The Use of Ion Exchange Membranes as Separators in Batteries

Lloyd H. Shaffer

Research & Development Division, American Machine & Foundry Company, Springdale, Connecticut

ABSTRACT

The factors which influence selective transport are reviewed. In available membranes, selectivity is controlled primarily by concentration effects rather than by mobilities. The fluxes of electric current and matter through membranes are analyzed in terms of the thermodynamics of irreversible processes. The effects of a selective membrane on the operation of a silver/zinc battery are discussed. The charge-selective character of the membrane causes sharp changes in electrolyte concentration when current flows through the boundary between membrane and electrolyte. This introduces both a high resistance film and a concentration potential; both of these operate to reduce the power output of the cell.

In many kinds of batteries, separation of the components is maintained by virtue of the fact that the electrodes and the electrode reaction products are insoluble solids, while the electrolyte is a liquid phase. When the physical and/or mechanical properties of the electrode structures are inadequate, improved operation is obtainable if separators are introduced. These are usually porous materials which act as mechanical barriers. The use of barriers opens up possibilities for low grade structural substances or even liquid/liquid/liquid batteries, as long as the individual components are not mutually soluble. If the separator is an ion exchange material, we can even think in terms of electrode reactions which may produce soluble products. Three distinct types of separators are illustrated in Fig. 1. The first type of separator, a porous substance, functions solely as a mechanical barrier which holds back solid small particles. With proper design of pore size and control of surface tension through the addition of wet-proofing agents, such separators may also be used to maintain a boundary between a liquid and a gas. Fluids in the broad sense, including gases, may be most readily separated by continuous structures in which one or more of the battery components may be soluble. This is illustrated in part b of Fig. 1. Ion selective substances are a specialization of this type of barrier; they reject solutes primarily on the basis of the charge on each solute particle rather than because of its size or miscibility.

A variety of potentially useful ion exchange materials are available. Many have been developed for purposes other than battery separators, and often their resistivities appear to be intolerably high. However, one or two types have been manufactured as separators for use in batteries, and the others are potentially useful for this purpose as the resistance normal to the direction of the sheet is a strong function of the sheet thickness while the selectivity is not. Results of a recent survey of membrane properties are summarized in Table I.

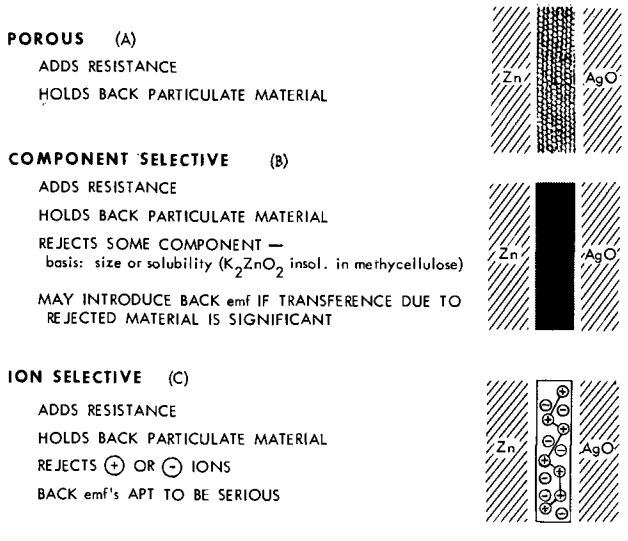

Fig. 1. Types of battery separators

Causes of Selectivity in Ion Exchange Membranes

A current of particles may be expressed as a mobility times a concentration times a force. Selective transport will occur if either the mobility or the concentration in a particular region that the current must pass through is very small. Selectivity in the usual kind of ion exchange membrane depends on the reduction of concentration of some species within the membrane; not too much is known about the effects of membrane on mobility.

The usual type of ion exchange membrane in which the selectivity is controlled by the exclusion of an ion of one sign, consists of an insoluble resin containing fixed ionic groups of the same charge as the excluded ion. The interior of the membrane may be regarded as a second phase and according to the Donnan principle the chemical potential of the salt in the solution external to the membrane must be equal to the chemical potential of the salt inside the membrane at equilibrium. This statement and its consequences are summarized in Eq. [1] to [4].

$$RT \ln a^2_{\pm} = \tilde{v}\Delta P + RT \ln \bar{a}^2_{\pm} \qquad [1]$$

$$\gamma^2_{\pm} C_k C_j = \bar{\gamma}^2_{\pm} (\bar{C}_r + \bar{C}_j)\bar{C}_j \quad \{j \text{ and } r \text{ have same sign}\} \qquad [2]$$

$$\bar{C}_j = \tfrac{1}{2} (\sqrt{\bar{C}^2_r + 4C^2_j} - C_r) \qquad [3]$$

$$\bar{C}_j = C^2_j/\bar{C}_r \ \{\text{dilute soln.}\} \qquad [4]$$

ΔP is the difference in internal pressure between the two phases, sometimes called the swelling pressure of the membrane, $\tilde{v}$ is the partial molar volume of any of the mobile species in the system, and a is its activity coefficient. The bar over the a is used to indicate activity within the membrane phase. This equation must hold for each and every component that is distributed between the two phases. Since both the solution and the membrane must be electrically neutral, and since the ion exchange material can be made to contain a very large concentration of ions of one sign, the concentration of mobile co-ion in the membrane will be smaller than it is in the solution outside. For example, suppose that j and k represent ions of opposite sign and r represents a monovalent fixed ion in the membrane. We will imagine that this ion has the same sign as j. Within the membrane electrical

Table I. Properties of commercial ion exchange membranes

Manufacturer and type	Permeable to	Electrochemical: Area resistance, ohm-cm²	Electrochemical: Selectivity	Mechanical: Nominal thickness, mils, wet	Mechanical: Strength, wet	Remarks
AMF		1000 ~ 0.6*N* KCl	Voltage ratio 0.5/1.0*N* KCl		Mullen burst, psi	
Homogeneous, polyethylene base						
C-63	C	5 ± 2	0.80 ± 5	12	45 ± 5	
C-103	C	7 ± 2	0.93 ± 2	8.5	60 ± 5	
A-63	A	6 ± 2	0.82 ± 4	12	45 ± 5	Tough, flexible, rewettable
A-103	A	9 ± 3	0.92 ± 3	8.8	55 ± 5	
Fluorocarbon base						
C-310	C	4.5 ± 2	0.86 ± 5	11	110 ± 20	
C-313	C	4.5 ± 2	0.85 ± 5	6	55 ± 5	
Asahi Chem. Ind.		1000 ~ 0.5*N* NaCl	Permselectivity 0.25/0.5*N* NaCl		Tensile kg/mm²	
Homogeneous, styrene-DVB base						
CK-1	C	1.4	0.85		2-2.4	
DK-1	C	1.8				
CA-1	A	2.1	0.92	9	1.9-2.3	Delicate, rewettable
DA-1	A	3.5				
Asahi Glass[1]		1000 ~ 0.6*N* KCl	Voltage ratio 0.5/1.0*N* KCl		Mullen burst, psi	
Reinforced						
DMT	C	1.3	0.62	4.2	134	Cracks on drying
AMT	A	3.0	0.72		71	
Ionac Chemical Company		a.c.	Corrected volt. ratio 0.5/1.0*N* NaCl			
Fabric reinforced						
MC3142	C	10	0.94	6		
MC3235	C	11	0.95	12	N.A.	Strong, rewettable
MA3148	A	20	0.90	7		
MA3236	A	20	0.93	12		
Ionics		1000 ~ 0.6*N* KCl	Voltage ratio 0.5/1.0*N* KCl		Mullen burst, psi	
Fabric reinforced						
CR-61	C	11	0.65[1]	23	115	Cracks on drying
AR-111A	A	11	0.57[1]	24	125	
Permutit Co. Ltd.		(a.c.) 1.0*N* NaCl	Permselectivity 0.1/1.0*N* NaCl			
Fabric reinforced						
C-20	C	12	0.90	High		Strong, rewettable
A-20	A	9	0.82			
Tokuyama Soda Co.		1000 ~ 0.5*N* NaCl	Permselectivity 0.5*N* NaCl		Burst, kg/cm²	
Fabric reinforced						
CL-7	C	6-8	0.97	8.3	4-5	
CL-2.5T	C	2.7-3.2	0.97	6.3	3-4	
CH-4	C	2.3-2.7	0.95	8.3	3-4	Strong, reversibility on drying not known
AV-3	A	3-4	0.95	8.3	6-7	
AV-3T	A	2.5-3	0.92	6.7	4-5	
AVS-3T	A	4-5	0.95	7.5	3-4	
Toyo Soda Mfg. Co.			Permselectivity 0.5/2.5*N* NaCl			
Fabric reinforced						
C-100	C	2-4	84	8.3		Strong, reversibility on drying not known
A-100	A	3-5	74	4.3		

[1] Courtesy Dr. R. N. Smith, Section Manager, Membranes and Electrodialysis, American Machine & Foundry Co., Springdale, Connecticut.

neutrality requires that $\bar{C}_k = \bar{C}_r + \bar{C}_j$. In the absence of large pressure differences between the exterior and the interior phases, application of the Donnan principle leads to the results given by Eq. [3], or for very dilute external solutions, Eq. [4]. Typical resin manufacturing techniques produce materials in which $\bar{C}_r$ is the order of 5*M* and Table II shows several values of expected co-ion concentration within such resins as a function of the external solution concentration. It is apparent that resins which are quite selective in dilute solutions may show greatly reduced selectivity in very concentrated solutions.

Table II. Values of co-ion concentration[1]

Conc. in ext. soln. (m/kg)	5	3	2	1	0.5	0.3	0.2	0.1	0.01
Conc. of mobile co-ion in resin (m/kg)	3.09	1.36	0.70	0.19	0.05	0.018	8×10^{-3}	2×10^{-3}	2×10^{-5}

Effective fixed ion concentration in resin phase: 5 m/kg H_2O

[1] Values tabulated for moderate external solution concentrations are in rough agreement with observations on actual ion exchange resin system (see for example Gregor and Gottlieb (1)).

Quantitative Description of the Performance of Ion Exchange Membrane Separators

To assess the effect of an ion exchange membrane on battery performance, we have to consider what happens when a current flows through the membrane. When this occurs, several coupled processes occur simultaneously. It is helpful to make use of the theory of irreversible thermodynamics in examining the interdependence of the various interacting forces and flows. This provides convenient definitions of certain quantities that are important in transport theory and makes the relationships between them plain. The simplest electrolyte solution imaginable consists of one salt dissolved in a pure solvent. Equation [5] is suitable for the description of this system (2). Note that a minimum of four equations is needed even for this simple system.

$$J_1 = -\mathcal{L}_{11}\nabla_T\mu^*_1 - \mathcal{L}_{12}\nabla_T\mu^*_2 - \mathcal{L}_{13}\nabla_T\mu^*_3 - \mathcal{L}_{14}\nabla \ln T$$

$$J_2 = -\mathcal{L}_{12}\nabla_T\mu^*_1 - \mathcal{L}_{22}\nabla_T\mu^*_2 - \mathcal{L}_{23}\nabla_T\mu^*_3 - \mathcal{L}_{24}\nabla \ln T$$

$$J_3 = -\mathcal{L}_{13}\nabla_T\mu^*_1 - \mathcal{L}_{23}\nabla_T\mu^*_2 - \mathcal{L}_{33}\nabla_T\mu^*_3 - \mathcal{L}_{34}\nabla \ln T$$

$$Q = -\mathcal{L}_{14}\nabla_T\mu^*_1 - \mathcal{L}_{24}\nabla_T\mu^*_2 - \mathcal{L}_{34}\nabla_T\mu^*_3 - \mathcal{L}_{44}\nabla \ln T \quad [5]$$

The *J*'s are currents of the two ions and the solvent, while *Q* represents the flow of heat. The coefficients

$\mathcal{L}ij$ are phenomenological coefficients and the symbol $\nabla_{T\mu}{}^*$ is meant to represent the gradient of the total chemical potential[1] taken at constant temperature. It is obvious that setting any of the driving forces $\nabla_{T\mu}{}^*$ or $\nabla \ln T$ equal to zero in the equations above does not guarantee that the corresponding current J_i or Q will vanish. In particular, the last line of Eq. [5] suggests that it may be almost impossible to perform an isothermal experiment. However, work by Ikeda (4) and Shaffer (5) has shown that thermal effects due to the flow of current in an ion exchange membrane are small. In addition, in the analysis of most systems which contain electrical potentials large enough to be of practical interest, some of the other terms that arise as a result of the formalism above are small enough to be dropped. For example, suppose we are dealing with a system in which only gradients of electrical potential, pressure, and concentration need be considered; then,

$$\nabla_{T\mu}{}^* = zF\nabla\phi + \frac{\partial\mu}{\partial P}\nabla P + \frac{\partial\mu}{\partial C}\nabla C$$

$$C \simeq a,\ \partial\mu/\partial C \simeq RT\,\partial \ln C/\partial C$$

$$\nabla_{T\mu}{}^* = zF\nabla\phi + \tilde{v}\nabla P + \frac{RT}{C}\nabla C \qquad [6]$$

And the magnitudes of the forces that might be associated with the flow of current through the membrane in a typical battery system under these conditions are summarized in Table III. It is clear that the term $\tilde{v}\nabla P$ is relatively unimportant. Under any normal circumstances, gravitational and centrifugal fields are also insignificant compared to the very large magnitudes of $zF\nabla\phi$ and $RT\nabla$ ln c. This permits considerable simplification of Eq. [5]:

$$J_1 = \mathcal{L}_{11}X_1 + \mathcal{L}_{12}X_2 + \mathcal{L}_{13}X_3$$
$$J_2 = \mathcal{L}_{12}X_1 + \mathcal{L}_{22}X_2 + \mathcal{L}_{23}X_3$$
$$J_3 = \mathcal{L}_{13}X_1 + \mathcal{L}_{23}X_2 + \mathcal{L}_{33}X_3 \qquad [7]$$

in which we have to consider the flows of two kinds of ions and the flow of solvent, and where X, the generalized force, is given by [8].

$$X = -zF\nabla\phi - \frac{RT}{C}\nabla C \qquad [8]$$

The quantities that are important in further electrochemical calculations are: electric current, electrical conductivity, transport number of the k^{th} ion, and transference number of any uncharged species that may move along with the charged particles. (Note that transport number and transference number are related by $T_k = z_k\tau_k$). These quantities are readily defined in terms of Eq. [7] and [8].

Electric current

$$i = z_kFJ_k + z_jFJ_j$$

Electrical conductivity

$$\sigma = i/(-\nabla\phi) = \mathcal{L}_{kk}z_k{}^2F^2 + 2\mathcal{L}_{kj}z_kz_jF^2 + \mathcal{L}_{jj}z_j{}^2F^2$$

Transport number of the k^{th} ion

$$\bar{T}_k = \frac{(\mathcal{L}_{kk}z_k{}^2 + \mathcal{L}_{kj}z_kz_j)}{(\sigma/F)} \qquad [9]$$

Transference number

$$\bar{\tau}_w = \frac{\mathbf{J}_w}{\sigma/F} = \frac{\mathcal{L}_{kw}z_k + \mathcal{L}_{jw}z_j}{\sigma/F}$$

These defining equations do not of course tell us the numerical values of the conductivity or the transference numbers, unless we have the values of all of the phenomenological coefficients. However, the defining equations can be used to help in the interpretation of experimental situations even when the coefficients are not known. For example, consider the measurement of "membrane potential," an experiment which is often performed to determine the selectivity of the membrane.

Analysis of "Membrane Potentials"

"Membrane potential" is the electrical potential across the membrane when there is a concentration difference between the solutions on either side and no electric current. The situation is summarized by Eq. [10].

$$i = z_kJ_kF + z_jJF_j = 0 =$$
$$\mathcal{L}_{kk}z_kFX_k + \mathcal{L}_{kj}z_kFX_j + \mathcal{L}_{kw}z_kFX_w$$
$$+ \mathcal{L}_{kj}z_jFX_k + \mathcal{L}_{jj}z_jFX_j + \mathcal{L}_{jw}z_jFX_w \qquad [10a]$$

and, dividing through by the expression for conductivity

$$0 = \tau_kX_k + \tau_jX_j + \tau_wX_w = -T_kF\nabla\phi - T_jF\nabla\phi$$
$$-\tau_kRT\nabla \ln a_k - \tau_kKT\nabla \ln a_j - \tau_wRT\nabla \ln a_w$$
$$-\nabla\phi = \tau_k\frac{RT}{F}\nabla \ln a_k + \tau_j\frac{RT}{F}\nabla \ln a_j + \tau_w\frac{RT}{F}\nabla \ln a_w \qquad [10b]$$

where, as before, we have used X's to stand for the negative gradients of the total chemical potentials. The last line of Eq. [10b] shows clearly that the potential gradient depends on the transference numbers and the activities of all of the species present in the system, even though no current is flowing.

This important result has been obtained previously by Scatchard (6) using a more conventional thermodynamic approach to an analysis of a cell containing a membrane. However, it is not apparent from his approach that one can avoid an integration over the thickness of the barrier. In an analysis of the problem due to Kirkwood (7) it has been shown that one can use microscopic differences between the bulk phases rather than local gradients in setting up the phenomenological equations. Using this idea and Eq. [9] we can calculate apparent electrochemical characteristics for the membrane. Transport coefficients defined in this manner are "effective" quantities that apply over the whole thickness of the system interface'/membrane/interface" and we can avoid the question of integration entirely.

Effect of Selective Membrane on Resistance, Voltage, and Concentration under High Current Conditions

To illustrate the effects that an ion exchange membrane will have on the operation of an actual battery, it is convenient to consider a specific system. As an example a silver-zinc battery with an anion exchange membrane separator will be used. Because the membrane is selective, serious concentration gradients will develop in the solution adjacent to it under high current conditions. Concentration polarization arises because the current in the solution is carried by the motion of both positive and negative ions, while in the membrane the current is carried by the motion of only

[1] The total chemical potential is sometimes called the electrochemical potential; see for example Harned and Owen (3).

Table III. Approximate magnitudes of the terms which contribute to the electrochemical driving force

$\Delta\phi \simeq 0.2$v
$\Delta x \simeq 0.02$ cm (8 mils)
$\tilde{v} \simeq 20$-30 cm^3/mole
$\Delta P \simeq 1$ atm $= 0.1$ watt-sec/cm^3
T ~ 300°K
C ratio $\sim$ 10-1000 max.
$F = 96{,}487$ a-sec/eq.

$R = 8.315$ watt-sec/mole-°C
$zF\nabla\phi \sim 0.2 \times 10^5 \times 1/0.02 \sim 10^6$ watt-sec/mole-cm

$\tilde{v}\nabla P \sim 25 \times 10^{-1}/0.02 \sim 125$ watt-sec/mole-cm
$RT\nabla \ln C \sim 8 \times 300 \times 6.9/0.02 \sim 8 \times 10^5$ watt-sec/mole-cm

one kind of ion. In addition, each electrode in general acts as a source or a sink for only one kind of ion. These discontinuities in the conduction process lead to concentration gradients in the vicinity of both the membrane and the electrodes. When a load is first connected to the cell, the disturbances are confined to the immediate vicinity of the interfaces between membrane and solution and electrode and solution. However, in an unstirred system, the depleted and concentrated layers will spread until they run into each other. Steady-state concentration gradients as sketched in Fig. 2 will be reached in a time such that $Dt/\delta^2 \sim 1$;[2] and, with the small spacings, 1.0-0.1 mm, that are apt to be used in a typical battery, the characteristic time for reaching the steady state will lie in the range 1-100 sec. At a current density of 1 amp/cm^2, the corresponding variations in the concentration range from ± 1.67 to ± 16.7M.

Although the concentrated and the diluted layers appear to merge in a typical battery, their effects might be considered in terms of separate diluted and concentrated regions each having a characteristic thickness $\delta = l/2$. These layers of altered concentration will affect the operation of the cell in two different ways: they will increase its resistance, and they may produce serious back emf's. In exploring the effects due to the concentration layers, it is convenient to think about resistance effects and voltage effects separately; consider first the effect of the concentration layers on resistance.

Resistance.—For purposes of illustration, we shall assume that there is no solvent transfer through the membrane, and, that the membrane is perfectly selective. Figure 2b indicates schematically the nature of the resistances that will arise when a current is passed through the membrane/solution system. For the moment let us ignore the resistances which are associated with the electrodes and the electrode reactions. The resistance of the membrane is known in advance and presumably will be small in accordance with design selections. The resistance marked R_δ' will probably not differ greatly from the resistance of the 30 and 40% KOH solution used as the electrolyte in the cell. On the other hand the resistance marked R_δ'' being associated with a diluted layer, may be quite high, and it will therefore tend to control the total resistance of the cell. In assessing the contribution of the diluted layer to the total IR drop in the cell it is convenient to make use of the fact that the variations of C and R from the initial bulk solution values C_b and R_b to C_i and R_i at the membrane/solution interface are approximately linear. It then is fairly simple to develop an expression for the amount of extra resistance introduced by the diluted layer. The results of this calculation for extreme conditions of polarization are shown in Eq. [11].

[2] According to Rosebrugh and Miller (8)

$$\Delta c_i \text{ (moles/cc)} = \frac{i\delta}{zFD}\left[1 - \frac{8}{\pi^2}\sum_1^\infty \frac{1}{(2n-1)^2}\exp\left\{-\frac{(2n-1)^2\pi^2 Dt}{4\delta^2}\right\}\right]$$

For a typical electrolyte, $D = 3 \times 10^{-6}$ cm^2/sec; and, if $l = 0.1$ mm, $\delta = 5 \times 10^{-3}$ cm, and $Dt/\delta^2 = 1$ when $t = 8 \times 10^{-1}$ sec.

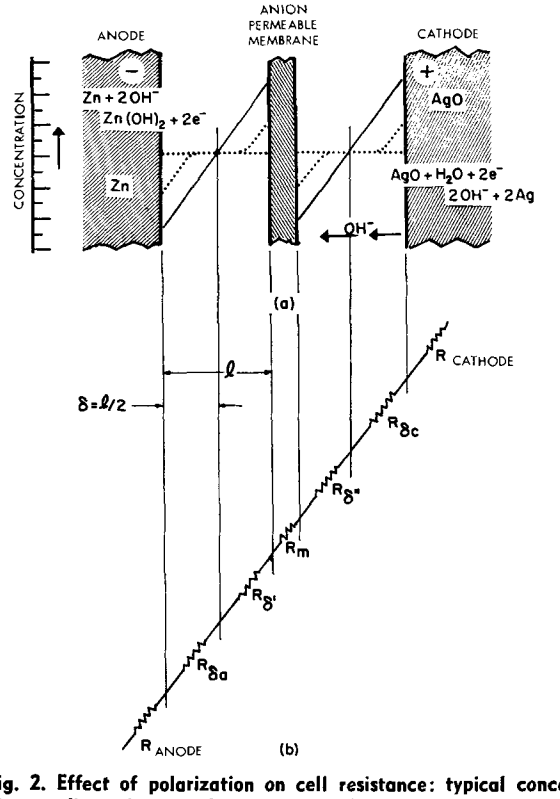

Fig. 2. Effect of polarization on cell resistance: typical concentration gradients (*a*) and the resulting cell resistances (*b*).

$$\Delta C \simeq C;\ C_i \simeq 10^{-2}\text{m};\ \omega_i \geqq 400 \text{ ohm-cm}$$

$$\omega_y = \frac{K}{(y/\delta)\Delta C + C_i},\quad dR = \frac{K dy}{(y/\delta)\Delta C + C_i}$$

$$R_\delta''(\text{ohm-cm}^2) = \int_0^l \frac{K\delta dY}{Y\Delta C + C} = \frac{K}{C_i}\odot\frac{\delta C_i}{\Delta C}\ln(1 + \Delta C/C_i)$$

$$K/\Delta C \simeq K/C_b \simeq \omega_b \text{ and } \Delta C/C_i \simeq (\omega_i - \omega_b)/\omega_b$$

$$R_\delta'' \sim \delta\omega_b \ln(\omega_i/\omega_b)^3 \qquad [11]$$

In these equations ω_i is the resistivity at the membrane/solution interface; ω_b is the bulk solution resistivity, and δ is the thickness of the concentration layer. It should be noted that the concentration effects which occur at the membrane solution interfaces when current is drawn from the cell are also duplicated at the electrodes. We can conclude that the actual resistance introduced by the membrane will be at least as great as the polarization resistance that would occur in the cell without any membrane being present.

Polarization potentials.—Consider also the voltages that may develop across the polarization layers when a current is passed through the system. The emf across each of the polarization layers and across the membrane can easily be calculated using Eq. [10]. It is obvious that concentration potentials should not occur whenever $\tau_+ = -\tau_- = 0.5$ and that the sign and magnitude of the concentration potentials under any other condition will depend on both the transference numbers and the actual concentrations. The situation as it is likely to exist if a high current is passed through an alkaline battery with an anion exchange separator is indicated in Fig. 3; Eq. [12]-[14] summarize the result obtained when the three voltages in the vicinity of the membrane, E_δ', $E_{m\phi}$ and E_δ'' are added up.

The polarization potential which arises as a result of adding a membrane to the battery system is:

$$\Delta\phi = \phi'' - \phi' = -\sum_i \tau_i \frac{RT}{F}\Delta \ln c_i = (-\tau_+ - \tau_-)\frac{RT}{F}\ln\frac{c + \Delta c}{c}$$

[3] Since $\Delta C = \dfrac{i\delta}{zFD}$ it is also true that

$$R_\delta'' \sim \frac{1}{i}\frac{RT}{F}\ln(\omega_i/\omega_b)$$

which agrees with the result recently obtained by Gregor and Peterson (9).

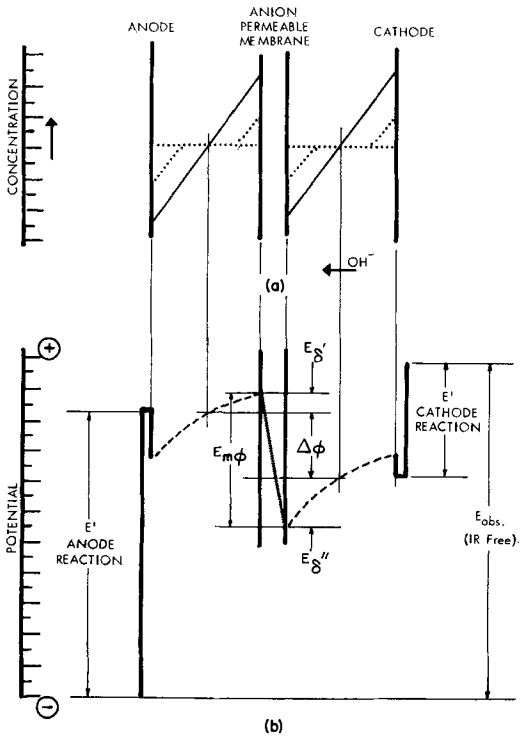

Fig. 3. Effect of polarization on cell potential—typical concentration gradients (*a*) and the resulting concentration potentials (*b*).

$$-\bar{\tau}_- \frac{RT}{F} \ln \frac{c - \Delta c}{c + \Delta c}$$

$$-(\tau_+ + \tau_-) \frac{RT}{F} \ln \frac{c}{c - \Delta c}$$

$$= -(\tau_+ + \tau_-) \frac{RT}{F} \ln \frac{c + \Delta c}{c - \Delta c} - \frac{RT}{F} \ln \frac{c + \Delta c}{c - \Delta c} \quad [12]$$

for a 1:1 electrolyte

$$-\tau_+ = -(1 - T_-); \; -\tau_- = T_-$$

and [12] simplifies to

$$\phi'' - \phi = \frac{RT}{F} 2(T_- - 1) \ln \frac{c + \Delta c}{c - \Delta c} = \frac{RT}{F} 2(T_- - 1)$$

$$\left\{ 2\left[\frac{\Delta c}{c} + \frac{1}{3}\left(\frac{\Delta c}{c}\right)^3 + \frac{1}{5}\left(\frac{\Delta c}{c}\right)^5 + \cdots \right] \right\} \quad [13]$$

This polarization, which appears as + on the left and as — on the right opposes the cell reaction and drastically reduces the power output.

If a cation permeable membrane were placed in the same spot, the initial polarization voltage associated with the membrane and its boundary layers would be

$$\phi'' - \phi' = -\frac{RT}{F} 2(T_-)$$

$$\left\{ 2\left[\frac{\Delta c}{c} + \frac{1}{3}\left(\frac{\Delta c}{c}\right)^3 + \frac{1}{5}\left(\frac{\Delta c}{c}\right)^5 + \cdots \right] \right\} \quad [14]$$

Equations [13] and [14] assume ideally selective membrane; if the membrane used is somewhat leaky, which it probably will be at these high concentrations, the back emf due to the membrane will be as given by Eq. [15] and [16]

$$\phi'' - \phi' = 2(T_- - \bar{T}_-) \frac{RT}{F}$$

$$\left\{ 2\left[\frac{\Delta c}{c} + \frac{1}{3}\left(\frac{\Delta c}{c}\right)^3 + \frac{1}{5}\left(\frac{\Delta c}{c}\right)^5 + \cdots \right] \right\} \quad [15]$$

$$\phi'' - \phi' = 2(T_+ - \bar{T}_+) \frac{RT}{F}$$

$$\left\{ 2\left[\frac{\Delta c}{c} + \frac{1}{3}\left(\frac{\Delta c}{c}\right)^3 + \frac{1}{5}\left(\frac{\Delta c}{c}\right)^5 + \cdots \right] \right\} \quad [16]$$

for anion and cation permeable membranes, respectively.

Up to this point, we have ignored the effects that may also occur at the electrodes. However, whatever else may be going on, the cathode is serving as a source of OH-ions and the anode is serving as a sink. Conceptually at least, we can imagine that the electrode/electrolyte interfaces are the equivalent of anion exchange membrane/solution interfaces. This means that when an anion exchange membrane is placed in a conventional silver/zinc cell, both the apparent IR drop and the observed concentration polarization will be twice as severe as when no membrane is present. We may conclude that even a low resistance anion exchange membrane may have undesirable effects when added to a high rate alkaline battery unless $T_- \simeq T_-$ under the expected conditions of use.[4] On the other hand, if the membrane can be made to replace the normal electrolyte entirely, the highest possible selectivity is desirable as this will tend to eliminate polarization effects at the electrode/electrolyte interfaces.

Manuscript received June 15, 1965; revised manuscript received Sept. 13, 1965. This paper was presented at the San Francisco Meeting, May 9-13, 1965.

Any discussion of this paper will appear in a Discussion Section to be published in the December 1966 JOURNAL.

REFERENCES

1. H. P. Gregor and M. H. Gottlieb, *J. Am. Chem. Soc.*, **75**, 3539 (1953).
2. G. J. Hills, P. W. M. Jacobs, and N. Lakshminarayanaiah, *Proc. Roy. Soc., London*, **A262**, 246, 257 (1961).
3. H. S. Harned and B. B. Owen, "The Physical Chemistry of Electrolytic Solutions," Chap. I, Section 15, Reinhold Publishing Co., New York (1958).
4. T. Ikeda, *J. Chem. Phys.*, **28**, 166 (1958).
5. L. H. Shaffer, *Nature*, **191**, 591 (1961).
6. G. Scatchard in "Ion Transport across Membranes," H. T. Clarke, Editor, pp. 128-143, Academic Press, New York (1954).
7. J. G. Kirkwood in "Ion Transport across Membranes," H. T. Clarke, Editor, pp. 119-127, Academic Press, New York (1954).
8. T. R. Rosebrugh and W. L. Miller, *J. Phys. Chem.*, **14**, 816 (1910).
9. H. P. Gregor and M. A. Peterson, *ibid.*, **68**, 2201 (1964).

SYMBOLS

$\underline{a}$	Activity
a	Activity in membrane phase
C	Concentration, moles/kg H_2O
c	Concentration, moles/cc.
D	Diffusion coefficient, cm/sec
Δ	Difference
δ	Boundary layer thickness, cm
∇	Gradient operator
$\nabla\cdot$	Divergence operator
E	Potential difference (emf) v

[4] If T_- is $\lesssim 0.5$, it is reasonable to place a cation permeable membrane in the battery. True, we'll always double the apparent IR drop in the cell but E_δ' and E_δ'' will just cancel the voltage due to the polarization layers at the anode and the cathode, respectively, and the net back emf in an alkaline cell containing an ideally selective cation permeable membrane will be the sum of the concentration potentials attributable to transferring ions (*a*) across the membrane/solution boundaries and (*b*) across the electrode/solution boundaries. Either of these processes in half the total and the initial back emf is

$$2E_{m\phi} = -2\frac{RT}{F} \ln \frac{c + \Delta c}{c - \Delta c}$$

$$= -2\frac{RT}{F}\left\{ 2\left[\frac{\Delta c}{c} + \frac{1}{3}\left(\frac{\Delta c}{c}\right)^3 + \frac{1}{5}\left(\frac{\Delta c}{c}\right)^5 + \cdots \right] \right\} \quad [17]$$

F Faraday's constant, 96,500 amp-sec
γ Activity coefficient
i Electric current density, amp/cm²
J Particle current density, moles/cm²-sec
K Resistivity constant (1000/eq cond)
ln Natural log.
L Phenomenological coefficient
μ Chemical potential
μ^* Total chemical potential including effects of charge, gravitational field etc.
ω Electrical resistivity ohm-cm
P Pressure, watt-sec/cc.
ϕ Electrical potential, v
Q Heat flow, watts/cm²
R Gas constant, 8.315 joules/mole-°C
R_δ Resistance of polarization layer, ohm-cm²
σ Electrical conductivity, mho/cm
T Absolute temperature, °K
T Transport number of ion in solution
$\overline{\mathrm{T}}$ Transport number of ion in membrane
t Time, sec
τ Transference number of ion in solution, moles/F
$\overline{\tau}$ Transference number of ion in membrane, moles/F
$\tilde{v}$ Partial molar volume, cc/mole
X Generalized force, watt-sec/cm-mole
z Valence including algebraic sign

Lithium-Chlorine Battery

D. A. J. Swinkels

Allison Division, General Motors Corporation, Indianapolis, Indiana

ABSTRACT

Requirements for a high energy density, high power density electrochemical energy conversion device have led to the study of a lithium-chlorine battery. The system operates at 650°C using molten LiCl electrolyte. Several cells have been assembled and measurements of the open-circuit voltage, electrode polarization and coulombic efficiency are reported. The chlorine electrode, made of porous carbon or graphite, was found to be the main source of polarization. Limiting currents were determined and these have been compared with theoretical estimates based on a model for the porous electrode. The model differs fundamentally from those used with aqueous electrolytes since fused LiCl does not wet graphite, and hence little or no penetration of electrolyte into the pores occurs.

Electrochemical couples of high energy capacity (>500 whr/lb) capable of operating at high power densities (>5 w/cm²) offer many possibilities for obtaining light energy storage devices. The Li-Cl_2 system using molten LiCl as the electrolyte is one of the most promising systems (1) and is currently being investigated (2).

The system consists of a molten Li-electrode, molten LiCl electrolyte, and a porous carbon or graphite chlorine electrode and operates at about 650°C. The overall cell reaction is simply

$$\mathrm{Li} + \tfrac{1}{2}\mathrm{Cl_2} \underset{\text{charge}}{\overset{\text{discharge}}{\rightleftharpoons}} \mathrm{LiCl} \qquad [1]$$

At 650°C the open-circuit voltage is 3.467v, which leads to a theoretical energy capacity for the reactants of 990 whr/lb. The energy capacity which can actually be obtained depends on the polarization of the electrodes and the IR-drop in the electrolyte under the chosen operating conditions, as well as on the weight of containers and cell components. The open-circuit and the electrode polarization of this system have therefore been studied in detail.

Open-Circuit Voltage

The O.C.V. of the Li-Cl_2 system was measured from the melting point of LiCl to about 850°C at a pressure of 1 atm. The LiCl used for these experiments was purified by the Anderson Physical Laboratories using the method of Laitinen *et al.* (3). The melting point was determined by measuring cooling curves and extrapolating the linear sections. Some supercooling was observed in each case. Six cooling curves were determined using five different calibrated thermocouples, giving a mp of 608° ± 1°C, which compares well with the range of values found in the literature: 606°-610°C (4-8). Three sets of O.C.V. data were taken in an experimental arrangement shown in Fig. 1. The cell consisted of a porous carbon chlorine electrode dipped in molten LiCl. A quartz tube around the carbon electrode restricted the chlorine flow to this part of the cell to avoid corrosion of the metal outer container. The LiCl was contained in a slightly porous (porosity ≈ 15%) beryllia crucible, which served to separate mechanically the LiCl from the lithium without causing electrical separation. The whole assembly was placed in a cylindrical heater. Two thermocouples, one in the lithium and one close to the chlorine electrode, are placed in the cell to insure uniform temperature throughout the cell. It was found that an auxiliary heater was required near the chlorine electrode to compensate for heat lost by thermal conduction through the graphite electrode. The current through this auxiliary heater was increased until the two thermocouples showed the same temperature. All voltages were read to 0.1 mv using a Keithley 660 d-c differential voltmeter. A total of 132 points were determined giving

$$E = 3.4906 - 0.64 \times 10^{-4}\,(t-608)\,\text{volt} \qquad [2]$$

with a standard error of ± 5.4 mv.

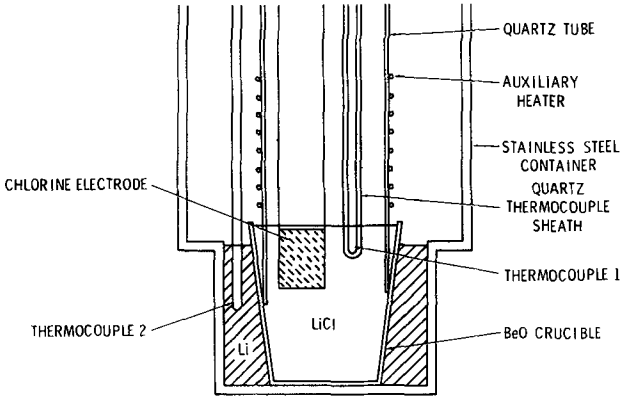

Fig. 1. Li-Cl_2 open-circuit voltage cell

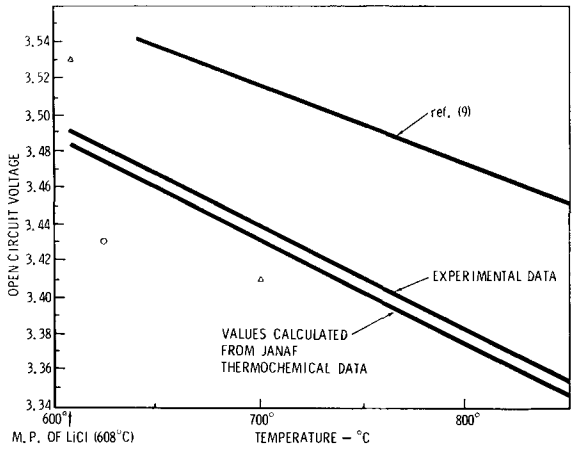

Fig. 2. Li-Cl_2 open-circuit voltage: △, ref. (2); ○, ref. (11)

This line is shown in Fig. 2 together with the O.C.V. calculated by Hamer *et al.* (9) and those calculated here from the free energy data given in a more recent compilation and evaluation of thermodynamic data known as the JANAF Thermochemical Tables (10). Some O.C.V. data reported by Werth *et al.* (2) and LiCl decomposition potentials given by Delimarski are also included (11). Taking only the uncertainty in the standard heat of formation of LiCl (c) at 25°C given in the JANAF tables then a standard error of ±12 mv results for the calculated O.C.V. line. Since the separation between the calculated and experimental lines is only 7 mv the two are in essential agreement.

Lithium Electrode

The exchange current density for metal electrodes in fused salts is generally high (12), and hence no polarization is expected at the Li/LiCl electrode. Constant current charge and discharge pulses of up to 40 amp/cm² were passed between two Li electrodes at 650° ± 5°C in the cell shown in Fig. 3. The cell consisted of a stainless steel outer container and a dense alumina crucible to contain the electrolyte. A chlorine electrode with a quartz sheath and two lithium electrodes were placed in the electrolyte. Each Li electrode consisted of a BeO tube with a cross-sectional area of 0.7 cm² with a stainless steel rod to make contact to the lithium and a thermocouple to measure the temperature of the actual electrode-electrolyte interface.

The experimental procedure here consisted of heating the cell components to 700°C on the day before a run was made, cooling and storing them overnight under vacuum. The cell was then assembled in a dry box, and pure dry LiCl was placed in the cell. After heating to 650°C to melt the LiCl, Li was formed on both Li electrodes by electrolysis against the carbon electrode. The experiment then consisted of charging Li back and forth between two Li electrodes using the chlorine electrode as a reference electrode. The voltage between each Li electrode and a Cl_2 reference electrode was observed on an oscilloscope 0.1 sec after switching on the current. Since the rise-time of the power supply used was about 50 μsec any activation polarization which was present could not be separated from the IR-drop between the reference and working electrodes. Since total cell resistances were typically 0.3 ohm, I^2R heating caused significant temperature changes at times greater than 1 sec (10°C/sec were observed). The current voltage relationship was found to be linear between cathodic and anodic current densities up to 40 amp/cm² (Fig. 4). Since activation polarization is nonlinear beyond about 100 mv most of the observed polarization must be due to the IR-drop and an exchange current density of at least 10 amp/cm² is indicated. On one occasion the amount of Li charged into the two Li electrodes was accurately measured (10 amp for 48 min), and a set of charge and discharge data was obtained. The cell was then left overnight with a slow flow of Cl_2 through the graphite electrode. Next morning, 23 hr after charging, the cell was discharged at a rate of 6 amp for 75.3 min. This corresponds to an over-all coulombic efficiency of 94%. The electrodes were then charged again at 10 amp for 48 min and immediately discharged at 6 amp for 77.3 min which corresponds to an over-all coulombic efficiency of 96.6%. Thus the Li/LiCl electrode shows negligible polarization at current densities up to 40 amp/cm², while the coulombic efficiency in the geometry used here approaches 100%. At closer electrode spacings coulombic efficiencies may well be less due to the solubility of both Li and Cl_2 in LiCl (13-15).

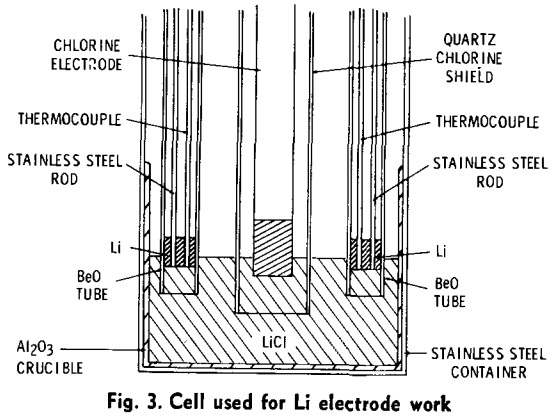

Fig. 3. Cell used for Li electrode work

Chlorine Electrode

The chlorine electrode consists of a porous carbon or graphite plug screwed onto a dense graphite feed tube which also serves as the current lead. The experimental cell used as well as the parts of one electrode are shown in Fig. 5. The cell consists of a quartz envelope into which three identical Cl_2 electrodes are placed. Cl_2 is fed to two of these (cathode and reference electrode) while a thermocouple is placed inside the anode. The cathode has a quartz sheath around it so that only the face of the porous plug is exposed to the electrolyte, thus giving a known electrode area. The essential difference between this electrode and many other porous fuel cell electrodes is the fact that LiCl does not wet the electrode. Hence the meniscus type of electrode geometry described by Will (16) cannot form in this electrode.

The over-all process at the Cl_2 electrode can still be divided into the following steps:

1. Flow of Cl_2 gas through the porous plug.
2. Dissolution of Cl_2 at the gas-liquid interface.
3. Diffusion of dissolved Cl_2 to the carbon-LiCl interface.
4. Dissociation and charge transfer.
5. Migration of Cl^- into the bulk electrolyte.

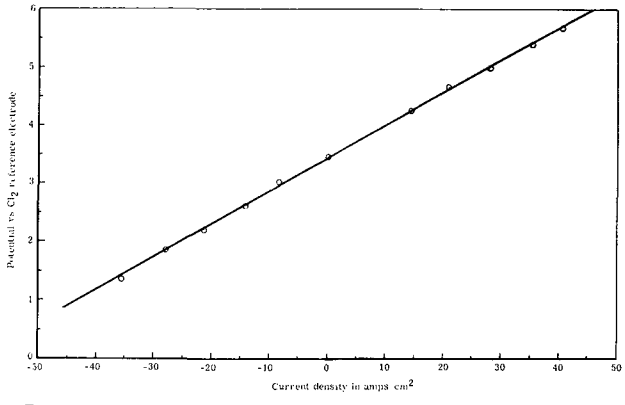

Fig. 4. Potential of a lithium electrode vs. a Cl_2 reference electrode in LiCl.

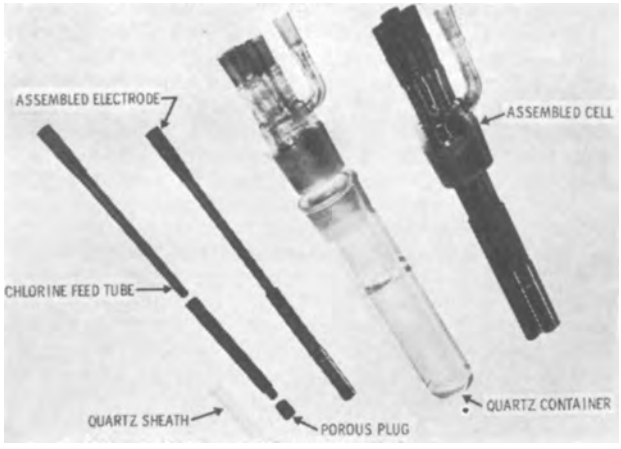

Fig. 5. Cell components for Cl_2 electrode work

The diffusion problem for a nonwetted pore (*i.e.*, step 3) has been treated by Austin *et al.* (17), who calculated the limiting current for both flooded and nonflooded pores for various boundary conditions at the gas-liquid interface. The solution in all cases is of the form

$$i_L = \frac{AnFDC_o}{r} \qquad [3]$$

where i_L is the limiting current density in amp/cm^2 of pore ends; A is a constant depending on the boundary condition assumed at the gas-liquid interface. A varies from $\approx$ 1.5 to 12 and a value of 8 has been used here; n is the number of electrons per molecule of Cl_2 = 2; **F** Faraday = 96,500 coulombs/mole; D the diffusion coefficient of Cl_2 in LiCl $\approx$ 4 x 10^{-5} cm^2/sec; C_o = equilibrium solubility of Cl_2 in LiCl = KP_2 where K = Henry's law constant; r the pore radius (cm); and P_2 chlorine pressure at the gas-liquid interface.

The diffusion coefficient of Cl_2 in LiCl at 650°C is estimated from measured diffusion coefficients of Cl^- in alkali halides (18, 19) by allowing for the larger size of the Cl_2 molecule and the lower temperature.

Von Wartenberg (14) measured the solubility of Cl_2 at 1 atm in LiCl at 620±5°C giving a Henry's law constant of 1.48 (±0.27) x 10^{-6} moles cm^{-3} atm^{-1}. Recent work in this laboratory indicates a somewhat lower solubility (15). Hence at 650°C K = 10^{-6} moles cm^{-3} atm^{-1} has been used here.

The fraction of the electrode surface made up of pore ends is equal to the porosity ψ. Hence

$$i_L = \frac{AnFDKP_2\psi}{r} \qquad [4]$$

Steps 2 and 4 above are assumed to be fast and hence essentially at equilibrium. Step 5 is the ionic conductivity of LiCl which at 650°C is 5.9 ohm^{-1}cm^{-1} (20). This leaves step 1 as the other possible rate-determining step.

For a single straight pore of length L with a circular cross section of radius r both viscous flow (Poiseuille flow) and molecular streaming (Knudsen flow) are observed (21). We have

$$Q = \pi r^2 \frac{\Delta P}{P}\left\{ = \frac{1.013 \times 10^6 r^2 (P_1 + P_2)}{16\eta L} + \frac{4\delta}{3}\sqrt{\frac{2RT}{\pi M}}\frac{r}{L}\right\} \qquad [5]$$

where Q is the flow in cc/sec at pressure P and temperature T (°K) through a single pore, P_1 the entrance pressure (atm), P_2 the exit pressure (atm), ΔP = $P_1 - P_2$, L is the length of pore = τt where t is thickness of the electrode, τ the tortuosity of the pores, η the gas viscosity (poise), m molecular weight = 70.9 g/mole, R = 8.317 x 10^7 erg/°mole, and δ = constant = 0.9.

Table I. Gas viscosity parameters

Gas	C	T_o, °K	η_o
Cl_2	325	273	1.23 × 10^{-4} poise
N_2	110	273	1.67 × 10^{-4} poise
He	70	298	2.0 × 10^{-4} poise

The number of pores per unit area is $\psi/\pi r^2$ so that the flow per square centimeter of electrode is $\psi Q/\pi r^2$. Winsauer *et al.* (22) measured the tortuosity (τ) for a number of sands with porosities in the range 0.06 < ψ < 0.4 and found the empirical relationship

$$\tau = 0.765\,\psi^{-0.65} \qquad [6]$$

This relationship has been used here to predict the flow of gas through porous graphite plugs, which was compared with experiment using three different gases at two different temperatures. The viscosity of the gases was calculated using the Sutherland equation

$$\eta = \eta_o\left(\frac{T_o + C}{T + C}\right)\left(\frac{T}{T_o}\right)^{3/2} \qquad [7]$$

The fit of experimental viscosity data to this equation, using the values of the parameters given in Table I, was very good. However experimental viscosity data for Cl_2 extend only to 146°C. Hence a large extrapolation is involved, and the purpose of these flow measurements was to check both the validity of this long extrapolation as well as the applicability of Winsauer's empirical relationship (Eq. [6]). The porosity and pore size distribution of the graphites used were measured using a mercury porosimeter. The actual pore size distribution was then approximated by a step function as shown in Fig. 6. To measure the flow of gases through porous graphite, plugs of the desired materials were sealed in Pyrex tubes by collapsing the Pyrex around the plugs under vacuum. The preheated gases were then forced through the plugs. The pressure difference, ΔP, across the plug was measured with a mercury U-tube manometer while the flow rate was measured after cooling the gas to room temperature by timing the movement of a soap film in a burette. A typical comparison of experimental and calculated flows is shown in Fig. 7. Similar agreement was obtained on other porous graphites and using other gases (He, N_2). Hence the use of Eq. [6] for the tortuosity and Eq. [7] for the viscosity of Cl_2 appears justified.

Multiplying Eq. [5] by (nFP/T) · (273/22,415) changes Q to amp/cm^2. This assumes ideal gas behavior for chlorine, which is necessary at the higher temperatures where no density measurements have been made for Cl_2 gas. The assumption is justified since at 0°C the ideal gas density of Cl_2 differs from the measured density by less than 2.5%.

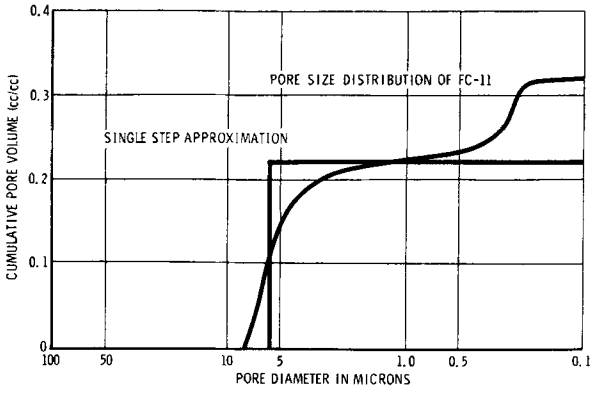

Fig. 6. Pore size distribution of FC-11

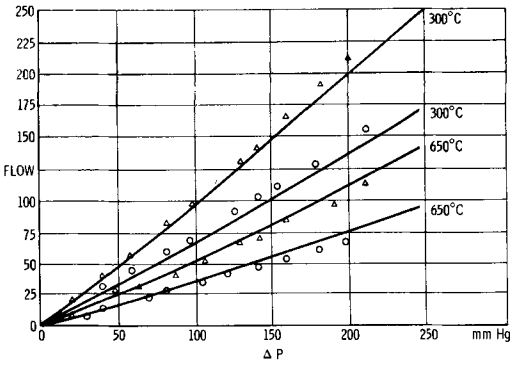

Fig. 7. Comparison of theoretical and experimental flow of N_2 through FC-11 plugs. Area of plugs, 2.8 cm^2; ○, thickness = 1.06 cm; △, thickness = 0.73 cm.

Hence

$$i_{flow} = \frac{nFP}{T} \cdot \frac{273}{22{,}415} \cdot \frac{\psi}{\pi r^2} \cdot Q \text{ amp/cm}^2 \qquad [8]$$

Converting to d = diameter in microns

$$i_{flow} = \frac{273}{T} \cdot \frac{nF\Delta P\psi}{22{,}415t\tau} \left\{ \frac{1.013d^2 (P_1 + P_2)}{6400\,\eta} + \frac{2\delta d}{3\times10^4} \sqrt{\frac{2RT}{\pi M}} \right\} \qquad [9]$$

For a dead-ended electrode, *i.e.*, one through which no excess chlorine flows, i_{flow} must equal the actual current passed through the electrode.

At the limiting current we can therefore equate Eq. [4] and [9]. Hence, for given values of all the external variables (T, P, ψ, d, t, τ) we can solve for P_2 and hence calculate i_L. This has been done for a hypothetical carbon with the following characteristics: ψ = 0.3; t = 0.5 cm; $\tau = 0.765\ \psi^{-0.65} = 1.67$; T = 650°C = 923°F. The results are shown in Fig. 8.

The curves of i_L *vs.* pore diameter all show a clear maximum. To the left of the maximum the current is limited by the flow of gas through the porous material while to the right of the maximum the diffusion of dissolved Cl_2 through the electrolyte is the main limiting step.

Using Eq. [4] and [9] limiting currents have been calculated for several commercially available porous carbons. These commercial materials generally do not have uniform size pores but rather a range of pore sizes.

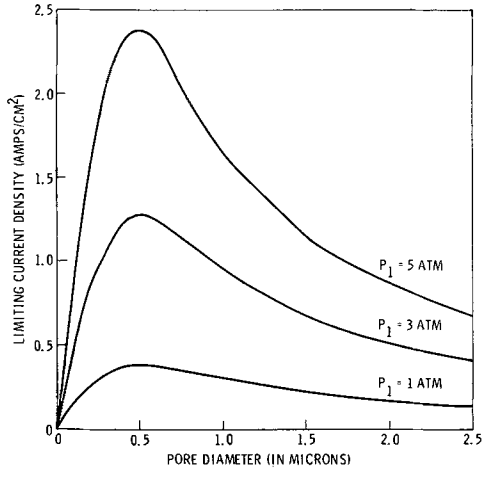

Fig. 8. Calculated limiting current according to Eq. [4] and [9]. Temperature, 650°C; porosity, 30%; electrode thickness, 0.5 cm; P_1, chlorine pressure.

The limiting current was therefore calculated in two ways. First, the pore size distribution for each material was approximated by a single step-function at the median pore diameter. The limiting currents so calculated are found to be low compared with the experimental data (Table II). A better approximation to the pore size distribution is obtained by using several steps and summing the flow and the diffusion current (Eq. [4] and [9]) over all the steps. The steps at large diameters contribute most to the total flow while the steps at smaller diameters contribute more to the diffusion current. With the exception of FC-1 the limiting currents calculated in this way are found to agree well with experimental data. This second method of calculation is more realistic since most of the flow in the bulk of the porous body no doubt occurs through the larger pores, while at the carbon-LiCl interface the small pores are the most active ones. This also suggests the use of a bi-porous carbon electrode consisting of say 0.5 cm of material with pores in the 10-20μ range with a thin surface layer (say 0.01 cm) of much finer pores ($\approx$ 0.05μ). In the multistep approximation it is necessary to limit the range of pores considered. If several 1 mm holes were drilled through a porous electrode and these holes were then treated as a step in the pore size distribution one would obviously obtain erroneous results. In this work only pores from 10 to 0.05μ were considered. Actually the only materials affected by setting these somewhat arbitrary limits were FC-13 and FC-50 both of which have a considerable number of pores smaller than 0.05μ. However, when these smaller pores are included the computed values of i_L become much too high.

Conclusion

The open-circuit voltage and electrode polarization of the Li-Cl_2 system using fused LiCl electrolyte have been investigated. Good agreement was obtained between the measured O.C.V. and those calculated from available thermodynamic data. The main source of polarization was found to be the mass transport of Cl_2 at the porous graphite electrode, either in the gas phase or in the electrolyte depending on the size of the pores. The porous electrode in this system differs in a fundamental way from porous electrodes in aqueous electrolytes in that molten LiCl does not wet graphite. Hence the thin film region at the top of the meniscus, which is of primary importance in the case of aqueous electrolytes does not exist in this electrode. A quantitative model for the nonwetted porous electrode was described and tested, and fair agreement with experiment was observed. The limiting currents found for dead-ended electrodes (Table II) appear disappointingly low in terms of obtaining high power densities. However the mass transport can be improved in a number of ways, *e.g.*, by increasing the system pressure to increase the solubility of Cl_2 in LiCl or by

Table II. Experimental and computed values of the limiting current of the Cl_2 electrode in LiCl at 650°C for various carbons

Carbon*	Experimental i_L amp/cm²	Theoretical i_L Single step approximation amp/cm²	Theoretical i_L Multistep approximation amp/cm²
FC-1	0.05 ± 0.01	0.16	0.15
FC-11	0.98 ± 0.29	0.08	0.84
FC-13	1.09 ± 0.15	0.14	0.79
FC-25	0.04 ± 0.01	0.06	0.06
FC-26	0.15 ± 0.03	0.03	0.14
FC-30	0.08 ± 0.01	0.07	0.08
FC-50	0.86 ± 0.29	0.06	0.83
37-G	0.75 ± 0.24	0.09	0.50
103-G	0.09 ± 0.04	0.14	0.19
105-G	0.26 (2 determinations only)	0.09	0.31
108	0.30 ± 0.08	0.08	0.29
108-G	0.16 ± 0.04	0.06	0.26

* The carbon identifications are those of the manufacturers: Pure Carbon Company, Inc., and Speer Carbon Company, St. Mary's, Pennsylvania.

bubbling through excess Cl_2. The stirring caused by the growing bubbles at the electrode surface improves the mass transport sufficiently so that current densities of 3 amp/cm^2 can be obtained with only 0.3v of concentration polarization.

Complete power cells have been assembled using a porous electrode with excess Cl_2 flow. In these cells power densities of 6 w/cm^2 have been obtained (23). Further improvements in the performance of the porous electrode can come from suitable choice of pore size distribution and by increasing the system pressure so as to increase the chlorine solubility.

Manuscript received June 16, 1965; revised manuscript received Sept. 17, 1965. This paper was presented at the San Francisco Meeting, May 9-13, 1965.

Any discussion of this paper will appear in a Discussion Section to be published in the December 1966 JOURNAL.

REFERENCES

1. R. E. Henderson, B. Agruss, and D. A. J. Swinkels, Paper presented at the ASME International Conference on Energetics, Detroit, August 1965.
2. J. Werth, J. Kennedy, and R. Weaver, Paper presented at 3rd Biennial Aerospace Power Systems Conference, Philadelphia, September 1964.
3. H. A. Laitinen, R. A. Osteryoung, and W. S. Ferguson, *This Journal*, **104**, 516 (1957).
4. T. B. Douglas, J. L. Dever, and A. W. Harman, NBS Report 6297.
5. E. N. Rodigina, K. Z. Gomelski, and V. F. Luginina, *Zhur. Neorg. Khim.*, **4**, 975 (1959).
6. H. M. Haendler, P. S. Sennett, and C. M. Wheeler, *This Journal*, **106**, 264 (1959).
7. H. Flood, O. Fykse, and S. Urnes, *Z. Elektrochem.*, **59**, 364 (1955).
8. H. Von Wartenberg and H. Schultz, *ibid.*, **27**, 568 (1926).
9. W. J. Hamer, M. S. Malmberg, and B. Rubin, *This Journal*, **103**, 8 (1956).
10. Janaf Thermochemical Data, The Dow Chemical Company, Midland, Mich.
11. Iu. K. Delimarski and B. F. Markov, "Electrochemistry of Fused Salts," p. 139, 141, Sigma Press, Washington, D. C. (1961).
12. H. A. Laitinen, R. P. Tischer, and D. K. Roe, *This Journal*, **107**, 546 (1960).
13. A. S. Dworkin, H. R. Bronstein, and M. A. Bredig, *J. Phys. Chem.*, **66**, 572 (1962).
14. H. Von Wartenberg, *Z. Elektrochem.*, **32**, 331 (1926).
15. S. B. Tricklebank, Private communication.
16. F. G. Will, *This Journal*, **110**, 145 (1963).
17. L. G. Austin, M. Ariet, R. D. Walker, G. B. Wood, R. H. Comyn, "The Simple Pore and Thin Film Models of Porous Gas Diffusion Electrodes," Report No. 7 to U. S. Army Material Command, Washington, D. C. Contract No. DA 49-186-502-ORD-917.
18. J. O'M. Bockris and G. W. Hooper, *Discussions Faraday Soc.*, **32**, 218 (1961).
19. S. R. Richards and J. O'M. Bockris, Report to U.S.A.E.C. 1961 Contract No. AT(30-1)-1769.
20. E. R. Van Artsdalen and I. S. Yaffe, *J. Phys. Chem.*, **59**, 118 (1955).
21. A. E. Scheidegger, "The Physics of Flow Through Porous Media," p. 25, MacMillan, New York (1957).
22. W. O. Sinsauer, H. M. Shearin, Jr., P. H. Masson, and M. Williams, *Bull. Am. Assoc. Petrol. Geologists*, **36**, 253 (1952).
23. H. R. Karas, To be published.

Anodic Oxidation of the Basic Sulfates of Lead

Jeanne Burbank

United States Naval Research Laboratory, Washington, D. C.

ABSTRACT

$PbO \cdot PbSO_4$, $3PbO \cdot PbSO_4 \cdot H_2O$, and $4PbO \cdot PbSO_4$ were prepared by reacting PbO and dilute H_2SO_4. The crystalline phases were identified by x-ray diffraction patterns, and electron microscope examination showed all three to be prismatic needles, The three basic sulfates were oxidized anodically in dilute sulfuric acid, and x-ray diffraction showed that each transformed to βPbO_2. The pellet made from $4PbO \cdot PbSO_4$ was mechanically strong, and the transformation to PbO_2 was largely metasomatic after the original crystals of the basic sulfate. The three anodic preparations were examined in the electron microscope and showed the presence of prismatic and nodular particles of PbO_2.

Studies on the lead acid battery have long been of interest to this Laboratory owing to the continued importance of this cell in submarine service. In recent years the so-called "lead-calcium" cell has replaced the conventional antimonial lead cell on the nuclear powered ships where the batteries were installed in float service. This change in cell type focused attention on the positive plate because, shortly after installation, the lead calcium cells began to fail by softening and disintegration of the positive active material. This loss of strength and electrical continuity in the positive mass was attributed to an unsuitable crystal morphology. Other simultaneous investigations revealed that mechanical strength and battery capacity were maintained when the active material paste was knit together by prismatic crystals of PbO_2 or $PbSO_4$ (1, 2). Because $PbSO_4$ is a discharge product in the plates, it is thermodynamically unstable in a float installation, and in order to retain its presence in the positive plates they must be carried in a partially discharged condition, and continuous float becomes impossible. In addition, fully charged batteries are almost universally desired. On the other hand, it is not known how the prismatic crystals of PbO_2 are produced in certain commercial battery pastes. Studies currently under way at this Laboratory are directed toward analysis of the factors affecting the structure of the positive active materials.

Battery plates are fabricated from a mixture of lead oxides, usually containing some free metallic lead, sulfuric acid, water, and miscellaneous additives. These materials are mixed for a brief period to form a stiff paste which is pressed into a metallic battery grid. The paste first stiffens or "sets," and the plates are then ready to be "cured." Curing is a combined setting and drying process during which several chemical reactions occur. Free metallic lead which may be present in finely divided form in the paste is spontaneously oxidized with the liberation of heat, and the reaction of the oxides and sulfuric acid is carried

essentially to completion. If the paste does not initially contain significant amounts of free lead, the curing process must be carried out in an oven in the presence of water vapor. After curing, the paste is a complex mixture of unreacted lead oxides, one or more basic sulfates of lead, perhaps basic carbonates and hydrated lead oxides (3-14). The cured plates are assembled into battery elements and electrochemically converted into the final active materials: PbO_2 at the positive and Pb at the negative plate.

Three basic sulfates are often encountered in the cured paste: $PbO \cdot PbSO_4$, $3PbO \cdot PbSO_4 \cdot H_2O$ and $4PbO \cdot PbSO_4$. To determine whether any or all of these materials is a source of prismatic PbO_2 in the finished battery plate, each of these compounds was separately converted to PbO_2 and the morphologies of the resulting crystals examined.

Experimental

For this study the three commonly encountered basic sulfates of lead were prepared and anodized individually in dilute sulfuric acid. The starting materials and final electrochemical products were identified by x-ray diffraction and examined by electron microscopy.

$PbO \cdot PbSO_4$, $3PbO \cdot PbSO_4 \cdot H_2O$, and $4PbO \cdot PbSO_4$ were synthesized from reagent grade PbO and the stoichiometric quantity of H_2SO_4. One mole of powdered PbO was mixed in a liter of distilled water, and the required amount of 1.250 sp gr H_2SO_4 solution was added dropwise with stirring which was continued 4 hr after addition of the acid. The mixture for the tetrabasic sulfate was heated during the initial reaction period to approximately 80°C and then allowed to cool to room temperature. The mixtures were digested for four days at room temperature, the solids collected on a filter, and air dried. The identity of the solid phases was verified by x-ray diffraction, and the crystals were examined directly in the electron microscope.

For the electrochemical formation, a thick paste of each basic sulfate and distilled water was pressed into a pellet in a frame cut from pure lead sheet 0.625 mm thick. Bibulous paper was applied to both sides of the pellet during fabrication and allowed to remain in place until the mass had dried in air at room temperature. These plates were then wrapped with filter paper held in position with rubber bands, and sheet lead electrodes of the same size were placed on both sides of each plate. These small elements were connected in series, and the pellets were anodized for 72 hr in 1.050 sp gr H_2SO_4 solution at a current density of 2.66 ma/cm^2 using the lead sheet as the counter electrodes, taking twice the apparent cross-sectional area as the surface area of the positive plates.

Following anodization, the cells were opened, and the pellets blotted dry. The formed material was analyzed by x-ray diffraction, examined in the optical microscope, and then extracted with saturated ammonium acetate solution. The residual particles of PbO_2 were again examined by x-ray diffraction and the optical microscope, and in addition they were studied with the electron microscope both directly and by means of carbon replicas (15).

Results and Discussion

The three basic sulfates prepared for this study were all prismatic crystalline materials and typical electron micrographs are shown in Fig. 1. The mono- and tribasic sulfates were colorless, and their prismatic forms are shown clearly in the electron micrographs, Fig. 1a and b. The tetrabasic lead sulfate, Fig. 1c, crystallized in rather large prisms with a pale yellow color. All three were readily and completely soluble in saturated ammonium acetate solution.

After anodization the pellet fabricated from $PbO \cdot PbSO_4$ had oxidized around the edges near the metal frame, but the center had not been converted to PbO_2 apparently owing to shrinkage accompanying the transformation which caused the center to lose contact with the edges. Upon extraction with ammonium acetate solution, the formed part of the pellet disintegrated readily, leaving a powder of PbO_2. Examination in the electron microscope showed that this was a mixture of nodular and prismatic crystals, Fig. 2.

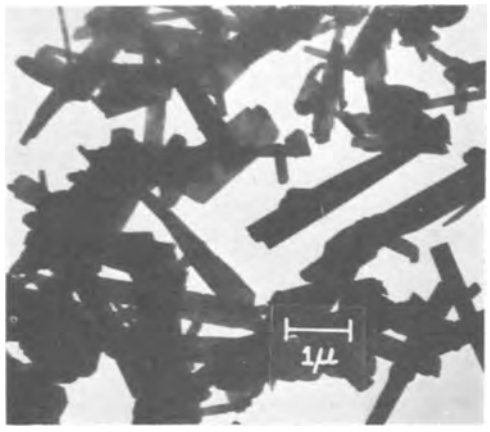

Fig. 1a. Electron micrograph of $PbO \cdot PbSO_4$ crystals. These appear to be rather thin blunted needles and were the smallest in average size of the basic sulfates prepared for this study.

Fig. 1b. Electron micrograph of $3PbO \cdot PbSO_4 \cdot H_2O$ crystals. The wide variation in size of these slender needles is apparent in this photograph. The surfaces of these crystals are covered with protrusions which may be incipient or vestiginal dendritic arms.

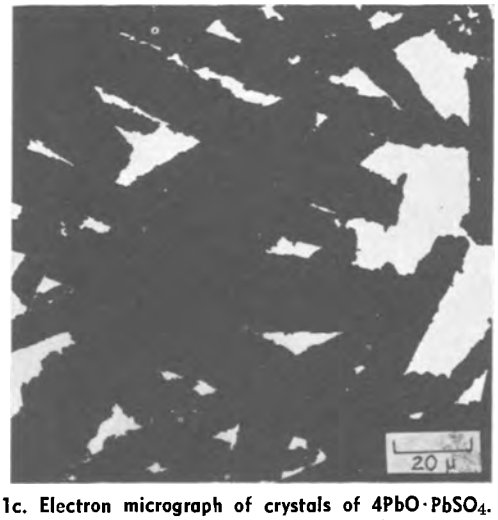

Fig. 1c. Electron micrograph of crystals of $4PbO \cdot PbSO_4$. These crystals were rather large for examination in the electron microscope, but are shown here for comparison with the other basic sulfates of lead. The surfaces of these crystals appear irregular and somewhat flokey at this magnification.

Fig. 2. Electron micrographs of carbon replicas of PbO_2 particles formed by anodization of $PbO \cdot PbSO_4$. (a) A mixture of nondescript and prismatic particles.

Fig. 2b. A cluster of small prismatic crystals

The anodized pellet made from $3PbO \cdot PbSO_4 \cdot H_2O$ had also formed around the edges near the metal frame, and shrinkage had left a smaller central area unformed than in the case of $PbO \cdot PbSO_4$. The formed mass was readily disintegrated into small particles on extraction with saturated ammonium acetate solution. Examination in the electron microscope showed again the presence of nodular and small prismatic crystals of PbO_2, Fig. 3.

The pellet fabricated from $4PbO \cdot PbSO_4$ appeared visually to be totally converted to PbO_2 by the anodic oxidation and was hard, mechanically strong, and well bonded to the metallic lead frame. Optical examination showed that the original crystal shapes of the basic sulfate had been retained intact during the oxidation. This pellet was extracted for several weeks with saturated ammonium acetate solution, and some fine particles were released from the mass, but the major portion of the pellet, comprising the distinct crystal forms related to the original $4PbO \cdot PbSO_4$ crystals, remained intact. Electron microscope examination of crystals obtained from this pellet showed that the fine particles were a mixture of nodular and prismatic forms, and that the surfaces of the large particles were very rough and irregular, Fig. 4.

X-ray diffraction analysis showed that all three basic sulfates had been converted to βPbO_2 by the electrolytic oxidation, in agreement with the earlier findings of Ikari, Yoshizawa, and Okada (10). As reported by these authors, it was also observed in this study that the pellet formed from $4PbO \cdot PbSO_4$ contained some residual unreacted material even though it appeared to be totally formed. This residue was readily extracted with saturated ammonium acetate solution so that subsequent x-ray diffraction patterns taken from the pellet showed only the presence of βPbO_2. It is considered that the retention of the crystal forms and pellet strength after extraction of all $4PbO \cdot PbSO_4$ detectable by x-ray diffraction shows that the prismatic forms of the large crystals of the basic sulfate are in fact retained by the PbO_2 and are not artifacts produced by a shallow conversion on the surface of the original basic sulfate crystals.

The conversion of one material into another by simultaneous addition and subtraction of matter, but without change in external form is called metasomatism or replacement by geologists (16-18). Petrified wood is one familiar and interesting example of metasomatism in which the wood structure is replaced by inorganic crystalline rock which retains the external form of the original tree trunk. The term metasomatism is used in this discussion because it so aptly describes the processes of charging battery pastes to form PbO_2 *in situ* within the original volume of the paste, and particularly the conversion of $4PbO \cdot PbSO_4$ to PbO_2. Electrochemical action has been thought to play a part in the formation of some geological deposits and in certain metasomatic transformations in the earth's crust, particularly when high temperatures and pressures were not active during a metamorphosis (19-22).

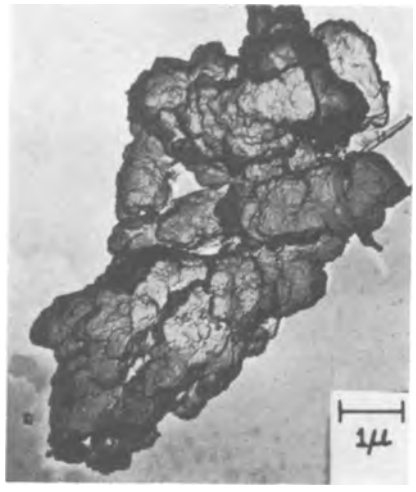

Fig. 3. Electron micrographs of carbon replicas of PbO_2 particles formed by anodization of $3PbO \cdot PbSO_4 \cdot H_2O$. (a) Nondescript nodular forms.

Fig. 3b. Prismatic dendritic crystal

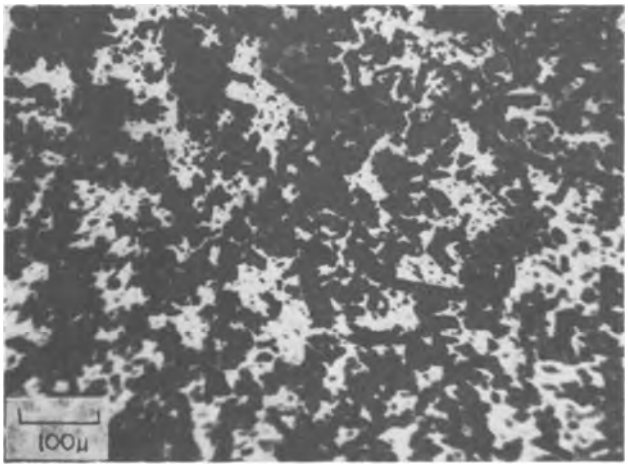

Fig. 4. Micrographs of PbO_2 particles obtained by anodization of $4PbO \cdot PbSO_4$. (a) Optical micrograph taken during extraction of PbO_2 with ammonium acetate solution. The large particles are metasomatic after the original basic sulfate crystals.

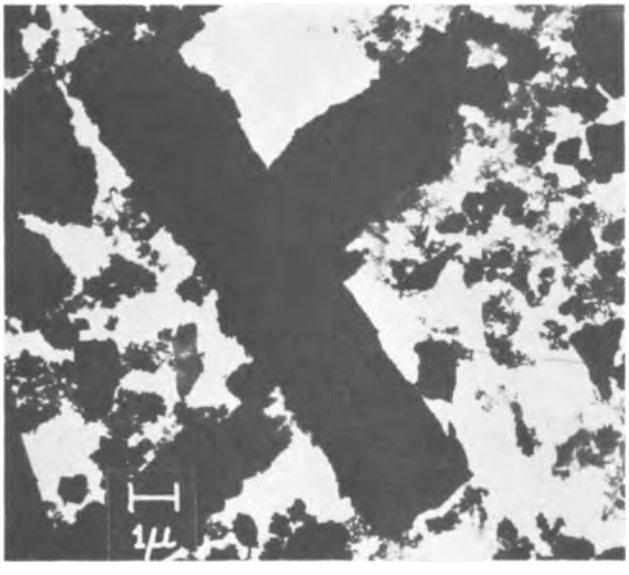

Fig. 4b. Electron micrograph showing a large metasomatic crystal and fine-particle material which is a mixture of prismatic and nondescript forms.

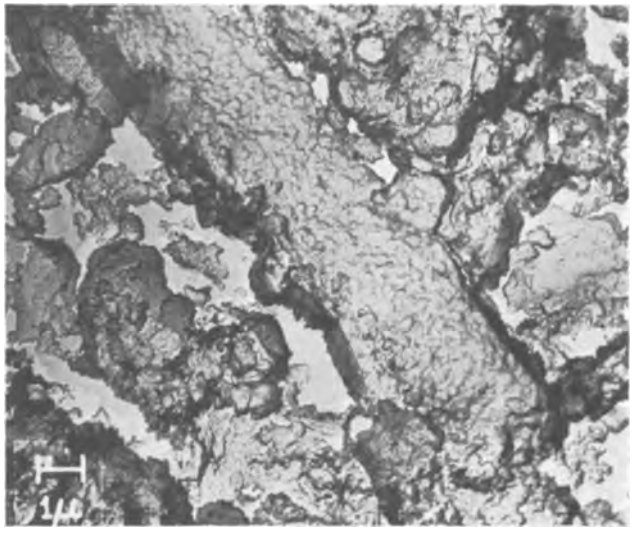

Fig. 4c. Electron micrograph of carbon replica including one of the metasomatic crystals. The surface is crenelated which may be evidence of grain structure within the metasome.

There is usually only a minimal volume change between host and metasome, and Table I lists the volume changes expected during formation of βPbO_2 from certain compounds likely to be present in the unformed active material of the lead acid cell. It is seen that free lead and PbO would be expected to give rise to a larger volume of PbO_2 than they themselves occupy, while the normal and basic sulfates of lead and Pb_3O_4 could produce shrinkage in volume. Thus a balance of these paste materials in the cured plate can result in zero change in total volume during electrochemical conversion to PbO_2. The pore structure does vary in battery plates depending on the relative amounts of oxide and acid used in fabrication (measured as paste density in the trade), and at least one study has shown an over-all expansion of the paste on formation (8, 23).

On the other hand, the large tetrabasic lead sulfate crystals have been shown in this study to transform by electrochemical metasomatic replacement, not accompanied by the expected shrinkage in volume. For every five molecules of PbO_2 formed from $4PbO \cdot PbSO_4$ only one sulfate ion need be removed from the body of the crystal with the simultaneous addition of six oxygen atoms as indicated by the reaction

$$5PbO_2 + 12H^+ + SO_4^= + 10e = 4PbO \cdot PbSO_4 + 6H_2O$$
$$E^* = 1.196 - 0.0709\,pH + 0.0059 \log a_{SO_4}$$

The volume change indicated in Table I for this compound may be eliminated if lead ions present in the electrolyte are electrodeposited within the volume occupied by the original crystals present in the unconverted paste mass. The initiation of the transformation may be the deposition of tetravalent lead ions at active sites on the surface of an original crystal, and transformation may then spread readily throughout the body of the crystal from this surface initiation by a diffusion mechanism across the interphase boundary. As indicated in Table I, there would be a 15% decrease in volume on conversion of a crystal of $4PbO \cdot PbSO_4$ to an equivalent amount of PbO_2. This may result in

* Calculated by assuming the standard free energy of formation of $4PbO \cdot PbSO_4$ is -374.88 kcal based on the free energies of formation of PbO and $PbSO_4$.

Table I. Volume changes during formation of βPbO_2

Compound	Molecular weight	Density	Gram molecular volume, cc	Moles PbO_2 formed per mole of compound	ΔV,* cc	% ΔV per Pb atom
Pb	207.21	11.341	18.28	1	6.56	35.87
$PbSO_4$	303.27	6.323	47.96	1	−23.12	−48.21
PbO (orthorhombic)	223.21	9.642	23.15	1	1.69	7.12
PbO (tetragonal)	223.21	9.355	23.88	1	0.96	4.02
Pb_3O_4	685.63	8.925	76.79	3	−0.72	−2.81
$PbO \cdot PbSO_4$	526.48	7.02	75.0	2	−12.66	−33.77
$3PbO \cdot PbSO_4 \cdot H_2O$	990.92	6.5**	152.0	4	−13.0	−34.0
$4PbO \cdot PbSO_4$	1196.11	8.15	146.76	5	−4.51	−15.38
βPbO_2	239.21	9.63	24.84	—	—	—

* Volume change upon conversion to βPbO_2 per gram atom of Pb in the compound.
** A very approximate value obtained from the material synthesized for this study.

porosity within the metasome, but if for example each molecule of $4PbO \cdot PbSO_4$ were replaced by six molecules of PbO_2, there would be a volume increase of 1%. The volume of the tetrabasic crystal could be replaced exactly by the addition of an appropriate number of lead ions from solution: approximately 9.083 for every 50 in the crystal. The replacement of one molecule of $4PbO \cdot PbSO_4 (Pb_5O_8S)$ with $5PbO_2 (Pb_5O_{10})$ would result in no change in weight. Taken on the basis of either the volume or the weight remaining constant, this conversion defines a reference state for a thermodynamic system as discussed by Thompson for metasomatic processes (24). This same mechanism could metasomatically replace any of the original basic sulfate crystals in the paste; however, a greater mass transfer would be involved in the conversion of the others.

The strength of the pellet of PbO_2 formed from $4PbO \cdot PbSO_4$ may be attributed to the interlocking of the large metasomatic crystals. This suggests that a suitable distribution of $4PbO \cdot PbSO_4$ crystals in a cured paste can impart strength to a fully formed plate by this same mechanism. Simon and Jones have shown that in certain battery plates there exists a network of hard PbO_2 that is continuous throughout the paste and suggested that this originated from a network of one of the basic sulfate crystals initially present in the unformed plates (25). It was further suggested that this hard network might be αPbO_2; however, only βPbO_2 was observed by x-ray diffraction as the anodic product from all three basic sulfates under the conditions used in this study. On the other hand, metasomes are frequently particularly hard and dense owing to their diffusional growth mechanism which somewhat resembles a zone refining process. On the basis of the results of this study it seems likely that the network described by Simon and Jones arises from tetrabasic lead sulfate crystallized in this pattern in the unformed plate.

In earlier investigations of the active material pastes of certain lead calcium batteries the small particles were consistently prismatic (1). However, none of the three basic sulfates examined in this study gave rise to prismatic crystals to such an extent: the fine-particle material was a mixture of nodular and prismatic crystals in all three instances. On the other hand, the crystals of $4PbO \cdot PbSO_4$ prepared for this study were of a fairly uniform and large size, and it is possible that fine-particle prismatic PbO_2 arises from small crystals of this same material when these are present in unformed battery plates.

Other mechanisms can give rise to prismatic PbO_2. For example it has been shown that antimony in the grid alloy leads to prismatic growth of PbO_2 (26), some appeared in the anodization of $PbO \cdot PbSO_4$ and $3PbO \cdot PbSO_4 \cdot H_2O$ in this study, and hydrothermal recrystallization also produces prismatic crystals (27). It is anticipated that future investigations of positive active materials will lead to further understanding and result in optimization of the physical structures required to give maximum plate durability thus extending battery life.

Manuscript received Aug. 16, 1965. This paper was presented at the Buffalo Meeting, Oct. 10-14, 1965.

Any discussion of this paper will appear in a Discussion Section to be published in the December 1966 JOURNAL.

REFERENCES

1. J. Burbank, "Batteries," Proc. 3rd I.D.C.B. Symposium, Bournemouth 1962, p. 43, Pergamon Press, New York (1963).
2. J. Burbank, *This Journal*, **111**, 765 (1964).
3. J. J. Lander, *ibid.*, **95**, 174 (1949).
4. R. H. Greenburg, F. B. Finan, and B. Agruss, *ibid.*, **98**, 474 (1951).
5. T. Takagaki, *J. Electrochem. Soc. Japan*, **23**, 173, 232, 399, 449, 567 (1955).
6. T. Takagaki, *ibid.*, **25**, 492 (1957).
7. T. Takagaki, *ibid.*, **26**, 278, 320, 354 (1958).
8. J. F. Dittman and J. F. Sams, *This Journal*, **105**, 553 (1958).
9. S. Ikari, *J. Electrochem. Soc., Japan*, **27**, 385 (1959).
10. S. Ikari, S. Yoshizawa, and S. Okada, *ibid.*, **27**, 426, 487 (1959).
11. S. Ikari and S. Yoshizawa, *ibid.*, **27**, 613 (1959).
12. H. Bode and E. Voss, *Electrochim. Acta*, **1**, 318 (1959).
13. T. Ishikawa, H. Tagawa, and Y. Nakamura, Denki-Kagaku, **29**, 168 (1961).
14. S. C. Barnes and R. T. Mathieson, "Batteries," Proc. 4th I.D.C.B. Symposium, Brighton 1964, Pergamon Press, New York (1965).
15. D. E. Bradley, *Brit. J. Appl. Phys.*, **5**, 65, 96 (1954).
16. W. Lindgren, "Mineral Deposits," 4th ed., pp. 23, 91, 173, McGraw Hill Book Co., Inc., New York (1933).
17. H. Ramberg, "The Origin of Metamorphic and Metasomatic Rocks," University of Chicago Press, Chicago (1952).
18. A. B. Edwards, "Textures of the Ore Minerals," chap. V, p. 115, Australasian Institute of Mining and Metallurgy, Melbourne (1960).
19. V. H. Gottschalk and H. A. Buehler, *Econ. Geol.*, **7**, 15 (1912).
20. G. V. Douglas, N. R. Goodman, and G. C. Milligan, *ibid.*, **41**, 546 (1946).
21. W. C. Krumbein and R. M. Garrels, *J. Geol.*, **60**, 1 (1952).
22. V. A. Mokievskii, N. N. Stulov, and I. S. Tsigel'man, *Zapiski Vsesoyuz Mineralog Obshchestva*, **85**, 39 (1956).
23. E. Voss and J. Freundlich, "Batteries," Proc. 3rd I.D.C.B. Symposium, Bournemouth, 1962, p. 73, Pergamon Press, New York (1963).
24. J. B. Thompson, Jr., "Researches in Geochemistry," p. 427, John Wiley & Sons, Inc., New York (1962).
25. A. C. Simon and E. L. Jones, *This Journal*, **109**, 760 (1962).
26. J. Burbank, *ibid.*, **111**, 1112 (1964).
27. H. R. Davidson, *Am. Mineralogist*, **26**, 18 (1941).

Correction

The running heads on pages 1085, 1087, and 1089 of the November 1965 issue of the Journal should read

Effect of N on the Oxidation of Ta

for the paper by John Stringer "The Effect of Nitrogen on the Oxidation of Tantalum at High Temperatures," pages 1083-1091.

Reaction of Flowing Steam with Refractory Metals

II. Rhenium (850°-1700°C)

Martin Kilpatrick[1] and Stanley K. Lott

Argonne National Laboratory, Argonne, Illinois

ABSTRACT

When rhenium reacts with steam at 1 atm pressure, the rate of evolution of hydrogen is constant with time, and the metal remains bright with no evidence of a coating. The apparent energy of activation for the reaction is 30 kcal/mole, and the enthalpy of sublimation of Re_2O_7 is 33.5 kcal/mole, which suggests that the rate-determining step is the sublimation of the oxide.

Although the oxidation of rhenium has been studied in air (1-3), no study of the reaction of steam with rhenium has been reported. The oxide formed (Re_2O_7) melts at 296° and boils at 362°C under 1 atm pressure, and the reaction with oxygen takes place uniformly over the surface rather than preferentially at the grain boundaries. This paper reports the oxidation of rhenium with flowing steam for the temperature 850°-1700°C.

Experimental

The method was based on passing steam over an inductively heated specimen of metal, passing the products through a water-cooled condenser to separate the aqueous solution from the gas, and collecting the gas evolved in an eudiometer (4).

The apparatus, as shown in Fig. 1, consisted of an electrically heated 3-liter steam boiler (A) connected to a quartz tube (B) by a ball joint. The metal cylinder (C) was mounted on a two-hole alumina rod (D) which carried the Pt/Pt, 10% Rh thermocouple wires. The bottom of the quartz tube fitted into a female ball joint on a brass cup (F) which was connected to a copper tube leading to the gas burette (G). A copper spiral (H) was soldered to the copper tube to carry cooling water to condense the steam. The induction coil (E) was connected to a Reeve Electronic Generator.

To carry out an experiment, the polished and weighed specimen was mounted at (C), the boiler (A) turned on, and the apparatus steamed out to remove air. The experiment was started by turning on the induction heater and rapidly bringing the specimen to the desired temperature, as indicated by the millivolt reading on the recorder chart, and following the evolution of gas with time. At the end of the experiment, the specimen was removed, washed, and weighed, and the gas sample analyzed by mass spectrograph.

The rhenium was obtained from the Rembar Company as 5 to 10 mm diameter rods with a quoted purity of 99.9% The product metal had been sintered in hydrogen at 2700°C, compacted, cold swaged to finish size by 10% reduction per pass, and process annealed in hydrogen-nitrogen. The final annealing was carried out at 1650°C in a hydrogen atmosphere. Spectrographic analysis at Argonne showed only a faint trace of calcium (<0.0001%) and a trace of aluminum (<0.001%). The specimens were cut from the rods in 1 cm lengths and 1/10 and 3/32 in. holes drilled by Elox method for mounting the samples in the field of the induction furnace.

Flow rates were determined from the weight of the condensate, and the size of the annular opening as illustrated in Fig. 2.

Results

The rhenium at the end of a run was bright but examination of the surface showed many small crystals of metal randomly oriented. A graph (Fig. 3) of the hydrogen evolved *vs.* time was linear, and a comparison of the volume of hydrogen evolved with the weight loss of the specimen gave 3.41 ± 0.15 moles of hydro-

[1] Professor Emeritus, Illinois Institute of Technology, Chicago, Illinois.

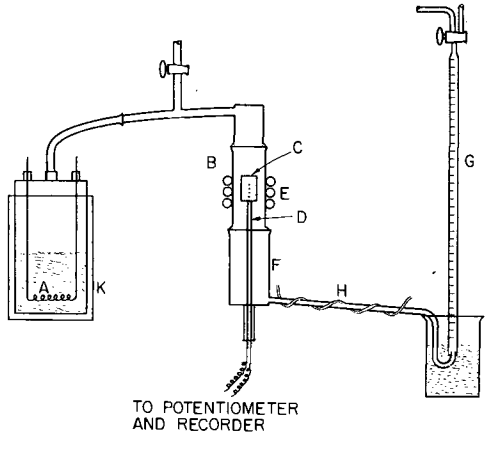

Fig. 1. Flow apparatus for the reaction of steam with metals: A, steam boiler; B, quartz tube; C, metal specimen; D, two hole alumina tube; E, induction heater; F, brass cup; G, gas burette; H, cooling coil; K, heating mantle.

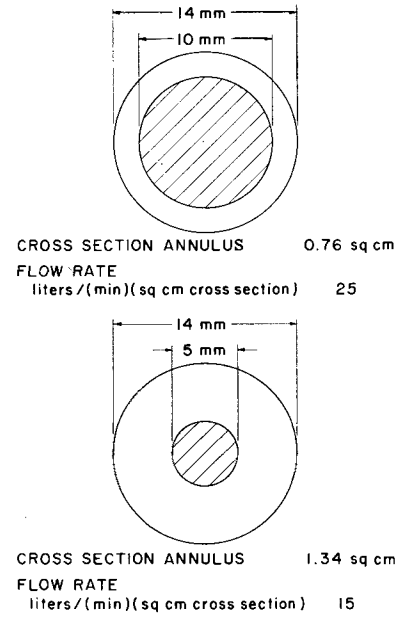

Fig. 2. Annulus area for steam flow

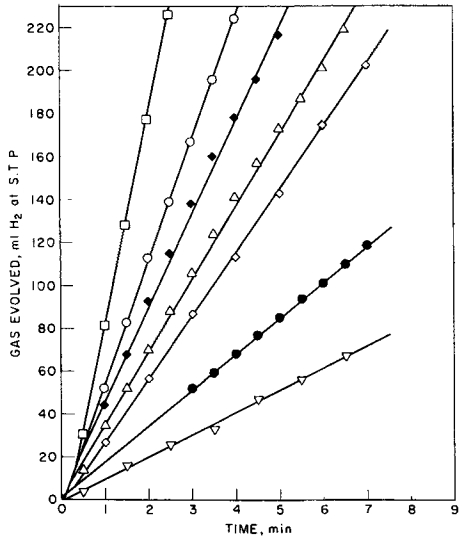

Fig. 3. Rate relationship of rhenium-steam reaction. Sample temperature and diameter are: □ 1593°C, 10 mm; ○ 1650°C, 5 mm; ◆ 1375°C, 10 mm; △ 1504°C, 5 mm; ◇ 1392°C, 10 mm; • 1312°C, 10 mm; ▽ 1240°C, 5 mm.

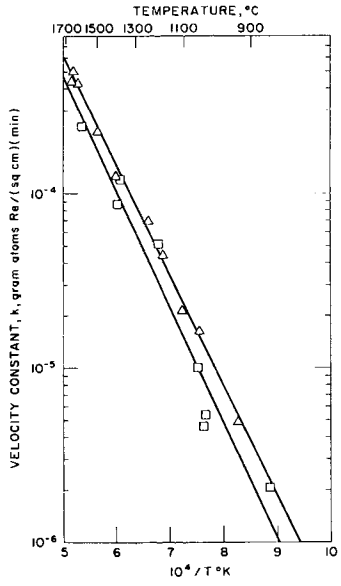

Fig. 4. Linear rate constants for the rhenium-steam reaction at various flow rates: flow rate, l/min cm²: △ 15; □ 25.

gen per gram atom of rhenium reacted. The stoichiometric equation is thus

$$2Re(c) + 7H_2O(g) \rightarrow R_2O_7(c) + 7H_2$$

The velocity constants calculated from the hydrogen evolved and from weight loss agreed fairly well. As shown in Table I, the effect of flow rate is small. The data are plotted in Fig. 4, and the least squares equations are given in Table II. All of the data can be represented by the equation $k = 0.962 \pm 0.384 \exp \frac{-29{,}800 \pm 1{,}000}{RT}$ gram atoms of Re per cm² per min.

Discussion

The value of 30 kcal for the energy of activation may be compared with $\Delta H_{sub} = 33.5 \pm 0.1$ for rhenium heptoxide at the melting point (5). This suggests the possibility that the rate-determining step is the desorption of the oxide.

Table I. Effect of flow rate on velocity constants for rhenium

Flow rate, liters steam/min/cm² of annulus cross section	Velocity constant, g atoms Re reacted/cm²/min	
	1500°K	1800°K
15	5.408×10^{-6}	2.731×10^{-4}
25	3.767×10^{-6}	2.062×10^{-4}

Manuscript received Nov. 20, 1964; revised manuscript received Sept. 15, 1965. This paper is based on work performed under the auspices of the United States Atomic Energy Commission.

Any discussion of this paper will appear in a Discussion Section to be published in the December 1966 JOURNAL.

REFERENCES

1. C. Agte, H. Alterthum, K. Becker, C. Heyne, and K. Moers, *Z. anorg. u. allgem. Chem.*, **196**, 129 (1931).
2. C. Sims, C. M. Craighead, and R. I. Jaffe, *Trans. AIME*, **7**, 168 (1955).
3. W. L. Phillips, Jr., *J. Less-Common Metals*, **5**, 97 (1963).
4. M. Kilpatrick and S. K. Lott, *J. Phys. Chem.*, **69**, 1638 (1965).
5. W. T. Smith, Jr., B. E. Line, Jr., and W. A. Bell, *J. Am. Chem. Soc.*, **74**, 4964 (1953).

Table II. Arrhenius equations—rhenium

[Temperature range (850°-1650°C)]

Flow rate, liters/min/cm² cross section of annulus	
25	$k = 1.012 \pm 0.798 \exp \frac{-30{,}402 \pm 2{,}035}{RT}$
15	$k = 0.8977 \pm 0.1673 \exp \frac{-28{,}967 \pm 566}{RT}$

Reaction of Flowing Steam with Refractory Metals

III. Tungsten (1000°-1700°C)

Martin Kilpatrick[1] and Stanley K. Lott

Argonne National Laboratory, Argonne, Illinois

ABSTRACT

The mechanism of the reaction of tungsten with steam over the temperature range 1000°-1450° is similar to that for the reaction of molybdenum. The rate-determining step consists of the oxidation of WO_2 (s) to the volatile $WO_2(OH)_2$ and WO_3 and its polymers. Above 1450° the reaction is complicated by the formation of a liquid phase on the surface of the metal.

Although the reaction of flowing steam with tungsten is similar in some respects to the reaction with molybdenum over the temperature range concerned, there are important differences. In the first place, the oxide product is relatively less volatile than the corresponding molybdenum compound, and the presence of a liquid phase around 1450°C complicates the kinetics. In addition, two oxides $W_{20}O_{58}$ and $W_{18}O_{49}$ are formed which are less volatile and less readily oxidized to WO_3 than is WO_2. Above 1530° WO_2 disproportionates to W and $W_{18}O_{49}$ (1).

Experimental Results

The experimental method was the same as that used for molybdenum and rhenium, and the experiments were carried out in similar fashion (2, 3). The tungsten was 99.9% pure, and both the 5 and 10 mm rods showed similar trace impurities which included traces of Fe, Cr, and Mo.

The stoichiometry of the reaction was established by comparing the moles of hydrogen evolved with the gram atoms of tungsten reacted as determined by weight loss. Although this ratio was 3.02 ± 0.04, the specimen at the end of the run was seldom free of black oxide or nonadhering dark violet oxide. Filings from the surface of the specimen after a typical run near 1200°C were examined by x-ray diffraction and found to contain tungsten dioxide with $W_{20}O_{58}$ as a minor constituent, in addition to tungsten. Filings from a specimen after a run just above 1500°C were found to contain $W_{18}O_{49}$ in addition to tungsten.

[1] Professor Emeritus, Illinois Institute of Technology, Chicago, Illinois.

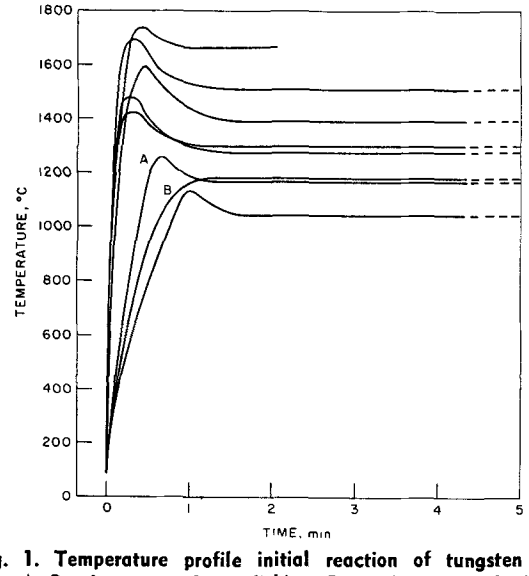

Fig. 1. Temperature profile initial reaction of tungsten with steam. A, Specimen run after polishing; B, specimen reused without removing tarnish.

As Fig. 1 indicates, there is considerable heat evolved when the polished metal initially reacts with steam, but the temperature rapidly becomes constant. When a specimen is rerun without polishing, this rise above the control temperature is absent, and the rate is the same. However, in cases where the temperature of the overshoot rises to 1500°C, with a very rapid evolution of hydrogen, when the temperature drops the evolution of gas decreases sharply. This is due to the fact that, as the molten oxide solidifies, the coating becomes impermeable to steam, and reaction does not continue normally until the temperature is raised above the melting point (1473°C).

In spite of the fact that not all of the product was converted to the volatile trioxide or its complex with water, the rate of evolution of hydrogen was constant (Fig. 2), and the velocity constants in terms of gram atoms of tungsten reacted per square centimeter per minute from the weight loss agreed well with the velocity constants calculated from hydrogen evolution. Above 1400°C, the aluminum oxide support reacted to some extent with the tungsten, and it was not always possible to remove the core and get the weight loss. In the experiments above 1400°C, the violet black oxide $W_{18}O_{49}$, flecked with the light yellow green oxide, remained as a coating on the sample and interfered with the flow pattern of the steam. The results are summarized in Fig. 3 by a plot of log k *vs.* $10^4/T$(°K). The Arrhenius equations for the two tem-

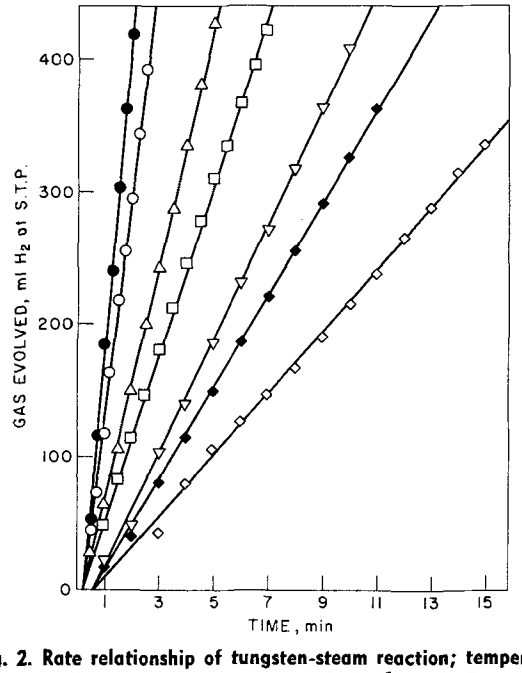

Fig. 2. Rate relationship of tungsten-steam reaction; temperature in °C, sample diameter in mm: ● 1663, 5; ○ 1505, 5; △ 1332, 10; □ 1392, 5; ▽ 1242, 10; ◆ 1217, 10; ◇ 1284, 5.

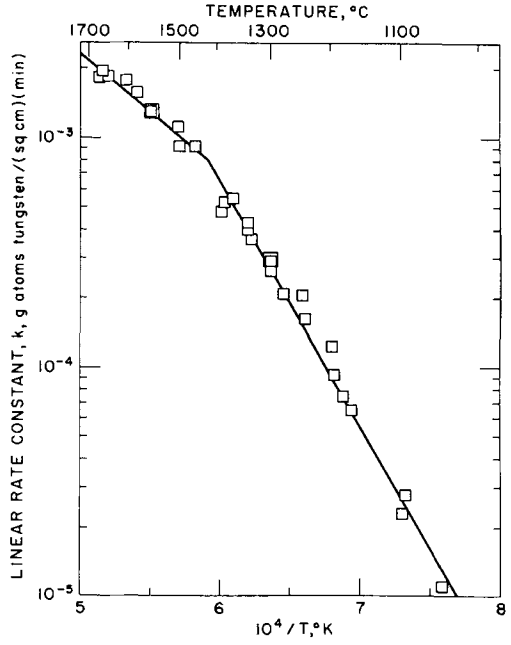

Fig. 3. Tungsten with steam velocity constants vs. $10^4/T$

perature ranges for the velocity constants as gram atoms of tungsten reacted per square centimeter per minute are, for the temperature range 1050°-1450°C

$$k = 1.688 \pm 0.593 \exp \frac{-48{,}900 \pm 1{,}000}{RT}$$

and for the temperature range 1450°-1700°C,

$$k = 0.282 \pm 0.178 \exp \frac{-22{,}700 \pm 2{,}200}{RT}$$

The oxidation of tungsten by water vapor at 38 Torr has been reported by Farber (4) who measured the change in electrical resistance with time over the temperature range 1700°-2000°K and found a value of 14.5 kcal for the energy of activation.

Discussion

If the reaction of tungsten with steam follows the path for the reaction of molybdenum with steam outlined in a previous paper (2)

$$2H_2O(g) + W(c) \rightleftharpoons 2H_2 + WO_2(c) \qquad [1]$$

and the dioxide would then be oxidized to WO_3 and removed as a vapor of WO_3 and its polymers, or as the more volatile $WO_2(OH)_2(g)$, via the reactions

$$WO_2(c) + H_2O(g) \xrightarrow{k_3} WO_3(g) + H_2 \qquad [2]$$

$$WO_2(c) + 2H_2O(g) \xrightarrow{k_5} WO_2(OH)_2(g) + H_2 \qquad [3]$$

As in the case of molybdenum, the measured rate follows the linear law and shows that the steady state would be reached very quickly under the conditions used, and that the amount of metal stored as dioxide would be small. Assuming the dioxide to be removed via both [2] and [3] the rate constant would be

$$k = [WO_2(c)][H_2O]\{k_3 + k_5[H_2O]\} \qquad [4]$$

where $[WO_2(c)]$ represents the surface concentration of active sites.

The measured energy for the reaction of steam with tungsten over the range 1100°-1400°C is 49 kcal. It is of interest to compare this figure with the enthalpy changes accompanying reactions [2] and [3], respectively. Using the heats of formation (5) of $WO_2(c)$ and $WO_3(c)$, and the heat of sublimation of the trioxide from Glemser and Völz (6), one finds ΔH_2 at 1500°K to be 43 kcal. For the reaction

$$WO_3(c) + H_2O(g) \rightarrow WO_2(OH)_2(g) \qquad [5]$$

ΔH is ca. 40 kcal (6-8), and from this and the heats of formation ΔH_3 at 1500°K is estimated to be 41 kcal. It may also be mentioned that Battles (9) investigated the rate of volatilization of the trioxide in a flowing mixture of argon and water vapor and found the energy of activation to be 40 kcal/mole.

In a recent paper, Bartlett (10) has proposed that the reaction between oxygen and tungsten, below 2000°C, proceeds by the steps

(a) $s|W + \frac{1}{2} O_2 \rightleftharpoons s|W-O$

(b) $s|W-O + \frac{1}{2} O_2 \rightleftharpoons s|W(O)(O)$

(c) $s|W(O)(O) \rightarrow WO_2(g)$

(d) $2(s|W(O)(O)) \rightarrow WO_3(g) + s|W-O$

where $s|W-O$ indicates a covered site in a monolayer (of which there are two) of chemisorbed oxygen atoms. At low pressures, about equal amounts of WO_2 and WO_3 would form, the proportion of the latter increasing with increasing pressure of oxygen. The activation energy found by Bartlett was 42 kcal. Although there was discoloration of the tungsten rods in his experiments, he believed the surface film to have formed on cooling.

In view, however, of the results shown in Fig. 1, it appears that in the reaction of water vapor and tungsten there is an initial, rapid reaction with the bright metal, accompanied by evolution of heat. This leaves a film on the surface so that if the specimen is re-used without polishing a steady rise to control temperature occurs, with no overshoot. This phenomenon, illustrated by curves A and B in Fig. 1, was readily reproducible. The view of a thin layer of lower oxide therefore appears more tenable in the case of the reaction of water vapor with tungsten than does the scheme proposed by Bartlett for the reaction of oxygen with tungsten.

Manuscript received Nov. 20, 1964; revised manuscript received Sept. 15, 1965. This paper is based on work performed under the auspices of the United States Atomic Energy Commission.

Any discussion of this paper will appear in a Discussion Section to be published in the December 1966 JOURNAL.

REFERENCES

1. B. Philip and L. L. Y. Chang, *Trans. AIME*, **203**, 1203 (1964).
2. M. Kilpatrick and S. K. Lott, *J. Phys. Chem.*, **69**, 1638 (1965).
3. M. Kilpatrick and S. K. Lott, *This Journal*, **113**, 15 (1966).
4. M. Farber, *This Journal*, **100**, 751 (1959).
5. J. P. Coughlin, Bull. 542, Bureau of Mines.
6. O. Glemser and H. G. Völz, *Naturwiss.*, **43**, 33 (1956).
7. O. Glemser and R. v. Haesler, *Z. anorg. u. allgem. Chem.*, **316**, 168 (1962).
8. G. R. Belton and R. L. McCarron, *J. Phys. Chem.*, **68**, 1852 (1964).
9. J. E. Battles, Doctoral Dissertation, Department of Metallurgical Engineering, Ohio State University (1964).
10. J. E. Battles, M. Sc. Thesis, Department of Metallurgical Engineering, Ohio State University, (1961).
11. R. W. Bartlett, *Trans. AIME*, **230**, 1100 (1964).

Solid-State Anodic Oxidation of Tantalum

D. M. Smyth

Research Laboratory, Sprague Electric Company, North Adams, Massachusetts

ABSTRACT

When an anodic potential is applied to a tantalum point contact to MnO_2, the current-voltage behavior is analogous to that observed during the anodic oxidation of a valve metal in an aqueous electrolyte. It is proposed that this represents a solid-state anodic oxidation whereby tantalum oxide is formed at the expense of the local oxygen content of the MnO_2, and that this process represents an important "healing" mechanism in the Ta-Ta_2O_5-MnO_2 solid electrolyte capacitor. This process requires that the conductivity of the reduced manganese oxide phase, which must be formed adjacent to the Ta_2O_5, have a finite ionic portion, and experimental support for this is described. The current efficiency of the solid-state anodization is very low and is dependent on ambient moisture. Similar behavior has been found for aluminum and niobium point anodes and with PbO_2 as the cathode.

The electrochemical formation of anodic oxide films on such metals as tantalum, niobium, and aluminum in electrolytic solutions is well known and is of considerable scientific and practical interest. In these cases the current efficiency of oxide formation may approach 100% under suitable conditions, and the ionic current which leads to oxide film growth can be expressed as

$$i_i = Ae^{BV/d} \qquad [1]$$

where i_i is the ionic current through the oxide, V is the voltage drop across the film whose thickness is d, and A and B are constants for a given experimental condition. Variations on this familiar theme have appeared in recent years. The preparation and properties of anodic oxides have been described where the source of oxide ions was a glow discharge rather than an electrolytic solution (1, 2). It has also been claimed that very thin anodic oxide films (15-20Å) can be grown when the cathode is a metal layer which has been evaporated in a poor vacuum and thus contains dissolved oxygen (1).

In recent years the solid electrolyte capacitor has become of great importance. This device is based on the Ta-Ta_2O_5-MnO_2 system and is prepared by the pyrolytic deposition of MnO_2 on anodized tantalum (3). The MnO_2 serves to maintain the highly insulating properties of the dielectric and thus replaces the electrolytic solution which acts as the cathode plate in conventional electrolytic capacitors. Publications on this device to date have been restricted largely to descriptions of the electrical behavior of completed capacitors (3-5). There have been no detailed hypotheses presented on the mechanisms by which the MnO_2 functions. In this paper, evidence will be presented which indicates that tantalum can be electrochemically oxidized by MnO_2 in a solid-state process which is analogous to the conventional aqueous anodic oxidation process. This mechanism is apparently related to the so-called "reformation" which is performed on solid electrolyte capacitors after the MnO_2 has been applied to the anodized tantalum.

Experimental

A schematic drawing of the experimental arrangement is shown in Fig. 1. The tantalum point was formed by clipping the end of 0.016 in. tantalum wire at an angle. The results did not seem to be affected by whether or not the point was then cleaned in an HNO_3-HF etch. The wire was attached to a phosphor-bronze sheet spring with Eccobond Solder 56C, a conducting epoxy produced by Emerson and Cuming, Inc., Canton, Massachusetts. The MnO_2 was produced by thermal decomposition of Fisher 50% $Mn(NO_3)_2$ solution in a Pyrex beaker. Decomposition was begun on a hot plate and, after most of the water had evaported, was completed in a muffle furnace at 350°-400°. The beaker was then broken away from the solid product, leaving a hard, smooth MnO_2 surface which had formed next to the glass. This surface was used in these experiments. The MnO_2 was affixed to a metal plate with the Eccobond Solder. The power supply was either a potentiometer-controlled battery-pack or a voltage regulated, electronic power supply, and the voltage was adjusted manually in steps. The current was measured with a Keithley Model 210 Electrometer with a decade shunt and was recorded on an Esterline-Angus Model AW Recorder. The high side of the circuit was completely shielded, and the sample jig was enclosed in a shielded box.

The tantalum dots on MnO_2 were obtained by cathodic sputtering of tantalum through a mask onto the glassy MnO_2 surface. The best results were obtained when the MnO_2 was in good thermal contact with a water-cooled block. With this arrangement and with a 2-min-on and 1-min-off cycle (controlled with a shutter), the temperature, as measured at the back side of the MnO_2, was kept below 200°. The tantalum thickness was generally about 2000Å. Electrical contact to the tantalum was made with a small drop of liquid In-Ga solder on the end of a tantalum wire.

A variety of other methods for obtaining Ta-MnO_2 area contacts were unsatisfactory. These included pressure contacts, pyrolysis of $Mn(NO_3)_2$ solutions on wires or masked areas, and electrochemical deposition by anodic oxidation of Mn^{++} solutions or by cathodic reduction of MnO_4^- solutions.

Cell emfs were measured with a Keithley Model 200B Electrometer in a completely shielded circuit.

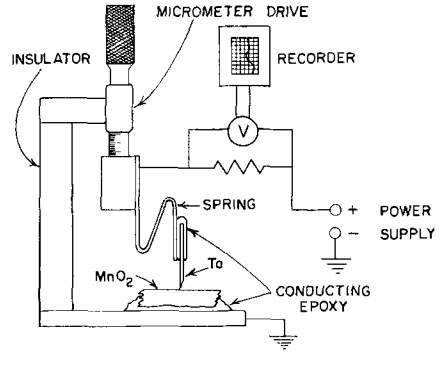

Fig. 1. Schematic diagram of point-contact experiment

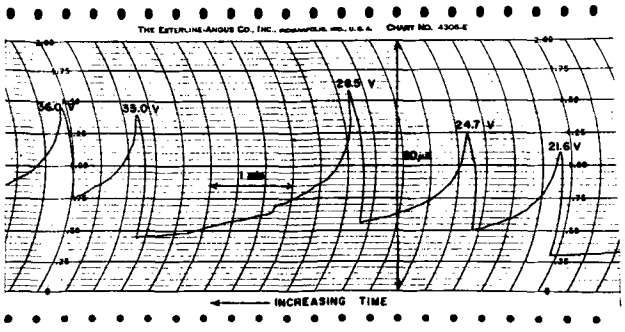

Fig. 2. Ta-MnO_2 point-contact experiment; current decay at successive constant voltages. (Note that time increases from right to left.)

Point-Contact Experiments

The behavior of the current, when the anodic potential on a tantalum point contact to MnO_2 is increased stepwise, is shown in Fig. 2. This is a photograph of a portion of the recorder trace for a typical experiment carried out in room air at room temperature. Each time the voltage is increased, the current rises immediately and then undergoes a smooth decay as the voltage is held constant. This behavior is repeated each time the voltage is increased. Each current decay at constant voltage will continue for hours as shown in Fig. 3 which has been redrawn from a similar recorder trace. (Strictly speaking, the meter reading, which is 0.8v for the full-scale reading of 80 μa, should be subtracted from the applied voltage to obtain the potential across the point contact.)

As the applied voltage is increased by approximately equal increments, the current decay becomes less and less steep; this also happens during anodic oxidation in aqueous electrolytes since the increase in oxide thickness, and hence resistance, created by the passage of a given amount of charge is a decreasing percentage of the total thickness as the oxide growth proceeds to higher anodization voltages. This decrease in the rate of current decay becomes much more pronounced in the case of these point contact experiments, however, as the applied voltage becomes larger than 50v. The beginning of the current decay becomes increasingly sluggish, and a gradual increase in current may even precede the decay. This behavior may be due to local resistive heating under the point contact which promotes the decay process. Above 80v the current decay process becomes vanishingly slow and can only be observed on recorder traces taken over several hours.

The current decay process represents a permanent and irreversible growth of resistance at the point. If a tantalum point which has been anodized on MnO_2 is moved to a new spot on the surface, the resistance created by the anodization moves with it, and further anodization proceeds from a high applied voltage without the low voltage formation observed with freshly cut points. This is not possible to verify quantitatively because of the uncertainty that the moved point is contacting the MnO_2 with exactly the same area, but the general validity is clearly apparent. An electrochemical growth of resistance is thus occurring on the metal point.

The efficiency of this solid-state, anodic oxidation depends on the presence of moisture in the ambient atmosphere. This is illustrated in Fig. 4 which summarizes an experiment carried out in a vacuum desiccator. During the course of the experiment the Ta-MnO_2 contact was alternately exposed to vacuum and to room air while the current was decaying at constant voltage. It is seen that the rate of current decay was reduced when the system was evacuated and quickly increased again when room air was admitted. If the room air was admitted through a desiccant, the increase in rate did not occur. This dependence on the presence of moisture was more striking when the entire system was baked out at 200°-300°C and placed in a sealed container with a desiccant. Under these conditions the anodization characteristics of the point contact were extremely poor.

This electrical behavior of metallic point contacts to MnO_2 is unique with valve metals with an anodic potential. In the case of a valve metal point contact to MnO_2 with a cathodic potential on the metal, or for noble metals such as platinum or rhodium with either polarity, the behavior is very different. The contact passes much higher current; there is no evidence of current decay; and when sufficient current is attained, *e.g.*, 20 ma with 5v across the point contact, the current drops abruptly and irreversibly to very low values such as 0.01 μa. Microscopic examination will then show a small crater blown in the MnO_2 and evidence of oxidation on oxidizable metal points. It is apparent that the MnO_2 has been thermally reduced to lower oxides which are insulators compared with MnO_2. This is not a surprising result since the power density under the point prior to breakdown will be of the order of 10^4 w/cm^2 if the contact area is assumed

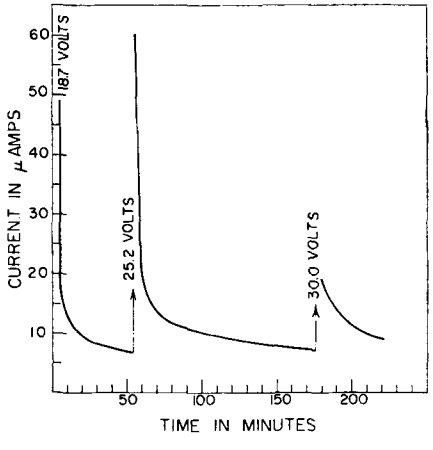

Fig. 3. Long-term current decay during Ta-MnO_2 point-contact experiment.

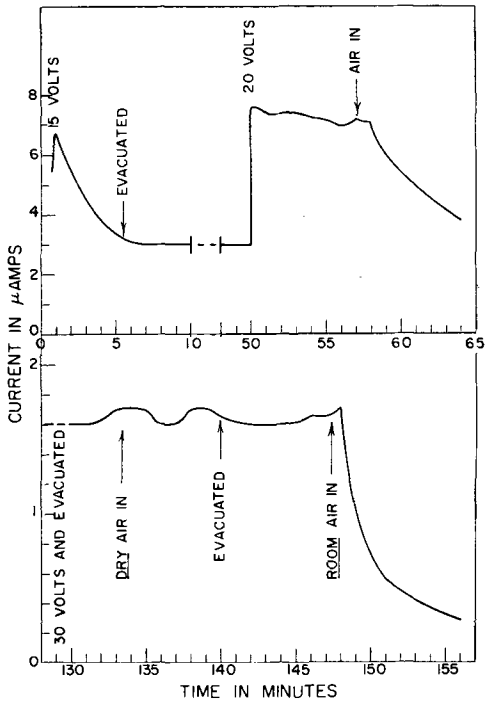

Fig. 4. Effect of ambient moisture on the solid-state anodization of Ta on MnO_2.

to be 1% of the cross-sectional area of the wire on which the point was cut.

Niobium and aluminum point contacts on MnO_2 behave very similarly, but have not been studied in great detail. All of these valve metals also give evidence of solid-state anodization on PbO_2. With the latter oxide the current level is about a decade less than is usually observed with MnO_2, and the current decay is not as smooth. No signs of anodic oxidation have been observed with CuO, NiO (doped with Li_2O), CdO, V_2O_5, and $Na_{0.7}WO_3$.

Area-Contact Experiments

The anodic oxidation of tantalum point-contacts on MnO_2 is a convenient demonstration of the basic current-voltage behavior of the system, but it has the great disadvantages of having an undefined contact area and of not being amenable to capacitance measurements. Thus numerous techniques were attempted in order to obtain an experimental contact of known and appreciable area. As previously described under Experimental, only the deposition of tantalum dots onto MnO_2 by cathodic sputtering gave satisfactory results. Several such samples were successfully anodized to the vicinity of 20v. Data from one of these are summarized in Table I. It is apparent that the general behavior is very similar to that of the point-contacts. The current decay in the case of sputtered contacts was much less dramatic since the current densities, and thus the fields, were held to a lower level (1-30 ma/cm^2 in Table I) to avoid local breakdown within the experimental area. The current efficiency of anodization is very low, 0.01-0.001% (based on the formation of 18Å of Ta_2O_5 per volt and a density for Ta_2O_5 of 8 g/cm^3). The quality of the dielectric is relatively poor as indicated by the high final current and the dissipation factor. The capacitances of such samples are substantially less than would be obtained by the conventional, aqueous anodization of tantalum to the same voltage.

Ionic Conduction in Lower Oxides of Manganese

If this phenomenon consists of the simultaneous electrochemical oxidation of the tantalum and reduction of the MnO_2, all phases between the metal and the MnO_2 must have some ionic conduction. This is obviously true for anodic oxides at high fields, but there is no comparable information available for the oxides of manganese. The following observations of battery-like behavior for the Ta-MnO_2 system give qualitative information on this point.

MnO_2 was applied to bare, porous tantalum pellets (about 3/8 in. high by 3/16 in. diameter, available surface area about 175 cm^2) by pyrolysis of a 50% aqueous solution of $Mn(NO_3)_2$. This can be accomplished with a maximum pyrolysis temperature of about 350°. At higher temperatures there is a tendency for the bare pellet to ignite and undergo catastrophic oxidation. Ta-MnO_2 samples prepared in this manner proved to be electrically inert. They exhibited erratic open-circuit voltages (OCV) of about 1 mv, and there was no current decay when an anodic potential of a few volts was applied to the tantalum. The samples were given 5-min heatings at increasing temperatures and tested electrically. After heat-treatment at some temperature between 400° and 500°, the particular temperature differing among the various samples, the electrical properties of some samples changed drastically. A stable OCV of 0.1-0.5v was observed, tantalum negative, which dropped slowly when loaded with 10^7 ohms. The voltage increased again after removal of the resistive load. There was clear evidence of current decay when an anodic potential was applied to the tantalum. The extent of decay varied from barely perceptible to a reduction of the current by half in 2 min. As in the case of the point-contact experiments, the increase of resistance corresponding to the current decay was a permanent effect. The anodic treatment was continued up to 26v in one case although very little permanent change occurred above 10v. When the anodic potential was removed, the OCV dropped steadily, changed polarity after 10-15 min, then continued to the order of tenths of a volt, tantalum negative. The observation of a stable OCV and an anodic current decay always appeared together; no sample exhibited one phenomenon without the other.

Table I. Anodization of 0.011 cm^2 Ta dot sputtered onto MnO_2 All measurements at room temperature; bridge measurements at 1000~

Anodization voltage	Initial current, μa	Anodization time, hr	Final current, μa	Parallel cap, μμf	% D.F.
0	—	—	—	5934	14.5
5.6	192	20	8	3974	9.38
7.0	68	40	13	3797	9.98
10.0	245	68	58	3554	10.6
17.0	—	~50	300	2665	8.99

There was a wide range of behavior among various samples, and some failed to exhibit anything other than electrical inertness. The above description is representative of those which did respond to heat-treatment. Once electrical activity appeared in a sample, the behavior described above could be repeated over and over.

It seems clear that the ability of the sample to undergo solid-state, anodic oxidation is accompanied by battery-like behavior. If the anodic oxidation process depends on the presence of a finite ionic contribution to the conduction of all phases between the tantalum and the MnO_2, then the basic requirements for an electrochemical cell are met: an active metal separated from an oxidizing agent by ionically conducting phases. The evidence that the observed OCV was an electrochemical emf is:

1. The polarity was correct (Ta negative).
2. The systems could deliver significant current (tenths of microamps) indefinitely.
3. The OCV rose quickly toward the original value when a resistive load was removed.
4. After extensive application of anodic biases (tantalum positive) of up to 20v, the OCV always quickly changed polarity back to that expected for an electrochemical emf.

The necessity for a thermal treatment to initiate described behavior can be compared with the initial behavior of the point-contact experiments. In the latter case there was usually no current decay at very low voltages. At some point, usually at an applied potential of about 5v, the decay began abruptly, frequently while the voltage was being increased. This may represent the need to supply sufficient resistive heating to create the required chemical situation which will allow the anodic oxidation to proceed.

In another experiment some current decay at constant voltage was observed for a tantalum point on a thin chip of Mn_2O_3. The high resistance of the Mn_2O_3 obscured the effect, but the current decreased by about 10% in 5 min at each of several successive voltage levels. This suggests that oxygen can be withdrawn electrochemically from even the Mn_2O_3 level, and that the reduced manganese oxide phase formed during the anodization process can have a lower oxygen content than Mn_2O_3.

Further experiments with electrochemical cells involved the use of specific manganese oxides as electrolytes. $Mn/Mn_2O_3/O_2$ cells made from pressed and sintered Mn_2O_3 pellets, sandwiched between metallic manganese and porous carbon electrodes, had barely perceptible emfs (0.1-1.0 mv). The d-c resistance of the Mn_2O_3 was about 30 megohms. This indicates a very small ionic contribution to the total conduction in Mn_2O_3, although such experiments must be interpreted cautiously since other manganese oxide phases may form spontaneously at the Mn-oxide and oxide-

air interfaces. Similar cells made from Mn_3O_4 pellets had no observable emf, but since the d-c resistance of the pellet was 10^{11} ohms it is dubious that the equipment was sufficiently sensitive.

Recent work by Otto on equilibria for the reactions

$$2Mn_2O_3 + O_2 \rightleftharpoons 4MnO_2 \quad [2]$$

$$4Mn_3O_4 + O_2 \rightleftharpoons 6Mn_2O_3 \quad [3]$$

gives evidence of oxide ion mobility at high temperatures in both Mn_2O_3 (6) and Mn_3O_4 (7). In the case of reaction [3], the recombination of Mn_3O_4 with O_2 at about 900° was only about five times slower than the dissociation of Mn_2O_3 at slightly higher temperatures. For reaction [2] the oxidation of Mn_2O_3 at 555° was extremely slow, but it was still detectable. In both cases the observation of a recombination reaction of finite rate implies oxide ion motion, although the results of the two oxide systems cannot be compared because of the different temperatures involved.

Discussion

All of the observations are consistent with the hypothesis that this phenomenon is a solid-state analog of the anodic oxidation of a valve metal in an aqueous electrolyte. Only typical valve metals demonstrate the effect and only when made anodic with respect to the oxide phase. The growth of resistance is permanent, and at least some of the resistance is associated with the valve metal as shown by the point-contact experiments.

The following mechanism is proposed for this solid-state anodic oxidation; Figure 5 is a cross section of such an experiment and illustrates aspects of the following discussion. At a contact between tantalum and MnO_2 there will occur a spontaneous chemical oxidation of the tantalum and reduction of the MnO_2. This will be enhanced by the local heating which will result from the passage of current when a potential is applied. Both Ta_2O_5 and reduced MnO_2 are poor conductors compared with tantalum and MnO_2 so that a voltage drop will build up across these regions. If these phases have finite ionic conductivities and, if the fields across them become sufficiently high, oxide ions will flow from the MnO_2 through the reduced oxides of manganese and tantalum ions will flow through the Ta_2O_5. These ions will combine to form Ta_2O_5 at the Ta_2O_5-MnO_x interface. [For simplicity of discussion, ion flow through the Ta_2O_5 will be assumed to consist only of tantalum ions, although this is probably not the case (8). Likewise, the ion current through the MnO_x, which will denote the reduced manganese oxide phase, may consist of oxide ion vacancies.] Thus there will be a simultaneous formation of Ta_2O_5 at this interface and of MnO_x which will extend into the original MnO_2. Both of these new phases will be poor conductors, and all phases between the tantalum and the MnO_2 must have some ionic conduction to support the ionic current necessary for further film growth. The current efficiency of the process will be roughly determined by the ratio of ionic to electronic conductivity in the phase having the least ionic conduction. For most experiments this efficiency is of the order 0.01-0.001%, although more information is needed for a quantitative evaluation of this figure.

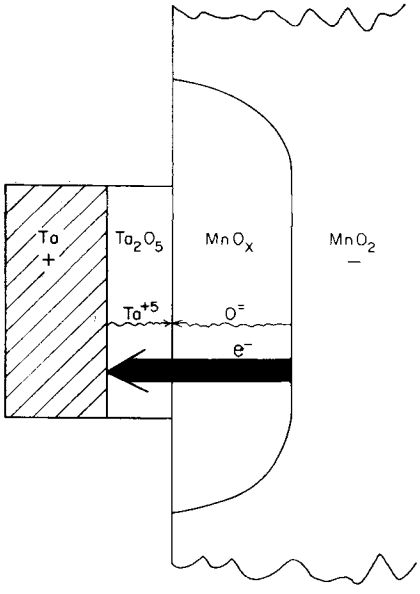

Fig. 5. Schematic representation of the solid-state anodization process.

We have been unable to characterize chemically the phases which are formed. Thus it is not known whether the MnO_x phase consists of one distinct oxide such as Mn_2O_3, Mn_3O_4, or MnO, a succession of oxide layers, or a continuous gradation of composition from MnO_2 to some oxygen-poor phase at the Ta_2O_5 surface. The small emfs observed for $Mn/Mn_2O_3/O_2$ cells and the evidence for thermal oxidation of Mn_2O_3 lend support to the idea of ionic mobility in this oxide, and the solid-state electrochemical reduction may proceed somewhat beyond this as indicated by the observation of some resistance build-up for a tantalum point on Mn_2O_3, and by the evidence of oxygen mobility in Mn_3O_4 at high temperatures.

The tantalum oxide phase created by this process has not been actually identified, although it is assumed to be essentially Ta_2O_5. The high electronic current densities observed for these experiments lead to the suspicion, however, that this Ta_2O_5 is defective in some sense. Possibly some Mn^{+3} is incorporated into the Ta_2O_5 since Mn^{+3} and Ta^{+5} have nearly equal ionic radii. An alternative explanation for the high current could be that the major rate-determining step in the electrochemical reaction is the flow of oxide ions across MnO_x which may be a predominantly electronic conductor. Thus sufficient voltage must be applied to supply adequate field across the MnO_x to obtain a detectable flow of oxide ions which can be accompanied by a relatively large electronic current. Meanwhile the flow of tantalum ions across the Ta_2O_5 will be restricted by polarization due to the limited supply of oxide ions with which they can combine. Thus the field across the Ta_2O_5 may exceed the normal fields for anodic oxidation in aqueous electrolytes and may lead to high electronic currents. In addition, the MnO_x may represent a good electron-injecting contact to the Ta_2O_5.

It is apparent that the cathodic oxide phase must meet certain requirements in order to support the anodic oxidation of valve metals. It must be a good source of oxygen and should be a fairly good conductor. The lower oxide phases formed by the extraction of oxygen to form the valve metal oxide must be poorer conductors than the parent oxide. If this were not the case, there would not be sufficient field across these lower oxides to sustain the required flow of oxide ions. Only MnO_2 and PbO_2 have been found to meet these requirements. Both are good conductors and good oxidizing agents, and the lower oxides of both are very poor conductors. These oxides are unusual in this respect since the oxides in which the metal is in its highest oxidation state, or is exhibiting the oxidation state typical of its column in the Periodic Table, are generally insulators whereas the lower oxides are conductors. This is best exemplified by such transition metal oxides as those of titanium and tantalum. Thus the range of suitable oxides is very narrow.

Although the solid-state anodization is analogous to the conventional anodization in a liquid electrolyte, the differences are very important and greatly complicate any quantitative interpretation. In the liquid system the reduction product is hydrogen gas which

escapes from the system. Ionic mobility in the electrolyte is high and, with the aid of agitation, the electrolyte remains homogeneous. On the other hand, the reduction product in the solid-state process must be a lower oxide of manganese, and it must be localized adjacent to the Ta_2O_5. Since the lower oxides of manganese are poor conductors, the applied voltage will be divided between the Ta_2O_5 and the MnO_x. The MnO_x layer may be substantially thicker than the Ta_2O_5. A simple calculation shows that, if MnO_x is MnO, the volume will be 1.3 times that of an equivalent amount of Ta_2O_5, and, if MnO_x is Mn_2O_3, the volume factor is 3.5. In the absence of detailed knowledge of the thicknesses and resistivities of all phases, the voltage distribution is unknown.

The initial capacitance of the sample described in Table I indicates that there is a significant thickness of dielectric prior to anodization. If this initial capacitance were due solely to Ta_2O_5 with a dielectric constant of 27.6, it would correspond to a thickness of about 450Å, which is unreasonably high for a thermally formed film. If this capacitance were determined by a layer of reduced manganese oxide having a dielectric constant of 5, it would correspond to a thickness of 80Å, which is reasonable. Since it is likely that the MnO_x has a dielectric constant which is substantially smaller than the unusually high value of 27.6 for Ta_2O_5, and since the MnO_x will be thicker than an electrochemically equivalent amount of Ta_2O_5, it is reasonable that the capacitance of these samples is determined essentially by the MnO_x.

Plots of equivalent series resistance *vs.* the reciprocal frequency and of the reciprocal series capacitance *vs.* log frequency were linear and the ratio $[\Delta 1/C_s/\Delta \log f]/[\Delta R_s/\Delta 1/f]$ was found to be 8.5 and 9.4 for two examples. These values are close to the value of 4 ln 10 = 9.2 which is typical of anodic oxides (9).

As the solid-state anodization proceeds, the current measured at any particular voltage below the anodization voltage decreases, giving further evidence that the process involves a permanent increase of resistance. Figure 6 shows a plot of log i *vs.* $(V/V_f)^{1/2}$ for a tantalum point contact formed on MnO_2. i represents the observed current, V the applied voltage, and V_f the formation voltage. The thickness of the oxide is assumed to be proportional to V_f, so V/V_f is proportional to the field across the oxide. For this experiment the point was anodized at successive 10v increments for 1 hr each. After each formation the current was measured at decreasing 5v intervals. The data shown are representative of several similar experiments.

The current is proportional to exp $(V)^{1/2}$ not only for voltages below the anodization voltage, but for the anodization voltage itself and for the initial, transient current which is observed as the voltage is increased

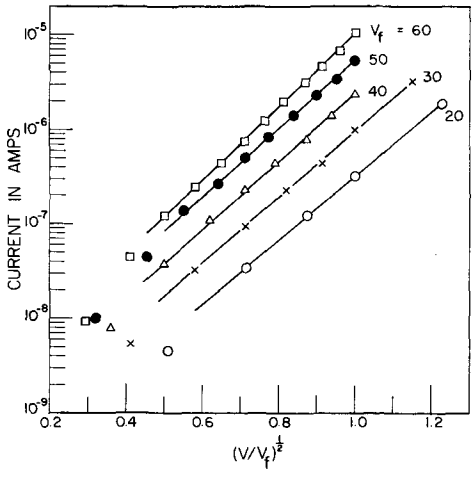

Fig. 6. Current-voltage characteristic for Ta-MnO_2 point-contact anodized for 1 hr at successive 10v intervals.

above the anodization voltage, *i.e.*, $(V/V_f)^{1/2} > 1$ in Fig. 6. This I-V behavior is a well-known characteristic of electronic leakage currents (10). This behavior suggests that the observed current in these experiments is essentially all electronic, even during the initial, rapid current decay, and that the current decay during anodic oxidation represents the electronic leakage current which is decreasing as the electrochemical reaction proceeds by means of an imperceptible ionic contribution to the total current. This concept is in accord with the estimated current efficiency of 0.01-0.001% since the latter figures also represent the overall ionic contribution to the total current.

When the point-contact anodizations are carried on until the current-decay essentially ceases (about 50 hr is generally sufficient), the data corresponding to that of Fig. 6 all fall on one line, indicating that the current-field relationship is independent of the thickness. The apparent thickness-dependence seen in Fig. 6 is merely a result of the fact that each successive anodization was less complete because of the decreasing current efficiency, and, as a consequence, the anodization voltage was not a valid measure of the relative dielectric thickness.

One can only speculate about the role of water in this mechanism. It is clear from the point-contact experiments that the process is aided by the presence of ambient water vapor. It is possible that the availability of water allows oxygen to move through the manganese oxides in the form of hydroxide ions rather than as oxide ions, since the attachment of a proton to an oxide ion reduces the charge by half but increases the size if the ion by only 10%. The lower charge and the polar nature of the hydroxide ion may reduce the barriers for oxide motion. A similar argument has been proposed for oxygen migration through anodic oxide films on aluminum by Hoar and Mott (11). Another possibility is that the water allows the manganese oxide to maintain the Mn:O ratio of MnO_2 even after reduction, thus eliminating the necessity of a change in structure. This would be analogous to current theories about the discharge of the MnO_2 cathode in the Leclanché cell where it has been suggested that the reduction requires only the migration of electrons and protons (12)

$$MnO_2 + e^- + H^+ \rightleftharpoons MnOOH$$

MnOOH is equivalent to $Mn_2O_3 \cdot H_2O$. The ramsdellite (MnO_2)-groutite (MnOOH) system is a good example of such a relationship (13).

The pertinence of the observations described here to the solid electrolyte capacitor will be readily apparent to those familiar with this component. In this device the MnO_2 replaces the liquid electrolyte which is used in conventional "wet-electrolytic" capacitors to maintain the electrical integrity of the oxide dielectric. The liquid electrolyte clearly serves as an electrochemical source of oxygen, but the mechanism by which the MnO_2 functions has never been clarified. The evidence presented here indicates that it can also seal off points of high leakage current when it is thermally decomposed by local, resistive heating to lower, insulating oxides. Evidence of both of these mechanisms can be observed during the reanodization of capacitors after the MnO_2 has been applied. The solid-state anodization results in a smooth decay of current at constant voltage, or increase of voltage at constant current; while sharp current spikes at constant voltage, or voltage dips at constant current, are believed to represent local breakdown of the dielectric which is healed by thermal decomposition of the adjacent MnO_2. If the amount of dielectric healing is sufficiently extensive, the characteristic battery-like behavior of these areas may become apparent. This effect, coupled with residual voltages of the type described by Dreiner (14), may account for some of the complicated open-circuit voltage behavior reported for Ta-Ta_2O_5-MnO_2 capacitors by Law and Richards (15).

Acknowledgments

The author wishes to express appreciation to Miss Marjorie Cutler, and to Drs. William Allison and Barry Noval for valuable experimental assistance.

Manuscript received July 19, 1965.

Any discussion of this paper will appear in a Discussion Section to be published in the December 1966 JOURNAL.

REFERENCES

1. J. L. Miles and P. H. Smith, *This Journal*, **110**, 1240 (1963).
2. G. J. Tibol and R. W. Hull, *ibid.*, **111**, 1368 (1964).
3. R. L. Taylor and H. E. Haring, *ibid.*, **103**, 611 (1956).
4. D. A. McLean and F. S. Power, *Proc. IRE*, **44**, 872 (1956).
5. A. V. Fraioli, *IRE Trans. Component Parts*, **CP-5**, 72 (1958).
6. E. M. Otto, *This Journal*, **112**, 367 (1965).
7. E. M. Otto, *ibid.*, **111**, 88 (1964).
8. J. J. Randall, Jr., W. J. Bernard, and R. R. Wilkinson, *Electrochim. Acta*, **10**, 183 (1965).
9. L. Young, *Trans. Faraday Soc.*, **51**, 1250 (1955).
10. P. F. Schmidt, F. Huber, and R. F. Schwarz, *J. Phys. Chem. Solids*, **15**, 270 (1960).
11. T. P. Hoar and N. F. Mott, *ibid.*, **9**, 97 (1959).
12. W. C. Vosburgh, *This Journal*, **106**, 839 (1959).
13. C. Klingsberg and R. Roy, *Am. Mineralogist*, **44**, 819 (1959).
14. R. Dreiner, *This Journal*, **111**, 27 (1964).
15. J. T. Law and W. C. Richards, *ibid.*, **109**, 215 (1962).

The Spectral Response of the Short-Circuit Photocurrent in Anodized Niobium Electrodes

R. A. Schell[1] and R. E. Salomon

Department of Chemistry, Temple University, Philadelphia, Pennsylvania

ABSTRACT

The spectral response of the short-circuit photocurrent in anodized niobium electrodes of the form $Nb/Nb_2O_5/M$, where M is a thin semitransparent metal, has been determined. Measurements were performed as a function of the light intensity and oxygen pressure in the range 10^{-4}-760 mm Hg. The light intensities were of the order of 10^{11} photons/sec cm^2. The most unusual result was that structure was exhibited in these curves. This is interpreted in terms of interband transitions. Since the band structure of the oxide is unknown, the discussion is qualitative. The structure changes slightly with oxygen pressure. The photocurrent exhibited a maximum when viewed as a function of the oxide film thickness. A trapping scheme is postulated to explain the current-light curve characteristics. This is based on an exponential distribution of traps. The superlinearity is interpreted in terms of a redistribution of these trapping states on illumination.

A great deal of interest in anodic oxide films has been exhibited during the past fifteen years. Photovoltaic cells, consisting of an anodized metal and a semitransparent metal coating, were first demonstrated by van Geel *et al.* (1).

It is well known that the spectral response of the photocurrent can be as sensitive a device as the absorption spectrum for obtaining knowledge of the intrinsic absorption region in semiconductors and insulators. Anodic oxide films of niobium are insulators with the fundamental absorption edge falling around 3400Å (2-4). These measurements indicate strong absorption ($E \approx 10^5$-10^6 cm^{-1}) which has generally been assigned to band-to-band electronic transitions.

Photovoltaic effects are known to occur with anodized zirconium, niobium, tantalum, and aluminum electrodes (5). A great deal of difficulty has been experienced in attempts to elucidate the nature and mechanism of these effects. The convenient observable here is the short-circuit photocurrent. The open-circuit photovoltage is not convenient because an open-circuit photovoltage for a given set of parameters is generally not reproducible in these systems. There is also much difficulty encountered when making measurements of the normal photocurrent (*i.e.*, with an externally applied field). Precisely establishing the value of the dark current and re-establishing that value subsequent to the decay of the photocurrent is most difficult. The problem of electrical noise is also greatly reduced when one measures the short-circuit photocurrent. A spectral response study of the short-circuit photocurrent in these systems has never been reported. This paper deals with the determination of the spectral response of the short-circuit photocurrent in cells of the form $Nb/Nb_2O_5/M$, where M is a thin, semitransparent evaporated metal film. The oxide films ranged in thickness from 750 to 3000Å. The evaporated metals utilized were copper, silver, and gold. Polycrystals as well as single crystals of niobium were used in this study. These measurements were performed as a function of the light intensity (absolute) and oxygen pressure.

[1] Present address: United States Army, Picatinny Arsenal, Dover, New Jersey.

Experimental Procedure

Electrode preparation.—The niobium electrodes were prepared using both polycrystalline and single crystals. The impurity content of the single crystals was, in parts per million: O(50), C(100), H(10), N(400), Fe(<1000), W(<100), S(<30), Cd(<100), Si(<100), Cu(<10), Mn(<10), Ni(<10), and Mg(<1). The single crystals were pulled in the (100), (110), and (111) directions. The sample dimensions were approximately ⅜ in. in diameter and ½ in. long. A platinum wire, encased in a ceramic tube, was mounted in a hole drilled lengthwise through the specimen near the periphery. This was used to provide electrical contact to the evaporated, semitransparent metal film. Edge effects were eliminated by suitable masking. Care was taken to insure uniform thickness of the evaporated metal from one experiment to another. A surface of the specimen was abraded with various grades of emery paper. This was followed by wet-polishing and chemical etching in a solution consisting of 15 parts HF, 75 parts HNO_3, and 10 parts water. After etching, the pieces were washed thoroughly with distilled water.

Samples were then anodized at constant polarization voltages in a 0.05M sodium borated-boric acid solution buffered to pH 8. This was done in a constant temperature water bath at 20°C. For polarization voltages above a few volts, the oxide grows approximately 30 Å/v if the field is maintained for several hours (2, 6). Final leakage currents at a formation voltage of 75v were typically 2 μa/cm^2. Hereafter, the thickness of the oxide films will be given in terms of formation voltage. The oxide films exhibit interference colors characteristic of their thickness. An illustration of a completely prepared electrode is shown in Fig. 1. The time between anodization and measurement was kept below two days, and the time between completion of the electrode and measurement was a few hours. Electrodes were stored in vacuum desiccators when not in use.

Optical assembly.—The light source was a Hanovia 1000w, air-cooled, high-pressure mercury-xenon arc lamp. The source intensity was monitored by reflecting a portion of the light from an aluminum mirror on to a Photovolt type B photocell which served as the search unit of a model 500M photometer. A Bausch and Lomb monochromator with a linear dispersion of 66 Å/mm was utilized in this study. A Kipp thermopile was used to reduce the measurements to an absolute basis.

Cell compartment.—The electrode cell consisted of a demountable Dewar fabricated from standard-tapered glass joints of fairly large diameter with provisions for electrical, temperature, and pressure measurements. A quartz window was sealed into the cell. The cell was connected to a vacuum and gas inlet system.

For the oxygen pressure dependence measurements, the following procedure was adopted. The entire system was flushed repeatedly with oxygen and then evacuated to a pressure of about 10^{-4} mm Hg. This pressure was maintained for more than 12 hr by continual pumping. For measurements at other pressures, the electrode was first allowed to equilibrate for 1 to 2 hr. The system was such that the pressure could be maintained at a fixed value for more than 12 hr under static conditions.

Although photocurrents were detected at wavelengths as long as 4000Å, a thorough investigation of the spectral response for wavelengths greater than 3700Å was precluded because of the small signals.

For all measurements both entrance and exit slits of the monochromator were fixed at 0.40 mm. Greater resolution could only be obtained at the expense of light intensity. The weak intensity between 2400-2660Å and 3341-3660Å precluded any investigations of the light intensity dependence in these regions.

Photocurrents were measured in terms of the potential drop across a 20 megohm resistor. The current was not sensibly changed when a 5 megohm resistor was used and hence the parameter studied was a short circuit photocurrent.

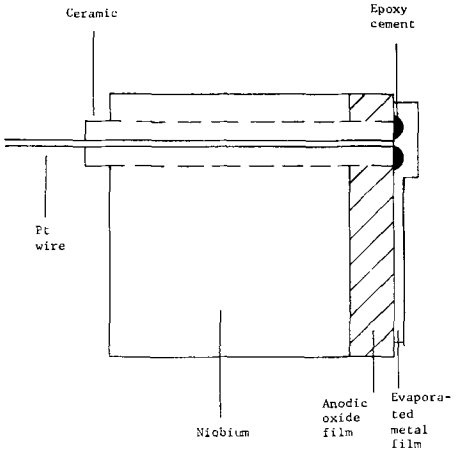

Fig. 1. Schematic illustration of a typical electrode

Results

Upon irradiation niobium always became negative. Short-circuit photocurrent measurements did not show any significant dependence on the crystallographic face. Consequently, results will be given only with reference to measurements obtained with polycrystalline samples.

The spectral response curves have been determined as a function of the radiation wavelength at a constant photon intensity. At a particular wavelength of incident radiation the short-circuit photocurrent varied with light intensity according to the relationship, $I_p = CL^n$, where C is a constant, L is the light intensity, and n is a constant whose value was found in general to lie between 0.5 and 1.0 although values as low as 0.3 and as high as 2.5 were found. A plot of the logarithm of the photocurrent *vs.* the logarithm of the light intensity always yielded straight lines.

The photocurrents were found to reach a steady value after a few seconds. Figure 2 shows a typical spectral response curve for the short-circuit photocurrent for a Nb/Nb_2O_5(100v)/Cu electrode. Similar curves were obtained if silver or gold were utilized as the second contact. The shape of these curves was quite reproducible although the actual photocurrent measured when two electrodes were treated similarly might differ by 10%. No simple relationship between photocurrent and oxygen pressure was found. However, comparison of Fig. 2 and 3 reveal a shift in a few peaks with oxygen pressure. The general shape of the curves remained the same however. The shapes of the spectral response curves were independent of oxide film thickness. If the photocurrent is plotted as a function of formation voltage a maximum occurs at 75v as can be seen by Fig. 4. The measurements are reduced to absolute incident intensities. No correction for reflec-

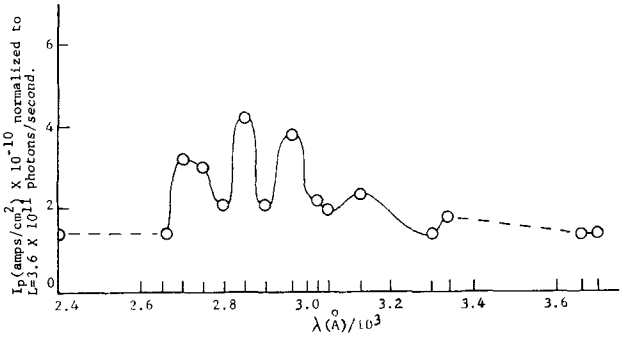

Fig. 2. Spectral response of the short-circuit photocurrent for a Nb/Nb_2O_5 (100v)/Cu electrode at P_{O_2} = 1.1 x 10^{-4} mm Hg; T = 20°C.

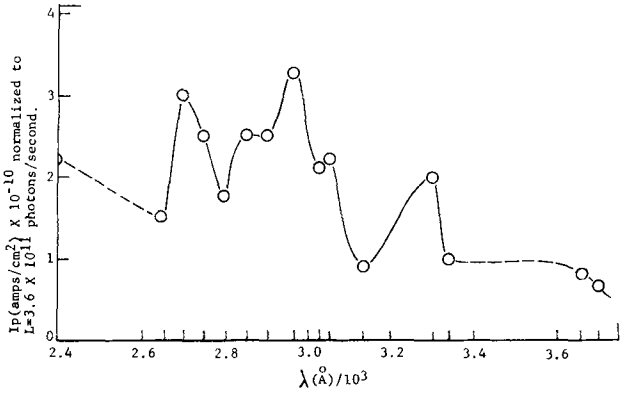

Fig. 3. Spectral response of the short-circuit photocurrent for a Nb/Nb_2O_5 (100v)/Cu electrode at P_{O_2} = 3.4 x 10^{-2} mm Hg; T = 20°C.

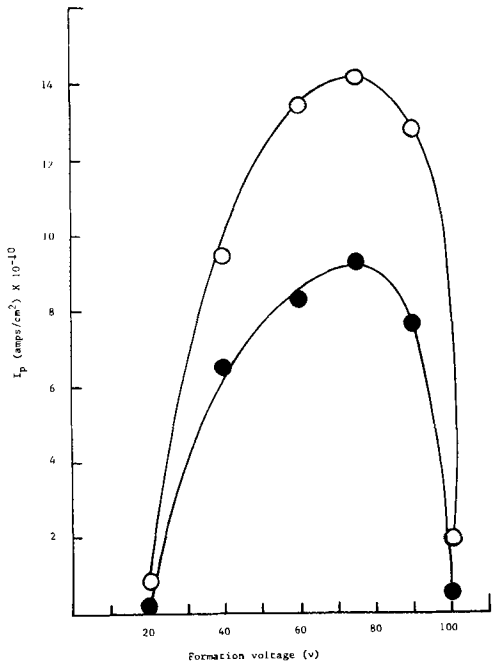

Fig. 4. Variation of short-circuit photocurrent with film thickness at light intensity of 3.6 x 10^{11} photons/sec. ○λ = 3130Å; ●λ = 2700Å; T = 20°C; P_{O_2} = 1.1 x 10^{-4} mm Hg.

tion and absorption by the evaporated metal film was made. However, a quartz microscope slide coated by evaporation with a thin semitransparent layer of copper was found to have a monotonic transmission spectrum down to 3200Å and transmitted more than 85% of the light.

The short-circuit photocurrent decreased with decreasing temperature and at liquid nitrogen temperatures the signals were too small to monitor by the method used. Activation energies were found to lie between 0.1 and 0.2 ev.

Discussion

The observation of structure in the spectral response curves of the short-circuit photocurrent was rather surprising in view of the fact that there is no concomitant structure in the absorption spectra of the isolated oxide films (2). A single peak, close to the absorption edge, in the spectral response curve could be explained in terms of a high recombination rate due to strong absorption (7).

The peaks and valleys cannot be ascribed to optical interference effects because the structure is independent of the oxide film thickness. It is also apparent that neither oxygen nor the nature of the evaporated metal contact determine the number and location of the peaks. This rules out photoexcitation from the evaporated metal contacts. In order to completely explain action spectra of this type, one must have a knowledge of spectral transition probabilities and the constant energy surfaces in $\vec{k}$ space. Although this information is not available, the observed monotonic absorption spectra might be due to oscillations in the dependence of effective mass on momentum.

It may be noted that recent work (8, 9) on shallow p-n junctions of silicon, germanium, and gallium arsenide show structure in the intrinsic region for reflectance and photoresponse measurements. There does not appear to be a one-to-one correspondence between photoresponse and reflectance for the measurements on silicon. The band structures of these materials have been extensively studied and are quite complex. The structure may be interpreted in terms of a nonequilibrium effect and recombination processes. This mechanism may also apply to the electrodes described in this paper.

The absorption spectra of isolated anodic niobium oxide films gives a long wavelength limit of absorption of about 3500Å (2). This value was in agreement with a previously reported value of 3400Å (3). Conlon and Doyle (4) determined the absorption spectrum of the evaporated oxide and arrived at a value of 3350Å. The latter spectrum extended down to 2000Å whereas that of Salomon *et al.* was determined to about 2700Å. However, both showed sharp absorption edges and very high absorbance indices values. Although Salomon *et al.* determined the absorption spectra using the anodic oxide films, these films were first removed from their bulk metal substrate. This would tend to remove a fair amount of stress and might cause some dissolution of the oxide. Hence differences in film behavior between mounted and free films should be recognized. This could account for the observation of photoconduction in these electrodes occurring at wavelengths as high as 4000Å.

It was found that if the photocurrent is plotted as a function of the oxide film thickness a maximum occurred. This can be readily accounted for by considering the oxide film to be optically anisotropic. By considering a small gradient in the absorption coefficient and using the relation, $dI = -I\alpha dx$ one may indeed show that the photocurrent-thickness curve will have a maximum.

The small activation energy for photoconduction combined with the slow decay may suggest the existence of a wide range of trap depths. Shallow traps would be thermally emptied and contribute to the small activation energy. Deep traps, which might be relatively unaffected by temperature variations, would lead to long decay times.

A model based on an exponential trap distribution (10) is able to account for the usual results of the dependence of the photocurrent on light intensity. Superlinearity (n-values > 1) in the photocurrent dependence on light intensity might be explained by modification of this model.

Manuscript received April 27, 1965; revised manuscript received Aug. 23, 1965. This research formed part of a dissertation submitted to the Temple University Graduate Board in partial fulfillment of the requirements for the Ph.D. degree. This work received financial support from the United States Atomic Energy Commission.

Any discussion of this paper will appear in a Discussion Section to be published in the December 1966 JOURNAL.

REFERENCES

1. W. Ch. van Geel, C. A. Pistorius, and P. Winkel, *Philips Research Repts.*, **13**, 265 (1958).
2. W. M. Graven, R. E. Salomon, and G. B. Adams, Jr., *J. Chem. Phys.*, **33**, 954 (1960).
3. O. A. Motovilov and V. N. Rozhdestvenskii, *Optiko-Mekh, Prom.*, **25**, 42 (1958); *C. A.*, **53**, 6773 (1959).
4. D. C. Conlon and W. P. Doyle, *J. Chem. Phys.*, **35**, 752 (1961).
5. L. Young, "Anodic Oxide Films," Academic Press, New York (1961).
6. L. Young, *Trans. Faraday Soc.*, **52**, 502 (1956).
7. A. Ioffe, "Physics of Semiconductors," p. 77, Infosearch, London (1960).
8. E. Loh, *J. Phys. Chem. Solids*, **24**, 493 (1963).
9. E. Loh and J. C. Phillips, *ibid.*, 24, 495 (1963).
10. A. Rose, *RCA Rev.*, **12**, 362 (1951).

The Electrical Conductivities and the Structural Properties of Molten $PbCl_2$-PbS Mixtures

I. Structural Properties

M. C. Bell[1] and S. N. Flengas

The Department of Metallurgy and Materials Science, University of Toronto, Toronto, Ontario, Canada

ABSTRACT

The phase diagram and the densities for the lead chloride-lead sulfide system were determined. The phase diagram is simple, with one weak incongruently melting compound for which the x-ray diffraction patterns were measured. Calculations from the phase diagram indicate that lead sulfide is dissociated in the liquid mixtures. The liquidus lines for PbS, NaCl, NaF, and KBr added to lead chloride were also determined and showed that pure liquid lead chloride contained ions other than simple lead and chloride ions. The molar volumes of the mixtures are almost ideal with only slight positive deviations from additivity occurring.

In previous publications (1, 2) some thermodynamic properties and the electrical conductivities of molten silver chloride-silver sulfide mixtures were determined. This paper presents the determination of the phase diagram and the densities for the molten lead chloride-lead sulfide system. The usefulness of these measurements in indicating the structural properties of the systems and their relationship to the electrical properties was illustrated in the previous work. Lead sulfide has the NaCl structure, a high melting point and a high heat of fusion, and is therefore expected to be fairly ionic in nature.

Experimental

Preparation of materials.—Lead sulfide was prepared by the direct reaction of stoichiometric amounts of zone-refined hydrogen-reduced lead and distilled sulfur, in sealed evacuated quartz capsules.

Reagent grade lead chloride was heated under vacuum for several days, melted, and then filtered through a fritted Pyrex disk by applying an argon pressure to the upper compartment of the tube containing the melt. The tube was allowed to cool slowly, and translucent crystals from the outside of the tube were taken for use.

Phase Diagram Studies.—Liquidus points were determined by cooling curves carried out in sealed Pyrex or quartz tubes. For the chloride-rich solutions, the cells were evacuated to a few microns pressure and then filled with enough dried purified argon to give approximately 1 atm pressure at the operating temperature. These cells had a sealed side arm feeding tube containing weighed pellets of solute and a small magnet, so that a number of liquidus points could be determined with the same cell. On the sulfide side, small quartz capsules, completely sealed, were used. The furnace was cooled at the desired rate, generally 0.5-2.0°C/min, by controlling the speed of a reversing d-c motor which drove down the furnace variac through a 250,000 to 1 gear reductor. The output from the thermocouples was recorded on a 1 mv full-scale L&N recorder, with most of the thermocouple output being compensated with a potentiometer. Generally, two thermocouples at different positions in the melt were recorded. The melt was mixed by rocking the entire furnace. The thermocouples were sheathed in close fitting Pyrex or quartz tubes blown into the cells. The bottom of these tubes was drawn out to a thin point to obtain the best possible thermal contact with the melt. A thermocouple depth of immersion of about 1¼ in. was used, as this immersion was required to obtain the same freezing point reading when cooling or heating a pure salt. The thermocouples were 24-gauge chromel-alumel, or 0.015 in. platinum-platinum rhodium, and were calibrated under identical experimental conditions, by cooling curves taken on zone-refined tin and silver. The sensitivity of the recorder was approximately 0.1°C for chromel-alumel thermocouples, and 0.25°C for the platinum-13% rhodium thermocouples. On calibration, the reproducibility of the measured freezing points was generally 0.25°C for the same sample, and up to 0.5°C for different samples with different cells and insulation in the furnace. Supercooling could generally be kept below 1.5°C by vigorous mixing or tapping the cell sharply. If more than this amount of supercooling occurred, the melt would not heat up to the correct liquidus temperature for the solutions.

Density measurements.—The densities for the molten mixtures were determined using the apparent loss in weight method described in a previous publication (1). The entire system was evacuated to a few microns pressure at 150°C and then filled with a positive pres-

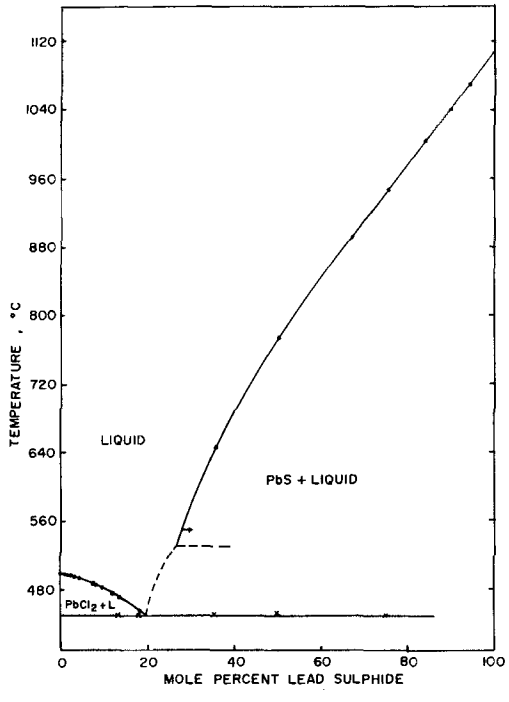

Fig. 1. Phase diagram of the PbS-$PbCl_2$ system

[1] Present address: Department of Metallurgy, Royal School of Mines, Imperial College, London, England.

sure of dried purified argon for the measurements. Small corrections due to material condensing on the quartz fiber were determined by weighing the quartz fiber suspension before and after a density determination.

Results and Discussion

Phase diagram measurements.—The determined phase diagram is shown in Fig. 1. Eight determinations of the melting point of lead chloride gave the value of 499.1°C with a standard deviation of 0.17°C. This value is quite close to values quoted in the literature (3, 4). The measured melting point of pure lead sulfide was 1111.9°C; this compares well with other reported values of 1112° and 1110°C (5, 3). The measured eutectic temperature is about 10°C higher than that reported by Winterhager (6), but very close to that reported by Urazov (7). It was observed in one cell that cracked that a small amount of air in the system rapidly lowered the measured eutectic temperature. Despite the high melting point of lead sulfide, there is seen to be a substantial liquid region in the phase diagram even at low temperatures.

X-ray analysis of material cooled from the chloride or the sulfide side of the diagram, showed no measurable shift in the lead chloride or the lead sulfide peaks, even at high diffraction angles. The measured relative intensity of the respective peaks was the same as observed for the pure components. Solid solubility in the system is then slight, if it occurs. Material which solidified at eutectic composition showed a new series of diffraction peaks, indicating that the phase diagram is not a simple eutectic diagram. The intensity of these peaks was much higher than the lead chloride peaks. The measured diffraction angles and relative intensities are given in Table I. The measured angles and intensities for pure lead chloride are also given in this table. Although the positions of the peaks were identical with the values reported by Swanson (8), in most instances, the relative intensities of the peaks are quite different.

Lead chloride prepared by fractional crystallization from an aqueous solution gave the same relative intensities with several methods of mounting the specimens. The diffraction peaks for lead sulfide were identical with those reported by Swanson.

Cooling curves taken on the sulfide side, close to the eutectic, could not detect any liquidus line, probably because of the slowness of the reaction to form the incongruently melting compound. The arrow on the phase diagram indicates that a decanted sample obtained from a melt held at 550°C showed that solid lead sulfide, identified by x-ray analysis, was in equilibrium with the melt. Since there is an incongruently melting compound in the system, the eutectic line on the sulfide side drawn through the points measured on continuous cooling may not represent part of the equilibrium diagram. It is evident from the phase diagram that the tendency toward compound formation is very slight in this system.

Table I. X-ray data for the incongruently melting compound in the lead chloride-lead sulfide system

Incongruently melting compound			Pure lead chloride			
			Swanson and Fuyat (8)		This study	
2θ	Relative intensities	d spacings, Å	2θ	Relative intensities	2θ	Relative intensities
22.45	22	4.15	19.62	18		
23.0	19	3.87	21.92	34		
23.65	39	3.77	22.84	73	22.8	12
26.0	96	3.42	23.32	43	23.2	19
33.45	100	2.678	24.87	100	24.85	71
36.1	39	2.488	30.2	7		
38.2	48	2.355	30.6	23	30.7	31
39.1	12	2.310	32.22	56	32.3	72
41.05	36	2.200	35.74	48	35.75	59
42.7	23	2.117	38.04	4	38.10	14
43.2	12	2.093	39.7	23		
43.6	32	2.074	39.83	24	39.8	100
46.4	8	1.957	40.7	28	40.8	31
48.9	41	1.863	41.67	10		
49.3	14	1.848	41.98	32	41.9	55
50.9	5	1.794	43.07	38	43.15	55
51.9	11	1.760	44.68	4	44.7	6
59.2	5	1.561	46.28	18		
60.2	10	1.537	46.64	13	46.6	10
60.8	14	1.523	47.66	5		
66.9	10	1.398				

Cryoscopic Calculations.—The activity of the solvent at a liquidus temperature may be readily calculated from the van't Hoff equation

$$\ln a_{\text{solvent (at } T_L)} = \frac{\Delta H_F}{R}\left[\frac{1}{T_F} - \frac{1}{T_L}\right] \qquad [1]$$

where, the heat of fusion of the solvent may be assumed to be temperature independent over a narrow temperature range. T_F and T_L are the melting and the liquidus temperatures, respectively, and a_{T_L} represents the activity of the solvent at a liquidus temperature with respect to pure supercooled liquid solvent as the standard state.

Considering the solution to be ideal, the theoretical liquidus may be calculated from Eq. [1], using the appropriate expressions for the activity of an ionic salt in an ideal solution.

For an ideal ionic mixture, in which the component salts A^+X^- and $B^{++}Y^-_2$ are completely dissociated, and randomly distributed, the activity of the species $B^{++}Y^-_2$ is given by Temkin (9) as

$$a_{B^{++}Y^-_2} = N_{B^{++}} \cdot N^2_{Y^-} \qquad [2]$$

where the ionic fractions are defined as:

$$N_{B^{++}} = \frac{n_{B^{++}}}{(+\text{ve ions})}$$

and

$$N_{Y^-} = \frac{n_{Y^-}}{(-\text{ve ions})}$$

For a reciprocal system of this type, however, the activity relationship must be modified to include the partial molar heat of mixing that appears because of the heat of the following exchange reaction

$$B^{++}Y^-_2 + 2A^+X^- = 2A^+Y^- + B^{++}X^-_2 \qquad [3]$$

Considering only first order interactions, and a regular solution model, the partial molar heat of mixing in an ideal reciprocal system is given (10) by the equation

$$(\overline{\Delta H})_{B^{++}Y^-_2} = N_{A^+} \cdot N_{X^-} \cdot \Delta H^\circ_{\text{exch.}} \qquad [4]$$

where $\Delta H^\circ_{\text{exch.}}$ corresponds to the heat of the exchange reaction [3], calculated from the heat contents of the components in their standard states at the specified temperature of the mixture.

The activity of the components $B^{++}Y^-_2$ is then calculated from the relationship

$$\log a_{B^{++}Y^-_2} = \log N_{B^{++}} \cdot N^2_{Y^-} + (N_{A^+} \cdot N_{X^-}) \cdot \frac{\Delta H^\circ_{\text{exch.}}}{2.3\,RT}$$

The activity equation is expected to hold in concentrated solutions of the component $B^{++}Y^-_2$ and may be considered as particularly useful in cryoscopic calculations.

For a mixture having a common ion, *e.g.*, A^+Y^- and $B^{++}Y^-_2$, the equation simplifies to the familiar Temkin expression

$$a_{B^{++}Y^-_2} = N_{B^{++}} \cdot N^2_{Y^-} \qquad [6]$$

An enlargement of the phase diagram on the lead sulfide side and the "ideal" liquidus, calculated from the van't Hoff equation, is shown in Fig. 2.

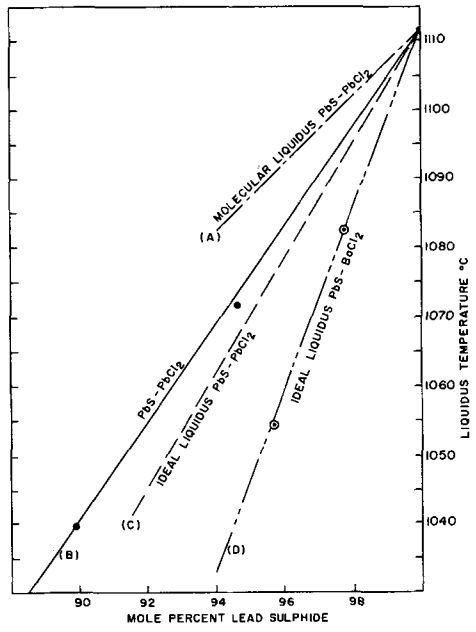

Fig. 2. Lead sulfide side of the phase diagram of the systems, PbS-$PbCl_2$, and PbS-$BaCl_2$: line A, calculated on the basis of the mole fraction; line B, experimental; line C, calculated on the basis of a'_{PbS} given in Table II; line D, calculated on the basis of a'_{PbS} given in Table II. The points are the measured liquidus temperatures. ● PbS-$PbCl_2$, ⊙ PbS-$BaCl_2$.

For the calculation, the reported heat of fusion of lead sulfide (3) was used, as well as the "ideal" activities given in Table II.

In Table II, column 1 gives the mole fraction composition, column 2 the Temkin activity which is valid only for systems having a common ion, and column 3, the "ideal" activity for a reciprocal salt mixture. The activity calculated from the experimental results, using the van't Hoff equation, is given in column 4. The activity coefficient is then obtained by dividing the experimental activity by the corresponding ideal activity.

For the PbS-$PbCl_2$ system, the measured liquidus lies above the ideal line, indicating positive deviations from ideality. The deviations could be caused by an error in the reported heat of fusion of lead sulfide, by a number of associated PbS species existing in solution, or by the presence of associated lead chloride. In order to differentiate between the most probable cause of the deviations, an ionic salt-like barium chloride was added to lead sulfide, and the new liquidus was determined. The ideal activity of lead sulfide in the PbS-$BaCl_2$ system was calculated and is given in Table II.

Table II. Activity calculations

System	X_{PbCl_2}	$N_{Pb^{++}} \cdot N^2_{a^-}$ (Temkin)	a'_{PbCl_2} (calc. ideal)	a_{PbCl_2} (expt.)	$\gamma PbCl_2$
1. $PbCl_2$-PbS (common ion)	0.98	0.9799	—	0.9849	1.005
	0.96	0.9598	—	0.9730	1.014
	0.94	0.9392	—	0.9550	1.016
2. $PbCl_2$-NaF (reciprocal)	0.98	0.9630	0.9634	0.9725	1.009
	0.96	0.9212	0.9225	0.9502	1.030
	0.94	0.8828	0.8860	0.9133	1.030
3. $PbCl_2$-NaCl (common ion)	0.98	0.980	—	0.9777	0.988
	0.96	0.960	—	0.9552	0.995
	0.94	0.940	—	0.9350	0.994
4. $PbCl_2$-KBr (reciprocal)	0.98	0.9630	0.9628	0.9714	1.009
	0.96	0.9212	0.9205	0.9458	1.027
	0.94	0.8828	0.8670	—	—

System	X_{PbS}	$N_{Pb^{++}} \cdot N_{a^{--}}$ (Temkin)	a'_{PbS} (calc. ideal)	a_{PbS} (expt.)	PbS
5. PbS-$PbCl_2$ (common ion)	0.98	0.9608	—	0.9750	1.014
	0.96	0.9231	—	0.9384	1.016
	0.94	0.8868	—	0.9053	1.020
6. PbS-$BaCl_2$ (reciprocal)	0.98	0.9416	0.9421	0.9451	1.002
	0.96	0.8862	0.8897	0.8882	0.998
	0.94	0.8336	0.8435	0.8374	0.993

The excellent agreement between the ideal and the experimental activities for lead sulfide indicates that this system is well described by the ionic model. The agreement indicates further that lead sulfide behaves as a dissociated liquid, suggesting indirectly that the positive deviations from ideality in the PbS-$PbCl_2$ system may be caused by association in lead chloride.

In Fig. 2, the calculation of the liquidus, when taking the activity as being equal to the mole fractions, gives line A which lies even higher than the experimental curve. This calculation corresponds to a totally molecular liquid, and accordingly lead chloride should be described as only partially associated.

Similar calculations were also made on the lead chloride side of the phase diagram.

The measured liquidus line for the $PbCl_2$-PbS binary system is shown in Fig. 3.

The ideal liquidus calculated from the Temkin activity and the heat of fusion of lead chloride (3), assuming complete dissociation of the components into their ionic species, is shown as line A which lies well below the experimental curve.

The x-ray data indicate that the deviations cannot be ascribed to solid solubility. The cryoscopic information on the sulfide side of the system has indicated that lead sulfide, rather than lead chloride, is dissociated. Accordingly, in order to provide some further evidence of association, several alkali metal halides were added to lead chloride, and the new liquidus lines were determined. The results of these measurements are also shown in Fig. 3.

The systems $PbCl_2$-NaF and $PbCl_2$KBr are reciprocal, while the $PbCl_2$-PbS and $PbCl_2$-NaCl have an ion in common. The ideal activities were calculated using the appropriate activity expressions, and the results are also given in Table II.

The ideal liquidus lines for these systems are given in Fig. 3 as curves A and B. It is evident from Table II that all systems, with the exception of the $PbCl_2$-

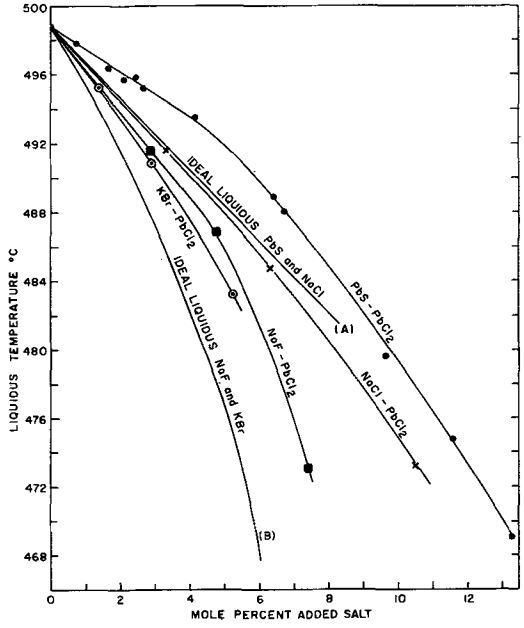

Fig. 3. Lead chloride side of the phase diagram of the systems, $PbCl_2$-PbS, $PbCl_2$-NaCl, $PbCl_2$-NaF, and $PbCl_2$-KBr. Lines A and B were calculated from the "ideal" activity data a'_{PbCl_2} given in Table II. ● PbS-$PbCl_2$; × NaCl-$PbCl_2$; ■ NaF-$PbCl_2$; ⊙ KBr-$PbCl_2$.

NaCl binary, indicate small positive deviations from ideality. The effect of such small deviations on the position of a liquidus line is shown by the large differences between the experimental and the ideal liquidus lines in Fig. 3. It is also evident that the liquidus temperature is very sensitive to small changes in activity. For example, an activity change of lead chloride from 0.971 to 0.963, would decrease the liquidus temperature by about 7°C.

The curves in Fig. 3 indicate clearly positive deviations, with the exception of the $PbCl_2$-NaCl system. Since the molten alkali metal halides are completely dissociated to their ions, the deviations may be accounted for by the tendency of lead chloride to associate in the liquid. Furthermore, the experimental activities for lead chloride are in better agreement to the mole fractions, representing a molecular model, than to the ionic activities.

In any case, the measured activities indicate deviations from ideality, which are too small to allow the calculation of any specific association scheme.

The transport properties of lead chloride also provide evidence of the existence of ions other than lead and chloride ions in pure lead chloride. In a calculation of the mobility coefficients and transport number, Laity (11) has shown that the calculated transport number of lead is about twice the measured value for lead chloride, while reasonable agreement was obtained for simple monovalent salts.

In the NaCl-$PbCl_2$ system, the Temkin activities and the molecular mole fractions are numerically equal, and therefore this is the only system where the calculation of an ideal activity cannot differentiate between association and dissociation. By comparison with the experimental activity, it appears that in this system only slight negative deviations from ideality do occur. This is in qualitative agreement with recent careful determinations of the heats of mixing in sodium chloride-lead chloride melts at 650°C by McCarty and Kleppa (12). No attempt has been made to compare the data because of the large temperature differences in the measurements.

Density measurements.—The measured densities were all linear functions of temperature. Linear regression of the experimental data yielded the constants for a and b and the standard deviations for the equation

$$\text{Density} = a - b(t°C - 500) \text{ in g/cm}^3$$

The values for the constants a and b at the compositions investigated are given in Table III. The standard deviation shows only the relative scatter of the experimental points and does not include absolute errors in density results.

The measured density of lead chloride is 0.6% higher than that reported by Heymans (13). Heyman's results for the density of molten silver chloride were also 0.8% lower than those determined by the present authors (1) and by Spooner and Wetmore (14). Lead chloride has a large expansivity, about three times that of strontium chloride, which might be expected to have somewhat similar properties. This abnormal expansivity would suggest, in agreement with the phase diagram measurements, that pure lead chloride contains ions other than simple lead and chloride ions. The expansivity of pure lead sulfide is small, about one-third that of lead chloride.

Table III. Density of PbS-$PbCl_2$-molten mixtures
Density = $a - b(t°C-500)$ (g/cm³)

Mole % PbS	a	$b \times 10^3$	Temperature range, °C	Standard deviation
0	4.985	1.50	500-650	0.003
14.97	5.160	1.56	490-650	0.002
34.35	5.306	1.07	670-840	0.004
50.00	5.554	1.01	800-960	0.003
70.54	6.003	1.06	920-1050	0.005
100.00	6.842	0.54	1120-1200	0.006

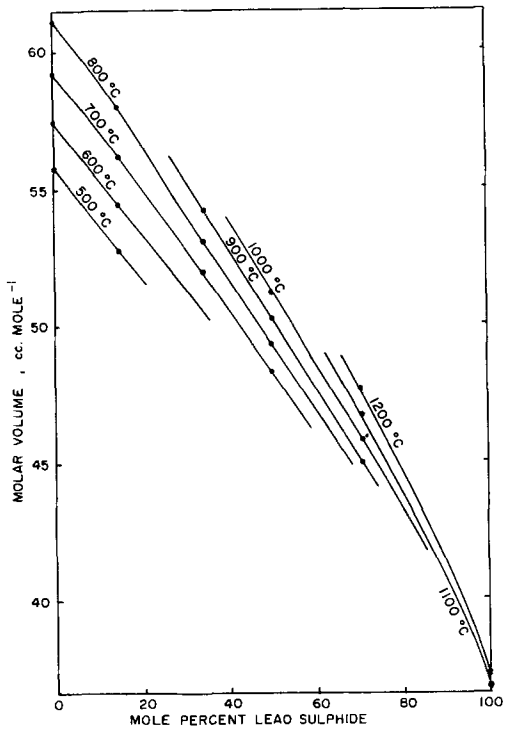

Fig. 4. Molar volume isotherms of the molten PbS-$PbCl_2$ system as a function of the lead sulfide content.

The molar volumes of the melts calculated from the density measurements are shown in Fig. 4. It is evident that the molar volumes of the mixtures are almost additive, the positive deviations from additivity being about 1 cm³/mole, or 2% of the total molar volume at 50 mole % sulfide. This positive deviation is of the same sign and magnitude as the excess molar volumes in lead chloride-potassium chloride mixtures (15) and is about half the excess volume at 35 mole % sulfide in the silver sulfide-silver chloride system. The density measurements indicate, in agreement with the phase diagram calculations, slight positive deviations from ideality. Lead sulfide in these melts is dissociated, while lead chloride behaves like a partially associated liquid. Furthermore, the tendency toward compound formation in the system is slight.

Summary

The phase diagram for lead chloride-lead sulfide is simple with one very weak incongruently melting compound occurring in the system. The x-ray diffraction pattern for the incongruently melting compound was determined. Calculations from the phase diagram indicate that liquid lead sulfide is dissociated. The liquidus lines for PbS, NaCl, NaF, and KBr added to lead chloride were also determined. Calculations from the phase diagram indicate positive deviations from ideality in the PbS-$PbCl_2$ system.

The density measurements show that the expansivity of lead chloride is high, while that for lead sulfide is small. The molar volumes of the mixtures are almost ideal, with slight positive deviations from additivity occurring.

The density and the phase diagram then indicate that the lead chloride-lead sulfide system is structurally simpler than the silver sulfide-silver chloride system previously investigated, and accordingly the electrical properties of the two systems would also be expected to be different.

Acknowledgments

The authors are indebted to the School of Engineering Research of the University of Toronto, for an equipment grant in support of this work. The award

of a Ford Foundation Fellowship to one of them (M.C.B.) is also gratefully acknowledged.

Manuscript received Feb. 9, 1965; revised manuscript received Sept. 10, 1965.

Any discussion of this paper will appear in a Discussion Section to be published in the December 1966 JOURNAL.

REFERENCES

1. M. C. Bell and S. N. Flengas, *This Journal*, **5**, 569 (1964).
2. M. C. Bell and S. N. Flengas, *ibid.*, **5**, 575 (1964).
3. O. Kubaschewski and E. W. Evans, "Metallurgical Thermochemistry," Pergamon Press, New York (1958).
4. C. C. Wicks and F. E. Block, Bull. 605, Bureau of Mines, U. S. Department of the Interior (1963).
5. J. Elliot and M. Gleiser, "Thermochemistry for Steelmaking," Vol. 1, AddisonWesley Publishing, London (1960).
6. H. Winterhager and R. Kammel, *Z. Erzberbau u. Metallhüttenw.*, **9**, 97 (1956).
7. G. C. Urazov and M. A. Sokolovn, *Isv. Sektora Figi. Khim. An. Inst. Obsch. Neorg. Khim. Akad. Nank. S.S.S.R.*, **14**, 3 (1941).
8. Swanson and Fuyat, N.B.S. Circular 539, Vol. 2, 45 (1953).
9. M. Temkin, *Acta Phys. Chim., U.S.S.R.*, **20**, 411 (1941).
10. H. Flood, T. Förland, and K. Grjotheim, Phys. Chem. of Melts., p. 46, Institute of Mining and Metallurgy, London (1953).
11. R. W. Laity, *Discussions Faraday Soc.*, **32**, 172 (1961).
12. F. G. McCarty and O. J. Kleppa, Private communication.
13. N. K. Boardman, F. H. Dorman, and E. Heymann, *J. Phys. Chem.*, **53**, 375 (1949).
14. R. C. Spooner and F. E. W. Wetmore, *Can. J. Chem.*, **29**, 777 (1957).
15. H. Bloom, *J. Pure Appl. Chem.*, **7**, 389 (1963).

The Electrical Conductivities and the Structural Properties of Molten $PbCl_2$-PbS Mixtures

II. Electrical Conductivities of the Systems PbS-$PbCl_2$ and Pb-PbS-$PbCl_2$

M. C. Bell[1] and S. N. Flengas

Department of Metallurgy and Materials Science, University of Toronto, Toronto, Ontario, Canada

ABSTRACT

The specific conductivities of molten lead chloride-lead sulfide mixtures have been determined. On the addition of the sulfide to the chloride the conductivity decreases initially and then increases as electronic conductance sets in at about 35 mole % sulfide. The conductivity in this region is characterized by temperature independent activation energies, typical of semiconductive behavior. The electronic conduction in this system is analyzed on the basis that the melts are intrinsic semiconductors. The solubilities of lead in lead chloride, and in lead chloride-lead sulfide melts up to 50 mole % sulfide were determined. The electrical conductivities of these solutions were also investigated. It is found that the activation energies for electronic conduction in the melts containing added metal change by only a very small amount, indicating that the added metal is not acting as are electron donor.

The lead chloride-lead sulfide system was one of the first sulfide-chloride mixtures studied and was the subject of patents for the electrolytic recovery of lead as early as 1906. More recently German (1) and Japanese workers (2) have shown that the electrolysis of lead sulfide in solutions in lead chloride and sodium or potassium chloride melts could be carried out at high current efficiencies.

Lead sulfide has the NaCl crystal structure, a high melting point, and a large heat of fusion, and is therefore expected to be fairly ionic. The phase diagram and density measurements for the lead chloride-lead sulfide system reported in the previous paper in this series (3) have shown that lead sulfide behaves like a dissociated liquid while pure liquid lead chloride contains species other than simple lead and chloride ions. The system shows only a slight tendency toward compound formation.

Solid lead sulfide is a well-known intrinsic semiconductor (4, 5) even at high temperatures, having an energy gap of 0.35 ev. The conductivity of pure solid lead sulfide has been found to increase rapidly because of the loss of small amounts of sulfur at high temperatures (6). This fact has limited the accuracy with which the conductivity of the molten stoichiometric sulfide could be determined.

Previous investigations of the molten silver sulfide-silver chloride system (7) in this laboratory have shown that the onset and amount of electronic conduction in the sulfide-chloride melts could be determined readily from careful conductivity measurements.

In the present investigation the electrical conductivities for the molten lead chloride-lead sulfide mixtures are presented over the composition and temperature range allowed by the phase diagram and the thermal stability of the system.

Lead and lead sulfide are miscible at high temperatures, while the silver-silver sulfide system has a large immiscibility gap (8). The post transition metals which do not form subhalides generally have extremely limited solubilities in their molten chlorides (9). It is therefore of interest to determine the solubilities in these molten mixtures. The measurement of the effect of the added metal on the conductivity in these mixtures, some of which are semiconductors, gives some indication of the electron donor properties of the excess metal present.

Experimental

The preparation of the materials used in this investigation and the cell design were described in detail in a previous publication (3). Graphite electrodes were used for all measurements above 20 mole % lead sulfide, as tungsten, or platinum, dissolved readily in these melts. The conductivity cells were of the U-tube, capillary type. For high concentrations of sulfide the melts were thermally unstable and evolved small amounts of sulfur. In this range the conductivity cells were modified by introducing female silica ground joints about 2 in. above the capillary. The graphite

[1] Present address: Department of Metallurgy, Royal School of Mines, Imperial College, London, England.

electrodes were then machined and ground to fit the joints, and were connected to the molybdenum or graphite leads for the bridge connections. When assembled the electrodes could be lowered and seal the capillary part of the cell making a tight fitting in the hot zone of the furnace, thereby reducing sulfur evolution. All measurements were taken in an atmosphere of purified argon.

The solubility of lead in molten lead chloride-lead sulfide mixtures was determined by direct loss in weight of small amounts of lead equilibrated with about 30g of the required salts sealed in evacuated ½-in. quartz tubes terminating in a 4 mm ID quartz tube at the bottom. For these measurements zone refined lead was further purified by passing anhydrous hydrogen through the liquid metal at about 500°C to reduce the oxygen content.

The capsules were evacuated overnight to a few microns pressure before sealing. The cells were placed in vertical holes drilled in a graphite block in the furnace and maintained at the required temperature for several days. The temperature gradient along the samples was maintained at less than 1°C. The samples were then removed from the furnace and quenched in iced brine. Preliminary experiments showed that the rate of quenching did not affect the measured solubility. The lead button at the bottom of the 4 mm tube was separated from the salt and boiled in distilled water to remove traces of lead chloride. Blank lead buttons and some of the equilibrated buttons showed weight losses of less than a tenth of a milligram on boiling in water. It was found however that some of the solidified buttons still contained trapped salt. All the buttons were therefore dissolved in dilute nitric acid, containing a small amount of 0.001 normal silver nitrate solution. Any salt trapped in the buttons was precipitated as silver chloride, or silver sulfide. The amount of silver remaining in the solution was then determined by titration with potassium thiocyanate solution using ferric ammonium sulfate as the indicator. The corrections in most of the samples were negligible.

The conductivity measurements on the Pb-PbS-$PbCl_2$ ternary were taken in the same manner as previously described (7). Graphite electrodes were used in all the determinations. The additions of metal to the conductivity cell were made by pressing a very small weighed amount of metal in the center of a pellet of lead sulfide. The pellet was then introduced to the melt from a side arm feeding tube.

Results and Discussion

Electrical conductivities in the binary system PbS-$PbCl_2$.—In order to show the large amounts of electronic conductivity occurring in the lead sulfide-lead chloride melts, the over-all diagram of the measured conductivities is shown in Fig. 1. Pure lead sulfide has a specific conductivity from 110 to 120 reciprocal ohm-cm, and a positive temperature coefficient typical of semiconductive behavior. In this respect, liquid lead sulfide is similar to solid lead sulfide which is a well-known intrinsic semiconductor. Lead sulfide unfortunately is not too stable at high temperatures, and the melts continuously lost very small amounts of sulfur. A small loss in sulfur however produced a large change in conductivity. Similar behavior has also been observed with solid lead sulfide (6). The present measurements on pure lead sulfide were taken by heating the cell as quickly as possible to about 1150°C. Once the lead sulfide had melted, the sulfide in the capillary was protected from further dissociation by the melt above it. Since the capillary determined 99.9% of the cell constant, stable conductivities could be measured over short periods of time, provided the melts were not mixed. Readings taken in the first half hour of three runs using different preparations of lead sulfide gave results within 5% of the mean shown in Fig. 1 and Table II, and all showed the same temperature dependence. Thus while accurate readings could not be obtained, the observed conductivities appear to be approximately correct.

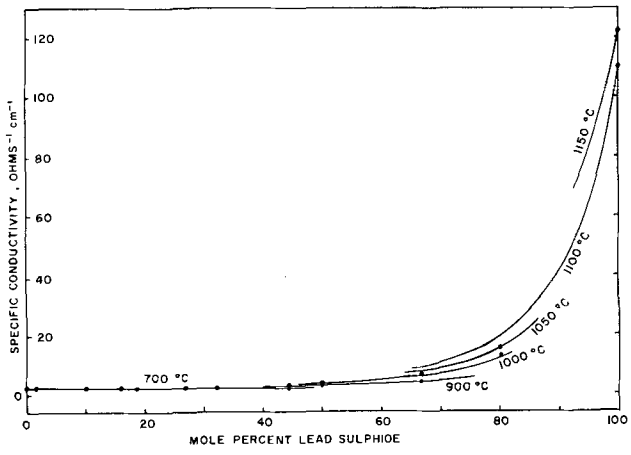

Fig. 1. Specific conductivity isotherms in the PbS-$PbCl_2$ system over the entire composition range.

The rapid decrease in conductivity on the addition of lead chloride to the sulfide is quite evident in Fig. 1. All the melts have a positive temperature dependence, unlike the silver chloride-silver sulfide system (7) which showed a metallic temperature dependence for the conductivity above 50% silver sulfide. The difference is attributed to the more ionic bonding of the lead sulfide as shown by the phase diagram and density measurements in the previous paper (3). It should also be noted that in the silver sulfide-silver chloride system at compositions below 50 mole % sulfide where the phase diagram and density measurements indicated that the melts became ionic, the temperature dependence of the conductivity also became positive.

The ionic conductivity on the chloride side of the system cannot be seen on the scale of this graph. An enlarged diagram of the specific conductivities in this region is shown in Fig. 2. The conductivities up to 36 mole % sulfide were all quadratic functions of temperature.

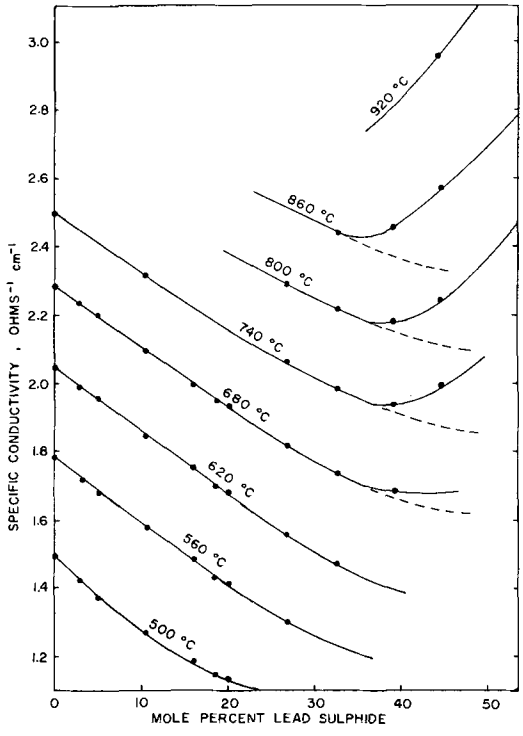

Fig. 2. Specific conductivity isotherms of the lead chloride rich solutions.

Table I. Specific ionic conductivity in the $PbCl_2$-PbS system

$k = a + b(t°C\text{-}500) - c(t°C\text{-}500)^2$, $ohm^{-1}\ cm^{-1}$

Mole % PbS	a	$b \times 10^3$	$c \times 10^5$	Standard deviation
0	1.486	0.511	0.414	0.004
2.79	1.445	0.508	0.307	0.004
10.58	1.283	0.502	0.295	0.002
16.03	1.190	0.501	0.293	0.003
18.64	1.148	0.499	0.256	0.005
25.20	1.032	0.497	0.22	0.006
26.89	1.006	0.496	0.22	0.003
32.71	0.906	0.495	0.19	0.001
35.94	0.863	0.494	0.17	
39.32	0.824	0.494	0.16	
44.61	0.770	0.492	0.14	
46.00	0.760	0.492	0.14	

In this region the measured conductivities were quite stable and were generally reproducible to ¼ of 1% on increasing and decreasing temperature. Multinomial regression about the quadratic equation

$$k = a + b(t°C - 500) - c(t°C - 500)^2 \qquad [1]$$

yielded the constants a, b, c, and the standard deviations of the measured conductivities from this equation. The constants for this equation, and the determined standard deviations are shown in Table I. A large number of readings were taken at each composition, and the standard deviation of the experimental data is seen to be small. The measured conductivities of lead chloride are about 3% higher than those reported by Harrap and Heymann (10). Harrap's values for the conductivities of silver chloride were also about 2.5% lower than those reported by Doucet (11), Wetmore (12), and in our previous investigation (7).

The densities for lead chloride and for the mixtures with lead sulfide have been previously determined (3), so that the equivalent conductivities could be calculated. Since the phase diagram measurements (3) have shown that lead chloride contains species other than simple lead and chloride ions, the conductance could not be defined per unit number of ions present. Similarly, the activation energy for conduction loses significance as an indication of an energy barrier, because the number of ions present per mole would be changing with temperature. Accordingly molar activation energies were calculated from the measured data and indicate a change from 4.32 kcal at 500°C to 3.48 kcal at 700°C. The apparent activation energies for ionic conduction change only slightly on the addition of lead sulfide to the chloride and are of the same magnitude as those for the alkaline earth halides (13).

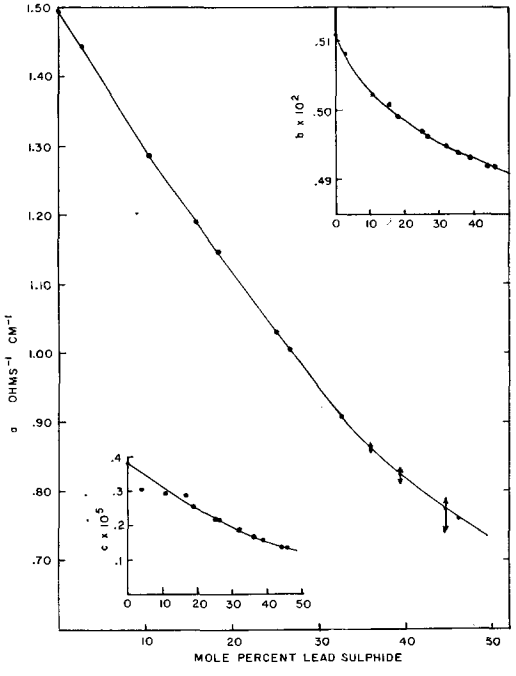

Fig. 3. Plot of the a, b, and c coefficients as a function of lead sulfide content.

The points shown on Fig. 2 are only those interpolated from the measured data at regular temperature intervals. The large temperature dependence of the conductivity is evident from the diagram. The general decrease in conductivity on the addition of the sulfide is quite evident. The decrease is similar to that observed on the addition of silver sulfide to silver chloride. In the present case, however, the isotherms are all essentially parallel, indicating that the effect of the added divalent ions is about the same at all temperatures.

The onset of electronic conductivity at about 40% lead sulfide is quite evident by the rapid increase in conductivity. The electronic conductivity rises steadily with further additions of sulfide to the large values observed on the lead sulfide side of this system. The onset of electronic conductivity is seen to occur at a much higher sulfide concentration than in the silver chloride-silver sulfide system. In order to determine the amount of electronic conductivity occurring in these mixtures it is necessary to extrapolate the ionic conductivity from lower sulfide concentrations. This was done by extrapolating the coefficients for quadratic equations for the specific conductivity. The extrapolation is shown in Fig. 3. The accuracy of the conductivities in the ionic region is evident in the smooth curves obtained for the coefficients. The change in the b and c coefficients is small, and possible errors in the extrapolation of these parameters are less likely than the uncertainty in the a term. Arbitrary limits for various possible extrapolations for the a coefficient past 32% sulfide are shown by the vertical arrows. The points given by the solid dots are those used in the calculation of the expected ionic conductivity for the higher concentrations and are given in Table I.

The difference between the measured conductivity and the expected ionic conductivity for concentrations above 32% lead sulfide, then gives the specific electronic conductivity. When multiplied by the molar volume of the melts, the molar electronic conductivity is obtained. The conductivity is then expressed per unit mole rather than per unit volume. The plot of the logarithm of the molar electronic conductivity *vs.* the reciprocal temperature is shown in Fig. 4. The points show the electronic conductivity calculated at 20°C intervals from the measured data. The electronic conductivity for these compositions is seen to be characterized by a temperature-independent activation energy over a wide temperature range, the deviations for the 44.6 mole % lead sulfide curve at low temperatures being on the borderline of being significant. The arrows on the lines show the uncertainty involved in the extrapolation for the expected ionic conductivity. If different extrapolations are made, the conductivities are all shifted in the same direction by the amount indicated by the arrows. The temperature dependence of the electronic conductivity in this region is then seen to be typical of an intrinsic semiconductor. A similar behavior was observed in the silver chloride-silver sulfide system when electronic conduction commenced. Exactly the same behavior with respect to the extrapolation for the ionic conductance is observed when excess soluble metal is added to the lead chloride-lead sulfide system.

The molar electronic conductivity of these mixtures was fitted to the equation

$$\Lambda_m = \Lambda_{oe} - \frac{\Delta H^*}{RT} \qquad [1]$$

and the results are shown in Table II. The standard deviations quoted are those determined graphically from the scatter of the measured points about the total conductivity predicted by the parameters given in Tables I and II. The uncertainty in the values for the

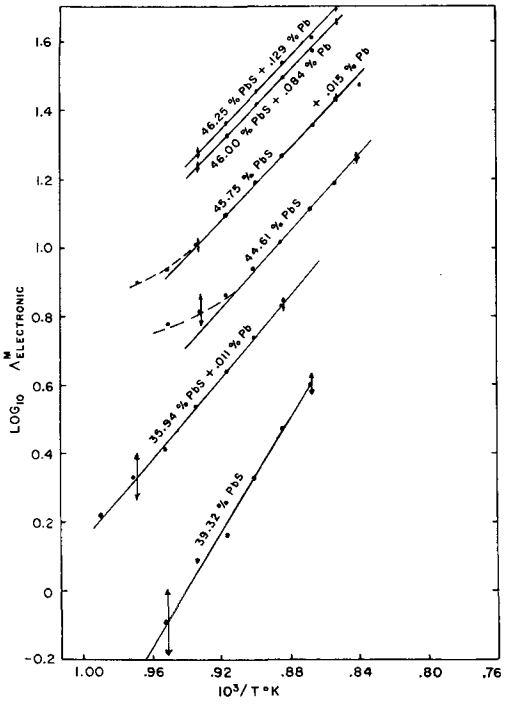

Fig. 4. Plot of the logarithm of the molar electronic conductivity vs. the reciprocal temperature.

activation energies correspond to the uncertainty in the extrapolation for the ionic conductivity shown in Fig. 3.

The data for the specific conductivities above 45 mole % sulfide are also shown in Table II, along with the determined activation energies. The errors shown are only approximate and are based on the fact that three determinations of the conductivity of pure liquid lead sulfide gave results within 5% of the mean value. The possible errors in the activation energies are difficult to assess, but the measured conductivities showed the same temperature dependence even after some decomposition of the sulfide had occurred.

The conductivity of liquid lead sulfide would appear to be about twice the value for the solid state when results from lower temperatures are extrapolated over a wide temperature range (6). This increase in conductivity is similar to the large increases in conductivity that occur on melting silicon, germanium, tellurium, tin sulfide, and a number of antimonide compounds (14-16).

The measured activation energy for pure liquid lead sulfide corresponds to an energy gap between the valence and conduction bands of 0.7 ev, if the liquid is considered as a semiconductor. This value compares with the value of 0.35 ev for solid lead sulfide (6). Similarly, the specific conductivity of liquid tin sulfide has a positive temperature dependence giving an energy gap of 1.9 ev (15) compared to a value of 1.2 ev for solid tin sulfide which is also an intrinsic semiconductor (17). Liquid selenium has also been shown to be a semiconductor having an energy gap of 2.3 ev, compared to 1.8 ev for the solid (18). This data would suggest that the positive temperature dependence of the conductivity in these systems is indicative of semiconductive behavior. In the solid state, the energy gap may be determined from conductivity measurements, as the mobility changes with temperature in a much slower manner than the exponential temperature dependence of the electrons raised to a conduction band.

Table II. Electronic conduction in the PbS-$PbCl_2$ system

Mole % PbS	Equation	$\log_{10} A_0$	ΔH^*, kcal	Uncertainty	Standard deviation
39.32	$^a \Lambda m = \Lambda_0 e^{-\Delta H^*/RT}$	7.7794	37.90	±4.0	0.004
44.61	$\Lambda_m = \Lambda_0 e^{-\Delta H^*/RT}$	5.8803	25.20	±1.5	0.006
		a	b	ΔH^*, kcal	Error, %
66.5	$k^* = a + b$ (t°C-900)	4.20	0.025	22.0	±2
80.2	$k = a + b$ (t°C-1000)	12.6	0.06	18.0	±5
100.0	$k = a + b$ (t°C-1100)	110.0	0.30	8.0	±5

[a] k ohm^{-1} cm^{-1}.
[b] Λ_m ohm^{-1} moles^{-1} cm^2.

From Table II, there is seen to be a large increase in the activation energy for electronic conduction, or in the energy gap, as lead chloride is added to the sulfide. The same observation was made in the silver sulfide-silver chloride melts in the region in which electronic conductivity commenced (7). This increase may be attributed to the more ionic bonding in these solutions as compared to the partially covalent pure sulfide.

The activation energy for electronic conduction in the silver sulfide-silver chloride system at 35 mole % added sulfide is less than half that in the lead sulfide-lead chloride system. This lower energy may also be attributed to the more covalent nature of silver sulfide, as indicated by the phase diagram and density measurements (3) of that system. Hall constants have not been measured in these systems, so that the number of charge carriers has not been determined experimentally. If the liquids are considered as semiconductors having a finite conduction band, the concentration of electrons n per unit volume, raised to the conduction band is given by the well-known expression

$$n = NT^x(m^* \cdot m)^y \cdot e^{-Eg/2KTG} \qquad [2]$$

where Eg represents the energy gap measured from the valence band, m^* is the effective electron mass, and m the normal electron mass. Such a relationship could be expected to hold for both the pure liquid sulfide and a solution, if both these liquids are intrinsic semiconductors.

The molar conductivities of these liquids may be expressed as

$$\Lambda m = 2k \cdot n \cdot \mu \cdot e \cdot Vm \qquad [3]$$

where e is the electron charge, μ is the mobility of the electrons, k is the conversion factor for the units, and Vm the molar volume of the liquid. The factor of 2 is introduced to account for positive hole conduction, as observed in solid lead sulfide at high temperatures (4, 5).

The ratio of electron mobilities in pure lead sulfide at 900°C, (μ_p), to that in a solution at 45 mole % sulfide, (μ_s), at the same temperature may be obtained by dividing the corresponding expressions

$$\frac{(\Lambda m)_p}{(\Lambda m)_s} = \frac{n_p \cdot \mu_p \cdot (V_m)_p}{n_s \cdot \mu_s \cdot (V_m)_s} \qquad [4]$$

where the constants shown in Eq. [3] cancel out.

The electron concentration ratio may be obtained from Eq. [2]. Since the comparison is made at the same temperature the pre-exponential terms in this equation will cancel out when substituted in Eq. [4].

The assumption is also made that the effective electron masses are the same in the two systems, or that both are equal to the normal electron mass. This assumption has some basis as Hall measurements in liquid metals and liquid germanium have been deter-

mined and show that the effective masses in these liquids are close to the normal electron mass (14). For the calculation, the energy gap is taken as being equal to twice the measured activation energies of conduction, *e.g.*

$$\frac{Eg}{2K'} = \frac{\Delta H^*}{R}$$

On substituting the corresponding values for the energy gaps and the measured molar electronic conductivities at 1100°C, the ratio of the mobilities in the two systems may be calculated as

$$\frac{\mu_p}{\mu_s} = 0.14 \text{ at } 1100°C$$

That is, the electron mobility in the solution is greater than the mobility in pure liquid lead sulfide. This could be accounted for by a lower scattering cross section of the chloride ion compared to the highly charged divalent sulfide ion present in the pure sulfide. The calculation indicates that the decrease in conductivity by a factor of 100 on going from the pure sulfide to a solution at 45 mole % sulfide is not necessarily caused by a decrease in the mobility of the electrons, but may be accounted for by the increase in the energy gap in the solutions on the addition of the ionic chloride.

Electrical conductivities and metal solubilities in the ternary system Pb-PbS-$PbCl_2$.—The interpretation of the electrical conductivities in the ternary system Pb-PbS-$PbCl_2$ requires the knowledge of the solubility of lead metal in the PbS-$PbCl_2$ melts.

Solubilities of lead were determined in melts containing only up to 50 mole % sulfide, because in this region the sulfide-chloride melts were quite stable, and accurate data on conductivities could be obtained. The measured solubilities are shown in Fig. 5. The solubility of lead in lead chloride is quite small, 0.008 mole % at 583°C to 0.056 mole % at 886°C. The measured solubilities are about one-third of those reported by Corbett (20). It was observed in the present investigation that if the reagent grade lead chloride was used as-received without previous purification, solubilities closer to those reported by Corbett (20) at 600°C were obtained.

It is evident that these small solubilities are very sensitive to the purity of the sample, and that the presence of oxygen or metallic impurities in the system may increase the measured solubility.

Despite the scatter in the results for the the mixtures of lead chloride and lead sulfide, it is apparent that the solubility at low temperatures (583°C) is very small, less than 0.02 mole %, for all the compositions studied. The solubility increases with increasing temperature and increasing sulfide concentration to a value of 0.65 mole % at 50 mole % sulfide and 886°C. Analysis of the lead buttons showed that most of the buttons contained no detectable amounts of chloride or sulfide, so that the solubility of lead chloride and lead sulfide in liquid lead is very small.

The measured solubilities of lead in pure lead chloride show less scatter than the data for the mixtures, and it is possible to obtain a value for the partial molar heat of solution of lead in lead chloride. A plot of the logarithm of the solubility *vs.* the reciprocal temperature is shown in Fig. 6. Despite the fact that only four readings were taken, a good straight line is obtained. The solubilities reported by Topol (21) are shown for comparison. The slope of the line for the present investigation gives a partial molar heat of mixing of +13.2 kcal, if the activity coefficient of lead in the solution is constant over the composition range involved. In view of the extremely small solubilities such an assumption is quite justified. Such a high positive heat at such low concentrations is indicative of the large immiscibility gap in the lead chloride-lead system. The scatter in the measured solubilities for the sulfide-chloride mixtures makes it impossible to determine the heat of solution with any precision in these mixtures.

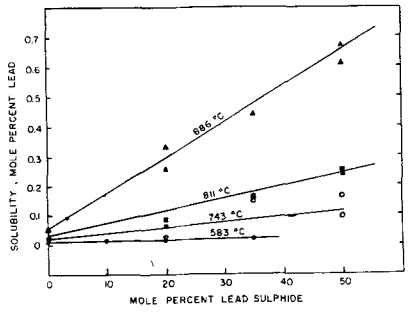

Fig. 5. Solubilities of lead metal in molten PbC-$PbCl_2$ mixtures as a function of the lead sulfide content.

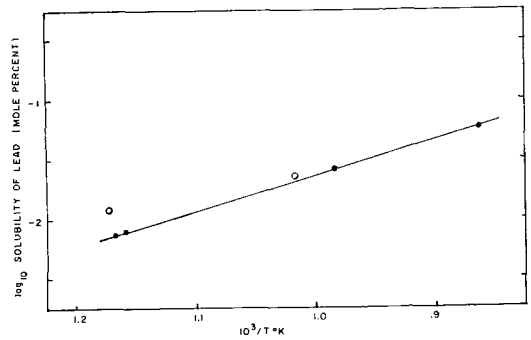

Fig. 6. Plot of the logarithm of the solubility of lead in lead chloride vs. the reciprocal temperature: ● this investigation; ○ Topol (21).

The effect of added soluble lead metal on the conductivity in the binary lead chloride-lead sulfide system was determined at three sulfide concentrations, 25, 36, and 46 mole % lead sulfide. The effect of added metal on the specific electronic conductivity is shown at one temperature in Fig. 7. The electronic conductivity was determined as the difference between the measured and the expected ionic conductivity. The values used for the ionic conductivity are shown in Table I. At 25.6 mole % lead sulfide, no electronic conductivity is occurring in the binary system, and the addition of 0.013 mole % lead metal produced no observable change in the conductivity even after standing overnight and thoroughly mixing. At 35.9 mole % lead sulfide, very little electronic conductivity is expected in the binary system, and the addition of metal increases the conductivity as shown. At 46 mole % sulfide, electronic conduction is occurring in the binary system, and the addition of metal increases the conductivity only slightly.

At the final metal concentration, the electronic conduction is about the same as the ionic conductivity in the system.

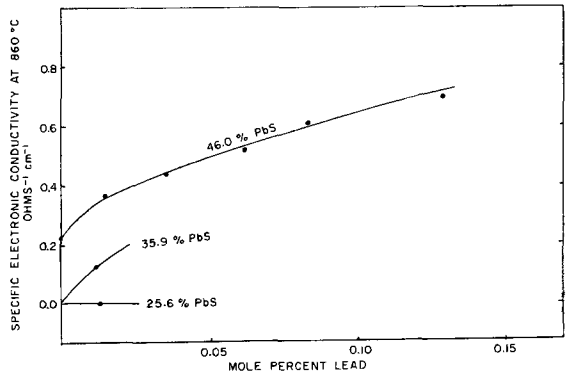

Fig. 7. Effect of added lead metal on the specific electronic conductivity of the PbS-$PbCl_2$ solutions at 860°C.

Table III. Electronic conduction in the Pb-PbS-$PbCl_2$ system: $\Lambda_m = \Lambda_o e^{-H^*/RT}$

Mole % PbS	Mole % Pb	$\log^{10} \Lambda_o$	ΔH^*, kcal	Standard deviations
25.64	0.13	No electronic conduction		
35.94	0.0114	5.7040	27.13 ± 2.8	0.005
45.74	0.015	6.0188	24.62 ± 1.5	0.006
46.00	0.084	6.2124	24.39 ± 1.2	0.006
46.25	0.129	6.2514	24.40 ± 1.2	0.006

Λ_m in ohm^{-1} mole^{-1} cm^2.

The temperature dependence of the electronic conductivity in this system is also shown in Fig. 4. The molar electronic conductivity was calculated in the same manner as for the binary system. The points on the lines again represent the electronic conductivity calculated at 20°C intervals from the measured data. It is evident that the electronic conductivity occurring in the systems with metal added, is characterized by a temperature independent activation energy of much the same value as that occurring in the binary systems. Not as many compositions are shown on this graph as in Fig. 7, because the conductivities of some of the metal concentrations were measured at a few temperatures only. The arrows on the lines again show the uncertainty in the extrapolations caused by the extrapolation for the ionic conductivity. Not as many readings were taken as in the binary systems, and the scatter in the measured values was greater. The resulting uncertainty in the determined activation energies is at least as great as the uncertainty caused by the extrapolation for the ionic component. Values for the constants in a simple exponential equation to give the measured molar electronic conductivity are shown in Table III. At 46 mole % sulfide the determined activation energy for conduction in the system with metal added are less than 0.8 kcal smaller than the activation energy in the binary system at 45 mole % lead sulfide. Such a change is very small and may not be significant within the accuracy of the data.

It may therefore be concluded that the added metal is not contributing electrons to the system at a donor level significantly different from the valence band in the binary system. This conclusion is consistent with the small increase in conductivity occurring. If the added metal atoms were all ionized giving free electrons in the conduction band, then at a metal concentration of 0.014 mole % metal, or approximately 2 x 10^{18} at., an increase of conductivity by about 1000 would be expected.

It then appears probable that the added metal is not acting as an electron donor, but is trapped by some mechanism which raises the valence band of the system slightly. Since this trapping does not occur in the pure sulfide where the conductivity changes extremely rapidly with small amounts of added metal, a complex involving chloride ion, such as $Pb+Cl^-$, is suggested as a possible trapping mechanism.

The rather low metal solubility in melts of this type may be accounted for by a "salting out" effect due to the free electrons. Thus, the dissolution process may be described by the reaction.

$$\underset{\text{(in metal)}}{M} = \underset{\text{(in melt)}}{M^+} + \underset{\text{(in melt)}}{e^-}$$

for which

$$Keq. = a_{M+} a_{e-} \qquad [5]$$

a_{M+}, and a_{e-} are the activities of the metal ions and of electrons in the salt phase, respectively.

In the present instance the salts are semiconductors and the relative concentration of "free" electrons is relatively high. This would cause the equilibrium in Eq. [5] to be shifted to the left. Preliminary experiments on the solubility of silver metal in molten silver chloride-silver sulfide mixtures at 25 mole % sulfide, have indicated a solubility of silver of less than 0.016 mole % at 890°C. This is much lower than the solubility of lead in lead chloride-lead sulfide melts at the same temperature (0.32%). Solutions of silver sulfide in this range have been shown to have much higher electronic conductivities. Accordingly they should also be expected to have a higher concentration of free electrons and a lower metal solubility.

Conclusions

Lead chloride has a low specific conductance (1.49 at 500°C) and a high "apparent" activation energy for ionic conduction (4.32 kcal at 500°C). The addition of lead sulfide to the chloride decreases the ionic conductivity in much the same manner as the addition of silver sulfide decreases the conductivity of silver chloride.

Liquid lead sulfide exhibits a positive temperature dependence for electronic conduction, typical of semiconductive behavior. The conductivity decreases very rapidly on the addition of lead chloride to the sulfide and always has a positive temperature coefficient. The metallic temperature dependence of the electronic conductivity observed in the AgCl-Ag_2S system above 50% silver sulfide is completely absent in the lead sulfide melts. The difference may be attributed to the more ionic nature of lead sulfide.

The activation energy for electronic conduction increases as lead chloride is added to lead sulfide from a value of 8 kcal in the pure liquid lead sulfide to 25 kcal at 45 mole % sulfide in lead chloride. The temperature dependence of the liquid mixtures it typical of intrinsic semiconductive behavior. If it is assumed that the effective mass of the electrons in the solution is the normal electron mass, the mobility of current carriers in a mixture of lead chloride with 45% lead sulfide is greater than in pure liquid lead sulfide. The large decrease in conductivity on adding lead chloride to the sulfide is then caused only by the increase in the energy gap on the addition of the chloride. The increase in the activation energy, or the energy gap, may be attributed to the more ionic behavior of the liquid mixtures, as compared to the partially covalently banded sulfide.

The solubilities of lead in lead chloride and in lead chloride-lead sulfide mixtures have been determined. The solubilities increase with increasing temperature and sulfide concentration to a value of 0.65 mole % lead at 50 mole % sulfide and 886°C.

The electronic conductivity is seen to increase only by a small amount when lead metal is added to the binary system. The data indicate that the added lead is not acting as an electron donor in these melts.

Acknowledgments

The authors are indebted to the School of Engineering Research of the University of Toronto for an equipment grant in support of this work. The award of a Ford Foundation Fellowship to one of them (M.C.B.) is also gratefully acknowledged.

Manuscript received Feb. 9, 1965; revised manuscript received Sept. 10, 1965.

Any discussion of this paper will appear in a Discussion Section to be published in the December 1966 JOURNAL.

REFERENCES

1. H. Winterhager and R. Kammel, *Z. Erzbergbau u. Metallhüttenw.*, **9**, 97 (1956).
2. H. Sawanoto and T. Saito, *J. Min. Inst. Jap.*, **68**, 555 (1952).
3. M. C. Bell and S. N. Flengas, *This Journal*, **113**, 27 (1966).
4. R. L. Petritz and W. W. Scalon, *Phys. Rev.*, **97**, 1620 (1954).
5. R. A. Smith, *Advances in Phys.*, **2**, 321 (1953).
6. W. W. Scalon, *Phys. Rev.*, **92**, 1573 (1953).
7. M. C. Bell and S. N. Flengas, *This Journal*, **111**, 575 (1964).
8. M. Hansen, "Constitution of Binary Alloys," McGraw Hill Book Co., London, New York (1958).

9. M. Bredig, "Molten Salt Chemistry," by M. Blander, Interscience Publishers, Inc., New York (1964).
10. B. S. Harrap and E. Heyman, *Trans. Faraday Soc.*, **51**, 259 (1955).
11. Y. Doucet and M. Bizouard, *Acad. Sci. Compt. Rend.*, **250**, 73 (1960).
12. R. C. Spooner and F. E. Wetmore, *Can. J. Chem.*, **29**, 777 (1959).
13. J. O'M. Bockris, E. H. Crook, H. Bloom, and N. E. Richards, *Proc. Roy. Soc.*, **255**, 558 (1960).
14. N. E. Cusack, *Prog. Phys.*, **26**, 361 (1963).
15. D. Boutin and M. Bourgon, *Can. J. Chem.*, **39**, 915 (1961).
16. V. M. Glazov and S. N. Chizhavskaya, *Soviet Phys. Solid State*, **3**, 1964 (1962).
17. J. S. Anderson and M. C. Morton, *Proc. Roy. Soc.*, **A184**, 83 (1945).
18. H. W. Henkels and J. Maczuk, *J. Appl. Phys.*, **93**, 922 (1954).
19. H. W. Henkels, *ibid.*, **21**, 725 (1954).
20. J. D. Corbett and S. V. Winbush, *J. Am. Chem. Soc.*, **77**, 3964 (1955).
21. L. E. Topol, *J. Phys. Chem.*, **67**, 2222 (1963).

Thermodynamic Properties of Molybdenum (III) Chloride in Molten Alkali Metal Chlorides

Sidney M. Selis

Research Laboratories, General Motors Corporation, Warren, Michigan

ABSTRACT

Using emf methods, partial thermodynamic values in molten LiCl-KCl have been precisely determined from 460° to 540°C in the Mo concentration range of 0.01 to 0.4 mole/liter. At 460°C, the free energy of formation of the molybdenum (III) chloride in a 1M solution is −63,700 ± 100 cal/mole and the corresponding entropy change is −34 ± 2 cal/deg/mole. Extrapolated to 450°C, the potential of Mo/Mo(III) (1M in LiCl-KCl) *vs.* Pt/Pt(II) (1M) is −0.603 ± 0.002v. There is a strong solvent cation effect due to coulombic, steric, and other contributions, and the excess free energy of $MoCl_3$ in KCl is much more negative than in LiCl-KCl.

The chlorides and bromides of metals in Groups IV-A, V-A, and VI-A ("refractory metals") have certainly not been the subjects of complete physicochemical investigations at elevated temperatures. Thermodynamic quantities, for instance, are not listed for many compounds, either pure or in solution. There are technical reasons for this. Physical behavior of melts results in real inconvenience for a number of experimental techniques, and the halides are unstable in the presence of moisture. Moreover, unambiguous definition of the chemical system may not be possible. Several valence states are exhibited by each of the elements, and oxidation or reduction from one to another takes place readily.

The present work is concerned with thermodynamic properties of liquid molybdenum (III) chloride. When heated, this compound vaporizes without melting, and it is not possible to study the pure liquid. But it is possible to prepare solutions in molten alkali metal chloride solvents and then to determine partial quantities. Values for LiCl-KCl have been compared with those available for pure potassium chloride, and there is an interesting solvent effect.

Furthermore, the electrode Mo/Mo(III) is now included in an emf series (for the solvent LiCl-KCl at 450°C).

Background.—In 1954 Senderoff and Brenner reported some preliminary experiments with molybdenum electrodes in molten mixtures of LiCl-KCl-K_3MoCl_6 (1). Although no rigorous proof was provided, they suggested that molybdenum metal is in equilibrium with Mo(III). It was shown that anodization of the metal occurs with unit efficiency assuming a three-electron change, and reduction of molybdenum (III) chloride to the metal also takes place with unit efficiency. Moreover, large anodic and cathodic current densities are accompanied by relatively small overpotentials.

Recently Ryzhik and Smirnov measured the equilibrium potentials of Mo/Mo(III) electrodes in molten KCl at 780°-940°C (2). They used the reference electrode Cl^-/Cl_2 (in pure liquid KCl), and their data were satisfactory for the calculation of partial thermodynamic quantities for molybdenum (III) chloride in the liquid potassium chloride solvent. Later in this paper there will be a comparison of these results with the present ones obtained at lower temperatures using the molten lithium chloride-potassium chloride solvent.

The present study was made with cells of the type Mo/$MoCl_3$ in LiCl-KCl//LiCl-KCl//$PtCl_2$ in LiCl-KCl/Pt. The solutions of molybdenum and platinum chlorides were dilute. Molybdenum (III) and platinum (II) ions were therefore unimportant carriers of current, and liquid junction potentials were consequently negligible. The temperature region was 460°-540°C, limited at the lower end by the solubility of the molybdenum (III) compound and at the upper end by the stability of the platinum (II) chloride in the reference electrode.

The platinum electrode was used for convenience instead of measuring against the chlorine electrode directly. The precise data of Laitinen and Pankey (3) are available for the cell Pt/$PtCl_2$ (1M) in LiCl-KCl// LiCl-KCl//Cl_2, C. Potential difference is given as a function of temperature, and with this, one can normalize the molybdenum electrode data, obtained with a platinum reference, to the reference Cl^-/Cl_2 (in liquid LiCl-KCl).[1] In this way, thermodynamic values are determined for the reaction

$$Mo(c) + 3/2Cl_2(g) \rightarrow MoCl_3(l, \text{ in solution})$$

Experimental

Materials.—The platinum wire (B & S 20 gauge) and sheet (0.3 mm in thickness) were over 99.99% pure. The molybdenum sheet (0.8 mm in thickness) was over 99.9% pure, the major impurity being carbon; it was obtained from the Climax Molybdenum Company. The carbon rods, 6 mm in diameter, were of spectrographic grade.

Chemically pure potassium hexachloromolybdate (III) was supplied by A. D. Mackay, Inc. Composition was verified by analysis for molybdenum using the photometric thiocyanate method (22.5% Mo calculated,

[1] Laitinen and Pankey measured platinum-chlorine cells in the temperature range 410°-490°C and arrived at relationship [1]. For the present work, it is assumed that the relationship remains valid and the electrode is usable up to 540°C.

22.3% Mo found). The chemical was dried at 110°C before use.

The LiCl-KCl mixture was of eutectic composition (58.8 mole % LiCl; 41.2 mole % KCl). It was purified by the procedure of Laitinen, Tischer, and Roe (4) which involves evacuation with gradual warming of the salts, melting under purified HCl gas, flushing with purified argon, and the use of magnesium metal which displaces heavy metal ion impurities from the alkali metal chloride electrolyte. The melts were not separately filtered and sealed in ampoules. Instead, purification was carried out in the cell container, and when the glass tubes with fritted disks were lowered and the electrolyte seeped through the porous diaphragms, the solid material was thereby filtered off and remained outside the electrode compartments. When an experiment was run in which electrolyte was subjected to the complete manipulation with opening and closing of the cell, except for actual addition of molybdenum (III), it was found that the polarographic residual reduction current was less than 1 μa with a platinum electrode area of 1 mm^2 at a potential of —2.0v *vs.* Pt/$PtCl_2$ (1M) in LiCl-KCl. Effective purification is therefore indicated, as is validity of the technique in terms of purity considerations.

Procedure.—Molybdenum electrode potentials were measured against the platinum reference with a technique similar to that used by Laitinen and Liu (5); the method involves a cell with compartments separated by fritted glass. In the present work the weight of electrolyte was 100g contained in a Vycor test tube with a diameter of 52 mm. The diameters of the compartment cups were 13 and 26 mm. The electrode leads of platinum wire were sealed in tubes at the upper ends, and the air in these tubes was replaced with argon before the electrodes were lowered. The platinum wire was connected to the molybdenum by spot-welding, using a short intervening piece of nickel.

Temperatures were measured with a chromel-alumel thermocouple calibrated at the melting points of zinc and aluminum. Temperatures could be maintained constant to within ± 0.5°C. The platinum electrode was generated by anodizing the platinum metal using a carbon counter cathode. Current density was 10-20 ma/cm^2, and the coulometric delivery was measured. The amount of electrolyte in the compartment

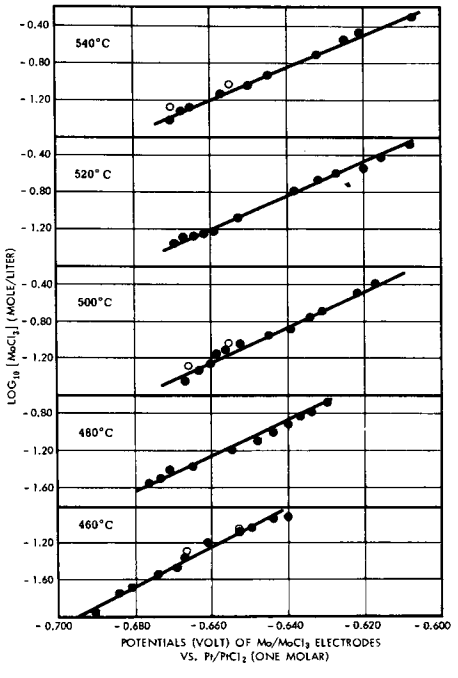

Fig. 1. Potentials of molybdenum electrodes with respect to the platinum reference: •, additions by current passage; ○, additions with K_3MoCl_6.

Table I. Nernst behavior of the molybdenum electrodes

Temperature, °C	$(\partial E/\partial \log [Mo^{+++}]_T$ (v) Calculated	Observed
460	0.0485	0.0471
480	0.0498	0.0550
500	0.0512	0.0508
520	0.0525	0.0578
540	0.0538	0.0569

was later determined using the Volhard procedure. Concentration of $PtCl_2$ in the compartment was about 0.05 mole/l (known precisely).

The molybdenum electrodes were similarly formed and later analyzed for quantity of electrolyte. After the potential was measured for one concentration, current passage was resumed to obtain the next composition. The concentration ranges are shown in Fig. 1. As much as an hour was required for a potential to become steady after a composition was changed, but once stable, the reading would generally not vary more than 1 or 2 mv in a half hour. These readings were made with a null-balancing potentiometer, the button switches being closed only momentarily.

As shown in Fig. 1, values were verified by using cells in which the molybdenum (III) was added at the beginning as K_3MoCl_6. This was weighed out with the lithium and potassium chlorides. Purification of the electrolyte was the same except that magnesium metal was not used.

Results

When the measurements with a cell were completed and the molybdenum and platinum compartments were analyzed, the molybdenum electrode composition could be defined and the potentials could be expressed with respect to Pt/$PtCl_2$ (1M in LiCl-KCl) through the use of the Nernst relationship. In Fig. 1 are plotted molybdenum electrode potentials *vs.* log concentration of molybdenum (III) for five temperatures; replicate experiments were run in order to obtain these data. The behavior is linear, and the slopes, determined by the method of least squares, are compared in Table I with the slopes calculated with the Nernst equation, assuming $n = 3$.

$$E_{Pt/PtCl_2//Cl^-/Cl_2} = -0.3223 + 0.000334\ (t - 450) \quad [1]$$

Relationship [1] gives the potentials of Pt/$PtCl_2$ (1M in LiCl-KCl) with respect to Cl^- (in LiCl-KCl)/Cl_2 at different temperatures as determined by Laitinen and Pankey (3); in their work and in the present study, temperature gradients occurred only in the platinum leads which were used from all electrodes, and so there are no corrections for thermoelectric emf. By using relationship [1], molybdenum electrode potentials with respect to the platinum electrode are normalized to the chlorine electrode, and these are numerically the same as the potential differences for the cells Mo/$MoCl_3$ (in LiCl-KCl)//LiCl-KCl/Cl_2. The reaction corresponding to these cells is the formation of molybdenum (III) chloride in solution as shown above; the partial thermodynamic quantities for the reaction are calculated from the data for these cells using relationships [2] through [4].

$$\overline{F} = nFE \quad [2]$$

$$\overline{S} = -nF(\partial E/\partial T)_P \quad [3]$$

$$\overline{H} = \overline{F} + T\overline{S} \quad [4]$$

E is the potential of the molybdenum electrode with respect to the chlorine electrode and has the negative sign when it is more anodic than the reference; n and F have the usual significance, and n is 3. Using these equations, thermodynamic quantities have been calculated; values are listed in Table II. $\overline{F}$, $\overline{S}$, and $\overline{H}$ are,

Table II. Partial thermodynamic quantities for the formation of $MoCl_3$ (1) in molten LiCl-KCl*

Concentration Moles/liter	Mole fraction	$\bar{F}$, cal/mole, 460°C	$\bar{S}$, cal/deg/mole	$\bar{H}$, cal/mole, 460°C
0.010		−70,100 ± 100	−16 ± 2	−81,900 ± 800
	0.0005	−69,700	−17	−82,500
	0.001	−68,700	−20	−83,000
0.060		−67,700	−22	−83,600
	0.003	−67,300	−23	−83,900
0.100		−67,000	−23	−84,100
	0.006	(−66,200)	−25	(−84,500)
0.200		(−66,000)	−26	(−85,100)
	0.010	(−65,500)	−27	(−85,100)
0.300		(−65,500)	−27	(−85,100)
0.400		(−65,100)	−28	(−85,300)

* Values in parentheses are based on extrapolated curves.

respectively, the partial molar free energy, entropy, and enthalpy of formation;[2] a negative value for $\bar{F}$ means that the formation occurs spontaneously. Concentrations are given on both molarity and mole fraction scales, the transformation being made with the density data of Van Artsdalen and Yaffe (6). Free energies and enthalpies in Table II are for a temperature of 460°C.

E was plotted against temperature for fixed concentrations, and Fig. 2 shows five of these curves. They are linear for the temperature region 460°-540°C and for the concentration ranges shown in Fig. 1. Using the method of least squares, a value of $(\partial E/\partial T)_P$ was found for each concentration and then plotted against log concentration. Again the behavior could be described as linear, and the method of least squares was again used to find the straight line. Referring to relationship [3], partial molar entropy was calculated for the concentrations as shown in Table II. The cells consist of electrodes which are metals in equilibrium with ions at about the same concentration, and so entropy differences of more than a few calories per degree per mole (positive or negative) are not to be expected. Partial entropies as large as −28 cal/deg/mole are given in Table II, but the major contribution to this (−23 cal/deg/mole) is by the chlorine electrode where the formation of $MoCl_3$ is accompanied by the disappearance of a gas phase.

[2] These partial thermodynamic quantities, having the general abbreviation $\bar{G}_{MoCl_3}$, are defined as $(\partial G \text{ system}/\partial n_{MoCl_3})_{n \text{ solvent}, T}$.

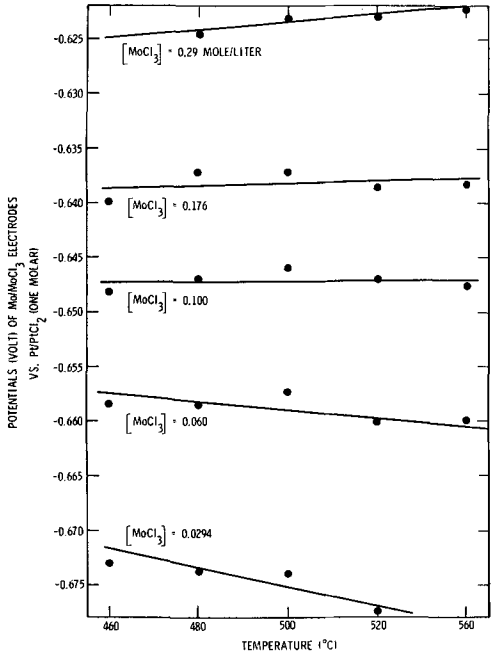

Fig. 2. Potentials of some molybdenum electrodes as a function of temperature.

Table III. Partial molar free energies of $MoCl_3$ (1) at standard concentrations in LiCl-KCl*

Temperature, °C	Concentration:	$\bar{F}$, cal/mole: 1 mole $MoCl_3$/liter	$\bar{F}$, cal/mole: $N_{MoCl_3} = 0.01$
460		(−63,700) ± 100	(−65,500) ± 100
480		(−63,000)	(−65,000)
500		(−62,300)	(−64,400)
520		(−61,700)	(−63,900)
540		(−61,000)	(−63,300)

* Parentheses indicate that the values are based on extrapolation of data.

Partial enthalpies, shown in Table II, were determined according to relationship [4]. The average deviation is based on the deviations in the free energy and entropy determinations.

Of interest are partial free energies of formation of $MoCl_3$ at standard concentrations and at different temperatures. These are listed in Table III. Enclosure of the values within parentheses indicates that they were obtained by extrapolating the curves in Fig. 1.

Discussion

One of the contributions of the present work is the determination of the Mo/Mo(III) potential which can be put in the emf series developed by Laitinen and co-workers (3, 5). For this series, the metal chlorides are dissolved in LiCl-KCl to the extent of 1 mole/l at 450°C. By extrapolation the molybdenum value is −0.603 ± 0.002v with respect to $Pt/PtCl_2$ (1M). It is more noble than Sb/Sb(III) by 32 mv and less noble than Bi/Bi(III) by 50 mv.

As already seen, only partial quantities for $MoCl_3$ in solution can be determined, and they cannot be related to pure liquid $MoCl_3$ which does not actually exist and for which hypothetical thermodynamic data are not available. One might express the partial quantities relative to pure solid $MoCl_3$, but the numbers would have only a very limited usefulness.

There is another standard state which might be employed and that is the infinitely dilute solution in the LiCl-KCl electrolyte. But over the entire concentration range activity coefficients are constant for each temperature. With the present data, therefore, reference to the infinitely dilute solution is a trivial calculation.

The potential-temperature data of Ryzhik and Smirnov (2) are precisely linear, and the present author has extrapolated them to 500°C. For their cell containing 2.58 w/o Mo in molten KCl (2.12 mole % of $MoCl_3$), the potential *vs.* Cl^-/Cl_2 is −1.403v. The molybdenum electrode with the same mole fraction composition in the LiCl-KCl solvent exhibits a potential of −0.910v *vs.* Cl^-/Cl_2 at 500°C. Lithium ion is smaller than potassium ion. In the LiCl-KCl solvent, therefore, the anions are closer to the solvent cations and less available for solvation of the molybdenum ion. Thus a more negative potential in pure KCl is predicted, but the effect is greater than expected. It is equivalent to 34 kcal/mole, much too large to be explained by small variations in Mo-Cl distances. Perhaps it represents a real difference in the structure of solutions in molten LiCl and molten KCl. A general discussion of these effects is given by Blander (7). Further measurements with pure LiCl and NaCl would certainly be of interest and might clarify the situation.

Manuscript received March 18, 1965; revised manuscript received Sept. 9, 1965. This paper was presented at the San Francisco Meeting, May 9-13, 1965.

Any discussion of this paper will appear in a Discussion Section to be published in the December 1966 JOURNAL.

REFERENCES
1. S. Senderoff and A. Brenner, *This Journal*, **101**, 16, 31, (1964).
2. O. A. Ryzhik and M. V. Smirnov, *Izv. Vysshikh Uchebn. Zavedenii, Tsvetn. Met.*, **6** (6), 103 (1963).
3. H. A. Laitinen and J. W. Pankey, *J. Am. Chem. Soc.*, **81**, 1053 (1959).
4. H. A. Laitinen, R. P. Tischer, and D. K. Roe, *This Journal*, **107**, 546 (1960).
5. H. A. Laitinen and C. H. Liu, *J. Am. Chem. Soc.*, **80**, 1015 (1958).
6. E. R. Van Artsdalen and I. S. Yaffe, *J. Phys. Chem.*, **59**, 118 (1955).
7. M. Blander, "Molten Salt Chemistry," pp. 191-193, Interscience Publishers, New York (1964).

Hyper-Maintenance of Electroluminescence

W. Lehmann

Westinghouse Electric Corporation, Research & Development Center, Pittsburgh, Pennsylvania

ABSTRACT

Electroluminescent ZnS:Cu becomes extremely deterioration-resistant after firing or refiring in pure sulfur. Additional air bake is permissible. The emission does not deteriorate toward zero, but toward a finite equilibrium which, in best cases, may be more than 50% of the original intensity. These "hyper-maintenance" phosphors permit high brightness (by excitation with high frequency) to be maintained over long time. The deterioration is considered to be due to sulfur vacancies diffusing from the particle surfaces into the interior.

The electroluminescence of powdered ZnS or (Zn, Cd)S phosphors embedded in an insulating medium and excited by an alternating electric field usually deteriorates with a rate which is nearly inversely proportional to the frequency, but which depends little or not on the amplitude of the exciting field (1). Therefore, it has become customary to characterize the maintenance behavior of a phosphor by the number of cycles required to deteriorate the emission intensity to 50% of its original value. This half-life is in the order of 10^7 to 10^8 cycles of continued operation in case of an ordinary ZnS:Cu,Cl phosphor embedded in a plastic dielectric and operated in dry air at room temperature. Thornton improved this half-life by a factor of roughly two to ten, *i.e.*, up to about 10^8 to 10^9 cycles, by means of air baking (2). A similar improvement is achieved if the phosphor is embedded in a ceramic (instead of a plastic) dielectric. Jaffe observed that replacement of the chlorine by bromine resulted in another improvement by a factor of 5 or more (3) which extended to obtainable half-life up to 10^9 to 10^{10} cycles.

We discovered that green emitting ZnS:Cu,Br or corresponding (Zn,Cd)S phosphors become extremely deterioration resistance if they are fired, or refired, in an atmosphere consisting of approximately 100% sulfur vapor provided only that the phosphor is in actual contact with the sulfur when it cools down after firing. The latter condition is essential. If the phosphor is fired and cooled in sulfur, the maintenance is good. If it is fired in sulfur but cooled in nitrogen or argon, the maintenance is poor. If it is fired in argon but shortly refired and cooled in sulfur, the maintenance is good. It is permissible also to use Thornton's air bake procedure on sulfur-fired phosphors and, in fact, this combination gave the longest living phosphors.

The emission intensity of an electroluminescent phosphor so prepared usually does not deteriorate with time to zero but to a finite level and, in some cases, this finite level may be higher than 50% of the zero-hour intensity so that the "half-lifes" of these phosphors appear to be infinitely long. This behavior was called "hyper-maintenance." The investigation on hyper-maintenance of electroluminescence is as yet not considered to be complete. Nevertheless, some observations and conclusions may be communicated.

Life tests on hyper-maintenance phosphors naturally require much time and, in contrast to ordinary electroluminescent phosphors, cannot be accelerated by excitation with a higher frequency since their deterioration is not inversely proportional to, but almost or completely independent of, the exciting frequency. For this reason, hyper-maintenance phosphors show their best performance at high frequency (typically in the order of 10 kcps) where ordinary phosphors would deteriorate within a relatively short time. It is thus possible with hyper-maintenance phosphors excited with high frequency to maintain substantial brightness over long times. However, an accelerated deterioration of hyper-maintenance phosphors with increasing electric field strength was observed, also in striking constrast to the behavior of ordinary electroluminescent phosphors whose maintenance is almost or completely independent of the field strength.

The zero-hour brightness of a good hyper-maintenance ZnS:Cu phosphor usually is somewhat lower (roughly between 50 and 100%) than that of a standard ZnS:Cu phosphor. However, several per cent of the ZnS may be replaced by CdS (4) which, beside the well-known color shift of the emission, causes all traps to become somewhat shallower (5) and, therefore, an extension between the approximate proportionality between emission intensity and frequency up to higher frequencies. Hence, hyper-maintenance is most successfully combined with (Zn,Cd)S phosphors to be excited by high frequencies and, under this condition, even the zero-hour brightness of a hyper-maintenance phosphor may be better than that of a standard ZnS phosphor. Typical data are compared in Table I.

Some deterioration curves measured on (Zn,Cd)S:Cu phosphors are shown in Fig. 1 and 2. The phosphors corresponding to Fig. 1 are fired in sulfur and air baked. They differ only in their CdS concentration (and, hence, somewhat in their emission color) but not in their maintenance (exceeding the unavoidable limit of accuracy of the measurements). Each curve in Fig. 2 is the average of measurements on four phosphors containing Cl, Br, or I, respectively. All samples containing Cl and Br are green emitters while the four iodine containing samples emit blue. The superiority

Table I. Zero-hour emission intensity of a hyper-maintenance ZnS(90%), CdS(10%):Cu,Br phosphor compared with a standard ZnS:Cu,Cl phosphor

Phosphor	(Zn,Cd)S:Cu,Br (hyper-maintenance)		ZnS:Cu,Cl (standard)	
Frequency (cps)	60	5000	60	5000
Brightness (ft-L)	2.2	230	3.2	140
Quanta (arb. units)	3.1	320	5.3	300
Emission color	Yellow-green		Green	

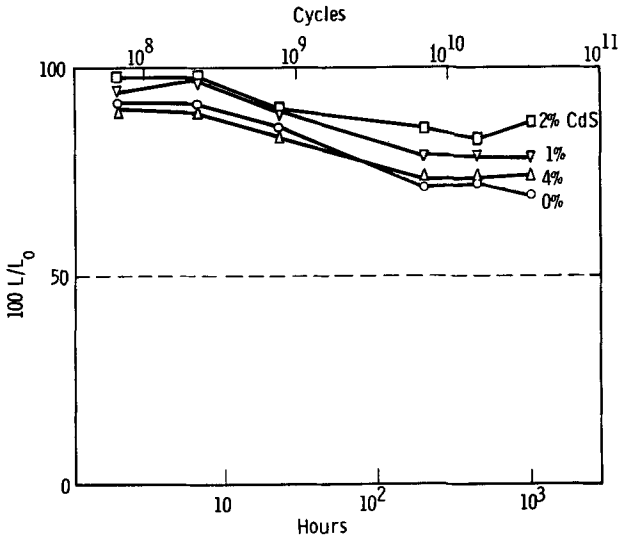

Fig. 1. Deterioration curves measured on several (Zn,Cd)S:Cu,Br phosphors, all sulfurized and air baked, operated in dry air at room temperature, 10 kcps.

of Br over Cl and I is clearly to be seen, and the approach of the curves corresponding to Br containing phosphors to finite and rather high brightness levels after long time of operation is quite obvious.

The observed effect of sulfur and air (*i.e.*, oxygen) on the maintenance of electroluminescence gives a clue as to a possible mechanism of deterioration. It is assumed that the phosphor deteriorates because of a creation of deep traps due to sulfur vacancies which, under the combined action of temperature and electric field, diffuse from the particle surface into the interior. This assumption is in agreement with many observations:

(*A*) Indications are that a commonly observed glow peak at about —125°C is due to sulfur vacancies (5, 6). However, the latter must be expected to be double donors producing two glow peaks. Although considerable uncertainty still exists, the second level may be the one responsible for a frequently observed glow peak at about —50° to —20°C which was observed by Jaffe (3) to increase strongly during deterioration.

(*B*) The deterioration effect is temperature dependent and proportional to $\exp(-E/kT)$ where E is some

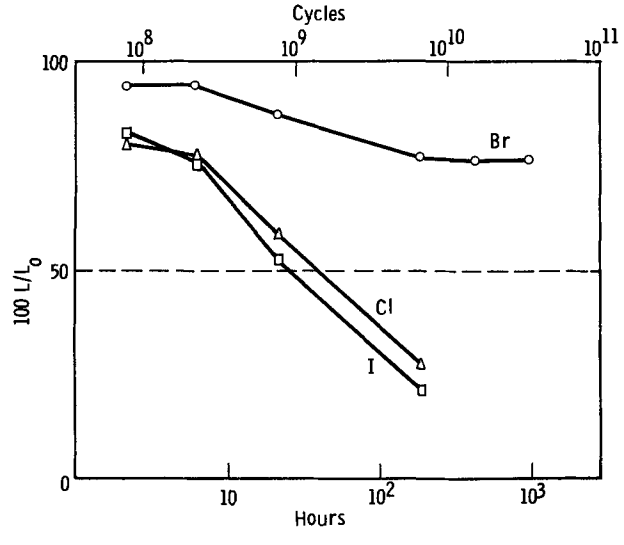

Fig. 2. Average deterioration curves (each 4 samples) measured on (Zn,Cd)S:Cu phosphors made with Cl, Br, or I, respectively. The phosphors are sulfurized and air baked, operated in dry air at room temperature 10 kcps.

energy (1). This indicates some kind of diffusion process involved, as already assumed by several workers.

(*C*) Maintenance improves with the particle size of the phosphor (1). Hence, an influence of a competition between particle surface (or surface-near parts) and the volume is indicated. Since glow peaks do build up during deterioration, a diffusion of something responsible for the additional glow peaks from the surface into the volume seems to take place.

(*D*) The most obvious way to improve the maintenance is to take care that little or no sulfur vacancies are available at the surface of a phosphor particle ready to diffuse into the volume, *i.e.*, the surface atoms of each particle shall be mostly sulfur rather than zinc atoms. Such a phosphor particle has only a limited number of sulfur vacancies available ready to diffuse into the volume, so that its emission does not deteriorate toward zero but toward a finite level. The particle has then used up all available sulfur vacancies from its surface and remains at a finite brightness level without any further deterioration provided only that no new sulfur vacancies are created at the surface.

(*E*) Sulfur vacancies may be occupied also by other anions, *e.g.*, by oxygen. Hence, a bake in oxygen [or in air (2)] improve the maintenance considerably while a bake in a neutral atmosphere (*e.g.*, argon) has little or no effect.

(*F*) ZnSe phosphors can be expected to contain fewer anion vacancies on their particle surfaces than ZnS because selenium is less volatile than sulfur. Hence, the life time of electroluminescence of ZnSe phosphors can be expected to be better than that of ZnS phosphors, in general agreement with experience.

(*G*) Water may cause a break of the Zn-S bond between surface atoms of a ZnS crystal so that, originally, equimolar amounts of Zn and S are effectively removed from the crystal. The reaction requires a certain energy which may be supplied by ultraviolet irradiation or, in case of electroluminescence by the same electric field which excites the phosphor. Various, and not too well understood, further reactions between the liberated Zn, the S, and the surrounding (*e.g.*, the water) are possible. These secondary reactions seem to cause a desulfurization of the particle surfaces. At least, liberated zinc frequently appears during exposure to ultraviolet (Lenard), or during electroluminescence in the presence of water (7), and can be observed visually as a very thin, dark deposit on the particle surfaces. Free surface zinc is identical to sulfur vacancies on the particle surfaces, ready to diffuse into the particles.

The proposed deterioration mechanism is accessible to a semiquantitative analysis. Let the time-average of steady-state emission be $L = \beta/M$ where M is the concentration of deep traps in the particle volume, and where β represents all other parameters. It must be supposed that the traps denoted by M are deep enough that a captured electron has little chance of escape during one cycle of the applied frequency. The concentration of sulfur vacancies at or near the surface may be C. When they diffuse into the volume, they decrease at a rate proportional to C which gives

$$C = C_o \exp(-\alpha t) \qquad [1]$$

where C_o and α are constants, and t is the time. Simultaneously, the concentration of deep traps in the volume increases with the same rate

$$dM/dt = -dC/dt = \alpha C_o \exp(-\alpha t)$$

which gives

$$M = M_o + C_o [1 - \exp(-\alpha t)] \qquad [2]$$

Hence, the emission intensity at any given time, normalized to the "zero-hour" intensity L_o, is

$$L/L_o = M_o/M = \{1 + (C_o/M_o)[1 - \exp(-\alpha t]\}^{-1} \qquad [3]$$

This is a function of the ratio L/L_o on the variable αt with one parameter, the ratio C_o/M_o. The function is

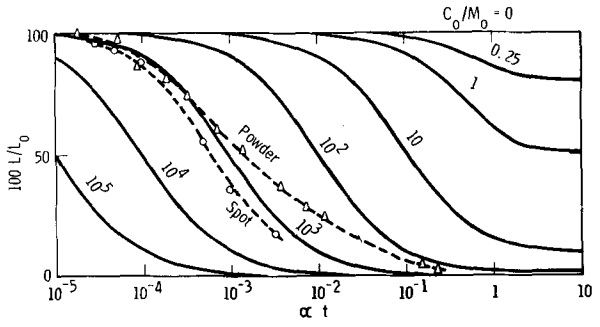

Fig. 3. Function of Eq. [3] for various values of C_o/M_o (solid curves). Experimental values measured on a powder (standard ZnS:Cu,Cl, dashed curve) and at a single emitting spot in a phosphor particle (dotted curve) are plotted on an arbitrary time scale.

shown in Fig. 3 where the curves with the lowest ratios of C_o/M_o, *i.e.*, those representing the best maintenance, do approach rather substantial values of L/L_o for $\alpha t \rightarrow \infty$. In contrast, the curves with high values of C_o/M_o, representing poor maintenance, do not only go down very soon, they also approach finite values of L/L_o very close to zero. In this case of $C_o >> M_o$, Eq. [3] reduces to $L/L_o = 1/(1 + t/\tau)$ where $\tau = M_o/(C_o\alpha)$ which is the hyperbolic decay first reported by Roberts (8).

These equations represent ideal cases only. In practice, the situation most certainly is obscured by many complications so that a more detailed calculation seems to have little sense. One complication is the fact that all real phosphors contain particles of many different sizes and, hence, different deterioration rates. If the deterioration curve of such real phosphor containing a wide particle size distribution is analyzed, one finds that the curve becomes somewhat shallower but never steeper than the ideal curves described by Eq. [3]. This is also in agreement with experiment. Figure 3 shows the deterioration curve measured on a real phosphor (a standard ZnS:Cu,Cl) which, indeed, is shallower than the ideal curves. The other experimental curve in Fig. 3 is that measured on a single emitting spot inside of one particle [measured by Haberland (9)]. One may safely assume that we are much closer to ideality in this case than in the case of a phosphor containing many particles and, indeed, the experimental curve follows the ideal ones very closely.

The proposed mechanism of a sulfur vacancy migrating from the particle surface into the volume is, of course, still a very crude approach to reality. Other atomic or ionic diffusions may occur besides those of sulfur vacancies. It is also possible that the assumption of only the outermost surface of a particle to be of influence is too extreme and that, in reality, surface-near layers several atoms deep are involved. These and other questions are still to be answered.

Acknowledgment

The writer is indebted to W. A. Thornton for help in measurements and to E. G. F. Arnott and P. H. Haberland for submission of experimental data.

Manuscript received May 6, 1965; revised manuscript received Sept. 3, 1965. This paper was presented at the Toronto Meeting, May 3-7, 1964.

Any discussion of this paper will appear in a Discussion Section to be published in the December 1966 JOURNAL.

REFERENCES

1. W. A. Thornton, *This Journal*, **107**, 895 (1960).
2. U. S. Pat. 3,082,344.
3. P. M. Jaffe, *This Journal*, **108**, 711 (1961).
4. W. Lehmann, *ibid.*, **110**, 759 (1963).
5. W. Hoogenstraaten, *ibid.*, **100**, 356 (1953).
6. H. Samelson and A. Lempicki, *Phys. Rev.*, **125**, 901 (1962).
7. I. L. Smith, R. M. Potter, and M. Aven, Paper presented at the Chicago meeting of the Society 1960, (Abstract No. 65).
8. S. Roberts, *J. Appl. Phys.*, **28**, 262 (1957).
9. P. H. Haberland, Private communication.

Anomalously Large Photovoltages in a New Photovoltaic Cell

P. N. Ramachandran and R. E. Salomon

Department of Chemistry, Temple University, Philadelphia, Pennsylvania

ABSTRACT

Unusual photoeffects have been observed in the cell Zr/ZrO_2/gas phase/M where M represents a metal plate of copper or brass and ZrO_2 is in the form of an anodic film. Photovoltages greatly in excess of the band gap of ZrO_2 are observed when Zr is cooled to liquid nitrogen temperatures and the anodized face of Zr and M are irradiated with ultraviolet light. The photovoltage increases with degassing time and with time of cooling and eventually reaches a steady maximum value. M can be replaced by a hot filament, and again large photovoltages are produced between Zr and the filament although only Zr need be irradiated in this case.

Photoeffects observed with anodized zirconium electrodes in which an electrolyte serves as a transparent contact have previously been reported (1, 2). The results of similar studies with aluminum and tantalum in which the electrolyte was replaced by a semitransparent evaporated metal coating have been described (3) and attributed to a work function difference between the contacts. Other workers (4) have interpreted the photoeffects arising with tantalum electrodes as due to a p-n junction within the oxide film. In a p-n junction photovoltaic cell the maximum photovoltage is limited to the width of the forbidden zone (5) which in the case of anodic ZrO_2 is about 5.5 ev (6). Photovoltages larger than this, as high as 90v, were reported by us (7) for anodized zirconium electrodes that were coated with a semitransparent metal, cooled to liquid nitrogen temperatures and then exposed to ultraviolet radiation of wavelength less than 2500Å. Although a number of other electrode systems have been reported to exhibit larger than band gap photovoltages (8, 9) the potential invariably appeared between contacts bounding a few centimeters of the photosensitive material and hence could be rationalized by various multiple junction mechanisms (10). Further studies on the low-temperature photoeffects occurring with anodized zirconium electrodes have led us to conclude that the electrical potential difference originally reported is actually developed between the zirconium and the grounded metallic cell chamber. The metallic chamber functioned as a photoemissive contact excited by stray ultraviolet light. This accidental finding led to the design of a new cell which

carefully defines the conduction path. It was also found that the evaporated metal film was unnecessary for the attainment of a larger than band gap photovoltage (LBGPV). Only a small voltage, less than 1v, was developed between zirconium and an evaporated metal coating on the oxide, when the electrode was cooled and irradiated with ultraviolet light. A somewhat larger photovoltage was obtained with this electrode when the experiment was carried out at room temperatures.

Since the LBGPV occurred in a system that was in some ways similar to an electrochemical cell, with the gas phase replacing the usual electrolyte, a new variable, namely the composition of the gas phase is available for study. It was therefore desirable to carefully define the conditions necessary for the attainment of a LBGPV in the cell Zr/anodic ZrO_2/gas phase/M. M refers to a photoemissive metal electrode, and both the anodic film and M are irradiated with ultraviolet light. In this paper a description of the construction, operation, and results obtained with this cell are given.

Experimental

Zirconium bars obtained from the Wah Chang Corporation, Albany, Oregon, containing about 1000 ppm total impurities were used in most of the studies. The use of other sources of supply did not lead to any noticeable differences in results. One face of the bar was mechanically abraded and polished and then etched in a manner previously described (7). The electrodes were rinsed in distilled water and transferred to an anodization beaker before the surface dried. Most of the anodizations were carried out at 30.0°C in a sodium borate-boric acid solution buffered at a *p*H of 8.

The formation voltage was raised slowly over a period of 5 min to the desired value and maintained for 24 hr. After anodization the electrode was washed, dried, and placed in the electrode chamber shown in Fig. 1.

The electrode chamber was fabricated from Pyrex except for the two quartz windows. The chamber was electrically shielded with ¼ in. copper plate. The electrode was mounted on a copper block which was soldered to a kovar seal. The copper block sealed the bottom of a demountable Dewar to which liquid nitrogen could be added for the attainment of low temperatures. A thermocouple was fastened to the Zr by means of a set screw. Electrode M was mounted in a similar manner at a distance of 5 cm from the Zr electrode. In this manner both Zr and M could be irradiated independently using the same light source. The light source was a GE UA-2 Uviarc mercury lamp. The lamp was positioned approximately 12 cm from the face of both electrodes. The lamp was air cooled and found to be steady in output after a short warmup time. Although the intensity could be varied by controlling the lamp voltage it was necessary to use neutral filters to vary the intensity because of the variation of spectral output with lamp voltage. Unfortunately, the intensity of the incident illumination cannot be given because the high light levels required could only be achieved through the use of polychromatic light.

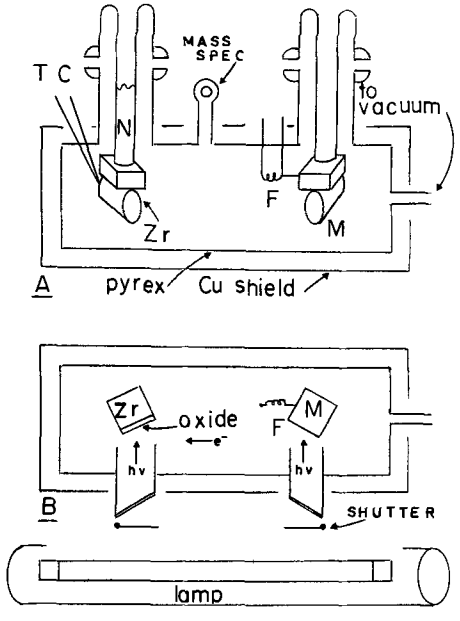

Fig. 1. Electrode chamber and light source: *A*, front view. *B*, top view.

Pressures as low as 10^{-6} Torr could be achieved by means of a liquid nitrogen trapped oil diffusion pump. A mass spectrometer was used to determine partial pressures. Potentials were measured with both a Keithley 621 electrometer and a L&N Millivolt Indicator in conjunction with a bucking circuit. These instruments essentially measure open-circuit potentials. By shunting the electrode with a 10 megohm resistor both instruments measure short circuit photocurrents because of the high impedance of the electrode.

In some cases metal M was replaced by a small tungsten filament which was permanently fixed in a position outside of the incident light beam.

The LBGPV was studied as a function of degassing time, cooling time, anodizing solution, formation voltage, light intensity, and partial pressure of oxygen. When M was replaced by the tungsten filament the LBGPV was studied as a function of filament current. Both open-circuit photovoltages and short circuit photocurrents were measured.

Results

A quantitative description of the photovoltaic effects associated with the cell described is precluded because of the complicated hysteresis of the system. Certain generalizations, however, are quite apparent, and an examination of the data to follow will show this.

The LBGPV could only be obtained on systems which were degassed for over 24 hr and in which the zirconium electrode was cooled to about 80°K for several minutes. In this temperature range the photovoltage was at most a slowly varying function of temperature. It was necessary to irradiate simultaneously both the anodized face of Zr and M with light of wavelength less than 2500Å or to replace M by an elec-

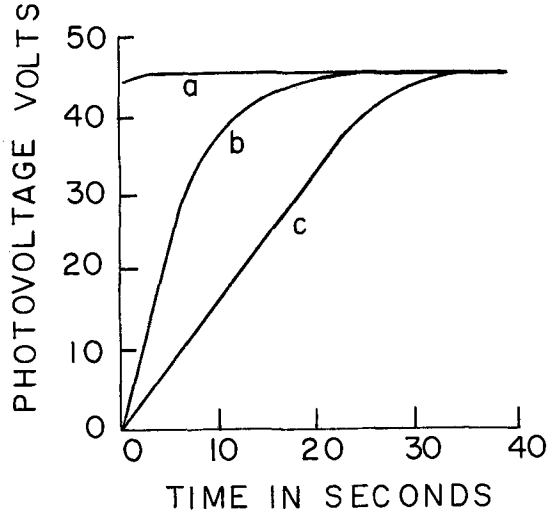

Fig. 2. Typical chronopotentiograms for a Zr/ZrO_2 (formation voltage of 60v)/gas phase (10^{-4} Torr)/Cu. a, pre-irradiated Zr, relative intensity 1.75; b, relative intensity 1.75; c, relative intensity 1.00.

trically heated tungsten filament, F, while Zr alone was irradiated in order to obtain the LBGPV. Stable measurements could only be obtained when the cell was well shielded and the potential measured with high impedance electrometers.

Zirconium always became negative with respect to M or F. The potential rises to a maximum value in a period of minutes. The rate of approach to this maximum depended on the light intensity although at the light levels used, the maximum photovoltage was independent of intensity as can be seen in Fig. 2. At room temperature the cell behaved as an electrically open circuit even when both electrodes were exposed to ultraviolet light.

In general it was found that electrodes anodized in sodium borate-boric acid buffer solutions developed somewhat higher photovoltages compared to electrodes anodized in citrate or phosphate buffers when all other parameters were held constant. When all other parameters were maintained at a constant value the maximum photovoltages increased as the logarithm of the oxygen pressure for the three pressures which were experimentally accessible. Some auxiliary experiments showed that only oxygen among all the residual gases caused an enhancement of the photovoltage. Photovoltages and short circuit photocurrents for the various gas mixtures are given in Table I.

The increase of the photovoltage with cooling time after a 48-hr degassing period can be seen by the data in Table II. The results indicate that the effect of cooling is not completely reversed by bringing the electrode to room temperature. This was the reason why the same sample was not anodized successively to higher voltages and the photovoltage measured at each point. In particular, it is to be noted that in several cases the photovoltage does not change after several hours of cooling.

When the filament was used in place of M it was found that small changes in filament current did not affect the maximum photovoltage, but did affect the rate of increase of the photovoltage. The results were similar to those shown in Fig. 2 with filament current replacing light intensity as the third variable. The short-circuit photocurrent, however, was quite sensitive to filament current as is shown in Fig. 3. It is to be noted that the system was not at saturation.

In some cases M consisted of an unanodized zirconium bar which was also cooled to liquid nitrogen temperatures. The observation of the LBGPV with this system indicates the importance of the anodic film and eliminated the necessity to consider thermoelectric effects.

One experiment which was considered quite revealing involved the simultaneous irradiation of M and Zr after Zr alone had been irradiated for over a minute. The open-circuit photovoltage reached its maximum value in a few seconds. When the sequence was reversed the photovoltage rise curve was identical to that obtained when both electrodes were irradiated without prior irradiation. This is shown in Fig. 2.

Table I. Maximum photovoltage and short-circuit photocurrent as a function of gas pressure at constant light intensity for a Zr/ZrO_2 (60v)/gas phase/Zr cell with two similar electrodes

Electrode No.	$p\ H_2$ Torr	$p\ O_2$ Torr	$p\ N_2$ Torr	$p\ H_2O$ Torr	Photovoltage, v	Photocurrent, amp
1	5×10^{-5}	2×10^{-6}	1×10^{-5}	9×10^{-7}	56	1.2×10^{-9}
1	—	2×10^{-7}	2×10^{-6}	7×10^{-7}	44	0.9×10^{-9}
1	5×10^{-7}	1×10^{-7}	3×10^{-6}	4×10^{-7}	41	0.7×10^{-9}
2	—	4×10^{-6}	2×10^{-5}	8×10^{-7}	32	1.4×10^{-9}
2	—	3×10^{-7}	2×10^{-6}	5×10^{-7}	28	1.0×10^{-9}
2	—	2×10^{-7}	4×10^{-6}	4×10^{-7}	25	0.8×10^{-9}

Table II. Maximum photovoltage as a function of pressure and time of cooling for a Zr/ZrO_2/gas phase/Cu cell

Electrode No.	Formation voltage, v	Total pressure, Torr	Time of cooling, min	Maximum voltage, v
1	100	3×10^{-5}	10	10
1	100	3×10^{-5}	20	20
1	100	3×10^{-5}	45	27
1	100	3×10^{-5}	60	30
1	100	3×10^{-5}	75	30
1	100	3×10^{-5}	Several hours	30
1 (after warm up)*	100	6×10^{-4}	15	21
1	100	6×10^{-4}	30	35
1	100	6×10^{-4}	60	45
1	100	6×10^{-4}	90	52
1	100	6×10^{-4}	120	52
1	100	6×10^{-4}	Several hours	52
4	60	6×10^{-4}	30	1.6
4	60	6×10^{-4}	45	2.4
4	60	6×10^{-4}	55	3.3
4	60	6×10^{-4}	80	4.7
4	60	6×10^{-4}	155	13.0
4	60	6×10^{-4}	275	28.0
4	60	6×10^{-4}	Several hours	97.0

* The electrode was brought to room temperature.

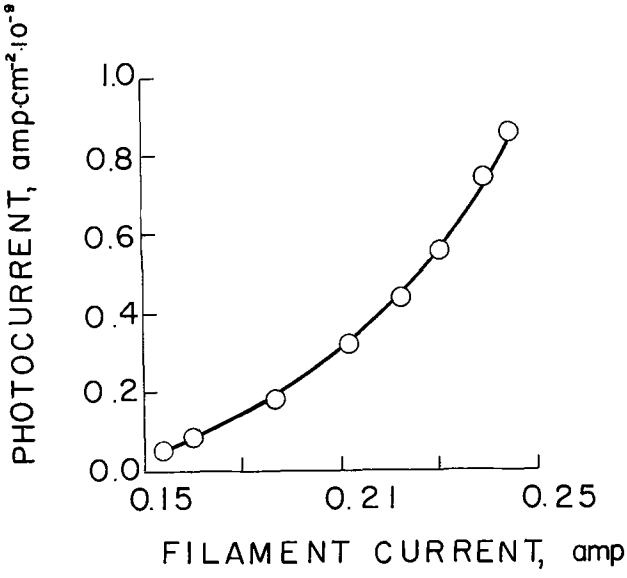

Fig. 3. Short-circuit photocurrent vs. filament current at constant light intensity for a Zr/ZrO_2 (formation voltage of 60v)/gas phase (10^{-4} Torr)/filament.

Discussion

It is easy to define the conduction path in the cell described and account for potentials up to 5 or 6v. The effect of oxygen is also quite understandable. Conduction in the gas phase is electronic and originates at the photoemissive or thermionic emissive electrode. The long degassing period at room temperature frees the oxide film from trapped oxygen. At low temperatures, oxygen is adsorbed at the oxide film-gas phase interface. An insulator which is bordered by a metal with a low work function and a strongly electronegative component such as oxygen will become polarized so that the electrochemical potential becomes uniform throughout. The absorption of light by the film leads to the creation of holes and electrons, the latter moving toward Zr and the former toward the adsorbed negative oxygen ions which thereby become discharged. Electrons arriving from the emissive contact recharge the adsorbed oxygen layer. The driving force in the process is the oxidation of zirconium. The linearity of the photovoltage with the logarithm of the oxygen pressure is suggestive of a reversible cell. Of course, even if such a reversible cell could be prepared the potential could hardly be expected to exceed 10v. The difference between the rise curves obtained when Zr or M is pre-irradiated, followed by the simultaneous irradiation of both, conforms to the general description presented. The lag is probably related to

deep lying traps in the oxide film. It was noted that the photopotential decayed extremely slowly when the illumination was discontinued and this is another characteristic of a photoconductor with deep lying traps.

The conventional mechanism for photovoltaic cells cannot be used to account for the effects reported. The reasons for this may lie in the nonuniform nature of the oxide although it is difficult to conceive of a circumstance which would enable the results to conform to the general theory. One cannot entirely rule out the possibility of multiple thin junctions which could add photovoltages in a series fashion, although their existence seems unlikely. Without invoking multiple junctions it would appear that the present day theory of photovoltaic effects is not generally applicable.

Acknowledgment

The authors wish to thank the United States Atomic Energy Commission (Contract No. AT 30-1-2775) for supporting this work. This paper is based on a Dissertation presented to the Graduate School, Temple University, in partial fulfillment of the requirements for the Ph.D. degree by one of the authors (P.N.R.).

Manuscript received June 23, 1965; revised manuscript received Sept. 27, 1965.

Any discussion of this paper will appear in a Discussion Section to be published in the December 1966 JOURNAL.

REFERENCES

1. A. Charlesby, *Acta. Met.*, **1**, 348 (1953).
2. R. E. Salomon, G. B. Adams, and W. M. Graven, *This Journal*, **110**, 1163 (1963).
3. W. Ch. van Geel, C. A. Pistorius, and P. Winkel. *Philips Res. Repts.*, **13**, 265 (1958).
4. L. Apker and E. A. Taft, *Phys. Rev.*, **88**, 58 (1958).
5. J. Tauc, "Photo and Thermoelectric Effects in Semiconductors," p. 122, Pergamon Press, New York (1962).
6. R. E. Salomon, W. M. Graven, and G. B. Adams, *J. Chem. Phys.*, **32**, 310 (1960).
7. P. N. Ramachandran and R. E. Salomon, *J. Phys. Chem. Solids*, **24**, 583 (1963).
8. L. Pensak, *Phys. Rev.*, **109**, 601 (1958).
9. V. M. Lyubin and G. A. Fedorova, *Soviet Physics Doklady*, **5**, 1343 (1960).
10. L. Pensak, "Structure and Properties of Thin Films," p. 503, C. A. Neugebaur, J. B. Newkirk, and D. A. Vermilyea, Editors, John Wiley & Sons, Inc., New York (1959).

Precipitates of Phosphorus and of Arsenic in Silicon

M. L. Joshi

Systems Development Division, International Business Machines Corporation, East Fishkill, New York

ABSTRACT

Precipitate particles were observed through transmission electron microscopy at different depths in silicon wafers diffused with a very high concentration of phosphorus. The precipitates, believed to be phosphorus complexes, were of various shapes, square, rod-like, and hexagonal, with no definite orientation in the silicon matrix. Silicon wafers diffused with high concentration of arsenic also showed elongated precipitate structures with no definite orientation.

The electric properties of semiconducting materials such as germanium and silicon doped with impurities belonging to the III and V columns in the periodic table and in excess of 10^{19} at./cc are found sensitive to precipitation phenomena (1-4). The precipitates of phosphorus in Si diffused with phosphorus ($C_s \approx 10^{21}$/cc) have been directly observed with the technique of transmission electron microscopy (5, 6). Arsenic precipitation was also observed with the same technique in germanium (1). These precipitates have been reported to account for the difference between the total concentration and the electrically active concentration (1, 3, 7). It has been fairly well established that, in general, there is a limit to the substitutional accommodation of the III and V column impurities in silicon and germanium, and the amount exceeding this limit is expected to be in the interstitial sites or in precipitates.

In this paper, we are submitting further evidence of precipitates caused by diffusion of high amounts of phosphorus and arsenic in silicon and observed through transmission electron microscopy. Phosphorus precipitates are observed in specimens diffused from both P_2O_5 and PH_3 sources. Their growth has been shown to be sensitive to the rate of cooling from the diffusing temperature.

Experimental

Diffusion.—Phosphorus.—Two wafers (10-mil thick and 1 in. in diameter were cut parallel to (111) from a Czochralski-grown boron-doped ($\approx 10^{15}$ cm^{-3}) silicon single crystal of low dislocation density ($\approx 10^3$ cm^{-2}). The silicon wafers were lapped and chemically polished to remove any surface damage. The wafers were diffused (in an open tube furnace configuration at 1150°C) from a P_2O_5 source. One of the wafers was removed from the diffusion furnace and allowed to cool on a quartz platform in room air. The removal of the other wafer, through the furnace tube, was done with a slower speed than the above, allowing it to cool to about 600°C at the open end of the tube furnace and then was permitted to cool on the quartz platform.

A wafer lapped and polished similarly to remove the surface damage was diffused to about 2μ depth with phosphorus from a phosphine (PH_3) source. The diffusion was done in an open tube furnace configuration at 970°C with a proper mixture of PH_3, O_2, and N_2 flowing over the wafers. The phosphorus surface concentration was found to be $\approx 2 \times 10^{21}$ at./cc.

Arsenic.—Arsenic was diffused (surface concentration $\approx 5 \times 10^{20}$ cm^{-3} and junction depth = 2μ) in an evacuated closed quartz capsule (vacuum $\approx 10^{-6}$ Torr) into a boron-doped ($\approx 1.5 \times 10^{16}$ cm^{-3}) silicon wafer (at 1100°C) previously treated for the removal of the surface damage. Elemental arsenic was used as the source of diffusion. The quartz capsule prior to sealing was cleaned with a HF-HNO_3 mixture, rinsed, and heated to 1000°C to remove moisture.

Specimen preparation.—The specimen preparation was similar to that reported in the earlier article (5). To obtain transparency to the electron beam of the microscope, the samples were chemically polished down to a few thousand angstroms from the other side of the surface under study using the solution (5) usually used for chemical polishing of the lapped wafers. It is of advantage to use slightly warmer solution than that at the room temperature.

Observations

A Philips electron microscope (100B) was used for transmission electron microscopy of the specimens.

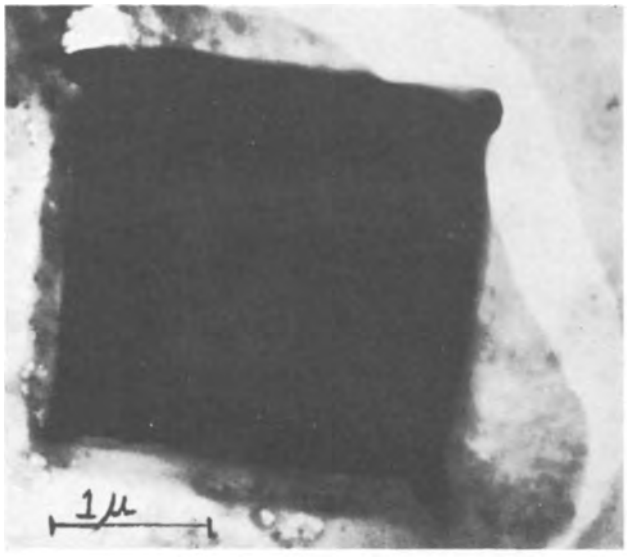

Fig. 1a. Phosphorus (source, P_2O_5) diffusion induced square particle in the layer $\frac{1}{4}\mu$ deep in the diffusion profile. Magnification 46,000X. The particle before acid washing.

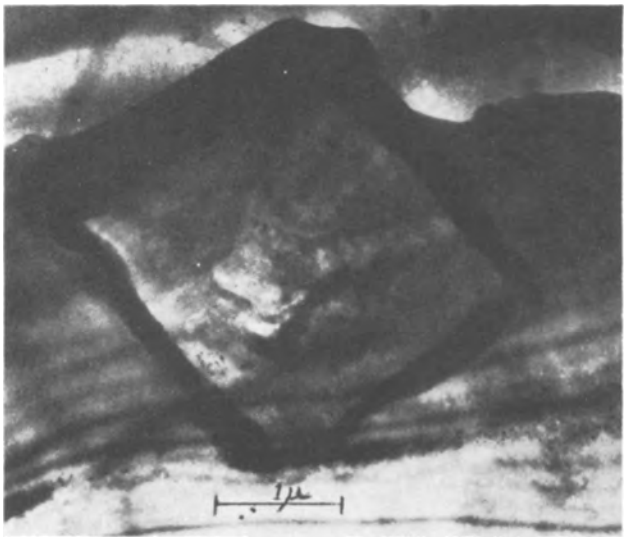

Fig. 1b. The same particle as shown in Fig. 1a after acid washing

Particles believed to be precipitates of phosphorus were observed throughout the diffused layers (P_2O_5 source). Figure 1a shows a dark square particle (at the depth of $\frac{1}{4}\mu$) with the broken film of silicon around. Mixtures used for electro- or chemical thinning have a tendency to leave a surface deposit on the specimen, sometimes as distinct foreign particles. Washing of the specimen in HNO_3 and subsequently in HF should remove some of these; washing in acetone and water removes "dirt" soluble in these solvents. This procedure of washing is illustrated in Fig. 1a and 1b. Figure 1b shows the square particle after washing for a short time (less than half a minute), and the dark film visible in Fig. 1a seems to be partially washed away. Since the specimen has a thickness of about 5000Å, a large particle like this could partially emerge on both sides of the film after intensive washing. Then it is found that the impurities intrinsic to the square particle start washing away very fast. However, the local misorientation in the matrix due to precipitation persists. Figure 2 shows phosphorus precipitates at the depth of $1\frac{1}{2}\mu$ in the same wafer; some of them are square, some rectangular, and some partly hexagonal. There is no significance with regard to the orientation of these precipitates in the silicon lattice. Figures 3a and 3b are the bright field and dark field micrographs (under a strong <220> operative reflection) of the

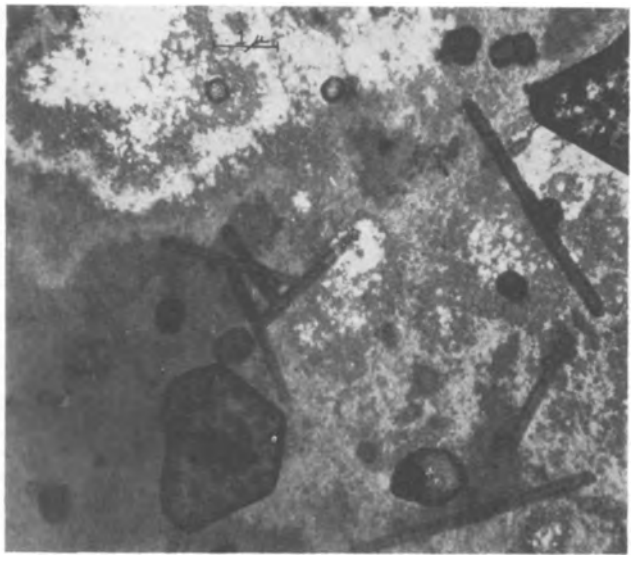

Fig. 2. Phosphorus (source, P_2O_5) diffusion induced precipitates in the layer $1\frac{1}{2}\mu$ deep in the diffusion profile. Magnification 50,000X.

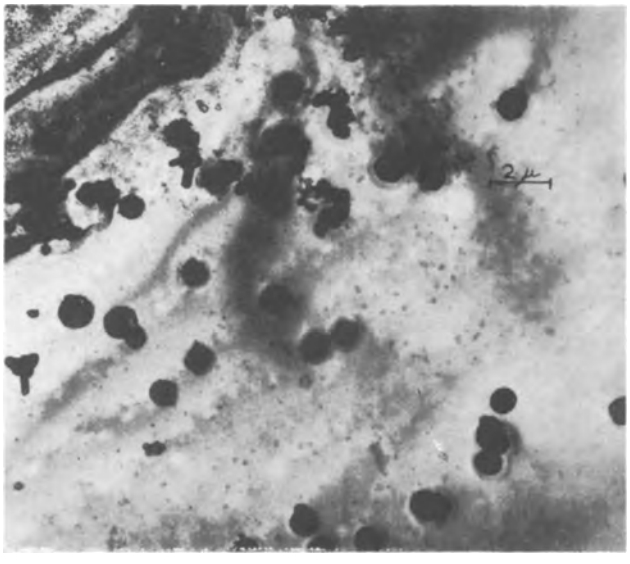

Fig. 3a. Phosphorus (source, PH_3) diffusion induced precipitates in the layer 0.2μ deep in the diffusion profile. Magnification 19,000X. Bright field view.

precipitates at the depth of 0.2μ in a sample diffused with phosphorus using the phosphine source. The similarity between these and those observed in Fig. 2 is obvious. Figures 4a and 4b are believed to represent the precipitates decorated with copper and are 5 to 10μ in size, as seen through reflection microscopy using white light.

The copper-decorated precipitates, observed by reflection microscopy, were found to lie at the depth of 1μ in the sample cooled with a deliberate slow speed from the diffusion temperature. Copper decoration of the precipitates was accomplished as follows: The method of the anodic oxidation with which we arrive at a particular depth in the diffused sample involves use of a jig in which the silicon strip rests on a copper block (anode); the other side of the strip is exposed to the anodizing solution connected to a platinum cathode. A small portion of the copper block exposed to the anodizing solution provides a source of copper atoms which were deposited preferentially on the precipitates instead of on to the platinum cathode. Although the mechanism of this copper deposition is not understood, the effect indicates that there exists a certain negative charge on these precipitates. The size of

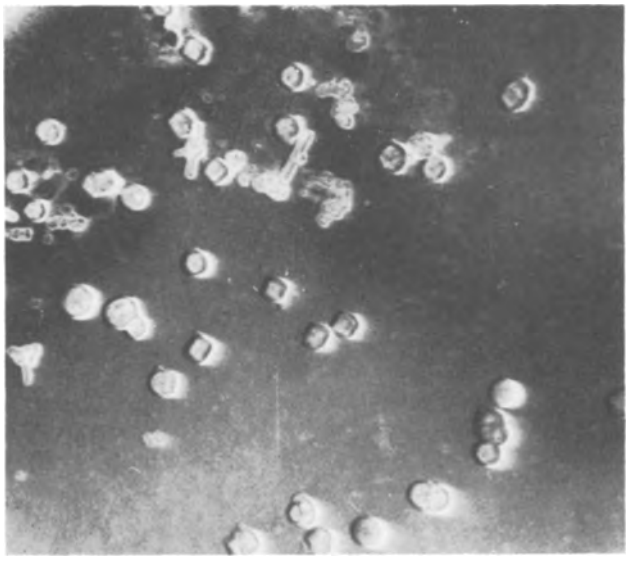

Fig. 3b. Dark field view corresponding to Fig. 3a

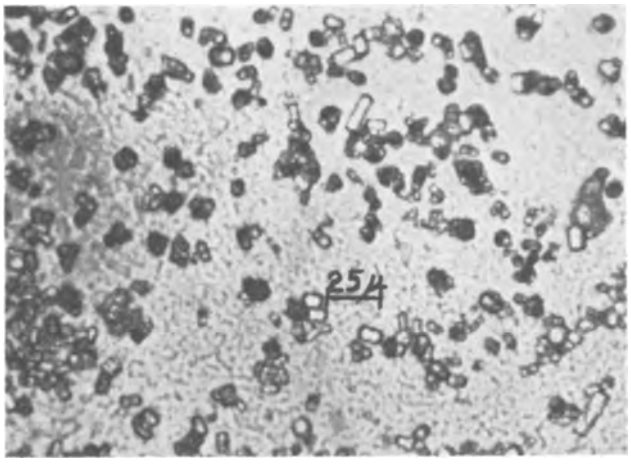

Fig. 4a. Particles developed by slow cooling from diffusion temperature and observed by optical microscopy. Magnification 530X.

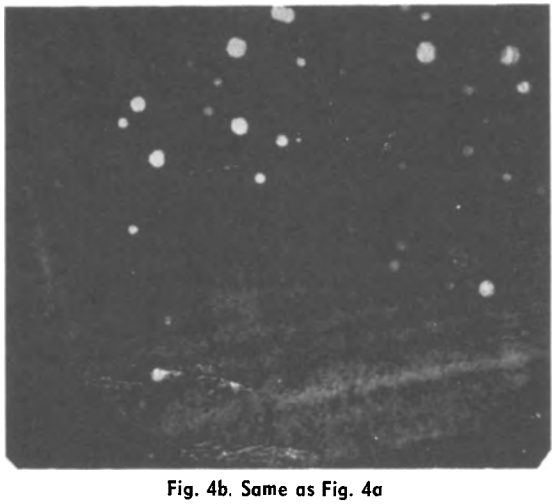

Fig. 4b. Same as Fig. 4a

these precipitates is much larger than those observed in the samples described earlier. The significant thing is that they are isomorphous with those observed by electron microscopy.

Figure 5 represents the observation under a strong <220> operative reflection of precipitates in the surface of an arsenic diffused sample. Again there are no specific directions in which the precipitates could be imagined to extend. No observation of precipitates could be made in the depths of the arsenic diffused profile.

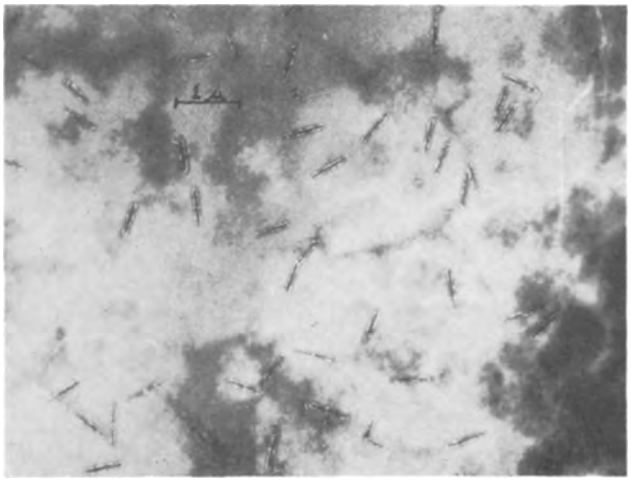

Fig. 5. Arsenic (source, elemental As) diffusion induced precipitates. Magnification 50,000X.

Only the particles of specific shapes are presented here, although diffused precipitation was often observed. Occasionally to determine whether a particular defect was structural or not, a dark field image was obtained (Fig. 3b). In thick regions Kikuchi lines were invariably observed in diffraction indicating that the strains involved in accommodation of these defects did not affect the lattice homogeneity. The selected area diffraction study is still inconclusive, since a rather speculative approach is needed regarding the definitive identification of their nature.

Discussion

Although it was not possible to establish positively the chemical nature of these precipitates, they can be reasonably assumed to originate during the diffusion. They could affect the electrical behavior of the junctions (8) and contribute to the deviations (1, 3). Recently neutron activation analysis was used to study the behavior of the phosphorus during its diffusion into silicon and silicon oxide films (7). This study confirms the existence of Si-P (7) phase in the surface layers of the silicon diffused with P_2O_5. The concentration of the phosphorus in the surface layer thinner than 0.1μ was shown to be of the order of 10^{22} at./cc which is an order of magnitude higher than the latest solid solubility limit established by the same technique. One could expect the precipitation of the second phase Si-P when the concentration is higher than this limit (7). However, the observation of the precipitates extends much deeper towards the junction indicating the formation of the second phase is not confined to the surface layers only. The growth of the precipitates (Fig. 4a, 4b) with slower cooling from the diffusion temperature is in agreement with the precipitation model (3). It is also important to note that the multiform precipitates of phosphorus and their indefinite orientation are not in accordance with the observations of Schmidt and Stickler (6). Consequently, it is not possible to support the crystal structure and the precipitation orientation of Si-P in relationship with silicon matrix, as deduced by the above authors.

Observation of the arsenic precipitates is also consistent with the interpretation of the deviation of diffusion profiles of arsenic from the strict erfc distribution (9). The precipitation in these samples is confined only to the surface. This implies that the arsenic surface concentration $\approx 5\times10^{20}$ cm^{-3} is not far away from the solid solubility limit. These precipitates also seem to be not isomorphous with those of Si-P.

Acknowledgments

The author wishes to thank F. Wilhelm, E. S. Wajda, J. N. Ramsey, J. G. Christ, and G. A. Silvey for their valuable help and encouragement. Thanks are due to J. Fairfield for reviewing the manuscript and giving

critical comments as well as to Harry Dee for editing the paper.

Manuscript received March 9, 1965; revised manuscript received Aug. 30, 1965.

Any discussion of this paper will appear in a Discussion Section to be published in the December 1966 JOURNAL.

REFERENCES

1. G. E. Brock and B. K. Bischoff, "Metallurgy of Advanced Electronic Materials," p. 249, Proc. of Technical Conference, Vol. 19. Metallurgical Society, Interscience Publishers, New York (1962).
2. F. A. Trumbore, *Bell Syst. Tech. J.*, **39**, 205 (1960).
3. E. Tannenbaum, *Sol. State Elect.*, **2**, 123 (1961).
4. D. P. Miller, J. E. Moore, and C. R. Moore, *J. Appl. Phys.*, **33**, 2648 (1962).
5. M. L. Joshi and F. Wilhelm, *This Journal*, **112**, 912 (1965).
6. P. F. Schmidt and R. Stickler, *ibid.*, **111**, 1188 (1964).
7. E. Kooi, *ibid.*, **111**, 1383 (1964).
8. A. N. Knopp and R. Stickler, *ibid.*, **111**, 1372 (1964).
9. E. S. Wajda, Private communication.

Deposition of Silica Films on Germanium by the Carbon Dioxide Process

Myron J. Rand and John L. Ashworth

Bell Telephone Laboratories, Incorporated, Allentown, Pennsylvania

ABSTRACT

An ambient composed of hydrogen (≥ 95%), carbon dioxide (0.5-5%), and silicon tetrabromide (0.1-1%) will deposit a film of silica on a substrate heated to 800°-850°C. The process has particular application for coating germanium for high-speed planar device technology; it is useful for silicon also. The reaction may be carried out immediately after epitaxial germanium deposition in the same equipment.

Silica growth rates are of the order of 100 Å/min; rates for various temperatures and concentrations are presented. Apparent activation energy is 30 kcal/mole. The oxide films are clear, vitreous, and adherent, with no detectable structure. Electrical properties of MOS diodes made on silicon are comparable to, or superior to, conventional steam-grown oxide. The film is a satisfactory mask against 1200° boron diffusion. The silica contains about 2% residual bromine, apparently in a form in which it is not free to migrate.

A film of silica on germanium is useful in the production of germanium planar transistors, diodes, and field-effect devices. The silica may serve as a diffusion mask during processing, as an insulating layer, or as a surface passivator.

The usual method of applying such a film is by pyrolysis of an organosilane (1) such as ethyl orthosilicate or ethyl triethoxysilane, either on a hot substrate or aided by gaseous plasma discharge (2). There is evidence that the pyrolysis oxides contain organic residues (3); often they are observed to have a low refractive index and high etch rate, indicating a disordered or "strained" structure.

Ideally, an oxide process should be compatible with epitaxial deposition equipment, so that a freshly deposited epitaxial surface can be coated with the passivator immediately, without risk of contamination by removal to another system. This requirement is met by the carbon dioxide process (4), which has been adapted to semiconductor device technology by Steinmeier and Bloem (5). These investigators deposited epitaxial Si from H_2 and $SiCl_4$ and then, in the same equipment, added CO_2 to the gas mixture and obtained at 1150°-1300° an insulating film of glassy SiO_2. However, extrapolating from rate studies in the H_2-CO_2-$SiCl_4$ system (5-7) it is evident that at temperatures below the melting point of Ge (936°) no useful SiO_2 film will form in any reasonable time.

An ambient of H_2, CO_2, and $SiBr_4$ vapor has been found to produce adherent, vitreous silica films on Ge at a temperature as low as 775°. This paper reports experience with this system gained from some eighty runs in a multiple-slice apparatus. In many of these, deposition of 2-3μ of epitaxial Ge from $GeCl_4$ and H_2 preceded silica film deposition. The process is carried out conveniently at about 850° to produce a 0.4μ film with growth rates in the range 50 to 100 Å/min. Rates of 300-400 Å/min may be attained by adjusting reactant concentrations, temperature, and transport rate of reactants to the hot zone. Concentrations used were 0.1-1% $SiBr^4$, 0.5-5% CO_2, ≥ 95% H_2. Most of the information presented here is from Ge coating experiments, but the process has been used extensively on Si as well, where it is equally simple and reliable.[1]

Experimental

The train for introducing the reactants was constructed so that only glass, stainless steel, and Teflon were in contact with the gases. Carbon dioxide was Matheson Company Coleman grade. Passing it through a —78° trap had no effect on the silica deposition rate. Tank hydrogen was passed through a Pd-Ag diffusion purifier, and also through a liquid nitrogen trap. It was established that the H_2-CO_2 mixture (without the $SiBr_4$) at 850° had no effect on the appearance of the Ge substrate surfaces. Silicon tetrabromide (Stauffer Chemical Company) was revealed by infrared absorption (8) to have minor organic contamination; however, one batch which was passed through a packed column at 700° and then fractionally distilled did not appear to produce a superior oxide. The $SiBr_4$ saturator was usually operated near 25°, at which the vapor pressure is 7.7 Torr. Lower concentrations were obtained by diluting the saturated gas with pure hydrogen. The temperature of the $GeCl_4$ saturator (for Ge epitaxy) was controlled automatically by thermoelectric refrigeration and a thermistor sensing probe.

The arrangement of the deposition section of the apparatus is shown schematically in Fig. 1. Up to nine slices could be coated simultaneously on the r.f.-heated horizontal rotating molybdenum platform. The usual Ge substrates were 6 mil thick, 0.005 ohm-cm Ga doped, electropolished. Many experimental slices of other resistivities of both Si and Ge were coated also, as well as Mo, Ta, and fused silica. Any epitaxial Ge deposition was done at 850°.

Temperatures were measured by a Latronics Colo-

[1] An early experiment with the bromide system was carried out by S. K. Tung and P. Buchman of these Laboratories.

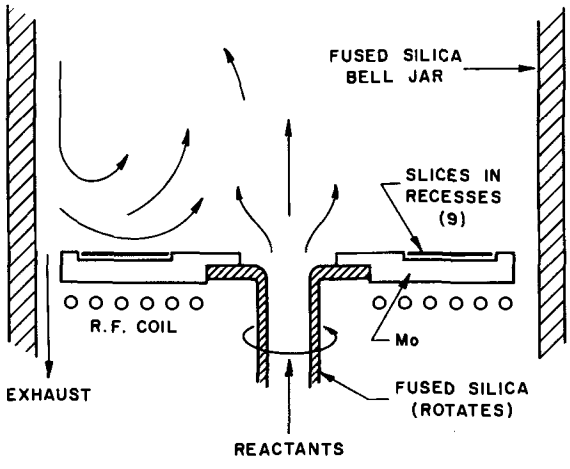

Fig. 1. Detail of deposition chamber

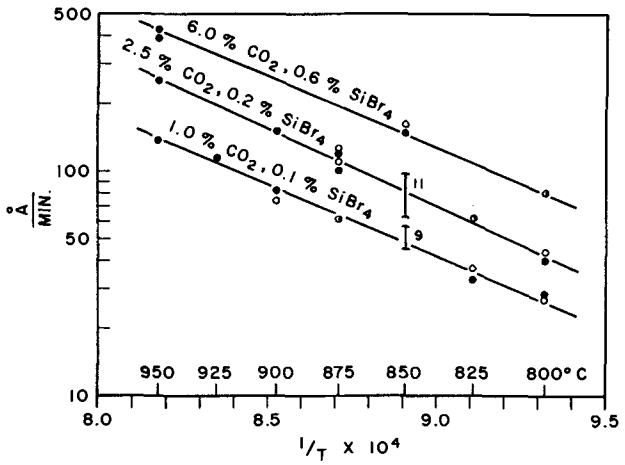

Fig. 2. Kinetics of silica deposition by the H_2-CO_2-$SiBr_4$ process. Rate of SiO_2 formation: ○, on Ge; ●, on Si. E_a = 30 kcal/mole.

ratio optical pyrometer,[2] which determines the ratio of the emission at two wavelengths in the visible range. This instrument has built-in calibration points, but it was also checked with chips of known melting-point materials resting on silica-coated Si slices. It is difficult to get an accurate temperature reading on a surface covered with a thin, transparent, growing film, owing mostly to interference colors; this is particularly true with a single wavelength optical pyrometer. This difficulty is probably responsible for much of the spread in activation energy reported by various investigators of the H_2-CO_2-$SiCl_4$ deposition process. Finally it should be realized that because the film is transparent the temperature being measured is mostly that of the substrate surface, which is not the surface where the reaction is taking place. A possible error of 20° in the temperature of the reaction site during oxide growth is a realistic estimate.

Oxide film thicknesses were determined from the pattern of interference minima in the reflection spectrum in the 190-750 mμ range (9), using a Perkin-Elmer 202 spectrophotometer. Thicknesses below 0.1μ were measured by ellipsometer.

Results

The H_2-CO_2-$SiBr_4$ reaction gives transparent, smooth, tightly adherent films on Ge substrates at any temperature from about 775° up to the melting-point of Ge. The films have no structure discernible by electron diffraction. Electron microscope examination rarely shows any surface features, pinholes, or cracks.

Figure 2 shows the rate of deposition of the oxide over the range 800°-950°C for three different combinations of reactant concentrations. Log rate *vs.* 1/T°K is linear; the plots for different concentrations have the same slope, and the rate is the same for Ge and Si substrates. (It is the same for Mo or SiO_2 substrates as well.) Probably a single reaction is the rate-determining step throughout the range, and this reaction does not involve the substrate surface. The 30 kcal/mole activation energy is substantially less than the 50-80 reported (5-7) for the H_2-CO_2-$SiCl_4$ system.

Within the range of conditions represented in Fig. 2, the deposition rate depends on temperature, $SiBr_4$ concentration, CO_2 concentration, and total flow rate, in decreasing order of importance. Careful examination of all the variables is not warranted since in a deposition chamber of different geometry and different gas flow pattern rates are somewhat different; each apparatus requires an experimental calibration, after which rates should be reproducible to ± 10%, as they were here. The total flow rate in the runs of Fig. 2 corresponds to about one displacement of the deposition chamber per minute.

Since total flow rate does have a minor, but not negligible, effect, it is probable that mass transport to the reaction zone limits the reaction rate, and that the observed rates are not quite true kinetic rates. In multislice equipment of several liters' capacity this situation is difficult to avoid without great waste of reactants.

Deposition rate is linear with $SiBr_4$ concentration up to 0.1-0.2%, above which there is progressively less effect. The influence of CO_2 concentration has been tested only well above the stoichiometric requirement; here doubling the concentration increases the rate by some 15%.

The oxide deposition rate is essentially linear with time. Germanium slices were put into the deposition chamber at various times during a run and removed after intervals, so that deposits sampling the effects of run duration and oxide thickness independently were obtained. There were some minor aberrations early in the run, but in general the slopes of the thickness *vs.* time plots were in excellent agreement. Deposition rate is thus little influenced by the duration of the run or the amount of oxide already present on the substrate.

On occasion a local area of the deposited oxide appeared cloudy and whitish. The film was obviously not vitreous here, but there was still no structure evident to electron diffraction. Tests with the electron beam microprobe showed no concentration of any impurity. They did show a significantly higher silicon count per unit area, indicating a thicker deposit. The cloudy areas were porous in tests as diffusion masks or dielectrics. Frequently they occurred on one Ge substrate and not on the neighboring one in the same run; they never appeared in films on Si substrates. No correlation was found with various Ge cleaning procedures; in fact, on many occasions hole-free films were made on substrates used as received, with no cleaning whatsoever. Some connection was observed, however, with substrate source, although it is not clear whether the original material or the preparation and polishing procedure was involved.

Cloudy oxide areas became much less common when regular removal of deposited silica from the molybdenum pedestal and other surfaces in the deposition chamber was instituted. The interpretation is that the silica adsorbs moisture from the atmosphere when the apparatus is opened, and then desorbs it on heating during the next run. It is well known that water vapor accelerates the devitrification of silica and other glasses. It is also known from studies on evaporated metal films that adatoms have more surface mobility on Ge than on Si.

Present evidence is that cloudy oxide areas are deposits of minute amorphous silica particles which constitute favored sites for the nucleation of still more of

[2] Latronics Corporation, Latrobe, Pennsylvania.

Table I. Typical properties of silica films from H_2-CO_2-$SiBr_4$ (0.2%), 850°

		Deposited oxide	1050° Steam oxide
% Br		2-2.5	0
Ref. index, 546 mμ		1.48 ± 0.02	1.455-1.46
I.r. transmission minimum, μ		9.25-9.35	9.20-9.30
Water contact angle		40-60°	35-40°
Relative etch rates, P etch*			1
0.1% $SiBr_4$		2.7	
0.2% $SiBr_4$		3.5	
0.6% $SiBr_4$		3.9	
675° ethylorthosilicate pyrolysis		9.3	
"Pinholes"/cm² **		28	28
MOS diode results			
Substrate	Ge	Si	Si
Number of samples	34	10	
Surface type	p	n	n
Surface state density/cm²	7×10^{12} to $>10^{13}$	$3\text{-}6 \times 10^{11}$	$\sim 8 \times 10^{11}$
Dielectric constant at 0.5 mc	3.7-4.2	3.5-4.1	~3.9
Breakdown voltage, v/Å	0.11-0.22	0.20-0.24	0.08-0.10

* Ref. (10).
** 2½ hr in amine-catechol etch, 110°C, ref. (11).

this form of deposit. Both a germanium surface anomaly of some sort and an excessive water vapor concentration would be required; neither condition alone will account for the experimental observations.

Evaluation of the Oxide

A summary of various properties and tests of the H_2-CO_2-$SiBr_4$ deposited silica appears in Table I. It will be noted that there is residual bromine in the film, detected by x-ray fluorescence analysis. H_2-CO_2-$SiCl_4$ oxides made at 1150° contain 0.5% Cl. Bromide process oxides made at 850° contain about 2% Br, and proportionately higher amounts if > 0.2% $SiBr_4$ was used. Bromine is probably present as unreacted Si-Br linkages rather than bromine-containing by-products, *e.g.*, HBr, trapped in the reaction zone by the depositing silica. A 1-hr pump at 700°C and 10^{-6} Torr did not reduce the bromine content.

The bromine content of the film probably accounts for the slightly high refractive index. The infrared transmission spectrum (2-25μ) compares closely with that of steam-grown oxide, with slightly greater absorption band half-widths. The high water contact angle predicts excellent adherence of Kodak Photoresist (12), and this is what is found; in fact, on occasion the bromide process has been used to deposit ~ 1000Å silica over phosphorus glass to provide a more hydrophobic surface for KPR.

The higher etch rate of bromide process oxides is probably more a consequence of low deposition temperature than bromine content. Etch rate does not change as the film is thinned, at least down to 900Å.

Evaluation of electrical properties by MOS diode structures on both Ge and Si is included in Table I. A p-type surface apparently is produced on Ge, with a rather high acceptor state density; on Si the usual n-type surface is seen, with a surface-state density usually lower than that produced by steam. Breakdown voltages are superior, particularly on Si; generally there was little leakage in advance of breakdown. The behavior of the MOS diodes reinforces the belief that the bromine impurity is not ionic, or at least is not free to migrate in a field.

The bromide-process oxide has been used as the first oxide, following epitaxy, on both Ge and Si planar structures, with satisfactory performance. It is also an entirely adequate diffusion mask against severe conditions such as boron diffusion into Si at 1200° for 2 hr. In this test, it was established by step-etching that boron penetration into the oxide was no more rapid than it is in a 1200° steam oxide. Furthermore, the oxide remaining, beyond the boron front, etched at a rate little different from that of 1200° steam oxide, rather than the three-times factor before treatment. The obvious inference is that the as-deposited oxide film is rapidly "densified" by further heating and becomes indistinguishable from a high-temperature oxide in many of its properties.

Discussion

It has been demonstrated that the H_2-CO_2-$SiBr_4$ system produces good silica films at temperatures some 300° lower than the analogous chloride system and is consequently useful for germanium solid-state device technology. The mechanism of the reaction is less clear. In published reports the carbon dioxide process has been regarded as a combination of two reactions

$$H_2 + CO_2 \rightleftarrows H_2O + CO \quad [1]$$

$$SiCl_4 + 2H_2O \rightarrow SiO_2 + 4HCl \quad [2]$$

with [1] believed to be the slow step. Authors are undoubtedly aware that this picture is certainly much too simple. In spite of its commercial importance the kinetics of reaction [1] is not well understood, but very likely it proceeds by a chain mechanism involving free radicals. It would be surprising if the rate-determining step were not influenced by any of the species of reaction [2]. If the CO_2-H_2-$SiBr_4$ reaction goes as fast at 850° as the chloride reaction at 1100° obviously [1], as written, cannot be the sole rate-determining reaction. Reaction [2] could be, but it is more likely that the silicon halide somewhere enters into the mechanism of [1], or catalyzes it. The hydrogen halide by-product has no significant effect on the H_2-CO_2 reaction (13). All that may be said at present is that the existence of the low-temperature bromide process, with its different energy of activation, is evidence that the carbon dioxide process for oxide deposition must be complex.

Acknowledgment

The authors are indebted to F. Reizman, J. Drobek, and H. E. Nigh for various measurements on oxide properties.

Manuscript received Aug. 13, 1965. This paper was presented at the San Francisco Meeting, May 9-13, 1965.

Any discussion of this paper will appear in a Discussion Section to be published in the December 1966 JOURNAL.

REFERENCES

1. E. Jordan, *This Journal*, **108**, 478 (1961); J. Klerer, *ibid.*, **108**, 1070 (1961).
2. L. L. Alt, S. W. Ing, Jr., and K. W. Laendle, *ibid.*, **110**, 465 (1963).
3. J. Klerer, *ibid.*, **112**, 503 (1965).
4. C. F. Powell, I. E. Campbell, and B. W. Gonser, "Vapor Plating," p. 137, John Wiley & Sons, Inc., New York (1955).
5. W. Steinmeier and J. Bloem, *This Journal*, **111**, 206 (1964).
6. S. K. Tung and R. E. Caffrey, *Trans. Met. Soc. AIME*, **233**, 572 (1965).
7. Y. Tarui, Y. Komiya, H. Teshima, and K. Nagai, *Japan. J. Appl. Phys.*, in press.
8. M. J. Rand, *Anal. Chem.*, **35**, 2126 (1963).
9. O. S. Heavens, "Optical Properties of Thin Solid Films," p. 113 ff, Butterworths, London (1955); E. A. Corl and H. Wimpfheimer, *Solid State Electronics*, **7**, 755 (1964); F. Reizman, *J. Appl. Phys.*, **36**, 3804 (1965).
10. W. A. Pliskin and R. P. Gnall, *This Journal*, **111**, 872 (1964).
11. R. M. Finne and D. L. Klein, *ibid.*, **111**, 63C (1964).
12. A. A. Bergh, *ibid.*, **112**, 457 (1965).
13. V. E. Hauser, Private communication.

Impurity Distributions in Single Crystals

I. Impurity Striations in Nonrotated InSb Crystals

K. Morizane, A. F. Witt, and H. C. Gatos

Department of Metallurgy, Massachusetts Institute of Technology, Cambridge, Massachusetts

ABSTRACT

Single crystals of InSb were pulled without rotation from the melt in the presence of tellurium or selenium impurity employing a Czochralski-type apparatus. The formation of pronounced periodic and nonperiodic impurity striations was observed; their appearance and origin were studied as a function of the thermal conditions prevailing in the immediate vicinity of the solid-melt interface. It was concluded that the formation of such striations is the result of temperature fluctuations at the interface brought about by convection currents in the melt which in turn are caused primarily by sharp temperature gradients in the growing crystal near the interface.

Semiconductor single crystals grown from the melt by the Czochralski technique frequently exhibit heterogeneous distributions of impurities. A commonly observed heterogeneity in crystals, grown in the <111> direction, is the so-called "coring" which consists in an (usually) increased impurity concentration in the central part of the grown crystal. This higher impurity concentration is associated with the presence of an (111) facet at the crystal melt interface and is limited in its lateral extent by the area of the facet (1, 2).

Another common type of impurity heterogeneity in rotated crystals is the impurity striations which appear as bands or lines of increased impurity concentration and assume the shape of the growing crystal-melt-interface. Such striations are attributed to nonsymmetric temperature profiles at the growing interface (3, 4).

Impurity striations have also been reported in nonrotated Czochralski grown crystals of InSb (5). These striations were attributed to temperature fluctuations resulting from a periodic release of latent heat of fusion. Recently impurity striations were reported in InSb grown in a horizontal boat (6).

The present investigation is concerned with the detailed study of the origin of striations appearing in nonrotated InSb single crystals grown by pulling from the melt.

Experimental Procedure

Single crystals of InSb were grown in the <111> direction from high-purity ingots on to seeds of 12.5 mm diameter and varying lengths in a purified hydrogen atmosphere. In order to permit the study of the role of temperature gradients in the growing crystals, a seed holder was designed with provisions (after cooler) to cool the seed by circulating various coolants or to heat the seed by means of a cylindrical heater (after heater). Neither the seed nor the crucible was submitted to rotation. The temperature in the melt and in the grown crystal was controlled and measured with chromel-alumel thermocouples. The pulling rates employed varied between 7 and 50 mm/hr.

Selenium or tellurium were used as impurities. The amount of InSb placed in a quartz or graphite crucible (30 mm ID) was in most experiments 50 g; the amount of impurity added was 2 mg of Se or Te corresponding to an average carrier concentration of about 1×10^{18}/cm^3 in the grown crystal. All crystals were cut along a (211) plane parallel to the growth direction. The (211) plane was polished and etched with a modified CP4 etchant (5 parts HNO_3, 3 parts HF, 3 parts CH_3COOH, and 11 parts H_2O).

Results and Discussion

Role of impurity.—In a series of experiments it was found that both selenium and tellurium impurities lead to the formation of striations exhibiting the same basic characteristics. The choice of selenium for most of the experiments was based on the greater ease with which its striations are revealed by the modified CP4 etchant.

The amount of impurity was varied between 2 and 10 mg for a 50g melt, but no difference could be detected in the ease of formation or the general characteristics of the striations.

Role of pulling rate.—Variations in the pulling rate between 7 and 50 mm/hr had no apparent effect on the formation, intensity, or the spacing of nonrotated striations. This result indicates that the pulling rate plays no significant role in the mechanism of striation formation under the present conditions.

It is often argued that impurity striations are due to nonuniform pulling rates ("jerking") caused by deficient pulling mechanisms. Such pulling irregularities were indeed detected in our system by employing a linear transducer. However, no correlation could be established between the pulling irregularities and the observed striations. Moreover, several striation-free crystals were grown under conditions in which, due to pulling irregularities, the instantaneous pulling rate ranged from 0 to well over 100 mm/hr. It, thus, appears that variations in impurity concentration expected from changes in pulling rate (7) are not revealed as striations.

Selenium striations and the role of orientation.—In crystals grown along the <111> direction, the selenium striations are revealed as lines on etched (211)

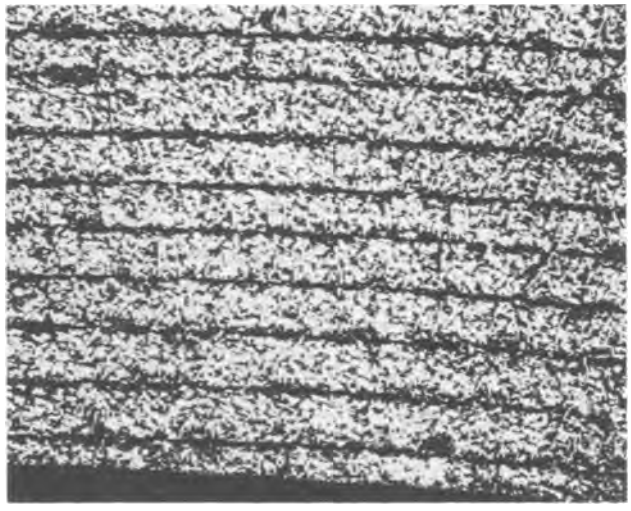

Fig. 1. Impurity striations in a Se-doped crystal of InSb grown without rotation. The surface shown is a (211) plane parallel to the growth direction. Magnification 50X.

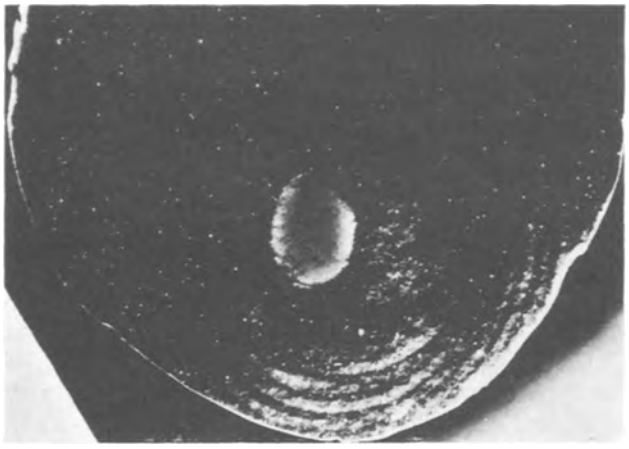

Fig. 2. Impurity striations in a Se-doped crystal of InSb grown without rotation. The surface shown is perpendicular to the growth direction. The part of the surface without rings corresponds to the (111) facet. Magnification approximately 5X.

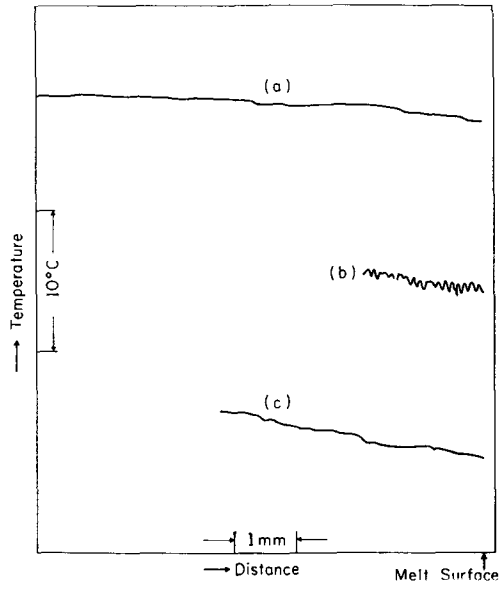

Fig. 3. Temperature profiles in the melt: (a) no seed is in contact with the melt; (b) growing crystal is in contact with melt but it is not being pulled nor rotated; (c) same as in (b) except the "afterheater" applied to reduce the temperature gradient in the seed.

planes (Fig. 1). On the (111) plane normal to the growth direction, the striations appear as more or less concentric rings on the "off-core" part of the plane which corresponds to the nonflat part of the growing interface (Fig. 2).

The formation of impurity striations was shown to be independent of orientation. Thus, striations invariably reflect the shape of the growing interface rather than show orientation affected characteristics. Actually in numerous instances of twinned or polycrystalline crystals, the striations exhibited no discontinuities. Occasionally, the striations appeared to terminate abruptly at a twin boundary. However, this behavior resulted from the fact that the twin in which the striations did not appear had an unfavorable orientation for revealing striations with that particular etchant. In all instances an appropriate etchant could be found to reveal the striations across the twin boundary.

Temperature measurements.—The thermal conditions in the crystal-melt system were determined with sheathed chromel-alumel thermocouples of 1 mm external diameter, which were introduced through the melt surface. Because of the considerable thermal conductivity of the sensor system, these measurements do not yield correct absolute temperature values, but the arrangement is considered quite adequate for the evaluation of temperature fluctuations.

The temperature profiles of the melt under varying experimental conditions are presented in Fig. 3. These measurements indicate that under the present experimental conditions the isolated melt (without a growing crystal) is free of major temperature fluctuations (curve a). Fluctuations are induced when the melt is contacted with the seed, as a result of the induced directional heat flow which leads to convection currents (curve b). Stable temperature conditions in the crystal-melt system can be readily re-established by reducing the temperature gradient in the seed by means of the afterheater (curve c). The same system exhibited extreme temperature instabilities with fluctuations up to 20°C when the upper end of the seed was water-cooled (aftercooler).

It was observed that non-rotated striations appear primarily under growth conditions which lead to a decreasing crystal diameter. Such conditions are obtained by raising the temperature of the melt while keeping all other parameters as constant as possible. Associated with any such raise in temperature is an upward shift of several millimeters in the location of the crystal-melt interface. (It is obvious that an excessive temperature increase will lead to the actual disruption of the solid-liquid contact.)

The temperature profile for a static system in which the melt was contacted with a water-cooled seed is given in Fig. 4. Curves (a) through (g) indicate the variations of the thermal conditions when the location of crystal-melt interface (meniscus height) was changed by increasing the melt temperature. The conditions corresponding to curves (e), (f), and (g) are characterized by major temperature fluctuations and were found to be most favorable for the formation of nonrotated striations.

The thermal conditions during crystal growth were determined by means of fixed thermocouples introduced through a channel drilled in the center of the seed. At the beginning of crystal growth the thermocouple protruded several millimeters into the melt; as the crystal was pulled the location of the thermo-

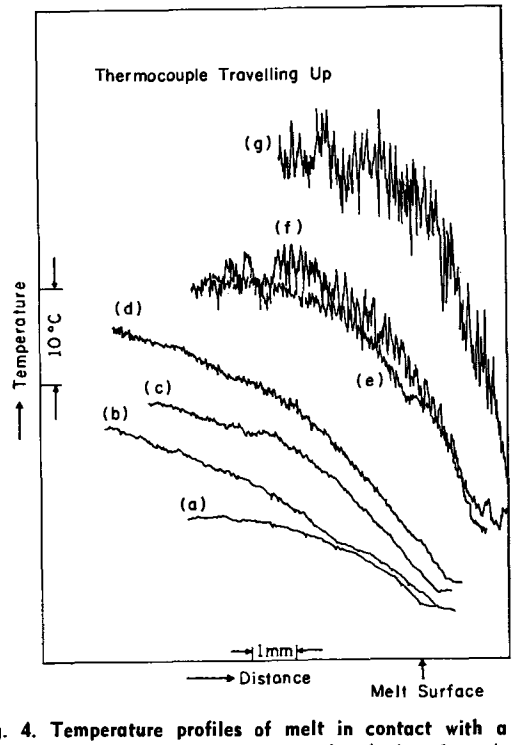

Fig. 4. Temperature profiles of melt in contact with a water-cooled seed. The height of the crystal-melt interface (meniscus height) increases from (a) to (g) as a result of increasing the melt temperature (see text).

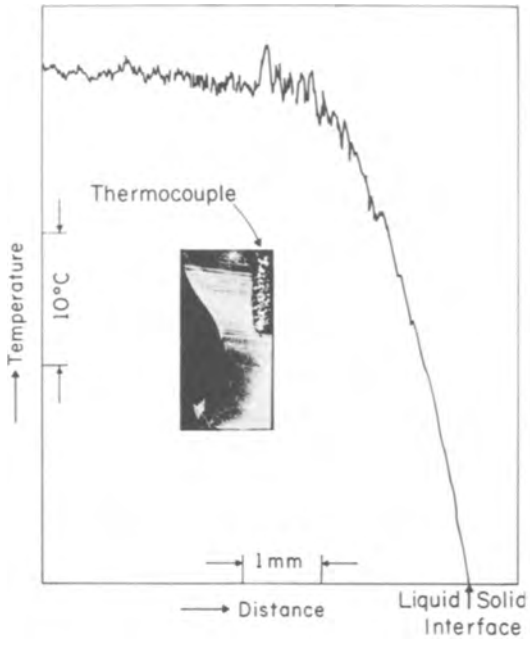

Fig. 5. Temperature fluctuations in the melt near the melt-solid interface during pulling of an InSb crystal (with aftercooler). Inserted photograph shows the impurity striations corresponding to the shown temperature fluctuation.

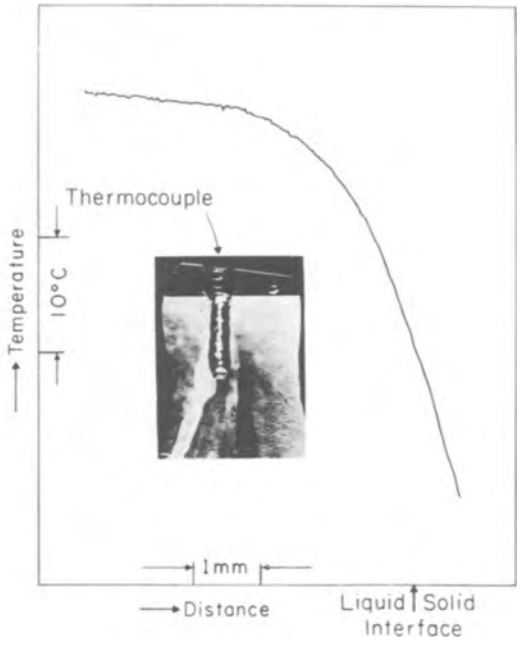

Fig. 6. Temperature profile of melt during pulling of an InSb crystal (with aftercooler). Note absence of temperature fluctuations and also absence of impurity striations in the inserted photograph (see text).

couple junction gradually approached the crystal-melt interface and finally was in the grown crystal itself. Figure 5 shows the results obtained with a water-cooled seed when the melt temperature was well above the melting point. Under these conditions the crystal-melt interface was several millimeters above the surface of the melt, and the grown crystal was of decreasing diameter. Temperature fluctuations as well as intensive striations can readily be observed. A decrease in the melt temperature brought the location of the crystal-melt interface closer to the melt surface and resulted in a crystal of constant diameter (Fig. 6). Neither temperature fluctuations nor striations are observed in this case. The pertinent facts as revealed by the temperature measurements are:

1. The temperature gradient in the seed crystal and the location of the crystal-melt interface (meniscus height) are primarily responsible for the presence of temperature fluctuations in the melt.
2. The convectively induced temperature fluctuations are generally irregular, but may in some instances assume a considerable degree of regularity.
3. Temperature fluctuations are virtually identical under static and dynamic (growth) conditions.
4. The amplitude and frequency of temperature fluctuations decreases with a decreasing amount of melt.
5. In actual crystal growth, a direct correlation exists between temperature fluctuations and striations.

Origin of striations.—As pointed out above, the formation of impurity striations in nonrotated pulled crystals is independent of such parameters as orientation, pulling rate fluctuations, or amount and type of impurity present. Consequently, it is believed that the formation of striations is not directly related to the mechanism of crystal growth. Impurity striations form only when the thermal conditions are such as to lead to temperature fluctuations at the crystal-melt interface. A direct correlation was unambiguously established between temperature fluctuations at the interface and the formation of impurity striations.

Under experimental conditions such as those employed in the present study, the cause of temperature fluctuations at the interface is given by the thermal gradients in the growing crystal which result in convection currents in the melt and affect the immediate vicinity of the interface. In the absence of pronounced thermal gradients, there are no temperature fluctuations at the interface (apparently no convection currents) and no impurity striations.

Impurity striations have invariantly been observed in these parts of the crystals where their diameter was decreasing (Fig. 5). They could not be observed in the part of the crystal where the diameter was increasing, a condition requiring thermal gradients into the melt. This observation is thus indicating that thermal fluctuations at the interface, brought about by convection currents and leading to impurity striations, are caused by sharp gradients in the direction of the crystal.

Under the present experimental conditions, the latent heat of fusion released during solidification apparently is not sufficient to cause temperature fluctuations at the interface as speculated earlier (5). If the latent heat were playing any significant role, then (at variance with the present results) sharp gradients in the crystal would enhance its dissipation and, thus, decrease its effectiveness in causing thermal fluctuations leading to striations.

Having established the presence of temperature fluctuations at the interface, the formation of impurity striations can be understood readily on the basis of changes in the microscopic rate of crystal growth

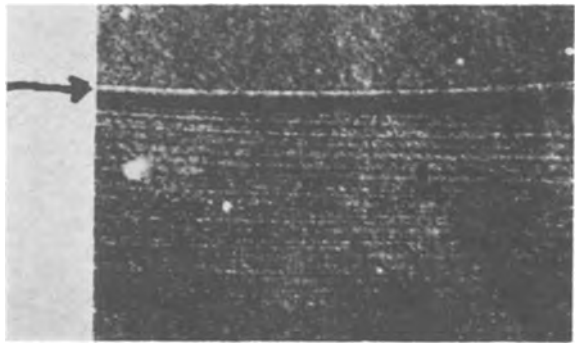

Fig. 7. Remelt line (arrow) and impurity striations in a Se-doped unrotated InSb crystal. Note sharpness of remelt line as compared to that of striations. Magnification 5X.

brought about by such temperature fluctuations (6, 8, 9). The rate of growth (the microscopic rate of growth is referred to here since the macroscopic rate is determined by the pulling rate) conforming to the prevailing temperature alters the deviation of the solidification process from equilibrium; thus, the amount of impurity incorporated in the solid is not constant with time. The increase in amount of impurity in the solid with increasing rate of growth is a well-established fact (7).

Temperature fluctuations determined in the present experiments were as large as 15°C. Others have reported even greater temperature fluctuations during crystal growth in similar systems. It is conceivable that the maximum temperature within each fluctuation does not reach the melting point of the supercooled solid so that no remelting takes place at any given time. However, depending on the prevailing convection current conditions, it is possible that the temperature at the interface approaches or even exceeds the melting point, as a flow of melt with bulk melt temperature passes by the interface (the bulk melt temperature is maintained above the melting point of the solid).

When remelting takes place, we believe that the impurity striations are more sharply delineated than the striations commonly formed. Their appearance in fact is quite similar to that of the demarkation lines formed when a growing crystal is allowed to remelt for an instant before proceeding with growth (Fig. 7).

This type of "remelt" striations appears to have a defect structure associated with it; however, a study on this aspect is now in progress.

Summary

Impurity striations in nonrotated crystals (at least under the given experimental conditions) are caused by temperature fluctuations in the melt. These temperature fluctuations which always increase with increasing meniscus height are due to convective currents induced by excessive temperature gradients in the growing crystal. In some instances periodic remelting leads to very sharp striations. In general, impurity striations are due to pronounced changes in growth rates and the associated variations of nonequilibrium distribution coefficients.

The fact that temperature fluctuations are substantially the same under static and dynamic growth conditions indicates that they are not induced by intermittent growth, as was suggested previously (10, 11). Our findings throw considerable doubt also on attempts to explain striations exclusively on the basis of supercooling and recovery phenomena (12).

It is quite likely that rotated, pulled crystals under particular conditions may exhibit rotational striations, which are caused by a nonsymmetric temperature distribution in the melt, and also a substructure of nonrotational striations.

Acknowledgment

This work was supported by the Atomic Energy Commission under Contract AT(30-1)-3208. The authors wish to express their appreciation to Mrs. Mary Cretella Lavine for her assistance with the etching techniques and valuable discussions.

Manuscript received July 19, 1965; revised manuscript received Sept. 13, 1965.

Any discussion of this paper will appear in a Discussion Section to be published in the December 1966 JOURNAL.

REFERENCES

1. J. B. Mullin and K. F. Hulme, *J. Phys. Chem. Soc.*, **17**, 1 (1960).
2. W. P. Allred and R. T. Bate, *This Journal*, **108**, 258 (1961).
3. P. R. Camp, *J. Appl. Phys.*, **25**, 459 (1954).
4. E. Billig, *Proc. Roy. Soc. (London)*, **229**, 346 (1955).
5. H. C. Gatos, A. J. Strauss, M. C. Lavine, and T. C. Harman, *J. Appl. Phys.*, **32**, 2057 (1961).
6. A. Müller and M. Wilhelm, *Z, Naturforsch.*, **19a**, 254 (1964).
7. J. A. Burton, R. C. Prim, and W. P. Slichter, *J. Chem. Phys.*, **21**, 1987 (1953).
8. W. R. Wilcox and L. D. Fullmer, Electronics Research Laboratory, Aerospace Corporation Rep. No. ATN-64(9236)-19 (1964).
9. G. S. Cole and W. C. Winegard, *J. Inst. Met.*, **93**, 153 (1950).
10. H. Ueda, *J. Phys. Soc. Japan*, **16**, 61 (1961).
11. A. I. Landau, *Fiz. Metal. Metalloved*, **6**, 148 (1958).
12. C. Z. LeMay, *J. Appl. Phys.*, **34**, 439 (1963).

Bourdon Gauge Determination of Equilibrium in the ZnSe(s)-I_2(g) System

T. O. Sedgwick and B. J. Agule

International Business Machines Corporation, Watson Research Center, Yorktown Heights, New York

ABSTRACT

Bourdon gauge measurements of samples of I_2(g) plus ZnSe(s) have been made in the temperature range 900°-1200°K and over a fourfold range in pressure. The pressure *vs.* temperature behavior of the system can be described satisfactorily by the equilibria,

$$ZnSe(s) + I_2(g) \rightleftarrows ZnI_2(g) + \tfrac{1}{2}Se_2(g)$$
$$I_2(g) \rightleftarrows 2I(g)$$

The standard enthalpy and entropy of the first reaction between 900°-1200°K were calculated using the second law with the result; $\Delta H^\circ = 23.1$ kcal, $\Delta S^\circ = 21.1$ e.u. The standard heat of formation, ΔH°_{298f}, and entropy, S°_{298}, of ZnSe(s) were found to be 44.2 kcal and 15.4 e.u., respectively.

The compound ZnSe exhibits interesting and potentially useful photoelectric properties typical of the II-VI compounds. Because of the very high melting point of this compound, it is advantageous to grow single crystal material either by evaporation or chemical transport processes. In designing a transport system, it is of considerable value to have accurate thermodynamic data for the chemical species in question to facilitate the proper selection of operating pressures and temperatures. Although there have been three recent determinations (1-3) of the heat of formation and entropy of ZnSe, the agreement between these results is not good.

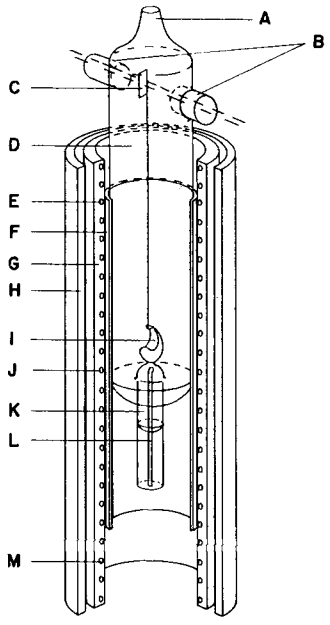

Fig. 1. Bourdon gauge and furnace arrangement: A, to pressure control; B, light pipes; C, flag; D, equalizing chamber; E, M, end windings; F, nickel pipe; G, quartz furnace; H, morganite heat reflector; I, asymmetric spoon; J, center winding; K, sample chamber; L, thermocouple well.

In the present investigation the automated Bourdon gauge described by Hochberg (4) and Sedgwick (5) was used to determine the equilibrium between ZnSe and the vapor solvent I_2, *i.e.*

$$ZnSe(s) + I_2(g) \rightleftarrows ZnI_2(g) + \tfrac{1}{2}Se_2(g) \qquad [1]$$

It was then possible to calculate the heat of formation and entropy of ZnSe from the measured data and other data already available in the literature.

Experimental

Apparatus and measuring procedure.—The quartz Bourdon gauge and furnace arrangement are shown in Fig. 1. The automatic pressure control system used to maintain equal pressure in the sample and measuring chambers has been described previously (4, 5). The measuring manometer, a Wallace and Tiernan Model FA129 dial gauge, was calibrated with a large bore Hg manometer. Both the pressure control and accuracy of measurement are within ± 0.4 mm Hg.

Before making any measurements, the Bourdon gauge assembly was thermally cycled several times over the temperature range of interest to stress relieve the sensitive spoon element. The particular gauge used in this study showed no significant variation of zero point with temperature.

The pressure of three samples of $I_2(g)$ plus ZnSe(s) was measured as a function of temperature over several cycles of increasing and decreasing temperature. The pressure was allowed to equilibrate at each temperature which required from one half hour up to several hours before taking the data. The reproducibility of the pressure readings at a given temperature and the variation of zero point during a run was within ± 1-2 mm Hg.

The temperature was measured with Pt-Pt 10% Rh thermocouples. One thermocouple was placed in a well at the bottom of the sample chamber near the ZnSe, and a second was placed in a well at the top of the sample chamber near the spoon. The temperature in the furnace was adjusted so that the top of the Bourdon gauge was 2°-10°C higher than the bottom (position of ZnSe) in order to avoid condensation of solids on the spoon. The temperature was controlled by a power proportioning controller to within 1°C.

Chemical purity and sample preparation.—High-purity crystals of ZnSe were supplied as a courtesy by Dr. M. Aven of the G. E. Research Laboratories, Schenectady, New York. They were grown by the vapor phase growth method from ZnSe powder synthesized by direct reaction between Zn and Se. They were then purified by firing in liquid Zn and etched with HCl and NaOH. The resulting crystals contained the following concentrations of impurities: S, Te ≤ 10 ppm; Cd, Mg, Si ≤ 3 ppm; Fe, Al, Co, Cu ≤ 1 ppm. In each run a predetermined weight consisting of several small crystal fragments of ZnSe was charged to the sample chamber which was evacuated and then heated slowly to 700°C, held for 10 min at 700° (ZnSe sublimes slowly at 700°C), cooled, and finally sealed off.

High-purity moisture-free iodine was prepared by the method of Washington and Naldrett (6). In this procedure PdI_2 was precipitated from solution by adding an excess of $PdCl_2$ in dilute HCl to a 0.5M NaI solution. The PdI_2 was dried and degassed under vacuum at 250°C and finally decomposed to Pd and I_2 at 350°C. The free iodine was transferred in an all-glass apparatus to the sample chamber.

Results

Figure 2 shows the pressure *vs.* temperature data for three samples of ZnSe(s) plus $I_2(g)$. The initial linear portions of the curves up to *ca.* 600°K are interpreted as the ideal gas pressure increase of $I_2(g)$ at constant volume. The absence of any measurable chemical reaction in this region is implied by the linearity of the curves. The initial slope and the calculated number of moles of I_2 in the sample chamber (estimated volume 16 cc) are compared with the moles of ZnSe used in each sample in Table I.

The rapid rise of pressure above *ca.* 750°K indicates reaction is taking place. The highest pressure points appear to be approaching a constant slope indicated by the short solid lines in Fig. 2. Unfortunately, it was not possible to exceed 1200°K without causing permanent distortions to occur in the thin walled quartz Bourdon spoon.

It should be noted that in all three samples the pressure curves increase smoothly with temperature and exhibit no "break points" (discontinuous dP/dT) indicative of the disappearance of solid phases. The pressure measurements of Nitsche and Richman (7) on the

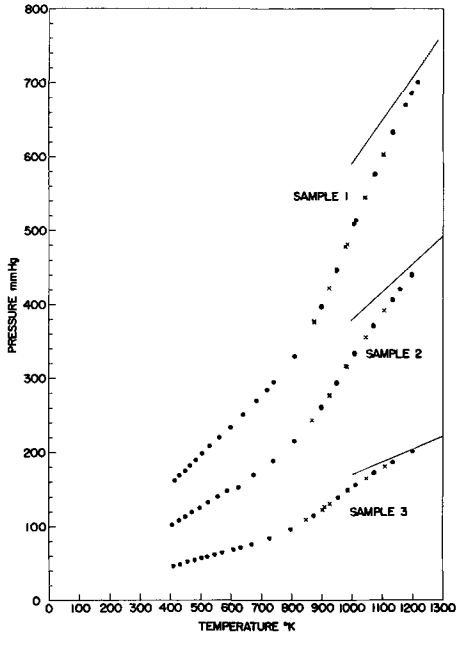

Fig. 2. Pressure *vs.* temperature data for three samples of ZnSe(s) plus $I_2(g)$ at constant volume: ●, temperature increasing; ×, temperature decreasing.

Table I. Quantities of ZnSe and I_2 used in Bourdon gauge runs

Sample No.	P/T, mm Hg/°C	Moles $I_2 \times 10^3$	Moles ZnSe $\times 10^3$
1	0.3921 ± 0.0007 (10)	0.101	0.25
2	0.2515 ± 0.0001 (8)	0.065	0.19
3	0.1129 ± 0.0003 (10)	0.029	0.086

Numbers in parenthesis indicate the number of data points averaged.

system CdS-I_2, for example, clearly exhibit abrupt decreases of dP/dT as solid phases of S and CdI_2 disappear with increasing temperature. Consequently, we will assume that no solid phases other than ZnSe(s) were present in our experiments.[1]

Equilibrium model.—An examination of the literature (8, 9) indicated that the major molecular and atomic species to be expected in the gas phase in the measured P-T range were $I_2(g)$, $I(g)$, $ZnI_2(g)$, $Se_2(g)$. (The presence of selenium vapor species other than Se_2 will be discussed later.) The equilibria between these species and ZnSe(s) may be written as follows

$$ZnSe(s) + I_2(g) \rightleftarrows ZnI_2(g) + \tfrac{1}{2}Se_2(g) \quad [1]$$

$$I_2(g) \rightleftarrows 2I(g) \quad [2]$$

In both equilibria $I_2(g)$ predominates at low temperatures. At higher temperatures both equilibria shift to the right, and since even rough estimates indicate that the Gibbs free energy, ΔF° for Eq. [1] is considerably smaller than ΔF° for Eq. [2] at high temperatures, it is expected that $ZnI_2(g)$ and $Se_2(g)$ will exist in much greater concentrations than $I(g)$ in the pressure range (200-700 mm Hg total pressure) under consideration here.

This model is qualitatively confirmed by the data since the P-T curve at high temperatures approaches a linear function with a slope 1½ times (see solid lines in Fig. 2) the slope of the low-temperature linear region. In order to test this model quantitatively as well as to obtain the thermodynamic constants for Eq. [1], the equilibrium constant Kp_1, has been calculated over a range of temperature and pressure.

$$Kp_1 = \frac{p_{ZnI_2}\, p_{Se_2}{}^{1/2}}{p_{I_2}} \quad [3]$$

In order to calculate the partial pressures in Eq. [3], we note that the total pressure, P_T, is the sum of partial pressures, *i.e.*,

$$P_T = p_{I_2} + p_I + p_{ZnI_2} + p_{Se_2} \quad [4]$$

and since the quantity of iodine is constant in the gas phase

$$\frac{V}{N_I R} \times T = 2p_{I_2} + p_I + 2p_{ZnI_2} \quad [5]$$

where V is the volume of the sample chamber, and N_I is the total number of moles of iodine atoms in the gas phase. Below 600°K $I_2(g)$ predominates and the terms p_I and p_{ZnI_2} in Eq. [5] are negligible. Therefore, the quantity $N_I R/2V$ is equal to the values of P/T tabulated in Table I for each sample.

From the stoichiometry of Eq. [1] and the presumed (see Discussion) stoichiometry of the ZnSe crystal it follows that

$$p_{ZnI_2} = 2p_{Se_2} \quad [6]$$

Finally, we note that the thermodynamic properties of the iodine dissociation are accurately known (10).

[1] It is possible that there was a very small amount of a second solid phase (ZnI_2,Se) formed in the region 600°-750°K. If this were the case, the apparent reaction rate was either extremely slow and/or the extent of reaction was very limited since the total pressure did not drop below the extrapolated $I_2(g)$ pressure line. Since our quantitative analysis is based on data taken only at much higher temperatures, we did not consider this temperature region further.

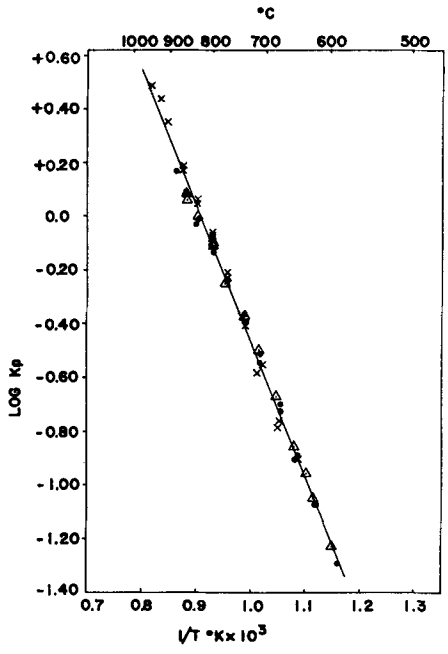

Fig. 3. Log K_p vs. $1/T$ for the equilibrium ZnSe(s) + $I_2(g)$ ⇄ $ZnI_2(g)$ + 1/2 $Se_2(g)$ for three different samples: ×, sample 1; ●, sample 2; △, sample 3.

$$\log K_{p2} = \log \frac{p_I{}^2}{p_{I_2}} = -\frac{7991}{T} + 5.481 \quad [7]$$

Equations [4]-[7] comprise a set of four independent equations in four unknown partial pressures which when solved simultaneously yield

$$p_I = \frac{K_{p2}}{4} \pm \sqrt{\frac{K_{p2}{}^2}{16} - K_{p2}\left(2P_T - \frac{3N_I RT}{2V}\right)} \quad [8]$$

$$p_{ZnI_2} = \frac{N_I R}{2V} \times T - p_{I_2} - \frac{p_I}{2} \quad [9]$$

The partial pressures p_{Se_2} and p_{I_2} are then readily obtained from Eq. [6] and [7].

A plot of the calculated $\log K_{p1}$ *vs.* $1/T$ for the three samples is shown in Fig. 3. The linear dependence of $\log K_p$ on $1/T$ and the lack of dependence of K_{p1} on pressure is reasonable confirmation that Eq. [1] and [2] constitute a satisfactory model for the equilibria. The standard enthalpy, ΔH° and entropy ΔS°, of reaction were obtained by the second law treatment using the relation

$$\log K_{p1} = -\frac{\Delta H^\circ}{2.303\, RT} + \frac{\Delta S^\circ}{2.303\, R} \quad [10]$$

where ΔH° and ΔS° are assumed independent of temperature. The best least square fit of Eq. [10] to the calculated results yields

$$\Delta H^\circ_{1000°K} = +23.1 \pm 1 \text{ kcal}$$

$$\Delta S^\circ_{1000°K} = +21.1 \pm 1 \text{ e.u.}$$

Discussion

Although the assumptions made in the above calculation appear straightforward, it is desirable to discuss several of them in somewhat greater detail. In order to insure the validity of Eq. [4]-[6], we have used a relatively small amount (see Table I) of ZnSe of the highest purity. Therefore, any errors in Eq. [4] and [5] caused by volatilization of an impurity or in Eq. [6] caused by a deviation from stoichiometry of the ZnSe (which is assumed to be less than 10^{-2}%) are negligible. Similarly the conservation of iodine in the vapor phase, Eq. [5], is valid if we assume that the solubility of I_2 in ZnSe does not greatly exceed the

Table II. Heat capacity (Cp) and entropy data

$Cp = a + b\ 10^{-3}\ T$

Specie	a	b	Ref.	$S°_{298}$	Ref.
$ZnI_2(g)$	13.82	1.45	(15)	71.71	(18)
$I_2(g)$	8.94	0.14	(16)	62.28	(8)
$Se_2(g)$	8.73	0.32	(17)	60.2	(8)
ZnSe(s)	11.99	1.38	(3)	—	—

Table III. Data for the calculation of heat of formation of ZnSe, $\Delta H°_{298f}$

Reaction	$\Delta H°_{298}$	Ref.
$ZnI_2(g) + \frac{1}{2}Se_2(g) \rightleftarrows ZnSe(s) + I_2(g)$	−25.0 kcal	this work
$ZnI_2(s) \rightleftarrows ZnI_2(g)$	28.6	(19)
$Zn(s) + 2I(s) \rightleftarrows ZnI_2(s)$	−50.0	(20)
$I_2(g) \rightleftarrows 2I(s)$	−14.9	(8)
$Se(s) \rightleftarrows \frac{1}{2}Se_2(g)$	17.06	(8)
$Se(s) + Zn(s) \rightleftarrows ZnSe(s)$	−44.2 kcal	

solubility of I_2 in CdS which was reported by Nitsche, Bölsterli, and Lichtensteiger (11) to be *ca.* 10^{-2} mole %.

The assumption that Se_2 is the only selenium containing gas phase species is not strictly valid below *ca.* 900°K since at least some Se_6 is formed. By using the data of Stull and Sinke (8) for the equilibrium

$$3Se_2(g) \rightleftarrows Se_6(g)$$

we have excluded any point from Fig. 3 for which the ratio p_{Se_6}/p_{Se_2} exceeds more than a few per cent. A more important source of error may be the presence of Se_4[2] (or possibly some other species of selenium). In lieu of any quantitative information on Se_4 concentrations, we have neglected it in the above calculations and expect that in any case it would be negligible at somewhat higher temperatures. The satisfactory fit of the data to the model further indicates that neglecting Se_4 does not give rise to a large error.

Comparison with literature values.—In order to make a direct comparison of our results with those of other investigators, it was first necessary to calculate the heat of formation, $\Delta H°_{298f}$, and entropy, $S°_{298}$, of ZnSe. The heat and entropy of reaction at 298°K may be calculated from our measured data and the data in Table II using the usual formulas.

$$\Delta H°_{298} = \Delta H°_{1000} + \int_{1000}^{298} \Delta C_p\, dT = 23.1 + 1.9 = 25.0 \text{ kcal}$$

$$\Delta S°_{298} = \Delta S°_{1000} + \int_{1000}^{298} \frac{\Delta Cp}{T}\, dT = 21.1 + 3.2 = 24.3 \text{ e.u.}$$

The entropy of ZnSe at 298°K is calculated from the entropy of Eq. [1] at 298°K, $\Delta S°_{298}$, and the data in Table II.

$$S°_{ZnSe}(s) = S°_{ZnI_2}(g) + \tfrac{1}{2}\, S°_{Se_2}(g) - S°_{I_2}(g) - \Delta S°_{298} = 15.4 \text{ e.u.}$$

The standard heat of formation of ZnSe is calculated directly from literature data and the measured enthalpy, $\Delta H°_{298}$, in Table III.

We finally compare our results in Table IV with the results of previous investigations as tabulated by Goldfinger and Jeunehomme (3).

The agreement of our data with that of Wösten and Geers is probably within our combined experimental errors.

Conclusion

The heat of formation, $\Delta H°_{298f}$, and entropy $S°_{298}$ for ZnSe have been determined indirectly by measuring the equilibrium between ZnSe and $I_2(g)$. The resulting data are in agreement with the known experimental result (11) that ZnSe may be vapor grown via the iodine disproportionation reaction using a hot to cold process. The relatively slow rates at which the pressure equilibrated in the Bourdon gauge between 800°-900°K indicate that seed temperatures in a vapor growth process should not be too low for optimum growth rates.

[2] Extensive investigations of the composition of sulfur vapor by Braune, Peter, and Neveling (12) using a Bourdon gauge, and by Berkowitz and Chupka (13) using a mass spectrograph reveal the presence of all even-numbered polymers up through S_8. Mass spectrographic studies (14) of Se vapor reveal a qualitatively similar distribution of species. The similarity between the thermodynamic properties of the sulfur species and the known Se species, *i.e.*, Se_2, Se_6 suggests that Se_4 may be present in our experiments in somewhat greater concentrations than Se_6 as calculated above.

Table IV. Summary of experimental determinations of $\Delta H°_{298f}$, $S°_{298}$ for ZnSe

$-\Delta H°_{298f}$	$S°_{298}$	Method	Investigator
34			Rossini
52	7	Knudsen recalc. 2nd law	Korneeva
47	16.6	Transport 2nd law	Wösten and Geers
39.3	19.8	Knudsen 2nd law	Goldfinger and Jeunehomme
44.2	15.4	Total pressure 2nd law	This paper

Acknowledgment

The authors would like to thank A. Reisman, M. Lorenz, and H. Leonhardt as well as other members of the laboratory staff for helpful suggestions and discussions during the course of this investigation. They are particularly indebted to Dr. M. Aven of the General Electric Research Laboratories for supplying the high-purity ZnSe, and would also like to thank C. Fisher and C. Mead for constructing several Bourdon gauges. This work was supported in part by AFCRL Contract No. AF19(628)-2468.

Manuscript received July 20, 1965; revised manuscript received Sept. 10, 1965.

Any discussion of this paper will appear in a Discussion Section to be published in the December 1966 JOURNAL.

REFERENCES

1. I. V. Korneeva, V. V. Sokolov, and A. V. Novoselova, *Russ. J. Inorg. Chem.*, **5**, 241 (1960).
2. W. J. Wösten and M. G. Geers, *J. Phys. Chem.*, **66**, 1252 (1962).
3. P. Goldfinger and M. Jeunehomme, *Trans. Faraday Soc.*, **59**, 2851 (1963).
4. F. Hochberg, Paper presented at the New York Meeting of the Society, Sept. 29-Oct. 3, 1963, Abstract 139.
5. T. O. Sedgwick, *This Journal*, **112**, 496 (1965).
6. R. A. Washington and S. N. Naldrett, *J. Am. Chem. Soc.*, **77**, 4232 (1955).
7. R. Nitsche and D. Richman, *Z. Elektrochem.*, **66**, 709 (1962).
8. Stull and Sinke, "Thermodynamic Properties of the Elements," Advances in Chemistry Series No. 18, American Chemical Society (1956).
9. "The Chemistry and Metallurgy of Miscellaneous Materials," Chap. 3, 5, 6, L. L. Quill, Editor, McGraw-Hill Publishing Co., New York (1950).
10. Selected Values of Chemical Thermodynamic Properties, NBS 500, Series III (1961).
11. R. Nitsche, H. U. Bölsterli, and M. Lichtensteiger, *J. Phys. Chem. Solids*, **21**, 199 (1961).
12. H. Braune, S. Peter and V. Neveling, *Z. Naturforsch.*, **69**, 32 (1951).
13. J. Berkowitz and W. A. Chupka, *J. Chem. Phys.*, **40**, 287 (1964).
14. P. Goldfinger, M. Ackerman, and M. Jeunehomme, Vaporization of Compounds and Alloys at High Temperatures, (Final Technical Report under Contract # AF 61 (052)-19 with ARDC), Universite Libre de Bruxelles, Jan. 1959.
15. Calculated from the data on the free energy function for ZnI_2 as given in L. Brewer *et al.*, *Chem. Rev.*, **63**, 111 (1963).
16. K. K. Kelley, Bureau of Mines, Bulletin 584, p. 91, U. S. Gov't. Printing Office (1960).
17. K. K. Kelley, *ibid.*, p. 158.
18. L. Brewer, *Chem. Rev.*, **63**, 111 (1963).
19. O. Kubaschewski and E. LL. Evans, "Metallurgical Thermochemistry," Table B, Pergamon Press, New York (1958).
20. O. Kubaschewski and E. LL. Evans, *ibid.*, Table A.

Solution Regrowth of Planar InSb Laser Structures

I. Melngailis and A. R. Calawa

Lincoln Laboratory,[1] Massachusetts Institute of Technology, Lexington, Massachusetts

ABSTRACT

A new technique has been developed for growing a thin layer of InSb on an InSb substrate from a saturated In-InSb melt. This type of growth from a solution has been used previously in the fabrication of GaAs and Ge p-n junctions; however, at the lower temperatures required for InSb (about 300°C) certain modifications were made, such as the use of hot liquid stearic acid which covers the InSb substrate and the In-InSb melt during the growth process. By doping the melt suitably, uniform planar InSb n^+-p junctions were grown on substrate areas of about 2 cm^2. Such InSb junctions have been used in large-volume injection lasers which emit coherent light in a direction normal to the junction plane.

The growth of thin crystal layers from a melt was first used by Nelson (1) as a technique of producing remarkably flat and abrupt p-n junctions for Ge tunnel diodes and GaAs junction lasers. In the case of InSb, this process is of particular interest for growing an n-type layer on a p-type substrate because of the difficulty of producing such layers by diffusion. The diffusion of the n-type impurities such as Se, Te, or S is impractical because these elements tend to form glasslike compounds on the substrate surface, and their diffusion coefficients in InSb are small at temperatures below the melting point of InSb (525°C). By the solution regrowth technique an n-type layer can be grown easily on a p-type substrate by simply adding an n-type dopant, such as Te, to the melt.

[1] Operated with support from the United States Air Force.

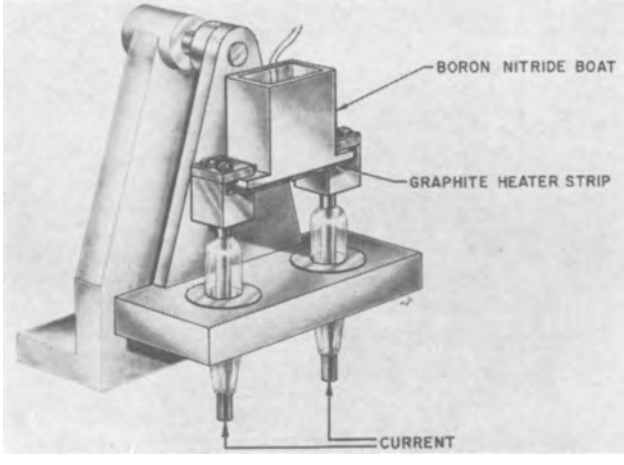

Fig. 1a. Apparatus for solution regrowth showing mount for the boron nitride boat.

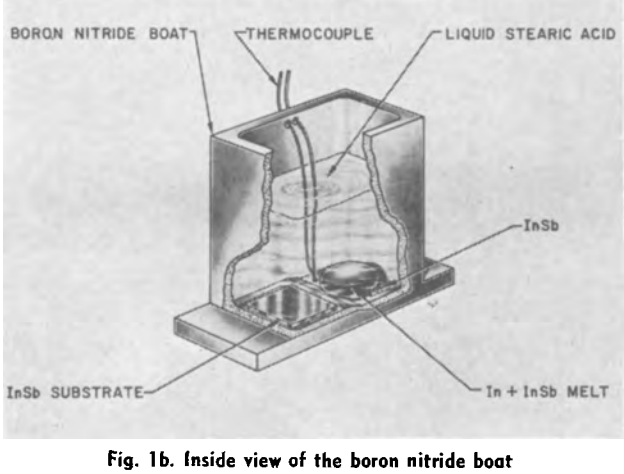

Fig. 1b. Inside view of the boron nitride boat

Method and Results

As shown in Fig. 1a and 1b the apparatus consists of a boron-nitride container which is heated from the bottom by passing current through a graphite heater strip and which can be tilted at various times during a run. The InSb substrate is placed on one side of the boat, while the opposite side contains In and a sufficient amount of InSb to produce a nearly saturated In-InSb solution at the maximum temperature of about 300°C. When growing n-type layers a small amount of Te is added to the solution. The melt and the substrate are kept apart during the first part of the run by a small ridge in the bottom of the boat. Molten stearic acid is then poured into the boat to cover the substrate and the melt. The purpose of the stearic acid is to keep the surface of the substrate and of the melt clean and to insure uniform wetting of the substrate surface by the melt. The boat is then heated by the graphite heater strip. At a temperature of about 300°C the boat is tilted so that the melt flows over the substrate, and the current in the heater is reduced immediately to begin cooling the boat. At the time when the melt first makes contact with the substrate the melt is not quite saturated with InSb, and a thin layer of the substrate surface goes into solution. This removes any surface damage. As the temperature is lowered InSb is forced out of the solution and grows in a uniform layer on top of the substrate. At about 200°-250°C the boat is tilted back and the remaining solution is wiped off the substrate. The stearic acid is then poured off before it solidifies. The grown surface generally has a clean mirrorlike appearance and the growth is quite uniform across the substrate. Figures 2a and 2b show the profile of a growth junction delineated by etching a cleaved (110) surface. All of our solution regrowths were done on a (100) crystal

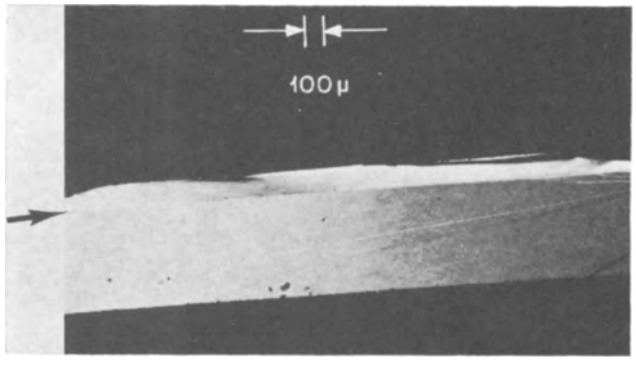

Fig. 2a. Profile of 120μ thick n^+ layer grown on the (100) face of a p-type InSb substrate. The junction indicated by an arrow has been delineated by etching a cleaved (110) face.

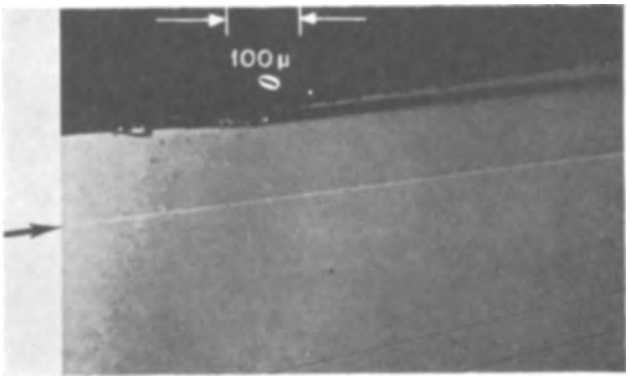

Fig. 2b. A further magnification of the profile in Fig. 2a

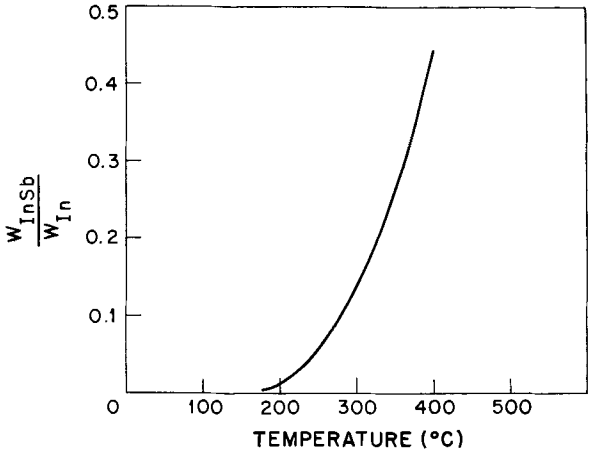

Fig. 3. Temperature dependence of the fractional weight of InSb required to produce a saturated solution, after Hall (4).

face to enable cleaving perpendicular to the junction plane.

The weights of the various ingredients of the melt used in growing a heavily doped n^+ region on a p-type substrate area of 12 x 12 mm were 4.0g of In, 0.6g of n-type InSb, and 4.0 mg of Te. The weight of the Te dopant in this case was chosen so as to produce the highest possible doping in the n^+ layer (8×10^{18} cm^{-3}) (2, 3). The ratio of the InSb weight to the weight of In in the melt was chosen from published solubility data (4). Figure 3 is the temperature variation of the fractional weight of InSb required to produce a saturated solution.

A typical heating cycle is shown in Fig. 4. The melt is poured over the substrate by tilting the boat at the maximum temperature of 315°C in this case. At about 225°C the melt is wiped off. Although most of our runs were similar to this one, the times and temperatures involved do not appear to be critical.

Discussion

The main innovation of our solution regrowth technique is the use of stearic acid, which facilitates growing at the low temperatures required for InSb. The use of a liquid instead of a gas atmosphere also greatly simplifies the apparatus and the process and permits visual observation during the process. Although the use of stearic acid is limited to temperatures not higher than 350°C, at which point it boils away too rapidly, other liquids such as boric oxide could be used for crystals which require higher growth temperatures than InSb.

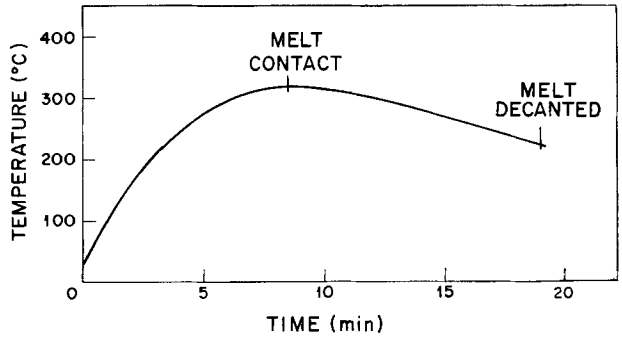

Fig. 4. Temperature cycle of a typical solution regrowth

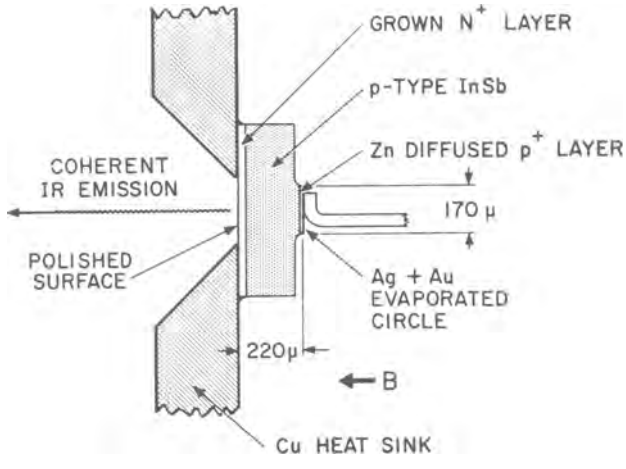

Fig. 5. Large volume InSb injection laser designed for coherent emission normal to the plane of the junction.

One of the applications of this method was in the fabrication of InSb injection lasers in which the light is emitted in a direction normal to the plane of the junction (5). Such a structure is shown in Fig. 5. The n^+ layer was grown on high resistivity p-type InSb by the above technique, and the p^+ layer in this case was made by Zn diffusion. In these diodes the lifetimes of injected carriers are sufficiently long (10^{-7} to 10^{-6} sec) and the mobilities are sufficiently high to permit population inversion across the entire region between the contacts. The radiation which is thus generated in the active region has to pass through the doped p^+ and n^+ layers; hence, these have to be of a good quality crystal which is transparent to the radiation. Solution regrowth proved to be the only satisfactory technique for making good n^+ layers.

Acknowledgment

The authors thank L. J. Belanger and Mary L. Barney for technical assistance.

Manuscript received Aug. 16, 1965. This paper was presented at the San Francisco Meeting, May 9-13, 1965.

Any discussion of this paper will appear in a Discussion Section to be published in the December 1966 JOURNAL.

REFERENCES

1. H. Nelson, *RCA Rev.*, **24**, 603 (1963).
2. A. J. Strauss, *J. Appl. Phys.*, **30**, 559 (1959).
3. J. T. Edmond, *Proc. Phys. Soc.*, **73**, 622 (1959).
4. R. N. Hall, *This Journal*, **110**, 385 (1963).
5. I. Melngailis, *Appl. Phys. Letters*, **6**, 59 (1965).

The Electrodeposition of Coherent Deposits of Refractory Metals

III. Zirconium

G. W. Mellors and S. Senderoff

Parma Research Laboratory, Union Carbide Corporation, Parma, Ohio

ABSTRACT

Exploratory experiments in chloride, bromide, and mixed chloride-fluoride melts always produced dendritic zirconium deposits. Pure fluoride systems consisting of ZrF_4 dissolved in alkali fluoride solvents produced coherent deposits of metal, some as thick as 0.1 in. with no indication of reaching a thickness limit, on electrolysis at 750°C and 30 ma/cm^2 cathode current density. Analysis and material balance experiments showed that reduced compounds were absent in these fluoride systems. Chronopotentiometric measurements indicate that the zirconium is deposited from the tetravalent state in a single four-electron step which would appear to be irreversible. The addition of KBF_4, K_2TiF_6, and Al_2O_3 to a working zirconium bath results in the deposition in coherent form of the compound ZrB_2 and the alloys Zr-Ti and Zr-Al. The ZrB_2 plate was 11 mils thick and showed no evidence of reaching an upper limit of thickness, while both alloys were smooth and fine-grained in nature, the Zr-Al deposit showing a particularly interesting rhythmic banded structure.

Earlier papers in this series have described the electrolysis of fused fluorides to produce columbium and the mechanism for the electrodeposition of tantalum. In this paper the deposition of coherent deposits of zirconium and the mechanism and electrode reactions to form such deposits will be discussed.

A considerable amount of work has been reported on the electrolysis of zirconium-containing molten salts to yield the metal. Efforts to obtain the metal by electrolysis of aqueous or organic solutions have always ended in failure.

Troost (1) electrolyzed molten sodium and potassium fluozirconates, while later Wedekind (2) and Marden and Rich (3) obtained amorphous zirconium powder by this method. Driggs and Lilliendahl (4, 5) obtained zirconium by the electrolysis of molten baths of sodium and potassium chlorides containing potassium fluozirconate. Plotinkov and Kirichenko (6) electrolyzed a melt containing aluminum and potassium chlorides, sodium fluoride, and zirconium tetrachloride, held at 300°-500°C in a porcelain cell. The cathode was copper and the anode aluminum or graphite. Variations of the method were reported using molten sodium chloride, potassium chloride and potassium fluozirconate mixtures (7). Steinberg, Sibert, and Wainer intensively studied the above method and obtained zirconium of 99.8-99.9% purity with carbon content 0.05%, oxygen 0.05%, and nitrogen 0.003% (8, 9).

The above work was concerned with electrowinning the metal and always resulted in cathodic deposits that were in powder or crystal form. To compact the metal, expensive procedures such as vacuum fusion or electron beam melting are necessary; the compacted material may then be rolled into sheets or fabricated into other desired forms. In view of the above, it would be extremely valuable to be able to deposit coherent metal from an electrolytic bath, thus circumventing the aforementioned procedures.

Deposition of coherent plates of pure zirconium has undoubtedly been attempted, but no successful process has been reported. One may note in passing that, although pure refractory metals cannot be deposited from aqueous systems, coherent alloy plates with Fe, Ni, and Co are obtainable. In these processes the refractory metal content (W or Mo) is always less than 30% and usually less than 20%.

In the prior literature there are very few substantiated instances of the deposition of coherent refractory metals by the electrolysis of molten salts. In the case of molybdenum the deposition of coherent metal was reported in a series of papers by Senderoff and Brenner (10). The anode was a pure molybdenum sheet, and the electrolyte, which consisted of potassium hexachloromolybdate (III) (K_3MoCl_6) dissolved in KCl-LiCl eutectic, was contained in an ATJ graphite crucible under an atmosphere of purified argon.

Davis *et al.* (11) deposited coherent layers of pure tungsten from fused salt baths containing borates and tungstic oxide. Schlain and co-workers (12) working in similar systems developed and improved the performance of the baths. Stetson (13) described the deposition of coherent titanium, although in his work there were limitations on substrate material, and indeed in this work and the work on tungsten there appeared to be limits on the ultimate thickness of deposits.

In the electrorefining of Hf metal through NaCl-$HfCl_4$ electrolyte, Baker (14) obtained a thick ($\approx$ ⅛ in.) coherent plate of the metal. However, this appeared to have been a purely fortuitous situation since it was not reproducible, repetition under supposedly identical circumstances yielding a dendritic deposit.

The deposition of columbium (15, 16) and tantalum (17) by the electrolysis of pure fluoride melts has been described by the present authors, and a general method for deposition of a group of refractory metals has been disclosed in the patent literature (18). However, concurrent with this work exploratory experiments were performed in fused chloride and bromide systems as described below.

Experimental

Materials.—$ZrCl_4$ was purchased from Stauffer Chemical Company in crude form. The material, which was pale yellow, was resublimed under argon-10% hydrogen atmosphere. The function of the hydrogen was to reduce $FeCl_3$ to $FeCl_2$, the latter being involatile. Pure $ZrCl_4$ was collected as a snow-white powder in a cooled receiver.

$ZrBr_4$ was made by the interaction of heated Zr metal (450°C) and a stream of bromine gas diluted with argon. The product was sublimed into a collection vessel where it was sealed off and removed from the system.

ZrF_4 and K_2ZrF_6 were obtained from General Chemical Division, Allied Chemical and Dye Corporation. The ZrF_4 was used as-received, but the fluozirconate was purified by recrystallization from water.

Zirconium in sheet and rod form was obtained from Reactive Metals, Inc.

Alkali chlorides, bromides and fluorides (ACS specification) were obtained from Harshaw Chemical Company.

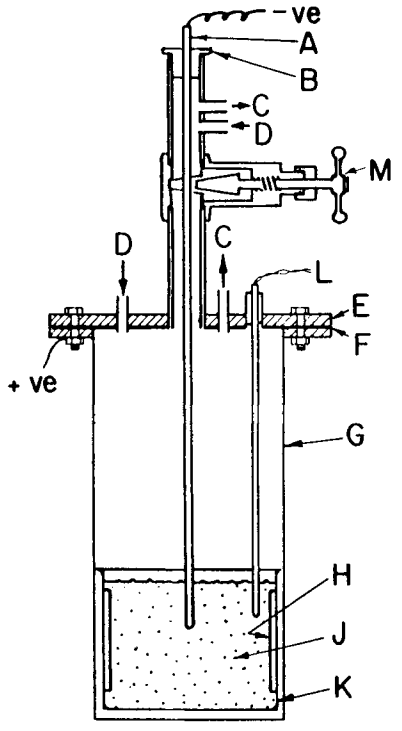

Fig. 1. Apparatus used in electrolysis of fluoride melts: A, stainless steel cathode; B, Teflon stopper; C, argon outlets; D, argon inlets; E, stainless steel lid; F, Teflon or Sauereisen gasket; G, "Hastelloy X" can; H, zirconium anode; J, fluoride melt; K, nickel or stainless crucible; L, thermocouple and well; M, gate valve (1 in.).

Argon was purified by passage through either Ti chips at 900°C or Cu turnings at 700°C.

Boron tribromide and boron trioxide were obtained from American Potash and Chemical Corporation.

Electrolytic cells.—The apparatus used is shown in Fig. 1 and has been fully described in an earlier publication (15).

Results

Chloride melts.—A series of exploratory experiments with melts of the series KCl-LiCl-$ZrCl_4$ and KCl-NaCl-$ZrCl_4$ confirmed that, after extended periods of electrolysis, the melts contained highly colored subhalides and that only dendrites could be deposited under all conditions of temperature, concentration, and cathode current density. In most cases, the dendrites overlay an initial layer of metal about 1 mil in thickness, and this coherent layer is in all probability a diffusion alloy with the material of the substrate. This work will not be discussed further in this paper since it confirms the results of earlier workers (8).

Bromide systems.—Experiments in this system were conducted in the NaBr-KBr eutectic mp 644°C (19) to which about 5 w/o (weight per cent) $ZrBr_4$ was added. The phase diagram of NaBr-KBr-$ZrBr_4$ is unknown, but by analogy with the NaCl-KCl-$ZrCl_4$ diagram a low melting eutectic rich in $ZrBr_4$ might be expected around 70-80% $ZrBr_4$ and 200°-250°C. Accordingly the temperature was held at 250°C for several hours and then slowly raised to the operating temperature.

The initial purification was performed at 800°C and 200 ma/cm² cathode current density (C.C.D.) with approximately 0.2v across the cell. However, polarization soon developed, the cell voltage rising to 6v, 5.8v of which was found to be potential drop at the anode. Simultaneously the current decreased but could be restored by tapping the anode. This suggests the presence of some insoluble film on the anode. No cathodic deposits were obtained, indicating that the species responsible for deposition was absent from the melt or present in insufficient concentration. The experiment was rerun at 950°C (to increase the solubility of such species) and 500 ma/cm². The polarization was to some extent overcome and a thin compacted powder deposit obtained, but on repetition of the experiment the polarization returned in more acute form. Under varying experimental conditions it proved impossible to extract clean dendritic Zr from this melt. A sample was taken from the liquid by means of a "Vycor" tube, and it was found that some crunchy, pulverizable solid was present in the crucible, thus lending some support to the idea of lower halide insolubility.

The bromide solutions on freezing were deep blue-black in color and reacted vigorously with water and dilute acid yielding impure hydrogen. An analysis showed the presence of 0.52% Zr and 69.0% Br and a reducing power of 0.988 milli-equiv/g corresponding to a mean Zr valence of 3.

Mixed chloride-fluoride melts.—In some of the preliminary work it was noted that a bath consisting of an alkali halide eutectic (*e.g.*, KCl-LiCl or NaCl-KCl) together with potassium fluozirconate (K_2ZrF_6 or 2 KF · ZrF_4) required far less "pre-electrolysis" to bring it to the required condition for the deposition of clean dendritic zirconium powders than did the all-chloride bath. Potassium fluozirconate may be purified very easily by recrystallization from water and subsequent drying. However, as in the pure chloride melt electrolysis, even at low temperatures and C.C.D.'s, this solution yielded dendritic powders plus the underlying 1 mil of coherent plate as reported previously (9).

On cooling, the NaCl-KCl-K_2ZrF_6 mixture was found to consist of two layers, the upper being very pale bluish-white and the lower black in color. The lighter material is inert with respect to water and dilute mineral acid, while the black material reacts vigorously, finally depositing a black powder, which again (*v.i.*) is probably zirconium metal formed by the disproportionation during cooling of a subfluoride.

In contradistinction to the fluoride systems, it should be noted that subhalides were always observed in the chloride, bromide, and mixed chloride fluoride systems. As will be seen below, an important feature of the pure fluoride systems is the complete absence of reduced species.

Fluoride systems.—Because of the encouraging results obtained with K_2ZrF_6, notably the ease of handling and involatility of ZrF_4 (sublimation point 910°C approximately) systems consisting of KF-LiF-ZrF_4 (KF-LiF-K_2ZrF_6) and LiF-NaF-KF-ZrF_4 were prepared. The melting point of the KF-LiF eutectic is 492°C and that of the ternary eutectic 454°C.

The ternary eutectic LiF-KF-NaF (Flinak) was used because of its very low melting point (454°C) (20). It had been hoped to deposit zirconium at temperatures in the 500°-600°C range, but this proved impossible, no deposit other than semiadherent powders being produced. It is likely that this occurs because, on the addition of ZrF_4 to the LiF-KF-NaF eutectic, a two-phase or highly viscous system exists up to about 650°C.

The anode was a zirconium sheet rolled in cylindrical form which fitted flush to the inner wall of the internal crucible. The cathode, which was a 1/4 or 3/16 in. diameter molybdenum rod, was centrally mounted. ZrF_4 (10 w/o) was dissolved in the ternary eutectic of NaF-KF-LiF contained in a seamless stainless steel crucible and some 4 hours of electrolysis at 750°C and approximately 400 ma/cm² C.C.D. was sufficient to bring the melt to a satisfactory operating condition. Runs were made at various temperatures, but the most efficient plating conditions were at 750°C with a C.C.D. of 10-30 ma/cm². However, further work showed that plates could be obtained from 675° to 800°C with C.C.D.'s of 5-30 ma/cm². Rotation of the cathode did little to improve the smoothness of the deposit in this particular instance.

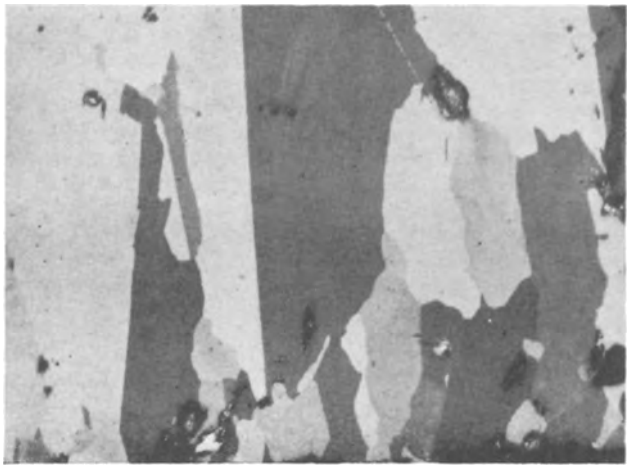

Fig. 2. Piece of detached Zr plate (X150)*

Spectroscopic analysis of the plates revealed them to be almost pure Zr metal, only traces (0.01%) of Fe, Mg, Mn, and Al being detected. A photomicrograph of the plate is shown in Fig. 2 and demonstrates (*a*) the columnar structure of the deposit, and (*b*) the cleanliness and sharpness of the grain boundaries. The grain size is very large compared with that of ZrB_2 and Zr-Ti deposits discussed below and probably indicates a deposit equivalent to a well annealed pure metal.

The residual electrolyte had no reducing power and contained 4.65 w/o Zr (average of two determinations differing by 0.1%).

An examination of the system KF-LiF-ZrF_4 was then made. The KF-LiF eutectic (50-50 M%) has a melting point of 492°C (21). ZrF_4 (14 w/o) was dissolved in the molten eutectic and the melt purified by 24-hr electrolysis at 850°C and 70 ma/cm² C.C.D. The temperature was lowered to 750°C and several runs carried out between 15 and 30 ma/cm² C.C.D. Smooth coherent plates of zirconium were obtained under these conditions.

To study the effects of solvent composition, a NaF-LiF eutectic (mp 652°C) was prepared and 12 w/o ZrF_4 added. The melt was purified by some 35 hr preelectrolysis, but under the identical conditions of temperature and current density leading to coherent plates in the KF-LiF-ZrF_4 and KF-LiF-NaF-ZrF_4 systems, the deposits produced from NaF-LiF-ZrF_4 melts tended to compacted powders although in a few cases an apparently coherent deposit was produced. Variation of experimental conditions of temperature and cathode current densities did not alter this situation materially. The presence of KF appears to be highly desirable for the reproducible production of coherent plates.

Experiments were conducted to assess the possibilities for coherent deposition of Zr from the molten KF-ZrF_4 system. Runs were made at the composition 0.88 KF·0.12 ZrF_4 (28.18 w/o ZrF_4). The lowest working temperature possible was around 800°C, the liquidus being 775°C (22). Unfortunately the melt became very viscous during the electrolysis, and no deposits of value were obtained at temperatures between 800° and 950°C with variations of C.C.D. from 10 to 400 ma/cm². It was thought that, if the ZrF_4 concentrations were less, the high viscosity problem would be overcome and the deposition run even at the higher temperature necessary to liquefy the composition. But electrolysis of 0.98 KF-0.02 ZrF_4 (mp 845°C) failed to produce a coherent deposit even with rotation of the cathode.

In general in the above work it was found that the cathode current efficiency based on the assumption of zirconium tetravalency was between 90 and 100%.

Effect of additives on deposition in chloride, chloride-fluoride, and fluoride baths.—A limited amount of work was done to determine the effect of additives on the electrodeposition of zirconium. In the deposition of molybdenum (23) it was found that electrolysis at 30 ma/cm² C.C.D. and 600°C under an inert atmosphere yielded a plate having a columnar structure and freedom from voids in the deposit, particularly in the presence of an addition of 1% by weight of "activated alumina." Other addition agents which showed promise in extending the range of current density and temperature for satisfactory metal deposition were ferrous chloride (0.1% by weight) and sodium fluosilicate (10% by weight) (24). The deposits obtained from baths containing the latter additive were particularly sound and could be built up to be as much as 0.02 in. in thickness without appreciable roughness. Current densities up to 300 ma/cm² could be used, but a temperature of 900°C was required. On the other hand, the addition of 10% by weight of nickel chloride to the system yielded bright, smooth Mo-Ni alloy deposits containing from 1 to 10% Ni when operated at 600°C and 30 ma/cm² C.C.D.

Addition of purified ZrO_2 (1.25 w/o) to the NaCl-KCl-K_2ZrF_6 bath was without visible effect on the electrolytic product. However, additions of SiO_2 or $ZrO_2 \cdot SiO_2$ made it impossible to obtain deposits of Zr metal at any reasonable temperature or current density, the effect of the additives leading to the production of black slimes. A similar effect was noted for additions of K_2SiF_6 to the chloride-fluoride baths.

The addition of 3 w/o K_2SiF_6 to an LiF-KF-K_2ZrF_6 melt had little effect on the deposit, but when 15 w/o K_2SiF_6 was added, silicon powder was the main cathodic product. It may be noted that silicon powders may be obtained by electrolysis of an LiF-KF-K_2SiF_6 melt, at 850°-900°C and at C.C.D.'s of 300 ma/cm².

The addition of 12 w/o KBF_4 to an electrolytically purified LiF-KF-K_2ZrF_6 solution resulted in the deposition of coherent coatings of ZrB_2 which adhered strongly to the molybdenum cathode. The optimum conditions for deposition (800°C and 30 ma/cm² C.C.D.) differed only slightly from those for depositing zirconium coatings, but it was noted that the requirements for depositing the boride were much less stringent. Purification requirements were less, the allowable range of current density and temperature greater, and the concentration of boron uncritical above the minimum requirement indicated above.

A ZrB_2 plate produced from this bath was 11 mils thick and showed no evidence of nearing an upper limit of thickness. A photomicrograph of the deposit is shown in Fig. 3. The deposit consists of dense columnar grains typical of electrodeposits of sound structure and mechanical properties. The cleanliness and sharpness of the grain boundaries attest to the high purity of this deposit. The major constituents were Zr and B, the minors (<0.1%) were Mn, Si, and Ca, and in addition traces of Fe and Ti were detected. An x-ray pattern showed only lines for ZrB_2. By analysis it was found

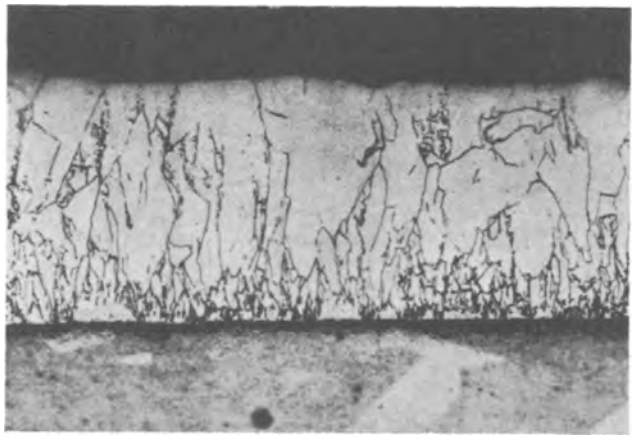

Fig. 3. Cross section of zirconium diboride coating (X150)

* All magnifications before reduction for printing.

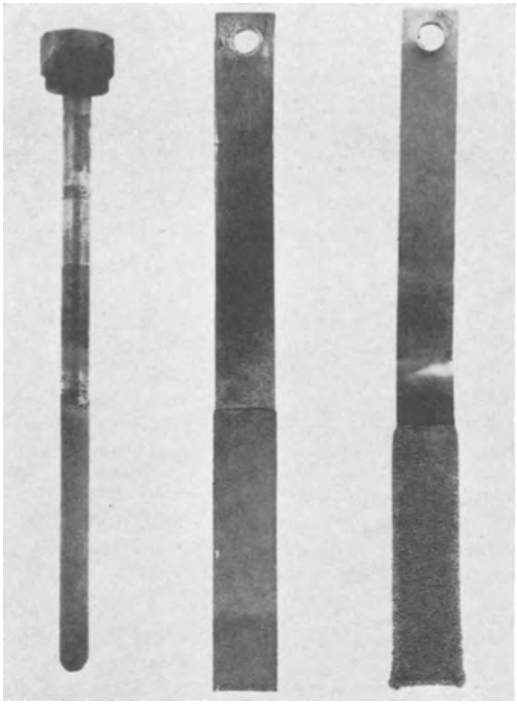

Fig. 4. Zirconium diboride articles

that the boron content of the solution was 0.85 w/o, the Zr 14.4 w/o.

Attempts were made to deposit ZrB_2 from this melt on graphite rods. Spectroscopic (AGKSP) rods, ¼ in. OD, were plated at 800°C and 150 ma/cm^2 with varying thicknesses of coherent ZrB_2. The analyses of the deposit indicated pure ZrB_2 as before, but the adherence was poorer than on molybdenum, perhaps owing to penetration of the substrates by the molten fluorides. A number of ZrB_2 plated articles are shown in Fig. 4.

The addition of KBF_4 to the purified Flinak-ZrF_4 bath also produced coherent plates of ZrB_2. However, when $NaBF_4$ was added to NaF-LiF-ZrF_4 melts it proved impossible to produce ZrB_2 plates, only dendrites and compacted powders being deposited. However, the addition of KBF_4 in sufficiently large amounts (~50 w/o) to NaF-LiF-ZrF_4 melts produced ZrB_2 plates on electrolysis. The systems NaCl-KCl-$ZrCl_4$-KBF_4 or NaCl-KCl-ZrF_4-KBF_4 would deposit only ZrB_2 powders under similar circumstances.

The addition of recrystallized Al_2O_3 to the purified LiF-KF-ZrF_4 or LiF-KF-K_2ZrF_6 melts produces a Zr-Al alloy in the form of smooth coherent plates. A cross section of this material is shown in Fig. 5. Approximately 1% by weight of Al_2O_3 was added to obtain this result. The rhythmic-banded structure is worthy of note.

Presumably the composition of this alloy could be altered by judicious handling of the relevant variables (*e.g.*, C.C.D., temperature and concentration of added alumina).

A few electrolyses were conducted in the system Flinak-ZrF_4-K_2TiF_6 (15 w/o). The anode was a rolled Zr sheet and the cathode a molybdenum rod. A smooth Ti-Zr alloy was produced and a cross section of this deposit is shown in Fig. 6. No further work has been done with this system, and the composition of the alloy is unknown. The surface of the plate is at the top of the picture. It will be noted that a dense columnar structure of sound metal alloy was produced. No voids are evident, grain boundary impurities are absent, and adhesion to the base metal is excellent. The streaks in Fig. 6 consist of thin regions of very fine-grain material which is apparently the same as the rest of the alloy except for grain size. Further, the metallographic treatment has brought out the detailed extremely fine-grain columnar structure, characteristic of a very

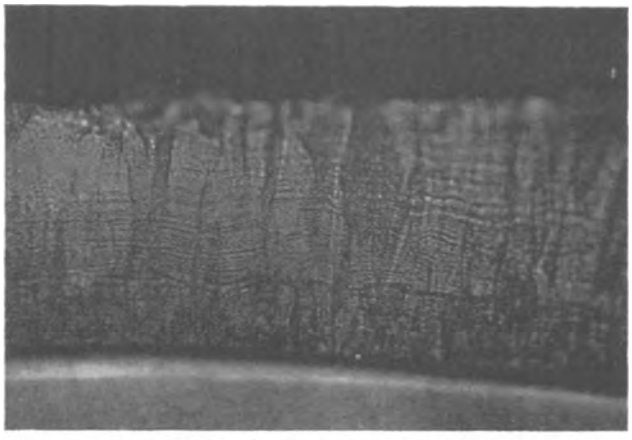

Fig. 5. Zirconium-aluminum alloy (X150)

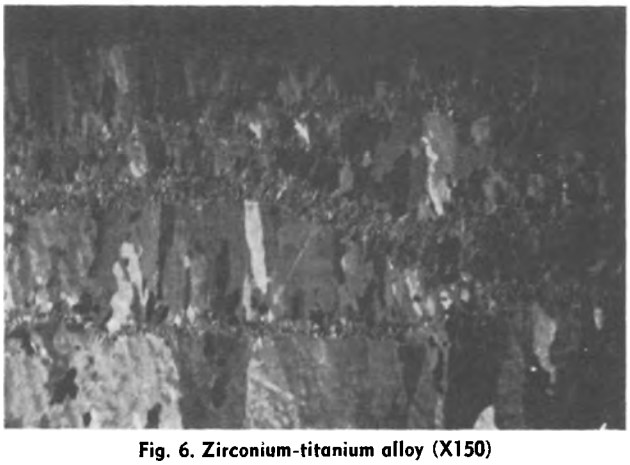

Fig. 6. Zirconium-titanium alloy (X150)

smooth, hard, deposit of high tensile strength. The variations in structure observed in Fig. 6 undoubtedly arose from accidental variations in the current density or other operating variables during the deposition. The effect of these variables on the structure and mechanical properties of the deposit requires further study. The lower criticality of the usual variables in alloy or compound deposition as compared with pure metal deposition was noted in the cases of Zr-Al, Zr-B, and Zr-Ti alloys also.

At this stage it seemed valuable to determine whether ZrB_2 might not be made by the addition of B_2O_3 to a chloride, etc., melt. A NaCl-KCl-$ZrCl_4$ melt was purified electrolytically until clean Zr dendrites were produced. About 3½ w/o dried B_2O_3 ("Trona") was added and after several electrolyses long crystalline needles were deposited. These turned out to be very pure iron containing but a trace of boron and undoubtedly came from the iron crucible. The experiment was rerun using an ATJ graphite crucible, and electrolysis finally resulted in the production of powdery cathode deposits showing Zr and B as main constituents. When the B_2O_3 of the bath was exhausted a further addition of this material was instrumental in producing further Zr-B powders. Unfortunately the x-ray pattern, in addition to demonstrating the presence of ZrB_2, showed also 5-10% of ZrO_2. This, of course, is not surprising in view of the oxidic nature of the melts, and it makes the ZrB_2 produced much inferior to powders and plates from the fluoride baths and to powders from the chloride-KBF_4 bath. It has proved impossible to produce plates from the chloride-B_2O_3 system, a result similar to that found for the chloride-KBF_4 bath described earlier.

The apparatus in which NaBr-KBr-$ZrBr_4$ was electrolyzed in an iron crucible was modified to permit admission of BBr_3 to the melt at operating temperature. BBr_3 is an orange-red liquid, but by shaking with

mercury metal the excess bromine responsible for the color may be removed. BBr_3 was boiled under a stream of purified argon and passed into the melt. No polarization troubles were encountered and a powder deposit of ZrB_2 was obtained at 750°C and 100 ma/cm² C.C.D. However, iron in the deposits, presumably entering the melt from the crucible, caused the termination of this experiment.

A further series of experiments with NaBr-KBr-$ZrBr_4$ melts was run in ATJ graphite crucibles. This time polarization was absent, though the reason is unclear, and clean Zr dendrites were obtained after some 4 hr electrolytic purification. But even at low C.C.D. (30 ma/cm²) and low temperature (750°C) coherent plates of Zr could not be obtained; the result was as observed in chloride and chloride-fluoride systems in that a 1-2 mil coherent plate was present under a dendritic deposit.

Again by bubbling BBr_3 into this melt it was possible to obtain ZrB_2 powders, but this method is wasteful of BBr_3 and inefficient with respect to electricity used as compared with additions of KBF_4 to fluoride melts.

Question of the Valency of Zirconium Species

The only systems from which coherent Zr metal could be plated were those based on pure fluorides, and in these systems the following rather interesting phenomena were observed.

Frequently during the operation of zirconium plating baths the presence of a blue volatile material and a silver liquid near the argon exit tube of the cells was noted. At first it was thought that this material was a subhalide (or perhaps a covalent complex) of zirconium. The presence of this material had been noted under electrolyzing conditions, but then was found to be formed if Zr metal, KF and ZrF_4, or more simply Zr + KF, were heated together to about 800°C.

The volatile material was collected and identified as potassium metal. Therefore, a reaction of the type

$$Zr + nKF \rightarrow ZrF_n + nK \qquad [1]$$

where $n = 1, 2, 3$ and possibly 4 had occurred.

The following experiment was performed to determine the value of n in the above equation. A weighed amount of pure potassium fluoride was held at 875°C in a stainless steel crucible under argon atmosphere and reacted for 30 hr with a weighed zirconium rod that was withdrawn from the system at the conclusion of the run and reweighed. At the temperature of operation the volatile material was evolved and conducted away from the reactor. The material remaining in the crucible was analyzed and it was found that; (*a*) all the zirconium lost from the weighed rod was now present in the crucible; (*b*) the loss of fluorine was negligible and could probably be accounted for on the basis of KF volatility; and (*c*) the molecular ratio of potassium lost by volatility to zirconium dissolved from the rod was 3.9, a close approximation to 4.

From these data it may be concluded that in reaction [1] $n = 4$ and that fluorides of lower valent zirconium do not exist in these melts. If such subfluorides existed they undoubtedly would have been formed in preference to ZrF_4 in the presence of excess Zr metal and would probably have disproportionated on cooling, leading to ZrF_4 and Zr powders. No Zr powders were found, and a trace of a metal powder found was identified as Cr, the source of which was probably the stainless steel crucible. Further, even if a lower fluoride had formed and later disproportionated, the observed ratio of K lost to Zr added would not have been 4, but would have been equal to the valence of the Zr in the intermediate compound. It may be concluded that reduced zirconium compounds are not involved in the metal deposition process. The reduction of KF by Zr metal proceeds in spite of the positive free energy change because of the volatility of potassium metal and the extremely stable fluozirconate complex formed between the excess KF and ZrF_4.

However, recently the synthesis of both zirconium di- and trifluoride has been reported (25, 26), but we have no evidence from the above results and those obtained from the chronopotentiometric investigations described below that reduced compounds or complexes of these materials are involved in the present system.

An experiment identical to the above was run to obtain cooling curve data on the system formed from Zr and KF. If the weights of Zr and KF are known, then it is possible from the known stoichiometry of the reaction to calculate the composition obtained in the KF-ZrF_4 system. In one such experiment, the calculated composition was 5.3 mole % ZrF_4 which has a liquidus at 834° and a solidus at 768°C. Accepted literature values for this composition are 830° and 765°C (27). This then is added confirmation that the end product of the Zr-KF reaction is a composition in the KF-ZrF_4 system in which $[ZrF_7]^{-3}$ is probably the dominant Zr-containing species. The latter may be inferred from the fact the K_3ZrF_7 melts congruently at 910°C and precipitates at the liquidus temperature. Similar conclusions may be drawn from surface tension (28, 29) and spectroscopic (30) measurements in these systems.

Chronopotentiometric Experiments

The apparatus used in this work has been described in a previous paper (17) and consists basically of a constant current pulsing device, an oscilloscope on which is displayed the resultant potential-time relationship, and a photographic recording device.

Since the reduction potentials of zirconium and aluminum are close together, it was thought desirable to replace the alumina bridge with a similar bridge constructed of BN. Unfortunately, even after prolonged soaking in an alkali-fluoride melt the resistance across a BN bridge was in excess of 10^5 ohms. In a second bridge a 0.067 in. (1/16 in.) hole through the bridge was merely filled with the melt and the resistance was approximately 70 ohms at 750°C. However, in operation this bridge proved unsatisfactory, and measurements were made with alumina, zirconia, and magnesia bridges and in one case measurements were made by using a platinum wire immersed in the melt as a quasi-reference.

A typical blank for the alkali-fluoride solvent is shown in Fig. 7; the $i\tau^{1/2}$ value being 1 x 10^{-2} amp cm^{-2} $sec^{1/2}$ at 750°C, 100 ma/cm² and —1.9v *vs.* the Ni/Ni^{2+} reference electrode.

With a zirconium concentration of 7.23 x 10^{-5} moles/cc added as K_2ZrF_6, chronopotentiograms were obtained at 750°C. At 50 to 100 ma/cm² C.C.D. no well-defined plateau was obtained. Figure 8 shows one such chronopotentiogram with the poorly defined plateau just under —1.5v. When the current density was raised to 300 ma/cm² and then to 500 ma/cm² and the

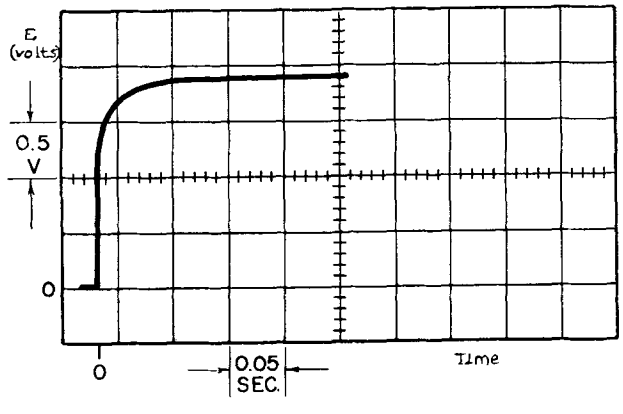

Fig. 7. Typical blank for KF-NaF-LiF solvent at 750°C C. D. 100 ma/cm².

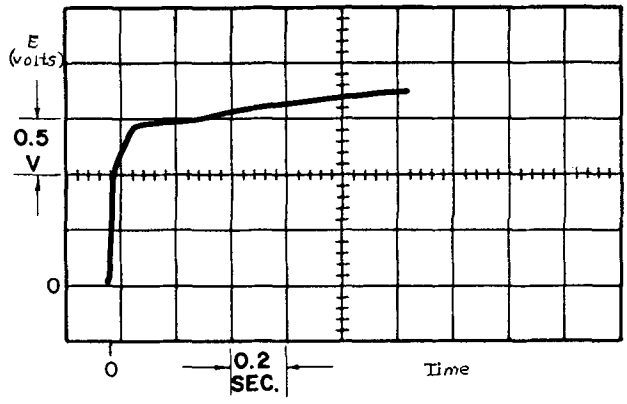

Fig. 8. Chronopotentiogram for KF-NaF-LiF-ZrF_4. C_{Zr} = 7.23 × 10^{-5} moles/cc; T = 750°C; C.D. = 100 ma/cm^2.

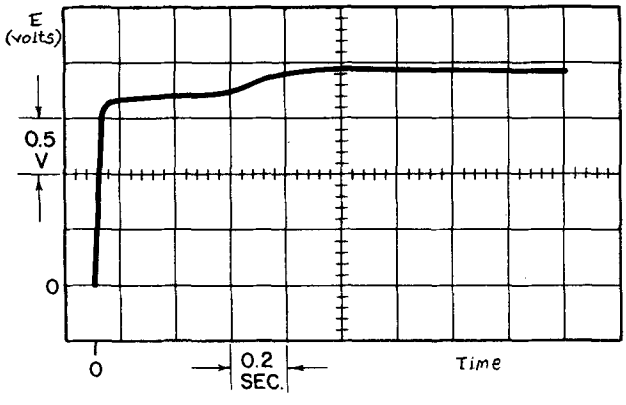

Fig. 9. Chronopotentiogram for KF-NaF-LiF-ZrF_4. C_{Zr} = 2.77 × 10^{-4} moles/cc; T = 750°C; C.D. = 500 ma/cm^2.

concentration also increased, a chronopotentiogram such as that shown in Fig. 9 was obtained, with $E_{1/4}$ value of —1.69v. The higher $E_{1/4}$ value can best be accounted for by the increased IR drop which resulted from the fivefold increase in current density.

Although potassium is apparently some 0.4 ~ 0.5v base to zirconium in this system, there is a chemical reaction between zirconium metal and KF as discussed earlier, and this occurs because of the volatility of potassium metal and the complexity of ZrF_4 produced with additional KF. Therefore, it is clear that with low concentrations of Zr in the bath at high temperatures there will be a corrosion reaction occurring which would distort the chronopotentiogram. However, if one increases the rate of Zr production by, for example, increasing the current density considerably, it is seen that the plateaus may be resolved (Fig. 9).

It has been suggested by Manning and Mamantov (31), on the basis of their polarographic measurements in KF-NaF-LiF-ZrF_4 at 500°C, that the zirconium reduction occurs in a single reversible four-electron step at —1.4v *vs.* the platinum quasi-reference electrode that they employed.[1] Since at 750°C we were not able to interpret our data with certainty except at very high current density, experiments were conducted at 500° and 650°C. Also, to eliminate any possible interference by alumina from the salt bridge, a platinum quasi-reference of the type mentioned above (31) was employed. Because of the undefined potential of this electrode, quantitative conclusions cannot be drawn regarding $E_{1/4}$ values, but the 500° and 650°C results show a single well-defined plateau (Fig. 10 and 11) at

[1] The authors have found in the course of the present investigation that this platinum quasi-reference is within 0.1v of their Ni/NiF_2 reference electrode. Since Manning and Mamantov reported the presence of iron in their solutions it is possible that the platinum quasi-reference is in fact an iron (II)-iron (III) electrode which would make it approximately 0.1v base to our reference.

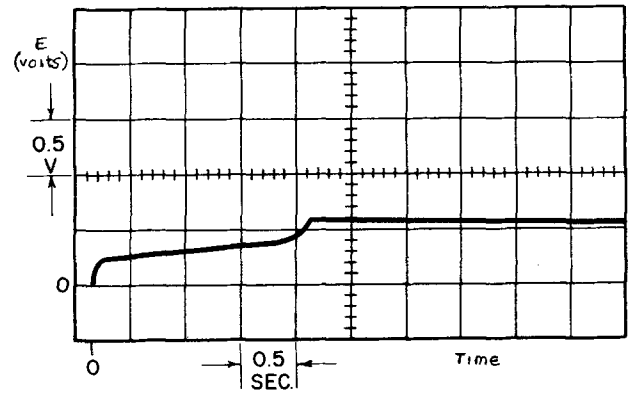

Fig. 10. Chronopotentiogram for KF-NaF-LiF-ZrF_4. C_{Zr} = 3.83 × 10^{-5} moles/cc; T = 500°C; C.D. = 100 ma/cm^2.

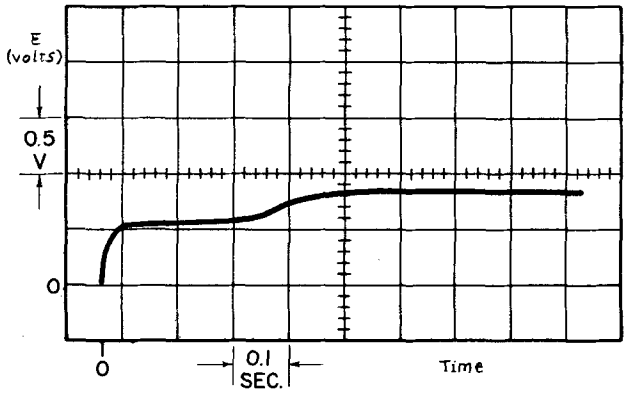

Fig. 11. Chronopotentiogram for KF-NaF-LiF-ZrF_4. C_{Zr} = 3.83 × 10^{-5} moles/cc; T = 650°C; C.D. = 200 ma/cm^2.

all current densities, whereas on returning to 750°C the ill-defined plateau was obtained.

At lower temperatures and higher zirconium melt concentrations the tendency for the corrosion of zirconium by KF to produce potassium is suppressed to the extent that the two processes, the deposition of zirconium and the deposition of alkali metal, are sufficiently resolved to permit observation of the former.

The plot of $i\tau^{1/2}$ *vs.* C for the system is still nonlinear and does not pass through the origin even at low temperature where a well-defined plateau is obtained.

In a reversible system $E = E_o + \frac{RT}{nF} \log \frac{\tau^{1/2} - t^{1/2}}{t^{1/2}}$

one may plot E *vs.* log t and derive n from the slope of this graph. This was done for 500° and 650°C and values of n equal to 2.99 at 500°C and varying between 2.6 and about 10 were obtained at 650°C. At 750°C it proved impossible to draw any plot of a satisfactory nature. This further confirms that the four-electron single step reduction of Zr is a highly irreversible process, but one can only speculate on why this should be so. Winand (32) reports on the basis of a study of electrode mechanisms in the electrolysis of NaCl-ZrF_4 mixtures that the reduction of zirconium occurs in a single, irreversible four-electron step in agreement with our findings in the present study in pure fluoride systems, but contrary to the polarographic results of Manning and Mamantov (31) who believed it to be reversible. In the systems so far examined, *viz.*, Nb, Ta, and Zr, the metal deposition step was always found to be more or less irreversible.

Conclusions

Several conclusions may be drawn from the results presented in previous sections:

1. By appropriate procedures zirconium powders and dendrites may be extracted from any of the baths investigated;

2. Electrolysis of fluoride melts, within certain temperature limits and over a specified range of current densities, results in the deposition of coherent plates of zirconium;

3. Electrolysis of fluoride melts containing both ZrF_4 and KBF_4 leads to the deposition of coherent plates of ZrB_2;

4. By the addition of Al_2O_3 to fluoride melts and subsequent electrolysis, plates of Zr-Al alloy may be obtained;

5. By the addition of K_2TiF_6 to a working zirconium bath, Ti-Zr alloy plates may be deposited;

6. The valency of the zirconium species involved is four and it is reduced to metal in a single four-electron step at —1.4v to the nickel-nickel fluoride reference electrode. This reduction is apparently irreversible.

Manuscript received Aug. 2, 1965; revised manuscript received Sept. 27, 1965. This paper was presented at the San Francisco Meeting, May 9-13, 1965.

Any discussion of this paper will appear in a Discussion Section to be published in the December 1966 JOURNAL.

REFERENCES

1. L. Troost, *Compt. rend.*, **61**, 109 (1865).
2. E. Wedekind, *Z. anorg. u. Allgem. Chem.*, **33**, 81 (1902).
3. J. W. Marden and M. N. Rich, Investigations of Zirconium with Especial Reference to the Metal and the Oxide, Bull. U. S. Bur. Mines, 186 (1921).
4. F. H. Driggs, U. S. Pat. 1,835,025, Dec. 8, 1931.
5. F. H. Driggs and W. C. Lilliendahl, Canadian Pat. 323,060, June 7, 1932.
6. V. A. Plotinkov and E. I. Kirichenko, *Mem. Inst. Chem. Kiev*, **3**, 133 (1939).
7. V. A. Plotinkov and E. B. Gutman, *J. Appl. Chem. USSR*, **19**, 826 (1946).
8. M. A. Steinberg, M. E. Sibert, and E. Wainer in "Zirconium and Zirconium Alloys," pp. 37-72, Am. Soc. Metals, Cleveland (1953).
9. M. A. Steinberg, M. E. Sibert, and E. Wainer, *This Journal*, **101**, 63 (1954).
10. S. Senderoff and A. Brenner, *ibid.*, **101**, 16 (1954).
11. G. L. Davis and C. H. R. Gentry, *Metallurgia*, **53**, 3 (1956).
12. F. X. McCawley, C. B. Kenahan, and D. Schlain, U. S. Bur. Mines, Rept. Investigations, No. 6454 (1964).
13. A. R. Stetson, *Materials in Design Engineering*, **57**, 81 (March 1963); U.S. Pat. 3, 024, 174, March 1962.
14. D. H. Baker, "The Metallurgy of Hafnium," pp. 119-125, D. E. Thomas and E. T. Hayes, Editors, USAEC (1960).
15. G. W. Mellors and S. Senderoff, *This Journal*, **112**, 266 (1965).
16. S. Senderoff and G. W. Mellors, *ibid.*, **113**, 66 (1966).
17. S. Senderoff, G. W. Mellors, and W. S. Reinhard, *ibid.*, **112**, 840 (1965).
18. G. W. Mellors and S. Senderoff, Canadian Pat. 688, 546, June 9, 1964.
19. N. S. Kurnakov and S. F. Zhenchuzhnui, *Z. anorg. Chem.*, **52**, 186 (1907), (Int. Crit. Tables IV, 68).
20. A. G. Bergman and E. P. Durgunov, *Compt. Rend. Acad. Sci. URSS*, **31**, 754 (1941).
21. A. G. Bergman and E. P. Durgunov, *ibid.*, **31**, 753 (1941).
22. Phase Diagrams of Nuclear Reactor Materials, p. 56, R. E. Thoma, Editor, ORNL-2548 (1959).
23. S. Senderoff in "The Metal Molybdenum," pp. 114-214, J. Harwood, Editor, American Society for Metals, Cleveland (1958).
24. D. E. Couch and S. Senderoff, *J. Metals*, **212**, 320 (1958).
25. F. K. McTaggart and A. G. Turnbull, *Australian J. Chem.*, **17**, 727 (1964).
26. P. Erhlich, F. Ploger, and E. Koch, *Z. anorg. u. allgem. Chem.*, **333**, 209 (1964).
27. Ref. (20), p. 56.
28. G. W. Mellors and S. Senderoff, "Proc. 1st Austr. Conference on Electrochemistry," p. 578, J. A. Friend and F. Gutman, Editors, Pergamon, London (1965).
29. G. W. Mellors and S. Senderoff, *This Journal*, **111**, 1355 (1964).
30. J. K. Wilmshurst, *J. Chem. Phys.*, **39**, 2545 (1963).
31. D. L. Manning and Gleb Mamantov, *J. Electroanal. Chem.*, **6**, 328 (1963).
32. R. Winand, *Electrochim. Acta*, **7**, 475 (1962).

The Electrodeposition of Coherent Deposits of Refractory Metals

IV. The Electrode Reactions in the Deposition of Niobium

S. Senderoff and G. W. Mellors

Parma Research Laboratory, Union Carbide Corporation, Parma, Ohio

ABSTRACT

The mechanism for the electrodeposition of coherent deposits of niobium from a molten fluoride electrolyte has been studied by means of chronopotentiometry and compared with that of tantalum. The reduction of the pentavalent niobium in solution occurs in three steps: a reversible one-electron step to the tetravalent state at —0.11v (referred to the Ni/Ni^{2+} electrode), a reversible three-electron step to the monovalent state at —0.76v, and finally an irreversible one-electron reduction to metal at —1.02v. However, the reaction $3Nb^{V} + Nb^{I} \rightarrow 4Nb^{IV}$ interferes with coherent metal deposition from the pentavalent solutions, and consequently in order that coherent metal be produced at high efficiency the mean valence of the bath must be reduced to approximately four. In these circumstances the chronopotentiogram of a working bath shows two steps only: a three-electron reduction, $Nb^{4+} + 3e^{-} \rightarrow Nb^{1+}$ at —0.76v followed by the metal producing step $Nb^{1+} + e^{-} \rightarrow Nb^{0}$ at —1.02v. The diffusion coefficient of $[NbF_7]^{-2}$ has been found to be 2.03×10^{-5} cm^2 sec^{-1} at 750°C and its activation energy for diffusion to be 8.75 kcal/mole. The diffusion coefficient of the tetravalent species is 5×10^{-5} cm^2 sec^{-1} at 750°C.

This is one of a series of papers dealing with a general process for electrodeposition of coherent deposits of the metals of groups IV-B, V-B and VI-B from molten fluorides (1). In the first paper of this series (2) the process variables for the electrodeposition of niobium were discussed together with the properties of the resultant deposits. The second paper discussed the electrode reactions in the deposition of tantalum (3) as determined by means of chronopotentiometry. The third paper (4) discussed the deposition of zir-

conium, its alloys and compounds, and in this paper a study of the electrode reactions in niobium deposition is described.

Experimental

The procedure used for this investigation was essentially that used for the study of tantalum deposition (3). The solvent electrolyte was the eutectic mixture of LiF-NaF-KF (46.5-11.5-42 mole %, mp 454°C) which was purified by melting with NH_4HF_2, sparging the melt with hydrogen, and electrolyzing between graphite electrodes as described previously (3). The purified electrolyte when subjected to chronopotentiometry at 0.100 amp/cm^2 yielded values of $i\tau^{1/2}$ below

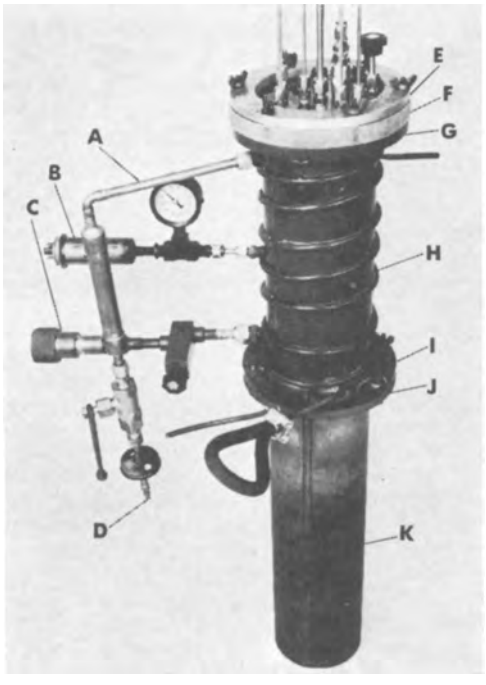

Fig. 1. Chronopotentiometric cell: A, gas exit line; B, vacuum gauge; C, vacuum or gas inlet line; D, gas exit bubbler tip; E, steel flange; F, plexiglas cover disk; G, steel flange; H, water-cooled stainless steel can; I, steel flange; J, steel flange; K, Hastelloy X can.

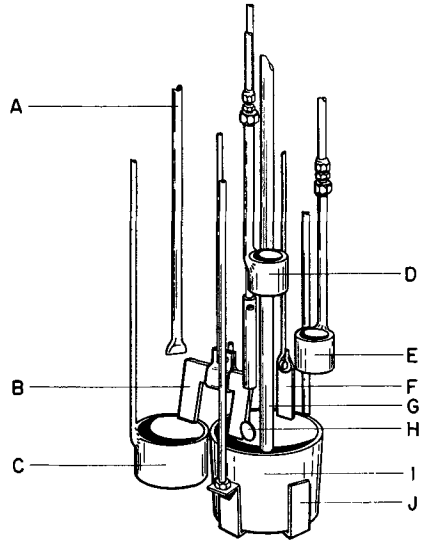

Fig. 2.Internal components of chronopotentiometric cell: A, gas inlet tube; B, salt bridge (alumina); C, nickel crucible for reference electrode; D, sampling cup (silver-plated nickel); E, addition cup (silver-plated nickel); F, counter electrode; G, thermowell; H, indicator electrode; I, crucible (platinum) for electrolyte under study; J, nickel cradle.

5 x 10^{-3} amp cm^{-2} sec$^{1/2}$ at —1.5v referred to the Ni/Ni^{2+} reference electrode. Niobium was added to this purified solvent as dried K_2NbF_7 obtained from Kawecki Chemical Company. NiF_2 for the reference electrode was prepared from $NiCl_2$ as previously and was added to the purified ternary alkali fluoride eutectic to a concentration of 1 mole % NiF_2. Furnace, circuitry, and porous Al_2O_3 salt bridges were the same as used in the earlier study as was the cell and its internal components shown in Fig. 1 and 2. It was necessary in this study to use a platinum crucible for the electrolyte (I, Fig. 2) rather than nickel or molybdenum as was done with the tantalum work, because the latter were slightly attacked by the pentavalent niobium solutions. No attack on the platinum was observed in pure solutions, and no platinum was detected chronopotentiometrically in the solutions. To prevent alloying with the platinum crucible by the nickel cradle which held it, the crucible was placed in a short alumina cup, which was placed in the nickel cradle. The sampling and addition cups (D and E, Fig. 2) were plated with silver to prevent attack on them by the pentavalent niobium solution.

The electrodes used most frequently as indicator electrodes were 0.005 in. platinum sheet disks, 0.9 cm^2 in area welded to 0.015 in. platinum wire. Counter electrodes in all cases were platinum strips. Niobium electrodes could not be used since they were attacked by the pentavalent niobium solutions. When it was desired to study a reduced solution it was reduced *in situ* by electrolyzing with a platinum cathode and niobium anode. Oxidation *in situ* was accomplished by using a spectrographic graphite anode. These "processing" electrodes were then replaced with the normal indicator and counter electrodes for measurements. The same reference electrode, Ni/NiF_2 (1 mole %), NaF-KF-LiF eutectic||, was used.

The general procedure for making the measurements was the same as used for tantalum (3). Chronopotentiograms at various current densities were recorded by use of a Polaroid camera on a Tektronix 535A oscilloscope on a solution of K_2CbF_7 in the alkali fluoride solvent at some concentration and temperature. The temperature was then changed, and another set of chronopotentiograms at various current densities were recorded. When the temperature range from 650° to 800°C was covered, a sample for analysis was taken, and a new solution was prepared at another concentration for a similar series. In a few cases the valence of the pentavalent niobium was reduced *in situ* by electrolysis at 15 ma/cm^2 with a niobium anode and platinum cathode, and a similar group of chronopotentiograms was run on the solution with the niobium in a mean valence state between 4 and 5. The total concentration and mean valence state were determined as previously (2).

Results

Chronopotentiograms were run at concentrations of K_2NbF_7 ranging from 0.025 to 0.08 millimole cm^{-3} at current densities between 0.05 and 0.4 amp/cm^2 and temperatures from 650° to 800°C. Figure 3 is a typical chronopotentiogram at 650°C showing two plateaus with $E_{1/4}$ values at —0.77 and —1.05v. The third near —1.5v is due to aluminum contamination from the Al_2O_3 salt bridge. When a porous BN salt bridge is used this disappears, but the BN salt bridge is inconvenient to use because of its structural weakness. Figure 4 is a chronopotentiogram on the solvent mixture (KF-LiF-NaF eutectic) alone showing essentially no reducible material present until the cathode reaches a potential of approximately —1.8v, at which potential the alkali metal of the solvent is reduced. Tables I and II summarize the data obtained at 750°C. The average $E_{1/4}$ values for the first and second plateaus are —0.756 ±0.015v and —1.02 ± 0.03v, respectively, and the transition time constant for the first plateau is 1.52 ± 0.03 amp sec$^{1/2}$ cm mole^{-1}. The ratio of the transition times

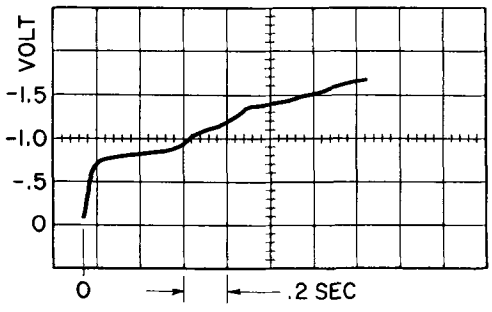

Fig. 3. Cathodic chronopotentiogram for K_2NbF_7 dissolved in KF-LiF-NaF eutectic mixture: concentration, 5×10^{-5} moles/cm^3; current density, 0.1 amp/cm^2; temperature, 650°C.

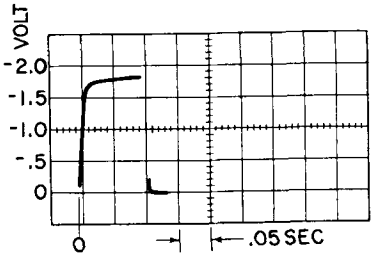

Fig. 4. Cathodic chronopotentiogram of solvent (KF-LiF-NaF) only: current density, 0.1 amp/cm^2; temperature, 750°C.

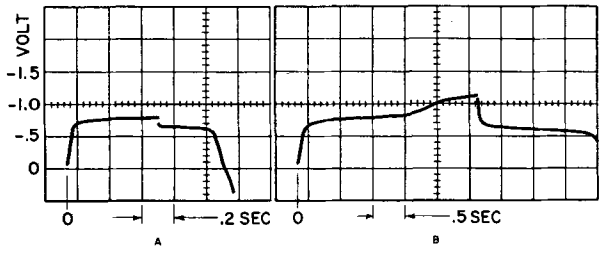

Fig. 5. Cathodic-anodic chronopotentiograms of K_2NbF_7 dissolved in Na-F-KF-LiF: cathodic portion on left, anodic on right. Concentration, (a) 5.6×10^{-5} moles/cm^3, (b) 5×10^{-5} moles/cm^3; current density, (a) 0.1 amp/cm^2, (b) 0.05 amp/cm^2; temperature, (a) 750°C, (b) 650°C.

for the two plateaus is 0.55 ± 0.11. The over-all average values are the averages of the results of five runs for each of the five concentrations. Each is thus the average of 25 chronopotentiometric runs. In Fig. 5 are shown two cathodic-anodic chronopotentiograms. In Fig. 5A the current was reversed before the first plateau was completed, and in Fig. 5B it was reversed before the second plateau was completed. Both give a single oxidation step corresponding to the lower (—0.76v) plateau.

Discussion

The values obtained for $E_{1/4}$ are each approximately 0.25v noble to those found for tantalum (3). This is consistent with the fact that in a plating solution containing equal concentrations of niobium and tantalum a plate is obtained at 35 ma/cm^2 which contains 99.8% niobium. The transition time constant, $i\tau^{1/2}/C$, for the first plateau is 50% greater than that for tantalum and the value of $i\tau^{1/2}/C$ for the second plateau is not constant but varies with concentration, indicating some degree of irreversibility of the final reduction step as in the case of tantalum. Let us now consider the details of each step as disclosed by the data.

Interpretation of the first plateau.—In all the data presented in Tables I and II the solutions contained niobium in its pentavalent state. The first wave, therefore, must represent the reduction of an ion containing pentavalent niobium to some lower valence state with the transfer of less than five electrons.

However, the first wave of the chronopotentiogram in Fig. 3 actually contains two reduction steps which were resolved as follows: by raising the temperature to 750°C and running a chronopotentiogram at the same current density as in Fig. 3, *i.e.*, 100 ma/cm^2, one obtains the chronopotentiogram shown in Fig. 6a. A very small plateau is seen here at about —0.1v. To resolve this more clearly, the current density was reduced to 30 ma/cm^2, and the chronopotentiogram in Fig. 6b was run. It can be seen from this that the $E_{1/4}$ value for this plateau is —0.11v. On electrolytically reducing the solution to a mean valence of 4.2 and running the chronopotentiogram, Fig. 6c is obtained. The —0.11v plateau has now disappeared and only that at 0.76v is seen. Reoxidizing the bath causes the —0.11v plateau to reappear as seen in Fig. 6d. It is clear from this that the —0.11v plateau corresponds to the reduction of the pentavalent ion and is the first step in the reduction to metal. For convenience, however, since the transition time, τ_1, of the first step is only about 2% that of the second step, τ_2, (the one at —0.76v) they will be treated together so that $\tau_s = \tau_1 + \tau_2$ in the following discussion.

If one can establish that this combined step is a reversible diffusion-controlled process one may obtain n_2, the electron number of the second step from

$$E = E_o' + \frac{RT}{n_2 F} \ln \frac{\tau_s^{1/2} - t^{1/2}}{t^{1/2}} \qquad [1]$$

Table II. Transition time of the second plateau of the reduction of K_2NbF_7 in Flinak at 750°C

Conc. K_2NbF_7 moles cm^{-3} × 10^5	(a) τ_3/τ_s	$i\tau_3^{1/2}/C$ (amp sec$^{1/2}$ cm mole^{-1}) × 10^{-3}
2.5	0.68 ± 0.22	1.28
5.0	0.50 ± 0.04	1.06
5.6	0.61 ± 0.09	0.95
6.1	0.65 ± 0.06	1.27
8.0	0.32 ± 0.09	0.85
Over-all average	0.55 ± 0.11	

(a)—τ_3 = transition time of second plateau in chronopotentiograms corresponding to Fig. 3.

Table I. Chronopotentiometric data for reduction of K_2NbF_7 in Flinak at 750°C

Conc. K_2NbF_7, moles cm^{-3} × 10^5	C.D., amp/cm^2 Min.	Max.	(a) $(E_2)_{1/4}$, volt Average	(b) $(E_3)_{1/4}$, volt Average	(c) $i\tau_s^{1/2}$, amp sec$^{1/2}$ cm^{-2} Average	$i\tau_s^{1/2}/C$, (amp sec$^{1/2}$ cm mole^{-1}) × 10^{-3}
2.5	0.030	0.250	0.742 ± 0.013	1.03 ± 0.01	0.0384 ± 0.002	1.55
5.0	0.050	0.250	0.736 ± 0.016	1.04 ± 0.03	0.0757 ± 0.002	1.51
5.6	0.100	0.300	0.764 ± 0.010	0.96 ± 0.04	0.0830 ± 0.007	1.48
6.1	0.100	0.250	0.773 ± 0.019	—	0.0961 ± 0.005	1.57
8.0	0.100	0.400	0.774 ± 0.010	1.03 ± 0.01	0.121 ± 0.004	1.51
Over-all average			0.756 ± 0.015	1.02 ± 0.03		1.52 ± 0.03

(a)—$(E_2)_{1/4}$ = quarter wave potential of first plateau in chronopotentiograms corresponding to Fig. 3.
(b)—$(E_3)_{1/4}$ = quarter wave potential of second plateau in chronopotentiograms corresponding to Fig. 3.
(c)—τ_s = transition time of first plateau in chronopotentiograms corresponding to Fig. 3.

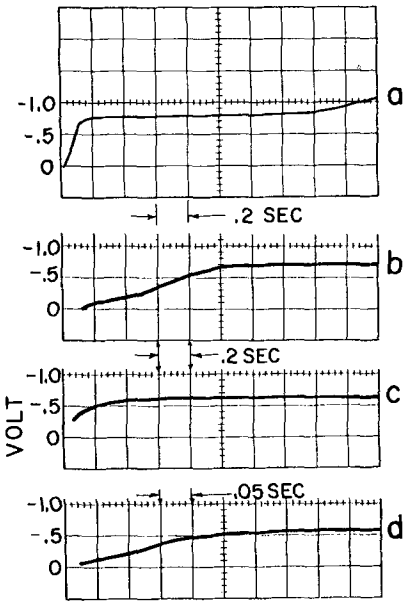

Fig. 6. Chronopotentiogram showing effects of current density and valence state: temperature, 750°C; concentration Nb, 5 × 10^{-5} moles/cm^3.

	a	b	c	d
Current density, ma/cm^2	100	30	30	30
Niobium valence	5.0	5	4.20	4.34

(since $\tau_1 << \tau_2$) (5) by plotting the potential, E, at time, t, in a chronopotentiogram such as Fig. 3 against log $\tau_s^{1/2} - t^{1/2}/t^{1/2}$ where τ_s is the transition time, or time corresponding to the length of the plateau in the chronopotentiogram. A straight line of slope 2.3 $RT/n_2\mathbf{F}$ results (5). One criterion for a diffusion-controlled reaction without kinetic complications is that the equation,

$$i\tau^{1/2} = \tfrac{1}{2}\, nCD^{1/2}\mathbf{F}\pi^{1/2} \qquad [2]$$

where i is the current density, τ the transition time, n the number of electrons in reaction, C the concentration of the reacting species, D the diffusion coefficient of the reacting species, and $\mathbf{F}$ the Faraday constant, describes the chronopotentiogram (6). Thus the constant, $i\tau^{1/2}/C$ should be independent of current density and concentration and $i\tau^{1/2}$ plotted against C be linear and extrapolate to zero at zero concentration. In Table I it can be seen that $i\tau_s^{1/2}/C$ is independent of concentration and the data from which this table was prepared confirm its independence of current density. In Fig. 7 it is seen that the plot of $i\tau_s^{1/2}$ *vs.* C is linear and passes through the origin. In Fig. 5A one notes the very small difference in potential between the cathodic and anodic waves, and it can be shown that this difference is accounted for by twice the IR drop in the solution, so that no appreciable polarization is detectable. Thus, having demonstrated the reversibility of the first (combined) wave one may derive n_2 for the second step from the plot of E *vs.* the log term in Eq. [1]. A typical plot is shown in Fig. 8. Twelve such plots were made using data from runs over the full range of current density and concentration, the slopes of each determined, and n_2 for each calculated. The average value thus obtained was 3.05 ± 0.45. This indicates that the plateau at —0.76v corresponds to a three-electron reduction. Another method of determining n in a stepwise reduction is by examining the ratio of transition times of the two steps (5). Taking the first combined wave as one step with a transition time, τ_s, and the final wave (plateau at —1.02v) with a transition time, τ_3, then the n values for each step may be calculated from

$$\frac{\tau_3}{\tau_s} = \left(\frac{n_3}{n_s}\right)^2 + 2\left(\frac{n_3}{n_s}\right) \qquad [3]$$

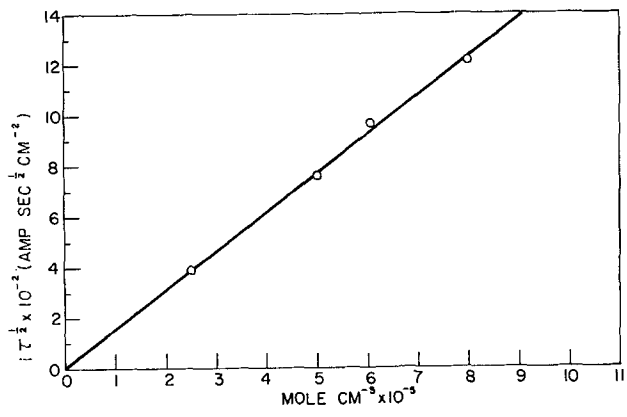

Fig. 7. Transition time, current, concentration relationship from cathodic chronopotentiograms of K_2NbF_7 in NaF-KF-LiF at 750°C.

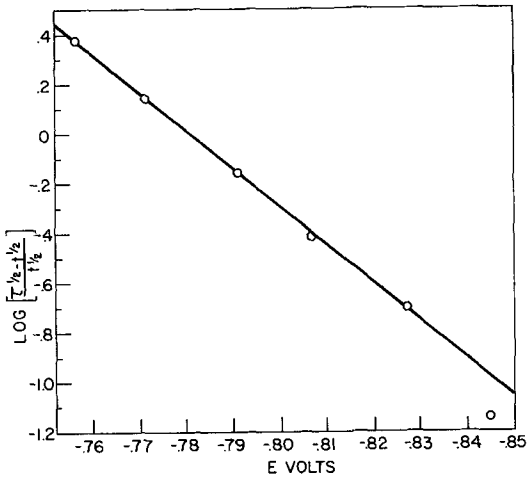

Fig. 8. Potential-time relationship during a chronopotentiometric run of K_2NbF_7 in NaF-KF-LiF: Concentration, 6 × 10^{-5} moles/cm^3; current density, 0.2 amp/cm^2; temperature, 750°C.

where n_3 is the electron number of the final step and $n_s = n_1 + n_2$, the total electron number of the first combined wave. Since in this case the sum of $n_s + n_3 = 5$, both may be calculated. On the basis of Eq. [3], $\tau_3/\tau_s = 1.8$ for $n_3 = 2$ and $n_s = 3$, and $\tau_3/\tau_s = 0.56$ for $n_3 = 1$ and $n_s = 4$. The value shown in Table II for the experimental $\tau_3/\tau_s = 0.55 \pm 0.11$ would indicate that $n_s = 4$ and $n_3 = 1$. Since n_2 has already been shown to be 3 by the method shown in Fig. 8, n_1, the unresolved first step, must be unity. It appears from these calculations, therefore, that the two steps of the first wave correspond to the reduction of pentavalent to tetravalent niobium at —0.11v and of tetravalent to monovalent niobium at —0.76v.

From chronopotentiograms run on solutions which had been reduced electrolytically to give a niobium of mean valence 4.2, the normal operating valence state of the plating bath, no evidence was found for any plateau below that at —0.76v; neither at 100 ma/cm^2 nor at 30 ma/cm^2 at any temperature. A plot of E *vs.* log $\tau^{1/2} - t^{1/2}/t^{1/2}$ on the —0.76v plateau for three such chronopotentiograms gave a value of $n = 3.04 \pm 0.49$ for this reduction step (in these reduced solutions the first reduction step) thus confirming the results obtained from the pentavalent solutions. It appears that the irreversibility of the final step at —1.02v discussed below does not affect the calculation based on transition time ratios because the proper coulombic relationship between the two steps is maintained, whatever the mechanism of the final step.

Figure 5A shows the cathodic-anodic chronopotentiogram at the —0.76v plateau. It is clear that the

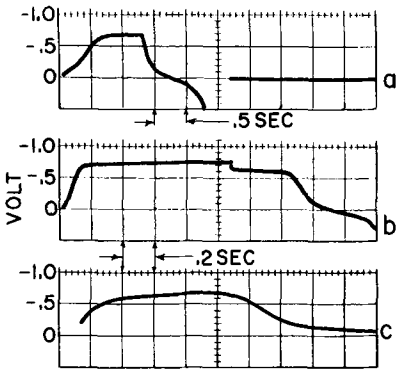

Fig. 9. Cathodic-anodic chronopotentiograms showing effect of current density and valence state: temperature, 750°C; concentration Nb, 5 × 10^{-5} moles/cm³.

	a	b	c
Current density, ma/cm²	30	100	30
Niobium valence	5.0	5.0	4.34

monovalent product is quite soluble in the melt, the average value of τ_{ox}/τ_{red} being 0.54 for 12 such chronopotentiograms compared to the theoretical value of 0.33 for a completely soluble reduction product and 1.0 for an insoluble product. This compares with the reduction intermediate in the case of tantalum which was found to be only very slightly soluble. Further the solubility of this product in the case of Nb varies with the valence of the electrolyte. In Fig. 9a is shown the cathodic-anodic chronopotentiogram for a solution at mean valence 5.0 at a current density of 30 ma/cm². In this case no reverse wave at —0.77v is seen at all, the entire oxidation occurring at —0.1 at which the Nb^{5+} to Nb^{4+} reduction occurred. On raising the current density in the same solution to 100 ma/cm² we see in Fig. 9b an oxidation wave at —0.7v followed by one at —0.1v. However, if the valence of the electrolyte is reduced to 4.2, one can obtain an oxidation wave at —0.7v even at 30 ma/cm² as seen in Fig. 9c. Apparently the rate of attack of the pentavalent solution on the monovalent intermediate according to the reaction $Nb^{1+} + 3\,Nb^{5+} \rightarrow 4\,Nb^{4+}$ is so rapid that at 30 ma/cm² the quantity of Nb^{1+} remaining at the electrode for the oxidation step is negligible, while at 100 ma/cm² enough remains to be detected in the oxidation step. However, when the bath is reduced to a mean valence of niobium of 4.2 the monovalent intermediate is essentially unattacked so that the amount recovered at 30 ma/cm² roughly corresponds to that of an ordinary soluble reduction product. The long oxidation step seen in Fig. 9c at —0.1v corresponds to the oxidation of the Nb^{4+} in the tetravalent Nb solution.

From this it is apparent that the need to operate a niobium plating solution in the tetravalent state arises from the reactivity of the intermediate reduction product with pentavalent niobium. This reaction is so rapid in a pentavalent solution that at low current density the current efficiency for metal deposition becomes negligible, while at high enough current density to overcome this attack only dendritic deposits are obtained, as reported by Cumings and Cattoir (7). It will be remembered that in the case of tantalum the intermediate reduction product was only very slightly soluble in the pentavalent solution and that no soluble intermediate valence state was observed.

The nature of the initial process.—The plateau at —0.11v shown in Fig. 6 is a one-electron reduction of an ion containing pentavalent niobium. On the basis of infrared spectroscopy studies J. S. Fordyce of this laboratory has demonstrated that the predominant species present in the pentavalent electrolyte is $[NbF_7]^{-2}$. This will be reported in a separate publication. The predominant ionic species present in the tetravalent solution has not yet been identified, but since it is soluble and stable it is reasonable to presume that it is also a complex fluoniobate. This first step may, therefore, be written

$$[NbF_7]^{-2}\,(l) + 1e \rightarrow [NbF_{(7-x)}]^{(3-x)-}\,(l) + xF\,(l)^-$$

where x = 0, 1, or 2. An apparent anomaly exists in the magnitude of τ_2/τ_1 in that it seems too large. The theoretical value of τ_2/τ_1 for successive reactions with electron numbers of one followed by three is 15. If one measures the value of τ_1 in Fig. 6b at 30 ma/cm² and converts it to an equivalent value for 100 ma/cm² by the equation $\tau = k/i^2$ (where k is a constant), and then calculates τ_2/τ_1 using the measured value of τ_2 in Fig. 6a, one obtains a value of 45. The value obtained by measuring directly the very small τ_1 in Fig. 6a is 40, confirming this high value for τ_2/τ_1. This probably results from τ_2 being enlarged with respect to τ_1 by a catalytic wave resulting from the reaction discussed above, $Nb^{1+} + 3Nb^{5+} \rightarrow 4Nb^{4+}$, in which additional Nb^{4+} is supplied to the electrode, above the amount obtained from the first step.

Transport properties.—Since the combined step terminating with the plateau at —0.76v has been shown to be reversible and diffusion controlled, one may calculate the diffusion coefficient of the $[NbF_7]^{-2}$ ion from the slope of Fig. 7 by means of Eq. [2] and the value of the total number of electrons involved, $(n_1 + n_2) = n_s = 4$. At 750°C the diffusion coefficient thus obtained is 2.03 x 10^{-5} cm² sec^{-1} compared to that of $[TaF_7]^{-2}$ of 1.5 x 10^{-5} cm² sec^{-1}. The increase over tantalum would be expected in view of the smaller niobium ion. The activation energy for diffusion between 650° and 800°C obtained from Fig. 10 is 8.75 kcal/mole compared to 8.5 kcal/mole for tantalum. If one uses Eq. [2] to calculate the diffusion coefficient of the same ion by using the value of $i\tau_1^{1/2}/C$ for the first step alone in Fig. 6b and a value of $n = 1$, one obtains a diffusion coefficient at 750°C of 1.72 x 10^{-5} cm² sec^{-1}. This can be considered good agreement since the latter is based on five runs at a single low current density with a very small value of $i\tau^{1/2}$ while the former is derived from the wide variety of data shown in Table I. If, however, one calculates the diffusion coefficient from the first plateau obtained from a solution of valence 4.2 in which $Nb^{4+} + 3e^- \rightarrow Nb^{1+}$ is the first step, one obtains, using $n = 3$ ($Nb^{4+} \rightarrow Nb^{1+}$), a diffusion coefficient at 750°C for the tetravalent ion of 5.02 x 10^{-5} cm² sec^{-1}. This is in accordance with the observations discussed previously (3) regarding the increase in diffusion coefficient with decreasing valence, and from this it would appear that the tetravalent complex is probably lower in coordination number than the heptacoordinate pentavalent niobium complex. A spectroscopic study of the tetravalent niobium solutions would be required to establish this.

The nature of the final step.—The final step represented by the plateau at —1.02v does not satisfy the chronopotentiometric criteria for reversibility or diffusion control. The value $i\tau^{1/2}/C$ decreases with increasing concentration, as in tantalum, and this may

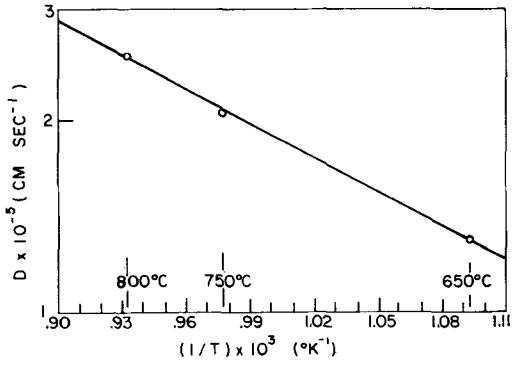

Fig. 10. Activation energy for diffusion of fluoniobate ion in KF-NaF-LiF.

result from incomplete solubility of the monovalent intermediate. This intermediate is much more soluble than in the case of tantalum as shown by the τ_{ox}/τ_{red} values (0.55 for Nb and 0.9 for Ta at similar current densities), however some film formation is still indicated since the value of 0.33 for τ_{ox}/τ_{red} is in all cases exceeded. The behavior of the final step may, therefore, also, as in the case of tantalum, be related to a film on the cathode as the product of the intermediate reduction step. The fact that niobium metal is not attacked when in contact with Nb^{4+} solution may be the result of the protective behavior of this film analogous to the suggested explanation for the inertness of tantalum in contact with Ta^{5+} solution (3). That there is a lack of reversibility is shown also in Fig. 5B in which the oxidation of the metal is seen to proceed directly to the tetravalent state (*ca.* —0.7v) with no indication of a plateau at the monovalent state (*ca.* —1.02v) as is observed in the reduction. Further study of the final step involving the reduction to metal is required.

Summary

The electrodeposition of niobium from a solution of K_2NbF_7 in the KF-LiF-NaF eutectic involves three steps, the first two of which are reversible and diffusion controlled. They are:

1. $[NbF_7]^{-2}$ (l) + $1e^-$ → $[NbF_{(7-x)}]^{(3-x)-}$ (l) + xF^- (l)
2. $[NbF_{(7-x)}]^{(3-x)-}$ (l) + $3e^-$ → NbF (s or l) + $(6-x)F^-$ (l)
3. NbF (s or l) + $1e^-$ → Nb^0 (s) + F^- (l)

Because of the rapid reaction between $[NbF_7]^{-2}$ and NbF to regenerate the tetravalent niobium ion, the current efficiency for niobium deposition falls to zero at low current density in the presence of appreciable $[NbF_7]^{-2}$, and at high current density only dendritic deposits can be obtained. If one operates from a solution with a niobium mean valence of 4.0-4.2 at low to moderate current densities, only steps 2 and 3 are operative and coherent deposits are produced. The product of step 2, NbF, is more soluble in the electrolyte than is the intermediate in the case of tantalum, but indications of some insolubility are noted and this may be responsible for the irreversible behavior of the final step. It may be significant that the final step of reduction to metal in both the tantalum and niobium plating systems and the single reduction step in the zirconium plating system are all irreversible. Work is in progress to determine whether irreversibility of the metal production step is a necessary condition for coherent metal deposition from molten salts.

The diffusion coefficient of the $[NbF_7]^{-2}$ ion has been found to be 2.03 x 10^{-5} cm^2 sec^{-1} at 750°C and its activation energy for diffusion as 8.75 kcal/mole. The diffusion coefficient of the tetravalent niobium-containing ion is approximately 5 x 10^{-5} cm^2 sec^{-1}.

The major difference between tantalum and niobium plating mechanisms arises from the interactions of the monovalent intermediate with the pentavalent species to form a stable tetravalent species in the case of niobium and the absence of such interaction in the case of tantalum. It is for this reason that a pentavalent solution may be used for plating tantalum and a tetravalent one is required for coherent deposition of niobium.

Acknowledgments

The authors are grateful for the discussion and criticism by Professor H. A. Laitinen throughout the course of this work and to R. L. Zupancic who made most of the measurements.

Manuscript received Aug. 2, 1965; revised manuscript received Sept. 27, 1965. This paper was presented at the San Francisco Meeting, May 9-13, 1965.

Any discussion of this paper will appear in a Discussion Section to be published in the December 1966 JOURNAL.

REFERENCES

1. (a) G. W. Mellors and S. Senderoff, Canadian Pat. 688,546 (1964); (b) G. W. Mellors and S. Senderoff, *Plating*, **51**, 972 (1964).
2. G. W. Mellors and S. Senderoff, *This Journal*, **112**, 266 (1965).
3. S. Senderoff, G. W. Mellors, and W. J. Reinhart, *ibid.*, **112**, 840 (1965).
4. G. W. Mellors and S. Senderoff, *ibid.*, **113**, 60 (1966).
5. T. Berzins and P. Delahay, *J. Am. Chem. Soc.*, **75**, 4205 (1953).
6. P. Delahay, "New Instrumental Methods in Electrochemistry," Chap. 8, Interscience, N. Y. (1954).
7. R. E. Cumings and F. R. Cattoir, U. S. Bur. Mines, Rept. of Investigation, 6506 (1964).

The Lead Oxide-Lead Sulfate System

J. D. Esdaile[1]

South Australian Institute of Technology, North Terrace, Adelaide, South Australia, Australia

ABSTRACT

The author's work confirms Lander's conclusion that monobasic, dibasic, and tetrabasic lead sulfates are the only stable lead sulfates in the lead oxide-lead sulfate system above 210°C. The author proposes a new room temperature x-ray pattern for dibasic lead sulfate. The decomposition temperature of dibasic lead sulfate in air is shown to be 631° ± 8°C by high-temperature x-ray analysis. The thermal inflection in the lead oxide-lead sulfate system at 450°C, first reported by Schenck and Rassbach, was found to be caused by a structural change in metastable dibasic lead sulfate.

This work was originally undertaken in order to insure positive identification of the basic lead sulfates present in the products resulting from high-temperature equilibrium studies (1). Serious disagreement was found between the x-ray patterns obtained by Lander (2) and the author (1) for dibasic lead sulfate.

The cause of the thermal inflection in the lead oxide-lead sulfate system at 450°C is obscure. Lander considered it to result from the decomposition of dibasic lead sulfate into a mixture of monobasic and tetrabasic lead sulfates. This conclusion is in conflict with the decomposition temperature of dibasic lead sulfate found by both Kellogg and Basu (3) (616°C) and the author (1) (634°C) during equilibrium measurements on the lead-oxygen-sulfur system. Kellogg and Basu attributed the discrepancy between their results and Lander's to supercooling, apparently unaware that Schenck (4) found the thermal inflection at 450°C to occur with both rising and falling temperature.

[1] Present address: C.S.I.R.O., Melbourne, Victoria, Australia.

The range of compositions over which the thermal inflections were found by Schenck and Rassbach (5), and Jaeger and Germs (6), differ widely. Schenck and Rassbach reported that these occurred between 51 and 89 mole % of lead monoxide while Jaeger and Germs detected thermal inflections between 50 and 75 mole % of lead monoxide and claimed that these were due to the decomposition of dibasic lead sulfate into a mixture of monobasic and tribasic lead sulfates. They also criticized the thermal analysis of Schenck and Rassbach, claiming that the latter had failed to homogenize their melts prior to thermal analysis. If this were so, it is possible that the thermal inflection at 450°C (observed by Schenck and Rassbach at 80.5, 84.8, and 89 mole % of lead monoxide) actually occurred in the segregated, sulfate-rich portions of these samples.

In view of these discrepancies, it was decided to investigate the thermal inflection at 450°C and to attempt to determine the decomposition temperature of dibasic lead sulfate, by means of high-temperature x-ray and thermal analysis.

Experimental Procedure

A Philips PW1009 generator operating on a copper target at 30 kv and 10 ma was used as the radiation source for the x-ray apparatus. A goniometer manufactured by Crystal Structures Ltd. was modified to give a focusing circle of 10 in. radius.

The body of the furnace used for the high-temperature x-ray analysis was formed from alumina powder. The alumina was moulded, when wet, around a wooden former on which nichrome resistance wire was wound. After drying, removal, and baking, the furnace proved to be satisfactory. A silver specimen holder was used, and this was supported by an Inconel alloy tube. Caps were placed on both the Inconel tube and the furnace, in order to reduce temperature gradients caused by convection currents. The temperature of the sample was controlled to ±3°C by an Ether transitrol anticipatory controller, using a 1 mm sheathed coaxial chromel alumel thermocouple for the hot junction. The specimen temperature was measured by using a similar, calibrated, thermocouple imbedded in the sample holder.

The basic lead sulphates were prepared from dry A.R. yellow lead monoxide and Merk's normal lead sulfate. These were mixed in the proportions corresponding to the formulas: $PbO \cdot PbSO_4$, $(PbO)_2 \cdot PbSO_4$, $(PbO)_3 \cdot PbSO_4$, and $(PbO)_4 \cdot PbSO_4$, heated in platinum crucibles for half an hour at temperatures 30°C above the liquidus temperatures determined by Lander, quenched, finely ground, reheated at 800°C, and finally quenched and ground before room temperature x-ray analyses and other treatments.

During the determination of the high-temperature patterns of the basic lead sulfates, sufficient time was allowed for equilibrium conditions to be reached. This was tested by repeating the x-ray analyses at regular time intervals until no changes in the patterns could be detected.

X-ray patterns of the fusions having the compositions corresponding to the formulas: $PbO \cdot PbSO_4$, $(PbO)_3 \cdot PbSO_4$, and $(PbO)_4 \cdot PbSO_4$, were made at temperatures ranging from ambient to 800°C.

The determination of the decomposition temperature of dibasic lead sulfate was attempted by using dibasic lead sulfate, and a mixture of monobasic and tetrabasic lead sulfates having the over-all composition of dibasic lead sulfate. Patterns of the dibasic lead sulfate fusion were taken at 36 hr intervals at 400°, 530°, and 690°C. Further analyses were made at 24-hr intervals in decreasing steps of 12°C. Patterns of the mixture of monobasic and tetrabasic lead sulfates were taken at 24 hr intervals at 425°, 530°, 610°, and 670°C.

For the thermal analysis of the lead oxide-lead sulfate system, suitably slow rates of cooling and heating, in addition to achieving a desired temperature, were obtained by adjusting the voltage input to a nichrome resistance wiring on a 3 in. diameter silica tube surrounding the sample mass. A series of samples of different lead monoxide content were prepared (Table I), each having a weight of at least 180g. These were prepared in cylindrical Triangle R.R. recrystallized alumina crucibles (1¼ in. ID) at temperatures 20°C above the liquidus values determined by Lander, and were stirred with an alumina rod until a homogeneous liquid was achieved. The alumina crucibles were used because no platinum crucible of sufficient size was available.

Table I. Observed and derived results

Run No.	PbO mole, %	Composition*	Inflection in curves	emf output at point of the deviation of the inverse rate curve, mv R†	emf output at point of the deviation of the inverse rate curve, mv F†	Deviation from avg thermocouple output, mv R†	Deviation from avg thermocouple output, mv F†
1	84.95	Between Q and PbO	No				
2	77.91	Between D ond Q	Yes	3.94	3.89	0.022	0.028
3	66.67	D	Yes	3.945	3.885	0.027	0.033
4	56.70	Between M and D	Yes	3.94	3.91	0.022	0.008
5	45.22	Between N and M	No				

* Q, D, M, and N indicate tetrabasic, dibasic, monobasic, and normal lead sulfates, respectively.
† R indicates rising temperature, and F indicates falling temperature. Average thermocouple output in millivolts = 3.918 ± 0.023; accuracy of thermocouple calibration = ±1°C; temperature of the change in the samples = 449.6° ± 2.2°C.

Time-temperature curves were obtained using a Honeywell temperature recorder, and additional data for plotting the curves were gained by using a calibrated 13% rhodium-platinum, platinum thermocouple connected to a Tinsley type 418D potentiometer via a cold junction immersed in melting ice.

The procedure entailed prolonged heating of the sample masses at 600° or 700°C immediately prior to thermal analysis. Room temperature x-ray analyses of the products from the thermal analyses were also made.

Discussion of Results

The x-ray patterns obtained by the author and Lander for the basic lead sulfates are shown in Table II, together with the A.S.T.M. pattern for monobasic lead sulfate.

To determine whether contamination of the thermally prepared basic lead sulfates has occurred, it is convenient to compare the relative intensities at the d values of the major lines in each pattern.

The patterns obtained by the author for the basic lead sulfates show no evidence of contamination. For example, it may be argued that the appearance of the line $d = 2.95$, $I = 0.63$, results from the contamination of dibasic lead sulfate by monobasic lead sulfate, for which $I = 1.00$ at $d = 2.95$. However, there is no such appearance of the second most intense line of the monobasic lead sulfate pattern ($d = 3.35$, $I = 0.49$) in the pattern for dibasic lead sulfate. The other apparent agreements at $d = 3.22$ and $d = 3.25$, for normal and tetrabasic lead sulfates, and dibasic and monobasic lead sulfates, respectively, are susceptable to the same argument.

The patterns of the lead sulfates thermally prepared by Lander provide evidence of contamination of the dibasic and tetrabasic lead sulfates, although there is no evidence of contamination of his monobasic salt. The coincidence of three of the four major lines in the pattern for dibasic lead sulfate with weaker lines in the pattern for tetrabasic lead sulfate indicates that Lander's thermally prepared sample of tetrabasic lead sulfate was contaminated by dibasic lead sulfate; this conclusion is supported by the absence of the line at $d = 2.96$ for the tetrabasic lead sulfate prepared by Lander (7) by his wet method. Slight contamination of the tetrabasic lead sulfate by lead monoxide is

Table II. X-ray patterns obtained by the author and Lander

Monobasic lead sulfate

Author			Lander		A.S.T.M.	
2θ†	d	I*	d	I*	d	I*
13.84	6.40	0.03			6.4	0.50
14.21	6.24	0.13	6.2	0.20	6.2	0.50
15.00	5.91	0.15	5.8	0.10	5.9	0.50
20.06	4.42	0.08	4.4	0.02	4.42	0.60
24.05	3.70	0.09	3.67	0.80	3.70	0.60
25.25	3.51	0.09	3.47	0.10	3.49	0.50
26.61	3.35	0.49	3.33	1.00	3.33	1.00
27.45	3.25	0.12				
28.04	3.18	0.12	3.16	0.10	3.17	0.40
30.25	2.95	1.00	2.95	1.00	2.95	1.00
31.33	2.85	0.30	2.84	0.30	2.84	0.70
			2.59	0.20		
			2.56	0.20		
36.25	2.48	0.09	2.46	0.25	2.47	0.50
36.94	2.43	0.09	2.42	0.70	2.43	0.50
			2.39	0.25		
38.35	2.35	0.09	2.34	0.05	2.34	0.50
39.80	2.26	0.08	2.26	0.12	2.28	0.60
40.45	2.23	0.09	2.22	0.10	2.23	0.40
41.60	2.17	0.01			2.17	0.40
					2.12	0.40
44.20	2.05	0.20	2.05	0.40	2.05	0.70
46.20	1.965	0.15	1.96	0.12	1.96	0.50
47.65	1.908	0.04	1.91	0.15	1.91	0.50
49.33	1.846	0.13	1.84	0.50	1.845	0.70
51.95	1.760	0.09	1.74	0.40	1.755	0.60
53.00	1.728	0.08	1.72	0.10	1.726	0.60
			1.67	0.15	1.668	0.60
55.80	1.647	0.06	1.66	0.15		
			1.65	0.05	1.646	0.50
56.90	1.618	0.05			1.617	0.40
			1.57	0.20	1.603	0.40
61.20	1.514	0.10	1.51	0.05		
62.95	1.476	0.06	1.48	0.20		
64.30	1.429	0.03	1.445	0.20		
64.95	1.436	0.04	1.435	0.15		

Dibasic lead sulfate

Author			Lander		Author			Lander	
2θ†	d	I*	d	I*	2θ†	d	I*	d	I*
11.28	7.85	0.30			30.97	2.89	0.59	2.87	0.70
14.09	6.29	0.20			33.43	2.76	0.06	2.76	0.06
15.03	5.90	0.22						2.69	0.05
18.75	4.72	0.10			37.87	2.37	0.25	2.37	0.50
19.94	4.45	0.07			38.21	2.355	0.38	2.35	0.50
23.50	3.79	0.13	3.75	0.03	39.21	2.30	0.15	2.29	0.10
25.48	3.49	0.13			40.48	2.23	0.06		
27.48	3.25	0.78						2.11	0.15
29.88	2.99	1.00			43.80	2.067	0.15	2.06	0.20
30.28	2.95	0.63	2.96	1.00	46.19	1.966	0.19	1.96	0.40
47.95	1.898	0.09			54.35	1.688	0.15	1.68	0.20
49.90	1.828	0.19	1.82	0.25	58.50	1.578	0.06		
50.90	1.794	0.23	1.79	0.40	58.95	1.565	0.15	1.56	0.30
52.40	1.746	0.06	1.74	0.10	60.75	1.524	0.16	1.52	0.20
52.90	1.731	0.10	1.73	0.20	61.35	1.511	0.06		

Tetrabasic lead sulfate

Author			Lander		Author			Lander	
2θ†	d	I*	d	I*	2θ†	d	I*	d	I*
10.81	8.15	0.25	8.1	0.30	46.65	1.947	0.15	1.94	0.15
14.10	6.28	0.10						1.86	0.11
27.68	3.22	1.00	3.25	1.00	49.97	1.825	0.05		
28.78	3.10	0.16	3.11	0.03	53.20	1.722	0.08	1.72	0.25
29.26	3.05	0.14	3.04	0.02	54.40	1.687	0.04	1.68	0.02
31.09	2.88	0.16	2.87	0.30	55.90	1.645	0.06	1.64	0.08
33.66	2.66	0.21	2.67	0.02	57.05	1.614	0.12	1.61	0.20
44.15	2.05	0.01	2.04	0.20	58.30	1.583	0.07	1.59	0.15
46.14	1.967	0.08						1.58	0.15

† Average of five determinations.
* Intensity relative to the strongest line of the pattern.

indicated by the presence of a weak line at $d = 2.92$, $I = 0.13$ for tetrabasic lead sulfate, corresponding to the strongest line obtained by Lander for lead monoxide. This conclusion is supported by the absence of this line in the pattern obtained by Lander by his wet method. The close agreement of the d values of the strongest lines for monobasic and dibasic lead sulfates ($d = 2.92$, $I = 1.0$, and $d = 2.93$, $I = 1.0$, respectively) precludes the use of either of these values as a reliable guide as to whether contamination has occurred of the dibasic lead sulfate. The coincidence of the next two major lines in the pattern of monobasic lead sulfate ($d = 1.96$, $I = 0.50$, and $d = 1.51$, $I = 0.11$) with the pattern for dibasic lead sulfate ($d = 1.96$, $I = 0.40$, and $d = 1.51$, $I = 0.10$) suggests that Lander's sample of dibasic lead sulfate was contaminated with monobasic lead sulfate.

Unfortunately, Lander, in assessing the final pattern for dibasic lead sulfate, removed lines which were close to those of the major lines in the patterns which he obtained for monobasic and tetrabasic lead sulfates by his wet method. In particular, those at the d values 7.8, 5.8, 3.47, 3.22, and 2.92 were removed by Lander.

For the reasons discussed above, the x-ray pattern obtained by the author for dibasic lead sulfate is considered to be more reliable than that given by Lander. Reasonable agreement exists between the x-ray patterns obtained by the author, Lander, and the A.S.T.M. values, for monobasic and tetrabasic lead sulfates.

The results obtained from x-ray analyses of monobasic and tetrabasic lead sulfates from room temperature to 800°C showed no evidence of phase changes in either compound.

The results obtained from the x-ray analyses of the sample having the over-all composition represented by the formula $(PbO)_3 \cdot PbSO_4$ showed that no compound of this composition occurred at 400°C or higher temperatures. It was found that tribasic lead sulfate yielded a mixture of dibasic and tetrabasic lead sulfates at 800°C, and a mixture of monobasic and tetrabasic lead sulfates at 400°C; this was shown by prolonged heating at these temperatures, followed by quenching and room temperature x-ray analyses. High-temperature x-ray analyses of "tribasic lead sulfate" at 400° and 530°C provided confirmatory evidence. Over-all, this investigation confirmed Lander's conclusion that tribasic lead sulfate was not stable at high temperatures.

The high-temperature x-ray patterns of a mixture of monobasic and tetrabasic lead sulfates (having the over-all composition of dibasic lead sulfate) and dibasic lead sulfate were compared at 400° and 530°C with patterns of pure monobasic lead sulfate and pure tetrabasic lead sulfate at these temperatures. These results showed that dibasic lead sulfate had decomposed into a mixture of monobasic and tetrabasic lead sulfates at these temperatures. Although there is very close agreement between the 2θ values of the peaks given by the dibasic lead sulfate sample and the mixture of monobasic and tetrabasic lead sulfates, the relative intensities of a number of these common peaks differ markedly. These differences are thought to result from the manner of formation of the two specimens, *i.e.*, one as the result of fusion, the other by simple mixing. A comparison of the 2θ values obtained from the decomposition products of dibasic lead sulfate was made with those obtained from the mixture of monobasic and tetrabasic lead sulfates between room temperature and 625°C. Apart from intensity variations, of the type discussed above, the agreement between the two patterns is sufficient to conclude that dibasic lead sulfate decomposes into a mixture of monobasic and tetrabasic lead sulfates at, and below, 625°C.

A comparison was made between the patterns obtained from dibasic lead sulfate and a mixture of monobasic and tetrabasic lead sulfates, having the over-all composition of dibasic lead sulfate, through the temperature range 610° to 800°C. The similar x-ray patterns obtained between 637° and 800°C are quite different from those obtained at, and below, 625°C. Since it has been shown that dibasic lead sulfate decomposes into a mixture of monobasic and tetrabasic lead sulfates at, and below, 625°C, and the room temperature patterns for dibasic lead sulfate prepared by quenching from just below the melting point of dibasic lead sulfate and at 800°C showed no significant differences, it is concluded that the change in the x-ray patterns at, and above, 637°C, is due to the formation of dibasic lead sulfate. An assessment of the accuracy of the temperature measurements at the sample surface extends these limits to 623° and 639°C. It is therefore concluded that dibasic lead sulfate de-

Table III. Results of thermal and x-ray analyses

Sulfate material	Heat-treatment before thermal analysis	Presence of a thermal inflection	Phases shown by room temperature x-ray analysis
That previously yielding a thermal inflection	600°C for two days	no	Monobasic and tetrabasic lead sulfates
That having the overall composition of dibasic lead sulfate	700°C for two days	yes	Dibasic lead sulfate
As above	700°C for two days	yes	Not done
As above	600°C for two days	no	Monobasic and tetrabasic lead sulfates

composes into a mixture of monobasic and tetrabasic lead sulfates below 631°±8°C. This conclusion is supported by the temperature of 634°C found by the author for the decomposition of dibasic lead sulfate at a pressure of 1.5 mm Hg during the course of equilibrium measurements on the lead-oxygen-sulfur system (1). It may easily be shown that the effect of a pressure change of 758.5 mm Hg on the decomposition temperature of dibasic lead sulfate is slight (1), *i.e.*, less than 1°C.

The results obtained during the initial thermal analysis of the specimens prepared in alumina crucibles, *i.e.*, after these had been heated to 700°C for 36 hr (Table I), show that thermal inflections at 450°±3°C occur between 20 and 50 mole % normal lead sulfate. These were found to occur with both rising and falling temperature, as originally reported by Schenck (4). Because the high-temperature x-ray analyses showed no evidence of any compound other than dibasic lead sulfate in this composition region, and that dibasic lead sulfate decomposed into a mixture of monobasic and tetrabasic lead sulfates below 631°± 8°C, it was provisionally concluded that the thermal inflections at 450°±3°C were due to a change in metastable dibasic lead sulfate. Further evidence for this was provided by room temperature x-ray analysis of the products, *i.e.*, it was found that the specimens yielding thermal inflections also contained dibasic lead sulfate.

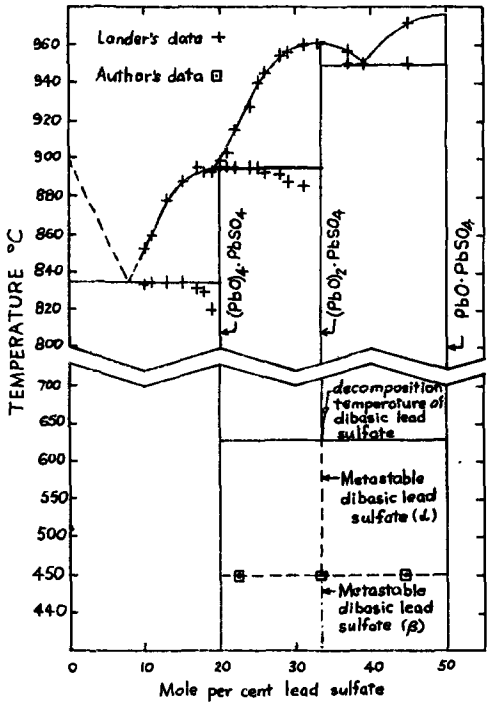

Fig. 1. PbO-$PbSO_4$ system: cross, Lander's data; square with a dot, author's data.

The results of a number of confirmatory tests on fused samples of dibasic lead sulfate are shown in Table III. These confirm that the thermal inflections are associated with the presence of dibasic lead sulfate and show that when specimens are heated for some time just below the decomposition temperature of dibasic lead sulfate (600°C for two days) no thermal inflections occur, and only monobasic and tetrabasic lead sulfates are present. To distinguish between the two types of dibasic lead sulfate, that which is metastable above 450°C is denoted by alpha, and that which is metastable below 450°C is denoted by beta, as shown by Fig. 1.

Although slight chemical attack on the alumina crucibles was noted during the preparation of the sulfate samples used for thermal analysis, this was not sufficient to cause any appreciable differences in the x-ray patterns obtained from these and all other samples which were prepared in platinum crucibles. This factor, and the fact that thermal inflections only occurred in the alumina prepared samples when dibasic lead sulfate was present, suggests that the fusion in alumina was justified for the preparation of the samples used for thermal analysis.

An attempt was made to determine whether the change in metastable dibasic lead sulfate was detectable by high-temperature x-ray analysis. This failed because the finely divided powder in the sample holder was found to decompose rapidly into a mixture of monobasic and tetrabasic lead sulfates at the temperatures involved. The coarsely crystalline form of dibasic lead sulfate thus seems to be necessary for preserving the metastable form of dibasic lead sulfate. It is thus possible that a single crystal could be used to determine whether any significant changes in metastable dibasic lead sulfate patterns occur above and below 450°C. This is, perhaps, a little doubtful, since the room temperature x-ray pattern for dibasic lead sulfate after thermal analysis, *i.e.*, after the change in dibasic lead sulfate has occurred, is very similar to that obtained by quenching from high temperatures. However, it is possible that the change at 450°C takes place very quickly and occurs even during quenching, or is completed at room temperature.

No thermal inflections could be detected at the decomposition temperature of dibasic lead sulfate. This finding is consistent with the prolonged times found necessary for the decomposition of dibasic lead sulfate during the high-temperature x-ray analyses around 631°C.

The liquidus of Lander's phase diagram, and the results of his thermal analyses, are unsatisfactory between 17 and 19 mole % of lead sulfate. The liquidus in this region of the phase diagram has been drawn in Fig. 1 so as to conform as closely as possible to Lander's data and the requirements of the phase rule.

Acknowledgment

To Dr. W. T. Denholm, formerly of the South Australian Institute of Technology, who was responsible for the design and construction of the furnace and enclosures used for the high-temperatue x-ray analysis the author expresses his thanks.

Manuscript received April 5, 1965; revised manuscript received Sept. 3, 1965.

Any discussion of this paper will appear in a Discussion Section to be published in the December 1966 JOURNAL.

REFERENCES

1. J. D. Esdaile, "The Thermochemistry of the Lead-Oxygen-Sulphur System," Ph.D. Thesis, Adelaide, 1963.
2. J. J. Lander, *J.* (and *Trans.*) *Electrochem. Soc.*, **95**, 174 (1949).
3. H. H. Kellogg and S. K. Basu, *Trans. Met. Soc., AIME*, **218**, 70 (1960).
4. R. Schenck and R. S. Dean, "The Physical Chemistry

of the Metals," John Wiley & Sons, Inc., New York (1919).
5. R. Schenck and W. Rassbach, *Bar. Cent. Chem. Gesell.*, **41**, 2917 (1908).
6. F. M. Jaeger and H. C. Germs, *Z. anorg. u. allgem. Chem.*, **119**, 145.
7. J. J. Lander, *J.* (and *Trans.*) *Electrochem. Soc.*, **95**, Table III, p. 178 (1949).

Some Effects of Small Displacements from Equilibrium on the Structure and Properties of Single Crystalline Copper Electrodes[1]

Leslie H. Jenkins

Solid State Division, Oak Ridge National Laboratory, Oak Ridge, Tennessee

ABSTRACT

Small displacements from equilibrium conditions were generated in systems of variously oriented copper single crystals exposed to acidic copper sulfate solutions by permitting a slow leak of air into the system and/or by application of an external emf. The effects of dissolution conditions on the orientation and shapes of structures formed on the surface was determined. An anomalous effect of a simultaneous corrosion reaction on electrolytic current-potential characteristics also was observed. Explanations for the phenomena in terms of kinetic processes occurring on the surface are offered.

Data obtained from copper single crystals exposed to a solution of copper sulfate under conditions both at and slightly removed from equilibrium have been used previously as supporting evidence for the argument that no crystal surface orientation is thermodynamically more favorable than another (1). Additional information concerning facet development and/or pit growth and movement of multi-atom high ledges over the surface can provide details of the effect of slow kinetic processes on changes in crystal surface habit. Generally it is agreed that areas immediately around points at which dislocations terminate in a surface are energetically more favorable reaction sites than a close-packed surface, and less favorable than kink-step sites. But once a reaction site has been nucleated and dissolution, for example, is proceeding by movement of atom steps over the crystal surface, it is not clear whether the gross changes in the structure of the crystal surface result primarily from thermodynamic factors, kinetic influences, or a combination of the two. The following is concerned with that problem.

Materials and Experimental Methods

All materials and their preparation and use were as previously reported (1), and all data included here were obtained from coin-shaped copper single crystals in the tripod-type cells described. Experimental results were reproduced numerous times in many different systems, and the observations which follow result from a study of more than forty different crystals. Likewise in the prior manner, all 0.2M $CuSO_4$ solutions, pH adjusted to ~1 with H_2SO_4, were, at the moment of introduction into the cells, under a hydrogen atmosphere and at equilibrium with copper metal.

When desired, air was permitted to leak into an assembly at a controlled rate by the same method previously used, a faulty platinum-through-glass seal at the side entry port of a tripod cell. The subsequent reaction of oxygen with copper(I) ions destroyed equilibrium in the cell

$$2Cu^+ + \tfrac{1}{2} O_2 + 2H^+ \leftrightharpoons 2Cu^{++} + H_2O \qquad [1]$$

Attempts to re-establish equilibrium in the assembly resulted in oxidation of the metal surface by copper(II) ions

$$Cu^{++} + Cu^0 \leftrightharpoons 2Cu^+ \qquad [2]$$

Overpotentials generated by the previous reactions occurring on crystal surfaces and/or those arising from dissolution due to application of an external emf were measured, and alterations in surface features resulting from such treatments subsequently observed. Orientations of facets developed as a result of reactions occurring on crystal surfaces were determined with a two-circle reflection goniometer. All potential differences were measured with a vibrating reed electrometer.

Experimental Results

Later it will become necessary to differentiate between removal of material from the surfaces by the over-all process described by Eq. [1] and [2] and dissolution resulting from the flow of current due to the application of an external emf. Unhappily, no unambiguous choice of terms is available, so arbitrarily in the following the former process will be referred to as corrosion and the latter as anodic or electrolytic dissolution.

Facet development.—Typical facets, which resulted from the corrosion process alone and which were produced at any corrosion rate up to ~50 $\mu a/cm^2$ (the greatest rate studied), were developed on different orientations as indicated in Fig. 1. The degree of structural development on all surfaces was dependent on the extent, but not the rate, of corrosion in the ranges studied. On the (001),[2] removal of material was restricted to a few, very large pits randomly distributed over the surface. As well as could be determined, corrosion did not occur on the surface area between pits. Calculations based on the average number and size of pits accounted for all material removed. Large, flat areas bounded by ledges of multi-atomic height were produced by the corrosion process on the (111). Presumably monatomic steps moved over the surface and eventually bunched together to form ledges separated by extensive flat areas. Step motion on the (011) apparently was not quite as easy as in the foregoing example, for immediately at the onset of corrosion small ridges, which quickly developed into facets, were observed on this surface.

In the case of the (001) and (111) decidedly different results were obtained when surfaces were subjected to anodic dissolution alone. Figure 2 illustrates that, even at a lower current density than for the corrosion reaction illustrated in Fig. 1, nucleation and reaction occurred over the entire (001) surface. Likewise no large, flat areas could be detected on the (111)

[1] Research sponsored by the U. S. Atomic Energy Commission under contract with Union Carbide Corporation.

[2] Standard crystallographic notations are used in that parenthesis, ( ), about indices indicate a single plane or set of parallel planes and curly brackets, { }, all the equivalent nonparallel planes of the indicated indices. Likewise, square brackets, [ ], indicate a single crystallograpnic direction and carets, < >, the complete set of equivalent directions.

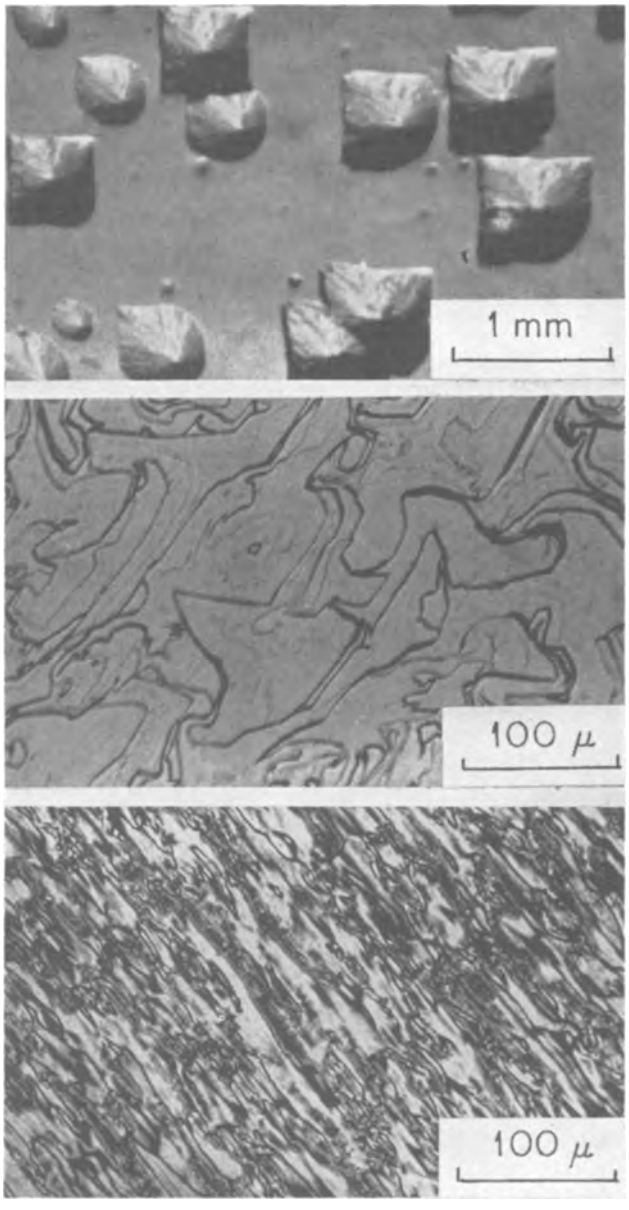

Fig. 1. Surface structures developed by cupric ion oxidation. Reading top to bottom, the surfaces shown are (001), (111), and (011). The latter two were photographed by interference contrast. In each system corrosion had occurred at approximately 50 $\mu a/cm^2$. The times permitted to react, although not equal, were not less than two nor more than four days.

following anodic dissolutions of about the same rate and duration as that illustrated for corrosion. Rather, the former surface was composed almost entirely of ledges of uniform average density and height. No such differences were observed for the (011) which developed approximately the same type of facets regardless of the mode of dissolution.

It was determined that, in a corroding system, small anodic currents could be superimposed on the corrosion current without effecting any changes in the typical structure developed by the corrosion process alone. The maximum anodic current which could be impressed on a given corrosion current without altering the development of surface topography typical of the latter process was not established. However, it was observed that an anodic current equal to the corrosion current did not result in any detectable change, but anodic currents about a factor of two larger than simultaneous corrosion currents did produce surfaces typical of the former process alone.

Orientation of facets.—Measurements with a two-circle reflecting goniometer showed that, regardless

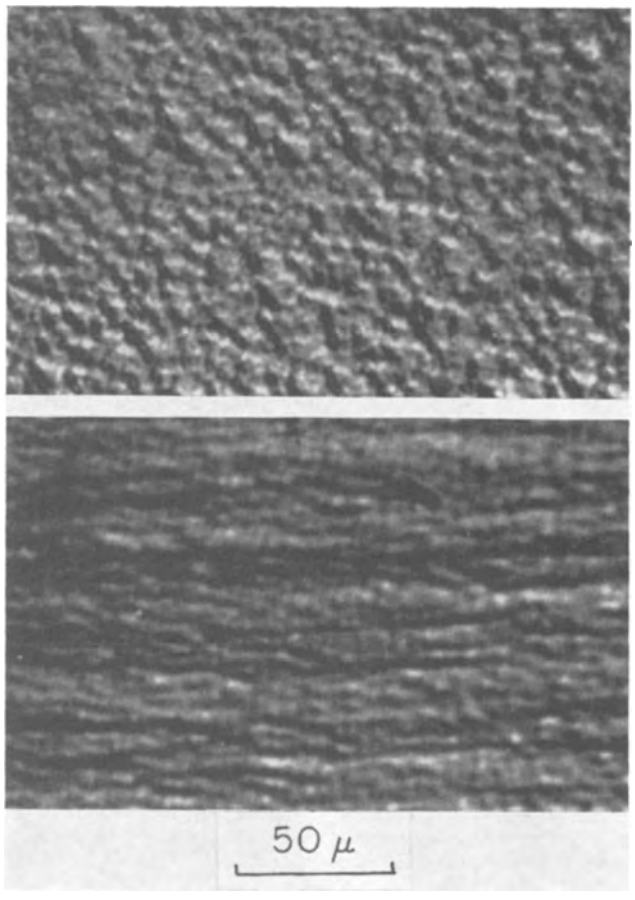

Fig. 2. Surface structures developed by anodic dissolution. The upper photograph is of an (001) surface and the lower a (111). Both are interference contrast photographs. The (001) resulted from dissolution at 3 $\mu a/cm^2$ for seven days. Note that less material has been removed, and at a slower rate, than for the corresponding surface shown in Fig. 1. Dissolution at 20 $\mu a/cm^2$ for four days produced the (111) surface illustrated above. Approximately the same amount of material has been removed at near the same rate as for the (111) surface of Fig. 1.

of means of dissolution, the orientations of facets developed on a certain surface were characteristic of that surface, but not of the process responsible for their development. Ultimately facets of like orientation developed from a surface of a certain orientation whether produced by corrosion or anodic dissolution or a mixture of the two processes. Also, the gross detail of surface structure was of no apparent importance in determining facet orientation. As an example, the small facets on the uniformly attacked (001) surface shown in Fig. 2 were oriented the same as facets developed on the bottoms of the pits on the (001) surface illustrated in Fig. 1.

It would be impossible to use data taken with a goniometer of the type employed to conclude that absolutely no orientations other than those recorded below were formed on the various crystals. But it is certain that the orientations reported account for approximately 90% of the total facet areas. Figure 3 indicates the geometry of pits formed on the (001). They were always relatively shallow with bottoms invariably approximately 4° from the (001) along the <001> zones. Sides of the pits were not quite normal to the surface under all conditions, but rather 4° from the {001} normal to the surface. Minor reflections from both sides and bottoms of pits indicated the presence of a very few facets of most orientations along the <001> zones. Under certain circumstances extensive faceting with near {012} orientations was observed, and occasionally a very few {111} and {011} orientations developed. But by far the preponderance of facets were those oriented 4° from the {001}.

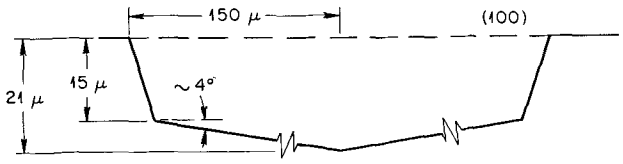

Fig. 3. Schematic profile of pits developed on the (001). Dimensions indicated are typical.

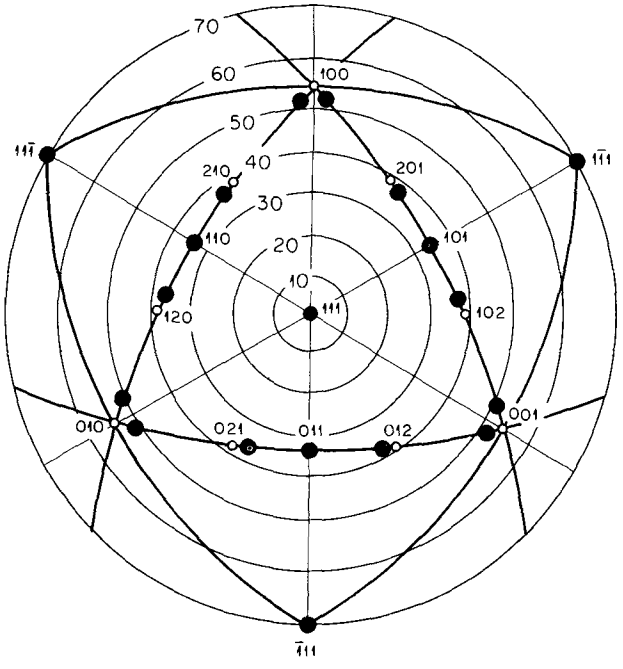

Fig. 4. Stereographic projection from (111) showing orientations of facets developed on that surface. Smaller, open circles indicate the orientations of major faces. No {001} facets were formed, but rather those "twins" ~4° away along the <001> zones.

As shown in Fig. 4 the orientations of facets developed on the (111) were not as restricted as those on the (001). Occasionally a few facets of the {111} 70° from the original surface could be detected, and as in the case of the (001), a very few facets of most orientations along the <001> zones were evident. Large areas of near {012} orientations always developed, and occasionally some few {011} were seen. Note particularly that in no case were {001} facets produced, but rather those orientations along the <001> zones about 4° from the {001} corresponding to the orientations of the bottoms and sides of pits developed on the (001).

With the occasional exception of a barely detectable amount of {111} facets, all orientations developed on (011) surfaces were along the <001> zones. Again no {001} surfaces were generated, only those about 4° removed along the <001> zones. Extensive production of near {012} and near {014} orientations were noticeable, and infrequently traces of {011} 60° from the original surface were perceptible.

Current-potential data.—Electrolytic current-potential relationships were affected in an unusual way by the existence of a simultaneous corrosion process on a crystal. Figure 5 shows typical galvanostatic data obtained from a crystal oriented (011) which was concurrently corroding at a very slow rate. While it is not absolutely certain in this case just what significance should be attached to the data, it is clear the electrode behavior is not that which reasonably could be anticipated. Although it was observed that anodic dissolution of similar value impressed on a corrosion process was also restricted to highly local areas, it is not obvious, for example, that deposition currents only slightly greater than the corrosion currents should

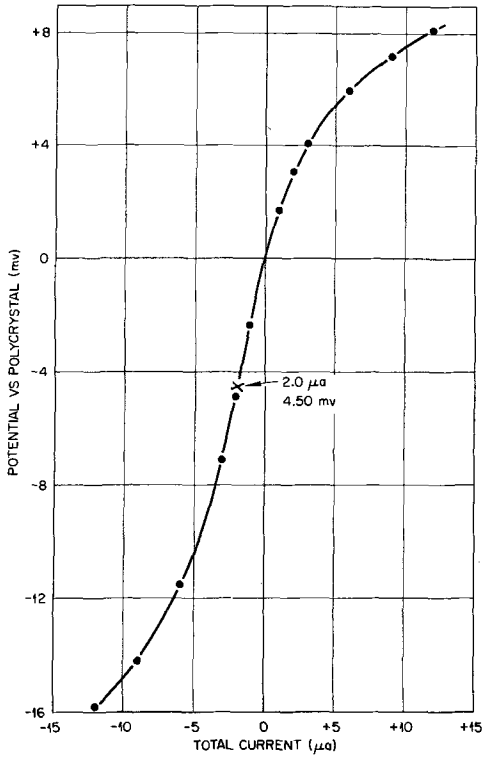

Fig. 5. Current-potential relationships for the (011) in a system corroding at a very slow rate. The inflection point, the current-potential value about which the curve is symmetric, is indicated.

also be local in nature.[3] Therefore, a highly asymmetric current *vs.* potential curve could be anticipated. However, after plotting data similar to that in Fig. 5 from any simultaneously corroding system, singular values for current and potential, about which the curve representing the data was symmetric, could be determined. Obviously, true current densities could not be calculated from geometric electrode areas and total current flow for in microscopic areas over the surface local current densities varied from zero to several times the average value. Nor could measured overpotentials be considered more than an effect of some nebulous local processes. Therefore, it must be concluded that under conditions discussed here curves of the type shown in Fig. 5 are not very useful in making conclusions about the processes occurring in the system.

The data shown in Fig. 6 further illustrate the effects of slight corrosion on anodic current-potential data. The information was collected on a system corroding for 11 days at a rate calculated to be equivalent to ~0.2 $\mu a/cm^2$. The leak in the system was then stopped and the assembly held at temperature for three weeks more. Initially the slight corrosion process probably restricted anodic dissolution to local regions, as has been shown, with the concomitant result that values of overpotentials measured were relatively high. When corrosion was stopped, normal anodic dissolution possibly occurred over the entire surface as the values for the geometric and "active" areas became more or less identical. When the crystal was removed and the surface examined, the extent of dissolution was so slight that only very few changes in surface structure could be established after diligent search. An alternative explanation is that, although not visually detectable, faceting resulting from corrosion increased the true surface area. The data do not suggest either explanation to be preferable.

[3] At the 1964 Washington meeting of the Society the author reported some results of deposition studies from $CuSO_4$ solutions on copper single crystals. It was shown that in systems initially at equilibrium deposition is uniform on the (001), for instance, at current densities as low as $3\mu a/cm^2$. This work is currently being prepared for publication.

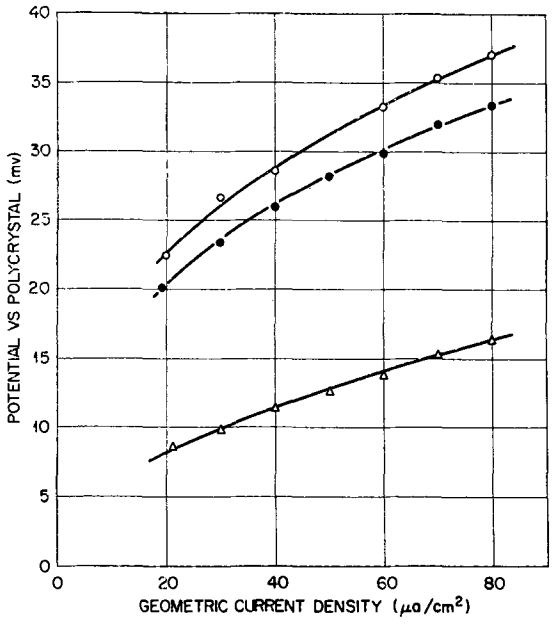

Fig. 6. Current-potential relationships for the (001) as a function of corrosion conditions. Initially the system was corroding at a rate equivalent to ~0.2 μa/cm² for a total of eleven days. The corrosion process was then stopped and the system allowed to stand for three weeks. Time after solution was admitted to system: ○, 2 days; ●, 12 days; △, 30 days.

Discussion

Corrosion in these systems containing copper metal, dissolved oxygen, copper ions, and hydrogen ions can be described by the general equation

$$Cu + \tfrac{1}{2} O_2 + 2H^+ \leftrightharpoons Cu^{++} + H_2O \qquad [3]$$

However, there are two possible types of reaction mechanisms which must be considered. The first type involves oxidation of the metal by oxygen, dissolution of the oxide by action of the acid, and possibly further oxidation of the newly formed cuprous ions by oxygen in the solution

$$2Cu + \tfrac{1}{2} O_2 \leftrightharpoons Cu_2O \qquad [4]$$

$$Cu_2O + 2H^+ \leftrightharpoons 2Cu^+ + H_2O \qquad [5]$$

$$2Cu^+ + \tfrac{1}{2} O_2 + 2H^+ \leftrightharpoons 2Cu^{++} + H_2O \qquad [6]$$

(It is impossible to differentiate experimentally between the preceding mechanism and one in which CuO is formed directly and subsequently dissolved.) Obviously the sum of reactions [4], [5], and [6] is twice reaction [3]. This type mechanism has been studied in this laboratory, and, as previously reported (3), produced a uniformly etched surface. It was presumed the homogenous attack was a consequence of the uniform diffusion of oxygen up to the surface of the metal. The second type of mechanism by which reaction [3] may occur is that in which equilibrium in the system is destroyed when cuprous ions are oxidized to cupric by dissolved oxygen, and the subsequent oxidation of copper metal by cupric ions in an attempt to re-establish equilibrium as outlined in Eq. [1] and [2]. Again, the sum of Eq. [1] and [2] is obviously Eq. [3]. However, when reaction proceeds by this latter mechanism the surface is not uniformly etched, for reaction does not occur homogeneously over the entire surface. Leidheiser and Gwathmey (2) first reported that large, square areas around the (001) poles of spherical copper single crystals were not etched when immersed in acidic copper sulfate solutions exposed to air, even though almost all the rest of the surface of the sphere was etched heavily. They also observed that solutions which had been boiled to remove dissolved gases and then maintained under a hydrogen atmosphere etched the spheres only slightly during 24 hr. These effects were confirmed at this laboratory (1) where it was also shown that, if in addition to freeing the solutions of dissolved gases and then maintaining under a hydrogen atmosphere the solution is at equilibrium with copper metal before the sphere is immersed, no evidence of etching could be detected at any orientation on the spheres even after several weeks' exposure. However, under corrosion conditions it was certain that, while most of the surface of the sphere was well etched, large areas near the {001}, and to a much smaller degree immediately around the {011} and {111}, were not attacked as heavily as the remainder of the surface, indeed, if at all. Therefore, it was concluded that etch patterns developed on the spheres were a consequence of the reaction proceeding by the second mechanism proposed in Eq. [1] and [2].

Since the rate at which cupric ions approached the spherical surface was (like oxygen in the first mechanism) diffusion controlled, it is reasonable to assume that reduction of cupric ion to cuprous occurred at all orientations. But since the anodic reaction occurred only at certain areas these observations serve as rather extreme examples of the existence of discrete, orientation-sensitive anodic and cathodic areas over a crystal supporting the cupric-cuprous redox reaction. Also, they suggest an interpretation for observations made on nonspherical crystals.

Obviously orientations which on spherical crystals did not sustain the anodic corrosion reaction were compelled to do so when those orientations alone were exposed to solutions. And again observations can be interpreted on the basis of the existence of discrete anodic and cathodic areas over corroding crystals. The pits formed by the corrosion process on the (001) support and extend such a supposition (Fig. 1). Surfaces undergoing corrosion alone permitted dissolution from only a few restricted areas. Even when small anodic currents were superimposed on the corrosion process, removal of material was still confined to these specific areas. However, when dissolution occurred solely as the result of an electrolytic current flow, even at current densities less than either of the components in the former cases, nucleation of reaction sites and removal of material was not restricted, but occurred uniformly over the entire surface. The effect was as if the cathodic part of the corrosion process effectively prevented the occurrence of anodic phenomena over most of the (001) surface. Similar conclusions can be drawn from data concerning the (111) surfaces illustrated in Fig. 1 and 2. Again, nucleation and dissolution occurred more or less uniformly over the surface in the absence of the corrosion process, but nonuniformly when accompanied by corrosion. That the reduction of cupric ions at the metal surface resulted in the dissolution process being resticted, if not prohibited, over large surface areas appears well established.

Perhaps a better understanding of the different etch patterns produced by the same over-all reaction can be gained from a consideration of the energies involved. Certainly the total free energy change in any one system due to reaction [3] will be the same. However, the mechanism of the reaction will determine the method by which the energy is dissipated. It is not unreasonable that, for the mechanism involving the direct attack on the surface by oxygen, most of the total free energy change can be expended in this step and a very high percentage of metal surface atoms possess sufficient energy to form the activated complex necessary for reaction. Conversely, if much of the free energy is expended first in oxidizing cuprous ions to cupric as in the second mechanism, relatively less energy remains to oxidize copper metal to cuprous ions. Then few surface atoms of the metal would possess energy sufficient to form the activated complex necessary for reaction, and dissolution becomes

not only a function of the crystallographic properties of the crystal, but possibly the defect structure as well.

The manner in which the local nature of the corrosion process affects current-potential relationships has been shown earlier. Data of the type shown in Fig. 5 have little value since, although the total current flow may be known, the current density associated with the measured over-potential cannot be determined. The data in Fig. 6 showing the variation in current-potential relationships for a system initially corroding, but not later, resulted at least partially from a change in the electrode process. Admittedly, it is still not certain whether the final data collected reflected only that corrosion had stopped or that also the true surface area of the electrode had changed. However, it is very clear that very low corrosion rates result in measurement of abnormally large values of potential associated with a geometric current density. This supports the previous suggestion that data, thought to indicate orientation sensitive equilibrium potential differences in similar systems, possibly were obtained from assemblies in which corrosion was occurring very slowly (1).

Although the orientation of facets developed on any one surface was independent of the dissolution process, this was not the case for their number and arrangement. Since there were local fluctuations in orientation $\sim \pm \frac{1}{4}°$ over all crystal surfaces, and since in all cases the dislocation density was at least of the order of $10^6/cm^2$, there were abundant steps on the surface to furnish reactive kink sites regardless of the means of dissolution. The appearance of the (001) after corrosion and after dissolution suggests that in both cases removal of material by motion of steps over the surface was relatively difficult, and the nucleation of new steps was more difficult in the corrosion case than in the latter. Comparison with (111) surfaces produced under similar circumstances indicate that movement of steps was more easily accomplished on this face than on the (001). Since it is not obvious that nucleation of new steps occurred on the (111) no inferences can be made. It is not at all impossible that the steps initially present on the surface were sufficient to sustain the dissolution processes without the necessity of nucleating new ones. In addition to the appearance of surfaces, this reasoning relies rather heavily on the concept of the degree to which the cathodic portion of the corrosion reaction changes what could be considered the normal appearance resulting from anodic dissolution alone.

In summary, the most significant observations concerning facet development were: (*A*) Although gross appearances were vastly different, the orientations of facets developed on any one orientation were always similar, regardless of the dissolution processes. (*B*) In no case were {001} facets ever produced, and extremely few {111} and {011} were detected. (*C*) On all surfaces most facets were oriented along the <001> zones. Since it has been shown that no orientation is measurably thermodynamically more stable in this system (1), the failure to develop facets of close-packed orientations is understandable. It seems reasonable then that the orientations of facets are determined more by the kinetic demands on the system than by any thermodynamic differences of the crystals. Certainly it is difficult to believe that an orientation about 4° from the {001} along the <001> zones is more stable than the closer packed {001}. The facets developed must represent the orientations which not only could be formed, but which also permitted relatively easier movement of steps on the surface in accommodating the dissolution process.

The apparent prohibition of {001} facet development, the frequency of formation of near {012} and near {014} orientations and the preponderance of faceting along the <001> zones, as well as the definition of broad cathodic and anodic areas by the corrosion process, are problems on which study is continuing.

Conclusions

Within the special meanings given to the terms "corrosion" and "anodic or electrolytic dissolution," and within the limitations of the experimental conditions, the following conclusions seem reasonable:

1. Copper single crystals with more than one orientation exposed to solution exhibit distinct, orientation-sensitive cathodic and anodic areas when subjected to oxidation by cupric ions.
2. If a crystal exposes only one orientation to solution, the corrosion process again results in the definition of distinct anodic and cathodic areas.
3. Since under conditions of anodic dissolution alone the surface of an electrode of singular orientation is uniformly attacked, corrosion and electrolytic dissolution are not electrochemically equivalent in the sense that equal areas of the electrode are not available to sustain the process in both cases.
4. Potential-current characteristics experimentally determined at very low current densities for a surface simultaneously corroding can be inexact and without obvious relationship to values obtained in noncorroding systems.
5. The orientations of structures developed on a surface as the result of dissolution processes are largely independent of the nature of the process and are determined more by the kinetic demands impressed on the surface than by any orientation-sensitive thermodynamic property of the crystal. The gross features developed on the surface are governed by the types and/or relative rates of the dissolution processes.

Manuscript received June 17, 1965; revised manuscript received Sept. 17, 1965.

Any discussion of this paper will appear in a Discussion Section to be published in the December 1966 JOURNAL.

REFERENCES

1. L. H. Jenkins and Ugo Bertocci, *This Journal*, **112**, 517 (1965).
2. H. Leidheiser, Jr., and A. T. Gwathmey, *ibid.*, **91**, 97 (1947).
3. L. H. Jenkins, *ibid.*, **107**, 371 (1960).

Electrical Conductivity Studies of Tetragonal Zirconia

L. A. McClaine and C. P. Coppel

Arthur D. Little, Incorporated, Cambridge, Massachusetts

ABSTRACT

The a-c and d-c resistances for tetragonal zirconia were measured over the temperature range of 1100°-1500°C and pressure range of 1 to 10^{-14} atm oxygen. Polarization studies indicated that in oxygen atmospheres an oxygen electrode reaction occurs at the platinum-zirconia interface so that it is not possible accurately to separate ionic and electronic conduction components from the resistance data. However, the data do indicate a significant ionic conduction component within the pressure and temperature range studied. Assuming that oxygen transport accounts for the ionic conduction some order of magnitude values for oxygen diffusion in zirconia at 1400°C were calculated.

Most chemical processes of interest in the fabrication and use of materials at high temperatures involve heterogeneous systems, and the kinetics of these processes are more often than not transport-controlled. However, experimental data on high-temperature diffusion processes is very limited, and we are not yet able to predict transport behavior.

In conjunction with recent studies in our laboratories, on the kinetics of oxidation of zirconium carbide and boride in the 1000°-2000°C range, we desired data on the mass transport properties of the ZrO_2 that can form as a surface coating during the oxidation process. In particular, information was sought on the diffusion of oxygen, the defect structure of the oxide, and the effect of temperature, atmosphere, and impurity content on the defect structure. As a result of this interest, we initiated a study of the a-c and d-c electrical conductivity of tetragonal zirconia in an attempt to provide some of the desired information.

From a-c and d-c resistance measurements we expected to be able to calculate transport numbers and separate ionic and electronic conduction components. From accurate knowledge of these components a defect structure model can be developed. In addition, knowledge of ionic conduction will permit the calculation of diffusion data for oxygen, providing that oxygen is the only ionic species contributing significantly to the ionic conduction.

Previous work on tetragonal zirconia has been extremely limited. Kofstad and Ruzicka (1) found that the direct current conductivity of tetragonal zirconia had a complex oxygen dependence. They proposed as a possible explanation for this behavior that zirconia is an ionic conductor with a coupled transport of oxygen vacancies and interstitials and pointed out that to confirm this explanation it would be desirable to study the relative importance of ionic and electronic conduction as a function of the partial pressure of oxygen. Vest and Tallan (2) have been studying tetragonal as well as monoclinic zirconia concurrently with this study utilizing a polarization technique. Their results have not yet been reported in detail.

Experimental Details

Sample material.—Very dense, high-purity sample boules were prepared from ZrO_2 by melting the oxide in an arc imaging furnace designed to permit a powder feed to the hot zone. Samples were cut from this material with a diamond sectioning saw.

The starting oxide for the preparation of the boules was either reactor grade oxide obtained from Wah Chang Corporation, or oxide prepared in our laboratories from Wah Chang sponge. The spectrographic analyses of these oxides labeled lot I and II, respectively, are presented in Table I. Also presented is a similar analysis on a boule prepared from lot II material. The fusion process has resulted in a much lower trace impurity concentration level. Quantitative spectrochemical analysis for Al and Fe in a boule made with lot II oxide gave values of 0.007 and 0.01% for Al and Fe, respectively, checking very well with the semiquantitative report.

Electrical leads.—In our initial work, thin disks were held in compression between two alundum rods carrying the electrical leads from outside the furnace area. Electrical contact was made by a bead or thin foil of platinum held against the sample. Results with this holder were easily affected by shocks and vibrations outside the furnace.

Therefore, most of our work including that reported here has been done with leads connected directly to the samples. These are made to the end of the sample by initially putting down a thin layer of platinum using either vapor deposition or "liquid platinum." In the a-c d-c resistance measurements reported here, the leads consisted of a Pt, Pt-Rh thermocouple attached to each end of the sample. In the d-c resistance measurements one set of thermocouple wires was used as current leads, while the other was used as potential leads.

Temperature and atmosphere control.—A resistance furnace wound with platinum-10% rhodium and operated with a constant voltage power unit was used to control the temperature of the sample. The atmosphere was fixed by using pure oxygen, an oxygen-helium mixture, CO-CO_2 mixtures, or H_2-H_2O mixtures at 1 atm total pressure.

Table I. Spectrochemical semi-quantitative analyses of ZrO_2 materials

Impurity	Starting oxide powders		Boule from lot II oxide
	Lot I	Lot II	
Al	125 ppm	0.01 to 1%	0.001-0.01%
B	0.2	0.001	ND
Cd	0.3	ND	ND
Co	<5	ND	ND
Cr	<10	0.001 to 0.01	0.0001
Cu	<25	0.001 to 0.01	0.0001
Fe	790	0.01 to 1.0	0.001-0.01
Hf	<40	0.001 to 0.01	
Mg	30	0.001 to 0.1	0.0001
Mn	10	0.001 to 0.01	ND
Mo	<10	ND	ND
Ni	<5	ND	0.0001
Pb	<5	0.001 to 0.01	ND
Si	40	0.01 to 0.1	0.001
Sn	<10	0.001	ND
Ti	52	ND	ND
V	<5	ND	ND
W	<25	0.001 to 0.01	ND
Zn	<50	ND	ND
Ge	<50	0.001 to 0.01	ND
Sr	<50	0.001 to 0.01	ND
Ba	<50	0.001 to 0.1	ND
Na	<50	0.001 to 0.01	0.001
Bi	<50	0.0001	ND
Ag	—	ND	0.0001

Note: < = less than, and ND = not detected.

In some of the studies the temperature of the furnace was increased or decreased at a steady rate of 1 or 2 deg/min using a motor drive attached to the variac which feeds power to the furnace.

In the polarization studies which were carried to very low potential levels, too much a-c pickup was observed for meaningful measurements, and for these studies a d-c power source for the furnace was used to eliminate this difficulty.

Resistance measurements.—The a-c resistance was measured at 1 kc with a General Radio Type 1650A impedance bridge. The d-c resistance was determined by passing a known d-c current through the sample and measuring the emf across the sample using a L&N Type K potentiometer. The d-c measurements were made frequently with current flow reversed to detect errors introduced by any thermal emf.

Current-voltage curves were determined so that d-c measurements might be carried out below any apparent decomposition potential. For pure ZrO_2 we found a straight line I to E relationship below potentials of 0.1v. The curves began to break as potentials were increased beyond this point. For our sample geometry the straight line portion corresponded to currents up to about 100 μa. Our d-c measurements were generally made at currents of 10-20 μa.

Measurements were made at either a constant temperature while the atmosphere was varied, or, more frequently, the atmosphere or ratio of gases determining the atmosphere was fixed, and the temperature was increased or decreased at a fixed rate with intermittent measurements of a-c and d-c resistance on the sample.

Results

A-C and d-c resistance measurements.—The a-c and d-c electrical resistance of ZrO_2 samples was measured over the temperature range of 1100°-1500°C and over the pressure range from 1 to 10^{-14} atm oxygen. The data obtained for one sample, No. 12, are presented in Fig. 1 through 5. For these measurements both current and potential leads were connected to the completely coated ends of the sample, and the conductivity was calculated from the known geometry. The sample measured 0.385 in. long and 0.206 x 0.177 in. in cross section.

The results reported on sample No. 12 were obtained within a period of three weeks while an attempt was being made to keep the sample in the tetragonal phase. During this period it was necessary to cool the sample once through the monoclinic-tetragonal transition in order to replace a lead which became detached. In general, we have observed excellent reproducibility of results on successive runs up and down in temperature, while remaining within the tetragonal phase. However, sometimes after taking a sample back and forth through the phase transition, we observe increases on the order of several per cent in the resistance which we attribute to the formation of microcracks in the sample during the transition. In this particular case with sample No. 12, there was no sig-

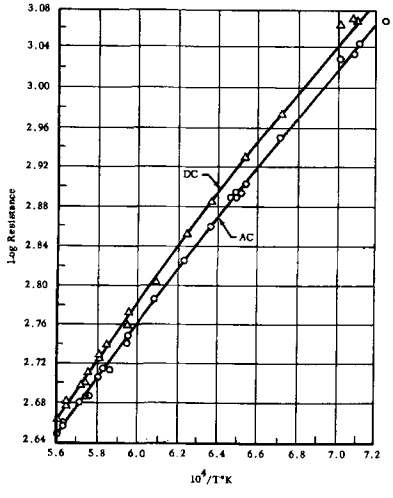

Fig. 1. Electrical resistance vs. reciprocal temperature (oxygen, log $P_{O_2} = 0$).

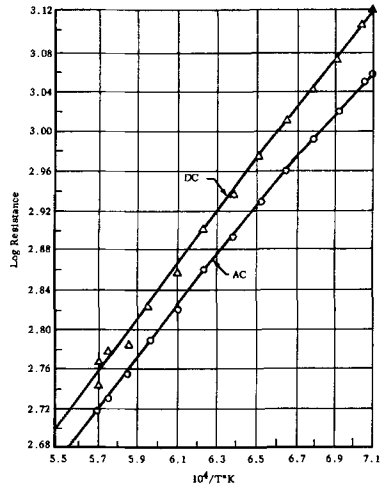

Fig. 2. Electrical resistance vs. reciprocal temperature (oxygen + helium, log $P_{O_2} = -2.49$).

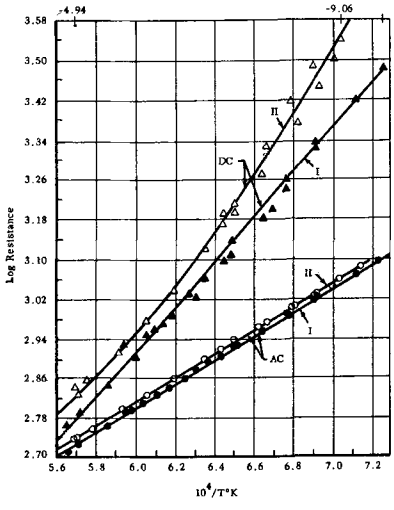

Fig. 3. Electrical resistance vs. reciprocal temperature (carbon dioxide/carbon monoxide ≅ 20/1, log $P_{O_2} = -9.60$ to -4.94).

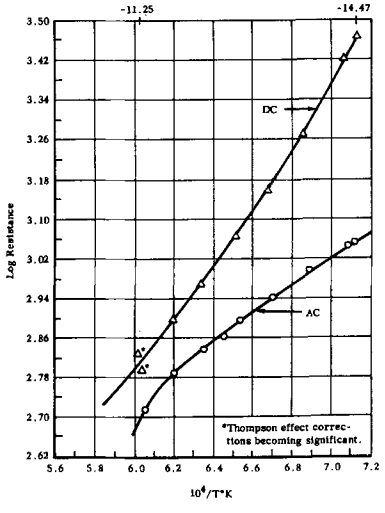

Fig. 4. Electrical resistance vs. reciprocal temperature (carbon monoxide/carbon dioxide ≅ 20/1, log $P_{O_2} = -14.47$ to -11.25).

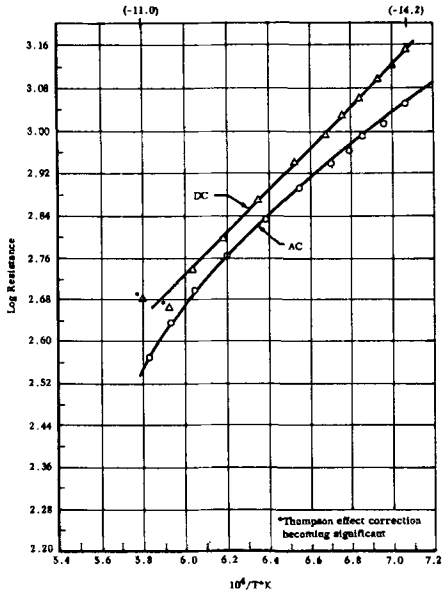

Fig. 5. Electrical resistance *vs.* reciprocal temperature (hydrogen + helium + water vapor, log P_{O_2} = —14.2 to —11.0).

nificant effect on the resistance from the passage back and forth through the phase transition. The initial runs were in pure oxygen and in H_2-H_2O mixture. After the cooling operation, the complete study in oxygen was repeated with agreement within 1%.

Frequently between the subsequent atmosphere studies the resistance in oxygen was measured again. The points in Fig. 1 represent the combined results of measurements made on seven different days during the period when all data reported here except the H_2-H_2O were obtained. On most of these days only individual points were determined after holding the sample overnight in an oxygen atmosphere at some temperature in the tetragonal region. The agreement is taken as an indication of a lack of change in the sample or electrical leads during this period. The scatter in the a-c measurements is on the order of ± 1%, and this is much less than the changes observed as the atmosphere is changed.

In Fig. 6 we present plots of zirconia conductivity as a function of oxygen pressure at different temperatures which are derived from the a-c resistance curves of Fig. 1-4. These curves show a minimum in total conductance at a pressure of 10^{-4}-10^{-5} atm. The total change in conductance with the greater than tenfold change in pressure is very slight, less than a factor of two. It may be noted that data presented in Fig. 4 and 5 represent almost identical oxygen pressures, but in

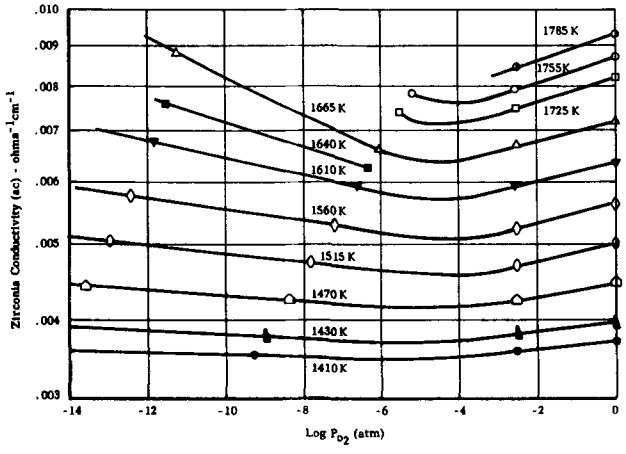

Fig. 6. Total conductivity *vs.* pressure of oxygen at selected temperatures.

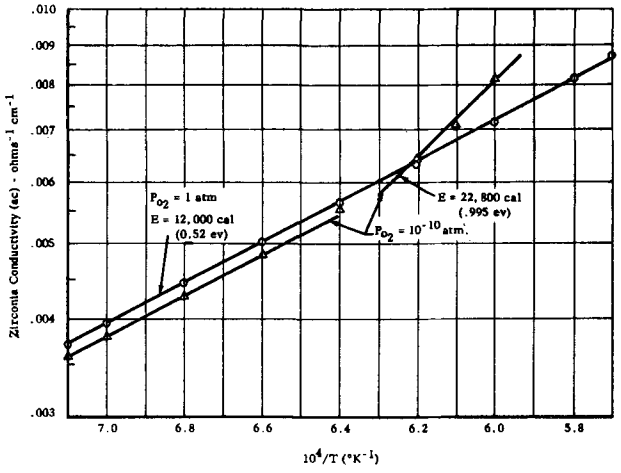

Fig. 7. Total conductivity *vs.* temperature at selected oxygen pressures.

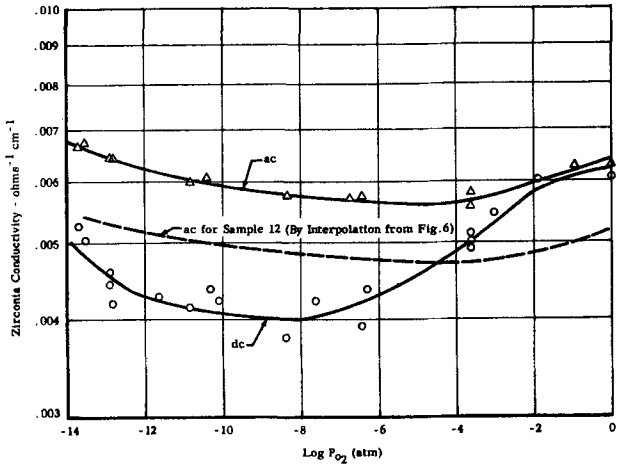

Fig. 8. Conductivity data for Sample No. 9 at 152°K.

one case CO-CO_2 was used to set the oxygen pressure, whereas in the other a H_2-H_2O mixture was used. In drawing the curves of Fig. 6, only the results from the CO-CO_2 mixtures have been used, for reasons which will be discussed shortly under atmosphere effects.

In Fig. 7 are plotted as log conductivity *vs.* reciprocal temperature data taken from Fig. 6 for pressures of 1 and 10^{-10} atm oxygen. These curves show that at low pressures there is an apparent increase in activation energy as temperature is increased while at 1 atm there is no apparent change over the temperature range studied.

Results obtained on samples prepared from both oxide sources were essentially identical. In Fig. 8 we plot results obtained on sample No. 9 which was cut from a boule prepared from the Wah Chang reactor grade oxide. These data were obtained at a constant temperature of 1525°K ± 10 while oxygen pressure was varied by means of atmosphere control. The dotted line represents comparable data for sample No. 12. It will be noted that although displaced somewhat in absolute conductance the behavior with variation in pressure is identical for the two samples.

It can be seen in Fig. 1-5 and 8 that d-c resistances measured are different than the a-c values. If there were no ionic component of conduction, we would expect the a-c and d-c values to be identical. The differences observed are evidence for a significant ionic component of conduction. In order to separate ionic and electronic components of conduction from the a-c and d-c resistance measurements two assumptions must be

made. One assumption is that under d-c conditions only electrons are transferred across the platinum-zirconia contact. That is to say that when a d-c potential is applied, both electrons and ions migrate toward the electrodes, but only the electrons can be discharged; the ions assume a concentration gradient which opposes the field. The second assumption is that the potential drop across this space charge resulting from the concentration gradient of the ions is small compared to the total potential drop across the sample. Providing that these assumptions are reasonably valid, ionic transference numbers may be calculated from the relationship

$$t_i = \frac{R_{dc} - R_{ac}}{R_{dc}}$$

In making the studies current-potential curves were determined and measurements were made at the small currents and potentials corresponding to the straight line portion of the curve; thus it was presumed that the measurement conditions were below the decomposition potential of the zirconia. On this basis we calculated ionic and electronic conductivities and a very reasonable picture evolved.

We were concerned, however, with establishing the limits of error introduced in our study by the two assumptions made in using the d-c resistance measurements to separate ionic and electronic conductivity. In studies on a lime-stabilized zirconia sample with the identical technique, we found about 90% ionic transport when measured in helium, but a much lower ionic transport indicated when measured in oxygen. This could be attributed only to some oxygen reaction at the electrodes in the oxygen atmosphere since we would expect that the lime content makes the transport properties atmosphere independent. To explore further the errors introduced by our assumptions, we carried out more detailed studies of the polarization behavior of several samples.

Polarization studies.—Further study of this problem was carried out using a sample of zirconia containing about 5 mole % CaO, which we obtained from the Norton Company. This material has about one third of the lime content of the sample studied by Kingery. We would expect a high ionic conductance which is virtually atmosphere independent.

We attached three potential electrodes along the sample as well as current leads on the end. The end leads covered the cross section of the sample and helped insure that current flux was uniform across the sample. The potential leads were spaced along the 1.3 cm length of the sample in the proportions indicated on the abscissa of Fig. 9, and were made by wrapping and twisting a piece of platinum wire around the sample. To reduce the contact resistance of these leads, a spot of "platinum paste" was used at about three or four points around the circumference of the sample to spot sinter the potential lead to the sample.

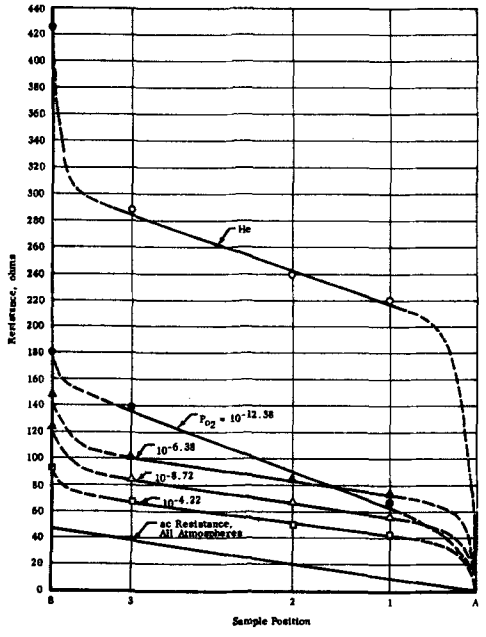

Fig. 9. Resistances calculated for various electrodes with respect to electrode A from potential measurements at 1390°C in various atmospheres.

In Fig. 9 we plot the resistance of the sample as calculated from end B to end A and to each of the three potential leads. The a-c potentials were measured using an oscilloscope to determine potential drops between the current and potential electrodes, and calculated resistances for all atmospheres fall on a straight line within the precision of the oscilloscope measurement. The fact that a straight line is obtained confirms the positioning of the leads as determined by measurement, and also indicates uniformity of the sample. Resistances calculated from d-c potential measurements, however, do not fall on a straight line. We attribute the high resistance at either end to space charge polarization. The fact that they are such a large portion of the total resistance indicates that separate potential leads such as on this sample should be used in the determination of d-c resistance. The three points calculated from the three potential leads do, in general, fall on a straight line, thus indicating sample uniformity and further indicating that the large potential gradient is very close to the end of the sample, as we would expect for space charge polarization.

Note, however, that when the sample is equilibrated in a high-oxygen atmosphere rather than helium, the d-c resistance calculated across the potential leads corresponds to that calculated from the a-c measurements. This behavior, assuming no oxygen reaction at the electrodes, indicates close to zero ionic transport contrary to results in helium. This occurs in a sample which we expect to be primarily an ionic conductor independent of atmosphere. This behavior in oxygen-containing atmospheres is confirmed in studies on other zirconia-lime samples of even higher lime content.

We conclude from these studies that the platinum electrodes cannot be assumed to be inert and blocking to an oxygen electrode reaction; in order to explain our observations, the reaction $\frac{1}{2}\ O_2 + 2e = O^{-2}$ must occur at a significant rate at the platinum-zirconia interface in atmospheres containing oxygen pressures of $10^{-8.72}$ atm and greater. We have found no evidence that reducing the area of the current electrode will modify the rate of this reaction and thus the behavior of the samples.

As a consequence of these results it is evident that an accurate separation of ionic and electronic components of conduction cannot be made from the a-c and d-c resistance data for pure zirconia reported in this paper. We now recognize that the assumptions necessary for such calculations are far from valid, and we see no way in which to eliminate with any degree of success the uncertainties introduced by using such assumptions. From the data in Fig. 9 one can see that the assumption of no oxygen electrode reaction is most in error at high-oxygen pressures, while the assumption that the potential drop across the space charge is small compared to the total potential drop across A-B is most in error at very low-oxygen pressures.

Vest and Tallan (3) have recently reported the application of a polarization technique to the study of $Ca_{0.15}Zr_{0.85}O_{1.85}$. Many of their data are from time dependent d-c measurements rather than a combination of a-c and d-c measurements, but the data resulting from either technique are comparable. In their work they also have recognized the oxygen gas reaction occurring at the platinum electrode and have proposed a means for interpreting their data which takes

into account this reaction. Their interpretation of their data recognizes that in certain pressure regions the various conductivity data recorded may be primarily due to either electronic, ionic, or the gas-electrode reaction. Thus by such assignment of their data to a specific conduction mechanism and by extrapolation of these data into the regions in which more than one conduction mechanism contributes significantly to the measured results they proposed to separate ionic and electronic conductivity in the mixed conduction region. Such a technique is not applicable to our data since we can recognize no region in which one conduction mechanism alone is predominant. Data collected over a much wider range of oxygen pressure might indicate such regions. However, in considering application of this technique one should recognize that a straight line extrapolation into the mixed conduction region is not necessarily correct since, in general, one can expect changes in the dependency of electronic and ionic conduction on oxygen pressure in different pressure regions. In addition Vest and Tallan assume that the ionic polarization is small and does not affect their measurements. Our studies show that a large polarization potential exists. We recognize no basis for assuming that the polarization potential will not affect the resulting measurements. To conclude, we believe that the means proposed by Vest and Tallan for treating their data can be useful as a first approximation to separating the conduction components when data are available over a sufficiently wide range. However, in our opinion the technique cannot be applied to our studies to produce the accurate and detailed separation of ionic and electronic conduction which we seek.

While we cannot, therefore, from the a-c d-c resistance data make a highly accurate and detailed separation of ionic and electronic conduction components as a function of temperature and oxygen pressure, our data do indicate that ion transport is a significant component in the over-all process and thus provide a basis for estimating the ionic conductivity. If the ionic conductivity was on the order of 1% or less, we would probably not have observed any significant difference in our a-c and d-c measurements; the differences noted, we believe, indicate that ionic conductivity must be on the order of several per cent of the total even at high partial pressures of oxygen. In Table II are presented transference numbers calculated from the a-c d-c resistance data of Fig. 4. The data in Fig. 4 are for oxygen pressures of 10^{-11} atm or less; under such conditions, as pointed out in a previous paragraph, the major error in using the data for transference numbers is the uncertainty with regard to the space charge polarization potential. However this error influences the results in such a manner that calculated electronic transference numbers are lower than the actual. As indicated in Table II calculated values increase from 0.39 at 1410°K to 0.78 at 1610°K. In spite of the fact that these values are probably on the low side it is still evident that electronic conduction is a large component at the high-temperature and low-pressure end of our studies. As shown in Fig. 7 this is the same region in which there is a marked change in activation energy for total conductivity indicating a radical change in the mechanism responsible for conduction. In our opinion these data indicate that over most of the pressure-temperature range studied the ionic conduction component represents several tens of per cent of the total conductivity.

Table II. Transference numbers calculated from data of Fig. 4

Temperature, °K	R_{ac}, ohm	R_{dc}, ohm	t_i	t_e
1410	1100	2820	0.61	0.39
1470	935	1740	0.46	0.54
1540	759	1150	0.34	0.66
1610	617	795	0.22	0.78

$\left(t_i = \dfrac{R_{dc} - R_{ac}}{R_{dc}},\ t_e = 1 - t_i\right)$

On the basis of these considerations of the data we estimate that the ionic conductivity of pure zirconia as represented by our sample No. 12 at 1400°C, falls within the limits of 0.0005 to 0.0025 ohm^{-1} cm^{-1} in the oxygen pressure range from 1 to 10^{-10} atm.

Having established an order of magnitude for ionic conduction in our zirconia material the next question is whether we can establish which ion provides the conduction component. Lime stabilized zirconia is generally recognized as an ionic conductor due to oxygen transport by a vacancy mechanism. Somewhat analogously we would expect the formation of oxygen vacancies in zirconia with decreasing oxygen pressure and thus an increase in ionic conduction with decreasing pressure. However our data indicate little change in ionic conductivity with pressure decrease, contrary to our initial expectation of oxygen transport by a vacancy mechanism. On the other hand, the behavior of the a-c and d-c measurements with increasing pressure can readily be interpreted as due to an oxygen reaction at the electrodes such as we concluded occurred with the lime stabilized sample we studied; this behavior tends to indicate that oxygen ion transport is important. One explanation could be that oxygen transport occurs, but that the vacancy content is controlled by impurities. Another alternative explanation could be that a combination of ionic conduction mechanisms exists which vary with oxygen pressure in opposite directions producing little net change in total ionic conduction. In our opinion a detailed interpretation of the defect structure and the ionic conduction mechanism will require a much more accurate separation of ionic and electronic conduction components than can be achieved by a polarization technique.

While our data do not permit us to assign the ionic conduction unequivocally to oxygen transport, it is worthwhile to assume that oxygen transport is the primary component and determine whether this assumption is consistent with other findings. If we assume that the estimated ionic conduction of 0.0005 to 0.0025 ohm^{-1} cm^{-1} at 1400°C is due to oxygen transport we can calculate the diffusion coefficient for oxygen in zirconia using the Nernst-Einstein relationship. On this basis we calculate that the diffusion coefficient of oxygen may fall within the limits of 0.22 to 1.1×10^{-8} cm^2/sec at 1400°C. Such values for the diffusion coefficient appear reasonable in relationship to the work at lower temperatures and somewhat different structures by Kingery *et al.* (4) on $Ca_{0.15}Zr_{0.85}O_{1.85}$, and Douglas (5) on $ZrO_{1.994}$. In addition a diffusion coefficient of the same order of magnitude as that calculated here was determined for oxygen in ThO_2 (6) at 1400°C.

Atmosphere effects.—In our work we have observed behavior which we interpret as evidence for interaction of the CO-CO_2 and H_2-H_2O atmospheres with our oxide samples. Apparently such interactions are not usually considered in work in this field, as most papers in which these atmospheres are used to fix oxygen pressure make no comment relative to possible interactions with sample materials.

For the same oxygen pressure we found a much lower d-c resistance when using H_2-H_2O than CO-CO_2 to control oxygen pressure as can be seen by comparing Fig. 4 and 5. The a-c resistance is also reduced but not as markedly. This behavior which indicates increased electronic conductivity in the H_2-H_2O atmospheres, we interpret as analogous to that observed by Mollwo (7) and Thomas and Lander (8) for a zinc oxide-hydrogen system. These authors found an increase in conductivity of ZnO when in an atmosphere of H_2. This was attributed to hydrogen entering the matrix as an interstitial positive ion with associated electron. Such an interaction will explain the trend of our results. In view of this observed behavior, the results with H_2-H_2O atmospheres were not used in

final calculations of ionic and electronic conductivities as a function of oxygen pressure.

In our opinion, the same atmosphere effect very likely influenced the results of Aronson's study (9) on ZrO_2 stoichiometry as a function of oxygen pressure. The results reported by Aronson were unusual in that they indicated a greater stability for a given ZrO_2 stoichiometry the higher the temperature. Comments made in Aronson's paper lend support to the belief that his results were affected by the H_2 atmosphere. He indicates that all of his reported data were obtained after reduction with small quantities of H_2-H_2O in an inert gas. When experiments were attempted using a pure H_2-H_2O environment, he reports that "spurious results" (a lower-weight gain on oxidation) were obtained. This might have been due to an increased H_2 solubility which would be in accord with observations on ZnO that the hydrogen atmosphere effect was increased with increased hydrogen pressure. We estimate that if hydrogen solubility in ZrO_2 is comparable in magnitude to that in zirconium metal (10), then weight changes due to hydrogen pickup would be of the same order of magnitude as the oxygen losses under study. In addition, of course, the presence of the hydrogen in ZrO_2 can be expected to influence the oxygen activity.

We also observed that the CO-CO_2 atmospheres had a slow effect on the measured a-c and d-c resistances. With increasing time in the atmospheres, the R_{dc} and R_{ac} values increased. After a day or more in CO-CO_2 mixture of high CO/CO_2 ratio results such as the curves in Fig. 3, labeled II, were obtained. After such changes, we observed corresponding changes in a-c and d-c resistance measured in pure oxygen atmosphere. However, we find that the increased resistance in both oxygen and CO-CO_2 atmospheres can be removed by a long period of heating in pure oxygen. We interpret this behavior as due to carbon building into the zirconia sample. Consequently, we did not permit a sample to remain for long periods in CO-CO_2 atmospheres and completed all measurements possible prior to using CO-CO_2 atmospheres. Kofstad (1) reported attempting to duplicate Aronson's study (9) using thermogravimetric studies in CO-CO_2 atmospheres with equilibration periods of up to one day. He observed much smaller oxygen losses in the CO-CO_2 mixtures than reported by Aronson for the H_2-H_2O-inert gas mixtures. Possibly Kofstad's results were affected also by sample interaction with the CO-CO_2 atmospheres, although, since we have no measurements on the amount of carbon picked up by ZrO_2 in our studies, it is difficult to judge.

One might consider that the effect of the atmospheres was on the rate of the oxygen electrode reaction, with a resulting change in concentration polarization, rather than chemical changes in the zirconia. Our information is not sufficient to prove that this does not occur. However, in the case of the CO-CO_2 atmosphere, we believe that the presence of changes in the a-c as well as the d-c resistance values argues against it. In the case of the H_2-H_2O atmosphere effect, this point is certainly not resolved, but the previous work on ZnO which was discussed and the reasonable interpretation of Aronson's observations as presented here argues for the existence of chemical effects.

Conclusions

We find from a-c and d-c resistance measurements on dense, high-purity tetragonal zirconia over the temperature range of 1100°-1500°C and an oxygen pressure range of 1 to 10^{-14} atm evidence that tetragonal zirconia is a mixed ionic and electronic conductor. The data show that electronic conduction is most important at the low-pressure and high-temperature end of the studies and that ionic conduction is a significant component of total conduction in the higher pressure regions.

We find from a-c and d-c resistance measurements on lime stabilized zirconia that the assumptions necessary for the desired, highly accurate separation of ionic and electronic conduction components from our data on tetragonal zirconia are not valid. Nevertheless we can conclude that the data on tetragonal zirconia will permit a reasonable estimate of the ionic component. We considered the nature of this ionic transport and conclude that an assignment primarily to oxygen transport is not incompatible with what we know at this time.

Acknowledgment

This work was supported in part by the Air Force Materials Laboratory, Air Force Systems Command, Wright-Patterson Air Force Base, Ohio under contract AF 33(616)-7472.

Manuscript received Jan. 29, 1965; revised manuscript received Sept. 17, 1965.

Any discussion of this paper will appear in a Discussion Section to be published in the December 1966 JOURNAL.

REFERENCES

1. P. Kofstad and D. J. Ruzicka, *This Journal*, **110**, 181 (1963).
2. See R. W. Vest, "The Electrical Behavior of Refractory Oxides," ARL 63-116, Systems Research Laboratories, Inc., Dayton, Ohio, July 1963, and other reports under Contract AF 33(616)-7748.
3. R. W. Vest and N. M. Tallan, *J. Appl. Phys.*, **36**, 543 (1965).
4. W. D. Kingery, J. Pappis, M. E. Doty,and D. C. Hill, *J. Am. Ceram. Soc.*, **42**, 393 (1959).
5. D. L. Douglas, in "Corrosion of Reactor Materials," published by International Atomic Energy Agency, Vienna (1962).
6. H. S. Edwards, A. F. Rosenberg, and J. T. Bittel, ASD TDR 63-635 under contract AF 33(657)-8470, July 1963.
7. E. Mollwo, *Z. Physik*, **138**, 478 (1954).
8. D. G. Thomas and J. J. Lander, *J. Chem. Phys.*, **25**, 1136 (1956).
9. S. Aronson, *This Journal*, **108**, 312 (1961).
10. R. M. Barrer, *Discussion Faraday Soc.*, **4**, 68 (1948).

Technical Notes

Chemical Spray Deposition Process for Inorganic Films

R. R. Chamberlin and J. S. Skarman

The National Cash Register Company, Dayton, Ohio

A new chemical technique (1) has been developed for the deposition of thin films of the sulfides and selenides which consists basically of spraying a solution on a heated substrate. This method has some similarity to the chemical bath deposition methods (2, 3) which have been used with lead sulfide and selenide and to the techniques used in the spray deposition of conductive oxide films. However, the process which is described in this paper is unique from the standpoint that all of the necessary elements are contained in the solution which is being sprayed. Neither the gas being used to operate the spray nozzle (4), the ambient atmosphere (5), the substrate (6), nor any post-treatment contributes to or changes the chemical composition of the film which is being deposited.

Experimental

As mentioned, the spray solution contains at least all the necessary elements which are desired in the resultant film. A typical example of a spray solution which if sprayed (see parameter list below) on a heated substrate will yield an optically clear and very adherent film of cadmium sulfide consists simply of an aqueous solution of cadmium chloride and thiourea which is usually made with a concentration of 0.001-0.05M and with the sulfur and cadmium ions in a ratio of 1 to 1.

The apparatus needed to carry out the chemical spray process consists basically of a device to atomize the spray solution and some sort of substrate heater. Figure 1 shows a typical experimental setup. Here is shown a spray nozzle of the two-fluid type although, since neither the gas used to atomize the spray nor the ambient atmosphere contributes to the composition of the film being deposited, a single-fluid nozzle could be used in which atomization is achieved by pressurizing the liquid.

The substrate heater should be one which has sufficient thermal capacity to maintain a temperature of at least 400°C while the spray is incident on its surface. Obviously, the necessary thermal capacity is dependent on the spray parameters such as spray rate and the volume of the gas being used to atomize the solution and propel the atomized solution to the substrate.

The spray nozzle used was one which had a maximum spray rate of about 20 ml/min. Stainless steel 316 has been used with most solutions with little evidence of metal contamination, but Teflon spray heads have been used and the hand-operated chromatic spray bottle has been extremely useful for quick trials with new spray solutions. Because of the range of spray rates possible with different spray heads and the control which is possible with different substrate heaters, the deposition parameters such as rate, temperature, and solution concentration for different compounds can be determined experimentally. Generally, the sulfides deposit at a higher temperature than the selenides. Deposition temperatures have been found to vary from 115°C for Cu_2S to 375°C for ZnS. However, the ease with which parameters can be changed even during a film deposition allows quite rapid determination of conditions necessary for a uniform deposit.

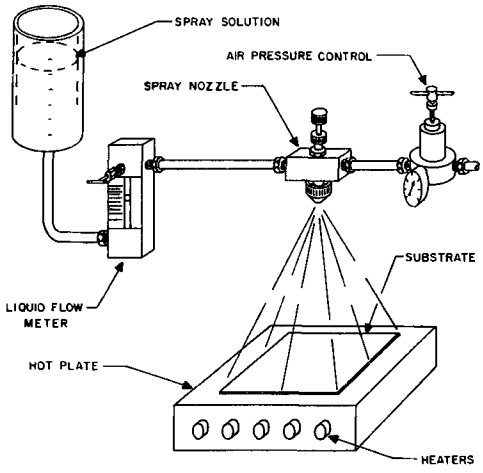

Fig. 1. Typical experimental setup

To obtain the desired semiconducting properties, separate additional experimentation will normally be required. The range in which a physically uniform film can be obtained is quite broad with definitely different electrical properties obtainable within this range.

The starting materials which can be used are many, and the choice will often depend only on what appears to yield the best results from a device standpoint.

The purity, freedom from other compounds or elements, and the film crystallinity which the various combinations yield are usually deciding factors. The compounds used to provide the elements need only be soluble in the liquid used, and the remainder of the starting components must be completely volatilized during the spray process. In the case of cadmium sulfide, many compounds could be used for the cadmium-ion source with still more choices for the sulfur ion as can be seen from Table II.

The choice of the starting material will determine the purity and crystallinity, deposition temperature, stability of the spray solution, and whether or in what way a doping impurity may be added. As an example, where a cadmium selenide film is to be spray deposited,

Table I. Typical CdS spray parameter values

Temperature	320°-380°C
Spray rate	15 ml/min
Concentration	0.01M

Table II. Starting materials for CdS

Cd	S
Cadmium propionate	thiourea
Cadmium acetate	N,N,dimethyl thiourea
Cadmium formate	allythiourea
Cadmium chloride	thiolocetic acid
Cadmium nitrate	2-thiozoline-2-thiol
	ammonium thiocyanate

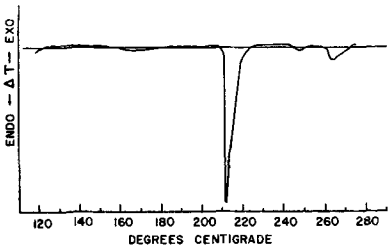

Fig. 2. Pyrolytic decomposition differential thermal analysis curve

substituted selenourea such as N,N,dimethyl selenourea is used to prevent free selenium from precipitating due to the decomposition action of both ambient heat and light. If a cadmium sulfide film is to be doped with copper, N,N,dimethyl thiourea is needed to prevent a copper hydroxide from immediately precipitating when the copper acetate is added to supply the copper to the starting solution.

Often it is found that best results can be obtained by using a combination that will precipitate a solid complex which is then subsequently redissolved to make a spray solution. A readily available complex, cadmium thiocyanate, if sprayed will yield a film of cadmium sulfide. This, of course, is equivalent to starting with cadmium chloride and ammonium thiocyanate. A solid complex which precipitates from mixing a 1M solution of cadmium chloride and thiourea has been found to be a convenient source of starting material for a cadmium sulfide spray and has generally proved satisfactory for films which have been used for semiconductor applications. Figure 2 is a differential thermal analysis curve describing the decomposition of a 2 to 1 sulfur-to-cadmium ratio complex. The decomposition of this complex is endothermic, and it occurs sharply at 210°C. This, then, clearly defines the minimum temperature that one could use when spray depositing cadmium sulfide from a solution containing this complex.

The semiconductor characteristics of a spray deposited film are most dependent on the solution composition (starting materials anion-to-cation ratio), substrate temperature, and the crystallinity of the substrate. Parameters such as spray rate, solution concentration, and the substrates thermal environment are the parameters which are adjusted such that a physically uniform film results. The crystallinity of a spray deposited film is dependent on the substrate and the starting material, particularly the cation material such as cadmium chloride or cadmium acetate in a cadmium thiourea solution. If cadmium chloride is used, a highly crystalline film can be expected with a given amorphous substrate, whereas, if cadmium acetate is used, the film would be amorphous as far as x-ray diffraction is concerned. Here amorphous is taken to mean that the crystallites are smaller than 400Å in size. If a cadmium chloride-thiourea solution is used for the deposition of cadmium sulfide, a crystalline film is normally expected; however, we find also that a variation in the extent of the crystallinity will be apparent if we vary substrate temperature even though at each temperature a physically uniform appearing film is being deposited. Examples of this variation are shown in Fig. 3 through 5 where the x-ray diffraction pattern shown in Fig. 5 is of a film deposited at the highest temperature and the diffraction pattern in Fig. 3 is that of a film deposited at the lowest temperature at which a physically uniform film could be deposited.

In general, the crystallinity of a film deposited using a cadmium halide-thio compound solution is more closely influenced by substrate temperature than substrate surface if the surface is inert to the deposition process and amorphous in nature. However, while very crystalline films can be deposited on noncrystalline material such as glass, when the substrate presents a more ordered surface such as a ceramic, the film crystallinity is often reduced (7). The highly crystalline metal surfaces will, in general, cause a film to be amorphous even though under other circumstances the same solutions would yield a film that would be very crystalline when deposited on an amorphous substrate.

The orientation of the crystallites with relation to a given substrate has been found to vary when the cation/anion ratio is varied. Variation as the result of changing this ratio can be seen in Fig. 6 through 8. Figure 6 is the typical orientation of a film from a 1:1 cadmium-to-sulfide ratio solution. Figure 7 is typical of a film deposited from a 2:1 cadmium-to-sulfur ratio, and Fig. 8 is typical of a film deposited from a solution with Cd:S ratio of 1:2.

Heat-treatment of chemically sprayed films in an inert atmosphere typically results in an increase in crystallinity with no significant change in orientation. The effect of heat-treatment can be seen by comparing Fig. 9 and Fig. 10 where two samples were examined by x-ray diffraction before and after heat-treatment. However, if a film is amorphous to x-ray diffraction, before heat-treatment, even a very long heat-treatment normally will not increase the crystallinity to the point where x-ray diffraction shows any significant change.

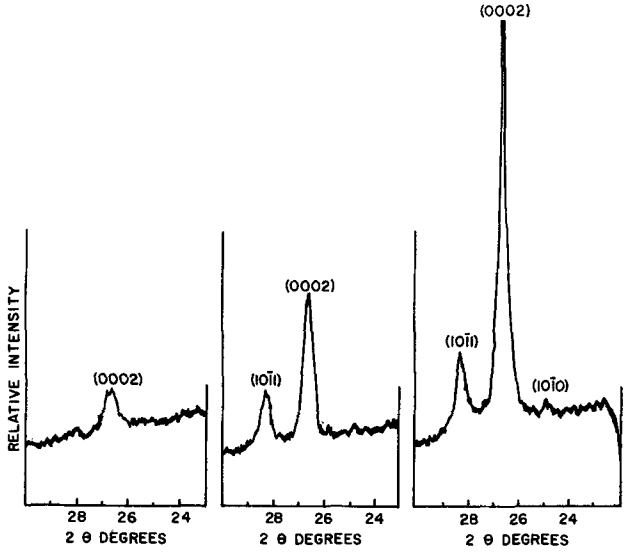

Fig. 3 (left), 4 (center), 5 (right). X-ray diffractographs of CdS films deposited at different temperatures.

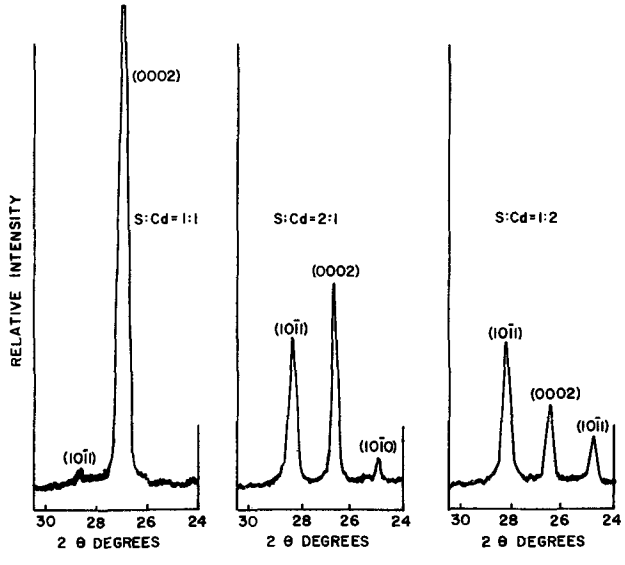

Fig. 6 (left), 7 (center), right). X-ray diffractographs of CdS films deposited from mixtures of different stoichiometric ratios.

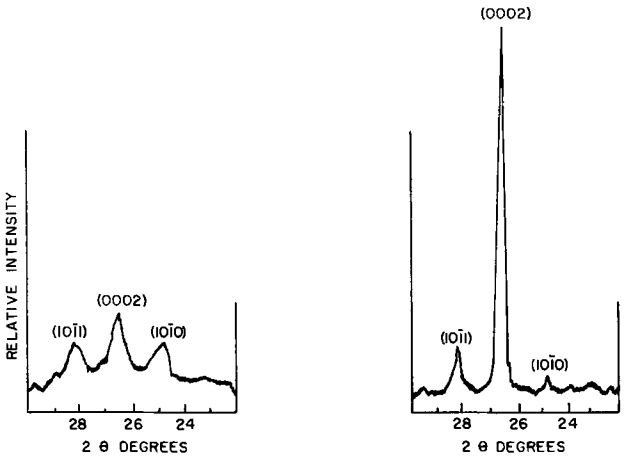

Fig. 9. X-ray diffractographs of two CdS films before heat treat, film A left, film B right.

Although x-ray fluorescence was the only means of checking stoichiometry, films deposited from a 1:1 cadmium-to-sulfur starting solution have always been found to be stoichiometric within the experimental error of the x-ray method used. With cadmium sulfide it is perhaps of interest to note that the undoped films are always a typical bright yellow and never show the darkening which is often attributed to excess cadmium in vacuum deposited films. It has been found that with any compounds the best initial approach is to start with the desired elements in the starting solution in the same ratio as desired (*e.g.*, antimony-to-sulfur ratio of 2:3 for Sb_2S_3) in the spray deposited film. This usually results in a film of the desired material over a quite broad (*e.g.*, ±70°C) deposition temperature range when binary or doped binary materials are being sprayed. However, when a solid solution film such as ZnCdS or CdSSe or films of ternary compounds such as $CdIn_2S_4$ is being deposited, the temperature range in which the desired ratio of the elements will deposit becomes quite narrow (*e.g.*, ±5°C). Because of the shift from stoichiometry with temperature in the solid-solution type films, adjustment of the initial ratio of the elements in the starting solution is sometimes necessary. Generally speaking though, the spray deposition process offers a great amount of versatility in the deposition of solid solution, ternary and impurity-doped films. The shifts of the x-ray diffraction peaks as the ratio of the anions was changed from 100% of one species to 100% of the other species, *e.g.*, in CdSSe, have been found to follow Vegard's law.

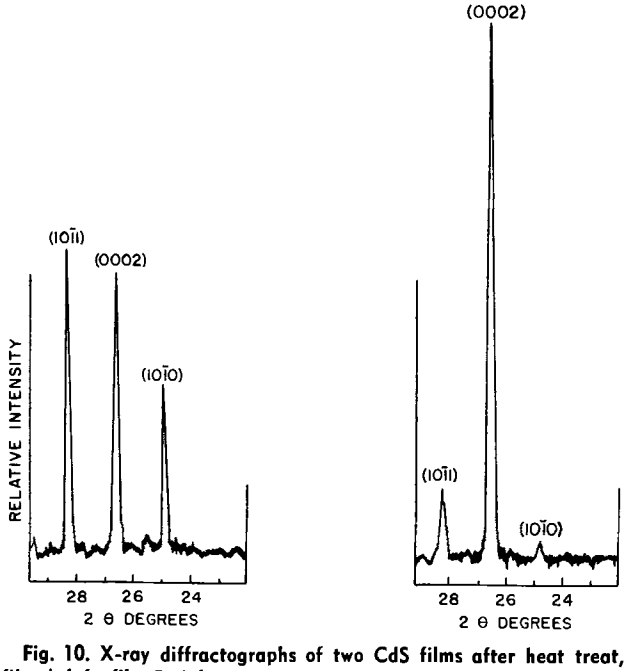

Fig. 10. X-ray diffractographs of two CdS films after heat treat, film A left, film B right.

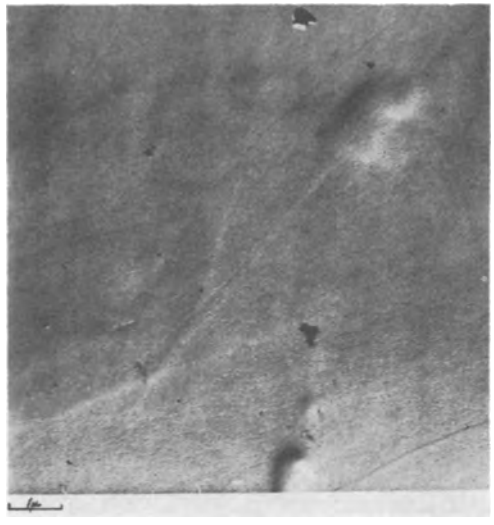

Fig. 11. Electronmicrograph of an amorphous CdS film

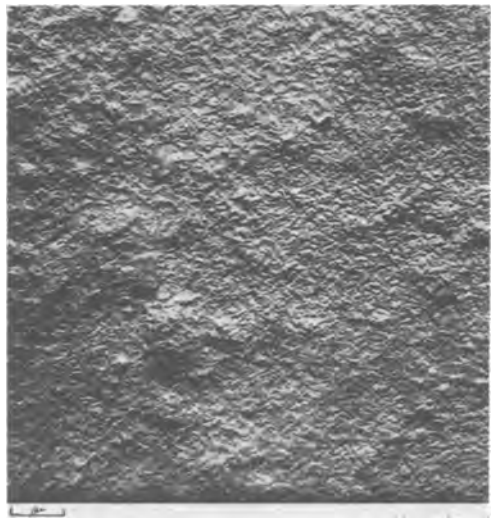

Fig. 12. Electronmicrograph of a highly oriented crystalline CdS film.

The physical characteristics of a spray deposited film are dependent on the degree of atomization, spray rate, temperature, and concentration of the spray solution and the film thickness. Generally, the finer the atomization, the higher the temperature and the less concentrated the solution, the greater the film's optical clarity will be. With proper parameter adjustment, the variation in surface can be less than 20Å. Figures 11 and 12 are electron micrographs of chemically sprayed films which appear amorphous and highly crystalline, respectively, when examined by x-ray diffraction. With an increase in the rate and solution concentration. it is possible to deposit films which range from glasslike to frosty in appearance. Whether the films are transparent or translucent, if they have been properly deposited, their adherence to the substrate should be such that mechanical abrasion is necessary to remove the film from the substrate.

Applications

The chemical spray process has been used successfully to deposit a great many compounds, some of which are listed in Table III.

Table III. Chemically spray deposited materials

I B VI A	II B VI A	III A VI A	III B VI A	IV A VI A	V A VI A	VIII	II B III A VI A	II B II B VI A
Cu_2S	CdS CdSe	In_2S_3 In_2Se_3	GdSe	PbS	Sb_2S_3	CoSe	$CdInSe_2$	CdZnS
Ag_2S	ZnS ZnSe	Ga_2S_3 Ga_2Se_3	SmS	PbSe				

The electrical and physical characteristics of chemically sprayed films are such that several significant devices have been developed.

The original application of sprayed films was in the area of photoconductivity; this application resulted in photoconductors (using films of about 1μ in thickness) made of CdS, Cd(SSe), and CdSe whose sensitivities are at least equal, whose rise and fall response times are normally faster, and whose spectral responses are broader than photoconductors made of these compounds by other processes (8).

Subsequent applications of the chemical spray process have been in the areas of photoluminescent and cathodoluminescent thin film layers which have shown extremely high (> 3,000 line pairs/in.) resolution, and in the area of thin film solar cells (9) (photovoltaic converters) where through the use of two sprayed films, one deposited on another (0.1μ film of $Cu_{2-x}S$ on a 1μ film of CdS) cells have been made with efficiencies of 4% in small areas and open-circuit voltages as high as 1.04v have been measured.

Acknowledgments

The authors wish to thank D. E. Koopman for his assistance. This work was supported in part by the Air Force Aero Propulsion Laboratory of the Research and Technology Division, USAF.

Manuscript received June 4, 1965.

Any discussion of this paper will appear in a Discussion Section to be published in the December 1966 JOURNAL.

REFERENCES

1. J. E. Hill and R. R. Chamberlin, United States Pat. 3,148,084.
2. J. Starkiewicz, L. Sosnowski, and O. Simpson, *Nature*, **158**, 28 (1946).
3. D. H. Roberts and J. E. Baines, *J. Phys. Chem. Solids*, **6**, 184 (1958).
4. F. J. Studer and D. A. Cusano, United States Pat. 2,685,530.
5. M. A. Tanner and L. B. Lockhart, Jr., *J. Opt. Soc. Amer.*, **36**, 703 (1946).
6. R. D. Kirk and J. H. Schulman, *This Journal*, **108**, 455 (1961).
7. R. R. Chamberlin, *Bull. Am. Ceram. Soc.*, **44**, 411 (Abstr. 4-55-65) (1965).
8. J. S. Skarman, *Solid State Elec.*, **8**, 17 (1965).
9. R. R. Chamberlin, *Bull. Am. Phys. Series II*, **8**, 635 (Abstr. 18) (1963).

Fast Etching Imperfections in Silicon Dioxide Films

A. D. Lopez

Bell Telephone Laboratories, Incorporated, Murray Hill, New Jersey

Fast etching imperfections in silicon dioxide films can produce pinholes when the film is partially thinned in buffered hydrofluoric acid. This paper proposes a model for the formation of these pinholes and also describes a means of detecting the pinholes. Furthermore, it is shown that the diffusion rate of phosphorus is greater in the imperfection than in the pure silicon dioxide. The cause of these imperfections is shown to be surface contamination prior to oxidation.

Samples of silicon dioxide films were checked for dielectric breakdown by application of a field between the bulk silicon and an evaporated metallic contact on the surface of the film. In general the breakdown field is found to be approximately 80-90v per 1000Å of oxide. However, if the oxide film is thinned by etching in a hydrofluoric acid etch, the breakdown field drops to a value near zero indicating that the oxide film no longer acts as a dielectric barrier. This is attributed to pinholes in the oxide film.

Consider two samples of silicon, one oxidized in atmospheric steam to a thickness of 6000Å, and the other, which is a control, to 3000Å (see Fig. 1a). The pipe-like structures running through the oxide film are fast etching imperfections which will be called potential pinholes. The potential pinhole has two characteristics. First, it has a much faster etch rate than pure silicon dioxide in the hydrofluoric acid etch and, second, its breakdown field is comparable to that of silicon dioxide. The 6000Å sample is now etched to a thickness of 3000Å in the hydrofluoric acid solution. The proposed model is one in which the pipe-like structures or potential pinholes will etch away because the potential pinhole is a region which etches much faster than SiO_2. This leaves a physical hole in the oxide which may extend to the SiO_2-Si interface as shown in Fig. 1b.

This model is tested by evaporating metallic contacts on the surfaces of the etched and unetched oxide films. If the model is valid, the evaporated metal will fill up the pinholes and consequently make contact to the bulk silicon as shown in Fig. 1c. Actually, the metal will make contact to the 20-30Å of oxide which forms immediately after etching. The breakdown voltage of this small thickness of oxide can be neglected since it is so small. The dielectric breakdown is now measured on the etched and unetched oxide films both of which are now 3000Å thick. One finds that the breakdown voltage of the unetched oxide is approximately 250-300v whereas on the etched oxide the breakdown voltage is in the order of 5-10v. It is concluded that contact has been made to the bulk silicon in the etched sample via a pinhole which must have been created by partially etching the film. Furthermore, it can be seen that the breakdown voltage

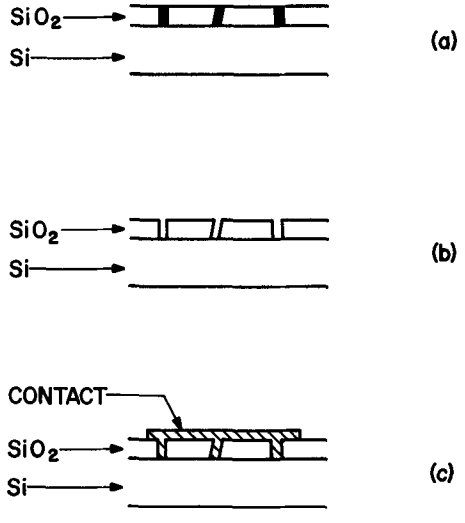

Fig. 1. Fast etching imperfections in SiO_2

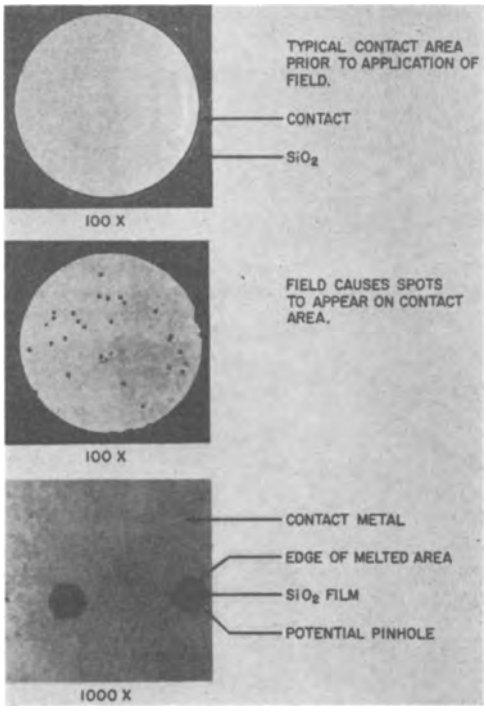

Fig. 2. Effect of applied field on contact metal

of the potential pinhole is comparable to pure SiO_2 since the unetched sample withstood 250-300v before breaking down.

Properties of the Potential Pinhole

Figure 2 shows metal contact areas on a film of silicon dioxide which was not etched. When a field is applied from the contact to the bulk silicon, the following observation is made: as the field is increased to a value near breakdown, spots begin to appear on the contact area. At first a few appear but as the field is increased to breakdown, the spots multiply until finally the oxide breaks down. Inspection of these spots at high magnification indicates that they are areas where the contact metal has melted. From a previous argument, it is reasonable to believe that the material which makes up the potential pinhole may have a dielectric strength somewhat less than pure SiO_2. Therefore, it seems reasonable that the spots are caused by conduction of current through a potential pinhole, where breakdown occurs first, causing the contact metal to heat up locally and melt. The contact material used was either gold or aluminum. The effect was not dependent on polarity.

It has been established that the material which makes up the potential pinhole is not pure SiO_2. Therefore, it is reasonable to expect a difference in the diffusion rate of phosphorus in SiO_2 and in the potential pinhole. This is borne out by the following experiment: a p-n junction was provided with a p-type layer approximately 1.5μ thick and a sheet resistance of 150 ohms per square. The sample was oxidized in 1 atm of steam to a thickness of 6000Å. Next, the sample received a phosphorus diffusion, such that only a part of the oxide was penetrated by the phosphorus. The penetrated oxide was then removed in buffered hydrofluoric acid, and metal contacts were evaporated on the oxide film. The breakdown voltage of each contact was measured, and on 25% of the dots the reverse characteristics of a p-n junction were observed with a breakdown of 6v. This breakdown voltage is what one would expect had the phosphorus penetrated completely through the oxide so that an n-p junction was made. It is concluded that where a 6v breakdown occurred, phosphorus must have diffused through the oxide forming an emitter base junction. Since the thickness of the masking oxide was great enough to mask the phosphorus diffusion, any phosphorus which appears in the "p" region must have diffused through a potential pinhole. If the phosphorus diffusion is omitted and contacts are applied to the oxide, no p-n junction reverse characteristics are observed. This indicates that any diffusion which takes place must be due to the presence of an external phosphorus source and not any source contained in the oxide.

In looking for the cause of the potential pinhole, it is reasonable to suspect surface contamination prior to oxidation. It has been found that if a sample of epitaxial silicon is oxidized directly after growth, the resulting oxide is essentially free of fast etching imperfections. Oxide films grown in this manner were subjected to repeated etchings and still were pinhole-free. It would seem, therefore, that surface contamination, which is minimized in this case, plays a significant role in the formation of fast etching imperfections.

Acknowledgments

The author would like to thank J. E. Iwersen, R. Edwards, and J. T. Nelson for their interest and helpful criticism and also A. Goetzberger for his encouragement to publish this work.

Manuscript received June 24, 1965; revised manuscript received Sept. 27, 1965.

Any discussion of this paper will appear in a Discussion Section to be published in the December 1966 JOURNAL.

Single Crystal Growth of SnTe and GeTe

P. F. Weller[1]

International Business Machines Corporation, Thomas J. Watson Research Center, Yorktown Heights, New York

Single crystals of SnTe and GeTe about 6 in. long and ⅜ in. in diameter were pulled from the melt by the Czochralski technique. A description is given of these crystals, together with the starting material synthesis and the crystal growth apparatus and procedures.

It was necessary to use a "graphite piston" puller with heated walls, similar to that used for PbTe (1), since SnTe and GeTe have vapor pressures at their melting points of 0.86 (2) and 17 (3) mm Hg, respectively.

Brief mention of Czochralski crystal growth of SnTe has been made by Allgaier and Houston (4) and by Brebrick (5), but no detailed information is generally available.

Starting Materials

Purification of elements.—SnTe was prepared from 99.9999% Sn shot obtained from Cominco Products, Inc. and 99.999% Te from American Smelting and Refining Company. The Sn, contained in a quartz boat, was fired in flowing H_2 at about 800°C for 1 hr. The charge was frozen and then refired in H_2 at 800°C for one more hour after the surface had been scraped clean. Tellurium was fired in flowing H_2 at 800°C for about ½ hr. Both the sublimed Te and the ingot remaining in the quartz boat were used for compound synthesis.

[1] Present address: Department of Chemistry, State University College, Fredonia, N. Y.

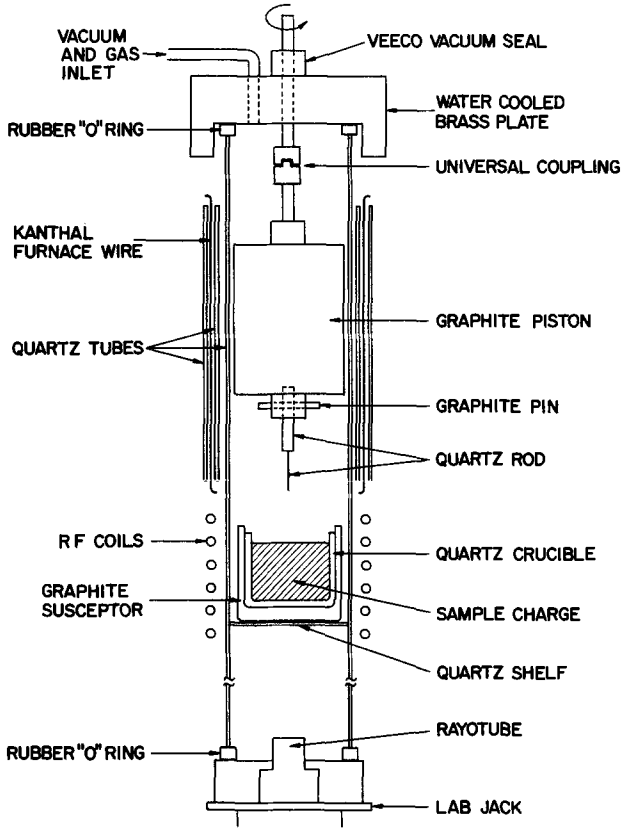

Fig. 1. Crystal puller

GeTe was prepared from instrument grade Ge, obtained from the Eagle-Picher Company, which had been zone refined until it was essentially intrinsic (resistivity of 45-50 ohm-cm). The Ge was then etched with a CP-4 solution and rinsed in water, ethyl alcohol, and finally acetone.

Compound synthesis—Stoichiometric amounts of Sn and Te were placed in a quartz tube, with the Sn resting above the Te in a quartz boat. The tube was evacuated to about 10^{-6} mm Hg and sealed off. Generally, this tube was placed in another quartz tube which was subsequently sealed under vacuum. This was purely a precautionary measure to prevent access to the air if the inner tube broke during synthesis. This had been a particular problem in PbTe synthesis (1).

The charge was then heated with a hand torch until the Sn began to melt (231.9°C) and to run down into the Te(mp 450°C). This had to be done carefully so that local overheating from the large heat of reaction did not occur. When the Sn and Te were entirely mixed and all visible reaction was complete, the tube was placed in a Kanthal furnace and heated to 825°C over a 6-hr period, and then cooled in the furnace to room temperature overnight.

The GeTe synthesis was similar, except for the initial heating procedures. Chunks of Ge and Te were premixed in the quartz tube and carefully heated with a hand torch until the visible reaction ceased. The higher melting point of the Ge (937°C) (6) permitted better control of the rate of reaction in this case. The above heating cycle was then used.

Apparatus

The crystal puller is shown in Fig. 1. A 2.1 in. OD quartz tube, 33-34 in. long, was clamped between rubber "O" rings by means of a "Lab Jack" at the bottom. A quartz shelf, located exactly 12 in. above the Rayotube temperature sensing device, divided the tube into two sections. A 1¾ in. tall, 1⅞ in. OD, ⅛ in. wall, graphite susceptor held the cylindrical quartz crucible (G.E. 204 A quartz, 1½ in. tall, 1½ in. OD, 1/16 in. wall) into which the sample charge was placed. A 3/32 in. quartz seeding rod, 1¾ in. long, was sealed to a ¼ in. quartz rod 2-2½ in. long, which was attached to the 5 in. long graphite piston with two graphite pins. The piston, machined to a 1/16 in. tolerance for a particular tube, was attached to a ¼ in. stainless steel rod, then to a similar rod through a universal coupling, and finally through a Veeco vacuum seal to the rotation motor.

The graphite susceptor was heated inductively, using a 5 kw Ecco RF generator at 450 kc/sec. Temperature was sensed by a Rayotube and controlled with a L&N, type H AZAR recorder and associated CAT controller. Temperature control was ±1°C or better, and desired changes were made easily and quickly.

An external furnace consisting of two concentric quartz tubes with longitudinal, Kanthal windings between the tubes kept the temperature of the upper chamber at the desired level with a minimum of visual obstruction. Temperatures were sensed with a chromel-alumel thermocouple and controlled with a West Gardsman controller.

Growth Procedure

About 200g of SnTe or GeTe chunks were packed in the crucible. This amount of material gave a melt volume about ¾ that of the crucible volume. Lower melt volumes caused difficulties in initial nucleation onto the quartz rod. This problem would probably be alleviated considerably if rather large diameter (about ¼ in. or more) SnTe or GeTe seeds were used.

After the external furnace had reached the desired temperature of 600°-650°C for SnTe and 400°-450°C for GeTe, the system was flushed several times and filled to about 3 psi with Ar or He. The charge was then melted [SnTe ~ 805°C (5, 7) and GeTe ~ 725°C (8)]. Generally, the melt surfaces were not completely clean. If too much surface scum was observed, the charge was frozen, the surface layer ground off, and the charge remelted. One such treatment usually reduced the surface contaminant to an acceptable level so that most of the remainder migrated to the crucible walls or to the first-formed polycrystalline boule. In either case the center portion of the melt was rendered essentially free of contaminants. [Care should be taken when melting a SnTe or GeTe charge if it fits snugly in the crucible. This would be the case, for example, with a charge that had solidified in place. Rapid heating, *i.e.*, to about 400°C in 5 min or so, caused several of the quartz crucibles to crack because of vastly different coefficients of expansion. Most of the charges were broken up to prevent this problem.]

When a sufficiently clean melt surface was obtained, an experimental crystallization temperature was determined by slowly lowering the temperature and noting the point at which freezing began. The temperature was then raised about 20°C. The quartz seed rod was dipped about ¼ in. into the melt, and the temperature was then decreased until nucleation on the rod was observed. Pulling was begun after temperature stabilization was attained. Pull speeds ranged from 1 to 3 in./hr, with the lower values generally preferable. A rotation rate of about 15 rpm was satisfactory.

The diameter of the polycrystalline boule was increased to about ¼ in. by slowly decreasing the temperature. The diameter was then slowly decreased again to 1/8-1/16 in. by carefully raising the temperature. This procedure generally yielded a single crystal, as indicated by reflections from developing faces as the crystal rotated. The crystal was then necked out to the desired diameter (usually less than ½ in.) by careful temperature control. Generally, rather large increases and decreases in temperature (2°-5°C or so) were necessary to show noticeable changes in crystal diameter. This is in sharp contrast to PbTe crystal growth where very small temperature variations cause large crystal diameter changes (1).

A problem was encountered in obtaining crystal diameters larger than about ⅜ in. A shelf formed at the side of the crucible and interfered with the growing crystal. The shelf was caused by the migration of surface impurities to a cold spot on the crucible. This problem could probably be helped considerably by rotation of the crucible. Other difficulties found in PbTe crystal growth (1) such as copious vaporization and rapid dendrite growth on the chamber walls and on the grown crystal, leading to poor visibility, were not severe problems with SnTe or GeTe.

The grown crystals were about 6 in. long and ⅜ in. in diameter and generally had large flats (faces). Crystal surfaces were sometimes shiny and metallic in appearance and sometimes had a powdery texture. All as-grown, undoped crystals showed p-type conductivity and grew with random orientation.

Acknowledgment

The author wishes to thank Mr. C. J. Lent for technical assistance.

Manuscript received June 23, 1965; revised manuscript received Oct. 4, 1965.

Any discussion of this paper will appear in a Discussion Section to be published in the December 1966 JOURNAL.

REFERENCES

1. See, for example, D. F. O'Kane, IBM Research Report NC-338, 1964.
2. R. F. Brebrick and A. J. Strauss, *J. Chem. Phys.*, **41**, 197 (1964).
3. R. F. Brebrick, *ibid.*, **41**, 1140 (1964).
4. R. S. Allgaier and B. Houston, "Physics of Semiconductors, Conference Proceedings, "Exeter, 1962, p. 172.
5. R. F. Brebrick, *J. Phys. Chem. Solids*, **24**, 27 (1963).
6. F. X. Hassion, C. D. Thurmond, and F. A. Trumbore, *J. Phys. Chem.*, **59**, 1076 (1955).
7. M. Weinstein and A. I. Mlavsky, *Rev. Sci. Instr.*, **33**, 1119 (1962).
8. J. P. HcHugh and W. A. Tiller, *Trans. Met. Soc. AIME*, **218**, 187 (1960).

Preparation of Doped Germanium for Far Infrared Detectors

E. M. Swiggard and H. Shenker

United States Naval Research Laboratory, Washington, D. C.

Efficient, extrinsic germanium detectors for the far infrared are now well known (1, 2). In order to maximize the performance of these detectors it is necessary to have material with a low concentration of compensating impurities, *i.e.*, donor impurities in a p-type material or acceptor impurities in an n-type material. It is also necessary to have low-noise electrical contacts to the detector to realize maximum signal-to-noise ratios. This work deals with the procedures developed to prepare low-compensation ($<4\times10^{12}$ cm^{-3} compensating impurities) boron- and gallium-doped germanium detector material and low-noise grown contacts. Horizontal zone refining and crystal growth techniques were used throughout this work.

The concentration of compensating impurities (assumed singly ionized) was obtained by measuring the Hall effect *vs.* temperature characteristics of each sample and analyzing these measurements by the methods described by Blakemore (3) and Putley (4).

Boron-doped germanium is a natural choice for the manufacture of low-compensation materials since boron is the only electrically active impurity in germanium with a distribution coefficient greater than one. It, however, suffers from the difficulty that a large amount of the boron is lost from the ingot during the zone refining process. This is presumably due to the oxidation of the boron by trace oxidants in the system as discussed by Bridgers and Kolb (5). The use of high-purity palladium-diffused hydrogen did not remedy this difficulty. In order to obtain the desired material, the loss of boron per pass was measured, and sufficient extra boron was put in to correct for the boron loss. It was found that after eight zone passes only from 0.1 to 1% of the original boron remained as electrically active boron in the ingot. Several ingots were grown using this estimation procedure. One of these ingots contained a zone-leveled portion 6 cm long over which the concentration of boron remained within 20% of the average value. The concentration of compensating impurities was measured on two samples from another of the ingots and was found to be 1×10^{12} and 1.5×10^{12} cm^{-3}, respectively. Detectors made from this ingot yielded the excellent detectors described in ref. (1).

Because of the inevitable variability of the loss of boron in purifying an ingot, it was difficult to prepare zone leveled boron-doped germanium of a predetermined doping level. For this reason it was desirable to be able to prepare low-compensation germanium using another group III dopant. Two methods of preparing low-compensation gallium-doped germanium were developed.

The first method utilizes the fact (6) that the slope of the ultimate distribution of an impurity is very sensitive to the distribution coefficient of the impurity, the smaller the distribution coefficient the steeper the slope. Since gallium has one of the largest distribution coefficients ($k = 0.087$) of any dopant in germanium the slope of its ultimate distribution is less steep than the slopes for most other impurities. For example, if there are equal numbers of gallium and arsenic ($k = 0.02$) atoms in a germanium ingot, then the ratio of arsenic to gallium concentrations is 0.0009 at a point four zone lengths from the final end of the ingot having the ultimate distribution of each of these dopants. Essentially this method uses this purification effect for reducing the compensation. In practice, a small piece of gallium was placed on the end of a previously zone refined ingot of germanium and ten additional zone refining passes made. A zone about 2.5 zone lengths (the exact distance depends on the desired gallium concentration) from the final end of the ingot was then melted and carried to the beginning end of the ingot. The first 10 cm of the ingot was then zone leveled. A sample cut from this ingot was measured to have a gallium concentration of 1.2×10^{14} at. cm^{-3} and a compensating impurity concentration of 4×10^{12} at. cm^{-3}.

The second method of preparing low-compensation gallium-doped germanium used a pellet-dropping technique adapted to horizontal crystal growth. While pellet-dropping to achieve varying doping levels and p-n junctions is a common procedure in connection with the Czochralski method of crystal preparation, its adaptation to horizontal crystal growth appears to have been neglected. The experimental apparatus is shown in Fig. 1. A quartz spoon which holds the dropping pellet containing the proper amount of gallium-doped germanium was inserted into the zone refining tube through an "O" ring connector. Previously zone refined germanium was placed in the zoner with a seed crystal, and 6-10 zone refining passes were taken to remove any impurities introduced during the handling and etching of the germanium. A zone was then melted toward the front end of the ingot and the

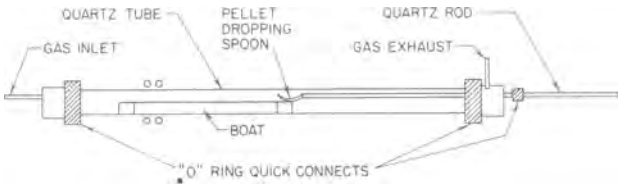

Fig. 1. Horizontal pellet dropping apparatus

pellet dropped into this molten zone. The pellet dissolved very rapidly, and the zone was backed up slightly to remelt the polycrystalline growth caused by the sudden temperature drop in the zone. The zone is then carried out to the end of the ingot. A sample cut from an ingot grown in this manner was measured to have a gallium concentration of 1.2×10^{14} at. cm^{-3} and a concentration of compensating impurities of 2×10^{12} at. cm^{-3}. Detectors made from material grown by either of these methods proved to be excellent detectors (2). A detector which used a piece of gallium-doped germanium grown by the pellet-dropping method was found to have a detectivity of 3.1×10^{11} cm-$cps^{1/2}$-W^{-1} at 104μ which is the highest detectivity for any detector of this type measured to date at NRL.

The chief source of extraneous current noise in these detectors appears to be associated with the contacts to the detector element. In order to reduce this current noise p^+-p single-crystal contacts were grown by placing a heavily doped piece of germanium on each end of a 1 cm section of gallium-doped germanium detector material. The boat containing these pieces was placed in the zone refining apparatus and the contact piece was melted. The rf coil was then moved until the molten contact piece wet the detector section and melted it back slightly; the coil was then slowly withdrawn (5 cm/hr) and a single crystal contact was grown. The same procedure was followed with the other contact. It was found that when boron was used for the p^+ dopant the lowest noise contacts were obtained (7); however when indium was used for the p^+ dopant relatively high noise contacts were obtained. Because the distribution coefficient of boron is greater than unity it forms a sharper junction than indium which has a distribution coefficient of 0.001 in germanium; it is presumed that an abrupt p^+-p junction is required for a low noise junction.

In order to carry out the procedures described above it is essential that single crystal growth be easily maintained. This was accomplished by using a quartz boat with a close-fitting graphite sleeve as shown in Fig. 2. The end pieces shown on top of the figure were used to raise the graphite sleeve off the quartz reaction tube and to prevent the boat from sliding out of the graphite sleeve. The boat was sand-blasted and blackened with soot from a paraffin candle. On top of the sooted layer there was deposited a thin layer of

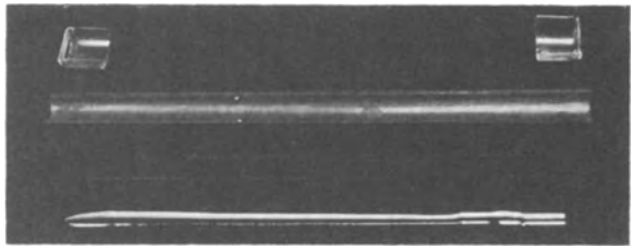

Fig. 2. Components of the crystal growing boat arrangement. The upper pieces are two quartz supports, the next lower piece is a graphite sleeve, the next lower piece is the quartz boat covered with soot and pyrolytic carbon. The bottom piece is a typical germanium ingot.

pyrolytic carbon which was obtained from the decomposition of acetone at 800°C. Before use the boat and graphite sleeve were heated at 1000°C in a stream of pure hydrogen to drive off any water or unreacted organic material. The graphite sleeve is a simple but effective method of obtaining a vertical, freezing interface in the germanium ingot. Single crystal growth was reliably maintained at all speeds up to 20 cm/hr. The pyrolytic carbon layer on top of the soot layer serves to stabilize the soot layer and has permitted the use of the same boat many times without recoating.

Acknowledgments

The authors are indebted to W. J. Moore for the measurements of the Hall effect *vs.* temperature on these samples. This work was performed under Project Defender, sponsored by the Advanced Research Projects Agency, Department of Defense, via the United States Office of Naval Research.

Manuscript received Aug. 4, 1965. This paper was presented at the San Francisco Meeting, May 9-13, 1965.

Any discussion of this paper will appear in a Discussion Section to be published in the December 1966 JOURNAL.

REFERENCES

1. H. Shenker, W. J. Moore, and E. M. Swiggard, *J. Appl. Phys.*, **35**, 2965 (1964).
2. W. J. Moore and H. Shenker, *Infrared Physics*, **5**, 99 (1965).
3. J. S. Blakemore, "Semiconductor Statistics," Chap. 3, Pergamon Press, New York (1962).
4. E. H. Putley, "The Hall Effect and Related Phenomena," Chap. 4, Butterworths, London (1960).
5. H. E. Bridgers and E. D. Kolb, *J. Chem. Phys.*, **25**, 648 (1955); *J. Appl. Phys.*, **26**, 1188 (1955).
6. W. G. Pfann, "Zone Melting," John Wiley & Sons, Inc., New York (1958).
7. An extended description of the work on contacts (principally by W. J. Moore) is contained in NRL Memorandum Report 1493 which may be obtained on request to the authors.

The Vapor Pressure of Iodine in the Temperature Interval 43°-80°C

M. Berkenblit and A. Reisman

International Business Machines Corporation, Thomas J. Watson Research Center, Yorktown Heights, New York

In an earlier study of the reactive transpiration in the system Ge-I_2-He, we had occasion to determine the vapor pressure of iodine at 50.5° and 61.8°C for comparison with literature values to insure against the possibility of large systematic errors affecting our results (1). The values obtained by us at the two temperatures were found to differ from those reported by Baxter and Grose (2), who also employed a transpiration technique, by 3.7% at 50.5° and 2.3% at 61.8°. Since our data showed an average deviation of 2-3% due, it is believed, to an end point inaccuracy in the thiosulfate titration as well as some tendency for solutions of the reducing agent to oxidize during the analysis (due to trace quantities of O_2 in the carrier gas),

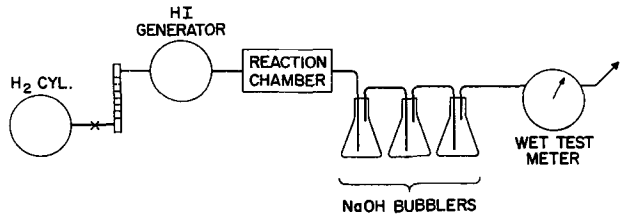

Fig. 1. HI determination apparatus schematic

we had no reason to question the earlier work at that time. Furthermore, as the absolute values of vapor pressures were less important than demonstrating that gas saturation was achievable at all flow rates in our system, subsequent Ge-I_2 reaction computations were based on iodine data reported by Baxter and Grose.

More recently, in quantitative kinetic studies of the Ge-HI reaction (3), the literature iodine data came under greater scrutiny because of the effect errors in the absolute values of the I_2 vapor pressure would have on determinations of the reaction order. We had developed an HI generator in the intervening time period which suggested a new approach to the determination of the vapor pressure of iodine in which the iodine was converted to hydrogen iodide and the latter was then quantitatively estimated via an acid-base volumetric procedure. This technique is clearly superior to the thiosulfate method employed in our earlier work. In addition, it seems subject to far less cumulative error than would be expected in the involved gravimetric analysis resorted to by Baxter and Grose.

During the course of the studies to be described, we demonstrated that the modified iodine source design employed was capable of equilibration with H_2 carrier gas input flow rates of up to *ca.* 8 liters/min in the temperature interval 43°-80°C.

Experimental Procedure

Figure 1 is a schematic representation of the HI analysis train. The system consists of a controlled carrier gas supply (Matheson "ultra pure" H_2 was used without further purification) to an HI generator followed by a reaction chamber. To this point, the apparatus is the same one employed in the Ge-HI kinetic studies of ref. (3). For the purpose of the present study it was necessary to provide a means for trapping and reacting HI and measuring the volume of carrier gas. This was accomplished via 3NaOH bubblers and a "Precision" wet test meter. The design of the HI generator and its operation has been described previously in detail (4), as have modifications in the iodine source bed length to accommodate high flow rates needed for the kinetic studies (3).

The experimental procedure followed was to place three traps in the line, each containing a measured quantity of standardized 0.1*N* NaOH solution diluted to a final volume of 100 cc. The entire system was flushed for 15 min with H_2 through the bypass portion of the HI generator. The carrier gas was then passed through the iodine source and catalyst chamber. The effluent HI-H_2 mixture is then depleted of HI in the standardized NaOH solution traps, the wet H_2 volume being finally measured in a calibrated wet test meter. After passage of given volumes of carrier gas, 6-21 liters, the iodine source was bypassed and the system was flushed for 30 min to insure complete removal of entrained HI. Analysis of the unreacted NaOH remaining in the bubblers was effected by titrating with a standardized 0.1*N* HCl solution. All of the HI generated was found to have reacted in the first two bubblers, with the final chamber providing a titration blank for the experiment. From these titrations the milliequivalents of HI and I_2 per volume of H_2 were determined.

Table I. Summary of I_2 vapor pressure calculations

T°C	p_{I_2} (Torr)	meq. HI titration
43.0	1.19	2.636 ± 0.004/21.00 l
49.35	1.90	4.195 ± 0.007/21.00 l
58.1	3.54	5.641 ± 0.002/15.00 l
68.0	6.86	8.788 ± 0.023/12.00 l
79.95	14.33	9.455 ± 0.002/ 6.00 l

Results and Discussion

Iodine vapor pressures were calculated with the aid of Eq. [1]. Assuming ideal gas behavior and a constant value of atmospheric pressure (1 atm), the partial pressure of iodine is given by

$$p_{I2(Torr)} = \frac{n_{I_2}}{\left[n_{I_2} + \frac{V}{RT_M}\left(\frac{760 - p_{H_2O(Torr)}}{760}\right)\right]} 0.760 \quad [1]$$

where n_{I_2} is the number of moles of iodine, determined by titration, that are carried in the volume V measured at a wet test meter whose temperature is T_M and where p_{H_2O} is the vapor pressure of water at T_M.

Table I contains the titration results and I_2 vapor pressures that were calculated from these data. The

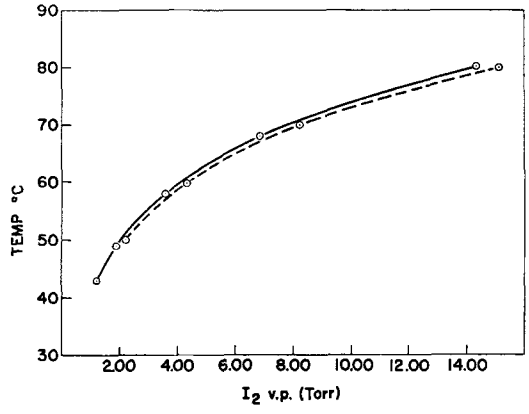

Fig. 2. Variation of I_2 vapor pressure with temperature: ---, Baxter and Grose; ——, present investigation.

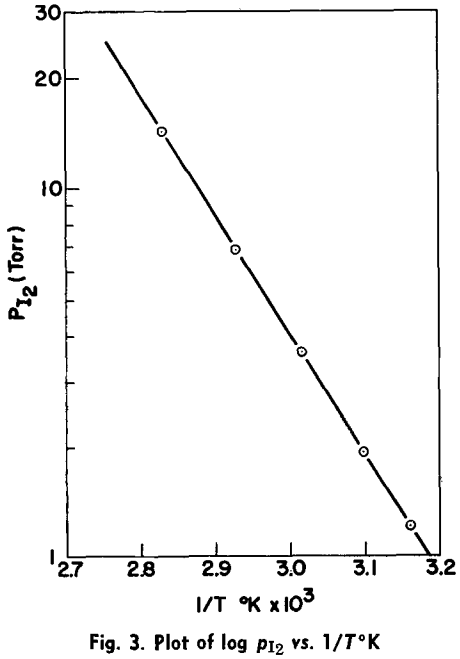

Fig. 3. Plot of log p_{I_2} vs. $1/T$°K

deviation observed was 0.2% in the worst case. A comparison of the Baxter and Grose data with those of the present study is shown by a plot of the variation of I_2 vapor pressure with temperature in Fig. 2. It can be seen that there is approximately a 5% difference between the two sets of results through the entire temperature range.

A plot of log p_{I_2} *vs.* 1/T°K, as shown in Fig. 3 yields a straight line described by Eq. [2]

$$\log p_{HI}(\text{Torr}) = \frac{-3.25 \times 10^3}{T°K} + 10.35 \qquad [2]$$

The slope of this curve has a value of 14.9 kcal/mole which is in exact agreement with $\Delta H°_{298}$, the heat of sublimation at 298°K, calculated from third law considerations using the free energy functions in Stull and Sinke (5). This is to be compared with the mean value of 14.7 kcal/mole reported by Baxter and Grose whose calculated values ranged between 14.6 and 15.0 kcal/mole.

Acknowledgment

The authors wish to thank Mr. M. Sampogna for his assistance in this work.

Manuscript received Aug. 23, 1965.

Any discussion of this paper will appear in a Discussion Section to be published in the December 1966 JOURNAL.

REFERENCES

1. A. Reisman, M. Berkenblit, and S. A. Alyanakyan, *This Journal*, **112**, 241 (1965).
2. G. P. Baxter and M. R. Grose, *J. Am. Chem. Soc.*, **37**, 1061 (1915).
3. A. Reisman and M. Berkenblit, To be published.
4. A. Reisman and M. Berkenblit, *This Journal*, **112**, 315 (1965).
5. D. R. Stull and G. C. Sinke, "Thermodynamic Properties of the Elements," No. 18 of the Advances in Chemistry Series, American Chemical Society (Nov. 1956).

Influence of Temperature on Illustrations of the Adoption of Limiting Values of Hydride Vapor Pressure and Hydrogen Contents by Highly Surface-active Cathodes of Palladium Alloys

J. A. S. Green and F. A. Lewis

Chemistry Department, The Queen's University of Belfast, Belfast, Northern Ireland

Measurements of the electrical resistance and electrode potential of cathodes of certain palladium alloys at 25°C have provided evidence (1) that, with highly catalytically active surfaces, the hydrogen content of the cathodes (expressed here as H/Me, the atomic ratio of hydrogen atoms to the total number of metal atoms) tends toward a limiting value over the range of current densities spanning the onset of the evolution of bubbles of gas. Such measurements also provided evidence that the adoption of limiting hydrogen contents results from the development of a limiting supersaturation of the catholyte with hydrogen molecules prior to the evolution of bubbles, and not to a limiting solubility of hydrogen within the cathodes.

At the limit of supersaturation, the concentration of dissolved hydrogen molecules, $C_{(\text{lim})}$, may be regarded as in equilibrium with a hypothetical equivalent pressure of hydrogen gas, $P_{(\text{lim})}$. The hydrogen content of the cathode under these conditions may, in turn, be designated H/Me$_{(\text{lim})}$, and its corresponding hydride vapor pressure designated $p_{(\text{lim})}$, where $p_{(\text{lim})}$ should equal $P_{(\text{lim})}$ in the steady state during electrolysis.

For palladium and some palladium alloys, electrical resistance (often conveniently expressed as relative resistance, R/R_o, where R_o is the "hydrogen-free" value) increases approximately linearly with increase of H/Me, and then exhibits a decrease following a relatively broad maximum. The relationships between H/Me and R/R_o can be virtually independent of temperature over appreciable ranges of H/Me (2).

The basis of illustrations of the attainment of limiting values by p and H/Me lies in the form of the pressure (p)-composition (H/Me) isotherms for the alloys. These should be such that there will be only a relatively small increase of H/Me for values of p up to $p_{(\text{lim})}$. This increase of H/Me then should be reflected by only a small increase of R/R_o up to $R/R_{o(\text{lim})}$. Any absorption of hydrogen in excess of H/Me$_{(\text{lim})}$ then can be reflected by substantial further changes of R/R_o.

At 25°C, alloys with ~20% Ni and ~25% Rh have been found satisfactory in these respects (1). Results in Fig. 1 indicate how other alloys can provide good demonstrations at other temperatures.

Figure 1a illustrates that, at 25°C, a highly catalytically active cathode of an 18.99% Pt alloy can exhibit relatively substantial increases of R/R_o during electrolysis at "160 ma cm^{-2}. This current density is sufficiently high for vigorous evolution of hydrogen bubbles to be occurring in the steady state. Changes of R/R_o during electrolysis were measured by an a-c bridge, and the electrolyte was in fairly low concentration in order to reduce errors in R/R_o due to co-conduction of the bridge current through the solution.

With increasing temperature, alloys of the Pd + Pt series exhibit (2, 3) a general decrease of the value of H/Me corresponding with any value of p. Results

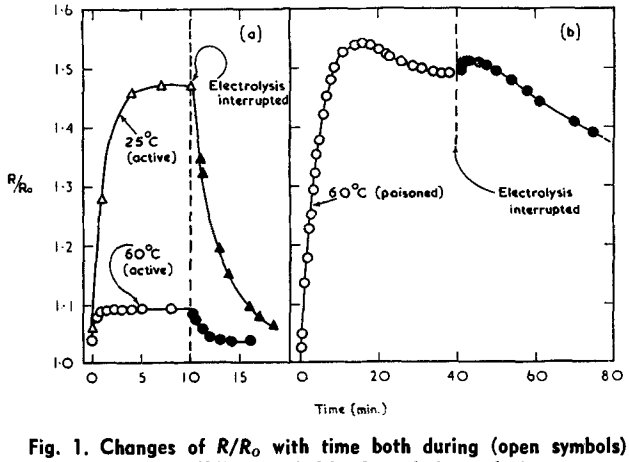

Fig. 1. Changes of R/R_o with time both during (open symbols) and subsequent to (filled symbols) electrolysis in hydrogen-saturated 0.02*N* HCl for ~8 cm lengths of a 0.0122 cm diameter wire of an 18.99% Pt-91.01% Pd alloy coated thinly with palladium black. Prior to electrolysis, the "active" specimens [Fig. 1(a)] had absorbed hydrogen from solution until they assumed a "zero" electrode potential with respect to a Pt/H_2 reference electrode in the same solution.

in Fig. 1(a) indicate that the value of H/Me corresponding to $p_{(lim)}$ had become so much lower at 60°C that the highest value of R/R_o which could be attained during electrolysis was now only ~1.1 in the case of a highly catalytically active specimen.

Prior to an otherwise duplicate experiment at 60°C, a further 18.99% Pt specimen was immersed in an arsenical solution. This caused its surface to be poisoned for equilibration with hydrogen molecules. Consequently the concentration of hydrogen atoms on its surface during subsequent electrolysis was likely to exceed (1, 4) the concentration of atoms complementary with $p_{(lim)}$.

Absorption of hydrogen by this poisoned specimen in excess of $p_{(lim)}$ is indicated in Fig. 1(b) by the substantial increase of R/R_o beyond 1.1, and by its subsequent passage through a maximum.

Figure 1(b) also shows that, after interruption of electrolysis, a maximum also is exhibited by plots of R/R_o against time during the relatively slow desorption of hydrogen from such poisoned specimens.

Acknowledgment

The authors are indebted to the International Nickel Company (Mond.) Limited for providing palladium alloys.

Manuscript received Aug. 17, 1965.

Any discussion of this paper will appear in a Discussion Section to be published in the December 1966 JOURNAL.

REFERENCES

1. J. A. S. Green and F. A. Lewis, *Trans. Faraday Soc.*, **60**, 2234 (1964).
2. A. W. Carson, T. B. Flanagan, and F. A. Lewis, *ibid.*, **56**, 363, 371, 1332 (1960).
3. T. B. Flanagan and F. A. Lewis, *This Journal*, **108**, 473 (1961).
4. Cf., *e.g.*, Z. Szlarska-Smialowska and M. Smialowski, *This Journal*, **110**, 444 (1963).

Brief Communication

Phase Diagram of the Pseudo-Binary System Ge-GaAs

R. M. A. Lieth and H. J. M. Heyligers

Solid State Physics Group, Department of Technical Physics, Technical University, Eindhoven, The Netherlands

The main object of the work of Jenny and Braunstein (1, 2) was to find the miscibility range for solid solutions of Ge and GaAs. In this paper we report the phase diagram for the system Ge-GaAs, determined by means of thermal analysis in the region 100% Ge to Ge-35 mol. % GaAs. The eutectic composition lies at 25 mol. % GaAs at a temperature of 862° ± 2°C. In the course of our work two articles appeared in the literature. Glazov *et al.* (3) report an eutectic alloy at 18.7 mol. % GaAs at a temperature of 888° ± 3°C. Takeda *et al.* (4) found the eutectic composition at 15 mol. % GaAs at a temperature of 865° ± 2°C.

The alloys were made by melting together the components[1] in silica ampoules with thermocouple holes in the top. These ampoules were sealed off after evacuation to 10^{-3} mm Hg. After fusion the Ge-GaAs melts were kept at 1250°C for 3 hr, while occasional shaking insured a thorough mixing of the contents. The thermal analysis of these alloys was made by recording the cooling curves with a Honeywell automatic measuring bridge.

From the constant part in the time-temperature curves a Tamman triangle was constructed, which enabled us to check the position of the eutectic composition.

The cooling rate was 10°C/min. Silver and sodium chloride were used as reference materials.

[1] Monocrystalline GaAs was obtained from Monsanto; monocrystalline Ge was provided by the Materials Science Group of our Physics Department.

In Table I the melting points of the various alloys are listed. The eutectic temperature of 860° ± 2°C is in good agreement with the work of Takeda *et al.* who reported 865° ± 2°C; however their eutectic composition of 15 mol. % GaAs differs from bur work.

The eutectic temperature of 888° ± 3°C found by Glazov *et al.* is higher than that found by Takeda and in our work. The corresponding eutectic composition of 18.7 mol. % GaAs, which is in good agreement with the work of Takeda, differs from our eutectic composition.

Acknowledgment

The authors thank Professor G. Diemer for his continuous interest in this work.

Manuscript received Sept 14, 1965.

Any discussion of this paper will appear in a Discussion Section to be published in the December 1966 JOURNAL.

REFERENCES

1. D. A. Jenny, U. S. Pat. 2,830,239, April 8, 1958.
2. D. A. Jenny and R. Braunstein, *J. Appl. Phys.*, **29**, 596 (1958).
3. V. M. Glazov and G. L. Malyutina, *Rus. J. Inorg. Chem.*, **8**, 1000 (1963).
4. Cf., *e.g.*, Z. Szlarska-Smialowska and M. Smialow- **112**, 363 (1965).
5. Handbook of Chemistry and Physics, 44th ed., p. 2417.

Table I. Melting point of various alloys

	100% Ge	5 mol. % GaAs	10 mol. % GaAs	15 mol. % GaAs	20 mol. % GaAs	25 mol. % GaAs	30 mol. % GaAs	35 mol. % GaAs
1st Thermal arrest	935° ± 2°C	915° ± 2°C	898° ± 2°C	890° ± 2°C	880° ± 2°C	860° ± 2°C	905° ± 2°C	934° ± 2°C
2nd Thermal arrest		860° ± 2°C	859° ± 2°C	858° ± 2°C	860° ± 2°C	860° ± 2°C	860° ± 2°C	862° ± 2°C

Pure Ag: mp: literature, 800.4; found, 800°C (5); pure NaCl: mp: literature, 960.8; found, 962°C.

Polarization Studies on Sintered Plate Electrodes Containing Various Amounts of $Ni(OH)_2$

E. Jost and F. Rufenacht

Metals & Controls Inc., A Corporate Division of Texas Instruments Incorporated, Attleboro, Massachusetts

ABSTRACT

Porous, sintered plate, nickel oxide electrodes containing varied amounts of active material (nickel hydroxide) were investigated with a single pulse interruption technique. Double layer capacitance measurements and long time overvoltage decay suggest that the nickel hydroxide deposited in the pores in sequential impregnations is deposited as a sponge of discrete particles. The available surface area proves, therefore, to be proportional to the $Ni(OH)_2$ weight. The long decay times indicate solid-state diffusion or relaxation phenomena on top of liquid concentration overvoltage, which becomes increasingly important with heavily impregnated electrodes.

Some investigations on the film-type nickel oxide electrode seem to suggest that the thickness of the nickel hydroxide layer not only influences the polarization behavior but also strongly influences the coefficient of utilization of the active material. Wynne-Jones (1, 2) prepared film-type electrodes of thicknesses ranging from approximately 1000 to 250,000Å and found electron yields on discharge ranging from 1.5 to 0.2 electrons per Ni for thin and thick films, respectively. Thin films up to 10,000Å were prepared by electrodeposition of nickel hydroxide on nickel substrates, thick films by oxidation of nickel surfaces with hypochlorites, and the results of the two preparation methods may not be directly comparable. However, thickness effects were clearly present in films prepared by the same method.

The electrochemical measurements of Kuchinskij and Ershler (3) on a large grain of nickel oxide in an alkaline electrolyte established the existence of a controlling solid-state diffusion mechanism which leads to the depletion of conductive species in the surface layer of the grain and ultimately, to the formation of an insulating $Ni(OH)_2$ layer at the conductor/nickel oxide interphase, which prevents the reduction of the higher valence, conductive interior of the grain.

Such a mechanism would explain the lower coulombic efficiency of thicker nickel oxide layers if the surface-to-volume ratio decreases in thicker layers or, in other words, if the specific surface area of nickel oxide does not remain constant as the layer is increased.

The existence of such potential determining surface layers was also discussed by Conway *et al.* in the series of papers on the nickel oxide electrode (4-7). These authors used a technique for their investigation similar to the one described in this paper.

In view of these findings, it would seem reasonable to expect that porous sintered electrodes may show similar effects if the pores are coated with nickel oxide films of various thicknesses.

On the other hand, since the methods of preparation of film-type electrodes and porous electrodes differ, the morphology of these layers could vary greatly. On the one extreme, the successive impregnation cycles in porous electrodes could build up epitaxial nickel oxide layers, and the available surface would remain constant or slightly decrease with every impregnation step. This surface would be an image of the internal surface area of the porous nickel-carbonyl plaque structure or approximately 0.1-0.2 m^2/g of plaque.

On the other extreme, the nickel oxide would be deposited as very small discrete particles independent of the previous deposit. In this case, the available surface area would increase in proportion to the increase in nickel oxide weight or, in other words, the specific area of nickel oxide would be constant and of the order of magnitude of several square meters per gram of plaque.

Such differences in available surface area would result in widely different polarization behavior of the electrode.

Experimental

The porous plates used in this investigation were 5 x 5 cm squares and approximately 1 mm thick. The average pore size was approximately 10μ, the porosity approximately 80%, and the BET surface area 0.1-0.2 m^2/g.

Ten plaques were washed with trichloroethylene in a Soxhlet extraction apparatus and vacuum impregnated with a nickel nitrate solution containing 0.25g of nickel/cm^3. The plaques were then immersed in 25% NaOH at 100°C, cathodically polarized at 170 ma/cm^2 for 30 min, washed with distilled water for 3 hr, and dried. This impregnation cycle was repeated up to ten times. Test plates were withdrawn after one, three, six, and ten impregnation cycles, respectively. In addition, two plaques were impregnated with diluted nitrate solution with a nickel content equivalent to one-third of the normally concentrated nickel nitrate solution. These plates are referred to as one-third impregnation plates.

Table I shows the plate loading for these plates.

The plates were assembled into cells using porous sintered plate cadmium counter electrodes of approximately ten times excess capacity. The cells were flooded with 30% KOH electrolyte and equipped with Hg/HgO reference electrodes in 30% KOH solution.

The cells were closed to avoid access of atmospheric CO_2.

After conventional forming, the cells received five charge and discharge cycles at a rate corresponding to the one used during the particular experiment, usually the 1- or 2-hr rate. In all cycles, the charge put into the cells was 140% of the theoretical electrochemical capacity.

Results

The most straightforward method of studying battery electrode behavior is the recording of charge and discharge curves measured against a suitable reference electrode. These charge and discharge curves, deter-

Table I. Plate Loadings

Impregnation cycles	Active materials per gram plaque	% Pore volume utilization
"1/3"	0.055	3
1	0.137	8
3	0.330	20
6	0.525	30
10	0.710	41

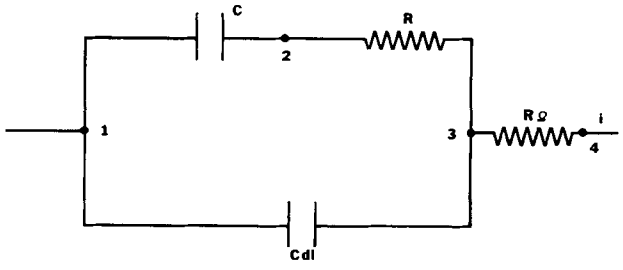

Fig. 1. Simplified equivalent circuit to illustrate double layer discharging after interruption of polarizing current: C, bulk capacity; R, faradaic impedance; R_Ω, ohmic impedance; C_{dl}, double layer capacitance.

mined at different temperatures and current densities, have practical importance, but are of little theoretical value, particularly with porous electrodes, because they only record the total overpotential. For more detailed studies, experimental methods distinguish between the individual components of the overpotential, namely, between ohmic, activation and concentration overpotential.

A method of great usefulness for this purpose is the measurement of the decay or build-up of overpotential as a function of time (4-7). If such measurements are carried out in the time interval from a few microseconds to several hours, it may be possible to measure the double layer capacitance and to distinguish between ohmic, activation, and concentration overpotentials by the rates of potential build-up or decay and by the slopes of the theoretically significant overvoltage decay or build-up against the logarithm of time.

The discharge process is given by the equivalent circuit, shown in Fig. 1 [see (8) for complete equivalent circuit], where C is the bulk or surface pseudocapacitance, and C_{dl} is the double layer contribution ($C >> C_{dl}$). R_Ω is the ohmic resistance. In the steady-state of discharge, the p.d. across C_{dl} is V_{13}. C will, in practice, be short-circuited by another reaction resistance corresponding to the rate of self-discharge on open circuit; however, this can be neglected. The p.d. across C during discharge is $V_{13} - iR$, *i. e.*, $V_{12}<V_{13}$. When the current is interrupted, R_Ω decays instantaneously. V_{13} will eventually become equal to V_{12} by an internal current flow from $C_{dl}C$. This is a fast process observable in the microsecond range and allows the determination of the double layer capacitance and thus the surface area of the electrolyte/nickel oxide interphase.

Activation and concentration overpotentials require longer decay times and with this type of electrode cannot be clearly discerned by decay rate measurement. Activation overpotential decay, however, should show one slope if plotted against the log of time regardless of current density or state-of-charge, provided there is only one operative mechanism. In any case, it would be expected that one mechanism will prevail over distinct regions of current density or state-of-charge. Therefore, if the decay slopes against the log of time change proportionally to current density or state-of-charge, a concentration overpotential mechanism is indicated.

The measurement of very short transients requires a fast-acting trigger circuit. Such a trigger circuit is shown in Fig. 2. It consists essentially of a 10-μsec monostable multivibrator, a 250 kc flip-flop, and a transistorized switch.

The typical sequence of operation consists of putting the cell on a selected load across the switching transistor in its conductive mode. The battery is then discharged for a predetermined period after which the switch is activated. The oscilloscope is triggered exactly 10 μsec before the switching transistor goes into its nonconducting mode.

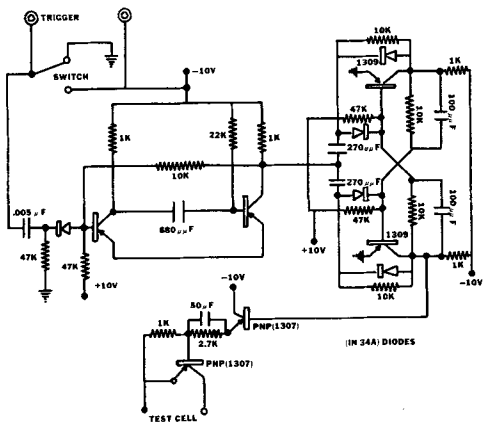

Fig. 2. Delayed-sweep trigger circuit used to obtain voltage time curves. (All diodes, 1N34A; all transistors, 2N1307's.)

Figure 3 shows typical voltage time plots covering the six time decades from 10 μsec to 10 sec for a cell at different state-of-discharge. Each of these curves represents six oscillographic traces.

This plot clearly shows three different regions in the curves of the overvoltage decay. Quite obviously, the ohmic overvoltage does not change markedly with state-of-discharge of the electrode. It should be understood that the voltage scale in this plot is relative, *i.e.*, the voltage level of the 10 μsec preinterruption sweep was arbitrarily taken as zero in order to allow a better comparison of the curves. The very small voltage drop in the interval from 10 μsec to approximately 100 msec is assigned to double layer charging, as explained, and reflects a large capacitance indicative of a very large surface area.

The portion from 100 msec to longer times is considered to be due to concentration and activation overvoltages and will be discussed in more detail later.

The very flat first portion of the curve is used for the estimation of the available area of the electrode.

Up to 1 msec, the overvoltage decay is almost linear with time, and the use of the relationship

$$C = i/(dE/dt)$$

where C is the double layer capacitance, i the preinterruption current, and dE/dt the time differential of the voltage, allows one to estimate the double layer capacitance and the area of the active materials.

In Fig. 4, the state-of-charge is plotted against the capacitance per gram of active material calculated from overvoltage decay traces for plates containing 0.18-2.5g of $Ni(OH)_2$. The discharge current per gram of active material was kept constant in all curves, and therefore, if the surface area of the active material in

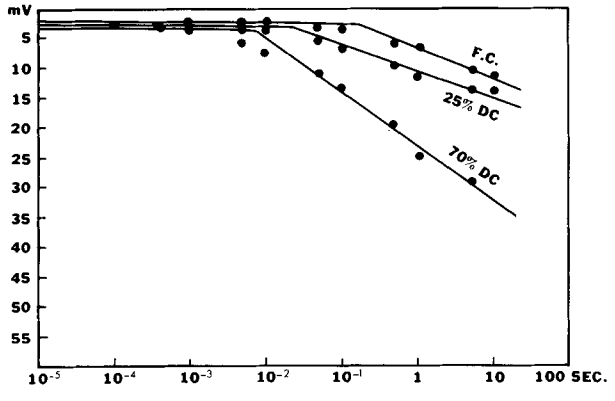

Fig. 3. Short-time overvoltage decay curves for an almost fully charged (FC), a 25% (25% d.c.) and a (70% d.c.) discharged electrode.

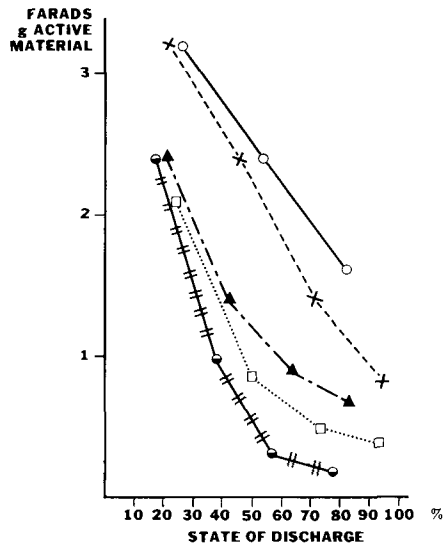

Fig. 4. Change of double layer capacitance during discharge of ——, 0.180g $Ni(OH_2)$/plaque d.c., 26 ma; — — —, 0.480g $Ni(OH)_2$/plaque d.c., 70 ma; — · —, 1.100g $Ni(OH)_2$/plaque d.c., 160 ma; . . . . ., 1.700g $Ni(OH)_2$/plaque d.c., 250 ma; —‖—‖—, 2.500g Ni $(OH)_2$/plaque d.c., 360 ma. Current density, 145 ma g $Ni(OH)_2 \sim 7.25 \cdot 10^{-7}$ amp/cm^2; based on a $Ni(OH)_2$ area of 20 m^2/g.

the pores is proportional to the weight, the curves should be identical.

For electrodes discharged up to 25%, the difference in capacitance between plates with 0.18g of $Ni(OH)_2$ and plates with 2.5g of $Ni(OH)_2$ is only approximately 20-25%. If we assume a double layer capacitance of 20 μf/cm^2 for the hydrated nickel oxide, the capacitance figures would suggest areas of the order of at least[1] 13-16 m^2/g of hydrated nickel oxide in reasonable agreement with reported surface areas for this oxide measured by the BET method (9, 10).

The capacitance and, therefore, the available surface area decreases with discharge, and the differences between lightly and heavily loaded electrodes become greater. It is suggested, however, that this might be due to interference of concentration polarization effects involving the electrolyte. Such effects would be considerably greater in heavily loaded cells since the current (and, therefore, mass transport) to pore volume ratio is approximately 25 times higher. The measurements with 75% charged plates are, therefore, considered more significant, and these indicate that the specific area does not drastically decrease with increased plate loading.

Figure 5 shows the long time overvoltage recovery of the same plates, again discharged at constant current per gram of active material, this time 200 ma/g, *i.e.*, 37 ma for the plate with one-third impregnation and 510 ma for the plate with 10 impregnations. The amount of time required to reach quasi-equilibrium is a function of the state-of-discharge. The fully charged cells, *i.e.*, cells which were approximately 4% discharged, attain equilibrium in approximately 20 min. The 50% discharged cells require approximately 16 hr, and the 80% discharged cells attain equilibrium only after a 24-hr stand.

The magnitude of recovery increases with the state-of-discharge and is 10 mv for a fully charged plate, 40 mv for 50% discharged cells, and 70 mv for 80% discharged cells.

Over long time periods, the curves are linear with the logarithm of time. At different states-of-charge the slopes are considerably different, indicating surface

[1] The curves suggest higher capacitance for fully charged nickel oxide electrodes.

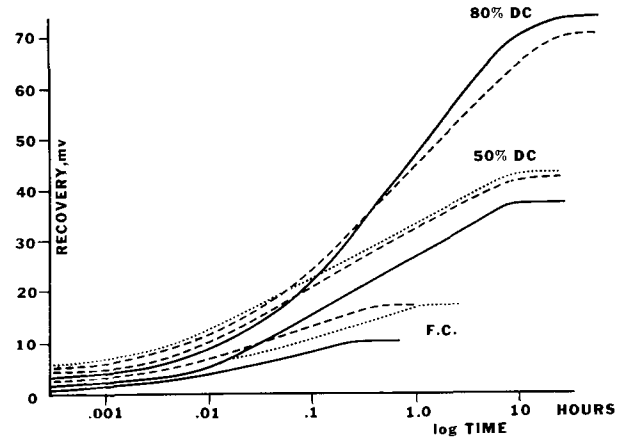

Fig. 5. Long-time overvoltage decay of positive plates for an almost fully charged, a 50% and an 80% discharged electrode. Discharge current 0.2 A/g active material. Active material per plaque: ——— 0.5g; — — — 1g, —.—. 1.5g.

changes as previously seen for the capacitance measurements.

For the same state-of-charge, however, the slopes of the recovery curves are very similar irrespective of active material loading if discharged at the same current per gram of active material. This behavior indicates similar current densities resulting from close to constant specific surfaces for these plaques containing various amounts of nickel oxide.

If the electrodes are discharged at the same current per gram of active material, *i.e.*, with 26 ma for the one-third impregnation and 360 ma for the 10-impregnation cells, the discharge curves are almost identical with respect to the voltage level as well as with respect to faradaic capacity.

If, however, a plate is discharged at various currents per gram of active material but within the same apparent current density limits as before, the difference is clearly visible in the reduced faradaic capacity delivered by the electrode at the higher current density (Fig. 6).

Discussion

These results indicate that the nickel hydroxide deposited in the pores in sequential impregnation cycles is deposited as a sponge of discrete particles. The available surface area is proportional to the $Ni(OH)_2$ weight, and cells discharged at the same current density per gram behave very similarly, although the apparent current density, *i.e.*, the current density per unit area of plaque, was varied 14-fold. If the current density per gram of active material is increased in the same limits, the effects are clearly discernible, mainly in the reduced faradaic capacity.

The long decay times and the slopes of the decay curves indicate solid-state diffusion or relaxation

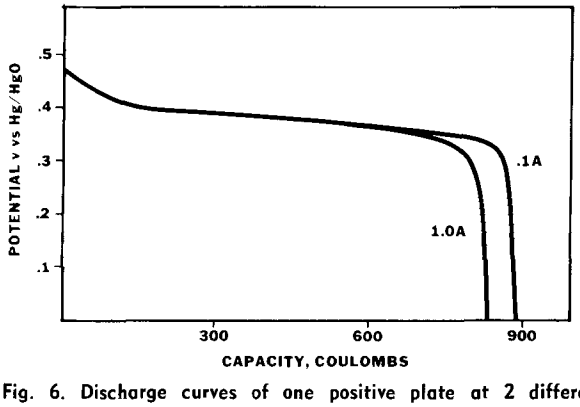

Fig. 6. Discharge curves of one positive plate at 2 different current densities.

phenomena, which again are very similar for plates of different loading if discharged at the same current per gram of active material.

The voltage decay measurements in the millisecond region indicate that KOH concentration overvoltage phenomena become important with increasing state-of-discharge of the electrode. These phenomena are not reflected in measurably decreased performance at room temperature, but they might be increasingly important at lower temperature.

Manuscript received March 3, 1965; revised manuscript received Sept. 23, 1965. This paper was presented at the Washington Meeting, Oct. 11-15, 1964.

Any discussion of this paper will appear in a Discussion Section to be published in the December 1966 JOURNAL.

REFERENCES

1. G. W. D. Briggs, E. Jones, and W. F. K. Wynne-Jones, *Trans. Faraday Soc.*, **51**, 1433 (1955).
2. E. Jones and W. F. K. Wynne-Jones, *ibid.*, **52**, 1260 (1956).
3. E. M. Kuchinskij and B. J. Ershler, *Zhur. Fis. Khim.*, **20**, 539 (1949).
4. B. E. Conway and P. L. Bourgault, *Can. J. Chem.*, **37**, 292 (1959).
5. *Ibid.*, **38**, 1557 (1960).
6. *Ibid.*, **40**, 1690 (1962).
7. B. E. Conway and E. Gileadi, *ibid.*, **40**, 1933 (1962).
8. K. Vetter, "Electrochemische Kinetik," p. 268, Springer-Verlag, Berlin, Gottingen, Heidelberg (1961).
9. T. C. Duddy and A. J. Salkind, *This Journal*, **108**, 717 (1961).
10. B. E. Conway and P. L. Bourgault, *Can. J. Chem.*, **40**, 1690 (1962).

The Heat-Treatment of Anodic Oxide Films on Tantalum

IV. Anodization in Phosphoric Acid Solutions

D. M. Smyth, T. B. Tripp, and G. A. Shirn

Research Laboratory, Sprague Electric Company, North Adams, Massachusetts

ABSTRACT

Dielectric measurements have been made on tantalum which has been anodically oxidized in aqueous phosphoric acid of various concentrations and then heated in air. The resulting dielectric consists of a highly conducting portion adjacent to the tantalum and an outer, nonconducting portion. This structure is interpreted in terms of the distribution of phosphorus incorporated into the oxide and its effect on the diffusion of oxygen during heat-treatment.

The previous papers in this series have presented a model which explains the dielectric properties of heat-treated, anodized tantalum (1-3). It was proposed that the tantalum extracts oxygen from the oxide film at an appreciable rate during heat-treatment above 200°. When the heating is done in an oxygen atmosphere, a dynamic equilibrium is established with fixed compositions in the oxide at the Ta-Ta_2O_5 and Ta_2O_5-O_2 interfaces, and with an appropriate variation of composition across the film. On cooling, the compositional variation with position is quenched, and there is then an exponential gradient of conductivity across the oxide, decreasing from a maximum value at the Ta-Ta_2O_5 interface. The dielectric properties are consistent with such an exponential gradient of semiconduction with an activation energy of conduction of 0.6 ev.

The above analysis was based on experimental results obtained from samples anodized in dilute aqueous electrolytes, particularly 0.01M H_2SO_4. Small but reproducible differences noted for samples anodized in dilute H_3PO_4 led to a more detailed study of the role of the anodization electrolyte.

Experimental

The basic techniques have been described previously (1-3). Electroless nickel counter electrodes were deposited by a standard deposition technique (4). The entire surface of the anodized sample was covered with nickel. Small dots of acid-proof paint were painted on the nickel, and the exposed metal was dissolved in concentrated HNO_3. The paint was removed with successive toluene and alcohol rinses. This left small dots of electroless nickel on the Ta_2O_5 surface to which gold wires were affixed by means of a conducting epoxy resin. Measurements on these samples were made with a General Radio 716-C bridge.

In all cases, the dielectric measurements were made in the temperature range −70° to +100° after heat-treatment in the range 300°-500°.

Unless specified otherwise, all samples were anodized to 75v, and all measurements were made in 40% H_2SO_4 at 34° and 120 cps.

Results

It was observed that samples anodized in 0.001M H_3PO_4 differed in the following ways from those formed in 0.01M H_2SO_4:

1. The average equilibrium capacitance increase for heat-treatment at 400° in air was 24% for phosphate films, compared with 17% for sulfate films.
2. The equilibrium value was attained somewhat more slowly for phosphate films.
3. The rate of weight increase during heat-treatment (oxygen up-take) was 25% slower for phosphate films (0.040 $\mu g/cm^2$ min *vs.* 0.053 $\mu g/cm^2$ min) for samples anodized to 15v and heated at 400°.

The last two points are consistent with a lower oxygen mobility in phosphate films. Moreover, the fact that there are any observable differences indicates that allowance for an influence of the anodization electrolyte must be added to the simple mechanism previously proposed for the heat-treatment process.

These observations led to an investigation of the effects of heat-treatment on samples anodized in H_3PO_4 and H_2SO_4 solutions of various concentrations. Results are shown in Fig. 1 which demonstrates factors 1 and 2 enumerated above. The equilibrium increase of capacitance increases drastically with H_3PO_4 concentration up to 1M and then drops again for 14.6M (85% H_3PO_4). Detailed data for samples anodized in H_2SO_4 are shown only for a concentration of 0.1M. The vertical line which intersects the 0.1M H_2SO_4 line at 60 min, however, shows the spread of values obtained over the concentration range 0.01-1M. Compared with the phosphate samples, there is almost no effect of H_2SO_4 concentration on the dielectric properties.

The bias dependence of capacitance of heat-treated phosphate films increases with increasing H_3PO_4 concentration up to 1M. The equivalent series resistance

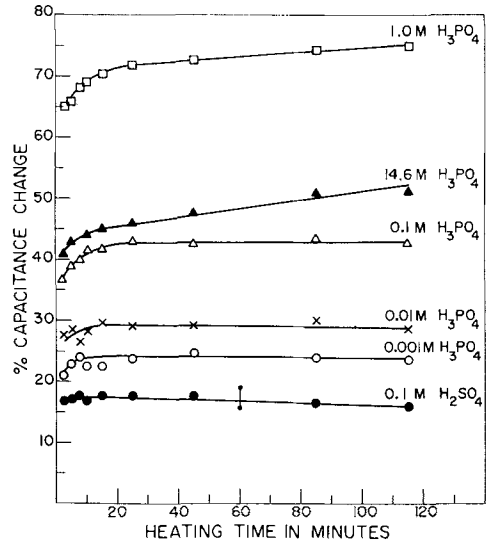

Fig. 1. Effect of anodization electrolyte on the capacitance increase due to heat-treatment of anodized tantalum at 400° in air.

increases up to a maximum at 0.1M and then decreases again. For the samples anodized in 14.6M H_3PO_4, even though the capacitance increased about 50% as a result of heat-treatment, the bias dependence of capacitance and the series resistance remained those of an unheated film. Characteristic data are shown in Table I. (Prior to heat-treatment, all of these samples had capacitances in the range 3.1-3.2 μf.)

Figures 2 and 3 show the temperature dependences of capacitance and dissipation factor for samples anodized in 1.0, 8.0, and 14.6M H_3PO_4 and then heated for 45 min at 400° in air. (The data for the 1M sample were obtained in two separate temperature runs. A different immersion depth probably accounts for the offset near 20°.) These results show that there is a smooth trend of properties with electrolyte concentration. The behavior shown in these figures is very similar to that reported earlier for heat-treated, partially reanodized samples (2). This similarity is shown clearly in Fig. 4 and 5, which show the frequency dependence of capacitance at several temperatures for a sample anodized in 14.6M H_3PO_4 and heat-treated in air; and for a sample anodized in 0.01M H_2SO_4, heat-treated in vacuum, and partially reanodized.

Another significant observation which is not related to heat-treament, is the effect of anodization in the more concentrated H_3PO_4 solutions on the interference color of the oxide film. Films anodized to the same voltages in solutions of increasing H_3PO_4 concentration appear optically to become progressively thinner. Thus a sample anodized to 75v in 14.6M H_3PO_4 has the same interference color as a sample anodized to about 55v in 0.01M H_2SO_4. For a given anodization voltage the capacitance of the unheated samples are essentially independent of electrolyte concentration, however. Similar observations have been made before (5, 6).

Discussion

As we have shown previously, the shape of the temperature dependence of capacitance is related directly

Table I. Dielectric properties of anodized tantalum after heat-treatment at 400° for 45 min in air, as a function of H_3PO_4 concentration in the anodization electrolyte

H_3PO_4 concentration, M	Capacitance bias 0v μf	Capacitance bias 10v μf	Series resistance bias 0v ohm	Series resistance bias 10v ohm
0.001	3.985	3.734	16.3	6.7
0.01	4.027	3.760	20.8	8.0
0.1	4.437	4.043	27.0	9.2
1	5.404	4.740	15.4	9.9
14.6	4.656	4.632	2.6	2.2
0.001 (unheated)	3.193	3.179	3.2	2.8

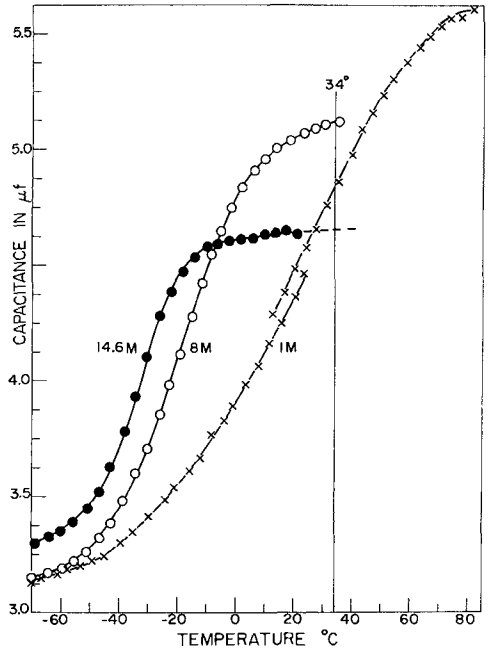

Fig. 2. Effect of H_3PO_4 concentration in the anodization electrolyte on the temperature dependence of capacitance of heat-treated, anodized tantalum.

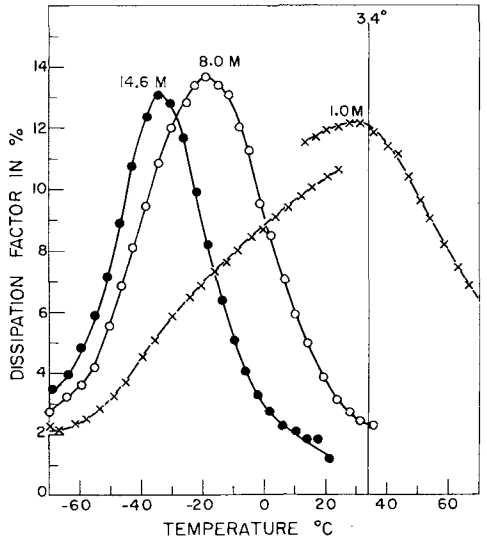

Fig. 3. Effect of H_3PO_4 concentration in the anodization electrolyte on the temperature dependence of dissipation factor of heat-treated, anodized tantalum.

to the shape of the conductivity profile across the oxide film (1-3). In fact, the relative shape of the conductivity profile is obtained by rotation of capacitance-temperature curves, such as Fig. 2, 90° clockwise. This then has the same appearance as a plot of log σ (conductivity) *vs.* position in the film with the Ta-Ta_2O_5 interface on the left-hand side where all conduction has been effectively quenched at low temperatures. This transformation can be empirically understood from the fact that the conductivity is related to the temperature by an exponential expression, and the capacitance is inversely related to a thickness of film, and hence a position. A rigorous derivation is given in the Appendix.

The data shown in Fig. 2 are thus used to obtain the schematic depiction of the conductivity profiles in Fig. 6. The level of σ_o, whose intersection with a conductivity profile defines a dielectric thickness (3), is shown for a measuring frequency of 120 cps. It is seen that the conductivity profiles are made up of two

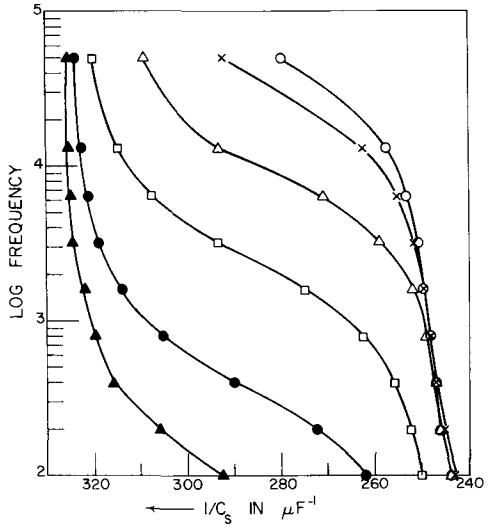

Fig. 4. Frequency dependence of capacitance of anodized tantalum heated for 2 hr in vacuum (5 x 10^{-8} Torr) at 500°, and reanodized 1 hr at 50v. Original anodization to 75v in 0.01M H_2SO_4; counter electrode was 0.02 cm^2 electroless nickel. ○, 19.2°; X, 11.5; △, —4.5; □, —23.8; •, —45.7; ▲, —59.6.

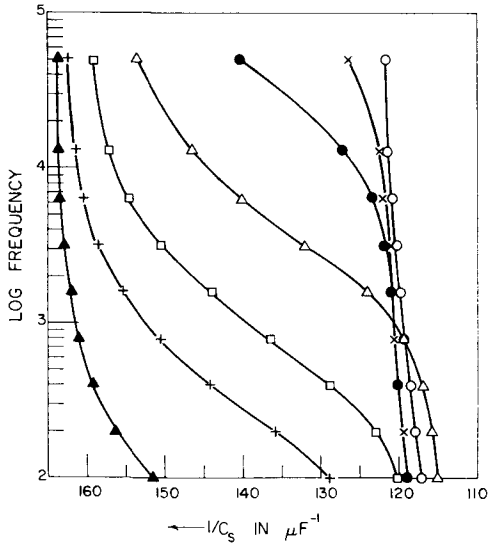

Fig. 5. Frequency dependence of capacitance of tantalum, anodized in 14.6M H_3PO_4, heat-treated in air at 400°. Counter electrode was 0.02 cm^2 electroless nickel. ○, 75.3°; X, 46.3; •, 26.4; △, —4.6; □, —23.8; +, —37.6; ▲, —59.8.

parts: a shallow, inner gradient which changes to a steeper gradient further out in the film. The distinction between the two slopes increases, and the transition between them moves closer to the tantalum with increasing concentration of H_3PO_4 in the anodization electrolyte. It is clear that these three samples represent a smooth trend, and that the apparent peculiarity of the 14.6M sample in Table I results from the particular choice of temperature and frequency of measurement. This resulted in the inner dielectric boundary (the intersection of the conductivity profile with σ_0) being on different characteristic parts of the profile. For the 1M sample the boundary is on the shallow, inner slope, and this very diffuse transition from dielectric to electrode results in high dielectric losses and large dependences of capacitance on bias, temperature, and frequency. For the 14.6M sample, on the other hand, the boundary is on the steep, outer slope which is so steep that it is as sharp a dielectric boundary as the Ta-Ta_2O_5 interface of an unheated sample (see Table I). When the frequency is increased or the

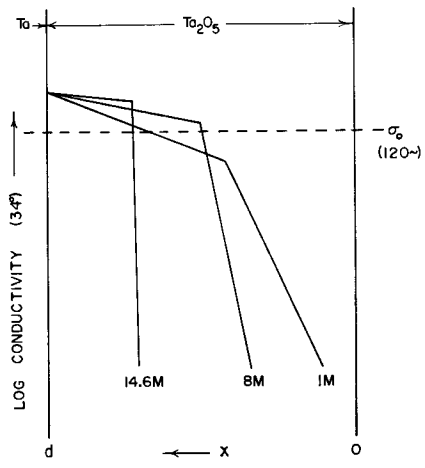

Fig. 6. Schematic representation of the conductivity profiles across oxide films on tantalum, anodized in various concentrations of H_3PO_4, and heat-treated at 400° in air.

temperature decreased enough to move the dielectric boundary up on the shallow, inner gradient, however, the dielectric properties of the 14.6M sample deteriorate as shown in Fig. 2, 3, and 5.

These samples have dielectric properties which are very similar to those of tantalum which has been anodized in dilute H_2SO_4, heat-treated in vacuum, and partially reanodized. Such treatment gives a similar conductivity profile, as seen in Fig. 4 and 5. In these figures log frequency, which is proportional to log conductivity (3), has been plotted against the reciprocal capacitance, which is proportional to the dielectric thickness. Thus these plots are equivalent to plots of log conductivity *vs.* position. These results at different temperatures could be normalized to a given temperature by use of the activation energy of conduction to give one continuous, overlapping curve which would represent the conductivity profile as shown in Fig. 6.

The obvious similarity between the samples represented by Fig. 4 and 5, and the fact that they yield identical activation energies of conduction both by the temperature dependence of conduction at a given position in the film, and by the frequency dependence of the maxima in the temperature dependence of tan δ (3), leads to the conclusion that the dissipative mechanism controlling the dielectric properties is the same for all of these samples, regardless of the anodization electrolyte. The problem of explaining the observations is thus reduced to an explanation of why the distribution of conductivity in the films which have been heat-treated in air is affected by the anodization electrolyte.

It has been proposed that, during the heat-treatment in air, a dynamic equilibrium is established whereby the compositions at both sides of the oxide film are fixed and oxygen is continuously flowing through the oxide from the air to the metal where it is held in solution. This flow is exemplified by a constant rate of weight increase during the heating. The flux of oxygen can be expressed as

$$J = D\frac{dn}{dx} \qquad [1]$$

where J is the flux density of oxygen at./sec cm^2, D is the diffusion constant, and dn/dx is the concentration gradient of the diffusing oxygen species. After equilibrium has been established, the flux must be the same across the entire film thickness. If these films consist of two layers, an inner layer where the diffusion constant of oxygen is high and an outer layer where it is low, then, to satisfy [1], the gradient of

oxygen content would be low across the inner layer and high across the outer layer. At this point it should be recalled that we have described two observations which indicate that oxygen has a lower rate of diffusion in phosphate films as compared with sulfate films: the longer time to reach the maximum capacitance increase during the heat-treatment, and the lower rate of weight increase.

Recent work by Randall, Bernard, and Wilkinson shows that anodic oxide films on tantalum are indeed composed of two layers with the outer layer containing material incorporated from the anodization electrolyte (7). They anodized tantalum in H_3PO_4 solutions containing P^{32} as a radiotracer. By measuring the residual radioactivity of the samples as thin layers of oxide were removed by dissolution in HF, these authors found that approximately the outer half of the oxide film contains a uniform distribution of phosphorus with the concentration increasing with the H_3PO_4 concentration in the anodization electrolyte. The boundary between the outer, phosphorus-containing layer and the inner, phosphorus-free layer was found to be quite sharp. Randall *et al.* concluded from this structure that the oxide film is formed by the migration of both tantalum and oxygen species with new oxide growth thus occurring at both the Ta-Ta_2O_5 and Ta_2O_5-electrolyte interfaces. Only the oxide which formed at the latter interface would contain material from the electrolyte. Samples which were anodized in 14.6M H_3PO_4 containing P^{32} and heat-treated in air were examined by this same technique. It was found that, as oxide was removed stepwise with HF, the reciprocal series capacitance, a measure of the effective dielectric thickness, and the residual P^{32} activity approached zero together at a point where significant oxide remained, as indicated by the interference color. Thus the effective dielectric thickness of the heat-treated oxide in this case corresponded precisely to that portion of the oxide which incorporated phosphorus from the electrolyte during anodization. If we can assume that the mobility of oxygen in the oxide during heat-treatment is reduced by the presence of phosphorus, the conductivity profiles shown in Fig. 6 follow logically: the phosphate films consist of an outer, phosphorus-containing layer in which the thermal diffusion of oxygen is low, and an inner, phosphorus-free layer in which the thermal diffusion of oxygen is "normal." The mobility of oxygen decreases with increasing phosphorus content. Thus when equilibrium is attained during heat-treatment, Eq. [1] requires that the compositional gradient be shallow in the inner, phosphorus-free layer, and steep in the outer phosphorus-containing layer. The conductivity profile is, of course, directly related to the composition profile. A combination of the phosphorus distribution and the conductivity profile in the oxide of the sample described above is shown schematically in Fig. 7.

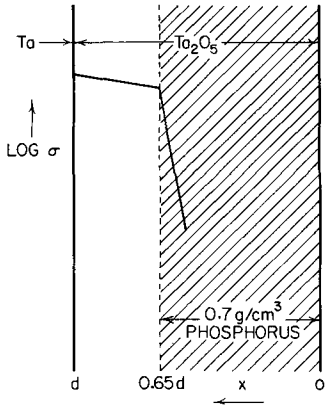

Fig. 7. Schematic representation of the correlation between the conductivity profile and the phosphorus distribution for tantalum, anodized in 14.6M H_3PO_4, and heat-treated in air.

Observations on other oxide systems indicate that the effect of incorporated phosphorus on oxygen mobility may be rather general. Bernard has reported that anodic oxides formed on aluminum in phosphate solutions are extremely resistant to hydration (8). It was found, for example, that films formed to 90v in 30% ammonium pentaborate in ethylene glycol and then continued to 100v in 0.1M NaH_2PO_4 were resistant to hydration, whereas borate films by themselves hydrated rapidly. The supposition is that a thin, outer layer of phosphorus-containing aluminum oxide was able to protect the underlying oxide. Since the hydration process presumably involves the migration of an oxygen-containing species, the effect of phosphorus on the mobility of such a species is reminiscent of the observations reported here. A related observation has been reported for the Si-SiO_2 system by Kerr, Logan, Burkhardt, and Pliskin (9). These authors have found that silicon field-effect transistors have greater stability if a layer of phosphosilicate glass, which is formed on the outer surface of the SiO_2 during processing, is left intact. If it is removed, a positive space charge forms in the oxide adjacent to the silicon. This space charge is attributed to oxygen vacancies which are introduced at the oxide-electrode interface and migrate across the oxide. Kerr *et al.* attribute the stabilizing effect of the phosphosilicate layer to the "oxidizing power" of the phosphorus which prevents the oxide from becoming oxygen-deficient. The mobility argument presented here seems more straightforward.

This investigation, and the radiotracer work of Randall, Bernard, and Wilkinson, also have significance with regard to the mechanism of the anodization process. Both works indicate that the interface between phosphorus-free and phosphorus-containing oxide moves toward the Ta-Ta_2O_5 interface as the concentration of H_3PO_4 increases in the anodization electrolyte. In other words, the amount of oxide formed as a result of oxide ion migration decreases as the amount of phosphorus in the oxide increases. Thus it appears that the presence of phosphorus in the oxide reduces not only the high-temperature mobility of oxygen in the oxide, but also the low-temperature field-driven mobility. Moreover, as the H_3PO_4 concentration in the anodization electrolyte increases, the interference colors of samples anodized under identical conditions correspond to thinner films. If this color difference is indeed related to a thickness difference rather than to changes in the optical properties, then the flow of both Ta ions and oxide ions must be retarded by the presence of phosphorus, although the earlier evidence indicates that the oxide ion current is restricted to the greater extent.

Thus in order to explain fully the kinetics of anodic oxidation, we must have expressions for the field dependence of ionic current for not only both tantalum ions and oxide ions, but for both of these ions in both regions of the oxide, with the expressions for the outer layer of oxide including allowance for the effect of electrolyte material incorporated into the oxide. This will necessitate terms for the identity of the electrolyte as well as for the current density and temperature of anodization. This means that a full understanding of the kinetics of anodization is much more complicated than hitherto appreciated. Of course the electrolyte effect can be minimized by the use of dilute solutions of relatively inert solutes such as H_2SO_4.

Although the explanation described here agrees with the observations in satisfactory detail, there are some basic inconsistencies which must be pointed out. The oxygen diffusion model which has been used to explain the origin of the gradient of oxygen content would normally lead to a linear distribution of the diffusing species across the film. The conductivity profile, how-

ever, has been found to be exponential, and the connection between this and the oxygen vacancy distribution has never been clarified. The treatment of mobility and concentration gradient exemplified by Eq. [1] and the subsequent discussion ignores this discrepancy. Moreover, the model assumes that all samples reach the same equilibrium compositions at the Ta-Ta_2O_5 and Ta_2O_5-air interfaces after equilibrium is attained during heat-treatment. As seen in Fig. 6, however, the outer, steep gradients will not extrapolate to a common conductivity at the oxide-air interface. The data are inconsistent with such a convergence. Possibly the phosphorus content of the oxide influences the Ta_2O_5-O_2 equilibrium. There is also evidence that the dielectric constant of the oxide depends on the phosphorus content (7). This may influence the ionization of oxygen vacancies in the outer portion of the film. These discrepancies are important and must not be overlooked, but they should not detract from the success of the original model in explaining these complex dielectric properties with the addition of only two observed facts: the nature of the distribution of phosphorus in the oxide, and the effect of phosphorus on the mobility of oxygen in the film.

Acknowledgment

The authors gratefully acknowledge the assistance of Dr. J. J. Randall, Jr., and Mr. Stanley Szpak, who carried out the radiotracer analysis, and the experimental assistance of Miss Marjorie Cutler.

Manuscript received Sept. 13, 1965. This paper was presented at the San Francisco Meeting, May 9-13, 1965.

Any discussion of this paper will appear in a Discussion Section to be published in the December 1966 JOURNAL.

REFERENCES

1. D. M. Smyth, G. A. Shirn, and T. B. Tripp, *This Journal*, **110**, 1264 (1963).
2. D. M. Smyth and T. B. Tripp, *ibid.*, **110**, 1271 (1963).
3. D. M. Smyth, G. A. Shirn, and T. B. Tripp, *ibid.*, **111**, 1331 (1964).
4. "Symposium on Electroless Nickel Plating," ASTM Special Tech. Publ. No. 265 (1959).
5. D. A. Vermilyea, *Acta Met.*, **2**, 482 (1954).
6. L. Young, *Proc. Royal Soc.*, **A258**, 496 (1960).
7. J. J. Randall, Jr., W. J. Bernard, and R. R. Wilkinson, *Electrochim. Acta*, **10**, 183 (1965).
8. W. J. Bernard, *This Journal*, **109**, 1082 (1962).
9. D. R. Kerr, S. S. Logan, P. J. Burkhardt, and W. A. Pliskin, *IBM J. Res. Develop.*, **8**, 376 (1964).

APPENDIX

Temperature Dependence of Capacitance Derived from an Exponential Gradient of Conduction

Let the spatial and temperature dependence of semiconduction across the Ta_2O_5 film be represented by

$$\sigma = Be^{ax}\, e^{-E/kT} \qquad [1a]$$

where a is the exponential slope, x is the position in the oxide measured from the Ta_2O_5-electrolyte interface, and E is the activation energy of conduction. The ratio of conductivity at the Ta-Ta_2O_5 interface ($\sigma = \sigma_d$ at $x = d$) to that at the Ta_2O_5-electrolyte interface ($\sigma = \sigma_1$ at $x = 0$) is

$$\frac{\sigma_d}{\sigma_1} = e^{ad} \qquad [2a]$$

Since $\sigma_d/\sigma_1 = 10^{21}$ by extrapolation of experimental observation, and $d = 1.5 \times 10^{-5}$ cm (20 Å/v for 75v film)

$$a = 3.2 \times 10^{6}\ \text{cm}^{-1} \qquad [3a]$$

Solving [1a] for B and using $E = 0.6$ ev, $T = 300°$K, $x = d = 1.5 \times 10^{-5}$ cm, and $\sigma_d = 3 \times 10^{-7}$ ohm^{-1} cm^{-1} (3) yields

$$\log B = -17.4 \qquad [4a]$$

$$B = 4 \times 10^{-18} \qquad [5a]$$

At the position, x, defined by

$$x = \frac{\epsilon\epsilon_o}{C_s} \qquad [6a]$$

$$\sigma_x = \sigma_o = \omega\epsilon\epsilon_o \qquad [7a]$$

so from [1a]

$$\frac{a\epsilon\epsilon_o}{2.3\, C_s} = \log \frac{\omega\epsilon\epsilon_o}{B} + \frac{E}{2.3\, kT} \qquad [8a]$$

Substituting and solving for C_s, the equivalent series capacitance, with $\epsilon = 27.6$, $\epsilon_o = 8.85 \times 10^{-14}$, and $\omega = 2\pi f$ gives

$$C_s = \frac{3.4\, T}{(6.6 + \log f)\, T + 3030}\ \mu\text{f/cm}^2 \qquad [9a]$$

The temperature dependence of capacitance is then

$$\frac{dC_s}{dT} = \frac{10{,}300}{(6.6\, T + T \log f + 3030)^2} \qquad [10a]$$

At 120 cps and 30°C

$$\frac{dC_s}{dT} = 3.22 \times 10^{-4}\ \mu\text{f/cm}^2\ °\text{C} \qquad [11a]$$

At 120 cps and −20°C

$$\frac{dC_s}{dT} = 3.77 \times 10^{-4}\ \mu\text{f/cm}^2\ °\text{C} \qquad [12a]$$

This represents a slope change of only 17% over our usual temperature range of measurement. Thus [9a] can be considered to be a quasi-linear relationship between C_s and T over this temperature range, in agreement with observation.

The Corrosion of Zirconium and Zircaloy-2 at Low Temperatures

R. Cigna, J. S. Llewelyn Leach, and A. Y. Nehru

Department of Metallurgy, Imperial College of Science and Technology, London, England

ABSTRACT

The aqueous corrosion of zirconium and Zircaloy-2 has been studied as a function of electrode potential, solution pH, and temperature below 100°C. The influence of these variables and of alloying is considered in terms of their effect on the rate and the temperature dependence of corrosion. The relation between the corrosion process and the electronic conduction in the oxide is discussed.

Some work on the low-temperature aqueous corrosion of zirconium has been briefly described in two previous publications (1, 2), which dealt chiefly with the corrosion of uranium. These early studies indicated the influence of a number of environmental and other factors on the corrosion behavior and showed that the results for both uranium and zirconium could be interpreted in the same general terms. Recently, further work on uranium has shown that changes in corrosion rate caused by altering the experimental conditions were associated with significant changes in the activation energy of the oxide growth process, and, in addition, suggested a relationship between the electronic and ionic conductivities of the oxides formed in aqueous electrolytes (3).

The present paper describes the results of a more detailed investigation of the corrosion behavior of zirconium with particular reference to the effect of cathodic polarization, solution pH, and alloying content. The temperature dependence of the corrosion process has been studied as a function of these variables. Changes in the corrosion rate have been shown to be accompanied in many instances by changes in the activation energy.

Experimental

The equipment developed for the estimation of corrosion rates has been adapted from a previous design (4) with some minor alterations and allows a study of the growth of oxide films without removal of the specimen from the test environment. The operating principle of the technique involves a continuous measurement of the intensity of light reflected from a metal corroding in an aqueous environment and calculation of film thickness by comparison with the intensity reflected from a clean surface. However, it is necessary to assume that the absorption coefficient of the oxide is not significantly influenced by its thickness.

The results reported in this paper are derived from measurements using an unfiltered high-pressure mercury lamp (Phillips HPK/125). The thickness of the oxide-film is given by

$$I = I_o e^{-2\theta x}$$

where I_o is the reflected intensity from the clean metal surface, I is the intensity at film thickness x, and θ is the absorption coefficient of the oxide. If x is some function of time (t), then

$$I = I_o e^{-2\theta f(t)}$$

and

$$\log_e I - \log_e I_o = -2\theta f(t)$$

A plot of ($\log I_o - \log I$) *vs.* t gives relative film thickness as a function of time.

Temperature control in the corrosion cell was achieved with an immersion heater and a temperature-controlling thermometer. The thermometer (Electromethods) which could be set to control to ±0.1°C at any temperature between 0° and 100°C was positioned near the specimen and activated a relay which switched the heater circuit.

The test solutions were prepared by dissolving Analar grade reagents in distilled water and were constituted as follows: pH 5.4 solution, 0.1*N* K_2SO_4; pH 13 solution, 0.1*N* KOH.

The materials examined were zirconium-10 and zirconium-20[1] (Zircaloy-2) supplied by Imperial Metal Industries (Kynoch) Ltd., in the form of 0.02 in. foil and 0.028 in. foil, respectively.

The average composition data are given in Table I.

The test electrodes were prepared in the form of strips and mounted in glass tubes with a cold-setting resin (Ciba Araldite) so that a rectangular working surface of about 4.5 cm^2 was exposed to the environment. Before testing, specimens were degreased in acetone and etched to a bright finish in a solution composed by volume of 1 part of 40% HF, 4 parts of 70% HNO_3, and 5 parts of water.

Tests were made in the temperature range 50°-90°C at values of cathodic potential maintained using a potentiostat (AERE type 1465A) and measured with a vacuum tube voltmeter (E.I.L. pH meter Model 23A).

Results

Figures 1 and 2 illustrate, respectively, the corrosion of zirconium and Zircaloy-2 in 90°C 0.1*N* K_2SO_4 solution at several values of cathodic potential. Assuming that the absorption coefficient of the oxide formed on zirconium is not significantly different from that of the film on the alloy, it is possible to attempt a direct comparison of the corrosion rates of the two metals. The following three observations may be made from the figures:

1. Protective kinetics appear to predominate for the corrosion of both metals within the present range of measurements. (Calculations show an approximation to the parabolic law except at the most negative potentials where the exponent of the growth law is about 1.5.)

[1] Zirconium-20 is the trade designation used by Imperial Metal Industries for Zircaloy-2.

Table I. Average composition data

Element	Zircaloy-2%*	Zirconium-10*
Al	50	40
C	200	
Cr	0.11%	
Co	20	
Hf	150	60
Fe	0.12%	0.05%
Pb	100	
Mg	15	
Mn	30	
Mo	30	
Ni	0.048%	
N	25	30
O	1150	800
Si	75	
Sn	1.48%	100
Ti	30	35
W	100	

* All values are in parts per million except where indicated.

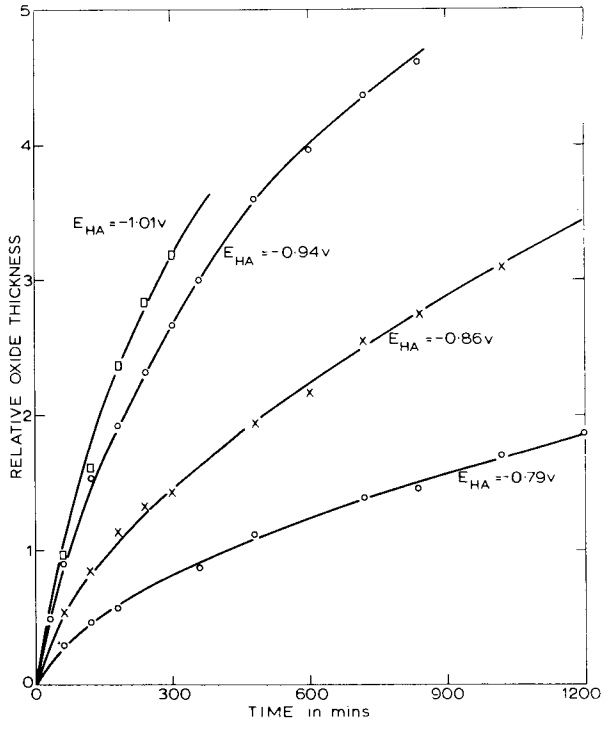

Fig. 1. Corrosion of zirconium as a function of cathodic polarization, 0.1*N* K_2SO_4, 90°C.

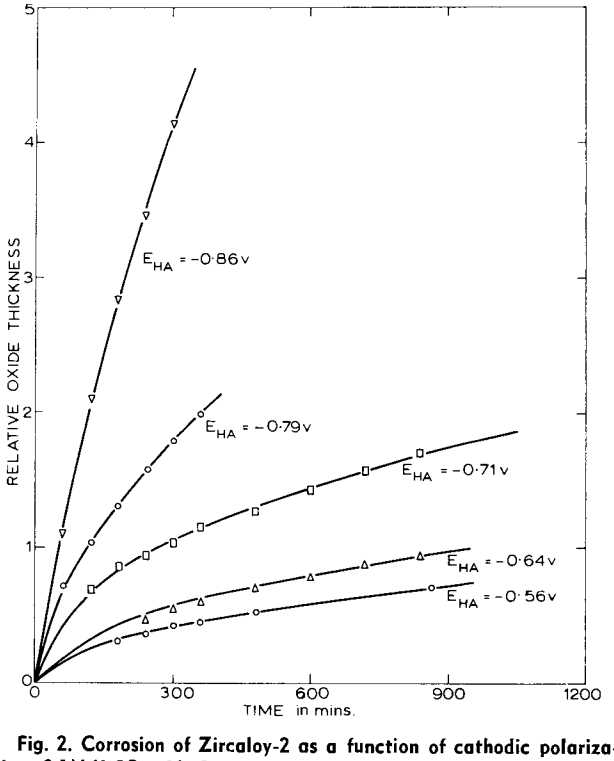

Fig. 2. Corrosion of Zircaloy-2 as a function of cathodic polarization, 0.1*N* K_2SO_4, 90°C.

2. The corrosion rate of both metals increases with increasing cathodic polarization.

3. The over-all corrosion rate of Zircaloy-2 is higher than that of zirconium for equivalent values of potential.[2]

Some examples of the corrosion of zirconium and Zircaloy-2 in 0.1*N* KOH are illustrated in Fig. 3. Comparison with Fig. 1 and 2 shows that over-all corrosion rates in the alkaline solution tend to be considerably higher than in acidic solution. Measurements at more negative potentials than those shown in Fig. 3 were not generally practical in 0.1*N* KOH due to irreproducibility of the corrosion kinetics.

Figures 4 and 5 show the temperature dependence of the arbitrary rate constant K for cathodically polarized zirconium and Zircaloy-2, respectively, in 0.1*N* KOH solution. (The kinetics of corrosion for each given value of cathodic potential being the same, K is taken as the reciprocal of the time required for the film to grow to a given thickness.) Activation energies were calculated by the standard method and were found to lie between 13.4 and 23 kcal/g mole for zirconium and 8.0 and 8.6 kcal/g mole for the alloy. Two values of potential are common to both sets of data.

It is clear from a comparison of Fig. 4 and 5 that alloying results in a considerable reduction of the activation energy for the corrosion of zirconium. Cathodic polarization appears to have a similar effect although this is too small to be significant in the case of the alloy.

It might be worth mentioning here that at a given temperature the measured increase in corrosion rate of zirconium due to cathodic polarization is considerably lower than the value expected from the associated decrease in experimental activation energy. Thus, for example, in Fig. 4 at temperature = 348°K, K changes

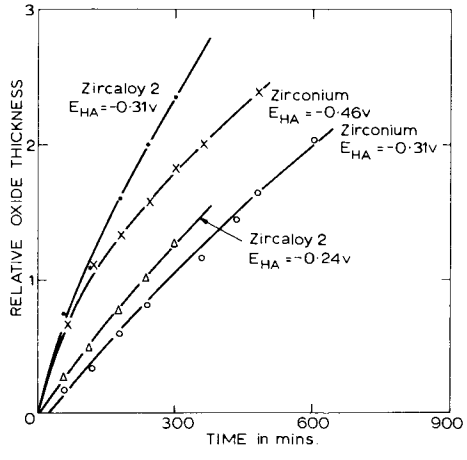

Fig. 3. Corrosion of zirconium and Zircaloy-2 as a function of a cathodic polarization, 0.1*N* KOH, 90°C.

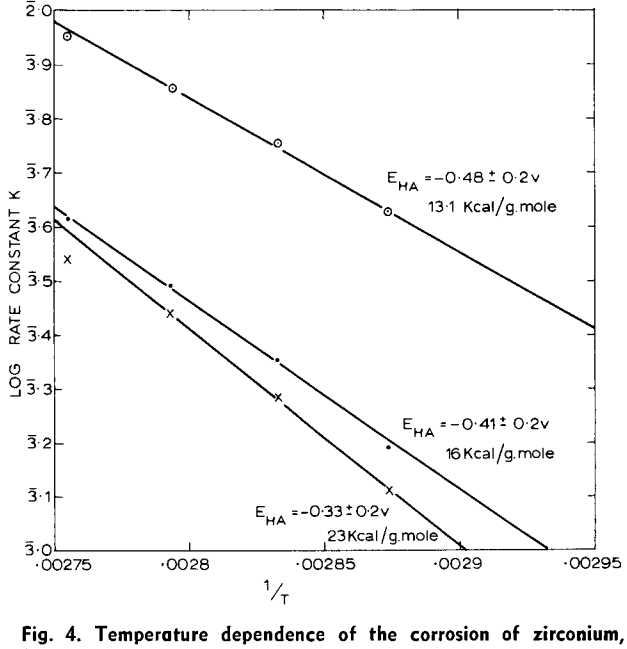

Fig. 4. Temperature dependence of the corrosion of zirconium, 0.1*N* KOH.

[2] $E_{HA} = E_H + 2.3RT/F$ pH, where E_H is the standard hydrogen potential.

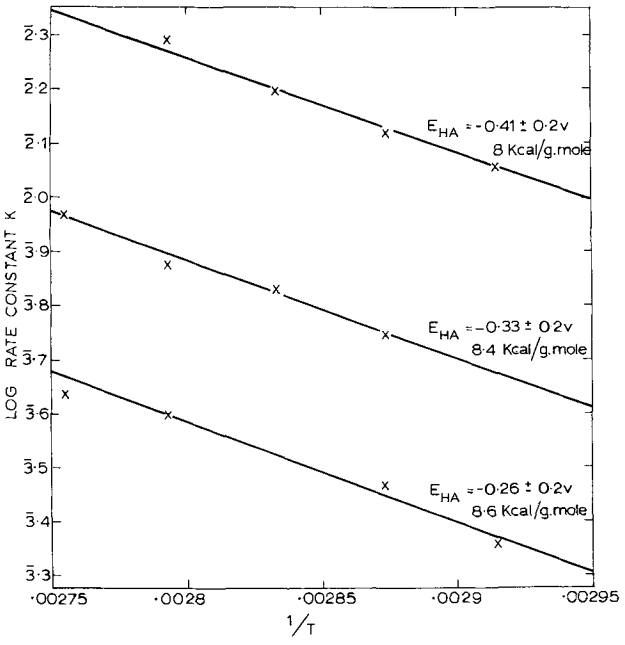

Fig. 5. Temperature dependence of the corrosion of Zircaloy-2, 0.1*N* KOH.

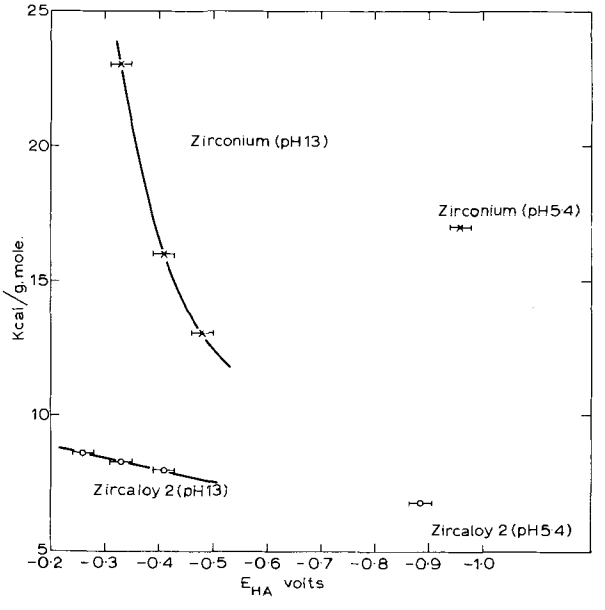

Fig. 6. Activation energy of corrosion as a function of potential, zirconium and Zircaloy-2, 0.1*N* K_2SO_4, 0.1*N* KOH.

from a value of 0.0013 for $E_{HA} = -0.33 \pm 0.02$v to 0.0016 for $E_{HA} = -0.41 \pm 0.02$v (same rate law applies at both potentials), an increase of 1.23 times, while, in fact, the change in rate caused by the observed reduction in activation energy from 23 to 16 kcal/g mole should amount to a factor of over two thousand times. This calculation suggests that decreases in the experimental activation energy E of the Arrhenius equation

$$K = A \exp -E/RT$$

are paralleled by decreases in the pre-exponential term A. Although in the present instance this does not appear to be true for Zircaloy-2, similar correlations between A and E have been found (5-7) for the corrosion of several other metals including uranium.

Figure 6 shows the simple relationships which appear to hold between the experimental activation energy and the impressed cathodic potential for the corrosion of both zirconium and the alloy in alkaline solution.

The temperature dependence of the corrosion rate in 0.1*N*/K_2SO_4 was not studied in detail, and only one value of activation energy was calculated for each metal (Fig. 6). These activation energies were obtained by measurement at very negative potentials due to the law rates of corrosion in the acidic solution. Although direct comparison is not possible, it would appear that higher activation energies prevail for the corrosion of both zirconium and the alloy in 0.1*N* K_2SO_4 than in alkaline solution.

Discussion

The present results, which were obtained under restricted and controlled experimental conditions, are not directly comparable with the results of the numerous detailed studies (8-11) of the high-temperature corrosion of zirconium and Zircaloy-2 available in the literature. The main contribution of a qualitative investigation such as this lies in the attempt made to determine which parameters involved in a given corrosion process are influenced by varying external factors.

Consider, then, the influence of cathodic polarization on the corrosion rate of the two metals studied (Fig. 1, 2, 3). It is clear that in all cases decreasing the electrode potential increases the rate without, in general, altering the mechanism. The corrosion kinetics for a given set of conditions remains constant over a wide range of potential.

Wanklyn and Hopkinson (12) also showed increases caused by cathodic polarization in the corrosion rate of zirconium in 325°C water. They rejected on two counts the cathodic reduction of the oxide formed as a possible explanation for this effect, but their observations did not permit a determination of the main sources of the rate increases, *e.g.*, it was not possible to distinguish between changes in the diffusion constants in the protective film and changes in its thickness. More recently, similar observations (1, 2) on the corrosion of both uranium and zirconium at lower temperatures have been interpreted in terms of higher ionic diffusion rates associated with increases in electronic conductivity of the corrosion-product oxide which follow the introduction of cathodically induced hydrogen ions.

The enhanced electronic conductivity can be discussed in the case of the n-type semiconducting oxide ZrO_{2-x} formed during the corrosion of zirconium (13, 14) in terms of the following equation

$$ZrO_{2-x} = Zr^{4+} + (2-x)O^{2-} + 2xe^-$$

where $2xe^-$ is the number of excess electrons required to maintain the charge balance. If the system is to remain electrostatically neutral, the addition of an H^+ ion will require the incorporation of an extra excess electron.

If the effect of this increase in electronic conductivity is now considered, it becomes clear that the potential gradients opposing ionic motion in the oxide are diminished and faster growth may take place. Similar relationships between the electronic conductivity and ionic diffusion coefficients have been demonstrated by Wagner (15) for the system Ag-Ag_2S-S and Jacobs (16) for anodic films on tantalum.

In discussing the reduction in activation energy associated with increasing cathodic polarization (Fig. 4, 6), it is relevant to compare the low values of activation energies calculated here and in other work with the values reported for self-diffusion in these oxides.

Oxide growth on zirconium in air or oxygen at high temperatures occurs by the inward diffusion of oxygen involving an activation energy of 30 to 40 kcal/g mole (17) very near the value of the activation energy

for the self-diffusion of oxygen in zirconia and undoubtedly much lower than the value for self-diffusion of the metal. It is known, however, that aqueous conditions can cause a significant change in the mechanism of oxide growth, and this applies over a wide range of temperature to several metals (3, 6, 18) including zirconium (19) and Zircaloy-2 (20). In the case of Zircaloy-2, an estimate from the data of Thomas and Forscher gave a value as low as 10 kcals/g mole for high-temperature aqueous corrosion. This is similar to the range of values found in this investigation but differs significantly from 28.6 kcal/g mole quoted (21) for the oxidation of the alloy in oxygen at high temperatures. Few explanations for the lowering of the activation energy due to the presence of water are generally available in the literature. One offered for the corrosion of magnesium (6) involves the assumption that hydrogen ions will convert O^{2-} ions in the lattice to OH^- ions, necessitating the introduction of vacancies at cation sites to maintain electrical neutrality. It is believed that the consequent distortion of the lattice reduces the activation energy for the diffusion of Mg^{2+}, but an explanation in these terms is unlikely for a system in which oxygen is the main diffusing species. Alternative arguments which invoke, for example, either the diffusion of both anions and cations in aqueous conditions or a lower energy barrier in opposition to hydroxyl ion diffusion than that opposing oxygen ion diffusion are so far unable to account for the lower activation energies. Decreases in activation energy due to diffusion via low-resistance short-circuit paths such as grain boundaries rather than entirely through the bulk by lattice vacancies are probably too small to account for the very low values obtained (22).

Values of activation energy calculated under the present experimental conditions are difficult to reconcile with the rate-controlling step during corrosion being oxygen diffusion either via low-resistance paths or through lattice vacancies. Nor do other simple explanations appear applicable. In a previous investigation on uranium (3) which yielded results of a similar nature, it was shown that activation energies for corrosion approximated closely to established values of activation energy for electronic semiconduction in uranium oxides. An extrapolation from the data of Johansen and Cleary (23) gives a value of about 15 kcal/g mole for the low-temperature dependence of n-type semiconduction in zirconia in reasonable agreement with two values obtained here for the corrosion of zirconium (Fig. 4).

It is difficult at the present stage of research to visualize a specific relationship between the electronic and ionic conductivities in corrosion-product oxides formed on metals such as uranium and zirconium. What does appear clear, however, is that those factors which alter the electronic conductivity appear to exert an influence on the rate and energetics of ionic diffusion. The increase in corrosion rate of both zirconium and the alloy caused by increasing the solution pH, shown in previous work (2), and illustrated here by comparison of Fig. 1 and 2 with Fig. 3, is associated with lower values of activation energy as was also the case for cathodic polarization. It is interesting, therefore, that, by treating the oxide as a solvent for hydrogen and hydroxyl ions, the effect of increasing alkalinity can be described in similar terms as the effect of potential. In alkaline solutions there will be a greater tendency for the oxide to contain hydroxyl ions arising from an attempt to achieve a balance between the OH^- activity in both the aqueous and the oxide solvent. These hydroxyl ions can also be produced in the film by the combination of a hydrogen ion and a lattice oxygen ion, and this is probably the most favored state for a proton in the lattice. Thus alkaline solutions should encourage the absorption of hydrogen into the oxide, which in turn leads to enhanced electronic conductivity. A recent study (24) of anodic films on zirconium has shown that oxides formed in alkaline solutions are better electronic conductors than their counterparts formed in more acidic solutions.

The increase in the corrosion rate associated with the alloying of zirconium (compare Fig. 1 and 2) may be interpreted in terms of faster ionic diffusion through a defective mixed oxide. However, it is necessary to reconcile this with the superior performance of Zircaloy-2 in high-temperature water. Earlier work on uranium (1) showed that, although initial diffusion rates were increased by alloying additions, the over-all corrosion resistance was improved by the greater thickness to which the protective film could grow before cracking. The present work gives no indication of a similar effect although the possibility cannot be excluded. An alternative explanation may, however, be tenable. It can be shown by extrapolation of the Arrhenius plots (Fig. 4 and 5) that the corrosion of zirconium cathodically polarized at $E_{HA} = -0.33 \pm 0.02$v and -0.41 ± 0.02v becomes more rapid than that of Zircaloy-2 at about 115° and 160°C, respectively. Hence, it is possible that the superior resistance of the alloy is apparent only at temperatures above the boiling point of water.

It has been suggested that the higher rate of corrosion observed for the alloy at low temperature might be due to the presence of oxygen in the solution. While this is not impossible, the solubility of oxygen in alkaline solution is much below that in pure water (25), and the effect of the higher temperatures will be to decrease this further. Moreover, it is believed that the effect of potentiostatic polarization will be to absorb any small amounts of oxygen present in a depolarizing reaction.

Conclusions

It is established from the results that the activation energy for the aqueous corrosion of zirconium is generally lower than the activation energies for either atmospheric oxidation or for the self-diffusion of oxygen in zirconia. Moreover, it has been shown that variables such as the formation potential of the oxide, the alloying content, and the pH of the environment which have a significant effect on the corrosion behavior also tend to influence the activation energy, and in this respect, the results appear to be closely related to the earlier observations (3) on the uranium-zirconium alloy system.

It is not clear at the present stage what mechanism permits corrosion to proceed with the low activation energies observed, but the results stress the suggestion previously made that the electronic conductivity is an important parameter in corrosion kinetics.

Acknowledgments

The authors wish to thank Professor J. G. Ball in whose department the work was carried out, the United Kingdom Atomic Energy Authority for financial support, and the Consiglio Nazionale delle Richerche, Italy, from whom one of the authors (R. C.) was seconded. The authors are indebted to the Imperial Metal Industries (Kynoch) Ltd. for supplying the materials examined.

Manuscript received Dec. 28, 1964; revised manuscript received Oct. 11, 1965.

Any discussion of this paper will appear in a Discussion Section to be published in the December 1966 JOURNAL.

REFERENCES

1. J. S. Llewelyn Leach and A. Y. Nehru, "Corrosion of Reactor Materials," **1**, 58, *IAEA*, Vienna (1962).
2. J. S. Llewelyn Leach and A. Y. Nehru, *This Journal*, **111**, 781 (1964).
3. J. S. Llewelyn Leach and A. Y. Nehru, *J. Nucl. Mater.*, **13**, 270 (1964).
4. A. E. Stebbens and L. L. Shrier, *This Journal*, **108**, 30 (1961).

5. J. S. Llewelyn Leach and A. Y. Nehru, Unpublished results.
6. S. J. Gregg and W. B. Jepson, *J. Inst. Metals*, **87**, 187 (1958).
7. A. R. Ubbelhode, *Discussions Faraday Soc.*, **23**, 128 (1957).
8. D. E. Thomas and S. Kass, *This Journal*, **104**, 261 (1957).
9. J. Boulton, "Corrosion of Reactor Materials," **2**, 133, *IAEA*, Vienna (1962).
10. W. E. Kuhn, *Corrosion*, **18**, 103 (1962).
11. B. Cox, *ibid.*, **16**, 380 (1960).
12. J. N. Wanklyn and B. E. Hopkinson, *J. Appl. Chem.*, **8**, 496 (1958).
13. K. Kiukkola and C. Wagner, *This Journal*, **104**, 379 (1957).
14. M. W. Mallet and W. M. Albrecht, *ibid.*, **102**, 407 (1955).
15. C. Wagner, *J. Chem. Phys.*, **21**, 1819 (1953).
16. A. R. Bray, P. W. M. Jacobs, and L. Young, *J. Nucl. Mater.*, **1**, 359 (1959).
17. D. L. Douglass, "Corrosion of Reactor Materials," **2**, 223 *IAEA*, Vienna (1962). Several references are given in this paper.
18. E. C. Potter and G. M. W. Mann, "Proc. 1st Int. Congress on Metallic Corrosion," Butterworth, London (1962).
19. D. E. Thomas, USAEC Rept. Westinghouse Electric Corp., WAPD-T-186 (1954).
20. D. E. Thomas and F. Forscher, *J. Metals*, **8**, 640 (1956).
21. E. A. Gulbransen and K. F. Andrew, *Trans. AIME*, **212**, 281 (1958).
22. W. W. Smeltzer, R. R. Haering, and J. S. Kirkaldy, *Acta Met.*, **9**, 880 (1961).
23. H. A. Johansen and J. G. Cleary, *This Journal*, **109**, 1076 (1962).
24. P. G. H. Draper, Private communication.
25. K. E. Gubbins and R. D. Walker, Jr., *This Journal*, **112**, 469 (1965).

Electrical and Structural Properties of Langmuir Films

Robert M. Handy and Luciano C. Scala

Research Laboratories, Westinghouse Electric Corporation, Pittsburgh, Pennsylvania

ABSTRACT

Barium and calcium stearate Langmuir films from 1 to 10 monolayers in thickness (approximately 25-250Å) have been investigated for use as ultrathin insulating barriers between evaporated metal electrodes. These metal-insulator-metal sandwiches showed highly nonlinear and temperature dependent conduction characteristics, from which a thermal barrier height of 0.25-0.30 ev is calculated. Reproducibility of electrical properties however was poor, apparently due to voids and inhomogeneities in the organic insulating films. It is calculated that even in the best samples, 2 to 3 monolayers were required to eliminate voids penetrating completely through the organic films. A reactive and hence oxidized surface was found to be necessary for the formation and retention of low porosity layers, tin being the most successful substrate electrode material. Insulating behavior could not be obtained from films transferred onto gold electrodes. Film structure and adhesion was investigated by studying the layering process and the autoradiographs obtained from C^{14} tagged films. The autoradiographs did not reveal any significant defects in the layers down to the resolution of the negatives ($\sim 25\mu$). It was found that the physicochemical nature of the substrate surface affected the adhesion of more than the first monolayer, and that porosity alone was unlikely to account for the long-range effect. Positive ion adsorption, as described by Goranson and Zisman, is suggested as a possible alternative and shown to be consistent with some aspects of the electrical measurements.

Metal oxide layers have often been employed as thin insulating films, particularly for the observation of electron tunneling phenomena. Our aim in the present work was to investigate the feasibility of using organic layers for the same purpose, that is, as insulating barriers 10-100Å thick sandwiched between conductive electrodes. Such an organic layer must be thin, homogeneous, uniform in thickness, and an excellent insulator. Monomolecular layers appeared to satisfy most of these requirements and could be easily obtained using the classic process developed by Langmuir and Blodgett. It was known that Langmuir films of certain materials behaved as insulators, in the sense that after being charged by surface electrification to fields exceeding 10^6 v/cm they showed very slow rates of decay. It was not known, however, whether voids, defects, or inhomogeneities in the films could be reduced to such a level as to permit the construction of tunnel sandwiches of useful area, nor whether the electronic properties of the insulating monolayers were suitable for device applications. In pursuing the answer to these questions, we have obtained new information on the behavior of Langmuir multilayers of small total thickness.

The Langmuir-Blodgett (1-3) process consists typically of spreading a monolayer of amphipathic molecules (*e.g.*, stearic acid) onto an aqueous surface, squeezing the monolayer into a compact floating film, and transferring it to a solid substrate by passing the substrate through the water surface. The molecules stand approximately vertical to the water or substrate surface, so that the compressed monolayer may be said to resemble a dense carpet whose thickness is determined by the molecular length. The surface of this hypothetical rug is formed by the ends of the molecular chains, and its nature depends on which end of the molecule is attached to the solid substrate. A very large amount of data on the formation and orientation of fatty acid or fatty acid salt mono- and multilayers is available in the literature (1-13) and will not be repeated here.

The higher the lateral pressure applied to the floating monolayer the more compact it becomes until it finally collapses. If transfer is accomplished at a pressure significantly below the collapse pressure, then voids or holes in the monolayer are inevitable. This is shown directly by the beautiful electron micrographs of Ries *et al.* (14) and is reflected indirectly in the variability of electrical measurements made on the Langmuir films. Buchwald, Zahl, and co-workers (15) attempted to measure the insulating properties of stearate films of from 1 to 41 monolayers by immersing metal rods coated with the multilayers into conductive salt solutions. A decrease in capacity and an

increase in resistance was observed with increasing numbers of layers. However, there was at least a twofold variation in apparent dielectric constant and several orders of magnitude variation in resistivity, both of which were influenced by the choice and concentration of the electrolyte. Small area probe measurements using water or mercury droplets were more successful. The mercury droplets in particular tend to bridge small defects in the layers because of their high surface tension. Porter and Wyman (8), working in the range from 7 to 141 monolayers, obtained dielectric constant values ranging from 1.9 to 3.5, with an average value of ~2.5. Race and Reynolds (16) made similar measurements on somewhat thicker films using Hg droplets and obtained values of 2.50 for calcium stearate and 2.44-2.56 for barium stearate, virtually identical to the bulk values which we have measured. The dielectric constant was independent of frequency between 40 and 10^6 cps.

Several workers (8, 16) studied both the resistivity and the breakdown strength of multilayer films. In general, the breakdown strength was higher with films formed at a higher bath pH. Breakdown voltages were generally rather low, *e.g.*, $\leq$ 0.5v. Moreover, they were often independent of thickness over a wide range and depended on whether water or mercury droplets were used as the top contact. Conduction through the films was highly nonlinear with increasing voltage and slightly asymmetric. No attempt was made to explain these observations other than to suggest that the water may be able to penetrate the films despite the hydrophobic nature of their surface. The variations in resistivity and breakdown strength observed with the mercury dots were generally ascribed to inhomogeneities or voids in the films. Further interest in the electrical properties of Langmuir layers lagged until Miles and McMahon (17) reported the use of a stearate monolayer as an insulating barrier for electron tunneling between superconductors.

The existing electrical data on Langmuir films (8, 15-17) was obtained from layers deposited on metal surfaces such as chromium, stainless steel, lead, tin, etc., which had been exposed to the atmosphere. All of these metals oxidize readily so that the organic monolayer was actually being deposited on the surface oxide, rather than directly on the metal. One can expect that the thickness of this surface oxide is significant compared to a monolayer thickness. In fact a brief exposure to the atmosphere is one of the standard techniques (18) for producing thin insulating oxides for tunnel conduction studies. The surface oxide adds another semi-insulating region electrically in series with the organic film. For optical studies on multilayer films its presence can usually be ignored, but, for some electrical measurements, the surface oxide may dominate the behavior, particularly if the organic layer contains holes so that the oxide can come into intimate contact with the counter electrode. The contribution of the surface oxide has apparently been neglected by most previous workers. Much of the data presented by Porter and Wyman (8) or Miles and McMahon (17), for example, could be explained by assuming direct contact to semi-insulating oxide layers.[1] As will be shown, this is a likely occurrence.

We have investigated the electrical behavior of stearate multilayers. For the most part, evaporated electrodes were used rather than mercury dot probes, and the range from 1 to 10 monolayers in thickness (25-250Å) was explored. The evaporated electrodes lead to a higher incidence of shorts through defects in the films, but they also provide a realistic test of film uniformity and of the practical utility of Langmuir layers for use as ultrathin insulating films. In order to reduce the occurrence of voids to a minimum, film transfer was effected as close to the collapse pressure as possible, using special apparatus developed for this purpose. The layering process was examined in detail, and auto-radiographs were made using C^{14} tagged layers in order to study adhesion and the occurrence of gross defects in the film. Considerable attention was devoted to the problems presented by the surface oxide and the porosity of the organic layers.

The organization of the paper was dictated by the complex interrelation between the electrical and structural properties of the layers and the difficulties encountered in trying to discuss one aspect without already having said a great deal about the other. The "results" section begins with the electrical measurements and carries through to the structural observations. In the "discussion" section, however, the order has been inverted, since the electrical measurements can be best understood in the light of the discussion of the structure and physicochemical properties of the films.

Experimental

The experimental structure consisted of glass slides on which a number of parallel stripes of one or more metals had been evaporated. The organic film was then applied as described below, and finally the second electrode stripe was evaporated over the top at right angles to the first set. Each sample provided from 6 to 9 metal-organic-metal junctions approximately 1 mm^2. The capacity of these sandwiches was measured, usually at 1 kc. Current-voltage characteristics were obtained at d.c. and 60 cps by four terminal methods. For variable temperature measurements, the samples were clamped to a heavy copper block, enclosed in a heat shield, and cooled with liquid nitrogen.

The Langmuir film apparatus consisted of a modified Cenco Hydrophil balance of the Langmuir-Adam-Harkins type, housed in a double wall thermostated cabinet mounted on a heavy steel table. It is similar in design to that described by Ries (19). The table was suspended from the ceiling by shock cords to eliminate extraneous vibration. The cabinet was slightly pressurized with dry filtered nitrogen to minimize atmospheric dust during preparation of the layers. The aluminum trough and stainless steel compression barriers were Teflon coated. The stearic acid in these experiments (Eastman Kodak best grade, mp 69°-70°C) was dissolved in Fisher Spectranalyzed n-hexane (0.0274g of acid/100 cc of solution). A few drops of this solution were used to form the film on the aqueous subphase, which contained Ba or Ca acetate or carbonate and which was appropriately buffered (29). The water for these aqueous subphases was originally triple distilled and was subsequently purified by passing it through ion exchange resin columns (final resistivity of water 1-2 megohms). Small quantities of acetic acid or ammonium hydroxide were used to control pH, which was held at a value of 6.8-6.9 for Y layers and 9.0 for X layers.

After the monolayer was spread, it was allowed to rest for 10 min to allow for the complete evaporation of the solvent. Compression of the monolayer was carried out at a rate of 7 mm/min. Pressure readings were taken every 10 mm of barrier travel at the beginning, and every millimeter of barrier travel near the desired transfer pressure. The transfer pressure used throughout this work was 39 dynes/cm, and it was reproducible within 0.5 dynes/cm. On attaining the transfer pressure, the electrode bearing slides were dipped at a rate of 2 mm/min, compression barrier speed being adjusted to maintain constant film pressure.

The precautions observed to insure absence of impurities from the surface of the aqueous substrate are summarized below.

(*A*) Before each experiment the trough was washed with deionized water, CP acetone, Spectro Grade

[1] The authors are indebted to Dr. J. L. Miles, one of the authors of ref. (17), for suggesting this interpretation of their results.

benzene; it was then treated in a trichloroethylene vapor degreaser.

(*B*) Before the layer was spread, the surface of the aqueous subphase was swept in front of and behind the balance and the degree of cleanliness checked using the balance.

(*C*) Sample slides were cleaned with Alconox detergent and warm water, rinsed with running deionized water, blown dry in a clean nitrogen stream, and then placed in a liquid nitrogen trapped evaporator for depositing the lower electrodes.

(*D*) After electrode evaporation and before monolayer deposition, the slides were dipped in the aqueous substrate, and any impurity contributed by them was swept away as described in step (*B*).

(*E*) All the parts of the balance that came in contact with the aqueous substrate were thoroughly cleaned with Spectro Grade benzene or purified n-hexane, allowed to dry, and then coated with a thin petroleum ether solution of hard wax. After about 1 hr, these wax-coated pieces were rinsed abundantly with deionized water. This treatment tends to do away with loose pieces of wax which may, later on, interfere with the film formation and compression.

In general, clean room techniques were followed and every effort was made to prevent contamination of the monolayers and the substrate surfaces during preparation of the sandwiches. A detailed description of the apparatus, and some preliminary results were presented earlier (20).

Results

A large number of samples were prepared using noble metals (*e.g.*, Ag and Au) as the first electrode in order to minimize or avoid the presence of an oxide layer. On many of these samples, half of the first electrode stripes were tin. From one to ten layers of calcium or barium stearate were transferred to these samples using the techniques described previously. On each passage through the surface of the bath, the area of the floating monolayer was observed to decrease, providing direct evidence of the transfer of the monolayer to the surface of the slide. In every case, however, electrical tests of the finished samples showed a junction resistance of less than 1 ohm for the noble metal based junctions. By contrast, the tin-based junctions yielded significant numbers of insulating devices showing nonlinear current-voltage characteristics. It was not possible to obtain any insulating behavior on an oxide-free electrode, even when adjacent tin based structures showed uniform stable insulating properties. This suggests strongly that the oxide plays an essential role in determining the electrical properties of Langmuir film sandwiches.

Two explanations are possible: either the insulating behavior is derived directly from the oxide, or the oxide and the reactive metal ions which it contains contribute significantly to the adhesion of the organic film. As will be shown, both processes are important. The electrical data which follow were derived principally from tin based junctions with various metals (Sn, Ag, Au, Cu, Pb, etc.) serving for the upper electrodes. A few copper based samples were successfully prepared and have been included.

Capacity measurements.—Figure 1 shows the results of capacity measurements on some 75 samples.[2] The average electrical thickness, given in terms of the reciprocal capacity (1/C) is plotted as a function of the number of layers predicted from the transfer process (N_p). The apparent dielectric constant may be calculated using the stearate monolayer thickness of ~25Å. It is seen that the data fall essentially between the dotted lines given by $\epsilon = 2.1$ and $\epsilon = 4.2$. The heavy dashed line corresponds to the bulk value of

[2] On Fig. 1 many of the clusters represent points which would fall on top of each other, and, in order to show the density distribution of the data, they have been slightly misplotted to the left or right.

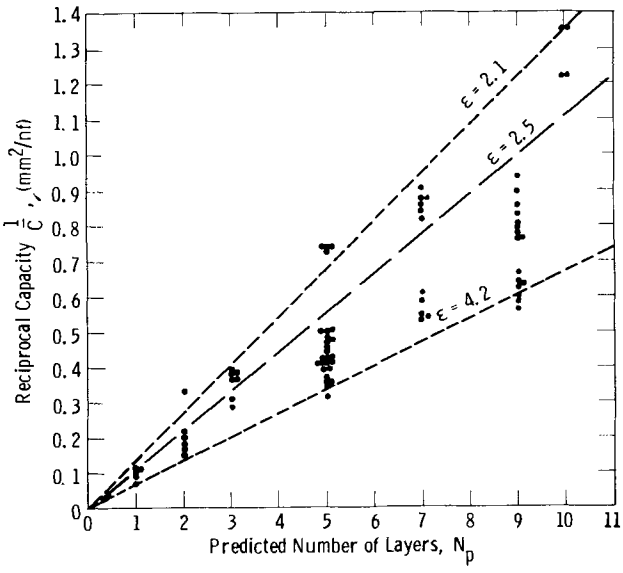

Fig. 1. Reciprocal capacity *vs.* predicted number of layers

$\epsilon = 2.5$. The spread in apparent dielectric constant values is of the same order as that obtained by others (8) working in a comparable thickness range, but using liquid contacts, *i.e.*, water or salt solution.

If the capacity is measured as a function of frequency, a slight change with frequency is observed, as shown in Fig. 2 for a typical sample. The upper curve gives C, and therefore ϵ *vs.* log *f*. Over the range from 100 cps to 20 kc, the dielectric constant drops by about 5%. The lower curve shows the variation with frequency of the imaginary part of the complex dielectric constant (proportional to *C* x *D*). It is noted that a slight maximum occurs near 700 cps, suggesting the presence of a weak polar adsorption mechanism with a characteristic relaxation time ($\frac{1}{2}\pi f_m$) of 0.23 msec. At higher frequencies (*i.e.*, $f > 10$ kc) the measurement uncertainty in the dissipation factor *D* becomes comparable with the observed values.

The contribution of the oxide region has been neglected in presenting the capacity measurements. To a first approximation this is reasonable, since, as will be shown in the next section, the resistivity of the oxide film is small compared to the resistivity of the organic layers. Calculation of the capacity of a composite oxide-organic multilayer structure shows that the porosity must exceed ~5% of the total area before a significant departure from the no-void value occurs. Under these circumstances, the sample resistance is usually so low that capacity values are not measurable.

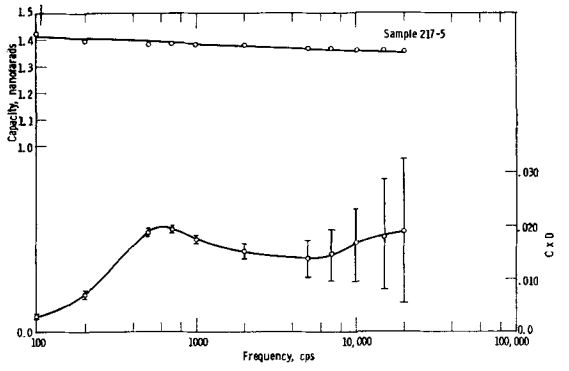

Fig. 2. Capacity C and capacity X dissipation factor *vs.* frequency.

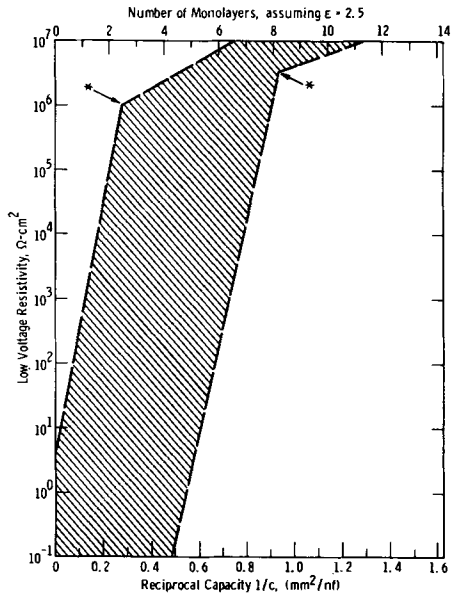

Fig. 3. Low voltage resistivity vs. reciprocal capacity (1/C) for barium stearate multilayers. Upper scale shows calculated number of monolayers assuming $\epsilon = 2.5$. * Indicates points of probably complete film coverage.

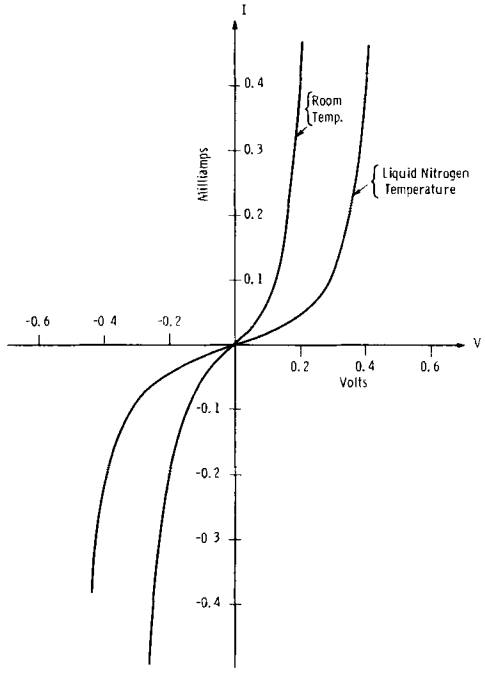

Fig. 4. Current-voltage characteristics at 0.1 cps of a Sn-3 layer calcium stearate-Sn sandwich of ~1 mm² area at two temperatures. Polarity is that of organic coated tin base layer.

Resistivity measurements.—The resistivity of the junctions was measured at low voltage (< 50 mv) where the current voltage characteristics are linear. If the values are plotted as a function of the measured thickness, as in Fig. 3, it is found that the points are approximately uniformly distributed within the shaded interval. The boundary lines denote the limits of the observed values. The points which define the upper limit of resistivity for a given thickness are generally those corresponding to the points on the upper limit line of Fig. 1, that is, the thickest layers obtained for a given number of transfer strokes. The wide range of resistivity values observed for the same measured thickness (1/C) supports the contention that the organic films are porous. It seems probable that, for small values of 1/C, the majority of the low-voltage resistivity values are characteristic of the oxide, and reflect the degree of coverage obtained, *i.e.*, the fractional area of the oxide in direct contact with the top electrode. The upper limit would correspond to those layers possessing the smallest fraction of voids.

The stearate films are necessarily transferred at a pressure slightly less than the collapse pressure, and hence the layers may well contain small open areas separated by comparatively large void-free regions of film. The collapse point corresponds to a fully compacted film of minimum area, which presumably no longer contains any voids. The pressure-area isotherm allows one to calculate the void area for pressures slightly less than the collapse pressure. We are interested in a worst-case estimate, hence we neglect changes in area due to elastic contraction or expansion of molecules and assume that for pressures less than the collapse pressure the deviation from the minimum area consists entirely of voids. Using the actual transfer pressure, and the measured pressure-area isotherm, we estimate the void area to be less than 2-3% of the total area. If the oxide is highly insulating, then one should be able to duplicate the electrical behavior of the organic coated samples by using an uncoated sample of sufficiently small area. To test this concept, the junction area was reduced from 1 to 0.02 mm² (*i.e.*, 2% of the usual value) and the junction resistance of coated and uncoated samples compared. Without exception, the uncoated samples gave resistivities of 10^{-4} to 10^{-5} ohm-cm², even when treated by a 1-hr exposure to a low-pressure oxygen glow discharge to promote oxide growth. By comparison, 1 mm² samples coated with a single monolayer gave low-voltage resistivities approaching 10^{3} ohm-cm², as can be seen from the upper limit line on Fig. 4. In order to account for the resistivity of the organic coated sample, the void area of this single monolayer would have to be less than 10^{-10} cm², or less than 10^{-6}% of the total area of a 1 mm² sample. Langmuir films are known to bridge small defects or voids (21), so that a multilayer sample corresponding to the upper limit line would have 10^{-14}% voids through two layers, 10^{-22}% voids through three layers, and so forth. The prospect of significant void area extending through more than about two layers is negligible under these conditions even if current flow is assumed to take place predominantly at the periphery of the junctions (27) rather than uniformly across the area. It can be seen in Fig. 3 that the upper limit line undergoes a significant change in slope at a calculated[3] thickness (N_o) between two and three monolayers, presumably corresponding to the onset of complete coverage. The resistance beyond this inflection point corresponds to an equivalent bulk resistivity of 10^{12} ohm-cm, which is comparable with the value for many bulk insulators. Most of the samples are not so compact as those falling near the upper limit line, and more than 2-3 monolayers are required to achieve total coverage of the surface. The lower limit line undergoes a change in slope at $N_o \approx 8$. Assuming that the low voltage resistivity (below the inflection point) provides a measure of the oxide area which remains exposed, then the average void area of the more porous films can also be estimated: *e.g.*, $R_o = 10^3$ ohm-cm² requires 10^{-6}% voids. The average void area per monolayer then should correspond to the N_o^{th} root of the void fraction. For the lower limit line, this gives an average void fraction per monolayer of the order of 6%, which is somewhat larger than the maximum value expected from the transfer conditions.

Conduction characteristics and temperature dependence.—Typical current-voltage characteristics of the metal-organic-metal sandwiches are shown in Fig.

[3] Calculated from capacity measurements assuming $\epsilon = 2.5$ and using the geometric area of the junction.

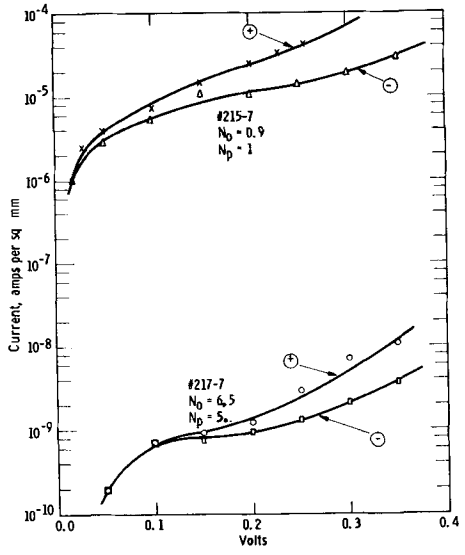

Fig. 5. Current-voltage characteristics of a one and a five-layer Sn-stearate-Sn sample. N_p = predicted number of monolayers; N_o = observed number of monolayers as calculated from measured capacity assuming $\epsilon = 2.5$. ⊕ and ⊖ indicate polarity of organic coated base layer.

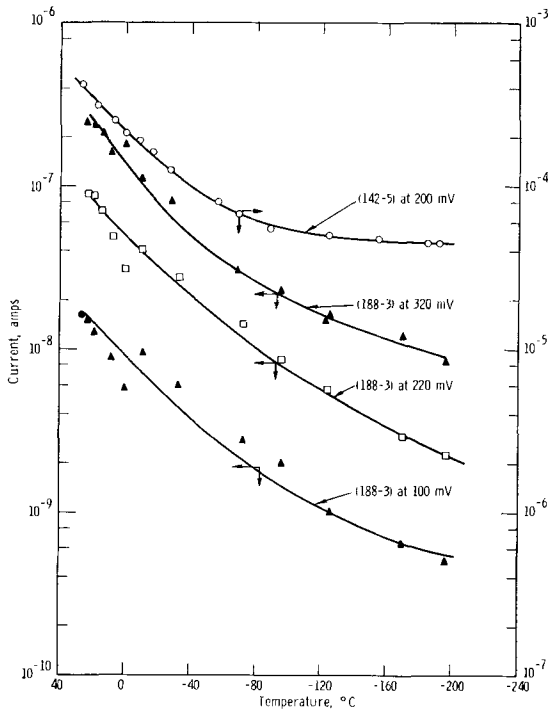

Fig. 6. Plot of current vs. temperature at constant voltage for two junctions. Junction (142-5), upper curve, is ~3 monolayers thick; junction (188-3), three lower curves, is ~5 monolayers thick. Polarity of test voltage is organic coated base electrode positive.

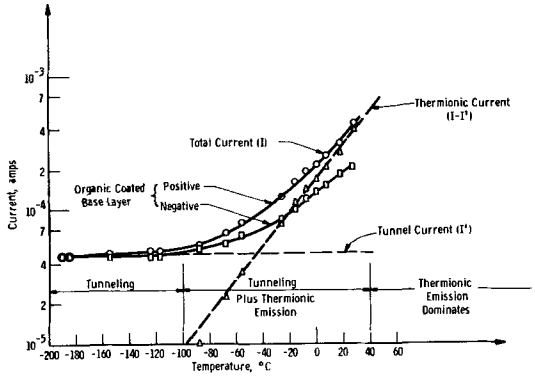

Fig. 7. Temperature dependence of current at constant voltage, 0.2 v.

4.[4] Near zero voltage the characteristic is linear and presumably controlled by the voids present in the organic films. As the voltage increases beyond 0.1-0.2v the current rises very rapidly with increasing voltage and, because of the current densities required, it must flow increasingly through the organic film. The voltage required for significant departure from linear conduction increased slightly with increasing layer thickness as would be expected, but in general was significantly less than the values typically observed for inorganic insulating films (*e.g.*, Al_2O_3) of comparable thickness. Figure 5 shows a semi-log plot of the I-V characteristics of a thin ($N_o \sim 0.9$) and a thick ($N_o \sim 6.5$) sample plotted on the same scale. The absolute current levels differ by about four orders of magnitude as would be expected from Fig. 3. The slope of the characteristics also differs slightly, the thicker film showing a more rapid increase in current than the thinner film. The thicker films are also more temperature sensitive. Figure 6 shows the variation of current with temperature at constant voltage for a ~3 layer film and a ~5 layer film. The slope at high temperature is approximately the same in both cases, indicating that the thermal activation energy for conduction is also comparable. At low temperatures, however, the slopes are quite different due to the different relative contribution of tunneling and thermionic currents through the sandwiches in the two cases.

The behavior of the 3 layer sandwich has been analyzed in detail as shown in Fig. 7. By subtracting the extrapolated zero temperature current value I', the thermionic contribution to the current (I-I') represented by the heavy dashed line, is obtained. This yields a straight line on a Schottky plot of log $[(I-I')/T^2)]$ *vs.* $1/T$ as shown in Fig. 8. From the slope and the measuring voltage, the zero voltage thermal activation energy ϕ_b is determined as $0.25 < \phi_b < 0.30$ ev. This analysis presumes that conduction is dominated by tunneling at low temperatures, and by thermionic emission over the insulating barrier of height ϕ_b presented by the composite oxide-organic film at high temperatures. Several attempts have been made to analyze the I-V characteristics using theoretical expressions derived by Stratton (22), Simmons (23), and others in order to obtain additional estimates of the various barrier parameters. However, a fit could not be obtained over any significant range of the variables. This was true even at low temperature and low thickness where we believe tunneling to be the predominant nonlinear conduction mechanism.

Layering and film structure.—In the present investigation considerable effort was expended to achieve reproducible results from the Langmuir-Blodgett monolayers. Extensive precautions were taken with regard to physical and chemical cleanliness of the materials and equipment, and film transfer was accomplished under much more carefully controlled conditions than were present during many of the earlier studies of electrical properties. Nevertheless, reproducibility of electrical properties was limited, and therefore some of the aspects of layering and film transfer onto solid substrates were examined by other means.

[4] In a few preliminary experiments in which the organic films were prepared by the classic piston oil and floating thread techniques but under very uncertain and crude layering conditions, some samples of remarkable electrical uniformity, stability, and voltage tolerance (*e.g.*, >1v) were obtained. They could not be duplicated once the experimental procedures were refined. It is possible that these may have represented nearly perfect layers; however, the high vibration levels and frequent leakage of piston oils during transfer made this unlikely. While the characteristics of Fig. 4 are not as attractive as these early results, they are more representative of the bulk of the samples.

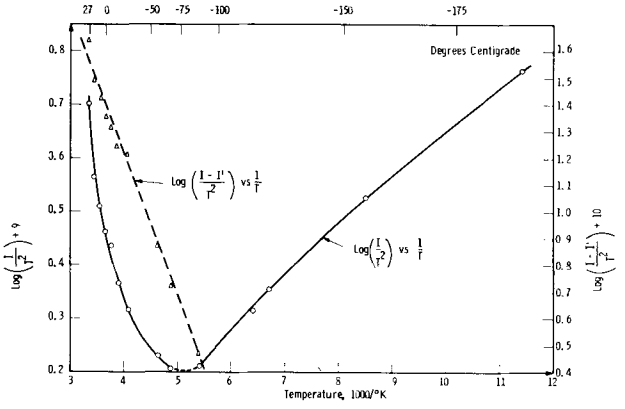

Fig. 8. Plot of log (I/T^2) vs. $(1/T)$ and log $[(I-I')/T^2]$ vs. $(1/T)$, where I = total current, I' = low-temperature current in amperes, and T = absolute temperature.

The uniformity and compactness of the monolayers used to build the insulating films are of paramount importance. These factors are most strongly influenced by the conditions during transfer, *e.g.*, film pressure, bath *p*H, etc. Pressure-area isotherms of barium and calcium stearates obtained during this study follow the course of the P/A curves of condensed monolayer films as discussed by Alexander (24), and indicate that the film forming techniques contained no gross defects. However, the area of monolayer swept off the bath by the compression bar during the actual transfer of layers was often different from the cumulative area of the sample being coated.[5] Using data from all of the samples prepared, it was found that on the average the barrier motion exceeded the predicted values by about 20%, which is considerably greater than the measurement uncertainty of our apparatus. This phenomenon may arise for example, from solution of a portion of the monolayer, or folding of the monolayer. It has been reported (30, 31) that stearic acid dissolves in the aqueous subphase under certain circumstances. In our case the rate of solution may have been increased because of the relatively high pressures employed throughout this work (30). Of these possibilities, only folding would be of serious consequence to the electrical measurements. This possibility was eliminated by autoradiograph studies described below.

Autoradiograph studies.—A visible demonstration of the effectiveness of transfer is provided by autoradiographs of mono- and multilayer Langmuir films containing C^{14} tagged barium stearate. The radioactive material was obtained as stearic acid in benzene solution from the Nuclear Chicago Corporation, with a total activity of 12.3 mc/millimole, and was diluted, spread, and transferred in the usual way, but at slightly lower pressures. Autoradiographs were taken by clamping a piece of Medical No-Screen x-ray film against the samples covered by the radioactive layer. Exposure time was approximately one day at 5°C. Results from four samples are shown in Fig. 9. It will be noted that the metallic stripes and circles evaporated onto the 1 x 3 in. glass slides and covered by the radioactive Langmuir films are visible. This is due to the difference between the back-scattering coefficient of the glass and that of the various metals. A number of small spots or scratches and a few large blemishes (*e.g.*, the dark region adjacent to the white clamp imprint at the top of Fig. 9a) can also be seen. With few exceptions these were traced to dust particles which settled on the surface after transfer, to imperfections in the film introduced during developing, or to artifacts of the reproduction and printing process. The general conclusion from the autoradiographs is that the organic layers are very uniform and cover the glass and metal stripes satisfactorily. There are no apparent gross defects. The resolution of the autoradiographs, however, is only 10-25μ depending on the film density,[6] so that uniformly distributed voids of the sizes discussed earlier would not be visible. Nevertheless, the large-scale uniformity over areas exceeding 3 in.^{2} is reassuring testimony as to the quality of the transfer procedures. None of the sample showed any evidence of "folded over" regions, such as reported by Roberts and Gaines (25).

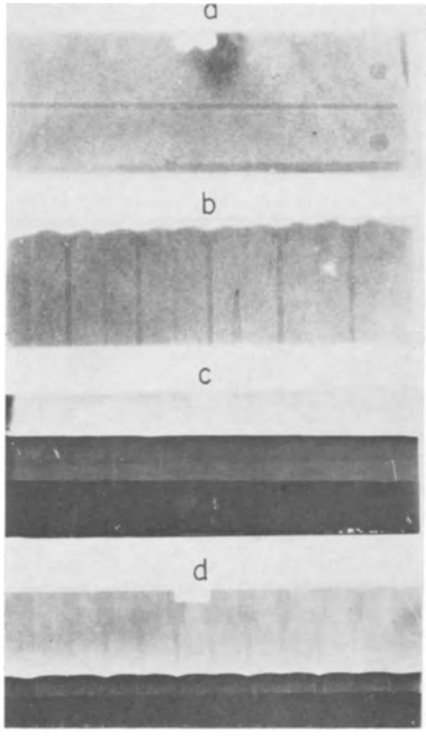

Fig. 9. Autoradiographs of radioactive Ba stearate and Ba stearate: PVB mixture mono- and multilayers. From the top: (a) one monolayer of Ba stearate over tin stripe on glass; (b) one monolayer of Ba stearate over tin and copper stripes on glass, showing different contact angles between aqueous subphase and glass or metal; (c) one, three, and five monolayer steps of Ba stearate; (d) one, three, and five monolayer steps of equiweight mixture of Ba stearate and PVB.

The four samples shown in Fig. 9 have been covered with varying numbers of monolayers as follows: (*a*) one monolayer over the whole slide, (*b*) one monolayer over part of the slide, the wavy edge showing the location of the meniscus at the beginning of the transfer stroke, (c) one monolayer over the whole slide, three monolayers and five monolayers over part of the slide as shown by the bands of increasing optical density, (*d*) steps of 1:3:5 monolayers similar to (c), but using an equiweight mixture of stearic acid and polyvinyl benzoate (PVB). The optical density of the exposures taken of the 1:3:5 stepped multilayer samples was measured and found to correspond to radioactive emission intensities also in the ratio 1:3:5, providing direct confirmation of the transfer of a single monolayer on each dipping stroke.

In those cases (Fig. 9b-d) where the slide was only partially immersed in the bath during some part of the transfer process, the optical density step gives an imprint of the meniscus where the floating monolayer met the surface of the slide. Over the different regions of the slide, *i.e.*, glass, copper, tin, the meniscus reached

[5] In most of the classical studies of Langmuir films a flexible floating thread was used as a barrier, and hence the accuracy of their area measurements is in some doubt.

[6] The resolution limit of these films was directly determined from the edge definition at the monolayer steps, (*e.g.*, 0 to 1, 1 to 3, 3 to 5, etc.), using a special instrument developed by Dr. A. Bennett of the Westinghouse Research Laboratories. We are indebted to Dr. Bennett for performing the measurements.

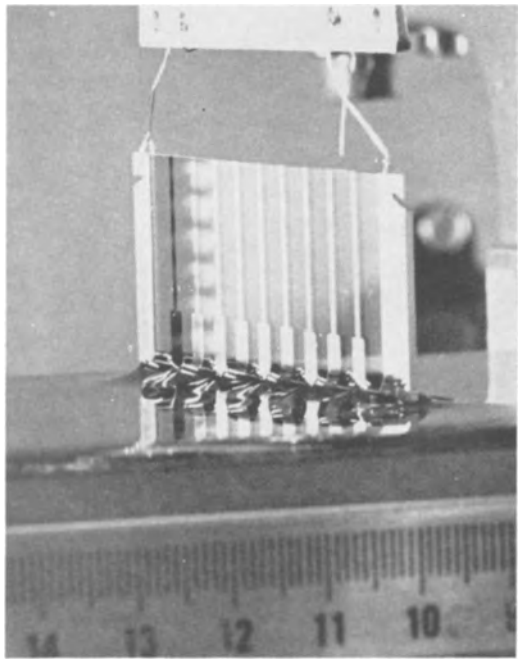

Fig. 10. Electrode arrangement on the sample and meniscus formed with the surface of the Langmuir bath content. There are 9 narrow electrodes and 2 wide end pads running parallel with the narrow dimensions of the slide. The 1st, 3rd, 5th, 7th, and 9th electrodes are gold. The remainder and the end pads are tin. Note the differences in the height of the meniscus over Sn, Au, and glass.

different heights, yielding a wavy pattern, corresponding to the different contact angles assumed by the meniscus. The higher the meniscus, the smaller the contact angle. The same effect can be seen visually during the actual transfer operation. Figure 10 shows a photograph of the meniscus drawn up on a slide as it is being pulled up out of the bath. (The slide is inverted with respect to those of Fig. 9.) The contact angle is small against the glass, and increases progressively against Sn, Cu, and Au surfaces in that order. The differences in contact angle reflect differences in the chemical nature of each surface, and to a first approximation one can expect that the binding forces, which tend to make the monolayer adhere, decrease as the contact angle increases. The first monolayer, understandably, should reflect these differences, as was seen in Fig. 10 and Fig. 9b. Once the first monolayer has been applied, however, the substrate surface is covered by a sheet of molecules 25Å thick, so that subsequent layers deposit on an organic base and are removed further and further from the substrate in 25Å steps. It is inconceivable that the interatomic binding forces responsible for the adhesion of the first layer could extend so far from the surface as to directly influence the adhesion of the second layer, much less the third and subsequent layers. The autoradiographs, however, show significant differences in contact angle to be present at the edge defining the third layer, and still perceptible differences to be present at the edge of the fifth layer. The effect was present on samples made with barium stearate as well as with the stearate-polyvinyl benzoate mixture. Clearly, the physicochemical nature of the substrate surface influences the contact angle and hence the adhesion of considerably more than the first monolayer.

We have observed that the contact angle against the glass surface increases as the number of dips increases. This corresponds to an over-all reduction in the adhesive forces tending to bind the floating monolayer to the solid surface, and to a gradual attenuation of the influence of the underlying substrate surface. Similarly, the difference in meniscus heights over the different regions of the slides, Fig. 10, becomes smaller as the number of dips increases. Equalization proceeds by means of the contact angle over the glass increasing more rapidly than the contact angle over the metal surfaces.

It was considered possible that this behavior might be explained on the basis of porous films, as were many of the electrical results discussed earlier. Inspection of the autoradiographs, however, places several conditions on this hypothesis: (i) the maximum hole size must be less than 25μ, (ii) the distribution of holes must be fairly uniform, and (iii) the percentage of holes must be approximately the same from layer to layer. Computing the porosity from the transfer pressure and the P/A isotherms, one finds that it can amount to only a small fraction of one per cent through the multilayers regions, and hence, by itself, porosity appears insufficient to account for the differences in wetting angle visible in the multilayer regions. Any tendency of the monolayers to bridge defects in the surface will further reduce the possibility that porosity has a significant bearing on the adhesion of subsequent layers. Some long-range force or ordering effect seems necessary.

Discussion

Germer and Storks (26) have observed that the azimuthal orientation of the molecules in the monolayers depends upon the physicochemical nature of the substrates. Films deposited on a hydrophobic surface (polystyrene resin) showed a high degree of hexagonal symmetry even in a single layer. On a metallic surface (chromium) the azimuthal orientation of the first monolayer was random, but a progressive increase in molecular order was observed in succeeding layers. This undoubtedly reflects the increased surface mobility of the molecules which are not in direct contact with the chemically active metal surface, or its oxide. Metal layers, however, may influence the adhesion of monolayers in another way. Goranson and Zisman (13) showed that excess divalent metal ions can become trapped in the films as they are withdrawn from the bath, so that the multilayer structure possesses a volume distribution of positive charge. The charges are distributed along the carboxyl group planes of the multilayer and, unless they are compensated, the net positive charge will increase with successive monolayers. The effect of this excess positive charge is to repel the positive ions adsorbed on carboxyl face of the floating monolayer. This is observed macroscopically as an increase in the contact angle with increasing numbers of layers. These authors also point out that the magnitude of the effect will depend on whether the substrate is conducting or insulating. The metallic regions on the substrate provide an equal negative image charge which reduces the repulsive force experienced by the floating monolayer. According to this hypothesis, the progressive increase in contact angles should be greatest over the insulating glass regions of the substrates, as we have observed. Unfortunately, we are not able to offer direct evidence of positive ion trapping in the multilayers. It is recognized that the arguments leading to this conclusion are largely circumstantial, being based on observations made during the transfer process and a study of the autoradiographs. However, no other mechanism has been discovered which can account for the long-range influence of the substrate surface through the multilayer films, and which is also consistent with all of the other experimental data.

If enough excess ions are being taken up by the films so as to perturb the layering process, then one can expect their presence to alter the electrical properties of the Langmuir films as compared with the bulk material. Figure 2 shows this to be the case in that the dielectric constant is slightly frequency dependent, and a weak maximum is observed in the loss factor. Neither

of these effects was present in bulk samples tested over the same frequency range.

The variable temperature measurements performed on the samples yielded a thermal barrier height ϕ_b of a few tenths of an electron volt. This is considerably smaller than the values (*e.g.*, 1-2 ev) reported (27) for metal-oxide-metal structures using materials such as Al_2O_3 for the insulating region. Not enough is known about the bulk electronic properties of the stearates to decide whether such low values are reasonable for a metal-stearate-metal barrier. We suspect, however, that the observed values of ϕ_b may be characteristic of the defects and impurities within the films, particularly in view of the evidence suggesting appreciable positive ion occlusion.

It was noted earlier that the I-V characteristics could not be satisfactorily fitted to the theoretical expression derived on the basis of simple homogeneous barriers. This is not surprising considering the complex nature of the composite Sn-SnO-stearate-metal barrier. Even for those multilayer samples in which we believe complete coverage of the lower electrode has been attained, there will still be significant local inhomogeneity in thickness. Small area variations in thickness will not have an important effect on the capacity measurements. However, both tunneling and field-assisted thermionic emission depend exponentially on thickness, so that the conduction characteristics will be strongly affected.

The results of the many attempts to form insulating multilayers on gold surfaces present an interesting problem. We have ample evidence to show that it is possible to seal off the surface of the tin electrodes. Given the same average porosity we would expect that at least some of the gold based samples would have been successful. None were successful, hence we conclude that the average porosity over the gold films must have been greater. The contact angle observations show that the adhesive forces between the floating monolayer and the gold surfaces were not as strong as in the case of glass or tin surfaces.

There is evidence in the literature (25, 28) to show that free stearic acid, which most of our films contain to some degree, is less strongly bound to noble surfaces, and furthermore can be pumped-off in vacuum. Thus, even though the porosity of the layers may initially have been no greater than that of the layers over the Sn or glass region of the samples, the layers on the gold surfaces will be less stable and are likely to develop significant voids extending through the entire multilayer.

Summary

A reactive, and in this case oxidized, electrode surface appears necessary for formation and retention of low porosity layers. The voids and inhomogeneities in the films strongly influence the electrical properties, giving rise to a 2 to 1 variation in capacity values and several orders of magnitude variation in low voltage resistivity for the same apparent thickness. Examination of the temperature dependence shows tunneling to be the dominant nonlinear conduction mechanism at low temperature and low thickness, while field assisted thermionic emission dominates at high temperature and greater thickness.

It was found that the physicochemical nature of the substrate surface affected the adhesion of more than the first monolayer, and that porosity alone was unlikely to account for the long range effect. Positive ion adsorption, as described by Goranson and Zisman, is suggested as a possible alternative and shown to be consistent with some aspects of the electrical measurements.

Acknowledgments

The authors are indebted to Mr. W. R. Miller and Mr. W. O. Bartlett for their able technical assistance, and to Drs. J. E. Johnson and T. P. Brody for valuable discussions and critique.

The research reported in this paper was sponsored by the United States Army Electronics Research and Development Laboratory, Fort Monmouth, New Jersey, under contract No. DA 36-039-AMC-00072.

Manuscript received April 21, 1965; revised manuscript received Sept. 27, 1965.

Any discussion of this paper will appear in a Discussion Section to be published in the December 1966 JOURNAL.

REFERENCES

1. I. Langmuir, *Proc. Roy. Soc.*, **170A**, 1 (1939).
2. K. B. Blodgett, *J. Am. Chem. Soc.*, **57**, 1007 (1935).
3. K. B. Blodgett and I. Langmuir, *Phys. Rev.* **51**, 964 (1937).
4. G. Clark, R. Sterrett, and P. Leffler, *J. Am. Chem. Soc.*, **53**, 330 (1935).
5. C. Holley and S. Bernstein, *Phys. Rev.*, **52**, 525 (1937).
6. S. Bernstein, *J. Am. Chem. Soc.*, **60**, 1151 (1938).
7. I. Fankuchen, *Phys. Rev.*, **53**, 909 (1938).
8. E. F. Porter and J. Wyman, Jr., *J. Am. Chem. Soc.*, **59**, 2746 (1937); *ibid.*, **60**, 1083 (1938); *ibid.*, **60**, 2855 (1938).
9. I. Langmuir, *ibid.*, **60**, 1190 (1938).
10. J. Bikerman, *Trans. Faraday Soc.*, **34**, 800 (1938).
11. W. D. Harkins and R. W. Mattoon, *J. Chem. Phys.*, **7**, 186 (1939).
12. F. J. Norton, *J. Am. Chem. Soc.*, **61**, 3162 (1939).
13. R. W. Goranson and W. A. Zisman, *J. Chem. Phys.*, **7**, 492 (1939).
14. H. E. Ries, Jr., and D. C. Walker, *J. Colloid. Sci.*, **16**, 361 (1961); H. E. Ries and W. A. Kimball, *Nature*, **181**, 901 (1958).
15. C. E. Buchwald, D. M. Gallagher, C. P. Haskins, E. M. Thatcher, and P. A. Zahl, *Proc. Nat. Acad. Sci.*, **24**, 204 (1938); P. A. Zahl, C. P. Haskins, D. M. Gallagher, and C. E. Buchwald, *Trans. Faraday Soc.*, **35**, 308 (1939).
16. H. H. Race and S. I. Reynolds, *J. Am. Chem. Soc.*, **61**, 1425 (1939).
17. J. L. Miles and H. O. McMahon, *J. Appl. Phys.*, **32**, 1126 (1961).
18. R. M. Handy, *Phys. Rev.*, **126**, 1968 (1962).
19. H. E. Ries, Jr., *Sci. American*, **204**, 1968 (1962).
20. R. M. Handy and L. C. Scala, Paper presented at Pittsburgh Meeting of the Society, April 1963 Abstract No. 101.
21. J. J. Bikerman, *Proc. Roy. Soc.*, **170A**, 130 (1939).
22. R. Stratton, *J. Phys. Chem. Solid*, **23**, 1177 (1962).
23. J. G. Simmons, *J. Appl. Phys.*, **34**, 1793, (1963); **34**, 2581 (1963).
24. A. E. Alexander, *Trans. Faraday Soc.*, **37**, 426 (1941).
25. R. W. Roberts and G. L. Gaines, Jr., Trans. 9th Nat. Vacuum Symp., p. 515, Los Angeles, Calif. (1962).
26. L. H. Germer and K. H. Storks, *J. Chem. Phys.*, **6**, 280 (1938).
27. S. R. Pollack and C. E. Morris, *J. Appl. Phys.*, **35**, 1503 (1964).
28. G. L. Gaines, Jr., *J. Colloid, Sci.*, **15**, 321 (1960).
29. H. P. Gregor and H. Schonhorn, *J. Am. Chem. Soc.*, **81**, 3911 (1959).
30. W. Rabinovitch, R. F. Robertson, and S. G. Mason, *Can. J. Chem.*, **38**, 1881 (1960).
31. E. D. Goddard and J. A. Ackilli, *J. Colloid Sci.*, **18**, 585 (1963).

Surface Diffusion Processes and Dendritic Growth in the Electrodeposition of Silver from Molten Halides

Thomas B. Reddy*

Bell Telephone Laboratories, Incorporated, Murray Hill, New Jersey

ABSTRACT

Studies of the rise time of the cathodic overpotential during galvanostatic pulsing of silver electrodes in molten AgCl-LiCl-KCl mixtures at 450°C show that the mechanism of electrodeposition from fused salts includes a step for surface diffusion of adatoms from point of deposition to growth sites on the metal surface. The concentration of adatoms on the surface at equilibrium and the surface diffusion rate have been determined and are compared to those found in aqueous electrolyte solutions at 25°C. The formation of dendritic deposits of silver is found to occur only when a concentration gradient equivalent to 4 mv polarization is produced. Destruction of this gradient through the use of a high concentration of silver chloride and convection reduces the concentration polarization and leads to the formation of coherent deposits. Studies of the dendrites produced by electrodeposition show that they all contain two parallel twin planes and indicate that nucleation and growth in these dendrites occur by the twin plane re-entrant edge mechanism previously shown to occur in the growth of germanium dendrites from the supercooled liquid.

There has been much recent interest in the mechanism of electrodeposition from aqueous solution. Bockris (1-3) and Gerischer (4) have advanced convincing theoretical and experimental evidence that the mechanism of silver deposition involves a step following the charge-transfer reaction for the diffusion of adatoms from point of deposition to growth sites on the crystal surface. Concurrently, scientific interest in electrode processes in molten salt solvents has greatly increased.

There have been several previous studies of various aspects of silver deposition from molten salts. Aten, den Hertog, and Westenberg (5) found low cathode polarization during deposition of silver from a large number of salt mixtures. Microcrystalline deposits were obtained from mixtures of KCl, NaCl, and AgCl at 705°C. Drossbach (6) electrodeposited silver from mixtures of KCl-NaCl-AgCl at a current density of 0.20 ma/cm^2 and a cathode polarization of 2 mv. Drossbach and Petrick (7) determined the limiting current for silver deposition from dilute solutions of AgCl in the LiCl-KCl eutectic at 450°C. If the carbon anode was not isolated, considerable convection in the melt was produced by chlorine evolution. With an isolated anode, stirring was found to increase greatly the limiting current for silver deposition. The tendency for metals to form dendrites when deposited from fused salts is well known. Yang, Chien, and Hudson (8) studied the formation of silver dendrites grown from the LiCl-KCl eutectic at 500°C. The trunks of these dendrites grew in the <211> directions with branching in the <211> and <110> directions. Shams-El-Din and Wranglen (9) investigated the morphology of silver dendrites grown by electrodeposition from a molten LiCl-KCl eutectic with 10-40% added AgCl at temperatures of 413°-475°C and current densities of 30-200 ma/cm^2 and found results similar to those reported by Yang, Chien, and Hudson. The dendrites were shown to be planar and the addition of a number of inorganic salts to the melt was found to have little effect on the morphology of the dendrites. Faust and John (10) made metallographic examinations of the dendrites grown by Yang, Chien, and Hudson and found they contained two or more twin planes.

Barton and Bockris (11) studied the growth of silver dendrites at 308°C from molten equimolar sodium nitrate-potassium nitrate containing silver nitrate. These authors found that the growth of the dendrite tip at constant overpotential was linear with time after an induction period. Data on growth rate at varying overpotential were obtained for a large number of dendrites and data on growth rate, radius of curvature at the tip, and overpotential were obtained for three dendrites. Barton and Bockris have developed a theory of dendritic growth by metal deposition. Three factors are included in the theory to account for the observed overpotential: charge-transfer, diffusion, and surface energy. The resulting equation predicts the growth rate as a function of overpotential, concentration, surface energy, and exchange current. In an attempt to obtain a fit between experiment and theory, the exchange current, transfer coefficient, and surface energy are treated as adjustable parameters, but only fair agreement is obtained. This theory suffers from several defects. The diffusion is assumed to be a spherical tip rather than to the more physically reasonable paraboloid. The nature of diffusion to these surfaces is quite different. Diffusion controlled growth of a sphere varies as the square root of time, while that of a paraboloid is linear in time (12). In addition, Barton and Bockris have equated the thickness of the diffusion layer to the radius of curvature of the dendrite tip.

Hamilton (13) has adopted the theory of dendritic growth in a supercooled liquid metal developed by Ivantsov (12) and Temkin (14) to the case of electrodeposition. This development of the theory of electrochemical dendrite growth, based on the assumption that the rate is controlled by diffusion alone, shows remarkable accuracy in predicting the tip radii for the three specimens studied by Barton and Bockris without the use of any adjustable parameters. An expansion of the theory to include terms for the curvature of the tip and activation overpotential gives agreement between theory and experiment only if surface energy and exchange current are treated as adjustable parameters. The values of exchange current and surface energy required to fit the experimental curves of growth rate against overpotential are higher by an order of magnitude in the case of the exchange-current and lower by a similar factor in the case of the surface energy than those known to be physically reasonable for this system. These disparities throw considerable question on the validity of the extended theory and reinforce the conclusion that diffusion is the dominant factor in the electrochemical growth of dendrites. The contribution to the overpotential due to the curvature of the surface, given by

* Present address: American Cyanamid Co., Stamford Research Laboratories, Stamford, Connecticut, 06904.

the expression $2\gamma V/F\rho$, is of the order of 1 mv for the dendrite tips measured by Barton and Bockris. The effect is a secondary contribution to the total overpotential. The activation polarization under the condition employed by Barton and Bockris is only of the order of 20 μv at a current density of 10 ma/cm^2 and can be ignored.

Three distinct steps occur in the electrodeposition process. These are:

Mass transport:

$$Ag^+ \text{ (solution)} \rightleftarrows Ag^+ \text{ (interface)} \qquad (a)$$

Charge-transfer:

$$Ag^+ \text{ (interface)} + e \rightleftarrows Ag^o \text{ (surface)} \qquad (b)$$

Surface diffusion:

$$Ag^o \text{ (surface)} \rightleftarrows Ag^o \text{ (lattice)} \qquad (c)$$

Laitinen, Tischer, and Roe (15) have determined the exchange current and transfer coefficient for the charge-transfer reaction for silver deposition from the molten LiCl-KCl eutectic at 450°C. These parameters completely define the kinetics of the charge-transfer reaction. This paper describes experimental studies of the surface diffusion and mass transport reactions for silver deposition in a LiCl-KCl eutectic at 450°C. The rise time of the overpotential on application of galvanostatic pulses has been studied to determine if the mechanism of electrodeposition from fused salts involves a surface diffusion process in which adatoms migrate from point of deposition to growth sites on the crystal surface or if deposition occurs directly at such sites. Steady-state polarization measurements during the deposition of silver from the molten chloride eutectic have been made and the results correlated with the occurrence of dendrites. The mechanism of nucleation and growth of silver dendrites by fused salt deposition has been elucidated.

Theoretical.—The mechanism of crystal growth by electrodeposition has been the subject of much theoretical and experimental consideration recently. The surface diffusion of adatoms as an important step in the over-all deposition process has been derived largely from the theory of vapor deposition. Burton, Cabrera, and Frank (16) first emphasized the role of screw dislocations as sites for nucleation in crystal growth. Cabrera and Burton (17) showed that a model of crystal growth, based on uniform production of adsorbed atoms followed by diffusion of these atoms to steps on the surface and then along steps to kink sites, correctly predicted the growth rate of iodine crystals. Bockris and Mehl (1, 2) and Gerischer (4) showed almost concurrently that the adatom mechanism occurs in electrodeposition of metals from aqueous solutions at low overpotentials. Galvanostatic pulsing was employed under conditions where mass transport in the solution phase could be ignored, *i.e.*, at high concentrations of reducible species. A steady-state overpotential cannot be reached in a time faster than that allowed by the slowest step in the over-all process. For deposition from aqueous solutions, it has been established that surface diffusion is a slower step than charge-transfer because the rate at which a steady-state overpotential is approached is significantly less than predicted if charge transfer alone were controlling the rate of deposition.

The principal difference between the method of Bockris and co-workers and that of Gerischer lies in the nature of the model employed. Gerischer's approach involves a generalized diffusion rate from point of deposition to growth site, while Bockris has recourse to a specific model involving diffusion of adatoms on a plane between two parallel steps on a crystal face. In this study, the model first proposed by Bockris and Mehl will be tested. Although a more involved approach was later developed by Despic and Bockris (3), the simple model was chosen because measurements of overpotential-time curves in fused salts involve the observation of overpotentials smaller by a factor of ten to fifty and at times faster by a factor of 10^3 than those necessary in studies of deposition from aqueous solution. The refined theory of Bockris and Despic yields essentially the same results as that first advanced by Bockris and Mehl.

This study has concentrated on the determination of overpotential-time curves rather than the log current density-overpotential curves. This has been necessary again because the overpotentials observed in fused salt electrode reactions are small due to the large values of the exchange current. It would be fruitless to look for small variations in quantities which are already small. The overpotential-time curves are themselves still quite sensitive to a slow surface diffusion step. The Bockris-Mehl model (1, 2) is developed on the assumption that adatoms act as intermediates in essentially all deposition or dissolution processes occurring on a metal surface. The overpotential-time relation, assuming no depletion of ions at the electrode surface, may be written[1]

$$i = i_o\left[\exp\left(-\beta\frac{nF}{RT}\eta\right) - \frac{C(\eta,t)}{C_o}\exp\left((1-\beta)\frac{nF}{RT}\eta\right)\right] \qquad [1]$$

Expansion of the exponential for small values of η, neglecting the products of small variables and assuming $C(\eta,t)/C_o$ is not greatly different from [1] gives[2]

$$-\eta(t) = \frac{RT}{nF}\frac{i}{i_o} + \frac{RT}{nF}\frac{[C(\eta,t) - C_o]}{C_o} \qquad [2]$$

The rate of change of adatom concentration at any point on a surface is given by the difference between the rate at which the adatoms arrive by deposition and the rate at which they diffuse away

$$\frac{dC}{dt} = \frac{i}{nF} - \nu \qquad [3]$$

The diffusion rate is assumed proportional to the supersaturation with adatoms.

$$\nu = \nu_o\left[\frac{C(\eta,t) - C_o}{C_o}\right] \qquad [4]$$

Substituting [4] in [3] and solving the differential equation subject to the condition that $C(\eta,t) = C_o$ at $t = 0$ gives

$$\frac{[C(\eta,t) - C_o]}{C_o} = \frac{i}{nF\,\nu_o}\left[1 - \exp\left(\frac{-\nu_o}{C_o}t\right)\right] \qquad [5]$$

Substituting [5] in [2] gives

$$-\eta(t) = \frac{RT}{nF}\frac{i}{i_o} + \frac{RT}{(nF)^2}\frac{i}{\nu_o}\left[1 - \exp\left(\frac{-\nu_o}{C_o}t\right)\right] \qquad [6]$$

Equation [6] is the general expression for the overpotential-time curve, valid at small values of overpotential. At small values of t, the exponential term of Eq. [6] may be expanded giving

$$-\eta(t) = \frac{RT}{nF}\frac{i}{i_o} + \frac{RT}{(nF)^2}\frac{i}{C_o}t \qquad [7]$$

or

$$-\frac{d\eta}{dt} = \frac{RT}{(nF)^2}\frac{i}{C_o} \qquad [8]$$

Equation [8] allows evaluation of C_o from the linear portion of the η-t curve at small t. It should be em-

[1] A list of symbols used and their meaning is given at the end of this paper.

[2] It is necessary to assume that $\frac{C(\eta,t)}{C_o}\frac{nF}{RT} \sim \frac{nF}{RT}\eta t$ while assuming $\Delta C(\eta,t) \neq 0$. These two assumptions are not wholly compatible, but the fact that nF/RT is small means they are not seriously in error.

phasized that the linear portion does not correspond to double layer charging as is the usual case. Inman, Bockris, and Blomgren (18) have shown that it is necessary to make η-t observations in the nanosecond range in fused salt deposition studies to observe double layer charging in the presence of reducible ions. Calculation of the apparent capacitance from the linear portion of the η-t curves gives the pseudo-capacitance associated with the adatom layer. Now C_o can be evaluated from Eq. [8], and v_o may be calculated since

$$\eta - \eta_\infty = \frac{RT}{(nF)^2}\frac{i}{v_o}\exp\left(\frac{-v_o t}{C_o}\right) \quad [9]$$

or

$$\frac{d\ln(\eta-\eta_\infty)}{dt} = \frac{-v_o}{C_o} \quad [10]$$

In the steady-state, the overpotential observed in most fused salt electrode processes are controlled solely by mass transport in the electrolyte solution (6, 7, 30-43) since charge transfer reactions are orders of magnitude faster at 450° than they are in aqueous solutions (16, 18, 44-47), while diffusion coefficients and viscosities are comparable to those found with aqueous solutions (19, 20, 28). The fundamental equation for diffusion-controlled current density at a planar electrode under conditions of linear diffusion is

$$i = nF\,D\left(\frac{dC}{dx}\right)_{x=0} \quad [11]$$

If the concentration gradient is approximated by a linear gradient over a finite thickness

$$i = nF\,D\frac{C^o - C^*}{\delta} \quad [12]$$

If the exchange-current is very high, the overpotential in the steady-state will be due solely to concentration polarization

$$\eta = \frac{RT}{nF}\ln\frac{C^*}{C^o} \quad [13]$$

or

$$C^* = C^o\exp\left(\frac{nF}{RT}\eta\right) \quad [14]$$

At small overpotentials

$$C^* = C^o\left(1 + \frac{nF}{RT}\eta\right) \quad [15]$$

Then

$$i = \frac{-(nF)^2}{RT}\frac{DC^o}{\delta}\eta \quad [16]$$

This equation predicts linear current-overpotential curves in the steady-state at low overpotentials with slopes proportional to concentration. The diffusion layer thickness in fused salt deposition will be controlled by both diffusion and convection in the steady-state because a concentration gradient can be maintained only for a matter of a few seconds (19) at 450°C before convection occurs.

Starting from the assumptions that transport to a dendrite tip growing in the z direction is controlled by diffusion to the surface and growth of the tip into the solution and also that the electrode surface is at a uniform potential, Hamilton (13) has shown the concentration field about a parabolic tip is given in cylindrical coordinates by

$$C(r,z) = C^o + (C^* - C^o)\frac{Ei\left[-\frac{v\rho}{2D}\left(\frac{z}{\rho} + \sqrt{\frac{z^2+r^2}{\rho^2}}\right)\right]}{Ei\left(\frac{v\rho}{2D}\right)} \quad [17]$$

where $Ei(x)$ is the exponential integral. If the overpotential is due only to the concentration gradient, it is found that

$$\frac{C^oVF}{RT}\eta = -\frac{v\rho}{2D}e^{v\rho/2D}\,Ei\left(-\frac{v\rho}{2D}\right) \quad [18]$$

If terms for the exchange current and surface energy are included, the relation becomes

$$\frac{\frac{C^oVF}{RT}\eta}{1 + \frac{1.33\,FC^oD}{\rho i_o} + \frac{3.86\,C^o\gamma V^2D}{v\rho^2\,RT}} = -\frac{v\rho}{2D}e^{v\rho/2D}\,Ei\left(-\frac{v\rho}{2D}\right) \quad [19]$$

Experimental

Eutectic salt mixtures.—High-purity LiCl (59%)-KCl (41%) melts were obtained in glass ampoules containing a nitrogen atmosphere from the Anderson Physics Laboratory, Inc., Champaign, Illinois. These salt mixtures had been subjected to the rigorous purification procedures described by Laitinen, Tischer, and Roe (15). Residual currents measured at −2.0v against a Pt/Pt(II) reference electrode with a 0.020-in. diameter flush ground indicator electrode were of the order of 1 μa for all melts.

Silver chloride.—Fisher or Mallinckrodt reagent grade silver chloride was finely ground and dried in a desiccator over magnesium perchlorate for several days before use.

Electrodes.—Electrodes were fabricated from 0.020-in. diameter platinum wire sealed into a Corning 0120 lead glass tube by means of a Corning 0100 (G-164-EC) glass.[3] Flush ground microelectrodes were obtained by polishing the glass-to-metal seal first with 600 mesh silicon carbide, lapping with 1800 mesh silicon carbide abrasive, and polishing with Linde A (0.3μ alumina) on a polishing wheel. Macroelectrodes were prepared by spot welding 1 cm x 1 cm x 0.015 in. platinum foil to 0.020 in. diameter platinum wire projecting through the glass-to-metal seals described above. Platinum cathodes were plated with silver from the melt at low current density (0.5 ma/cm^2) before overpotential measurements were made. Laitinen *et al.* (15) have shown the roughness factor for polished platinum microelectrodes is about 2. A roughness factor of 3 has been taken for the silver plated microelectrodes used in the studies of the rise time of the overpotential, based on microscopic observations of the electrodes before and after plating.

Anodes were silver foil spot welded to silver wire. Ag/Ag(I) reference electrodes were silver wires dipped into the melt containing silver chloride. These wires were positioned about 1 cm away from the cathode. Closer placement is not required because of the high conductivity of the melt. Silver electrodes were cleaned and etched in 1:1 HNO_3, washed in distilled water, soaked in concentrated NH_3 solution, washed again, and dried.

Procedure.—Experiments were conducted in 15 x 2½ in. OD medium walled Pyrex test tubes flanged to fit No. 12 silicone rubber stoppers. These stoppers were frozen and drilled to fit electrode sheaths, thermocouple wells, etc. The test tubes were immersed in a three-zone Hevi-Duty furnace whose temperature was controlled at 450° ± 1°C by a Wheelco Model 404 temperature controller.

Cells and electrodes were cleaned in hot concentrated $HClO_4$ or cold chromic acid solution prior to use. These materials were then washed thoroughly and

[3] This glass has previously been described incorrectly as Corning 010 (15, 20). Corning 0010 is a common type of lead glass and is unsuitable for use at metal seals in fused salt electrochemistry because of its high conductivity and the resulting reduction of lead ions which occurs. Corning 0010 is similar to Corning 0120 in its properties.

dried prior to use. The procedure for evacuating and breaking the ampoule has previously been described (15).

Instrumentation.—A Teletronics Laboratory Model PS-110 constant current power supply was employed to supply currents in the range from 1 μa to 50 ma. A 16 μF oil capacitor was connected across the output terminals to remove residual a-c ripple. Currents were measured with a Sensitive Research ammeter. In measurements of the rise time of the overpotential, a Tektronix Type 565 dual beam oscilloscope with Type 2A63 plug-in units with rise-times of 1 μsec was utilized. A mercury-wetted relay system (Western Electric Type 276B) was used to switch the current from a dummy resistor (10 ohms) to the electrochemical cell. This was achieved by applying a pulse from a battery which activated the relay coil and triggered time base A of the dual beam oscilloscope simultaneously. Time base B was operated in the delayed mode after an interval of 3.75 msec which corresponds to the closure time of the reed in the mercury wetted relay. In this way, time base B was triggered a few microseconds before application of the constant current to the electrochemical cell and overpotential-time curves in the range of 0-100 μsec were obtained on the B channel and recorded with a Tektronix Type C-12 oscilloscope camera using Polaroid Type 47 film (ASA 3000).

Steady-state polarization measurements were made with a Sargent Model MR potentiometric recorder.

Convection.—Solutions were stirred with a paddle stirrer rotating in a Teflon gland and driven at 600 rpm by a Sargent synchronous rotator.

Results

In studies of the rise-time of the overpotential, current pulses from 2.5 to 500 ma/cm^2 were applied to a flush ground silver plated platinum electrode in a 0.101*M* AgCl solution. In the range of current densities from 2.5-100 ma/cm^2, the overpotential time curves are similar to those shown by Mehl and Bockris (1). A steady state is reached in times from 60-100 μsec over this range of current densities. If charge-transfer alone were rate controlling, a steady state should be reached in $\tau_{c.t.} \sim 5 \times (RT/nF)(C/i_o)$ (2). Using the known values of exchange current for 0.1*M* Ag^+ solutions and the double layer capacity which has been estimated from the known value for a Pt surface (21) in the same melt at 450°C, this calculation

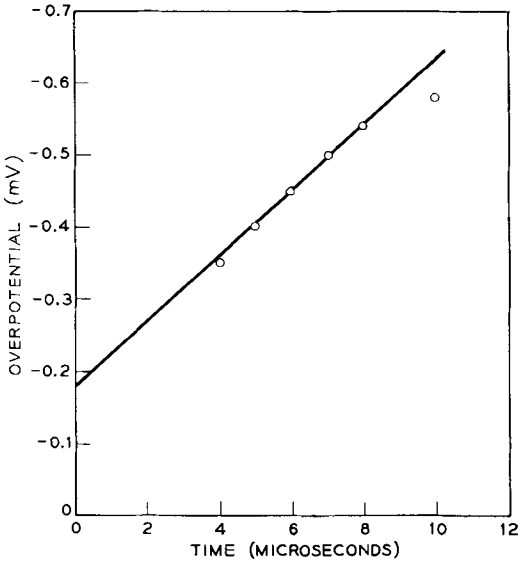

Fig. 1. Plot of overpotential against time for deposition of silver from 0.101M AgCl in molten LiCl-KCl at 450°. Current density, 98.7 ma/cm^2.

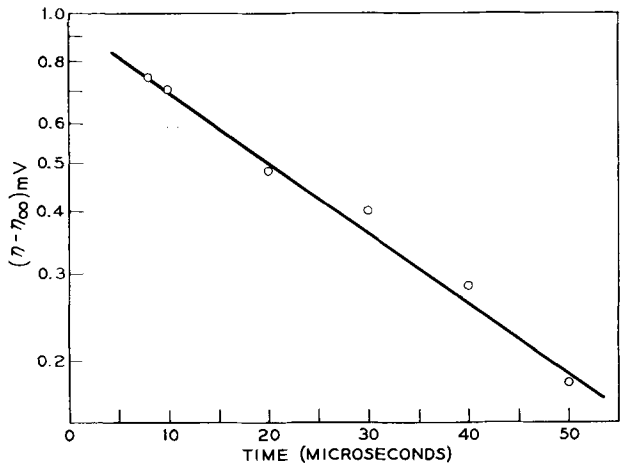

Fig. 2. Plot of log $(\eta-\eta_\infty)$ against time for the deposition of silver from 0.101M AgCl in molten LiCl-KCl at 450°C. Current density, 98.7 ma/cm^2.

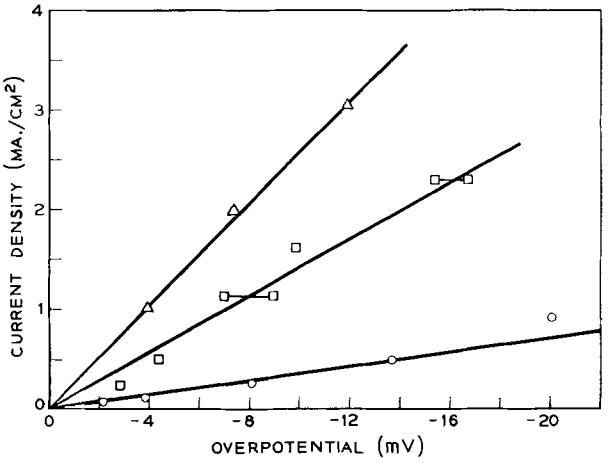

Fig. 3. Plot of steady-state overpotential against current density for the deposition of silver from AgCl in fused LiCl-KCl at 450°C. Concentrations: —○—, 0.48%; —□—, 1.36%; —△—, 3.33% AgCl.

gives $\tau_{c.t.} \sim 2$ μsec. At current densities above 100 ma/cm^2, the concentration overpotential, η_d, becomes significant before a steady state is reached. This may be calculated from

$$\eta_d = \frac{RT}{nF} \ln \left(\frac{\tau_d^{1/2} - t^{1/2}}{\tau_d^{1/2}} \right) \qquad [20]$$

where τ_d is the transition time for concentration polarization

$$\tau_d = \frac{\pi D}{4} \left(\frac{nFC^o}{i} \right)^2 \qquad [21]$$

Results are presented for a current density of 98.7 ma/cm^2; the highest current density employed before concentration overpotential becomes significant during the course of the measurement, since this affords the maximum accuracy of measurement. Figure 1 shows a plot of η against time for short times. The iR component has been subtracted from the observed overpotential to give the activation overpotential. Evaluation of C_o. the concentration of adatoms at the equilibrium potential, using Eq. [8], gives a value of 9×10^{-10} moles/cm^2. Calculation of the pseudocapacitance associated with the layer of adatoms from the linear $\eta - t$ curve gives a value of 700 μF/cm^2. Figure 2 shows the plot of log $(\eta - \eta_\infty)$ against time. Evaluation of the rate of surface diffusion using Eq. [10] and the C_o value obtained above gives $nF\ v_o = 3.3$ amp/

cm^2. The experimental data are seen to fit Eq. [8] and [10] well.

Figure 3 shows steady-state polarization curves observed at macroelectrodes for 0.48, 1.36, and 3.33 w/o (weight per cent) AgCl in the LiCl-KCl eutectic. The linear i-η curves predicted by Eq. [16] are observed showing that mass transfer is limiting the rate of electrodeposition. Linear i-η curves are also expected at low overpotentials when charge transfer is rate controlling. Calculations of the activation overpotential at current densities of 1-5 ma/cm^2 show that the observed values are far greater than the calculated ones. The linear i-η relation is thus due to mass transfer and not charge transfer. The slopes of the three lines shown in Fig. 3 are approximately proportional to concentration as Eq. [16] predicts. The scatter shown in Fig. 3 for the 1.36 w/o AgCl chloride solution is due to the difficulty of establishing a reproducible diffusion layer thickness. The diffusion layer thickness is controlled by both diffusion and convection. Since convection is difficult to reproduce, some scatter in the observed overpotential is expected. In all instances, the nature of the deposit was studied by observing the cathode in the molten bath with a 20-power eyepiece. At overpotentials of less than 4 mv, coherent deposits are always observed. The average thickness of the deposit was 1.6×10^{-4} cm. At overpotentials greater than 4 mv but less than 10 mv, a few well-developed dendrites grow at fairly rapid rates and are readily observable. The dendrite shown in Fig. 5 grew to a length of 6 mm in 1 hr at a current density of 2.28 $\mu a/cm^2$ and an overpotential of 5.3 mv from a 3 w/o AgCl solution. Above 10 mv polarization, a large number of small dendrites are formed. These results parallel those of Barton and Bockris (11) who found no dendrites at overpotentials less than 3 mv in their studies of silver deposition from a molten nitrate solution at 308°C. These studies were conducted with plating thicknesses of 2×10^{-3} cm and plating times up to 20 hr (current density of 0.25 $\mu a/cm^2$). These observations leave no doubt that dendrites do not form below the critical overpotential. Both 3 mv at 308°C and 4 mv at 450°C correspond to the same degree of concentration overpotential [$C^*/C^o = 0.94$] and indicate that dendritic growth occurs when ionic diffusion in the liquid phase controls the growth process. This suggests that destruction of the concentration gradient by convection would reduce the overpotential and the tendency for dendrite formation. Figure 4 shows the current-overpotential lines for stirred and unstirred 3.33 w/o AgCl solutions. At a given current density, simple stirring significantly reduces the overpotential and, thus, allows the use of higher current densities before the critical overpotential for the initiation of dendrites is reached. The critical overpotential was found to be 4 mv in both stirred and unstirred solutions.

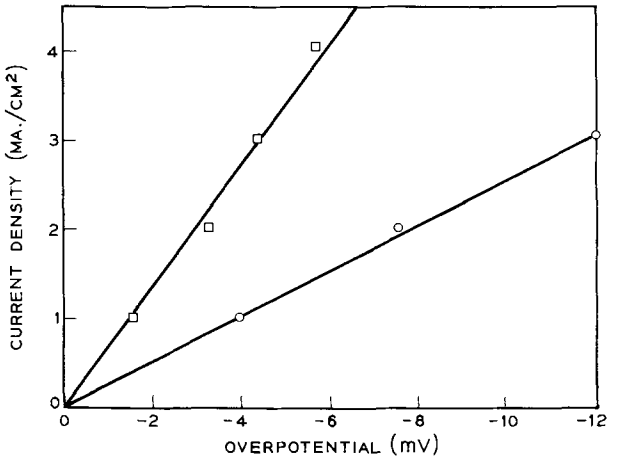

Fig. 4. Plot of steady-state overpotential against current density in 3.33% AgCl solution in LiCl-KCl at 450°C. —○—, unstirred; —□—, solution stirred at 600 rpm.

Fig. 5. Typical silver dendrite grown from 3% AgCl solution in LiCl-KCl at 450°C. Current density, 2.28 ma/cm^2; overpotential, 5.3 mv.

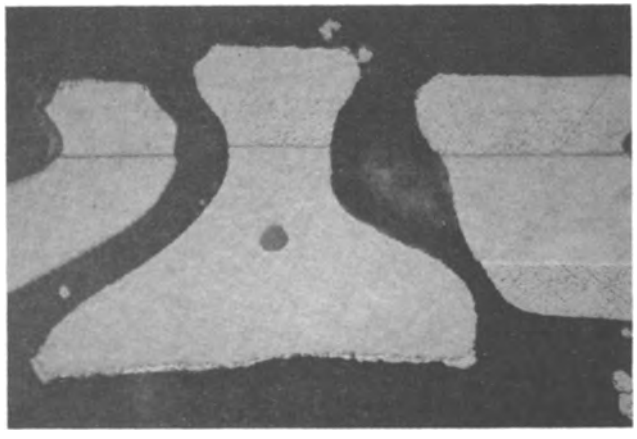

Fig. 6. Etched cross section of silver dendrite trunk showing closely spaced parallel twin planes at approximately 370X magnification.

Metallographic studies of the dendrites formed by electrodeposition of silver from the fused LiCl-KCl have been performed. Figure 5 shows a typical dendrite. The morphological studies of Yang, Chien, and Hudson indicate that this dendrite both grew and branched in the <211> direction. Figures 6 and 7 show cross sections of the trunks of two different dendrites at approximately 370X and 1470X, respectively. These dendrites were potted in CIBA Araldite epoxy polymer, polished and etched with a 5% KCN-5% $(NH_4)_2S_2O_8$ solution. In Fig. 6, two closely spaced parallel twin planes are seen. In Fig. 7, the twin planes are more prominent at approximately 1470X. Etching has apparently produced faceting of the surface between the planes. In Fig. 8. the cross section of a dendrite branch is shown. Here, the twin planes are considerably farther apart. All dendrite branches show at least two, and sometimes as many as seven, parallel twin planes.

Discussion

The fact that the rise time of the overpotential observed over a wide range of current densities is much slower than that predicted from simple theory for charge-transfer reactions constitutes proof that a proc-

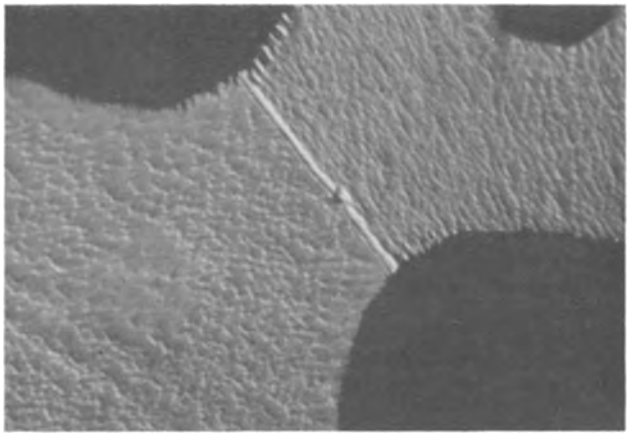

Fig. 7. Etched cross section of silver dendrite showing parallel twin planes at approximately 1470X magnification.

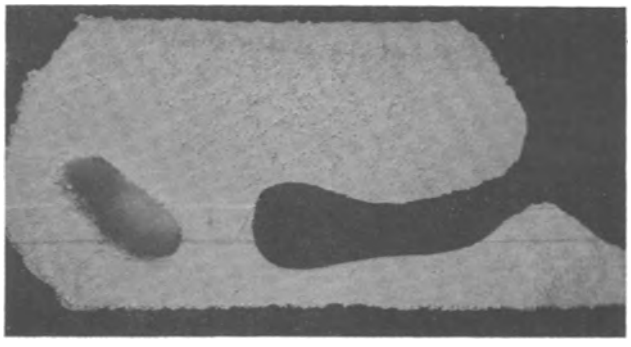

Fig. 8. Etched branch of silver dendrite containing parallel twin planes at approximately 370X magnification.

ess slower than charge-transfer must be rate controlling. Since these experiments were conducted over time scales and current densities where concentration changes at the electrode surface can be neglected, the slow step in the over-all process can only be surface diffusion. Good agreement is observed between the theory for the form of the overpotential-time curves and the experimental results. The adatom concentration found for the silver surface (9×10^{-10} moles/cm^2) at 450°C is approximately twice that found by Bockris and Mehl in aqueous solution at 25°C (4×10^{-10} moles/cm^2). This indicates that the adatom mechanism is relatively more important in deposition processes from fused salts than from aqueous solutions. This fact is understandable in terms of the relative rates of the charge-transfer and surface diffusion processes. The molar exchange current for silver deposition under the conditions employed in this study is 190 amp/cm^2, while that in aqueous solution at 25°C is 0.17 amp/cm^2 (2). The effect of temperature and change of medium gives an increase in rate by a factor of 1100. This is consistent with the activation energies for electrochemical charge-transfer reactions which are typically around 10 kcal/mole (48, 11, 27). The surface diffusion process, however, increases from 0.014 amp/cm^2 ($nF\,v_o$) at 25°C in an aqueous system to 3.3 amp/cm^2 at 450°C in the fused salt case. This represents an increase by a factor of 230 only, because of the relatively low activation energy for the surface diffusion process, estimated to be about 3 kcal/mole (4). Since the increase in rate of charge-transfer is several times greater than the increase in surface diffusion rate, the surface diffusion step is relatively more important in determining the rate of the over-all deposition process [see Eq. (b) and (c)]. The adatom concentration must be greater since adatoms are essential intermediates in the total process and the rate at which they are formed is increased more than the rate by which they are removed from the surface.

The results of the present study indicate that dendritic deposits may be expected when the electrode process is controlled primarily by ionic diffusion in the liquid phase. A calculation of the apparent diffusion layer thickness using Eq. [16] and the diffusion coefficient for Ag(I) in LiCl-KCl at 450°C as determined by Thalmayer, Bruckenstein, and Gruen (28) gives 0.071 and 0.026 cm as the apparent diffusion layer thicknesses for the unstirred and stirred 3.33 w/o AgCl solutions. The fact that a definite concentration gradient must be established before dendritic deposits occur has also been shown. To produce coherent deposits of silver by deposition from fused salts, it is necessary to work under conditions such that the critical overpotential for dendrite initiation, resulting from concentration polarization, is not exceeded. The results shown in Fig. 3 and 4 prove that this may be accomplished by two means: the employment of a high concentration of reducible ion, and the use of convection. Under these conditions, the extent of concentration overpotential will be minimized, and it will be possible to produce coherent deposits at higher current densities than would otherwise be the case. This conclusion is in contradiction of the statement of Yang, Chien, and Hudson (8) that dendritic deposits will occur at high concentration of reducible ions and high current density. These authors did not measure the overpotential during deposition, however, and were not cognizant of the fact that overpotential is the relevant parameter determining the morphology of the deposit. Undoubtedly, the use of a rotated cathode would provide the most efficient means of convection. A calculation of the current density necessary to produce 4 mv polarization at a disk electrode rotating at 600 rpm in a 1*M* AgCl solutions in LiCl-KCl at 450°C gives 56 ma/cm^2. Charge-transfer alone provides no limitation, since 12 amp/cm^2 are necessary to produce 4 mv of activation polarization under the same conditions. Although it has been proven only for silver, a critical overpotential for the initiation of dendritic growth may exist for other metals as well. The low value of the critical overpotential for silver is probably related to the low value of the stacking fault energy for silver of 25 ergs/cm^2 (29) which should be about half the energy necessary to form a twin plane.

The trunks and branches of all dendrites examined in this study were found to contain at least two parallel twin planes in agreement with the results of Faust and John (10). Since the morphological studies (8, 9) have shown that these dendrites grow in the <211> direction, the results suggest that nucleation and growth of these dendrites is occurring by the twin plane re-entrant edge mechanism similar to that known to occur in the growth of germanium dendrites (22-24).

The groove between two facets at the twin plane provides a site for low energy nucleation and two parallel planes provide a structure which growth cannot destroy (24). The recent reports of twin planes in electrodeposited dendrites (10, 22, 26) suggests that this is a general mechanism for their growth. Dendrite formation in electrodeposition must start with faceting of the planar surface (11). The idea that penetration of the diffusion layer by the facet leads directly to dendrite formation as suggested by Barton and Bockris (11) is incorrect, however. If this were the case, convection, which decreases the thickness of the diffusion layer, should lead to increased incidence of dendritic growth. This is not the case. In reality, faceting leads to increased mass transport to the faceted surface as opposed to the planar surface. Those facets containing two or more twin planes provide a site for low energy nucleation and rapid propagation. The closely spaced twin planes found in the trunk of the dendrites in this study help explain the rapid growth of electrolytically grown dendrites since Wagner (25) has shown that the growth rate of germanium dendrites is greater when the parallel twin planes are closer together.

Acknowledgments

The author wishes to thank Dr. K. A. Jackson for elucidating the process of dendritic growth. He is also indebted to Mr. A. A. Tartaglia for the expert performance of the metallography and to Mr. J. A. Gribbin for aid with some of the experiments.

Manuscript received Dec. 28, 1964; revised manuscript received June 24, 1965. This paper was presented at the San Francisco Meeting, May 9-13, 1965.

Any discussion of this paper will appear in a Discussion Section to be published in the December 1966 JOURNAL.

REFERENCES

1. W. Mehl and J. O'M. Bockris, *J. Chem. Phys.*, **27**, 818 (1957).
2. W. Mehl and J. O'M. Bockris, *Can. J. Chem.*, **37**, 190 (1959).
3. A. R. Despic and J. O'M. Bockris, *J. Chem. Phys.*, **32**, 389 (1960).
4. H. Gerischer, *Z. Elektrochem.*, **62**, 256 (1958).
5. A. H. W. Aten, H. J. den Hertog, and L. Westenberg, *Trans. Electrochem. Soc.*, **47**, 265 (1925).
6. P. Drossbach, *Z. Elektrochem.*, **56**, 599 (1952).
7. P. Drossbach and P. Petrick, *ibid.*, **58**, 95 (1954).
8. L. Yang, C. Chien, and R. G. Hudson, *This Journal*, **106**, 632 (1959).
9. A. M. Shams-El-Din and G. Wranglen, *Electrochim. Acta*, **7**, 79 (1962).
10. J. W. Faust, Jr., and H. F. John, *This Journal*, **108**, 109 (1961).
11. J. L. Barton and J. O'M. Bockris, *Proc. Roy. Soc. (London)*, **268A**, 485 (1962).
12. G. P. Ivantsov, *Doklady Akad. Nauk. SSSR*, **58**, 567 (1947).
13. D. R. Hamilton, *Electrochim. Acta*, **8**, 731 (1963).
14. D. E. Temkin, *Doklady Akad. Nauk. SSSR*, **132**, 1307 (1960).
15. H. A. Laitinen, R. P. Tischer, and D. K. Roe, *This Journal*, **107**, 546 (1960).
16. W. K. Burton, N. Cabrera, and F. C. Frank, *Nature*, **163**, 398, (1949).
17. N. Cabrera and W. K. Burton, *Discussions Faraday Soc.*, **5**, 33, 40 (1949).
18. D. Inman, J. O'M. Bockris, and E. Blomgren, *J. Electroanal. Chem.*, **2**, 506 (1961).
19. H. A. Laitinen and W. S. Ferguson, *Anal. Chem.*, **29**, 4 (1957).
20. H. A. Laitinen and R. A. Osteryoung, "Fused Salts," B. R. Sundheim, Editor, Chap. 4, McGraw-Hill, Book Co., New York (1964).
21. H. A. Laitinen and D. K. Roe, *Collection Czech. Chem. Comm.*, **25**, 3065 (1960).
22. H. F. John and J. W. Faust, Jr., Paper presented at the Washington, D. C., Meeting of the Society, October 1964.
23. D. R. Hamilton and R. G. Seidensticker, *J. Appl. Phys.*, **31**, 1165 (1960).
24. R. S. Wagner, *Acta. Met.*, **8**, 57 (1960).
25. R. S. Wagner, "Metallurgy of Elemental and Compound Semiconductors," R. O. Grubel, Editor, **12**, 177 (1950).
26. F. Ogburn, B. Paretzkin, and H. S. Peiser, *Acta Cryst.*, **17**, 774 (1964).
27. N. Tanaka and R. Tamamushi, *Electrochim. Acta*, **9**, 963 (1964).
28. C. E. Thalmayer, S. Bruckenstein, and D. M. Gruen, *J. Inorg. Nucl. Chem.*, **26**, 347 (1964).
29. I. L. Dillamore, R. E. Smallman, and W. T. Roberts, *Phil. Mag.*, (18th series), **9**, 517 (1964).
30. P. Drossbach, *Z. Elektrochem.*, **40**, 605 (1934).
31. P. Drossbach, *ibid.*, **56**, 23 (1952).
32. P. Drossbach, *ibid.*, **56**, 31 (1952).
33. P. Drossbach, *ibid.*, **57**, 548 (1953).
34. P. Drossbach, *ibid.*, **58**, 66 (1954).
35. P. Drossbach, *ibid.*, **59**, 512 (1955).
36. R. Piontelli and R. Montanelli, *J. Chem. Phys.*, **22**, 178 (1954).
37. R. Piontelli and R. Montanelli, *Z. Elektrochem.*, **59**, 64 (1955).
38. R. Piontelli and G. Sternheim, *J. Chem. Phys.*, **23**, 1358 (1955).
39. R. Piontelli and G. Sternheim, *ibid.*, **23**, 1971 (1955).
40. R. Piontelli, G. Sternheim, and M. Francini, *ibid.*, **24**, 1113 (1956).
41. R. Piontelli, G. Montanelli and G. Sternheim, *Rev. Met. (Paris)*, **53**, 246 (1956); *C. A.*, **50**, 10573 (1956).
42. R. Piontelli, G. Sternheim, M. Francini, and G. Montanelli, "Soveschanie Po Elektrokhimii, 4th," Moscow (1956); "Soviet Electrochemistry," Vol. 1, p. 90, Consultants Bureau, New York (1961).
43. R. Piontelli, *Ann. N.Y. Acad. Sci.*, **79**, 1025 (1960).
44. J. E. B. Randles and W. White, *Z. Elektrochem.*, **59**, 666 (1955).
45. H. A. Laitinen and R. A. Osteryoung, *This Journal*, **102**, 598 (1955).
46. H. A. Laitinen and H. C. Gaur, *ibid.*, **104**, 730 (1957).
47. D. L. Hill, G. J. Hills, L. Young, and J. O'M. Bockris, *J. Electroanal. Chem.*, **1**, 79 (1959).
48. K. J. Vetter, "Elektrochemische Kinetik," p. 104, Springer-Verlag, Berlin (1961).

SYMBOLS

i	Current density (positive for a cathodic process)
i_o	Exchange current density
β	Transfer coefficient ($0 < \beta < 1$)
n	Number of electrons in electrode process
η	Overpotential [E-E(equilibrium)]. Taken negative for a cathodic process
$C(\eta,t)$	Adatom concentration at any overpotential and time (moles cm^{-2})
C_o	Adatom concentration at the equilibrium potential (moles cm^{-2})
ν	Rate of surface diffusion (moles sec^{-1} cm^{-2})
ν_o	Intrinsic rate constant for surface diffusion (moles sec^{-1} cm^{-2})
D	Diffusion coefficient of reducible ion (cm^2 sec^{-1})
C^o	Bulk concentration of reducible ion
C^*	Concentration of reducible ion at electrode surface
δ	Apparent diffusion layer thickness (cm)
η_d	Concentration overpotential (polarization)
τ	Transition time for concentration overpotential ($C^* = 0$)
t	Time
C	Double layer capacitance
R	Gas constant
T	Absolute temperature
$\mathbf{F}$	The Faraday
V	Molar volume of metal
γ	Surface energy of metal (ergs/cm^2)
ρ	Radius of curvature of dendrite tip
v	Growth rate of dendrite tip (cm sec^{-1})

Preparation and Luminescent Properties of Ti-Activated Zirconia

J. F. Sarver

Lighting Research Laboratory, General Electric Company, Cleveland, Ohio

ABSTRACT

Very pure monoclinic ZrO_2 prepared from recrystallized zirconium oxychloride and activated with 0.08% Ti^{4+} responds well to 2537Å and cathode-ray excitation. A room temperature quantum efficiency of 70%, relative to $MgWO_4$, has been attained with 2537Å excitation. The emission band extends from below 4000 to above 6500Å, peaking at 4800Å. The phosphor has a broad excitation spectrum and responds almost equally well to wavelengths between 2100 and 2600Å. At 20°C the response to 2537Å excitation is about 82% of the maximum response which occurs at about −60°C. The initial decay is exponential with rate constant $\alpha = 1.5 \times 10^5$ sec^{-1}, but the visually detectable persistence lasts several minutes. The long persistence is associated with glow peaks which were found to exist above 20°C. Additional stronger glow peaks occur at lower temperatures.

Prior to this investigation it was observed by the author that several commercial sources of monoclinic zirconia responded to 2537Å and cathode-ray excitation, yielding a blue-white luminescence with a long persistence. ZrO_2 prepared from an experimental sample of hydrous zirconium carbonate, which is a relatively high purity zirconium compound manufactured by the Titanium Alloy Manufacturing Division of the National Lead Company, appeared to be only weakly luminescent. Similar observations have been mentioned previously in the literature (1, 2).

Further interest in this phenomenon was stimulated by a paper of Harrison, Melamed, and Subbarao (2) who prepared several compounds having the same generalized formula. Of special interest was a series of isostructural compounds having the generalized formula R_2^{2+} ZrR_2^{5+} O_9 where R^{2+} is Sr^{2+}, Ba^{2+}, or Pb^{2+}, and R^{5+} is P^{5+} or As^{5+}. These compounds responded to 2537Å excitation and exhibited broad emission bands with peak wavelengths between 4840 and 4920Å. They also found a similar emission for the monoclinic ZrO_2 used in the preparation of the ternary compounds. The marked similarity in the absorption, excitation, and emission spectra of these isotypic compounds and of ZrO_2 suggested to the authors that the phosphors were of the self-activated type, as are certain tungstate and molybdate compounds. They suggested the possibility that the luminescence is related to an asymmetric coordination of oxygens about the Zr^{4+} ions. The oxygen coordination of zirconium in monoclinic ZrO_2 is indeed asymmetric and unusual. According to McCullough and Trueblood (3), the zirconium ions are coordinated by seven oxygens and the Zr-O distances vary from 2.04 to 2.26Å. An idealized representation of the coordination polyhedron is shown in Fig. 1, in which the ZrO_7 group can be thought of as being derived from a cube. Four oxygens are at the base and one is located at one of the upper corners of the cube. Two additional oxygens are situated at the midpoints of the cube edges between the unoccupied corners. If the three oxygens on the top of the cube are moved as indicated by the arrows, their distances from the Zr^{4+} ion at the center of the cube are more nearly equalized but still average less than the Zr-O distances for the other four oxygens. The actual interionic distances determined by McCullough and Trueblood are given in Table I.

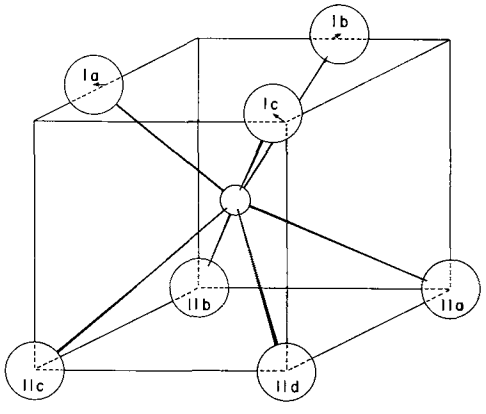

Fig. 1. Zr^{4+} coordination polyhedron in monoclinic ZrO_2 (McCullough and Trueblood).

The hypothesis of Harrison *et al.* regarding self-activation appears to be plausible if one considers their observations that certain zirconium compounds such as ZrP_2O_7, in which Zr^{4+} is symmetrically coordinated by six oxygens, are nonluminescent. On the other hand, a high-purity zirconia sample prepared by decomposing triply recrystallized zirconium oxychloride, $ZrOCl_2 \cdot 8H_2O$, did not respond to ultraviolet or cathode-ray excitation. The recrystallization procedure for purification of the oxychloride was developed by Hickok (4) in this laboratory, and was based on solubility data for the oxychloride compound in hydrochloric acid solutions cited by Blumenthal (5). These observations suggested that the luminescence observed in certain samples of ZrO_2 is due to the presence of some impurity which functions as a primary activator rather than to a self-activation mechanism. As discussed in subsequent sections, this impurity was shown to be Ti^{4+}.

Kröger and Overbeek (6) have prepared several Ti-activated phosphors including zirconia. In the case of ZrO_2, titanium was incorporated in amounts of 0.001 to 10 mole % by firing oxide mixtures at 1300°C. The phosphors yielded a greenish emission peaking at 4700Å when excited by wavelengths less than 3850Å, and the optimum activator concentration was found to be 0.1 mole %. The development of only weak emission can probably be attributed to the presence of other impurities such as iron which is quite detri-

Table I. Zr-O distances in monoclinic zirconia in Å (3)

O^{2-}	Distance	O^{2-}	Distance
I_a	2.04	II_c	2.16
I_c	2.10	II_a	2.18
I_b	2.15	II_b	2.26
		II_d	2.26

mental to the Ti^{4+} emission Besides hafnium, two of the major impurities in most commercial sources of monoclinic ZrO_2 are iron and titanium.

Phosphor Preparation

Purification of zirconium oxychloride.—According to Blumenthal, the room temperature solubility of $ZrOCl_2 \cdot 8H_2O$ in 8.72 NHCl solution is 0.0547 moles/liter and is highly temperature dependent in this solution. Based on this information a purification process by repeated recrystallization of the oxychloride was developed by Hickok. A description of his process follows.

Approximately 450g of TAM high-purity zirconium oxychloride is dissolved in 400 ml of deionized or distilled water and the solution is filtered to remove insoluble impurities. The solution is heated and added slowly with continuous heating to 800 ml of hot concentrated HCl so that the final solution is approximately 8*N* HCl. On cooling to room temperature, $ZrOCl_2 \cdot 8H_2O$ crystallizes and the yellow color of the supernatant liquid indicates that iron has been at least partially removed from the starting material. The supernatant liquid is vacuum-filtered from the crystals which are then washed several times with cold 8*N* HCl. The entire process of dissolving, recrystallization, etc., is repeated for further purification. The zirconium oxychloride is decomposed above 1000°C to form a white, fine-grained, polycrystalline monoclinic ZrO_2 which does not respond to either 2537Å or cathode ray excitation.

Spectrographic analyses.—In Table II, semiquantitative spectrographic analyses of two commercial zirconia samples (A and B) are compared with the analysis (C) of zirconia prepared from the purified oxychloride which was derived from oxychloride supplied by the TAM Division of the National Lead Company.

It is quite evident that the zirconia prepared from the recrystallized oxychloride is significantly purer than the other two samples. As far as possible activator impurities in the other two samples are concerned, the major differences occur for the elements Cu, Fe, Pb, Sn, and Ti. The blue-white luminescence observed in sample A suggested that the most likely activator should be Ti^{4+}. Titanium was not detected in the oxychloride sample whereas it was present in trace amounts in sample B and in greater amounts in sample A. Sample A exhibited a more intense emission with 2537Å excitation than did the sample B.

Phosphor synthesis.—Ti^{4+} as phosphor grade TiO_2 was substituted for Zr^{4+} in ZrO_2 in molar concentrations of from 0.06 to 0.6%. TiO_2-ZrO_2 mixtures were reacted in air in platinum crucibles at 1200°C for 1 hr and finally at 1300° for 2 hr after a second mixing. Firing in oxygen or mildly reducing conditions did not affect phosphor brightness. The latter atmosphere consisted of 0.5% forming gas passed through water at room temperature.

All of the preparations gave a blue-white emission with 2537Å excitation. Optimum plaque brightness for 2537Å excitation was observed for a Ti^{4+} concentration of 0.08 mole %. A plot of plaque brightness *vs.* titanium concentration is shown in Fig. 2. All of the subsequent discussions of optical properties will pertain to the optimized phosphor, *i.e.*, ZrO_2:0.0008Ti.

Table II. Spectrographic analyses of zirconia samples

	A	B	C		A	B	C		A	B	C
Ag	T	T	ND	Cr	T	T	ND	P	ND	ND	ND
Al	×	T	ND	Cu	T	*	*	Pb	T	ND	ND
As	ND	ND	ND	Fe	×	×	ND	Sb	ND	ND	ND
B	ND	ND	ND	Hg	ND	ND	ND	Si	×	×	T
Ba	T	T	ND	Mg	×	×	T	Sn	T	*	ND
Bi	ND	ND	ND	Mn	T	T	ND	Sr	×	ND	ND
Ca	T	T	×	Mo	ND	ND	ND	Ti	×	T	ND
Cd	ND	ND	ND	Na	Zr	Interference		V	ND	ND	ND
Co	ND	ND	ND	Ni	*	*	ND	Zn	T	ND	ND

Remarks: *, line is barely visible; ×, greater than trace; T, less than 100 ppm.

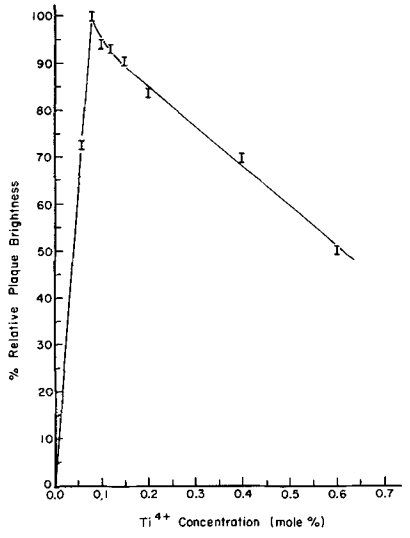

Fig. 2. Plaque brightness *vs.* activator concentration for ZrO_2:Ti phosphors.

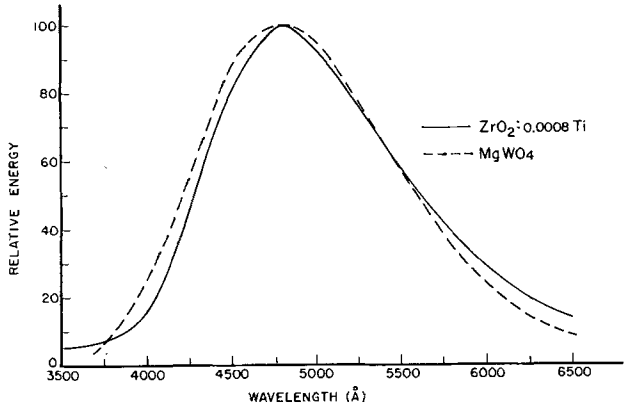

Fig. 3. Emission curves for Ti-activated ZrO_2 and magnesium tungstate (2537Å excitation).

Optical Properties

Emission spectrum.—With 2537Å or cathode-ray excitation, Ti-activated zirconia exhibits a wide emission band extending from below 4000Å to above 6500Å with a peak emission at 4800Å as shown in Fig. 3. The absence of cathodoluminescence in unactivated high-purity zirconia suggests that the Ti^{4+} impurity ions function as a primary activator and not as a sensitizer for the observed emission.

The emission spectrum is very similar to that observed by Koelmans and Verhagen (7) for a similar concentration of Ti^{4+} in $Ca_2Ge_3O_8$. They noted that the emission is very much like that of Sb-activated calcium halophosphate with Cl/F = 1 and that the quantum efficiency was the same or slightly better than that of the halophosphate. Figure 3 also shows the emission spectrum of $MgWO_4$ which was used as a standard for quantum efficiency measurements.

Excitation spectrum.—It was not possible to record an accurate excitation spectrum for this phosphor continuously because of a slow build-up of the emission. With 2537Å excitation, the emission attained 90% of its maximum after 4 sec exposure but did not attain a nearly constant value until after 4 min of exposure (see Fig. 4). Therefore, it was necessary to determine the excitation spectrum point by point, allowing the

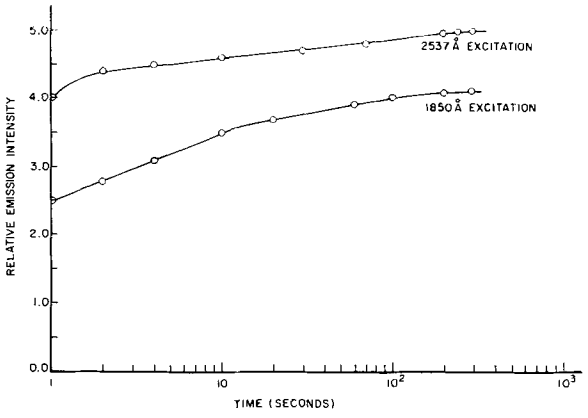

Fig. 4. Buildup of luminescence

emission to equilibrate at each wavelength of excitation.

The excitation spectrum shown in Fig. 5 was established using sodium salicylate as a standard for comparison at each wavelength. The spectrum is rather broad and the phosphor responds relatively well to 2537Å excitation.

Reflectance spectra.—In Fig. 6, the ultraviolet diffuse reflectance spectrum of purified unactivated ZrO_2, made from the recrystallized oxychloride, is compared with the reflectance spectra of the two commercial sources of zirconia mentioned previously. The spectrum for the activated sample clearly shows the effect of the Ti^{4+} impurity (800 ppm). Without quantitative spectrographic analyses, it would not be possible to explain the lower relative reflectance values for the two commercial samples. A reasonable approximation would be that both are considerably higher in iron content than either the purified sample or the phosphor made from it and that both contain Ti^{4+} as a major impurity since both are luminescent, although much weaker than the phosphor under discussion. According to a paper by Heffelfinger *et al.* (8), most commercial monoclinic zirconia samples have two major impurities in addition to hafnium; titanium and iron. These impurities will introduce absorption in the ultraviolet. Cr, Mn, Ni, Cu, etc., are generally present in only trace amounts or less.

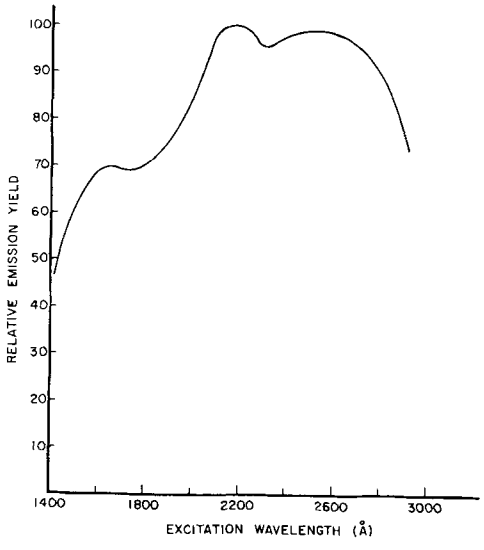

Fig. 5. Excitation spectrum

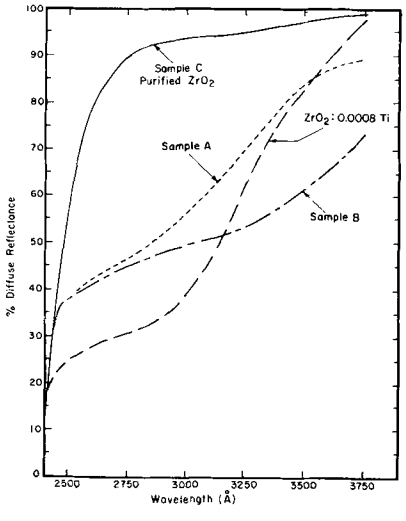

Fig. 6. Diffuse reflectance spectra for ZrO_2 and ZrO_2:Ti

Temperature dependence.—The dependence of the luminescence intensity on temperature is seen in Fig. 7. The shift of the emission to longer wavelengths (5100Å at 77°K) as reported by Harrison *et al.* for ZrO_2 was confirmed visually. At 20°C, the relative response to 2537Å excitation is about 82% of the response at −60°C as measured with a 1P21 photomultiplier tube and Corning UV filter. At 40°C, the approximate temperature at which ordinary 40 watt fluorescent lamps operate under normal ambient conditions, the relative brightness is 70%.

Decay and glow phenomena.—At room temperature the phosphor exhibits a very rapid initial exponential decay with rate constant $\alpha = 1.5 \times 10^5$ sec^{-1}, similar to $CaWO_4$ and $MgWO_4$ and some sulfide phosphors. Decay curves are shown in Fig. 8 and 9. Beyond about 20 μsec, the decay rate becomes much slower and the phosphorescence is visually detectable for a few minutes. It was found that the addition of certain mineralizers or fluxes, in particular 1 mole % LiF, besides leading to an expected increase in particle size during

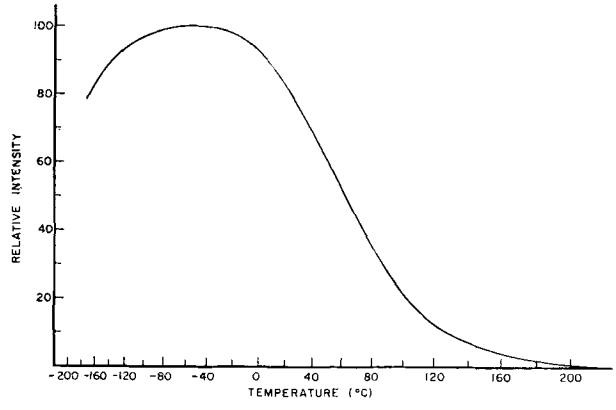

Fig. 7. Temperature dependence of emission

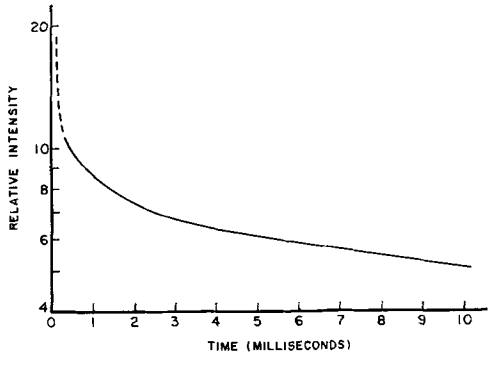

Fig. 8. Luminescence decay (2537Å excitation)

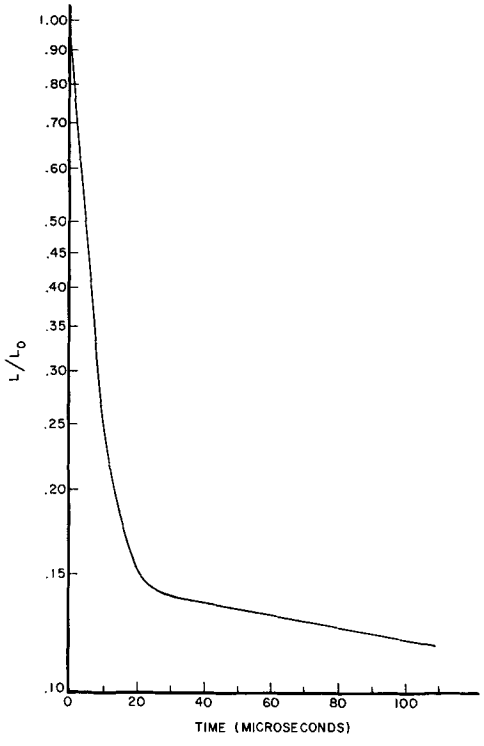

Fig. 9. Luminescence decay (cathode-ray excitation)

firing, also causes an increase in the intensity of the phosphorescence although the intensity of the fluorescence is virtually the same as ZrO_2:Ti phosphors synthesized without mineralizers. The effect of LiF on particle size development is shown in Fig. 10 and 11.

The long persistence of the phosphor is explained by the presence of trapped electrons which require heating above room temperature for release. The glow curve for this phosphor is shown in Fig. 12. In addition to the peaks above room temperature, there are several much stronger peaks at lower temperatures. There is apparently a very strong peak near liquid N_2 temperature. The phosphor was irradiated for 60 min at this temperature and allowed to decay 5 min before the heating was started at a rate of approximately 15°C/min.

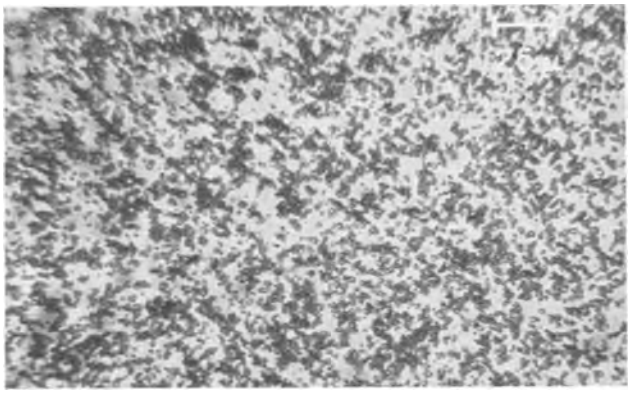

Fig. 10. Monoclinic ZrO_2 prepared from $ZrOCl_2 \cdot 8H_2O$

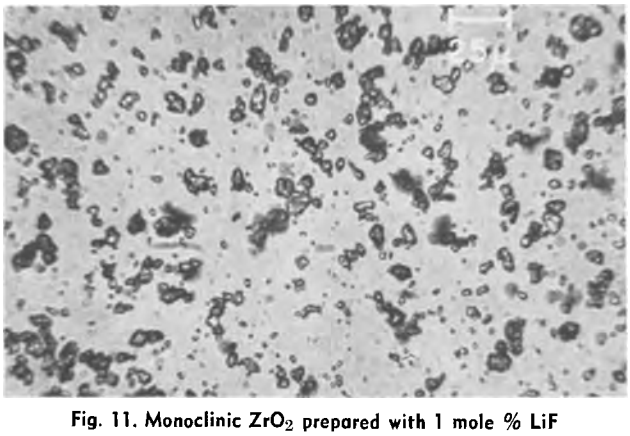

Fig. 11. Monoclinic ZrO_2 prepared with 1 mole % LiF

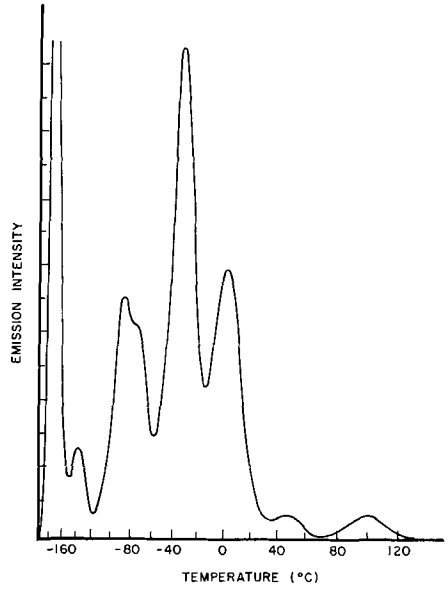

Fig. 12. Glow behavior above —196°C

Quantum efficiency.—Using a $MgWO_4$ phosphor as a standard for brightness comparison and $BaSO_4$ as a reflectance standard, relative quantum efficiency with 2537Å excitation was determined. $BaSO_4$ has a reflectance of 79% relative to MgO which is taken as 100% for 2537Å radiation, but the sulfate is much more stable under normal atmospheric conditions for longer periods according to Jones (9). Data used in the calculation of quantum efficiency are summarized in Table III.

An integration of the normalized photon plot, $\lambda^3 dE/d\lambda$ *vs.* λ(ev) for $MgWO_4$ and the zirconia phosphor yielded relative areas of 0.79 and 0.80, respectively. Both photon plots peak at 5000Å. The calculated relative quantum efficiency for the zirconia phosphor is 68 or 71%, depending upon whether that of $MgWO_4$ is taken as 95 or 100% (10).

Summary

The luminescence phenomenon associated with various commercial sources of zirconia and which has been cited in the literature has been shown to be attributable to the presence of titanium, a common impurity in commercial sources of ZrO_2. The intensity of the emission not only depends on the concentration of Ti^{4+} present but also is strongly dependent on the concentration of other impurities, in particular iron. It is therefore necessary to reduce the level of iron impurity to less than trace amounts before an efficient phosphor can be prepared. This undoubtedly serves to

Table III. 2537Å Reflectance and plaque brightness data

Sample	Reflectance, R Uncorrected	Reflectance, R Corrected	1-R	Plaque* brightness	Q.E.
ZrO_2:0.0008Ti	0.35	0.28	0.72	51	68-71%
$MgWO_4$	0.13	0.10	0.90	89	95-100%
$BaSO_4$	1.00	0.79	—	—	—

* At 5000Å.

reduce the amounts of other impurities also if the oxychloride recrystallization process is used. It is evident that commercial sources of zirconia, if used in the preparation of other zirconium compounds, will introduce the same undesirable impurities if luminescence phenomena involving other activator ions are being considered, for example, the rare earths. It is possible that these impurities may not have as pronounced a detrimental effect in such compounds as they do in ZrO_2 alone.

It is probable that Ti^{4+} replaces Zr^{4+} in monoclinic ZrO_2 substitutionally rather than interstitially. The usual coordination of Ti^{4+} in oxide compounds is octahedral. In monoclinic ZrO_2, however, the coordination of Ti^{4+} is likely the same unusual asymmetric sevenfold coordination discussed previously. This highly asymmetric environment may account for the strong emission which can be developed.

The slow build-up of steady-state luminescence and the long persistence of irradiated samples at room temperature is probably related to the filling and emptying of a relatively large number of traps which were shown to exist. Several strong glow peaks were detected above liquid nitrogen temperature. One of the peaks occurs between 0° and 20°C.

Acknowledgments

The author acknowledges the efforts of R. L. Brown in determining emission and excitation spectrum, of G. Schlotzer and F. Geraghty who measured decay rates, and to R. L. Hickok for his efforts in the preparation of high purity starting materials. R. Potter devoted considerable time in helping with the determinations of glow curves and quantum efficiency. The many discussions with J. S. Saby, E. F. Apple, and D. W. Magee during this investigation were most helpful.

Manuscript received Sept. 24, 1965. This paper was presented at the San Francisco Meeting, May 9-13, 1965.

Any discussion of this paper will appear in a Discussion Section to be published in the December 1966 JOURNAL.

REFERENCES

1. B. C. Weber, *Keram. Z.*, **15**, 192 (1963).
2. D. E. Harrison, N. T. Melamed, and E. C. Subbarao, *This Journal*, **110**, 23 (1963).
3. J. D. McCullough and K. N. Trueblood, *Acta Cryst.*, **12**, 507 (1959).
4. R. L. Hickok, Personal communication.
5. W. B. Blumenthal, "The Chemical Behavior of Zirconium," D. Van Nostrand Co., Inc., Princeton, New Jersey (1958).
6. F. A. Kröger and T. G. Overbeek, N. V. Philips Gloeilampenfabreiken, Dutch 73,114, August 15, 1953; U.S. 2,542,336, February 20, 1951 (assigned to General Electric Company).
7. H. Koelmans and C. M. C. Verhagen, *This Journal*, **106**, 677 (1959).
8. R. E. Heffelfinger, E. R. Blosser, and W. M. Henry, *J. Am. Cer. Soc.*, **47**, 646 (1964).
9. S. Jones, Personal communication.
10. F. Studer, Personal communication.

Sb^{3+} and Mn^{2+} Activated Calcium Halophosphate Phosphors from Flux-Grown Apatites

A. Wachtel

Lamp Division, Advanced Development Department, Westinghouse Electric Corporation, Bloomfield, New Jersey

ABSTRACT

The crystallization of calcium chloro- and chloro-fluoroapatites from calcium halide fluxes was studied as a function of composition and heating schedules. Activation of $Ca_5(PO_4)_3F_{0.9}Cl_{0.1}$ was investigated by varying phosphor stoichiometry and firing methods. The results indicate that flux-grown apatites are slightly deficient in PO_4^{3-} and that for a particle size of predominantly 50-100μ, 72-hr firing at 1150°C causes only limited incorporation of Sb^{3+}, Cd^{2+}, and additional PO_4^{3-}. The incorporation of Mn^{2+} is more extensive and may be nearly uniform. The rate of migration of Mn and Sb toward the interior of the crystals increases with increasing PO_4^{3-} [as $(NH_4)_2HPO_4$] added prior to activation; however, maximum emission occurs at a calculated over-all metal/phosphorus ratio of exactly 5/3. High output of heterogeneously emitting crystals suggests that quantum efficiency is independent of activator concentration.

The present study consisted of preparation of Mn- and Sb-activated Ca-halophosphate phosphors, based on apatites crystallized in fused salt media. Morton (1) reported on the crystallization of Ca_2PO_4Cl and $Ca_5(PO_4)_3Cl$ in fused $CaCl_2$, and Klement and Harth (2) describe the preparation of Cl- and Br-apatites by fusion of $Ca_3(PO_4)_2$ with the respective Na halides. Nacken (3) reported on the system $Ca_3(PO_4)_2$-$CaCl_2$-CaF_2 in some detail, but included no observations on morphology of the products. In view of the present need to obtain luminescence-pure materials and the versatility with which apatites are known to incorporate or exchange foreign ions, the choice of fluxes was confined to the system $CaCl_2$-CaF_2. Melting points for this, in combination with the respective Li salts, are reported by Bukhalova and Bergman (4).

Johnson (5) prepared single crystals of Mn-activated apatite grown from a melt containing this element and reported that Mn- and Sb-activated Ca-halophosphates can be briefly fused while retaining the original luminescence properties. In the present case, the excess Ca halide (flux) results in a metal/phosphorus ratio much higher than 5/3 which would promote extensive oxidation of these activators. Therefore, the incorporation of Mn and Sb was effected by additional firings, conducted after removal of the flux, and suitable adjustment of stoichiometry of the crystallized apatites.

Experimental

Crystallizations were conducted in covered round bottom platinum dishes in a furnace kept at a constant temperature, followed by quenching in water so as to minimize formation of Ca_2PO_4Cl in the temperature range below about 1040°C. Experimental batches amounted to a total of 2×10^{-2}g atoms Ca^{2+} (apatite + flux), while for purposes of phosphor preparation, larger batches were crystallized, based on an expected yield of 0.5 moles $Ca_5(PO_4)_3X$. The reacted materials were soaked in water, carefully disintegrated, wet-

screened through 40 or 60 mesh, and freed of flux by several decantations, discarding all fines not settling in one minute. In this process, particles below about 10μ and almost all of the CaF_2 occurring in finely divided (gelatinous) form was also removed. After alcohol washing and drying, the apatites were analyzed by conventional chemical techniques.

Activators were added in the form of 2 w/o (weight per cent) $MnCO_3$, 4 w/o Sb_2O_3,[1] 1.0 w/o NH_4Cl, and varying amounts of $(NH_4)_2HPO_4$ in aqueous slurry and drying. The mixtures were fired in capped silica tubes at 1150°C for 1 hr to decompose volatile matter, screened through 60 or 80 mesh, mixed with 1% NH_4Cl, and refired for longer times. Refiring of small samples for long times (72 hr) posed problems with respect to losses and oxidation of activators. In this case, the refiring was done in sealed evacuated silica tubes, the quantity of NH_4Cl being limited to provide approximately 1 atm pressure at 1150°C. After firing, the phosphors were re-screened and washed in a solution of 0.5*M* ethylene-diamine tetraacetic acid (EDTA) (6, 7) in 4*M* NH_4OH at boiling temperature for 15 min, washed with water followed by alcohol, and dried.

Brightness readings were performed with a Spectra Brightness Spot Meter on samples prepared in aluminum plaques. Maintenance was determined by irradiating the plaques in close proximity to a quartz low-pressure mercury vapor lamp in a N_2 atmosphere for 100 hr, and repeating the brightness readings. Crystallographic data were obtained on a Philips x-ray diffractometer operated at 35 kv and 15 ma, using a Cu target and Ni filter.

Results

Calcium chloroapatite.—The molar proportion of apatite/flux was arbitrarily defined in terms of the ratio of Ca^{2+} present in either of the two components, so that a mixture of $1Ca_5(PO_4)_3Cl + 5CaCl_2$ is considered equimolar (1/1). Microscopic examination of material crystallized at 1150°C for 2 hr showed needles predominant at 30-50% apatite, and short hexagonal prisms at higher apatite concentrations. The largest prisms were obtained at 70-80% apatite. At 75% apatite and 1050°C and short firing times, the largest apatite crystals (50-80μ) resulted, but with numerous inclusions and surface imperfections. Higher or prolonged heating caused at first a considerable reduction in particle size (10-30μ) followed by a slight increase, while the general appearance of the crystals was continually improved. One-half mole batches with apatite/flux = 7/3, crystallized at 1050°C for 16 hr yielded well-crystallized $Ca_5(PO_4)_3Cl$ of considerably larger particle size. Figure 1 shows photomicrographs of this type, a crystal in the upper right hand corner illustrating the growth habit. The diamond-type platelet near top center occurs only rarely. At bottom center we note a crystal with a typical inclusion, often appearing in elliptical form. Focussing of the two crystals on the right was chosen to show typical surface defects appearing in the form of raised ridges, predominantly on larger particles.

Calcium chlorofluoroapatite.—Figure 2 shows the partition of F between apatite and flux as obtained by

[1] Based on a molecular weight of $Ca_5(PO_4)_3F_{0.9}Cl_{0.1}$ = 505.95, this corresponds to addition of 0.088 Mn^{2+} and 0.137 Sb^{3+}/5 Ca^{2+}. Based on 3 P, after adjustment of stoichiometry by $(NH_4)_2HPO_4$ addition, these figures are somewhat reduced.

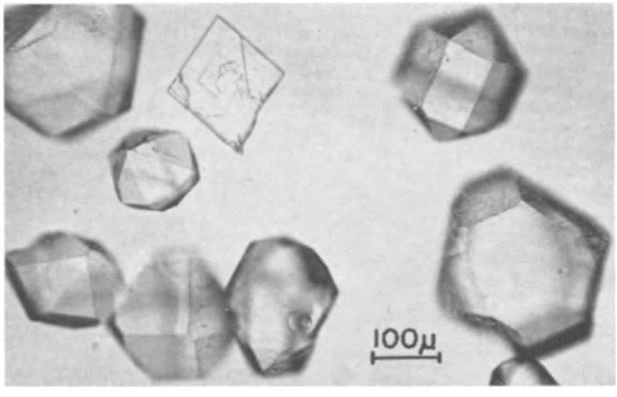

Fig. 1. $Ca_5(PO_4)_3Cl$ crystallized in 0.5 mole quantity from $CaCl_2$ at 1050°C, 16 hr, apatite/flux = 7/3 in terms of Ca^{2+} present in either phase.

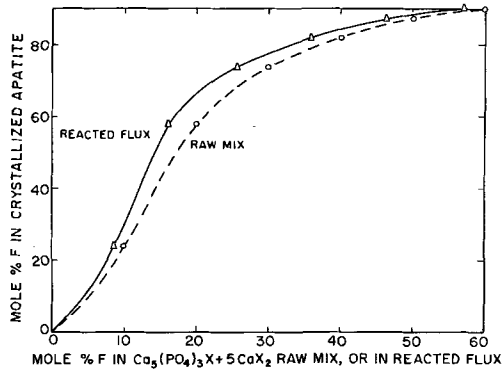

Fig. 2. Atom per cent F in crystallized apatite as a function of atom per cent F in raw materials with apatite/flux = 1/1 (dashed curve), and resulting in atom per cent F in reacted flux (drawn curve). The latter values are calculated from analyses of apatites and accounting for total Ca-halides present.

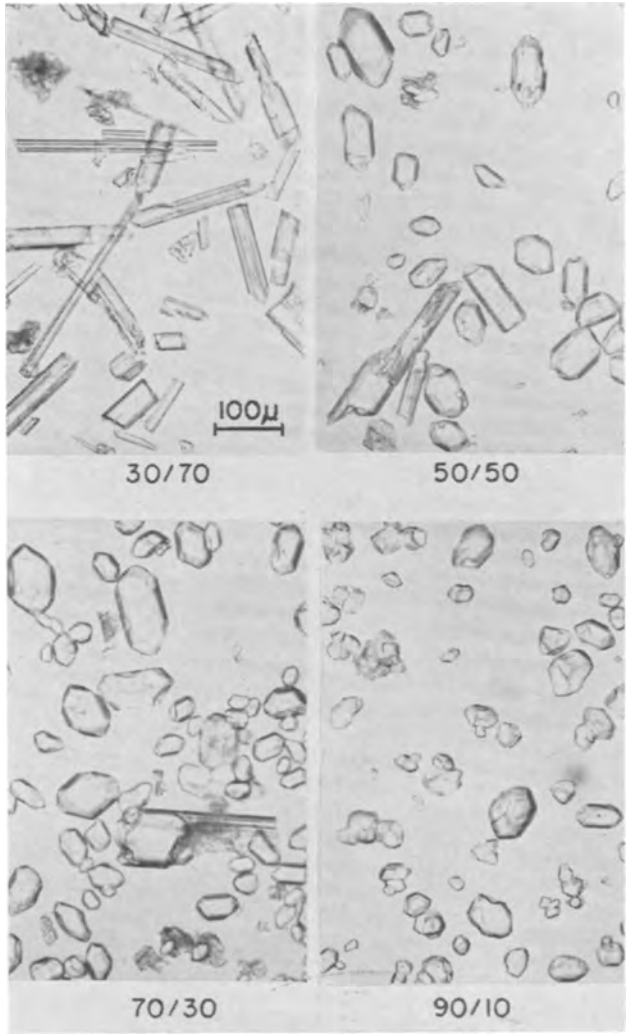

Fig. 3. Growth habit of $Ca_5(PO_4)_3F_{0.9}Cl_{0.1}$ crystallized from $0.57CaF_2 + 0.43CaCl_2$ as a function of apatite/flux ratio, expressed as per cent of total Ca^{2+} present in either phase.

crystallizing mixtures of [$Ca_5(PO_4)_3Cl$ + $5CaCl_2$] and [$Ca_5(PO_4)_3F$ + $5CaF_2$] in different ratios. The dashed curve is based on composition of the starting materials (apatite/flux = 1/1) while the drawn curve represents the composition of the reacted flux as obtained by difference and is therefore applicable for all apatite/flux ratios, assuming that the apatite "sees" only the composition of its immediate environment. For purposes of phosphor preparation, a F/Cl ratio of 9/1 was of particular interest, and we note this composition to be stable in equilibrium with $0.57CaF_2$ + $0.43CaCl_2$. The preferred incorporation of F into the apatite is fortunate inasmuch as leaching of the reacted melt depends on the solubility of the $CaCl_2$ and therefore becomes increasingly difficult with increasing CaF_2 concentration.

The influence of the apatite/flux ratio on the growth habit of $Ca_5(PO_4)_3F_{0.9}Cl_{0.1}$, crystallized in different proportions of $0.57CaF_2$-$0.43CaCl_2$ flux is shown in Fig. 3 and closely resembles the effect observed for $Ca_5(PO_4)_3Cl$, except that in the present case, especially at low apatite concentrations, one also notes small aggregates of finely divided matter which are optically isotropic and probably consist of CaF_2. The prismatic form of apatite is slightly more elongated than that of $Ca_5(PO_4)_3Cl$. Toward higher apatite concentrations, the needle form diminishes in frequency, occasionally growing out of prismatic crystals as shown for two instances in the intermediate concentration ranges. At 90% apatite, needles are essentially absent and contamination by CaF_2 is noted only rarely. However, the particle size is reduced and the crystal faces appear more distorted, often resembling conchoidal fractures. At this point, owing to the preponderance of insoluble matter, the crystallized mass is also already more difficult to leach. For practical purposes, an apatite/flux ratio of 8/2, *i.e.*, $1.6Ca_5(PO_4)_3F_{0.9}Cl_{0.1}$ + $1.14CaF_2$ + $0.86CaCl_2$ was found to be a good compromise.

Preparation of larger batches was modified in accordance with the following observations: (*A*) Analyses of apatites often showed a considerable deficiency in P, *i.e.*, a high Ca/P ratio, possibly owing to CaF_2 contamination. Substitution of some of the raw material apatite by $Ca_2P_2O_7$ [2] helped to approach theoretical stoichiometry, as well as to promote crystal growth. (*B*) The 9F/1Cl apatite grows best at 1250°C [3] which during a 16-hr run, causes some loss of $CaCl_2$ by evaporation. The initial composition, therefore, has to be adjusted empirically. (*C*) Addition of $CaCl_2$ in the form of Ca_2PO_4Cl was found to be more convenient than $CaCl_2$ itself which is hygroscopic and often of questionable purity. Decomposition temperatures of Ca_2PO_4Cl of 945°C (1) and of 1040°C (3) have been reported. Present observation of Ca_2PO_4Cl formed at 1000°C support the latter figure.

Table I shows analytical data for a number of lots of $Ca_5(PO_4)_3F_{0.9}Cl_{0.1}$ prepared in this manner.[4] Analyses of the first two samples show high figures for Cl, F, and Ca; the remainder merely indicate high Ca and low P content. All of this suggests contamination by some Ca halide which is reasonable in view of the likelihood of residual flux occlusion.

Particle size increases primarily with firing temperature. The effect of batch size and firing time is much smaller. Increased firing time tends to decrease the amount of fines (10-20μ) as well as decreases the amount of visible crystal imperfections. Cooling was rapid in all cases and its contribution to crystal growth

[2] The reaction of $Ca_2P_2O_7$ and CaF_2 (forming apatite) has been described by Rabatin and Gillooly (8).

[3] This may also hold for $Ca_5(PO_4)_3Cl$, but was found unnecessary and inconvenient owing to extensive volatilization of $CaCl_2$. For this reason, temperatures above 1250°C were not employed.

[4] For a theoretical yield of 247.4g $Ca_5(PO_4)_3F_{0.9}Cl_{0.1}$ (slightly less than 0.5 moles because of $Ca_2P_2O_7$ substitution), a suitable raw material composition consisted of 97.2g $Ca_5(PO_4)_3F$ + 26.7g $Ca_2P_2O_7$ + 150.3g Ca_2PO_4Cl + 37.9g CaF_2.

Table I. Analytical data on 0.5-mole batches of crystallized $Ca_5(PO_4)_3F_{0.9}Cl_{0.1}$

Batch No.	Yield		Analyses in w/o			
	Grams	%	Ca^{2+}	PO_4^{3-}	Cl^-	F^-
1	247.5	100	39.9	55.5	0.82	3.85
2	242.5	98	39.9	55.8	0.84	3.64
3	244.9	99	40.13	55.94	0.70	—
4	242.3	98	40.0	55.9	0.72	—
5	240.7	97	39.8	55.9	0.67	—
6	230.7	93	39.8	56.0	0.63	—
Theory	247.4	(100)	39.61	56.31	0.70	3.38

is questionable. Figure 4 shows the particle size distribution, as determined by screening, of typical 0.5 mole lots of $Ca_5(PO_4)_3Cl$ crystallized 16 hr at 1050°C (Fig. 1) and of $Ca_5(PO_4)_3F_{0.9}Cl_{0.1}$ crystallized 16 hr at 1250°C.

Phosphors.—Activation of $Ca_5(PO_4)_3Cl$ was limited to relatively short firing periods with fixed phosphate additions designed to adjust the stoichiometry of the phosphors to a metal/phosphorus (M/P) ratio of about 4.9/3. Emission colors ranged from relatively bluish-pink to orange, and close to the black body locus (9, 10), and brightness values ranged between 80 and 90% of N.B.S. standard No. 1031.

Activation of $Ca_5(PO_4)_3F_{0.9}Cl_{0.1}$ was performed with varying PO_4^{3-} additions and refiring times. With nominal additions, a minimum of 4 hr was generally found necessary to obtain good output. Losses of Sb^{3+} as well as oxidation of Mn^{2+} to Mn^{3+} (11, 12) (the latter noted to occur more readily at low M/P ratios) was avoided by conducting the prolonged (72 hr)

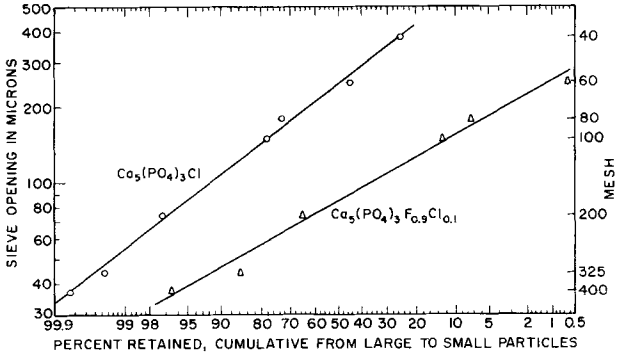

Fig. 4. Particle size distribution of $Ca_5(PO_4)_3Cl$ shown in Fig. 1 and of $Ca_5(PO_4)_3F_{0.9}Cl_{0.1}$ crystallized in 0.5 mole quantity from $0.57CaF_2$ + $0.43CaCl_2$ (apatite/flux = 8/2) at 1250°C, 16 hr.

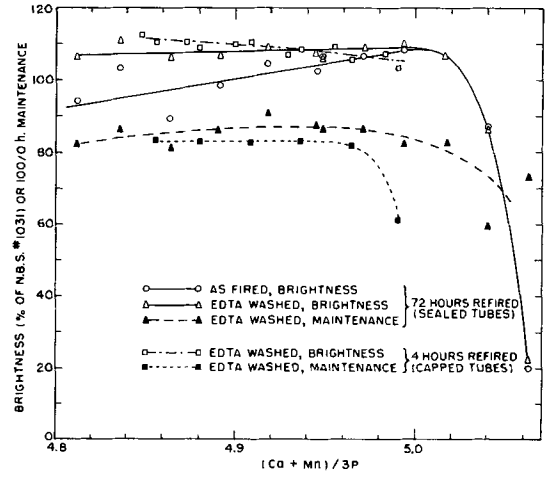

Fig. 5. Brightness and maintenance of phosphors as a function of stoichiometry. Under present conditions, the maintenance of NBS 1031 was 88%.

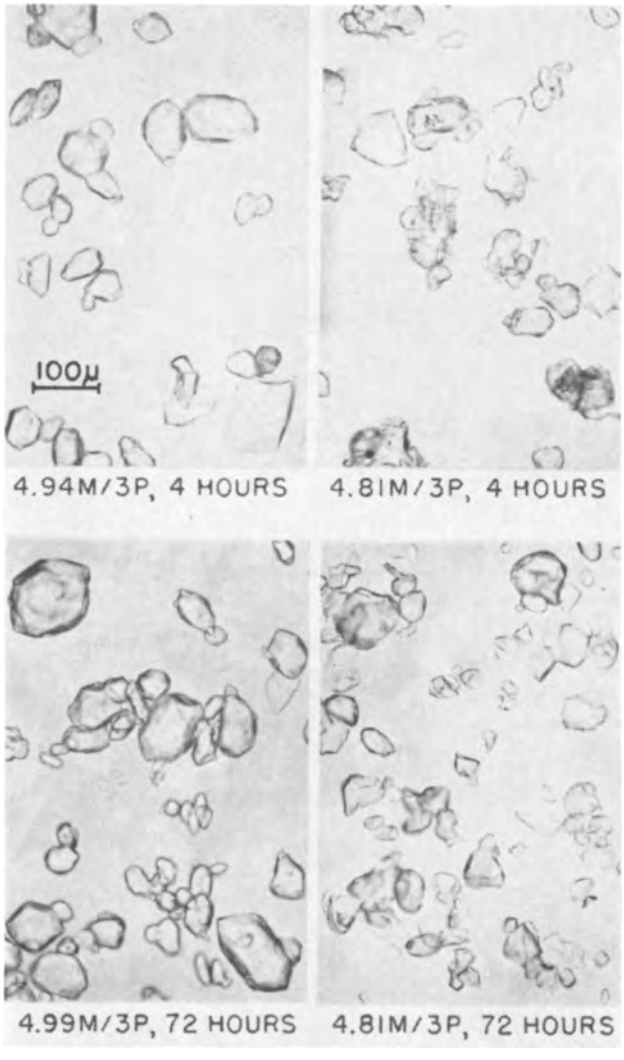

Fig. 6. Appearance of phosphors resulting from different $(NH_4)_2HPO_4$ additions (expressed as M/P ratio) and different firing times at 1150°C.

firing in sealed tubes as described. Figure 5 shows brightness and maintenance data on two series of phosphors (representing two firing times and methods) as a function of phosphor stoichiometry. We note that the output of phosphors activated by firing for 72 hr goes through a maximum at 5M/3P and is therefore in agreement with a theory to this effect proposed by Ouweltjes and Wanmaker (13) as well as calculations reported by Gillooly, Rabatin, and Vincent (14). On the other hand, phosphors activated for 4 hr improve at higher phosphate additions. We also note that differences due to EDTA washing decrease as the phosphor stoichiometry approaches the theoretical value and it therefore appears that this effect is connected with removal of an inert PO_4^{3-}-rich surface layer. Depreciation under ultraviolet irradiation was accompanied by development of yellow body color due to color center formation (15, 16) which decreased with M/P ratio (17). Depreciation of phosphors prior to EDTA washing (not shown) was severe and accompanied by black discoloration which increased with decreasing M/P ratio, *i.e.*, opposite to the observed dependence of the yellow discoloration. The maintenance of standard Ca-halophosphate phosphor N.B.S. No. 1031, under the same conditions, was 88%.

With increasing phosphate addition, sintering and attack of the apatite crystals increases. Attempts to circumvent this by using $SbPO_4$ and $Mn_2P_2O_7$ instead of $(NH_4)_2HPO_4$ (and the equivalent amounts of the respective oxide and carbonate) were of questionable value. Longer firing periods, however, did result in somewhat more friable products and also tended to eliminate small surface irregularities caused by high phosphate addition, but caused no actual re-crystallization. Figure 6 shows these effects on a group of typical phosphors representing short and long firing times as well as low and high excess phosphate additions. One of the photomicrographs (4.94M/3P, 4 hr) shows a rarely occurring plate-type crystal in the lower right-hand corner. It can be seen that at low M/P ratios, corrosion of the crystal surfaces is severe, while at high ratios (low phosphate additions), the original morphology is well preserved. In the latter case, it was also found that the particle size distribution remained the same as that shown for unactivated $Ca_5(PO_4)_3F_{0.9}Cl_{0.1}$ in Fig. 4.

Incorporation of Cd (17, 18) was attempted during the growth of raw material apatite by replacing a portion of the CaF_2 by CdF_2 in varying amounts up to 10 a/o (atom per cent) substitution based on total Ca^{2+}. However, analyses showed that at the highest concentration, only about 0.1 a/o Cd entered the apatite. Cd added with activators had no effect on output, but slightly improved maintenance and eliminated discoloration of 72-hr fired phosphors. Four-hour (air) fired phosphors were severely degraded, probably owing to retention of an ultraviolet absorbing Cd-rich surface layer.

The extent of activator incorporation was investigated by etching phosphors in 3*N* HCl at room temperature. Details on the preparation of samples taken for this purpose are summarized in Table II. The depth of etching was calculated on a IBM 1401 computer on the basis of the weight loss of material assumed to be spheres with particle size distribution equal to that of the raw material apatite (Fig. 4). For sample 4 (from −400 mesh apatite) a particle size distribution corresponding to the same slope but including only the range of 10-37μ (400 mesh) was con-

Table II. Phosphors examined by etching; all are EDTA-washed

Sample	Refiring					Removed by etching		
No.	x(Ca + Mn)/3P	Amt, g	Cont.*	Atm.	Time, hr	w/o	μ	Remarks
1	4.81	2	CT	Air	4	64.5		
2	4.81	150	CC	Air	4	65.8		
3	4.81	150	CC	Air	20	74.7		Refired 1.5 hr with 1.8% Sb_2O_3**
4	4.81	80	CC	Air	72	76.8	5.9	From −400 mesh fraction apatite; also refired as above.
5	4.81	2	ST	Vac.	72	57.6		
6	4.92	2	ST	Vac.	72	50.4		
7	4.99	2	ST	Vac.	72	56.9	10.1	
8	5.06	2	ST	Vac.	72	55.6	9.7	
9	4.99	200	CT	N_2	72	85.0	22.1	Phosphor prepared with 0.059 Cd^{2+}/3P (1.3 w/o Cd), replacing Ca^{2+}.
10	Pooled material from 4.84 to 5.02 M/3P (Fig. 5)					83.7	21.2	

* CT, capped tube; CC, covered crucible; ST, sealed tube.
** These firings conducted after those shown in the table and designed to restore Sb lost on prolonged air firings.

Table III. Mn^{2+}, Sb^{3+}, and PO_4^{3-} in weight per cent as a function of etching

Sample No.	Core			Outer layer			Ratio		
	Mn	Sb	PO_4	Mn	Sb	PO_4	Mn	Sb	PO_4
1	0.58	0.028	56.3	0.97	0.235	58.0	0.60	0.12	0.97
2	0.46	0.034	—	1.07	0.078	—	0.43	0.46	—
3	0.82	0.125	—	0.94	0.175	—	0.875	0.715	—
4	0.64	0.047	—	0.80	0.19	—	0.80	0.25	—
5	0.88	0.37	—	0.77	1.05	—	1.14	0.35	—
6	0.75	0.48	—	0.78	0.94	—	0.96	0.51	—
7	0.70	0.10	—	0.75	1.02	—	0.935	0.098	—
8	0.12	0.008	—	0.85	0.032	—	0.14	0.25	—
9	0.79	0.034	55.4	0.92	0.26	55.6	0.86	0.13	0.996
10	—	—	55.3	—	—	55.9	—	—	0.99

Note: Sample 9 analyzed 0.56% Cd (core) and 1.02% Cd (outer layer), ratio = 0.55

sidered applicable.[5] The figures represent maxima because for real particles whose surface area is larger than that of spheres, the actual depth is correspondingly smaller. For larger phosphate additions (lower M/P ratios), corrosion of crystals was too severe to allow this approximation and no data of this nature were computed. Table III shows analyses which indicate the presence of concentration gradients of components added prior to the activation step. Analyses for total Sb in unetched phosphors ranged in the neighborhood of 1 w/o; however etching causes an apparent enrichment by (insoluble) Ca-antimonate, and therefore data on Sb analyses are confined to the trivalent (soluble) portion. With one exception (sample 3) the concentration gradient of Sb^{3+} is quite high, showing relatively small amounts in the interior of the particles. Comparison of samples 1 and 2 show that this is further increased for small sample sizes where contact with the atmosphere is more extensive, and samples 5 through 8 show that PO_4^{3-} appears to promote the migration of Sb to the interior. The incorporation of Mn is generally more rapid than that of Sb and is similarly promoted by PO_4^{3-} as well as by extended firing time (samples 2 and 3). The single instance in which Cd was determined indicates more limited incorporation compared to Mn; moreover this observation is supported by those previously mentioned concerning Cd. Ratios in PO_4^{3-} content are necessarily close to unity, since total phosphate greatly exceeds the portion subsequently added. Owing to activator content, the amount of phosphate present can be lower than that corresponding to stoichiometric $Ca_5(PO_4)_3F_{0.9}Cl_{0.1}$ (56.31%), but the analyses suffice to suggest the presence of a concentration gradient of this component as well.

[5] Owing to the large surface area of this phosphor, even the large phosphate addition employed resulted in little corrosion of the crystals.

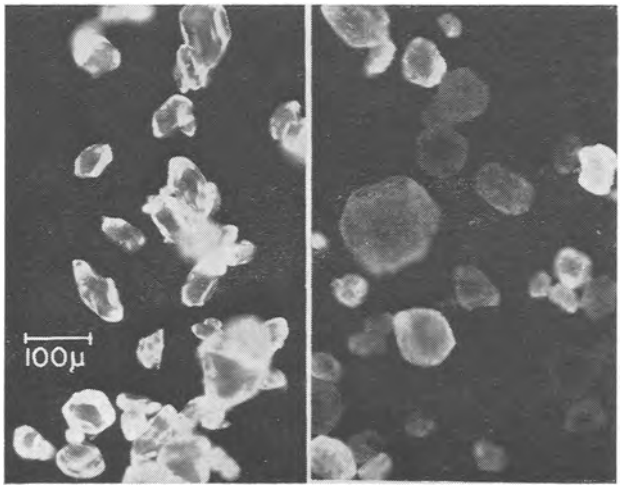

Fig. 7. Fluorescence of sample 10 (Table II) before and after etching in 3N HCl. The extent of etching was chosen so as to obtain an appreciable range of emission intensities; left, unetched; right, etched.

The process of etching is accompanied by a reduction in light output, more so in thin than in thick layers. Figure 7 shows the fluorescence of a thin layer of sample 10 prior to and after etching. Although these photomicrographs were difficult to obtain with all particles in sharp focus, the following observations can be made: (*A*) All of the unetched particles show about equal fluorescence which is principally noted at edges, corners, and surface irregularities. (*B*) The fluorescence of etched particles shows varying degrees of attenuation, ranging from occasional brightly emitting to completely nonluminescent crystals, the latter dimly outlined by illumination from the surrounding field. The roughened surfaces emit more or less uniformly and, in some cases, a fine structure, presumably an etch pattern, can be discerned. (*C*) There is no apparent relationship between size or shape and the luminescence intensity of etched particles. (*D*) Visually, it was noted that occasional crystals showed the characteristic green emission associated with compounds of Sb^{5+}, identified as fluoromeite (19), or Ca-antimonate or fluoroantimonate (11). It was interesting to note that etched crystals showing this effect appear uniformly green luminescent over the entire surface without being otherwise distinguishable (by shape or size) from neighboring white or nonluminescent crystals. Only after complete solution of the apatite does the Ca-antimonate appear in the form of small and irregularly shaped fragments. In the present materials, the effect of a high M/P ratio, oxygen, and limited firing schedule in promoting the formation of this phase (7, 20, 21) was very pronounced. Thus, in 4-hr air-fired phosphors with 4.94M/3P, green emitting crystals were abundant, a very small amount being visible even prior to etching, while in 72-hr sealed tube fired phosphors these were rare and revealed only on etching. Finally in both cases, the amount of green emitting matter rapidly diminished with increasing $(NH_4)_2HPO_4$ added prior to firing.

The spectral distribution of emission of etched phosphors, taken in 2 mm deep plaques, differs from that of the original phosphors by a reduction of the orange (Mn) band by about 10 to 20%, and a smaller reduction of the blue (Sb) band. The extent of reduction of crange emission increases with increasing relative orange emission of the unetched phosphor which, in turn, is a function of its previous history. Table IV illustrates this on a number of phosphors arranged in

Table IV. Emission characteristics of phosphors prior to and after etching

Sample No.	Ratio of emission peak heights (Mn/Sb) Original	Etched	Ratio
2	3.28	2.34	0.715
3	2.78	2.03	0.73
1	2.38	1.95	0.82
9	2.17	1.91	0.88
4	1.66	1.73	1.04

Table V. X-ray powder diffraction data on flux-grown apatites and phosphors

Cl-apatite unactivated			9F/1Cl apatite				Ca-halophosphate phosphor NBS No. 1031	
			Unactivated (Batch 6, Table I)		Activated (Sample 9, Table III)			
hkl	d in Å	I	hkl	d in Å	I	d in Å	I	d in Å	I
100	8.30	8	100	8.11	35	8.11	10	8.11	6
101	5.24	7	101	5.24	5	5.24	6		
			200	4.06	34	4.06	13	4.05	7
			111	3.87	6	3.86	7		
201	3.54	5	002	3.43	29	3.43	26	3.43	26
002	3.37	16						3.32*	5
								3.21*	4
210	3.15	7	102	3.16	11	3.16	8	3.16	10
			201	3.07	20	3.07	13	3.07	15
				3.00**	6				
211	2.85	56	211	2.80	76	2.80	70	2.80	70
300, 112	2.77	79	112	2.77	35	2.77	29	2.77	29
			300	2.71	408	2.71	90	2.71	51
202	2.62	9	202	2.62	21	2.62	25	2.62	21
212	2.31	22	212	2.29	5	2.28	6	2.29	6
			310	2.26	22	2.25	32	2.25	19
			221			2.21	5		
311	2.18	6	311			2.15	5	2.14	5
			400	2.034	12				
			203					1.994	5
222	1.959	23	222	1.938	30	1.936	17	1.938	20
312	1.905	6	312	1.884	6	1.883	11	1.886	10
213	1.833	20	213	1.836	13	1.835	21	1.836	22
410	1.819	10	321	1.801	8	1.799	13	1.799	11
402	1.776	5	410	1.776	20	1.773	9	1.775	11
			402	1.748	5	1.748	6	1.751	11
004	1.688	7	004	1.720	9	1.714	8	1.719	9
			322			1.638	6	1.639	6

* Probably $Ca_2P_2O_7$ ASTM No. 9-345 d = 3.30 (100), 3.21 (90).
** Probably $Ca_2P_2O_7$-I ASTM No. 2-0647 d = 3.00 (100).

decreasing relative intensity of the orange band. This correspondence indicates that these differences between samples arise mainly from differences in the concentration gradient of Mn. It can also be seen that longer firing times or smaller particle size causes a shift in emission color toward the blue, undoubtedly by promoting the migration of originally high surface concentrations of Mn toward the interior. Unfortunately, a quantitative correlation of relative peak heights and Mn content (Tables IV and III) is usually not very satisfactory by virtue of the appreciable influence of Sb content which, depending on firing conditions, could vary over a wide range.

Table V shows x-ray powder diffraction analyses of prism-type apatites and of a typical phosphor (sample 9), ground to pass 400 mesh. In order to enable direct comparison, the usual normalization to 100 for the strongest reflection in each sample was omitted. It can be seen that in spite of the extensive grinding, the reflection intensities of the unactivated apatites for the 100, 200, 300, and 400 planes were all very high, indicating a high degree of preferred orientation for these planes. A slight degree of orientation is still retained in the activated apatite when compared with the standard (N.B.S. 1031) Ca-halophosphate phosphor. Microscopic comparison of the unactivated and activated apatites (unground) under polarized light revealed no significant differences; the crystal planes in both samples show uniform extinction colors. This indicates that the activation step did not introduce random orientation within individual particles.

Discussion

Uniform incorporation of activators into a matrix whose average particle size is much larger than that of the conventional Ca-halophosphate phosphors is expected to proceed more slowly, and one also expects that under these conditions a greater proportion of Sb is lost through volatilization as halides or oxidation, even during the preliminary 1-hr prefiring step. Thus, we note the amount of Sb^{3+} incorporated in 72-hr sealed tube fired phosphors averaged 1 w/o in a surface layer not exceeding 10μ, and less than half of that for the cores. For the outer layer, the figure is in fair agreement with values of Sb^{3+} incorporation reported by Ouweltjes and Wanmaker (13). Inasmuch as the output of Ca-halophosphate phosphors does not decrease very sharply until the Sb concentration drops below about 0.25% (19), it is likely that the sharp concentration gradient of Sb^{3+} in the phosphors does not interfere with output for an appreciable portion of the crystal volume.

The presence of nonluminescent crystals in etched samples is related to the rate of migration of activators, particularly Sb^{3+} which, even during a 72-hr firing period is severely limited. This is evidenced by the generally low figures of Sb^{3+} in cores especially as the M/P ratio approaches 5/3 (Table III, samples 7, 9). While this condition is favored by high M/P ratios which causes oxidation to Sb^{5+} as mentioned, it has also been observed on etched phosphors prepared with large excess phosphate additions, although to a lesser extent.[6] The observation that reduction in luminescence intensity, as a result of etching, is less pronounced if the comparison is made on thick layers, suggests that the nonluminescent cores also have correspondingly low absorption in the ultraviolet. This is, of course, consistent with the analytical results for Sb^{3+} which is primarily responsible for absorption at 254 nm in this system (5).

Inspection of Fig. 5 shows that the output and maintenance of the present phosphors can approach values for modern conventional (powder) phosphors prepared with similar activator concentrations, although different with respect to particle size, homogeneity, crystal habit, as well as total Sb^{3+} content. For optical reasons however, this requires that they be viewed in layers which are considerably deeper, in fact which indicates that the absorption for 254 nm radiation of the luminescent portions is no higher (and, owing to low Sb^{3+} concentration, probably worse) than in powder phosphors. Moreover, the luminescent layer itself is heterogeneous with respect to relative height of the two emission bands. This means that high output (presently measurable only in plaques) has been brought about by viewing the summed light emitted by materials of which only a portion constitutes an efficient phosphor, while other portions contribute little or no radiation. From this, it may be concluded that at

[6] The mechanism whereby excess phosphate promotes the incorporation of activators is, of course, further aided by crystal corrosion (Fig. 6) which decreases the average particle size and greatly increases the surface area of the host material.

least within certain limits, the quantum efficiency of Ca-halophosphates is independent of Sb and Mn concentration.

The scope of the present study did not include x-ray diffraction analyses and activation of the needle-type form of apatite crystals, as prepared by present methods. Results of such further investigations will be reported separately.

Acknowledgments

The writer wishes to thank Miss I. Walinski for phosphor preparation and measurements, Mr. R. Farnum for chemical analyses, Dr. C. K. Lui Wei for x-ray powder diffraction analyses, Messrs. M. Barrick and C. Dawley for assistance in obtaining photomicrographs, and Mr. G. Hagen for computer programming. He is also grateful to Mr. R. C. Ropp and Dr. W. A. Thornton for valuable discussions.

Manuscript received Sept. 8, 1965; revised manuscript received November 9, 1965.

Any discussion of this paper will appear in a Discussion Section to be published in the December 1966 JOURNAL.

REFERENCES

1. R. D. Morton, *Norsk Geol. Tidsskr.*, **41**, 223 (1961).
2. R. Klement and R. Harth, *Chem. Ber.*, **94**, 1452 (1961).
3. R. Nacken, *Zentr. Mineral. Geol.*, **1912**, 545-599.
4. G. A. Bukhalova and A. G. Bergman, *Doklady Akad. Nauk, SSSR*, **66**, (1), 69 (1949). See "Phase Diagrams for Ceramicists," Fig. 1648.
5. P. D. Johnson, *This Journal*, **108**, 159 (1961).
6. W. C. Martyny, Canadian Pat. 679,905, Feb. 11, 1964.
7. D. Robbins, Electrochem. Soc. Electronics Div. Enlarged Abstracts, **11** [1], 31 (1962).
8. J. G. Rabatin and G. R. Gillooly, *This Journal*, **112**, 489 (1965).
9. M. Doherty and W. Harrison, *Brit. J. Appl. Phys.*, Suppl. 4, 1955.
10. R. F. Quirk and M. J. B. Thomas, Electrochem. Soc. Electronics Div. Enlarged Abstracts, **13** [1], 32 (1964).
11. W. L. Wanmaker, A. H. Hoekstra, and M. G. A. Tak, *Philips Research Repts.*, **10**, 11 (1955).
12. J. G. Rabatin and G. R. Gillooly, *This Journal*, **111**, 542 (1964).
13. J. L. Ouweltjes and W. L. Wanmaker, *ibid.*, **103**, 160 (1956).
14. G. R. Gillooly, J. R. Rabatin, and T. C. Vincent, Canadian Pat. 692,046, August 1964.
15. L. Suchow, *This Journal*, **108**, 847 (1961).
16. J. H. Singleton and L. Suchow, Electrochem. Soc. Electronics Div. Enlarged Abstracts, **11** [1], 37 (1962).
17. E. F. Apple, *This Journal*, **110**, 374 (1963).
18. M. A. Aia and S. M. Poss, U. S. Pat. 2,965,786, 1960.
19. K. H. Butler, M. J. Berg, and V. M. B. Hannaford, *This Journal*, **97**, 117 (1950).
20. W. L. Wanmaker, *J. Phys. Radium*, **17**, 636 (1956).
21. H. Weitzmann and J. Fussel, Tagung der Physikalischen Gesellschaft in der Deutsehen Demokratischen Republik, Greifswald, April 26-29, 1959, pp. 47-76.

Preparation and Photoluminescence of Silicon Carbide Phosphors Doped with Group IIIa Elements and/or Nitrogen

Arrigo Addamiano

Lamp Research Laboratory, General Electric Company, Nela Park, Cleveland, Ohio

ABSTRACT

Silicon carbide phosphors were prepared by firing in an atmosphere of argon containing a trace of nitrogen mixtures of semiconductor grade silicon and spectroscopically pure graphite to which a trace of group IIIa element was added. Room temperature photoluminescence was observed only with boron doping. Doping with other group IIIa elements resulted in low-temperature phosphors, whose brightness had not quite reached peak values at 77°K.

In the past few years and particularly since the advent of the Lely method for growing single crystals of silicon carbide (1), interest in the physical properties of silicon carbide has steadily grown (2). Recently attention was drawn on the luminescent properties of silicon carbide. Lely and Kröger (3) reported luminescence over all the visible spectrum at 77°K in single crystal α-SiC. The temperature dependence of the luminescence of commercial α-SiC crystals was investigated by Gorban' and Rud'ko (4). Yellow luminescence in natural α-SiC discovered in Bohemia was observed by Bauer, Fiala, and Hrichovà (5). The low-temperature photoluminescence of nitrogen-exciton complexes in high-purity single crystal SiC was investigated in detail for seven SiC polytypes by Choyke, Hamilton, and Patrick (6-10). Room temperature luminescence in α-SiC single crystals containing grown p-n junctions with B and N dopants was investigated by Addamiano, Potter, and Ozarow (11). More recently relationships between band gaps and luminescence in different SiC polytypes doped with boron were reported independently by Addamiano (12) and Kholuyanov (13). It seems likely that the mechanism of light emission in different B-doped SiC polytypes is very much the same. The nature of the luminescence center, however, is not yet known in detail. What is known from x-ray (1) and E.S.R. studies in α-SiC single crystals (14, 15) is that both B and N substitute for C in the lattice of SiC.

We thought that a comparison with other SiC phosphors containing group IIIa activators might help improve our understanding of SiC as a luminescent material. In this paper we describe their preparation and some of their properties.

Experimental

Because of the availability of "semiconductor grade" silicon and of "spectroscopically pure" graphite the preparation of SiC phosphors is a relatively simple one. The metal dopants (B,Al,Ga,In) were usually added to graphite powder in the form of a dilute solution, to make a paste, which was dried under i.r. heat. The doped graphite was then blended with a fine powder of silicon, usually in stoichiometric ratios. The mixture was transferred to a crucible of spectroscopically pure graphite and fired at the desired temperature in a graphite tube furnace in a controlled atmosphere, usually argon containing a trace of nitrogen. Temperatures of 2350°-2500°C were preferred for the synthesis of α-SiC phosphors, while temperatures around 2000°C were used for the preparation of β-SiC phosphors. Firing times ranged from 15 min to 2 hr follow-

ed by quenching.[1] With the furnace cool the charges were extracted, and excess unreacted graphite, mainly from the crucible walls, was eliminated by 900°C firing in air. The SiC so obtained was further treated with "white etch" (*i.e.*, $HF+HNO_3$) to remove oxide layers, if any. Finally it was washed and dried.

The products resulting from high temperature, *e.g.*, 2500°C, firing were coarse green powders. Firing at 2000°C resulted in relatively fine powders of yellow-green color. Luminescence depended on doping level. The best results were obtained with metal doping levels typical of ZnS-type phosphors, *e.g.*, 5 x 10^{-4} Al/SiC.

The metal doping had to be compensated or slightly more than compensated with nitrogen to produce materials with light body color and luminescence. Operating in a static atmosphere and using a charge of 10g, good results were obtained by exhausting the furnace (volume *circa* 10 liters), leaking in enough N_2 to establish a pressure of ~0.5 Torr then adding 99.999% pure argon to a final pressure of 5 psig at r.t. and firing. Similar results were obtained by flowing through the furnace a mixture of Ar + N_2 in the approximate ratio 1000:1. Preparations in the absence of nitrogen resulted in nonfluorescent materials with the dark color typical of p-type SiC. On the other hand a high partial pressure of nitrogen also resulted in materials of dark body color, with stabilization of the cubic, β-SiC, phase to very high temperatures (16). In some experiments BN was added to Si and C to supply the necessary doping, or B_4C + Si_3N_4 were used. The first outlined method, however, was preferred, insofar as more homogeneous products were obtained.

Optical measurements.—For the optical measurements a sample from each preparation was reduced to a very fine powder by vigorously shaking in a plastic vial containing a plastic sphere with the sample.[2] Contamination from the plastic were eliminated by 600°-700°C firing in air, followed by a short treatment with "white etch" washing and drying.

The emission spectra in the visible were measured using a grating monochromator in connection with a calibrated 1P22 phototube. The data were extended to 1.0μ using a Perkin-Elmer double pass monochromator with NaCl prism and a calibrated i.r. Du Mont 6911 photomultiplier.

With the exception of β-SiC:B,N, which has room temperature luminescence, all the powders were cooled to 77°K. Good thermal contact with the sample holder was insured by the use of a thin coating of Viscasil 10,000, a high viscosity, practically nonfluorescent silicone compound.[3] For the excitation we used a General Electric AH-6 high-pressure mercury lamp. The broad beam produced was confined to a region close to 3650Å by filtering through Corning 7-37 filters and through a solution of $CuSO_4$-$CoSO_4$ in water.

The photoluminescence spectra of the materials investigated are shown in Fig. 1.

Discussion

We summarize the results of our investigations on SiC phosphors in Table I, which includes some of the data published in a previous work (12).

As predicted in (12), β-SiC:B,N did show room temperature luminescence with a peak at 1.49 ev, in good agreement with the expected value, 1.48 ev. All the other SiC phosphors prepared in the course of the present investigation, both cubic and hexagonal, showed luminescence only at low temperature and in a region of the visible spectrum closer to the band edge than for SiC:B,N phosphors. The behavior is probably related to differences in the depth of the acceptor centers. The depth of the boron level in α-SiC as given by Lomakina (17) is $E_B = 0.39 - 5.5 \times 10^{-8} \sqrt[3]{N_D}$ ev. Of the other group IIIa elements only the depth of the aluminum level is known (3, 18, 19), with a value of 0.27 ev. From the shift in the position of the peak of luminescence in α-SiC:Al,N; α-SiC:Ga,N and α-SiC:In,N the depth of the Ga and In levels can be estimated to be ~0.23 and ~0.12 ev, respectively.

The α-SiC phosphors doped with group IIIa elements other than boron were brighter than the corresponding β-SiC phosphors. Measurements of brightness *vs.* temperature showed that their brightness has not yet reached peak values at 77°K.

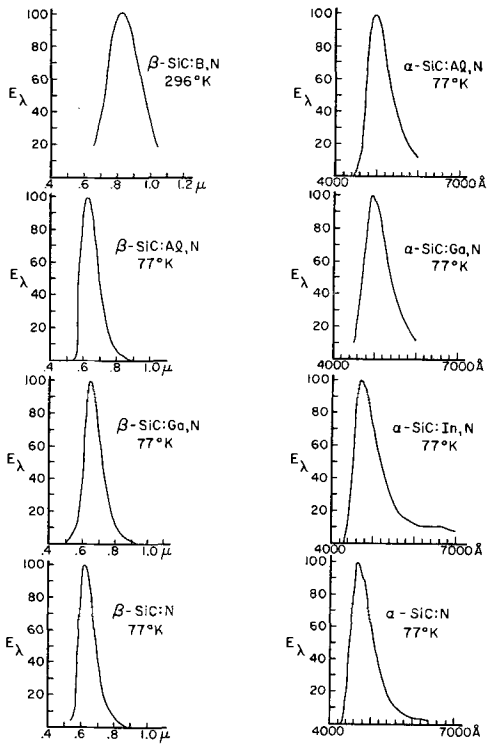

Fig. 1. Normalized emission curves for different SiC phosphors ($\lambda_{exc.}$ = 3650Å).

Acknowledgment

The author wishes to thank L. S. Staikoff and R. M. Potter for help in the collection of the experimental data, and R. P. Taylor for spectrographic analyses of the materials prepared.

Manuscript received June 25, 1965; revised manuscript received Nov. 1, 1965.

Any discussion of this paper will appear in a Discussion Section to be published in the December 1966 JOURNAL.

Table I. Summary of data for the luminescence of SiC phosphors

Composition	Structure	Emission peak, E_p, ev	Luminescence observed at T°K
α-SiC:B,N	4H	2.317	298
α-SiC:B,N	6H	2.137	298
α-SiC:B,N	33R	2.101	298
α-SiC:B,N	15R	2.049	298
α-SiC:B,N	21R	1.983	298
β-SiC:B,N	3C	1.49	298
β-SiC:Ga,N	3C	1.89	77
β-SiC:N	3C	1.96	77
α-SiC:Al,N	6H	2.48	77
α-SiC:Ga,N	6H	2.52	77
α-SiC:In,N	6H	2.63	77
α-SiC:N	6H	2.66	77

[1] The furnace used in our work (kindly loaned to us by Dr. G. A. Slack, General Electric Research Laboratory, Schenectady, New York) is described in ref. (2), p. 24-25. Because of the small heat capacity of such furnace it was possible effectively to quench the products of the high-temperature preparations. Thus the probability of forming layers of β-SiC on α-SiC grains or more complicated structures on cooling was very small.

[2] The apparatus used is known as Wig-L-Bug, a product of the Crescent Dental Manufacturing Company, Chicago, Illinois.

[3] A product of the General Electric Company.

REFERENCES

1. J. A. Lely, *Ber. Deutsch Keram. Ges.*, **32**, 229 (1955).
2. See for instance, "Conference on Silicon Carbide," J. R. O'Connor and J. Smiltens, Editors, Pergamon Press, New York (1960).
3. J. A. Lely and F. A. Kröger, "Semiconductors and Phosphors," M. Schön and H. Welker, Editors, p. 514, 525, Interscience Publishers, New York (1958).
4. I. S. Gorban' and S. N. Rud'ko, *Soviet Physics-Solid State*, **5**, 1368 (1963); English Translation, **5**, 995 (1963).
5. J. Bauer, J. Fiala, and R. Hrichovà, *Amer. Mineralogist*, **48**, 620 (1963).
6. L. Patrick, W. J. Choyke, and D. R. Hamilton, *Phys. Rev.*, **137**, A1515 (1965).
7. D. R. Hamilton, W. J. Choyke, and L. Patrick, *ibid.*, **131**, 127 (1963).
8. L. Patrick, D. R. Hamilton, and W. J. Choyke, *ibid.*, **132**, A2023 (1963).
9. W. J. Choyke, D. R. Hamilton, and L. Patrick, *ibid.*, **133**, A1163 (1964).
10. W. J. Choyke and L. Patrick, *ibid.*, **127**, 1868 (1962).
11. A. Addamiano, R. M. Potter, and V. Ozarow, *This Journal*, **110**, 517 (1963).
12. A. Addamiano, *ibid.*, **111**, 1294 (1964).
13. G. F. Kholuyanov, *Soviet Physics-Solid State*, **6**, 3336 (1964); English Translation, **6**, 2668 (1965).
14. H. H. Woodbury and G. W. Ludwig, *Phys. Rev.*, **124**, 1083 (1961).
15. J. S. van Wieringen, "Semiconductors and Phosphors," M. Schön and H. Welker, Editors, p. 367, Interscience Publishers, New York (1958).
16. A. Addamiano and L. S. Staikoff, *J. Phys. Chem. Solids*, **26**, 669 (1965).
17. G. A. Lomakina, *Fis. Tverdogo Tela*, **7**, 600 (1965).
18. H. J. van Daal, C. A. A. J. Greebe, W. F. Knippenberg, and H. J. Vink, *J. Appl. Phys., Supplement*, **32**, 2225 (1961).
19. H. J. van Daal, W. F. Knippenberg, and J. D. Wasscher, *J. Phys. Chem. Solids*, **24**, 109 (1963).

Structural and Optical Properties of Thin Films of $Zn_xCd_{(1-x)}S$

Walter M. Kane, James P. Spratt, Lincoln W. Hershinger, and Imdad H. Khan[1]

Applied Research Laboratory, Philco Corporation, Blue Bell, Pennsylvania

ABSTRACT

Films of the solid solution system $Zn_xCd_{(1-x)}S$ have been produced by simultaneous evaporation from two separately controlled sources onto a single substrate. Films of uniform composition were made covering the full range from 0 to 100% ZnS concentration, and the dependence of energy gap, crystal habit, and lattice parameter on composition was investigated. Optical transmission edge measurements yielded a nearly linear dependence of gap width on composition between the values of 2.35 ev for pure cadmium sulfide and 3.35 ev for pure zinc sulfide. X-ray diffraction specimens were prepared by scraping the films from the substrates. The powder patterns obtained showed that a gradual transition from the wurtzite structure typical of CdS to the characteristic ZnS zinc-blende form takes place between 60 and 85% ZnS concentration. At compositions where both modifications are present, the basal plane spacing is the same for the hexagonal (002) and cubic (111). Equivalent hexagonal lattice parameters could therefore be defined for the cubic form, and a and c calculated for all compositions. The results show good agreement with data obtained by others on bulk material.

In certain device application (1), use is made of a semiconducting material whose energy gap is a controllable function of composition. The present paper deals with the properties of thin evaporated films of the solid solution system $Zn_xCd_{(1-x)}S$. Films of uniform composition were made covering the full range from 0 to 100% ZnS concentration. The following properties were studied as a function of composition: (*a*) energy gap; (*b*) crystal habit; (*c*) lattice parameter.

Experimental

Sample preparation.—The specimens were prepared by vacuum evaporation onto glass substrates (Corning cover glass No. 2) in an oil diffusion pumped system. All evaporations were made at pressures below 3×10^{-6} Torr, and the substrates were glow-discharge cleaned just prior to deposition of the film.

To evaporate the composite films, two molybdenum boats, one containing zinc sulfide powder and the other containing cadmium sulfide powder, were heated simultaneously, the heating currents controlled separately so that the evaporation rates were in the proper ratio to yield a film having the desired composition. Detectors in the vicinity of the substrate monitored the rate at which material was being deposited by each of the sources. This information was fed back into a control system which automatically adjusted the heater current to maintain the preset rates. The total film thickness was about 5000Å. All films were annealed in vacuum for 15 min at 450°C before any measurements were made.

Measurements.—Energy gap.—The optical-band gap was determined on 20 uniform composition sulfide films, covering the full composition range from pure cadmium sulfide to pure zinc sulfide. The measurement consisted of a transmission-edge determination, using a Cary recording spectrophotometer, Model 114R. Reflection was not taken into account.

Interference peaks in the transmission curves caused an apparent shift in the edge, but measurements on films of different thicknesses and films whose surfaces were treated to cut down internal reflection show that the transmission edge could be read to an accuracy of ±50Å.

The energy gap, determined from the transmission edge, is plotted as a function of composition in Fig. 1, and a nearly linear dependence is observed. Data on bulk material, collected by Curie (2), are shown for comparison. The deviation in the high ZnS range may represent a phase change from hexagonal to cubic structure (discussed further below).

Crystal habit.—Both zinc sulfide and cadmium sulfide are known (3) to exist in either the cubic (zinc blende) or hexagonal (wurtzite) crystal form, depending on the conditions of preparation of the material.

X-ray diffraction measurements made early in this study showed that thin films of zinc sulfide characteristically exhibit the cubic phase, while cadmium sulfide films appear to consist of the hexagonal form.

[1] Present address: General Telephone & Electronics Laboratories, Bayside, New York.

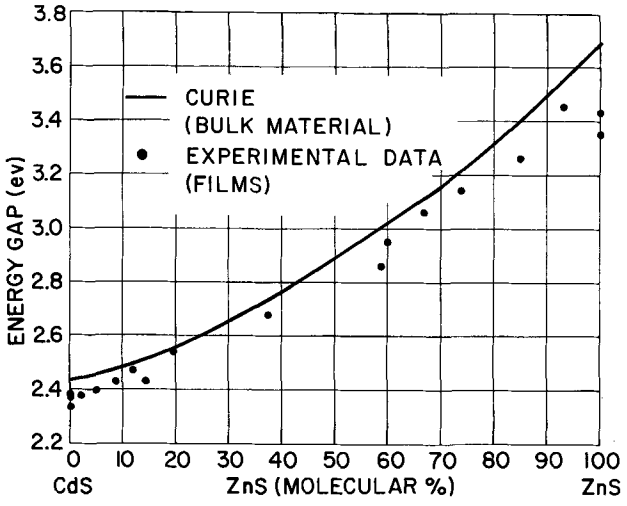

Fig. 1. Energy gap *vs.* per cent ZnS of $Zn_xCd_{(1-x)}S$ films

One of the objectives of the structural studies has been to evaluate the crystal habit of the composite films to determine the nature of the transition from cubic to hexagonal; in particular, to determine whether the transition is a gradual one with the intermediate compositions exhibiting both forms (polymorphism), or whether it is an abrupt one, the possibility of an abrupt change in crystal structure in a graded film in a device being an important consideration.

Measurements were made on 12 uniform composition films covering the full range of zinc sulfide concentration from 0 to 100%. The films, prepared as described above, were scraped from the substrates and glued to a quartz fiber with Canada balsam. The fiber was then mounted in a 36-cm circumference powder camera and exposed to Fe-filtered Co-Kα radiation.

Analysis of the x-ray powder patterns, although complicated by the close similarity between the face-centered cubic and the hexagonal close-packed crystal structures, showed that films containing less than about 60% ZnS are hexagonal in form, that films with

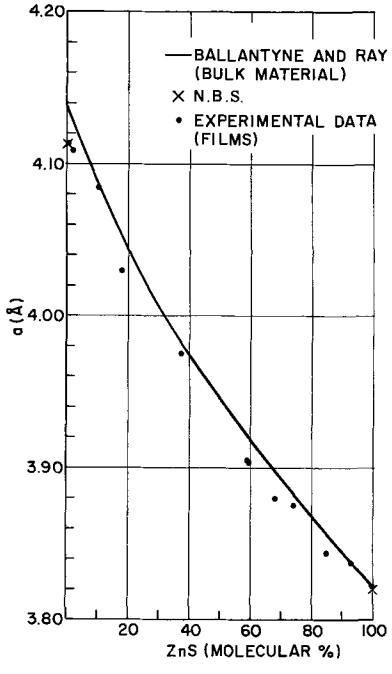

Fig. 2. Hexagonal lattice parameters *vs.* per cent ZnS of $Zn_xCd_{(1-x)}S$ films.

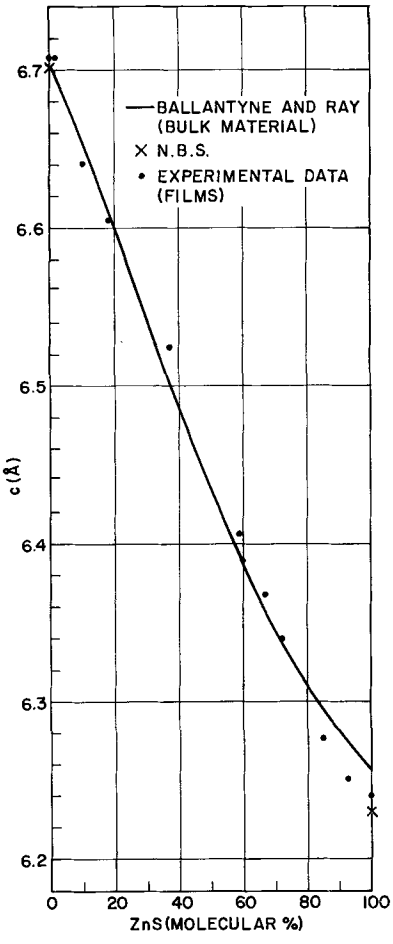

Fig. 3. Hexagonal lattice parameters *vs.* per cent ZnS of $Zn_xCd_{(1-x)}S$ films.

a ZnS concentration greater than about 85% are cubic, and that in the transition range both modifications are present, the relative quantities of the two polymorphs varying with composition.

Transmission and reflection electron diffraction patterns made on some of the films show that they are highly oriented with the basal plane parallel to the substrate.

Lattice parameters.—From the values of plane spacing d measured on the x-ray patterns, the lattice parameters were calculated for both the hexagonal and cubic forms. For convenience in presentation of the data we have made use of the equivalent planes and defined equivalent hexagonal lattice parameters a_H and c_H for the cubic modification. That is, since

$$d_{002} = d_{111}$$

we have $c_H = 2a_c/(3)^{1/2}$

and since $d_{110} = d_{220}$

we can write $a_H = a_c/(2)^{1/2}$

Because of the coincidence of the equivalent lines on the x-ray patterns, no error results from an assumption of the wrong crystal form in calculating lattice parameter.

In Fig. 2 and 3 we compare the lattice parameters of $Zn_xCd_{(1-x)}S$ films with bulk values given in the literature (4, 5), and find generally good agreement.

Discussion

From the well-behaved dependence of energy gap and lattice parameter on composition, we confirm that films prepared in the manner described are substitutional solid solutions in which solubility exists in all proportions.

A transition from the hexagonal to the cubic crystal form does apparently take place at high ZnS concentrations, but because of the close relationship between the two modifications, *i.e.*, having the same plane spacings, the transition is a gradual one and no discontinuity in the variation of composition dependent properties occurs.

Acknowledgments

The authors wish to thank Messrs. L. Altman and W. A. Hodorowski for their work in preparing the specimens, and Dr. M. H. Francombe for his help in interpreting the crystallographic data. This work was supported by the U.S. Army Electronics Command at Fort Monmouth, New Jersey.

Manuscript received Aug. 25, 1965; revised manuscript received Oct. 22, 1965. This paper was presented at the San Francisco Meeting, May 9-13, 1965.

Any discussion of this paper will appear in a Discussion Section to be published in the December 1966 JOURNAL.

REFERENCES

1. L. W. Hershinger, J. P. Spratt, and W. M. Kane, "Thin Film Metal Base Transistors Using Graded ZnCdS Films," Solid State Device Research Conference, Lansing, Michigan (1963).
2. D. Curie, "Luminescence in Crystals," John Wiley & Sons, Inc., New York (1963).
3. "Index to the X-Ray Powder Data File," American Society for Testing Materials, Special Testing Publication 48-H.
4. "Standard X-Ray Diffraction Powder Patterns," National Bureau of Standards Circular No. 539.
5. D. W. G. Ballentyne and B. Ray, *Physica*, **27**, 337 (1961).

Improved Properties of Silicon Dioxide Layers Grown Under Bias

A. Goetzberger

Bell Telephone Laboratories, Incorporated, Murray Hill, New Jersey

ABSTRACT

Oxidation of silicon was carried out under the influence of an electric field which was applied by means of an electrode suspended close to the surface. Negative electrode potential resulted in a voltage dependent reduction of surface donor density during steam oxidation. Above several hundred volts surface donor density saturates at about 4 x 10^{11} states per cm^2. The results tend to suport the impurity ion model for channel and drift effects. No influence of field on dry oxidation was found. MOS-drift experiments gave indications of greatly improved stability of bias grown wet oxides.

Thermal oxidation of silicon usually results in an n-type inversion layer at the surface of p-type crystals. It is generally accepted that the inversion layer is caused by positively charged sites in the oxide close to the interface (1-3). Although these sites do not seem to be capable of exchanging charge with the silicon, they are commonly called slow surface states. Because it is more likely that they are fast levels located close to the conduction band, they will be referred to as surface donors in this paper. Surface donors with which this paper is mostly concerned, cause only a voltage shift of the capacitance voltage curve of an MOS (metal-oxide-semiconductor) capacitor without changing the curve shape. Fast surface states on the other hand are states which change their state of charge when the band bending is altered by an external field. These states produce a distortion of the MOS curve.

Various models have been suggested to account for the surface donors. Kuper and Nicollian (3) concluded that the channels associated with the surface donors result from hydration in wet ambients. Seraphim *et al.* (4) propose formation of positively charged oxygen vacancies in the oxide. Deal *et al.* (1), and Griffin *et al.* (2) recently presented evidence that the surface donors consist of alkali ions which are present as impurities in the oxide.

Drift effects that are observed in MOS structures during temperature-bias aging are closely related to the n-type channels. MOS aging is carried out by applying a voltage between field plate and semiconductor at slightly elevated temperatures (100°-300°C). Positive bias at the metal electrode enhances the channel, negative bias reduces it. This effect is caused by migration of charges through the oxide. Explanations of it depend on assumptions about the nature of the charges. In particular, migration of oxygen vacancies (5, 4) or alkali ions (1, 2) and electron trapping effects (6) have been suggested.

In the present investigation, oxide layers were grown under the influence of an electric field. Growth of SiO_2 in an electric field had previously been studied by Jorgensen (7); however, he was only interested in the growth kinetics of the oxide film. In the present investigation, the influence of the field on the density of surface donors was the main concern. The results obtained tend to support the alkali ion model.

Experimental Arrangement and Procedure

Oxide growth technique.—The equipment used for oxide growth is shown in Fig. 1. Bias is applied between the silicon sample and a Pt electrode. The electrode is suspended about 1 cm above a silicon pedestal which supports the sample. The pedestal is heated by RF in an arrangement very similar to an

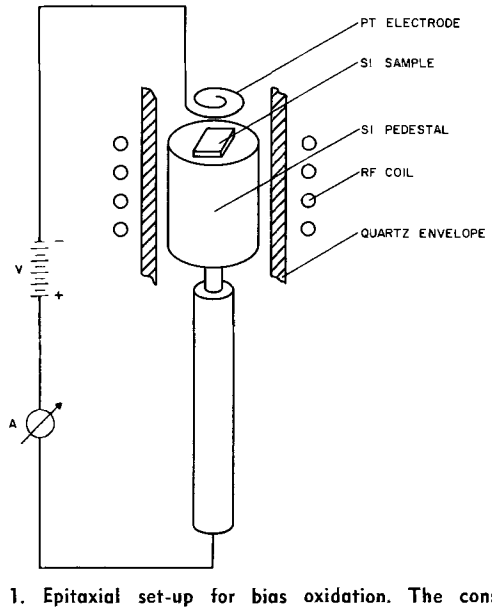

Fig. 1. Epitaxial set-up for bias oxidation. The constriction in the pedestal prevents excessive heat conduction from the hot zone. The oxidation chamber is enclosed in an oven that is kept at 100°C to prevent condensation of water vapor.

epitaxial grower. This technique differs from Jorgensen's in that the electrode is not in contact with the growing oxide. By this means the probability of contamination of the oxide from an evaporated electrode is eliminated.

In the arrangement used here, the potential drop is divided between the oxide layer and the gas phase. The situation is further complicated by the fact that not only the surface of the sample but also its rear side and the surface of the pedestal is being oxidized. Since no dependence of oxide growth rate on bias was observed, it can be concluded that most of the voltage drop occurred in the gas. According to Jorgensen's results, the drop across the oxide layer must have been below 2v. The electric field distribution during growth is presumably quite complex. In order to obtain detailed information about it a great deal of further experimentation would be necessary. This was not undertaken because the purpose of this work was the study of the influence of the growth techniques on interface properties.

In a typical oxidation run, a layer of 1000Å was grown at 1000°C. Growing time for this thickness was about 5 min in steam, 60 min in dry oxygen. Under these conditions, current flow at the beginning was between 10^{-7} and 10^{-6} amp, dropping during the run by about an order of magnitude. This applied to negative electrode voltages above 100v. Below this voltage, the system displayed an ohmic resistance of about 10^9 ohms.

Evaluation by MOS capacitance measurement.—Surface donor densities of the oxidized silicon were evaluated by the MOS capacitance technique. Metal dots were evaporated after oxidation. In most cases, evaporated Cr-Au contacts were used. No significant dependence of parameters on the contact metals was found with exception of the drift effects to be described below.

Capacitance *vs.* voltage curves of the MOS systems were measured at 100 kc. No significant hysteresis effect was noticed, indicating that all the surface states had come to equilibrium during the measurement. As pointed out above, oxidation in steam results in a channel on p-type silicon. The MOS capacitance curve of such a surface has a minimum at negative field plate voltage (Fig. 2). The correlation between this characteristic and channel properties is well known (8, 9). The voltage of the capacitance minimum is proportional to the density of surface charge. In the present paper, this voltage was converted to surface donor density with a relation given by Sah (10). This relation applies to the very low-frequency case where the electron concentration can follow the applied signal. It is also a good approximation for the present case where the increase of capacitance is caused by lateral current flow in the inversion layer. The surface charge measured this way comprises electrons in the inversion layer plus a small contribution from the charge in fast surface states. These states are located in the gap interval determined by the Fermi level at zero bias and at the capacitance minimum. The total surface charge is defined here as surface donor density, N_S. No correction for work functions was made.

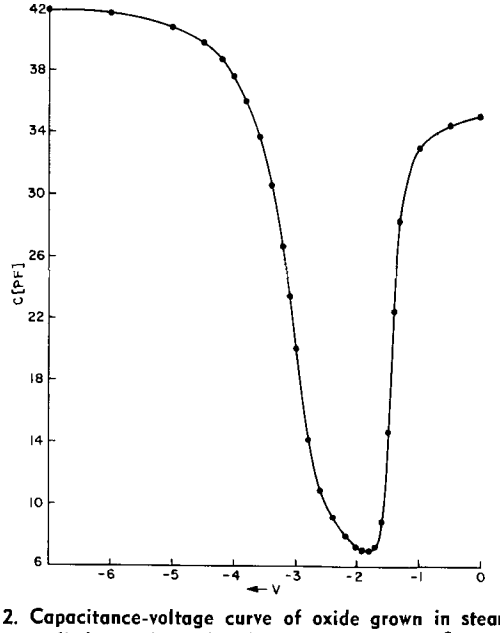

Fig. 2. Capacitance-voltage curve of oxide grown in steam with —1500v applied to electrode. Oxide thickness 900Å, frequency 100 kc; substrate p-type 50 ohm-cm.

Results

Influence of growth conditions.—Oxidations with different positive and negative biases were carried out in steam and dry oxygen. Substrate material was p-type silicon of 50 ohm-cm resistivity which had been electrochemically polished. The results can be summarized as follows:

Steam, zero and positive bias on electrode: Very high density of surface donors, large and uncontrollable fluctuations.

Steam, negative bias: Reduction of surface donor density. Reduction is bias dependent up to about 300v.

Dry oxygen, negative and positive and zero bias: No influence of bias on MOS characteristics.

The dependence of surface donor density on bias for steam oxidations with negative bias is shown in Fig. 3. MOS minimum voltages and the corresponding surface state densities are plotted.

It should be noted that the zero bias values are representative only of this particular run and can vary widely for different levels of contamination. The surface donor density saturates with voltage at an average of 3.9 x 10^{11} cm^{-2}. A typical MOS curve obtained at —1500v is given in Fig. 2. The saturation level at high bias, henceforth called residual surface donor density, varies only within narrow limits (3.2 x 10^{11} cm^{-2} to 6 x 10^{11} cm^{-2}). It does not depend noticeably on oxide thickness, growth temperature or crystal orientation. Ranges investigated were thicknesses from 500 to 6000Å and temperatures between 800° and 1100°C.

In another set of experiments, bias was applied only during part of the oxidation. The results (Fig. 4) indicate that no reduction of surface donor density occurs when the bias of 1500v is turned off after the first 1.4 min of a 5-min oxidation run. Turning off the bias during the last minute gives a low surface donor density. The same result is obtained when the bias is on only during the last 30 sec of the run.

The conditions under which a heavy channel could be removed were investigated. For this purpose steam oxide layers were grown without bias. An attempt was then made to reduce the channel by exposing the samples to 1500v at different temperatures. Results in-

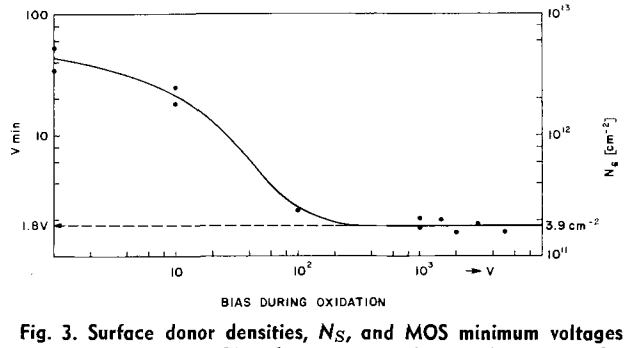

Fig. 3. Surface donor densities, N_S, and MOS minimum voltages *vs.* negative electrode bias for steam oxidation. All values for 1000Å oxide on 50 ohm-cm silicon.

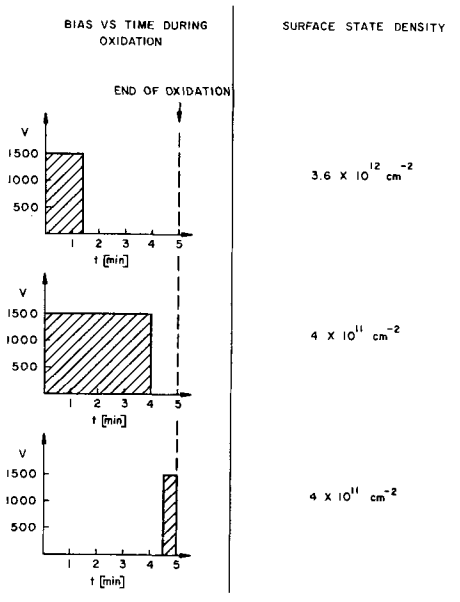

Fig. 4. Influence of interrupted bias during run. Oxidation time 5 min, bias —1500v.

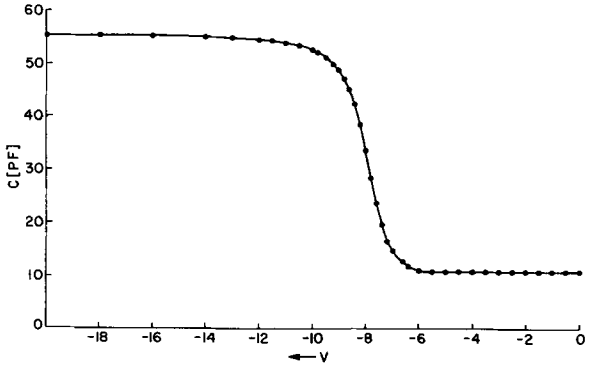

Fig. 5. Capacitance-voltage curve of oxide grown in dry oxygen

dicate that at 900° and 1000°C a 1-min exposure reduced the channel to its residual value. At 800°C, however, an increase in channel strength was observed. There is reason to believe that contamination of oxide surfaces and growing equipment has a major influence on these results. In another set of experiments, freshly grown oxides were contaminated by exposure to a NaCl solution. This contamination could be removed by a 1-min bias oxidation treatment. Control samples which did not receive the second oxidation treatment showed a very large MOS drift effect.

Oxidation in dry oxygen could not be influenced by biasing during growth. A typical MOS curve of a dry oxide is shown in Fig. 5. The capacitance rise at negative voltage indicates positive surface charge, but there is no inversion. If the surface were inverted, the capacitance would rise toward zero bias as in Fig. 2. In dry oxide, the Fermi level appears to enter a region of high density of fast surface states at the onset of inversion. The same type of curve is obtained when a wet oxide is dried thoroughly by heating in dry gas. Occasionally curves are obtained which are in between those shown in Fig. 2 and Fig. 5. The density of fast surface states in dry oxide is between 10^{12} and 10^{13} cm^{-2}. This is in striking contrast to oxides grown in steam or wet oxygen where fast surface state density is around 10^{11} cm^{-2} (11, 12).

Drift in MOS structures.—Drift experiments with positive bias during drift gave an increase of surface donor density by 3 x 10^{11} cm^{-2} within 60 min at 150°C. This is more than two orders of magnitude less than in steam oxide grown in the same equipment without bias. It was noticed that great care has to be exercised in applying the metal contacts to avoid contamination of the surface. Another effect interfering with drift measurements is in-diffusion of ions from the oxide air interface into the MOS structures during long runs at elevated temperature. For these reasons it is not certain that the figure quoted above is the limit of the bias oxidation technique.

Surface preparation.—For temperature bias aging experiments, surface cleaning in acids and solvents before oxidation was found not advisable. Oxide layers of less than 2000Å thickness had a tendency to develop shorts during aging. This effect could be avoided by oxidizing freshly grown epitaxial wafers.

Discussion

Wet oxide.—The results described here can best be explained by assuming that channels are caused by impurity ions. It is likely that, by oxidation under bias, ions are collected by the electrode from the gas phase. Ions within the SiO_2 are drawn to the surface and, if the vapor pressure of the ions or compounds formed by them is high enough, they evaporate. It is possible, of course, to carry out an oxidation in an exceedingly clean environment. Under these conditions, a very low surface donor density is expected even without an electric field.

The kinetics experiment (Fig. 4) can be interpreted as follows. Because short application of bias at the beginning of the run does not remove the channel, it can be concluded that the ions do not result only from surface contamination of the silicon. If this were the case, they would be removed by bias at the start only. Much of the contamination must therefore be introduced through the gas phase. Further conclusions can be drawn from the second experiment in Fig. 4, where the bias was turned off 1 min before the end of the oxidation, and a low surface donor density was observed. This shows that the channel cannot be due to the presence of water or oxygen vacancies because, in either case, equilibrium would have been established during the unbiased part of the run. The same is true for any polarization of the oxide that might have been introduced by the bias.

The reasons for the residual channel after bias oxidation are at present unknown. Possibly it is caused by the structure of the interface itself or by ions that are either immobile or unable to evaporate from the oxide surface.

Dry oxide.—No explanation exists at present for the difference of characteristics between dry oxides and wet oxides. If one accepts the fact that a dry oxide has a very high density of fast surface states, it is possible to speculate on a mechanism which might account for the independence of dry oxidation of bias. If a positive ion is located at an interface containing a high density of fast surface states, the probability that a surface state is close to the ion is high. The energy level of the fast surface state will then be modified by the coulomb field of the ion such that it becomes an electron trap. Thus the ion is bound to the surface state and cannot be removed by an external field. This model might also explain the fact that as a rule dry oxides exhibit only a small MOS drift effect.

MOS drift.—Since drift effects in MOS structures are closely related to mobile charges in the oxide, it can be expected that removal of the charges by growing under bias reduces drift. This is borne out by the results described above. The fact that no drift was ever observed with negative bias leads to the conclusion that there are no mobile negative charges in the oxide. This refers only to pure SiO_2. If the oxide is modified, for instance by incorporating P_2O_5, negative ions can be observed (13).

The experiments with positive bias during drift are still in a preliminary stage and more work has to be done. It can be stated, however, that the drift effect is not inherent in SiO_2 (1). Neither does it seem to depend on the contact metal. Some influence of the metal was found here, but most of it could be correlated with the difference of evaporation conditions.

Conclusions

The conclusions are:

1. N-type inversion in oxidized surfaces exceeding a density of about 4 x 10^{11} cm^{-2} is caused by positive impurity ions. It is not directly caused by the presence of water during oxidation. Most of the ions are highly mobile at elevated temperatures and can be removed by an electric field.
2. Of the different models proposed for MOS drift effects, alkali ion drift (1, 2) is the likeliest. Removal of these ions from SiO_2 layers will probably result in drift-free structures.
3. The bias oxidation technique described here is capable of reducing the density of surface donors after steam oxidation reproducibly to the range of 3.5-6 x 10^{11} cm^{-2}. Oxides produced this way exhibit greatly reduced drift effects.

Acknowledgments

The very careful experimental work of J. McGlasson is gratefully acknowledged. Thanks are also due to J. T. Nelson, E. H. Nicollian, and C. Goldberg for helpful discussions.

Manuscript received July 13, 1965; revised manuscript received Sept. 20, 1965.

Any discussion of this paper will appear in a Discussion Section to be published in the December 1966 JOURNAL.

REFERENCES

1. E. H. Snow, A. S. Grove, B. E. Deal, and C. T. Sah. *J. Appl. Phys.*, **36**, 1664 (1965).
2. J. R. Mathews, W. A. Griffin, and K. H. Olson, *This Journal*, **112**, 899 (1965).
3. A. B. Kuper and E. H. Nicollian, *ibid.*, **112**, 528 (1965).
4. D. P. Seraphim, A. E. Brennemann, F. M. D'Heurle, and L. Friedmann, *IBM Journal*, **8**, 400 (1964).
5. J. E. Thomas, Jr., and D. R. Young, *ibid.*, **8**, 368 (1964).
6. J. Lindmayer, *J. Appl. Phys.*, **36**, 196 (1965).
7. P. J. Jorgensen, *J. Chem. Prys.*, **37**, 874 (1962).
8. E. H. Nicollian and A. Goetzberger, *IEEE Trans.*, ED-**12**, 108 (1965).
9. S. R. Hofstein, K. H. Zaininger, and G. Warfield, *Proc. IEEE*, **52**, 971 (1964).
10. C. T. Sah, *IEEE Trans.*, ED, 324 (1964).
11. C. N. Berglund, To be published.
12. E. H. Nicollian and A. Goetzberger, To be published.
13. D. R. Kerr, *IBM Journal*, **8**, 385 (1964).

The Substrate Orientation Effect on Impurity Profiles of Epitaxial GaAs Films

R. R. Moest

Bell Telephone Laboratories, Incorporated, Murray Hill, New Jersey

ABSTRACT

Undoped n-type GaAs films have been grown epitaxially on heavily doped n-type GaAs substrates of various crystallographic orientations by the HCl/H_2 flow method. The thickness of the epitaxial films ranged from 0.5 to 20.5μ. The impurity profiles of undoped films on the (100) and (110) planes were strongly dependent on the film thickness but independent of the substrate dopants and their concentration. Impurity profiles of films grown on the (111) and ($\bar{1}\bar{1}\bar{1}$) planes were independent of the substrate dopants and their concentrations as well as of the film thickness. The steep impurity gradients at the substrate-film interface exclude the possibility of outdiffusion or autodoping of donors from the substrate. The minimum net donor concentrations obtained were in the low 10^{15} range. Reverse bias breakdown voltages vary from 5 to 60v for 0.5μ and 6μ thick films, respectively.

The epitaxial growth of GaAs films on GaAs substrates by the HCl/H_2 flow method has been described in detail by Williams and Ruehrwein (1) and by Weinstein, Bell, and Menna (2).

The objective of this communication is to report on a study made on the growth technique and evaluation of thin n-type epitaxial GaAs films of low carrier concentration on highly doped, n-type GaAs substrates.

Experimental

The system used in this work has been described previously by other authors (1, 2).

A mixture of HCl and H_2 gas is passed into a quartz reaction tube inside two coupled split-tube micro combustion furnaces. The schematic drawing of this arrangement and the temperature profile are shown in Fig. 1. Hydrogen gas is passed through a Deoxo Unit[1] and two glass-wool packed liquid nitrogen traps to condense any moisture. Lecture bottle HCl gas of 99.0% purity[2] is passed through an isopropanol-dry ice cold trap packed with Pyrex beads before the gas is admitted to the reaction tube. These purification

[1] Manufactured by Engelhard Industries, Inc., Newark, New Jersey.

[2] Supplied by Matheson Company, Inc., East Rutherford, New Jersey.

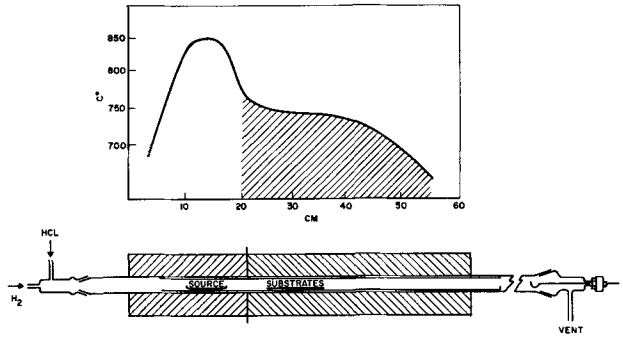

Fig. 1. Furnace and temperature profile

procedures for hydrogen and hydrogen chloride seem to be adequate for the system studied.

The source material used in this study was exclusively boat grown, undoped, n-type GaAs from Monsanto Chemical Company with a carrier concentration of 1.7 x 10^{16} at./cm^3, room temperature mobilities of 4000 to 5000 cm^{2}v^{-1} sec^{-1} and resistivities of approximately 0.1 ohm-cm.

The GaAs crystals used for substrates were either Bridgman or Czochralski grown ingots cut to various orientations with an accuracy of approximately 15 min. With the exception of one float-zoned GaAs crystal supplied by R. G. Sobers of this Laboratory, all substrate material was obtained from Monsanto Chemical Company.

Wafers 25 mil thick were cut from the oriented crystals. They were lapped with 12μ silicon carbide abrasive, mechanically polished with 0.1μ alumina, and chemically polished with Br_2-CH_3OH solution (3). The wafers were then thoroughly degreased in trichloroethylene and acetone, rinsed with deionized water, and etched in H_2SO_4-H_2O_2-H_2O solution (4). Weight measurements were made on a microbalance just prior to a run.

It has been observed that the substrate preparation immediately before the growth of a film is of greatest importance to at least the physical perfection of the epitaxial layers. Chemical polishing has frequently revealed surface imperfections in GaAs substrate wafers with carrier concentrations in excess of approximately 3 x 10^{18} (at./cm^3). In Czochralski grown material these imperfections display a pattern which might best be described as "phonograph record grooves" [see Fig. 2a (n_{Te} 4 x 10^{18})]. It is assumed that this pattern is caused by radial impurity segregation during the growth of the crystal. A similar but more randomly distributed impurity segregation might be responsible for the feathery type of imperfections observed on boat grown material, shown in Fig. 2b, (n_{Te} 3 x 10^{18}). In both boat grown and pulled crystals, randomly distributed solid particles in the GaAs have also been revealed by etching the material [see Fig. 2c (n_{Sn} 2 x 10^{18})]. These imperfections become more pronounced if the wafers are immersed and etched in a Br_2-CH_3OH solution for 5 to 10 min. The H_2SO_4-H_2O_2-H_2O etching solution, on the contrary, seems to smooth out these surface irregularities, and they may even disappear altogether after prolonged etching with H_2SO_4-H_2O_2-H_2O. It is apparent that these irregularities will be reflected in the visual perfection of epitaxial films grown on such substrate wafers.

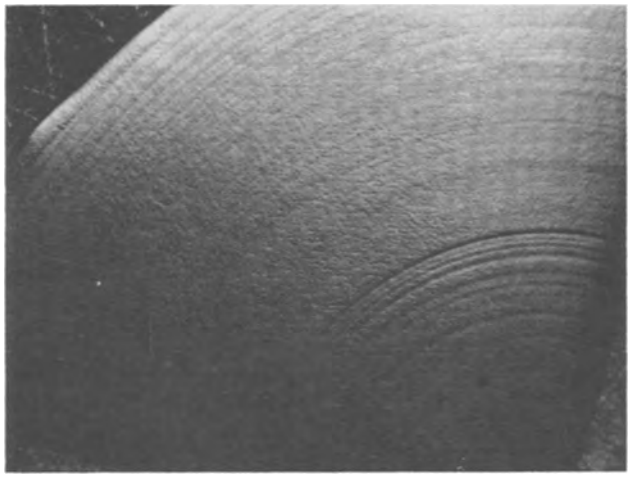

Fig. 2a. GaAs wafer, Czochralski grown, with "phonograph record groove" effect, ($\bar{1}\bar{1}\bar{1}$). Magnification approximately 14X.

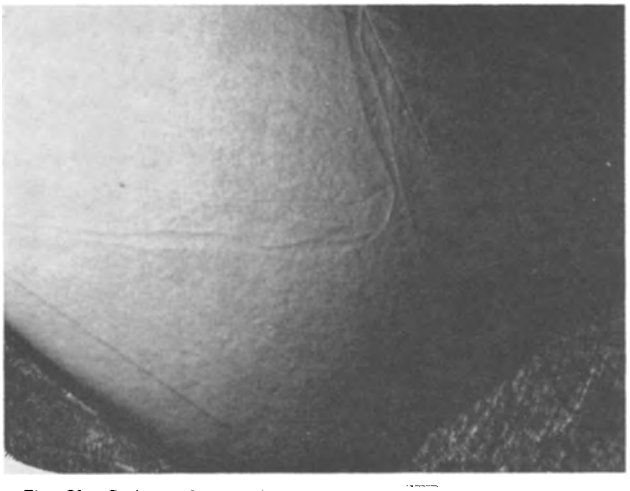

Fig. 2b. GaAs wafer, Bridgman grown, ($\bar{1}\bar{1}\bar{1}$). Magnification approximately 14X.

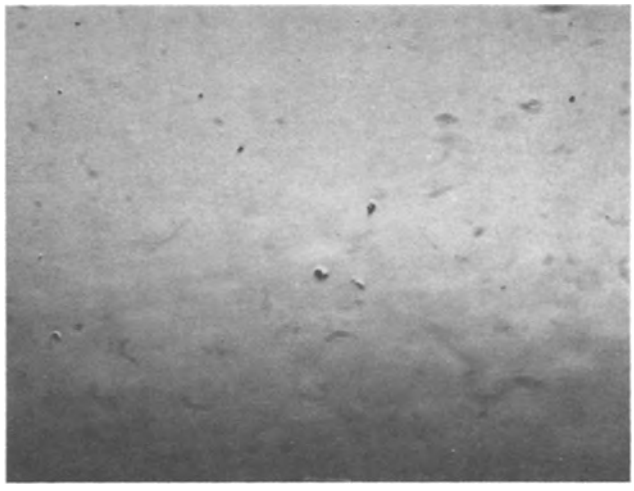

Fig. 2c. GaAs wafer, Czochralski grown; solid particles imbedded in the wafer, ($\bar{1}\bar{1}\bar{1}$). Magnification approximately 73X.

Five to ten GaAs source wafers of approximately 5 to 10 cm^2 total surface area were placed in a quartz boat. The substrate wafers, with a surface area of approximately 0.5 cm^2 each, were supported on a flat quartz plate. They were then positioned in the liner so that the source material was at the peak and the substrates were at the flat portion of the temperatube profile as shown in Fig. 1. The deposition zone is indicated by a shaded area in Fig. 1. Heavier GaAs deposition was experienced toward the lower temperature zone. The weight changes of substrate and source wafers were measured to an accuracy of ± 3 μg.

Since the objective of this work was primarily the growth and electrical evaluation of relatively thin films, no attempts were made to study growth variables such as hydrogen and hydrogen chloride flow rates, source and substrate temperature ranges, and various ΔT's in detail. The epitaxial films were all grown under the following conditions: H_2 flow, 300-500 cm^3/min; HCl flow, 1-3 cm^3/min; temperature source, 850°C; substrate, 750°C; reaction time, 15-30 min. At hydrogen flow rates of less than 100 cm^3/min, counterflow diffusion of arsenic has previously been observed resulting in arsenic condensation in the upstream portion of the reaction tube. Hydrogen flow rates in excess of 600 cm^3/min normally lead to etching of the substrate material due to undersaturation of the reacting gas at the source wafers. It appeared that the temperatures of source and substrate and their temperature differences were not critical within certain limits. It was, however, of greatest importance that the reactive H_2-HCl gas mixture passing over the substrates was supersaturated with source material. The conditions of saturation depend as well on temperature

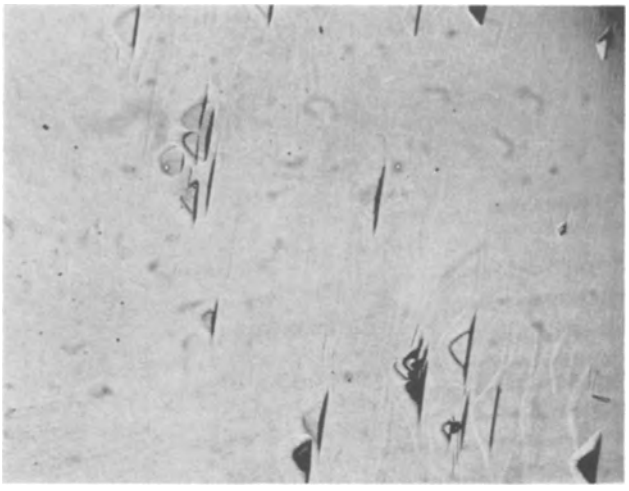

Fig. 3a. Epitaxial film on (110) oriented substrate. Magnification approximately 140X.

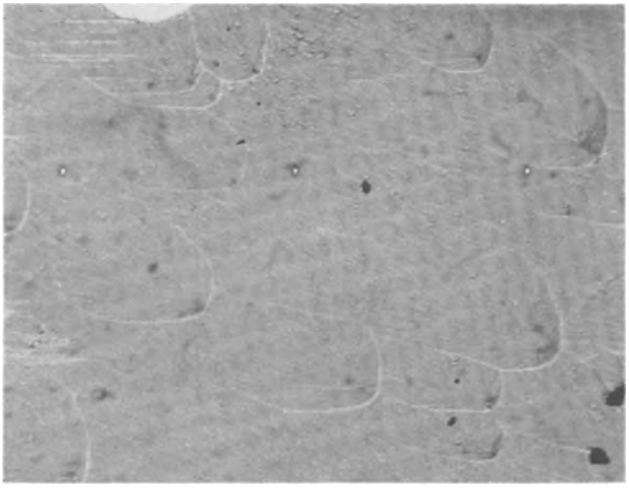

Fig. 3b. Epitaxial film on (111) oriented substrate. Magnification approximately 140X.

and flow rates as on the geometry of the system. No difference in the carrier concentration of the profiles of the films could be detected by using either fresh source material or the remainder of previously used source wafers.

Epitaxial films from 0.5 to 20.5μ thick have been grown on ($\bar{1}\bar{1}\bar{1}$), (111), (110), and (100) substrates. The surfaces of epitaxial films grown on the ($\bar{1}\bar{1}\bar{1}$) and (100) planes were visually and microscopically smooth and generally free of growth patterns, while films grown on (111) and (110) oriented substrates exhibited some surface texture (Fig. 3a and 3b). Growth rates were found to vary for different substrate orientations. The observed absolute growth rates were: 0.5-0.7 μ/min on (111) plane; 0.2-0.4 μ/min on (100) plane; 0.1-0.15 μ/min on (110) plane; 0.03-0.05 μ/min on ($\bar{1}\bar{1}\bar{1}$) plane.

The thickness of the epitaxial films was measured with a Beckman Infrared Spectrophotometer (Model IR-5, NaCl optics). Since the lower limit for measurements of film thicknesses with this technique is approximately 1μ, the thickness of films less than 1μ was calculated by area and weight gain measurements.

The carrier concentration profiles in the films have been determined by the differential capacitance-voltage method at 100 kc as described by Thomas *et. al.* (5). Schottky surface barrier diodes were used as rectifying contacts. Nominal 10 mil diodes were formed by evaporating gold at pressures of $\leq 10^{-6}$ Torr. Ohmic contacts were formed by spot-welding

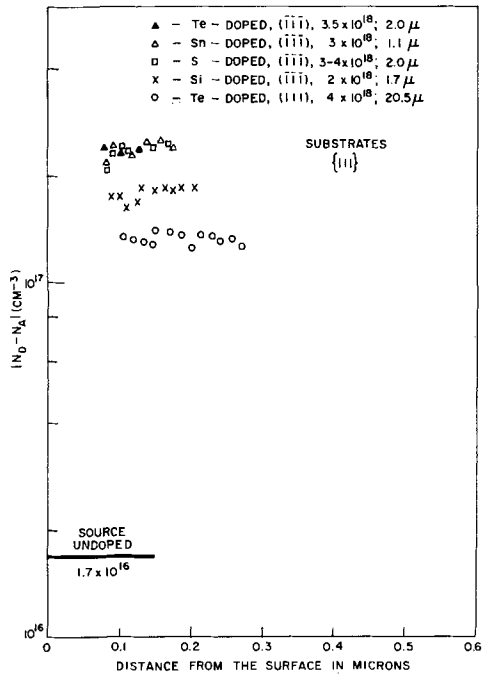

Fig. 4A. Several of the evaluated profiles

5% Sn-Au alloy wires to the bulk wafer. The ohmic behavior of these contacts and the characteristics of the diodes were checked on an I-V curve tracer. It was necessary to measure microscopically the diameter of the Au diode since variations from 9.3 to 12.5 mils diameter were encountered.

Results and Discussion

Epitaxial films with thicknesses from 0.5 to 20.5μ have been grown from "undoped," n-type GaAs source material on substrates doped with various impurities to a level of 2 to 4 x 10^{18}. The substrates were cut to different crystallographic orientations. Despite the fact that only one type of source material has been used, different results were obtained on films grown on different substrate orientations. The measurements were generally made without etching the units. It has been found that etching mesas frequently deteriorated the breakdown characteristics of the diodes to completely ohmic behavior. It seems appropriate to discuss the results on the basis of different substrate orientations.

Films grown on ($\bar{1}\bar{1}\bar{1}$) oriented substrates.—It has been observed that the ($\bar{1}\bar{1}\bar{1}$) plane is the slowest growing plane and yields the smoothest film surfaces. Epitaxial films grown on this plane also exhibit the lowest breakdown voltages, ranging from 2 to 8v. Films of various thicknesses have been grown on this plane using substrates doped with different impurities. Figure 4A shows several of the evaluated profiles together with the corresponding film thicknesses as determined by the infrared method. The different substrate dopants and their concentrations are included in this figure. The zero-bias space charge width extended only to 0.1μ with zero-bias capacitance values of 70 to 90 pf. This indicates an impurity concentration of 2 to 3 x 10^{17} at only 0.1μ from the surface. To assure that these relatively high carrier concentrations are not merely surface layer effects of the epitaxial films, several samples have been step-etched whereby part of the epitaxial film was etched off. A typical example is shown in Fig. 4B. In this case the total epitaxial film thickness was 1.0μ. Part of the sample was coated with Apiezon W wax and the sample etched in H_2SO_4-H_2O_2-H_2O solution to remove 0.75μ of the epitaxial film. After removal of the wax coating 10 mil

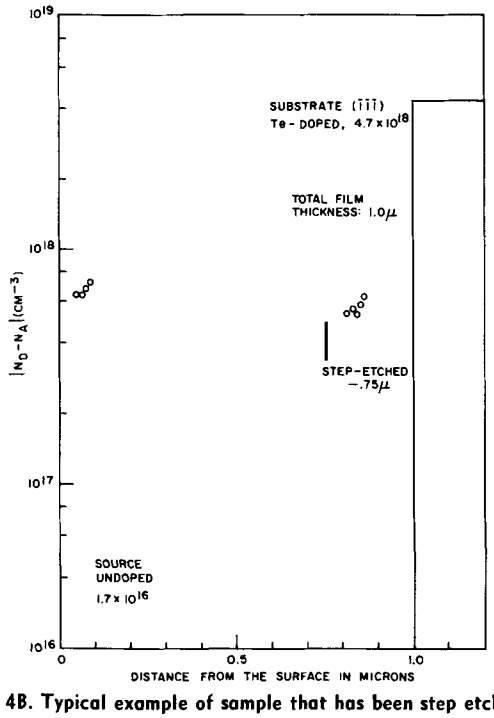

Fig. 4B. Typical example of sample that has been step etched

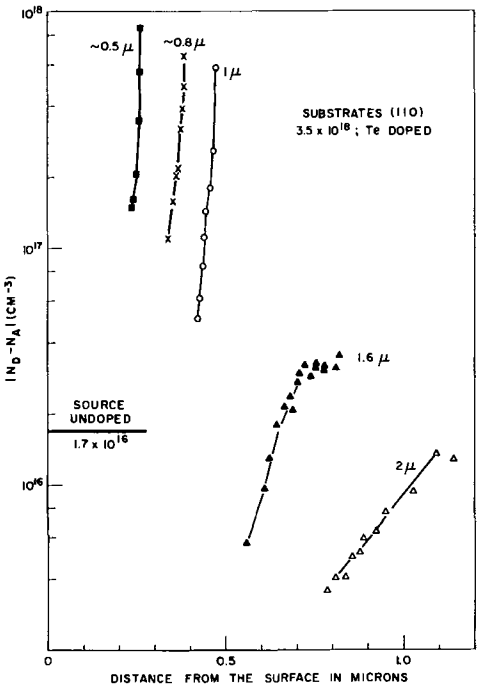

Fig. 5. Impurity profiles of several films

diameter gold dots were evaporated on the surface and the diodes were then evaluated as described earlier. The fact that the carrier concentration of the epitaxial film on the etched layer is identical with the one observed on the original surface indicates that the high carrier concentration is uniform throughout the epitaxial layer. These results seem to be completely independent of the film thickness and the type of substrate dopant.

Films grown on (111) oriented substrates.—The (111) plane proved to be the fastest growing plane, but the surface perfection of the films is very poor. The characteristics of the diodes on this plane are identical with the ones on the $(\bar{1}\bar{1}\bar{1})$ plane. The impurity profiles for the (111) films are the same as for the $(\bar{1}\bar{1}\bar{1})$ films (see Fig. 4A, B). Two films with thicknesses of 19 and 20.5μ have been grown showing the same film thickness independence of the impurity profile as observed on $(\bar{1}\bar{1}\bar{1})$ films.

Films grown on (110) oriented substrates.—Diodes of films grown on the (110) plane generally have V_{BS} ranging from 3 to 8v for films of less than 1μ thickness to approximately 20v for films 1-2μ thick. The impurity profiles are also remarkably different from those observed on (111) films. The space charge width at zero bias extends much farther into the film compared to {111} films. The impurity profiles of several films grown on the (110) plane are plotted together with the film thicknesses in Fig. 5. The space charge width at zero bias increases with the film thickness and the corresponding lowest carrier concentration at zero bias drops from the low 10^{17} range for 0.5μ thick films to the mid 10^{15} range for approximately 1.5μ thick films. The slope of the impurity profile at the apparent film-substrate interface is very steep, approximately 13-15 decades/μ. The discrepancy between the film-substrate interface as indicated by the impurity profile and determined by IR measurements can be explained by cummulative errors in the various measurements. This is particularly the case with the infrared thickness measurements where almost the entire width of the relatively small substrate wafer is exposed to the IR beam through a wide slit. The measurements therefore yield only an average film thickness of the sample.

Films grown on (100) oriented substrates.—The highest reverse bias breakdown voltages and the lowest carrier concentrations have been obtained with films grown on the (100) plane.

The Schottky surface barrier diodes had V_B values of 4-8v for approximately 0.5μ thick films and 40-60v for 3 to 6μ thick layers. The zero bias space charge width increases with the film thickness analogous to films grown on the (110) plane. The lowest carrier concentration at zero bias is about one order of magnitude lower than on (110) films of comparable thickness. The impurity profiles of (100) films thicker than 2μ exhibit some anomalous behavior at low bias (see Fig. 6). The carrier concentrations as determined by differential capacitance-voltage measurements at zero bias are in the low 10^{14} range, increasing rapidly with applied reverse bias to some peak value in the low or mid 10^{15} range and then decreasing slightly toward the substrate. Within a few tenths of a micron of the interface, the carrier concentrations increase very rapidly toward the substrate doping level. The same

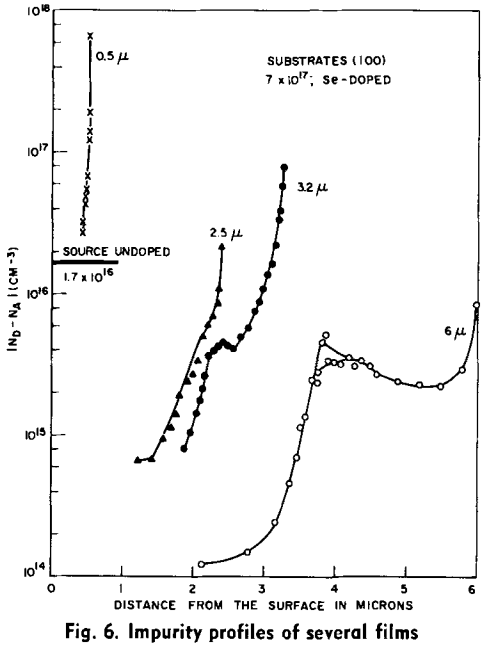

Fig. 6. Impurity profiles of several films

peculiar impurity profile was observed on a (100) film after etching. In this case the original gold dots were removed with a saturated aqueous solution of KI and I_2. The wafer was then etched with H_2SO_4-H_2O_2-H_2O and thus thinned down by removing part of the epitaxial film. New gold dots were then evaporated. The impurity profile, similar to the one shown in Fig. 6 for a 6μ thick film, remained essentially unchanged, except that the initial ascending slope and the peak shifted closer to the film-substrate interface, corresponding to the new film thickness. Lawley (6) has made similar observations on films grown with the water vapor system. He also conducted some experiments on bulk GaAs crystals with carrier concentrations of 2 to 3 x 10^{15} and observed the same anomalies (7).

The slope of the impurity profiles of (100) films at the film-substrate interface is practically infinite. This indicates that adverse reactions like outdiffusion of impurities from the substrate into the film or substrate autodoping as described by Thomas *et al.* (5) were not encountered in the experiments with films of this orientation.

The impurity profiles for epitaxial films grown by the HCl/H_2-method at substrate temperatures about 750°C are generally independent of the kind of substrate donors and their concentration up to 6 x 10^{18}. This conclusion is evident from the results obtained on (100) and (110) films. Not clearly explained, however, are the results on {111} films. It might be argued that some mechanism like substrate autodoping or outdiffusion of impurities from the substrate into the film is orientation dependent and is predominant on the {111} orientation. If this were the case one should be able to obtain {111} films of lower carrier concentration by using lightly or undoped {111} substrates. In Fig. 7 are depicted the results of such experiments. Two films were grown on {111} oriented substrates, Te-doped with a carrier concentration of 2 x 10^{16}. The films were 1. 3 and 1.2μ thick, and the impurity profiles were essentially identical to the ones observed on films grown on n^+-substrates. The impurity profiles of films grown on {111} oriented n^+-substrates with high carrier concentrations seem, therefore, to be independent of the kind and concentration of substrate donors. In view of the results obtained on (110) and (100) films it is improbable that the system itself could contribute to the high carrier concentration of these {111} films.

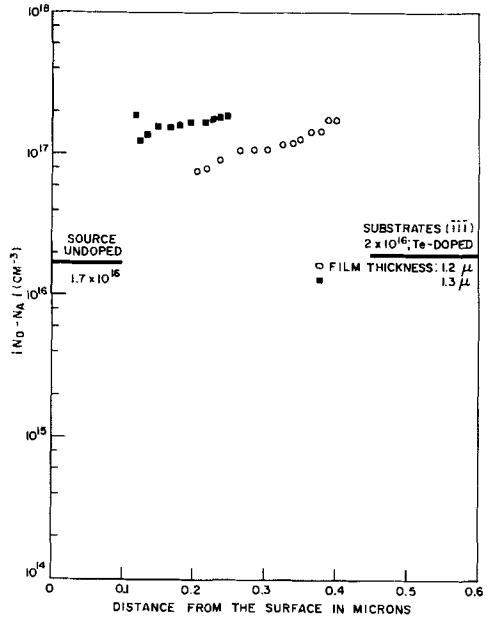

Fig. 7. Results of experiments

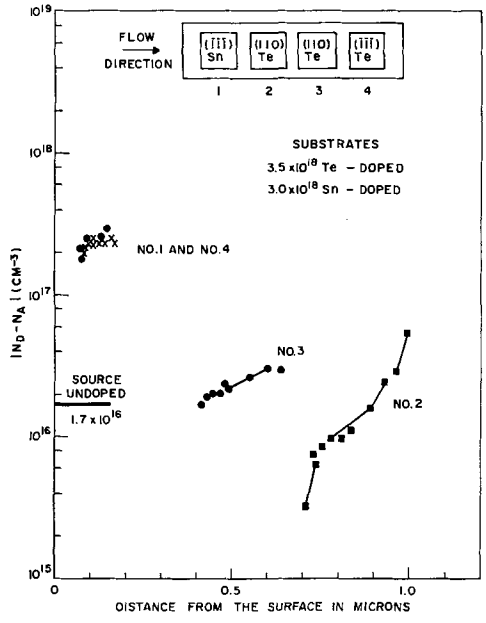

Fig. 8. Results of experiment

If we assume that no substrate-originating effects occur which adversely influence the properites of the epitaxial films, then it should be possible to place several substrates of various orientations on the quartz plate during one experiment and still observe the results shown in Fig. 4, 5, and 6 for the appropriate substrate orientations. The result of one such experiment is shown in Fig. 8. In this run four substrates of two different orientations, but approximately the same carrier concentration, were used. They were spaced close together on the quartz plate in the sequence indicated. The consistency of the results obtained on multiple substrate experiments with the results obtained on single substrate experiments indicates that no "downstream" impurity contamination occurs due to outdiffusion or autodoping from the substrates.

Conclusions

From the results obtained in this work we may conclude that thin GaAs films of approximately 0.5μ thickness can be grown by the HCl/H_2 system at substrate temperatures low enough to eliminate impurity diffusion from the substrates into the films. The impurity profiles of the films are strongly orientation dependent. Only the (110) and (100) orientations seem to yield low carrier concentrations in the films if source material of low carrier concentration is used. The slope of the impurity profiles at the film-substrate interface is very steep and indicative of an abrupt change in carrier concentrations. For {111} oriented films only relatively high carrier concentrations can be obtained, regardless of the substrate donor concentration and film thickness. For films of comparable thickness there appears to be a definite orientation dependent trend in carrier concentrations towards lower values in the order $(\bar{1}\bar{1}\bar{1}) = (111) >> (110) > (100)$.

The peculiar impurity profiles for {111} films are not explained in this work. It has been suggested by Williams (8) that anisotropic impurity segregation might occur in this vapor growth process similar to the one observed in the crystal growth from the melt.

Acknowledgment

The author wishes to thank K. L. Lawley and B. Schwartz for valuable discussions.

Manuscript received Sept. 16, 1965; revised manuscript received Nov. 1, 1965.

Any discussion of this paper will appear in a Discussion Section to be published in the December 1966 JOURNAL.

REFERENCES
1. F. V. Williams and R. A. Ruehrwein, *This Journal*, **108**, 177C (1962).
2. M. Weinstein, R. O. Bell, and A. A. Menna, *ibid.*, **110**, 55C (1963); **111**, 674 (1964).
3. M. V. Sullivan and G. A. Kolb, *ibid.*, **110**, 585 (1963).
4. M. V. Sullivan and L. A. Pompliano, *ibid.*, **108**, 60C (1961).
5. C. O. Thomas, D. Kahng, and R. C. Manz, *ibid.*, **109**, 1055 (1962).
6. K. L. Lawley, Private communication.
7. K. L. Lawley, *This Journal*, **112**, 68C (1965).
8. F. V. Williams, *ibid.*, **111**, 886 (1964).

Kinetics of the Reaction Hi-⟨111⟩Ge

A. Reisman and M. Berkenblit

International Business Machines Corporation, Watson Research Center, Yorktown Heights, New York

ABSTRACT

Experiments are described which appear to differentiate between mass transport and surface reaction kinetics in the open tube reaction of gaseous hydrogen iodide with <111> germanium surfaces. Surface limiting reaction behavior is not observed until average linear gas stream velocities in the neighborhood of 800,000 cm/min are attained. The limiting reaction rate for the etching reaction is described by the equation $\log R_f = -3.64 \times 10^3/T^\circ K + \log p_{HI} + 5.42$, R_f having the dimensions mg/cm^2 hr. The reaction order was found to be unity which together with other information suggested that the desorption of germanium iodides constitutes the rate-limiting step. Autodoping phenomena are examined in view of the speed of the etching reaction, and calculated rate data for probable deposition reactions are presented.

The widespread usage of reversible vapor-solid chemical processes for the epitaxial growth of semiconductors has focused considerable attention on both the kinetic and equilibrium properties of the reactions involved (1-14). In general, kinetic studies conducted in open tube systems have not yielded reproducible data for either the forward, deposition, or the reverse, etching, processes. In the light of recent work by Sedgwick, in fact, it is not evident that open tube deposition processes as normally practiced should be treated kinetically, their behaviors more nearly approximating equilibrium states (1). Closed system investigations are frequently questionable on the grounds that experimental evidence demonstrating a differentiation between mass transport and surface limitations is lacking, a point applicable also to open tube work.

While a full understanding of the nature of the growth processes entails independent evaluations of both the forward and reverse reactions, the former represents a formidable problem in that deposition cannot be confined to the substrate alone. This suggests that investigations of the etching process are potentially more rewarding, information about the forward reaction then being inferred from relationships between etch rate and equilibrium constant information. Using this approach one may also obtain clues as to the extent of possible back etching reactions in depositions which lead to autodoping of the deposits by impurities initially present in the substrate, etched during the growth process, and then incorporated in the growing crystal via a gas phase segregation process.

One typical class of deposition reactions involves the hydrogen reduction of a polyhalide via the stoichiometry depicted in Eq. [1]. It is to be noted that a product of this reaction is the halogen

$$GeX_4 + 2H_2 \rightleftarrows 4HX + Ge \qquad [1]$$

acid, HX, and that the reverse reaction involving this acid occurs under conditions of an essentially constant, large H_2 ambient atmosphere, the tetrahalide usually being present in concentrations of less than a few mole per cent. The specific reaction of gaseous HI with solid Ge in an open tube system using an H_2 carrier gas has been discussed qualitatively by the authors with respect to the parameters affecting vapor polishing of Ge and Si (15). The present work was suggested by the results of the earlier etching study and is concerned with quantitative aspects of the surface limiting kinetics of the Ge(solid)-HI(gas) reaction. Concomitantly, techniques are described for separating surface and mass transport phenomena in solid-gas reactions.

Analysis of Open Tube Reactions

Parameters affecting an open tube process, that involving HI and Ge for example, Eq. [2], are the etchant concentration, etchant flux, temperature and reactor geometry. If

$$2(x+y)HI + xGe \rightleftarrows (x-y)GeI_2 + yGeI_4 + (x+y)H_2 \qquad [2]$$

surface kinetics alone are to be explored, effects due to the last named parameter must be obviated, the others being amenable to control. It is to be noted in Eq. [2] that two possible Ge-containing species may be formed in the general case by either parallel or sequential reaction paths. Conditions must be chosen to minimize one or the other of these reactions. A thermodynamic analysis of the type reported on earlier (12) can provide information on the temperature and concentration intervals in which one or the other of the over-all reactions specified in Eq. [3] and [4] prevails. While this represents a starting point, it is no guarantee

$$2HI + Ge \rightleftarrows GeI_2 + H_2 \qquad [3]$$

$$4HI + Ge \rightleftarrows GeI_4 + 2H_2 \qquad [4]$$

that the kinetics leading to the equilibrium states proceed via the gross mechanisms suggested by Eq. [3] and [4], and must be considered in the light of other evidence (13).[1] In an open tube system consisting of a source of HI and a reaction chamber of defined geometry, etchant flux may be varied simply by varying the input flow rate. In order to provide some crude normalization of the geometry factor, it is well to consider average linear gas stream velocity, l.g.s.v., rather than flow rate in the reaction chamber. The l.g.s.v. we will consider is simply the input carrier gas flow rate divided by the cross-sectional area of the reactor,

[1] K. Haq, for example, has suggested on the basis of spectrophotometric studies that, in the reduction of $GeCl_4$, the tetrahalide is reduced in the vapor to the dihalide from which point the reduction actually proceeds. If this is actually the case, then it follows that either free halogen or halogen acid is present prior to deposition.

correcting for the temperature of the reactor and the addition of etchant.

Two distinct types of mass transport limitations are associated with etchant flux into the reaction chamber. The first of these depends solely on the rate of introduction of gaseous reactant into the chamber. The second depends on the movement of this introduced mass to all portions of the chamber, particularly the reaction site. It is this second phenomenon which is a geometrically governed limitation, and it is the combination of both phenomena that establishes the mass transport limiting aspects of a reaction taking place in a given open tube apparatus. Boundary layers at the surface of the solid being etched need not be considered in our qualitative discussion since for all practical purposes it is the solid surface plus its inseparable boundary layer that must be together treated as the "surface".

In order to proceed, we will simplify our task subject to subsequent experimental verification by assuming that: (*a*) there exists a distinct slow step in the reaction; (*b*) the total pressure is to a first approximation constant with varying l.g.s.v.; and (c) pertinent vapor phase species are accounted for.

Low L.G.S.V. range-complete mixing-linear region.—At low linear gas stream velocities, the etchant introduced into the reaction chamber has sufficient residency time to come into equilibrium with the solid surface. In this l.g.s.v. interval nothing can be learned of the surface kinetics since the reaction is mass transport limited by the first mass transport process mentioned, *i.e.*, input rate of reactants into the reaction chamber. A plot of etch rate, R_t, *vs.* l.g.s.v. must be linear and it is a consequence of the situation specified that: (*a*) no species partial pressure gradients exist; (*b*) the partial pressures of reactant and products are the equilibrium values; and (c) the reaction efficiency, β, defined as the ratio of observed etch rate to that predicted thermodynamically is unity. These conditions, indeed, are those sought in a transpiration experiment of the type previously discussed by the authors (14), and coincide with a state of affairs in which complete mixing obtains.

Intermediate L.G.S.V.–incomplete mixing, sublinear region.—As the l.g.s.v. is increased, a critical value is reached where the residency time of etchant molecules introduced into the reactor becomes equal to, then less than the time required for complete equilibration to occur. Since this situation is concomitant with an increase of flux into the reactor, it represents the point at which mass transport into the reactor plays less of a role in limiting the reaction and where mass transport of etchant molecules from the walls of the reactor to the solid surface, for example, becomes a major rate-limiting step. Since not all of the introduced etchant molecules in the reactor are able to equilibrate with the solid surface being etched, the efficiency β, whose value may vary between 0 and 1, becomes less than unity and the etch rate-l.g.s.v. curve must become sublinear. The shape of the curve is dependent on the nature of some complicated function describing the relationship between β and l.g.s.v. where hydrodynamic aspects, not simply partial pressure differences, must be incorporated. If in the experiment being considered the surface of the solid is parallel to the gas drift velocity direction (the axial direction), it is evident that the partial pressure of etchant immediately above the solid surface where reaction is depleting its value will be less then at the walls radially removed from the surface (the radial direction).[2] Information relating to the surface limiting kinetics is not obtainable in the sublinear l.g.s.v. region because the radial and very probably axial partial pressure gradients make it impossible to define etchant partial pressure at the surface. In addition, the extent of the reverse reaction contribution to the etch rate is unknown. In the sublinear region, therefore, the case exists where the system tends from a state of complete mixing to one of zero mixing, and where the partial pressure gradients are not readily definable.

High L.G.S.V.-zero mixing, plateau region.—The observed etch rate, R_t, is assumed to represent the differences in rates between the etching and reverse reactions, Eq. [5], where k_f and k_r are the forward and reverse rate

$$R_t = k_f p_{HI}{}^x - k_r p_{GeI_2}{}^y \qquad [5]$$

constants, respectively, p_{HI} and p_{GeI_2} are the partial pressures of HI and GeI_2, respectively, at the surface, and x and y are the reaction orders for the forward and reverse reactions, respectively. With increasing l.g.s.v. we see that, because of the decreased depletion of etchant, the average partial pressure of HI at the surface will increase. This will increase the value of the forward reaction rate term, R_f, defined by Eq. [6]. Simultaneously,

$$R_f = k_f p_{HI}{}^x \qquad [6]$$

the increased l.g.s.v. will sweep away the reaction product(s) causing a diminution of its partial pressure and thereby decreasing the extent of the reverse reaction defined by Eq. [7]. When

$$R_r = k_r p_{GeI_2}{}^y \qquad [7]$$

the l.g.s.v. achieves a sufficiently high rate such that the depletion of etchant is experimentally insignificant, and the extent of the reverse reaction tends toward zero, mass transport effects are obviated, and the observed etch rate is directly that demanded by Eq. [6]. Since p_{HI} is effectively the input value at this point, further increase in l.g.s.v. does not result in a change in etch rate. It is in this l.g.s.v. range that the reaction is surface limited and reactor geometry independent for the first time. It is in this l.g.s.v. range also that zero mixing prevails for the first time.

During the sequence of events represented by the three l.g.s.v. regions, the difference p_{HI}(walls)-p_{HI}(solid) moves from a value approaching zero through a maximum, then back to a value approaching zero. At the two extremes, however, the values for the walls and solid approach $p_{equilibrium}$ in the linear region and p_{input} in the plateau region. In the intermediate sublinear region in which the wall-solid etchant partial pressure differential is not zero, the partial pressure at the wall or solid surface has a value less than the input value, but greater than the equilibrium one. Furthermore, the value of p_{HI} ranges closer to the equilibrium value over a wider l.g.s.v. interval at the solid surface than it does at the walls.

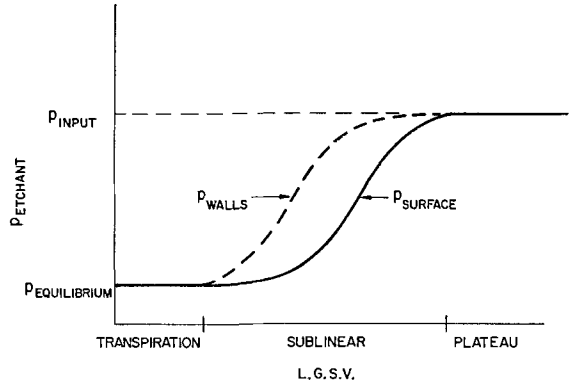

Fig. 1. Schematic representation of variation in partial pressure

[2] In ref. (15) experiments are described in which the existence of radial gradients was demonstrated. In essence, these experiments involved decreasing the diameter of the reaction chamber while maintaining the input etchant flux and temperature constant. Despite the increased l. g. s. v. (therefore, decreased residency time of HI molecules in the vicinity of the surface), the etch rate increased markedly. The effect is, of course, twofold, *i.e.*, bringing more of the HI to the surface and sweeping away reaction products at a faster rate.

Figure 1 schematically depicts the variation in partial pressure at both the walls of the reactor and at the solid surface over the entire l.g.s.v. range.

Based on the rationale, it is clear that experimental data must be acquired solely in plateau regions. These plateau regions can be defined by studying the etch rate-l.g.s.v. behavior, at each etchant concentration, at different temperatures, and for specific crystallographic surface orientations. Such an approach, while necessary in finding a suitable temperature and concentration range to examine, is very laborious, requiring the amassing of an enormous number of data points. A more palatable, but nonetheless laborious approach, involves testing each concentration and temperature interval at a few high l.g.s.v. values on each curve until a suitable region is found.

Experimental Procedure

A number of preliminary tests were applied by us before a region which appeared to represent a starting point for studying Ge surfaces was found. Experiments were conducted in a number of different reactors in which l.g.s.v. were continually increased, in which wafer dimensions were continually reduced to minimize axial direction effects, and temperatures were lowered to get to a reasonable reaction rate range. Having located a starting point, measurements were then made at the highest velocity attainable both below and above the test temperatures and at HI concentrations greater and lower than those used in the test. As long as surface kinetics prevailed, plots of log etch rate (ordinate) *vs.* $1/T$ (abscissa) were expected to provide linear graphs if a simple reaction process obtained. When mass transport conditions became significant, the curves were expected to bend downward indicating that a sublinear region had been entered. The starting crystallographic orientation for the final stages of the current study was the <111> surface which is reputed to be the slowest growing of the low indices planes and, therefore, presumably the slowest etching. It was felt consequently that <111> kinetics would be most amenable to resolution. Furthermore, to duplicate etching behavior in a deposition process, the etching was studied in a hydrogen ambient atmosphere. The hydrogen concentration as a consequence could be considered constant which approximates conditions in conventional deposition processes.

Figure 2 shows the results of a preliminary study conducted on <211> surfaces in a 0.13 cm^2 cross-sectional area rectangular chamber in which l.g.s.v. up to 60,000 cm/min were obtained. It is seen that plateaus were achieved only at the lowest temperatures. It is also observed in Fig. 2 that in a single wafer reactor in which only a small portion of the reactor volume is occupied by the wafer, equilibrium l.g.s.v. regions are obtainable. Here also it was demonstrated by etch rate *vs.* time studies that edge and damage effects were not important since the graphs were linear. It was also found that axial gradients were a potentially serious problem since the wafer leading edges were thinned preferentially.[3] Also there was some indication that the primary vapor phase species was GeI_2 since the quenched etch products were primarily GeI_2, little evidence for the red tetraiodide being observed.

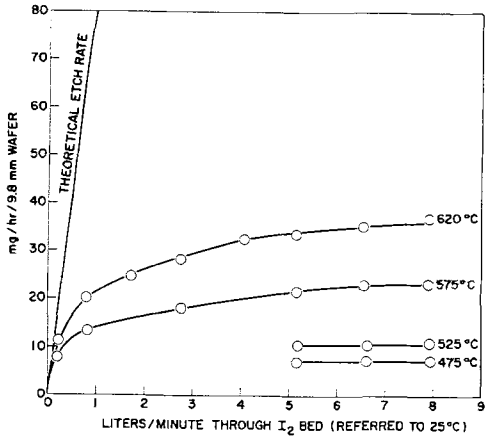

Fig. 2. Results of study on <211> surfaces. Reactor 4 13 x 1 mm; pHI = 3.8 Torr; <211> surfaces NaCl polished both sides; sample diameter *ca.* 9.8 mm.

Reagents.—HI was synthesized *in situ*, on demand, and with input flow rates up to 7.90 l/min at 25°C, using the modified generator design shown in Fig. 3 (15). The generator was constructed entirely of Pyrex and quartz and employed magnetically actuated, hand lapped ball joint members as valves. The leakage rate of the valves when closed was extremely small, since at 2-hr by-pass flow of 7.90 l/min over a Ge wafer at 910° failed to result in a measurable weight change or visually observable surface degradation. The platinum wool catalyst tower was maintained at 450°C and the generator temperature was controlled to ± 0.1°C in an oil bath. The vapor pressure of iodine in the temperature interval 43°-80°C was re-evaluated for purposes of the present study by a method to be reported on by the authors (16).

Matheson "ultra pure" H_2 was used as the carrier gas in all experiments without further purification.

Germanium wafers were prepared from Czochralski pulled single crystals doped with Ga to the 0.01-ohm-cm p-level. The crystals were sliced in the desired <111> or <211> orientation, then cut ultrasonically into circular wafers having a nominal diameter of 195 mils (*ca.* 5 mm) and a thickness of 30 mils. The slices were lapped planar with 3μ Al_2O_3 compound then polished on both sides by the NaOCl technique recently described (17). This provided a finished wafer size of 184-190 mils and a thickness of 19 mils. The dimensions, particularly the diameter, were checked before, and frequently after each run, each sample being used only once. After polishing, in which saw and lapping damage was apparently removed, the edges and one surface were coated with SiO_2 via the pyrolysis of tetraethoxy silane at 700°. The back side of the wafer and edges were protected with black wax, and the reaction side was treated with HF prior to use to remove any SiO_2 that may have deposited on it. Prior to conducting the etching experiment, the

[3] In the process of reducing the cross-sectional area of our reactors starting with the 7.77 cm^2 reactor described in ref. (15), we observed a sequence of events in which an axial gradient became pronounced as the wall surface to wafer surface distance was decreased with constant wafer size. In order to eliminate this effect it was necessary also to reduce wafer diameters. This effect is to be expected since surface etchant depletion at the leading edge of the wafer will be compensated for by diffusion from the walls if the wafer is large enough in a large diameter reactor. As the diameter of the reactor is reduced, however, this diffusion effect cannot overcome the depletion rate at the leading edge if the wafer axial dimensions are too large. Consequently, within limits imposed by experimental necessity, the axial extent of the wafer must be made of minimum dimension (a wire if feasible). With the reactor design to be described below, axial effects were not noticeable.

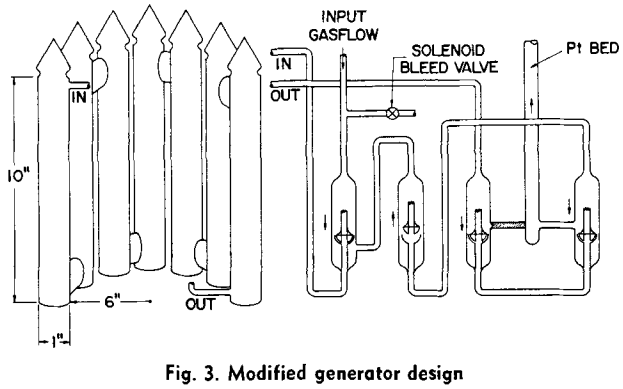

Fig. 3. Modified generator design

black wax was dissolved in trichlorethylene. The oxide coat minimized edge attack and completely eliminated attack of the under surface of the sample. The final weight of the samples was of the order of 40 mg. For each set of experimental conditions, etching times were varied so as to provide weight losses of *ca.* 10-15 mg. These run times varied between 20 min and 6 hr with the majority of experiments falling into the 1-2 hr range. In general, two to four determinations were made under each set of conditions. Etch time was varied to provide weight loss variation so that continued monitoring of possible edge and damage effects could be made. Generally, weight loss reproducibilities were within 2-3% of a mean with the worst case in one instance being 8%.

Apparatus.—Figures 4 to 6 show the design details of the high velocity reactor and reaction train used to acquire our final data. This reactor was capable of developing l.g.s.v. of approximately 800,000 cm/min at 760°C with input carrier gas flow rates at the 7.9 l/min level. The main portion of the reactor (the inner reactor) consists of precisely machined quartz parts having a rectangular cross section uniform over 2 in. to within a few square mils. The inner rectangle dimensions are 6.98 x 0.51 mm (275 x 20 mils) providing a cross-sectional area of 0.036 cm^2. Built into the center of the inner reactor is a 15-mil deep circular recess having a diameter of 105 mil. In the center of this recess, in which the wafer is positioned, is a 25-mil diameter hole connected to a vacuum line. This vacuum chuck is necessary to keep the wafer positioned at the high l.g.s.v. employed. The entire inner reactor and its associated vacuum chuck and effluent path are movable within a rubber sleeve attached to a female standard taper joint which in turn connects the inner reactor to the outer reactor into which etchant is first introduced.

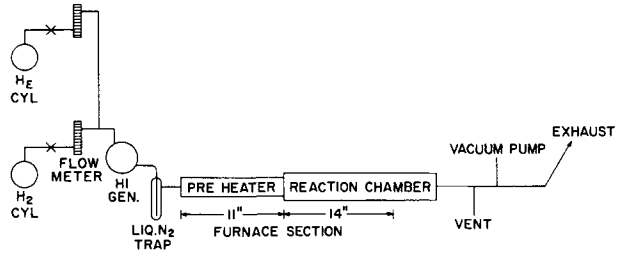

Fig. 4. Design details of high volecity reactor and reaction train

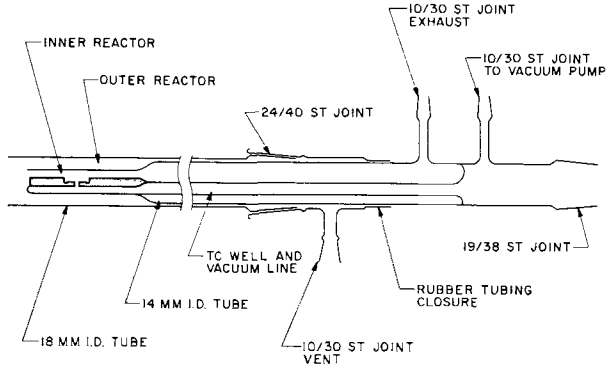

Fig. 5. Design details of high velocity reactor and reaction train

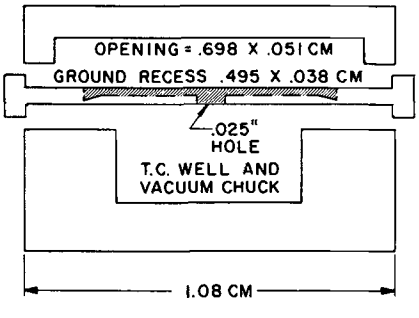

Fig. 6. Design details of high velocity reactor and reaction train

The combination of inner and outer reactor is resistance heated over a 14 in. length, and the sample temperature is monitored by a movable thermocouple located in the vacuum chuck portion of the apparatus which also functions as a thermocouple well. In order to assist the gas entering the outer reaction chamber in achieving the required temperature, the incoming gas was first preheated over an 11 in. length to the reaction temperature.

The experimental procedure followed was to load the wafer, then flush the system with the vent to the outer reactor open for 10 min at an input H_2 flow rate of 4 l/min. The system was then brought to temperature with the outer chamber vent closed and the experiment run. At the conclusion of the etching process, the system was flushed for 5 to 30 min at the experimental flow rate; the furnace was then turned off and allowed to cool while maintaining a flow rate of 4 l/min.

Some insignificant back streaming, as evidenced by the minute quantities of reaction product accumulating in the outer chamber, did occur. Over the course of several hundred runs, a thin Ge mirror formed in the colder regions of the outer reactor chamber.

Results

Figure 7 shows a plot of the log R_f *vs.* $1/T$ obtained on <111> surfaces with an input HI partial pressure of 3.8 Torr. The apparent temperature intervals for mass and surface-limiting reaction are delineated in the graph. The activation energy for the surface limited reaction was calculated to be 16.6 kcal, and the rate expression describing the data on this curve is given by Eq. [8].

$$\log R_f = \frac{-3.64}{T°K} + 5.99 \qquad [8]$$

where R_f is the etch rate in mg/cm^2 hr.

Figure 8 shows a number of such curves, each representative of a different input partial pressure of HI. Within experimental limits, the slopes of those curves defined by the greatest number of data points are identical, and those curves tested at only a few points clearly exhibit similar slopes. It is noteworthy that with increasing HI mole fraction the temperature

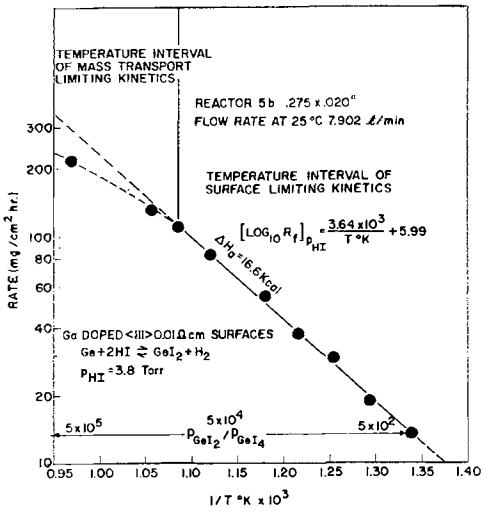

Fig. 7. Plot of log R_f *vs.* $1/T$ obtained on <111> surfaces

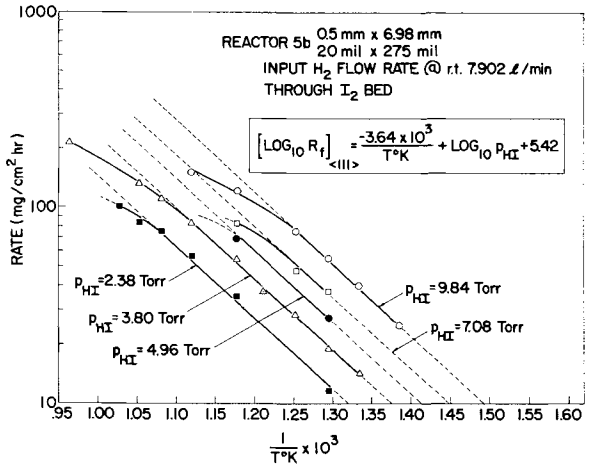

Fig. 8. Curves representing different input partial pressures of HI

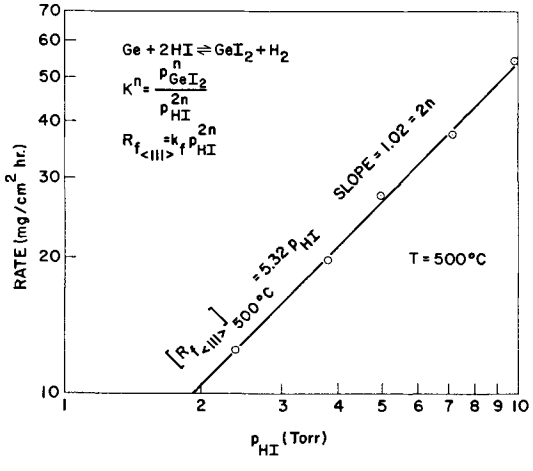

Fig. 9. Plot of log R_f vs. log pHI from 2.38 to 9.84 Torr at 500°C

at which mass transport conditions begin to prevail decreases.

Figure 9 is a plot of log R_f *vs.* log pHI, in the range 2.38-9.84 Torr at 500°C. These data provide an excellent straight line relationship having a slope very close to unity. The value of k_f was determined using Eq. [5], and its temperature dependency was determined from the Ahrennius relation, Eq. [9].

$$\log k_f = -3.64 \times 10^3/T°K + 5.42 \quad [9]$$

k_f has the dimensions mg/cm² hr Torr. From Eq. [6] and [9], the temperature dependency of the forward reaction rate was calculated and is given in Eq. [10].

$$\log R_f = -3.64 \times 10^3/T°K + \log p_{HI} + 5.42 \quad [10]$$

R_f has the dimensions mg/cm² hr, and p_{HI} is the input partial pressure of the halogen acid.

Discussion

Separation of mass transport and surface limiting phenomena.—From the results cited it appears that the qualitative description of open tube kinetic processes satisfactorily predicts the effect of l.g.s.v. in achieving a separation between the geometrically governed mass transport and the surface controlled reaction. In different systems and with different substrate orientations one would of course expect that the boundaries between the linear, sublinear, and plateau regions might vary greatly. No attempt to analyze the sublinear region analytically has been made because of the complicated nature of diffusion phenomena in nonstatic systems, static treatments such as applied by Lever and Mandel not being applicable (18-23). Furthermore, attempts on our part to computer analyze the sublinear region invoking a complete mixing assumption were completely unsuccessful as might have been anticipated.

Effect of etchant partial pressure increase at constant l.g.s.v. and temperature.—While it is the case, as can be seen from Eq. [3] and [4], that two or four molecules of HI must react at the surface in order that only one molecule of Ge containing product is generated, it is also evident that at constant temperature and l.g.s.v. the forward rate increases with an increase in etchant partial pressure as required by Eq. [6]. A consequence of this enhanced etch rate is the buildup of reaction product partial pressure at the surface and an increase in the rate of reverse reaction. Thus, what may be an adequate l.g.s.v. velocity to satisfy both conditions necessary for resolving the forward reaction kinetics at a low etchant partial pressure may become inadequate at higher values because of an increased reverse reaction rate.

Speculation on the reaction mechanism.—From the experimental results obtained we have seen that the forward rate is dependent on the HI partial pressure to the first power. In attempting to define a reasonable mechanism consistent with this, Eq. [11 a-e], a number of alternatives

$$\left.\begin{aligned} H_2(g) + Ge(s) &\rightleftarrows Ge \cdot H_2(a) \\ HI(g) + Ge(s) &\rightleftarrows Ge \cdot HI(a) \end{aligned}\right\} \text{Langmuir adsorptions} \quad [11a], [11b]$$

$$Ge \cdot HI(a) + HI(g) \rightleftarrows GeI_2(a) + H_2(a) \quad [11c]$$

$$GeI_2(a) \xrightarrow{\text{slow}} GeI_2(g) \quad [11d]$$

$$H_2(a) \rightleftarrows H_2(g) \quad [11e]$$

suggest themselves. The first involves a mechanism in which the adsorption of HI via Eq. [11b] represents the slow step. Such a rate-limiting step is not too probable, however, since initial surface coverage is likely to be rapid. In fact, with the large quantity of H_2 present it is likely that the HI absorption isotherm is so modified that even at very low HI pressures the surface rapidly achieves saturation with respect to HI. This leads to either Eq. [11c] or [11d] as representing the possible rate-limiting step. In attempting to assess the relative probability of each of these steps as rate limiting, some preliminary observations of <211> etching results are worthwhile mentioning. These data together with those of Fig. 7 are presented in Fig. 10 for comparison. It is to be noted that the etch rate on <211> surfaces is slower than on <111> surfaces. In order for the equilibrium constant describing the reaction to be constant, this observation indicates that the surface-controlled growth rate on <111> surfaces must be slower than on <211> surfaces. Also to be noted is the apparent similarity of

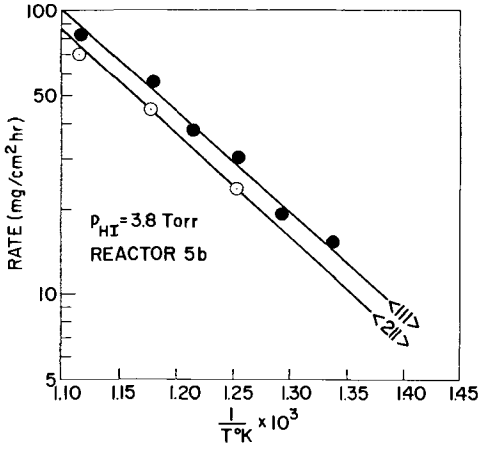

Fig. 10. Observations of <211> etching results

Table I. Thermodynamic data for the system Ge-I_2-H_2

T_{I_2} Bed, °C	p_{HI} input, mm	T_{Ge}, °C	p_{GeI_2}/p_{GeI_4}
43.6	2.38	500	1.6×10^3
		600	1.7×10^4
		720	2.2×10^5
49.35	3.80	500	5.3×10^2
		600	7.8×10^3
		720	1.0×10^5
53.0	4.96	500	3.7×10^2
		600	5.8×10^3
		720	6.6×10^4
58.1	7.08	500	2.0×10^2
		600	2.6×10^3
		720	3.5×10^4
63.0	9.84	500	1.3×10^2
		600	1.8×10^3
		720	2.2×10^4

activation energies for both <111> and <211> surface rates, indicative of similar rate-controlling steps. Whether this is general for other low indices planes is yet to be explored, but it would tend to point more to the reaction product desorption step, Eq. [11d], rather than a bond breaking step, Eq. [11c], as rate limiting. The former is more likely to involve similar activation energies on different planes than is the latter.

Reverse reaction and autodoping phenomena.—In all of the experiments conducted, conditions were chosen in which the thermodynamic GeI_2/GeI_4 ratio was *ca.* 10^2 or greater, Table I (12). The data for the forward reaction, however, are independent of which product is predominant so long as the over-all reaction mechanism exhibits a distinct rate-limiting step and proceeds primarily by a sequential path. Assuming that the over-all reaction mechanism coincides with the thermodynamic relationship, Eq. [3], in which GeI_2 is formed, for which we have presented some indirect evidence, the equilibrium constant may be defined by Eq. [12]. In Eq. [12], the H_2 has been taken as a constant having a value of 755 Torr.

$$K = \frac{pGeI_2}{pHI^2} \qquad [12]$$

In order for the kinetics to be consistent in both the nonequilibrium and boundary equilibrium states, Eq. [12] may be rewritten as

$$K' = K^{1/2} = \frac{pGeI_2^{1/2}}{pHI} \qquad [13]$$

It will be noted that the pHI term is raised to the first power consistent with the reaction order determined. The temperature dependency of K' as determined from data in ref. (12) is given by

$$\log K' = -93.7/T°K - 0.631 \qquad [14]$$

The total rate expression for the reaction defined by Eq. [3] is given in Eq. [15].

$$R_t = k_f p_{HI} - k_r p_{GeI_2}^{1/2} \qquad [15]$$

A similar expression assuming GeI_4 as the end product is given by Eq. [16].

$$R_t' = k_f p_{HI} - k_r' p_{GeI_4}^{1/4} \qquad [16]$$

At equilibrium where the rates for the forward and reverse reactions are equal, it is a consequence that

$$k_f p_{HI} = k_r p_{GeI_2}^{1/2} \qquad [17]$$

or

$$k_f p_{HI} = k_r' p_{GeI_4}^{1/4} \qquad [18]$$

and

$$k_r = \frac{k_f}{K'} \text{ or } \frac{k_f}{K''} \qquad [19]$$

where K'' is the equilibrium constant for the reaction in which GeI_4 is the end product. The temperature dependency of $K''$is given by Eq. [20].

$$\log K'' = 1890/T°K - 3.771 \qquad [20]$$

Equations [14] and [20], together with the temperature dependency of k_f, Eq. [9], enable us to calculate the temperature dependency of the specific rate constant, k_r, for either of the assumed reverse reactions. These relationships are given in Eq. [21] and [22].

$$\log k_r = \frac{-3.55 \times 10^3}{T°K} + 6.05 \text{ where } GeI_2 \text{ is involved} \qquad [21]$$

$$\log k'_r = \frac{-5.53 \times 10^3}{T°K} + 9.19 \text{ where } GeI_4 \text{ is involved} \qquad [22]$$

Dimensionally k_f has the value mg/cm² hr Torr. k_r for the GeI_2 reaction has the dimensions mg/cm² hr Torr$^{1/2}$, and k_r' for the GeI_4 reaction has the dimensions mg/cm² hr Torr$^{1/4}$. The activation energies calculated for the reactions involving GeI_2 or GeI_4 are 16.2 and 25.3 kcal, respectively.

The above has considerable implications concerning the extent to which autodoping is likely to occur in a deposition reaction involving the reduction of GeI_2 or GeI_4. Since the etching kinetics of the HCl-Ge reaction are even faster than those we have determined for the Ge-HI system, the problem of autodoping is potentially more severe in the tetrachloride process.

In its simplest sense, as mentioned earlier, autodoping is a term used to describe an effect in a net deposition reaction in which a reaction product (here a halogen acid) reacts with the substrate and substrate dopants bringing both the semiconductor and the impurities into the vapor phase. These impurities then, either by a deposition or segregation process, become incorporated in the epitaxially grown layer. A drastic example of such an effect is observed in the growth of Ge on GaAs via the reduction of $GeCl_4$. Even though a net growth is observed, the GaAs is noticeably etched, and the deposited layer of Ge is doped almost to degenerate levels for some distance from the physical junction. Since the grown layer shields the substrate, once the former is thick enough, the autodoping decreases with increasing grown layer thickness.[4] The net effect is the formation of a nonabrupt impurity gradient around the grown junction. Alternately, workers in the field have attributed the observed impurity gradient characteristics to outdiffusion from the substrate or to the gas phase phenomena mentioned. The fact that our studies indicate such fast kinetics for the etching reaction is strong evidence to support the gas phase mechanism as the major factor in autodoping. If we consider further that the deposition reaction is dependent on either the ½ or ¼ power of the Ge halide while the etching is proportional to the first power of the halogen acid concentration, the gas phase mechanism becomes even more compelling. As we have pointed out earlier, the l.g.s.v. normally employed coincide with those in which the rates approach equilibrium values. This, of course, further favors a gas phase autodoping mechanism in view of our results. If these arguments are indeed representative of the state of affairs in open tube halide deposition reactions, it would appear that a means by which autodoping can be minimized is to increase l.g.s.v. to values many orders of magnitude greater than are normally employed at the start of the deposition to obtain initial surface coverage. When this has been achieved and the surface is protected, more normal conditions may then be employed.

As previously discussed, the temperature interval in which surface-limiting kinetics could be achieved in the reactor employed appeared to decrease with increased HI partial pressure. Since the faster l.g.s.v.

[4] In the initial growth stages, nucleation processes are occurring so that even though a net deposition occurs, most of the original surface is exposed to the attack of reaction products.

apparently needed to minimize autodoping would probably require proportionately decreased concentrations of reactants whose concentration effect behavior hopefully is similar in the deposition process to that observed in the etching process, both requirements for approaching surface-limiting kinetics and minimizing autodoping in a deposition would appear to be consistent.

Acknowledgment

The authors wish to acknowledge gratefully the assistance of R. L. Rohr in designing the reactor, and M. Sampogna in acquiring the data. They wish also to thank H. R. Leonhardt and T. O. Sedgwick for many stimulating discussions and critical evaluation of the manuscript, and R. F. Lever for evaluating it. The authors wish to acknowledge the assistance of S. A. Alyanakyan in providing needed thermodynamic information.

Manuscript received July 9, 1965; revised manuscript received Oct. 25, 1965. The work was supported in part by AFCRL Contract No. AF 19(628)-2468.

Any discussion of this paper will appear in a Discussion Section to be published in the December 1966 JOURNAL.

REFERENCES

1. T. O. Sedgwick, *This Journal*, **111**, 1381 (1964).
2. R. F. Lever, *IBM J. Res. and Dev.*, **8**, 460 (1964).
3. H. C. Theuerer, *This Journal*, **108**, 649 (1961).
4. W. Steinmaier, *Philips Research Rpts.*, **18**, 75 (1963).
5. E. G. Bylander, *This Journal*, **109**, 1171 (1962).
6. R. R. Monchamp, W. J. McAleer, and P. I. Pollack, *ibid.*, **111**, 877 (1964).
7. O. Alstrup and C. O. Thomas, *ibid.*, **112**, 319 (1965).
8. W. J. Heinecke and S. Ing, *J. Appl. Phys.*, **32**, 1498 (1961).
9. K. J. Miller and M. J. Grieco, *This Journal*, **111**, 1099 (1964).
10. I. L. Kalnin and J. Rosenstock, *ibid.*, **112**, 329 (1965).
11. S. E. Craig, *ibid.*, **112**, 647 (1965).
12. A. Reisman and S. A. Alyanakyan, *ibid.*, **111**, 1154 (1964).
13. K. E. Haq, Paper presented at the Washington Meeting of the Society, Oct. 11-15 (1964).
14. A. Reisman, M. Berkenblit, and S. A. Alyanakyan, *This Journal*, **112**, 241 (1965).
15. A. Reisman and M. Berkenblit, *ibid.*, **112**, 812 (1965).
16. M. Berkenblit and A. Reisman, *ibid.*, To be published.
17. A. Reisman and R. L. Rohr, *ibid.*, **111**, 1425 (1964).
18. G. Mandel, *J. Phys. Chem. Solids*, **23**, 587 (1962).
19. R. F. Lever and G. Mandel, *ibid.*, **23**, 599 (1962).
20. G. Mandel, *J. Chem. Phys.*, **37**, 1177 (1962).
21. R. F. Lever, *ibid.*, **37**, 1078 (1962).
22. R. F. Lever, *ibid.*, **37**, 1174 (1962).
23. G. Mandel, *ibid.*, **40**, 683 (1964).

Kinetic Effects in Temperature Gradient Zone Melting

R. G. Seidensticker

Research Laboratories, Westinghouse Electric Corporation, Pittsburgh, Pennsylvania

ABSTRACT

Experiments on the motion of liquid zones in the germanium-gold TGZM system indicate that kinetics characteristic of screw dislocations may play an important role. In many instances, dissolution rather than deposition appeared to be the rate-limiting mechanism. Finally, it was found that the motion of such zones was intrinsically unstable under some conditions.

Temperature gradient zone melting (TGZM), sometimes called the traveling solvent method of crystal growth (TSM), has been discussed in a number of papers (1-9). Migration of the zone occurs because a temperature gradient imposed on a solid-liquid-solid sandwich creates a concentration gradient, linear for most cases of interest, which provides a driving force for the diffusion of solvent across the zone. Since the solvent concentration may be equated to a temperature, T_{liquidus}, by the phase diagram liquidus curve, the concentration gradient may be equated to an "equilibrium temperature gradient," G^*. The migration velocity is proportional to the flux of solvent so that $v = \beta G^*$, where β includes the diffusivity of the liquid, and parameters relating to the phase diagram. A model frequently used for analyzing zone motion assumes that the liquid alloy is in equilibrium with the solid at both the high and low temperature interfaces so that $G^* = G$, the actual temperature gradient. On the other hand, Tiller (5) assumed that both interfaces depart from equilibrium due to kinetic effects and the resulting equations show an additional dependency on zone thickness and kinetic constant.

This effect of kinetics on zone migration can be easily seen from Fig. 1. Let δT_m and δT_s be the departures of the dissolving and solidifying interfaces from equilibrium at a given velocity, *i.e.*, $\delta T = T_{\text{liquidus}} - T_{\text{actual}}$. It is easily seen that

$$G^* = G - \frac{\delta T_s - \delta T_m}{l} \qquad [1]$$

where $\delta T_m \leq 0 \leq \delta T_s$, and l is the zone thickness. Since the migration velocity is proportional to G^*

$$v = \beta G^* = \beta G - \frac{\beta}{l}(\delta T_s - \delta T_m) \qquad [2]$$

If kinetics are neglected (the δT's $= 0$) or if l is very large, then Eq. [2] reduces to the usual form $v = G\beta$; when kinetic laws are specified, it reduces at once to Tiller's equations.

Zone stability has been discussed qualitatively for isotropic kinetics by Pfann (1), and by Tiller (5) who assert that the zone should be stable when moving in the direction of the temperature gradient. For the case of anisotropic interfacial energy [equivalent to aniso-

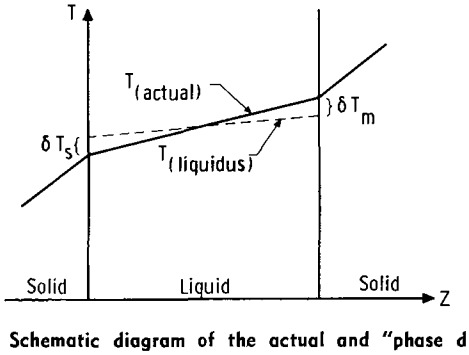

Fig. 1. Schematic diagram of the actual and "phase diagram" temperatures in a migrating zone with kinetics limitations.

tropic kinetics (5)] they conclude that stability depends on the orientation of both the zone and the temperature gradient.

As to the results of experiments, Wernick (4) reported that both gold and aluminum wire zones in germanium and silicon exhibited a dependence of velocity on zone size and a stability dependency on the orientation of both the zone and the gradient. Mlavsky and Weinstein (7), however, reported no indication of an orientation dependent velocity in the growth of GaAs from a Ga rich zone; indeed, they and their colleagues have asserted in several papers (7, 9) that if adequate wetting is obtained between the solid and liquid, then the zone moves uniformly through the sample. For the case of zone motion in GaAs, Mlavsky and Weinstein did report that the migration velocity depended on zone thickness, however, their analysis as well as Tiller's (6) indicates that this was due to a change in liquid composition rather than to kinetic effects. Wernick's interpretation of his data was based on undersaturation in the liquid combined with anisotropic dissolution at the hotter interface. Tiller, on the other hand, concluded that Wernick's data indicated that screw dislocation kinetics limited the zone velocity, but for lack of distinguishing criteria assigned equal weight to kinetics at both interfaces, *i.e.*, assumed $\delta T_m = \delta T_s$.

In this paper, various effects of kinetically limited mechanisms and of interfacial energy will be discussed. In many instances, dissolution was found to be the rate limiting process so that kinetics at the higher temperature interface do indeed limit the velocity. A quantitative evaluation of zone stability including kinetic effects is made, based on an extension of the stability analysis of Mullins and Sekerka (10). This treatment, derived in a later paper (11), shows that the migrating zone may be unstable even in the strictly isotropic case.

Experimental Apparatus and Procedures

Zone migration experiments were carried out using both flat or "slab" zone and wire zones. The germanium-gold system was chosen because the low eutectic temperature (12) permitted experiments to be done in a convenient temperature range, and the negligible solid solubility of gold in germanium (13) assured that the gold content of the zone was constant during a run.

The experimental apparatus is shown in Fig. 2. All the components are enclosed in a Vycor "T" tube to permit a choice of ambient. The furnaces were brought

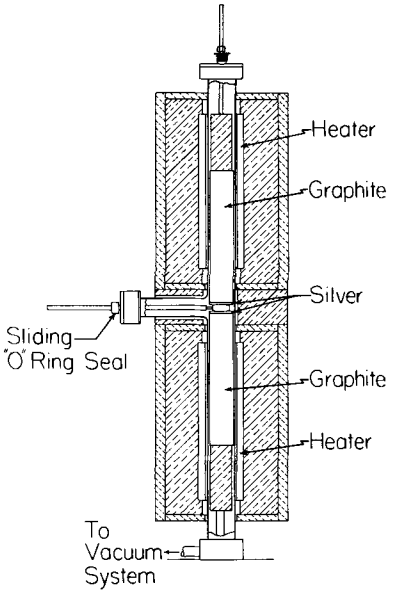

Fig. 2. Schematic diagram of the experimental apparatus

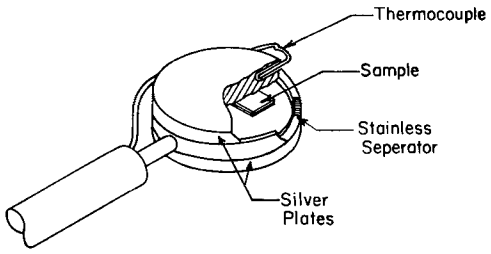

Fig. 3. Schematic diagram of the sample holder

up to temperature and outgassed at a pressure of 10^{-5} Torr. When the sample holder was inserted in the hot section to start a run, about 5 Torr of He was admitted to aid thermal transport. Heavy graphite pistons extending into the hot zones of the furnaces maintained the sample holder temperatures. A bellows at the top of the apparatus allowed the upper piston to be raised so that the sample holder could be easily moved, and yet provided a good pressure contact. Caps of 3/16 in. silver on the ends of the pistons reduced radial gradients at the sample holder.

The sample holder itself is shown in Fig. 3. Silver top and bottom plates separated by a stainless steel ring serve to further minimize radial temperature gradients. Temperature measurements at the plates were made using chromel-alumel thermocouples, protected by thin walled silica tubes, and inserted 1 cm into the plates. An additional 5 cm of the thermocouples were in the hot zone of the furnace to minimize immersion corrections. Since the difference in temperature between the two plates was much more important than the absolute temperature, some care was taken to insure that the couples had similar response. Both junctions were made from adjacent regions of the thermocouple wire; calibration of one pair of couples indicated an agreement of ¼°C or better, *i.e.*, about 1% of the temperature differences usually measured.

The temperature gradients in the sample were usually computed from the measured temperature difference across the sample holder. This technique required good thermal contact between the sample and the holder, and several methods were tried. The use of Aquadag as a cement was reasonably successful, however the use of a pressure contact with the sample separated from the holder plates by thin (75μ) graphite disks was more reproducible. When the disks were used, the sample had to be prepared so that there was a solid region around the liquid zone for support; the liquid was essentially enclosed. Calibration runs using samples with differential thermocouples embedded in them showed that the ratio of sample gradient to the temperature difference across the holder was constant to about 10%, especially when the pressure contact technique was used.

The samples themselves were prepared by first alloying gold plating or gold foil onto the individual germanium slices. If a plated deposit was used, additional gold foil was added to make up the final zone thickness. The alloying was done either in a hydrogen atmosphere or in forepump vacuum. Both techniques gave satisfactory results, however vacuum was preferred since gold-germanium eutectic has a small but important solubility for hydrogen. For some of the runs, an alloy of Au + ½ a/o (atomic per cent) Sb was used to enhance both the wetting of the germanium and the ease with which the redeposited material could be delineated. There was no significant improvement in wetting, so that in spite of the improved delineation, pure gold was used for most of the runs to reduce the number of parameters in the system. In the wire zone runs, the Ge slices were grooved lightly on one surface and pure gold wires fused into the grooves.

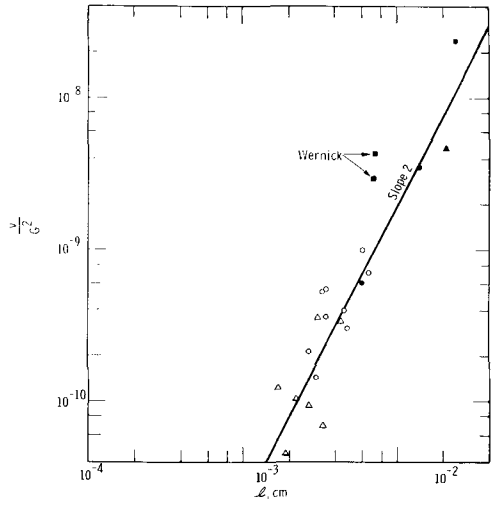

Fig. 4. Experimental data on the zone migration velocities. Zone velocity, v; temperature gradient in the liquid, G; zone thickness, l. ○ ●, ~ 525°C; △ ▲, ~ 625°C; solid points, wire zone.

The behavior of the zone was determined on the basis of one or more sections through the sample. Standard polishing and etching techniques were used to determine the zone travel, and hence the velocity.

Most of the flat zone runs were made using {111} wafers for both the source and the seed crystals. The axis of the wire zones was usually <110> and the temperature gradient in either <001> or <112>. The calculated gradients in the liquid zone ranged from 15° to 60°C/cm, and average zone temperatures of about 525° and 625°C were used.

Experimental Results

Although the flat zones frequently moved as segments rather than as a single slab, the segments were wide and thin enough to be considered as individual flat zones. Only those runs where the segment velocity was uniform over the sample were used for the evaluation of the kinetics. The experimental data on the migration velocity is shown in Fig. 4, where the function v/G^2 is plotted *vs.* the zone thickness. Data from the wire zone runs which showed uniform motion are also plotted in the same figure.

In some of the runs, the segments were the result of uneven wetting; in many cases, however, bubbles apparently formed in the liquid and forced some of it out of the zone. Fusion analysis in a mass spectrometer showed that samples that had been fused in hydrogen released sufficient gases to give such bubbling, even in the presence of the 5 Torr He ambient. Simple calculations indicated that when bubbling had forced droplets of liquid out of the zone, the free energy of the system was lowered and the configuration was stable. The use of samples fused in vacuum markedly reduced the size and number of voids.

The morphology of the zone was used to determine qualitatively at which interface the kinetics effects were most pronounced. If one interface but not the other showed faceting, then it is reasonable to assume that kinetic limitations were more important at that interface. In the case of flat zones bounded by {111} planes, the dissolving interface showed indications of faceting while the growing interface did not. The effect was more pronounced, however, with the wire zones. Figure 5 shows transverse and longitudinal sections of a <110> zone which has moved in a <001> gradient. The zone was dissolving in a faceted trough bounded by {111} planes, while the growing interface was highly curved. These observations confirm Wernick's conclusion that in wire zones, particularly, the rate limiting step was dissolution rather than solidification.

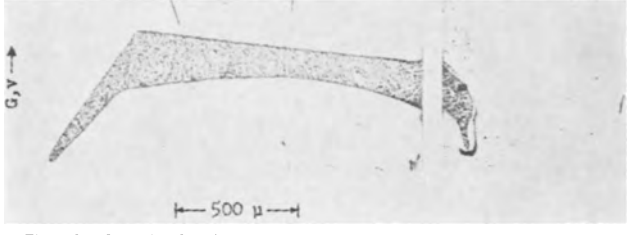

Fig. 5. Longitudinal and transverse section of a wire zone. Dissolving interface faceted and solidifying interface curved.

These observations were generally applicable to zone motion with moderate temperature gradients in the liquid, *e.g.*, $G < 60$°C/cm. Two runs were made using {111} flat zones with gradients above 100°C/cm. These runs, which apparently had good wetting and few if any voids, showed an instability characterized by the break up of the zone into small droplets. The possible cause of such instability will be considered later.

Discussion

In order to analyze the zone motion data, Eq. [2] must be modified by assuming a specific kinetic law. For example, if layer generation by a screw dislocation is the assumed mechanism, then $\delta T_s - \delta T_m = \Gamma v^{1/2}$, where $\Gamma = (1/\mu_s)^{1/2} + (1/\mu_m)^{1/2}$ and the μ's are the kinetic constants at the solidifying and melting interfaces. This assumption allows Eq. [2] to be solved for v giving

$$v = \frac{\beta^2\Gamma^2}{2l^2}\left\{1 + \frac{2l^2G}{\beta\Gamma^2} - \left[1 + \frac{4l^2G}{\beta\Gamma^2}\right]^{1/2}\right\} \qquad [3]$$

When kinetic effects are pronounced, $\beta\Gamma^2 >> 4Gl^2$ and Eq. [3] may be approximated by

$$v \approx \frac{G^2l^2}{\Gamma^2} \qquad [4]$$

For the case of linear kinetics ($\delta T = v/\mu$) a similar approximation leads to

$$v \simeq \frac{lG}{\Gamma'} \qquad [5]$$

and, for a two-dimensional nucleation process

$$v = \beta G - \frac{\beta A}{l}\left(\frac{1}{\ln \mu/v}\right) \qquad [6]$$

Hence, a plot of the experimental data as log (v/G^2) *vs.* log l should give a straight line of slope 2 if the screw dislocation law applies; log (v/G) *vs.* log l should yield a straight line of unity slope if linear kinetics obtain; and finally a plot of v/G *vs.* $1/lG$ should be reasonably straight if exponential kinetics fit the data. Only the plot appropriate to the screw dislocation kinetics gave a reasonable representation of the data (Fig. 4). The value of Γ computed from this plot is about 220 deg $(\text{sec/cm})^{1/2}$ giving a kinetic constant of $\mu = 2 \times 10^{-5}$ cm/sec-deg^2 if only the solution interface were kinetically limited, and twice this value if both interfaces were equally involved. Although this value is low for a kinetic constant, it is not implausible. (5).

With such sluggish kinetics, the effect on zone motion is very pronounced, and the migration velocity is much slower than is predicted by the simple theory which assumes that diffusion is the limiting mechanism. Thus the use of TGZM as a technique for the measurement of diffusivities is not straightforward, and diffusivities obtained in this manner can only be considered as lower limits.

One final point should be made with regard to the data in Fig. 4, namely that there does not appear to be any pronounced dependence on the average zone temperature; the gradient and zone thickness are the controlling parameters. Two of the points are taken

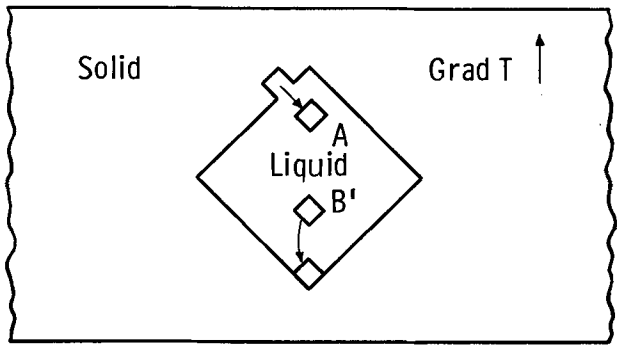

Fig. 6. Schematic diagram of a completely faceted <110> wire zone in a <001> temperature gradient.

from Wernick's paper (3) and are in reasonable agreement with the present results.

Derivation of the temperature gradient in the liquid, G, used in the analysis of the data, required several assumptions. First, the use of the relations between the gradients in the liquid and solid for static plane and wire zones is justified since the latent heat contribution is two to three orders less than the heat flux due to the temperature gradient and may be neglected. Second, when the flat zone consisted of isolated segments, it was assumed that the total heat flux passed through the liquid (conductivity through the voids being very small) and hence the liquid gradient was increased in inverse proportion to the liquid area. Differential thermocouple measurements confirmed that this assumption held to about 15%.

Some knowledge of the thermal conductivities is necessary, however the calculations are most sensitive to the value for solid germanium which fortunately is well known (14). The value used for the thermal conductivity of the liquid alloy was 0.5 watt/cm-deg and was based on a Wiedemann-Franz calculation. The electrical conductivity of the liquid alloy was taken to be proportional to the conductivities of pure liquid gold and germanium adjusted for temperature and weighted by the liquid composition.

The faceting at the solution interfaces of the zone may be interpreted using a simple layer source model. This model in its simplest form states that the addition or removal of an atom from a close packed plane (the {111} planes in germanium) is energetically less favorable and hence slower than at a step or corner. The application of such a model to zone motion may be most clearly illustrated by considering the fully faceted form of a <110> wire zone moving in a <001> temperature gradient, as shown in section in Fig. 6. Dissolution at the hotter interface would require an event of type "A," the removal of an atom or group of atoms from the close packed plane. Once this event occurred, subsequent dissolution could proceed by the removal of additional atoms from the edge so formed. Eventually, however, another "A" event would be required before additional dissolution could take place. At the colder interface, grooves or layer edges will always exist, and an event analogous to "A" will never be required. Atoms can always be added by the relatively easier events "B." Thus, a self-perpetuating step generated by a screw dislocation provides little advantage at the solidifying interface where steps are already plentiful but would greatly enhance the dissolution rate at the hotter interface.

Break up of several runs at high gradient, despite good wetting of the interface and freedom from voids, prompted an analysis of zone stability on a quantitative basis. The interfacial stability treatment of Mullins and Sekerka (10) was extended to include isotropic kinetics and specifically applied to the problem of TGZM. Details of the analysis will appear in a subsequent paper (11), however the central result is a stability function, S, which must be evaluated for both interfaces of the zone. Only when $S < 0$ is the interface stable, and both interfaces must be stable for stable migration of the zone as a whole. For systems with low solid solubility of the solute, S may be approximated by

$$S = -\frac{4\pi^2\gamma T_m}{\lambda^2 L} - \frac{Lv}{K_s + K_l} - \left(\frac{K_l - K_s}{K_l + K_s}\right)G + \frac{\delta T_2 - \delta T_1}{l} \quad [7]$$

where γ is the interfacial free energy, T_m the melting temperature of the pure solvent, L the latent heat per unit volume, λ the wavelength of the instability, K_s and K_l the thermal conductivities of the solid and liquid, v the average zone velocity, G the thermal gradient in the liquid, and l the zone thickness. δT_1 is the kinetic departure at the interface under consideration and δT_2 is the kinetic departure at the other interface. When the growing interface is being analyzed, $\delta T_2 < 0 < \delta T_1$ but when the dissolving interface is under consideration, $\delta T_1 < 0 < \delta T_2$. It should also be emphasized that because of the coordinate system used in the derivation (positive direction into the liquid), G and v are negative at a dissolving interface. Thus it can be seen that, for $K_l > K_s$, which is usually appropriate for semiconductors, the growing interface is always stable, but stability of the dissolving interface depends on λ, G and v. If the zone is stable for values of λ much larger than the total width of the interface, then the zone should be able to migrate considerable distances without appreciable distortion. It can be seen, however, that when the gradient is increased, the value of λ necessary for stability decreases. For most metallic systems, $K_l < K_s$ so that instability terms are present at both interfaces. Thus, the variation in thermal conductivities and interfacial energies for various systems may well account for the apparent conflict in experimental data reported for zone stability.

Summary

The experimental data for the motion of a gold-germanium liquid zone through solid germanium in a temperature gradient suggests that the motion is limited by kinetics characteristic of screw dislocations. The appearance of faceting on the dissolving interface but not on the growing interface indicates that for some experimental situations, it is dissolution and not deposition which limits the zone motion, especially in the case of wire zones.

Instability of the zone due to poor wetting and to bubbles in the liquid was found. In addition, an instability was observed in apparently flawless samples at high gradient. Analysis of interface stability following the technique of Mullins and Sekerka indicated that zone motion has regimes of intrinsic instability, particularly with high gradients and sluggish kinetics.

Acknowledgments

This work was partially supported by the United States Air Force Office of Scientific Research under Contract AF-49(638)-1029. The author would like to thank W. A. Tiller for suggesting the project, D. R. Hamilton for many helpful discussions, and W. W. Mullins for clarifying some points on interface stability. He would also like to thank L. M. Potochnik for assistance with the experiments.

Manuscript received Sept. 1, 1965. This paper was presented at the Buffalo Meeting, Oct. 10-14, 1965.

Any discussion of this paper will appear in a Discussion Section to be published in the December 1966 JOURNAL.

REFERENCES

1. W. G. Pfann, *J. Metals*, **7**, 961 (1955).
2. W. G. Pfann, "Zone Melting," John Wiley & Sons, New York (1958).
3. J. H. Wernick, *J. Chem. Phys.*, **25**, 47 (1956).
4. J. H. Wernick, *Trans. AIME*, **209**, 1169 (1957).

5. W. A. Tiller, *J. Appl. Phys.*, **34**, 2757 (1963).
6. W. A. Tiller, *ibid.*, **36**, 261 (1965).
7. A. I. Mlavsky and M. Weinstein, *J. Appl. Phys.*, **34**, 2885 (1963).
8. M. Weinstein and A. I. Mlavsky, *ibid.*, **35**, 1892 (1964).
9. L. B. Griffiths and A. I. Mlavsky, *This Journal*, **111**, 805 (1964).
10. W. W. Mullins and R. F. Sekerka, *J. Appl. Phys.*, **35**, 444 (1964).
11. R. G. Seidensticker, To be published.
12. C. D. Thurmond and M. Kowalchik, *Bell Syst. Tech. J.*, **39**, 169 (1960).
13. F. A. Trumbore, *ibid.*, **39**, 205 (1960).
14. C. J. Glassbrenner and G. A. Slack, *Phys. Rev.*, **134**, A1058 (1964).

In Situ Etching of Silicon Substrates Prior to Epitaxial Growth

T. L. Chu, G. A. Gruber, and R. Stickler

Research Laboratories, Westinghouse Electric Corporation, Pittsburgh, Pennsylvania

ABSTRACT

The cleanness of the substrate surface is important for the epitaxial growth of silicon. The *in situ* etching of substrates with commercial hydrogen chloride has been used successfully, and the resulting silicon films have been found to be generally of good crystal perfection by chemical etching and optical microscope techniques. However, transmission electron microscopy has revealed the presence of high concentrations of precipitates in the substrate-film interface region. Thermochemical considerations indicated that these precipitates were most likely silicon nitride. Most of these precipitates can be removed by using water vapor as an etchant.

The structural perfection of an epitaxial silicon film is an important factor determining its suitability for device applications. The most commonly observed imperfections in epitaxial silicon are dislocations, stacking faults, precipitates, hillocks, and inclusions of random orientations. With the exception of the dislocations propagated from the substrate, the majority of these imperfections were found to originate at the substrate-deposit interface and were attributed mainly to contaminants in the reactant mixture and foreign impurities on the substrate surface (1). The importance of cleanness of the substrate surface has been well-recognized, and *in situ* etching techniques have been developed. In these techniques, the substrates are chemically etched in the growth apparatus immediately prior to the deposition process, employing anhydrous hydrogen chloride (2, 3) or water vapor (4). Using the thermal reduction of silicon tetrachloride with hydrogen, epitaxial silicon films grown on substrate surfaces treated in this manner were found to have considerably improved structural perfection by chemical etching and optical microscope techniques. For example, the use of hydrogen chloride etchant has produced silicon films with stacking fault concentrations less than 200/cm^2 and dislocation densities no greater than those of the substrates (2). These results are indeed remarkable in view of the fact that the purity of commercial hydrogen chloride is not comparable to that of other reagents customarily used in epitaxial processes. On the other hand, imperfections of submicron dimensions cannot be readily revealed by optical microscope examinations, and submicroscopic imperfections in epitaxial silicon films, particularly in the substrate-film interface region, have not been extensively studied.

We have prepared a number of epitaxial silicon specimens using various *in situ* treatments of the substrates, including the thermal etching and the use of commercial hydrogen chloride and water vapor as etchants prior to the deposition process. The substrate-deposit interface regions in these specimens were examined by the transmission electron microscopy technique. The effects of various etchants on the structural perfection of the epitaxial silicon films are summarized in this communication.

Experimental

The epitaxial silicon specimens were prepared in the conventional manner, using the thermal reduction of silicon tetrachloride with hydrogen on heated substrate surfaces in a flow system (5). Electronic grade silicon tetrachloride, purchased from the Stauffer Chemical Company, was purified by fractional distillation through a quartz column and was found to yield n-type silicon with an electrical resistivity of 50 ohm-cm or higher. Commercial grade hydrogen was purified by diffusion through a palladium-silver alloy. The silicon substrates were of {111} orientation, n-type, 50 ohm-cm resistivity, and had dislocation densities less than 10^3 cm^{-2}. They were mechanically lapped with American Optical Company No. 305 abrasive, and chemically etched with CP_4 to remove at least 50μ of silicon from the surface. The substrates were supported on a susceptor in a quartz reaction tube, and the susceptor was heated externally by an rf generator. Hydrogen at a flow rate of 6 to 20 l/min was used for the thermal etching or as a diluent for the etchant, hydrogen chloride (HCl/H_2 = 0.01-0.05) or water vapor ($H_2O/H_2 = 2 \times 10^{-4}$ to 10^{-3}). The *in situ* etching was carried out at a substrate temperature of approximately 1270°C for 10-30 min. Subsequently, 0.3 to 0.5μ of silicon films were deposited, without intentional doping, on the substrates at 1200°C.

To provide adequate electron transmission for the electron microscope studies, the specimens must be reduced to 1μ or less in thickness. This was accomplished by removing the major part of the substrate from a portion of the specimen by jet chemical etching (6). The geometry of the resulting specimen is shown in Fig. 1. The specimen was mounted on a specimen stage and the substrate-film interface of the thin portions were examined in transmission in an electron microscope at 100 kv.

Results and Discussion

The thermal etching of the silicon substrate is related to the presence of an oxide film on the substrate

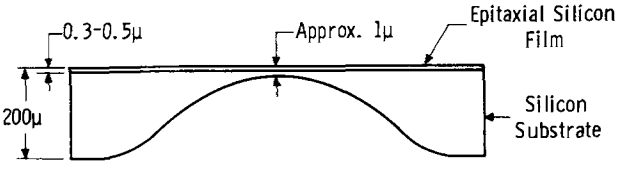

Fig. 1. Cross-section of an epitaxial silicon specimen thinned by jet chemical polishing for examination by transmission electron microscopy.

Table I. Impurity contents of hydrogen chloride specimens by mass-spectrographic analysis, ppm

Impurities	Specimen I	Specimen II
O_2	380	450
N_2	1250	1600
SO_2	750	400
Ar	15	20
CO_2	N.D.	N.D.
Organic Cpds.	N.D.	N.D.*

* N.D., not detectable, less than 10 ppm. Sensitivity, approximately 10 ppm.

surface. The chemical etching of silicon with nitric acid and hydrofluoric acid mixtures usually leaves an oxide film of the order of 100Å depending on the resistivity of silicon (7). At high temperatures, this oxide film reacts with the silicon underneath to form volatile silicon monoxide according to the equation

$$Si(s) + SiO_2(s) = 2SiO(g) \quad [1]$$

Silicon monoxide has appreciable vapor pressures at temperatures above 1100°C. For example, the vapor pressure of silicon monoxide in equilibrium with silicon and silicon dioxide at 1300°C is approximately 2 Torr (8). In a flow system, this reaction approaches completion and an equivalent amount of silicon is removed from the substrate. The removal of silicon by this process is presumably more rapid than the evaporation of silicon because of its low vapor pressures in the temperature range under consideration. For example, the vapor pressure of silicon at 1510°K is 10^{-5} Torr (9), and the evaporation rate of silicon calculated on the basis of kinetic theory is approximately 10^{-2} μ/min. However, the presence of minute quantities of oxygen or water in hydrogen would increase the rate of removal of silicon as will be discussed later. When the substrates were subjected to the thermal etching prior to the deposition process, the substrate-film interface regions were found by transmission electron microscopy to be generally clean, indicating that the growth apparatus and the reactants did not introduce any appreciable amount of impurities.

Commercial hydrogen chloride used for the *in situ* etching of silicon substrates was analyzed by mass spectrography for impurities in the mass range 2 to 120. The principal impurities were found to be oxygen, nitrogen, and sulfur dioxide (Table I). When the hydrogen chloride containing these impurities was used as an etchant, the epitaxial silicon films were found to be generally of good crystal perfection by chemical etching and optical microscope techniques. However, the substrate-film interface regions were invariably found to have high concentrations of precipitates, a few hundred angstroms in dimensions. A typical example is shown in Fig. 2. These precipitates were not of sufficient concentration to be identified by electron diffraction or other methods. However, one could deduce the nature of these precipitates from the impurity contents of hydrogen chloride and the chemical behavior of silicon toward these impurities. It is assumed in the following discussion that the hydrogen-hydrogen chloride mixture used as the etchant contains oxygen, sulfur dioxide, and nitrogen at partial pressures of 2 x 10^{-5}, 3 x 10^{-5}, and 7 x 10^{-5} atm, respectively.

The reaction between silicon and oxygen at high temperatures yields silicon dioxide or silicon monoxide, depending on experimental conditions. Silicon monoxide is volatile at high temperatures. The free energy of formation of silicon dioxide at 1500°K (10) is

$$Si(s) + O_2(g) = SiO_2(s) \quad \Delta F^\circ_{1500^\circ K} = -146 \text{ kcal} \quad [2]$$

and the equilibrium partial pressure of oxygen over solid silicon and silicon dioxide is approximately 10^{-21} atm. Assuming that chemical equilibria are approached

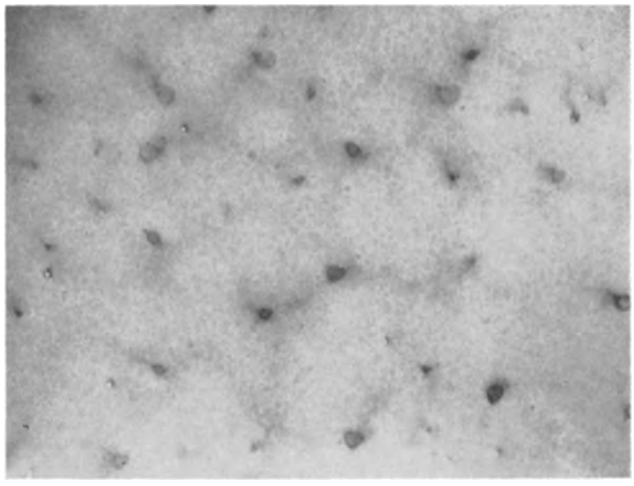

Fig. 2. Typical example showing a high concentration of precipitates in the substrate-film interface region of an epitaxial silicon specimen. The substrate was etched with commercial hydrogen chloride prior to the deposition process. Magnification approximately 36,000X.

at temperatures used in the etching process, the reaction of oxygen in the etchant with the silicon substrate is thus essentially complete. The silicon dioxide formed further reacts with the substrate according to Eq. [1] to yield silicon monoxide which has an equilibrium vapor pressure of approximately 10^{-3} atm at 1500°K. Since the partial pressure of oxygen in the etchant was considerably lower than this vapor pressure, it is unlikely that silicon dioxide would be deposited on the substrate surface during the *in situ* etching process.

The reaction between silicon and sulfur dioxide at high temperatures yields a mixture of oxides and sulfides. Silicon disulfide is similar to silicon dioxide in that the disulfide reacts with silicon at 850°C or above to form the volatile monosulfide (11). Thus, the monoxide and the monosulfide are the predominate products at low partial pressures of sulfur dioxide. The chemical reactions and the associated free energy changes at 1500°K (10) are

$$Si(s) + SiS_2(l) = 2SiS(g) \quad \Delta F^\circ_{1500^\circ K} = -45 \text{ kcal} \quad [3]$$

$$3Si(s) + SO_2(g) = SiS(g) + 2SiO(g)$$

$$\Delta F^\circ_{1500^\circ K} = -78 \text{ kcal} \quad [4]$$

The presence of minute quantities of sulfur dioxide in the etchant is not likely to cause the formation of precipitates on the substrate surface.

The reaction between silicon and nitrogen at high temperatures yields silicon nitride. The standard free energy of formation of alpha-silicon nitride at 1500°K (12) is

$$3Si(s) + 2N_2(g) = \alpha\text{-}Si_3N_4(s)$$

$$\Delta F^\circ_{1500^\circ K} = -60 \pm 6 \text{ kcal} \quad [5]$$

The equilibrium pressure of nitrogen over solid silicon and silicon nitride is of the order of 4.5 x 10^{-5} atm. Since the partial pressure of nitrogen in the etchant was higher than this equilibrium pressure, it is reasonable to assume that the precipitates shown in Fig. 2 were alpha-silicon nitride particles formed as a result of the nitridation of the silicon substrate by the nitrogen in the etchant. These particles could be epitaxial with respect to the substrate (12) and therefore had no appreciable influence on the epitaxial growth process. On the other hand, the presence of silicon nitride particles in the vicinity of p-n junctions is highly undesirable since dielectric precipitates may enhance the local electric resulting in reverse breakdown at low voltages (13).

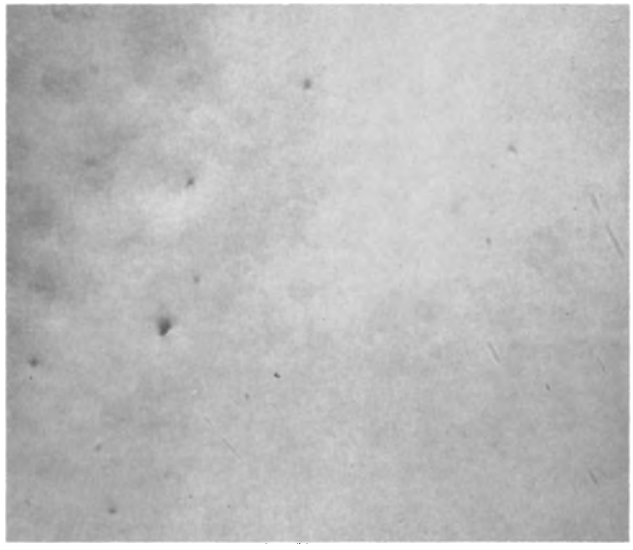

Fig. 3. Substrate-film interface region of an epitaxial silicon specimen having only a few small particles. The substrate was etched with water vapor subsequent to etching with commercial hydrogen chloride. Magnification approximately 36,000X.

Epitaxial growth experiments were also carried out in which the *in situ* etching of silicon substrates by a hydrogen-hydrogen chloride mixture was followed by using a hydrogen-water vapor mixture. The use of water etching was found to eliminate many of the precipitates in the interface region (Fig. 3) due presumably to the hydrolysis of silicon nitride.

$$Si_3N_4(s) + 3H_2O(g) = 3SiO(g) + 2N_2(g) + 3H_2(g)$$
$$\Delta F^\circ_{1500^\circ K} = 9.5 \text{ kcal} \quad [6]$$

The removal of silicon nitride is feasible because of the formation of volatile silicon monoxide. This result also verifies the previous assumption that the small concentration of oxygen in the etchant would not cause the formation of silicon dioxide on the substrate surface.

Conclusions

Epitaxial silicon films prepared by using commercial hydrogen chloride as an *in situ* etchant have been found to be generally of good crystal perfection by chemical etching and optical microscope techniques. However, transmission electron microscopy has revealed the presence of high concentration of precipitates, presumably silicon nitride, in the substrate-film interface region. Most of these precipitates can be removed by using water vapor as an etchant. These results illustrate the significance of using high purity reagents for the *in situ* etching of substrates in the epitaxial growth process.

Manuscript received July 29, 1965; revised manuscript received Oct. 14, 1965. This paper was presented at the San Francisco Meeting, May 9-13, 1965. The research reported in this paper was sponsored by the George C. Marshall Space Flight Center of the National Aeronautics and Space Administration under Contract NAS8-11432.

Any discussion of this paper will appear in a Discussion Section to be published in the December 1966 JOURNAL.

REFERENCES

1. T. L. Chu and J. R. Gavaler, in "Metallurgy of Advanced Electronic Materials," G. E. Brook, Editor, p. 209, Metallurgical Society Conferences, Vol. 19, Interscience, New York (1963).
2. K. Bean and P. Gleim, *This Journal*, **110**, 265C (1963).
3. G. A. Lang and T. Stavish, *RCA Rev.*, **24**, 488 (1953).
4. T. L. Chu and R. L. Tallman, *This Journal*, **111**, 1306 (1964).
5. See, for instance, H. C. Theuerer, *ibid.*, **108**, 644 (1961).
6. G. R. Booker and R. Stickler, *Brit. J. Appl. Phys.*, **13**, 446 (1962).
7. See, for instance, J. C. Ritter, M. N. Robinson, B. J. Faraday, and J. I. Hoover, *J. Phys. Chem. Solids*, **26**, 721 (1965).
8. N. C. Tombs and A. J. E. Welch, *J. Iron Steel Inst.*, **172**, 69 (1952).
9. R. E. Honig, *RCA Rev.*, **23**, 567 (1962).
10. JANAF Interim Thermochemical Tables, The Dow Chemical Co., Midland, Mich., Dec. 31, 1960.
11. W. C. Schwaub and W. J. Bernard, *J. Am. Chem. Soc.*, **77**, 904 (1955).
12. R. D. Pehlke and J. E. Elliott, *Trans. Met. Soc., AIME*, **215**, 781 (1959).
13. A. N. Knopp and R. Stickler, *Electrochem. Tech.*, **3**, 84 (1965).
14. W. Shockley, *Solid State Electronics*, **2**, 35 (1961).

A Raman Spectroscopic Study of the Molten Salt System $ZnCl_2$-KCl

J. R. Moyer, J. C. Evans, and G. Y-S. Lo

The Dow Chemical Company, Midland, Michigan

ABSTRACT

Using both polarized and normal incident radiation, spectra have been recorded over the temperature range 280°-500° for solutions with molar ratios of KCl:$ZnCl_2$ between 0 and 2. The results are interpreted in terms of polymeric zinc chloride and a single complex ion, $ZnCl_4^=$.

The structure of zinc chloride has been studied often and by many different techniques. Brehler (1) has determined that the solid is a three-dimensional network of $ZnCl_4$ tetrahedra with chlorine atoms disposed symmetrically between the Zn atoms. Considerable indirect evidence from viscosity measurements (2), conductivity (3), and self-diffusion (4), indicate that this polymeric structure is maintained in molten zinc chloride. Raman spectra of the solid (5, 6) and of the liquid (6-8) are virtually identical, indicating persistence of the network structure in the melt. Concentrated aqueous solutions of zinc chloride contain $(ZnCl_2)_n$ polynuclear aggregates (9).

There remains some uncertainty, however, about the structure of the melt. Gruber and Litovitz (2) have concluded that the network structure is lost about 20° above the melting point, whereas MacKenzie and Murphy (3) and Bockris and co-workers (4) find remnants of polymer up to, and probably beyond, 100° above the melting point. Irish and Young (8) found the anhydrous melt to be polymeric nearly 200° above the melting point. Discrete molecules ($ZnCl_2$ or

$ZnCl_n^{2-n}$) were postulated in addition to the dominant polymer.

Zinc chloride is known to form stable salts in the presence of excess chloride ions. The phase diagram of the system $ZnCl_2$-KCl shows the compound K_2ZnCl_4 (10). An x-ray crystallographic study of several solid compounds containing the $ZnCl_4^=$ anion shows it to have an almost perfect tetrahedral structure (11). The vibrational spectrum of this ion has been reported for the solid (12) and for aqueous solutions (13).

Planar MX_3^- ions have been reported in zinc halide systems as well as in cadmium and mercury halide systems, which also have the d^{10} electronic structure. Bues (6), in Raman studies of molten mixtures of $ZnCl_2$ and KCl, and of $CdCl_2$ and KCl, interpreted his spectra in terms of both MX_3^- and $MX_4^=$ ions. Morris, Short, and Waters (14) found $ZnCl_3^-$ and $ZnBr_3^-$ in nonaqueous solutions of zinc halides to which the corresponding hydrogen halide had been added.

In Raman studies of related systems, Janz and James (15) reported both HgX_3^- and $HgX_4^=$ ions in molten mixtures of HgX_2 and KX. Tanaka *et al.* (16) found $CdCl_3^-$ to be the only complex ion in the molten salt system $CdCl_2$-KCl. Bues (6) found both $CdCl_3^-$ and $CdCl_4^=$ in the same system.

Bredig and van Artsdalen (17) have criticized Bues' interpretation of his data in terms of a MX_3^- species and have questioned the existence of such ions in d^{10} systems on theoretical grounds.

Experimental

Reagent grade $ZnCl_2$ was fused to expel most of the water, then triply sublimed. The sublimer was 2 in. OD and 15 in. long with the outer portion, including the standard taper joint, made of fused silica. About 200g of fused zinc chloride was heated to 700° under vacuum while tap water circulated through the cold finger. About 100g deposited overnight in the form of transparent platelets. Accumulated sublimates were combined for a second sublimation. Since the residue of the second sublimation showed a faint yellow color, that product was sublimed a third time.

Reagent grade KCl was fused in platinum ware. All transfers of these materials were performed in a dry box.

Samples were prepared in the mixing-filtering apparatus shown in Fig. 1. The apparatus was cleaned, dried, and finally baked under vacuum at 500°C. Predetermined amounts of $ZnCl_2$ and KCl were then added.

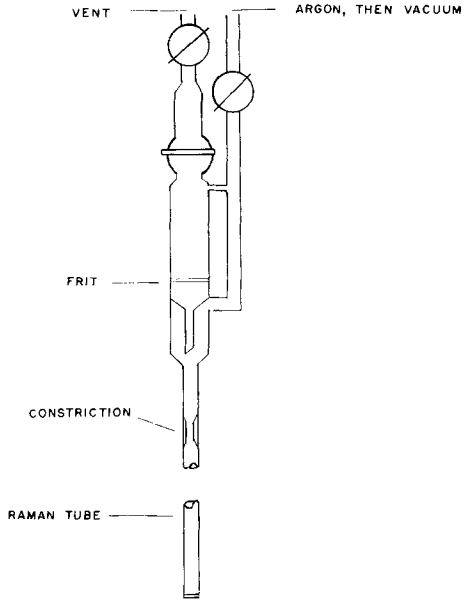

Fig. 1. Mixing filtering apparatus

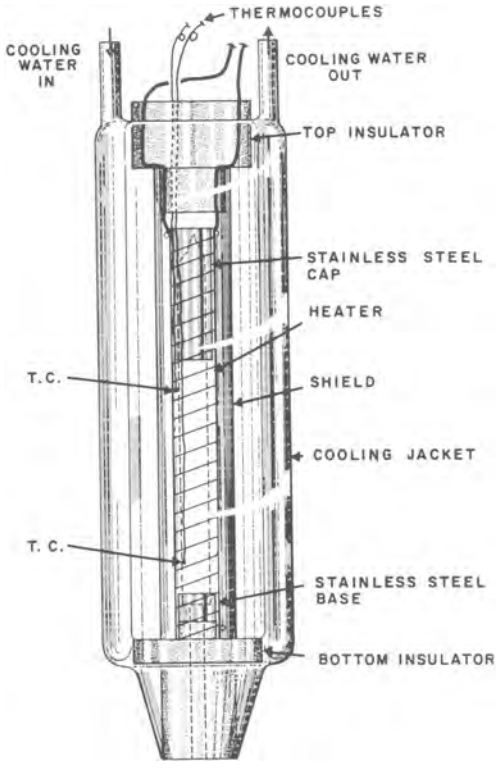

Fig. 2. High temperature Raman sample holder

The mixing-filtering apparatus was placed vertically in a tube furnace and heated about 100° above the melting point of the sample. During the melting, a stream of dry argon was passed through the frit from the underside. After melting, this purge served to mix the sample. After mixing, the argon flow was stopped and the apparatus was evacuated. The sample was filtered through the "fine" porosity fritted disk and dripped directly into the Raman tube. The Raman tube was sealed while the system remained under vacuum. The sample was allowed to freeze with the Raman tube lying in a horizontal position. This is necessary to avoid fracture of the Raman tube when the sample is remelted for the recording of its Raman spectrum.

The Raman spectra were recorded with the sample in the cell shown in Fig. 2. Stainless steel caps concealed the meniscus and the window and also centered the tube on the optical axis of the spectrometer. A vertical slot in the upper cap permitted the insertion of two thermocouples. This allowed measurement of the thermal gradient along the Raman tube. The spacing of windings of wire on the heater was adjusted until a gradient of 1° was obtained at 500°C.

The heater was a Vycor cylinder to which three binding posts were attached. A winding of 31 gauge Nichrome wire was anchored to these posts. Spacings were ⅛ in. for 1 in. at the bottom and ¼ in. above this. A second Vycor cylinder was placed around the heater to reduce heat losses by convection.

The sample and heating assembly were placed inside a doublewalled Vycor jacket. Circulating water through the jacket kept its outside surface near room temperature and permitted the use of Polaroid sleeves for polarization studies. Raman scattered light passed through the plane window at the bottom of the sample tube, through holes in the bottom cap and bottom insulator, and through a plane window on the bottom of the jacket.

Spectra were recorded over the temperature range 280° to 500°C with a Hilger Model E612 (f/5.7) Raman spectrometer having a reciprocal dispersion of 16 Å/mm. Preliminary runs were made using the Hilger source unit, but this proved unsatisfactory. Excessive background emission extended out to about 120 cm^{-1}

Table I. Raman frequencies of molten zinc chloride

Present work, melt	Irish, MacCarroll and Young (9), 13.0M aqueous	Irish and Young (8), melt	Salstrom and Harris (7), melt	Assignment
75 ± 8, w	90 w	95 ± 10, vw 110 ± 10, vw	98	$(ZnCl_2)_n$ polymer, bridge Zn-Cl deformation
226 ± 10, s,p	230 s,p	230 ± 5, s	231	$(ZnCl_2)_n$ polymer, bridge Zn-Cl stretch
250 ± 10, w		266 w		$(ZnCl_2)_n$ polymer, bridge Zn-Cl stretch
			285	
305 ± 10, w	335 w	305		$(ZnCl_2)_n$ polymer, terminal Zn-Cl stretch
360 ± 10, w	360-400 w	375-400		$(ZnCl_2)_n$ polymer, terminal Zn-Cl stretch

vw = very weak; w = weak; s = strong; p = polarized.

from the exciting line. To overcome this a Toronto arc was constructed. Excitation by 4358 and 4047A Hg lines was employed; the latter was particularly useful in measuring the bands below 150 cm^{-1}. Unfortunately, it was not possible to use photoelectric recording and all spectra were recorded photographically.

Results and Discussion

Zinc chloride.—The Raman spectrum of molten zinc chloride shows five bands: an intense, polarized band at 226 cm^{-1}, an uncertain shoulder near 250 cm^{-1}, and weak bands near 75, 305, and 360 cm^{-1}. The results are compared with those of previous studies in Table I.

It was observed qualitatively that the weak features near 300 and 360 cm^{-1} were easier to discern on plates recorded with the sample at 425° compared with 290°C. The intensities of the bands at 226 and 250 cm^{-1} seem independent of temperature. Irish and Young (8) also observed that elevated temperatures increased the intensity of the 305 cm^{-1} band had no effect upon the 230 cm^{-1} band. On the other hand, they noted decreased intensity of the 266 cm^{-1} band on heating. A plausible interpretation is that these features arise from the depolymerization which is favored by the higher temperature. The higher frequencies are therefore assigned to terminal Zn-Cl stretching modes and the bands near 230 and 250 cm^{-1} to bridged Zn-Cl stretching modes.

These intensity changes are consistent with the observations of MacKenzie and Murphy (3), of Bockris, Richards, and Nanis (4) and of Irish and Young (8) that the network structure of the solid persists well above the melting point. Molten zinc chloride consists of polymeric $(ZnCl_2)_n$ species of various sizes. These species are made up of $ZnCl_4$ tetrahedra joined at corners to give a three dimensional array. At increasing temperatures the degree of polymerization is lowered, but even at 500°, the spectra show that the vast majority of Zn-Cl bonds are bridging rather than terminal bonds. Band assignments are given in Table I.

Chloride-rich solutions.—Addition of KCl has a significant effect on the Raman spectrum of molten zinc chloride. The results are given in Table II.

The bridging Zn-Cl stretching frequencies of polymeric $ZnCl_2$ are reduced in intensity: the weak band at 250 cm^{-1} disappears upon the first addition of KCl, the intense, polarized band at 226 cm^{-1} gradually fades. The terminal Zn-Cl stretching bands at 305 and 360 cm^{-1} in pure zinc chloride are shifted to lower frequencies and become at first more intense, then fade away. In the case of the 305 cm^{-1} band this pattern is obscured by the emerging spectrum of $ZnCl_4^=$, but careful scrutiny of the photographic plates indicates that the pattern of the 360 cm^{-1} band is followed.

The bands observed in mixtures containing 1.5 and 2 moles of KCl per mole of $ZnCl_2$ are readily identified from previous studies (12, 13) as those of the tetrahedral $ZnCl_4^=$ ion.

Increasing temperatures cause the bands in the 340-360 and 290-300 cm^{-1} regions to become more intense and the band at 226 cm^{-1} to grow weaker. These changes are consistent with the assignment of the higher frequencies to terminal ZnCl stretching modes and the 226 cm^{-1} band to a bridging ZnCl stretch.

A physical model consistent with the observed spectra is one of depolymerization and complex ion formation. According to this picture the initial process on addition of KCl to molten $ZnCl_2$ is the formation of smaller clusters of $ZnCl_4$ tetrahedra. The chloride ion added up to a molar ratio of KCl:$ZnCl_2$ of about 0.2 is consumed largely in the depolymerization reaction

$$(ZnCl_2)_n + Cl^- = (ZnCl_2)_{n-m} + (ZnCl_2)_m \cdot Cl^-$$

This process continues upon further addition of KCl but a second process predominates beyond the molar ratio KCl:$ZnCl_2$ of 0.2

$$(ZnCl_2)_m \cdot Cl^- + Cl^- = ZnCl_4^= + (ZnCl_2)_{m-1}$$

This model is consistent with the spectral observations and with the physical properties of these melts. It is reminiscent of the model proposed by Bloom and Bockris (18) to describe the break up of the structure of molten SiO_2 on the addition of a metal oxide. These authors describe a series of step-wise transitions from a three-dimensional network of SiO_2 tetrahedra through fused rings, planar rings, chains, and finally $SiO_4^=$ ions. The effect of adding MCl to molten $ZnCl_2$ seems to be roughly analogous, but with $ZnCl_4^=$ ions

Table II. Observed bands in Raman spectra of molten mixtures

$ZnCl_2$	$4ZnCl_2/KCl$	$2ZnCl_2/KCl$	$ZnCl_2/KCl$	$2ZnCl_2/3KCl$	$ZnCl_2/2KCl$
75 ± 8, w	80 ± 8, w	75 ± 8, w	80 ± 8, w 125 ± 10, w	70 ± 8, w 120 ± 5, w	75 ± 8, w 124 ± 5, w
226 ± 10, s, p	226 ± 8, s, p	226 ± 8, s, p	218 ± 5, vw		
250 ± 10, w					
305 ± 10, w	288 ± 5, w, p	290, m, p	292 ± 5, m, p	294 ± 5, s, p	283 ± 3, s, p
360 ± 10, w	349 ± 5, m, p	344 ± 8, w, p			

p = polarized; w = weak; vw = very weak; m = medum; s = strong.
All bands are broad.

splitting out at all stages of the depolymerization.

The downward trend in several frequencies on addition of KCl is attributed to this change in the basic nature of the melt.

The data reported here do not eliminate the possibility of the formation of $ZnCl_2$ monomer or of the complex ion $ZnCl_3^-$. It does seem possible, however, to explain the data without invoking either species.

Manuscript received Sept. 13, 1965; revised manuscript received Oct. 21, 1965. This paper was presented at the San Francisco Meeting, May 9-13, 1965.

Any discussion of this paper will appear in a Discussion Section to be published in the December 1966 JOURNAL.

REFERENCES

1. B. Brehler, *Z. Krist.*, **115**, 373 (1961).
2. G. J. Gruber and T. A. Litovitz, *J. Chem. Phys.*, **40**, 13 (1964).
3. J. D. MacKenzie and W. K. Murphy, *ibid.*, **33**, 366 (1960).
4. J. O'M. Bockris, S. R. Richards, and I. Nanis, *J. Phys. Chem.*, **69**, 1627 (1965).
5. C. S. Venkateswarlu, *Proc. Indian Acad. Sci. Al*, 850 (1935).
6. W. Bues, *Z. anorg. allgem. Chem.*, **279**, 104 (1955).
7. E. J. Salstrom and L. Harris, *J. Chem. Phys.*, **3**, 241 (1935).
8. D. E. Irish and T. F. Young, *ibid.*, **43**, 1765 (1965).
9. D. E. Irish, B. MacCarroll, and T. F. Young, *ibid.*, **39**, 3436 (1963).
10. R. A. Fleming and F. R. Duke, *This Journal*, **104**, 251 (1957).
11. B. Morosin and E. C. Lingafelter, *Acta Cryst.*, **12**, 611 (1959).
12. A. Sabatini and L. Sacconi, *J. Am. Chem. Soc.*, **86**, 17 (1964).
13. M. L. Delwaulle, *Compt. rend.*, **238**, 2522 (1954).
14. D. F. C. Morris, E. L. Short, and D. N. Waters, *J. Inorg. Nucl. Chem.*, **25**(8), 975 (1963).
15. G. J. Janz and D. W. James, *J. Chem. Phys.*, **38**, 905 (1963).
16. M. Tanaka, K. Balasubramanyam, and J. O'M. Bockris, *Electrochim. Acta*, **8**, 621 (1963).
17. M. A. Bredig and E. R. van Artsdalen, *J. Chem. Phys.*, **24**, 478 (1956).
18. H. Bloom and J. O'M. Bockris, "Modern Aspects of Electrochemistry, No. 2," p. 243, J. O'M. Bockris, Editor, Academic Press Inc., New York (1959).

Determination of Resistance Factors of Porous Diaphragms and Electrodes

K. S. Spiegler

Sea Water Conversion Laboratory, University of California, Berkeley, California

ABSTRACT

Oxygen-argon interdiffusion measurements across two porous glass disks are compared to measurements of the electrical resistance of these disks when saturated with a dilute electrolyte solution. The resistance factors (also called formation factors) determined by the two methods agree within about 10%. The gas diffusion method of resistance factor measurement is applicable to conductive porous bodies, *e.g.*, sintered metal disks. Recording apparatus and method of interdiffusion measurement are described in detail. The same apparatus can be used for permeability measurements.

Porous diaphragms and electrodes used in electrochemical practice differ widely in accordance with their intended use. They can be classified according to their characteristic pore dimension which ranges from macroscopic size to submicroscopic; according to thickness, ranging from several millimeters to fractions of millimeters; according to matrix conductivity, which can be practically zero, to the considerable ionic conductivities of ion exchange membrane separators and the electronic conductivities of metallic electrodes; and according to many other factors.

This study deals with methods for the measurement of resistance factors of porous diaphragms, in particular with the gas diffusion method which is applicable to both conductive and nonconductive matrices.

The definition of the resistance factor, also called formation factor, of a nonconductive matrix is straightforward: it is simply the resistivity, ρ' (ohm cm), of the material when the pores are filled with a conductive liquid divided by the resistivity of the conductive liquid, ρ. It can be determined from two resistance measurements in a system consisting of two electrodes, each of area A (cm^2) immersed in an electrolyte solution of resistivity ρ. First, the resistance, R_1 (ohm), is measured without the separator in place, then with the separator of thickness l (cm) inserted between the electrodes and fully wetted with electrolyte. This yields the higher resistance R_2. The formation factor, F_E, is then

$$F_E \equiv \rho'/\rho = [A(R_2 - R_1)/(l\rho)] + 1 \qquad [1]$$

The difference $R_2 - R_1$ is often termed "separator resistance." Convenient methods for these measurements have been described and are in routine use in the battery industry (1, 2). Other types of apparatus have been used for the resistance measurement, including variants of the classical a-c methods using a Wheatstone bridge; one such method was developed in this study and is described in the experimental section. Formation factors are often interpreted in terms of the "spaghetti model" which describes the porous medium as bundles of n_τ tubes per unit volume, all of length τ. The radii n are not necessarily equal. The formation factor can then be expressed in terms of τ^2 and the porosity (= volume fraction of nonsolid space), by considering the passage of current under the influence of a potential gradient E (volt). In this model (Fig. 1), the porosity is

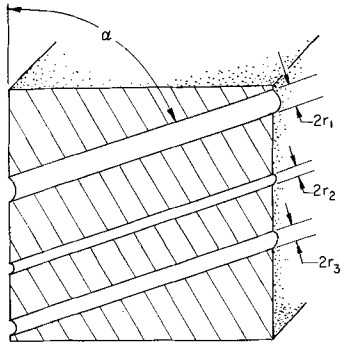

Fig. 1. Capillary bundle model ("Spaghetti model") of porous diaphragm. Cube of unit edge length is shown. r_1, r_2, and r_3 are pore radii.

$$\epsilon = \sum_r n_r r^2 \pi \tau \quad [2]$$

and the current density, i (amp cm^{-2})

i = cross section of pores x conductivity of electrolyte x potential drop

$$= \sum_r n_r r^2 \pi (1/\rho)(E/\tau) \quad [3]$$

Since

$$\rho' = E/i \quad [4]$$

it follows that

$$F_E = \rho'/\rho = \tau^2/\epsilon \quad [5]$$

The pore model can be generalized by assuming a distribution of pore radii as determined by porosimeter measurements (3, 4), but even so it is only of limited value for the description of flow phenomena in real porous media. Since porosity, ϵ, can be measured independently, τ^2, (the length of the fictional pore bundles per unit macroscopic thickness of the porous medium) can be calculated from the resistance factor. τ is called the "tortuosity" of the pore model, but some authors call τ^2 by this name.

When one deals with solid matrices which are themselves conductive, the determination of resistance factors by the electrical method is often inconclusive, because the solid can then act as a "short" with respect to the current path in solution. For instance, both a-c and d-c measurements of the conductance of a porous mass of ion exchanger grains in a solution reflect not only the conductance of the solution, but also that of the solid ion-exchange material; in a-c measurements of porous metal electrodes the current is carried primarily electronically through the metal matrix rather than through the pores which are filled with electrolyte, and this can even happen in d-c measurements, unless the conditions are properly chosen to prevent the current from following this path. Yet it is frequently important to know the formation factors (or tortuosities) of such conductive matrices. In this case one defines the formation factor of the conductive matrix as equal to the formation factor of a nonconductive matrix of the same geometry as the conductive one under consideration. Since the pore resistant factors of metal electrodes affect the operation of fuel cells, it was deemed important (*a*) to develop a method for formation factor measurement which is applicable to both conductive and nonconductive matrices, and (*b*) to compare the results for some nonconductive matrices with measurements by an a-c resistance method which is applicable only to nonconductive media.

The thought underlying the gas diffusion measurements is the following: When gases interdiffuse across a porous diaphragm, they follow the same tortuous path which ions follow when carrying the electric current through the same diaphragm. Hence the ratio of the interdiffusion coefficient of two gases in free space to their interdiffusion coefficient across the diaphragm is equal to the formation factor. In other words, it is assumed that ionic migration under the influence of an electrical potential gradient follows in a macroscopic sense the same path as the interdiffusion of gas molecules, caused by a chemical potential gradient. Although this thought is quite plausible, there is not much direct experimental verification in the literature, e.g., measurements of diffusion of water vapor through a synthetic porous rock (5) and through plugs of fine powders (6).

It will be shown that this simple hypothesis has to be modified somewhat because of the presence of "Knudsen" diffusion in gas interdiffusion measurements, and that, moreover, the choice of the gases has to be made judiciously, so that there is indeed only a single interdiffusion rather than two separate individual diffusion processes of the two gases proceeding at different rates.

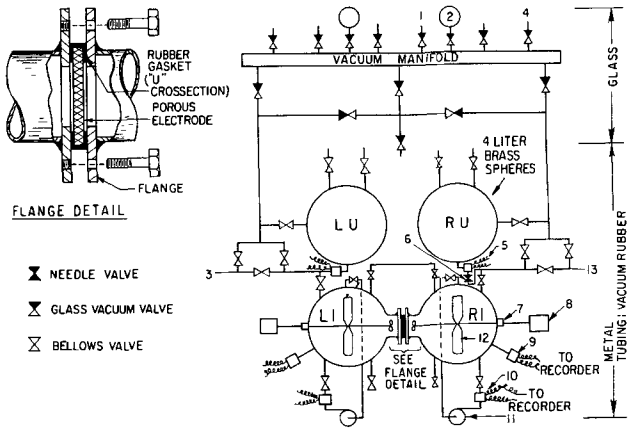

Fig. 2. Schematic of apparatus for interdiffusion and permeability measurement. 1, vacuum pump connection; 2, 100 ml calibrated volume flask; 3, to manometer; 4, to McLeod gauge; 5, solenoid valve; 6, needle valve; 7, rotary seal; 8, stirrer motor; 9, collapsible pressure transducer; 10, collapsible analysis cell; 11, collapsible peristaltic pump; 12, collapsible paddle.

Experimental

Gas diffusion measurements.—A schematic of the apparatus is shown in Fig. 2. The lower part is largely metal, the upper glass, connected to a conventional vacuum system. Flexible connections are made by vacuum rubber tubing. The electrode is held between two flanges, silver-soldered to the gas containers. A special gasket with "U" cross section (Irving B. Moore Corporation, Boston, Massachusetts) is used to prevent transport of gases through the edge of the electrode. The standard size of the electrode samples is a disk 2 in. in diameter. For samples yielding very high interdiffusion rates, part of the surface is masked on both sides with masking tape, care being taken that the two openings calender perfectly.

Vessels LI and RI are first evacuated and shut off from the vacuum system, Spheres LU and RU are filled with argon and oxygen, respectively, at about twice the pressure desired in the experiment. The solenoid valves (Circle Seal Products Corporation, Pasadena, California) are opened simultaneously for about 1 min and closed by a small programmer built for the purpose, thus admitting the gases to spheres LI and RI. The needle valve between spheres RU and RI has a micrometer head calibrated so that the pressure difference between LI and RI at the end of the filling process is as small as possible. To insure further that the experiment is started at equal pressure of the two gases, the top connection between spheres LI and RI is opened for about 15 sec immediately after the solenoid valves close.

The "peristaltic" pumps (Sigmamotor Pump Corporation, Middleport, New York) and paddle stirrers are now started, to circulate and mix the gases in spheres LI and RI. (Since pumping alone is not sufficient for perfect mixing in the spheres the paddle stirrers have been added.) The composition of the gases is determined from the continuous record of the thermal conductivity cells which have been calibrated before with mixtures of argon and oxygen of known composition.

The composition of the gases in spheres LI and RI is recorded until they contain 40 v/o oxygen and argon, respectively. The upper connection between the spheres is then opened and the composition equalized by vigorous gas recirculation through both spheres. This is done to verify that the final composition is 50% O_2-50% A. In general, some small deviation from this ideal condition is occasionally observed and suitable correction made.

The interdiffusion process is mathematically equivalent to heat flow between two identical good conduc-

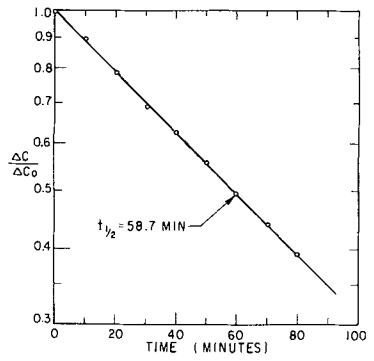

Fig. 3. Oxygen-argon interdiffusion across GS-I sintered glass disk. Exposed diameter 2r = 2.22 cm, thickness Δz = 0.549 cm, pressure 400 Torr, stirring rate 200 rpm.

tors connected by a poor conductor. Like the latter phenomenon it follows an exponential decay law

$$\frac{\Delta c}{\Delta c_o} = \exp\left[-2\bar{D}_{12}At/(V\Delta z)\right] \qquad [6]$$

where Δc and Δc_o are the oxygen concentration differences between the two spheres at time t (sec) and at zero time respectively, $\bar{D}_{12}$ the interdiffusion coefficient in the porous medium (cm^2 sec^{-1}), A(cm^2) and Δz (cm) the gross cross section and thickness of the disk, respectively, and V(cm^3) the sphere volume. Therefore a straight line is obtained when log $\Delta c/\Delta c_o$ is plotted against time. Figure 3 shows such a plot illustrating the graphical interpolation for finding the half-time, $t_{1/2}$(sec), from which the interdiffusion coefficient is calculated

$$\bar{D}_{12} = 0.347\ V\ \Delta z/(At_{1/2}) \qquad [7]$$

The area A is corrected for edge effects from a curve computed by Auslender *et al.* (7) shown in Fig. 4.

Because of the exponential nature of Eq. [6] the zero time can be arbitrarily set at any time after the start of the experiment. Although the experiments are started with pure gases, measurements at the very beginning of the experiment were disregarded because of some transient effects in the instrumentation and also because the assumption of a single interdiffusion coefficient for the gases, rather than separate individual coefficients, is weakest at the beginning when Δc is large. Zero time is usually taken at about 85 and 15 v/o oxygen in the two spheres, respectively.

The ideal gas pairs for interdiffusion measurements are para and ortho hydrogen, or isotopic pairs of very similar molecular weight and hence similar self-diffusion coefficients (7a). We used oxygen and argon (which do not quite meet the latter criterion) because

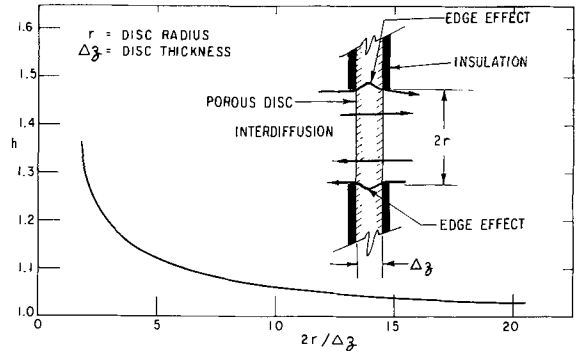

Fig. 4. Edge effect correction factors. h = (equivalent area of disk with no edge effect)/(true area of disk), r = disk radius, Δz = disk thickness.

their thermal conductivities are very different (thus simplifying the continuous monitoring of the gas compositions) while their self-diffusion coefficients are not too far apart. It should be realized, however, that the interdiffusion of different gases across a porous diaphragm proceeds at different rates, a phenomenon which becomes the more apparent, the lower the gas pressure and the smaller the characteristic pore dimension, i.e., the higher the ratio of gas-wall to gas-gas collisions. As a corollary, there should develop a transient pressure gradient between the two spheres (8). We measured this effect in a typical experiment with a V-shaped oil manometer and found the maximum pressure difference between the spheres to rise rapidly to about 0.1 Torr and then to decrease more or less exponentially as diffusion progressed. In this experiment, the sample was a porous disk of thickness 0.26 cm, exposed diameter 1.0 cm, porosity about 75% and characteristic pore dimension several microns. The volume of each sphere was about 4 liter.

Measurements were carried out at different pressures, thus enabling us to eliminate the Knudsen diffusion resistance term by use of the Bosanquet formula [8]

$$\frac{1}{\bar{D}_{12}} = \frac{F_G p}{[D_{12}]_{1\ atm}} + \frac{1}{\bar{D}_K} \qquad [8]$$

where $\bar{D}_{12}$ and $[D_{12}]_{1\ atm}$ are the measured interdiffusion coefficient across the medium and the oxygen-argon interdiffusion coefficient in free space at 1 atm, respectively, (cm^2 sec^{-1}), p the pressure (atm), $F_G(>1)$ the resistance factor for gas interdiffusion and $\bar{D}_K$ a positive, pressure-independent constant for a given porous medium and the oxygen-argon gas pair at 25°C. In other words, when plotting the measured $1/\bar{D}_{12}$ *vs.* pressure p, straight lines were obtained with positive ordinate intercepts. The slope of these lines is F_G/D_{12}. We used a recent literature value of D_{12} = 0.195 cm^2 sec^{-1} at 25° (9) and thus were able to calculate F_G from the slopes.

Equation [8] was originally derived from the kinetic theory of gases (8), but its main features can also be understood from the familiar friction model for linear transport processes in membranes and diaphragms (10, 11). According to this model, $1/\bar{D}_{12}$ represents a resistance to interdiffusion, which Eq. [8] splits into two additive terms *viz.*, (*a*) a term proportional to the pressure. This represents the resistance due to collisions between the interdiffusing gases; at 1 atm and in the absence of the porous medium this resistance equals $1/[D_{12}]_{1\ atm}$, but when the porous medium is present this resistance increases to $F_G/(D_{12})_{1\ atm}$, F_G expressing the decreased available cross section and increased tortuosity of the interdiffusion path. Thus F_G is considered identical with the electrical resistance factor (formation factor), F_E, which expresses the same steric factors. (*b*) A pressure-independent resistance term, $1/\bar{D}_K$, due to collisions between gas molecules and porous matrix, which becomes predominant at low pressures and is therefore identified with the reciprocal of the Knudsen interdiffusion coefficient, $\bar{D}_K$.

It is of interest that the apparatus shown in Fig. 2 can also be conveniently used for the rapid determination of permeability over the pressure range of about 100 to 800 Torr. In this case the spheres are first filled with the test gas at the desired pressure. A pressure differential of a few Torr is then created by opening one of the solenoid valves to the vacuum for about 1 sec by means of a programmed timer. The influx of air from the other sphere, which follows an exponential law similar to Eq. [6] is then determined from the gradual pressure increase by monitoring continuously the transducer output.

Electrical resistance factor measurement.—A schematic of the cell is shown in Fig. 5. In this apparatus

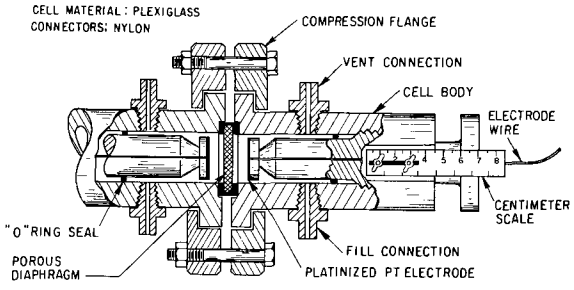

Fig. 5. Schematic of cell for electric resistance factor determination: material, plexiglas; connectors, nylon.

the electrical resistance is measured with alternating current. The electrodes never touch the diaphragm. The porous disk, contained in the gasket of U-shaped cross section is saturated with a dilute KCl solution and placed between the flanges of the two half-cells, which are filled with the same solution. Two platinized platinum electrodes of the same diameter as the porous sheet can be moved forward and backward in the cell by means of a screw drive so that the electrodes remain parallel to the plane of the sample. One electrode usually remains stationary close to the sample, but not in direct contact with it. The other is placed at different distances from the porous material, and the resistance between the electrodes measured with an a-c bridge (Industrial Instruments, Inc., Cedar Grove, New Jersey) at 60 cps. The position change can be measured to 0.005 cm by means of a ruler attached to the cell and subdivisions of the screw head.

When the measured resistance, R_1 (ohm) is plotted against the distance between the electrodes, a straight line is obtained which is described by Ohm's law

$$R_1 = \frac{1}{A}\left[\rho' \Delta z + \rho(z - \Delta z)\right] \qquad [9]$$

A is the effective cross section (cm^2), Δz the diaphragm thickness (cm), z the length coordinate (cm), ρ' and ρ the specific resistances of the solution-saturated diaphragm (ohm-cm) and of the solution, respectively. ρ can be taken from literature values, but it is preferable to determine it under the same conditions by repeating the measurements in the absence of the porous medium. This is done in order to guard against inaccuracies due to minor deviations from cylindrical geometry.

In this case, the resistance is

$$R_o = \frac{\rho z}{A} \qquad [10]$$

It is seen that both curves should have the same slope, ρ/A, and that the electrical resistance factor, (formation factor) F_E, is given by

$$F_E \equiv \frac{\rho'}{\rho} = (R_1)_{\Delta z}/(R_o)_{\Delta z} \qquad [11]$$

since, for $z = \Delta z$, Eq. [9] yields

$$\rho' = \frac{A}{\Delta z}(R_1)_{\Delta z} \qquad [12]$$

where $(R_1)_{\Delta z}$ and $(R_o)_{\Delta z}$ are the values of R_1 and R_o, respectively, at the electrode separation Δz.

In practice, resistances of diaphragm and pure electrolyte solution are measured in the same manner, except that for electrolyte measurement a dummy made up of circular plastic rings of similar thickness as the diaphragm is placed in the cell (small differences in thickness are allowed for by graphical correction).

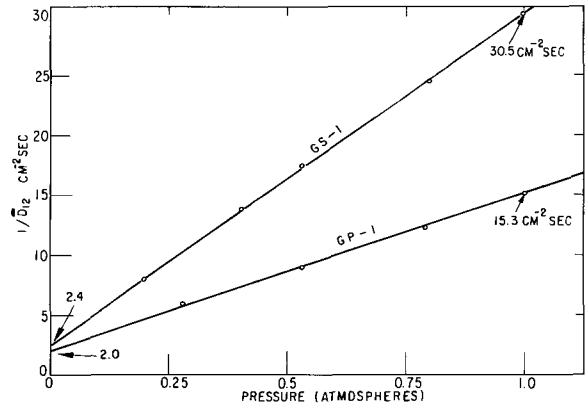

Fig. 6. Dependence of interdiffusion on pressure, Bosanquet plot shows reciprocal of oxygen-argon interdiffusion coefficient, D_{12} (cm^2 sec^{-1}) as function of pressure (atm). Porosities of sintered disks GS-1 and GP-1 are 30.2 and 65.0% respectively.

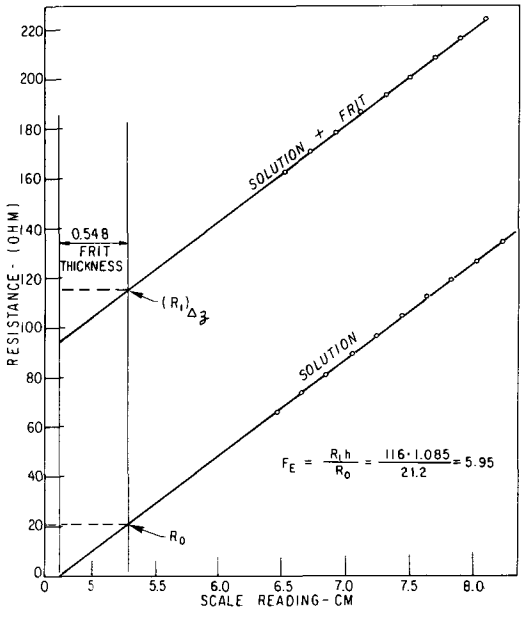

Fig. 7. Electrical resistance factor determination of sintered disk GS-1. Resistance between electrodes of measuring cell (Fig. 5) is shown as function of electrode distance. Upper line: dilute KCl solution and frit; lower line: solution only. Extrapolation of straight lines to distance Δz yields resistance of saturated disk, R_1 and solution (of same thickness), R_o, respectively. Electrical resistance factor, F_E, is $R_1 h/R_0$ = 116 x 1.085/21.2 = 5.95, where h is edge correction factor taken from Fig. 4.

Results and Discussion

Oxygen-argon interdiffusion measurements across two commercial glass frits, GS-1 and GP-1, respectively, (Ace Glass Company, Vineland, New Jersey), at different pressures are shown in Fig. 6 in terms of Bosanquet plots. From the slope of the straight lines the gas interdiffusion resistance factors F_G were calculated by the procedure described in the experimental section.

For comparison, the electrical resistance factor measurement of one of these glass frits, GS-1, is illustrated in Fig. 7. The electrical resistance factor for GP-1 was determined in the same manner.

The resistance factors (formation factors) calculated from the diffusion and from the resistance measurements are listed in Table I, along with some pertinent data on the glass frits.

It is seen that the resistance factors of the two frits are quite different, due mainly to the large difference

Table I. Properties of glass frits used in tests

Designation	GS-I	GP-I
Total diameter, cm	5.08	5.08
Exposed diameter for gas diffusion, cm	2.22	1.20
Exposed diameter for electrical resistance, cm	3.85	3.85
Thickness, cm	0.549	0.315
Pore size, micron	4-8*	3*
Open porosity, volume per cent	30.2	65*
Slope of Bosanquet plot, cm^{-2} sec atm^{-1}	28.1	13.3
Resistance factor for gas interdiffusion, F_G	5.48	2.61
Electrical resistance factor, F_E	5.95	2.34
Tortuosity, τ, from Eq. [5]	1.32	1.27

* Statement by manufacturer.

in porosity. The measurements by the gas diffusion and electrical method agree within about 10%.

In view of the results in Table I and the earlier findings of other investigations with radically different samples (5, 6) one can indeed assume that gas diffusion measurements can be used to determine the formation factors of the pores, irrespective of the conductivity of the matrix itself, provided (*a*) the geometry of the matrix in the dry and wet state is the same, and (*b*) due correction is made for Knudsen diffusion resistance.

Gas diffusion is not the only method for the measurement of the formation factors of conductive matrices. Instead, one can measure the diffusion of solutes or ionic self-diffusion across the porous body (12) and compare the measured diffusion coefficients to those in free solution. The appropriate ratios again yield the formation factor, provided the matrix have no surface conductivity due to the type of ions whose diffusion is being measured. For instance, for porous ion-exchange materials, the electrical and self-diffusion measurements do not yield the same formation factor unless elaborate corrections are made (10, 13). On the other hand, ionic self-diffusion measurements in metallic diaphragms should yield the correct formation factor. Yet another method is based on electrical potential drop measurements across polarized porous metal diaphragms. For instance, if a porous nickel disk is immersed in a solution of pure NaOH and a sufficiently small d-c potential difference applied to large electrodes on opposite sides of the disk, the current will pass only through the NaOH solution in the pores and not through the metal matrix, provided the potential difference is too small to maintain continuous electrode reactions at the nickel-solution boundary (14). The electrode resistance is calculated from the current and the potential difference across the porous disk, as measured between two small probe electrodes placed close to the diaphragm faces, (4-electrode method).

Acknowledgment

The author expresses thanks to Dr. J. G. Tschinkel, for many helpful discussions and suggestions, and to G. Grist and C. Osgood for their valuable assistance.

Manuscript received Oct. 11, 1965. This paper was presented at the San Francisco Meeting, May 9-13, 1965.

Any discussion of this paper will appear in a Discussion Section to be published in the December 1966 JOURNAL.

REFERENCES

1. R. G. Robinson and R. L. Walker, "Battery Symposium," p. 15, Pergamon Press, Oxford (1963).
2. A. Fleischer, Private communication.
3. M. R. J. Wyllie and M. B. Spangler, *Bull. Am. Assoc. Petroleum Geol.*, **36**, 359 (1952).
4. H. L. Ritter and L. C. Drake, *Ind. & Eng. Chem.*, **17**, 782 (1945).
5. L. J. Klinkenberg, *Bull. Geol. Soc. Amer.*, **62**, 559 (1951).
6. D. S. Scott and F. A. L. Dullien, *A.I.Ch.E. J.*, **8**, 113 (1962).
7. S. Auslender, C. Crown, and N. Engersbach, Pratt & Whitney Aircraft, East Hartford, Connecticut, Private communication.

7a. E. P. Ney and F. C. Armistead, *Phys. Rev.*, **71**, 14 (1947).

8. R. B. Evans, III, G. J. Watson,and E. A. Mason, *J. Chem. Phys.*, **35**, 2076 (1961).
9. R. Paul and I. B. Srivastava, *Indian J. Phys.*, **35**, 465 (1961).
10. K. S. Spiegler, *Trans. Faraday Soc.*, **54**, 1408 (1958).
11. O. Kedem and A. Katchalsky, *J. Gen. Physiol.*, **45**, 143 (1961).
12. R. K. Scholfield and C. Dakshinamurti, *Discussions Faraday Soc.*, **3**, 56 (1948).
13. K. S. Spiegler and C. D. Coryell, *J. Phys. Chem.*, **57**, 687 (1953).
14. O. S. Ksenzhek, E. A. Kalilnovskii, and E. L. Baskin, *Zh. Prikl. Khim.*, **37**, (5), 1045 (1964); cf. *C.A.*, **53**, 18693c (1964).

Differential Capacity Measurements at Carbon Electrodes

S. Evans

Research Department, Rocketdyne,
A Division of North American Aviation, Incorporated, Canoga Park, California

ABSTRACT

Voltammetry at continuously changing potentials has been used to determine the differential double-layer capacity of carbon materials. The total capacity of carbon microelectrodes was of sufficient magnitude to necessitate the use of slower scan rates than are normally used with the dropping mercury electrode. The differential double-layer capacities of Air-Spun graphite, acid-treated Air-Spun graphite, and MA-Norit graphite were 1.4, 1.8, and 60 farads per gram, respectively. At low applied potentials charging of the double layer was the major electrochemical process. In this potential range the magnitude of the double-layer capacity did not vary with potential.

Electrodes, formed by the impregnation of Dacron with chemically treated carbon paste, have been used for water demineralization (1). The determination of the double-layer capacity of various carbon pastes was part of a basic study of the mechanism of demineralization at carbon-type electrodes.

The theory and application of voltammetry at continuously changing potentials to the determination of the differential capacity of the double layer has been presented in detail by Loveland and Elving (2-5). At potentials where no reduction or oxidation occurs, the currents observed using this technique are the sole result of the charging and discharging of the double layer (6). The expression for differential capacity, C_d, is

$$C_d = dQ/dE \qquad [1]$$

where Q is the surface-charge density of the double layer, and E is the electrode potential. When the rate of change of potential across the double layer is equal to the rate of change of applied potential, this expression can be rearranged to

$$C_d = \frac{1}{v}\frac{dQ}{dt} \qquad [2]$$

where v is the scan rate in volt sec^{-1}, and dQ/dt is the differential capacity current (i_c). It will be seen that the limitations imposed by this condition ($dE/dt = v$) are more severe in the case of high surface-area carbon pastes than with the dropping mercury electrode. The differential capacity can be determined experimentally according to

$$C_d = \frac{i_c}{\text{scan rate}} \qquad [3]$$

The integration of the capacity current as a function of changing potential can also be used to evaluate the differential capacity in accordance with Eq. [1].

Experimental

The test electrode and the silver-silver chloride reference electrode were contained in the same compartment of the H-type cell (Fig. 1). The potential at the test electrode was detected through a Luggin capillary which contained a silver wire coated with silver chloride. This Ag-AgCl electrode was in contact with the electrolyte (*e.g.*, 10% NaCl). The potential of the test electrode was varied linearly with respect to the reference electrode. The cell current was measured as a function of the potential.

The test electrode (Fig. 2) consisted of a Teflon cup equipped with mating threads and a ¼-in. diameter graphite rod cemented to a Teflon plunger. The spectroscopic-grade graphite rod was wax impregnated and insulated on the sides so that a geometrical area of 0.3 cm^2 was exposed. A known amount of carbon material was supported on a disk of Whatman No. 42 filter paper.

The voltage-scanning instrument was constructed of commercial high-gain operational amplifiers. The basic potentiostat circuitry was similar to that described by

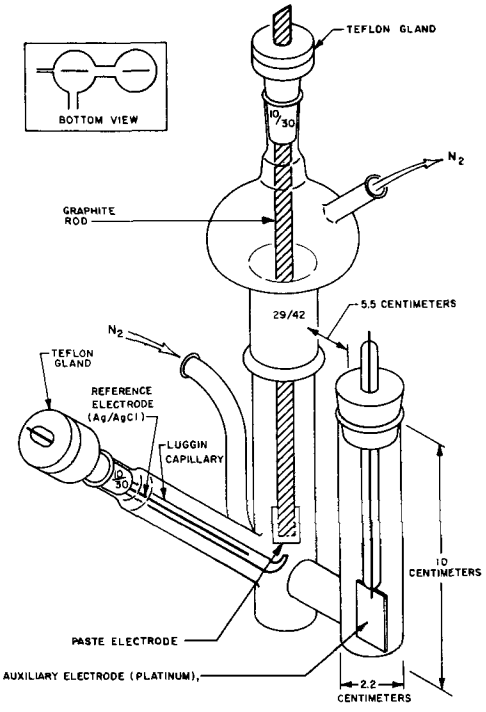

Fig. 1. H-cell

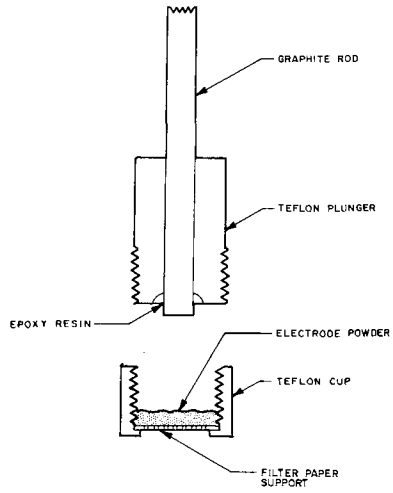

Fig. 2. Test electrode assembly

Lauer, Schlein, and Osteryoung (7). Current was recorded on the X-axis, and potential on the Y-axis of a Moseley X-Y recorder. At high-scan rates, the curves were photographed from the screen of a Dumont oscilloscope.

In other experiments the current was electronically integrated, and direct plots of charge *vs.* input voltage were obtained. In a typical experiment, the test electrode was maintained potentiostatically at a fixed potential for 10 min prior to scanning anodically or cathodically. Generally the scan range was 0.1 or 0.3v from the starting potential. The polarization curves were determined at varying scan rates in a 10% NaCl solution in the presence of air and with a nitrogen atmosphere.

The capacitative characteristics of Air-Spun graphite, mixed-acid treated Air-Spun graphite, "cation-responsive" paste, and the graphite support rod of the test electrode were studied. The cation-responsive paste has been used extensively in demineralization experiments and was prepared according to established procedures (1). Briefly, a 2:1 mixture of H_2SO_4 and HNO_3, washed, filtered, and dispersed with tannic acid. Twenty-four hours later the dispersion was stabilized by the addition of ammonium hydroxide. This is referred to as MA-Norit graphite (where MA means mixed-acid treatment).

Results

Air-spun graphite.—The characteristics of Air-Spun graphite (2.8 mg) were studied over a 0.3v range (*vs.* Ag-AgCl) at scan rates varying from 0.02 to 20 v/sec. At rates above 0.1 v/sec accurate results were not obtained. Double-layer capacitance values calculated from polarization data are given in Table I. Repre-

Table I. Double-layer capacity of air-spun graphite

Curve type	Open-circuit potential, v *vs.* Ag-AgCl	Scan rate, v/sec	Capacitance, i/scan rate	mf, dQ/dE
Cathodic	0.14	0.1	4.0	
	0.10	0.1		3.9
	0.13	0.1	3.9	
	0.14	0.1		4.0
	0.10	0.1		3.8 (scope)
	0.14	0.05	4.3	
		0.05	4.0	
		0.02	4.5	
		0.02		4.6
Anodic	0.11	0.1	4.5	
	0.12	0.1		4.2
	0.10	0.1		4.0 (scope)
	0.06	0.05	5.0	
	0.13	0.02	4.7	
	0.08	0.02		4.2

Sample size, 2.8 mg; solution, 10% NaCl; range, 0.3v.

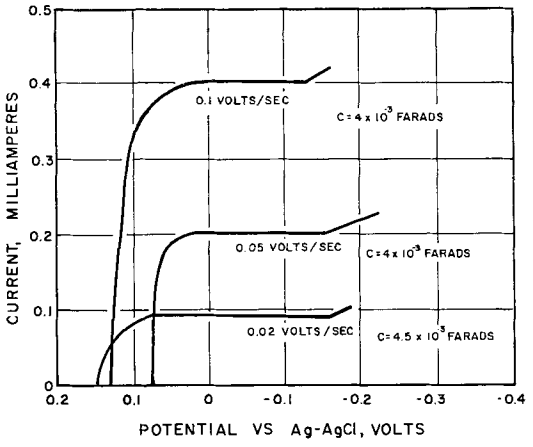

Fig. 3. Cathodic polarization curves determined on Air-Spun graphite ($C_d = i_c$/scan rate).

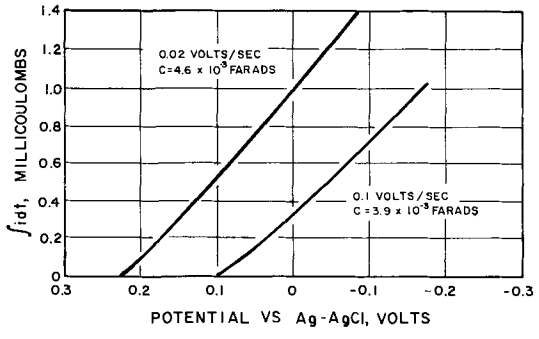

Fig. 4. Integrated cathodic scan for Air-Spun graphite

sentative curves obtained from cathodic scans (Fig. 3 and 4) were not significantly different from those determined anodically, and the presence of air had no noticeable effect on these determinations. The magnitude of the solution resistance between the test and reference electrodes was 35 ohms as established by a current-interrupter technique. The results of experiments on acid-treated Air-Spun graphite (1.7 mg) are shown in Table II.

MA-Norit graphite.—Linear current-potential curves were obtained with a 3-mg sample of the paste at 0.1 and 0.05 v/sec. A definite current plateau (0.55 ma) was observed at 0.0032 v/sec. This corresponds to a capacity of the order of 170 mf (57 mf/g of paste). Plots of dQ *vs.* dE yielded similar results.

To obtain more quantitative results, smaller samples of paste were required. Accordingly, 0.39 mg of paste was studied. The range studied was restricted to 0.1v from a potential which had been potentiostatically

Table II. Double-layer capacity of mixed-acid treated air-spun graphite

Curve type	Starting potential, v *vs.* Ag-AgCl	Scan rate, v/sec	Limiting current (i), μa	i/scan rate, mf
Cathodic	0	0.025	0.80	3.2
	0.065	0.0049	16	3.3
	0.087	0.0025	7	2.8
	0.065	0.0025	7	2.8
	0.065	0.0016	4.5	2.8
	0.065	0.0016	4.2	2.6
Anodic	0.074	0.1	275	2.8
	0.074	0.1	305	3.1
	0.074	0.1	290	2.9
	0	0.025	90	3.6
	0	0.0049	15.5	3.2
	0.087	0.0025	7.5	3.0
	0.065	0.0025	7.5	3.0
	0.065	0.0016	4.2	2.6

Sample, 1.7 mg; solution, 10% NaCl.

Table III. Double-layer capacity of MA-Norit graphite

Curve type	Starting potential, v *vs.* Ag-AgCl	Rate, v/sec	Limiting current (i), μa	i/scan rate, mf
Cathodic	0.2	0.0053	12	23
	0.19	0.0007	15	21
	0.2	0.001	21	19
	0.18	0.0033	80	24
	0.1	0.0053	14	26
	0.1	0.0011	25	23
	0.1	0.0022	50	23
	0	0.00053	14	26
	0	0.0007	15	21
	0	0.0011	27	25
	0	0.0022	50	23
	−0.1	0.00053	15	28
	−0.1	0.0011	29	26
Anodic	−0.05	0.00053	13	25
	−0.03	0.0007	20	29
	−0.05	0.0011	25	23
	−0.05	0.0022	50	23
	−0.065	0.0033	86	26
	0.05	0.00053	14	26
	0.05	0.0011	23	21
	0.1	0.0053	12	23
	0.1	0.0011	22	20
	0.15	0.00053	13	25
	0.15	0.0011	23	21
	0.2	0.0007	14	20
	0.195	0.0033	55	17

Sample, 0.39 mg; range, 0.1v.

fixed for 10 min. Anodic and cathodic polarization curves were determined from several starting potentials as a function of scan rate, and the results are shown in Table III. Representative anodic polarization curves determined are illustrated in Fig. 5.

A typical anodic polarization curve determined over a 0.3-v range (Fig. 6) exhibits a steady capacitance current over the entire range. This range was not useful for cathodic polarization, since the reduction of water commenced at approximately —0.4v with respect to the Ag-AgCl electrode. Anodic polarization curves, determined immediately after the test electrode was subjected to cathodic pretreatment below this voltage (*i.e.*, more negative), exhibited current waves presumably resulting from the oxidation of adsorbed hydrogen.

Graphite support rod.—Anodic and cathodic polarization curves were determined on the graphite support rod at scan rates of 1, 2, 10, 20, 40, and 80 v/sec. The

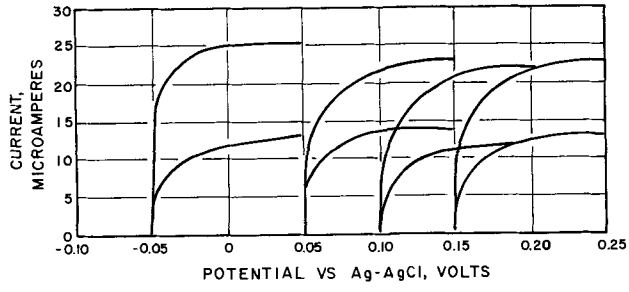

Fig. 5. Representative anodic polarization curves for Ma-Norit graphite paste. (Range, 0.1v starting from —0.05, 0.1, and 0.15v *vs.* Ag-AgCl; upper curves, 0.001 v/sec; lower curves: 0.00053 v/sec).

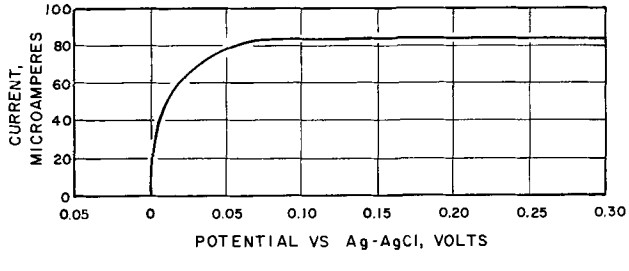

Fig. 6. Anodic polarization curve of MA-Norit graphite paste. (Range, 0.3v; rate: 0.0033 v/sec).

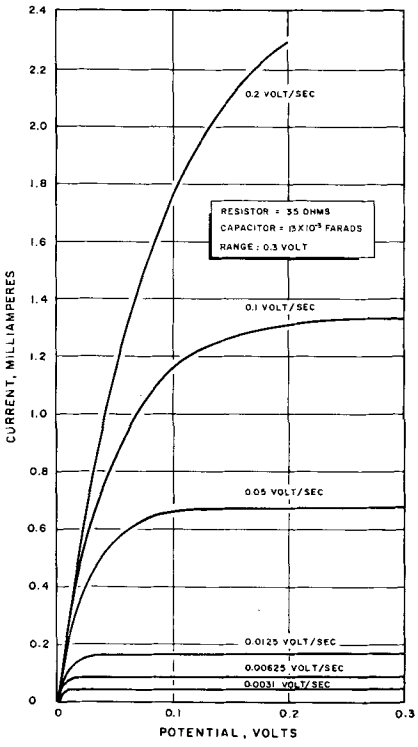

Fig. 7. Polarization of analog *RC* series circuit

resulting photographs of the oscilloscope trace revealed that dQ/dE was constant over the range of 10 to 80 v/sec. The double-layer capacitance was 30 ± 5 μf for this area of the rod. The purpose of this experiment was to assess the relative magnitude of contributions from the support rod in experiments where a sample was present. There was no significant difference in polarization characteristics when the filter paper was present.

Analog RC series circuit.—Polarization curves were determined on a series *RC* circuit as a function of scan rate, with R = 35 ohms and C = 13 mf (Fig. 7). The mean capacitance value determined at scan rates less than 0.1 v/sec, using the relationship $C = i/\text{scan rate}$, was 13.3 ± 0.3 mf.

Surface-area measurements.—The surface areas of Norit A, Air-Spun graphite, and the MA-Norit graphite paste were found to be 1200, 4, and 270 m^2/g, respectively. The Engelhard Isorpta Analyzer (BET method) was used. The samples were heated overnight in a slow stream of helium at 200°C. A mixture of 10% N_2 in helium was used in developing the nitrogen adsorption isotherm. From the lower portion of this isotherm (p/p_o = 0.15-0.25) the surface area was obtained by the application of the BET method.

Discussion and Conclusions

The determination of differential capacity, using voltammetric scanning techniques, is ideally undertaken when faradaic contributions can be ignored. Under such conditions (high faradaic impedance) the electrode equivalent circuit can be regarded as a series *RC* circuit, where *R* represents the solution resistance, and *C* is the capacity of the double layer. In an analog *RC* circuit the magnitude of the time constant (*RC* product), τ, limits the useful range of scan rates. Analysis of the time-variant voltage applied to such an *RC* circuit reveals that after a period to time, τ, has elapsed, the rate of change of potential across the capacitor is equal to the rate of change of applied voltage. Thus, for high time constants (R = 35 ohms, C = 13 mf) the experimental upper limit of scan rate for the 0.3-v range was 0.1 v/sec (Fig. 7). An analog *RC*-series circuit with R = 35 ohms and C = 25 μf was studied successfully in this laboratory from 0.02 to 40 v/sec.

The conditions under which such determinations are made on the dropping mercury electrode (2) cannot be extended to include electrodes of high surface area. Because of the large effective capacity of even small samples of carbon, slower scan rates must be used. The limit of scan rate is determined by the length of time required for the rate of change of the potential across the double layer to become equal to the scan rate (6). Thus, while the effective capacity of the graphite support rod (30 μf) was successfully determined at scan rates from 10 to 80 v/sec, slower scan rates and smaller samples were necessary with high surface-area carbons.

The double-layer capacity of Air-Spun graphite was found to be 1.4 f/g or 35 $\mu f/cm^2$ based on the measured surface area. Since the Isorpta Analyzer is better suited for larger surface areas, the value should be considered approximate. The double-layer capacity for mixed-acid-treated Air-Spun graphite was 1.8 f/g, and for the MA-Norit graphite paste it corresponded to 60 f/g, or 19 $\mu f/cm^2$. The latter value is based on the measured surface area.

It can be seen that over a small potential range and at several scanning speeds, typical capacitative behavior was obtained. Since the reduction of water begins at approximately —0.4v *vs.* the Ag-Ag-Cl electrode, it is desirable to limit the cathodic range to approximately 0.1v. Deviation from capacitative behavior was noted for Air-Spun graphite at approximately —0.1v *vs.* Ag-AgCl. Since the oxidation of water was found to occur at approximately 0.9v *vs.* the Ag-AgCl electrode, capacitative characteristics were observed over a wider range (Fig. 6).

It is concluded that at low applied potentials, charging of the double layer is the major electrochemical process. In this potential range the differential capacity did not vary with potential and did not depend on whether the polarization curve was determined anodically or cathodically.

There was no difference in polarization when air was present or excluded, indicating that oxygen was not reduced. Chronopotentiometric studies on carbon black electrodes indicated the absence of an air blank at cathodic potentials (8).

Manuscript received July 14, 1965; revised manuscript received Nov. 5, 1965. This work was supported by the office of Saline Water, Department of the Interior, under Contract 14-01-0001-334.

Any discussion of this paper will appear in a Discussion Section to be published in the December 1966 JOURNAL.

REFERENCES

1. J. W. Blair and G. W. Murphy, American Chemical Society Advances In Chemistry Series, **27**, 206 (1960).
2. J. W. Loveland and P. J. Elving, *J. Phys. Chem.*, **56**, 250 (1952).
3. J. W. Loveland and P. J. Elving, *ibid.*, **56**, 255 (1952).
4. J. W. Loveland and P. J. Elving, *ibid.*, **56**, 935 (1952).
5. J. W. Loveland and P. J. Elving, *Chem. Rev.*, **51**, 67 (1952).
6. P. Delahay, "New Instrumental Methods in Electrochemistry," p. 143, Intersciences Publishers, Inc., New York (1954).
7. G. Lauer, H. Schlein, and R. A. Osteryoung, *Anal. Chem.*, **35**, 1789 (1963).
8. J. D. Voorheis and S. M. Davis, *ibid.*, **32**, 1855 (1960).

The Characterization of Anodic Aluminas

I. Composition of Films from Acidic Anodizing Electrolytes

G. A. Dorsey, Jr.

Department of Metallurgical Research, Kaiser Aluminum & Chemical Corporation, Spokane, Washington

ABSTRACT

High-purity aluminum sheet was anodized in eleven different acidic electrolytes: boric, chromic, phosphoric, sulfuric, oxalic, malonic, succinic, tartaric, fumaric, glutaric, and adipic acids. These anodic coatings were analyzed by infrared to determine the composition and nature of each. We found, aside from alumina differences particular to each electrolyte, that the anodic barrier layer can be distinguished from the porous layer by an absorption band in the 1000-900 wavenumber region. Background information for the interpretation of anodic coating infrared data was obtained from the infrared analysis of known mineral forms of alumina. A band correlation table was devised.

Anodic alumina films are generally prepared in acidic electrolytes, such as dilute sulfuric acid, and have properties attributable to the specific electrolyte, the anodizing conditions, and the aluminum substrate compositions. Films formed at temperatures near 0°C are hard, abrasion resistant, and are often dark-colored and semi-opaque. Films prepared near 25°C may be clear and colorless, as with high-purity aluminum alloys anodized in sulfuric acid electrolytes; however, these are softer than coatings prepared at lower temperatures.

Anodic coatings formed in room temperature electrolytes are often immersed, after anodizing, for short periods in hot water solutions; this process is referred to as sealing. Thick anodic coatings have been shown to have a porelike structure, and sealing is thought to close these pores at the outer surface of the coating; sealed films are more protective against corrosive environments than are unsealed films, and this is generally thought to be due to this pore-closure mechanism. Although the protectiveness of anodic films may be due, in part, to properties within the coating itself, much work has been done relating film properties to sealing conditions (1).

Attempts to obtain information about anodic films, using x-ray and electron diffraction techniques, have generally been unsuccessful owing to the coatings' amorphous or ill-defined state (2). Electron microscopy has contributed much information on the geometric structure, but not molecular structure, of anodic coatings (3, 4). Other means have been employed, such as film particle electrophoresis (5), resistivity measurements (6), and infrared analysis (7). Since we are concerned here with the molecular structure of these aluminas, infrared analysis has proven to be our most powerful tool for general use.

Infrared analysis has been widely used in the examination of mineralogical aluminas. Frederickson (8) characterized the Al-OH stretch and bend modes for most of the common monohydrates and proposed a hydrogen bonded structure for at least one alumina, the β-monohydrate diaspore. Others have used infrared in studies of thermally induced alumina phase transitions (9). Newsom has combined the various analytical and physical property data into an excellent review for mineralogical aluminas (10), as has Lippens (11).

Our purpose here is to combine the general knowledge of anodic alumina properties with the molecular structure and composition to better characterize anodizing mechanisms, film compositions, and structures.

Experimental

Reference aluminas.—A series of pure alumina phases was obtained from our Permanente Metals Division Laboratory. These alumina phases had been identified by x-ray diffraction and differential thermal analytical techniques. These samples, listed below, were taken as being representative of the alumina mineral system and were used as reference standards for our infrared analysis.

1. Alumina trihydrates: α, trihydrate (gibbsite); β, trihydrate (bayerite).
2. Alumina monohydrates: α, monohydrates (boehmite and pseudoboehmite); β, monohydrate (diaspore).
3. Anhydrous aluminas: α, γ, pseudo-γ, η, θ, χ.

Other aluminum compounds were also examined. Aluminum isopropoxide was used as an additional reference for the aluminum-oxygen linkage. In addition, much information was made available through the investigation of sodium aluminates; these were examined initially and after a series of bakings.

Infrared analysis—reference aluminas.—These were examined using the potassium bromide disk and nujol mull techniques. Nujol mulls were used as a supplement to the disk method since the latter occasionally altered the water content of the sample; disks are prepared in a vacuum press while mulls are simply oil dispersions of the sample. Both sampling methods were used over the 4000-600 cm^{-1} range of a Beckman IR-7, in double-beam operation. A blank disk was used as a reference with the potassium bromide method, while the mulls were spread on cleaned sodium chloride plates, and spectra were prepared using air as a reference.

Anodic aluminas.—Cleaned 99.99% aluminum sheet was used as the substrate material for the samples. Electrolytes were prepared from each of the following, using distilled water:

Inorganic electrolytes: Orthoboric acid, 2.2M; Chromium (VI) oxide, 0.3M; Phosphoric acid, 3.1M; Sulfuric acid, 1.5M.

Organic electrolytes: Oxalic acid, 0.6M; Malonic acid, 0.6M; Succinic acid, 0.6M; Tartaric acid, 0.6M; Fumaric acid, 0.6M; Glutaric acid, 0.6M; Adipic acid, 0.6M.

Current densities, electrolyte temperatures, and coating thicknesses are listed in the Results section, along with other pertinent data. When used, the sealing process was carried out in boiling distilled water adjusted to pH of 6.0 with sodium hydroxide.

Infrared analysis—anodic aluminas.—The samples were examined over the 4000-600 cm^{-1} range of the IR-7 operated in double-beam mode. The flat anodized sheets were mounted in the sample stage of a C.I.C. ATR-1 reflectance attachment at the 45° incidence angle, and spectra were prepared using a front-sur-

faced aluminized mirror as a reference; the latter was mounted in an identical fashion. The reflectance method eliminated the side effects common to other sampling techniques and preserved the integrity of the sample. The orthoboric acid samples were also examined in the 800-33 cm^{-1} region, using the Model IR-11 at the Beckman Fullerton Laboratories. As with the IR-7 spectra, these were prepared using 45° reflectance.

The attenuated total reflectance technique of Fahrenfort (12) was also used, in isolated instances, with the same attachments. To accomplish this, a thin silver chloride sheet was first pressed against the anodic coating surface; a flat chrome-surfaced plate was used to press against the opposite side of the silver chloride. The anodized specimen, with the silver chloride overlayer, was then clamped in place against a C.I.C. silver chloride ATR prism; this procedure gave far better sample-prism optical contact than could be achieved without the sample overlayer.

In each case, the instrument was operated with a slit program and gain setting yielding an unloaded SB/DB ratio of 1.5; speed and period were adjusted for each sample so that the instrument response was adequate.

Results and Discussion

Alumina-system correlation.—The objective here was to relate infrared absorptions with specific alumina-system chemical linkages. Four bond types were detected, or were previously reported: AlO-H stretching vibration, Al-OH bend, Al=O stretching vibration, and Al-OAl stretching vibration. The anhydrous alumina reference phases and aluminum isopropoxide spectral data yielded information about the Al-OAl region, while the hydrate phases were used to define the AlOH stretch and bend regions. The Al=O stretch region was determined from spectral data obtained with sodium aluminate samples and from pseudoboehmite samples.

Once each of the four infrared absorption regions had been located, the upper and lower wavenumber limits for each region were determined by using the following relation with appropriate reduced mass values for each limit

$$\bar{\nu} = 1307\sqrt{\frac{k}{\mu}}$$

where k is the binding constant expressed in dynes per centimeter and $\mu = \dfrac{M_1 \times M_2}{M_1 + M_2}$ = reduced mass.

If we consider the bond RO-H, then $M_1 = 1$ and M_2 becomes increasingly large for increasing mass increments within the remainder of the molecule; here $\text{Lim.}_{M_2 \to \infty}\ \mu = 1$. Similar considerations apply to the other bonds, leading to the following results:

Bond	M_1	Limiting value of reduced mass	
RO-H	1	1	
R_2Al-OH	17	17	R represents the remainder of the molecule
RAl=O	16	16	
R_2Al-OAlO	59	59	

(The Al-OAl bond has no limiting reduced mass value for the system R_2Al-OAlR_2, and R_2Al-OAlO was used as an approximation.)

Furthermore, it follows that the limits of variation of μ will determine the limits of variation of the absorption frequency. As the molecular weight increases, the reduced mass increases to a maximum, and the absorption frequency decreases to a minimum as indicated below.

This behavior was exploited to good advantage for our work. The lowest observed wavenumber of the band belonging to each bond type was considered as being associated with a large reduced mass; therefore, the lowest observed wavenumber for each bond type

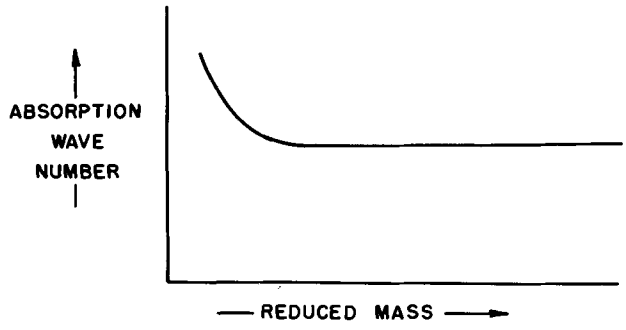

Fig. 1. Reduced mass *vs.* absorption wavenumber for relation $\bar{\nu} = 1307\sqrt{\frac{k}{\mu}}$

was taken to be an approximation to the lower absorption frequency limit for the bond type. From this, plus the limiting value of the reduced mass, binding constants were calculated for each of the bond types previously mentioned. The minimum limit of the reduced mass for each bond type was next calculated, and this, together with the binding constant, produced a value for the highest absorption frequency within each of the calculated frequency ranges for each type of bond, as is shown below:

Alumina-system chemical bond	Infrared absorption wavenumber range	Interpretation
AlO ⟷ H (stretch)	From 3660 to 2940 cm^{-1}	Bands in this region indicate the presence of water; either free, adsorbed, or combined as hydroxide
Al ⟷ O (stretch)	From 1696 to 1345 cm^{-1}	The presence of double bonds indicates an adsorptive or reactive material that probably does not have much crosslinking.
Al ⟷ OH (bend)	From 1162 to 900 cm^{-1}	Absorption here indicates the presence of aluminum hydroxides. Monohydrates are characterized by bands near 1070 cm^{-1}, while normal trihydrates show bands below 1025 cm^{-1}.
Al ⟷ OAl (stretch)	Below 900 cm^{-1}	Bands in this region indicate a high degree of crosslinking in the material; strong bands in this region are often associated with an absence of Al=O bonds. As the degree of crosslinking, i.e., molecular weight, increases, the bond absorption frequency will shift to lower values.

Infrared data for anodic aluminas.—Table I presents the infrared data that were obtained with the anodic aluminas; anodizing conditions and coating thicknesses are included in the table. The average anodic coating thicknesses were taken from metallographic cross-section determinations.

The anodic coating on aluminum may consist of one or more layers. The first layer to form, during anodizing, is termed the "barrier layer," further anodizing thickens this layer and may also cause a second layer to form on top of it. Unlike the barrier layer, this second layer is generally quite porous and is referred to as the "porous layer."

While the porous layer readily dissolves in acid solutions such as chromic-phosphoric mixtures, the barrier layer is less rapidly attacked. The barrier layer is also a better dielectric than the porous layer; the bulk of the voltage drop through an anodic coating, during anodizing, is thought to be due largely to the barrier layer. Many anodizing electrolytes can be used to produce the composite barrier and porous-layered coating; however, some yield only barrier layers. Orthoboric acid is commonly used when it is desired only to produce the barrier layer.

Table I. Infrared data for anodic aluminas

The following notations are used to describe the intensity of the infrared bands: S, strong; M, moderate; W, weak; b, broad; s, sharp; sh, shoulder on another band.

	Electrolytes and anodizing parameters	Infrared absorptions (wavenumbers) AlO ⟷ H stretch	Al <=> O stretch	Al ⟷ OH bend	Al ⟷ OAl stretch
A.	2.2M orthoboric acid				
	100°C, 250v, unsealed	None	None	955^{M,s}	None
	100°C, 450v, unsealed	None	None	955^{M,s}	None
	(Orthoboric acid films were examined over the 4000-33 cm^{-1} region, using IR-7 and IR-11 instruments)				
B.	0.3M chromium (VI) oxide				
	41°C, 0.216 amp/dm², 1.7μ, unsealed	3360^{S,b}	None	1100^{W,b} 1060^{S,s} 925^{S,b}	670^{S,b}
	41°C, 0.216 amp/dm², 1.7μ, sealed	3360^{S,b}	None	1100^{W,b} 1060^{S,s} 925^{S,b}	670^{S,b}
	41°C, 0.216 amp/dm², 8.9μ, unsealed	Fringe pattern interference	None	1003^{S,sh,s} 1002^{S,s} 920^{M,sh,s}	725^{M,b}
	41°C, 0.216 amp/dm², 8.9μ, sealed	Fringe pattern interference	None	1112^{S,s} 1025^{S,b} 975^{S,sh,s}	900^{M,sh,b} 835^{M,b}
C.	3.1M othophosphoric acid				
	25°C, 0.756 amp/dm², 2.0μ, unsealed	3000^{W,b}	None	1150$^{(1)S,s}$ 1140$^{(1)S,sh,s}$ 908^{M,b}	700^{S,b}
	25°C, 0.756 amp/dm², 2.0μ, sealed	3000^{M,b}	None	1150$^{(1)S,b}$ 908^{M,b}	700^{S,b}
	25°C, 0.756 amp/dm², 5.3μ, unsealed	3400^{M,b}	None	1150$^{(1)S,b}$ 950^{S,b}	725^{M,b}
	25°C, 0.756 amp/dm², 5.3μ, sealed	3450^{M,b}	None	1150$^{(1)S,b}$ 950^{S,b}	725^{S,b}
D.	1.5M sulfuric acid				
	25°C, 1.30 amp/dm², 1.8μ, unsealed	3400^{M,b}	1325^{M,b}	1150$^{(2)S,b}$ 1090^{S,sh,s} 900^{M,b}	650^{M,b} 610^{M,s}
	25°C, 1.30 amp/dm², 1.8μ, sealed	3450^{S,s} 3420^{S,s} 3390^{M,sh,s}	1325^{M,b}	1125$^{(2)S,b}$ 1090^{S,sh,s} 900^{M,b}	650^{M,b}
	25°C, 1.30 amp/dm², 6.9μ, unsealed	Fringe pattern interference	1200^{S,b}	1125$^{(2)S,b}$ 1075^{S,b} 920^{S,s}	750^{M,b}
	25°C, 1.30 amp/dm², 6.9μ, sealed	Fringe pattern interference	1200^{S,b}	1125$^{(2)S,b}$ 1015^{S,s} 970^{S,s}	750^{M,b}
	25°C, 1.30 amp/dm², 1.8μ, sealed, ATR spectrum	3600^{M,s} 3520^{M,s} 3440^{S,s} 3420^{S,s} 3390^{S,s} 3300^{S,s} 3310^{S,s} 3250^{M,s}	1300^{W,b}	1120$^{(2)M,b}$ 1070^{S,s} (no band in 1000-900 cm^{-1} region)	680^{S,b}
	25°C, 1.30 amp/dm², 6.9μ, sealed, ATR spectrum	3550^{M,sh,s} 3370^{S,s} 3310^{S,s} 3280^{S,s} 3180^{S,b} 3120^{S,s} 3100^{S,s} 3050^{S,s} 3000^{S,s}	None	1120$^{(2)S,s}$ 1070^{S,s} (no band in 1000-900 cm^{-1} region)	675^{S,b}
E.	0.6M oxalic acid				
	3°C, 1.08 amp/dm², 1.3μ, unsealed	None	1480^{S,s}	940^{S,s}	610^{S,b}
	10°C, 1.08 amp/dm², 2.8μ, unsealed	None	1470^{M,s}	935^{S,s}	740^{W,b} 650^{W,b}
F.	0.6M malonic acid				
	68°C, 1.08 amp/dm², 2.5μ, unsealed	None	1470^{M,s}	1130^{M,s} 960^{S,s}	610^{S,b}
	90°C, 1.08 amp/dm², 1.7μ, unsealed	3400^{W,b}	None	933^{S,s}	675^{W,b}
G.	0.6M Succinic acid				
	50°C, 1.08 amp/dm², thickness not measurable, unsealed	None	1470^{W,b}	960^{S,s}	755^{W,sh,b}
	85°C, 1.08 amp/dm², thickness not measurable, unsealed	None	None	965^{S,s}	755^{W,sh,b}
H.	0.6M tartaric acid				
	25°C, 1.08 amp/dm², thickness not measurable, unsealed	None	1450^{W,b}	955^{M,s}	610^{S,b}
	75°C, 1.08 amp/dm². 2.8μ, unsealed	None	1475^{M,s}	970^{S,s}	610^{S,b}
I.	0.6M fumaric acid				
	10°C, 1.08 amp/dm², thickness not measurable, unsealed	None	1468^{M,s}	965^{S,s}	610^{S,b}
	100°C, 1.08 amp/dm², thickness not measurable, unsealed	None	None	960^{S,s}	725^{W,b}
J.	0.6M glutaric acid				
	98°C, 1.08 amp/dm², thickness not measurable, unsealed	None	None	957^{M,s}	None
K.	0.6M adipic acid				
	95°C, 400v, thickness not measurable and C.D. not constant. unsealed	None	None	970^{S,s}	None

(1) This band may be due to aluminum phosphate. The 2.0μ film thickness contained 6%, by weight, PO_4^{-3} while the 5.3μ coating contained 8 w/o PO_4^{-3}.

(2) This band may be due to aluminum sulfate. The 1.8μ film thickness contained 13%, by weight, SO_4^{-2} while the 6.9μ coating contained 14 w/o SO_4^{-2}

The preceding table shows that the barrier layer electrolyte, orthoboric acid, yields an anodic coating having only one infrared absorption band in the 4000 to 33 cm^{-1} region: at 955 cm^{-1}. Similarly, each of the other electrolytes produce coatings with one infrared band in the 1000-900 wavenumber region. Often, the wavenumber placement of this band shifts to higher values as the thickness of the coating increases: example, orthophosphoric, sulfuric, and malonic acids.

The ATR spectra, which show only the surface composition, and bulk reflectance spectra of sulfuric anodic films are similar, however the 1000-900 cm^{-1} band is missing in the sulfuric anodic film ATR spectra. This indicates that the 1000-900 cm^{-1} band corresponds to an alumina composition not found on the sulfuric anodic coating surface. We conclude, therefore, that the anodic barrier layer is characterized by an infrared absorption band lying within the 1000 to 900 wavenumber region. The basis for this conclusion is reiterated below.

1. Orthoboric acid electrolytes produce only barrier layer oxide types. These anodic films have only one absorption band in the 4000 to 33 cm^{-1} region: between 1000 and 900 cm^{-1}.

2. The reflectance spectra of the entire group of coatings, from various electrolytes, have one common absorption region: 1000 to 900 cm^{-1}.

3. The surface composition of a porous coating is similar to the bulk composition (example, sulfuric anodic film); however the 1000 to 900 cm^{-1} region is blank.

Although the barrier layer alumina apparently can be identified with an infrared absorption in the 1000-900 wavenumber region, this presents an anomaly. The barrier layer infrared band is within the region ascribed to alumina hydrates; specifically, the band is in the trihydrate region. Alumina hydrates normally have a second band located in the higher frequency region near 3400 cm^{-1}; barrier layers normally do not have a band here. However, when there is a band in the 3400 region, the barrier layer band has usually shifted from a low to higher frequency (example: 25°C phosphoric coatings); this frequency shift normally corresponds to a breaking-up of a high molecular weight polymer to give a series of lesser polymers. We believe that our data show the barrier layer to be a hydrated alumina, specifically a trihydrate, which is altered in structure as anodizing progresses in a porous film-forming electrolyte.

Conclusions

Infrared analysis of anodic and nonanodic aluminas can reveal much about their composition and structure. The following correlation chart was derived from our preliminary work here.

Alumina bond type	Infrared absorption frequency range (wavenumbers)
AlO ⟷ H	3660-2940
Al <=> O	1696-1345
Al ⟷ OH	1162-900
(Barrier layer Al ⟷ OH	1000-900)
Al ⟷ OAl	Below 900

Infrared absorptions of composite anodic films may be used to distinguish the porous layer from the barrier layer; the barrier layer absorption is limited to the 1000-900 cm^{-1} region while the porous layer may show bands above 1000 cm^{-1} or below 900.

Acknowledgments

The author wishes to thank the Kaiser Aluminum & Chemical Corporation for its support of this work and for its permission to publish these results. Our thanks go also to Beckman Instrument's H. J. Sloane and K. W. Stein, who obtained the far infrared data for the orthoboric acid anodic films.

Manuscript received June 14, 1965.

Any discussion of this paper will appear in a Discussion Section to be published in the December 1966 JOURNAL.

REFERENCES

1. B. A. Scott, *Electroplating and Metal Finishing*, **18**, 47 (1965).
2. M. A. Heine and P. R. Sperry, *This Journal*, **112**, 359 (1965).
3. H. Akahori, *J. Electronmicroscopy*, **10**, 175 (1961).
4. H. Ginsberg and K. Wefers, *Metall.*, **17**, 202 (1963).
5. C. H. Giles *et al.*, *J. Chem Soc.*, **1954**, 4360.
6. M. A. Heine and M. J. Pryor, *This Journal*, **110**, 1205 (1963).
7. R. F. Fichter, *Helv. Phys. Acta*, **19**, 21 (1946).
8. L. D. Frederickson, Jr., *Anal. Chem.*, **26**, 1883 (1954).
9. T. Sato, *J. Appl. Chem.*, **14**, 303 (1964); *ibid.*, **13**, 316 (1963); *ibid.*, **12**, 9 and 553 (1962); *ibid.*, **11**, 207 (1961).
10. J. W. Newsom *et al*, Alcoa Technical Paper No. 10 (1960).
11. B. C. Lippens, "Structure and Texture of Aluminas," Thesis, Tech Univ. of Delft (1961).
12. J. Fahrenfort, *Spectrochem. Acta*, **17**, 698 (1961).

The Characterization of Anodic Aluminas

II. Effect of Anodizing Temperature on Coatings from Aliphatic Dicarboxylic Electrolytes

G. A. Dorsey, Jr.

Department of Metallurgical Research, Kaiser Aluminum & Chemical Corporation, Spokane, Washington

ABSTRACT

High-purity aluminum sheet was anodized in eight dicarboxylic electrolytes: oxalic, malonic, succinic, and tartaric acids, ammonium tartrate, and fumaric, glutaric and adipic acids. The anodic coatings were quantitatively analyzed by infrared techniques to evaluate the amounts of porous and barrier layers in each. We found that the anodizing temperature influenced the amount of porous layer formed and appeared to be related to the dissolving tendency of the electrolyte. Furthermore, we found a shift in the absorption wavenumber of the barrier layer that correlates with the amount of porous layer. A mechanism for formation of porous layer from barrier layer is proposed.

A correlation chart, which we described previously, related alumina-system chemical linkages with absorption regions in the infrared (1). We were able to make a distinction between the infrared absorption of the anodic barrier layer and absorptions characteristic of the various porous layers. The composition of the porous layer varied with the anodizing electrolyte used. The purpose of this present work is to show the effect of anodizing temperature on the amounts of both barrier and porous layers within the same anodic film.

It is commonly accepted that the thickness of the barrier layer is defined by a relationship with the applied voltage: ~14 Å/v. However, as is pointed out by van Geel and Schelen (2), this relationship exists only under a certain set of conditions. When the peak anodizing voltage is reached, it must be held con-

stant until the anodizing current density has decayed to a low steady-state value. No further barrier layer should be formed at this fixed voltage. If the anodizing electrolyte and conditions are such that both porous and barrier layers form, the anodizing current will not correspondingly decay at fixed voltages and the 14 Å/v relation should not be applied to compute barrier layer thicknesses.

Since we are interested in the amounts of both porous and barrier layers which were formed at constant current density, the 14 Å/v relation could not be applied. Instead, we used the infrared absorbance of bands which could be identified with the porous and barrier layers, respectively. The absorbance of an infrared band is governed by two factors: (*i*) the absorbancy index, a relationship between refractive index and wavelength for a specific molecular absorption band, and (*ii*) the "amount" of absorbing material. The amount is determined by two factors: concentration of material per unit volume and thickness of the contained material.

As described earlier (1), our procedure for the infrared analysis of anodic aluminas is one of 45° incident angle reflectance. The readings for each anodized sample are made over equal areas so that only differences in coating density or coating thickness influence the quantitative reproducibility between samples of the same anodic material. The effective beam area is a fixed parameter and depends only on the angle of incidence for the sample and the optical geometry of the system.

We can make quantitative measurements on a relative basis without knowing the sample thickness or effective beam area but, to do this, we sacrifice the ability to express our data in terms of units. As a matter of expediency, our final data were obtained in unitless absorbance values that express the effects of coating thickness, density, and bond absorbancy indices. In this paper, therefore, we chose to refer to our quantitative results as amounts rather than in more normal concentration terms. A thin, dense coating could present the same amount of a particular molecular bond to the beam as would a thicker, but lighter, film.

Experimental

Anodic aluminas.—Cleaned 99.99% aluminum sheet was used as the substrate material for the samples. The following electrolytes were prepared, using distilled water: oxalic acid, 0.6M; malonic acid, 0.6M; succinic acid, 0.6M; tartaric acid, 0.6M; ammonium tartrate, 0.2M-solution of *p*H 6; fumaric acid, 0.6M; glutaric acid, 0.6M; adipic acid, 0.6M.

The aluminum panels were anodized at a constant current density of 1.08 amp/dm^2 or, where the current density could not be maintained, to a maximum of 400v. The samples were anodized for 5.0 and 10.0 min at temperatures ranging from near 0° through 100°C. At the lower temperatures, some solutes were not sufficiently soluble to obtain the desired concentration; at higher temperatures, the desired concentration was obtained. The samples were not sealed but were analyzed immediately after anodizing.

Infrared analysis.—The samples were examined, as before, over the 4000-600 cm^{-1} range of the Beckman IR-7. The flat anodized sheets were mounted in the sample stage of a C.I.C. ATR-1 reflectance attachment at a 45° angle of incidence. Double beam spectra were obtained *vs.* a front-surfaced aluminized mirror which was mounted in an identical fashion as the sample.

Quantitative determinations were made using a weight-method of graphical integration. Checks showed that the total precision, using this method, was within ± 1.3%.

Results and Discussion

Infrared absorption bands were assigned to porous or barrier layers according to the results of previous studies (1, 3, 4). A summary of these background data is given below:

Alumina bond type	Infrared absorption frequency range (wavenumbers)
AlO ⟷ H stretch	3660-2940
Al <=> O stretch	1696-1345
Al ⟷ OH bend	1162-900
(Barrier layer 1000-900)	
Al ⟷ OAl stretch	Below 900

The 1470 cm^{-1} Al=O band is used as a measure of the apparent amount of porous layer obtained from the dicarboxylic electrolytes. This band has been found only in the porous layer and is well defined, whereas the Al-OAl band is broad and often extends below the 600 cm^{-1} limit of our instrument. The 1570 Al=O band was not used, since this may be altered by the degree of sorbed water.

We recognize that a one-to-one correlation has not been established between the Al=O absorbance and the amount of porous layer. Further, the concentration of this bond group may vary with the thickness of a porous layer. Pending further work, we will refer only to the amount of porous layer Al=O, or to the apparent amount of porous layer, and not to the amount of porous layer itself.

A band in the 1000 to 900 cm^{-1} region is due to absorption by the anodic barrier layer (1). Accordingly, its absorbance is used as a measure of the amount of barrier layer.

The coating thicknesses were generally too small to be measured by metallographic cross-sectional techniques and are therefore not included here.

Figures 1 through 8 show the results that were obtained on coatings produced in each electrolyte and over a range of anodizing temperatures. Peak voltages are included with the barrier layer data.

It is well accepted that electrolytes which do not dissolve alumina produce only barrier layer coatings. Electrolytes which can dissolve alumina may produce both barrier and porous coatings. If the dissolving action of the electrolyte is weak, the anodic oxidation of aluminum may be less efficient at low anodizing temperatures; with such electrolytes, successively thicker coatings may be obtained as the temperature is increased under otherwise identical conditions of current and time. However, at higher temperatures, the dis-

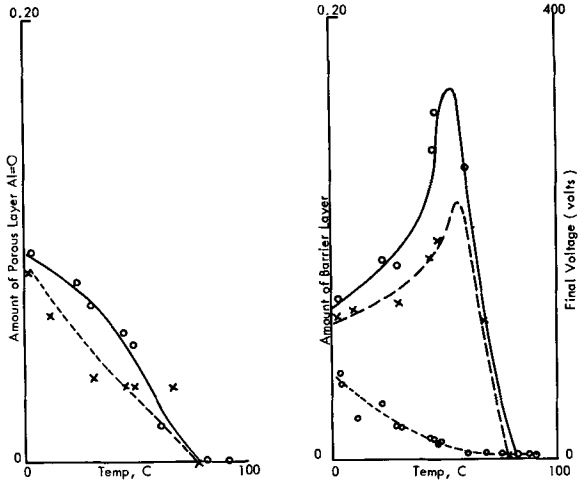

Fig. 1. Effect of anodizing temperatures on coating layers formed in oxalic acid; 0.6M at 1.08 amp/dm^2. A (left), Apparent porous layer: porous coating trends, the amount of porous coating Al=O was greatest at low temperature. Increased anodizing time did not appear to change the amount obtained after 5 min of anodizing. The bond group did not form above 80°C. B (right), Barrier layer: Barrier layer trends; the barrier layer predominated at intermediate temperatures and reached a maximum amount near 60°C; above this temperature, it, too, ceased to form, and the metal then electropolished. —○—, 10-min anodize; — — ✕ — —, 5-min anodize; — — • — —, anodizing voltage.

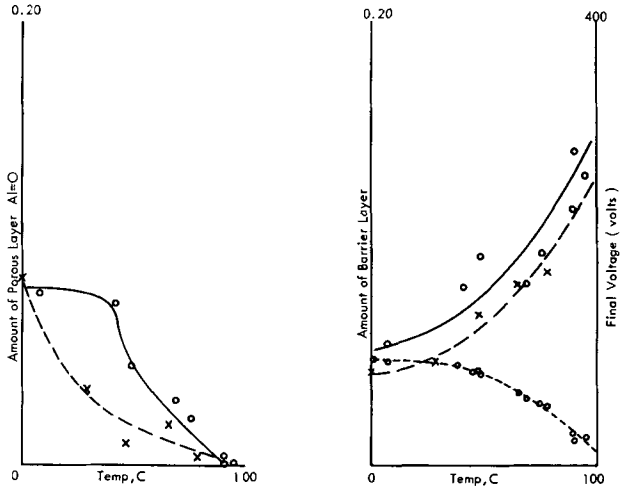

Fig. 2. Effect of anodizing temperatures on coating layers formed in malonic acid; 0.6M at 1.08 amp/dm^2. A (left), Apparent porous layer: porous coating trends, the apparent amount of coating was greatest at low temperatures. The porous coating Al=O did not form above 90°C. (B) (right), Barrier layer: barrier layer trends, the barrier layer predominated and increased steadily in amount with increasing temperature. —⊖—, 10-min anodize; —✕—, 5-min anodize; — — ○ — —, anodizing voltage.

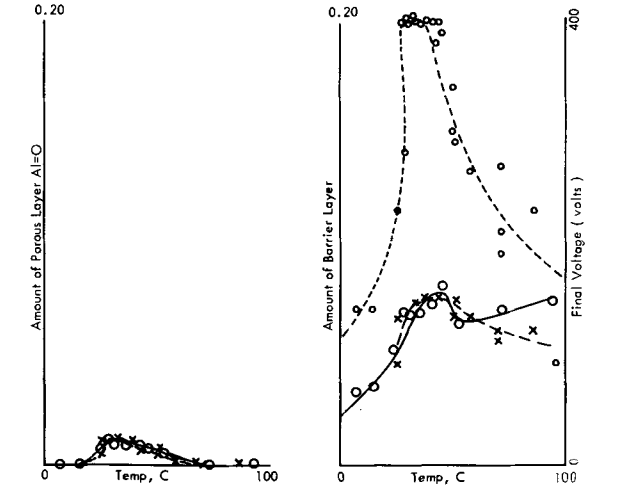

Fig. 3. Effect of anodizing temperatures on coating layers formed in succinic acid; 0.6M at 1.08 amp/dm^2. A (left), Apparent porous layer: porous coating trends, the apparent coating formed only at mid-range temperatures and at high voltages. The coating did not form below 15°C nor above 60°C, and the amount of Al=O obtained did not change after the first 5 min of anodizing. B (right), Barrier layer: Barrier layer trends, the amounts of barrier layer showed maxima in the temperature region where a porous coating formed. —⊖—, 10-min anodize; —✕—, 5-min anodize; — — ○ — —, anodizing voltage.

solving action will predominate so that the porous layer is attacked (Fig. 1, 2, 3, 5, and 8). At still higher temperatures the porous layer, and thereafter the barrier layer, will dissolve; this sequence is demonstrated in Fig. 1 for the oxalic acid electrolyte.

Tartaric acid, Fig. 4, however appears to show two relationships between the dissolving rate and the formation rate of the coatings. We theorize that this behavior is due to the existence of two dissolving mechanisms with tartaric acid. Tartaric acid may form two distinct aluminum complexes: one which forms readily and a less-solubilizing complex that forms only at higher temperatures. The presence of such a dual complexing mechanism for tartaric and other polyhydroxy acids is well known (5).

Under such a system, thicker anodic coatings would be produced at successively higher anodizing temperatures until the dissolving action of the more readily

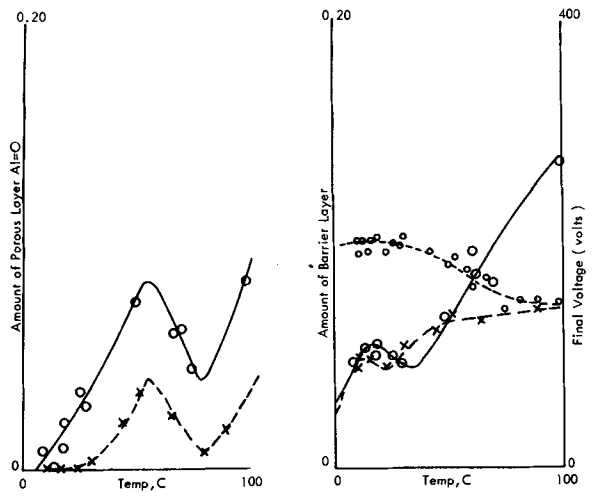

Fig. 4. Effect of anodizing temperatures on coating layers formed in tartaric acid; 0.6M at 1.08 amp/dm^2. A (left), Apparent porous layer: porous coating trends, the amount of Al=O showed two temperature-dependent maxima: at 60°C and near 100°C. The amount obtained was also dependent on the anodizing time. B (right), Barrier layer: barrier layer trends, the barrier layer amount also exhibited two maxima that were temperature-dependent: at 20°C and near 100°C. An explanation for the occurrence of these dual maxima follows in this section. —⊖—, 10-min anodize; —✕—, 5-min anodize; — — ⊖ — —, anodizing voltage.

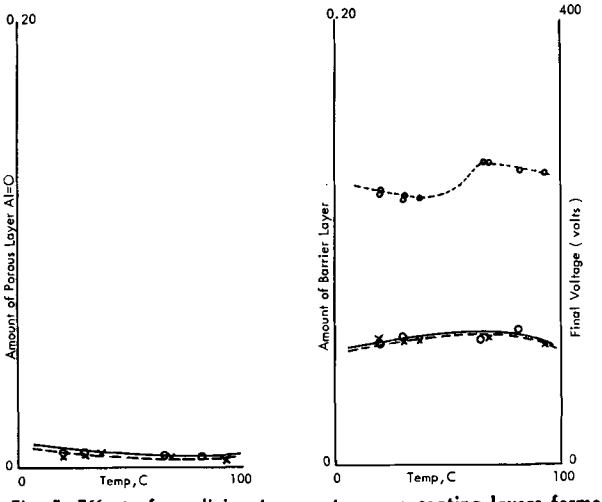

Fig. 5. Effect of anodizing temperatures on coating layers formed in ammonium tartrate; 0.2M at 1.08 amp/dm^2. A (left), Apparent porous layer: porous coating trends, a trace amount of Al=O was always present regardless of anodizing temperature or voltage. Anodizing beyond 5 min had no further effect on the total amount present. B (right), Barrier layer: barrier layer trends, the amount increased gradually with increasing temperature and went through a maximum of 80°C, afterwards decreasing slightly. —⊖—, 10-min anodize; —✕—, 5-min anodize; — — ⊖ — —, anodizing voltage.

formed aluminum tartrate complex approached the rate of aluminum oxidation. In this temperature region, thinner coatings would be formed. At still higher temperature, the first complex would revert to the weaker, less active form. This would result in a net decrease in the dissolving action of the solution, and the coating thickness would again increase with increasing temperature.

Further examination of these data revealed a peculiar trend for the anodic barrier layer. The trend was particularly well developed when the tartaric acid electrolyte was used; this electrolyte does not appear to exert a dissolving action on the barrier layer under the conditions employed here. Figure 9 shows that, when a porous coating was formed in conjunction with the barrier layer, the barrier layer infrared band tended to shift toward higher frequencies. A frequency

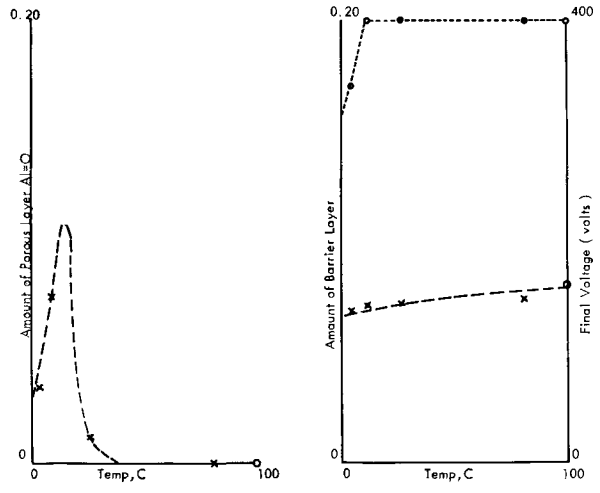

Fig. 6. Effect of anodizing temperatures on coating layers formed in fumaric acid; 0.6M at 1.08 amp/dm^2. A (left), Apparent porous layer: porous coating trends, the apparent amount showed a sharp maximum near 15°C and rapidly decreased to an undetectable amount above 30°C; the porous coating Al=O did not form above 30°C. B (right), Barrier layer: barrier layer trends, the amount steadily increased with increasing temperature, from 0 to 100°C, the increase was uniform and without any apparent maximum. —⊖—, 10-min anodize; —✕—, 5-min anodize; ——⊖——, anodizing voltage.

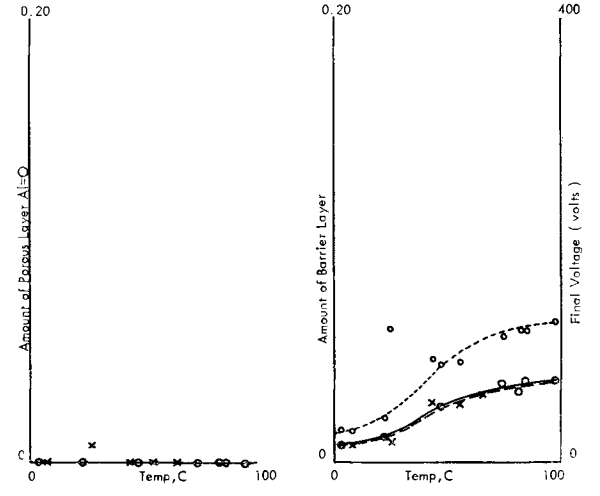

Fig. 7. Effect of anodizing temperatures on coating layers formed in glutaric acid; 0.6M at 1.08 amp/dm^2. A (left), Apparent porous layer: porous coating trends, no detectable Al=O formed during anodizing from 0 to 100°C. B (right), Barrier layer: barrier layer trends, the barrier layer amount increased with anodizing temperature; the increasing amount conformed well with increasing voltage increments. No change was detectable after the first 5 min of anodizing. —⊖—, 10-min anodize; —✕—, 5-min anodize; ——⊖——, anodizing voltage.

shift of this type normally corresponds to a reduction in polymer weight, indicating a breaking up of a high polymer to give a series of lesser polymers. This tendency appeared to be independent of the anodizing temperature and was influenced by increasing amounts of the porous layer Al=O bond.

We also found that coatings formed in chromic, oxalic, phosphoric, and sulfuric acids all show a similar relationship between porous layer Al=O absorbance and barrier layer wavenumber (1). Tartaric acid is the only example for which a complete set of data was available; previous data show the effect for the other acids, but the data are for two coating thicknesses and not for a uniformly increasing series of samples.

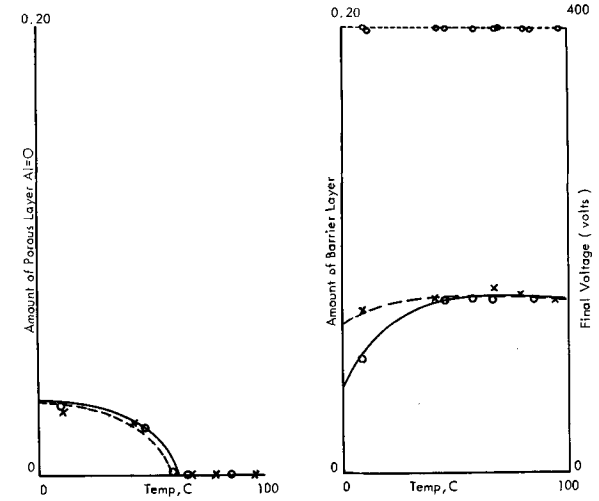

Fig. 8. Effect of anodizing temperatures on coating layers formed in adipic acid, 0.6M (current density could not be held constant at 1.08 amp/dm^2). A (left), Apparent porous layer: porous coating trends, the apparent amount decreased with increasing temperature and was not detectable above 60°C. B (right), Barrier layer: Barrier layer trends, the amount increased with increasing temperature and reached a plateau above 40°C. Effects of anodizing beyond the first 5 min were only apparent at temperatures below 40°C. —⊖—, 10-min anodize; —✕—, 5-min anodize; ——⊖——, anodizing voltage.

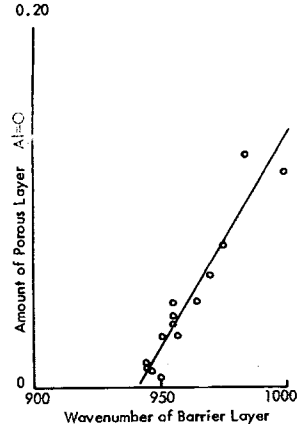

Fig. 9. Relationship between amount of porous layer and infrared positioning of barrier layer band: 0.6M tartaric acid; amount of porous layer *vs.* absorption wavenumber of barrier layer.

This effect was not evident if the amount of porous coating remained unchanged with increasingly higher temperatures or anodizing times. Moreover, coatings formed in barrier layer electrolytes did not show a shift in the wavenumber of the absorption band with increasing anodizing temperatures. We postulate from these observations that porous coatings are not formed from the barrier layer unless the surface of the barrier layer is first altered; this surface alteration appears to be a conversion of the barrier layer into a reactive hydrous alumina layer. Unless this surface layer, which we will call the "parent layer," is first formed, the barrier layer will apparently continue to grow without undergoing conversion to a porous overlayer.

This proposal of a two-phase barrier layer is consistent with earlier findings by Heine and Pryor (6), who found two regions of different high-frequency a-c resistance within an ammonium tartrate-anodized barrier layer. One such region lay next to the metal while the second region was about 90Å beyond the metal-oxide interface. Altenpohl, also, has reported two apparent sublayers within the anodic barrier layer (7); of the two, the innermost sublayer showed the least tendency to dissolve in chromic-phosphoric acid mixtures.

Conclusions

Quantitative infrared analyses of the barrier and porous layers, within the same anodic film, can be used to follow the effects of electrolyte temperature on the formation and dissolution of the coating. Acids which readily form stable complexes (here, oxalic or malonic) showed a high dissolving effect on the anodic film; the film was formed only at low temperatures, and it dissolved in the electrolyte at higher temperatures. Tartaric acid, a weaker complexing agent, required a higher temperature to produce a similar dissolving action; two dissolving mechanisms were apparent here. Other acids, which were not complexing agents under these conditions, produced only barrier layers.

We found, too, that the barrier layer apparently undergoes a change as the porous overlayer forms. The apparent polymer weight of the barrier layer decreases as the apparent amount of porous overlayer is increased.

Acknowledgments

The author wishes to thank the Kaiser Aluminum & Chemical Corporation for its support of this work and for its permission to publish these results.

Manuscript received July 26, 1965.

Any discussion of this paper will appear in a Discussion Section to be published in the December 1966 JOURNAL.

REFERENCES

1. G. A. Dorsey, Jr., *This Journal*, **113**, 169 (1966).
2. W. Ch. van Geel and B. J. J. Schelen, *Philips Research Repts.*, **12**, 240 (1957).
3. L. D. Frederickson, Jr., *Anal. Chem.*, **26**, 1883 (1954).
4. J. W. Newsom *et al.*, Alcoa Technical Paper No. 10 (1960).
5. S. Chaberek and A. F. Martell, "Organic Sequestering Agents," p. 308, John Wiley & Sons, Inc., New York (1959).
6. M. A. Heine and M. J. Pryor, *This Journal*, **110**, 1205 (1963).
7. D. Altenpohl, *Inst. Radio Engrs. Com. Rec.*, **111**, 35 (1954).

Theory of Potentiostatic and Galvanostatic Charging of the Double Layer in Porous Electrodes[1]

F. A. Posey and T. Morozumi[2]

The Chemistry Division, Oak Ridge National Laboratory, Oak Ridge, Tennessee

ABSTRACT

A theory of potentiostatic and galvanostatic transients which occur during charging of the double layer in porous electrodes is developed. Solutions are presented for transients due to charging processes in the interior of idealized, one-dimensional porous and tubular electrodes of finite length. In addition, the effect of IR drop which occurs in solution between the tip of the reference electrode capillary and the front surface of the porous electrode is calculated. The effect of the external surface of the electrode on the charging transients is also assessed. Solutions for charging transients are presented for the case of potentiostatic and galvanostatic single pulse methods, for measurements made with square waves of current or voltage, and for triangular current or voltage sweeps. The effect of the conductivity of the metallic phase on the observable transients is considered. Graphical solutions of the theoretical equations are presented.

Double layer capacity measurements provide an important means for the study of electrode systems. The capacity of the double layer is a function of the nature of the metallic phase, electrode potential, temperature, and composition of the solution. Double layer capacities reflect the presence of adsorbed substances at the interface, and for this reason capacity measurements may be useful for the study of processes occurring in porous electrodes of large surface area in which adsorption plays a significant role. This paper presents equations which may be used for analysis of potentiostatic and galvanostatic transients which occur during charging of the double layer in porous or tubular electrodes of finite length.

Galvanostatic charging transients of semi-infinite porous electrodes were first considered by Ksenzhek and Stender (1, 2) for the case of combined double layer charging and Faradaic reaction which was assumed to follow a linear polarization relation. These authors later used their formulas in studies on the properties of graphitized anodes in the electrolysis of aqueous chloride solutions (3, 4). Further treatments of Ksenzhek and Stender considered galvanostatic charging transients for combined double layer charging and Faradaic reaction for electrodes of finite length, as well as effects of the external surface of the electrode and of concentration polarization (5, 6). De Levie (7) derived potentiostatic and galvanostatic charging transients for semi-infinite porous electrodes in the absence of any Faradaic reaction. Similar relations and some other special cases of galvanostatic charging were developed by Bonnemay, Bronoël, Levart, Pilla, and d'Orsay (8). Various cases of the response of porous electrodes to alternating current were investigated by Ksenzhek and Stender (1-6), Winsel (9), DeLevie (7, 11), Feuillade (10), Coffre and Feuillade (12), and Vergnolle (13).

Equations are presented below for potentiostatic and galvanostatic charging transients of porous and tubular electrodes of finite length in the absence of appreciable Faradaic currents. Solutions are also given for potentiostatic and galvanostatic single pulse methods, for measurements made with square waves of current or voltage, and for triangular current or voltage sweeps. Complications due to the effect of IR drop in solution between the tip of the reference electrode capillary and the front surface of the electrode are considered. Effects of the external surfaces of the electrode and of the conductivity of the metallic phase upon the observable transients are also discussed. Graphical solutions of the theoretical equations, obtained by use of a high-speed digital computer, are presented.

Fundamental Relations

A schematic diagram of an idealized, one-dimensional porous or tubular electrode is shown in Fig. 1. The current density of the non-Faradaic process for charging of the double layer, $j(x,t)$, is related to the rate of change of interfacial potential difference by Eq. [1].

$$j(x,t) = C\frac{\partial\Delta\phi(x,t)}{\partial t} = C\frac{\partial\eta(x,t)}{\partial t} \qquad [1]$$

[1] Research sponsored by The Office Of Saline Water, United States Department of the Interior, under Union Carbide Corporation's contract with the United States Atomic Energy Commission.

[2] Present address: Faculty of Engineering, Hokkaido University, Sapporo, Japan.

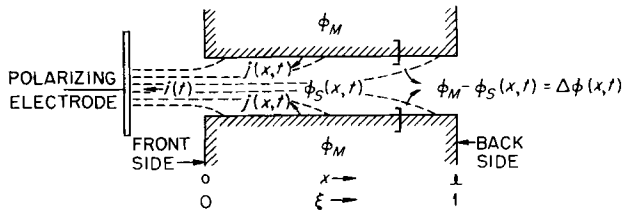

Fig. 1. Schematic diagram of idealized, one-dimensional porous electrode.

Here, C is the differential capacity (Farads/cm^2), $\Delta\phi(x,t) = \phi_M - \phi_S(x,t)$ is the potential difference between metal and solution phases, and $\eta(x,t)$ is the overpotential or change in interfacial potential difference [we assume in the usual case that $\eta(x,0) = 0$].

Because of the finite conductivity of the solution phase,[3] the passage of current introduces a gradient of $\eta(x,t)$ throughout the length of the pores. The fundamental differential equation governing the distribution of potential in porous electrodes was derived by Daniel'-Bek (14). This relation is given by Eq. [2] for the one-dimensional case, where x is the

$$\frac{\partial^2\eta(x,t)}{\partial x^2} = \frac{S}{\sigma A} j(x,t) \qquad [2]$$

length coordinate (cm), S is the internal surface area of the porous electrode per unit length (cm^2/cm), σ is the specific conductance of the solution (ohm^{-1} cm^{-1}), and A is the average cross-sectional area of the electrolyte in the electrode (cm^2).[4]

Combination of Eq. [1] and [2] and introduction of a dimensionless length, $\xi = x/l$, and of the time constant $\tau = SCl^2/\sigma A$ (sec), lead to Eq. [3]

$$\frac{\partial^2\eta(\xi,t)}{\partial\xi^2} = \tau\frac{\partial\eta(\xi,t)}{\partial t} \qquad [3]$$

which is the fundamental relation for charging of the double layer in one-dimensional porous electrodes.[3] The time constant may be expressed as the product of the resistance of the solution in the pores of the electrode, $R_o = l/\sigma A$, times the total differential capacity of the electrode, $C_T = SCl$; thus $\tau = R_oC_T$.

Solutions of Eq. [3] for a number of boundary conditions corresponding to potentiostatic and galvanostatic charging modes are presented below. These relations were obtained by use of the method of Laplace transforms (16, 17), and graphical solutions were computed by use of a high-speed digital computer.[5]

Galvanostatic Transients

Basic solution.—Boundary conditions for the solution of Eq. [3] when a constant current, $i(t) = i$ = constant, is applied to the electrode are given by

$$\left(\frac{\partial\eta(\xi,t)}{\partial\xi}\right)_{\xi=0} = -iR_o\,;\left(\frac{\partial\eta(\xi,t)}{\partial\xi}\right)_{\xi=1} = 0$$

The initial condition is simply $\eta(\xi,0) = 0$. Equation [4] gives the potential distribution in the electrode as a function of time.

$$\frac{\eta(\xi,t)}{iR_o} = \frac{t}{\tau} + \frac{2}{\pi^2}\sum_{k=1}^{\infty}\frac{(-1)^k}{k^2}\cos[\pi k(1-\xi)]\,[1-\exp(-\pi^2k^2t/\tau)] \qquad [4]$$

Potential transients at various positions in the electrode, calculated from Eq. [4], are shown in Fig. 2. The directly observable potentials are $\eta(0,t)$ and $\eta(1,t)$, the potentials of the front and back sides of the electrode. The slope of the linear portion of the transients in Fig. 2 is given by $d\eta(0,t)/dt = d\eta(1,t)/dt = iR_o/\tau = i/C_T$. Relations for the intercepts (extrapolated) of the linear portions are shown in Fig. 2. The parameters R_o and C_T may be estimated from experimental transients by use of these relations. During the first moments after application of the current, $\eta(0,t)$ follows Eq. [5], a relation valid for semi-infinite

$$\frac{\eta(0,t)}{iR_o} = 2\,(t/\pi\tau)^{1/2} \qquad [5]$$

electrodes which was derived earlier by Ksenzhek and Stender (1, 2), Ksenzhek (5), de Levie (7), and Bonnemay *et al.* (8). The transient predicted by Eq. [5] is shown as the dotted line in Fig. 2; it holds well for finite electrodes for times less than about $t = \tau/3$.

Charging of the electrode occurs in a "wave," and a certain delay time is required for the charging current to penetrate to the back side of the electrode. This delay time may be obtained by extrapolation of the $\eta(1,t)$ transient back to its intersection with the time axis. Use of Eq. [4] then leads to t (delay) = $\tau/6$;

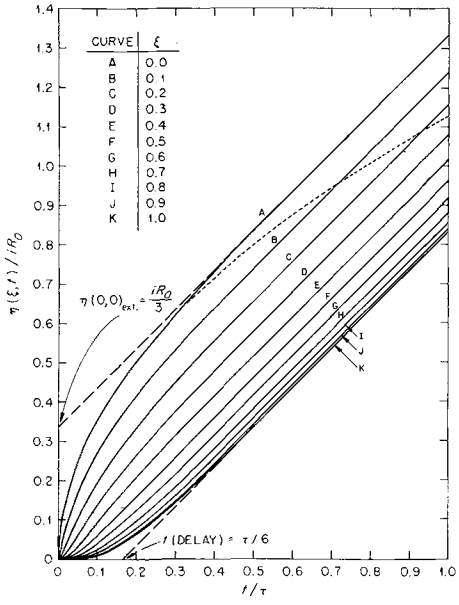

Fig. 2. Variation of potential with time during galvanostatic charging of finite porous electrode as a function of position.

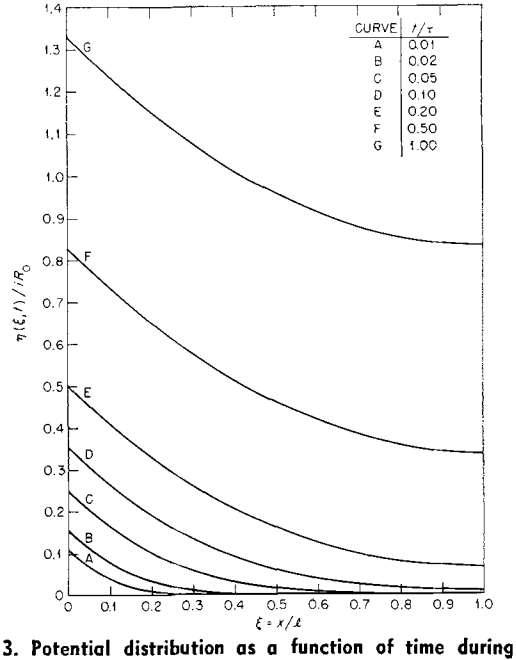

Fig. 3. Potential distribution as a function of time during galvanostatic charging of finite porous electrode.

[3] We assume for the most part that the resistivity of the metallic phase is essentially zero so that ϕ_M = constant. This restriction is relaxed below in considering cases where the conductivities of metallic and solution phases are comparable. We assume also that the differential capacity is independent of the potential. This assumption may limit strict applicability of the equations to small potential excursions in some cases.

[4] Equation [2] has been integrated for a number of important cases occurring in the operation of porous electrodes [see, for example, ref. (15)].

[5] Control Data Corporation Model 1604-A.

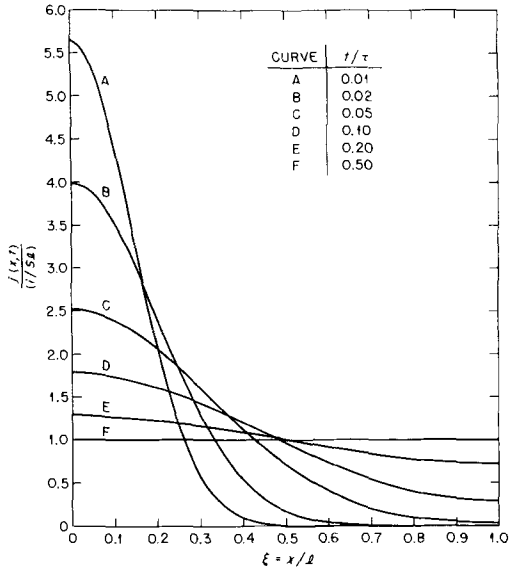

Fig. 4. Current density distribution as a function of time during galvanostatic charging of finite porous electrode.

the delay time is directly proportional to the differential capacity and to the square of the pore length since $\tau = SCl^2/\sigma A$. Figure 3 shows the potential distribution as a function of time; at the delay time the potential of the back side of the electrode [$\eta(1,t)$] begins to change significantly.

The current density distribution during the charging transient may be calculated by differentiation of Eq. [4] and use of Eq. [1]. Figure 4 shows how the current density distribution changes with time. For times greater than about $\tau/3$, the current density is constant throughout the length of the pores and all parts of the electrode change potential at the same rate (cf. Fig. 2). In this region of constant current density, the potential profile is parabolic and obeys Eq. [6]. It follows that the potential

$$\frac{\eta(0,t) - \eta(\xi,t)}{iR_o} = \xi(1 - \xi/2) \qquad [6]$$

difference between the front and back sides of the electrode for $t > \tau/3$ is simply related to the resistance of the electrolyte in the pores by the expression $[\eta(0,t) - \eta(1,t)]/i = R_o/2$. Both of the parameters R_o and C_T of the simple one-dimensional model may be estimated from experimental data by use of these relations, whereas only the ratio R_o/C_T may be obtained by use of Eq. [5] alone.

Effect of IR drop.—In the case where the tip of the reference electrode capillary is located between the front side of the porous electrode and the polarizing electrode (cf. Fig. 1), some IR drop is included in the measurement of the $\eta(0,t)$ transient. The measurable transient is then given by the relation $\eta_T(0,t) = \eta(0,t) + iR_{REF}$, where $\eta_T(0,t)$ is the potential transient measured with respect to the reference electrode, R_{REF} is the solution resistance between the tip of the reference capillary and the front side of the electrode ($\xi = 0$), and $\eta(0,t)$ is obtained from Eq. [4]. In the case of a reference electrode located at the back side of the electrode ($\xi = 1$), the $\eta(1,t)$ transient and the delay time are unchanged.

Single pulse.—For the case where a single galvanostatic pulse of current, i, is applied to the finite electrode for a time, t_o, the potential distribution during the pulse up to the time t_o is given by Eq. [4]. After the current is switched off, a type of relaxation process occurs and the potential of the electrode becomes uniform throughout the length of the pores. The initial condition for the relaxation transient is given by Eq. [4] with $t = t_o$. Appropriate boundary conditions are

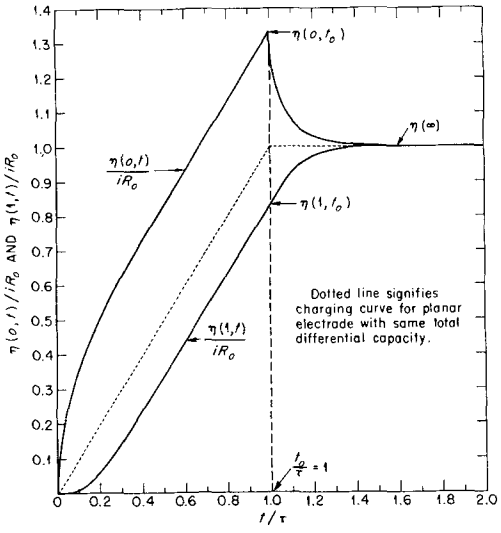

Fig. 5. Variation of potential with time during galvanostatic charging of finite porous electrode with single pulse.

$$\left(\frac{\partial\eta(\xi,t)}{\partial\xi}\right)_{\substack{\xi=0\\ t>t_o}} = \left(\frac{\partial\eta(\xi,t)}{\partial\xi}\right)_{\substack{\xi=1\\ t>t_o}} = 0$$

The corresponding solution of Eq. [3] for the potential distribution during the relaxation transient is given by Eq. [7]. The current density distribution

$$\frac{\eta(\xi,t)}{iR_o} = \frac{t_o}{\tau} + \frac{2}{\pi^2}\sum_{k=1}^{\infty}\frac{(-1)^k}{k^2}\cos[\pi k(1-\xi)][\exp(\pi^2k^2t_o/\tau)-1]\exp(-\pi^2k^2t/\tau) \qquad [7]$$

may be calculated from Eq. [1] and [7]. Figure 5 shows a graph of the charging transient for the case, $t_o = \tau$. The dotted line is the charging curve of a planar electrode having the same total differential capacity as the porous electrode. Up to $t = t_o$, the $\eta(0,t)$ and $\eta(1,t)$ transients are the same as those shown in Fig. 2; for $t > t_o$, the relaxation transients are described by the appropriate cases of Eq. [7].

The single pulse galvanostatic method provides a very simple way of determining C_T for finite porous electrodes when Faradaic currents are negligible. For $t >> t_o$, Eq. [7] approaches the limit t_o/τ, so that C_T is easily calculable from the relation, $C_T = i\,t_o/\eta(\infty)$, where $\eta(\infty)$ is the final change in potential produced by the current pulse. For t_o greater than about $\tau/3$, the final potential, $\eta(\infty) = \eta(0,\infty) = \eta(1,\infty)$, bears a definite relation to the potentials exhibited by the electrode at t_o [$\eta(0,t_o)$ and $\eta(1,t_o)$]; this relation is given by Eq. [8]. For t_o less than about $\tau/3$, Eq. [8]

$$\frac{\eta(\infty)-\eta(1,t_o)}{\eta(0,t_o)-\eta(1,t_o)} = 1/3 \qquad [8]$$

is no longer valid, and the value of the ratio lies between 0 and 1/3.

Square wave.—Application of a symmetrical square wave of current to a finite porous electrode produces a symmetrical potential wave which may conveniently be displayed on an oscilloscope or other recording device. The square wave of current may be expressed as

$$i(t) = (-1)^{(n-1)}\,i$$

where

$$\frac{(n-1)}{2}T \leqq t < \frac{n}{2}T$$

where T is the period of the square wave and n the number of half cycles applied at time t ($n = 1, 2, 3, \ldots$). The value of the current $i(t)$ therefore alternates between $+\,i$ and $-\,i$. Initial and boundary conditions are the same as those for the basic solution, and the expression for the potential transient is the same as Eq. [4] when the right-hand side of this

equation is multiplied by the factor, $(-1)^{(n-1)}$. The amplitudes of the potential excursions are given by Eq. [9] and [10]. When $T << \tau$,

$$\frac{\eta(0,T/2) - \eta(0,T)}{iR_o} = \frac{T}{\tau} + \frac{2}{3} - \frac{4}{\pi^2}\sum_{k=1}^{\infty}\frac{1}{k^2}\exp(-\pi^2k^2T/2\tau) \quad [9]$$

$$\frac{\eta(1,T/2) - \eta(1,T)}{iR_o} = \frac{T}{\tau} - \frac{1}{3} - \frac{4}{\pi^2}\sum_{k=1}^{\infty}\frac{(-1)^k}{k^2}\exp(-\pi^2k^2T/2\tau) \quad [10]$$

the amplitude of the potential wave is related to the time constant (τ) by Eq. [11]. Since $\tau = R_oC_T$, measurements with frequencies much higher than

$$\frac{\eta(0,T/2) - \eta(0,T)}{iR_o} = [\sqrt{2}\,(1+\sqrt{2})](T/\pi\tau)^{1/2} \quad [11]$$

$1/\tau$ yield information only about the ratio, R_o/C_T. When $T >> \tau$, the summed terms in Eq. [9] and [10] approach zero, so that C_T could be estimated from measurements at frequencies considerably lower than $1/\tau$.

Triangular wave.—Solution of Eq. [3] for the case of application of a triangular wave of current to the finite porous electrode makes use of the same initial and boundary conditions as those for the basic solution. The current wave may be expressed as:

$$i(t) = \mu t \qquad (0 \leqq t < T/2)$$
$$i(t) = \mu(T-t) \qquad (T/2 \leqq t < T)$$

where μ (amp/sec) is the constant rate of change of applied current and T is the period of the triangular current wave. As in the case of the square wave, the low- and high-frequency solutions are of most immediate applicability. For $T << \tau$, the maximum potential excursion of the front side of the electrode is given by Eq. [12], and only the ratio R_o/C_T

$$\frac{\eta(0,T/2)}{i(T/2)R_o} = (2/3)(2T/\pi\tau)^{1/2} \quad [12]$$

can be determined at high frequencies. For low frequencies ($T >> \tau$) of the triangular wave, Eq. [13]

$$\frac{\eta(0,T/2)}{i(T/2)R_o} = T/4\tau \quad [13]$$

gives the maximum potential excursion. Low-frequency triangular waves therefore permit a direct estimation of C_T, the total differential capacity of the porous electrode.

Effect of external surface.—The galvanostatic charging transient of a finite porous electrode may be affected considerably by the external surfaces of the electrode provided the external surface area is comparable to the internal surface area.[6] Part of the total current (i) applied to an electrode is used to charge the front surface, part is involved in charging the interior surface of the electrode, and part charges the back surface. The fraction of the total current involved in each charging process depends on the electrode parameters and on the time. The total current may be divided into three parts, $i = i_F(t) + i_I(t) + i_B(t)$, where $i_F(t)$ is the current used in charging the front surface, $i_I(t)$ is the current involved in charging the interior surface, and $i_B(t)$ is the current which charges the back surface of the electrode. If $\alpha = A_M/Sl$ is the ratio of the front (or back) surface area (A_M) to the interior surface area of the electrode (Sl), the rates of change of $\eta(0,t)$ and $\eta(1,t)$ may be expressed by Eq. [14] and [15]. Equation [3] may be solved subject to the constraints imposed

$$\frac{\partial\eta(0,t)}{\partial t} = \frac{i_F(t)}{A_MC} = \frac{i_F(t)R_o}{\alpha\tau} \quad [14]$$

[6] Internal surface areas of most real porous electrodes are very large compared to their external surface areas. However, the relations derived in this section and in a later section on the potentiostatic charging transient may be useful in analysis of charging curves of very thin porous electrodes or of finely perforated planar electrodes.

$$\frac{\partial\eta(1,t)}{\partial t} = \frac{i_B(t)}{A_MC} = \frac{i_B(t)R_o}{\alpha\tau} \quad [15]$$

by Eq. [14] and [15] by use of the initial condition, $\eta(\xi,0) = 0$, and the boundary conditions

$$\left(\frac{\partial\eta(\xi,t)}{\partial\xi}\right)_{\xi=0} = -[i_1(t) + i_B(t)]R_o;$$
$$\left(\frac{\partial\eta(\xi,t)}{\partial\xi}\right)_{\xi=1} = -i_B(t)R_o$$

The potential distribution in the electrode is given as a function of time and of the area ratio (α) by Eq. [16]. Values of the index m

$$\frac{\eta(\xi,t)}{iR_o} = \frac{t/\tau}{(1+2\alpha)} + 2\sum_m \frac{\alpha m\sin[m(1-\xi)] - \cos[m(1-\xi)]}{m^2\Delta(m)}[1-\exp(-m^2t/\tau)] \quad [16]$$

where

$$\Delta(m) = 2m\,\alpha(1+\alpha)\sin(m) - (1+2\,\alpha-\alpha^2m^2)\cos(m)$$

are the positive roots of the auxiliary equation $\tan(m) = 2\,\alpha m/(\alpha^2m^2-1)$. Equation [16] reduces to Eq. [4] for $\alpha = 0$. An increase of the area ratio α reduces the slope of the transients in the region where $\eta(0,t)$ and $\eta(1,t)$ change linearly with time; this slope is simply equal to $1/(1+2\alpha)$ according to Eq. [16]. The intercept obtained by extrapolation of the linear part of the $\eta(0,t)$ curve back to $t = 0$ decreases with increasing α, and the delay time increases with increasing α. Figure 6 shows how the $\eta(0,t)/iR_o$ intercept and the delay time change with the value of α. For small external areas, the $\eta(0,t)/iR_o$ intercept is equal to 1/3 and the delay time is given by t (delay) $= \tau/6$. For large external areas (α greater than about 10), the $\eta(0,t)/iR_o$ intercept approaches the value ¼, and the delay time becomes proportional to α according to the relation t (delay) $= \alpha\tau/2$.

Essentially all the current is concerned with charging of the front surface of the electrode during the initial part of the transient. During the first moments $\eta(0,t)$ changes linearly with time according to $\eta(0,t)/iR_o = t/\alpha\tau$ as implied by Eq. [14]. With time, the interior of the electrode is charged and $\eta(0,t)$ may vary according to Eq. [5]. Finally the current begins to penetrate to the back side of the electrode. For $t >> t$ (delay), the current is distributed according to the ratio of areas.

Effect of conductivity of metallic phase.—Galvanostatic charging transients of finite porous electrodes differ from the predictions of Eq. [4] if the conductivity of the metallic phase is comparable to that of the liquid phase. The expected charging transient for this case may be derived by use of a modification of the basic model shown in Fig. 1. The potential of the metallic phase, $\phi_M(\xi,t)$, is no longer constant in the x direction, so that the interfacial potential difference is given by

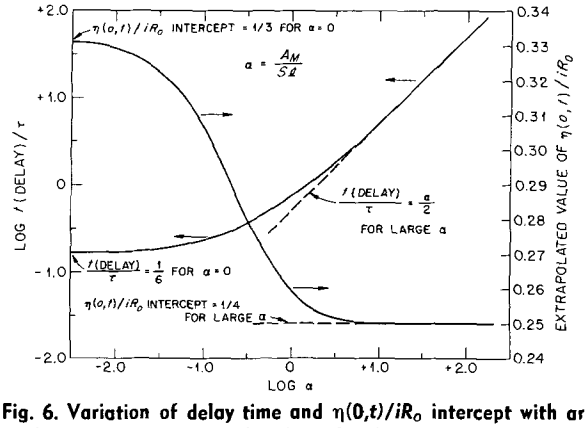

Fig. 6. Variation of delay time and $\eta(0,t)/iR_o$ intercept with area ratio (α) for galvanostatic charging of finite porous electrode.

$\Delta\phi(\xi,t) = \phi_M(\xi,t) - \phi_S(\xi,t)$. If A_T is the total cross-sectional area of the electrode, A_M is the cross-sectional area of the metallic phase, A is the cross-sectional area of electrolyte as before, κ is the specific conductance of the metallic phase, and σ is the specific conductance of the electrolyte phase as before, then the porosity (f) is given by $f = A/A_T$ and Eq. [3] becomes Eq. [17]. the new

$$\frac{\partial^2\eta(\xi,t)}{\partial\xi^2} = \tau'\frac{\partial\eta(\xi,t)}{\partial t} \qquad [17]$$

where:

$$\tau' = \frac{SCl^2}{A_T}\left[\frac{\sigma f + \kappa(1-f)}{\sigma\kappa f(1-f)}\right]$$

time constant, τ', can be set equal to $C_T(R_M + R_o)$, where $C_T = SCl$ and $R_o = l/\sigma A_T$ have the same significance as before and $R_M = l/\kappa A_T(1-f)$ is the resistance of the metallic phase in the x direction. When R_M approaches zero, τ' approaches τ of the basic solution.

The electrical lead to the porous electrode is assumed to be attached at $x = l$ (or $\xi = 1$), so that ϕ_M varies only in the x direction. Boundary conditions for this case are:

$$\left(\frac{\partial\eta(\xi,t)}{\partial\xi}\right)_{\xi=0} = -i\,R_o; \quad \left(\frac{\partial\eta(\xi,t)}{\partial\xi}\right)_{\xi=1} = +i\,R_M$$

Solution of Eq. [17] with these boundary conditions and the initial condition $\eta(\xi,0) = 0$ leads to the potential distribution of Eq. [18],

$$\frac{\eta(\xi,t)}{i\,R_o} = (1+\gamma)\frac{t}{\tau'} + \frac{2}{\pi^2}\sum_{k=1}^{\infty}\frac{(-1)^k}{k^2}\{\gamma\cos[\pi k\xi] + \cos[\pi k(1-\xi)]\}[1-\exp(-\pi^2k^2t/\tau')] \qquad [18]$$

where γ is the ratio of the resistance of the metallic phase to that of the solution phase ($\gamma = R_M/R_o$). For $\gamma = 0$, Eq. [18] reduces to Eq. [4].

The potential-time characteristics, $\eta(0,t)/i\,R_o$ and $\eta(1,t)/i\,R_o$, are similar in form to those shown in Fig. 2, except that the slopes and intercepts of the linear regions of the transients depend on the value of γ. The $\eta(0,t)/i\,R_o$ intercept is given by $1/3 - \gamma/6$, and the delay time for propagation of the current to $\xi = 1$ is given by

$$\frac{t(\text{delay})}{\tau'} = \frac{1}{(1+\gamma)}\left(\frac{1}{6} - \frac{\gamma}{3}\right)$$

For sufficiently large values of $\gamma = R_M/R_o$, the back side of the electrode is charged up before the front side. This fact accounts for the negative delay times predicted for the $\eta(1,t)$ transient for large γ. On the basis of Eq. [18], one can derive the symmetry relation, $\eta(\xi,t,\gamma) = \gamma\cdot\eta(1-\xi,t,1/\gamma)$. This expression may be useful for visualizing the effect of γ on the observable transients. The difference between the front side and back side potentials in the linear region of the charging transient is also affected by the resistance ratio γ. Use of Eq. [18] for this region leads to $[\eta(0,t) - \eta(1,t)]/i = R_o(1-\gamma)/2$. Therefore γ may be calculated provided R_o is known. For sufficiently large γ, this potential difference is given by $[\eta(1,t) - \eta(0,t)]/i = R_M/2$. Under the same conditions, the potential of the back side changes in the initial moments according to $\eta(1,t)/i\,R_o = 2\gamma(t/\pi\tau')^{1/2}$.

Potentiostatic Transients

Basic solution.—Boundary conditions for the solution of Eq. [3] when the potential of the front side of a finite porous electrode is suddenly changed to the value η_o are

$$\eta(0,t) = \eta_o; \quad \left(\frac{\partial\eta(\xi,t)}{\partial\xi}\right)_{\xi=1} = 0$$

As before, the initial condition is $\eta(\xi,0) = 0$. The resulting potential distribution is given by Eq. [19], where all quantities have their previously

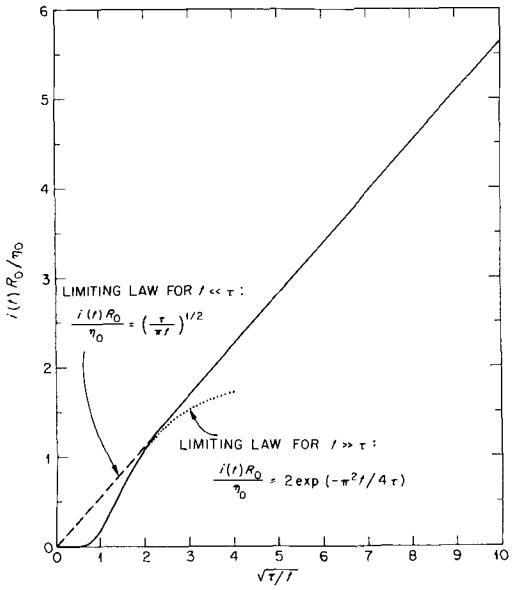

Fig. 7. Variation of current with time during potentiostatic charging of finite porous electrode.

$$\frac{\eta(\xi,t)}{\eta_o} = 1 - \frac{2}{\pi}\sum_{k=0}^{\infty}\frac{(-1)^k}{(k+\frac{1}{2})}\cos[(k+\tfrac{1}{2})\pi(1-\xi)]\exp[-(k+\tfrac{1}{2})^2\pi^2t/\tau] \qquad [19]$$

defined significance. The observable current transient may be obtained by differentiation of Eq. [19] with use of the relation

$$i(t) = -\frac{1}{R_o}\left(\frac{\partial\eta(\xi,t)}{\partial\xi}\right)_{\xi=0}$$

This result is given in Eq. [20]. Figure 7 shows the current transient

$$\frac{i(t)R_o}{\eta_o} = 2\sum_{k=0}^{\infty}\exp[-(k+\tfrac{1}{2})^2\pi^2t/\tau] \qquad [20]$$

plotted against reciprocal square root of time. For $t << \tau$, this type of plot is linear. Equation [21] gives the relation followed during this period

$$\frac{i(t)R_o}{\eta_o} = (\tau/\pi t)^{1/2} \qquad [21]$$

(cf. dashed line in Fig. 7); it was derived previously by de Levie (7) for the case of potentiostatic charging of semi-infinite electrodes. For $t >> \tau$, the current decreases according to $i(t)R_o/\eta_o = 2\exp(-\pi^2t/4\tau)$; this limiting law is shown as the dotted line in Fig. 7.

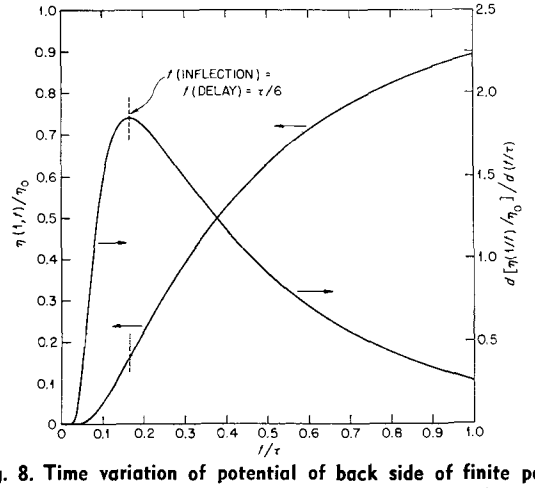

Fig. 8. Time variation of potential of back side of finite porous electrode and its time derivative during potentiostatic charging of the double layer.

The slope of such a plot of current against reciprocal square root of time enables one to estimate the value of the ratio C_T/R_o by use of Eq. [21].

Charging of the electrode occurs in a "wave," just as in the case of galvanostatic charging. The current density distribution may be obtained by differentiation of Eq. [19] with use of Eq. [1]. As in the case of galvanostatic charging, a certain delay time is required for the current to penetrate to the back side of the electrode. Figure 8 shows how $\eta(1,t)$, the potential of the back side, varies with time. The delay time may be identified with the inflection in this curve. Figure 8 also shows how the time derivative of $\eta(1,t)$, which has a maximum at the time of inflection or the delay time, changes with time. The delay time is given by $t(\text{delay}) = t(\text{inflection}) = \tau/6$, just as for galvanostatic charging. The delay time may be determined experimentally by use of a differentiating circuit for the measurement of $\eta(1,t)$. A knowledge of the delay time, together with the slope of the plot of current against reciprocal square root of time (cf. Fig. 7), allows estimates to be made of both R_o and C_T from an experimental transient.

Effect of IR drop.—When the resistance between the tip of the reference electrode and the front surface of the porous electrode (R_{REF}) is considered, boundary conditions for the solution of Eq. [3] become

$$\eta(0,t) = \eta_o - i(t)R_o; \quad \left(\frac{\partial\eta(\xi,t)}{\partial\xi}\right)_{\xi=1} = 0$$

The potential distribution in this case is given by Eq. [22], where values

$$\frac{\eta(\xi,t)}{\eta_o} = 1 - 2\sum_m \frac{\cos[m(1-\xi)]\exp(-m^2t/\tau)}{m[(1+\rho)\sin(m) + \rho m\cos(m)]} \quad [22]$$

of the index m are the positive roots of $m\tan(m) = 1/\rho$. The resistance ratio ρ is equal to R_{REF}/R_o. When $\rho = 0$, Eq. [22] reduces to Eq. [19]. The observable current transient is given by Eq. [23]; this equation was used

$$\frac{i(t)\,R_o}{\eta_o} = 2\sum_m \frac{\sin(m)\exp(-m^2t/\tau)}{(1+\rho)\sin(m) + \rho m\cos(m)} \quad [23]$$

to calculate the results in Fig. 9, which depicts the effect of ρ on potentiostatic charging transients. For large values of ρ, a long time may be required for

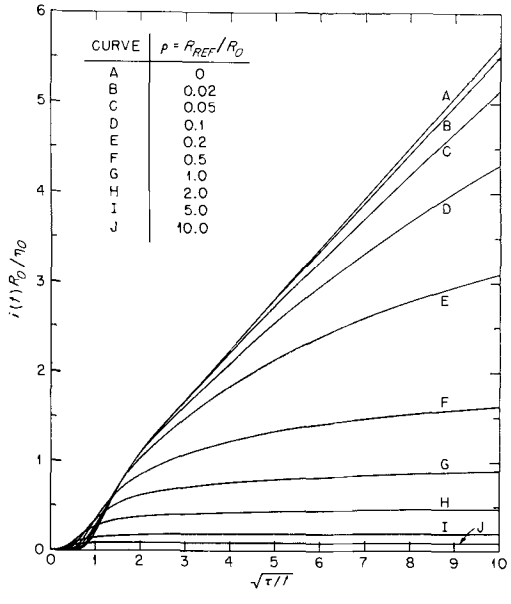

Fig. 9. Effect of R_{REF} on variation of current with time during potentiostatic charging of finite porous electrode.

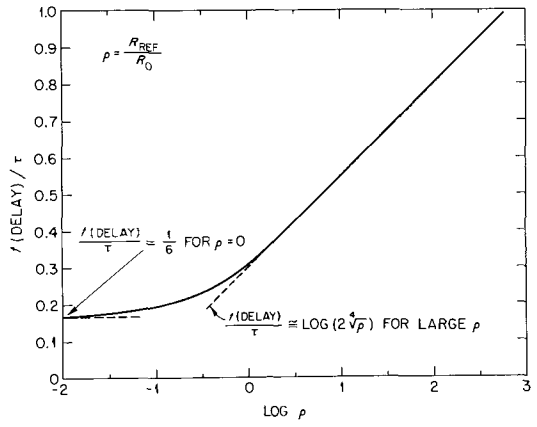

Fig. 10. Effect of R_{REF} on delay time for potentiostatic charging of finite porous electrode.

$\eta(0,t)$ to reach the value η_o; during this time charging of the electrode occurs essentially at constant current. For intermediate values of ρ, nonlinear plots of current against reciprocal square root of time will be obtained. Potentiostatic charging transients are therefore most easily interpreted if R_{REF} is kept small compared to R_o.

The current limitation imposed on the potentiostatic charging transient by large values of ρ affects the delay time for propagation of the charging "wave" through the electrode. Figure 10 shows how the delay time varies with ρ and gives limiting expressions for the delay time. If ρ can be estimated, then τ can be obtained from the curve in Fig. 10 if transients of the form shown in Fig. 9 are observed experimentally.

Single pulse.—If a potentiostatic pulse of magnitude η_o is applied to the front side of a porous electrode for a time t_o, then the current transient up to the time t_o is given by Eq. [20]. Equation [3] may be solved for the transient in the region $t > t_o$ by use of the following boundary conditions

$$\eta(0,t) = 0; \quad \left(\frac{\partial\eta(\xi,t)}{\partial\xi}\right)_{\xi=1} = 0$$

At the time t_o the potential distribution is given by Eq. [19] with $t = t_o$. Equation [24] gives the current transient for $t \geqq t_o$. If η_o is positive, the

$$\frac{i(t)\,R_o}{\eta_o} = 2\sum_{k=0}^{\infty}\exp[-(k+\tfrac{1}{2})^2\pi^2t/\tau] - 2\sum_{k=0}^{\infty}\exp[-(k+\tfrac{1}{2})^2\pi^2(t-t_o)/\tau] \quad [24]$$

current of Eq. [24] is negative for $t > t_o$. For $t_o << \tau$, the value of the current at the time t_o, $i(t_o)$, is given approximately by Eq. [21] with $t = t_o$. This relation may be used to estimate the ratio C_T/R_o from potentiostatic measurements with short single pulses.

Square wave.—If the potential of the front side of a porous electrode is forced to alternate between the values $+\eta_o$ and $-\eta_o$ by use of a potentiostat which supplies a symmetrical square wave of potential to the electrode, the boundary conditions for the solution of Eq. [3] are

$$\eta(0,t) = (-1)^{(n-1)}\eta_o; \quad \left(\frac{\partial\eta(\xi,t)}{\partial\xi}\right)_{\xi=1} = 0$$

where $(n-1)T/2 \leqq t < nT/2$ and T is the period of the square wave ($n = 1, 2, 3, \ldots$). The corresponding current transient is given by Eq. [20] when the right-hand side of the equation is multiplied by the

factor, $(-1)^{(n-1)}$. For $T << \tau$, the difference between the amplitudes of the current transient at $t = T/2$ and at $t = T$ is given by Eq. [25]. This relation may be used to

$$\frac{[i(T/2) - i(T)]\,R_o}{\eta_o} = (1 + \sqrt{2})\,(\tau/\pi T)^{1/2} \quad [25]$$

estimate the parameter τ from potentiostatic measurements with square waves of frequency higher than $1/\tau$.

Triangular wave.—For the case where the potential of the front side of a porous electrode is forced to follow a triangular wave, the potential excursion may be expressed by

$$\eta(0,t) = \frac{2\Delta\eta}{T}\,t \qquad (0 \leqq t < T/2)$$

$$\eta(0,t) = \frac{2\Delta\eta}{T}\,(T - t) \qquad (t/2 \leqq t < T)$$

where $\Delta\eta$ is the amplitude, and T is the period of the triangular potential wave. The initial condition and the boundary condition at $\xi = 1$ are the same as those used above. Equation [26] gives the resulting current transient

$$\frac{i(t)R_o}{\Delta\eta} = (-1)^{(n-1)}\frac{2\tau}{T}$$

$$\left[1 - \frac{2}{\pi^2}\sum_{k=0}^{\infty}\frac{1}{(k+1/2)^2}\exp\{-\pi^2(k+1/2)^2 t/\tau\}\right] \quad [26]$$

where $(n-1)T/2 \leqq t < nT/2$ with $n = 1, 2, 3, \ldots$. For $T << \tau$, the amplitude of the current transient is given by Eq. [27], which may be used

$$\frac{i(T/2)R_o}{\Delta\eta} = (\tau/\pi T)^{1/2} \quad [27]$$

to estimate τ when triangular waves of frequency higher than $1/\tau$ are used. For $T >> \tau$, the electrode is charged very slowly and the summed terms in Eq. [26] may be neglected at large T. The current amplitude in this case is given simply by $i(T/2)\,R_o/\Delta\eta = 2\tau/T$, and C_T may be estimated directly from this relation.

Effect of external surface.—Potentiostatic charging transients of porous electrodes may be affected by the external surfaces of the electrode.[6] Although the front surface of the electrode is charged very quickly by the potentiostat, time is required before the interior and back surfaces of the electrode are charged up to the potential of the front side ($\eta(0,t) = \eta_o$). The total current during the transient may be divided into two parts, $i(t) = i_I(t) + i_B(t)$, where $i_I(t)$ is the current used for charging the interior surface, and $i_B(t)$ charges the back surface of the electrode. If $\alpha = A_M/Sl$ is the ratio of the back (or front) surface area (A_M) to the interior area of the electrode (Sl), the rate of change of $\eta(1,t)$ is the same as that in Eq. [15] for the case of galvanostatic charging. The current transient may be obtained by integration of Eq. [3] together with the constraint of Eq. [15] and the following boundary condition

$$\left(\frac{\partial\eta(\xi,t)}{\partial\xi}\right)_{\xi=1} = -\,i_B(t)\,R_o$$

Integration leads to the current transient of Eq. [28], where values of

$$\frac{i(t)R_o}{\eta_o} = 2\sum_m \frac{\sin(m) + \alpha m\cos(m)}{(1+\alpha)\sin(m) + \alpha m\cos(m)}\exp(-m^2 t/\tau) \quad [28]$$

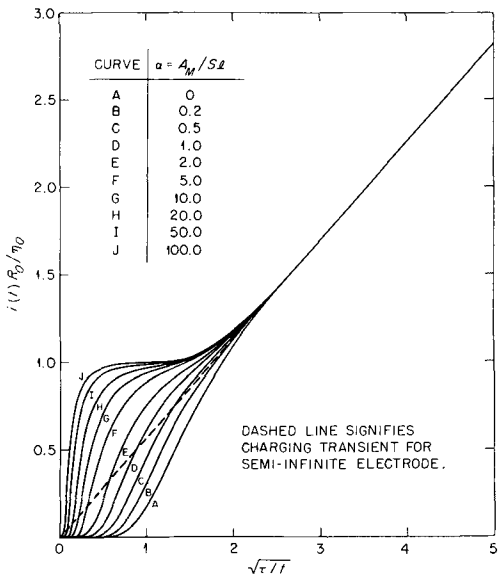

Fig. 11. Effect of external surface of the electrode on the variation of current with time during potentiostatic charging of finite porous electrode.

the index m are the positive roots of $m\tan(m) = 1/\alpha$. For $\alpha = 0$, Eq. [28] reduces to Eq. [20].

Current transients corresponding to Eq. [28] are plotted in Fig. 11 as a function of the area ratio α. Additional current is required to charge the back side of the electrode compared to the basic potentiostatic charging transient (cf. Fig. 7). For large values of α, a limiting current is observed. In this region, $i(t)/\eta_o \cong R_o$ and considerable time may be required before $\eta(1,t)$ begins to change significantly. Therefore, potentiostatic charging of the back side of an electrode with a large external surface takes place by essentially a galvanostatic process; the current available for charging the back side is determined by the potential change on the front side (η_o) and by the properties of the pore system expressed by the quantity R_o. For times less than about $\tau/10$, essentially all the current is used in charging the interior of the electrode. For times greater than about $\tau/2$, the current ratio $i_I(t)/i_B(t)$ is essentially constant with time and depends on the value of the area ratio α.

Effect of conductivity of metallic phase.—The model used above to derive the galvanostatic charging transient of a porous electrode when the conductivity of both the metallic and the electrolyte phases are comparable may also be used to derive the corresponding potentiostatic charging transient. In this case, Eq. [17] is solved subject to the constraint, $\eta(0,t) = \eta_o$, and the following boundary conditions

$$\left(\frac{\partial\eta(\xi,t)}{\partial\xi}\right)_{\xi=0} = -\,i(t)\,R_o\,;\quad \left(\frac{\partial\eta(\xi,t)}{\partial\xi}\right)_{\xi=1} = +\,i(t)\,R_M$$

The potential distribution is given by Eq. [29], where values of the index

$$\frac{\eta(\xi,t)}{\eta_o} = 1 - 2\sum_m \frac{\gamma\cos(m\xi) + \cos[m(1-\xi)]}{m\sin(m)}\exp(-m^2 t/\tau') \quad [29]$$

m are the positive roots of $m = \cos^{-1}(-\gamma)$. As before, $\gamma = R_M/R_o = \sigma f/\kappa(1-f)$ is the ratio of the resistance of the metallic phase [$R_M = l/\kappa A_T\,(1-f)$] to the resistance of the solution phase ($R_o = l/\sigma A_T f$). Equation [29] reduces to Eq. [19] when $\gamma = 0$. The value of γ can be determined quite simply by measuring the sudden change in the potential of the back side of the electrode when the potential of the front

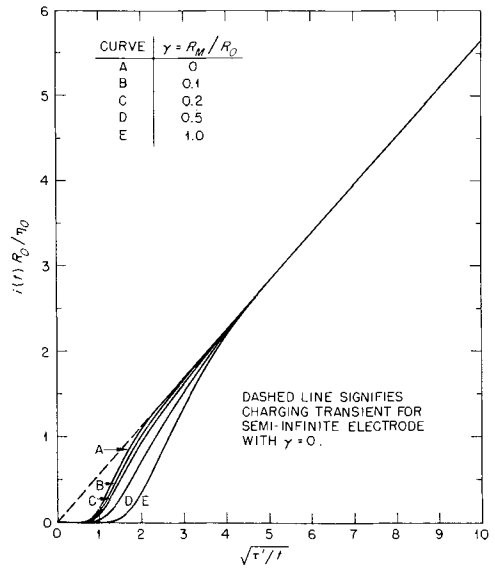

Fig. 12. Effect of resistance of metallic phase on variation of current with time during potentiostatic charging of finite porous electrode.

side is changed potentiostatically by the amount η_o. Thus $\gamma = \eta(1,0)/\eta_o$.

Differentiation of Eq. [29] and use of the boundary conditions at $\xi = 0$ lead to Eq. [30] for the observable current transient. Equation [30]

$$\frac{i(t)R_o}{\eta_o} = 2\sum_m \exp(-m^2t/\tau') \qquad [30]$$

reduces to Eq. [20] for $\gamma = 0$. Figure 12 shows the effect of the resistance ratio γ on the observable current transient. Solutions of Eq. [29] and [30] exist only when the resistance ratio lies in the range $0 \leqq \gamma \leqq 1$. In the limiting case when $\gamma = 1$, the potentials of both front and back sides of the electrode immediately attain the value η_o at the start of the charging transient. For values of γ greater than unity, the potentiostatic constraint $\eta(0,t) = \eta_o$ cannot be fulfilled; in this case most of the charging current crosses the interface near $\xi = 1$, and the potential of the front side of the electrode cannot be polarized to η_o by use of a normal potentiostatic configuration.

Summary

Solutions to a number of boundary value problems occurring in the theory of potentiostatic and galvanostatic charging of porous or tubular electrodes of finite length are presented above. Charging of the double layer is assumed to be the only interfacial process of significance; Faradaic reactions are not considered. Experimental transients obtained on systems which reasonably satisfy these stipulations may be analyzed by use of the appropriate relations to yield values of R_o and C_T, the resistance of the electrolyte phase and the total differential capacity of the electrode. Complications may arise in the interpretation of the charging transients because of IR drop in solution between the front surface of the electrode and the tip of the reference electrode capillary, because of charging processes on the external surfaces of the electrode, and because of a limited conductivity of the metallic phase. The forms of the charging transients in these cases are sufficiently different from the basic charging transients so that in favorable instances some information may also be obtained about the complicating parameters. Real porous electrodes have intricate geometries and the parameters of the simple, one-dimensional model used here should be regarded as averages which may nevertheless be useful for the study of porous electrodes.

Manuscript received April 22, 1965; revised manuscript received Oct. 8, 1965.

Any discussion of this paper will appear in a Discussion Section to be published in the December 1966 JOURNAL.

SYMBOLS

A	Cross-sectional area of electrolyte in porous or tubular electrode, cm^2
A_M	Cross-sectional area of metallic phase (also area of front or back surface of electrode), cm^2
A_T	$A_T = A + A_M$; total cross-sectional area of porous electrode, cm^2
C	Differential capacity, Farad/cm^2
C_T	$C_T = SCl$; total differential capacity of electrode, Farad.
f	$f = A/A_T$; porosity of porous electrode
$i, i(t)$	Total current applied to porous electrode, amp
$i_F(t)$	Current used to charge front surface of electrode, amp
$i_I(t)$	Current used to charge interior surface of electrode, amp
$i_B(t)$	Current used to charge back surface of electrode, amp
$j(x,t)$, $j(\xi,t)$	Current density used to charge double layer (non-Faradaic), amp
k	Summation index
l	Pore length, cm
m	Positive roots of auxiliary equations (cf. Eq. [16], [22], [28], and [29].
n	Number of half-cycles of square wave of current or voltage applied to electrode or of transients observed at time t.
R_M	$R_M = l/\kappa A_M = l/\kappa A_T(1-f)$, resistance of metallic phase, ohms
R_o	$R_o = l/\sigma A = l/\sigma A_T f$; resistance of electrolyte phase, ohms
R_{REF}	Resistance of electrolyte between front surface of porous electrode and tip of reference electrode capillary, ohms
S	Interior surface area of porous electrode per unit length, cm
t	Time, sec
t_o	Time of application of single current or voltage pulse, sec
T	Period of square or triangular wave of current or voltage, sec
x	Distance coordinate, cm
α	$\alpha = A_M/Sl$; ratio of area of metallic phase (also area of front or back surface) to total interior surface area of electrode
γ	$\gamma = R_M/R_o$; ratio of resistance of metallic phase to resistance of solution phase
$\eta(x,t)$, $\eta(\xi,t)$	Change of interfacial potential difference during potentiostatic or galvanostatic charging transient volts.
η_o	Change of potential of front side of electrode by potentiostat, volts
$\eta(\infty)$	Final potential change exhibited by porous electrode after application of single galvanostatic pulse, volts
$\eta_T(0,t)$	Total potential change of front side of porous electrode including effect of R_{REF}, volts
$\Delta\eta$	Amplitude of triangular potential wave, volts
κ	Specific conductance of metallic phase, ohm^{-1}cm^{-1}
μ	Rate of change of current with time during application of triangular current wave to electrode, amp/sec
ξ	$\xi = x/l$; dimensionless distance coordinate
ρ	$\rho = R_{REF}/R_o$; ratio of electrolyte resistance between front surface of porous electrode and tip of reference electrode capillary to resistance of solution in pores of electrode.
σ	Specific conductance of solution phase, ohm^{-1}cm^{-1}

τ	$\tau = R_oC_T = SCl^2/\sigma A$; time constant for propagation of charging current through porous electrode, sec
τ'	$\tau' = (R_o + R_M)C_T$; time constant for propagation of charging current through porous electrode taking into account resistance of metallic phase, sec
ϕ_M, $\phi_M(\xi,t)$	Potential of metallic phase of porous electrode, volts
$\phi_S(x,t)$, $\phi_S(\xi,t)$	Potential of solution phase of porous electrode, volts
$\Delta\phi(x,t)$, $\Delta\phi(\xi,t)$	Interfacial potential difference of porous electrode, volts

REFERENCES

1. O. S. Ksenzhek and V. V. Stender, *Dokl. Akad. Nauk S.S.S.R.*, **106**, 487 (1956).
2. O. S. Ksenzhek and V. V. Stender, *Zhur. Fiz. Khim.*, **31**, 117 (1957).
3. O. S. Ksenzhek and V. V. Stender, "Trudy Chetvertogo Soveshchaniya po Elektrokhimii," p. 823, Moscow (1956).
4. V. V. Stender and O. S. Ksenzhek, *Zhur. Priklad. Khim.*, **32**, 110 (1959).
5. O. S. Ksenzhek, *Zhur. Fiz. Khim.*, **37**, 2007 (1963).
6. O. S. Ksenzhek, *ibid.*, **38**, 1846 (1964).
7. R. de Levie, *Electrochim. Acta*, **8**, 751 (1963).
8. M. Bonnemay, G. Bronoël, E. Levart, A. A. Pilla, and E. P. d'A. d'Orsay, *Compt. rend.*, **258**, 4256, 6139 (1964).
9. A. Winsel, *Z. Elektrochem.*, **66**, 287 (1962).
10. G. Feuillade, *Compt. rend.*, **256**, 2786 (1963).
11. R. de Levie, *Electrochim. Acta*, **9**, 1231 (1964).
12. R. Coffre and G. Feuillade, *Compt. rend.*, **259**, 3245 (1964).
13. J. Vergnolle, *This Journal*, **111**, 799 (1964).
14. V. S. Daniel'-Bek, *Zhur. Fiz. Khim.*, **22**, 697 (1948).
15. F. A. Posey, *This Journal*, **111**, 1173 (1964).
16. G. Doetsch, "Tabellen zur Laplace-Transformation und Anleitung zum Gebrauch," Springer-Verlag, Berlin (1947).
17. A. Erdelyi, Editor, "Tables of Intergral Transforms," Vol. I, McGraw-Hill Book Co., New York (1954).

Electrochemical Studies of Single Crystals of Lithiated Nickel Oxide

1. Distribution of Charge and Potential at Oxide Electrolyte Interface

T. O. Rouse and J. L. Weininger

General Electric Research and Development Center, Schenectady, New York

ABSTRACT

Lithiated nickel oxide is a p-type semiconductor. Electrodes were made from single crystals of this material and their d-c and a-c behavior was studied in acid electrolytes. These electrodes are nearly ideally polarizable over an appreciable potential range. At 0.5-1.0v, with respect to a hydrogen electrode in the same solution, there is observed a capacitive impedance, which is associated with the charging of a space charge region due to the exhaustion of holes near the NiO surface. The experimentally determined flat-band potential for NiO is pH-dependent, which indicates the existence of an adsorbed surface layer in equilibrium with protons in the electrolyte. Near zero potential hydrogen evolution is observed, and above 1v faradaic processes occur.

Electrochemical processes at metallic electrodes are often influenced by the reactivity of a semiconducting surface oxide. A fundamental description of these processes should reflect the interaction of the semiconducting properties and the surface reactivity of the oxide. A necessary first step in arriving at such a description is the determination of the relationship between surface charge and the potential at the oxide-electrolyte interface in the absence of any reaction.

Lithiated nickel oxide is one of the few transition metal oxides with well-characterized semiconducting properties. This report describes a study of the distribution of charge and potential across the interface of the lithiated NiO single crystal electrode in an acid electrolyte. This distribution of charge and potential depends on the degree of doping of the semiconductor bulk, the pH of the solution, and the applied potential across the interface.

The energy band structure of oxides of the 3d-transition metals are discussed in detail by Morin (1). Among these oxides, NiO has been studied most extensively. It has a very wide band gap and, therefore, is an insulator in the pure state. When doped with lithium ions ($Li_xNi^{+2}{}_{1-2x}Ni^{+3}{}_xO$) it becomes a p-type semiconductor. Verwey *et al.* first suggested (2) that this conduction arises because the addition of Li^+ generates an equal number of Ni(III) ions. The mechanism of conduction is then thought to consist of the exchange of holes between Ni(II) and Ni(III) ions in the cation lattice and is termed a "hole-hopping" mechanism. The exchange takes place over an energy barrier (3); hence the drift mobility of the holes is very small and increases with temperature. This mechanism, which may also occur in other 3d-transition metal oxides, *e.g.*, Fe_3O_4, is quite unlike that usually described by the band theory of semiconduction.

The electrochemical behavior of zinc oxide single crystals has been studied by Dewald (4). ZnO is an n-type semiconductor which conducts through bands no comparable investigation for oxide electrodes which conduct by the hole-hopping process has been made Lithiated NiO was chosen for this study because it is the best characterized of this class of oxides. Second, large crystals of NiO can be grown, and these crystals can be doped with lithium under controlled conditions. Third, preliminary d-c measurements indicated that there were no appreciable faradaic processes, including dissolution, at the single crystal surface in nondepolarizing acid solutions.

There are important differences between the semiconduction process found in nickel oxide and that found in oxidic or elemental semiconductors to which the band theory of conduction applies (5). In common with all semiconductor electrodes, however, on applying a potential to the nickel oxide electrode in solution, the potential difference from the interior of the semiconductor to the bulk of the electrolytic solution will consist of two individual contributions. There will be a potential difference across a region of accumulated electronic charge in the oxide, the space charge region, and another across a region of accumulated ionic charge in the electrolyte. The characteristics of

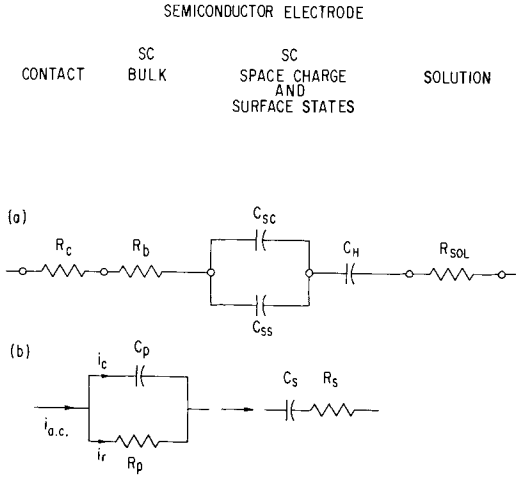

Fig. 1. Equivalent circuits. (a) Representation of system-semiconductor/electrolytic solution. (b) Experimentally measured quantities, C_p, R_p, and their series equivalents.

the space charge portion of this double layer are determined by the bulk properties of the semiconductor; the solution side of this double layer is determined by the properties of the electrolyte and by the interaction of the electrolyte with the oxide surface.

The potential difference, U, of the galvanic cell

$$\underset{\text{I}}{M_1}/\underset{\text{II}}{\text{Semiconductor}}/\underset{\text{III}}{\text{Solution}}/\underset{\text{IV}}{\text{Reference Electrode}}/\underset{\text{V}}{M_2}$$

can be given by

$$U = \Delta\phi_{\text{I, III}} + \Delta\phi_{\text{III, V}}$$

where the subscripts refer to the appropriate phases and interfaces. Thus, ϕ_N would be the inner potential associated with phase N. $\Delta\phi_{\text{III, V}}$ is defined as zero for the normal hydrogen reference electrode.

The potential difference $\Delta\phi_{\text{I, III}}$ is frequently represented by the voltage drop across an equivalent circuit such as that shown in Fig. 1a. Usually, the solution resistance is considered separately, and another solution layer, the Gouy layer (not shown), is assumed to be absent at high concentrations of the electrolyte.

In practice, at a given frequency one measures a resistance and capacitance in a simple series or parallel connection as shown in Fig. 1b. For example, the impedance of the elements in series, Z, is given by

$$Z = R_S + 1/(j \cdot \omega \cdot C_S)$$

R_S and C_S are the measured quantities. Therefore, the central problem in interpreting experimental results is the correlation of impedance measurements, at several frequencies and applied potentials, with the individual components of the circuit in Fig. 1a. Two of these components, the bulk resistance, R_b, and the space charge capacitance, C_{sc}, are related to the bulk properties of the semiconductor.

The theory of the space charge layer at a semiconductor-electrolyte interface has been developed by several workers (4-8). In lithiated NiO holes and electrons are distributed among energy levels localized about nickel cations and isolated acceptors (Li^+ ions). The levels will be altered by a change in potential $\Delta\phi(x)$, hence, the local distribution of holes and electrons will be altered.

The relation between space charge capacitance and potential is derived from Poisson's equation for the distribution of space charge and potential. This distribution must follow semiconductor statistics in the same way as the more usual band-type semiconductors. The behavior of the space charge in lithiated NiO can simply be considered that of a p-type semiconductor with acceptor exhaustion.

$$C = \pm\left(\frac{e_o^2\,\epsilon N_{Li}}{8\pi kT}\right)^{1/2} \frac{\exp\left[e_o(\phi_B - \phi_S)/kT\right] - 1}{\{\exp\left[e_o(\phi_B - \phi_S)/kT\right] - e_o(\phi_B - \phi_S)/kT - 1\}^{1/2}} \quad [1]$$

$\phi_B - \phi_S$ is the potential difference between the bulk and surface, and is zero for the isolated semiconductor. We use the usual electrochemical notation, having $\phi_B - \phi_S$ larger than zero for an anodic surface. The positive sign in [1] is used for positive values of $\phi_B - \phi_S$; the negative sign for negative values of $\phi_B - \phi_S$. N_{Li} is the concentration of Li^+; ϵ, the dielectric constant of NiO; e_o, the charge of the electron; k and T have their usual significance.

Two approximations are applicable to Eq. [1].

At large positive values of $\phi_B - \phi_S$ the surface is enriched with holes and

$$C \sim \left(\frac{e_o^2\,\epsilon N_{Li}}{8\pi kT}\right)^{1/2} \cdot \{\exp\left[e_o(\phi_B - \phi_S)/kT\right]\}^{1/2} \quad [2]$$

For large negative values of $\phi_B - \phi_S$ the surface is depleted of holes and the space charge is due to uncompensated occupied acceptors.

$$C \sim \left(\frac{e_o^2\,\epsilon N_{Li}}{8\pi kT}\right)^{1/2} \cdot \frac{1}{[-e_o(\phi_B - \phi_S)/kT - 1]^{1/2}} \quad [3]$$

This is the well-known Mott-Schottky approximation.

The total applied potential, U, across the interface is

$$U = (\phi_B - \phi_S) + (\phi_S - \phi_{Soln}) + (\phi_{M_1} - \phi_B)$$

ϕ_{Soln} and ϕ_{M_1} are inner potentials of the solution and of the contacting metal, respectively. Equation [3] can be rewritten

$$U = U_{FB} - \frac{kT}{e_o}\left[1 + \left(\frac{\epsilon e_o^2 N_{Li}}{8\pi kT}\right)/C^2\right] \quad [4]$$

where U and U_{FB} are referred to the normal hydrogen electrode.

Although in NiO there is no conduction in bands we retain the definition of a "flat-band potential," U_{FB}, as that value of the applied potential at which the potential at the surface and in the bulk of the semiconductor are equal. At that value, the entire potential difference in the cell (*vs.* NHE) is concentrated across the metal-semiconductor contact and the solution side of the double layer, the Helmholtz layer. This is illustrated in Fig. 2. It is tacitly assumed in obtaining Eq. [4] that $(\phi_S - \phi_{Soln})$ is not altered by a change in U. This assumption is usually valid in the case of semiconductors whose carrier and surface state concentrations are low compared to the electrolyte concentration in the solution (5). Its validity in the present case will be discussed in connection with the experimental results. $(\phi_{M_1} - \phi_B)$ is not a function of U for an ohmic contact.

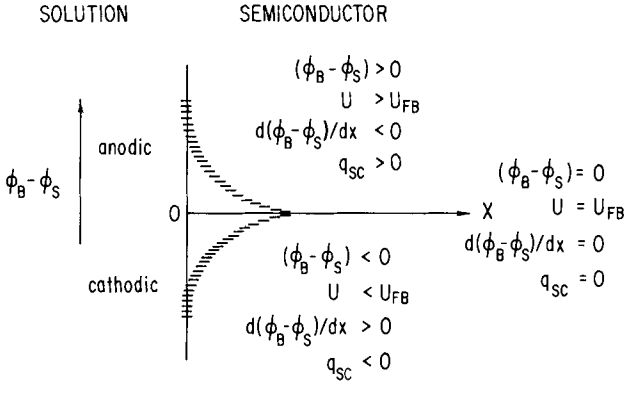

Fig. 2. Distribution of potential in the electrode

The space charge region is treated as if its impedance were purely capacitive. This capacity is in series with the resistive impedance beyond the space charge layer (R_b in Fig. 1a). At the flat-band potential, the space charge region has been compressed to zero thickness, and the charge carrier distribution is uniform throughout the bulk of the semiconductor. The capacitive impedance then is associated only with the surface charge distribution, and the resistive impedance is a measure of the bulk resistivity of the entire crystal. The conductivity, σ, of the crystal, and the bulk resistance R_b, respectively, are given by

$$\sigma = N_A e_o \mu$$

and

$$R_b = \frac{d}{N_A e_o \mu A} \qquad [5]$$

where d is the thickness of the crystal; A, its area; and μ, the drift mobility of the hole.

Experimental

Single crystals of NiO were grown by the method of Cech and Alessandrini (9); this method produces very pure crystals, with a (100) orientation, and a geometry suitable for flat, large, and thin electrode structures. In this method $NiBr_2$ vapor is hydrolyzed at 640°C and at a water vapor pressure of 25 mm in a flowing system. NiO deposits epitaxially on the {100} surface of an MgO single crystal substrate. Subsequently, the crystals are separated by dissolving the MgO substrate in boiling 1*N* H_2SO_4 or 1*N* H_3PO_4. This acid treatment does not affect the NiO crystals adversely. The size of the crystals depends only on the availability of large MgO substrate crystals and surface areas of one square inch can be achieved. Maximum thickness is about 400μ, but thinner crystals are used for electrodes in order to reduce the time required for uniform doping. The purity of the crystals can be judged by their conductivities which were determined to be of the order of 10^{-13} ohm^{-1}-cm^{-1}. Any extraneous cations or cation vacancies would increase this value to about 10^{-6} ohm^{-1}-cm^{-1}, depending on the impurity concentration.

Cooling from the formation temperature introduces some strain into these crystals. The degree of strain is, however, much lower than that found in crystals grown by other methods, *e.g.*, the flame-fusion technique.

The crystals were doped by heating (1600°-1800°C) in air for various times (3-50 hr) with a powdered mixture of NiO and Li_2O. The latter serves as the source of Li^+ ions, and the former presents a means of maintaining a lithium oxide atmosphere over the NiO single crystals for a longer period of time than would be possible using Li_2O alone at these high temperatures. The time and temperature of doping is calculated from the diffusion coefficient of Li in NiO, $D = 2.0 \exp(-3.55 \text{ ev}/kT)$, in cm^2/sec, which has been determined by Garfinkel (10).

With this method NiO crystals were doped with Li up to a concentration of 0.48 a/o (atom per cent). The conductivity of the highest doped crystals is of the order of 10^{-2} ohm^{-1}-cm^{-1}. Lithium concentrations were determined by flame-photometric analyses.

NiO crystals were mounted in Pyrex electrode holders. Ag was chosen as the contact material, but Ni, Pt, and a Ga-Al alloy were also tried. Such electrodes were used in a conventional cell containing a hydrogen reference electrode and a large platinized Pt counter electrode. The reference electrode dipped into the same solution, but was separated from the bulk of the solution by a porous diaphragm. This permitted stirring the solution with Ar gas while measuring the test electrode directly with respect to the hydrogen reference. Unless otherwise noted, potentials are referred to the hydrogen electrode in the same solution as the test electrode.

The following solutions were used: 1*N* H_2SO_4, 1*N* $HClO_4$, and 1*N* $NaClO_4$ adjusted to pH 4 with $HClO_4$.

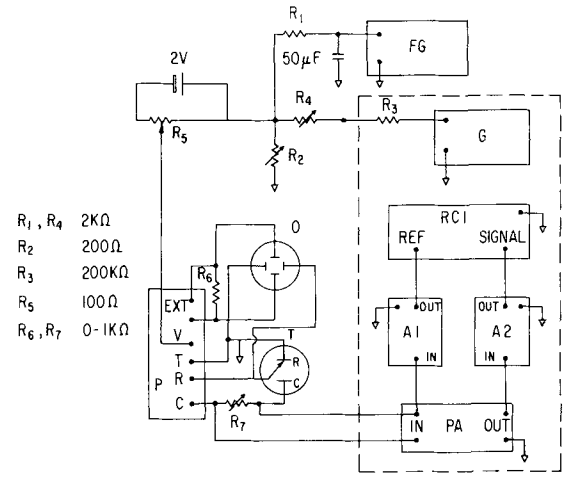

Fig. 3. Schematic circuit diagram: A_1, A_2, Ballantine decade amplifiers; PA, Tektronix type D plug-in unit in power supply used as preamplifier; RCI, Solartron-resolved component indicator, Model VP 250; G, Hewlett-Packard oscillator, type 200CD; O, Tektronix 502 double beam oscilloscope; FG, Exact Electronics function generator, type 250; P, Wenking potentiostat with connections for V, applied voltage; T, test electrode; R, reference electrode; C, counter electrode; and EXT, output. Dashed box: a-c instrumentation.

The circuit used in this study is shown in Fig. 3. It is a modification of an earlier circuit which combined instrumentation for d-c potentiostatic and a-c impedance measurements (11). Because the previous circuit introduced a phase shift between the reference and test signals above 3000 cps the circuit was altered by taking the a-c reference signal from R_7 (Fig. 3) instead of the previously used R_6. This placed the comparison of reference and test signals on adjacent components without introducing the phase shift due to the potentiostat. The high-frequency limit now became that of the resolved component indicator, namely 20 kcps.

A-c impedances were measured in a d-c potential range from 0 to 1.5v (with respect to the hydrogen electrode) at 200 cps, 1, 2, 5, 10, and 20 kcps, with the resolved component indicator. This instrument gives directly the in-phase and out-of-phase currents, i_r and i_c, of Fig. 1b. The electrolytic solution resistance, $R_{sol.}$ of Fig. 1a, was determined separately. From the experimental currents i_r and i_c, the parallel impedance R_p and C_p were calculated. The parallel circuit of Fig. 1b was converted into the equivalent series circuit, and the experimentally determined electrolytic resistance was subtracted from the calculated series resistance. Final corrected values were then computed for tan δ (tan $\delta = 1/\omega R_s' C_s$), R_s', and C_s. R_s' is the equivalent series resistance after elimination of the electrolytic resistance between the working electrode and the reference electrode. All computations were performed on a G.E. 225 computer, which also plotted the data against applied potential.

D-c measurements were performed galvanostatically, potentiostatically at steady state, and potentiostatically with a transient triangular voltage sweep method with rates up to 1 v/sec.

Galvanostatic measurements were made with a conventional constant current circuit. Potentials were measured by a Keithley Model 610A electrometer, with an input impedance of 10^{14} ohms, which in turn drove an X-Y recorder.

Results

A schematic comparison of the experimental results obtained by the four methods mentioned above is shown in Fig. 4. In this figure the potential scale is drawn accurately to indicate the different regions of potential where electrochemical processes may be occurring. Only the magnitude of the dependent varia-

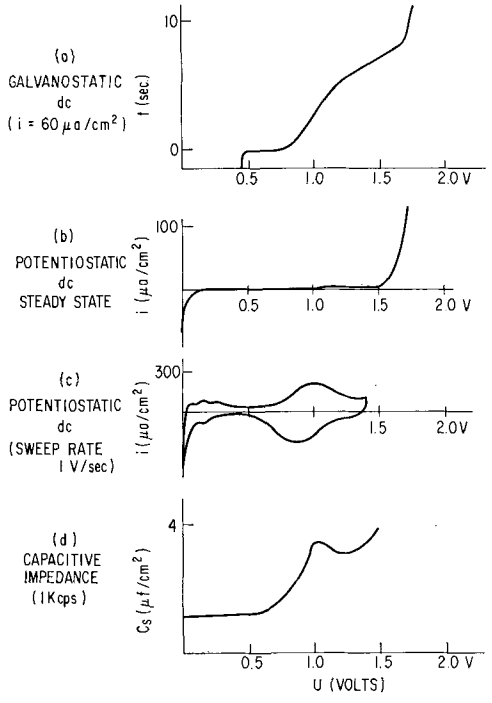

Fig. 4. Schematic curves of time, current, and capacitance vs. applied potential for Li-doped NiO single crystal electrodes.

bles are noted because their actual values depend on doping.

Figure 4a shows the galvanostatic curve obtained on passing a current of 60 μa/cm^2. A charging step is observed beginning at about 0.75v. This step is followed by a slow rise in potential above 1.20v. Oxygen evolution becomes appreciable at 1.7v. The i·t product for the potential step is independent of current, and for this crystal it has a value of 0.18 mC/cm^2.

In the steady-state potentiostatic measurements (Fig. 4b) only a small anodic current (1-5 μa/cm^2) is observed above 1.1v. At higher potentials oxygen is evolved, and at low potentials a cathodic reaction, possibly hydrogen reduction, is observed.

In the transient method (Fig. 4c) a triangular voltage sweep is applied to the electrode under potentiostatic conditions at a high sweep rate of approximately 1 v/sec. Transient phenomena appear. The close correspondence of anodic and cathodic current peaks at such a high sweep rate demonstrate the reversibility of the process beginning at potentials above 0.75v. The very small transients below 0.5v, are not observed at slower sweep rates.

Figure 4d shows a characteristic maximum of C_s for a crystal with 0.48 a/o Li in a solution of *p*H 4.

It should be pointed out that after the crystals are subjected to a high current density other phenomena appear. Under these circumstances crystals frequently develop cracks. Results reported here refer only to crystals which were not subjected to high current density.

Figure 5 through 11 show the a-c behavior of a NiO electrode doped with 0.48 a/o Li, in 1*N* $NaClO_4$ solutions adjusted with $HClO_4$, respectively, to *p*H 1 and 4.

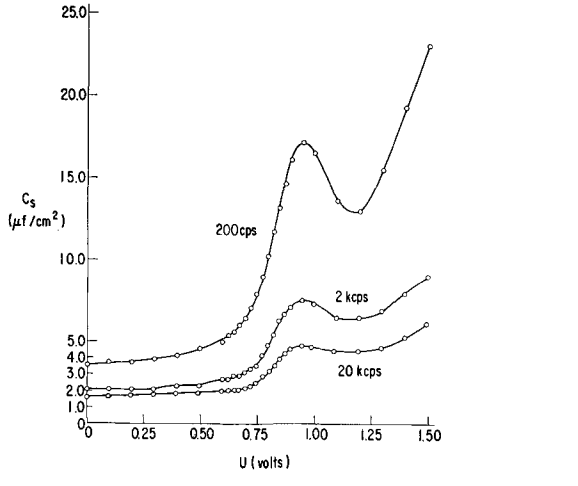

Fig. 5. Series capacitance at 200 cps, 2 kcps, and 20 kcps as a function of applied d-c potential.

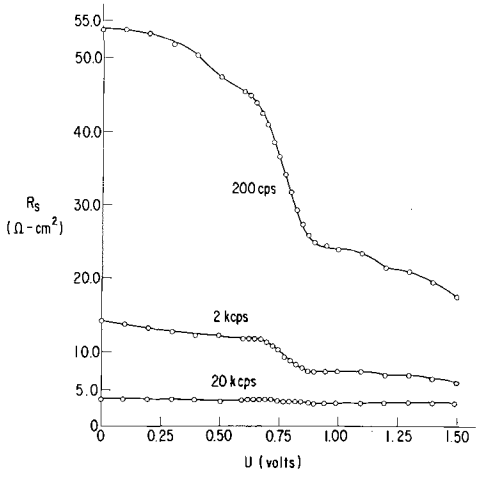

Fig. 6. Series resistance at 200 cps, 2 kcps, and 20 kcps as a function of applied d-c potential.

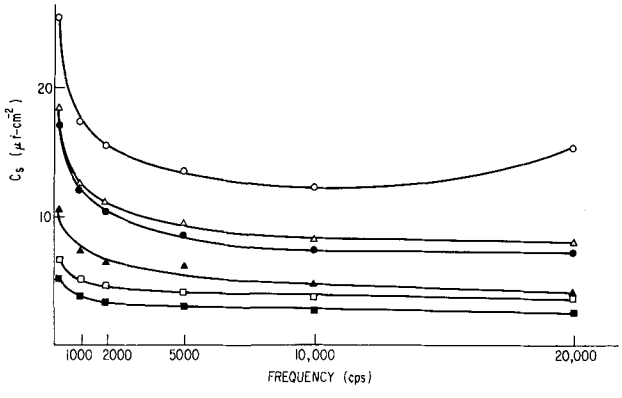

Fig. 7. Series capacitance as function of frequency at applied d-c potentials; open symbols, *p*H 1; solid symbols, *p*H 4; ○, ● 1.20v; △, ▲ 0.75v; □, ■, 0.50v.

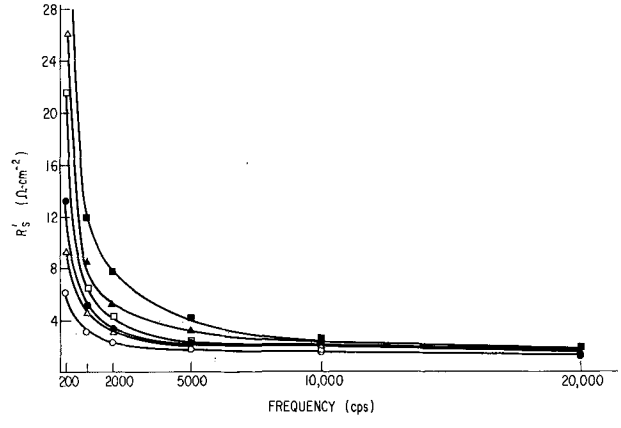

Fig. 8. Series resistance as function of frequency at applied d-c potentials; open symbols, *p*H 1 ;solid symbols, *p*H; ○, ●, 1.20v; △, ▲, 0.75v; □, ■, 0.20v.

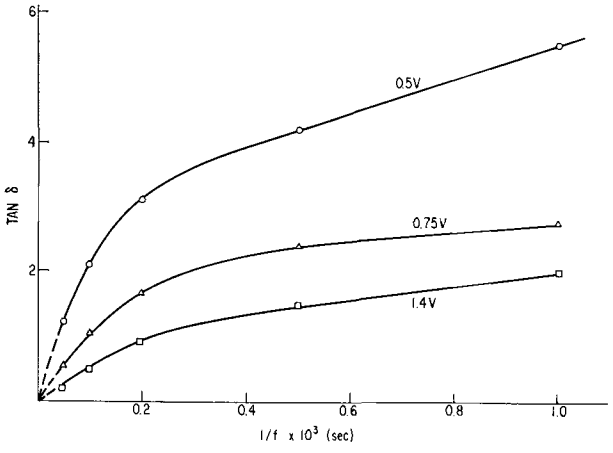

Fig. 9. Phase shift, tan δ, as a function of frequency at different applied d-c potentials.

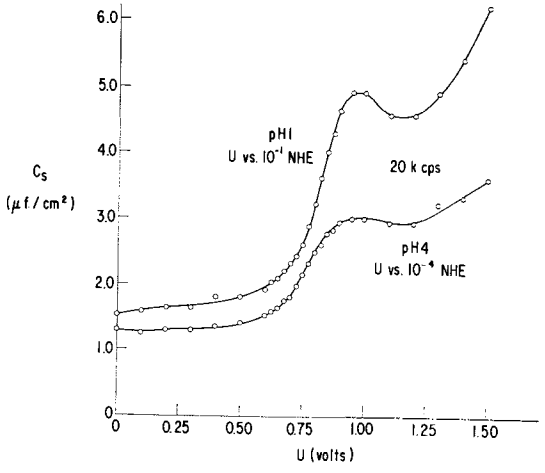

Fig. 10. Comparison of C_s function vs. applied d-c potentials at pH 1 and 4. Potential scales: pH 1 vs. 0.1 NHE; pH 4 vs. 10^{-4} NHE.

The series capacitance and resistance are shown, respectively, in Fig. 5 and 6 as a function of applied potential at several frequencies, and in Fig. 7 and 8 as functions of frequency for several potentials. At the lower frequencies, both resistance and capacitance show pronounced frequency dependence. At 10 and 20 kcps the resistance is independent of frequency and the capacitance is only slightly dependent on it.

The values of the series resistance and capacitance did not change on adding detergent or N-methyl-2-pyrrolidone to the solution.

Although the crystals represented by these figures belonged to the most highly doped group of NiO crystals, the data obtained with crystals having lower lithium concentrations differ only in magnitude from those shown in these figures.

The variation of the phase shift, tan δ, with reciprocal frequency at several values of applied potential is shown in Fig. 9. It is apparent that, at lower frequencies, the simple equivalent circuit of Fig. 1b does not describe the semiconductor-electrolyte interface adequately. No peaks are observed in the tan δ curve which can be associated with relaxation processes. At 10 and 20 kcps tan δ approaches a straight line with an intercept at zero (dashed line, Fig. 9). From this we conclude that the simple equivalent circuit of Fig. 1b describes the interface adequately at 20 kcps. The capacitance *vs.* potential curves of Fig. 10 were obtained for the same NiO electrode in *p*H 1 and *p*H 4 solutions. In the experimental setup the hydrogen reference electrode dipped into the same electrolyte in which the NiO was immersed. Thus, in Fig. 10 the

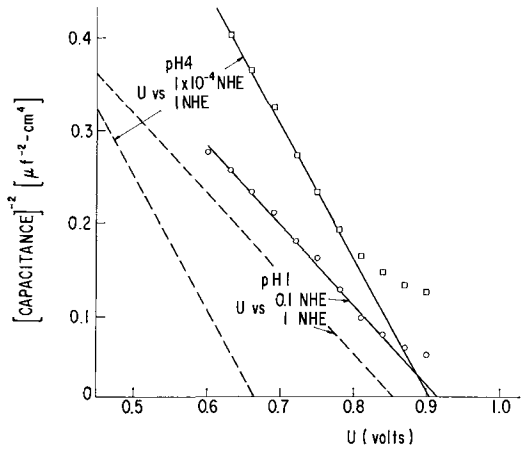

Fig. 11. Mott-Schottky plot for lithium-doped NiO crystals at pH 1 and 4. Dashed curves, reference potential 1 NHE; solid curves, experimental.

potentials for the *p*H 1 curve refer to a 0.1 NHE and those for the *p*H 4 curve refer to a 10^{-4} NHE. The C_s — U curves are then shifted by nearly 180 mv *vs.* the NHE for a *p*H change of three. Furthermore, the capacitance values were always lower in the more alkaline electrolyte.

The resistivities of several of these crystals were obtained after the impedance measurements had been made. The outer face of the crystal was coated with silver while still in the electrode assembly. The resistances were then determined from the slope of the current-voltage curve for this two-contact, dry, Ag-NiO-Ag system. The linearity of the curve indicates that Ag forms an ohmic contact with NiO, a conclusion in agreement with the findings of Thistlethwaite *et al.* (12).

Figure 11 shows a typical plot of $1/C^2$ *vs.* U for a given crystal in the two electrolytes in the range 0.50-1.00v. The Mott-Schottky plots in this potential region are linear for all crystals at all frequencies. The inverse slope decreases with increasing frequency; the intercept is independent of frequency. The results obtained at 20 kcps for several crystals are given in Table I, in which the slopes S_{exptl} and S_{calcd} are compared. S_{exptl} is the inverse slope of Fig. 11, $dU/d(1/C^2)$, and S_{calcd} is the value calculated from Eq. [4]. In the latter calculation a value of 12 was assumed for the dielectric constant for NiO (13). Crystals 1 and 2 were cut from the same original crystal after doping; crystals 3 and 4 were from the same doping run. Crystal 3 was rather small, its analysis should obviously be viewed with caution.

The measured resistive component of the impedance at U_{FB} was used to calculate the conductivity of the crystals. Drift mobilities were calculated from Eq. [6], using the resistances obtained electrochemically and those obtained from the solid-state measurements (Ag-NiO-Ag). These are shown in Table II.

Discussion

The general trend of the experimental results by all methods, shown in Fig. 4, indicates that a reversible process occurs in the potential range 0.5-1.0v. This process is not diffusion controlled; it is not affected by surfactants; and it is associated with an increasing equivalent series capacitance. At potentials above and below this range, small d-c currents indicate the presence of other minor reactions.

The mobilities reported in Table II are in good agreement with those found by van Houten (14) on polycrystalline samples of Li-doped NiO and with those estimated by Koide (15) for single crystals similar to those used in the present work.

Linearity of the Mott-Schottky plots and a linear dependence of the slope, S, on dopant concentration

Table I. Observed and calculated slopes of Mott-Schottky plots and flat-band potentials for Li-doped NiO crystals

Crystal No.	Lithium content, a/o	$S_{calc.}$ Calculated slope	$S_{expt.}$ Experimental slopes, pH 1	$S_{expt.}$ Experimental slopes, pH 4	Flat-band potentials U_{FB}, pH 1	Flat-band potentials U_{FB}, pH 4
			μf^2 v cm^{-4}		v *vs.* NHE	
1	0.48 ± 0.1	3.47	2.50	1.08	0.79	0.66
2	0.48 ± 0.1	3.47	1.01	0.71	0.85	0.67
3	0.05 ± 0.05	0.31	0.12	0.12	1.04	0.86
4	0.19 ± 0.03	1.39	0.17	0.10	0.86	0.78
5	0.16 ± 0.10	1.14	0.48	0.15	0.84	0.67
					0.88 ± 0.06	0.73 ± 0.07

Table II. Conductivities and mobilities of Li-doped NiO crystals

Crystal No.	Li content a/o	Conductivities at pH 1, ohm^{-1}-cm^{-1}	Conductivities at pH 4, ohm^{-1}-cm^{-1}	Average mobilities electrochem. measurement, $\mu \times 10^4$ cm^2-sec^{-1}-v^{-1}	Average mobilities solid-state measurement, $\mu \times 10^4$ cm^2-sec^{-1}-v^{-1}
1	0.48	0.0165	0.0100	2.88	1.20
2	0.48	0.0125	0.0115	2.57	1.69
3	0.05	0.00103	0.00126	2.20	1.10
4	0.19	0.00068	0.00068	0.37	0.08
5	0.16	0.00158	0.00103	0.85	—

are diagnostic for a space charge region in a semiconductor with charge exhaustion. The Mott-Schottky plots found here were invariably linear over a potential range of about 250 mv. These plots began to deviate from linearity only at potentials less than 0.55v (with respect to the hydrogen electrode in the same solution), where fast potential sweeps (Fig. 4c) show the occurrence of another process. The observed values of the slopes at a given frequency are fairly reproducible. They show clearly the predicted dependence on lithium content.

The discrepancy between observed and predicted values of the slopes will be discussed later.

The existence of a surface dipole due to a specific interaction of the surface with protons is shown by the pH dependence of the flat-band potential

$$U_{FB} = 0.94 - 0.050\ \text{pH} \quad (U\ vs.\ \text{NHE})$$

At the flat-band potential, the entire potential difference between bulk oxide and solution is concentrated across the Helmholtz layer. Ideally, for the case of ions specifically adsorbed on a surface in equilibrium with protons in solution, the potential difference is given by

$$\Delta\phi_H = \frac{\bar{\mu}_{H^+} - \bar{\mu}_{surface}}{F} - 0.059\ \text{pH}$$

This pH-dependent Helmholtz potential difference has been found for germanium (6, 16), where the effect was attributed to the presence of an acidic surface oxide. It has also been observed for the Ta_2O_5-electrolyte system (17). In that case, the effect is attributed to protons adsorbed on the oxide surface.

The discrepancy between prediction and experiment at 20 kcps is manifested in two ways: the observed Mott-Schottky slope is about half a decade low, and the observed capacities are low by a factor of about two to three. This discrepancy cannot be due to the presence of slow surface states. Because surface states store charge in parallel to the space charged layer, their presence would result in capacitances higher than predicted and slopes higher than predicted. Furthermore, although surface states could conceivably be distributed in such a way as to give a linear Mott-Schottky slope over a limited range of applied potential, it is unlikely that any such single distribution could apply to crystals of different bulk doping (4). Slow surface states do not appear to contribute to the capacitance at 20 kcps; they may contribute at the lower frequencies where the tan $\delta - 1/f$ curve (Fig. 9) indicates the simple series circuit is not applicable.

It does not appear that incomplete dissociation of Li(1)-Ni(III) ion pairs can account for this discrepancy. MacDonald (18) has treated the case of incompletely ionized donors in local equilibrium with charge carriers. This treatment is applicable here and results in an equation of the form

$$C \sim \left(\frac{e_o^2 \epsilon N_{Li}}{8\pi kT}\right)^{1/2} \frac{1}{[-e_o(\phi_B - \phi_S)/kT - f + \ln f]^{1/2}}$$

for an exhaustion space charge region, *i.e.*, for large negative valves of $(\phi_B - \phi_S)$.[1] f is the fraction of ion pairs dissociated to form free carriers, and N_{Li} is the total number of Li ions. The slope of the Mott-Schottky plot is not a function of the degree of ionization, but the intercept is a function of f. The reproducibility of the flat band potentials found for the dopings used here is too low to give any information on the degree of ionization.

The discrepancy cannot be attributed to the Helmholtz capacitance in the case of simple specific adsorption of protons; although in this case C_H should be dependent on pH and applied potential, it should not be less than that of the double layer in the absence of specific adsorption, *i.e.*, 20-40 μf/cm^2. The magnitude of the discrepancy then is too large to be accounted for in this way.

The Helmholtz portion of the double layer may, however, have a more subtle influence in the charge-potential relationship. In deriving Eq. [4] it was assumed that $(\phi_S - \phi_{Soln})$ was independent of applied potential. If this is not the case, it can be shown simply that the observed slope, $\delta U/\delta(1/C^2)$, is given by

$$\frac{\delta U}{\delta(1/C^2)} = \frac{-kT}{e}\left(\frac{e_o^2 \epsilon N_{Li}}{8\pi kT}\right)\left[1 + \frac{\delta(\phi_S - \phi_{Soln})}{\delta(\phi_B - \phi_S)}\right]$$

The discrepancy between theory and prediction can be resolved if $\delta(\phi_S - \phi_{Soln})/\delta(\phi_B - \phi_S)$ is independent of capacitance and if its magnitude is somewhat greater than unity. A definitive consideration of this point cannot be given at this time; however, some tentative estimates of the magnitude of this ratio can be made. Verwey and Niessen (20) have considered the potential distribution across a double layer, both sides of which are diffuse. We have given preliminary consideration to the case more nearly applicable here, *i.e.*, a diffuse layer in the semiconductor and a layer in solution bounded by a Helmholtz plane. In both cases, because of the high doping concentrations available in nickel oxide, the magnitude of the ratio appears to be of the order of unity.

A final consequence of the high carrier concentration is that the thickness of the space charge layer is quite small. For the potential range over which the Mott-Schottky approximation holds for NiO and for the doping concentrations used in this study, most of the space charge is due to uncompensated lithium ions in the first two or three lattice layers. The quantitative discrepancy may conceivably be attributed to nonhomogeneous acceptors near the surface.

At potentials more positive than U_{FB} the behavior of the capacitance is also complex. Equation [4] predicts that the space charge capacitance should increase

[1] Dewald (19) has arrived at a similar limiting solution to this problem.

exponentially as (ϕ_B — ϕ_S) increases. As ϕ_S approaches a value corresponding to the Fermi level, the Boltzman distribution is not applicable, and the surface becomes degenerate. Charge should then accumulate more slowly than predicted by the Boltzman approximation. In the case of the hole-hopping mechanism of conductance a density-of-states function is not known, and the exact dependence of the space charge capacitance on the potential in the degenerate region cannot be derived. However, in the degenerate region the capacitance should increase only slowly with potential and should become independent of doping. The predicted rapid rise in capacitance of U_{FB} and the subsequent slower increase in capacitance is not observed. This finding is in general agreement with Dewald's observations (4) of the enrichment region in n-type ZnO. It appears likely that for NiO at potentials greater than U_{FB} the complex dependence of the capacitance on applied d-c potential is due to faradaic or adsorptive processes which give rise to a small d-c current above 1v in the steady-state potentiostatic measurements (see Fig. 4b). At these high anodic potentials the space charge capacitance will have become sufficiently large that the measured capacitance is primarily due to the charge distribution in the Helmholtz layer.

Conclusions

In summary, it is concluded that:

1. Single crystals of NiO, doped with lithium, are nearly ideally polarizable electrodes over an appreciable potential range. Near zero potential (with respect to the normal hydrogen reference) there is some evolution of hydrogen and above 1v, on the same scale, there is evidence for faradaic processes.

2. A space charge region due to the exhaustion of holes near the surface of the NiO is observed at weakly anodic potentials (*vs.* NHE).

3. The flat-band potential for NiO is given by

$$U_{FB} = 0.94 - 0.050\ p\mathrm{H}$$

At the flat-band potential, the potential drop in the Helmholtz region is controlled by an adsorbed layer on the oxide in equilibrium with protons in solution.

4. The resistive component at the flat-band potential is determined by the crystal resistance.

5. The measured capacitance at potentials more anodic than U_{FB} is not controlled by the semiconductor. The behavior is complex and is probably related to the faradaic processes at the electrode surface.

Acknowledgment

The authors are indebted to C. E. Van Buren for growing the nickel oxide crystals, to M. Garfinkel for the doping procedure and the use of his unpublished diffusion data, and to D. A. Vermilyea for very helpful discussions.

Manuscript received June 28, 1965; revised manuscript received Oct. 8, 1965. This paper was delivered before the San Francisco Meeting, May 9-13, 1965.

Any discussion of this paper will appear in a Discussion Section to be published in the December 1966 JOURNAL.

REFERENCES

1. F. J. Morin, *Bell System Tech. J.*, **37**, 1047 (1958).
2. E. J. W. Verwey, P. W. Haayman, and F. C. Romeyn, *Chem. Weekblad*, **44**, 705 (1948).
3. R. R. Heikes and W. D. Johnston, *J. Chem. Phys.*, **26**, 582 (1957).
4. J. F. Dewald, *J. Phys. Chem. Solids*, **14**, 155 (1960).
5. H. Gerischer, in "Advances in Electrochemistry and Electrochemical Engineering," No. 3, Ch. III, P. Delahay, Editor, Interscience Publishers, New York (1963).
6. K. Bohnenkamp and H. J. Engell, *Z. Elektrochem.*, **61**, 1184 (1957).
7. M. J. Spaarnaaij, III. Internatl. Congress of Surface Active Materials, Cologne 1960, Vol. II, p. 232, University Press of Mainz.
8. R. Memming, *Philips Research Repts.*, **19**, 323 (1964).
9. R. E. Cech and E. I. Alessandrini, *Trans. Am. Soc. Met.*, **51**, 150 (1959).
10. M. Garfinkel, Unpublished results.
11. J. L. Weininger and M. W. Breiter, *This Journal*, **111**, 707 (1964).
12. P. J. Thistlethwaite, K. R. Turnbull, and P. J. Fenshaw, Proc. 1st Australian Conf. on Electrochem., p. 44, Pergamon Press, New York (1965).
13. R. Newman and R. M. Chrenko, *Phys. Rev.*, **114**, 1507 (1959).
14. S. van Houten, *J. Phys. Chem. Solids*, **17**, 7 (1960).
15. S. Koide, *J. Phys. Soc. Japan*, **20**, 123 (1965).
16. F. Beck and H. Gerischer, *Z. Elektrochem.*, **63**, 500 (1959).
17. D. A. Vermilyea, *Surface Science*, **2**, 444 (1964).
18. J. R. MacDonald, *J. Chem. Phys.*, **29**, 1346 (1959).
19. J. F. Dewald, *Bell System Tech. J.*, **39**, 615 (1960).
20. E. J. W. Verwey and K. F. Niessen, *Phil. Mag.*, **28**, 435 (1939).

Technical Notes

Comparison of Platinum and its Group VIII Nearest Neighbors as Anode Electrocatalysts in Propane-Phosphoric Acid Fuel Cells

W. T. Grubb

Research and Development Center, General Electric Company, Schenectady, New York

Low-temperature survey experiments have indicated that platinum black is the best simple electrocatalyst for the anodic oxidation of hydrocarbons near room temperature (1). More recently, high performance platinum black hydrocarbon anodes operating in phosphoric acid fuel cells at 110°-200°C (2,3) have been reported. It was therefore of interest to re-examine the question of whether platinum is still superior to other group VIII noble metals under such conditions. A limited series of experiments was carried out to help provide an answer to this question.

Experimental

Teflon-bonded fuel cell electrodes were prepared by techniques previously described (4). Commercial blacks of platinum,[1] palladium,[2] rhodium,[1] and iridium[1] were used. Their areas as measured by a BET method were respectively, 20, 28, 0.6, and 82 m^2/g. Electrocatalytic ability was compared by observing the performance of these electrodes as propane anodes in complete fuel cells at 150°C using the same Teflon-bonded platinum black cathode and 85% H_3PO_4 as electrolyte. Anode overvoltage *vs.* an unpolarized hydrogen reference electrode in the same electrolyte was also obtained. All of the anodes performed well with hydrogen as fuel indicating that effective gas electrode structures had been achieved in each case.

Results

A comparison of propane current densities at an anode overvoltage *vs.* reversible hydrogen of 0.5v are presented in Table I. The superiority of platinum is clearly indicated. The performance comparison between platinum and iridium is particularly striking as Fig. 1 shows. The current density *vs.* voltage is plotted for hydrogen-oxygen and propane-oxygen cells under the same conditions. Both platinum and iridium black electrodes gave extremely high performance on hydrogen as fuel and in fact supported current densities in excess of 800 ma/cm^2 in both cases. By contrast, a very strong difference in activity with propane was observed. Platinum black supported more than three orders of magnitude higher current density than iridium in spite of its being of somewhat lower specific surface area.

[1] Engelhard Industries, Incorporated, Newark, New Jersey.

[2] J. Bishop and Company, Malvern, Pennsylvania.

Table I. Comparison of propane current densities

Electrocatalyst	Current density at E_a/r = 0.5v in ma/cm^2
Pt	125
Pd	0.7
Rh	0.05 ± 0.05
Ir	0.05 ± 0.05

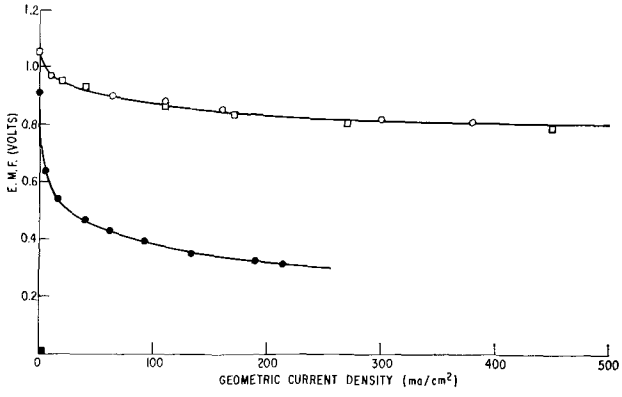

Fig. 1. Comparison of Pt and Ir as anode electrocatalysts in 85% H_3PO_4 at 150°C; cathode *vs.* anode voltage as a function of current density; anodes: ○, H_2-Pt; □, H_2-Ir; •, C_3H_8-Pt; and ■, C_3H_8-Ir; cathode: O_2-Pt (the ordinate is the iR-free cell voltage).

Discussion and Conclusions

The data support the conclusion that platinum is the best simple electrocatalyst for the direct oxidation of hydrocarbon fuels under conditions where, in the case of platinum, high hydrocarbon reactivity is observed. It appears to be orders of magnitude better than its nearest neighbors in the periodic table.

This result is the more surprising in view of the many similarities among these metals. Taking platinum and iridium as an example: both have partially filled d electron orbitals, both are of face-centered cubic crystal structure, the lattice parameters (a_o) differ by less than 3%, and both are known to be excellent catalysts for many nonelectrochemical reactions involving hydrocarbons (5). Apparently some very specific property or set of properties is required for catalyzing the direct electrooxidation of hydrocarbons in the moderate temperature region. It is hoped that further study of the electrooxidation mechanisms will shed light on this point.

The results described here do not of course preclude the possibility of improving the electrocatalytic activity of platinum by various means such as alloying. Considerable literature exists (6-8) indicative of the possibility that such measures may result in increased activity in fuel cell electrodes. However, the nature of the fuel and electrolyte are expected to have an important bearing on the detailed requirements for a suitable electrocatalyst.

Acknowledgment

Thanks are due to Miss C. J. Michalske and Mr. J. G. Lucas for experimental assistance and to Mr.

M. E. Lazarus for performing surface area measurements. The author thanks also Dr. D. W. McKee for some helpful discussions. This work is part of the program under contract DA-44-009-AMC-479(T) and DA-44-009-ENG-4909, ARPA Order No. 247 with the U. S. Army Engineer Research & Development Laboratories, Fort Belvoir, Virginia, to develop a technology which will facilitate the design and fabrication of practical military fuel cell power plants for operation on ambient air and hydrocarbon fuels.

Manuscript received Sept. 10, 1965.

Any discussion of this paper will appear in a Discussion Section to be published in the December 1966 JOURNAL.

REFERENCES

1. W. T. Grubb, Proc. 16th Annual Power Sources Conference, p. 31, Atlantic City, N. J. (1961).
2. W. T. Grubb and C. J. Michalske, *This Journal*, **111**, 1015 (1964); Proc. 18th Annual Power Sources Conference, p. 17, Atlantic City, N. J., May (1964).
3. H. Binder, A. Kohling, and G. Sandstede, Paper presented at Washington Meeting of the Society Oct. 1964; Battery Division Extended Abstracts, **9**, 25 (1964).
4. L. W. Niedrach and H. R. Alford, *This Journal*, **112**, 117 (1965).
5. G. C. Bond, "Catalysis by Metals," Academic Press, Inc., London and New York (1962).
6. D. W. McKee and F. J. Norton, *J. Phys. Chem.*, **68**, 481 (1964).
7. Platinum Metals Review, **9**, 119 (1965).
8. E. W. Brooman and T. P. Hoar, *ibid.*, **9**, 122 (1965).

Hydrogen Plasma Transport of Se, As, and Te

S. W. Ing, Jr., and Y. S. Chiang

Fundamental Research Laboratory, Xerox Corporation, Webster, New York

We have transported Se, As, and Te from either a vapor source or a solid source to substrates located some distance away from the source by using a low-pressure hydrogen plasma. It is suggested that energetic species of hydrogen react with these elements to form hydrides. The gaseous hydrides formed are thermodynamically unstable in the absence of the plasma and decompose rapidly when these hydrides have been transported out of the plasma region. The element, Se, As, or Te is then deposited out.

A continuous flow system was employed in which hydrogen gas was continuously fed into and pumped out of the reaction chamber. The hydrogen discharge was ignited and sustained by using an external inductively coupled excitation source. The generator consisted of a water-cooled copper coil wound around a section of the Pyrex reaction tube near the hydrogen inlet. This coil was connected to a 30 Mc r.f. source. It was found that under a pressure of 20 to 100μ the plasma could be easily sustained using such an excitation source. The visible light intensity of the plasma appeared to be highest at the r.f. coil region, gradually decreased downstream of the coil and finally terminated at the end of the tube.

When a solid source was used, it was usually placed inside the tube in the region of the r.f. coil. The plasma was terminated by using a grounded electrode, strapped to the outside of the tube wall, a short distance downstream of the r.f. coil. It was seen that the element began to deposit out in a thin film form along the tube wall, downstream of the plasma front, which was distinguishable by its glow color. No deposition occurred on the section of the tube wall where the glow color extended very close to the wall. This suggests that any Se deposited in this region was quickly removed by the plasma and returned to the gas phase. All three elements, Se, As, and Te, have been transported and deposited in this manner.

In order to demonstrate the effectiveness of the hydrogen plasma transport of Se, for example, an argon plasma has been tried under otherwise identical conditions. No significant amount of Se transport took place. Only a slight amount of deposition was observed in the immediate vicinity of the solid source.

We have also shown that this transport process is not merely a localized heating and evaporating process. We have applied heat to the solid selenium exposed to a flowing stream of normal hydrogen under a reduced pressure. The selenium vapor simply condensed out on a narrow section of the tube wall adjacent to the heated zone, without being transported along the tube to any appreciable length.

The over-all chemical reactions that possibly are occurring in this plasma transport process can be visualized as follows. The first step is the formation of active hydrogen species, such as atomic hydrogen and energetic molecular hydrogen, by electron bombardment of the hydrogen molecule. These active hydrogen species, on collision with the elements, in either the solid or the gaseous phases, can form metastable gaseous hydrides. Radford (1) has, for example, observed an appreciable amount of hydride radicals of Se and Te in the gas phase when he exposed these solid elements to a reduced pressure hydrogen plasma formed by a d.c. discharge. The ratio of hydrogen to Se, Te, and As in these hydrides is not known. Presumably, this ratio could vary over a wide range. The hydride species formed are likely to decompose on collision with the wall surface to deposit out the elements.

The rate of deposition can be increased substantially by pumping these elements into the plasma in a vapor form. This technique has been applied to transporting Se. The solid source was placed in a small closed end tubular side arm. This side arm was situated close to the hydrogen gas inlet to the reaction chamber, hence on the up-stream side of r.f. coil. Heat was applied to the solid source causing it to evaporate rapidly, and Se

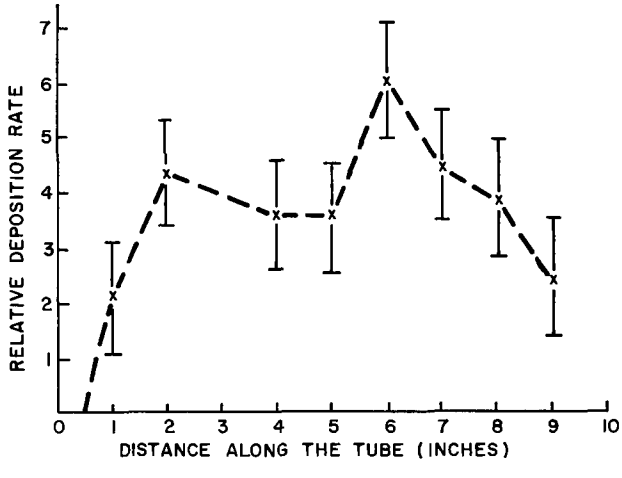

Fig. 1. Relative deposition rate vs. distance along the reaction tube

vapor was thus injected into the plasma. The high-frequency coil used to generate the plasma was water-cooled. and, being in contact with the reaction tube, it also served the purpose of cooling the reaction tube wall. No Se deposition was observed on the tube wall closest to the r.f. coil. The plasma was allowed to extend approximately 12 in. down stream of the coil, *i.e.*, near the grounded electrode. The glow intensity appeared to diminish only very gradually from the r.f. coil, to the region where the plasma was terminated. The plasma was seen to break away from the tube wall outside of the coil region; in this region deposition primarily took place.

Thin Pyrex glass slides were placed along the length of the plasma for monitoring the amount of Se deposited. Relative rates of deposition were obtained by measuring the weight increase of these glass slides at various locations following a certain time length of operation. These results are shown in Fig. 1. The zero distance on the abscissa indicates the region where the r.f. coil ends. The deposition rate is seen to rise rapidly and reaches a broad plateau. This broad peak extends over a distance of 6-7 in. The rate then decreases as the glass slides are further removed from the source. This suggests that the deposition process itself is limiting the net deposition rate. It is likely that the deposited Se is being removed constantly by the hydrogen plasma, and the net deposition rate is therefore strongly dependent on the removal rate. Since the plasma intensity and the removal rate are highest in the region of the r.f. coil, there is no net deposition in this area. The glow intensity gradually decreases down stream of the coil primarily due to the recombination of active species at the tube wall, which allows deposition to occur. The deposition rate is then dependent on the concentration of the gaseous Se species and the active hydrogen; both quantities are expected to decrease simultaneously down the reaction tube. This effect could give rise to the observed deposition rate distributed along the tube wall.

The hydrogen plasma deposited Se films have been studied under an electronmicroscope. The film, with a mean thickness of a few hundred angstroms, is constructed of close packed nodules of around a thousand angstroms in diameter. Electron diffraction measurements show that these films are amorphous. The substrate surface where Se deposition occurred is apparently less than 60° or 70°C. Above these temperatures Se crystallizes very rapidly. Electrical resistivity measurements of the deposited Se films in the dark have been made using evaporated gold electrodes as the contacts. Because of carrier trapping effects no quantitative measurements could be made, however, the film resistivity is estimated to be of the order of 10^{13} ohm-cm.

Acknowledgment

The authors wish to acknowledge the assistance rendered by P. DePerro in carrying out some of the experiments.

Manuscript received Aug. 25, 1965.

Any discussion of this paper will appear in a Discussion Section to be published in the December 1966 JOURNAL.

REFERENCE

1. H. E. Radford, *J. Chem. Phys.*, **40**, 2732 (1964).

Diffusion of Transition Metal Ions into Rutile (TiO_2)

James P. Wittke

RCA Laboratories, Radio Corporation of America, Princeton, New Jersey

Although the diffusion of hydrogen (1), boron (2), and lithium (3) into single crystal rutile has been previously reported, we have not found any reference to diffusion of the larger, heavier transition metals into this material. This Note reports the observation of the diffusion of Cr, Fe, Co, and Ni into rutile. These observations are important for at least two reasons. In the past, measurements of the electrical and other properties of rutile have led to somewhat conflicting conclusions (4, 5) We believe that the observed discrepancies reflect different states of purity of the crystals on which the measurements were made, and the observation that many metals readily diffuse into rutile offers an explanation of why this may be so. Second, rutile doped with chromium or with iron is perhaps the most important material yet found for use in microwave masers (6, 7). For masers, uniformity of doping and accurate control of paramagnetic ion concentration are very important. The techniques reported below for introducing paramagnetic impurities by diffusion offer promise of better maser materials than can be achieved by introducing them during crystal growth.

When transition metal ions are introduced into rutile, the absorption edge at about 4100Å that gives pure rutile its yellowish cast is shifted further toward the red. This results in an orange-brown coloration by means of which the presence of these ions can be monitored. [The color of rutile depends strongly on the treatment of the sample as well as on the doping; *e.g.*, if chromium-doped rutile (brown) is reduced by heating in a vacuum, the absorption at about 1.2μ that gives "reduced" (nonstoichiometric) pure rutile its blue appearance also appears in the doped sample, resulting in a green crystal.] The brown coloration associated with fully oxidized rutile doped with transition metal ions was used to monitor the diffusion of these ions into the crystal.

Rutile has the cassiterite structure; its tetragonal unit cell contains two TiO_2 molecules. The structure can be considered as composed of titanium ions in a body-centered sublattice, with pairs of oxygen ions placed between the titanium ions in alternative face-diagonal directed pairs normal to the c-axis. The titanium ions lie in rows directed along the c-axis, the rows forming a square array when viewed along this axis. The rutile lattice has "channels" of low electron density, lying along the centers of these squares (8). These channels lead to greatly enhanced interstitial diffusion of impurity ions, compared to diffusion via substitutional lattice sites (8).

As in the cases of boron (2) and lithium (3), the diffusion of transition metal ions is exceedingly anisotropic, proceeding along the c-axis (as evidenced by the coloration) faster by orders of magnitude than perpendicular to this axis. This is strong evidence that transition metal ions diffuse into rutile by means of the same interstitial mechanism found for lithium and boron. That this is plausible can be seen from an argument based on lattice geometry. From the electronegativity of titanium and oxygen (9), we estimate the Ti-O bond to be about 60% ionic. Using Pauling's values (9) for ionic and covalent radii for Ti and O, and interpolating linearly with degree of ionicity gives radii of R (Ti) = 0.90Å and R (O) = 1.06Å. Using these values and the lattice parameters a_o = 4.593Å and c_o = 2.959Å determined by Cromer and Herrington (10), we find the interstitial diffusion channels

Table I. Ionic radii

Ion	Radius (9), Å
Cr^{3+}	0.69
Fe^{3+}	0.64
Co^{2+}	0.74
Ni^{2+}	0.72
Ni^{3+}	0.62

(8) to consist of chains of "voids" of approximately 0.77Å radius, joined by deformed regions of comparable cross-sectional area. Thus, the observed rather rapid interstitial diffusion of the transition metal ions(ionic radii given in Table I) is understandable. The much larger rare earth ions [R (Yb^{3+}) = 0.94Å to R (Ce^{3+}) = 1.11Å (9)] do not give measurable diffusion even at a temperature (1200°K) well above those required to make the transition metal ions mobile.

An interesting aspect of rutile is that all of the paramagnetic ions we have diffused into it, with the notable exception of Ni, are preferentially found on substitutional sites, as shown by our paramagnetic resonance studies. This is in agreement with the results reported by Gerritsen (11) for rutile with impurities incorporated during crystal growth. [In the case of Fe^{3+} incorporated at growth, paramagnetic resonance studies (12) indicated that over 70% of all the iron was in a substitutional site.] The fact that the bulk of the ions are found on substitutional sites argues strongly for rapid, energetically preferred reactions in the crystal in which interstitial transition metal ions (except Ni) are captured at vacant Ti sites. Whether there is a valence change accompanying these reactions is at present unknown.

The transition metal ions can be applied to the surface of the crystal prior to diffusion in any of a number of ways. We have used metallic evaporation in a vacuum successfully; alternatively, we have coated the surface of the crystal with an alcohol solution of the transition metal nitrate or acetate, which we subsequently evaporated to remove the solvent. Upon heating to diffusion temperatures, the nitrate or acetate decomposed, leaving an oxide residue that acted as the dopant source for the diffusion. We have also immersed the rutile crystal, at the diffusion temperature, in a vapor of $FeCl_3$ or $CrCl_3$, both of which react at the crystal surface to yield $TiCl_4$, which comes off as a vapor.

Based on visual examination of the coloration induced by diffusion, all transition metal ions have approximately the same diffusion rate, although nickel diffuses perhaps twice as fast as iron; chromium also diffuses somewhat faster than iron. While accurate diffusion constants have not been measured, we estimate $D \approx 10^{-6}$ cm²/sec for temperatures of about 1000°C Chemical analysis indicated that we were able to incorporate over 0.04% Fe (by weight) by diffusion, and much higher concentrations can presumably be achieved (13). At our highest doping levels of Fe we observed paramagnetic resonances that could not be associated with simple substitutional sites. These might be due to interstitial ions or to substitutional sites with associated lattice defects (other impurity ions on adjacent sites, oxygen vacancies, interstitial Ti^{3+} ions, etc.). We have prevented loss of oxygen ions during diffusion, with attendant nonstoichiometry (14), by carrying out the diffusion in an atmosphere of flowing oxygen.

By controlling the amount of transition metal ion applied to the surface of a rutile crystal, a predetermined amount of dopant can be introduced into the crystal in a few hours by holding it at readily attainable temperatures. Since it apparently is very difficult to control closely the doping level when the transition metals are introduced during crystal growth, this technique makes possible many experiments requiring a controlled doping concentration that otherwise would be difficult to do.

Manuscript received Sept. 24, 1965; revised manuscript received Nov. 8, 1965.

Any discussion of this paper will appear in a Discussion Section to be published in the December 1966 JOURNAL.

REFERENCES

1. A. Van Hippel, J. Kalnajs, and W. B. Westphal, *J. Phys. Chem.*, **23**, 779 (1962).
2. V. N. Bugomolov, *Soviet Phys.-Solid State*, **5**, 1468 (1964).
3. O. W. Johnson, *Phys. Rev.*, **136**, A284 (1964).
4. H. P. R. Frederikse, *J. Appl. Phys. Suppl.*, **32**, 2211 (1964).
5. J. A. Van Raalte, MIT Lab. for Insulation Res., Tech. Rept. 195, Nov. 1964.
6. L. C. Morris and D. J. Miller, *IEEE Trans. on Microwave Theory and Tech.*, **MTT-12**, 421 (1964).
7. L. C. Morris and D. J. Miller, *IEEE J. Quantum Electronics*, **QE-1**, 164 (1965).
8. H. B. Huntington and G. A. Sullivan, *Phys. Rev. Letters*, **14**, 177 (1965).
9. L. Pauling, "The Nature of the Chemical Bond," Cornell University Press, 3rd ed. (1960).
10. D. T. Cromer and K. J. Herrington, *J. Am. Chem. Soc.*, **77**, 4708 (1955).
11. H. J. Gerritsen, "Low Symposium on Paramagnetic Resonance," Vol. 1, p. 3, Academic Press, New York (1963).
12. E. S. Sabisky, Private communication.
13. A. H. Webster and N. F. H. Bright, *J. Am. Ceram. Soc.*, **44**, 112 (1961).
14. F. A. Grant, *Rev. Mod. Phys.*, **31**, 646 (1959).

The Phase Diagram of the BI_3-SiI_4 System and Its Relationship to Zone Refining

A. F. Armington

Air Force Cambridge Research Laboratories, Office of Aerospace Research, Bedford, Massachusetts

and E. O. Fisk

Wentworth Institute, Boston, Massachusetts

Experiments with zone refining have indicated unfavorable effective segregation coefficients[1] for silicon tetraiodide (SiI_4) in boron triiodide (BI_3) and for boron triiodide in silicon tetraiodide (1, 2). In order to determine whether these segregation coefficients were due to experimental problems or to a high equilibrium segregation coefficient, the authors have constructed the phase diagram for the system BI_3-SiI_4. A rough curve for the liquidus portion of this diagram was published previously (3), but the solidus portion needed for zone refining evaluation was not reported.

Two methods were used in this study. Usually the phase transitions were determined by thermal analysis

[1] The segregation coefficient is $K = C_S/C_L$ where C_S is the impurity concentration of solid after zone refining and C_L is the impurity concentration in the liquid zone.

using the cell shown in Fig. 1. With this apparatus, melting of the samples could be examined prior to placement of the cell into a Dewar flask. Measurements were made using a bare copper constantan thermocouple immersed into the sample through the hollow paddle-type stirrer. This was found to be more sensitive than the use of a thermocouple inserted in a well. The thermocouple output voltage was monitored on a 0-400 μv potentiometric recorder (L&N Speedomax G). A potentiometer (Rubicon model No. 2748) was used to compensate part of the thermocouple voltage with a precisely known voltage. This "bucking" voltage was changed each time the pen reached the edge of the chart; thus the cooling curve consisted of a number of successive curves on the chart. Repeated runs on the same mixture were within ± 0.5°C. Variations in the cooling rate provide a small time lag (particularly near the ends of the diagram) so that in general the liquidus temperature is accurate to ± 0.6°C and the solidus to ± 1.2°C.

A potential source of error tending to give lower transformation temperature is the possible presence of hydrolysis products. To test the magnitude of this effect the following checks were made: pure BI_3 containing 0.47% each of I_2 and B_2O_3 showed a melting point lowering of 1.47°C; a BI_3-SiI_4 mixture (59.27% SiI_4) containing 0.34% I_2 showed the liquidus temperature to be lowered by 0.60°C and the solidus temperature to be lowered by 0.72°C.

For dilatometer measurements a simple volume apparatus consisting of a tubular container (of about 10 ml volume) with a capillary tube attached by means of a tapered joint was used. The capillary tube had an internal diameter of approximately 0.7 mm and was approximately 60 cm long. The sample was placed in the container and covered with Dow Corning 704 fluid as a inert liquid. By proper adjustment of the amount of fluid a plot could be made of temperature *vs.* volume (cm of fluid height in the capillary tube). The dilatometer was contained in a water bath in a Dewar flask along with a thermometer, immersion heater, and stirrer. Using the dilatometer it was not possible to obtain eutectic temperature indications for mixed compositions as close to the edges of the diagram as it was with the cooling curves. However, with the dilatometer it was possible to approach the eutectic temperatures from both sides and obtain a more accurate temperature by slowing down the heating and cooling rates, thus narrowing down the distance between the lags in temperature.

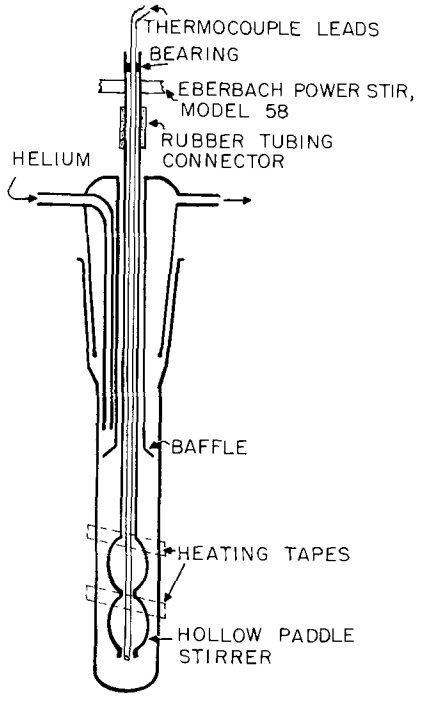

Fig. 1. Sketch of thermal analysis apparatus used for solidus and liquidus temperatures.

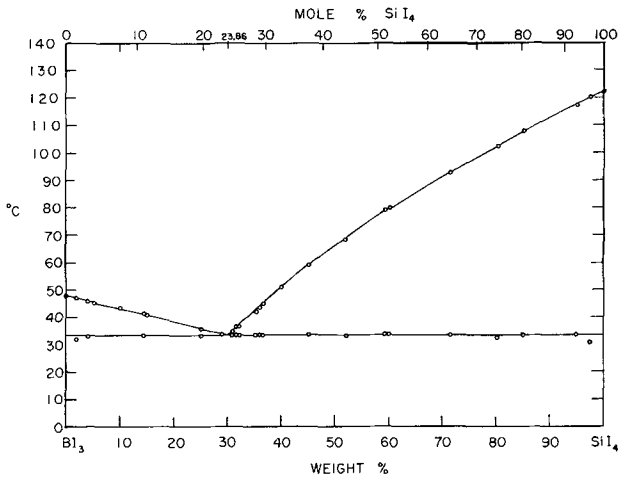

Fig. 2. Phase diagram of the system BI_3-SiI_4

The boron triiodide was distilled from a 30 plate Oldershaw column and was approximately 99.99% pure. The silicon tetraiodide was purified by recrystallizing from toluene and was approximately 99.9% pure; some points were determined using sublimed SiI_4. No difference in results could be detected with this material however.

Since both materials hydrolize readily in the presence of water vapor, they were stored in sealed containers; the weighings were done as rapidly as possible into the thermal analysis cell in air and immediately covered by a flow of dry helium.

The results of the experimental work on the phase diagram are shown in Fig. 2. From this, it can be seen that the phase diagram consists of a simple eutectic system with no evidence of compound formation. The eutectic appears at 30% by weight of SiI_4 and a temperature of 33.8°$\pm$ 1°C. Since Niselson and Chernyaev did not accurately determine the eutectic, but based it on a single point near the eutectic, it is difficult to compare their value with the eutectic reported here. However, their eutectic appears to be in the 23-25 mole % SiI_4 region rather than at the 30 mole % SiI_4 value found in this study. Using the equipment discussed in the previous section, the authors were not able to detect the solidus points below 2% or above 97.5% SiI_4.

Thus the maximum equilibrium segregation coefficients would be 0.028 for BI_3 in SiI_4 and 0.067 for SiI_4 in BI_3. Since these values are markedly lower than the experimental values of 0.42 for the former and about one for the latter, it is evident that the failure of zone purification in these cases is not due to high equilibrium segregation coefficients, but is due to experimental conditions. In both cases cited here, considerable fracture of the solid was observed at the freezing interface and the authors believe the filling of the cracks with impure liquid could be responsible for the failure of the zone purification of these materials.

Acknowledgment

The authors would like to acknowledge Major Guy H. Moates, AFCRL, for his helpful discussions on this work. Part of this work was sponsored by Contract AF19(604)-8503 with Wentworth Institute.

Manuscript received Sept. 2, 1965.

Any discussion of this paper will appear in a Discussion Section to be published in the December 1966 JOURNAL.

REFERENCES
1. A. F. Armington, R. F. Mitchell, and G. F. Dillon, *Trans. AIME*, **230**, 351 (1964).
2. B. Rubin, G. H. Moates, and J. R. Weiner, *This Journal*, **104**, 656 (1957).
3. L. A. Niselson, *Zn. Neorgan. Khim.*, **5**, 1564 (1960).
4. J. T. Buford and R. J. Starks, "Ultrapurification of Semiconductor Materials," M. S. Brooks and J. K. Kennedy, Editors, p. 25, MacMillan Company, New York (1962).

Tetragonal Germanium Dioxide Layers on Germanium

W. A. Albers, Jr., E. W. Valyocsik, and P. V. Mohan

Research Laboratories, General Motors Corporation, Warren Michigan

The desirability of exploiting as-grown oxide layers of germanium and silicon for diffusion masking and electronic surface passivation in semiconductor device technology has been recognized for some time. In recent years this concept has been unambiguously successful in the fabrication of silicon devices. A similar development for germanium devices has not been forthcoming because the oxide that naturally forms on a germanium surface is chemically very reactive. Naturally occurring GeO_2 invariably assumes either an amorphous or an hexagonal (hex) crystalline state. Germanium dioxide can also occur in a tetragonal (tet) crystallographic modification (1, 2). An examination of the chemical and physical properties of the tet GeO_2, as listed in Table I, suggests that it might provide the same advantages for germanium devices as SiO_2 does for silicon devices. In order to test this conjecture, a means of preparing germanium specimens with tet oxide layers had to be developed. The purpose of this note is (*a*) to report a method which we have employed for obtaining tet oxide layers on germanium and (*b*) to describe preliminary observations on the semiconductor surface properties as influenced by the oxide.

Our approach to the preparation of tet oxide layers on germanium centered on the fact that the hex form can be completely converted to tet by a solid-solid phase transformation at relatively low temperatures (2-4). This transformation can be effected either by heating hex powders in the presence of small quantities of a mineralizer, such as an alkali-metal salt, to temperatures in the 800°-1000°C range at atmospheric pressure, or by heating to temperatures in the 300°-600°C range under several hundred atmospheres of pressure (hydrothermally). We confined our attention to the first of these. The hydrothermal conversion of GeO_2 layers has been investigated in another laboratory (5).

The experimental program consisted of two parts: (*a*) a detailed study of the transformation kinetics of bulk powders employing 1% by weight Li_2CO_3 as the mineralizer, and (*b*) an investigation of the direct conversion of as-grown crystalline oxide layers on germanium employing lithium carbonate to promote the phase transformation. The study of bulk powders was carried out in the hope that it would provide a description of the transformation mechanism which could be applied to the conversion of as-grown hex oxide layers. Only the pertinent aspects of the bulk conversion work are reported here; a detailed report will be published elsewhere (6).

Table I. Properties of germanium and its crystalline oxides

Property	Germanium	Hexagonal	Tetragonal
Coordination	Tetrahedral	Tetrahedral	Octahedral
Crystal type	Diamond	Quartz	Rutile
Density @ 25°C, g/ml	5.35	4.228	6.239
Molar volume, cc	13.57	22.24	16.77
Melting point, °C	937	1116 ± 4	1086 ± 5
Transition point, °C	—	1033 ± 10	1033 ± 10
Index of refraction	4.0	1.735	2.05-2.10
Thermal coefficient of expansion	61 × 10^{-7}	95 × 10^{-7}	~60 × 10^{-7}*
Solubility in H_2O @ 25°C, g/liter	Insoluble	4.53	<0.005
Action of HF	None	Reacts very rapidly	None
Action of HCl	None	Reacts rapidly	None
Action of 5*N* NaOH @ 100°C	None	Dissolves rapidly	Dissolves very slowly

* Approximate average of several crystallographic directions [see J. F. Sarver, *J. Amer. Ceram. Soc.*, 46, 195 (1963)].

The experimental procedure for the bulk powder transformation studies involved baking commercially available hex GeO_2 (obtained from K & K Laboratories, Plainview, New Jersey), to which had been added 1% by weight Li_2CO_3, at temperatures in the range 800° to 1000°C. Small portions of the powder were extracted at certain intervals and analyzed for relative weight percentages of hex and tet GeO_2 by x-ray diffraction techniques (4). This procedure was repeated for several different temperatures in the above range. The resulting data are summarized in Fig. 1 where the fraction, *f*, of hex material transformed is plotted *vs.* the temperature, *T*, with reaction time as a parameter.

The samples for investigating the conversion of as-grown oxide layers were prepared from oriented (111) single crystal germanium slices. After lapping and etching by standard methods, they were oxidized in several ways. One of these was direct oxidation in wet oxygen at 500°C. A second method consisted of anodic oxidation in a 0.25*N* solution of sodium acetate in glacial acetic acid and a third involved chemical oxidation in concentrated (15*N*) nitric acid. X-ray and electron diffraction observations of the resulting oxide layers revealed that the thermally grown oxide was amorphous while those prepared anodically were either amorphous or hexagonal depending on a number of factors. The samples that were oxidized in concentrated HNO_3 were invariably the hex crystalline form.

Attempts to convert these oxide layers were carried out by placing a specimen in a ceramic crucible along

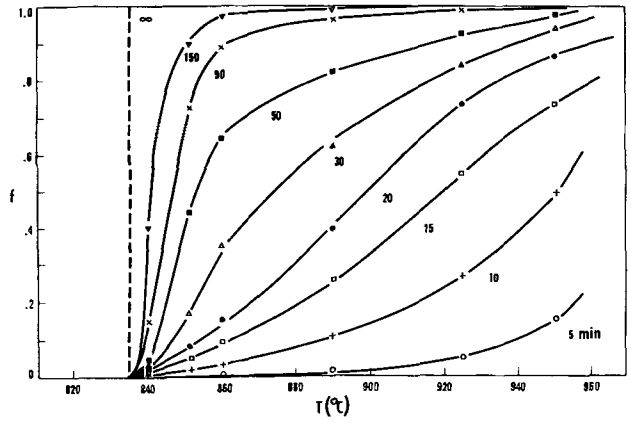

Fig. 1. Fraction of material transformed, *f*, as a function of temperature, *T*, for the hexagonal-to-tetragonal phase transformation of germanium dioxide, with time as a parameter.

with either pure Li_2CO_3 or hex GeO_2 powder containing 1% by weight Li_2CO_3. The crucible was covered with a loosely fitting lid and heated to temperatures in the 700°-900°C range for periods varying between several hours and a day. The crystalline form of the oxide layer was then determined by electron diffraction or by chemical techniques based on the relative reactivity of the two forms as listed in Table I. The samples were weighed before and after the above processing and any weight change noted. All experiments were conducted in a room atmosphere of about 40% relative humidity.

An analysis of data for the bulk powder transformation presented in Fig. 1 suggests the following description of the hex-to-tet conversion (6). The tet phase is nucleated through the formation of alkali-metal oxide groups in the host hex crystallites. These oxide groups promote a local octahedral coordination of germanium atoms consistent with the structure of the tet GeO_2 phase. Since the tet phase is the more stable phase below temperatures of about 1000°C (2), some of these nuclei grow at the expense of the host hex phase. The macroscopic features of this growth are adequately described by the phenomenological theory of diffusion-like phase transformations (7, 8), which takes into consideration the influence of strain in the host and transformed lattices. We believe that strain energies play an important role in the GeO_2 phase transformation in view of the large specific volume difference between the hex and tet phases (see Table I).

The results of the conversion of as-grown oxide layers can be summarized as follows:

(*a*) In all cases in which pure Li_2CO_3 was employed, the oxidized specimens were destroyed, presumably because of a reaction of the Li_2CO_3 with germanium;

(*b*) Systems employing the 1% Li_2CO_3-99%GeO_2 mixture also resulted in the destruction of the samples when the conversion was attempted above 800°C;

(*c*) Between 700° and 800°C the crystalline oxide layers were completely converted to the tet form when the Li_2CO_3-GeO_2 mixtures were used and reaction times were about 16 hr. No change of weight was observed. Under the same conditions, the samples with amorphous oxide layers remained unchanged.

Several features of the successful oxide-layer conversions are worth noting. For example, the complete conversion of the layer was accomplished at temperatures well below those necessary for conversion of the bulk powders; indeed, Fig. 1 indicates that the bulk transformation rates are essentially zero below about 830°C. Also, the GeO_2 hex powder, which was included in the oxide-layer transformation systems, was not converted to the tet form, consistent with the results of the bulk powder studies.

It appears reasonable that the oxide layers grown on germanium are more highly strained than the bulk powders and that this strain could be responsible for the lower conversion temperature of the oxide layers. As already noted, strain is an important feature of the transformation mechanism and therefore could also account for the differences observed in the conversion kinetics.

The fact that GeO_2 powders had to be included in the systems which resulted in successful oxide layer conversions suggests that GeO plays an important role. It is well established that the vapor of GeO_2 is predominantly GeO at the temperatures of interest (9). Also, considering the reaction $Ge^{(s)} + GeO_2^{(s)} \rightleftharpoons 2GeO^{(g)}$, which we feel is dominant in the destruction of samples in the unsuccessful conversion, the importance of the GeO can be appreciated. Below 800°C the GeO vapor pressure associated with the GeO_2 powder is sufficient to inhibit this reaction from proceeding to the right. On the other hand, above 800°C the reaction apparently proceeds to the right at a rate large enough to etch the germanium sample.

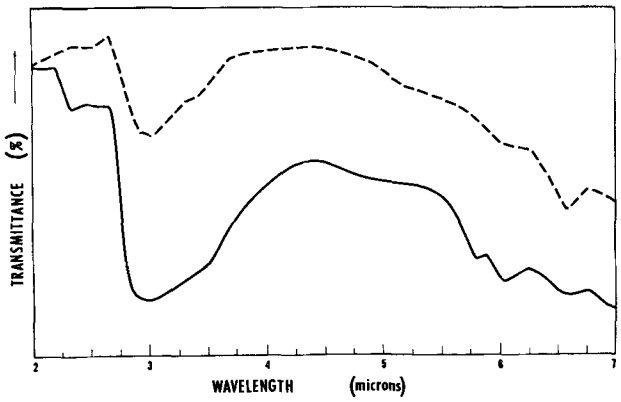

Fig. 2. Infrared spectra of hexagonal (——) and tetragonal (- - -) oxide layers on single crystal germanium. Note the difference in transmittance associated with the O-H stretching frequency near 3μ.

A final remark about the oxide-layer conversion studies pertains to the unsuccessful conversion of amorphous oxide layers under any of the conditions described. We conclude that the crystallinity of the oxide is an important feature of the conversion process. Evidently, a stage of recrystallization is necessary before thermal oxides can be converted.

The successful preparation of tet oxide layers on germanium led us to a consideration of the influence of such layers on the surface properties of germanium. To this end, several single-crystal, p-type specimens of germanium were oxidized in 15*N* nitric acid, and the following experiments were set up:

(*a*) The oxide was converted to tet and checked as a potential diffusion mask by exposing the sample to arsenic vapor for 2 hr at 750°C.

(*b*) Sheet resistivity of the germanium surface was measured before and after conversion to determine the possible effect of the expected diffusion of lithium into the germanium substrate.

(*c*) Infrared absorption of the oxide layers before and after conversion was observed.

(*d*) Field-effect measurements were carried out on samples before and after conversion to characterize the surface electronic properties by a method previously developed (10). All of the oxides in these experiments were converted by heating at 750°C for 16 hr in the presence of the Li_2CO_3-GeO_2 mixture as described earlier.

The results of the diffusion mask experiments were negative. The entire sample was invariably converted to an n-type semiconductor which is characteristic of arsenic doping. We attribute this result to the polycrystalline nature of the oxide layer since large voids between grains were observed by electron microscopy subsequent to the diffusion studies. The sheet resistivity measurements indicated that lithium was not a problem; the resistivity was the same before and after conversion to tet.

A typical set of infrared spectra for an oxide layer, before and after conversion, is presented in Fig. 2. The relatively strong absorption in the 3.0μ wavelength region is associated with the O-H stretching frequency. It is evident that the density of O-H groups is larger for hex than for tet. The field-effect studies revealed that, although both germanium surfaces were n-type, the surface bearing the tet oxide layer was invariably less n-type than the surface covered by a hex oxide. Since the O-H of the oxides can be associated with adsorbed water, known to cause germanium surfaces to exhibit n-type properties (11), the above results support the conjecture that water vapor in the atmosphere will not influence germanium specimens protected by tet oxide as seriously as those bearing hex oxide layers.

Acknowledgment

The authors gratefully acknowledge the capable assistance of Miss Agnes Forster (x-ray diffraction) and Mr. T. R. McKinney (electron diffraction) of the General Motors Research Laboratories, and the encouragement and active participation in many aspects of this work provided by personnel of the Delco Radio Division of General Motors Corporation.

Manuscript received June 29, 1965; revised manuscript received Nov. 4, 1965. This paper was presented at the San Francisco Meeting, May 9-13, 1965.

Any discussion of this paper will appear in a Discussion Section to be published in the December 1966 JOURNAL.

REFERENCES

1. J. H. Müller and H. R. Blank, *J. Am. Chem. Soc.*, **46**, 2358 (1924).
2. A. W. Laubengayer and D. S. Morton, *ibid.*, **54**, 2303 (1932).
3. J. F. Sarver and F. A. Hummel, *J. Am. Ceram. Soc.*, **43**, 336 (1950).
4. Y. Kotera and M. Yonemura, *Trans. Faraday Soc.*, **59**, 147 (1963).
5. Belgian Pat. No. 635971; J. G. Wilkes, Private communication.
6. To be published.
7. D. Turnbull, "Solid State Physics," F. Seitz and D. Turnbull, Editors, Vol. 3, 225, Academic Press, New York (1956).
8. M. E. Fine, "Phase Transformation in Condensed Systems," MacMillan Company, New York (1964).
9. G. A. Bergman, *Zhur. Neorgan. Khimii*, **3**, 2422 (1958); S. Drowart, F. Degreve, G. Verhaegen, and R. Colin, Government Research Report AD-607511, September 1964.
10. W. A. Albers, Jr., and A. M. Rickel, *ibid.*, **109**, 582 (1962).
11. R. H. Kingston, *J. Appl. Phys.*, **27**, 101 (1956).

Growth and Preferential Doping of Zircon and Thorite

A. B. Chase and Judith A. Osmer

Aerospace Corporation, El Segundo, California

Single crystals of stable, transparent metal oxides that can incorporate rare earth ions are of research interest and may also be of value for electronic applications. Zircon ($ZrSiO_4$) and thorite ($ThSiO_4$), an isomorph of zircon, meet these basic requirements. Zircon and thorite are tetragonal crystals and belong to the space group $I4_1/amd$ (1, 2). Naturally occurring zircon has been reported to have Y_2O_3 and U_2O_3 as impurities (3). In the present work, synthetic crystals of both $ThSiO_4$ and $ZrSiO_4$ were readily doped with various lanthanides and UO_2.

Espig has grown crystallites of zircon from Li_2MoO_4 by the use of mass transport techniques for both nucleation and growth of crystals (4). Using similar techniques, Finch *et al.* (5) have grown thorite with $Li_20.2MoO_3$, $Li_20.2WO_3$, or $Na_20.2WO_3$ as solvents. These techniques normally involve placing the solute in a hot zone and rely on either diffusion or diffusion and convection in the solvent to carry the solute to a cooler region to nucleate and grow crystals. Ballman and Laudise have grown crystals of zircon by slow cooling of $Li_20.3MoO_3$ melts (6).

In the present work, crystals as large as 7 mm across have been grown from molten Li_2MoO_4-MoO_3 and doped with UO_2 and various lanthanide ions. The method of crystal growth is similar to that used by Ballman and Laudise. It involves mixing the solute and solvent and relies on programmed cooling for crystal nucleation and growth. Crystal growth runs of 3 to 5 days' duration generally produce crystals large enough for crystal growth and spectroscopic studies.

The melts from which the largest zircons were grown consisted of 3 mole % ZrO_2, 3 mole % Li_2SiO_3, 5-10 mole % Li_2MoO_4, and 84-89 mole % MoO_3. The materials used were 99.7% pure ZrO_2 obtained from the Zirconium Corporation, high-purity grades of Li_2SiO_3 and Li_2MoO_4 (Lithium Corporation and Chemical Procurement Laboratories, respectively), and an analytical reagent grade of MoO_3 (Allied Chemical Corporation). Appropriate amounts of the powders were mechanically mixed and placed in tightly covered 50 to 100 ml standard form platinum crucibles. The crucibles were heated to 1250°C in Super-Kanthal muffle furnaces that have vertical temperature gradients of no more than 0.5°C/in. The crucibles were held at 1250°C for 2 to 8 hr and program cooled at 2° or 4°C/hr to 1000°C. At this temperature the crucibles were removed from the furnaces and allowed to cool to room temperature. The crystals were separated from the contents of the crucibles by leaching with hot 25% ammonia solutions. The weight loss of a standard run was between 25-35 w/o (weight per cent).

The procedure used to grow thorite was similar to that used for zircon. The ThO_2 was 99.9% pure (purchased from the Lindsay Company). Silicon dioxide was used instead of Li_2SiO_3 in these runs. All other materials were the same as those used for the zircon.

The primary differences in the procedure were that a lower soaking temperature and a different flux composition were necessary for the growth of thorite. Finch (3) indicated that only thorite could be grown below 1225° ± 10°C, and only huttonite could be grown above this temperature.[1] Having substantiated this conclusion, we used a soak temperature of 1220°C with cooling rates of 2°-4°C/hr. The crucibles were removed from the furnaces at 900°C.

The melts used for thorite contained 3 mole % ThO_2, 3 mole % SiO_2, 74 mole % Li_2MoO_4, and 20 mole % MoO_3. Huttonite was obtained from a melt consisting

[1] Huttonite ($ThSiO_4$), the high-temperature polymorph of thorite, is a monoclinic crystal belonging to space group $P2_1/n$ (7) and is retained metastably at room temperature when grown from this system.

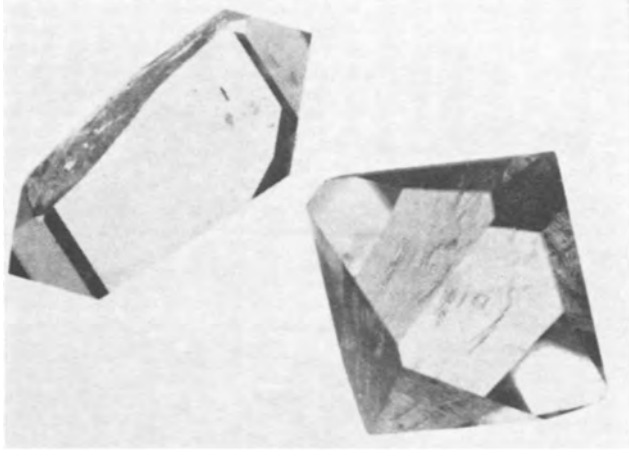

Fig. 1. Zircon crystals showing the change in habit due to rare-earth doping. The crystal on the right is from a doped run, the one on the left from an undoped run. Magnification approximately 8X.

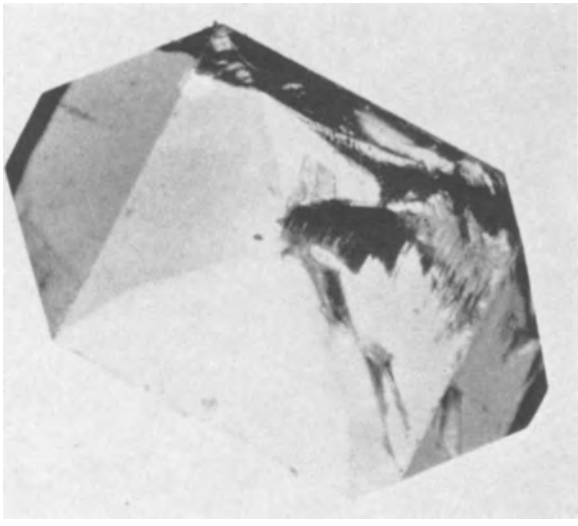

Fig. 2. A UO_2-doped zircon crystal with the dark areas more heavily doped with UO_2 than the light areas. Magnification 12X.

of 5 mole % ThO_2, 5 mole % SiO_2, 70 mole % Li_2MoO_4, and 20 mole % MoO_3 with a maximum temperature of 1250°C. Because the solubility of $ThSiO_4$ in Li_2Mo_4-MoO_3 fluxes increases with increasing MoO_3, it was necessary to use 10% ThO_2 and 10% SiO_2 to produce thorite with a MoO_3-to-Li_2MoO_4 ratio of 1 to 1.

Utilization of the above mixtures for both thorite and zircon provided between 5 and 20 single crystals of good optical quality per run. The crystal sizes in a run varied from 2 to 7 mm long, and the yield for a normal run was 60 to 80% of the starting material. Most of the crystals grew on the bottom of the crucible with a few attached to the sides of the crucible below the melt surface. The largest crystals trapped small amounts of solvent in layers parallel to the major growth planes, during early growth. The normal habit of the crystals from an undoped melt was that of a {110} rod with {111} terminating pyramids.

The habits of the crystals changed when the mixtures were doped with the lanthanide ions. The {111} faces became larger as the lanthanide doping was increased, until, at about a 1 to 3 ratio of the lanthanide sesquioxide to ZrO_2 in the melt, the {110} faces disappeared completely. Figure 1 is a photograph of a crystal from an undoped run and one from a doped run. With up to 0.8 mole % lanthanide ions in the melt, the resultant crystals were clear. Above this level of doping the crystals were cloudy with what appeared to be an unidentified exsolved phase. The experimental evidence implies that the disappearing {110} faces are relatively uncontaminated and grow out of existence as the growth rates of the {111} faces decrease owing to contamination. The particular mechanism of habit change is similar to that described by Frank (9) when an impurity ion is adsorbed onto a face, thereby retarding the propagation of steps on that face and decreasing the growth rate of that face.

While the lanthanide ion changed the habit of zircon, UO_2 contamination had no appreciable effect on the habit. However, the amounts of UO_2 that were incorporated in the crystal varied in direct relationship to the different faces on the crystal. The differences are readily apparent by the color of the crystal. The volume of the material below the {111} faces is a dark green and that below the {110} faces is light green. Figure 2 is a photograph of such a crystal. Spectroscopic analysis of the absorption spectra of the crystals indicated that the color was due to differences in the concentration of the U^{4+} ion. Spectrographic analysis showed 0.08 mole % UO_2 incorporated in a crystal obtained from a run where the UO_2-to-ZrO_2 ratio in the melt was 1 to 2. The U^{4+} ion is much larger than the Zr^{4+} ion and presents a fairly difficult size fit problem for replacement of a Zr^{4+} ion in the lattice.[2] This may account for the relatively small amount of U^{4+} incorporated in the lattice.

Acknowledgment

The authors wish to express appreciation to P. Kisliuk who identified U^{4+} by analysis of the absorption spectra of the crystals. This work was supported by the United States Air Force under Contract No. AF 04(695)-469.

Manuscript received Sept. 2, 1965.

Any discussion of this paper will appear in a Discussion Section to be published in the December 1966 JOURNAL.

REFERENCES

1. Hassel, *Struktuberichte*, **1**, 347, 408 (1926).
2. Frondel, *Am. Mineralogist*, **38**, 1007 (1953).
3. A. N. Winchell and H. Winchell, "Elements of Optical Mineralogy," Part II, 2nd ed., p. 494, John Wiley & Sons, Inc., New York (1951).
4. Hermann Espig, *Chem. Tech. (Berlin)*, **12**, 327 (1960).
5. C. B. Finch, L. A. Harris, and G. W. Clark, *Am. Mineralogist*, **49**, 782 (1964).
6. A. A. Ballman and R. A. Laudise, *J. Am. Ceram. Soc.*, **48**, 130 (1965).
7. Pabst, *Am. Mineralogist*, **36**, 60 (1951).
8. F. C. Frank, "Growth and Perfection of Crystals," p. 411, John Wiley & Sons, Inc., New York (1958).
9. L. Ahrens, *Geochim. et Cosmochim. Acta*, **2**, 155 (1952).

[2] Ahrens (9) gives an atomic radius of 0.97 for U^{4+} and 0.79 for Zr^{4+}.

Incorporation of Zinc into Epitaxial GaAs Using Diethyl Zinc

R. W. Conrad and R. W. Haisty

Texas Instruments Incorporated, Dallas, Texas

Generally two approaches have been taken in incorporating acceptor impurities into epitaxially grown III-V semiconductors (*A*) doped source material, and (*B*) a separate reservoir of the dopant inside the deposition system, heated to provide an appreciable vapor pressure.

Method (*A*) has been applied to zinc-doping of epitaxial GaAs (1) and $GaAs_xP_{1-x}$ (2) and found to be unsatisfactory. Reproducible doping levels could not be obtained, apparently because of rapid depletion of the dopant in the source material, perhaps by outdiffusion.

Method (*B*) has been employed with some success to the doping of epitaxial GaAs (3) and $GaAs_xP_{1-x}$ (2) with elemental cadmium. This method, however, has several disadvantages, *viz.*, very accurate temperature control of the dopant is required, the dopant cannot easily be turned on and off abruptly, and nonconstant doping profiles cannot easily be produced except by using elaborate temperature-programming equipment.

Recent work in our laboratories with the volatile organometallic diethyl zinc (bp 118°C) shows this

material to be very promising for the controlled introduction of zinc into epitaxial GaAs.

Epitaxial GaAs was prepared on chromium-doped, semi-insulating (100) oriented GaAs substrates in an open-tube deposition system. Undoped, pulled-crystal GaAs was used as source material and $AsCl_3$ in hydrogen as the transport agent. Source and deposition temperatures were 840° and 735°C, respectively. The background excess donor concentration of undoped epitaxial GaAs prepared in this system was typically 1-2 x $10^{16}cm^{-3}$. Diethyl zinc from the Gallard-Schlesinger Chemical Company was used without further purification.[1] Figure 1 illustrates the deposition and doping systems.

A very small flow of purified hydrogen is metered into the diethyl zinc reservoir where it is saturated with diethyl zinc vapor, then swept by a dilution hydrogen flow (35 cc/min) into the deposition zone of the reactor. Initial experiments in which the hydrogen was introduced through a capillary tip below the surface of the diethyl zinc were unsuccessful because of persistent clogging of the tip by a white solid. This solid, although not positively identified, was probably zinc oxide produced by the reaction of diethyl zinc with traces of oxygen known to be present in the helium used as a flush gas. The ultrafine quartz frit situated at the exit end of the dope tube serves to restrict the passage of particulate matter such as zinc oxide or carbonaceous material. After several doping experiments the quartz frit would become discolored, but the material causing the discoloration was present in only trace amounts and could not be identified.

A series of GaAs depositions was made with various rates of flow through the diethyl zinc system maintained either at room temperature or 0°C. Figure 2 shows the variation of hole concentration in the deposits (from room temperature Hall measurements) as a function of dopant flow rate. In general, the surface quality of the deposits was very good at doping levels $< 10^{19}$ cm^{-3}. Scanning reflection x-ray topographic examination (4) of several of these samples did not reveal any macroscopic inclusions. At $> 10^{19}$ cm^{-3}, however, several samples exhibited what appeared to be small inclusions, when examined with transmitted infrared light. Also, at these high doping levels, deposition rates were substantially reduced, and surface quality degraded. Figure 3 shows the variation of room temperature hole Hall mobility with hole concentration. Included for comparison are the data of Meyerhofer (5) for zinc- and cadmium-doped bulk GaAs.

Two possible explanations for the decrease in deposition rate and surface quality at high dopant flow rates are (*a*) a dilution effect, in which the depositing species are literally swept away from the vicinity of the substrate by the high gas flow issuing from the dope tube outlet and, (*b*) an inhibition of deposition by the high concentration of zinc and/or carbonaceous material smaller than the pore size of the quartz frit. To clarify this, epitaxial GaAs was deposited with a high flow of hydrogen only issuing from the dope outlet tube (20 cc/min plus the usual dilution flow of 35 cc/min). The rate of deposition was drastically reduced and the surface quality seriously degraded, indicating that the dilution effect is a contributing factor in the production of poor quality deposits. To evaluate more fully the role of dopant concentration, it will be necessary to employ a more volatile zinc compound such as dimethyl zinc.

The room temperature hole mobilities in diethyl zinc-doped epitaxial GaAs compare favorably with the published values for zinc- and cadmium-doped bulk GaAs, implying that carbon, if incorporated, is not seriously affecting the electrical properties. An improvement in the hole mobilities in diethyl zinc-doped epitaxial GaAs should be realized by reducing the background donor impurity concentration.

Experiments are presently being conducted in these laboratories on the doping of various epitaxial III-V

[1] Caution should be used in handling this material, since it is spontaneously flammable in air and highly toxic.

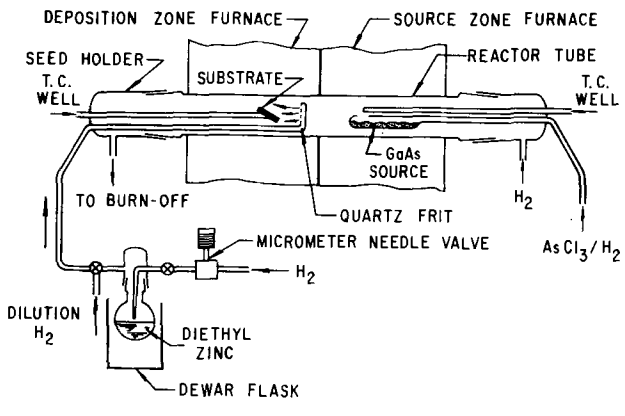

Fig. 1. System for introducing diethyl zinc into GaAs vapor deposition reactor.

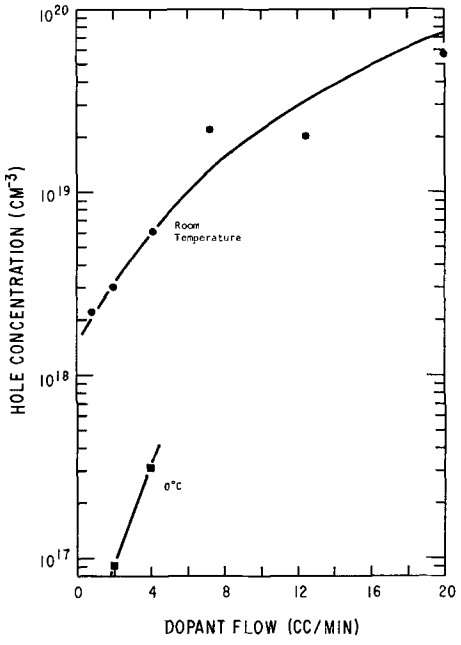

Fig. 2. Variation of hole concentration (at 24°C) with dopant flow; •, diethyl zinc at room temperature; ■, diethyl zinc at 0°C.

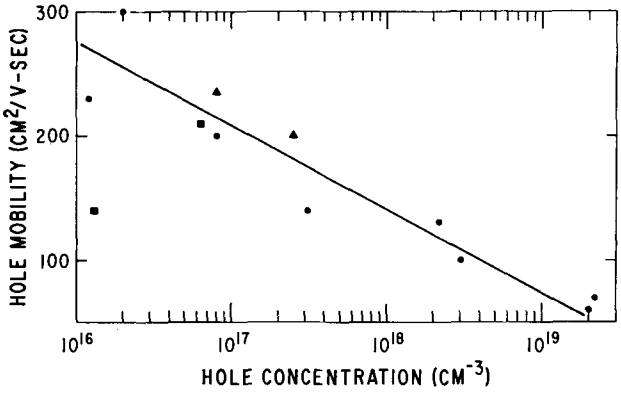

Fig. 3. Variation of hole mobility (from room temperature Hall measurements) with hole concentration; •, our data, ▲, ■, data of Meyerhofer for zinc and cadmium, respectively.

compounds and alloys with several zinc and cadmium alkyls.

Acknowledgments

The authors wish to thank E. W. Mehal and L. G. Bailey for their helpful criticism and William Neff for his aid in preparing the samples. This work was supported by the Electronics Technology Division of the Air Force Avionics Laboratory under Contract No. AF 33(615)-1272.

Manuscript received Aug. 2, 1965; revised manuscript received Nov. 3, 1965.

Any discussion of this paper will appear in a Discussion Section to be published in the December 1966 JOURNAL.

REFERENCES

1. V. J. Silvestri and F. Fang, *This Journal*, **111**, 1164 (1964).
2. R. H. Cox, To be published.
3. E. W. Mehal and G. R. Cronin, Submitted to *Electrochem. Technology*.
4. J. K. Howard and R. D. Dobrott, *Appl. Phys. Letters*, **7**, 101 (1965).
5. D. Meyerhofer, International Conference on Semiconductor Physics, Prague, 1960, p. 958, Academic Press, New York.

Purification of Lithium Metal by High-Vacuum Fractional Distillation

Paul H. Schmidt

Bell Telephone Laboratories, Incorporated, Murray Hill, New Jersey

Lithium, the lightest of all metals, has a high thermal conductivity, low melting point, and small thermal neutron cross section. It is, therefore, of interest to nuclear scientists as a heat transfer fluid. Its advantages as compared to other alkali metals are, however, limited in part by the presence of impurities both gaseous and metallic which greatly accelerate the corrosion process of lithium with its container material. High purity is also a requirement for the investigation of the electronic band structure of a metal, this being the primary motivation for the present study.

The purest commercially available lithium produced today approaches 99.99% purity (Table I) and is prepared chiefly by the electrolytic reduction of a fused eutectic mixture of lithium chloride and potassium chloride (1). Purification beyond this level either by zone refining (2) or by distillation (3-7) has not been achieved. Attempts to purify lithium by vacuum distillation have generally been ineffective because of the small differential vapor pressures between lithium and its contaminants at high temperatures. Furthermore, the improper choice of suitable container materials for still construction and marginal design and operation has led to the belief that the purification of lithium metal by vacuum distillation was not feasible. Lithium metal of 99.9999% purity,[1] however, has been prepared in this laboratory by high-vacuum fractional distillation.

Apparatus

Distillations were carried out in a 2½ in. diameter 16½ in. long stainless steel column (Fig. 1). All seams were helium arc welded during fabrication of the retort. A 0.010 in. thick rolled molybdenum sheet with a ¼ in. overlapping seam was used as the liner. It extended from the top to the bottom of the chamber. A molybdenum crucible was used to contain the raw material. Ten perforated molybdenum sieve plates served as the rectifying portion of the column producing approximately a ten to one reflux ratio and a very low holdup at operating temperatures. Each plate, 0.010 in. thick, contained four ⅜ in. diameter holes and was rotated from the adjacent plates by 45° to prevent vapor channeling. The plates were held together with three molybdenum rods and separated with molybdenum tube spacers 0.292 in. long. The entire assembly fit snugly into the chamber for positive thermal contact with the wall and rested on the

[1] Purity as determined from the analysis of detectable metallic contaminants.

Table I. Emission spectrographic analysis of raw material in ppm

	Charge for runs 1-3	Charge for runs 4-5
	Foote Mineral Company Paoli, Pennsylvania	Lithium Corporation of America Bessemer City, North Carolina
Al	1	1
Ba	2	2
Ca	7-10	10-300
Cu	4	4
Fe	5	2-30
Ga	2	—
K	5-50	2-5
Mg	2	2
Na	2-30	1-40
Si	6-10	5-50

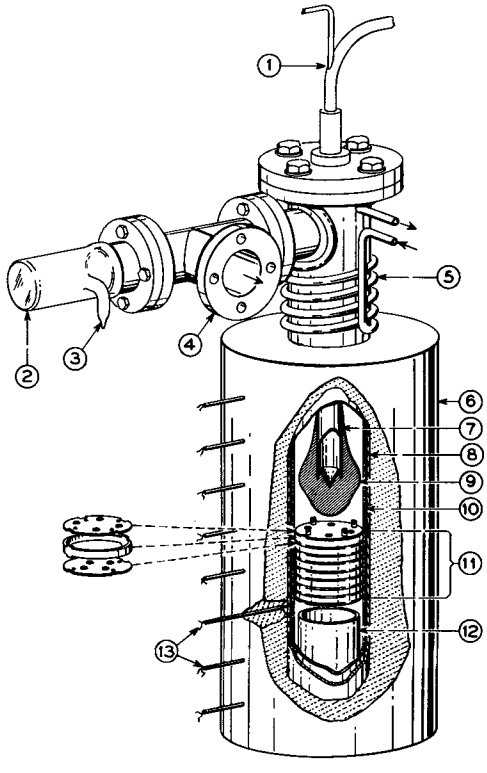

Fig. 1. Diagramatic view of the distillation apparatus: 1, collector adapter (water cooled); 2, Pyrex viewing port; 3, roughing pump line; 4, to diode type getter-ion pumping system; 5, copper cooling coils; 6, nichrome wound furnace; 7, collector (321 stainless steel); 8, shell (321 stainless steel); 9, distillate; 10, molybdenum liner; 11, molybdenum baffle plates; 12, molybdenum crucible (100 cc capacity); 13, thermocouples to monitor zone temperatures.

crucible. A ¾ in. diameter stainless steel tube, closed and pointed at one end, was welded to the inside of the top flange. It projected downward into the column and served as the solid-state condenser. The temperature of the condenser could be maintained at any desired temperature in the interval from —196° to 800°C by cooling liquid nitrogen, gas, or water or by heating with an electric heater.

The column was heated with a nichrome wound resistance furnace. A temperature gradient of 2°-5°C was maintained from plate to plate of the rectifying column by shunting windings on the furnace. The temperature during distillation was controlled to ± 0.5°C using a digital set point proportional controller and continuously monitored using seven thermocouples spaced along the column's length. The upper portion of the still, not in the furnace, was water-cooled.

A 15 l/sec diode-type getter-ion pumping system employing 1½ in. diameter tubing and copper O-ring seals was used in conjunction with the distillation chamber. The pumping system incorporated a viewing window to permit observation of the light fraction as it condensed in the water cooled section of the still. A valve between the ion-pump and the chamber permitted removal of the still, under vacuum, to a dry box for sample removal.

Container Materials

Choice of suitable container materials both for distillation and sampling procedures was essential for the success of these experiments. Since most metals are severely corroded by liquid lithium and lithium hydroxide the choice of a container material is difficult. The metals modybdenum,[2] tantalum, and tungsten are perhaps the most resistant to corrosion by liquid lithium (8, 9). Unfortunately, these metals are difficult to weld and fabricate and furthermore become embrittled on exposure to the atmosphere at distillation temperatures. The use of these metals was restricted to structures within the distillation chamber (liners, crucibles, and baffles). Stainless steel types 304 and 321 were the materials selected for structures exposed to the atmosphere. The use of a molybdenum liner in the distillation chamber prevented, for the most part, excessive contact of liquid lithium with the stainless steel shell. Failures due to corrosion were not experienced even after 2000 hr at 500°C using the molybdenum liner.

Experimental Procedure

Careful chemical cleaning of the still and all its associated components preceded each distillation. The still was then assembled and attached to the pumping system. The column was then baked overnight at 700°C in vacuum. The bakeout served the twofold purpose of reducing to a minimum those volatile contaminants not previously chemically removed and insured that no leaks had occurred either during the chemical cleaning procedures or through corrosion from a previous distillation. The molybdenum crucible was filled with lithium metal, allowed to cool, and then loaded into the still along with the rectifying column. Following the initial pumpdown to 1×10^{-9} Torr, the column temperature was slowly increased to 400°-550°C. Typical vacuum conditions at distillation temperatures ranged from 5×10^{-6} to 4×10^{-8} Torr measured at the ion pump. During this phase of the distillation those impurities having a high vapor pressure were separated from the bulk charge, enriched in the rectifying baffles, and driven up the column. The collector was maintained at a high temperature preventing condensation at this time. Approximately 10-25% of the charge was driven to the top of the column and later discarded, the amount being determined by the volatile impurity content in the raw material. The collector temperature was then decreased and lithium allowed to condense. By controlling the vapor density through the rectifying baffles and the temperature of the collector, the grain size of the distillate could be varied from finely polycrystalline to very coarsely polycrystalline. Once the desired fraction was collected on the condenser, the still was shut down and allowed to cool under vacuum. Enriched low-vapor-pressure contaminants were thus contained in the balance of the lithium remaining in the crucible and on the baffles. The valve isolating the vacuum system was then closed and the still moved to an argon-filled dry box. Samples were removed from the distillate with molybdenum knives and stored in degassed and prereacted mineral oil.

[2] Solubility ~1 ppm at 950°C.

Discussion

Analysis for residual metallic impurities indicated that group II elements, especially calcium, were the most difficult to remove (Table II). Distillation effects with uranium metal and boric oxide additives to the charge were studied in an effort to change the differential vapor pressures between lithium and its metallic contaminants. Additive amounts were controlled to compensate for the known impurity concentration in the raw material. The results indicate that the addition of uranium metal as an additive to the charge did not affect the purity of the distillate. It was observed, however, that addition of a small amount of boric oxide to the charge improved the purity considerably (Table II) (Fig. 2). Only trace amounts of impurities were detectable. In distillations carried out under similar conditions, but in the absence of boric oxide, 14-31 ppm metallic impurities remained in the distillate. The mechanism believed to be responsible

Table II. Emission spectrographic analysis of distilled lithium in ppm

	Run 2			Run 3		Run 4		Run 5			
	Temperature 520°C			Temperature 500°C		Temperature 450°C		Temperature 450°C			
Element	Tops	Distillate	Bottoms	Tops	Distillate	Tops	Distillate (plus B_2O_3)	Tops	Distillate	Mineral oil	B_2O_3
Ag			0.5	<1							
Al	2	6	5	2	2	4	0.1	1	1		<1
Ba			3						4		
Ca	5	6	9	8	8	7	0.7	8	5		1
Co											
Cr											
Cs											
Cu	0.5	0.5	7	2	<1	<1		0.5	0.1		
Fe			2	2	1	1		1	0.5		1
Ga	4	4	1								
K	5	5	5	3	2	3		3	0.5		
Mg	10	2	2	5	1	2	0.6	2	0.7	tr	<1
Mn				1		0.8		0.5			
Mo											
Na	10	2	2	8	3	1	<0.1	0.8	<0.1	tr	
Ni											<<1
Rb											
Si	6	6	6	5	5	6	0.5	2	2		
Ti											<1
Total	42.5	31.5	42.5	37	23	26	1-2	19	14	tr	~4

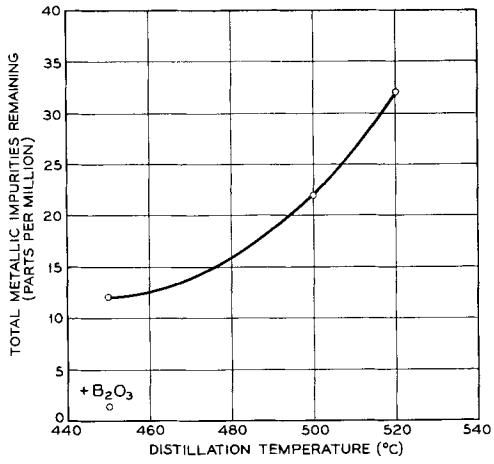

Fig. 2. Total metallic impurities *vs.* distillation temperature. The distillate purity approaches an apparent asymptotic level of approximately 10 ppm at temperatures near 450°C.

for the purity reduction is the formation of a stable oxide.

$$6Li + B_2O_3 \xrightarrow{\text{vacuum}} 3Li_2O + 2B \qquad [1]$$

$$Li_2O + \text{Ca impurities} \xrightarrow{\leftarrow} CaO + 2Li \qquad [2]$$

Reaction [2] favors the formation of calcium oxide which is more stable thermodynamically than lithium oxide. Calcium oxide would be stable at distillation temperatures and not decompose. Separation based on the differential vapor pressures of calcium oxide and lithium would now apply. The stable compound would therefore remain in the "bottoms" on distillation of the lithium charge.

A direct correlation of temperature *vs.* purity is observed during distillation, lower distillation temperatures being associated with higher purities (Fig. 2). This is not surprising in view of the increasing relative volatility α, as temperatures are reduced. Variation of vacuum conditions from 4×10^{-8} to 5×10^{-4} Torr did not seem to affect the distillate purity. Distillation below 450°C did not seem practical, even though greater purity might ultimately be achieved (Fig. 2), since distillation rates are very low (0.005 g/hr at 400°C and 0.042 g/hr at 450°C). At the lowest temperature of the present series of experiments (450°C), the total distillation time was 21 days. Cleaning and bakeout of the chamber and vacuum system required another six days.

Analysis.—The eddy current decay method of measuring resistivity ratios (10) was used as a rapid means of ascertaining the electronic quality and "purity" of lithium samples. Resistivity ratios $\rho_{300°K}/\rho_{4.2°K}$ of the purest commercially available lithium, 99.9-99.99% purity, ranged from 500 [3] to approximately 1000 [4] while ratios as high as 4000 were recorded on samples taken from the distillate of the run using the boric oxide additive. Resistivity ratios measured on samples taken from the distillates of other runs never exceeded 1100. Even though spectrographic analyses indicated a reduction in the total metallic impurity level, the resistivity ratios were not greatly affected. Calcium impurities were thought to affect the resistivity ratios more than any other impurities in these samples.

Table III. Emission spectrographic analysis of lithium carbonate

(Estimated limits of sensitivity for the elements in ppm using standards of 100, 50 10, 4, and 1 ppm)

Ag	<0.1	Cr	<1	Ni	1
Al	<0.1	Cu	<0.1	P	>100
As	100	Fe	<0.5	Pb	1
Au	4	Ga	1	Sb	10
B	<4	Ge	10	Si	<1
Ba	<1	Hg	100	Sn	<1
Be	<4	In	1	Sr	10
Bi	<4	K	<1	Ti	1
Ca	<1	Mg	<0.1	V	1
Cd	4	Mn	<0.1	W	100
Co	4	Mo	<1	Zn	50
		Na	<1	Zr	5

[3] Foote Mineral Company, Paoli, Pennsylvania.

[4] Lithium Corporation of America, Bessemer City, North Carolina.

Samples of lithium metal from different sections in the still as well as the raw material were analyzed for metallic impurities (Table II, Table III). Bulk specimens of lithium metal were used for x-ray fluorescent analyses while lithium carbonate samples were used for analysis by emission spectroscopy. Specimens of metallic lithium were converted to lithium carbonate by reacting the metal with water and carbon dioxide gas. Polypropylene containers were used for the reduction process and platinum containers for drying. Fused silica containers were found to contaminate the samples with 5-30 ppm of silicon. Excellent correlation was obtained for potassium and calcium impurities using the two methods of analysis. The usefulness of x-ray fluorescence was, however, limited by the dilute nature of the other metallic impurities.

A study of the electron spin resonance of bulk metallic lithium specimens (11) at 12 kMc frequency has further substantiated the above analytical data. Using our 4000 residual resistivity ratio lithium metal, the spin resonance line is approximately 0.2 gauss wide, the narrowest line width thus far observed in bulk lithium. Line widths of the raw material are at least a factor of four broader.

Conclusion

Distillations carried out using an additive of boric oxide in the charge yielded a higher purity distillate than distillations without the additive. Distillations carried out at lower temperatures yielded higher purity distillates. Group II elements, especially calcium, were the most difficult impurities to remove by distillation techniques.

Acknowledgments

The author wishes to thank C. C. Grimes for his assistance and constructive criticism regarding still design, K. B. Jefferts for his guidance in vacuum system design and technology, and G. Adams for resistivity ratio measurements. He would also like to thank D. Nash for spectrographic analyses.

Manuscript received July 14, 1965; revised manuscript received Sept. 28, 1965.

Any discussion of this paper will appear in a Discussion Section to be published in the December 1966 JOURNAL.

REFERENCES

1. C. A. Hampel, "Rare Metals Handbook," p. 220, Reinhold Publishing Corp., New York (1956).
2. I. G. D'Iakov and I. R. Khvedchuk, *Fiz. Metal. i Metalloved. Akad. Nauk. S.S.S.R.*, **17** 2, 303 (1964).
3. L. F. Epstein and W. H. Howland, *Science*, **114**, 443 (1951).
4. W. Arbiter and S. Lazeruc, Nuclear Development Corp. of America, Report No. NDA-39 (June 14, (1957).
5. E. E. Hoffman, ASTM Special Technical Publication #272, p. 195 (1953).
6. L. F. Epstein and W. H. Howland, Knolls Atomic Power Lab., Report AECH-1549 (July 2, 1961).
7. Y. F. Bychkov, A. N. Rozanov, B. I. Gromov, and V. I. Cheburkov, "Metallurgy and Metallography of Pure Metals," p. 171, V. S. Yemel'yanov and

A. I. Yevstyukhin, Editors, Gordon and Breach, Science Publishers, Inc., New York (1962).
8. H. W. Leavenworth, R. E. Cleary, *Acta Metalurgica*, **9**, 519 (1961).
9. Y. F. Bychkov, A. N. Rozanov, V. B. Razanova, *Metallurgy and Metallography of Pure Metals*, edited by V. S. Yemel'yanov and A. I. Yevstyukhin (Gordon and Breach, Science Publishers, Inc., New York 1962), p. 178; N. M. Beskorovagnyy and Ye. I. Yakovelev, *Metallurgy and Metallography of Pure Metals*, (Gordon and Breach, Science Publishers, Inc., New York 1962) p. 190.
10. C. P. Bean, R. W. DeBlois and L. B. Nesbitt, J. *Appl. Phys.*, **30**, 1976 (1959).
11. W. M. Walsh, Jr., and L. W. Rupp, Jr., Unpublished work.

Hydrogen Oxidation on Platinum

M. P. Makowski,[1] Ewald Heitz,[2] and Ernest Yeager

Western Reserve University, Cleveland, Ohio

The anodic reaction of hydrogen on platinum has been studied by a number of authors in both acid (1-14, 16) and basic (1, 6, 11-13, 17) media, but some questions continue to exist as to the nature of the results and in particular the kinetics of the reaction. Of particular interest is the work of Frumkin and Aikazyan (5, 6, 17) who found a zero or near zero-order dependence of the anodic limiting current for hydrogen oxidation on the hydrogen concentration in the solution adjacent to the electrode in acid media. These authors used slow sweep voltammetry in con-

[1] Present address: Clevite Research Center, Cleveland, Ohio.

[2] Present address: DECHEMA, Frankfurt/Main, Germany.

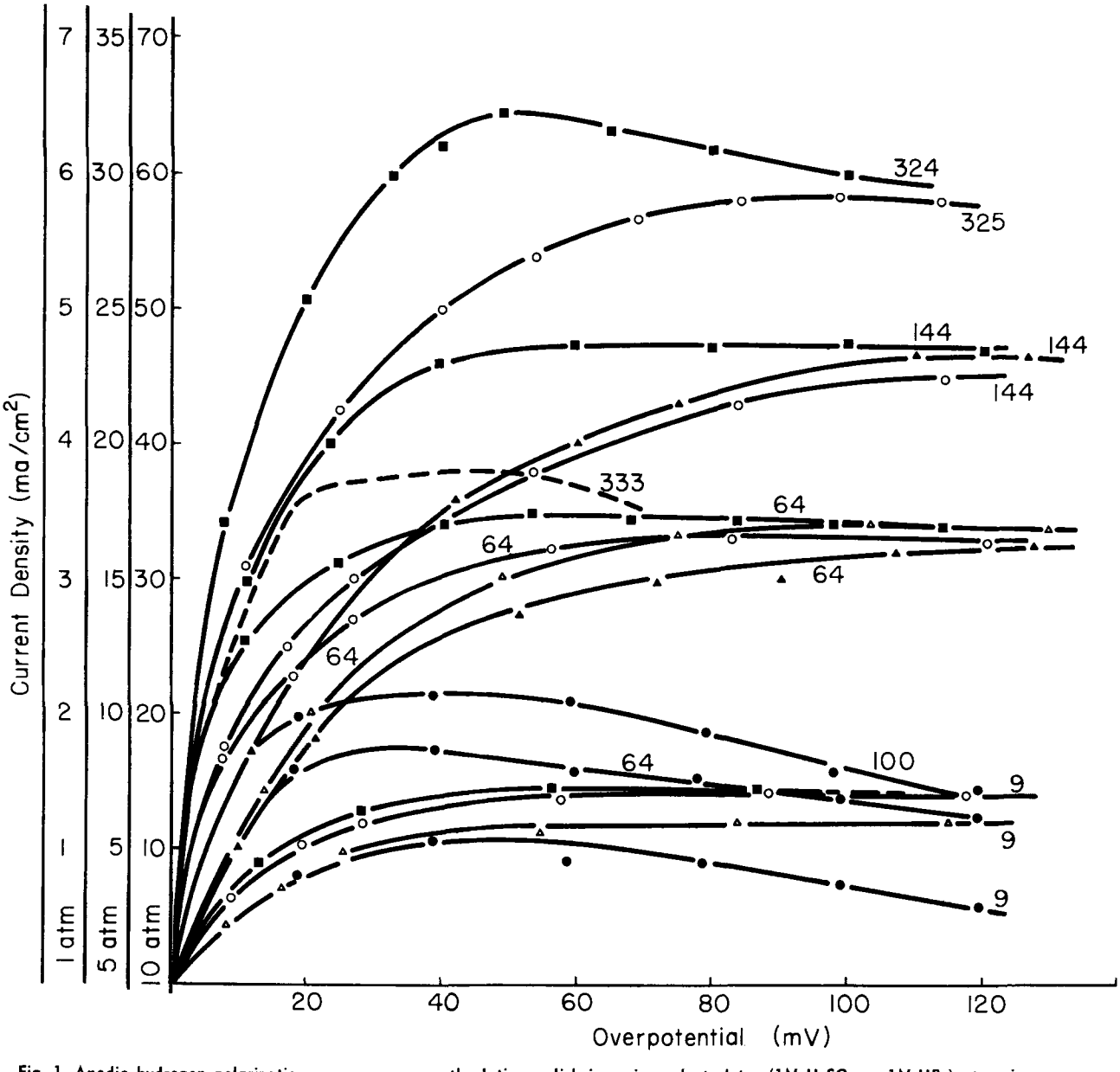

Fig. 1. Anodic hydrogen polarization curves on a smooth platinum disk in various electrolytes (1*N* H_2SO_4 or 1*N* HBr) at various pressures (1, 5, and 10 atm) and rotation rates (indicated by number on curves in rps). ○, HBr, 1 atm, permanganic acid pretreatment; •, HBr, 1 atm, chromic acid pretreatment; △, HBr, 5 atm, permanganic acid pretreatment; ▲, HBr, 10 atm, permanganic acid pretreatment; ■, H_2SO_4, 1 atm, permanganic acid pretreatment; dashed curve data of Frumkin and Aikazyan.

junction with the rotating disk method to obtain these results.

In a relatively recent review (17) Frumkin has cited the work of other electrochemists which indicates first order dependence on hydrogen concentration for the oxidation of hydrogen in acid media. Included in this other work is reference to preliminary studies conducted in our laboratories in 1961 under conditions similar to those employed by Frumkin and Aikazyan with the added feature of variable pressure. These data have never been submitted for publication. Subsequently, additional more extensive data supporting the earlier unpublished results have been obtained. The purpose of this note is to present these data.

Slow sweep voltammetry (20-95 mv/min) has been used to study the anodic hydrogen reaction on platinum in conjunction with the rotating disk technique at pressures from 1 to 60 atm and disk velocities up to 20,000 rpm. Several experiments also have been conducted by varying the disk velocity while holding the potential constant in the range of the limiting currents. The platinum anodes had an apparent area of 0.283 cm^2 and were machined from reference grade platinum supplied by Englehard Industries with a purity of 99.999%. The electrolytic cell was made of Teflon and was mounted in a high-pressure stainless steel enclosure together with the drive system used in conjunction with the rotating disk technique. The whole system was located in a thermostated bath maintained at 26°C. Details of the apparatus and experimental procedures are given elsewhere (16). The solutions used in the present work included 1*N* H_2SO_4, 1*N* HBr, and 1*N* $HClO_4$. Considerable effort was directed to the purification of the solutions and the hydrogen gas used to saturate the solutions. All polarization runs were preceded by a pre-electrolysis treatment extending for 48 hr with a reversible hydrogen cathode (smooth or platinized platinum) and a polarized smooth platinum anode of at least several square centimeters apparent area unless otherwise noted.

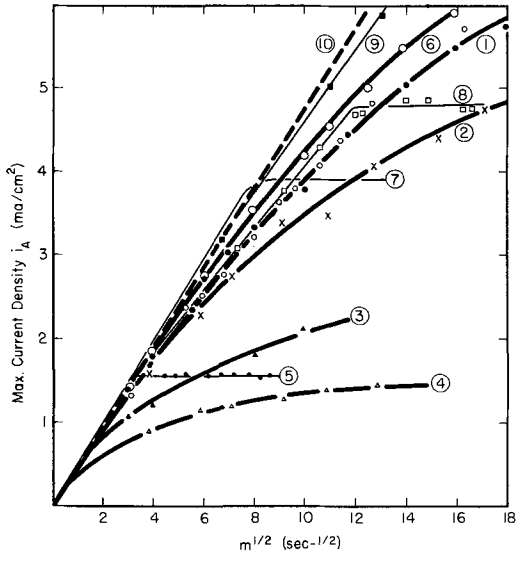

Fig. 2. Anodic current density (i_A) for hydrogen oxidation on a smooth platinum disk in 1*N* acids as a function of angular velocity (m); 1 atm; T = 25°C. 1, solid points, maximum current density, permanganic acid pretreatment, electrochemical activation, 1*N* HBr; open circles, current density at +100 mv from Fig. 1; other conditions same as curve 1; 2, HBr pretreatment; other conditions same as open circles for curve 1; 3, maximum current density, chromic acid pretreatment, electrochemical activation, 1*N* HBr; 4, current density at +100 mv from Fig. 1; HBr pretreatment, no electrochemical activation, 1*N* HBr; 5, maximum current density in 1*N* HBr according to Frumkin and Aikazyan; 6, maximum current density, permanganic acid pretreatment, electrochemical activation, 1*N* H_2SO_4; 7, maximum current density in 1*N* H_2SO_4 according to Frumkin and Aikazyan; 8, same as curve 6 except no distillation of acids or pre-electrolysis; 9, same as curve 6 except in 1*N* $HClO_4$; 10, limiting current density for pure diffusion control.

Prior to the introduction of the solution into the cell, both the cell and the electrodes were given a pretreatment with either chromic acid or an acid permanganate solution at room temperature for a few minutes. The cell and electrodes were then washed profusely with distilled water and the solution to be used in the subsequent measurements prior to commencing final preparations for the experiment.

Before obtaining the anodic polarization curve, the disk electrode was polarized usually at a potential of −0.40v (re. reversible hydrogen electrode) for a period of 1 min. This activation procedure is to be compared with the cyclic procedure used by Frumkin and Aikazyan, in which they polarized their platinum alternately anodically and cathodically in sulfuric acid at unspecified potentials.

In Fig. 1 are presented typical potential-current density curves obtained at various angular velocities. The current maximum was observed for the oxidation of hydrogen in all instances where the voltammetry sweep was extended to sufficiently anodic potentials. In instances where the upper limit on the current density was imposed by the kinetics of the electrode reaction rather than transport in the solution, the maximum was observed at relatively low anodic potentials. In instances where combined reaction and diffusion control are involved, the maximum is very broad and difficult to see from the curves shown in Fig. 1 (*e.g.*, HBr, 1 atm, permanganic acid pretreatment) because of the limited range of the anodic sweep. The shape of the curve and in particular the position of the maximum were critically dependent on the nature of the electrolyte, the type of pretreatment given to the electrode, the rate of voltage scan, and the rotation rate.

The least active electrodes (lowest current density maximum) were found in experiments with electrodes pretreated with chromic acid solution. The permanganic acid treatment resulted in much more active electrodes, using the maximum current density as a criterion of activity. A comparison of the results obtained in the present work and those reported earlier by Frumkin and Aikazyan shows that their electrodes had activities comparable to the electrodes pretreated with chromic acid solution and considerably less than those prepared with the permanganic acid pretreatment.

Two or more runs were made to check each of the curves given in Fig. 1. The agreement of all the curves

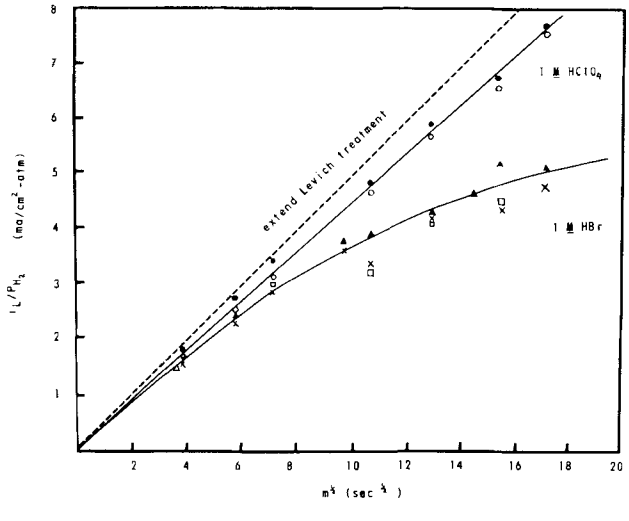

Fig. 3. Anodic maximum current densities in HBr and $HClO_4$ as a function of rotation rate. ○, 1*M* $HClO_4$, 1 atm; ●, 1*M* $HClO_4$, 20 atm; ×, 1*M* HBr, 1 atm; ▲, 1*M* HBr, 10 atm; □, 1*M*, HBr, 60 atm; T = 25°C.

reported was within a few per cent. Hysteresis was also checked in some instances by recording currents with decreasingly anodic potentials. While some hysteresis was observed, in general the magnitude was not sufficient to modify the over-all shape of the curve. The relatively small hysteresis effects observed are what one would anticipate for a system in which large anodic Faradaic currents are involved. The currents associated with the adsorption and desorption of anions during the course of the slow sweep voltammetry would be very small compared to the anodic Faradaic current associated with hydrogen oxidation.

In Fig. 2 are plotted maximum current densities as a function of the square root of the angular velocity. Superimposed on these curves is the curve of Frumkin and Aikazyan for hydrobromic acid and the curve expected from the Levich equation for a purely diffusion-controlled process. The sharp break in the curve of Frumkin and Aikazyan is evidence for zero order or very low fractional order dependence of the limiting current on the hydrogen concentration in the solution adjacent to the electrode.

The only instance in the present work under which the zero or near zero order dependence of the limiting current on hydrogen concentration has been observed is that represented by curve 8 in Fig. 2. The data corresponding to this curve were obtained in 1*N* H_2SO_4 which had not been subjected to any special purification procedures.

Figure 2 includes data for electrodes prepared without either chromic acid or permanganate pretreatment and also electrodes not subjected to cathodic polarization prior to the anodic run. The differences in the activities of the electrodes given these various pretreatments are self-evident from the figure. Electrodes given the acid permanganate treatment and cathodic polarization prior to the anodic run were the most reproducible.

In Fig. 3 are graphed the anodic maximum current densities in HBr and $HClO_4$ as a function of the square root of the angular velocity for various partial pressures of hydrogen gas. While there is some scatter of the data, these results generally support the conclusion that the limiting current has a first order dependence on concentration of hydrogen dissolved in the HBr solutions.

No kinetic control has been found in 1*N* $HClO_4$ (see curve 9, Fig. 2) over the range of potentials investigated in the present work. A plot of the overpotential *vs.* the function log $(i_L - i)/i_L$ has a slope of approximately 30 mv/decade as would be expected for pure diffusion control.

Attempts have been made by the authors to explain the curves in Fig. 1 quantitatively on the basis of combined kinetic and diffusion control with hydrogen dissociative adsorption and hydrogen ionization together responsible for the kinetic control. Temkin-type adsorption kinetics for hydrogen adsorption and ionization and double layer behavior in the vicinity of the point of zero charge have been considered. A quantitative correlation with theory, however, has not been accomplished. Perhaps the difficulty is associated with inadequate quantitative consideration of the competitive adsorption of anions and hydrogen in the presence of water dipoles, particularly near the point of zero charge.

Acknowledgment

The authors are pleased to acknowledge the support of this research by the Office of Naval Research under Contract Nonr 2391(00).

Manuscript received Nov. 3, 1965.

Any discussion of this paper will appear in a Discussion Section to be published in the December 1966 JOURNAL.

REFERENCES

1. L. Hammett, *J. Am. Chem. Soc.*, **46**, 7 (1924).
2. W. Roiter and J. Poluyan, *J. Phys. Chem. USSR*, **7**, 775 (1936).
3. M. Loshkarev and O. Essin, *Acta Physicochim. URSS*, **8**, 189 (1938).
4. E. Wicke and B. Weblus, *Z. Elektrochem.*, **56**, 169 (1952).
5. A. Frumkin and E. Aikazyan, *Doklady Akad. Nauk SSSR*, **100**, 315 (1955).
6. A. Frumkin and E. Aikazyan, *Izvest. Akad. Nauk SSSR, Otdel. Khim. Nauk*, 202 (1959).
7. K. Vetter and D. Otto, *Z. Elektrochem.*, **60**, 1072 (1956).
8. S. Schuldiner, *This Journal*, **106**, 891 (1959).
9. F. Will and C. Knorr, *Z. Elektrochem.*, **65**, 258 (1960).
10. M. Breiter, C. Knorr, and R. Meggle, *ibid.*, **59**, 153 (1955).
11. M. Breiter, L. Kandler, B. Kennel, and H. Feigl, *U.S. Dept. Com., Office Tech. Serv., AD 277,211* (1962).
12. M. Breiter and B. Kennel, *Z. Elektrochem.*, **64**, 1180 (1960).
13. W. Vielstich, CITCE Meeting, Moscow, August, 1963; M. Lauver and W. Vielstich, *Ber. Bunsenges.*, **69**, 538 (1965).
14. E. Heitz and E. Yeager, Paper 221, presented at the Los Angles Meeting of the Society, May 1962.
15. G. Lewis and P. Ruetchi, *J. Phys. Chem.*, **67**, 65 (1963).
16. M. Makowski, E. Heitz, and E. Yeager, Technical Report 19, Western Reserve University, U. S. Office of Naval Research, Contract Nonr 2391(00), July 15, 1964, AD 604,268.
17. A. Frumkin in "Advances in Electrochemistry," Vol. 3, pp. 287-391, P. Delahay, Editor, Interscience Publishers, New York (1963).
18. V. Levich, "Physicochemical Hydrodynamics," Prentice Hall, Inc., Englewood Cliffs, N. J. (1962).
19. A. Frumkin and G. Tedoradse, *Z. Elektrochem.*, **62**, 251 (1958).

Theory of the Performance of Porous Fuel Cell Electrodes

John A. Rockett and Ralph Brown

Pratt & Whitney Aircraft, Division of United Aircraft Corporation, East Hartford, Connecticut

ABSTRACT

A theoretical analysis of the polarization mechanisms in a porous fuel cell electrode was made employing a model consisting of a single pore coated by a thin film of electrolyte. The analysis accounted for those polarizations associated with transport of electrolyte species, transport of dissolved gas, chemical reaction at the solid-liquid interface, and ohmic losses in the electrolyte. The theory was compared with data from biporous nickel electrodes operating on oxygen in 80% KOH at temperatures ranging from 300° to 500°F.

An important adjunct to the development of a high performance fuel cell electrode is the development of a satisfactory theoretical description of the electrode. We have devoted a good deal of effort in the last five years to the development of biporous, sintered, metal electrodes and to the development of a theory for them.

The criterion for judging any theoretical description is its ability to match accurately the measured performance of practical electrodes. Some of our previous attempts, one of which considered only the polarizations associated with diffusional transport processes, and one which considered only the chemical reaction, gave no satisfactory agreement with any of our porous electrode data. The foundations of the theory which is presented here were first suggested in an unpublished paper by Wagner (1). His paper presented a good, comprehensive theoretical study. It contained no data. Wagner had combined aspects of both the transport and chemical reaction in his theory. A similar fusion of these processes is the heart of this theory. This theoretical approach has also been discussed by other authors (2, 3). In the work presented here, however, particular care had to be exercised in the description of the transport processes in the electrolyte. The compositions of the electrolytes in our applications are considerably different from the low solute concentrations often discussed in the published literature. Molar ratios of solute to solvent of over one are common. A satisfactory description of the transport in these highly concentrated electrolytes is often a formidable problem.

This theory represents an attempt to make a comprehensive analysis of the processes taking place in a porous gas-diffusion electrode. After making a basic assumption regarding the geometry of the gas-liquid-solid interface, the theory accounts for those polarizations associated with transport of electrolyte species, transport of dissolved gas, chemical reaction at the solid-liquid interface, and ohmic losses in the electrolyte.

Theoretical Model

The first and one of the most dramatic of the assumptions which must be made is the selection of a geometrical model for the porous structure. Figure 1 shows a cross section of a typical biporous sintered electrode and a cross section of the analytical model adopted. The sinter particles which are seen in cross section are interconnected below the focal plane of the microscope to form a coherent mass; the walls of the analytical model are connected below the section plane of the drawing to form a circular cylinder. Better representations of the sinter can be readily proposed, and a few of these are being developed. The model presented here is the simplest which has proved quantitatively useful. The bulk electrolyte completely fills the fine pore layer represented in the model by an array of small diameter tubes, and coats the entire surface of the coarse layer with a thin liquid meniscus. The variable thickness meniscus is thickest at the fine pore-coarse pore interface and thinnest at the gas side. The reactant gas occupies the volume to the right of the coarse pore and also fills the central portion of the tubular meniscus coated coarse pore.

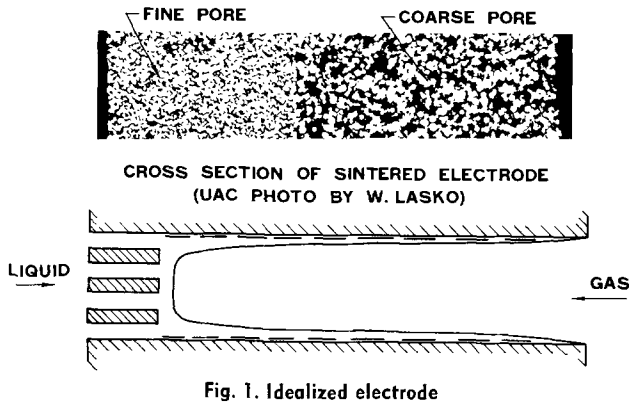

Fig. 1. Idealized electrode

The second assumption deals with the half-cell electrode reactions. The theory, as presented here, applies to the cathode of a hydrogen-oxygen fuel cell. These arguments, with minor variations, could equally well be phrased for the anode or other gas diffusion electrodes. The over-all reaction for the complete reduction of oxygen in alkaline electrolyte is as follows

$$O_2 + 2H_2O + 4e^- \rightleftharpoons 4\,OH^- \qquad [1]$$

At the relatively high temperatures and concentrations which have been of specific interest to us, the experimental open-circuit potentials are very close to those calculated from the free energy change of the H_2-O_2 reaction as shown in Fig. 2.

The fact that the experimental open-circuit values are not below their theoretical values suggests that any competing reactions that could lower the open-circuit potential are of relatively little importance. Reaction [1], therefore, substantially represents the

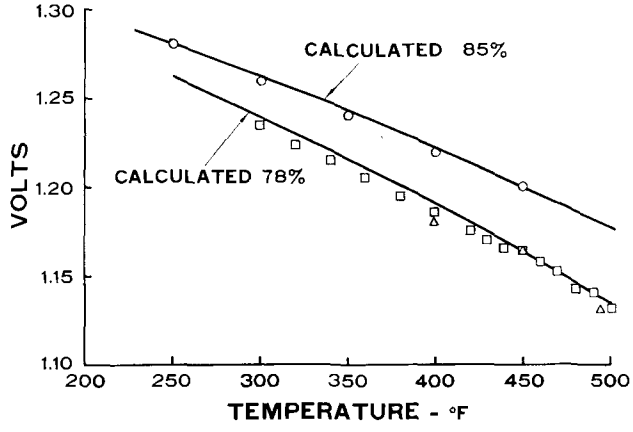

Fig. 2. Open-circuit voltage. ○, Measured 85% KOH; □, △, measured 78% KOH.

net cathode reaction. In order to write a precise kinetic expression for the net half-cell reaction, however, the sequence and relative rate constants for each reaction step must be known. To illustrate the problem, suppose the over-all reaction can be divided into two steps

$$2M + O_2 + 2e^- \rightleftharpoons 2MO^- \qquad [2]$$

$$MO^- + H_2O + e^- \rightleftharpoons M + 2\,OH^- \qquad [3]$$

where the first of these is presumed to be the rate-limiting step. The kinetic expression for reaction [1] is

$$i = i_1 \left[\frac{\alpha_{O_2}}{\alpha_{O_2}^{\circ}} \left(\frac{\alpha_{H_2O}}{\alpha_{H_2O}^{\circ}} \right)^2 e^{\frac{2F}{RT}\eta} - \left(\frac{\alpha_{KOH}}{\alpha_{KOH}^{\circ}} \right)^4 e^{-\frac{2F}{RT}\eta} \right] \qquad [4]$$

where α_i is the local activity of species i, α_i° is the reference activity for the bulk electrolyte, i_1 is the exchange current, and η is the local metal-solution potential difference.

On the other hand, the kinetic expression for the sequence of reactions [2] and [3] is

$$i = i_2 \frac{\dfrac{\alpha_{O_2}}{\alpha_{O_2}^{\circ}} \left(\dfrac{\alpha_{H_2O}}{\alpha_{H_2O}^{\circ}} \right)^2 e^{\frac{2F}{RT}\eta} - \left(\dfrac{\alpha_{KOH}}{\alpha_{KOH}^{\circ}} \right)^4 e^{-\frac{2F}{RT}\eta}}{\left[(1-\theta_o) \left(\dfrac{\alpha_{H_2O}}{\alpha_{H_2O}^{\circ}} \right) e^{\frac{F}{RT}\eta} + \theta_o \left(\dfrac{\alpha_{KOH}}{\alpha_{KOH}^{\circ}} \right)^2 e^{-\frac{F}{RT}\eta} \right]^2} \qquad [5]$$

where θ_o is the equilibrium fractional coverage of adsorbed oxygen.

Note that the numerator of Eq. [5] is identical to Eq. [4]. The important addition in Eq. [5] is the denominator which changes the exponentials and alters the functional dependence of the water activity term. In spite of the apparent differences in the specific expressions for various hypothetical reaction sequences, it is a practical fact that the complete electrode theory is a synthesis of many interacting parts and is not highly sensitive to the detailed reaction mechanism. After trying a variety of possible reaction sequences, the insensitivity of the results became apparent. Considering this fact, and considering the conjectural basis for choosing any particular reaction sequence, we decided to employ Eq. [4] because of its relative simplicity. This choice does impose certain assumptions on the nature of the reaction sequence, the principal one being that the controlling step involves diatomic oxygen species, and does not take place after the O-O bond is broken. This is a good assumption because the strength of the O-O bond suggests that O-O dissociation is likely to be the controlling step. This assumption also yields the important result that the exchange current is directly proportional to oxygen partial pressure.

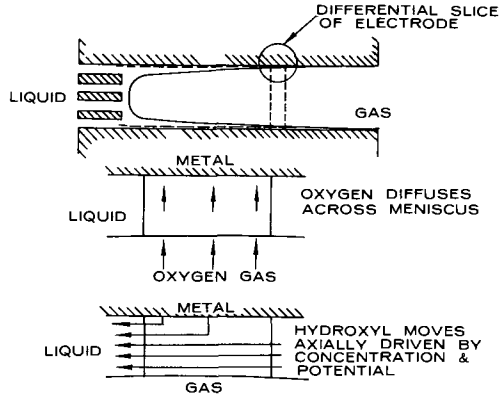

Fig. 3. Meniscus model

Mathematical Formulation

The analysis considers a differential slice cut from the meniscus portion of the electrode as shown in Fig. 3. The local current density on the metal surface is given by the kinetic expression. The potential, E, of the electrode is measured relative to a reference probe located in the bulk liquid to the left of the electrode fine pore. The potential of the electrolyte is chosen as zero at the left edge of the fine pore and chosen to have increasingly positive values in the positive X direction. The local metal-solution potential difference at any point in the meniscus is given by the difference between the electrode potential and the solution potential. The kinetic expression in Eq. [4] can then be written with the driving potentials in terms of the solution potential.

$$i = i_1 \left[\frac{\alpha_{O_2}}{\alpha_{O_2}^{\circ}} \left(\frac{\alpha_{H_2O}}{\alpha_{H_2O}^{\circ}} \right)^2 e^{\frac{2F}{RT}(E-\phi)} - \left(\frac{\alpha_{KOH}}{\alpha_{KOH}^{\circ}} \right)^4 e^{-\frac{2F}{RT}(E-\phi)} \right] \qquad [6]$$

The gas consumed in the differential portion is assumed to diffuse directly across the meniscus. For most practical geometries the partial pressure of the reactant gas is constant all along its length. This being the case, the local current density in the differential element can be expressed in terms of the Fick's law diffusion expression for the diffusion of the reactant gas across the meniscus.

$$i = \frac{4FD_{O_2}\alpha_{O_2}^{\circ}}{\delta} \left(1 - \frac{\alpha_{O_2}}{\alpha_{O_2}^{\circ}} \right) \qquad [7]$$

where δ is the meniscus thickness.

Simultaneous solution of Eq. [6] and [7] allows the elimination of the gas activity ratio from the expression for local current density.

$$i = i_1 \left[\frac{\left(\dfrac{\alpha_{H_2O}}{\alpha_{H_2O}^{\circ}} \right)^2 e^{\frac{2F}{RT}(E-\phi)} - \left(\dfrac{\alpha_{KOH}}{\alpha_{KOH}^{\circ}} \right)^4 e^{-\frac{2F}{RT}(E-\phi)}}{1 + \dfrac{i_1\delta}{4FD_{O_2}\alpha_{O_2}^{\circ}} \left(\dfrac{\alpha_{H_2O}}{\alpha_{H_2O}^{\circ}} \right)^2 e^{\frac{2F}{RT}(E-\phi)}} \right] \qquad [8]$$

The local current density is related to the current in the axial direction of the meniscus by making a current balance on the differential element.

$$i = \frac{1}{2\pi R} \frac{dJ}{dx} \qquad [9]$$

The current in the axial direction of the meniscus is related to the ohmic potential in the electrolyte by Ohm's law.

$$-J = 2\pi R\delta\sigma \frac{d\phi}{dx} \qquad [10]$$

where σ is the conductivity of the electrolyte.

Substitution of Eq. [10] into Eq. [9] relates the ohmic potential in the electrolyte to the local current density. In making this substitution, the meniscus thickness will be assumed constant with X. This assumption is justified by the fact that only a fraction of the total meniscus length is utilized.

$$i = -\delta\sigma \frac{d^2\phi}{dx^2} \qquad [11]$$

Equation [11] represents the second order differential equation which is to be solved in order to obtain the total current produced in the pore. If we can obtain the water and KOH activity ratios as a function of electrolyte potential, the local current density can then be expressed solely as a function of this potential. The total current produced by the pore is given by the axial current (Eq. [10]) evaluated at the fine pore-coarse pore interface. Although some current is produced in the fine pore as gas diffuses into it, this is assumed to be negligible because of the low diffusion rate of the gas into this flooded portion of the electrode. The total current is then given by

$$-J = 2\pi R\delta\sigma \frac{d\phi}{dx} \Bigg/ \text{evaluated at fine pore-coarse pore interface} \qquad [12]$$

The ohmic gradient at the fine pore-coarse pore interface is obtained by one integration of Eq. [11] over the active length of the meniscus. Equation [11] is multiplied by $d\phi/dx$ and the following differential identity is applied

$$\frac{d}{dx}\left(\frac{d\phi}{dx}\right)^2 = 2\frac{d\phi}{dx}\frac{d^2\phi}{dx^2} \qquad [13]$$

Equation [11] can then be written.

$$d\left(\frac{d\phi}{dx}\right)^2 = -\frac{2i}{\delta\sigma}\, d\phi \qquad [14]$$

This form of Eq. [11] can then be directly integrated to obtain $d\phi/dx$. Substitution of the result into Eq. [12] yields an expression for the pore current as a function of a definite integral in ϕ.

$$-J = \pi R\left[8\sigma\delta\int_{\phi_1}^{\phi_o} i(\phi)\, d\phi\right]^{1/2} \qquad [15]$$

The lower limit of integration is the potential, ϕ_1, at the fine pore-coarse pore interface. This must be obtained by simultaneous solution of Eq. [15] and an Ohm's law expression which describes the proportionality between the axial current through the fine pore and this potential. The expression is corrected for the number of fine pores associated with each coarse pore.

$$-J = \pi R^2 \frac{P_{FP}\tau_{CP}\sigma}{P_{CP}\tau_{FP}^2 t}\phi_1 \qquad [16]$$

where P_{FP} is the fine pore porosity, P_{CP} is the coarse pore porosity, τ is the tortuosity, and t is the fine pore thickness.

The upper limit of the integration is that potential at which the local current density becomes zero. Inspection of the numerator of Eq. [8] shows that as the ohmic potential increases along the meniscus, the forward reaction driving potential decreases, the water activity ratio decreases, and the KOH activity ratio increases.

The result is that the forward and reverse reaction rates approach each other, and the local current becomes zero. It was pointed out earlier that a variety of reaction sequences are described by expressions that differ only in the denominator. Whereas the numerator specifies the upper limit of integration, the value of the upper limit is common to these various mechanisms. This is the reason that the final result is fairly insensitive to the choice of the reaction mechanism. The upper limit of integration, which is related to the working length of the meniscus, is a far more important factor than the functionality of the denominator of the rate expression. In most practical cases, the working length of the meniscus is just a fraction of its total length.

The requirements for computing the current from one pore have been indicated. The solution is given as a function of definite integral in Eq. [15], but a numerical integration is required for even the most simple reaction mechanism. In order to include the resistance of the fine pore, this solution must be solved simultaneously with the linear expression of Eq. [16] to find the lower limit of integration. A numerical approach is also required to solve for the root of a transcendental equation to find the upper limit. The pore radius is chosen to correspond to an average pore size of the structure. Using a "spaghetti" model, the number of pores in a given area of electrode is

$$\frac{N}{A} = \frac{P_{CP}}{\tau_{CP}}\frac{1}{\pi R^2} \qquad [17]$$

The electrode current density is found by multiplying the current for each pore by the number of pores per unit area.

$$I = \frac{-JP_{CP}}{\pi R^2\tau_{CP}} \qquad [18]$$

The discussion to this point has been predicated on the assumption that a means of obtaining the water and KOH activities as a function of solution potential is available. This problem is discussed below.

Transport of Electrolyte Species

The hydroxyl ion that is produced in the reaction must diffuse axially through the meniscus from the reaction surface to the bulk electrolyte. If ideal solutions are assumed and bulk transport is neglected, the transport equations for both potassium and hydroxyl ions show a term proportional to KOH concentration gradient and a term proportional to ohmic potential.

$$J = \pi R^2\left[-FD_{OH}\frac{dC_{OH}}{dx} - \lambda_{OH}C_{KOH}\frac{d\phi}{dx}\right] \qquad [19]$$

$$O = \pi R^2\left[-FD_K\frac{dC_{KOH}}{dx} + \lambda_K C_{KOH}\frac{d\phi}{dx}\right] \qquad [20]$$

Equation [20] can be integrated using a reference concentration, C_{KOH}^o, as that in the bulk electrolyte where the reference electrolyte potential is zero. The variation of the diffusivity and ion equivalent conductance with concentration are neglected.

$$\frac{C_{KOH}}{C_{KOH}^o} = e^{\frac{\lambda_K}{FD_K}\phi} \qquad [21]$$

In extremely dilute solutions, the Nernst-Einstein relation could be applied to the coefficient of ϕ in Eq. [21] and the concentration variation as a function of ϕ would be known. In a nonideal electrolyte, however, the correct driving force for the diffusive transport is not the concentration gradient, but the gradient of chemical potential. Equation [21] can be corrected to the proper diffusive drive force by a simple adjustment to the diffusivity.

$$D_K = D_K^o\frac{\partial(\ln a_{KOH})}{\partial(\ln C_{KOH})} \qquad [22]$$

Application of the correction in Eq. [21] assumes the correction factor does not vary strongly with concentration. There are other correction factors for the diffusivity which are functions of the electrolyte fluid properties such as viscosity and density. These same corrections apply to the equivalent ion conductance so that the conductance to diffusivity ratio is assumed constant. With these assumptions, the Nernst-Einstein relation can be applied.

$$\frac{\lambda_K}{FD_K^o} = \frac{F}{RT} \qquad [23]$$

The KOH concentration variation as a function of potential can now be written by substituting Eq. [22] and [23] into Eq. [21]

$$\frac{C_{KOH}}{C_{KOH}^{o}} = e^{\frac{F\phi}{RT\frac{\partial(\ln a_{KOH})}{\partial(\ln C_{KOH})}}} \quad [24]$$

It is necessary to relate the concentration changes to activity changes as are required in the kinetic equation. Activity coefficients for KOH have been measured but only to 50 w/o (5). Water vapor pressures have been measured over highly concentrated KOH over a wide range of temperature (6). The solvent activity is defined as the ratio of electrolyte vapor pressure to pure solvent vapor pressure. The water vapor pressure data gives us the water activity as a function of the solvent concentration. Specifically, the water vapor pressure data was related to the water concentration by the following empirical expression

$$\ln p_{H_2O} = AF_{H_2O}^2 + BF_{H_2O} + C \quad [25]$$

where F_{H_2O} is the weight fraction water; $A = -34.135$; $B = 45.110 - 0.024055\ T$; $C = 0.021597\text{-}14.01648\ T$; T = temperature °F.

In order to calculate the water activity, the above expression is divided by the pure water vapor pressure which can be related to temperature by the Clausius-Clapeyron equation. The water activity is then known as a function of the water molar density or the KOH molar density from the following expressions

$$F_{H_2O} = C_{H_2O} M_{H_2O}/\rho \quad [26]$$

$$1 - F_{H_2O} = C_{KOH} M_{KOH}/\rho \quad [27]$$

The water activity ratio corresponding to the KOH molar density ratio of Eq. [24] is then given by substitution of Eq. [27] into Eq. [25] and taking water vapor pressure ratios

$$\ln \frac{a_{H_2O}}{a_{H_2O}^{o}} = A\left[\left(1 - \frac{C_{KOH}M_{KOH}}{\rho}\right)^2 - \left(1 - \frac{C_{KOH}^{o}M_{KOH}}{\rho}\right)^2\right] + B\frac{M_{KOH}}{\rho}(C_{KOH}^{o} - C_{KOH}) \quad [28]$$

The KOH activity ratio is related to the water activities by application of the Gibbs-Duhem expression

$$\ln \frac{a_{KOH}}{a_{KOH}^{o}} = -\int_{\ln a_{H_2O}^{o}}^{\ln a_{H_2O}} \frac{C_{H_2O}}{C_{KOH}}\, d(\ln a_{H_2O}) \quad [29]$$

Application of the Gibbs-Duhem relation can also be employed to obtain the Onsager-Fuoss correction employed in Eq. [24]. Equation [29] is simply differentiated with respect to $\ln C_{KOH}$.

$$\frac{\partial(\ln a_{KOH})}{\partial(\ln C_{KOH})} = -C_{H_2O}\frac{\partial(\ln a_{H_2O})}{\partial(\ln C_{KOH})} \quad [30]$$

The above relation is computed at the reference KOH concentration since, as previously indicated, it varies slightly with concentration.

It was assumed initially that bulk transport properties would be neglected. This is only precisely correct in a pore where the axial water diffusion molal flux is equal and opposite to the hydroxyl ion flux. If, for example, the product water of the total cell is allowed to evaporate into the hydrogen gas, the axial water diffusion flux does not balance the hydroxyl ion flux. It was found experimentally, however, that the cathode polarization was unaffected by wide variations in the flow rates of pure oxygen over the electrode. These flow variations affect the water vapor pressure in the gas and so control the amounts of water transported through the working electrode. This experimental result indicates that the assumption of no bulk flow is a good one.

Comparison with Experiment

Oxygen electrode half-cell data were measured for KOH concentrations ranging from 60 to 85 w/o and temperatures from 300° to 500°F. The current-potential measurements had been made on electrodes having essentially the same properties. A set of polarization curves for various temperatures and 80% KOH is chosen as an example to describe the theory-data fits. Equations [15] and [16] are rearranged into a convenient form.

$$I = \frac{1}{R}\left[\frac{P_{CP}}{\tau_{CP}}(32FD_{O_2}a_{O_2}^{o}\sigma)^{1/2}\right]_{\{1\}}\left[\frac{i_1\delta}{4FD_{O_2}a_{O_2}^{o}}\right]_{\{2\}}^{1/2}\left[\int_{\phi_1}^{\phi_o}\frac{i}{i_1}d\phi\right]_{\{3\}}^{1/2} \quad [31]$$

$$\phi_1 = \left[\frac{t_{FP}\tau_{FP}^2}{P_{CP}\sigma}\right]_{\{4\}} I \quad [32]$$

Various terms are bracketed and subscripted for reference. In Eq. [31], the coarse pore radius is chosen to correspond to a mean for the structure as obtained by porosimeter measurements. This radius was 3μ for the electrodes employed in this study. The bracketed term {4}, which is a function only of the conductivity and fine pore properties is calculated. This term specifies the magnitude of the polarization losses resulting from the ohmic and concentration polarization in the fine pore. The bracketed term {1} can act as a scale factor to obtain the correct magnitude of current and was determined in this manner during the experimental-theoretical fitting. Rough estimations of this factor are possible, and comparison of the estimation with the empirically determined quantity provides a basis for checking the validity of the theoretical model. The bracketed term {3} is the integration of the local current density over the active portion of the meniscus. The activity ratios in the local current density expression are predicted by the methods previously indicated, and the exchange current is factored out of the integrand. The remaining unknown is that which appears in the denominator of Eq. [8] and is in the bracketed term {2}. This term is proportional to the product of the exchange current and meniscus thickness. There is no accurate way to estimate either of these quantities so the term has been applied strictly as an empirical parameter. Physically, this term is the ratio of the exchange current and a characteristic oxygen diffusion current. The value of the exchange current, which controls the degree of activation polarization, has a strong influence on the shape of the current-polarization characteristic. In summary, one term is applied as an adjustable parameter, another is also adjustable but must have a value reasonably comparable with prediction, and all other quantities are predicted.

The theoretical curves and their corresponding data points are shown in Fig. 4. Values of the three param-

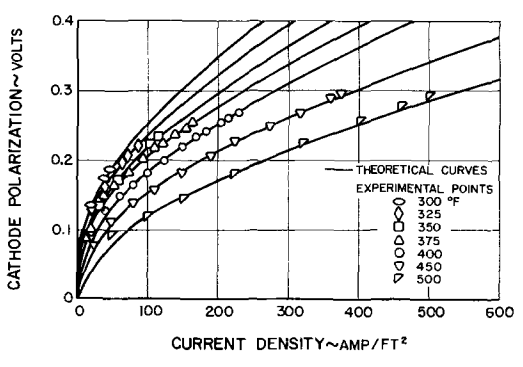

Fig. 4. Comparison of data and theory, 80% KOH

Table I. Values of three parameters

T, °F	Calculated geometric factor, ohms-cm² $\left(\frac{t_{CP}\tau_{FP}^2}{P_{FP}\sigma}\right)$	Fitted exchange current to oxygen diffusion current $\left(\frac{i_0\delta}{4FD_{O_2}a_{O_2}^0}\right)$	Scale factor (amp/cm) $\frac{P_{CP}}{\tau_{CP}}(32FD_{O_2}a_{O_2}^0\sigma)^{1/2}$
300	0.23	6.7×10^{-8}	9.32×10^{-3}
325	0.20	1.8×10^{-7}	8.42×10^{-3}
350	0.18	4.6×10^{-7}	7.49×10^{-3}
375	0.16	1.2×10^{-6}	6.51×10^{-3}
400	0.14	4.0×10^{-6}	5.95×10^{-3}
425	0.13	8.0×10^{-6}	5.22×10^{-3}
450	0.12	2.0×10^{-5}	4.37×10^{-3}
500	0.10	1.4×10^{-4}	3.51×10^{-3}

eters required for the theoretical line in Fig. 4 are shown in Table I. The logarithm of the ratio of exchange current to characteristic oxygen diffusion current, which is the adjustable parameter, is plotted *vs.* reciprocal temperature in Fig. 5. The straight line is indicative of an Arrhenius law dependence on temperature as should be expected of a quantity proportional to the ratio of a kinetic rate constant and a liquid-phase diffusivity.

In order to estimate the bracketed term {1}, the diffusivity-solubility product must be known. Rotating electrode data obtained in our laboratories in 85% KOH and at 450° indicate that $D_{O_2}^{2/3}a_{O_2}^0 = 2.3 \times 10^{-12}$. The diffusivity of oxygen was estimated from that in pure water (7) by applying viscosity data and the Stokes-Einstein relation. The resulting diffusivity-solubility product for 80% KOH and 450°F is 4×10^{-12}. Applying values of the other constants

$$\frac{P_{CP}}{\tau_{CP}}(32\,FD_{O_2}a_{O_2}^0\sigma)^{1/2} = \frac{0.6}{2}(32 \times 96{,}500 \times 4 \times 10^{-12} \times 2.16)^{1/2} = 1.55 \times 10^{-3}\ \text{amp/cm}$$

In the 80% KOH and 450°F case, the empirical value of this quantity required to obtain a theory-data fit was 4.37×10^{-3} amp/cm. It can be shown that the correspondence between the empirical and estimated quantities is satisfactory by considering the uncertainty in the choice of just one parameter. Note that a coarse pore tortuosity factor of two was assumed. Measurements of the tortuosity factor by comparison of gas diffusion rates through porous structures and free gas diffusivities have shown a range of values between one and two. So if the lower limit of the measured range was applied, the calculated value would have been 3.1×10^{-3} amp/cm. Furthermore, a factor of two was also assumed in the fine pore tortuosity. The ohmic drop through the fine pore, being proportional to the square of this factor, would have been considerably less if a smaller tortuosity was assumed. This would decrease the lower limit of integration in the bracketed term {3}. This term would then have been greater, and so a smaller value of the scaling factor could have been applied to obtain the experimental-theoretical fit.

Considering the inexactness of the choice of a tortuosity factor, the comparison of the theoretically calculated scale factor with that empirically determined is well within the inherent limitations of the model. Similar comparisons could be shown for data at other concentrations, but this comparison is sufficient to illustrate the point.

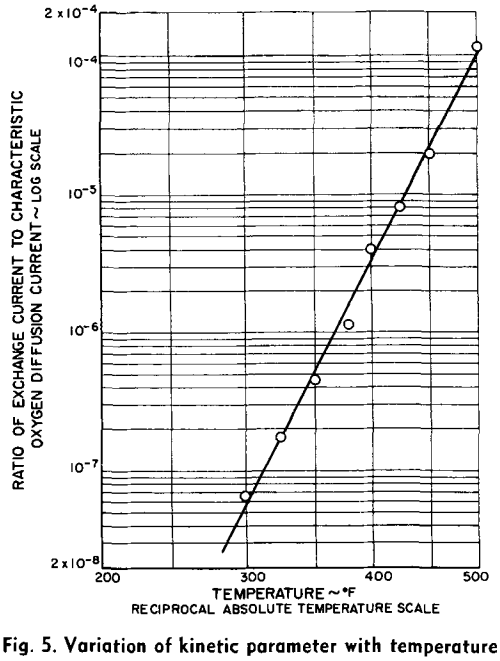

Fig. 5. Variation of kinetic parameter with temperature

Discussion

What does the theory tell us about how a porous electrode behaves? Inspection of the equations giving the current in a pore (Eq. [15] or [31]) will show that the current is proportional to a geometric mean of two kinetic or transport properties. At low electrode potentials, where the local current density near the base of the meniscus is activation controlled, the pore current is proportional to a geometric mean of electrolyte conductivity and exchange current. At intermediate electrode potentials, where the local current density near the base of the meniscus is gas diffusion controlled, the current is proportional to a geometric mean of electrolyte conductivity and a characteristic oxygen diffusion rate across the meniscus. At potentials approaching the limiting current regime, the current is proportional to a geometric mean of a characteristic oxygen diffusion rate and a characteristic electrolyte species diffusion rate. It is this electrolyte species diffusion rate from which the existence of a limiting current is derived, as this diffusion limits the length of active meniscus. In each potential region, the net current is determined by the geometric mean of a local current characteristic (exchange current or oxygen diffusion current) and an electrolyte property from the integration along the meniscus (conductivity or electrolyte diffusion). The fact that the pore current is proportional to the geometric mean of two properties illustrates a general feature of gas diffusion electrodes; their performance is not limited by one effect but by an interplay of several. In fact, the coupling of effects is so important that approximations which eliminate one or another of the transport processes, although pedagogically useful since they lead to analytic solutions, often turn out to be unacceptable for data analysis. The characteristic rate constant for the local current density is directly proportional to the gas partial pressure, whether it is represented by the exchange current or a gas diffusion rate. This rate constant is contained in a geometric mean with either the conductivity or electrolyte species diffusion rate, which are electrolyte properties and independent of reactant gas partial pressure. Thus the mean, being the root of the product, varies with the square root of partial pressure. This effect is illustrated in Fig. 6. The currents with dilute gases are scaled to those at 100% oxygen by dividing them by the square root of the mole fraction oxygen. Let us examine this effect more closely to better understand its origin. Consider the region close to the base of the meniscus where most of the current is generated. The reactant gas is then diluted to below its original partial pressure keeping the total pressure and electrode potential constant. At this reduced pressure, less gas is available to react in the active region. This means that less current will be generated at every point along the pore, and there will be less accumulated ohmic and concentration potential in this region. The active region of the meniscus is then extended. Although the local currents at

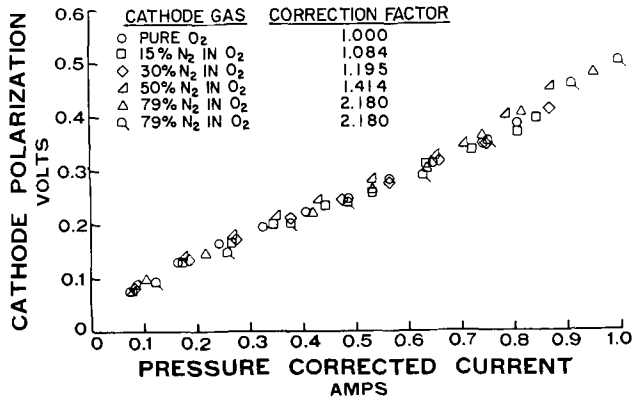

Fig. 6. Effect of oxygen pressure on cathode performance, verification of square root pressure law.

each point along the meniscus have decreased proportionally to the partial pressure reduction, the useful active area of the electrode has increased. The net quantitative result is the square-root proportionality of current on the reactant gas partial pressure.

The useful length of the electrode depends not only on the gas partial pressure but also on the catalytic activity of the electrode. Had we introduced a catalytic poison into our electrolyte, the current would again have decreased all along the pore and again the active area would have increased. Conversely, a more active electrode would have a smaller useful area. If the electrode potential were decreased, this too would increase the useful, working electrode area until very close to open circuit, where the entire wetted area of metal would become active.

The local current density can be computed along the meniscus by a second integration of Eq. [11]. This was done by employing a Runge-Kutta technique. The location along the meniscus where the local current equals zero is plotted *vs.* electrode potential in Fig. 7 for the 400° and 500°F case. This illustrates some of the arguments in the preceding paragraphs. At low potentials, the zero-current location decreases with potential and has values of 10^4-10^5. As soon as the potential is high enough so that electrolyte freezes at the zero-current point on the meniscus, the length to thickness ratio drops very rapidly with increasing potential. The length to thickness ratio at zero current then becomes constant with polarization at limiting current density. The potential region beyond that at which electrolyte freezes is only of theoretical interest, this potential region being well above that at which the electrodes operate. The theoretical freezing takes place at current densities very close to the calculated limiting current. Figure 7 shows how the less active electrode at 400°F has a longer working area except in the limiting current range. At limiting current, where current is affected only by diffusion processes, the active length decreases with temperature reduction because of the smaller diffusivities. In order to give some suggestion of the shape of the local current *vs.* location characteristic, the location from the base of the meniscus to where a local of 95% of the pore current is produced is shown on Fig. 7 for 500°F. This shows that 95% of the current is produced in about 30% the length of the active meniscus at the operating potentials, 0.1-0.3v. Apparently, the ohmic and electrolyte concentration polarizations along the rest of the meniscus make the local current densities relatively small. At potentials approaching that of limiting current density, however, the shape of the local current-location characteristic changes drastically as the 95% pore current point is almost coincident with the 100% pore current point.

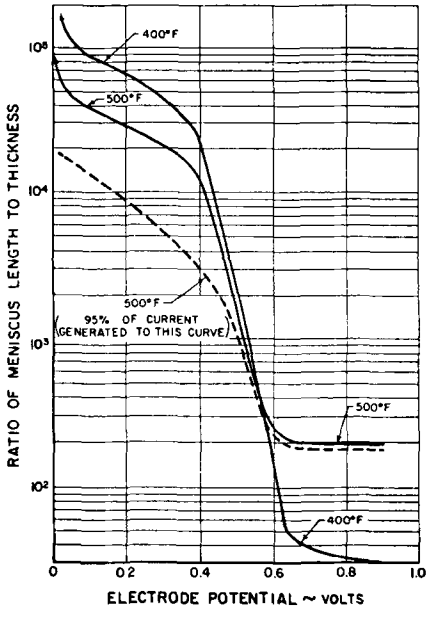

Fig. 7. Active lengths of meniscus, 80% KOH

The length of the electrode required to give enough active meniscus is, of course, dependent on the meniscus thickness. If we use the 0.5μ thickness from light interference measurements (8), this means that the length of the active meniscus is about 0.5 cm. The electrodes in this study were 0.25 cm thick, but the meniscus lengths are no doubt a few factors longer due to their tortuous shapes. It is also possible that the meniscus thicknesses in a porous structure are less than the reported values in which a flat is plate partially immersed in 3.5*N* KOH at room temperature. We have found that the thickness of electrodes having the same properties of those in this study could be reduced by a factor of two with no change in performance.

The comparison of the porous electrode theory with experiment has suggested that the model does give a good representation of the polarization mechanisms in porous electrodes. This means that in addition to providing a systematic scheme for data correlation, the theory gives useful quantitative estimations for the design of fuel cell electrodes and fuel cell systems. For example, it shows how much polarization is associated with the fine pore and how variations in fine pore porosity or thickness will affect performance. By variation of the exchange current, it shows what fraction of this electrode polarization is activation polarization. This tells what gains are possible by improved catalysis. The theory also provides a quantitative prediction of the effect of reactant gas partial pressure on performance.

Having a theory that seems to work leads us to a better understanding of the behavior of porous gas diffusion electrodes. There are, however, certain limitations. Since certain empirical values of inestimable physical quantities are required in the fitting, the proof of the theory is, in part, circumstantial. Furthermore, the results of the theory, being fairly insensitive to the details of the reaction mechanism, can tell us little about this mechanism. Finally, the assumption of cylindrical pores of one size eliminates the possibility of estimating the effects of both pore-size distribution and the relative gas-filled to liquid-filled volumes in the electrode. In spite of these limitations, we have a beginning and can go on from here to refine and better define the model.

Manuscript received July 16, 1964; revised manuscript received Oct. 28, 1965. This paper was presented at the New York Meeting, Sept. 29-Oct. 3, 1963.

Any discussion of this paper will appear in a Discussion Section to be published in the December 1966 JOURNAL.

REFERENCES

1. C. Wagner, Unpublished work.
2. E. Justi, M. Pilkuhn, W. Scheibe, and A. Winsel, "High-Drain Hydrogen Diffusion Electrodes Operating at Ambient Temperature and Low Pressure," p. 33, Verlag d. Akademie d. Wissen-Schaften u.d. Literatur, Wiesbaden (1959).
3. F. G. Will, *This Journal*, **110**, 152 (1963).
4. L. Onsager and R. M. Fuoss, *J. Phys. Chem.*, **36**, 2687 (1932).
5. G. C. Akerlof and P. Bender, *J. Am. Chem. Soc.*, **62**, 2366 (1948).
6. International Critical Tables.
7. International Critical Tables.
8. R. H. Muller, Paper presented at the Washington, D. C. Meeting of the Society, Oct. 11-15, 1964.

NOMENCLATURE

a_{O2}	solubility of oxygen, mole/cm^3
A	empirical constant which is a function of temperature
B	empirical constant which is a function of temperature
C_j	concentration of species j, mole/cm^3
C	empirical constant which is a function of temperature
D_j	diffusivity of species, cm^2/sec
D_j^o	diffusivity of species j at infinite dilution, cm^2/sec
E	electrode potential, v
F	Faraday constant, 96500 coulombs/equivalent
F_{H2O}	weight fraction of water in electrolyte
i	local current density on surface of pore, amp/cm^2
i_1, i_2	exchange currents, amp/cm^2
I	electrode current density, amp/cm^2
J	current generated in one pore, amp
M	symbol representing an active adsorption site
p_{H2O}	water vapor pressure over electrolyte, atmo.
P_{FP}, P_{CP}	porosity of the fine pore sinter and coarse pore sinter, respectively
R	gas constant, 8.314 joules/°C-mole
R	mean radius of the coarse pores, cm
t	thickness of the fine pore sinter, cm
T	absolute temperature, °K
x	distance from electrolyte—electrode interface, cm
α_j	activity of species j
α_j^o	reference activity of species j
δ	thickness of meniscus, cm
η	local metal-solution potential difference, v
θ_o	equilibrium fractional coverage of adsorbed gas
σ	conductivity of electrolyte, ohm-cm^{-1}
λ_{OH}	Equivalent conductance of hydroxyl ions, cm^2/equ.-ohm
λ_k	equivalent conductance of potassium ions, cm^2/equ.-ohm
τ_{FP}, τ_{CP}	tortuosity factor of the fine pore sinter and coarse pore sinter, respectively
ϕ	potential in electrolyte, v
e	density of electrolyte, gm/cm^2

A Comparison of the Passivity of Iron in Acid and Neutral Electrolytes

J. L. Ord

Department of Physics, University of Waterloo, Waterloo, Ontario, Canada

ABSTRACT

The results of similar sets of measurements on a passive iron electrode in acid and neutral electrolyte indicate that a high-field conduction process, limited by an activation barrier of fixed energy, is operating in both systems. The exchange current density across the activation barrier is not constant in either system and depends on the applied current density. Changes in the exchange current density require appreciable charge transfer, and overshoot is observed when the applied current density is changed. Differences in the conduction mechanism reported in previous work are attributed to the techniques of data analysis used.

Recent work on the passivity of iron indicates that the conduction mechanism through the passive layer in acid electrolyte is quite different from the mechanism in neutral electrolyte. Ord and Bartlett (1), working in $2N$ H_2SO_4, conclude that the current is controlled by the electric field at an activation barrier. They find the activation energy to be constant and the electric field to vary inversely with the layer thickness. Sato and Cohen (2), working in a buffered neutral electrolyte, also find an activation-controlled process, but conclude that the activation energy is proportional to the layer thickness and that the conduction process is independent of the electric field in the layer.

A recent study (3) of the experimental determination of overpotential parameters on passive electrodes finds that the values obtained for the parameters depend strongly on the measuring technique. The conclusions described above concerning the conduction mechanism are based on different types of measurement in the two electrolytes. The work described below consists of a set of similar measurements performed on a passive iron electrode in acid and neutral electrolyte. The aim of the work is to determine whether the reported differences in the conduction mechanism are genuine, or are due to the difference in measuring technique.

Experimental

The experimental equipment is a modification of that used in previous work. The simple battery and Helipot combination used previously acts as a potentiostat only if the cathode is stabilized either by working in hydrogen-saturated electrolyte or by using a two-component cathode (4). This potentiostat is not satisfactory for work in argon-saturated neutral electrolyte, and it has been replaced by an electronic potentiostat. The development of small solid-state differential operational amplifiers (Philbrick SP2A) has simplified the design of electronic potentiostats. A schematic diagram of the circuit used is shown in Fig. 1. One operational amplifier is used as a potentiostat, the other as an electrometer follower to drive a fast recorder. A galvanostat can be designed using an operational amplifier, but in this work a galvanostat consisting of resistors in series with a 200v battery bank is used to simplify switching problems. The switch shown in Fig. 1 connects the cell to either the potentiostat or the galvanostat. This switch is a lever switch with open contacts which can be bent for proper phasing. Current is measured using a battery-operated electrometer VTVM with shunt (Keithley 200B with 2008 shunt) operated off ground. The potentiostat automatically compensates for the voltage drop across the VTVM. A mercurous sulfate electrode

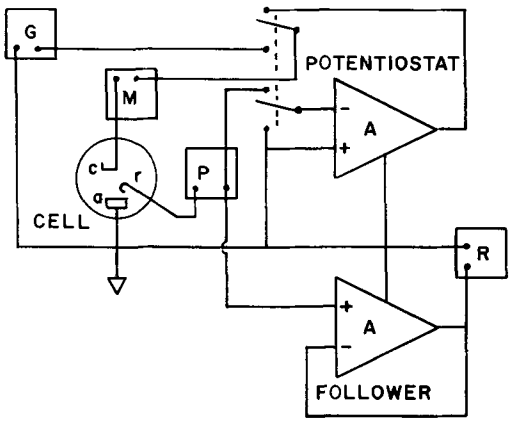

Fig. 1. Circuit schematic: A, operational amplifier; G, galvanostat; M, electrometer VTVM with shunt; P, potentiometer; R, recorder; c, cathode; r, reference electrode; a, anode.

with a 0.1N K_2SO_4 salt bridge is used as a reference for potential measurements, and all potentials are expressed relative to the potential of this electrode.

Jacketed five-neck flasks with ground glass joints are used as cells. The electrolyte is saturated with Linde argon. The impurity specifications of this gas make further purification unnecessary. The argon leaves the cell through a water trap which maintains a slight excess pressure within the cell. Quantitative results on the effect of the dissolved oxygen in the electrolyte are reported below. Twelve hours of bubbling with argon were found to be sufficient to remove dissolved oxygen from the 500 ml of electrolyte used in the cell. The acid electrolyte used is 1N H_2SO_4, and the neutral electrolyte is the 0.15N sodium borate-boric acid buffer (pH 8.4) used by Sato and Cohen (2). Iron electrodes of 0.2 cm^2 area are prepared by coating iron single crystals with epoxy. The electrodes are mounted in the cell with the exposed surface vertical.

Results and Discussion

Studies of the passivity of iron all indicate that the current density, i, depends exponentially on the overpotential, V, above the Flade potential. This dependence can be written in the simple form

$$i = i_o \exp(V/V_o) \qquad [1]$$

where the parameters i_o and V_o have the same units as the measured quantities i and V. The observation that the steady-state current density in 1N H_2SO_4 is independent of potential is consistent with the exponential dependence expressed in Eq. [1], for the parameter V_o is found to be proportional to the steady-state passivating potential (1, 3). The differential equation of a general transient is

$$C\,dV/dt + i_o \exp(V/V_o) = i_1 \qquad [2]$$

where C is the layer capacitance and i_1 is the total current flowing in the circuit. Most measurements involve one or the other of two special cases of the general transient. One can define a fast (or capacitive) transient as one for which dV/dt is large enough to require that the first term in Eq. [2] be retained. (The layer thickness does not change appreciably over a fast transient, and hence it is often assumed that i_o and V_o also remain constant over the transient.) A slow (or oxidation) transient is one for which dV/dt is small and the first term in Eq. [2] can be neglected. For such a transient the current going into layer formation far exceeds the current charging the layer capacitance. According to these definitions, all potentiostatic transients are classed as slow, whereas galvanostatic transients have fast and slow regions. These regions are usually quite distinct, and are characterized by dV/dt's which differ by orders of magnitude.

In a typical experiment one determines the dependence of the parameters i_o, V_o, and $1/C$ on the experimentally controllable variables such as temperature, pH, accumulated charge, etc. The experimental data obtained are then used in conjunction with the equation relating current density to overpotential across an activation barrier

$$i = \kappa\lambda e \frac{kT}{h} a_1 \exp(-U/kT)\,[\exp(\beta\lambda e\eta/kT) - \exp(-(1-\beta)\lambda e\eta/kT)] \qquad [3]$$

to deduce basic features of the conduction mechanism and oxidation reaction. In Eq. [3], κ is the transmission coefficient, λ is the valence of the charge carriers, a_1 is the activity of the carriers moving in the forward direction across the barrier, U is the activation energy in the forward direction at the reversible potential, and β is the fraction of η, the overpotential, aiding motion in the forward direction; the other symbols have their standard meanings. In most experiments η is sufficiently large that the second term on the right of Eq. [3] (which represents the reverse current across the barrier) can be neglected.

Fast galvanostatic transients have been used to study the passivity of iron in acid electrolyte (1, 3). In the simplest set of experiments, the electrode is held at a constant passivating potential until the current shows no further time dependence. In this steady state the rate at which the layer is being formed is balanced by the rate at which it dissolves in the acid. Once a steady state is reached, the circuit is opened, and the resulting fast transient is analyzed (3) to determine V_o and $1/C$. When the circuit is opened, the current across the metal-layer and layer-electrolyte interfaces is reduced to zero, but the current through the layer decreases gradually to zero as it discharges the layer capacitance. The region over which the transient is fitted involves a change in the current density by a factor of about 20. Beyond this region the reverse current across the activation barrier (the second term on the right of Eq. [3]) cannot be neglected. In Fig. 2, V_o and $1/C$ are plotted $vs.$ steady-state passivating potential for an iron electrode in argon-saturated 1N H_2SO_4 at 25°C. The steady-state current density is 5.5 $\mu a/cm^2$. If the zero of overpotential is taken to be —0.16v on this potential scale, i_o is found to be constant and equals 0.06 $\mu a/cm^2$. The data plotted in Fig. 2 were taken in an increasing sequence of passivating potentials. The electrode was allowed to stabilize for 1 hr and 20 min after each 0.1v increment in passivating potential. The value of V_o shows little further time dependence after this

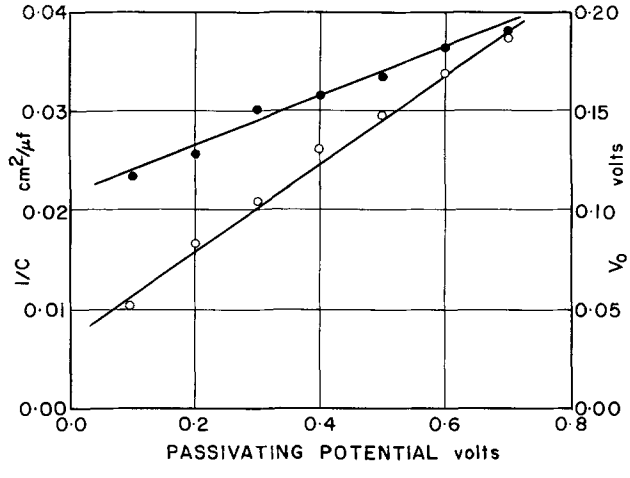

Fig. 2. Dependence of V_o and $1/C$ on steady-state passivating potential in 1N H_2SO_4 at 25°C. The open circles represent V_o, the solid circles, $1/C$.

interval, but the reciprocal capacitance continues to change with time for at least a week (5), and hence the state is not truly steady. This time dependence complicates the interpretation of capacitance measurements, and hence it is simpler to use only the parameters i_o and V_o to compare the behavior in acid and neutral electrolyte.

The interpretation of the acid-electrolyte data is carried out by direct comparison with Eq. [3]. Since i_o is constant, both U, the activation energy, and a_1, the activity of ions crossing the barrier, must be constant. The overpotential in the steady state, V_p, is the passivating potential used as abscissa in Fig. 2 plus 0.16v. Figure 2 shows that V_p/V_o is constant, and hence the overpotential across the barrier, η, must also be constant, independent of the overpotential above the Flade potential, V_p. Therefore the electric field at the activation barrier must be independent of V_p. This will be the case if V_p appears across a layer of thickness D which is proportional to V_p. Using this model V_o is proportional to D through the equation

$$V_o = (kT/ea)\, D \qquad [4]$$

where a is the half-jump distance of the activation barrier. The two main features of the conduction mechanism which emerge from these considerations are: (*i*) the ionic current through the layer is controlled by the high electric field (V/D) within the layer, and (*ii*) the activity of the charge carriers is constant at a limiting activation barrier of fixed energy. It must be emphasized that in the experiments on which these conclusions are based, V_p, the initial steady-state passivating overpotential, is a parameter describing the initial state of the electrode. The points plotted in Fig. 2 were obtained from transients in which V sweeps out a range of values from V_p to zero. The V_o and $1/C$ values in Fig. 2 essentially are plotted *vs.* layer thickness.

In neutral electrolyte the passive layer is insoluble, and hence it is not generally possible to achieve a steady state in which the current and potential are independent of time. The simplest transients in such a system are slow galvanostatic and potentiostatic transients. Sato and Cohen (2) found that, except for the initial stages, potential increases linearly with time for slow galvanostatic transients. The slope of these transients is proportional to the oxidation current, and hence dV/dQ, where Q is the charge accumulated at the electrode, is independent of the oxidation current. The displacement between transients starting from the same layer thickness is proportional only to the logarithm of the current ratio. They found in addition that, for potentiostatic transients, the logarithm of the current density decreases linearly with Q, and that the slope of this decrease is independent of the passivating potential.

These experimental results can be summarized in two equations

$$\left(\frac{\partial V}{\partial Q}\right)_i = \frac{\beta}{B} \qquad [5]$$

$$\left(\frac{\partial \ln i}{\partial Q}\right)_V = -\frac{1}{B} \qquad [6]$$

where β and B are constants determined from the experimental data. These equations can be integrated to give an equation between i and V

$$i = k' \exp(\beta V - Q/B) \qquad [7]$$

where k' is an additional constant. This equation can be compared to Eq. [3] to deduce a conduction mechanism in the same way as the conduction mechanism is deduced in acid electrolyte. A comparison of the potential dependent factors shows that η, the activation overpotential, is proportional to V and independent of Q. A comparison of the other exponential factors indicates that U, the activation energy, is proportional to Q which is, in turn, assumed proportional to layer thickness. Since k' is constant, the activity of ions in the initial state, a_1, must be constant. Sato and Cohen conclude that a suitable conduction mechanism consistent with these observations is one in which ions move through the layer by a correlated flipping of ion pairs. This mechanism has an activation energy which is proportional to the length of the chain of ion pairs (in this case the thickness of the layer), and the activation overpotential appears across the entire passive layer. The features of this proposed mechanism to be compared with the mechanism proposed for acid electrolyte are (*i*) the ionic current through the layer is controlled by the overpotential across the layer and not by the field within the layer, and (*ii*) the activity of the charge carriers is constant, but the energy of the activation barrier is proportional to the layer thickness.

Both proposed conduction mechanisms require the activity of the charge carriers to be constant, but in all other features they differ markedly. There is little doubt as to the validity of the experimental data, but it is important to note that the acid-electrolyte data were obtained using fast transients whereas the neutral-electrolyte data were obtained using slow transients. A recent study (3) of the experimental determination of overpotential parameters on passive electrodes, with iron in acid electrolyte as the system under study, shows that the values obtained for these parameters depend strongly on the measuring technique used. Hence it is possible that the reported difference in the conduction mechanism is due to the measuring technique and not to the electrolyte. This possibility can be explored by making similar measurements in the two systems.

The selection of an experiment to be performed in both acid and neutral electrolyte requires some care. In neutral electrolyte it is not possible to perform steady-state measurements similar to those used to obtain the data plotted in Fig. 2 for acid electrolyte. The slow galvanostatic transients used by Sato and Cohen can be used in acid electrolyte (3, 6), but the analysis is complicated by the fact that the rate of dissolution of the layer under these conditions is not necessarily the same as it is in the steady state (7). The layer dissolution in sulphuric acid electrolytes is governed by an activation energy of approximately 0.7 ev, and hence the effects of this process can be reduced by a factor of 10 by working near 0°C rather than at 25°C. For this reason the electrolytes were held at 0.3°C for the experiment. The experiment chosen, consisting of galvanostatic oxidation transients interrupted by brief open-circuit transients, combines the techniques used by Ord and Bartlett in acid electrolyte and Sato and Cohen in neutral electrolyte. During galvanostatic oxidation, the layer thickens at a uniform rate. When the circuit is opened, the capacitance discharges through the layer, and the overpotential across the layer and current through the layer decay together to zero over the transient. This process increases the layer thickness only slightly, and hence the open-circuit transient can be used to determine the dependence of the current through the layer on the overpotential across the layer at a fixed value of the layer thickness. Analysis of the open-circuit transients determines the overpotential parameters at a series of potentials along the oxidation transient. The overpotential parameters chosen are i_o and V_o from Eq. [1]; they are related to the parameters used in Eq. [7] through $V_o = 1/\beta$ and $i_o = k' \exp(-Q/B)$. These parameters can be plotted *vs.* either the charge accumulated at the electrode or the potential of the electrode just before the circuit is opened. In this work, the potential at which the circuit is opened, designated the passivating potential, is chosen as abscissa for plots of experimental data. The data are expected to depend also on the oxidation current density. The oxidation current densities used

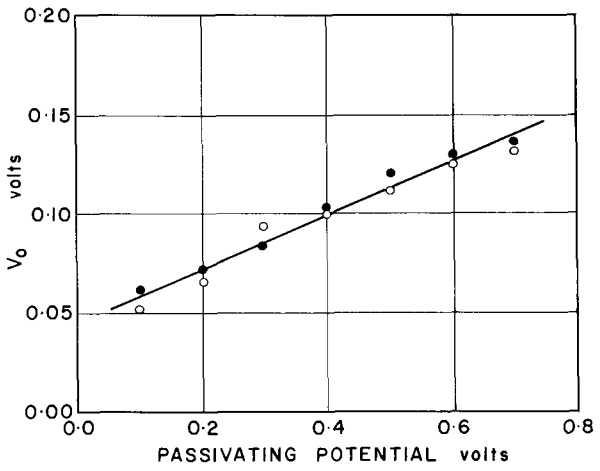

Fig. 3. Dependence of V_o on passivating potential in 1*N* H_2SO_4 at 0.3°C. The oxidation current density is 25 μa/cm^2 for the data represented by open circles, 5 μa/cm^2 for the solid circles.

in acid electrolyte are at least an order of magnitude greater than the steady-state current density at 0.3°C.

The results of this experiment performed in 1*N* H_2SO_4 are plotted in Fig. 3 for oxidation current densities of 5 and 25 μa/cm^2. The linear increase of V_o with passivating potential is similar to the plot in Fig. 2, although the slope is somewhat lower. The straight line in the figure is fitted to the average of the data at the two current densities. If the data are fitted to two straight lines, one for each current density, their slopes differ only slightly. The conduction mechanism proposed above for acid electrolyte, for which a_1 and hence i_o are constant, predicts that the reciprocals of the slopes differ by the natural logarithm of the ratio of the oxidation current densities. For these data, this amounts to a difference of 22% in the slopes themselves. (This effect shows up more clearly in neutral electrolyte where the absence of layer dissolution permits the use of a wider range of oxidation current densities.) The conduction mechanism proposed for acid electrolytes can be made consistent with the data plotted in Fig. 3 if the requirement that a_1 be constant is relaxed. Variations of i_o with current density in acid electrolyte have been reported previously (1).

Results of a similar experiment performed in neutral electrolyte are plotted in Fig. 4 for oxidation current densities of 2.5 and 25 μa/cm^2. Figure 4 shows

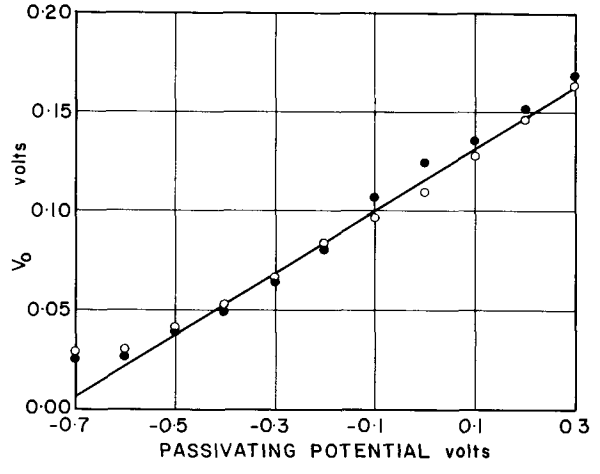

Fig. 4. Dependence of V_o on passivating potential in 0.15*N* sodium borate-boric acid buffer at 0.3°C. The oxidation current density is 25 μa/cm^2 for the data represented by open circles, 2.5 μa/cm^2 for the solid circles.

that V_o increases linearly with passivating potential, varying by a factor of 6 over the passive region. Results plotted in Fig. 4 are similar to the results plotted in Fig. 3 for acid electrolyte. The slopes of the least-squares lines differ by only 14%. [The deviation of the V_o value at −0.7v in Fig. 4 is similar to the deviation observed in acid electrolyte (1) where it is attributed to the existence of a minimum thickness for a continuous passive layer.] There can be little doubt that the same conduction mechanism is operating in both electrolytes. The sixfold variation in V_o ($1/\beta$) is not consistent with Eq. [7] (in which β is constant) nor the conduction mechanism based on it. It is consistent with the high-field conduction process proposed for acid electrolyte. The V_o values fall on a straight line which intersects the passivating potential axis at or near the Flade potential. Since $V/V_o = \ln (i/i_o)$, this result requires $\ln (i/i_o)$ to be independent of film thickness, and hence the activation energy cannot be proportional to film thickness.

The discrepancy between the V_o values plotted in Fig. 4 and the $1/\beta$ value determined from slow transients is related to the fact that both sets of data in Fig. 4 fall approximately on the same straight line. If two lines are used to fit the data, their slopes differ by 10%, increasing with decreasing current density. This result can be checked over a wide range of current densities by interrupting a potentiostatic transient with brief open-circuit transients. The data obtained confirm the galvanostatic result, i.e., an increase of approximately 10% in V_o is associated with a tenfold decrease in current density. If i_o is independent of the oxidation current density, Eq. [1] requires a 36% increase in V_o for a tenfold decrease in the oxidation current density. Since only a 10% increase is observed experimentally, i_o must be a function of the oxidation current density. A tenfold decrease in the oxidation current density is associated with a 10% increase in V_o and a fivefold decrease in i_o. There are two factors in Eq. [3] which can produce changes in i_o: the activity factor and the activation energy factor. Because i_o is independent of layer thickness for a fixed value of the oxidation current density, it is assumed by this author that the variations in i_o are directly proportional to changes in the activity of charge carriers in the initial state. (Other explanations, based on different assumptions, are possible also.) Under this assumption, the activation energy is constant, but it is extremely difficult to measure experimentally. Data obtained at 25°C are almost indistinguishable from the data plotted in Fig. 4 which were obtained at 0.3°C. A direct proportionality between i_o and the oxidation current density, considered in conjunction with Eq. [1] and the data in Fig. 4, results in a constant slope, dV/dQ, for slow galvanostatic transients. If, as the experiments indicate, i_o varies somewhat more slowly than a direct proportionality requires, dV/dQ should increase slightly with oxidation current density. Sato and Cohen (2) find a small deviation in this direction.

The dependence of i_o on the oxidation current density raises a question concerning the validity of the analysis of open-circuit transients. Over the course of such a transient the current density through the layer decreases to zero. The analysis requires, and in fact indicates, that i_o is constant over the transient. This is consistent with evidence from overshoot experiments which indicates that changes in i_o require charge transfer across the layer interfaces. Figure 5 shows a slow galvanostatic transient in which oxidation current density is switched from 11 to 25 μa/cm^2 and then back to 11 μa/cm^2. On the slow time base used in the figure, the capacitive switching transients appear as vertical lines. After each switching transient there is an overshoot, and appreciable time is required before the transient again becomes linear. This delay indicates the changes in i_o require charge transfer since i_o cannot follow rapid changes in the

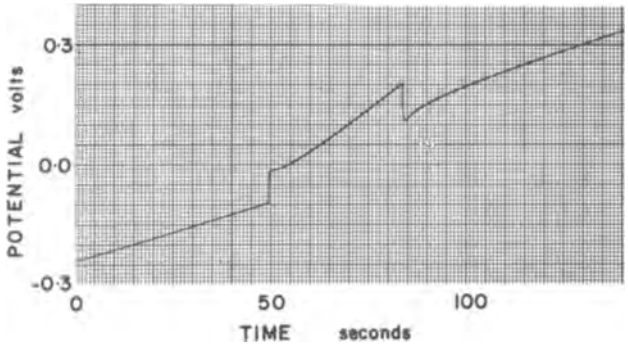

Fig. 5. Recorder trace of potential *vs.* time for an oxidation transient in which the current density is switched from 11 $\mu a/cm^2$ to 25 $\mu a/cm^2$ and then back to 11 $\mu a/cm^2$. The electrolyte is 0.15*N* sodium borate-boric acid buffer at 25°C.

oxidation current density. For a discussion of Fig. 5 it is convenient to differentiate Eq. [1] with respect to Q

$$dV/dQ = \ln (i/i_o)\ dV_o/dQ - V_o/i_o\ di_o/dQ \qquad [8]$$

The positive term on the right is the steady-growth term; the negative term arises from changes in i_o. dV_o/dQ is a constant proportional to the rate of change of thickness of the layer with accumulated charge. When the oxidation current density is increased, there is first a capacitive transient, then i_o begins to increase. The increase in i_o decreases the magnitude of the positive term, and introduces the negative term, thus decreasing dV/dQ (and perhaps making it initially negative). Similarly when the oxidation current density is decreased, i_o begins to decrease, increasing the first term and making the second term positive, thus increasing dV/dQ. It is important to note that no overshoot is observed when the circuit is reclosed after an open-circuit transient. This result is expected if i_o is unchanged over the course of such a transient as is asserted above.

It has been reported (2) that trace amounts of oxygen dissolved in neutral electrolyte affect the electrical behavior strongly. This is true of the measurements used in this investigation. Figure 6 shows a plot of potential *vs.* time for an iron electrode immersed in oxygen-saturated neutral electrolyte under open-circuit conditions. One can calculate the potential dependence of the oxidation current density required to produce a transient of the form shown in Fig. 6 for an oxygen-free electrolyte. This equivalent oxidation current density is very high at low potentials, but falls off rapidly as the potential increases (actually as the layer thickness increases) and becomes insignificant over the upper two-thirds of the passive region. Galvanostatic oxidation in oxygen-saturated electrolyte is masked by this effect at low potentials. A sensitive test for traces of dissolved oxygen in the electrolyte is provided by an open-circuit transient at a passivating potential of —0.7v. In oxygen-free electrolyte the decrease of potential with time is monotonic. If a small amount of oxygen is present in

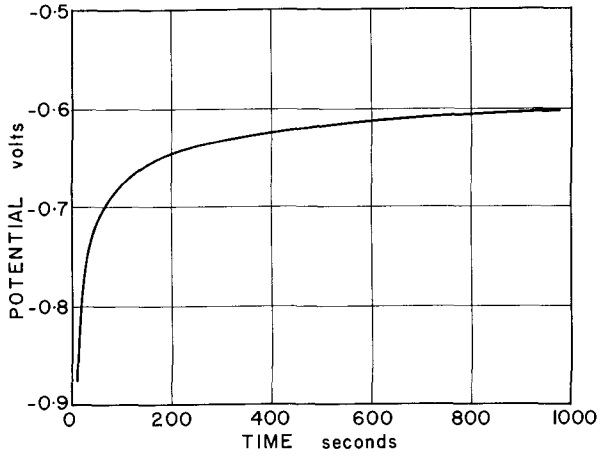

Fig. 6. Plot of potential *vs.* time for an iron electrode immersed in oxygen-saturated 0.15*N* sodium borate-boric acid buffer at 25°C.

the electrolyte, the potential initially decreases, but then begins to increase slowly. This test indicates that bubbling argon through the electrolyte for a 12-hr period is sufficient to remove traces of oxygen from the electrolyte.

Conclusions

This comparison of the passivity of iron in acid and neutral electrolytes leads to three main conclusions:

1. The conduction mechanism through the passive layer is the same in the two electrolytes.
2. The differences in the conduction mechanism reported in other investigations are due to the technique of data analysis and are not due to the data themselves.
3. A high-field conduction mechanism, limited by an activation barrier of fixed energy, operates through the passive layer, and the activity of the charge carriers depends on the oxidation current density.

Acknowledgment

The author is indebted to Mr. W. J. Woitowetch for his assistance in preparing electrodes. This work received partial support from the National Research Council of Canada under Grant No. A-1151.

Manuscript received July 30, 1965; revised manuscript received Dec. 15, 1965.

Any discussion of this paper will appear in a Discussion Section to be published in the December 1966 JOURNAL.

REFERENCES

1. J. L. Ord and J. H. Bartlett, *This Journal*, **112**, 160 (1965).
2. N. Sato and M. Cohen, *ibid.*, **111**, 512 (1964).
3. J. L. Ord, *ibid.*, **112**, 46 (1965).
4. J. Giner, *ibid.*, **111**, 376 (1964).
5. J. L. Ord, Unpublished data.
6. K. G. Weil, *Z. Elektrochem.*, **59**, 711 (1955).
7. K. J. Vetter, *This Journal*, **110**, 597 (1963).

Infrared Study of Adsorbed Corrosion Inhibitors: Butyl Nitrite and Nitric Oxide on Iron-Iron Oxide

G. W. Poling and R. P. Eischens

Texaco Research Center, Beacon, New York

ABSTRACT

Infrared techniques for observing spectra of adsorbed molecules were used to study the mechanism of corrosion inhibition. Attempts were made to study the chemisorption of butyl nitrite and nitric oxide on reduced iron and on iron oxide surfaces. It was possible to detect differences between nitric oxide chemisorption on iron oxide and on reduced iron even though the latter became oxidized by reaction with nitric oxide. On a preoxidized surface, nitric oxide produces a band at 1820 cm^{-1} which is attributed to $Fe^{++}:N{=}O^{+}$. Oxidative chemisorption on initially reduced iron produces a band at 1750 cm^{-1} which is attributed to Fe—O—N=O. Butyl nitrite decomposes during chemisorption to give chemisorbed hydrocarbon and chemisorbed nitrogen oxides. Neither oxygen nor water vapor displaces the observed chemisorbed species from oxide surfaces. The results suggest that the corrosion inhibitor properties involve both the oxidizing action of nitrogen oxides and the strong chemisorption of neutral or cationic inhibitor species on the oxide surface.

Corrosion of iron and steel can sometimes be retarded by inhibitors which have nitrogen oxide functional groups. Many investigators attribute the inhibitive properties of these groups to their ability to promote the development of protective oxide films (1-3). Other workers believe that the protective mechanism involves chemisorption of oxygen-containing inhibitor on the metal surface (4, 5). In a study of amine inhibitors, Yu Yao emphasized the importance of chemisorption of inhibitor on the oxide film rather than chemisorption on the metal (6). She suggests that chemisorbed inhibitor renders the oxide barrier more effective by decreasing the electric field gradient across the oxide and thereby slowing the transport of metal ions through the oxide. The work to be presented here shows that strong chemisorption of nitrogen oxide inhibitor also occurs on the oxide film and thus, to some extent, supports the Yu Yao mechanism.

This paper is mainly concerned with the infrared spectra of butyl nitrite and nitric oxide adsorbed on samples which consist of small particles of iron or iron oxide dispersed on high area silica. In transmission through this type of sample, the infrared beam traverses sufficient adsorbent surface to provide monolayer detecting sensitivity. The butyl nitrite and nitric oxide are related because butyl nitrite dissociates during chemisorption, and one of the fragments appears to be nitric oxide.

The techniques for observing these spectra of molecules adsorbed on small particles were developed in studies of chemisorption systems related to catalysis (7). It will be seen that the small particle samples introduce factors which are not pertinent to corrosion research. However, the important aspects of the observed chemistry at iron/iron oxide/inhibitor interfaces appear to be widely applicable to corrosion studies.

Experimental Procedure

Recording spectra.—The spectra (of the 4000-1300 cm^{-1} region) were obtained using a CaF_2 prism in a Perkin-Elmer Model 12C spectrometer which had been modified to allow the beam to pass vertically through a 10 in. long sample cell (8). The cell, shown in Fig. 1, was made from Pyrex tubing 45 mm in diameter. Infrared transmitting CaF_2 end windows were sealed to the body of the cell with glyptal resin. These windows were cooled with air jets when the cell was heated. The cell could be evacuated to 10^{-6} mm Hg by means of a conventional mechanical pump-oil diffusion pump-cold trap system.

The sample powder was pressed at 12,000 psi into a self-supporting disk and then placed on a glass ring stand (ring not shown in Fig. 1). The sample disks were 26 mm in diameter and weighed about 0.15g. The composition of the samples is described later.

The infrared spectral data were supplemented by mass spectral analysis of the gas phase. A Consolidated Vacuum Corporation Model 21-611 mass spectrometer was connected to the cell through a variable leak valve.

Sample preparation.—Samples were prepared by impregnating Cabosil type silica with an aqueous solution of $Fe(NO_3)_3$, drying, and then reducing with flowing hydrogen at 350°-400°C for 50 hr. On the basis of experience with a similar preparation of nickel and platinum samples, it was expected that this method would produce small particles of iron (~50Å diameter) dispersed on silica. Sufficient $Fe(NO_3)_3$ was used to yield a sample which would contain 12 w/o iron after complete reduction.

In practice it was found to be impossible to reduce all of the iron to the metallic state. This difficulty is attributed to a type of dispersion (perhaps as individually adsorbed ferric nitrate molecules) which prevented sufficient aggregation of impregnated ma-

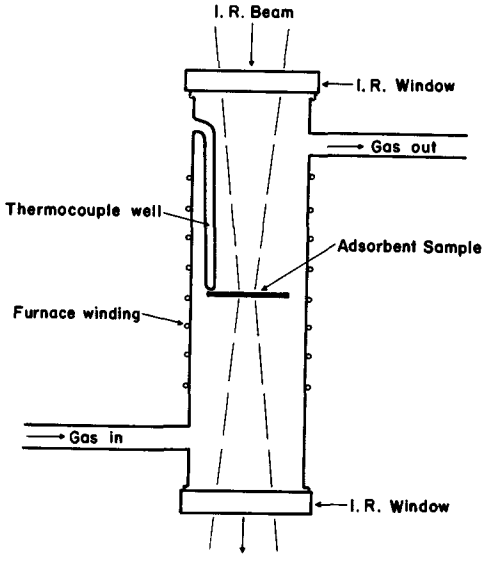

Fig. 1. Cell for infrared study of chemisorbed molecules

terial for subsequent reduction to the metallic state. Using the concept that formation of discrete ferric nitrate crystallites is likely to facilitate reduction to metal, efforts were made to determine the most satisfactory method of preparing iron on silica samples. This problem was not completely solved, but it was possible to prepare samples having sufficient reduced iron to allow a comparative study of reduced and oxidized iron. In the most satisfactory samples, reduction was carried to the state where about 20% of the exposed iron was in the reduced state and 80% was unreducible and remained in an oxidized state. Determination of the relative amounts of surface iron in the reduced and oxidized states was based on the concept that carbon monoxide adsorbs only on reduced iron while nitric oxide adsorbs on both reduced and oxidized iron. Details of this determination will be given later.

The specific procedure found to be the most satisfactory in attempts to prepare reduced iron samples involved addition of the amount of $Fe(NO_3)_3$ solution needed to form a thick paste with the silica, rapid drying of the paste under vacuum at 30°C, pressing the sample disk, installation of the disk in the cell with minimal loss of time, further vacuum drying at 105°C, and finally reduction with hydrogen at 350°-400°C. Palladium diffused hydrogen was used at a flow rate of 40 ml/min. After reduction, the hydrogen was evacuated from the cell at 400°C, and the sample was then cooled to room temperature. Satisfactory samples were used in several different experiments with intermediate reductions at 400°C for 16 hr. Unless stated otherwise, all spectra discussed in this paper were recorded at room temperature.

Determination of reduced iron surface area.—Studies of the spectrum of carbon monoxide chemisorbed on silica-supported iron have been reported (7,9) so the interpretation of these spectra will not be discussed here. It now appears that not more than 10% of the surface iron was in the reduced state in the previous studies.

As indicated, the extent of reduction was determined from the ratio of the volumes of carbon monoxide and nitric oxide which were adsorbed. This determination involved only surface atoms so statements regarding extent of reduction apply to the fraction of the surface which was reduced. The ratio of the total atoms in the reduced or oxidized state can be different from the surface ratios if particle size is a factor in ease of reduction (as it probably is with larger particles being the more easily reduced).

The measurements of the amounts of carbon monoxide and nitric oxide chemisorbed were obtained by dosing in measured volumes of gas until the infrared bands attributable to the chemisorbed species reached maximum intensity. The volume of gas retained in the gaseous phase was subtracted from the total added. The method for determining the end point for carbon monoxide chemisorption is discussed below while the end point for nitric oxide will be discussed later in connection with the studies of nitric oxide chemisorption.

Chemisorbed carbon monoxide produced strong bands in the 1900-1990 cm^{-1} region. As carbon monoxide was dosed into the cell, the intensity of the bands increased until a terminal point was reached. Further addition of carbon monoxide produced a band at 2020 cm^{-1} which was attributed to iron carbonyl formation. The carbonyl band was removed by evacuation at 30°C without affecting the bands of chemisorbed carbon monoxide. The best samples were capable of chemisorbing 0.16 cc (0.15g sample). This would correspond to about 2000 cm^2 of reduced iron surface.

All gas volumes reported in this paper (including vapors of water and butyl nitrite) are given as cc s.t.p.

The silica did not adsorb either carbon monoxide or nitric oxide under the experimental conditions used in the chemisorption determinations.

Purification of adsorbates.—Commercial tank nitric oxide (Matheson-99% purity) contains nitrous oxide and nitrogen dioxide. These impurities were removed by distillation through cold traps (10). The satisfactory purity of butyl nitrite vapor (Eastman Kodak white label grade) was established by observing the infrared spectrum at 13 mm pressure in a 9 cm path length gas cell (11). The carbon monoxide (Airco, spectra assayed grade) and the commercial tank oxygen were used as-received.

Bulk iron oxides.—Iron oxide (Cabot's E-7) was obtained in the form of γ-Fe_2O_3. This material had a specific surface area of 35 m^2/g. Because the infrared transmission was poor, only about 0.0075 g/cm^2 of the γ-Fe_2O_3 could be tolerated in the beam path. This thickness did not allow preparation of a self-supporting disk so it was diluted with about three times as much silica in order to make the disk for infrared examination.

Adsorbents of Fe_3O_4 and α-Fe_2O_3 were produced by conversion of the γ-Fe_2O_3. Evacuation at 250°C for several hours removed any adsorbed water and also produced an Fe_3O_4 adsorbent (12, 13). The same sample was converted to an α-Fe_2O_3 adsorbent by heating at 350°C in 1 atm of oxygen for 16 hr followed by rapid cooling to room temperature in the pure oxygen atmosphere (14).

Results and Discussion

Nitric oxide on oxidized iron.—Since it was not possible to obtain completely reduced iron samples, studies of nitric oxide chemisorption were limited to completely oxidized samples and samples which were only partially reduced. The completely oxidized samples are considered first because they provide the simpler system.

Samples, having completely oxidized iron surfaces, may be obtained either by starting with bulk iron oxide or by taking a silica-supported sample through the preparative sequence previously described, and then exposing the partially reduced sample to oxygen (2 mm Hg) at 30°C. Exposure to oxygen under these conditions was expected to form 15-20Å thick films of Fe_3O_4, or mixtures of Fe_3O_4 and γ-Fe_2O_3, on the iron which had been reduced (13, 14). Oxidized iron samples prepared by this method were more amenable to infrared study than the bulk iron oxides. This advantage was due to the smaller particle size of the silica-supported iron oxide. The smaller particle size gave better infrared transmission and higher adsorptive capacity per unit weight of oxide.

Samples which were studied directly after reduction with hydrogen will be referred to as "reduced" even though it is understood that the reduction was only partially successful. Samples prepared by exposing reduced iron to oxygen will be referred to as "pre-oxidized" to differentiate them from "bulk" iron oxide and from samples in which the iron became oxidized during chemisorption.

Spectrum A of Fig. 2 shows the 1900-1700 cm^{-1} region for a pre-oxidized sample and spectrum B shows this region after chemisorption of 0.095 cc of nitric oxide. The chemisorption of nitric oxide produced a strong band at 1824 cm^{-1}. No other bands were observed in the 4000-1300 cm^{-1} region which was scanned in the present work.

Chemisorption of nitric oxide on bulk Fe_3O_4 produced a spectrum similar to B with a single band near 1830 cm^{-1}. No band attributable to chemisorbed nitric oxide was detected when α-Fe_2O_3 was exposed to nitric oxide.

The band observed after chemisorption of nitric oxide on either pre-oxidized iron or on bulk Fe_3O_4 is attributed to the nitrogen-oxygen stretching frequency of an adsorbed nitrogen-oxide species which was

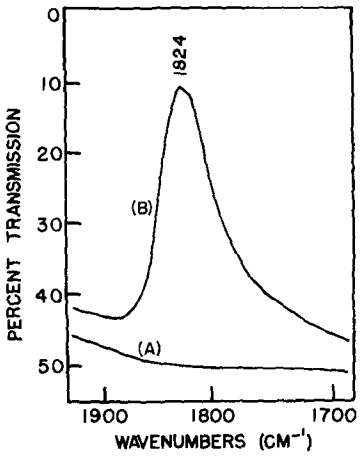

Fig. 2. Nitric oxide chemisorbed on pre-oxidized iron. A, background after exposure to oxygen at 30°C; B, after chemisorption of nitric oxide.

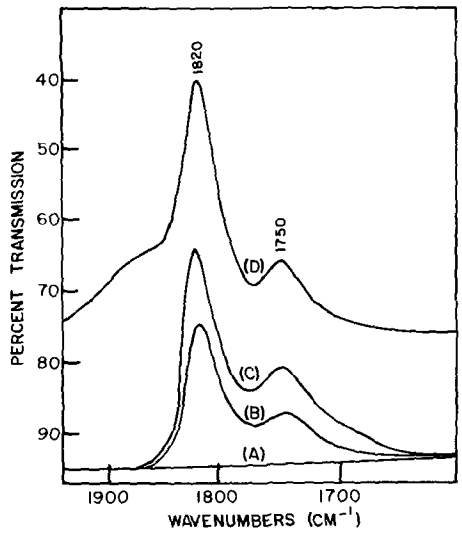

Fig. 3. Nitric oxide chemisorbed on reduced and oxidized iron: A, background of freshly reduced sample; B to D, after chemisorption of: B, 0.08 cc; C, 0.14 cc and D, 0.41 cc of nitric oxide.

bonded to the surface through the nitrogen. More specifically, the nitrogen is thought to be bonded to Fe^{++} sites on the oxidized iron surfaces as $Fe^{++}:N{=}O^{+}$.

The conclusion regarding the Fe^{++} sites is indicated by the detection of chemisorption on Fe_3O_4 but not on α-Fe_2O_3. Partial support for this conclusion comes from the reported observation of a similar band near 1850 cm^{-1} when nitric oxide was adsorbed on Fe^{++} sites of $FeSO_4$ (15).

The positive charge associated with the adsorbed nitric oxide represents a formal charge which is indicated because a coordinate covalent adsorption bond is visualized with both bonding electrons donated by the nitric oxide (15).

A general decrease in transmission over the entire 4000-1300 cm^{-1} region was observed when a reduced sample was exposed to oxygen to produce a pre-oxidized sample. The effect was frequency dependent with the transmission loss being greater in the higher wavenumber regions of the spectrum. In the case of the sample used for spectrum A of Fig. 2, the transmission was 90-100% prior to exposure to oxygen. It can be seen that exposure to oxygen decreased the transmission of this sample by about one half in the 1900-1700 cm^{-1} region. The observed decrease in transmission poses an interesting solid-state problem because at first thought it would be expected that conversion of metal to oxide would increase the infrared transmission.

An understanding of the mechanism of the observed decrease in transmission is not vital to the present work, and at this time it is not possible to put forth a nonspeculative explanation of this phenomenon. However, it is reasonable to expect that the quantitative explanation will be related to the small diameter of the metal particles. The diameter of the particles (~50Å) is less than the normal mean free path of electrons in metals, and it is reasonable that this factor accounts for the relatively high transmission of the reduced samples (16). The iron oxide obtained after exposure to oxygen probably had semiconductor properties and could have been a better conductor, and correspondingly a poorer transmitter, than the small metal particles. Another possibility is that the transmission loss was primarily due to increased scattering loss as indicated by the observed frequency dependence. This demands that growth of oxide film on the metal particles increased light scattering losses due to increased particle sizes more than it decreased their absorptivities due to conversion of metal to oxide.

Nitric oxide on reduced iron.—Figure 3 shows typical spectra observed when a reduced sample was exposed to nitric oxide. Spectra A, B, C, and D correspond to nitric oxide adsorptions of 0, 0.08, 0.14, and 0.41 cc, respectively. The band at 1820 cm^{-1} is attributed to nitric oxide chemisorbed on oxidized iron, $Fe^{++}:NO^{+}$, as discussed for Fig. 2.

The 1750 cm^{-1} band is related to chemisorption of nitric oxide on portions of the sample which were in the reduced metallic state prior to chemisorption. This is not equivalent to chemisorption of nitric oxide on reduced metal since the chemisorption process appears to involve an oxidation.

The sample used for Fig. 3 had chemisorbed 0.050 cc of carbon monoxide in the test for reduced iron surface. Prior to nitric oxide adsorption the sample was re-reduced for 2 hr at 350°C to remove the chemisorbed carbon monoxide.

During the addition of nitric oxide, the residual gas was analyzed by a mass spectrometer. A total of 0.026 cc of nitrogen was evolved during the sequence of spectra shown in Fig. 3. On the basis of the approximately 2/1 ratio for the volumes of nitrogen evolved and carbon monoxide previously chemisorbed it appears that the nitric oxide was involved in an oxidative chemisorption on the reduced iron. The oxidative phase of this reaction can be expressed as

$$2NO + 2Fe_{red.} \rightarrow 2FeO_{ads.} + N_2\uparrow \qquad [1]$$

Equation [1] indicates that each molecule of nitrogen corresponds to loss of two reduced metallic surface sites. This is therefore consistent with the observation that the number of evolved nitrogen molecules is one half the number of carbon monoxide molecules which could be chemisorbed.

In Eq. [1] the oxygen attached to the iron is indicated as being adsorbed. This designation is used to emphasize the difference between the surface oxide formed by the oxidative chemisorption of nitric oxide and the bulk or pre-oxidized type of iron oxide which were discussed previously. This differentiation is necessary because chemisorption of nitric oxide on the Eq. [1] oxide produced a band at 1750 cm^{-1} while chemisorption of nitric oxide on the bulk or pre-oxidized iron oxide produced a band above 1820 cm^{-1}.

The band observed at 1750 cm^{-1} is attributed to the nitrogen-oxygen stretching frequency in a species formed by chemisorption of nitric oxide on FeO_{ads}

$$NO + FeO_{ads} \rightarrow Fe{-}O{-}N = O_{ads} \qquad [2]$$

Partial support for this assignment comes from the observation of bands near 1700 cm^{-1} in organic nitrites of the type RONO (11).

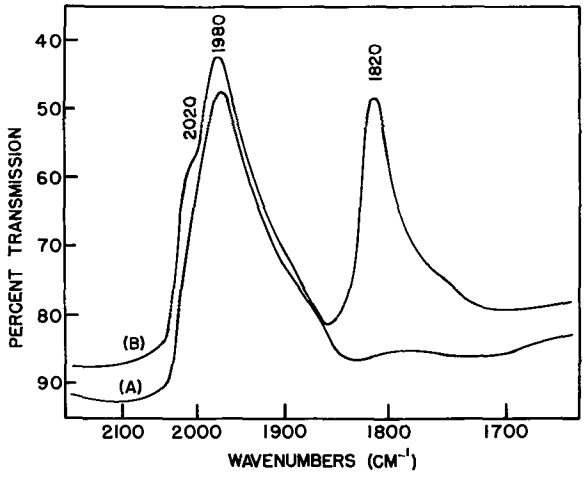

Fig. 4. Co-adsorbed carbon monoxide and nitric oxide on iron: A, carbon monoxide chemisorbed on the reduced iron; B, after co-adsorbing nitric oxide on the unreducible iron phase.

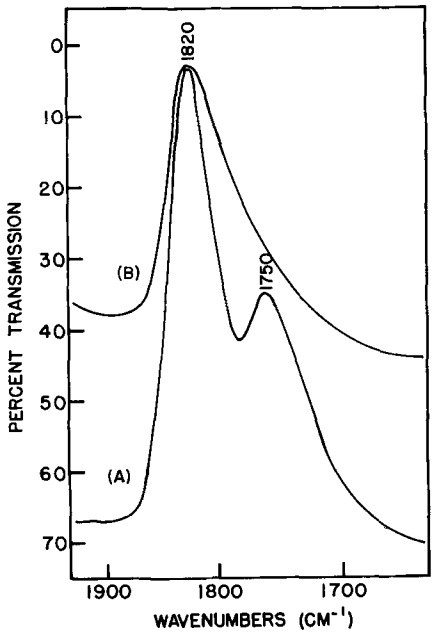

Fig. 5. Effect of oxygen on chemisorbed nitric oxide: A, nitric oxide chemisorbed on both oxidized and initially reduced iron phases; B, after adding oxygen at 30°C.

The present work indicates that it is not possible to preserve iron surfaces in the reduced state after exposure to nitric oxide at room temperature. For this reason the 1750 cm^{-1} band is attributed to nitric oxide chemisorbed on iron which was in the reduced state prior to exposure to nitric oxide and is not referred to as nitric oxide on reduced iron. There is a discrepancy between this concept and the conclusions of Terenin and Roev (15). These workers observed a band at 2008 cm^{-1} which they attribute to nitric oxide chemisorbed on reduced iron as Fe—N≡O^+. In this case the iron atom is considered as a constituent of a reduced metallic particle. Thus it is significantly different from the iron in our Fe^{++}:NO^+ structure because here the Fe^{++} refers to an iron cation in an oxide. The 2008 cm^{-1} band has not been observed in the present work even though it shows up strongly in the Terenin and Roev spectrum. Moreover, if the 2008 cm^{-1} band were observed, it would not be possible to attribute it to nitric oxide on reduced iron without abandoning the concept of the oxidative nature of nitric oxide chemisorption.

Co-adsorption of carbon monoxide and nitric oxide.—The above discussion implies that the 1750 cm^{-1} band is produced by an oxidative chemisorption of nitric oxide on the reduced iron sites which were initially capable of chemisorbing carbon monoxide. This conclusion is supported by observations made when nitric oxide is added to reduced samples on which carbon monoxide is chemisorbed. Spectrum A of Fig. 4 was recorded after chemisorbing 0.09 cc of carbon monoxide on a reduced iron sample. The strong band at 1980 cm^{-1} is attributed to the carbon-oxygen stretching frequency in Fe—C≡O. Spectrum B of Fig. 4 was observed after dosing in small quantities of nitric oxide until a total of 0.12 cc of nitric oxide had been added. Even though a slight perturbation of the carbon monoxide band caused a shoulder to appear at 2020 cm^{-1}, the conclusion is that the band at 1820 cm^{-1} (characteristic of nitric oxide on oxidized iron) grew without profoundly affecting the chemisorbed carbon monoxide. A small band is observed at 1750 cm^{-1} in spectrum B. However, this band is small compared to the 1750 cm^{-1} band in spectrum C of Fig. 3. Thus, it appears that the chemisorbed carbon monoxide is effective in protecting the underlying iron surface from oxidation by nitric oxide. This protection is not complete because an additional 1.0 cc of nitric oxide caused the disappearance of the chemisorbed carbon monoxide band and the 1750 cm^{-1} band increased to the levels expected on the basis of spectrum C of Fig. 3.

Effect of oxygen and water on chemisorbed nitric oxide.—If a chemisorbed nitrogen-oxygen species is to be regarded as a significant factor in corrosion inhibition, it is reasonable to expect that these species would resist displacement by oxygen or water. The effect of exposing chemisorbed nitric oxide to oxygen is shown in Fig. 5. Spectrum A was observed after adding 0.75 cc of nitric oxide to a reduced iron sample. This spectrum shows the 1820 cm^{-1} and 1750 cm^{-1} bands which have been discussed for Fig. 3.

Spectrum B of Fig. 5 was observed after adding 1.15 cc of oxygen. The oxygen caused complete removal of the 1750 cm^{-1} band. The 1820 cm^{-1} band has been decreased but a large portion remains. The disappearance of the 1750 cm^{-1} band indicates that the Fe—O—N=O species, which is thought to be responsible for this band, is not a significant factor in corrosion inhibition. The retention of the 1820 cm^{-1} band suggests that any inhibitive properties of adsorbed nitrogen-oxygen species would be associated with the Fe^{++}:NO^+ structure.

The decrease in transmission, which is observed in going to spectrum B of Fig. 5, suggests that further oxidation of the particles on which the —O—N=O species (1750 cm^{-1}) were adsorbed may have been a factor in the displacement of this species.

Exposure of a sample, equivalent to that which gives spectrum A of Fig. 5, to water vapor did not cause displacement of either the 1820 cm^{-1} or the 1750 cm^{-1} bands. If a reduced sample was exposed to water vapor prior to adsorption of nitric oxide, the spectrum of the chemisorbed nitric oxide showed only a single band at 1820 cm^{-1}. Prior exposure to water vapor would result in formation of a thin oxide film on the iron. Results presented in Fig. 2 indicate that nitric oxide adsorption would then produce only the one nitrogen oxide band at 1820 cm^{-1} as was observed. Preadsorption of nitrogen oxide species on the reduced iron (as O—N=O groups) was apparently able to prevent this oxide film formation.

Effect of excess nitric oxide.—In Fig. 3 a decrease in transmission is observed in going from spectrum C to spectrum D. This decrease proceeded further as more nitric oxide was added until a transmission level of about 50% was reached after addition of 0.95 cc of nitric oxide. This decrease in transmission is evidence for a change in the nature of the reaction since there was no decrease in transmission in going from spectrum A to spectrum C. Other evidence for the changing character of the reaction of nitric oxide with the

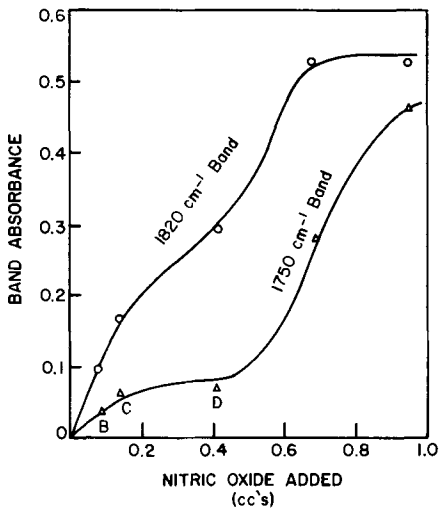

Fig. 6. Growth behavior of chemisorbed nitric oxide bands

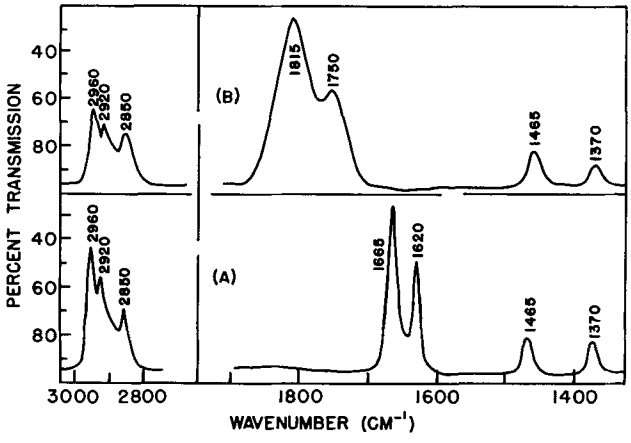

Fig. 7. Chemisorption of butyl nitrite on iron: A, butyl nitrite vapor (adsorbate); B, chemisorbed butyl nitrite on iron.

iron sample was also noted. When more nitric oxide was added, after the stage represented by spectrum D, nitrous oxide and nitric oxide were detected in the gaseous phase while the evolution of nitrogen ceased.

The most puzzling aspect of the changing character of the reaction lies in the observation of a further increase in the intensity of the 1750 cm^{-1} band. This increase cannot be explained on the basis that the 1750 cm^{-1} band is due solely to a monolayer of Fe—O—N=O on the initially reduced iron surface.

Figure 6 shows a plot of the absorbances of the 1820 cm^{-1} and 1750 cm^{-1} bands as a function of the amount of nitric oxide added. Up to the region of 0.8-0.9 cc the amount of nitric oxide added is equivalent to the amount chemisorbed since no residual nitric oxide could be detected. The residual pressure of nitric oxide after addition of 0.95 cc was ~0.01 mm. The absorbance is the log I_o/I where I is the transmission at the band peak and I_o is the base line background transmission at the peak frequency.

The specific extinction coefficient of the species responsible for the 1750 cm^{-1} band was calculated from the intensity of this band in previous spectra using the assumption that the adsorbed species is formed as indicated by Eq. [1] and [2]. This extinction coefficient is 0.1 x 10^{-17} cm^2/molecule (where extinction coefficient k is defined by: 2.3 log $I_o/I = kC$; C is concentration in molecules per square centimeter of beam path). This value is about one half that of the extinction coefficient of carbon monoxide chemisorbed on reduced iron. For the sample used to provide the data of Fig. 6, the absorbance due to chemisorbed carbon monoxide was 0.22. This would predict a maximum intensity of about 0.11 for the 1750 cm^{-1} band if this band is due solely to Fe—O—N=O groups on the portion of the surface which was initially capable of chemisorbing carbon monoxide. The flat portion for the 1750 cm^{-1} absorbance curve in Fig. 6 is slightly lower than this, but the agreement is acceptable.

The change to the evolution of nitrous oxide rather than nitrogen suggests that nitrogen evolution was related to the presence of reduced iron surface. When this type of surface was no longer available, the stoichiometry of the oxidative reaction suggests that it involved reaction of a molecule of nitric oxide from the gaseous phase with a molecule of nitric oxide which was previously chemisorbed.

A bulk oxidation could explain the decrease in transmission, but it cannot explain the additional growth of the 1750 cm^{-1} band. On the basis of present evidence, it is most reasonable to assume that the increase in the 1750 cm^{-1} band and at least some of the increase in the 1820 cm^{-1} band, which is observed above the plateau region (0.5 cc) of Fig. 6, was due to the formation of iron nitrosyl, $Fe(NO)_4$. Iron nitrosyl has bands at 1810 cm^{-1} and 1730 cm^{-1} (17). A single monolayer of iron nitrosyl could give the absorbance values shown in Fig. 6. However, the possibility of the formation of some bulk iron nitrosyl cannot be excluded.

Adsorption of butyl nitrite on reduced iron.—The vapor pressure of n-butyl nitrite is about 13 mm at room temperature. This vapor pressure permits it to be used as a vapor phase corrosion inhibitor. It also permits convenient handling in the gas transfer procedures which are associated with the infrared method. However, there is some likelihood of its condensing on the silica portions of the sample. The spectrum of butyl nitrite physically adsorbed on silica is similar to that of butyl nitrite vapor. The physically adsorbed butyl nitrite can be easily removed from silica by evacuation at room temperature.

The spectrum of butyl nitrite vapor is shown as spectrum A of Fig. 7. This spectrum was observed with 13 mm of butyl nitrite in a gas cell which had a path length of 9.5 cm. The bands at 2960 cm^{-1}, 2920 cm^{-1}, and 2850 cm^{-1} are carbon-hydrogen stretching bands, and the 1465 cm^{-1} and 1370 cm^{-1} bands are due to carbon-hydrogen bending vibrations of the butyl group. The bands at 1665 and 1620 cm^{-1} have been attributed (11) to the stretching vibrations of the nitrogen-oxygen double bond in the trans, R—O, N=O, and cis, R—O, N, O, isomers, respectively.

Spectrum B of Fig. 7 was observed after adding 0.28 cc of butyl nitrite vapor to a reduced iron sample. This spectrum shows bands at 1815 and 1750 cm^{-1} which are similar to the bands observed after adding nitric oxide to reduced samples. It appears that there was no butyl nitrite physically adsorbed on the silica because bands are not observed at 1665 and 1620 cm^{-1}.

The hydrocarbon bands of spectrum B are similar to those of spectrum A. This similarity indicates that the majority of the adsorbed butyl hydrocarbon radicals remained intact.

Evacuation at room temperature had no effect on any of the bands in spectrum B. However, after evacuation at 100°-150°C it was observed that the 1815 cm^{-1} and 1750 cm^{-1} nitrogen-oxygen bands disappeared while the hydrocarbon bands remained unaffected. The hydrocarbon bands became smaller after the temperature was increased to 200°C, but did not completely disappear until the temperature was increased to 380°C.

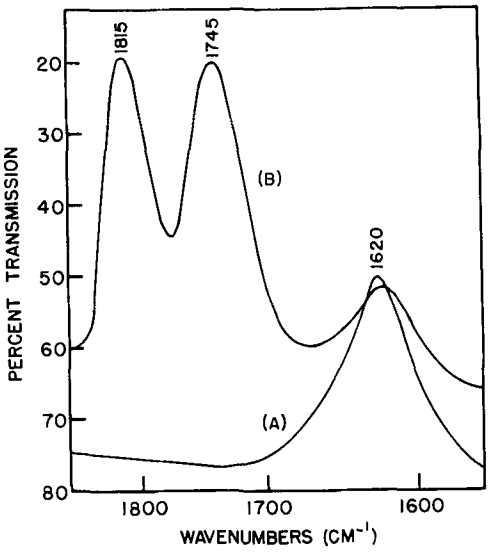

Fib. 8. Chemisorption of butyl nitrite on iron covered by an adsorbed water film: A, adsorbed water; B, after adding butyl nitrite vapor.

At temperatures above 200°C, bands attributed to carboxylate ions were observed near 1550 and 1420 cm^{-1}. These bands indicate that the hydrocarbon fragments on the surface were being partially oxidized. This oxidation is thought to have involved oxygen furnished by the iron oxide.

The difference in the ease of removal of the nitrogen-oxygen and hydrocarbon bands shows that the butyl nitrite had dissociated. However, there is a question as to whether the dissociation occurred during the evacuation above 100°C or whether the dissociation occurred during the initial chemisorption of room temperature. The nitrogen-oxygen bands at 1850 and 1750 cm^{-1} are similar to those observed when nitric oxide was chemisorbed. This is taken as an indication that the dissociation of butyl nitrite occurred during the chemisorption at room temperature. It is difficult to account for the 1815 and 1750 cm^{-1} bands on the basis of structures in which the nitrogen-oxygen functional groups remain attached to butyl groups.

Butyl nitrite might dissociate by rupture of the carbon-oxygen bond, RONO → R— + ONO, or by rupture of the oxygen-nitrogen bond, RONO → RO— + NO. The spectra of the residual hydrocarbon fragments are not useful in clarifying which type of dissociation occurs. It is difficult to distinguish between the spectra of adsorbed butyl radicals, C_4H_{11}–, and adsorbed butoxy radicals, $C_4H_{11}O$—. Moreover, rupture to initially give butyl radicals might result in butoxy radicals if the butyl radical were adsorbed on an oxygen.

Nitrogen was evolved during the initial phases of the chemisorption of butyl nitrite on the reduced iron sample. This nitrogen was probably produced by the oxidative chemisorption of nitric oxide formed during decomposition of butyl nitrite. The decrease in transmission, which has been associated with oxidation of the iron, was also observed during the chemisorption of butyl nitrite.

Chemisorption of butyl nitrite on pre-oxidized iron.—Chemisorption of butyl nitrite on pre-oxidized samples produced spectra similar to that of spectrum B of Fig. 7. Nitrogen-oxygen bands were observed at 1815 and 1750 cm^{-1}. As in the case of butyl nitrite on reduced iron, the 1815 and 1750 cm^{-1} bands were removed by evacuation at 150°C while the hydrocarbon bands were retained.

If the butyl nitrite had dissociated to butoxy radicals and nitric oxide, observation of the 1750 cm^{-1} would not be expected since nitric oxide did not produce this band when adsorbed on a pre-oxidized sample. Thus, the observation of the 1750 cm^{-1} band in this case presents a question which is difficult to resolve. Tentatively, the 1750 cm^{-1} band of butyl nitrite on a pre-oxidized sample is ascribed to Fe—O—N=O produced by adsorption of —O—N=O fragments. These result from the rupture of the carbon-oxygen bonds RONO → R— + O—N=O. Attempts have been made to support this explanation by adsorbing nitrogen dioxide on iron and iron oxide samples, but no chemisorbed O—N=O species were detected.

Effect of water on butyl nitrite chemisorption.—In many practical situations if butyl nitrite were to be an effective corrosion inhibitor, it would necessarily adsorb on a surface which was initially covered with a layer of water. In order to determine whether preadsorbed water would retard chemisorption of butyl nitrite, a reduced iron sample was exposed to 6 cc of water vapor prior to admission of butyl nitrite. This quantity of water was sufficient to cover all of the surface of the sample including the silica.

Spectrum A of Fig. 8 was observed after adsorption of the water and prior to adsorption of the butyl nitrite. It shows a strong band at 1620 cm^{-1} which is due to the hydrogen-oxygen-hydrogen bending mode of physically adsorbed water. Spectrum B of Fig. 8 was observed after adding 0.65 cc of butyl nitrite vapor. The observed nitrogen-oxygen bands are similar to those of Fig. 5. This shows that the preadsorbed water did not retard the chemisorption of butyl nitrite.

Significance of results to corrosion inhibition.—The work presented in this paper shows that both nitric oxide and butyl nitrite cause oxidation of the surface of reduced iron and that chemisorption of these molecules produces strongly held nitrogen-oxygen species on oxide surfaces; with butyl nitrite, strongly adsorbed hydrocarbon fragments are also detected. On the basis of the specific examples studied, it is reasonable to conclude that chemisorption on reduced iron is not likely to be a significant factor in corrosion inhibition by nitrites.

The role of the chemisorbed hydrocarbon fragments, produced by dissociation of butyl nitrite, cannot be evaluated on the basis of present results. It is reasonable to assume that the chemisorbed hydrocarbons would render the surface partially hydrophobic and would thereby provide some protective action. However, the many examples of the inhibitive properties of sodium nitrite show that a hydrocarbon constituent is not essential to the corrosion inhibitive properties of inorganic nitrites.

The evidence presented here shows that nitrogen-oxygen species adsorb strongly on iron oxide and also resist displacement by water and oxygen. Extension of these observations to a conclusion regarding the role of the adsorbed species in corrosion inhibition is admittedly speculative. However, it is reasonable to consider that the nitrogen-oxygen species, which is thought to adsorb as $Fe^{++}:NO^{+}$, creates surface conditions which are significantly different from those which prevail in the absence of the inhibitor. In the latter case the surface is probably covered with species such as $O^{=}$, OH^{-}, or Cl^{-}. Replacement of these anions by the NO^{+} could be expected to decrease the potential drop across the oxide layer and thereby reduce the field assisted migration of metal ions through the oxide barrier.

Present plans call for a continuation of the infrared study of adsorbed corrosion inhibitors with emphasis on the development of techniques which preclude the necessity of using silica supported samples. Hopefully, an application of infrared methods to samples which are suitable for simultaneous testing of the efficiency of corrosion inhibition will provide additional worthwhile information.

Acknowledgment

The authors wish to express appreciation to D. Bauer and B. Clark for help with the experimental work, to L. C. Roess and A. N. Webb for stimulating discus-

sions, and to the management of Texaco, Inc. for support of this work.

Manuscript received Sept. 9, 1965.

Any discussion of this paper will appear in a Discussion Section to be published in the December 1966 JOURNAL.

REFERENCES

1. M. Cohen, *Can. J. Chem.*, **37**, 286 (1959).
2. J. Kruger, *This Journal*, **110**, 654 (1963).
3. J. L. Ord and J. H. Bartlett, *ibid.*, **112**, 160 (1965).
4. H. H. Uhlig, *Ann. N. Y. Acad. Sci.*, **58**, 843 (1954).
5. Y. M. Kolotyrkin, *Z. Elektrochem.*, **62**, 664 (1958).
6. Yung-Fang Yu Yao, *J. Phys. Chem.*, **68**, 101 (1964).
7. R. P. Eischens and W. A. Pliskin, *Adv. Catalysis*, **X**, 1 (1958).
8. R. P. Eischens, S. A. Francis, and W. A. Pliskin, *J. Phys. Chem.*, **60**, 194 (1956).
9. G. Blyholder and L. D. Neff, *ibid.*, **66**, 1664 (1962).
10. R. E. Nightingale, A. R. Downie, D. L. Rotenburg, B. Crawford, and R. A. Ogg, *ibid.*, **58**, 1047 (1947).
11. P. Tarte, *J. Chem. Phys.*, **20**, 1570 (1952).
12. A. F. Wells, "Structural Inorganic Chemistry," 3rd ed., p. 491, Oxford Press (1962).
13. D. E. Davis, U. R. Evans, and J. M. Agar, *Proc. Roy. Soc. London*, **225A**, 443 (1954).
14. P. B. Sewell and M. Cohen, *This Journal*, **111**, 508 (1964).
15. A. N. Terenin and L. M. Roev., *Spectrochim. Acta*, **16**, 274 (1959).
16. R. H. Doremus, *J. Chem. Phys.*, **42**, 414 (1965).
17. W. P. Griffith, J. Lewis, and G. Wilkinson, *J. Chem. Soc.*, **1958**, 3493.

The Gallium-Phosphorus-Zinc Ternary Phase Diagram

M. B. Panish

Bell Telephone Laboratories, Incorporated, Murray Hill, New Jersey

ABSTRACT

The data obtained from a series of differential thermal analysis studies have been used, along with several x-ray studies, information from the literature, and a regular solution computation to construct a portion of the condensed ternary phase diagram for the gallium-phosphorus-zinc system. The phase diagram consists principally of the primary phase fields of GaP and Zn_3P_2.

The major interest in the Ga-P-Zn ternary phase diagram is the result of the current interest in electroluminescence in gallium phosphide p-n junctions made by the diffusion of zinc into n-type GaP. Since the ternary phase diagram defines the stability conditions for GaP in the presence of a third component, it is of importance in the selection of diffusion source compositions and for the definition of crystal growth conditions.

Thurmond's (1) binary liquidus data for the gallium-phosphorus system, and Hultgren's (2) tabulated data for the gallium-zinc system have been used, along with experimental data obtained from a series of differential thermal analysis studies, and a regular solution extrapolation procedure, to construct a portion of the ternary phase diagram for the gallium-phosphorus-zinc system.

The Binary Phase Systems

GaP.—Gallium and phosphorus form a single congruently melting compound, GaP, with a melting point of 1465°C (3). Thurmond (1) has utilized the solubility data of Rubenstein (3) and Hall (4) along with an adaptation of the regular solution treatment of Vieland (5) to construct the binary phase diagram.

Ga-Zn.—Gallium and zinc form a simple eutectic system with a eutectic temperature of 25.5°C at a zinc concentration of 3.7 a/o (atom per cent). Hultgren, Orr, Anderson, and Kelley (2) have constructed the phase diagram on the basis of measurements by Heuman and Predel (6).

P-Zn.—There is not enough data available in the literature for the construction of the P-Zn binary phase diagram. Hansen (7) reports the existence of two zinc phosphides, Zn_3P_2 and ZnP_2. For the purposes of the work reported here it has been assumed that the shape of the binary phase diagram is similar to that reported for the Zn-As system (7).

Experimental

Semiconductor grade phosphorus and zinc with purities better than 99.99% were used in this work. The gallium in some runs was 99.9999% pure, but for some runs in which large amounts of gallium were required, reclaimed gallium with purity better than 99.99% was utilized.

Fused silica capsules with a volume of about 13 cc which were about 2/3 filled with melt were used for the differential thermal analysis experiments. The experimental details are very similar to those which have already been described for the study of the Ga-As-Zn system (8).

In order to obtain x-ray data for the phases present during cooling process, several of the DTA cells were removed from the cooling apparatus before they had cooled enough to go through all the expected phase transitions. These cells were then air or water quenched in an attempt to freeze in the phases of interest.

Results and Discussion

The temperature at which thermal effects were observed when melts of various compositions were cooled are given in Table I. T_1 represents the temperature at which the surface of primary crystallization is reached. T_2 is the temperature of appearance of a second solid phase. T_3 and T_4 are temperatures at which there are apparently solid phase transitions in Zn_3P_2. T_5 is the temperature at which a ternary peritectic is reached and the reaction

$$Zn_3P_2 + 2Ga \rightarrow 2GaP + 3Zn \qquad [1]$$

Table I. Thermal effects in the Ga-P-Zn ternary

Atom per cent			Temperature of thermal effect, °C					
Zinc	Gallium	Phosphorus	T_1	T_2	T_3	T_4	T_5	T_6
90.0	5.0	5.0	889	498	850	(835)*	404	—
82.5	8.75	8.75	954	629	846	(805)	408	—
77.4	11.3	11.3	986	736	824	**	†	—
77.4	11.3	11.3	988	745	839	817	406	—
73.5	13.75	13.75	1018	(919)	829	822	†	—
71.6	23.5	5.0	903	—	—	—	—	331
68.1	15.9	15.9	1055	988	827	817	415	—
65.0	27.0	8.0	968	—	—	—	—	†
62.1	18.9	18.9	1040	1017	825	817	401	—
60.0	25.0	15.0	1026	962	**	811	361	‡
56.0	40.0	4.0	937	—	—	—	—	270
55.0	30.3	14.8	1060	—	—	—	—	324
47.0	41.6	11.4	1075	—	—	—	—	†

* Doubtful observation is indicated by brackets.
** Not observed.
† Not done.
‡ Apparent inhomogeneity during this run. This point has been disregarded.

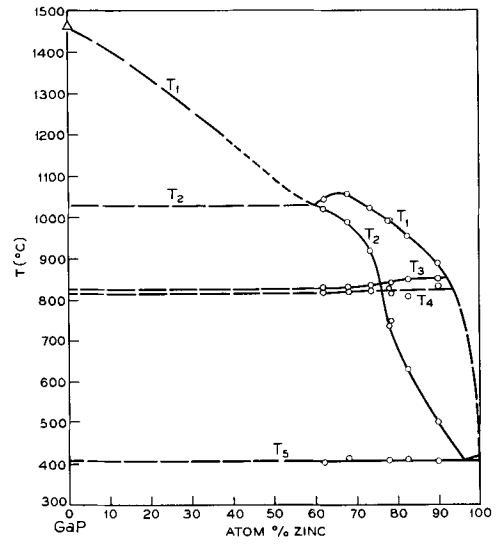

Fig. 1. Thermal effects in the GaP-Zn pseudobinary. ○, This work; △, Thurmond; - - - Estimated from regular solution calculation; — —, Estimated.

occurs. T_6 is the temperature at which a zinc-gallium phosphide mixture precipitates. Figure 1 is a plot of the temperature at which most of the thermal effects described above were observed in melts whose over-all compositions were along the GaP-Zn pseudobinary.

As can be seen from Table I and Fig. 1, experimental thermal effect data were obtained only in the region of the ternary system in which the over-all phosphorus composition was less than about 19 a/o. The restriction of experimental work to this part of the phase diagram was necessary because of the high equilibrium phosphorus pressures which would have been encountered had experiments been done at higher phosphorus composition.

Construction of the ternary diagram.—The Ga-P binary diagram of Thurmond (1) and the Zn-Ga binary diagram of Hultgren (2) were used as boundaries for the ternary without modification. It was assumed that the P-Zn phase diagram is similar in shape to the As-Zn phase diagram; however, no effort has been made to show details of the ternary diagram in the region of the Zn-P axis.

The ternary Ga-P-Zn phase diagram is shown in Fig. 2. The position of the ternary eutectic valley was obtained from the T_1-T_2 thermal effect intersection on the GaP-Zn pseudobinary (Fig. 1), from the T_2 thermal position for a point on cut C (Fig. 2 and 3), and from the position of the ternary peritectic point. The ternary eutectic valley was extrapolated towards the Zn-P axis of the diagram, by assuming that the

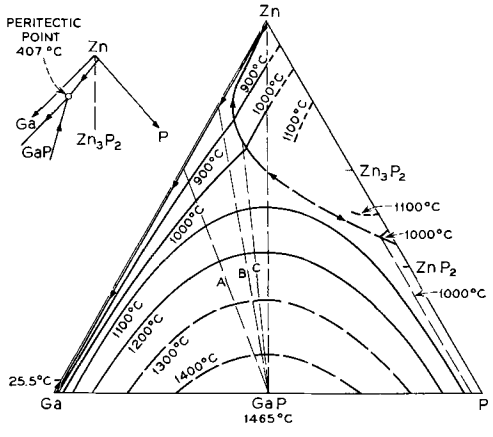

Fig. 2. The Ga-P-Zn ternary phase diagram

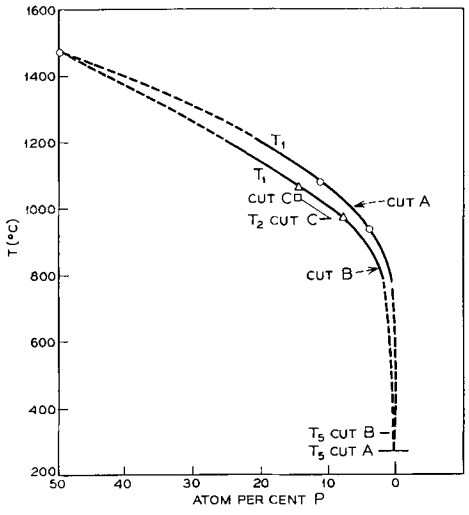

Fig. 3. Thermal effects for mixtures along several cuts in the Ga-P-Zn ternary system.

Ga-P-Zn system behaves in a manner similar to that already shown for the Ga-As-Zn system (8).

The composition at which the ternary peritectic occurs was obtained by assuming that this composition is very close to the Ga-Zn axis and therefore is essentially on the Ga-Zn binary at a composition corresponding to the liquid-solid equilibrium composition at the observed peritectic temperature. This assumption is supported by the fact that in the Zn-P system the liquidus has been reported to rise steeply from the melting point of pure Zn (9). The binary eutectic temperature is thus very close to the melting point of pure zinc and there is very little phosphorus in the liquid binary at the eutectic temperature.

X-ray analysis of samples quenched after formation of the first solid phase were found to contain only zinc, gallium, and GaP when the initial over-all composition was along cuts A and B. When the initial over-all composition was along the Zn-GaP pseudobinary or in the indicated Zn_3P_2 primary phase field, the slow cooled or quenched solid was found to contain zinc, gallium, GaP, Zn_3P_2 (occasionally), and an unidentified phase. The unidentified phase was present in all these samples, even in cases in which the sample was allowed to slow cool through the peritectic transformation temperature. The x-ray data are consistent with the phase diagram if it is supposed that the peritectic transformation is incomplete and that the unidentified phase is a modification of Zn_3P_2.

The latter assumption is substantiated by electron beam microprobe analyses which demonstrated the presence of a phase containing only zinc and phosphorus when the unidentified phase was observed by x-ray analysis. The thermal effects designated T_3 and T_4 in Fig. 1 are consistent with the suggested existence of one or more solid phase transitions in Zn_3P_2. A similar thermal effect which has been interpreted as a solid state transition has been observed in the Zn-As system (7) and the Ga-As-Zn system (8).

The regular solution procedure for interpolation of ternary isotherms which was recently suggested by Furukawa and Thurmond (10), and which has been applied by them to the Ga-As-Cu system, and by this author to the Ga-As-Zn system (8), was used for estimation of the isotherms in the GaP primary phase field. For this procedure the equation

$$RT \ln \left[\frac{k}{x_1 x_2}\right] = \{(a_{12}x_2 + a_{13}x_3)(x_2 + x_3) + (a_{12}x_1 + a_{23}x_3)(x_1 + x_3) - a_{23}x_2x_3 - a_{13}x_1x_3\} \quad [2]$$

was used. The symbols a_{12}, a_{13}, and a_{23} represent the interaction energies for components 1, 2 and 3; x_1, x_2,

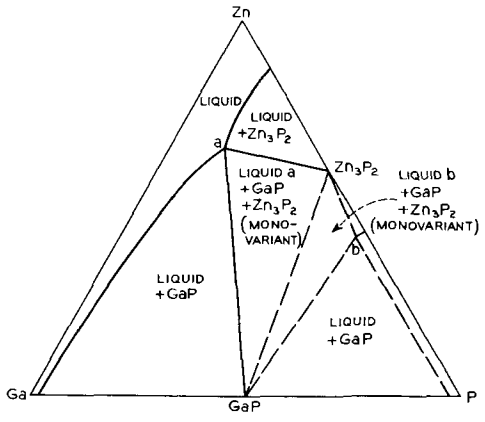

Fig. 4. The 1000°C isotherm in the Ga-P-Zn system.

and x_3 are atom fractions of the constituents, and K is the equilibrium constant for the reaction

$$GaP \rightleftarrows Ga_{(l)} + P_{(l)} \quad [3]$$

which was obtained from Thurmond's (1) binary data. Isotherms at 900°, 1000°, 1100°, and 1200°C were computed with data from Thurmond's Ga-P binary diagram and from several points along cuts A and B (Fig. 2 and 3). The 1300° and 1400°C isotherms were drawn to be consistent with the extrapolations of the various cuts, the Ga-P binary and the shape of the curves at lower temperatures. It should be noted that because of the limited region in which data was obtained the isotherms should be considered to be preliminary estimations.

Two isotherms in the Zn_3P_2 primary phase region were drawn by connecting the isotherm composition on the GaP-Zn pseudobinary with the intersection point of the isotherm in the GaP primary phase region with the ternary eutectic valley. Several other isotherms were roughly estimated by comparison with the Ga-As-Zn system.

Conclusions

The ternary phase diagram of the gallium-phosphorus-zinc system consists principally of two primary phase fields due to GaP and Zn_3P_2, respectively. The Zn_3P_2 phase field exists over part of the GaP-Zn pseudobinary, and there is a ternary peritectic point near the zinc corner of the diagram. These facts have several interesting implications for electronic device work done with gallium phosphide.

The existence of the Zn_3P_2 primary phase field over a large region of the ternary diagram indicates that it will be difficult to produce zinc alloyed electrical contacts to gallium phosphide without interference from Zn_3P_2 unless zinc-gallium "solders" are used. The presence of the additional phase will, however, be useful in diffusion studies. On any isotherm below about 1050°C there are extensive composition regions in which two solid phases and a liquid phase coexist. See, for example, Fig. 4. These regions are monovariant, the partial pressures of the equilibrium gaseous species being a function only of the temperature within the region. Highly reproducible diffusion sources may therefore be produced from mixtures with over-all compositions within the monovariant regions specified by the phase diagram.

A more detailed discussion of the implication of the ternary condensed phase diagram to diffusion studies and solid solubility in a system such as that discussed here has been given elsewhere (8).

Acknowledgments

The author is indebted to C. D. Thurmond for his helpful suggestions during the course of this work. The aid of Mr. S. Sumski with some of the experimental work, of Mrs. V. Compton for the x-ray analysis, and of H. Schreiber for the electron beam microprobe analyses is gratefully acknowledged.

Manuscript received Oct. 18, 1965.

Any discussion of this paper will appear in a Discussion Section to be published in the December 1966 JOURNAL.

REFERENCES

1. C. D. Thurmond, *J. Phys. Chem. Solids*, **26**, 785 (1965).
2. R. Hultgren, R. W. Orr, P. D. Anderson, and K. K. Kelley, "Selected Values of Thermodynamic Properties of Metals and Alloys," John Wiley & Sons, New York (1963).
3. M. Rubenstein, Electrochemical Society, Extended Abstracts of the Electronics Div., **11**, 129 (1962).
4. R. N. Hall, *This Journal*, **110**, 385 (1963).
5. L. Vieland, *Acta. Met.*, **11**, 137 (1963).
6. T. Heuman and B. Predel, *Z. Metalk.*, **49**, 90 (1958).
7. M. Hansen, "Constitution of Binary Alloys," McGraw-Hill Book Co., New York (1958).
8. M. B. Panish, *J. Phys. Chem. Solids*, **27**, 291 (1966).
9. R. Vogel and D. Horstmann, *Arch. Eigenhüttenw.*, **24**, 247 (1953).
10. Y. Furukawa and C. D. Thurmond, *J. Phys. Chem. Solids*, **26**, 1535 (1965).

Luminescence in Mg_2SiO_4:Tb,Li Phosphors

W. A. McAllister

Lamp Division, Advanced Development Department, Westinghouse Electric Corporation, Bloomfield, New Jersey

ABSTRACT

Magnesium orthosilicate (Mg_2SiO_4) can be activated by terbium, when lithium is used as a flux, to give the characteristic green line emission of Tb^{+3} ion. The emission is modified without loss in 254 nm-excited efficiency on addition of manganese, to give a supplementary orange band. The incorporation of high concentrations of activator terbium, a cation much larger than any other species present, without significant distortion of the olivine structure is probably related to known features of this lattice. The good brightness at such high activator levels suggests better coupling of the emitting rare earth to the ultraviolet absorbing host.

The emission characteristics of rare earths have been studied for the free ions (1, 2) and when present as constituents in various host lattices such as oxides (3), tungstates, and molybdates (4, 5). Where the rare earth is part of a crystal matrix its spectral properties are largely those of the free ion, characterized by a series of lines indicative of the shielding of the f-orbital energy levels involved in optical processes. Accommodation of the rare earths is usually by replacement of other cations of similar size,

with compensation of any charge differences if necessary. This is doubtless true in the europium-activated alkaline earth silicate phosphors described by Jenkins and McKeag (6), in which calcium, strontium, or barium were the cations involved. On the other hand, substitution of lanthanides (r = 1.1Å) for magnesium (r = 0.78Å) in a lattice is not likely since the differences in ionic radii are over twice the 15% value considered to be the limit of miscibility for mixed crystal formation (7). It has been found possible, however, to introduce rare earths into hosts having magnesium as the largest cation, by using a compensating alkali metal ion (lithium). The work described herein represents a portion of the effort devoted chiefly to magnesium silicate activated by terbium or terbium and manganese.

Experimental

Phosphors were prepared by firing mixtures of carbonates of magnesium and lithium, silica, and terbium oxide (Tb_4O_7) at 1300°C for several hours. The carbonates were SL grade and the terbium oxide was 99.9% pure with respect to rare earth ions. Although luminescent materials were produced by air firing, those prepared in a stream of nitrogen, containing a few per cent hydrogen, were superior.

Optical properties of the phosphors were examined using equipment described by Thornton (8) elsewhere. Briefly, the appropriate wavelength from the radiation in a lamp is isolated by a Bausch and Lomb monochromator and focussed on the sample plaque. The emission spectrum for a given exciting wavelength is then determined by focussing the emitted radiation on the entrance slit of a second (analyzing) monochromator and scanning with an EMI 9558B photomultiplier. Excitation spectra were determined by setting the analyzing monochromator on the desired emission peak and scanning the first monochromator in the region 200-400 nm. The intensity of the uv radiation incident on the phosphor was found by repeating this operation with sodium salicylate as the standard. Excitability is taken as the ratio of photomultiplier signals for phosphor and standard. Reflectance characteristics were compared using calibrated magnesium oxide as the standard with source and sample at the usual positions and the drive mechanisms of the two monochromator gratings coupled during scanning. Plaque brightness data were collected on thick samples with other equipment including a 400w mercury vapor arc tube, appropriate filters and a 1P28 photomultiplier.

Quantum efficiency was determined relative to magnesium tungstate by measurements of relative emission spectra coupled with reflectance data. Color coordinates and luminosity factor were computed from spectral emission curves. Correction of raw data and calculations of important parameters of this type were accomplished by use of computer programs.

Results

Phosphors were made with terbium concentrations ranging from 0.01 to 0.48 moles of terbium for a constant 2 moles of $MgCO_3$ and 1 mole of silica. Lithium additions up to 0.30 mole were also used. In the absence of lithium only a faint blue-green luminescence (line spectrum) was noted for any terbium concentration. Addition of even small quantities of lithium shifted the color to yellow-green and increased brightness markedly, best output being at 0.12 mole of terbium and 0.14 of lithium (Table I). At this level, the changes in color with activator concentration are associated with the suppression of some of the blue peaks and concurrent enhancement of those in the green-yellow region (Fig. 1). Especially pronounced is the increased height of the lines peaking at 543 and 553 nm, in the region of maximum eye sensitivity.

Introduction of lithium also favorably alters the excitability of the phosphor by shortwave uv radiation (Fig. 2). In fact said response is more sensitive to lithium than to terbium concentration, as shown by the plaque brightness data of Table I. The same increment in 254 nm excited emission results when lithium is increased from 0.10 to 0.14 at 0.04 Tb as is produced by increasing terbium from 0.04 to 0.12 at 0.10 lithium. Another feature of the excitation spectra is the appearance, or perhaps better resolution, of a peak at 300 nm with addition of lithium.

Absorption of uv radiation is also dependent on the presence of lithium (Fig. 3). In the absence of this alkali metal oxide only half the incident 254 nm radiation was absorbed while 80-85% absorption, measured by diffuse reflectance, could be attained in the best samples. From Table II it is evident that the raw

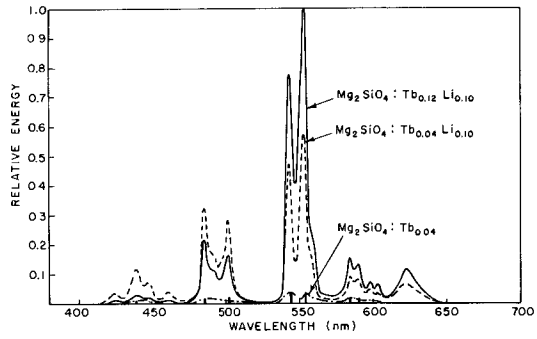

Fig. 1. Emission spectra of phosphors activated by terbium with lithium and without lithium (heavy lines) under 254 nm excitation.

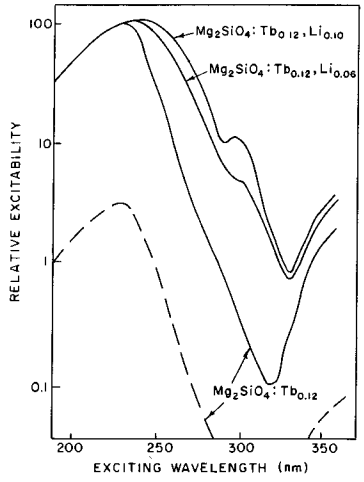

Fig. 2. Influence of lithium on excitability of the phosphor for the emission peak at 543 nm. The dashed curve is the true excitability of a sample with no lithium.

Table I. Plaque brightness of Mg_2SiO_4:Tb,Li phosphor (254 nm excitation)

Composition	Relative plaque brightness, %
Mg_2SiO_4:$Tb_{0.04}$	5
Mg_2SiO_4:$Tb_{0.04}Li_{0.01}$	50
Mg_2SiO_4:$Sb_{0.04}Li_{0.10}$	90
Mg_2SiO_4:$Tb_{0.01}Li_{0.14}$	100
Mg_2SiO_4:$Tb_{0.12}$	5
Mg_2SiO_4:$Tb_{0.12}Li_{0.06}$	100
Mg_2SiO_4:$Tb_{0.12}Li_{0.10}$	100

Table II. Effect of lithium on structure of Mg_2SiO_4:Tb,Li phosphors

Composition	Intensity of strongest x-ray line			
	Mg_2SiO_4	MgO	SiO_2	Tb_2O_3?
Mg_2SiO_4:$Tb_{0.04}$	22	22	86	34
Mg_2SiO_4:$Li_{0.10}$	82		Not detected	
Mg_2SiO_4:$Tb_{0.04}Li_{0.10}$	68		Not detected	
Mg_2SiO_4:$Tb_{0.12}$	16	82	70	57
Mg_2SiO_4:$Tb_{0.12}Li_{0.10}$	60		Not detected	

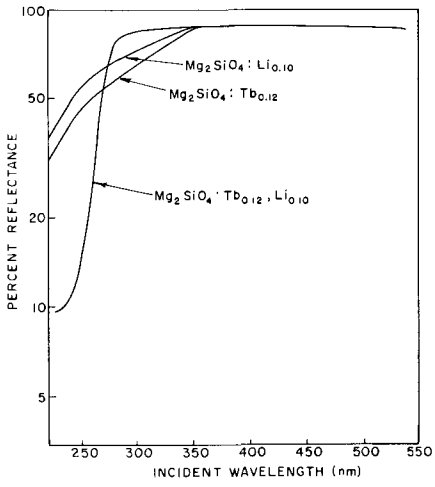

Fig. 3. Diffuse reflectance of magnesium silicate activated by terbium or lithium or both.

mix with only terbium results in a mixture of products, while addition of lithium gives a single phase. Thus the comparisons made in Fig. 3 are not, strictly speaking, justified, since the reflectance of the sample without lithium could be ascribed to the other product (MgO, SiO_2). The Mg_2SiO_4:Li, on the other hand, is a single material with the characteristics of that noted with terbium and lithium as activators.

With these reservations in mind, the absorption properties described do highlight the fact that good phosphors are noted only when lithium is used, along with the terbium which is responsible for the emission found. When this restriction is observed, the x-ray diffraction patterns are those of the mineral olivine, Mg_2SiO_4. The lattice constants of several luminescent materials were compared with published values for olivine. From the data of Table III it is apparent that only the b-dimension is perceptibly different from that of Mg_2SiO_4. The disparity is not of sufficient magnitude to change the structure.

While phosphors with terbium emission are promising, addition of radiation other than the characteristic green luminescence is attractive. Transfer of energy between rare earths, *e.g.*, $Tb^{+3} \rightarrow Eu^{+3}$(9) has been noted, and simultaneous uv absorption by several activators, each with its own characteristic emission color, is another useful process for alteration of the spectrum. Of the activators considered only manganese was found to be effective. Figure 4 shows the change in spectral properties with addition of manganese to the silicate. The green peaks are suppressed and a new orange band appears. Excitation spectra for the emission at 650 nm (manganese) and 550 nm (terbium) were determined and found to be quite similar (Fig. 5), with the manganese containing phosphor being more responsive to uv wavelengths below 200 and above 350 nm. The color of phosphors with varying amounts of manganese was determined along with quantum efficiency. Despite the marked change in the former (Fig. 6), the quantum efficiency remains essentially constant at the 0.5 level. These quantum efficiency figures, along with luminosity factors and color are presented in Table IV.

Finally the temperature dependence of brightness was determined using a quartz arc tube as source and

Table III. Structural data on Mg_2SiO_4:Tb,Li phosphors

Composition	Lattice constants, Å a	b	c
$Mg_2SiO_4:Tb_{0.04}Li_{0.10}$	4.75	10.37	5.99
$Mg_2SiO_4:Tb_{0.12}Li_{0.10}$	4.75	10.38	5.99
$Mg_2SiO_4Li_{0.10}$	4.76	10.22	5.98
Olivine (Mg_2SiO_4)	4.76	10.20	5.99

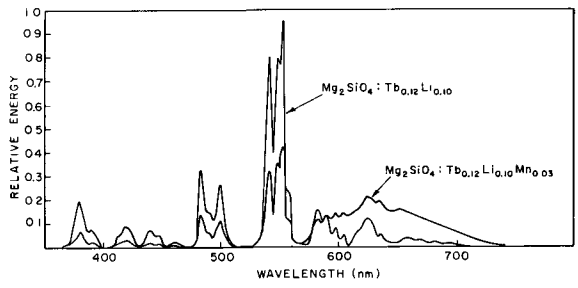

Fig. 4. Effect of manganese activation on the 254 nm-excited emission of Mg_2SiO_4:Tb,Li phosphor.

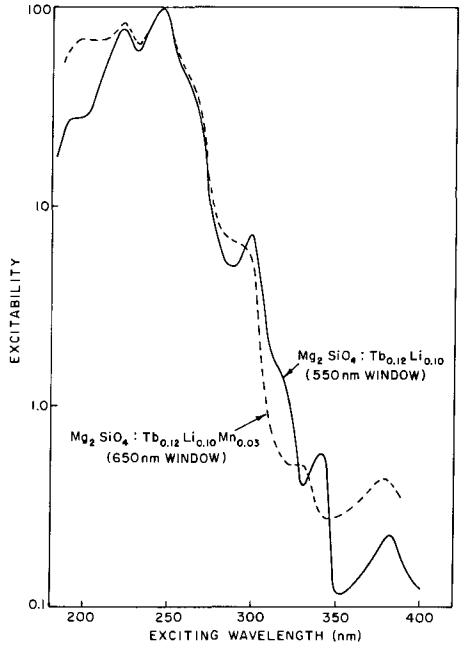

Fig. 5. Excitation spectra for emission at wavelength peaks of terbium or manganese.

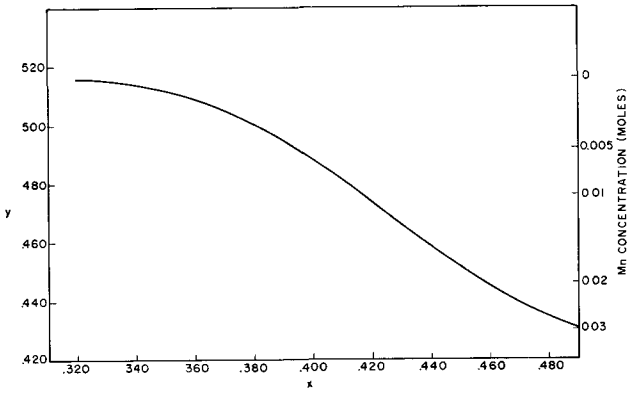

Fig. 6. Changes in color of Mg_2SiO_4:Tb,Li phosphors on addition of manganese. $Mg_2SiO_4:Tb_{0.12}Li_{0.10}Mn$, λ_{exc} = 256 nm.

taking measurements in transmission on thin samples. The results in Fig. 7 show that the phosphors retain a significant portion of their room temperature output at elevated temperatures.

Discussion

The crystallographic data show that, in the presence of lithium, the terbium is included in the olivine host without structurally significant distortion of the latter. While the lithium can substitute at magnesium sites, their ionic radii both being 0.78Å, the terbium ion would be expected to modify the structure if sub-

Table IV. Color and efficiency of Mg_2SiO_4:Tb,Li,Mn phosphors (λ_{exc} = 256 nm)

Phosphor	x	y	Quantum efficiency	Luminosity factor, η
$Mg_2SiO_4:Tb_{0.12}Li_{0.10}$	0.321	0.516	0.43	0.62
$Mg_2SiO_4:Tb_{0.12}Li_{0.10}Mn_{0.01}$	0.418	0.476	0.51	0.52
$Mg_2SiO_4:Tb_{0.12}Li_{0.10}Mn_{0.03}$	0.486	0.430	0.50	0.41
$MgWO_4$	0.222	0.312	0.84	0.38

stituting for either cation present in the olivine matrix. The reason such lattice changes are not evident may be associated with known features of the olivine structure. The latter may be regarded as an assembly of hexagonal close-packed oxygen ions in which half the octahedral and an eighth of the tetrahedral sites are occupied (8). This fact accounts for the occurrence of materials like Li_3PO_4 in the olivine structure, at the same time suggesting that the framework has some freedom to accommodate additional ions, even of disparate size, under favorable conditions.

When trivalent cations substitute for divalent species some type of charge compensation is required. Since luminescence depends on the presence of lithium, substitution of one Tb^{+3} and one Li^{+1} for two Mg^{+2} would provide the necessary compensation. The oxygen added with the first two is most likely in substitutional locations and is probably compensated by defects on the cation lattice. In a structure such as that of magnesium silicate, the effect of a few more unoccupied cation sites on lattice parameters should be infinitesimal. The slight, measured change in the b dimension (Table III) can be accounted for by the space requirements of the large added terbium ion.

Although the replacement described

$$Tb^{+3} + Li^{+1} \rightarrow 2Mg^{+2}$$

satisfies the arithmetic of charge compensation it avoids some possible symmetry problems. The effect of replacing divalent cations about a common SiO_4^{2-} anion radical is a difference in unshielded nuclear charge as seen by the silicate grouping. An anticipated consequence would be polarization of the radical toward terbium, rather than lithium, *i.e.*, a decrease in volume about the rare earth and better coupling to the absorbing lattice. Both the presence of alkali with rare earths (Tb^{+3}, Eu^{+3}) and the volume occupied by the latter have been found to alter emission characteristics of tungstates and molybdates in which host cations, but not structure, have been varied (10). The increase in brightness of Mg_2SiO_4 with terbium concentration and its dependence on concomitant lithium addition indicate the importance of such rare earth-lattice coupling here also.

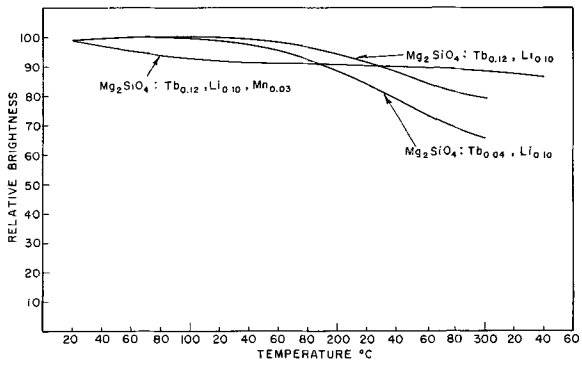

Fig. 7. Temperature dependence curves for representative phosphors under excitation by the total uv of a HPMV quartz arc tube.

Acknowledgment

The writer is indebted to W. A. Thornton for fruitful discussions and measurements, C. K. Lui Wei for x-ray powder diffraction data, and to R. B. Parsons for sample preparation.

Manuscript received Sept. 2, 1965; revised manuscript received Nov. 19, 1965.

Any discussion of this paper will appear in a Discussion Section to be published in the December 1966 JOURNAL.

REFERENCES

1. G. H. Dieke, H. M. Crosswhite, and B. Dunn, *J. Opt. Soc. Amer.*, **51**, 820 (1961).
2. G. H. Dieke and H. M. Crosswhite, *Appl. Optics*, **2**, 675 (1963).
3. G. Urbain, *Ann. Chim. Phys.*, **18**, 293 (1909); N. C. Chang, *J. Appl. Phys.*, **34**, 3500 (1963); R. C. Ropp, *This Journal*, **111**, 311 (1964).
4. See for example, L. G. Van Uitert, *J. Chem. Phys.*, **37**, 981 (1962).
5. H. J. Borchardt, *ibid.*, **38**, 1251 (1963); **39**, 504 (1963).
6. H. G. Jenkins and A. H. McKeag, *This Journal*, **97**, 415 (1950).
7. A. F. Wells, "Structural Inorganic Chemistry," 3rd ed., Oxford University Press (1962).
8. W. A. Thornton, Extended Abstracts, ECS Meeting, San Francisco, Calif., May 10-14, 1965.
9. L. G. Van Uitert and R. R. Soden, *J. Chem. Phys.*, **36**, 1289 (1962).
10. L. G. Van Uitert, *ibid.*, **37**, 981 (1962); *This Journal*, **110**, 46 (1963).

Correction

Equation [2] of the paper "Lithium Chlorine Battery" by D. A. J. Siwinkels, p. 6, Vol. 113, January 1966 Journal should read

$$E = 3.4906 - 5.64 \times 10^{-4} (t\text{-}608) \text{ volt} \qquad [2]$$

High-Temperature Resistivity of the Chalcopyritic Compound $CuInTe_2$

Stojan M. Zalar[1]

Research Division, Raytheon Company, Waltham, Massachusetts

ABSTRACT

To investigate extrinsic and intrinsic behavior of the semiconductor $CuInTe_2$, high-temperature electrical resistivity experiments were carried out, using the technique of porcelain "cocoons." $CuInTe_2$ was considered as part of the pseudobinary system Cu_2Te-In_2Te_3. Inspection of the plots ln ρ *vs.* $1000/T$ for samples with 44 to 56 molar % Cu_2Te revealed the existence of two extrinsic regions: room temperature to 200°C and 200°-710°C. The latter was found complex and exhibited in general two different slopes. The intrinsic region in these samples existed in a narrow temperature interval between 710° and 779.8°C (the melting point of $CuInTe_2$), and was well defined and reproducible. Assuming a $T^{-3/2}$ dependence of carrier mobility, the "thermal" energy gap of $CuInTe_2$ could be calculated from the intrinsic slopes in the plots ln ρ *vs.* $1000/T$, and was found to be 1.04 ev. Observed deviations from this value were ±0.02 ev. Prolonged annealing of various samples of $CuInTe_2$ at 400°C promoted disappearance of extrinsic differences among them, while their intrinsic slopes remained the same.

$CuInTe_2$ is a semiconductor belonging to the broad family of ternary chalcopyritic compounds I-III-VI_2, which in turn are generally regarded as cross-substitutional derivatives of II-VI binary compounds, such as CdTe and ZnSe. We have previously studied the crystal growth (1), thermoelectric power, and electrical resistivity (2) at room temperature. In this paper we report studies of the high-temperature behavior of the chalcopyritic compound $CuInTe_2$.

In a previous work on semiconducting solid solutions $Cu_xAg_{1-x}InTe_2$ (3) we found it convenient to consider them as a linear part of the ternary system Ag_2Te-Cu_2Te-In_2Te_3, as illustrated in Fig. 1. In a similar way Mason and Cook (4) investigated the peritectic compound $CdIn_2Te_4$ as part of CdTe-In_2Te_3, while O'Kane and Mason (5) studied $AgIn_3Te_4$ as part of the Ag_2Te-In_2Te_3 system. Figure 1 shows stoichiometric composition of $CuInTe_2$ as $(Cu_2Te)_{50}$-$(In_2Te_3)_{50}$. Since our prime interest was in studying physical phenomena in slightly off-stoichiometric $CuInTe_2$, it was decided to investigate compositions in the range between $(Cu_2Te)_{44}$-$(In_2Te_3)_{56}$ and $(Cu_2Te)_{56}$-$(In_2Te_3)_{44}$ and to explore changes in electrical resistivity up to their melting point. To our knowledge a "thermal" energy gap of $CuInTe_2$ has not yet been determined.

[1] Present address: Westinghouse Research Laboratories, Pittsburgh, Pennsylvania.

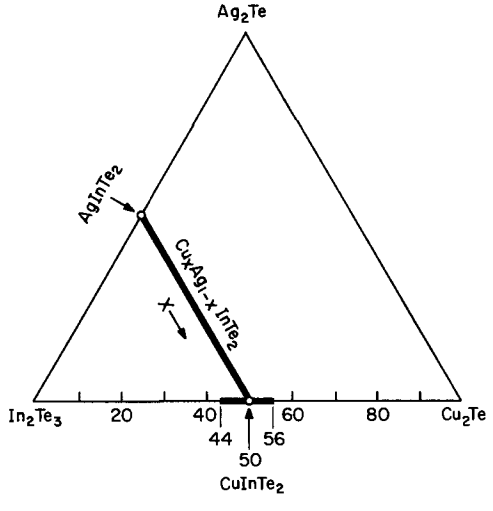

Fig. 1. $Cu_xAg_{1-x}InTe_2$ as part of the pseudoternary system Ag_2Te-Cu_2Te-In_2Te_3, and $CuInTe_2$ as part of the pseudobinary system Cu_2Te-In_2Te_3.

Experimental Method

The work on $CuInTe_2$ at high temperature (up to 800°C) required a method which would suppress evaporation of tellurium, thus maintaining the original composition. Of several different techniques, from pressurized capsules to immersions into ceramic powders, the method of porcelain "cocoons" proved to be the most successful.

There are three main techniques for single crystal growth of solids: Czochralski crystal pulling, Bridgman method, and zone melting. The last two were applied to $CuInTe_2$ in these laboratories. In both cases the material was placed in evacuated and sealed quartz capsules, hence preventing the nonequilibrium evaporation of volatile tellurium. This is why in principle the Czochralski method of pulling crystals out of the melt, which otherwise produces essentially stressfree ingots, is not very suitable for chalcopyrites containing tellurium with its relatively high partial vapor pressure. For resistivity studies, as reported here, only Bridgman specimens were used, while zone melting of $CuInTe_2$ was employed in the thermoelectric investigations (2).

For the initial preparation of specimens $CuInTe_2$, the method of direct melting of elements, weighed separately on a microbalance with an accuracy of ±0.0001g, was utilized. Because of the critical effect of impurities in semiconductor investigations, the purest available materials were used: copper: spectroscopically pure, +99.999% (ASARCO); indium: special high purity, +99.999% (ASARCO); tellurium: semiconductor grade, +99.999% (ASARCO).

The first phase, which consists of melting and reacting the elements, was done in relatively large batches (100g or more). The quartz capsule containing the elements was first evacuated (typical vacuum: 1×10^{-5} Torr) and then sealed with a hydrogen-oxygen torch. The capsule was then placed in the center of a tiltable furnace with temperature controlled at 850°C or more. During the melting operation, the furnace was vigorously tilted upside-down many times in order to enhance the thorough mixing of the elements and to remove the surface bubbles. The melt was first held at temperatures about 100° above the melting point of $CuInTe_2$ (779.8°C) for several hours, then its temperature was lowered to 800°C for about

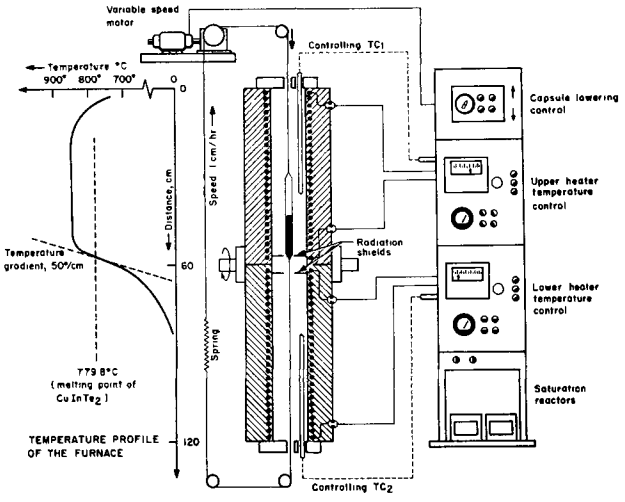

Fig. 2. Vertical Bridgman furnace experimental set-up for the crystal growth of $CuInTe_2$.

half an hour, after which the capsule was quenched in ice water.

In the second phase (crystal growing), the capsule from the first phase was cautiously crushed and the brittle $CuInTe_2$ broken into small pieces. All the powder was thrown away. Small pieces of $CuInTe_2$ were placed into clear, carefully pointed quartz tubes (7 mm OD, 5 mm ID). These were in turn evacuated to a pressure of 1×10^{-5} Torr, and subsequently hooked to the Bridgman lowering mechanism.

The Bridgman furnace, as shown in Fig. 2, consisted of two kanthal wound sections, separately temperature controlled to an accuracy of $\pm 0.5°C$ by saturable reactors. A sharp temperature gradient of about 50°C/cm, produced by two platinum radiation shields, was needed for the successful crystal growth of $CuInTe_2$. The lowering speed of the capsule was regulated very accurately by a variable speed motor. The best speed was between 5 and 20 mm/hr. It was held at 7 mm/hr for the most part.

The resulting ingots, of 5 mm diameter, were coarsely polycrystalline, containing an average 3-7 grains and mostly with no bubbles on the surface. They were cut into lengths of 15-20 mm and carefully sandblasted.

One of the most stubborn experimental problems in the Bridgman method of crystal growing $CuInTe_2$ was the formation of surface bubbles. These bubbles, believed to be primarily caused by the evaporation of dissolved gases, were difficult to remove during the slow motion of the Bridgman ingot. Several experimental measures were tried in order to solve the problem. First it was noticed that a steeper temperature gradient partially removed the surface bubbles, mostly in the upper portion of the ingot. The temperature gradient was hence increased from 17° to 53°C/cm by inserting two platinum radiation shields in the central portion of the furnace.

A second improvement was achieved by using refrasil (quartz) sleeving, placed tightly against the inner walls of the quartz tubing (13 mm in diameter). In one typical run the temperature in the upper portion of the furnace was held at 880°C, and the capsule was lowered at the high speed of 35 mm/hr for 6 hr. Results were positive: no bubbles appeared on the surface of the ingot. While this method was successful in eliminating bubbles, large single crystals could not be grown by this technique, presumably because the sleeving with its interwoven structure induced the formation of crystal nuclei.

A third substantial improvement in the reduction of surface bubbles in $CuInTe_2$ was accomplished by using a carbon coated quartz tube. The carbonizing of the inner walls of the quartz tube was done by thermal decomposition of pentane: $C_5H_{12} \rightarrow 5C + 6H_2$. First the tube was evacuated. Then the vapors of pentane were introduced (pentane is a liquid with a high vapor pressure) and decomposed by the heat of a gas-oxygen torch. This procedure was repeated several times; each time a very thin layer of carbon was deposited on the inner wall of the tube. The results were good; ingots of $CuInTe_2$ were bubble-free.

In order to prepare specimens for resistivity experiments four thin platinum wires of 0.005 in. in diameter were electrically welded onto the surface of the ingot at even distances from each other. The distances between these potential probes were measured with an accuracy of 0.001 cm using an optical microscope and were typically of the order of 0.15 cm. Four-point electrical resistivity was calculated from the Valdes' formula (6).

A direct current of 10-50 ma was applied, automatically and successively in both directions, thus eliminating thermoelectric end effects by simple subtraction of voltage readings.

A thin chromel-alumel thermocouple (No. 30 wire) was also welded on the surface of the ingot, close to the four electric leads, allowing an on-the-spot temperature reading with an accuracy of $\pm 0.2°C$.

The schematic wiring of $CuInTe_2$ specimens for high-temperature resistivity investigations is shown in Fig. 3. The "cocoon" itself was made by repeated dipping of the specimen into a pot of diluted liquid porcelain (Sauereisen No. 1). After each dip, thin porcelain layers were left to dry under infrared illumination. Typically from five to eight coatings were applied. A finished cocoon ready for measurement is shown on the right of Fig. 3. These porcelain coatings proved to be very dense and prevented tellurium from evaporation at temperatures above 400°C. A certain amount of contamination of $CuInTe_2$ by impurities in Sauereisen coatings during high-temperature runs could have occurred thus influencing its extrinsic behavior. No systematic study was performed on this question. Intrinsic properties, however, were not affected by the porcelain encapsulation.

On several occasions the resistivity measurements could be extended well into the molten phase of $CuInTe_2$, some 50° above the melting point. The four platinum probes, rigidly set in solid porcelain, maintained their position in the molten $CuInTe_2$ within the cocoon. A sharp drop of electrical resistivity at the melting point of $CuInTe_2$ was observed, but no further work has been done on this possibly useful method of studying the resistivity behavior in the vicinity of the melting point of compounds.

The thoroughly dried cocoon, with six wires protected by Refrasil sleevings was lowered into a quartz tube filled with washed Alundum bubbles. The tube

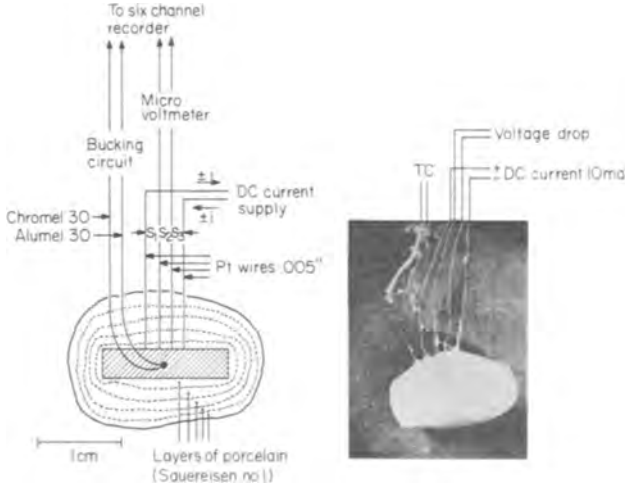

Fig. 3. Schematic wiring of experimental "cocoons" of $CuInTe_2$ for high-temperature resistivity investigations.

was in turn placed into a vertical resistance furnace. A slow stream of clean argon flowed through the furnace during the duration of the entire experiment to prevent any oxidation of the specimen. The temperature of the furnace was increased manually.

All electrical signals, $+\rho$, $-\rho$, and TC were automatically printed on a six-channel L&N recorder at 4-sec intervals. The measuring ranges were adjusted manually by the bucking circuit for the thermocouple case and by the Keithley microvoltmeter amplifier for the resistivity case.

Results and Interpretation

Microstructure of specimens.—The samples had the following compositions: $(Cu_2Te)_x$ $(In_2Te_3)_{100-x}$, x = 44, 45, 46, 47, 48, 49, 50, 52, 53, 54, and 56. Metallographic inspection showed that all quenched specimens were coarsely polycrystalline and mostly monophase, as revealed by etching with CP4 (without bromine).

The microstructure of some samples exhibited a small amount of a secondary phase in the form of little "chicken-pox" like islands. In previous work (3) we found that $CuInTe_2$ undergoes a metastable transition near 650°C. This was determined by thermal analysis in which a slight thermal arrest occurred at that temperature. On the basis of this evidence, it was proposed that $CuInTe_2$ is a supersaturated solid solution. To test this idea, several Bridgman-grown and several quenched polycrystalline ingots of stoichiometric $CuInTe_2$ were annealed at 650°C for 15 hr. Their microstructure was examined before and after annealing. Results are shown in Fig. 4. It is seen that after annealing at high temperatures some secondary phase or phases precipitate out of the chalcopyrite matrix of $CuInTe_2$, thus supporting the hypothesis of a supersaturated solid solution.

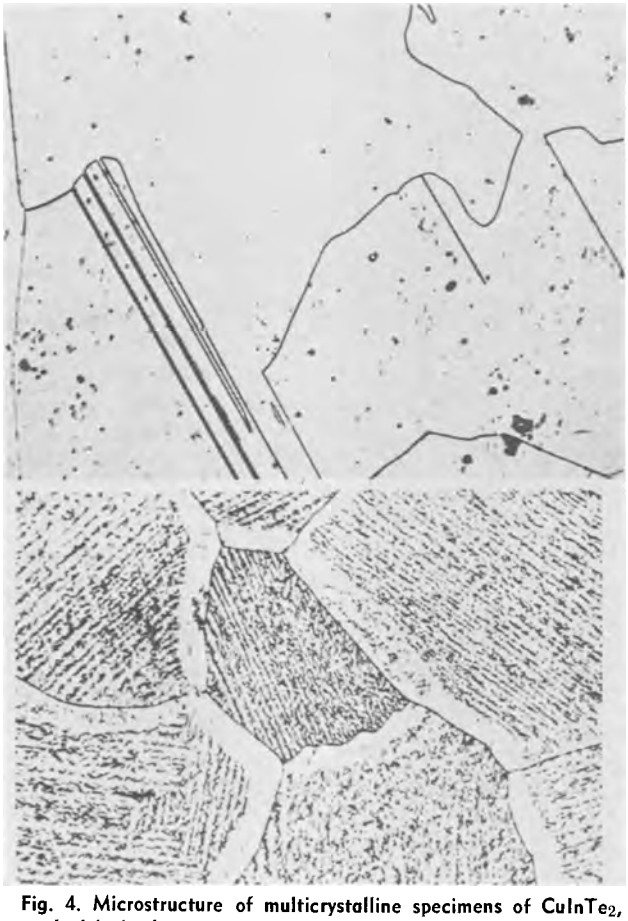

Fig. 4. Microstructure of multicrystalline specimens of $CuInTe_2$, quenched in iced water, and annealed at 650°C for 15 hr. Etched, 50% HNO_3. Top, quenched $CuInTe_2$; bottom, annealed $CuInTe_2$. Magnification 150X.

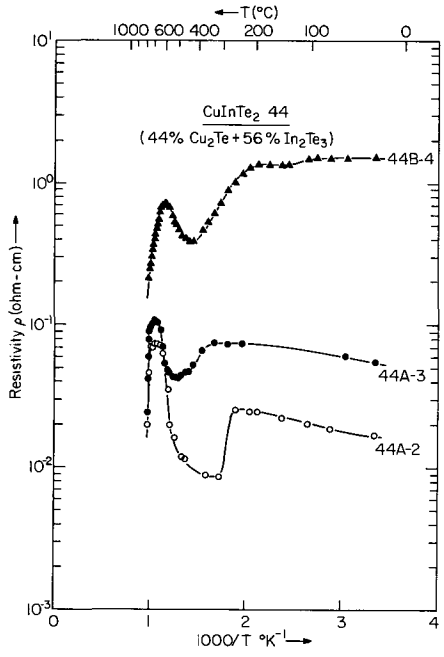

Fig. 5. Electrical resistivity vs. 1000/T in $CuInTe_2$ 44

To check this assumption still further, x-ray diffraction data were taken of samples with 44, 50, and 56% Cu_2Te in quenched and in annealed form. In all cases only the lines of the chalcopyrite structure occurred. These somewhat unexpected results were explained by the inherent limitation of x-ray diffraction technique. In the case of $CuInTe_2$ secondary phases could be detected only if they were present in the amount of more than 4%.

As in a previous x-ray study (3) very weak fixed count peak intensities of InTe (ASTM card 7-112) could be detected in annealed samples of $CuInTe_2$ (44, 50, and 56% Cu_2Te, rest In_2Te_3). InTe is the most prominent, congruently melting compound of the binary system indium-tellurium. Its relatively high melting point (696°C) suggests a stable compound with the lowest potential energy of any compound in the system. It is probable that after a prolonged annealing at elevated temperatures the structure of $CuInTe_2$ or of compounds (Cu_2Te)-(In_2Te_3) close to the ratio 50/50 becomes unstable and the compound InTe forms locally and precipitates out of the chalcopyritic matrix.

Resistivity at elevated temperatures.—By using the "cocoon" technique it was possible to measure and record electrical resistivity of specimens $CuInTe_2$ from room temperature up to their melting point, 779.8°C. Figures 5, 6, and 7 show typical plots of ln ρ *vs.* 1000/T for the compositions: 44, 50, and 56 molar % Cu_2Te. These plots and others for intermediate compositions not included in this paper, have several common features:

1. There are three distinct temperature ranges; the first an extrinsic region, from room temperature up to about 200°C; the second, an extrinsic region, from 200° up to 710°C; and the third, an intrinsic region, from 710°C up to the melting point at 779.8°C.
2. The extrinsic region 200°-710°C is complex and shows in general two linear slopes: one in the temperature range 200°-500°C and one in the range 500°-710°C. They could be explained by the presence of shallow and deep impurity levels.
3. Well-defined, reproducible "resistivity pockets," sandwiched between two extrinsic slopes appear in the stoichiometric $CuInTe_2$ in the temperature interval 455°-600°C. Similar, although distorted pockets could also be detected in other compositions.
4. The intrinsic region (710°-779.8°C) is nearly the same in all samples.

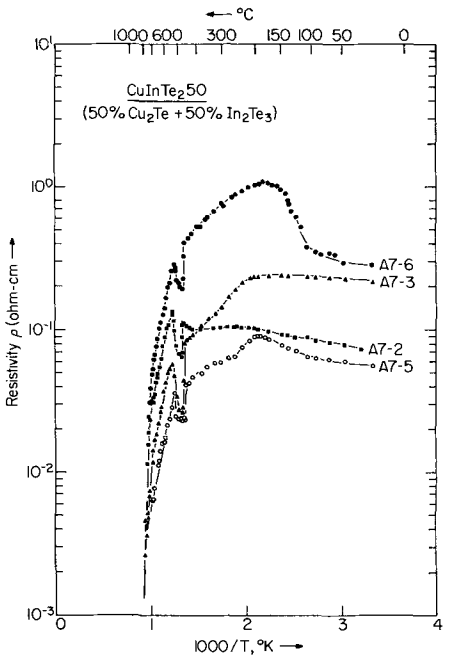

Fig. 6. Electrical resistivity vs. 1000/T in $CuInTe_2$ 50

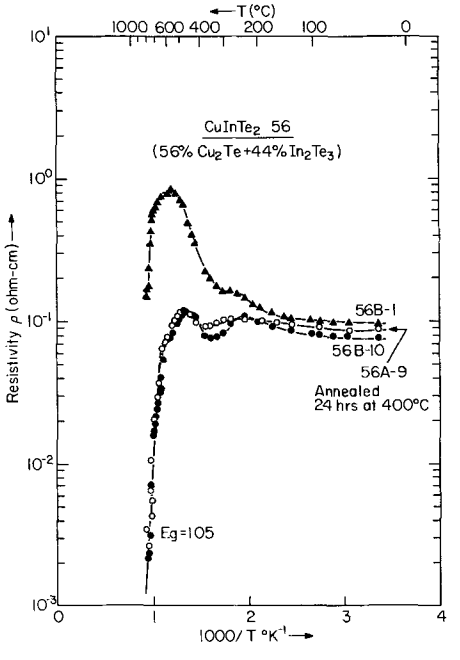

Fig. 7. Electrical resistivity vs. 1000/T in $CuInTe_2$ 56

Thermoelectric measurements at room temperatures have shown (2) that in the extrinsic region $CuInTe_2$ and all compositions from 44 to 56 molar % Cu_2Te are p-type semiconductors. From the linear relation between $\ln \rho$ and $1000/T$ in the high-temperature intrinsic region, the intrinsic "thermal" energy gap of $CuInTe_2$ was calculated with certain assumptions as follows:

For the effective mass of the carriers independent of temperature the resistivity in the intrinsic range is given by

$$1/\rho = en_i(\mu_n + \mu_p) = (\text{constant})\,T^{3/2}\,(\mu_n + \mu_p)\,e^{-E_g/2kT} \qquad [1]$$

where n_i is the concentration of intrinsic carriers, μ_n and μ_p are mobilities of electrons and holes respectively, T is the absolute temperature, E_g is the intrinsic energy gap at temperature T and k is the Boltzmann constant: 8.62×10^{-5} ev/°K.

If we now assume that $\mu \sim T^{-3/2}$, Eq. [1] simplifies to

$$1/\rho = (\text{const})\,e^{-E_g/2kT} \qquad [2]$$

We further assume that in the narrow intrinsic region (710°-779.8°C) the energy gap E_g changes linearly with temperature

$$E_g = E_{go} + \alpha T \qquad [3]$$

Here E_{go} is the intrinsic energy gap at 0°K, and α is the temperature dependence coefficient of the energy gap. Then for two different temperatures we may write

$$\ln \rho_1 - \ln \rho_2 = \frac{E_{go}}{2kT_1} - \frac{E_{go}}{2kT_2} \qquad [4]$$

solving for E_{go}, we obtain

$$E_{go} = \frac{2k \ln \rho_1/\rho_2}{(1/T_1 - 1/T_2)} = \frac{3.965 \times 10^{-4} \log_{10} \rho_1/\rho_2}{(1/T_1 - 1/T_2)} \qquad [5]$$

The intrinsic energy gaps E_{go} of samples $(Cu_2Te)_x(In_2Te_3)_{100-x}$ for $44 < x < 56$, calculated from Eq. [5] on the basis of experimental linear slopes of $\ln \rho$ *vs.* $1000/T$, are 1.04 ev. Variations observed were in the range ±0.02 ev, which corresponds to an experimental accuracy of approximately ±2%. If some other temperature dependence of mobility were assumed, say $\mu \sim T^{-5/2}$ or $\mu \sim T^{-1/2}$, it was calculated that the value for energy gap E_{go} of $CuInTe_2$ would change by less than +2 or −2%, respectively, because the intrinsic temperature interval is so small. Austin *et al.* (7) measured the energy gap of $CuInTe_2$ optically and found the value 0.95 ev.

The origin of distinct "resistivity pockets," as seen in Fig. 6 for the specimens of stoichiometric $CuInTe_2$, is not yet completely understood. One explanation may be that the first sharp drop of resistivity above 455°C is due to precipitation of a more conductive secondary phase, such as InTe. At higher temperatures the carrier mobility in this secondary phase decreases and the resistivity climbs again until it joins the original curve. The usual explanation of a resistivity drop as the temperature increases, based on the degeneracy of charge carriers (8), cannot be applied here since the change of resistivity is much too sudden and much too sharp on the low-temperature side

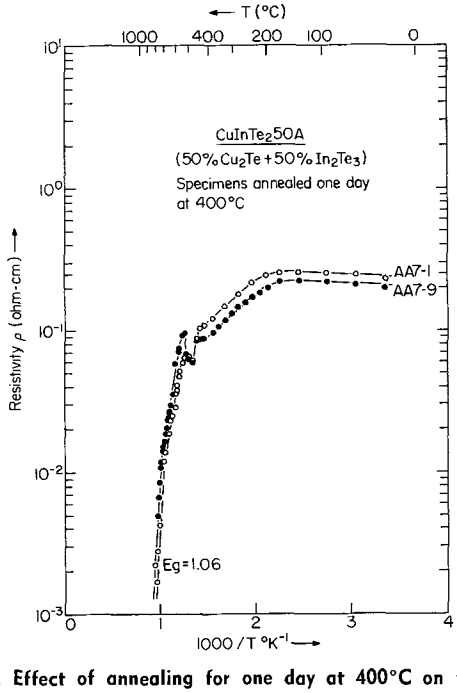

Fig. 8. Effect of annealing for one day at 400°C on the high-temperature resistivity of stoichiometric $CuInTe_2$. Compare with Fig. 6.

of the pocket, as compared with the smooth changes in germanium and silicon.

In order to see if the observed extrinsic and intrinsic effects in $CuInTe_2$ were reversible upon annealing, specimens were heat-treated 24 hr at 400°C in argon. The results shown in Fig. 8 for the compositions with 50% Cu_2Te and in Fig. 7 for the composition with 56% Cu_2Te indicate that impurity dominated extrinsic differences mostly disappear, "resistivity pockets" largely shrink, while intrinsic slopes remain unchanged. These changes during annealing are due to an equilibrium redistribution and relaxation of atoms within the basic chalcopyritic matric of $CuInTe_2$.

Conclusions

$CuInTe_2$ was treated as part of the pseudobinary system $(Cu_2Te)_x(In_2Te_3)_{100-x}$ for $44 < x < 56$ molar % of Cu_2Te. Coarsely polycrystalline specimens with these compositions were prepared by a vertical Bridgman growth technique. After long annealing at 650°C specimens of $CuInTe_2$ show a tendency to precipitate a small amount (below 4%) of a secondary phase, probably InTe.

High-temperature (up to the melting point 779.8°C) electrical resistivity measurements were performed, using the method of porcelain "cocoons." Inspection of the plots of ln ρ *vs.* $1000/T$ for samples with 44 to 56 molar % Cu_2Te revealed the existence of two extrinsic temperature regions (room temperature-200°C, 200°-710°C) and one well-defined and reproducible intrinsic temperature region from 710° to the melting point. Stoichiometric $CuInTe_2$ specimens in particular, show sharp, well-defined "resistivity pockets," sandwiched between two extrinsic slopes in the temperature interval 455°-600°C. The origin of these pockets is not yet clear, but is believed to be due to a high-temperature precipitation of a more conductive secondary phase, such as InTe.

The "thermal" band gap in all investigated samples of $CuInTe_2$ (in the composition range from 44 to 56 molar % Cu_2Te), calculated from the experimental intrinsic slopes of ln ρ *vs.* $1000/T$ with the assumption that $\mu \sim T^{-3/2}$, was 1.04 ev. Observed variation of the energy gap in samples with different compositions was ± 0.02 ev. This value compares with the "optical" energy band gap in $CuInTe_2$ of 0.95 ev, measured by Austin *et al.*

Acknowledgments

Experimental assistance of Robert P. Whelan, Harold E. LaBelle, Jr., and Neal I. Obert in the preparation of specimens and resistivity measurements is gratefully acknowledged. Ruth Brown and Marylin Harrison helped ably with numerical computations.

The author also wishes to thank Dr. R. Mazelsky, Dr. D. J. Page and particularly Dr. R. W. Ure, Jr. of Westinghouse Research Laboratories for critical reading of the revised manuscript.

Manuscript received Oct. 10, 1963; revised manuscript received *ca.* Nov. 29, 1965.

Any discussion of this paper will appear in a Discussion Section to be published in the December 1966 JOURNAL.

REFERENCES

1. S. M. Zalar, "Experimental Studies of the Chalcopyritic Compound $CuInTe_2$," Raytheon Research Division Technical Memorandum T-445, pp. 1-153, May 16, 1963; not published, but available on request
2. S. M. Zalar, *J. Appl. Phys.*, **35**, 1988 (1964).
3. S. M. Zalar, "Metallurgy of Semiconductor Materials," pp. 263-283, AIME, Interscience Publishing Co., New York (1962).
4. D. R. Mason and J. S. Cook, *J. Appl. Phys.*, **32**, 475 (1961).
5. D. F. O'Kane and D. R. Mason, *This Journal*, **111**, 546 (1964).
6. L. B. Valdes, *Proc. IRE*, 420, February 1954.
7. I. G. Austin, C. H. I. Goodman, and A. E. Pengelly, *This Journal*, **103**, 609 (1956).
8. E. H. Putley, *Proc. Phys. Soc., Sec.* **A62**, 284 (1949).

High Conductivity Transparent Contacts to ZnS

V. A. Williams

Department of Physics and Applied Physics, University of Ife, Ibadan Branch, Ibadan, Nigeria

ABSTRACT

Two methods of producing high conductivity transparent contacts on ZnS single crystals are investigated. It is found that sputtering of In_2O_3:Sn onto the crystal followed by suitable heat-treatments gave much better results than a straightforward attempt at diffusion of compensated donor systems into the crystal lattice.

The nature of an ohmic metal-semiconductor contact has been discussed by Kroger and co-workers (1) who proposed a model for a metal-CdS contact. Ohmic contacts on semiconductors are now achieved through $n\text{-}n^+$, otherwise called L-H junctions. L-H stands for low-high, implying a junction arising from a change in impurity concentration from low to high between two adjacent regions of a crystal, which gives a corresponding change in conductivity value, but not type, across the junction.

At an L-H (or $n\text{-}n^+$), unlike the p-n junction, there is no high field barrier region and no minority carrier injection, the current across such a junction being carried entirely by majority carriers, with no rectification. The discontinuity in impurity concentration across the L-H junction can be brought about by controlled diffusion of donor impurities into the crystal, or by forming a heterojunction on the crystal surface. The heterojunction in this case would be between the host crystal and another crystal of similar structure, but of the same conductivity type. The latter crystal could for example be epitaxially grown on the host crystal, or deposited thereon by a variety of other means.

ZnS is a wide bandgap material (3.7 ev), normally of very low intrinsic conductivity. A variety of suitable doping materials exist however which could in principle give it n- or p-type conductivity. Table I (2) shows such a range of suitable dopants and some of their characteristics. The last two columns of Table I show,

Table I. Suitable donor and acceptor impurity materials for ZnS

Impurity material	Group	Substituting in ZnS for:	Acceptor or donor	$E_c - E_i$ (ev)	$E_i - E_v$ (ev)
Chlorine, Bromine	VII B	S	D	0.25	—
Aluminum	III B	Zn	D	0.25	—
Scandium	III B	Zn	D	0.35	—
Gallium	III B	Zn	D	0.42	—
Indium	III B	Zn	D	0.5	—
Copper	I B	Zn	A	—	0.95
Silver	I B	Zn	A	—	0.55

respectively, depth or height of the impurity level E_i, below or above the conduction or valence band edges E_c or E_v.

In attempting to diffuse impurities into zinc sulfide it is often necessary to balance (3) the charge created by the partial replacement of the S^{2-} ion by the halide ions ($Cl^-Br^-I^-$) or the replacement of the Zn^{2+} ion by, say, trivalent ions (Al^{3+}, Ga^{3+}, In^{3+}) or monovalent ions (Cu^+Ag^+, Au^+). Charge compensation normally requires the presence of an anion vacancy whether ionized or not, *i.e.*, $V_A{}^+$ or V_A. If the energy involved in replacing a lattice ion by one of these foreign ions is less than that required to form a cation vacancy, then the introduction of a second type of foreign atom may be necessary to incorporate the former ions in the lattice in sufficient quantities. However, the formation of $V_A{}^+$ or V_A centers may be enhanced if the activation energy for the formation of these centers is supplied externally (*e.g.*, thermally), in which case, the incorporation of the donor ions is self-compensated.

With the process involving the formation of a heterojunction as for example between tin-doped indium oxide and ZnS the use of indium as the donor impurity in the ZnS could be effected by diffusing it into the lattice via the same process as is necessary to form the indium oxide semiconductor. Note that the word heterojunction used here to describe the junction between ZnS and indium oxide is not strictly correct as indium oxide has a different lattice structure from ZnS. However only thin films of indium oxide are here involved.

Diffusion of Donor Impurities into ZnS *from the Vapor*

The experimental arrangement for the diffusion of donor impurities into ZnS is illustrated in Fig. 1. The materials tried are listed in Table II below. (All materials were of analar quality.) The ZnS pieces are cut from larger crystals supplied by the Eagle Picher Company, Joplin, Missouri.

The material to be diffused into the ZnS crystal is placed at one end of a sealed evacuated quartz tube while the ZnS is placed at the other, the two materials being separated by clean quartz wool. The separation between the two substances depends on the temperature at which the impurity material is desired to be kept relative to that of the ZnS.

The temperature of the ZnS is so chosen that its vapor partial pressure is negligible relative to that of the vapor of the doping material, while the temperature for the latter depends on its melting point or the vapor pressure.

The sealed tube is then in turn placed in a fused silica furnace tube, toward the cool end of the furnace where a desired temperature gradient can be obtained at the desired hot-end temperature. Figure 2 illustrates typical temperature gradients when the center temperatures of the furnace are 700° and 900°C, respectively.

A standard diffusion time of 1 hr was used for all experiments. Cooling after the run is effected fairly rapidly by withdrawing the tube completely into the cool zone of the furnace where the temperature is only slightly above room temperature.

The average diffusion depth (based on the depth at which the sheet resistance is $1/e$ of its surface value) obtained is about 50μ and the resistivities calculated

Table II. Temperature characteristics of some doping materials

Material	Melting point, °C	Temperature, °C at which the V.P. = 1 Torr
Zinc chloride ($ZnCl_2$) (anhydrous)	365	428
Copper chloride ($CuCl_2$) (anhydrous)	422	546
Aluminum chloride ($AlCl_3$) (anhydrous)	192	100 (sublines)

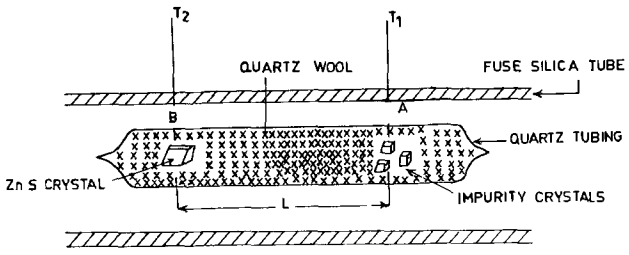

Fig. 1. Arrangement for diffusing impurities from the vapor phase into zinc sulfide crystals.

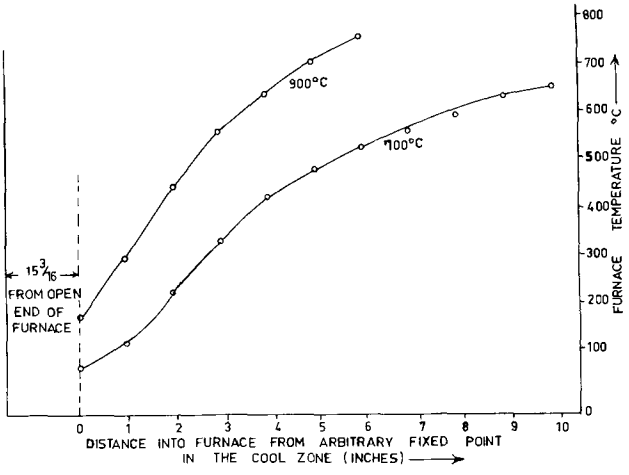

Fig. 2. Typical temperature profile at the cool end of diffusion furnace.

on this mean thickness of 50μ varies from 5 x 10^3 ohm-cm for copper chloride to 5 ohm-cm for aluminum chloride.

It was further found that, using aluminum chloride (which gave the lowest observed resistivity), a lowering of the resistivity resulted from further heating for about 5 min at 700°C in an inert atmosphere, the resistivity being approximately halved.

The treated crystals were however very dark in appearance, indicating strong absorption in the visible; the lower the resistivity, the darker the crystal. It is thought that, although this effect might be due to free carrier absorption, it may perhaps also be due to colloidal aggregation of the impurity material. In any case this darkening is of course a great disadvantage because any luminescence arising from the crystal interior would be strongly absorbed.

Deposition of Another Semiconductor on the ZnS *Surface*

This involves the deposition on the ZnS of a thin layer of oxygen-deficient indium oxide doped with tin, by a sputtering process. The process is only partially chemically reactive in that, although chemical combination of oxygen is effected during the process, yet the deposited layer has a very high concentration of the free metal and it is opaque. This is an important difference from the method employed by Shivonen and Boyd (4) for making transparent indium oxide contacts on CdS.

Details of the sputtering apparatus are shown in Fig. 3. Aluminum head pieces are used for the electrodes as this material is strongly resistant to sputtering. Provision for water cooling is made to prevent excessive rises in temperature of the electrodes and of the glass-to-metal seals.

Spectroscopically pure indium and tin are evaporated together in the ratio 4:1 in high vacuum (10^{-6} Torr) onto the aluminum cathode to obtain a very thick coating, such evaporation being carried to completion to maintain the composition of 4:1 ratio.

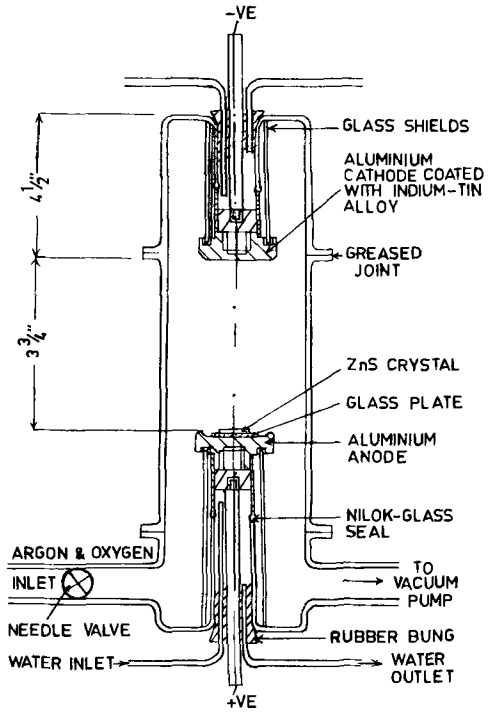

Fig. 3. Details of the sputtering apparatus

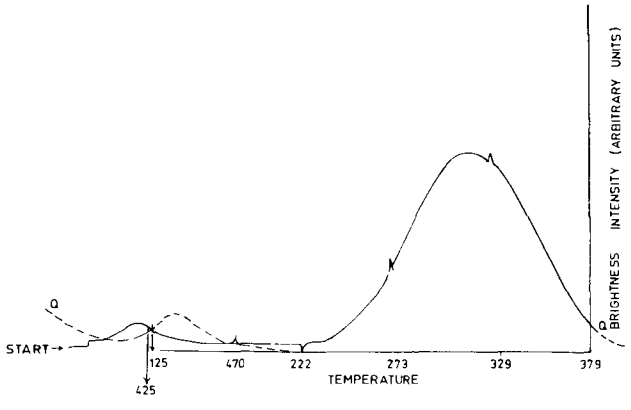

Fig. 4. Thermal glow curve of a ZnS crystal equipped with an In_2O_3:Sn contact.

For sputtering, ZnS crystals, in the form of 7 x 5 x 1 mm plates cut and polished from larger crystals of reasonable perfection, are masked to expose surfaces of 3 x 5 mm on each flat face and then mounted on a glass disk placed in turn on the anode as shown in Fig. 3. Thermal resistances between the pieces are reduced by use of thin films of silicone grease.

Sputtering is then carried out at 0.1 Torr in an atmosphere consisting approximately of 5 parts of argon (99.999%) to two parts of pure oxygen (supplied by BOC), for 7-10 min. The anode is maintained during this time at 2.2-2.5 kv relative to the cathode with 60-70 ma discharge current.

The resulting sputtered layer has a rather opaque metallic appearance: after removing the silicone grease from the crystal by cleaning in a mixture of acetone and toluene it is then heated for about 5 min at 700°C in argon at 2 atm pressure in order to diffuse some indium into the ZnS. The crystal is then subsequently fired in air at 375°-400°C to give a completely transparent layer. Crystals used for measurements had contacts approximately 3 x 5 mm placed on the two flat faces fairly accurately located opposite one another. For the electrical measurements aluminum foil electrodes were attached on the edges of the transparent layers using a hard setting silver conducting paste (from Johnson Mathey Company).

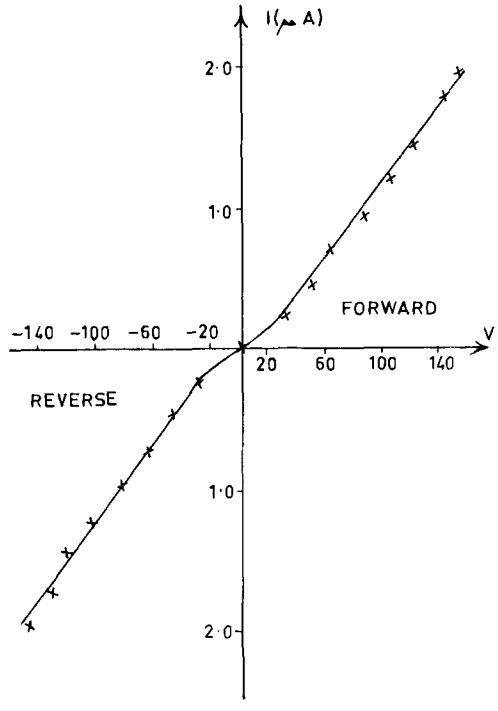

Fig. 5. Current-voltage characteristics of a crystal equipped with In_2O_3:Sn contacts.

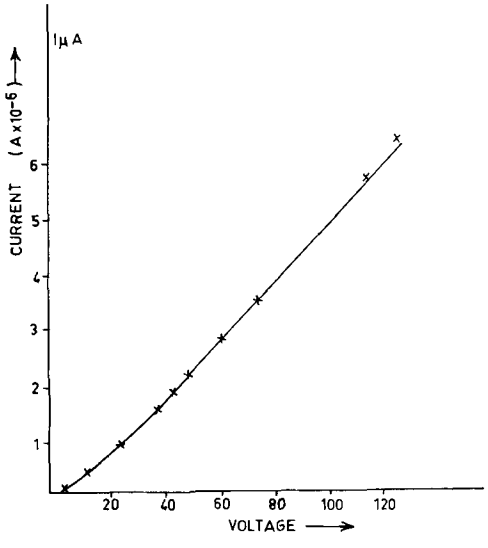

Fig. 6. Current-voltage characteristics under 3650Å uv irradiation.

Irradiation of the crystal by 3650Å uv light gave luminescence characteristic of indium centers. Figure 4 gives the typical glow curve obtained from a crystal doped with indium in the manner described (after previous light body doping with aluminum and chlorine).

The resistivities of the indium oxide layers obtained were of the order of 10^{-1} ohm-cm (assuming a 50μ thickness). The current-voltage characteristics of the contacts are shown in Fig. 5. Photoconductivity measurements for undoped crystals equipped with the indium oxide contacts were made, and the resulting current-voltage characteristic for 3650Å excitation is shown in Fig. 6. The conducting properties of the In_2O_3:Sn layer itself appears to be unaffected by low temperatures as the conductivity did not appear to change from room temperature down to 77°K.

Discussion

It is evident from the foregoing that diffusion of donor impurities into ZnS could lead to an increase

in surface conductivity. Two problems are attendant with this method of achieving high conductivity however; the first is the problem of diffusion of impurities into ZnS owing to the effects of charge or vacancy compensation (5). This makes it easier for deeper centers to be incorporated than shallower ones. The second problem arises from the first. The shallowest centers are 0.25 ev for donor levels, and 0.5 ev for acceptor centers, so that, both because of the depth of levels, and because of charge compensation, very high impurity concentrations ($\approx 10^{20}/cm^3$) are required to give adequate conductivities. Such high concentrations of impurities frequently lead to discoloration of the crystals, and self-absorption of luminescence (6), this appears to be confirmed by the experiment. This discoloration is objectionable since transparency is of prime importance.

On the other hand, the formation of In_2O_3:Sn-ZnS contact is easier to achieve and appears to be more straight forward. To a rough approximation the junction between the two materials could be treated as H-I heterojunction which in many ways agrees with the proposals of Kroger *et al.* as to the nature of an ohmic semiconductor contact. The required region of relatively high conductivity in the ZnS would arise from the diffusion of indium into the crystal as would be expected from the heat-treatment immediately following after the sputtering process, and as it is known that indium has a high diffusion rate in ZnS single crystals.

Acknowledgment

This work was carried out while the author was in the Department of Electrical Engineering, Manchester University (U.K.). Thanks are thus due to Professor F. C. Williams, for facilities provided, and further to Dr. C. N. W. Litting and Dr. D. E. Mason, for helpful discussions and to Ferranti Ltd. who constructed the sputtering apparatus and the diffusion furnace.

Manuscript received July 7, 1965; revised manuscript received Nov. 3, 1965.

Any discussion of this paper will appear in a Discussion Section to be published in the December 1966 JOURNAL.

REFERENCES

1. F. A. Kroger, G. Diemer, and H. A. Klassens, *Phys. Rev.*, **105**, 279 (1956).
2. R. H. Bube, "Photoconductivity of Solids," p. 160, J. Wiley & Sons Inc., New York & London.
3. F. A. Kroger, *Brit. J. Appl. Phys.*, Suppl. **4**, S58 (1955).
4. T. Shivonen and D. R. Boyd, *Rev. Sci. Inst.*, **31**, 992 (1960).
5. F. A. Kroger, *ibid.*
6. A. G. Fischer, *Solid State Electronics*, **2**, 232 (1961).

Detection of Thermal Reaction in Mixed Oxide Powders by Electrical Resistance Measurements

A. N. Copp, M. Nakahira, and G. W. Brindley

Materials Research Laboratory, The Pennsylvania State University, University Park, Pennsylvania

ABSTRACT

Resistivity measurements are made on 1:1M mixtures of MgO-Cr_2O_3, NiO-Cr_2O_3, ZnO-Cr_2O_3, and CoO-Cr_2O_3 powders heated in oxygen, and in nitrogen atmospheres at 2.5°C/min. Sharp inflections are found in the log ρ *vs.* $1/T$ curves; two inflections are found for MgO-Cr_2O_3 and ZnO-Cr_2O_3 heated in oxygen. X-ray diffraction measurements are made of similar powders heated under identical conditions and quenched from various temperatures, and curves are obtained of α (fraction reacted) *vs.* T, maximum heating temperature. The temperatures of the inflections in the log ρ *vs.* $1/T$ curves (the lower inflection when two are observed) correspond with reasonable extrapolations of the α *vs.* T curves to $\alpha = 0$, *i.e.*, these inflections appear to correspond with, or to be closely related to, the onset of reaction in the powder mixtures. The method has potential application for studying the onset of reactions under conditions where more bulky equipment cannot be used and particularly in closed systems.

The present paper is concerned with the possibility of detecting the onset of thermal reaction in intimately mixed oxide powders under conditions of progressively rising temperature by following the change of electrical resistance of compacted powder samples. The more commonly used methods, such as x-ray diffraction and differential thermal analysis, tend to be insensitive to the onset of these reactions. Electrical resistance measurements for this purpose have hitherto received rather little attention, but several studies indicate that the question is worth examination. Garn and Flaschen (1) showed that polymorphic transformations in quartz, barium titanate, and several other materials gave rise to a change in slope of resistance *vs.* temperature curves. Bielanski and Deren (2) studied 1:1M mixtures of ZnO-Cr_2O_3, MgO-Cr_2O_3, and ZnO-Fe_2O_3, and Bielanski, Deren, Haber, and Polaczkawa (3) made a further study of the ZnO-Cr_2O_3 1:1 mixture. They observed well-defined breaks in the log σ *vs.* $1/T$ plots (σ = electrical conductivity). In the earlier study, the breaks were attributed to an interaction involving the migration of one oxide over the surface of the other beginning at about 400°, 400°, and 700°-800°C for the respective oxide mixtures given above. In the later study, it was emphasized that the conductivity depends on the surface states of the particles and on the formation of a reaction product. The ZnO-Cr_2O_3 mixture was shown to give two inflections, the first of which at around 415°C was associated with surface migration of one oxide over the other, and the second at around 650°C with formation of a spinel product. Szabó and Solymosi (4) studied 1:1 MgO-Cr_2O_3 mixtures and considered that the beginning of spinel formation, about 600°-700°C, changes the electrical properties of the mixed oxides markedly by the formation of a product with good defect state conductivity.

In the present work, attention has been given to the behavior of intimately mixed oxide powders in 1:1M proportions of MgO, NiO, ZnO, and CoO with Cr_2O_3. In all cases the resulting product is a spinel. Under dynamic conditions of progressively rising temperature, solid-state reactions between mixed powders depend greatly on the particle sizes of the components, on the rate of heating, and in many cases (as will be shown) on the ambient atmosphere. It is scarcely possible,

therefore, to make detailed comparisons between results obtained by different investigators using different experimental conditions. Likewise a comparison between results obtained by electrical resistance measurements and by other techniques, such as x-ray diffraction, will be significant only if identical conditions are employed during the reactions. Particular attention has been given to this aspect of the study.

Experimental

Raw materials and sample preparation.—Reagent grade powders from Fisher Scientific Company of MgO, ZnO, NiO, Cr_2O_3, and a CoO-Co_3O_4 mixture were used. The CoO-Cr_3O_4 mixture was heated in air at 1000°C for 12 hr to convert it wholly to CoO. The MgO powder was preheated in air at 1300°C for 2 hr to obtain an oxide of coarser particle size. Following these treatments, the MgO and CoO samples were finely ground in an agate mortar. Microscopic examination showed that the resulting MgO and CoO powders had particle diameters of the order 1-10μ, and all other powders were somewhat finer than 1μ. It was considered unnecessary for the immediate purpose to prepare well-sized fractions.

The 1:1M mixtures were hand-ground in an agate mortar with acetone for approximately 2 hr. They were dried in air, finely pulverized, and stored in a desiccator over P_2O_5. Cylindrical pellets, 1.27 cm diameter and about 1.5 cm in length, were formed in a hardened steel pellet mold without use of a binding material under a pressure of about 50 kg/cm^2.

Heat-treatment.—For the resistance-temperature measurements, a horizontal mullite tube furnace with silicon carbide heating elements was used. The temperature was uniform over a 1-in. section up to 1100°C. A cam-type program controller gave a temperature increase of about 2.5°C/min. This rate is a compromise between slow running to obtain resistance measurements at sufficiently well-defined temperatures and a uniform temperature in the sample, and fast running to obtain the desired range of temperature in a convenient working time.

Samples for x-ray analysis were prepared in a vertical tube furnace wound with Kanthal, type A-1, wire with identical arrangements for temperature control. The samples were suspended in platinum containers in the hot zone of the furnace and were quenched by fusing the suspending wires when desired temperatures were reached.

Because solid-state reactions between oxides frequently depend on the ambient atmosphere, the present tests were carried out under two conditions, with a slow flow of either dry oxygen or dry nitrogen through the furnace tubes. After flushing the system at room temperature with the gas to be used, a small excess pressure was maintained as shown by an outlet "bubbler." The investigation was not concerned with the specific role of the gas atmosphere in the reactions considered.

Resistance measurements.—These were made using a four-terminal measuring technique with a 10v potential drop across the sample. The sample was held in a specially constructed silica framework, with two platinum foil electrodes pressed against the end faces by means of spring-loaded silica rods, with the springs mounted outside the hot zone of the furnace. The potential probes, also spring loaded, consisted of platinum wires pressed into finely drilled holes penetrating about 0.5-1 mm into the cylindrical surfaces of the sample, and about 5 mm apart. Two thermocouples, Pt, Pt-Pt/10% Rh, were pressed against the opposite side of the sample. Resistances were measured up to temperatures of about 1000°C, higher temperatures being avoided because of possible deformation of the silica framework.

D.C. power was applied only during measurements and was supplied by a Kepco 5M-160-12MK regulated power supply. Current and potential measurements were made with a Keithley 410-R electrometer.

Resistivities were calculated using sample dimensions prior to heating. Compaction (sintering) of the powders occurred during the heating process resulting in changes of about 10-15% in linear dimensions. Since the resistivity is expressed in ohm-cm units, the resistivity values obtained will be influenced to the same extent. Changes of this magnitude, however, are small compared with the over-all resistivity changes recorded.

X-ray measurements.—The quenched samples were ground in an agate mortar to a particle size estimated to be of the order of 5μ. A standard weight of material, 0.160g, was packed from the rear into a rectangular opening in a glass slide, with no smoothing of the front surface exposed to the x-ray beam. The sample thickness was effectively infinite for the CuKα radiation employed. Integrated intensity measurements were made on reflections from the initial components and from the resulting spinels. Three measurements were made for each reflection involved, using independently prepared samples. The fraction of material reacted, α, was determined by comparing the reflected intensity from a quenched sample with that from a fully reacted sample, heated at 1400°C for 48 hr. This procedure is legitimate because the mass absorption coefficient of the powder sample for the x-rays employed is not changed by the reaction; the reflected intensity, therefore, is proportional to the amount of reflecting material (initial material or product) in the sample.

Results

Resistivity data.—Values of log ρ *vs.* $1/T$, where ρ is the resistivity of the powder compact and T the absolute temperature, for the four oxide mixtures are shown on Fig. 1 where arrows on the curves indicate the direction of temperature change. Solid and open symbols indicate, respectively, results obtained for mixtures heated in oxygen and in nitrogen. For NiO-Cr_2O_3 heated in oxygen, circles and squares denote observations on different samples and illustrate the good reproducibility of the data. The curves on Fig. 1 are seen to consist of nearly straight portions with sharp inflections. In six of the eight sets of data shown, there are sharp deflections downward of the log ρ *vs.* $1/T$ curves with rising temperature, but in two sets

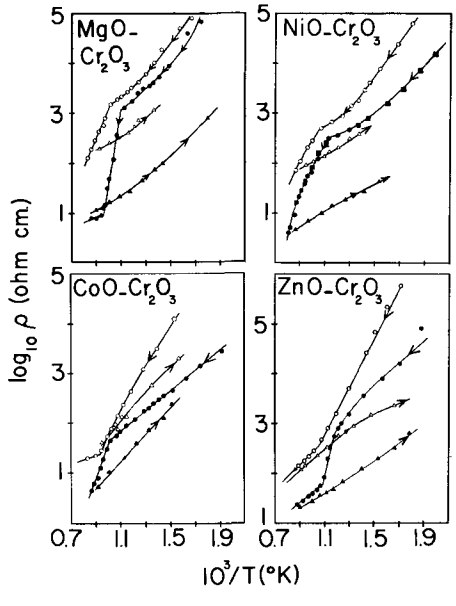

Fig. 1. Log ρ (resistivity) *vs.* $1/T$ (degrees absolute) for 1:1M mixtures of oxides heated in oxygen (solid symbols) and in nitrogen (open symbols). For NiO-Cr_2O_3 in oxygen, closed circles and squares denote observations on different samples.

Table I. Temperatures in °C of inflections in log ρ vs. $1/T$ curves

1:1 Mixture	In oxygen, °C	In nitrogen, °C
$MgO-Cr_2O_3$	635, 770	713
$NiO-Cr_2O_3$	615	660
$CoO-Cr_2O_3$	707	795
$ZnO-Cr_2O_3$	575, 645	674

($CoO-Cr_2O_3$ and $ZnO-Cr_2O_3$) the deflections give lines of lesser slope. In two sets of data, $MgO-Cr_2O_3$ and $ZnO-Cr_2O_3$ both heated in nitrogen, a second deflection also appears. The temperatures, in °C, at which the deflections occur are listed in Table I and are considered to be accurate to about ±5°C.

X-ray data.—The results obtained for the fraction α of material reacted are plotted in Fig. 2 against the temperature T, in °C, from which the samples were quenched. Solid and open circles refer, respectively, to reactions in oxygen and in nitrogen. In all cases, the reactions proceed at lower temperatures in oxygen than in nitrogen, and the α *vs.* T curves are of sigmoidal shape. In nitrogen, two and, possibly, three of the reactions are represented by curves which may be sigmoidal, but only the initial, acceleratory region is achieved; the fourth reaction, $ZnO-Cr_2O_3$ in nitrogen, yielded an almost linear relation. The smallest values of α which could be determined were of the order of 0.05-0.10.

Discussion

The temperatures listed in Table I of the inflections in the log ρ *vs.* $1/T$ curves are shown by arrows in Fig. 2. In all cases, these inflection points (the lower temperatures where two inflections are found) correspond with reasonable extrapolations of the α *vs.* T curves to $\alpha = 0$. These extrapolations are shown by dashed lines in Fig. 2. It is concluded that the inflection points (lower temperatures where two are found) are coincident with, or are closely related to, the temperatures of initial reaction under the experimental conditions employed.

When second inflections are found in the log ρ *vs.* $1/T$ curves, in $MgO-Cr_2O_3$ and $ZnO-Cr_2O_3$ reactions in oxygen, there is a possible coincidence between these inflections and a rapid change in slope $d\alpha/dT$ in the α *vs.* T curves, but on the basis of these two results alone, no firm conclusion can be drawn. For the $ZnO-Cr_2O_3$ reaction, there is a qualitative agreement with the results of Bielanski *et al.* in that they also observed two inflections, but these occurred at about 415° and 650°C as compared with 575° and 645°C in the present work. It is probably not surprising that previous authors associated the second and higher inflection temperature with the formation of a spinel product if this inflection corresponds to a maximum of $d\alpha/dT$, especially if conditions were not identical in the two methods of study (x-ray and resistance measurements).

The present experimental data do not justify making comments either for or against the previous suggestions that the first inflection corresponds to a surface migration, beyond the observation that such a migration may constitute the first step toward a solid-state reaction.

Whether resistivity measurements have any worthwhile merit for detecting the onset of solid-state reactions under rising temperature conditions is a valid question. When the experimental equipment is available, it is easy and relatively quick to determine a log ρ *vs.* $1/T$ curve, and if many tests are required, the method could be automated. The method is quicker than x-ray diffraction using quenched specimens; with a heated stage, x-ray diffraction would take no longer than the resistivity measurements, but there would remain the difficulty that the method is insensitive to small amounts of product. The resistivity change appears to occur sharply at a temperature corresponding to the earliest stage of the reaction, what previous workers have described as a surface migration of one reactant over the other. A possible advantage of the resistivity method is that it may be applicable under circumstances where more bulky equipment cannot be used, for example, in closed systems.

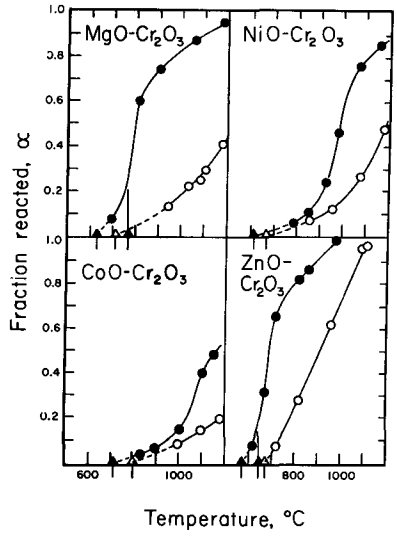

Fig. 2. Fraction reacted, α, vs. T (°C) for 1:1M mixtures of oxides heated in oxygen (solid circles) and in nitrogen (open circles). Temperatures of inflections in log ρ vs. $1/T$ curves (see Table I) are shown by arrows. Solid lines are curves through points obtained from x-ray diffraction measurements; dashed lines are extrapolations joining the solid lines to the resistivity inflection temperatures.

Acknowledgments

This investigation forms part of a program sponsored by the United States Atomic Energy Commission under Contract AT(30-1)-2581. The authors thank Dr. L. E. Cross and Dr. M. E. Bell, of The Pennsylvania State University, for valuable discussions.

Manuscript received May 19, 1965; revised manuscript received Oct. 8, 1965.

Any discussion of this paper will appear in a Discussion Section to be published in the December 1966 JOURNAL.

REFERENCES

1. P. D. Garn and S. S. Flaschen, *Anal. Chem.*, **29**, 268 (1957).
2. A. Bielanski and J. Derén, *Bull. Acad. Polon. Sci., Sér. sci., Chim., Géol. et Géog.*, **6**, 239 (1958); C. A., **52**, 16041e.
3. A. Bielanski, J. Deren, J. Haber, and E. Polaczkawa, *Z. anorg. u. allgem. Chem.*, **294**, 269 (1958).
4. Z. G. Szabó and F. Solymosi, *ibid.*, **301**, 225 (1959).

Vapor Growth Parameters and Impurity Profiles on N-Type GaAs Films Grown on N^+-GaAs by the Hydrogen-Water Vapor Process

K. L. Lawley

Bell Telephone Laboratories, Incorporated, Murray Hill, New Jersey

ABSTRACT

Controlled growth of very smooth n-type films of GaAs on n^+-GaAs substrates has been achieved with the hydrogen-water vapor transport process. These films are grown at 1000° and 1050°C at growth rates from 0.080 to 1.5 μ min^{-1} with partial pressures of water vapor of 0.30 x 10^{-3} to 6.0 x 10^{-3} atm and total flow rates from 300 to 600 cc min^{-1}. The impurity profiles of these films have been determined from differential capacitance-voltage measurements on gold surface barrier diodes. These profiles show that films grown on Si-doped substrates have much steeper impurity gradients at the substrate-film interface than those grown on Te-doped substrates. Films grown on Te-doped substrates at low flow rates become graded with a slope of about one decade per micron. These results suggest that outdiffusion from the substrate controls the profiles of thin films. The minimum net donor concentration in the films is 4 to 5 x 10^{15} cm^{-3}. Reverse bias breakdown voltages of the gold diodes range from > 200 to 5-7v for 11μ and 1μ thick films, respectively.

The synthesis of monocrystalline films of GaAs on GaAs substrates in a H_2-H_2O transport system has been demonstrated by Frosch (1), Sirtl (2), and Gottlieb and Corboy (3). The present investigation is designed to establish the growth parameters and substrate preparation by which controlled growth of smooth, thin films may be achieved in an open-tube system similar to that of Frosch and to explore the effects of these parameters on the resulting impurity profiles of n-type films grown on n^+-substrates.

Apparatus and Experimental Procedure

The apparatus in which the films were grown is shown schematically in Fig. 1. It consists of a fused silica reaction tube (26 mm ID, 140 cm long) into which is inserted a fused silica liner (22 mm ID, 46 cm long) which holds the single crystal source and substrate. The source and substrate are positioned in the liner so that the source is at the maximum furnace temperature and the substrate is at a position downstream from the source within the zone of deposition shown as a shaded area in Fig. 1. The source slices of about 10 cm^2 surface area are held normal to the gas flow in a quartz holder. The substrate is placed on a thin quartz plate to minimize growth on the back of the substrate. The furnace profile as measured in the tube is achieved by shunting the windings on a one-zone tube furnace. In this way the entire profile may be raised or lowered by changing the control temperature. The maximum temperature is controlled to ±1°C by a Pt-Pt/10% Rh thermocouple adjacent to the furnace windings at the midpoint of the furnace.

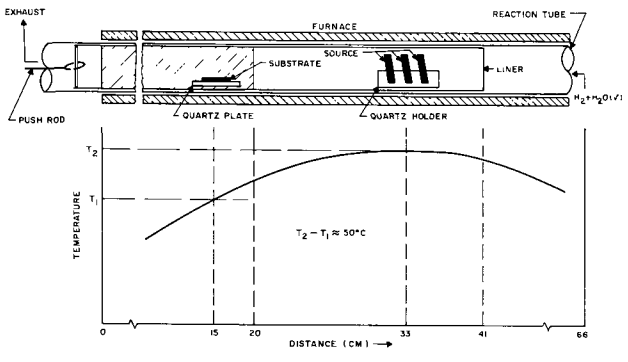

Fig. 1. Schematic drawing of the apparatus and furnace temperature profile.

The substrate temperature for the growth of films is 1000° or 1050°C with the source material being 50°C hotter than the substrate. The temperature gradient at the substrate is about 10°C cm^{-1}.

The water content of the reactant gas is maintained by mixing hydrogen passed through a Pd-Ag tube purifier with purified hydrogen which had been bubbled through a water saturator immersed in an ice-water bath. The dew point of the water-saturated gas was found to be the temperature of the ice-water bath and was independent of the hydrogen flow rate. The dew points of the mixtures of pure and water-saturated hydrogen agreed with those calculated from the volume ratios of the gases. Dry nitrogen is used to purge the apparatus of hydrogen prior to insertion or removal of the liner.

The $(\bar{1}\bar{1}\bar{1})$, B or As faces of the substrates have been used almost exclusively for this investigation, because growth on substrates oriented <110> or <100> is about twice as rapid as on the $(\bar{1}\bar{1}\bar{1})$ planes and smoother films also result from growth on the $(\bar{1}\bar{1}\bar{1})$ planes.

An important factor which contributes to the perfection of these films is the substrate preparation immediately before the growth of the film. Initially the substrate is mechanically lapped and polished with 1800 grit alumina and with Linde B and then chemically polished with a dilute solution of bromine in methanol (4). Immediately before loading the substrate into the liner, the substrate is boiled in acetone, washed in deionized water in an ultrasonic agitator, etched in 70 H_2SO_4/15 H_2O_2 (30%)/15 H_2O, washed in deionized water ultrasonically, and blown dry with line nitrogen. Approximately 10μ of substrate are removed with the sulfuric acid etch.

Films grown on $(\bar{1}\bar{1}\bar{1})$ substrates prepared in this way are very smooth. Under bright field illumination at 50X, the films appear flawless. Examination of the films with an interference contrast microscope shows the presence of parallel growth steps concentrated mostly near the edges of the wafer. Films grown on the other major planes have rough textures due to irregularities such as square patterns on the (100) planes and tilted pyramids on the (110) planes.

The impurity distributions in the films have been determined by the differential capacitance-voltage method at 100 kc as outlined by Thomas *et al.* (5) using gold surface barrier diodes (10 mil diameter) as the rectifying contacts. The diodes are formed by evaporating gold in an oil-pumped evaporator at pres-

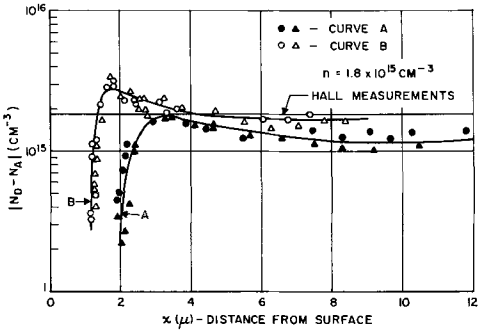

Fig. 2. Impurity profile obtained from Au surface barrier diodes on bulk GaAs (n = 1.8 x 10^{15} cm^{-3}). Curve A, H_2SO_4-H_2O_2-H_2O etch; curve B, Br_4-CH_3OH etch. Different symbols are used for different diodes.

sures of less than 10^{-6} mm Hg. Mesas are formed by etching off the film around the gold diodes with 1 H_3PO_4/1 H_2O_2 (30%)/3 CH_3OH. Alloyed tin balls on the n^+-surface served as the ohmic contact. All units were checked on an I-V curve tracer to determine the ohmic behavior of the tin balls and the rectification characteristics of the diodes.

Kahng (6) has shown that Au-n-type surface barriers are non-injecting majority carrier rectifiers on bulk GaAs having a net donor concentration of 5-9 x 10^{16} cm^{-3}. In this range, the inverse square of the capacitance varies linearly with the applied reverse bias.

Most of the films grown in this system have net donor concentrations in the low-10^{15} cm^{-3} range; therefore, it was necessary to examine the diode behavior on bulk material of this donor concentration. Gold diodes were fabricated on bulk GaAs with a net donor concentration of 1.8 x 10^{15} cm^{-3}. One slice (A) was prepared by the technique used for preparing substrates using the $H_2SO_4/H_2O_2/H_2O$ etch. A second slice (B) was prepared using only bromine in methanol as the etch. The net donor concentration variation shown in Fig. 2 as computed from differential capacitance-voltage measurements does not always approximate the net donor concentration obtained from Hall measurements. All four diodes show a rapid rise in the calculated net donor concentration of about 1 decade of carrier concentration per micron over the first micron of the depletion width. The depletion width of 1μ corresponds to reverse bias voltages of 1v or less. Reverse bias breakdown voltages were about 130v on A and about 100v on B. For biases greater than 1v, the carrier concentration appears to decrease slightly. In this region, diodes on slice B approximate the donor concentration as obtained from Hall measurements better than those on A. Curves from diodes on slice A are displaced about 1μ into the film from those obtained from slice B. This fact suggests that the surface treatment prior to the evaporation of the gold has changed the nature of the surface. These results are consistent with the existence of surface states at the Au-GaAs interface. A comparison of these curves with the results of Kahng (6) suggests that at the higher dopant concentration the effects of the surface may be masked by the higher bulk donor concentration. The objective here is not to give a detailed description of the physics of these surface barriers, but rather to give a basis for comparison of the results on bulk material in which the carrier concentration is well-established with those in films grown by this process. It is concluded that differential capacitance-voltage measurements at greater than 1v reverse bias on gold diodes may be used to determine the net donor concentration of films grown by this process.

The thickness of the n-type films grown on n^+-substrates are measured with a Beckman Infrared Spectrophotometer (Model IR-5, NaCl optics). The lower limit of film thickness which may be determined by this instrument is about 1μ. In the range of thicknesses of 1-3μ the accuracy of indexing the reflectance patterns is about $\pm$0.15μ. For thicker films, the accuracy is greater because of the increased number of reflectance maxima. Also, greater accuracy is achieved when there exists an abrupt change in the carrier concentration at the film-substrate interface. Some films were angle-lapped on a 3° block and stained with 5 HCl/5 H_2O_2 (30%)/3 HF/30 H_2O (7) to delineate the n-n^+ structure. Generally, the film thicknesses obtained in this manner are 0.2 to 0.3μ thinner than those obtained from IR measurements, probably because the etch attacked the film surface and reduced its thickness.

Materials.—The single crystals of GaAs used in these experiments were obtained from the Monsanto Chemical Company except for one semi-insulating crystal of float-zone GaAs used as source material. The electrical characteristics of these crystals are included in Table I which gives the pertinent growth data for each of the films under discussion. Substrates are about 15 mm in diameter.

Experimental Results and Discussion

Films have been grown at 1000° and 1050°C with total flow rates of 20-600 cc min^{-1} and partial pressure of water vapor of 0.30-6.0 x 10^{-3} atm. Growth rates do not differ significantly at these two temperatures. Frosch (8) has shown for the GaP-H_2O-H_2 system that the theoretical growth rate for a constant temperature difference of 50°C between the source and substrate does not differ greatly for substrate temperatures of 1000° and 1050°C. The difference in growth rates at

Table I. Pertinent data for films

Films	Substrate temp, °C	Total flow rate, cc min^{-1}	*$P^i_{H_2O}$ x 10^{+3}, atm	Growth rate, V, μmin^{-1}	Film thickness, b, μ	$-V_{BD}$† at 1μa	$\frac{bV}{D} \equiv \alpha$	[Source Crystal / Substrate Crystal] n, cm^{-3}	μ, $cm^2 v^{-1} sec^{-1}$	ρ, ohm-cm	Dopant	Profile in figure
A	1050	600	0.60	0.11	1.1	5-7	70	1.0 x 10^{16} 1.4 x 10^{18}	6700 2100	0.10 0.0022	— Si	4
B	1050	600	0.60	0.17	1.7	15-20	40	1.2 x 10^{16} 1.6 x 10^{18}	5200 2700	0.10 0.0015	— Te	5
C	1000	300	1.5	0.14	2.1	30-35	100	1.2 x 10^{16} 1.6 x 10^{18}	5200 2700	0.10 0.0015	— Te	6
D	1000	61	6.0	0.22	3.3	20-22	—	~3 x 10^{7} 3.9 x 10^{18}	~5000 1900	4 x 10^{7} 0.008	— Te	7
E	1050	300	6.0	0.75	11.2	>200	—	1.2 x 10^{16} 3.4 x 10^{18}	5200 2200	0.10 0.0007	— Te	8
F	1050	600	1.8	0.33	3.3	50-60	625	1.0 x 10^{16} 1.4 x 10^{18}	6700 2100	0.10 0.0022	— Si	9

* Partial pressure of water vapor.
† Reverse bias breakdown voltage.

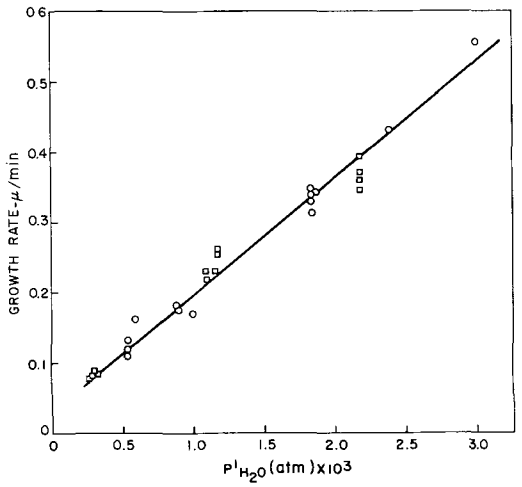

Fig. 3. Dependency of the growth rate on P_{H_2O} at a total flow rate of 600 cc min^{-1} and substrate temperatures of 1000° and 1050°C. ○, 1050°C; □, 1000°C.

these two temperatures also decreases as the partial pressure of water vapor decreases. The same conclusions would be anticipated for the GaAs-H_2O-H_2 system. Films with the smoothest surfaces are grown at 1000°C or higher.

The growth rate varies with the partial pressure of water vapor. Gottlieb and Corboy (3) demonstrated a square-root dependence of growth rate with the partial pressure of water vapor. This result has been confirmed for this system at flow rates of less than 70 cc min^{-1}.

Figure 3 shows the linear variation of growth rates with the partial pressures of water vapor for films grown at 1000° and 1050°C and with total flow rates of 600 cc min^{-1}. At low flow rates the only observable reaction product is GaAs; whereas, at high flow rates, arsenic deposits outside the furnace, and gallium forms on the source.

These observations suggest that the controlling reaction at low flow rates is

$$2\,GaAs(s) + H_2O(g) = Ga_2O(g) + As_2(g) + H_2(g) \quad [1]$$

At high flow rates, the GaAs dissociates and the water vapor reacts directly with the liquid gallium as given in the following reaction

$$2\,Ga(l) + H_2O(g) = Ga_2O(g) + H_2(g) \quad [2]$$

The particular growth conditions of partial pressures of water vapor of 0.30-6.0 x 10^{-3} atm and a total flow rate of 600 cc min^{-1} result in growth rates of 0.080-1.5 μ min^{-1}, respectively. Most of the films to be discussed were grown at 300 or 600 cc min^{-1} because the films show less taper and steeper gradients at the interface than those grown at lower flow rates. The thicknesses of films grown at these flow rates decrease in the direction of the gas flow about 10-20%.

The net donor concentration of films grown by a vapor deposition process is the cumulative effect of numerous sources: dopant transfer from the source, system doping (contamination from the reaction tubes, from reactant gases, from the back of the substrate, etc.), autodoping, or a counter-current deposition as described by Thomas *et al.* (5), and outdiffusions during growth as formulated by Rice (9). Because the profiles of films grown at high flow rates have been in reasonable agreement with the results of this outdiffusion model, all the profiles will be discussed from this standpoint. Under some conditions it appears that other dopant sources are involved in establishing the profiles.

In order to apply Rice's model of outdiffusion, the diffusion constants of the substrate donors (Te and Si) are required; however, these quantities have not been measured. The apparent diffusion constants have been calculated from the value of bV/D[1] which gives the best fit of Rice's numerical tabulations to the profiles. The bV/D values are redefined as α in order to simplify the discussion.

The net donor concentration profiles are plotted as the log of the net donor concentration *vs.* the distance from the substrate-film interface. Different symbols are used to identify different diodes on each film. The curve corresponding to an α which gives the best fit to these data is shown. In some cases, no α could be determined. The donor concentration from the vapor phase which is assumed to be the minimum donor concentration in the film is added to the donors from the outdiffusion to give the final profile labelled Σ. Pertinent growth data are given in Table I, and the film profiles are shown in Fig. 4 through 9.

The impurity profile of film A grown on an n^+-Si-doped substrate is shown in Fig. 4. The effect of outdiffusion of Te may be seen in Fig. 5, which is an impurity profile of another thin film, B, grown on a Te-doped substrate. Both films, A and B, were grown at 1050°C, at a total flow rate of 600 cc min^{-1} and a partial pressure of water vapor of 0.60 x 10^{-3} atm. The values of D calculated from α are 2.9 x 10^{-13} and 1.2 x 10^{-12} cm^2 sec^{-1} for the Si and Te-doped substrate, respectively. The consequence of this difference in diffusion constants is that the net donor concentration in the film grown on the Si-doped substrate is

[1] b is the film thickness (cm), V the growth rate (cm-sec^{-1}), and D the diffusion constant (cm^2-sec^{-1}).

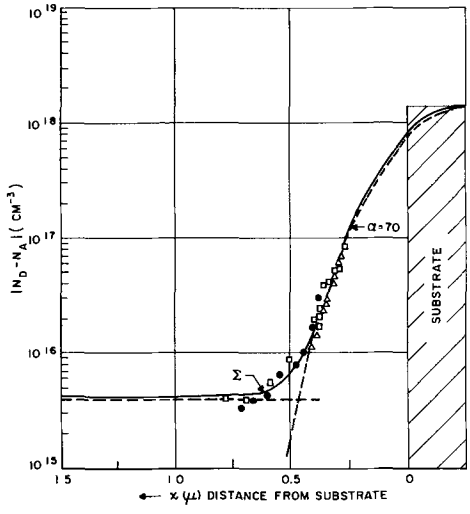

Fig. 4. Impurity profile for film A on Si-doped substrate

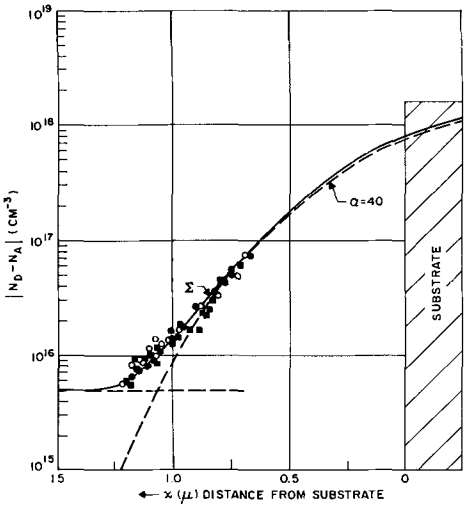

Fig. 5. Impurity profile for film B on Te-doped substrate

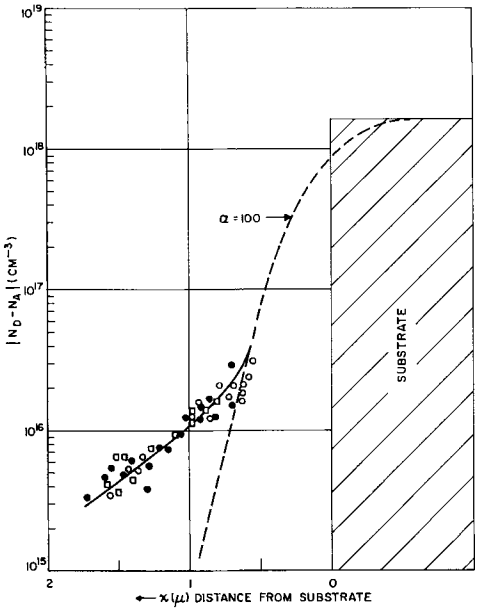

Fig. 6. Impurity profile for film C on Te-doped substrate

lower near the substrate-film interface than when Te-doped substrates are used. For film A and film B, a net donor concentration of 10^{16} cm^{-3} is reached at $\sim 0.4\mu$ and $\sim 1.10\mu$, respectively. In both cases it appears that the donor concentration levels off at about 4-5 x 10^{15} cm^{-3}.

The profile of film C grown at 1000°C on a Te-doped substrate is shown in Fig. 6. The value of α is approximately 100; therefore, D is approximately 4.9 x 10^{-13} cm^2 sec^{-1}. Again the minimum donor concentration in the film is about 3-5 x 10^{15} cm^{-3}. Comparing D values for films B and C (1.20 x 10^{-12} and 4.9 x 10^{-13} cm^2 sec^{-1}), it is apparent that the diffusion constant is lower at 1000°C than at 1050°C as expected. The activation energy for diffusion of group VI donors is roughly about 4.1 ev as has been reported for Se and S diffusions (10). From these values of D for films B and C, the calculated activation energy is roughly 3 ev, a somewhat surprising agreement in light of the method of calculation of D. The diffusion constant for Te in GaAs has not been reported. These results suggest that the effective diffusion constant lies between those of S and Se. Because Te has a greater atomic radius than S and Se, it might be expected to have a lower diffusion constant than S or Se. The higher value may be due to the intermediate electron affinity and electron density of Te with respect to S and Se or due to a more rapid diffusion in a film which undoubtedly has a higher imperfection density than does bulk material. A contribution from some additional dopant would also increase the apparent diffusion constant.

It has been shown that films grown at 600 cc min^{-1} total flow have impurity profiles which may be approximated by the impurity distribution equation given by Rice. Films C and D, however, were grown at 300 and 61 cc min^{-1}, respectively. In both cases, the datum points suggest a linear log concentration *vs.* distance variation of about one decade per micron. It appears that an additional dopant source may be operative under these conditions. A plausible explanation would be that the dopant, in this case Te, could be coming from the back side of the substrate. At high flow rates this dopant would be swept away; whereas, at low flow rates, the Te vapor could envelop the substrate until enough GaAs is deposited on the back to cut off the vapor supply. Eventually the net donor concentration would then arrive at some constant value. A countercurrent, autodoping model (5) could also account for this behavior.

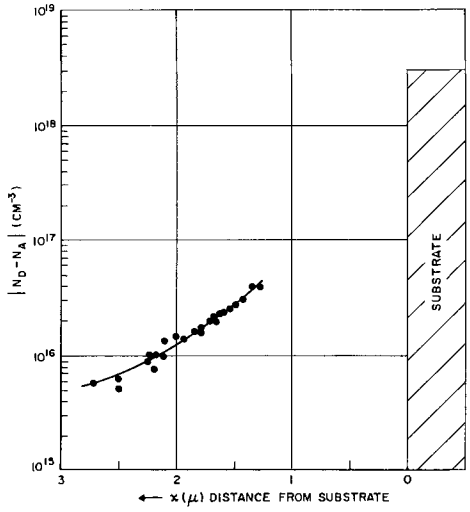

Fig. 7. Impurity for film D on Te-doped substrate

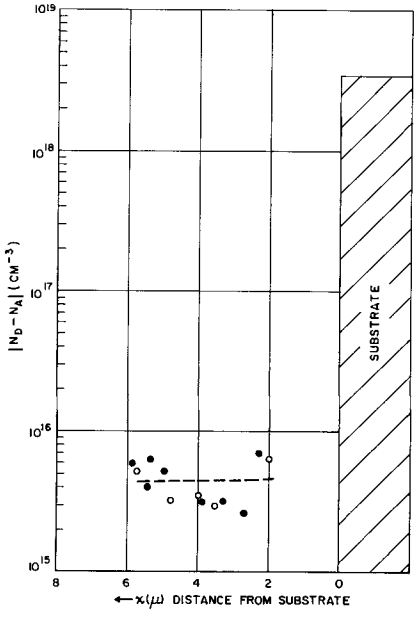

Fig. 8. Impurity profile for film E on Te-doped substrate

The profile of film D in Fig. 7 grown at 61 cc min^{-1} shows this effect even more markedly than does film C in Fig. 6. In the former film, the net donor concentration does not drop to 10^{16} cm^{-3} until 2μ of film have been deposited. This conclusion may be exaggerated in part because the donor concentration in the substrate for film D is higher than in the other films discussed.

In order to conclude the analysis of films grown on Te-doped substrates, a thick film (11.1μ) was grown. The profile of this film (E) is shown in Fig. 8. Here the profile is reasonably flat at a net donor concentration of about 5 x 10^{15} cm^{-3}. The diffusion tail could not be obtained because of the very small capacitance variation with voltage when the depletion layer approached the substrate.

The difference between the profiles of thin films grown on Si- and Te-doped substrates was illustrated in Fig. 4 and 5. This difference was attributed to the different apparent rates of diffusion of the substrate donors into the films during growth. The effect of Si on the film profile of a thicker film may be seen in Fig. 9, which is the profile of film F. This film was also grown at 1050°C. The value of D calculated from α is 2.9 x 10^{-13} cm^2 sec^{-1}, which is in agreement with 2.9 x 10^{-13} cm^2 sec^{-1} for film A. Figure 9 shows that the profile changes abruptly at about 0.5μ from the

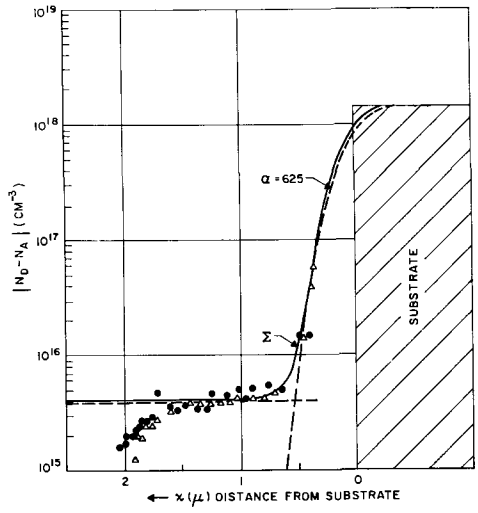

Fig. 9. Impurity profile for film F on Si-doped substrate

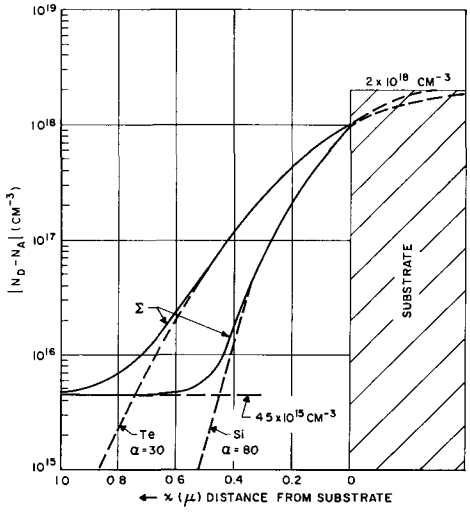

Fig. 10. Proposed impurity profiles for 1μ films grown on Te-and Si-doped substrates.

film-substrate interface. Most of the film is doped to a net donor concentration of ~5 x 10^{15} cm^{-3}. Although not shown here, films grown at 1000°C on Si-doped substrates have a slightly steeper gradient at the interface. The calculated D value for these films is about 2 x 10^{-13} cm^2 sec^{-1}. The apparent diffusion constant for Si does not vary greatly with temperature and, at both 1000° and 1050°C, it is lower than that of Te. The diffusion of Si into GaAs would be expected to be more rapid than the diffusion of a group VI element because Si may replace both gallium and arsenic (11). This fact and the apparently low activation energy associated with the lack of variation in D values suggests that the Si which comes from the substrate may not be in an electrically active state. It is altogether conceivable that the oxygen atoms from the oxide vapor species have effectively neutralized the electrical contribution of Si in the films by pairing of the oxygen with the Si atoms.

From the observations of the apparent diffusion of substrate donors, it appears that the growth of films of thicknesses of 1μ or less with an abrupt rise in the donor concentration at the film-substrate interface is not feasible. At 1000°C the only way of increasing the abruptness is to increase the growth rate. In this system, the maximum growth rate compatible with the growth of a 1μ film is about 0.1 μ min^{-1}. The corresponding α calculated from the apparent diffusion constants for Si- and Te-doped substrate are α (Te, 1000°C) ≈ 30 and α (Si, 1000°C) ≈ 80. The minimum system doping is assumed to be 4.5 x 10^{16} cm^{-3}. From these data, the calculated impurity profiles of 1μ films grown on substrates of net donor concentrations of 2 x 10^{18} cm^{-3} are shown in Fig. 10. For the case of Si-doped substrates, about half the film is influenced by the substrate. For Te-doped substrates, the influence of the substrate is observed almost throughout this film.

An alternate approach to the problem of increasing the steepness of the concentration gradient at the interface is to grow thicker films so that the growth rate may be increased, and then, by controlled etching, remove the film to the desired thickness. In this manner, a steeper gradient at the interface could be achieved so that the influence of the substrate dopant would be decreased.

The investigation of the gold surface barrier diodes on these films was performed to provide a method of determining the variation of impurity profiles with process variables. A complete characterization of these diodes has not been undertaken. It is interesting to note, however, the reverse bias breakdown voltages (reverse voltage at which the diode draws 1 μa of current). These voltages are listed for diodes on each film in Table I. The breakdown voltage is limited by the accumulation of charge as the depletion zone is pushed toward the substrate interface. This is illustrated in films D and F which are of identical thickness. Film F as shown in Fig. 9 is reasonably flat up to 0.5μ from the interface with an abrupt increase in the donor concentration near the substrate. The reverse bias breakdown voltages are between 50 and 60v. Film D as shown in Fig. 7 has a graded profile, so that breakdown occurs at smaller voltages, 20 to 22v. Film E has a very high breakdown of slightly greater than 200v because of the low doping in the film and because the space charge region may extend for such a long distance into the film. For this film the maximum electric field strength is approximately 4 x 10^5 v cm^{-1}.

Conclusions

The growth of n-type films of GaAs on n$^+$-GaAs by the H_2-H_2O transfer process has been investigated. The surface preparation of the substrate immediately before deposition has been determined to be an important factor in obtaining smooth films. The best films have been grown at 1000°C or higher. The slowest growth rate and smoothest films result when growth occurs on the $(\bar{1}\bar{1}\bar{1})$ planes. At low flow rates (≤70 cc min^{-1}), the growth rate is proportional to the square root of the partial pressure of water vapor, however, at high flow rates (≈600 cc min^{-1}) the growth rate is directly proportional to the partial pressure of water vapor. The variation of the partial pressure of water vapor and the total flow rates may be used to vary the growth rate from 0.080 to 1.5μ min^{-1}.

Examination of the impurity profiles of the resulting films suggests that outdiffusion of substrate dopants near the substrate-film interface may be controlling the profiles. This effect may be minimized if Si-doped substrates are used. The net donor concentration in the remainder of the film appears to be about 4 x 5 x 10^{15} cm^{-3}. Growth at 600 cc min^{-1} results in a flattening of the profile in the section of the film not affected by outdiffusion by reducing the effect of other dopant sources. High flow rates also yield flatter films.

Profiles obtained on bulk GaAs (n = 1.8 x 10^{15} cm^{-3}) suggest that the gold surface barrier diodes do not show classical diode behavior. The interpretation of the impurity profiles of these films, although based on these diode measurements, has been tempered to reflect these peculiarities.

Acknowledgments

The author is indebted to R. G. Sobers for the semi-insulating GaAs used in some of these experiments, to

Dr. J. M. Whelan, R. R. Moest, and C. J. Frosch for their sustained interests in this work and for their valuable suggestions, and to D. F. Raver who made many of the electrical measurements.

Manuscript received Sept. 29, 1965; revised manuscript received Nov. 22, 1965.

Any discussion of this paper will appear in a Discussion Section to be published in the December 1966 JOURNAL.

REFERENCES

1. C. J. Frosch, *This Journal*, **111**, 180 (1964).
2. E. Sirtl, *J. Phys. Chem. Solids*, **24**, 1285 (1963).
3. G. E. Gottlieb and J. F. Corboy, *RCA Rev.*, XXIV, 585 (1963).
4. M. V. Sullivan and G. A. Kolb, *This Journal*, **110**, 585 (1963).
5. C. O. Thomas, D. Kahng, and R. C. Manz, *ibid.*, **109**, 1055 (1962).
6. D. Kahng, *Bell System Tech. J.*, **43**, 1 (1964).
7. R. A. Furnanage, Private communications.
8. C. J. Frosch, Private communications.
9. W. Rice, *Proc. IEEE*, **52**, 284 (1964).
10. B. Goldstein, "Compound Semiconductors, Vol. I," R. K. Willardson and H. L. Goering, Editors, Reinhold Publishing Co., New York (1962).
11. C. Kohm, S. A. Kulin, and B. L. Averbach, *Phys. Rev.*, **108**, 965 (1957).

Preparation of Ge/Si and Ge/GaAs Heterojunctions

A. R. Riben,[1] D. L. Feucht, and W. G. Oldham[2]

Electrical Engineering Department, Carnegie Institute of Technology, Pittsburgh, Pennsylvania

ABSTRACT

The effect of various substrate preparation techniques is investigated in the vapor growth of germanium on Ge, Si, and GaAs substrates. Important differences are noted for substrates which are iodine etched *in situ*, chemically etched, and cleaved *in situ;* namely, the appearance and crystal perfection of the overgrowth as well as epitaxial junction properties, all improve in the order of the above procedures. Flat, structureless overgrowths on cleaved GaAs substrates and growths with negligible stacking fault densities and dislocation densities of approximately 10^6 cm^{-2} on cleaved germanium substrates are obtained. However, strain and cracking of the overgrowth, in addition to higher defect densities occur in germanium grown on cleaved silicon substrates.

Considerable interest has been aroused in recent years in the study of heterojunction devices, especially structures made from various combinations of group IV and III-V compounds. Poorly defined interfacial conditions arising from contamination and defect states have confused efforts to relate heterojunction device characteristics to material bulk properties (1-4). In the interest of improving the knowledge of interfacially derived effects, as well as achieving better device consistency, a variety of device preparation techniques have been examined and compared. Heterojunction structures have been prepared by the open tube vapor growth of germanium on gallium arsenide and silicon substrates at relatively low temperatures using the germanium di-iodide disproportionation reaction. A comparison of growth features and final device behavior has been made for various substrate preparation techniques including water and solvent washing, aqueous etching, iodine etching, and cleaving. It has been found that surface conditions alter both the physical growth features and the final device electrical properties. The most consistent device behavior as well as the sharpest reverse breakdown has been obtained by cleaving the substrates *in situ* during deposition.

Experimental

The germanium vapor deposition system employed here has been described briefly in a previous publication (5) and is quite similar to the original systems devised by Ruth *et al.* (6) and Marinace (7). The furnace arrangement used and the corresponding temperature profile are shown in Fig. 1. After Marinace (7), the furnace consists of "Nichrome" ribbon wound on quartz, allowing observation of the growth process through the furnace walls. The hydrogen carrier gas is passed through a "De-Oxo" purifier and a liquid nitrogen cold trap before entering the reaction tube which contains three zones: an iodine zone, a source, and a seed zone. At the exit end of the reaction tube the exhaust gases are passed through a bubbler to maintain positive pressure within the system.

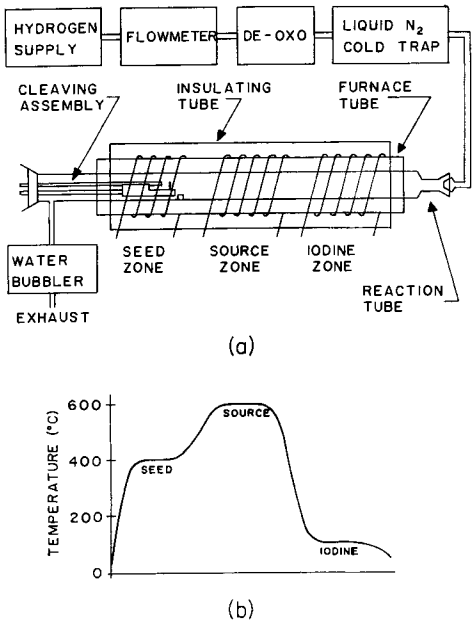

Fig. 1. Germanium vapor growth system: (a) experimental arrangement; (b) temperature profile during growth.

High-purity hydrogen,[3] ultrahigh-purity I_2,[4] and appropriately doped germanium ingots are used as starting materials. Before operation, the system is flushed with hydrogen for 12-18 hr to purge any traces of water or oxygen. If gas etching of the seed is not required, the iodine, seed, and source temperatures are

[1] Present address: Electronics Department, Hamilton Standard Division, United Aircraft Corporation, Broad Brook, Connecticut.

[2] Present address: Electrical Engineering Department, University of California, Berkeley, California.

[3] Linde Division of Union Carbide Corporation, Pittsburgh, Pennsylvania.

[4] Gallard-Schlesinger Chemical Manufacturing Corporation, Garden City, New York

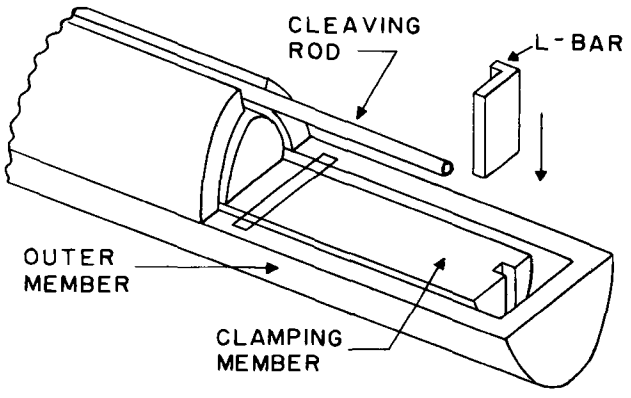

Fig. 2. Quartz apparatus for cleaving Ge, Si and GaAs L-bars *in situ*.

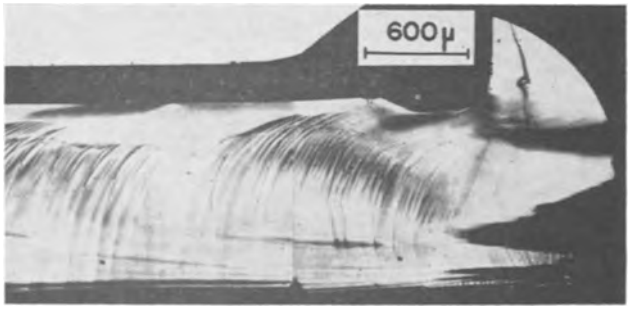

Fig. 3. Composite photograph of a typical silicon cleavage surface

raised to 110°, 400°, and 600°C, respectively, and deposition proceeds. Gas etching is accomplished by first adjusting the iodine temperature to 50°C and both the seed and source temperatures to 400°C for approximately 1 hr. This gas etching causes the chemically polished surface to become dull gray in appearance. The various methods of seed preparation include: chemical etching[5] followed by a de-ionized water rinse, chemical etching with a water rinse followed by iodine etching, cleaving in air, cleaving in air followed by chemical etching and a water rinse, cleaving in air followed by an organic solvent rinse, and cleaving in the growth stream.

The latter operation, cleaving of the substrate to expose a fresh surface during steady-state deposition, requires a special quartz cleaving apparatus depicted in Fig. 2. The samples are prepared by cutting them into L bars which when cleaved yield several square millimeters of flat surface (8). Figure 3 illustrates a typical cleavage surface obtained for silicon. In general, the germanium cleaved surfaces are similar, but the cleaved GaAs surfaces are much flatter. While the Ge and Si surfaces are not of the perfection reported by Gobeli and Allen (8), due to the lack of rigidity of the quartz sample holder, they are adequate for the studies described here.

Results

Growth rates.—Single crystal growth of germanium has been achieved on all surfaces attempted, *i.e.*, on the three major planes of Ge, on the (111) ($\bar{1}\bar{1}\bar{1}$) and (110) planes of GaAs and on the (111) plane of Si. In the case of silicon, growth has been possible only on the (111) plane, because cleavage was necessary to produce an oxide-free surface at these low growth temperatures. Growth rates range from 0.5 to 10 μ/hr and are dependent on seed orientation. In Fig. 4 the growth rate is plotted as a function of the I_2 partial pressure for growth on the ($\bar{1}\bar{1}\bar{1}$) plane (As plane) of GaAs for source and seed temperatures of 600° and 400°C, respectively. No quantitative measurement of

[5] The chemical etches used were 1:1:10 H_2O:H_2O_2:H_2SO_4 for GaAs seeds and 1:5 HF:HNO_3 for Ge seeds.

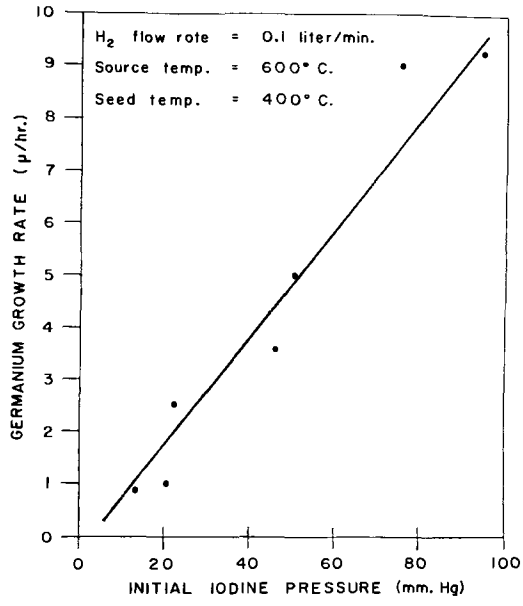

Fig. 4. Growth rate of Ge on (111) plane GaAs substrates as a function of iodine partial pressure.

growth rates on other surfaces has been made. It has been noted that growth on cleaved (110) plane GaAs surfaces proceeds considerably slower than on corresponding uncleaved surfaces. A possible explanation is that the number of growth steps is reduced on a cleaved surface due to near atomic flatness and perfect orientation.

Control of resistivity.—Four-point probe and Hall measurements have been made on test samples to determine doping control. Germanium films grown from intrinsic sources are invariably n-type with carrier concentrations greater than 10^{16} cm^{-3}. However, if the source doping is raised above this value, n-type films may be grown with controlled doping in the range 10^{17}-10^{20} cm^{-3}. A modification of the system, described in another publication (9), has permitted the growth of higher resistivity n-type films. Previously, a troublesome donor has prevented the growth of controlled resistivity n-type Ge films having a doping concentration less than 10^{17} cm^{-3}. P-type films grown in this manner normally have a very thin intermediate n-type layer similar to that reported by Marinace (10).

Crystalline perfection.—The appearance of the overgrowths is in general similar to the films reported by Marinace (7). However, some qualitative differences may be noted between growths on differently prepared surfaces. In one experiment a comparison was made of the overgrowth of four (110) plane GaAs seeds prepared in the following manner and grown simultaneously under the same conditions: (*a*) cleaved in air, chemically etched, and rinsed in de-ionized water; (*b*) cleaved in air and rinsed in organic solvents (semiconductor grade); (*c*) cleaved in air; and (*d*) cleaved *in situ* during steady-state Ge deposition.

Treatments (*a*) and (*b*) resulted in similar heavily faceted overgrowths, Fig. 5(a), whereas the treatment (*c*) produced a nearly flat structureless overgrowth, Fig. 5(b). The overgrowth on surfaces prepared by treatment (*d*) was similar in nature to that of (*c*) but possessed some additional structure. This experiment indicates that contamination left on the surface from wash treatments is primarily responsible for the heavily faceted overgrowth usually observed for (110) plane seed orientations with the Ge-I_2 system (7). Extensive gas etching of the substrate prior to growth forms a dull gray surface which also results in heavily faceted overgrowth. In the absence of high-temperature seed treatments in hydrogen the overgrowth of Ge on Si substrates has been possible only for freshly cleaved surfaces, that is cleaved as the Ge is deposit-

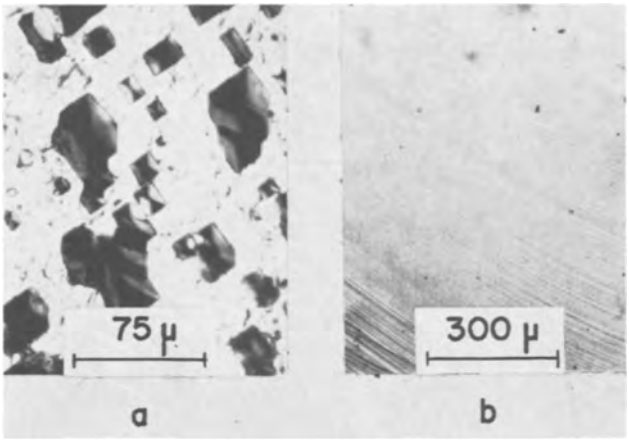

Fig. 5. Appearance of Ge overgrowths on GaAs substrates: (a) substrate cleaved followed by chemical etching or organic solvent rinsing; (b) substrate cleaved in air or *in situ*.

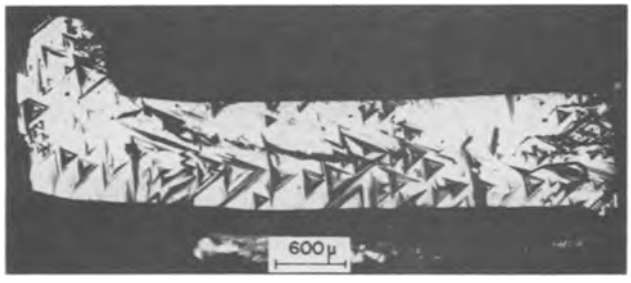

Fig. 6. Appearance of a Ge overgrowth on a cleaved Si substrate

ing. The germanium films thus obtained are not so featureless as the (110) plane growths on cleaved GaAs substrates, but resemble the usual (111) plane Ge films grown on cleaved Ge susbtrates. A photograph of a complete overgrowth of Ge on Si is shown in Fig. 6. In addition to variations in growth appearance, surface treatment also plays a role (to be discussed) in determining the electrical properties of both heterojunctions and homojunctions.

A defect present in germanium layers grown on silicon but not present in layers grown on germanium or gallium arsenide is a cracking of the overgrowth. Some of the cracks can be observed directly, while a brief etch serves to enlarge those not immediately observable. The crack lines are almost entirely in the [110] direction, suggesting that, as the germanium overgrowth cools from the growth temperature, it cleaves on those (111) planes intersecting the surface. The mean distance between cracks has been as low as 40μ, *i.e.*, the crack density is 1/40 μ^{-1} for layers thinner than 10μ. On thick layers the mean distance between cracks has been up to 230μ. Crack density correlated with crack width as well as growth thickness. The very dense cracks on the thinner growths cannot be observed without etching, whereas cracks became easily observable as the thickness of the growths increased and crack density decreased. The cracks cannot be associated with specific defects on the silicon substrate. However, the very thin growths ($<10\mu$) on areas with dense cleavage defects have a high crack density, and more perfect areas have a lesser density. Figure 7 shows a 4μ thick Ge overgrowth; (a) as grown and (b) following a 9-sec etch. The corresponding region of the cleaved silicon substrate[6] is shown in Fig. 7 (c). In Fig. 7(b), the crack free regions correspond to the more perfect cleavage areas [see Fig. 7(c)]. The crack density varies in (b) from $1/50\mu^{-1}$ to zero. The thicker growths have both a different appearance and a lower density of cracks.

[6] As a result of the cleaving process a section of the silicon L bar is pushed upstream into a region where no deposition occurs. Thus it may later be removed and examined to determine the cleavage perfection.

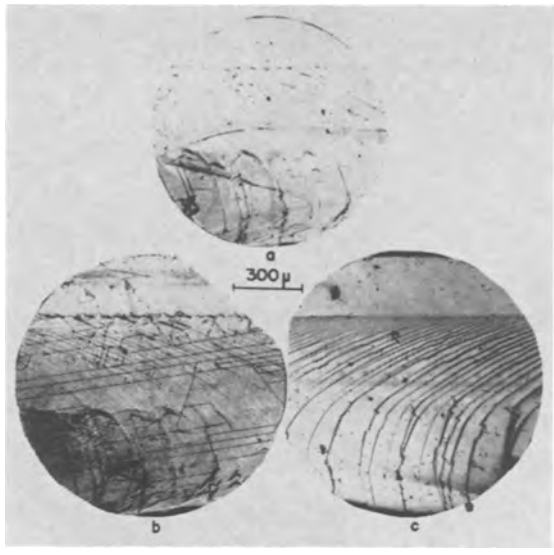

Fig. 7. A 4μ-thick Ge overgrowth on a cleaved Si substrate: (a) as grown (b) after a 9-sec WAg etch showing cracks in the overgrowth; (c) corresponding Si cleavage surface (see text).

Growth pyramids on thicker growths (see Fig. 6) have triangular bases whereas pyramids on thinner growths [see Fig. 7(b)] have more circular bases. The areas of very low crack density on the more perfect substrate regions suggest that improved cleavage quality and growth uniformity can mitigate the cracking difficulties. In any case, it has been possible to fabricate devices by etching mesas which do not include cracks.

X-ray analysis.—Laue back reflection photographs and diffractometer studies have confirmed the single crystal, epitaxial nature of the overgrowths. Studies of Ge/GaAs structures indicate no distortion of the Ge film or GaAs substrate. However, Laue photographs of Ge/Si structures show considerable distortion in the form of elongated Laue spots with striations as previously reported by Ruth *et al* (6). The latter attributed the distortion to the lattice mismatch between Ge and Si; however, such distortion in the Laue photographs has not been found to be present in other heterojunction pairs with equally large lattice mismatches (11) (InP-GaAs and InAs-GaAs), nor in heavily dislocated Ge layers grown on any Ge or GaAs substrates. In addition, it has been observed that in Laue photographs taken at 350°C, some of the distortion disappears, suggesting that the greater shrinkage of the Ge overgrowth during cooling from the growth temperature is responsible for the distortion. The striations in the spots are concluded to be reflections from the various slightly misoriented facets separated by cracks. This has been further confirmed by an experiment in which the x-ray beam diameter was increased and the striations became more pronounced.

Etching studies.—Germanium layers grown on Ge, GaAs, and Si have been treated with an etchant sensitive to crystalline defects. For the Ge-Ge and Ge-GaAs structures a comparison of the number of dislocations and stacking faults in the epitaxial layer as a function of the original surface preparation of the seed has been made. The etchant used to bring out both the stacking faults and the dislocations was the Westinghouse silver etch (12), (25 ml H_2O, 10 ml HF, 15 ml HNO_3, 0.2g $AgNO_3$). The optimum procedure was found to be a 5-sec etch, followed by a water rinse, and then removal of excess silver by wiping. The procedure is repeated until the imperfections are visible. Normally, after a total of 15 sec the stacking faults are visible, and after 30 sec the dislocation pits appear.

A comparison of dislocation pits in germanium grown on three (111) plane germanium substrates having different surface preparations is shown in Fig.

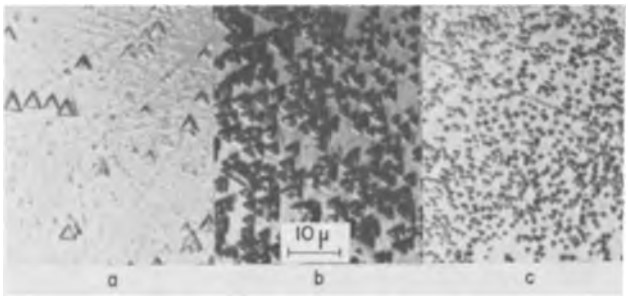

Fig. 8. Etch pits in the Ge overgrowth on (111) Ge substrates for various substrate preparation techniques. (The etch pits were developed with a 30-sec WAg etch): (a) substrate cleaved *in situ;* (b) substrate chemically etched; (c) substrate iodine etched *in situ.*

8. The growths on the cleaved and chemically etched substrates, shown in Fig. 8(a) and 8(b), were deposited simultaneously. The lowest dislocation density (less than $10^6/cm^2$) occurs in growths on substrates cleaved *in situ.* Dislocation counts on chemically etched seeds indicate approximately 10^7 dislocations cm^{-2} whereas the number of dislocations in the overgrowth on a typical iodine etched substrate [Fig. 8(c)] is greater than 3 x 10^7 cm^{-2}. The substrates themselves have an average dislocation count of approximately 10^4 cm^{-2} and a maximum count of 10^5 cm^{-2}. Cross sections of the cleaved growths show a smooth transition from substrate to overgrowth whereas for cross sections of the chemically or iodine etched seeds a dark line occurs at the interface which appears to be a region of very high dislocation density. Germanium layers grown on the (111) and ($\bar{1}\bar{1}\bar{1}$) planes of gallium arsenide show dislocation densities approximately a factor of two higher than those grown on correspondingly prepared germanium substrates. It has not been possible, however, to decorate the dislocations for overgrowths on (110) plane cleaved gallium arsenide substrates.

The stacking fault densities follow a similar pattern; the density is higher for germanium overgrowths on gallium arsenide than on germanium, and they increase as the substrate preparation is changed from cleaving to chemical etching to iodine etching. No stacking faults are observed on cleaved Ge substrates, occasional isolated stacking faults are observed in layers grown on chemically etched germanium substrates and up to 100 faults cm^{-2} occur on I_2 etched substrates. In comparison, clusters of stacking faults with a density of 3 x 10^4 cm^{-2} appear relatively uniformly spaced across the germanium layer grown on a chemically etched gallium arsenide seed.

A striking difference is noted for germanium grown on cleaved silicon substrates. Both the dislocation density (greater than 5 x 10^7 cm^{-2}) and the number of stacking faults (approximately 10^6 cm^{-2}) are much higher than for germanium grown on any germanium substrates.

These etching studies confirm the importance of substrate imperfections in initiating stacking faults and dislocations in the overgrowth (13-15). Cleaved substrates should initially be oxide and contaminant free leading to the lowest fault density as observed. Iodine-etched substrates apparently are left with a film of contaminants which nucleate both stacking faults and dislocations. The higher defect density in germanium grown on silicon is expected in light of the defect nucleation at microscratches (13) and local stresses (14) for silicon grown on silicon. In addition, oxides which rapidly form on the cleaved silicon surface would be expected to cause defect nucleation, by analogy to the growth of silicon on silicon (15).

Electrical properties.—The electrical properties of these junctions have also been studied and correlated with the surface preparation. Capacitance as a function of voltage shows a square law dependence which

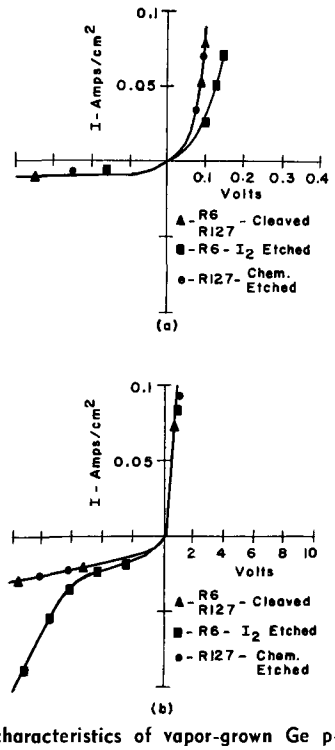

Fig. 9. V-I characteristics of vapor-grown Ge p-n junctions for cleaved, iodine-etched, and chemically etched substrates: (a) low voltage region; (b) high voltage region.

indicates the existence of an abrupt junction. In Fig. 9 the V-I characteristics of junctions fabricated from Ge grown on Ge substrates having different surface preparations are shown. In Fig. 9(a) the forward characteristics are shown for cleaved, chemically etched, and iodine etched substrates. At the same voltage, the forward current density is approximately the same for devices grown on cleaved and chemically etched substrates whereas devices on iodine etched substrates have a smaller current density. At low reverse voltages (less than 0.5v) the reverse current densities are presumably determined by the doping in the seed ma-

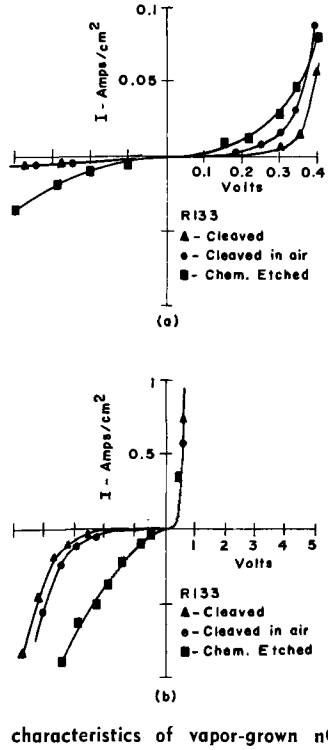

Fig. 10. V-I characteristics of vapor-grown nGe-pGaAs junctions for cleaved, iodine-etched and chemically etched GaAs substrates: (a) low voltage region; (b) high voltage region.

terial and are therefore identical. For higher reverse voltages, shown in Fig. 9(b), the diode on the iodine-etched substrate has a much larger reverse current density at a given voltage than those on the cleaved or chemically etched substrates. The devices fabricated on iodine-etched substrates vary widely but always exhibit a larger current density.

The forward and reverse V-I characteristics of nGe-pGaAs heterodiodes having various GaAs substrate preparations are shown in Fig. 10. The forward current density at constant voltage increases as we proceed from cleaved to cleaved in air to chemically etched substrates, Fig. 10(a). A similar dependence of the current density on surface preparation is noted in the reverse direction, for the same diodes as shown in Fig. 10(b). The reverse current increases with voltage as a power law prior to breakdown ($I \sim V^m$ where $m > 3$) (16) due to tunneling via interface states. The forward electrical characteristics of Ge-GaAs diodes are also controlled by tunneling via interface states. Both of these mechanisms will be discussed in detail in a future publication (17). Avalanche breakdown would normally occur in these diodes at approximately 9v.

Conclusions

A correlation of crystal defects in vapor-grown germanium layers with substrate surface preparation is established. The electrical properties of epitaxial heterojunctions and homojunctions also show a similar correlation with substrate preparation. The most perfect overgrowths and the best device characteristics (*i.e.*, highest rectification ratio) are obtained for growths on substrates which have been cleaved *in situ* during vapor deposition.

Acknowledgment

The authors wish to thank Mr. M. J. Zamba for preparing the samples. This work was supported in part by a United States Army Research Office (Durham) Contract. DA-31-124-ARO (D)-131.

Manuscript received June 16, 1965; revised manuscript received Nov. 18, 1965. This paper was presented in part at the San Francisco Meeting, May 9-13, 1965.

Any discussion of this paper will appear in a Discussion Section to be published in the December 1966 JOURNAL.

REFERENCES

1. R. L. Anderson, *Solid State Electronics*, **5**, 341 (1962).
2. W. G. Oldham and A. G. Milnes, *ibid.*, **7**, 153 (1964).
3. L. J. Van Ruyven, *Phys. Stat. Sol.*, **3**, K109 (1964).
4. R. H. Rediker, S. Stopek, and J. H. R. Ward, *Solid-State Electronics*, **7**, 621 (1964).
5. W. G. Oldham, A. R. Riben, D. L. Feucht, and A. G. Milnes, *J. Electrochem. Soc.*, **110**, 53C (1963).
6. R. Ruth, J. Marinace, and W. Dunlap, *J. Appl. Phys.*, **31**, 995 (1960).
7. J. C. Marinace, *IBM J. Research and Develop.*, **4**, 248 (1960).
8. G. W. Gobeli and F. G. Allen, *J. Phys. Chem. Sol.*, **14**, 23 (1960).
9. A. R. Riben, D. L. Feucht, and W. G. Oldham, *J. Appl. Phys.*, **36**, 3685 (1965).
10. J. C. Marinace, *Electrochem. Technol.*, **1**, 104 (1963).
11. W. G. Oldham, Thesis, Carnegie Institute of Technology, Pittsburgh, Pennsylvania, (1963), Office of Technical Services, #AD 412-297.
12. R. H. Wynne and C. Goldberg, *Trans. AIME*, **197**, 436 (1953).
13. S. Mendelson, *J. Appl. Phys.*, **35**, 1570 (1964).
14. T. L. Chu and J. R. Gaveler, "Metallurgy of Advanced Semiconductor Materials," p. 209, Interscience Publishers, New York (1963).
15. B. A. Unvala and G. R. Booker, *Phil. Mag.*, **9**, 100 (1964).
16. A. R. Riben and D. L. Feucht, IEEE Trans. on Electron Devices, *ED-11*, 534 (1964).
17. A. R. Riben and D. L. Feucht, *Solid State Electronics*. To be published.

Preparation and Properties of AlAs-GaAs Mixed Crystals

J. F. Black and S. M. Ku

General Telephone & Electronics Laboratories, Incorporated, Bayside, New York

ABSTRACT

AlAs-GaAs mixed crystals of composition varying throughout the solid-solution range 0-40 mole % AlAs and 60-100 mole % AlAs have been prepared by halide-vapor disproportionation and by melt-growth techniques, respectively. Electron-beam-probe data and optical data showed that the epitaxially grown mixed crystals were of graded composition, while the melt-grown crystals were homogeneous in composition (within ±1 mole %). Measurements of the optical energy gap, the x-ray lattice parameter, the density, and the electrical properties of these crystals are described. The variation of the optical energy gap with composition is discussed in relation to an ideal mixed crystal model of the energy band structure.

Direct-band-gap III-V compounds are of considerable interest for opto-electronic devices, especially since the advent of high-frequency high-efficiency light-emitting and laser diodes in 1962 (1). The value of the energy gap of a semiconductor is very important in opto-electronic devices, where, for example, it is often necessary to "tailor" the optical properties for acceptable performance. It has long been known that by combining appropriate III-V compounds a number of mixed crystal systems can be formed which make it possible to produce direct-band-gap semiconductors over a continuous range of energy gaps (2-4). These direct-band-gap mixed crystal systems can be divided into two groups according to the type of band structure of the terminal compounds: (*i*) direct-direct and (*ii*) direct-indirect, where the indirect gap compound usually possesses the higher energy gap. The direct-indirect combinations are of particular interest because they offer higher energy gap ranges than the direct-direct combinations.

Only one direct-indirect III-V system, GaAs-GaP, has been thoroughly examined to date (5-7). Previous work by Stambaugh *et al.* (8) in 1960 established that another of these systems, AlAs-GaAs, was potentially useful for its high energy gap range. The results of Stambaugh and co-workers indicated that AlAs possessed the same type of band structure as GaAs, *i.e.*, direct. However, later measurements on pure AlAs conducted by Mead and Spitzer (9) provided strong evidence that AlAs had an indirect band structure. The present paper describes a more detailed investigation of the AlAs-GaAs system with results which confirm the conclusions of the latter investigators. A description of the methods of preparation and the properties of mixed crystals of AlAs-GaAs is given herein. A succeeding paper (10) will deal with

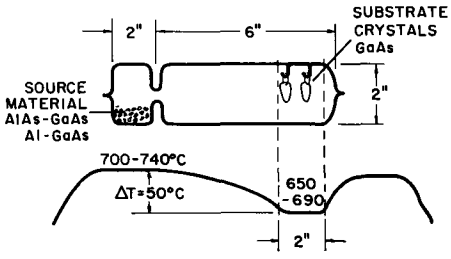

Fig. 1. Arrangement used for preparation of AlAs-GaAs mixed crystals by iodide-vapor phase epitaxial growth.

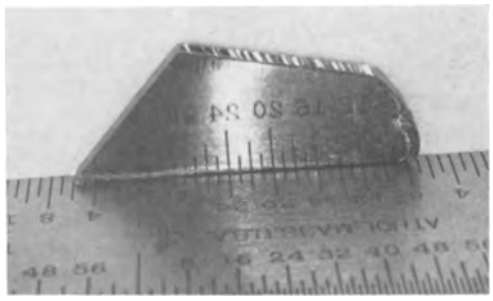

Fig. 2. As grown epitaxial AlAs-GaAs layer on GaAs substrate

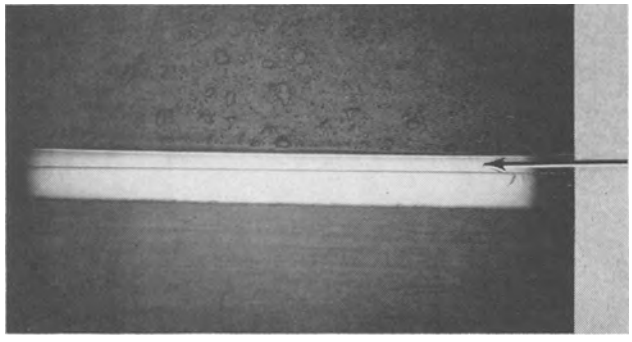

Fig. 3. Cross section of AlAs-GaAs layer (arrow) 6½ mils thick grown on a GaAs substrate. Only one mixed crystal layer is seen since the substrate has been sliced in half to recover the other layer.

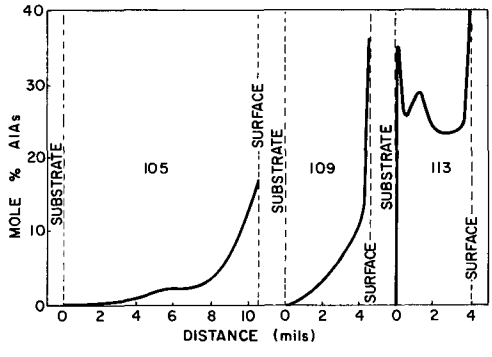

Fig. 4. Composition profiles of AlAs-GaAs mixed layers as determined by the electron beam microprobe.

the fabrication and measurements of light-emitting diodes made from some of these mixed crystals.

Synthesis Studies Experimental Approach

Epitaxial AlAs-GaAs.—*Preparation.*—Single-crystal layers of AlAs-GaAs of a composition extending to about 40 mole % AlAs were grown epitaxially on GaAs substrates by an iodide-disproportionation-type closed-tube vapor-transport process similar to that used for GaAs-GaP (11). The essential details of the technique are shown in Fig. 1. The GaAs substrates were suspended from quartz hooks by loops of rhodium wire. Rhodium was chosen because it did not contaminate the epitaxial layers, *i.e.*, rhodium was not detectable by spectroscopic analysis of layers grown in preliminary experiments. The substrates were <110> oriented single crystal wafers of high purity ($n < 5 \times 10^{16}/cm^2$) with faces which had been ground flat and parallel, lapped with No. 1800 grit and then chemically polished in 1% bromine-methanol solution.

The source material was either a mixture of presynthesized AlAs powder and GaAs powder or a mixture of powdered GaAs and granules of pure Al. The AlAs powder was prepared by reacting pure aluminum with arsenic vapor in the presence of iodine (12). When the pure aluminum was used to charge the epitaxial growth capsule, care was taken to ensure that there was a layer of GaAs powder between the aluminum and the capsule wall to avoid contact of the quartz with molten aluminum. The iodide vapor phase was established by introducing pure iodine into the capsule in evacuated breakseal ampoules which were broken after the capsule had been sealed from the vacuum system. Enough iodine was used to yield 1 mg of free iodine per cubic centimeter of capsule volume. In a few instances small chunks of SnI_4 were used instead of pure iodine to produce a dopant-iodide vapor phase. Just prior to seal off, the capsule was backfilled with ½ atm of H_2 purified by passage through a palladium diffusor. It was found that by sealing ½ atm H_2 in the capsule better epitaxy and more uniform growth resulted than if the capsule were sealed under vacuum. Mixed crystal growth was initiated by quickly inserting the capsule into the preheated furnace. When sufficiently thick layers had been grown the run was terminated by removing the capsule from the furnace and cooling in the air.

Results.—Most samples of epitaxially grown AlAs-GaAs displayed a dull matte finish on their surfaces, but some, especially those with high aluminum content toward the surface, had smooth mirrorlike surfaces. Figure 2 shows an example of one of these mirrorlike surfaces. Surfaces of this type were sufficiently good for optical measurements, but the matte-finish surfaces required lapping and polishing to prepare the epitaxial layer for measurement of optical transmission. All of the epitaxial layers were "dished," especially near the edges of the sample; therefore, only the central regions of the grown layers, where the epitaxial film was of uniform thickness, were used for measurements. Figure 3 shows the uniformity of layer thickness that was generally obtained in the central regions of the layers.

Many of the epitaxial layers which were prepared in this investigation were not only quite thin—as thin as 3 mils—but they proved to have composition gradients through the thickness of the layer. By use of the electron beam probe, it was possible not only to identify and recover those films of uniform composition, but also to gather useful information from those films of a graded composition.

Figure 4 shows the composition profiles of several samples as determined by the electron-beam-probe technique. Lateral variations of composition, *i.e.*, in a plane parallel to the epitaxy substrate interface, were not more than 1 mole % AlAs in any epitaxially grown layer. This was consistent with the results of measurements of injection electroluminescence of diodes made from these layers (10).

Samples were also analyzed by x-ray fluorescence analysis using conventional x-ray equipment and grinding thin increments from the layer between successive analyses. In this case the irradiated region was several millimeters square, and the sampling depth about 1.5 mils. Where sample uniformity and size was such as to allow comparison, for example in slices cut from polycrystalline ingots, good agreement was obtained between x-ray fluorescence analysis (including electron-beam-probe results) and other means

Table I. Epitaxial growth parameters

Sample	Transporting agent	Source composition, g	Duration of growth, hr	Thickness of epitaxy, mils	Epitaxial composition max. AlAs mole %	Epitaxial composition profile
104	I_2	AlAs—2.1 GaAs—3.0	48	6.0	40	Graded increasing AlAs toward surface
105	I_2	Al—0.1 GaAs—3.4	64	10.5	16	Graded increasing AlAs toward surface
109	I_2	Al—0.5 GaAs—4.0	64	4.5	37	Graded increasing AlAs toward surface
113	SnI_4	AlAs—1.7 GaAs—2.3	141	4.0	40	See Fig. 5
116	SnI_4	AlAs—1.6 GaAs—2.3	231	6.0	40	Graded decreasing AlAs toward surface

of composition determination. By comparison with chemical analysis, with density determinations, and with precision x-ray lattice parameter measurements, the analytical accuracy was determined to be ±1 mole % AlAs.

The time required for growth of AlAs-GaAs layers and the composition of the layers were strongly dependent on the source material as may be seen from the data in Table I. Epitaxial layers with graded composition (continuous increase in Al content from interface to surface) were consistently formed from Al + GaAs source material. When AlAs was used in the source instead of aluminum, the grown layers sometimes showed regions of nearly constant composition (sample No. 113). The use of SnI_4 rather than pure iodine as transport agent resulted in Sn doping of the grown layers and also resulted in greatly reduced growth rates, presumably because the SnI_4 did not decompose sufficiently to provide the proper concentration of iodide vapor phase for rapid material transport. Epitaxial layers with greater than 40 mole % AlAs grew very slowly and were heavily contaminated with silicon. Suitable mixed crystal material with composition in excess of 40 mole % AlAs was best prepared by slow freezing of AlAs-GaAs melts.

Melt-grown AlAs-GaAs.—*Preparation.*—Mixed crystals with greater than 50 mole % AlAs composition were prepared by directional solidification (*i.e.*, normal freezing) of AlAs-GaAs melts in sealed evacuated quartz tubes, because of the difficulties that were encountered in growing suitable epitaxial crystals in this composition range. Previous work by Stambaugh *et al.* (13) had demonstrated that melt techniques could be used to good advantage for preparing crystals of AlAs-GaAs. The multiple zone furnace arrangement employed was essentially as described by Stambaugh (14) except that an aluminum oxide sleeve was placed around the graphite susceptor to keep the inside walls of the quartz tube cool enough to prevent softening and to minimize reaction of the quartz with aluminum vapors. To prepare mixed crystal ingots, the boat was charged either with a mixture of presynthesized AlAs powder and powdered GaAs or with a sandwichlike arrangement of slices of pure aluminum and high-purity GaAs. When the latter procedure was used, severe attack of the quartz tube occurred in the region of the hot zone, presumably by aluminum vapors, during the process of melting and reacting the charge. The use of the presynthesized AlAs powder rather than aluminum in the charge kept the aluminum vapor density at a minimum at all times and reduced the degradation of the quartz tube to tolerable levels. Boron nitride boats were found to be most suitable for crystallizing molten AlAs-GaAs. The ingots could not be easily removed from the boats without cracking, and most of the ingots were recovered by filing and sandblasting the boats away.

Results.—All of the ingots prepared were polycrystalline with a relatively fine (about 0.5 mm) grain size. To produce ingots with sections of reasonably good lateral homogeneity (*i.e.*, with no more than ±1 mole % variation from the mean value as determined by electron beam probing), it was necessary to crystallize at a speed of no more than 2 mm/hr. Even so it was not possible to produce homogeneous material of less than about 50 mole % AlAs. The composition at the first-to-freeze end was always considerably higher than the initial melt composition, indicating a wide gap between the liquidus and solidus lines in the AlAs-GaAs temperature-composition phase diagram. For example, in an ingot of initial composition of 33 mole % the first-to-freeze end had a composition of 78 mole % AlAs, Similar observations were reported previously for this system (13).

A section of one of the melt-grown ingots which was polished for optical measurements is shown in Fig. 5. The composition of this piece was 72 mole % AlAs, and it was a clear red-orange color by transmitted light. Black spots which are barely visible in the sample are inclusions of an unidentified foreign material. Since the total amount of these inclusions was less than 1% of the total volume of the sample, their presence was neglected in correlating optical measurements with composition.

Precision lattice parameter measurements made on a sample of 58 mole % AlAs yielded a value of 5.6581 ±0.0003Å. A comparison of this value with values for GaAs (5.6534 ± 0.0002Å) and AlAs (5.662 ± 0.001Å) (15) is made in Fig. 6 which indicates that the lattice

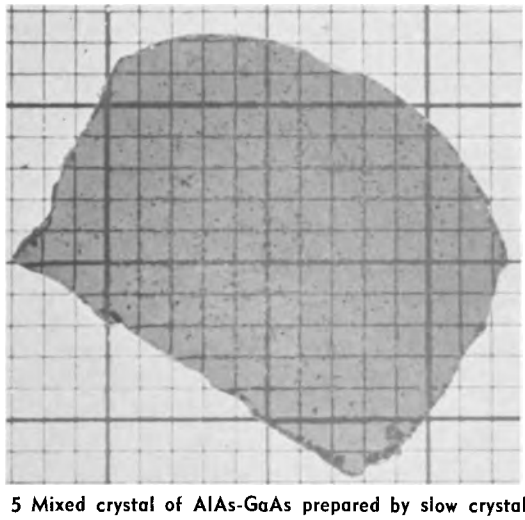

Fig. 5 Mixed crystal of AlAs-GaAs prepared by slow crystallization from the melt. The actual size of the section shown is 5/16 x 1/4-in. and it is 0.015-in. thick.

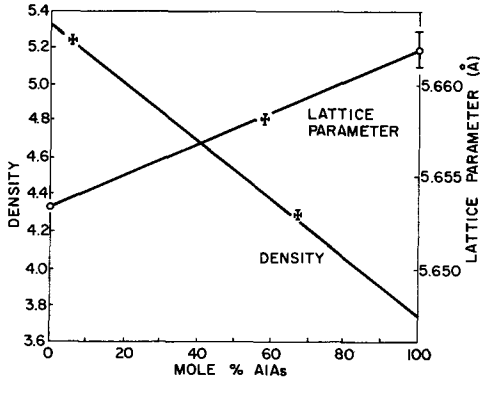

Fig. 6. Variation of lattice parameter and density with composition in the AlAs-GaAs system. The horizontal and vertical bars at each data point represent the limits of experimental error. The solid lines represent the behavior expected if Vegard's law is followed.

parameter-composition variation (mole per cent) may be linear (Vegard's law). Once it was established that there was no serious deviation from Vegard's law, it was a simple matter to calculate the density-composition variation. For the purpose of a density calculation even as large a mid-range deviation from Vegard's law as $a_o = 5.600$Å or $a_o = 5.700$Å would not have been serious since it would have introduced an error of only ±½% in the calculated mid-range density. A density measurement is capable of very good precision in determining the AlAs-GaAs composition since the density change is quite large. For example with a measurement accuracy of ±½% (which is easily achieved in measurements of density), the composition determined by the density measurements was within 2 mole % of the analysis values for samples of either high or low aluminum content. These results are shown in Fig. 6.

Optical and Electrical Studies

Measurement methods.—Optical measurements.— Optical transmission measurements were performed on a model 350 Perkin-Elmer spectrometer using a beam condenser attachment for small samples. Measurements on epitaxial layers of graded composition were made as follows. Samples 3-4 mm long x 2-3 mm wide were mounted on separate quartz plates with a transparent wax, and the GaAs substrate was ground off. By careful grinding and polishing, successive layers were removed from the epitaxial layer and the optical absorption edge was correlated with the mixed crystal composition determined by electron beam probe analysis of the polished surface. The optical absorption edge was defined as the intercept of the transmission curve with the zero transmission abscissa, neglecting the short-wavelength tail caused by the spectrometer band pass. In this way the region of the polished sample face which defined the absorption edge (or the optical energy gap) was the first several microns that the spectrometer beam traversed in passing through the sample. This is equivalent to defining the optical energy gap as that energy corresponding to an absorption coefficient of about 10^4 cm^{-1}. Since the region of the film sampled by the electron beam probe was essentially the same as that determining the absorption edge, good correlation could be expected between the two kinds of information. Strictly speaking, good correlation could be expected only for compositions where the (lowest energy) band-to-band transitions were still direct. Band-to-band optical transitions in the indirect III-V compounds are generally characterized by absorption coefficients no higher than 10^3 cm^{-1}. Thus for AlAs-GaAs compositions where the band gap transitions were indirect, the region determining the optical energy gap would no longer be comparable to the region sampled by electron probe analysis.

By the technique described above it was possible to investigate (optical) energy gap-composition variations over a moderate range of composition in a single graded composition epitaxial layer. The correlation was best accomplished in layers possessing a monotonic increase in AlAs content from the substrate-epitaxy interface to the surface of the epitaxial layer. For sharp composition gradients, *i.e.*, more than a few mole per cent over several microns, the correlation was made less reliable because of the difficulty experienced in keeping the plane of polish exactly parallel to the epitaxial surface. In effect this limited our optical measurements on the epitaxial mixed crystals to the composition range 0-25 mole per cent AlAs (see Fig. 4). Only those melt-grown samples which were of uniform (within ±1 mole per cent) mixed crystal composition were used for the correlation of optical energy gap with composition. Furthermore, only samples with minimal amounts of foreign inclusions, such as in Fig. 5, were used. The optical transmission measurements were made on mechanically polished samples 5-20 mils in thickness, and the optical energy gap was calculated at the shoulder of the absorption edge. This is a common method of determining the optical band edge of a semiconductor, and it is a more accurate definition of the energy gap than the point of intercept with the zero-transmission abscissa, especially for an indirect semiconductor. [Previous measurements of pure AlAs by Mead and Spitzer (9) indicated that high AlAs composition mixed crystals would be of an indirect band structure.] In addition, the energy gap of the AlAs-GaAs mixed crystals could then be better compared with pure AlAs since the values that have been reported for the optical energy gap of pure AlAs are essentially equivalent to the shoulder of the absorption edge.

Electrical measurements and impurity analysis.—Electrical measurements were made in much the same way as the optical measurements, *i.e.*, by mounting the samples on flat quartz plates and grinding off the substrate. Undoped epitaxial mixed-crystal layers were n-type. P-type material was produced by in-diffusing zinc from the vapor phase at 800°C in small evacuated quartz ampoules. For the most part, electrical measurements were confined to four-point probe resistivity measurements using a co-linear probe arrangement, and to hot-point probe thermoelectric measurements to determine the sign of the charge carriers. The making of low-resistance alloyed contacts was very difficult due to the rapid formation of tenacious oxide films even on samples of low AlAs content. However, this difficulty was partially overcome by forming spring-loaded point contacts with a spark discharge from a Tesla coil of the kind used for vacuum leak detection. Because of the difficulties involved in the handling of these thin samples and in making suitable ohmic contacts, Hall effect measurements were successful in only a few instances. The impurity content was obtained by quantitative emission spectroscopy of pieces of the epitaxial layers recovered after grinding off the substrate material.

Electrical measurements were not made on polycrystalline material because of the severe effects that grain boundaries often have on the measured electrical properties of semiconductors.

Results and discussion.—Electrical measurements and impurity analysis.—The results of electrical measurements of AlAs-GaAs layers are listed in Table II, and the results of spectroscopic analysis are found in Table III. No other impurity elements besides those

Table II. Electrical characteristics epitaxial layers

Sample	Thickness,[a] mils	Composition mole % AlAs Average	Range	Cond. type	$\bar{\rho}$ 4 pt. probe, ohm-cm	Hall effect $\bar{n}$/cm³	Hall effect $\bar{\mu}$, cm²/v-sec
104	2.5	20	15-40	n	1.2	—	—
105	5.0	6	2-17	n	0.01	—	—
109	2.5	8	3-37	n	0.03	—	—
109	1.5[b]	11	6-37	p	0.005	—	—
113	3.5	26	23-40	n	0.45	7×10^{16}	165
113	1.0[b]	25	23-40	p	0.04	—	—
116	4.0	27	18-40	n	—	1.8×10^{17}	670

[a] Thickness of sample measured from surface of epitaxial layer.
[b] Depth of p-n junction measured from surface of epitaxial layer.

Table III. Impurity content of[a] epitaxial layers

Sample	Si	Cu	Mg	Ag	Sn	Time, hr
Starting GaAs	20	3	2	1	N.D. (<10)	—
Starting AlAs	30	2	4	N.D. (<1)	N.D. (<10)	—
105	130	15	3	1	—	64
109	320	45	3	1	—	64
113	900	35	2	1	850	140
116	1800	30	5	3	375	230

[a] By quantitative emission spectroscopy, concentrations given in ppm by weight.

listed were detected. The high level of Si contamination in the layers was consistent with a noticeable etching of the quartz capsule by the aluminum iodide vapors. The attack was continuous, and therefore longer term runs contained high Si-contamination. Note that there is a significant amount of Cu contamination also. It is believed that the quartz is the source of Cu contamination too. It is encouraging that despite the heavy contamination of these mixed crystals, the electron mobilities measured are still reasonably high. In addition, the resistivities observed in the zinc-diffused layers are comparable to the resistivities one would obtain for diffusion of zinc into GaAs under similar conditions.

The melt-grown AlAs-GaAs material showed much lower Si content than the epitaxially grown crystals even though the processing temperature was much higher (1700°C) than for the epitaxial material (700°C). This points up the critical role of iodine in promoting the attack of quartz by aluminum vapor at low temperature. For example, spectroscopic analysis of the polycrystalline ingots typically showed 30-50 ppm Si compared to 100-2000 ppm Si in epitaxially grown material. Other trace impurities present in the melt grown AlAs-GaAs were Ag (1-2 ppm), Cu (5-10 ppm), and Mg (5 ppm). Boron was detected in the ingots, but in relatively low concentrations, less than 100 ppm, indicating very little dissolution of the boron nitride boats in AlAs-GaAs melts.

Optical measurements.—In Fig. 7 is shown the variation in optical transmission of a graded composition layer as the layer was successively ground and polished toward the region of high aluminum content. The first measurement included the region of the film near the epitaxy-substrate interface. This region was low in aluminum content, and the transmission curve is nearly identical to that of pure GaAs. The decrease in transmission beyond the absorption edge as the sample was made thinner was probably caused by the difficulty experienced in getting a high polish in regions of high Al content. There appeared to be an increase in the hardness of AlAs-GaAs mixed crystals at high AlAs compositions.

The optical energy gap-composition variation determined for both epitaxially prepared AlAs-GaAs and melt-grown AlAs-GaAs is shown in Fig. 8. Included are the results of the measurements of two homogeneous polycrystalline melt grown samples of low AlAs composition.[1] The energy gap for these samples was defined in the same way as for the graded composition samples, and the composition-energy gap data are in good agreement with the data obtained on epitaxial material.

The solid circles are values of the optical energy gap measured by Stambaugh *et al.* (8) for polycrystalline melt-grown material. The value for the optical energy gap of GaAs corresponds to an absorption coefficient $\alpha = 10^4$ cm^{-1} and was determined at the intercept of the absorption edge with the zero-transmission abscissa in order to be consistent with the data on the low-Al-content mixed-crystal material.

[1] Obtained from E. Stambaugh, Battelle Memorial Institute, Columbus, Ohio.

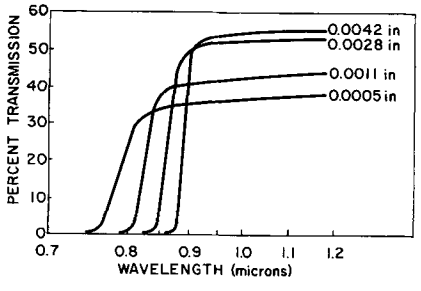

Fig. 7. Variation in optical transmission (300°K) as graded composition mixed crystal layer was successively lapped and polished toward the surface, the region of high AlAs composition.

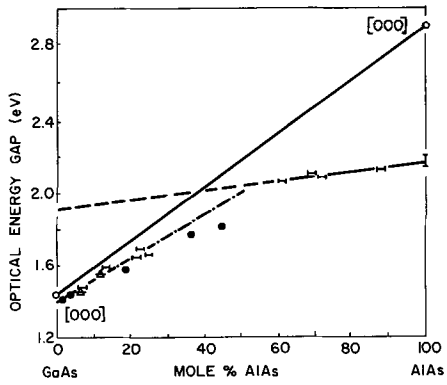

Fig. 8. Optical energy gap (300°K) vs. composition for the AlAs-GaAs system. The solid line is the linear interpolation between the direct transition energies of the terminal compounds. The dashed lines are extrapolations of the experimental data. The [000] energy value for AlAs is from ref. (9) while the lower conduction band energy of AlAs is from ref. (9) and (16). |—|, this investigation; |—△—|, polycrystalline samples from Battelle; •, Stambaugh *et al.*

The fact that the energy gap composition data differ widely from a linear relationship between the conduction band energy of GaAs and the conduction band energy of AlAs is evidence for the indirect nature of the AlAs band structure (3, 4) confirming the conclusions of Mead and Spitzer (9). The data suggest a marked change of slope at 2.0 ev and 50 mole % AlAs, the approximate values of the energy gap and composition, respectively, at which the energy separating the direct and indirect band edges in AlAs-GaAs mixed crystals would approach zero.

The composition-energy gap relation in the Al-rich end of the composition range is in good agreement with the band-gap value of AlAs obtained by measurements of the photoresponse of n-type AlAs-Au surface barrier layers (9). It is also in good agreement with reported values of the optical energy gap of pure AlAs (16).

A virtual crystal model of the energy band structure of an ideal mixed crystal predicts to a first approximation a linear relationship between energy transitions of like kind and molar composition. Woolley (17) has recently discussed the merits of this theoretical approach in interpreting the properties of mixed crystal semiconductors. As he has pointed out, this kind of application of a virtual crystal model leaves something to be desired, but we believe it to be a useful framework for the following discussion. Actually, ideal behavior has been observed for energy transitions of like kind (band-gap) in InAs-InP mixed crystals and more recently for several like-kind energy transitions (above band-gap) in GaAs-GaP mixed crystals (18). If ideal behavior is assumed to apply to the AlAs-GaAs system, then a linear extrapolation of the data in the high AlAs composition range will intercept the GaAs ordinate at the energy of the indirect minimum in GaAs which corresponds to the indirect minimum forming the conduction band in AlAs. The estimated energies of the indirect minima in GaAs at room temperature are 1.75-1.80 ev for the [100] minimum (19, 20) and 1.90-1.95 ev for the [111] minimum (19). An extrapolation of our data intercepts the GaAs ordinate at about 1.90 ev which is closer to the energy gap associated with [111] transitions than to that associated with [100] transitions. This is contrary to a theoretical postulate of a [100] type of minimum for the conduction band of AlAs made by Paul (20). However, the uncertainty in the intercept on the GaAs ordinate is about ±0.05 ev and prevents a definitive conclusion from our data as to whether the [111] or [100] transition establishes the energy gap in AlAs.

The measurements of Mead and Spitzer (9) indicate a direct-band-gap energy of 2.9 ev in AlAs. Thus, if the data in the Ga-rich range of the AlAs-GaAs energy gap-composition diagram follow fairly closely the line interpolated between the direct-band-gap energy of GaAs and 2.9 ev for AlAs, this would provide good evidence for ideal behavior in the system. The data obtained in this part of the composition range, however, differ widely from this line. The data of Stambaugh *et al.* (8) determined for polycrystalline melt grown material fall well below the extrapolated data of this investigation at mid-range compositions. It is significant that their data points toward mid-range compositions fall furthest below our data line since the results of a number of recent investigations of mixed crystal III-V compounds have shown that it is particularly difficult to achieve a high degree of homogeneity in melt-grown crystals of mid-range composition (21). Inhomogeneous material typically gives optical energy gap values which are lower than those obtained for (more) homogeneous material of the same average composition (5). A polycrystalline melt-grown sample produced in this investigation with an average composition of 13 mole % AlAs was shown to be inhomogeneous (composition range 7 to 20 mole %) by electron beam probe analysis and gave a value of 1.47 ev ($\alpha = 10^4$ cm^{-1}) for the optical energy gap, whereas a value of 1.65 ev was obtained for 13 mole % AlAs determined to be homogeneous by electron beam probing. Unfortunately, the usually reliable method of determining the homogeneity of a mixed crystal by measuring the sharpness of high angle x-ray diffraction lines is not applicable to AlAs-GaAs mixed crystals because of the nearly identical values of the lattice parameters of AlAs and GaAs. Thus, we suggest that the early data of Stambaugh *et al.* fall below the present data because their samples were less homogeneous. With respect to the present samples, the results of electron-beam-probe analysis show that any inhomogeneity present cannot exceed ±1 mole % (and this has already been taken into account in plotting the data) or else the inhomogeneity must exist on a scale which is near the resolution capability of the electron beam probe, *i.e.*, a few microns. Even if there were inhomogeneity on such a microscale, measurements of the near-band-edge recombination radiation in diodes made from this material indicated that the range of inhomogeneity could not be more than 2 mole % (10). Therefore, unless the energy gap in AlAs-GaAs mixed crystals is very sensitive to small degrees of inhomogeneity, we conclude that the energy gap in this system does not follow a linear interpolation between the direct transition minima of the terminal compounds, and hence the system does not behave as an ideal solid solution. It appears that such nonideal behavior of the band structure is the rule in most III-V mixed crystal systems whether they be of the direct-indirect or the direct-direct types. Of six systems where sufficient energy gap-composition data are available for an evaluation (InAs-InP, InAs-GaAs, InSb-InAs, InSb-GaSb, GaAs-GaP, and GaSb-AlSb) (4, 5, 9, 22) only one, the direct-direct system of InAs-InP, has been positively identified as having an energy gap-composition relation compatible with an ideal system. It is interesting to note that, of the five remaining systems that are nonideal, three are substituted on the group III sublattice, the same sublattice which is substituted in AlAs-GaAs.

Acknowledgment

It is a pleasure to acknowledge the aid rendered by many colleagues. In particular, the electron-beam-probe, x-ray fluorescence, and spectroscopic analysis of our samples, which have been quite indispensible for this study were made by W. Sutkowski, P. Lublin, J. Cosgrove, and S. Weisberger. Thanks are also due to Dr. E. Stambaugh of Battelle Memorial Institute for supplying several samples of melt-grown AlAs-GaAs mixed crystals. The technical assistance of A. Marx and J. Hurley during the course of this work are also gratefully acknowledged. The authors are especially indebted to Dr. S. Mayburg and Dr. B. Smith without whose support and encouragement this work could not have been carried out.

Manuscript received Sept. 20, 1965; revised manuscript received Nov. 12, 1965. This paper was presented in part at the Toronto Meeting, May 3-7, 1964.

Any discussion of this paper will appear in a Discussion Section to be published in the December 1966 JOURNAL.

REFERENCES

1. For the early publications on high efficiency light emitting diodes and for many papers relating to p-n junction lasers see the excellent review article by G. Burns and M. I. Nathan, *Proc. IEEE*, **52**, 770 (1964).
2. O. G. Folberth, *Z. Naturforsch.*, **10a**, 502 (1955).
3. H. Welker and H. Weiss, "Group III-Group V Compounds," Solid State Physics, *3*, F. Seitz and D. Turnbull, Editors, Academic Press, New York (1956).
4. F. Oswald, *Z. Naturforsch.*, **14a**, 374 (1959); H. Weiss, *ibid.*, **11a**, 430 (1956); ASTIA Rep. ERD-TM-60-759, L. Weisberg, Editor, 1960; H. Ehrenreich, *Phys. Rev.*, **120**, 1951 (1960).
5. For an extensive review of III-V mixed crystals see Chap. 6, "Physics of III-V Compounds" by O. Madelung, John Wiley & Sons, Inc., New York (1964).
6. G. E. Fenner, *Phys. Rev.*, **134**, A1113 (1964).
7. S. Ku and J. Black, *Solid State Electronics*, **6**, 505 (1963); see also M. Pilkuhn and H. Rupprecht, *J. Appl. Phys.*, **36**, 684 (1965) for other references regarding the GaAs-GaP system.
8. E. P. Stambaugh, J. I. Genco, and R. C. Himes, Bureau of Ships, Contract Nobs-77034, 10th Bimonthly Report, Nov. 15, 1960.
9. C. A. Mead and W. G. Spitzer, *Phys. Rev. Letters*, **11**, 358 (1963).
10. S. Ku and J. Black, "Injection Electroluminescence in Mixed Crystal AlAs-GaAs Diodes of Graded Energy Gap," To be published.
11. S. Ku, *This Journal*, **110**, 991 (1963).
12. J. Black, To be published.
13. E. P. Stambaugh, J. F. Miller, and R. C. Himes, "Growth of Refractory III-V Compounds and Alloys from Solution," in "Metallurgy of Elemental and Compound Semiconductors," R. O. Grubel, Editor, Interscience, New York (1961).
14. E. P. Stambaugh, "Preparation of Aluminum Arsenide," in "Compound Semiconductors," Vol. 1, R. K. Willardson and H. L. Goering, Editors, Reinhold Publishing Co., New York (1962).
15. P. Lublin, ASTM X-Ray Powder Data File, In press.
16. R. Summergrad, Private communication; P. Keck, Unpublished work; W. Kischio, *Z. Anorgan. Allgemeine Chem.*, **328**, 187 (1964).
17. J. C. Woolley, "Alloy Semiconductors," Chap. 7, "Progress in Solid State Chemistry," *1*, H. Reiss, Editor, MacMillan, New York (1964).
18. T. K. Bergstresser, M. L. Cohen, and E. W. Williams, *Phys. Rev. Letters*, **15**, 662 (1965); J. C. Woolley, A. G. Thompson, and M. Rubenstein, **15**, 670 (1965).
19. D. A. Cusano, G. E. Fenner, and R. O. Carlson, *Appl. Phys. Letters*, **5**, 144 (1964); C. Hilsum, Proc. of 7th International Conference on Physics of Semiconductors, Paris, 1964, 1127.
20. W. Paul, *J. Appl. Phys.*, **32**, 2080S (1961).
21. J. C. Woolley and J. Warner, *This Journal*, **111**, 1142 (1964); M. S. Abrahams, R. Braunstein, and F. D. Rosi in "Properties of Elemental and Compound Semiconductors," H. C. Gatos, Editor, Interscience, New York (1960).
22. H. T. Minden, *This Journal*, **112**, 300 (1965); J. C. Woolley and J. Warner, *Can. J. Phys.*, **42**, 1879 (1964).

A Spreading Resistance Technique for Resistivity Measurements on Silicon

R. G. Mazur and D. H. Dickey[1]

Research Laboratories, Westinghouse Electric Corporation, Pittsburgh, Pennsylvania

ABSTRACT

A technique for determining local silicon resistivity from the measured spreading resistance associated with a metal to semiconductor, small-area pressure contact is described. The major problems encountered in earlier attempts to derive quantitative resistivity data from small area pressure contacts on silicon have been circumvented by making the measurements at bias levels of a few millivolts and by using a particular osmium-tipped probe arrangement to provide contact reproducibility. The method provides a three-dimensional spatial resolution in resistivity measurements on silicon on the order of 1μ, and, using a calibration curve determined for a particular silicon surface finish, yields an experimental reproducibility $\leq 15\%$ for sample resistivities in the range 10^{-3} ohm-cm $\leq \rho \leq 500$ ohm-cm. Several examples of the application of the technique to problems of current interest in silicon technology are given.

One of the most important control parameters in semiconductor technology is that of material resistivity. If the carrier mobility in the material is known, a simple measurement of the semiconductor resistivity then gives direct quantitative data on the net concentration of majority carriers. For silicon, the requirement of known carrier mobility has been obviated through the publication of empirical data relating impurity concentration directly to material resistivity (1). These data are widely used in conjunction with resistivity measurements, both to assure known impurity concentrations in starting material and to maintain control of desired impurities introduced during device manufacture.

The resistivity measurements needed are normally made by one of several well-known potential probe techniques (2-4). A variety of other resistivity techniques have been advanced for special purposes (5), but the potential probe methods have remained standard because of their directness and relative ease in operation.

One aspect of the standard potential probe measurements that has become increasingly frustrating is the limited spatial resolution normally obtained. Generally speaking, the spatial resolution of these techniques is measured in millimeters. For instance, the most commonly used small four-point probe spacing is about 0.5 mm. As the current flow in a region of two or three probe spacings around the central pair of probes contributes significantly to the potential between the voltage probes, the quantitative resolution of this technique is 1 or 2 mm. The standard techniques may be used for high resolution resistivity measurements under certain conditions, *e.g.*, the four-point probe technique has been used with a sectioning procedure (such as boiling water or anodic oxidation of the silicon and subsequent dissolution of the silicon dioxide layer with HF) to measure resistivity in diffused layers with a resolution (normal to the plane of the section) measured in some tens of Angstrom units (6). However, this requires a one-dimensional geometry in that the material measured must still be homogeneous over millimeter distances in the plane of the section.

Some specific problems in which spatial resolution is of importance are: resistivity measurements of lightly doped epitaxial layers grown on heavily doped substrates of the same conductivity type; measurements on internal layers in multi-layer epitaxial or diffused structures; and the rapid evaluation of actual resistivity, (or concentration) profiles of diffused layers. Less frequent but equally troublesome problems involve initial resistivity measurements on certain materials as-grown, such as whiskers or dendrites, which are either physically too small for the use of standard resistivity techniques or are normally inhomogeneous.

In response to these problems, a variety of techniques for high spatial-resolution resistivity measurements have been reported in recent literature. One of the most well-known is the "three-point probe" technique (7, 8), based on a measurement of the breakdown voltage of a metal semiconductor point contact and using an empirically established relationship between the measured breakdown voltage and the resistivity of the silicon. Several of the available quantitative techniques for measuring epitaxial silicon have been compared (9); the methods covered included a modification of the three-point probe technique involving the use of d-c methods and a two-point probe "constriction resistance" method (10) which, while less developed, is quite similar to the technique discussed in this paper, both being based on a point contact resistance measurement. More recently, the details of a technique which employs a four-point probe of a special configuration have been published (11).

In the course of our attempts to find a suitable resistivity technique with high spatial resolution, we investigated the possibilities of metal-semiconductor point contacts. It is well known that certain features of the I-V characteristics of such contacts can be used to obtain information about the basic electrical properties of the semiconductor material (12). In particular, at least semiquantitative measurements of semiconductor resistivity have been made by measuring the "spreading resistance" or "constriction resistance" of such contacts (12, 13).

This paper presents details of some developments introduced into the use of the "spreading resistance" technique, allowing local resistivity measurements on silicon with a sampling volume of about 10^{-10} cm^3 and an estimated maximum probable error of $\pm 15\%$ on bulk samples, with a somewhat larger error on highly inhomogeneous silicon. This is followed by a description of both the apparatus used and the calibration procedure found to be of primary importance in obtaining accurate data. Results of typical measurements on several inhomogeneous silicon structures are then given to illustrate the use of the technique.

Background

Some of the phenomena involved in current flow through small area contacts are quite familiar in semi-

[1] Present address: Physics Department, Montana State University, Bozeman, Montana.

conductor technology. A more extensive background to small-area current flow exists in the study of metal-to-metal contacts (14-16). It has been shown (14) that, for the case of a perfectly conducting hemisphere embedded in a homogeneous semi-infinite solid of resistivity ρ, the spreading resistance (or equivalently, the constriction resistance) in the semi-infinite solid is given by

$$R_s = \frac{\rho}{2\pi r} \quad [1]$$

in which r is the radius of the embedded hemisphere. This relationship has been widely used in making rough estimates of spreading-resistance effects in current-flow in solids. Reference (16) has indicated that a more realistic geometry for the contact interface between a hemispherically surfaced member and a flat solid is a circular disk of radius a, which is given by the Hertzian formula

$$a = 1.1\{(Fr/2)[(1/E_1) + (1/E_2)]\}^{1/3} \quad [2]$$

in which F is the force applied to the contact, r is the radius of curvature of the spherically surfaced member, and E_1 and E_2 are the Young's moduli of the materials involved in the contact. The spreading resistance on either side of such a flat circular contact between two members of bulk resistivity, ρ, has been shown (15) to be

$$R_s = \frac{\rho}{4a} \quad [3]$$

These relationships have been used extensively in research on electrical contacts and in work on the frictional behavior of solids, primarily as a means of determining the true electrical contact area between contact members whose bulk resistivities are known (14-16). The spreading resistance resistivity technique inverts this process to determine local material resistivity from a measurement of the spreading resistance associated with a contact-spot of known dimensions. Furthermore, for a metal-semiconductor contact, the spreading resistance in the metal is negligible compared to that in the semiconductor because of the order-of-magnitude or more difference in bulk resistivity between metal and semiconductor. Therefore, the total contact resistance at a single-spot circular contact between a metal and a semiconductor should be given by

$$R_s = \rho/4a \quad [4]$$

where ρ now refers specifically to the resistivity of the semiconductor and a is the radius of the circular contact spot. The derivation of Eq. [3] and [4] involves the assumption that ρ is homogeneous in the contact members, at least in the region surrounding the contact. The general problem of inhomogeneous ρ has not been treated in the literature, but particular cases of interest are discussed later in connection with the spatial resolution of the spreading resistance technique on silicon. Also, the value of R_s as given by Eq. [4] will be the total measured contact resistance only if experimental conditions are such that the bulk resistances involved, the resistance of surface insulating layers (if present), and other contact resistances in the ciricuit are all much smaller than $\rho/4a$, or are otherwise accounted for.

The use of a spreading resistance technique for semiconductor resistivity measurement has been reviewed (12) with the conclusion that, at best, only semiquantitative results are possible. This failure to achieve good quantitative results was due to a number of effects peculiar to the metal-to-semiconductor contact system. These are (17)

(*i*) In general, metal-semiconductor contacts are nonohmic; there is either a reverse-biased barrier in series with the spreading resistance; or, with bias applied in the forward direction, excess carriers are injected into the semiconductor, reducing the local resistivity.

(*ii*) Due to the small size of the contact, the electric field in the spreading resistance region may be high enough to alter the carrier mobility, again resulting in a modification of local resistivity.

(*iii*) Also because of the small contact area, significant Joule heating in the spreading resistance region can occur at moderate currents. The heat generated may cause an appreciable thermoelectric voltage, which will be added to the resistive voltage drop, or, the temperature rise in the contact-region may alter the carrier concentration or carrier mobility in the semiconductor.

(*iv*) The actual contact area of a metal-semiconductor pair is difficult to determine, primarily due to deformation of the metal probes used in such point contacts.

Despite these problems, initial measurements produced results in approximate agreement with Eq. [4]. The results achieved could be rationalized as follows.

(*A*) For voltages appreciably $<\beta kT/q(\beta > 1)$ (17), the injected carrier density for contacts such as those used in our work is small relative to the equilibrium carrier density, producing a nearly linear V-I region near the origin where a reasonable spreading resistance measurement may be made. The maximum expected temperature rise at the point contacts used in this work has been calculated from a relationship given by Holm (14) as $<0.1°C$ for applied voltages <15 mv. Furthermore, the maximum electric field in the spreading resistance region of the contacts used for applied voltages ≤ 15 mv is about 10^3 v/cm, a value somewhat less than that which has been found to appreciably affect carrier mobility in silicon. Thus, the measurement difficulties mentioned above in (*i*), (*ii*), and (*iii*) may apparently be eliminated by making the contact resistance measurement at a sufficiently low voltage level.

(*B*) It appears that previous difficulties in obtaining reproducible contacts and in determining the area involved in metal-semiconductor point contacts may have been due as much to the over-all mechanical construction as to the inherent limitations imposed by the contact materials. Most metal-semiconductor point contact studies have been carried out with metal wires of very small diameter; the often-observed deformation of these probably then is due more to the lack of structural rigidity rather than plastic deformation of the metal itself. Some additional remarks on the point-contacts themselves are included below in the section on measurements on inhomogeneous silicon structures.

While the problems expected on the basis of effects indicated in (*i*), (*ii*), and (*iii*) were thus experimentally resolved by our initial measurements as outlined above, the lack of complete agreement between the experimental data and Eq. [4] and especially the consistent differences observed between p- and n-type material pointed to the presence of a less commonly appreciated problem due to the metal-semiconductor barrier other than those listed above. This is a resistive voltage drop measured across the barrier at any bias level, *i.e.*, the "zero-bias barrier resistance" (18), which is then always in series with the geometrical spreading resistance itself. By definition, the zero-bias barrier resistance obviously cannot be eliminated by the approach used in our measurements to eliminate carrier injection, etc.; the zero-bias barrier resistance is present at any voltage level used. While, in theory, the zero-bias barrier resistance of a particular contact may be calculated for a given barrier height (18), real metal-semiconductor interfaces are complicated by semiconductor surface states, geometry, and the generally unclean nature of real surfaces, precluding an analytical allowance for zero bias barrier resistance in a spreading resistance measurement.

However, in order to make practical use of the spreading resistance technique, we have constructed

a calibration curve, established under conditions such that the metal-semiconductor barrier height is, at least, reproducible. Further remarks on the observed zero-bias barrier resistance are included in the discussion of the calibration data.

Experimental

Homogeneous Resistivity Silicon

Apparatus.—The apparatus used in this work consisted of one or two probes (Jensen A-70LP phonograph needles) supported in such a manner that they could be carefully placed with a known, fixed force on a sample surface without dragging. The total resistance between a pair of probes or between one probe and a low resistance base contact was measured with a Keithley 610A electrometer-ohmmeter. For the calibration procedure discussed in detail in this paper, an arrangement of two identical probes was used.

The probes themselves had an osmium tip of 2.5 x 10^{-3} cm radius of curvature (checked with an optical comparator to within 10%) and were mounted on separate booms, which were loaded with calibrated 50g weights.

Calibration procedure and results.—Slices of both n- and p-type silicon with resistivities from 10^{-3} ohm-cm to several hundred ohm-cm were obtained from commercial sources. The slices were hand-lapped with a slurry of 5μ particle size aluminum oxide and water on a glass plate. The resistivity of each sample was checked with an A. & M. Fell four-point probe, obtaining values which are considered reproducible within ±10%. The spreading resistance measurement was then made at least ten times on the surface of each sample in the region where the four-point probe measurement had been made. Measurements were made under both forward and reverse bias to establish experimentally the validity of the use of ultralow power in avoiding the "normal" effects involved in a metal-semiconductor point contact. In addition, the current was changed in decade steps to insure that the V-I characteristics of the contacts used was linear (to within the accuracy of the meter) well beyond the typical applied voltage of 10-15 mv. The average of the measurements on each sample was divided by two to normalize the data to a single probe, and the result plotted as R_s on the ordinate of Fig. 1 (with the four-point probe value plotted on the abscissa as "true" resistivity). The main features of the data in Fig. 1. are: (*A*) The measured spreading resistance is proportional to sample resistivity, as predicted by Eq. [4], over a resistivity range from 10^{-3} to about 10^3 ohm-cm. (*B*) The exact relationship between contact spreading resistance and bulk resistivity is obviously more complicated than would be expected on the basis of Eq. [4], with an observed deviation from the theoretical linear relationship of as much as 300%.

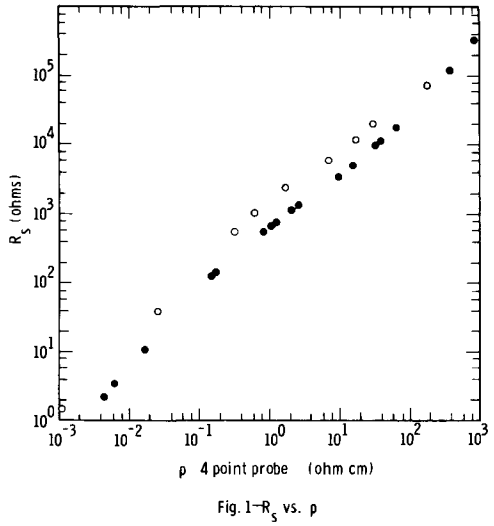

Fig. 1. Spreading resistance vs. true (four-point probe) resistivity for lapped surfaces of p (•) and n (○) silicon.

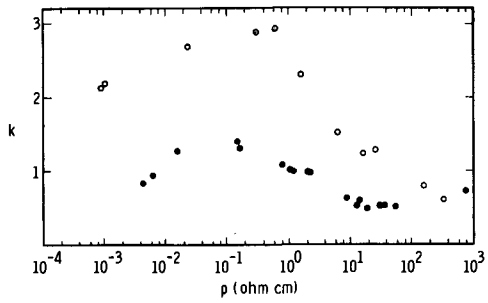

Fig. 2. Proportionality constant "k" between spreading resistance and resistivity for p (•) and n (○) silicon.

One way of characterizing the variation of the experimental data from that expected on the basis of Eq. [4] is to introduce an empirical parameter as

$$R_s \text{ (actual)} = \frac{k\rho}{4a} \qquad [5]$$

With $a = 4 \times 10^{-4}$ cm, k may be then evaluated from the actual sample resistivity. This has been done for the data of Fig. 1 and is plotted in Fig. 2. No attempt will be made at the present time to explain the detailed variation of k with resistivity and conductivity type; however, the existence of a higher k value for n-type silicon of a given resistivity is consistent with the zero-bias barrier resistance concept in that the published (19) values of work-function indicate that a contact between osmium and n-silicon should be rectifying and that between osmium and p-silicon should be ohmic; since $\phi m > \phi_s$ in this case. A further treatment of this aspect of the spreading resistance technique is in progress.

Considering the individual measurements of spreading resistance in the data shown in Fig. 1, the fractional standard deviation of the group of measurements made on a particular sample varied from 0.04 to 0.25, depending on the sample, with more than 90% of the samples having fractional standard deviations in the range 0.04-0.15. The existence of a specific, reproducible fractional standard deviation for each particular sample used in the calibration work indicates that much of the scatter of individual data points is probably due to inhomogeneities in resistivity in samples used. The existence of specific samples with spreading resistance fractional standard deviations on the low end of the range (0.04-0.06) clearly shows that the inherent reproducibility of the measurement technique itself must be consistent with a fractional standard deviation of about 0.05 Therefore, it is highly unlikely that a single measured R_s value will be in error by more than ±15%, at least on bulk silicon.

Inhomogeneous Resistivity Material

After establishing calibration data and the reliability of the spreading resistance measurements on bulk "homogeneous" silicon samples, experimental attention was turned to the investigation of inhomogeneous samples. In this regard, the size of the contacts used is of paramount importance as the spatial resolution of the measurements made depends directly on the size of the spreading resistance contact.

An initial calculation of the contact radius under the conditions used in this work was made on the basis of the Hertz formula, Eq. [2], assuming elastic deformation of the materials involved. The values of Young's modulus for silicon and osmium were taken as (20) Silicon, $E = 1.884 \times 10^{12}$ dynes/cm^2; Osmium, $E = 5.4 \times 10^{12}$ dynes/cm^2. The other parameters used were:

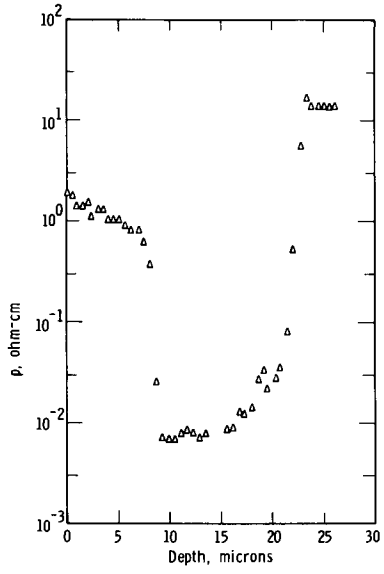

Fig. 3. Resistivity profile of an n-n$^+$ epitaxial silicon layer as determined with a spreading resistance probe.

$r = 0.001$ in. $= 2.54 \times 10^{-3}$ cm; $F = 4.9 \times 10^4$ dynes (a load of 50g). The calculation leads to a value $a \cong 4 \times 10^{-4}$ cm.

The validity of this calculation is admittedly open to question in that, although the stress applied is well within the elastic range of osmium, the silicon surface is visibly damaged by what appears to be local microcracking. However, experimental measurements of the average diameter of these microcracked regions agree well with the value $a = 4 \times 10^{-4}$ cm. We thus assume that the contact radius of our spreading resistance contacts is 4×10^{-4} cm.

On the basis of the above and the known (14) spatial distribution of the equipotentials around circular flat contacts, it is apparent that useful quantitative data may be derived from spreading resistance measurements with a resolution of 1-2μ. In addition, for silicon giving a relatively large zero-bias barrier resistance, the spatial resolution may be better, as the zero-bias barrier-resistance depends essentially on the surface layer of the silicon only. An illustration of the resolution obtained experimentally is given in Fig. 3, which is a plot of the local resistivity of an epitaxially produced n on n$^+$ on p silicon wafer. These data were taken by beveling the wafer at a nominal three-degree angle and probing down the bevel with the pair of spreading resistance probes arranged parallel to the intersection of the bevel surface and the upper surface, the "edge" of the bevel. Measured values of spreading resistance were related to material resistivity through the use of Fig. 1 and the resistivity values plotted against the depth below the surface. The resolution of the technique may be seen in the delineation of the nn$^+$ boundary at a depth of 8μ, where the resistivity is seen to change by about two orders of magnitude in a depth increment less than 2μ.

As previously mentioned, the original derivation of spreading resistance magnitude assumed homogeneity in the material concerned. Thus, the presence of low-high or pn junctions near the spreading resistance contacts on silicon will affect the measurements. It is obvious, for instance, that a transition from high resistivity to low resistivity occurring within the spreading resistance region will shunt the resistance associated with a probe placed on the high resistivity material, and that an insulating boundary (or a pn junction) nearby would have the opposite effect. One of the authors (21) has provided the necessary correction to the measured R_s for the case of approach to an insulating boundary, which can be important in the study of diffused layers. Our results indicate that for layers less than several contact radii thickness, the corrections may be significant, depending on the actual resistivity profile. Because of the extent of these calculations the problem of these immediately adjacent inhomogeneities will not be covered completely in this paper.

Multilayer epitaxial structure.—Figure 4 is a plot of local resistivity *vs.* depth beneath the surface of an angle-lapped sample with an epitaxially produced n$^+$n n$^+$n configuration on a p$^+$ substrate. The resistivity values were derived from the measured spreading resistance of a single probe (using as base contact an ultrasonically soldered strip along one edge of the beveled surface in order to obtain a low-resistance contact to all conductivity regions) traversing the beveled surface from the original outer surface of the sample (all the points to the left of the vertical dashed line) over the edge of the bevel (indicated by the vertical dashed line) and down the bevel into the substrate region. The thickness of material plotted in the figure represents only the epitaxially grown layers, with the substrate material continuing to the right. The horizontal dashed line on the right is drawn to

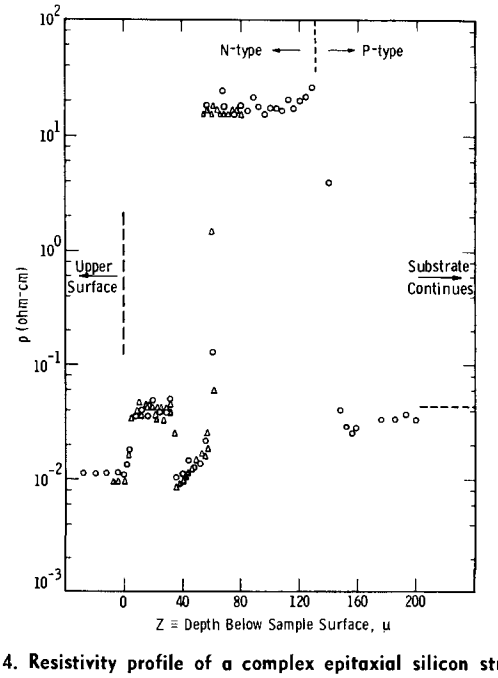

Fig. 4. Resistivity profile of a complex epitaxial silicon structure containing an n-p junction.

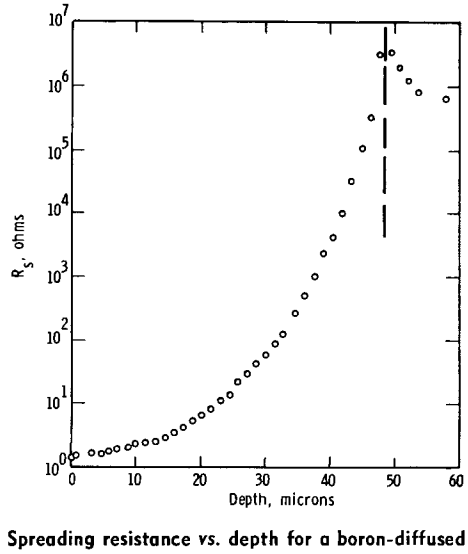

Fig. 5. Spreading resistance *vs.* depth for a boron-diffused sample

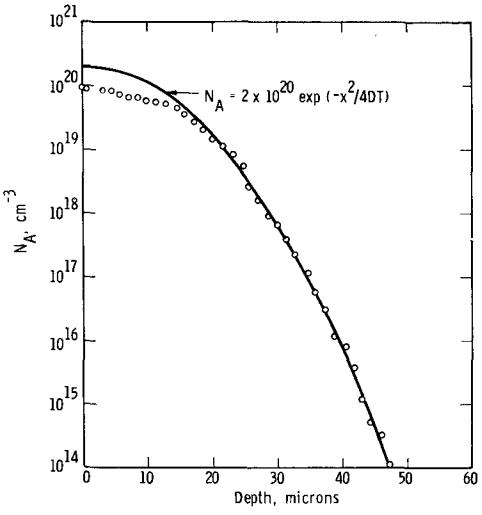

Fig. 6. Boron concentration *vs.* depth derived from spreading resistance measurements.

indicate the continuing substrate material and is positioned so as to correspond to the substrate wafer's resistivity according to its manufacturer (0.043 ohm-cm). The circles and triangles refer to two separate runs down the angle-lapped surface, separated horizontally by 20-30μ (to avoid overlap of residual-damage regions) and indicate the over-all reproducibility of the measurements on this type of material. The run plotted as triangles was not carried all the way through the p-n junction. The scatter seen in the points of a particular resistivity region is thought to be real inasmuch as some epitaxially grown silicon (not deliberately doped), measured under identical conditions as used in obtaining the data shown in Fig. 4, gave as many as 30 points with a scatter less than 2%.

The data of Fig. 4 near the p-n junction or one of the low-high junctions are not to be considered accurate to the $\pm 15\%$ estimated for points in regions several contact diameters away from inhomogeneities as the formula on which these measurements are based have been derived on the assumption of homogeneous resistivities.

Diffused pn *junctions.*—An example of a spreading resistance determination of a concentration profile resulting from a boron diffusion is given in Fig. 5 and 6. Figure 5 is the measured spreading resistance on a beveled surface of the diffused sample. Figure 6 shows the actual boron concentration as a function of depth, derived from the spreading resistance data as outlined in reference (21). This figure shows the good agreement obtained between the measured concentration profile and the theoretical Gaussian distribution expected for this diffusion. The poor agreement near the surface of the sample may be due to precipitation or other electrical inactivation of the diffused dopant at the high concentrations found there, or to a depletion of boron as the result of thermal oxidation of the sample.

While the present publication does not claim to have thoroughly covered all aspects of the spreading resistance resistivity measurement technique, the data does indicate a wide range of application to practical measurement problems; with the hope of further work leading to a solution of the remaining problems.

Acknowledgments

The authors would like to thank T. L. Chu who supplied both continual stimulation and much of the material studied in this work. Appreciation is also extended to H. F. John and O. C. Wells for critical readings of the manuscript and to J. Morris and R. Pfeil, who assisted in the experimental work.

Manuscript received Oct. 4, 1965. This paper was presented at the Pittsburgh Meeting, April 15-18, 1963.

Any discussion of this paper will appear in a Discussion Section to be published in the December 1966 JOURNAL.

REFERENCES

1. J. C. Irvin, *Bell System Tech. J.*, **41**, 385 (1962).
2. L. B. Valdes, *Proc. I.R.E.*, **42**, 420 (1954).
3. A. Uhlir, Jr., *Bell System Tech. J.*, **34**, 105 (1955).
4. F. M. Smits, *ibid.*, **37**, 711 (1958).
5. H. G. Rudenberg, *Semicond. Prod.*, **2**, xx (1959).
6. E. Tannenbaum, *Solid-State Electron.*, **2**, 123 (1961).
7. J. Brownson, *This Journal*, **111**, 919 (1964).
8. P. J. H. Dobbs and F. S. Kovacs, Semiconductor Products and Solid State Technology, 28 (1964).
9. E. E. Gardner, J. F. Hallenback, Jr., and P. A. Schumann, Jr., *Solid-State Electron.*, **6**, 311 (1963).
10. P. A. Schumann, Jr., and J. F. Hallenback, Jr., *This Journal*, **110**, 538 (1963).
11. P. A. Schumann, Jr., and E. E. Gardner, *Trans. AIME*, **233**, 602 (1965).
12. "Methods of Experimental Physics," Vol. 6, K. Lark-Horovitz and V. A. Johnson, Editors (1959).
13. H. C. Torrey and C. A. Whitmer, "Crystal Rectifiers," 1st ed., p. 306, McGraw-Hill Book Co., New York (1948).
14. R. Holm, "Electric Contacts Handbook," 3rd ed., Springer, Berlin (1958).
15. F. Llewllyn Jones, "Physics of Electrical Contacts," Oxford University Press (1957).
16. F. P. Bowden and D. Tabor, "The Friction and Lubrication of Solids," p. 10 and ff, Clarendon Press, Oxford (1950).
17. H. K. Henisch, "Rectifying Semiconductor Contacts," especially p. 6 and pp. 125 ff, Clarendon Press, Oxford (1957).
18. J. N. Shive, "The Properties, Physics and Design of Semiconductor Devices," D. Van Nostrand Co., Princeton, N. J. (1959).
19. American Institute of Physics Handbook, 2nd ed.
20. Metals Handbook, 8th ed., American Society for Metals (1961).
21. D. H. Dickey, Abs. No. 57, Paper presented at the Pittsburgh Meeting of the Society, April 15-18, 1963: See p. 151, Extended Abstratcts of the Electronics Division, Vol. 12, No. 1.

Optical Study of the $GeCl_4$/Ge System

K. E. Haq and W. von Muench[1]

International Business Machines Corporation, Watson Research Center, Yorktown Heights, New York

ABSTRACT

The optical absorption characteristics of $GeCl_4$, both with and without free germanium present in the system, have been studied for the wavelength region between 2300Å and 2μ. Pure $GeCl_4$ was found to have a dissociation continuum with the long wavelength edge beginning at 2700Å at a temperature of 150°C. When free germanium was added to the system, $GeCl_4$ was found to react with it to give rise to one or more species, depending on whether or not the molar quantity of free germanium was greater than that of $GeCl_4$. It has also been observed that $GeCl_2$ has a strong absorption band with a peak at 3150Å.

To understand the phenomenon of germanium film growth in vapor transport processes, it is important to know the species present in the vapor phase at various temperatures and equilibrium conditions. One obvious method is to study the vapor pressure of the gas at different temperatures. However, such a measurement permits unique interpretation only in the very simple case where two molecules are formed from one as a result of reaction. The other possible approaches will be either to study the species by mass spectrographic technique or to study the optical absorption of the molecules. In the present investigation the latter method has been used to study the germanium chlorine system at various temperatures under equilibrium conditions, and significant conclusions with regard to vapor phase species have been drawn. The optical study of this system is considered particularly important since there is no report in the literature of such a study for the wavelength region 2300 to 20,000Å.

Experimental Arrangement

The experimental arrangement is shown in Fig. 1. A chopped monochromatic beam of light emerging from the exit slit of a Perkin Elmer double pass monochromator fell first on a plane mirror M_1, then on concave mirrors M_2 and M_3 and finally on the photomultiplier. An RCA 1P28 photomultiplier tube was used as a detector. The sample cell was placed in the central part of the furnace, located in the path of the monochromatic beam of light between the concave mirrors M_2 and M_3. The furnace consisted of three coils, a central coil and a back up coil on each end, both of which could be controlled independently from the central coil. Thus, in the investigation of the $GeCl_4$ + Ge system the windows could be maintained at a slightly higher temperature than the experimental chamber in order to prevent deposition of germanium on the windows of the cell. A quartz window was placed at each end of the furnace to minimize chimney effects.

[1] Present address: IBM Laboratory, Boeblingen, Germany.

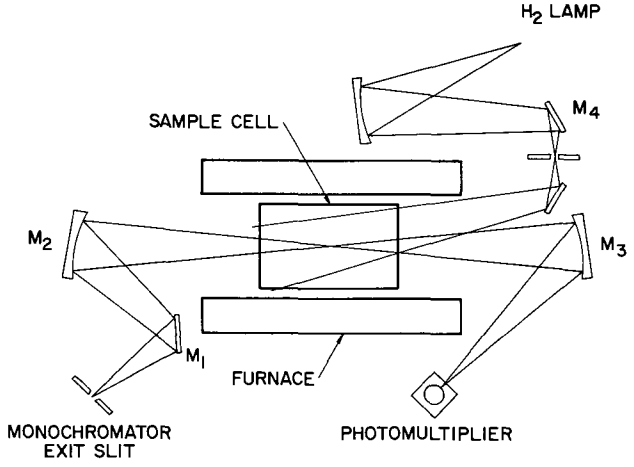

Fig. 1. Optical arrangement for transmittance measurement

The sample cell consisted of a cylindrical quartz tube 120 mm long and 35 mm in diameter with a quartz window at each end. Introduction of $GeCl_4$ into the sample cell was accomplished in the following manner: The $GeCl_4$ liquid was distilled *in vacuo* (after breaking the tip of the supply) into small calibrated Pyrex or quartz ampoules in a sealed system. The ampoules provided with a breaking tip, were sealed and removed from the system while the $GeCl_4$ was kept at liquid nitrogen temperature. An ampoule was then placed (with or without a weighed amount of additional solid Ge) in the sample cell, which was pumped to a pressure of 5×10^{-6} mm Hg and sealed. The purpose of sealing the tube at high vacuum was to eliminate the possibility of contaminating the sample with water vapor or other gases. The sample cell had a built-in thermocouple well which permitted accurate measurement of the temperature of the gas. In most of the experiments, the amount of $GeCl_4$ introduced into the cell produced a pressure of approximately ½ atm at 100°C.

By means of an additional mirror, M_4, continuous light from a strong uv source could be shined on the sample to perform the optical dissociation experiments described in a subsequent section.

Result

The absorption studies were conducted for the wavelength region 2300 to 20,000Å. Since no significant absorption was observed at wavelengths beyond 5000Å, the data for that region are not shown in the graphs.

The transmittance of pure $GeCl_4$ gas as a function of wavelength is shown in Fig. 2. At 150°C an absorption edge beginning at 2300Å and extending into the shorter wavelength regions was observed. As the temperature of the sample was raised, the absorption increased and the absorption edge shifted to longer wavelengths. However, in the temperature range (150°C $T \leq$ 800°C), in which the investigation was made, no absorption band due to pure $GeCl_4$ at wavelengths exceeding 3000Å was observed. The nature of the absorption in the short wavelengths region was investigated in more detail and is described in a subsequent paragraph.

Figure 3 shows the transmittance of $GeCl_4$ at various temperatures when solid germanium was present in the system. The amount of $GeCl_4$ introduced into the cell was approximately the same as that in the cases represented by Fig. 2. The molar quantity of Ge added was less than that of $GeCl_4$. The solid germanium was first etched with White etch and then thoroughly washed with DI water and alcohol before being introduced into the cell, in order to prevent contamination of the sample by the surface oxide layer.

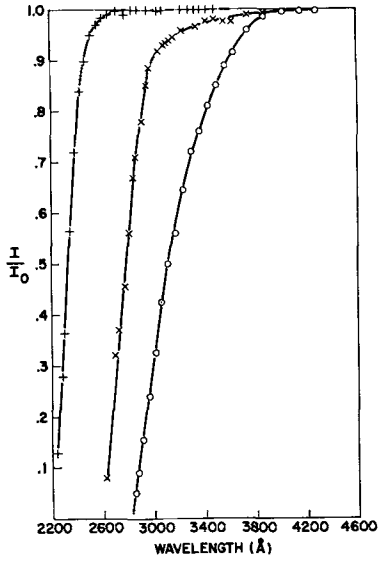

Fig. 2. Transmittance of pure $GeCl_4$. +, 150°C; ×, 500°C; ○, 800°C; $GeCl_4$ pressure at 100°C, 380 mm Hg.

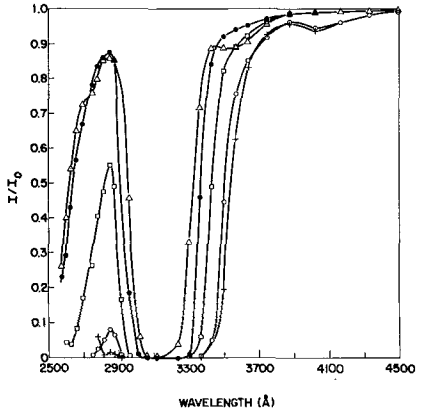

Fig. 3. Transmittance of germanium deficient system. △, 200°C; •, 250°C; □, 300°C; ○, 400°C; +, 500°C. $GeCl_4$ + 12 mg Ge.

The results in Fig. 3 show that $GeCl_4$ and germanium reacted to give rise to a species which has an absorption band with a peak at 3150Å. As the temperature of the system was raised, this absorption increased rapidly.

In addition, at higher temperatures there is an indication of increased absorption at wavelengths below 2800Å. This is apart from the increase of $GeCl_4$ absorption effected by temperature rise shown in Fig. 2. The following experiment demonstrates this: Two ampules, one containing pure $GeCl_4$ and the other containing solid germanium, were introduced into the cell. First the ampule with $GeCl_4$ was broken, and the absorption of pure $GeCl_4$, both at room temperature and at 500°C, was measured. Similar measurements were then made after breaking the ampule containing solid germanium. The results exhibited in Fig. 3a show that at wavelengths shorter than 2800Å, there was a rise in absorption after the introduction of solid germanium. The absorption of $GeCl_4$ was expected to go down, due to decrease in its concentration as a result of reaction with solid germanium. Contrary to expectation. it increased. This result has been further confirmed by measurements on a flow system in which $GeCl_4$ carried by He was passed through a germanium bed.[2] If the amount of free Ge added exceeded that required to complete the assumed reaction

[2] This result will appear in a subsequent article. Extended Abstract, Electronics Division, Electrochemical Society Meeting, Oct. 11-15, 1964, 13, [2], Abstract No. 141.

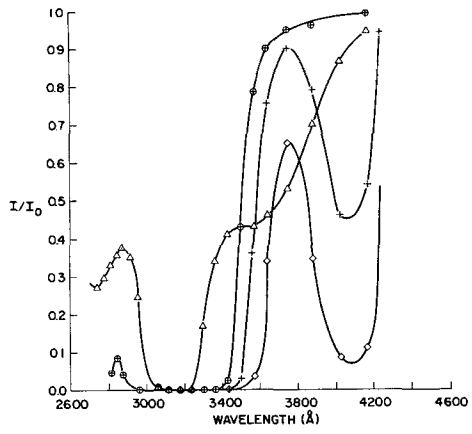

Fig. 4. Transmittance of germanium excess system. △, 180°C; ⊕, 380°C; +, 500°C; ◇, 600°C. Cell 4, $GeCl_4$ + Excess Ge, 101 cm^3, $GeCl_4$, 15 mm.

$$GeCl_4(g) + Ge(s) \rightleftarrows 2GeCl_2(g)$$

an additional band with a peak at 4120Å appeared at 500°C. As the temperature was raised, this absorption also increased (Fig. 4).

In order to understand the absorption due to pure $GeCl_4$ at the short wavelength end of the spectrum, the following experiment was performed: From a hydrogen lamp, a beam of light which could be turned on or off by means of a shutter, was impinged on the sample cell, while the species were monitored by means of a chopped monochromatic beam as before. Precautions were taken to prevent the light from the hydrogen lamp from falling on the photomultiplier. When the beam of light from the hydrogen lamp was turned on by removing the shutter, approximately a 4% decrease in transmission was observed for wavelengths 3300Å and longer.

To determine if any error was introduced in the measurements by possible deposition of germanium on the cell windows, the following experiment was conducted:

A cell containing $GeCl_4$ and solid germanium was heated and cooled several times, while the intensity of the transmitted beam at 3150Å was observed. The intensity (of the transmitted beam) always returned to the initial value when the sample cooled to room temperature, indicating that there was no effect due to deposition of germanium film on the window. Further, when the cell was taken out of the furnace, there was no indication of any germanium film on the window of the cell.

Discussion

For proper understanding of the results, the following cases should be distinguished: (*a*) pure $GeCl_4$ system; (*b*) the $GeCl_4$ and germanium deficient system; (*c*) the $GeCl_4$ and Ge excess system.

A germanium deficient system is one in which the molar quantity of free germanium added is less than the molar quantity of $GeCl_4$. A germanium excess system is one in which the molar quantity of free germanium added is greater than the molar quantity of tetrahalide. The three systems are now discussed individually.

The $GeCl_4$ *system.*—As seen in Fig. 2, pure $GeCl_4$ exhibited only an absorption edge, which, with an increase in temperature, extended into longer wavelength regions. Since no absorption band with a peak at 3300Å (the peak of Cl_2 absorption band) was observed, there was no indication of thermally induced decomposition of $GeCl_4$ within the temperature range of the present investigation. The nature of the long wavelength absorption edge due to pure $GeCl_4$ was investigated by monitoring the species while the sample was irradiated with uv light from a hydrogen lamp

source described earlier. The result of this experiment indicated the formation of new species due to uv irradiation. Thus it was concluded that the absorption edge was the beginning of a dissociation continuum. This result, along with those shown in Fig. 2 (*i.e.*, the extension of the absorption edge to longer wavelengths with rise in temperature of the sample) can be understood in the following way: As the temperature of the sample is raised, higher vibrational levels in the electronic ground state become occupied, and as a result, lower energy photons induce the electron to make transitions to unstable excited states, causing dissociation of $GeCl_4$ molecule. It would appear logical to conclude that one of the dissociation products was chlorine for the following reasons: (*A*) the dissociated species showed absorption at 3300Å; (*B*) the $GeCl_4$ molecules can break up only by releasing free chlorine.

The $GeCl_4$ and germanium deficient system.—With the addition of solid germanium to $GeCl_4$ in molar quantity less than that of the tetrahalide, an additional structure developed upon heating. Most significantly, as seen by comparing Fig. 2 and 3, an absorption band at 3150Å appeared. Less obvious, however, was an enhanced absorption at wavelengths below 2800Å. These two phenomena may be indicative of the formation of either one or two new species as a consequence of the reaction between germanium and $GeCl_4$. However, optical study alone cannot resolve this question.

Based on the results of a recent Bourdon gauge investigation[3] of the $GeCl_4$ and $GeCl_4$-Ge system, it would seem reasonable to attribute the 3150Å absorption band to $GeCl_2$. From the same result one might infer that the enhanced absorption at wavelengths below 2800Å was also due to $GeCl_2$. As will be discussed below, this inference is somewhat tenuous.

The $GeCl_4$ and germanium excess system.—When the molar quantity of Ge exceeded that of $GeCl_4$, an additional band at 4120Å was generated (Fig. 4), implying either the formation of an additional species or an enhanced absorption at a weak absorption band due to increased concentration of $GeCl_2$. However, the latter possibility has been discarded on the basis of the following two experiments: (*i*) with a $GeCl_4$ and germanium deficient system, and (*ii*) with a $GeCl_4$ and germanium excess system. The amount of $GeCl_4$ and free germanium introduced into the cells in the two cases were such that the amount of $GeCl_2$ formed in case (*i*) was far in excess of that formed in case (*ii*). Measurements showed no absorption at 4120Å in the case of the deficient system, while significant absorption was observed in the case of the excess system. This would indicate that a second species was formed if the molar quantity of free germanium added was greater than that of $GeCl_4$. This is indicative of an apparent inconsistency between the results of optical and Bourdon gauge measurements. One possible explanation for the differences observed in the two approaches is that the absorption band with a peak at 4120Å may have been due to a species whose concentration was too small to perturb the pressure data, and yet whose extremely high absorption coefficient made it observable in optical measurement.

In an effort to find possible structure in the 3150Å absorption band, an experiment was performed with much reduced $GeCl_4$ pressure, approximately 1.5 mm Hg, compared to ½ atm in other cases. Results are shown in Fig. 5. Apart from reduced absorption due to corresponding reduction in density of material, no significant difference in absorption characteristics was noticed.

[3] Paper presented by T. Sedgwick at the Toronto Meeting of the Society, May 1964.

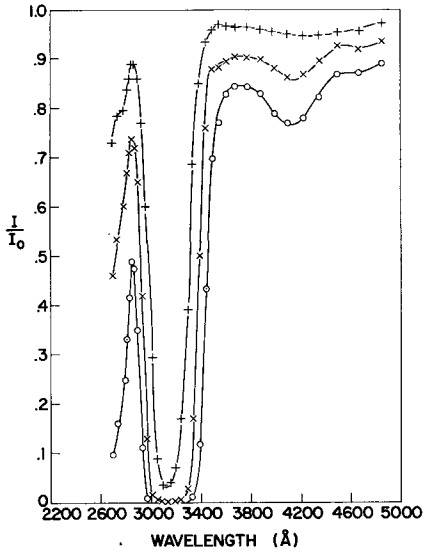

Fig. 5. Transmittance of germanium excess system with low $GeCl_4$ pressure. + 350°C; ×, 400°C; ○, 500°C $GeCl_4$ + Ge. $GeCl_4$ pressure at 100°C = 15 mm Hg.

Conclusions

From the above experiments the following tentative conclusions have been drawn.

1. Up to 800°C there was no thermally induced reaction in the $GeCl_4$ system.
2. When $GeCl_4$ was irradiated with uv light at suitable temperatures, it decomposed into chlorine and some subchloride other than $GeCl_2$.
3. At 300°C, $GeCl_4$ reacted with Ge to give rise to $GeCl_2$ which absorbed at 3150Å.
4. The species formed as a result of reaction between $GeCl_4$ and Ge also absorbed at wavelengths shorter than 2800Å as well as in the region of 3150Å.
5. When the amount of free Ge added was greater than what would be required to complete the assumed reaction

$$GeCl_4 + Ge = 2GeCl_2$$

a second absorption band at 4120Å appeared at 500°C. This absorption was due to some subchloride, presumably GeCl or some other germanium chlorine complex.

Acknowledgment

The authors wish to thank Dr. A. Reisman for many helpful discussions during the course of the investigation. They would also like to thank W. Lee for his assistance in making the measurements.

This work was supported in part by A.F.C.R.L. Contract No. AF 19(628)-2468.

Manuscript received June 9, 1964; revised manuscript received Nov. 8, 1965. This paper was presented in part at the New York Meeting, Sept. 29-Oct. 3, 1963.

Any discussion of this paper will appear in a Discussion Section to be published in the December 1966 JOURNAL.

Polarization Phenomena and Other Properties of Phosphosilicate Glass Films on Silicon

E. H. Snow and B. E. Deal

Research and Development Laboratory, Fairchild Semiconductor, Palo Alto, California

ABSTRACT

A study has been made of phosphosilicate glass films prepared by predepositing P_2O_5 on thermally oxidized silicon. Many of the properties of these films including composition, density, etch rate, conductivity, dielectric constant, and dielectric strength have been measured and are compared with the corresponding properties of thermally produced silicon dioxide layers. A polarization effect is discussed which gives rise to an increase of about 20% in the dielectric constant of the glass at high temperatures and low frequencies ($\sim$ 250°C at 50 cps). Under d-c bias at lower temperatures this polarization causes a slow drift in the capacitance-voltage characteristic of metal-oxide-semiconductor (MOS) capacitors which use the glass as a dielectric. The MOS capacitance-voltage method is used to study the time, temperature, and voltage dependence of the polarization, and mechanisms are discussed which can account for the observed results.

Modern silicon planar technology (1) involves the use of silicon dioxide films to mask certain areas of the underlying silicon against the diffusion of n- and p-type dopants. The thickness of SiO_2 required to mask against various phosphorus diffusion conditions has been investigated by Sah, Sello, and Tremere (2) and by Allen, Bernstein, and Kurtz (3). Sah *et al.* concluded that P_2O_5 vapor reacts with SiO_2 to form a layer of P_2O_5-SiO_2 glass of an unknown composition over the remaining pure SiO_2. The thickness of the glass layer increases at the expense of the SiO_2 as phosphorus diffuses through the glass and reacts at the interface. A cross section of such an oxidized silicon surface subsequently predeposited with P_2O_5 is sketched in Fig. 1. The existence of the sharp interface has been verified by Pliskin and Gnall (4) who developed a selective etch which removes the phosphorus containing glass much faster than the SiO_2 underneath.

The phase diagram of the SiO_2-P_2O_5 system has been determined by Tien and Hummel (5), and Kooi (6) has recently studied the composition of glass layers obtained by depositing P_2O_5 on silicon and diffusing in nitrogen or oxygen at 920°-1310°C. In general, Kooi found that after a sufficiently long diffusion time the composition of the glass approached that corresponding to the limiting solubility of SiO_2 in the liquid phase.

In device manufacture, the glass layer which remains on the passivating oxide after phosphorus diffusion may or may not be removed by etching, but it has recently been reported by Kerr, Logan, Burkhardt, and Pliskin (7) that the presence of a phosphorus glass layer greatly increases the stability of planar transistors and MOS devices under temperature and voltage stressing.

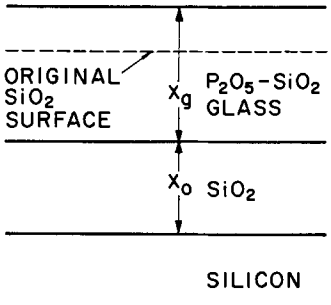

Fig. 1. Cross section of a phosphosilicate glass-silicon dioxide double layer on a silicon substrate. The double layer is prepared by predepositing P_2O_5 on a thermally oxidized silicon slice.

Because of its importance in silicon technology and particularly in view of the results of Kerr *et al.* there is need for a more thorough knowledge of the properties of the SiO_2-P_2O_5 system. The present paper surveys some of these properties and describes an electrical polarization effect which limits the stability of MOS devices utilizing phosphorus glass.

Experimental

Preparation of oxide layers.—The silicon used in these studies was single crystal, Czochralski pulled, (111) surface oriented with an initial dislocation count of less than 100 cm^{-2}. It was obtained in the form of circular slices, lapped both sides to 250μ thickness from the Kollstan Semiconductor Elements Company, Westbury, New York. Both n-type (phosphorus) and p-type (boron) silicon with dopant concentrations in the 10^{15} to 10^{16} cm^{-3} range were included in these studies. Slices used for thickness or weight measurements were mechanically polished, with 25μ removed per side. To assure clean, noncontaminated surfaces, these slices were then cleaned in both organic and inorganic solvents. Silicon slices used for electrical measurements were cleaned and then chemically polished in a HF:HNO_3 solution and quenched in acetic acid. At least 50μ per side was removed by this procedure.

All slices were oxidized in dry oxygen at 1200°C. Oxide thicknesses varied, depending on the particular measurement being conducted, but generally were between 0.10 and 0.50μ (1000-5000Å). Following oxidation, some of the samples were placed in a P_2O_5 predeposition[1] furnace for various times. For the most part the substrate temperature was 1020° $\pm$ 1°C with the P_2O_5 source at 230° $\pm$ 2°C. Dry nitrogen was the carrier gas. In some cases subsequent diffusions were carried out at temperatures ranging from 1020° to 1200°C in nitrogen or oxygen.

For those experiments in which electrical measurements were made, such as dielectric breakdown, conductivity, etc., field plates were prepared by evaporating 3000Å of aluminum over the oxide and preparing circular dots 250-1400μ in diameter by photoresist techniques. The oxide was then stripped from the back of the slice, aluminum was evaporated on the bare silicon, and alloyed at 550°C for several minutes to assure good ohmic contact.

Thickness measurements.—In the next section, several properties of the predeposited P_2O_5-SiO_2 system are reported. The experimental procedures involved

[1] The term predeposition, as used in semiconductor technology, is that step preceding diffusion in which the semiconductor slice is given a relatively short thermal treatment in the presence of an ambient containing a doping impurity (1).

in each particular measurement are described as that property is discussed. However, since the measurement of the oxide and glass layer thicknesses was required for all determinations, the general method will be discussed here.

Multiple beam interferometry was used for the film thickness measurements. The principle of this technique, which involves the measurement of an interference fringe displacement across a metallized step etched in the oxide, has already been adequately described (8, 9). For this particular work, a silver film was evaporated over a step etched in the oxide layer with 49% HF. The reference surface was a glass slide evaporated with a 97% reflecting multilayer dielectric film prepared by Optics Technology, Palo Alto, California.

Initial examination of fringe displacements across steps etched in phosphorus glass indicated a much more abrupt step than was obtained on regular thermal oxides. This was true whether the oxides were etched separately, or as a double layer, as pictured in Fig. 1. Photographs of the actual fringes obtained are shown in Fig. 2. In (a) and (b) the difference in step profile can be readily observed between the P_2O_5-SiO_2 glass and the conventional thermal SiO_2. The taper of the SiO_2 step depicted by the fringes in Fig. 2(b) was reported by Booker and Benjamin (9) to be due to undercutting of the oxide by the HF. Figure 2(c) shows fringes produced due to a step etched (with HF) across a mixed glass-thermal oxide layer. This system was produced by predepositing P_2O_5 over an existing SiO_2 film. Again the difference in etching characteristics can be seen, with the abrupt fringe change due to the P_2O_5-SiO_2 glass and the tapered change due to the underlying SiO_2.

It appeared that the difference in etching characteristics across a double layer oxide as indicated in Fig. 2(c) might provide a rapid means of determining thicknesses of the two layers. To check this possibility, special measurements were conducted. These involved

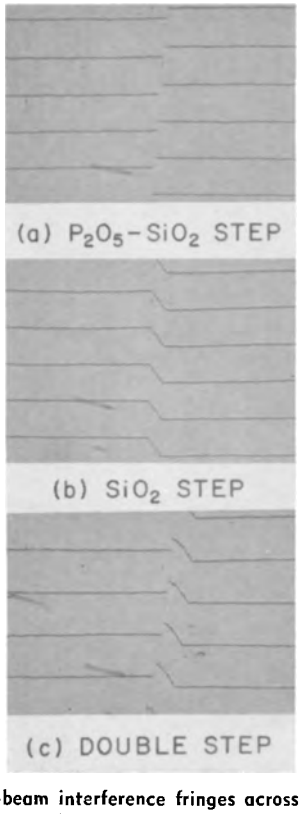

Fig. 2. Multiple-beam interference fringes across metallized steps etched in three types of oxides. Phosphosilicate glass is shown in (a), (b) is standard thermal silicon dioxide, while (c) shows double step in phosphosilicate glass over standard thermal oxide. Area to left of steps represents top surface of oxides.

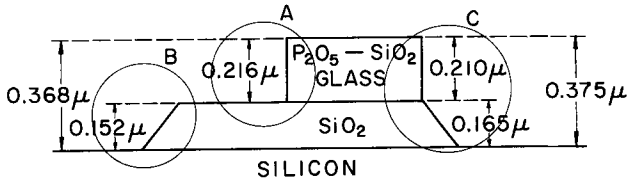

Fig. 3. Cross section of phosphosilicate glass over silicon dioxide, showing thickness values obtained for single step measurements (regions A and B), as compared with double step measurement (region C). Corresponding fringes for regions A, B, and C are shown in Fig. 2.

preparing a double layer oxide (P_2O_5-SiO_2 over SiO_2), selectively etching a portion of the glass from the SiO_2 (see next section), etching a second step in the exposed SiO_2, and measuring the fringe displacements across the resulting steps. Results were compared with fringes crossing a step made by etching through the entire double layer. The photographs in Fig. 2 are typical of these measurements and the measured thicknesses are indicated in Fig. 3. The circled areas labeled A, B and C in Fig. 3 represent the corresponding regions pictured in Fig. 2 with A and B being the single steps and C the double step. It can be readily observed that the thickness values obtained from the double step are within 100Å of the single step determinations. The ultimate accuracy of the method would be determined by the selectivity of the etch used to remove the glass layer and the sharpness of the interface between the two layers.

The above method has been used successfully on various glass-silica systems and becomes even more useful when the etch rates of the two oxides approach each other and a selective etch cannot be used rapidly for single step measurements. In the above case the phosphorus glass etched 100 times faster than the SiO_2. Instead of causing more undercutting and thus a more tapered step in the glass, the conditions of etching evidently are such that a more vertical etch profile is obtained.

Properties of SiO_2-P_2O_5 Layers

Composition.—The ratio of P_2O_5 to SiO_2 in a predeposited phosphosilicate layer over oxidized silicon was determined as follows. Weights of a silicon slice were determined using a Mettler Model M-5-S/A Microbalance at the following processing steps.

Wt 1. Original cleaned, chemically polished silicon.
Wt 2. After oxidizing in dry O_2 to desired oxide thickness, *i.e.*, 3000Å.
Wt 3. After predepositing P_2O_5 in N_2 onto oxidized silicon.
Wt 4. (Optional) After diffusing predeposited, oxidized silicon in N_2 or O_2.
Wt 5. After selectively etching P_2O_5-SiO_2 glass from SiO_2 using Pliskin's "P-etch" (15 parts conc. HF, 10 parts conc. HNO_3, and 300 parts H_2O) (4).
Wt 6. After stripping remaining SiO_2 in conc. HF.

The accuracy of the weight measurements was ± 2 μg, with a typical 3000Å oxide weighing 680 μg or 70 $\mu g/cm^2$.

From the gain in weight due to predeposition (Wt 3-Wt 2) and the weight of the glass layer (Wt 3-Wt 5), the ratio of P_2O_5 to SiO_2 in the glass could be determined.[2] Also by comparing total thermal oxide weight (Wt 2-Wt 6) with total silicon consumed (Wt 1-Wt 6) a measure of the oxidation efficiency may be determined (10). In these experiments, it was shown that no additional SiO_2 was formed during predeposition, and thus all weight gain during this step was P_2O_5. This is due mainly to the N_2 ambient used during predeposition.

The over-all results indicated that at a predeposition temperature of 1020°C, 5-6 moles of SiO_2 were present

[2] For the purpose of this analysis, all silicon oxide was assumed to be SiO_2 and all phosphorus oxide P_2O_5.

in the glass layer to 1 mole of P_2O_5. In terms of atoms, one out of four silicon atoms are replaced by a phosphorus atom during the predeposition, with an extra oxygen atom being associated with every two phosphorus atoms. The above ratio corresponds to about 14.5 to 16.5 mole % of P_2O_5, which agrees with the findings of Kooi (6) in related work involving the SiO_2-P_2O_5 system. This composition was constant over predeposition times of 10-60 min.

If the predeposited structure was subjected to additional thermal treatment (diffusion) in oxygen or nitrogen for 30 min, either at 1020°C or higher temperatures, a ratio of SiO_2 to P_2O_5 was obtained representative of the diffusion temperature. These compositions corresponded to those given in ref. (6); the value at 1020° remaining at about 15 mole % while at 1200° the P_2O_5 concentration dropped to 7 mole %. Additional diffusion time decreased the P_2O_5 percentage only very slowly.

It should be noted that thickness measurements indicated that the movement of the glass "front" into the SiO_2 during predeposition obeyed a diffusion-controlled relationship, *i.e.*, $y = kt^{1/2}$, where y is the distance of the front from the original outer surface of the SiO_2 and t is the predeposition time. At 1020°C, $k \approx 0.18\ \mu/\sqrt{\text{hr}}$ in agreement with data first reported by Sah, Sello, and Tremere (2). The total volume increase of the oxide due to phosphorus was about 40% at 1020°C, agreeing with the composition and density (see next paragraph) results.

Density.—Apparent densities of the P_2O_5-SiO_2 glass layers were obtained using the weight and thickness results. In general the density values were between 2.35 and 2.40 g/cm^3. This compares with 2.24-2.27 g/cm^3 for the underlying SiO_2 layer, the latter agreeing quite well with earlier results (11). The density of amorphous P_2O_5 is reported to be 2.39 g/cm^3 (12), and so the values for the P_2O_5-SiO_2 glass mixture determined in this work are reasonable when the results of the previous section are considered.

Etch rate.—The etch rate of the phosphosilicate glass in Pliskin's p-etch (4) appeared to be a function of P_2O_5 content. For the higher phosphorus concentration (16 mole % P_2O_5 obtained at a 1020°C predeposition temperature) the rate was 500 Å/sec. However, as the P_2O_5 concentration decreased to 7% at 1200°C, the etch rate also decreased (logarithmically) to 15 Å/sec. The corresponding value for SiO_2 in this etch is about 2 Å/sec. As discussed in the section above describing thickness measurements, the phosphosilicate glass also etches much more rapidly than SiO_2 in HF solutions, but both etch so rapidly it is not known if the same dependence on P_2O_5 concentration exists.

Sodium masking.—It has been reported (7) that a thin layer of P_2O_5-SiO_2 glass over SiO_2 on MOS-type devices will greatly reduce drift in the capacitance-voltage characteristic under bias at elevated temperatures (~200°C). Special experiments were conducted to test this possibility. MOS structures, prepared both with a 0.20μ thermal SiO_2 layer and with a double-layer consisting of 0.15μ of SiO_2 plus 0.07μ of P_2O_5-SiO_2 glass, were contaminated with sodium ions prior to metallization (13). Noncontaminated controls were also included. Under 10v bias at 300°C for 5 min, the standard, noncontaminated SiO_2 samples did not drift in voltage by more than 0.5v with bias of either polarity. The contaminated SiO_2 samples drifted more than —60v under the positive field plate bias, with no drift under negative bias. Both the noncontaminated and the contaminated P_2O_5 glass structures drifted about 1v under both positive and negative bias. This drift was undoubtedly due to a polarization phenomenon to be discussed later. It was clear, however, that the P_2O_5 layer prevented the large drift due to sodium ion migration which was observed in the contaminated silicon dioxide sample.

Electrical conductivity.—For determining electrical properties of the P_2O_5-SiO_2 glass layers, special structures were prepared. This was done by predepositing the P_2O_5 at 1020°C over a 0.20μ thermal oxide so that the glass front extended to within 100Å of the silicon surface. The total glass thickness was 0.275μ. A thermal oxide of the same thickness but without phosphorus was used as a control. MOS structures were prepared as described in the Experimental Section, with aluminum dot diameters of 250, 440, 800, and 1400μ.

Using these samples, the electrical conductivity of the phosphosilicate glass was compared with that of pure SiO_2. Currents corresponding to an approximate steady state were measured after a bias of ±10v had been applied for 10 min at 200°C. In the case of the silicon dioxide samples, the currents under either polarity were too small to measure and corresponded to less than 10^{-11} amp/cm^2. In the case of the phosphosilicate glass the currents were easily measureable and gave current densities in the range 2 to 3 x 10^{-10} amp/cm^2. If bulk resistivities at 200°C are calculated from these data, the values obtained are 2 x 10^{15} ohm-cm for the phosphosilicate glass and greater than 5 x 10^{16} ohm-cm for the SiO_2.

Dielectric breakdown.—Dielectric breakdown values were obtained using an Anodicator (manufactured by the R. O. Hull Company, Rocky River, Ohio). The applied voltage (60 cps a.c.) was increased at the rate of 32 v/sec until breakdown occurred. Values of the peak field at breakdown were 1200 -1450 v/μ (848-1025 v/μ rms) for the phosphosilicate glass samples compared to 810-870 v/μ (572-615 v/μ rms) for the SiO_2. Even though leakage currents are larger, the phosphosilicate glass shows a marked increase in dielectric strength. This has also been found to be the case with other glasses formed by predeposition over thermal oxides on silicon.

Dielectric constant.—Small-signal capacitance measurements were made in the frequency range 50 cps to 100 kc/sec using Boonton model 74C and Wayne-Kerr type B221 bridges. During the measurements a large negative d-c bias was applied to the field plate so that the p-type silicon surface was strongly accumulated and the true oxide capacitance was obtained. From the measured capacitance, the field plate area, and the oxide thickness, dielectric constants were calculated and were found to be independent of frequency at room temperature. The values obtained were in the range 4.0 to 4.1 for the phosphosilicate glass. Slightly lower values of 3.75 to 3.9 were obtained for the thermal oxides in agreement with previously published values (14, 15).

The temperature dependence of the dielectric constant was also investigated, and in the case of the phosphosilicate glass it was found to increase markedly at high temperatures and low frequencies. Figure 4 shows the dielectric constant *vs.* temperature at 50 cps for both the glass and the SiO_2 samples. For the glass, the dispersion is about 20% while for the SiO_2 it is less than 1%. At higher frequencies, the dispersion shifts to higher temperatures and vice-versa. Under a d-c bias, the polarization effect responsible for the dispersion manifests itself as a drift in the ca-

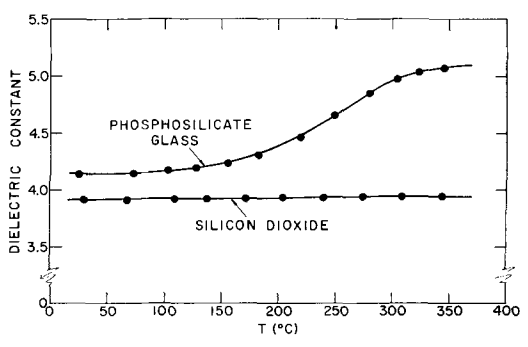

Fig. 4. Dielectric constant of phosphosilicate glass and silicon dioxide films as a function of temperature at 50 cps.

Table I. Properties of silicon dioxide layers on silicon (prepared at 1200° in dry O_2) compared with phosphosilicate glass (prepared by predepositing P_2O_5 onto thermal SiO_2 at 1020°C).

	SiO_2	P_2O_5-SiO_2
Composition (Mole % P_2O_5)	0	14.5-16.5
Density	2.24-2.27 g/cm³	2.35-2.40 g/cm³
Etch rate (15 HF: 10 HNO_3: 300 H_2O)	2 Å/sec	500 Å/sec
Resistivity (200°C, 37 v/μ)	>5 × 10^{16} ohm-cm	2 × 10^{15} ohm-cm
Dielectric strength (25°C, 375μ dia Al dots)	810-870 v/μ	1200-1450 v/μ
Dielectric constant (25°C, 100kc)	3.75-3.90	4.00-4.10

pacitance-voltage characteristic of the MOS structure. This drift was observed in the sodium masking experiment above and was the subject of an extensive investigation to be described in the next section.

A summary of the properties reported above for the silicon-dioxide and the phosphosilicate glass layers on silicon is shown in Table I. In the case of the phosphosilicate layers, only the properties of the glass formed by predeposition at 1020°C are included.

Polarization Effects

The phosphosilicate glass films[3] were examined for polarization effects using the MOS capacitance-voltage method (15). In applying this method to study polarization, one first measures the initial capacitance-voltage characteristic of the device. A polarizing voltage V_P is then applied to the field plate for a given length of time at an elevated temperature. After quenching to room temperature, the C-V characteristic is remeasured and any shift ΔV along the voltage axis is related to charge displacement or polarization in the glass. The details of the technique are described in ref. (13) and (16). In addition to being a measure of the polarization, the shift ΔV has a very practical significance since it corresponds directly to the change in turn-on voltage which would be observed in an MOS transistor using the glass for gate insulation.

In these films, two distinct and easily separable polarization effects were observed. The first of these was relatively small and saturated rapidly at low temperature (a few minutes at ~100°C). The second effect was much larger, but required over 100 hr at 300°C to reach saturation. We shall discuss the smaller low temperature effect first.

Low-temperature polarization.—The time dependence of the shift in the C-V characteristic of a typical sample at 60°C and —50v bias is shown in Fig. 5. The

[3] All phosphosilicate films used for the following polarization studies were prepared by depositing P_2O_5 at 1020°C for various times onto thermally formed SiO_2.

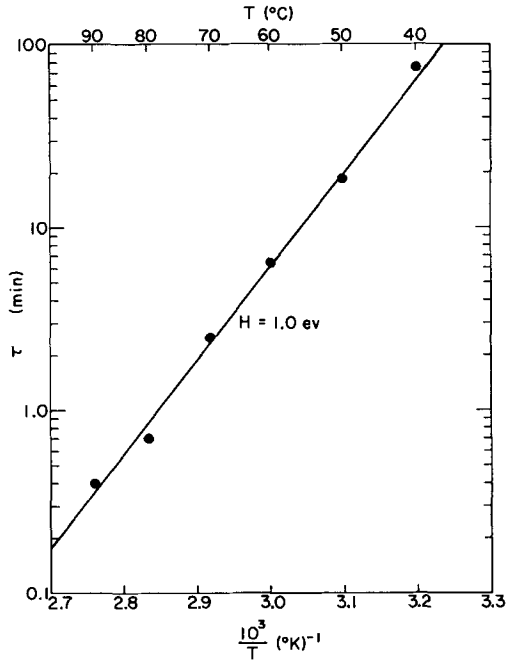

Fig. 6. Temperature dependence of the time constant for polarization of the phosphosilicate glass layer. The polarization process is characterized by an activation energy of about 1 ev.

approach to saturation is not exponential and a detailed description would require a broad distribution of time constants. Nevertheless, we define an effective time constant τ as that time required for ΔV to come within $1/e$ of its saturation value. This is about 6 min in the example of Fig. 5. The effective time constant τ was evaluated at several other temperatures between 40° and 100°C, and its dependence on temperature is shown in Fig. 6. This temperature dependence can be described by an activation energy of 1.0 ev (23 kcal/mole).

The time constant was not very sensitive to the magnitude or sign of the applied polarizing voltage V_P, but the saturation drift ΔV_{SAT} was almost precisely proportional to V_P and was opposite in sign. In Fig. 7, a number of capacitance-voltage curves are shown which were obtained from the same device after biasing at various voltages at 120°C for 5 min (more than sufficient to reach saturation). These curves were reproducible and did not depend on past history. They could be obtained in any order by simply biasing at the desired voltage for a time long enough to achieve saturation. Upon heating under short circuit the characteristic always returned to the zero bias case. The

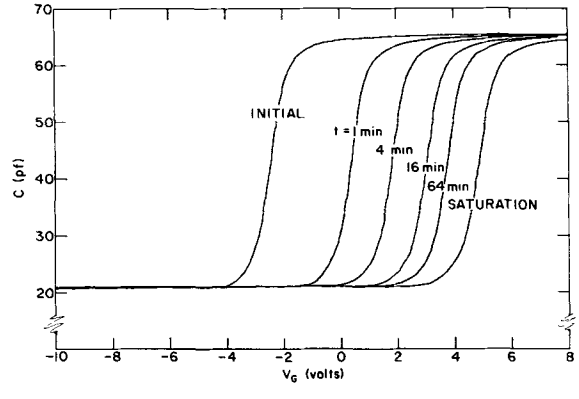

Fig. 5. Capacitance-voltage curves obtained on a double-layer capacitor after application of —50v to the field plate at 60°C for various lengths of time. The shift of the C-V characteristic is due to the build-up of a polarization in the phosphosilicate layer.

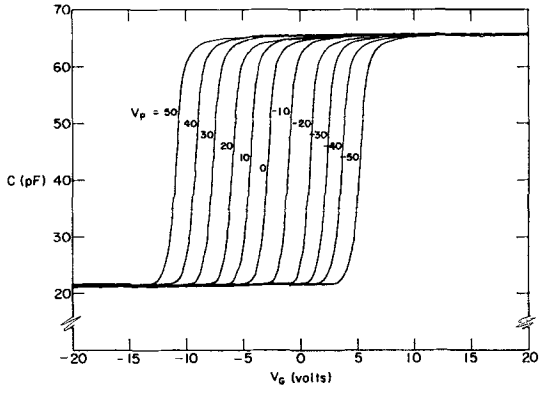

Fig. 7. Capacitance-voltage curves obtained on a double layer capacitor after biasing until saturation at various applied voltages. The shift of the C-V curve ΔV_{SAT} is proportional to the applied voltage. $x_g = 0.24\mu$; $x_o = 0.04\mu$.

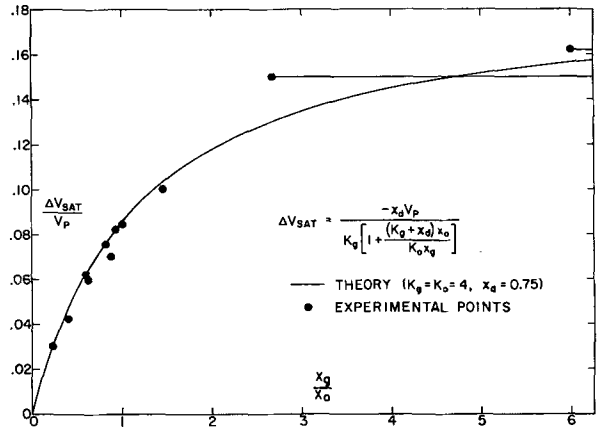

Fig. 8. Dependence of the saturation shift of the C-V curve per unit applied voltage $\Delta V_{SAT}/V_P$ on the phosphosilicate glass to silicon dioxide thickness ratio x_g/x_o. Each point corresponds to a different sample. The theoretical curve is calculated from Eq. [9]. ——, Theory ($K_g = K_o = 4$; $x_d = 0.75$).

saturation drift per unit applied voltage $\Delta V_{SAT}/V_P$ was found to be larger for larger values of the glass-to-oxide thickness ratio x_g/x_o. This dependence was investigated on a large number of samples with a wide range of x_g/x_o ratios and the results are shown in Fig. 8. The points corresponding to very large x_g/x_o ratios are rather uncertain because of difficulty in measuring the thinnest oxide layers. The curve through the data points is a theoretical one, and its basis will be discussed later. These data show that $\Delta V_{SAT}/V_P$ is a saturating function of x_g/x_o and that even when the insulating layer is essentially all phosphorus glass ΔV_{SAT} is only about 18% of the applied polarizing voltage.

Similar drift effects in a lead borosilicate glass have been explained by the migration of mobile cations in the glass (16). These ions drift under an applied polarizing voltage until space charges have been built up at the metal-glass and glass-oxide interfaces which completely cancel the electric field in the glass layer. This model predicts a saturation drift in the C-V characteristic which is given by

$$\Delta V_{SAT} = -\frac{K_o x_g}{K_g x_o} V_P \qquad [1]$$

where K_o and K_g are the relative dielectric constants of the oxide and glass, respectively. Hence for large x_g/x_o, ΔV_{SAT} can be many times the polarizing voltage. In the present experiments, on the other hand, ΔV_{SAT} was not proportional to x_g/x_o and was always much less than V_P. This shows that the polarization is not due to the unlimited migration of ions within the glass layer which would correspond to an infinite polarizability but must be described by a finite polarizability χ_p. Under an applied voltage, such a polarizability will give rise to the slow build-up of a uniform volume polarization $P = \epsilon_o \chi_p E_g$ where ϵ_o is the permittivity of free space and E_g is the field in the glass layer.[4] This slow polarization is in addition to the instantaneous polarization which is related to the high-frequency dielectric constant K_g. Such a volume polarization is equivalent to a surface charge on the glass-oxide interface of density

$$Q_p = P = \epsilon_o \chi_p E_g \qquad [2]$$

and a surface charge on the glass-metal interface of equal magnitude but opposite sign.

After equilibrium is reached, we can relate Q_p to the applied polarizing voltage as follows. The applied voltage must be the sum of the voltage drops across the oxide and glass layers

$$-V_P = E_g x_g + E_o x_o \qquad [3]$$

Also, the fields in the glass and oxide are related by

$$K_o E_o = (K_g + \chi_p) E_g \qquad [4]$$

since the electric displacement must be continuous across a dielectric interface. Eliminating E_o between [3] and [4] we obtain

$$E_g = \frac{-K_o V_P}{(K_g + \chi_p) x_o + K_o x_g} \qquad [5]$$

and substituting this into [2] we have

$$Q_p = \frac{-K_o \epsilon_o \chi_p V_P}{(K_g + \chi_p) x_o + K_o x_g} \qquad [6]$$

If C_g and C_o are the capacitances of the glass and oxide layers, respectively, then the charge induced in the silicon by Q_p is

$$Q_s' = \frac{C_o Q_p}{C_o + C_g} \qquad [7]$$

and the shift in the C-V characteristic caused by this excess charge is

$$\Delta V_{SAT} = \frac{(C_o + C_g)}{C_o C_g} Q_s' = \frac{Q_p}{C_g} = \frac{x_g Q_p}{\epsilon_o K_g} \qquad [8]$$

Finally, substituting [6] into [8] we obtain for the saturation drift as a function of applied voltage

$$\Delta V_{SAT} = \frac{-K_o x_g \chi_p V_P}{K_g[(K_g + \chi_p) x_o + K_o x_g]} \qquad [9]$$

Note that if we let $\chi_p \to \infty$, this reduces to Eq. [1] for a completely polarizable glass layer.

Equation [9] gives a linear dependence of ΔV_{SAT} on V_P and predicts that $\Delta V_{SAT}/V_P$ is a saturating function of x_g/x_o as was observed experimentally. The theoretical curve in Fig. 8 was plotted from Eq. [9] using the approximate values $K_o = K_g = 4$ and choosing for the polarizability $\chi_p = 0.75$. It will be seen from the figure that this single value of the polarizability is in reasonable agreement with the data on all of the samples which have been measured. Since these samples were prepared in several different furnaces and on some of them $POCl_3$ was substituted for P_2O_5 as a source of phosphorus, it seems unlikely that this polarizability results from an unintentional trace contamination. It is more likely that it is an intrinsic property of the phosphosilicate glass itself.

It has been assumed throughout the preceding discussion that the polarization was uniform throughout the glass layer and was zero in the oxide layer. This fact was demonstrated by an etching experiment using two identical samples. One was polarized at —60v while the other remained unpolarized. The aluminum electrodes were then etched off both samples and the glass layers were etched away in small steps. After each step C-V curves were made using a gold ball pressed against the glass surface as the metal electrode. The displacement between the C-V curves made on the polarized and unpolarized samples was then plotted as a function of the remaining glass thickness and the result is shown in Fig. 9. The straight line thus obtained verifies the linear dependence of ΔV on x_g (for a given Q_p) which is predicted by Eq. [8]. Since this equation was derived on the basis of a uniform polarization in the glass, that assumption is justified. The fact that ΔV goes to zero when all of the glass is removed proves that there is no polarization in the SiO_2 layer.

The mechanism responsible for the polarizability χ_p has not been established, but two possibilities will be considered. These are illustrated schematically in Fig. 10 (a) and (b). The first is the orientation of permanent dipoles uniformly distributed in the glass. This mechanism results (17) in a polarizability given by

[4] Rationalized MKS units are used throughout this section.

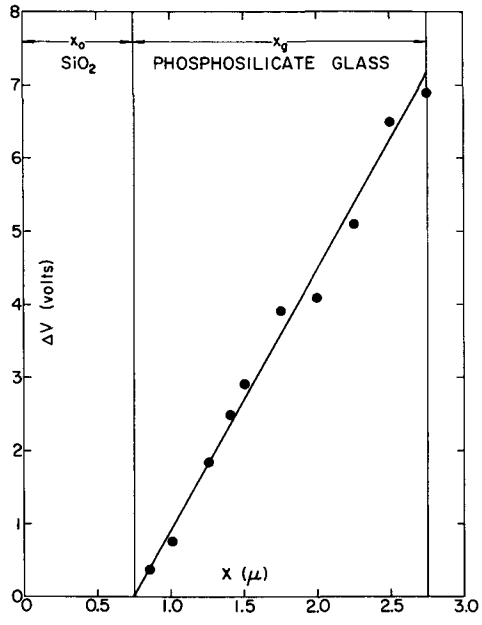

Fig. 9. Displacement ΔV between C-V curves made on polarized and unpolarized devices as a function of glass removed by etching. The straight line intersecting the x-axis at the glass oxide interface implies a uniform polarization in the glass and zero polarization in the SiO_2.

$$\chi_p \text{ (dipolar)} = \frac{Nq^2a^2}{2\epsilon_o kT} \qquad [10]$$

where N is the concentration of dipoles, qa is their dipole moment, k is Boltzmann's constant, and T is the absolute temperature. Assuming a dipole length $a = 5$Å, this model would require a concentration of dipoles of the order of $10^{19}/cm^3$. One difficulty with this model is that the predicted temperature dependence of χ_p was not observed experimentally.

A second, and more likely, possibility is that the glass is not homogeneous, but that it contains a small amount of a conductive phase (perhaps a crystalline precipitate) uniformly dispersed in the glass layer. The apparent polarizability that is observed would then be due to interfacial polarization between the conductive inclusions and the bulk of the glass. The resulting expression for the polarizability depends somewhat on the shape of the small conductive regions, but if it be assumed they are spheres, one gets (18, 19)

$$\chi_p \text{ (interfacial)} = \frac{9K_{g1}^2 v_2/v_1}{2K_{g1} + K_{g2}} \qquad [11]$$

where K_{g1} and K_{g2} are the dielectric constants of the bulk glass and the conductive phase and v_2/v_1 is the fractional volume of the conductive phase. Assuming $K_{g1} \simeq K_{g2}$ and using $\chi_p = 0.75$ we obtain from [11] $v_2/v_1 = 0.06$ or the conducting phase must occupy about 6% of the total volume of the glass. If, instead of being spherical, the inclusions were needle-shaped with the axis perpendicular to the surface, then a much smaller volume of conductive material could account for the observed polarizability (19). The time constant for the build-up of this interfacial polarization is (18, 19), again assuming spherical conducting regions

$$\tau = (2K_{g1} + K_{g2})\ \epsilon_o/\sigma_2 \qquad [12]$$

where σ_2 is the conductivity of the conducting phase. From this equation and the measured time constants of Fig. 6 we get a conductivity which increases exponentially with temperature with an activation energy of 1 ev and which has a value of 2×10^{-15} mho/cm at 60°C. As was noted earlier, the τ used here is an effective value representing an average of a distribution of relaxation times. This distribution could be explained either by variations in the shapes of the conducting regions or by variations in the conductivity itself.

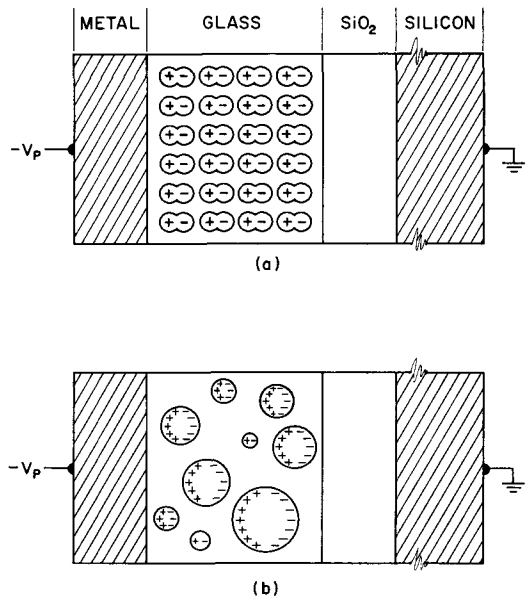

Fig. 10. Schematic illustration of two models which could account for the observed polarization of the phosphosilicate glass layers: (a) the orientation of permanent dipoles; if the dipole length were 5Å, a concentration of the order of $10^{19}/cm^3$ would be required; (b) interfacial polarization due to conducting inclusions in the glass layer. If the conducting regions were spherical they would have to occupy about 6% of the glass volume.

High-temperature polarization.—It was possible to obtain much larger polarization effects than those just described by biasing for very long periods of time at higher temperatures. This high temperature polarization was also proportional to the applied voltage and was approximately symmetrical under positive and negative bias. Figure 11 shows ΔV *vs.* time at three different temperatures for a set of identical samples. The dotted line indicates the saturation value of the low-temperature drift. At 125°C about 10 hr are required before any additional drift can even be observed. At 200°C the drift is much faster, but it has still not saturated after 3000 hr. At 300°C the drift is still faster, and it finally saturates at slightly over 100

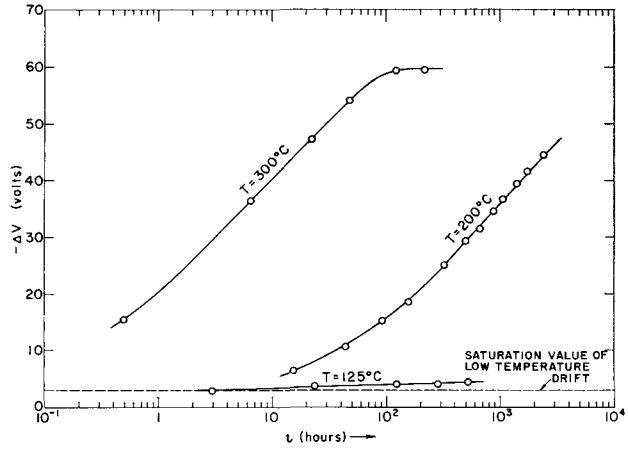

Fig. 11. Long-term, high-temperature drift in the C-V characteristic of phosphosilicate glass-silicon dioxide double-layer capacitors. This effect can be explained by ion migration through the bulk of the glass layer causing interfacial polarization on the glass-oxide interface. $x_g = 0.20\mu$; $x_o = 0.075\mu$; $v_p = +22.5$v.

hr. In this case the ΔV at saturation is 20 times larger than that corresponding to the low-temperature drift.

This long-term drift can be explained in terms of ion migration in the bulk of the glass film. The migrating ions build up a space-charge on the glass-oxide interface which eventually cancels the applied field in the glass layer and leads to saturation. This type of polarization has been discussed at length in ref. (16) and leads to a shift ΔV_{SAT} given by Eq. [1]. For the sample dimensions and the applied voltage indicated in Fig. 11, this equation predicts a ΔV_{SAT} of 60v which is in excellent agreement with the observed value. The 200° and 300° curves in Fig. 11 are nearly parallel, being displaced from each other along the time axis by a factor of about 160. This shift corresponds to an activation energy of 1.15 ev, a value only slightly higher than that for the low-temperature effect.

This long-term drift effect is definitely associated with the phosphosilicate glass layer since it was not observed with uncontaminated silicon dioxide films under similar test conditions (13, 15).

Summary and Conclusions

A survey has been made of the properties of the phosphosilicate glass which is obtained when P_2O_5 is predeposited on thermally oxidized silicon. Such properties as the composition, density, etch rate, resistivity, dielectric constant and dielectric strength have been determined and compared with the corresponding properties of silicon dioxide films.

It has also been found that a phosphosilicate glass layer over silicon dioxide is an effective barrier to sodium ion migration, and this fact may account for the reported increase in stability of planar transistors and MOS devices which include such a glass layer (7). On the other hand, reproducible polarization effects have been discovered in the phosphosilicate glass which appear to be unrelated to contamination. Thus, while the glass layer eliminates the gross instabilities which result from alkali contamination, these polarization effects lead to MOS devices less stable than those which can be made using pure uncontaminated SiO_2. The polarization of the phosphosilicate glass has been studied in detail using the MOS capacitance-voltage method, and a model has been presented for interpretation of the results.

Acknowledgments

The authors wish to thank Mrs. D. S. Sklar, L. D. Allasia, and P. J. Fleming for assistance with the experimental portion of this work. Thanks are also due to A. S. Grove, C. A. Bittmann, and G. E. Moore for many stimulating discussions.

Manuscript received Nov. 5, 1965; revised manuscript received Dec. 16, 1965.

Any discussion of this paper will appear in a Discussion Section to be published in the December 1966 JOURNAL.

REFERENCES

1. G. E. Moore, "Microelectronics," E. Keonjian, Editor, Chap. 5, McGraw-Hill Publishing Co., New York (1963).
2. C. T. Sah, H. Sello, and D. A. Tremere, *J. Phys. Chem. Solids*, **11**, 288 (1959).
3. R. B. Allen, H. Bernstein and A. D. Kurtz, *J. Appl. Phys.*, **31**, 334 (1960).
4. W. A. Pliskin and R. P. Gnall, *This Journal*, **111**, 872 (1964).
5. T. Y. Tien and F. A. Hummel, *J. Am. Ceram. Soc.*, **45**, 422 (1962).
6. E. Kooi, *This Journal*, **111**, 1383 (1964).
7. D. R. Kerr, J. S. Logan, P. J. Burkhardt, and W. A. Pliskin, *IBM J. Res. Develop.*, **8**, 376 (1964).
8. S. Tolansky, "Multiple-Beam Interferometry of Surfaces and Films," Clarendon Press, Oxford, England (1948).
9. G. R. Booker and C. E. Benjamin, *This Journal*, **109**, 1206 (1962).
10. B. E. Deal, *ibid.*, **110**, 527 (1963).
11. B. E. Deal, *ibid.*, **110**, 1292 (1963).
12. "Handbook of Chemistry," 10th ed., p. 286, N. A. Lange, Editor, McGraw-Hill Book Co., New York (1961).
13. E. H. Snow, A. S. Grove, B. E. Deal, and C. T. Sah, *J. Appl. Phys.*, **36**, 1664 (1965).
14. J. L. Sprague, J. A. Minahan, and O. J. Wied, *This Journal*, **109**, 94 (1962).
15. A. S. Grove, B. E. Deal, E. H. Snow, and C. T. Sah, *Solid-State Electron.*, **8**, 145 (1965).
16. E. H. Snow and M. E. Dumesnil, *J. Appl. Phys.*, **37**, (April 1966).
17. A. J. Dekker, "Solid State Physics," Prentice-Hall, Inc., Englewood Cliffs, N. J. (1957).
18. K. W. Wagner, *Archiv. für Electrotechnik*, **2**, 371 (1914).
19. R. W. Sillars, *J. Inst. Elect. Engrs. (London)*, **80**, 378 (1937).

High-Temperature Immiscibility of Uranium Mono- and Dicarbides[1]

Mildred Bradley Sears, Leslie M. Ferris, and Robert J. Gray

Oak Ridge National Laboratory, Oak Ridge, Tennessee

ABSTRACT

The high-temperature, uranium monocarbide-dicarbide immiscibility region was determined by examining the microstructures of specimens with compositions from $UC_{1.1}$ to $UC_{1.8}$, which had been prepared by decomposing mixtures containing the sesquicarbide at 1820°-2130°C. The low carbon miscibility boundary, which occurs between $UC_{1.1}$ and $UC_{1.2}$ (5.2 and 5.7% carbon), is nearly composition invariant between 1820° and 2070°C. The high carbon miscibility boundary occurs at about $UC_{1.65}$ (7.7% carbon) at 1820°C and the solubility of the monocarbide in the dicarbide phase increases linearly with increasing temperature. The peak of the immiscible region occurs at about $UC_{1.2}$ (5.7% carbon) and a temperature above 2070°C.

There is general agreement that cubic uranium monocarbide (UC) and cubic uranium dicarbide [usually designated as UC_2 although, in fact, it is always substoichiometric, the most common composition being $UC_{1.8}$ (1)] form a complete series of solid solutions near the melting point (1-8). A region of immiscibility has been observed at temperatures between about 1800° and 2100°C, but has not been clearly defined. Mallett *et al.* (2) placed the upper limit of the immiscible region at about 2025°C and 6.2% carbon based on microstructure studies, while Witteman and Bowman (9) determined the critical temperature as 2050° ±50°C at a composition of $UC_{1.35\pm0.05}$ (6.4±0.2% carbon) from thermal arrest data. At one time Chubb and Phillips (10) felt that the region of immiscibility extended to the melting point, but soon afterward revised their constitutional diagram when they found evidence of a single-phase region at 2300°C (3). Mal-

[1] Research sponsored by the United States Atomic Energy Commission under contract with the Union Carbide Corporation.

lett *et al.* (2) found little or no solubility of UC_2 in UC at 1800°C based on microstructure studies. From the change in the UC lattice parameter at high temperatures, Wilson (4) concluded that a UC-UC_2 solid solution containing up to 5.2% carbon exists at 1820°C, and that UC may also dissolve a small amount of excess carbon at lower temperatures. Unfortunately at high temperatures the surface composition, which determines the x-ray diffraction pattern, differed from the bulk composition of the specimens so that Wilson had to estimate the carbon compositions from the lattice parameters by assuming that the lattice parameter varied linearly with composition from cubic UC to cubic UC_2 (Vegard's law). A number of phase diagrams appear to be based on Wilson's solubility data (1, 3, 5, 6, 8, 10). From thermal arrest data, Witteman and Bowman (9) established that one boundary of the immiscible region intersects the UC_2 cubic-to-tetragonal transition isotherm at a composition between $UC_{1.0}$ and $UC_{1.065}$ (4.8-5.07% carbon). While they did not give a temperature for the UC_2 phase transition, co-workers of theirs have reported a value of 1785° ±20°C (11). Magnier and Accary (7) found practically no solubility of UC_2 in UC at 1800°C, and Chubb (6) in his most recent diagram lowered the miscibility boundary to about 5% carbon; no data were given. The boundary at the high-carbon end of the system at about 1800°C has been placed at 8.2% carbon by Mallett *et al.* (2), about $UC_{1.6}$ (7.5% carbon) by Witteman and Bowman (9), 8.5% carbon by Wilson (4), 8.8% by Magnier and Accary (7), and 7.8% by Chubb (6). Takahashi *et al.* (12) believe that a UC_{2-y} phase containing 7.8% carbon or more is stable at the transition temperature.

Examination of the microstructures of diffusion couples which had been annealed at 1800°C and higher led Chubb and Phillips (10) to postulate a eutectoid at 7-7.5% carbon and just below 1800°C. They revised Wilson's constitutional diagram (4), and this revision has been incorporated into several other diagrams (1, 3, 5, 8). Chubb deleted the eutectoid from his 1964 diagram (6). Takahashi *et al.* (12) found no evidence of a eutectoid in the microstructure of a specimen containing 6% carbon, and Magnier and Accary (7) did not include it in their diagram.

This paper presents the results of a microstructure study of uranium carbide specimens with compositions from $UC_{1.1}$ to $UC_{1.8}$ (5.3-8.3% carbon) which had been prepared by decomposing mixtures containing uranium sesquicarbide at temperatures from 1820° to 2130°C.

Experimental

Preparation of the carbides.—Specimens were prepared by first arc-melting high-purity uranium metal (<400 ppm total impurities) and spectroscopic grade carbon, using nonconsumable tungsten electrodes, and quenching the melts on a water-cooled button mold as described previously (13-16). The resulting buttons were then heat-treated for 65 hr at 1600°C in a Brew High Vacuum Furnace, No. 424 B, to form monocarbide-sesquicarbide and sesquicarbide-dicarbide mixtures (15). Finally, the mixtures were heat-treated in the Brew furnace at temperatures between 1820° and 2130°C to decompose the sesquicarbide and reform monocarbide-dicarbide mixtures. Temperatures were measured with an accuracy of ±20°C with a Leeds and Northrup optical pyrometer. Although samples were not quenched after the heat-treatments, they were furnace-cooled to 1000°C in less than 5 min and to 500°C within 10 min. Graphite crucibles were used to contain the specimens. Most of the specimens with compositions from $UC_{1.1}$ to $UC_{1.3}$ were set on small disks of uranium monocarbide to prevent reaction with the crucible. Under these conditions there was no visible reaction of the specimens with the crucibles, and only specimen 8G ($UC_{1.3}$ heat-treated at 2130°C directly on graphite) showed any noticeable increase in the carbon concentration as a result of the heat-treatments.

Table I. Composition of heat-treated uranium carbides

Fig. No.	Specimen	Final heat-treatment[a] Temp, °C	Time, hr	Analysis, w/o U	Total C	Free C	Combined-C/U atom ratio
1	16I[b]	1820	6	94.7	5.25	0.01	1.10
	16H[b]	1900	6	94.7	5.26	0.01	1.10
	17I[b]	1820	6	94.3	5.71	0.01	1.20
	17H[b]	1900	6	94.2	5.74	0.01	1.20
	17J[b]	2000	4	94.3	5.69	0.01	1.20
2	17M[b]	2070	2	94.3	5.70	0.01	1.20
3a	8G	2130	2	93.5[c]	6.52[c]	0.02[c]	1.38[c]
	8M[b]	2070	2	94.0	5.98	0.01	1.26
3b	8J	2000	4	93.8	6.16	0.03	1.30
4a	11M[b]	2070	2	93.0	6.67	0.01	1.41
4b	11J	2000	4	93.4	6.64	0.01	1.41
5a	U_2C_3-3J	2000	4	92.9	7.08	0.01	1.51
5b	U_2C_3-3H	1900	6	93.0	7.02	0.04	1.49
6a	12H	1900	6	92.4	7.56	0.01	1.62
6b	12I	1820	6	92.4	7.55	0.01	1.62
7	10I	1820	6	91.9	8.06	0.05	1.73
8	UC_2-21I	1820	6	91.6	8.30	0.03	1.80

[a] Heated first 65 hr at 1600°C, then at indicated temperature.
[b] Set on UC disks.
[c] Average composition of the specimen after it reacted with the graphite crucible.

Characterization of the carbides.—Chemical analyses of the specimens, after the final heat-treatment, for uranium, total carbon, and free carbon are given in Table I. Tungsten contamination from the electrodes averaged 0.05% w/o (weight per cent). Specimens were also analyzed for oxygen (0.01% or less) and nitrogen (avg. 30 ppm). The x-ray diffraction powder patterns of the specimens after cooling to room temperature were those of uranium monocarbide-dicarbide mixtures; no residual sesquicarbide from the 1600°C heat-treatments was detected. There was no shift in either the monocarbide or dicarbide lines in the x-ray powder patterns as a function of the total carbon content between $UC_{0.8}$ and $UC_{2.4}$, or as a function of the heat-treatment indicating that at room temperature there is very little if any solubility of monocarbide in dicarbide and *vice versa*. The hydrolysis properties of many of these specimens have been reported elsewhere (16).

Procedures.—All chemical analyses were conducted by procedures developed in the study of the hydrolysis of the as-cast uranium carbides (14). X-ray powder patterns were determined with a Debye-Scherrer 114.59-mm-diameter powder camera using CuK-α radiation. Specimens were mounted for metallographic examination in a room-temperature setting epoxy resin[2] 1.25-in. mount, rough ground through 320, 400, and 600 grit silicon carbide papers using a water-free silicone fluid[3] as a lubricant, and vibratorily polished 6-12 hr on a nylon cloth using a silicone fluid-Linde A-graphite slurry (17). The carbides were etched with equal parts of glacial acetic acid, 15.8*M* (70%) nitric acid and water for 10 to 15 sec for uranium monocarbide, 15 to 30 sec for uranium dicarbide, and 10 to 30 sec for uranium sesquicarbide. The variation for each of the three carbides was due to the relative amount of the other carbide(s) present in the microstructure. Etching formed an interference film on the surface of the sample which varied in color with the orientation and composition of the substrate. Black and white photomicrographs were made under bright field illumination with Royal Pan film, using Polydel developer.

Results

Two different types of microstructures were observed when mixtures containing sesquicarbide were decomposed by heat-treating in the range of 1820°-2130°C: (*i*) orientated platelets of monocarbide (dark) or dicarbide (light) were observed as a homogeneous dispersion throughout the entire specimen if the sesquicarbide decomposition had occurred in a region where

[2] "Araldite," Ciba Products Corporation, Fairlawn, New Jersey.

[3] Dow Corning 702 Diffusion Pump Fluid.

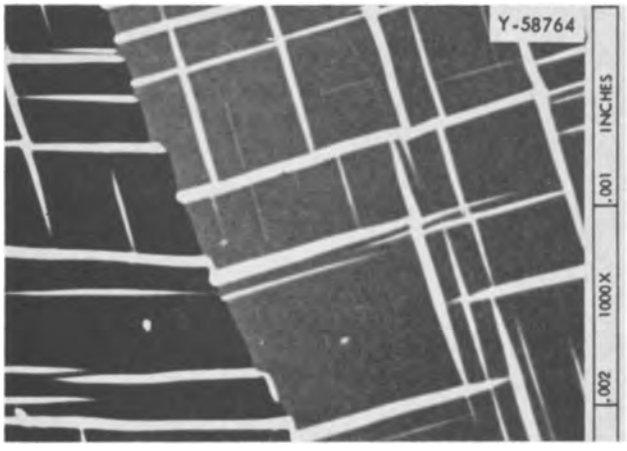

Fig. 1. $UC_{1.10}$ heat-treated at 1820°C (specimen 16I). The specimen appears to have been heated in a single-phase region. Nitric-acetic etch.

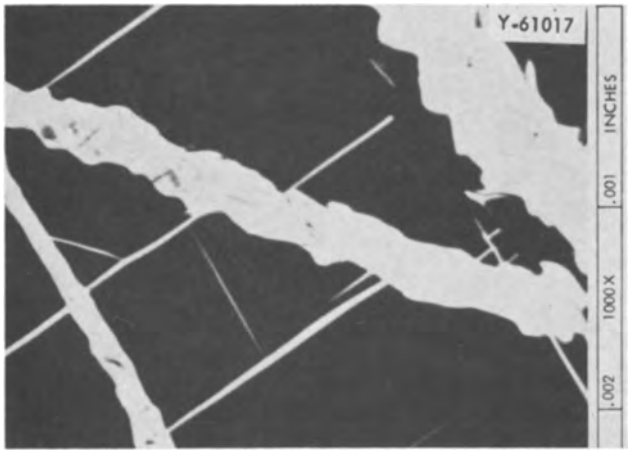

Fig. 2. $UC_{1.20}$ heat-treated at 2070°C (specimen 17M). The specimen appears to have been heated in a two-phase region. Nitric-acetic etch.

the monocarbide and dicarbide formed a solid solution (Fig. 1, 3a, 4a, 5a, 6a, 7, and 8), and (*ii*) large, irregularly shaped areas of monocarbide-rich and dicarbide-rich phases were observed if the decomposition had occurred within the monocarbide-dicarbide immiscibility region (Fig. 2, 3b, 4b, 5b, and 6b).

The first type of microstructure was similar to those observed by Takahashi *et al.* (12) for slow-cooled specimens and, in general, the postulates of these authors concerning the morphologies of the precipitates are applicable here. The microstructure of specimen 8G, which reacted with the graphite crucible at 2130°C, varied from Fig. 3a which was typical of the low carbon part of the specimen ($UC_{1.3}$) to a microstructure resembling Fig. 7 ($UC_{1.7}$) in the part of the specimen in contact with the crucible. Across this range of composition, only the first type of microstructure indicating solid solution was observed.

The second type of microstructure (Fig. 2, 3b, 4b, 5b, and 6b) was distinctly different from the first type.

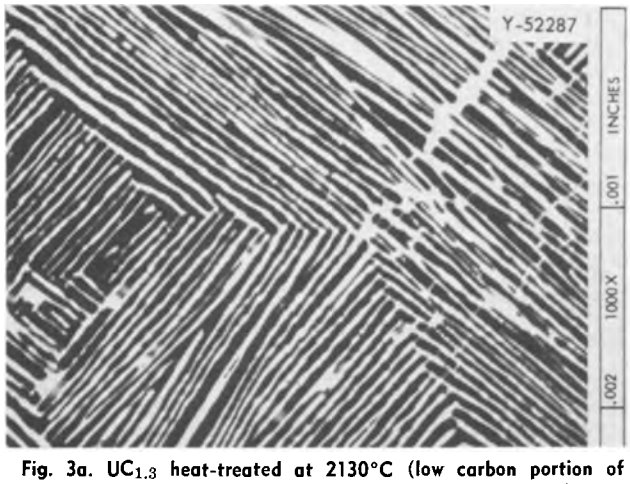

Fig. 3a. $UC_{1.3}$ heat-treated at 2130°C (low carbon portion of specimen 8G). The specimen appears to have been heated in a single-phase region. Nitric-acetic etch.

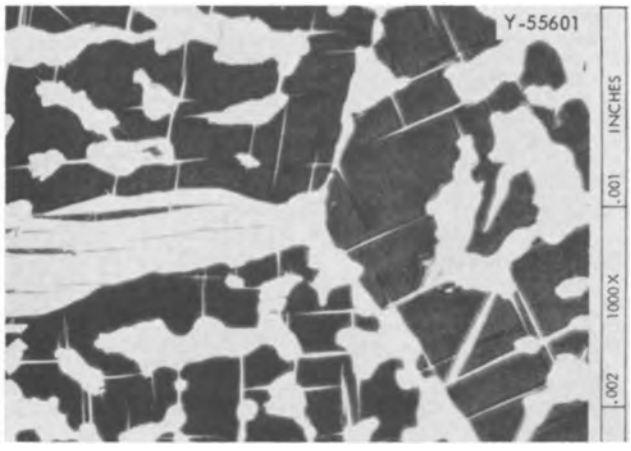

Fig. 3b. $UC_{1.30}$ heat-treated at 2000°C (speimen 8J). The specimen appears to have been heated in a two-phase region. Nitric-acetic etch.

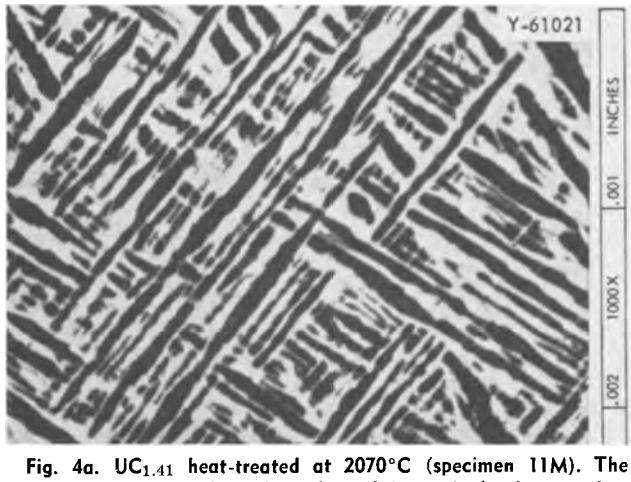

Fig. 4a. $UC_{1.41}$ heat-treated at 2070°C (specimen 11M). The specimen appears to have been heated in a single-phase region. Nitric-acetic etch.

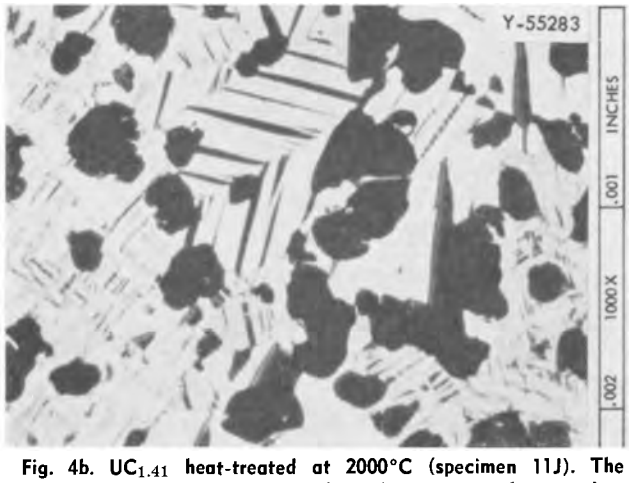

Fig. 4b. $UC_{1.41}$ heat-treated at 2000°C (specimen 11J). The specimen appears to have been heated in a two-phase region. Nitric-acetic etch.

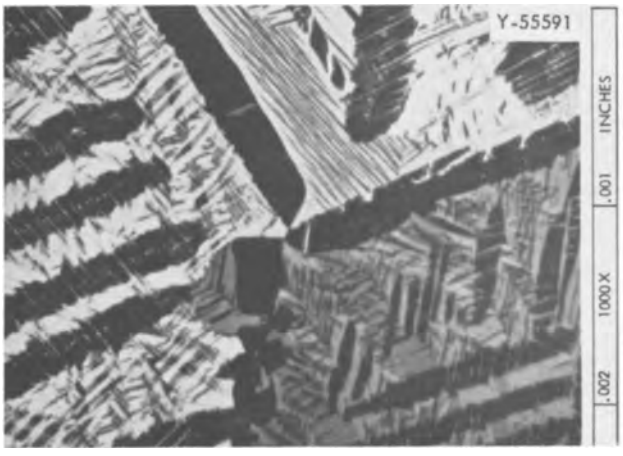

Fig. 5a. $UC_{1.51}$ heat-treated at 2000°C (specimen U_2C_3-3J). The specimen appears to have been heated in a single-phase region. Nitric-acetic etch.

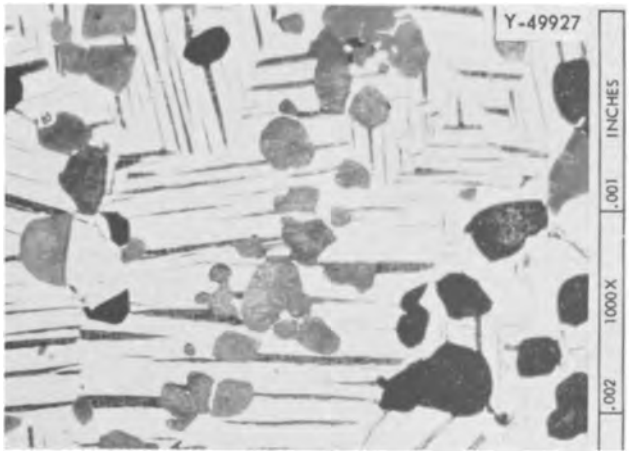

Fig. 5b. $UC_{1.49}$ heat-treated at 1900°C (specimen U_2C_3-3H). The specimen appears to have been heated in a two-phase region. Nitric-acetic etch.

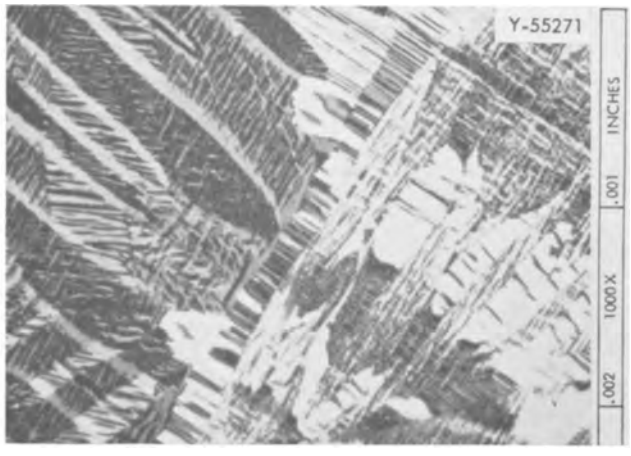

Fig. 6b. $UC_{1.62}$ heat-treated at 1820°C (specimen 12I). The specimen appears to have been heated in a single-phase region. Nitric-acetic etch.

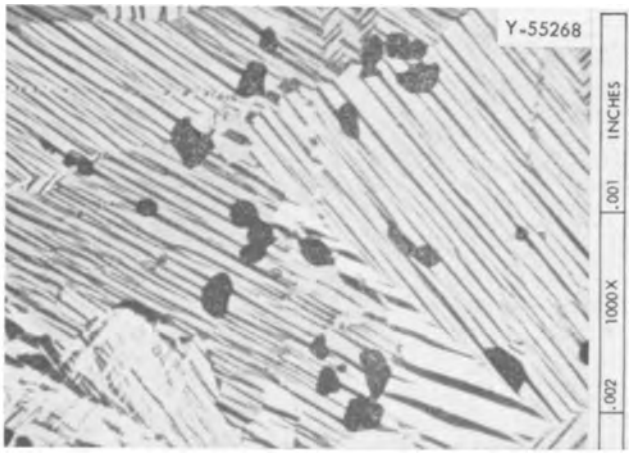

Fig. 6b. $UC_{1.62}$ heat-treated at 1820°C (specimen 12I). The specimen appears to have been heated in a two-phase region. Nitric-acetic etch.

While the second type contained some orientated platelets indicating partial solid solution formation, there were also relatively large, irregularly shaped areas of monocarbide-rich and dicarbide-rich phases indicative of immiscible phases at the heat-treating temperature. The dicarbide-rich areas were similar in appearance to the $UC_{1.7}$ specimen which had been heated in the single-phase region (Fig. 7) and always contained parallel platelets of monocarbide which did not cross the twin boundaries. Because of a fine substructure (observed at 2000X), the relative areas of UC and UC_2 in the dicarbide-rich phase could not be estimated by point counting on a grid. The monocarbide-rich sections of the $UC_{1.2}$ and $UC_{1.3}$ specimens (Fig. 2 and 3b) resembled the $UC_{1.1}$ specimen which had been heated in the single-phase region (Fig. 1) and contained parallel sets of dicarbide lamellae having up to three different orientations. Specimens with a composition of $UC_{1.20}$ which had been heated at 1820°, 1900°, and 2000°C had similar microstructures to specimen 17M, which was heated at 2070°C (Fig. 2). The composition of the monocarbide phase in equilibrium with excess dicarbide at 1820°, 1900°, 2000°, and 2070°C was estimated as being very close to $UC_{1.1}$ by point counting on a 0.25 in., 187 point-grid the relative areas of the dicarbide platelets and monocarbide matrix in the monocarbide-rich portions of these $UC_{1.2}$ specimens, and correcting for the densities of UC and UC_2.

Partial Constitutional Diagram

The high-temperature, uranium monocarbide-dicarbide immiscibility region as determined by examining the microstructures of specimens with compositions from $UC_{1.1}$ to $UC_{1.8}$, which had been prepared by decomposing mixtures containing the sesquicarbide at 1820°-2130°C, is illustrated in Fig. 9. The low carbon immiscibility boundary is nearly composition invariant between 1820° and 2070°C. This is in marked contrast to current phase diagrams (1-8) which show increasing solubility of the dicarbide in the monocarbide with increasing temperature in this range. At 1765°C only a trace of dicarbide dissolved in the monocarbide

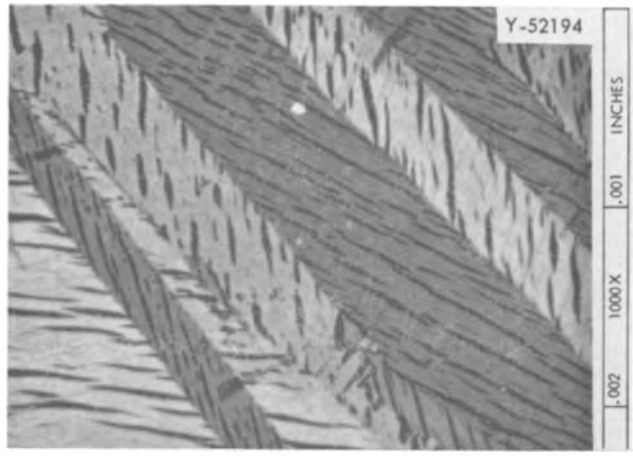

Fig. 7. $UC_{1.73}$ heat-treated at 1820°C (specimen 10I). The specimen appears to have been heated in a single-phase region. Nitric-acetic etch.

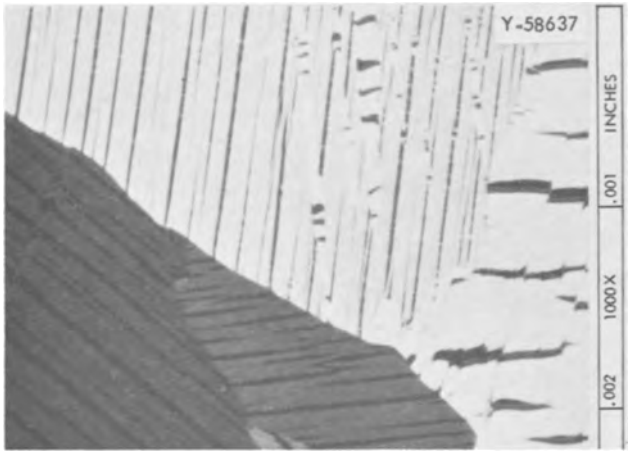

Fig. 8. $UC_{1.80}$ heat-treated at 1820°C (specimen UC_2-211). The specimen appears to have been heated in a single-phase region. Nitric-acetic etch.

phase (18) indicating that the miscibility boundary must change rapidly with temperature between 1820° and 1765°C. This proposal is consistent with the Los Alamos work placing the miscibility boundary somewhere between $UC_{1.0}$ and $UC_{1.065}$ (9) at 1785° ± 20°C (11). On the high carbon side of the immiscible region, our work shows a much wider range of solid solution formation than was reported by Mallett *et al.* (2), Wilson (4), Chubb (6), and Magnier and Accary (7). Although our high carbon boundary is about the same as that given by Frost (1), Rough and Chubb (3), Imoto *et al.* (5), and the IAEA Panel (8), we found no indication of the eutectoid shown in their diagrams. Our results are consistent with those of Takahashi *et al.* (12) who first observed that alloys containing 7.8% carbon or more were stable solid solutions above the dicarbide transition temperature. The peak of the immiscible region occurs at about $UC_{1.2}$ (5.7% carbon) and a temperature above 2070°C. Unfortunately 2100°C was about the maximum temperature attainable in the Brew furnace, so we were unable to define the exact peak temperature. The estimate of 2100°C in Fig. 1 was based on the results of

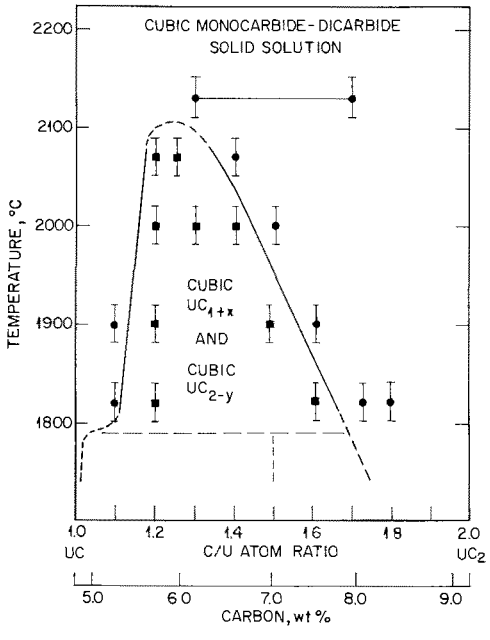

Fig. 9. High-temperature uranium monocarbide-dicarbide immiscibility region. Square dots represent specimens heat-treated in a two-phase region and round dots specimens heated in a single-phase region.

Witteman and Bowman (9) and Mallett *et al.* (2), who found the peak at 2050° ± 50° and 2025°C, respectively. In fact, the miscibility boundary lines of Fig. 9 can be extrapolated to a peak as high as 2200°C.

The microstructures of specimens prepared by decomposing mixtures containing the sesquicarbide show the high temperature monocarbide-dicarbide immiscibility region much more clearly than do the microstructures of as-cast specimens which had been annealed at 1800° to 2100°C such as were used by Mallett *et al.* (2) and Rough and Chubb (3) in determining their constitutional diagrams. Although we cannot prove in this study that the phases reached equilibrium during heat-treating, the heat-treating times were long enough to produce marked changes in the microstructures compared with most of the original sesquicarbide mixtures, and were probably much longer than those used in the previous studies: Mallett *et al.* (2) heat-treated for "nominal periods of time" and Rough and Chubb (3) for 2 to 20 min, compared with 2 to 6 hr in this study. While caution must always be exercised in determining high-temperature phenomena by metallographic examination at room temperature, our procedure has included chemical analyses of the specimens both before and after heat-treating so that the chemical compositions are known precisely, which was not the case in Wilson's (4) high-temperature x-ray studies.

Acknowledgments

The authors wish to thank the following members of the ORNL Metals and Ceramics Division for their aid in this study: R. E. McDonald and L. Queener for arc-melting the carbides; J. P. Hammond and C. Hamby for heat-treating the specimens; and B. C. Leslie for the photomicrographs. The ORNL Analytical Chemistry Division provided analyses: x-ray analyses by R. L. Sherman and chemical analyses by the group of W. R. Laing.

Manuscript received July 22, 1965; revised manuscript received Oct. 25, 1965.

Any discussion of this paper will appear in a Discussion Section to be published in the December 1966 JOURNAL.

REFERENCES

1. B. R. T. Frost, *J. Nucl. Mat.*, **10**, 265 (1963).
2. M. W. Mallett, A. F. Gerds, and H. R. Nelson, *This Journal*, **99**, 197 (1952).
3. F. A. Rough and W. Chubb, BMI-1554 (1961).
4. W. B. Wilson, *J. Am. Ceram. Soc.*, **43**, 77 (1960)
5. S. Imoto, T. Sano, Y. Takada, K. Yamamoto, K. Watanabe, T. Isoda, and H. Uchikoski, "Studies on Uranium Dicarbide and Sesquicarbide," Paper A10 presented at the Symposium on Carbides in Nuclear Energy, Harwell, November 1963.
6. W. Chubb as quoted by K. H. Osthagen and A. A. Bauer, BMI-1686 (1964).
7. P. Magnier and A. Accary, "Solubility of Uranium and Carbon in Uranium Monocarbide," Paper A2 presented at the Symposium on Carbides in Nuclear Energy, Harwell, November 1963.
8. "The Uranium-Carbon and Plutonium-Carbon Systems, A Thermochemical Assessment, A Report from a Panel Held in Vienna, Oct. 8-12, 1962," Technical Reports Series No. 14, International Atomic Energy Agency, Vienna, 1963.
9. W. G. Witteman and M. G. Bowman, "Studies Within the System UC-UC_2," in "The Fourth Uranium Carbide Conference, East Hartford, Conn., May 20-21, 1963," TID-7676.
10. W. Chubb and W. M. Phillips, *Trans. Am. Soc. Metals*, **53**, 465 (1961).
11. T. C. Wallace, N. H. Krikorian, and P. L. Stone, *This Journal*, **111**, 1404 (1964).
12. S. Takahashi, B. Ishii, K. Yamamoto, H. Uchikoshi, and Y. Akimoto, "Microstructures of U-C Alloys," in J. T. Waber, P. Chiotti, and W. N. Miner, Editors, "Nuclear Metallurgy Volume X, Compounds of Interest in Nuclear Reactor Technology," IMD Special Report No. 13, The Metallurgical Society of the AIME, 1964, pp. 627-640.

13. M. J. Bradley, L. M. Ferris, T. Hikido, and J. W. Ullmann, ORNL-3403 (1963).
14. M. J. Bradley and L. M. Ferris, *Inorg. Chem.*, **3**, 189 (1964).
15. M. J. Bradley and L. M. Ferris, *ibid.*, **3**, 730 (1964).
16. M. J. Bradley and L. M. Ferris, *J. Inorg. Nucl. Chem.*, **27**, 1557 (1965).
17. C. K. H. DuBose and R. J. Gray, ORNL-TM-91 (1962).
18. M. B. Sears and R. J. Gray, Unpublished data.

The Electrolytic Reduction of Diisopropyl Ketone in Acid Solution

Sherlock Swann, Jr., D. K. Eads,[1] and L. H. Krone, Jr.[2]

Department of Chemistry and Chemical Engineering, University of Illinois, Urbana, Illinois

ABSTRACT

The electrolytic reduction of diisopropyl ketone has been studied in acid solution at cathodes of zinc, cadmium, mercury, and lead. The main products are the saturated hydrocarbon and secondary alcohol with pinacol and olefin in smaller amounts. The temperature at which the solid electrodes were cast had a marked effect on the course of the reduction.

This paper is a continuation of a study of the electrolytic reduction of aliphatic ketones, in which it was shown that methyl propyl ketone was reduced to pentane at cathodes of zinc, cadmium, mercury, and lead in yields varying from 23 to 75% (1). Since it might be expected that steric hindrance would influence the course of the reduction of an aliphatic ketone (12), it seemed desirable to investigate the effect of branched chains adjacent to the carbonyl group. A study of the electrolytic reduction of diisopropyl ketone was therefore undertaken. Only one previous example of the electrolytic reduction of a branched chain aliphatic ketone has been reported in the literature. Wibaut, Hoog, Langedijk, Overhoff, and Smittenberg (2) found that the main product of the reduction of 3.3-dimethylbutanone at a cadmium cathode was the saturated hydrocarbon. The olefin and alcohol were also present in small amounts.

Apparatus and Procedure

The apparatus has been described previously (3, 4). In the early part of the investigation the calcium chloride tube was omitted.

First procedure.—After much experimentation the following procedure for the recovery of products was adopted. The catholyte and washings of the porous cup and cathodes were poured into a separatory funnel where they divided into two layers. The lower, aqueous, layer was removed and the remaining liquid transferred to a small flask. The aqueous part was subjected to simple distillation and the fraction boiling up to 88°C collected. This fraction was diluted with water and the oily layer which formed added to the rest of the organic material in the flask. The residual aqueous layer was again redistilled and the fraction taken off and treated as before. This procedure was repeated four times.

The oil was fractionated in a small column. The first fraction 62°-64°C, was a constant boiling mixture of hydrocarbons and ethyl alcohol. The next fraction was evidently all ethyl alcohol. The second cut was, therefore, made at 85°C.

The distillation was then continued under 14 mm pressure and the next fraction cut at 60°C. This consisted of diisopropyl carbinol and ketone. A residue, very probably of dehydration products of the pinacol, was left.

The hydrocarbon-ethyl alcohol fraction was diluted with water and the hydrocarbon which separated, dried with anhydrous magnesium sulfate and weighed. A portion of it was analyzed for unsaturation by bromine titration.

[1] Present address: Rohm and Haas Co., Bristol, Pa.

[2] Present address: Monsanto Chemical Company St. Louis, Missouri. National Science Foundation Fellow, 1952-53.

The carbinol-ketone fraction was weighed, dried over anhydrous magnesium sulfate, and analyzed for ketone by refractive index.

To establish the identity of the saturated hydrocarbon, the mixed hydrocarbons were shaken in a separatory funnel with concentrated sulfuric acid and syrupy phosphoric acid to remove the olefin. The acids were removed with sodium carbonate solution and water after which the residual hydrocarbon was dried over anhydrous magnesium sulfate and distilled. The bulk of the material boiled at 80°-81° and upon redistillation at 80.5°C. The refractive index was $N_D^{20} = 1.3806$. These constants correspond closely with those reported in the literature for 2,4-dimethylpentane, bp 80.5°C and $N_D^{20} = 1.38145$. The unsaturated heptene was determined in representative samples of hydrocarbons by titration with bromine in the first part of the investigation and with iodine in the latter part.

The presence of diisopropyl carbinol in the ketone-carbinol fraction was established by making its phenylurethane, mp 93°-94°C. The melting point reported in the literature is 94°-95°C (7). To identify the ketone an attempt was made to prepare the 2,4-dinitrophenylhydrazone. This was unsuccessful, but it was found possible to prepare the semicarbazone, mp 156°-157°C. The melting point reported in the literature is 160°C (8).

Second procedure.—In the latter part of the investigation the catholyte and washings were neutralized with sodium carbonate before separation of the oily layer. The aqueous layer was distilled and the fraction boiling up to 85°C collected and diluted with water as before to recover hydrocarbons. Since the amount of oil obtained in this way was very small, only one distillation was usually carried out. The rest of the procedure was the same as that previously described except that the residue was dissolved in low boiling petroleum ether causing the crystallization of 2,5-dimethyl-3,4-diisopropyl-3,4-hexanediol, mp 89°-90°C. After recrystallization the melting point was 90.5°-91°C. The pinacol has been prepared previously by Young and Roberts (5) and by Nazarov (6). The melting point reported was 91°-92°C.

All temperatures reported in this paper are uncorrected.

Preparation of cathodes.—Solid cathodes were cast in a cold mold and in a mold 50°C under the melting point of the metal. For other experiments they were electropolished. Zinc was electropolished in phosphoric acid-ethyl alcohol (9), cadmium in phosphoric acid-butyl alcohol (10), and lead in perchloric acid acetic anhydride (11). The solid cathodes were always anodized in 20% sulfuric acid before use except when electropolished.

Table I. Influence of temperature

Anode: lead; anolyte: 10% sulfuric acid; catholyte: 20g of diisopropyl ketone in 90g of a solution of 172.5 cc of conc. sulfuric acid, 600 cc of 95% ethyl alcohol and 203 cc of water (30% acid); current: 5 amp; current density: 0.05 amp/cm²; duration of run: 3¾ hr (theoretical for reduction of diisopropyl ketone to 2,4-dimethylpentane).

Cathode material	Temp, °C	Grams of 2,4-dimethyl pentane	Per cent yield of 2,4-dimethyl pentane	Grams of diisopropyl carbinol	Per cent yield of diisopropyl carbinol	Grams of 2,5-dimethyl-3,4-diisopropyl-3,4-hexanediol	Per cent yield of 2,5-dimethyl-3,4-diisopropyl-3,4-hexanediol
Zinc 370	55-60	2.8	16.0		49.3		
Zinc 370	55-60	3.0	17.1		41.0		
Zinc 370	55-60	2.6	14.7	8.5	41.9	0.2	1.0
Zinc 370	55-60	2.6	14.7	8.6	42.4	0.3	1.5
Zinc 370	25-30	3.2	18.4		48.7		
Zinc 370	25-30	3.1	19.0		49.3		
Zinc 370	25-30	2.7	15.3	9.0	44.1	2.3	11.4
Zinc 370	25-30	2.6	14.7	8.8	43.4	2.3	11.4
Cadmium	55-60	7.1	40.5		26.1		
Cadmium	55-60	7.8	44.5		33.4		
RT	55-60	6.7	38.4		31.4		
RT	25-30	6.3	36.0		34.4		
RT	25-30	6.1	35.0		31.9		
RT	25-30	7.2	41.1	7.4	36.4	1.0	5.0
RT	25-30	7.3	41.7	7.4	36.4	0.9	4.5
Cadmium 270	55-60	4.3	24.4	8.1	39.8	0.4	2.0
Cadmium 270	55-60	4.1	23.4	8.0	39.2	0.3	1.5
Cadmium 270	25-30	5.2	29.7	7.1	34.8	1.2	6.0
Cadmium 270	25-30	5.2	29.7	6.9	34.0	1.2	6.0
Mercury	55-60	3.4	19.1	0.5	2.5	Trace	
Mercury	55-60	3.1	17.7	0.6	3.0	Trace	
Mercury	25-30	1.6	9.0	0.5	2.5	Trace	
Mercury	25-30	1.8	10.1	0.6	3.0	Trace	
Lead 270	55-60	3.3	18.8	3.8	18.6	0.2	1.0
Lead 270	55-60	3.5	20.0	3.7	18.3	0.2	1.0
Lead 270	25-30	3.7	21.0	4.5	22.1	0.4	1.7
Lead 270	25-30	3.5	19.9	4.6	22.7	0.3	1.5

The number following the metal is the casting temperature. RT means at room temperature. No metallo-organic compounds were found.

Results and Conclusions

The results of the investigation are shown in Tables I and II and in the discussion, which follows.

The products of the runs in which yields of pinacol are reported were recovered by the second of the procedures previously described.

It will be noted in Table I that under strictly comparable conditions the yields of hydrocarbon and alcohol do not vary much with the temperature at cathodes of zinc, cadmium, and lead, but the yield of pinacol increases markedly at the lower temperature. The yield of hydrocarbon at mercury is, however, decidedly poorer at the lower temperature. It is interesting to note that in the one example of the relation of the effect of temperature with the physical structure of the cathode material, cadmium, and temperature seems to be the deciding factor in the formation of pinacol.

In the runs reported in all tables where no attempt was made to isolate the pinacol the temperatures were taken in the anolyte. In all others the temperature was that of the catholyte. Under the conditions of the experiments, there was little difference.

It may be seen in Table II and also with cadmium cathodes in Table I that the temperature at which the metal is cast had a marked effect on the yield, higher yields of hydrocarbon being obtained at metals cast in a cold mold and higher yields of alcohol at those cast 50°C under their melting points. The physical structure of the cathode had little effect on the yield of pinacol as previously indicated (temperature 25°-30°C, other conditions as in Table I).

Effect of electropolishing.—The most important effect of electropolishing the solid cathodes was the lowering of the yields of hydrocarbons about 8-10%. The yield of alcohol was unchanged at cadmium and

Table II. Influence of physical structure of cathode

Temp.: 25°-30°C. Other conditions as in Table I

Cathode material	Grams of 2,4-dimethyl pentane	Per cent yield of 2,4-dimethyl pentane	Grams of diisopropyl carbinol and ketone	Per cent yield of diisopropyl carbinol	Grams of 2,5-dimethyl-3,4-diisopropyl-3,4-hexanediol	Per cent yield of 2,5-dimethyl-3,4-diisopropyl-3,4-hexanediol
Zinc	5.1	29.6	6.5	32.0	1.3	6.5
RT, Set 1	5.3	30.2	6.7	33.0	1.9	9.5
Zinc	5.2	29.6	7.1	34.9	1.6	8.0
RT, Set 2	5.1	29.1	7.0	34.4	1.8	9.0
Zinc 370	2.2	12.5	9.0	44.3	1.9	9.5
Set 1	2.4	13.5	9.0	44.3	1.6	9.0
Zinc 370	2.7	15.3	9.0	44.3	2.3	11.4
Set 2	2.6	14.7	8.8	43.4	2.3	11.4
Cadmium	7.2	41.1	7.4	36.2	1.0	5.0
RT, Set 1	7.3	41.7	7.4	36.2	0.9	4.5
Cadmium	7.0	40.0	7.4	36.4	1.0	5.0
RT, Set 2	7.1	40.5	7.5	36.7	1.1	5.5
Cadmium 270	5.2	29.7	7.1	34.8	1.2	6.0
Set 1	5.2	29.7	6.9	34.0	1.2	6.0
Cadmium 270	5.5	31.4	7.4	36.4	1.0	5.0
Set 2	5.6	32.0	7.5	36.9	1.0	5.0
Lead	5.2	29.6	4.0	19.7	0.3	1.5
RT, Set 1	4.9	28.0	4.0	19.7	0.2	1.0
Lead	4.6	26.2	4.0	19.7	0.2	1.0
RT, Set 2	4.8	27.4	4.0	19.7	0.3	1.5
Lead 270	3.4	19.4	4.6	22.6	0.3	1.5
Set 1	3.7	21.1	4.4	21.6	0.4	2.0
	3.7	21.1	4.5	22.1	0.4	2.0
	3.5	19.9	4.6	22.6	0.3	1.5
Lead 270	3.6	20.5	3.6	17.8	0.3	1.5
Set 2	3.8	21.6	3.9	19.2	0.4	2.0
	3.2	18.2	4.0	19.5	0.3	1.5
	3.3	18.8	3.9	19.2	0.3	1.5

zinc, but was raised about 4% at lead. The yields of pinacol were lowered at the zinc and cadmium, but were unchanged at lead.

The high yields of hydrocarbons at cathodes cast in a cold mold and low yields at electropolished cathodes would indicate that the reduction to the hydrocarbon was favored by the presence of grain boundary material (temperature 25°-30°C, other conditions as in Table I).

Effect of acid concentration.—The effect of reducing the acid concentration from 30 to 10% was of significance only at a zinc cathode, the yield of hydrocarbon decreasing about 5% while the yield of the alcohol increased about 3% (temperature 55°-60°C, other conditions as in Table I).

Effect of current density.—Reductions were carried out at all cathodes at current densities of 0.02 and 0.05 amp cm^2; cadmium and zinc cathodes also at 0.1 amp/cm^2. The theoretical amount of current was allowed to flow. The effect of the current density varied considerably with the cathode material. Hydrocarbon formation was favored by current densities greater than 0.02 amp/cm^2 at all cathodes except lead at which the reverse was true. It is interesting to note that the formation of hydrocarbon from methyl propyl ketone at a lead cathode was also favored by low current densities (1). The yield of the alcohol was unaffected except at lead where a high current density was favorable. The effect of the current density on the yield of pinacol was important only at zinc, the best results being obtained at a low current density.

Formation of olefin.—The amount of olefin, presumably, 2,4-dimethyl-2-pentene, found as an impurity in the saturated hydrocarbon, was related to the cathode material. The average with zinc was 4, with cadmium 5, with mercury 10, and with lead 8 per cent by weight.

General Conclusions

The products of the electrolytic reduction of diisopropyl ketone were found to be 2,4-dimethylpentane, diisopropyl carbinol, 2,5-dimethyl-3,4-diisopropyl-3,4-hexanediol, and an olefin. The highest yield of hydrocarbon, 44.5%, was obtained at a cadmium cathode which had been cast in a mold at room temperature. The highest yields of the alcohol, 49.3%, and pinacol, 11.4%, were obtained at zinc cathodes cast in a mold 50°C below the melting point of the metal. The least active of the four cathodes was mercury, at which only a fair yield of hydrocarbon, a very small amount of the alcohol, and a trace of pinacol were obtained.

Decreasing the temperature of the catholyte caused a lowering of the activity of a mercury cathode but had little effect on the yields of hydrocarbon and the alcohol at the solid cathodes; higher yields of pinacol were obtained at the lower temperature.

The effect of acid concentration was appreciable only at a zinc cathode where the yield of hydrocarbon was greater at the higher concentration the reverse being true for the alcohol.

The effect of the current density was dependent on the cathode material. At cathodes of zinc, cadmium, and mercury, higher yields of hydrocarbon were obtained at higher current densities, the reverse being true at lead. The yield of alcohol was affected only at a lead cathode where it was favored by a high current density. Again, the yield of pinacol was affected only at zinc, with best results at a low current density.

The change in the physical structures of the solid cathodes due to casting in a cold mold or in a mold held 50°C under the melting point of the metal had an important effect on the course of the reduction. In all cases higher yields of hydrocarbon were obtained at cathodes cast in a cold mold while the reverse was true of the alcohol. The yields of pinacol were little affected by the change in physical structure. Electropolishing on the other hand brought about certain changes, the most important of which was the lowering of the yields of hydrocarbon.

The yields of products obtained in the electrolytic reduction of diisopropyl ketone were quite different from those with a typical straight chain ketone such as methyl propyl (1, 13). At cathodes of zinc and cadmium diisopropyl ketone was reduced to the hydrocarbon and to the alcohol in considerable amounts while the main product of the reduction of the straight chain ketone was predominantly the hydrocarbon. At cathodes of lead and mercury diisopropyl ketone was not reduced to the metallo-organic compounds which were found in the products of the reduction of the straight chain ketone.

Acknowledgments

Acknowledgments of gifts of metals for electrodes and for their casting have been made in previous papers. The authors are indebted to Dr. H. M. Kvalnes and Dr. K. B. Walker of the Experimental Station of the E. I. DuPont de Nemours Company for much of the diisopropyl ketone. The analysis of the pinacol was carried out by Mr. Jozsef Nemeth.

Manuscript received Feb. 15, 1963. This paper was presented at the New York Meeting, April 12-16, 1953.

Any discussion of this paper will appear in a Discussion Section to be published in the December 1966 JOURNAL.

REFERENCES

1. S. Swann, Jr. and J. Feldman, *Trans. Electrochem. Soc.*, **67**, 195 (1935).
2. J. P. Wibaut, H. Hoog, S. L. Langedijk, J. Overhoff, and J. Smittenberg, *Rec. trav. chim.*, **58**, 329 (1939).
3. S. Swann, Jr., *Trans. Electrochem. Soc.*, **62**, 177 (1932).
4. S. Swann, Jr., Chapter on electrolytic reactions in "Technique of Organic Chemistry. Vol. II. Catalytic Photochemical and Electrolytic Reactions," 2nd Ed., A. Weissberger, Editor, Interscience Publishers, Inc., New York (1956).
5. I. N. Nazarov, *Compt. rend. acad. sci. U.R.S.S.*, **4**, 288 (1934).
6. W. G. Young and J. D. Roberts, *J. Am. Chem. Soc.*, **66**, 1444 (1944).
7. F. C. Whitmore, *ibid.*, **64**, 1239 (1942).
8. R. L. Shriner and R. C. Fuson, "Identification of Organic Compounds," 3rd Ed., p. 260, John Wiley & Sons, New York (1948).
9. P. A. Jacquet, *Rev. gén. élec.* **54**, 239 (1945).
10. H. I. White (to American Rolling Mill Co.) U. S. 2,424,674, July 29, 1947.
11. P. A. Jacquet, *Bull. Soc. chim. France*, **53**, 750 (1936).
12. S. Swann, Jr., E. I. Onstott, and F. H. Baastad, *This Journal*, **102**, 113 (1955).
13. S. Swann, Jr., *Bull. Centr. Electrochem. Res. Inst. (Karaikudi)*, **2**, 6 (1955).
14. S. Swann, Jr. and J. Feldman, *Trans. Electrochem, Soc.*, **67**, 195 (1935).

An Ellipsometric Study of Steady-State High Field Ionic Conduction in Anodic Oxide Films on Tantalum, Niobium, and Silicon

L. Young and F. G. R. Zobel[1]

Electrical Engineering Department, University of British Columbia, Vancouver, British Columbia, Canada

ABSTRACT

The classical theory of ionic conduction in solids at high field strengths (10^6 to 10^7 v cm^{-1}) predicts that the relation between the ionic current density I and the field strength E should be $I = I_o \exp(-W(E)/kT)$ where the activation energy $W(E) = W_o - qaE$, q is the magnitude of the charge on the ions, a is half the distance between successive sites occupied by the ions, and I_o is a constant. Deviations from this supposed law have been reported in various forms. New experimental results for steady-state conditions are reported which were obtained by *in situ* ellipsometry. These confirm for tantalum and establish for the first time for niobium that the deviations may be simply and accurately described by taking the activation energy to be nonlinear in E in a way which may be represented over the experimental range of E by $W_o - q(\alpha - \beta E)E$. Data were also obtained for silicon, but were not sufficiently accurate to detect nonlinearity. Models are discussed which might give this effect. A model in which ions move fairly freely in channels with infrequent trapping by a coulombic potential leads to a law of the form $I = I_o \exp(-(W_o - \gamma E^{1/2})/kT)$, analogous to the Schottky and Poole-Frenkel laws for electronic currents. Such a law fits the data well enough for the model to be considered as realistic.

Anodic oxide films grow by a process of ionic conduction in the oxide at high field strengths (1, 2). The ionic current density defines the rate of increase of the thickness of the film. The purpose of the present experiments was to re-investigate the relation between the ionic current density, the field strength, and the temperature for films on tantalum and niobium, and to obtain such data for the first time for silicon, only the order of magnitude of the fields necessary to produce appreciable ionic current having been determined previously (3). The method used was to determine the thickness as a function of time by ellipsometry during anodization at constant potential. The field was then obtained from the potential with respect to the reversible oxide potential by dividing by the thickness of oxide. The ionic current density was obtained by calculating the rate of increase of thickness. With tantalum and niobium the optical measurements were made with the specimens still immersed in the solution (that is by *in situ* ellipsometry), but this could not be done with silicon because the refractive index of the oxide was too close to that of the solution.

It is difficult to give a brief account of the theory [which we have reviewed elsewhere (1, 2)] because no general agreement exists on a model which reproduces the complicated behavior of the ionic current under steady-state and transient conditions. It is usually considered that the problem is basically one of field assisted thermal activation of ions over potential energy barriers. The mobile ions are supposed to be deactivated after each jump. Consideration of the rate at which energy is supplied by the field to moving ions suggests that ions once mobile may traverse several minima and maxima of potential energy before being halted. The behavior of the current when a large field is suddenly applied suggests that some form of ionic avalanche multiplication process may occur under these circumstances (3).

In order to explain the transients, it appears to be necessary to construct a model in which the concentration of mobile ions is field dependent but responds slowly to a change in field. The model of Bean, Fisher, and Vermilyea (4) satisfies this requirement by postulating that two processes of ionic movement are involved. These are (*a*) the production of Frenkel defects by the movement of ions from lattice (or glass network) sites into interstitial sites, and (*b*) the mobility process of ions in interstitial sites. The transients may then be partially explained as due to a variation of the concentration of mobile ions. However the build-up of current when a large field is suddenly applied is definitely inconsistent with the treatment of this model according to the classical idea of field assisted thermal activation of ions over potential energy barriers.

The classical theory of ionic conduction at high field strengths [*cf.* Frenkel (5)] predicts a law of the form $I = I_o \exp(-W(E)/kT)$ where the activation energy $W(E) = W_o - qaE$ and where q is the magnitude of the charge on the ions, a is the average distance from minimum to maximum potential energy along the path of the ions (resolved along the field direction), I_o is a constant, k is Boltzmann's constant, and T is the absolute temperature. Thus qaE is the work done on the ion by the field as it travels from a minimum to the following maximum potential energy. The quantity a is sometimes called the activation distance and may include factors allowing for the effective field being different from the applied field (6) and for the effective charge being different from the valence charge or even varying with distance (7).

If both types of process postulated by Bean *et al.* obey this type of law, with destruction of Frenkel defects by a capture cross-section process of vacancies for interstitial ions, the steady-state kinetics are controlled by an expression of the same form as the classical expression but with the parameters representing averages of the values for the two processes.

The use of thin films allows an accurate test to be made of theories of conduction at high field strengths. This is hardly possible with bulk specimens. Deviations from the form of law predicted by Frenkel have been observed, starting with the work of Vermilyea [for references see (1), (2)]. These deviations were difficult to explain in the form which they were first thought to have, that is that $\partial E/\partial \log I$ was (as expected) independent of E at constant T but was almost independent of T under steady-state conditions (and even as was found later, decreased with increasing T under transient conditions) instead of being proportional to T as expected. Dewald proposed a theory to explain the steady-state kinetics in which a transition was supposed to occur (as space charge became effective in modifying the field) from control by the metal/

[1] Present address: Unilever Research Laboratory Port Sunlight, Cheshire, England.

oxide interface (Mott and Cabrera's model) to control by the bulk oxide [Verwey's model, if a modification of Dewald's postulates is made (1)]. This theory could not explain the transients, and it is now usually supposed that the process is one of conduction in the electrically neutral oxide. Bean, Fisher, and Vermilyea proposed a model for the high field production of Frenkel defects with a parabolic potential superimposed on a periodic potential energy *vs.* distance curve. This gave an activation distance for the production of Frenkel defects which was stepwise dependent on the field. Experimental results for the steady state required a field dependent pre-exponential factor to fit this model (8). Later, Vermilyea (9) was driven by consideration of the transient behavior to conclude that the oxide was modified structurally by the passage of current, a model which was not amenable to calculation. Winkel, Pistorius, and van Geel (10) considered that the existence in the amorphous oxide of a range of site parameters would explain the kinetics, but it was later shown that this idea was not sufficient (11).

On the basis of further experimental work, using an optical technique for the determination of the thickness, Young (11, 12) proposed that the best form of description of the experimental results both for steady-state and transient conditions ($\partial E/\partial \log I$ data) was obtained by writing $W(E) = W_o - q(\alpha E - \beta E^2)$, that is that the activation energy need not be linear in E (as has usually been taken to be the case in processes of this nature). Various physical processes could be considered *a priori* as possible causes of such an effect. This substitution gave an adequate phenomenological description of the steady-state $\log I$ *vs.* E data and of the transient data for $\partial E/\partial \log I$ for tantalum. It reduced the anomalies to a form which suggests an explanation not dependent on a transition between mechanisms. Dignam (13) observed similar effects with aluminum. His theory of the effect is discussed later. Dreiner (14), however, has recently obtained further experimental results for tantalum which confirm the original Frenkel law, in the sense that $\log I$ *vs.* E plots were linear. It was later realized that his values of $\partial \log I/\partial E$, although linearly dependent on $1/T$, do not extrapolate to zero at zero $1/T$, so that the Frenkel law was not observed accurately. (We thank Dr. Dreiner for a private communication on this point which we had missed.) In any case a further experimental test on tantalum was evidently required. The present experiments were extended to niobium since if the nonlinearity were established for three metals (tantalum, niobium, and aluminum) it could safely be concluded that it is basic and not due to fortuitous relations between parameters leading to some transition of mechanism or the like. Actually a transition between two mechanisms can hardly explain the results even for tantalum since there is no indication of two linear portions in the plots of $\log I$ *vs.* E but rather a smooth change of slope over the whole range of field. Measurements were also made on silicon, since according to Schmidt and Michel (3) the field strengths with this material are extremely high (10^7 v cm^{-1}) so that nonlinear effects should be increased. However, the scatter was too large to detect nonlinearity with silicon.

Experimental Procedure

The tantalum and niobium specimens were Fansteel material. They were 1.5 x 2.5 cm and 2 x 2.5 cm, respectively, with a tab, and were about 0.02 cm thick. They were prepared by abrasion on metallurgical papers followed by electropolishing as previously described (15). Anodization was carried out in 0.2N H_2SO_4. The experiments on silicon were carried out on p-type (111) oriented single crystal slices. Mostly the specimens had a resistivity of 0.094 ohm-cm, but some measurements were made on 0.006 ohm-cm material. The specimens were mechanically polished and then etched for 2 to 3 min in CP4A solution (5 parts concentrated HNO_3, 3 parts glacial acetic acid, and 3 parts of 49% HF, by volume). The etchant was quenched with 5% HF solution. Electrical contact was made to the silicon by means of a 0.005 in. diameter, chemically polished tantalum wire welded on the slice with an electron beam in vacuum. The silicon was then immersed briefly in CP4A, the weld and tantalum wire being kept from contact with the etchant, rinsed in 49% HF, washed well, and boiled for 30 min in deionized water to remove any adsorbed fluoride.

Anodization was carried out in a solution of N-methylacetamide saturated with KNO_3 at 32°C (about 0.05N). The N-methylacetamide was used as-received and appeared to be practically anhydrous (M.P. > 30°C). No special precautions were taken to prevent the absorption of water by the solution, but the anodizing cell was kept closed off from the air. The specimen was measured dry on the ellipsometer, since the similar refractive indices of N-methylacetamide (1.43) and anodic silicon dioxide (1.47) make *in situ* ellipsometry impractical. For similar refractive indices of oxide and immersion medium, a very small ψ, Δ loop is obtained which makes thickness determination inaccurate. The same difficulty applies to some of the other nonaqueous solvents in which silicon may be anodized, *e.g.*, ethylene glycol and tetrahydrofurfuryl alcohol. For dry examination the niobium and tantalum were anodized in a cell similar to that described previously (15). For *in situ* examination they were mounted in a specially constructed glass cell as shown in Fig. 1a, which was attached to the specimen platform of the Gaertner L119 ellipsometer. The light beam entered and left through windows made by sealing optical flats on the side arms. A constant temperature was maintained by circulating water from a thermostatted bath through the double wall of the cell. The specimen was held between stubs of tantalum wire inserted into two pieces of Teflon which were held together by a screw at their upper ends as shown in Fig. 1b. Electrical contact to the specimen was made through one of the tantalum wire stubs.

The calibration of the ellipsometer (16) and its application to anodic oxide films on tantalum (17) have been described in detail previously. The incident light is considered to be resolved into two components, p-light with the electric vector in the plane of incidence, and s-light with the electric vector perpendicular to the plane of incidence. If R_p and R_s are the complex reflectivities for p- and s-light, respectively, the quantities ψ and Δ are defined by $|R_p/R_s| = \tan \psi$ and $\arg R_p/R_s = \Delta$.

The analyzer and polarizer Glan-Thompson prisms were set for extinction, a quarter wave plate being

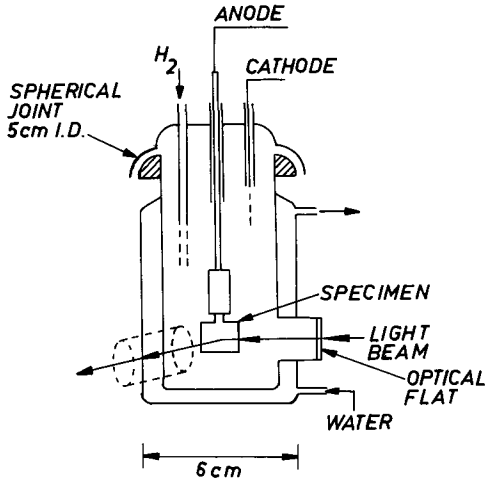

Fig. 1a. Water-jacketted cell for *in situ* ellipsometry

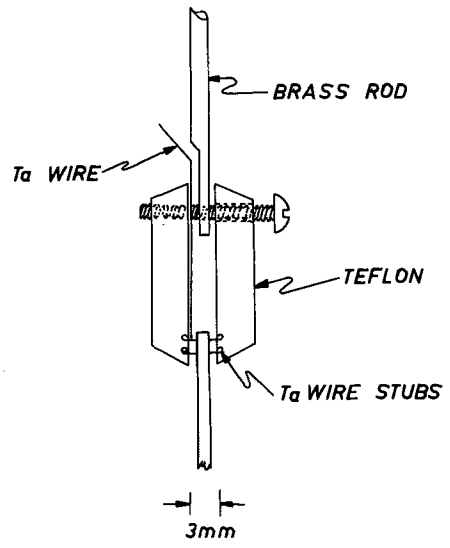

Fig. 1b. Device for supporting specimens

set at ± 45° azimuth. The detector was a photomultiplier (RCA 931A) coupled to an amplifier tuned to the frequency of the chopped light. The ellipsometer was enclosed in a box to minimize stray light. The quantities ψ and Δ are derived directly from the settings of the analyzer and polarizer prisms. Several sets of readings may be obtained, which may be classified into zones according to the scheme given by McCrackin, Passaglia, Steinberg, and Stromberg (16). The calibration appears to be a more critical matter than is sometimes made clear. The scheme of McCrackin *et al.* was followed. Specimens were exchanged with other workers in this field, and it was found that the agreement was not as good as would be expected from the precision with which readings may be taken, being only to about 0.2° in ψ and 1.2° in Δ.

For measurements *in situ* it was found advisable to make measurements in all four zones. This was found to minimize the small errors due to the polarization of the light by the cell windows. The windows are, of course, the same throughout, but the state of polarization of the light incident on them is changed with the zone. Measurements on the same specimen (dry) inside and outside the cell gave adequately concordant results.

For a discussion of the question of variation of optical constants with angle of incidence reference is made to a paper by Hall (18).

Results for Tantalum

Determination of the optical constants.—Data on ψ and Δ *vs.* the angle of incidence are not included here but are available for comparison by anyone wishing to reproduce these experiments.

The optical constants were obtained by trial and error fitting of the experimental and calculated curves. Figure 2 shows ψ *vs.* Δ for tantalum anodized at 8 ma cm^{-2} in 0.2*N* H_2SO_4 at 25°C and examined dry. Measurements were made at 5461Å and at an angle of incidence of 67.5° using a quarter wave plate as compensator. (A Soleil-Babinet compensator set as a quarter wave plate gave indistinguishable results.) The calculated curve was fitted to the experimental points using the constants $n_2 = 3.30 \pm 0.02$, $k_2 = 2.30 \pm 0.05$ for the metal ($\bar{n} = n - ik$) and $n_1 = 2.22 \pm 0.02$ for the oxide. The uncertainties are obtained by comparison of the experimental points with curves calculated from slightly different optical constants.

The Hartmann equation reported by Young (19) for films formed at 25°C and 10 ma cm^{-2} was $n_1 = 2.14 + 0.292/(\lambda/10^3\text{Å} - 2.305)^{1.2}$. This gives 2.21 for

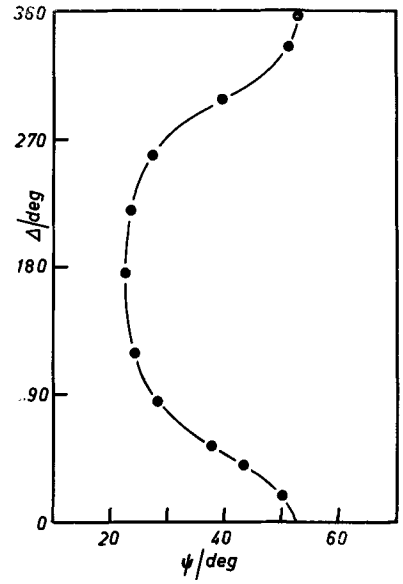

Fig. 2. Ellipsometry data for tantalum at 5461Å, angle of incidence 67.5° for specimen measured dry. The curve is calculated with $n_1 = 2.22$, $n_2 = 3.30$, and $k_2 = 2.30$.

the oxide refractive index at 5461Å in good agreement with the present estimate. Young's values were based on a value of n_1 in sodium light determined by the Becke method using S/Se mixtures plus dispersion data from interferometric measurements. Masing, Orme, and Young (15) found that the refractive index determined by a modification of a method due to Abelès was just detectably dependent on the current density and temperature at which the oxide was made. A direct comparison with their values is not possible because their work was at 4358Å, but using the dispersion relation given by Young to convert to 5461Å the agreement is satisfactory. Kumagai and Young (17) fitted their ellipsometric data for tantalum anodized in 0.2*N* H_2SO_4 at 25°C and 1 ma cm^{-2} using $n_2 = 3.5$, $k_2 = 2.4$, and $n_1 = 2.26$ at 5461Å.

The deviations of the experimental points from the calculated curve are shown in Fig. 3, which was plotted assuming that the errors occur entirely in Δ or entirely in ψ. The shape of the curve causes the deviations in Δ to appear rather large, but probably

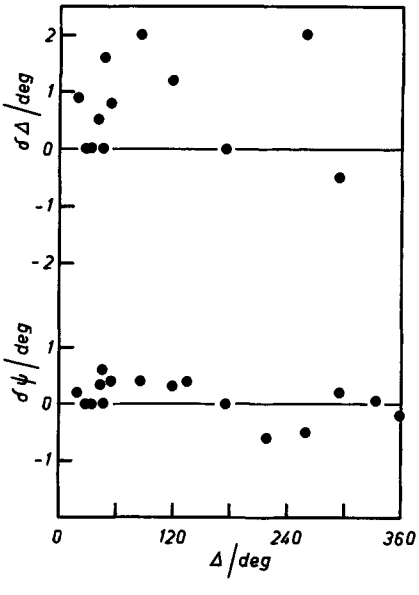

Fig. 3. Deviations of the experimental points in Fig. 2 from the fitted curve, assuming error lies entirely in Δ or in ψ respectively.

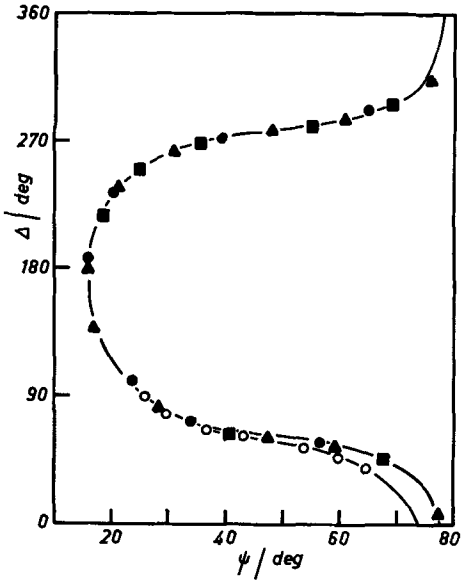

Fig. 4. Ellipsometry data (*in situ*) for tantalum at 5461Å, angle of incidence 67.5°. •, ■, ▲, first, second, and third cycles of curves at 25°C for which $n_0 = 1.334$ and the other constants as in Fig. 2. O data at 60°C, $n_0 = 1.329$, $n_1 = 2.27$.

the deviations in ψ are more meaningful. The mean deviation in ψ is 0.27°.

ψ, Δ curves measured during the anodization of tantalum specimens *in situ* at 25° and 60°C are shown in Fig. 4. The same angle of incidence and wavelength were used as for the dry measurements. The refractive index of the solution was taken as $n_0 = 1.334$ at 25°C and 1.329 at 60°C. The curve at 25°C was fitted using the same optical constants for the metal and oxide as the "dry" curve, but at 60°C, an oxide refractive index of 2.27 was used (with the same constants for the metal). The experimental points are shown for 3 cycles of the 25°C curve lie on a single curve. This demonstrates that within the thickness range studied (about 3700Å) the optical constants do not alter appreciably. The deviations of the experimental points from the calculated curve are shown in Fig. 5.

Steady-state formation kinetics (tantalum).—In order to obtain the kinetics of the oxide growth, specimens were first anodized to at least 90v at a constant

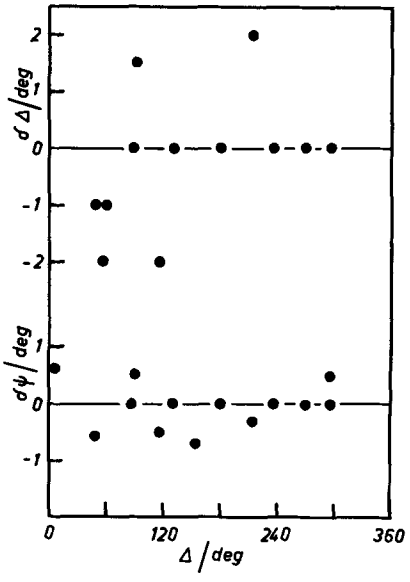

Fig. 5. Deviations of the experimental points from the fitted curves at 25°C for Fig. 4.

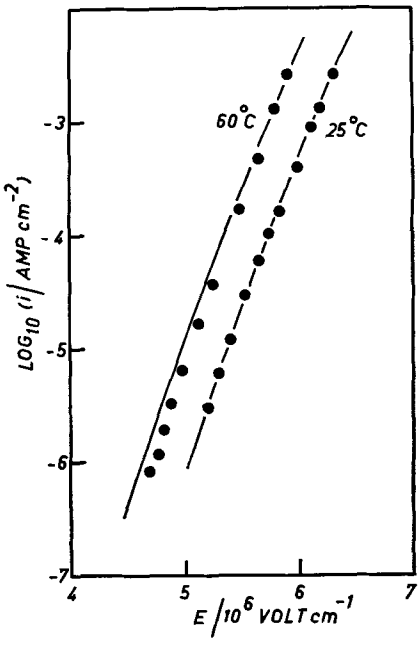

Fig. 6. Tafel plot for tantalum. Points, this paper; lines, calculated from constants given by Young (11) corrected to n_1 (5461Å) = 2.22.

current of about 10 ma cm^{-2} and then held at constant voltage with respect to a small platinum wire (0.7 x 0.05 cm diameter) cathode, the current being allowed to decay as the thickness increased. A small cathode gives a more constant potential than a large cathode. All measurements were carried out with the specimen *in situ*. The applied voltage was measured with a digital voltmeter. The solution was kept saturated with hydrogen. Measurements were made at 25° and 60°C. At suitable intervals the current was interrupted and the thickness measured. A sufficiently long time was allowed between interruptions so that approximately steady-state conditions were observed. Switching at the shorter intervals of time (less than 1 min) was accomplished by means of an electronic timer. The longer times were measured with a stopwatch, and the circuit was then broken manually.

The resulting values of thickness *vs.* $\log_{10}$ (time) were fitted by a smooth curve and differentiated using an IBM 7040 computer. The approximation made by Dreiner is not necessary. Results were checked by graphical differentiation. The ionic current is obtained from the rate of increase of thickness by applying Faraday's law: $I = (10\ F\rho/M)\partial D/\partial t$ where I is the ionic current per unit area, t is the time, F is Faraday's constant, ρ is the density, M the molecular weight, and D the thickness of the oxide.

The potential of the cathode was measured relative to a Pt/H_2 electrode in the same solution for currents over the range used. The ohmic potential drop across the solution was also determined over this current range. The electric field in the oxide was taken as $E = V/D$, where V is the potential of the tantalum in excess of the reversible potential for oxide formation (1).

The so-called Tafel plots of log I *vs.* E are shown in Fig. 6. The smooth curves were calculated from the constants used by Young (*11*) to fit his experimental results. The agreement is mostly within 1% in the field when both sets of data are brought to the same refractive index basis.

Figure 7 shows $T\Delta\log_{10}I/\Delta E$ (where $\Delta\log_{10}I = 1$) *vs.* mean field. This plot emphasizes the nonlinearity of the log I *vs.* E relation and shows that, although the curvature of plots of log I *vs.* E may appear small to the eye, it is large compared to experimental uncertainties.

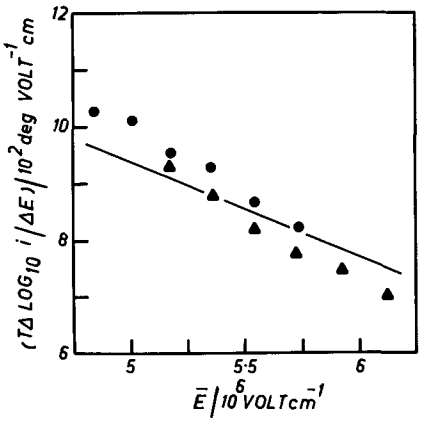

Fig. 7. $T\ \Delta \log_{10} I/\Delta E$ for $\Delta \log_{10} I \simeq 1$ for data of Fig. 6. The line corresponds to the equation fitted by Young to his data. ▲, 25°C; ●, 60°C.

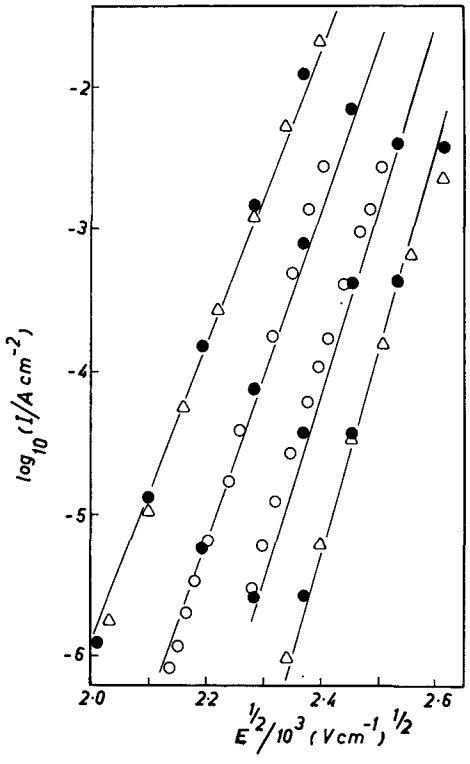

Fig. 8. Schottky-type plot: (*i*) O data from Fig. 6 converted to refractive index used by Young (19, 11); (*ii*) ●, points calculated from equation with $W(E) = W_0 - q\alpha E + q\beta E^2$ fitted by Young; and (*iii*) Δ experimental data of Vermilyea [(8) plus private communication of tabular data] converted by factor 7.93 x 0.99/8.74 to allow for assumed density. The straight lines are calculated from $I = I_0 \exp((-W + \gamma E^{1/2})/kT)$ with $I_0 = 10^{8.05}$ Acm^{-2}, $W = 2.56$ ev, and $\gamma = 7.65 \times 10^{-4}$ ev/(v cm^{-1})$^{1/2}$.

It is of interest (see Discussion) to test the equation $I = I_o \exp[-(W_o - \gamma E^{1/2})/kT]$. Figure 8 shows that this expression represents the data quite well, certainly better than the Frenkel law. This "Schottky" expression contains one less adjustable parameter than the expression with $W = W_o - q\alpha E + q\beta E^2$, and it cannot, therefore, be expected to give so good a fit as this expression.

Figure 8 also serves to compare the data of Vermilyea (8), Young (11), and the present paper. All have been brought to the same basis of thickness determination. (Vermilyea's data were based on an assumed value of the density which later work has shown to be about 10% too high). Evidently the agreement is excellent.

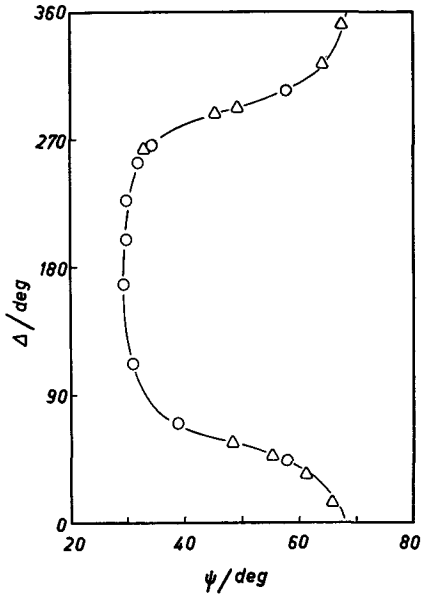

Fig. 9. Ellipsometry data at 5461Å and 67.5° angle of incidence for niobium measured dry. The curve is calculated from $n_1 = 2.37$, $n_2 = 3.60$, and $k_2 = 3.60$. 0, first cycle; Δ, second cycle.

Results for Niobium

The procedures and the general nature of the results were very similar to those for tantalum. The formation voltage was, however, 60v at 25°C and 40v at 75°C since niobium does not behave so ideally as tantalum at higher voltages.

The optical constants of the metal were determined by fitting curves for specimens measured dry. They were $n_2 = 3.60 \pm 0.05$ and $k_2 = 3.60 \pm 0.05$ for the metal and $n_1 = 2.37 \pm 0.02$ for the oxide. The oxide index agreed within experimental error with that calculated for this wavelength 5461Å from the dispersion curves given by Young (20), obtained by a spectrophotometric method with scaling using an absolute value determined using a modification of a method due to Abelès by Masing, Orme, and Young (15).

Figure 9 shows ellipsometric data for immersed specimens anodized and measured at 25°C. The data

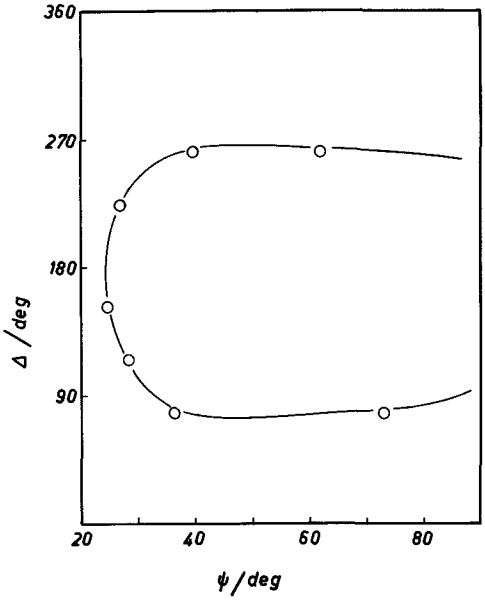

Fig. 10. Ellipsometry data *in situ* for niobium. The curve is calculated with $n_0 = 1.334$ and the other constants as in Fig. 9.

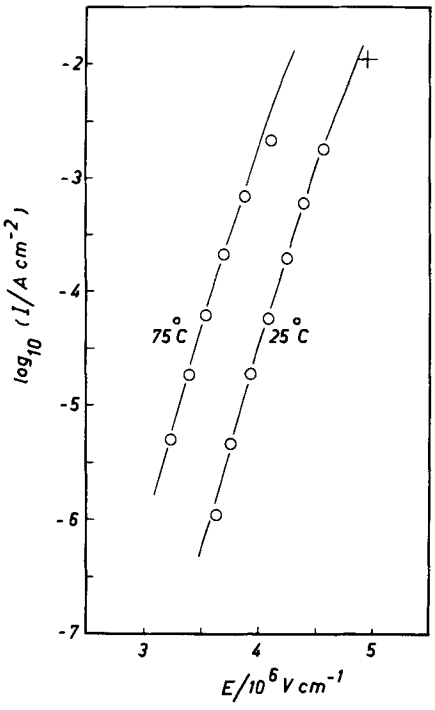

Fig. 11. $\log_{10} I$ vs. E for niobium. The curves are the fitted equation (see text).

at 75°C were of equivalently good fit to the curves using the optical constants determined from measurements on dry specimens. The index of the solution was taken as 1.334 at 25°C and 1.320 at 75°C.

Figure 11 shows plots of $\log_{10} I$ vs. E. The values of the current density were obtained from $\partial D/\partial t$ using density 4.74g cm^{-3} (21). Figure 12 shows $T\Delta \log_{10} I/\Delta E$ vs. mean field. The line in Fig. 12 and the curves in Fig. 11 correspond to the fitting equation

$$I = 10^{7.24} \exp\left(-\frac{2.168ev}{kT}\right) \exp\left(\frac{e(10.74 \times 10^{-8}cm - 8.36 \times 10^{-15}volt^{-1}cm^2 E)E}{kT}\right) Acm^{-2}$$

The constants in this equation are quoted with sufficient accuracy to reproduce the data. If they are given some physical interpretation, they cannot be regarded as determined to the number of decimals quoted since they are not independent. Figure 11 also contains a single point determined by the spectrophotometric method for the thickness (20). This is in good agreement. An earlier investigation of the anodic oxide films on niobium (22) gave a nonlinear relation which was interpreted in terms of Dewald's theory, and the present simpler description was not tested. It is hardly necessary to demonstrate that the Schottky law fits quite adequately. Plots of log I vs. $E^{1/2}$ are again certainly more linear than the Frenkel type of plot, log I vs. E. The above equation again gives a better description, but this is because it contains an extra adjustable parameter.

Results for Silicon

The ellipsometric method is particularly useful for silicon because with this material the ionic current is only a very small fraction of the total current as contrasted with tantalum and niobium with which the ionic current constitutes nearly all the current, despite the high field strengths.

The experimental ellipsometry data were fitted by curves calculated using Archer's values (23) for the optical constants of silicon $n_2 = 4.05$ and $k_2 = 0.028$ with the oxide refractive index taken as $n_1 = 1.475 \pm 0.005$. Claussen and Flower (24) found $n_1 = 1.468 \pm 0.003$ for silicon anodized in 0.0025N KNO_3 in anhydrous N-methylacetamide.

Log I vs. E for a number of experiments is shown in Fig. 13. The line is $I = 10^{-14} \exp(10^{-6}\ cm\ v^{-1}\ E)\ Acm^{-2}$. The activation distance is only very roughly determined by the data, and there is no question of deciding whether or not curvature is present. The data suggest an activation distance of 0.6 to 1.5Å.

Discussion

The form $W = W_o - q\alpha E + q\beta E^2$ was first proposed (11, 12) as an empirical equation but with the basic assumption in mind [ref. (12), p. 406] that some form of nonlinearity in $W(E)$ was to be expected at high field strengths and that no transition with increasing field between two mechanisms was required to give a nonlinear relation between log I and E. If the free energy of activation is expanded in powers of E, one should expect that sufficiently accurate measurements will require the inclusion of terms of higher order than the first power. Various sources of such an effect were discussed, including the nature of the potential energy vs. distance relation. (The model with high curvature at the minimum and a sinusoidal maximum was correctly shown to give too small an

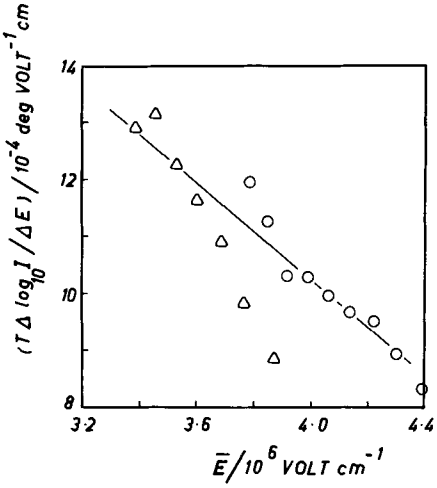

Fig. 12. $T\Delta \log_{10}/\Delta E$ vs. mean E for $\Delta \log_{10} I = 1$ for data of Fig. 11. The line corresponds to the fitted equation. 0, 25°C; Δ, 75°C.

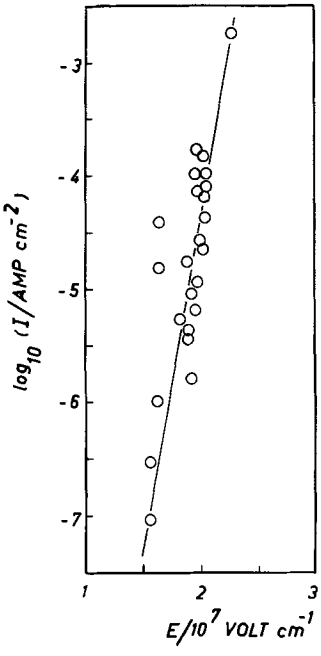

Fig. 13. $\log_{10} I$ vs. E for silicon

effect, but the statement about mirror symmetry was an error.) A physical mechanism was later proposed (25) which gives the observed type of effect and which has the decided advantage that it must occur to some extent. This is that the activation energy will increase due to the compression of the lattice which must occur on application of an electric field. The compression will be proportional to the square of the field. Dignam (7) has criticized this theory on the grounds that the data of Jost [cf. (26)] for halide crystals which were quoted as indicating the correct order of magnitude give only 1/20 of the required effect (which would still seem to satisfy the "order of magnitude" description). However, the present materials are open glassy structures of low density which may reasonably be expected to give larger effects than halide crystals. A direct test of the theory by applying pressure was unsuccessful due to experimental difficulties.

Dignam proposed instead that the effects were due to the form of the potential energy *vs.* distance relation, seen by the mobile ion in moving from one site to the next. Dignam expanded $W(E)$ in powers of E for three P.E. curves: a clipped parabolic function, a sinusoidal function, and a Morse function: P.E. $= W_o[1 - \exp(x/L)]^2$ in our notation, where x is distance, and L a constant. He found that the first two functions gave an inadequate effect, but that the Morse function fitted data for tantalum, niobium, and aluminum very well. His conclusion was that the curvature "arises quite naturally from a more detailed analysis of the ion transfer process at high fields." This would seem to be misleading. We suggest that what Dignam has done is to show that, if the observed curvature is to be explained entirely in terms of the P.E. *vs.* distance relation function, this function must approximate to the shape of a Morse function. Such a function does not seem to be applicable quite as generally as Dignam suggests. In effect, it suppresses any periodic nature of the material. The position of maximum energy at zero field is at infinity. In a crystalline material one would surely expect that the peaks in the potential energy curve would be relatively sharp so that an applied field would not move them very far. A model to which the Morse function is more appropriate is as follows. We suppose that ions move fairly freely in channels through the labyrinthine open structure of these films, but may become trapped by coulombic attraction at pockets of excess negative charge which will be present, due to the random nature of the glassy structure, at infrequent places along the channels.

With this model the transients might arise from a variation of the proportion of trapped ions and from the building of queues at blocks in the channels. The accelerating build-up of current when a large field is suddenly applied could be due to the clearing of jams by rapidly moving ions. The ions would acquire greater velocity and hence be more effective as the process continued. The obvious and simplest way to treat the above model is in fact not to assume a Morse function but to assume that except very near to the traps the attraction between the mobile ions and the trapping centers in coulombic. With an applied field E we have P.E. $= -A/x - qEx$ (where A is a constant and x is the distance along the path of the ion). A derivation analogous to that of the Schottky law for high field emission of electrons from metals or to that of the Poole-Frenkel law for high field liberation of electrons from traps leads to $I = I_o \exp(-W_o/kT) \exp(\gamma E^{1/2}/kT)$ where γ is a constant. We should perhaps not expect γ to have the value $q_2 q_1^{1/2}/(\epsilon\epsilon_o\pi)^{1/2}$ (M.K.S.) predicted by the above treatment (where $q_1 = z_1 e$ = charge on trap, $q_2 = z_2 e$ = charge on mobile ion, and ϵ = dielectric constant) since, as in the model of Bean, Fisher, and Vermilyea, the steady-state parameters will include an allowance for the change in concentration of mobile ions with field. However, we have shown elsewhere (2) that the transient $\partial \log I/\partial E$ data for tantalum also fit a Schottky law and that the slope is consistent with $z_1 = z_2 = 1.4$. It should perhaps be mentioned that the Schottky form of law was tested as an empirical law by Güntherschulze and Betz (27) and again by Charlesby (28).

A later paper by Dignam (29) presents a radically new approach in which the amorphous nature of the oxide is brought fully into play. However, it need not be discussed in relation to the present results since the feature which reproduces the nonlinearity of $W(E)$ is again the use of a Morse function potential energy.

A further difficulty is presented by the tracer experiments of Davies, Pringle, and their collaborators [*e.g.*, (30), reviewed in (2)]. These experiments appear to show that both metal and oxygen ions move to about equal extents in the oxide films on tantalum, niobium, and aluminum. As has been noted before by various authors in connection with various theories which required similar coincidences, it is unlikely that both ions should move to similar extents if their motions are independent, since even a slight difference of activation energy or activation distance should prevent this. Dignam (29) explained this result in terms of a reorganization which he supposed will occur in the individual mosaic blocks (which he postulated are present in the structure of the oxide) each time they receive an extra ion, because of the disturbance of the dipole moment of the mosaic blocks and because of the comparatively large amount of energy which the mobile ions will pick up from the field and hand over to the mosaic block on arrival. Vermilyea (in a private communication) suggested that when a metal ion breaks loose from the network the neighboring oxygen ions will also tend to be freed. Some such *ad hoc* assumption seems the only way at present to fit the mobility of both ions, if it is accepted, into the theory.

Acknowledgment

This work was supported by the Defence Research Board of Canada (E.C.R.D.C. T65A).

Manuscript received Aug. 2, 1965; revised manuscript received Nov. 29, 1965.

Any discussion of this paper will appear in a Discussion Section to be published in the December 1966 JOURNAL.

REFERENCES

1. L. Young, "Anodic Oxide Films," Academic Press, London and New York (1961).
2. L. Young, F. G. R. Zobel, and W. S. Goruk, "Ionic and Electronic Currents at High Fields in Anodic Oxide Films," to be published in "Modern Aspects of Electrochemistry," Vol. IV, J. O'M. Bockris, Editor, Butterworths, London.
3. P. F. Schmidt and W. Michel, *This Journal*, **104**, 230 (1957).
4. C. P. Bean, J. C. Fisher, and D. A. Vermilyea, *Phys. Rev.*, **101**, 551 (1956).
5. J. Frenkel, "Kinetic Theory of Liquids," Dover Publishing Inc., New York (1955).
6. L. Young, *Trans. Faraday Soc.*, **50**, 153 (1954).
7. M. J. Dignam, *Can. J. Chem.*, **42**, 1155 (1964)
8. D. A. Vermilyea, *This Journal*, **102**, 655 (1955).
9. D. A. Vermilyea, *ibid.*, **104**, 427 (1957).
10. P. Winkel. C. A. Pistorius, and W. Ch. van Geel, *Philips Research Rept.*, **13**, 277 (1958).
11. L. Young, *Proc. Rou. Soc.*, **A258**, 496 (1960).
12. L. Young, *ibid.*, **A263**, 395 (1961).
13. M. J. Dignam, D. G. W. Goad, and M. Sole, *Can. J. Chem.*, **43**, 800 (1965).
14. R. Dreiner, *This Journal*, **111**. 1350 (1964).
15. L. Masing, J. E. Orme, and L. Young, *ibid.*, **108**, 428 (1961).
16. F. L. McCrackin, E. Passaglia, R. R. Stromberg, and H. A. L. Steinberg, *J. Res. Nat. Bur. Stand. A*, **67**, 303 (1963).
17. S. Kumagai and L. Young, *This Journal*, **111**, 1411 (1964).
18. A. C. Hall, *J. Opt. Soc. Amer.*, **55**, 911 (1965).
19. L. Young, *Proc. Roy. Soc.*, **A244**, 41 (1958).

20. L. Young, *Can. J. Chem.*, **38**, 1141 (1960).
21. A. J. Schrijner and A. Middlehoek, *This Journal*, **111**, 1167 (1964).
22. L. Young, *Trans. Faraday Soc.*, **52**, 502, 515 (1956).
23. R. J. Archer, *J. Opt. Soc. Amer.*, **52**, 970 (1962).
24. B. H. Claussen and M. Flower, *This Journal*, **110**, 983 (1963).
25. L. Young, *ibid.*, **110**, 589 (1963).
26. W. Paul and D. M. Warschauer, Editors, "Solids under Pressure," McGraw Hill Co., New York (1963).
27. A. Güntherschulze and H. Betz, *Z. Phys.*, **92**, 367 (1934).
28. A. Charlesby, *Proc. Phys. Soc.*, **B66**, 317, 533 (1953).
29. M. J. Dignam, *This Journal*, **112**, 722 (1965).
30. J. A. Davies, J. P. S. Pringle, R. L. Graham, and F. Brown, *ibid.*, **109**, 999 (1962).

The Characterization of Anodic Aluminas

III. Barrier Layer Composition and Structure

G. A. Dorsey, Jr.

Department of Metallurgical Research, Kaiser Aluminum & Chemical Corporation, Spokane, Washington

ABSTRACT

High-purity aluminum sheets were anodized in both sulfuric and deuterosulfuric acid electrolytes. The anodic coatings from each electrolyte were analyzed by infrared to determine the composition and nature of the anodic barrier layer. We found that deuteration of the alumina lowered the absorption frequency of the 900-1000 wavenumber barrier layer band and also reduced the amount of both the porous layer Al = O and barrier layer. We conclude, from these data, that the barrier layer is a trihydrate. The primary phase of the barrier layer, as obtained initially or by boric acid anodizing, may be a cyclic aluminic acid trihydrate. A secondary barrier phase may be a decyclized form of the primary, having more terminal groupings and a lower polymer weight.

Previous studies have shown that the infrared absorption of the barrier layer distinguishes it from the porous layer even when the two layers are present together within the same film (1). The following correlation chart was derived from this preliminary work; the absorption band belonging to the barrier layer is included.

Alumina bond type	Infrared absorption frequency range, wavenumbers
AlO↔H stretch	3660-2940
Al<=>O stretch	1696-1345
Al↔OH bend	1162- 900
(Monohydrates near 1070 cm^{-1}, while trihydrates below 1025 cm^{-1})	
(Barrier layer	1000- 900)
Al↔OAl stretch	Below 900

Barrier layers, then, always exhibit an absorption band within only a narrow region of the infrared spectrum, a region normally ascribed to alumina trihydrates. A barrier layer formed by boric acid anodizing has only one absorption band within the 4000 to 33 cm^{-1} range (1), a band near 950 cm^{-1}. Further, the barrier layer was found to change during the course of anodizing, as the growth of the porous layer was first initiated and then accelerated (2). Quantitative infrared analyses revealed that the absorption band defining the barrier layer tended to shift toward higher frequencies as the amount of porous layer increased. A frequency shift in this direction normally corresponds to a conversion from a high polymer weight to a series of lesser polymers.

The primary objective of the present study was to establish whether or not the anodic barrier layer is truly hydrated. The barrier layer infrared absorption band is within the alumina trihydrate region; however, alumina hydrates also normally have a second series of bands located in the higher frequency region near 3400 cm^{-1}. Barrier layers do not have infrared bands in this region or at least not until the barrier layer 1000-900 cm^{-1} band has shifted, indicating an alteration in the structure of the barrier layer. This presents an anomaly. If the barrier layer is truly an alumina hydrate, then some irregularity of structure has caused the AlO ↔ H stretch band to disappear, or, as with hydrogen bonding, the band could be broadened to such an extent that it cannot be located.

Frequently, structures involving hydrogen can be elucidated by replacing the abundant hydrogen with one of its isotopes: here, deuterium was substituted for protium. The mass of the deuterium ion is twice that of protium, and the increase in the reduced mass of a deuterated system causes a reduction in the wavenumber of absorption bands involving hydrogen. A comparison of the infrared spectrum of the protonated material with that of the deuterated compound reveals those bands that involve structural hydrogen; these bands will have shifted to lower frequencies as a result of the isotopic mass effect.

Accordingly, we attempted to determine the composition of the barrier layer by anodizing in deuterium oxide (heavy water) solutions of deuterosulfuric acid. Parallel anodizing studies were also made in protonated systems of sulfuric acid.

Experimental

Anodic aluminas.—Cleaned 99.99% aluminum sheets were used as the substrate material for the samples prepared. The two electrolyte systems were prepared as described below and were verified by titration before proceeding further.

1. Deuterated system: 1.0*N* deuterosulfuric acid in heavy water. Both reagents were obtained from Diaprep, Inc. of Atlanta and were reported to be more than 99% deuterated.

2. Protonated system: 1.0N sulfuric acid in distilled water.

Both electrolytes were used with a 1.08 amp/dm^2 current density for 5.0 min. Anodizing temperatures were varied to cover the region between 10° to 45°C. The samples were not sealed after anodizing.

Infrared analysis.—The samples were examined, as before (1), over the 4000-600 cm^{-1} range of the Beckman IR-7. The flat anodized sheets were mounted in the sample stage of a C.I.C. ATR-1 reflectance attachment at a 45° angle of incidence. Double beam spectra were obtained *vs.* a front-surfaced aluminized mirror, which was mounted the same as the sample.

Quantitative determinations were made using a weight method of graphical integration. Checks showed that precision, using this method, was within ± 1.3%. The IR-7 was operated with a slit program and gain settling yielding an unloaded SB/DB ratio of 1.5; speed and period were adjusted for each sample so that the instrument response was adequate.

Results and Discussion

As was done earlier (2), we chose to identify the porous component of the sulfuric acid anodic coating with an Al=O band occurring at 1325 wavenumbers. Sulfuric-anodized films also show a probable sulfate band near 1150, but the absorbance of this band could be altered by both anodically incorporated and free residual sulfate. Changes in the absorbance of the Al=O band should be caused only by changes in the amount of porous coating. We recognize that a one-to-one correlation has not been established between the Al=O absorbance and the "amount" of porous layer (2). Further, the concentration of this bond group may vary with the thickness of a porous layer. Pending further work, we will refer only to the amount of porous layer Al=O, or to the apparent amount of porous layer, and not to the "amount" of porous layer itself.

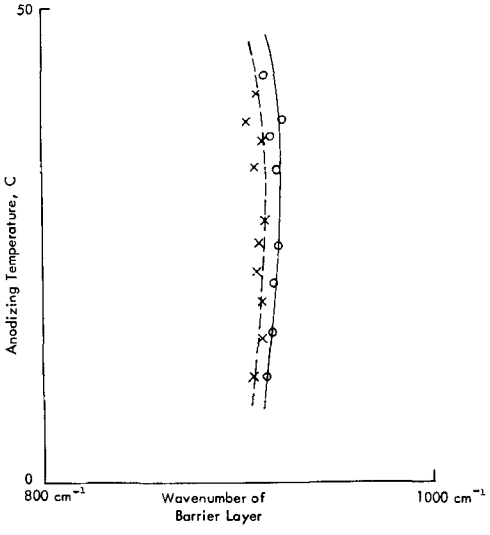

Fig. 1. Anodizing temperature *vs.* wavenumber of barrier layer. ○, 1.0*N* H_2SO_4, 1.08 amp/dm^2, 5 min; X, 1.0*N* D_2SO_4, 1.08 amp/dm^2, 5 min.

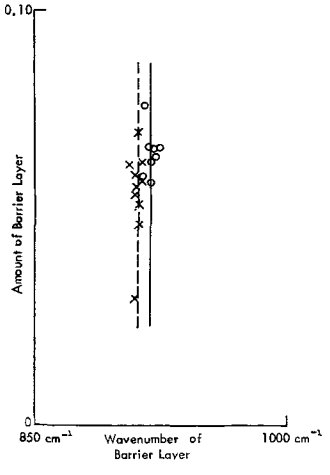

Fig. 2. Amount of barrier layer *vs.* wavenumber of barrier layer. ○, 1.0*N* H_2SO_4, 1.08 amp/dm^2, 5 min; X, 1.0*N* D_2SO_4, 1.08 amp/dm^2, 5 min.

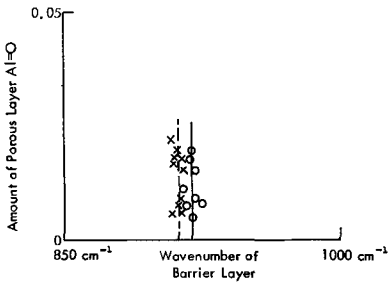

Fig. 3. Amount of porous layer Al=O *vs.* wavenumber of barrier layer. ○, 1.0*N* H_2SO_4, 1.08 amp/dm^2, 5 min; X, 1.0*N* D_2SO_4, 1.08 amp/dm^2, 5 min.

The amount of barrier layer was determined from the absorbance of the band lying within the region of from 900 to 1000 cm^{-1}.

Figures 1, 2, and 3 clearly show the effects of deuteration on the barrier layer. The infrared absorption band of the barrier layer was at a lower frequency when the barrier layer was prepared in a deuterated system than it was when prepared in a protonated system. The difference between protonated and deuterated systems is apparent regardless of the anodizing temperature (Fig. 1), the amount of barrier layer (Fig. 2), or the apparent amount of porous overlayer (Fig. 3). When prepared under the same conditions, the barrier layer absorption was at 920 cm^{-1} for the protonated system and 912 cm^{-1} for the deuterated system.

We also found that deuteration changed the apparent amount of porous coating obtained at different anodizing temperatures. The deuterated system required a higher anodizing temperature to produce the same apparent amount of porous coating as that produced in the protonated system (Fig. 4). Deuteration produced a similar change in the relation between the barrier layer and the electrolyte temperature (Fig. 5).

Reactions involving deuterium generally proceed at slower rates than those involving hydrogen, and the extent of chemical reactions is generally less complete (3). Therefore, higher temperatures or longer reaction times are usually required to make the same amount of product (here, anodic alumina) when deuterium is substituted for protium. These differences were

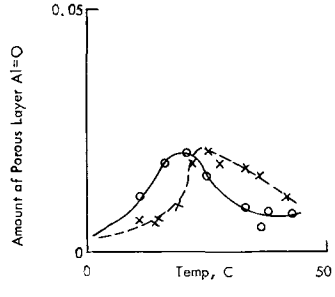

Fig. 4. Amount of porous layer Al=O *vs.* anodizing temperature. ○, 1.0*N* H_2SO_4, 1.08 amp/dm^2, 5 min; X, 1.0*N* D_2SO_4, 1.08 amp/dm^2, 5 min.

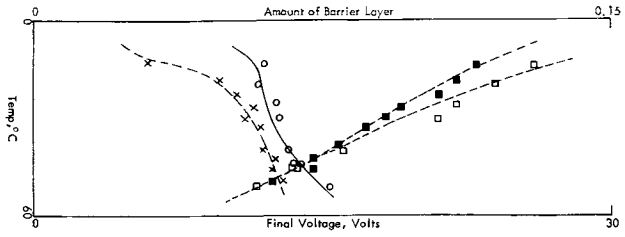

Fig. 5. Amount of barrier layer vs. anodizing temperature and voltage. ○, 1.0*N* H_2SO_4, 1.08 amp/dm^2, 5 min; X, 1.0*N* D_2SO_4, 1.08 amp/dm^2, 5 min; □, H_2SO_4 anodizing voltage; ■, D_2SO_4 anodizing voltage.

noted in our observations regarding the relative amounts of porous and barrier layers obtained in deuterated and protonated systems, respectively.

Conclusions

The data show that hydrogen is an integral component of the anodic alumina barrier layer; if this were not so, deuteration would have had no effect.

It was previously shown that the barrier layer infrared band was in the alumina hydrate region (2), but anomalies were found: (*i*) barrier layers showed no absorption in the 3400 AlO-H stretch region, and (*ii*) barrier layers showed no Al-OAl absorption bands even when examined down to 33 cm^{-1}.

It is well established that hydrogen bonding shifts the frequency of the oxygen-hydrogen stretch vibration and reduces the intensity of the band by broadening it (4). Strong hydrogen bonding may entirely remove the band from the 3400 region. Hydroxyl vibrations are also shifted by hydrogen bonding, but band intensities are not similarly affected. We propose that the absence of a 3400 region infrared band indicates that strong hydrogen bonding is present within the barrier layer. Further, since no Al-OAl linkages were detected in barrier layer infrared spectra, and since the barrier layer infrared band is in the alumina trihydrate region, the barrier layer must have a trihydrate composition. The simplest structure for a strongly hydrogen-bonded trihydrate is:

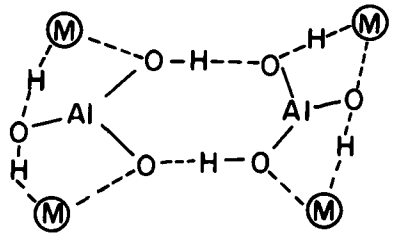

when this represents a unit section of a long polymer chain and M designates an identical unit within the same chain.

However, the barrier layer structure must have terminal groups, and to fit the existing data, the linkages within the terminal groups must be identical with those in the chain. If more than one fundamental type of linkage were present, then the barrier layer spectrum would have more than one absorption band: weak Al=O or weak Al=O-plus-monohydrate absorptions. The spectrum has only one band, however, and that lies in the lower frequency region for trihydrates, between 900 and 1000 cm^{-1}. We must attempt to account for chain-terminating groups using only AlOH---OAl linkages. The simplest structure here would require that aluminum have a subvalent oxidation state within the terminal groups.

Our proposed structure for the anodic barrier layer is then as follows, where aluminum is present in both divalent and trivalent oxidation states.

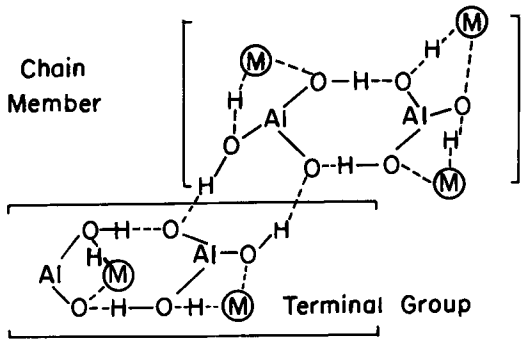

We propose to call this structure the primary barrier layer phase and refer to it as a cyclic aluminic acid trihydrate. The oxygen deficiency of the anodic barrier layer has long been established (5-8), and our divalent aluminum-containing barrier layer is consistent with this deficiency. The divalent aluminum content of the barrier layer would produce a greater aluminum/oxygen ratio than that corresponding to the solely trivalent aluminum in Al_2O_3. Although Al (I) is a more common subvalent oxidation state for species such as gaseous aluminas, Al (II) has also been suggested (9).

We have found that a second type of bonding, the Al=O bond, forms as anodizing progresses further to produce the porous layer (2). It was also noted that the frequency of the barrier layer band increased as this occurred. This was taken to mean that the barrier layer underwent a change from high to low polymer weights as anodizing progressed through to the porous layer stage; the altered form of the barrier layer was termed the "parent layer" since the conversion appeared to be a requirement for porous layer formation.

We now propose that the parent layer represents a secondary phase of the barrier layer which has undergone a conversion from the cyclic to a decyclic form. The oxygen-deficient terminal groups of the cyclic primary phase would be a logical site for further oxidation leading to depolymerization with the formation of Al=O linkages. The introduction of these chain-terminating groups would also give rise to a series of lower polymer weights; this would result in a wavenumber shift of the barrier layer infrared band, as has been reported earlier (2).

Acknowledgments

The author wishes to thank the Kaiser Aluminum & Chemical Corporation for its support of this work and for its permission to publish these results. Our thanks go also to Beckman Instrument's H. J. Sloane and K. E. Stein, who obtained the far infrared data referred to here.

Manuscript received Aug. 16, 1965.

Any discussion of this paper will appear in a Discussion Section to be published in the December 1966 JOURNAL.

REFERENCES

1. G. A. Dorsey, Jr., *This Journal*, **113**, 169 (1966).
2. G. A. Dorsey, Jr., *ibid.*, **113**, 172 (1966).
3. T. Moeller, "Inorganic Chemistry," p. 390, John Wiley & Sons, Inc., New York (1959).
4. K. Nakamoto, "Infrared Spectra of Inorganic and Coordination Compounds," p. 194, John Wiley & Sons, Inc., New York (1963).
5. T. V. Krotov, *Z. fiz. khim.*, **18**, 1550 (1954).
6. M. A. Heine and M. J. Pryor, *This Journal*, **110**, 1205 (1963).
7. M. A. Heine, D. S. Keir, and M. J. Pryor, *ibid.*, **112**, 24 (1965).
8. H. Akahori, *J. Electronmicroscopy*, **10**, 175 (1961).
9. M. J. Linevsky, *J. Chem. Phys.*, **41**, 542 (1964).

Technical Notes

Reflectivity Studies of Epitaxial $Ga_xIn_{1-x}As$

R. W. Conrad, C. E. Jones, and E. W. Williams

Texas Instruments Incorporated, Dallas, Texas

The reflectivity spectra in the uv-visible range of various $Ga_xIn_{1-x}As$ alloys, prepared by a gradient-freeze method, have been reported by Woolley and Blazey (1). A linear variation of the energy of the E_1 (low energy) reflectivity peak with alloy composition was observed. The E_1 transition has been ascribed by Cardona (2) to an L (Brillouin zone edge) transition, but later work by Brust *et al.* (3), with germanium indicates a Λ (within the Brillouin zone) transition, perhaps at about the point (1/6, 1/6, 1/6) in k space. We wish to report the results of our reflectivity measurements on single-crystal, epitaxial $Ga_xIn_{1-x}As$ alloys deposited on GaAs substrates, in particular the anomalous results obtained on as-grown and mechanically polished deposit surfaces.

Experimental

Epitaxial $Ga_xIn_{1-x}As$ alloys were prepared from the vapor phase in an open-tube reactor system[1] using undoped GaAs and InAs source materials[2] and $AsCl_3$-saturated hydrogen as transport agent. Substrates were Cr-doped, semi-insulating (4) and Te-doped (5×10^{18} cc^{-1} GaAs,[2] cut 3° off the (111) toward the (100). These were chemically polished, using a technique similar to that described by Reisman and Rohr (5) for the room-temperature polishing of GaAs. All substrates were chemically etched in hot aqueous NaOCl solution immediately prior to deposition. Deposits were obtained on both sides of the substrates, but in general, only one side of the substrate had been chemically polished beforehand. In several deposition experiments, two substrates were used, one with a chemically polished A (111) surface, the other with a chemically polished B (111) surface. Deposit thicknesses were from 2-15μ on B (111) substrates and 10-50μ on A (111) substrates. Deposition rates tended to decrease when depositing higher indium-content alloys.

[1] Details of the reactor system will appear in a later publication.

[2] From Texas Instruments Incorporated, Dallas, Texas.

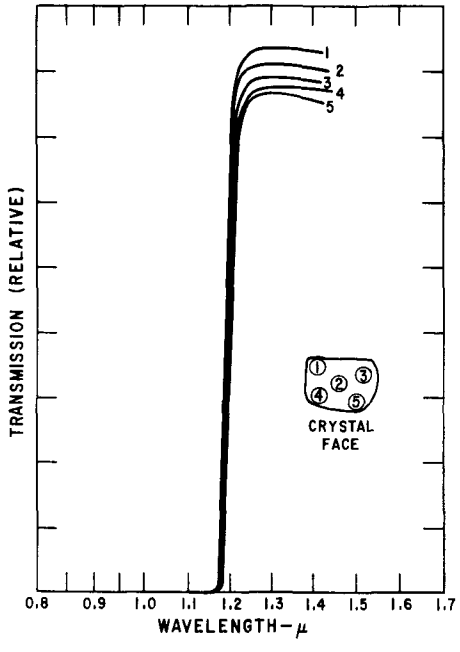

Fig. 1. Infrared transmission of epitaxial $Ga_xIn_{1-x}As$ illustrating lateral composition homogeneity.

Deposits were evaluated for single-crystallinity by microscopic examination of surface and cleaved edge, and by "light-figure" patterns of the surfaces (6). Several representative samples were also examined for single-crystallinity and epitaxial orientation by electron diffraction reflection scans of the as-grown surfaces. To determine composition homogeneity, infrared transmission spectra were measured at several different locations on the sample surfaces. Figure 1 shows the results of such measurements for a typical sample and indicates very good composition homogeneity both in the plane of and perpendicular to the deposit surface.

The reflectivity spectra in the range 0.35-0.75μ were measured with a Perkin-Elmer Model 350 recording spectrophotometer. Alloy compositions were calculated from the E_1 peaks for a series of as-grown samples, with the reactor conditions varied to obtain various alloy compositions. In every case, the apparent compositions of the as-grown layers were higher in GaAs on the A (111) side. This apparent composition difference was independent of whether the particular substrate surface had been chemically polished or not, prior to deposition. Examination of several of these samples by infrared transmission and x-ray diffraction methods, however, showed no difference in composition between the A and B side deposits. Further, the reflectivity compositions of the A (111) samples were in good agreement with values determined from x-ray and infrared transmission measurements, the B (111) samples being anomalous. To determine if the apparent composition difference was peculiar to polar substrates, several depositions were made on (100) GaAs substrates. In each case, the compositions of the as-grown deposits as determined from reflectivity were identical on the two sides of the substrates and in good agreement with x-ray and transmission measurements. These results are summarized in Table I.

Several B (111) samples which exhibited anomalous reflectivity compositions were re-examined by reflectivity after successive removal of thin layers of deposit (0.5-2.0μ) by hand-lapping with 0.3μ alumina abrasive. The E_1 peaks were appreciably broadened and compositions determined after each lapping varied erratically and were unreproducible. In the case of one sample whose actual composition (from infrared transmission and x-ray diffraction) was $Ga_{0.5}In_{0.5}As$, composition determined by reflectivity after successive lappings varied randomly from $Ga_{0.2}In_{0.8}As$ to $Ga_{0.8}In_{0.2}As$. This effect was also observed for A (111) and (100) surfaces of epitaxial alloys, whereas epi-

Table I. Anomalous reflectivity compositions of B(111) epitaxial $Ga_xIn_{1-x}As$

Sample No.	Substrate	Deposit composition, mole % GaAs	
		True value*	B side value
129	Te, 5×10^{18} cc^{-1}	85	67
55	Semi-insulating	86	71
	Te, 5×10^{18} cc^{-1}	85	73
57	Semi-insulating	88	67
	Te, 5×10^{18} cc^{-1}	91	77
59	Semi-insulating	88	67
	Te, 5×10^{18} cc^{-1}	91	77
61	Te, 5×10^{18} cc^{-1}	50	38
76	Semi-insulating	22	12

* From A side reflectivity confirmed by x-ray diffraction and infrared transmission.

taxial and bulk GaAs and InAs showed only peak broadening but no shift in energy.

To determine if the anomalous reflectivity results after mechanical polishing could be caused by surface melting (7) and subsequent regrowth of a thin surface layer of different composition from the rest of the deposit, several InAs (111) substrates were mechanically polished with a 0.3μ alumina-liquid gallium slurry (at *ca.* 35°C). Were surface melting to occur, alloying with the gallium should take place, forming a thin surface layer of $Ga_xIn_{1-x}As$. Reflectivity spectra of the surface of these substrates after such a treatment showed no shift in the E_1 peak.

Light chemical etching of the alloy deposit surface was found to yield very reproducible reflectivity spectra. A short treatment of either as-grown or mechanically polished deposit surfaces with dilute bromine-methanol solution, sufficient to remove 1-2μ of deposit, gave reproducible reflectivity spectra in every sample examined. Further, the compositions of the A and B side deposits after etching were found to be identical, the apparent fraction of GaAs in the B side deposit having increased to that of the as-grown A side deposit, with the A side composition remaining unchanged. These results are illustrated in Fig. 2 which shows the shift in reflectivity peaks for as-grown A and B side deposits, and in Fig. 3 which shows the coincidence of the reflectivity peaks for the same sample after chemical etching.

To determine if a difference in mechanism of thermal dissociation of the A and B side deposits, such as reported by Miller *et al.* (8) for GaAs, could be a factor in producing the anomalous reflectivity results on as-grown B (111) surfaces, we heat-treated a chemically etched sample for a short time at 720°C in flowing hydrogen. These conditions are similar to those in the vapor deposition reactor during the shutdown procedure. Reflectivity measurements on this sample, however, showed no apparent change in composition.

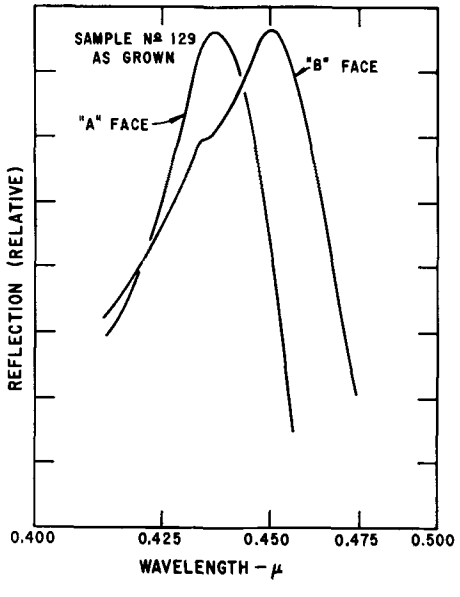

Fig. 2. Reflectivity spectrum of a sample of as-grown epitaxial $Ga_xIn_{1-x}As$.

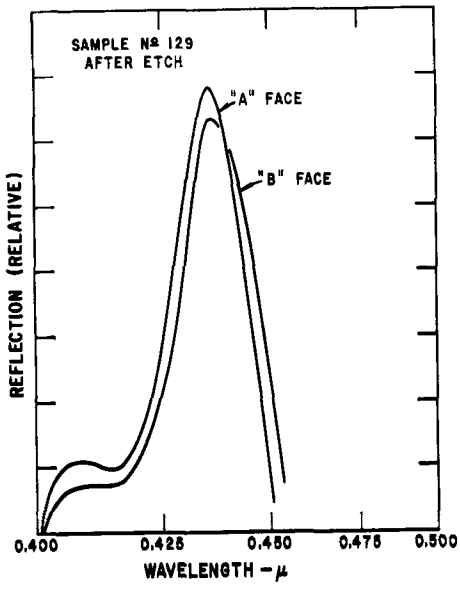

Fig. 3. Reflectivity spectrum of a sample of epitaxial $Ga_xIn_{1-x}As$ after etching.

Discussion

The anomalous compositions as determined by reflectivity for the B (111) side $Ga_xIn_{1-x}As$ alloy deposits appear to be connected in some fashion to the fundamental differences between the A (111) and B (111) sides, and not to some peculiarity of the vapor deposition system, since deposits on nonpolar (100) GaAs substrates do not exhibit this effect. A difference in mechanism of thermal dissociation of A (111) and B (111) $Ga_xIn_{1-x}As$ surfaces, although probably present, does not seem to be a factor in producing anomalous reflectivities. Whatever the reason for this phenomenon, light chemical etching apparently eliminates it.

A satisfactory explanation for the anomalous composition values obtained by reflectivity on mechanically polished $Ga_xIn_{1-x}As$ alloy surfaces is still lacking. Surface melting probably can be eliminated as a factor, but oxide formation has yet to be investigated.

Cardona (9) has listed semiconductor surface preparation techniques in order of decreasing quality as: cleaved > vapor grown > liquid grown > electropolished > chemically etched > mechanically polished. Our results for epitaxial $Ga_xIn_{1-x}As$ indicate: chemically etched > as-grown > mechanically polished.

Acknowledgments

The authors wish to thank L. G. Bailey and R. W. Haisty for their helpful criticism and W. S. Bradley for his help in preparing the samples.

This work was supported by the Electronics Technology Division of the Air Force Avionics Laboratory under Contract AF 33(615)-1272.

Manuscript received March 18, 1965; revised manuscript received Oct. 25, 1965.

Any discussion of this paper will appear in a Discussion Section to be published in the December 1966 JOURNAL.

REFERENCES

1. J. C. Woolley and K. W. Blazey, *J. Phys. Chem. Solids*, 25, 713 (1964).

2. M. Cardona, *J. Appl. Phys. Suppl.*, **32** [10], 2151 (1961).
3. D. Brust, J. C. Phillips, and F. Bassani, *Phys. Rev. Letters*, **8**, 94 (1962).
4. G. R. Cronin and R. W. Haisty, *This Journal*, **111**, 874 (1964).
5. A. Reisman and R. Rohr, *ibid.*, **111**, 1425 (1964).
6. G. R. Cronin, *Rev. Sci. Instr.*, **34** [10], 1151 (1963).
7. A. W. Adamson, "Physical Chemistry of Surfaces," pp. 325-330, Interscience Publishers, Inc., New York (1960).
8. D. P. Miller, J. G. Harper, and T. R. Perry, *This Journal*, **108**, 1123 (1961).
9. M. Cardona, Proc. Int. Conf. on Physics of Semiconductors, p. 196, Paris, 1964.

Phase Diagram for the Pseudobinary System InSb-InSe

D. F. O'Kane and N. R. Stemple

Thomas J. Watson Research Center, International Business Machines Corporation, Yorktown Heights, New York

This note describes the results of an investigation of the InSb-InSe pseudobinary phase diagram using differential thermal analysis (DTA) and x-ray methods.

InSb has a zinc blende structure with a lattice parameter a = 6.4782Å (1). InSe has been reported to have a rhombohedral structure (2) with a = 4.02Å and c = 25.05Å and a hexagonal structure with a = 19.2Å, c = 4.00Å (3) and a = 4.05Å, c = 16.93Å (4). There is no known investigation of the pseudobinary system composed of InSb-InSe.

Our samples were prepared from the pure elements (99.999%)In, Sb, and Se. Fifteen grams of the elements were reacted in evacuated, fused silica tubes and water quenched from the liquid state. The samples were ground to a fine powder and annealed near 440°C for 6 to 57 days before making the x-ray powder patterns and the DTA measurements. The exact annealing conditions for each sample are described in Table I. The DTA sample tubes were made of fused silica with a thermocouple well in the bottom. The DTA heating and cooling rate was 2°C/min.

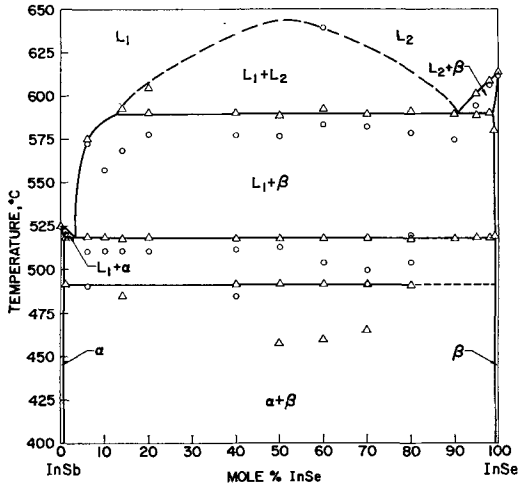

Fig. 1. Phase diagram for the pseudobinary system InSb-InSe. △, from DTA heating curves; ⊙ from DTA cooling curves.

Results

The phase diagram for the InSb-InSe pseudobinary system is shown in Fig. 1. InSb and InSe are not miscible in all proportions. A monotectic occurs at 591°C and 91 mole % InSe, and the composition of the InSb rich melt at the monotectic temperature is 13 mole % InSe. The extent of the miscibility gap in the liquid state above 591°C was difficult to estimate from differential thermal analysis, and this boundary is shown as a dashed line to indicate this uncertainty.

A eutectic exists near 3 mole % InSe and 519°C. This eutectic transformation appeared as a thermal arrest on all the heating curves for the annealed compositions between 1 and 98 mole % InSe. The DTA samples at 1 and 95 mole % InSe were annealed 57 days at 450°C in order to determine if a solid solution was formed at each of these compositions. The occurrence of the 519°C eutectic transformations in the DTA heating curve of each sample indicates a lack of complete solid solution. Zone refining of the composition $(InSb)_{30}(InSe)_{70}$ resulted in the separation of a crystal containing 0.60 w/o (weight per cent) Sb, which is equivalent to $(InSb)_{0.96}(InSe)_{99.04}$, in the first section to freeze. DTA measurements on the latter composition showed the 519° and 591°C eutectic and monotectic transformations during the heating cycle. The data on the annealed and zone refined samples indicated that the solubility of InSe in InSb

Table I. Summary of DTA measurements for the pseudobinary phase diagram of InSb-SnSe

Sample composition Mole % InSb	Mole % InSe	DTA run No.	Annealing conditions	Differential thermal analysis results: Heating Liquidus temp, °C	Heating Transition Temp, °C	Cooling Liquidus temp, °C	Cooling Transition temp, °C
100	0	54	None	524		524	
99	1	58	31 days at 440°C	522	519, 491	520	
94	6	50	57 days at 450°C	576	519	573	511, 491
90	10	51	57 days at 450°C		519	558 (?)	511
86	14	57	14 days at 440°C		593, 518, 485		569, 511
80	20	7	14 days at 440°C	605	591, 519		578, 511
60	40	6	14 days at 440°C		591, 518, 492		578, 512, 485
50	50	5	14 days at 440°C		589, 518, 492, 458		578, 513
40	60	2	14 days at 440°C		593, 518, 492, 460	640	584, 504†
30	70	12	7 days at 420°C		590, 518, 492, 466		583, 500, 492*
20	80	3	6 days at 450°C		592, 516, 491		580, 519, 504
10	90	13	7 days at 420°C		590, 518		576**
5	95	52	57 days at 450°C	602	589, 519	595	**
2	98	53	23 days at 450°C	609	518	607	
~0.96	~99.04	32	First section to freeze, zone refined ingot		580, 519	607	
0	100	11	None	612		614	

† No data below 494°C.
* No data below 485°C.
** No data below 510°C.

Table II. Powder pattern diffraction lines for InSe

ASTM (3) standard, d, Å	InSe quenched from liquid state, d, Å	InSe both annealed and zone refined samples, d, Å
8.36	8.36	8.36
4.16 S	4.12 S	4.15 S
3.38 B	3.40	3.40
3.14	3.17	
3.05 B	3.04	
2.96 B	2.92	2.95 B
2.77	2.75	
	2.63	
2.44 B		
2.38 B	2.38 B	2.38 B
2.30		
	2.15	
2.08	2.07	2.06
2.00 S	2.00 S	2.00 S
1.95	1.95 B	1.95 B
1.80	1.80	1.80
1.73	1.73	1.72
	1.64	1.65
1.62	1.62	1.62
	1.53 B	1.53 B
	1.49	
	1.465	
1.44	1.44	1.44
1.40		
1.388	1.385	1.385

is less than 1%, and the solubility of InSb in InSe is also less than 1%.

The phase diagram characteristics associated with two phase transitions could not be determined. One transition occurred sharply at 492°C between 1 and 80 mole % InSe, and it is assumed to be a high-temperature solid-solid phase transition. The heat necessary for this transformation is only 1/10 of the quantity required for the eutectic transformation at 519°C. A smaller transition near 460°C in the 50, 60, and 70 mole % InSe samples occurs gradually over a range of 10°C and may be an order-disorder type of reaction.

The x-ray powder patterns on annealed samples of 10, 50, 80, 90, and 95 mole % InSe showed both InSb and InSe phases present. In an x-ray sample of 6 mole % InSe, which was annealed at 450° ± 5°C for 26 days, the principal phase had a lattice parameter of $a = 6.4765$Å. This is not significantly different from the reported values of $a = 6.4782$Å (1) and 6.4760Å (5) for InSb. A significant decrease in lattice parameter to $a = 6.4721$Å was noted on the annealed 50 mole % InSe; this may be connected with the transformations near 492° and 460°C.

Initially, there was a question about the powder pattern diffraction lines associated with InSe in the InSb-InSe samples. Several lines reported for InSe (3) did not show up in the InSb-InSe patterns. However, examination of InSe which was quenched from the liquid state, annealed InSe, and zone refined InSe showed a difference in diffraction lines as illustrated in Table II. After annealing the quenched InSe, the diffraction pattern was identical to that of the zone refined InSe. The change in InSe diffraction patterns may be explained by the phase diagram characteristics of the InSe binary system in the vicinity of InSe. The limits of solid solubility of InSe are unknown. Fast quenching from the liquid state could result in a two phase mixture if the maximum melting point is not exactly at InSe, and annealing could produce a single phase material.

The different lattice parameters (2-4) reported for InSe may be partially explained by the methods of preparation. Sugaike (3) used a single crystal grown by the Stockbarger method for his lattice parameter determination, Schubert (2) does not describe his method of sample preparation, and Semiletov (4) used an evaporation procedure.

Summary

Differential thermal analysis and x-ray methods have been used to characterize the InSb-InSe pseudobinary phase diagram. A monotectic exists at 591°C and 91 mole % InSe, and the composition of the InSb rich melt at the monotectic temperature is 13 mole % InSe. A eutectic occurs at 519°C and 3 mole % InSe and two other phase transitions at 492° and 460°C were present in the system. The solubility of InSe in InSb is less than 1% and less than 1% of InSb is soluble in InSe.

Acknowledgments

The authors wish to express their appreciation to J. Angilello for his assistance with the x-ray work and to B. L. Gilbert for the chemical analysis work. The zone refined InSe was obtained from Dr. D. R. Mason. Thanks are due to Drs. L. M. Foster and A. H. Nethercot for reviewing the manuscript.

Manuscript received Sept. 13, 1965.

Any discussion of this paper will appear in a Discussion Section to be published in the December 1966 JOURNAL.

REFERENCES

1. H. E. Swanson, R. K. Fuyat, and G. M. Ugrinic, Standard X-ray Diffraction Patterns, National Bureau of Standards Circular 539, Vol. IV, U. S. Dept. of Commerce (1955).
2. K. Schubert, E. Dorre, and E. Gunzel, *Naturwissenschaften*, **41**, 448 (1954).
3. S. Sugaike, *J. Mineral. (Japan)*, **2**, 63 (1957).
4. S. A. Semiletov, *Soviet Physics, Crystallography*, **3**, 292 (1958).
5. T. S. Liu and E. A. Peretti, *Trans. AIME*, **191**, 791 (1951).

Phase Diagram for the Pseudobinary System of Sb-SnTe and Some Electrical Properties of the Ternary Alloys

D. F. O'Kane and N. R. Stemple

Thomas J. Watson Research Center, International Business Machines Corporation, Yorktown Heights, New York

The purpose of this work was to determine the phase diagram characteristics of the pseudobinary system of Sb-SnTe, and to examine the electrical properties of some of the alloys in the system. Investigation of the Sb-SnTe system was motivated by a separate investigation in these Laboratories of the band structure of the compounds of average valence V.

The elements Sb, Sn, and Te are in the same row of the periodic table and would be expected to show substantial mutual solubilities. Sb has a rhombohedral structure with $a = 4.307$Å and $c = 11.273$Å (1). SnTe has the sodium chloride structure with $a = 6.314$Å at the composition 50.4 a/o (atomic per cent) Te-49.6 a/o Sn (2). This is the maximum melting (806°C) point composition in the Sn-Te system. Krebs *et al.* (3) have investigated the solubility of SnTe in Sb and report the limit of solubility as $Sb_{87.0}(SnTe)_{13.0}$.

Experimental Procedure

Differential thermal analysis (DTA), x-ray methods, microstructure examination, and zone refining were used to establish the phase diagram for the Sb-SnTe system. The DTA samples were made in two ways. For those samples for which only DTA cooling data

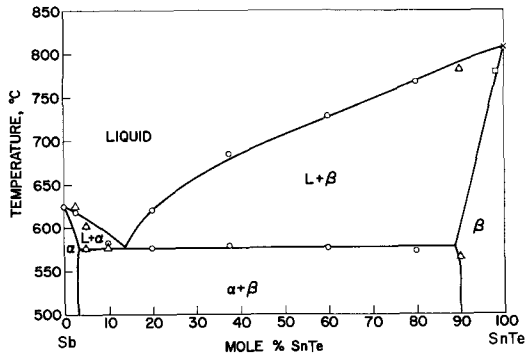

Fig. 1. Phase diagram for the Sb-SnTe pseudobinary system. △, from DTA heating curves; ⊙, from DTA cooling curves; square with a dot, from crystal No. 38; X from Brebrick (2).

were to be obtained, the elements (99.999% purity) were reacted in the DTA furnace and cooled at 2.0°C/min. The remaining samples at 5, 10, and 90 mole % SnTe were prepared by reacting the elements and water quenching them from the liquid state. They were then ground to a powder, sealed in evacuated, fused silica tubes, and annealed at 525°C for 51 days. The DTA heating and cooling rate on the annealed samples was 2.0°C/min. The x-ray powder pattern samples of 5, 10, 85, 87, and 90 mole % SnTe were annealed at 525°C for 31 to 51 days.

Zone refining for 4 to 9 passes at 0.5-0.8 in./hr. was used to separate the eutectic composition in the Sb-SnTe system for chemical analysis, and to establish the solubility of SnTe in Sb. The use of zone refining to separate the eutectic composition in a binary system has been previously demonstrated by Yue (4). Sn and Te were analyzed in the Sb-rich samples, and Sb was analyzed in the SnTe-rich samples.

Single crystals for electrical measurements were pulled at 4 mm/hr from melts of $Sb_{15}(SnTe)_{85}$ and $Sb_{95}(SnTe)_5$ in a Czochralski-type crystal puller. Electrical resistivity and Hall effect were measured by the direct current method on samples approximately 0.25 x 1 x 7 mm^3 with a magnetic field of 4,000 gauss for determination of the Hall coefficient.

Results

The phase diagram for the Sb-SnTe pseudobinary system is shown in Fig. 1. A eutectic exists at the composition $Sb_{85.8}(SnTe)_{14.2}$ and 576° ± 2° C. The limits of solid solubility are $Sb_{97}(SnTe)_3$ and $Sb_{10}(SnTe)_{90}$.

The solid solubilities and the eutectic composition were established by zone refining, microstructure examination, x-ray powder patterns on annealed samples, x-ray diffractometry on single crystal cleaved surfaces, and chemical analyses.

The results of chemical analyses on zone refined samples and Czochralski pulled crystals are summarized in Table I. X-ray analyses are summarized in Table II. The number in brackets with each sample number in Table I indicates the section number of the material analyzed. Section 3 was near the first to freeze section of the zone refined ingot, section 5 was at the center of the ingot, and section 7 was the last section to freeze. The first section, 3, to freeze in zone refined ingot No. 082 was single crystalline with the approximate composition of $Sb_{97.1}(SnTe)_{2.9}$. This should represent essentially the limit of solubility of SnTe in Sb, since section 5, which contained $Sb_{94.7}(SnTe)_{5.3}$, showed free SnTe in the powder pattern. This latter section was similar to an annealed sample of $Sb_{95}(SnTe)_5$ which also contained some second phase. The powder pattern for a mechanical mixture of 10 mole % SnTe-90 mole % Sb showed the same diffraction lines as those obtained on the annealed $Sb_{90}(SnTe)_{10}$ sample. The addition of SnTe to the Sb lattice caused an increase in volume of 0.06% at the maximum solubility of $Sb_{97}(SnTe)_3$.

Table II. Summary of x-ray analyses

Sample No.	Composition	Heat-treatment Time, days	Heat-treatment Temp, °C	Lattice parameters a, Å	Lattice parameters c, Å
	Sb			4.307*	11.273**
082(3)	$Sb_{97.1}(SnTe)_{2.9}$			4.303*	11.308
078	$Sb_{95}(SnTe)_5$	51	525	4.306*	11.283
094	$Sb_{15}(SnTe)_{85}$	31	525	6.322†	
088	$Sb_{13}(SnTe)_{87}$	23	525	6.321†	
		49	525	6.321†	
077	$Sb_{10}(SnTe)_{90}$	33	525	6.321†	
		51	525	6.323†	

* Rhombohedral structure.
† Sodium chloride structure.
** From ref. (1).

Equilibrium conditions for the solution of SnTe in Sb were more closely approached in the zone refiner than in the crystal puller, as shown in Table I. This is seen by the difference in composition between the zone refined sample 082 at position 3, which was near the leading end, and the Czochralski crystals 26 and 36, which also represented the first to freeze.

The eutectic phase was observed by microstructure examination of the DTA samples of $Sb_{95}(SnTe)_5$ and $Sb_{90}(SnTe)_{10}$. The results of chemical analysis (Table I) on the end sections, 082(7), 083(7), and 090(7), of zone refined samples of $Sb_{95}(SnTe)_5$ and $Sb_{85}(SnTe)_{15}$ indicate a eutectic composition of $Sb_{85.8}(SnTe)_{14.2}$.

The limit of solubility of Sb in SnTe at 525°C is $Sb_{10\pm2}(SnTe)_{90\pm2}$. The single phase $Sb_{10}(SnTe)_{90}$ had lattice parameters of a = 6.321Å and a = 6.323Å after 33 and 51 days, respectively, at 525°C. $Sb_{13}(SnTe)_{87}$ was two phase after 49 days at 525°C; the lattice parameter of the principal phase was a = 6.321Å. These lattice parameters are comparable to the values of a = 6.318Å (2) and a = 6.322Å (5) obtained for the composition 50.1 a/o Te-49.9 a/o Sn in the Sn-Te binary system. At 777°C, the solubility of Sb in SnTe is $Sb_{1.8}(SnTe)_{98.2}$ from the chemical analysis of a single crystal pulled from a melt of $Sb_{15}(SnTe)_{85}$.

A small heat effect that occurred at 551°C during the cooling of the DTA samples containing 5, 10, and 20 mole % SnTe apparently is not representative of the equilibrium phase diagram. This transition does not appear in annealed samples during the heating cycle and may be related to the 540°C eutectic between Sb and Sb_2Te_3, which extends into the ternary

Table I. Summary of chemical analyses

Sample No.	Starting composition	Method of crystal growth	Final composition a/o Sb	Final composition a/o Sn	Final composition a/o Te	Approximate pseudobinary composition
082[3]	$Sb_{95}(SnTe)_5$	Zone refining, 4 passes at 0.8 in./hr	94.2	3.3	2.4	$Sb_{97.1}(SnTe)_{2.9}$
082[5]	$Sb_{95}(SnTe)_5$	Zone refining, 4 passes at 0.8 in./hr	89.8	5.6	4.5	$Sb_{94.7}(SnTe)_{5.3}$
082[7]	$Sb_{95}(SnTe)_5$	Zone refining, 4 passes at 0.8 in./hr	75.3	11.6	13.0	$Sb_{85.9}(SnTe)_{14.1}$
083[7]	$Sb_{95}(SnTe)_5$	Zone refining, 4 passes at 0.8 in./hr	75.4	11.1	13.4	$Sb_{86.0}(SnTe)_{14.0}$
090[3]	$Sb_{85}(SnTe)_{15}$	Zone refining, 9 passes at 0.5 in./hr	63.3	18.9	17.7	$Sb_{77.6}(SnTe)_{22.4}$
090[7]	$Sb_{85}(SnTe)_{15}$	Zone refining, 9 passes at 0.5 in./hr	74.6	9.1	16.2	$Sb_{85.5}(SnTe)_{14.5}$
26	$Sb_{95}(SnTe)_5$	Czochralski	97.0	2.4	0.5	
36	$Sb_{95}(SnTe)_5$	Czochralski	97.6	2.2	0.2	
38	$Sb_{15}(SnTe)_{85}$	Czochralski	0.90	49.55	49.55	$Sb_{1.8}(SnTe)_{98.2}$

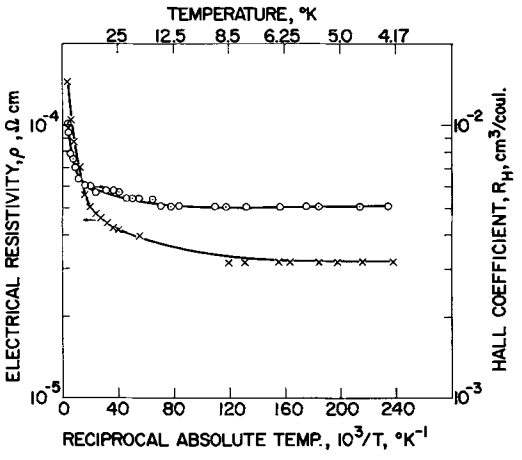

Fig. 2. Electrical resistivity and Hall coefficient vs. reciprocal absolute temperature for single crystalline $Sb_{1.8}(SnTe)_{98.2}$, sample No. 38.

field. These experimental points have been omitted from the phase diagram of Fig. 1.

The electrical resistivity and Hall coefficient data below 300°K for the single crystal $Sb_{1.8}(SnTe)_{98.2}$ are shown in Fig. 2. The concentration of Sb is 2 x 10^{20} at./cm³ from chemical analysis. The apparent hole concentration is 6 x 10^{20}/cm³ at 300°K (from $p = 1/eR_H$, where e is the electron charge and R_H is the Hall coefficient). The hole mobilities are 74 and 110 cm²/volt-sec at 300° and 77°K, respectively. These mobilities are identical to the results obtained by Brebrick (2) on doped and undoped SnTe. The $Sb_{1.8}(SnTe)_{98.2}$ crystal was grown from a melt at 777°C. SnTe grown from a Sn-rich melt at the same temperature has a carrier concentration of 3.5 x 10^{20}/cm³ at 300°K. The hole conduction in this compound is attributed to doubly ionized tin vacancies. This one experiment suggests that possibly the Sb is going on tellurium sites and increasing the tin vacancies.

At the opposite end of the phase diagram, a single crystal of $Sb_{97.6}Sn_{2.2}Te_{0.2}$ was pulled from a melt of $Sb_{95}(SnTe)_5$. The electrical resistivity, ρ, was 6 x 10^{-5} and 3 x 10^{-5} ohm-cm at 300° and 77°K, respectively. Electrical measurements were made with the current flow along the binary direction. Electrical measurements on pure Sb single crystals by Tanaka (6) resulted in $\rho_{297°K}$ = 1.28 x 10^{-4} ohm-cm and $\rho_{20.4°K}/\rho_{297°K}$ = 4.6 x 10^{-3} for current flow in the binary direction.

Summary

The Sb-SnTe pseudobinary phase diagram is a simple eutectic system with the eutectic point at 576°C and $Sb_{85.8}(SnTe)_{14.2}$. The limits of solubility are $Sb_{10}(SnTe)_{90}$ and $Sb_{97}(SnTe)_3$ at 525°C. The latter result does not agree with Krebs (3) who obtained a solubility limit of $Sb_{87.0}(SnTe)_{13.0}$ for samples annealed 24 hr near 470°C. The increase in crystal volume of Sb with the addition of 3 mole % SnTe is 0.06%. The addition of 10 mole % Sb to SnTe causes no significant change in lattice parameter from SnTe. The electrical properties of $Sb_{1.8}(SnTe)_{98.2}$ are similar to those of SnTe.

Acknowledgments

The authors would like to thank Dr. J. F. Woods for obtaining the electrical measurements and J. Angilello for assisting with the x-ray work. The chemical analyses were performed by B. L. Gilbert and B. L. Olson. Thanks are due to Dr. L. M. Foster and Dr. A. H. Nethercot for reviewing the manuscript.

Manuscript received Sept. 13, 1965.

Any discussion of this paper will appear in a Discussion Section to be published in the December 1966 JOURNAL.

REFERENCES

1. H. Swanson, R. Fuyat, and G. Urgrinic, Standard X-Ray Diffraction Powder Patterns, National Bureau of Standards, Circular 539, Vol. III (1954).
2. R. F. Brebrick, *J. Phys. Chem. Solids*, **24**, 27 (1963).
3. H. Krebs, K. Grun, D. Kallen, and W. Lippert, *Z. anorg. u. allgem. chem.*, **308**, 200 (1961).
4. A. S. Yue and J. B. Clark, *Trans. Met. Soc. AIME*, **221**, 383 (1961).
5. R. Mazelsky and M. S. Lubell, "Nonstoichiometric Compounds," Advance in Chemistry Series 39, American Chemistry Society (1962).
6. K. Tanaka and T. Fukuroi, *Sci. Rept. Res. Inst. Tohoku Univ. Series A*, **16**, 115 (1965).

Annular Facets and Impurity Striations in Tellurium-Doped Gallium Arsenide

G. R. Cronin, G. B. Larrabee, and J. F. Osborne

Texas Instruments Incorporated, Dallas, Texas

The preparation of uniformly doped GaAs single crystals is important for use as substrates for epitaxial deposition and for the fabrication of devices from bulk material. The growth of uniformly doped material from the melt is not as simple as it would appear to be.

Work by LeMay (1) on tellurium-doped GaAs described the effects of constitutional supercooling and facet formation on crystals whose growth axis was 15° off the <111>. Striations believed to be caused by impurity segregation have been revealed by a variety of techniques including anodic etching (2), chemical etching (3), infrared transmission (4), and electron microscopy (5). This work describes several GaAs crystals pulled from a melt doped with radioactive tellurium. The radiotracer technique has the advantage of permitting a direct correlation between the impurity distribution as revealed by autoradiograms and the etching characteristics of the material.

Experimental

Three crystals were grown doped with radioactive tellurium in concentrations ranging from about 5 x 10^{16}/cm³ to 1 x 10^{19}/cm³. The crystals were grown on the <111> orientation from x-ray oriented seeds in a vertical pulling apparatus described previously (6). The GaAs melt was compounded *in situ* and Te-127m-127[1] was added in elemental form to the gallium which was contained in an alumina crucible. The crystals, grown from the <$\bar{1}\bar{1}\bar{1}$> or arsenic end of the seed, were entirely single, and weighed approximately 50g each. They were then cut into wafers 30 mil thick from which the autoradiograms were made and the tellurium concentration measured. Dislocation density measurements by etch pit counting were made follow-

[1] Te-127m-127 was produced by the neutron irradiation of tellurium metal isotopically (91.6%) enriched in tellurium^{126} obtained from Oak Ridge National Laboratories.

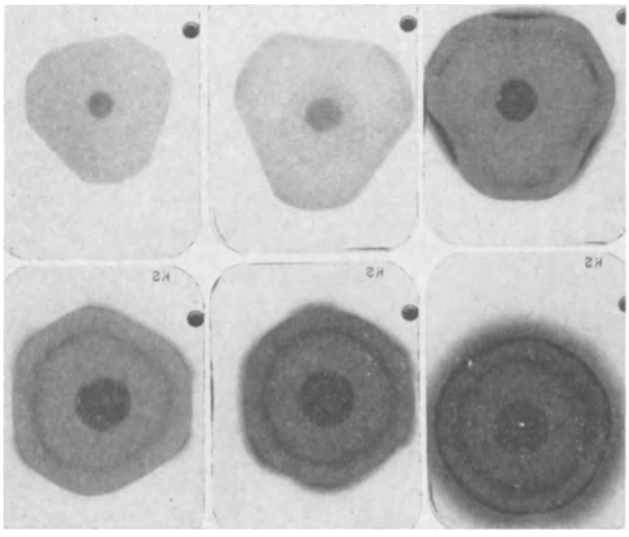

Fig. 1. A "top to bottom" series of autoradiograms from tellurium-doped GaAs crystal 218. Note appearance of annular facet on third and fourth autoradiogram.

ing a method described by Richards *et al.* (7). The radio purity of the tellurium was checked by gamma ray spectroscopy in each crystal, and only tellurium-127m-127 activity was found. The activity of each slice was measured by conventional gamma counting techniques. Autoradiograms were also made on each slice to determine doping uniformity.

Results and Discussion

Six autoradiograms taken from the first crystal (218) are shown in Fig. 1 The tellurium concentration in this crystal ranged from about 5 x 10^{16}/cm^3 to 1 x 10^{17}/cm^3. The appearance of the sharply outlined central facet in the upper portion of the crystal is similar to those reported by Allred and Bate for tellurium in InSb (8). The most striking feature of this crystal, however, is the appearance of a second well-defined area of high tellurium concentration which appeared about midway through the growth of the crystal. This concentric or annular facet then persists throughout the remaining lower half of the crystal. The origin of this type of annular facet, we believe, is related to the shape of the growth interface. We have observed, by withdrawal from the melt, that as the crystal first begins to grow, the interface tends to have a maximum concave curvature and hence a relatively small area which approximates a (111) plane. The result is a small central facet at the top of the crystal as shown in Fig. 2 and the autoradiograms of Fig. 1.

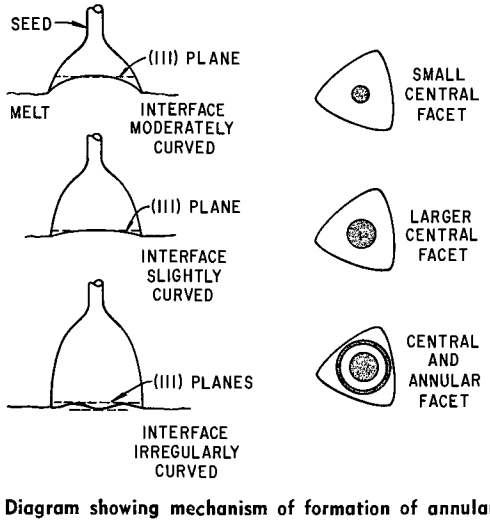

Fig. 2. Diagram showing mechanism of formation of annular facets

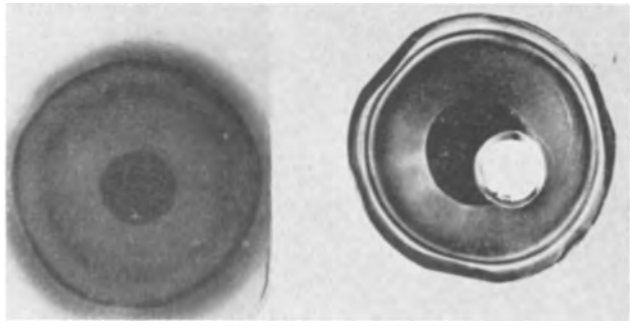

Fig. 3. Photograph and autoradiogram of the bottom of crystal 218. The white area is the portion of the last drop to freeze as the crystal was withdrawn from the melt.

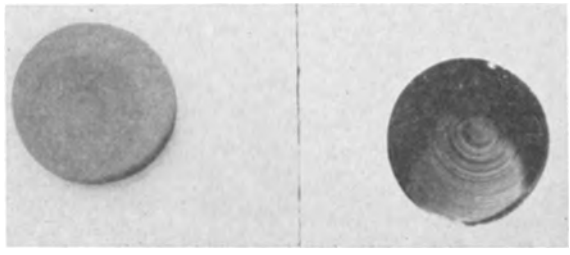

Fig. 4. (Left) autoradiogram of 10^{19}/cm^3 tellurium-doped GaAs showing portions of impurity striations; (right) same slice after etching in 15 H_2SO_4-3 H_2O_2-3 H_2O mixture.

As the crystal continues growing, the interface becomes more planar and the central facet grows larger. The sudden appearance of the annular facet shown in Fig. 1 suggests that at some point during the growth of this crystal a second distinct area of the interface surrounding the central facet also approximated a (111) plane. This, of course, implies an irregularly shaped interface such as depicted in Fig. 2. The irregular shape of the bottom of this crystal (218) as it was withdrawn from the melt (Fig. 3) is good evidence for this explanation.

Some of the autoradiograms shown in Fig. 1 also show edge facets which we have often seen on crystals grown on the ($\bar{1}\bar{1}\bar{1}$) orientation.

The tellurium concentrations on and off facet were determined by analyzing cavitroned specimens from these areas. Data shown in Table I are from upper and lower portions of the crystal. The on/off facet ratios agree fairly well with LeMay's reported figure of 2.6 (1).

Crystal 205 was doped with tellurium at about 1 x 10^{19} at./cm^3. Autoradiograms taken from several slices show no evidence of tellurium precipitation at this concentration but do exhibit nonuniform distribution of dopant again resulting from faceting. These facets were primarily limited to the outer edges of the crystal indicating some misorientation of the seed. Several autoradiograms, however, showed the striated pattern of concentric circles similar to those which LeMay (1) has attributed to constitutional supercooling.

These slices were then subjected to the chemical polishing procedure undergone by GaAs substrates prior to epitaxial deposition. The pattern produced by

Table I. Tellurium concentration and etch pit on and off the facet of GaAs crystal 218

	Te concentration, at./cm^3	On/off ratio	Etch pit density, cm^{-2}
Slice No. 5			
On facet	1.05×10^{17}		7.7×10^3
Off facet	4.74×10^{16}	2.4	8.8×10^3
Slice No. 11			
On facet	1.08×10^{17}		5.5×10^3
Off facet	5.54×10^{16}	2.1	low 10^4

Table II. Comparison of tellurium concentration from tracer count and Hall data for GaAs crystal 205

Slice No.	Te concentration from tracer count, cm^{-3}	Excess electrical carrier concentration cm^{-3} 300°K
6	9.86×10^{18}	7.2×10^{18}
13	9.86×10^{18}	6.5×10^{18}
23	1.09×10^{19}	8.0×10^{18}
26	1.07×10^{19}	6.4×10^{18}
	Etch pit density	
5	$6 \times 10^3/cm^2$	
22	$3 \times 10^3/cm^2$	

the final etch, a mixture of sulfuric acid and hydrogen peroxide, coincided with the tellurium distribution revealed by the autoradiograms as shown in Fig. 4. We have observed similar patterns on material doped as low as 10^{17} at./cm^3. No correlation could be drawn between the spacing of the striation and the rotation and withdrawal rates.

The etch pit density of this crystal was relatively low even at this high tellurium concentration. Counts of 3-6 x $10^3/cm^2$ were made in the approximate center of several slices.

Hall data taken from this crystal show excess carrier concentration lower than the tellurium concentration in every measurement (Table II) with a maximum electrical activity at 8 x 10^{18} excess carriers/cm^3. Black and Lublin (9) have reported that in tellurium-doped GaAs at concentrations of 3 x 10^{19} at./cm^3 (by chemical analysis) the free carrier concentration was only 8.5 x 10^{18}/cm^3 indicating that part of the tellurium is either un-ionized or electrically compensated at this concentration. We feel, however, that the presence of these impurity striations in our crystal casts some doubt upon the validity of our Hall measurements.

The third crystal (223) was grown on the <115> orientation with a tellurium concentration in the low 10^{16} at./cm^3 range. Slices were cut both on the (111) and (115) orientation. Autoradiograms of both orientations show entirely uniform distribution of tellurium with neither rings, nor central facets, nor striations. The dislocation density aparently shows no appreciable increase by pulling crystals on this orientation. Etch pit densities on the (111) slices were nominally in the high 10^3-low $10^4/cm^2$ range.

Growth on this <115> orientation appears to be uniform at this doping level and may offer a solution to the problem of obtaining uniformly doped material. Previous experience in this laboratory has shown that crystals of other materials such as indium antimonide are much more uniform when grown on the <115> orientation. We plan to investigate more heavily doped gallium arsenide crystals grown on this orientation.

Manuscript received Nov. 3, 1965.

Any discussion of this paper will appear in a Discussion Section to be published in the December 1966 JOURNAL.

REFERENCES

1. C. Z. LeMay, *J. Appl. Phys.*, **34**, 439 (1963).
2. M. H. Pilkuhn and H. Rupprecht, *Trans. AIME*, **230**, 296 (1963)
3. T. S. Plaskett and A. H. Parsons, *This Journal*, **112**, 954 (1965).
4. M. E. Drougard and J. B. Gunn, *ibid.*, **111**, 155C (1964).
5. E. S. Meieran, *J. Appl. Phys.*, **36**, 2544 (1965).
6. G. R. Cronin, M. E. Jones, and O. Wilson, *This Journal*, **110**, 582 (1963).
7. J. L. Richards and A. J. Crocker, *J. Appl. Phys.*, **31**, 611 (1960).
8. W. P. Allred and R. T. Bate, *This Journal*, **108**, 258 (1961).
9. J. Black and P. Lublin, *J. Appl. Phys.*, **35**, 2462 (1964).

Cristobalite Formation on Vitreous Silica Boats and the Relation to the GaAs Crystal Growing

M. Yamaguchi, Y. Mizushima, S. Hirota, and H. Noake

Electrical Communication Laboratory, Nippon Telegraph and Telephone Public Corporation, Musashino-shi, Tokyo, Japan

In the course of making single crystals of GaAs by means of the horizontal zone-leveling method, we have found spherulitic cristobalite formation on the sand-blasted surface of a vitreous silica boat which greatly facilitates single-crystal growth.

It is customary to use a sand-blasted vitreous silica boat for single crystal preparation (1). A graphite boat can be used for synthesis, but for single crystal zoning it is inferior to a vitreous silica boat. But even if the vitreous silica boat itself was sand-blasted, GaAs frequently stuck to the boat so that it cracked and the crystals failed to be single.

As the contact points between the molten semiconductor and the boat may promote the nucleation, it would be advantageous if the solidifying interface of the molten zone bends forward in the direction of zone-travel, as (solid/liquid) $\rightarrow$, so that the solidification proceeds downward from the free surface. The lower zone heater carried more current than the upper, to make the vertical temperature difference about 20°C in the furnace tube (25 mm in diameter). Zone-traverse-velocity was 15 mm/hr.

Otherwise successively appearing nuclei may grow up and interfere with the single-crystal formation. By using a boat of high purity (Al_2O_3 50 ppm, Fe_2O_3 10 ppm, CuO 0.1 ppm, MgO tr) and sand-blasted with 600-mesh carborundum we have experimentally verified that the bending interface method is effective for single-crystal preparation[1] and for avoiding sticking of the GaAs to the boat. In this case the whole GaAs surface is as smooth and shiny as that of a free surface.

After the above procedure we always found a layer of white powder on the inner surface of the boat, but only on the area in contact with the liquid phase of GaAs. Electron diffraction analysis showed the powder to be coarsely grained α-cristobalite (Fig. 1). Electronmicrographs of the surface before and after the treatment are shown in Fig. 2 and 3. The crystal has spherulite-like appearance and is fixed with stems to a pit of the vitreous silica surface. The shape of the crystals becomes dendritic at the area where the GaAs solidification proceeds upward from the base surface and the GaAs crystal partly sticks (Fig. 4), so that the cristobalite would have not enough space to grow up.

As a reaction product between the GaAs and silica one may suppose $GaAsO_4$ which is isostructural to SiO_2 (2). They have almost the same crystal parameters. Although $GaAsO_4$ is not known to exhibit α-cristo-

[1] The bending-interface appeared in Pfann's (3) and Chalmers' (4) works to improve the crystallinity so that it tilted backward as (solid/liquid) $\rightarrow$

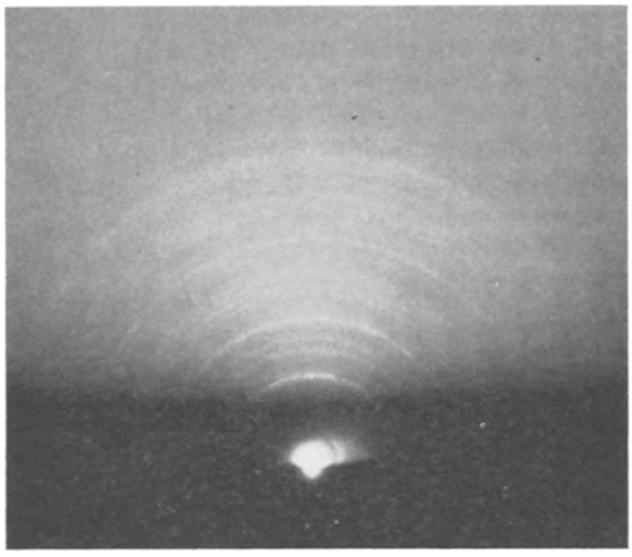

Fig. 1. Electron diffraction pattern of the white powder on the quartz boat showing α-cristobalite. The lattice parameters coincide with the value in ASTM cards.

Fig. 2. Electron micrograph of the sand-blasted quartz boat surface.

Fig. 3. Spherulite-like crystals of α-cristobalite found on the quartz boat after downward solidification of GaAs.

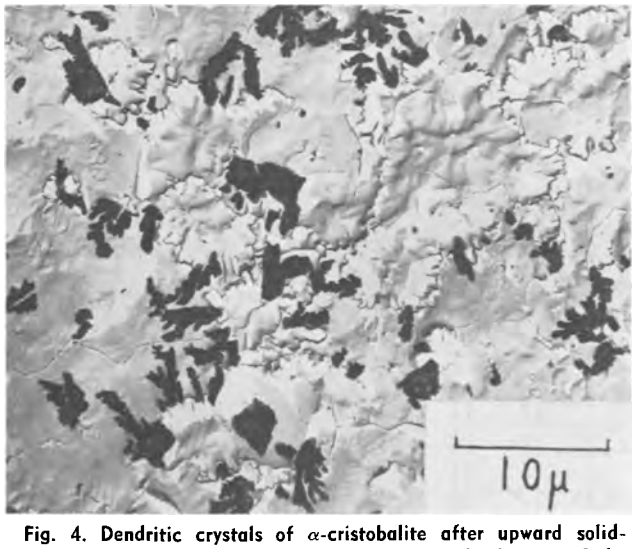

Fig. 4. Dendritic crystals of α-cristobalite after upward solidification of GaAs. There are sticking traces at the bottom of the dendritic crystals.

balite structure (2), we have tested the existence of Ga and As in the powder of α-cristobalite under the x-ray microanalyzer, but neither of them were detected as a major constituent. The probability of this reaction product is therefore excluded.

The melting point of the cristobalite (1713°C) is very much higher than the softening point of the vitreous silica (about 1300°C). In fact, the sand-blasted vitreous silica surface evidently shows softened traces after the crystal-growing (Fig. 3). But the surface retains its roughness even after zone-leveling unless it has contact with the melt of GaAs. Therefore the change of the surface into α-cristobalite is induced not by heat softening, but by the existence of the liquid phase of GaAs.

At the melting point of GaAs (1238°C) the cristobalite crystals prevent the melt from coming in direct contact with the vitreous silica, and the melt is supported by its surface tension on the spherulites so that relatively little stress is introduced into the crystal.

The minimum contact area also ensures minimum contamination from the boat material. Two pieces of GaAs polycrystal cut from the same part of a rod ($n = 10^6$ cm^{-3}) were placed in the same vitreous silica boat, the one (A) was on the white layer of α-cristobalite and the other (B) on the part of the boat which had been only sand-blasted. After melting for the same length of time, both samples were analyzed by means of emission spectroscopy. Table I shows that the amount of detected impurities differs considerably between the two samples. Thus, the cristobalite layer is evidently effective in preventing contamination during the heat-treatment once the cristobalite is formed, since cristobalite is more stable than the vitreous form. The solubility of the more stable cristobalite in the liquid GaAs would be less than that of the metastable vitreous silica.

Table I. Emission spectroscopic result of impurities in GaAs crystal: (A) was molten on the layer of α-cristobalite and (B) on the sand-blasted surface of the quartz boat for about 2 hr

$+ > (+) > \pm >$ tr $>$ $\overline{\text{tr}}$ (doubtful) $>$ — (not detected)

Impurity elements	Wavelength	Before heat-treatment	(A)	(B)
Si	2881.568	$\overline{\text{tr}}$	$\overline{\text{tr}}$	(+)
	2516.123	—	—	tr
Mg	2852.129	+	±	+
	2795.53	±	tr	±
Cu	3247.540	—	—	$\overline{\text{tr}}$
	3273.962	—	—	—

It is peculiar that cristobalite spherulite crystallizes at a temperature never above 1250°C. Also, the thermodynamic stability of cristobalite below 1470°C is questionable, although minute substitution of Ga or As in SiO_2 may stabilize this structure. To identify this stabilizing, impurity experiments were performed in which Ga was heated for 2 hr at 1300°C in a sand-blasted vitreous silica boat in an evacuated ampule. In the area in contact with Ga the same α-cristobalite spherulitic crystals were found. Therefore it is possible that Ga acts as a stabilizing agent.

The mechanism of crystallization is not clear at this time. Consider the following points: SiO_2 [or Si produced by the reaction of SiO_2 in the GaAs melt (5, 6)] dissolves in the melt and segregates at the solidifying interface as SiO_2. With sand-blasting the stressed rough surface may act as the active point for the solution and/or the nucleation, or the transformation, from vitreous silica to the cristobalite structure since this structure does not occur without sand-blasting.

Acknowledgment

The authors are indebted to Mr. T. Simozaki for the emission spectroscopy.

Manuscript received July 6, 1965; revised manuscript received Nov. 6, 1965.

Any discussion of this paper will appear in a Discussion Section to be published in the December 1966 JOURNAL.

REFERENCES

1. L. R. Weisberg, J. Blanc, and E. J. Stofko, *This Journal*, **109**, 642 (1962).
2. E. C. Shafer and R. Roy, *J. Am. Chem. Soc.*, **39**, 330 (1956).
3. W. G. Pfann, "Zone Melting," p. 162, John Wiley & Sons, Inc., New York (1958).
4. B. Chalmers, "Principles of Solidification," p. 306, John Wiley & Sons, Inc., New York (1964).
5. C. N. Cochran and L. M. Foster, *This Journal*, **109**, 144 (1962).
6. C. N. Cochran and L. M. Foster, *ibid.*, **109**, 149 (1962).

The Preparation of Epitaxial Semi-Insulating Gallium Arsenide by Iron Doping

P. L. Hoyt and R. W. Haisty

Texas Instruments Incorporated, Dallas, Texas

The preparation of semi-insulating GaAs by iron doping melt-grown crystals has been reported previously (1). This material has been shown to have a deep acceptor with an energy level of about 0.5 ev and typical resistivities of 10^4-10^5 ohm-cm at room temperature.

This note describes the preparation of epitaxial iron-doped gallium arsenide by an open tube halide transport technique employing GaAs and $AsCl_3$, similar to the method used for Ga(As, P) by Finch and Mehal (2).

Figure 1 shows the experimental apparatus. Hydrogen, purified by Pd diffusion, was bubbled through distilled $AsCl_3$, carrying the vapor into the feed holder in the reactor (R_3). For convenient control of the $AsCl_3$ concentration in the feed region, additional hydrogen was metered in (R_2), and the reaction products from the feed zone were swept toward the seed by a steady flow of hydrogen (R_1). Typical operating conditions were: R_1, 25.0 cm³/min; R_2, 15.0 cm³/min; R_3, 75.0 cm³/min; seed temperature 750°C; GaAs source temperature 950°C.

The GaAs used for feed material and substrates was cut from undoped pulled crystals grown in this laboratory and especially selected for high purity since care must be taken to keep the donor concentration such as Si very low. The substrates were polished to a mirror finish with *ca.* 2.5% NaOCl solution on a polishing wheel (3). Deposits were made on (100), (111), and (115) oriented GaAs seeds. The (115) and (100) orientations were preferred because of faster deposition rate and because better surfaces were obtained on these seeds.

High-purity iron (99.999%) used as the dopant, was placed in the feed holder, typically in four pieces weighing about 50 mg each with 15g of GaAs feed. The iron was cleaned 4-5 min in dilute hydrochloric acid and rinsed in distilled water followed by methanol. Wet chemical and x-ray analysis confirmed the formation of FeAs in the feed holder which appears to be necessary before transport of the iron occurs. The first run after the addition of the iron invariably produces a low resistivity n-type deposit. However, it is convenient to add elemental iron, which can be obtained in a high degree of purity, and form the arsenide in the reactor.

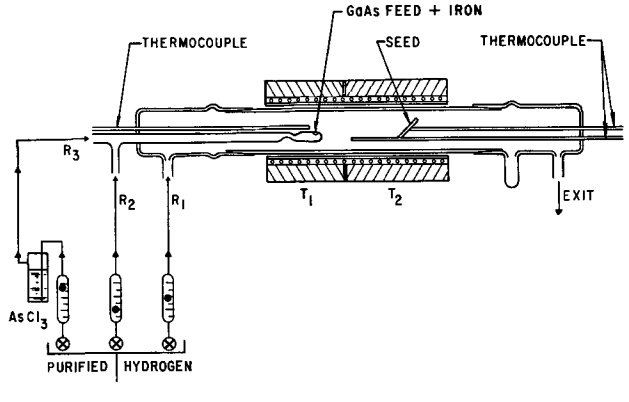

Fig. 1. Vapor deposition system. $R_1 = H_2$ dilution flow; $R_2 = H_2$ feed dilution flow; $R_3 = AsCl_3 + H_2$ flow.

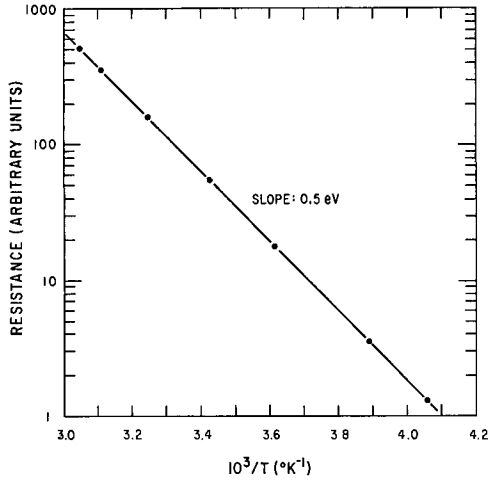

Fig. 2. Temperature dependence of resistance for epitaxial Fe-doped gallium arsenide.

Table I. Electrical properties of epitaxial and melt-grown Fe-doped GaAs at 300°K

Crystal No.	ρ, ohm-cm	μ, cm²/v-sec	p, cm⁻³
Epitaxial GaAs			
145	9.0×10^4	230	3.1×10^{11}
146	6.9×10^4	330	2.7×10^{11}
147	2.7×10^4	370	6.3×10^{11}
Melt-grown GaAs			
3-33	2.7×10^4	208	1.1×10^{12}
3-34	9.6×10^4	206	3.2×10^{11}
3-36	7.2×10^4	243	3.6×10^{11}

To determine the thickness of the deposits, the samples were angle-lapped and either gold plated (4) or stained with a HNO_3 + Fe stain developed by Mehal of this laboratory.[1] The energy level of the deep acceptor in the deposits was determined in the following manner:

1. Samples were cleaved to obtain clean edges.
2. Alloyed Au-5% Zn contacts were applied to the surface of the deposits. (The contacts were shown to be ohmic by measuring current *vs.* voltage at a fixed temperature.)
3. Resistance was measured as a function of temperature. A plot of log resistance *vs.* 1/T (Fig. 2) gave a slope of 0.51 ev which corresponds to the iron level in bulk GaAs. The deposits checked p-type by thermoelectric probe, using an electrometer indicator.

Hall effect measurements made on several Fe-doped deposits for comparison with melt-grown iron-doped GaAs showed that about the same doping levels were achieved in both cases. The epitaxial GaAs used for the measurements was deposited on Cr-doped semi-insulating substrates with resistivities about 10^8 ohm-cm at room temperature, three to four orders of magnitude higher than the deposit to be measured. The deposits were typically about 30μ thick as determined by angle-lapping and staining techniques. Cavitroned samples with side arms were used for the Hall measurements. Ohmic contacts were made using indium contacts. Table I shows a comparison of the electrical measurements of the epitaxial deposits with typical melt-grown, Fe-doped crystals.

It is interesting to note that, while the properties are quite similar, the mobilities are somewhat higher in epitaxial GaAs (5, 6).

To show the possibility of using iron doped semi-insulating epitaxial GaAs in discrete devices or to provide electrical isolation in integrated circuits, such as three-dimensional electronic blocks (7), a sample n-SI-n sandwich structure was prepared. This structure was made using the apparatus described above in the following manner:

1. A 15μ n-type GaAs layer was deposited by the usual technique on a high-resistivity (115) oriented substrate, using undoped feed material.
2. This substrate and deposit were then removed from the reactor, and several runs were made with iron added to the feed material to insure that semi-insulating deposits were being obtained consistently.
3. The original substrate with n-type deposit was cleaned in hot methanol and placed in the reactor.
4. An 8μ semi-insulating layer was deposited on the n-type deposit with no appreciable change in the latter.
5. The reactor was cleaned and new undoped feed material was placed in the feed holder.
6. The sample was again cleaned and returned to the reactor for the final n-type deposition. An n-type deposit (7μ) was produced on the semi-insulating layer.

The sequence of angle-lapped, stained sections made during the entire process showed no appreciable movement of the boundaries during deposition steps, which indicated that diffusion of the dopants is not a problem in this case.

[1] The NHO_3-Fe staining solution is made by dissolving about 1g of iron in 100 cc of 1.0*N* HNO_3.

Acknowledgment

The authors wish to acknowledge the support of the Electronics Technology Laboratory of the Research and Technology Division, Air Force Systems Command, United States Air Force, Contract AF 33(615)-1275. They also wish to thank O. W. Wilson for the bulk GaAs and W. B. Henderson for assistance in the experimental work.

Manuscript received Aug. 13, 1965; revised manuscript received Nov. 15, 1965. This paper was presented at the San Francisco Meeting, May 9-13, 1965.

Any discussion of this paper will appear in a Discussion Section to be published in the December 1966 JOURNAL.

REFERENCES

1. R. W. Haisty and G. R. Cronin, Proc. Int. Conf. on Phys. Semicond., Paris, 1964, p. 1161.
2. W. F. Finch and E. W. Mehal, *This Journal*, **111**, 814 (1964).
3. A. Reisman and R. Rohr, *ibid.*, **111**, 1424 (1964).
4. R. W. Haisty, *ibid.*, **108**, 790 (1961).
5. J. R. Knight, D. Effer, and P. R. Evans, *Solid-State Electronics*, **8**, 178 (1965).
6. E. W. Mehal and G. R. Cronin, To be published.
7. R. E. Johnson, R. C. Sangster, and W. J. Beyen, Proc. 4th Annual Microelectronics Symposium, May 24-26, St. Louis, Mo.

The Epitaxial Growth of Ge on Si by Solution Growth Techniques

J. P. Donnelly and A. G. Milnes

Carnegie Institute of Technology, Pittsburgh, Pennsylvania

Solution growth techniques have a long history in the field of crystal growth. The solution growth process reported in this work is based on the work of Nelson (1, 2) for fabricating tunnel and laser diodes. This same method has also been used to fabricate p Ge-n GaAs heterojunctions (3-5).

The stable oxide layer of silicon, however, presented many problems in trying to fabricate Ge-Si heterojunctions by similar solution growth techniques. To overcome these problems, it was decided to use in-growth cleaving techniques to achieve oxide free surfaces. Silicon L-bars with their major axis in the <111> direction, as first described by Gobeli and Allen (6), were used as seeds. An all-graphite boat, with a clamping arrangement at one end to hold these L-bars securely, was constructed. Provisions were made for a quartz cleaving rod to facilitate in-growth cleaving of the L-bars. During the growth cycle the graphite boat is locked in position at the center of a long constant temperature zone of a quartz tube furnace which is free to rotate about its center. Solutions consisting of 20g Sn, 2.5g Ge and 0-100 mg of

either Ga for p-type material or As for n-type material are free to run from one end of the graphite boat to the other depending on the tilt of the furnace. Forming gas (95% nitrogen, 5% hydrogen) or hydrogen is passed through the furnace during the growth cycle to prevent oxidation.

With the solution at the end of the boat opposite the clamped silicon L-bar, power is applied to the furnace heating winding, and the temperature of the graphite boat is raised from room temperature to 625°C in approximately 1 hr. At this temperature, the power is turned off and the furnace tipped so the solution completely covers the L-bar. When the temperature cools to 600°C, the silicon L-bar is cleaved using the quartz cleaving rod. This creates the oxide free silicon surface on which the germanium depositing from the cooling solution grows epitaxially. At 400°C, the furnace is tipped back so the solution runs off the seed stopping the growth. During the growth period, the cooling rate used is between 10° and 15°C/min.

Using this method single crystal germanium layers up to 5 mils thick were grown on the cleaved silicon seeds. The growth rates were approximately 0.35 mils/min. Although the surfaces were often very rough due to the solidification of some of the solution which tended to cling to the sharp edges of the cleaved seed and clamping arrangement, the junctions were consistently very flat as shown in Fig. 1. Laue back reflection x-ray photographs indicated good single crystal germanium overgrowth in the 111 direction. However, there was slight elongation and splitting of some of the Laue spots. It is believed that the elongation and splitting are due to thermal strain and cracking, respectively, which occur because of the large thermal mismatch between Ge and Si. The cracks become evident on etching with any standard Ge etch. Figure 2 shows a typical photograph of these cracks after a 30-sec etch with etching solution composed of (5 vol HNO_3, and 1 vol HF). Beside the cracking difficulty in these layers, the stacking fault density was found to be high as shown in Fig. 3. The stacking faults were brought out by polishing the grown layer with alumina abrasive powder (0.05μ) and then etching in a solution (0.2g $AgNO_3$, 25 ml H_2O, 10 ml HF, 15 ml HNO_3) which plates the imperfections with silver. Although most of these faults are probably due to lattice mismatch and strain effects, similar measurements on Ge layers grown on Ge and GaAs from both indium and tin solutions (3, 5) indicate that better crystallographic material might be obtained by using a lower melting point solvent such as indium or a lead-tin alloy instead of tin. Impurity concentrations as low as approximately 10^{17} cm^{-3} could be obtained by varying the amount of As and Ga in the solution.

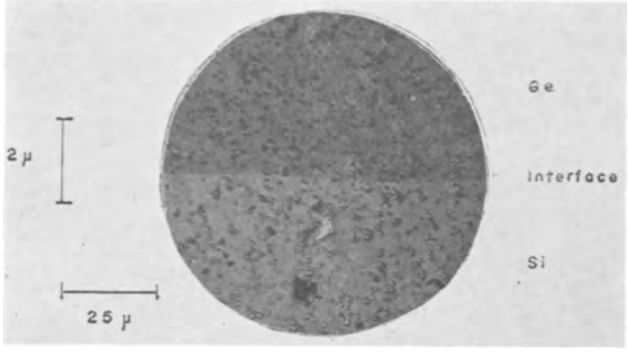

Fig. 1. View of 6° angle-lapped section of a germanium layer grown on a cleaved Si seed from a tin solution.

Fig. 2. Cracks in germanium grown on silicon from a tin solution after 30-sec white etch.

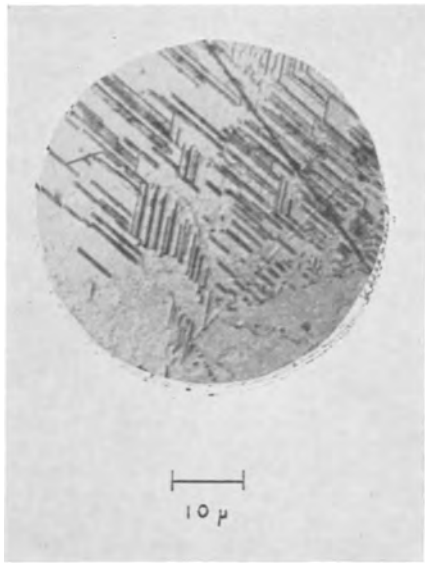

Fig. 3. Stacking faults in germanium grown on silicon from a tin solution.

In conclusion, a rapid reliable method of obtaining abrupt Ge-Si heterojunctions has been developed. Although the Ge overgrowths were cracked due to thermal effects, large enough uncracked areas were obtainable to fabricate diodes. The characteristics of these diodes are reported elsewhere (5, 7) and are comparable with those obtained on diodes fabricated by the germanium diiodide disproportionation reaction (8).

Manuscript received Oct. 13, 1965. This work was supported in part by U. S. Army Research Office (Durham), Contract DA-31-124-ARO(D)-131.

Any discussion of this paper will appear in a Discussion Section to be published in the December 1966 JOURNAL.

REFERENCES

1. N. H. Ditrick and H. Nelson, *R.C.A. Engineer*, **7**, 19 (1961).
2. H. Nelson, *R.C.A. Review*, **24**, 603 (1963).
3. H. Nelson, Private communication.
4. S. S. Perlman, D. L. Feucht, and R. M. Williams, *Trans. Inst. Radio Eng's. on Electron Devices*, **ED-9**, 509 (1962).
5. J. P. Donnelly, Thesis, Carnegie Institute of Technology, Pittsburgh (1965).
6. G. W. Gobeli and F. G. Allen, *J. Phys. Chem. Sol.*, **14**, 23 (1960).
7. A. R. Riben, J. P. Donnelly, and D. L. Feucht, "Electrical Characteristics of Ge-GaAs and Ge-Si p-n Heterojunctions," Solid State Device Research Conference, Princeton, N. J. (1965).
8. W. G. Oldham, A. R. Riben, D. L. Feucht, and A. G. Milnes, Paper presented at the Pittsburgh Meeting of the Society, April 15-18, 1963.

On the Removal of Dislocations in Crystals Grown by Travelling Solvent Method

G. A. Wolff and B. N. Das

Tyco Laboratories, Inc., Waltham, Massachusetts

X-ray diffraction contrast methods provide an efficient means for observing dislocations in crystals. The phenomenon of anomalous transmission of x-rays is observed in nearly perfect crystals and results in enhanced transmission when the crystal is set for Laue diffraction. The effect was first observed by Borrmann (1); its theory was described in detail by Batterman and Cole (2) with reference to previous work.

In previous experiments on the TSM growth of GaAs (3) and $SrTiO_3$ (4), it has been shown by etching techniques that the etch pit concentration decreases fairly abruptly to values which are lower by at least an order of magnitude for the regrown material compared to the original seed material. Since a one-to-one relationship between etch pits and dislocations in crystals is not expected to exist in all cases, an anomalous x-ray transmission technique was used to determine dislocations and dislocation density. Preliminary anomalous transmission tests on GaAs (5) and GaSb (6) have largely confirmed the findings of etching investigations. In the following, specific evidence is presented for such a dislocation decrease in GaSb and for anomalous transmission in transmission Laue micrographs for this material. The propagation of dislocations in TSM crystal growth and the method of evaluation of Burgers vectors in single crystals are also discussed.

High-purity GaSb of 1 x 10^{17} (electronic) hole carrier concentration, 650 cm^2/volt-sec Hall mobility, and 0.1 ohm-cm resistivity, was used in this study. The TSM grown GaSb crystal of 0.7 mm thickness and 1 mm height was mounted on a goniometer head after being etched in 1 part HF: 4 parts HNO_3: 5 parts distilled water for 1 min and accurately set in front of a 40 cm collimator. Preliminary x-ray photographs were taken on Ilford industrial x-ray film (type G), and the final exposures were made on single coated, Kodak industrial x-ray film (type M). The time of exposures varied from 2 hr to 8 days. Dislocations were studied on TSM grown GaSb crystals using white radiation (schematic in Fig. 1 and Fig. 2) and characteristic radiation ($CuK\alpha$) at operating voltage of 25-40 kv and 15-20 ma current.

Figures 3 a, b, and c, show, respectively, the $(31\bar{1})$, $(24\bar{2})$, and $(51\bar{1})$ reflection micrographs of the GaSb crystal obtained by Laue transmission. All three micrographs show an increase of x-ray transmission in the upper regrown section of the crystal over the transmission in the lower seed crystal section. When the product μt (with μ being the linear absorption coefficient and t the thickness of the crystal) is large ($\mu t >> 1$), the conditions for observing anomalous transmission are satisfied. This is observed, since, for the shortest wavelength (which satisfies the Laue condition) of these reflections, $\mu t \simeq 6.4 >> 1$. The elimination of dislocations during crystal growth apparently increases the anomalous transmission through the (upper part of the) crystal. This produces the photographic contrast between the two sections of the photographs, which correspond to the regrown region and the seed region of the crystal. The dark striations

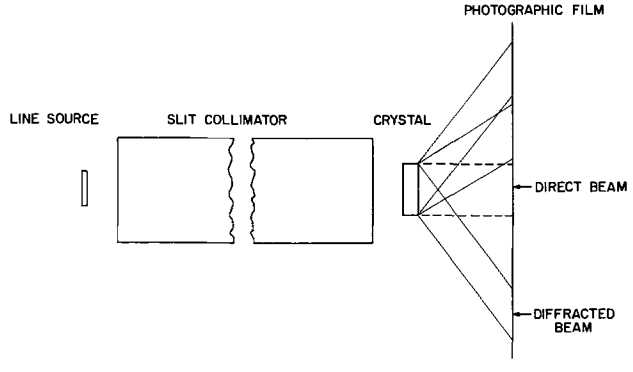

Fig. 1. Schematic of experimental arrangement for anomalous transmission study by Laue transmission.

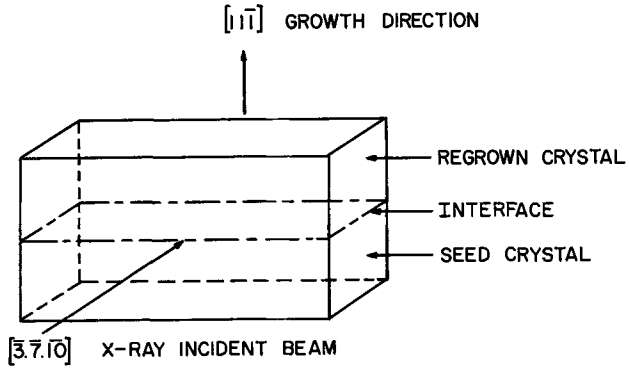

Fig. 2. Schematic view of the GaSb crystal investigated

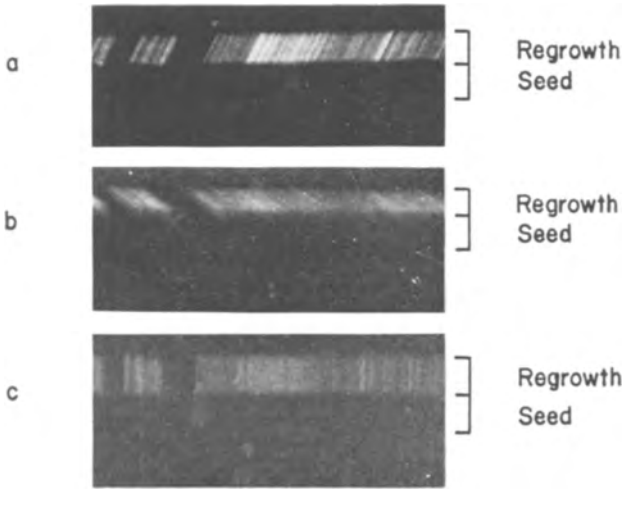

Fig. 3. (a) (top), (b) (middle), and (c) (bottom) show, respectively, the $(31\bar{1})$, $(24\bar{2})$ and $(51\bar{1})$ reflection micrographs of the GaSb crystal obtained by Laue transmission. The upper regrown section is largely made up of light areas of low dislocation content. Striation indicates direction of dislocation lines. The two dark patches in the upper section represent nonreflecting crystals of slightly different orientations which have been nucleated by poor solvent wetting.

in the photograph positive, then, indicate the trace of dislocation lines (in the regrown section) projected onto the plate in a direction which is parallel to the forward reflected x-ray beam. They do not indicate oriented impurity segregation or strain fields not associated with dislocations or simple surface scratches, as one could perhaps assume, since, upon comparison of such a micrograph with others from different reflections in this case, the actual striations in the crystal due to impurity or strain should not differ in orientation, which is contrary to the findings. This is particularly apparent when x-ray micrographs of neighboring reflections are compared, where orientation differences of more than 30° [*e.g.*, $(31\bar{1})$ *vs.* $(51\bar{1})$] are observed. An anomalous x-ray transmission photograph obtained with CuKα radiation from $(11\bar{1})$ of the GaSb crystal also showed two sections, with the brighter section corresponding to the regrown part and the darker section corresponding to the seed part. This result thus supports the first finding. Due to the relatively long transmission paths of transmitted and reflected beams, the resolution was not high enough to show individual dislocations; in addition $\mu t \simeq 80$ in this case was too high for anomalous transmission analysis. In silicon single crystals dislocations have also been observed using white x-ray radiation (extinction contrast) (7, 8).

The contrast of individual dislocation lines in the micrograph is determined by the dislocation density and the orientation of the dislocation lines relative to the reflecting plane. The dislocation density must be low enough for these lines to be individually distinguishable. The maximum value of dislocation concentrations for which single dislocation lines can still be recognized in the Laue transmisison micrographs is approximately 10^4 lines/cm^2. For the 0.7 mm thick sample, about 200 lines/cm corresponding to 3×10^3 lines/cm^2 are counted, which is roughly of the same order of magnitude as the etch pit count of 10^3 etch pits/cm^2 found in our crystals.

Since the condition for dislocation contrast is $\vec{g} \cdot \vec{b} \neq 0$ (with $\vec{g}$ being the diffraction vector and $\vec{b}$ the Burgers vector), the observed orientation of dislocation lines in each photograph permits the determination of the respective Burgers vector and the type of dislocation as shown in Table I. In this table the Burgers vectors and the type of dislocations observed were correlated with the dislocation models derived by Hornstra (9). The corrections due to perspective and geometrical conditions were taken into account. It has been found that glide planes for most of the grown-in dislocations and their deduced Burgers vectors lie in octahedral planes.

Table I. Dislocations in GaSb as evaluated by x-ray diffraction microscopy

Further identification of the multiple choices of Burgers vectors would be possible by taking photographs from other directions of incident beam. The (022) reflection micrograph shows three different types of dislocation lines as indicated by the three different sets of striations. Reflections from $(31\bar{1})$, $(24\bar{2})$ and (511) are presented in Figs. 3, (a), (b), and (c), respectively.

Reflecting plane	Dislocation line direction and glide plane		Hornstra (9) notation	Burgers vector
$(31\bar{1})$*	[011]	$(1\bar{1}1)$**	II	½[110]
	[011]	$(1\bar{1}1)$	II	½[10$\bar{1}$]
$(24\bar{2})$	[211]	(111)	V	½[01$\bar{1}$]
(200)*	[110]	$(1\bar{1}1)$**	II	½[$\bar{1}$01]
	[10$\bar{1}$]	(111)	II	½[$\bar{1}$10]
	[10$\bar{1}$]	$(1\bar{1}1)$	II	½[110]
	[$\bar{1}$12]	$(1\bar{1}1)$	IV	½[$\bar{1}$01]
	[$\bar{1}$12]	$(1\bar{1}1)$	V	½[110]
$(0\bar{2}2)$*	[110]	$(\bar{1}11)$**	II	½[0$\bar{1}$1]
	[1$\bar{1}$0]	(111)	II	½[0$\bar{1}$1]
	[$\bar{1}$01]	(111)	II	½[0$\bar{1}$1]
$(0\bar{2}2)$	[101]	$(\bar{1}11)$	II	½[011]
$(0\bar{2}2)$*	[2$\bar{1}$1]	(111)	IV	½[1$\bar{1}$0]
$(1\bar{1}1)$	[0$\bar{1}$1]	(111)**	II	½[110]
	[0$\bar{1}$1]	$(\bar{1}11)$	II	½[101]
$(51\bar{1})$	[121]	(111)**	IV	½[110]
	[121]	$(1\bar{1}1)$	V	½[$\bar{1}$01]

* Although dislocations of type VII are possible, they are not included in this table.

** These dislocation types are possible one at a time or in combination.

The mechanism of dislocation removal can be explained by either a closed loop formation, or by degeneration through transformation to other types of dislocations which then propagate sideways and normal to the crystal growth direction until they intersect with the surface (5, 6). Specifically, it is possible that during crystal growth, pairs of screw dislocations of opposite sign will terminate in closed half-loops, and single screw dislocations transform to dislocations with edge-components, which propagate sideways to the crystal surface (Fig. 4). The latter dislocation system may conveniently be called "partial loops." The formation of both half-loops and partial loops is a result of climb and is confined to the very first stages of solvent growth. This is indicated by the abrupt change of dislocation density at the crystal interface where regrowth started, and by the uniform dislocation density of the regrown crystal (Fig. 3). This process represents a dislocation climbing mechanism directly associated with crystal growth, since the dislocation half loops and partial loops propagate as each layer deposits. The half loop and partial loop formation and associated elimination of dislocations are limited to the first 100μ, or less, of solvent growth as estimated from Fig. 3. This is in fair agreement with the value of 150μ given for GaAs (5). In a somewhat related way the elimination of edge and edge-type dislocation observed can be explained. It appears, therefore, that dislocations are not required and do not participate critically in the mechanism of travelling solvent growth of GaSb and GaAs from the metal solution. It must be concluded that the catalytic (equilibrating) influence of the (liquid metal) solvent becomes greater than the catalytic influence of dislocations in crystal growth.

Since each specific anomalous transmission reflection records only dislocations with their Burgers vectors not parallel to the reflecting planes, the evaluation of such reflections allows the analysis of the mechanism of crystal growth and dislocation removal, using separately white and characteristic x-ray radiation. This work will be reported in a later publication. Decoration and (Berg-Barrett) x-ray techniques also indicate a similar elimination of dislocations in SiC by TSM regrowth (10).

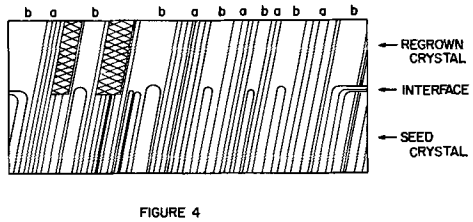

FIGURE 4

Fig. 4. Two-dimensional schematic illustrating dislocation removal observed in travelling solvent single crystal growth, as related to Fig. 2. Idealized dislocations of one type are shown as a system of parallel lines. The two-cross-hatched areas represent slightly disoriented regrown single crystal sections, where Bragg reflection does not occur (see also Fig. 3). Dislocations are eliminated from propagation in the regrown crystal by half-loop formation (regions b), or else by the formation of screw or edge type (60°) dislocations (here called "partial loops") parallel to the crystal growth front, both of which are the result of climb. All dislocations eliminated in this way terminate at the plane of solvent growth commencement. Anomalous x-ray transmission is low in sections a, and enhanced in sections b.

Acknowledgments

The authors wish to thank Doctors A. I. Mlavsky and M. Weinstein for helpful discussions, Miss A. D. Sarney for aid in the calculations, and Mr. E. J. Alexander for crystal growing and experimentation. Support for this work was furnished in part by the Energetics Branch of the Air Force Cambridge Research Laboratory under Contract No. AF 19(628)-2845 and in part by the Air Force Office of Scientific Research under Contract No. AF 49(638)-1246, ARPA order No. 444.

Manuscript received July 12, 1965; revised manuscript received Nov. 8, 1965.

Any discussion of this paper will appear in a Discussion Section to be published in the December 1966 JOURNAL.

REFERENCES

1. G. Borrmann, *Physik. Z.*, **42**, 157 (1941).
2. B. W. Batterman and H. Cole, *Rev. Mod. Phys.*, **36**, 681 (1964).
3. A. I. Mlavsky and M. Weinstein, *J. Appl. Phys.*, **34**, 2885 (1963).
4. B. DiBenedetto and A. I. Mlavsky, Unpublished work.
5. M. Weinstein, H. E. LaBelle, Jr., and A. I. Mlavsky, *J. Appl. Phys.*, **37**, (1966) in press.
6. G. A. Wolff and A. I. Mlavsky, Proc. Intern'l. Conf. on Adsorption and Crystal Growth, Nancy, France, June 1965, p. 711.
7. L. Fiermans, *Phys. stat. sol.*, **6**, 169 (1964).
8. T. Fujiwara, S. Dohi, and J. Sunada, *Jap. J. Appl. Phys.*, **3**, 129 (1964).
9. J. Hornstra, *J. Phys. Chem. Solids*, **5**, 129 (1958).
10. L. B. Griffiths, To be published.

A Method of Casting Sound Ingots of Thermoelectric Materials

W. N. Borle and B. L. Sharma

Solid State Physics Laboratory, Delhi, India

In general, ingots of semiconducting materials are prepared by melting the charge and casting it into fused silica tubes, Vycor tubes, or graphite molds (1, 2). Cast polycrystalline ingots are often used for thermoelectric device work, zone refining, etc. Especially for thermoelectric generators and coolers in which the authors are interested (3, 4), the ingots should, apart from having uniform thermoelectric properties, contain no mechanical defects like shrinkage cavities and blow holes.

Ingots of PbTe, for example, are prepared by first mixing and melting thoroughly stoichiometric amounts of the constituent elements in a quartz tube or graphite mold and then freezing the melt to form an ingot within the tube. Usually, as shown in Fig. 1, a long shrinkage piping occurs along the vertical axis of the ingot. This piping can be reduced by slow directional freezing, but then the segregation during solidification increases. In order to overcome these difficulties a simple method of casting sound ingots having uniform composition and thermoelectric properties has been devised and is discussed below.

In this method, as mentioned above, the compound is prepared by melting Pb and Te under inert atmosphere (hydrogen, argon, or nitrogen) in a quartz container. The furnace is rocked mechanically to ensure complete homogenization of the molten charge. PbTe is then remelted in a graphite mold having required

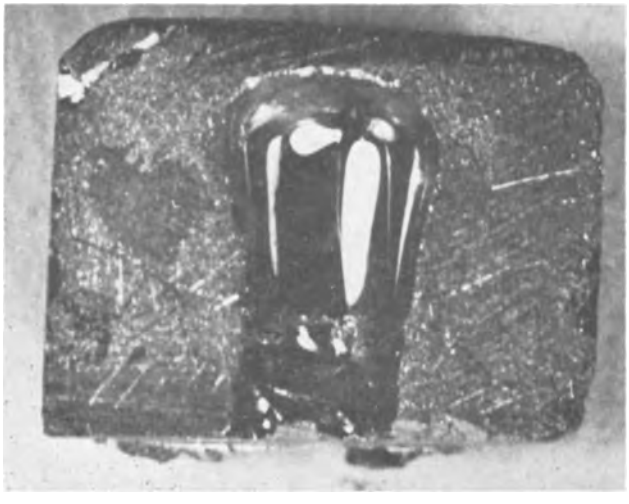

Fig. 1. Cross-sectional photograph of the top end of a PbTe ingot obtained by the ordinary casting method.

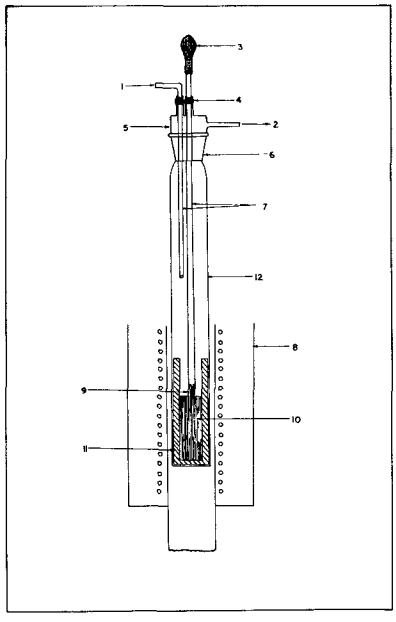

Fig. 2. Apparatus for casting sound ingots: 1, inlet; 2, outlet; 3, rubber bulb; 4, rubber tube; 5, Pyrex glass; 6, ground joint; 7, quartz tubes; 8, furnace; 9, arrested cavity; 10, molten material; 11, graphite mold; 12, quartz jacket.

dimensions. As shown in Fig. 2, a quartz tube, having a sliding arrangement at the top of the ground joint of the atmosphere enclosure, is used as a shrinkage cavity arrestor. By vertical displacement with the slider, this tube is inserted in the melt to approximately 1 cm depth. Then with the help of the rubber bulb fixed at the top of the quartz tube a small quantity of the molten material is sucked into the tube. In this process one must ensure that the immersed portion of the quartz tube attains the same temperature as that of the molten material in the graphite mold. This can be achieved by heating the complete assembly for a long time inside the furnace.

After this, the complete assembly is lowered vertically through the furnace so that it is rapidly air quenched and the molten material solidifies directionally from the bottom. As the rate of cooling of the material inside the graphite mold is faster than that of the material in the quartz tube due to the differences in the thermal conductivities of the two, the material inside the quartz tube will be the last to

Table I. Comparison of the electrical resistivity along the length of PbTe samples before annealing

Distance from the bottom end in mm	By above technique ρ in ohm-cm	By slow directional freezing method ρ in ohm-cm
0-5	2×10^{-3}	2.1×10^{-3}
5-10	1.6×10^{-3}	3.7×10^{-3}
10-15	2.5×10^{-2}	3.9×10^{-3}
15-20	2.3×10^{-3}	5.6×10^{-3}

freeze. We speak only in relative terms since, although the rate of lowering in the furnace and actual process of quenching are important factors, they depend entirely on experimental parameters, such as the geometry of the furnace, the assembly, etc. In the above experiments rapid air quenching was used to minimize the segregation problem, as this is a comparatively faster method of solidification than the slow directional freezing method (modified Bridgman technique). By minimizing segregation in the cast ingot, subsequent annealing periods can be reduced considerably. The electrical resistivity before annealing treatment, of two typical samples of PbTe, prepared by the above and by the usual slow directional freezing technique are compared in Table I.

Very sound ingots of doped lead-telluride without shrinkage cavity or blow holes were cast by this technique. Figures 1 and 3 show the vertical cross sections of the upper portion of samples prepared by the ordinary casting method and by this method, respectively. It is clear from the photographs that the shrinkage cavity is localized and completely arrested in the quartz tube and from Table I that the segregation is minimum.

Acknowledgment

The authors are grateful to Dr. N. B. Bhatt, Director, Solid State Physics Laboratory, for providing facilities and encouragement. They are also thankful to Drs. A. K. Sreedhar and V. V. Agashe for helpful discussion and Mr. B. K. Sachar for preparing the lead telluride.

Manuscript received May 10, 1965; revised manuscript received Nov. 9, 1965.

Any discussion of this paper will appear in a Discussion Section to be published in the December 1966 JOURNAL.

Fig. 3. Vertical cross section of the top end of a PbTe ingot obtained by this method.

REFERENCES

1. "Metallurgy of Semiconductor Materials," J. B. Schroeder, Editor, Metallurgical Society Conferences Vol. 15, p. 285, Interscience Publishers, N. Y. (1962).
2. "Properties of Elemental and Compound Semiconductors," H. C. Gatos, Editor, Metallurgical Society Conferences, Vol. 5, p. 71, Interscience Publishers, N. Y. (1960).
3. V. V. Agashe *et al.*, *J. Inst. Telecom. Engrs.*, **10**, 297 (1964).
4. A. K. Sreedhar *et al.*, *ibid.*, **10**, 207 (1964).

Measurement of the Reflectance of an Electrode Surface

D. F. A. Koch and D. E. Scaife

Division of Mineral Chemistry, Commonwealth Scientific and Industrial Research Organization, Melbourne, Australia

The measurement of the adsorption of ions or molecules on an electrode surface is of major importance in studies of electrochemical energy conversion, corrosion, and electropolishing. The surface coverage can be determined electrochemically by pulse and rapid potential sweep methods, by chemical analysis, or by radio tracer techniques. Recently it has been shown (1) that, for a strongly adsorbed species such as oxygen on platinum, the changes in light reflectance can be directly related to the amount of oxygen adsorbed on the surface. This technique could offer advantages in systems where competing reactions not involving a strongly adsorbed species occur. For example, we have found (2) that the adsorption of formaldehyde on platinum has no significant effect on the reflectance spectra, and, consequently, the oxygen coverage can be determined by the reflectance method in the presence of this reacting species. In cases where the metal dissolves, large changes in reflectance are caused by etching or polishing of the surface; a recent study of such a system (3) demonstrated this behavior clearly and also showed that the passivation of a gold surface in cyanide solution could be attributed to the effect of adsorbed films on the dissolution mechanism.

In this paper, we shall describe in greater detail the experimental techniques used and some of the results obtained for oxygen adsorption on platinum and gold dissolution in cyanide.

Experimental

The electrolysis cell is shown in Fig. 1. The electrode was in the form of a metal disk suspended from a platinum hook sealed into a glass tube, which fitted through a cone and socket joint and could be rotated into position once placed in the cell. The distance of the electrode from the optically flat silica window was 2-3 mm, and the metal disk was sufficiently rigid on its suspension to avoid disturbance from bubbling. The cell was equipped with gas inlets and outlets, to provide a controlled atmosphere and agitation, and with a Luggin capillary connected to a saturated calomel reference electrode. Potentials were controlled by an electronic potentiostat (4).

In the systems studied here, uneven current distribution between front and back faces of the electrode is not a serious problem. In the case of platinum, very little current was passed; in the case of gold dissolution in cyanide, currents of the order of 1 ma/cm^2 were passed, and the changes in reflectance still coincided with the passivation potentials measured in a conventional cell.

The front face of the cell was held against the sample port of a Beckman DK2A Spectroreflectometer, the

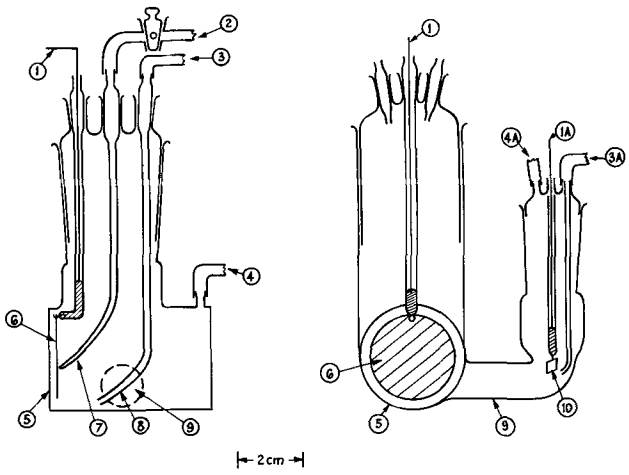

Fig. 1. Electrochemical cell for reflectance measurements: 1,1A, leads to potentiostat. 2, H_2SO_4-filled bridge to saturated calomel reference electrode; 3,3A, gas inlets; 4,4A, gas outlets; 5, silica window; 6, working electrode; 7, Luggin capillary; 8, gas bubbler; 9, side arm connecting to compartment with counter electrode, gas inlet and outlet; 10, counter electrode.

metal sample being just a little larger than the sample port. In this system, light from the sample is reflected back into the MgO-coated integrating sphere of the reflectometer, and measured by a detector at the top of the sphere in comparison with the light reflected from a standard sample in the reference beam. In this work MgO plates, or flat disks of the metal under examination, were used as standards.

To enable the cell to be fitted against the sample port, the door of the reflectometer was replaced by a large aluminum box 25 x 25 x 30 cm high made completely light-tight, and painted matte black inside. This box contained various built-in clamp supports and holes for gas and electrical leads, and had a removable lid. The front section of the box was swung on the hinges provided for the standard door which it replaced.

The exact positioning of the electrode relative to the light beam was found to depend on the nature of the surface; in the case of samples which were completely flat and of mirror-finish, it was necessary to determine whether diffuse or total reflectance measurements were appropriate. In the former case, the light reflected specularly (*i.e.*, at the angle of incidence) must be reflected back out through the beam entrance ports of the sphere, only diffusely reflected light being collected by the sphere for measurement. In the latter case, the specularly reflected beam is reflected back onto the walls of the sphere and measured. In fact, none of the samples used in this work were sufficiently flat or polished to present this problem, random scratches in particular causing the specularly reflected beam to lose coherence almost completely. A very small amount of light was diffusely reflected from the silica window and liquid medium, and a slightly larger specular component of reflected light occurred at the air-silica and silica-liquid interfaces. Both of these components were negligible for the purpose of this study, being in any case constant during a set of measurements. Light losses in the gap between sample and window were similarly negligible.

The platinum electrodes used in this work were of cold-rolled sheet, flame annealed, and anodized and cathodized several times before use. Temperatures in the cell were 27°-30°C.

Results and Discussion

The performance of the system may be judged from data obtained for a platinum electrode in *N* H_2SO_4 solution. The relationship between reflectance (relative to MgO), measured when it showed no further

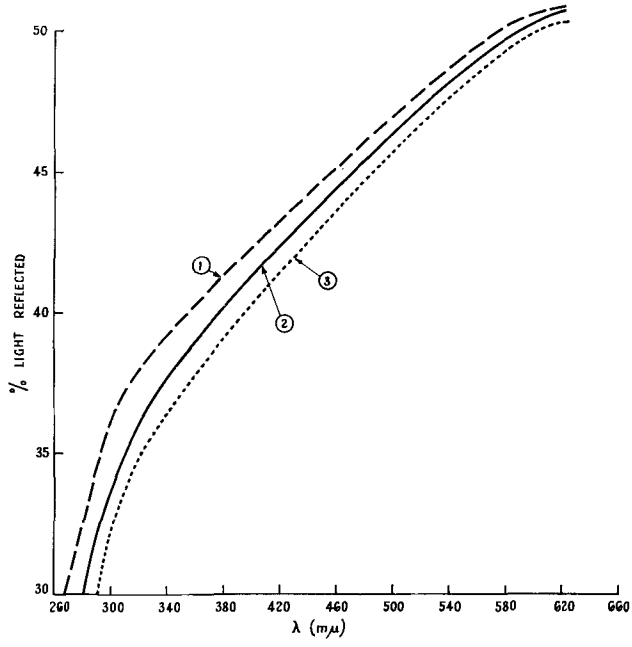

Fig. 2. Reflectance (MgO reference) *vs.* wavelength for Pt in *N* H_2SO_4, at various potentials: 1, 0.3v (*vs.* N.H.E.); 2, 1.2v; 3, 1.6v.

change, and wavelength, at three potentials is shown in Fig. 2. It can be seen that the absorption edge of the platinum is shifted in the direction of longer wavelength as the potential is increased in the anodic direction. From the curves of Fig. 2 values can be calculated for the change in reflectance, ΔR, with potential, which is plotted against wavelength in Fig. 3. There is a continuous increase in ΔR with decreasing wavelength, the sharpest rise occurring below 420 mμ. Previous results against MgO suggested a maximum in these curves (1), but the more sensitive differential method against platinum (see below) confirmed the results shown in Fig. 3. The small inflections indicated by the points off the curves are probably within experimental error, and no discrete absorption band structure is clearly shown.

The changes in reflectance with time, as a function of electrode potential, were recorded at a constant wavelength of 350 mμ, and are shown in Fig. 4. Before the application of the required potential, the electrode surface was stripped of oxygen by maintaining it at 0.3v (*vs.* N.H.E.) (5) for about 3 min. This provided a reproducible initial surface which served as a base line for changes in reflectance. In this case, the reflectance of the sample was compared with that of a

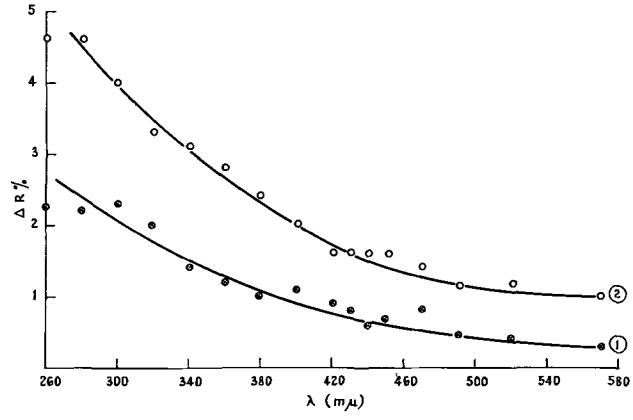

Fig. 3. Change in reflectance (ΔR) vs. wavelength for Pt in *N* H_2SO_4 at various potentials (v *vs.* N.H.E.): 1, $R_{(0.3v)} - R_{(1.2v)}$; 2, $R_{(0.3v)} - R_{(1.6v)}$.

platinum metal disk as reference instead of MgO. This provided closer matching (within 1-2%) of the sample and reference reflectance over the whole wavelength range, and allowed the use of the 0-10% reflectance differential setting on the instrument to amplify tenfold the small changes in reflectance of the sample on application of anodizing potentials. The changes of reflectance shown in Fig. 4 are, therefore, ten times the absolute changes relative to MgO. For a pen circuit time constant of 0.6 sec, the peak-to-peak noise in the traces was approximately 10% of the maximum change in reflectance measured. The rates of change of reflectance on changing the potential indicated (see Fig. 4) an initial fast reaction, with time constant of about 5 sec, followed by a slower reaction. (Surfaces previously saturated with hydrogen, which diffuses into the metal, showed considerably slower reactions.) The changes in reflectance measured when the reflectance became steady, were found to be related to the electrode potential, and a curve was obtained (1) which followed closely the plot of oxygen surface coverage (in coulombs) against potential. Similar curves for the changes in reflectance with potential were found at other wavelengths.

It is probable that this experimental method could be applied to other systems in which corrosion by material transport of metal from the surface does not occur. Similar results have, in fact, been obtained for gold in dilute sulfuric acid.

The reflectance changes with electrodes which dissolved under the experimental conditions (Au in KCN or Ni in H_2SO_4) were basically different to those obtained with insoluble electrodes (Pt and Au in H_2SO_4). In the former case, large changes (up to 50%) in reflectance were observed which were often only slowly reversible and which continued for 15 min or more without reaching steady values, while in the latter case, reproducible and constant reflectance values were obtained in a few minutes, and the changes in reflectance were always rapidly reversible.

This behavior of the dissolving electrodes, together with the visual observation that the electrode surface was roughened after a treatment which produced a decrease in reflectance, suggests that the changes in reflectance in these systems are caused by etching and polishing of the surface. The change in reflectance with time of a gold surface in cyanide solution, shown in Fig. 5, is a clear example of this behavior, the changes in this case being very much slower than those observed with platinum (Fig. 4).

By starting with an electrode fully roughened by etching, and using carefully standardized procedures,

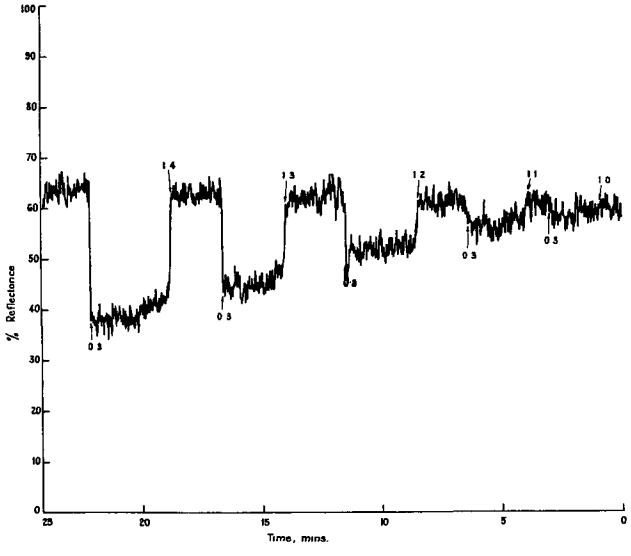

Fig. 4. Reflectance (Pt reference) vs. time for Pt in N H_2SO_4 for a series of potentials (volts vs. N.H.E.). Scale expanded approximately 10 x scale of Fig. 2 and 3.

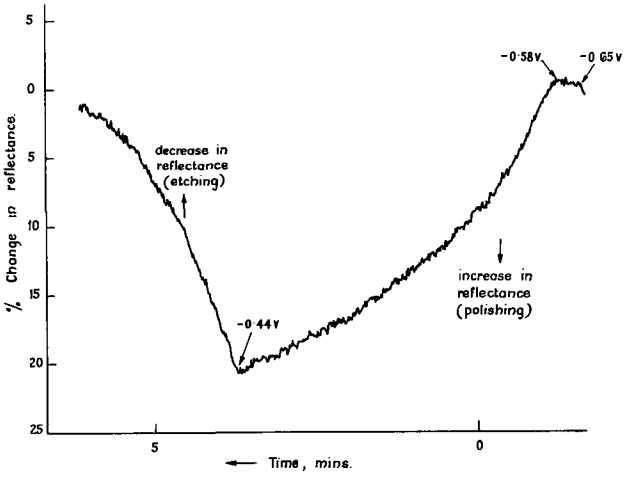

Fig. 5. Change in reflectance (Au reference) vs. time for Au in 0.25% KCN (pH 12) for a series of potentials (volts vs. S.C.E.).

the method may be used to follow such etching and polishing changes (2). In the absence of gas evolution, which causes large variable changes in reflectance, the method may provide a rapid means of determining the optimum potential for electropolishing in a particular system.

For the change of reflectance of a platinum surface in H_2SO_4, an explanation of the observed effects is possible in terms of light absorption by an oxide layer on the surface of the metal. In what follows, the scattering factor of the metal covered with oxide is assumed to be the same as that of the metal alone.

In Fig. 6, I_0 = light intensity incident on the liquid-oxide interface; I_1 = light incident on the oxide-metal interface, after absorption in the oxide layer; I_2 = light leaving the metal-oxide interface after absorption by the metal; and I_3 = light leaving the oxide-liquid interface after absorption in the oxide layer. Then $I_3/I_0 = R_{(\text{metal oxide})} = R_0$ where R = per cent reflectance/100

$$I_2/I_1 = R_{(\text{metal})} = R_M$$

$$I_1/I_0 = 10^{-\epsilon ct}$$

where ϵ = molar extinction coefficient of the oxide layer, c = concentration of the absorbing species in this layer, moles/1; and t = thickness of oxide layer in cm.

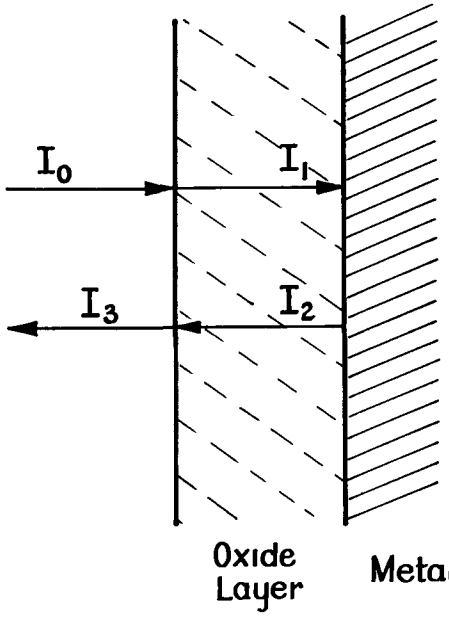

Fig. 6. Light absorption in an oxide layer on Pt metal

Then

$$I_3/I_0 = I_3/I_2 \times I_2/I_1 \times I_1/I_0$$

$$R_M 10^{-2\epsilon ct}$$

$$\Delta R = R_M - R_O = R_M(1 - 10^{-2\epsilon ct}) \quad [1]$$

At 350 mμ, $R_M \simeq 0.40$, $R \simeq 0.03$ (maximum effect)
Then $\epsilon ct \simeq 0.0164$
Thus, $\epsilon ct << 1$, and Eq. [1] can be reduced to

$$\Delta R = 4.606\ R_M\ \epsilon ct \quad [2]$$

Laitinen and Enke (6) have obtained coulometric data for the formation of oxide films on Pt, in 1*N* perchloric acid solution, using anodizing times and other conditions comparable to those in our experiments, and if, as seems probable, the behavior of Pt in the anodic region is the same in sulfuric acid and perchloric acid solutions, it is possible to use their data to obtain an estimate of ϵ as follows:

$$Q_{total} = \frac{A \times t \times nF \times \rho}{\text{Mol. wt.}}$$

where Q_{total} = charge in coulombs; A = electrode area in cm²; t = thickness; F = the Faraday; n = the number of electrons involved in the reduction of one molecule; and ρ = the density.

$$\therefore\ Q = \frac{t\,n\,F\,\rho}{\text{Mol. wt.}} \quad [3]$$

where Q is in coulombs/cm².

The concentration of the absorbing species in the layer is given by

$$c = \frac{\rho \times 10^3}{\text{Mol. wt.}} \text{ moles/l} \quad [4]$$

Substituting [4] in [3]

$$Q = t\,n\,FC \times 10^{-3}$$

$$i.e.,\ t = \frac{Q \times 10^3}{nFC} \quad [5]$$

Substituting [5] in [1]

$$\Delta R = R_M \frac{4.606\ Q \times 10^3 \epsilon}{n\,F}$$

If ϵ/nF is constant over the range of oxide coverage, a plot of ΔR against Q would give a straight line through the origin.

Figure 7 shows our experimental values of ΔR at various potentials plotted with Laitinen and Enke's values of Q. The straight line passes through the origin and has a slope from which can be calculated

$$\epsilon = \frac{n\,F}{4.606 \times 10^3 \times R_M} \frac{\partial(\Delta R)}{\partial Q}$$

$$= 2.62 \times 10^3\ n \text{ for } R_M = 0.40$$

For the reduction of PtO or PtO_2, n = 2 or 4, so ϵ is in the range 5000-10000.

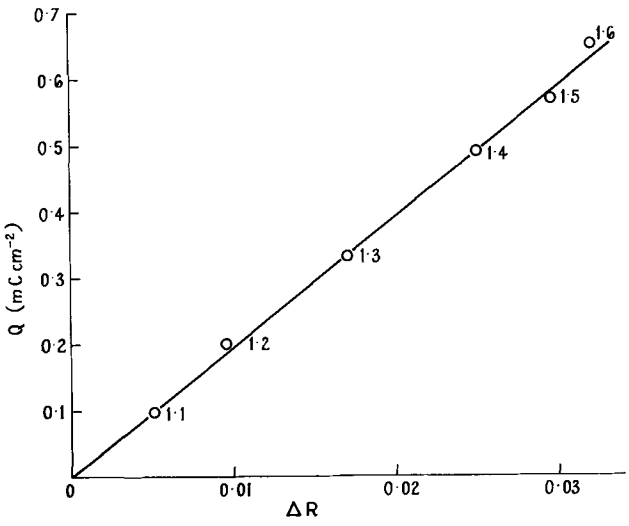

Fig. 7. Relationship between ΔR and Q for Pt in N H_2SO_4 at various potentials (v *vs.* N.H.E.).

The large values of ϵ required to account for the results by the above mechanism and the increase in the effect at shorter wavelengths suggest that the electronic transition responsible is of the charge transfer type. The much less intense ligand-field transitions between d-orbitals on the Pt atoms in the oxide ($\epsilon \sim 100$) would be beyond the limit of detection. Three different types of charge transfer process could occur in a metal-oxygen system: (*a*) transitions of an allowed nature between metal orbitals in the oxide and oxygen orbitals; (*b*) transitions between metal levels and levels of the oxide, across the metal-oxide interface; (*c*) transition between levels in the oxide itself.

The absorption occurs at wavelengths near the absorption edge for a "clean" platinum surface which suggests that the transition involves the metal itself, as in mechanism (*b*).

Manuscript received Nov. 16, 1964; revised manuscript received Dec. 7, 1965.

Any discussion of this paper will appear in a Discussion Section to be published in the December 1966 JOURNAL.

REFERENCES

1. D. F. A. Koch, *Nature*, **202**, 387 (1964).
2. D. F. A. Koch and D. E. Scaife, Unpublished work.
3. K. J. Cathro and D. F. A. Koch, *This Journal*, **111**, 1416 (1964)
4. M. Fleischmann and H. R. Thirsk, *Trans. Faraday Soc.*, **51**, 71 (1955).
5. F. G. Will and C. A. Knorr, *Z. Elektrochem.*, **64**, 258 (1960).
6. H. A. Laitinen and C. J. Enke, *This Journal*, **107**, 773 (1960).

Brief Communications

An Electroless Method for Deposition of Lead on Copper

B. G. Slay and B. G. Carbajal

Texas Instruments Incorporated, Dallas, Texas

Occasionally it is desirable to plate lead on copper where it is either impossible or impracticable to do so electrolytically. This would be the case with incoherent copper patterns.

Several preparations were tried using water as the solvent, lead nitrate, $PbNO_3$, as the lead containing compound, and thiourea, CN_2SH_4, as a complexing and reducing agent. Results were generally poor, as the lead plate obtained was either very granular or would not adhere to the copper.

A successful answer to the problem was found when dimethyl sulfoxide was tried as the solvent. A typical plating solution was 35g each of $PbNO_3$ and thiourea in 175 ml of dimethyl sulfoxide heated to 45°C. The solution is not critical to either the amount of reagents used or to the temperature. The copper surface was prepared by cleaning with a bright dip solution.

The lead plate obtained using this technique adhered well to the copper and was shiny in appearance. For the intended applications, it was necessary that the coating be superconducting. This coating was found to be superconducting at some temperature greater than 4.2°K.

This is an "electroless" process catalyzed by copper and lead surfaces. The glass beaker or plastic stirring rods were not coated. After several days or weeks some chemical reduction takes place in the solution. Metals other than copper and lead were not investigated as catalytic surfaces.

It should be pointed out that dimethyl sulfoxide penetrates the skin very readily and that care should be taken in working with this solution to avoid possible lead poisoning; also, dimethyl sulfoxide has been removed from the list of chemicals permitted for therapeutic tests on humans.

Manuscript received Nov. 15, 1965.

Any discussion of this paper will appear in a Discussion Section to be published in the December 1966 JOURNAL.

The Growth of Pink Magnesium Aluminate ($MgAl_2O_4$) Single Crystals

Cortland O. Dugger

Air Force Cambridge Research Laboratories, Office of Aerospace Research, Bedford, Massachusetts

Transparent magnesium aluminate (1 mole MgO/1.04 mole Al_2O_3) single crystals, doped with 1.2 ppm chromium sesquioxide (Cr_2O_3) have been grown six times from molten salt solution following the hydrolysis of some of the MgF_2 to MgO and the chemical formation and dissolution of the magnesium aluminate phase. The starting composition of the mixture was 38.1 mole % BaF_2, 38.1 mole % MgF_2. xH_2O weighed as MgF_2, 23.8 mole % Al_2O_3, and 200 ppm Cr_2O_3. The largest octahedral crystals measure 4 mm from apex to apex and 3 mm across. Polarizing microscopy, Laue, and Debye-Scherrer x-ray analyses confirm the isotropic character, monocrystallinity, and spinel structure of the crystals, respectively.

An extensive literature search in the Chemical Abstracts from 1907 to 1965 and the Defense Documentation Center files has not revealed the previous growth of spinel crystals by the hydrolysis technique. Kubo (1) recently used this method to grow needle-like crystals of zinc oxide from zinc fluoride. Although many sintering reactions of magnesium aluminate have been reported, to this author's knowledge, only Linares (2), has reported the growth of chromium-doped spinel crystals from a molten salt solution.

The thermal hydrolytic reactions of some of the MgF_2 to MgO, the chemical formation of spinel ($MgAl_2O_4$), and the dissolution of spinel in the molten salts, plotted by differential thermal analysis (3), occurred within the temperature range of 155°C to approximately 1642°C.[1] Upon programmed cooling, at 1642°C recrystallization of the spinel phase was initiated. A mechanism of the hydrolysis of MgF_2 to MgO has been proposed by Buckner (4) and most recently by Messier (5).

[1] "Approximate" because the known accurate maximum temperature limit of our differential thermal analysis apparatus is 1620°C.

The crystals were grown in an open molybdenum crucible, which contained the noncalcined and unreacted starting chemicals. The crucible was heated under a vacuum to 900°C in a carbon furnace. At 900°C, a helium atmosphere was introduced and the temperature raised to 1650°C. This temperature was maintained for 3 hr and then lowered at approximately 5°C/hr to 1510°C. The furnace was then rapidly cooled (500°C/hr) to room temperature. The temperatures were measured by an optical pyrometer, uncorrected for emissivity. The crystals were removed by destroying the crucible and gently tapping the matrix with a hammer. The crystals easily separated from the crystallized fluoride solvent. The x-ray density, lattice parameter, and the refractive index of the crystals are 3.577 g/cm^3, 8.0835Å, and 1.710, respectively. Navias (6) reported for 1MgO/1Al_2O_3, a specific gravity and lattice parameter of 3.578 g/cm^3 and 8.0832Å, respectively. Wickersheim and Lefever (7) published an index of refraction of 1.708 for the stoichiometric spinel.

If the solution is cooled from 1650° to 1510°C at approximately 15°C/hr, the crystals are smaller (2 mm) but are more heavily doped (15 ppm) with chromium oxide (8.0846Å) than those crystals grown by cooling at 5°C/hr. Semiquantitative emission spectrochemical analysis detected 50 ppm barium.

If the starting composition is placed in a platinum crucible, covered, heated in air to 1470°C, and then slowly cooled at approximately 1°C/hr to 1200°C, a new compound is formed in which barium is included in the lattice (Fig. 1). Single crystals of this new compound demonstrate a hexagonal habit and the largest crystal measures 5 x 5 x 3 mm.

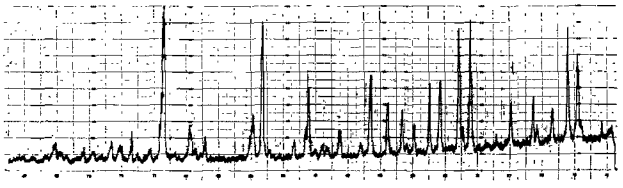

Fig. 1. X-ray diffraction pattern (in degrees) of chromium doped barium magnesium aluminate.

These crystals are uniaxial optically positive crystals whose indices of refraction are 1.700 and 1.716 for the ordinary ray and the extraordinary ray, respectively. X-ray analysis has identified the compound as hexagonal with a c axis equal to 22.56Å and an a axis equal to 5.63Å. Neglecting the chromium ion content, its formula from wet chemical analysis is $BaMgAl_{10}O_{17}$, which is isostructural with $NaAl_{11}O_{17}$ (8), whose unit cell dimensions are: c equal to 22.48Å and a equal to 5.58Å.

Fluorescence spectra were obtained for both the spinel crystals of greater chromium ion concentration (15 ppm) and chromium oxide doped barium magnesium aluminate ($BaMgAl_{10}O_{17}$) crystals at liquid nitrogen temperature (77°K) and room temperature (300°K). The fluorescence wavelength, which is the same at both temperatures, is 6880Å and 6950Å for $(MgAl_2O_4)Cr$ and $(BaMgAl_{10}O_{17})Cr$, respectively.

Absorption spectra demonstrate that $(BaMgAl_{10}O_{17})Cr$ has two absorption bands, one at 3900Å and the other at 5600Å. Liquid nitrogen and room temperature measurements were made at 5600Å. The absorption lines are broad and do not change appreciably with temperature.

The hydrolysis of a fluoride to an oxide, which might be considered a new technique for growing single crystals of some refractory oxides, has been extended to the growth of other crystals. Using different soak temperatures, crystals of yttrium iron garnet (12.377Å), yttrium aluminum garnet (12.015Å), barium zirconate, magnesium oxide, zinc oxide, and a double salt of magnesium orthosilicate (forsterite) and magnesium fluoride have been grown and verified by x-ray analyses.

Acknowledgments

The author wishes to express his appreciation to Jane Bruce, Anahid Thomasian, and John Fitzgerald of the Properties and Analysis Branch at AFCRL. He also wishes to acknowledge the spectra measurements made by the Sperry Rand Research Center and the index of refraction measurements made by Manlabs, Inc.

Manuscript received Oct. 19, 1965.

Any discussion of this paper will appear in a Discussion Section to be published in the December 1966 JOURNAL.

REFERENCES

1. I. Kubo, Japan J. *Appl. Phys.*, **4**, 225 (1965).
2. R. C. Linares, *U.S. Department of Commerce, Final Report,* Contract No AF19(628)-4057 and AF19(628)-2965, 10-14, 1964.
3. C. O. Dugger, "Differential Thermal Analysis (DTA) of Oxide Systems in Air to 1620°C at Atmosphere Pressure," AFCRL-65-466, June 1965.
4. D. A. Buckner, H. C. Hafner, and N. J. Kreidel, *J. Am. Ceram. Soc.*, **45**, 435 (1962).
5. D. R. Messier, *ibid.*, **48**, 452 (1965).
6. L. Navias, *ibid.*, **44**, 434 (1961).
7. K. A. Wickersheim and R. A. Lefever, *J. Opt. Soc. Am.*, **50**, 831 (1960).
8 C. A. Beevers and M. A. S. Ross, *Z. Krist.*, **97**, 59 (1937).

A Long-Life Thermal Cell

Lawrence H. Thaller

Lewis Research Center, National Aeronautics and Space Administration, Cleveland, Ohio

ABSTRACT

Cells consisting of magnesium anodes, mixed copper oxide cathodes, and an electrolyte of the eutectic mixture of lithium chloride and potassium chloride, had service lives measured in days. Seven cells were discharged at temperatures of 425°-535°C. Electrode efficiencies varied from 73% for a cell that was discharged over a period of six days to 93% for a cell that was discharged over a period of one day. For these nonoptimized research cells, energy densities of 28 whr/lb of total battery were shown.

Thermal cells, which usually have solid electrolytes, become activated when these solids are melted. Such cells have been described by several authors including Vinal (1), Goodrich and Evans (2), and McKee (3). These cells are generally employed when very high currents are desired for very short periods of time. Once activated, a lifetime measured in minutes is the rule. In general, the anode reacts with the electrolyte, and the soluble cathode material reacts with the anode. These undesirable side reactions are only of minor significance during the short-term operation of these short-life thermal cells.

A program was initiated to investigate electrochemical systems which might prove suitable for making a battery that would have an operating temperature of about 425°C and a service of several days. The potential application of this type of battery would be on missions where the environment itself would supply the heat to activate and maintain the battery at its operating temperature. The more usual thermal cell employs a pyrotechnic device to supply a short-term high-temperature environment for the battery. The high self-discharge characteristics of this class of cells renders them unsuitable for long-term applications.

Research was begun on a new class of cells which, for the present, contain no added mechanical separators or diffusional hindrances. The general criteria established for these long-life thermal cells were the following:

1. All components should possess interface compatibility. Since it is questionable whether metastable equilibrium will exist at these temperatures, thermodynamic data and criteria should be used to determine compatibility.
2. The electrodes should be very insoluble in the electrolyte. Solubility of the electrode materials would lead to self-discharge of the cell.
3. The products of reaction should be only sparingly soluble in the electrolyte. Excess solubility of the discharge products might adversely affect the physical properties of the electrolyte such as the melting point, conductivity, etc.

The eutectic mixture of lithium chloride (LiCl) and potassium chloride (KCl) (59 mole % LiCl) was chosen for the molten salt electrolyte. This mixture has a rather low melting point (363°C), a high conductivity, and the individual compounds have large free energies of formation ΔF_f^o. Magnesium was chosen for the anode material. It is lightweight, has a rather high melting point (651°C), will not replace lithium (Li) or potassium (K) from the molten salt (as does calcium), and is relatively insoluble in the molten salt. Any number of likely cathode materials could have been tested. In general, the halides could be ruled out because of their solubility in the halide electrolyte (4). The oxides would not as a rule be very soluble in the electrolyte, and thus they represent a source of potential cathode materials (5). Calculation of free energy changes of some metal oxides makes it possible to find a number of oxides that might form cells with high energy densities. From this latter group, mixed copper oxides (Cu_2O, CuO) were chosen for investigation because this system possesses good electronic conductivity and thus could serve as the current collector.

Experiment

Cells.—Figure 1 shows the general construction of the cells used in these studies. The can was constructed of commercially pure copper (99.9% Cu with some P and S) or nickel (99.4% Ni, 0.1% Cu, 0.15% Fe, and 0.25% Mn). The lid assembly had three small tubes used for adding electrolyte, venting the cell during the addition of electrolyte, and affixing the positive lead to the cell. An electrical feedthrough, consisting of a ceramic insulator brazed between two metal tubes, was also affixed to the top of the can. A stainless-steel rod, which was screwed into the shank end of the anode and was silver soldered to the upper part of the ceramic feedthrough, served as the negative terminal of the cell. The cathode of copper oxides rested on a small piece of coiled copper tubing, which, in turn, rested on the bottom of the can. The cathode of copper oxides was raised above the floor of the cell to prevent the possibility of solid products of reaction from clogging the passages of the checker-work cathode. Another stainless steel rod was silver soldered into one of the small tubes. This rod was the positive lead of the cell. The lid assembly was by heliarc

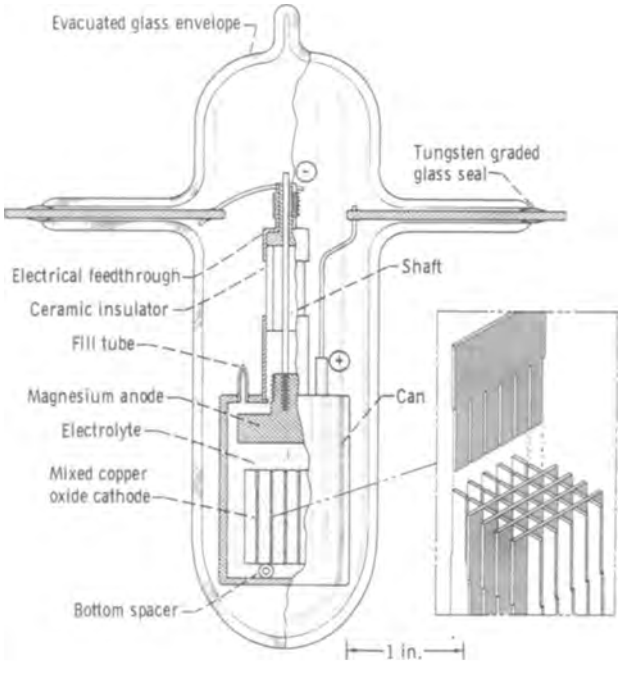

Fig. 1. Cutaway view of typical cell

Table I. Weight breakdown of typical cell

Component	Weight, g
Anode	5.6
Can	39.8
Cathode	16.8
Electrolyte	22.8
Total	85.0 (0.187 lb)

welded to the can. This welding was performed in a dry box filled with argon.

The cells were then filled as needed by the addition of the electrolyte. The small tubes were then pinched off and silver soldered. The weights of the individual components are given in Table I. When the copper can cells were discharged, the entire cell was enclosed in an evacuated glass envelope to prevent the oxidation of the copper cans. One cell was constructed using only an anode, a cathode, and a glass envelope to permit visual observation of the discharging cell. Copper wires were used to connect the electrodes to the tungsten feedthroughs. This cell will be referred to as the glass cell.

The anodes were of primary magnesium (99.8% Mg, 0.15% Mn, 0.02% Cu), while the cathodes were a mixture of Cu_2O and CuO. The anodes were made in the form of thick round disks with a shank on one end. The cathodes were made by oxidizing a checkerwork of oxygen-free high conductivity (OFHC) copper plates, which had been slotted and fitted together. This checkerwork was placed in a furnace and oxidized in air for 6 hr at 1000°C followed by a 1-day oxidation at 600°C. The cathodes were analyzed to be nominally 16 mole % CuO and the remainder Cu_2O.

Although some effort was made to have an anhydrous melt, there were always some hydrolysis products in the melt. The salts were dried in an oven for several days at about 150°C, weighed in the proper proportion, and melted. To the melt were added some magnesium chips to react with water; when reaction was no longer apparent the melt was filtered through quartz wool. The electrolyte in effect was the eutectic of LiCl and KCl with some dissolved MgO plus some unwanted hydrolysis products.

A U-shaped cell (Fig. 2) was discharged at 425°C. Folded magnesium ribbon served as the anode, while oxidized copper wires were used at the cathode. The cell was constructed of heat-resistant glass, which permitted visual observation of the cathode and anode regions separately. The ampere-hours withdrawn were noted and then the cell was broken into two portions. These sections were then analyzed for total magnesium.

Experimental setup.—Most of the experiments were carried out at 425°C (Table II) using a setup shown in Fig. 3. The cell undergoing discharge was wired to a load resistor and the switching relay. The value of load resistance (1, 5, 10, and 20 ohms) depended on the duration the cell was expected to last. The voltage across this load resistor was fed into a high impedance voltmeter. A recording potentiometer was connected to the output of the voltmeter. A cycle timer was employed during several runs. It would alternately place the cell under load for 15 min, followed by 2 min in the no-load condition. The system was connected so

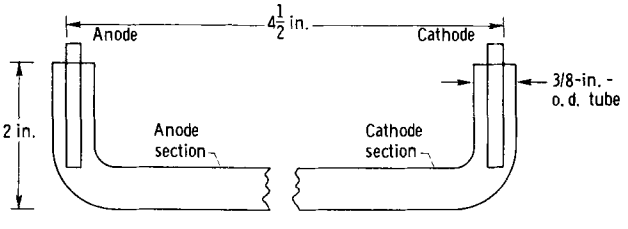

Fig. 2. Pyrex U-shaped cell

Table II. Analysis of nickel cell 3

[Test for nickel salts, negative; pH of 1.0 liter of wash solution, 8 ± 0.3.]

(a) Analysis

Material		Weight		
In fresh cell	In spent cell	g	milli equivalent	amp-hr
Mg^0		5.661	466	12.48
	Mg^0	4.165	343	9.20
	$Mg^{+2}(MgO)$	1.548	131	3.41
	Total	5.713	474	12.61
$Cu^{+2}(CuO)$		1.49	46.8	1.25
$Cu^{+1}(Cu_2O)$		13.36	210.0	5.63
Total		14.85	256.8	6.88
	$Cu^{+2}(CuO)$	0.48	15.2	0.41
	$Cu^{+1}(Cu_2O)$	8.50	133.7	3.57
	Cu^0	5.79	—	—
	Total	14.77	—	—

(b) Electrode efficiencies (amp-hr delivered, 3.04)

Electrode	Efficiency, %
Anode (from Mg^0 lost)	92.7
Anode (from Mg^{+2} gained)	89.2
Cathode (from Cu_2O and CuO lost)	104.8

the voltmeter would read the voltage across the load resistor during one portion of the cycle and the no-load voltage during the other. The ampere-hours delivered during discharge were calculated from the recorded voltage across the load resistor.

Analysis techniques.—The discharged cells were analyzed in an attempt to follow the course and extent of the chemical and electrochemical reactions that took place within the cells. After discharge the nickel cells were analyzed quantitatively for reaction products and unused electrode components. The copper cells and the glass cell were analyzed qualitatively.

The magnesium and copper oxides were expected to react to form magnesium oxide and metallic copper. Selis *et al.* (6), however, found in the analysis of the molten salt cell, Mg/KCl-LiCl/Fe_2O_3, Ni, that the oxidized magnesium in the spent cells was water soluble magnesium chloride ($MgCl_2$). The oxide ion from the discharging iron oxide cathode was taken up in the form of nonsoluble $Li_2O \cdot (FeO)_x$.

An analysis routine (Fig. 4) was made up, which tried to take into account all possible courses of reaction. The resultant routine allowed for analyses of the following constituents as they would appear after a spent cell had been opened and the contents dissolved if possible in water: magnesium metal, water soluble magnesium compounds, magnesium oxide, cop-

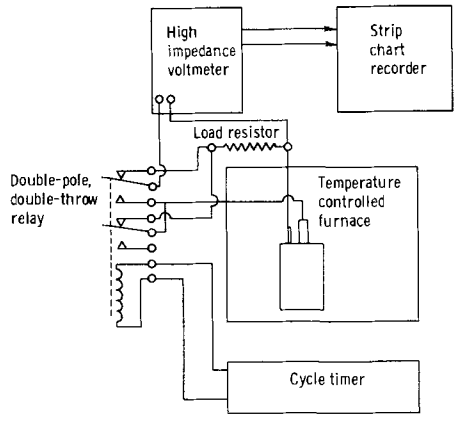

Fig. 3. Schematic diagram of apparatus

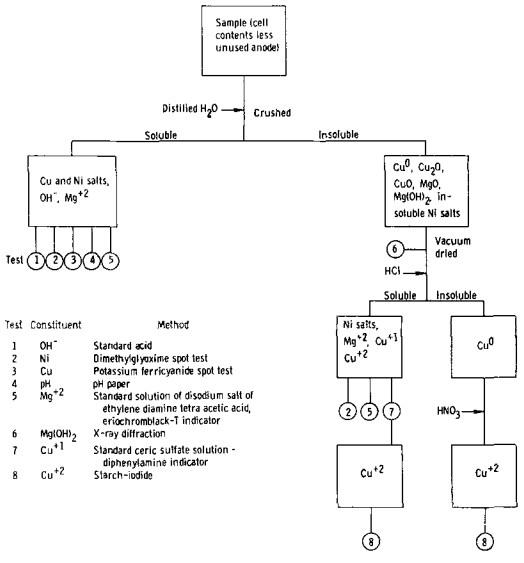

Fig. 4. Flow sheet of analysis

per metal, acid or water soluble compounds of copper and nickel, and finally any alkali metal hydroxides. The pH of the initial wash solution was also measured. If any $MgCl_2$ was present in the spent cells formed during these studies, it would react with the corresponding amount of alkali metal oxide to form, in the presence of water, $Mg(OH)_2$, but this was absent. Analyses of the spent cells for unused reactants would permit calculation of the electrode efficiencies, while analyses for products of reaction would allow some conclusions to be made concerning the course of the reaction. Figure 4 gives details of the analytical routine.

Results and Discussion

General observations.—Figure 5 is a plot of the open-circuit voltage and load voltage against time for the intermittently operated glass cell. This cell was used so that the condition of the cell materials could be observed as a function of depth of discharge. It was noted that a white flocculent material and also small particles of copper were formed and held in suspension. The copper particles ranged in size from less than 1μ to more than 50μ. Most of the copper formed remained on the cathode.

The U-shaped cell experiment (Fig. 2) was performed to gather more information than available from chemical analysis and the glass cell concerning the physical state and region of origin of the MgO. It was already suspected from the discharge curves of the copper and nickel cells that a tightly bound, electrochemically formed layer of MgO was not present at either electrode. Such an insulating layer would greatly inhibit further electrochemical action. A white flocculent cloud of material was formed at both the

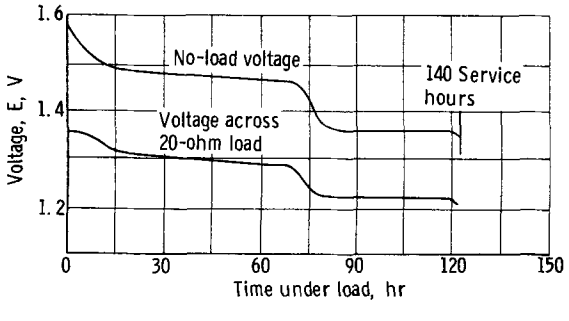

Fig. 5. Discharge characteristics of glass cell. Duty cycle: 15-min load, 2-min open circuit.

anode and cathode regions and these grew toward the center of the cell. Before the clouds overlapped, the reaction was stopped, the cell frozen and broken into two portions as indicated. Each of these portions was analyzed for Mg^{+2}. The presence of Mg^{+2} (MgO) was found in both compartments; about 60% was in the anode half and 40% in the cathode portion.

After the nickel cells had been discharged the ampere-hours withdrawn were determined and the cells were opened and analyzed. Table II (a) shows a set of typical results. The weights of the magnesium and copper compounds are reported not only in grams but also in terms of milliequivalents and ampere-hour equivalents.

Electrochemical and chemical cell reactions.—The chemical analyses showed that the oxidized magnesium in the spent cells was present as solid MgO dispersed throughout the electrolyte. The U-shaped cell experiment showed that MgO was formed in both the anolyte and catholyte, evidently by the reaction of magnesium ions and oxide ions in the electrolyte. It was concluded that the anode reaction in the cell is $Mg \rightarrow Mg^{++} + 2e$.

The chemical analyses also showed that copper oxide cathodes were reduced to metallic copper. This was also evident visually from observation of the glass cell. The probable cause of this reaction can be determined from consideration of the free energy changes of various possible reactions. Working from Laitinen and Liu's (4) list of standard electrode potentials in this electrolyte at about the same temperature, it may be seen that the couple Cu^o/Cu^{+2} would not be expected to exist under the conditions present in the cell, since

$$Cu^{+2} + Cu^o \rightarrow 2Cu^{+1} \quad E^o = +0.509v; \ \Delta F = -46 \text{ kcal}$$

where E^o = standard electrode potential against Pt^o/Pt^{+2} and ΔF = change in free energy. This means that as soon as any Cu^{+2} is reduced electrochemically to metallic copper, chemical reaction will occur to yield Cu^{+1}. Thus, after the cell has been operated for a short time, the principal oxidized form of copper on the cathode will be Cu^{+1}. The cathode reaction is then

$$Cu^{+1} + e \rightarrow Cu^o$$

The over-all cell reaction is

$$2Cu^{+1} + Mg^o \rightarrow Mg^{+2} + Cu^o$$

The voltage of the cell is given by

$$E_{cell} = E^o_{Mg/Mg+2} - E^o_{Cu/Cu+1} - \frac{RT}{nF} \ln \frac{A_{Mg+2}}{(A_{Cu+1})^2}$$

Using Laitinen and Liu's values for the standard electrode potentials, Laitinen and Bhatia's (5) values for the solubility of Cu_2O, and our value for the solubility of MgO (6.52×10^{-2} mole liter^{-1}), the value of E_{cell} is found to be between 1.50 and 1.54v, depending on which value for the solubility of Cu_2O is used. The value of 1.48v was found for these cells after there had been enough electrochemical action to saturate the cell with reactants and products of reaction (Fig. 5). Considering the uncertainty associated with certain of the values used in the cell voltage calculation, this is very good agreement.

Electrode efficiency.—Table III shows the results of life testing of these cells. After an encouraging life test on the glass cell, the three nickel cells were discharged over a rather short period of time and then analyzed thoroughly for products of reaction and unused reactants. The output of the cells varied considerably, but failure was in no case due to depletion of electrode materials by either chemical or electrochemical reaction. The cells were cathode limited, containing 6.9 amp-hr of copper oxides. The best performance gave 5.29 amp-hr (75% of theoretical) and the poorest only 2.48 amp-hr. This latter cell devel-

Table III. Determination of cell life, output, and efficiency for cells of different can material

Cell Can material	No.	Temperature, °C	Life, hr	Cell output, amp-hr	Anode efficiency, %	Cause of failure
Copper	1	425	46	1.04	—	Cell leaked
	2	425	28	2.55	—	Disconnection of anode
	3	425	52	1.73	64.3	Cell leaked
Glass		425	140	5.82	73.4	Disconnection of anode
Nickel	1	425	35	2.48	92.5	Internal short
	2	425	22	5.29	97.8	Disconnection of anode
	3	425-535	5	3.04	90.5	Disconnection of anode

oped an internal short believed to be caused by a bridge of copper metal particles bridging between the electrodes. This has been observed by McKee (3) in other cells containing copper with the lithium chloride, potassium chloride electrolyte. The cell giving 75% of theoretical life failed because the anode lead became disconnected. Considering this, the cell showed a very fine efficiency of the cathode. This was also indicated by cell No. 7 where the efficiency of the cathode, calculated on the amount of copper ions reduced, was slightly over 100% (Table II-b). A figure of over 100% is probably due to a slight oxidation of the finely divided copper formed during cell discharge. Both massive bright shiny copper and micron-size dull red copper were formed. The very fine particles most likely underwent some oxidation during the handling procedure, even though precautions were taken to prevent this.

The anode efficiency calculated for the nickel cells varied from 90.5 to 97.8% (Table III). These efficiencies are the average of the efficiencies based on magnesium lost by the anode and magnesium gained in the electrolyte. On the basis of these calculations, it appears that the anode would be the limiting material if equal equivalents were used for the anode and cathode.

The over-all cell, assuming no other cause of failure, should have an efficiency better than 90%. One possible reason for some loss of efficiency is the slight solubility of the copper oxides. Once this material is in solution, it can migrate to the magnesium and react chemically. This would affect both electrodes. Another possible factor reducing anode efficiency could be the amount of water or KOH in the electrolyte by the reaction $Mg + H_2O \rightarrow MgO + H_2$. By proper preparation of the electrolyte, this loss should be negligible.

Conclusions

A long-life thermal cell was built and was discharged over a period of six days at 425°C, with an anode efficiency of 73%. Other cells that were discharged over shorter periods of time had anode efficiencies greater than 90%.

It was concluded that the following reactions took place at the electrodes. At the cathode, the slightly soluble cuprous oxide was reduced to metallic copper. At the anode, the magnesium was oxidized to soluble magnesium ion. Insoluble magnesium oxide was found to form in the region of both the cathode and anode. The value of the cell voltage, 1.48, was in agreement with that calculated assuming the cell reaction responsible for the emf to be

$$2Cu^{+1} + Mg \rightarrow 2Cu^{o} + Mg^{+2}$$

Acknowledgment

The author gratefully acknowledges the efforts of Miss Mary Beth Ruskai in preparing the analytical routine and then analyzing the spent cells.

Manuscript received Aug. 19, 1965; revised manuscript received Dec. 4, 1965. This paper was presented at the San Francisco Meeting, May 9-13, 1965.

Any discussion of this paper will appear in a Discussion Section to be published in the December 1966 JOURNAL.

REFERENCES

1. G. W. Vinal, "Primary Batteries," pp. 324-329, John Wiley & Sons, Inc., New York (1950).
2. R. B. Goodrich and R. C. Evans, *This Journal*, **99**, 207 (1952).
3. E. McKee, "Thermal Cells," Proc. Tenth Annual Battery Res. and Dev. Conf., Power Sources Div., Signal Corps Eng. Labs., Fort Monmouth, N. J., pp. 26-28 (1956).
4. H. A. Laitinen and C. H. Liu, *J. Am. Chem. Soc.*, **80**, 1015 (1958).
5. H. A. Laitinen and B. B. Bhatia, *This Journal*, **107**, 705 (1960).
6. S. M. Selis, L. P. McGinnis, E. S. McKee, and J. T. Smith, *ibid.*, **110**, 469 (1963).

The Morphology of Magnetite Growth on Mild Steel in Alkaline Solutions at 316°C

T. F. Marsh

Central Electricity Research Laboratories, Leatherhead, Surrey, England

ABSTRACT

In previous work on the oxidation of mild steel to magnetite in high-temperature alkaline solutions different workers have obtained markedly differing types of oxide under apparently similar conditions. The types of oxide obtained, the conditions under which they were grown, and possible reasons for the difference in oxide morphology are discussed. Experiments are described which support the idea that the type of magnetite growth obtained upon an area of mild steel depends upon the presence or otherwise of a suitable cathodic surface in contact with it. For example, the oxidation of a mild steel specimen in a new pressure vessel will take place in a different manner to that of a specimen in a vessel with a pre-formed protective magnetite film coating its sides, since the magnetite film in the latter case probably acts as a cathode for the oxidation of the specimen. The properties of the types of growth, and in particular their healing properties, are discussed with particular reference to the practical problem of pitting growth in steam generator tubes.

Under the conditions existing in modern power stations, the mild steel comprising the boiler tubes is thermodynamically unstable in the presence of the high-temperature feed water and reacts to form magnetite with liberation of hydrogen. Fortunately, operating experience has indicated that the magnetite produced in slightly alkaline feed waters forms a protective film which, if maintained, ensures that thinning of the tube walls is negligible under normal conditions of operation.

In recent years (1-6), studies have been made of the growth of protective magnetite films on mild steel in alkaline solutions at typical operating temperatures in order to establish their properties and to throw some light upon the occasional circumstances in which they lose their protective character and produce a rapid pitting attack.

The investigations which concern the morphology of these films have been complicated by the fact that the protective magnetite films obtained by different investigators at the same temperatures and solution pH's have had markedly different morphologies. In general, two different types of film growth have been observed under apparently similar conditions and the experiments described subsequently were performed in order to resolve the differences observed and to determine which of the two growth mechanisms would be likely to predominate on a boiler tube wall in operation.

Previous work.—Experiments have been performed involving the oxidation of mild steel in sodium hydroxide solutions of up to 40% by weight in the expectation that oxide films of a similar character to those produced in the just-alkaline feed water would be obtained, but of a thickness large enough for their morphology to be studied.

Studies were made by Potter and Mann (1) and later by Adams, Field, Holmes, and Stanley (2) which involved the oxidation of small mild steel specimens (ground on 600 grade silicon carbide paper and degreased in acetone) in partly filled mild steel pressure vessels sealed with Ermeto caps.[1] The former used solutions ranging from distilled water to 20% sodium hydroxide solution at temperatures from 250° to 355°C, whereas the latter used 15% NaOH at 316°C. In both cases "conditioned" pressure vessels were used, that is, with a magnetite film grown in NaOH solution on the internal walls.

[1] Manufactured by British Ermeto Corporation Ltd., Maidenhead, Berkshire, England.

Under these conditions oxide films consisting of two layers were observed (Fig. 1). The films adjacent to the metal ("inner-layer") were regular, compact, and adherent and were found to be protective in most cases despite a porosity of 8-15% (2, 7).

In contrast, the "outer-layer" consisted of a loose array of tetrahedral crystals and, when the original metal surface was ground, apparently afforded no protection to the metal.

Bloom and Krulfeld (3) studied the alkaline corrosion of mild steel by continuous measurement of the hydrogen released in the oxidation reaction. This was achieved by taking a length of annealed mild steel tubing, flattening to an oval cross-section and sealing solutions inside by squeezing the ends in a hydraulic press and spot-welding. On raising to temperature the capsules remain completely filled with liquid since the hydrostatic pressure generated inside is greater than the vapor pressure of the solution and the hydrogen produced by the corrosion reaction diffuses through the capsule wall.

The growth obtained by Bloom on mild steel in 40% NaOH and 15% NaOH, although still protective, was quite dissimilar to that shown in Fig. 1 (4, 5). Figure 2 shows a section of magnetite growth on annealed mild steel in 15% sodium hydroxide solution typical of that obtained by Bloom. The growth is irregular at both the oxide/metal and oxide/solution interfaces, and there is no division into two layers. Direct examination of the oxidized metal surface by reflected light reveals a mass of magnetite tetrahedra similar to the surface of "outer-layer" described above.

These irregular films appear to be considerably more protective than the regular films obtained by Potter

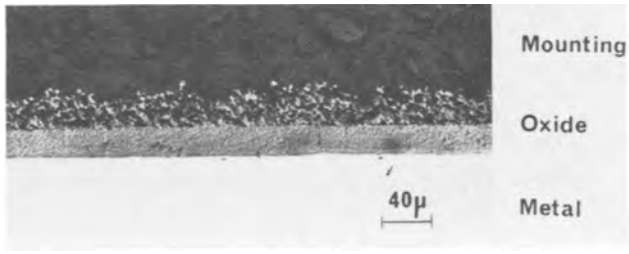

Fig. 1. Normal section of Fe_3O_4 growth on mild steel specimen contained in conditioned pressure vessel. Oxidized for 250 hr in 15% NaOH.

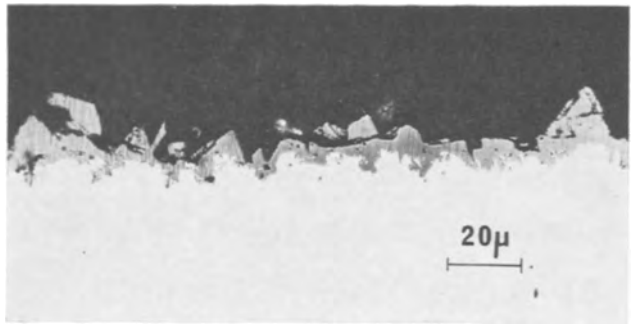

Fig. 2. Normal section of Fe_3O_4 growth on the inner surface of a mild steel capsule. Oxidized for 72¼ hr in 15% NaOH.

and Mann. For example, in 15% NaOH solution the thicknesses of Bloom films appear to differ only marginally after oxidation periods of 3.7 and 42 days (6). For Potter and Mann growth, calculations based on the growth curves shown in Fig. 4 of ref. (1) indicate that in 13% NaOH the thickness of metal oxidized (*i.e.*, the thickness of the inner-layer) increases from 11-12 μm to 35-36 μm in the same time period. These results are in accord with surface area measurements involving the adsorption of radioactive krypton (8) which indicate that the Bloom films do not have the porosity possessed by the Potter and Mann films.

In addition to the protective film, there is a tendency for hemispherical pits to form in the later stages of growth (4, 5). No such type of pitting growth was observed on the block specimens used by Potter and Mann.

Comparison of Experimental Conditions

It seemed necessary first of all to eliminate the possibility that the different growth mechanisms were a result of differences in the composition of the mild steels used, or in the purities of the NaOH solutions. The former was disposed of by the oxidation in a conditioned pressure vessel of small sections of tubing,[2] of the same mild steel as that used in Bloom's capsule experiments. This resulted in two-layer Mann and Potter type films on the samples used.

Differences in surface treatment also were found to have no radical effect on the morphology of oxide grown on specimens in conditioned pressure vessels: a blue air-formed interference color film (grown at 316°C) did not affect the form of the film grown subsequently in NaOH solution, and the change in oxide morphology produced by the oxidation of annealed specimens was inadequate to explain the growth differences previously described. Two distinct oxide layers are still formed on annealed specimens, but with a much increased size of "outer layer" crystal which acts as an additional local protection to the underlying metal. This effect is described in more detail by Field and Holmes (7).

The effect of the stress existing in the walls of Bloom's capsules was considered also. However, elastic and plastic straining were found to have no effect on the morphologies of two-layer films. A piece of steel was bent into an arc corresponding to a maximum strain of 1.06%, held in a jig of the same material and oxidized for 51¼ hr in 15% NaOH and 316°C in a conditioned pressure vessel. A two-layer Potter and Mann film was observed on the strained specimen.

Similarly a mild steel specimen in the form of a test piece for a Hounsfield Tensometer was strained until near to fracture and then oxidized in a conditioned pressure vessel in 17% NaOH. The unstrained ends of the test piece grew between 9 and 13 μm of inner layer; in the region where necking had occurred and the plastic strain was as high as 15% the growth of inner layer had increased to 24-28 μm. The morphology of both types of growth was nevertheless found to be the same (9).

It will be seen below that it is possible to obtain Bloom-type films on specimens oxidized in nonconditioned pressure vessels. This supports the conclusion reached above that surface treatment, steel compositions, and presence of stress are not the factors determining whether Bloom growth or Potter and Mann growth is obtained, and also eliminates factors such as the effect of dissolved oxygen or of minute amounts of other impurities in solution.

Effects of Hydrogen

In Bloom's experiments with mild steel capsules it is believed that all the hydrogen produced in the corrosion reaction diffuses directly away from the site of the reaction through the thin (0.05 cm) mild steel tubing. The excellent agreement obtained between the corrosion rates, as estimated by hydrogen effusion and those obtained on other specimens by Blaser and Owens (10) as estimated by measurements of the weight loss of descaled specimens supports this. On the other hand, a residual pressure is almost invariably observed after cooling in thick-walled conditioned pressure vessels used for the oxidation of block specimens. This suggests that some of the hydrogen generated in the iron/water reaction has been liberated as hydrogen gas into the solution instead of diffusing away in monatomic (or ionic) form through the steel.

If hydrogen produced near the metal were unable to escape directly through the steel, as it appears to do in Bloom's experiments, then the evolution of molecular hydrogen into the solution might alter the morphology of the oxide film. If this were so, then the differences between the two types of growth might be caused by the different conditions in which hydrogen is evolved; the continual interference of hydrogen evolved at or near the metal with the oxide growth producing the porous Potter and Mann growth, the escape of hydrogen through the metal with little or no interference with the growing oxide film producing the more compact and protective Bloom growth.

On this picture, the pits obtained in Bloom growth would arise from local hydrogen evolution from parts of the steel surface.

Galvanic Effects

Another possible difference between the conditions of oxidation used by Bloom and by Potter and Mann lies in the electrochemistries of the systems involved: in particular, the possibility of galvanic coupling existing when Potter and Mann growth is obtained.

An unoxidized mild steel specimen placed in a conditioned mild steel vessel is in contact, both electrically and via the solution, with a comparatively large surface area of magnetite. It is known that a magnetite surface can act as an efficient cathode, for example a magnetite electrode can serve as a passivator for stainless steels and titanium (11). When magnetite grows inside a capsule, no such cathodic surface is present at the start of the oxidation and during oxidation the cathode reaction will presumably be confined to the vicinity of the corroding metal.

It is therefore possible that the presence of a cathodic surface external to the oxidizing steel gives rise to the conditions necessary for the growth observed by Potter and Mann, whereas oxidation with no such external cathode produces Bloom growth.

Bloom (12) has suggested that galvanic effects may accelerate corrosion in the early stages and that hydrogen generation can subsequently render the oxide film less protective, but has not described any experiments in support of this.

Further Experiments

In order to determine more precisely the conditions in which the two categories of growth are obtained, with a view to deciding the relative importances of the

[2] Kindly supplied by Dr. Bloom.

factors described above, the types of magnetite formed on mild steel in several different systems are described below. In all experiments the oxide was grown in 15% sodium hydroxide solution at 316°C.

Except for the mild steel tubing and capsules supplied by Dr. Bloom, the four mild steels used in the experiments had the following compositional ranges: C, 0.05-0.23; Mn, 0.37-0.71; S, 0.01-0.02; Si, < 0.08; Ni, 0.10-0.20; Cr, 0.05-0.11; Cu, 0.04-0.16; P, 0.014-0.017; Mo, 0.05-0.07; V, <0.05.

Composition differences in the mild steels of both pressure vessels and specimens within the ranges above were found to have no effect on the oxide morphologies obtained in the experiments described below.

Growth on pressure-vessel walls.—The magnetite growth on the walls of pressure vessels of the type used by Potter and Mann was studied and in the early stages was found to be Bloom-type, but with a greater proliferation of pits than is seen inside a capsule. The wall thickness was 0.4 cm; local reduction to thicknesses of 0.2 cm, 0.1 cm, 0.05 cm appeared to have no effect.

Specimens in unconditioned pressure vessels.—In these experiments, which were referred to above, specimens were oxidized in pressure vessels under the same conditions as those known to promote the formation of two-layer films, except that the conditioning film of magnetite was no longer present on the interior walls at the start of the oxidation. On removal and examination under the microscope the specimens were found to have oxidized to give Bloom-type magnetite films. Hemispherical and saucer-shaped pits, which often tended to occur at or near the corners of the rectangular mild steel blocks, were also observed many times. The oxide inside the pit was normally very similar to that constituting the inner layer of Potter and Mann growth (Fig. 3).

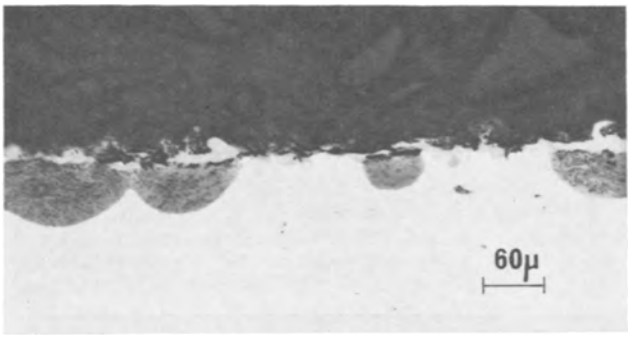

Fig. 3. Normal section of specimen oxidized in a nonconditioned pressure-vessel showing pitting growth. Oxidized for 185 hr in 15% NaOH.

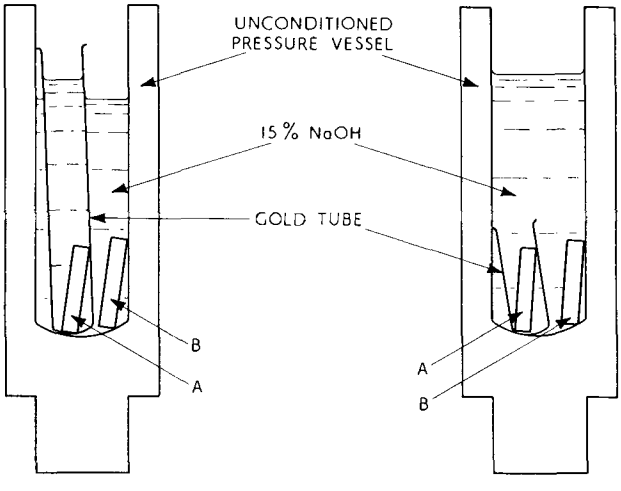

Fig. 4. and Fig. 5. Arrangements for experiments

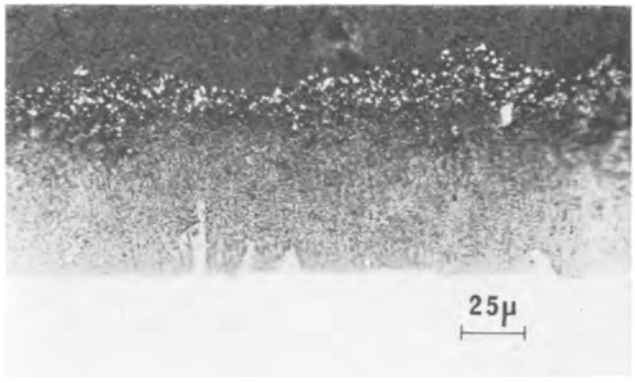

Fig. 6. Oxidation of specimen A (Fig. 4) to give relatively thick porous Fe_3O_4 film. Oxidized for 65 hr in 15% NaOH.

Use of gold tubes.—It has been suggested (13) that in some circumstances it might be possible for hydrogen to effuse directly from a corroding specimen to a tube wall and thereby escape. In view of the possible relevance of hydrogen escape in determining the oxide morphology, experiments were performed with the arrangements described in Fig. 4 and 5. Since hydrogen is insoluble in gold (14) no direct escape of atomic hydrogen could occur away from specimens A in either Fig. 4 or Fig. 5, whereas it could conceivably escape from B.

In order to take account of possible galvanic effects between the specimen and the gold care was taken to distinguish between the arrangements described in Fig. 4 where no intermixing of the liquids inside and outside the tube could take place, and those in Fig. 5 where contact between wall and both specimens existed through the solution. The results obtained are summarized below: A represents the specimen inside the tube, B, that in direct contact with the wall.

(*a*) *Unconditioned pressure vessels, no liquid contact between specimens*[3].—Specimens A were found to give more oxide growth than B. In a typical experiment a uniform 63 μm Mann and Potter film was observed on A after 65 hr with an appearance suggesting a greater porosity than is usual (Fig. 6). On B, a Bloom film was observed in a few places with coalescing saucer-shaped pits extending over the greater part of the specimen. Figure 7 is a normal section of the oxide occurring in the coalescing pits. From the smoother textured appearance and lesser depth of the oxide (16 μm) in comparison to that in Fig. 6 it appeared to be less porous.

(*b*) *Unconditioned pressure vessels, liquid contact between specimens.*—The two experiments performed gave completely different results: in one instance both A and B were coated with a thick growth similar to

[3] In fact at temperature it is possible that contact will exist between specimens via a thin film of liquid covering the tube above the level of the meniscus. However the results of the experiment indicate that the resistance of such a film is high enough for this contact to be ignored.

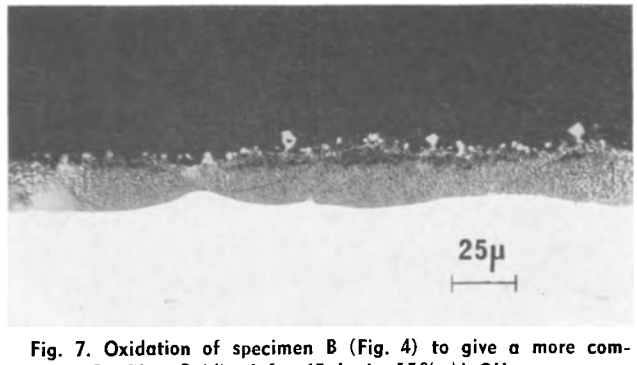

Fig. 7. Oxidation of specimen B (Fig. 4) to give a more compact Fe_3O_4 film. Oxidized for 65 hr in 15% NaOH.

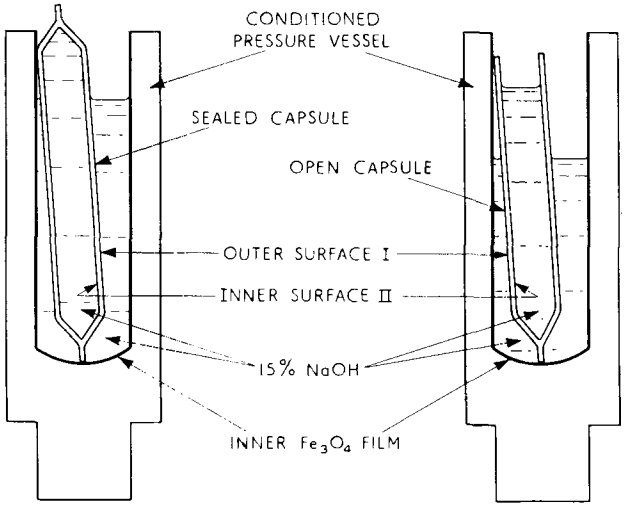

Fig. 8. and Fig. 9. Arrangements for experiments

Fig. 6; the other time the greatest part of the oxide in both cases was the nonporous Bloom film.

The most significant feature of (a) and (b) seems to be the fact that almost identical oxide growths on specimens A and B were obtained when the liquids were in contact, whereas A and B oxidized in different manners when no liquid contact existed. This implied that galvanic coupling was a more relevant factor in determining the type of growth than was the possibility of direct escape of atomic hydrogen from the specimen.

Capsules within conditioned pressure vessels.—(a) Through the kind cooperation of Dr. Bloom who provided sealed capsules containing 15% NaOH of the type used in his effusion experiments, these were oxidized in the experimental arrangement shown in Fig. 8, in order to observe the effect of a reaction on outer surface I upon that on internal surface II. I oxidized as expected to give Mann and Potter growth, but this had no effect upon the oxidation of the interior, on which Bloom growth was observed. (b) Capsules sealed at one end only were oxidized as shown in Fig. 9 care being taken that no contact existed between the liquid outside and inside.[4] Regular Mann and Potter films were always observed on surfaces I, Bloom films (plus pits) on II.

A blank experiment was performed in which a short length of a similar half-sealed capsule was oxidized while totally immersed in a conditioned pressure vessel. A regular Mann and Potter film of constant thickness was produced on all the capsule surface, except where the capsule was sealed.

[4] In fact at temperature it is possible that contact will exist between specimens via a thin film of liquid covering the tube above the level of the meniscus. However the results of the experiment indicate that the resistance of such a film is high enough for this contact to be ignored.

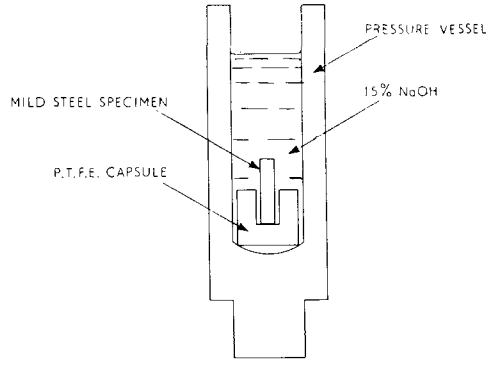

Fig. 10 Treatment of specimen

Use of P.T.F.E. capsules.—Specimens were electrically insulated from the pressure vessels by being contained in small capsules of polytetrafluoroethylene (P.T.F.E.) as in Fig. 10. In 11 of the 13 experiments performed involving both conditioned and nonconditioned pressure vessels Bloom growth was observed on the specimen, although a fairly large incidence of pitting was observed on several specimens.

One of the other two experiments produced a thick porous film, similar to Fig. 6, on the specimen; the other produced a film very similar to normal Potter and Mann growth except for a more irregular metal/oxide interface.

The action of the 15% NaOH solution at 316°C was found to have darkened the P.T.F.E. surface, and to ensure that the oxidation of the specimen was not influenced by contamination of the solution by an oxidation product of P.T.F.E. blank experiments were performed in which specimens were oxidized along with P.T.F.E. chips. Similarly, experiments were performed in which oxidation took place in the solutions previously used for the oxidation of the specimens in P.T.F.E. capsules. None of these experiments showed any change in the expected growth morphology.

Additional Experiments

Some further experiments were performed in order to check the effect of an external magnetite surface upon the oxidation of mild steel. A specimen was oxidized in an unconditioned pressure vessel for 3 days, thereby building up a Bloom-type magnetite film on the specimen and wall. On the third day a second specimen was placed in the pressure vessel and after a further day of oxidation the two specimens were removed, mounted, and examined under a microscope. The specimen which had had 4 days' oxidation was covered by a continuous Bloom film thickness *ca.* 1 μm; that which had only one day's oxidation but which was in contact with a magnetite surface (that formed on the other specimen and the pressure vessel) during this period had grown 11 μm of Mann and Potter-type growth. It was thus apparent that completely different types of oxide had grown on the two specimens on the fourth day.

Similarly, when a specimen oxidized in a new pressure vessel to give Bloom growth had one face ground to remove the film and was then reoxidized in the same pressure vessel, the exposed face was found to have given Potter and Mann growth while the other faces continued to give Bloom growth (Fig. 11). By exposing small areas of metal under a Bloom film and reoxidizing it was found possible to produce hemispherical pits similar to those observed by Bloom (Fig. 12).

Fig. 11. Section perpendicular to specimen showing Potter and Mann growth on vertical face, Bloom growth on horizontal face. The specimen was oxidized in 15% NaOH in a nonconditioned pressure vessel for 63¾ hr to give a Bloom film on all faces; the Bloom film was removed from the vertical face and the specimen re-oxidized for 70¼ hr in the same pressure vessel.

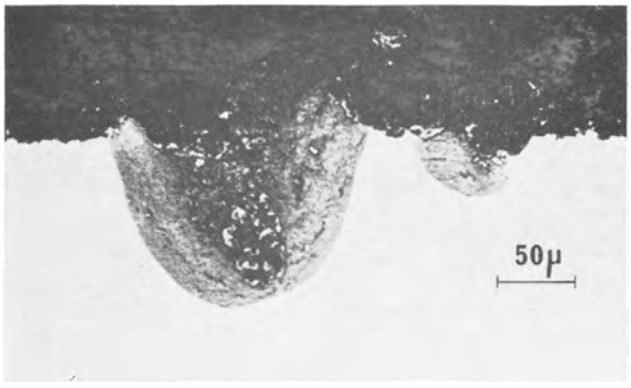

Fig. 12. Normal section of pits produced after removing small areas of a Bloom film and re-oxidizing in 15% NaOH for 328 hr.

Interpretation of Results

Galvanic effects.—A surface able to act as an efficient cathode for an anodic reaction taking place external to it must have the following characteristics: (a) Good electronic conduction. (b) The cathodic reaction on the surface must occur with ease, *i.e.*, with a low overvoltage. (c) Contact must take place with the anode both via an electronic conductor and via a solution of good conductivity. (d) The surface must not itself be supporting an anodic reaction taking place at a comparable rate. For example, when a specimen is placed in NaOH solution in an unoxidized pressure vessel the specimen and pressure vessel wall will oxidize to magnetite at very similar rates and there is no reason why the magnetite surface produced on the wall [a potential cathode with respect to (a), (b), and (c)] should act as a cathode for the corrosion of the specimen or vice versa. On the other hand, if a film of (protective) magnetite is already present on the wall, the initial corrosion rate of the wall will be less than that of the specimen and hence the magnetite on the wall is able to support the cathode reaction associated with the corrosion of the specimen.

The oxidations of the mild steel surfaces present in the systems described above are classified in Table I in terms of the presence or absence of a suitable external cathode fulfilling the requirements (a) to (d).

Table I shows a correlation between Mann and Potter growth and the presence of an external cathode, and between Bloom growth and the absence of one, but with the following discrepancies.

In Table I [5] the surface of B gave a mixture of Bloom films in a few places together with Mann and Potter films despite the presence of the gold tube exterior as a possible cathode. Here, however, as Fig. 4 indicates, the exterior of the gold tube was "shared" by both B and the pressure-vessel wall and hence it is possible that the differences in the oxidation behaviors of A and B are indicative of the relative areas of anode and cathode. During the oxidation of A a larger ratio of cathode surface/anode surface might promote thick porous Mann and Potter films; for B the smaller ratio might be related to the more protective Mann and Potter films together with the Bloom growth observed.

In Table I [6], although A and B oxidized in the same manner, the fluctuation in the oxidation behavior of the few specimens used so far is difficult to explain. It is hoped to do further experiments of this kind.

In Table I [8] an unexpectedly high incidence of pitting was observed on the specimens and, on 2 out of 13, Mann and Potter-type films were obtained. This may be associated with a high rate of oxidation of the pressure-vessel wall, with the subsequent possibility of electronically conducting magnetite "bridges" between specimen and wall. In one of these experiments the pressure vessel was known to have oxidized at an abnormally high rate.

Effects of hydrogen.—The provision of an external cathode has been shown to have a pronounced effect upon the growth of magnetite in 15% sodium hydroxide solution. Since there is such a distinct change in the morphology of the oxide this effect is not simply an acceleration of the growth rate resulting from galvanic coupling and so, for a fuller understanding of both types of growth, it is necessary to know the mechanism by which the morphology is changed.

It was described above how the evolution of hydrogen and its interference with the growing oxide film might change the type of oxide obtained. For this mechanism to be relevant one can assume that hydrogen is produced at the anode and that the growth acceleration produced by coupling the oxidizing mild steel to magnetite (or gold) increases the rate of the anode reaction sufficiently for the hydrogen evolved from the metal surface to produce a porous oxide.

On this view, proposed by Bloom (12), a strong correlation between the morphology and the rate of growth would be expected and the provision of ex-

Table I. Oxidation of mild steel surfaces

Conditions	Oxidizing surface	Possible external cathode	Type of growth [M = Mann & Potter, B = Bloom]
[1] Growth in a conditioned pressure vessel	Specimen surface	Fe_3O_4 on pressure-vessel wall	M
[2] Growth in a nonconditioned pressure vessel	Specimen surface	None (d) not fulfilled	B
[3] Growth in Bloom's capsules	Interior capsule surface	None No other surface present	B
[4] Growth on pressure-vessel walls	Wall surface	None	B
[5] Gold tube experiment as in Fig. 4	Surface of A Surface of B	Interior of gold tube Exterior of gold tube	M M + B
[6] Gold tube experiment as in Fig. 5	Surface of A Surface of B	Entire surface of gold tube Entire surface of gold tube	Same type of growth in both cases. Both M + B observed
[7] Capsules in pressure vessels as in Fig. 8 and 9	Surface I Surface II	Fe_3O_4 on pressure-vessel wall None (c) not fulfilled	M B
[8] Specimens in P.T.F.E. capsules	Specimen surface	None (a) rules out P.T.F.E. (c) rules out the pressure-vessel wall	Mostly B

ternal cathodes would serve to increase the rates of growth of magnetite to values at which porous magnetite films are formed.

Both the Bloom growth obtained in capsules and the Potter and Mann growth in conditioned pressure vessels have been obtained with growth rates varying over a wide range, depending on the temperatures and alkalinities used, and consequently the author feels that the function of the cathodic surface in changing the growth is not simply the indirect result of its increasing the growth rate. However, further experimental evidence is necessary before a definite mechanism can be established.

Discussion and Conclusions

A satisfactory explanation of the discrepancies between the results of the experiments performed previously in growing protective magnetite now seems to be available and it is possible to describe the conditions under which the known types of protective growth are obtained, although the reasons why these conditions should give rise to the particular types of growth obtained are not yet fully understood.

A mild steel specimen oxidizing in high temperature alkaline solution and in electrical contact with a suitable area of magnetite (or gold) in the same solution will, in general, subject to the limitations mentioned above, produce a fine-grained porous film together with an array of tetrahedral crystals usually located at the outer surface of the film. The function of this external magnetite (or gold) surface is presumably as a cathode, the cathodic reaction probably being

$$2e + 2H_2O \rightarrow 2OH^- + H_2$$

(In the initial stages, when some dissolved oxygen is present in solution, the reaction

$$4e + 2H_2O + O_2 \rightarrow 4OH^-$$

may occur.)

Magnetite films produced in the presence of an external cathode have been observed with what appears to be varying degrees of porosity: this may be related to the relative sizes of the anodic and cathodic areas. Investigations into this are proceeding.

On the other hand, if a mild steel specimen has no contact with a suitable cathodic surface an irregular, nonporous film is obtained which displays greater protectiveness and a strong similarity to the "outer-layer" tetrahedra observed in the other type of growth.

Pits are eventually formed in this type of growth: as suggested by Bloom (5) these probably occur after the rupture of the protective film. The intact film can then act as a cathode for the high rate of corrosion at the point of breakage, condition (d) mentioned above is now fulfilled. Since the corrosion at the point of pitting is taking place in the presence of an external cathode, it is not surprising that the oxide formed in pits often bears a strong resemblance to that observed in Potter and Mann films. Figure 11 shows the hemispherical pits observed after oxidation of a specimen in a nonconditioned pressure vessel for 185 hr.

The oxidation of the internal surfaces of boiler feedwater tubes will take place initially under conditions similar to the oxidation of the inside of capsules, *i.e.*, in the absence of an external cathode. Consequently, it appears that the growth mechanism and properties of Bloom films might be of most relevance to a study of the protective oxide growth on boiler tubes.

Perhaps one of the most important properties of Bloom films to be considered in this respect is the way in which a broken film is repaired. In 15% sodium hydroxide the rupture of a Bloom film produces a site anodic to the rest of the metal upon which a porous oxide grows. If films with the properties of the Bloom films investigated are also grown in the very dilute alkaline solutions in boiler tubes then, should any breakage occur, oxide with the properties of Potter and Mann growth will be formed at the break. Although at places such as these the oxide will be protective under normal conditions, by virtue of their anodic nature they are likely to be the sites of more severe attack should abnormal conditions arise.

For example, it has been suggested (15) that if Cl^- ions are present in the feed water then ferrous chloride, known to promote a nonprotective growth on mild steel (16), might be formed by anodic action at the steel surface. It is possible that the fracture of a Bloom film might produce such a relatively anodic site. Any Potter and Mann growth (assumed to be porous) formed prior to the ingress of chloride ions would no longer be protective after ferrous chloride had been formed: indeed, it has been suggested that such a growth might aggravate the corrosion by assisting the accumulation of anodic products near the metal (15).

Acknowledgments

The author would like to thank Dr. M. C. Bloom for supplying some of the mild steel capsules used in the experiments, his colleagues at C.E.R.L. and Dr. J.S.Ll. Leach for many interesting discussions, and Miss M. J. Rowbotham and Mr. P. D. Cooper for assistance with the experimental work.

The work was carried out at the Central Electricity Research Laboratories, and this paper is published by permission of the Central Electricity Generating Board.

Manuscript received Aug. 25, 1965.

Any discussion of this paper will appear in a Discussion Section to be published in the December 1966 JOURNAL.

REFERENCES

1. E. C. Potter and G. M. W. Mann, First International Congress on Metallic Corrosion, p. 417, London, April 10-15, 1961.
2. A. M. Adams, E. M. Field, D. R. Holmes, and R. C. Stanley, Paper presented at the 2nd International Congress on Metallic Corrosion, New York City, March 11-15, 1963. In press.
3. M. C. Bloom and M. Krulfeld, *This Journal*, **104**, 264 (1957).
4. W. A. Fraser and M. C. Bloom, *Corrosion*, **18**, 163*t*.
5. M. C. Bloom, G. N. Newport, and W. A. Fraser, *This Journal*, **111**, 1343 (1964).
6. M. C. Bloom, G. N. Newport, and W. A. Fraser, U. S. Naval Research Laboratory, N.R.L. Report 6082.
7. E. M. Field and D. R. Holmes, *Corrosion Science*, **5**, 361 (1965).
8. J. E. Castle, C.E.R.L. Laboratory Note No. RD/L/H 148/64.
9. D. G. Harris, Private communication.
10. R. V. Blaser and T. J. Owens, Symposium on High Purity Water Corrosion, A.S.T.M. Special Technical Publication No. 179, 1956.,
11. N. D. Tomashov, *Corrosion Science*, **4**, 315 (1964).
12. M. C. Bloom, Discussion of "Large-Scale Steam Generation at Steel Surfaces—a Physicochemical Enquiry" by E. C. Potter, presented at the 25th International Water Conference, Pittsburgh, September 1964.
13. H. Krulfeld, M. C. Bloom, and R. E. Seebold, *Corrosion*, **15**, 179*t* (1959).
14. D. P. Smith, "Hydrogen in Metals," p. 191, University of Chicago Press (1948).
15. G. M. W. Mann, *Chemistry and Industry*, 1584 (1964).
16. E. C. Potter and G. M. W. Mann, *Chemistry and Industry*, 1768 (1963).

Characteristic Scales on Pure Nickel-Chromium Alloys at 800°-1200°C

G. C. Wood and T. Hodgkiess

Corrosion Science Division, Department of Chemical Engineering, Faculty of Technology, University of Manchester, Manchester, England

ABSTRACT

Thermogravimetric measurements, metallography, and electron-probe microanalysis have revealed the nature of characteristic scales produced on pure Ni-14.6, 27.4, and 40.2 w/o (weight per cent) Cr in oxygen at 800°-1200°C. The growth kinetics are relatively independent of the surface preparation but are critically affected by the method of heating the specimen to temperature. Preferentially oxidized specimens usually produce only Cr_2O_3 scales, but samples immediately located in the hot zone possess an outer layer which is largely NiO. For high chromium contents and low temperatures the inner layer is Cr_2O_3, but under the opposite conditions it is multiphase. Cr_2O_3, subscale formation is extensive and can stop rapid development of stratified scale by joining up to give a complete layer. Cr_2O_3 is definitely the oxide which renders scales on these alloys protective. Extensive chromium depletion in the underlying alloy has serious consequences if protective scale fails. The mechanism of oxidation of Ni-Cr alloys is discussed and briefly compared with that of Fe-Cr alloys, from which there are distinct differences.

A surprising feature of the alloy oxidation field is the extensive disagreement about the nature of protective scale on Ni-Cr alloys rich in chromium when they are oxidized in air or oxygen (1-15). It is also curious that this system has been neglected during the recent trend to study the behavior of pure materials by topographical and microanalytical methods, which can scarcely fail to resolve such problems.

Except for quite low-chromium alloys (15-16), scarcely any optical micrographs of scales on reasonably pure materials have been published. In addition, no detailed electron-probe microanalyses have appeared yet. Use of these techniques, in conjunction with kinetic measurements, provides a close characterization of the scaling behavior, with precise details of scale topography and analysis, and data regarding the location and time of appearance of the various oxides, information lacking in previous studies. This paper presents such data for Ni-Cr alloys containing respectively 14.6, 27.4, and 40.2% chromium over a wide range of exposure times at 800°-1200°C. This allows a more precise description of the mechanism of scaling than given previously (9), without arbitrary divisions according to composition.

Experimental Procedure

The Ni- 14.6, 27.4, and 40.2 w/o (weight per cent) Cr alloys were made from nickel of 99.97% purity (C 0.008, Fe < 0.03, S < 0.002, Pb < 0.002, B < 0.001, Cr, Co, Mo, Ti, Al, Si, Mn, Zr, Mg, and Cu < 0.01%) and from pure chromium (C < 0.005, O 0.035, H 0.01%; N 7, Pb 3, Sn 4, Al 4, Fe 2, Na 4, Mg, Cu, Ni, Ag, Sb and B < 1 ppm) by rapid vacuum melting and were rolled to strip 0.06 cm thick. They were then given a preliminary annealing treatment in an inert gas at 1000°-1100°C which produced a coarse, heavily twinned, equiaxed grain structure with few Cr_2O_3 inclusions and a homogeneous bulk composition.

Specimens 2.0 x 0.5 x 0.06 cm were annealed "in vacuo" (10^{-5} mm Hg) for 8 hr at 1050°C in a further effort to obtain complete homogeneity and a large grain size; this led to mild preferential oxidation of the surface but no subscale. The final treatment was usually an adaptation of one previously used satisfactorily in studies of the oxidation of Fe-Cr alloys (17-18) and chromium (17). The specimens were electropolished for about 5 min at 0.1 amp/cm² (15v) in a freshly prepared solution containing 450 ml glacial acetic acid, 40 ml perchloric acid (sp. gr. 1.61) and 15 ml water below 20°C. Since there was a chromium-depleted surface layer at least 20μ thick, developed during fabrication and not easily removed by annealing, it was thought essential to use this long polishing time to remove about 40μ from each side. Microanalysis then indicated uniform composition throughout the specimen similar to that of the original alloy. Specimens were usually given a final dip or a minimum cathodic etch at 10 μamp/cm² for 60 sec in 5% HF, although a few were used in the electropolished condition or after abrasion on dry silicon carbide papers to grade 600. Potential/time curves recorded during etching were similar but not identical to those previously reported for Fe-Cr alloys (17). Unlike the Fe-Cr case, no attack was visible on the alloy after etching.

Samples were generally located immediately in the hot-zone of a previously heated silica-spring thermobalance (sensitivity ± 0.1 mg/cm²), containing slowly flowing pure dry oxygen and a crucible containing Cr_2O_3 near the specimen. The Cr_2O_3 was present to minimize losses from the specimen of a volatile species [probably CrO_3 (17)] which would invalidate the kinetic measurements. Weight gains were measured within 5 min of exposure and were continued for periods up to 100 hr. In several experiments the specimen was brought to temperature over 2-3 hr in an oxygen pressure lower than 5 x 10^{-5} min Hg, after which oxygen at atmospheric pressure was admitted. Scale structures were unaffected by the method or rate of cooling.

Metallography was more difficult than with scales on Fe-Cr alloys which may partly explain the absence of previously published micrographs. Many methods were tried but none proved better than conventional polishing.

Certain specimens, made conducting by a thin carbon film, were studied in a Cambridge Mk II "Microscan" electron-probe microanalyzer at 29 kv, the x-ray source size producing 95% of the characteristic radiation in the oxide being 1.7-2.5μ. The results are presented as scanning x-ray images or as ultra-slow-scanning line concentration profiles. The individual points on these traverses indicate where absorption and fluorescence corrections have been made and the whole curve adjusted accordingly, rather than the location of static probe measurements. The latter were occasionally used to check results.

Electron-probe microanalysis and optical examination are entirely adequate for identification of single-phase regions which are nearly pure Cr_2O_3 or NiO, and of larger subscale particles and loops which are always Cr_2O_3. The terms Cr_2O_3 and NiO are used for single phases of such oxides containing about 1% Ni and 1% Cr, respectively. In multiphase regions, it is only possible to give mean compositions and rely on the extensive literature on diffraction data for likely structural identification.

Results and Interpretation

General considerations.—The general pattern of behavior of the alloys, prepared and exposed in the usual manner described earlier, will be given before specific modes of scaling are introduced.

1. Ni-40.2% Cr always produces a NiO-rich outer layer a few microns thick, formed in the early stages, above a further uniform layer of Cr_2O_3 which thickens during the remainder of the run, at a faster rate the higher the temperature.

2. Ni-27.4% Cr behaves as above at 800°C and generally at 1000°C, although sometimes at 1000°C the Cr_2O_3-rich layer eventually fails and complex stratified scale grows. At 1200°C, however, nodular scale, with an outer NiO layer and an inner multiphase layer [probably NiO, $NiCr_2O_4$, and Cr_2O_3 in varying proportions (7, 8, 16)] grows. Cr_2O_3 subscale joins up to form a complete Cr_2O_3 layer at the main scale base and this alone thickens quite rapidly subsequently.

3. At all temperatures, Ni-14.6% Cr displays similar nodular stratified scale which develops faster at high temperatures. Completion of the "healing" Cr_2O_3 layer takes many hours at 800°C but is rapid at 1000° and 1200°C, although at 1200°C the outer scale is very thick. The subsequent Cr_2O_3 growth at 1000°C is much slower than with Ni-27.4% Cr at 1200°C.

4. Chromium depletion and nickel enrichment in the underlying alloy is extensive and persistent. Cr_2O_3 subscale is formed even behind protective Cr_2O_3 scale.

Thus, in general Ni-27.4% Cr at 800° and 1000°C behaves like Ni-40.2% Cr at 800°-1200°C and Ni-27.4% Cr at 1200°C acts like Ni-14.6% Cr at 800°-1200°C. This gradation of behavior demonstrates that arbitrary subdivision of alloys at compositions of ~10% (9, 19), 20%, or any other figure in this vicinity (30, 31) is fundamentally meaningless and practically misleading. The actual behavior depends on factors such as temperature, environment, and surface finish which in turn determine the contribution of thermodynamic, kinetic, nucleation, and mechanical factors to the final scale product.

Influence of surface preparation.—Typical growth curves at 1000° and 1200°C for the oxidation of Ni-40.2% Cr specimens, prepared by the three techniques described earlier, and allowed to enter the hot zone of oxygen immediately, are shown in Fig. 1. The reproducibility was good, particularly for specimens given an electropolish followed by a minimum etch which were studied in most detail. Clearly, ignoring small deviations due to balance errors, there is little influence of surface finish, although the abraded specimen at 1000°C oxidizes somewhat slower than the others, after the first few minutes. This is also true for the other alloys whether they produce protective or stratified scale.

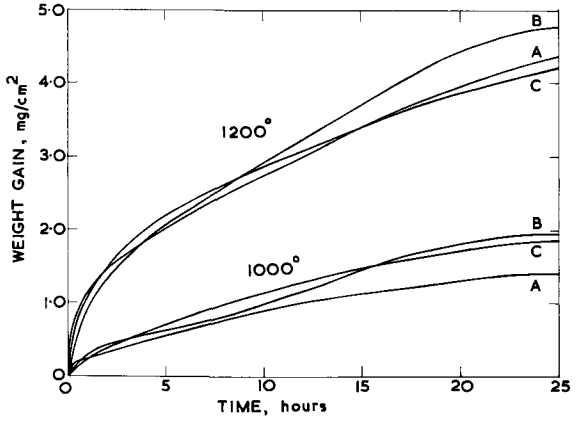

Fig. 1. Influence of surface pretreatment on the oxidation rate of Ni-40.2% Cr at 1000° and 1200°C. A, abraded; B, electropolished; C, electropolished and etched.

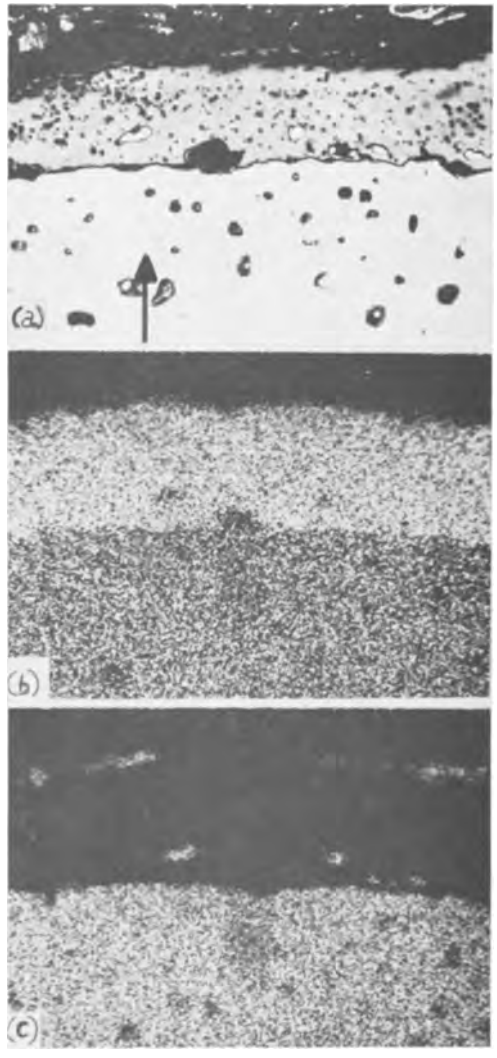

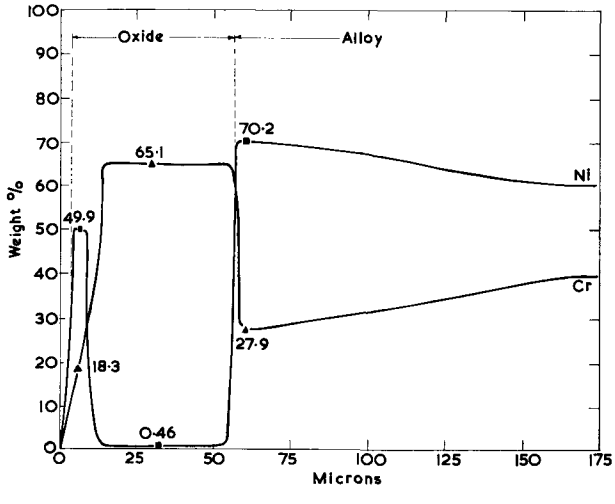

Fig. 2. Electropolished Ni-40.2% Cr oxidized for 25 hr at 1200°C. a, Optical image in cross section, magnification *ca.* 500X. b, Cr Kα x-ray image. c, Ni Kα x-ray image. d, Concentration profiles along line of traverse on Fig. 2a.

After the first 40-60 min at 1200°C the abraded and electropolished and etched specimens show good agreement with the parabolic growth relationship (rate constant = 1.62×10^{-10} g^2 cm^{-4} sec^{-1}). It will become apparent that this stage is associated with the formation of a thick, uniform Cr_2O_3-type scale. The earlier deviations from the above rate can be represented by a faster parabolic rate constant (6.34×10^{-10} g^2 cm^{-4} sec^{-1}), but this is probably fundamentally meaningless because it represents a stage where nickel and chromium are both entering the scale and the Cr_2O_3 layer is becoming developed.

On cooling, the scale on electropolished specimens sometimes tended to lift in flakes, and that on abraded specimens to fail explosively in some places, but elsewhere adhesion was good. The scale generally adhered to specimens which had been lightly etched after electropolishing. Despite these gross differences, microtopography and composition were largely independent of surface finish, except for a few areas on long-term electropolished specimens, a conclusion which is predictable from the growth curves. The results presented here for an electropolished specimen are also characteristic of the other two preparations.

The scale on an electropolished specimen oxidized for 25 hr at 1200°C (Fig. 2 a-c) consists mainly of a thick, uniform, compact chromium-rich oxide, containing a few metallic particles and occasionally keyed to the alloy by tongues of similar oxide. There is also an internally oxidized layer 50-60μ deep and outside the main scale there is a thin friable layer of nickel-rich oxide. Such layers could not be improved in appearance except when formed on other specimens at 800°C (see later). The concentration profiles (Fig. 2d) confirm that the outer layer is largely NiO. It is not clear whether the chromium measured in this layer is genuine, indicating the presence of some Cr_2O_3 or $NiCr_2O_4$, or whether the x-ray source is overlapping the two layers. The inner layer is Cr_2O_3 containing 0.46% nickel. Chromium is depleted to 27.9% at the alloy/oxide interface over a distance of about 110μ, there being a corresponding nickel enrichment. Except where otherwise stated, the alloy compositions at the alloy/oxide interface are genuine, care having been taken to avoid subscale particles and overlap with the main scale.

Over $<$ 10% of electropolished specimen surfaces only, complex ballooned oxide above more compact layers was observed, particularly at 1000°C. This agrees with the observation (Fig. 1) that electropolished specimens oxidized slightly faster in the later stages than the other samples at both temperatures. The outer scale along the line of traverse in Fig. 3 contained 68.9% chromium and 0.47% nickel, whereas the inner scale had an outer layer analyzing as 33.4% chromium and 19.0% nickel and an inner one as 61.0% chromium and 1.56% nickel. The chromium content at the alloy/oxide interface was depleted to 17.6% over a distance of about 40μ. Although the outer ballooned layer appeared to be Cr_2O_3 alone, it probably had a thin NiO-rich layer outside it which spalled off during ballooning at temperature. The inner scale which formed after the initial scale failure was similar to that previously described. The high apparent chromium content and low total weight per cent metal of its outer layer were again mainly due to its thinness.

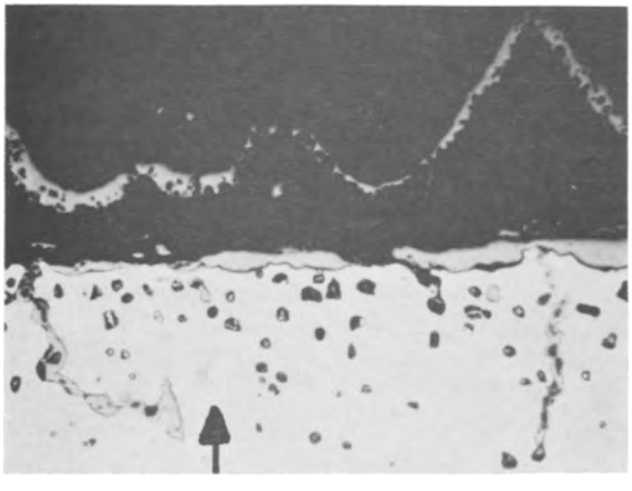

Fig. 3. Cross section of electropolished Ni-40.2% Cr oxidized for 25 hr at 1000°C, showing ballooned scale and subscale particles. Magnification 500X.

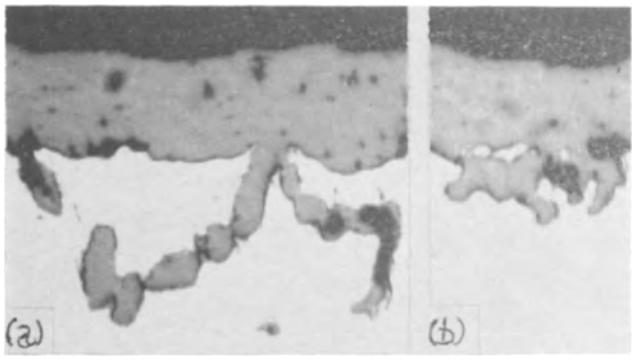

Fig. 4a and b. Cross sections of electropolished and etched Ni-40.2% Cr oxidized for 5 hr at 1200°C, showing development of subscale loop and alloy incorporation into the scale. Magnification 1000X.

An interesting feature of this study, which partly explains the general good adhesion of the Cr_2O_3 scales for all surface finishes, is the Cr_2O_3 loop development, probably along grain boundaries, behind the main scale. Such loops, and also the smaller internal oxide particles of the same oxide, are particularly prevalent for all alloys at high temperature and after long oxidation times. Figure 4a shows an almost complete loop on an electropolished and etched specimen subsequently oxidized for 5 hr at 1200°C. It also shows how the metallic particles become incorporated in the scale, although the much smaller particles shown previously in Fig. 2a were probably formed as in Fig. 4b.

Influence of pre-oxidation.—When specimens with any of the three surface finishes were preheated to temperature "in vacuo" (oxygen pressure less than 5×10^{-5} mm Hg) for 3 hr at 1000°C, prior to admitting oxygen at atmospheric pressure (a technique used by some investigators) quite different scale structure resulted. Ni-40.2% Cr and Ni-27.4% Cr produced nearly pure Cr_2O_3 with no outer NiO-rich layer. Ni-14.6% Cr also generally gave only Cr_2O_3 but stratified scale sometimes appeared in places, probably after the breakdown of the initial Cr_2O_3 layer. Reproducible growth of Cr_2O_3, largely independent of surface finish, usually occurred for at least 25 hr.

One specimen of Ni-14.6% Cr gave only Cr_2O_3, 6-10μ thick, over its entire surface with a few massive complete subscale loops, when oxidized for 285 hr at 1000°C (Fig. 5a). Figure 5b, which avoided the loops, indicates a single Cr_2O_3 layer containing 1.8% nickel with no outer NiO and static probe analysis of the subscale gave a similar composition. A significant observation with all specimens is the extensive and persistent chromium depletion beneath the scale, indicating the slow interdiffusion in the alloy.

Typical growth relationships.—Growth curves for the remaining specimens to be described, all of which were given the minimum etched finish after electropolishing before direct exposure at temperature, are shown in Fig. 6a and b. Figure 6b continues the curves for the long-term runs and includes a curve for a Ni-27% Cr alloy at 1000°C which displayed limited break-through. Reproducibility with other runs not

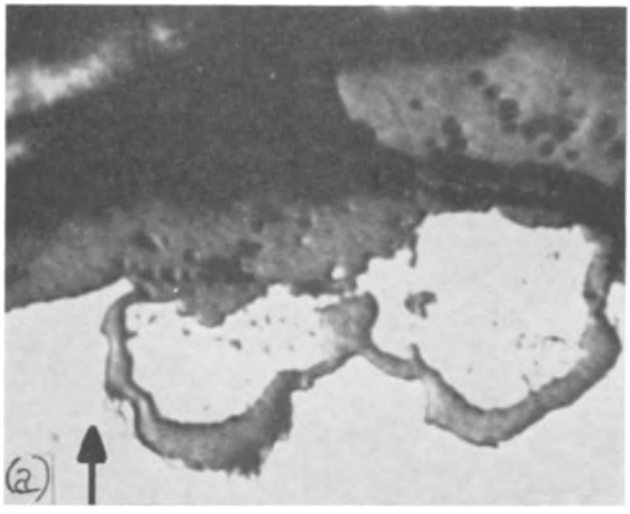

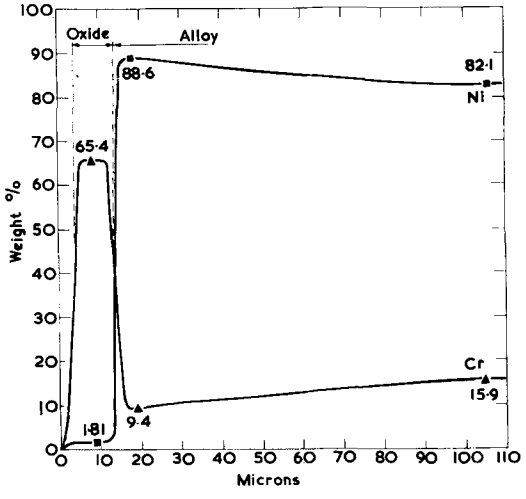

Fig. 5. Abraded Ni-14.6% Cr oxidized for 285 hr at 1000°C after being heated to temperature in vacuum (~5 x 10^{-5} mm Hg). a, Optical image showing fully developed subscale loops, magnification 1500X. b (bottom), Concentration profiles along line of traverse on Fig. 5a, showing no outer NiO-rich layer.

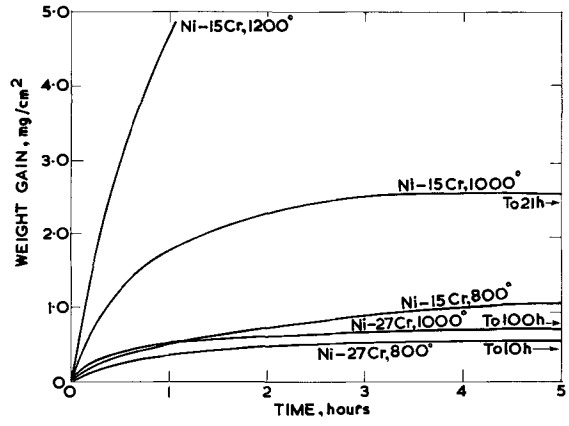

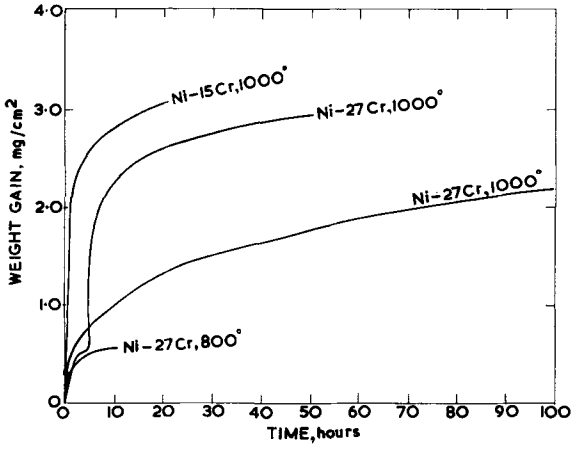

Fig. 6. Rates of formation of scales on electropolished and etched Ni-14.6% Cr (at 800°, 1000°, and 1200°C) and Ni-27.4% Cr (at 800° and 1000°C). a (top), 0-5 hr. b (bottom), 0-100 hr. Curves for Ni-14.6% Cr at 800° and 1200°C are omitted from Fig. 6b and that for Ni-27.4% Cr showing breakthrough at 1000°C from Fig. 6a in the interests of clarity.

reported was generally remarkably good, even in some cases when scale nodules formed, rendering the kinetics fundamentally meaningless. The only exceptions were the occasional failure of Ni-27.4% Cr at 1000°C after the early stages, which could be expected to be irreproducible, since it depended on irregular lifting and failure of Cr_2O_3-rich scale, and the nodular growth of scale on Ni-14.6% Cr at 1200°C.

The oxidation of Ni-40.2% Cr and Ni-27.4% Cr at 800° and 1000°C suggested the same two-stage parabolic behavior as Ni-40.2% Cr at 1200°C, but the scatter in the very low weight gains in the early stages made this difficult to prove absolutely. Quantitative treatment of other growth curves was unwarranted due to complex scale formation.

Protective scale.—Despite careful precautions the thin scales on samples of Ni-40.2 and Ni-27.4% Cr oxidized for short times (5-30 min at 800°-1200°C) invariably exhibited severe spalling on cooling. Such specimens in section showed a thin uniform oxide 1-2μ thick which had lifted almost entirely from the alloy surface on cooling. This process probably led to spalling of any outer NiO-rich layer but in any case it may not have emerged sufficiently in this short time to be detected by the microanalyzer. Indeed, line traverses merely revealed a chromium-enriched oxide, containing some nickel, and slight chromium depletion in the alloy. After 1-2 hr at these temperatures the layered structure described below was fully developed.

The scale on Ni-27.4% Cr after 10 hr at 800°C is interesting because the uniform outer NiO-rich layer remained adherent (Fig. 7). Concentration profiles indicated a 5μ outer layer of NiO containing about 1.5% Cr and a 1-2μ inner layer (appearing black in the micrograph due to relief polishing) of nearly pure Cr_2O_3. The presence of NiO at this low temperature is evidence for its genuine direct formation and suggests that its appearance at 1000° and 1200°C could not possibly be related to volatilization of chromium oxides or similar material from the outer layer. Depletion of chromium to 13.9% at the interface occurred over only 3-4μ of alloy. Exposure for 100 hr at 800°C failed to thicken the NiO layer, only the Cr_2O_3 inner layer growing during this period.

After 100 hr at 1000°C the thickness is still remarkably uniform over the entire surface and the inner layer is considerably thicker than at shorter times and lower temperatures (Fig. 8a). The x-ray images (Fig. 8b and c) confirm the existence of the outer layer and show that this and part of the inner layer

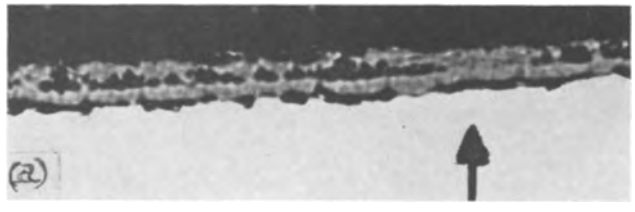

Fig. 7. Cross section of electropolished and etched Ni-27.4% Cr oxidized for 10 hr at 800°C, showing distinct outer NiO-rich layer, magnification 1000X.

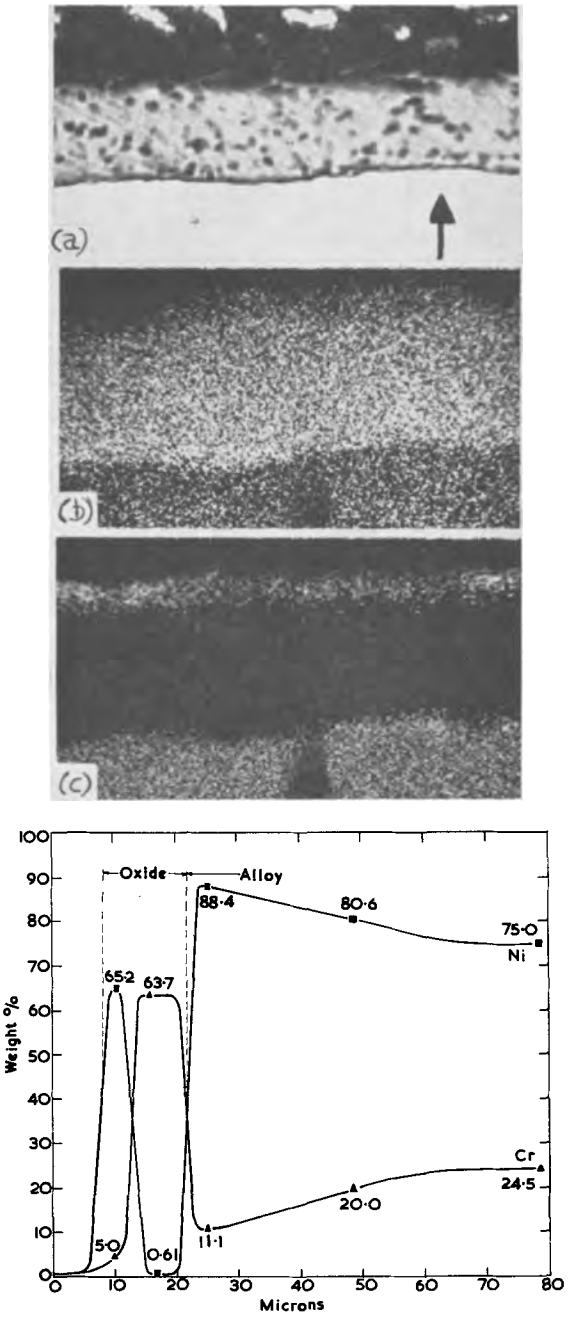

Fig. 8. Electropolished and etched Ni-27.4% Cr oxidized for 100 hr at 1000°C, showing protective scale. a, Optical image, magnification *ca.* 1500X. b, Chromium Kα x-ray image. c, Nickel Kα x-ray image. d (bottom), Concentration profiles along line of traverse on Fig. 8a.

are invisible in the optical image due to polishing problems. Figure 8d shows the outer 3μ-layer apparently containing 65.2% nickel and 5.0% chromium (some of the chromium could be due to x-ray source overlap) and the inner 10μ-layer 63.7% chromium and 0.61% nickel. Chromium depletion to 11.1% occurs over a distance of 48μ from the bulk alloy.

In summary, the early relatively rapid stages of oxidation are associated with the appearance of an outer NiO-rich layer of constant thickness and the establishment of a Cr_2O_3-rich layer at its base. The final slower oxidation is connected entirely with the growth of the Cr_2O_3.

Complex scale formation after protective scale failure.—For certain specimens of Ni-27.4% Cr at 1000°C (Fig. 6, 50 hr specimen) the oxidation rate increased suddenly after an initial protective period, and then declined again. Such specimens are too complex to be detailed here but a relatively simple area with several scale layers is shown in Fig. 9a-c, with corresponding concentration profiles in Fig. 9d. Almost certainly the initial protective Cr_2O_3 scale, covered by a thin NiO-rich layer, was lost from a few regions of the surface by lifting and cracking after about 6 hr (20). The chromium-depleted underlying alloy then behaved like a lower chromium alloy, producing a thick outer NiO layer and multiphase oxides in the inner layer. Eventually, however, the higher bulk chromium concentration re-asserted itself and a new Cr_2O_3 scale developed at its base, so healing the main scale. The thickening of this Cr_2O_3, and of that where failure had not occurred, occupied the final 40 hr of the run.

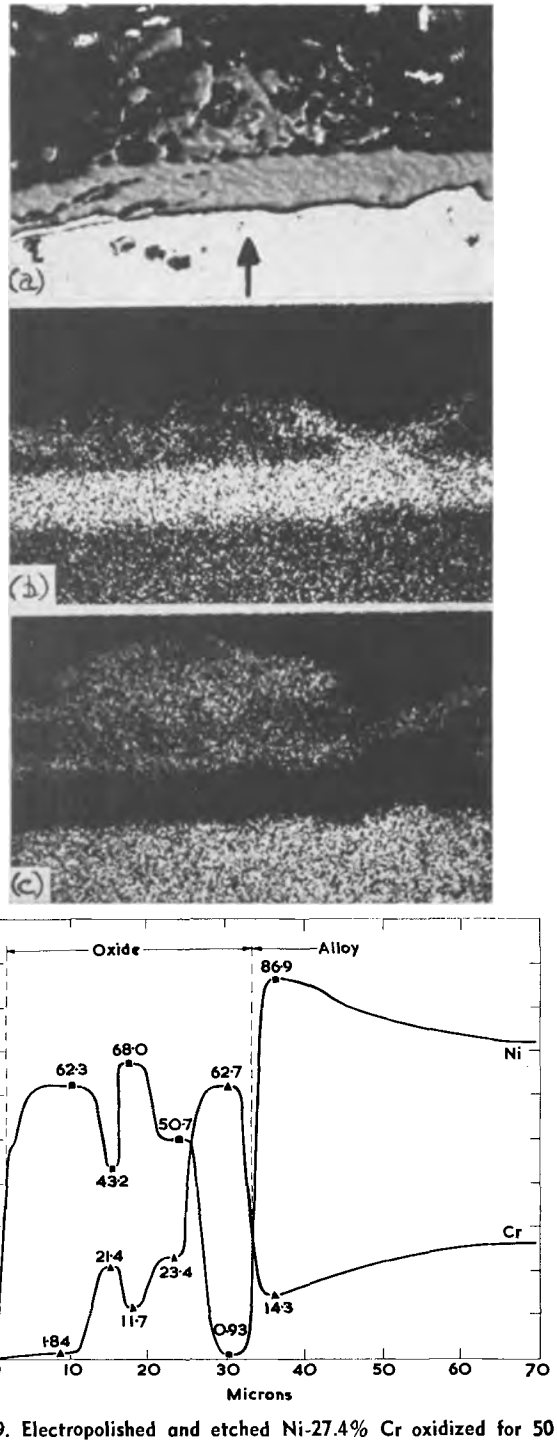

Fig. 9. Electropolished and etched Ni-27.4% Cr oxidized for 50 hr at 1000°C, showing complex scale. a, Optical image, magnification *ca.* 800X. b, Chromium Kα x-ray image. c, Nickel Kα x-ray image. d (bottom), Concentration profiles along line of traverse on Fig. 9a.

Stratified scale.—Uniform stratified scale formed on Ni-14.6% Cr at 800°C in 5 hr possesses a compact outer layer and a friable inner layer (Fig. 10a). A dense layer of subscale particles beyond resolution also appears over the entire surface and this persisted in other samples for at least 25 hr. Figure 10b reveals an outer layer containing 74.1% nickel and 1.2% chromium, an inner layer with 44.1% nickel and 24.4% chromium, a step representing the mean composition of the internal oxide and alloy matrix containing it, and no depleted alloy layer. The same is true in the very early stages at 1000°C, but the subscale soon joins up to give a complete Cr_2O_3 layer.

Healed stratified scale.—Figure 11 a-c shows a Cr_2O_3 layer which grew at the base of the nodular stratified scale initially developed on Ni-14.6% Cr at 1000°C. This Cr_2O_3 layer controls the asymptotic growth observed during the final 19 hr of exposure at this temperature (21 hr specimen in Fig. 6). An outer, single-phase, nickel-rich layer covers a region of at least two phases containing nickel and chromium which is in turn insulated from the alloy by the Cr_2O_3. In the thicker scale the outer and intermediate layers are of approximately equal thickness, with their interface located at the original alloy surface, but at the thin end of the wedge the intermediate layer eventually disappears. The chromium-rich loop in the inner layer of the thick scale, similar to others occasionally found, is difficult to explain but presumably represents some transitional form of scale which did not maintain protection. The underlying alloy is depleted in chromium but shows no subscale.

Concentration profiles were made along the three lines of traverse in Fig. 11a. In the thin region, the scale is like protective oxide on alloys richer in chromium with outer and inner layers of nearly pure NiO and Cr_2O_3, respectively. The middle region (Fig. 11d) possesses outer NiO containing 0.45% chromium, an intermediate layer with a uniform composition of 49.3% nickel and 22.7% chromium, and inner oxide rich in Cr_2O_3. Five layers, with the two outermost zones having analyses similar to those in the previous traverses, appear in the thickest region [traverse (iii)]. The thick intermediate layer is again remarkably uniform at 49.2% nickel and 21.7% chromium, a composition found for many specimens studied under these conditions. In the present case a chromium-rich region and a further NiO-rich layer are sandwiched between this oxide and the inner Cr_2O_3-rich layer.

The extent and depth of chromium depletion in the alloy (chromium reduced to 6.7-9.1% at the interface over 26-28μ) is independent of the type of superficial scale. Thus, the boundary of the region of chromium-depleted alloy follows a similar contour to the alloy/oxide interface because the depletion was

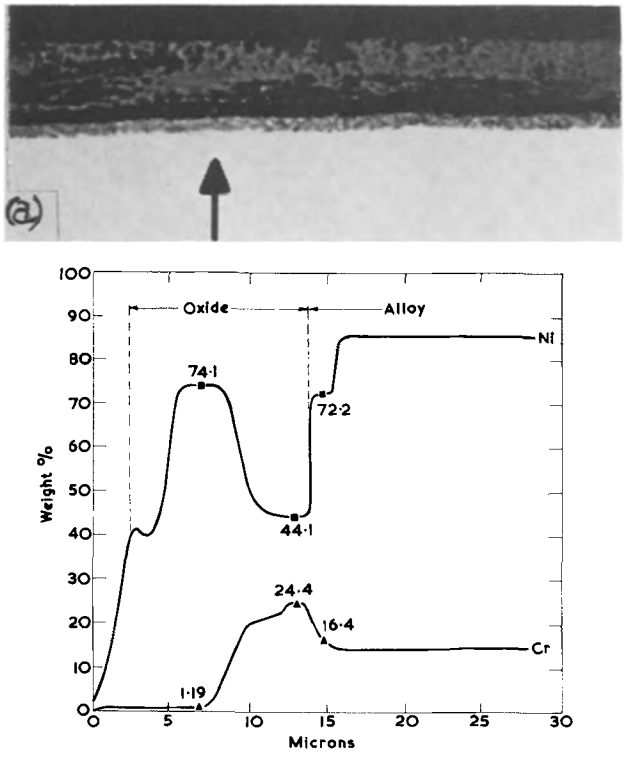

Fig. 10. Electropolished and etched Ni-14.6% Cr oxidized for 5 hr at 800°C, showing uncoalesced subscale layer. a, Optical image, magnification 1000X. b (bottom), Concentration profiles along line of traverse on Fig. 10a.

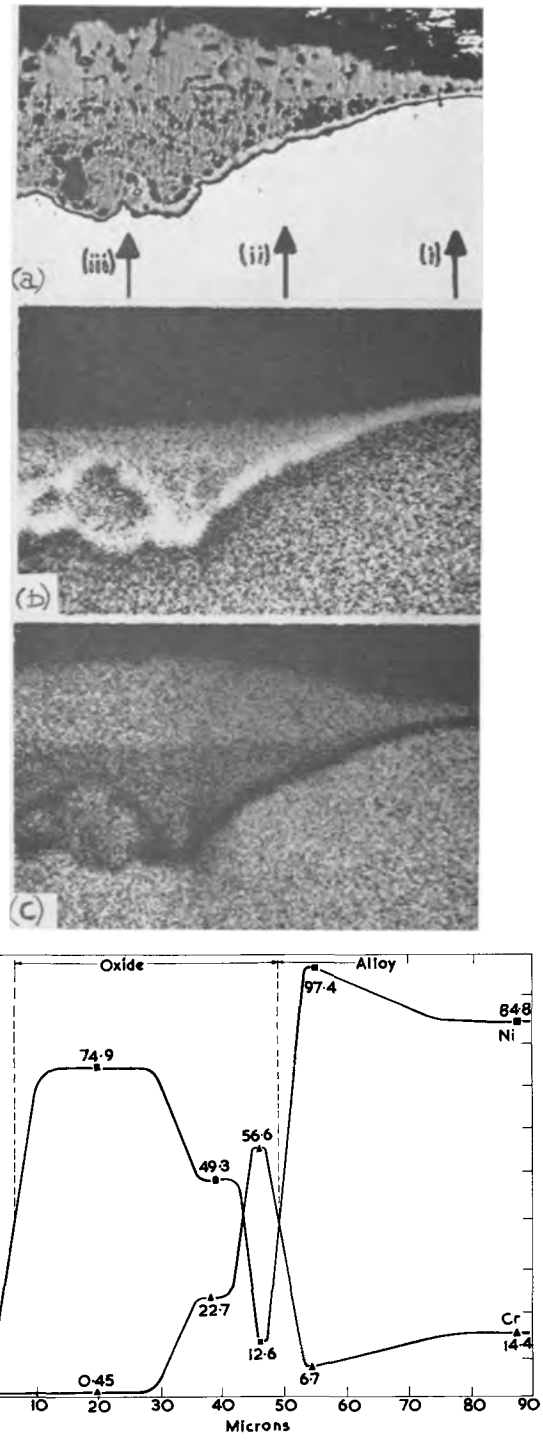

Fig. 11. Electropolished and etched Ni-14.6% Cr oxidized for 21 hr at 1000°C, showing healed stratified scale. a, Optical image, magnification ca. 380X. b, Chromium Kα x-ray image. c, Nickel Kα x-ray image. d (bottom), Concentration profiles along line of traverse (ii) on Fig. 11a.

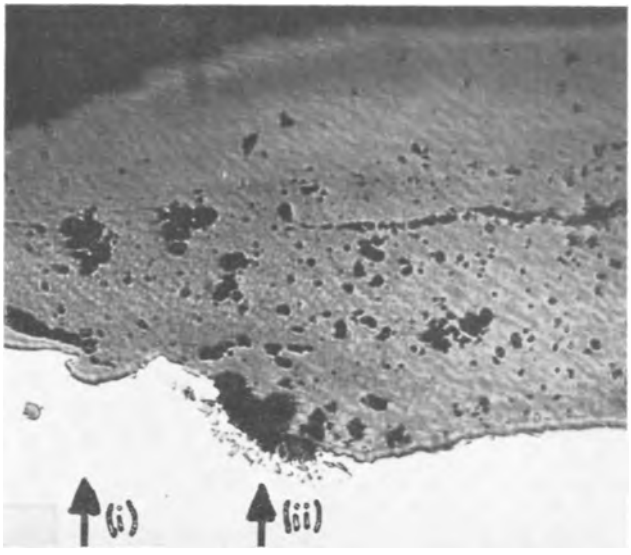

Fig. 12. Cross section of electropolished and etched Ni-14.6% Cr oxidized for 1 hr at 1200°C, showing partly healed stratified scale.

achieved during the final 19 hr of the run, in which only the Cr_2O_3 was thickening at a slow rate.

Partly healed stratified scale.—When Ni-14.6% Cr is oxidized at 1200°C, thick stratified scale grows very rapidly, but the formation of a Cr_2O_3 layer at its base is accomplished much sooner than at lower temperatures. Figure 12 shows a typical stratified nodule almost insulated from the alloy by a Cr_2O_3 layer after 1 hr. Healing was achieved earlier to the left of the image than to the right and the process was not complete in the center, where a small cluster of Cr_2O_3 subscale particles is still visible. Line traverses along (i) and (ii) proved that the intermediate layer is of variable composition, showing some chromium-rich regions, including a small loop like that in the previous specimen, and a thin chromium-rich band between the two main layers. Furthermore, there does not seem to be a complete network of macropores in the multiphase region, although this appeared to be so in other specimens. The outer layer is nearly uniform NiO containing 0.9-1.5%Cr and the inner layer is nearly pure Cr_2O_3. Even where only subscale Cr_2O_3 particles exist there is a severe depletion in chromium to 6.3% immediately below in the alloy. This indicates that although alloy interdiffusion was very rapid at 1200°C, so was Cr_2O_3 formation.

Discussion

Mechanism of oxidation of Ni-Cr alloys.—Before discussing the nature of oxidation of Ni-14.6% Cr at 800°-1200°C and of Ni-27.4% Cr at 1200°C it is appropriate to summarize certain of the new quantitative facts. The outer NiO layer on Ni-14.6% Cr contains 0.25-1.5% chromium (depending on the temperature and time of oxidation) which presumably thus increases the cation vacancy concentration in this layer. On Ni-27.4% Cr, which acts in the same way at 1200°C, 3.5-6% Cr is measured in this layer, but some of this may conceivably be $NiCr_2O_4$ or Cr_2O_3. Once the Cr_2O_3 healing layer is complete, the composition of the intermediate layer on Ni-14.6% Cr is remarkably uniform at about 50% nickel and 20% chromium through its entire thickness at 1000°C and through certain regions of the more undulating profiles at 1200°C. It was not possible to resolve the small particles in the layer, which could contain NiO and $NiCr_2O_4$ in the weight ratio 1:1, or NiO and Cr_2O_3 in the ratio 2:1, or a mixture of all three phases. This layer is porous but this could have been produced on cooling and possibly accentuated on metallographic preparation. It was impossible to measure the alloy composition between the subscale particles because they were densely populated, but there was little chromium depletion behind them in the bulk alloy, particularly at 1000°C.

The nucleation and growth of these scales are explicable by extending a theory proposed for low-chromium alloys (16, 21). It states that when the alloy is exposed, NiO and Cr_2O_3 both form initially but rapidly combine and coalesce to give $NiCr_2O_4$ granules in a matrix of excess NiO, so effectively forming the inner layer. Partial dissociation of NiO occurs at the alloy/oxide interface and oxygen diffuses into the alloy, provoking the precipitation, by preferential oxidation, of Cr_2O_3 in a matrix of what becomes essentially pure nickel. As the external scale develops the Cr_2O_3 granules become incorporated into the inner layer where they are rapidly converted to $NiCr_2O_4$. Only Ni^{2+} ions can diffuse through the inner layer to extend the outer layer since Cr^{3+} ions are localized in the Cr_2O_3 or $NiCr_2O_4$ particles and Cr^{3+} ions are relatively insoluble in NiO.

A second theory (9) requires oxygen to diffuse into the bulk alloy, preferentially oxidizing chromium to Cr_2O_3, the matrix then oxidizing like almost pure nickel to give double-layer scales. The outer layer grows by the outward diffusion of electrons and Ni^{2+} ions and the porous inner layer by the inward diffusion of oxygen gas, produced by dissociation of NiO in voids at the interface between the two layers. There is also some Ni^{2+} diffusion out through bridges of scale in the porous inner layer.

There are still certain doubts about both theories. The dissociation mechanism has not been proved, so both layers may in fact grow by cation movement outwards, as suggested in the first theory. It has not been experimentally demonstrated that the metal between the subscale particles is nearly pure nickel and also mechanical factors in the scale have been neglected. It is not clear how Cr_2O_3 subscale particles are transformed to $NiCr_2O_4$ particles of similar appearance on entering the oxide and, in any case, Cr_2O_3 has also been reported in such scales (7).

Despite these doubts it is reasonable that the NiO outer layer, the intermediate layer, and the Cr_2O_3 subscale develop in general as suggested for the lower-chromium alloys. Scale thickening is then uniform over the surface at 800°C but nodules appear at 1000° and 1200°C. The chromium content of the complex inner layer increases with time before the healing Cr_2O_3 layer is complete when it becomes constant. This increase tends to reduce the over-all oxidation rate and favor complete subscale coalescence before it is absorbed by the encroaching scale. Thus the subscale population now becomes sufficiently dense to link up and produce a complete "healing" Cr_2O_3 layer at the base of the stratified scale, this process taking longer at lower temperatures. Variations in the time to establish it lead to permanent differences in local total scale thicknesses. The layer is completed when the rate of oxygen arrival into the subscale/alloy interface region is of the same order as chromium arrival there, with consequent continued precipitation. Subsequently, slow growth of the Cr_2O_3 alone occurs, with no other noticeable processes other than the development of extensive chromium depletion and nickel enrichment in the alloy. It is just possible that a chromium-rich layer is simultaneously developing independently in the base of the scale, by chromium reducing NiO here (22) or by oxygen gas at low partial pressure diffusing through pores in the inner layer and preferentially oxidizing chromium in the depleted alloy in contact with the scale. Neither theory could, of course, hold if the metal between the subscale particles is pure nickel. If the Cr_2O_3 really is a p-type metal deficit semiconductor, the nickel would tend to block cation vacancies and reduce its formation rate.

The Cr_2O_3 subscale coalescence to give a complete layer is an example of the theory that below a critical base metal concentration internal oxidation occurs, whereas above it only external scale is obtained, except that here the situation is being decided behind a pre-existing nonprotective surface scale. Where a complete layer of base metal oxide is formed, oxygen entry into the alloy is inhibited or prevented. The simplest situation has been discussed theoretically (23) and tested in the case of Ag-In alloys (24). In the present system it has been suggested (15, 19) that internal oxidation is possible only for alloys containing less than 9% chromium. This paper shows such an arbitrary division to be false because the mode of scaling depends on the oxidizing variables.

Ni-27.4% Cr at 800°-1000°C and Ni-40.2% Cr at 800°-1200°C start to oxidize in the same way as Ni-14.6% Cr but the Cr_2O_3 layer develops rapidly and there is little time for an extensive intermediate layer or for dense Cr_2O_3 subscale to grow. It can be stated categorically that the protective part of the scale is Cr_2O_3 (generally containing less than 1% nickel) and not $NiCr_2O_4$. Previous reports of spinel being the protective oxide are inexplicable but it should be noted that trace elements such as manganese in impure materials may promote its formation. It is not true to say (9), however, that the sole oxide is Cr_2O_3, at least when the alloy is immediately exposed to the hot atmosphere, although this is true for specimens brought to temperature in a so-called vacuum. There is always an outer NiO-rich layer a few microns thick, (containing a little chromium which in few extreme cases might exist as $NiCr_2O_4$ or Cr_2O_3). Incidentally, there is little evidence of the NiO-rich and Cr_2O_3-rich layers combining to give an extensive $NiCr_2O_4$ layer, although it is likely that a thin layer does exist.

The mode of scaling is similar to that described in theoretical papers (25). Probably NiO and Cr_2O_3 nucleate separately on the bare surface but the more rapidly growing NiO rapidly overgrows the Cr_2O_3 to form an outer layer. The Cr_2O_3 then spreads laterally until a complete layer is developed, whereupon this is the only oxide to continue growing. The time required to do this depends partly on the initial spatial distribution of nuclei in the scale, but also on the alloy chromium content, the atmosphere, and the temperature. It takes longer than with corresponding Fe-Cr alloys because metallic interdiffusion in the alloy is slower and oxygen solubility is apparently greater. It is sufficiently rapid for Ni-40.2% Cr and for Ni-27.4% Cr at 800° and 1000°C for any intermediate layer to be unnoticed with the microanalyzer, but for Ni-27.4% Cr at 1200°C and Ni-14.6% Cr it only occurs after both layers are well developed and internal oxidation has been extensive. Possibly some of the NiO-rich material in the initial inner layer is also reduced to metal by chromium, again promoting the Cr_2O_3 layer formation. The two-stage parabolic plot for Ni-40.2% Cr at 1200°C indicated a slower oxidation rate after 40-60 min, when the mean scale thickness was 6-8μ. This agrees well with the observation that the outer NiO-rich layer was always 4-9μ thick for oxidation times longer than 1 hr. Under preferential oxidation conditions no NiO is formed because Cr_2O_3 is thermodynamically favored and oxygen solubility in the alloy is drastically reduced while alloy interdiffusion is unaffected. If cation movement is postulated in both Cr_2O_3 and NiO, Cr_2O_3 could grow at their interface by the reaction

$$2Cr^{3+} + 6\epsilon + 3NiO = 3Ni^{2+} + 6\epsilon + Cr_2O_3$$

Consequently in these later stages only the thermodynamically stable Cr_2O_3 grows and the NiO, which owes its presence merely to a nucleation effect, continually reforms. An alternative mechanism, involving the inward diffusion of oxygen ions through the Cr_2O_3, obtained directly from NiO at the Cr_2O_3/NiO interface or after gaseous oxygen diffusion through a porous outer NiO layer, would have to be invoked if Cr_2O_3 is an n-type semiconductor, which is the minority view. Recently, mechanisms involving cation and anion movement have been published (1, 17). One of these (17), however, appears to rely heavily on the idea that stresses cannot be developed in oxides growing by cation movement (26) in its prediction of anion movement. Work on copper (27) seems to challenge this concept and indicates that the original theory (26) is oversimplified.

Volatilization losses from Cr_2O_3-rich scale in pure oxygen would be low due to the outer NiO-rich layer, which is an important practical point when considering commercial heat-resistant nickel-base alloys. There are also theories current (28) referring to chromium vapor effects, but there is no adequate mechanism for its movement through compact oxide. There are objections to its movement through grain boundaries, so it can only be concluded that the oxide is not compact where chromium vapor does make a contribution to scale growth.

Once the protective Cr_2O_3-rich scale is established it usually adheres well to the alloy at temperature and often on cooling, even on electropolished specimens. Any influence of the outer NiO layer in restraining the Cr_2O_3 is doubtful and obscure but the Cr_2O_3 subscale must play an important keying-on role. Occasionally the double layer of NiO above Cr_2O_3 did fail after a few hours on Ni-27.4% Cr at 1000°C, presumably by the mechanism of lifting and cracking reported for Fe-23% Cr (20), because there is no evidence of nickel in the alloy tending to transform the surface Cr_2O_3 to $NiCr_2O_4$, giving complex layered structures with alternate nickel-rich and chromium-rich oxides. No transformation of Cr_2O_3 to $NiCr_2O_4$ would be expected on thermodynamic grounds (9) because the alloy chromium content measured at the interface (shown by consideration of the interdiffusion equations to be close to the actual value) was still relatively high. Layered structures were also sometimes noted on electropolished specimens of Ni-27.4% Cr and Ni-40.2% Cr. They contrast with multilayered Cr_2O_3 found on pure chromium and on iron-chromium alloys (17, 18).

The extensive chromium depletion existing behind protective scales for long periods and to great depths, due to the slowness of metallic interdiffusion in the Ni-Cr system, would considerably assist stratified scale growth, so it is fortunate that scale failure at temperature does not occur more frequently. The chromium depletion, together with the likely higher solubility of oxygen in Ni-Cr alloys than in Fe-Cr alloys, explains the Cr_2O_3 internal oxide and subscale loops linking alloy to complete Cr_2O_3 inner layers. Cr_2O_3 at the alloy/oxide interface tends to dissociate, the resulting oxygen diffusing slowly into the alloy to permit the internal oxidation. As expected from the lower dissociation pressure of Cr_2O_3, this is a much slower process (occurring mainly at higher temperatures and after long times) than the formation of such oxide behind stratified scale where NiO is the dissociating oxide and can give a more plentiful oxygen supply. Also the alloy composition between widely spaced internal oxide particles, as well as behind a complete Cr_2O_3 layer, is far from being nearly pure nickel which may be the case between densely packed particles. There is some similarity between these thick scale protrusions into the alloy, before they link up to give loops, and the irregular interfaces suggested in theoretical papers (25). There must be some lateral diffusion of chromium to continue the subscale loop growth. It is again arguable that the subscale is evidence in favor of oxygen ion movement in the Cr_2O_3 scale, since it is supposed not to be formed behind scale growing by cation movement. The authors do not think this is strong evidence because heavy intergranular oxidation is also observed behind compact NiO on pure nickel at 1000°-1300°C

and feel that the whole subject of internal oxidation on pure metals requires further study.

In summary, most of the somewhat vague statements in the literature, regarding deviations from parabolic growth (1, 8) and the presence of NiO in late and early stages of oxidation (1, 2, 11-14, 16, 31-33), appear to fit in with the theories developed above but this is not true of protection by $NiCr_2O_4$ (1-6) which seems something of a myth. Protection is by Cr_2O_3, as has been previously suggested (7-14). Where NiO has not been observed outside, this may have been due to spalling, preferential oxidation effects, or to it forming a small percentage of the scale after long runs, particularly with Ni-60% Cr and Ni-80% Cr (9). Observations and detailed theories given elsewhere (2) appear at variance with the present work.

The results make interesting comparison with corresponding studies of Fe-Cr alloys (17, 18, 20). In general, initial protective Cr_2O_3-rich scale is less easily established but more readily retained on Ni-Cr alloys. The better adhesion is related to subscale keying on of Cr_2O_3 (absent for Fe-Cr alloys), which means that surface finish is also less important. Scale lifting and cracking are much less prevalent which is fortunate because chromium depletion in the underlying alloy is greater and longer-lived than for Fe-Cr alloys. Stratified scale development is thus potentially more likely but in practice less frequently found. These differences are largely due to the undoubted slower rate of intermetallic diffusion and the probable greater oxygen solubility in the Ni-Cr system. Stratified scale grows less rapidly because Ni-rich oxides are more protective than Fe-rich oxides, and are more readily healed by linking up of the denser population of Cr_2O_3 subscale particles to give a complete protective layer at the scale base. Few data are available on Co-Cr alloys (29) but they appear to behave more like Ni-Cr than Fe-Cr alloys.

Conclusions

1. The growth kinetics (approximately parabolic after an initial deviation) are relatively independent of the surface preparation but are critically affected by the method of heating the specimens to temperature.

2. Scales owe their protective properties to Cr_2O_3 generally containing less than 1% nickel.

3. Specimens preferentially oxidized by elevation to temperature "in vacuo" produce Cr_2O_3 alone but samples immediately located in the hot zone possess an outer nearly pure NiO layer. With high alloy chromium contents and low temperatures the inner layer is Cr_2O_3 but for the reverse conditions it is multiphase.

4. Cr_2O_3 subscale formation is moderate behind Cr_2O_3 and extensive behind stratified scale. Its coalescence to give a complete Cr_2O_3 layer at the scale base invariably halts stratification.

5. Chromium depletion in the alloy is extensive and long-lasting. If the protective scale fails, stratified nonprotective scale can appear on relatively chromium-rich alloys. In practice this is rare, because Cr_2O_3 subscale loops key the initial scale to the alloy.

Acknowledgments

Our thanks are due to Professor T. K. Ross for providing facilities and for his interest and to the Science Research Council for a maintenance allowance to one of us (T.H.). We are indebted to Mr. R. M. Cook of the International Nickel Company (Mond.) Ltd. for making the alloys.

Manuscript received Aug. 13, 1965.

Any discussion of this paper will appear in a Discussion Section to be published in the December 1966 JOURNAL.

REFERENCES

1. A. S. Tumarev, L. A. Panyushin, and A. V. Tuts, *Izv. Vysshikh. Uchebn. Zavedenii, Chernaya Met.*, **6**, 26 (1963).
2. D. V. Ignatov and R. D. Shamgunova, "Mechanism of the Oxidation of Nickel and Chromium Alloys," Moscow (1960). Available as N.A.S.A. Translation TT-F59, March 1961.
3. I. Iitaka and S. Miyake, *Nature*, **137**, 457 (1936).
4. S. Miyake, *Sci. Pap. Inst. Phys. Chem. Research, Tohoku*, **29**, 167 (1936); **31**, 161 (1937).
5. K. Pschera and K. Hauffe, *Z. anorg. Chem.*, **262**, 147 (1950); **264**, 217 (1951).
6. K. Hauffe, *Z. Metallkunde*, **42**, 34 (1951).
7. G. E. Zima, *Trans. Am. Soc. Metals*, **49**, 924 (1957).
8. L. Horn, *Z. Metallkunde*, **36**, 142 (1944).
9. N. Birks and H. Rickert, *J. Inst. Metals*, **91**, 308 (1962-1963).
10. E. A. Gulbransen and K. F. Andrew, *This Journal*, **101**, 163 (1954); **106**, 294, 941 (1959).
11. E. A. Gulbransen, R. T. Phelps, and J. W. Hickman, *Ind. Eng. Chem. (Anal. Ed.)*, **18**, 889 (1947).
12. E. A. Gulbransen and W. R. McMillan, *Ind. Eng. Chem.*, **45**, 1734 (1953).
13. J. W. Hickman and E. A. Gulbransen, *Metals Tech*, **15**, T.P.2372(1948).
14. B. Lustman, *Trans. Amer. Inst. Min. Met. Engrs.*, **188**, 995 (1950).
15. H. R. Copson and F. S. Lang, *Corrosion*, **15**, 194t (1959).
16. J. Moreau and J. Bénard, *Compt. rend.*, **237**, 1417 (1953); *Corrosion et Anti-Corrosion*, **4**, 211 (1956).
17. D. Caplan, A. Harvey, and M. Cohen, *This Journal*, **108**, 134 (1961); **112**, 471 (1965); *Corrosion Science*, **3**, 161 (1963).
18. D. P. Whittle, Ph.D. Thesis, University of Manchester, 1965.
19. W. Schwartzkopf, *Z. Elektrochem.*, **63**, 830 (1959).
20. G. C. Wood and D. P. Whittle, *Corrosion Science*, **4**, 263, 293 (1964); *J. Iron. Steel Inst.*, **202**, 979 (1964).
21. J. Moreau in "L'Oxydation des Metaux" Vol. 1, J. Bénard, Editor, p. 343, Gauthier-Villars, Paris (1962).
22. N. Spooner, J. M. Thomas, and L. Thomassen, *J. Metals*, **5**, 844 (1953).
23. C. Wagner, *Z. Elektrochem.*, **63**, 772 (1959).
24. R. A. Rapp, *Acta Met.*, **9**, 730 (1961).
25. C. Wagner, *This Journal*, **99**, 369 (1952); **103**, 627 (1956).
26. D. A. Vermilyea, *Acta Met.*, **5**, 492 (1957).
27. W. Jaenicke, S. Leistikow, and A. Stadler, *This Journal*, **111**, 1031 (1964).
28. E. A. Gulbransen and K. F. Andrew, *ibid.*, **99**, 402 (1952); **104**, 334 (1957); **109**, 560 (1962).
29. C. A. Phalnikar, E. B. Evans, and W. M. Baldwin, *ibid.*, **103**, 429 (1957).
30. Y. Matsunaga, *Japan Nickel Review*, **1**, 347 (1933).
31. E. P. Abrahamson and N. J. Grant, "High Temperature Materials," p. 501, R. F. Heheman and G. M. Ault, Editors, Chapman and Hall, London (1957).
32. I. Pfeiffer, *Z. Metallkunde*, **51**, 322 (1960).
33. H. J. Yearian, H. E. Boren, and R. E. Warr, *Corrosion*, **12**, 561t (1956).

The Passivation of Iron in the Presence of Pertechnetate and Chromate Ions[1]

G. H. Cartledge

Chemistry Division, Oak Ridge National Laboratory, Oak Ridge, Tennessee

ABSTRACT

Experiments were carried out to determine whether reducible inorganic inhibitors passivate iron solely by their own cathodic reduction or have some additional role in the passivation process. Passivation was effected potentiostatically in pertechnetate and chromate solutions at potentials noble to the calculated reversible potential of the inhibitor couple under the conditions prevailing. It was found that the inhibitors reduce greatly both the critical current density and charge required for anodic passivation when they are not themselves reduced. It was shown also that neither of the inhibitors is capable of supplying more than a very small fraction of the current density required for passivation in the absence of the additional effect which arises, presumably, through adsorption of the inhibiting anions. The results show the inadequacy of the hypothesis that the oxidation-reduction properties of the inhibitor alone are sufficient to account for its passivating action.

The most widely used inorganic inhibitors of the corrosion of iron and steel have one or more of the following properties: (*a*) they are derived from weak acids and consequently their salts have buffering action at the corrosion interface; (*b*) their anions form sparingly soluble products with the escaping cations and thus provide a more or less protective film; (c) they have oxidizing properties which have been presumed to be sufficient to produce passivation by a pure oxidation-reduction reaction; or (*d*) they are adsorbed at the interface in such a way as to alter the mechanism or rate constants of one or more of the corrosion partial processes. Theories of their inhibiting action have been variously derived from these characteristics (1).

In the purely electrochemical mechanism [(c), above] (2), no specific action is ascribed to the inhibitor other than its ability to provide a mixed potential with the corroding metal in the region of passive potentials.[2] On the contrary, there are reasons for assuming that adsorbed inhibitor anions produce specific electrostatic or other kinetic effects over and above any results of their oxidizing action alone. An example of such specific effects may be seen in the destruction of passivation by added electrolytes which do not alter the oxidation-reduction properties of the inhibitor. Such effects have been demonstrated in this laboratory for iron in the use of several inhibitors (3, 4). A competitive adsorption has been assumed to be in operation, and this has been measured in the case of iodide ion (5). Hackerman and Powers have shown the competitive action of sulfate and chromate ions at a surface of chromium (6), and the ion exchange of unreduced chromate ions by hydroxide or sulfate ions on stainless steel has also been studied quantitatively (7). Posey and Sympson (8) found that their study of the effect of anions upon certain cathodic processes on stainless steel could be interpreted mathematically in terms of a dynamic adsorption equilibrium at the electrode.

It is, of course, true that if a metal is capable of being passivated by anodic polarization, and if a reducible inhibitor has a sufficiently noble electrode potential and a cathodic polarization curve that passes to the high-current side of the critical passivation current density of the metal, then no further participation of the inhibitor is required beyond its cathodic polarization. Even so, it remains to be considered whether, in the case of a metal capable of passivation, the inhibitor may not also act specifically and noncathodically on some step of the mechanism which leads to passivation. In view of the highly irreversible character of both the Cr(III-VI) and Tc(IV-VII) couples in acidic media, it is indeed most unlikely that the cathodic polarization of these inhibitors could possibly supply the large current densities necessary for passivation of iron in sulfate or perchlorate systems.

The present work was undertaken to provide a more detailed study of passivation and activation of iron in the presence of a reducible inhibitor, in the hope that effects specifically related to adsorption of unreduced inhibitor might be differentiated from simple anodic passivation by reduction of the inhibitor. The method followed was to determine what effects, if any, the inhibitor produces in the polarization of the metal in acidic media at potentials noble to the oxidation-reduction potential of the inhibitor so that its reduction is ruled out. The pertechnetate ion is admirably suited for such a study. Its reduction forms a film of $Tc(OH)_4$, with the normal potential of 0.738v (9)

$$Tc(OH)_{4(s)} \rightleftharpoons TcO_4^- + 4H^+ + 3e^-;\ V_h^\circ = 0.738v$$

It is therefore convenient to carry out potentiostatic polarizations under conditions which either produce $Tc(OH)_4$ or keep it oxidized to TcO_4^-. It is possible also to examine the effects of $Tc(OH)_4$ on the surface, as well as effects arising from addition of a foreign ion, such as the sulfate ion. By utilizing the beta activity of ^{99}Tc, it is possible also to determine the amount of technetium on an electrode.

The experiments demonstrated that the presence of either pertechnetate or chromate ions greatly reduces both the current density and charge required for passivation of iron at potentials noble to the respective couple potentials under the prevailing conditions. Beta counting confirmed the absence of reduction of the inhibitor during passivation in the pertechnetate solutions. Cathodic polarizations showed both pertechnetate and dichromate ions to be capable of supplying much lower current densities than are required for passivation of iron in uninhibited solutions.

Experimental

The electrode material was Armco iron; it was machined into a cylinder 1.25 cm long and 0.625 cm in diameter. The upper end was threaded to fit a stainless steel rod by which it could be drawn tightly against a Teflon sleeve. Before use, the electrode was electrolytically cleaned in a mixture of H_3PO_4(100),

[1] Research sponsored by the United States Atomic Energy Commission under contract with the Union Carbide Corporation.

[2] Stern (2) recognized the possibility that an inhibitor might reduce the critical current density required for passivation.

HNO_3(20), and excess CrO_3. It was then treated alternately with HNO_3 and HCl several times, the final treatment being activation in HCl immediately before use. Solutions were made from NH_4TcO_4 or $KTcO_4$ and were acidified to the desired *p*H value by addition of Dowex-50 resin in the hydrogen-ion form. The volume of solution used (125 ml in each side of an H-cell) was sufficiently large to prevent significant change in *p*H during polarization, as shown by repeated measurement during the experiments. To produce heavy deposits of $Tc(OH)_4$ on the electrode, when desired, it was polarized cathodically in a separate cell containing a slightly acidic solution of a pertechnetate.

Anodic polarization was effected by a FairPort Potentiostat-Galvanostat, Model 610. The potentiostat was preset to the desired potential, and the circuit was closed by inserting the electrode. A rapid stream of helium kept the oxygen concentration at a harmless level during the operation. The polarizing potentials in different experiments varied between +350 and +850 mv, referred to the saturated calomel electrode. The theoretical reversible potential of the Tc(IV-VII) couple in the most concentrated and most acidic solution used was +326 mv (SCE). Polarizations were continued until the current density for electrodes that were initially free of $Tc(OH)_4$ fell to an approximately steady value. This required from 20 to 40 min in the different experiments. The current densities on filmed electrodes were not quite limiting values, owing to continuous oxidation of $Tc(OH)_4$ from the film. From the recorder trace of the current flowing during the polarization stage, the charge accumulated during passivation was computed graphically. Upon completion of the polarization, the electrode and reference cell were quickly detached from the potentiostat circuit and connected to a vibrating reed electrometer with a Brown recorder for following the open-circuit potential.

To confirm the assumption that passivation was effected without reduction of pertechnetate ions, an electrode was carefully decontaminated from ^{99}Tc and polarized at +400 mv (SCE) in 10^{-2} *f* TcO_4^-, *p*H 2.80, under helium for 43 min, at which time the current density had fallen to 3.0×10^{-6} amp/cm^2. The electrode was quickly withdrawn from the cell, washed in five beakers of distilled water, and held under running distilled water for 30 sec. The specimen was again counted for beta activity. Since the cylindrical form of the electrode made its exact counting geometry indeterminate, it was placed on the fourth (lowest) shelf of the counter to minimize the uncertainty. As will be detailed in the section on Results, the experiment succeeded in confirming the absence of $Tc(OH)_4$.

In a few passivations, the early stages of current flow were examined by use of an oscilloscope (Tetronix, Model 536),[3] the very brief initial surge of current decaying too fast to be followed with the Brown recorder. Here again, the circuit was closed by insertion of the freshly activated electrode into the pertechnetate solution.

Possible effects of $Tc(OH)_4$ in the surface film were examined by comparing polarization curves of filmed and bare electrodes in sulfate media. Both potentiostatic and galvanostatic procedures were used. The effect of $Tc(OH)_4$ was apparent also in the activation experiments, some of which were conducted with a preformed film of $Tc(OH)_4$ in too great an amount to be oxidized completely during passivation at the elevated potential. In other experiments, the antagonistic action of sulfate and pertechnetate ions was shown by anodic polarization in simple and mixed electrolytes.

To evaluate practically the current density obtainable in reduction of the inhibitor, both pertechnetate and dichromate solutions were polarized with platinum electrodes containing the respective reduction products.

[3] The author is indebted to his colleague, Dr. Franz A. Posey, for assistance in these observations.

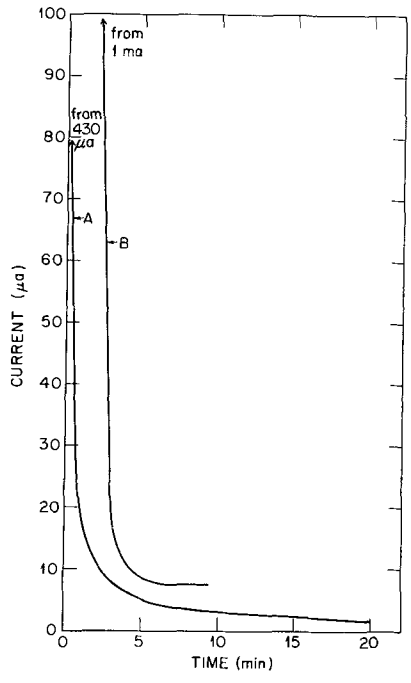

Fig. 1. Anodic charging curve in pertechnetate solutions: A, 10^{-2} *f*, *p*H 3.00; area 2.77 cm^2; without $Tc(OH)_4$ in film. B, 10^{-3} *f*, *p*H 3.92; area 2.61 cm^2; lightly filmed with $Tc(OH)_4$.

Results

Passive-active transitions.—In repeated tests, it was found that the full anodic output of the potentiostat (*ca.* 40 ma) was insufficient to lead to passivation of either the Armco or electrolytically deposited iron electrodes in sulfate solutions of 0.1-0.5 *f* concentration at *p*H values between 1 and 4.18 when the potentiostat was set at +400 mv (SCE). On the contrary, in pertechnetate solutions of comparable concentrations and acidities, after an initial surge, the anodic current rapidly fell to values characteristic for passivation. Figure 1 shows the observed charging current for two typical electrodes. In one, curve A, the surface was free of any film when introduced into the electrolyte at +400 mv (SCE); in the other, the sur-

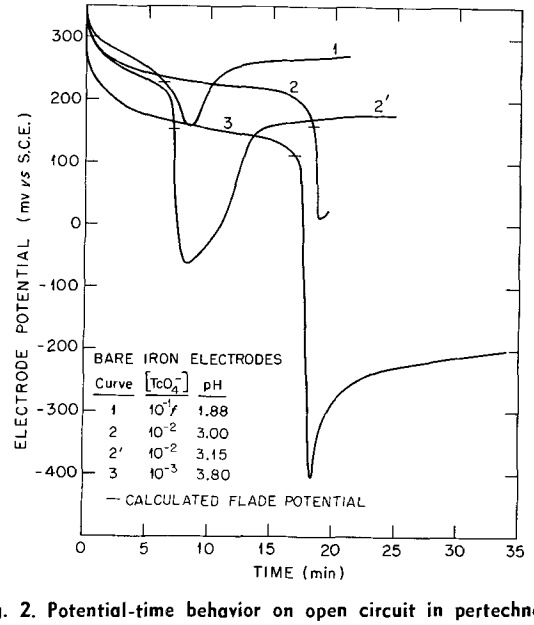

Fig. 2. Potential-time behavior on open circuit in pertechnetate solutions; electrodes free of $Tc(OH)_4$.

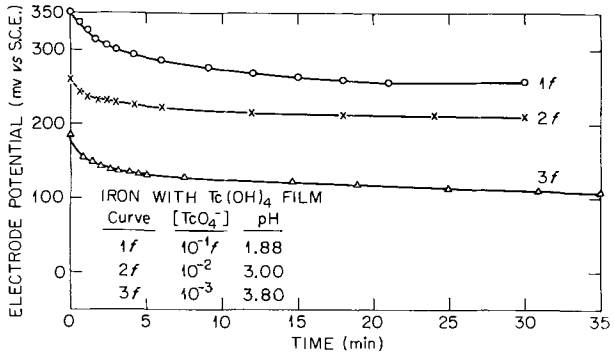

Fig. 3. Potential-time curves with $Tc(OH)_4$ on the electrode

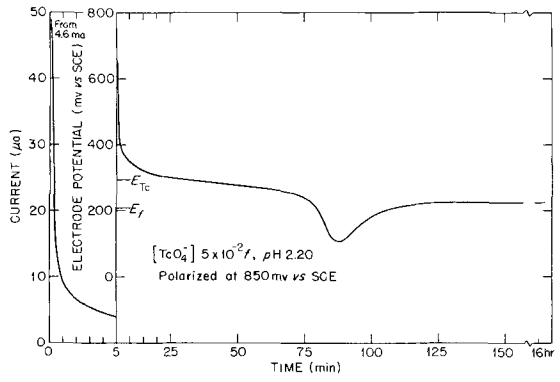

Fig. 4. Polarization of iron in 5.0×10^{-2} f $KTcO_4$, pH 2.20 for 5 min at 850 mv (SCE); area 2.25 cm^2.

face had a light brown film containing $Tc(OH)_4$, but was activated in HCl just before use. The polarization of the unfilmed electrode was discontinued when the current density became almost steady at 0.54 $\mu a/cm^2$; graphical integration of the recorder chart gave 2.1×10^{-3} coulomb/cm^2 as the charge passed up to this point. Similar results were repeatedly obtained with initially bare electrodes.

When the electrode was previously coated with $Tc(OH)_4$, somewhat higher current densities and charges were found because of oxidation of the $Tc(OH)_4$ which occurs slowly at +400 mv (SCE). The current density again fell rapidly, however, as the anodic process of passive film formation was completed. Use of the oscilloscope in certain of these experiments merely confirmed the observation of a surge of current which fell sharply within 0.5 sec to values picked up by the Brown recorder.

Figures 2 and 3 show the change of potential with time when the potentiostatic circuit was quickly replaced by a vibrating reed electrometer and recorder, with the electrode on open circuit. Table I gives the experimental conditions for the different curves in these figures, together with calculated values of the reversible potential of the Tc(IV-VII) couple and Flade potential for the same conditions (E_f = 0.338 −0.59 pH, SCE). The prior potentiostatic polarizations had been conducted at potentials that were well above the theoretical value for the Tc(IV-VII) couple.

In Fig. 1, curve B is for an electrode that was polarized until the visible film of $Tc(OH)_4$ had been so largely oxidized back to TcO_4^- that the potential fell to −270 mv (SCE) before beginning to re-ennoble. Its behavior in this respect resembled closely that shown by an unfilmed electrode, such as shown by curve 3 of Fig. 2 for the same concentration and pH value. The anodic charge was 30 mc/cm^2, whereas the smaller charge of 15 mc/cm^2 was found for the electrode represented by curve 3f in Fig. 3. In this case, the electrode retained a dark film of $Tc(OH)_4$. Both electrodes, however, were fully passive when put on open circuit.

Figure 4 gives both the current-time and potential-time curves for an electrode that was held for only 5 min at 850 mv (SCE) immediately after having fallen to a minimum open-circuit potential of 59 mv (SCE) following polarization at 400 mv (SCE). The polarization was stopped somewhat before the current density reached its limiting value, the charge passed amounting to 1.3 mc/cm^2 at this point. It is seen that the potential on open circuit fell rapidly by about 500 mv to the vicinity of the Tc(IV-VII) couple potential (E_{Tc} in Fig. 4) and then leveled off before debasing again as the Flade potential was approached. The 16-hr recording of the open-circuit potential shows that even though passivation was effected approximately at the reversible potential for evolution of oxygen [calc. 857 mv (SCE)], the surface state became stable in the electrolyte only after incipient activation and consequent deposition of some $Tc(OH)_4$ at the lower potential.

Table I. Passive-active transition experiments

Figure and Curve	$[TcO_4^-]$, M	pH	Final c. d. $\mu a/cm^2$	M-coulomb/ cm^2 passed	Calculated potentials mv (SCE) $E_{Tc(IV-VII)}$	E(Flade)
2-1	10^{-1}	1.88	1.8	14.0	326	227
2-2	10^{-2}	3.00	0.19	0.9	219	161
2-2′	10^{-2}	3.15	0.50	—	205	152
2-3	10^{-2}	3.80	0.22	2.1	136	114
3-1f	10^{-1}	1.88	1.6	8.8	326	227
3-2f	10^{-2}	3.00	5.3	—	219	161
3-3f	10^{-3}	3.80	5.5	15	136	114

The results shown in Fig. 2, 3, and 4 are typical of many experiments which differ somewhat in detail but agree in exhibiting the following uniform behavior. Consider, first, the results for electrodes having no film of $Tc(OH)_4$, Fig. 2, 4. (*A*) When the circuit was opened, the potential first fell rapidly; the rate of change soon decreased, however, and the inflection came at potentials that are clearly related to the reversible potential of the inhibitor couple in the different media. (*B*) The slow debasing was succeeded by a rapid fall in potential, and this change occurred close to the calculated Flade potential for the pH value involved. In these two respects the behavior resembles closely that observed in noninhibiting solutions. (*C*) The debasing of the potential was arrested before full activation occurred, however, and the minimum value of the potential and rate of re-ennobling were highly dependent on the concentration and acidity of the inhibiting solution. (Some of the observations were continued until the potential of the iron electrode approximated that of a platinum wire coated with $Tc(OH)_4$ in the same solution, although this required several hours).

Figure 3 refers to electrodes which were given a visible film of $Tc(OH)_4$ by a cathodic prepolarization. It is seen that the initial debasing on open circuit soon became very slow and that it halted without the electrodes becoming active. Again, the level of the approximately stable potentials parallels the shift in the Tc couple potential in the different media.

Although the properties of the Tc(IV-VII) couple make it convenient to carry out the potentiostatic passivations at potentials that are too noble for reduction of the inhibitor to occur, nevertheless the possibility remains that small active sites on the electrode might react with the inhibitor and cause deposition of radioactive $Tc(OH)_4$ locally. To test this possibility, an experiment was done at +400 mv (SCE) with an electrode that was first decontaminated of ^{99}Tc, counted, passivated, rinsed, and counted again. Current passed for 42 min, at which time the current density had fallen to 3.0 $\mu a/cm^2$ and the total charge passed was 27 mc/cm^2. The specimen gave 22 cpm (counts/minute) before passivation and 29 cpm afterward. At the 95% confidence level the two counts are the same. It may be calculated that if the charge of

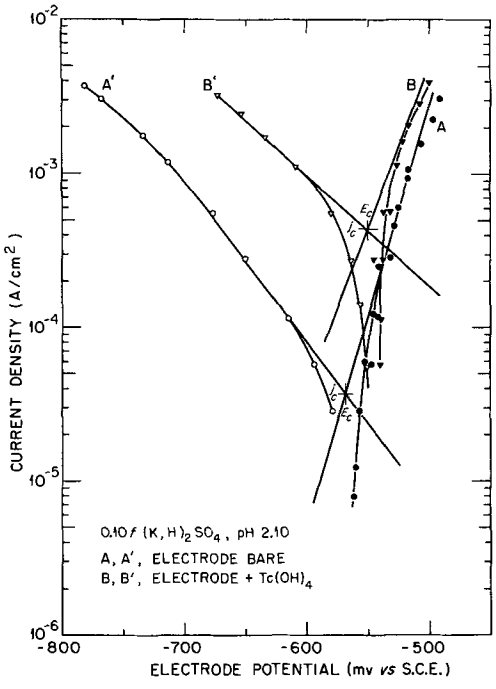

Fig. 5. Polarization of iron in 0.10 *f* $(K,H)_2SO_4$, *p*H 2.1, with and without a film of $Tc(OH)_4$. A, A' unfilmed, B, B' filmed.

27 mc/cm² had been augmented to the extent of even 1% by deposition of $Tc(OH)_4$, the specimen should have acquired 4500 cpm. (This result is based on a determination that the cylindrical surface of the electrode reduced the counting efficiency by a factor of 2).[4]

Influence of $Tc(OH)_4$ *on polarizations in absence of pertechnetate ions.*—Since the activation experiments disclosed a considerable effect of $Tc(OH)_4$ on the re-ennobling process, further polarizations were done in a sulfate medium to determine whether the film affects the anodic corrosion process at active potentials as well as the cathodic process. An acceleration of cathodic processes by deposited $Tc(OH)_4$ on passive iron was reported previously (12). It was difficult to obtain a high degree of reproducibility on filmed specimens, but a characteristic set of polarization curves is shown in Fig. 5, which was derived from both potentiostatic and galvanostatic measurements in 0.10 *f* $(K,H)_2SO_4$ at *p*H 2.10 under helium. The acceleration of the cathodic process is clearly seen in curves A' and B'. There is probably no appreciable effect on the anodic side, the observed displacement being no greater than the scatter of different polarizations of bare electrodes. For these reasons, the film makes the open-circuit potential in the sulfate solution somewhat less active than that of a bare electrode, but the corrosion rate on open circuit is considerably increased.

Polarization in a sulfate medium with and without pertechnetate.—The antagonistic effects of sulfate and pertechnetate ions were demonstrated by subjecting an electrolytically deposited iron electrode of 0.110 cm² surface to anodic polarization with the potentiostat set at +400 mv (SCE), first in 0.10 *f* $(K,H)_2SO_4$ at *p*H 1.85 and then in a mixed solution which was 3.9×10^{-2} *f* in sulfate and 6.1×10^{-3} *f* in pertechnetate at *p*H 2.15, in both cases under helium. In the pure sulfate solution, the electrode drew the limit of the anodic output in the potentiostat (*ca.* 360 ma/cm²) without passivation, that is, the instrument was incapable of bringing the potential to +400 mv. In the mixed solution, an initial current of 160 ma/cm² flowed. This fell to 20 ma/cm² in 5 min and to a nearly steady 5 ma/cm² in an additional 10 min. On opening the circuit, the potential fell rapidly to −550 mv (SCE) and became steady at −581 mv. This is about 10 mv noble to the potential to be expected in a simple sulfate solution (0.5 *f*), according to the results of Kelly (13). Hence, although a current density of 360 ma/cm² failed to induce passivation in the sulfate solution, a maximum initial current density of 160 ma/cm² sufficed in the presence of the pertechnetate ions, although the mixed solution was incapable of maintaining passivity.

Polarization of the Tc(IV-VII) *couple.*—Most discussions of the electrochemical action of reducible inhibitors have been based on schematic polarization diagrams, rather than on numbers obtained experimentally. The technetium and chromium couples are very sluggish, and few reversible values have been determined for them. Nevertheless, polarization data which are empirically useful for present purposes were obtained by polarizing a platinum electrode which had been cathodically coated heavily (black) with $Tc(OH)_4$.[5,6] The electrolyte was 0.10 f NH_4TcO_4 at *p*H 2.15 under helium. The potential of a freshly coated electrode is considerably negative to the reversible value, which it approaches very slowly. After some anodic pre-polarization, however, the equilibration is more rapid. The polarization of the electrode from its reversible potential soon runs into complications that lead to limiting currents of small magnitude. Thus, on the cathodic side, a 17-hr galvanostatic polarization at 54 μa/cm² led to a potential of −122 mv (SCE), or 430 mv negative to the reversible value. On the anodic side, a limiting value below 30 μa/cm² was reached. These results make it evident that, even at a concentration much higher than that necessary for effective inhibition, the available cathodic current density is very small in comparison with current densities required for passivation of iron in the absence of an inhibitor. For the conditions of this measurement, the exchange current density was of the order of 10^{-6} amp/cm².

Passivation and polarization in chromate solutions.—The action of the dichromate ion was examined briefly in passivation experiments similar to those done with the pertechnetate ion. The electrolytes were $K_2Cr_2O_7$, 0.20 *f*, *p*H 3.68 and 0.020 *f*, *p*H 4.10. The Cr(III-VI) couple gives such irreproducible values in acidic media that a potential calculated from free energies is not very meaningful. The values computed for the process

$$2Cr(OH)_3(\text{hydrous}) + H_2O \rightleftharpoons Cr_2O_7^{=} + 8H^+ + 6e^-$$

for the two solutions indicated above are +570 mv and +530 mv (SCE), respectively. When the iron electrode was passivated with the potentiostat at +400 or +600 mv (SCE), it was found that the charging curve resembled Fig. 1, but the charge passed for a steady current density was 60-100 mc/cm², or very considerably more than that required in the pertechnetate solutions.

After passivation at +600 mv in the 0.20 *f* solution, the iron electrode fell quickly to the same potential as that of a bare platinum wire, but there was a slow debasing to a somewhat lower value, without intervening activation. Without prior anodic passivation, an active iron electrode was inserted into the 0.20 *f* dichromate solution in helium. Its potential rose only to −100 mv SCE in 15 hr and was almost stationary at

[4] These experiments give direct support to the prior claim that no unreduced pertechnetate ions can be found on rinsed specimens (10, 11).

[5] The identity of such cathodic deposits with $Tc(OH)_4$ precipitated by chemical reduction of pertechnetates was established by transmission electron diffraction. The author is indebted to T. E. Willmarth of the Analytical Chemistry Division for this service.

[6] One would naturally wish to know the cathodic current density for reduction of the pertechnetate ion on an active iron surface. Such a measurement is impossible, however, since the metal immediately acquires a film of the reduction products at the active potential. Hence the measurement on a filmed surface is entirely realistic for a discussion of the extent of the cathodic action of the inhibitor. A platinum support for the film was preferred in order to eliminate direct action between the support and reducible anions.

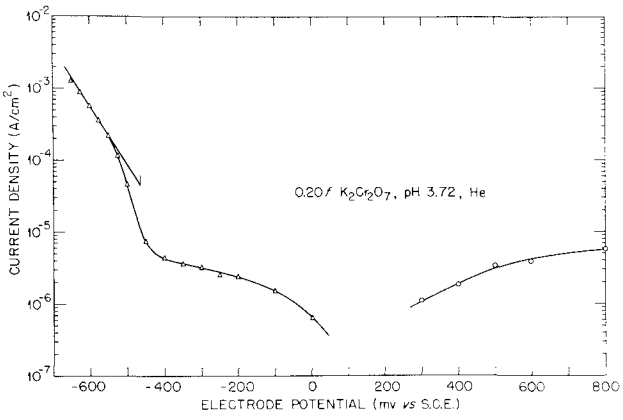

Fig. 6. Polarization of the Cr(III-VI) couple on a platinum electrode: 0.20 $K_2Cr_2O_7$, pH 3.72. Calculated potential for discharge of hydrogen —463 mv (SCE).

that point, the Flade potential for this pH value being +120 mv (SCE). The slowness and incompleteness of the debasing after anodic polarization are perhaps related to the fact (7) that the passive film binds some unreduced Cr(VI) species in an exchangeable form, whereas the Tc(VII) species is not so held. These observations agree with the previous study of the action of the chromate ion in the absence of oxygen (3, 10).

Since it is evident that reduction of chromate species in absence of oxygen does not produce complete passivation but does retard the corrosion process greatly, it seemed desirable to determine experimentally the magnitude of the current available for anodic polarization of the iron. Potentiostatic polarizations were therefore carried out, using the platinum electrode which had served as cathode in the previous passivation polarizations. The electrolyte was 0.20 *f* $K_2Cr_2O_7$ at pH 3.72, and helium was passed through the solution. Results are shown in Fig. 6, which is of no quantitative theoretical significance, except insofar as it accounts for the inefficiency of the Cr(III-VI) couple as a source of cathodic current. The large values of $dE/d \log j$ are also typical of similar values frequently observed on electrodes with poorly conducting films of reaction products. It is seen that the hydrogen-discharge reaction is superimposed on the reduction of Cr(VI) at potentials below —450 mv (SCE). A normal Tafel slope of —120 mv/decade is observed, with an exchange current density at the calculated reversible potential in close agreement with the values shown by Vetter (15). The presence of the dichromate ions is therefore without significant influence on the discharge of hydrogen.

Discussion

That a normal state of passivation resulted from the potentiostatic polarizations is shown by the clearly recognizable relation between the calculated Flade potential and the potential at which rapid activation set in with electrodes having no $Tc(OH)_4$ in the film. Both the noble potential at which the potentiostat was set and the absence of beta activity on the electrode passivated in the pertechnetate solution confirm the conclusion that reduction of the inhibitor was not involved in the passivation process in these experiments.

The passivation experiments of both Franck (16) and Olivier (17) showed that the time required for passivation of iron by galvanostatic polarization is related to the applied current density by the expression $(j - j_0)t_p = \text{const.}$, in which j_0 is a current density below which no passivation is attained. The constant then represents the charge presumably consumed in the passivation process alone. For iron in 1 to 2*N* H_2SO_4 the experimental arrangements of Franck and Olivier agreed in giving a value of around 1.7 coulombs/cm² for the constant. More recently, Froment, Keddam, and Morel (18) have conducted the passivation in 1*N* H_2SO_4 by raising the potential potentiostatically at different rates and recording the current. The lowest effective current density was about 154 ma/cm² for their conditions, this value being obtained when the potential was raised 16 mv/min. In a phthalate-sulfate buffer at pH 3, Weil and Bonhoeffer (19) found the requisite charge to be 1 c/cm², and this quantity fell only to 130 mc/cm² at pH values of 4-6. Even for an Fe-18% Cr, alloy, Olivier found the constant to be 8 mc/cm² and j_o = 11 ma/cm². Values of similar magnitude for stainless steels were found by Edeleanu (20).

The effective charges and current densities vary somewhat with the experimental conditions, hence it was necessary, in the present work, to ascertain definitely that no passivation resulted when a sulfate medium was used under the same conditions as were found to induce passivation in the inhibiting solutions. The negative result found in sulfate media at pH's as high as 4.18 could have been anticipated, in view of the limiting anodic output of the potentiostat employed. The measurements show, therefore, that the low values obtained for both the total charges and current densities in the presence of the inhibitors must be ascribed to an effect of their anions that does not depend upon their reduction. In all experiments, the potential-time behavior on open circuit showed that passivity had been attained, even when the total charge was as low as 1-2 mc/cm² on unfilmed specimens. The evidence indicates, therefore, that a film of no more than 10-15Å in thickness (calculated for the magnetite crystal structure) suffices to exhibit the low corrosion rate and Flade potential characterizing the passive state, although the film is not stable even in the pertechnetate solutions here used until some $Tc(OH)_4$ had been deposited at the lower potentials during incipient activation.

It is therefore necessary to conclude, for both pertechnetate and chromate systems, that the presence of the unreduced inhibitor tremendously favors the processes leading to passivation. From the references cited in the early part of the text, it is well established that anions are adsorbed, and it is only reasonable to assume that this adsorption is the origin of the great retardation of the anodic dissolution process in the presence of the inhibitors.

The experiments in which a visible film of $Tc(OH)_4$ was present demonstrated again some acceleration of cathodic processes in a sulfate environment, with little, if any, displacement of the anodic polarization curve. To the extent that reduction of the inhibitor is accelerated by $Tc(OH)_4$, however, by so much is maintenance or restoration of passivity favored in the open-circuit experiments in the presence of the pertechnetate.

It is possible that the $Tc(OH)_4$ which deposits in the interface normally may favor maintenance of passivity in two ways. The observed acceleration of cathodic processes would be one factor. Another may well be the sealing of pores or weak places in the normal film by the presumably low solubility of $Tc(OH)_4$, since, in general, the solubility of hydroxides decreases as the cation increases in valence, up to a point. This second possibility is rendered plausible by the earlier observation (14) that, if a little H_2O_2 is added to the inhibiting pertechnetate solution, stable passivation may be achieved at pH *ca.* 6 with deposition of no more $Tc(OH)_4$ than would suffice to cover a few tenths of a per cent of the surface. A thirteen-year observation shows that after stabilization is once established, no continuing consumption of the inhibitor is detectable (closed bottle occasionally opened for weighing and counting the specimen). In further support of this solubility effect, it was found also (14) that $Tc(OH)_4$ deposited on carbon steel cathodes is quickly oxidized to TcO_4^- by H_2O_2 with >90% decontamination, whereas if the hydroxide is formed together with the

anodic corrosion product, the decontamination efficiency in similar treatment is generally between 30 and 40%.

In the experiments with dichromate as inhibitor, the charge passed during passivation was up to 60-100 mc/cm^2 in different experiments. The thicker film so formed and its ability to bind exchangeable Cr(VI) ions are most probably the reason why complete activation did not occur on open circuit. In the absence of oxygen or external anodic polarization, however, even 0.20 *f* $K_2Cr_2O_7$ at *p*H 2.7 only slowly ennobled the iron potential, and an exposure of 16 hr left the electrode very considerably below the Flade potential. Unlike the pertechnetate ion and osmium (VIII) oxide (21), therefore, the chromates cannot be considered to be vigorous as passivating inhibitors under de-aerated conditions, though their own slow reducibility distinguishes them sharply from molybdates and tungstates, which are quite ineffective without a supplementary oxidizing agent.

Kolotyrkin and Bune (22) and Makrides and Stern (23) have presented data on electrode potentials and corrosion rates in solutions containing strong oxidizing agents which they used as evidence for the conclusion that passivating inhibitor anions function only by their cathodic action. It is to be noted, however, that both sets of experiments were done under conditions which make passivation easier than it is with iron, and at the same time both enhance the oxidizing power of the additive and destroy its possible inhibitory action. The experiments of Kolotyrkin and Bune were done with nickel, while Makrides and Stern used stainless steel; both metals are passivated at relatively low current densities. Both sets of experiments were done in 1*N* H_2SO_4, which differs in two essential respects from electrolytes in which the anions may actually produce inhibition, namely, the high acidity accentuates oxidizing power both thermodynamically and kinetically, and the high concentration of sulfate ions and low pH value completely suppress the inhibition observed under suitable conditions. Neither set of experiments can be used, therefore, as valid arguments against specific, noncathodic action by inhibiting anions when proper conditions for inhibition are used (24).

It was proposed earlier that the basic kinetic effect of adsorbed ions of the type of the Cr(VI) and Tc(VII) species comes from the space charge or potential gradient induced close to the site of adsorption (14, 25, 26). Such effects were shown to be of opposite sign for adsorbed sulfate and chromate ions, and the hypothesis led to the natural prediction that the pertechnetate ion should be inhibiting. This was at once found to be the case. Whether this particular mechanism is correct or not, the present experiments make it entirely clear that the action of the passivating inhibitors involves at least two very distinct functions. The noncathodic effects of such inhibitors will be discussed in another place.

Acknowledgment

The author is indebted to his colleague, Dr. E. J. Kelly, for helpful discussions.

Manuscript received Oct. 4, 1965.

Any discussion of this paper will appear in a Discussion Section to be published in the December 1966 JOURNAL.

REFERENCES

1. G. H. Cartledge, *Corrosion*, **18**, 316t (1962).
2. Milton Stern, *This Journal*, **105**, 638 (1958); cf. also N. Ya. Bune and Ya. M. Kolotyrkin, *Doklady Akad. Nauk*, **111**, 1050 (1956).
3. R. F. Sympson and G. H. Cartledge, *J. Phys. Chem.*, **60**, 1037 (1956).
4. G. H. Cartledge and R. F. Sympson, *ibid.*, **61**, 973 (1957).
5. K. E. Heusler and G. H. Cartledge, *This Journal*, **108**, 732 (1961).
6. Norman Hackerman and R. A. Powers, *J. Phys. Chem.*, **57**, 139 (1953).
7. G. H. Cartledge and D. H. Spahrbier, *This Journal*, **110**, 644 (1963).
8. F. A. Posey and R. F. Sympson, *ibid.*, **109**, 716 (1962).
9. G. H. Cartledge and W. T. Smith, Jr., *J. Phys. Chem.*, **59**, 1111 (1955).
10. G. H. Cartledge, *ibid.*, **65**, 1009 (1961). [Cf. also, M. Cohen and A. F. Beck, *Z. Elektrochem.*, **62**, 696 (1958).]
11. G. H. Cartledge, *Corrosion*, **21**, 216 (1965).
12. G. H. Cartledge, *J. Phys. Chem.*, **64**, 1882 (1960).
13. E. J. Kelly, *This Journal*, **112**, 124 (1965).
14. G. H. Cartledge, *J. Phys. Chem.*, **59**, 979 (1955).
15. K. J. Vetter, "Elektrochemische Kinetik," p. 432, Springer, Berlin (1961).
16. U. F. Franck, *Z. Naturforsch.*, **4A**, 378 (1949).
17. R. Olivier, Dissertation, Leiden (1955).
18. Michel Fromet, Michel Keddam, and Philippe Morel, *C. r.*, **253**, 2529 (1961).
19. K. G. Weil and K. F. Bonhoeffer, *Z. physik. Chem., N. F.*, **4**, 175 (1955).
20. C. Edeleanu, *J. Iron Steel Inst. London*, **188**, 122 (1958).
21. G. H. Cartledge, *J. Phys. Chem.*, **60**, 1571 (1956).
22. Ya. M. Kolotyrkin and N. Ya. Bune, *Z. physik. Chem.*, **214**, 264 (1960).
23. A. C. Makrides and Milton Stern, *This Journal*, **107**, 877 (1960).
24. G. H. Cartledge, *J. Phys. Chem.*, **65**, 1361 (1961).
25. G. H. Cartledge, *ibid.*, **60**, 28, 32 (1956).
26. G. H. Cartledge, *Z. Elektrochem.*, **62**, 684 (1958).

The Anodic Behavior of Iron-Carbon Alloys in Moving Acid Media

T. K. Ross, G. C. Wood, and I. Mahmud

Corrosion Science Division, Department of Chemical Engineering, Faculty of Technology, University of Manchester, Manchester, England

ABSTRACT

The anodic behavior of pure iron, mild steel (0.055% C) and iron-1.3% C was studied in flowing oxygenated and deaerated solutions of sulfuric and hydrochloric acids, the results being presented mainly as apparent anodic polarization curves at low current densities and as plots of potential against Reynolds number for a fixed current density at high current densities. The data were obtained largely by conventional galvanostatic methods for plate electrodes situated in a cell of square cross section, designed to allow the complete development of the hydrodynamic and mass transfer boundary layers. In solutions containing oxygen, the rest potentials and apparent polarization curves were shifted in the positive direction on increasing the flow rate, the effect being greater the lower the carbon content of the alloy. In deaerated acid the curves were insensitive to flow changes up to a critical current density, which was lower for more dilute acids and higher carbon contents, since the reactions involved are entirely activation controlled. Influences of carbon content, heat-treatment, and acid and cation concentrations on the position and length of the Tafel region of the anodic polarization curve are considered. At high current densities (*e.g.*, 100 ma/cm^2) the behavior of all three alloys departed from Tafel behavior, and potentiostatic and galvanostatic results were observed to be sensitive to the liquid flow rate in both hydrochloric acid and sulfuric acid solutions. From galvanostatic results obtained at a current density of 440 ma/cm^2 it was deduced that a film was formed at the anode surface. The presence of this film was shown to present an additional impediment to convective mass transfer of anolyte, thus occasioning a redistribution of the potential difference between metal surface and bulk electrolyte. While changes in liquid flow rate could be expected to control the rate of mass transfer in the liquid boundary layer, their effect on the thickness and nature of the porous surface layer was complex.

Over forty years ago Friend and Dennett (1) reported that the corrosion rate of rotating iron disks in aerated 0.01-0.2*N* H_2SO_4 increased linearly with rotational speed up to 4000 rpm. However, Whitman *et al.* (2, 3) found for aerated and oxygenated acid (0.33-5*N*), and to a lesser extent for nitrogen-saturated solution, that the corrosion rate of 0.12% C steel cylinders first decreased, passed through a minimum, and finally increased linearly with rotation rate. The speed corresponding to the minimum increased with acid concentration while the corrosion rate was independent of acid concentration at high flow rates, a result confirmed recently by other workers (4).

It is now generally accepted that the final rise in corrosion rate with flow velocity is due to an increase in the cathodic reduction current of oxygen. It was demonstrated further (5) that hydrogen surface films (or carbon or cementite films in the case of high-carbon alloys) interfere with this reaction. However, in all cases, electrolyte flow reduces the thickness of the boundary layer, thus allowing faster transport of oxygen to the metal surface.

The initial fall and minimum in corrosion rate has caused some controversy. It was originally suggested that (2, 3) the energy required to produce small hydrogen bubbles during rotation was greater than for the large bubbles produced in stagnant solutions, and presumably the bubbles interfered differently with oxygen arrival. Russian workers (4) refuted the latter idea, claiming that the phenomenon occurred in deaerated solutions but, as pointed out by Makrides (6), such solutions may contain traces of residual oxygen. This point was pursued by Foroulis and Uhlig (5) who provided strong evidence, using a variety of rotating iron-carbon alloy cylinders in 0.33*N* H_2SO_4, that very low concentrations of O_2 (and Fe^{3+} ions produced incidentally) act as anodic inhibitors rather than as depolarizers in this region, thus accounting for the initial fall and minimum. This effect of oxygen was evident in static solutions for low-carbon steels, but the minimum corrosion rate occurred at higher velocities for higher carbon steels, due to the need to remove hydrogen or cementite screens.

Other workers (6-8) applied quantitative treatments to the rate of arrival of depolarizers other than oxygen at a corroding iron surface. It was shown incidentally that the potential and dissolution rate of rotating specimens increased with velocity in air-saturated 2*N* HCl, but there was no effect in deaerated acid (7). This was confirmed subsequently in hydrogen-saturated 0.52*N* H_2SO_4 (6) and in nitrogen-saturated 0.33*N* H_2SO_4 (5). These results indicate that the anodic dissolution of iron and the cathodic evolution of hydrogen are not mass-transfer-controlled at these current densities. Surface roughening may affect corrosion rates at high velocities, and this phenomenon must clearly be considered in flow studies because of possible influences on boundary layers (8).

Corrosion of iron and steel tubes by flowing acid has been less extensively and less quantitatively studied. It was reported (4) that in concentrated H_2SO_4 $Y = 0.0026\ Re^{0.8}$, where Y is the corrosion rate at Reynolds number (Re) and in more dilute acid $Y = a + bV^{0.8}$, where V is the velocity and a and b are constants. The latter result agrees with corresponding work for rotated specimens (9), but it was also shown (4) that the corrosion rate was independent of flow rate above a certain velocity (presumably in aerated solutions). Ross and Jones (10) emphasized the importance of mass transfer considerations and showed that the dissolution rate of mild steel in *N* H_2SO_4 varied as $\sqrt{Re}$ and directly as Re for laminar flow (Re <2000) and turbulent flow, respectively.

There has been surprisingly little study of the influence of flow at high current densities where concentration polarization and consequent filming occur in what may be termed the prepassive region. It was suggested (11) that for concentrated acid velocity is not important below that critical value required to erode the protective $FeSO_4$ film. Hines and Williamson (12, 13) also commented briefly on the flow sensitivity of mild steel in very concentrated H_2SO_4. Apparently a thin compact ferrous sulfate layer beneath the porous visible layer controls the current density at constant potential, but diffusion from a layer of saturated solution outside the film may also be important. Hoar and Rothwell (14) studied the electropolishing of copper in orthophosphoric acid in a flow system of square section under potentiostatic control, but their results refer only to $Re < 1000$.

All of the previous work is open to criticism. Dissolution in pipes has often been studied in the presence of oxygen and under not clearly specified flow conditions. For the experimentally simpler system of a rotating cylinder or a revolving disk in deaerated acid, it is not always possible to establish the precise hydrodynamic and mass transfer conditions necessary for quantitative treatment. For example, segregation of the corrosion products according to mass by the centrifugal forces may play an important part in the relative extent of depolarization of anodic and cathodic processes. The edges of revolving disks also dissolve faster than the inner regions due to the thinner diffusion layer at the edges.

In the flow cell used in the present study, the hydrodynamic and mass transfer boundary layers were fully developed on the corroding anodic surface. Dissolution of pure iron, mild steel and iron-1.3% carbon were studied galvanostatically over a wide range of current densities in aerated, oxygenated and deaerated sulfuric and hydrochloric acids. This study is the first quantitative consideration of mass transfer at a rapidly dissolving anode surface where concentration polarization and consequent filming prevail.

This part of the paper deals with mass transfer at a dissolving unfilmed anode at relatively low current densities. In the second part the influence of flow on dissolution through an anodic film is discussed with special reference being made to mass transfer considerations.

Mass Transfer Relationships for an Unfilmed Anode Dissolving under Transport Control

It may be assumed that changes in velocity and concentration of an electrolyte flowing past a dissolving plate occur within thin boundary layers. Although velocity boundary relationships can be derived in terms of fluid properties, the definition of the concentration boundary terms is only possible when a further simplifying assumption is made. This requires either that the interfacial concentration of the transferred substance is constant over the entire anode surface or, alternatively, that the diffusive flux (current density) is constant. It is not possible to state in advance which of these conditions applies during anodic dissolution, although experimental observations reported later suggest that an equipotential surface is attained.

When the flow over the anode plate is laminar, Eckert's (15) cubic velocity profile leads to the following expression

$$\frac{V}{V_b} = \frac{3}{2}\frac{y}{\delta_l} - \frac{1}{2}\frac{y^3}{\delta_l} \qquad [1]$$

from which the hydrodynamic boundary layer has the dimension

$$\delta_l = 4.64\ (Re_x)^{-0.5}$$

and the relevant integrated boundary layer mass transfer equation is of the form

$$\frac{d}{dx}\int_o^{\delta_d} (C_i - C)\,V \cdot dy = -D \left|\frac{dC}{dy}\right|_{y=\delta_l} \qquad [2]$$

Wranglen and Nilsson (16) applied Eckert's procedure to the case of a flat cathode and, if their derivation is followed for a dissolving anode, similar expressions result. However, because the concentration gradient is reversed during dissolution, the numerical constants are slightly different and the concentration boundary layer at an anode is generally thinner than at a cathode. It is also noteworthy that the diffusion boundary layer thickness δ_d depends not only on the Reynolds (Re) and Schmidt (Sc) groups, but also on the electrode length (x).

Expressions for the thickness of the concentration boundary layer under either assumption, and in both flow regimes, are given below

Equipotential surface

Laminar flow

$$\delta_d = B_l x\, Sc^{-0.33}\, Re_x^{-0.5}\left[1 - \left(\frac{x_o}{x}\right)^{0.75}\right]^{0.33} \qquad [3]$$

Turbulent flow

$$\delta_d = B_t x\, Sc^{-0.33}\, Re_x^{-0.6}\left[1 - \left(\frac{x_o}{x}\right)^{0.90}\right]^{0.33} \qquad [4]$$

Values of the constants B_l,B_t

cathodic deposition	*anodic dissolution*
$B_l = 4.53$	$B_l = 2.86$
$B_t = 6.97$	$B_t = 5.40$

Constant current density

Laminar flow

$$\delta_d = B_l x\, Sc^{-0.33}\, Re_x^{-0.50}\left[1 - \frac{x_o}{x}\right]^{0.33}$$

Turbulent flow

$$\delta_d = B_t x\, Sc^{-0.33}\, Re_x^{-0.60}\left[1 - \frac{x_o}{x}\right]^{0.33}$$

cathodic deposition	*anodic dissolution*
$B_l = 3.59$	$B_l = 2.26$
$B_t = 5.88$	$B_t = 4.87$

Equations [3] and [4] with the appropriate values of B_l and B_t show that the thickness of the mass transfer boundary layer is much less at the leading edge of a dissolving specimen; although at high flow rates a nearly constant value is rapidly attained, there is always a tendency for excessive dissolution at edges, as was indeed found in practice.

Experimental Procedure

Three materials, designated here as "pure iron," "mild steel," and "iron-1.3% C," were employed. The analysis of the pure iron was C 0.0059, Si 0.0070, Mn 0.0020, S 0.0080, P 0.0010, Ni 0.0044, Cr 0.0014, Co 0.0032, Cu 0.0028, Al 0.002, O 0.014%, and of the mild steel C 0.055, Si trace, Mn 0.360, S 0.020, P 0.016, Ni 0.020, Sn 0.007, Al trace, Cd 0.030%. The iron-1.3% C alloy was made by adding graphite to the vacuum-melted pure iron.

The pure iron and iron-1.3% C were in strip form, used mainly in a cold-worked condition, obtained by cold rolling from 0.254 to 0.163 and from 0.279 to 0.198 cm, respectively, after annealing for two hours at 650°C. For a few runs in the annealed condition, final vacuum annealing was carried out at 650°C for two hours. The commercial mild steel had been cold rolled from 0.274 to 0.170 cm and was annealed at 650°C.

Metallographic examination of the pure iron showed a single phase ferritic structure of massive grain size. The grains of the mild steel were smaller and contained a trace of pearlite. The iron-1.3% C contained large spheroidized cementite particles in a ferritic matrix.

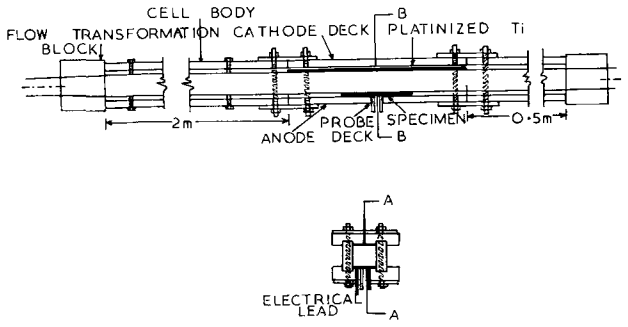

Fig. 1. Flow cell in section

Unless otherwise stated the solutions were always made from Analar grade reagents and distilled water. Solution concentrations were normally 0.5% or 5.0% w/w with respect to H_2SO_4 or HCl.

A flow cell of square cross section was used because mass transfer relationships have recently been published for a flat plate cathode in such a cell (16).

The flow cell, shown schematically in Fig. 1, was made of 0.95 cm thick Perspex and had an internal cross section of 1.90 x 1.90 cm. The sides were joined by bolts, and it was made leak-proof by applying a thin layer of polystyrene in the grooves. The cell sides were continuous except for the short lengths left vacant for insertion of the cathode and anode decks. The total length of the flow cell was 3m of which 2m (about 96 equivalent pipe diameters) preceded the length containing the specimen, so permitting the full development of the hydrodynamic boundary layer. About 25 equivalent diameters of cell length were provided at the end of the test section to avoid sudden changes in the direction of flow. Gradual conversion of flow, from a circular duct to a square one of somewhat larger cross section, was successfully provided at the two ends of the cell by means of Perspex blocks in which the shape of the cross section was changed gradually.

The cathode and anode decks were bolted into the main body of the cell and any minor joints made leak-proof. The specimen width was the same as that of the internal surfaces of the flow cell, and its length was generally greater than twice the distance required to develop the full mass transfer boundary layer but not as long as the cathode. Metal specimens were glued into shallow depressions in specimen decks, care being taken on mounting to ensure that they were flush with the deck and subsequently that the decks were flush with the sides of the flow cell. Platinized titanium cathodes, generally 15.24 x 1.90 cm, were attached to Perspex decks.

A plastic centrifugal pump was used to circulate the electrolyte at a controlled rate (measured by rotameters) through 1.59 cm bore glass tubing to the flow cell, the total volume of the system including the tanks being 30-40 liters. The solution was saturated with pure oxygen or pure nitrogen and was kept under a positive head of pressure. The temperature, measured well upstream from the flow cell, varied from 23° to 26°C.

Potentials were measured with a saturated calomel electrode through a backside Piontelli probe, thus avoiding IR_o drops and providing a minimum disturbance of the hydrodynamic boundary layer. The fine capillary Teflon probe fitted tightly into a hole in the center of the specimen and was held in position by screwing the thicker end into the Perspex back of the deck. The capillary was trimmed exactly flush to the surface of the specimen before use. All potential values are quoted on the standard hydrogen scale; they were obtained by adding 240 mv to the calomel values, liquid junction potentials being neglected.

Galvanostatic polarization curves were obtained as described later using conventional circuitry. Corresponding potentiostatic curves were sometimes obtained using a Wenking Potentiostat (standard 61/TR).

Due to the well-known hysteresis effects in the systems investigated, it was necessary to adopt standard procedure for all experimental runs. The mounted specimen was etched in 1:3 HNO_3 for 15 sec (or longer when it was felt that decarburized layers might exist on the specimen), washed, dried and inserted in the cell. Pure nitrogen was passed through the circulating electrolyte by-passing the flow cell for 2 hr before the cell was connected, deaeration then being continued for about 30 min until the specimen potential became constant. Current was next passed through the cell for 15 min with maximum circulation speed of the electrolyte until a new steady value was achieved. Readings of potential were then made at successively lower flow rates to the minimum, then rising again to the maximum, the velocity being changed every 2 min. Mean values are plotted on the various curves. With oxygenated and naturally aerated solutions a steady potential was obtained within 5 min of imposing the external current; readings were taken after a further 5 min during these runs. For low current density runs a single specimen could be used for several current densities, but at high current densities it was employed only once because of the change in geometry resulting from rapid dissolution.

Anodic Dissolution at Low Current Densities

Preliminary Considerations

Hysteresis and reproducibility.—It was early established that a polarization curve obtained by gradually raising the current density stepwise lay no more than 20 mv above the corresponding curve obtained subsequently by reducing the current (at Re 17,000). Similarly, on applying any current the potential of the anode rose sharply to a more positive value and then gradually dropped to a final value. The reverse phenomenon occurred when the current was switched off. Such general behavior can be related to potential-dependent specific surface activities of the specimen which cannot be discussed in detail here.

When specimens were used at several current densities, values were obtained with both progressively increasing and decreasing current density, mean figures being plotted on the characteristic curves. Experimental runs were all duplicated and were often triplicated. The reproducibility of potential readings was $\pm$ 2 mv below 10 ma/cm^2 and $\pm$ 5 mv at higher current densities. At very high current densities ($>$ 400 ma/cm^2) and low Re ($<$ 1000) it deteriorated to $\pm$ 20 mv, but such results are rarely quoted.

Potentiostatic and galvanostatic curves.—At relatively low current densities virtually identical results were obtained; however, at very high current densities and low flow rates a film of hydrogen accumulated on the cathode and affected the functioning of the potentiostat. Consequently galvanostatic control was adopted for most runs.

HCl or H_2SO_4.—Work at very high current densities was conducted mainly in hydrochloric acid because of the greater solubility of the iron salts and the smaller tendency to passivate in HCl. Polarization curves in H_2SO_4 and HCl at concentrations of 0.5% and 5% w/w showed relatively little difference.

Cell and specimen geometry.—The anode dissolved uniformly in static environments and in flowing solutions provided the current density was low. At high current densities, the leading and trailing edges dissolved faster than the rest of the surface. This suggests that the diffusion boundary layer was not fully established at the edges.

The higher dissolution rate of the edges was unaffected by the position of the cathode; placing the cathode well downstream failed to prevent preferential attack of the leading edge. The higher rate was not caused by the narrow crevices between deck and anode since masking of these crevices led to the de-

velopment of "lips" immediately adjacent to the covered areas.

Results were independent of anode size, provided it was smaller than the cathode. For the reverse case, there was excessive dissolution over an area roughly equal to the cathode area.

The anode was equipotential over its main surface: two probes placed 2.54 cm from each end showed the same potential. Also, a small (1.9 x 0.5 cm) anode, insulated from the main deck but kept at the same current density, showed the same potential as the rest of the deck provided it was not placed at an edge. The sides of the specimen corroded at the same rate as the center, even at high current densities (400 ma/cm^2). Therefore, the specimen behaved hydrodynamically as a flat plate.

Influence of Oxygen at Low Current Densities

In Fig. 2, the rest potentials are plotted against Re for all three materials in deaerated, oxygenated, and naturally aerated conditions. Corresponding apparent polarization curves are depicted in Fig. 3 to 5. The latter results are presented at all Re for the mild steel which shows behavior intermediate between that of the pure iron and the iron-1.3% C alloy. Results for these last materials have been condensed in Fig. 4 and 5.

For each material it was found that the rest potential changed very little (2-7 mv) on raising Re

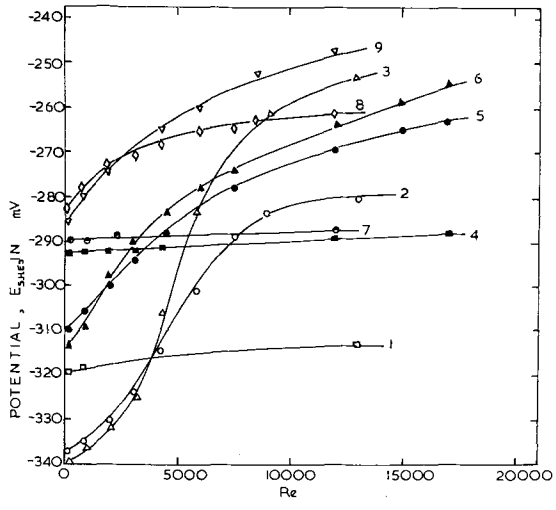

Fig. 2. Variation of rest potentials with Re for all materials in 0.5% w/w H_2SO_4. Pure iron: deaerated solution, curve 1 □; aerated solution, curve 2 ○; oxygenated solution, curve 3 △. Mild steel: deaerated solution, curve 4 ■; aerated solution, curve 5 ●; oxygenated solution, curve 6 ▲. Fe-1.3% C: deaerated solution, curve 7 half dark circle; aerated solution, curve 8 ◇; oxygenated solution, curve 9 ▽.

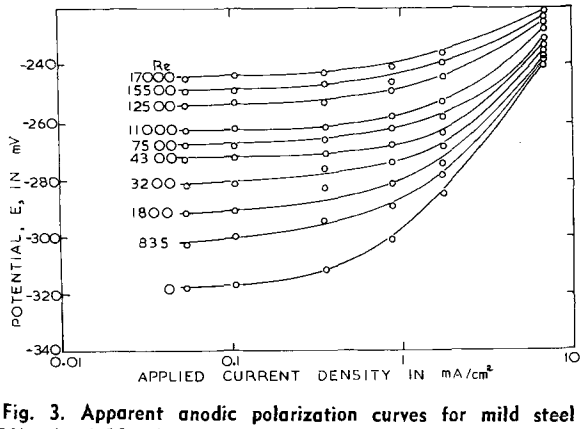

Fig. 3. Apparent anodic polarization curves for mild steel in 0.5% w/w H_2SO_4: (*a*). oxygen saturated.

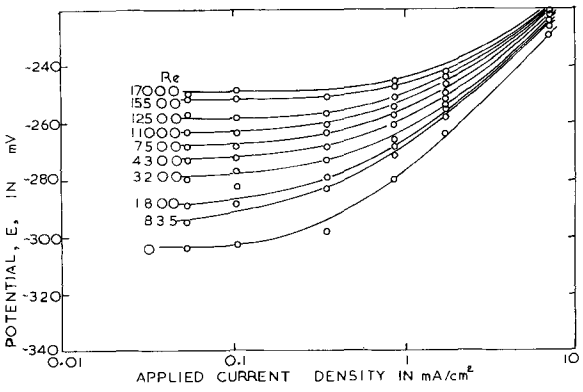

Fig. 3 (b). Naturally aerated

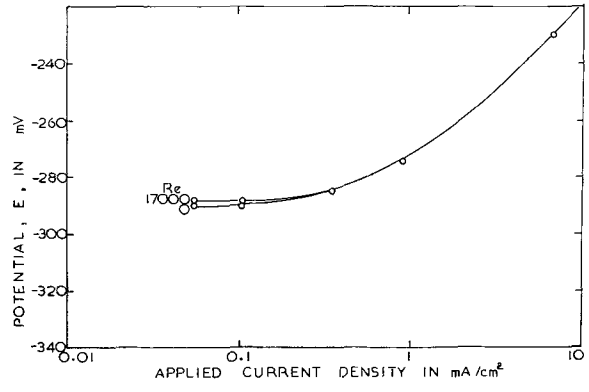

Fig. 3 (c). Deaerated

from 0 to 13,000-17,000 in deaerated solution. These small changes are undoubtedly due to minor traces of oxygen remaining in solution. On the other hand, for aerated and oxygenated solutions the rest potential increased with flow velocity, the effect being greater in the oxygenated solutions. The same general picture holds for the polarization curves; their position is independent of Re in deaerated solution, but they rise with Re in the presence of oxygen. The influence of oxygen on the rest potential and on the position of the apparent anodic polarization curve is increasingly important the lower the carbon content of the alloy.

It can be concluded that in a deaerated solution the rest potential and anodic polarization curve, and consequently the corrosion rate, are independent of flow rate in a duct of square cross section, thus confirming the corresponding results of Makrides (6) and Foroulis and Uhlig (5) with rotating electrodes. This result implies that iron dissolution and hydrogen evolution are not mass-transfer controlled under these conditions.

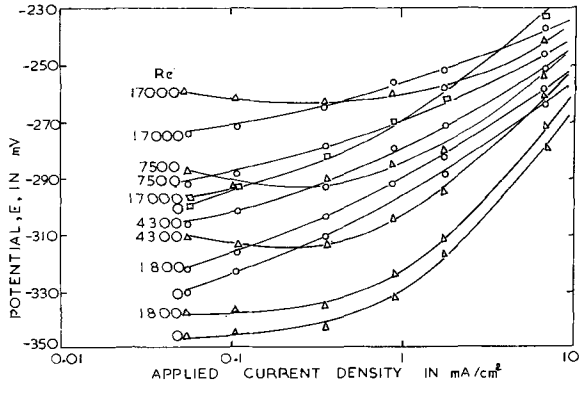

Fig. 4. Selected apparent anodic polarization curves for pure iron in 0.5% w/w H_2SO_4: □ deaerated; ○ naturally aerated; △ oxygenated.

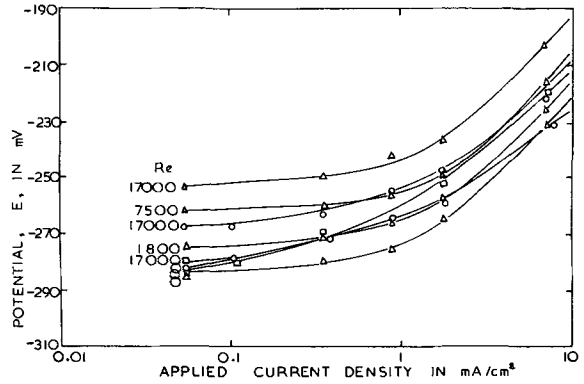

Fig. 5. Selected apparent anodic polarization curves for iron-1.3% C in 0.5% w/w H_2SO_4: □ deaerated; ○ naturally aerated; △ oxygenated.

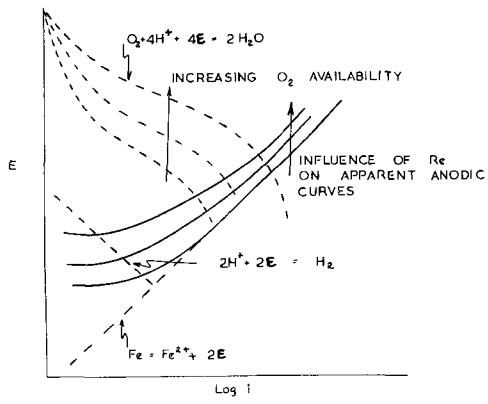

Fig. 6. Schematic representation of relationship between apparent anodic curves and true anodic and cathodic curves in solutions containing oxygen.

The reduction of oxygen raises the rest potential and the polarization curves by contributing to the cathodic reaction and increasing the dissolution rate. The effect is more pronounced the lower the carbon content (lower corrosion rate) for several possible reasons. First, the effect will be smaller at higher natural corrosion rates because the contribution of oxygen will be relatively less important than the very large hydrogen-evolution contribution to the cathodic current. Second, the presence of a hydrogen film on the surface interfering with the access of oxygen to the surface will become increasingly important the higher the corrosion rate, as has been pointed out by Foroulis and Uhlig (5). It is possible in the present flow cell for hydrogen to adhere to the surface even at high Re which apparently is not the case with rotating specimens. An additional obstacle to oxygen arrival exists in the case of the iron-1.3% carbon alloy because a carbon and cementite film accumulates on the anode surface.

Examination of all curves for aerated and oxygenated solutions shows that at high Re the rest potential is reaching a limiting value, also implying that the corrosion rate is becoming constant. This rate is determined by the arrival-rate of oxygen through the diffusion boundary layer which is reaching a limiting thickness at high Re.

An interesting, and apparently anomalous, effect for the pure iron and mild steel at Re $<$ 3000-4000, corresponding approximately to the region of laminar flow, is that the rest potentials (and polarization curves) are lower the greater the degree of oxygenation. Actually it was shown by allowing 15 min instead of the usual 2 min between readings that the differences between aerated and oxygenated solutions (always $<$ 5 mv) could have been due to hysteresis effects. In this region the resistance to diffusion of oxygen through the thick boundary layer must have been more important than the bulk oxygen content. The result for nominally deaerated solution, some 20 mv higher, could not be explained in this way and was quantitatively reproducible. The most likely explanation is that small quantities of residual oxygen (or Fe^{3+}) were adsorbed on active anodic sites, inhibiting iron dissolution and raising the slope of the true anodic curve (5). Once flow enters the turbulent region, oxygen readily arrives at the interface in oxygenated and aerated solutions and obscures this effect. Apparent confirmation of these ideas is obtained by scrutinizing the results for iron-1.3% C; no effect (other than the bogus displacement of oxygenated and aerated specimens due to hysteresis) is observed. This is because the hydrogen and cementite films would prevent oxygen adsorption and because the very rough surface might restrain the formation of laminar flow.

The apparent anodic polarization curve is initially almost flat and its slope rises with current density until it approaches the Tafel value. At low current densities, this curve is the algebraic sum of the anodic reaction current and of the two cathodic reaction currents, as shown schematically in Fig. 6. In the case of the pure iron in oxygenated solution the cathodic curves may be so dominant at high Re that a negative slope is observed, although this is almost within the limits of experimental error. As the oxygen content of the solution is raised, the apparent curve rises in the manner shown. On increasing the current density the proportion of cathodic areas and consequently of the cathodic reaction on the anode surface decreases and the shift with flow becomes proportionately less. In deaerated solutions no anodic shift was observed, and the slope of the curve was steeper. It is noticeable that for pure iron and mild steel in aerated and oxygenated solutions the slope at the highest current densities reported increased as Re decreased. This is in harmony with the theory given above. Further confirmation is afforded by the slopes of the curves for iron-1.3% C which are independent of Re because oxygen is relatively unimportant. Finally, most of the curves in aerated and deaerated solution do not exactly conform to true Tafel behavior (the slopes being too low) because the cathodic reaction on the anode surface is still significant. Results approximating more closely to Tafel behavior are discussed below.

Apparent Anodic Polarization Curves

The typical curve for mild steel in 0.5% w/w HCl, depicted in Fig. 7, shows three distinct regions. At low applied current densities (up to about 1 ma/cm²) the curve AB is relatively flat. At slightly higher current densities and potentials, where hydrogen evolution on the anode surface is much less, the apparent Tafel region BC is reached, with a slope of 65 mv. This region has been extrapolated above the current density of 12 ma/cm² where it ceases to hold true in practice. There is no sensitivity to flow in the first two regions because the reactions involved are activation controlled.

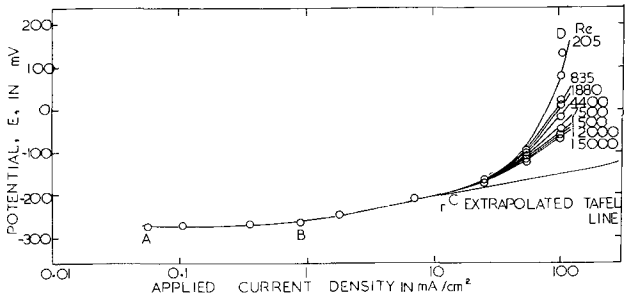

Fig. 7. Complete apparent anodic polarization curves for mild steel in deaerated 0.5% w/w HCl at various Re.

Nevertheless, above 12 ma/cm² the polarization curves (which should be largely "true" curves) rise sharply, the rise being greater the lower the Re. It is important to observe that once the current density corresponding to C is exceeded very rapid flow is incapable of depressing the polarization curve to the extrapolated Tafel line. Evidence will be presented in the second part to show that, once concentration polarization is established, filming of the anode surface occurs, and this is not readily removed. It is just possible that part of this residual overpotential is due to an IR_o drop in the electrolyte, even though a backside probe was adopted, but this possibility will be neglected here.

Corresponding curves for the three materials in deaerated 0.5% and 5% w/w HCl are given in Fig. 8, the two branches at high current densities represent-

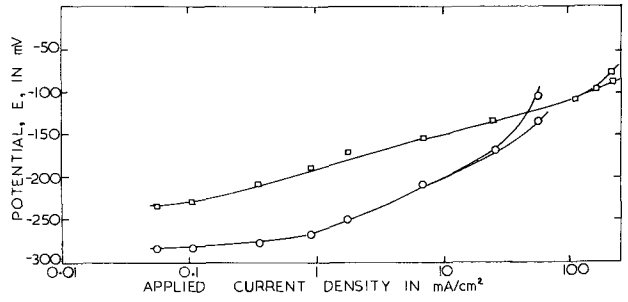

Fig. 8. Influence of HCl concentration, carbon content and heat treatment on apparent anodic polarization curves (deaerated): (a) mild steel; □ 5% w/w acid; ○, △ 0.5% w/w acid.

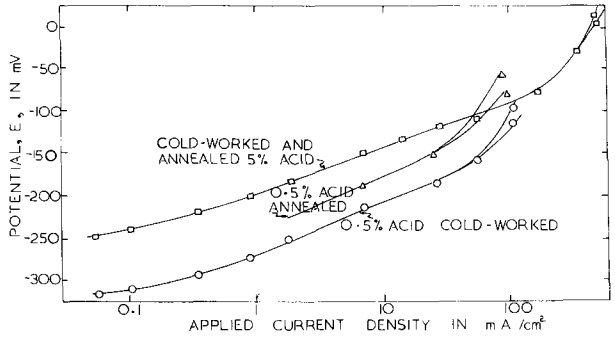

Fig. 8 (b). Pure iron

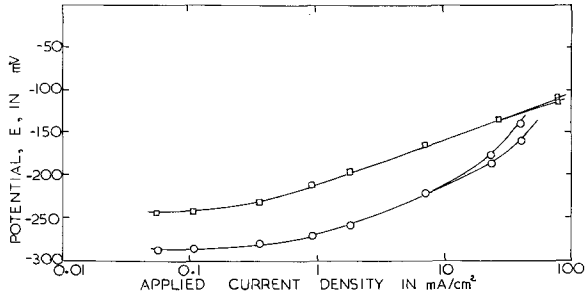

Fig. 8 (c). Iron-1.3% C

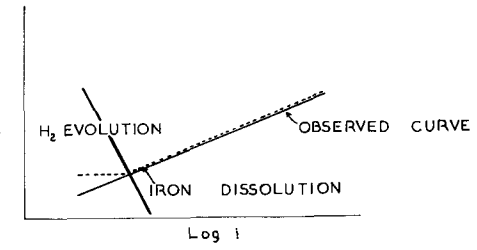

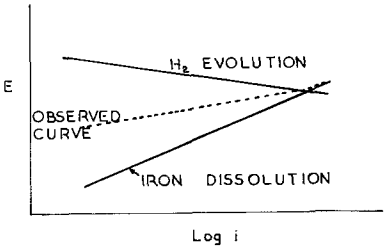

Fig. 9. Change in slope of apparent anodic curve due to increase in acid concentration in the absence of oxygen (schematic): (a) (top) dilute acid; (b) (bottom) concentrated acid.

ing values for Re 205 and 15,000, respectively. Included in the diagrams for pure iron are the results for annealed specimens. Some of the more important quantities are tabulated in Table I.

Influence of carbon content.—If the polarization curves for pure iron, mild steel, and iron-1.3% C taken from Fig. 8 are superimposed for each acid concentration several interesting conclusions may be drawn. First, allowing for slight variations in Tafel slope, which are probably related to changes in specific surface activity determined by the polarizing cycle imposed, the apparent polarization curves in the Tafel region are relatively close. There is some evidence that curves for the iron-1.3% C alloy lie to the right of those for the pure iron but the effect is not very pronounced. These curves clearly do not show up the massive differences in natural cell corrosion. Thus, Wood and Roberts (17) showed that true curves for iron-1.3% C obtained by weight loss measurements lie well to the right of those for pure iron corresponding to a tenfold increase in dissolution rate. In the present case at low current densities before Tafel behavior is observed the curves are higher and flatter for the higher carbon materials, due to the greater contribution of the cathodic reaction to the apparent anodic curve, and Tafel behavior does not start until the current density is higher (Fig. 9).

The second important point is that Tafel behavior ceases at a lower applied current density the higher the carbon content. This could be due to the contribution made by local cell corrosion in providing a sufficient concentration of Fe^{2+} ions for concentration polarization and film formation to occur at an earlier stage. An alternative explanation, which would be more likely in potential ranges where local cell corrosion is negligible, is that cementite and carbon corrosion products block the surface, so increasing the actual anodic current density in regions of free surface thus permitting an earlier onset of filming.

Table I. Important values for materials in deaerated solutions

Material	Rest potential, mv, E_H				Tafel slope, $\frac{dE}{d \log i}$, mv				Range of Tafel behavior current densities, ma/cm²			
	0.5% HCl		5% HCl		0.5% HCl		5% HCl		0.5% HCl		5% HCl	
	Annealed	Cold worked	Annealed	Cold worked	Annealed	Cold worked	Annealed	Cold worked	Annealed	Cold worked	Annealed	Cold worked
Pure iron	−280	−322	−242	−263	65	65	54	54	−23	0.9-55	0.45-155	0.45-155
Mild steel	−290	—	−245	—	65	—	42	—	1-12	—	0.11-110	—
Iron-1.3% C	−288	−291	−238	−248	57	57	50	50	1.8-8	1.8-8	0.7 -30	0.7 -30

Influence of annealing.—A few results were obtained on annealed specimens of pure iron and iron-1.3% C to compare with the cold-worked specimens normally used. Examination of the rest potentials in Table I shows that annealing raised the value for pure iron by 42 mv in 0.5% w/w acid and by only 21 mv in 5% w/w acid. The very small shifts for iron-1.3% C specimens are almost within the experimental error. The only apparent polarization curves which show any difference in the Tafel region are those for the pure iron in 0.5% w/w acid, where the curve for the annealed specimen lies 28 mv above that for the cold-worked specimen.

In view of the conflicting evidence and opinion on the importance of cold work on dissolution behavior (17-19), deductions must be made with reservation. At the outset it is important to emphasize the differences which occur when comparing the behavior of: (*a*) cold-worked specimens with specimens obtained from them by subsequent annealing, and (*b*) annealed specimens with specimens obtained from them by cold working. The comparison made here lies in the first category. The higher rest potentials of pure iron after annealing can be explained readily by the possible removal of many active anodic sites by annealing, and probably much more important, the reprecipitation of cementite at appropriate sites to form an increased number of cathodic areas. Hydrogen evolution will be simpler, cathodic polarization will be less, so the rest potential will be higher, in agreement with the findings of Foroulis and Uhlig for 0.002% C iron (18). The effect is less pronounced in the 5% w/w acid because the much greater H^+ concentration in the electrolyte makes hydrogen evolution easier, and it is less important to have specific cathodic sites. It is difficult to draw conclusions from the apparent anodic curves particularly if, as appears the case, some local cell action is still occurring in this region. However, the effect of annealing is less pronounced than for the rest potentials and is nonexistent in the case of the 5% w/w acid. The latter findings agree with those of Wood and Roberts (17) who demonstrated a shift between annealed and cold-worked specimens, using method (*b*) above, for 0.5% acid but not for 5% acid, but are not apparently supported by the theories of Foroulis and Uhlig. (18).

The insignificant changes in rest potential and the position of the polarization curves for the iron-1.3% carbon alloy are not surprising since subcritical annealing will not greatly affect the redistribution of massive cementite. However, a difference is observed in rest potentials and true anodic curves using scheme (*b*) above (17).

In agreement with the observations at low current densities, only the annealed pure iron in 0.5% w/w acid filmed more readily than the cold-worked material. This occurred at 23 ma/cm^2 instead of 55 ma/cm^2 due presumably to the greater inherent dissolution rate of annealed iron. It is not particularly clear why this should be so because local cell corrosion should be very small at this potential. The alternative explanation of partial surface blocking by cementite products does not look very likely either for such a relatively pure metal.

Influence of acid concentration.—Consideration of the apparent Tafel slopes shows them to lie within the range 42-65 mv which is in reasonable agreement with the literature. Not too great credence should be given to the present values since they were obtained from apparent curves obtained in a stepwise fashion. It does appear that the values are relatively independent of carbon content and are lower the higher the concentration of the acid, a trend also found by other workers (17).

For all alloys the onset of concentration polarization and consequent filming was delayed in the higher concentration of acid until a higher applied current density was attained. This could be ascribed possibly to the greater diffusivity of ferrous ions in the more concentrated acid, so restricting their accumulation in the boundary layers. Alternatively the film could be more soluble in the 5% acid, where the lower *p*H might be significant, but this is definitely not the case with yet higher concentrations (12, 13).

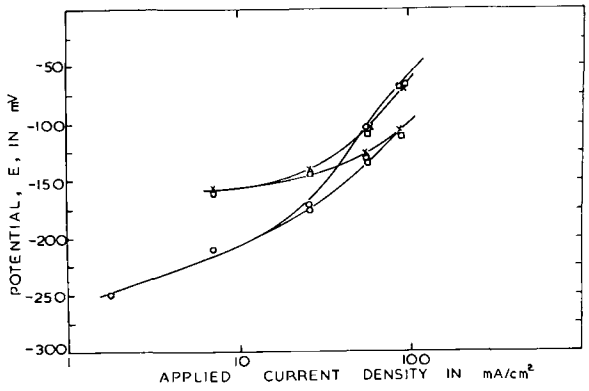

Fig. 10. Influence of adding $FeCl_2$ on anodic curves for mild steel in deaerated 0.5% w/w HCl: ○ no Fe^{2+} added; □ 0.57 g ions Fe^{2+}/liter; X 1.73 g ions Fe^{2+}/liter.

Influence of initially dissolved ferrous ions.—Anodic polarization curves were obtained for additions of 0.57 and 1.73 g ions Fe^{2+}/liter to solutions of HCl in the form of $FeCl_2 \cdot H_2O$. These additions raised the rest potentials to —190 and —188 mv, respectively, values partly determined by the increase in Fe^{2+} concentration but mainly by impurity filming of the anode as commercial grade $FeCl_2 \cdot H_2O$ had to be used.

The apparent polarization curves always remained higher for the $FeCl_2$-containing solutions, but the current density at which departure from Tafel behavior occurred was independent of $FeCl_2$ concentration (Fig. 10). This proved that the concentration of Fe^{2+} ions obtained at the interface just prior to filming must be much greater than those resulting from the relatively small additions of $FeCl_2$ solution.

Anodic Dissolution at High Current Densities

The results presented in the first part of this paper show that at low and medium current densities there is little dependence of either potential or current density upon the flow rate (Fig. 7). This is not to say of course that there is no mass transport, but rather that its contribution is negligible save in those instances where dissolved oxygen is present. When the dissolution rate is increased to a level where the specimen surface adopts an entirely anodic role and solute is generated at a rate approaching that at which it

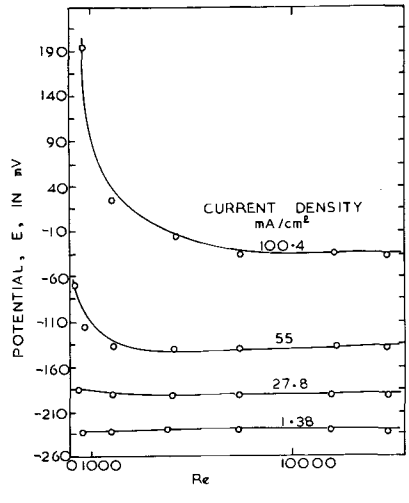

Fig. 11. Potentials of mild steel specimen in flowing deaerated 0.5% w/w H_2SO_4 at various current densities.

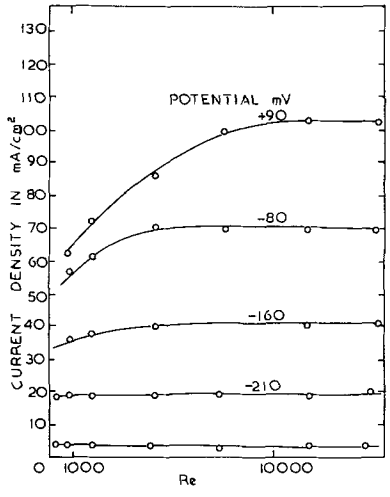

Fig. 12. Current densities on specimen of mild steel in flowing deaerated 0.5% w/w HCl at various potentials.

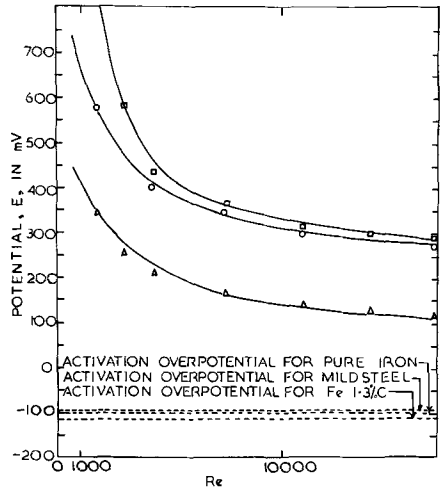

Fig. 13. Potentials of specimens in flowing 0.5% w/w HCl at current density of 440 ma/cm²: △ pure iron; ○ mild steel; □ iron-1.3% C.

is dispersed by diffusion and convection, a more marked response to flow rate should result. Figure 11 presents results typical of those obtained with all three metals in both hydrochloric and sulfuric acid; it shows that at 100 ma/cm² the potential responded to flow variations over a wide range of Reynolds number. Similarly, Fig. 12 is typical of potentiostatic data which show that at a sufficiently anodic potential there is a wide range of response to flow. The maximum current density employed was 440 ma/cm², and at this value there was a marked decrease in flow sensitivity even at high Reynolds numbers.

Reference to Fig. 7 and 8(a) suggests that at dissolution rates corresponding to a current density of 12 ma/cm² (in the case of mild steel exposed to 0.5% w/w HCl) the true Tafel behavior of the anodic reaction is disturbed by an increasing degree of concentration polarization and consequent filming. Above this value, therefore, the observed electrode potential includes activation overpotential, the concentration overpotential in the film and between the film and the bulk electrolyte, ohmic overpotential in the film, and any ohmic term in the probe. This last term is considered to be negligible in a back probe of the Piontelli type; the activation potential may be obtained by extrapolation of the Tafel region of the curve. A comparison of such values with those observed for all three metals in 0.5% HCl at maximum dissolution rate (Fig. 13) indicates how the apparent concentration overpotential and the ohmic overpotential in the film responded to flow rate. It is recognized that both of these factors will be operative, but since it is difficult to separate them in a quantitative manner, each will be dealt with as alternative explanations, as though the other were negligible.

When a solute is transported by means of diffusion and convection through a boundary layer under the influence of a concentration driving force, the simplified equation for the flux j_D, assuming no participation by the solvent or other species, is

$$j_D = K(C_i - C_b)$$

The concentration driving force is the difference between the interfacial concentration and the bulk concentration, and K is referred to as the mass transfer coefficient. Wranglen and Nilsson's treatment of the cathodic (16) process allows us, with an appropriate change of constant, to calculate K for an equipotential anodic process and compare theoretical mass transfer coefficients with those encountered at high current densities. The interfacial concentration C_i may be calculated from the apparent concentration overpotential (E_c) previously described by introducing the concentration of ferrous ions (C_r) corresponding to the reversible potential of the metal concerned.

Thus if

$$E_c = \frac{RT}{zF} \operatorname{lon} \left[\frac{C_i}{C_r} \right]$$

$$C_i = C_r \cdot \exp \left[E_c \frac{zF}{RT} \right] \qquad [5]$$

Now E_c may be read off from results such as those portrayed in Fig. 13, and C_r may be calculated from the reversible potential (E_{rm}) for each metal, as calculated by the method of Bockris (20)

$$E_{rm} = E^\circ + \frac{RT}{zF} \operatorname{lon} C_r$$

or

$$C_r = \exp \left[(E_{rm} - E^\circ) \frac{zF}{RT} \right] \qquad [6]$$

Concentration terms were used throughout because of the paucity of activity coefficient data.

The results of such calculations in the case of mild steel sustaining a current density of 440 ma/cm² in flowing deaerated 0.5% HCl are displayed in Table II, from which two facts are immediately apparent. First, the observed mass transfer coefficient (U) is many orders of magnitude less than the calculated value (K), and second, the interfacial concentration (C_i) is much higher than that expected from the solubility of the salts concerned in the medium employed (*e.g.*, 4.16 x 10^{-3} moles/ml for $FeCl_2$). Table III presents similar data obtained from mild steel in 5% HCl, where there is good agreement between U and K at high Reynolds numbers. The agreement between the predicted and observed mass transfer de-

Table II. Comparison of observed and calculated mass transfer coefficients

Mild steel in 0.5% w/w HCl

Re	E conc mv	C_i g ions/ml	U cm/sec	K cm/sec
1000	785	1.58×10^{21}	1.442×10^{-27}	6.4×10^{-5}
1500	705	3.16×10^{18}	7.22×10^{-25}	7.85×10^{-5}
2000	640	2.00×10^{16}	1.14×10^{-22}	9.05×10^{-5}
2500	595	6.30×10^{14}	3.62×10^{-26}	1.01×10^{-4}
3000	565	6.30×10^{13}	3.62×10^{-20}	1.11×10^{-4}
5000	475	6.60×10^{10}	3.46×10^{-7}	1.18×10^{-4}
7000	435	3.16×10^{9}	7.220×10^{-16}	1.42×10^{-4}
11000	390	1.00×10^{8}	2.28×10^{-14}	1.78×10^{-4}
15000	370	2.24×10^{7}	1.015×10^{-13}	2.27×10^{-4}
17000	365	1.41×10^{7}	1.62×10^{-13}	1.67×10^{-4}

Table III. Comparison of observed and calculated mass transfer coefficients

Mild steel in 0.5% w/w HCl

Re	E conc mv	C_i g ions/ml	U cm/sec	K cm/sec
1000	125	1.1×10^{0}	2.07×10^{-6}	6.82×10^{-5}
1500	120	7.6×10^{-1}	3.00×10^{-6}	8.37×10^{-5}
2000	115	5.25×10^{-1}	4.35×10^{-6}	9.66×10^{-5}
2500	110	3.56×10^{-1}	6.4×10^{-6}	1.08×10^{-4}
3000	105	2.4×10^{-1}	9.5×10^{-6}	1.18×10^{-4}
5000	95	1.125×10^{-1}	2.02×10^{-5}	1.25×10^{-4}
7000	80	3.56×10^{-2}	6.4×10^{-5}	1.51×10^{-4}
11000	75	2.405×10^{-2}	9.5×10^{-5}	2.01×10^{-4}
15000	70	1.645×10^{-2}	1.385×10^{-4}	2.42×10^{-4}
17000	67	1.34×10^{-2}	1.7×10^{-4}	2.64×10^{-4}

pendence is thus clearly dependent on the metal and electrolyte and both matters are commented on later.

Supersaturation of the metal-electrolyte interface with metallic ions and nucleation and growth of soluble films have been observed by several workers in different systems. Although in this work conditions for passivity were not attained, the formation of crystalline layers due to supersaturation alone have been noted previously (21-23). The interfacial concentration C_i is the concentration prevailing at the metal surface where the anion concentration is low, while C_i' is that value at which the film substance is just soluble. It should be noted that a constant mass transfer rate requires that $(C_i' - C_b)$ remains constant also. Thus, if the transport properties of the film are represented by means of a film coefficient (h), the steady-state flux through both film and boundary layer in series may be written as

$$j_D = h(C_i - C_i') = K(C_i' - C_b) = U(C_i - C_b) \quad [7]$$

whence

$$\frac{1}{U} = \frac{1}{h} + \frac{1}{K}$$

and so

$$h = \frac{UK}{K - U}$$

This expression enables us to extract the film coefficient from the observed coefficient by means of the theoretical mass transfer coefficient.

The dimensions of the film are related to the solubility of the substance, as follows. Consider that a metal M of valency m reacts with an anion X of valency n thus, (again employing concentrations rather than activities)

$$\mathrm{M} \rightarrow \mathrm{M}^{m+} + m\epsilon$$

$$\frac{m}{n}\mathrm{X} + m\epsilon \rightarrow \frac{m}{n}X^{n-}$$

and

$$\mathrm{M}^{m+} + \frac{m}{n}\mathrm{X}^{n-1} \rightleftharpoons \mathrm{MX}_{m/n}$$

If the concentration of X ions is C_x, and the solubility product of $\mathrm{MX}_{m/n} = S$, solid exists at a cation concentration C_i,

when

$$S = [C_i][C_x]^{m/n}$$

or

$$C_i = \frac{S}{[C_x]^{m/n}}$$

now let

$$j_D = \frac{I}{AnF} = \frac{\partial c}{\partial y}(D + \epsilon) \quad [8]$$

where ϵ is the contribution to transport derived from turbulent eddies, and integrating between the limits

$$C = C_i \text{ when } y = 0$$

$$C = C_i' \text{ when } y = y_f$$

$$\left[C_i - \frac{S}{(C_x)^{m/n}}\right] = \frac{I}{AnF}\frac{y_f}{(D + \epsilon)} \quad [9]$$

or

$$y_f = (D + \epsilon)\frac{AnF}{I}\left[C_i - \frac{S}{(C_x)^{m/n}}\right] \quad [10]$$

This result may appear to suggest that increased turbulence at a fixed current density would result in a thicker film. However, increased turbulence would also reduce the interfacial concentration for it is the outer value C_i' which is controlled only by considerations of solubility.

Thus at any given flux (or current density) the film thickness decreases as the turbulent contribution to mass transport increases. Unfortunately lack of precise solubility data for iron salts in solutions of acids prevents an assessment of the absolute value of C_i but, as has been shown already in many instances, the film constituted the dominant resistance to the diffusion of ferrous ions.

The formation of a porous film on the anode increases the electrical resistance and introduces an IR_o drop. Employing this alternative approach, it is possible to calculate the resistance from the potential in excess of the appropriate activation potential. The results (Fig. 14) suggest that at current densities of less than 80 ma/cm^2 the film was not fully formed, and also that the fully developed resistance was dependent on flow rate.

If the limiting resistance values (R_o) from this graph are used in conjunction with experimental E *vs.* Re data, it is possible to compare the calculated overpotential (or IR_o drop) with the observed value, as in Fig. 15. It will be seen that close agreement be-

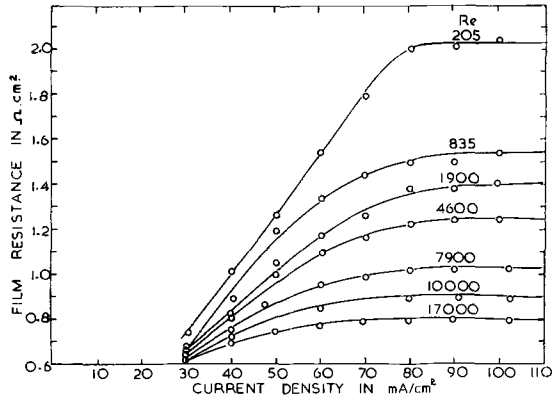

Fig. 14. Film resistance at various flow rates, for mild steel and 0.5% w/w HCl.

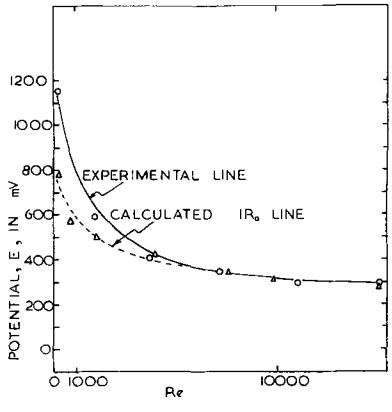

Fig. 15. Comparison of observed overpotential and that calculated from IR_o for mild steel in 0.5% w/w HCl at 440 ma/cm^2.

tween these two values exists at Reynolds numbers in excess of 5000, but that at lower flow rates a discrepancy becomes apparent. This could be due either to different film properties at low Re, or to a more substantial contribution from concentration polarization in the pores of the film at low current densities.

Effect of Variations in C content, Annealing, Acid Concentration, and Dissolved Fe(II) *Ions*

The results so far discussed, although illustrative of the behavior of all the systems examined at high current densities, were mainly drawn from experiences with mild steel in deaerated 0.5% w/w solution of hydrochloric acid. As in the current density regimes reviewed earlier, it is to be expected that changes in carbon content, heat-treatment, acid concentration, or in the initial presence of ferrous ions would result in changes in the effect of flow rate.

Carbon content.—As has been remarked, the current density at which departure from Tafel behavior and hence flow sensitivity is observed varies with carbon content. These figures were 55 ma/cm^2 for pure iron, 12 ma/cm^2 for mild steel, and 8 ma/cm^2 for 1.3% C alloy. The increased carbon content increased the natural dissolution rate so that the concentration overpotential and filming effects became more noticeable. Similar behavior is observed at high current densities (Fig. 13).

Annealing.—In only one instance, namely of pure iron in 0.5% w/w HCl solution, did annealing result in a changed behavior at high current densities. Figure 16 shows how the observed potential of the specimens differed from each other at various flow rates. It would seem that in this case the annealing amounted to a differential heat-treatment resulting in more numerous cathodic sites (18). This effect was not noticeable either in increased acid concentrations or when the carbon content was higher, because of the greatly increased natural dissolution rates.

Acid concentration.—The results obtained from specimens of all three metals exposed to 0.5 and 5.0% w/w HCl are shown in Fig. 17. It is clear that in both carbon-containing alloys the increased acid concentration reduced the degree of concentration polarization and the resulting filming process, thereby diminishing the sensitivity to flow rate. The potential of pure iron indeed ceased to be flow sensitive when immersed in the stronger acid.

Now a re-arrangement of Eq. [7] results in an expression for the film factor h

$$h = \frac{1}{1/U - 1/K} \qquad [11]$$

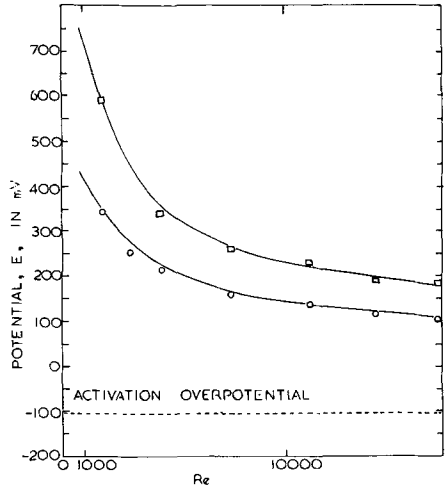

Fig. 16. Variation of potential of annealed (open box with dot) and cold worked (open circle) pure iron in flowing 0.5% w/w HCl (current density 440 ma/cm^2).

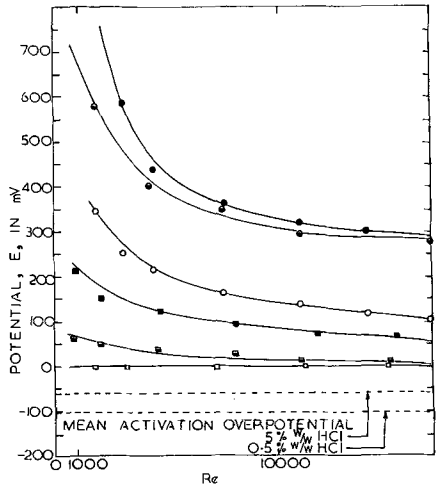

Fig. 17. Variation of potential of specimens in flowing HCl (current density 440 ma/cm^2). Circle, Pure iron in 0.5% w/w HCl; box, pure iron in 5.0% w/w HCl; half dark circle, mild steel in 0.5% w/w HCl; half dark box, mild steel in 5.0% w/w HCl; • iron-1.3% C in 0.5% w/w HCl; ■ iron-1.3% C in 5.0% w/w HCl.

and as at any fixed current density I/A

$$h(C_i - C_i') = K(C_i' - C_b)$$

$$C_i' = (hC_i + KC_b)/(K + h) \qquad [12]$$

substituting for $C' = S/(C_x)^{m/n}$

$$h = \frac{K\left[\dfrac{S}{(C_x)^{m/n}} - C_b\right]}{C_i - S/(C_x)^{m/n}} \qquad [13]$$

Thus an increase in C_x, the anion concentration, would reduce h, the film factor, in any flow state where K is constant.

$$C_i = C_i'\frac{(K+h)}{h} - C_b\left(\frac{K}{h}\right)$$

$$= \frac{S}{(C_x)^{m/n}}\left[\frac{K}{h} + 1\right] - C_b\left(\frac{K}{h}\right) \qquad [14]$$

now re-arranging [11] as

$$\frac{K}{h} = \frac{U}{h} - 1$$

and substituting

$$C_i = \frac{U}{h}\left[\frac{S}{(C_x)^{m/n}} - C_b\right] + 1 \qquad [15]$$

which also predicts that an increase in anion concentration (*i.e.*, acid strength) would result in a reduction of C_i, and hence the probability of the necessary concentration of cations to result in filming. For example, in the case of iron in HCl, where $m/n = 2$, a tenfold change in anion concentration results in almost a 100-fold change in C_i. Adopting the film resistance approach, apparent film resistances are given in Table IV. Films formed in concentrated acid may be thicker than the resistance indicates because entrapped acid is more conductive.

Ferrous ion concentration.—Equation [15] is also of interest inasmuch as it predicts that, once filming is complete, the presence of ferrous ions in solution (C_b) should have little effect on the interfacial concentration (C_i). Experiments were carried out in which 0.57 g ion Fe^{2+}/liter were added to 0.5% HCl solution, and 1.73 g ion Fe^{2+}/liter added to 5.0% HCl solution, in the form of $FeCl_2 \cdot H_2O$ crystals. At high dissolution rates the readings were rather unsteady, but in gen-

Table IV. Apparent film resistances for Re = 10,000 at c.d. of 440 ma/cm^2

Alloy	Electrolyte HCl	Physical state	Apparent film resistance, ohm · cm^2
Pure Iron	0.5%	Cold worked	0.53
Mild steel	0.5%	Annealed	0.90
Fe-1.3% C	0.5%	Cold worked	1.00
Mild steel	5.0%	Annealed	0.18
Fe-1.3% C	5.0%	Cold worked	0.32
Pure iron	0.5%	Annealed	0.75

eral there was little departure of behavior of all three alloys from that experienced in plain acid. It is of interest to note that this is not expected if diffusional control is entirely by mass transport in the boundary layer, but is predicted from Eq. [15] which includes the film factor.

Conclusions

1. The rest potentials and apparent anodic polarization curves for all materials in H_2SO_4 containing oxygen shift in the positive direction with increase in flow rate, due to oxygen reduction adding to the cathodic current. The shift is less at higher carbon contents due to the smaller relative contribution of oxygen to the total cathodic current and also to blocking the specimen surface by hydrogen, carbon and cementite films. Anomalous effects at low Re for pure iron and mild steel may be due to inhibition by oxygen or Fe^{3+} ions.

2. In deoxygenated HCl the apparent anodic polarization curve is composed of three distinct regions. The first is relatively flat, representing the net result of the true anodic and cathodic processes on the specimen; the second is a Tafel region where anodic dissolution is activation controlled; in the final region there is a sharp rise in potential due to concentration polarization which immediately produces filming. The overpotential in excess of the activation value may be accounted for either in terms of cation concentration gradients within the film and between the film and bulk solution or as an IR_o drop in pores in the film.

3. In the first two regions, the potential is not sensitive to flow during a galvanostatic run. Flow sensitivity apparent in the third region is attributed either to reduction in concentration overpotential in the film or to film thinning.

4. Increase in carbon content and decrease in acid concentration reduces the apparent range of current densities over which Tafel behavior is detected. The apparent Tafel slope is lower in more concentrated acid. The current density at which Tafel behavior ceases is independent of large concentrations of Fe^{2+} ion added to the acid.

5. Annealing a cold-worked specimen has no effect on any region in the case of Fe-1.3% C in 0.5% or 5% w/w HCl or of pure iron in 5% w/w HCl. However, pure iron in 0.5% w/w acid dissolves more rapidly in the annealed condition probably due to the production of favorable cathodic sites.

6. In the flow-sensitive region the leading edge dissolves preferentially in close accordance with theory.

7. Filming is caused by supersaturation of the boundary layer with Fe^{2+} ions and once the film is formed its stability is determined by its solubility product. The film is thicker for higher carbon contents and at low acid concentrations but is independent of the bulk Fe^{2+} concentration. Increase in flow rate reduces the film thickness or the concentration polarization associated with it to a limiting value. Although it has proved possible to treat the data quantitatively in terms of either phenomenon exclusively, it is not possible to separate their individual contributions to the measured overpotential.

Acknowledgments

The metal samples were kindly presented by the British Iron and Steel Research Association and by John Summers Limited. One of the authors (I.M.) gratefully acknowledges financial support from the Commonwealth Scholarship Commission during this research.

Manuscript received March 15, 1965; revised manuscript received Dec. 13, 1965.

Any discussion of this paper will appear in a Discussion Section to be published in the December 1966 JOURNAL.

SYMBOLS

A	electrode area, cm^2
B_l, B_t	constants in boundary layer equations
C	concentration of cations, g ions/cm^3
C_i	concentration of cations at the metal/electrolyte or metal/film interface, g ions/cm^3
C_i'	concentration of cations at the film/electrolyte interface, g. ions/cm^2
C_b	concentration of cations in the bulk electrolyte, g ions/cm^3
C_r	concentration of cations at reversible potential, g ions/cm^3
C_x	concentration of anions in the bulk electrolyte, g ions/cm^3
D	diffusion coefficient, cm^2/sec
d	equivalent diameter of flow cell, cm
E	electrode potential on standard hydrogen scale, v
E_c	concentration overpotential, v
E_{rm}	reversible electrode potential of metal, v
F	Faraday, 96,500 coulombs/g equiv
g	acceleration due to gravity, cm/sec^2
h	film factor, cm/sec
I	current, amp
j_D	diffusional flux, g ions/cm^2 sec
K	mass transfer coefficient, cm/sec
m	valency of a cation
N	total mass flux, g ions/cm^2 sec
n	valency of an anion
R	gas constant
R_o	film resistance, ohms
S	solubility product
T	temperature, °K
U	over-all mass transfer coefficient, cm/sec
V	velocity in x direction, cm/sec
V_b	velocity in the bulk of the electrolyte, cm/sec
x	distance along electrode surface from the leading edge, cm
x_o	length of inlet channel, cm
y	distance normal to the electrode surface, cm
y_f	thickness of film on the anode surface, cm
Z	valency state,
δ_d	thickness of diffusion boundary layer, cm
δ_l	thickness of laminar hydrodynamic boundary layer, cm
ϵ	eddy diffusivity, cm^2/sec
ρ	density of electrolyte, g/cm^3
μ	viscosity of electrolyte, g/cm sec

Dimensionless numbers

Nu	Nusselt number Kx/D
Re	Reynolds Number $\rho Vd/\mu$
Sc	Schmidt number $\mu/\rho D$

REFERENCES

1. J. A. N. Friend and J. Bennett, *J. Chem. Soc. (London)*, **121**, 41 (1922).
2. W. Whitman, R. Russell, C. Welling, and J. Cochrane, *Ind. Eng. Chem.*, **15**, 672 (1923).
3. W. Whitman and R. Russell *ibid.*, **17**, 4 (1925).
4. I. N. Putilova, S. A. Balezin, and V. P. Barranik, "Metallic Corrosion Inhibitors," p. 32 et. seq., Pergamon Press, London (1960).
5. Z. A. Foroulis and H. H. Uhlig, *This Journal*, **111**, 13 (1964).
6. A. C. Makrides, *ibid.*, **107**, 869 (1960).
7. A. C. Makrides, N. M. Komodromos, and N. Hackerman, *ibid.*, **102**, 363 (1955).
8. A. C. Makrides and N. Hackerman, *ibid.*, **105**, 156 (1958).
9. T. K. Ross and D. H. Jones, *Ann. Univ. Ferrara*, 5, 163 (1960).
10. T. K. Ross and D. H. Jones, *J. Appl. Chem.*, **12**, 314 (1962).
11. "Corrosion Handbook," H. H. Uhlig, Editor, p. 136, John Wiley & Sons Inc., New York (1948).

12. J. G. Hines and R. C. Williamson, *Corrosion Science*, **4**, 201 (1964).
13. R. C. Williamson and J. G. Hines, *ibid.*, **4**, 221 (1964).
14. T. P. Hoar and G. P. Rothwell, *Electrochim. Acta*, **9**, 135 (1964).
15. E. R. G. Eckert, "Heat and Mass Transfer," pp. 138, 173, 463, McGraw-Hill Book Co. Inc., New York (1959).
16. G. Wranglen and O. Nilsson, *Electrochim. Acta*, **7**, 121 (1962).
17. G. C. Wood and K. J. Roberts, To be published. K. J. Roberts, M. Sc. Tech. Thesis, University of Manchester, January 1963.
18. Z. A. Foroulis and H. H. Uhlig, *This Journal*, **111**, 522 (1964).
19. N. D. Greene and G. A. Saltzman, *Corrosion*, **20**, 293t (1964).
20. J. O'M. Bockris, "Modern Aspects of Electrochemistry," Vol. I. Butterworths, London (1954).
21. J. H. Bartlett and L. J. Stephenson, *This Journal*, **99**, 504 (1952).
22. R. Olivier, C.I.T.C.E. VI, Butterworths, London, 1954, p. 314.
23. M. Serra and S. Feliu, *ibid.*, p. 360.

A Redox Printing Technique for the Study of the Electronic Conductivity of Anodic Oxide Films on Valve Metals

Gerhart P. Klein

Laboratory for Physical Science, P. R. Mallory & Co. Inc., Northwest Industrial Park, Burlington, Massachusetts

ABSTRACT

A printing method using iodide-starch as the redox indicator in a solidified electrolyte was developed for applications to various valve metals and their anodic oxide films. It was used to study the electronic conductivity of anodic oxide films on tantalum and niobium and to detect defective sites in oxide films on aluminum. Applied to titanium, zirconium, and silicon, as well as the other valve metals, the technique was used for an evaluation of the surface condition of the metal substrates. The technique also was useful in cases where the oxide films corroded under the influence of the printing electrolyte.

Some of the valve metals are noted for high resistivity oxide films (1) that can be produced by anodic oxidation. However, the high resistivity can be realized only when materials of extreme purity are being used. In most practical cases, heterogeneities which disrupt the uniformity of the dielectric were found to be present in the oxide film giving inferior over-all properties. Impurities and several other conditions have been identified as sources for excessive electronic conductivity of anodic oxide films leading to "gassing," *i.e.*, oxygen evolution during formation in aqueous electrolytes in the absence of redox systems other than H_2O/O_2-system and to excessive leakage currents.

The distribution of the electronic current will depend on the distribution of the heterogeneities and impurities. It can vary from complete uniformity, both microscopically and macroscopically, to distinct singularity in cases of random contamination.

Measurements in electrolytes do not permit the determination of the distribution of the electronic currents unless the reaction products are immobilized at the site of their creation. These must be detectable by their color or other distinguishing characteristics.

The quantitative evaluation of electronic currents is possible, at least in principle, by measuring the reaction products of redox reactions by standard analytical or electroanalytical methods. However, the quantities of materials to be evaluated are usually so small, except in cases of large electronic currents and small volumes, that the sensitivity of most analytical methods is inadequate.

This situation led to our development of a thin layer printing-out technique which uses a redox indicator printing electrolyte in gelled form supported by a porous back-up material for the determination of the distribution and density of the electronic current passing through anodic oxide films in the formation direction. The electronic current is utilized to oxidize the reduced species of the redox indicator, the oxidized form of which must show a color distinctly different from the reduced form which ideally should be colorless. The oxidized form being fixed by the gel can then be evaluated optically.

Experimental Procedures

From the large number of redox indicators available only few qualify for use in the printing technique as applied to anodic oxide films. The main criteria for their selection were: sensitivity, redox potential, distinctness of color change, diffusion of the oxidized form in the printing electrolyte, chemical stability and stability towards light, compatibility with the anodic oxide films and substrate metals to be tested. One of the systems found to be most satisfactory from the point of view of these criteria was the iodide/iodine-starch redox system for reasons that will become evident in the following.

The printing electrolyte consisted of an agar-agar gel 0.01-0.1 molar in potassium iodide, 0.05 molar in borax, and containing varying amounts of soluble starch. The mixture was kept liquid in a water bath. On cooling it solidified to a rigid, non-tacky gel. The borax served as both a buffer and a means to make the solidified gel more rigid.

To perform a printing test liquid gel was spread on a specimen in the form of sheet or foil. The specimen then was sandwiched between two sheets of a suitable back-up material, such as MILLIPORE filter paper, and compressed in the printing press (Fig. 1).

The press was made from a clamp to the jaws of which electrode plates had been attached. Excess elec-

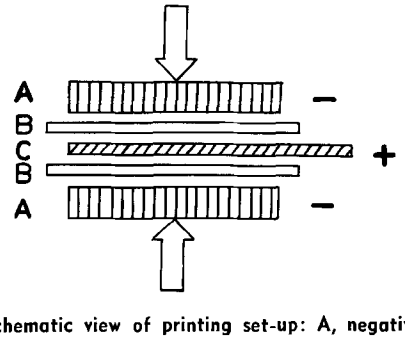

Fig. 1. Schematic view of printing set-up: A, negative electrode plates; B, printing medium consisting of back-up material and electrolyte; C, specimen.

trolyte gel was squeezed out assuring a thin smooth layer of printing electrolyte in intimate contact with the specimen surface and well bonded to the back-up material which, at the same time, became soaked with electrolyte. Electrical connections were made to a constant current or constant voltage power supply, depending on the test to be performed. The specimen was connected to the positive, and the press with the electrode plates to the negative output of the power supply.

Electronic current oxidized iodide to iodine which, upon reacting with starch, led to the formation of a blue to black coloration on a clear white background. The prints were preserved by bonding them to glass slides with the gel side down followed by drying in an air stream. The color changed to brown after drying. They could be stored for several months without noticeable deterioration.

Two printing-out modes were used. In the dynamic mode, the printing was done at constant currents, *i.e.*, while formation of the oxide film was taking place. In this case we obtained the integral electronic charge that passed while the film was formed to a certain voltage. Printing was usually done in voltage intervals with a new layer of printing medium used in every printing interval. This resulted in a series of prints which covered the whole range of anodic oxidation of a specimen up to the scintillation voltage and which reflected the electronic conductivity and its variation while the oxide film was being grown. In the static mode, the printing was done at constant voltage on a specimen that had been oxidized previously. The test was performed at the formation voltage of the film or a fraction thereof. This test was used to test the electronic conductivity of specimens that had been anodized previously under any experimental condition and could be used to evaluate the effect of formation conditions on the electronic conductivity and to detect defects in the oxide film.

The minimum sensitivity of the printing technique to detect electronic charges was found to be 1 millicoulomb/cm^2, approximately, for the iodide/iodine-starch redox system. Since the electronic current is integrated while a print is being taken even small currents could be detected if the printing time was extended. However, this was practical only within certain limits because the printing medium tended to dry out and because of slight fading and diffusion. Best results were obtained when the printing time was kept below about 15 min. This corresponded to minimum current densities which could just be detected of approximately 1 μa/cm^2. Point defects could be detected if their current was of the order of 1 nanoamp and higher.

Two factors contribute to the distinctness of the printing marks:

1. The iodine forms an adsorption complex with starch in which the iodine vapor pressure is reduced greatly.

2. The starch, being a high polymer, is immobilized in the matrix of the agar gel. The same is true for the adsorption complex with iodine.

The second factor, on the other hand, is also responsible for the spreading of the printing marks while they are being produced. The iodine has to diffuse to regions around the current source that have free starch still available. This explains the increase in the size of the marks with increasing printing time without further increase after the power has been shut off. Only if a large excess of iodine has been formed will there be additional spreading by diffusion. The greater the starch concentration the sharper the prints. The high sensitivity, the color change from colorless to blue-black, the distinctness of the printing marks, and their stability are the main advantages of the iodide/iodine-starch redox indicator system over most of the other redox systems which, in most cases, gave very diffuse patterns only.

Nothing has been said so far about the compatibility of this redox system with the anodic oxidation of the common valve metals. Most oxide forming metals exhibit a particular sensitivity toward halide ions which are responsible for corrosion effects which prevent the formation of protective and insulating oxide films. This effect is very noticeable with aluminum where even traces of chloride can be harmful when insulating anodic oxide films are to be formed. The only metals where such effects have been found to be absent are tantalum and niobium. The printing technique with iodide can be applied to these metals without limitations. In the case of most other valve metals, iodide-iodine containing electrolytes lead to specific corrosion, a fact that limits the use of the printing method. However, it is still a useful tool for the detection of imperfections in oxide films on these metals, as will be shown in the next paragraphs.

The concentration of iodide in the printing electrolyte has to be chosen such that the scintillation potential of the electrolyte is sufficiently high; this requires low concentrations. On the other hand, high concentrations are required to suppress oxygen evolution at sites of high local current density. If the concentration of iodide is too low, depletion in the layers adjacent to the substrate surface will lower the iodine solubility and thus lead to the formation of free iodine which cannot reach unreacted starch. Obviously, the most suitable iodide concentration has to be determined empirically for each application.

Applications of the Printing Technique

Tantalum and niobium.—Anodic oxide films on tantalum and niobium can be formed in electrolytes containing iodide as readily as in more conventional formation electrolytes. The linearity of the voltage increase during constant current formation of very clean specimens and the well-defined sparking voltages observed as a function of the concentration of potassium iodide were considered to be sufficient criteria for a "normal" formation behavior. The iodide printing-out technique could, therefore, be applied to tantalum and niobium in the dynamic and static modes. For example, a vacuum annealed tantalum foil specimen could be oxidized anodically while prints were taken in the arrangement described above without any trace of general darkening and only a few spots due to the oxidation of iodide to iodine and its reaction with starch (Fig. 2a). The voltage increased linearly to the scintillation point which was found to be near 200v for the particular electrolyte used in this experiment.

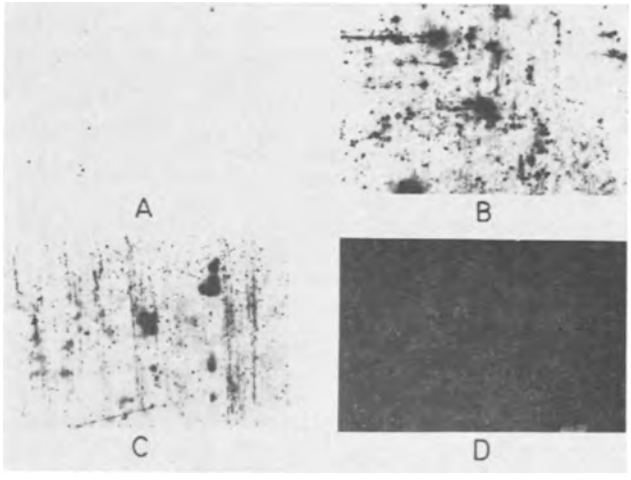

Fig. 2. Anodic prints obtained with tantalum and niobium foil. a. Vacuum annealed tantalum foil; dynamic print at 1 ma/cm^2, 0-150v formation. b. "As received" tantalum foil; dynamic print at 1 ma/cm^2, 0-50v formation. c. "As received" niobium foil; dynamic print at 1 ma/cm^2, 50-100v formation. d. Same foil as c., reverse side. Area of each print approximately 2 cm^2.

Specimens of foil in the "as received" condition by contrast produced prints which revealed a large number of localized electronically conducting centers, or even uniform electronic conductivity (Fig. 2b-d). Figure 2c and d, obtained from "as received" niobium sheet, show how the electronic conductivity patterns may differ on the two sides of a specimen.

Anodic oxide films on tantalum and niobium formed in the electrolytes containing iodide may not show satisfactory properties for use as thin film dielectrics, *e.g.*, in capacitors, but this is not due to any damage done by the printing process. The printing process itself is neutral as was shown by a comparison of prints obtained with clean and contaminated specimens. In addition, the properties of the electronically conducting sites in anodic oxide films were found to be unaffected by the printing process. No corrosion phenomena, such as have been observed with aluminum and the other valve metals, have been observed with tantalum and niobium.

Aluminum.—Aluminum behaves quite differently from tantalum and niobium which were inert toward iodide and iodine, respectively. Aluminum cannot be oxidized anodically in halide containing electrolytes, such that insulating films are formed with a voltage increase typical for constant current formations. The presence of even small amounts of halide ions leads to the corrosion of anodic oxide films formed in halide-free electrolytes. By applying the printing-out technique with iodide-starch to aluminum that had been anodized previously in electrolytes containing ammonium borate, we found that violent breakdown reactions took place if we applied the full previous formation voltage of the film. However, by applying a fraction of the formation voltage, typically between 20 and 50%, the current was found to be stable in the low milliampere per square centimeter range with only a slight tendency to increase with time. Only if one print after the other was taken at the same voltage did the current increase to higher values. It was still limited by the oxide film itself, however. The prints revealed a pattern of specks on the white background of the printing medium. The oxide film had clearly been corroded at sites of current flow, but the surprising result was that the corrosion at these sites had been accompanied by electronic current which led to the marks on the prints. By comparison, prints taken at constant current with bare aluminum did not show any blackening. Also, large areas of the oxides were free of corrosion sites if the aluminum was of high purity and, in addition, was cleaned properly. The prints obtained from various specimens are shown in Fig. 3. They were all oxidized in ammonium borate solution to 100v and aged for 1 hr. The prints were taken at 40v for 30 sec each. The first print of the series was obtained with 99.999% aluminum foil after electrochemical polishing, the second print with the same foil in the "as received" condition, the third with 99.99% foil in the "as received" condition, and the fourth print with commercial aluminum wrap, also in the "as received" condition. It is easily seen that characteristic differences were observed with these specimens and that the printing-out method clearly revealed defective areas in the anodic oxide film. The importance of the surface condition as an electronic current determinant is indicated by the differences between the prints obtained with chemically polished and "as received" 99.999% foil on the one hand and "as received" 99.99% foil on the other. It indicates that the stated purity is meaningful only if it specifically includes the surface purity.

The printing-out technique, as applied to aluminum with iodide-starch as the redox indicator, can be considered as a corrosion test which uncovers inhomogeneities in the oxide films by virtue of the electronic current that accompanies the corrosion reaction. A correlation between the electrical properties of the anodic oxide films and the number of corrosion sites has been found to exist.

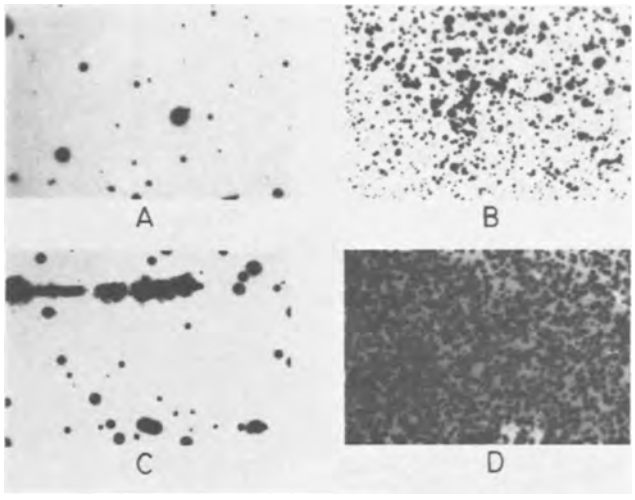

Fig. 3. Anodic prints obtained with aluminum foil. a. 99.999% pure foil, electropolished and oxidized to 100v in aqueous ammonium borate solution. Static print taken at 40v with 30 sec printing time. b. Same foil, in "as received" condition. Test as in (a). c. 99.99% pure foil in the "as received" condition. Test as in (a). d. Household aluminum wrap, as received. Test as in (a). Area of each print approximately 2 cm^2.

Titanium, zirconium, silicon.—Anodic oxide films were produced on these metals but the films were usually of lower quality than those on tantalum and aluminum. The oxide films on these materials are all quite sensitive to halides so that formation in halide containing electrolytes is either impossible or proceeds only to a few volts. The behavior of the oxide free and oxide covered metals is intermediate to that of tantalum and aluminum, even though closer to the latter. The anodic oxidation of titanium did not proceed beyond 4-5v under the conditions of the printing test at constant current. Figure. 4a and b give the result of tests performed with 99.9+% titanium sheet. Figure 4b was obtained with the sheet in the "as received" condition, Fig. 4a shows the result obtained with chemically polished material. A print similar to Fig. 4a was obtained when a chemically polished specimen was oxidized to 100v in ammonium borate and tested at 10v. Again, the various prints reflect characteristic differences in the distribution and density of the electronic conductivity which show that the printing-out technique, even when the system is not inert, can still give information helpful for the evaluation of surface treatments and specimen quality.

In Fig. 4c and d two examples of prints with zirconium are given. Zirconium behaved similarly to titanium, except in the case when a chemically polished specimen was tested. A more or less uniform distribution of the electronic conductivity was found with titanium compared to a distribution showing a few very active areas in the case of zirconium.

Silicon could be oxidized to about 25v under the printing condition. A comparison of prints obtained with specimens with different surface treatments and doping again revealed characteristic differences which could be utilized for an evaluation of the quality and surface condition of silicon specimens.

Conclusions

1. The electronic conductivity of anodic oxide films on tantalum and niobium could be studied during the growth of the oxide. The behavior of electronically conducting sites could, therefore, be studied dynamically and statically with respect to the growth of the oxide film.

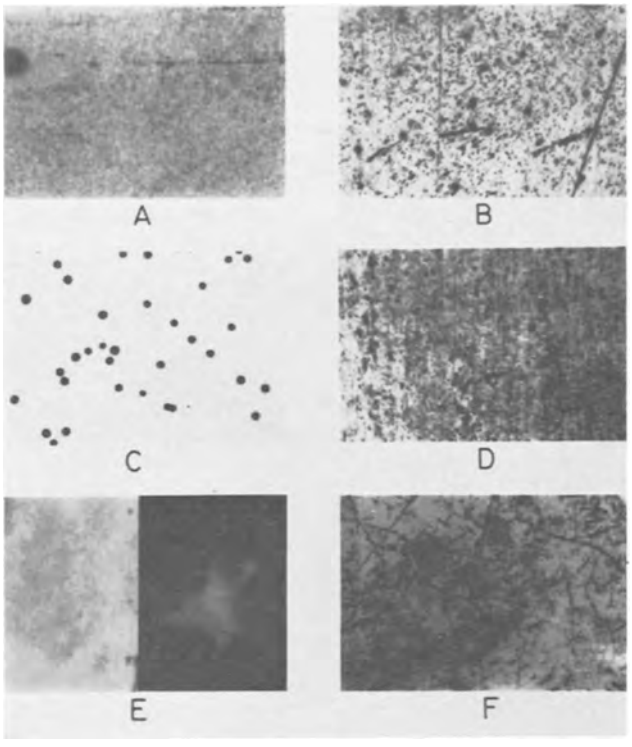

Fig. 4. Anodic prints obtained with titanium, zirconium, and silicon. a, Chemically polished titanium sheet 99.9+% purity. Dynamic print at 1 ma/cm^2 for 60 sec reached 4v, approximately. b. Same foil as above in "as received" condition. Test as in (a). c. Chemically polished zirconium sheet 99.9+% purity. Test as in (a). d. Same foil as in (c), in "as received" condition. Test as in (a). e. Two sides of silicon slice, (left) polished, (right) "rough." Dynamic print at 1 ma/cm^2 reached 25v in about 2 min. f. Mechanically polished and etched silicon slice. Test as in (e). Area of each print approximately 2 cm^2.

Surface contamination of random distribution was found to be the main reason for the high electronic conductivity of "as received" foil. Chemical polishing and vacuum annealing produced specimens essentially free of gross defects.

2. The printing-out technique could be used for the detection of defects in anodic oxide films on aluminum at potentials well below the formation voltage. The corrosion of the oxide film at defective sites was found to be accompanied by electronic currents. No electronic currents were observed with bare aluminum.

3. In the case of titanium, zirconium, and silicon, the printing-out technique could be used for an evaluation of the surface condition even though the anodic oxidation proceeded only to a few volts. A behavior similar to that of aluminum was found for anodic or thermally grown oxide films when tested at a fraction of the formation voltage or its equivalent.

4. The detection sensitivity of the printing medium for uniform electronic currents approached the low microampere/square centimeter range in the case of tantalum and niobium. Point defects could be detected if their current was in the nanoampere range.

In the case of aluminum and the other metals the sensitivity could not be evaluated quantitatively. It was found, however, that in the case of aluminum very small defects could be activated, allowing enough time and a sufficiently large fraction of the formation voltage, such that the electronic current accompanying the corrosion reaction would lead to their detection.

The situation may be similar with some of the other metals and their oxide films, even though this was not studied in any detail.

5. The printing-out method is a quick and reliable method to evaluate the quality of oxide film dielectrics and the surface condition of substrate materials. It is particularly useful in the case of tantalum and niobium where the test is nondestructive. One of the main advantages of the test is that prints can be obtained which record directly the electronic current distribution.

Acknowledgments

The author wishes to thank Mr. L. Wingood for his assistance in the experimental part of this work and Dr. P. Bro for his comments on the paper.

Manuscript received Nov. 22, 1965. This paper was presented at the San Francisco Meeting, May 9-13, 1965.

Any discussion of this paper will appear in a Discussion Section to be published in the December 1966 JOURNAL.

REFERENCE

1. L. Young, "Anodic Oxide Films," Academic Press, London and New York (1961).

The Electronic Conductivity of Defective Anodic Tantalum Oxide Films

Gerhart P. Klein

Laboratory for Physical Science, P. R. Mallory & Co. Inc., Northwest Industrial Park, Burlington, Massachusetts

ABSTRACT

The conditions under which anodic oxide films on tantalum showed electronic conductivity were studied using an electrochemical printing-out technique with starch-iodide as the redox indicator. The sensitivity for the detection of electronic charge was approximately 1 millicoulomb/cm^2. The effect of alloying (contamination), thermal oxidation, plastic deformation, and surface topography were investigated with regard to their contribution to the electronic conductivity of anodic oxide films on mechanically treated ("rough") tantalum surfaces. It was concluded that impurities alone were responsible for the electronic conductivity even in cases where supposedly clean tantalum had been abraded with tantalum. Roughness by itself was not a sufficient condition for electronic conductivity.

The electronic conductivity (e.c.) of anodic oxide films on substrate metals such as tantalum, niobium, aluminum, and other "valve" metals in electrolytic systems and with solid counter electrodes may be made up of two parts: A uniformly distributed part which is due to the electronic conductivity of the bulk oxide, and a nonuniformly distributed one which is localized in heterogeneities in the oxide film. By

heterogeneities we mean deviations in the structure and composition in the widest sense, *i.e.*, factors which disrupt the uniformity of the dielectric. A separation of the two parts of the electronic conductivity (e.c.) is required before an analysis of either part can be attempted successfully.

Heterogeneities in anodic oxide films were considered by several authors to explain abnormal formation behavior, excessive leakage currents, abnormal a-c properties (1, 2), electrolytic rectification (2-4), and luminescence (5). Pores, cracks, microfissures, with or without direct electrolyte contact to the substrate, or highly conducting areas of unspecified nature were discussed to explain these phenomena. A blocking mechanism had to be assumed in order to explain why the active sites could withstand the high field strength present across the film. Oxygen bubbles formed at the base of pores and cracks were discussed by Vermilyea (6) and Young (1), who also suggested the condenser pressure as a possible means of closing microfissures.

Vermilyea (7) published electronmicroscopic studies of flaws which he found to have been caused by a variety of different treatments and conditions.

In a previous paper (8) we described a printing-out technique and showed how it could be applied to the study of the gross electronic conductivity of anodic oxide films on tantalum and niobium. In this paper, we describe its use in the investigation of the conditions under which anodic oxide films on these metals became electronically conducting and its use to study the dynamic changes of the electronic conductivity (e.c.) during film formation and the external factors affecting it.

Previous studies (1, 2, 6) have shown that the electrical properties, especially the e.c. of anodic oxide films formed on "rough" (mechanically treated) surfaces differed greatly from those of films formed on "smooth" (chemically polished) surfaces. Rough surfaces, in general, were produced by abrasion or by rolling as in the case of sheet material in the "as received" condition. Obviously, mechanical surface treatments can have many more effects than just the production of a rough topography of the surface. They can be grouped into four categories: effects of (*i*) contamination; (*ii*) local heating of the surface; (*iii*) plastic deformation of the surface layers; (*iv*) surface topography, that is, roughness in the true sense.

We shall consider each of these factors separately and then apply these results to the problem of the e.c. found with oxide films on mechanically treated surfaces in general.

Experimental Procedures

The anodic printing technique described in an earlier paper (8) was used to study the electronic currents in the oxide films; we refer to that paper for experimental details.

Specimens were cut from Kawecki tantalum sheet 0.01 and 0.002 in. thick which was designated as high reliability, capacitor grade, annealed material of 99.9+% purity. The chemical polishing followed standard procedures, *i.e.*, the specimens were dipped in a mixture of 5 parts H_2SO_4, 2 parts HNO_3, 1.5-2 parts HF (parts per volume of concentrated commercial acids) for 10-20 sec at 40°-50°C, and was followed by a 10-sec dip in concentrated HF to remove the film left from the polishing treatment. Vacuum annealing and alloying of the tantalum sheet was done in a Varian high vacuum resistance heated furnace under pressures of 10^{-6} mm Hg and lower.

Experimental

Contamination: Electronic conductivity of anodic oxide films on alloys of tantalum with iron, nickel, and carbon.—Bulk contamination.—Contamination is known to be responsible for excessive electronic conductivity of anodic oxide films (9, 10). From the large number of possible contaminants, we chose three in order to demonstrate the specific effects of alloying constituents in Ta on the e.c. of anodic oxide films as detectable with the printing technique.

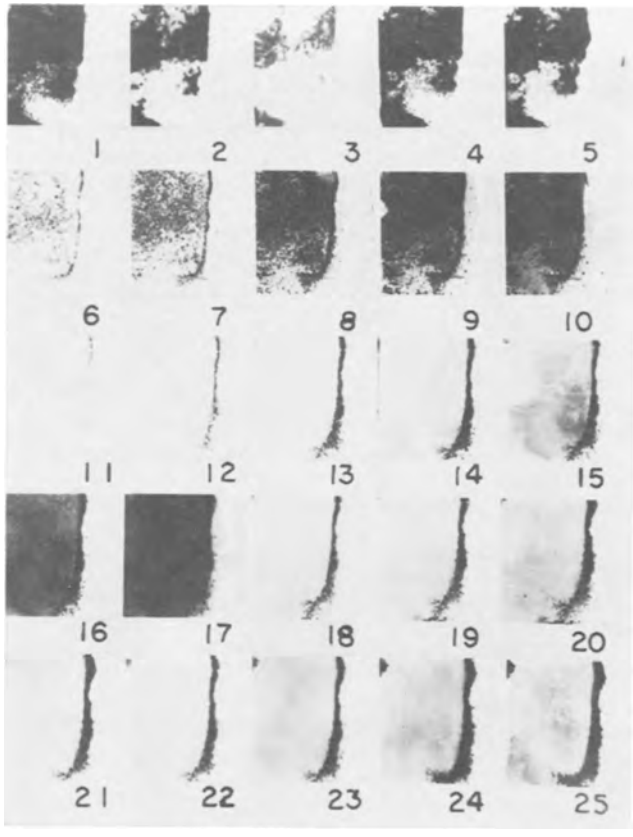

Fig. 1. Anodic prints of Ta alloyed with Fe by heating Ta sheet with Fe powder under the following conditions: Pressure less than 10^{-6} mm Hg, temperature 1400°C, time 2 hr. See Table I.

Table I

Print No.	Current density $\mu a/cm^2$	Time sec	Formation voltage range	Remarks
1	625	70	to 10	
2	250	60	to 13.5	
3	62.5	60	to 10.5	
4	625	70	15 to 20	
5	625	70	20 to 23	After No. 5-1 min dip in conc. HF
6	625	35	to 10	
7	625	50	10 to 20	
8	625	65	20 to 30	
9	625	75	30 to 40	
10	625	85	40 to 50	After No. 10-1 min dip in conc. HF
11	625	40	to 10	
12	625	55	10 to 20	
13	625	55	20 to 30	
14	625	50	30 to 40	
15	625	55	40 to 50	
16	625	60	50 to 60	
17	625	55	60 to 70	After No. 17-1 min dip in conc. HCl
18	625	55	70 to 80	
19	625	55	80 to 90	
20	625	55	90 to 100	
21	625	55	100 to 110	
22	625	55	110 to 120	
23	625	55	120 to 130	
24	625	55	130 to 140	
25	625	60	150 to 160	

The alloys were prepared by heating chemically polished tantalum sheet with thin layers of iron, nickel, and carbon powder at 10^{-6} mm Hg pressure and 1400°C for 2 hr. Powder was used because it proved the simplest way of producing alloys with a composition gradient at the surface, a condition that gave a qualitative picture of the effects of composition on the e.c.

Tantalum alloyed with iron.—Three series of prints are shown in Fig. 1 obtained from the Ta-Fe alloy speci-

men. The first group of prints was taken without further pretreatment of the specimen, the second and third groups were taken after removal with HF of the oxide films formed in series one and two, respectively. The anodic oxidation to 10v (Print 1.1) was accompanied by high electronic current. Prints 1.2 and 1.3 were taken at one fifth and one tenth of the initial current density and give more details of the conducting area due to the lower intensity of the prints. Prints 1.4 and 1.5, again taken with full current density, show that the rate of voltage increase at constant current slowed down progressively and approached almost zero above 20v. Treatments in conc. HCl, dilute HNO_3, and aqua regia either prior to taking the first print or between prints did not affect the electronic conductivity as reflected in the following prints. The initial oxide film was removed with conc. HF before the second series of prints was taken. This treatment also dissolved some of the Ta-Fe alloy as could be seen from the gas evolution and the formation of pits at sites where the Fe powder particles had alloyed with the Ta. Prints 1.6 through 1.10 show the electronic conductivity of the film formed after the HF treatment. The formation proceeded rapidly at first but again slowed down after the e.c. developed with increasing film thickness. The formation time through 10v increased from 50 sec in the first interval to 85 sec in the fifth interval. At the end of the first series formation through 3v had required 70 sec.

The HF treatment was repeated as before and another series of 10v interval prints was taken. Again, the e.c. built up gradually, even though much slower than before (except for a narrow area at the right-hand side which gave prints rather like those in the second series). Even print 1.17 with the strongest blackening required only 55 sec for a formation through 10v. The specimen was dipped in conc. HCl after print 1.17 and then printing was continued. Print 1.18 no longer showed the blackening of the background while the marks at the right-hand side were not affected by HCl.

Tantalum alloyed with nickel.—The prints taken of a Ta-Ni alloy specimen are shown in Fig. 2. In contrast to the Ta-Fe alloys, the e.c. was low initially so that film formation proceeded smoothly to 30v with only little increase in the formation time for a 10v interval. Upon further oxidation, the e.c. increased rapidly which is reflected both in the more intense blackening of the prints and the increase in time to cover a 10v formation interval. Dipping the specimen in aqua regia for 1 min after print 2.5 strongly reduced the e.c. in the following formation interval. The e.c. increased rapidly after the aqua regia dip which was repeated after print 2.7 with the same result: The first print after the dip showed very little blackening while the following one was again extremely dark, it required 100 sec for the 10v interval formation. A static print at 45v was clear.

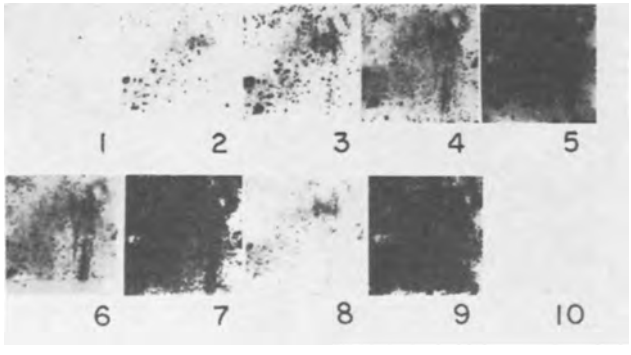

Fig. 2. Anodic prints of Ta alloyed with Ni by heating Ta sheet with Ni powder under the following conditions: Pressure lower than 10^{-6} mm Hg, temperature 1400°C, time 2 hr. See Table II.

Table II

Print No.	Current density, $\mu a/cm^2$	Time, sec	Formation voltage range	Remarks
1	625	45	to 10	
2	625	55	10 to 20	
3	625	60	20 to 30	
4	625	55	30 to 40	
5	625	75	40 to 50	After No. 5-1 min dip in aqua regia
6	625	75	50 to 60	
7	625	90	60 to 70	After No. 7-1 min dip in aqua regia
8	625	50	70 to 80	
9	625	100	80 to 90	
10	—	60	45	Constant voltage

Tantalum alloyed with carbon.—The prints obtained from tantalum foil containing tantalum carbide are shown in Fig. 3. Prints 3.1-3.10 were obtained with a specimen containing an area of low and uniform concentration while the concentration in the following specimen, prints 3.11-3.20, was high and nonuniform. The behavior of the e.c. with film formation differed greatly from that observed with alloys of tantalum with iron and nickel. The initial one or two 10v inter-

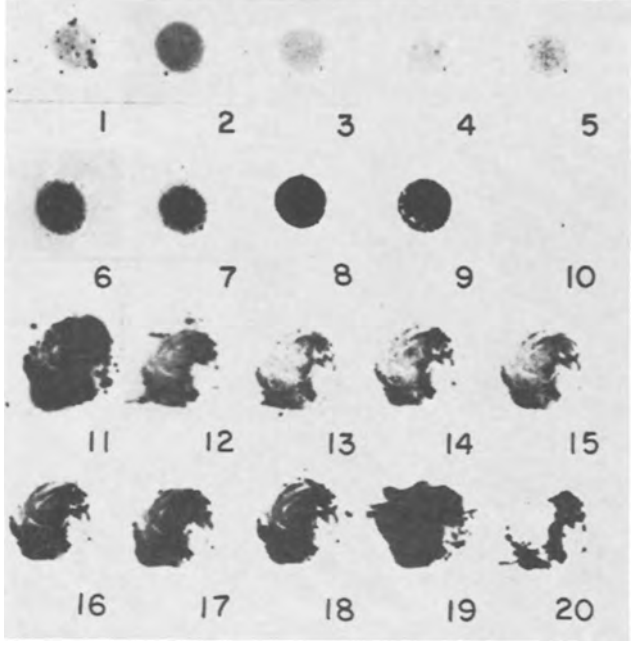

Fig. 3. Anodic prints of Ta alloyed with C by heating Ta sheet with thin layer of graphite under the following conditions: Pressure lower than 10^{-6} mm Hg. temperature 1400°C, time 2 hr. Series A (No. 1-10): low concentration of Ta_2C; Series B (No. 11-20): higher concentration of Ta_2C. See Table III.

Table III

Print No.	Current density, $\mu a/cm^2$	Time, sec	Formation voltage range	Remarks
1	625	50	to 10	Series A—low conc. of Ta_2C
2	625	75	10 to 20	
3	625	75	20 to 30	
4	625	70	30 to 40	
5	625	72	40 to 50	
6	625	80	70 to 80	
7	625	80	90 to 100	
8	625	80	100 to 110	
9	625	75	120 to 130	
10	—	60	50	Const. voltage
11	625	55	to 10	Series B—higher conc. of Ta_2C
12	625	55	10 to 20	
13	625	53	20 to 30	
14	625	55	30 to 40	
15	625	55	40 to 50	
16	625	60	70 to 80	
17	625	45	90 to 100	
18	625	50	100 to 110	
19	625	60	120 to 125	
20	—	60	20	Const. voltage

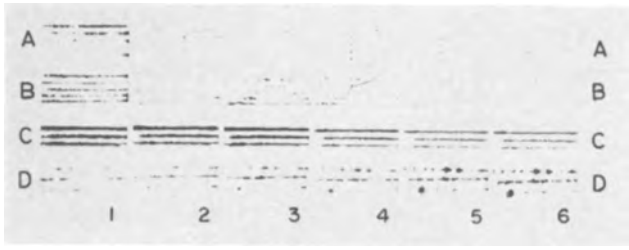

Fig. 4. Anodic prints of Ta sheet scratched with: a. Ta; b. Ni; c. C; d. Fe. See Table IV.

Table IV

Print No.	Current density, $\mu a/cm^2$	Time, sec	Formation voltage range	Remarks
1	125	30	to 2.6	a. Ta
2	625	60	20 to 30	b. Ni
3	625	65	40 to 50	c. C
4	625	70	70 to 80	d. Fe
5	625	65	110 to 120	
6	625	65	130 to 140	

val prints revealed higher e.c. compared with the following ones obtained during formation from 20 through 80v. Above 80v the e.c. started to increase and became extremely high above 120v. Constant voltage prints taken at fractions of the formation voltage after this activation had taken place showed different results for the two specimens with low and high carbide content. The specimen with the lower concentration still exhibited the rapid decrease in the e.c. with field observed previously with Fe and Ni alloys of Ta. The areas with high concentration of carbide were active regardless of the voltage applied. The resistance in these areas was rather low and apparently ohmic.

Surface contamination.—Electronic conductivity in scratches can be seen in Fig. 4 which gives prints taken of a specimen of chemically polished Ta sheet that was scratched with Ta, Ni, Fe, and C. The Ta scratches were taken as the basis for comparison. The first print, taken at low current density with a formation voltage still below 2v gives the initial distribution of the e.c. along the scratches. Subsequent prints were taken in 10v intervals at the higher current density of 625, $\mu a/cm^2$. Very high current density was required to overcome the initial range of high e.c. always observed with mechanically treated specimens. The Ta scratch gave only a few distinct sites of e.c., while the other scratches were highly conducting with C scratches being dominant. The e.c. of the C and Ni scratches decreased with increasing formation voltage while the e.c. in the Fe scratch area increased strongly. The Ta line, after being almost invisible in intermediate voltage ranges, became more uniform and more pronounced toward higher formation voltages.

Tantalum scratches on Ta sheet that was annealed for 8 hr at 2100°C gave very low nonuniform e.c. on the first 10v print, no e.c. between 10 and 120v, and very faint uniform e.c. above 120v. Less pure material showed more of the discontinuous e.c. along the scratches.

Thermal oxidation of tantalum.—Mechanical surface treatments may lead to local temperature increases and the formation of additional thermal oxide beyond that always present on Ta. By studying specimens of Ta foil which were heated in air we attempted to evaluate the effect of pre-existing thermal oxide in the e.c. of subsequently formed anodic oxide films.

The heating of tantalum in air leads to the formation of amorphous and crystalline oxides. Amorphous oxide is formed initially at temperatures below 350°C, longer times and higher temperatures favor the formation of crystalline oxide (11).

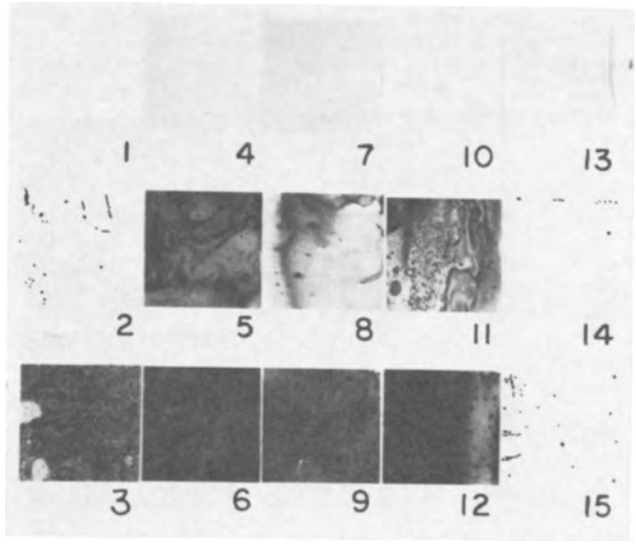

Fig. 5. Anodic prints of Ta sheet given various pretreatments and oxidized thermally in air. See Table V.

Table V

Print No.	Pretreatment	Thermal oxidation	Printing conditions
1	v.a	none	60 sec; 1 ma/cm^2
2	v.a.	500°C; 5 min	60 sec; 1 ma/cm^2
3	v.a./10 min KOH/10 min H_2O	500°C; 5 min	60 sec; 1 ma/cm^2
4	c.p. + HF/10 min H_2O	none	60 sec; 1 ma/cm^2
5	c.p. + HF/1 min H_2O	500°C; 5 min	60 sec; 1 ma/cm^2
6	c.p. + HF/10 min H_2O	500°C; 5 min	60 sec; 1 ma/cm^2
7	c.p. + HF/10 min HCl/10 min H_2O	none	60 sec; 1 ma/cm^2
8	c.p. + HF/10 min HCl/1 min H_2O	500°C; 5 min	60 sec; 1 ma/cm^2
9	c.p. + HF/10 min HCl/10 min H_2O	500°C; 5 min	60 sec; 1 ma/cm^2
10	c.p. + HF/10 min KOH/10 min H_2O	none	60 sec; 1 ma/cm^2
11	c.p. + HF/10 min KOH/1 min H_2O	500°C; 5 min	60 sec; 1 ma/cm^2
12	c.p. + HF/10 min KOH/10 min H_2O	500°C; 5 min	60 sec; 1 ma/cm^2
13	v.a./ox. to 100v in 0.1% H_3PO_4	none	60 sec; 1 ma/cm^2
14	v.a./ox. to 100v in 0.1% H_3PO_4	500°C; 5 min	60 sec; 1 ma/cm^2
15	c.p. + HF/ox. to 100v in 0.1% H_3PO_4	500°C; 5 min	60 sec; 1 ma/cm^2

Abbreviations: v.a. = vacuum annealed; c.p. + HF = chemical polish followed by a 10-sec dip in conc. HF; HCl = conc. HCl; KOH = 10*N* aqueous KOH solution.

The prints shown in Fig. 5 were obtained with specimens pretreated in various ways and heated to 500°C for 5 min in stationary air.

Annealed foil gave completely clear prints when unheated (print 5.1), but when heated, the prints frequently revealed a number of localized electronically conducting sites (print 5.2). Uniformly distributed electronic current, however, was not observed. With foil of highest purity we found no e.c. either with or without thermal oxidation.

When chemically polished foil was used, we obtained prints without e.c. if taken with the unheated foil (print 5.4). When the same foil was heated in air we obtained prints with little e.c. if the specimen was rinsed in water for a short time only (print 5.5) while rather high e.c. was observed after extended rinsing in cold or boiling water (print 5.6). When rinsed for short time only it was difficult to avoid drying marks which always became centers of high e.c. They account for the nonuniform pattern in print 5.5 Dipping in conc. HCl for 10 min after chemical polishing and a 10 sec HF dip led to clear prints without thermal oxidation (print 5.7), prints reflecting very little e.c. after short rinsing in water (print 5.8), and uniform e.c. after a 10 min rinse (print 5.9). Treatment of annealed

(print 5.3) or chemically polished (prints 5.10-5.12) foil in alkaline solutions produced an effect similar to treatment in HF whereas dipping in concentrated acids like HNO_3, H_2SO_4, H_3PO_4, etc., did not produce films with e.c. either with or without thermal oxidation.

Print 5.14 was obtained from a vacuum annealed specimen previously oxidized in phosphoric acid to 100v followed by a 5 min thermal treatment in air at 500°C. It shows a pattern of electronic conductivity which was not observed when an unheated specimen was tested (print 5.13). With chemically polished instead of annealed foil, considerably more localized e.c. was observed after heating (print 5.15).

The e.c. of crystalline anodic tantalum oxide was found to be too low for detection with our method when we took prints of various specimens which had been crystallized anodically for 1 hr at 90°C in 2% HNO_3 (12) and which showed a high density of crystalline areas. Some e.c. was found when scintillation associated with the formation of crystalline oxide had taken place.

Plastic deformation of tantalum sheet by bending.—Since plastic deformation is a consequence of all mechanical surface treatments, we had to consider its effect on the e.c. of oxide films formed on plastically deformed substrates.

Chemically polished sheet was bent up to 10 times at four different positions. One specimen was used for taking prints after bending, the other one after it was submitted to thermal oxidation in air at 500°C for 2 min. Figure 6 shows that along the bends a few localized marks indicating e.c. were found being both more numerous and intense after thermal oxidation. Vacuum annealed sheet showed few conducting sites, highly contaminated sheet showed more uniform e.c. along the bends.

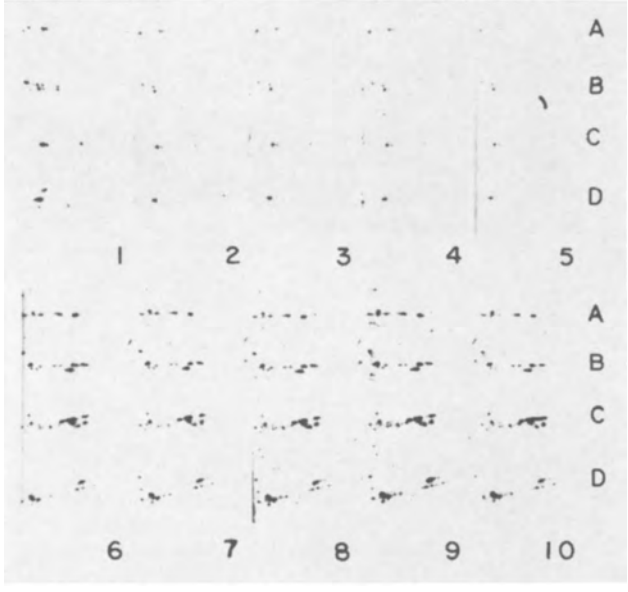

Fig. 6. Anodic prints of vacuum annealed Ta sheet deformed plastically by repeated bending at positions A-D. The second series shows prints of a specimen that was thermally oxidized in addition to bending. See Table VI.

Table VI

Print No.	Current density, $\mu a/cm^2$	Time, sec	Formation voltage range	Remarks
1	625	45	to 10	
2	625	60	10 to 20	
3	625	60	20 to 30	
4	625	60	30 to 40	
5	625	60	40 to 50	
6	625	40	to 10	
7	625	60	10 to 20	
8	625	60	20 to 30	
9	625	60	30 to 40	
10	625	60	40 to 50	

Surface topography—roughness.—The surface topography of mechanically treated surfaces, their roughness, was held responsible for the electronic conductivity of oxide films on supposedly clean surfaces. Two mechanisms were proposed to explain the e.c. (1, 2, 7): (*i*) The field at sharp points and ridges was thought to be higher than the average giving rise to field emission effects which eventually would lead to breakdown; and (*ii*) oxide formation at asperities would produce highly stressed films which would crack and expose the bare metal. Electronic conduction would be due to a local field increase or due to changes in the oxide film as a consequence of local heating following high local currents at bare spots. Oxygen bubbles were thought to play a role in stabilizing active pores and microfissures.

Since it is difficult to produce roughness by other than mechanical means, and since all such attempts are likely to introduce side effects, we could not study rough surfaces *per se*. However, we prepared specimens with sharp edges by tearing thin foil and by electrochemical etching. The foil was 0.0005 in. thick and had very jagged edges after etching. The radii of curvature of such edges were a few microns after etching. Prints taken from such specimens never showed any trace of electronic current along the edges up to the sparking potential of the printing electrolyte. Even when some of the jags tore off while changing the printing medium the next print would still show no blackening at those sites. Surfaces with a high degree of surface roughness could also be produced by sintering tantalum powder to tantalum foil. Prints taken from such specimens did not reveal any electronic conductivity which, by its distribution, could have been attributed to roughness. The particle size was less than 10μ; sintering time and temperature were such that no significant change of the particle shape could have taken place during sintering.

Electronic conductivity of blasted tantalum surfaces.—Abrasion can lead to contamination of the surface layers of a specimen in various ways: by the transfer of impurities from the abrasive to the substrate and the embedding of abrasive particles. Also, impurities present in the substrate can become exposed, for example, when the abrasive removes the softer material while leaving the harder precipitates on the surface.

The blasting of tantalum with tantalum, alumina, and dolomite powder was found to produce similar surface conditions as far as the e.c. of anodic oxide films was concerned. The degree of surface damage depended on the relative hardness of substrate and abrasive and the intensity and duration of blasting. Dolomite powder was chosen because of the ease with which it could be dissolved in acids. Particles of abrasive which adhered to the surface did not give any e.c. as long as the abrasive was of high purity and itself an insulator. Scratches produced with tantalum on the same specimens were used as a standard for comparisons since contamination by the abrasive was least likely to have occurred in this case. Figure 7 shows dynamic prints obtained with blasted specimens. Prints 7.1-7.3 taken at constant current reveal how a pattern of electronically conducting sites developed. Initial specks in print 7.1 became somewhat fainter in the following two prints with many more appearing in the center portion of the blasted area. A closer comparison shows the continued presence of most of the specks initially present. Higher current densities brought forth more specks in print 7.4, but print 7.5 was practically identical with print 7.3 except for its intensity. The following series of prints was taken at a higher current density in voltage intervals of 20v.

The e.c. decreased rapidly once the first few volts of formation had been achieved at a high current density and continued to decrease more slowly above 20v. The

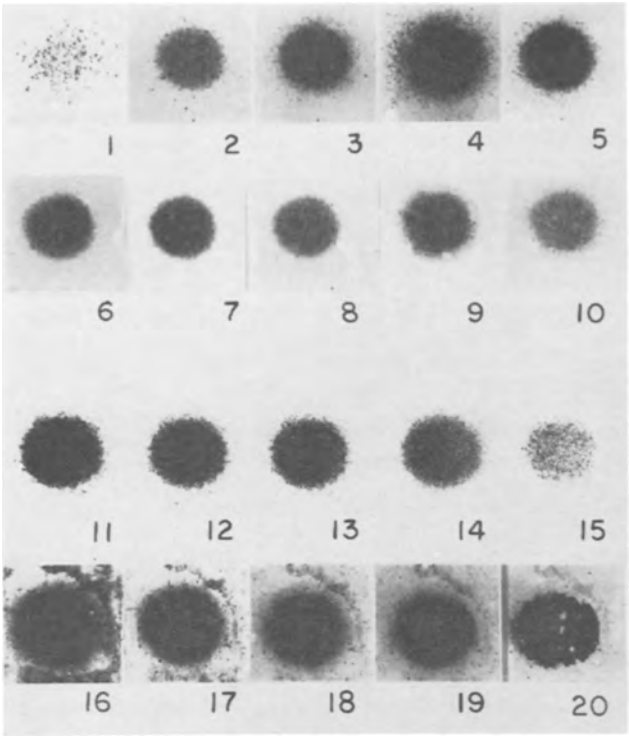

Fig. 7. Prints No. 1 through 10: Anodic prints of chemically polished Ta sheet blasted with dolomite powder. Specimen was cleaned with HCl after blasting. Diameter of blasted area 0.5 cm. Prints No. 11 through 20: Anodic prints of chemically polished Ta sheet blasted with dolomite powder and cleaned with HCl. The specimen was then oxidized thermally in air at 500°C for 2 min. See Table VII.

Table VII

Print No.	Current density, $\mu a/cm^2$	Time, sec	Formation voltage range	Remarks
1	12.5	120	to 1.3	Blasted with dolomite powder
2	12.5	60	to 1.35	
3	12.5	60	to 1.4	
4	125	30	to 2.5	
5	12.5	60	to 2.0	
6	625	60	to 20	
7	625	120	40 to 60	
8	625	115	80 to 100	
9	625	115	120 to 140	
10	625	115	140 to 160	
11	12.5	120	to 1.5	Blasted with dolomite powder followed by thermal oxidation
12	12.5	60	to 1.55	
13	12.5	60	to 1.55	
14	125	30	to 5.0	
15	12.5	60	to 4.1	
16	625	60	to 20	
17	625	130	40 to 60	
18	625	125	80 to 100	
19	625	125	124 to 140	
20	625	130	140 to 160	

spots were made up of a large number of tiny specks which remained the same over most of the range of anodic oxidation covered in the prints. Only within the first 10v had there been a pronounced change in the relative intensity of the specks. The specks persisted over a sufficiently large voltage range to exclude their being transients. Prints 7.5 and 7.10 may serve as an illustration of the decrease in the e.c. from the initial stages of film formation to its later stages. The total charge that had been passed in print 7.10 was 72 mcb/cm^2 compared to only 0.75 mcb/cm^2 in print 7.5 even though the electronic charge passed was several times larger in the latter print.

The second half of Fig. 7 shows a series of prints taken from a similarly pretreated specimen that was heated in air at 500°C for 2 min after the blasting. In this case, the e.c. started out very high in the first print and decreased rapidly in the following ones. This behavior was the opposite of what was found with the unheated specimen where the e.c. had shown an increase in a similar series of prints. The voltages reached in comparable prints of the unheated and heated samples were slightly higher in the case of the latter since a thermal oxide film was present. The following series of prints in 20v intervals revealed very strong e.c. in the interval to 20v. Apart from an intensive blackening of the blasted area a pattern was also found around it. The e.c. decreased slightly in the higher formation voltage intervals, but remained several times higher than with the unheated specimen. The blasted area itself was so intensely blackened that no details could be observed except when a short time print was taken (not shown) that revealed localized specks indicating discrete sources of e.c.

Additional information concerning the origin of the e.c. of blasted areas was obtained when the oxide formed on blasted specimens during printing was removed with HF before another series of prints was taken. Results are shown in Fig. 8. Removal of the oxide and printing were repeated three times. Thermal oxidation after oxide removal was applied in the last

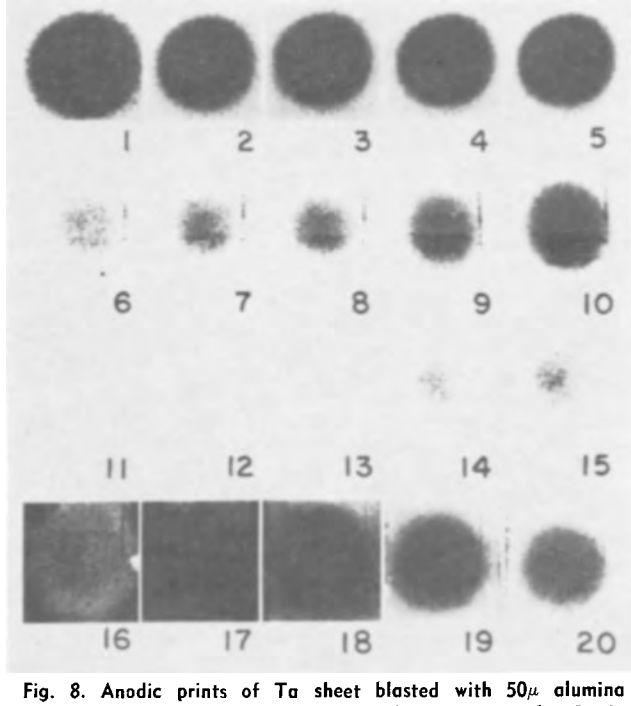

Fig. 8. Anodic prints of Ta sheet blasted with 50μ alumina powder. First row: as after blasting; second row: repeat, after 1-min dip in conc. HF; third row: repeat, after 1-min dip in conc. HF; fourth row: repeat, after 1-min dip in conc HF and thermal oxidation at 500°C in air for 2 min. See Table VIII.

Table VIII

Print No.	Current density, ma/cm^2	Time, sec	Formation voltage range	Remarks
1	1	50	to 10	Blasted with alumina powder
2	1	55	10 to 20	
3	1	55	20 to 30	
4	1	55	30 to 40	
5	1	55	40 to 50	
6	1	45	to 10	After No. 5—1-min dip in conc HF
7	1	50	10 to 20	
8	1	50	20 to 30	
9	1	50	30 to 40	
10	1	50	40 to 50	
11	1	40	to 10	After No. 10—1-min dip in conc HF
12	1	50	10 to 20	
13	1	50	20 to 30	
14	1	50	30 to 40	
15	1	50	40 to 50	
16	1	60	to 10	After No. 15—1-min dip in conc HF; thermal oxidation 2 min 500°C
17	1	60	10 to 20	
18	1	55	20 to 30	
19	1	55	30 to 40	
20	1	50	40 to 50	

series of prints (prints 8.16-8.20); the specimen had been blasted with alumina powder.

The first series of prints (prints 8.1-8.5), similar to parts of Fig. 7, again showed the high initial e.c. followed by a sharp decrease after the first formation interval and a very slight increase on further oxidation. After removal of the initial oxide film by dipping in concentrated HF a second series of prints (prints 8.6-8.10) showed an e.c. gradually increasing with an increase in the formation voltage. The pattern of the e.c., being at first highly nonuniform, became more and more uniform while the size of the print approached the size of the total blasted area.

The oxide was dissolved in conc. HF after oxidation to 50v and a third series of prints (prints 7.11-7.15) was taken. The intensity of the e.c., at a much reduced level compared to the last series, shows the same tendency to increase gradually with an increase in formation voltage. The oxide was again dissolved in conc. HF after formation to 50v. The specimen was then rinsed in triple-distilled water, dried in an air stream, and heated at 500°C for 5 min. Prints 7.16-7.20 were taken after this treatment. The blasted area initially showed lower e.c. than the surrounding area, but with increasing formation voltage the blasted area showed an increasing e.c., whereas the surroundings became less conducting.

Discussion

The effects of bulk contamination on the e.c. of anodic oxide films on Ta were demonstrated by taking anodic prints of Ta alloyed with Fe, Ni, and C. The effects of surface contamination were shown for Ta that was scratched with Ta, Ni, Fe, and C. With alloys of Ni and Fe the e.c. was either strong from the beginning with a tendency to increase further, as indicated by the first series of prints obtained with Fe, or it started out low and increased gradually with progressing film growth until it reached very high values as in the case of Ni and with Fe after HF treatment. The e.c. was affected by chemical treatments of the oxidized specimen in the case of the Ta-Ni alloy where aqua regia, for example, removed the cause for e.c., at least temporarily. The e.c. was not noticeably affected by chemical treatments of the oxide covered specimen in the case of Fe and C alloys as long as fluorides and hydrofluoric acid were absent. After prolonged HF treatment of the Ta-Fe alloy, which dissolved Fe rich portions of the alloy, oxides were formed on anodic oxidation exhibiting e.c. that was removed by conc. HCl.

It appears that in the case of Ta-Ni alloys a Ni rich oxide at the oxide-electrolyte interface was responsible for the e.c. The e.c. of the oxide film on the Fe-Ta alloy must either be due to an oxide film which in itself is highly doped with Fe, or a highly doped surface film that still shows the chemical reactivity of Ta_2O_5 rather than of any of the iron oxides. In any case, the e.c. was not affected in the same way it was in the case of the Ta-Ni alloy.

Without discussing in detail the possible mechanism of the anodic oxidation of tantalum alloys we shall briefly consider some aspects that may help to understand the characteristics of the e.c. of alloy oxides. Assuming a thin initial oxide layer consisting mainly of tantalum oxide, we are likely to have a competition between tantalum and foreign ions in regard to their transport through the already existing oxide film under high field conditions. In case the foreign ions migrate at a higher rate than the tantalum ions they will accumulate at the oxide-electrolyte interface unless they dissolve in the electrolyte. Depending on the *p*H of the solution and the particular anions present, a layer will be formed on the tantalum oxide, this layer being either insulating or electronically conducting, or porous and permeable to the electrolyte. In case the migration rate of the foreign ions is less than that of Ta ions, or if the transport number for the cations is less than one, intermediate situations may be found where oxide layers rich in foreign ions are formed inside the oxide film or at the metal-oxide interface.

The valency of the ions as they arrive at the oxide/electrolyte interface will depend on the nature of the ions and their environment. In the case of Fe or Ni the valency could be two, three, or even higher. These high valency ions may then react with the electrolyte and be reduced by any redox system with a sufficiently negative redox potential. It is conceivable, therefore, that the redox indicator system that we used (iodide/iodine-starch) reacted with these ions, leading to a blackening of our prints which was not due to electronic conductivity of the film. However, the result of this reaction would be the same as with truly electronic charge transport.

In order to determine whether oxidation of iodide by higher valency ions could have contributed to our results to any appreciable degree, we used the printing technique with indicators for Fe^{2+}, Fe^{3+}, and Ni^{2+} ions, respectively. The sensitivity of these color reactions was about as high as for the iodine-starch reaction. The test indicators were $K_3Fe(CN)_6$ for Fe^{2+}, KSCN for Fe^{3+}, and dimethyl glyoxim for Ni^{2+}. In no case did we observe more than a trace of any of the low valency ions and no trace at all of the higher valency ions. These tests were conducted under conditions where very strong coloration of the iodide-starch prints would have been observed.

An additional test showed beyond doubt that no high valency ions were formed in a concentration that could have affected our results. Prints were taken as usual except that the printing electrolyte did not contain any potassium iodide. The tantalum alloy to be tested was anodized through at least 10v (it would have given a very strong blackening of the prints with iodide). Since no iodide was present in this test, the prints were absolutely clear. If any higher valency ions had been formed, they should have reacted immediately with a drop of potassium iodide solution brought onto this print. Neither with Ta-Fe nor with Ta-Ni alloys did we observe any positive reaction. This showed that the blackening of our prints was indeed a result of the electronic conductivity of the anodic oxide film. It also showed that practically no corrosion of the Fe and Ni was taking place during printing since even low valency ions could only be found in trace concentrations at the most.

The observation that with aqua regia we could remove something from the surface of oxides on Ta-Ni alloys which caused the prints to become black showed that a Ni containing compound was present at the oxide-electrolyte interface; however, this compound did not cause blackening of the printing medium without the passage of current. The over-all mechanism of electron transfer is not known, but it does not seem to go via a consecutive homogeneous redox reaction, at least with Fe and Ni alloys of Ta.

It is clear that further studies of the structure and composition of the mixed oxide films and their kinetics of growth are required before final conclusion can be drawn.

With carbon the behavior was very different. The e.c. started out high, decreased subsequently, and increased again on approaching voltages around 100v. Above 120v the anodic oxide film was destroyed by a process which led to excessive e.c. A behavior of this kind can be understood qualitatively by assuming that the original substrate surface contained both tantalum and carbon (in the form of tantalum carbide) and that the initially formed oxide film was electronically conducting due to the carbon. As more film was built up, the e.c. decreased since the new film consisted mainly if tantalum oxide, carbon having been left behind. This eventually led to the formation of a layer of carbon underneath the insulating oxide film, at the

irregularities of which the dielectric would break down at high fields.

Areas on the Ta sheet where carbon had reacted incompletely with the substrate showed strong activity which in some cases did not exhibit the same exponential current-field characteristics that we observed with most other defects (13). The resistance of these areas appeared to be ohmic with the current being limited by diffusion in the electrolyte, or interrupted by gas evolution. A similar situation arose when tantalum was scratched and contaminated with carbon. Direct contact between sufficiently large areas of metal and carbon was believed to have prevented the growth of tantalum oxide thus maintaining active areas on the substrate. But in most cases of surface contamination the anodic oxide appeared to have grown underneath, above, and around the impurities thereby establishing the characteristics typical for most defects in anodic oxide films.

The results obtained with Ta specimens that were pretreated in various ways and then oxidized thermally (500°C in air, for 5 min) are summarized below. Vacuum annealed Ta foil was used as the standard for comparisons. As was shown in Fig. 5, no e.c. was observed whenever prints were taken from foil that was annealed in vacuum or polished chemically, as long as the specimens were not oxidized thermally. Occasionally, chemically polished material would give rise to nonuniform e.c. which could be traced to gross impurities.

After thermal oxidation, vacuum annealed foil tended to show some nonuniform e.c. with a distribution typical for contamination. No uniform e.c. was found either after short oxidation at 500°C or after oxidation up to several hours at 2-400°C. Thermal oxide, either amorphous or crystalline, does not give rise to e.c. of the subsequently formed anodic oxide within the sensitivity of the printing method. Thermal oxidation brings out impurities, however, which would not have been apparent before. It can be used as a means to amplify their effect. Thermal oxidation in connection with anodic printing is an effective means to test the purity of tantalum foil.

Chemical treatment of vacuum annealed foil prior to thermal oxidation led to more or less uniform e.c. of the anodic oxide film if alkaline reagents were used. Mineral acids had only a minor effect. The effect of concentrated HF depended strongly on the duration of subsequent rinsing in water: very little e.c. was observed if the specimen was blown dry after dipping in Hf, without rinsing in water, while high e.c. was found after several minutes of rinsing in cold or hot triple-distilled water. Further rinsing did not change the intensity of the e.c. once it was established.

Chemically polished foil, that was given the usual 10-min rinse in conc. HF, behaved similarly to vacuum annealed foil with HF treatment. Besides more or less uniform effects of the chemical treatments, nonuniform e.c., probably due to impurities, was more frequently observed with chemically polished material.

Uniformity of the e.c. could not be achieved when chemical treatments were used. It was difficult to avoid drying marks, especially after very short rinsing times, even though triple-distilled water was used. Drying marks, fingerprints, etc., always led to e.c. after thermal oxidation. But even if the preparation and handling of the specimens was done with great circumspection we obtained a considerable degree of nonuniformity. Extended rinsing in water after chemical treatments usually gave the most uniformly distributed e.c. The conditions characteristic of vacuum annealed foil were most closely approached by washing chemically polished foil in conc. HCl and short rinsing in water. Practically no uniform e.c. was observed except for the almost unavoidable drying marks.

These observations are tentatively explained in the following way. Tantalum oxides formed by thermal oxidation are insulating and do not cause subsequently formed anodic oxide films to become electronically conducting. If, however, a tantalum hydroxide film is present initially, thermal oxide may be formed which exhibits a higher e.c. due to the hydroxyl ions replacing oxygen ions, transforming the tantalum oxide into a highly conductive n-type semiconductor. A similar reaction would be expected to take place with fluoride; however, it seems likely that tantalum fluorides, being rather volatile, may be removed during the thermal oxidation. This would explain why HF treated specimens showed e.c. only after washing in water for several minutes or after short treatment in conc. KOH.

It is not clear why thermal oxidation should be required to produce these effects. Apparently, the hydroxyl ions, if responsible for the electronic conductivity, are not incorporated in sufficiently high concentration as would be the case if a thin pre-existing surface film with high anion concentration was being oxidized thermally.

If specimens anodized in dilute phosphoric acid were heated in air after the same chemical pretreatments, similar effects were observed. By comparing vacuum annealed and chemically polished specimens, more localized defects were observed in the latter case. This again suggested the printing method combined with thermal oxidation as a means to evaluate the effectiveness of purification techniques and the quality of Ta foil.

Plastic deformation (bending) of Ta sheet did not produce e.c. attributable to this treatment. Usually a few localized centers with high e.c. were found, but they were probably caused by impurities which became exposed due to slip within grains and the displacement of neighboring grains relative to one another. Thermal oxidation after bending produced increased e.c. which again was localized in a limited number of sites. It seems most likely that impurities became exposed at the surface by the combined action of bending and thermal oxidation. Since the sheet was bent back and forth ten or more times, plastic deformation was so extensive that a uniform effect along the bends should have been seen if the strain associated with plastic deformation had an effect on the e.c. at all. This result is interesting in that it reveals a strong secondary effect of a particular treatment that was induced by the primary effect of this treatment; the primary effect was inoperative in producing e.c. directly.

The experiments with foil having torn and highly jagged edges produced by electrochemical etching and of foil with powder sintered onto it did not give any indication of e.c. due to surface geometry. Likewise, the reformation of cracked anodic oxide films at high local current densities gave no indication of any electronic current due to excessively high local fields.

These tests cannot be considered a sufficient proof that the geometry of the substrate has no effect at all on the e.c., but they suggest that it is so.

In discussions of the e.c. of "rough" surfaces in the literature (1, 2, 6, 7) it has been maintained, after other possible causes were thought to have been excluded, that the geometry alone could be responsible for electronically conducting sites on the surface. Several mechanisms by which this could happen were suggested. They were all based on the assumption that for one reason or another the field strength was increased locally with the consequence of electronic current due to field emission. This current could be the precursor of local breakdown which in turn might lead to local heating, destruction of the dielectric, and crystallization.

These mechanisms require that an increase in the field strength lead to an exponential increase in the electronic conductivity. While the field strengths encountered in these thin film dielectrics under the test conditions are such that field emission may occur,

we must take into account the ionic conductivity as a stabilizing factor for the field strength. If the e.c. was due to high fields only, then the electronic current should have been transitional since the field would have caused the ionic current to rise as well and this would have led to film repair and a corresponding drop in the local field towards average values. Therefore, if the e.c. was caused by cracking, as suggested by Young (1, 2), then we should see changing patterns on the prints. According to Young, the cracks should also become more numerous with increasing film thickness. Neither phenomenon was observed by us. On the contrary, the conductive sites were found to be active over rather large formation intervals starting at low voltages with their intensity staying constant or even decreasing with increasing film thickness. No increase in the number of specks or a radical change in pattern were observed with mechanically treated specimens towards higher formation voltages once the initial maximum in the e.c. in the first 10v interval was overcome.

Sudden, high, local currents, either ionic or electronic, could have damaged the oxide film through local heating either by causing the film to crystallize, or at least to nucleate crystalline oxide. Again, these changes would most likely have resulted in ephemeral bursts of electronic current since at least partial healing of the damage would have followed any catastrophic event. In addition, it had been found that the e.c. of thermal and anodic crystalline oxides was below the sensitivity of the printing method. In no case did we find electronically conducting defects with an initial burst and a trail of disappearing electronic current which we would expect in all of these cases.

Vermilyea (7) found roughness to be one of the causes for flaws which in his model took the form of a thin oxide film separated from the substrate by an air gap. No direct reference was made to their e.c.; it was even thought that they were passive electrically contributing to the capacity only. However, in an earlier paper (6) Vermilyea had found gassing to take place when rough surfaces were anodized. The question arose whether the flaws were responsible for the e.c. which should have been distributed rather uniformly on a macroscale since the number of flaws had been found to be very high in scratches and nowhere lower than $10^4/cm^2$ on the best smooth specimens.

Vermilyea's flaws seemed to have appeared under a multitude of conditions. Our studies showed the most distinct flaws to be caused by thermal crystalline oxide and tantalum carbide precipitates. The e.c. of individual flaws was below the sensitivity of our method, but even very high concentrations of flaws caused by thermal oxide did not give an imprint. Higher carbide concentrations on the other hand gave prints as the ones shown in Fig. 3. Mechanically treated specimens developed a varying number of flaws depending not only on the kind of abrasive used, but even more on the substrate material and its and the abrasive's purity.

The pattern of e.c. which we observed within blasted areas and along scratches indicated that the sources of e.c. could not be distributed uniformly on a macroscopic scale as would have been expected if the flaws had been responsible for the observed e.c. At least the predominant sources of electronic current were few compared with the number of flaws or even the number of blasting marks. Also, we found very few electronically conducting sites along tantalum scratches on tantalum. This led us to conclude that the e.c. in mechanically treated areas of tantalum could not be related to the flaws that were observed by Vermilyea, and, in some cases, by us.

If we consider tantalum scratches on carefully purified tantalum as the closest approach to a rough surface, eliminating at least contamination, we have to explain the observation of e.c. in the initial print, the absence of e.c. in the range from 10 through 120v and the appearance of uniform but very low e.c. above 120v. In case the specimen was thermally oxidized after scratching the same general picture was observed with the addition of suddenly appearing higher e.c. above 140v. The initial e.c. was nonuniformly distributed along the scratch and the number of conducting sites correlated well with the number of "slivers" observed along the scratch. In this case, geometry could have played a role as a cause for e.c. However, the e.c. was observed only in the initial print and was totally absent in the following ones up to approximately 120v.

The uniform e.c. observed above this voltage is difficult to explain: The geometry would cause nonuniform e.c. while thermal oxide has been shown not to cause e.c. under these conditions. Whether strain could account for it is uncertain. The sudden appearance of e.c. above 140v in scratches that were thermally oxidized as well appear to have been caused by spontaneous crystallization accompanied by a disruption of the amorphous oxide film as observed when scintillation occurred. In the case of the thermally oxidized specimen a connection of the faint uniform e.c. with flaws is likely since thermal oxidation of plastically deformed tantalum led to a very high density of flaws and anodic crystals. However, in the case of the specimen which was scratched only, no flaws were observed which could have accounted for the faint uniform e.c.

The interpretation of the prints from blasted specimens will be based on the results obtained for the individual factors contributing to the effects of mechanical surface treatments. Abrasive particles, if by themselves insulators, did not give rise to e.c. when sprinkled on tantalum foil. Conducting powder, such as carbon, by comparison yielded excessively high e.c. It is very unlikely, therefore, that abrasive particles even if partially or completely embedded in the substrate were responsible for the effects found with blasted surfaces. By comparing series two, three, and four of Fig. 8, we found that a considerable number of individual marks in the second series could also be found in the fourth (after thermal oxidation), whereas practically no marks were found in the third series. Particles of abrasive cannot account for this behavior since they should produce marks in all three series: an embedded particle either is there, then it gives rise to e.c., or it is removed and no further treatment like thermal oxidation will bring it back.

Roughness was shown to have no or only a temporary effect: slivers along Ta scratches were found to be centers of initial e.c. which decreased rapidly on film formation. The initially very high e.c. observed in all blasting experiments (without thermal oxidation) may in part be explained by this. However, other factors, especially contamination, may have contributed substantially as well.

After the first oxide layer was removed the e.c. no longer showed the conductivity maximum in the initial printing interval. This could be explained by a decrease in the initial roughness, but also by the removal of surface impurities. The prints of the blasted areas after the removal of the initial oxide film (second series, Fig. 8) increased in size with increasing formation voltage. If roughness were responsible for the e.c. it should have been uniform over the whole area. Stress concentrations may be eliminated as a source of e.c. by virtue of the bending test results.

The strongest point in favor of impurities as the cause for the e.c. observed with blasted surfaces is the effect thermal oxidation has after repeated anodic oxidation and oxide removal. The intensity of the e.c. had become so low that it could no longer be detected with the printing technique. Thermal oxidation led to renewed strong e.c. in the blasted area, with some localized marks which had been present in previous series before deactivation. Thermal oxidation would

have removed the extreme roughness since sharp projections especially on plastically deformed surfaces oxidize more rapidly. The last series in Fig. 8 has to be seen in comparison with Fig. 5, since HF pretreatment usually led to e.c. in combination with thermal oxidation. It accounts for the e.c. surrounding the blasted area which for itself shows only considerably lower e.c., probably because the blasted area was oxidized thermally more readily than the rest. The HF effect decreased rapidly in successive prints in favor of a more pronounced effect in the blasted area.

Comparison of the results obtained with blasted surfaces and of surface and bulk contamination lead to the conclusion that the e.c. after blasting showed the characteristics of a surface scratched with contaminating material, i.e., surface contamination. The following series after surface cleaning showed the characteristics typical for bulk contamination.

Other factors discussed in this paper may contribute to the e.c. to some degree; however, their over-all contribution appears to be masked by the effect of impurities in the majority of cases.

The overwhelming contribution to the e.c. of mechanically treated areas came from a limited number of rather active sites which remained active over large formation voltage intervals. No conclusions can be drawn at this point about the structure of the electronically active sites and the conduction mechanism.

Quantitative measurements of the intensity of blackening of the prints by densitometric methods have been used to determine the field dependence of the electronic current in electronically conducting areas of tantalum oxide films. They will be the subject of a future publication.

Conclusions

1. The redox printing technique was used to study the electronic conductivity of anodic oxide films while they were being formed (dynamic behavior) and after formation under other suitable conditions.

2. The study of alloys of tantalum with nickel, iron, and carbon (bulk contamination) revealed characteristic differences in the dynamic behavior of the electronic conductivity during the formation of the oxide film. It was shown that for specific impurities the e.c. as reflected in the prints varied characteristically with increasing formation voltage.

3. Surface contamination produced by scratching with nickel, iron, and carbon was studied by comparing the e.c. of these scratches with scratches made with tantalum alone. With increasing formation voltage, a decrease in the intensity of the e.c. was observed with Ni and C compared with an increase in the case of bulk contamination.

4. Thermal oxidation led to an amplification of the effects of impurities. No e.c. was found to be associated with thermally or anodically formed crystalline oxide in the absence of impurities.

5. Plastic deformation (bending of sheet) led to e.c. which was irregularly distributed along the bends indicating that no direct correlation existed between the plastic deformation of tantalum and the e.c. The impurity content of the material was an important variable. The effect of bending was more pronounced the higher the impurity content. Thermal oxidation after bending led to an increased e.c., rather than to a greater uniformity of the e.c. along the bends.

6. Roughness as produced by extreme electrochemical etching, or by tearing of thin foil, or by sintering of powder onto foil gave no indication of e.c. due to these conditions.

7. The e.c. of mechanically treated surfaces was found to be due mainly to impurities, the contributions from other factors being not detectable. The dynamic behavior of the e.c. of blasted surfaces was similar to that of surfaces scratched with contaminating materials. After surface cleaning, the e.c. was similar to that of alloyed tantalum.

Acknowledgments

The author wishes to thank Mr. L. Wingood for his assistance in the experimental part of this work and Dr. P. Bro for his comments on the paper.

Manuscript received Nov. 22, 1965. This paper was presented at the San Francisco Meeting, May 9-13, 1965.

Any discussion of this paper will appear in a Discussion Section to be published in the December 1966 JOURNAL.

REFERENCES

1. L. Young, *Acta Met.*, **5**, 711 (1957).
2. L. Young, *Trans. Faraday Soc.*, **55**, 842 (1958).
3. D. A. Vermilyea, *J. Appl. Phys.*, **27**, 863 (1956).
4. A. W. Smith, *Can. J. Phys.*, **35**, 1151 (1957).
5. A. W. Smith, *ibid.*, **37**, 591 (1959).
6. D. A. Vermilyea, *Acta Met.*, **2**, 476 (1954).
7. D. A. Vermilyea, *This Journal*, **110**, 250 (1963).
8. G. P. Klein, *ibid.*, **113**, 345 (1966).
9. C. C. Houtz and S. Karlik, Proc. 1959 Electronics Components Conference.
10. C. J. B. Fincham and G. L. Martin, *This Journal*, **107**, 658 (1960).
11. D. A. Vermilyea, *Acta Met.*, **6**, 166 (1958).
12. D. A. Vermilyea, *This Journal*, **102**, 207 (1955).
13. G. P. Klein, IEEE Transactions PMP-1, (1965).

Phase Changes in Thin Reactively Sputtered Alumina Films

R. G. Frieser[1]

Bell Telephone Laboratories, Incorporated, Murray Hill, New Jersey

ABSTRACT

A study has been made of the preparation and properties of aluminum oxide films prepared by reactive sputtering. Deposition temperature, rate, oxygen pressure, etching characteristics in HF, and phase changes of the deposited films as a function of heat-treatment were investigated. Two phases of deposited alumina could be prepared; either an amorphous, HF soluble, or a polycrystalline form of γ-alumina, which was considerably more HF resistant. On the basis of the observed changes in HF solubility, refractive indices, and phase changes, a tentative model is proposed which could be pertinent to catalytic behavior of alumina powders.

While studying the properties of reactively sputtered oxides, thin (< 1000Å) aluminum oxide films were prepared which exhibited anomalous solubility behavior in HF. This paper describes the preparation and properties of these films and a tentative interpretation of the observed time-temperature dependence of the HF solubility of these films and a corresponding increase in their refractive index. The proposed model is based on the known phase transformations of alumina.

[1] Present address: Sprague Electric Company, North Adams, Massachusetts.

Experimental Procedures and Results

The deposition of the films was carried out in an oil-free vacuum system in order to reduce contamination from pump oil. To reduce contamination further, particularly during loading of the apparatus, the entire vacuum system was enclosed by a Whitfield-type hood. By recirculating and filtering the air in the enclosure, particulate matter of a size larger than 0.3μ was reduced to two particles in 3½ hr.

Using a combination of sorb- and ion-pumps, the pressure in the system was reduced to about 10^{-6} Torr prior to sputtering. During the deposition the system was operated as a dynamic system, keeping a constant pressure (1 to 5 x 10^{-4} Torr) in the sputtering chamber. This was accomplished by permitting a certain amount of oxygen or of an oxygen-argon mixture to enter a sputtering chamber through a controlled leak-valve while the sorb-pump continuously removed approximately the same amount of gas. The sputtering gases were used directly from tanks without further purification. The electrodes were 5 cm in diameter; their separation during the experiment was either 2.5 or 5.0 cm. The anode, which held the materials to be coated, was above the cathode which held a disk of pure aluminum (99.9999%, 5 cm diameter x 0.3 cm thick). Both electrodes were electrically shielded to prevent sputtering in undesirable directions. Electrochemically polished silicon disks were employed as substrates with a few exceptions, when mechanically polished platinum disks were employed. All disks were chemically cleaned prior to deposition, and transported in a dust free container to the sputtering chamber.

The deposited film thickness in the range of 500-7000Å was observed to be a linear function of time (Fig. 1). The deposition rate of the reactively sputtered alumina was found to vary directly with the sputtering voltage (1-2 kv), the total sputtering gas pressure (1 to 5 x 10^{-4} Torr), the current density (0.25-3.5 ma/cm^2), and inversely as the electrode separation. The deposition, however, was found to decrease as the oxygen partial pressure increased in an oxygen-argon mixture of the sputtering gas. The substrate temperature, as a result of the ion and electron bombardment of the substrates, increased as the deposition rate increased since the anode was not cooled. A range of 100°-600°C was observed.

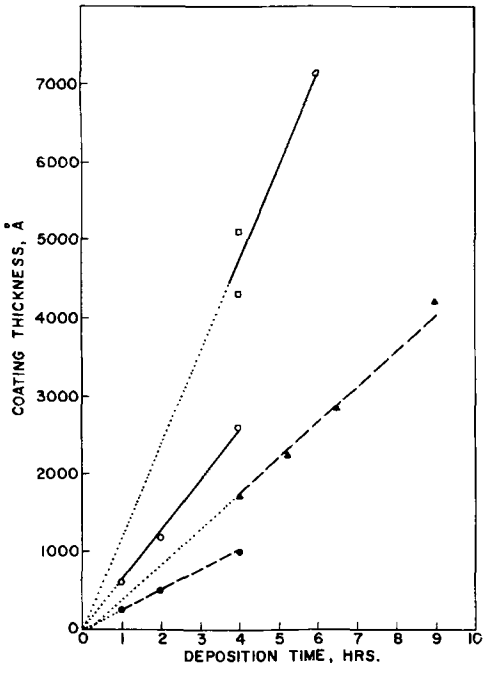

Fig. 1. Film thickness of reactively sputtered alumina as a function of deposition time at oxygen pressures (in μ, where 1 μ = 1 milliTorr), sputtering voltages (in kv) and electrode separations (in cm). Electrode separation: ———, 2.5 cm; - - - -, 5.0 cm; . . . . ., extrapolation. ●, 20μ, 1.1 kv; ▲, 50μ, 1.5 kv; ○, 20μ, 1.1 kv; □, 50μ, 20 kv.

Depending on the experimental conditions, two types of alumina films could be deposited. A polycrystalline γ-alumina film, which was difficultly soluble in HF, resulted under conditions favoring high deposition rates and substrate temperatures. At low deposition rates and substrate temperatures, an amorphous, HF-soluble film was deposited.

A coating was considered soluble in HF or ammonium bifluoride solution if, when immersed, a continuous change in the interference colors was observed. Films which showed an induction period (no change of interference colors) when immersed in HF for 1 min or longer were considered difficultly soluble. No color changes were noted but instead, after the induction period, localized dissolution of the film occurred, which spread with time over the entire surface. Under such conditions insoluble flakes of oxide could be observed to remain in the acid solution. The conditions which produced the transition from the soluble to the difficultly soluble form of reactively sputtered alumina are not well defined.

Soluble alumina films were obtained when the deposition rate was below 400 Å/hr, whereas difficultly soluble films were obtained at rates above 600 Å/hr. In the range between 400 and 600 Å/hr the solubility of the film decreased progressively as deposition time and thickness increased. Since no provision for cooling the anode existed, the higher deposition rates resulted in higher temperature. The same solubility effects could be obtained by heating the soluble films in vacuum, nitrogen, or nitrogen-oxygen ambients (no weight changes were noted), or by bombardment with an intermittent electron beam (90 kv).

Furthermore, it was noted that the loss of solubility of the films appeared to start at the free film surface and proceeded into the bulk of the film as a function of time and/or temperature on heating. The following experiment is a typical example demonstrating the existence of such a difficultly soluble skin while the bulk of the film below the skin exhibited a solubility characteristic similar to that of the original films.

A 4550Å thick alumina film (deposition rate 570 Å/hr, deposition time 8 hr) was etched in a modified ammonium bifluoride solution. This etch contained 12% concentrated H_2SO_4 and was sufficiently slow to permit thickness measurements of the films every 10 sec. Film thickness measurements were made by comparing changes in the interference colors with interference colors of prepared standards. An etch rate of 840 Å/min was estimated for the first 750Å on top of the film. The remainder of the coating (3800Å) then dissolved in 20 sec; this corresponded to an etch rate of about 11,000 Å/min. This observation suggests that a thin surface layer is responsible for the decrease of the solubility of the film and further that this results from low heat treatment. At what time/temperature conditions a soluble alumina film can be completely converted was not ascertained.

The densities of the films were determined from weight-area-thickness measurements. These were found to be 1.8 ± 0.2 g/cm^3 for either type of film. This is about ½ of the value reported in the literature for bulk γ-alumina which ranges from 3.42-3.67 (g/cm^3).

The observed refractive indices of the films varied from 1.51 ± 0.03 for the soluble to 1.62 ± 0.03 for the difficultly soluble alumina, with γ-alumina being reported as 1.76 (2). Refractive indices were measured by the VAMFO techniques (Variable Angle Monochromatic Fringe Observation) (3).

Physical homogeneity of the alumina films was examined by chlorine etching. All films were etched in ammonium bifluoride solution to remove about 500Å

from the soluble films prior to exposure to hot chlorine at 800°C for 30 min. Etch pits in the silicon substrate were then observed under a microscope. Examination of the soluble films revealed many very small pits ($> 50/mm^2$). A heat treatment of the coating, such as 4 hr at 260°C, prior to chlorine etching reduced the number of pits to 3 to $4/mm^2$. These observations support the contention that a structural rearrangement of the deposited oxide apparently occurs as a result of heat treatment. Films deposited on silicon substrates at rates above 600 Å/hr showed few (1 to $2/mm^2$) etch pits if the film was 400Å thick.

The dielectric strength of soluble and heat treated (3 hr at 100°C) alumina films on silicon substrates was examined using 25 mil gold evaporated contacts on 3400Å thick films and a voltage ramp of 5 v/min. The dielectric strengths of the films increased by a factor of 2 on heating (4 to 8 x 10^5 v/cm).

Differential thermal analysis of several representative alumina films showed only one phase transformation at about 375°C in air, in the range from 25° to 1200°C (heating rate 1°C/min). This change was irreversible and exothermic. Electron diffraction studies have shown that (*i*) the soluble alumina was amorphous, and (*ii*) that the films became progressively more crystalline on heating and that this crystalline phase was a $\gamma(\eta, \theta, \kappa)$-alumina. Formation of the γ-alumina phase was clearly a temperature-time dependent phenomenon. From line broadening it was inferred that the films were composed of crystallites, the diameter of which grew on heating from 30 to 50Å.

Prolonged (164 hr) heating of an alumina film at either 1000° or 1150°C in nitrogen did not convert the γ-alumina form to the α-form although according to the literature γ-alumina is not stable above 1100°C (4). On platinum substrates the γ-phase persisted under such drastic conditions, while on silicon substrates the films again became amorphous. This phase might be attributed to the diffusion of silicon in the γ-alumina and the formation of an amorphous aluminasilicate.

The consistently low density observed for the reactively sputtered films as compared to the literature value of alumina (1), the etching experiments, the physical inhomogeneity (revealed pinholes), and the measured crystallite size support the suggestion that the structure of the reactively sputtered alumina films is an aggregate of particles, and therefore porous.

Discussion

Studies of the refractive indices in aluminum oxide systems have shown that aluminum can exist in both 4- and 6-fold coordination in the same compound (5), and that the refractive index increases with the coordination number of aluminum (5), (from 1.5 to 1.6). Since the range of refractive indices observed in this study are the same as those cited in the literature, the observed increase in the refractive index on heat treatment of the film could be interpreted as a change from 4- to 6-fold coordination of the aluminum atom.

An acid-soluble amorphous form is mentioned by Durrant and Durrant (6). In the present work, reactively sputtered alumina can be deposited as an amorphous, HF soluble film. Such films on heating undergo crystallization resulting in γ-alumina. It should be pointed out that formation of γ-alumina by reactive sputtering does not proceed via the dehydration of gibbsite or aluminum hydroxide (7), which is the usual procedure reported in the literature. The strong time-temperature dependence of the phase transformation and the fact that no weight changes were observed on heating even in nitrogen-oxygen mixtures argues that a reconstructive transformation is taking place (8). This could be accompanied by some aluminum atoms changing their coordination number from 4 to 6 as they move from a tetrahedral to an octahedral site. The reason that the initial increase in density associated with a reconstructive transformation was not observed can be due to the porous nature of the films, since the observed density was that of a film and not that of the individual crystallites. The observed decrease in the pinhole density on heating may indicate that in the amorphous phase very small crystallites could be present, which on heating coalesce with the bigger particles. Such a process would close many of the channels, but would still leave a spongy coating having a low density.

The apparent change in observed solubility of the films as a function of the depth in the film could be explained on the basis of the low solubility of anhydrous γ-alumina forming a film on top of a layer of readily soluble amorphous alumina. This explanation would not be applicable to the reported decrease in the acid solubility of well crystallized and anhydrous γ-alumina which did not have any amorphous component. However, a mechanism proposed here could fit the data in this work as well as some data published on the study of catalysis and hydration on γ-alumina. For instance Peri (9) studying γ-alumina surfaces came to the conclusion that for anhydrous γ-alumina "some other type of strain-relieving mechanism (than hydration) apparently becomes operative on the surface of dry alumina above 500-600°C." Peri does not offer any suggestions concerning this mechanism. Solubility studies of γ-alumina powders in concentrated HCl have shown that the solubility decreases markedly as a result of prior heat exposure in the range from 600° to 1500°C (10). Similar behavior was noted for the solubility in HF of reactively sputtered alumina in this work. The observation of the induction period for the solvent attack on reactively sputtered alumina films is in accord with catalytic studies on γ-alumina powders (11-13). Here again the loss of catalytic action and the length of the induction period (hydration of the surface) was found to be a function of prior heat treatment. Recalling that the solubility decreased as the refractive index increased, it is tempting to postulate that a change in the coordination number of the aluminum atoms in the surface is responsible.

α-alumina has a hexagonal closest packed structure with all aluminum atoms located on octahedral sites. This form of alumina is known to be quite insoluble in mineral acids, and catalytically inert. γ-alumina, however, has a defect spinel structure, thus some of the aluminum atoms are located in tetrahedral sites. Aluminum atoms sitting on a tetrahedral site in a crystal would have sp^3 hybrid bonding (6). For those aluminum atoms which are on the surface in γ-alumina and would be in tetrahedral sites only two bonds remain in a rigid position. These would point into the body of the crystal. The other two bonds pointing up from the surface would not be "dangling bonds" in the usual sense of the term. With oxygen and air as ambient these bonds would most likely have hydroxyl ions attached to them. However, these would, on the surface, be mobile, and thus, it does not seem unreasonable to treat these two bonds as having somewhat the characteristic of "dangling bonds." If this can be assumed the following argument could be made. Haneman (11) has argued that on GaAs the "dangling bonds" on the cleaved surface revert to a less-hybridized form. In our case this would mean that the sp^3 character of the hybrid bonds would change to something more closely resembling an sp hybrid bond which is linear. The two oxygen atoms, bonded to the aluminum atom, would then experience a force pushing them out and away from the aluminum atoms. But they are hindered by the other oxygen atoms in the surface from moving too far. This would strain the surface. This strain could be however relieved, with little energy requirements, by the aluminum atom "flipping" over into the surface, since below each tetrahedral site is an empty octahedral site. Such a surface with all aluminum atoms in 6-fold coordina-

tion would be virtually an α-alumina surface. This film would still give an electron diffraction pattern of a γ-alumina. Because of the increasing coordination number of the aluminum atom, a hexagonal closest packed structure would result as in α-alumina, which in turn reduces the polarizability of the oxygen atoms. Such a surface could be expected to be more inert to chemical attack and would require an initiation period (5). Such a mechanism would be time-temperature dependent as well as surface initiated and presumably progress towards the oxide-substrate interface.

Acknowledgments

The author wishes to express his appreciation to Dr. E. A. Wood for reading the manuscript and helpful discussion, as well as to Mr. A. W. Smith for the preparation of the oxide films, to Mrs. A. Hunt and to Messrs. G. M. Loiacono and F. L. Worthing for the crystallographic and physical measurements.

Manuscript received Dec. 7, 1965. This paper was presented at the San Francisco Meeting, May 9-13, 1965.

Any discussion of this paper will appear in a Discussion Section to be published in the December 1966 JOURNAL.

REFERENCES

1. Therald Moeller, "Inorganic Chemistry," p. 754, John Wiley & Sons, Inc., New York (1952).
2. P. W. Lee, "Ceramics," p. 15, Rheinhold Publishing Co., New York (1961).
3. W. A. Pliskin and E. E. Conrad, *IBM Journal*, **8**, 43 (1964).
4. Crystal Data Determinative Table, 2nd. Ed., p. 919, J. D. H. Donnary, Editor, ACA Monograph No. 5, American Crystallographers (1963).
5. W. A. Weyl and E. C. Marboe, "The Constitution of Glasses," Vol. I. pp. 91, 213, 357 (1962).
6. P. J. Durrant and B. Durrant, "Introduction to Advanced Inorganic Chemistry," pp. 532, 534, John Wiley & Sons, Inc., New York (1962).
7. G. W. Brindley and J. O. Chole, *Am. Mineralogist*, **46**, 772 (1961).
8. M. J. Burger, "Phase Transformation in Solids," pp. 188-199, R. Smoluchowski, Editor, John Wiley & Sons, Inc., New York (1951).
9. J. B. Peri, *J. Phys. Chem.*, **69**, 211 (1965).
10. W. Blitz and A. Lemke, *Z. anorg. allgem. Chem.*, **186**, 377 (1930).
11. R. Fricke *et al.*, *Ber. Dtsch. Chem. Ges*, **70**, 2318 (1937).
12. A. Euchen and E. Wicke, *Naturwissenschaften*, **32**, 161 (1944).
13. A. Euchen, *ibid.*, **34**, 374 (1947).
14. D. Haneman, Intern. Conf. Phys. of Semicond., Exeter, 1962, p. 842.

The Relationship Between Coercivity and the Structure and Composition of Electroless Cobalt-Phosphorus Films

M. G. Miksic,[1] R. Travieso, A. Arcus, and R. H. Wright

International Business Machines Corporation, Systems Development Division, Poughkeepsie, New York

ABSTRACT

Electroless cobalt-phosphorus films were prepared under varying conditions of temperature, hypophosphite concentration, total concentration, time, and pH to determine the relationship between coercivity, structure, and chemical composition of the films. It was found that coercivity increases with increasing percentage of phosphorus content. The thickness effect on coercivity is complex and dependent upon the phosphorus concentration. The preferred orientation of the films is related to phosphorus concentration. Films with phosphorus weight per cent smaller than 2 exhibit, on the average, a normal orientation of the c-axis to the substrate; those with higher per cent phosphorus generally have the c-axis parallel to the substrate.

The magnetic properties of thin films, in general, and of cobalt, in particular, are strongly dependent upon the crystalline structure and the macroscopic structure of the film. Many properties of these films have been related to the thickness of the deposits with consideration of the deposition parameters (1, 2). In this report, we consider the variation of the magnetic properties with thickness for electroless films of constant phosphorus concentration in the range from 0.5 to 4 w/o (weight per cent) P which have been prepared under varied conditions.

The properties of bulk Co itself are a function of crystalline direction. The magneto-crystalline anisotropy of cobalt at room temperature is considerably higher than that of the other ferromagnetic elements. The curves showing the ratio of the areas under magnetization (for the c-axis the easy direction, and the a-axis the hard direction) indicate a measure of magnetic anisotropy; it is 10 times that of iron and 100 times that of nickel. Thus, it will be expected that in some cases the magnetic properties are a function of the preferred orientation of the crystallites which make up the films, but in other cases, shape anisotropy can also be of importance.

[1] Present address: Queens College, New York.

Experimental Techniques

Sample preparation.—The cobalt-phosphorus films were chemically deposited on polyethylene terephalate substrate.

The substrate was rendered hydrophilic using Koretzky treatment (3) which consists of 30 sec immersion in a 27.5*N* solution of H_2SO_4 containing 38 g/l of $Na_2Cr_2O_7 \cdot 2\ H_2SO_4$ at a temperature of 80°C. Substrate was rinsed in deionized water at 25°C for 30 sec, followed by 30 sec immersion in a 3.3*N* solution of NaOH at a temperature of 84°C and rinsed.

The sensitization and activation of the substrate was performed using Bergstrom technique (4) which consists of 30 sec immersion in an aqueous solution containing 30 g/l of $SnCl_2 \cdot 2H_2O$ and 10 ml/l of concentrated HCl at a pH of 1.0 and a temperature of 25°C. This was followed by 30 sec rinsing in deionized water at 25°C and 30 sec immersion in an aqueous solution containing 0.75 g/l of $PdCl_2$ and 10 ml/l of concentrated HCl at a pH of 1.0 and a temperature of 25°C, and rinsed.

The electroless cobalt-phosphorus deposition was made using the following modified Brenner bath (5): $CoSO_4 \cdot 7H_2O$, 35 g/l; $NaH_2PO_2 \cdot H_2O$, 20 g/l; $Na_3C_6H_5O_7 \cdot 2H_2O$, 35 g/l; $(NH_4)_2SO_4$, 66 g/l.

NH_4OH was added to adjust pH to 8.3 at a temperature of 75°C for 3 to 5 min.

To study the effect of process parameters on the structure and composition of the electroless cobalt-phosphorus films the following parameters were varied, one at a time, systematically: bath temperature, 67° to 87°C; pH, 7.3 to 9.3; $NaH_2PO_2 \cdot H_2O$, 5 to 25 g/l.

Magnetic measurements.—The coercive force was obtained by using a 60 cycle hysteresis loop tracer having a maximum driving field of 2000 oersteds.

X-ray diffraction.—A Norelco diffractometer and filtered molybdenum Kα radiation were employed for all the x-ray diffraction studies. The ratios $I(002)/I(100)$, for the films were normalized to a ratio of 1.1, calculated from the structure of hexagonal cobalt in order to avoid the error of using the literature values for polycrystalline cobalt which all show some degree of preferred orientation.

Chemical analysis.—Chemical analysis of the thin films was made only for cobalt and phosphorus. At present, these are the only elements known to have a major influence on the characteristics of the film. A General Electric vacuum x-ray emission apparatus was used for this study.

The operating conditions were as follows: *Cobalt*: x-ray target, tungsten at 40 ma and 50 kv; receiving slit, 0.005 in.; analyzing crystal, lithium fluoride; pulse height selector; detector, scintillation counter; air path. *Phosphorus*: x-ray target, chromium at 40 ma and 50 kv; receiving slit, 0.020 in.; analyzing crystal, EDDT; pulse height selector; detector, gas flow proportional counter-, P-10 gas; vacuum path, at 5μ pressure.

The standards used were previously compared with standard chemical analysis. Cobalt was analyzed colorimetrically by nitroso-R-salt method (6). Phosphorus analysis was made colorimetrically by the Heteropoly Blue method (7).

The experimental results indicated that the coercive force does not seem to be a function which depends only on thickness. It may vary independently of thickness by changing the hypophosphite concentration, the total concentration, the pH, and the temperature in the cobalt bath. The coercive force increases, in general, with increasing hypophosphite concentration and total concentration and with decreasing pH, temperature, and thickness (time of deposition).

In Fig. 1, the coercive force is plotted against the phosphorus concentration of a group of films prepared under widely varying conditions. The significance here is that the coercivity appears to be directly related to the phosphorus concentration of the film for a broad range of deposition conditions. Thus, this may not indicate ways to make a good magnetic film, an admittedly complex undertaking, but it is a step toward characterizing magnetic parameters with the film composition. The points lying below the curve in the high phosphorus range and above the curve at the low phosphorus range are films generally heavier than 0.2 mg/cm². It is now possible to consider the variation of coercive force with film thickness (or cobalt weight) for films having a constant phosphorus concentration.

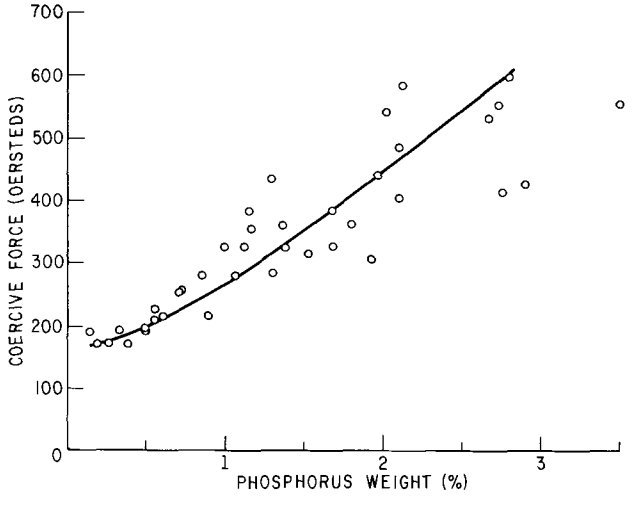

Fig. 1. Coercive force *vs.* phosphorus weight for cobalt-phosphorus films.

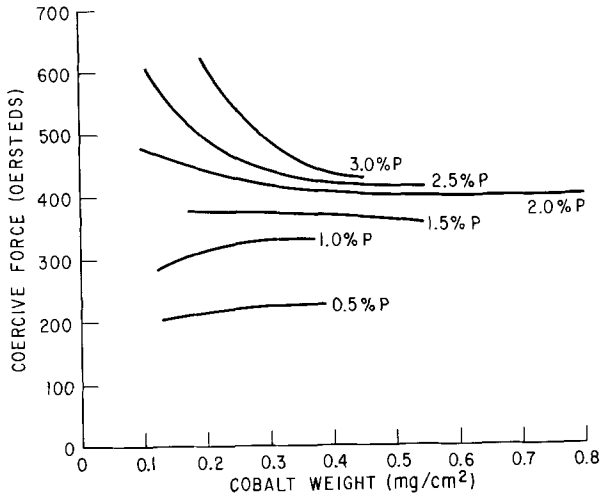

Fig. 2. Coercive force *vs.* cobalt weight for cobalt-phosphorus films

In Fig. 2, the data plotted in Fig. 1 is grouped roughly according to the phosphorus concentration. The coercive force increases with increasing cobalt weight for phosphorus concentration smaller than 2% and decreases with increasing cobalt weight for phosphorus concentration larger than 2%. The data indicates a generally smaller dependence of the coercive force on phosphorus concentration for films heavier than 0.2 mg/cm². It was observed that the phosphorus concentration decreases with increasing film thickness when deposition time is increased on a given bath. This suggests that, in general, the phosphorus concentration is higher at the initial stage of deposition. X-ray emission and electron probe measurements on selected samples have indicated that the phosphorus concentration at the substrate interface is larger than at the film surface.

X-ray diffraction data indicates that, in general, films with phosphorus concentration less than 2% have the c-axis normal to the substrate and those with phosphorus concentration greater than 2% have the c-axis parallel to the substrate. This is indicated in Fig. 3 and 4 by the value of the x-ray intensity for the reflected plane, (002) and (100), as given by the symbol I_{002}/I_{100}. A ratio of I_{002}/I_{100} larger than one indicates a c-axis preferentially oriented normal to the plane of the film, whereas a value smaller than one indicates a c-axis preferentially oriented in the plane of the film.

The aggregate size as shown by electron micrographs increases with cobalt weight at a constant phosphorus concentration (Fig. 3) and decreases with

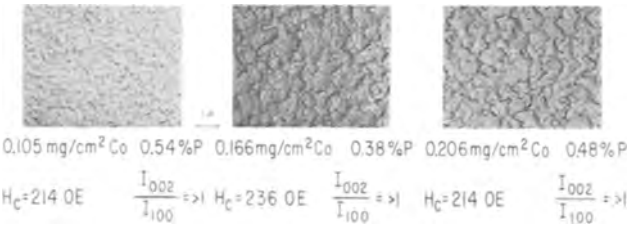

Fig. 3. Electron micrographs for cobalt-phosphorus films with increasing cobalt weight at constant phosphorus concentration. Magnification 10,000X.

Fig. 4. Electron micrographs for cobalt-phosphorus films with increasing phosphorus concentration at constant cobalt weight. Magnification 10,000X.

increasing phosphorus concentration at constant cobalt weight (Fig. 4). These micrographs also show a crevice type surface structure at a phosphorus concentration below approximately 2% and a noncrevice type surface structure at a phosphorus concentration above 2%.

Discussion

The results indicate that the magnetic properties of chemically deposited cobalt, as previously reported (1), depend on the cobalt plus hypophosphite ion concentration, the total bath concentration, the pH, temperature, and thickness (time of deposition). It seems that these process parameters affect the chemical composition of the deposits which were found to relate closely to the structural and magnetic properties. Films with phosphorus concentration smaller than 2% have their average orientation with the c-axis normal to the substrate, aggregate size larger than 0.2μ and coercive force smaller than 400 oersteds. Films with phosphorus concentration larger than 2% have their average orientation with the c-axis parallel to the substrate, aggregate size less than 0.2μ and coercive force larger than 400 oersteds. In general, the coercive force increases with increasing phosphorus concentration. The thickness effect on coercive force is shown to be complex and dependent also upon the phosphorus concentration.

Also of interest is the chemical nature of the phosphorus which is present within the film. Cobalt-phosphorus compounds have not been observed by x-ray diffraction, and in fact all diffraction traces have been identified as corresponding to α-cobalt which has a hexagonal close packed crystallographic structure.

No satisfactory model for the electroless cobalt-phosphorus films can be set forth based on the available data. However, there appears to be a correlation between coercivity of the film and the phosphorus concentration which, in turn, seems to relate to the crystallographic orientation, surface structure, and aggregate size.

Acknowledgments

The authors would like to express their gratitude to Mr. R. E. Smith for the electron microscopy studies, to Dr. J. E. Hurt for the electron transmission studies, and to Mr. R. G. Volk for the magnetic measurements.

Manuscript received May 17, 1965; revised manuscript received Dec. 4, 1965. This paper was presented at the Buffalo Meeting, Oct. 10-14, 1965.

Any discussion of this paper will appear in a Discussion Section to be published in the December 1966 JOURNAL.

REFERENCES

1. R. D. Fisher and W. H. Chilton, *This Journal*, **109**, 485 (1962).
2. J. S. Sallo and J. M. Carr, *ibid.*, **109**, 1040 (1962); *J. Appl. Phys.*, **34**, 1309 (1963).
3. H. Koretzky and B. Leland, U.S. Pat. 3142582, July 28, 1964.
4. E. A. Bergstrom, U. S. Pat. 2702253, Feb. 15, 1955.
5. A. Brenner, U. S. Pat. 2532284, Dec. 5, 1950.
6. E. B. Sandell, "Colorimetric Determination of Traces of Metal," 3rd ed., p. 415, Interscience Publishers Inc., New York (1959).
7. D. F. Boltz, "Colorimetric Determination of Nonmetals," p. 32, Interscience Publishers Inc., New York (1958).

The Kinetics of Growth of $FeSn_2$ Layers on Tinplate

H. E. Biber

Applied Research Laboratory, United States Steel Corporation, Monroeville, Pennsylvania

ABSTRACT

$FeSn_2$ alloy layers were formed on unalloyed tinplate specimens heated by immersion in constant-temperature oil baths and by resistance heating. The data show that the critical factor affecting alloy-layer-growth behavior is the rate at which the unalloyed tinplate is heated. As the heating rate is decreased the average alloy-layer-growth rate decreases instead of remaining constant. With rapid heating, there is an appreciable interval during which the growth of the alloy ceases or practically ceases.

During the production of tinplate, a thin layer of $FeSn_2$ is formed at the steel-tin interface. In the hot-dip tin-plating process, this alloy layer forms while the steel strip is immersed in the molten tin bath. In the electrolytic process, it forms when the freshly plated strip is briefly heated to melt the coating and give it a high reflectance (flow brightening). Excessive amounts of this iron-tin alloy are detrimental to the physical properties of tinplate, therefore, the kinetics of its formation is a subject of interest in the tinplate industry.

Loginow and Frankenthal (1) studied the kinetics of this reaction in detail by immersing strips of matte tinplate (*i.e.*, electrolytic tinplate that had never been heated) in a constant-temperature oil bath for various times and then measuring the resultant amount of alloy. Their data for bath temperatures of 175°-316°C showed that the growth rate increased with increasing bath temperature and that a parabolic rate law was followed at all temperatures.

Seybolt (2) studied the kinetics of alloy-layer formation by immersing strips of steel in molten tin maintained at 260°, 288°, 316°, and 330°C. His data also showed that a parabolic rate law was followed at each temperature.

However, when Thwaites (3) formed alloy layers by immersing matte tinplate in oil baths heated to 175°, 200°, and 225°C, he found that the growth did not follow a parabolic rate law. In addition, he observed that when matte tinplate was heated resistively to 250°C and held at that temperature, no additional alloy was formed after the first 3 sec, even though the heating was continued for 30 sec.

This present study was undertaken to resolve the differences in the results of the previous studies of alloy-layer growth.

Experimental Work

Matte tinplate was prepared from 0.010-in.-thick Type L steel in a circulation cell with phenolsulfonic acid electrolyte. The coating weights were 0.5, 1.0, 1.5, and 2.0 lb per base box (1.3, 2.6, 3.8, and 5.1 x 10^{-4} oz/in.^{2}, respectively).

For most of the study, ½-in. squares of the matte tinplate were immersed for various times in a constant-temperature oil bath vigorously stirred by a 2-in.-diameter propeller driven at 10,500 rpm. Alloy-layer growth was measured for bath temperatures of 200°, 210°, 220°, 231°, 240°, 260°, and 300°C. Some additional measurements were made for a bath at 240°C with a less vigorous stirrer speed of 1800 rpm and without stirring. When the oil was stirred, the temperature variation was less than ±0.5°C; however, when the oil was not stirred, temperature gradients set up in the bath resulted in a variation of about ±4°C. Immediately upon removal from the oil bath, the specimen was quenched in an organic liquid.

Alloy layers were also formed by resistively heating strips of matte tinplate for various times. Alloy-layer-growth data were obtained for various potentials applied across the strip.

The heavier tin-coating weights were used for the longer times and/or higher temperatures so the amount of free tin would always be considerably in excess of the expected amount of alloyed tin. To minimize the possible effect of alloy layer formed at room temperature, no measurements were made with matte tinplate that was more than three days old.

The amount of alloy layer formed on each specimen was determined in duplicate by the coulometric method of Kunze and Willey (4).

The heating rates with different degrees of stirring of the oil bath at 240°C and with resistance heating were determined by means of an iron-constantan thermocouple welded to steel specimens identical in size to the tinplated specimens. The thermocouple was connected to a fast-response chart recorder.

Results

In the oil bath stirred at 10,500 rpm, the alloy layer grew in three distinct stages (Fig. 1). In the initial stage the alloy layer formed very rapidly. The growth followed a rate law of the form $w = kt^n$, where $n > 1$. The value of n and the total amount of alloy formed in this first stage increased with increasing bath temperature. Following this initial stage was a second stage in which little additional alloy was formed. The duration of this growth-retardation stage varied from about 15 to 200 sec at different bath temperatures; however, the changes in duration were not consistent with the changes in temperature. In the third stage the growth again followed a rate law of the form $w = kt^n$, but $n = 0.3$ at each bath temperature, Table I. This last stage comprised the main part of the growth curve.

Table I. Slope of plotted third stage alloy-layer-growth data at various bath temperatures

Bath Temperature, °C	Slope, n
200	0.31
220	0.30
231	0.32
240	0.29
260	0.30
300	0.32

Stirring the oil at 10,500 rpm causes the tinplate specimen to be rapidly heated to bath temperature. If the agitation of the oil is reduced, the heating rate is reduced (Fig. 2) and the alloy-layer-growth behavior changes. An example of this relationship is seen in the results of alloy-layer-growth measurements at 240°C in oil baths stirred at 10,500, 1800, and 0 rpm (Fig. 3). With the rapid heating rate provided by stirring at 10,500 rpm, the alloy layer grew in three stages and the initial stage persisted well beyond the time required to heat the specimen to bath temperature. With the intermediate heating rate provided by stirring at 1800 rpm, the three-stage nature was less pronounced and the slope of the third stage was increased. With the slow heating rate provided by the unstirred bath, the alloy layer grew in two stages. The initial rapid-growth stage persisted only until the specimen was heated to bath temperature. The slope of the main portion of the plotted data was greater than in the stirred baths, having a value of almost 0.5.

Thus the results for oil heating can be summarized as follows. For a given bath temperature, as the heating rate is increased three changes occur in the

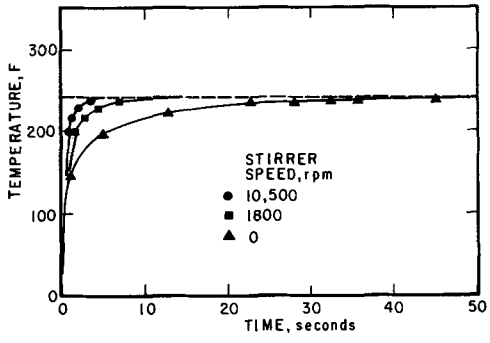

Fig. 2. Heating of ½ x ½ in. squares of black plate with different degrees of stirring of oil. Stirrer speed, rpm: ●, 10,500; ■, 1800; ▲,0.

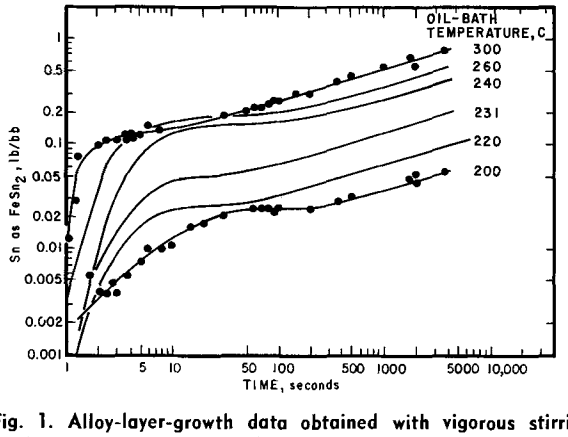

Fig. 1. Alloy-layer-growth data obtained with vigorous stirring at various bath temperatures. Note: Data points omitted from all curves except 200° and 300°C for simplification.

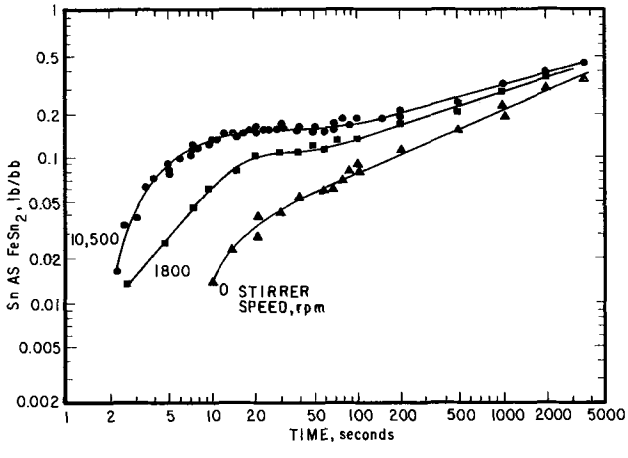

Fig. 3. Alloy-layer-growth data obtained for tinplate with different degrees of stirring at 240°C.

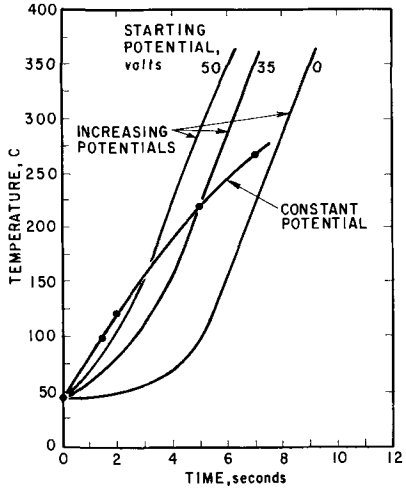

Fig. 4. Approximate heating curves on resistance melter with constant potential or potentials increasing 16v/sec to 120v.

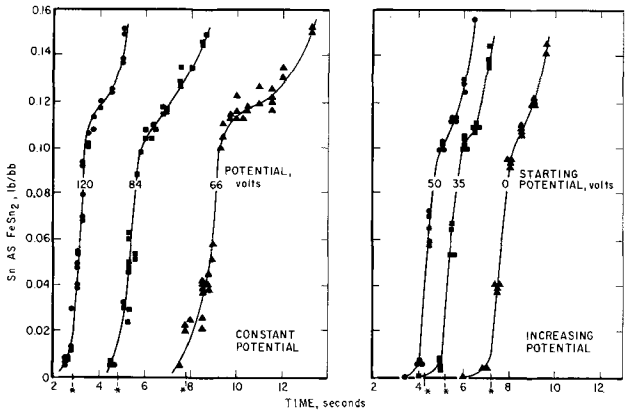

Fig. 5. Alloy-layer growth with constant or increasing potentials on resistance melter. * equals tin melting time.

plotted alloy-layer-growth data: (*i*) the slope of the main portion of the plotted data continuously decreases from a value of about 0.5; (*ii*) an initial stage of accelerated growth becomes pronounced, and (*iii*) an intermediate stage of growth retardation appears at a higher heating rate.

No explanation can be offered for the growth retardation. It was thought to indicate the formation of a new phase that could not be detected by the coulometric analysis. However, x-ray diffraction analysis showed only $FeSn_2$ in the alloy layer before, during, and after the growth-retardation stage.

This relationship between heating rate and alloy-layer-growth behavior clarifies the differences in the results of previous alloy-layer-growth studies. Loginow and Frankenthal (1) used large specimens in an unstirred oil bath, which resulted in a slow heating rate. Therefore they observed little, if any, of the initial stage of accelerated growth, and the slope of their plotted data was 0.5. Seybolt's paper (2) does not include information about the heating rate, but, because he observed only the parabolic growth, it is assumed that his specimens were also heated slowly. On the other hand Thwaites' oil-bath specimen heating rates (3) must have been faster than Loginow and Frankenthal's because his data did not indicate the parabolic rate law. His resistance-heating experiments certainly involved rapid heating rates because the specimens were heated to 250°C in 3 sec. The fact that no additional alloy was formed after the first 3 sec., even though heating was continued for 30 sec., indicates that the alloy layer was in the growth-retardation stage. In fact, Thwaites' alloy-layer-growth curves at 250° and 300°C obtained by resistance heating compare favorably with the present curves for 260° and 300°C obtained by rapid oil heating.

Oil-bath heating differs considerably from commercial practice in which the tin coating is flow-brightened by rapidly heating the strip resistively for a few seconds. The tinplate temperature increases continuously during the entire resistance-heating period, whereas with oil-bath heating it increases exponentially to the bath temperature. To obtain a better understanding of alloy-layer growth during resistance heating, alloy-layer-growth curves were prepared by heating matte tinplate resistively with three different constant potentials and three different continuously increasing potentials. The constant potentials produced heating rates that were practically linear, Fig. 4, whereas the continuously increasing potentials produced heating rates that continuously increased. For the same melting time, the growth curves obtained with either heating condition are generally the same, Fig. 5. There is very little alloy-layer growth until the tinplate temperature approaches the melting point of tin; then the growth proceeds rapidly. Each of the growth curves exhibits the arrest that is characteristic of growth during rapid heating. However, the arrest is not as pronounced as with oil-bath heating, presumably because the temperature is continuously increasing.

Discussion

In studies of the kinetics of surface reactions one is concerned with the effects of time and temperature on the amount of reaction product formed. Ideally the reactants are kept apart until the system is at the desired temperature. However with a system such as tinplate this is not possible because the reactants are always in intimate contact. Thus the reaction can occur from the onset of heating. The results of the present study show that with such a system there is

Table II. Effect of different heating rates on alloy-layer-growth rates

A. Linear Heating Rates—Resistance Heating at Constant Potential

Approximate heating rate, °C/sec	Evaluation at 240°C			Evaluation at 260°C		
	Time,[a] sec	Alloy,[b] lb/bb	Average growth rate, lb/bb sec	Time, sec	Alloy, lb/bb	Average growth rate, lb/bb sec
68	2.9	0.025	0.0086	3.2	0.072	0.022
40	5.0	0.025	0.0050	5.5	0.075	0.014
25	8.0	0.019	0.0024	8.8	0.045	0.0051

B. Increasing Heating Rates—Resistance Heating at Increasing Potential

Starting potential, v	Evaluation at 240°C			Evaluation at 260°C		
	Time,[c] sec	Alloy,[b] lb/bb	Average growth rate, lb/bb sec	Time, sec	Alloy, lb/bb	Average growth rate, lb/bb sec
50	4.3	0.043	0.010	4.6	0.078	0.017
35	5.3	0.038	0.0072	5.6	0.070	0.012
0	7.3	0.020	0.0027	7.6	0.052	0.0068

C. Exponential Heating Rates—Oil Heating, Different Stirring Rates at 240°C

Stirrer speed, rpm	Evaluation at 240°C		
	Time,[d] sec	Alloy,[e] lb/bb	Average growth rate, lb/bb sec
10,500	2.7	0.024	0.0089
1,800	7.0	0.041	0.0059
0	50.0	0.056	0.0011

[a] Calculated from heating rate.
[b] From Fig. 5.
[c] From Fig. 4.
[d] From Fig. 2.
[e] From Fig. 3.

a factor other than time and temperature that affects the amount of reaction product formed.

If the growth of the iron-tin alloy layer depended only on time and temperature, with different linear heating rates, there should be an inverse proportionality between the heating rates and the relative amounts of alloy layer formed when a given temperature was reached. For example, if one heating rate were twice another, it would reach a given temperature in half the time and should cause half as much alloy-layer growth. However with either heating rate the average growth rate should be identical when evaluated at the same temperature. (The average growth rate is the amount of alloy layer that has formed when a given temperature is reached divided by the time required to reach that temperature.)

The data for linear heating rates show that the amount of alloy layer formed when a given temperature is reached is not inversely proportional to the heating rate and further that the average growth rate actually decreases as the heating rate decreases, Table IIA. The data for increasing heating rates and for exponential heating rates also show the same effects, Table IIB and IIC, respectively. The heating rates for resistance heating at increasing potentials were practically identical above about 150°C and differed considerably in the range 40°-150°C, whereas those for the 240°C oil baths were just the opposite. Thus it appears that a reduction in heating rate in any part of the temperature range up to at least 240°C produces these effects.

The cause of these effects is not known. It is possible that they can be explained on the basis of increased $FeSn_2$ crystallite nucleation rates with decreased heating rates, and this is currently being investigated.

Summary

The rate at which matte tinplate is heated strongly affects the kinetics of alloy-layer formation. For a given oil bath temperature, as the heating rate is increased, the slope of the main portion of the plotted growth data continuously decreases from a value of 0.5, an initial stage of accelerated growth becomes pronounced, and at a higher heating rate an intermediate stage of growth retardation appears. When matte tinplate is rapidly heated resistively, as in commercial flow brightening, the growth data exhibit a growth retardation, however, it is not as pronounced as with oil-bath heating.

An analysis of the growth data for both oil-bath heating and resistance heating shows that a reduced heating rate reduces the average alloy-layer-growth rate and therefore causes a smaller amount of alloy layer to be formed by the time a given temperature is reached. It appears that a reduced heating rate in any part of the temperature range to at least 240°C will cause this effect.

Acknowledgments

The author wishes to express his thanks to Messrs. L. E. Berta, E. C. Brendlinger, C. W. Cross, E. J. Masar, and J. W. Ruffner for constantly supplying fresh matte tinplate and for patiently assisting in the various resistance heating experiments. Also, the valuable assistance of Messrs. W. T. Harter and B. J. Lapinski in making numerous measurements for this study is gratefully acknowledged.

Manuscript received Sept. 29, 1965; revised manuscript received Dec. 9, 1965.

Any discussion of this paper will appear in a Discussion Section to be published in the December 1966 JOURNAL.

REFERENCES

1. R. P. Frankenthal and A. W. Loginow, *This Journal*, **107**, 920 (1960).
2. A. U. Seybolt, *Trans. Am. Soc. Metals*, **29**, 937 (1941).
3. C. J. Thwaites, *J. Iron Steel Inst.*, **183**, 244 (1956).
4. C. T. Kunze and A. R. Willey, *This Journal*, **99**, 354 (1952).

Epitaxial Synthesis of GaAs Using a Flow System

M. Rubenstein and E. Myers

Westinghouse Electric Corporation, Research & Development Center, Pittsburgh, Pennsylvania

ABSTRACT

The epitaxial synthesis of gallium arsenide utilizing a flow system was achieved using gallium trichloride, arsenic, and hydrogen as reactants, and oriented single crystals of GaAs as substrates. Under the conditions of these experiments, there is almost no difference in growth rates between the "A" orientation of the {111} surface and the "B" orientation of a $\{\bar{1}\bar{1}\bar{1}\}$ surface. The rate of growth on a {110} surface is more than twice as great as on a {111} surface, and the rate of growth on a {100} surface is slower by a factor of 1.4 than on a {111} surface.

Gallium arsenide has been prepared in a variety of manners (1-4). This paper concerns the epitaxial synthesis of GaAs using $GaCl_3$, arsenic, and H_2. The over-all reaction can be written as

$$4GaCl_3 + As_4 + 6H_2 \rightleftarrows 4GaAs + 12HCl \quad [1]$$

Since this reaction appears to be the complete hydrogen reduction of $GaCl_3$ in the presence of arsenic, one must look at the various equilibria involved in this over-all reaction (5)

$$2GaCl_3 \rightleftarrows Ga_2Cl_2 + 2Cl_2 \quad [2]$$

$$3Ga_2Cl_2 \rightleftarrows 4Ga + 2GaCl_3 \quad [3]$$

$$H_2 + Cl_2 \rightleftarrows 2HCl \quad [4]$$

$$As_4 \rightleftarrows 2As_2 \quad [5]$$

$$2Ga + As_2 \rightleftarrows 2GaAs \quad [6]$$

In the system $GaCl_3$-As_4-H_2 the sources of chlorine are in reactants [2] and [4]. The ratio of any of the three reactions is not critical. However, in the system $GaCl_3$-$AsCl_4$-H_2, the ratio of $GaCl_3$:$AsCl_3$ must not fall below unity (3). When this ratio falls below unity, not only is there no epitaxial growth, but the substrates are often attacked. This $GaCl_3$-$AsCl_3$-H_2 system has three sources of Cl_2: Eq. [2], [4], and [7].

$$2AsCl_3 \rightleftarrows As_2 + 3Cl_2 \quad [7]$$

If the Cl_2 concentration were to increase, reaction [2] would shift to the left, reaction [3] would shift to the left, reaction [6] would shift to the left and the over-all reaction [1] would shift to the left so that less or little GaAs would grow epitaxially. In the system $GaCl_3$-As_4-H_2, as long as the chlorine source is only in Eq. [2] and [4] (and not in Eq. [7]) and as long

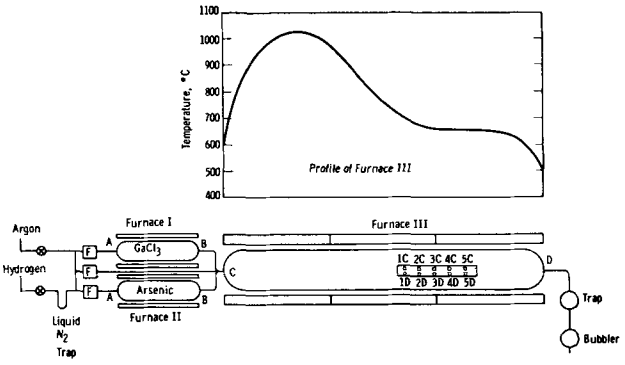

Fig. 1. Diagrammatic flow system for the epitaxial synthesis of GaAs.

as H_2 is the carrier, any combination of ratios of reactants is non-critical for the epitaxial growth of GaAs.

Experimental Procedures

$GaCl_3$ was prepared by ALCOA and AIAG from their respective 99.9999% gallium. Arsenic was 99.999+% from ASARCO. The heating was done with hinged resistance furnaces and heating tapes. The glass apparatus was quartz except for the Vycor ball and socket joints. Figure 1 shows the diagrammatic sketch of the apparatus with the temperature profile of the reaction furnace. The tube in furnace III was 45 mm OD and the length of the deposition zone (where the seeds were placed) was about 25 cm.

Furnace I was maintained at a temperature of about 70°C, furnace II was maintained at a temperature of about 450°C. Heating tapes were used from points B to C to maintain the wall temperature at a minimum of 475°C. Hydrogen and/or argon (argon for flushing the hydrogen out of the system at the end of the experiment) can flow through the system monitored by flow meters at points F. The experiments usually lasted about 5 hr.

All substrates were single crystals of GaAs sliced, lapped, and given a nonpreferential polishing etch. The dimensions of the seeds were about 1x5x5 mm. The seeds were placed on a graphite slab as indicated in Fig. 1. The flat surfaces of the substrates were oriented in {111}, {110}, and {100} planes. The seeds were placed on a graphite slab (as indicated in Fig. 1) to give relative rate growths using the "A" and "B" orientations of the {111} planes as the standard. In some runs {110} and {100} oriented substrates were placed adjacent to {111} seeds so the {111} oriented substrates could be used as a standard experiencing the same flow rates of gases, concentrations, and temperatures.

The flow rate of arsenic was about 0.13 mM/min, and the flow rate of $GaCl_3$ was between 0.2 to 0.7 mM/min, and the total flow rate was about 200 cc/min. The arsenic flow rate and the $GaCl_3$ flow rates were calculated from weight measurements of the sources before and after runs. The total flow rate was made by calibrating the flow meter settings with the gas coming out of the bubbler at the effluent end of the apparatus. The optimum temperature for the growth of GaAs on the substrates (maximum amount of GaAs deposited) was 665°-670°C. Deposits grew at the rate of between 0.07 to 0.45 μ/min. This difference in growth rates was primarily due to differences in flow rates of the $GaCl_3$. The thickness of the GaAs growth was obtained by angle lapping and decorating the junction using an aqueous solution containing $CuSO_4$ and HF (6).

Results

Table I contains data from three representative runs. Under "substrate orientation" column, the numbers and letters refer to positions of substrates as indicated in Fig. 1. The thickness of the grown layers used in this paper were obtained by angle lapping and decorating with a copper solution. Weight gain measurements of substrates before and after growth could not be used to determine thicknesses of growth since the ratio of the surface area of the tops of these substrates to the surface area of the sides varied between 1.0 and 1.5. There was very little growth on the bottom surface of these substrates.

Table I. Representative results

Run designation*	Substrate orientation	Temp. of seed, °C	Thickness from angle lapping, μ
EP 23 (a)	1C{111}	668	65
	1D{$\bar{1}\bar{1}\bar{1}$}		68
	2C{111}	663	40
	2D{$\bar{1}\bar{1}\bar{1}$}		38
	3C{111}	662	30
	3D{$\bar{1}\bar{1}\bar{1}$}		28
	4C{111}	663	28
	4D{$\bar{1}\bar{1}\bar{1}$}		27
EP 24 (b)	1C{111}	674	17
	1D{110}		35
	2C{$\bar{1}\bar{1}\bar{1}$}	663	23
	2D{110}		55
	3C{111}	661	24
	3D{110}		56
	4C{$\bar{1}\bar{1}\bar{1}$}	662	23
	4D{110}		51
EP 25 (c)	1C{111}	672	88
	1D{100}		60
	2C{$\bar{1}\bar{1}\bar{1}$}	660	55
	2D{100}		35
	3C{111}	657	35
	3D{100}		30
	4C{$\bar{1}\bar{1}\bar{1}$}	651	31
	4D{100}		25

* Hydrogen flow over $GaCl_3$ for these three runs was 125 ml/min. Hydrogen flow over arsenic for these three runs was 145 ml/min.
(a) {111} grows at about the same rate as {$\bar{1}\bar{1}\bar{1}$}.
(b) {110} grows about 134% faster than {111} or faster by a factor of 2.34.
(c) {100} grows about 26% slower than {111} or slower by a factor of 1.35.

The three runs indicated in Table I are meant to be representative of many runs. These three representative runs demonstrate a few points. One can note that the substrates downstream in EP 23 and EP 25 show smaller growth layers than substrates which are upstream. But EP 24 does not demonstrate this trend. The $GaCl_3$ flow for EP 25 was the largest flow, for EP 23 the flow was somewhat smaller, and the flow for EP 24 was appreciably smaller. The two fast flow rate experiments yielded larger growth rates and a lessening of growth on downstream substrates. Faster flow rates of $GaCl_3$ produce faster growth rates of GaAs within the limits of the flow rates in these experiments. The reduction of growth as one looks at downstream substrates is probably due to the reaction products from the upstream substrates reducing the rate of growth on the downstream substrates. EP 24 indicates that at temperatures of 674°C and greater the rate of deposition of GaAs is being reduced by the rate of transport of GaAs. EP 24 also shows a more uniform rate of deposition on upstream and downstream substrates. If the flow rate of $GaCl_3$ is slow enough the reaction products from the upstream substrates probably have enough time to diffuse away and not deter the growth rates on the downstream substrates. These same observations were noted in runs other than EP 23, EP 24, and EP 25.

The relative rates of growth on the three orientations of GaAs (under the conditions stated earlier in this paper) are {110} > {111} > {100}. The {110} surface grows faster than a {111} surface by a factor of about 2.3; and the {100} surface grows slower than a {111} surface by a factor of about 1.4. No real difference in growth rates were observed between the "A" and "B" orientations of the {111} surfaces. Many of these layers on the four orientations were checked by back reflection Laue x-ray diffraction studies and were all found to be single crystal growths with the same orientations as their respective substrates. These

layers were also lightly lapped and given a preferential etch to demonstrate that there were no grain boundaries in the grown layers.

Two runs were made in which the carrier gas was argon. No deposition was observed on the seeds and the seeds were seriously attacked. These experiments confirm that hydrogen is more than just the carrier gas but is necessary for the reaction to synthesize GaAs.

Variation was performed on the maximum temperature indicated in Fig. 1. This temperature was varied between 1150° and 900°C with no apparent effect on the rate of deposition. At temperatures lower than 850°C there was little or no deposition of GaAs on the seeds. One can conclude from this that a temperature of 900°C or higher is necessary to shift Eq. [2] to the right. The function of this high temperature zone is to allow the partial reduction of the $GaCl_3$ so that a disproportionation reaction can occur in the substrate zone.

The efficiency of growth on these seeds is between 1 and 3%. This efficiency is calculated on the basis of the amount of GaAs deposited on the seeds and the amount of arsenic or $GaCl_3$ delivered from the sources (whichever was the lesser amount). Between 15 and 50% of the $GaCl_3$ which left the tube in furnace I was recovered in the trap, after point D (see Fig. 1). The trap mentioned above was air cooled. At the flow rates used in these experiments much of the $GaCl_3$ and any Ga_2Cl_4 formed would be trapped since the melting points are 77.9° and 171°C, respectively. If the trap contained any Ga_2Cl_4 mixed with the $GaCl_3$ the recovery of gallium would be that much higher than reported here. Of course, some of the gallium halide was not trapped, so the figures of 15-50% are low figures. The variation between 15 and 50% was due primarily to the rate at which $GaCl_3$ left the tube in furnace I. The inefficiency of the growth of GaAs on the seeds can be attributed to the equilibria (Eq. [2] and [3] indicate that 1 mole out of an initial 3 moles of $GaCl_3$ must be unreacted), to GaAs which formed on the walls of the quartz tube (particularly downstream from the seeds), and to the fact that every molecule passing through the high temperature zone does not undergo reduction. This technique could be made more efficient by using more seeds in the deposition zone, by tilting the seeds from the horizontal (7) (or placing the seeds in a vertical state), and by passing the reactants through the system at optimum flow rates.

Discussion

The data on the relative rates of growth on the various orientations {111}, {$\bar{1}\bar{1}\bar{1}$}, {110}, and {100} in the literature varies tremendously (8-10) and the authors will not attempt to try to interpret why various experimental procedures used by various scientists give such varied results. However, we would like to offer an explanation for the results in this paper. The results of the experiments in this paper are consistent with the model presented by Gatos (11). A surface atom on a {100} orientation is bonded to two atoms of the crystal and has 2 unshared electrons. A surface atom on a {111}, {$\bar{1}\bar{1}\bar{1}$}, or a {110} orientation is bonded to three atoms of the crystal and has one unpaired electron.

If one assumes that these various surfaces are surrounded by gallium atoms (as Ga_2Cl_2 or GaCl) and arsenic atoms about to form bonds with the surface atoms, the probability would be greater to form such bonds if the atom in the gas would have to make one bond with one surface atom to complete the tetrahedron of the surface atom. Therefore, one would expect growth on a {100} surface to be slower than growth on a {111}, {$\bar{1}\bar{1}\bar{1}$}, or {110} surface. The {111} and {$\bar{1}\bar{1}\bar{1}$} surface consists only of gallium atoms and arsenic atoms, respectively, and the {110} surface consists of gallium and arsenic atoms. The probability of growth on the {110} should be greater since gallium and arsenic are in the gas above the surface ready to form bonds with the surface. In the case of the {111} surface, a layer of arsenic atoms must deposit before a layer of gallium atoms can deposit. Therefore, one would expect the {110} surface to accept growth faster than a {111} or a {$\bar{1}\bar{1}\bar{1}$} surface. From the above discussion one would expect the {111} surface to grow at the same rate as the {$\bar{1}\bar{1}\bar{1}$} surface.

Marinace (12) found the same relative growth rates with respect to the {110}, {111}, and {100} orientations using a sealed-tube iodine transport type growth of germanium on germanium.

Sangster (13) discussed the relative growth rates of III-V compounds. He concluded that the {110} growth rates should be greater than the {111} as this paper is reporting, but he concluded that the fastest growing orientation should be the {100}. He concluded this from the most stable and least stable planes. Experimentally he reported confirmation of his conclusions by referring to InSb {311} crystals (grown from the melt) so that the development of facets would be encouraged. The facets found in sequence of strength or prominence were {111} > {110} > {100}. The order of rates of growth should be in the reverse order. Sangster in this same reference (13) also points out that "crystals of III-V compound semiconductors are not usually grown under near-isothermal, near-equilibrium conditions, but are grown rapidly in the presence of strong temperature gradients."

This paper demonstrates the isoepitaxial synthesis of GaAs in a flow system in which the reactants are $GaCl_3$, As_4, and H_2. This paper also shows that under the conditions as set forth here, there is almost no difference in growth rates between the "A" and "B" orientations of the {111} orientations; the rate of growth on a {110} orientation is more than twice as fast as on a {111} plane; the rate of growth on a {100} orientation is slower by a factor of about 1.4 than on a {111} orientation.

Manuscript received June 14, 1965; revised manuscript received Oct. 20, 1965. This paper was presented at the San Francisco Meeting, May 10-13, 1965.

Any discussion of this paper will appear in a Discussion Section to be published in the December 1966 JOURNAL.

REFERENCES

1. D. Effer and A. G. Antell, Jr., *This Journal*, **107**, 252 (1960).
2. S. W. Ing., Jr., and H. T. Minden, *ibid.*, **109**, 995 (1962).
3. F. W. Tausch and T. A. Longo, Electrochemical Society Spring Meeting, 1962, Abstract No. 77.
4. N. Goldsmith and W. Oshinsky, *RCA Rev.*, **24**, 546 (1963).
5. V. J. Silvestri and V. J. Lyons, *This Journal*, **109**, 963 (1962).
6. D. R. Turner, *ibid.*, **106**, 786 (1959).
7. S. K. Tung, "Metallurgy of Semiconductor Material," p. 87, J. B. Schroeder, Editor, Interscience Publishers, New York (1962).
8. R. Moest and B. Shupp, *This Journal*, **109**, 1065 (1962).
9. N. Goldsmith, *ibid.*, **110**, 588 (1963).
10. F. A. Pizzarella, *ibid.*, **110**, 1059 (1963).
11. H. Gatos, "The Surface Chemistry of Metals and Semiconductors," p. 381, John Wiley and Sons, Inc., New York (1959).
12. J. C. Marinace, *IBM J.*, **4**, 248 (1960).
13. R. C. Sangster, "Compound Semiconductors," Vol. 1, R. K. Willardson and H. L. Goering, Editors, Reinhold Publishing Corp., New York (1962).

Phase Shift Corrections for Infrared Interference Measurement of Epitaxial Layer Thickness

P. A. Schumann, Jr., R. P. Phillips, and P. J. Olshefski

IBM Systems Manufacturing Division, East Fishkill Facility, Hopewell Junction, New York

ABSTRACT

Under certain conditions of wavelength and substrate impurity level, correction factors were found to be necessary for the infrared interference method of measuring epitaxial layer thickness. A general theory has been developed which relates the index of refraction and extinction coefficient to physical properties of the semiconductor and the wavelength. From these constants, a phase change at the epitaxial layer-substrate interface is calculated. This phase shift is shown to influence the measurement and a correction factor is derived.

In 1961 Spitzer and Tanenbaum (1) proposed a nondestructive technique for the measurement of the thickness of epitaxial layers deposited on heavily doped substrates of the same type. This technique relies on the reflection of infrared radiation from the epitaxial layer-air interface and from the epitaxial layer-substrate interface and subsequent interference of the two beams. Further work was done by Albert and Combs (2) and Pliskin and Grochowski (3) in expanding the technology and comparing the infrared interference method with other techniques. It was assumed in the aforementioned papers that the phase shift on reflection at the layer-substrate interface was constant and did not enter into the calculation of the layer thickness. However, it was pointed out by Albert and Combs (2) that in the transition region between low refractive index and high extinction coefficient the phase shift on reflection was a function of wavelength. In 1961, Pliskin (4) measured this phase shift showing it was a function of wavelength and proposed that this phase shift could be used to determine the substrate resistivity empirically. Albert and Combs (2) limited their discussion of the thickness measurement to the spectral region where the phase shift was small. However, the wavelength region in common use, 11-35μ, encompasses the transition region for most low resistivity substrates.

This varying phase shift is evidenced by the fact that successive peaks or valleys do not yield the same layer thickness when calculated in the standard manner.

To determine the phase shift at the epitaxial layer-substrate interface, the index of refraction and extinction coefficient must be known. This paper will present theoretical solutions for these optical constants and propose a method of correcting the thickness measurement by including the varying phase shift.

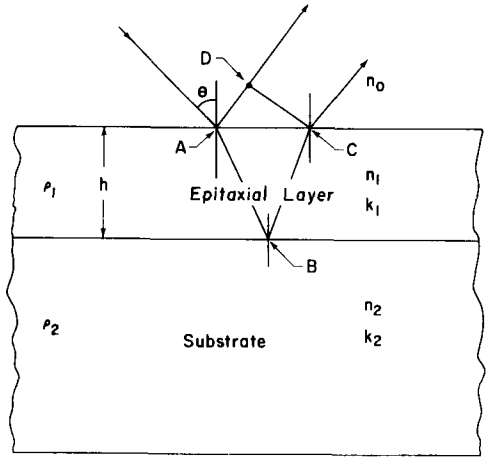

Fig. 1. Geometry of infrared interference method of measuring epitaxial layer thickness.

Theory

The geometry of the technique is illustrated in Fig. 1. Here the incident beam makes an angle, θ, with a normal to the surface. The beam is split by reflection and refraction. The reflected ray undergoes a phase shift Φ_1 at point A. The refracted ray passes through the epitaxial layer and is reflected at point B experiencing a phase shift Φ_2. The refracted and reflected ray then passes back through the epitaxial layer to point C where it is again refracted and interferes with the reflected ray. This interface is either constructive or destructive depending upon the relative phase of the two rays. The multiple reflected rays are not considered because they add nothing to the analysis.

In this analysis of the epitaxial layer thickness measurement, several assumptions have been made. First, it is assumed that there is an abrupt change in conductivity at the layer-substrate interface and that within each region the conductivity is uniform. Second, the assumption is made that the wavelength is sufficiently long so that no direct transitions can be made across the band gap. For silicon, this can be satisfied if $\lambda > 2\mu$. This is equivalent to stating that the lattice contribution to the dielectric constant is independent of wavelength. Third, it is assumed that the band structure is such that there are no interband transitions. Fourth, the assumption is made that the carrier concentration in the epitaxial layer is sufficiently low that the carriers do not contribute to the dielectric constant and only the lattice contribution need be considered. This is equivalent to saying that the extinction coefficient is zero and the refractive index is constant with wavelength. Fifth, the effects of polarization are neglected because the angle of incidence of the ray at the layer substrate interface is close to zero. The first assumption is questionable but necessary to make the analysis possible. It will be shown in the data that this condition is not too restrictive since the results are self-consistent. For normal epitaxial structures, conditions two through five are satisfied.

Equations [1] and [2] express the phases of the outgoing rays at points C and D in terms of the optical path lengths and the phase shifts the rays suffer when reflected. Because the epitaxial layer is nonabsorbing the phase shift of the transmitted ray at point A is zero and is neglected (5).

$$\Phi_C = \frac{4\pi h n_1^2}{\lambda\sqrt{n_1^2 - \sin^2\theta}} - \Phi_2 \qquad [1]$$

$$\Phi_D = \frac{4\pi h \sin^2\theta}{\lambda\sqrt{n_1^2 - \sin^2\theta}} - \Phi_1 \qquad [2]$$

The difference in phase, δ, is

$$\delta = \Phi_1 - \Phi_2 + \frac{4\pi h}{\lambda}\sqrt{n_1^2 - \sin^2\theta} \qquad [3]$$

The order of interference, P, is

$$\delta = 2\pi P \qquad [4]$$

where if $P = 0, 1, 2, 3 \ldots$ interference is constructive, and if $P = 1/2, 3/2, 5/2 \ldots$ interference is destructive.

Equations [3] and [4] can be solved for the epitaxial layer thickness, h, as

$$h = \left(P_j - \frac{\Phi_{1j}}{2\pi} + \frac{\Phi_{2j}}{2\pi}\right)\frac{\lambda_j}{2\sqrt{n_1^2 - \sin^2\theta}} \qquad [5]$$

An expression for the order, P, is obtained by writing Eq. [5] for the two different interference extremum and subtracting one from the other. The convention is adopted that $\lambda_1 > \lambda_2$, hence $P_2 > P_1$ and $P_2 = P_1 + m$. The result is given by

$$P_2 = \frac{m\lambda_1}{\lambda_1 - \lambda_2} + \frac{\Phi_{11}\lambda_1 - \Phi_{12}\lambda_2}{2\pi(\lambda_1 - \lambda_2)} - \frac{\Phi_{21}\lambda_1 - \Phi_{22}\lambda_2}{2\pi(\lambda_1 - \lambda_2)} \qquad [6]$$

where Φ_{X1} is the phase shift at λ_1 and Φ_{X2} is the phase shift at λ_2.

Equations [7a] and [7b] express the phase shifts Φ_1, and Φ_2 in terms of the indices of refraction and the extinction coefficients of mediums 0, 1, and 2 (6). For normal incidence

$$\tan\Phi_1 = \frac{2\,n_0 k_1}{n_0^2 - n_1^2 - k_1^2} = 0 \text{ as } k_1 = 0 \qquad [7a]$$

$$\tan\Phi_2 = \frac{2\,n_0 k_2}{n_1^2 - n_2^2 - k_2^2} \text{ for } k_1 = 0 \qquad [7b]$$

In order to calculate the phase shifts values of n and k must be obtained.

Moss (7), Smith (8), Spitzer and Fan (9), and Lyden (10) made various approximations to the theory of the optical constants of a semiconductor. These approximations make their solutions valid for limited ranges of wavelength and carrier concentration. The general solutions (11) for the index of refraction and extinction coefficient are given by Eq. [8a] and [8b]. These solutions have been verified by comparison with published data on the reflectivity of heavily doped semiconductors (12).

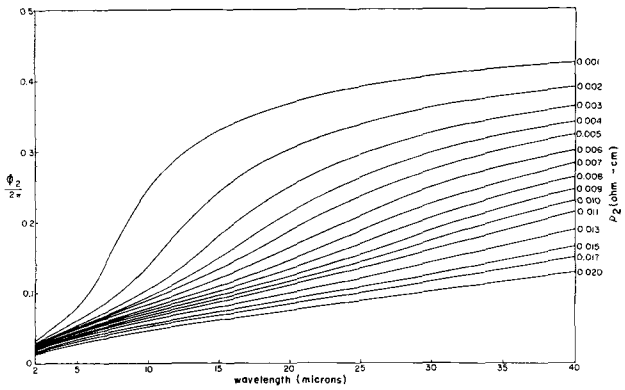

Fig. 2. Phase shift on reflection at the epitaxial layer-substrate interface for N/N$^+$ silicon.

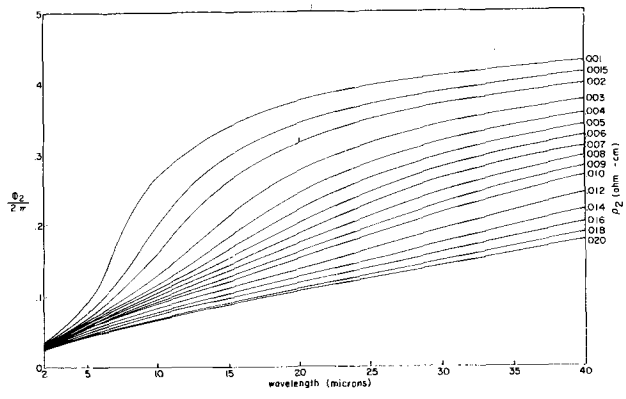

Fig. 3. Phase shift on reflection at the epitaxial layer-substrate interface for P/P$^+$ silicon.

$$n = \frac{1}{\sqrt{2}}\left[K_L - \frac{e^2\lambda^2 NJ(D)}{4\pi^2\epsilon_0 C^2 m^*}\right]^{1/2}\left\{1 \pm \left[1 + \frac{e^8\lambda^6 N^4\rho_0^2 g^2 [L(D)]^2}{64\pi^6\epsilon_0^2 C^6 m^{*4}\left[K_L - \frac{e^2\lambda^2 NJ(D)}{4\pi^2\epsilon_0 C^2 m^*}\right]^2}\right]^{1/2}\right\}^{1/2} \qquad [8a]$$

$$k = \frac{1}{\sqrt{2}}\left[K_L - \frac{e^2\lambda^2 NJ(D)}{4\pi^2\epsilon_0 C^2 m^*}\right]^{1/2}\left\{-1 \pm \left[1 + \frac{e^8\lambda^6 N^4\rho_0^2 g^2 [L(D)]^2}{64\pi^6\epsilon_0^2 C^6 m^{*4}\left[K_L - \frac{e^2\lambda^2 NJ(D)}{4\pi^2\epsilon_0 C^2 m^*}\right]^2}\right]^{1/2}\right\}^{1/2} \qquad [8b]$$

where

$$J(D) = \frac{1}{\Gamma(5/2)}\int_0^\infty \frac{x^{9/2}\,e^{-x}\,dx}{x^3 + D} \qquad D = \frac{N^2 e^4 \lambda^2 \rho_0^2 \Gamma(4) g}{4\pi^2 C^2 m^{*2}}$$

$$L(D) = \int_0^\infty \frac{x^3\,e^{-x}\,dx}{x^3 + D} \qquad g = \frac{\Gamma(4)}{[\Gamma(5/2)]^2}$$

where N is the carrier concentration, ρ_0 the d-c resistivity, λ the wavelength, m^* the conductivity effective mass, e the charge on electron, and C the velocity of light. All the symbols have their standard meanings. K_L is the dielectric constant of the intrinsic semiconductor at long wavelengths, and D is a convenient parameter in the integrals. The choice of the positive or negative sign is dictated by the fact that n and k must be real.

These solutions are applied to Eq. [7a] and [7b] to calculate the phase shift. It can be shown that as the impurity concentration decreases, the index of refraction approaches the intrinsic index of refraction and the extinction coefficient approaches zero. For the first phase shift, ϕ_1, with a lightly doped layer, less than $10^{17}/\text{cm}^3$, and the wavelength region between 5 and 35μ, the phase shift is π, and not a function of the wavelength.

Since no such convenient approximation may be made for the second phase shift, these equations were programmed for an IBM 7094 computer and solved numerically (13). Figure 2 shows $\Phi_2/2\pi$ plotted as a function of wavelength for various substrate resistivities for N-type silicon. Figure 3 shows the same parameters plotted for P-type silicon. The phase shift varies from zero to π as the wavelength or carrier concen-

Table I. Order calculation for N/N+ silicon

The substrate resistivity, ρ_2 = 0.0069 ohm-cm. The average error for uncorrected order is 0.35 and for corrected order is 0.10.

Reference number	λ(μ) Max	λ(μ) Min	Uncorrected order $\frac{m\lambda_0}{\lambda_0-\lambda_j}+\frac{1}{2}$	$\frac{\Phi_{2j}\lambda_j}{2\pi}$	Order correction	Corrected order-P_j Max	Corrected order-P_j Min
−1	27.90		2.34	5.90	−0.40	1.94	
0		21.95	—	3.53	—		—
1	18.30		3.51	2.40	−0.31	3.20	
2		15.40	3.85	1.70	−0.28		3.57
3	13.05		4.19	1.20	−0.26	3.93	

tration increases. These phase shifts are then used in Eq. [5] and [6] to calculate the layer thickness.

Discussion

The best and most general procedure found for calculating epitaxial layer thickness from the interference pattern is: (*I*) Knowing the resistivity of the substrate, determine the orders of the maxima and minima observed. (*II*) Calculate the thickness from the order using the phase shift correction.

Table I shows a sample order calculation for an N/N+ epitaxial layer. Φ_1 has been replaced by π and the terms factored to yield the 1/2 in the uncorrected order. In all of the calculations presented, all computations involving wavelengths are taken from the reference number zero which was the longest wavelength valley occurring in the spectrum. The calculated order generally differs from a whole integer, for a maximum, or a half integer, for a minimum by less than 0.2. This deviation is felt to be caused by small errors in reading the wavelengths of maxima or minima, which cause significant errors when the difference in wavelengths is taken. If the order calculation spans many fringes, the average error is generally less than 0.1. Because of this effect, samples with thick layers may be treated differently. By combining Eq. [5] and [6] and solving for the thickness

$$h = \frac{m\,\lambda_1\,\lambda_2}{2(n_1^2 - \sin^2\theta)^{1/2}\,(\lambda_1 - \lambda_2)}\left[1 - \frac{\phi_{21} - \phi_{22}}{2\,\pi\,m}\right] \quad [9]$$

Equation [9] may be used when the pair of wavelengths, used for the calculation, span many fringes so that the "difference" errors are small, and m is large.

When the correct order of one maximum or minimum has been determined, the orders of other maxima and minima may be assigned. Note that when the order is corrected, no difficulty is experienced in assigning whole or half integers to the peaks or valleys.

Table II shows the thickness calculations for the same sample treated in Table I. The thicknesses calculated without correction show a systematic error while the corrected values agree quite well. The uncorrected thickness. calculated by

$$h' = \frac{m\,\lambda_1\,\lambda_2}{2(n_1^2 - \sin^2\theta)^{1/2}\,(\lambda_1 - \lambda_2)} \quad [9a]$$

has a spread of 13.6% while the corrected thickness has only a 2.6% spread.

Table II. Thickness calculation for the same sample as in Table I

The average corrected thickness is 7.01μ ± 1.3% and average uncorrected thickness is 7.62μ ± 6.8%.

Reference number	λ(μ)	Order P	$\frac{\Phi_2}{2\pi}$	Corrected thickness h(μ)	Uncorrected thickness h′(μ)
−1	27.90	2.0	0.214	6.98	7.59
0	21.95	2.5	0.155	6.97	—
1	18.30	3.0	0.136	7.11	8.15
2	15.40	3.5	0.115	7.07	7.63
3	13.05	4.0	0.099	6.93	7.12

Table III. Order calculations for thin N/N+ silicon sample

An approximate thickness of 4μ was used to calculate an approximate order of 1.26. The correct order for that peak is therefore 1.0. The substrate resistivity, ρ_2 = 0.006, ohm-cm.

Reference number	λ(μ) Max	λ(μ) Min	Uncorrected order $\frac{m\lambda_0}{\lambda_0-\lambda_j}+\frac{1}{2}$	$\frac{\Phi_{2j}\lambda}{2\pi}$	Order correction	Corrected order-P_j Max	Corrected order-P_j Min
−1	28.80		1.37	6.05	0.38	0.99	
0		17.25	—	2.39	—		—
1	12.20		2.26	1.16	0.25	2.01	

It should be noted that the correction decreases the calculated thickness. The correction has its largest effect when the order is small. For $P = 2$, a typical correction is −10%. The correction improves the agreement between the staining technique and infrared technique since the infrared technique, without correction, always reads thicker. It was reported by Pliskin and Grochowski (3) that the difference between the two techniques ranged up to 11%.

Table III shows order calculations for a thin N/N+ epitaxial silicon sample. It was noted by Pliskin (4) that if the approximate thickness is known within wide limits, the order may be deduced. This is true for low orders (1, 2, and 3) as incorrect choices of the order change the thickness by at least 33%. This change is at least 50% for orders 1 and 2. Order zero, if never observed as the second phase shift (ϕ_2), never reaches π.

Table IV shows thickness calculations for the same thin sample. These data exhibit the self consistency observed on the thicker sample even when the order correction is 30% for first order. This exhibited self consistency extends the range of the infrared technique below 5μ.

Tables V and VI show similar calculations for a P/P+ epitaxial silicon sample. The data have been treated in the same manner as the N-type samples.

In conclusion, the shift in phase of infrared radiation upon reflection from an epitaxial layer-substrate interface has been calculated. When this phase shift is included in the calculation of epitaxial layer thick-

Table IV. Thickness calculations for sample shown in Table III

The average corrected thickness is 2.90 ± 0.016μ and the average uncorrected thickness is 3.32 ± 0.073μ.

Reference number	λ(μ)	Order P	$\frac{\Phi_{2j}}{2\pi}$	Corrected thickness h(μ)	Uncorrected thickness h′(μ)
−1	26.80	1.0	0.246	2.95	3.46
0	17.05	1.5	0.138	2.87	—
1	12.20	2.0	0.099	2.88	3.17

Table V. Order calculation for P/P+ silicon

The substrate resistivity is 0.01 ohm-cm. The average error for the corrected order is 0.12 and for the uncorrected order is 0.39.

Reference number	λ(μ) Max	λ(μ) Min	Uncorrected order $\frac{m\lambda_0}{\lambda_0-\lambda_j}+\frac{1}{2}$	$\frac{\Phi_{2j}\lambda_j}{2\pi}$	Order correction	Corrected order-P_j Max	Corrected order-P_j Min
−1	29.80		1.38	6.38	0.31	1.07	
0		19.00	—	2.76	—		—
1	14.00		2.40	1.61	0.23	2.17	

Table VI. Thickness calculations for the same sample as in Table V

The average corrected thickness is 3.10 ± 0.033μ and the average uncorrected thickness is 3.64 ± 0.12μ.

Reference number	λ(μ)	Order P	$\frac{\Phi_{2j}}{2\pi}$	Corrected thickness h(μ)	Uncorrected thickness h′(μ)
−1	29.80	1.0	0.214	3.02	3.40
0	19.00	1.5	0.145	3.08	—
1	14.00	2.0	0.114	3.20	3.88

ness, the self consistency of the measurement is improved, and the applicable thickness range is increased.

Acknowledgments

The authors wish to acknowledge the contributions of C. D. Gill in programming the solutions for the IBM 7094 computer and M. R. Poponiak for the collection of the experimental data.

Manuscript received July 6, 1965. This paper was presented at the Washington Meeting, Oct. 11-15, 1964.

Any discussion of this paper will appear in a Discussion Section to be published in the December 1966 JOURNAL.

REFERENCES

1. W. G. Spitzer and M. Tanenbaum, *J.A.P.*, **32**, 744 (1961).
2. M. P. Albert and J. F. Combs, *This Journal*, **109**, 709 (1962).
3. E. Grochowski and W. A. Pliskin, Paper presented at the Detroit Meeting of the Society, October 1961.
4. W. A. Pliskin, IBM, Private communication.
5. M. Born and E. Wolf, "Principles of Optics," MacMillan Co., New York (1964).
6. American Institute of Physics Handbook, pp. 6-104, McGraw-Hill Book Co., New York (1963).
7. T. S. Moss, "Optical Properties of Semiconductors," Butterworths, London (1959).
8. R. A. Smith, "Semiconductors," Cambridge University Press (1959).
9. W. G. Spitzer and H. Y. Fan, *Phys. Rev.*, **106**, 882 (1957).
10. H. A. Lyden, *ibid.*, **134**, A 1106 (1964).
11. P. A. Schumann, Jr. and R. P. Phillips, IBM Technical Report TR 22.167.
12. R. P. Phillips and P. A. Schumann, Jr., Paper presented at May 1965 meeting of the Society.
13. P. A. Schumann, Jr., and R. P. Phillips, IBM Technical Report TR 22.182.

Reaction of Tantalum with Molten Cerium-Cobalt Alloys

Felix B. Litton and John C. Biery

University of California, Los Alamos Scientific Laboratory, Los Alamos, New Mexico

ABSTRACT

The reaction of tantalum with molten cerium-cobalt was investigated by heating alloys containing from 6 to 18 w/o cobalt in sealed tantalum capsules at temperatures from 600° to 800°C and at times from 4 to 2069 hr. At 800°C, with 18 w/o cobalt-cerium alloy, reaction layers formed which varied in thickness with time from 5 to 16μ. The reaction layer consisted of two separate zones. The inner diffusion zone contained discrete particles of cerium distributed in a tantalum-cobalt alloy, TaCo or Ta_2Co. The composition of the molten cerium-cobalt alloy, temperature, and reaction time controlled the composition and growth of the reaction layer. The tantalum-cobalt phase identified as Ta_2Co was predominant in layers formed from cerium-cobalt containing 12 w/o cobalt, while either TaCo or Ta_6Co_7 was predominant in the layer formed from cerium-cobalt containing 18 w/o cobalt. The sequential steps in the formation of the reaction layer are as follows: dissolution of tantalum, precipitation of Ta-Co crystals on the Ta surface, diffusion of Co into and Ta out from an inner diffusion zone, and continued precipitation of a tantalum-cobalt alloy from the liquid cerium-cobalt melt onto the outer layer. The growth rate at long times was controlled by diffusion of tantalum and cobalt through the outer precipitation layer.

Low melting plutonium alloys have been proposed for fuels in fast breeder power reactors to eliminate the problem of irradiation damage and to simplify handling and reprocessing procedures (1, 2). Alloys of potential value occur in the Pu-Fe and Pu-Ce-Co systems (3-5). The Los Alamos Molten Plutonium Reactor Experiment (LAMPRE) was operated to determine the problems that might be encountered when these fuels are used under operating conditions. The core of the LAMPRE reactor consisted of an array of tantalum capsules containing plutonium fuel alloy (6-8). Tantalum and tungsten had been observed to be satisfactory materials for alloy containment, but tantalum was preferred because of the greater ease in its fabrication.

In out-of-pile experiments with the Pu-Co-Ce fuel and Co-Ce binary alloys held in tantalum capsules, a cobalt-tantalum reaction layer was observed to form. To understand better the mass transfer processes of tantalum in the Co-Ce-Pu fuels, a knowledge of the characteristics of the reaction layer was necessary. This study was initiated in an attempt to determine these characteristics by observing layers formed from the Co-Ce alloys.

Experimental

Materials.—Tantalum capsules, 1½ in. long, were fabricated from 0.025 in. wall x 0.430 in. O.D. seamless tubing. End caps were stamped from sheet stock. Capsules were fabricated from powder metallurgy, double arc-melted, and electron-beam-processed material. The parts were degreased and dipped in hydrofluoric-nitric acid mixture prior to attaching the end cap by welding, after which the capsule blanks were vacuum annealed for 1 hr at 1450°C.

Cerium base alloys were prepared to contain nominally 6, 12, and 18 w/o Co by heating 99.8 w/o Ce with 99.5 w/o Co to 900°C for 2 hr in tantalum crucibles under a helium atmosphere. During alloying, the melts were stirred with helium and filtered through a tantalum frit. Prior to their use, the cerium base alloys were analyzed for cobalt, then stored in a vacuum desiccator.

Procedure.—The reaction between tantalum and Ce-Co alloys was studied by heating 5g of each alloy composition in a tantalum capsule for a specified time at a given temperature. The cerium base alloys were cut, weighed, and placed in the capsules in air, and sealed in a welding box under argon. The capsules were placed in a copper block and heated under a positive pressure of 10 cm of helium. The temperature of the furnace was regulated from a thermocouple centrally located in the copper block to within ± 5°C of the desired temperature.

After heating, transverse sections were cut from the tantalum capsule for metallographic examination and chemical analysis to determine the structure and amount of cobalt in the reaction layer. The cerium-cobalt alloy was dissolved from the transverse section in dilute hydrochloric acid, and, after visually measuring the layer thickness, the weight of cobalt in the layer was determined by chemical analysis and re-

ported as milligrams cobalt per square centimeter of surface area.

Description of Reaction Layer Growth

Photographs of the reaction layer formed on tantalum in contact with 6, 12, and 18 w/o cobalt-cerium alloys for 96 hr at 800°C are shown in Fig. 1, 2, and 3. The tantalum capsules were cut longitudinally to produce the section shown at the right in each figure and the Ce-Co alloy dissolved from one-half of the capsule with dilute hydrochloric acid revealing the section shown at the left in each figure. A reaction layer was formed above the liquid meniscus in each of the capsules. However, a reaction layer was not formed along the surface in contact with the bulk liquid with 6 and 12 w/o Co-Ce alloys. With these alloys, the areas in direct contact with the melt or with heavy films above the liquid surface show an etched appearance. The reaction layer in Fig. 1 and 2 is the silvery zone above the etched areas. In Fig. 2 a fairly heavy layer of reaction layer crystals has grown immediately above the etched area. The Co-Ce alloy has climbed the walls of the capsule and has covered all surfaces with a thin liquid layer. For the 6 and 12 w/o Co-Ce alloys at this length of exposure, the reaction layer forms only on the surfaces covered with this very thin film. In contrast, as shown in Fig. 3, a reaction layer was formed above the meniscus and in the bulk liquid contact area with molten 18 w/o Co-Ce alloy.

Structure of reaction layer.—The reaction layer consists of a diffusion zone adjacent to the tantalum and a crystalline deposit in contact with the cerium-cobalt alloy. Electron microprobe analysis indicated that the diffusion zone contained cerium globules distributed in a tantalum-cobalt phase and the crystalline deposit consisted of an impurity-free tantalum-cobalt phase.

X-ray and microprobe analyses showed that two distinct tantalum-cobalt phases were included in the reaction layer zones. However, they also indicated that the exact composition of these phases varied somewhat. Therefore, in this report these phases are titled A and B. The A phase is nominally Ta_2Co while the B phase is nominally TaCo with some solubility of cobalt existing in both phases. For instance, the composition of the B phase was found to range from Ta_6Co_7 to Ta_7Co_6.

The composition of the reaction layer zones varies with changes in temperature and cobalt concentration in the melt. Two cobalt-temperature regimes exist. In the upper one B is the stable phase in contact with the melt; in the lower regime A phase is stable. The

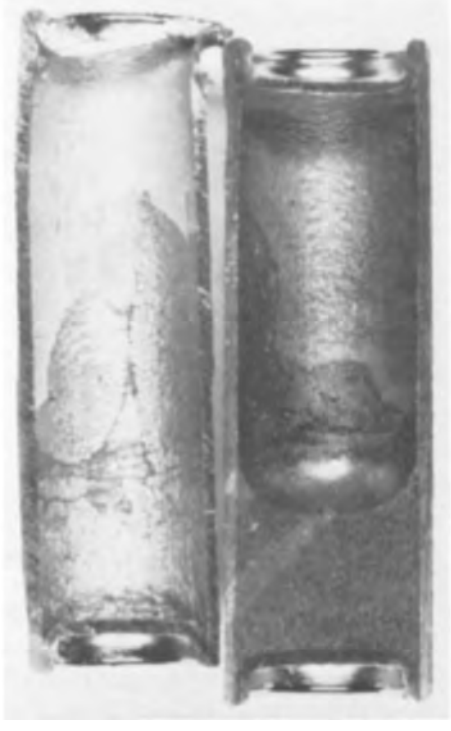

Fig. 1. View of tantalum capsule heated in contact with 6 w/o Co-Ce alloy. Left, After dissolving the Ce-Co alloy in dilute hydrochloric acid, the reaction layer is shown as the silvery zone above the etched area. Magnification 2.5X.

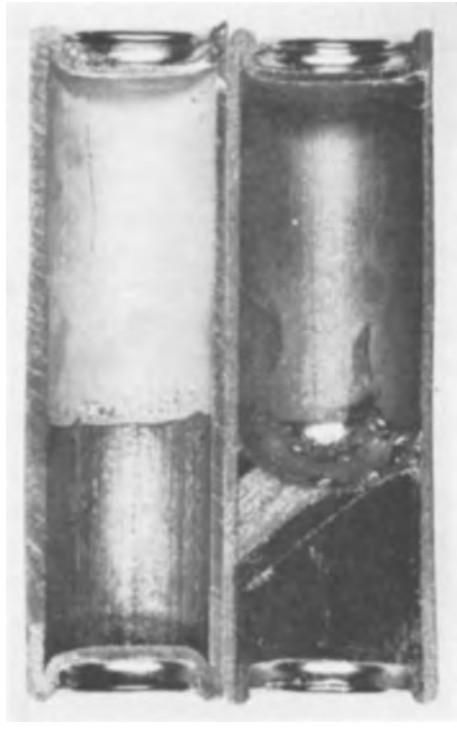

Fig. 2. View of tantalum capsule heated in contact with 12 w/o Co-Ce alloy. Left, Ta-Co reaction layer covers the entire area above the meniscus of the Ce-Co alloy. Magnification 2.5X.

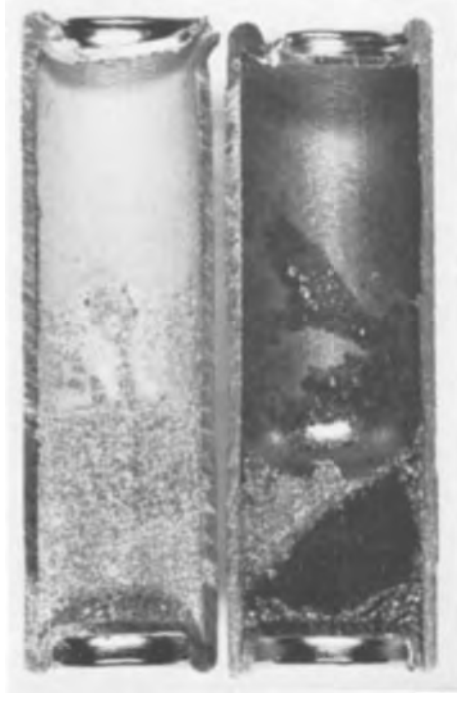

Fig. 3. View of tantalum capsule heated in contact with 18 w/o Co-Ce alloy. Left, Crystalline Ta-Co reaction layer is on the tantalum surfaces above and below the meniscus. Magnification 2.5X.

Table I. Temperature-cobalt concentration boundary between A and B phase stable regimes

Temp, °C	Cobalt concentration in melt,* w/o
800	15
700	18

* A phase is stable below this concentration while B phase is stable above this concentration.

temperature-cobalt concentration boundary between the regimes is shown in Table I.

The inner diffusion zone which may not be in direct contact with the melt can contain layers of both A and B phase. In the upper cobalt-temperature regime, microprobe analysis has shown the outer precipitation zone to be B phase and the inner diffusion zone to be mainly B phase with a possible thin zone next to the metal being A phase. In the lower regime, both the inner and outer zones contain only A phase.

Examples of the above phenomena are shown in Fig. 4 and 5. The two-layered structure in Fig. 4 has been emphasized by a selective etching procedure. The outer precipitation crystals resisted etching and appear much as they did in the as-polished state. The inner diffusion zone was attacked much more rapidly by the etch. This layer was produced with 18 w/o Co-Ce at 700°C in 1024 hr.

The outer precipitation layer appears to grow in horizontal platelets of relatively uniform thickness across the tantalum diffusion zone surface. The average thickness of the platelets is approximately 5-6μ, but the width of the platelet may be as great as 300μ. In Fig. 5 a very large crystal which had fallen off the tantalum surface is shown. Note the well-formed corners of 120°. This particular crystal is 330μ long and 200μ wide. These crystals were formed in 18 w/o Co-Ce at 740°C in 832 hr.

Growth Rates of Reaction Layer in Bulk Liquid Contact Area

6 w/o Cobalt-cerium.—With 6 w/o cobalt-cerium alloy no reaction layer was formed on tantalum in contact with the bulk liquid phase at temperatures from 600° to 800°C and periods of time up to 2069 hr.

12 w/o Cobalt-cerium.—Reaction layers were formed with 12 w/o cobalt-cerium alloy at 800°C but not at lower temperatures. However, even at 800°C the layers formed only after relatively long periods of time, *i.e.*, 1024 and 2069 hr. The reaction layer thicknesses observed at these times were 5.5μ and 8.5, respectively.

Fig. 4. Structure of reaction layer. Two zones are shown: the diffusion zone adjacent to the tantalum, covered by crystals identified by x-ray analyses as B phase. Etched. Magnification 420X.

Fig. 5. B phase precipitation platelet, 330μ long x 200μ wide x 5μ thick.

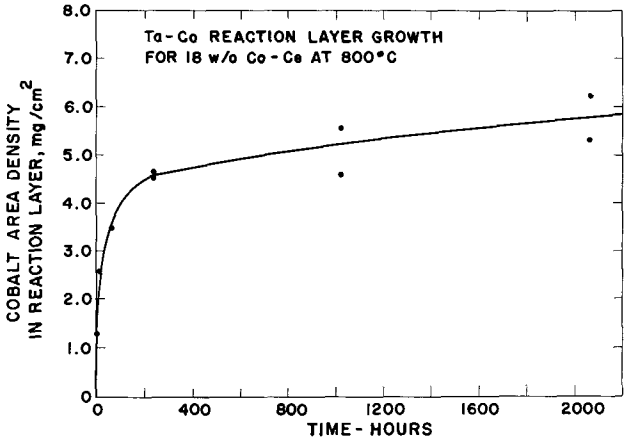

Fig. 6. Reaction layer growth as a function of time, 18 w/o Co-82 w/o Ce at 800°C.

18 w/o Cobalt-cerium.—800°C.—The growth rate data for tantalum with 18 w/o cobalt-cerium alloy at 800°C are shown in Fig. 6 and in Table II. At this temperature a reaction layer was formed in periods as short as 4 hr. The reaction layer grew very rapidly in the first 250 hr. Thereafter, the growth essentially stopped. The thickness observed after 2069 hr as estimated from the cobalt density data was 16.7μ.

The thicknesses of the reaction layer in microns as obtained from photomicrographs are also tabulated in Table II for the 18 w/o Co-Ce alloy at 800°C. Visual

Table II. Ta-Co reaction layer growth for 18 w/o Co-Ce at 800°C

Time, hr	Cobalt area density in reaction layer, mg/cm²* Experimental***	Smoothed***	Layer thickness,** μ
4	1.28	1.40	5.2
16	2.58	2.40	9.0
64	3.48	3.60	11.0
240	4.51	4.58	13.3
1024	4.64 4.57 5.53	5.20	—
2069	5.31 6.22	5.76	—

* Determined by chemical analysis of ring cut from capsule.
** Determined by graphical integration of layer area on photomicrograph.
*** The estimated experimental standard deviation is 6.1%. The estimated standard deviation of the smoothed curve is 2.0%, and a 95% confidence width about the smoothed curve is ± 6.6%.

Table III. Time required for reaction layer to start forming when in contact with bulk cobalt-cerium melts ($A/V = 5$ cm^{-1})

	Time to first formation, hr		
	600°C	700°C	800°C
6 w/o Co-Ce	>2069	>2069	>2069
12 w/o Co-Ce	>2069	>2069	1024
18 w/o Co-Ce	>2069	256 (Intermittent thereafter)	4

readings at 1024 and 2069 hr were not obtained. These data are not as reliable as the cobalt density data since the visual thicknesses were measured from one small area of the layer while the chemical data were obtained from the layer formed on a complete ring cut from the capsule. Comparison of the visual and chemical data indicates that the microns of thickness per milligram per square centimeter of cobalt density decreased from 3.7 at 4 hr to 2.9 at 240 hr. This variation would indicate that the composite layer was changing in cobalt composition with time and was becoming more dense.

700°C.—At 700°C with 18 w/o Co-Ce, reaction layers formed after 256 hr of contact time. However, even after this initiation period subsequent tests at longer periods did not consistently produce reaction layers. For instance, at 256 and 1024 hr the observed cobalt density in the layer was 3.94 and 6.88 mg/cm^2, respectively. But at intermediate and longer times of 625 and 2069 hr no layer was produced whatsoever. This type of behavior seems to indicate that the 18 w/o—700°C conditions represents one of the boundary points between the fast and slow reactive regimes.

600°C.—At 600°C with the 18 w/o melt no reaction layer was formed in the bulk liquid contact zone in periods up to 2069 hr.

A summary of the minimum observed times to form reaction layers in contact with the bulk liquid phase is given in Table III.

Effect of Cobalt Concentration on Reaction Layer Formation Rate

The results from the 12 and 18 w/o Co-Ce melts at 800°C show a large change in reaction layer formation rate with change in cobalt concentration. To test the effect more exactly, a series of capsules was run for 96 hr at 800°C with melt concentrations ranging from 11 to 16 w/o cobalt in 1% increments. The results are shown in Fig. 7. Up to 14 w/o cobalt no layer was formed. Then almost dramatically, the layer started to grow rapidly at 15 and 16 w/o cobalt. The measured cobalt density in the layer increased from < 0.01 mg/cm^2 at 14 w/o to 2.4 mg/cm^2 at 15 w/o. A 1% increase in cobalt concentration increased the reaction rate by a factor of 200 or more.

Effect of Surface Area to Volume Ratio on Reaction Layer Formation

The ratio of tantalum contact surface area to melt volume (A/V) greatly influences the ability of the reaction layer to form, especially in the low concentration-temperature regime. For instance, reaction layer is always found above the meniscus where a thin layer of melt, 10-20μ thick, has crept up the wall. Here the A/V ratio is 500 to 1000 cm^{-1}. In the same systems, 6 and 12 w/o cobalt at 600°-800°C, no reaction layer is formed at times up to 1000 hr on areas in contact with the bulk liquid phase where the A/V ratio is approximately 5 cm^{-1}.

To investigate the area to volume ratio effects, finely divided tantalum powder (30μ diameter particles) was added to 6 w/o Co-Ce and was run at 600°C for 96 hr. In this short period a reaction layer formed on the tantalum wall in direct contact with the powder, while no reaction layer was found on the wall where no powder resided. The A/V ratio in the powder zone was approximately 250 cm^{-1}.

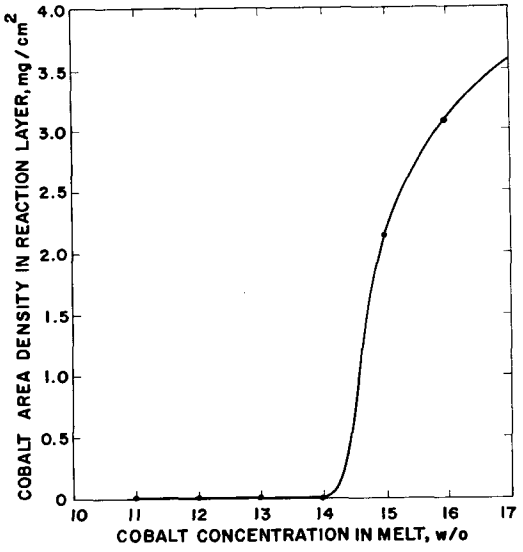

Fig. 7. Reaction layer thickness as a function of cobalt concentration in melt; 96 hr at 800°C.

Mechanical Instability of Reaction Layer

A number of experiments have been run which indicate that the outer precipitation layer cannot stand excessive mechanical or thermal shock. Temperature cycling and melt freezing cause the precipitation crystals to disengage from the diffusion zone. The crystal shown in Fig. 5 is one of many hundreds of crystals which fell off from the wall of a capsule when the melt was frozen, capsule inverted, and alloy remelted. Also, a few runs at temperatures of 900°C and above indicate that the precipitation layer grows and spalls with no obvious thermal perturbations.

The instability of the precipitation zone indicates that the over-all reaction layer might not be protective and self-healing if it is thermally perturbed. The layer growth is slowed by the formation of the precipitation zone. If it falls off, then the total layer can continue to grow until more crystals cover the surface. A worse case which could cause catastrophic failure is one in which the precipitation crystals detach but loosely hang onto the wall. The dissolving tantalum can precipitate on the detached crystals which now serve as a local sink. The dissolution process is unimpeded since the precipitation zone is not re-formed to inhibit the diffusion of cobalt into and tantalum out from the diffusion zone.

Mechanism for Formation of Reaction Layer

The following stepwise mechanism is proposed to explain the observed phenomena.

1. Dissolution of tantalum into the melt. Before the layer can grow tantalum must dissolve into and saturate the melt. The rate of dissolution appears to be a strong function of cobalt concentration. In the high cobalt-temperature regime, the rate is very fast while in the low regime the rate appears to be quite slow. During this period cobalt does not diffuse into the tantalum wall. The cobalt does attack the tantalum and probably forms Ta-Co A or B phase molecules or subcritical sized crystallites on the surface. While the melt is unsaturated, these crystallites are unstable and immediately dissolve. In this manner tantalum and cobalt transfer back into the liquid metal.

2. Supersaturation of the melt and precipitation of stable crystals on the tantalum surface. The melt becomes supersaturated with respect to the A or B phase crystals and precipitates these crystals on the tantalum surface. The melt is not saturated with respect

to the tantalum metal since the tantalum is in a higher energy state in the metal wall then in the Ta-Co crystals.

3. Formation of diffusion zone. With the precipitation of the crystals, the diffusion zone immediately starts to form. The cobalt attacks the tantalum surface and forms the A or B phase crystallites. Now, however, stable crystals of A or B phase are in direct contact with the reactive surface, and the new crystallites are stabilized in the local area of the precipitate. The newly formed reaction compound does not dissolve into the melt since the melt is now saturated with respect to the stable crystals.

As the reaction proceeds, the reactive zone moves inward into the metal. Also, the growth can move out radially from the initial precipitation crystal. (Note: Circular colonies of crystals and reactive zones have been noted on tabs immersed in the Co-Ce alloy.)

By observing growth on thin foils of known thickness, the original tantalum surface is readily identified as the boundary between the precipitation zone and the diffusion zone. Therefore, as the Ta-Co reaction zone is formed, tantalum must diffuse outward toward the melt to maintain volume and mass continuity since the Ta-Co compounds are less dense than tantalum itself. The outward current of tantalum can dissolve into the melt because the melt is saturated with respect to the A or B phase crystals and not with respect to the tantalum metal.

4. Continued growth of the A or B phase crystals. The tantalum which is dissolving into the melt from the diffusion zone precipitates on the crystals which are near by. The A or B phase crystals then continue to grow in platelets on the surface and to move laterally across the surface. Figures 8 and 9 show two stages in this development of the crystalline layer as grown from 18 w/o Co-Ce at 800°C.

5. Slowing down of layer growth as precipitation crystals cover the surface. Since the precipitation crystals are well-formed flat platelets, they present a diffusion barrier to the diffusing cobalt and tantalum. Therefore, the process is essentially terminated when the crystals cover the surface. Slow growth can occur since there must be a small but finite diffusivity for the cobalt and tantalum in the precipitation layer.

Summary

Observed phenomena.

1. For temperatures and cobalt concentrations below 18 w/o at 700°C and 15 w/o at 800°C, a reaction layer forms in contact with the bulk fluid only after long incubation periods of 1000 hr or more. (A/V = 5 cm^{-1}).

2. For temperature-cobalt conditions above the limits in 1, the reaction layer forms at short times of 4 hr or less in the bulk phase contact area.

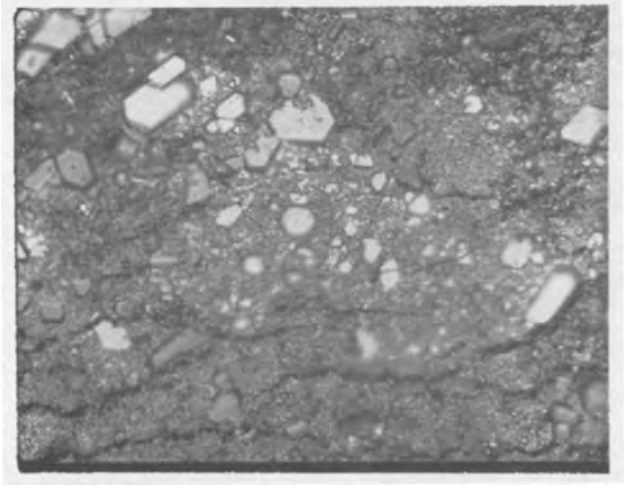

Fig. 8. Hexagonal B phase crystals in an early stage of development

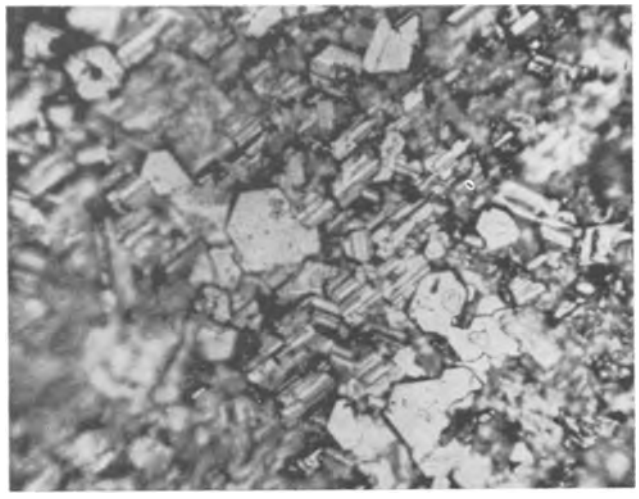

Fig. 9. A heavy layer of B phase crystals as developed at long times

3. For all concentrations and temperatures tested (6-18 w/o Co and 600°-800°C) the reaction layer formed in contact with the thin liquid layer above the meniscus in periods of 4 hr or less. (A/V = 500-1000 cm^{-1}).

4. Microprobe and chemical analysis show crystals in equilibrium with the melt to be A phase (approximately Ta_2Co) for the low temperature-cobalt conditions and to be B phase (approximately TaCo) for the high temperature-cobalt conditions.

5. Microprobe and chemical etching indicate that two layers form, one on the outside of the original surface and one inside the original surface. The outer layer appears to be crystals precipitated from the melt since they are well formed and contain no impurities. The inner layer appears to be a diffusion zone of Co in Ta since it etches easily and contains impurities of cerium. The outer crystals are A or B phase as indicated in item 4 above. The matrix of the inner layer is nominally A phase for the low temperature-concentration cases and B phase for the high temperature-concentration systems.

6. Evidence indicates that crystal precipitation must occur first before the cobalt diffusion zone can form.

Proposed Mechanism

The reaction layer appears to grow with the following sequence of events.

1. Tantalum dissolves into the melt.
2. The melt becomes supersaturated and precipitates A or B phase intermetallic crystals.
3. The cobalt diffusion zone starts to form.
4. Tantalum diffuses out of the diffusion zone, dissolves into the melt, and back precipitates on the A or B phase crystals.
5. The layer growth almost terminates when the diffusion zone is completely covered with thick crystals.

Proposed Cobalt Effect

1. The tantalum is attacked by the cobalt. The main effect is to form Ta_nCo nuclei which immediately dissolve into the melt.
2. The reverse reaction of Ta_nCo precipitation does not occur until the melt is supersaturated and can grow crystals above a critical size.
3. As temperature and cobalt concentration are lowered, the cobalt reaction produces Ta_2Co instead of TaCo. The Ta_2Co reaction proceeds much more slowly than does the TaCo reaction.

Stability of Layer

1. The precipitated crystals are not securely affixed to the tantalum surface. These crystals tend to spall off with thermal or physical shock. With spallation the cobalt-tantalum reaction is allowed to continue.

Acknowledgment

The authors wish to thank Carl Cushing for his help in obtaining data on the stability of the reaction layer. Also, the help of Marguerite Coleman and Doreen Bourne in preparing the manuscript is greatly appreciated.

Manuscript received Oct. 1, 1965; revised manuscript received Jan 17, 1966. Work on this paper was performed under the auspices of the United States Atomic Energy Commission.

Any discussion of this paper will appear in a Discussion Section to be published in the December 1966 JOURNAL.

REFERENCES

1. D. B. Hall, "Plutonium Fuels for Fast Reactors," Proceedings of the Second United Nations International Conference on the Peaceful Uses of Atomic Energy, 13, p. 300, United Nations Geneva (1958).
2. F. H. Spedding, "The Molten-Metal Fuel Reactor," Ames Laboratory Iowa State College, ISC-318, Office of Technical Services, U. S. Department of Commerce, Washington, D. C. (1953).
3. F. W. Schonfeld, *et al.*, "The Physical Metallurgy of Plutonium," Progress in Nuclear Energy, Vol. 2, Series V, Pergamon Press Ltd., London (1957).
4. J. K. Critchley, "Low Melting Point Alloys of Cerium with Iron, Cobalt and Plutonium," Atomic Energy Research Establishment, Harwell, England, AERE-M488 (1959).
5. A. S. Coffinberry *et al.*, "The Physical Metallurgy of Plutonium and Its Alloys," Second Geneva International Conference **6**, 681 (1958).
6. LAMPRE I Final Design Status Report, Los Alamos Scientific Laboratory, Los Alamos, New Mexico, LA-2833, March 8, 1963.
7. R. M. Bidwell *et al.*, *Nuc. Science and Eng.*, **14**, 109 (1962).
8. G. S. Hanks *et al.*, **14**, 135 (1962).
9. D. M. Poole *et al.*, "Properties of Plutonium Based Fuels," Chapter 12 in Plutonium 1960, Editors, E. Grison, W. B. H. Lord, and R. D. Fowler, Cleaver-Hume Press, Ltd., London (1961).

Standard Molar Free Energy of Formation of Uranium Dicarbide and Uranium Sesquicarbide by Electromotive Force Measurements

W. K. Behl and J. J. Egan

Brookhaven National Laboratory, Upton, New York

ABSTRACT

The free energy of formation of UC_2 and U_2C_3 has been determined by means of the following solid state galvanic cells operated between 700° and 900°C

$$U,UF_3(s)\,|\,CaF_2(s)\,|\,UF_3,UC_2,C \qquad [A]$$

$$U,UF_3(s)\,|\,CaF_2(s)\,|\,UF_3,U_2C_3,C \qquad [B]$$

Although UC_2 is in metastable equilibrium with carbon in cell A, results are significant. Experimental details are presented and results are compared with values obtained by other techniques.

In many cases electromotive force measurements provide a useful method for an accurate determination of the free energy of formation of compounds in liquid or solid state. In this laboratory, solid state galvanic cells

$$U,UF_3(s)\,|\,CaF_2(s)\,|\,UF_3,UC_2,C(s) \qquad [A]$$

and

$$U,UF_3(s)\,|\,CaF_2(s)\,|\,UF_3,U_2C_3,C(s) \qquad [B]$$

were employed to determine the free energy of formation of uranium dicarbide and uranium sesquicarbide, respectively, in the temperature range 700°-900°C. It has been observed from the phase diagram (1) that UC_2 is in equilibrium with carbon only at temperatures above about 1500°C. At lower temperatures, U_2C_3 is the stable phase in equilibrium with carbon. Thus in the temperature range 700°-900°C, cell A is in a metastable state. However, studies of several workers (2, 3) indicate that the transformation of UC_2 to U_2C_3 and carbon is an extremely slow process. In one experiment in this laboratory a sample of UC_2 was heated to about 900°C for more than a week, at which time an x-ray of the experiment showed no U_2C_3 in the sample. As this study has shown, despite the metastable nature of cell A, meaningful results for the free energy of formation of uranium dicarbide were obtained from this cell.

In cell A at the left-hand electrode

$$U = U^{+3} + 3e$$

and at the right-hand electrode

$$3e + U^{+3} + 2C = UC_2$$

and the over-all reaction on passing $3F$ is

$$U + 2C = UC_2$$

with the CaF_2 conducting F^- ions from right to left. Thus

$$\Delta F^\circ_{UC_2} = -3FE \qquad [1]$$

Likewise in cell B

$$2U = 2U^{+3} + 6e$$

$$6e + 2U^{+3} + 3C = U_2C_3$$

and over-all

$$2U + 3C = U_2C_3$$

with

$$\Delta F^\circ_{U_2C_3} = -6FE \qquad [2]$$

Experimental

Uranium dicarbide was prepared by mixing finely filed uranium metal with an excess of carbon powder, pressing the resulting mixture into a pellet, and heating the pellet in a graphite crucible under vacuum at 1600°-1700°C for 30-40 min in an induction furnace. An x-ray of the sample identified UC_2 and carbon.

The following procedure was employed to prepare uranium sesquicarbide. Equivalent amounts of uranium metal and carbon to form UC_2 were mixed together and heated in a graphite crucible under vacuum at 1600°C in an induction furnace for 2 hr. To this a calculated amount of uranium metal was added to yield a composition corresponding to U_2C_3. Two pellets were made of the mixture and placed in a molybdenum

crucible (one over the other) and heated at 1450°C under vacuum for 5 hr. The top pellet was then removed, crushed, and again made into a pellet and placed over the other pellet in the molybdenum cup and heated for 12 hr under vacuum. The procedure was repeated once more and finally the pellets heated at 1450°C under vacuum for 18 hr. The bottom pellet in immediate contact with molybdenum was discarded and the top pellet used for experiments. An x-ray of the sample identified it as U_2C_3.

The uranium carbides so prepared were separately crushed and mixed with UF_3, and again pressed into a pellet. A similar pellet was obtained by mixing finely filed uranium with uranium fluoride.

All the above mixing operations were performed under carbon tetrachloride to prevent uranium metal or the carbides from coming in contact with the air. Also the mixture under CCl_4 resulted in a paste, from which it was easier to obtain the pellets. Carbon tetrachloride was later pumped off by evacuating the assembled cell.

A calcium fluoride single crystal, which has been shown to conduct entirely through fluoride ions, served as the auxiliary electrolyte; molybdenum disks were used to provide the leads. The cell was then quickly assembled and evacuated for a few hours. The cell arrangement was similar to the one reported by Egan, McCoy, and Bracker (5). The cell was then filled with argon gas that provided the inert atmosphere during the course of the experiment. The temperature was gradually raised to 800°C and the cell allowed to come to an equilibrium value (generally 2-3 days); this was indicated by a steady value of emf. The emf of the cell was then measured at various temperatures. Temperature cycling did not affect the values of the cell potentials. In all cases, the cells were operated for a period of 1 month.

Results

The cell potential *vs.* temperature plots for cells A and B are presented in the curves shown in Fig. 1. The measurements for cell A were carried out between 700° and 900°C while those for cell B were carried out up to 800°C.

The free energies of formation for uranium dicarbide and uranium sesquicarbide at various temperatures calculated from Eq. [1] and [2] are shown on the right of the figure. They are also given by the equations

$$U(\beta) + 2C(gr) = UC_2(s)$$
$$\Delta F^o = -15{,}820 - 8.2T \text{ (kcal)} \quad [3]$$

$$U(\gamma) + 2C(gr) = UC_2(s)$$
$$\Delta F^o = -18{,}980 - 5.2T \text{ (kcal)} \quad [4]$$

$$2U(\beta) + 3C(gr) = U_2C_3(s)$$
$$\Delta F^o = -43{,}860 - 7T \text{ (kcal)} \quad [5]$$

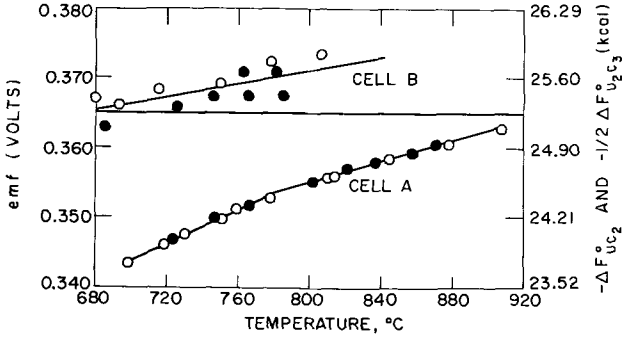

Fig. 1. Curves of emf measurements taken on cells of type A and B. Results from two separate cells are shown in each case (closed and open circles).

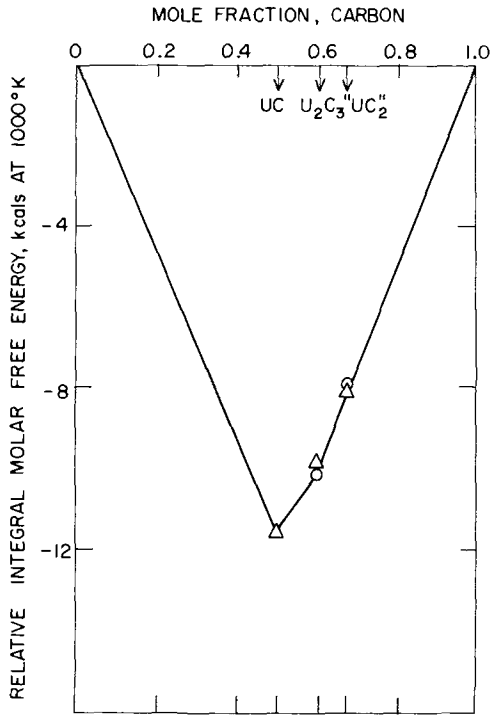

Fig. 2. Relative integral molar free energy *vs.* composition in the U-C system. The triangles represent values compiled in ref. (4). The circles represent values taken from the measurements reported here.

in the temperature range of the experiments. The precision between different cells was of the order of ±2 mv for UC_2 and ±4 mv for U_2C_3. Thus the accuracy is estimated as ±200 cal for the values reported here.

In curve A of Fig. 1, a break is observed at 780°C. This corresponds to the phase transformation of β-uranium to γ-uranium, which is known (6) to occur at 772°C.

Alcock and Grieveson (7) have measured the free energy of formation for the reaction

$$U(l) + 2C(s) = UC_2(s)$$

by measuring the uranium dissociation pressure of the carbide in equilibrium with pure carbon in the temperature range 1700°-1800°C. The free energy of formation (—27.54 kcal) extrapolated from these measurements to 1132°C (the melting point of uranium) compares very well with the value (—26.28 kcal) obtained by extrapolation from the present measurements.

An idea about the stability of the different phases in a binary system can be obtained (8) from a plot of relative integral molar free energy *vs.* mole fraction. Such a plot for the uranium-carbon system is shown in Fig. 2, in which the values of relative integral molar free energies of U_2C_3 and UC_2 obtained from the present measurements are plotted along with the literature (4) values for UC, U_2C_3, and UC_2. These values are from a thermochemical assessment using previous results from calorimetry, phase equilibria, vapor pressures, and other methods. The agreement is quite close between these values and the experimental values reported here. It is clear from the plot that at 1000°K, U_2C_3 is the stable phase in equilibrium with carbon. This is in agreement with the earlier phase diagram studies (1) for the U-C system.

Acknowledgment

The authors would like to thank Mr. John Bracker for preparing the UC_2 and U_2C_3 and for his help in assembling the cells. They are also indebted to Dr. Richard Wiswall for helpful discussions, and to Mr.

Bernard Sturm of the Reactor Division of Oak Ridge National Laboratory for supplying them with the UF_3 used in these experiments.

Manuscript received Nov. 15, 1965. This paper was presented at the San Francisco Meeting, May 9-13, 1965. This work was performed under the auspices of the United States Atomic Energy Commission.

Any discussion of this paper will appear in a Discussion Section to be published in the December 1966 JOURNAL.

REFERENCES

1. J. M. Leitnaker and W. G. Witteman, *J. Chem. Phys.*, **36**, 1445 (1962).
2. E. K. Storms, "A Critical Review of Refractories," LA-2942, p. 195 (1964).
3. S. Imato, Y. Sano, Y. Takad, K. Yamamoto, K. Watanalie, T. Isoda, and H. Uchikoshi, "Carbide in Nuclear Energy," Macmillan and Co., Ltd., London (1964).
4. "The Uranium-Carbon and Plutonium-Carbon Systems—A Thermochemical Assessment," Technical Reports Series, No. 14, IAEA, Vienna (1963).
5. J. J. Egan, W. McCoy, and J. Bracker, "Thermodynamics of Nuclear Materials," IAEA, Vienna (1962).
6. B. Blumenthal, J. E. Baumrucker, and L. T. Lloyd, *J. Nucl. Materials*, **2**, 23 (1960).
7. C. Alcock and P. Grieveson, "Thermodynamics of Nuclear Materials," IAEA, Vienna (1962).
8. C. Wagner, "Thermodynamics of Alloys," Addison Wesley Press, Inc. (1952).

The Ductile-Brittle Transition in Tantalum Carbide

H. A. Johansen and J. G. Cleary

Research Laboratories, Westinghouse Electric Corporation, Pittsburgh, Pennsylvania

ABSTRACT

Tantalum carbide was prepared in the composition range $TaC_{0.73}$ to $TaC_{1.26}$ and consolidated by hot pressing. Compositions at ends of the range were two phase. A modified cantilever-beam test method was used to determine the ductile-brittle transition temperature (T_{db}) at a given strain rate and for this geometry as a function of carbon content. The T_{db} range from $TaC_{0.98}$ was 1825°-1925°C, and the median nominal bend stress in this range was 23,000 psi (1617 kg/cm²). At $TaC_{0.90}$ the median nominal bend stress was at a minimum of 14,000 psi (984 kg/cm²) for the T_{db} range 1750°-1850°C. T_{db} increases approximately 150°C with increasing x across the single-phase cubic region of TaC_x.

Information concerning the high-temperature mechanical properties of refractory "hard metals" is of direct importance to their use as structural materials and to an understanding of the metallicity and mechanism of deformation of the general class of transition metal interstitial compounds.

Tantalum carbide, because of its very high melting point and good resistance to thermal decomposition, has long been of interest for many high-temperature applications, but the extreme brittleness and the absence of data on the mechanical properties at elevated temperatures have limited its consideration. In particular, knowledge has been lacking concerning the transition temperature (T_{db}) from brittle to ductile behavior, and its dependence on composition and other factors. While the T_{db} is not as well defined a physical quantity as, say density or melting point, because surface condition, porosity, second phase content, and other factors may influence T_{db}, nevertheless such information is of practical importance in understanding the limits of gross plastic flow. This work supplies new information on the ductile-brittle transition of well-characterized tantalum carbide under specific conditions.

Previous work in this field has been reported by Williams and Schaal (1) and by Williams (2) who carried out compression tests on single crystal TiC as a function of temperature, composition, and other parameters. Single crystal ZrC and NbC were also examined by Williams (2), and the behavior was found to be similar to that of TiC, although NbC was reported to have a higher hardness than either TiC or ZrC.

Experimental

Preparation of TaC_x.—Tantalum carbide compositions were prepared by direct reaction of the elements under argon in a graphite resistor furnace according to the reaction

$$Ta + xC \rightarrow TaC_x$$

for nominal values of $x = 0.8$ to 1.0. This is approximately the single-phase cubic NaCl structure region. In addition, compositions in the two-phase cubic plus hexagonal Ta_2C region, and in the cubic plus excess carbon region were prepared for comparison with the cubic single-phase TaC.

The materials used were metallurgical grade tantalum powder (Kawecki) and spectroscopic grade graphite powder (National Carbon). The tantalum metal was of 99.8% purity with oxygen the chief nonmetallic impurity (0.1%) as determined by vacuum fusion, and silicon and niobium the principal metallic impurities at 100 ppm each determined spectrographically.

Preparation of test specimens.—The tantalum carbide powders were consolidated by hot-pressing in graphite dies with 4 w/o cobalt as binder. The cobalt used was high-purity (99.999%) sponge (United Mineral). Hot-pressing was carried out by direct heating of the die by means of R. F. induction to 2000°C, and applying a pressure of 1.5 tons/in.² (211 kg/cm²). Densities obtained were between 90 and 95% of theoretical. Close to stoichiometry, dense compositions were somewhat more difficult to obtain. The compositions prepared of TaC_x were $x = 0.73$, 0.84, 0.90, 0.98, and 1.26 (1.0 + 0.26 free carbon). After compaction by hot pressing, rectangular cross-section specimens were prepared by diamond sawing to produce a rod 2 to 3 mm on a side and 5 cm long. The sawn rods were then decobalted by heating to 2000°C in vacuum to leave a cobalt content less than 0.1 w/o as determined by x-ray fluorescence analysis.

To insure homogeneity prior to testing, preliminary analysis for carbon content of the sawn specimens was made by x-ray diffraction using a 114.6 mm camera, and CuKα radiation with nickel filter. The patterns were single phase except for $TaC_{1.26}$ which showed free carbon lines, and $TaC_{0.73}$ which showed Ta_2C. The lattice parameters for the single-phase compositions were $a_o = 4.4540$Å for $TaC_{0.98}$, $a_o = 4.4427$Å for $TaC_{0.90}$, and $a_o = 4.4356$Å for $TaC_{0.84}$. The parameters are in good agreement with those reported by Bowman (3).

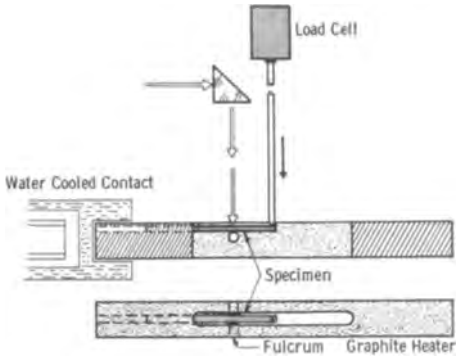

Fig. 1. Modified cantilever-beam tester (schematic)

All carbon contents were determined after the bend tests by analysis of the individual specimens for carbon by combustion. The total carbon analyses found were: carbon (in w/o) 4.57, 5.23, 5.60, 6.10, and 7.84; corresponding to x values in TaC_x of 0.734, 0.84, 0.90, 0.98, and 1.26, respectively. Analysis for free carbon was made metallographically, and, except for the composition $TaC_{1.26}$ where a deliberate excess was added, the microstructures showed no graphite. Oxygen and nitrogen were not determined, but, as found by difference on ignition, were estimated to be less than 200 ppm each in all compositions.

Test method.—A modified cantilever-beam test method was selected as the best means to compare high-temperature strength properties. The most desirable method is the standard tensile test, but this was considered too difficult and costly. The compression test was also considered, but interpretation of data is difficult and gives, finally, only the behavior in compression.

The modified cantilever-beam test apparatus is shown in Fig. 1 and consisted of a slotted graphite resistor drilled in one end to receive the specimen. The specimen was heated by radiation when a current was passed through the graphite resistor. A graphite push rod transmitted the bending force to the free end of the specimen and bending (or fracture) occurred at the graphite fulcrum. A Schaevitz-Bytrex load cell and a Brown recorder were used to record the data. All tests were conducted under flowing argon atmosphere.

The temperature was read with a Micro-optical Pyrometer and the optics corrected by checking the melting points of nickel, molybdenum, tantalum, and tungsten. Temperatures were read on the specimens at the point of maximum stress directly above the fulcrum. No correction was made for emissivity of TaC since the dependence of the spectral emissivity on carbon content was not known. The apparent temperatures reported here are lower than the true specimen temperatures by an estimated 25°-50°C, depending on the temperature range of the test.

The test specimens were brought to a predetermined temperature under no-load conditions, then the drive of the test machine was started. The test proceeded (when ductile) to a total deflection of 2.5 mm (0.1 in.) at a deflection rate of 0.9 mm/min (0.0354 in./min). The moment arm in all tests was 1 cm (0.394 in.). The deflection of 2.5 mm was selected because this deflection gave only a 3% change, due to downward motion of the end of the specimen, in the length of the moment arm.

Ductile bend specimens are shown in Fig. 2. The top specimen is before test, the middle specimen is to the 2.5 mm deflection, and the bottom specimen bent to approximately 45° without failure.

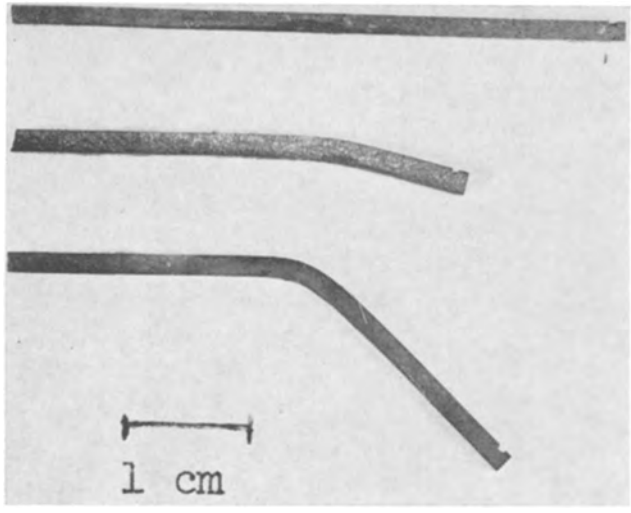

Fig. 2. Bend specimens

Results and Discussion

The maximum load obtained at brittle fracture, or at 2.5 mm (0.1 in.) deflection in ductile bending, was used in the standard beam stress formula to calculate the nominal bending stress, σ, *i.e.*, the maximum tensile strength and maximum compressive stress

$$\sigma = \frac{Mc}{I} \text{ and } M = fl,\ c = \frac{h}{2},\ I = \frac{bh^3}{12}$$

where f is load, l is specimen arm length, h is specimen cross-section height, and b is specimen cross-section width.

Since the beam formula for bending stress is properly applicable only in the elastic region, the results reported here, which include both elastic and ductile deformation, are designated nominal bending stresses. The values should be used only for comparison within the TaC_x compositions. However, tungsten rod tested in this equipment showed a value of bending stress of 16,410 psi (1153 kg/cm²) at 2270°C, in reasonable agreement with published values of tensile stresses in tungsten at elevated temperature (4).

It should be pointed out that a positive influence of strain rate on critical resolved shear stress for TiC was found by Williams (2). TaC should show the same behavior. Values for the nominal bending stress reported here refer only to the specific experimental conditions and particularly to the specific deflection rate of 0.9 mm/min (0.0354 in./ min).

Stresses for each composition were plotted against temperature, and results are shown in Fig. 3. For the compositions x = 1.26, 0.98, 0.90, and 0.84, a T_{db} transition region of about 100°C width was obtained. That is, at temperatures above the region all tests gave ductile behavior, and below, all brittle. Within the region both ductile (D) and brittle (B), as well as ductile-brittle (DB) behavior occurred. The last type of deformation (DB) was characterized by initial ductile bending, followed by brittle failure before the 2.5 mm (0.1 in.) deflection was obtained. For the composition x = 0.73 a narrow transition region of 100°C could not be defined; instead, the transition occurred over the temperature interval 1500°-1950°C and was all (DB) behavior. Nominal stress values averaged about 27,000 psi in this region. This high value was attributed to the presence of the subcarbide Ta_2C in the composition $TaC_{0.73}$. Values for the room temperature bend stresses were for values of x: 0.73 = 56,694 psi (3986 kg/cm²), 0.84 = 16,906 psi (1189 kg/cm²), 0.90 = 23,418 psi (1646 kg/cm²), 0.98 = 20,236 psi (1423 kg/cm²), and 1.26 = 43,498 psi (3048 kg/cm²).

A specimen of $TaC_{1.26}$ was polished with 6μ diamond powder on copper, but no particular effect of polishing on bend behavior was noted for this composition. This is not surprising since the presence of internal defects due to a large excess of free graphite in the microstructure would override the influence of purely surface defects.

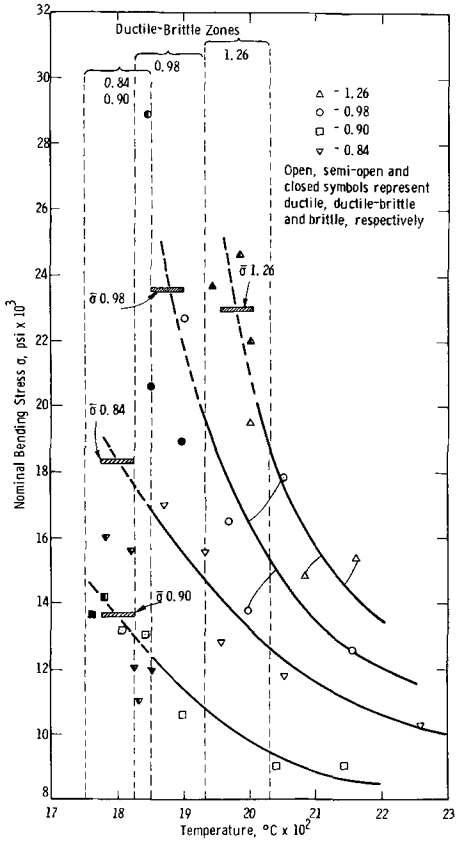

Fig. 3. Stress *vs.* temperature for $TaC_{0.84}$ to 1.26

A gas-carbided specimen of TaC showed a brittle fracture at 2030°C, which was a higher temperature than for $TaC_{1.26}$. The only discernible difference between gas-carbided TaC and the hot-pressed material close to stoichiometry ($TaC_{0.98}$) was a slightly smaller grain size of the gas-carbided TaC. However, a variation in grain sizes between 3 and 14 ASTM (70-5μ) of hot-pressed TaC in compositions near stoichiometry showed no particular effect in either bending stress or T_{db}.

If for each composition a curve be drawn from the ductile region and extrapolated into the midpoint of the ductile-brittle zone, then a median stress, $\bar{\sigma}$, as shown in Fig. 3, is obtained. A plot of the median stress data, $\bar{\sigma}$, *vs.* the carbon content x in TaC_x is shown in Fig. 4. The curve is seen to be nearly constant between $\bar{\sigma}_{0.98}$ and $\bar{\sigma}_{1.26}$ with a slight falling off in stress possibly due to excess carbon in the two-phase composition $TaC_{1.26}$ The curve then falls sharply from $TaC_{0.98}$ to a minimum at $\bar{\sigma}_{0.90}$ and rises sharply to $\bar{\sigma}_{0.84}$ and is shown directed toward the higher average values (~27,000 psi) in the Ta_2C-TaC two-phase region.

A minimum in the room temperature ultimate tensile and transverse rupture strength has also been reported at $TaC_{0.8}$ by Santoro (5). The shift in the minimum to $TaC_{0.90}$ shown in our work may be due to the difference between room temperature and elevated temperature measurement. The implications of a pronounced minimum well within the cubic single-phase region are not readily understood, but as suggested by Santoro (5), this effect may be connected with a transition in the electronic structure.

Figure 5 shows the results of plotting the mid-point temperature of the ductile-brittle transition region for each composition against the carbon content x in TaC_x. An increase in T_{db} of approximately 150°C is found with increasing x across the single phase cubic region of TaC_x.

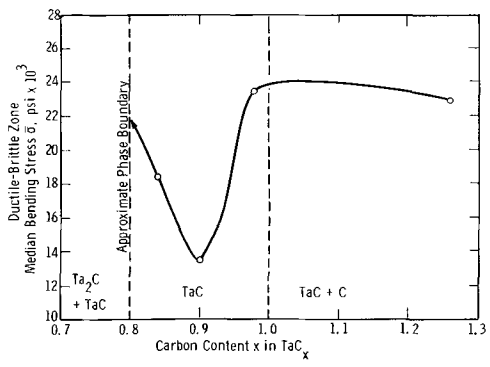

Fig. 4. Median bending stress $\bar{\sigma}$ in ductile-brittle zone *vs.* carbon content x in TaC_x.

The data show that the ductile-brittle transition range for polycrystalline TaC at or near stoichiometry is between 1850° and 1950°C, and the average nominal bending stress in this region is 23,000 psi (1617 kg/cm²). This is in reasonable agreement with a value of 17,600 psi (1237 kg/cm²) at 2000°C reported by Shaffer (6).

Examination of the microstructures of ductile, ductile-brittle, and brittle deformation and fracture showed no discernible differences in the region of stress. Brittle fracture was entirely intergranular.

Cobalt was used as a sintering aid as it is one of the best for this purpose, and its use allowed much lower hot-pressing temperatures and shorter sintering times at high temperature. Carbon pick-up from graphite dies was thus avoided or minimized. Residual cobalt (less than 0.1 w/o after vacuum decobalting) could have had a possible influence on the deformation at high temperatures. However, the existence of a carbide skeleton in various carbides such as TiC-WC-Co at cobalt contents up to 15% has been reported by Kreimer, Vakhorskaya, and Baranov (7), and the bending strength was reported to be independent of the cobalt content between 20° and 500°C. A continuous carbide skeleton was found for WC-Co containing less than 10% Co by Dawihl (8). Klimenko (9) reported that Cr_3C_2 with even 30% Ni preserved a carbide skeleton, and specimens with 5% and 15% Ni had considerable bending strength up to 1100°C. It should be reasonable to conclude that, on the basis of the evidence for strong carbide skeletons formed in various other systems as well as TaC_x, and for the change in T_{db} with change in carbon content, the effect of residual Co was removed, or at least minimized.

Williams and Schaal (1) have discussed the influence of increasing the C/metal ratio in single crystal TiC_x. They found the critical resolved shear stress to

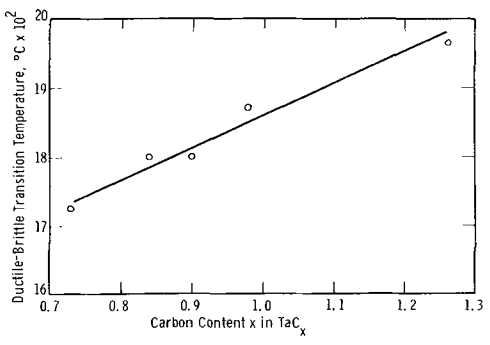

Fig. 5. Ductile-brittle transition temperature *vs.* carbon content x in TaC_x.

increase with increasing x. This also appears to be the case with TaC_x where the nominal bending stress increases with x above $x = 0.90$. The T_{db} for polycrystalline TaC_x of 1725°-1980°C is much higher than the 800°-1100°C range reported for single crystal TiC_x. At 1100°C all compositions of single crystal TiC_x were reported to exhibit plastic flow independent of the Ti/C ratio (1).

Tantalum carbide, in common with the other transition metal carbides, shows a high melting point and high hardness. This indicates some degree of covalent or other tight bonding. On the other hand, the high electrical and thermal conductivity indicate some degree of metallic-type bonding. Plastic deformation in metals occurs by dislocation movement, and the presence of vacancies in TaC due to substoichiometry might be expected to lead to the strengthening of the TaC lattice by a dislocation-vacancy mechanism. This strengthening behavior is observed in TaC_x for x values less than 0.9. Since, however, the TaC_x lattice is strengthened above $x = 0.9$ by addition of carbon (or decreasing carbon vacancies) in a fashion similar to that of TiC, we may conclude with Williams and Schaal (1) that a vacancy-dislocation interaction is less important as a strengthening mechanism in this composition range than an increase in Peierls stress (or other source of lattice resistance).

Above the ductile-brittle transition temperature the strength does not appear to depend as strongly on the C/Ta ratio as in the ductile-brittle region. This may indicate that once the source of lattice resistance is thermally removed, the material tends to react in a uniform manner, regardless of carbon content.

Summary

1. Polycrystalline TaC_x has been examined by a modified cantilever-beam test method to obtain the ductile-brittle transition temperature (T_{db}) as a function of x.

2. Nominal bend stresses as a function of temperature and carbon content were determined. An average value in the ductile-brittle transition region for $TaC_{0.98}$ (1850°-1950°C) was 23,000 psi (1617 kg/cm²).

3. T_{db} falls with decreasing carbon content to $TaC_{0.90}$, where the median bend stress is at a minimum of 14,000 psi (984 kg/cm²) for the temperature range 1750°-1850°C.

4. Below the cubic single phase boundary (x approx. 0.80) the presence of the second phase Ta_2C drastically alters the ductile-brittle transition to give a broad range of 1500°-1950°C. The nominal bend stress is raised to as high as 32,000 psi (2250 kg/cm²) at 1600°C.

5. A minimum in the median bending stress was found at $x = 0.90$. A vacancy-dislocation interaction does not appear to be the principal strengthening mechanism in $TaC_{x>0.9}$. A high Peierls stress for dislocation movement is expected.

Acknowledgment

The authors wish to acknowledge helpful discussions with G. Comenetz and E. A. Davis, and special technical assistance from J. R. McDowell and S. M. Ho.

Manuscript received July 14, 1965; revised manuscript received Jan. 17, 1966. This paper was presented at the San Francisco Meeting, May 9-13, 1965.

Any discussion of this paper will appear in a Discussion Section to be published in the December 1966 JOURNAL.

REFERENCES

1. W. Williams and R. Schaal, *J. Appl. Phys.*, **33**, 955 (1962).
2. W. William, *ibid.*, **35**, 1329 (1964).
3. A. Bowman, *J. Phys. Chem.*, **65**, 1596 (1961).
4. ASM Metals Handbook, 1961 ed., p. 1226.
5. G. Santoro, *Trans. AIME*, **227**, 1361 (1963).
6. P. Shaffer, "High Temperature Materials—Materials Index," p. 114, Plenum (1964).
7. G. Kreimer, M. Vakhorskaya, and A. Baranov, *Phys. Metals and Metallography*, **10** [5], 61 (1960).
8. W. Dawihl, *Z. Metallkunde*, **44**, 69 (1953).
9. V. Klimenko, *Sov. Powder Metallurgy and Metal Ceramics*, Sept.-Oct., No. 5, 396 (1964).

The Potentiostatic Method as Applied to the Anodic Oxidation of the Valve Metals, and the Field Dependence of the Tafel Slope for Aluminum

M. J. Dignam and D. Goad

Department of Chemistry, University of Toronto, Toronto, Ontario, Canada

ABSTRACT

The potentiostatic method for determining the steady-state parameters for anodic oxidation of the valve metals is examined in relation to present models for the conduction properties of the oxides. It is shown that despite the fact that potentiostatic conditions correspond to nonsteady-state conditions, the steady-state field coefficient (reciprocal Tafel slope) may be determined accurately, and relatively easily, from such measurements. Data for aluminum are presented in illustration and found to be in accord with an equation of the form $i = \alpha \exp[\gamma E - \delta E^2]$, where i is the current density, E the field strength, and α, γ, and δ positive constants for isothermal conditions. The values of γ and δ obtained are in good agreement with values obtained previously using a method in which steady-state conditions were maintained during measurement. The agreement lends further support for the inclusion of the term in E^2 in the conduction equation.

Previous workers have carried out experiments on anodic oxidation of valve metals, in which the oxide was formed under steady-state conditions to a given overpotential, which was then held constant (1, 2). By following the current decay during the potentiostatic condition, kinetic data were obtained. It is important to emphasize that potentiostatic conditions are not steady-state conditions for this system, since the field is changing as the film grows. It is, therefore, not valid to analyze such data using a steady-state ionic conduction equation as has been done previously, but rather they must be interpreted using a model which makes allowance for transient behavior. At present, there are two such models: the high field Frenkel de-

fect model (1) and the recent "dielectric mosaic" theory (3). It is not necessary to discuss these theories here; a full discussion may be found in the references cited. This paper presents an analysis of the potentiostatic method in relation to both of these theories. The two theories give rise to essentially the same result, which is tested against new data for the anodic oxidation of aluminum.

Theory

The purpose of this section is to derive an equation giving the current density as a function of time for an experiment carried out as outlined in the introduction. This will be done first and in some detail with reference to the dielectric polarization theory, the high field Frenkel defect theory being treated briefly later.

The relevant equations for the dielectric polarization model are recorded below

$$\frac{\mu dEe}{dt} - \frac{\mu_1 dE}{dt} = Bi(\mu_s E - \mu Ee) \quad [1]$$

$$i = io \exp(-\phi/kT) \exp\left[\frac{\mu Ee}{kT}\left(1 - \frac{\mu Ee}{C\phi}\right)\right] \quad [2]$$

The various parameters are defined as follows: E, Ee are the applied field and the effective field strength respectively; t is the time; μ is the activation dipole (effective charge activation distance product); μ_1, μ_s are the effective activation dipoles for transient and steady-state conditions, respectively; B is a kinetic parameter with the dimensions reciprocal charge times area; i is the ion current density; io is a temperature independent constant with the dimensions of current density; ϕ is the activation energy at zero field strength, and C a constant whose value depends on the shape of the potential energy surface for the activation process.

A further relationship required is that between the applied field and the effective field under steady-state conditions

$$\left(ie\frac{di}{dt} = 0 = \frac{dE}{dt}\right)$$

$$\mu Ee = \mu_s E \text{ at steady-state} \quad [3]$$

Equation [1] may now be solved for the conditions of the experiment in question. Accordingly setting

$$i = dq/dt$$

the solution to [1] becomes

$$\left[Ye^{Bq}\right]_o^q = (\mu_1 - \mu_s)\int_o^q e^{Bq}\frac{dE}{dq}dq \quad [4]$$

where $Y = \mu Ee - \mu_s E$ represents the deviation of the effective field from its steady-state value. The boundary conditions used to obtain Eq. [4] are that $\mu Ee = \mu_s E$ at $q = 0$.

Setting

$$E = \frac{V}{X} = E_o\left(1 + \frac{fq}{X_o}\right)^{-1} \quad [5]$$

we obtain

$$\frac{dE}{dq} = \frac{-E_o f}{X_o}\left(1 + \frac{fq}{X_o}\right)^{-2} \quad [6]$$

where V is the potential across the oxide film assumed to be equal to the overpotential; Xo, the film thickness at $t = 0 = q$; X, the film thickness at time t; Eo, the field strength at time $t = 0$.

$$f = \frac{dX}{dq} = \frac{W_e}{\rho F}$$

where W_e and ρ are the electrochemical equivalent weight and density of the oxide, respectively, and F is Faraday's constant.

Substituting [6] in [4] we now obtain

$$Ye^{Bq} = (\mu_s - \mu_1)\frac{E_o f}{X_o}\int_o^q \frac{e^{Bq}}{(1 + fq/X_o)^2}dq \quad [7]$$

Although the integral in [7] may be expressed explicitly in terms of the exponential integral, a more useful expression results on integration by parts. Accordingly, the integral may be written

$$I = \int_o^q \frac{e^{Bq}\,dq}{(1 + fq/X_o)^2} = \frac{1}{B}\left[\frac{e^{Bq}}{(1 + fq/X_o)^2}\right]_o^q + \frac{2f}{BX_o}\int_o^q \frac{e^{Bq}\,dq}{(1 + fq/X_o)^3} \quad [8]$$

It is clear that the error in I introduced by neglecting the remainder integral on the right-hand side is less than $2f/Bx_o$ in unity. For alumina, $f = 5.6 \times 10^{-5}$ cm³/coul; $B = (1.22 \pm 0.07) \times 10^4$ cm²/coul (4); so that neglect of the remainder term will introduce an error in $I \gtrsim ½\%$ for $X_o \gtrsim 170$Å. Since the first term is already very small, representing the deviation from steady state, neglect of the remainder integral is of no consequence.

Accordingly, [7] becomes

$$Y = (\mu_s - \mu_1)\frac{E_o f}{BX_o}\left[\frac{1}{(1 + fq/X_o)^2} - e^{-Bq}\right] \quad [9]$$

When sufficient charge has passed such that Bq is appreciably greater than unity we will have

$$\exp(-Bq) << 1$$

and hence

$$Y = (\mu_s - \mu_1)\frac{E_o f}{BX_o}\frac{1}{(1 + fq/X_o)^2} \text{ for } q > \frac{4}{B} \quad [10]$$

From Eq. [10] we see that following a transition period corresponding to a charge past of $4/B$, Y remains essentially constant (since $fq/Xo << 1$). This means that following the transient period the effective field strength lags behind the steady-state effective field strength by a constant amount. Combining this result with the conduction Eq. [2], we conclude that to a first approximation the current density will lag behind its steady-state value by a constant factor. To show this we start by replacing Eq. [2] by an approximation which will be valid over a sufficiently narrow range of the effective field. Accordingly we write

$$i = A \exp \beta Ee \quad [11]$$

where

$$A = i_o \exp\left[\frac{-1}{kT}\left(\phi - \frac{2(\mu\overline{Ee})^2}{C\phi}\right)\right] \quad [12]$$

$$\beta = \frac{\mu}{kT}\left(1 - \frac{2\mu\overline{Ee}}{C\phi}\right) \quad [13]$$

and $\overline{Ee}$ is the mean effective field strength over the range of interest. Eliminating Ee from Eq. [9] and [11] and substituting for E according to [5] we obtain

$$\ln i/A = \frac{\beta_s E_o}{(1 + fq/Xo)} + \beta_s\frac{(\mu_s - \mu_1)}{\mu_s}\frac{Eof}{BXo}\left[\frac{1}{(1 + fq/X_o)^2} - e^{-Bq}\right] \quad [14]$$

where β_s is the steady-state reciprocal Tafel slope at a field strength equal to the mean field strength over the region of interest, and is given by

$$\beta_s = \frac{\mu_s}{kT}(1 - 2\mu_s\overline{E}/C\phi) \quad [15]$$

where $\overline{E}$ is the mean external field strength for the region of the experiment being considered.

From Eq. [14] we may now see that at $t = 0 = q$ the second term on the right is 0 and hence, the current density is simply the steady-state current density for the initial field strength Eo as indeed it must be since this represents the starting conditions. As q increases, however, the term on the right increases and reaches a limiting value which changes only very slowly with time; thus when $\exp(-Bq) << 1$ the current density lags by an almost constant factor behind the steady-state value for the field in question.

For comparison with experimental data a more useful equation is obtained on differentiating Eq. [14] with respect to time after setting $\exp(-Bq) << 1$.

$$\frac{d}{dt}\left(\frac{1}{i}\right) = \frac{\beta_s E_o f}{X_o}\frac{1}{(1+fq/X_o)^2} + 2\beta_s\frac{(\mu_s-\mu_1)}{\mu_s}\frac{E_o f^2}{BX_o^2}\frac{1}{(1+fq/X_o)^3} \quad [16]$$

Thus a plot of $1/i$ *vs.* t will be nearly a straight line, there will be an initial deviation with a "time constant" corresponding to $Bq = 1$, then a nearly straight line with slope $\beta_s E_o f/X_o(1+fq/X_o)^2$ (the second term in [16] is negligible by comparison). The initial points corresponding to $Bq < 1$ will fall below this straight line. From Eq. [14], extrapolation of the straight line portion following the initial transient will give an intercept i'_1 at $t = 0$, which is related to the actual initial current, i_1, by

$$\ln\frac{i'_1}{i_1} = \beta_s\frac{(\mu_s-\mu_1)}{\mu_s}\frac{E_o f}{BX_o} = \frac{\mu_s-\mu_1}{\mu_s}\frac{f}{BX_o}\frac{\ln i_1}{A} \quad [17]$$

The treatment based on the Frenkel defect model is similar and begins with equation (1)

$$\frac{\partial m}{\partial t} = (No-m)\,v_1\exp\left\{-\left[\frac{W_1-ea_1E}{kT}\right]\right\}\frac{-i'\sigma m}{e}$$

$$i = 2ea_2mv_2\exp\left\{-\left[\frac{W_2-ea_2E}{kT}\right]\right\}$$

where W_1 and W_2 are activation energies, a_1 and a_2 are activation distances, v_1 and v_2 vibration frequencies, No the concentration of lattice sites, m the concentration of Frenkel defects, e the charge on the mobile ion, and σ' capture cross-section of vacant sites.

To obtain a solution for these equations appropriate to the problem at hand is more difficult since they are nonlinear. It can be shown, however, that after sufficient charge has passed such that $\exp(-2\sigma' q/e) << 1$, the concentration of charged defects m lags its corresponding steady-state concentration by a nearly constant factor, leading to the same type of current dependence as given by [14]. Thus the two theories predict substantially the same behavior for this experiment, and oscilloscope techniques to record the initial transient are required to differentiate between them. As such measurements were not carried out here, we shall not pursue the Frenkel defect theory further.

The conclusion which may be drawn from these analyses are as follows: both the dielectric polarization theory and the high-field Frenkel defect theory when applied to constant voltage experiments of the type outlined earlier predict that the current density will lag behind the steady-state current density by approximately a constant factor, following an initial transient. For films which are not too thin, however, tangents to a plot of reciprocal current density against time have almost precisely the same slope as would be obtained from a hypothetical plot of the reciprocal of the true steady-state current density against time. It would appear to be safe, therefore, to use constant voltage experiments to obtain information about the steady-state field coefficient (steady-state reciprocal Tafel slope).

In the following section data for the anodic oxidation of aluminum under potentiostatic conditions are presented in order to test the validity of the principle Eq. [16] and [17].

Experimental Method

Details of the cell design, glycol-borate[1] electrolyte, etc., may be found in a previous publication (6). For the present experiments the previously described reference electrode was replaced by a mercury mercuric oxide electrode (7) immersed in a 20% solution of aqueous ammonium pentaborate. The electrolytes were separated by a thin membrane permeable to cations only.

The experiment was carried out by forming the film at a constant current density of $2.09_5 \times 10^{-4}$ amp/cm^2 to a fixed constant potential of the anode with respect to the reference electrode. From this potential the anode overpotential V may be found. Since

$$V = V' - Vrev + Vref$$

V' is the measured difference in potential between anode and reference electrode, $Vrev$ the calculated potential of a hypothetical reversible aluminum-aluminum oxide electrode with respect to a hydrogen electrode in the same solution, and $Vref$ is the potential of reference electrode with respect to a hydrogen electrode in the electrolyte.

$Vrev$ was calculated as -1.386v, $Vref$ was measured as 0.567v, and $V' = 26.79$v, thus $V = 27.61$v. Because of space charge and interfacial potentials, the uncertainty in V may be as much as 2v. The importance of this may be minimized by using thicker films.

Using the data of Bernard and Cook (9) in the manner previously described (6), the formation field strength, E_o, has the value 0.085_6 v/Å so that the initial film thickness, X_o, is 27.61/0.0856 = 312Å.

Results

Figure 1 shows a plot of $1/i$ *vs.* t for the first few seconds and after several hours, showing clearly a difference in slope. Least squares straight lines were fitted to six sets of data, obtained by taking points covering factors of about 4 fall in the current during the same run. The intercept on the $t = 0$ axes obtained from the data for the first few seconds differs from the reciprocal of the initial steady-state current density by the amount $(1.88 \pm 0.23) \times 10^3$ cm^2/amp. The difference is statistically significant, being in fact, 8 times the standard deviation of the intercept. The shift predicted from Eq. [17], using the values of f, B, X_o given earlier and setting $\mu_s = 23.5$; $\mu_1 = 7.8$ eÅ (4); and $\beta_s = 374$ v/Å (see below) is 1.58×10^3 cm^2/amp in excellent agreement with the experimental shift.

[1] This is the only known electrolyte for which close to 100% current efficiencies for the formation of anodic oxide films on aluminum are obtained at low current densities.

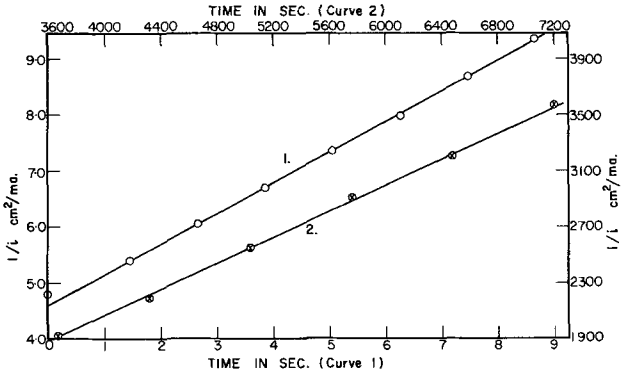

Fig. 1. Plot of $1/i$ *vs.* t for first few seconds and after several hours

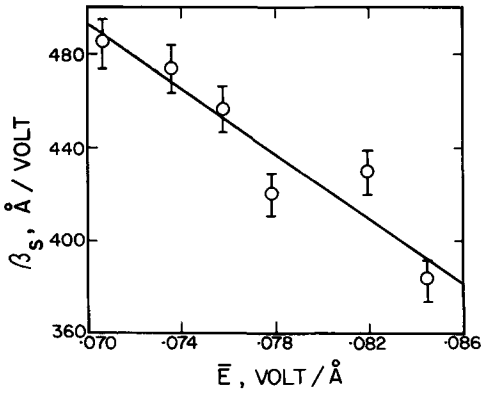

Fig. 2. Results of calculation of values of β_s

Neglecting the very small final term, Eq. [16] may be written

$$\frac{d}{dt}\left(\frac{1}{i}\right) = \beta_s f E^2/V \qquad [18]$$

The slopes of the lines as determined above were assumed to be equal to the derivative of $1/i$ with respect to t at the mean field value. Values of E were calculated by numerical integration of the charge passed, assuming 100% current efficiency with respect to film formation. Values of β_s were then calculated as a function of the mean field strength $\bar{E}$ using Eq. [18]. The results are shown in Fig. 2, the vertical lines representing ± 2 standard deviations of β_s. It should be noted that E^2 changes by several per cent for a decade change in current so that it is not a good approximation to regard it as constant as Dreiner (2) has done.

The solid line in Fig. 2 represents the least squares regression line and corresponds to the following values for the parameters in Eq. [15] and their standard deviations

$$\mu_s = 25.0\ e\text{Å};\quad \sigma = 10\%$$

$$C\phi = 7.08\ ev;\quad \sigma = 5\%$$

These values are in good agreement with those found previously using a different method (6).
vis:

$$\mu_s = 23.8\ e\text{Å},\quad \sigma = 14\%$$

$$C\phi = 7.65\ ev,\quad \sigma = 3\%$$

Discussion

The present analysis and data confirm the validity of the potentiostatic method for obtaining values of the steady-state field coefficient. In addition, the existence of a quadratic term in the field in the net activation energy, reported previously (6), has been verified.

Some comment on the papers by Dreiner (2, 8), who employed the potentiostatic method to determine the field coefficient for the anodic oxidation of tantalum, is in order, since he purports to find the steady-state field coefficient independent of field strength and inversely proportional to temperature, in direct contrast to the findings of Young (10). As he was unable to detect any curvature in a plot of $1/i$ *vs.* t he concluded that β_s was independent of field strength. Using Young's values for the relevant parameters, however, it can be shown that the decrease in β_s with increasing field cancels to a large degree the increase in E^2 with increasing field [18], so that the slope $d(1/i)/dt$ remains almost independent of time. Furthermore, contrary to the conclusion stated in the paper, Dreiners' results do indeed indicate an anomalous temperature dependence of the field coefficient. The temperature dependence of the field coefficient predicted by the simple equation which omits the term in E^2, is that the field coefficient be proportional to $1/T$ (*i.e.*, β_s *vs.* $1/T$ is a straight line with zero intercept). Dreiner's results, however, indicate a very substantial positive intercept. In order to obtain proportionality between β_s and $1/T$ the slope of the straight line representing variation of β_s with $1/T$ presented by Dreiner would have to be approximately doubled. Such an adjustment in the equation for the straight line falls well outside the experimental scatter in his data. Thus, his data indicate beyond any reasonable doubt the presence of an anomalous temperature dependence for the field coefficient. As an adequate explanation for this anomalous behavior has been presented previously by one of us (5) the matter will not be discussed further here.

Manuscript received Oct. 22, 1965.

Any discussion of this paper will appear in a Discussion Section to be published in the December 1966 JOURNAL.

REFERENCES

1. For a summary of work in this field see: L. Young, "Anodic Oxide Films," Academic Press (1961).
2. R. Dreiner, *This Journal*, **111**, 1350 (1964).
3. M. J. Dignam, *ibid.*, **112**, 722 (1965).
4. M. J. Dignam, *ibid.*, **112**, 729 (1965).
5. M. J. Dignam, *Can. J. Chem.*, **42**, 1155 (1964).
6. M. J. Dignam, D. Goad, and M. Sole, *ibid.*, **43**, 800 (1965).
7. B. D. Cahan, J. B. Ockerman, R. F. Amlie, and P. Ruetschi, *This Journal*, **107**, 725 (1960).
8. R. Dreiner, K. Lehovec, and J. Schimmel, *ibid.*, **112**, 395 (1965).
9. W. J. Bernard and J. W. Cook, *ibid.*, **106**, 643 (1959).
10. L. Young, *Proc. Roy. Soc.*, **A258**, 496 (1960).

Kinetics of the Chemical and Electrochemical Reduction of Platinum Black Surface Oxides

Jaspal S. Mayell

Central Research Division, American Cyanamid Company, Stamford, Connecticut

ABSTRACT

A comparative study of the reductions of platinum black surface oxides by electrochemical (at constant current) and chemical means (by propane) has been made. From the nature of the rates of the chemical reduction, from potential-time behavior, and from the two breaks observed in potential *vs.* logarithm coulombs for reductions at <1.60v oxidation, two types of surface oxides at the platinum black electrode have been observed. The chemical reduction of the platinum black surface oxide, when the electrode is oxidized to a potential in the range of 1.30-1.60 v *vs.* hydrogen electrode, is zero order with respect to oxide formation and has a rate of 7.1×10^{-7} equivalent/sec/cm^2 or "67 ma/cm^2." The zero order reaction observed suggests that the oxygen is strongly adsorbed. The chemical reduction rate of the surface oxide formed at potentials less than 1.30v, is not constant, and the oxygen is held loosely at the platinum surface.

In many reactions, it is quite often observed that the products obtained by chemical or electrochemical oxidation or reduction are the same. However, their comparative kinetic behavior is not well understood. Recently, Schuldiner and Warner (1) have studied the chemical reduction of surface oxides of smooth platinum with hydrogen saturated sulfuric acid. They have shown that the most likely rate controlling step is the migration of O_{ad} atoms to platinum active sites, where they react with hydrogen. They also have observed that the chemical reaction rate is independent of the surface coverage of platinum from a monolayer up to about two layers of oxygen per platinum atom.

In this study, known amounts of the surface oxides are formed on the platinum black molded electrodes by anodic oxidation at constant current density to predetermined potentials. The chemical reduction of the surface oxides by propane is compared with the electrochemical reduction at constant current.

Experimental

The working electrode was platinum black (30 mg/cm^2) having 15% polytetrafluoroethylene (P.T.F.E.) as a binder. It was placed in a shielded polychlorotrifluoroethylene electrode holder as shown in Fig. 1. The shield was only ¼ in., and the electrode was backed by a gas permeable but liquid impermeable porous P.T.F.E. The area of the electrode in contact with the electrolyte was 0.462 cm^2. Propane (3 ml/min) atmosphere in large excess of the stoichiometric amount required was kept over the porous P.T.F.E. The blank runs were performed with a nitrogen atmosphere.

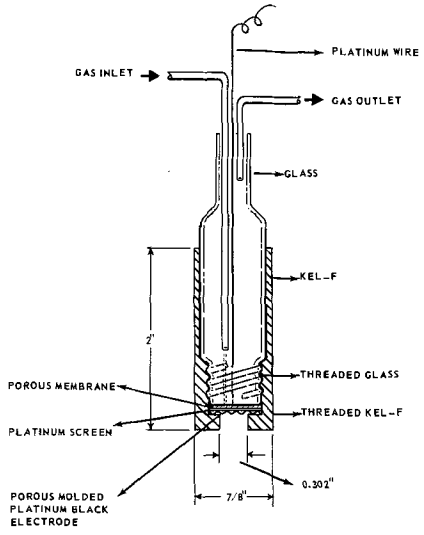

Fig. 1. Gas permeable liquid impermeable molded platinum black-P.T.F.E. porous electrode assembly.

The auxiliary electrode was also platinum black separated from the working compartment by a sintered glass disk. The reference electrode was hydrogen gas bubbled through 85% H_3PO_4 over a molded platinum black P.T.F.E. electrode contained in a Vycor tube (No. 7900) having a porous tip of Vycor 7930. The Vycor tube was placed in 85% H_3PO_4 so that the porous tip was completely submerged in the acid. Nitrogen was bubbled continuously through a sintered disk in order to remove any hydrogen leaking through the Vycor tube. The hydrogen reference electrode assembly was kept at room temperature. The connection to the working compartment of the cell was made by means of a bridge of small bore tubing. All potentials mentioned in this work are referred to the above hydrogen electrode which differs from the hydrogen electrode in 1M $HClO_4$ by about +30 mv. The apparatus used has already been described (2, 3).

The propane was allowed to flow at a high rate, far in excess of the stoichiometric amount required, directly over the porous P.T.F.E. The structure of the test electrode shown in Fig. 1 was such that there was always an excess of propane available at the electrode surface for the reduction of surface oxides. The water proofed porous gas electrode caused a considerable decrease in the average effective diffusion layer thickness. Propane was thus easily available at the reaction sites. The rate of chemical reduction of the surface oxides of platinum black was not dependent on the diffusion of propane but was similar to that of constant current reduction as will be shown in the results.

Results and Discussion

Mayell and Langer (2) oxidized platinum black electrodes in 2*N* H_2SO_4 at a constant current density to different potentials. They observed from coulometric reduction that the oxidation sequence for platinum black electrode was Pt → $Pt(OH)_2$ → $Pt(O)_2$ → $Pt(O)_{2.5(approx.)}$. Complete formation of the monolayer of $Pt(OH)_2$ occurred when the electrode was oxidized to a potential of 1.24v while the monolayer of $Pt(O)_2$ occurred at 1.54v. Above 1.60v, the amount of surface oxide formed remained constant, corresponding to $Pt(O)_{2.5(approx.)}$.

In the present work, similar results were observed when a platinum black electrode was oxidized in 85%

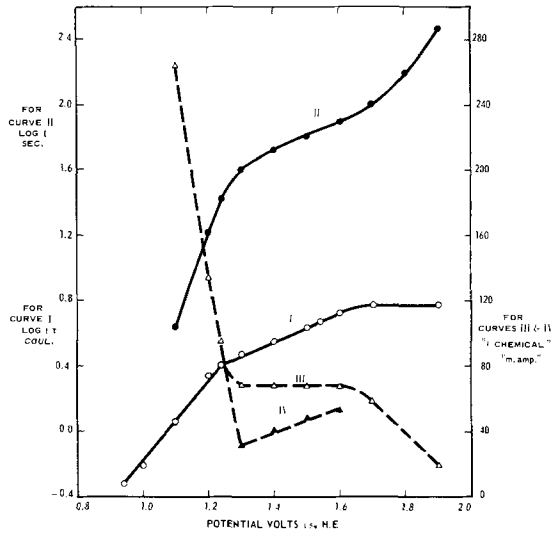

Fig. 2. Plot of potential to which the platinum black electrode was oxidized at constant current density in 85% H_3PO_4 *vs.* Curve I, log coulombs required to reduce, electrochemically, the oxidized surface at 130°C (oxidation and reduction were performed at 40.5 ma/cm^2); curve II, log seconds required for propane to reduce the electrode at 150°C, after the electrode was oxidized at 134 ma/cm^2 to different anodic potentials; curve III, the chemical reduction rate, $i_{chemical}$, by propane to reduce the total surface oxides formed at different potentials at 134 ma/cm^2; curve IV, $i_{chemical}$ of the second oxygen layer alone, by propane, when the electrode is oxidized to a potential in the range of 1.30-1.60v at 134 ma/cm^2.

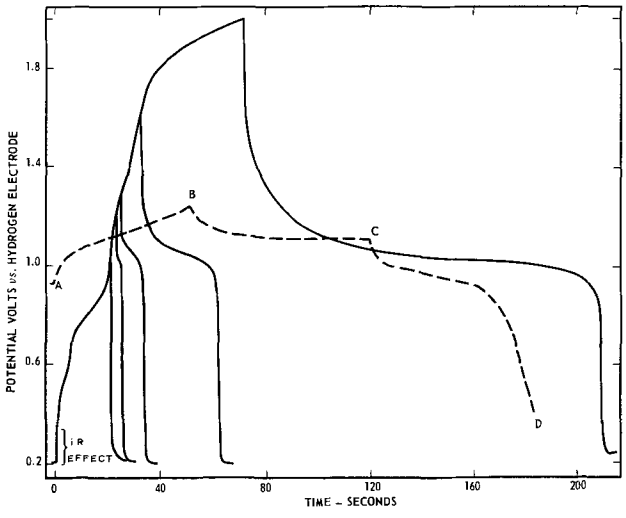

Fig. 3. Plots of potential *vs.* time when a platinum black electrode, over which propane is flowing at the rate of 3 ml/min, is oxidized at 134 ma/cm^2 to predetermined potentials (rising part of the curve) at 150°C in 85% H_3PO_4 and then put on open circuit (declining part of the curves). Dotted lines are a blank run under nitrogen atmosphere. AB is oxidation and CD is reduction, both at 40.5 ma/cm^2 of the platinum black electrode. BC is open circuit decay potential before reduction.

H_3PO_4 (H_2O_2 treated)[1] at 130°C at a constant current density of 40.5 ma/cm^2 to predetermined potentials. The cell was put on open circuit for 3 min, during which the oxygen evolved was removed by bubbling with nitrogen and then the electrode was reduced at the above current density. The number of coulombs required to reduce the platinum black surface oxides was plotted against the potential to which the electrode had been oxidized, as shown in curve I, Fig. 2. This will serve as a reference to compare the results obtained in the reduction of surface oxides by propane.

The current density used to oxidize the platinum black electrode in the blank experiment (nitrogen atmosphere) was 40.5 ma/cm^2. When propane was allowed to flow (3 ml/min) over the porous P.T.F.E., the potential did not rise above 0.8v when currents up to 130 ma/cm^2 were utilized to oxidize the electrode in 85% H_3PO_4 at 150°C. It thus appeared that the electrochemical oxidation of propane occurred predominantly as compared to the formation of surface oxides at currents less than 130 ma/cm^2 (and potentials $<$0.8v). When the current density was increased to 134 ma/cm^2, the electrode could be oxidized to about 2v. Above approximately 1v the formation of surface oxides and above 1.60v the evolution of oxygen predominated over the oxidation of propane. It could be assumed in this work that the chemical reduction of Pt surface oxides by propane during their anodic formation (at constant current) is negligible.

The electrode was oxidized to predetermined potentials and on open circuit, the potential dropped to 0.2v as seen in Fig. 3. The time τ required for the potential to reach 0.4v was taken as that corresponding to complete reduction of the surface oxides. An increase in the time for chemical reduction was observed as the electrode was oxidized to higher potentials. When the electrode was oxidized to potentials in the range of 1.30 to 1.60v, normalization of the open circuit potential decay curves with respect to time indicated an identical shape for all of the experimental curves.

[1] 0.2 ml of 30% H_2O_2 was added to a liter of 85% H_3PO_4 and heated in water condenser at 150°C for 6 hr to remove excess of H_2O_2 (tested by decolorization of $KMnO_4$).

One very characteristic feature of the open circuit decay in Fig. 3 was the very sharp transition from about 0.9 to 0.2v. When platinum surface oxides (formed in the absence of propane) were reduced at constant current, the transition was not sharp as seen in curve CD of Fig. 3. The quick drop to near the thermodynamic potential of the propane oxidation ($E^\circ_{C_3H_8 \rightarrow CO_2(25°C)} = 0.15$v), suggested that the chemical reduction of surface oxides was not limited by mass transport of propane. In another experiment in which a saturated solution of propane was used under identical oxidation conditions, the drop in potential was gradual showing mass transport limitation.

A plot of log time (decay of open circuit potential to 0.4v) by propane (Fig. 3) *vs.* the potential (iR corrected) to which the working electrode was oxidized is shown as curve II, Fig. 2. The close similarity of curves I and II suggested that the nature of the chemical reduction of surface oxides by propane is very similar to that of electrochemical reduction and that the surface oxide reduction is rate controlling in both cases. Also, the shape of curve II is further evidence for the existence of two different surface oxides at potentials lower than 1.60v, a conclusion drawn from previous work on cathodic reduction of surface oxides (2).

The data above 1.60v in curves I and II of Fig. 2 were difficult to compare because of oxygen evolution. Previously (2), oxygen was removed by a nitrogen purge before electrochemical reduction. This was not possible in the experiments with reduction by propane, as the electrode must be continuously in contact with propane in order to obtain meaningful results.

Kinetics

Since surface oxides are present at the platinum black electrode at all times, diffusion of the electroactive species does not occur and the reduction is controlled by Faraday's law.

The over-all complete reduction of the platinum black surface oxides at constant current density occurs according to the equation

$$Pt(O)_x + 2x\,H^+ + 2x\,e \rightarrow Pt + x\,H_2O \qquad [1]$$

while the over-all chemical reduction by propane follows the equation

Table I. Kinetic data for the reduction of platinum black surface oxides

	"Oxidation potential" volts *vs.* H. E.						
	1.10	1.20	1.24	1.30	1.40	1.50	1.60
Number of equivalents of platinum surface oxide/cm² $\Gamma \times 10^7$ determined electrochemically.	118.4	229.6	260.0	305.6	375.2	452.8	546.0
Time, t, required by propane to reduce the total surface oxide in sec/cm² of electrode.	4.34	16.4	26.6	40.7	53.2	65.0	79.0
Chemical reaction rate, k, equivalents/sec/cm² $\times 10^7$ for the reduction of total surface oxides.	27.32	13.98	9.78	7.52	7.08	7.00	6.92
Chemical reaction rate, k', equivalents/sec/cm² $\times 10^7$ for the reduction of second oxygen layer only.	—	—	—	3.24	4.32	5.00	5.48

$$\frac{10}{x}\,Pt(O)_x + C_3H_8 \rightarrow \frac{10}{x}\,Pt + 3\,CO_2 + 4\,H_2O \quad [2]$$

Propane oxidizes completely to CO_2 as has been shown by Grubb (4) in a fuel cell. In the present study the propane electrode is exactly similar to a fuel cell anode compartment and thus a similar over-all oxidation of propane occurs.

The chemical reaction rate, k in equivalents/sec/cm² for the reduction of total surface oxides as shown in Table I is determined as follows

$$k = \frac{\Gamma}{t} \quad [3]$$

where t is time required for propane to reduce the oxides and Γ is the number of equivalents of the surface oxide. Γ is calculated by using Faraday's law

$$\Gamma = \frac{i\tau}{F} \quad [4]$$

where $i\tau$ is the number of coulombs required to reduce the surface oxide electrochemically in the presence of nitrogen. From the values of k as shown in Table I and the curves in Fig. 2, it appears that the oxygen is adsorbed differently on the platinum black surface, when the electrode is oxidized to a potential in the range of 1.30-1.60v than at <1.30v.

If it is assumed that the adsorption of oxygen in the surface oxide formed in the potential region of 1.30-1.60v is similar to that formed at <1.30v, then the rate of the chemical reduction of the second oxygen layer, k' in equivalents per sec/cm², is determined as below

$$k' = \frac{\Gamma_{\text{determined at 1.30-1.60v}} - \Gamma_{\text{determined at 1.24v}}}{t_{\text{at 1.30-1.60v}} - t_{\text{at 1.24v}}} \quad [5]$$

since a monolayer of oxygen is complete at 1.24v (2).

The rate should decrease if the nature of the surface oxide is similar to that formed at potentials <1.30v, as shown in Fig. 2. However, the value of k' increases, as seen in Table I, when the electrode is oxidized to higher potentials, which contradicts the above assumption. Thus, the oxygen atoms of the two platinum black electrode surface oxides are arranged differently.

The reduction rates determined above could be expressed in terms of constant current

$$i_{\text{"chemical"}} = \frac{i\tau\,(\text{electrochemical})}{t\,(\text{chemical})} \quad [6]$$

The values of $i_{\text{"chemical"}}$ for the reduction of total surface oxides and second oxygen layer alone are plotted as curves III and IV, respectively, in Fig. 2. The three distinct regions observed in curve III show a similar trend as seen in the other two curves of the same figure. The decrease in $i_{\text{"chemical"}}$ above 1.60v is caused by the inability to remove oxygen and so is not considered for comparison purposes.

It is quite clear from the data in Table I and curve III of Fig. 2, that the chemical rate for the reduction of total surface oxides formed in the potential range of 1.30-1.60v is independent of the amount of surface oxide formed. The over-all reduction is thus zero order, and the rate constant is 7.1 x 10^{-7} equivalents/sec/cm² of the electrode which is equivalent to "67 ma/cm²."

A zero order reaction is strongly suggestive of strong adsorption of oxygen (5) when the electrode is oxidized to a potential in the range of 1.30-1.60v. It has been suggested (1) that oxygen atoms could go into the interstitial holes in the Pt lattice (especially in the 110 plane) after a monolayer of oxygen atoms have been formed.

Potential-Time Behavior

Comparison of the chemical reduction by propane and electrochemical reduction at constant current of the platinum black surface oxides formed by oxidation at constant current in the potential range of about 1.30-1.60v can be made by assuming a quasi-equilibrium hypothesis. It is supposed that all steps prior to the rate-determining one in the reaction sequence are almost in equilibrium, *i.e.*, the rate constant of the rate-controlling step is at least ten times smaller than all other antecedent steps in both directions. Conway (6) determined the kinetics for consecutive reactions (using constant current) assuming the above hypothesis and derived the following equation

$$E = a + \frac{2.303\,RT}{F}\log\frac{\tau - t}{t} = a + \frac{2.303\,RT}{F}\log\frac{\theta}{(1-\theta)} \quad [7]$$

where E is the potential on open circuit after oxidation to predetermined potential; a is a constant; τ is the time in seconds for complete reduction of $Pt(O)_x$ taken at 0.4v; θ is the fraction of the surface covered with $Pt(O)_x$ at any time t after the electrode has been oxidized to predetermined potential. $\theta = 1$ refers to oxide coverage at $t = 0$ in a given experiment; $(1 - \theta)$ is the fraction of the surface covered by the potential determining intermediate at any time t as in Eq. [8]; while F, R, and T have their usual values.

It has been found that the plots of E *vs.* $\log(\tau - t)/t$ gave straight lines when the surface oxide formed in the potential region of 1.30-1.60v was reduced chemically by propane (curve I) and electrochemically at constant current (curve II) as shown in Fig. 4. The experimental slopes of 0.085 (curve I, Fig. 4) for chemical reduction at 150°C and 0.081 (curve II, Fig. 4) for the electrochemical reduction at 130°C compare very well with the theoretical slopes ($2.3\,RT/F$) of 0.084 and 0.080, respectively.

The first step could then be a quasi-equilibrium reaction. One possibility for electrochemical reduction may be

$$Pt(O)_x + H^+ + 1e \underset{k_b}{\overset{k_f}{\rightleftharpoons}} [Pt(O)_{x-1}\,(OH)] \quad [8]$$

while for chemical reduction may be

$$Pt(O)_x + H^+ \underset{k_b}{\overset{k_f}{\rightleftharpoons}} [Pt(O)_{x-1}\,(OH)] \quad [9]$$

followed by the rate determining step in both the cases. The electrochemical equilibrium condition is

$$k_f\,\theta\,C_{H^+}\,e^{-\frac{\alpha FE}{RT}} = k_b\,(1-\theta)\,e^{\frac{(1-\alpha)FE}{RT}} \quad [10]$$

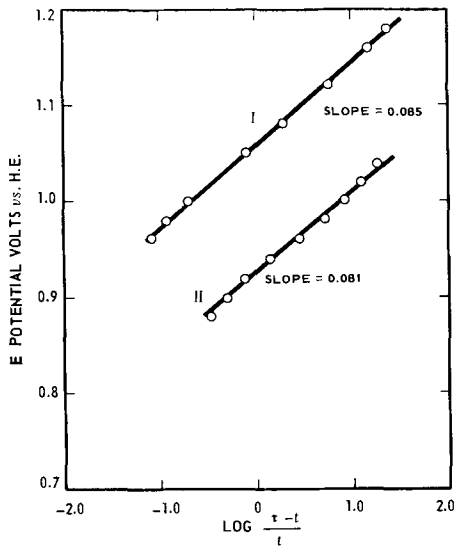

Fig. 4. Plot of potential vs. log $\left(\frac{\tau - t}{t}\right)$ for the reduction of surface oxide formed in the potential region of 1.30-1.60v in 85% H_3PO_4. Curve I, chemical reduction by propane at 150°C when the electrode was oxidized at 134 ma/cm^2 to 1.3v; curve II, electrochemical reduction at constant current density of 40.5 ma/cm at 130°C when the electrode was oxidized to 1.54v at 40.5 ma/cm^2.

$$\frac{\theta}{1-\theta} = K\, C_{H^+}\, e^{\frac{FE}{RT}} \qquad [11]$$

where α is the transfer coefficient; C_{H^+} is the concentration of H^+ which is in large excess and so is constant; and $K = k_b/k_f$.

The above equilibrium expression (6) is a thermodynamic equation for the surface species and is independent of α and any possible double layer effect.

Although the slopes of the two curves in Fig. 4 are the same, their potential displacement of about 0.13v is quite remarkable. The ease of the chemical reduction by propane is evident from the small "over potential" required to reduce the surface oxide formed in the potential region of 1.30-1.60v although the equivalent "current density" is about 1.5 times that of the electrochemical reduction.

Curves I and II of Fig. 4 and the potential-time curves for electrochemical and chemical reduction in Fig. 3 again demonstrate the similar nature of electrochemical and chemical reduction of the platinum black surface oxides.

E *vs.* log $(\tau - t)$ is linear when the surface oxides formed at potentials <1.30v are reduced at constant current density. However, E *vs.* log $(\tau - t)/t$ is not linear in the above range. It thus appears that the surface oxides formed at potentials <1.30v are reduced by a mechanism different from that operative when the oxide is formed in the potential range of 1.30-1.60v. The experimental slope (2.3 $RT/\alpha F$) of 0.25 at 130°C gives a value of 0.33 for α. This mechanism may involve a simple electrochemical reaction. One possibility may be the following mechanism

$$Pt(OH)_2 + H^+ + 1\,e \underset{\longleftarrow}{\overset{\text{slow}}{\longrightarrow}} [Pt\,OH] + H_2O \qquad [12]$$

$$[Pt\,OH] + H^+ + 1\,e \xrightarrow{\text{fast}} Pt + H_2O \qquad [13]$$

The formation of Pt OH intermediate has also been postulated by Laitinen and Enke (7) during the oxidation of Pt electrode surface.

From the different rates and apparent reaction orders of the chemical reduction; from the potential-time behavior, and from the two breaks observed in curves I and II of Fig. 2 below 1.60v, two types of surface oxides at a platinum black electrode are proposed; one formed at less than 1.30v and the other at 1.30-1.60v. The difference in the two surface oxides is not only in the amount of oxygen held per platinum atom but also in the nature of the surface oxide (relative degree of adsorption) formed. It is quite likely that the platinum surface oxides below 1.30v (oxygen loosely held) could play a significantly different role in electrochemical reactions than the surface oxides above 1.30v (oxygen strongly adsorbed).

Acknowledgment

The author thanks Professor Brian E. Conway, Dr. John D. Voorhies, and Dr. Paul Stonehart for helpful discussions and Henry P. Landi for preparation of the platinum black electrodes.

Manuscript received Aug. 13, 1965.

Any discussion of this paper will appear in a Discussion Section to be published in the December 1966 JOURNAL.

REFERENCES

1. S. Schuldiner and T. B. Warner, *This Journal*, **112**, 212 (1965).
2. J. S. Mayell and S. H. Langer, *ibid.*, **111**, 438 (1964).
3. J. S. Mayell and S. H. Langer, *J. Electroanal. Chem.*, **7**, 288 (1964).
4. W. T. Grubb and C. J. Michalske, *This Journal*, **111**, 1015 (1964).
5. W. J. Moore, "Physical Chemistry," p. 582, Prentice-Hall, New York (1955).
6. B. E. Conway, "Theory and Principles of Electrode Processes," p. 115, Ronald Press Co., New York (1965).
7. H. A. Laitinen and C. G. Enke, *This Journal*, **107**, 773 (1960).

Concentration Gradients at Horizontal Electrodes

R. N. O'Brien

Chemistry Department, University of Alberta, Edmonton, Alberta
and Inorganic Materials Research Division, Lawrence Radiation Laboratory,
University of California, Berkeley, California

ABSTRACT

Interferograms of the transient condition of concentration gradient build-up have been recorded with a motion picture camera for horizontal electrodes in the cathode-over-anode position. The appropriate solution of Fick's second law for the unsteady state has been shown to predict the concentration gradient at times of the order of 150 sec or greater. The interference fringes can be integrated as time dependent concentration contours and, hence, a measure of the diffusion current obtained. Logically, at $t=0$ sec, $i_{diff} = 0$. Experimental data show that i_{diff} reaches a maximum at times greater than 150 sec in the diffusion layer, and t goes from 0 to some value close to one during the same time. It has been impossible to decide on a definite value for the transference number and diffusion coefficient that would be appropriate.

Concentration gradients at working electrodes were difficult to obtain until the advent of the modern optical methods of Schlieren patterns (1) and interferometry (2). The recording system has always been a still camera until very recently when a motion picture camera was used (3). This recording technique should provide sufficient data of good quality to establish quantitatively the dependence of concentration changes in the electroactive species with time.

A series of interferograms of an experiment with the electrodes in the cathode-over-anode position were recorded on motion picture film and the results analyzed and compared to the theory of ionic transport. To the best of the author's knowledge this is the first recording of such transient concentration changes.

Fig. 1. Exploded view of the cell without the thermostating clamp

Experimental

A 0.5M $CuSO_4$ solution, *p*H 4.5, made up in the usual way was electrolyzed in an interferometer (Fig. 1) which has been described in detail elsewhere (4). Briefly, the cell had two copper electrodes 0.2 cm thick and 4 cm long sandwiched 0.313 cm apart between two coated glass flats. The flats were held in a specially shaped Teflon cylinder which was placed in a clamp with which an appropriate wedge angle between the flats could be produced. Collimated sodium vapor light produced wedge fringes which were recorded by a Bolex Paillard 16 mm motion picture camera on Ansco Hypan film at 24 frames/sec. The film was underexposed, and therefore required overdeveloping by a factor of 2 to 4. The developed film was then projected at a magnification factor of 80, and from frames at selected times representative fringes were sketched

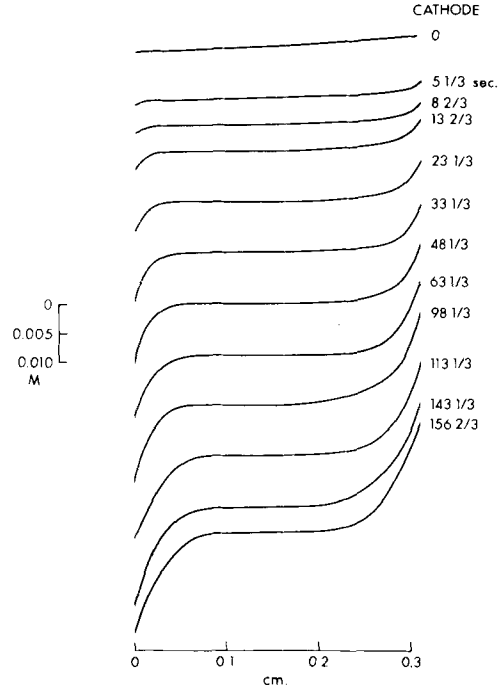

Fig. 2. Interference fringes (as sketched from 16 mm film) at various times after the beginning of electrolysis in the system $Cu/CuSO_4/Cu$. Electrolyte concentration 0.1*N*, *p*H 4.5.

on graph paper (Fig. 2). Details of the type of fringes obtained and adjustments made to them appear in Appendix I.

Carefully prepared pure polycrystalline copper electrodes were used in the cell which was thermostated at 25°C. When a suitably oriented fringe system had been produced, the motion picture camera was started, then a preset constant current passed through the cell, in this case 0.9022 ma/cm^2.

Theory

The theory of ionic mass transport in electrolysis has been reviewed by Tobias, Eisenberg, and Wilke (5). They give for the rate of transfer of ions in the x direction (x perpendicular to the plane of the electrode)

$$N_t = CU\frac{\partial\psi}{\partial x} - D\frac{\partial C}{\partial x} + VC$$

where N_t = total rate of transfer, gram ions/cm^2-sec; C = concentration in gram ions/cm^3; U = mobility, cm^2/sec-volt; ψ = potential, volts; x = distance in direction of transfer, cm; D = diffusion coefficient, cm^2/sec; and V = velocity for steady-state conditions. In the experimental set-up here used, horizontal electrodes, cathode-over-anode; $V = 0$ since convection is absent leaving only electromigration and diffusion, represented by the first and second terms on the right side. Tobias *et al.* then give an expression for the rate of ionic transport by diffusion $N_d = N_t - N_m = I(1 - t_+)/nF$ where N_m = rate of migration, gram ions/cm^2-sec; t_+ = cation transference number, and the other symbols have their usual meanings. Again this expression is for steady-state conditions.

Considering the unsteady state, the solution of the equation

$$\frac{\partial C}{\partial t} = D\frac{\partial^2 C}{\partial x^2}$$

for the boundary conditions $\Delta C = 0$ at $t = 0$, $x = 0$ and $\Delta C = 0$ at $t \neq 0$, $x = l$ is

$$\Delta C_{(x,t)} = \frac{\sqrt[2]{Dt}/l^2\, I\, l\, t-}{nF\, D}\ \text{ierfc}\ \frac{1 - x/l}{\sqrt[2]{Dt}/l^2}$$

as given by Carslaw and Jaeger (6), using only the first term of the complete series solution since ierfc $z \to 0$ as $z \to \infty$. It is worth noting that the expression is independent of 1, only requiring that $\Delta C \to 0$ as $x \to 1$ ($2l$ = electrode separation). Inclusion of the anion transference number in the pre-error function coefficient ($t-$), is to be expected and as in the steady state is intended to make allowance for the migration current. ierfc is the complement of the integrated error function (6).

The present experimental results should permit a testing of the efficacy of this treatment since the number of coulombs discharged at any time can be calculated by considering the number of ions required to be removed (discharged) to produce the observed concentration gradient. This can be done by a form of graphical integration which makes only the assumptions that the fringe selected is a typically average fringe for the whole electrode surface, that the diffusion coefficient is known and constant over the concentration range considered, and that all refractive index changes are due to $CuSO_4$ concentration changes.

Results

The initial attempts to fit the interference fringe selected as typical at 150 sec were made using the diffusion coefficient of $CuSO_4$ as reported by Eversole (7) and co-workers and the transference number for SO_4^{2-} according to Fritz and Fuget (8). The diffusion coefficient and transference number for the concentration at the selected x were used for each point calculated. Results are shown in Fig. 3. The agreement with the anode side of the interferogram is quite good, but for the cathode the prediction is everywhere short of that found. The predicted values for 15 sec are almost 50% too high and so are not plotted.

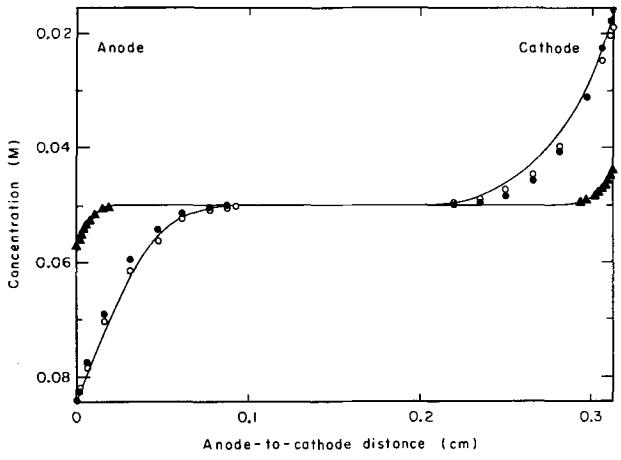

Fig. 3. Comparison of calculated and experimental values at 15 and 150 sec. ○ calculated using best literature values of D and t- for each concentration; • calculated using D = 4.4 x 10^{-6} cm^2 sec^{-1}, appropriate literature t- and current densities from Fig. 4; ▲ calculated using D = 4.4 x 10^{-6} cm^2 sec^{-1} appropriate literature t- and current densities from Fig. 4.

Realizing that the results of other studies (9) of the Cu/$CuSO_4$/Cu system have shown values for the diffusion constant of about 4.4 x 10^{-6} cm^2/sec, the requisite current densities to give agreement at ΔC_{max} using D = 4.4 x 10^{-6} were calculated, and are shown in Fig. 4 to suggest that eventually a potential gradient will be produced such that $N_d = N_t$. If instead the diffusion constant is calculated for each time and using the appropriate transference number such that $\Delta C_{calc} = \Delta C_{exp}$ at the electrode ($x = 0$), D obviously approaches 4.4 x 10^{-6} cm^2/sec at some time greater than 150 sec (Fig. 5).

Using the calculated required current density for D = 4.4 x 10^{-6} cm^2/sec and average literature transference numbers, values at selected distances from the electrodes were plotted on Fig. 3 and for 15 sec is quite good. The agreement is worse than the first attempt, but not much worse. Figure 4 shows the results of graphical integration to obtain the number of coulombs of charge required to discharge the necessary number of ions to form the concentration gradient found at various times. The successive current densities plotted in Fig. 4 are again plotted here in a different way. Beginning at 3 1/3 sec the value found is plotted from zero time to ½ the distance to the next calculated value, in this case 4 1/16 sec since the next time is 5 sec. The 5-sec value is now plotted to join at

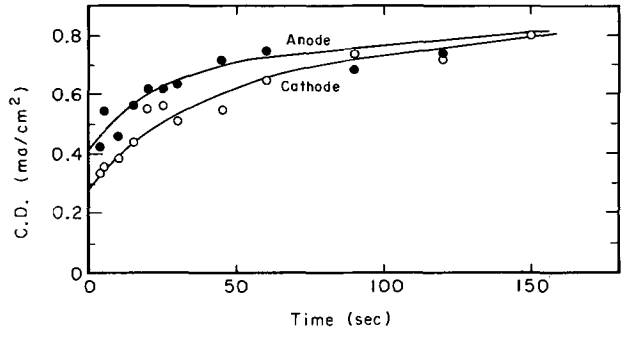

Fig. 4. Current densities calculated at various times, using D = 4.4 x 10^{-6} cm^2 sec^{-1} and appropriate literature t- such that the concentration change found experimentally at x = 0 is equal to the calculated concentration change; • anode; ○ cathode.

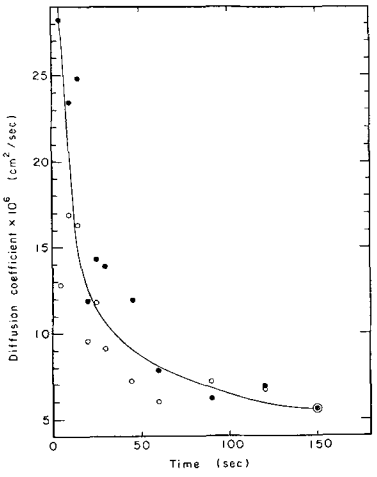

Fig. 5. Diffusion constants calculated to give agreement with concentration change found at the electrode using appropriate literature t- values; • anode; ○ cathode.

this point and is drawn half-way across the next time interval. Plots for both the anode and cathode were made. The line drawn for the anode appears to be generally too high, but the cathode plot is reasonably representative of the charge-carried points. The current density plots appear to be approaching the same slope as the externally measured current density.

Assuming the diffusion constant to be fixed at 4.4×10^{-6} cm^2/sec the transference number necessary to give agreement at $x = 0$ and $t = 150$ sec is $t- = 0.58$ for 15 sec $t- = 0.298$. This suggests that $t-$ goes to zero at $t = 0$, when of course $N_t = N_m$ since there is no diffusion gradient to support a diffusion current.

Conclusions

The quality of the fit of calculated points using

$$\Delta C_{(x,t)} = \frac{\sqrt[2]{Dt}/l^2\, I\, l\, t-}{nF\, D}\ \text{ierfc}\ \frac{1 - x/l}{\sqrt[2]{Dt}/l^2}$$

is sufficiently good that, apart from the theoretical reason for selecting it, it obviously is the correct form to represent the physical process considered, that is the sudden imposition of a constant current density between parallel, plane, horizontal electrodes in the absence of convection.

However, the problem of deciding on the values of the basic constants to use has not been solved. The assumption that a concentration contour, calculated from a refractive index contour with no allowance for pH change or extraneous reactions is probably as good as the data. If this is so, then the problem becomes one of deciding what D and $t-$ to use, again assuming that the externally measured current density must be used unmodified. These problems can probably be resolved by electrolysis for longer times so that plots like Fig. 4 and 5 could indicate the steady-state diffusion constant and diffusion current. Electrolysis at the limiting current density should also give helpful information regarding these two quantities.

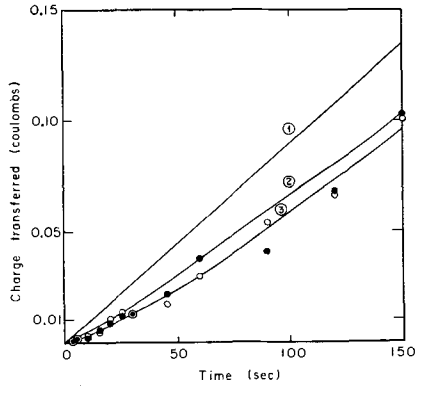

Fig. 6. Charge transferred vs. time. Line 1 is the externally measured current density; line 2 is the calculated required value of the current density at the anode from Fig. 4; line 3 is the same value for the cathode. • number of charges transferred at the anode at a given time found by integrating under the concentration contour. ○ cathode values obtained in the same way.

Acknowledgment

The author wishes to acknowledge the suggestion of E. J. Casey that the data be subjected to this type of analysis, the efforts of K. Kinoshita, who did most of the experimental work, and of John Newman for interesting and advisory conversations on the theoretical aspects. This work was supported in part by the National Research Council of Canada and the Inorganic Materials Research Division of the Lawrence Radiation Laboratory, University of California, Berkeley.

Manuscript received Dec. 7, 1964; revised manuscript received Jan. 18, 1965.

Any discussion of this paper will appear in a Discussion Section to be published in the December 1966 JOURNAL.

REFERENCES

1. R. S. Cooper, *This Journal*, **105**, 506 (1958); A. G. Samarcev, *Z. Physik. Chem.*, **A168**, 45 (1934).
2. N. Ibl and R. H. Muller, *Z. Elektrochem.*, **59**, 671 (1955); R. N. O'Brien and C. Rosenfield, *J. Phys. Chem.*, **67**, 643 (1963).
3. R. N. O'Brien, *This Journal*, **111**, 1300 (1964).
4. R. N. O'Brien, *Rev. Sci. Inst.*, **35**, 803 (1964).
5. C. W. Tobias, M. Eisenberg, and C. R. Wilke, *This Journal*, **99**, 359C (1952).
6. H. S. Carlslaw and J. C. Jaeger, "Conduction of Heat in Solids," pp. 69 and 486, 2nd Ed., Oxford Press (1962).
7. W. G. Eversole, H. M. Kindswater, and J. D. Peterson, *J. Phys. Chem.*, **46**, 370 (1942).
8. J. J. Fritz and C. R. Fuget, *ibid.*, **62**, 303 (1958).
9. H. J. S. Sand, *Phil. Mag.*, **1**, 45 (1901); R. N. O'Brien and C. Rosenfield, *J. Phys. Chem.*, **67**, 643 (1963); R. N. O'Brien, D. Quon, and C. R. Darsi, "Estimation of Diffusivities and Thermal Conductivities of Liquids and Solutions by Analysis of Unsteady State Experiments Using a New Optical Technique," to be published.
10. S. Tolansky, "An Introduction to Interferometry," p. 80, Longmans Green and Co., London (1955).

APPENDIX I

Fringes of equal inclination: Brewster's fringes.— Tolansky has given an excellent treatment of fringes of equal inclination (10). However the difference between wedge or fizeau-type fringes and Brewster's fringes will be considered briefly.

Figure 7 shows schematically the light path and how Brewster's fringes are produced. If the incident light is at an angle to the wedge whose angle is small (about 2 min of arc), instead of getting wedge fringes, that is, a continuous set of equally spaced parallel fringes, rings of fringes are produced. In this experiment it was intended to use wedge fringes, but since

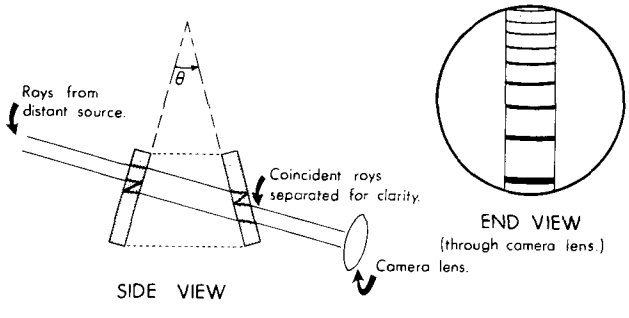

Fig. 7. Production of Brewster's fringes

the radius of curvature of the fringes is relatively large and the two types can exist simultaneously, it is easy to confuse the two. The error was not discovered until a large number of tedious hand measurements had been made.

For wedge fringes, the fringes appear on a uniform wedge at positions where the thickness of the wedge is an integral multiple of the wavelength of the monochromatic light, that is since $n\lambda = 2\mu t \cos \phi$, whenever the thickness has increased by $\lambda/2$ from the last fringe, bright or dark, a new fringe appears. n is the order of interference, μ the refractive index, t the thickness, and ϕ the angle of incidence of the light. If ϕ becomes a very little less than 90° for thick wedges, Brewster's fringes result.

Brewster's fringes are located at infinity and appear on the wedge as rings. The fringes will appear at positions governed by $n\lambda = \mu t$(cosine of the angle of refraction in the first glass flat minus cosine of the angle of refraction in the second glass flat) assuming $\cos \phi$ is about equal to 1, since the light passes only once through the cell.

Variations in the refractive index of the wedge of electrolyte cause displacement of the fringes up and down the wedge (toward the apex if the change is an increase in concentration) which takes the form of a perturbation to the arc of the circle seen between the electrodes. The fringes measured for the S/V position were a 2° 35′ arc of a circle of 3.43 cm radius and those for the C/A position had a similar radius of curvature. A detailed account of how to relate wedge fringe perturbation to concentration has been given by O'Brien and Rosenfield (7) and complete review of the theory by O'Brien (9).

To allow plots of concentration changes to be made on cartesian coordinates, these arcs had to be converted to straight lines. Frequently the increments at successive positions at which measurements were made were smaller than the expected precision of measurement. However, to ensure that some systematic method of correction for fringe curvature was used, a transparent plastic template whose plotting edge was cut in the mirror image of the curve was used in replotting the uncorrected values read from the display of the original fringes. In this way the curvature was plotted out and also any rotation of axis needed to correct the angle of the fringes to the electrode to 90°. Of course since both the plastic template and the pencil point had thickness, a further, but it is thought, random scatter of points resulted. A smooth curve was then drawn through the points. A scale in which fringe perturbations are shown as concentration change in moles per liter has been added to the figures where necessary. The limit of accuracy of the measurements is that with which the center of any fringe can be located relative to the center of another fringe. In this case it is thought from the results of repeated measurements to be about ±1/20th of a fringe width or about $\pm 7 \times 10^{-4}$M. Details of this type of calculation have been given previously (4).

Faradaic Impedance of Polarized Porous Electrodes

I. First Order Kinetics

R. Darby[1]

LTV Research Center, Ling-Temco-Vought, Inc., Dallas, Texas

ABSTRACT

The a-c impedance characteristics of polarized porous gas-diffusion electrodes are calculated on the basis of a simplified dual-layer model. It is shown that the consideration of a region within the electrode wherein simultaneous diffusion and reaction occur can result in either an inductive or capacitive reactance, depending on the magnitudes of dimensionless frequency and d-c current density parameters. The absence of such a region, which corresponds to the limiting case at high reaction rates, results in capacitive reactance only.

Recently, Gutmann (1) discussed the experimental observation of lagging currents in electrochemical systems and proposed an explanation of this inductive effect by analogy with viscoelastic phenomena. A number of authors have considered the a-c impedance of electrode systems [*e.g.*, (2)-(18)], although none of their results account for the effects described by Gutmann. It will be shown that inductive reactances arise naturally from a consideration of the Faradaic impedance of a polarized porous electrode in which mass transport and electrochemical reaction can proceed simultaneously over a distributed region of the electrode.

[1] Present address: Chemical Engineering Department, Texas A & M University, College Station, Texas.

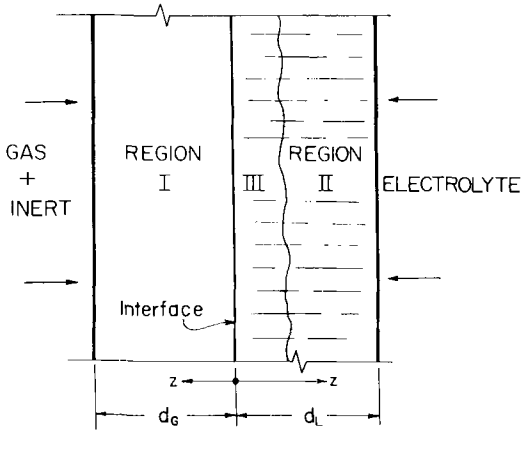

Fig. 1. Schematic diagram of dual-layer model

The Model

A simplified dual-layer model is considered for analysis and is schematically illustrated in Fig. 1. One face of the electrode is exposed to a binary gas phase containing a reactant and an inert component, and the other face is exposed to a liquid (electrolyte) phase, also considered to be a binary mixture of a reacting (ionic) component and an inert. The porosity of the two layers and the differential pressure is assumed to be such that the gas-liquid interface is maintained at the junction of the two layers. The resistivity of the electrode matrix will be neglected in comparison with that of the electrolyte so that the electrode matrix will be essentially at a uniform potential.

The electrode is assumed to be operating in a polarized condition, resulting in a d-c current I and d-c polarization E. The electrode reaction will thus proceed irreversibly and will be represented by the general expression

$$gG + lL + ne^- \rightarrow pP \qquad [1]$$

The corresponding rate equation relating current,

polarization, and concentration can thus be written as

$$I = I_o \left(\frac{G}{G_o}\right)^{g'} \left(\frac{L}{L_o}\right)^{l'} \exp\left(\frac{\alpha n' F}{RT} E\right) \quad [2]$$

where G and L are the concentrations at the reaction site, while G_o and L_o are those in the bulk phases, which are constant. The reaction orders g', l', and n' may or may not be the same as g, l, and n of [1], depending on whether or not [1] represents the true kinetics of the electrode reaction.

In order to determine the a-c impedance of the electrode, we consider an a-c component of potential superimposed upon the d-c (constant) value. If the amplitude of this a-c component is small compared with the value of $(\alpha n'F/RT)$, correspondingly small a-c components of polarization, current, and concentration will result. Thus rewriting [2] in terms of total (a-c plus d-c) quantities, gives

$$I + i = I_o \left(\frac{G + \zeta}{G_o}\right)^{g'} \left(\frac{L + \lambda}{L_o}\right)^{l'} \exp\left[\frac{\alpha n' F}{RT} (E + \eta)\right] \quad [3]$$

Recognizing that

$$\left(\frac{\zeta}{G}, \frac{\lambda}{L}, \frac{\alpha n' F}{RT} \eta\right) << 1$$

and neglecting terms of second order in these quantities, [3] can be written in the linearized form

$$i = I\left[g'\left(\frac{\zeta}{G}\right) + l'\left(\frac{\lambda}{L}\right) + \frac{\alpha n' F}{RT}\eta\right] \quad [4]$$

Equation [4] is the kinetic rate equation relating the a-c components of current, polarization, and concentration.

Mass transport through the porous layers of the electrode is assumed to occur by a diffusional type of mechanism, so that Fick's second law applies

$$\frac{\partial c}{\partial t} = D_{AB} \frac{\partial^2 c}{\partial z^2} \quad [5]$$

Here, D_{AB} can be thought of as a "pseudo" diffusion coefficient for transport through the porous medium. For diffusion paths which are large compared with pore size, the relation between gaseous binary molecular diffusivity and the porosity and tortuosity of the medium is (19)

$$D_{AB} = \mathcal{D}_{AB} \frac{\sigma}{\tau} \quad [6]$$

For transport of the electrolyte through the pores, an equivalent mechanism will be assumed. In this case, the "pseudo" diffusivity will also include the effects of migration. For dilute electrolytes, this is accomplished simply by multiplying the molecular diffusivity by the factor $(1 + Z_1/Z_2)$ as shown by Levich (20), where Z_1 and Z_2 are the charge numbers of the reacting and nonreacting ions, respectively. For very concentrated electrolytes, the effect is much more complicated, and the diffusion coefficient can no longer be considered a constant.

We shall consider three regions within the electrode. Region I includes the entire gas-filled pore layer, in which the only rate process is diffusion of the gaseous reactant in accordance with Fick's law. Region II includes the major portion of the liquid-filled pore layer, in which the only rate process is diffusion of the liquid reactant in accordance with Fick's law (with the appropriate "pseudo" diffusion coefficient). Region III is that portion of the liquid filled pore layer adjacent to the gas-liquid interface in which the catalyzed electrochemical reaction is assumed to occur. Hence simultaneous diffusion and reaction occur in this region, by the following assumed mechanism. The gaseous reactant dissolves in the liquid electrolyte at the interface, resulting in a concentration C_i at the electrolyte interface as given by Henry's law

$$C_i = G_i \frac{c_t RT}{H} \quad [7]$$

The dissolved reactant diffuses through the liquid-filled pores, and reacts simultaneously at catalytic sites on the pore walls as it diffuses. For small values of the pore diameter to length ratio, the problem is essentially one dimensional. Thus for region III, Eq. [5] is replaced by

$$\frac{\partial c}{\partial t} = D_{AB} \frac{\partial^2 c}{\partial z^2} - r = D_{AB} \frac{\partial^2 c}{\partial z^2} - i\left(\frac{ag}{nF}\right) \quad [8]$$

Since the concentration of dissolved gaseous reactant will be small compared with that of the liquid (electrolyte) reactant, L, the reaction zone (region III) will be small compared with the total diffusion path (d_L) of L. Hence the concentration of L will be assumed constant over this region at a value of L_i, as determined by solution of the diffusion equation for region II.

In summary, the appropriate dependent variables within the three regions, and their respective dependence on time and spatial coordinates are:

Region I:

$$z = 0;\ G = G_i,\ \zeta = \zeta_i(t)$$

$$0 < z < d_G;\ G = G(z),\ \zeta = \zeta(z,t)$$

$$z = d_G;\ G = G_o,\ d\zeta/dz = -\frac{ig}{nFD_{GG}}$$

Region II:

$$z = 0;\ L = L_i,\ \lambda = \lambda_i(t)$$

$$0 < z < d_L;\ L = L(z),\ \lambda = \lambda(z,t)$$

$$z = d_L;\ L = L_o,\ d\lambda/dz = -\frac{il}{nFD_{LL}}$$

Region III:

$$z = 0;\ C = C_i = G_i \frac{c_t RT}{H},\ \gamma = \gamma_i(t) = \zeta_i(t) \frac{c_t RT}{H}$$

$$z > 0;\ C = C(z),\ \gamma = \gamma(z,t),\ L = L_i$$

These conditions are expressed in terms of concentrations at the interface, which are dependent variables and hence are not known *a priori*. However, in solving the appropriate equations these conditions are essentially replaced by the following boundary conditions involving the total current density I_t, produced by the electrode

$$I_t = -\frac{nFD_{GG}}{g}\left(\frac{dG}{dz}\right)_{z=0} = -\frac{nFD_{LL}}{l}\left(\frac{dL}{dz}\right)_{z=0} = -\frac{nFD_{GL}}{g}\left(\frac{dC}{dz}\right)_{z=0} \quad [9]$$

with equivalent expressions for the total alternating current density, i_t, in terms of the flux of alternating concentration components.

It is noted that [2] can be written

$$E = \frac{RT}{\alpha n' F}\{\ln(I/I_o) + g'\ln(G_o/G) + l'\ln(L_o/L)\} \quad [10]$$

i.e., the total polarization can be expressed as the sum of three terms which are determined by the current production ("activation polarization"), and the change in reactant concentrations from bulk values ("concentration polarization"). The same interpretation can be made from [4] for the alternating components. Since L is assumed constant at L_i over the

reaction zone, for a given total current the term involving L is essentially a linearly additive constant (the same being true for λ). Thus the contribution of L and λ to d-c polarization and a-c impedance, respectively, results in an additional additive term dependent only on the total current and Fick's law over region II. Furthermore, since the calculation of this term is analogous to that for gas phase polarization (region I), the resulting gas and liquid phase terms are analogous, so that nothing new is learned by including the L term. Henceforth, it will be omitted, with the knowledge that it could later be included by simple linear addition for a given total current. This is equivalent to saying that setting $l' = 0$ results in no loss of generality for the present model.

Steady D-C Analysis

The solution for the steady d-c component of concentration has been given elsewhere (21). The results, for a first order ($g' = 1$) reaction and considering the effect of the inert gas phase component are

$$C = C_i \exp(-z\sqrt{K}) \quad [11]$$

where

$$C_i = \frac{c_t P_o}{H}\left[1 - (1 - G_o/P_o)\exp(I_t/A_2)\right] \quad [12]$$

$$K = [I_t g/(nFD_{GL}C_i)]^2 \quad [13]$$

$$A_2 = (nF\,P_o\,D_{GG}/g\,RT\,d_G) \quad [14]$$

and

$$E = \frac{2RT}{\alpha n'F}\ln(I_t/A_3C_i) \quad [15]$$

where

$$A_3 = [anFD_{GL}I_oH/(gG_oc_t)]^{1/2} \quad [16]$$

In Eq. [11]-[16], G_o refers to the partial pressure of the gaseous reactant in the bulk gas phase, P_o is the total pressure, and D_{GG} and D_{GL} refer to the pseudo-diffusivities of the gas reactant component within the gas filled and liquid filled pores, respectively. These equations are exact only if the liquid filled region is effectively semi-infinite relative to the reaction zone. As seen from [11], the effective penetration depth of the reaction zone is of the order of $1/\sqrt{K}$, which is quite small for normal values of current density (*i.e.*, significant polarization values). Hence the assumption of a semi-infinite liquid filled layer for the purpose of applicability of these equations should be quite adequate under polarized conditions.

Impedance Calculations

The electrode impedance is defined as the ratio of the alternating components of polarization (η) and current density (i_t), for a sinusoidally varying input. This involves the simultaneous solution of Eq. [4] and [8] for the appropriate alternating components, together with the condition

$$i_t = -\frac{nFD_{GL}}{g}\left(\frac{d\gamma}{dz}\right)_{z=0} \quad [17]$$

The steady d-c component also enters through I in Eq. [4].

Taking the LaPlace transform of [8] and combining with [4] (for $l' = 0, g' = 1$) gives

$$\frac{d^2\bar{\gamma}(s)}{dz^2} - \bar{\gamma}(s)\,K\left(1 + \frac{s}{KD_{GL}}\right) = \Delta\bar{\eta}(s)\exp(-z\sqrt{K}) \quad [18]$$

where

$$\Delta = \alpha n'FC_iK/RT \quad [19]$$

The solution to [18] is

$$\bar{\gamma}(s) = \left[\bar{\gamma}_i(s) - \frac{\Delta\bar{\eta}(s)}{K(1-\beta)}\right]\exp(-z\sqrt{K\beta}) + \frac{\Delta\bar{\eta}(s)}{K(1-\beta)}\exp(-z\sqrt{K}) \quad [20]$$

where

$$\beta = 1 + s/KD_{GL} \quad [21]$$

and $\bar{\gamma}_i(s)$ is given by the solution [5] for region I, relating $\bar{\gamma}_i(s)$ and $\bar{\zeta}_i(s)$ by Henry's law [7]:

$$\bar{\gamma}_i(s) = \bar{i}_t(s)\frac{A_4}{d_G\sqrt{s/D_{GG}}}\left[\frac{1 - \exp(d_G\sqrt{s/D_{GG}})}{1 + \exp(d_G\sqrt{s/D_{GG}})}\right] = \bar{i}_tA_4\Gamma(s) \quad [22]$$

where

$$A_4 = \frac{gc\,RT\,d_G}{nF\,H\,D_{GG}} \quad [23]$$

Substituting the derivative of (the transform of) [2] into [17], employing [22] for $\bar{\gamma}_i(s)$, and solving for $\bar{\eta}(s)/\bar{i}_t(s)$ gives

$$Z(s) = \bar{\eta}(s)/\bar{i}_t(s) = \sqrt{K}[(g/nFD_{GL}) - A_4\Gamma(s)\sqrt{K\beta}][1 + \sqrt{\beta}]/\Delta \quad [24]$$

Now if the substitution $s = j\omega$ is made in [24], the result is the complex impedance, $Z(j\omega)$. Separating this into real and negative imaginary parts gives the resistance (R) and capacitive reactance (X_c) of the electrode, as a function of frequency, ω. From [22] and [21], the frequency dependence of Z is seen to be a function of the following two dimensionless groups

$$\xi = d_G\sqrt{\omega/2D_{GG}} \quad [25]$$

and

$$\psi = \frac{\omega}{D_GK} = \frac{2D_{GG}}{KD_G}\left(\frac{\xi}{d_G}\right)^2 \quad [26]$$

The group ξ is essentially the square root of the ratio of the characteristic diffusion time through the gas pore layer to the angular period of the alternating voltage. The group ψ represents essentially the ratio of the characteristic reaction (relaxation) time to the angular alternating period.

Evaluation of $Z(j\omega)$ as a function of ξ was done with the aid of a computer for the representative system parameters shown in Table I. The results are expressed as impedance attenuation, $(DB)_z$, and phase angle, θ defined as follows

$$(DB)_z = 20\log(Z/Z_o) \quad [27]$$

$$\theta = \tan^{-1}(X_c/R) \quad [28]$$

Figures 2 and 3 show $(DB)_z$ and θ as functions of ξ for various values of ϕ, the ratio of current density to the gas phase diffusion limited current density

$$\phi = I_t/I_{lim};\ I_{lim} = A_2\left(\frac{1}{1 - x_o}\right) \quad [29]$$

It is pointed out that negative values of θ correspond to inductive reactances.

Figure 4 shows the Argand diagram (X_c *vs.* R) for the impedance components. The familiar semicircular form is seen, which blends into a 45° line as ξ increases. At sufficiently large values of ξ the reactance becomes inductive, and the curves approach a line with a negative slope of 45°.

Table I. Parameter values used in calculations

Gas phase: $x_o = 0.21$ mole fraction, $P_o = 1$ atm
Henry's law constant: $H = 3.95 \times 10^4$ atm/mole fraction
Porous medium: $\Phi = 0.5$, $\tau = 15$, $d_G = d_L = 0.1$ cm
Diffusivities: $D_{GG} = 0.2$ cm²/sec, $D_{LL} = 2 \times 10^{-5}$ cm²/sec
$D_{GL} = 1 \times 10^{-5}$ cm²/sec
Kinetic parameters: $I_o = 10^{-5}$ amp/cm², $n = n' = 4$, $\alpha = \frac{1}{2}$
$(aI_o) = 5 \times 10^{-5}$ amp/cm³, $T = 25$°C

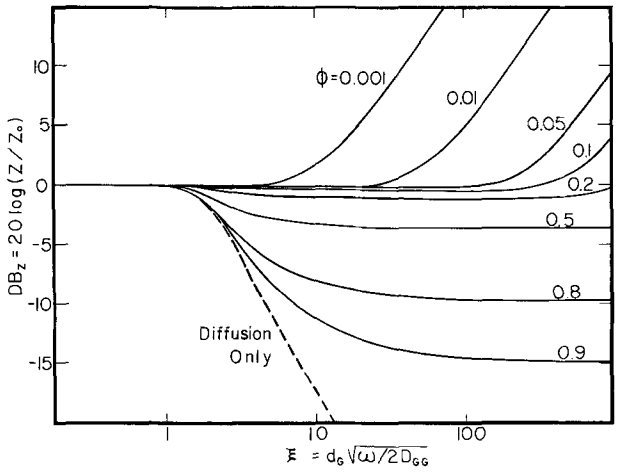

Fig. 2. Impedance attenuation as a function of frequency and current density.

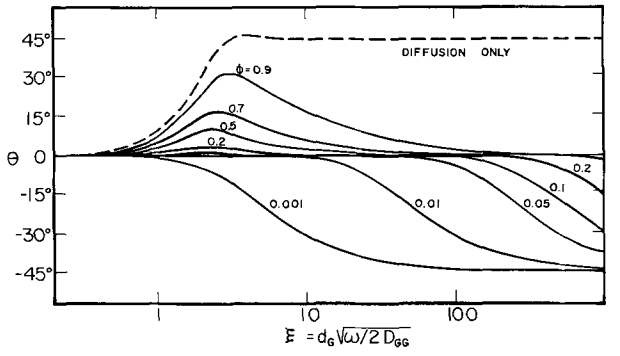

Fig. 3. Capacitive phase angle as a function of frequency and current density.

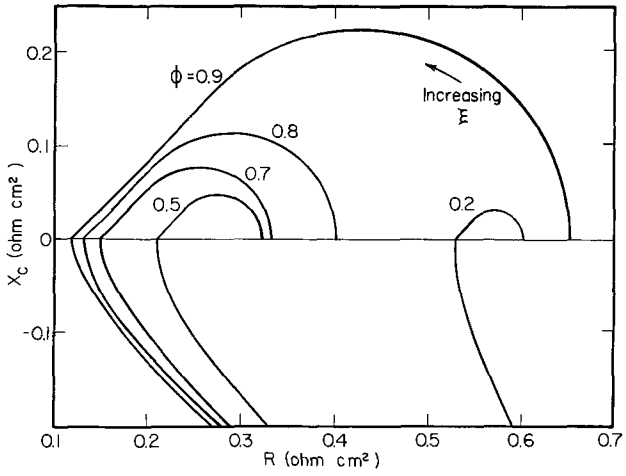

Fig. 4. Argand diagram

Limiting (Uncoupled) Behavior

As previously noted, the above analysis is valid for reaction penetration depths $(1/\sqrt{K})$ less than d_L. However, [as shown in (19)], when the reaction rate (I_t) is sufficiently large so that $1/\sqrt{K}$ is of the order of the pore diameter, this approach is not valid, since it will not then be possible to introduce a "pseudo" diffusion coefficient as per Eq. [6]. Further, it will not be possible to define an effective rate constant per unit volume, represented by $(I_o a)$. However, in this case the penetration depth would be so small that the reaction takes place essentially at the plane of the interface located at the junction of the two layers, and there will be no region of simultaneous reaction and diffusion represented by region III. Thus this condition is equivalent to a planar nonporous electrode, with finite but independent diffusion paths for each reactant.

In this event, the d-c and a-c characteristics will be determined by the sum of three separate terms, as given by Eq. [4] and [10]. Here, the values of G, L, γ and λ are those at the interface which result from the solution of the diffusional flux equations, while I and i represent total values since the current is not distributed as before. This condition is treated in (21) as the "uncoupled" model.

Again assuming $l' = 0$, the resulting complex impedance becomes,

$$Z(j\omega) = \frac{RT}{\alpha n' F}\left(\frac{1}{I_t} - \frac{gg' d_G \Gamma(j\omega)}{n F D_{GG} G_i}\right) \quad [30]$$

The impedance is thus composed of a purely resistive term, which is inversely proportional to total d-c current ("activation impedance"), and a complex term due to diffusion ("concentration impedance"). The contribution to $(DB)_z$ and θ from the concentration impedance term only is shown as the dashed curve on Fig. 2 and 3. As expected, the results for the total $Z(j\omega)$ (*i.e.*, the sum of both activation and concentration terms) for the uncoupled case approach the previous results for the coupled case very closely for larger values of ϕ. At smaller values, the $(DB)_z$ and θ curves approach zero, the inductive characteristic being absent. Likewise the Argand diagram for the concentration impedance is a semicircle blending into a 45° line through the origin. The addition of the resistive activation term merely serves to shift the entire curve along the real axis. No negative (inductive) reactance is predicted for this limiting (uncoupled) condition.

Restrictions

The analysis of electrode impedance presented here does not include the non-Faradaic effects of ohmic resistance and double layer capacitance, both of which contribute to the total impedance. The former is quite often negligible in comparison with mass transport effects, as pointed out by Austin and Lerner (22), and in any event can be independently measured and separated from polarization data [*e.g.*, Brodd (23)]. The double layer capacitance, on the other hand, can be quite significant, especially in porous systems. Although in principle it too may be determined independently in the absence of reaction, this is not easily done in practice. However these factors should not affect the qualitative picture of electrode impedance presented here, inasmuch as the inductive effects appear only at relatively high frequencies, and capacitive reactance effects from the double layer should be small at these frequencies.

Manuscript received April 2, 1965; revised manuscript received January 7, 1966.

Any discussion of this paper will appear in a Discussion Section to be published in the December 1966 JOURNAL.

REFERENCES

1. F. Gutmann, *This Journal*, **112**, 94 (1965).
2. R. DeLevie, *Electrochemica Acta*, **8**, 751 (1963).
3. R. DeLevie, *ibid.*, **9**, 1231 (1964).
4. P. Drossbach and J. Schulz, *ibid.*, **9**, 1391 (1964).
5. G. Feuillade, *Compt. rend.*, **256**, 2786 (1963).
6. R. Coffre and G. Feuillade, *ibid.*, **259**, 3245 (1964).
7. J. Euler and W. Nonnenmacher, *Electrochemica Acta*, **2**, 268 (1960).
8. O. S. Ksenzhek and V. V. Stender, *Zhur. Phiz. Khim.*, **31**, 117 (1957)
9. O. S. Ksenzhek, *ibid.*, **36**, 243 (1962).
10. A. W. Winsel, *Z. Elektrochem.*, **66**, 287 (1962).
11. D. E. Smith, *Analyt. Chem.*, **36**, 962 (1964).
12. J. E. B. Randles, *Discussions Faraday Soc.*, **1**, 11 (1947).
13. J. E. B. Randles and K. W. Sommerton, *Trans. Faraday Soc.*, **48**, 937 (1952).

14. R. J. Brodd, *J. Research Natl. Bureau Standards*, **65A**, 275 (1961).
15. D. C. Grahame, *This Journal*, **99**, 370C (1952).
16. D. C. Grahame, *J. Phys. Chem.*, **57**, 257 (1953).
17. P. Delahay, "New Instrumental Methods in Electrochemistry," Interscience, New York (1954).
18. K. J. Vetter, "Elektrochemische Kinetic," Springer-Verlag, Berlin (1961).
19. D. A. Frank-Kamenetskii, "Diffusion and Heat Exchange in Chemical Kinetics," Princeton (1955).
20. V. G. Levich, "Physicochemical Hydrodynamics," Prentice-Hall, Englewood Cliffs, N. J. (1962).
21. R. Darby, *Advanced Energy Conversion*, **5**, 43 (1965).
22. L. J. Austin and H. Lerner, *Electrochem. Acta*, **9**, 1469 (1964).
23. R. J. Brodd, *This Journal*, **106**, 471 (1959).

SYMBOLS

a specific catalytically active area, cm²/cm³
A_2 term defined by Eq. [14]
A_3 term defined by Eq. [16]
A_4 term defined by Eq. [23]
c_t total concentration of liquid phase, mole/cm³
C concentration of dissolved gaseous reactant, mole/cm³
d_G width of gas-filled pore layer, cm
d_L width of liquid filled pore layer, cm
$\mathcal{D}_{AB}$ binary molecular diffusion coefficient of phase A reactant in phase B, cm²/sec
D_{AB} "pseudo" diffusion coefficient for porous medium, cm²/sec
E d-c polarization (deviation from open-circuit potential), v
g stoichiometric coefficient for gas phase reactant
g' reaction order with respect to gas phase reactant
G gas phase reactant, concentration, mole/cm³
H Henry's law constant, atm/mole fraction
i alternating component of current density, amp/cm²
I d-c current density, amp/cm²
I_o exchange current density, amp/cm²
j $\sqrt{-1}$
K term defined by Eq. [13]
l stoichiometric coefficient of liquid phase reactant
l' reaction order with respect to liquid phase reactant
L liquid phase reactant, concentration, mole/cm³
n number of electrons involved in over-all electrode reaction
n' equivalent electron change in rate equation
P_o gas pressure, atm
R resistance, ohm-cm²
s transform variable, sec^{-1}
X_c capacitive reactance, ohm-cm²
x_o mole fraction of reactant in gas phase
Z impedance, ohm-cm²
z distance from gas-liquid interface, cm

Greek

α transfer coefficient
β term defined by Eq. [21]
γ alternating component of dissolved gas phase reactant concentration, mole/cm³
ζ alternating component of gas phase reactant concentration, mole/cm³
η alternating component of polarization, v
θ capacitive (lagging) phase angle, degrees
λ alternating component of liquid phase reactant concentration, mole/cm³
ξ dimensionless term defined by Eq. [25]
τ tortuosity
ϕ ratio of d-c current density to gas diffusion limited current density
ψ dimensionless term defined by Eq. [26]
ω angular frequency, sec^{-1}
Γ term defined by Eq. [22]
Δ term defined by Eq. [19]
σ porosity

Subscripts

i gas-liquid interface
o bulk phase, external to electrode
t total value

Technical Notes

Potassium Distribution in Nickel-Oxide Electrodes

Frederick P. Kober and Paul Lublin

General Telephone & Electronics Laboratories, Inc., Bayside, New York

Various authors have considered the role and distribution of potassium ion in the electrochemical oxidation of nickel-oxide electrodes in alkaline solution. Bourgault and Conway (1) were able to relate extrapolated values of the "reversible" electrode potential to the activity of H_2O and KOH in the electrochemical oxidation reactions using the data of Akerlof and Bender (2). Their results indicate the association of hydrated KOH with the charged state. A formal reaction is given and shows the discharged state to be free of any adsorbed KOH. These results are in qualitative agreement with the previous work of Kornfeil (3). Neither of these authors has considered the inclusion of potassium into the crystal structure of the active materials.

Experimental

The potassium content of sintered nickel electrodes impregnated with nickel hydroxide was investigated by means of electron probe analysis.[1] A Norelco AMR/3 electron probe analyzer equipped with two channels and a beam scanner, operating at 30 kv, was employed. The electrodes to be investigated were cycled in 31% KOH at the 3-hr rate and then thoroughly washed with deionized water in a continuous extractor for at least 48 hr. This elaborate washing procedure was employed to insure the complete removal of any adsorbed electrolyte. The electrodes were then potted in epoxy resins and polished in alcohol in order to reduce the tendency for the re-distribution of the potassium ions.

Beam scanning techniques were used to survey the samples. Since the specimen current is a function of atomic number as well as mass density, the specimen current scans are indicative of both average atomic number and porosity. Consequently, any interpretation of the results must be tempered by a consideration for the porous structure of the samples. Potassium x-ray scans were used to reveal the relative distribution of potassium in a given area under examination. As additional information, concentration profiles were obtained by positioning the goniometers on selected po-

[1] Electron probe analysis of sintered cadmium electrodes was recently reported by E. Lifshin and J. L. Weininger, 128th Meeting, Electrochemical Society, Buffalo (1965).

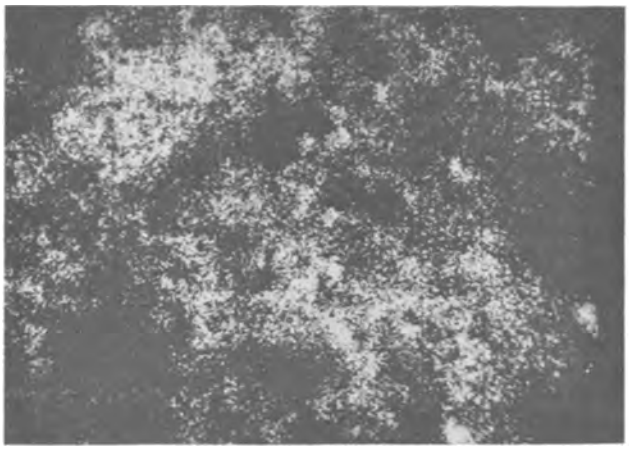

Fig. 1. Potassium x-ray scan. Magnification approximately 400X. (a) Initial charge.

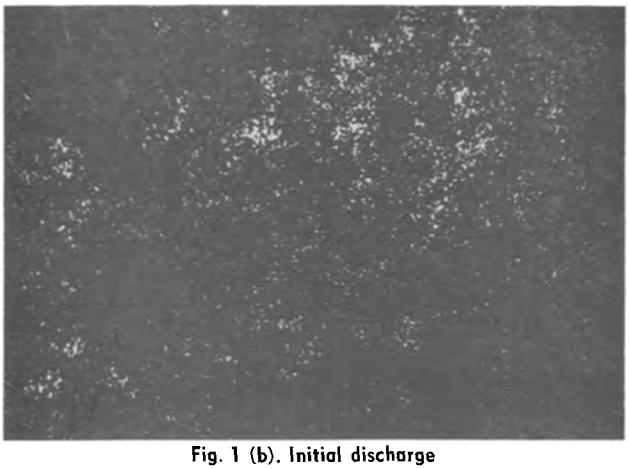

Fig. 1 (b). Initial discharge

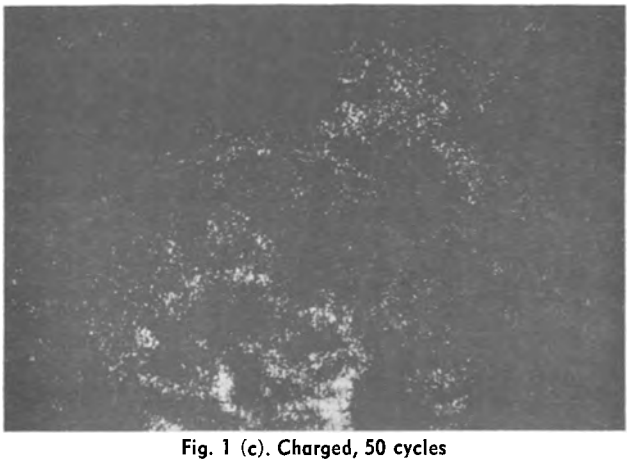

Fig. 1 (c). Charged, 50 cycles

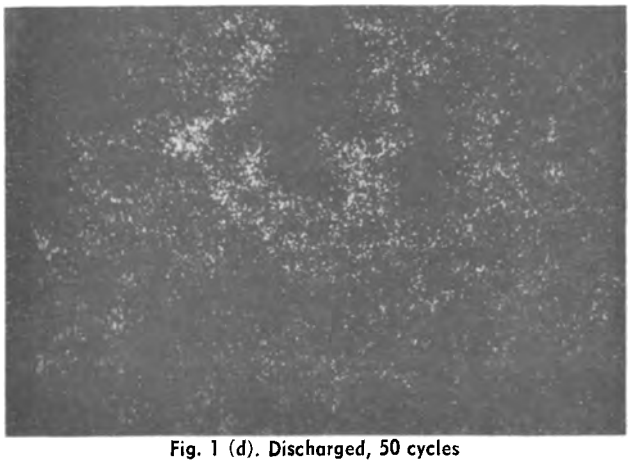

Fig. 1 (d). Discharged, 50 cycles

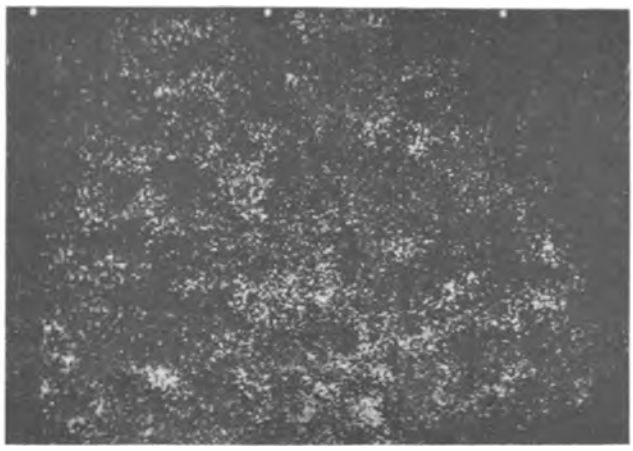

Fig. 1 (e). Recharged to 40% capacity

tassium and nickel lines and mechanically translating the specimen under the electron beam.

Results and Discussion

The specimen current scan of a charged and discharged electrode revealed the highly porous nature of the electrode surface. Because of the porosity of the surface, quantitative analysis of the potassium content is not possible. However, qualitative generalizations can be made concerning the concentration and distribution of potassium in the electrode.

Figure 1 shows the potassium x-ray scans of sintered nickel-oxide electrodes. In general, the charged state appears to have a higher potassium content than the discharged state. The highest potassium concentration is observed during the initial charging of an electrode (Fig. 1a). Upon subsequent cycling the concentration

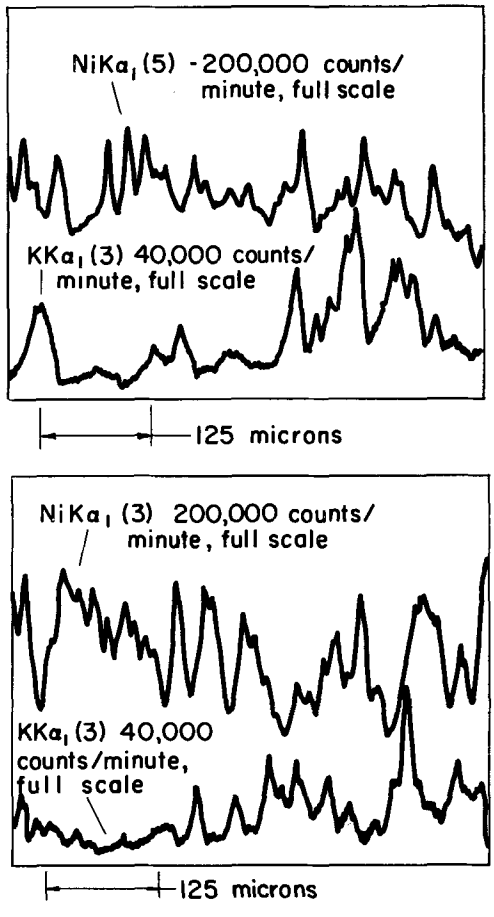

Fig. 2. Nickel and potassium concentration profiles. (a, top) Charged, 50 cycles, (b, bottom) discharged, 50 cycles.

slowly decreases to a stable limiting value (Fig. 1c and e). This increase in potassium concentration during charging is in qualitative agreement with the results of Bourgault and Conway (1) and Kornfeil (3). However, it is also observed that potassium is associated with the $Ni(OH)_2$ structure of the discharged state. It appears that although potassium is exchanged between the solid-phase and the electrolyte during the course of electrochemical reaction, a residual amount always remains incorporated within the crystal structure.

Perhaps more interesting than the changes in potassium concentration which occur during electrode reaction is the distribution of potassium within the solid phase. The x-ray scans (Fig. 1) reveal agglomerates of potassium, *i.e.*, localized areas of high potassium concentration. This result is further evidenced by the concentration profiles shown in Fig. 2. The exact meaning of this result is, at present, not well understood with respect to the role of potassium ion in the overall reaction mechanism.

Electron probe analysis is easily extended to a study of the effect on electrode reactions of cations other than potassium. There is, however, one notable exception. The analysis of lithium ion is, at present, beyond the capabilities of the electron probe.

Acknowledgment

The authors wish to thank Mr. M. A. Aia for his many helpful discussions during the course of this investigation.

Manuscript received Dec 3,1965.

Any discussion of this paper will appear in a Discussion Section to be published in the December 1966 JOURNAL.

REFERENCES

1. P. L. Bourgault and B. E. Conway, *Can. J. Chem.*, **38**, 1557 (1960).
2. G. C. Akerlof and P. Bender, *J. Am. Chem. Soc.*, **70**, 2366 (1948).
3. F. Kornfeil, Proc. Ann. Battery Res. and Dev. Conf., 12th Conf. 18 (1958).

Red Emitting Al_2O_3 Based Phosphors

Virgil D. Mochel[1]

Technical Staffs Division, Corning Glass Works, Corning, New York

Two new Al_2O_3-containing phosphors which emit in the red and near-infrared have been prepared.

The first type is prepared by thoroughly mixing Al_2O_3, Li_2CO_3, and Fe_2O_3 and firing in air at a temperature between 1100° and 1550°C. A bright red or fuchsia photoluminescence (PL) results when they are irradiated with 254 mμ radiation. Only a weak red emission is observed if they are excited at 366 mμ.

Reagent grade materials are satisfactory for the preparation. PL is observed for concentrations of Li_2O varying between 0.05 and 20.8% in weight per cent. A concentration of 5.0% Li_2O is optimum. Li_2O was usually added as Li_2CO_3, but other compounds of Li could be used as well. Fe_2O_3 concentrations varied between 0.013 and 1.3% by weight with 0.13% being optimum.

The best firing temperature was found to be about 1450°C although bright PL is observed from any of these phosphors fired in the range 1100°-1550°C. Firing time is not critical above 1200°C, but at 1100°C a marked improvement in PL is noticed in firing at 1 hr as compared to 30 min. The phosphors were fired in oxidizing reducing, and neutral atmospheres with no differences noted in the PL.

[1] Present address: Central Research Laboratories, The Firestone Tire and Rubber Company, Akron, Ohio.

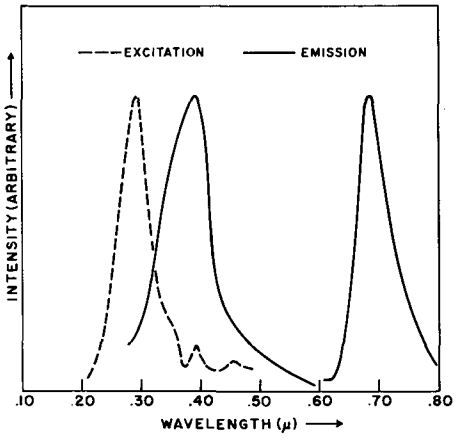

Fig. 1. Emission and excitation spectra for $Li_2O \cdot 5Al_2O_3$:Fe phosphor. Curves are normalized.

According to x-ray diffraction analysis, Li_2O serves to form the crystalline phase, lithium spinel ($Li_2O \cdot 5Al_2O_3$) otherwise known as lithium zeta alumina (1,2). The Fe_2O_3 is an activator, apparently. There is enough Fe impurity in reagent grade Al_2O_3 to activate the phosphor, but the PL is enhanced by further Fe_2O_3 additions.

Figure 1 shows the excitation and the emission spectra of these phosphors. The spectra were obtained with an Aminco-Bowman Spectrophotofluorometer. The solid curves are the emission spectra in the visible and the near-infrared regions when excited with 254 mμ radiation. The emission peak in the visible region centered at 390 mμ was obtained with a 1P28 photomultiplier tube, and the peak centered at 682 mμ was obtained with a 7102 photomultiplier tube. Because of the lack of calibration, the relative intensities of the two peaks could not be determined. All curves are normalized. The dotted curve is the excitation spectrum for the 682 mμ peak.

Figure 2 shows a direct comparison of the red emission with that of Sylvania No. 235 phosphor, which is

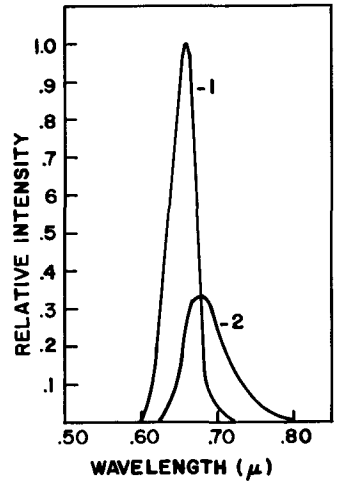

Fig. 2. Comparison of the red emissions of Sylvania 235 phosphor and $Li_2O \cdot 5Al_2O_3$:Fe phosphor. Both phosphors were excited with 254 mμ radiation: 1, Sylvania No. 235 phosphor; 2, $Li_2O \cdot 5Al_2O_3$:Fe phosphor.

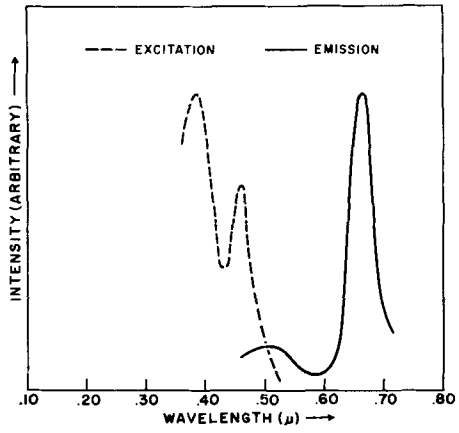

Fig. 3. Emission and excitation spectra for $CaO \cdot 2Al_2O_3$:$MnCl_2$ phosphor. Curves are normalized.

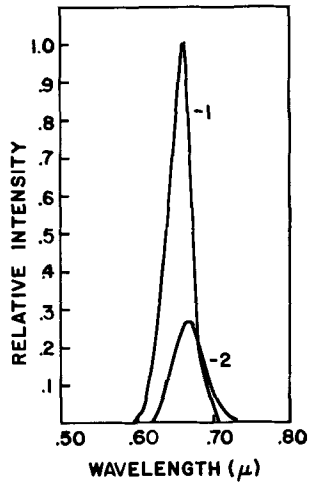

Fig. 4. Comparison of the red emissions of Sylvania 235 phosphor and $CaO \cdot 2Al_2O_3$:$MnCl_2$ phosphor. Both phosphors were excited with 366 mμ radiation: 1, Sylvania No. 235 phosphor; 2, $CaO \cdot 2Al_2O_3$:$MnCl_2$ phosphor.

a Mn-activated magnesium arsenate phosphor. The curves were run under identical conditions and have been corrected for the sensitivity of the photomultiplier tube. The ratio of the integrated intensities under the two curves is 1.8/1.

The temperature dependence of the Al_2O_3 phosphor is excellent. The relative brightness remains essentially constant at least up to a temperature of 320°C. No color shift is observed over this range. The color coordinates[2] (trichromatic coefficients) are $x = 0.729$ and $y = 0.272$.

Another series of red PL phosphors was prepared by slurrying a mixture of Al_2O_3, CaO, and $MnCl_2$ in water and firing at 1450°C. The concentration of CaO can be varied between 4.0 and 17.0% by weight and the concentration of $MnCl_2$ between 0.0048 and 1.0% by weight. The optimum composition appears to be: Al_2O_3—83.0%, CaO—17.0%, $MnCl_2$—0.048%.

X-ray diffraction analysis shows $CaO \cdot 2Al_2O_3$ as the major phase and alpha-Al_2O_3 as a minor phase. The $CaO \cdot 2Al_2O_3$ phase with $MnCl_2$ as the activator gives rise to the PL. It is known that Al_2O_3 emits a red or a green luminescence when activated with Mn (3). However, Al_2O_3 compositions which contained only $MnCl_2$ or only CaO exhibited a very weak red PL. This was also true of those containing $MnCl_2$ and just small concentrations of CaO. As the concentration of CaO increased, the brightness of the phosphor also increased until the optimum was reached.

The spectra are shown in Fig. 3. Again the solid curve shows the emission spectrum and the dotted curve shows the excitation spectrum. There is a strong red emission centered at 665 mμ and a weaker, broad peak at about 500 mμ. The phosphor is excited by both 254 mμ and 366 mμ radiation, but the red emission is most strongly excited by 366 mμ.

Figure 4 gives a direct comparison of the red emission of this type of phosphor with that of the Sylvania No. 235 phosphor. Both were excited with 366 mμ radiation. The integrated intensity of the Sylvania phosphor is about 2.9 times greater than that of the Al_2O_3 phosphor.

Since the blue emission of the first type of phosphor is centered at about 390 mμ, it can be used to activate any other phosphor which is sensitive to this wavelength. This was done with a mixture of the two phosphors described above. Peaks from both phosphors appeared in the spectrum when excited with 254 mμ radiation.

Manuscript received Aug. 19, 1964; revised manuscript received Sept. 24, 1965.

Any discussion of this paper will appear in a Discussion Section to be published in the December 1966 JOURNAL.

[2] The color coordinates and the temperature dependence were kindly measured by W. A. McAllister of Westinghouse Electric Corporation, Lamp Division.

REFERENCES

1. E. Kordes, *Z. Krist.*, **91**, 205 (1935).
2. R. K. Datta and R. Roy, *J. Am. Ceram. Soc.*, **46**, 389 (1963).
3. S. Izawa, *J. Soc. Chem. Ind., Japan*, **36**, 44B (1933); L. de Boisbaudran, *C. R. Paris*, **104**, 330 (1887); J. T. Randall, *Proc. Roy. Soc., London*, **A170**, 272 (1939); E. Tiede and H. Luders, *Ber.*, **66**, 1681 (1933).

Silicon Dioxide Films Doped with Phosphorus

Y. Miura, S. Tanaka, Y. Matukura, and H. Osafune

Semiconductor Division, Nippon Electric Co., Ltd., Kawasaki, Japan

There recently has been great interest in the properties of the silicon dioxide film with the development of the oxide coated semiconductor devices such as the planar transistor, MOS transistor, and integrated circuit. It has been reported (1) that the semipermanent changes in the surface potential occur in the oxide coated silicon when an external field is applied at elevated temperature. This instability can be accounted for by the migration of sodium ions (2) and/or oxygen vacancy ions (3) in the silicon dioxide film. It would be very difficult to produce sodium-free or vacancy-free silicon dioxide film in the device production. One method to obtain a stable dioxide film is the doping of phosphorus into the silicon dioxide film, because the phosphosilicate layer is supposed to be an effective mask against the sodium and oxygen vacancy ions (4). The experimental techniques of the phosphorus doping into the silicon dioxide film during the vapor deposition of the silicon dioxide (5) and during the thermal oxidation are discussed in this paper.

Figure 1 (a) shows the schematic diagram of experimental apparatus to obtain the silicon dioxide film doped with phosphorus by vapor growth technique. Through the $SiCl_4$ saturator and $POCl_3$ or PCl_3 satu-

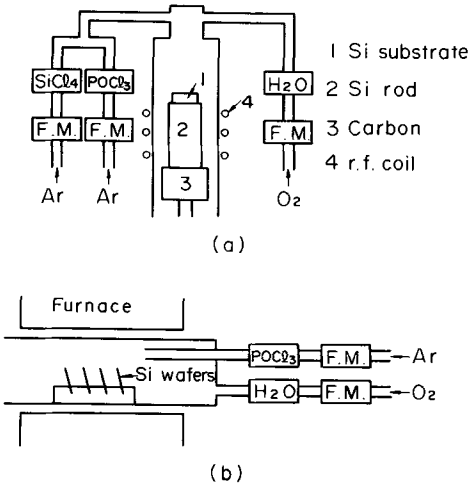

Fig. 1. Apparatus for growth of the silicon dioxide films doped with phosphorus.

rator, argon gas is introduced into the reaction chamber, where the gas is mixed with the oxygen gas saturated with H_2O.

The silicon dioxide doped with phosphorus is grown onto the silicon wafer mounted on the silicon pedestal heated by RF power.

On the incorporation of phosphorus into the silicon dioxide, the following reactions may be written

$$2POCl_3 + 3H_2O \rightarrow P_2O_5 + 6HCl$$

$$SiCl_4 + 2H_2O \rightarrow SiO_2 + 4HCl$$

The upper reaction proceeds only in oxygen atmosphere, and the product P_2O_5 incorporates into the silicon dioxide film. The silicon dioxide free of phosphorus is deposited initially onto the silicon wafer and subsequently phosphorus-doped silicon dioxide.

This procedure prevents the diffusion of phosphorus into the silicon. Deposition of the silicon dioxide is carried out at the temperature above 900°C and the growth rate of the silicon dioxide film is independent of doping with phosphorus.

Figure 1(b) shows another technique to obtain the phosphorus doped silicon dioxide film. Phosphorus is incorporated into the silicon dioxide film during the thermal oxidation process. At first, the wet oxygen is introduced, and then $POCl_3$ is introduced. The oxidation rate in this process is not affected by the addition of $POCl_3$ but is similar to that in the ordinary thermal oxidation.

The presence of phosphorus in the silicon dioxide film is verified by the absorption band at 7.5μ due to phosphorus, although it has not been reported yet that

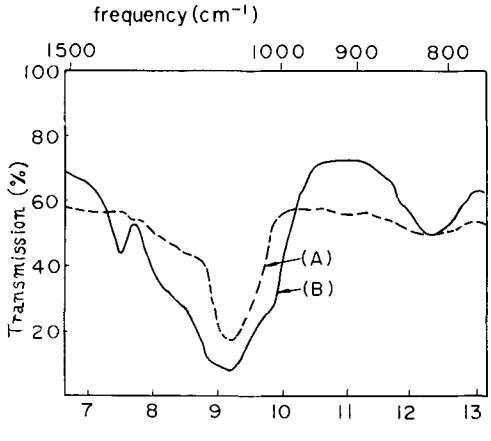

Fig. 2. Effect of phosphorus doped into silicon dioxide layers

Table I. Phosphorus content in the silicon dioxide films
Deposition temperature 900°C

Sample	Mole ratio (P/Si)	P (wt %) in SiO_2
152	0.23	5.6
112	0.49	10.0
117	0.75	15.4
113	1.1	19.6

this absorption band corresponds to phosphorus. Curve A in Fig. 2 shows the absorption curve of the nondoped silicon dioxide film and it does not show the peak at 7.5μ, while curve B for the film doped with phosphorus has the peak at 7.5μ. Phosphorus content is determined by the chemical analysis. The phosphorus content increases linearly with the mole ratio of phosphorus to silicon in gas phase, as shown in Table I.

The etch rate of the silicon dioxide film increases with the increasing phosphorus content. Successive etching of the silicon dioxide film doped with phosphorus shows that phosphorus uniformly distributes along the growth direction of the silicon dioxide. The refractive index slightly increases with the increasing phosphorus content. The dielectric constant is nearly constant, independent of phosphorus content.

MOS diodes are fabricated for studying the stability of the surface potential in the oxide coated silicon under the bias-temperature stress. Silicon substrates are prepared by using an FZ crystal of n-type 15 ohm-cm. No particular caution is taken about the aluminum evaporation. On the experiments of the MOS stability, the shift of the flat-band-voltage, ΔV_{FB}, in capacitance-voltage characteristics of the MOS diode is measured before and after the bias-temperature treatment. Positive sign of ΔV_{FB} means the accumulation of electrons to the silicon surface at the silicon-silicon dioxide interface. The measurements are performed at 1 mc/sec.

Figure 3 shows the relation between ΔV_{FB} and the field strength in the silicon dioxide film during the bias-temperature treatment for 30 min at 300°C. Curve (A) in Fig. 3 corresponds to the diode prepared by using the wafer with the silicon dioxide film doped with 11.4% (BW) phosphorus by the vapor grown technique, and curve (B) corresponds to the diode with 15% (BW) phosphorus doped by the thermal oxidation technique. Positive sign of the field strength shows a bias direction as metal is positive to silicon. For nondoped MOS diode, curve (C), the value of ΔV_{FB} is remarkably large even at a positive low field strength, but for the diodes with phosphorus doped silicon dioxide the value of ΔV_{FB} is small. It is noticeable that ΔV_{FB} at the high negative value of the field strength is negative.

Stable MOS diodes are obtained by doping the silicon dioxide film with phosphorus, as shown in Fig. 3. It

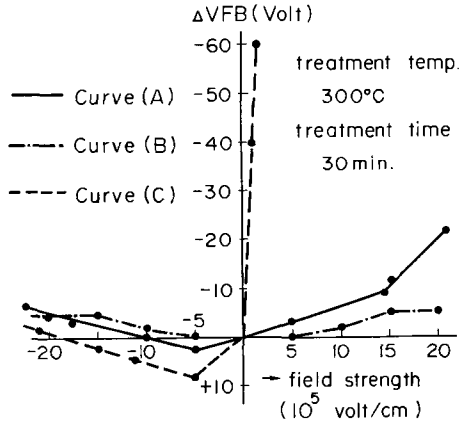

Fig. 3. Relation between the shift of flat-band-voltage ΔV_{FB} and field strength in the silicon dioxide film.

cannot be defined whether or not phosphorus combines with sodium ion or oxygen vacancy ion in the silicon dioxide film. But, it can be concluded that phosphorus doped into the silicon dioxide impedes the movement of such ions and gives stable MOS diodes.

Thermal diffusion of phosphorus into the silicon dioxide film has been put into practice to obtain a stable oxide film (4). But, it has a remarkable gradient of the phosphorus content in the silicon dioxide film. As mentioned above, the etching rate increases with the increasing phosphorus content. In the fabrication of the device, selective etching of the oxide film is an important process, then the uniform distribution of phosphorus in the silicon dioxide film is desirable. The oxide film obtained by the technique, presented in this paper, has a fixed etching rate independent of the position in the oxide film. Thus, these doping techniques are suitable for the fabrication of the planar transistor, MOS transistor, and the integrated circuits.

Manuscript received Dec. 15, 1965.

Any discussion of this paper will appear in a Discussion Section to be published in the December 1966 JOURNAL.

REFERENCES

1. J. E. Thomas, Jr., and D. R. Young, *IBM Journal*, **8**, 368 (1964).
2. E. H. Snow, A. S. Grove, B. E. Deal, and C. T. Sah, *J. Appl. Phys.*, **36**, 1664 (1965).
3. D. P. Seraphim, A. E. Brennemann, F. M. d'Heurle, and H. L Friedman, *IBM Journal*, **8**, 400 (1964).
4. D. R. Kerr, J. S. Logan, P. J. Burkhardt, and W. A. Pliskin, *ibid.*, **8**, 376 (1964).
5. Y. Haneta, Paper presented at the Fall Meeting of the Physical Society of Japan, (1964) Abstract p. 59.

Preparation of Rare Earth Nitrides by Reactive Arc Melting

R. J. Gambino and J. J. Cuomo

Watson Research Center, International Business Machines Corporation, Yorktown Heights, New York

The rare earth nitrides are a group of refractory compounds with the rock salt structure. They are hard, brittle compounds, stable, but extremely sensitive to hydrolysis. Current interest in the magnetic and electrical properties of these compounds has prompted an investigation of improved methods for their preparation.

The nitrides have been prepared in the past by the reaction of rare earth metal filings (1) or hydride powders (2) with nitrogen or with ammonia gas. These methods have not in general yielded stoichiometric products even after long and repeated reaction (1, 2). Elaborate precautions must be taken to prevent the oxidation of powdered rare earth metals and hydrides and the hydrolysis of the nitride product. The product is obtained in the form of a finely divided, highly reactive powder which is unsuitable for many types of physical properties measurements.

The objective of this study was to devise a method for the preparation of high purity, oxygen free, rare earth nitrides in an unreactive, consolidated form. In some initial experiments it was found that the nitrides could be formed by reacting molten rare earth metal, contained in a tantalum crucible, with flowing, high purity nitrogen (3). The reaction did not go to completion, however, because the product formed as an impervious crust on the surface of the melt inhibiting further reaction. The product was very fine grained and sensitive to hydrolysis.

The method ultimately developed was reactive arc melting. This method differs from inert gas arc melting in that the gas phase in which the arc is sustained takes part in the reaction. The rare earth metal is arc melted on a water cooled copper hearth in a high purity nitrogen atmosphere. The steep temperature gradient in the melt, inherent in this configuration, causes the nitride to precipitate at the cooler bottom of the melt. In one operation, the nitride is formed and consolidated into a dense, coarsely grained ingot. The method is rapid and simple and is well suited for the preparation of solid solutions between nitrides as well as doped samples.

Experimental

The apparatus consists of a commercial arc furnace with a water cooled copper hearth and a water cooled tungsten electrode. The chamber was provided with a vacuum port connected to a mechanical pump through a liquid nitrogen trap. The pressure was monitored with a thermocouple gauge and a bellows gauge for pressures above atmospheric. A pressure relief valve, set for 3 psi above atmospheric, was also provided. The input to the chamber was connected to cylinders of argon (ultra high purity 99.999%) and nitrogen (prepurified 99.996%) through appropriate valves and flow meters. A flow of either gas or a mixture of both could be delivered to the chamber.

Metals in both ingot and sponge form were used for this study (analyses of gadolinium are shown in Table I). Most of the samples were prepared from ingot rare earth; in a few cases it was possible to obtain the higher purity distilled sponge. The metal to be nitrided (typically 2 to 5g) was placed in the melting chamber which was then evacuated to about 10μ and backfilled with argon, at least three times. The arc was struck and the sample melted in argon. With the sample still molten, the argon flow was stopped and a flow of nitrogen was initiated. The arc was maintained for 1 min after the nitrogen was introduced. The reaction

Table I. Spark source mass spectrographic analyses of gadolinium metal

Atomic ppm

Element	Ingot	Sponge (distilled)
O	40,000	1,000
F	15,000	20
Al	400	20
Si	3,000	40
S	16,000	15
Cl	100	90
K	400	<100
Ca	400	<100
Ti	<5	230
Cr	100	20
Mn	50	4
Fe	200	8
Co	<5	<5
Ni	30	40
Cu	100	30
As	<5	
Y	100	170
Sn	<5	<5
La	60	20
Ce	60	1
Pr	75	1
Nd	1,500	290
Tb	60	100
Dy	60	11,440
Ho	30	50
Er	<5	140
Tm	<5	10
Ta	200	<10
Pt	100	<10
Au	<5	<5
Pb	<5	5

was carried out in three or four such melting steps because maintaining the arc for more than 1 min caused overheating of the walls of the chamber. Due to the difficulty of striking the arc in nitrogen, it was necessary to evacuate the chamber and back fill with argon before each melting. The arc current used varied from 180 to 260 amp depending on the melting point of the metal. The nitrogen flow was 10 liters/min. Solid solutions were prepared by alloying the two rare earths, then nitriding the alloy by the same procedure as was used for the pure metals.

Metallographic sections of product ingots were made by conventional techniques with slight modification. The sample was fractured into several pieces in order to obtain a vertical section. The specimen was mounted in glycol phthalate on a metal polishing plug and hand ground on 400, 600, and 0/2 metallographic papers with kerosene as a lubricant and rinse. The sample was then polished with 1μ diamond paste on a vibratory polisher. The polished surface had a blue-black lustrous finish which reacted with air when the kerosene was removed giving interference colors and eventually a white or dull gray surface. The micrographs had to be taken within about 15 min of final polishing to avoid this air corrosion. The initial stages of oxidation were selective with respect to grain orientation and grain boundaries and thus constituted a convenient and effective etch. No other etching procedure was necessary. Analysis of the micrographs was made by the lineal method (4).

Specimens for x-ray diffraction analysis were prepared by pulverizing the nitride to a fine powder in a dry nitrogen (dew point —100°C) filled dry box and sealing the powder in Lindemann glass capillaries (0.3 mm diameter). Powder patterns were made with Fe-Kα radiation in a 90 mm Debye-Scherrer camera.

Results

Most of the rare earth nitrides as well as yttrium nitride have been prepared by this technique. The results of x-ray diffraction and metallographic analyses on some of these samples (prepared from ingot R.E.) are shown in Table II. Samples prepared from gadolinium sponge and gadolinium ingot (see Table I) did not show significant differences in the properties tabulated. From the data in Table II one notes these samples are almost fully dense.

The oxygen concentration in the product nitride and in the as-received rare earth metal sponge was determined by spark source mass spectrographic analysis. In the two samples examined, GdN and ErN, the oxygen level was found to be the same in the nitride as in the metal, both about 1000 atomic ppm. This result suggests that no oxygen contamination occurs during the nitride preparation.

The product ingots usually have a thin layer of unreacted metal on their top and bottom surfaces which can be ground off to isolate the nitride. Occlusions of rare earth metal are observed as a minor second phase [usually <1 v/o (volume per cent)] within the nitride grains. Since the unreacted metal in the nitride portion of the ingot is present in small concentrations and occurs as isolated occlusions rather than at grain boundaries, its effect on the physical properties of the nitride is probably small.

The unreacted metal in the ingots, both at the surface and within the grains, can be eliminated by annealing the ingots in flowing N_2 for 2 hr at 2200°C. This treatment also results in considerable grain growth (see Table II). The samples had to be exposed to air, however, while being transferred from the arc melter to the annealing furnace. The oxide layer, formed on the ingot surface during this air exposure, diffused into the ingot during the anneal and thus was a source of oxygen contamination.

Solid solutions of the type $GdN_{1-x}O_x$ have been prepared by reacting mixtures of Gd metal and Gd_2O_3 with nitrogen. At 2000°C, oxygen can substitute for nitrogen up to an X value of 0.12. The lattice constant of the solid solution decreases with oxygen concentration from 4.99 to 4.96Å at the solubility limit. The paramagnetic Curie temperature, θ_p, decreases from 68°K for GdN to 31°K for the most oxygen rich solid solution. It is apparent from those results that oxygen contamination can have a drastic effect on the magnetic properties of rare earth nitrides.

The lattice constants of the arc melted nitrides are in good agreement with the values reported in the literature (5). The lattice constant of the nitride phase in samples which were intentionally incompletely reacted was the same as that of single phase ingots. This

Table II. Results of metallographic and x-ray diffraction analysis

Composition	Sample number	Average grain size, μ	Porosity volume, %	Metal volume, %	Lattice constant, a_o	Hardness[b] 50 g load
CeN	45R	150	<1	0	5.02	
NdN	32	100	<1	10		635
GdN	30	50	3	0		644
	54R	30	0	<1	4.99	
	ZX-2[a]	100	5	<1		
DyN	55	30	0	1	4.89	858
HoN	56	20	<1	<1	4.87	936
ErN	33	20	<1	2	4.84	1035
YN(0.1 m/o GdN)	29	20	0	1		895
YN(0.5 m/o ErN)	74	20	1	<1		
YN(0.1 m/o GdN)	ZX-7[a]	500	5	0		
YN(1.0 m/o GdN)	87A[a]	100	8	0		
LaN(1.0 m/o GdN)	94A[a]	<1000	0	0		
$Gd_{0.75}Eu_{0.25}N$	37	20	0	5		1120
$Gd_{0.9}Yb_{0.1}N$	38	50	<1	3	4.982	1072
$Gd_{0.75}Yb_{0.25}N$	39	100	0	2	4.977	1017
$Gd_{0.9}Ce_{0.1}N$	58R	50	0	2		

[a] Samples annealed 2 hr at 2200°C in flowing nitrogen.
[b] Vickers Diamond Penetration Microhardness.

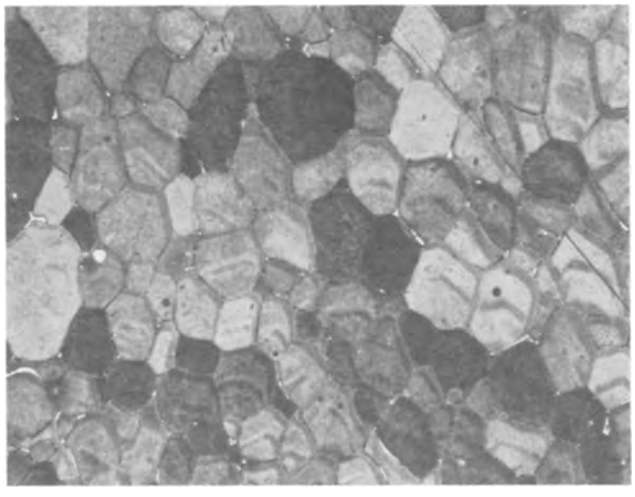

Fig. 1. Micrograph of GdN prepared by reactive arc melting (X 200)

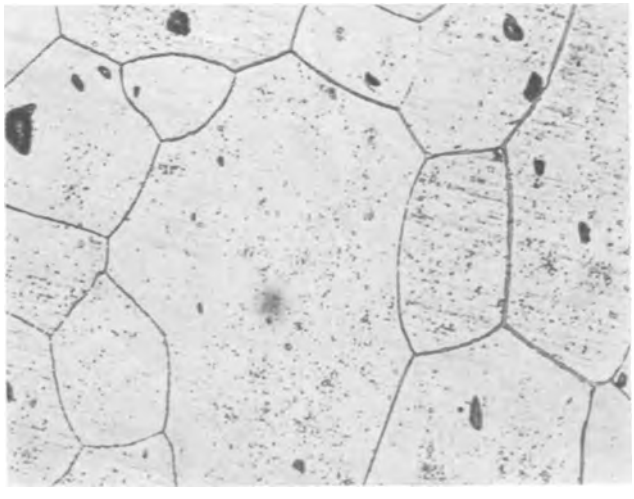

Fig. 2. Micrograph of CeN (X 200)

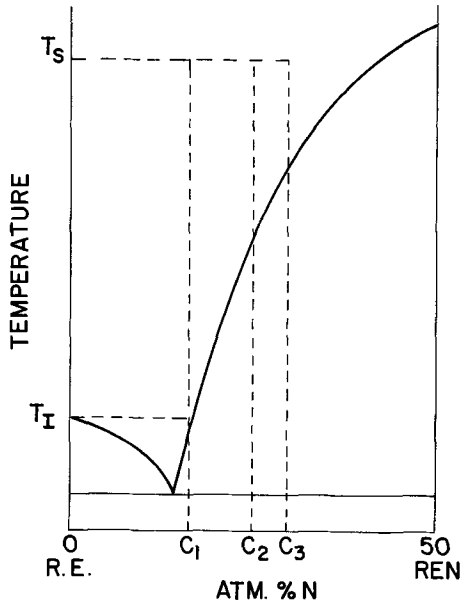

Fig. 3. Hypothetical rare earth-nitrogen phase diagram showing the concentration of nitrogen in the liquid (C_1, C_2, C_3) at successive time intervals.

suggests very limited solid solubility on the metal rich side of the compound. No impurity phase, other than the metal, was observed by x-ray diffraction in any of the samples.

Discussion

In order to elucidate the mechanism of nitride formation, ingots were examined metallographically, in vertical section, after various periods of reaction. A band of nitride several millimeters thick was observed near the bottom of the ingot for 1 min of nitridation. The thickness of the nitride band increased with reaction time until after approximately 3 min it encompassed virtually the entire volume of the sample. A thin (> 1 mm thick) layer of unreacted metal was found on the bottom surface of the ingot in all cases. This surface layer is in contact with the water cooled copper hearth and thus remains solid throughout melting. The last portion of the melt to freeze always contains some unreacted metal and often has the microstructure of a eutectic, suggesting that the nitride is crystallizing from a nitrogen deficient melt. These observations suggest the following mechanism for the reaction:

1. Nitrogen gas dissociates at the surface of the melt and/or in the plasma of the arc and dissolves in the molten metal at temperature T_s (see Fig. 3).
2. The dissolved nitrogen is rapidly distributed throughout the melt by the arc current stirring of the melt until the concentration has the value C_1 (Fig. 3).
3. Initially, the melt-solid interface is at temperature T_I, the melting point of the rare earth metal. Nitride begins to precipitate at the interface when concentration C_1 is achieved.
4. As the concentration of nitrogen in the melt increases, the temperature of the melt-solid interface moves up the liquidus curve. At the same time, the interface moves upward through the melt leaving solid nitride behind it.

A similar mechanism has been proposed for the formation of III-V compounds by the "Solute Buildup" method (6).

Conclusions

Arc melting is particularly well suited for this method of reaction. The melt is in a very steep temperature gradient so that the formation of an impenetrable crust of nitride at the surface is avoided. The dissociation of nitrogen gas in the arc plasma and the rapid stirring of the melt by the arc current probably contribute to the high reaction rate. Rapid reaction makes it practical to use the rare earth metal in bulk form thus eliminating the oxygen contamination associated with the fine powders used in previous methods. The product is in the form of a dense ingot suitable for the fabrication of specimens for physical property measurements and is much more resistant to reaction than the fine powders previously obtained.

Acknowledgment

The authors are happy to acknowledge H. G. Schaefer who assisted with the preparation of the samples, R. Wnuk who assisted with the x-ray diffraction analysis, and J. Kuptsis for the mass spectrographic analysis. We also thank E. A. Giess and J. Gilvey for their advice and encouragement. We are also indebted to T. R. McGuire for permitting us to use previously unpublished data on the magnetic properties of oxygen-doped GdN.

Manuscript received June 25, 1965; revised manuscript received Dec. 29, 1965.

Any discussion of this paper will appear in a Discussion Section to be published in the December 1966 JOURNAL.

REFERENCES

1. W. Klein and H. Senff, *Z. anorg. allgem. Chem.*, **241**, 259 (1939).
2. a) M. K. Wilkinson, *et al.*, *J. Appl. Phys.*, **31**, 358S (1960).
   b) D. E. LaValle, *J. Inorg. and Nuclear Chem.*, **24**, 930 (1962).
   c) N. Sclar, *J. Appl. Phys.*, **35**, 1534 (1964).
3. E. L. Boyd and R. J. Gambino, *Phys. Rev. Letters*, **12**, 20 (1964).
4. W. D. Kingery, "Introduction to Ceramics," John Wiley & Sons, Inc., New York (1960).
5. K. A. Gschneidner, Jr., "Rare Earth Alloys," D. Van Nostrand Company, Inc., New York (1961).
6. E. P. Stambaugh, J. F. Miller, and R. C. Himes, "Metallurgy of Elemental and Compound Semiconductors," R. O. Gunbel, Editor, Interscience Publishers, New York (1961).

Brief Communication

The Solubility of Oxygen in Molten Carbonates

M. Schenke, G. H. J. Broers, and J. A. A. Ketelaar

Central Technical Institute-TNO, The Hague, The Netherlands

The solubility of gases in molten salts has caused much interest recently with regard to technological problems (1-5). We have determined the solubility of oxygen in molten alkali carbonates with respect to galvanic high-temperature fuel cell research.

Our method is based on an amperometric titration of the dissolved oxygen, by adding stepwise solid Na_2SO_3 as a reducing agent [compare the potentiometric acid-base titrations in molten salts by Shams-El-Din *et al.* (6) and earlier publications]. The oxygen was dissolved by leading an O_2-CO_2 gas mixture of known composition through the melt, and titrations with Na_2-SO_3 were carried out under a cover of a N_2-CO_2 mixture, while the CO_2 partial pressure was kept constant. As indicator a system of two rotating platinum wire electrodes was used; during the experiment a fixed potential difference was maintained between these electrodes potentiostatically, the current being a measure of the amount of dissolved oxygen. The procedure will not be described here extensively; only the results will be given.

We determined the solubility of oxygen in the eutectic mixture of Li_2CO_3, Na_2CO_3, and K_2CO_3 (composition in mole %: 43.5% Li_2CO_3, 31.5% Na_2CO_3, 25.0% K_2CO_3; mp 397°C) and in the eutectic mixture of Li_2CO_3 and Na_2CO_3 (in mole %: 53.3% Li_2CO_3, 46.7% Na_2CO_3; mp 496°C).

Henry's law, $L = Zp$, was found to be obeyed within the limits of accuracy, (p = gas pressure in atm; Z = Henry's coefficient, expressed in mole/cm^3 atm; L = gas solubility in mole/cm^3). In Fig. 1 the decadic logarithm of the Henry coefficient is given as a function of 1/T. The plotted lines were calculated with the method of least squares.

There is a small, but certainly significant dependence of solubility on the composition of the carbonate melt, both with respect to the absolute value and to the temperature coefficient. The solubilities of O_2, as well as the heats of solution are of the same order of magnitude for different melts and comparable with data found for other gases and other melts (1-5). As can be seen, the process of solution is endothermic, the enthalpies of solution, calculated with $\Delta H = -R\,[\partial \ln Z]/[\partial\,(1/T)]$, being + 14.9 kcal/mole for the binary mixture and + 17.7 kcal/mole in the ternary case, respectively. The solubility of H_2 in molten carbonates will be determined in an analogous way.

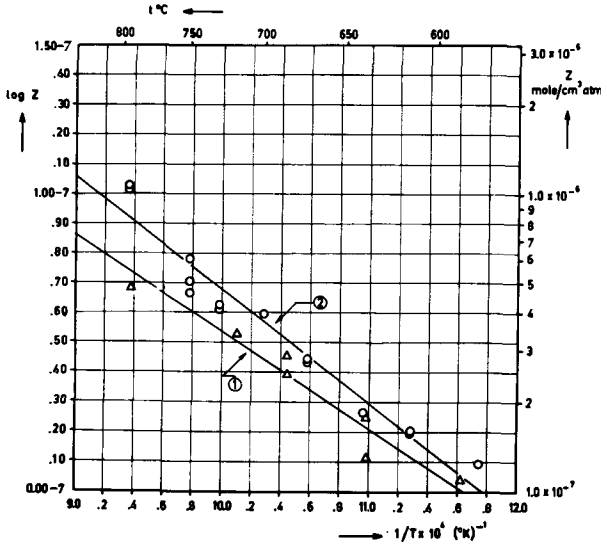

Fig. 1. Henry coefficient of oxygen in molten eutectic Li_2CO_3-Na_2CO_3 (1) and eutectic Li_2CO_3-Na_2CO_3-K_2CO_3 (2) mixtures.

Acknowledgment

The authors wish to thank the Director of the Central Technical Institute-TNO for permission to publish these results.

Manuscript received Dec. 20, 1965.

Any discussion of this paper will appear in a Discussion Section to be published in the December 1966 JOURNAL.

REFERENCES

1. K. Grjotheim, P. Heggelund, C. Krohn, and K. Motzfeldt, *Acta Chem. Scand.*, **16**, 689 (1962).
2. W. R. Grimes, N. V. Smith, and G. M. Watson, *J. Phys. Chem.*, **62**, 862 (1958).
3. M. Blander, W. R. Grimes, N. V. Smith, and G. M. Watson, *ibid*, **63**, 1164 (1959).
4. G. M. Watson, R. B. Evans, III, W. R. Grimes, and N. V. Smith, *J. Chem. and Eng. Data*, **7**, 285 (1962).
5. Yu. M. Ryabukhin, *Zhur. Neorg. Khim.*, **7**, 1101 (1962).
6. A. M. Shams-El-Din and A. A. A. Gerges, *Electrochim. Acta*, **9**, 613 (1962).

Solubilities of Mn(II) and Mn(III) Ions in Concentrated Alkaline Solutions

A. Kozawa, T. Kalnoki-Kis, and J. F. Yeager

Research Laboratory, Consumer Products Division, Union Carbide Corporation, Cleveland, Ohio

ABSTRACT

Measurements using a polarographic method of the solubility of Mn(II) in 3-13.5M KOH and 3-19M NaOH at 23°, 50°, and 70°C, as well as solubility of Mn(III) in 5-13.5M KOH at 23°C, are reported. The exponential increase in solubility found with increasing KOH and NaOH concentrations is principally due to the formation of OH^- coordinated-complex ions; $Mn(OH)_2 + nOH^- = [Mn(OH)_{n+2}]^{n-}$. Based on the calculation of the equilibrium constant, a likely predominant species of the Mn(II) complexes is $[Mn(OH)_4]^=$ in 5-12M KOH. Based on measurements for solubility of Mn(II) the heat of dissolution was found to be 6.7 kcal in 9M KOH.

It has been shown previously (1) that the cathodic reduction of electrolytic MnO_2 in 9M KOH took place in two steps, namely, from MnO_2 to Mn_2O_3 (or MnOOH) in the first step and from Mn_2O_3 to $Mn(OH)_2$ in the second step. It was assumed that the first step was a homogeneous phase discharge through a proton and electron transfer in the MnO_2 lattice, and for the second step a new discharge mechanism was proposed (1) based on the presence of dissolved Mn(II) and Mn(III) in 9M KOH. In order to study the details of the second step, solubility values of Mn(II) and Mn(III) oxides or hydroxides in concentrated alkaline solutions were needed. This prompted the present measurements.

Few papers have been published on the solubility of Mn(II) in alkaline solutions. Fox *et al.* (2) in solubility measurements of $Mn(OH)_2$ in neutral solution and up to 4M NaOH solutions found that the solubility increased with increasing NaOH concentration: 7.53×10^{-5}m of Mn(II) in 1.924m NaOH and 29.8×10^{-5}m in 4.14m NaOH. They proposed a reaction, $Mn(OH)_2 + OH^- = HMnO_2^- + H_2O$, to be a main reaction in this NaOH concentration range. Scholder and Kolb (3) measured solubilities of $Mn(OH)_2$ in 6.1-18.7M NaOH solution at boiling temperatures (108°-141.5°C) and found the Mn(II) ion concentration to be 0.211×10^{-2}m-13.34×10^{-2}m in the concentration range of NaOH. They also isolated $Na_2[Mn(OH)_4]$ and Ba_2 (or Sr_2)$[Mn(OH)_6]$ from 50% NaOH (or 19M NaOH) solution saturated with $Mn(OH)_2$.

In the present measurements, by a polarographic method, Mn(II) solubilities in 3-13.5M KOH and in NaOH were obtained at 23°, 50°, and 70°C, and Mn(III) solubility was measured in 5-13.5M KOH at 23°C. The data are discussed to elucidate the equilibrium in the solution and to identify the predominant species of Mn(II) complexes.

A polarographic method was selected in the present measurement because the polarographic diffusion current is not only proportional to the concentration of dissolved Mn(II) or Mn(III), but is usually unaffected by the excess solid material suspended in the solution (except colloidal materials, which will be mentioned later). Therefore, the very difficult separation of the excess manganese hydroxide by filtration from viscous alkaline solutions of high concentration was avoided.

Experimental

General polarographic behavior of Mn(II) *and* Mn(III).—In alkaline solutions, Mn(II) ion gives an oxidation wave and Mn(III) ion gives a reduction wave at a dropping mercury electrode as shown previously in the case of 9M KOH (1). While the half-wave potential of the anodic wave was considerably apart from that of the cathodic wave in lower KOH or NaOH concentrations, with increasing KOH or NaOH concentration the anodic and cathodic polarograms became more reversible and the difference between the two half-wave potentials became smaller. In 19M NaOH (*ca.* 50% NaOH by weight), the anodic and cathodic half-wave potentials were within 5 mv of each other and were equal to —0.467v *vs.* Hg/HgO (19M NaOH). Although the polarograms of Mn(II) and Mn(III) ions were not reversible at lower KOH and NaOH concentrations, a fairly well-defined diffusion limiting current (i_d) was observed in the concentration range studied (3-13.5M KOH and 3-19M NaOH), the i_d values were found to be proportional to the Mn(II) or Mn(III) concentration. Therefore, these polarographic characteristics were utilized to measure the solubilities of Mn(II) and Mn(III) ions in concentrated alkaline solutions.

Solubility measurements for Mn(II).—All the measurements reported here were made in a slightly modified polarographic H-cell with a controlled potential and derivative voltammeter (4) as shown in Fig. 1. The sintered glass disc, which separates the H-cell into two compartments, was placed closer to the test solution arm, so that the viscous solutions of high concentration could be thoroughly stirred by the N_2 gas bubbling. The initial volume of the NaOH or KOH solution in the test arm was 20.0 or 25.0 ml. Both arms were filled with the same solution and the levels were kept equal. In the solubility measurement of Mn(II), $MnSO_4$ solution of known concentration was added step by step. Before the initial addition, dissolved oxygen was thoroughly eliminated by bub-

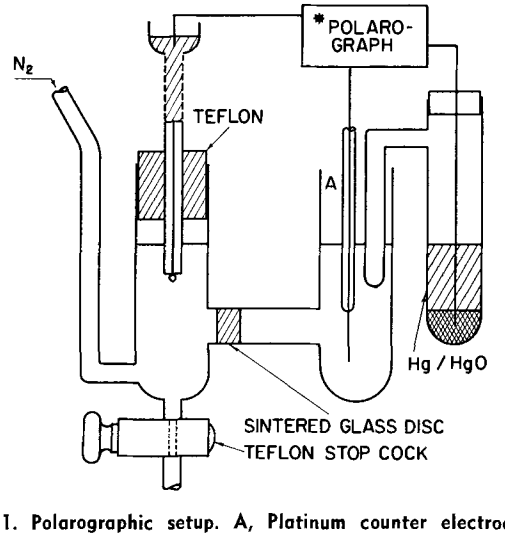

Fig. 1. Polarographic setup. A, Platinum counter electrode; *, controlled potential voltmeter (three electrode polarograph).

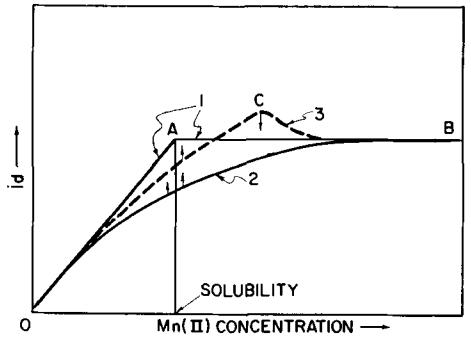

Fig. 2. Schematic i_d-[Mn(II)] curves: curve 1, an ideal curve; curves 2 and 3, experimentally obtained curves. Small arrows on the curves indicate the direction to which the i_d value changed with time.

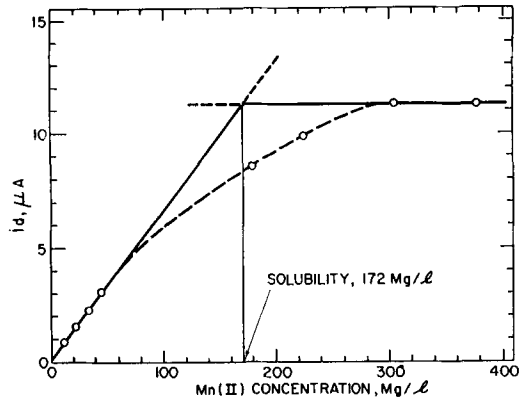

Fig. 4. i_d-[Mn(II)] curve in 11.26M KOH at 70° ± 1°C

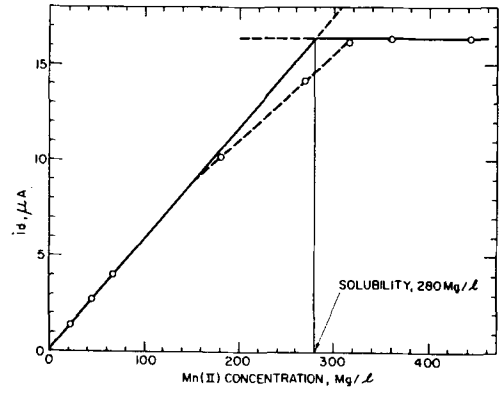

Fig. 3. i_d-[Mn(II)] curve in 13.52M KOH at 70° ± 1°C

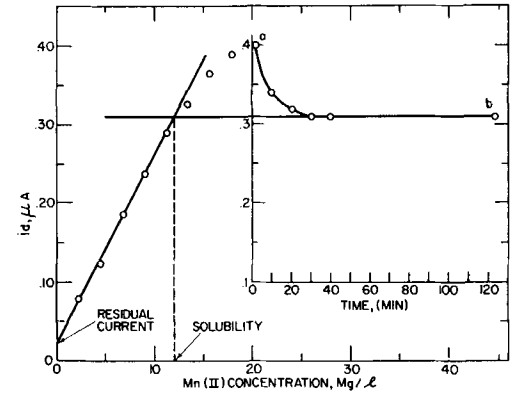

Fig. 5. i_d-[Mn(II)] curve in 5.3M KOH at 23°C

bling pure N_2 gas, because Mn(II) ion is easily oxidized to Mn(III) by dissolved oxygen in alkaline solutions. On each addition of the $MnSO_4$ solution, the solution was thoroughly mixed with pure N_2 gas, and the i_d was measured at —0.130v *vs.* a Hg/HgO reference electrode in the same solution. During the measurements at 50° and 70°C, the polarographic cell was kept in a water bath, but the Hg/HgO reference electrode was held at 23°C. The time required to obtain a constant i_d value, after the addition of $MnSO_4$, varied considerably, depending on the Mn(II) concentration as well as on the temperature. At Mn(II) concentrations far below the saturation value, a constant i_d was obtained usually within 10-15 min after each $MnSO_4$ addition. However, near the saturation value, and particularly at room temperature and low KOH concentrations, in many cases the i_d did not reach a constant value even after 60-100 min. In those cases, the i_d values were taken after 60-100 min even though they are not equilibrium values. At Mn(II) concentrations far greater than the solubility, the i_d reached constancy in a relatively short time, probably because the suspended solid functions as seed for the precipitation and coagulation of the colloid and/or the breaking of the supersaturation may be much easier.

The i_d values thus obtained were plotted against the Mn(II) concentration. The general shape of the i_d-[Mn(II)] curves are shown schematically in Fig. 2 and some measurements are shown in Fig. 3, 4, and 5. Curve 1 in Fig. 2 represents the ideal case where i_d increases linearly with Mn(II) concentration to the saturation value with no further increase after the solubility value. Types of the curves obtained experimentally are shown with curves 2 and 3 in Fig. 2. The reasons for such deviations from the ideal curve may be as follows. When $MnSO_4$ solution was added, even within the solubility value, white precipitate of $Mn(OH)_2$ was formed because of the localized high concentration of Mn(II), and the $Mn(OH)_2$ suspension slowly dissolved or polymerized Mn(II) species slowly decomposed to reach an equilibrium. Curve 2 in Fig. 2 probably represents such a case. In some cases (curve 3 in Fig. 2), the i_d exceeds the value of the solubility concentration. This is probably because of the formation of colloidal $Mn(OH)_2$ and some of the colloidal particles are reacting at the dropping mercury electrode in addition to the dissolved Mn(II) species. At point C on curve 3, the i_d decreases slowly with time to an equilibrium value as such colloidal particles coagulate, as shown in Fig. 5 (curve ab).

At high temperatures and high caustic concentrations, the i_d-[Mn(II)] curve was close to the ideal curve (curve 1 of Fig. 2) as shown in Fig. 3. At low temperatures and low caustic concentrations the i_d-[Mn(II)] curve was of the same type as curve 3 in Fig. 2 and is seen in Fig. 5.

In order to obtain a solubility value, (namely, to find out the intersection A of the lines OA and AB in Fig. 2) enough points to construct a straight line OA and one or two points after the saturation concentration are necessary. Usually three or four points were taken at low Mn(II) concentrations which were far from the saturation value, and one or two points taken beyond the saturation allowing a long time to obtain a true equilibrium.

Solubility of Mn(III).—In order to measure Mn(III) solubility, Mn(II) in KOH or NaOH solution must be oxidized to Mn(III). Two methods for such an oxidation were tested; oxidation by O_2 gas and electrochemical oxidation at a platinum electrode under controlled potential. In the first method, Mn(II) ion was added to the alkaline solution and oxygen gas was bubbled through. The i_d was measured at —1.25v *vs.* Hg/HgO electrode in the same solution, and i_d values were plotted against time; an example of such a curve is given in Fig. 6 in which i_d at —0.13v is also given to show Mn(II) concentration. These curves indicate that Mn(II) is oxidized to Mn(III) with time by

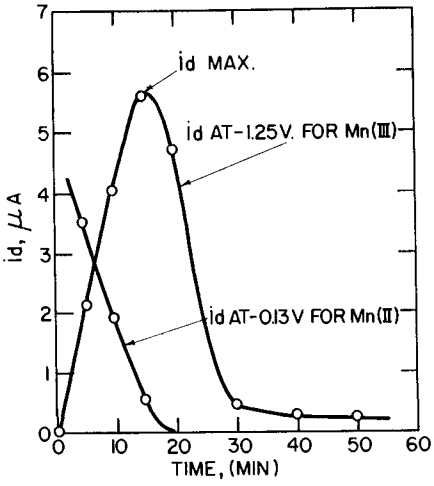

Fig. 6. i_d-Time curves during Mn(II) oxidation in 9M KOH by bubbling O_2 gas.

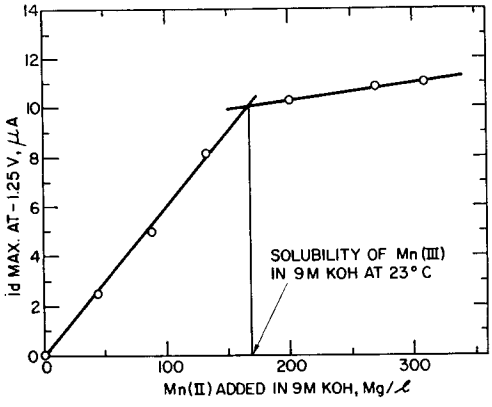

Fig. 7. i_d max-Mn(II) concentration in 9M KOH by the O_2 gas oxidation method (see text).

bubbling oxygen gas, but Mn(III) ion can be further oxidized to MnO_2, because the i_d decreased finally to zero and MnO_2 precipitated. When these i_d-time curves were taken for various initial Mn(II) concentrations and the i_d max (see Fig. 6) was plotted against initial Mn(II) concentration, a curve similar to curve 1 of Fig. 2 was found, and the approximate solubility of Mn(III) was obtained as shown in Fig. 7. The solubility values by this method were close to those obtained by the electrochemical oxidation. However, accuracy of the i_d max measurement was poor, and therefore the results by the electrochemical oxidation will be reported here.

In the electrochemical oxidation, Mn(II) ion in 9M KOH was oxidized at —0.35v *vs.* Hg/HgO (9M KOH). The potential value was found from a current-potential curve (Fig. 8) taken in 9M KOH containing Mn(II) and Mn(III). The current-potential curve may be interpreted as follows, although the details will be discussed in a separate paper. In the potential range from b to c, Mn(III) ion is reduced to Mn(II) ion and from c to f, Mn(II) ion is oxidized to Mn(III) ion, and from f to i, Mn(II) and Mn(III) ions are oxidized to MnO_2 which deposits on the platinum electrode. The potential at d is the approximate standard potential of the Mn(II)-Mn(III) couple in 9M KOH and that at g is of the Mn(III)-MnO_2 couple. The wave j is due to dissolution of the deposited MnO_2, and at k the platinum surface becomes completely bright. The peak potential of k depends on the amount of MnO_2 and is not a constant value.

The potential for the Mn(II) oxidation in other KOH solutions was determined in a similar manner. At various initial Mn(II) concentrations (added as

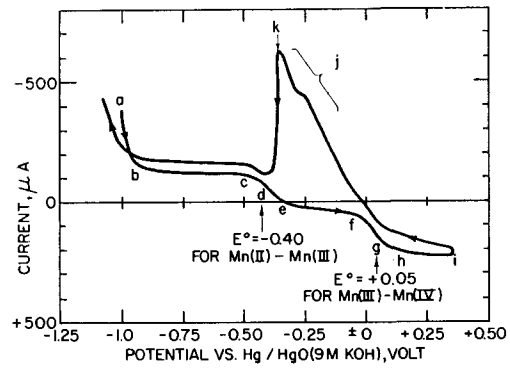

Fig. 8. Current-potential curves at a platinum electrode (apparent area: 9.0 cm^2) in 9.0M KOH containing Mn(II) and Mn(III) at 23°C. The current-potential curve in pure 9M KOH in which no manganese was added was close to the zero current line. The curve was taken with a scanning rate of 250 mv/min along the direction shown by arrows on the curve. Nitrogen gas was bubbled through the solution at a constant rate during the measurement.

$MnSO_4$), i_d values were determined at a dropping mercury electrode at —1.30v after the controlled potential oxidation at —0.35v. Solubilities were obtained from the i_d-[Mn(III)] curve in the same manner as described above for the Mn(II) solubility.

During the measurement, mercury accumulated at the bottom was taken out through the Teflon stopcock.

Accuracy.—All-over accuracy of the solubility data may be ±5% because of various errors associated with volume measurement of $MnSO_4$ solution and i_d measurement in addition to relatively poor temperature control (±0.5°-1.0°C).

In connection with the error of the i_d measurement at the dropping mercury electrode in concentrated KOH or NaOH solutions, stability of the glass capillary or constancy of the drop time must be mentioned, because the tip of the glass capillary may be attacked by alkali solution and may change the characteristics. The i_d is proportional to $m^{2/3}\,t^{1/6}$ (m is flow rate of Hg and t is drop time), of which m is largely determined by the height of the mercury pool and friction in the capillary so that the value may be kept constant even when the tip is attacked, and t may be influenced by the condition of the tip of the capillary. The drop time measurement in 3-19M NaOH was carried out over several hours; the change of the drop time was not appreciable in the period. In the present measurement, the glass capillary was dipped in the solution only during the i_d measurement and, whenever ill behavior started, the tip was renewed by cutting the end approximately a centimeter. For each complete series of measurements of i_d-Mn(II) or Mn(III) curve, the same capillary was used.

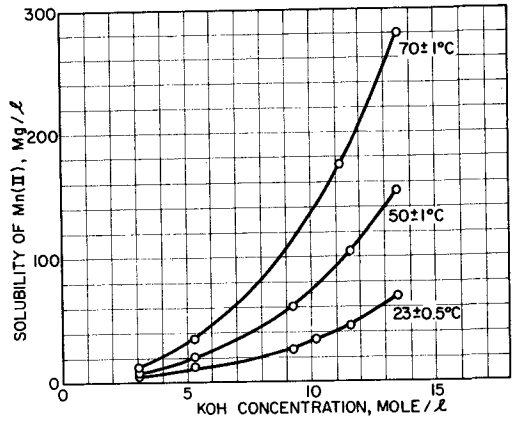

Fig. 9. Solubility of Mn(II) in KOH

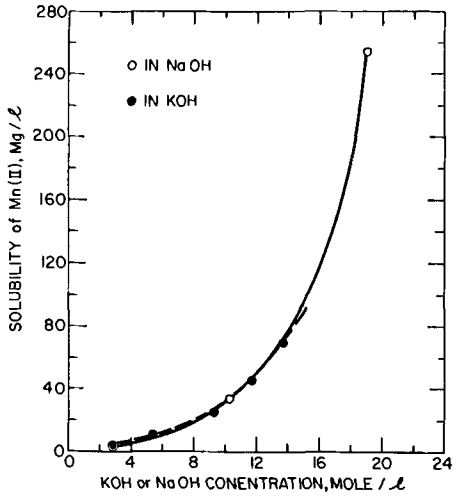

Fig. 10. Solubility of Mn(II) at 23°C in KOH and NaOH

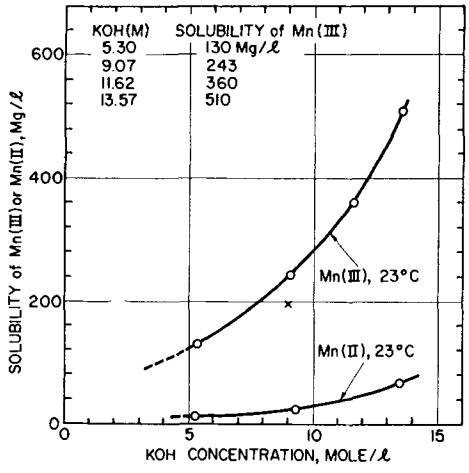

Fig. 11. Solubilities of Mn(III) and Mn(II) in KOH. The point marked with X was measured by oxidizing Mn(II) with O_2 gas (see text).

Results

Solubilities of Mn(II) in KOH and NaOH solutions are shown in Fig. 9 and 10, respectively. In both solutions the solubility increases rapidly with increasing caustic concentration. In Fig. 9 solubility values in KOH solutions are also plotted and show that solubilities in KOH and NaOH are essentially the same when compared at the same caustic concentration (molarity). However, the highest possible concentration was 50% by weight for both KOH and NaOH (13.4M in KOH and 19.0M in NaOH) at room temperature.

The solubility of Mn(III) in KOH is given in Fig. 11 and shows that the solubility of Mn(III) also increases rapidly with increasing KOH concentration. When compared to Mn(II) solubility (lower line in Fig. 11) at the same concentration, Mn(III) solubility is approximately 8-10 times higher than the Mn(II) values. The Mn(III) solubility obtained by O_2 oxidation is a little lower, probably because at the i_d max (Fig. 6) MnO_2 formation has already taken place.

Discussion

Since the main coordination numbers of Mn(II) are four and six (5), a number of Mn(II) complex ions of general formulas $[Mn(OH)_n(H_2O)_{4-n}]^{(n-2)-}$ and $[Mn(OH)_n(H_2O)_{6-n}]^{(n-2)-}$ can coexist in concentrated KOH or NaOH solutions, having an equilibrium among themselves. Of these possible species an equilibrium constant for the $K_2Mn(OH)_4$ formation of Eq. [1] was arbitrarily calculated, because activity coefficients of $K_2Zn(OH)_4$ in KOH solutions are available (7) and can be used in place of those of $K_2Mn(OH)_4$ as a first approximation. Also $[Mn(OH)_4]^=$ may be a predominant form, judging from the work of Scholder and Kolb (3), in which $Na_2[Mn(OH)_4]$ was isolated from the 50% NaOH solution saturated with $Mn(OH)_2$.

In the solubility measurement presented above, $MnSO_4$ solution was added to the KOH solutions. Therefore, there is a question whether the suspended excess solid is $Mn(OH)_2$ or not. In order to check this, Mn(II) solubility was measured by adding excess MnO to 9M KOH. The data were very close to that shown in Fig. 9. This indicates that we can assume $Mn(OH)_2$ as a solid phase.

$$Mn(OH)_2 + 2KOH \rightleftharpoons K_2Mn(OH)_4 \qquad [1]$$

Expression of the equilibrium constant for reaction [1] can be reduced to Eq. [3], assuming $a_{Mn(OH)_2} = 1$.

$$K = \frac{a_{K_2Mn(OH)_4}}{a_{Mn(OH)_2} \cdot a^2_{KOH}} \qquad [2]$$

$$K = \frac{\gamma^2_{K+} \cdot m^2_{K+} \cdot \gamma_{Mn(OH)_4^=} \cdot m_{Mn(OH)_4^=}}{\gamma^2_{K+} \cdot m^2_{K+} \cdot \gamma^2_{OH^-} \cdot m^2_{OH^-}}$$

$$K = \frac{\gamma^3_{\pm K_2Mn(OH)_4} \cdot m_{K_2Mn(OH)_4}}{\gamma^4_{\pm KOH} \cdot m^2_{KOH}} \qquad [3]$$

K's were calculated and are shown in Table I, in which $m_{K_2Mn(OH)_4}$ was calculated from the solubility of Mn(II) at 23°C, $\gamma_{\pm KOH}$ was obtained from the table given by Harned and Owen (6) and the $\gamma_{\pm K_2Zn(OH)_4}$ values (7) in KOH solutions of various concentrations were used in place of $\gamma_{\pm K_2Mn(OH)_4}$. In general, activity coefficients of dissolved salts are largely determined by the dissociation type of the salt, and therefore it is unlikely that the use of $\gamma_{\pm K_2Zn(OH)_4}$ in the same KOH solution of various concentrations introduces serious error in the calculation of K. The K's thus calculated give a fairly good constant in 9-12M KOH, so that a predominant species in this range of KOH concentration is probably $[Mn(OH)_4]^=$.

Another rough way to estimate the number of OH^- ions coordinated to the Mn(II) ion is to plot the logarithm of the Mn(II) solubility against the logarithm of the KOH concentration. The slope of such a plot should give the number of OH^- added to $Mn(OH)_2$. Such a plot is shown in Fig. 12, in which most of the data at 50° and 70°C fall on straight lines of the slope of 2.0. This suggests that the predominant Mn(II) complex ion may be $[Mn(OH)_4]^=$ in 3-12M KOH at 50° and 70°C.

The rough method based on the log [Solubility of Mn(II)] *vs.* log [KOH] plot can be justified as follows. Taking the logarithm of both sides of Eq. [3]

Table I. Calculation of K

KOH M	KOH m	Solubility of Mn^{++}, mg/l	Solubility of Mn^{++}, m	$\gamma_{\pm KOH}$	a_{KOH} $(=\gamma_{\pm KOH} m_{KOH})$	$\gamma_{\pm K_2Zn(OH)_4}$	K
3.07	3.10	5.2	9.75×10^{-6}	1.08	3.41	0.466	7.6×10^{-7}
5.30	5.75	12.0	23.7	2.078	12.4	1.047	3.9
9.31	10.90	25.0	53.8	7.902	87.3	5.39	1.6
10.22	12.30	34.0	74.8	12.44	135.3	8.209	1.8
11.62	14.65	44.0	101.0	18.97	278.4	15.93	1.5
13.52	17.80	68.0	237.0	38.0	676.4	73.77	14.4

Table II. Estimated values of M/m and the activity coefficient ratio of Eq. [3] showing rough constancy

KOH M	M/m for KOH	M/m for Mn(II)	$\gamma^3_{\pm K_2Zn(OH)_4}/\gamma^4_{\pm KOH}$
3.07	0.991	0.973	0.074
5.30	0.922	0.923	0.061
9.31	0.854	0.846	0.042
10.22	0.830	0.829	0.023
11.62	0.794	0.794	0.031
13.52	0.760	0.523	0.194

$$\log m_{K_2Mn(OH)_4} = \log K - \log \frac{\gamma^3_{\pm K_2Mn(OH)_4}}{\gamma^4_{\pm KOH}} + 2 \log m_{KOH}$$

as shown in Table II, M/m for KOH and $K_2Mn(OH)_4$ and log $(\gamma^3_{\pm K_2Mn(OH)_4}/\gamma^4_{\pm KOH})$ are roughly constant in 3-12M KOH. Therefore, we can write

$$\log S = k + 2 \log [KOH]$$

where S is solubility of Mn(II) in mg/l and [KOH] is molarity of KOH. Although molarity values change with temperature and molality values do not, the change in M/m with temperature change from 23° to 70°C is small and can be neglected for the approximate method described above.

Two points on Fig. 12 for Mn(II) in lower KOH concentrations at 23°C deviate from the solid line of the slope 2.0. These points were difficult to measure and may not be accurate because of very low i_d and the possibility of air oxidation of Mn(II) and formation of colloidal $Mn(OH)_2$ as mentioned before. The values measured in NaOH by Fox *et al.* are considerably higher than the present value in KOH, although the present measurements indicate that the solubility of Mn(II) is essentially the same in both KOH and NaOH as shown in Fig. 10. The higher values of Fox *et al.* may be due to the colloidal particles of $Mn(OH)_2$ which passed through their filter and were included in their final colorimetric determination.

Using the equilibrium constant value $K = 1.6 \times 10^{-7}$ (Table I), $\Delta F°$ $(= -RT \ln K)$ was found to be 9.15 kcal for the process of Eq. [1]. The approximate heat of dissolution for the process of Eq. [1] in 9M KOH was calculated from $d \log S/d\ (1/T) = -\Delta H/2.3R$, where S is solubility of Mn(II), by using data for 9M KOH at 23°, 50°, and 70°C; ΔH was found to be 6.7 kcal.

Acknowledgment

The authors wish to thank Dr. G. H. Newman and Dr. G. E. Blomgren for the activity coefficient values of $K_2Zn(OH)_4$ in KOH solution and for their valuable discussion on the calculation of the equilibrium constant.

Manuscript received Dec. 27, 1965. This paper was presented at the Cleveland Meeting, May 1-6, 1966.

Any discussion of this paper will appear in a Discussion Section to be published in the December 1966 JOURNAL.

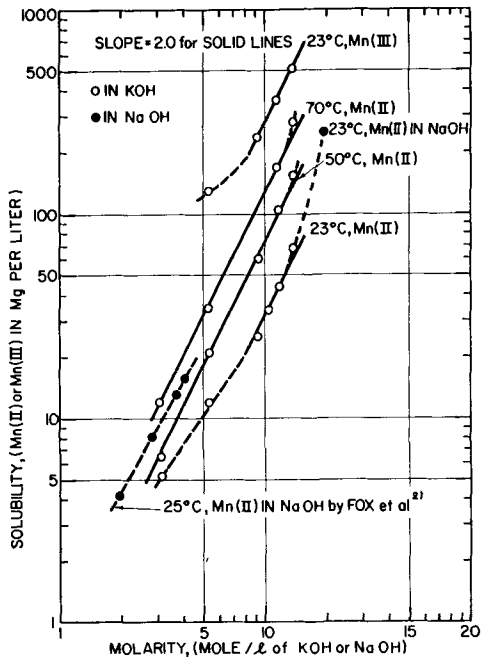

Fig. 12. Solubility of Mn(II) and Mn(III) vs. KOH or NaOH concentration.

REFERENCES

1. A. Kozawa and J. F. Yeager, *This Journal*, **112**, 959 (1965).
2. R. K. Fox, D. F. Swinehart, and A. B. Garrett, *J. Am. Chem. Soc.*, **63**, 1779 (1941).
3. R. Scholder and A. Kolb, *Z. anorg. u. Allgem. Chem.*, **264**, 209 (1951).
4. M. T. Kelley, H. C. Jones, and D. T. Fischer, *Anal. Chem.*, **31**, 1475 (1959).
5. J. C. Bailar, Editor, "The Chemistry of the Coordination Compounds," p. 169, 375, Reinhold Publishing Co., New York (1956).
6. H. S. Harned and B. B. Owen, "The Physical Chemistry of Electrolytic Solutions," p. 730, Reinhold Publishing Co., New York (1958).
7. G. H. Newman and G. E. Blomgren, Private communication.

Ledge Formation on the (111) Surface of Copper

L. D. Hulett, Jr., and F. W. Young, Jr.

Solid State Division, Oak Ridge National Laboratory, Oak Ridge, Tennessee[1]

ABSTRACT

The ledges formed by bunching of atomic steps during dissolution of copper crystals with surfaces vicinal to (111) have been investigated. The conditions for ledge stability were determined in dissolution experiments for which data of step velocities *vs.* step spacings had been determined previously. From these data step interaction functions were generated, and step motion was simulated on a digital computer, making use of the Mullins and Hirth modification of the kinematic theory of dissolution. Ledges could be made to appear or disappear in the computer experiments for conditions corresponding directly to laboratory experiments in which the ledges appeared or disappeared.

On close-packed and vicinal surfaces the preferred sites for atom removal are at monatomic steps, and dissolution processes can be described in terms of the motion of these steps across the surface. The kinematic theory of step motion as developed by Frank and Cabrera (1) deals with average velocity as a function of average step spacing, ignoring microscopic fluctuations. However, there are certain dissolution conditions for which microscopic fluctuations are amplified, causing steps to bunch into multiatomic "ledges." The Frank-Cabrera theory, without modification, cannot treat bunching since it deals only with averages, but recently Mullins and Hirth (2) have considered the velocities of individual steps. A nearest-neighbor interaction model is used, and the velocity of each step is defined as a function of the distances from the step ahead and the step behind, a formulation capable of treating bunching. In previous work (3), the Frank-Cabrera kinematic theory was used to analyze the growth of dislocation etch pits on (111) surfaces of copper. Ignoring ledges, we were able to explain the general dissolution shapes of the pits and determine average step velocities as a function of step spacing. In the present paper we consider the ledges.

The topographic changes associated with dissolution are described in Fig. 1. Figure 1(a) is a photomicrograph of a dislocation pit and ledges formed on a (111) copper surface. Figures 1(b) and 1(c) are schematic profiles of the surface before and after dissolution. Before dissolution is started [see Fig. 1(b)], monatomic steps are present because of slight misorientations from the exact (111) surface. Figure 1(c) shows that as the steps moved across the surface during dissolution they aggregated to form ledges. The sides of the dislocation pit are vicinal surfaces composed of steps nucleated at the point of dislocation-surface intersection.

In this study the step motion illustrated in Fig. 1(b) and 1(c) was simulated on a digital computer, making use of the Mullins-Hirth modification of the kinematic theory. Conditions for stability and instability of ledges were determined by laboratory experiments, and the velocity *vs.* step spacing data were obtained from pits formed under the same conditions. From these data, step interaction functions were generated which were used to simulate laboratory dissolution conditions in the computer experiments. In this paper we shall show correspondence between the laboratory and computer experiments. In addition, there was semiquantitative agreement for the frequency of ledge generation and the slopes of ledge fronts between laboratory and computer experiments.

Laboratory Experiments

In our previous etch pit studies (3) measurements of step flux, J, as a function of step density, ρ, were made for several dissolution conditions. Step flux is defined as $J = \rho V$, where V is the average step velocity and ρ is the reciprocal of step spacing, ϵ. From J *vs.* ρ curves, $\bar{V}$ *vs.* ϵ curves can be calculated. Two such curves are shown in Fig. 2. For the conditions of curve I, step velocity increases monotonically as step spacing increases. For the conditions of curve II the velocity of steps is a maximum for intermediate step spacings. For the conditions of the type I curve there is an effective repulsion between steps for all values of ϵ, while for the conditions of the type II curve there is an effective attraction between steps of large ϵ. The dissolution parameters that determine whether the curve is type I or type II are bromide ion concentration and current density. When these parameters are such that the V-ϵ curve is type II, ledges form and are stable, but under the conditions that cause type I curves, ledges do not form and are not stable. These observations are exemplified in the following

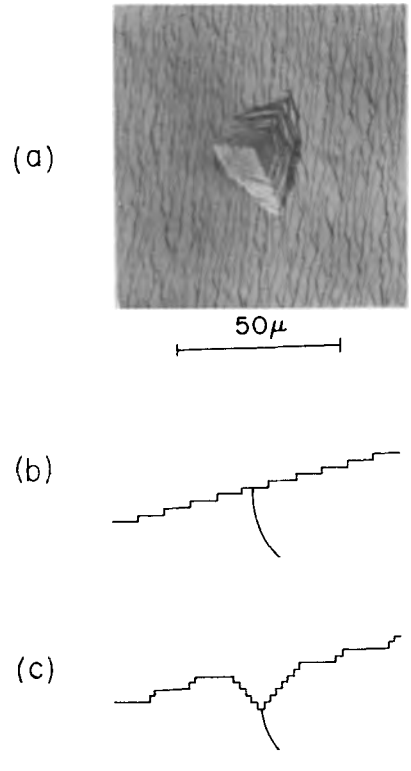

Fig. 1(a). Photomicrograph of dislocation pit and ledges formed by electrolytic etching of a copper surface vicinal to (111). Fig. 1(b). Schematic diagram of dislocation and steps on the vicinal surface in (a) before etching. Fig. 1(c). Schematic diagram of steps in the dislocation pit and in the ledges of the vicinal surface in (a) after etching.

[1] Research sponsored by the U. S. Atomic Energy Commission under contract with Union Carbide Corporation.

laboratory experiments. All dissolutions were carried out electrolytically, as previously described (3, 4).

(*A*) Starting with an electropolished surface, ledges are generated if the dissolution is governed by a type II curve and if the average step spacing is less than about 550Å. The ledges in Fig. 1 are the result of such a dissolution. They developed under the same condition as those for which the type II curve of Fig. 2 was measured. The average step spacing was 200Å, corresponding to a misorientation of ½° from the (111) pole. Figure 3 is an electron micrograph of the replica of a ledge formed under similar conditions. From the distortion of the shadow of the ¼ micron polystyrene ball, one can estimate that the height of the ledge and the slope of its front are about 100 atoms and 6°, respectively.

(*B*) Starting with an electropolished surface, ledges are not generated if the dissolution conditions are those of type I curves. The surface in Fig. 4, which has no ledges, was etched under the same conditions as those for which the type I curve of Fig. 2 was measured. The average misorientation and step length of the surface is about the same as that of the surface in Fig. 1.

(*C*) For a given bromide concentration, large changes in current density can cause ledges to disappear. The first frame in Fig. 5 is a photomicrograph of a surface having ledges formed at an average current density of 1.0 ma/cm². The second frame is of the same surface after the current density has been increased to 5 ma/cm². The higher current density caused the $\bar{V}$-ϵ curve to shift from a type II to a type I curve for which ledges are unstable.

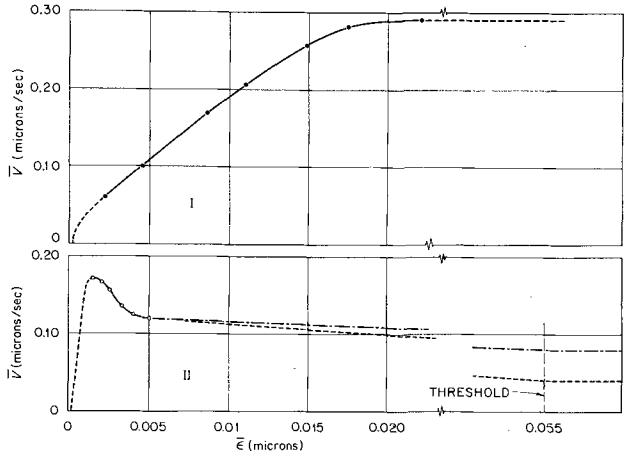

Fig. 2. Laboratory measurements of average step velocities as functions of average step spacings for conditions under which ledges do not form (curve I) and for conditions under which ledges do form (curve II). Dissolution conditions of curve I: 6M HCl; 0.03M HBr; 5 ma/cm² current density. Dissolution conditions of curve II: 6M HCl; 0.25M HBr; 10 ma/cm² current density.

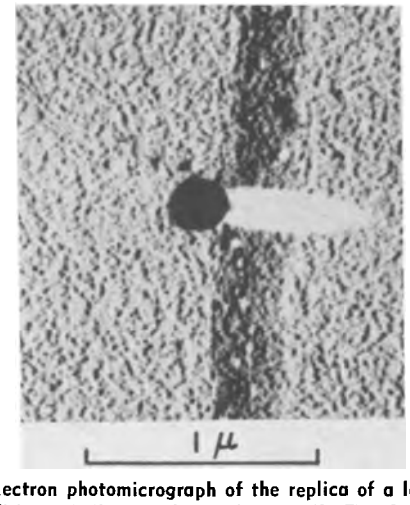

Fig. 3. Electron photomicrograph of the replica of a ledge formed under conditions similar to those of curve II, Fig. 2.

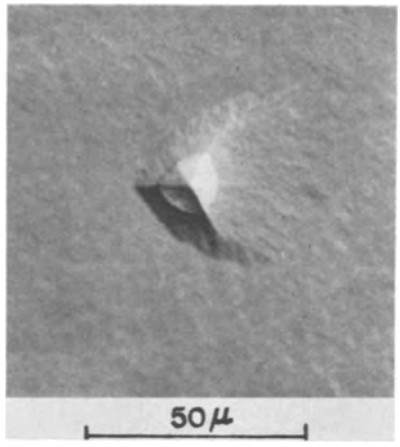

Fig. 4. Photomicrograph of a dislocation pit and vicinal surface having no ledges. Dissolution conditions were the same as those of curve I, Fig. 2.

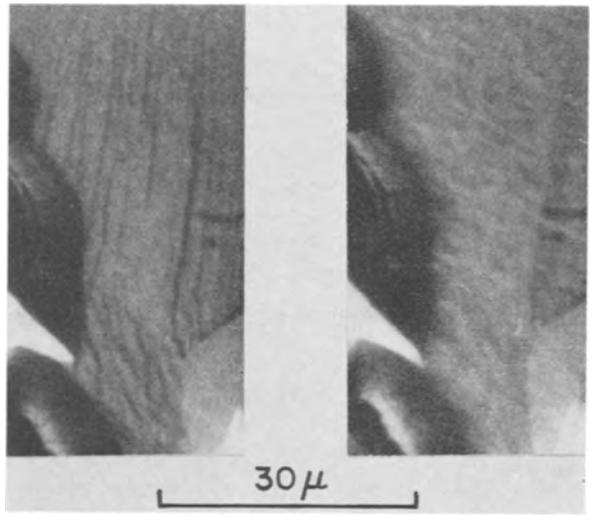

Fig. 5. Ledge disappearance caused by current density increase. Solution composition: 6M HCl, 0.03M HBr. Current density for frame (a) 1 ma/cm²; for frame (b), 5 ma/cm²; time difference between frames is 20 sec.

(*D*) There is a "threshold" step spacing beyond which steps are too widely separated to interact and form ledges, even if the conditions correspond to type II. On (111) surfaces of copper the threshold spacing is 500-700Å. In Fig. 6 the average misorientation[2] of the surface on the right part of the photomicrograph, which has no ledges, is less than ¼° which corresponds to a step spacing of 550Å or larger. The surface having ledges in the left part of the photomicrograph has a step spacing smaller than 550Å. The dissolution conditions were the same as those of experiment (*A*).

The Mullins-Hirth Formulation; Step Interaction Functions

Mullins and Hirth proposed that dissolution processes be described by infinite sets of simultaneous equations, each equation representing the motion of an individual step

$$V_n = f(\epsilon_n) + f(\epsilon_{n-1})$$
$$V_{n+1} = f(\epsilon_{n+1}) + f(\epsilon_n) \qquad [1]$$

[2] Misorientation can be calculated from the asymmetry of etch pits.

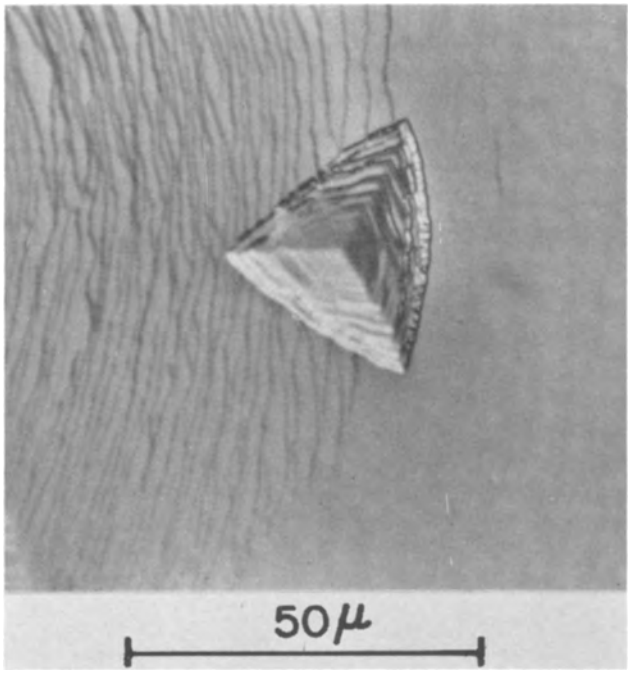

Fig. 6. Illustration of threshold step spacing effect. Average step spacing on left portion of surface, containing ledges, is less than the threshold. Average spacing on right portion of the surface, having no ledges, is greater than the threshold.

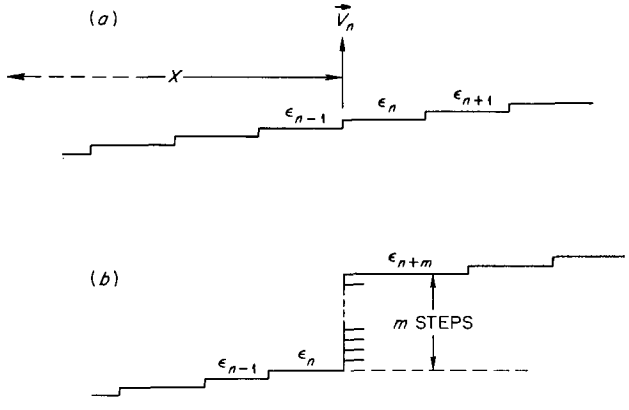

Fig. 7.(a) Schematic diagram of monatomic steps. (b) Schematic diagram of multiatomic step.

The subscript notation is defined in Fig. 7(a); ϵ denotes step spacing, and x denotes the coordinate of the step, measured from an arbitrary reference. The boundaries of the surface are $x = \pm \infty$.

The f-functions are of the same form for the spacings in front and behind a given step. They express the nature of the interaction between steps and are the medium by which conditions of the laboratory experiments are simulated in the computer experiments.

To employ the Frank-Cabrera theory it was necessary to ignore ledges and other surface roughness. Curves I and II, Fig. 2, are therefore measures of average step velocities as functions of average spacing. To extrapolate from these average velocities to f-functions of the Mullins-Hirth formulation it is necessary to assume that a surface with an average step spacing of $\bar{\epsilon}$ is equivalent to a surface with a uniform step spacing of this same $\bar{\epsilon}$. If this assumption is valid, the velocities for trains of steps can be written, according to Eq. [1], as

$$\overline{V} = 2f(\bar{\epsilon}) \qquad [2]$$

The f-functions used in the machine calculations of this paper were determined from curves I and II of Fig. 2 using Eq. [2].

The values of the velocity functions and the f-functions for very small step spacings could not be measured directly and had to be extrapolated. The velocities of steps with average spacings of 0.7Å, which corresponds to the intersection of two (111) surfaces, must be zero since it is assumed that atoms are not removed from close-packed surfaces. Therefore, the $\overline{V}$-functions and the f-functions were extrapolated to zero for 0.7Å spacings.

The values of the $\overline{V}$-functions for very large ϵ's were extrapolated[3] from plots of both V *vs.* ρ and $(\partial J/\partial \rho)$ *vs.* ρ. For spacings larger than the threshold [experiment (D)], the f-functions must behave in such a manner that steps do not bunch; that is, there is no difference in their velocities. This requirement is satisfied if the f-functions are constant for large values of ϵ, a reasonable assumption, since steps spaced from each other beyond a certain distance have negligible interactions and their velocities are constant and equal. Therefore, the type II f-functions were extrapolated to $f(\infty)$ at the spacing of 550Å, which was the experimentally measured threshold spacing. On surfaces etched under type I conditions no threshold spacing could be deduced, but from the V *vs.* ρ plot, V appeared to approach a constant value for spacings larger than 230Å which was used as the threshold spacing.

Calculation Procedure

(*a*) To simulate an infinite surface 100 steps with periodic or cyclic boundary conditions were used. That is, in the course of the calculation the current length of the first step was used as the leading boundary condition (101st step) and that of the 100th step was used as the rear boundary conditions (0th step).

(*b*) The motion of steps was simulated by simultaneous numerical integration of each of the velocity equations (1). For an increment of time, Δt, the coordinate increase of the n^{th} step was calculated as

$$\Delta X_n = [f(\epsilon_n) + f(\epsilon_{n-1})]\,\Delta t$$

This operation was iterated on each of the 100 steps with the cyclic boundary conditions applied to the 1st and 100th steps. At the end of the cycle the ϵ's were recalculated

$$\epsilon_n = X_{n+1} - X_n$$

The cycle was repeated $t/\Delta t$ times, where t was the simulated dissolution time. In all the calculations shown in this paper, Δt was equal to 0.005 sec. Configurations generated by the 0.005-sec calculations were convergent on those generated by calculations using smaller Δt's, thereby justifying the choice of Δt.

(*c*) Steps were permitted to collapse to form multisteps, but negative step spacing, which would correspond to "undercutting," was forbidden; *i.e.*, the machine was programed such that the coordinate of a given step was never allowed to be larger than the coordinate of the step ahead.

(*d*) Mullins and Hirth suggested that the velocity of multisteps such as in Fig. 7b, containing m steps, be defined as follows

$$V = 1/m\,[f(\epsilon_n) + f(\epsilon_{n+m})] \qquad [3]$$

We have used a different treatment. When multisteps were encountered during a calculation cycle, the velocities of all understeps, such as steps $(n + 1)$ and $(n + m - 1)$ in Fig. 4, were set to zero for the instant represented by that cycle. The top steps [step $(n + m)$ in Fig. 7] were allowed to move in a normal manner with their velocities defined by Eq. [1].

[3] $\lim_{\rho \to 0} V(\rho) = \lim_{\rho \to 0} \left(\frac{\partial J}{\partial \rho}\right) = \lim_{\epsilon \to \infty} (\overline{V}(\epsilon))$

Simulation of Experimental Results

To approximate an electropolished surface one must make some assumptions about its nature. Electropolishing makes surfaces very smooth on a macroscopic scale, but there are microscopic fluctuations in step lengths. Very little is known about step configurations on electropolished surfaces, so an empirical choice was made which is illustrated for 100 steps by the uppermost diagram in Fig. 8, and is analytically described as follows

$$\frac{\Delta N(\epsilon)}{\Delta\epsilon} = \epsilon \exp\left(\frac{-\pi r^2}{4}\right)$$

for which $r = \epsilon/\bar{\epsilon}$ and $\Delta N(\epsilon)$ is the number of steps with a spacing between ϵ and $\epsilon + \Delta\epsilon$. The order of the steps is random. All the step diagrams in this paper were plotted by machine, and the step lengths are accurately proportional to those calculated.

(*A*) To simulate laboratory experiment (*A*), the calculation procedure was applied to the electropolished surface configuration using an *f*-function derived from curve II in Fig. 2. The results are illustrated in Fig. 8. The two lower diagrams, representing the surface after 6 and 10 sec of simulated dissolution, show that a step pile-up, corresponding to a ledge, was generated. The use of the type II *f*-function caused the interaction between steps to be such that there was a tendency to aggregate. The periodicity of ledge generation is one ledge per 100 steps, and the slope of the ledge front is about 20°; compare with the 6° slope of Fig. 3.

(*B*) To simulate laboratory experiment (*B*), the calculation was applied to the electropolished surface configuration using an *f*-function derived from curve I, Fig. 2. As shown by the lower diagrams in Fig. 9, no step pile-ups occurred. The surface remained smooth on a macroscopic scale.

(*C*) Ledge disappearance, described in laboratory experiment (*C*), was simulated by applying the calculation procedure, using a type I *f*-function, to an initial distribution of step lengths that contains ledges. As shown in Fig. 10, the ledges were made to disappear after 10 sec of simulated dissolution. The type I *f*-function effects a repulsion between steps in the ledges, causing them to dissociate.

(*D*) In laboratory experiment (*D*) there was no ledge formation because the steps were too widely separated to interact. This observation was simulated by using an initial configuration of steps with an average spacing larger than the threshold spacing (see type II curve, Fig. 2). An average step spacing of 1000Å was used, which is about twice as large as

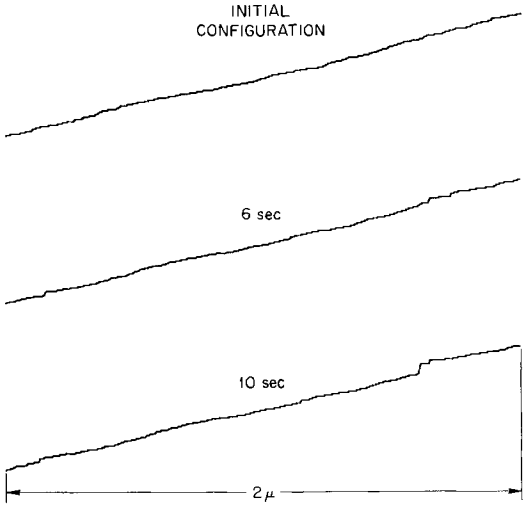

Fig. 8. Step diagrams generated by a simulated dissolution experiment in which the step interaction function was type II.

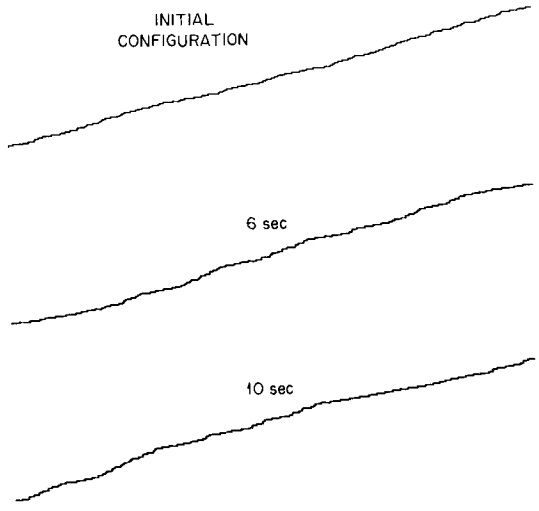

Fig. 9. Step diagrams generated by a simulated dissolution experiment in which the step interaction function was type I.

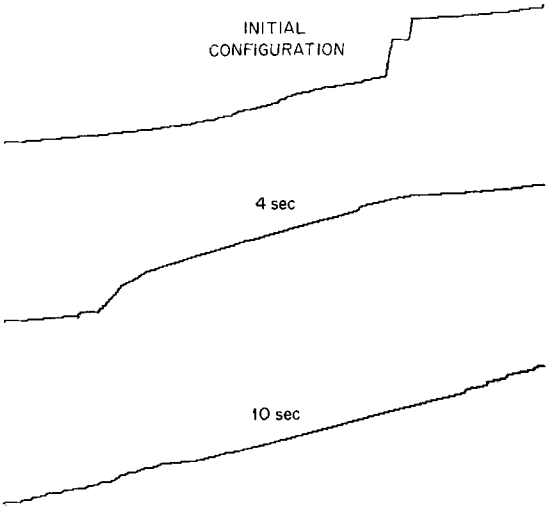

Fig. 10. Ledge disappearance in a simulated dissolution experiment using a type I step interaction function.

the threshold, 550Å. For spacings beyond the threshold, the *f*-function is constant. Fig. 11 shows that after a simulated 10-sec dissolution there were no ledges generated. The simulated surface remained macroscopically smooth, as did the actual surface seen in the laboratory. In the initial configuration used in this calculation, 21 pairs of steps were close enough to interact ($\epsilon < 550$Å). At the end of the calculation this number had decreased to 18.

(*A*-1) The number of ledges generated depends on the initial distribution of steps chosen to simulate the electropolished surface. For the calculation shown in Fig. 12 a random distribution of step lengths was used. It was generated as follows

$$\epsilon_n = \epsilon_{AV}\,(1 \pm R)$$

where ϵ_n is the initial step length of the n^{th} step, ϵ_{AV} is the average step length and R is a random number varying between 0.00 and 0.99. The plus or minus sign was chosen according to whether the second digit of R was odd or even. The calculation procedure was applied to this distribution using the same type II *f*-function as was used in calculation *A*. Because of the different initial distribution of steps, a greater number of ledges were generated. The slopes of the ledge fronts were about the same as that of the ledge generated in experiment *A*. The random distribution of steps used in this calculation represented a more perturbed surface than the Gaussian

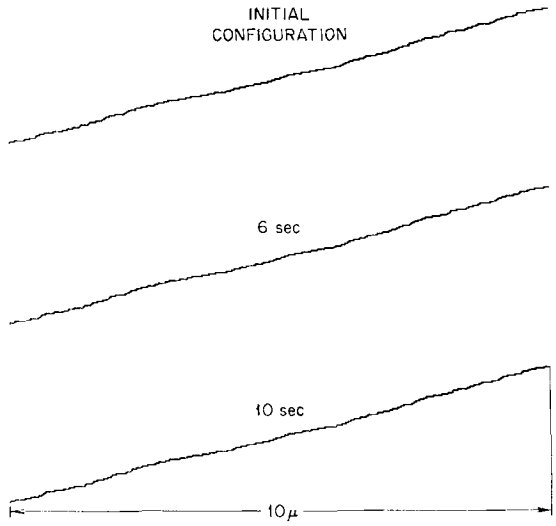

Fig. 11. Simulated dissolution experiment using a type II step interaction function and a surface whose average step spacing is greater than the threshold.

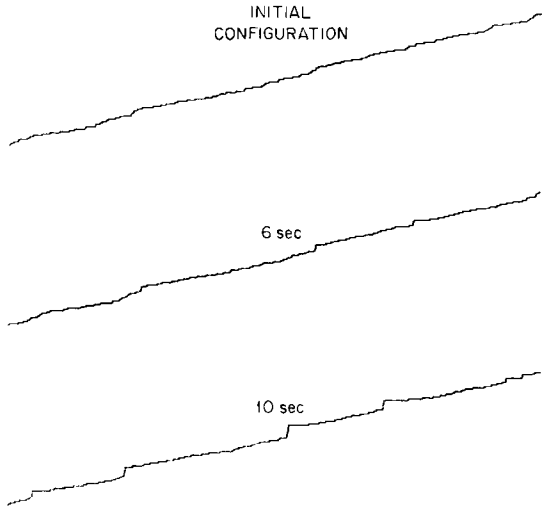

Fig. 12. Simulated dissolution experiment using a random distribution of step lengths to represent the electropolished surface, type II step interaction function.

distribution used in A. That is, the average deviation of the step lengths was greater for the random distribution.

(A-2) If the f-function is given a faster rate of change in the large-ϵ region, more ledges with steeper fronts will be generated. The 10-sec configuration in Fig. 13 was generated from the same initial distribution as was used in A, but the f-function was given a lower value at the threshold spacing. In calculation A, the f-function was extrapolated to a value of 0.04 μ/sec (one-half the extrapolated value of V in Fig. 2) at the threshold spacing. For the present calculation it was extrapolated to a value of 0.02 μ/sec.

Discussion and Conclusions

In these calculations we have modified Mullins and Hirth's treatment of the motion of multiatomic steps. They treat multisteps as units, which once formed cannot dissociate and whose velocity is defined by Eq. [3]. Equation [3] implies that ledge velocity is dependent on height. We have found experimentally that this is not true; ledges may differ in height by large factors, but still move with the same velocity. Also, it seems reasonable that multiatomic steps might dissociate if future conditions permit. For example,

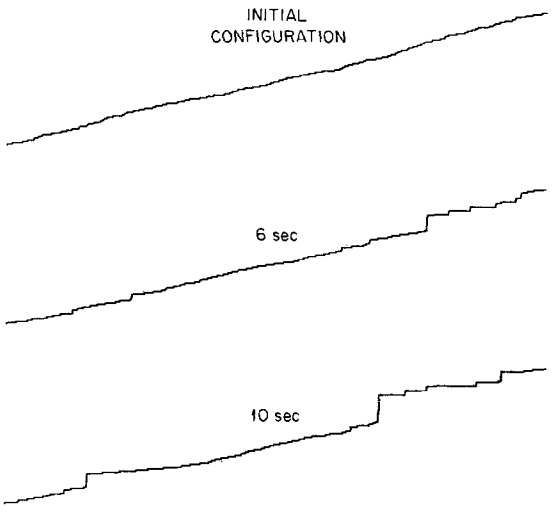

Fig. 13. Simulated dissolution experiment using a type II f-function with a fast rate of change for large step spacings.

the uppermost step in a multiatomic step [step $n + m$ in Fig. 7(b)] can break away from its lower neighbors. Collapsed understeps, of course, should not be able to move since this would result in "undercutting," which amounts to the removal of atoms from close-packed surfaces and is energetically unfavorable. We therefore treated multiatomic steps in the manner described in the calculation procedure. As ϵ attempts to become less than 0.7Å, the f-function should behave in such a manner that strong repulsive terms, which prevent undercutting, arise between the steps. This is accomplished, in effect, by the special instructions in the calculation program which disregard negative values and substitute zero values in their places.

The machine calculations show that this model of step kinematics is capable of explaining the behavior of ledges observed in the laboratory. Experimentally it was found that the conditions for ledge formation and stability can be categorized as those for which the V-ϵ curves are type II, while under the conditions of type I curves, ledges do not form and are unstable. The results of the simulated dissolutions paralleled these observations. This model assumes a nearest-neighbor interaction between steps. The nature of the interaction, "attractive" or "repulsive",[4] is expressed by the f-function. Calculation (A), which simulates laboratory experiment (A), shows that the type II f-function causes the interaction to be attractive, which results in a ledge. For type I f-functions there is a repulsion between steps that tends to dampen large fluctuations in step spacing and prevent ledge formation, and this effect is demonstrated by calculation (B). Type I interactions also tend to annihilate ledges once they are formed. This fact is accounted for by calculation (C). Calculation (D) shows that the theory predicts the fact that ledges do not form when the steps are too far apart to interact. The number of pairs of steps capable of interacting decreased during this calculation which suggests that bunching will never occur, even if the calculation were extended indefinitely.

Admittedly Eq. [2], which illustrates the assumption made in order to be able to evaluate the f-function from experimental data, is an oversimplification. However, it should be a reasonable first approximation and allow at least a semiquantitative estimate of the nature of the interactions. These calculations only purport to describe this system qualitatively or at best semiquantitatively. Whether there is kinematic

[4] Since there are no energy terms involved, it is not proper to consider the interactions as forces in the strict physical sense. Lighthill and Whitham (5) discuss this point. Perhaps a better terminology is "kinematic attraction" and "kinematic repulsion."

attraction or repulsion between steps is the important factor, it is not determined by the exact nature of $f(\epsilon)$, rather by its general form. Therefore, small deviations in $f(\epsilon)$ generally will not alter the type of interaction.

Calculation (*A*) is in semiquantitative agreement with laboratory experiment (*A*) in that the frequency of ledge generation and the slopes of the ledge fronts are approximately the same. In laboratory observations the frequency of ledge generation is approximately 1.2 ledges per 2μ along the surface. The slope of the ledge fronts for the experimental conditions corresponding to this calculation were about 6°. The ledge in calculation (*A*), having a frequency of one ledge per 2μ and a frontal slope of 20°, is a reasonable semblance of these observations. In investigations of some of the factors that determine the frequency of ledge generation and frontal slopes, calculation (*A*-1) shows that the initial step configuration is important in determining the frequency of ledge generation. The random initial distribution, which represents a more perturbed electropolished surface than that used in experiment (A), causes more ledges to be generated. That is, the greater average deviation of step lengths apparently results in a larger number of regions in which the step configurations are such that bunching can occur. Calculation (*A*-2) shows that the *f*-function is also important in determining the frequency of ledge generation. In this calculation the greater rate of change of the *f*-function in the large-ϵ region causes larger differences in step velocities which lead to a higher incidence of steps piling up to form ledges. The slopes of the ledge fronts in calculations (*A*) and (*A*-1) are approximately the same, but those of (*A*-2) are considerably steeper. This observation suggests that the slopes of ledge fronts are dependent on the shape of the *f*-function curve but not on the initial step configuration.

Manuscript received Sept. 27, 1965; revised manuscript received Jan. 25, 1966. This paper was presented at the Buffalo Meeting, Oct. 10-14, 1965.

Any discussion of this paper will appear in a Discussion Section to be published in the December 1966 JOURNAL.

REFERENCES

1. F. C. Frank, "Growth and Perfection of Crystals," R. H. Doremus *et al.*, Editors, p. 411, John Wiley & Sons, Inc., New York (1958); N. Cabrera, "Reactivity of Solids," J. H. De Boer *et al.*, Editors, p. 345, Elsevier, Amsterdam (1961); N. Cabrera and R. V. Coleman, "The Art and Science of Growing Crystals," J. J. Gilman, Editor, p. 3, J. Wiley & Sons, Inc., New York (1963).
2. W. W. Mullins and J. P. Hirth, *J. Phys. Chem. Solids*, **24**, 1391 (1963).
3. L. D. Hulett, Jr., and F. W. Young, Jr., *ibid.*, **26**, 1287 (1965).
4. F. W. Young, Jr., and L. D. Hulett, Jr., "Metal Surfaces," W. D. Robertson *et al.*, Editors, p. 375, American Society for Metals, Metals Park, Ohio (1963).
5. M. J. Lighthill and G. B. Whitham, *Proc. Roy. Soc.*, **229A**, 281, 317 (1955).

Oxidation of Copper Single Crystals in Aqueous Solutions of Inorganic Salts

I. Topography of Oxide Formed in $CuSO_4$ and $Cu(OAc)_2$ Solutions

C. Earl Guthrow, Jr.,[1] and G. Tyler Miller, Jr.[2]

Department of Chemistry, Hampden-Sydney College, Hampden-Sydney, Virginia

ABSTRACT

Electron microscopic examination was made of the topography of Cu_2O formed on the (110), (100), and (111) faces of copper single crystals immersed for varying times in aqueous solutions of $CuSO_4$ and $Cu(OAc)_2$. Considerable differences in the nature of the oxide were observed in the two systems. Polyhedra of Cu_2O were formed on all three faces in solutions of $CuSO_4$, while under the same initial conditions of Cu(II) ion concentration, pH, and temperature in $Cu(OAc)_2$ solutions relatively smooth and continuous films formed on the (110) and (111) faces, while polyhedra were observed on the (100) face. Annealing the copper surfaces in H_2 at 500°C before immersion enhanced the formation of polyhedra in the $CuSO_4$ system and the formation of continuous films in the $Cu(OAc)_2$ system. Epitaxial relationships between the metal and oxide, as shown by reflection electron diffraction, were the same in both the $CuSO_4$ and $Cu(OAc)_2$ systems, and this was the same as found in other studies of Cu_2O formed in gaseous O_2 at high temperatures and in pure water at room temperature.

An understanding of the fundamental processes involved in the oxidation of metals is one of the important, unsolved problems of modern science. The formation of oxide films on metal surfaces exposed to aqueous solutions is quite complex and a great amount of fundamental work needs to be carried out.

This paper reports results obtained in the first of a series of studies designed to obtain a clearer picture of what happens at a surface of copper when it is immersed in an aqueous solution of some inorganic salt. In most corrosion or oxidation studies polycrystalline metal specimens have been used, and as a result the data obtained represented the composite behavior of a number of different crystal faces and grain boundaries. Such measurements are often useful for solving pressing technological problems, but they give only limited information about the mechanism of corrosion reactions. The work of Gwathmey and his associates (1-7) has shown the importance of crystal face and the absolute necessity for careful surface preparation in any fundamental study of metal surfaces.

Since most work with copper single crystals has been concerned with oxidation in the gas phase, there are relatively few studies in aqueous solutions. One notable exception is found in the careful work of Kruger and his associates (8-10) on the oxidation of copper single crystals in pure water. In addition, in-

[1] Present address: Department of Materials Science, University of Virginia, Charlottesville, Virginia.

[2] Present address: Department of Chemistry, St. Andrews Presbyterian College, Laurinburg, North Carolina.

directly related work on the potentials of copper single crystals in copper sulfate solutions has been reported by Miller (11), Tragert and Robertson (12), Piontelli (13), Jenkins and Stiegler (14), and Jenkins and Bertocci (15).

In an earlier study Miller (11), and Miller and Lawless (16), made an extensive investigation of the oxidation of copper single crystals in $CuSO_4$ solutions. They found that a continuous oxide film did not form, but instead large well-defined polyhedra of cuprous oxide formed at random points on the metal surface. The height, shape, and relative number of these polyhedra varied reproducibly with crystal face. Later, Kassis and Miller (17) carried out exploratory experiments in which copper single crystals were oxidized in solutions of $Cu(NO_3)_2$ and $Cu(OAc)_2$. In the copper (II) nitrate system, polyhedra formed which were similar to those found in the $CuSO_4$ system, while in the $Cu(OAc)_2$ system a relatively smooth and continuous oxide film formed.

Since the continuous film could afford greater corrosion protection than the polyhedra, an extensive study of the variables affecting these two contrasting types of oxide growth was initiated. The present study, which is the first in a series of investigations, is concerned with an electron microscopic and electron diffraction study of the effect of time on the oxidation of the (100), (110), and (111) planes of copper in solutions of copper(II) sulfate and copper(II) acetate. The present study extends the earlier studies (11, 16, 17) to include additional reaction times and additional important variables.

Experimental Procedure

Materials.—Copper single crystal rods of 99.999% purity were grown from the melt by the Bridgman technique and machined into spheres ⅝ in. in diameter and having a cylindrical stem approximately ¼-⅜ in. in diameter x ½ in. in length.[2] Flat surfaces parallel to specific crystallographic planes were cut on the spheres.

In all studies 0.05*N* solutions of either $CuSO_4 \cdot 5H_2O$ or $Cu(OAc)_2 \cdot H_2O$ were made from reagent grade chemicals and water which had been demineralized, distilled through a tin lined still, and stored in a seasoned polyethylene vessel. This water, when cooled to room temperature, was also used to wash all single crystal surfaces. After oxidizing copper crystals in solutions whose concentration varied from 0.001 to 0.40*N*, it was decided to use 0.05*N* as the solution concentration for all experiments rather than the 0.39*N* concentration used in earlier studies (11, 16). This normality could possibly allow the solution to be treated theoretically using Debye-Huckel, Onsager, or other approaches, and at the same time it supported an oxidation reaction with a reasonable rate. Since Shreir and Smith (18) found that $CuSO_4$ solutions were often unstable, fresh $CuSO_4$ solutions were prepared every week.

The polyethylene water reservoir was not used until it had been seasoned for at least two weeks until the reproducible "standard" oxidation pattern shown in Fig. 1 could be obtained on copper single crystal spheres washed with water stored in the reservoir. This pattern, which consisted of a symmetrical and beautiful array of interference colors, was formed by oxidizing the crystal in a cupric acetate solution for 5 min. Experiments on a given day were not run unless this "standard" pattern could be obtained. Since the pattern is sensitive to impurities of the order of a few parts per million and to the slightest change in surface preparation, this practice represented a convenient and extremely sensitive method of checking reproducibility. This approach has been discussed in detail by Young, Cathcart, and Gwathmey (6). These standard patterns will probably vary slightly from one laboratory to another, since they only assure that measurements will be carried out under a constant state of trace contamination.

Preparation of surfaces.—Spheres and flat surfaces were etched in a 1:1 by volume solution of concentrated nitric acid and distilled water, mechanically polished, electrolytically polished, and washed carefully to remove traces of phosphate ions as described by Young, Cathcart, and Gwathmey (6). To be certain that strain and deformation were absent and to insure that each plane remained within 2° of the desired orientation, they were checked with x-ray diffraction using a Laue back-reflection technique after the initial surface preparation and after every 2-4 experiments. In the case of (100) plane the orientation was held within 1°.

Reaction procedure.—After the crystal was washed and polished, it was exposed to the desired electrolyte solution under two sets of conditions. In the first series of experiments the copper specimens were dried in a jet of nitrogen and then annealed in purified dry hydrogen for 1 hr at 500°C in a Pyrex reaction chamber. After the crystal was cooled in a hydrogen atmosphere to 25°C, the desired electrolyte solution was transferred under hydrogen pressure from a solution reservoir to the crystal reaction chamber. In these "annealed" experiments any initial thin film of oxide had to be formed while the crystal was exposed to the electrolyte.

In the second series of experiments, the crystal was not dried after being washed but was immersed immediately for the desired length of time in a glass vessel containing approximately 30 ml of the electrolyte solution and maintained in a water bath at 30° ± 0.05°C. In order to prevent evaporation the reaction vessel was closed for the longer immersion times. In these "unannealed" experiments the oxide formed in the electrolyte solution probably grew on top of a thin 20-30Å oxide film formed in the air. After the desired immersion time the crystal was quickly removed from the solution, immediately washed for 30 sec in distilled water and dried in a jet of N_2.

In both types of experiments no attempt was made to remove dissolved oxygen from the electrolyte solutions. It was estimated that the oxygen concentration was approximately 10^{-4} moles/liter. In all experiments the *p*H of the solution was measured before and after reaction. The *p*H of 0.05*N* $CuSO_4$ was found to be 4.3 ± 0.05. Pourbaix (19) has shown that cuprous oxide is thermodynamically stable at this value but that cupric oxide would not be expected to form. As a result, the initial *p*H of all solutions was set at 4.3 ± 0.05. The value for 0.05*N* $Cu(OAc)_2$, which was normally 5.6, was adjusted to 4.3 by the addition of reagent grade glacial acetic acid.

Surface examination and characterization.—After reaction the surface of the crystal was examined using optical and electron microscopy. In addition, electron and x-ray diffraction techniques were used to identify the reaction products and to determine their epitaxial relationship to the metal substrate. In order to examine the surfaces using electron microscopy, it was necessary to use a replica technique. In most cases the surface was preshadowed with platinum at angles from 5° to 20° and replicated using a carbon evaporation technique. These carbon replicas were stripped successfully from the surface using a sequence of solutions including fresh 5% by volume ethylenediamine, a 3:1 mixture of 10% by volume ammonium persulfate and concentrated ammonium hydroxide, and subsequent washing in 10% by volume nitric acid and distilled water. A modified shadowing and replicating procedure was initiated after it was found that the ethylenediamine dissolved the platinum during the stripping operation. In order to protect the platinum it was sandwiched between two layers of carbon.

[3] The copper single crystal rods used in this study were obtained from the Virginia Institute for Scientific Research, 6300 River Road, Richmond, Virginia.

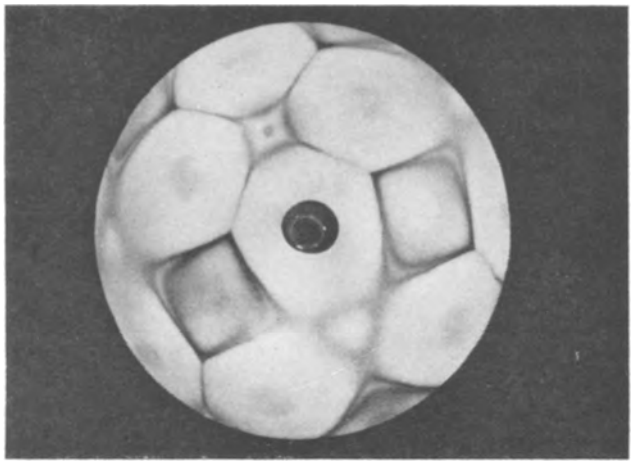

Fig. 1. Oxidation pattern formed on a spherical copper single crystal immersed in 0.39*N* $Cu(OAc)_2$ for 5 min at 30.0°C, *p*H 4.3.

Experimental Results

Oxidation of spheres.—Oxidation of copper single crystal spheres under various conditions gives a symmetrical and beautiful oxidation pattern of interference colors resulting from the different rates of oxidation of the various crystallographic planes. The "standard" oxidation patterns for the oxide formed in dry oxygen gas at 250°C and in $CuSO_4$ solutions at 25°C have been given in the original article of the present study (16). A typical standard pattern formed in $Cu(OAc)_2$ solution at 25°C is shown in Fig. 1. Compared to the pattern formed in $CuSO_4$, this acetate pattern is much sharper and the colors are more brilliant. In general, this indicated the formation of much smoother oxide films in the cupric acetate system. In an earlier article Lawless and Miller (22) suggested that the oxide patterns formed by immersing carefully prepared copper single crystal spheres in a 0.39*N* solution of $CuSO_4$ for times from 1 to 5 min provided a quick and convenient means for identifying particular crystallographic planes for purposes of cutting flat crystal faces or for other purposes. Since the patterns formed after 5 min immersion of the spheres in 0.05*N* or 0.39*N* $Cu(OAc)_2$ are much sharper, they represent an even better method for quickly and accurately locating particular faces on a spherical crystal.

Effect of oxidation time on surface topography.—The (110), (111), and (100) planes of copper were oxided in copper (II) sulfate and copper (II) acetate solutions for times varying from 30 sec to 24 hr. In all experiments reflection electron diffraction showed that the only surface product formed was Cu_2O. The initial *p*H of 4.3 was maintained during the course of oxidation in the copper (II) acetate solutions, while in the copper (II) sulfate solutions it had dropped slightly after 5 min immersion and after immersion for 24 hr it had dropped to values ranging from 3.5 to 3.7 depending on the relative surface area of copper exposed to the solution. The topography of the surfaces after oxidation is shown in Fig. 2-6.

$CuSO_4$ *system.*—In the original study of this series Miller and Lawless (16) showed that large individual oxide polyhedra formed on annealed copper single crystals immersed in 0.39*N* $CuSO_4$ solutions. In the present study these results have been expanded to include additional immersion times, unannealed crystals, and 0.05*N* $CuSO_4$ solutions.

Figure 2 shows the formation of Cu_2O as a function of time on the (110) face. It should be noted that the exposed surface between the polyhedra increased as the polyhedra grew larger. On the (111) plane evidence of oxide polyhedra was observed, although individual polyhedra were very difficult to distinguish, since the surface had the appearance of run-together

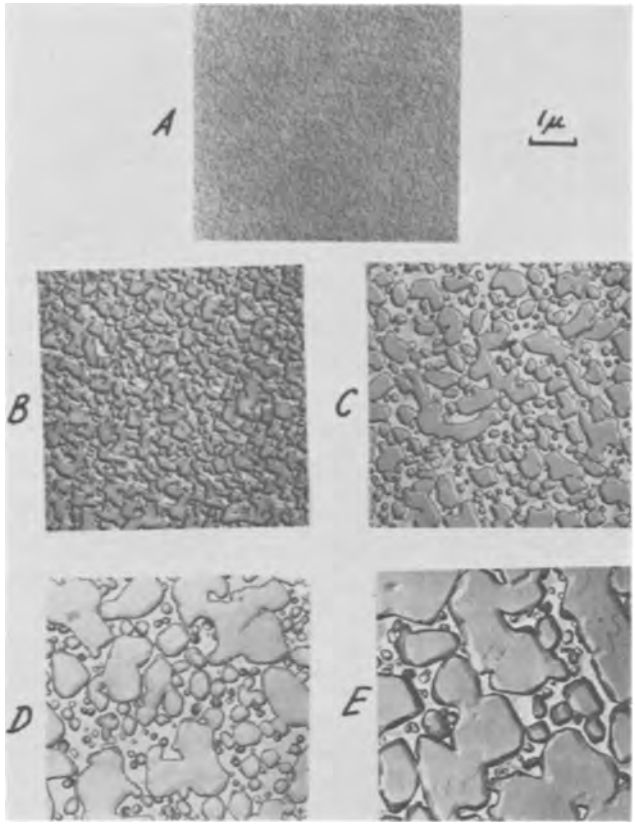

Fig. 2. Growth of oxide polyhedra with time on the (110) face of copper after immersion in 0.05*N* $CuSO_4$ at 30.0°C, initial *p*H 4.3: a, 30 sec; b, 3 min; c, 5 min; d, 15 min; e, 1 hr. Magnification 15000X before reduction for publication.

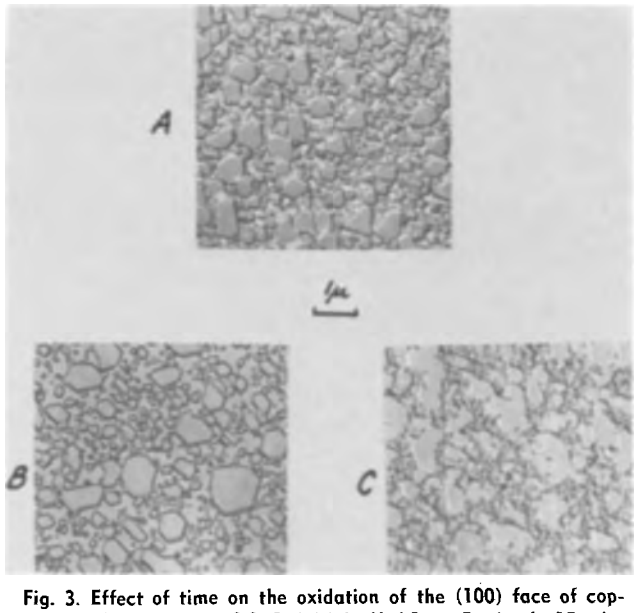

Fig. 3. Effect of time on the oxidation of the (100) face of copper in 0.05*N* $CuSO_4$ at 30.0°C, initial *p*H 4.3: a, 5 min; b, 15 min; c, 1 hr. Magnification 15000X before reduction for publication.

polyhedra after only 5 min. Figure 3 shows that the growth of polyhedra on the (100) face followed the same over-all growth pattern as that on the (110) face.

For immersion times longer than an hour, the polyhedra on the (100) and (110) faces grew together to form a relatively continuous film. As mentioned above, this occurred much earlier on the (111) face. After 24 hr this continuous film on all three faces appeared to be etched, and the *p*H of the solution had dropped from 4.3 to approximately 3.5-3.7, depending on the

particular crystal face. Under these more acidic conditions the rate of dissolution of oxide was probably beginning to become more competitive with the rate of oxidation.

$Cu(OAc)_2$ *system.*—Figure 4 shows that in the acetate system a relatively smooth and continuous oxide film formed instead of polyhedra. Numerous immersion times, other than those shown, were studied and at no time from 30 sec to 48 hr was there any evidence of polyhedra formation on the (110) face. The films formed on the (111) face were also continuous and even smoother than those on the (110) face. On the (100) face the film was relatively smooth and continuous up to oxidation times of about 10 min, as shown by Fig. 5a. However, some very interesting results were observed when the (100) plane was oxidized for times from 10 min to 1 hr. As shown in Fig. 5b and c, well defined polyhedra formed in the acetate system under these conditions. By comparing Fig. 3c and 5c it can be seen that the density of oxide polyhedra after 1 hr in both systems was not significantly different. However, a comparison of Fig. 3a and Fig. 5a shows that there was a significant difference between the two systems after 5 min immersion. At first it was felt that these somewhat unexpected results were obtained because the (100) plane was held within 2° of the desired orientation rather than 1°. A close look at the standard sphere pattern in Fig. 1 revealed that there were more significant changes in oxide thickness in the region around the (100) face than there are in the (111) and (110) regions. After repeating the experiment several times with (100) faces within ½-1° of the proper orientation, polyhedra were still found, although their density and shape differed slightly from those formed on faces greater than 1° off of the (100) orientation. As a result all (100) planes were maintained within 1°.

Effect of annealing.—By comparing Fig. 6a and Fig. 2c, it can be seen that in the $CuSO_4$ system the growth of individual, regularly shaped oxide polyhedra was favored when the crystal was annealed in hydrogen at 500°C. Although the same general tendency to form polyhedra was observed in the case of unannealed crystals, the polyhedra became rounded and ran together to cover a greater fraction of the surface.

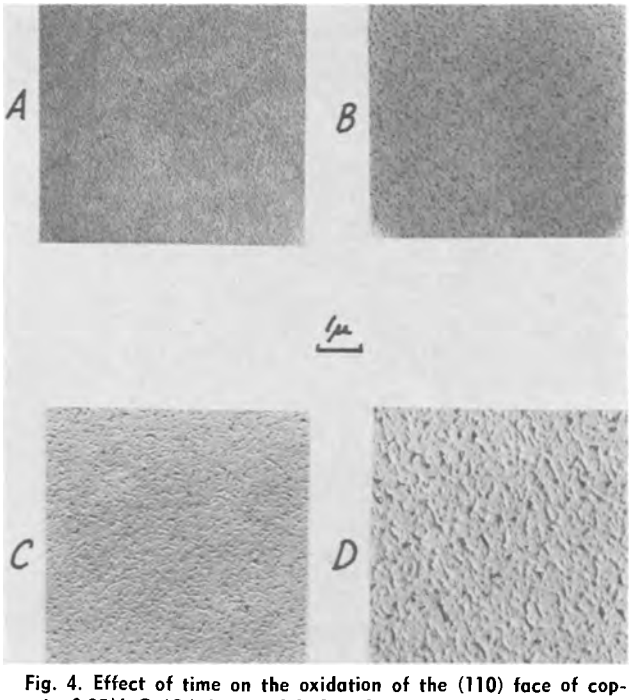

Fig. 4. Effect of time on the oxidation of the (110) face of copper in 0.05*N* $Cu(OAc)_2$ at 30.0°C, *p*H 4.3: a, 30 sec; b, 3 min; c, 5 min; d, 1 hr. Magnification 15000X before reduction for publication.

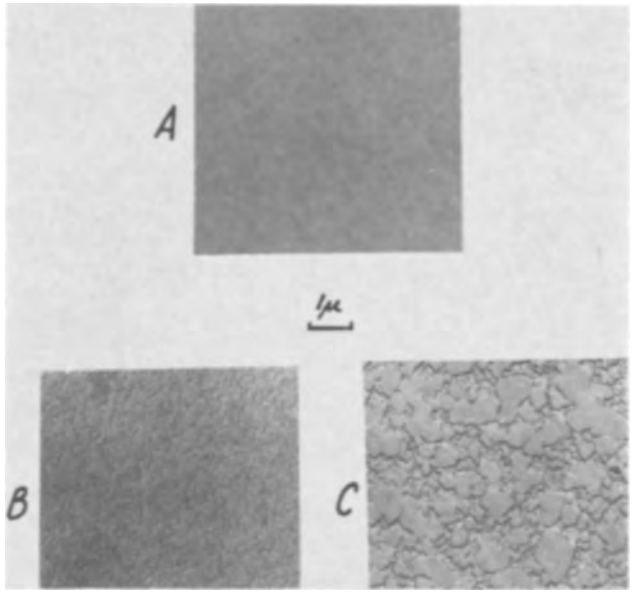

Fig. 5. Effect of time on the oxidation of the (100) face of copper after immersion in 0.05*N* $Cu(OAc)_2$ at 30.0°C, *p*H 4.3: a, 5 min; b, 15 min; c, 1 hr. Magnification 15000X before reduction for publication.

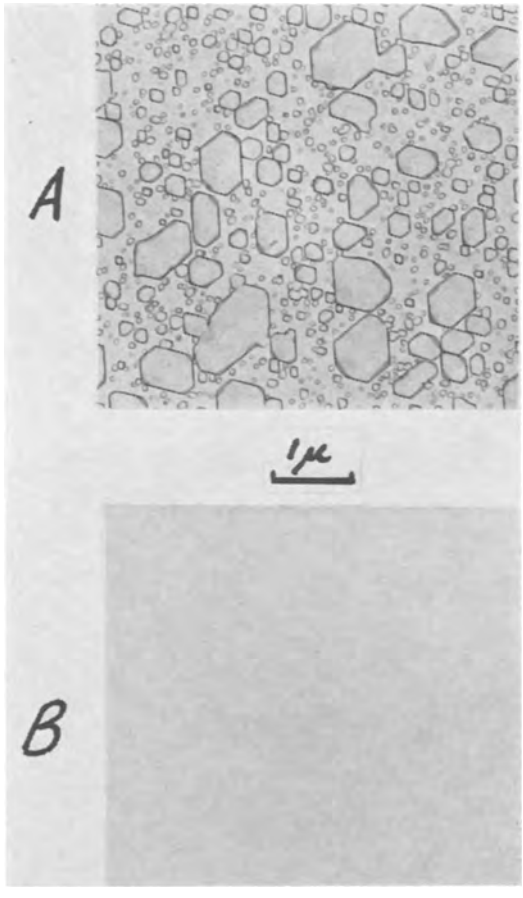

Fig. 6. Oxide formation on annealed (110) faces of copper; a, 5 min in 0.05*N* $CuSO_4$ at 30.0°C, initial *p*H 4.3; b, 5 min immersion in 0.05*N* $Cu(OAc)_2$ at 30°C, *p*H 4.3. Magnification 15000X before reduction for publication.

Figure 6b and Fig. 4c show that in the $Cu(OAc)_2$ system the oxide formed with both annealed and unannealed crystals was relatively smooth and continuous compared to that formed in the $CuSO_4$ system. The smoothness and continuity of the film was greatly enhanced when the crystal was annealed.

Additional experiments were run to determine whether the observed effect of annealing was due to changes in the nature of the metal surface when heated to 500°C or due to the differences in the initial thin oxide films formed on the annealed and unannealed crystals. With annealed surfaces, the initial oxide growth must form in the solution, while in the unannealed system any oxide formed in the solution would be expected to grow on top of a thin (20-30Å) air formed film. In this experiment, a (110) flat face was annealed in hydrogen at 500°C, removed from the annealing apparatus, exposed to the air at room temperature for several minutes, and then immersed in the desired solution. Electron microscopic examination showed that the oxide topography was very similar to that of an unannealed (110) flat exposed to the same solution. Thus, the main effect of annealing appears to lie in the difference between the initial thin films of oxide rather than the effect of heating the metal surface.

Since in both the $CuSO_4$ and the $Cu(OAc)_2$ systems the only apparent effect of annealing was to enhance the over-all type of behavior, *i.e.*, individual polyhedra formation in the sulfate system and smooth continuous films in the acetate system, it was decided to run the majority of experiments under unannealed conditions. Furthermore, since each annealed experiment was long and tedious, it was felt that this would allow a quicker and broader study of the variables affecting the two systems. Annealing experiments thus need only to be run later to check the results at the more important experimental conditions.

Epitaxy.—The epitaxial relationships of cuprous oxide crystals immersed in the $CuSO_4$ solutions have been reported previously by Lawless and Miller (22). In the present investigation electron diffraction studies showed that essentially the same epitaxial relationships were found when the oxide was formed in $Cu(OAc)_2$ solutions. Furthermore, the orientation relationships between the metal and cuprous oxide in the $CuSO_4$ and $Cu(OAc)_2$ systems were in general the same as those previously found for oxidation of copper in pure O_2 at room temperature and at high temperatures by Lawless and Gwathmey (23), and for oxidation of copper in pure water by Kruger (8-10) at room temperature.

Discussion

Since this is the second paper in a long range study of the variables affecting the oxidation of copper single crystals in aqueous salt solutions, it would be premature to engage in a detailed theoretical discussion until additional data have been obtained. It might be helpful, however, to summarize the questions that appear to be important and in some cases to indicate possible explanations.

The present study, as well as the previous study (16), indicated that the following questions must be considered:

1. What factors cause the rate of oxidation in $CuSO_4$ and $Cu(OAc)_2$ solutions to be significantly greater than that in both pure water and in air at room temperature?

2. Why are there differences in the relative thicknesses of the oxide formed on the various crystal faces of copper immersed in $CuSO_4$ and $Cu(OAc)_2$ solutions and what are these differences?

3. What mechanism can account for the formation of oxide polyhedra in the $CuSO_4$ system and the formation of relatively smooth, continuous films in the $Cu(OAc)_2$ system?

4. How can this mechanism also account for the formation of polyhedra on the (100) face in the $Cu(OAc)_2$ system?

5. Why does annealing the crystal in H_2 promote the formation of polyhedra in $CuSO_4$ and the formation of very smooth, continuous films in $Cu(OAc)_2$?

6. Is the anion present in the solution the primary variable controlling the nature of the oxide topography?

7. What is the source of the copper found in the Cu_2O film?

8. What is the source of the oxygen in the Cu_2O film?

9. What are the effects on the oxidation process of variables such as *p*H, dissolved oxygen concentration, temperature, and stirring?

10. What is the significance of the fact that the epitaxial relationships of the metal and oxide were the same for Cu_2O formed in air, pure water, $CuSO_4$, and $Cu(OAc)_2$ at room temperature?

Some discussion of questions 1, 3, and 7 for the $CuSO_4$ system has been given previously by Miller (11) and Miller and Lawless (16). The results of the present study, which included immersion times in $CuSO_4$ between those in the original study, gave a more detailed picture of the growth sequence of polyhedra as shown in Fig. 2. They show that the amount of exposed surface between the polyhedra increased as they grew larger, which suggested that the mechanism of polyhedra growth may involve a dissolution of small polyhedra at certain points. This, in turn, could indicate that changes in *p*H at the reaction surface could be one of the major factors in the formation of polyhedra. This is supported by the fact that the *p*H in $CuSO_4$ solutions decreases with time of oxidation while the *p*H in the $Cu(OAc)_2$ remains essentially constant. This constancy of *p*H would be expected in the $Cu(OAc)_2$ system, since the acetic acid added to adjust the initial *p*H to 4.3 would allow the solution to act as a buffer system. A detailed study of the effect of *p*H on oxidation in both systems is now being carried out in this laboratory. Ives and Rawson (24) have discussed the influence of *p*H on the appearance and dissolution of polyhedra and their ideas will be considered in a future paper devoted exclusively to the effect of *p*H.

A well supported explanation of the formation of smooth films as opposed to polyhedra as posed in question 3 does not appear to be possible at this time. Several factors which could be important are (*i*) localized surface changes in *p*H as mentioned above; (*ii*) formation of complex ions between the Cu (I) or Cu (II) ions and the anions in solution which could result in changes in diffusion rates of copper ions to the reaction surface; (*iii*) selective adsorption of cations, ion pairs, or other species at steps or other spots on the metal or oxide surface; or (*iv*) factors which would change the conductivity of the oxide.

It is very important to obtain the thickness measurements mentioned in question 2, before a meaningful interpretation of the topographical data presented in this paper can be made. It is anticipated that these results will be published in the near future. A comparison of approximate thicknesses of oxide formed on the (110) face of copper in various systems is shown in Table I. It can be seen from the table that oxidation in solutions of copper salts occurs at a much greater rate than that in water or pure oxygen gas at the same temperature. It should be noted that the value of 700-800Å reported for oxide thickness in $CuSO_4$ should be interpreted only as a measurement of total oxide and not of thickness, since Fig. 2c indicates that the surface contains oxide polyhedra

Table I. Relative thickness of Cu_2O formed on the (110) face of copper at room temperature

System	Approximate thickness, Å	Oxidation time	Reference
Pure water	25	5 min	(8), (9)
	80	8-80 min	(8), (9)
Pure, dry oxygen	100	Several months	(20)
0.05*N* $Cu(OAc)_2$	475 ± 50	5 min	(21)
0.05*N* $CuSO_4$	700-900	5 min	(21)

rather than a smooth, continuous film. Indeed, this study again emphasizes the importance of carrying out topographical studies along with rate studies, since it is necessary to assume the formation of a smooth, continuous film in order to get a meaningful rate equation from measurements of oxide thickness as a function of time.

In the earlier study (16) the importance of the reaction $Cu + Cu^{+2} = 2\ Cu^{+}$ was discussed. From a thermodynamic standpoint, it is highly probable that the over-all free energy change of the oxidation of copper metal in Cu(II) ion solutions results from the tendency of the system to approach the equilibrium represented by the above equation. The tendency of the *p*H to decrease towards 3.2 in the unbuffered $CuSO_4$ system along with the tendency of initial corrosion potentials on various crystal faces of copper to approach a limiting value in $CuSO_4$ solution (11, 12) indicate the importance of this reaction, as a possible driving force for the over-all process. The work of Jenkins and Bertocci (15) emphasized that true equilibrium for this reaction exists only in solutions which are free of dissolved oxygen, which have been pre-equilibrated with copper, and which exhibit a *p*H less than about 3.2. Of course, none of these conditions was met in the systems in the present study, since under these conditions oxide would not form on copper.

No explanation for the sudden appearance of polyhedra on the (100) face in the acetate system, as posed in question 4, can be offered at this time. Since oxide on the (100) plane can have four possible orientations while that on the (111) can have two and the (110) only one orientation (11, 22), more grain boundaries could be formed in the oxide on the (100) face. However, since this should affect the acetate and sulfate system in the same manner, this factor may not be the controlling one.

With respect to the effect of annealing, as raised in question 5, it is proposed that this is due primarily to the difference in the nature of the thin base films formed in the two systems. When the unannealed crystal is washed in water and exposed to the air prior to immersion, a thin film of the order of 10Å probably forms immediately. This film then grows fairly rapidly to a thickness of about 30-50Å. In this process the individual crystals in the film possibly have time to obtain a more uniform state of perfection and to patch up any weak spots. On the other hand, with annealed crystals the 30Å initial film forms very rapidly in the electrolyte solution. As a result, the crystals in this film might be expected to vary widely in their degree of perfection. This could promote the growth of individual polyhedra by the mechanism proposed earlier (16). Another explanation of this annealing effect could involve the influence of temperatures on the metal surface. Impurities might diffuse to the metal surface from the interior of the crystal or trace impurities could be left on the surface by reduction when the thin film of cuprous oxide is reduced by hydrogen. These impurities could promote or retard oxide growth at specific reaction sites. The experiments described earlier in this paper indicated that this effect is not the controlling factor.

With respect to question 6, the results of this study certainly indicate that by varying the anion the nature of the oxide can be controlled and perhaps in this way the degree of corrosion protection afforded by the oxide film can be controlled. However, since the *p*H remains constant in one system and varies in the other, this conclusion is not certain. Further study of the effect of anions on oxide topography is being carried out by exposing copper crystals to solutions of copper (II) formate and copper (II) perchlorate. Due to similarities in anions it is hypothesized that the oxide formed in $Cu(OAc)_2$ solution would be similar to that formed in $Cu(CHO_2)_2$ solution, while that formed in $Cu(ClO_4)_2$ would be similar to the oxide formed in $CuSO_4$ solutions.

There appear to be three possible sources for the oxygen in the Cu_2O, as posed in question 7: dissolved O_2 oxygen obtained from the sulfate on acetate radical, or oxygen from the H_2O. Since the reaction is so rapid in copper salt solutions as opposed to pure water, it appears to be improbable that dissolved oxygen is the source. It also seems unlikely that the oxygen would come from the breakdown of the sulfate or acetate radicals, although there is little information available in the literature on this matter. To check this possibility, it was decided to oxidize a sphere in a solution of copper (II) tetrafluoroborate, $Cu(BF_4)_2$, which contains an anion with no available oxygen. Results obtained showed that an oxide pattern did form in the solution of $Cu(BF_4)_2$ and thus it appears that the anion is at least not the primary source of oxygen. The most likely source of oxygen appears to be H_2O. Several equations for possible reactions involving water were given in the previous article (16). Experiments planned for the future include oxidizing a copper crystal respectively in a solution made by dissolving $Cu(OAc)_2$ in O^{18} labelled water and in a solution prepared from normal water and O^{18} labelled $Cu(OAc)_2$. The oxide formed could then be reduced in H_2 in a closed vessel and the water formed could then be analyzed for the presence of O^{18} with a mass spectrograph. In this manner information on the source of oxygen in the oxide could be obtained.

With respect to the variables indicated in question 9, the effect of *p*H is presently under study and the other variables are to be studied in the future.

Finally, the most important observation that can be made about the epitaxial relationships found in this study is that they are the same regardless of whether to Cu_2O is formed in gaseous O_2 at temperatures from 100° to 900°C (23), in pure water at room temperature (8), or in solutions of $CuSO_4$ or $Cu(OAc)_2$ at room temperature. This indicates that one fundamental factor was determining these relationships and that epitaxy may be more fundamental than was thought. These ideas are discussed in greater detail by Lawless and Gwathmey (23) and Lawless and Miller (22).

Summary

1. A more detailed picture of the growth sequence of the formation of Cu_2O polyhedra on the (110), (100), and (111) faces of copper in $CuSO_4$ solution was obtained. The exposed surface between the polyhedra increased as the polyhedra grew larger. This indicated that the mechanism of polyhedra growth may involve dissolution of small polyhedra at certain points.

2. Under the same conditions in $Cu(OAc)_2$ solutions relatively smooth and continuous films of Cu_2O rather than polyhedra were observed on the (110) and (111) faces, while polyhedra were observed on the (100) face.

3. During oxidation the *p*H of the $CuSO_4$ solution dropped from its initial value of 4.3 to 3.5-3.7 for immersion times greater than 1 hr, while the *p*H of the $Cu(OAc)_2$ solutions remained essentially constant throughout the reaction.

4. Annealing of the metal surfaces in H_2 at 500°C prior to immersion into the electrolyte solution enhanced the formation of individual polyhedra in the $CuSO_4$ system and the formation of smooth, continuous films in $Cu(OAc)_2$ solutions. This apparently resulted from the differences in the initial thin oxide films formed on the annealed and unannealed metal surfaces.

5. The epitaxial relationships of the metal and oxide were the same in both the $CuSO_4$ and $Cu(OAc)_2$ systems, and this relationship was the same as that found in other studies of Cu_2O formed on copper in

gaseous O_2 at high temperatures and in pure water at 25°C.

Acknowledgments

The authors are deeply indebted to the late Dr. Allan T. Gwathmey of Cobb Chemical Laboratory, University of Virginia, and to Dr. K. R. Lawless, Department of Materials Science, University of Virginia, for their encouragement and helpful discussions, as well as for the use of the electron microscope and the x-ray and electron diffraction apparatus at the University of Virginia. We would also like to thank Mr. R. W. Topham for his aid in carrying out some of these experiments and Mrs. C. E. Guthrow for her help in preparation of the manuscript. This research was supported in part by grants from the Research Corporation, Sigma Xi, Hampden-Sydney College, the National Science Foundation Undergraduate Science Education Program, and PHS Research Grant DE-01893-01, National Institute of Dental Research, Public Health Service.

Manuscript received Aug. 4, 1965; revised manuscript received Dec. 14, 1965.

Any discussion of this paper will appear in a Discussion Section to be published in the December 1966 JOURNAL.

REFERENCES

1. A. T. Gwathmey and A. F. Benton, *J. Phys. Chem.*, **46**, 969 (1942).
2. E. Leidheiser and A. T. Gwathmey, *Trans. Electrochem. Soc.*, **91**, 97 (1947).
3. A. T. Gwathmey and F. W. Young, *Rev. met.*, **48**, No. 6, 434 (1951).
4. A. T. Gwathmey, *Record Chem. Progress*, **14**, No. 3, 117 (1953).
5. R. E. Cunningham and A. T. Gwathmey, *J. Am. Chem. Soc.*, **76**, 391 (1954).
6. F. W. Young, Jr., J. V. Cathcart, and A. T. Gwathmey, *Acta Met.*, **4**, 145 (1956).
7. A. T. Gwathmey and K. R. Lawless in "The Surface Chemistry of Metals and Semiconductors," H. C. Gatos, Editor, p. 483, John Wiley & Sons, Inc., New York (1960).
8. Jerome Kruger, *This Journal*, **106**, 847 (1959).
9. Jerome Kruger, *ibid.*, **108**, 503 (1961).
10. Jerome Kruger and J. P. Calvert, *ibid.*, **111**, 1038 (1964).
11. G. T. Miller, Jr., Dissertation, Ph.D., University of Virginia (1958).
12. W. E. Tragert and W. D. Robertson, *This Journal*, **102**, 86 (1955).
13. R. Piontelli, *et al.*, *Inst. Lombardo Rend. Sci.*, **91**, 355 (1957).
14. L. H. Jenkins and J. O. Stiegler, *This Journal*, **109**, 467 (1962).
15. L. H. Jenkins and U. Bertocci, *ibid.*, **112**, 517 (1965).
16. G. T. Miller, Jr., and K. R. Lawless, *ibid.*, **106**, 854 (1959).
17. R. M. Kassis and G. T. Miller, Jr., Unpublished results, University of Virginia (1960).
18. L. L. Shreir and J. W. Smith, *This Journal*, **98**, 193 (1951).
19. M. J. N. Pourbaix, "Thermodynamics of Dilute Aqueous Solutions," Edward Arnold and Co., London (1949).
20. K. R. Lawless, Unpublished results, University of Virginia.
21. G. T. Miller, Jr., Unpublished results, Hampden-Sydney College.
22. K. R. Lawless and G. T. Miller, Jr., *Acta Cryst.*, **12**, 594 (1959.)
23. K. R. Lawless and A. T. Gwathmey, *Acta Met.*, **4**, 153 (1956).
24. D. J. G. Ives and A. E. Rawson, *This Journal*, **109**, 458 (1962).

Oxidation of Copper Single Crystals in Aqueous Solutions of Inorganic Salts

II. Topography of Oxide Formed in $Cu(ClO_4)_2$ and $Cu(CHO_2)_2$ Solutions

R. W. Topham[1] and G. Tyler Miller, Jr.[2]

Department of Chemistry, Hampden-Sydney College, Hampden-Sydney, Virginia

ABSTRACT

Electron microscopic examination was made of the topography of Cu_2O formed on the (100), (110), and (111) faces of copper single crystals immersed for varying times in aqueous solutions of $Cu(ClO_4)_2$ and $Cu(CHO_2)_2$. A previous study indicated the importance of the anion on topography in that Cu_2O polyhedra formed on copper oxidized in $CuSO_4$ solutions, while in $Cu(OAc)_2$ solutions relatively smooth, continuous films of Cu_2O formed on the (110) and (111) faces and polyhedra were observed on the (100) face. It was hypothesized that due to similarities in the anions that the oxide formed in copper(II) formate solutions would be similar to that formed in copper(II) acetate solutions and that oxide formed in copper(II) perchlorate solutions would be similar to that formed in copper(II) sulfate solutions. In general, the present study has substantiated this hypothesis.

This is a continuation of a long range study of the growth of oxide on copper single crystal surfaces exposed to aqueous solutions of inorganic salts. The preceding paper (1) indicated that the anion present in solutions containing copper(II) ions could greatly influence the topography formed on copper surfaces. Specifically, it was found that oxide polyhedra formed on copper surfaces exposed to $CuSO_4$ solutions, while relatively smooth and continuous films formed in $Cu(OAc)_2$ solutions on the (110) and (111) faces and polyhedra formed on the (100) face.

Since control of the nature and thickness of the oxide film by varying the anion could significantly vary the degree of corrosion protection afforded by an oxide film, it was desirable to investigate the influence of other anions. If the anion is the primary variable causing the different types of oxide growth, then it was reasoned that because of the similarities in anions, that the topography of the oxide formed in copper(II) formate solutions would be similar to that formed in copper(II) acetate solutions and likewise, that the oxide formed in copper(II) perchlorate solutions would resemble that in copper(II) sulfate

[1] Present address: Department of Biochemistry, Cornell University, Ithaca, New York.
[2] Present address: Department of Chemistry, St. Andrews Presbyterian College, Laurinburg, North Carolina.

solutions. The present study was undertaken to support this hypothesis.

Experimental Procedure

Known crystallographic faces of carefully prepared copper single crystals were exposed to 0.05*N* solutions of $Cu(CHO_2)_2$ and $Cu(ClO_4)_2$ maintained at 30° ± 0.05°C, and at an initial *p*H of 4.30 ± 0.02. With the exceptions given below, all procedures were the same as those used in the previous study (1).

Copper(II) formate was prepared by the reaction of basic copper(II) carbonate and 50% aqueous formic acid. The reaction was carried out at 75°C for ½ hr and the copper(II) formate obtained was doubly recrystallized and dehydrated. The *p*H of copper(II) formate solutions was adjusted to 4.3 by addition of reagent grade formic acid. The copper(II) perchlorate was prepared in a similar manner by reacting basic copper(II) carbonate with 70% aqueous perchloric acid for an hour at 75°C. After allowing the reaction mixture to stand for several days the salt was doubly recrystallized and used in the pentahydrated form.

The washing procedure for the copper crystals after electropolishing was varied slightly from the previous study as follows:

1. Immediately after removal from the electropolishing bath crystals were washed for 1 min in demineralized water with a specific resistivity of at least 1.2 million ohms. This water was obtained from a D-ion Master demineralizer, Model No. 8120.
2. This was followed by washing in a rapidly stirred 10% by volume H_3PO_4 for 1 min.
3. The crystal was then re-washed in the demineralized water for 3 min.
4. Finally, the crystal was washed in distilled water[2] with a resistivity of approximately 1.4 million ohms for 2 min.

Experimental Results

As expected, reflection electron diffraction showed that the oxide formed in the present study was Cu_2O. The initial *p*H of 4.3 was maintained during oxidation in the copper(II) formate solutions but in the copper(II) perchlorate solutions it dropped to approximately 3.5 after immersion for 1 hr. These *p*H effects were essentially the same as those found respectively in the $CuSO_4$ and $Cu(OAc)_2$ solutions.

[2] The distilled water was obtained by using a Consolidated Still, Model CSA-NP-X2.

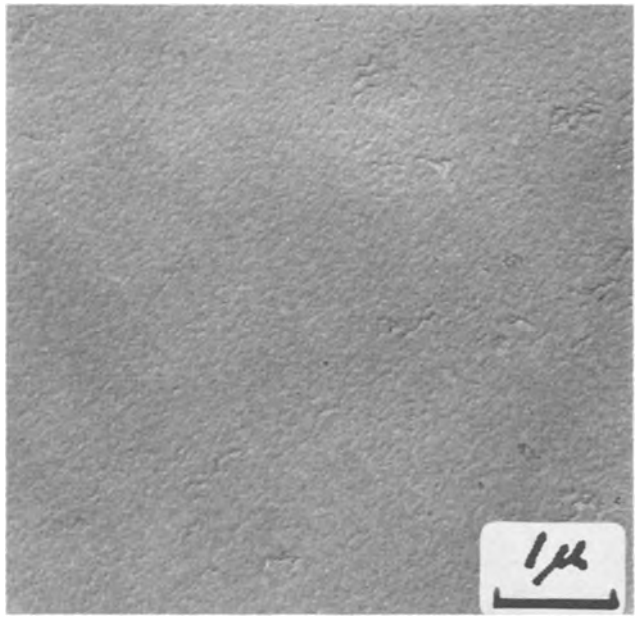

Fig. 2. Oxidation of the (110) face of copper in 0.05*N* $Cu(CHO_2)_2$ at 30.0°C for 5 min. Initial *p*H 4.3. Magnification 15000X before reduction for publication.

Figures 1 and 2 show a general comparison of the topography of the oxide formed on the (110) face in $Cu(ClO_4)_2$ and $Cu(CHO_2)_2$ solutions after 5 min of oxidation. By comparing Fig. 1 and 2, respectively, with Fig. 2c and 4c in ref. (1) it can be seen that polyhedra form in the sulfate and perchlorate systems, while smooth films form in the acetate and formate systems. These pictures along with others taken at immersion times varying from 30 sec to 24 hr show that the film formed in the formate system is normally even smoother than that in the acetate and the polyhedra formed in the perchlorate solutions grow together to a much greater extent than those formed in the sulfate solutions. Results indicated that in $CuSO_4$ solutions the oxide polyhedra require several hours to grow together to cover the entire surface,

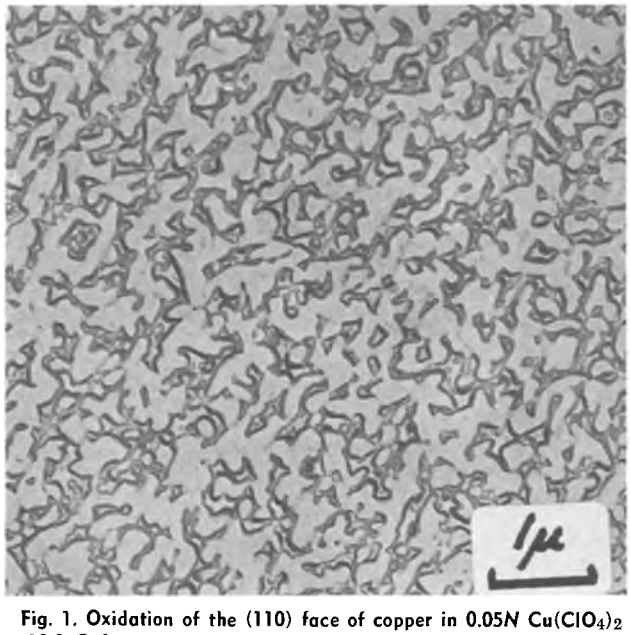

Fig. 1. Oxidation of the (110) face of copper in 0.05*N* $Cu(ClO_4)_2$ at 30.0°C for 5 min. Initial *p*H 4.3. Magnification 15000X before reduction for publication.

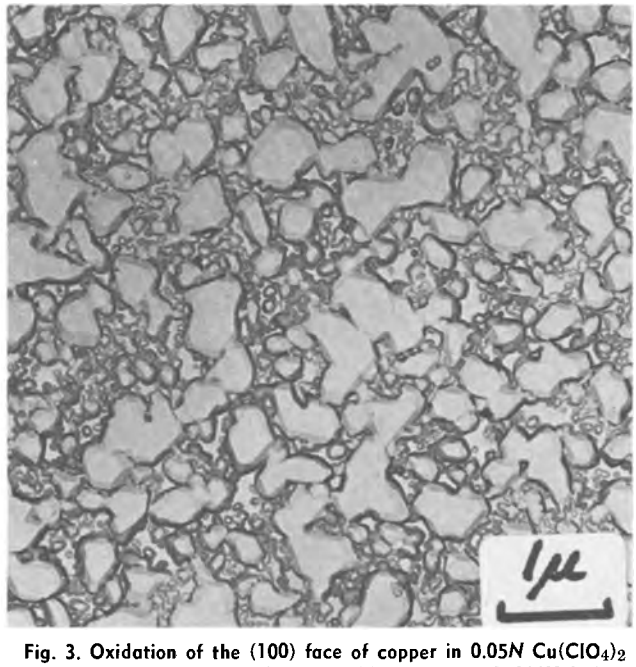

Fig. 3. Oxidation of the (100) face of copper in 0.05*N* $Cu(ClO_4)_2$ at 30.0°C for 10 min. Initial *p*H 4.3. Magnification 15000X before reduction for publication.

while this happens in the $Cu(ClO_4)_2$ system within 1 hr. This indicates that in the $Cu(ClO_4)_2$ solutions the oxide must grow much more rapidly, at least in a lateral direction, so as to cover more of the surface.

The (111) face in both $Cu(ClO_4)_2$ and $Cu(CHO_2)_2$ solutions showed oxide growths similar to those found respectively in the sulfate and acetate systems. A comparison of Fig. 3 with Fig. 3a of ref. (1) shows that the (100) face oxidized in perchlorate showed polyhedra similar to that in the sulfate system. Again the oxide in perchlorate were more run together than those in sulfate solutions. It was shown in the previous study (1) that the oxide formed on the (100) face in acetate solution was continuous up to about 10 min but for immersion times from 10 min to 1 hr polyhedra were observed. A comparison of Fig. 4 in this paper with Fig. 5b in ref. (1) shows that this phenomenon was also observed in the formate system.

Discussion

It would appear that the results of the present study when combined with those in the previous study support the conclusion that the anion can greatly affect the nature of the oxide formed on copper surfaces and that similar anions cause similar oxide growths. However, as mentioned in the earlier paper this conclusion has not necessarily been substantiated. It will be recalled that the bulk *p*H drops in the sulfate and perchlorate systems but remains essentially constant in the buffered acetate and formate systems. It is possible that a major variable or perhaps even the controlling variable could be changes in *p*H at the reaction surface. For example, selective dissolving at weak points in an oxide film could cause the formation of polyhedra of oxide. In order to check this possibility a detailed study of the effect of *p*H is now being carried out in this laboratory.

The present study raises two additional questions.

1. Why is the oxide formed in solutions of copper(II) formate normally smoother than that formed in copper(II) acetate solutions?

2. Why do oxide polyhedra formed in copper(II) perchlorate solutions apparently grow laterally at a faster rate than those formed in copper(II) sulfate solutions?

One possible factor that could influence the formation of continuous films as opposed to polyhedra lies in the nature of the complex species present in the electrolyte solutions. The copper(II) ion in solutions of $CuSO_4$ and $Cu(ClO_4)_2$ would exist predominantly as $Cu(H_2O)_4^{++}$ and the perchlorate and sulfate ions would exist in a noncomplexed form. In concentrated solutions of $Cu(OAc)_2$ and $Cu(CHO_2)_2$ the complex species present are quite different, as shown by Yamada, Nakamura, and Tsuchida (2). In concentrated copper(II) formate solutions there are infinite chains of composition $Cu(CHO_2)_2 \cdot 2H_2O$ joined together by hydrogen bonding through the two water molecules and in concentrated copper(II) acetate solutions there are binuclear complexes of the form $Cu_2(CH_3COO)_4 \cdot 2H_2O$. Of course, these are the monodisperse species only in concentrated solutions; in the relatively dilute solutions used in the present study they would exist in much lower concentrations along with $Cu(H_2O)_4^{++} \cdot C_2H_3O_2^-$, and CHO_2^- ions.

If these formate and acetate complexes with copper were present in sufficient number, they could be more easily adsorbed than the $Cu(H_2O)_4^{++}$ at local charge sites in the thin initial film of Cu_2O. Using Pearson's terms (3) in which "hard" acids are relatively resistant to polarization and "soft" acids are relatively easy to polarize, one would expect the formate and acetate complexes to be fairly "soft" compared to the square planar $Cu(H_2O)_4^{++}$ ion. Thus, these "softer" or more polarizable species could be more readily adsorbed. If they were adsorbed more readily, they would provide a larger number of nucleation sites for further oxide growth than the adsorbed $Cu(H_2O)_4^{++}$ and could thus account for the growth of a fairly smooth, continuous oxide film.

Another explanation could lie in the selective adsorption of the anions as opposed to the metal complex ions. The softer acetate and formate ions could be more easily polarized and adsorbed on the initial thin oxide film. The adsorbed anions could then attract $Cu(H_2O)_4^{++}$. Again, if the acetate and formate ions were more readily adsorbed they would provide a much larger number of reaction sites and could account for continuous films.

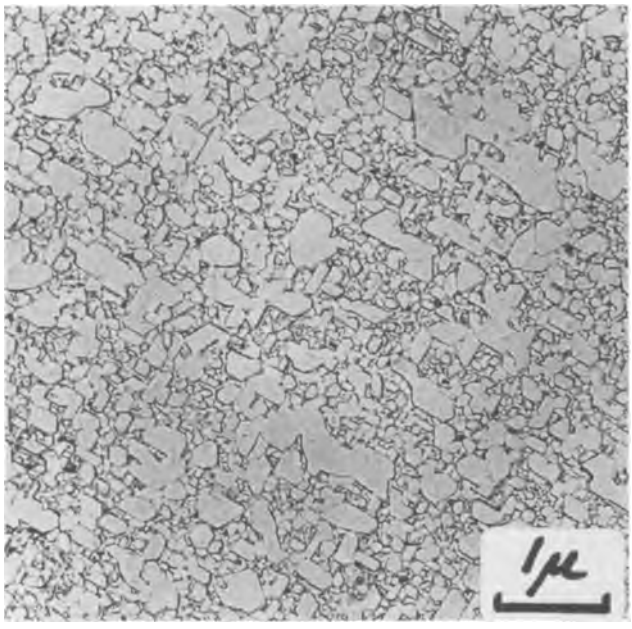

Fig. 4. Oxidation of the (100) face of copper in 0.05*N* $Cu(CHO_2)_2$ at 30.0°C for 10 min. Initial *p*H 4.3. Magnification 15000X before reduction for publication.

Summary

1. Oxide formed in $Cu(ClO_4)_2$ solutions on copper single crystals is generally in the form of polyhedra of Cu_2O.

2. The polyhedra are similar to those found in a previous study using $CuSO_4$ solutions except that they appear to grow together laterally at a faster rate in the $Cu(ClO_4)_2$ solutions.

3. Oxide formed in $Cu(CHO_2)_2$ solutions on the (110) and (111) faces copper single crystals is generally in the form of a smooth continuous film.

4. These continuous films are similar to those found in a previous study using $Cu(OAc)_2$ solutions except that they are even smoother than those formed in $Cu(OAc)_2$ solutions.

5. Oxide polyhedra formed on the (100) face of copper in solutions of $Cu(CHO_2)_2$. This behavior is similar to that found in the previous study for the (100) face exposed to $Cu(OAc)_2$ solutions.

6. During oxidation the *p*H of the $Cu(ClO_4)_2$ solution dropped from its initial value of 4.3 to approximately 3.5 after immersion for 1 hr, while the *p*H of the $Cu(CHO_2)_2$ solutions remained essentially constant throughout the reaction.

Acknowledgments

The authors wish to thank Dr. W. W. Porterfield for aid pertaining to this work and to thank Dr. K. R. Lawless of the Department of Materials Science at the University of Virginia for the use of their electron microscope. This research was supported by a grant from the National Science Foundation Undergraduate Science Education Program and by PHS Research Grant DE-01893-02, National Institute of Dental Research, Public Health Service.

Manuscript received Aug. 4, 1965; revised manuscript received Dec. 14, 1965.

Any discussion of this paper will appear in a Discussion Section to be published in the December 1966 JOURNAL.

REFERENCES

1. C. E. Guthrom, Jr. and G. T. Miller, Jr., *This Journal*, **113**, 4415 (1966).
2. S. Yamada, H. Nakamura, and R. Tsuchdida, *Bull. Chem. Soc., Japan*, **30**, 953 (1957).
3. R. G. Pearson, *J. Am. Chem. Soc.*, **85**, 3533 (1963).

Deposition Modes of Cobalt from Sulfate-Chloride Solutions

R. Sard, C. D. Schwartz,[1] and R. Weil

Department of Metallurgy, Stevens Institute of Technology, Hoboken, New Jersey

ABSTRACT

The as-plated surfaces of cobalt electrodeposits obtained using various combinations of the common plating variables as well as some thinned foils of these samples were studied. The basal plane was found to be predominantly perpendicular to the substrate leading to $<11\bar{2}0>$ and $<10\bar{1}0>$ fiber axes. Structural features associated with each fiber axis are explained in terms of crystal symmetry and twinning. Using the concepts of free and inhibited outgrowth it was not possible to predict the structure resulting from plating under a given set of variables. The cubic phase of cobalt was observed after deposition at room temperature and low *p*H.

Electrodeposited cobalt has been a topic for research during the past half-century because of its magnetic properties, its similarities to nickel, and its salient crystallographic features. The allotropic transformation in cobalt and the report by Kersten (1) that the high temperature face-centered-cubic phase is present at room temperature under certain conditions of electrodeposition has been of particular interest to investigators. A group at the Institute of Physical Chemistry of Bulgaria (2-4) has been concerned with the effect of certain plating parameters on the occurrence of the cubic phase at room temperature. Their studies consisted of Debye-Scherrer x-ray analyses. From the relative intensities of various diffraction lines they were also able to draw some conclusions about preferred orientation. Other investigators who used x-ray techniques to study growth textures in relation to magnetic properties, were Polukarov (5) and Quinn and Croll (6). Polukarov also studied the surface microstructure of a few samples with replicas. Brenner, Couch, and Williams (7) worked with cobalt deposits from chloride baths and noted the effect of phosphorous content and heat-treatment on the microstructure of optically viewed cross sections and on several other properties.

Finch, Wilman, and Yang (8) studied the orientation of a number of electrodeposited metals, among them cobalt, by electron diffraction. They reported that cobalt has a $<11\bar{2}0>$ fiber axis in the hexagonal form and a $<110>$ orientation in f.c.c. form. Random deposits were also observed. The first attempt to relate orientation to structural type was made by Weil (9). He related the types of surface structures that could be expected under certain plating conditions with the fiber axes as determined by electron diffraction. The structure of cobalt electrodeposited on single-crystal substrates has been the subject of recent work by Cliffe and Farr (10) and also by Goddard and Wright (11).

None of the investigations to date were comprehensive and systematic studies of the effect of the various plating parameters on the structure of cobalt. The present investigation was undertaken to survey the orientation types which can exist in cobalt electrodeposits plated under various combinations of *p*H, current density, temperature, and concentrations of the negative ions of two cobalt salts. This study consisted of a determination of the orientations of various deposits in a way similar to that used by Banerjee and Goswami (12) in their work with nickel, as well as electron-microscopic examinations of replicas of all the surfaces and a number of thin films in order to relate texture and microstructure.

[1] Present address: Central Research Laboratory, Air Reduction Corporation, Murray Hill, New Jersey.

Experimental Procedure

Four plating solutions were prepared from analytically pure chemicals to determine the effects of the important deposition variables, namely *p*H, current density, bath temperature, and composition. The compositions of the solutions, all of which had the same cobaltous ion concentration, 1.25 moles/liter, are given in Table I. The solutions were purified as described by Weil (9).

Initially, the starting cathodes were electropolished copper sheet. Subsequently, some experiments were repeated using cobalt starting cathodes to determine the possible effect of the substrate, to check on reproducibility, and to make it easier to thin the deposits electrolytically for transmission electron microscopy. The starting-cathode sheets were inserted in a plastic frame which exposed an area of 0.4 dm^2 to the plating solution. The cathodes were weighed before and after deposition. The thicknesses of the deposits were calculated from their weights and were about 50μ in all instances. Bagged cobalt anodes were used, and the solutions were not stirred.

Deposition was performed in each of the four plating baths at *p*H values of 2.0, 3.5, and 5.0. The *p*H was adjusted by addition of either H_2SO_4, HCl, or the appropriate mixtures to maintain the existing ratio of sulfate to chloride ions. The plating baths were operated at both room temperature and 60° ± 3°C. At room temperature and at each of the three *p*H values in each of the four baths, deposition took place at current densities of 0.1, 0.5, 2.5, and 5.0 amp/dm^2. The deposits obtained at 0.1 amp/dm^2 and 60°C were not coherent and therefore not studied further. Thus a total of 84 different plating conditions were em-

Table I. Bath compositions*

Bath	Moles/liter $CoSO_4 \times 7H_2O$	Moles/liter $CoCl_2 \times 6H_2O$	Molar ratio
A	0	1.25	All chloride
B	0.625	0.625	1:1
C	1.136	0.114	10:1
D	1.25	0	All sulfate

* All baths also contained 30g/liter H_3BO_3 and 0.15g/liter sodium lauryl sulfate.

ployed. In addition, several samples were deposited in an all-sulfate bath at room temperature with the pH lowered to between 1.0 and 1.5 for the purpose of obtaining deposits with relatively large amounts of face-centered-cubic material.

The crystallographic orientations of the deposits were determined by several methods. The relative intensities of the lines from the various diffracting planes parallel to the surfaces of the deposits were measured by using a diffractometer and Geiger-counter assembly in a G.E. X-Ray Diffraction Unit with cobalt $K\alpha$ radiation. The fiber axes were also determined by glancing a Mo $K\alpha$ incident beam normal to the surface in the manner described by Taylor (13), as well as by reflection electron diffraction.

The microstructures of the as-plated surfaces of all deposits were studied by electron microscopy using carbon replicas. The deposits plated on cobalt substrates were stripped and thinned by covering the deposit with acid-resistant adhesive tape and electropolishing in a stirred solution of 860 cc H_3PO_4, 51 cc H_2SO_4, and 100g CrO_3 at 30-35v and 2-4 amp/cm^2 at about 10°C. The thinned foils were examined by transmission electron microscopy and selected-area diffraction in an Hitachi HU-11 Electron Microscope operated at 100 kv.

Results

The diffraction patterns, which were obtained from the as-plated deposits, could be classified into four types. In all of them the basal plane {0001}, which in the hexagonal system is the most densily packed one, was predominantly perpendicular to the cathode. The most frequently observed pattern also had the most closely packed direction, $<11\bar{2}0>$ as the fiber axis. Occasionally, a $<10\bar{1}0>$ fiber axis occurred. Sometimes a doubly fibered deposit consisting of both $<11\bar{2}0>$ and $<1010>$ textures was observed. A diffraction pattern in which the intensity of each Debye ring had azimuthal symmetry was also observed. In this pattern, however, all reflections from planes of the type {0002}, {0004}, etc. were either absent or quite weak, consequently this type of orientation has been termed pseudo-random. Table II lists the type of fiber axis which was obtained under the various plating conditions. The relative strengths of the fiber axes are also indicated and will be discussed later.

The electron-microscopic examination of the replicas from the as-plated deposit surfaces showed that there were distinct structural features associated with each of the four types of fiber axes. Thus for each set of plating conditions listed in Table II, which produced a given type of orientation, there were certain distinctive features observed. A relatively coarse structure with a layered or faceted morphology represented by Fig. 1a was found to occur in samples plated at 60°C and which had a strong $<11\bar{2}0>$ fiber axis. In some areas the facets were arranged so as to produce pyramidal shapes. The strong $<11\bar{2}0>$ texture in deposits obtained at room temperature, was characterized by smaller, though more readily recognizable pyramids as shown in Fig. 1b. These pyramids generally possessed either four or five sides and usually had fine structure on their faces. The weaker $<11\bar{2}0>$ texture was associated with pyramids with more rounded sides as shown in Fig. 1c. Samples having the $<10\bar{1}0>$ fiber axis and the pseudo-random orientation frequently exhibited acicular or ridge-like shapes on their surfaces. Figure 1d is representative of the $<10\bar{1}0>$ texture. The pseudo-random orientation was observed in deposits that ranged from coarse ridges as seen in Fig. 1e, to the finer structures of Fig. 1f. It can be seen that the ridges were generally symmetric about a plane which was perpendicular to the surface and ran parallel to their long direction. The mixed structure with $<11\bar{2}0>$ and $<10\bar{1}0>$ fiber axes showed both pyramids and ridges. In addition to the aforementioned variation with temperature, it was found that the structural features, in general, became smaller and less distinct with decreasing pH or current density.

In order to elucidate further the structural features associated with the various orientations, transmission electron-microscopic studies of thin foils were conducted. The pyramids were found not to be a single crystal, but to consist of several sections which were in a twin relationship to each other. Figure 2 illustrates this phenomenon for a five-sided pyramid. In each section there are closely spaced parallel lines, which were observed in all deposits and represent the intersection of the basal plane {0001} with the plane of the foil. In Fig. 2, {0001} planes are perpendicular to the surface of the foil in each section. The $<0001>$ directions which therefore lie in the plane of the foil are indicated in Fig. 2. The electron diffraction patterns upon which the crystallographic observations were based, also showed streaking in the $<0001>$ direction, that is perpendicular to the fine

Table II. Fiber axes

Plating conditions	Room temperature Bath A	Bath B	Bath C	Bath D	60°C Bath A	Bath B	Bath C	Bath D
5.0 amp/dm^2 pH 2.0	* 'R'	$<11\bar{2}0>$ M	*$<11\bar{2}0>$ M	$<11\bar{2}0>$ M	$<11\bar{2}0>$ M	$<11\bar{2}0>$ W	'R'	'R'
2.5 amp/dm^2 pH 2.0	* 'R'	'R'	*$<11\bar{2}0>$ M	$<11\bar{2}0>$ M	$<11\bar{2}0>$ M	$<11\bar{2}0>$ S	'R'	$<11\bar{2}0>$ W
0.5 amp/dm^2 pH 2.0	'R'	* 'R'	*$<11\bar{2}0>$ M	$<11\bar{2}0>$ M	$<11\bar{2}0>$ VS	$<11\bar{2}0>$ VS	'R'	$<11\bar{2}0>$ M
0.1 amp/dm^2 pH 2.0	'R'	* 'R'	*$<11\bar{2}0>$ W	$<11\bar{2}0>$ M	—	—	—	—
5.0 amp/dm^2 pH 3.5	'R'	$<11\bar{2}0>$ S + $<10\bar{1}0>$ W	$<11\bar{2}0>$ M	$<11\bar{2}0>$ S	$<11\bar{2}0>$ S + $<10\bar{1}0>$ W	$<11\bar{2}0>$ S + $<10\bar{1}0>$ S	'R'	$<10\bar{1}0>$ M
2.5 amp/dm^2 pH 3.5	'R'	'R'	$<11\bar{2}0>$ M	$>11\bar{2}0>$ S	$<11\bar{2}0>$ S	$<11\bar{2}0>$ S	'R'	$<10\bar{1}0>$ M
0.5 amp/dm^2 pH 3.5	'R'	'R'	$<11\bar{2}0>$ M	$<11\bar{2}0>$ S	$<11\bar{2}0>$ VS	$<11\bar{2}0>$ VS	'R'	$<11\bar{2}0>$ S
0.1 amp/dm^2 pH 3.5	$<11\bar{2}0>$ S	$<11\bar{2}0>$ S + $<10\bar{1}0>$ S	'R'	'R'	—	—	—	—
5.0 amp/dm^2 pH 5.0	'R'	'R'	$<11\bar{2}0>$ S	'R'	$<11\bar{2}0>$ S	$<11\bar{2}0>$ VS	$<11\bar{2}0>$ VS	$<10\bar{1}0>$ S
2.5 amp/dm^2 pH 5.0	'R'	'R'	$<11\bar{2}0>$ S	'R'	$<11\bar{2}0>$ S	$<11\bar{2}0>$ S	$<11\bar{2}0>$ S	$<10\bar{1}0>$ M
0.5 amp/dm^2 pH 5.0	'R'	$<11\bar{2}0>$ S	'R'	'R'	$<11\bar{2}0>$ VS	$<11\bar{2}0>$ VS	$<11\bar{2}0>$ M	$<11\bar{2}0>$ W
0.1 amp/dm^2 pH 5.0	$<11\bar{2}0>$ S	$<11\bar{2}0>$ S	$<10\bar{1}0>$ W	$<10\bar{1}0>$ S	—	—	—	—

* Showed {200} cubic line. VS, very strong; S, strong; M, medium; W, weak; 'R', pseudo-random.

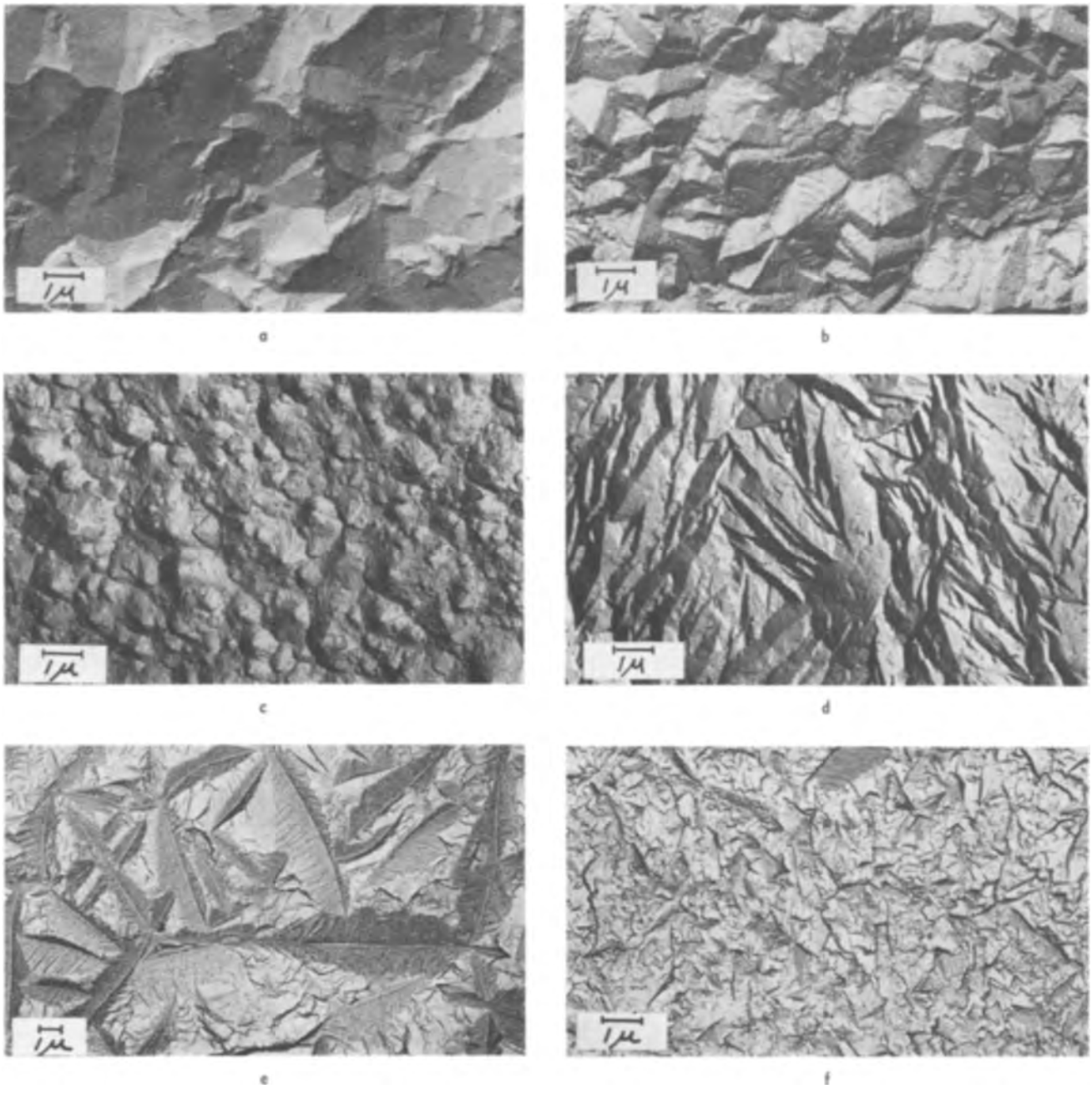

Fig. 1. Electron micrographs using replicas of cobalt deposits. Surfaces with: a) strong $<11\bar{2}0>$ fiber axis formed at 60°C; b) strong $<11\bar{2}0>$ fiber axis formed at room temperature; c) weak $<11\bar{2}0>$ fiber axis; d) $<10\bar{1}0>$ fiber axis; e) psuedo random orientation and coarse needles; f(pseudo-random and finer sturcture.

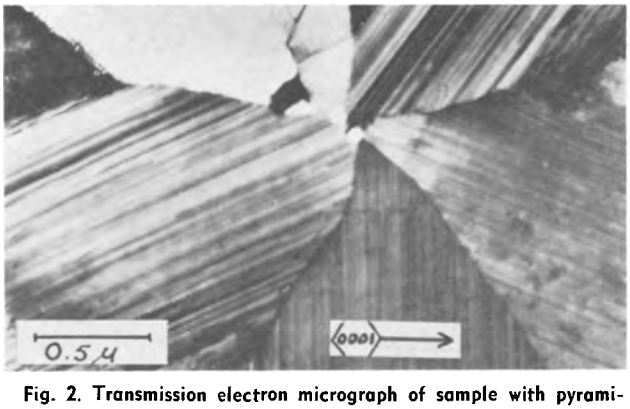

Fig. 2. Transmission electron micrograph of sample with pyramidal morphology.

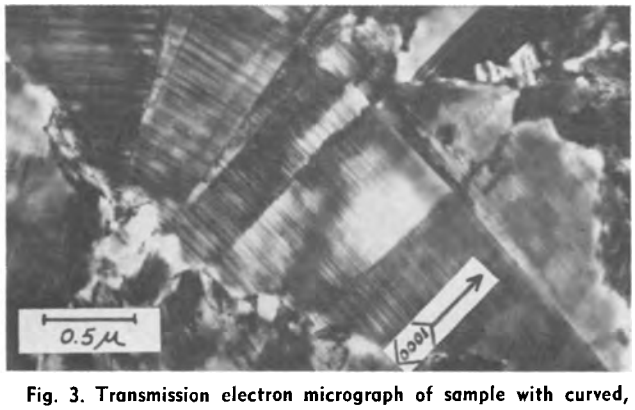

Fig. 3. Transmission electron micrograph of sample with curved, acicular morphology.

lines indicating that the coherently diffracting regions were quite thin in that direction. When the sample was tilted in the microscope, so that the basal planes were no longer parallel to the electron beam, the finely spaced lines developed into fringes of the kind generally associated with faults in the stacking of closely packed planes. The acicular or ridge-like features had {0001} planes parallel to the long direction which were again perpendicular to the surface. The series of fine lines were again present as seen in Fig. 3, where a <0001> direction is indicated for reference. Figure 3 is a transmission electron micrograph of a sample having the curved-ridge type of surface structure seen in Fig. 1e. The curvature is seen to result from the fact that a ridge was not a single crystal, but again consisted of a series of segments. It is doubtful, however, that these segments bore a twin relationship to one another. On a number of occasions single-crystal needles were also observed.

In the course of the study of the preferred orientations by x-ray diffraction, an extra Debye ring not belonging to the hexagonal system was found in patterns from deposits plated at low *p*H and room temperature in baths containing chloride ions. The samples having the extra line, which was always weak and broadened, are designated by asterisks in Table II. The extra line had an interplanar spacing corresponding to that of {200} planes of the face-centered-cubic lattice. The {200} line is the only cubic line which does not coincide with a hexagonal one.

Deposition in an all-sulfate bath operated at a *p*H of 1.0 to 1.5 resulted in specimens with a very fine grain size and the extra {200} cubic line. Selected-area diffraction of these deposits showed an intense {200} line, superimposed on the hexagonal pattern, but attempts to isolate the cubic material by dark-field microscopy were unsuccessful due to the proximity of this reflection to the neighboring $\{10\bar{1}1\}$ line.

Discussion

Several authors (8, 12, 14) have classified the structures of electrodeposits as lateral and outgrowth. According to Reddy (15) there is lateral growth if preferentially developed planes are parallel to the surface and outgrowth if they are perpendicular. In lateral growth, if the closest packed plane is the preferentially developed one, a condition of free growth is said to exist. In outgrowth, if the densest packed direction is preferentially perpendicular to the surface, it is said to be the freest growth. Thus for cobalt, a <0001> fiber axis corresponds to freest lateral growth and $<11\bar{2}0>$ freest outgrowth. Other fiber axes, therefore, represent conditions of more inhibited growth and are said, according to Reddy (15), to result from variations in the coverage of different atom planes by inhibitors. As in this study the basal plane was in no instance preferentially developed parallel to the surface, only outgrowth can be considered to have occurred. This fact was substantiated by examinations of the cross sections of the samples which showed a columnar type of structure perpendicular to the substrate. From the above, it can be concluded that samples which exhibited a strong $<11\bar{2}0>$ fiber axis therefore had the most free growth and those having other crystal directions perpendicular to the surface represented a more inhibited condition.

An alternate theory of the relationship of preferred orientation to the degree of inhibition has been proposed by Pangarov (16). According to this theory, the work of forming a two-dimensional nucleus for a given lattice plane is a function of the overpotential. The lattice plane for which the work of forming such a nucleus is a minimum is the one parallel to the surface. In the hexagonal system such a calculation leads to the order of fiber axes with increasing inhibition as follows: $<0001>\rightarrow<10\bar{1}1>\rightarrow<11\bar{2}0>\rightarrow<10\bar{1}0>\rightarrow<11\bar{2}0>+<10\bar{1}0>$. As the first two orientations were not observed, according to Pangarov's theory, then $<11\bar{2}0>$ is again the least inhibited growth found in this study. However, it should be pointed out that it is questionable whether two-dimensional nucleation has to occur for growth to continue as screw dislocations (17) can provide continuing sites for atom incorporation. It also was found (18) that there is no definite relationship, in the cobalt baths studied, between overpotential and the type of fiber axis.

The results shown in Table II can now be considered in terms of the effects of the plating variables on the relative freedom of growth as indicated by the degree to which the $<11\bar{2}0>$ fiber axis is developed. The effect of temperature in the two baths with the highest chloride-ion concentration, baths A and B, was opposite from that in baths C and D. In baths A and B, increasing the temperatures resulted in freer growth. Such an effect of temperature was expected because the adsorption of impurities should have been decreased and the metal-ion concentration near the cathode increased due to accelerated diffusion rates. However, at the low chloride-ion concentration or in their absence, increasing temperatures resulted in more inhibited growth except at *p*H 5.0 and 0.5 amp/dm^2 in bath C. It may be postulated that the low anode efficiencies usually associated with low chloride-ion concentration resulted in the formation of other reaction products, which at high temperatures could have diffused rapidly to the cathode thereby inhibiting growth. A diffraction ring, tentatively identified as cobalt hydroxide, was found in deposits plated under these conditions.

The effect of current density as seen from Table II shows a trend toward freer growth with a decrease in the variable at 60°C in all four plating baths and at room temperature in baths A and B. A possible reason for this behavior is less impoverishment of the solution at the cathode at lower current densities. At room temperature in baths C and D, growth became freer with increasing current densities. An explanation is that the chloride ions decreased the adsorption of an inhibitor. As there was a tendency toward freer growth at high *p*H values, the inhibitor could have been hydrogen.

The *p*H value appeared to have had little effect at 60°C when the chloride-ion concentration was relatively high. In bath C, growth became freer with increasing *p*H possibly because the chloride-ion concentration was not sufficient to prevent hydrogen from acting as an inhibitor. In the absence of chloride ions, growth tended to become freer with decreasing *p*H. A possible reason for this behavior may be that the basic substances which tended to form at high *p*H values were the more potent inhibitors when their adsorption was not impeded by chloride ions. At room temperature there was again no significant effect of *p*H on the type of growth.

The chloride-ion concentration exerted the greatest influence at the elevated temperature of any of the variables which were studied. The baths with the higher chloride-ion concentration, baths A and B, behaved alike as far as free growth was concerned and exhibited the greatest number of $<11\bar{2}0>$ orientations. Here, the chloride ion probably prevented inhibition. In bath C there was free growth only at high *p*H. A possible reason for this phenomenon, which has already been stated, is that there were not sufficient chloride ions to prevent inhibition due to hydrogen evolving at low *p*H values. In the absence of chloride ions, in bath D, inhibited growth occurred at high current densities. An explanation for these observations has also already been given. At room temperature, the effect of the negative ions was not definite. Decreasing chloride-ion concentration ap-

peared to favor free growth at low pH and, except at the lowest current density, also at the medium pH value.

Thus, while it is possible to explain the occurrences of inhibited or free growth, the requirements of a satisfactory theory to predict the behavior are not realized. It is clearly necessary to determine experimentally the fiber axis under a given set of plating conditions. However, with a given set of plating conditions, the structures were reproducible, as those samples plated on copper and on cobalt substrates were the same.

The reason why certain structural features were associated with each fiber axis in hexagonal cobalt can be deduced by analogy to Schlötterer's (19) explanation of face-centered-cubic nickel. The closest packed direction in the face-centered-cubic lattice is <110>. When this direction was the fiber axis, multisided pyramids were observed. Schlötterer has shown that these pyramids resulted because there are two sets of twinning planes perpendicular to the substrate. The possibility for the sections of a pyramid to be in a twin relationship to each other permits a higher degree of symmetry. In the hexagonal system when the close-packed direction $<11\bar{2}0>$ is the fiber axis, there are also a number of reported (20) twinning planes of the type $\{10\bar{1}L\}$, where L can be an integer from 1 to 5, perpendicular to the substrate. These planes probably provided the opportunity for forming the type of pyramids shown in Fig. 2.

In nickel when the <211> direction was the fiber axis, Schlötterer (19) found elongated shapes. These shapes were symmetric about a plane parallel to the long direction and perpendicular to the substrate. When there was a <211> fiber axis, there is only one twinning plane perpendicular to the substrate, thus only shapes with a two-fold symmetry can form. The hexagonal direction equivalent to <211> is $<10\bar{1}0>$. When $<10\bar{1}0>$ was the fiber axis in cobalt, the same types of shapes resulted as were observed with <211> in nickel. As the basal plane of the hexagonal lattice is a mirror plane without twinning, shapes having two-fold symmetry can result whenever this plane was perpendicular to the substrate. In the cubic system, as there is no mirror symmetry about the {111} planes, there had to be twinning on these planes in order to produce the types of shapes which Schlötterer observed.

Face-centered-cubic cobalt, unlike "hexagonal" nickel is thermodynamically stable above 420°C. Whereas Schlötterer (19), has shown that the extra line segment observed in diffraction patterns of some nickel deposits and which had been indexed as the $\{10\bar{1}0\}$ of a hexagonal phase can also result from double diffraction, the circumstances for cubic cobalt are probably different. As a complete diffraction ring corresponding to {200} has been observed, it is probable that there actually were crystals or parts thereof which had a face-centered-cubic lattice. Incomplete transformation to the hexagonal phase in wrought cobalt, especially if the grain size is small, is a well-known phenomenon (21, 22). The plated samples in which the cubic diffraction line was observed generally had a very fine grain size. It has been postulated (23) that the excess deposition energy is equivalent to an effective temperature considerably above ambient at the cathode surface. Based on this theory, under the conditions used in this study, the temperature at the growing cathode surface would be one at which the cubic phase is stable. Possibly the fine grain size prevented complete transformation. From Table II it can be noted that the presence of the chloride ion and low pH are also obviously associated with formation of some cubic phase possibly by their effects on the grain size.

Many workers (24-27) have used quantitative x-ray measurements in order to study the nature of lattice faults as well as the effects of particle size and strain on the structure of cobalt powders. The application of these techniques to elucidate the lattice faults and the presence of the cubic phase in electrodeposited cobalt is presently being studied.

Conclusions

1. In all deposits the basal planes were predominantly perpendicular to the substrate which led to the formation of $<11\bar{2}0>$ and $<10\bar{1}0>$ fiber axes.
2. Certain structural features were associated with each fiber axis and could be explained in terms of the crystal symmetry and available twinning planes.
3. Applying the concepts of free or inhibited outgrowth to the various orientations which were found did not permit a prediction of the type of structure which would result under a given set of plating variables.
4. The cubic phase was observed at room temperature and pH 2.0 in the presence of chloride ions, and at pH 1.0-1.5 in an all-sulfate bath.

Manuscript received Oct. 11, 1965; revised manuscript received Feb. 14, 1966. This paper was presented at the Washington Meeting, Oct. 11-15, 1964. This paper is based on theses submitted by two of the authors (R. S. and C. D. S.) in partial fulfillment of the requirements for the MSc degree (Metallurgy) to the faculty of Stevens Institute of Technology.

Any discussion of this paper will appear in a Discussion Section to be published in the December 1966 JOURNAL.

REFERENCES

1. H. Kersten, *Physica*, **2**, 274 (1932).
2. N. Pangarov and S. Rashkov, *Compt. Rend. Acad. Bulgare Sci.*, **13**, 439 (1960).
3. N. Pangarov and Rashkov, *ibid.*, **13**, 555 (1960).
4. S. Rashkov and V. Mircheva, *ibid.*, **15**, 759 (1962).
5. Yu. M. Polukarov, *Russ. J. Phys. Chem.*, **34**, [1], 68 (1960).
6. H. F. Quinn and I. M. Croll, "Advances in X-ray Analysis," Vol. 4, 151, W. M. Mueller, Editor, Plenum Press, New York (1961).
7. A. Brenner, D. E. Couch, and E. K. Williams, *Plating*, **37**, 36 (1950), *ibid.*, **37**, 161 (1950).
8. G. I. Finch, H. Wilman, and L. Yang, *Disc. Faraday Soc.*, **1**, 144 (1947).
9. R. Weil, Ph.D. Thesis, The Pennsylvania State College (1951).
10. D. R. Cliffe and J. P. G. Farr, *This Journal*, **111**. 299 (1964).
11. J. Goddard and J. G. Wright, *Brit. J. Appl. Phys.*, **15**, 807 (1964).
12. B. C. Banerjee and A. Goswami, *This Journal*, **106**, 20 (1959).
13. A. Taylor, "X-ray Metallography," John Wiley and Sons, New York (1961).
14. H. Fischer and H. F. Heiling, *Trans. Inst. Metal Finishing*, **31**, 90 (1954).
15. A. K. N. Reddy, *J. Electroanal. Chem.*, **6**, 141 (1963); *ibid.*, **6**, 153 (1963).
16. N. A. Pangarov, *Electrochimica Acta*, **7**, 139 (1962), *ibid.*, **9**, 721 (1964).
17. F. C. Frank, "Growth and Perfection of Crystals," p. 411, Doremus, Roberts and Turnbull, Editors, John Wiley and Sons, New York (1958).
18. H. S. Graime, Unpublished work.
19. H. Schlötterer, *Z. Kristall.*, **119**, 321 (1964).
20. C. S. Roberts, "Magnesium and Its Alloys," John Wiley and Sons, New York (1960).
21. E. A. Owen and D. Madoc Jones, *Proc. Phys. Soc. (London)*, **67B**, 456 (1954).
22. E. Votava, *J. Inst. Metals*, **90**, 129 (1961).
23. H. Wilman, *Proc. Phys. Soc. (London)*, **68B**, 474 (1955).
24. O. S. Edwards and H. Lipson, *Proc. Roy. Soc. (London)*, **A180**, 268 (1942).
25. T. R. Anantharaman and J. W. Christian, *Acta Cryst.*, **9**, 479 (1956).
26. C. R. Houska and B. L. Averbach, *ibid.*, **11**, 139 (1958).
27. G. B. Mitra and N. C. Halder, *ibid.*, **17**, 817 (1964).

Effect of Crystal Plane on the Mechanism and the Kinetics of Copper Electrocrystallization

A. Damjanovic, T. H. V. Setty, and J. O'M. Bockris

The Electrochemistry Laboratory, The University of Pennsylvania, Philadelphia, Pennsylvania

ABSTRACT

To study the mechanism and the kinetics of electrocrystallization, electrochemical measurements were supplemented with *in situ* microscopic observations of growing copper electrodeposits. The growth was followed on main crystal planes of copper single crystals up to an average thickness of the deposit corresponding to 10 coulomb/cm^2. Highly purified solutions of 0.25M $CuSO_4$ in 0.1M H_2SO_4 were used.

Triangular and hexagonal pyramids form on the (111) plane at low ($\leq$10 ma/cm^2) current densities. Edges in the bases of these pyramids are either parallel to the <112> or to the <011> direction. At higher current densities (>10 ma/cm^2), the pyramids truncate and gradually transform into blocks. On the (110) plane, ridge types of deposit develop. At 2 and 5 ma/cm^2, the ridges are parallel to the [100] direction. At 10 ma/cm^2 and higher current densities, they are parallel to the [110] direction. Details of the types of deposit which are formed are given. Rates of growth of individual growth forms are determined and analyzed.

On all crystal planes, at any given current density the electrode potential changes with the time of deposition. On the (100) plane, the trend is for the potential to increase with deposition time until the average thickness of the deposit corresponds to about 3 coulomb/cm^2. On the (111) plane, however, there is a large decrease in the potential, which reaches a steady value once the average thickness of the deposit corresponds to about 6 coulomb/cm^2. On the (110) plane, the magnitude of the change in the potential with time of deposition is the lowest of the three planes considered.

Current-potential plots, both from the data at the initial stages of deposition, and from those obtained at an average thickness of deposit corresponding to 10 coulomb/cm^2 and the same type of growth, show Tafel slopes close to $2RT/F$. This slope is consistent with a mechanism where the first charge transfer is rate-controlling.

From the current-potential plots for the initial stages of deposition, exchange current densities on different crystal planes are found to be in the order

$$i^o_{111} < i^o_{100} < i^o_{110}$$

The decrease in the potential with time on the (111) plane is accounted for in terms of the formation and growth of new and more active crystal faces over the growing substrate. With this hypothesis, the observed change in the potential on the (100) plane is also explained. The observed exchange current densities at any instant of deposition is an average over all crystal faces of different activities. The dependence of the exchange current density on the crystal plane is discussed.

An inherent difficulty in the study of metal electrocrystallization is the continuous change of the electrode substrate with time of deposition (1). For this reason, the transient technique, or the technique of monolayer deposition, was frequently preferred (2-7) over that of the long time deposition (or electrocrystallization) and has been used successfully in the study of the mechanisms and the kinetics of metal electrodeposition. Most of these short time studies were done on polycrystalline electrodes and thus, because of the effect of grain boundaries and the distribution of various crystal planes, only average values of the kinetic parameters were obtained. This was clearly shown by the work of Bockris and Kita (6) in copper electrodeposition where both the mechanism and, for the same mechanism, the rate of the reaction changed with the electrode pretreatment. To separate the effects of various crystal planes and possibly of the grain boundaries, on the study of short time electrodeposition, single crystals with well defined faces would be preferred over polycrystalline electrodes. This is equally important in the study of the mechanisms and the kinetics of electrocrystallization at longer times. However, in the latter study, new crystal faces with different orientation than the initial substrate may form and grow. Because of this formation of new faces, the mechanism and the kinetics of electrodeposition may change. These latter changes may, in turn, alter the mechanisms of growth and produce new and different crystal faces. For this reason, in the study of the mechanisms of electrocrystallization, the electrochemical data and their changes with time of deposition have to be supplemented by other types of observations, such as optical measurements. These give information concerning the change of the substrate with time and about the formation and growth of new faces.

In the present study of copper electrocrystallization on (111) and (110) planes of copper single crystal, following the work on the (100) plane already published (8, 9), electrochemical techniques were combined with optical ones. The aim was to obtain data, suitable for theoretical treatment, on the dependence of the mechanism and the kinetics of electrocrystallization on the initial crystal plane and on the changes in the plane which arise from the formation and the growth of new faces.

The methods used involve continuous observation and photography at regular intervals of time by means of Nomarski interference contrast microscopy and polarized interferometry together with simultaneous electrochemical measurements. Supplementary analysis by means of electron microscopy was also carried out.

Experimental

Crystals.—Single crystals in the form of cylinders about 10 mm long and 8 mm in diameter were cut so that their bases were closely parallel to (110) or

(111) crystal planes. Each crystal was mounted in the Teflon body of an electrodeposition cell.

Cell.—The all Teflon cell for deposition was described in a previous publication (10). It allows observation of the growing deposit to be made *in situ* with relatively high useful magnification of 600-900X, without the objective of the microscope being immersed in the solution. With this cell it is possible to study deposition from highly purified solutions. The cell with the crystal is assembled and closed to the atmosphere inside a glove-box which is filled with prepurified argon. On the solution outlet tubing (10), a small compartment ($\sim$ 1 cm^3) is located with a copper reference electrode (prepared just immediately before use by electrodeposition from 0.25M $CuSO_4$ + 0.1M H_2SO_4 solution with 10 ma/cm^2 for 30 min). Electrical contact to the cathode is made on the opposite (bottom) side of the crystal (not exposed to the solution).

Solution preparation.—Analytical grade (Baker) copper sulfate was recrystallized twice in a closed system, in an atmosphere of highly purified nitrogen (9), using freshly redistilled conductivity water. Only the copper sulfate which crystallized first was used. The recrystallized copper sulfate was washed quickly three times with freshly redistilled conductivity water, after which it was dissolved in additional freshly redistilled conductivity water. Then the solution was transferred along a closed system of all glass tubing under the pressure of purified N_2 to a pre-electrolysis vessel for further purification by pre-electrolysis. At the same time, 50% H_2SO_4 was pre-electrolyzed in a separate vessel. Details on pre-electrolysis and final solution preparation have been given in a previous publication (8). Just before the experiments with electrocrystallization, the solution was passed through a column of activated charcoal and neutral alumina to remove any residual organic impurities from the solution (8, 11). Before each experiment, charcoal and alumina in the purification column (length $\sim$ 100 cm and diameter $\sim$ 6 cm) were washed with about 4 liters of 1M H_2SO_4, and then, after the H_2SO_4 passed through, three times with freshly redistilled conductivity water, each pass using about 2 liters. The first copper sulfate solution to pass through the column was discarded. The solution from the purification column was collected into a small collector vessel ($\sim$ 2 liter) which was connected to the Teflon cell. This vessel, as all the others, was washed by overnight soaking in a 1:1 mixture of HNO_3 and H_2SO_4, and then thoroughly rinsed with conductivity water. Finally, before the solution from the purification column was collected, the collection vessel was washed *in situ* with freshly redistilled conductivity water.

The solution used was 0.25M in $CuSO_4$ and 0.1M in H_2SO_4. (In a few experiments the concentration of $CuSO_4$ was changed and this has been noted in the text.) In some experiments, n-decylamine was added to the solution after it passed through the activated charcoal and alumina. For this purpose, a small graduated separatory funnel (50 cm^3) was attached to the final collector vessel.

Pre-treatment of the copper substrate.—For each experiment, the copper single crystal together with the main body of the Teflon cell, was mechanically polished first on 4/0 emery paper with ethanol as a lubricant, and then on 0.3μ alumina on a felt. The crystal in the Teflon cell body was washed under running distilled water, then with a mixture of ethanol and ether, and finally with ethanol. At this stage, the crystal and all components of the cell were introduced into the glove box (8).

Further treatment of the electrode surface included electropolishing at a constant potential in 50% H_3PO_4 in the argon atmosphere. After electropolishing, the crystal was washed with 10% H_3PO_4 and with redistilled conductivity water. All components of the cell were washed inside the glove box with water redistilled directly into it. The cell was assembled inside the glove box. The inlet and outlet tubing were attached to the cell at this stage. So assembled, the cell was then transferred to the platform of a microscope, and the connections made to the solution and outlet vessels. Further experimental details are available in ref. (8).

General procedure.—Electrodeposition was carried out at a given constant current density to an average thickness of the deposit corresponding to 10 coulomb/cm^2 (3.6μ). The overpotential (with respect to a polycrystalline copper reference electrode in the same solution) was continuously recorded. A Keithley 600A Electrometer and Moseley Autograf (680) were used. The growing crystal substrate was continuously observed and photographed at regular intervals. Nomarski interference contrast technique was used (12). Occasionally, level differences in the deposit were determined by Nomarski polarized interferometry (12).

Polaroid positive film (3000 ASA) was used. Usually, magnification on the photographs was 600X.

Results

Types of Deposit on (111) Plane

Deposition was carried out at 2, 5, 10 15, 20, and 30 ma/cm^2 from highly purified solutions, at 5 ma/cm^2 from the solution containing n-decylamine in concentrations varying from 10^{-9} to 10^{-4} mole/l, and at 2, 5 and 10 ma/cm^2 with a constant concentration of n-decylamine.

Types of deposits at 2 and 5 ma/cm^2.—At 2 and 5 ma/cm^2, the type of deposit formed from pure solutions may be classified as pyramid formation on either

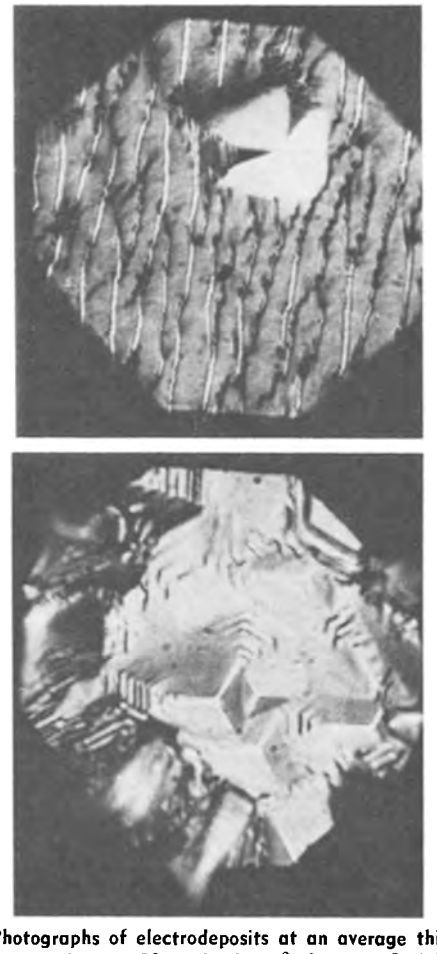

Fig. 1. Photographs of electrodeposits at an average thickness of deposit corresponding to 10 coulomb/cm^2. 2 ma/cm^2. (a) Pyramid on substrate containing macrosteps; (b) high density of pyramidal growth ($1.2 \cdot 10^5$ cm^{-2}). Magnification 600X.

smooth or layered substrate (Fig. 1). Some characteristics of the growth are listed here:

(*i*) Pyramidal growths, which often show a perfect geometrical shape, are of two types, triangular and hexagonal (Fig. 2).

(*ii*) Pyramids, both triangular and hexagonal, may form at any time of deposition.

(*iii*) Pyramidal faces in triangular pyramids are usually smooth. These faces are parallel either to one of <112> or of <110> directions both of which lie in (111) plane. Hence, there are four orientations of these triangular pyramids. These orientations are illustrated in Fig. 3.

(*iv*) As a triangular pyramid grows, it often develops, starting from the base, three extra side faces (Fig. 4, at places a). Edges at the base of these extra faces are parallel either to the <112> or to the <111> direction. As these new faces develop, a triangular pyramid gradually transforms into a hexagonal pyramid.[1] These newly developed pyramidal faces are usually stepped particularly close to the base of the pyramid and often form only close to the base of the pyramids.

(*v*) Triangular pyramids, or hexagonally shaped pyramids originating from the triangular ones, rarely truncate. The apex of some of these pyramids is observed to be a short line (presumably parallel to the base) rather than a point. The line on well developed pyramids can be as long as 1μ.[2]

(*vi*) "Regular hexagonal" pyramids also appear. They form as "hexagonal" in the earliest detectable stage. The occurrence of these pyramids is less frequent than that of the triangular pyramids.

(*vii*) "Hexagonal" pyramids tend to truncate even at an early stage of growth. All side faces, and not only alternate ones, are always stepped (Fig. 2).

(*viii*) Truncated "hexagonal" pyramids grow sidewise and transform eventually to sixfold "blocks" (*e.g.*, Fig. 6 and 7). At the center of a block, a new pyramid may begin growing again (Fig. 2).

(*ix*) When macrosteps are present on the deposit (8), they all propagate in the same direction. Some macrosteps fade out and disappear (8).

Here, some differences between deposits at 2 and 5 ma/cm^2 are given. At both current densities triangular pyramids are more frequent than the "true hexagonal" ones. The ratio of the density of the triangular pyramids to the hexagonal pyramids is less in deposits at 6 than at 2 ma/cm^2. On the average, from a number of experiments, the density of pyramidal growths at 5 ma/cm^2 (5 x 10^5 cm^{-2}) is higher than at 2 ma/cm^2 (about 1 to 2 x 10^5 cm^{-2}). Finally, the tendency for triangular pyramids to acquire additional faces and transform to "hexagonal" pyramids is higher at 5 than at 2 ma/cm^2. At 5 ma/cm^2, hexagonal pyramids truncate more readily than at 2 ma/cm^2.

[1] A pseudo sixfold symmetry is understood.

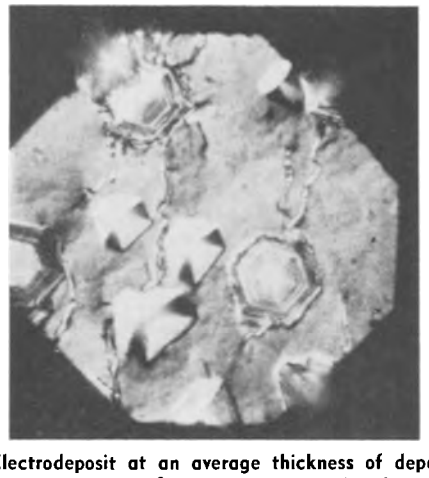

Fig. 2. Electrodeposit at an average thickness of deposit corresponding to 10 coulomb/cm^2 showing hexagonally shaped and triangular pyramids. Current density i = 5 ma/cm^2 (600X).

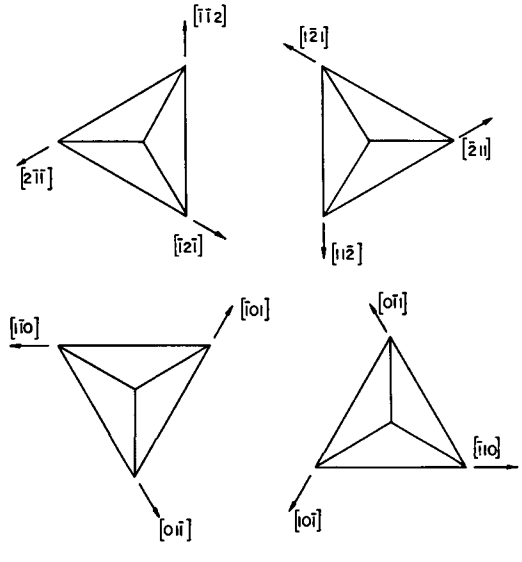

Fig. 3. Side faces of triangular pyramids parallel to either <112> or <110> directions.

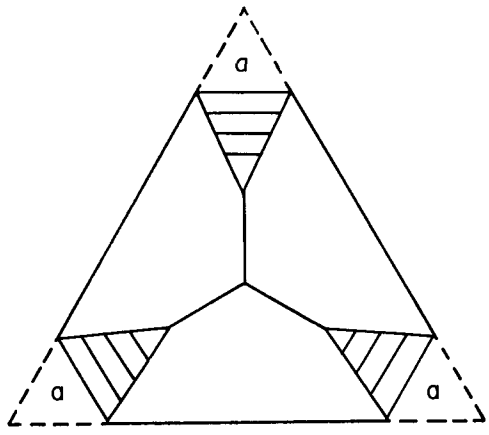

Fig. 4. Schematic representation of a triangular pyramid on which additional (a) faces start forming from the base of the pyramid.

Types of Deposits at 10 ma/cm^2 and Higher Current Densities

Hexagonally shaped pyramids form predominantly at 10 ma/cm^2, whereas triangular pyramids rarely occur at this current density. Almost all "hexagonal" pyramids truncate and transform into blocks and larger hexagonal layers which may eventually disappear by joining with other hexagonal layers (Fig. 5a and 6). Triangular pyramids, if they form, also show a tendency to truncate. Further a new pyramid may begin growing over a truncated pyramid.

At 15 ma/cm^2 and higher C.D., the type of deposit may still be described as pyramidal but truncation is complete. At 30 ma/cm^2 no distinct features in the deposit can be seen. The deposit appears to be polycrystalline.

Effect of addition of n-decylamine.—Addition of n-decylamine to the solution in concentrations below 10^{-5} mole/l has no visible affect on the type of deposit formed. With 10^{-5} mole/l of n-decylamine and at 5 ma/cm^2 truncation occurs readily for hexagonal pyramids and often for triangular pyramids. With 10^{-4} mole/l and at the same current density, hexagonal

[2] Arrow shaped pyramids were previously reported by Economou *et al.* (13).

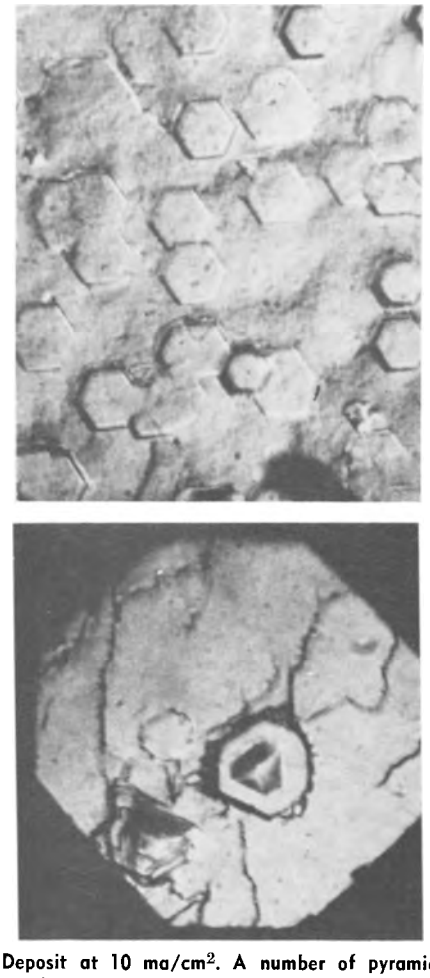

Fig. 5. Deposit at 10 ma/cm^2. A number of pyramidal growth transform to hexagonal blocks (a), and (b) triangular pyramid formed over a block (600X).

pyramids form in preference to triangular, and all pyramids soon truncate. Side faces, even of triangular pyramids, are stepped. Alternate faces of a truncated hexagonal pyramid contain macrosteps which are not parallel to the edge in the base, but are rather normal to it (Fig. 7). Complex shapes of pyramidal growths may also form and are probably due to twinning (Fig. 8).

With 10^{-4} mole/l of n-decylamine and at 2 ma/cm^2, the type of deposit is less affected than that at 5 ma/cm^2. The triangular pyramids remain with smooth faces. With 10^{-4} mole/l of n-decylamine and at 10 ma/cm^2, all pyramids truncate at an early stage of growth.

Fig. 6. Over a block close to its center a "line" parallel to an edge in the base often appears (600X).

Fig. 7. An example of macrosteps on side faces of truncated pyramids. 5 ma/cm^2 in the presence of n-decylamine (600X).

Fig. 8. An example of possible twinning (600X).

In general, n-decylamine affects the structure of the deposit more at high than at low current densities.

Effect of $CuSO_4$ *concentration and of temperature on the deposit.*—Deposition at 5 ma/cm^2 on the (111) plane has been made from solutions containing 0.05 mole/l and 1 mole/l of $CuSO_4$. The concentration of H_2SO_4 was 0.1 mole/l. The types of deposits obtained from these solutions were the same as those obtained from 0.25 mole/l and the same current density.

The morphology of the deposit at 5 ma/cm^2 from 0.25M $CuSO_4$ and 0.1M H_2SO_4 solution at 0°C differed markedly from that at room temperature. No pyramidal growth and only macrosteps were observed.

Types of Deposit on (110) Plane

Deposition was carried out at 2, 5, 10, 15, 25, and 30 ma/cm^2. At all current densities the ridge type of deposit formed. In Fig. 9, these ridges are shown for two current densities. The surface is not necessarily completely covered by ridges and "smooth" areas exist between them. Occasionally over the "smooth" surface macrosteps may have formed. Pyramidal growth rarely formed at 10 ma/cm^2.

At a given current density, ridges are all aligned along a particular direction. This direction is independent of the direction of solution flow. Ridges with two different orientations are observed. At 2 and 5 ma/cm^2, ridges are aligned parallel to the [100] direction. At 10 ma/cm^2 and higher current densities, they are all aligned parallel to the [110] direction.[3] Ridges

[3] This type of ridges was previously observed by Pick *et al.* (14).

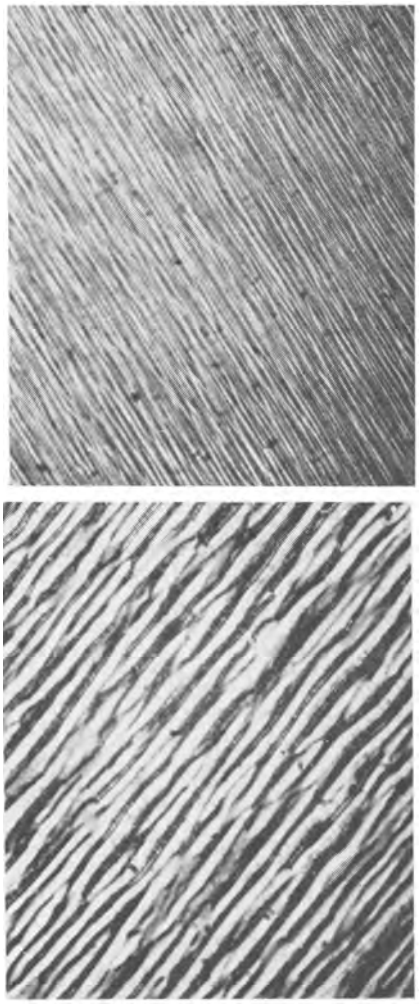

Fig. 9. Ridges developed on the (110) plane. (a) 5 ma/cm^2, (b) 10 ma/cm^2 (600X).

were not observed to advance laterally as, for instance, macrosteps (8).

The effect of n-decylamine was examined at 5 ma/cm^2. No significant change in the type of deposit from that in pure solutions was observed even at 10^{-4} mole/l of n-decylamine.

Rates of Growth

From a series of *in situ* (10) photographs taken at known intervals of deposition times, the rates of growth of pyramids and of macrosteps were measured. In Fig. 10, the normal distance of a macrostep from a reference point (a pyramid) is plotted *vs.* time of deposition. From similar plots rates of growth of pyramids at their bases, and rates of macrostep propagation both on pyramidal faces and on "smooth" substrates were determined. Average rates from a number of measurements are collected in Table I.

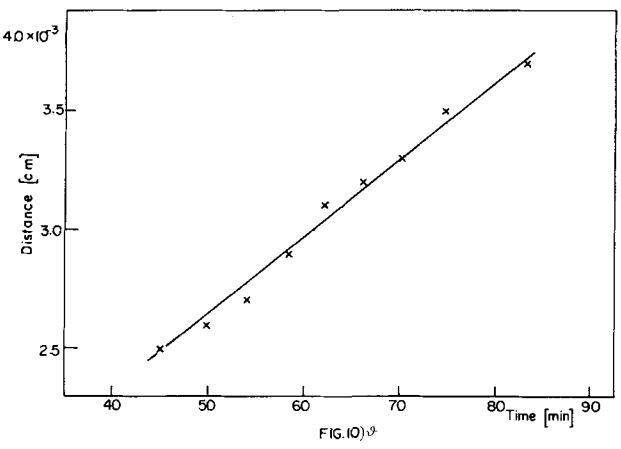

Fig. 10. A plot of distances of a macrostep from a fixed point on the substrate *vs.* time of deposition. 2 ma/cm^2.

In all experiments, it was found that, to a good approximation, the rates of propagation of macrosteps both on "smooth" substrate and on pyramidal faces, and the rates of growth of pyramids in their bases were independent of the deposition time for all the average thicknesses of deposit examined. The rate at which the base of both triangular and hexagonal pyramids, truncated or not, propagate was independent of the current density. The rates of macrostep propagation, both on "smooth" substrate and on pyramidal faces, increased with current density. To a first approximation, these two rates are equal. All these rates are independent of the concentration of $CuSO_4$. Addition of n-decylamine did not significantly affect either of these rates except possibly in the case of macrosteps on pyramidal faces at 2 ma/cm^2 and 10^{-4} mole/l of n-decylamine.

The edge of the upper plateau of truncated pyramids usually propagated faster than the base of the pyramids. In this way truncated pyramids gradually transformed into blocks.

Change of Overpotential with Time

Overpotential at a constant current density usually changed with time of deposition: it either increased or decreased. Often, for the same current density and when on the same crystallographic plane, much the same type of deposit formed. Potential-time dependence may have differed in details from one experiment to another. The general trend and appearance

Table I. Rates of advance of macrosteps and of pyramid growths on (111) plane

Current density (ma/cm^2)	Purity of the solution*	Macrosteps on smooth substrate (Å/sec)	Macrosteps on pyramidal faces (Å/sec)	Base of triangular pyramids (Å/sec)	Base of hexagonal pyramids (Å/sec)	Base of truncated pyramid (Å/sec)	Calculated rate of deposition (Å/sec)
2	Pure*	50-55	55-70	50-55	50-55		7.5
	10^{-4} M/l n-D**		(~100)	50			
5	Pure*	130 (±20)	135 (±15)	55 (±7)	55		18.7
	10^{-5} mole/l n-D	120	125	55	55		
	10^{-5} mole/l n-D			55	55		
	10^{-5} mole/l n-D			45	45	45	
	1M $CuSO_4$	130	135	55			
	0.05M $CuSO_4$	130	135	55		55	
10		190	~180	58		58	37.5

* 0.25M $CuSO_4$ + 0.1M H_2SO_4, no n-decylamine.
** n-D stands for n-decylamine.

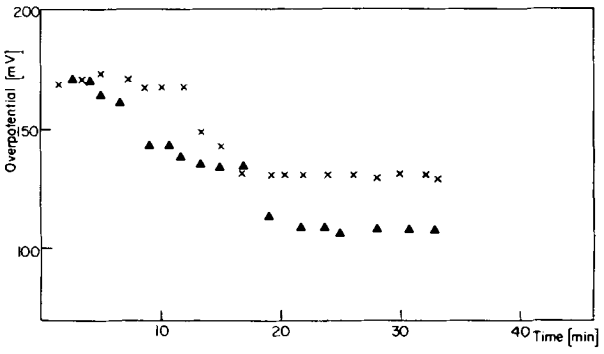

Fig. 11. Overpotential *vs.* time in two experiments at 5 ma/cm^2. (111) plane.

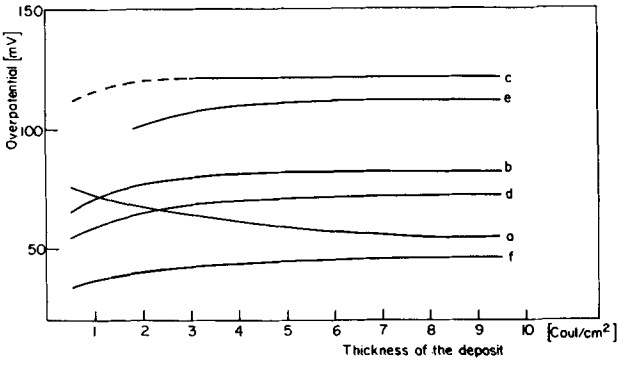

Fig. 12. Overpotential *vs.* the average thickness of the deposit at different current densities. Lines are idealized. The (100) plane. (a) Large layer formation at 5 ma/cm^2; (b) pyramids (and some macrosteps) at 5 ma/cm^2; (c) small layers and pyramids at 10 ma/cm^2; (d) ridges at 5 ma/cm^2 (in the presence of n-decylamine); (e) ridges at 10 ma/cm^2 (in the presence of n-decylamine); (f) smooth substrate (with or without small macrosteps) at 5 ma/cm^2.

of the plot were, however, much the same for both experiments. This is illustrated in Fig. 11, where values of overpotentials for two experiments are plotted *vs.* time of deposition. In both experiments nearly identical deposits were formed [pyramids on the (111) plane at 5 ma/cm^2]. The best fit line is drawn through all the experimental points for each current density. These lines at different current densities are shown in Fig. 12, 13, and 14 for the (100), (111), and (110) planes,[4] respectively. Line d in Fig. 13 corresponds to the experimental points in Fig. 11. In most cases, however, more than two experiments were available for construction of these lines. In these figures, overpotentials are plotted *vs.* average thickness of the deposit in coulomb/cm^2, and not *vs.* time. On this scale overpotentials at different current densities can be compared easily.

The (100) plane.—Some characteristics of the potential-time curves for deposition are:

At all current densities, overpotentials tend to increase with average thickness of the deposit if pyramidal types of growth (8) or if macrosteps on "smooth" substrate develop. The opposite trend, that overpotential decreases with the thickness of the deposit, is observed when a large layer type of deposit forms (8).

Addition of n-decylamine to concentrations less than 10^{-7} mole/l does not affect overpotential-time relation. At higher ($> 10^{-7}$ mole/l) concentrations of n-decylamine, when the ridge type of deposit is formed (8), the potential increases with time, but always stays below that for pyramidal growth.

In all cases overpotential became reasonably constant at the average thickness of the deposit corresponding to about 2-3 coulomb/cm^2 (Fig. 12).

[4] Thanks are due to Mr. M. Paunovic for making data on the (100) plane available.

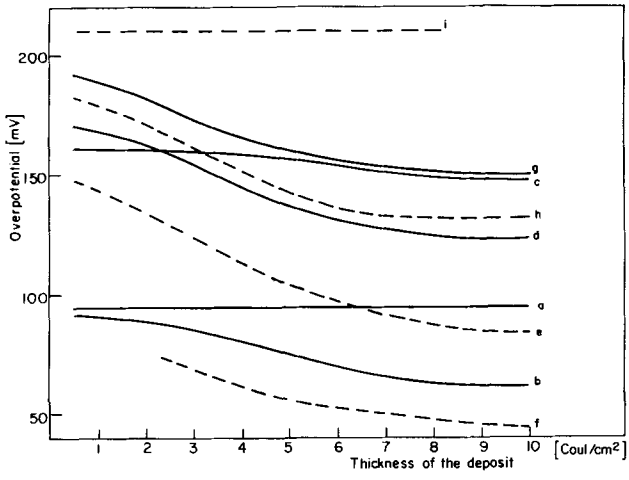

Fig. 13. Overpotential *vs.* the average thickness of the deposit at different current densities. Lines are idealized. The (111) plane. (a) Occasional macrosteps + occasional pyramids at 2 ma/cm^2; (b) large pyramidal growth at 2 ma/cm^2; (c) smooth substrate + occasional pyramids at 5 ma/cm^2; (d) large pyramidal growth at 5 ma/cm^2; (e) large pyramidal growth, n-decylamine, 5 ma/cm^2; (f) large pyramidal growth, n-decylamine, 2 ma/cm^2; (g) large truncated pyramids + blocks (occasional steps), 10 ma/cm^2; (h) large truncated pyramids, n-decylamine 10 ma/cm^2; (i) small truncated pyramids + blocks, 15 ma/cm^2.

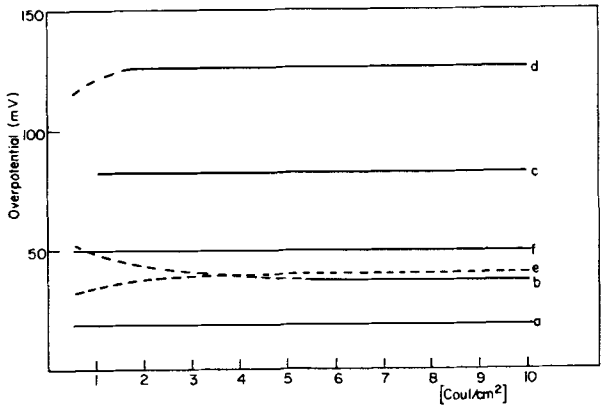

Fig. 14. Overpotential *vs.* the average thickness of the deposit at different current densities. Lines are idealized. The (110) plane. (a) 2 ma/cm^2; (b) 5 ma/cm^2; (c) 10 ma/cm^2; (d) 15 ma/cm^2; (e) 5 ma/cm^2 in the presence of n-decylamine; (f) 5 ma/cm^2 with almost smooth substrate.

The (111) plane.—At any given current density, overpotentials on the (111) plane are higher than on the (100) plane, and, as will be seen later, on the (110) plane.

At all current densities, the overpotential either initially decreases but becomes reasonably constant at about 6 coulomb/cm^2, or it remains reasonably constant from the initial ($\sim$ 0.5 to 1 coulomb/cm^2) time of deposition. In either case, overpotentials for the same current density at the initial time of deposition are approximately equal. When a deposit is smooth, with or without macrosteps (it may contain occasional pyramids, *e.g.*, 10^4 cm^{-2}), the overpotential is fairly constant with time for 2 ma/cm^2, and almost constant for 5 ma/cm^2 (Fig. 13). When large and numerous pyramids form, overpotential at the initial stage of deposition decreases with time rather sharply. In the presence of n-decylamine, overpotentials are usually lower than those in "pure" solutions.

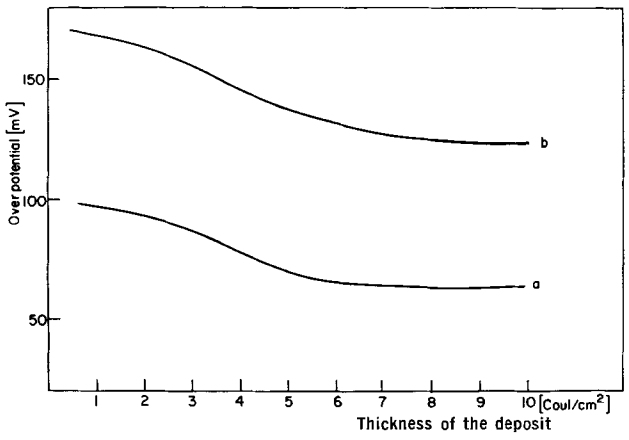

Fig. 15. Overpotential *vs.* average thickness of the deposit at 5 ma/cm². The (111) plane. (a) 1M $CuSO_4$, (b) 0.25M $CuSO_4$.

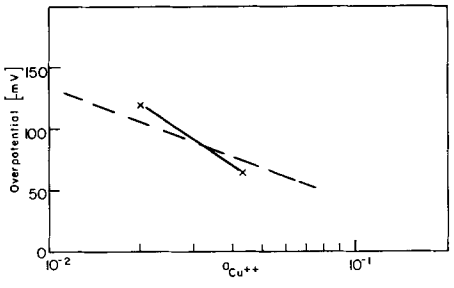

Fig. 16. Overpotential *vs.* activity of Cu^{++}. Broken line represents theoretically expected relationship.

The (110) plane.—For a given current density and any average thickness of the deposit, overpotentials on this plane are lower than on either the (111) or the (100) plane. Except for the initial period of deposition, overpotentials are fairly constant with time (Fig. 14). Contrary to the observation on the (111) plane in the presence of n-decylamine, overpotential at the average thickness of the deposit of 10 coulomb/cm² is higher than that from "pure" solutions.

Effect of Cu^{++} Concentration

Overpotential for electrodeposition onto the (111) plane with 5 ma/cm² from 1M $CuSO_4$ solution decreases with time in much the same way as it does from 0.25M solution. The former overpotential is lower by about 60-70 mv than in the latter case (Fig. 15). In Fig. 16, overpotentials[5] at the average thickness of deposits of 10 coulomb/cm² are plotted *vs.* log a_{Cu++}. The slope through two points is

[5] The activity of Cu^{++} in H_2SO_4 solution was calculated by the equation given by Glueckauf (15).

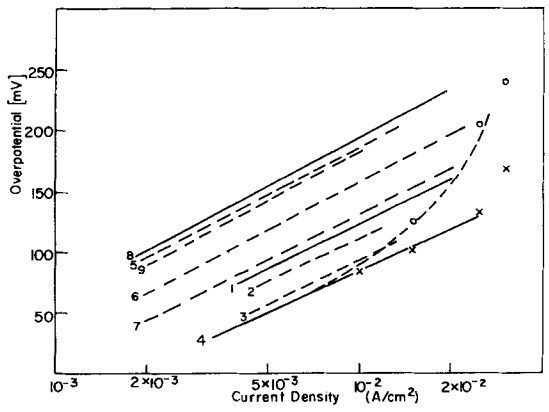

Fig. 17. Plot of overpotential *vs.* current density for different planes, different types of deposit and for initial and final stage of deposition. Numbers correspond to those in Table II. (x) represents initial values of overpotentials on the (110) plane; (0) represents values at the average thickness of the deposit corresponding to 10 coulomb/cm².

$$\left(\frac{\Delta\eta}{\Delta \log a_{Cu++}}\right)_i \approx 150 \text{ mv}$$

Current-Potential Relationship

In Fig. 17, overpotentials are plotted *vs.* log current density. Overpotentials are taken for the initial stages of deposition as well as at the final stage of deposition corresponding to 10 coulomb/cm². A linear relationship exists between electrode potential and log (current density) over one decade with slopes between 115 and 130 mv. Exchange current densities obtained by extrapolation to zero overpotential[6] differ from one crystal plane to another. In Table II data are summarized on the exchange current densities, and on the slope $dV/d \ln i$. It can be noted that:

(*i*) The exchange current densities, i_o's, obtained from the data at the initial stage of deposition, are in the following order

$$i^o_{110} > i^o_{100} > i^o_{111} \qquad [1]$$

i.e., overpotentials at the same current density are in the reverse order; and (*ii*) overpotential-log *i* line for deposits on (110) planes obtained from the steady state data at 10 coulomb/cm² deviate toward higher overpotentials at current densities above 10 ma/cm². Overpotentials at the initial stages of deposition, however, fall on the same Tafel line (x in Fig. 17).

Discussion

Potential-Time Relationships

The observed changes of overpotentials with time of the deposition can, in principle, be accounted for

[6] It is taken that reversible electrode potentials on different crystal planes are the same (16-18).

Table II. Tafel slopes and exchange current densities for deposition on various crystal planes and types of deposit

Plane	No. of line*	Type of deposit	$\frac{d\eta}{d \log i}$ [mv]	i_o [a/cm²]	Remarks
(100)	1	Pyramid, truncated pyramid + macrosteps	122	10^{-3}	
	2	Ridges	120	10^{-3}	10^{-4}M n-decylamine
	3**	Macrosteps + occasional pyramids	125	$2 \cdot 10^{-3}$	
(110)	4**	Ridges	115	$2 \cdot 10^{-3}$	
(111)	5	Occasional macrosteps + occasional pyramids	130	$4 \cdot 10^{-4}$	
	6	Large pyramidal growth	130	$6 \cdot 10^{-4}$	
	7	Large pyramidal growth	125	10^{-3}	10^{-6}M n-decylamine
	8**	Occasional macrosteps + occasional pyramids	130	$3.5 \cdot 10^{-4}$	
	9**	Large pyramidal growth	120	$4 \cdot 10^{-4}$	10^{-6}M n-decylamine

* Numbers correspond to those in Fig. 17.
** Values of overpotentials at initial stage of deposition.

by: (*A*) a change in the mechanism of the reaction, (*B*) a change of the "active" surface area, (*C*) the change in the (apparent) exchange current density, and (*D*) blocking of the growth sites (adsorption of impurities on steps).

The observed slope of $2RT/F$ agrees with that found by Mattson and Bockris (4), Bockris and Enyo (5), and Bockris and Kita (6). According to the latter authors, on electrodes of electrodeposited copper, Tafel lines extend to low overpotentials. This is a characteristic of charge transfer as the rate-controlling reaction step, and not of surface diffusion of adions (2, 3, 7, 19-21). In the present experiments, Tafel relationships were observed both at initial ($\sim$ 30 sec) and at final (corresponding to 10 coulomb/cm^2) stages of deposition. Hence, in the considered interval of time, the mechanism of deposition does not change with time, and the explanation under point (*A*) can be discarded.

If the first charge transfer step is rate-controlling (5, 6), then blocking of growth sites, unless it is extensive, is not expected to affect the over-all rate of the reaction; it simply lowers the rate of the succeeding reaction step, which is still "faster" than the first charge transfer step. Furthermore blocking of growth sites, say of monatomic steps which act in the growth process, should tend to increase overpotential for the given current density. On the (111) plane, however, the addition of n-decylamine causes the overpotential to decrease (Fig. 13). Hence, point (*D*) may also be discarded.

Change in the surface area during the deposition.—If the change in the surface area (point *B*) is to explain the change of potential with time of deposition at a constant current density, then for the (111) plane the area has to increase and for the (100) to decrease with time of deposition. The observed increase of overpotential with time on the (100) plane would require an area decrease of 30-40%. Decrease of overpotential on the (111) plane can be accounted for only if the surface area increases by 200-400%.

The largest decrease in overpotentials on the (111) plane occurs when large pyramids form (Fig. 13). This suggests that the observed change in overpotential with time is due to an increase in the surface area arising from the formation of pyramidal faces. This increase can be calculated from the heights of pyramids and their size and density. In all cases examined it was found that $\tan \alpha \leq 0.2$, where α is the angle which a pyramidal face makes with the substrate.[7] Even assuming that pyramids touch each other in a close packing and that $\tan \alpha = 0.2$, the true surface area would increase by only a few per cent. This is calculated on the basis of smooth pyramidal faces. If pyramidal faces are assumed stepped, then the increase in the surface area is about 20%.

Increase in the surface area, therefore, cannot account for the observed change in the overpotential with time on the (111) plane. For the (100) plane, explanation of overpotential behavior in terms of the increased surface area alone is inadmissable, since the overpotential increases with time of deposition.

Change in the "active" surface area may arise from adsorption of "residual impurities." Behavior on the (100) plane could be accounted for by the increased adsorption, but not on the (111) plane. In fact, the following points argue against the explanation in terms of the decrease in the active surface area.

(*i*) Addition of n-decylamine does not significantly change overpotential on the (100) plane, providing that the type of the deposit remains the same.

(*ii*) On the (111) plane, addition of n-decylamine decreases, rather than increases, the overpotential for a given current density at any time of deposition.

Hence, cause (*B*) above must be rejected.

[7] See also Seiter *et al.* (22).

Change of the Activity with Time

The (111) plane.—When pyramids form, the data at the initial stage of deposition indicates a lower exchange current density, i^o_{111}, than at the final stage of the experiment. If, however, "smooth" deposits (with or without occasional pyramids) form, no appreciable change in overpotential with time is observed, and i_o's from the initial and final stages of deposition are nearly equal. It may be postulated that on the close packed (111) plane, the newly formed pyramidal faces correspond to the planes less closely packed (higher indices planes).

Since $i^o_{111} < i^o_{100} < i^o_{110}$, higher over-all activity results. Pyramidal faces close to the apex are parallel to some high index plane. As these pyramidal faces grow, the over-all activity of what was originally a (111) substrate increases and the overpotential for the same "average" current density decreases.

An area of newly formed faces of only a fraction of the total area suffices for the observed changes. Thus, if A is the area of the newly formed faces per unit area of the initial substrate then

$$i = [(1 - A)\, i^o_{111} + A\, i^o_{hkl}] \cdot e^{-\alpha F\eta/RT} \qquad [2]$$

where i^o_{hkl} is the exchange current density for the newly formed high index face. If

$$i^o_{hkl} \geqq 10\, i^o_{111} \qquad [3]$$

then [2] can be written as

$$i \approx [i^o_{111} + A \cdot i^o_{hkl}] \cdot e^{-\alpha F\eta/RT} \qquad [4]$$

Coefficient A in these equations increases with time of deposition. An increase in A to about 0.1 would suffice to explain the observed potential decrease on the (111) plane. Thus, instead of assuming a change in the surface area by 200-400%, the apparent exchange current density

$$(i^o_{Ap})_t = [i^o_{111} + A_t \cdot i^o_{hkl}] \qquad [5]$$

increases by factor 2 or 4. In the last equation suffix t stands for time. In general the apparent exchange current density is the sum over all the planes of the products of the exchange current density for a given plane, i^o_{hkl}, and the corresponding surface area

$$(i^o_{Ap})_t = \sum_{hkl} i^o_{hkl}\, (A_{hkl})_t \qquad [6]$$

For the steady state to be established, no further changes in the area of newly formed faces (planes) is required. This is to be expected under ideal conditions. A further increase in the surface area is prevented when pyramids touch each other. The steady state, however, is established before pyramids cover the entire substrate. This can be accounted for by the fact that the side faces of pyramids close to their bases are stepped (Fig. 1b). Once macrosteps have formed on these pyramidal faces, further growth results in the increase of the surface area of the newly formed more active planes. Inspection of the photographs shows that the surface area of the new faces can easily reach the value $A = 0.1$ even when the stepped portion of the pyramidal faces is excluded. The flat portion of pyramidal faces between macrosteps corresponds most probably to a low index plane, whereas side faces on these macrosteps are not necessarily perpendicular to the substrate and may correspond to a higher index plane, and thus also contribute to the increased activity.

From the foregoing discussion, it is concluded that the change in the apparent activity (point *C* above) can account for the observed change in overpotential with time of deposition on (111) plane. The least active (111) plane is gradually replaced by more active planes and overpotential decreases with time of deposition. It yet remains to explain the potential time behavior on the other two crystal planes.

Overpotential on the (100) plane.—On the (100) plane, in contrast to the (111) plane, overpotentials generally increase with time of deposition. The extent of the increase (Fig. 12) is, however, far less than the decrease on the (111) plane (Fig. 13). This behavior can also be explained in terms of changing the over-all activity of the electrode surface (point C above).

i^o_{100} is larger than i^o_{111} and when new faces are formed their effect would be less than the corresponding effect on the (111) plane. Were the newly formed faces close to, for instance, the (111) plane, it would be expected that the effect should be the opposite one to that for deposits on the (111) plane, namely the overpotential should increase with time of deposition since more active surface is replaced by less active surface. In fact, no large change in overpotential would be expected since the replacement of a small area of active surface by less active surface is far less effective as far as potential change is concerned, than the reverse process (cf. Eq. [2]).

It is possible that initially the electrode surface corresponds to some higher index plane due to local misorientation arising, for instance, from electropolishing. Soon, growth results in a smoothing out of the surfaces which become parallel to the (100) plane. Hence, overpotential initially increases with time and then becomes constant (Fig. 12).

Overpotential on the (110) plane.—The exchange current density is higher for the (110) plane than for the other two crystal planes considered. Time dependence of overpotential on the (110) plane is less than on the other planes.

Even when ridges form at 5 ma/cm^2, the potential does not change with time of deposition to any appreciable extent. This indicates that the side faces of ridges, which are parallel to a [100] direction, are as active as the (110) plane. If these faces were at 45° toward the substrate (toward the (110) plane), they would correspond to {100} planes. Then the over-all activity would not change significantly, particularly since the increase in the surface area arising from the inclination would be compensated by the lower activity at (100) planes. This explanation would clarify the experimental observation that overpotentials at current densities of 2 and 5 ma/cm^2 are virtually independent of the time of deposition. At 15 ma/cm^2 and higher current densities, overpotentials at the initial stage of deposition increase with time of deposition, but soon ($<$ 2 coulomb cm^2) assume a steady value. At these current densities, ridges are parallel to the [110] direction. Side faces of these ridges may correspond to the (111) plane (14). If so, the more active (110) plane is gradually replaced by the less active (111) plane and overpotential increases reaching the value close to that corresponding to the (111) plane. In this way the deviation of η — log i curve for the (110) plane at higher current densities (at 10 coulomb/cm^2) can be explained (Fig. 17).

Ridges at 10 ma/cm^2 are of the same orientation as those at 15 ma/cm^2 and yet no significant increase in η at 10 coulomb/cm^2 was observed (Fig. 14 and 17). This agrees with the observation that at 10 ma/cm^2 not all the surface of the electrode was covered by ridges. Hence, the observed changes of overpotentials with time of deposition on the main three crystal planes of Cu are due to the change in the over-all activity of electrode surface. The latter change arises from the growth of new crystal planes with different orientations and exchange current densities.

Effect of n-decylamine.—Faster decrease of overpotentials with time of deposition on the (111) plane at 2 and 5 ma/cm^2 in the presence of n-decylamine can also be attributed to the formations of new faces of different activity.

In the presence of n-decylamine one would expect "bunching" of monatomic steps which originate at the apex of a pyramid and propagate down their side faces to occur more readily since, in this case, their propagation would be disturbed more than in "pure" solutions. If so, surface area of the newly formed smooth and more active faces close to the apex of pyramids will decrease. Hence, less change in overpotential with time is expected in the presence of n-decylamine than in "pure" solutions. This is contrary to the experimental observation.

In the presence of n-decylamine crystallographically different pyramidal faces form than those in "pure" solutions. This was shown to be the case for copper deposition on the (100) plane. The inclination of pyramidal faces in "pure" solution was found to be larger than in "impure" solution. Even a slight change in the inclination could produce crystal planes with different activities. Side faces of macrosteps, both on the flat substrate and on the pyramidal faces, may also correspond to different crystallographic planes when formed in "pure" solutions or in solutions containing n-decylamine.

The Exchange Current Density

Different values of the exchange current density, i^o, on the main crystal planes (cf. Table II) may, in principle, arise from the change in: (*A*) the mechanism of the reaction, (*B*) the concentration of adions on various crystallographic planes, (*C*) the bond strength between substrate and adions, (*D*) the density of "growth sites" or steps on the surface, and (*E*) the work function. These possibilities are discussed below.

The mechanism of the reaction.—The mechanism of the reaction has been studied in detail by Mattson and Bockris (4), and Bockris and Enyo (5). It is

$$Cu^{++} + e^- \rightarrow Cu^+ \qquad [7]$$

$$Cu^+ + e^- \rightleftharpoons Cu \qquad [8]$$

with the first charge transfer as the rate-controlling step. Bockris and Kita (6) confirmed this mechanism for electrodeposited copper electrodes.

Tafel relationships established in the present experiments are in accordance with the first charge transfer as the rate-controlling step over the range of current densities examined on all the three crystal planes.

Dependence of i^o_{hkl} on adion concentration.—For the first charge transfer rate-controlling, the change in the concentration of adions from one crystal plane to another should not affect the activation energy for the rate-controlling step (6). Adion concentration may, however, affect the rate even under these conditions if the "active" surface area changes with adion coverage. Thus, it is in principle possible that (6)

$$i^o = K[Cu^{++}]\,(1-\theta)\exp(-\beta F V_{REV}/RT)\cdot \exp(-\Delta H^*_1/RT) \qquad [9]$$

where V_{REV} is the reversible electrode potential with respect to a reference electrode, ΔH^*_1 the activation energy for forward reaction, and θ the coverage by adions. There is little (16) or no (18) difference in V_{REV} on different crystal planes of copper. Therefore, the ratio of exchange current densities for the (111) and the (110) planes is given by (6)

$$\frac{i^o_{111}}{i^o_{110}} = \frac{(1-\theta_{111})}{(1-\theta_{100})}\exp[-\beta(H_{111}-H_{110})/RT] \qquad [10]$$

where $\beta(H_{111} - H_{110})$ is the change in the activation energy due to the change in the potential energy of Cu^+ for different crystal planes. If this change is taken as negligible (6), it follows that

$$\frac{i^o_{111}}{i^o_{110}} \approx \frac{(1-\theta_{111})}{(1-\theta_{110})} \qquad [11]$$

From experimental results, i^o_{111}/i^o_{110} is about 0.12, and, consequently, θ_{111} should be greater than θ_{110}.

It is possible to estimate the ratio of coverages on different planes. For the (111) and (110) planes

$$c^{o}_{111}/c^{o}_{110} = [\exp - \Delta F/RT] \quad [12]$$

where $\Delta F = F_{111} - F_{110}$, and F_{111} and F_{110} are the free energies of adsorption of adions on the (111) and (110) planes, respectively. On the (111) plane, an adion has 3 close neighbors in the substrate; on the (100) 4, and on the (110) 5. Energy of the adsorption will depend on the number of bonds formed by an adion. As a first approximation $\Delta F \approx \Delta H$, where ΔH is the heat of adsorption and is estimated from the difference in the number of bonds formed on both planes. It follows that

$$\Delta H = -\frac{L}{6}\cdot 3 + \frac{L}{6}\cdot 5 = \frac{L}{3}\left[\frac{\text{kcal}}{\text{mole}}\right] \quad [13]$$

where L ($\approx$ 84.8 kcal/mole) is the heat of sublimation for copper. Next, hydration energy terms should be considered. In the solution, primary hydration number for Cu^{2+} is approximately 12. The degree of hydration of an adion will depend on the site on the surface. Conway and Bockris (19, 20) calculated the heat of hydration of copper adions at various sites on the surface. Assuming that primary coordination by water molecules is 4 and 3 on the (111) and (110) planes, respectively, the corresponding heats of hydration are found to be —40 and —28 kcal/mole, The difference in the hydration energies is 12 kcal/mole, and $\Delta H \simeq 16$ kcal/mole. This calculation, however approximate, shows that adion concentration on the (110) is expected to be higher than on the (111) plane. Even if the difference in primary coordination of adions were 2, and the difference in the heat of hydration of adion on two planes were —19 kcal/mole [cf. Conway and Bockris (19, 20)], ΔH would be large and positive. Similar reasoning hold if the (111) plane is compared to the (100). It follows that c^{o}_{111} is less than c^{o} on the other two planes, and the change of i^{o} with the crystallographic plane cannot be accounted for by the change in adion concentration.

Dependence of i^{o}'s on energy of adion adsorption and on density of "growth sites."—For the first charge transfer as the rate-controlling step, the energy of adion adsorption should not affect the activation energy of the step, since the reaction product in the rate-controlling step, Cu^{+}, is fully hydrated and not yet attached to the electrode (6).

The density of "growth sites" or steps on the surface changes the rate with which adions can diffuse to and incorporate into the lattice. However, since the first charge transfer is rate-controlling, no affect on the over-all rate of the reaction should occur. Hence, the dependence of i^{o} on crystal plane cannot be explained in terms of adsorption energy or the density of growth steps.

Dependence of exchange current density on work function.—A possible dependence of the exchange current density on work function can be analyzed in the following way.

In a cell with a single crystal test electrode exposing the (*hkl*) plane, the measured potential difference,[8] ΔV, with respect to any reference electrode is given by

$$-\Delta V = -\phi^{In}_{hkl} + \phi^{In}_{S1} - \phi^{In}_{S1} + \phi^{In}_{REF} + V_c \quad [14]$$

Here, ϕ^{In} is the inner potential of the phase considered, (hkl) stands for the given crystal plane, REF for the reference electrode, and S1 for the solution. V_c is the contact potential difference between the two solids of which the electrodes are made, and is equal to (23, 24)

$$V_c = \Phi_{REF} - \Phi_{hkl} \quad [15]$$

where Φ_{REF} and Φ_{hkl} are the work functions for the reference and the test electrode, respectively. With

[8] By potentiometry.

$$\Delta\phi_{hkl} = \phi^{In}_{hkl} - \phi^{In}_{S1} \quad [16]$$

and

$$\Delta\phi_{REF} = \phi^{In}_{REF} - \phi^{In}_{S1} \quad [17]$$

where $\Delta\phi$'s are the corresponding galvani potentials, and with [15], Eq. [14] becomes[9]

$$\Delta\phi_{hkl} = \Delta V + \Delta\phi_{REF} - \Phi_{hkl} + \Phi_{REF} \quad [18]$$

The rate of an activation controlled cathodic reaction, when the rate of anodic reverse reaction is negligible and the ionic strength of the electrolyte sufficient to make the diffuse part of the double layer comparatively small, can be written as

$$i_{hkl} = k\,[Cu^{++}]\exp\left[-\frac{\Delta G^{o\neq}_{hkl} + (\Delta V + \Delta\phi_{REF} - \Phi_{hkl} + \Phi_{REF})\alpha F}{RT}\right] \quad [19]$$

Here, k is the rate constant independent of the work function, and $\Delta G^{o\neq}_{hkl}$ is the activation energy for the rate-determining step and depends on the work function, and thus on the crystal plane considered. When no net current flows across the test electrode, and since for the same reference electrode and the same experimental conditions, $\Delta\phi_{REF} + \Phi_{REF}$ remains constant, [19] transforms to

$$i^{o}_{hkl} = K\exp\left[-\frac{\Delta G^{o\neq}_{hkl}}{RT}\right]\exp\left[\frac{\alpha F\,\Phi_{hkl}}{RT}\right]\exp\left[-\frac{\alpha F\Delta V_{REV}}{RT}\right] \quad [20]$$

where i^{o}_{hkl} is the exchange current density for the (hkl) plane, and ΔV_{REV} is the reversible electrode potential with respect to the reference electrode.[10]

Activation energy $\Delta G^{o\neq}_{hkl}$ is not readily calculated. However, the change in the activation energy arising from the change of the crystal plane, $\Delta G^{o\neq}_{hkl} - \Delta G^{o\neq}_{h'k'l'}$, can numerically be evaluated from the change in the heats of the reaction $Cu^{++}_{aq} + e^{-} \rightarrow Cu^{+}_{aq}$ with the crystal plane considered. Thus, from the cycle

$$\begin{array}{ccc} Cu^{++}_{aq} + e^{-}_{M} & \xrightarrow{\Delta H^{o}_{M}} & Cu^{+}_{aq} \\ \uparrow H_{Solv}\,Cu^{++} & & \downarrow -\Delta H_{Solv,Cu^{+}} \\ Cu^{++} + e^{-} + aq & \xleftarrow{\bar{\mu}\quad I_{Cu^{+}}} & Cu^{+} + aq \end{array} \quad [24]$$

where $\bar{\mu}$ is the electrochemical potential of an electron in the metal, and other symbols have their usual meaning, it follows that

$$\Delta H^{o}_{M} = -\Delta H_{Solv,Cu^{+}} - I_{Cu^{++}} - \bar{\mu} + \Delta H_{Solv,Cu^{++}} \quad [25]$$

The difference in the heat of reaction on two crystal planes is then given by

$$\Delta H^{o}_{hkl} - \Delta H^{o}_{h'k'l'} = (\bar{\mu}_{hkl} + \bar{\mu}_{h'k'l'})F \quad [26]$$

With

$$\bar{\mu} = \mu + e\phi^{In} \quad [27]$$

and since μ is independent of the crystal plane

[9] Identical relationship has been obtained by Bockris and Potter (25).

[10] The absolute reversible electrode potential of an electrode with a single crystal plane exposed to the solution can be written [cf. Kortüm and Bockris (26)] as

$$\Delta\phi_{REV} = K - \Phi_{hkl} \quad [21]$$

where the constant K is independent of the crystal plane. The change in the reversible electrode potential arising from the change in the crystal plane from (hkl) to (h'k'l')

$$\Delta\Delta\phi_{REV} = \Phi_{h'k'l'} - \Phi_{hkl} \quad [22]$$

For the same reference electrode, this change is compensated by the change in the contact potential which arises at the metal-metal junction between the metal of the working electrode and the metal of the reference electrode. This is

$$\Delta\phi_{contact} = \Phi_{hkl} - \Phi_{h'k'l'} \quad [23]$$

$$-\bar{\mu}_{hkl} + \mu_{h'k'l'} = e\,(-\phi^{In}{}_{hkl} + \phi^{In}{}_{h'k'l'}) \quad [28]$$

From [14] and [15] it follows

$$-\phi^{In}{}_{hkl} + \phi^{In}{}_{h'k'l'} = \Phi_{hkl} - \Phi_{h'k'l'} \quad [29]$$

and [26] transforms to

$$\Delta H^{o}{}_{hkl} - \Delta H^{o}{}_{h'k'l'} = e\,(\Phi_{hkl} - \Phi_{h'k'l'}) \quad [30]$$

Assuming now that the entropy terms are nearly the same for the reactions on both crystal planes, then

$$\Delta G^{o\neq}{}_{hkl} - \Delta G^{o\neq}{}_{h'k'l'} = \beta F(\Phi_{hkl} - \Phi_{h'k'l'}) \quad [31]$$

where β is the symmetry factor.

The ratio of the exchange current densities on two different crystal planes is given from [20] as

$$\frac{i^{o}{}_{hkl}}{i^{o}{}_{h'k'l'}} = \exp\left[-\frac{(\beta-\alpha)(\Phi_{hkl} - \Phi_{h'k'l'})F}{RTT}\right] \quad [32]$$

It is apparent, therefore, that, if $\alpha = \beta \approx \frac{1}{2}$, the exchange current density, on the above basis, should not depend on the difference in the work function on the corresponding crystal planes. It is possible however, that $\alpha \neq \beta$ which would result in the dependence of the exchange current density on the crystal plane. In fact, if for the reaction [7] tunneling of electrons were possible [cf. Bockris and Matthews (27)], β would be less than $\frac{1}{2}$. In this case, and with $\alpha \gtrsim \frac{1}{2}$, the ratio of the exchange current densities on the (111) and (110) planes

$$\frac{i^{o}{}_{111}}{i^{o}{}_{100}} = \exp\left[\frac{\gamma(\Phi_{111} - \Phi_{100})F}{RT}\right] \quad [33]$$

where

$$\tfrac{1}{2} > \gamma > 0 \quad [34]$$

can be accounted for only if

$$\Phi_{111} < \Phi_{100} \quad [35]$$

Recently, Blevis and Crowell (28) measured (on a relative scale) work functions on the main crystal planes of copper at various temperatures. Their analysis of the work functions on different planes agreed with the older findings of Underwood (29) that the work function on the (100) plane is positive in respect to the (111) plane by about 0.5v. This value would satisfy the observed ratio $i^{o}{}_{111}/i^{o}{}_{100}$ (< 1) if γ is approximately equal to 0.1, or $\beta \gtrsim 0.4$.

Effect of $CuSO_4$ *Concentration on the Deposition*

Morphology of the deposit does not change with Cu^{++} concentration. The overpotentials at 5 ma/cm² from 1M $CuSO_4$ solution, on average, are by 60-70 mv lower than those from 0.25M solution (Fig. 15) with

$$i^{o} = k\,[Cu^{++}] \cdot e^{-\alpha F V_{REV}/RT} \quad [36]$$

and

$$V_{REV} = V_{REV_0} + RT/2F \ln [Cu^{++}] \quad [37]$$

$$\left\{\frac{\partial\eta}{\partial \ln [Cu^{++}]}\right\}_{i,T} = RT\,(2-\alpha)/2\alpha F \quad [38]$$

or with $\alpha \approx \frac{1}{2}$

$$\left\{\frac{\partial\eta}{\partial \log [Cu^{++}]}\right\}_{i,T} \approx 90 \text{ mv}$$

Data from only two points are available and indicate a slope larger than 90 ($\sim$ 150) mv. Were the second step rate-controlling, $\partial\eta/\partial \log [Cu^{++}]$ would have much lower ($\sim$ 10 mv) slope (4, 6). This confirms that, at both concentrations, the rate-controlling step is the first charge transfer.

The Rate of Growth and the Rate of Deposition

Were the deposit evenly distributed all over the smooth substrate, the calculated rate of growth normal to the substrate, v, would be given by approximately

$$v = 3.75\,i \quad [39]$$

where the current density, i, in ma/cm² gives v in Å/sec. At 2 ma/cm² this rate is 7.5 Å/sec. From Table I, it follows that the rate of macrostep propagation, either on smooth substrate or on pyramidal faces, is about 7 times higher than this calculated rate.

While the rate of propagation of macrosteps, both on pyramidal faces and on smooth substrate, increases with current density, the rate at which pyramidal bases advance laterally was found independent of the current density. The constant rate is not due to local exhaustion of cations which would result in local limiting currents being set up in the neighborhood of the growing pyramids (or steps). Thus, to a first approximation the (local) limiting current should be proportional to the bulk concentration of copper sulfate, c_o, as

$$i_{lim} = K c_o$$

If the rates of growth are limited by diffusion in the solution, they should change with the concentration. When the concentration was changed by factor 20, no change in the rates was observed.

The amount of the deposited metal required for the pyramid formation on the (111) plane can be calculated from the size of pyramids and their density. Thus, in a typical case, the height of pyramids at 10 coulomb/cm² is determined by polarized interferometry at 1.25 x 10⁴Å. The length of a pyramid base was 1.5 x 10⁵Å, and the density of pyramids about 3 x 10⁵ cm^{-2}. The volume of all pyramids at the time of deposition corresponding to 10 coulomb/cm² is then about 2 x 10^{-5} cm³/cm². This volume corresponds to about 6% of the total deposited metal.[11] Thus, to account for all the metal deposited, it has to be assumed that incorporation of Cu-adions occurs also over the flat substrate. This implies that, while a pyramid grows, it is at the same time "buried" by evenly advancing substrate. Consequently, the true rate of growth is not measured (cf. Fig. 18). From Fig. 18, it follows that

$$x = x_o + h \cot \alpha \quad [40]$$

where $h = vt$, and α is the inclination of the pyramidal face toward the substrate. Then, the true rate of growth is given by

$$v_{pyr} = dx/dt = dx_o/dt + v \cot \alpha = v_o + v \cot \alpha \quad [41]$$

where v_o is the observed rate of pyramid propagation. With numerical values for 5 ma/cm² (Table I), v_{pyr} is equal to

$$v_{pyr} = 55 + 18.7 \times 5 = 148.5 \text{ Å/sec}^{-1}$$

This rate is close to the observed rate (135 ± 15 Å/sec) of macrostep propagation on the pyramidal faces. Under ideal conditions therefore the rate at which macrosteps on pyramidal faces propagate is the rate at which the base of the pyramid would propagate were it not for the simultaneous "burying." The latter rates are thus close to the rate with which most of the macrosteps on "smooth" substrate propagate.

At a constant current density, potential changes with time and hence the (relative) rate of deposition and of incorporation of adions[12] into the lattice at the newly formed faces of macrosteps should change with time or thickness of the deposit, contrary to the reported observation of constant (with time) rate of macrostep propagation. The main change in the potential occurs, however, at the initial stage of deposition, while the rate of macrostep propagation was determined for the latter stages of deposition when potential becomes constant.

[11] At initial stages of deposition, the percentage has to be less, as the area of the "flat" substrate is initially larger and decreases with time of deposition. In this particular case, the electrode becomes almost fully covered by pyramids at 10 coulomb/cm².

[12] The effect of the delivery of adions to growth sites by surface diffusion is neglected.

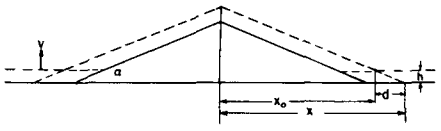

Fig. 18. A model for pyramid growth.

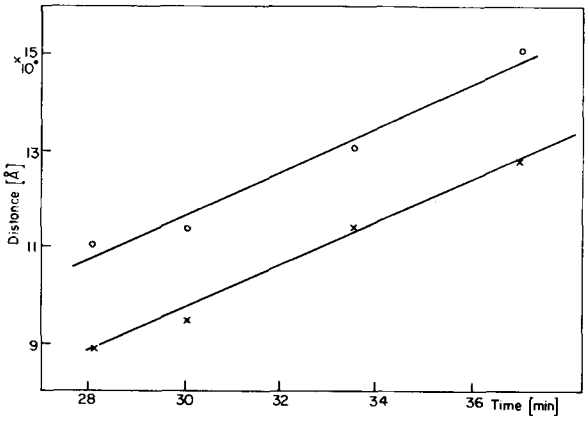

Fig. 19. Position of two macrosteps on a pyramidal face vs. time of deposition, 2 ma/cm^2.

The Mechanism of the Growth of Pyramids

The formation of pyramids on the (111) plane can be accounted for by the screw dislocation mechanism of growth. The appearance of a straight line on the apex of some pyramids instead of "sharp" point favors the mechanism involving a pair of screw dislocations of opposite signs. Macrosteps on side faces of pyramids form by initial bunching of small, ideally monatomic steps which originate at the apex of the pyramid. In support of the bunching mechanism is the fact that close to the apex of pyramids no visible steps appear [cf. ref. (1), (29), and (30)].

Formation of "hexagonal" blocks on the (111) deposits at higher current densities corresponds to the formation of cubic blocks (or layers) on the (100) plane, the mechanism for both of which has already been discussed (1, 8, 11). First, regular pyramids form, the apex of which may become in time blocked by adsorbed impurities. New microsteps then will spread no longer from the apex, and the pyramid truncates. Truncated pyramids gradually transform into blocks.

On the (110) plane, pyramidal growth under the given experimental conditions rarely occurs, and ridges and/or "smooth" deposits form. It is likely that on an ideal (110) plane any site is a growth site. There is no need for surface diffusion of adions and of propagation of microsteps. For pyramidal growth, propagation of microsteps is essential, and consequently no pyramids would be expected to form on the (110) planes. For an understanding of ridge formation, particularly of different current densities, further detailed analysis of the geometry of ridges is required.

Acknowledgments

The authors are indebted to the American Electroplaters' Society for the continued support of this work. They also wish to acknowledge the help they have derived from numerous discussions of results and theory in this field with Mr. E. R. Bowerman, Dr. O. Kardos, Dr. J. Kruger, Dr. J. V. Petrocelli, Dr. D. R. Turner, and Dr. R. Weil.

Thanks are also due to Mr. M. Paunovic for making available some of his experimental data on the (100) plane, and to Mr. G. Razumney for help in some of the measurements, for valuable discussions of some aspects of this work. Thanks are also due to Mr. O. Shannon for machining the cell, and to Mr. T. Dawson for glassblowing.

Manuscript received April 19, 1965; revised manuscript received Jan 29, 1966.

Any discussion of this paper will appear in a Discussion Section to be published in the December 1966 JOURNAL.

REFERENCES

1. A. Damjanovic and J. O'M. Bockris, "Modern Aspects of Electrochemistry," Vol. III, p. 224, Butterworths Scientific Publications, London (1964).
2. W. Mehl and J. O'M. Bockris, *Can. J. Chem.*, **37**, 190 (1959).
3. A. Despic and J. O'M. Bockris, *J. Chem. Phys.*, **33**, 389 (1960).
4. E. Mattsson and J. O'M. Bockris, *Trans. Faraday Soc.*, **55**, 1586 (1959).
5. J. O'M. Bockris and M. Enyo, *ibid.*, **58**, 1187 (1962).
6. J. O'M. Bockris and H. Kita, *This Journal*, **109**, 48 (1962).
7. H. Gerischer, *Z. Elektrochem.*, **62**, 256 (1958).
8. A. Damjanovic, M. Paunovic, and J. O'M. Bockris, *J. Electroanal. Chem.*, **9**, 93 (1965).
9. A. Damjanovic, M. Paunovic, and J. O'M. Bockris, *Electrochemica Acta*, **10**, 111 (1965).
10. A. Damjanovic, M. Paunovic, and J. O'M. Bockris, *Plating*, **50**, 735 (1963).
11. D. R. Turner and G. R. Johnson, *This Journal*, **109**, 798 (1962).
12. G. Nomarski and A. R. Weil, *Rev. Metallurgies*, **52**, 121 (1955).
13. N. A. Economou, H. Fischer, and D. Trivich, *Electrochim. Acta*, **2**, 207 (1960).
14. H. J. Pick, G. G. Storey, and T. B. Vaughan, *ibid.*, **2**, 165 (1960).
15. E. Glueckauf, *Nature*, **163**, 414 (1949).
16. W. E. Tragert and W. D. Robertson, *This Journal*, **102**, 86 (1955).
17. R. Piontelli, G. Poli, and G. Serravalle, In "Transactions of the Symposium on Electrode Processes," E. Yeager, Editor, John Wiley & Sons, Inc., New York (1961).
18. L. H. Jenkins and U. Bertocci, *This Journal*, **112**, 517 (1965).
19. B. E. Conway and J. O'M. Bockris, *Proc. Royal Soc.*, **248**, 394 (1958).
20. B. E. Conway and J. O'M. Bockris, *Electrochim. Acta*, **3**, 360 (1960).
21. A. Damjanovic and J. O'M. Bockris, *This Journal*, **110**, 1035 (1963).
22. H. Seiter, H. Fischer, and L. Albert, *Electrochim. Acta*, **2**, 97 (1960).
23. R. V. Culver and F. C. Tompkins, "Advances in Catalysis, XI," 68 (1959).
24. R. Parsons, "Modern Aspects of Electrochemistry," Vol. I, p. 103, Butterworths Scientific Publications, London (1954).
25. J. O'M. Bockris and E. Potter, *This Journal*, **99**, 169 (1952).
26. G. Kortüm and J. O'M. Bockris, "Textbook of Electrochemistry," p. 255, Elsevier Publishing Co., New York (1951).
27. J. O'M. Bockris and D. Matthews, Thesis, University of Pennsylvania (1965).
28. E. H. Blevis and C. R. Crowell, *Phys. Rev.*, **133** (2A), 580 (1964).
29. N. Underwood, *ibid.*, **47**, 502 (1935).
30. F. C. Frank, "Growth and Perfections of Crystals," p. 411, John Wiley & Sons, London (1958).
31. T. B. Vaughan and H. J. Pick, *Electrochim. Acta*, **2**, 179 (1960).

Electrodeposited Ni-Fe-As Magnetic Thin Films

W. O. Freitag, G. DiGuilio, and J. S. Mathias

UNIVAC Division, Sperry Rand Corporation, Blue Bell, Pennsylvania

ABSTRACT

Thin films (1000-2000Å) containing 6-20% Fe, 1-15% As, balance Ni were electrodeposited from mixed nickel-ferrous sulfate solutions containing sodium arsenite. Arsenite concentration and ferrous sulfate concentration in the solution were related to the film composition and the magnetic properties. The effects of As in Ni-Fe films was found to be similar to those of P, *i.e.*, H_c and H_k values were lower and switching times were much more rapid in the ternary films than in similarly prepared binary films. Quarternary alloy films of Ni-Fe-As-P are also described.

This work is an outgrowth of earlier studies on the Ni-Fe-P and Ni-Fe-Mo film alloy systems which have already been reported (1,2). Electrodeposited thin films in the alloy system Ni-Fe-As have been investigated and evaluated as magnetic elements for computer memory use, and results are described. A limited amount of work in the quarternary system Ni-Fe-As-P is also discussed.

The objective of the over-all program has been the development of the electrodeposition method for preparation of films having controllable and reproducible magnetic properties.

Experimental

The substrates were 3 by 3 in. microcover sheet, 0.002-0.010 in. thick, coated with vacuum-evaporated layers of chromium and gold. Corning 7059 glass, 1 by 2 by 0.032 in. was also used. The depositions were carried out in rectangular Lucite cells which were fitted with removable cathode holders, permitting accurate alignment of the cathode to the cell. A uniform magnetic field of 30 oe surrounded the cell. Anodes were of nickel sheet. No agitation was used. The current density was normally 6 ma/cm^2 delivered by a constant-current power supply. The films were electrodeposited at room temperature from nickel and ferrous sulfate solutions of the Watts type, containing boric acid, sodium chloride, saccharin, and sodium lauryl sulfate.

The compositions of the electrolytes are shown in Table I. Arsenic was introduced as sodium arsenite. Two series of solutions were made up. In one, the sodium arsenite concentration was varied, and in the other, the ferrous sulfate concentration was varied.

Films were chemically analyzed as follows: A known film area is dissolved in 1:2 HNO_3 and diluted to volume. Arsenic is determined on one aliquot colorimetrically by the molybdenum-blue method after low-temperature evaporation of HNO_3. Spectrophotometric measurements at 820 mμ were made on a Beckman DU. The method was calibrated with standard solutions in the range from 0.006 to 0.3 mg/100 cc. Dissolved film samples 1 by 2 in. in area, containing about 5% As, commonly gave readings in the 0.04 mg/100 cc range. Accuracy in the 5% As range is believed to be ±0.5%.

Nickel and iron are determined on other aliquots colorimetrically as nickel dimethylglyoxime and iron orthophenanthroline. These are also spectrophotometric measurements and are believed to be accurate to within 0.5%. A nickel/iron ratio calculated from these determinations is accurate to within 3%.

The magnetic properties were measured in a 60-cycle BH loop tracer (1) the drive field of which was oriented parallel to the horizontal component of the earth's field. The sample could be placed into the sense coil either parallel to the easy axis for measurement of H_c, or perpendicular for H_k. Relative magnetostriction values were obtained from the change in H_k when tension was applied along the hard axis by flexing the sample into a fixed arc. Magnetic measurements are believed accurate to ±5% or better.

Table I. Composition of plating solutions for the deposition of Ni-Fe-As alloy thin films

Component	Composition of Plating Solutions Concentration, (g/l) Series N solutions	Series P solutions	Preferred
$NiSO_4 \cdot 6H_2O$	218	218	218
$FeSO_4 \cdot 7H_2O$	3.0-8.1	6.0	6.0
$NaAsO_2$	0.4	0.05-1.5	0.4
H_3BO_3	25.0	25.0	25.0
NaCl	9.7	9.7	9.7
Saccharin	0.8	0.8	0.8
Na lauryl sulfate	0.2	0.2	0.2
pH	2.2	2.2	2.2

Film Composition as a Function of Electrolyte Composition

Figures 1 through 6 show the effects of variation of the electrolyte composition on the composition of the electrodeposited films. Figure 1 shows the linear increase in arsenic content with increase in sodium arsenite concentration. This was done with the series-P solutions, where the Ni and Fe concentrations were held constant, as was the deposition time. The range studied was from 0.05 to 1.5 g/l arsenite. We did not go higher because the magnetic properties were poor at 1.0 g/l and the deposits appeared streaked and discolored at 1.5 g/l. Figure 2 shows the effect of arsenite concentration on the Ni/Fe ratio in the film. This ratio increases as arsenite concentration increases, although this is not too obvious in view of the scatter of experimental points. The films were plated for 70 sec and had a thickness of 1300Å. Two other sets of films were plated at the same time from these solutions at

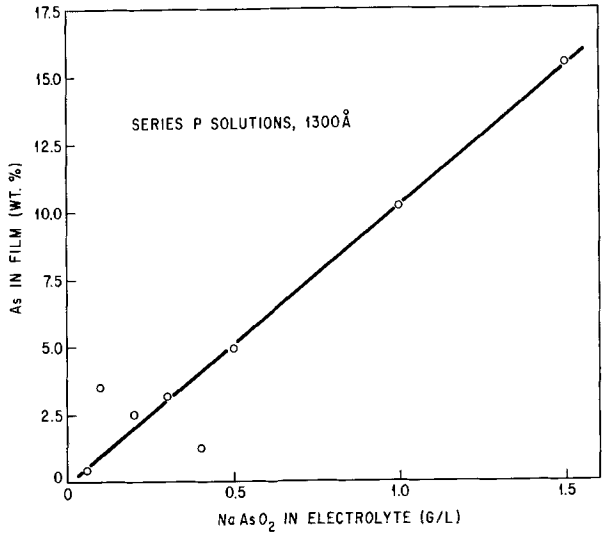

Fig. 1. Arsenic content of 1300Å films as a function of sodium concentration in the electrolyte. Deposition time was 70 sec at 6 ma/cm^2.

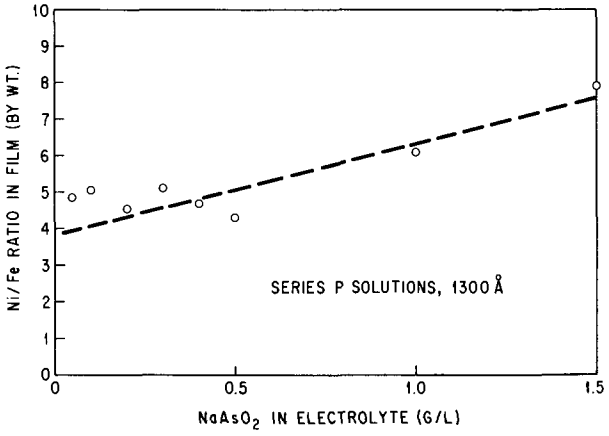

Fig. 2. Nickel and iron content of 1300Å films as a function of sodium arsenite concentration in the electrolyte. The nickel and iron content of the electrolyte was held constant. Deposition time was 70 sec at 6 ma/cm^2.

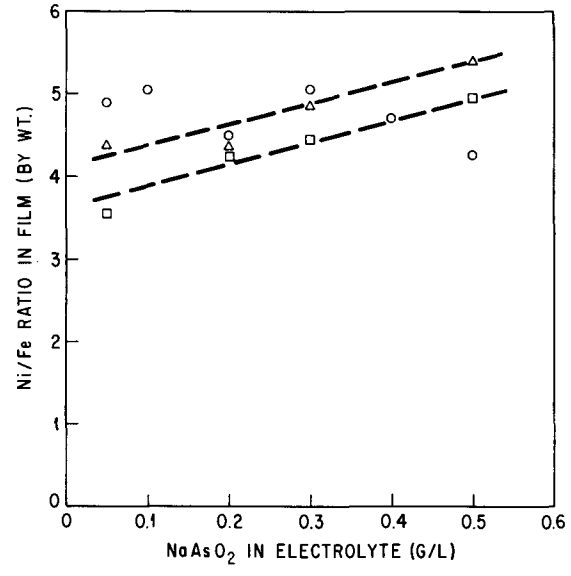

Fig. 3. Nickel and iron content of 1100 and 1500Å films as a function of sodium arsenite concentration in the electrolyte. Plated under the same conditions as in Fig. 4, but for 60 and 80 sec, respectively. Series P solutions: △, 1500Å; ○, 1300Å repeated from Fig. 2; □, 1100Å.

60 and 80 sec, with thicknesses of about 1100 and 1500 Å, respectively. The analyses of these films are shown in Fig. 3, and the upward trend in Ni/Fe ratio is clear. The slope of these lines is about the same as the slope in Fig. 2. Thus the presence of arsenite ion in this system depresses the relative deposition rate of iron, just as hypophosphite ion does in the Ni-Fe-P system (1).

Figure 4 shows the effect of ferrous sulfate concentration on the iron content of the film. These films were deposited for 70 sec at 6 ma/cm^2, from a solution containing a constant 0.4 g/l sodium arsenite. As expected, the iron increases with increasing ferrous ion concentration. The arsenic content of these films is essentially constant; the change in iron concentration, therefore, has no effect on the deposition rate of arsenic.

The compositional variations that occur during the first few seconds of alloy deposition have been studied for nickel-iron by Cockett and Spencer-Timms (3), by Hemstock and Spencer-Timms (4), and by Dahms and Croll (5). The addition of hypophosphite ion reduces but does not eliminate the compositional gradient (1). A similar gradient occurs with Ni-Fe-Mo (2). Figure 5 shows iron content, arsenic content, and

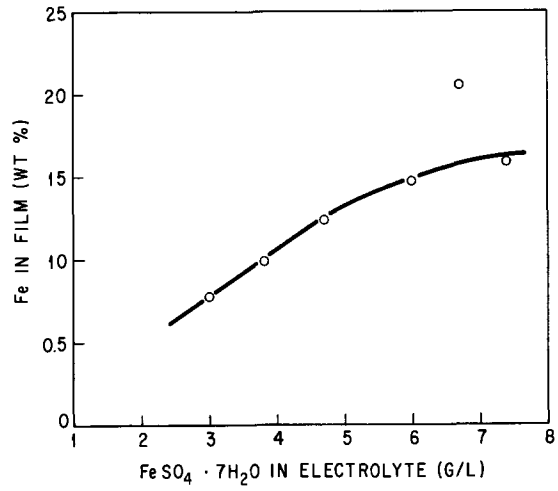

Fig. 4. Iron content in 1300Å films as a function of ferrous ion content in the electrolyte. Arsenite concentration was held constant. Series N solutions: $NaAsO_2$ = 0.4 g/l; plating time 70 sec; c.d. 6 ma/cm^2.

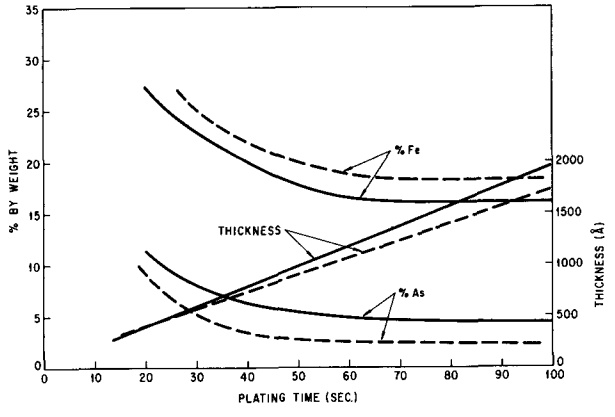

Fig. 5. Effect of plating time on the composition and thickness of Ni-Fe-As films. Series P solutions: c.d. 6.0 ma/cm^2; - - - 0.2 g/l $NaAsO_2$; —— 0.4 g/l $NaAsO_2$.

thickness *vs.* plating time for two levels of sodium arsenite concentration in the Ni-Fe-As system. The decrease in iron as deposition proceeds is apparent. The arsenic content also decreases with plating time. At a higher arsenic concentration the iron content is depressed further. The plating time *vs.* thickness curves have slightly different slopes, with the higher arsenic concentration giving slightly thicker films. This suggests a small increase in current efficiency, with increasing arsenite concentration.

The effect of current density on the film properties is shown in Fig. 6. As current density increases, the relative amount of arsenic occurring in the film decreases. This is what one would expect; since the arsenic is present in low concentrations, arsenic deposition should be diffusion-limited. The Ni/Fe ratio increases as current density increases. This agrees with the current density effects found by Hemstock and Spencer-Timms (4) and by Uehara (6) for Ni-Fe films. The same is true in the Ni-Fe-Mo system (2). The anisotropy of these films passes through a minimum as determined by the Ni/Fe ratio. As we shall see later, there is a minimum in the H_k *vs.* Ni/Fe ratio curve. The variation in H_k with current density can thus be simply explained solely on the basis of compositional changes.

Magnetic Properties as a Function of Electrolyte Composition

Figure 7 shows the effect of the arsenite concentration on the coercivity of films in three thicknesses. The

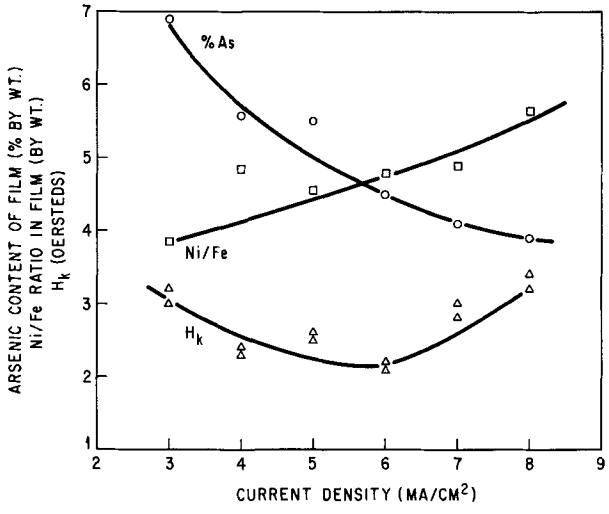

Fig. 6. Effect of current density on the composition and anisotropy field of 1600Å Ni-Fe-As films. Series P solutions: 0.4 g/l $NaAsO_2$.

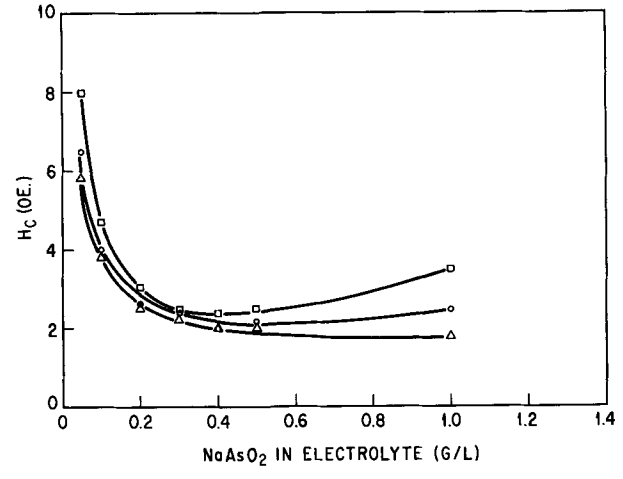

Fig. 7. Coercivity of Ni-Fe-As films deposited from solutions with varying amounts of sodium arsenite. Series P solutions: 6 ma/cm^2; □, 1100Å; ○, 1300Å, △, 1500Å.

addition of arsenic lowers H_c considerably. These films all have Ni/Fe ratios of 4 to 5, and the decrease in H_c brought about by the arsenic is quite clear. It is interesting to note that there appears to be a minimum in H_c which occurs at 0.4 to 0.5 g/l arsenite in the 1300Å films. In Fig. 1, it was shown that at this arsenite level the film contained about 5% As. This corresponds roughly to the solid solubility of As in Ni, which is given by Hansen (7) as 5.5%. Perhaps, at As concentrations above approximately 5%, a second phase appears which begins to raise H_c by interfering with domain wall motion. This is conjecture only, and no attempt at identification of a second phase was made, but the idea is supported by the behavior of the thinner and thicker films. If it is recalled that thinner films from a given solution contain more arsenic (and more iron) than thicker films, it will be expected that the 5% As level will be reached at a slightly lower arsenite concentration, and that the minimum will shift slightly to the left, which indeed it does.

Figure 8 shows the effect of sodium arsenite addition on the anisotropy of the films. Again, H_k values are lower than when As is absent. The Ni/Fe ratio of the deposit increases as sodium arsenite is increased; also, the Ni/Fe ratio increases slightly for increase in thickness, so that As concentration is not the only variable. The same considerations hold for Fig. 9, which shows the change in magnetostriction as As is added.

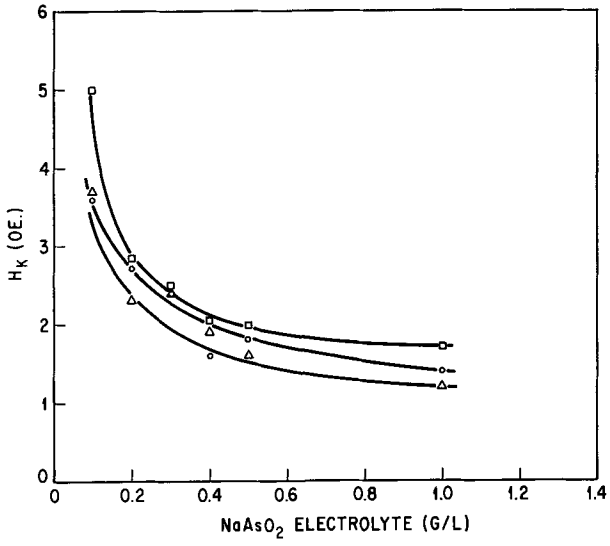

Fig. 8. Anisotropy of Ni-Fe-As films deposited from solutions containing varying amounts of sodium arsenite. Series P solutions: 6 ma/cm^2; □, 1100Å; ○, 1300Å; △, 1500Å.

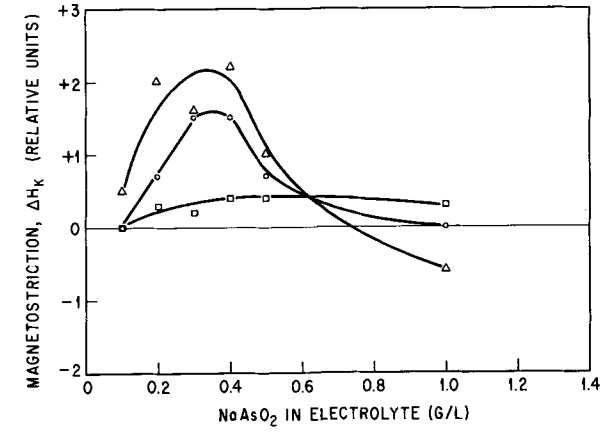

Fig. 9. Relative magnetostriction of Ni-Fe-As films as a function of sodium arsenite content in electrolyte. Series P solutions: 6 ma/cm^2; □, 1100Å; ○, 1300Å; △, 1500Å.

The magnetostriction units are arbitrary and represent the change in H_k when the sample is placed under tension. These values are positive for nickel-rich composition.

In addition to lowering H_c and H_k of Ni-Fe films, the presence of arsenic also results in greatly improved switching times as shown in Table II which lists switching coefficients for arsenic films. Some further improvements were obtained when the films were subjected to a very mild annealing step. In general,

Table II. Switching coefficient of 1300Å films

	Series P Solutions, 6 ma/cm^2 ¼-in. squares cut from 3- by 3-in. deposits							
	As prepared				After annealing*			
		Switching coeff. ($S_w \times 10^6$) Cross field (oe)				Switching coeff. ($S_w \times 10^6$) Cross field (oe)		
G/L $NaAsO_2$	H_k (oe)	0.19	0.38	0.57	H_k (oe)	0.19	0.38	0.57
0.05	Isotropic	—	—	—	Isotropic	—	—	—
0.1	4.0	Poor switch			3.8	Poor switch		
0.2	3.8	0.500	0.150	0.010	3.2	0.077	0.001	0.004
0.3	3.8	0.250	0.003	0.001	Blistered	—	—	—
0.4	2.4	0.281	0.013	0.005	1.9	0.030	0.003	0.004
0.5	2.2	0.205	0.015	0.005	2.0	0.020	0.006	0.005
1.0	1.8	0.020	0.005	0.005	1.6	0.010	0.001	0.010
1.5	No output	—	—	—	No output	—	—	—

* 250°C, 20 min in air.

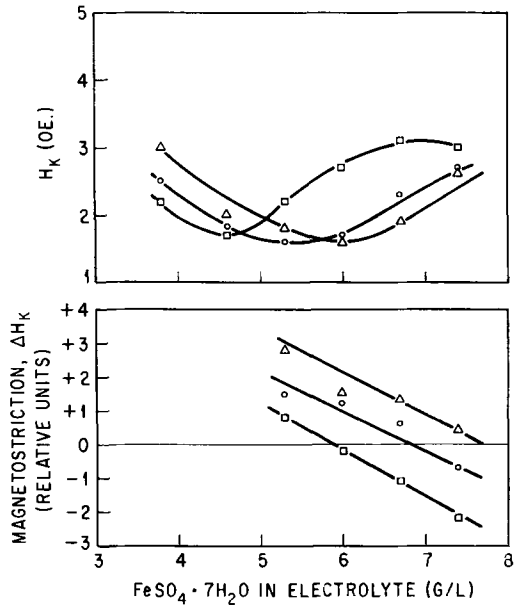

Fig. 10. Anisotropy and magnetostriction as a function of sulfate concentration. Series N solutions: 6 ma/cm^2; □, 1100Å; ○, 1300Å; △, 2000Å.

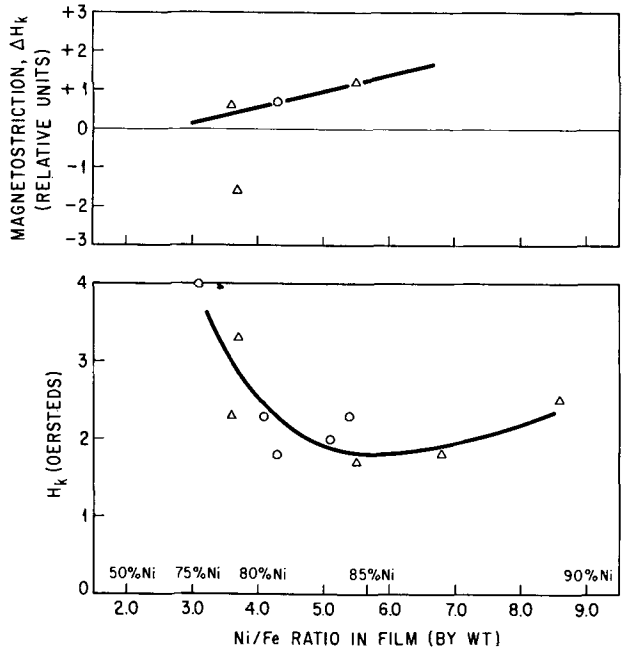

Fig. 11. Anisotropy and magnetostriction as a function of Ni/Fe ratio for films containing 4-5% As. Thickness 700-2000Å; ○, series P solutions; △, series N solutions.

however, the films were not annealed, and all data reported in this work refer to unannealed films as deposited.

The effect of varying the ferrous sulfate concentration is shown in Fig. 10; H_k passes through a minimum with increasing iron concentration. As film thickness is increased and the relative deposition rate of iron is decreased, it takes more and more Fe in the plating solution to produce the film composition having the minimum H_k value. Higher positive values of ΔH_k indicate nickel-rich compositions. Minimum H_k values do not coincide with the zero magnetostrictive compositions.

In Fig. 11, anisotropy and magnetostriction are plotted as a function of film composition, using the limited amount of analytical data available. Only films that had arsenic contents of 4-5% were selected. A wide range of thicknesses are represented, 500-2000Å, but the majority of the points are in the 1300Å region. The points were differentiated with respect to the two solutions used in their preparation to show the essential reproducibility of this plating system.

A minimum in H_k has been observed in both electroplated and evaporated Ni-Fe films. Wolf (8) reported the minimum at 80-88% Ni in electrodeposited films. The occurrence of this minimum in evaporated films has been attributed to a stress mechanism whereby differences in thermal expansion between film and substrate operate magnetostrictively. These arguments have been discussed by Robinson (9) who studied films evaporated on soda lime glass at 240°C. With respect to films electrodeposited at room temperature, thermal expansion can certainly not be the origin of any stress anisotropy, yet it seems clear that some stress mechanism must be operating. The role of stress relievers has been studied by Wolf (10), who showed the effects of the presence of various stress-relieving agents in the plating bath on H_k of 82% Ni films, but did not study this as a function of alloy composition. It is interesting to note that the addition of Mo to Ni-Fe films sharpens the minimum (2) as well as lowers it.

In Fig. 12, variations in magnetostriction are plotted as a function of plating time and arsenite concentration. In the left-hand side of the figure it is seen that as plating time increases (and the alloy becomes more nickel-rich) higher positive values of ΔH_k are obtained, as expected, at the arsenite concentrations we have been considering up to now. At high arsenite concentrations, the reverse appears to be true. Unfortunately, analyses are not available for these films, so it is not clear whether the Ni-Fe concentration trend is reversed in the high As films, or whether the high arsenic concentration itself is having a dominating effect on magnetostriction. The very high arsenic films were not investigated further, since they were less interesting for our purposes than the 0.4 g/l films.

Effect of Hypophosphite Addition

On the right-hand side of Fig. 12 is a similar set of curves obtained from these same solutions under the same conditions, except that sodium hypophosphite has been added. A well-behaved set of trend lines is obtained, but again the high arsenic films give anomalous results. In general, the effects of adding arsenic to Ni-Fe films are quite similar to the effects of adding phosphorus. Present together, their effects, qualitatively speaking, are additive; that is, H_c and H_k are lowered and rapid switching times are obtained.

The Ni-Fe-As-P composition was not explored in any detail, partly because of analytical difficulties. In

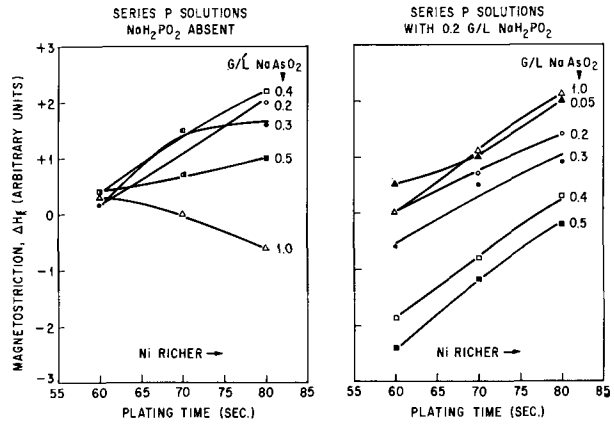

Fig. 12. Left, relative magnetostriction for Ni-Fe-As films as a function of plating time and sodium arsenite concentration. Right, same for Ni-Fe-As-P films obtained from the same solutions after addition of sodium hypophosphite.

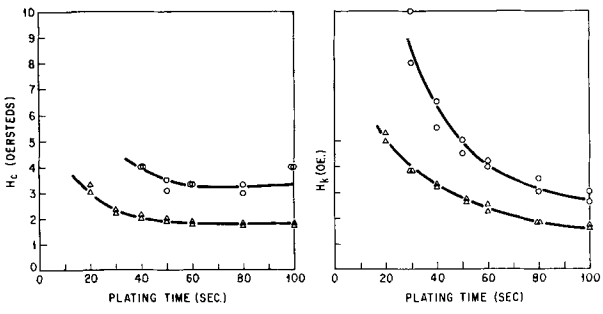

Fig. 13. Effect of substrate surface on coercivity and anisotropy. Series P solutions: 6 ma/cm^2, 0.2 g/l $NaAsO_2$; ○, Cr-Au evaporated on glass; △, electrodeposited Cu on Cr-Au evaporated on glass.

the 5% arsenic films, zero magnetostriction was associated with an anisotropy of about 2.5 oe.

A solution containing 6 g/l ferrous sulfate, 0.4 g/l arsenite, and 0.2 g/l hypophosphite yielded zero, or near zero, magnetostrictive films with H_k of 1.6-1.8 oe and H_c of 1.9-2.5 oe, with a high degree of reproducibility. The composition of these films was about 83% Ni, 13% Fe, 2% As, and 2% P.

Effect of Substrate

In all this work, the substrates were evaporated Cr-Au layers on glass. Substrates must be prepared uniformly with a high degree of quality control, in order for a study of this sort to have meaning. The magnetic properties are, of course, functions of film thickness and composition, and the magnetic properties can be controlled by controlling the deposition parameters which affect composition. But this is practical only if a reproducible substrate is available. This is illustrated in Fig. 13, in which H_c and H_k values are compared for two sets of films, deposited from the same solution under identical conditions, except for the use in one case of Corning 7059 glass with evaporated Cr-Au layers, and in the other case of the same substrates having, in addition to the Cr-Au, an electrodeposited layer of copper. Striking differences in magnetic properties are found, and the copper surface is seen to have an even more reproducible surface than the Cr-Au. The effect of substrate material and substrate preparation procedures on magnetic properties has long been recognized by workers preparing films by vacuum evaporation or sputtering, but this point has not been emphasized in the electrodeposition literature.

Conclusion

It has been shown here that the addition of sodium arsenite to Ni-Fe sulfate solutions of the Watts type leads to the deposition of Ni-Fe-As alloy thin films with magnetic properties superior to those obtained with binary Ni-Fe films; that is, H_c and H_k are lower, and switching times are very fast.

The magnetic properties can be controlled by manipulating the electrolyte composition and plating parameters in a manner analogous to those applied to the Ni-Fe-P system. We have shown that even further improvements may be expected in the quarternary system Ni-Fe-As-P.

Manuscript received Nov. 24, 1965; revised manuscript received Jan. 21, 1966. This paper was presented at the Buffalo Meeting, Oct. 10-14, 1965.

Any discussion of this paper will appear in a Discussion Section to be published in the December 1966 JOURNAL.

REFERENCES

1. W. O. Freitag, J. S. Mathias, and G. DiGuilio, *This Journal*, **111**, 35 (1964).
2. W. O. Freitag and J. S. Mathias, *ibid.*, **112**, 64 (1965).
3. G. H. Cockett and E. S. Spencer-Timms, *ibid.*, **108**, 906 (1961).
4. M. E. Hemstock and E. S. Spencer-Timms, *Trans. Institute of Metal Finishing*, **40**, 179 (1963).
5. H. Dahms and I. M. Croll, *This Journal*, **112**, 771 (1965). Also Abstract No. 80, Meeting of the Electrochem. Society, Buffalo, N. Y., (October (1965).
6. Uehara, *Jap. J. Appl. Phys.*, 2, 451 (1963).
7. Hansen, "Constitution of Binary Alloys," 2nd ed. McGraw-Hill Book Co., New York (1958).
8. I. W. Wolf, *This Journal*, **108**, 959 (1961).
9. G. Robinson, *J. Phys. Soc. Japan*, **17**, *Supplement B-1*, 558 (1962).
10. I. W. Wolf, *Electrochem. Technol.*, **1**, 164 (1963).

Some Aspects of Sensitized Fluorescence in $Ca(PO_3)_2$:Sn:Mn Glass Phosphors

Richard F. Reade

Research and Development Laboratory, Corning Glass Works, Corning, New York

ABSTRACT

Sensitized fluorescence in $Ca(PO_3)_2$:Sn:Mn glass phosphors occurs via a direct transfer of excitation energy from tin to manganese centers. The transfer process is described in terms of its efficiency and the fraction of tin centers which participate. A statistical model for energy transfer is developed on the basis of a random distribution of tin and manganese ions and is shown to be consistent with the experimental data. The effective transfer range of approximately 8.8Å encompasses about 33 cation sites surrounding a tin center.

The phenomenon of sensitized fluorescence in impurity activated crystalline phosphors has been the subject of a considerable body of theoretical and experimental investigation. Klick and Schulman (1) have reviewed this work. Sensitized fluorescence involves two centers or ions, the sensitizer and the activator. The activator ion provides an emission band in a desired spectral region but does not absorb radiation in the excitation range of interest; frequently the 2537Å resonance line of a low-pressure mercury discharge lamp. The sensitizer ion introduces an absorption band in the required excitation range, and if present alone, will fluoresce with its characteristic emission spectrum. When both sensitizer and activator ions are present in a coactivated phosphor, the sensitizer will transfer part of its absorbed energy to the activator causing a fluorescence which is characteristic of the latter. The total fluorescence spectrum of the coactivated phosphor is thus a composite of the emissions of both ions, whose relative intensities are

dependent on the respective ion concentrations.

This paper describes a series of fluorescence intensity measurements designed to clarify the roles of tin and manganese in the energy transfer process leading to sensitized fluorescence in $Ca(PO_3)_2$:Sn:Mn glass phosphors. A statistical model for energy transfer is applied to the data.

Experimental

CaO and P_2O_5 were introduced as reagent grade monobasic calcium phosphate. The fluorescent ions were introduced as reagent grade oxides or carbonates. Reagent grade dextrose was used as a reductant to maintain tin and manganese in their divalent states. The well-mixed batches were melted at 1200°C using a platinum-wound resistance furnace, and annealed at 500°C. A portion of each sample was powdered to pass through a 100 mesh screen.

The fluorescence characteristics of the powdered samples were measured with a powder plaque fluorometer developed in this laboratory. In using this device, a planchet containing the powdered glass was placed under a circular, low pressure mercury discharge lamp. The lamp emission was filtered so that the 2537Å line was predominant. The fluorescence emission from the powdered glass was passed successively through blue, green, and red filters, detected by a photocell and measured by a galvanometer. The galvanometer shunt resistors were adjusted so that the reading obtained with each filter-photocell combination was directly proportional to the fluorescence intensity in the corresponding spectral region. In this manner equal blue, green, and red readings would be obtained for a phosphor which had a uniform spectral distribution of intensity. A magnesium tungstate phosphor was used as a calibration standard.

Fluorescence measurements.—The following quantities were determined experimentally or derived from experimental data.

I_{Sn} = Fluorescence intensity of a singly activated Sn glass.

$I_{Sn:Mn}$ = Total fluorescence intensity of a Sn:Mn coactivated glass.

I'_{Sn} = Tin component of fluorescence intensity in a Sn:Mn coactivated glass.

I'_{Mn} = Manganese component of fluorescence intensity in a Sn:Mn coactivated glass.

I_{Sn} and $I_{Sn:Mn}$ were obtained directly by summing the blue, green, and red readings from the powder fluorometer. I'_{Sn} and I'_{Mn} were obtained by summing the resolved tin and manganese readings for the coactivated glasses.

Resolution was accomplished by assuming that the spectral distribution of either ion, hence its distribution in the blue, green, and red regions of the spectrum was unaffected by the presence of the other ion. This assumption has been found valid for many crystalline phosphors (1, 2). Its validity in the present case was demonstrated by the fact that the ratio of the green to red readings for the resolved manganese intensity component was constant among all the coactivated glasses studied. To confirm the validity of these measurements, comparative fluorescence and excitation spectra were taken on an Aminco-Bowman Spectrofluorometer. Since the spectra were not corrected for instrument parameters, only qualitative results will be given.

It was found that the divalent manganese ion is inefficiently excited by radiation below 320 mμ. The feeble manganese fluorescence caused by 2537Å excitation of $Ca(PO_3)_2$:Mn glasses was too weak to be detected by the powder fluorometer. The manganese excitation spectrum of the coactivated, $Ca(PO_3)_2$:Sn:Mn glasses exhibited an additional, strong excitation band below 320 mμ which was associated with the Sn^{++} ion. The appearance of this band indicated that energy absorbed by the Sn^{++} centers is transferred to Mn^{++} ions causing them to fluoresce. In all other respects, the shape and position of the fluorescence or excitation bands for either ion were the same in both singly and coactivated glasses. Only the relative intensities varied. The presence of the characteristic tin fluorescence in the coactivated glasses showed that not all the tin centers participate in the energy transfer process. The tin excitation spectrum in the coactivated glasses exhibited no bands associated with manganese, indicating that Mn → Sn energy transfer does not occur.

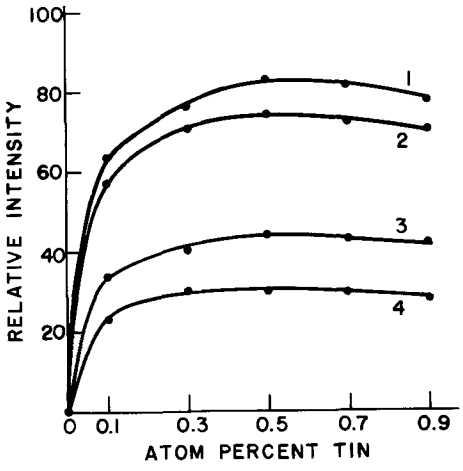

Fig. 1. Fluorescence intensity vs. tin concentration: curve 1, I_{Sn}: total intensity of Sn activated glasses; curve 2, $I_{Sn:Mn}$: total intensity of Sn:Mn coactivated glasses; curve 3, I'_{Mn}: Mn intensity component of Sn:Mn coactivated glasses; curve 4, I'_{Sn}: Sn intensity component of Sn:Mn coactivated glasses.

Results

Coactivated glasses with Mn *constant.*—Plots of fluorescence intensity *vs.* tin concentration for the tin activated glasses and for the Sn:Mn coactivated glasses with manganese held constant at 0.5 a/o (atom per cent) are shown in Fig. 1. The resolved tin and manganese intensity components of the coactivated glasses are also shown. The intensity maximum for the singly activated glasses occurs at a tin concentration of 0.5 a/o. The decrease in fluorescence intensity above this tin level may be caused by concentration quenching in the tin centers. This self-quenching effect has been attributed by Johnson and Williams (3) to the presence of a nonfluorescent center formed by two closely associated fluorescent ions. As the tin concentration increases, the number of these self-quenching, closely associated centers should increase, thereby lowering the fluorescence intensity.

The total intensity of the coactivated Sn:Mn glasses is consistently lower than that for the tin activated glasses, but the intensity maximum also occurs at about 0.5 a/o tin. The correspondence of these maxima indicates that tin self-quenching may be responsible for the intensity decrease in both Sn:Mn and Sn activated glasses.

The lower over-all intensity of the coactivated glasses is not surprising since an absorption and emission process within an isolated Sn^{++} ion is apt to be more efficient than one which involves the transfer of excitation energy between a tin and a manganese center (4). The energy transfer process should increase the probability for nonradiative energy losses accompanied by a decrease in the over-all fluorescence efficiency.

Variations in the tin concentration of the coactivated glasses did not alter the spectral distribution and color (pink) of the composite Sn:Mn fluorescence; only the intensity varied. $I_{Sn:Mn}$, I'_{Sn}, and I'_{Mn} vary similarly with tin concentration denoting a constant I'_{Sn}/I'_{Mn} ratio, and hence a constant fluorescence color. Since the spectral distribution of either ion is independent of the presence of the other, only their relative intensities determine the fluorescence color.

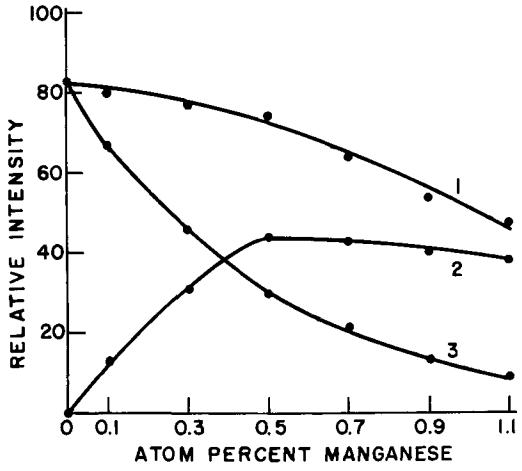

Fig. 2. Fluorescence intensity *vs.* manganese concentration: curve 1, $I_{Sn:Mn}$: total intensity of Sn:Mn coactivated glasses; curve 2, I'_{Mn}: Mn intensity component of Sn:Mn coactivated glasses; curve 3, I'_{Sn}: Sn intensity component of Sn:Mn coactivated glasses.

Coactivated glasses with Sn *constant.*—If tin is held constant while the manganese concentration is varied, a different situation presents itself. Figure 2 shows the variation in $I_{Sn:Mn}$, I'_{Sn}, and I'_{Mn} *vs.* manganese concentration in glasses with tin at 0.5 a/o. An increase in the manganese concentration causes both a decrease in $I_{Sn:Mn}$ and a change in the spectral distribution and color of fluorescence (I'_{Sn}/I'_{Mn} varies). The fluorescence color varied from blue in the manganese-free glass, through white at intermediate manganese levels, to orange in the high manganese glasses. Increasing manganese causes a sharp reduction in I'_{Sn} and an increase in I'_{Mn} up to 0.5 a/o manganese. As the manganese concentration increases, the probability for energy transfer and sensitized manganese fluorescence increases, thereby lowering the intensity of the characteristic tin fluorescence. Although I'_{Sn} continues to decrease above 0.5 a/o manganese, denoting even more concerted energy transfer, I'_{Mn} also decreases. This effect suggests the onset of a significant manganese self-quenching process similar to that previously described for the tin centers. Support for this view was found from the fact that the fluorescence of $Ca(PO_3)_2$:Mn glasses excited by 365 mμ radiation exhibits an intensity maximum at about 0.5 a/o manganese.

The energy transfer process.—The results of the fluorescence intensity measurements indicated that energy transfer in the coactivated Sn:Mn glasses proceeds from tin to manganese centers with some loss of efficiency due to nonradiative processes. The extent to which the energy undergoing transfer is utilized in the sensitization of manganese centers may be estimated from a comparison of the fluorescence intensity of the tin glasses with the resolved intensity components of the coactivated glasses having the same tin concentration. The following quantities will be used to describe the energy transfer process.

$I_{Sn} - I'_{Sn}$ = The decrease in tin fluorescence intensity caused by the presence of manganese where the tin concentration is the same in both singly and coactivated glasses. This decrease is a measure of the energy undergoing transfer between tin and manganese centers.

$\frac{I'_{Mn}}{I_{Sn} - I'_{Sn}} = E$, the efficiency of the energy transfer process. E gives the ratio of the activator (manganese) intensity to the corresponding loss of sensitizer (tin) intensity caused by energy transfer.

$\frac{I_{Sn} - I'_{Sn}}{I_{Sn}} = F_s$, the fraction of available or active tin luminescent centers undergoing energy transfer.

Table I. Energy transfer in $Ca(PO_3)_2$:Sn:Mn glasses

Sn, a/o	Mn, a/o	E, %	F_s, %
0.1	0.5	84	64
0.3	0.5	87	62
0.5	0.5	84	64
0.7	0.5	83	64
0.9	0.5	86	64
0.5	0.1	81	19
0.5	0.3	84	44
0.5	0.5	84	64
0.5	0.7	70	74
0.5	0.9	58	84
0.5	1.1	52	89

The equation for F_s is based on the proportionality between fluorescence intensity and the number of fluorescing centers. The ratio does not account for any tin species which do not normally fluoresce. It is based on the assumption that the total number of tin centers which fluoresce and experience energy transfer in a coactivated glass is equal to the number of tin centers which fluoresce in a singly activated glass having the same tin concentration.

Data are given in Table I. The calculated values of E are somewhat high since the ultraviolet component of the tin fluorescence could not be measured accurately and was not included in the calculations. Comparison with the magnesium tungstate standard indicated that the error in E caused by this omission was small. F_s is not affected.

When manganese is held constant at 0.5 a/o, the percentage of tin luminescent centers undergoing energy transfer and the efficiency of the transfer process are constants from 0.1 to 0.9 a/o tin. The calculated values are 64 and 85%, respectively. Conversely, when tin is held constant at 0.5 a/o, the percentage of tin centers undergoing transfer increases as the manganese concentration increases. The energy transfer efficiency is essentially constant up to 0.5 a/o manganese, but decreases at higher manganese concentrations. This apparent decrease is most probably a result of manganese self-quenching. Any decrease in I'_{Mn} caused by self-quenching would give an erroneously low value for E.

These results suggest that, within the concentration ranges of sensitizer and activator studied, a given tin concentration serves only to provide a certain number of active Sn^{++} centers capable of absorbing and emitting energy. The manganese concentration determines what percentage of these active tin centers will undergo energy transfer and, consequently, what percentage will emit the characteristic tin fluorescence. Although $I_{Sn:Mn}$, I'_{Sn}, and I'_{Mn} decrease uniformly above 0.5 a/o tin, F_s and E remain constant. Only the absolute number of active Sn^{++} centers decreases; in agreement with the idea of tin self-quenching discussed earlier.

The fact that the energy transfer efficiency is constant over the ranges 0.1 to 0.9 a/o tin and 0.1 to 0.5 a/o manganese indicates that a single energy transfer mechanism is operative. The high measured efficiency for this process, about 85%, suggests that a direct Sn → Mn energy transfer is occurring. No evidence was found for the existence of a significant energy transport mechanism involving sensitizer-sensitizer interactions of the type discussed by Botden (5).

Statistical model for sensitized fluorescence.—The experimental results indicate that the over-all efficiency of sensitized fluorescence in the coactivated glasses is a function of (*i*) the intrinsic efficiency, E, of the Sn → Mn energy transfer process itself, and (*ii*) the fraction of tin centers, F_s, that participate in this process. Direct energy transfer from sensitizer, S, to activator, A, should occur if a given S center has at least one A ion within some effective sensitizing distance, r_s. If there is no A within this distance, S will fluoresce with its characteristic emission spec-

trum. An effective sensitizing volume, $V_s = 4/3\ \pi r^3_s$, is associated with r_s. Only active S centers which fluoresce or experience energy transfer are considered; the two alternatives being taken as mutually exclusive. If the S and A centers are randomly distributed throughout the glass, there is a calculable probability that an A will be found in V_s. F_s is taken to be directly proportional to this probability. A standard derivation for the probability of no successes in n mutually exclusive (Bernouilli) trials (6) gives the distribution equation

$$F_s = (1 - F_f) = 1 - (1 - c/\rho)^{V_s\rho} \quad [1]$$

F_s is the fraction of S centers that experience energy transfer, F_f the fraction of S centers that fluoresce, c the manganese concentration, ions/cc, ρ the density of cation sites in the glass, sites/cc, and V_s the effective sensitizing volume, cc.

Stroud (7) utilized this treatment to study positive hole trapping by cerium ions in glass. A similar equation was derived by Shulman *et al.* (8) and used by Botden (5) in studies of energy transfer in crystalline phosphors. In the present investigation $\rho \simeq 10^{22}$ sites/cc, $c < 10^{21}$ ions/cc; therefore $c/\rho < 1/10$ and Eq. [1] may be simplified to give

$$F_s = 1 - \exp(-V_s c) \quad [2]$$

V_s is a constant characteristic of a particular transfer mechanism and of the particular ions involved, but is independent of their concentrations. The energy transfer efficiency was found to be constant over a wide range of sensitizer and activator concentrations, indicating the presence of a single energy transfer mechanism. V_s must likewise be constant over the same concentration ranges to satisfy the imposed condition of randomness on the S and A distributions. The problem of demonstrating that the experimentally determined values of F_s are consistent with the statistical model becomes one of showing that V_s, calculated from Eq. [2], is a constant for all values of F_s and c. The values of V_s and r_s obtained from Eq. [2] are given in Table II along with the experimentally determined values of F_s, F_f, and E.

Equation [2] predicts immediately that V_s will be constant for glasses having the same manganese concentration, regardless of the tin concentration, so long as F_s remains constant. Of greater significance is the fact that V_s remains constant for glasses having the same tin concentration but with varying manganese concentrations. V_s thus fulfills the requirement of invariance imposed by the existence of a single energy transfer mechanism and the condition of randomness placed on the distributions of the tin and manganese ions. Sensitized fluorescence in the coactivated glass phosphors can be rationalized solely on the basis of a random distribution of fluorescent ions; no preferred orientation or pairing of ions need be invoked. In this respect, the $Ca(PO_3)_2$:Sn:Mn glass phosphors are similar to those crystalline phosphors, particularly the phosphates, wherein sensitized fluorescence and energy transfer have been generally explained on the basis of a random distribution of sensitizer and activator ions (2, 5, 8, 9). The use of successive approximations in Eq. [1] indicated that ρ for these glasses is about 1.2 x 10^{22} sites/cc. The number of cation sites around a tin ion which are within the effective sensitizing range of 8.8Å is then about 33, in agreement with values found in the literature for sensitized fluorescence involving the manganese ion (5, 8, 9).

Table II. Application of the statistical model

Concentrations a/o		Concentrations ions/cc × 10^{-20}						
Sn	Mn	Sn	Mn	F_s	F_f	V_s, cc × 10^{21}	r_s, A	E, %
0.1	0.5	0.7	3.6	0.64	0.36	2.8	8.8	84
0.3	0.5	2.2	3.6	0.62	0.38	2.7	8.6	87
0.5	0.5	3.6	3.6	0.64	0.36	2.8	8.8	84
0.7	0.5	5.0	3.6	0.64	0.36	2.8	8.8	83
0.9	0.5	6.5	3.6	0.64	0.36	2.8	8.8	86
0.5	0.1	3.6	0.7	0.19	0.81	3.0	9.0	81
0.5	0.3	3.6	2.2	0.44	0.56	2.6	8.5	84
0.5	0.5	3.6	3.6	0.64	0.36	2.8	8.8	84
0.5	0.7	3.6	5.1	0.74	0.26	2.6	8.5	70
0.5	0.9	3.6	6.5	0.84	0.16	2.8	8.8	58
0.5	1.1	3.6	8.0	0.89	0.11	2.8	8.8	52

The dependence of the normalized tin fluorescence intensity, I'_{Sn}/I_{Sn}, on the manganese concentration, c, is given by the equation

$$I'_{Sn}/I_{Sn} = F_f = \exp(-V_s c) \quad [3]$$

and is shown in Fig. 3. The tin concentration is 0.5 a/o. The agreement of the data with Eq. [3] justifies the earlier statement that the fluorescence intensity is proportional to the number of fluorescing centers. It also demonstrates that the comparison of the tin fluorescence intensity between singly activated and coactivated glasses introduces no difficulties into the application of the statistical model.

Although no experimental evidence was found for the existence of a significant energy transport mechanism involving one or more sensitizer-sensitizer transfers culminating in a sensitizer-activator transfer (5); the possibility exists that such a mechanism may become significant at lower manganese concentrations. In this respect it should be noted that the glass containing 0.5 a/o tin and 0.1 a/o manganese has $V_s = 3.0$ x 10^{-21} cc and $100E = 81\%$. These values are respectively higher and lower than the corresponding values found for the other glasses. Although such discrepancies are within experimental error, they vary from the norms in the manner predicted by the statistical model for a small contribution due to a longer range, less efficient energy transport mechanism.

Effect of quenching in A and S centers on energy transfer.—An examination of F_s, V_s, and E (Table II) for glasses having 0.5 a/o Sn and Mn > 0.5 a/o shows that as the manganese concentration increases above 0.5 a/o, F_s increases, E decreases, but V_s remains constant. It may be assumed that an increase in F_s requires that an increasing number of manganese centers be excited by energy transferred from the tin centers. If the decrease in E were indicative of the presence of some new, less efficient S → A transfer process, then it is likely that V_s would also vary with manganese concentration, since it is difficult to envision two different S-A transfer mechanisms having differing efficiencies but with the same V_s. The fact that V_s remains constant implies that the decrease in E is most likely the result of self-quenching in the manganese centers. As the manganese concentration increases, this quenching effect predominates over the energy transfer process with a resultant net de-

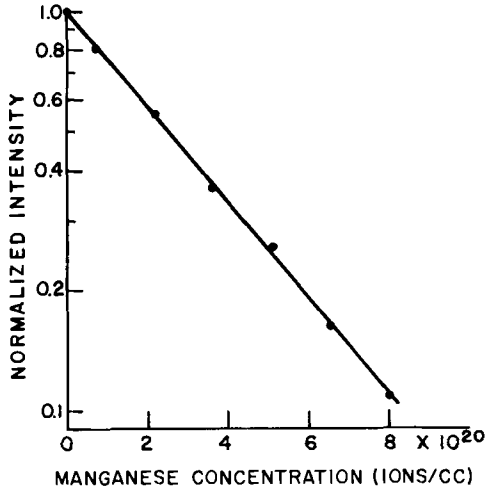

Fig. 3. Normalized tin fluorescence intensity, I'_{Sn}/I_{Sn}, vs. manganese concentration.

crease in the manganese fluorescence intensity, and an erroneously low value of $E = I'_{Mn}/(I_{Sn} - I'_{Sn})$.

The effect of tin self-quenching on the over-all efficiency of sensitized fluorescence can similarly be examined. In Fig. 1 it was shown that both I'_{Sn} and I'_{Mn} pass through a maximum at 0.5 a/o tin and then gradually decrease with increasing tin concentration. The data in Table II show that in the same glasses, F_s, V_s, and E remain constant. Tin self-quenching does not affect the range or efficiency of the S → A energy transfer process, nor does it affect the fractions of tin centers that fluoresce or undergo energy transfer. It does decrease the over-all efficiency of the sensitization process simply by reducing the number of active tin centers that are available for fluorescence or energy transfer.

Independent measurements of concentration quenching among the tin and manganese centers in the host glass would provide useful information on the manner in which S-S, A-A, and S-A interactions compete in coactivated phosphors, since it is unlikely that any one mechanism operates completely independently of the others.

Summary

Sensitized fluorescence in $Ca(PO_3)_2$:Sn:Mn glass phosphors occurs via a direct transfer of excitation energy from an excited tin center to a near-neighbor manganese ion. No other mechanism for energy transport appeared to be significant over the concentration ranges studied. The experimental results were rationalized on the basis of a random distribution of tin and manganese ions in the host glass; no preferred orientation or ion pairing was required to fit the data. The effective sensitization range for Sn → Mn transfer is approximately 8.8Å and encompasses a spherical distribution of about 33 cation sites around an excited tin center. The tin concentration determines the total number of tin centers available for either fluorescence or energy transfer. The manganese concentration determines what fraction of available tin centers will participate in either process. The fluorescence spectrum of either ion does not appear to be affected by the presence of the other. Hence the manganese concentration, by determining the relative fluorescence intensities of the two ions, determines the fluorescence color. The tin concentration places an upper limit on the total intensity which is then decreased somewhat by the efficiency of the transfer process. Concentration quenching in the tin or manganese centers does not appear to affect either the intrinsic efficiency or the sensitization range of the energy transfer process. Both quenching processes affect the over-all fluorescence intensity by decreasing the number of available fluorescent centers.

Acknowledgments

The author wishes to thank J. S. Stroud for his many helpful comments.

Manuscript received Nov. 4, 1965; revised manuscript received Jan. 15, 1966.

Any discussion of this paper will appear in a Discussion Section to be published in the December 1966 JOURNAL.

REFERENCES

1. C. C. Klick and J. H. Schulman, in "Solid State Physics," **5**, p. 97, F. Seitz and D. Turnbull, Editors, Academic Press, New York (1955).
2. J. H. Schulman, *Brit. J. Appl. Phys.*, **6**, Suppl. 4, S64 (1955).
3. P. D. Johnson and F. E. Williams, *J. Chem. Phys.*, **18**, 1477 (1950).
4. G. F. Fonda, *Brit. J. Appl. Phys.*, **6**, Suppl. 4, S69 (1955).
5. T. P. J. Botden, *Philips Research Repts.*, **7**, 197 (1952).
6. *Cf.* W. Feller, "An Introduction to Probability Theory and Its Applications," **1**, John Wiley & Sons, New York (1950).
7. J. S. Stroud, *J. Chem. Phys.*, **37**, 836 (1962).
8. J. H. Schulman, R. J. Ginther, and C. C. Klick, *This Journal*, **97**, 123 (1950).
9. R. J. Ginther, *ibid.*, **101**, 248 (1954).

SYMBOLS

I_{Sn}	fluorescence intensity of Sn activated glasses
$I_{Sn:Mn}$	fluorescence intensity of Sn:Mn coactivated glasses
I'_{Sn}	tin component of fluorescence intensity in coactivated glasses
I'_{Mn}	manganese component of fluorescence intensity in coactivated glasses
$E = I'_{Mn}/(I_{Sn} - I'_{Sn})$	efficiency of Sn → Mn energy transfer process
$F_s = (I_{Sn} - I'_{Sn})/I_{Sn}$	the fraction of tin luminescent centers undergoing energy transfer to manganese ions
$F_f = (1 - F_s)$	the fraction of active tin luminescent centers which fluoresce
V_s	effective sensitizing volume, cc
r_s	effective sensitizing range,Å
ρ	density of cation sites, sites/cc
c	manganese concentration, ions/cc

Emission Spectra of Impurity Activated (Zn,Cd)(S,Se,Te) Phosphors

I. Copper Activated Phosphors

W. Lehmann

Research Laboratories, Westinghouse Electric Corporation, Pittsburgh, Pennsylvania

ABSTRACT

Copper produces two emission bands in all (Zn,Cd)S and all (Zn,Cd)Se phosphors. Both bands shift monotonically to lower or higher quantum energies, if the Zn/Cd ratio is varied, so that their differences to the also varying energy of the band gap remain constant. In contrast, the positions of the emission bands in Zn(S,Se), Zn(Se,Te), and Cd(S,Se) depend relatively little on the S/Se or Se/Te ratio, respectively, except for a pronounced, and as yet not understood, discontinuity near 100% ZnS. Otherwise, the behavior can be understood qualitatively by assuming predominantly ionic crystal bonding, with the Schön-Klasens model of luminescence, and with Fonger's model of term-splitting in all cases where the activator is surrounded by different kinds of anions.

All possible binary compounds between Zn and Cd on the one, and S, Se, and Te on the other hand can be arranged conveniently in the scheme shown in Fig. 1. Each two next neighbors in this scheme are well known to be completely miscible into each other thus forming the ternary compounds (Zn,Cd)S, Zn(S,Se), etc. All these compounds are also luminescent materials which can be activated by the incorporation of

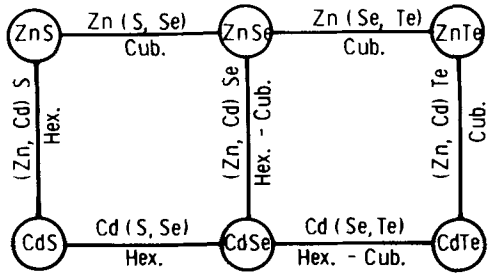

Fig. 1. Binary and ternary (Zn,Cd)(S,Se,Te) compounds

small amounts of certain impurities notably Cu, Ag, and Au. It is the purpose of this study to provide a fairly comprehensive survey over the emission spectra of the binary and ternary (Zn,Cd) (S,Se,Te) phosphors activated by Cu, Ag, or Au, and of corresponding self-activated phosphors, as functions of the composition of the host material. Impurity activated ZnS phosphors (especially ZnS:Cu) are well known, of course, and a fair amount of investigation is reported in the literature also on (Zn,Cd)S phosphors. However, comparatively little, or nothing, is known yet on the emission spectra of all other ternary compounds indicated in Fig. 1. Halsted, Aven, and Coghill attempted to bridge this gap of knowledge by an interpolation between the emission spectra observed in the binary compounds (1), but an actual investigation of the intermediate ternary compounds shows that the matter is not always so simple (2).

The experimental work to be presented here was limited to powder phosphors whose compositions, at the moment at least, are still much better under control than those of single crystals. The investigation was extended over all binary and ternary compounds shown in Fig. 1 with the only exception of compounds containing CdTe which, because of their narrow band gaps, can only give emission rather far in the infrared. Low impurity concentrations were preferred wherever possible in order to minimize complications due to interactions between neighboring impurity atoms. All spectra were measured at 77°K (liquid N_2-temperature) since many emission details do not show up at room temperature.

Experimental

The raw materials used to prepare the phosphors were ZnS, ZnSe, CdS, and CdSe powders of luminescent or electronics grade purity from various suppliers. ZnTe was made by a direct synthesis from metallic Zn and Te (each 99.999% pure) in high-purity argon. The powdered raw materials were dry mixed in the desired ratios. Copper was added as an aqueous solution of $Cu(C_2H_3O_2)_2$, the halogens Cl, Br, I as the Zn or Cd halides, and aluminum, gallium, and indium as nitrates dissolved in water. The resulting slurries were stirred to insure uniformity and dried again. Most samples were fired in amounts of 2% of 1 g-mole, in small capped quartz tubes in argon, H_2S, etc., or in evacuated and sealed quartz tubes in order to insure well-defined compositions even in critical cases.

For measurements, the phosphors were coated in thin layers (in order to minimize influences of possible optical reabsorption on the emission spectra) on small pieces of aluminum metal by means of a nonluminescent binder and placed in a small quartz Dewar with a nonsilvered "window" at one side. The Dewar was filled with liquid N_2 (77°K) so that the phosphors were completely immersed in the coolant. The phosphors were excited to the luminescence, through the window of the Dewar, by the filtered radiation of a small (100w) mercury discharge lamp. The emission spectra were point by point measured with a Beckman DU monochromator and an attached photomultiplier (RCA 1-P-28 for the visible and near ultraviolet, Du Mont K-1430 for the near infrared up to about 1μ). The obtained resolution ($\sim$ 0.01 ev, fairly independent of the spectral position) was sufficient to resolve all details of the generally broad and structureless emission bands of the phosphors. Spectral transparency of the monochromator and spectral sensitivity of the photomultipliers were determined separately by means of a calibrated tungsten ribbon lamp supplied by the National Bureau of Standards.

The measured emission spectra of luminescence are correlated to the quantum energies corresponding to the optical absorption edges of the materials which, in turn, were determined by means of reflection spectra measured on thin layers of the pure (unactivated) binary or ternary compounds. It is estimated from the geometry of the arrangement that the so determined absorption "edge" corresponds to a quantum energy where the intrinsic absorption constant of the material goes through the value of approximately 100 cm^{-1}. This quantum energy is close [but not necessarily identical (3, 4)] to the true band gap of the ideal, defect-free lattice and may be identified with the latter for all practical purposes. The variations of the so determined absorption edges with the compositions of the materials agree closely with data published by other authors in the literature.

Emission spectra presented in the literature are often (not always specified) given as energy distributions, $\epsilon = d(\text{energy})/d\lambda$, as functions of the wavelength, λ. In contrast, the writer prefers to present all spectra in terms of quantum intensity distributions, $q = d(\text{number of quanta})/d(\text{ev})$, as functions of the quantum energy, ev. This is the physically most meaningful way since luminescent processes are quantum processes. The curves in the diagrams are arbitrarily shifted up or down along the logarithmically calibrated ordinates in order to normalize to equal peak heights or to provide clear pictures and to avoid too much crowding of several curves in one area. This means that the shapes and peak positions of the spectra in each diagram can be compared but not their absolute intensities.

Zinc Sulfide

ZnS can be prepared equally well in the cubic (zinc blende) and in the hexagonal (wurtzite) modification. Copper-activated ZnS may well be the most often investigated of all luminescent materials. Its emission spectrum may slightly depend on the modification, cubic or hexagonal, or on the kind of coactivator used to dissolve the copper in the ZnS, but consists generally[1] of two separate, diffuse bands centered in the blue and in the green, respectively. Positions and shapes of both emission bands of any particular sample are almost or completely independent of kind and intensity of excitation, the widths of both bands increase somewhat with increasing temperature, but the peak positions again are little dependent on the temperature at least between room temperature and 77°K or lower. These are well-known facts. However, the following observations made on ZnS:Cu probably are not so well known:

(*A*) The peak positions of both emission bands are slightly uncertain and may vary from sample to sample over a range of approximately 0.03 ev even within phosphors made of identical compositions. This uncertainty was observed already by van Gool and Cleiren (7). A similar uncertainty is observed also in the widths of the emission bands which may vary between about 0.23 and 0.28 ev (measured at half-maximum) at 77°K. Some data are collected in Table I.

(*B*) It is a common belief and is frequently reported in the literature (8-10) that the emission bands of hexagonal (wurtzite) ZnS:Cu phosphors peak at slightly higher quantum energies (*i.e.*, shorter wavelengths) than those of corresponding phosphors of cubic (zinc blende) structure. This is indeed true for

[1] *i.e.*, at copper concentrations in the order of 100 ppm. Higher concentrations produce more complicated effects (5, 6) which are not considered here.

Table I. Emission peak positions of ZnS:Cu (0.01%) excited by ultraviolet at 77°K

Sample No.	Structure	Added coactivator, %	Green peak, ev	Blue peak, ev
826	Cubic	0.1 Cl	2.38 (0.27)	2.79 (0.26)
800	Cubic	0.01 Cl	2.34 (0.26)	2.78 (0.26)
801	Cubic	0.1 Cl	2.34 (0.25)	2.78 (0.26)
802	Cubic	0.01 Br	2.34 (0.26)	2.78 (0.26)
803	Cubic	0.1 Br	2.34 (0.25)	2.80 (0.25)
804	Cubic	0.1 I	2.35 (0.24)	2.81 (0.24)
Average			2.35	2.79
805	Cubic	0.01 Al	2.35 (0.26)	2.77 (0.27)
809	Cubic	0.1 Al	2.34 (0.26)	2.77 (.026)
806	Cubic	0.01 Ga	2.33	2.74 (0.31)?
810	Cubic	0.1 Ga	2.36 (0.26)	2.75 (0.25)
807	Cubic	0.01 In	2.37 (0.25)	2.75 (0.24)
811	Cubic	0.1 In	2.35	2.77 (0.28)?
Average			2.35	2.76
684	Hexagonal	0.1 Cl	2.43 (0.25)	2.87 (0.25)
721	Hexagonal	0.1 Cl	2.43 (0.26)	2.85 (0.26)
821	Hexagonal	0.1 Cl	2.41 (0.26)	2.86 (0.26)
722	Hexagonal	0.1 Br	2.43 (0.26)	2.86 (0.26)
723	Hexagonal	0.1 I	2.42 (0.25)	2.85 (0.26)
Average			2.42	2.86
759	Hexagonal	0.003 Al	2.42 (0.28)	2.74 (0.28)?
724	Hexagonal	0.003 Al	2.43 (0.28)	2.77
725	Hexagonal	0.01 Al	2.41 (0.25)	2.78 (0.25)
760	Hexagonal	0.01 Al	2.40 (0.25)	2.77 (0.26)
726	Hexagonal	0.03 Al	2.41 (0.27)	2.76 (0.26)
761	Hexagonal	0.03 Al	2.41 (0.26)	2.78 (0.24)
727	Hexagonal	0.003 Ga	—	2.75 (0.24)
728	Hexagonal	0.01 Ga	—	2.74 (0.23)
729	Hexagonal	0.03 Ga	—	2.74 (0.25)
Average			2.41	2.76

The numbers in ( ) denote the widths of the emission bands at 50% of peak.

both emission bands of phosphors containing halides (Cl, Br, or I) as coactivators, and in the case of the green emission band of phosphors containing group III elements (Al, Ga, In) as coactivators, but not for the blue emission band of ZnS:Cu phosphors containing group III elements where the peak position does not, to an amount exceeding the general uncertainty, depend on whether the phosphor is cubic or hexagonal. Some typical emission spectra are shown in Fig. 2, for more data see Table I.

(C) The position of the blue (but not, or by far not as much of the green) emission band of ZnS:Cu depends on the kind of the added coactivator, in contrast to Kröger and Dikhoff (12) but in agreement with van Gool and Cleiren (7). Halides give peak positions at higher quantum energies than Al, Ga, or In. The effect is less pronounced in cubic but rather strong in hexagonal ZnS.

Hexagonal Zinc-Cadmium Sulfides

Ternary (Zn,Cd)S containing more than a few per cent of CdS crystallizes only in the hexagonal modification under all ordinary preparation conditions. The two main emission bands of hexagonal (Zn,Cd)S:Cu phosphors (blue and green) shift monotonically toward red if zinc is gradually replaced by cadmium (8, 13-17). Some measured spectra are shown in Fig. 3. The blue emission band of hexagonal ZnS:Cu,Cl (peak ~ 2.86 ev at 77°K) corresponds to a band with the peak at ~ 1.53 ev (λ = 810 nm) in CdS:Cu,Cl. Most of this band is located in the infrared, only a small fraction of its high-energy tail extends into the visible red. The green band of hexagonal ZnS:Cu,Cl (peak ~ 2.42 ev) corresponds to a band near 1.16 ev (λ = 1080 nm) in CdS:Cu,Cl. This band is completely in the infrared. The energy difference between both bands scatters around 0.43 ± 0.05 ev and is fairly independent of the ZnS/CdS ratio. Also the widths of both emission bands are (very approximately, at least) independent of the ZnS/CdS ratio if measured in ev.

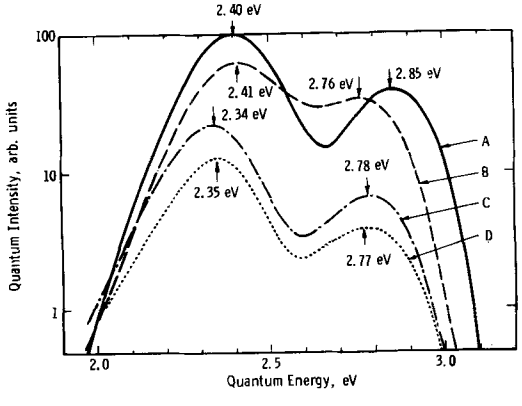

Fig. 2. Emission spectra of four different ZnS:Cu phosphors, all excited by ultraviolet of 3.40 ev (λ = 365 nm) at 77°K. A, hexagonal ZnS:Cu (0.01%), Cl (0.1%), 1100°C, H_2S; B, hexagonal ZnS:Cu (0.01%), Al (0.03%), 1100°C, H_2S; C, cubic ZnS:Cu (0.01%), Cl (0.1%), 800°C, H_2S; D, cubic ZnS:Cu (0.01%), Al (0.01%), 800°C, H_2S.

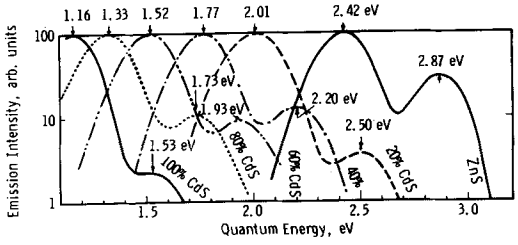

Fig. 3. Emission spectra of hexagonal (Zn,Cd)S:Cu,Cl phosphors excited by band-gap irradiation at 77°K.

II-VI Compounds can be approximately considered to be ionic compounds where the cation belongs to the conduction band and the anion to the valence band. Hence, a variation of the composition from ZnS to CdS means a variation of the conduction band while the edge of the valence band can be represented as a horizontal straight line extending from the ZnS to the CdS in Fig. 4. The generally accepted Schön-Klasens model ascribes the luminescence of ZnS:Cu phosphors to electron transitions from the edge of the conduction band into previously emptied copper acceptor levels. According to this model, the peak energies of the emission bands measured on (Zn,Cd)S:Cu,Cl phosphors (Fig. 3) are plotted downward from the edge

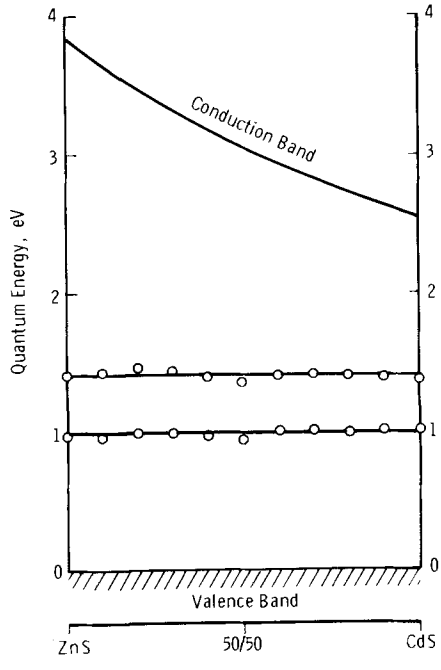

Fig. 4. Recombination term scheme of hexagonal (Zn,Cd)S:Cu,Cl at 77°K.

of the conduction band in Fig. 4. The resulting positions of the two copper terms are remarkably good on two horizontal straight lines extending from the ZnS to the CdS, the one line corresponding to the green, the other to the blue emission band of hexagonal ZnS:Cu,Cl. The distance between the "green" line and the edge of the valence band is approximately 1.40 ev independent of the used coactivator. The distance between the "blue" line and the valence band is approximately 0.98 ev for phosphors containing Cl, Br, or I, and 1.08 ev for phosphors containing Al, Ga, or In as coactivators.

Cubic Zinc Sulfoselenides

Ternary Zn(S,Se) containing more than a few per cent of ZnSe crystallize predominantly in the cubic modification under all ordinary preparation conditions. Emission spectra of Zn(S,Se):Cu phosphors are published by Leverenz (8), by Klasens (18), and by Morehead (19). All varied the S/Se ratio in a few big steps from the ZnS to the ZnSe, and all agree that a gradual replacement of ZnS by ZnSe causes a gradual and steady shift of the green emission band of ZnS:Cu into the red. No corresponding investigation on the blue emission band of ZnS:Cu seems ever to have been made although a steady shift is assumed by Halsted *et al.* (1) also here. This reported, or assumed, behavior is quite in contrast to what is observed in a more detailed investigation.

Some emission spectra of cubic Zn(S,Se):Cu,Cl phosphors are shown in Fig. 5 and 6. The emission peak positions of cubic ZnS:Cu,Cl phosphors at 77°K are, on the average, about 2.35 and 2.79 ev, respectively. Replacement of less than 1% of the ZnS by ZnSe causes a decrease of the intensity of both bands and the appearance of two new bands at about 2.23 and 2.60 ev, respectively. This replacement is essentially completed already at 1% of ZnSe (Fig. 5). Further gradual increase of the ZnSe concentration to 100%

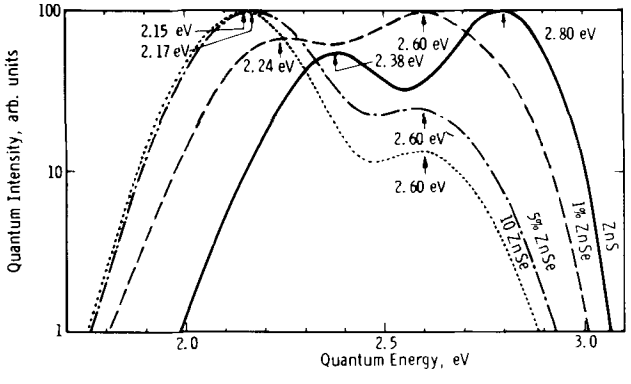

Fig. 5. Emission spectra of cubic Zn(S,Se):Cu (0.01%), Cl phosphors excited by ultraviolet of 3.40 ev (λ = 365 nm) at 77°K.

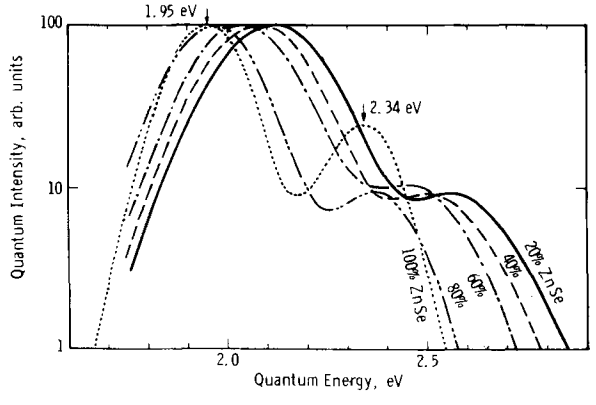

Fig. 6. Emission spectra of cubic Zn(S,Se):Cu (0.01%), Cl phosphors excited by ultraviolet of 3.40 ev (λ = 365 nm) at 77°K.

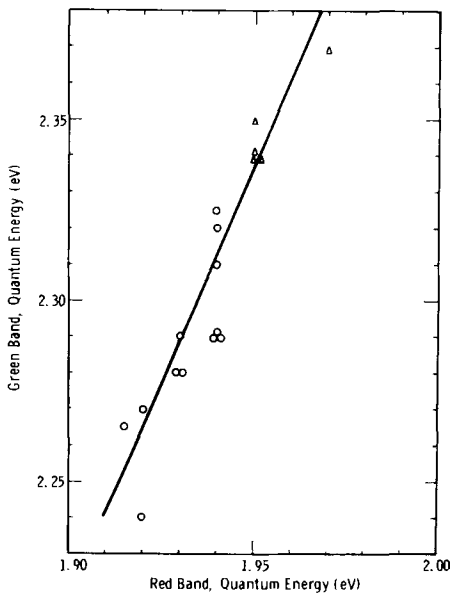

Fig. 7. Correlation between peak positions of the two emission bands of ZnSe:Cu (0.01%) measured at 77°K. △, Cl, Br, I coactivator; ○, Ga or In coactivator.

then causes only a comparatively slow shift of both bands toward red until, in ZnSe:Cu,Cl, they are at about 1.95 ev (red) and 2.34 ev (green), respectively (Fig. 6). Essentially the same behavior is observed also with Zn(S,Se):Cu, Ga phosphors.

Typical width (at half-peak height) of the emission bands at 77°K are 0.26 ev for both bands of ZnS:Cu and 0.19 ev for both bands of ZnSe:Cu. Emission bands of intermediate Zn(S,Se):Cu phosphors are wider; typical widths are about 0.28 to 0.30 ev. This observation strongly supports the assumption that the emission bands of all intermediate Zn(S,Se) phosphors, but not those of the two end members ZnS and ZnSe, actually are close overlaps of two or more sub-bands, as proposed by Fonger (20).

The exact peak positions of the two emission bands of ZnSe:Cu phosphors are even more uncertain than those of cubic ZnS:Cu. Coactivation with Cl, Br, or I generally give both emission bands at slightly higher quantum energies than coactivation with Ga or In. Correlation with details of the preparation conditions, *e.g.*, with the amount of coactivator used, could not be detected. However, there seems to be a linear relationship between the peak positions of the green and of the red band in ZnSe:Cu (Fig. 7). This relationship is not understood at present nor is a similar relationship observed in corresponding ZnS phosphors.

In the ionic picture, a variation of the composition of the host material from ZnS to ZnSe means a variation of the valence band while the conduction band remains constant. Using the Schön-Klasens model of luminescence, the measured peak positions of the emission bands are plotted downward from the edge of the conduction band, and the resulting points connected by two curves (Fig. 8). These curves are not the perfect horizontal straight lines observed in the case of (Zn,Cd)S:Cu phosphors (Fig. 4), but their deviation from the horizontal is much less than that of the edge of the conduction band except only in the neighborhood of ZnS where evidently the introduction of very little ZnSe causes a pronounced unsteadiness. In contrast, no unsteadiness is observed if small amounts of ZnSe are replaced by ZnS.

Cubic Zinc Selenotellurides

ZnSe, ZnTe, and all intermediate Zn(Se,Te) compositions crystallize practically only in the cubic (zinc blende) lattice. The emission band of ZnSe:Cu,Cl is characterized by two separate, diffuse bands in the red

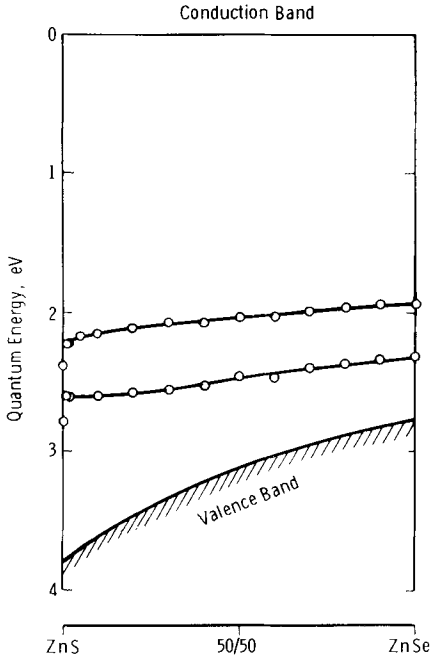

Fig. 8. Recombination term scheme of cubic Zn(S,Se):Cu,Cl at 77°K

(~ 1.95 ev) and in the green (~ 2.35 ev), respectively. Ordinarily the latter can be observed only at low temperature; it is thermally quenched at room temperature. Replacement of a few per cent of Se in ZnSe:Cu,Cl by Te causes the green emission band to decrease in intensity, the red band remains approximately unchanged, and a third emission band builds up in the near infrared at 1.70 to 1.75 ev (Fig. 9). The positions of all bands appear to be independent of the ZnTe concentrations up to the limit to which they could be observed (~ 50% ZnTe). If the observed peak positions are plotted downward from the horizontal edge of the conduction band, one obtains the recombination term scheme of Fig. 10 where, again, all points scatter fairly closely around horizontal straight lines.

The writer was unable to detect any emission in Zn(Se,Te):Cu containing more than about 50% ZnTe which could be ascribed unambiguously to be due to copper. However, Halsted and co-workers report ZnTe:Cu, at 25°K, to emit in two bands at 1.97 and 1.47 ev, respectively (1). Points corresponding to these energies are also indicated in Fig. 10. There is obviously a straight-line connection between the 1.97 ev band of ZnTe:Cu and the red emission band of ZnSe:Cu (~ 1.95 ev), but no such correlation is visible between the reported 1.47 ev of ZnTe:Cu with any emission in ZnSe:Cu.

Zinc-Cadmium Selenides

ZnSe crystallizes practically always in the cubic modification, CdSe always in the hexagonal. The transition point from cubic to hexagonal within intermediate (Zn,Cd)Se powders (fired at 900°C in evacuated and sealed quartz tubes) was determined by x-ray analysis and found to be between 30 and 40% of CdSe. It is obvious, however, that this point may shift either to the ZnSe or to the CdSe side depending on the preparation temperature, on various impurities, etc.

The luminescence of CdSe:Cu phosphors was investigated by Garlick and Dumbleton (21) who report two emission bands at 0.95μ (1.30 ev) and at 1.2μ (1.03 ev), both measured at 90°K, and by Avinor and Meijer (22) who report only one band at 1.20μ (1.03 ev) measured at 77°K. Emission spectra of intermediate (Zn,Cd)Se:Cu phosphors do not seem to be published.

Some emission spectra of (Zn,Cd)Se:Cu, I phosphors are shown in Fig. 11. The two emission bands

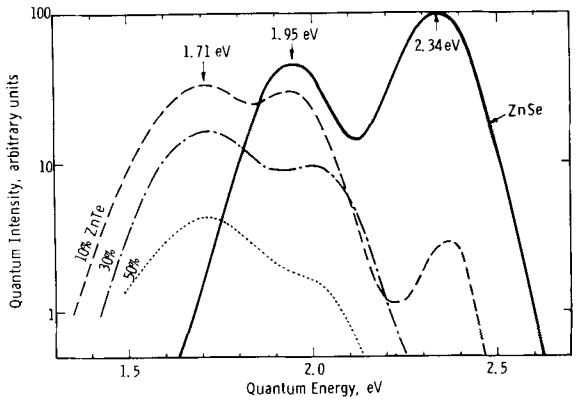

Fig. 9. Emission spectra of cubic Zn(Se,Te):Cu (0.01%), Cl phosphors excited by ultraviolet of 3.40 ev (λ = 365 nm) at 77°K.

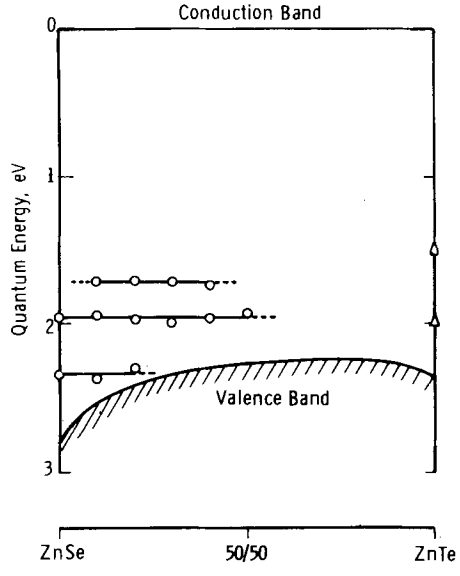

Fig. 10. Recombination term scheme of cubic Zn(Se,Te):Cu,Cl at 77°K. △, data from ref. (1).

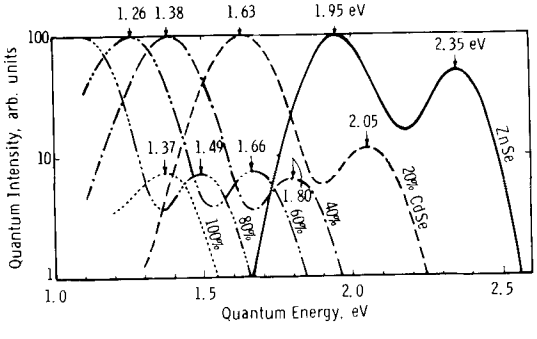

Fig. 11. Emission spectra of (Zn,Cd)Se:Cu (0.02%), I phosphors excited by ultraviolet of 3.40 ev (λ = 365 nm) at 77°K.

due to copper shift monotonically into the infrared as more and more ZnSe is replaced by CdSe (completely similar to the shift observed in corresponding sulfide phosphors). The green emission band of ZnSe:Cu (~2.35 ev) corresponds to the 1.37 ev band in CdSe:Cu (this is probably identical to the 0.95μ band reported by Garlick and Dumbleton). The emission band of CdSe:Cu corresponding to the red band (~1.95 ev) of ZnSe:Cu could not be measured any more with the used instrumentation, but it is obviously identical the 1.2μ band reported elsewhere (21, 22). If the Schön-Klasens model of luminescence is used here and the quantum energies corresponding to the peaks of the

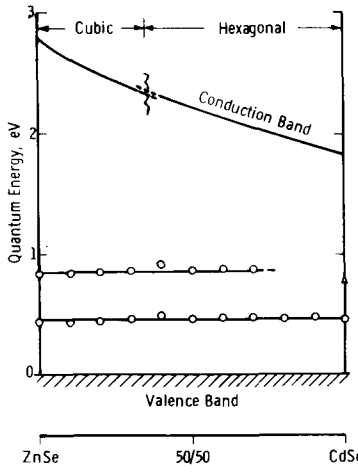

Fig. 12. Recombination term scheme of cubic and hexagonal (Zn,Cd)Se:Cu,I at 77°K. △, from ref. (21).

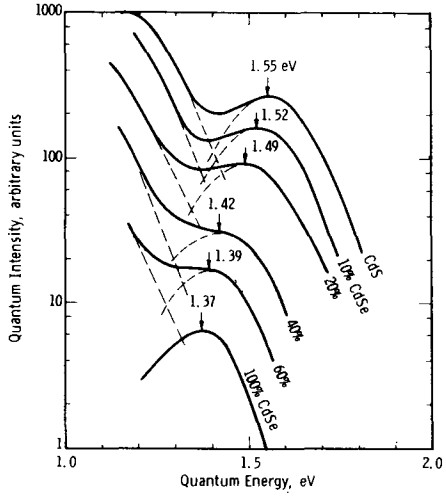

Fig. 13. Emission spectra of hexagonal Cd(S,Se):Cu (0.01%), I phosphors excited by ultraviolet of 3.40 ev (λ = 365 nm) at 77°K.

emission bands are plotted downward from the curved edge of the conduction band, one obtains the diagram of Fig. 12 which may be compared with Fig. 4. Again, all measured points scatter closely around two horizontal straight lines about 0.4 ev apart.

Hexagonal Cadmium Sulfoselenides

CdS, CdSe, and all intermediate Cd(S,Se) crystallize practically only in the hexagonal modification. Emission spectra of copper activated Cd(S,Se) phosphors, except those of the two end members CdS and CdSe, apparently are not reported before. Some spectra measured within this work are given in Fig. 13. All spectra evidently consist of two emission bands although, due to instrumental limitations, only the high-energy band could be measured over the whole composition range. There is some, but very little, shift of the peak position with the CdSe concentration. In contrast to corresponding Zn(S,Se) phosphors (Fig. 5), no discontinuity in the peak position could be observed near the 100% CdS. If the quantum energies corresponding to the peaks of the emission bands are plotted downward from the horizontal edge of the conduction band, one obtains the recombination scheme of Fig. 14. The curve connecting all measured points deviates somewhat from a horizontal straight line, but this deviation is much less than the variation of the band gap, represented by the curved edge of the valence band, over the same range.

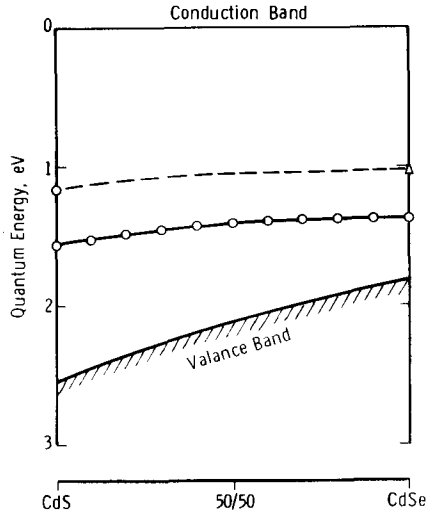

Fig. 14. Recombination term scheme of hexagonal Cd(S,Se):Cu,I at 77°K. △, data from ref. (21).

Discussion

The main observations on the emission spectra due to copper in the II-VI compound phosphors can be summarized as follows.

The emission in the binary compounds ZnS, ZnSe, CdS, and CdSe consists of two diffuse but fairly well separable bands of approximately Gaussian shape whose peaks are about 0.4 ev apart. The exact peak positions depend not only on the host material but also on a number of other parameters some of which are still unknown. Gradual replacement of zinc by cadmium either in the sulfides or in the selenides causes a steady shift of both emission bands toward lower quantum energies so that the differences between the energy of the band gap and the quantum energies of the emission peaks always remain constant. By contrast, gradual replacement of sulfur in ZnS or in CdS by selenium, and gradual replacement of selenium at least in ZnSe by tellurium, causes little or no shift of the emission except for a strong discontinuity near 100% ZnS.

Most of this behavior can be understood qualitatively with the assumption of a predominantly ionic crystal bonding where the conduction band belongs to the cation and the valence band to the anion, and with the familiar Schön-Klasens model of luminescence which ascribes the photon emission to electron transitions from the conduction band into previously emptied electron levels between the activator ion and the four surrounding chalcogenide ions. Any replacement of zinc by cadmium then causes only a variation of the conduction band while the activator electron levels and the valence band remain unchanged. Hence, the energy difference between valence band and activator levels is independent of the Zn/Cd ratio as predicted already by Bube (23). This is expressed by the horizontal straight lines in the term scheme of Fig. 4 and 12. However, if sulfur is gradually replaced by selenium, or selenium by tellurium, the conduction band remains unchanged while the valence band changes and the highly localized electron wave functions of the activator centers split into several levels depending on the four chalcogenide ions surrounding the copper ion. This latter effect is discussed by Fonger (20) for the case of Zn(S,Se) phopshors. It seems that Fonger's assumptions hold essentially also for Zn(Se,Te) and for Cd(S,Se) phosphors although, perhaps, modifications are necessary to explain all observed details.

The discontinuity in Zn(S,Se) observed near 100% ZnS seems peculiar and probably cannot be understood with the above models. Also it does not seem to be related to the discontinuity which Klasens (18)

was looking for in Zn(S,Se):Cu but did not find. Klasens assumed activator centers in ZnS:Cu phosphors to be identical to single sulfur ions disturbed by copper ions as next neighbors and, correspondingly, expected two emission bands to be present in Zn(S,Se) for every one in ZnS, namely, those due to disturbed sulfur and selenium ions. If this assumption (which obviously is in disagreement with Fonger's model) were correct and the reason for the observed discontinuity in Zn(S,Se):Cu near 100% ZnS:Cu, it could hardly be the reason for the completely different behavior observed in Zn(S,Se):Ag near 100% ZnS:Ag (24). Further, similar discontinuities obviously should appear in Zn(Se,Te):Cu near 100% ZnSe:Cu, and in Cd(S,Se):Cu near 100% CdS:Cu, which are not observed in reality. At the moment, the writer is unable to offer any explanation of the discontinuity in Zn(S,Se):Cu near 100% ZnS:Cu.

Acknowledgment

The author wishes to express his thanks to H. F. Ivey and to W. A. Thornton for proof reading and helpful suggestions, and to H. H. Dorman for much careful work in preparation and measurement.

Manuscript received Dec. 17, 1965.

Any discussion of this paper will appear in a Discussion Section to be published in the December 1966 JOURNAL.

REFERENCES

1. R. E. Halsted, M. Aven, and H. D. Coghill, *This Journal*, **112**, 177 (1965).
2. W. Lehmann, discussion of ref. (1), *ibid.*, **112**, 1256 (1965).
3. T. S. Moss, "Optical Properties of Semiconductors," p. 38 ff, London (1961).
4. W. Lehmann, *This Journal*, **112**, 1150 (1965).
5. H. C. Frölich, *ibid.*, **100**, 496 (1953).
6. W. Lehmann, *ibid.*, **110**, 754 (1963).
7. W. van Gool and A. P. Cleiren, *Philips Research Repts.*, **15**, 238 (1960).
8. H. W. Leverenz, "An Introduction to Luminescence of Solids," New York-London (1950).
9. F. A. Kröger, J. E. Hellingman, and N. W. Smit, *Physica*, **15**, 990 (1949).
10. M. H. Payen de la Garanderie, *J. Phys. Rad.*, **22**, 423 (1961).
11. S. Rotschild, "Solid State Physics in Electronics and Telecommunication," Vol. 4, part 2, p. 705, Academic Press, New York (1960).
12. F. A. Kröger and J. Dikhoff, *Physica*, **16**, 297 (1950).
13. K. Albers, "Zur Physik und Chemie der Kristallphosphore," p. 228. H. Ortmann and H. Witzmann, Editors, Berlin (1960).
14. S. Asano, *Science of Light*, **4**, 32 (1955).
15. E. Grillot and P. Guintini, *Compt. rend.*, **239**, 418 (1954).
16. S. T. Henderson, *Proc. Roy. Soc. London*, **A-173**, 323 (1939).
17. K. Kamm, *Ann. Phys.*, **30**, 333 (1937).
18. H. A. Klasens, *This Journal*, **100**, 72 (1953).
19. F. F. Morehead, *J. Phys. Chem. Solids*, **24**, 37 (1963).
20. W. H. Fonger, *Phys. Rev.*, **137**, A-1038 (1965).
21. G. F. J. Garlick and M. J. Dumbleton, *Proc. Phys. Soc.*, **B67**, 442 (1954).
22. M. Avinor and G. Meijer, *J. Chem. Phys.*, **32**, 1456 (1960.)
23. R. H. Bube, "Photoconductivity of Solids," p. 169 ff. New York-London (1960).
24. W. Lehmann, To be published. See also ref. (18).

On the Luminescent Properties of Some $CaMoO_4/LnVO_4$ Systems

L. H. Brixner

Pigments Department, Experimental Station, E. I. du Pont de Nemours & Co., Inc., Wilmington, Delaware

ABSTRACT

The $(LnVO_4)_x(CaMoO_4)_{1-x}$ systems (with Ln = Nd^{+3}, Sm^{+3}, Eu^{+3}, Tb^{+3}, and Dy^{+3}) have been prepared over wide ranges of x and some of their structural, analytical, and optical parameters have been measured. The x-ray phase diagram for the $EuVO_4/CaMoO_4$ system was determined and shows that only very limited solid solubility of the scheelite- and zircon-type constituents exists. Fluorescent emission data are given for the compounds containing the rare earths Sm, Eu, Tb, and Dy, which emit in the visible. The Nd compound emits in the infrared and laser action is reported for a Fabry-Perot resonator machined from a Czochralski-grown single crystal of the composition $Nd_{0.01}V_{0.01}Ca_{0.99}Mo_{0.99}O_4$.

In the series of scheelite-type ABO_4 compounds (where A = Ca, Sr, and Ba, B = Mo, W), $CaMoO_4$ is thermodynamically the least stable and the only one which loses oxygen if pulled as a crystal from melts under normal atmospheric conditions. It is probably for this reason that the thresholds for Nd^{+3} in $CaMoO_4$ as first reported by Johnson (1) were quite high (360 joules at 295°K) and most investigators concentrated on $CaWO_4$ as a laser host crystal. In a previous paper, we (2) demonstrated that the introduction of rare earths into $CaMoO_4$ as their $LnNbO_4$-type niobates not only provides the necessary valence compensation, thereby simplifying the fluorescent emission spectrum, but also stabilizes $CaMoO_4$ so that no oxygen is lost at the melting point. Recently, Duncan (3) observed continuous-wave operation with such crystals, thus showing that Ca-molybdate can be obtained in as high optical perfection as Ca-tungstate. These findings, plus the fact that Ca-molybdate has some inherent advantages over Ca-tungstate (higher refractive index, lower melting point and higher thermal conductivity), generated renewed interest in this composition as a laser host.

Based on the size of the ionic radii as given by Ahrens (4), the V^{+5} ion should provide an even better structural match in substituting for Mo^{+6} than does Nb^{+5}. The V^{+5} ion is only some 5% smaller than Mo^{+6} and since the $LnVO_4$-type vanadates are quite stable (5), it seemed that the $CaMoO_4/LnVO_4$ systems were worth studying, particularly since energy exchange at least for the case of Eu^{+3} had been demonstrated in the $LnVO_4$ (5) system as well as in the $Ca_3(VO_4)_2$ (6) host. Since the $LnTaO_4$-type tantalates did not show any advantages over the corresponding niobates as dopants, the vanadates were the only remaining group VB compositions to be investigated in solid solution with $CaMoO_4$.

Experimental

Since the vanadates crystallize in a structure different from scheelite, the range of solid solubility had to be established first. The techniques used in ob-

Table I. Lattice parameters for some compositions of the $(CaMoO_4)_{1-x}(EuVO_4)_x$ system

x	a_t, Å	c_t, Å	Space group	Unit cell volume, Å^3
0	5.219	11.418	$I4_1/a$	311.00
0.1	5.214	11.422	$I4_1/a$	310.52
0.2	5.207	11.429	$I4_1/a$	309.87
0.9	7.229	6.374	I4/amd	333.09
1.0	7.253	6.398	I4/amd	336.57

Table II. Fluorescent emission characteristics for some $(CaMoO_4)_{1-x}(LnVO_4)_x$ systems

Ln	x for Maximum fluorescent emission intensity (of underlined wavelength)	Relative intensity of most intense line	Lines at mμ*
Sm	0.02	39	560, 595, 635
Eu	0.20	282	585, 610
Tb	0.02	486	485, 540, 580
Dy	0.01	108	570

* The underlined wavelength was the most intense emission.

taining lattice parameters are essentially those described earlier (2). Some of the data are summarized in Table I and Fig. 1 gives a graphic representation of the phase diagram for $CaMoO_4$-$EuVO_4$.

Between $x > 0.2$ to $x < 0.9$, there was no solid solubility; this makes the two-phase region considerably wider than for the corresponding $CaMoO_4$/$EuNbO_4$ system, a rather surprising result in view of the fact that the closer match of the Mo^{+6} and V^{+5} ion radii should permit even more extended solid solubility. Since there is no change in coordination number for the cationic and the anionic metal constituent in going from either $LnVO_4$ or $LnNbO_4$ to $CaMoO_4$ (8 for A and 6 for B), the $LnNbO_4$ structure is obviously more closely related to the $CaMoO_4$ structure. In view of the fact that Kankov (7) first described $YNbO_4$ as a distorted scheelite this supports this consideration.

Fluorescent emission studies were carried out for the $CaMoO_4$-$LnVO_4$ systems where Ln = Sm, Eu, Tb and Dy. The experimental arrangements for examining fluorescence have been published (2). The data are given in Table II.

Since no corrections were made for photomultiplier response, the intensity data are meant merely to give a qualitative basis for comparison. Obviously, both Tb^{+3} and Eu^{+3} are the most intense emitters in this system.

Typical fluorescent emission spectra of polycrystalline samples are represented in Fig. 2-5. The line sharpening in going from room temperature to liquid nitrogen temperature is particularly prominent for the Dy case, but the complexity of the spectrum and the multitude of still available transitions prevents stimulated emission. Laser experiments with the Dy and Sm compositions in the niobate-molybdate system had failed (2) and were not attempted with these new compounds. The europium spectrum as shown in Fig. 3 is of course substantially simpler, but surprisingly, line narrowing was rather insignificant in this case. The Tb sample as represented in Fig. 4 showed similar behavior, whereas the Sm compound (Fig. 2) gave narrowing almost as pronounced as the Dy composition.

A characteristic plot of intensity of fluorescent emission as a function of activator concentration is given

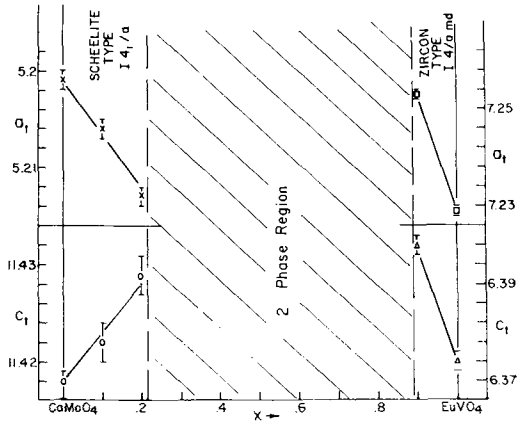

Fig. 1. Structure types as a function of x for the $(EuVO_4)_x(CaMoO_4)_{1-x}$ system.

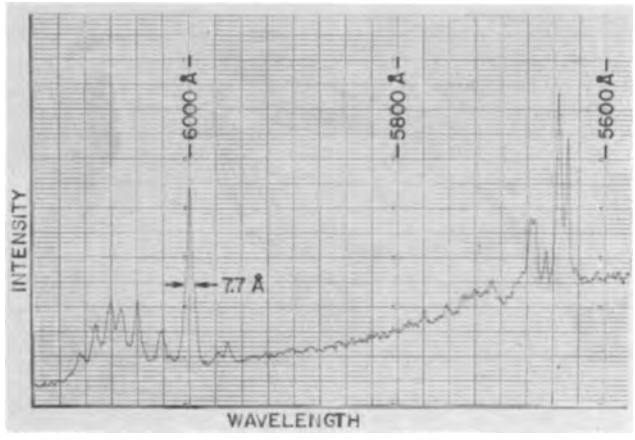

Fig. 2. Fluorescent emission spectrum of $Sm_{0.02}Ca_{0.98}V_{0.02}Mo_{0.98}O_4$ at 300°K.

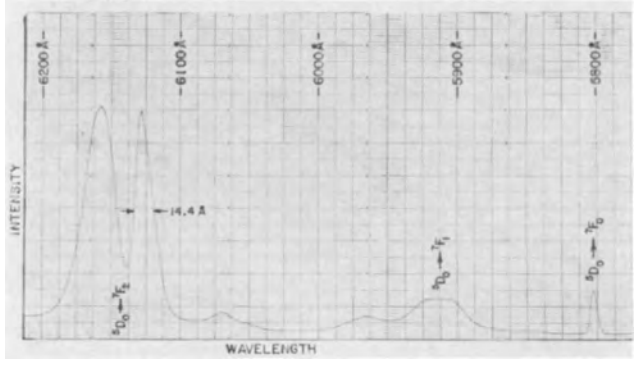

Fig. 3. Fluorescent emission spectrum of $Eu_{0.20}Ca_{0.80}V_{0.20}Mo_{0.80}O_4$ at 300°K.

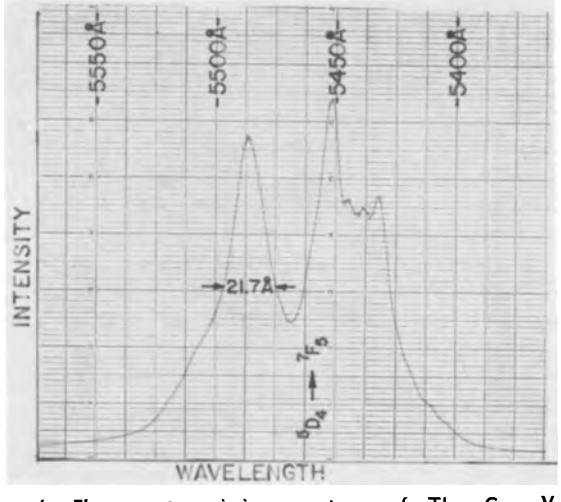

Fig. 4. Fluorescent emission spectrum of $Tb_{0.02}Ca_{0.98}V_{0.02}Mo_{0.98}O_4$ at 300°K.

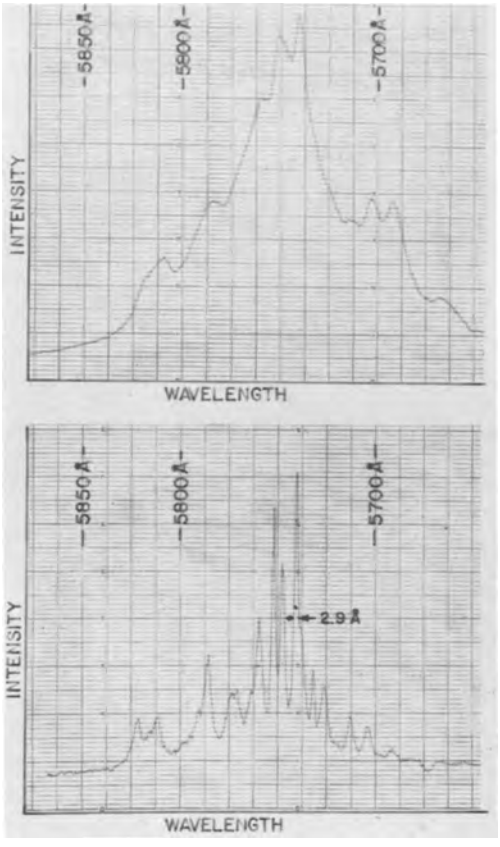

Fig. 5. Fluorescent emission spectrum of $Dy_{0.02}Ca_{0.98}V_{0.02}Mo_{0.98}O_4$ at 300°K (top) and 77°K (bottom).

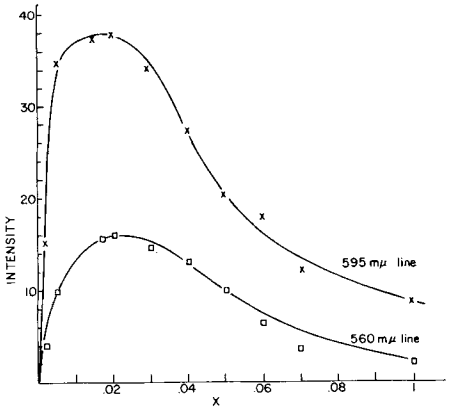

Fig. 6. Intensity of fluorescent emission as a function of x for the $(SmVO_4)_x(CaMoO_4)_{1-x}$ system.

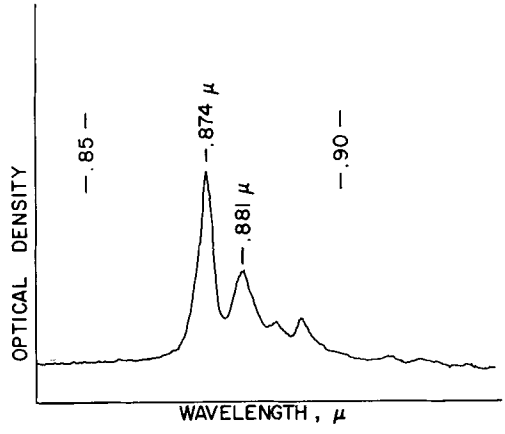

Fig. 7. $4F_{3/2}$ absorption level for $Nd_{0.01}Ca_{0.99}V_{0.01}Mo_{0.99}O_4$

in Fig. 6 for the example of Sm. As can be seen, the shape of the curve is essentially the same for the two different emission lines plotted: a rather steep rise to the optimum at 2 mole % and then gradual decrease of intensity until eventually complete concentration quenching occurs.

Whenever Nd is introduced into a novel host or a new compensation scheme is applied, it is always of interest to observe the absorption characteristics at the $4F_{3/2}$ level, which is the last absorption band before the 1.06μ region of emission for Nd^{+3}. It would be highly desirable to find a host material with an absorption peak at 0.84μ, the emission wavelength of a modified GaAs injection laser. As can be seen from Fig. 7, the shortest peak is still at 0.87μ.

Crystal Growing Experiments

Procedure and equipment have been described earlier (2). The most significant difference from niobate-compensated $CaMoO_4$ was that the oxygen loss in the presence of vanadates was even more severe than for undoped $CaMoO_4$. Contrary to behavior of niobate-compensated crystals, segregation coefficients were below 1 and the melting point was about 10°C lower than that of pure $CaMoO_4$ (1480°C). Despite the use of an automatic voltage control unit to minimize current fluctuations, it was very difficult to control the crystal shape. This was true for crystals grown both in the a- or the c-axis of the scheelite structure. Characteristically, the a-axis crystals were elliptical in cross section, with a considerably higher axial ratio than for Nb-compensated crystals, and the c-axis crystals showed an almost round cross section. Contrary to experience with Na-compensation the vapor pressures posed no problem; no V_2O_5 was lost and materials were charged to the melting crucible in stoichiometric proportions. A detailed examination of the Ln_2O_3:V_2O_5 ratio on top and bottom of a crystal based on the analytical information given in Table III gives the following values:

For Dy: top, Dy_2O_3:V_2O_5 = 1:0.88; bottom, Dy_2O_3:V_2O_5 = 1:0.93 (3.5 in. over-all length representing 42% of weight of original charge).

For Tb: top, Tb_2O_3:V_2O_5 = 1:0.87; bottom, Tb_2O_3:V_2O_5 = 1:0.85 (4.8 in. over-all length representing 51% of weight of original charge).

This indicates that even if ½ of the original charge is grown into a single crystal, there is essentially no

Table III. Analysis of some single crystals

Nominally charged composition	Analytically determined %							Sum total %*	
	CaO	MoO_3	V_2O_5	Nd_2O_3	Sm_2O_3	Tb_2O_3	Dy_2O_3		
$Dy_{0.01}Ca_{0.99}V_{0.01}Mo_{0.99}O_4$	27.37	71.99	0.24	—	—	—	0.56	100.16	(T)
	27.58	71.88	0.31	—	—	—	0.68	100.45	(B)
$Sm_{0.01}Ca_{0.99}V_{0.01}Mo_{0.99}O_4$	27.76	71.14	0.22	—	0.56	—	—	99.68	(T)
	28.31	71.02	0.24	—	0.59	—	—	100.16	(B)
$Tb_{0.01}Ca_{0.99}V_{0.01}Mo_{0.99}O_4$	27.62	70.89	0.23	—	—	0.53	—	99.27	(T)
	27.30	72.07	0.24	—	—	0.57	—	100.18	(B)
$Nd_{0.01}Ca_{0.99}V_{0.01}Mo_{0.99}O_4$	27.75	71.36	0.26	0.73	—	—	—	100.10	(T)
	27.71	71.19	0.28	0.79	—	—	—	99.97	(B)

* T is top, B is bottom.

Table IV. Laser evaluation

Composition	Room temperature threshold
$Ca_{0.99}Nd_{0.01}Mo_{0.99}Nb_{0.01}O_4$	173 joules
$Ca_{0.99}Nd_{0.01}Mo_{0.99}V_{0.01}O_4$	290 joules

Table V. Some physical parameters of $Nd_{0.01}Ca_{0.99}V_{0.01}Mo_{0.99}O_4$

Molecular weight	200.61
Weight % Nd^{+3}	0.72
Structure	$I4_1/a$ (scheelite)
Lattice parameters	a_t = 5.215A
	c_t = 11.427A
Thermal conductivity	38 m watts/cm deg
Hardness (mohs)	4.4 (300°K)
Refractive index	1.99
Dielectric constant	9.9 (at 1 kc)
Melting point	1470°C
Typical threshold	290 joules

(⅛ × 1 in. rod at 300°K)

shift in the concentration ratio. Some typical analytical data obtained by x-ray fluorescence analysis are summarized in Table III.

Laser Experiments

Single crystal boules were cut and ground into cylindrical rods ⅛ in. diameter and 1 in. long. The cylindrical surfaces were left rough and the ends polished to form a Fabry-Perot resonator. Silver was evaporated onto the end surfaces; one end was 5% transmissive and the other completely opaque.

Laser characteristics were measured under pulsed illumination in a Lear-Siegler LS-3 laser head with a Kemlite FT100B helical xenon flash lamp. All experiments were run at 295°K. The lamp was flashed by discharging a 5-μf condenser charged to 2000v. Light from the laser rods was detected with a Dumont K1485 photomultiplier through a 3-mm silicon filter. For the purpose of comparison, a niobium-compensated rod of equal size and Nd concentration was also lased. The data for those rods are given in Table IV.

A number of other pertinent parameters have been determined for $Nd_{0.01}Ca_{0.99}V_{0.01}Mo_{0.99}O_4$ and are summarized in Table V.

Based on these data, in conjunction with the laser experiments, it would seem that V^{+5} compensation in $CaMoO_4$:Nd, while quite feasible, does not offer any further improvement over the $CaMoO_4$:$NdNbO_4$ system.

Acknowledgment

The author greatly appreciated the assistance of Mr. F. Walls in growing the crystals and of Dr. P. A. Flournoy in performing the laser experiments.

Manuscript received Oct. 25, 1965; revised manuscript received Jan. 6, 1966.

Any discussion of this paper will appear in a Discussion Section to be published in the December 1966 JOURNAL.

REFERENCES

1. L. F. Johnson, *J. Appl. Phys.*, **34**, 897 (1963).
2. L. H. Brixner, *This Journal*, **111**, 690 (1964).
3. R. C. Duncan, *J. Appl. Phys.*, **36**, 874 (1965).
4. A. L. H. Ahrens, *Geochim. Cosmochim. Acta*, **2**, 115 (1939).
5. L. H. Brixner, *This Journal*, **112**, 70 (1965).
6. L. H. Brixner, *ibid.*, **112**, 303 (1965).
7. A. I. Kankov, *Schr. Allumions Mineralog. Ges.*, **86**, 432 (1957).

Pseudobinary InSb-InTe System

A. J. Strauss, M. D. Banus, and M. C. Finn

Lincoln Laboratory,[1] Massachusetts Institute of Technology, Lexington, Massachusetts

ABSTRACT

The InSb-InTe pseudobinary system has been investigated by thermal, metallographic, x-ray diffraction, and electron microprobe analysis. The results show that there is an unstable phase diagram in addition to the stable diagram. The principal features of the stable diagram are the same as those reported by Deneke and Rabenau, but the temperatures of the thermal arrests are appreciably different. The system contains one ternary compound, with nominal composition In_3SbTe_2, which is a peritectic phase unstable above 556° and below about 420°C. According to the stable diagram, In_3SbTe_2 is the first phase to crystallize during cooling runs on melts containing between 15 mole % InTe (the eutectic composition) and 40 mole % InTe (the liquidus composition at the peritectic temperature), and InTe crystallizes as the primary phase from melts containing more than 40 mole % InTe. When experimental conditions permit sufficient supercooling, however, the ternary compound crystallizes as the primary phase from melts containing between 40 and 75 mole % InTe, since in this region there is an unstable liquidus which lies below the stable liquidus. The unstable liquidus temperature increases monotonically from 556° to 586°C as the InTe content increases from 40 to 75 mole % InTe. For samples of the ternary compound crystallized close to 586°C, the formula In_4SbTe_3 appears to be more appropriate than In_3SbTe_2.

A number of alloy systems involving a III-V compound and an $A_2^{III}B_3^{VI}$ compound containing the same group III element have been investigated (1). The III-V compounds in these systems have the zinc blende structure, and except for In_2Se_3 the $A_2^{III}B_3^{VI}$ compounds have a defect zincblende (or possibly defect antifluorite) structure. Except in the InSb-In_2Te_3 system, the only phases obtained are solid solutions which lie in or close to the pseudobinary section of the two terminal compounds. In several systems, for example InAs-In_2Te_3 (2), the two compounds are soluble in all proportions.

In investigating the InSb-In_2Te_3 system, Goryunova, Radautsan, and Kiosse (3) and Woolley, Gillett, and Evans (4) obtained a phase with rock-salt structure. Goryunova *et al.* (3) showed that this phase was a ternary compound in the InSb-InTe pseudobinary section, rather than in the InSb-In_2Te_3 section. They reported that the ternary compound contained approximately 75 mole % InTe, corresponding to the nominal formula In_4SbTe_3.

[1] Operated with support from the U. S. Air Force.

It was later found in our laboratory (5) and confirmed elsewhere (6) that InTe, whose stable phase at atmospheric pressure has the TlSe tetragonal structure and is not superconducting, is transformed at about 30 kbar into a high pressure phase with rock-salt structure which has a superconducting transition at about 3.5°K. This result suggested the possibility that the ternary In-Sb-Te compound, which also has the rock-salt structure, might be a superconductor. In order to investigate this possibility, attempts were made to obtain the ternary compound by solidifying melts containing 75 mole % InTe. These attempts failed to yield single-phase samples, although the preparation of such samples by the same method had been reported by Goryunova *et al.* (3). To find an explanation for this discrepancy, we undertook a detailed investigation of the InSb-InTe pseudobinary phase diagram by means of thermal, metallographic, x-ray diffraction, and electron microprobe analysis.

This paper reports the results of our investigation and compares them with earlier incomplete data on the InSb-InTe system obtained by Molodyan, Radautsan, and Madan (7) and with the phase diagram recently reported by Deneke and Rabenau (8). The findings of these authors did not come to our attention until our investigation was essentially complete. On the basis of their x-ray diffraction and metallographic data, Deneke and Rabenau (8) report that the ternary compound has the composition In_3SbTe_2. Although our data do not establish the precise homogeneity range of the ternary compound, for samples annealed at 475°C they show that the composition In_3SbTe_2 lies within this range but In_4SbTe_3 does not. Throughout this paper the ternary compound is accordingly designated as In_3SbTe_2, but this should be regarded as a nominal formula. [In our earlier reports (9) of this investigation, the ternary compound was designated as In_4SbTe_3. Evidence will be given that this is probably a more appropriate formula than In_3SbTe_2 for samples of the compound prepared by crystallization under certain conditions.]

Our investigation establishes a stable phase diagram for the InSb-InTe system which is in general agreement with the diagram proposed by Deneke and Rabenau (8). In addition, our results demonstrate the existence of an unstable diagram, for the composition region between 40 and 75 mole % InTe, which explains the observations of Goryunova *et al.* (3) and Molodyan *et al.* (7).

Experimental

With one exception, thermal analysis data were obtained in cooling runs on initially molten samples. Each sample for the cooling runs was prepared by placing appropriate quantities of semiconductor grade In, Sb, and Te (nominal purity 99.999%) totaling 150g in a quartz tube which was then evacuated and sealed. A Pt-(Pt-13% Rh) thermocouple for measuring sample temperatures was inserted into a reentrant tube at the bottom of the sample tube. The thermocouple had been calibrated at the melting point of Sb (630.5°C). Since the difference between the observed and tabulated voltages at this temperature corresponded to less than 0.2°C, no corrections were made in converting the subsequently measured voltages to temperatures. In order to reduce thermal gradients within the sample, the sample tube was placed in a heavy-walled stainless steel cylinder. A reference thermocouple for differential measurements was inserted into a hole in the bottom of this cylinder. The sample and cylinder were heated in a vertical resistance furnace to about 800°C, allowed to equilibrate at that temperature for at least 12 hr, and then cooled at 2°-3°C/min over the range of interest by turning off the furnace power. In order to measure the sample temperature with high precision, most of the thermocouple signal was bucked out with a d-c microvolt potentiometer, and the remaining voltage was amplified with a d-c microvolt amplifier whose output was recorded with a recording potentiometer. The same procedure was followed for the reference thermocouple.

One heating run between about 200° and 700°C was made on an initially solid sample, which was prepared by pulverizing material taken from the first-to-freeze portion of an ingot obtained by the horizontal Bridgman technique from a melt containing 65 mole % InTe. This sample, which weighed about 45g, consisted primarily of In_3SbTe_2 but contained a small amount of InSb as a second phase. A reference specimen of pulverized germanium sealed in an evacuated quartz tube was used. The sample and reference thermocouples were bucked against each other and the difference voltage was amplified and recorded.

Metallographic studies were made with a Leitz MM5 metallograph on a number of the ingots formed during thermal analysis runs on initially molten samples, on ingots prepared by the horizontal Bridgman technique, and on annealed samples prepared in the manner described below. One of the metallographic samples was also examined with a Cameca electron microprobe at Acton Laboratories, Acton, Massachusetts, and others were examined with an electron microprobe at the Department of Metallurgy, Massachusetts Institute of Technology.

Room temperature x-ray diffraction patterns for powdered samples were obtained with a standard 114.6 mm Debye-Scherrer camera. Exposures of 7 hr were made with Cu-Kα radiation. Measurements were made both on as-grown samples (from ingots solidified during thermal analysis runs, prepared by the horizontal Bridgman technique, or quenched from the melt) and on annealed samples. To prepare an annealed sample, a melt of the desired composition was quenched, the resulting ingot was powdered, and about 2g of the powder was pressed into a pellet. The pellet was sealed into an evacuated quartz ampoule and annealed for 2-4 weeks at 475°-500°C. One portion of the pellet was analyzed for In, Sb, and Te by a wet chemical method described elsewhere (10).

X-ray diffraction measurements were also made on 2 samples of In_3SbTe_2 at a number of temperatures up to 540°C with a 90 mm Rigaku-Denki high temperature camera. The period of exposure at each temperature was 12-18 hr. One of the samples had been prepared by annealing in the manner described above. The other was an as-grown sample from an ingot prepared by the horizontal Bridgman technique.

Results and Discussion

Figure 1 shows the pseudobinary InSb-InTe phase diagram, which includes not only the stable diagram (indicated by solid and dotted lines) but also an unstable diagram (indicated by dashed and dot-dashed lines). The data points in Fig. 1 represent the thermal arrests observed in cooling runs on initially molten samples. These arrests are also listed in Table I. For

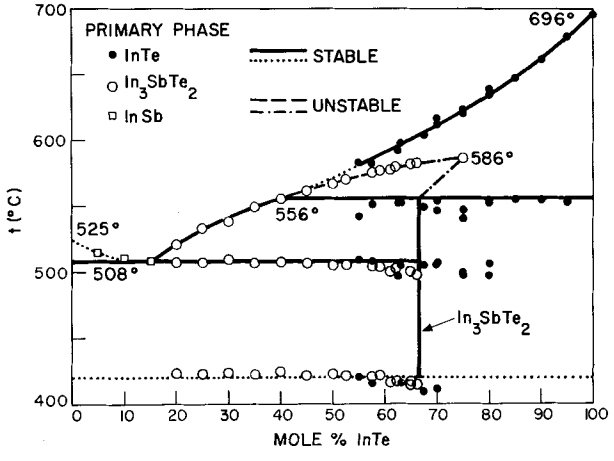

Fig. 1. Phase diagram of the pseudobinary InSb-InTe system

Table I. Thermal arrests observed in the InSb-InTe system

Mole % InTe	Sample	Liquidus (°C)	Peritectic (°C)*	Eutectic (°C)†	Near 420°C (°C)
5	19	514	L	XX	X
10	18	510	L	XX	X
15	17	(508)	L	508	X
20	16	520	L	507	423
25	11	533	L	507	422
30	15	538	L	509	423
35	14	549	L	507	422
40	13	555	L	507	424
45	12	561	X	506	421
50	10	566	X	505	422
52.5	26	570	X	505	421
55	7	583	542	509	420
57.5	25	575	X	504	420
	27	582	551	507	415
59	33	576	X	503	421
61	32	577	X	500	416
62	31	579	X	502	416
62.5	24	592	552	497	No data
63	30	597	553	505	416
65	6	581	X	500	414
	21	582	X	500	416
66	29	582	X	498	415
67.5	23	603	549	505	409
70	8	612	554	506	411
	35	616	546	507	X
75	2	620	547	497	No data
	36	622	540	499	X
	40	586	X	X	No data
80	3	635	554	497	No data
	41	638	552	506	No data
85	4	647	555	X	X
90	5	661	554	X	X
95	20	679	552	X	X
100	IT	695			

* L, liquidus temperature below peritectic temperature.
X, no arrest observed.
† XX, arrest not resolved.

each run in which InTe was the first phase to crystallize from the melt, all the thermal arrests observed during the run are indicated by closed circles in Fig. 1. Arrests observed during runs in which the primary phase was In_3SbTe_2 or InSb are indicated by open circles and squares, respectively. The compounds InSb, InTe, and In_3SbTe_2 are shown as line phases in Fig. 1 and will generally be referred to as such in the following discussion, since information on their ranges of homogeneity is limited.

Stable phase diagram.—Liquidus, peritectic, and eutectic.—The principal features of the stable phase diagram are the same as those reported by Deneke and Rabenau (8). The ternary compound In_3SbTe_2 is a peritectic phase, unstable below about 420°C, which forms a eutectic with InSb. The eutectic mixture contains 15 mole % InTe. Along the stable liquidus lines, in agreement with Deneke and Rabenau (8), melts containing 15 mole % InTe or less are in equilibrium with InSb, those containing between 15 and 40 mole % InTe are in equilibrium with In_3SbTe_2, and those containing more than 40 mole % InTe are in equilibrium with InTe.

The liquidus temperature for pure stoichiometric InTe was found to be 695°C, in good agreement with the melting point of 696°C recently reported by Grochowski, Mason, Schmitt, and Smith (11) for congruently melting InTe, which according to these authors contains 50.8 a/o (atomic per cent) Te.

According to the stable phase diagram, InTe is the first phase to crystallize from InSb-InTe melts containing more than 40 mole % InTe. Primary crystallization of InTe did occur in all cooling runs on melts containing at least 80 mole % InTe. It also occurred in about half the runs on melts containing 55-75 mole % InTe, while primary crystallization of In_3SbTe_2 according to the unstable phase diagram occurred in the rest of these runs.

When InTe was the primary phase in cooling runs on melts containing up to 80 mole % InTe, thermal arrests were observed at the stable liquidus, peritectic, and eutectic temperatures.[2] Typical thermal analysis

[2] According to the stable diagram, eutectic arrests should not occur in cooling runs on samples containing more than 67 mole % InTe, since these samples should become completely solid at the peritectic temperature. As pointed out by Deneke and Rabenau, however, eutectic arrests can occur for compositions above 67 mole % InTe when the cooling rate is too fast to permit equilibrium to be attained.

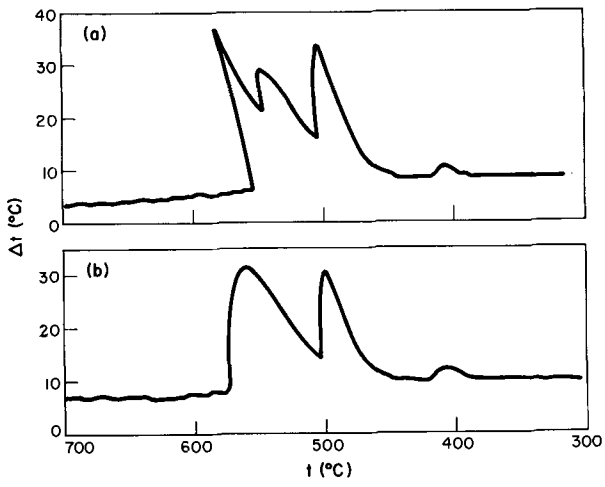

Fig. 2. Differential thermal analysis data obtained in cooling runs on samples containing 57.5 mole % InTe. (a) Sample No. 27, which froze according to the stable diagram. (b) Sample No. 25, which froze according to the unstable diagram.

data showing these three arrests are presented in Fig. 2(a), where the difference between sample and reference temperatures is plotted against sample temperature for a sample (No. 27) containing 57.5 mole % InTe. (The small arrest at 415°C will be discussed below.) When the three arrests were observed, metallographic, x-ray diffraction, and electron microprobe studies showed that InTe, In_3SbTe_2, and InSb were all present in the solidified sample. Figure 3(a) is a photomicrograph of the polished surface of such a sample (No. 7), prepared from a melt containing 55 mole % InTe. The sample consists of dark islands of InTe, each surrounded by a lighter ring of In_3SbTe_2, which is surrounded in turn by a darker matrix of eutectic. (The single-phase appearance of the eutectic will be explained below.) The three phases are present because the cooling rate was too fast either to permit the InTe first crystallized to be removed by the peritectic reaction with InSb-rich liquid or to permit the In_3SbTe_2 to be removed by decomposition below 420°C.

Thermal arrests at the stable liquidus temperatures were not observed in cooling runs on samples containing between 40 and 55 mole % InTe, since these samples froze according to the unstable phase diagram. Therefore, the stable liquidus curve in this composition region, which is represented by a dotted line in Fig. 1, was obtained by extrapolating the portion of the curve above 55 mole % InTe to the peritectic point.

The stable liquidus from pure InSb to the eutectic point at 15 mole % InTe is also represented by a dotted line in Fig. 1, since the solid samples obtained in cooling runs on InSb-InTe melts in this composition range do not lie in the pseudobinary InSb-InTe section. These samples contain two phases: a small quantity of essentially pure In and a solid solution with zincblende structure lying in or close to the InSb-In_2Te_3 section. The In phase was identified by electron microprobe analysis. The nature of the solid solutions was established by x-ray diffraction measurements on samples prepared by quenching InSb-InTe melts containing 1-40 mole % InTe. As shown in Fig. 4, the lattice parameters of the zincblende phase in these quenched samples are in good agreement with those reported by Woolley, Gillett, and Evans (4) for annealed InSb-In_2Te_3 specimens containing the same mole fractions of InSb. For InSb-InTe samples with compositions between 15 and 40 mole % InTe, the lattice parameter of the zincblende phase has a fixed value corresponding to an In_2Te_3 content of about 15 mole %, the same as the maximum solubility of In_2Te_3 in InSb found by Woolley *et al.* (4). As required by

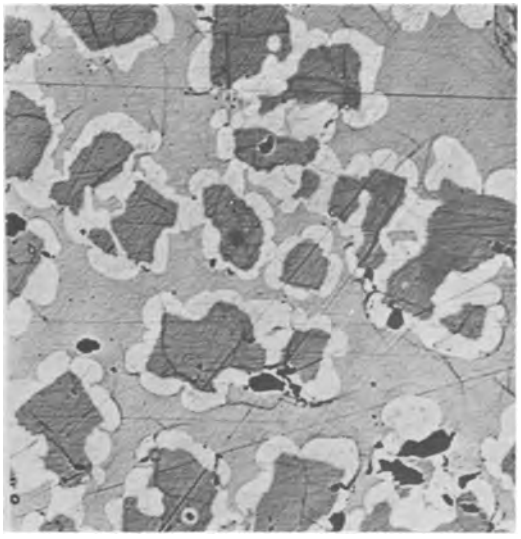

Fig. 3. Photomicrographs of polished specimens from samples prepared by solidification of InSb-InTe melts. (a) Sample No. 7, with over-all composition of 55 mole % InTe, containing InTe (primary phase), In_3SbTe_2, and eutectic.

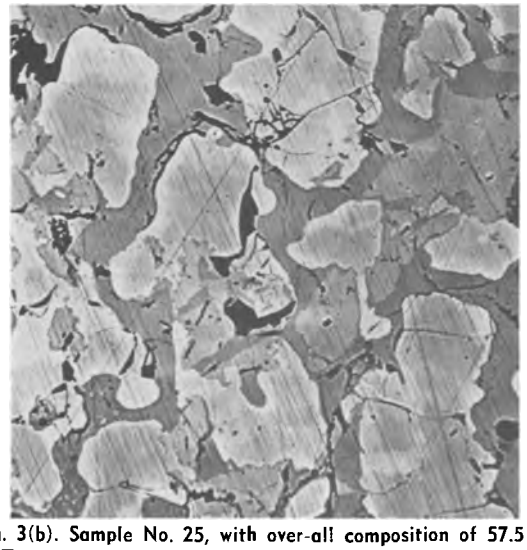

Fig. 3(b). Sample No. 25, with over-all composition of 57.5 mole % InTe, containing In_3SbTe_2 (primary phase) and eutectic.

the stable phase diagram, these samples contain In_3SbTe_2 as well as the zincblende and In phases. The solid obtained by freezing an InSb-InTe melt of eutectic composition (15 mole % InTe) consists almost entirely of a solid solution with approximately 15 mole % In_2Te_3, and therefore this solid contains only small scattered regions of characteristic two-phase eutectic mixture. This explains the single-phase appearance of the eutectic material in Fig. 3.

The mixtures of In and InSb-In_2Te_3 phases in samples obtained by solidifying InSb-InTe melts are unstable, at least at 475°C. When the quenched samples discussed above were powdered, pressed, and annealed at this temperature for 2-3 weeks, the In phase disappeared. A zincblende phase was still present in all samples, and In_3SbTe_2 appeared for compositions between 5 and 15 mole % InTe as well as for those exceeding 15 mole %. As shown in Fig. 4, the lattice parameters of the stable zincblende phase initially decrease somewhat with increasing InTe content but become essentially constant for compositions above about 5 mole % InTe, although there is considerable scatter in the data. We assume that the stable zincblende phase is a solid solution lying in the InSb-InTe section and conclude that the solubility of InTe in InSb is less than 5 mole % at 475°C. It seems reasonable to assume that under equilibrium conditions melts

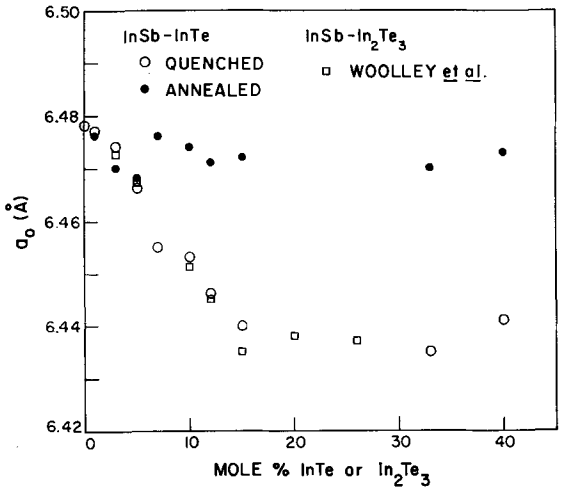

Fig. 4. Lattice parameter of the zincblende phase in InSb-InTe samples quenched from the melt or annealed at 475°C, as a function of over-all sample composition. The data of Woolley, Gillett, and Evans for the zincblende phase in InSb-In_2Te_3 samples annealed at 500°C are also included.

containing up to 15 mole % InTe coexist at the liquidus line with InSb-InTe solid solutions, rather than with the InSb-In_2Te_3 solutions obtained when such melts are solidified during cooling runs or by quenching. No attempt has been made to determine the stable liquidus in this composition region by means of heating runs on annealed samples. However, the stable liquidus probably does not differ much from the dotted line shown in Fig. 1, since the temperature range between the melting point of InSb and InSb-InTe eutectic temperature is only 17°C.

On the basis of the thermal arrests which occurred in cooling runs on initially molten samples, we have adopted 508°C as the eutectic temperature for the InSb-InTe system. In good agreement with this value, a thermal arrest was observed at 507°-509°C in a heating run on a Bridgman-grown sample of In_3SbTe_2.

A peritectic temperature of 553°-554°C for the InSb-InTe system is indicated by the results of our cooling runs on initially molten samples. We have adopted 556°C as the peritectic temperature, however, because the peritectic arrest occurred at 558°C in the heating run on the Bridgman-grown sample of In_3SbTe_2. In good agreement with the latter value, Molodyan, Radautsan, and Madan (7) observed arrests at 558°-560°C, 557°-561°C, and 558°-560°C, respectively, in heating runs on samples solidified from melts containing 50, 75, and 80 mole % InTe. [Molodyan *et al.* (7) did not identify these as peritectic arrests.]

The eutectic and peritectic temperatures reported by Deneke and Rabenau (8) are 512° and 568°C, respectively. Both values are significantly higher than the present ones. The stable liquidus temperatures obtained by Deneke and Rabenau [as read off Fig. 1 of ref. (8)] are also higher than the present values. For a number of compositions the difference is about 15°C, and in some cases it exceeds 20°C. We have not found a satisfactory explanation for these discrepancies. For compositions exceeding 55 mole % InTe, the present stable liquidus temperatures may be lower than the true values because considerable supercooling (15°-40°C) occurred before the initial crystallization of InTe. Although Deneke and Rabenau (8) do not report the amount of supercooling which occurred in their experiments, it was probably less than in the present experiments, since as discussed below they never observed freezing according to the unstable diagram. In the present cooling runs on samples containing 55 mole % InTe or less, the amount of supercooling ranged from 1° to 11°C and was probably insufficient to cause significant errors in the stable liq-

uidus temperatures. It is also unlikely that supercooling caused significant errors in the present peritectic or eutectic temperatures. At the peritectic point, the amount of supercooling was 15°C in one case, 11°C in another, and less than 9°C in all the rest. At the eutectic point, the amount of supercooling was always less than 5°C, and in most cases a constant temperature plateau was observed.

Composition and temperature stability of In_3SbTe_2. —In earlier reports (9) on the InSb-InTe system, we stated that x-ray diffraction data on samples annealed at 475°C established upper and lower limits of 80 and 70 mole % InTe, respectively, for the homogeneity range of the ternary In-Sb-Te compound, although these data did not fix the exact positions of the solidus lines. We therefore accepted the nominal formula In_4SbTe_3, which had been adopted for the compound by Goryunova *et al.* (3) and by Molodyan *et al.* (7) primarily on the basis of data for samples frozen from the melt. We later learned, however, that on the basis of x-ray and metallographic data for samples annealed at 440°-500°C Deneke and Rabenau (8) had reported the formula to be In_3SbTe_2 rather than In_4SbTe_3. We therefore re-examined our x-ray diffraction patterns for annealed samples containing 60-80 mole % InTe and examined these samples metallographically. We also made x-ray and metallographic studies on additional samples in this composition range annealed at 475°C. The results obtained for samples containing between 40 and 90 mole % InTe are shown in Fig. 5, where the room temperature lattice parameter (a_o) of the ternary compound is plotted against sample composition determined by chemical analysis, and the phases detected in each sample are indicated. In agreement with Deneke and Rabenau (8), the data show that at 475°C the ternary compound contains less than 70 mole % InTe and therefore cannot have the formula In_4SbTe_3. (Metallographic examination clearly reveals the presence of InTe as a second phase in samples containing close to 70 mole % InTe, although lines due to InTe cannot be detected in the x-ray diffraction patterns for these samples.) The data are consistent with the nominal formula In_3SbTe_2 given by Deneke and Rabenau (8), since no second phase was detected metallographically in the samples containing 64 and 68 mole % InTe. According to these results, the homogeneity range of In_3SbTe_2 is somewhat wider than reported by Deneke and Rabenau (8), who state that it is less than 2 mole % wide. The values of a_o for In_3SbTe_2 in two-phase mixtures containing InSb and InTe are 6.125 ± 0.001Å and 6.133 ± 0.003Å, respectively. This difference in a_o

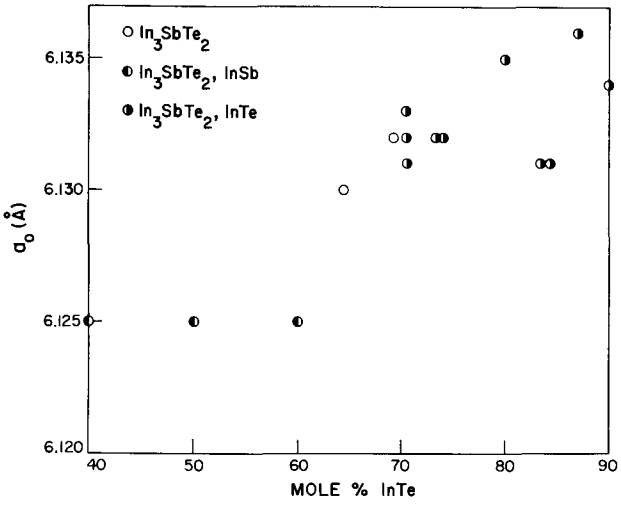

Fig. 5. Lattice parameter of the ternary compound in InSb-InTe samples annealed at 475°C, as a function of over-all sample composition. The phases detected in each sample are also indicated.

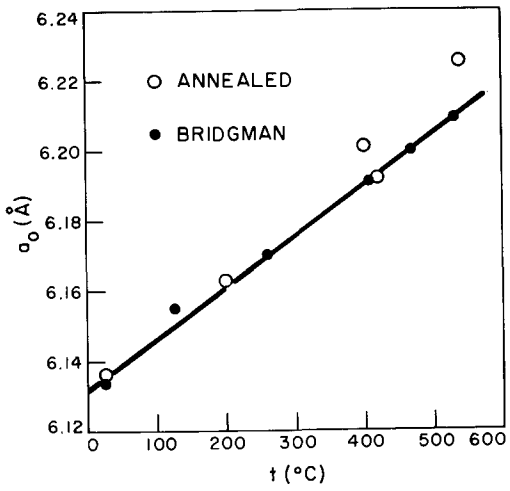

Fig. 6. Lattice parameter for two samples of In_3SbTe_2 as a function of temperature. (Both samples contained a small quantity of InTe as a second phase.)

values is evidence that In_3SbTe_2 has an appreciable homogeneity range at 475°C, although no quantitative estimate of the width of the range can be made from the a_o data. Deneke and Rabenau (8) report a_o = 6.1263 ± 0.0007Å for single-phase In_3SbTe_2. They do not give a_o values for In_3SbTe_2 in two-phase mixtures.

The temperature dependence of a_o between room temperature and 540°C was determined by x-ray diffraction measurements on two samples of In_3SbTe_2, one annealed at 475°C and the other prepared by the horizontal Bridgman technique. The data for these samples, which are plotted in Fig. 6, show that a_o increases linearly with temperature over the whole range. The linear expansion coefficient calculated from these data is 2.4 x 10^{-5} deg^{-1}, in good agreement with the value of 2 x 10^{-5} deg^{-1} obtained by Molodyan *et al.* (7) from lattice parameter data between room temperature and 500°C.

After the present investigation was almost complete, Woolley (12) informed us of his observation that In_3SbTe_2 slowly decomposes into InSb and InTe below about 400°C. Later we learned that Deneke and Rabenau (8) had observed the decomposition of In_3SbTe_2 at 300° and 400°C. We subsequently studied the decomposition of In_3SbTe_2 at 400°C with a high temperature x-ray camera. No lines due to InSb or InTe appeared within the first 24 hr. (This explains why the decomposition of In_3SbTe_2 was not observed in our measurements of a_o as a function of temperature, since each x-ray exposure required only 12-18 hr.) After 2 or 3 days, however, the lines due to In_3SbTe_2 had entirely disappeared, and only lines due to InSb and InTe were present.

In drawing their phase diagram for the InSb-InTe system, Deneke and Rabenau (8) adopted 420°C as the most likely value for the minimum temperature at which In_3SbTe_2 is stable, but they indicated the phase boundary by a broken line, since its exact temperature is unknown. The same procedure has been followed in Fig. 1. The choice of 420°C suggests that partial decomposition of In_3SbTe_2 could be the cause of the small thermal arrest observed close to this temperature in the cooling run on almost every sample containing between 20 and 70 mole % InTe, whether or not it froze according to the stable phase diagram. (Both sets of thermal analysis data in Fig. 2 include arrests of this kind.) This explanation is consistent with the slow rate of decomposition observed at 400°C if it is assumed that the decomposition rate is strongly temperature dependent. In that case, the rate in the immediate vicinity of the phase boundary could be high enough to result in a thermal arrest on cooling, but lowering the temperature only a few degrees

would reduce the rate so much that no further thermal effects could be detected.

Unstable phase diagram.—In addition to the stable phase diagram, Fig. 1 includes the liquidus and solidus of an unstable diagram. This unstable diagram has been constructed in order to explain the results of the cooling runs on about half the InSb-InTe samples containing between 40 and 75 mole % InTe. Typical results for one of these runs are shown in Fig. 2(b), which gives the thermal analysis data obtained for a sample (No. 25) containing 57.5 mole % InTe. Only two principal thermal arrests are observed: one at the unstable liquidus temperature, which lies below the stable liquidus line, and the other at the InSb-In_3SbTe_2 eutectic temperature. There is no arrest at the peritectic temperature. A small arrest is observed at about 420°C, as discussed previously. The pattern of these data is obviously different from the pattern of those in Fig. 2(a), obtained for a sample (No. 27) of the same composition which froze according to the stable diagram. On the other hand, the pattern in Fig. 2(b) is closely similar to the one found for samples containing between 15 and 40 mole % InTe. It was this similarity which first suggested the existence of the unstable liquidus, which is simply an extension to higher InTe compositions of the portion of the stable liquidus between 15 and 40 mole % InTe.

According to the unstable phase diagram, the ternary InSb-InTe compound begins to crystallize as the primary phase at the unstable liquidus temperature, while InTe does not crystallize from the melt at all. This interpretation of the thermal analysis data has been confirmed by the results of metallographic and x-ray studies on solidified thermal analysis samples. These studies show that little if any of an InTe phase is present in samples which did not exhibit a peritectic arrest during cooling. Figure 3(b) is a photomicrograph of the polished surface of such a sample, the same one (No. 25) containing 57.5 mole % InTe for which thermal analysis data are given in Fig. 2(b). As expected, the ternary compound and eutectic phase are present, but not InTe. In contrast, Fig. 3(a) shows that large quantities of InTe are present in a sample containing 55 mole % InTe which froze according to the stable diagram.

In Fig. 1 the unstable liquidus temperature is shown as increasing monotonically to 586°C as the InTe content increases to 75 mole % InTe, the highest value for which primary crystallization of the ternary compound was observed. The shape of the liquidus between 66 and 75 mole % InTe is uncertain, since no data points were obtained between these two compositions. Accordingly, this portion of the liquidus is represented by a dot-dashed line in Fig. 1. It seems almost certain, however, that there is no maximum close to 67 mole % InTe. Such a maximum would be expected if the ternary compound crystallizing along the unstable liquidus had a composition approximating In_3SbTe_2, the formula adopted for samples annealed below the eutectic temperature. Furthermore, in cooling runs on samples which froze according to the unstable diagram, prominent eutectic arrests were observed for 65 and 66 mole % InTe. On the other hand, only a single arrest at 586°C occurred for a sample (No. 40) containing 75 mole % InTe. In addition, the lattice parameter of the ternary compound in sample No. 40 was 6.142 ± 0.003Å, significantly higher than the value of 6.133 ± 0.003Å for the ternary compound in annealed samples containing InTe as a second phase. (Metallographic examination of sample No. 40 revealed traces of both InSb and InTe in addition to the ternary compound.) These observations indicate that the ternary compound contains significantly more than 67 mole % InTe, and probably as much as 75 mole % InTe, when it crystallizes from melts at temperatures sufficiently far above the peritectic temperature. For samples crystallized close to 586°C, therefore, the formula In_4SbTe_3 appears to be more appropriate than In_3SbTe_2. The solidus is shown in Fig. 1 as a dot-dashed line joining the unstable liquidus at 75 mole % InTe with the stable solidus at the peritectic temperature.

In order for an InSb-InTe melt to freeze according to the unstable diagram, it must be supercooled below the stable liquidus by an amount equal to the difference between the stable and unstable liquidus temperatures plus the amount of supercooling required to nucleate crystallization of the ternary compound. In the present investigation, for those runs in which freezing occurred according to the unstable diagram, the amount of supercooling averaged 21°C below the stable liquidus and 7°C below the unstable liquidus. In about half the cooling runs for samples containing between 40 and 75 mole % InTe, the experimental conditions did not permit sufficient supercooling, and the samples froze according to the stable diagram. Apparently, the conditions employed by Deneke and Rabenau (8) were even less favorable for supercooling, since the thermal analysis data of these authors show that freezing according to the unstable diagram did not occur in any of their cooling runs. Consequently they did not discover the existence of this diagram.

Freezing according to the unstable diagram did occur in the experiments of Goryunova, Radautsan, and Kiosse (3), who reported on the basis of x-ray diffraction data that they obtained the ternary compound as a single phase by slow cooling of a melt containing 75 mole % InTe. If this melt had frozen according to the stable diagram, three phases would have been obvious in the solidified sample. These authors had no reason to suspect the existence of an unstable diagram on the basis of their observations. Therefore they assumed that the ternary compound had crystallized as a stable phase, which they identified as In_4SbTe_3.

Freezing according to the unstable diagram also occurred in several experiments performed by Molodyan, Radautsan, and Madan (7), although these authors still failed to realize the existence of this diagram. They too reported that they obtained single-phase samples of the ternary compound by cooling melts containing 75 mole % InTe at a slow rate (15°-20°C/hr). In addition, they report thermal analysis data which show that freezing according to the unstable diagram occurred in cooling runs on melts containing 50 and 75 mole % InTe. For the former composition, arrests occurred at 567° and 503°C, in excellent agreement with the present values of 566° and 505°C, respectively, for a sample (No. 10) with this composition. For the latter composition, a single arrest was observed at 586°C, just as in the present run on sample No. 40. Molodyan *et al.* (7) regarded this observation as confirming the identification of the ternary compound as In_4SbTe_3, and they adopted 586°C as the melting point of the compound.

Molodyan *et al.* (7) also reported thermal analysis and x-ray data which were obviously inconsistent with a simple phase diagram containing In_4SbTe_3 as a congruently melting compound. These data, which they could not interpret satisfactorily, can be explained in detail on the basis of the stable diagram for the InSb-InTe system. For example, they observed three thermal arrests, at 637°, 530°, and 496°C, in a cooling run on a sample containing 80 mole % InTe. These are the characteristic liquidus, peritectic, and eutectic arrests for a sample freezing according to the stable diagram. The liquidus and eutectic temperatures agree satisfactorily with the present values for this composition, but the peritectic temperature is about 20°C lower than the present one. They also observed that InSb, InTe, and the ternary compound were all present in a sample prepared by rapidly cooling a melt containing 75 mole % InTe. In this case, freezing must have occurred according to the stable diagram.

Table II. Electrical properties of samples containing In_3SbTe_2

Sample	Phases	Analysis (Mole % InTe)	T (°K)	ρ (ohm-cm)	R_H (cm^3 $coul^{-1}$)	$n = 1/R_H e$ (cm^{-3})	$R_H\sigma$ (cm^2 v^{-1} sec^{-1})
67	In_3SbTe_2	68	300	4.5×10^{-5}	—	—	—
			77	2.6×10^{-5}	-5.5×10^{-4}	1.1×10^{22}	21
69	In_3SbTe_2	70	300	6.2×10^{-5}	—	—	—
			77	3.3×10^{-5}	-5.0×10^{-4}	1.3×10^{22}	15
HA2-1	In_3SbTe_2, InTe	73	300	2.3×10^{-4}	-6.6×10^{-4}	9.9×10^{21}	3
			77	6.7×10^{-5}	-7.1×10^{-4}	8.8×10^{21}	11
H-3	In_3SbTe_2, InSb	—	300	5.1×10^{-5}	-7.2×10^{-4}	8.7×10^{21}	14
			77	3.0×10^{-5}	—	—	—

Superconductivity and electrical properties of In_3SbTe_2.—As discussed at the beginning of this paper, we originally wished to prepare In_3SbTe_2 in order to determine whether it was a superconductor, a possibility suggested by its similarity in structure to InTe(II), the superconducting form of InTe prepared under high pressure. Accordingly, a number of annealed samples prepared during the phase diagram investigation, all of which contained one or two minor phases in addition to In_3SbTe_2, were checked for superconductivity by a self-inductance technique (13). None of these samples became superconducting down to 1.3°K, the lowest temperature which could be attained with the apparatus. Subsequently, however, In_3SbTe_2 was found to be a superconductor by Rabenau, Deneke, and van der Meij (14), who were able to make measurements at lower temperatures. These authors, who had independently noted the similarity between In_3SbTe_2 and InTe(II), observed a superconducting transition at 1.06°K.

Table II gives the results of electrical resistivity (ρ) and Hall coefficient (R_H) measurements on four samples containing In_3SbTe_2. The most significant data are those for the single-phase samples 67 and 69, which were cut from annealed ingots with nominal compositions of 67 and 69 mole % InTe, respectively. Sample HA2-1 was also cut from an annealed ingot (nominal composition 75 mole % InTe), and sample H-3 was taken from an ingot prepared by the horizontal Bridgman technique. In each case the values of ρ and R_H are very low, and ρ decreases with decreasing temperature. Thus all four samples exhibit metallic behavior, although it cannot be determined from the data whether In_3SbTe_2 is a metal or a semiconductor with very high carrier concentrations. For samples 67, 69, and H-3, at room temperature ρ is about 5×10^{-5} ohm-cm, more than an order of magnitude lower than the value of 7×10^{-4} ohm-cm reported for In_3SbTe_2 by Deneke, Rabenau, and van der Meij (14).

Table II gives carrier concentrations calculated from the measured R_H values according to the one-carrier expression $n = 1/R_H e$. Although it has not been established that this expression is valid for In_3SbTe_2, it is of interest that the concentrations listed for the single-phase samples 67 and 69 are in good agreement with those expected on the basis of the ionic model proposed by Geller and Hull (15) for high pressure InTe(II) and similar materials. According to this model, such materials exhibit metallic behavior because they contain both In^{+1} and In^{+3} ions, and electrons are easily transferred from one type of In ion to the other. The free electron concentration is equal to twice the concentration of In^{+1} ions. Therefore, the electron concentrations predicted for $InSb_{0.32}Te_{0.68}$ and $InSb_{0.30}Te_{0.70}$ are 1.18×10^{22} and 1.21×10^{22} cm^{-3}, respectively, in comparison with the values of 1.1×10^{22} and 1.3×10^{22} cm^{-3} given in Table II for samples 67 and 69, respectively.

Acknowledgments

It is a pleasure to acknowledge the valuable assistance of R. L. MacLean, who performed almost all the thermal analysis experiments, and of M. Jane Button, J. C. Cornwell, Lynne B. Farrell, Muriel C. Plonko, T. E. Stack, and G. E. Wheatley, who participated in various phases of the experimental work. We are grateful to Professor J. C. Woolley, for communicating his results prior to publication and for a number of helpful discussions, and to Dr. A. Rabenau, for calling our attention to his investigations of the InSb-InTe system.

Manuscript received Oct. 21, 1965; revised manuscript received Jan. 24, 1966.

Any discussion of this paper will appear in a Discussion Section to be published in the December 1966 JOURNAL.

REFERENCES

1. These investigations have been reviewed by J. C. Woolley, "Progress in Solid State Chemistry," Vol. 1, p. 275, H. Reiss, Editor, The Macmillan Co., New York (1964).
2. J. C. Woolley and B. A. Smith, *Proc. Phys. Soc. (London)*, **72**, 867 (1958); N. A. Goryunova and S. I. Radautsan, *Soviet Phys.-Doklady*, **3**, 854 (1958).
3. N. A. Goryunova, S. I. Radautsan, and G. A. Kiosse, *Soviet Phys.-Solid State*, **1**, 1702 (1960).
4. J. C. Woolley, C. M. Gillett, and J. A. Evans, *J. Phys. Chem. Solids*, **16**, 138 (1960).
5. M. D. Banus, R. E. Hanneman, M. Strongin, and K. Gooen, *Science*, **142**, 662 (1963).
6. H. E. Bömmel, A. J. Darnell, W. F. Libby, B. R. Tittman, and A. J. Yencha, *Science*, **141**, 714 (1963).
7. I. P. Molodyan, S. I. Radautsan, and I. A. Madan, *Izv. Akad. Nauk. Mold. SSR*, **10**, 91 (1961).
8. K. Deneke and A. Rabenau, *Z. anorg. allgem. Chem.*, **333**, 201 (1964). A brief report of the principal results was given by A. Rabenau and K. Deneke, *Angew. Chem.*, **74**, 659 (1962).
9. A. J. Strauss, M. D. Banus, and M. C. Finn, *This Journal*, **111**, 277C (1964); Solid State Research Report, Lincoln Laboratory, M.I.T. (1964:3), p. 33.
10. M. C. Gardels and J. C. Cornwell, Pittsburgh Conference on Analytical Chemistry and Applied Spectroscopy, Pittsburgh (1965).
11. E. G. Grochowski, D. R. Mason, G. A. Schmitt, and P. H. Smith, *J. Phys. Chem. Solids*, **25**, 551 (1964).
12. J. C. Woolley, Private communication.
13. T. B. Reed, H. C. Gatos, W. J. LaFleur, and J. T. Roddy, "Metallurgy of Advanced Electronic Materials," p. 71, G. E. Brock, Editor, Interscience, New York (1963).
14. A. Rabenau, K. Deneke, and M. M. van der Meij, *Angew. Chem.*, **76**, 651 (1964).
15. S. Geller and G. W. Hull, Jr., *Phys. Rev. Letters*, **13**, 127 (1964).

Alloys of InSb with InTe, In_2Te_3 and Tellurium

J. C. Woolley

Department of Physics, University of Ottawa, Ottawa, Ontario, Canada

ABSTRACT

Standard x-ray powder photograph techniques have been used to investigate the phases occurring in the InSb rich regions of the InSb-InTe, InSb-In_2Te_3, and InSb-Te sections of the In-Sb-Te diagram and also in some general ternary alloys of the system. It is found that only the InSb-InTe section is pseudobinary and that in the other two sections three-phase conditions occur. An isothermal section shows that the InSb phase observed is practically identical for all three sections investigated, and that the very narrow InSb single-phase field lies between the InSb-InTe and InSb-In_2Te_3 sections. This accounts for the similarities in the electrical and optical data reported for the InSb-rich regions of the three sections.

It is also confirmed that the sodium chloride type phase which occurs in the diagram is at In_3SbTe_2 and that this phase disappears by a eutectoid reaction in the temperature range 400°-500°C.

Various sections of the In-Sb-Te phase diagram involving InSb have been investigated to some extent (1-5), mainly with reference to the semiconducting properties of the InSb phase. Thus the InSb-rich region of the InSb-Te section is of interest from the point of view of doping of InSb, while the InSb-In_2Te_3 and InSb-InTe sections have received attention from the alloy semiconductor viewpoint. Both the InSb-In_2Te_3 and InSb-InTe sections have usually been treated as pseudobinary in behavior.

The InSb-In_2Te_3 section is of interest in that both InSb and In_2Te_3 have a zincblende structure, that of In_2Te_3 being of the defect type where every third site on the indium sublattice is vacant. (Although the lattice vacancies in In_2Te_3 can be caused to order at temperatures below approximately 600°C, this ordering requires very long annealing or special preparation techniques. For preparations by the quench-anneal method used below, the In_2Te_3 can be assumed to be in the disordered state.) Thus a considerable range of single-phase solid solution might be expected. In the initial work (4) on the InSb-In_2Te_3 section, it was reported that single-phase solid solution occurred out to 15 mole % In_2Te_3 in In_3Sb_3, while at compositions beyond the range of single-phase InSb solid solution a phase with rock-salt structure was observed, but not identified. Later work (1-3) however showed that this phase was in fact a ternary compound in the InSb-InTe section, with a composition of either In_4SbTe_3 (1) or In_3SbTe_2 (2, 3). The occurrence of this phase in the equilibrium alloys of the InSb-In_2Te_3 section shows that this section cannot have pseudobinary properties. This conclusion is reinforced by the semiconducting properties of the InSb rich alloys of the InSb-In_2Te_3 section (6, 7) where the high total electron concentration ($>10^{19}$/cc) indicates the presence of uncompensated ionized tellurium atoms. This can be explained only in terms of the absence of the stoichiometric concentration of lattice vacancies which is equivalent to saying that the equilibrium phase is not represented by a point in the InSb-In_2Te_3 section, and that the apparent single-phase alloys reported previously (4) do in fact contain a small amount of second phase.

From the point of view of the behavior of InSb and its alloys, it is of interest to have more information on this region of the In-Sb-Te diagram. Also, the rock-salt phase has been shown to have superconducting properties (8) so that further information in this part of the diagram also is of interest. The work of Strauss *et al.* (9), carried out at the same time as the present work, considers in detail the vertical section InSb-InTe. It is confirmed that the rock-salt compound has the composition In_3SbTe_2 and that it is stable over only a limited temperature range. In the present work, x-ray methods have been used to obtain data on isothermal sections of the In-Sb-Te diagram, one at a temperature where In_3SbTe_2 is stable and one at a temperature below that at which In_3SbTe_2 undergoes a eutectoid change.

Experimental Procedure

All specimens were prepared from elements of 99.999% purity. In some cases, the alloys were made from the appropriate compounds InSb, InTe, In_2Te_3, while in others they were prepared directly from the elements. No difference in results was observed for the two methods of preparation. The samples were sealed in evacuated quartz tubes, held molten and agitated to give thorough mixing, and then quenched in water. Each sample was then annealed at an appropriate temperature so that equilibrium could be attained, as indicated by x-ray powder photographs. As mentioned below, at temperatures below the eutectoid temperature of the rock-salt compound, considerable difficulty was experienced in bringing samples to equilibrium even though the annealing was carried out for two or three weeks.

Results

The majority of the alloys considered lay on one of the sections InSb-Te, InSb-In_2Te_3, or InSb-InTe, although a few general ternary alloys were also investigated. All alloys investigated are indicated either on Fig. 1 or Fig. 2. The annealing temperatures used were 470°, 430°, 400°, and 350°C.

For all alloys where appropriate, the lattice parameter a_0 of the zincblende phase was determined and the variations of a_0 with composition in the InSb-In_2Te_3 and InSb-Te sections are shown in Fig. 1. This data for the InSb-In_2Te_3 sections [Fig. 1(a)] had been obtained previously (4), and additional points confirmed the apparent pseudobinary form with a

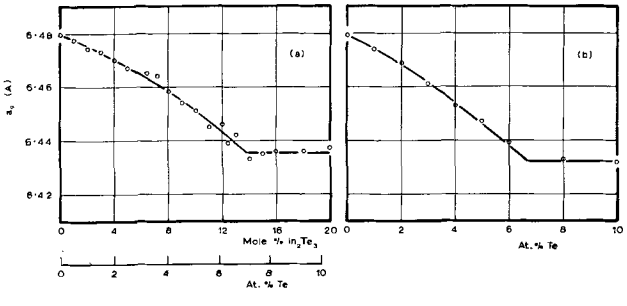

Fig. 1. Variation of lattice parameter a_0 of InSb phase as a function of composition. (a) InSb-In_2Te_3 section. (b) InSb-Te section.

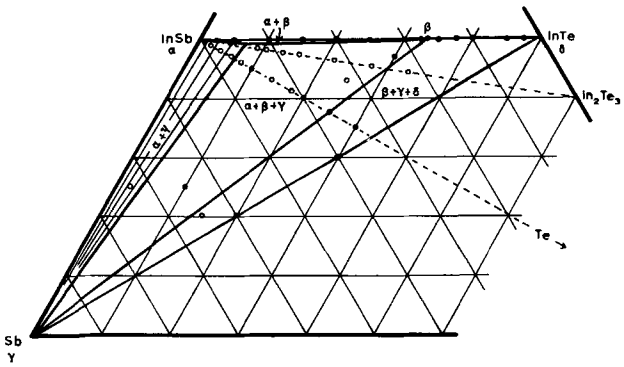

Fig. 2. Diagram showing 470°C isothermal section

range of solid solution of 14 mole % In_2Te_3 in In_3Sb_3, *i.e.*, slightly more than 7 a/o (atomic per cent) Te. The value of a_0 at larger tellurium content was determined for various annealing temperatures, but although the points show some scatter, no systematic variation with temperature could be determined. The results for InSb-Te in Fig. 1(b) are seen to be very similar, giving an apparent range of single-phase solid solution of a little below 7 a/o tellurium.

Study of the x-ray photographs for samples of higher tellurium content on these sections revealed the presence of lines corresponding to antimony, and a photomicrograph of an alloy containing 4 a/o tellurium showed the presence of a second phase, presumably antimony. Investigation of alloys of higher antimony content showed that the isothermal section at 470°C is as given in Fig. 2. The vertical sections InSb-In_2Te_3 and InSb-Te intersect this isothermal section first in a two-phase field InSb(α) + Sb(γ) and then in a three-phase field (α + β + γ) where β is the rock-salt phase. Thus the two parts of the a_0 against composition graphs in Fig. 1 correspond to the zincblende parameters in these two fields. The apparent limits of solid solution in atomic per cent tellurium, quoted above for the two vertical sections, determine the position of the three-phase field boundary and hence indicate the range of the single-phase α field. The exact position of the α field was not determined by x-ray methods, but it is clear from the electrical data on InSb-In_2Te_3 and InSb-InTe alloys (7) that this single-phase region must lie between these two sections as indicated in Fig. 2. From this data it is also seen that the range of single-phase α in the InSb-In_2Te_3 and InSb-Te sections must be very small.

In the InSb-InTe section, the variation in zincblende lattice parameter for the annealed samples was found to be very small, so that an accurate estimate of the limits of solid solution could not be made, but this would appear to be approximately 5 mole % InTe, in agreement with the data of Strauss *et al.* (9). In the two phase region (α + β), the tie lines lie in the plane of the section, this being the limit of a narrow two phase (α + β) field of the isothermal section as shown in Fig. 2. Because of the narrowness in this two-phase field, a very small deficiency in indium would result in a quite different value for the range of solid solution in the zincblende α phase. This could explain the results of Goryunova *et al.* (1), giving a limit of solid solution of 15 mole % InTe in InSb.

Other work (2, 3, 9) has shown that the rock-salt phase β definitely occurs on the InSb-InTe section, and the data obtained here agree with this result. A study of the x-ray photographs showed that two-phase behavior was shown by almost all samples in the range 60-80 mole % InTe, and the β phase appears to be a line phase with a composition close to In_3SbTe_2 and not In_4SbTe_3.

The range of solid solution in InTe was not investigated in detail, but this was observed to be small and less than 5 mole % as indicated by Strauss *et al.* (9). In Fig. 2, the In_3SbTe_2-InTe line forms the limit of a second three-phase field (β + γ + δ) where the δ phase is very close to InTe.

Alloys were annealed at 400° and 350°C in order to determine the equilibrium conditions at temperatures below the range of stability of the rock-salt phase. Difficulties were experienced in obtaining consistent data from the various alloy samples, in that in many cases the x-ray lines corresponding to the rock-salt phase was still observed even after one or two weeks annealing. In most cases however the appearance of InSb or InTe lines (as appropriate) indicated that the rock-salt phase was slowly decomposing into InSb and InTe phases. Although the rock-salt phase was never completely lost, the equilibrium condition at 400° and 350°C could be determined. Thus the two three-phase fields (α + β + γ) and (β + γ + δ) shown in Fig. 2 combine at lower temperatures to give one three-phase (α + γ + δ) field, and the extent of the two-phase (α + γ) and the single-phase α fields are practically unaffected.

Conclusions

The form of equilibrium diagram obtained here explains the similarities in the lattice parameter, electrical and optical data reported for the alloy systems InSb-Te, InSb-In_2Te_3, and InSb-InTe. In the case of InSb-Te and InSb-In_2Te_3 alloys, the zincblende phase observed in the apparent single-phase region is the same for both cases, the difference being only in the amount of antimony second phase present. For concentrations of tellurium of a few atomic per cent, this antimony will have practically no effect on the observed values of energy gap, Hall coefficient, etc. With the single-phase α field being very narrow, as shown in Fig. 2, similar alloys on or close to the InSb-InTe section will consist of the same zincblende phase with a small amount of second phase present and so again will give data similar to that for alloys on the other two sections.

Since alloys on the InSb-Te and InSb-In_2Te_3 sections give the same equilibrium phases, In_2Te_3 can be used for doping InSb. This use of In_2Te_3 can have the advantage that when very heavy doping is required, less second-phase antimony is produced.

Acknowledgments

The author wishes to thank Mr. P. J. Montford-Azmier for assistance in the preparation and x-raying of specimens, and Dr. E. W. Williams for a photomicrograph. He is also grateful to Dr. A. J. Strauss and Dr. M. D. Banus of Lincoln Laboratory, Massachusetts Institute of Technology, for useful discussions.

Manuscript received Oct. 25, 1965; revised manuscript received Jan. 24, 1966.

Any discussion of this paper will appear in a Discussion Section to be published in the December 1966 JOURNAL.

REFERENCES

1. N. A. Goryunova, S. I. Radautsan and G. A. Kiosse, *Sov. Phys. Solid State*, **1**, 1702 (1959).
2. A. Rabenau and K. Deneke, *Angew. Chem.*, **74**, 659 (1962).
3. K. Deneke and A. Rabenau, *Z. anorg. allgem. Chem.*, **333**, 201 (1964).
4. J. C. Woolley, C. M. Gillett, and J. A. Evans, *J. Phys. Chem. Solids*, **16**, 138 (1960).
5. R. Barrie and J. T. Edmond, *J. Electronics*, **1**, 161 (1955).
6. J. C. Woolley and E. W. Williams, *This Journal*, **111**, 210 (1964).
7. J. C. Woolley and E. W. Williams, *Can. J. Phys.* In press.
8. A. Rabenau, K. Deneke, and van der Meij, *Angew. Chem.*, **76**, 651 (1964).
9. A. J. Strauss, M. D. Banus, and M. C. Finn, *This Journal*, **113**, 458 (1966).

Vapor Growth of AlP Single Crystals

F. J. Reid, S. E. Miller, and H. L. Goering

Columbus Laboratories, Battelle Memorial Institute, Columbus, Ohio

ABSTRACT

Single crystal AlP layers up to 0.1 cm thick and 2 cm in diameter have been grown onto silicon and GaAs substrates by using an open-tube vapor-transport technique. Iodine was found to be more satisfactory than chlorine for transporting aluminum at moderately low temperatures (source at 1100°C; substrate at 900°C). It was essential that the phosphorus vapor be introduced downstream from the aluminum source to prevent the formation of AlP at the source and the eventual retardation of the transport process. The as-grown layers are invariably n-type containing greater than 1 x 10^{18} donors/cm^3. Characteristics of n-p, AlP-Si heterojunctions were obtained and are discussed.

The III-V compound semiconductor aluminum phosphide, AlP, has received very little attention in the past (1), while others of this family, such as GaAs and InSb, have been studied extensively and characterized reasonably well. This situation is understandable when it is considered that AlP is a high-band-gap (2.5-3 ev) semiconductor with a melting point > 2000°C and a dissociation pressure of tens of atmospheres at its melting point. However, since AlP is a compound which is isoelectronic with the most useful of the group IV elemental semiconductors, silicon, studies of its properties would be of value in extending existing knowledge in solid-state science, and the material could prove to be of substantial practical importance. Other III-V compounds, which are isoelectronic to the semiconducting group IV elements, are GaAs and InSb, two compounds which are by far the most interesting and potentially useful of the family in their band-gap ranges.

One of the advantages realized in vapor phase growth of III-V compounds is that crystal growth occurs at temperatures and pressures well below the respective melting point and dissociation pressure of the compound at the melting temperature. The lower growth temperature makes it possible to employ substrates of lower melting compounds or elements, which is also a distinct advantage in the epitaxial growth of AlP. In addition interesting heterojunctions are formed by this technique. An important feature of vapor phase growth, which is sometimes overlooked, is the possibility of growing relatively large volume single crystals that can be removed from a substrate and treated as a bulk crystal. The scope of this paper is directed toward these two points, *i.e.*, the growth of bulk crystals of AlP by a vapor phase growth technique and the growth of semiconductor heterojunctions.

Experimental

The vapor phase process for obtaining AlP involves reacting liquid aluminum with a halogen, preferably iodine, to produce volatile aluminum halides. The various vapors are transported through an open-tube flow system by maintaining a constant flow of hydrogen as a carrier gas. The aluminum halides are carried downstream and mixed with phosphorus vapor in a vapor growth chamber, containing a silicon or a GaAs substrate. In this chamber, free aluminum is released through a disproportionation type of reaction and is available to react with the phosphorus to form AlP as an epitaxial layer on the substrate. An important feature of this technique is that the phosphorus vapor does not contact the liquid aluminum source. If this feature is not provided, a coherent layer of AlP forms over the aluminum, which impedes and eventually stops the reaction of aluminum with the halogen.

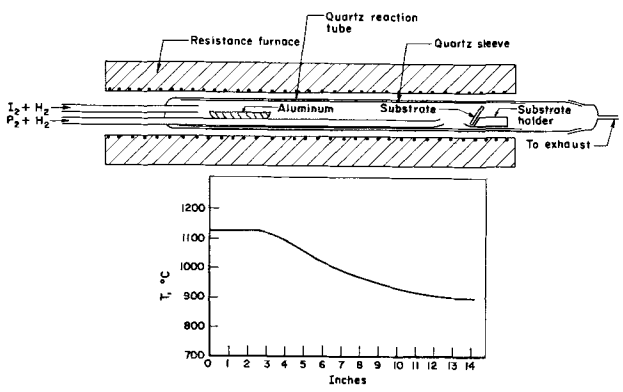

Fig. 1. Vapor growth apparatus

The vapor phase growth apparatus shown in Fig. 1 consists of a quartz tube (40 mm OD, 34 mm ID) about 3 ft long. The aluminum source (5-9's pure) is contained in an alumina boat positioned about midway along the length of the quartz tube. Iodine vapors are admitted to the reaction chamber by directing a stream of hydrogen (passed through palladium) over about 50g of triply sublimed iodine crystals contained in a U-shaped tube attached to the large quartz tube. The quantity of iodine which is carried into the system is determined by the temperature of the iodine and the flow rate of the hydrogen gas. Phosphorus vapors are added in a similar manner, but these vapors are introduced into the quartz tube downstream of the aluminum and immediately upstream of the substrate. Approximately 10g of high-purity white phosphorus makes up the phosphorus source.

The reactions at the aluminum source, which is maintained at about 1130°C, appear to involve at least the two competing reactions

$$Al + 1/2\ I_2 = AlI \qquad [1]$$

and

$$Al + 3/2\ I_2 = AlI_3 \qquad [2]$$

The disproportionation reaction of interest in the vapor growth chamber is therefore,

$$3AlI \rightleftharpoons 2Al + AlI_3 \qquad [3]$$

and finally the free aluminum reacts with phosphorus to form AlP.

During a typical experiment, hydrogen flows through the iodine reservoir at about 1000 cc/min and through the phosphorus reservoir at about 25 cc/min. When the iodine source is maintained at about 45°C, iodine flows into the system at a rate of about 1.3 g/hr. When the phosphorus source is maintained at about 230°C, the phosphorus flows into the system at a rate of about 0.16 g/hr. The aluminum source is maintained at a temperature of about 1130°C, and aluminum is introduced into the vapor stream as aluminum iodide

compounds at a rate of about 0.17 g/hr. It is noted that if the iodine reacts completely with the aluminum source, the rate at which aluminum is transported as AlI is about 0.12 g/hr; the rest of the aluminum (0.05 g/hr) being transported as AlI_3. In addition, it is noted from reaction [3] that the maximum amount of free aluminum which can be produced in the vapor growth chamber by a disproportionation type reaction is 2/3 of the amount of aluminum present as AlI or at a rate of 0.08 g/hr. Therefore under these conditions, the phosphorus is in excess of the amount of free aluminum available in the vapor growth chamber. Hence, as AlP is formed and grown on the chemically polished silicon or GaAs substrate, which is maintained at about 900°C, all the free aluminum can be consumed to form AlP with the excess phosphorus being carried away in the vapor stream.

Results

Preparation.—In the manner described, single crystal layers of AlP as thick as 1000μ have been grown during a 24-hr run. The layers were grown on 2-cm diameter silicon substrates oriented such that a {111} crystallographic plane was exposed. It is noted that silicon is an excellent choice for a seed material since it has the same crystal structure and almost exactly the same atom spacing as AlP. It has also been possible to deposit layers of AlP on GaAs substrates by the procedure given above.

By contrast, if the phosphorus vapor is introduced upstream of the aluminum source, essentially no AlP forms in the vapor growth chamber under similar conditions. Instead the aluminum source is covered with a coherent layer of solid AlP which eventually precludes reaction of the incoming iodine with the aluminum. In a separate experiment, AlP crystals were used in place of the aluminum source and iodine passed over them at 1140°C. No AlP was transported during a 5-hr run. Hence, it is essential to keep phosphorus vapors away from the aluminum source in order to achieve a continuous preparation process at moderate temperatures, which will yield relatively thick layers of AlP epitaxially grown on a substrate. Another advantage in delaying the mixing of the aluminum halides and the phosphorus vapors until they reach the vapor growth chamber is that direct reactions of phosphorus with the aluminum halides are suppressed, thus eliminating an uncontrolled production of AlP over a relatively wide temperature range.

Investigations were made using chlorine, introduced as HCl or $AlCl_3$, instead of iodine as the halogen. The aluminum source was maintained at temperatures as high as 1200°C with no apparent formation of AlP in the vapor growth system. This is not surprising if one considers the thermochemical data available (2) for the aluminum chlorides and the aluminum iodides as shown in Fig. 2. For equal mole fractions of chlorine, reaction [2] is favored over reaction [1] until a temperature in excess of about 1280°C is reached. In the case of the aluminum iodides, reaction [1] is favored at temperatures in excess of about 1080°C. In order to grow AlP using a chlorine transport, aluminum source temperatures in excess of 1300°C would be required. A liner would be necessary to prevent deterioration of the quartz tube by attack from reaction products. This was seen to be a problem even at 1200°C for the chlorine case and, to a lesser extent, at 1130°C for the iodine case. A quartz liner is sufficient to prevent breakage; however, a high-purity alumina liner would be better from the standpoint of eliminating silicon contamination from the quartz.

Figure 3 shows the consumption of aluminum at the source as a function of iodine flow rate. The aluminum source temperature was 1130°C, with a surface area of approximately 10 cm^2. The experimental data lie above the line representing complete reaction of the iodine via reaction [2]. Hence, some of

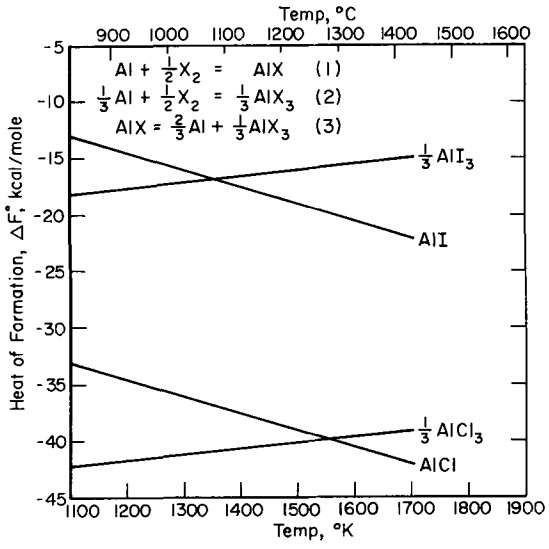

Fig. 2. Heats of formation of aluminum halides as functions of temperature.

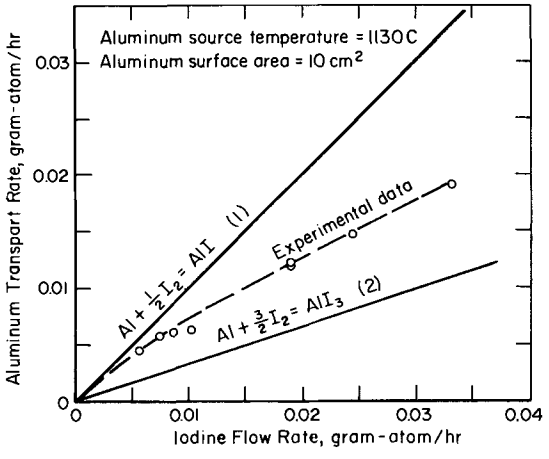

Fig. 3. Consumption of aluminum source as a function of iodine flow rate.

the aluminum must have been transported as an unstable intermediate, such as AlI or AlI_2. Actually the amount of aluminum transported is found to be greater than could be transported solely as AlI_2. On the other hand, the amount of aluminum transported is less than would have been consumed in complete reaction of the iodine via reaction [1], suggesting that the iodine had not completely reacted and/or formation of AlI_3 and possibly AlI_2 occurred at the aluminum source. At the larger iodine flow rates, unreacted iodine was observed experimentally. However, at the smallest iodine flow rate of 5.7 x 10^{-3} gram-atm/hr nearly all the aluminum consumed was transported as AlI, and no evidence of free iodine was observed visually in the exhaust products.

Properties.—The single crystal layers of AlP are easily removed from the silicon or GaAs substrates by lapping away the substrate with a silicon carbide abrasive. It is observed that the rates at which AlP and silicon are abraded are approximately equal, which facilitates the removal of the silicon. After removal of the substrate, the AlP layers are found to be transparent, appearing greenish yellow in color. The surface of the AlP reacts with moist air to form a white film if exposed for any length of time. The AlP surface can be polished mechanically under kerosene and rinsed in a dry organic solvent. The resulting surface appears less susceptible to attack by moist air.

The results of d-c electrical measurements show that the AlP samples prepared to date are n-type,

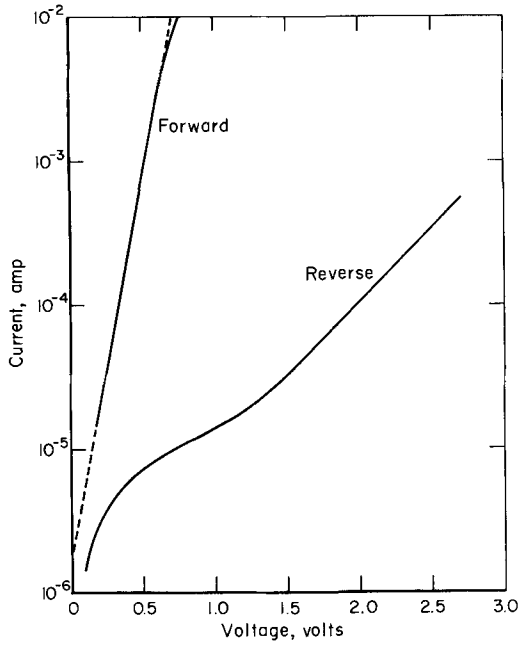

Fig. 4. Room temperature I-V characteristics of n-p, AlP-Si heterojunction.

exhibiting relatively low resistivities and containing relatively large concentrations of free carriers. The free carriers are believed to result from the incorporation of impurities during preparation, and one suspects that the silicon content may be large because the vapor growth was carried out in a quartz tube. However, the effects of carbon and oxygen as substitutional impurities should be considered because these elements may be expected to produce more pronounced effects in AlP than they apparently produce in lower-band-gap III-V compounds. Carrier concentrations obtained from Hall effect measurements have been in the range 5 x 10^{18} to 5 x 10^{19}/cm^3 with the highest electron mobility being about 60 cm^2/volt-sec at 300°K. The Hall coefficient is seen to be constant with temperature and the electron mobility increases with increasing temperature in the range 77°-300°K.

Heterojunctions formed at the AlP-Si interfaces have been examined and I-V characteristics obtained. Figure [4] shows the forward and reverse characteristics of an n-p, AlP-Si heterojunction. One ohm-cm silicon was used; hence both materials are heavily doped. The rectification ratio is about 100 and 1000 at 0.5 and 0.8v, respectively. The log I-V plot is linear for forward bias over an appreciable range, with current varying as exp ($qV/3.2\ kT$). The $\eta = 3.2$ value is too large to be indicative of only Schottky emission ($\eta = 1$). However, if one considers an energy band profile for the n-p AlP-Si structure, it is apparent that a barrier exists. Analysis of forward characteristics in the form

$$J = A^*T^2e^{-\psi/\eta kT}\ (e^{qV/\eta kT-1}) \qquad [4]$$

yields a value of the barrier ψ of about 2 ev, where $A^* = Am^*/m_o$ is the effective Richardson constant (3). When n-n AlP-Si heterojunctions were made with 0.01 ohm-cm n-type Si, no barrier was observed experimentally.

Summary

It has been demonstrated that large single crystals of AlP can be grown by a vapor phase growth technique. Iodine is seen to be superior to chlorine as a transporting agent, primarily from the standpoint of lower source-temperature requirements. Aluminum source temperatures as low as 1100°C have been used for long period continuous growth of AlP. To maintain such growth, it is necessary to prevent the phosphorus vapors from contacting the aluminum source. To make the AlP more attractive for further study of properties and applications, greater attention must be directed to the elimination of impurities.

Acknowledgments

The authors wish to acknowledge the assistance of R. J. Buist in the heterojunction measurements. This paper is based on results of research sponsored by the Battelle Development Corporation.

Manuscript received Dec. 27, 1965.

Any discussion of this paper will appear in a Discussion Section to be published in the December 1966 JOURNAL.

REFERENCES

1. See, for example, A. Rabenau, Chap. 20 of "Compound Semiconductors," R. K. Willardson and H. L. Goering, Editors, Reinhold Publishing Corp., New York (1962).
2. JANAF Thermochemical Tables, The Dow Chemical Co., Midland, Michigan, Dec. 31, 1962.
3. E. D. Hinkley, R. H. Rediker, and D. K. Jadus, *Appl. Phys. Letters*, **6**, 144 (1965).

Autodoping of Silicon Films Grown Epitaxially on Sapphire

D. J. Dumin and P. H. Robinson

RCA Laboratories, Princeton, New Jersey

ABSTRACT

Doping by the substrate of silicon films grown epitaxially on sapphire (Al_2O_3) has been measured. Spectroscopic analysis of the silicon films has shown that aluminum is the major impurity. In films grown with $N_A = 10^{15}$/cc further processing below 1200°C introduces no additional doping from the substrate. The doping of the films by the sapphire becomes significant above 1250°C with the sapphire acting as a source of aluminum. The total number of aluminum atoms entering the silicon films is of the order of $1\text{-}2\cdot10^{15}$ resulting in a concentration of $2\cdot10^{18}$/cc in the silicon film. The mechanism responsible for the liberation of the aluminum from the sapphire has not been determined. A qualitative description of the changes in crystal structure on heat-treatment is given.

Recently silicon has been grown epitaxially on single-crystal sapphire (Al_2O_3) (1), and silicon-on-sapphire has been used in the fabrication of MOS transistors (2). The silicon used in these studies was grown by the pyrolysis of silane (SiH_4) and has been described in detail (3).

All films not purposely doped are p-type, and emission spectrographic analysis of the silicon indicates the major impurity to be aluminum. Substrate doping of silicon grown epitaxially on silicon has been studied (4) and attributed to normal diffusion of impurities from the silicon substrate. A series of ex-

periments has been performed to determine the extent of doping attributable to the sapphire substrate. Measurements of the diffusion constant and concentration of the dopant have been made which indicate that the sapphire acts as a limited source of aluminum. The aluminum is liberated from the sapphire and diffuses into the silicon during the epitaxial growth and during subsequent high temperature heat treatments. This source of aluminum will determine the upper temperature limit for device processing in silicon grown on sapphire.

Experimental Techniques

The silicon films were grown on polished heat-treated sapphire substrates having (0001) and ($1\bar{1}02$) orientations. Other orientations have been tried, and all results reported here appear to be independent of orientation. The silicon grown on sapphire has been single crystal as determined by x-ray Laue back-reflection patterns and electron diffraction patterns. Chemical etches (5) have revealed the dominant crystallographic imperfections to be low angle grain boundaries and stacking faults. The silicon grown from undoped silane is p-type with resistivity between 1 and 100 ohm-cm and Hall mobility between 50 and 250 cm^2/v-sec. The higher resistivity films are produced by growth at lower temperatures and/or by limiting the high temperature hydrogen pre-firing of the sapphire substrate. Typical growth temperatures are between 1100° and 1200°C. N-type silicon films were prepared by adding phosphine to the silane during growth.

The resistivity and mobility of the silicon films as a function of silicon thickness was measured on a six terminal Hall sample delineated by masking and etching. The resistivity and Hall mobility were measured after the silicon was polished to successively thinner sections to a final thickness of 1-2μ. Measurements on thick (40μ) polished and as-grown pieces of silicon showed that the polishing introduced no changes in measured resistivity or mobility. These measurements were performed on as-grown and on heat-treated silicon.

The doping from the substrate was demonstrated by depositing n-type silicon layers and then heat-treating this material in hydrogen. Angle lapping and staining with a copper stain revealed a p-region extending from the substrate into the silicon. This p-region was also revealed using a thermal probe. The thickness of this p-region was studied as a function of time and temperature of heat-treatment.

Before and after the films were heat-treated a four-point probe was used to measure the resistivity of the films utilizing the analysis of Valdes (6) for resistivity measurements of thin layers on a nonconducting plane. The samples were broken into two pieces. One piece was heat-treated in dry hydrogen and the resistivity after heat-treating was compared with the resistivity before heat-treating. The two pieces of the film were polished and Sirtl etched to delineate any changes in crystal structure that might have resulted from the heat-treatment.

Since most of these experiments involved a post-growth heat-treatment, care had to be taken to eliminate contaminants from the gas supply during the heat-treatment step.

The films were heat-treated on a silicon-carbide coated graphite susceptor in an r-f heated furnace with water-cooled quartz walls. Dry hydrogen from a palladium diffuser was used as the ambient gas. When small amounts of H_2O or O_2 were admitted to the gas, etching of the silicon took place; however, no etching was observed in the dry H_2. At temperatures above 1425°C melting of the silicon was observed and pronounced etching of the sapphire by the silicon resulted. The temperature was measured using an optical pyrometer corrected for absorption and emissivity and checked against the melting points of silicon and germanium. Temperatures are estimated to be correct to within ± 10°C.

Heat-treatment of bulk silicon in dry hydrogen at temperatures up to 1400°C resulted in no significant changes in resistivity. During approximately one half of the heat-treatments of silicon-on-sapphire a piece of bulk silicon of resistivity similar to that of the film was included as a control. No significant changes in the resistivity of the bulk silicon were observed. The control pieces were either 10 ohm-cm n-type or 0.1, 3, 5, or 40 ohm-cm p-type silicon.

A further test for doping from the gas supply was performed by heating pieces of bulk silicon in contact with, and out of contact with, pieces of sapphire. Heat-treatment of polished pieces of 5 ohm-cm p-type silicon for 60 min at 1400°C showed no significant changes in resistivity. However, pieces of 5 ohm-cm p-type silicon placed on disks of polished sapphire or sandwiched between disks of polished sapphire dropped in resistivity to about 1 ohm-cm p-type after similar heat-treatment.

Experimental Results

The results of these experiments are presented in the order in which the experiments were described. Typical profiles of doping density *vs.* distance are shown in Fig. 1 for four samples. The doping density has been derived from the resistivity, mobility, and thickness data of each section by using $N_A = 1/\rho e\mu$ where N_A is the acceptor concentration, ρ is the resistivity, e is the electronic charge, and μ is the mobility. Three treatments are described by the data presented in Fig. 1. Two samples are pieces of as-grown silicon and represent the doping due to the substrate during normal growth. These samples were chosen as representative of many samples measured. The third sample was grown using the following growth cycle: 7μ of silicon was grown at 1160°C, heat-treated in hydrogen in the same reaction tube for 30 min at 1325°C, and then 23μ more of silicon was grown at 1160°C. The fourth sample was a 14μ thick film of silicon heat-treated at 1375°C for 30 min after growth. The initial doping of this film was of the order of 10^{17}/cc. The diffusion constant of aluminum in bulk silicon at 1375°C is about $3 \cdot 10^{-10}$ cm^2/sec (7), yielding a diffusion length greater than 15μ. Thus, this film should be uniformly doped. The increase in doping at the

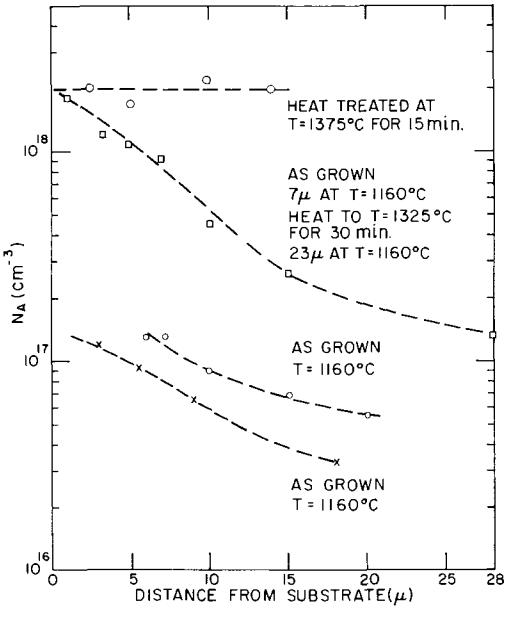

Fig. 1. Carrier concentration vs. distance from the silicon-sapphire interface.

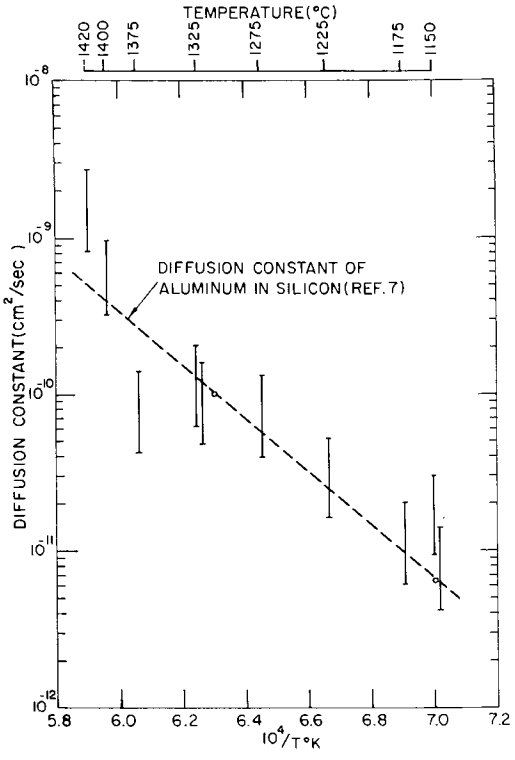

Fig. 2. Diffusion constant vs. temperature for out-diffusion of a p-type dopant from the sapphire into n-type silicon.

silicon-sapphire interface is evident in the as-grown samples and the uniform doping of the heat-treated silicon indicates sufficient diffusion to completely dope the silicon. Measurements of this type have been performed on numerous as-grown films of varying resistivity and all have shown increased acceptor concentrations at the silicon-sapphire interface. Matching of these profiles to an erfc diffusion has resulted in values of D which are 4-10 times that of aluminum in silicon. This is not surprising in light of the fact that this silicon contains large numbers of low angle grain boundaries, and diffusion is enhanced along these grain boundaries (8).

The n-type silicon films were heat-treated at temperatures between 1225° and 1420°C for times ranging from 30 to 5 min. The junctions between the p-region near the substrate and the n-type film were delineated using a copper-stain. From this data the diffusion constant as a function of temperature was determined and is shown in Fig. 2. The data points at 1150° and 1175°C were taken on the as-grown n-type films. The diffusion constant of aluminum in bulk silicon is shown in this figure also. The diffusion constant determined from this experiment agrees well with that of aluminum in silicon. The quality of the silicon films used in the n-type experiments was better than those used in the sectioning experiments which accounts for the difference in the observed diffusion coefficients.

The resistivities of several silicon films 10-20μ thick before and after heat-treatment are shown in Table I. Changes in resistivity were measured when the heat-treatment temperature exceeded 1250°C. Heat-treatments as long as 240 min at temperatures below 1225°C had no significant effect on the film resistivity.

Changes in the crystal structure of the silicon films heated above 1375°C for times greater than 30 min showed a decrease in the density of low angle grain boundaries. Stacking faults were the dominant crystal imperfection in a film heated above 1375°C. In Fig. 3a and b the crystal structure of a film before and after heat-treatment has been delineated by Sirtl etching a polished surface. Diffusion of phosphorus into material that had been heat-treated above 1375°C produced

Table I. Changes in resistivity due to heat-treatment

Heating temperature, °C	Heating time, min	Initial resistivity, ohm-cm	Final resistivity, ohm-cm
1150	30	>100	100
1150	60	10	10
1225	30	>100	100
1250	120	20	2.4
1300	30	90	3.7
1340	60	10	0.2
1340	60	34	1.0
1350	15	10	0.45
1350	60	10	0.2
1375	30	20	0.1
1375	60	200	0.1
1400	10	10	0.45
1400	20	10	0.3
1400	30	100	0.05
1400	60	150	0.2

sharp diffusion fronts of depth similar to diffusion into bulk silicon, while diffusion into as-grown silicon-on-sapphire produced anomalously deep diffusions and irregular diffusion fronts. Diffusions into as-grown and heat-treated films are compared in Fig. 3c and d. As noted, however, the improvement in crystal structure was accompanied by decreases in resistivity.

These results were confirmed by measuring the capacitance of MOS capacitors as a function of distance from the silicon-sapphire interface. The ratio C_{max}/C_{min} for a constant oxide thickness decreases as the doping of the semiconductor increases (9). The normalized MOS capacitance as a function of voltage is plotted in Fig. 4 for different thicknesses of silicon. As the silicon-sapphire interface is approached, the ratio of C_{max}/C_{min} decreases indicative of higher acceptor concentration near the substrate.

Discussion and Conclusions

The following conclusions concerning substrate doping of silicon grown on sapphire have been reached: (I) The sapphire acts as a source of aluminum acceptors. (II) The resistivity of p-type silicon films grown on sapphire substrates can decrease when the films are subsequently heat-treated to sufficiently high temperatures. (III) The amount of aluminum is limited to about $1\text{-}2\cdot10^{15}$ atoms and limits the doping of heat-treated films to a maximum of about $2\cdot10^{18}$/cc. (IV) The doping of the silicon by the substrate during post-growth heat-treatments is not significant below 1200°C but becomes appreciable above 1250°C.

This substrate doping limits the range of temperatures which can be used to anneal defects in the silicon film but does not affect normal device processing which takes place at temperatures below 1200°C. The substrate doping also affects processing of n-type films grown on sapphire. Unwanted p-n junctions can ap-

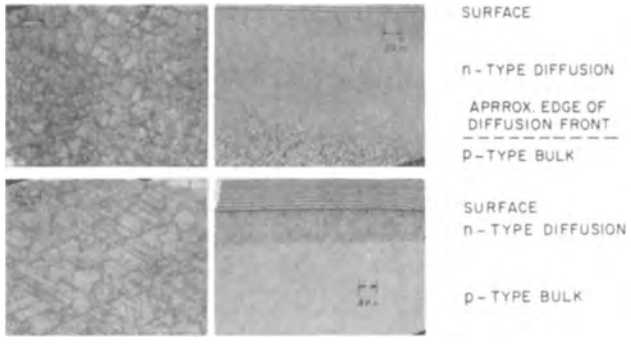

Fig. 3. Crystal structure and diffusion fronts in as-grown and heat-treated silicon-on-sapphire.

a. (top left) Etch pattern of a film before heat-treatment

b. (bottom left) Etch pattern of the same film after heat-treatment at 1360°C for 60 min.

c. (top right) Diffusion front into a film before heat treatment

d. (bottom right) Diffusion front into the same film after heat-treatment at 1360°C for 60 min.

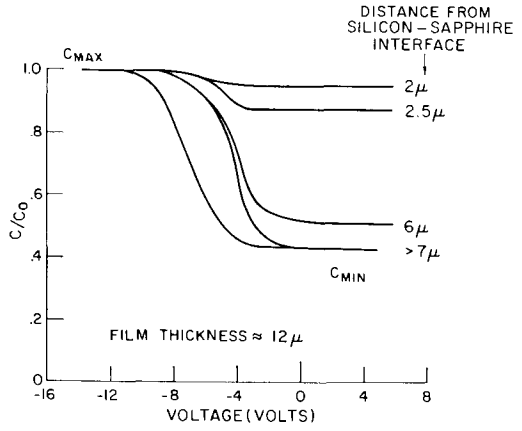

Fig. 4. Capacitance-voltage characteristics of MOS structures as a function of distance from the silicon-sapphire interface.

pear during high temperature processing, and, in fact, conversion to p-type silicon can occur if the temperature is sufficiently high or the processing sufficiently long.

Attempts have been made to determine the mechanism which liberates the aluminum from the sapphire, but no conclusions have yet been drawn. Assuming a temperature independent concentration of aluminum in Al_2O_3 and using the data presented in Table I, the analysis of Paladino and Kingery (10) can be applied to determine the diffusion constant of aluminum in Al_2O_3. The high activation energy of 18 ev resulting from this analysis suggests that the process of liberating the aluminum from the Al_2O_3 is more complicated than a simple diffusion process. The limit in the amount of aluminum that dopes the silicon films may indicate that only the first few atomic layers are involved in the doping process.

Acknowledgments

The authors wish to acknowledge the technical assistance and encouragement of C. W. Mueller. The authors are indebted to R. Adams and R. O. Wance who performed the sectioning measurements, to A. G. Revesz and R. Evans for use of the annealing furnace, and to Mrs. E. Moonan who processed the diffused samples.

Manuscript received Nov. 12, 1965; revised manuscript received Dec. 20, 1965. The research reported here was sponsored by the Air Force Avionics Laboratory, Research and Technology Division, Air Force Systems Command, Wright-Patterson Air Force Base, Ohio, under Contract No. AF33(657)-11398 and RCA Laboratories, Princeton, New Jersey.

Any discussion of this paper will appear in a Discussion Section to be published in the December 1966 JOURNAL.

REFERENCES

1. H. M. Manasevit and W. I. Simpson, *J. Appl. Phys.*, **35**, 1349 (1964).
2. C. W. Mueller and P. H. Robinson, *Proc. IEEE*, **52**, 1487 (1964).
3. P. H. Robinson and C. W. Mueller, *Trans.*, Metallurgical Soc., AIME, March 1966.
4. A. S. Grove, A. Roder, and C. T. Sah, *J. Appl. Phys.*, **36**, 802 (1965).
5. E. Sirtl and A. Adler, *Z. Metallk.*, **52**, 529 (1961).
6. L. B. Valdes, *Proc. IRE*, **42**, 420 (1954).
7. R. C. Miller and A. Savage, *J. Appl. Phys.*, **27**, 1430 (1956).
8. E. C. Ross and C. W. Mueller, To be published in IEEE Trans. E. D. March 1966.
9. K. H. Zaininger and G. Warfield, *IEEE Trans., ED-12* 179 (1965); A. S. Grove, B. E. Deal, E. H. Snow, and C. T. Sah, *Solid State Elect.*, **8**, 145 (1965).
10. A. E. Paladino and W. D. Kingery, *J. Chem. Phys.*, **37**, 957 (1962).

Measurement of Epitaxial Film Thickness Using an Infrared Ellipsometer

A. Ray Hilton and Charlie E. Jones

Texas Instruments Incorporated, Dallas, Texas

ABSTRACT

The thickness of most epitaxial layers is measured using spectrophotometer scan techniques. The method does not work well for very thin epitaxial layers ($<5\mu$). The principles, underlying the ellipsometric method used to measure thin transparent films in the visible region, apply to the optical interference that occurs between a substrate and an epitaxial layer in the infrared. An ellipsometer and the ellipsometric technique were used to measure the thickness of 40 P on P^+ Ge and 40 N on N^+ Si epitaxial layers. They ranged in thickness from 1 to 10μ. The measured values compared to those obtained by the infrared scan technique agreed within +9.6% for the Ge layers and ±6.7% for the silicon. The reproducibility of the measurements was +2.8% and ±4.1%, respectively. In ultimate form the method should be more accurate and more direct than the infrared scan technique.

Optical interference occurs when infrared light is reflected obliquely from the surface of a semiconductor epitaxial layer grown on a substrate of the same semiconductor material. The interference occurs because of a difference in the optical constants of the layer and substrate brought about by the differences in the infrared absorption of charge carriers in the heavily doped substrate and lightly doped layer. The thickness of the epitaxial layer is commonly measured using an infrared reflectance scan technique which takes advantage of the variation in the reflected intensity as a function of wavelength (1, 2). The method is accurate, fast, and nondestructive. However, the magnitude of the free carrier absorption generating the optical interference increases with the square of the wavelength (3-5). For very thin epitaxial layers ($<5\mu$), the first order of the optical interference occurs in the near infrared where the optical difference between layer and substrate is small. For this reason, the infrared scan method does not work well for very thin epitaxial layers. The ellipsometer technique has been widely used in the visible region of the spectrum to measure films less than one wavelength thick (6, 7). This paper describes the extension of this technique to measure semiconductor epitaxial film thickness.

Calculation of semiconductor optical constants.— Generally, the infrared light obliquely reflected from the semiconductor epitaxial layer is elliptically polar-

ized. In ellipsometry (6, 7), an instrument called an ellipsometer is used to analyze optically the elliptically polarized light. The light is characterized in terms of its azimuth angle ψ and its phase shift angle Δ. The values of ψ and Δ are determined by the optical constants of the film, the optical constants of the surface, the angle of incidence, the wavelength of light used in the measurement, and the thickness of the film. In actual practice, curves in ψ and Δ are constructed from points calculated for films of varying thickness. The measured value of ψ and Δ is compared to the computed curves and the corresponding thickness value determined. The calculation of individual points is very tedious and is usually programmed for electronic computer computation.

The optical constants of the semiconductor epitaxial layer and semiconductor substrate become different in the infrared because of free carrier absorption. Free carrier absorption is the absorption of infrared energy by conduction electrons (or holes) of a semiconductor. The magnitude of the effect depends on the number of free carriers available for absorption and the wavelength of light used in making the measurements. The absorption increases with the square of the wavelength of light (3-5). In epitaxial device specifications, the substrate material is usually more heavily doped than the layer. As the wavelength of light increases, the free carrier absorption in the substrate material increases producing a change in its optical constants. The optical constants of the substrate are then different from the layer so that reflection of light at the layer-substrate interface occurs, producing optical interference.

The substrate material begins to show optical behavior typical of a metal. The refractive index can no longer be represented as a real number. The complex refractive index must be used

$$N = n - ik$$

where n is the real part of the refractive index and k is the imaginary part and is really the extinction coefficient. The extinction coefficient is calculated from the absorption coefficient

$$\alpha = \frac{4\pi k}{\lambda}$$

where α is the absorption coefficient and λ is the wavelength of the light. The contribution to the absorption coefficient by free carrier absorption is given by (3)

$$\alpha_{\text{free carrier}} = \frac{\lambda^2 e^3}{4\pi^2 c^3 n \epsilon_0}\left(\frac{N_n}{M_n^2 \mu_n} + \frac{N_p}{M_p^2 \mu_p}\right) \qquad [1]$$

where e is the electronic charge, c the velocity of light, n the real part of the refractive index, ϵ_0 the permitivity of free space, N_n the number of conduction electrons, M_n the effective mass of the electrons, μ_n the electron mobility, N_p the number of holes, M_p the effective mass of holes, and μ_p the mobility of holes.

The normal case considered is the case of a single carrier semiconductor. In this case the interdependent optical constants n and k can be calculated (8) from

$$n^2 - k^2 - \epsilon = \frac{N_c e^2}{M_c \epsilon_0} \cdot \frac{1}{\omega^2 + g^2} \qquad [2]$$

and

$$2nk\omega = \frac{N_c e^2}{M_c \epsilon_0} \cdot \frac{g}{\omega^2 + g^2} \qquad [3]$$

where ϵ is the optical dielectric constant (no free carrier contribution); ω the angular frequency at wavelength λ, ($\omega = 2\pi/\lambda$); N_c the number of free carriers; M_c the effective mass of the free carriers; and g the reciprocal of the relaxation time τ, ($\tau = \mu_c M_c/e$)

An idea of the magnitude of the free carrier effect can be obtained from examining Fig. 1. The value of α for different resistivities of n-type silicon measured in our laboratory is plotted as a function of the wavelength. The data shows that free carrier absorption in 0.01 ohm-cm n-type silicon is a very large effect even at wavelengths as small as 10μ. Values calculated using Eq. [2] and [3] for 1.0 and 0.013 ohm-cm n-type silicon are shown for comparison values. Also shown are values reported in the literature by Spitzer and Fan (5). Close agreement between the calculated values and experimental values is obtained. The dashed line in Fig. 1 shows the calculated absorption coefficient as a function of wavelength for 0.013 ohm-cm n-type silicon. Silicon with this resistivity was used as substrate material for silicon epitaxial layers measured in this investigation.

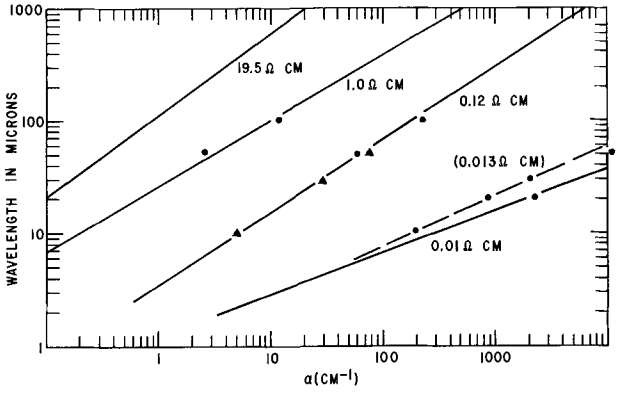

Fig. 1. Magnitude of the absorption coefficient due to free carrier absorption in n-type silicon as a function of wavelength: •, calculated using Lyden method; ▲, Spitzer and Fan.

An Infrared Ellipsometer

The optical constants of the semiconductor layer and substrate at infrared wavelength can be calculated from Eq. [2] and [3] using the appropriate values of resistivity, mobility, and effective mass. All the parameters needed to calculate a set of ellipsometer curves in ψ and Δ for epitaxial layers on a particular substrate are known. All that is needed to measure epitaxial thickness by the ellipsometer technique is an instrument that will operate in the infrared.

General description.—A schematic drawing of an instrument that meets all the basic requirements of a visible ellipsometer but operates in the infrared is shown in Fig. 2. The instrument is built on a Gaertner L118 base. Energy from a globar source passes through an optical chopper, strikes an off-axis front surface parabolic mirror, and forms a globar image

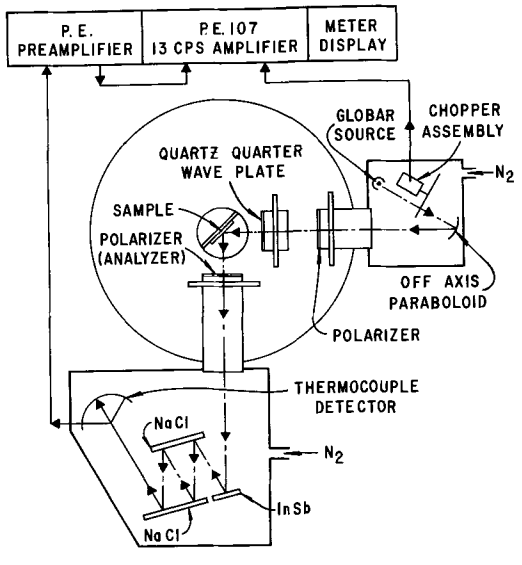

Fig. 2. Schematic drawing of the infrared ellipsometer

at the sample holder. The light striking the sample is not collimated, contrary to the practice followed in visible ellipsometry, because of the use of the parabolic mirror. Such an optical arrangement is required in the infrared because of the necessity of collecting as much energy as possible from the finite globar source. How the use of un-collimated light affects the instrument operation and ultimately, the accuracy of the method will be discussed in a later section.

The light in this path passes through the first infrared polarizer and the infrared quarter wave plate. After striking the sample, the light is reflected down the second arm. It passes through the infrared analyzer polarizer and into the monochromator section. In this section the light is reflected once from a polished InSb surface and four times from polished NaCl plates. The reflection is at near normal incidence. The resultant light strikes an ellipsoid and is focused on a standard thermocouple detector. The signal of the detected energy is amplified by a Perkin-Elmer 13 cps preamplifier and amplifier. The amplified signal is displayed on a high sensitivity voltmeter. Air tight chambers were constructed on each arm so that absorption by atmospheric moisture could be minimized in the optical paths. The chambers are flushed with dry nitrogen. Angles of incidence and polarizer readings are read using the verniers supplied with the instrument. Optical alignment was accomplished using front surface mirrors in place of the NaCl plates so that visible light could be used to determine the optical path. After alignment the mirrors were replaced with the NaCl plates and the detector peaked on the infrared energy. The infrared quarter wave plate, the infrared polarizers, and the monochromator sections warrant further discussion.

Infrared quarter wave plate.—A quarter wave plate is made from optical material that is bi-refractive. The velocity of light traveling through a bi-refractive material is a function of the angle the electric vector of the light makes with the optical axis of the crystal. The velocity (and thus the refractive index) changes from either a maximum or minimum in a direction along the optical axis to a minimum or maximum in a direction perpendicular to the optical axis. If the two refractive indexes are accurately known at a particular wavelength, a bi-refractive crystalline material can be carefully oriented (using an x-ray diffractometer) and a plate cut of sufficient thickness to produce a quarter wave plate. Two light waves of a particular wavelength polarized in and perpendicular to the direction of the optical axis will emerge, after traveling through the plate, separated in phase by 90° ($\lambda/4$).

Selection of the proper optical material was a difficult problem. Most of the optical materials that transmit well in the infrared are not bi-refractive. Of those that are bi-refractive, either the refractive indexes are not accurately known or the materials cannot be obtained in proper sizes. Natural quartz was selected. It can be obtained in large high quality pieces and its optical constants are accurately known (9). The major disadvantage to using quartz is that it is opaque in the normal infrared regions. Quartz does not transmit well from about 3.5 to ~45μ, so that the wavelength selected for the operation of the instrument has to be at least 50μ. The thickness of the quarter wave plate is calculated from the difference in the refractive indexes; the correct thickness for one operating at 55μ is ~10 mils.

The monochromator section.—Any instrument operating in the far infrared is energy limited. The problem encountered in designing the monochromator section was how to produce a source of light of at least 50μ wavelength in a simple manner while conserving as much of the available energy as possible. A unique reflection system was selected which takes advantage of the Reststrahlen reflection bands of ionic crystals for its energy isolation. These bands are the reflectivity maxima that occur in ionic crystals because of the strong absorption of infrared energy by the oscillating constituent atoms or ions.

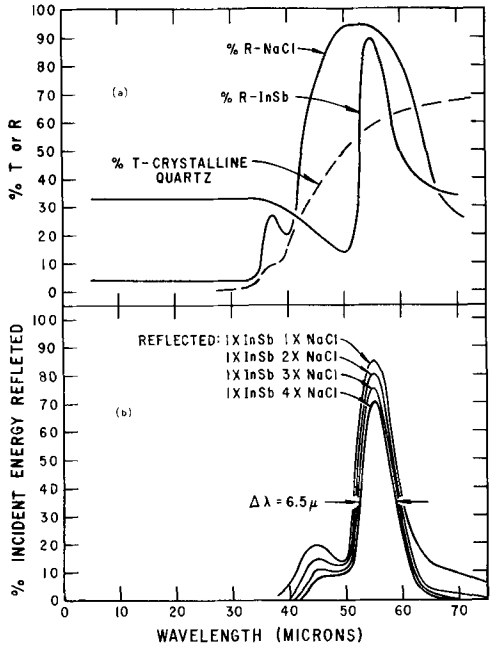

Fig. 3(a) and (b). Monochromator components

The reflectivity of the two materials selected, NaCl and InSb, are shown in Fig. 3a. Notice the reflectivity maxima are 90-95%. The selection of NaCl as a material was based on its reflection maximum (55μ) and its low reflectivity out to 35μ. This low reflectivity allows the elimination of the unwanted radiation on both sides of the 55μ peak. The NaCl reflection peak is too broad to produce a narrow band of radiation. For this reason, InSb was chosen because of its very sharp reflection band which peaks at 54.6μ (10). The transmission of crystalline quartz is included in Fig. 3a to emphasize that a wavelength of at least 50μ is needed if a quartz quarter wave plate is used.

Reflectivity is defined as the ratio of the reflected energy over the incident energy. The method of energy isolation by multiple reflections is based on the fact that the resultant intensity at a particular wavelength after multiple reflections is just the reflectivity of the surface raised to the n^{th} power, where n is the number of reflections. This fact is demonstrated in Fig. 3b. The per cent of incident radiation as a function of wavelength is shown after reflection from one InSb surface and one to four NaCl surfaces. More reflections from NaCl drastically decrease the amount of energy on both sides of the 54.6μ peak while leaving the percentage of energy at the peak quite large. This is because the low reflectivity of NaCl (0.04) on both sides of the peak raised to the fourth power approaches zero. The value of the peak reflectivity (0.95) raised to the fourth power is still quite large (0.81). The small shoulder occurring at ~45μ presents no problem because of the low transmission of the quartz quarter wave plate.

Infrared polarizers.—The best infrared polarizers reported in the literature are transmission wire grid polarizers reported by Bird and Parish (11). They show good transmission, have high polarization, and work well in optical systems where the light is not collimated. The polarizers are produced by shadowing a plastic grating replica with a metal that has high reflectivity in the infrared (Al or Au). The result is a plastic film covered with a set of closely spaced parallel conducting wires. Of course, the plastic film must be transparent at the wavelength of interest. A spacing of $\lambda/3.5$ is required to produce 99% polariza-

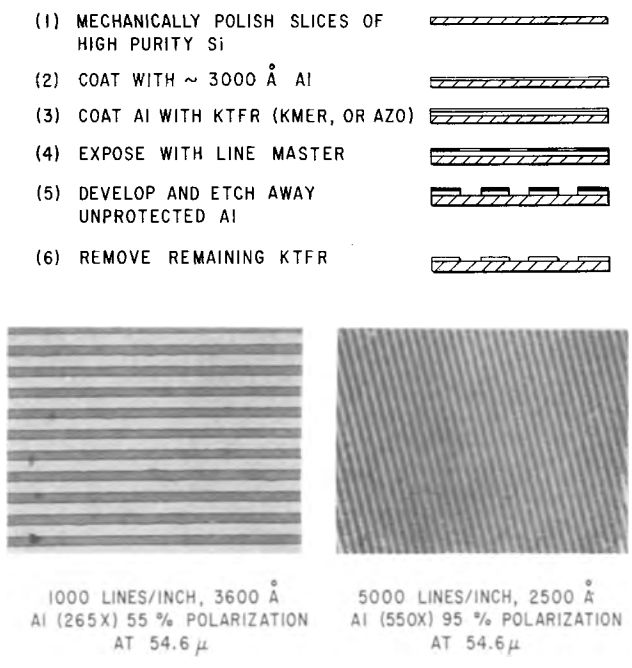

Fig. 4. Preparation of Si-Al grid infrared polarizers

tion (11). For 55μ wavelength, this corresponds to at least 1600 lines/in.

Wire grid polarizers are not commercially available. Attempts in this laboratory to produce polarizers of this type on polyethylene film using Bird and Parish's technique failed. A photomask technique was used instead. High purity silicon was chosen as the optical material to use because of its availability, transparency in the far IR, and because photomask technology is well developed for silicon. A step wise description of the process followed is shown in Fig. 4. Two prints were used, 1000 and 5000 lines/in. Photographs of the finished aluminum lines are shown for both polarizers. The measured polarization for these polarizers at 54.6μ was ~55% for the 1000 lines/in. and 95-98% for the 5000 lines/in. Another advantage of these polarizers is the plane of polarization can be accurately measured.

Two 5000 lines/in. polarizers were used in the instrument operation and worked quite well. At 54.6μ they transmitted about 25-27% of the incident unpolarized light. After operating the instrument for quite sometime, it was decided to try to improve the reading of the nulls by constructing polarizers which would transmit more energy. Polyethylene film polarizers were constructed. These are made by stretching 25-30 films over a holder and allowing the incident radiation to strike the polyethylene films obliquely at the polarization angle ($\phi = \tan^{-1} n$). The transmitted light is then plane polarized. Polarizers constructed in this way did transmit more light (~35% incident radiation) but are not too effective for uncollimated light. The instrument operation did not improve substantially but the polyethylene polarizers are still used because of the slight increase in transmitted energy.

Instrument operations.—The instrument was operated exactly as the visible ellipsometer except that the eye was not used to detect the null. Instead, a sensitive voltmeter was used to display the detected and amplified infrared signal. The system is definitely energy limited in its present form. Nulls are difficult to measure. Readings are taken on both sides of the null to improve accuracy. However, even in its present form the readings are surprisingly reproducible. The present instrument was designed and built to demonstrate the applicability of the ellipsometer technique to epitaxial film thickness. Improvement of the instrument can be readily obtained by using a more sensitive detector or by redesigning the optical system to provide more energy.

A sample that is nonuniform in thickness produces a resultant elliptical polarization which is the average for the entire sample. In visible ellipsometry, for such a sample, total extinction is difficult to obtain because a faint background intensity is still visible at the null. A similar effect is produced by the use of uncollimated light in the infrared ellipsometer. The magnitude of this effect is decreased by careful optical alignment of the instrument symmetric about the center ray. Additionally, a small area of the sample (~¾ in. in diameter) is used as the limiting aperture of the instrument. Considering the size of the source mirror and the image distance, the total possible beam divergence is ±4°. However, a movement of the monochromator arm ±2° from the proper incidence angle reduces the detected signal to half value indicating the rays contributing most heavily to the detected signal travel very close to the center rays. An equal number of rays from the two vertical extremes (<±4°) average out to produce a plane of incidence determined by the center ray. The same averaging process occurs between rays of the two horizontal extremes to produce an average angle of incidence determined by the center ray. Averaging of both vertical and horizontal nonparallel rays occurs when the beam passes through the quarter wave plate to produce an average 90° phase shift for the center ray.

The averaging of the horizontal rays to produce an average plane of incidence does not produce a difference in the measured and calculated ψ and Δ values. The plane of incidence is not involved in the calculation. However, for a particular thickness of film on a particular substrate, the calculated ψ and Δ points may not be linear functions of the angle of incidence. In this case, a small error may result because the effective value of ψ and Δ for all rays does not average out to the same value as that calculated for the center ray. Each particular system must be evaluated for each thickness range. The magnitude of this effect is discussed under the results section for the two systems measured.

Applications

Device specifications usually call for epitaxial materials grown in the N on N^+ or P on P^+ configuration. In this arrangement the resistivity of the layer is at least an order of magnitude higher than the substrate. The two examples chosen for this evaluation, N on N^+ Si and P on P^+ Ge, represent the configuration of the majority of epitaxial slices produced. It was pointed out earlier that the method works best when the layer is nonabsorbing. The nonabsorbing criterion was met by the layer resistivity selected (~1 ohm-cm) at the wavelength of measurement.

N *on* N^+ Si *epitaxial layers.*—About 40 N on N^+ epitaxial layers 1-10μ in thickness were specially prepared for this evaluation. The substrate and layer resistivities were 0.013 ± 0.001 ohm-cm and 2 ± 1 ohm-cm, respectively. The optical constants were calculated for the wavelengths of measurement (54.6μ) using Eq. [2] and [3]. An ellipsometer curve in terms of ψ and Δ for layers 0-10μ thick in 0.1μ increments was calculated using the program described by McCrackin and Colson (12). The results are shown in Fig. 5. The angle of incidence chosen was 50°. In the illustration, every micron increment was designated and the 0.5μ increments marked with an arrow head. The first order of thickness appears on the right hand side of the curve. This would correspond to thickness from 0 to 8.1μ. For thickness greater than 8.1μ, the numbers on the left hand side of the curve are read. This corresponds to epitaxial thickness from 8.2 to 10.4μ on the curve. Thickness greater than 10.4 can be extrapolated from the existing points. Because the film is nonabsorbing the points for films of different thickness fall almost on top of one another (as in the case of

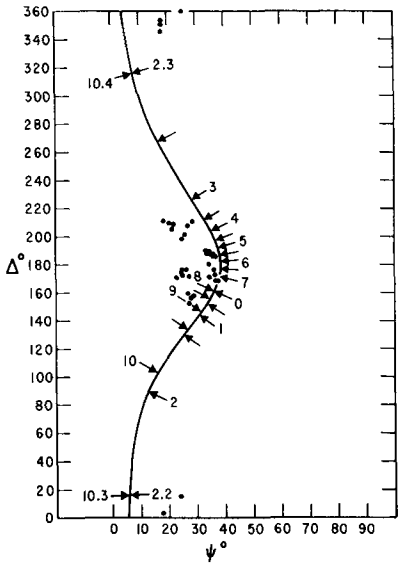

Fig. 5. Ellipsometer curve for silicon epitaxial layers, N on N^+. $\Phi = 50°$, $\lambda = 54.6\mu$.

nonabsorbing oxide films on semiconductors) retracing the curve. For a single set of readings, prior knowledge of the order of thickness of a film is required. The value of Δ goes off scale at the thickness of $\sim 2.2\mu$ (or 10.3) and back on scale $\sim 2.3\mu$ (or 10.4). These points are also marked to avoid confusion.

The measured values of ψ and Δ for 38 samples are indicated in Fig. 5 with small circles. The experimental points follow the general shape of the curve. Considering the fact that the optical constants of the substrate are calculated and that the junction is graded to some variable degree the fit is quite good. The calculation of Δ from the Polarizer reading ($\tan\Delta = \cot 2P$) yields two possible values. Generally this creates no problem because only one value of Δ along with the measured value of ψ make a point which falls on the curve. However, in our case, the experimental error in the measured ψ and Δ may be great enough so that neither point falls on the curve. For this reason, the prior knowledge of the order of thickness is used to select the proper value of Δ.

The thickness values were selected by extrapolating the Δ value to the curve disregarding ψ. The thickness determined for the samples for three separate readings are shown in Table I. The columns headed ellipsometer 1, 2, and 3 show the measured values for each sample. The values determined by the infrared scan technique with a Beckman IR-5A are given in the first column. Portions of some samples were removed from the slice and the epitaxial layer thickness determined by the angle lap and stain technique (L.S.). These results are given in column 2. An interference pattern or a junction stain was not obtained for eight very thin samples. Several of these produced an interference pattern when remeasured at shorter wavelengths using a Perkin-Elmer 337. The calculated thickness are given in Column 3. Average values for the three ellipsometer thickness measurements are given in the sixth column.

In the next column, the error existing between the average ellipsometer and the IR-5A values are given in terms of per cent of the IR-5A measured thickness. No values are given for the eight samples which failed to produce an interference pattern with the IR-5A. The per cent error for the 30 remaining samples ranges from 0 to 14.7% with an average value of $\pm 6.7\%$. The reproducibility of the ellipsometer reading is indicated in the last column. The individual readings for the three thickness determinations are compared to the average value and an average error calculated. For the same 30 samples the average

Table I. Comparison of thickness valves for silicon epitaxial layers determined using the infrared ellipsometer and the infrared scan technique*

Sample No.	t by IR-5A	t by L.S.	t by P.E. 337	t by ellip-som. (1)	t by ellip-som. (2)	t by ellip-som. (3)	t Aver. ellip-som.	% Error (from IRSA)	Re-prod. ± %
N-6608-									
206-1	9.9	8.3		10.3	10.3	10.3	10.3	+4.0	0
206-3	9.5			10.3	10.3	10.3	10.3	+8.4	0
207-1	7.4	7.4		7.0	6.9	7.0	7.0	−5.4	0.5
207-3	7.9			7.1	7.5	6.9	7.2	−8.9	3.2
208-1	7.9	6.8		7.1	7.1	6.8	7.0	−11.4	1.9
208-2	7.2			7.4	7.2	6.9	7.2	0	2.3
208-3	7.1			7.3	7.4	7.4	7.4	+4.2	0.4
208-4	7.3			7.0	7.1	7.5	7.2	−1.4	2.8
209-1	5.3	4.7		5.3	6.2	5.9	5.8	+9.4	5.7
209-2	5.1			5.4	5.7	5.2	5.4	+5.9	3.1
209-3	4.8			5.5	5.6	5.5	5.5	+14.5	0.6
209-4	5.0			5.4	5.4	5.6	5.5	+10.0	1.8
210-1	5.5	4.7		5.4	5.8	5.6	5.6	+1.8	2.4
210-2	6.0			5.4	5.5	6.0	5.6	−6.7	3.0
210-3	5.6			5.5	5.6	6.1	5.7	+1.8	4.1
210-4	5.4			5.4	5.6	5.4	5.5	+1.8	1.8
211-1	3.4	2.4		3.7	3.7	4.3	3.9	+14.7	6.8
211-2	4.0			4.0	3.9	4.1	4.0	0	1.7
211-3	3.6			3.6	3.7	3.4	3.6	0	2.8
211-4	3.7			3.5	3.4	3.9	3.6	−2.7	5.5
213-1		N.D.	1.0	2.2	2.2	2.2	2.2		
213-2		N.D.	0.9	2.2	2.2	2.2	2.2		
213-3		N.D.	0.9	2.3	2.3	2.3	2.3		
213-4		N.D.	0.9	2.2	2.2	2.3	2.2		
214-1		N.D.	1.0	0.4	0.3	0.6	0.4		
214-2		N.D.		0	0.4		0.4		
214-3		N.D.		0.5	0.5		0.5		
214-4		N.D.		0.2			0.2		
215-1	6.8	6.8		6.2	6.7	7.1	6.7	−1.5	4.5
215-4	8.2			6.5	7.4	7.5	7.1	−13.4	6.1
216-1	9.5	8.8		10.3	10.3	10.3	10.3	+8.4	0
216-2	9.7			10.3	10.3	10.3	10.3	+6.2	0
216-3	9.6			10.3	10.3	10.3	10.3	+6.8	0
216-4	10.2			10.3	10.3	10.3	10.3	+1.0	0
217-1	3.9	3.2		3.6	5.4	4.3	4.4	+12.8	14.4
217-2	3.9			3.8	5.8	3.6	4.4	+12.8	21.2
217-3	3.9			4.4	5.2	3.6	4.4	+12.8	12.2
217-4	3.8			4.2	5.0	3.4	4.2	+10.5	12.7

* Average error for 30 samples $\pm 6.7\%$. Reproducibility error $\pm 4.1\%$.

error (in terms of per cent of the average ellipsometer value) is $\pm 4.1\%$.

P *on* P^+ Ge *epitaxial layers.*—Forty epitaxial samples of P on P^+ were specially prepared for evaluation. The resistivity of the substrate and layer were 0.0022 ± 0.0001 ohm-cm and ~ 1 ohm-cm, respectively. As in the other example, the optical constants were computed at 54.6μ and the values used to compute an ellipsometer curve for layers varying in thickness from 0 to 10μ. The thickness increment again was 0.1μ. The results in terms of ψ and Δ are plotted in Fig. 6. The angle of incidence was 50°. As in the other illustration, the whole microns are numbered and the half microns accented. The first order of thickness is read on the inside of the curve (0-6.8μ) and the second

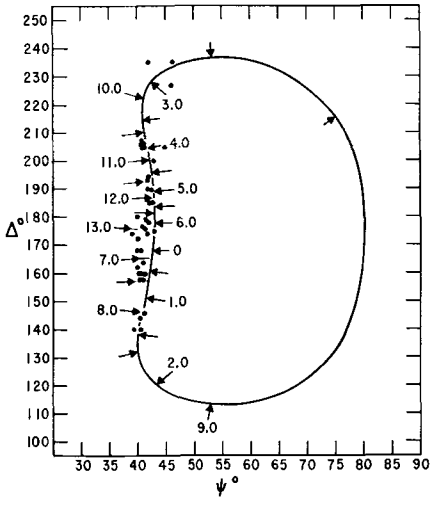

Fig. 6. Ellipsometer curve for germanium epitaxial layers, P on P^+. $\Phi = 50°$, $\lambda = 54.6\mu$.

Table II. Comparison of thickness values for germanium epitaxial layers determined using the infrared ellipsometer and the infrared scan technique

Sample No.	t by IR-5A	t by <)(S	t by P.E. 337	t by ellip-som. (1)	t by ellip-som. (2)	t by ellip-som. (3)	t Aver. ellip-som.	% Error (from IRSA)	Re-prod. ± %
2-668-1	10.4	9.1		11.0	10.8	10.9	10.9	+4.8	0.6
2-668-2	10.0			—	—	—	—	—	—
2-668-3	10.0			10.8	11.3	11.3	11.1	+11.0	2.7
2-668-4	10.2			10.6	10.9	11.1	10.9	+6.8	1.5
2-669-1	9.1	8.3	10.4	6.4	5.9	6.4	6.2	−31.9	3.8
2-669-2	9.2		9.8	5.8	6.5	6.9	6.4	−30.5	6.2
2-669-3	9.2		9.1	6.5	6.3	6.0	6.3	−31.5	2.7
2-669-4	9.1		9.7	6.8	6.6	7.1	6.8	−25.3	2.5
2-670-1	8.0			6.8	7.4	7.7	7.3	−8.7	4.6
2-670-2	8.2			7.3	7.0	7.0	7.1	−13.4	1.9
2-670-3	8.0	6.8		7.4	6.8	6.9	7.0	−12.5	3.3
2-670-4	8.0			7.1	6.9	7.1	7.0	−12.5	1.4
2-671-1	7.0	6.8		6.2	6.1	6.8	6.4	−8.6	4.7
2-671-2	7.1			6.2	6.3	6.8	6.4	−9.9	3.6
2-670-3	6.8			6.2	6.6	6.2	6.3	−7.3	2.7
2-671-4	6.8			6.4	6.5	6.5	6.5	−4.4	0.5
2-672-1	5.7	5.0		6.0	5.5	5.7	5.7	0	2.9
2-672-2	5.8			5.9	5.7	5.3	5.6	−3.4	4.2
2-672-3	5.7			5.4	5.8	5.8	5.7	0	4.1
2-672-4	5.7			5.4	5.7	5.4	5.5	−3.5	2.4
2-673-1	5.1	4.1		4.7	4.8	5.1	5.0	−2.0	4.0
2-673-2	5.1			4.6	5.0	5.1	4.9	−3.9	4.1
2-673-3	5.1			4.9	4.8	5.1	4.9	−3.9	2.0
2-673-4	5.1			4.9	5.2	5.0	5.0	−2.0	2.0
2-674-1	3.7			3.9	4.0	4.0	4.0	+8.1	0.8
2-674-2	3.7			3.9	3.9	3.9	3.9	+5.4	0
2-675-1	3.4	2.7		3.1	—	—	3.1	−8.8	—
2-675-2	3.3			2.9	3.3	3.1	3.1	−6.0	4.3
2-675-3	3.1			2.9	2.9	3.1	3.0	−3.2	3.3
2-675-4	3.1			2.8	2.9	3.2	3.0	−3.2	5.6
2-676-1	≈2.0	No stain	2.2	1.2	1.4	1.2	1.3	—	—
2-676-2	≈2.0		2.3	1.4	1.8	1.6	1.6	—	—
2-676-3	≈2.0		2.3	1.4	1.6	1.7	1.6	—	—
2-676-4	≈2.0		2.3	1.3	1.6	1.7	1.5	—	—
2-677-1	≈1.0	No stain	—	0.6	0.2	0.6	0.5	—	—
2-677-2	≈1.0		—	0.6	0.4	0.6	0.5	—	—
2-677-3	≈1.0		—	0.7	—	—	0.7	—	—
2-677-4	≈1.0		—	0.7	0.6	0.6	0.6	—	—

order on the outside (6.8-13.6μ). Again the film is nonabsorbing and the curve could be used for greater thicknesses.

The measured values of ψ and Δ for 40 samples are shown on the illustration as small circles. They follow the calculated curves much more closely than the silicon points. As pointed out before, prior knowledge of the order of thickness is used in assigning the proper value of Δ from the polarizer reading. The thickness data treated in the same manner as the previous samples in shown in Table II.

Again the values determined by the IR-5A are used for comparison. Poor values were obtained for the eight samples between 1 and 2μ thick. The P-E 337 could be used for the 2μ samples. Large disagreement was obtained between the average ellipsometer readings and four samples about 9μ thick. They were checked using the P-E 337 at shorter wavelength. The indicated values were greater than with the IR-5A, while the IR-5A value was much larger than the one obtained on the ellipsometer at much greater wavelength. The source of this disagreement most probably is a wide graded junction. For the 31 samples for which IR-5A values were available, the average error with the average ellipsometer value was ±9.1%. The reproducibility again was quite good, for the 31 samples, ±2.8%.

Discussion of results.—There are five aspects of the measurements which should be briefly discussed in order to properly evaluate the results: the sample, the instrument, the calculated curves, the angle of incidence, and the wavelength of measurement.

The Samples.—The ellipsometer measures a slightly different thickness than the infrared scan technique. The only way the two methods can agree (within reproducibility of both methods) is for the sample to have a sharp junction. Undoubtedly, the major source of disagreement is the variation in degree of gradation of the substrate layer junction. The calculated curves are based on the optical constants of the substrate. If the junction is very graded, the origin of reflection occurs at some point toward the layer which has a carrier concentration (and thus optical constants) different from the substrate. The measured value of ψ and Δ will fall off the predicted curve and give a slight error in thickness.

The Instrument.—The instrument in its present form is energy limited. Reproducibility nevertheless is better than ±5%. Undoubtedly, some of the error was caused by instrumental troubles, but it was not the major source. Present plans call for an improvement in instrument performance obtained by using a more sensitive detector (a Golay cell) and by the fabrication of infrared polarizers with better transmission (wire grid polarizers on polyethylene film).

The calculated curves.—When the epitaxial samples were prepared, the resistivities of layer and substrate were specified within a certain tolerance range. The normal variation within this tolerance range will produce a variation of optical constants between samples. The effect would be negligible for the essentially nonabsorbing layers. However, the substrate variation could cause ψ and Δ to fall off the curve calculated for the normal or middle value. In order to check the magnitude of this effect, ψ and Δ curves for substrates within the tolerance range were calculated and compared. The curves were only slightly displaced from one another. Variation in substrate resistivity cannot account for all of the observed displacement of ψ and Δ points from the calculated curves. At this time, the main source of displacement is believed to be the junction gradation.

The angle of incidence.—An improvement in accuracy or reproducibility might be expected for another angle of incidence. A set of ψ and Δ curves for the N on N^+ silicon epitaxial layers was calculated for 70° incidence. The curve is shown in Fig. 7. Silicon N on N^+ samples that had been measured at 50° incidence were remeasured at 70°. No improvement in precision or accuracy was obtained.

In the section describing instrument operation it was pointed out that the use of un-collimated light could lead to a thickness error if the calculated ψ and Δ values for a particular system were nonlinear functions of the angle of incidence. The magnitude of this effect is determined by the specific film-substrate combination and each system must be considered separately. For the systems evaluated, curves were calculated for full divergence (±4°). Comparisons were made between the two extreme curves (46° and 54°) at the even micron increments of the 50° curve. The differences in the magnitude of the deviation from the even micron increment were taken as a measure of the nonlinearity. The maximum nonlinearity values

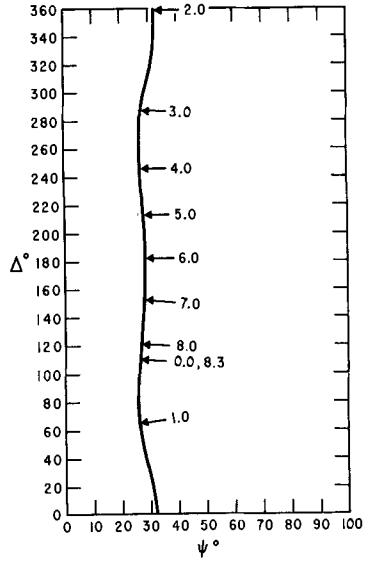

Fig. 7. Ellipsometer curve for silicon epitaxial layers, N on N^+. $\Phi = 70°$, $\lambda = 54.6\mu$.

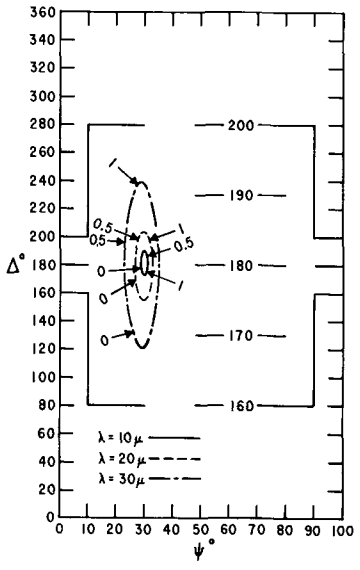

Fig. 8. Ellipsometer curves for silicon epitaxial layers. $\Phi = 50°$, $\lambda = 10\mu$, $\lambda = 20\mu$, $\lambda = 30\mu$.

for the Si system were $\pm 0.1\mu$ and for the Ge system were $\pm 0.2\mu$. For these systems, this effect does not appear to be a major source of error.

The wavelength of measurement.—The amount of energy available at shorter wavelengths from a globar source is many times that available at 54.6μ. If a different $\lambda/4$ plate optical material were available, perhaps an instrument could be constructed which would operate at a shorter wavelength and thus not be so energy limited. To check this possibility, ellipsometer curves were calculated for measurements made on the same N on N^+ silicon epitaxial layers measured before, using the same 50° angle of incidence but changing the wavelength of measurement to 10, 20, and 30μ. The results are shown in Fig. 8. Notice the Δ scale has been expanded by a factor of 5 over the ψ and Δ curves shown previously, in order to show the variation with thickness. The free carrier effect, in this case at least, is so small at the shorter wavelength that a large change in the elliptical polarization of the light is not obtained with thickness. These results indicate 54.6μ is a good choice as a wavelength of measurement.

The results presented here show that on the first try, with no concentrated effort to improve the method or the instrument, the infrared ellipsometer is at least as good and probably better for thin epitaxial layers than the infrared scan. The method should work well on good quality layers $<2\mu$ thick. With improvement in the instrument performance and a better fit of the calculated curves, an accuracy and reproducibility of 1% may be ultimately obtained.

Conclusions

1. The thickness of most epitaxial layers is measured using the infrared spectrophotometer scan technique. The method is not good for very thin epitaxial layers ($< 5\mu$).

2. The ellipsometer is an optical instrument used to accurately measure the thickness of very thin transparent films on highly reflective surfaces in the visible region of the spectrum. The underlying optical principles of the ellipsometric method apply to the optical interference that occurs between an epitaxial layer and its substrate in the infrared region of the spectrum.

3. An ellipsometer was designed and built that operates in the long wavelength infrared region in much the same way as the conventional visible ellipsometer.

4. Using the infrared ellipsometer the thickness of about 40 P on P^+ Ge and 40 N on N^+ Si epitaxial layers was measured. The layers ranged in thickness from 1 to 10μ. The agreement with the values obtained from the infrared scan measurement (when it could be made) was $\pm 9.6\%$ for the Ge layers and $\pm 6.7\%$ for the Si layers. The reproducibility of the measurement was $\pm 2.8\%$ and $\pm 4.1\%$, respectively. All percentages are given in terms of the thickness.

5. The ellipsometer technique ultimately will be a more accurate, more direct method for epitaxial film thickness.

Acknowledgments

The authors are grateful to Phil Kane for his encouragement and support throughout this investigation. Gene Keeney made the successful completion of this program possible by building the instrument and making all the measurements. Special thanks are due to Walt Runyan, Paul Gleim, Murray Bullis, and especially Stacy Watelski of SRDL. These men helped us many times in discussions of the measurement problems and the critical parameters of the materials. Stacy Watelski furnished all the epitaxial samples used in the evaluation.

Manuscript received Nov. 1, 1965; revised manuscript received Feb. 10, 1966. This paper was presented in part at the Denver Meeting of the Society for Applied Spectroscopy, Sept. 3, 1965, and at the Buffalo Meeting of The Electrochemical Society, Oct. 11, 1965.

Any discussion of this paper will appear in a Discussion Section to be published in the December 1966 JOURNAL.

REFERENCES

1. Robert J. Walsh, *Solid State Technology*, p. 23 (August 1964).
2. Warren O. Groves, *Semiconductor Products*, p. 25 (December 1962).
3. T. S. Moss, "Optical Properties of Semiconductors," Academic Press Inc., New York (1959).
4. A. H. Kohn, *Phys. Rev.*, **97**, 1647 (1955).
5. W. Spitzer and H. Y. Fan, *ibid.*, **105**, 268 (1957).
6. R. J. Archer, *J. Optical Soc. Am.*, **52**, 970 (1962).
7. Frank L. McCrackin Eliv Passaglia, Robert R. Stromberg and Harold L. Steinberg, *J. Research, Nat. Bur. Standards*, **67A**, No. 4, (July-August 1963).
8. Henry A. Lyden, *Phys. Rev.*, **134**, A1106 (1964).
9. S. Robert and D. D. Coon, *J. Optical Soc. Am.*, **52**, 1023 (1962).
10. M. Hass and B. W. Henvis, *J. Phys. Chem. Solids*, **23**, 1099 (1962).
11. George R. Bird and Maxfield Parish, Jr., *J. Optical Soc. Am.*, **50**, 886 (1960).
12. Frank L. McCrackin and James P. Colson, "A Fortran Program for Analysis of Ellipsometer Measurements and Calculations of Reflection Coefficients from Thin Films," *Nat. Bur. Standards Technical Note 242*, May 27, 1964.

Polarographic Behavior of Some Metal Acetates in Aqueous and Anhydrous Acetic Acid

Harris E. Ulery

Jackson Laboratory, Organic Chemicals Department,
E. I. du Pont de Nemours and Company, Wilmington, Delaware

ABSTRACT

A study of the polarographic behavior of the acetates of Co(II), Ni(II), Zn(II), Pb(II), Cd(II), Bi(III), and Cu(II) at the dropping mercury electrode has been made in the systems: H_2O-HOAc-MOAc and HOAc-MOAc, where MOAc is the supporting electrolyte with M = Li, Na, K, and NH_4. The data are interpreted in terms of the control exerted by solvent on the dissociative equilibria of the reducible metal species and the associative equilibria leading to aggregates involving the inert electrolyte. The half-wave potentials of the reversibly reduced metals (Cd, Pb, and Cu) conform to the qualitative predictions of the equation derived by Schaap (22).

The earliest reported study of acetic acid as a polarographic medium is that of MacGillavry (1), who was unable to obtain sigmoidal curves with the dropping mercury electrode. Later Bachman and Astle (2) and also Hala (3) demonstrated that satisfactory waves could be obtained in this medium provided that caution was exercised to remove all dissolved oxygen and that a suitable correction was made for the sizable iR drop developed across the cell. These workers also showed that the currents obtained in HOAc in the presence of carrier electrolyte, NH_4OAc, although lower than those in aqueous solution, were proportional to the concentration of the reducible species. Since then, proportional currents in glacial HOAc have been obtained with NH_4NO_3 (4) and H_2SO_4 or $HClO_4$ (5) as the inert electrolytes. It has been possible to use this solvent to advantage in the polarographic determination of sulfate ion (6) and of some organic materials (2, 7), particularly the anthraquinones (8).

At this time we would like to report the results of a polarographic study of the behavior of certain metal acetates in anhydrous HOAc as well as in HOAc-H_2O mixtures; included are some comparative results obtained in formic acid.

Experimental Section

Materials.—Anhydrous acetic and formic acids were prepared by the methods of Orton and Bradfield (9) and Garner, Saxon, and Parker (10), respectively.

The anhydrous sodium, potassium, and ammonium acetates were all analytical grade commercial materials and were used without further purification. The anhydrous acetates of lithium, cobalt(II), lead(II), nickel(II), copper(II), cadmium, and zinc were obtained by refluxing the common hydrates for several hours in a 50:50 volume mixture of acetic acid and anhydride, followed by recrystallization from the same solvent; the salts were then dried at 110°C for 1 to 7 days. $Bi(OAc)_3$ was available in these laboratories and was recrystallized in the same fashion. Metal analyses are given in Table I. It is noteworthy that only one solvate was obtained, *viz.*, $Ni(OAc)_2 \cdot HOAc$, while Kolling and Lambert (11) reported obtaining *inter al.* $2Ni(OAc)_2 \cdot HOAc$, $2Co(OAc)_2 \cdot HOAc$, and $Cu(OAc)_2 \cdot HOAc$ by a somewhat similar procedure.

Equipment.—The Sargent Model XXI (S-29303) recording polarograph was employed in conjunction with a Sargent Model A IR Compensator (S-29320) as designed by Arthur (12). The electrolysis vessel, also an Arthur design, was a 100 ml, three electrode assembly (Sargent, S-29322) employing an asbestos fiber bridge. The reference and current electrodes were aqueous saturated calomel (SCE). Transfer of water across the bridge was found to be negligible during the course of a run by Karl-Fischer titration. The d.m.e. had the capillary constants given in Table II. The assembly was thermostated at 25.0° ± 0.5°C.

Method.—All aqueous solutions were prepared volumetrically using deionized water; appropriate concentration values were obtained with the aid of International Critical Tables' density and composition data for the aqueous acids (13). Solutions of the reducible metals were made up fresh from stock solutions of the inert electrolyte; aging the solutions for a few hours appeared to have no significant effect on the data obtained. Routinely, 0.005% Triton X-100 (Rohm and Haas) was used as a maximum suppressor in all the aqueous acid runs, since it was found to have a negligible effect on the measured half-wave potentials. Solutions were thoroughly deoxygenated by sparging with argon.

The polarograms were recorded with the damping switch in the "off" position. The instrument was precalibrated with respect to both recorded voltage and current. Values given for the half-wave potentials, limiting currents, and slopes are the averages of three or more determinations. Half-wave potentials and slopes were obtained by a plot of E *vs.* log $(\bar{i}/\bar{i}_l - \bar{i})$ linearly fitted by a least squares routine programed on an IBM 1410 computer. For uniformity, only $\bar{i}$ values between $E_{1/4}$ and $E_{3/4}$ were utilized; in certain cases where nonsymmetrical polarograms gave rise to nonlinear log plots, the $E_{1/2}$ and slope param-

Table I. Analyses of anhydrous metal acetates

Metal acetate	% M calc'd.	% M found
$Bi(OAc)_3$	54.2	54.8
$Cd(OAc)_2$	48.7	48.8
$Co(OAc)_2$	33.3	33.0
$Cu(OAc)_2$	35.0	35.1
$Pb(OAc)_2$	63.6	63.6
LiOAc	10.4	10.0
$Ni(OAc)_2 \cdot HOAc$	24.7	24.6

Table II. Capillary constants in various media[a, c]

Electrolyte/solvent[b]	Open circuit	−0.5v
NH_4OAc/H_2O	1.460	1.476
$NH_4OAc/HOAc$	1.452	1.453
KOAc/HOAc	1.450	1.451
NaOAc/HOAc	1.443	1.443
LiOAc/HOAc	1.437	1.440
$NH_4HCO_2/HCOOH$	1.444	1.450

[a] $mg^{2/3}$ $sec^{-1/2}$ at h = 50 cm; [b] electrolyte conc. = 0.50 F; [c] values of m were determined with the apparatus described by J. J. Lingaine, *Ind. Eng. Chem., Anal. Ed.*, 15, 588 (1943) and varied over 1.106-1.170 mg/sec.

eters obtained in this manner were slightly higher than values obtained by the usual graphical method.

Mercury heights were corrected by the method outlined by Kolthoff and Lingane (14). Viscosities were obtained by a capillary-flow method at 25.0° ± 0.5°C.

Results and Discussion

Liquid junction potentials.—Nelson and Iwamoto (15) recently suggested a polarographic method for approximating the value of E_j which is based on the measurement of the half-wave potential of the reversible 4,7-dimethyl-1,10-phenanthroline (Fe^{2+}/Fe^{3+}) couple in the desired solvent *vs.* an appropriate reference electrode. The values obtained by them for a number of solvents containing 0.1F lithium perchlorate ranged between 30 and 110 mv *vs.* SCE. We have made some yet unpublished computer studies based on the electrostatic models proposed by Garrick (16) and Born (17), which suggest that these values may be high by a factor of about two. As it happens, it is not possible to use the Nelson-Iwamoto method in acetic or formic acid, since the iron complex is not stable in these media. At any rate, there is no reason to expect that the junction potentials obtained in these solvents would be much different from those found in other nonaqueous solutions, and hence, are probably less than ca. 100 mv.[1] Finally, it can be mentioned that the reversible half-wave potential of cadmium is relatively insensitive at high concentrations to the kind of acetate electrolyte used; this would be expected if the contribution to a junction potential by the carrier acetate was small. This is likely since NH_4OAc is weakly dissociated in HOAc (19).

Half-wave potentials and slopes in aqueous acetic acid.—In Fig. 2 are illustrated the $E_{1/2}$ data obtained from millimolar solutions of the metal acetates in 0.5M NH_4OAc supporting electrolyte. The wave due to Co(II) remained distinguishable over the entire concentration range. At intermediate compositions, however, this wave was so close to the hydrogen wave that the limiting current was ill-defined; this resulted in some scattering of the values for $E_{1/2}$. The wave was irreversible at all times with a slope of 85-100 mv. The rather dramatic change in the half-wave potential at the left end of the scale (*ca.* 80 mv for the first 0.5 mole water added) suggests that selective solvation of some form of Co(II) is occurring to produce a more stable hydrate.[2] Very probably it is the reducible species itself which is being affected, since no appreciable change in the wave slope is noted. The slight maximum at the aqueous end of the scale is due to the influence of *p*H on the concentrations of the various forms of Co(II) in the solution. This was indicated by a pronounced change in the shape of this part of the curve when either a strong base or acid was added.

The curve for Ni(II) (slopes, 80-115 mv) is quite similar to that given by Co(II), displaying analogous,

[1] Failure to find any significant shift in the electrocapillary maximum from the aqueous value (Fig. 1) supports this contention, although a shift due to the development of a junction potential might not be seen if the actual potential of the maximum had undergone a nearly equal change in the opposite sense as a result in the change in solvent (18).

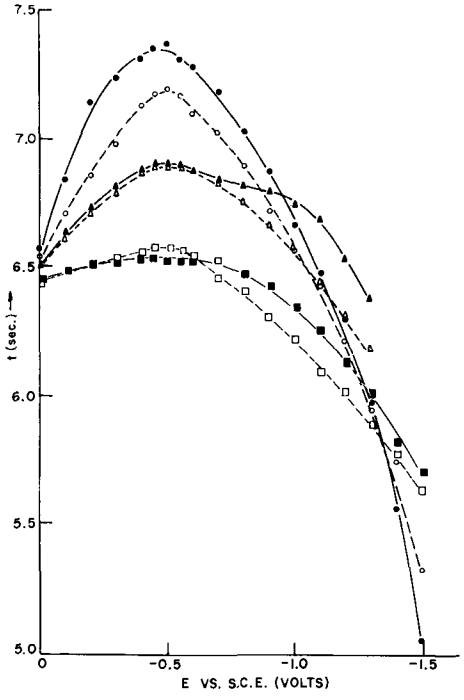

Fig. 1. Comparison of aqueous and nonaqueous electrocapillary curves: •, H_2O; ○, H_2O + 0.005% TX-100; ▲, HCOOH; △, HCOOH + 0.005% TX-100; ■, HOAc; □, HOAc + 0.005% TX-100.

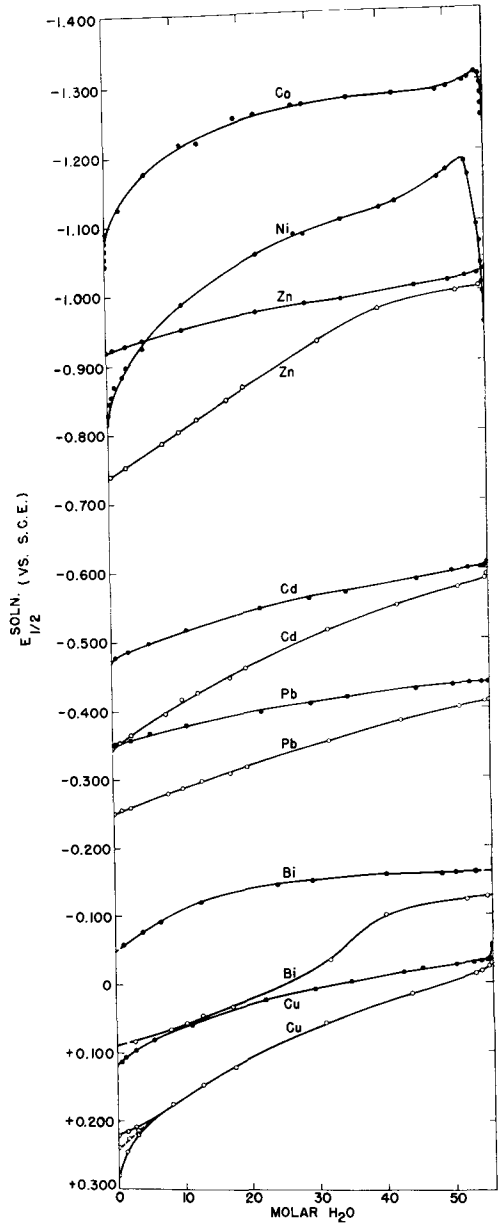

Fig. 2. Effect of composition on half-wave potentials: •, HOAc; ○, HCOOH.

[2] Clearly the peculiar end behavior of the $E_{1/2}$ values of Co(II) and Ni(II) in nearly anhydrous solution cannot be due to a rapid change in either the junction potential or the "effective ionic strength" of the medium, since it is not observed with the other metals investigated.

but exaggerated, features at both ends of the composition scale.

Zinc appears to give a reversible wave with $[H_2O] > 50M$, but the slope of the wave increases as the concentration of the water is reduced, reaching a value of 83 mv in pure HOAc. By contrast, Cd and Pd give waves with reversible slopes for all compositions of the solvent.

Bismuth(III) acetate was not sufficiently soluble in water to obtain a wave, but the solubility improved on adding HOAc. The wave in this medium was nearly reversible with a slope of 23 mv. This parameter increased to a value of 52 mv as the water was reduced to 1.5M. Below this concentration a maximum appeared which could not be suppressed by added Triton X-100. An unsuppressable maximum was also observed with Cu(II) in anhydrous acid, but it disappeared on adding 0.5M water. The development of maxima on the waves of metals which reduce on the positive side of the electrocapillary maximum in HOAc has been studied in some detail by Bachman and Astle (2). The waves obtained with Cu(II) were reversible or nearly so over the rest of the scale.

These results stand in striking contrast to those of Bachman and Astle who found that the half-wave potentials of Pb, Cd, Zn, Co(II), and Ni(II) in 0.25F NH_4OAc were shifted to more negative values by 0.1-0.2v (*vide infra*). Migal and Agas'eva (4), on the other hand, found that the half-wave potentials of Cd, Zn, and Ni(II) were 145, 198, and 162 mv more positive in HOAc containing 0.01M NH_4NO_3 than in water when measured against the SCE.

To facilitate the interpretation of these data, the formic acid-water system was examined similarly, using in this case 0.5M ammonium formate as the supporting electrolyte (Fig. 2). Ni(II) and Co(II) were obscured by the hydrogen wave over most of the range. Zn, Bi(III), and Cu(II)[3] gave waves which displayed dramatic increases in irreversibility as the concentration of acid was raised, while Pb and Cd remained reversible throughout.

In the cases of Cd and Pb which reduce with no detectable overvoltage in both acid media, it is clear that these metals are not as efficiently stabilized in formic acid as they are in acetic. The lower dielectric constant operates to reduce the number of uncomplexed ions in solution, which accounts for the more negative potentials. Also important is the fact that formate is a poorer complexing agent than is acetate as evidenced by the lower pK_a of formic acid in water (3.75 *vs.* 4.76 for HOAc); this can be seen in the slightly more negative half-wave potentials observed in aqueous acetate media as compared to the aqueous formate values (Fig. 3). An additional factor contributing to the destabilization in acid media could stem from the decreased activity of the lyate. It is possible that the activity of the lyate may become so low in poorly ionizing solvents that, despite the correspondingly low value of the dissociation constants for the metal complexes, the degree of dissociation may actually be higher. The observed potential would then reflect a larger contribution from the uncomplexed component. Based on the known dissociation constants of the metal acetates and of ammonium acetate in acetic acid (11, 19) and in water (24), the activity coefficient of acetate ion in acetic acid would have to be very much less than unity to account for such large anodic shifts.

Limiting currents in aqueous acetic acid.—The striking influence of the solvent composition on the limiting currents obtained with various metal acetates is seen in Fig. 3, where the Ilkovic term $\bar{i}_l/nCm^{2/3}t^{1/6}$ is plotted. In each case the curves pass through a generally broad minimum between 5-20M water. Many physicochemical properties of water-acetic acid mixtures display a maximum or minimum at compositions near 13.7M water (mole fraction = 0.5) due to the presumed formation of the monohydrate, $HOAc:H_2O$ (20). In all cases the lower value of the current in acetic acid is anticipated on the basis of the higher viscosity of this solvent. The current data were corrected according to the Ilkovic-Stokes-Einstein equation (Fig. 4); in order not to neglect the effect of the inert electrolyte, the viscosities of 0.5M NH_4OAc solutions were determined (Fig. 5) and employed in this correction.

The corrected curves of Fig. 4 clearly indicated that factors other than viscosity are also responsible for the nonconstancy of the limiting currents. For a dif-

[3] In concentrated solution of HCOOH, Cu(II) presents two irreversible waves (Fig. 2) which merge into one as the water level increases. The dotted line indicates the "midpoint" potential for the wave pair.

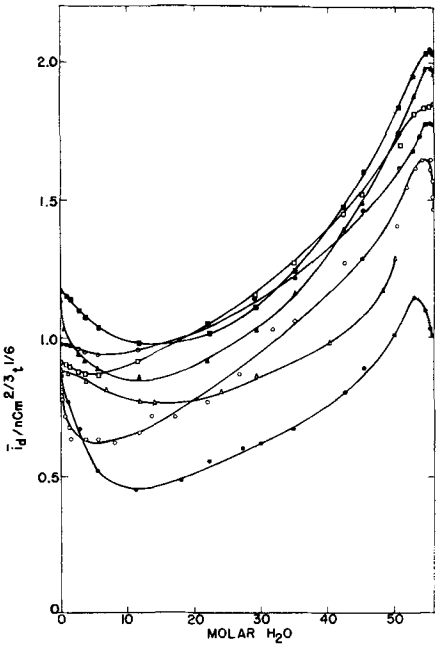

Fig. 3. Effect of solvent composition on diffusion currents in H_2O-HOAc mixtures: ○, Co(II); •, Ni(II); □, Zn(II); △, Bi(II); ▲, Cu(II); ■, Pb(II); ◒, Cd(II).

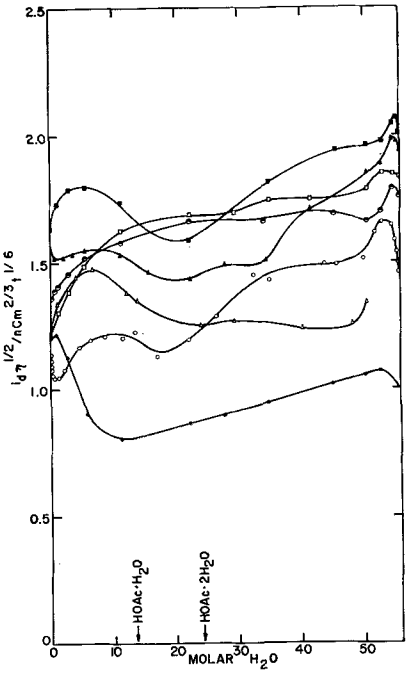

Fig. 4. Effect of solvent composition on $\bar{i}_d\eta^{1/2}/nCm^{2/3}t^{1/6}$ in H_2O-HOAc mixtures. Symbols are the same as those in Fig. 3.

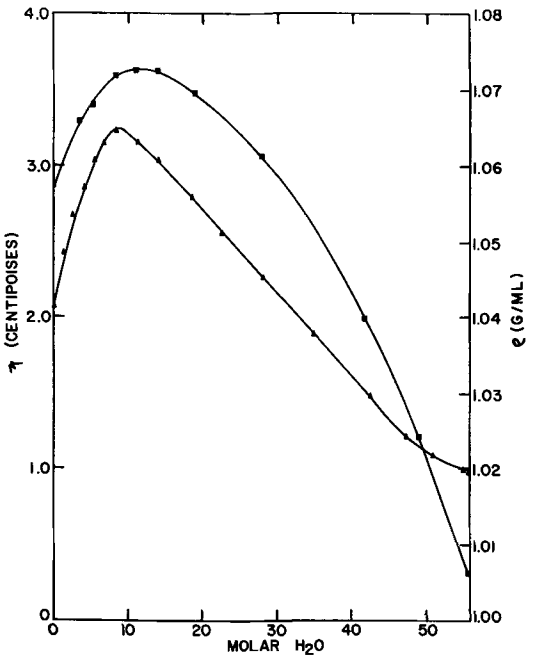

Fig. 5. Physicochemical properties of solutions of 0.5F NH_4OAc in aqueous acetic acid at 25.0°C. ▲, viscosity, η; ■, density ρ.

fusion controlled process, variations in $\bar{i}_d\eta^{1/2}$ must reflect changes in the nature of the diffusing species. In addition to viscosity effects, there are two ways in which a solvent can be expected to determine the diffusion properties of a solution component. Various solvent properties such as acid-base character, dielectric strength, etc., will operate simultaneously (*a*) to determine the kinds of diffusing species (ionic or nonionic, mono- or polyvalent, simple or complex) present in solution, as well as the positions of the equilibria interrelating these, and (*b*) to determine the extent to which ionic and polar components are solvated, and consequently, the over-all geometry of the diffusing particle and the immediate solvent environment through which it must pass.[4] Similar points can be made concerning currents which are kinetically controlled; in such an instance one is concerned with the effect of the solvent on the transition state of the slow step rather than on the stabilities of longer-lived species, although parallels may exist.

The currents due to Pb(II), Cu(II), and Cd(II) are apparently diffusion controlled over the entire range of solvent composition. As Fig. 4 reveals, the maximum in $\bar{i}_d$ which occurs at the aqueous end of the scale (cf. Fig. 4) is just part of a generally complicated dependence on composition which indicates a wide variation in the bulk structure of the diffusing mass. Each of these metals displays seemingly unique behavior, although the ratio of the corrected currents in water to those in acetic acid are perhaps surprisingly constant (Pb, 1.23; Cu, 1.23; Cd, 1.27). The Zn(II) and Bi(III) currents display increasing chemical control at higher acid concentrations, which is evident in the larger value of this ratio for Zn (1.50); the value for Bi could not be measured. The corresponding ratios for Co(II) and Ni(II) are 1.26 and 0.83; neither metal shows simple diffusion control.

Several general features can be observed in the curves of Fig. 4: (*i*) all pass through a pH sensitive max above 50M; (*ii*) all except Ni show a slight maximum or plateau near 40M; (*iii*) all except Zn and Cd show an exaggerated minimum between 10 and 20M (the value at this point is less than or equal to the value in pure HOAc), followed by a maximum below 10M; the homologues, Zn and Cd, reach a broad plateau in this region; (*iv*) all except Cu and Co have a large positive slope at the nonaqueous extreme. Zn and Cd, whose curves do not possess the minimum described in item (*iii*), do give this feature when the inert electrolyte is 0.01F NH_4NO_3; the same is true for Ni(II) (4). This minimum may be associated with a rather loose solvent shell composed largely of the mono- and dihydrates of acetic acid, to which the composition of the solvent closely corresponds. As the concentration of HOAc is increased the rapid decrease in the dielectric constant would lead to a reduction in the concentration of dissociated ions requiring extensive solvation, and an enhanced mobility of the metal would be expected; the final drop in the current in nearly pure acid might be due to solute aggregation. On the other hand, as the water concentration is increased from about 20M, the more bulky HOAc molecules would be replaced by smaller more efficient solvators, and again, an increase in the mobility of the metal would be the likely result.

Half-wave potentials and slopes in anhydrous acetic acid.—In order to appreciate the effect of the carrier electrolyte on the polarographic behavior of the various metal acetates, the current-potential parameters were measured as a function of the supporting acetate concentration. Figure 6 shows that as the NH_4OAc is decreased from 2 to 0.5M there is a corresponding positive shift in the $E_{1/2}$ of each of the reversible or nearly reversible couples (Cd, Pb, and Cu); the same is true for Zn and Bi, which appear to be irreversibly reduced, although the drawing out of these waves may be due to the presence of two incompletely resolved components. This shift has been predicted by Schaap (22) as a result of ion-pair formation in solvents of low dielectric constants. A much less pronounced negative shift was recorded with Ni and Co, both of which reduce irreversibly. Data on Bi and Cu are incomplete due to the development of unsuppressable maxima at lower carrier levels. The 0.5M points shown in Fig. 6 for this pair of metals were obtained by extrapolation of the $E_{1/2}$ data from the HOAc-H_2O mixtures containing this amount of NH_4OAc.

At concentrations below about 0.5M the polarograms of all the metals became increasingly drawn out; in

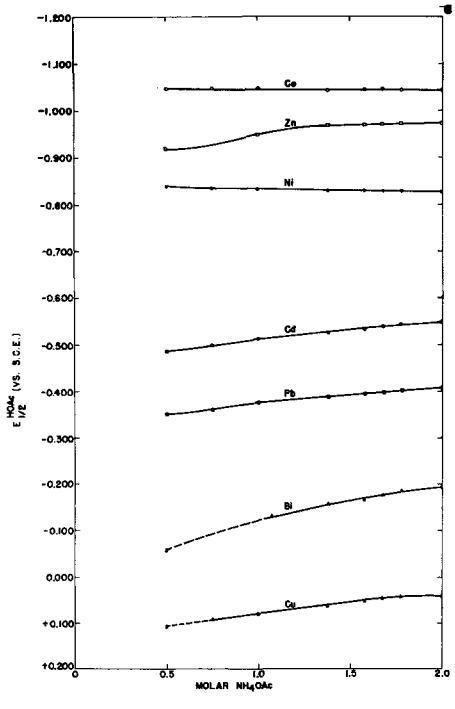

Fig. 6. Effect of NH_4OAc concentration on half-wave potentials of metals in acetic acid.

[4] Fuoss (21) has attempted to accommodate the electrostriction of the solvent shell quantitatively by employing an effective internal viscosity coefficient different from that ordinarily measured.

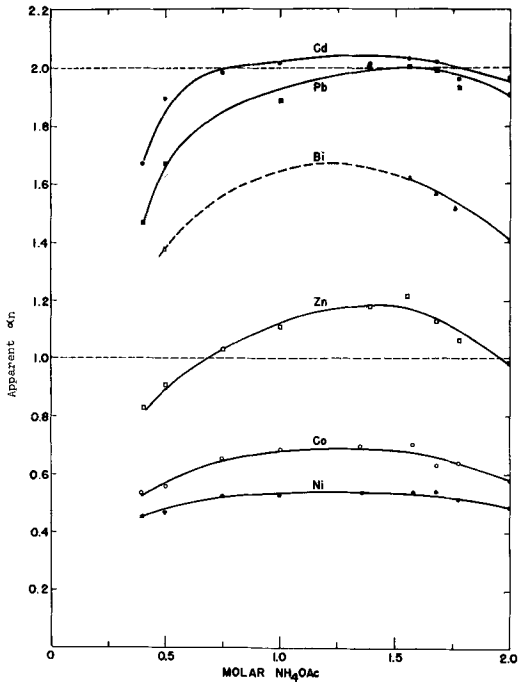

Fig. 7. Effect of NH_4OAc concentration on αn in acetic acid solution.

these instances the current was approximately proportional to the applied voltage. Below 0.1M no diffusion plateau was reached before $E_{applied} = -4$v. The dramatic change in the slope can be seen in Fig. 7 where the apparent "αn" is plotted. The results obtained below 0.3M depended slightly on the position of the microelectrode with respect to the reference. Further, the resistance of the cell at this concentration was of the order of 200,000 ohms, while at 0.5M it was only about 30,000 ohms. It is clear that the three electrode system employed fails to provide adequate iR compensation when the electrolyte concentration is below 0.3-0.5M. This point has been

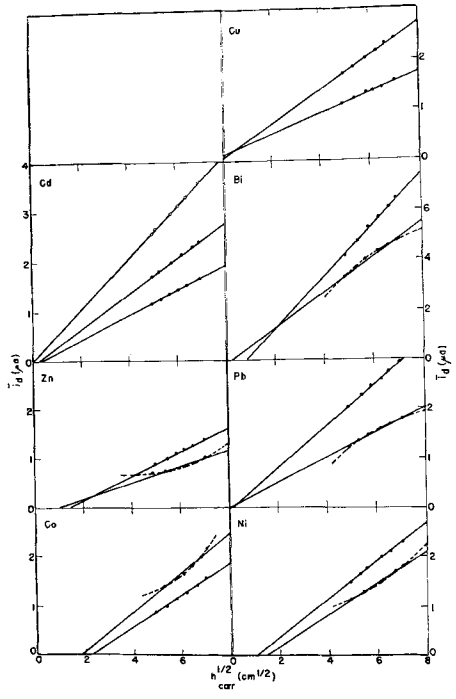

Fig. 8. Effect of mercury pressure on diffusion currents in acetic acid, ○, 0.18M LiOAc; ◓, 0.50M LiOAc; ●, 1.78M LiOAc.

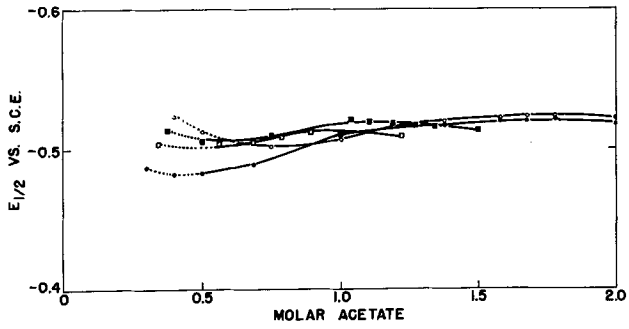

Fig. 9. Effect of concentration of supporting acetate on half-wave potential of $Cd(OAc)_2$ in acetic acid. ●, NH_4OAc; ○, LiOAc; ■, NaOAc; □, KOAc.

treated in some detail by Schaap and McKinney (23), who obtained very similar results in a solvent system of approximately the same dielectric constant. Although it is possible that, due to the development of kinetic control, an actual change in the reversibility of the electrode process may also be taking place with some metals at lower acetate concentrations, this does not appear to be so in the case of Cd whose reduction is still diffusion controlled in 0.18M LiOAc (cf. Fig. 8).

The effect of the kind of supporting electrolyte on the half-wave potentials was examined. At concentration above 1.0M the observed potentials for Cd (Fig. 9) are essentially independent of the kind of electrolyte. Since an increase in the acetate activity should lead to more negative potentials, one would expect the following order of increasing negative values: LiOAc<NaOAc<KOAc<NH_4OAc. Although some crossing of the curves near 1.0M acetate is evident, the expected order is not attained even for LiOAc and NH_4OAc at 2.0M. This discrepancy may be due to an interfering junction potential or to a lack of sufficient information concerning the relative activities of the alkali acetates at high concentrations.

Below 1.0M the apparent $E_{1/2}$ values for Cd show considerable divergence. This is due to slight differences in wave slopes which have an exaggerated influence on the measured half-wave potentials. The $E_{1/2}$ values in this region are seen to decrease in the order of increasing ionic radius of the electrolyte cation. Since the equivalent conductivities of the alkali acetates increase with the size of the cation (19b), it is probable that the differences in the slopes of the polarograms at low electrolyte concentrations are re-

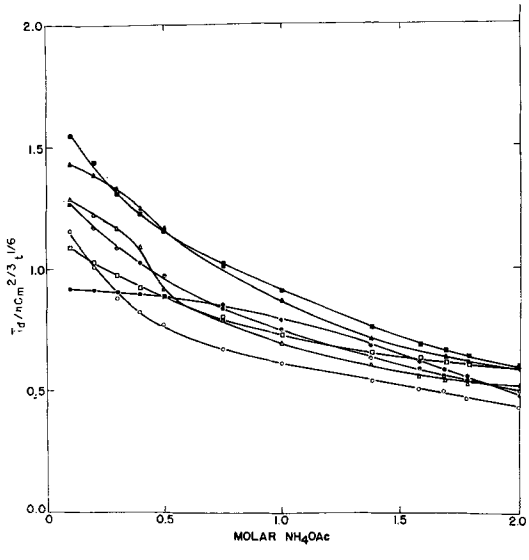

Fig. 10. Effect of NH_4OAc concentration of diffusion currents in HOAc. ○, Co; ●, Ni; ■, Pb; △, Bi; ▲, Cu; □, Zn; ◓, Cd.

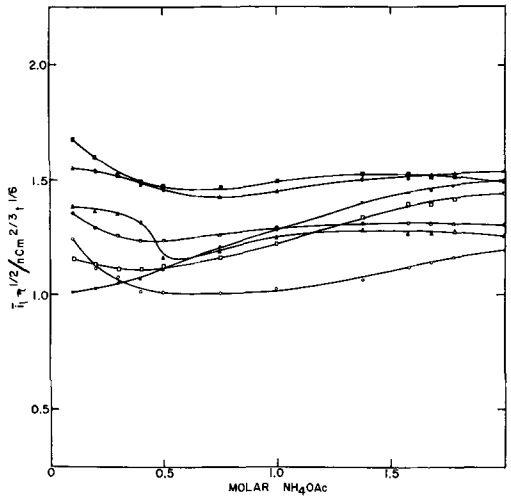

Fig. 11. NH_4OAc concentration vs. $\bar{i}_l\eta^{1/2}/nCm^{2/3}t^{1/6}$ for various metal acetates in HOAc. Symbols are the same as those in Fig. 10.

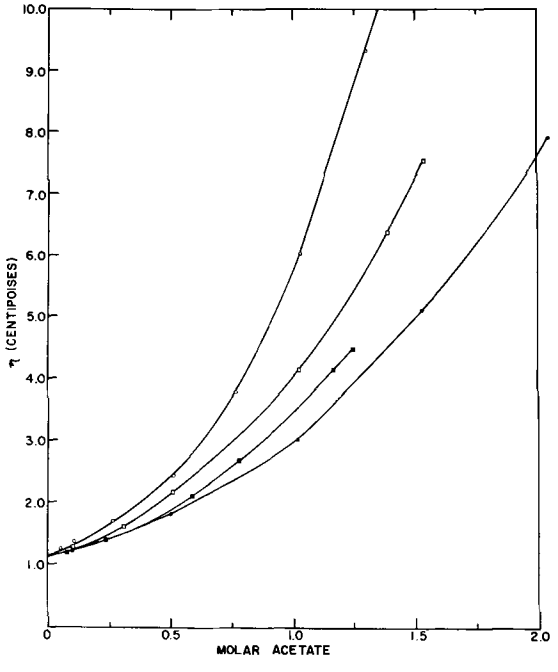

Fig. 12. Viscosities of acetate-acetic acid solutions at 25°C. Symbols are the same as those in Fig. 9.

flections of the uncompensated iR drop existing at low values of the absolute conductivities.

Limiting currents in anhydrous acetic acid.—As can be seen in Fig. 10, the current increases with decreasing concentration of electrolyte, the behavior of Ni, Bi, and Cu deviating from that of the other metals. The viscosities of the electrolyte solutions were determined (Fig. 12), and the data were corrected accordingly as shown in Fig. 11. The near constancy of $\bar{i}_l\eta^{1/2}/nCm^{2/3}t^{1/6}$ at the higher end of the concentration range for Cu, Pb, Cd, and Bi indicates that the current change in this region depends primarily on the change in viscosity of the medium. At the opposite extreme of electrolyte concentration, however, the current is more sensitively and inversely related to the amount of added acetate. Since migration should not be a complication at supporting electrolyte concentrations of 0.01M or greater, even in this weak electrolyte system, the change in $\bar{i}_l$ must be due to an alteration in the structure of the average diffusing species. This is strictly true in the cases of these four

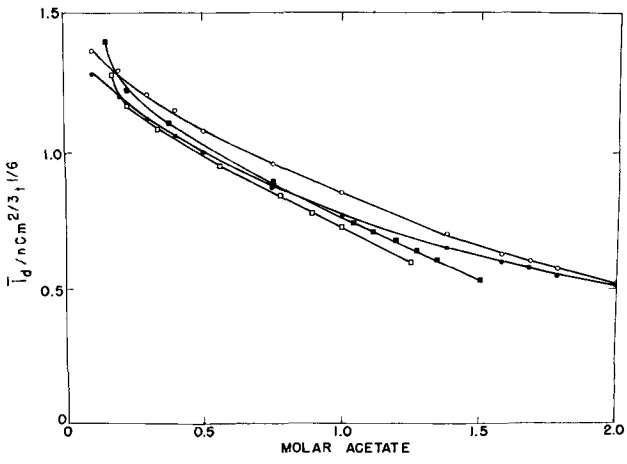

Fig. 13. Effect of concentration of supporting acetate on diffusion current of $Cd(OAc)_2$ in acetic acid. Symbols are the same as those in Fig. 9.

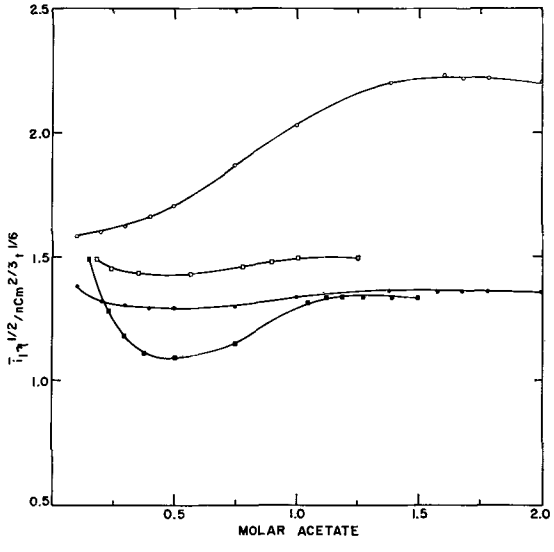

Fig. 14. Acetate concentration vs. $\bar{i}_l\eta^{1/2}/nCm^{2/3}t^{1/6}$ for $Cd(OAc)_2$ in HOAc. Symbols are the same as those in Fig. 9.

metals for which it can be shown that the limiting-current is diffusion controlled (Fig. 8). The reductions of Zn, Co, and Ni exhibit reaction rate-controlled currents (Fig. 8) which may or may not comply with Walden's rule; the same is true of Bi at low electrolyte levels. The more pronounced change in the currents at low electrolyte concentrations may be a manifestation of aggregation of the reducible metal acetate and one or more supporting electrolyte ion-pairs. The dipole moment of the electrolyte ion-pair will be larger than that of acetic acid with which it is structurally homologous. As the concentration of supporting acetate is increased, this component will compete increasingly more favorably with acetic acid for a position in the solvation sphere of the reducible metal ion, *i.e.*, MeL_n (S) + xMOAc $\rightleftarrows$ MeL_n (MOAc) (S) $\rightleftarrows$ . . . $\rightleftarrows$ $MeL_n(MOAc)_x$ (S). The bulk of the latter will then increase to a point of maximum coordination. Further addition of the electrolyte will lead only to self-aggregation which would not directly effect the diffusion of the reducible metal, except by way of changing the effective viscosity of the medium. This hypothesis is borne out by the observation that the viscosity-corrected limiting currents obtained with Cd in the presence of different supporting acetates were more strongly dependent on the nature of the associated cation than on the concentration of the electrolyte (Fig. 13 and 14). This is just what would be ex-

pected, since the cation would determine not only the size of the "solvating" electrolyte, but also the magnitude of its dipole moment. Figure 14 shows that the initial decrease in the current is relatively small in the case of the larger potassium and ammonium ions and most pronounced with the smaller sodium. The latter ion would be expected to benefit most from aggregation, since it is a much higher energy species; LiOAc is undoubtedly so tightly solvated by acetic acid that its behavior is that of an unusually large species which also has little to gain through aggregation. This rationale does not provide an explanation for the rise is the limiting current at concentration levels above 0.5M. It must not be forgotten, however, that the viscosity corrections employed are not entirely adequate in solvents of low dielectric strength, such that the curves shown may not truly reflect the active mobilities of Cd at the various concentrations (22).

Acknowledgments

The author is particularly grateful to Professor L. B. Rogers for his review and discussion of this manuscript. Thanks also must go to the author's colleague, Dr. D. M. King, who labored many hours with him in helpful discussion.

Manuscript received Aug. 24, 1965; revised manuscript received Jan. 13, 1966. This is Research and Development Division Contribution No. 304, E. I. du Pont.

Any discussion of this paper will appear in a Discussion Section to be published in the December 1966 JOURNAL.

REFERENCES

1. D. MacGillavry, *Trans. Faraday Soc.*, **32**, 1447 (1936).
2. G. B. Bachman and N. J. Astle, *J. Am. Chem. Soc.*, **64**, 1303 (1942).
3. E. Hala, *Chem. Obzor*, **23**, 145 (1948); *C. A.*, **43**, 2874a (1949).
4. P. K. Migal and V. G. Agas'eva, *Zhur. Obshchei Khim.*, **29**, 8 (1959); *C. A.*, **53**, 17725e (1959).
5. J. Cihalik, J. Simek, and J. Ruzicka, *Chem. Listy*, **51**, 1283, 1663 (1957); *C. A.*, **51**, 17528c (1957).
6. W. Kemula and A. Krzeminska, *Roczniki Chem.*, **28**, 125 (1954); *C. A.*, **48**, 9273 (1954).
7. I. Bergman and J. C. James, *Trans. Faraday Soc.*, **48**, 956 (1952); for a comparison of the advantages of various nonaqueous solvents see also, A. P. Toropov and A. M. Yakubov, *Zhur. Fiz. Khim.*, **30**, 1702 (1956); *C. A.*, **51**, 7193e (1957).
8. T. Isshiki and K. Tada, *Pharm. Bull.*, **2**, 266, 272 (1954); K. Tada, *ibid.*, **2**, 270 (1954); L. Starka and A. Vystricil, *Chem. Listy*, **51**, 1449 (1957); *C. A.*, **51**, 17528i (1957).
9. K. J. P. Orton and A. E. Bradfield, *J. Chem. Soc.*, **125**, 960 (1924); *ibid.*, **1927**, 983.
10. J. B. Garner, B. Saxon, and H. O. Parker, *Am. Chem. J.*, **46**, 236 (1911).
11. O. W. Kolling and J. L. Lambert, *Inorg. Chem. (A.C.S.)*, **3**, 202 (1964).
12. P. Arthur, *et al.*, *Anal. Chem.*, **33**, 488 (1961); P. Arthur and R. H. Vanderham, *ibid.*, **33**, 765 (1961).
13. International Critical Tables, **3**, 123 (1928).
14. I. M. Kolthoff and J. J. Lingane, "Polarography," Vol. I, pp. 78-86, Interscience Publishers, New York (1952).
15. I. V. Nelson and R. T. Iwamoto, *Anal. Chem.*, **33**, 1795 (1961).
16. F. J. Garrick, *Phil. Mag.*, **9**, 131 (1930); *ibid.*, **10**, 71, 76 (1930); *ibid.*, **11**, 741 (1931); *ibid.*, **14**, 914 (1932).
17. M. Born, *Z. Physik*, **1**, 45 (1920).
18. J. O'M. Bockris, M. A. V. Devanathan, and K. Müller, *Roy. Soc. Proc.*, **A-274**, 55 (1963).
19. (*a*) P. J. Proll, L. H. Sutcliffe. and J. Walkley, *J. Phys. Chem.*, **65**, 455 (1961); (*b*) for additional data on dissociation constants in this medium see: M. M. Jones and E. Grunwold, *J. Am. Chem. Soc.*, **76**, 3247 (1954), and ref. (11). Cf. A. J. Davidson, *Chem. Rev.*, **8**, 175 (1931).
20. See ref. 2-5 cited in (4).
21. (a) R. M. Fuoss, *Proc. Nat'l. Acad. Sci.*, **45**, 807 (1959); (b) C. Treiner and R. M. Fuoss, *Z. Phys. Chem.*, **228**, 343 (1965).
22. W. B. Schaap, *J. Am. Chem. Soc.*, **82**, 1837 (1960).
23. W. B. Schaap and P. S. McKinney, *Anal. Chem.*, **36**, 29, 1251 (1964); cf. I. M. Kolthoff *et al.*, *J. Electroanal. Chem.*, **3**, 209 (1962).
24. "Stability Constants Part I: Organic Ligands," G. Schwarzenbach and L. G. Sillen, Editors, The Chemical Society, London (1957).

Raman Spectra of Molten Mixtures of Zinc Halides with Alkali Metal Halides

R. B. Ellis

Southern Research Institute, Birmingham, Alabama

ABSTRACT

Raman spectra of molten compositions in the $ZnCl_2$-MCl (M = Li, K, Rb, or Cs) systems contain strong, polarized bands at 230, 275, 290, and 305 cm^{-1} and weak bands, probably polarized, at ~260 and 345 cm^{-1}. The strong bands have essentially the same frequencies as those appearing in solutions in water and organic solvents. The variations in relative intensity of the bands in the melts with temperature and composition are consistent with assigning them to the same species identified in aqueous solutions, namely, 230 cm^{-1}, a $(ZnCl_2)_n$ polymer; 275 cm^{-1}, $ZnCl_4^{2-}$; 290 cm^{-1}, $ZnCl_3^-$; 305 cm^{-1}, $ZnCl_2$ monomer. The weak 345 cm^{-1} band is tentatively assigned to the $ZnCl^+$ ion. The weak 260 cm^{-1} band is assumed to be associated with an unstable species containing at least one Zn-Cl-Zn bond. In $ZnBr_2$-KBr melts the principal species are $(ZnBr_2)_n$ polymer, $ZnBr_4^{2-}$, and $ZnBr_3^-$. The $ZnBr_2$ and $ZnBr^+$ species are much less stable relative to the corresponding chloride species.

The structure of molten zinc halides is of considerable interest because the physical properties of these salts indicate occurrence of extensive molecular association at temperatures near the melting point. Primarily on the basis of a marked decrease in electrical conductivity and increase in viscosity, Mackenzie and Murphy (1) proposed a network structure of $ZnCl_2$ at the melting point that gradually degrades with rising temperature into Zn^{2+} and $ZnCl_6^{4-}$ ions. They were influenced in their assumption of the hexachlorozincate ion by the C-19 ($CdCl_2$) layer structure assigned to solid $ZnCl_2$ by Bruni and Ferrari (2). In light of the four-coordinate structure for crystalline $ZnCl_2$ recently described by Brehler (3) and their own

Table I. Raman spectra of zinc halide solutions

Assumed species	Observed wave numbers for the symmetrical stretching vibration, cm^{-1}				
	Delwaulle (8)	Kecki (9)	Morris (10)	Irish (11, 12)	Yellin and Plane (13)
$Zn(H_2O)_6^{2+}$				390	
$ZnCl^+$				305	
$ZnCl_2$	305	304	305	305	
$ZnCl_3^-$			286		
$ZnCl_4^{2-}$	282	282	275	278	
$ZnCl_n^{2-n}$				266	
$(ZnCl_2)_n$				230	
$ZnBr^+$					205
$ZnBr_2$	208		206		
$ZnBr_3^-$	184		182		
$ZnBr_4^{2-}$	172		172		172

experimental work on ultrasonic absorption, Gruber and Litovitz (4) suggest that, close to the melting point, the liquid consists of chains of ZnCl tetrahedra sharing corners and that these chains dissociate into Zn^{2+} and $ZnCl_4^{2-}$ ions.

There is evidence from several other lines of investigation for the existence of zinc-halogen complexes, usually assumed to be $ZnCl_3^-$ or $ZnCl_4^{2-}$. Moss (5) calculated the activities of KCl and $ZnCl_2$ in molten mixtures from measurements of vapor pressure and vapor composition, and Lantratov and Alabyshev (6) obtained similar information from electromotive force measurements on galvanic cells. The results of both investigations were consistent with the assumption of $ZnCl_3^-$ or $ZnCl_4^{2-}$, but the identity of the species could not be clearly established. Van Artsdalen (7), using a cryoscopic technique, found that the important species in dilute solutions of $ZnCl_2$ in molten $NaNO_3$ were Zn^{2+}, $ZnCl_2$, and $ZnCl_4^{2-}$.

It is expected that vibrational spectra should be more helpful in identifying the species present than other physicochemical properties. The species present in solutions of zinc chloride and zinc bromide in water and organic solvents, at various levels of total zinc concentration and of zinc-halogen ratio, have been identified and the observed Raman spectra have been correlated with them (8-13). The results are summarized in Table I, indicating excellent agreement among the several investigators. The assignments of the 205 and 186 cm^{-1} bands for zinc bromide species given by Morris, Short, and Waters (10) and by Delwaulle (8) appear preferable to those by Yellin and Plane (13). Especially pertinent to the present problem is Irish and Young's investigation (12) of the transition from highly concentrated aqueous solutions to anhydrous melts, in which two bands, 230 and 266 cm^{-1}, increase in intensity as water is removed from the system. The published data on the Raman and infrared spectra of melts containing $ZnCl_2$ are tabulated in Table II. Bues (14) assigned the 233 cm^{-1} band to a polymeric species, $(ZnCl_2)_n$, the 280 cm^{-1} band to $ZnCl_4^{2-}$, and the 292 cm^{-1} band to $ZnCl_3^-$. Bredig and Van Artsdalen (18) have argued that Bues' data do not justify the assumption of two complex ions and favor the $ZnCl_4^{2-}$ species. It should be noted that the work of Morris, Short, and Waters, that of Irish and Young, and that of Moyer, Evans, and Lo had not been done at that time. In the more recent work of Irish and Young and of Moyer, Evans, and Lo, the species are identified as a polymer, a $ZnCl_2$ monomer, and a $ZnCl_4^{2-}$ ion. On the other hand, Wilmshurst considers his infrared spectra to arise from lattice-type interactions among simple ions rather than from true complexes. This conclusion was based primarily on the variations in wave number and intensity with change in composition.

Table II. Literature data on Raman and infrared spectra* for molten compositions containing zinc halides

Author	Composition	Temperature range, °C	Wave numbers, cm^{-1}
Bues (14)	$ZnCl_2$	350-600	233
	$2ZnCl_2 \cdot KCl$	280	233, 292
	$ZnCl_2 \cdot KCl$	250-500	85, 292
	$ZnCl_2 \cdot 2KCl$	450-550	92, 280
	$ZnCl_2 \cdot 4KCl$	650	92, 280
Salstrom and Harris (15)	$ZnCl_2$	400-500	100, 231, 285
	$ZnBr_2$	440	79, 155
Irish and Young (12)	$ZnCl_2$	340-470	95, 110, 230, 266, 305, 375-400
Moyer (16)	$ZnCl_2$	280-500	75, 226, 250, 305, 360
	$4ZnCl_2 \cdot KCl$		80, 266, 288, 349
	$2ZnCl_2 \cdot KCl$		75, 226, 290, 344
	$ZnCl_2 \cdot KCl$		80, 125, 218, 292
	$2ZnCl_2 \cdot 3KCl$		70, 120, 293
	$ZnCl_2 \cdot 2KCl$		75, 124, 283
Wilmshurst (17)	$ZnCl_2$	280	285
	$3ZnCl_2 \cdot KCl$	398	275, 335
	$2ZnCl_2 \cdot KCl$	438	270, 330
	$ZnCl_2 \cdot KCl$	260	265, 317
	$ZnCl_2 \cdot 2KCl$	473	290
	$ZnCl_2 \cdot 3KCl$	638	285
	KCl	830	220
	$3ZnCl_2 \cdot LiCl$	357	283, 313
	$2ZnCl_2 \cdot LiCl$	385	292, 315
	$ZnCl_2 \cdot LiCl$	420	295, 320
	$ZnCl_2 \cdot 2LiCl$	490	320
	$ZnCl_2 \cdot 3LiCl$	593	330
	$LiCl$	695	350

* The spectra of Wilmshurst are IR, the rest are Raman.

The only data on molten $ZnBr_2$ are the two bands found by Salstrom and Harris (15) at one temperature, which do not agree with those for aqueous solutions.

In order to learn more about the species existing in molten systems containing zinc chloride and alkali metal chlorides and to compare them with corresponding bromide systems, we have made an extensive study of the Raman spectra of these systems.

Experimental

Materials.—Reagent grade $ZnCl_2$, containing about 5% H_2O, was dried by heating under vacuum to the melting point over a period of about 4 hr. Dry HCl gas was then bubbled through the melt for about 4 hr, followed by carefully dried argon for 1 hr or longer. This operation was carried out in a reservoir sealed to the Raman tube with an intervening sintered glass filter of medium porosity. After the drying operation, the melt was transferred through the filter into the Raman tube, which was then sealed off under vacuum. Zinc bromide was treated in the same way, using HBr to counteract hydrolysis. Mixtures were prepared by combining appropriate amounts of the desired zinc halide and alkali metal halide in the oven-dried state and following the same drying procedure.

Apparatus.—The Raman spectra were recorded with a Hilger E612 spectrograph, using the f/5.7 camera and Eastman 103a-J plates. The Hilger-FL1 mercury-lamp source unit was replaced with one of essentially identical design except that the lamps were centered on a 3-in. radius instead of 2 in., in order to have ample space for the sample heater, which was made according to Corbett's (19) design. For estimating depolarization ratios of the Raman lines, a Wollaston prism was inserted into the light path between the source unit and the spectrograph, as suggested by Bender and Lyons (20). The positions of the spectral lines were measured on recording densitometer traces, using the graphical technique of resolving overlapping bands described by Irish and Young (12, 13). Iron and mercury spectra were used for calibration. The 4358Å line of mercury was used as the exciting radiation.

Results

Raman spectra have been obtained on $ZnCl_2$ and its mixtures with LiCl, KCl, RbCl, and CsCl and on $ZnBr_2$ and its mixtures with KBr, in the molten state.

Table III. Raman spectra of molten zinc chloride-alkali metal chloride systems

Composition mole % $ZnCl_2$	Wave numbers[a], cm^{-1}								
				$ZnCl_2$-KCl system					
100	80w, d	90w, d		227s, p	270w, p			310w, p	350vw
90	82w, d	106w, d		230s, p	262w, p			300w, p	340w, p
86		95w, d		232s, p	260w			304w, p	350w, d
80	80w, d	106w, d		230m, p	260vw			304w, p	340w
75	80w, d	106w, d		230m, p				304m, p	350w
67		95w, d		235w, p			290s, p	304w	
50	80w, d	95w, d		230vw			290s, p	310vw	350vw
25				230vvw		270s, p	290[b]		360vvw
				$ZnCl_2$-LiCl system					
50	76w, d	105w		230vw			290s, p		
				$ZnCl_2$-RbCl system					
50	90w, d		115w, d	237w, p				303s, p	345w
33	90w						284s, p		
25			115w			280s, p			
				$ZnCl_2$-CsCl system					
50	95w			230w			290s, p (<700°)	305w, p (>700°)	
25			116w			276s, p			

w, weak; m, medium; s, strong; d, depolarized; p, polarized.
[a] Wave numbers are averages of 10 or more observations with a maximum range of ±5 cm^{-1}.
[b] The 290 cm^{-1} band appears only on the anti-Stokes side.

Tables III and IV contain the average wave numbers for chloride and bromide compositions, respectively, along with an indication of the relative intensity and polarization state where determined. No Raman bands were found in molten, pure RbCl. There were no systematic variations in wave number with temperature, although there were some variations in intensity for some of the bands. The reported wave numbers are the averages of values obtained from ten or more recorded spectra for each composition, and each value has a range of ±5 cm^{-1} or less. Since they are close to the parent line, the bands between 50 and 106 cm^{-1} appear as weak shoulders on a steep background curve. In some spectra the background was so dark that these bands were not detected. In others, the presence of a band was recognizable, but the center could not be located accurately. For this reason, the number of bands in the range from 90 to 105 cm^{-1} in the $ZnCl_2$-KCl system cannot be definitely stated. However, the 115 cm^{-1} band in the $ZnCl_2$-RbCl and $ZnCl_2$-CsCl systems is definitely different from the 90-105 cm^{-1} band. In the $ZnBr_2$-KBr system there is clearly a single band at 79-82 cm^{-1}, but the bands in the 50-70 cm^{-1} range cannot be clearly resolved.

In pure $ZnCl_2$, the ratio of the intensities of the 230 cm^{-1} band to that of the 305 cm^{-1} band is about 10:1 at 295° and about 5:2 at 600°. At the $80ZnCl_2$-$20KCl$ composition, the ratio of intensities for these two bands is about 4:1 at 300°, but 1:2 at 625°. At both of these compositions, the intensity of the 260 cm^{-1} band decreases with increasing temperature, while that of the 345 cm^{-1} band increases. The intensity of the 230 cm^{-1} band decreases with increasing percentage of added alkali chloride until it is very weak at 50 mole % $ZnCl_2$ and only traces appear at lower $ZnCl_2$ contents. In the $25ZnCl_2$-$75KCl$ mixture, the 290 cm^{-1} band appears on the anti-Stokes side but not on the Stokes side. In the $50ZnCl_2$-$50LiCl$ mixture the 280 cm^{-1} band appears in some spectra and the 290 cm^{-1} in others, but they have not been observed together.

In the $ZnBr_2$-KBr system, the 150 cm^{-1} band predominates in pure $ZnBr_2$, with its intensity decreasing with increasing temperature and with increasing KBr concentration. The 170 cm^{-1} band is weak in pure $ZnBr_2$ at the lower temperatures. Its intensity increases with addition of KBr. At 50 mole % $ZnBr_2$ it predominates at 270°, but becomes progressively weaker as the temperature increases. However, at 25 mole % $ZnBr_2$ it is strong at 600°. The 180 cm^{-1} band is weak or absent at the lower temperatures at each composition, increases with rising temperature, and

Table IV. Raman spectra of the molten zinc bromide-potassium bromide system

Composition mole % $ZnBr_2$	Temperature, °C	Wave numbers,[a] cm^{-1}								
100	425	60w, d		80w, d	150s, p	170w, p				
	540	60w	70w	80w	150s, p	170m, p	180m, p		225w, d	
93	430	60w, d		80w	150s, p	170w, p	180w, p			
80	400	60w, d	70w, d		150s, p		180m, p		225w, d	260w, d
	470	60w				170[b]		200w		
	550				155m, p		180m, p		225w, d	260w, d
50	270	60w	70w	80w, d	155w	170s, p	180vw		225w	
	400			80w		170w	180m, p			
	480			80w		170w	180s, p		225vw	
	585			80w, d			180s, p		225w, d	265vw
34	460	60w		80w	155w, p	170s, p			210w, d	
25	600	60w		80w		170s, p	180w		226vw	

w, weak; m, medium; s, strong; d, depolarized; p, polarized.
[a] Wave numbers are averages of 10 or more observations with a maximum range of ±5 cm^{-1}.
[b] Strong band that cannot be resolved, broad enough to include 150 and 180 cm^{-1}.

becomes predominant at 50 mole % $ZnBr_2$ above 400°. It is weak at 600° at the 25 mole % $ZnBr_2$ composition. The 225 cm^{-1} and 265 cm^{-1} bands are weak at all compositions, having their greatest strength in the range of 50-80 mole % $ZnBr_2$.

Discussion

Zinc chloride systems.—Possible chemical species and the corresponding numbers of fundamental vibrations are summarized as follows:

Fundamental Vibrations

Chemical species	Point group	Total No.	IR active	Raman active	Raman polarized
Zn^{++}	—	—	—	—	—
$ZnCl^+$	$C_{\infty v}$	1	1	1	1
$ZnCl_2$ linear	$D_{\infty h}$	3	2	1	1
$ZnCl_2$ bent	C_{2v}	3	3	3	2
$ZnCl_3^-$ planar	D_{3h}	4	3	3	1
$ZnCl_3^-$ pyramidal	C_{3v}	4	4	4	2
$ZnCl_4^{2-}$ tetrahedral	T_d	4	2	4	1
$ZnCl_6^{4-}$ octahedral	O_h	6	2	3	1

In addition to these mononuclear species, there may conceivably be a variety of polynuclear species. For instance, phase diagrams for the $ZnCl_2$-KCl (21), $ZnCl_2$-TlCl (22), and $ZnCl_2$-NH_4Cl (23) systems show compounds of the type $2ZnCl_2$-MCl, but a binuclear $Zn_2Cl_5^-$ complex has not been proposed as a constituent of aqueous solutions or of melts. However, a polymer made up of $ZnCl_4$ tetrahedra linked by sharing corners has been proposed (4, 12).

The observed Raman bands may be separated into two groups, weak, depolarized bands between 80 and 115 cm^{-1} and polarized bands above 200 cm^{-1}. The first group has wave numbers of a magnitude expected for bending vibrations. Since it was impossible to determine the exact number of bands, they cannot be used as a basis for inferences concerning the species they represent. However, they are consistent with the inferences based on consideration of the other bands. The second group contains polarized bands at approximately 230, 260, 275, 290, and 305 cm^{-1} and one at 345 cm^{-1} for which the state of polarization is in doubt. Since polarized bands arise from totally symmetric vibrations and since stretching vibrations have higher frequencies than bending vibrations, these bands must represent symmetric stretching vibrations. In the above list of fundamental vibrations for the several possible chemical species, there is only one totally symmetric stretching vibration for each species. Therefore, each of the polarized Raman bands must represent a different chemical entity. The almost exact agreement between the wave numbers of the bands appearing in aqueous solutions and those in the melts implies that the same Zn-Cl species exist in both systems.

Brehler (3) has described the structure of crystalline $ZnCl_2$ in terms of $ZnCl_4$ tetrahedra linked by sharing corners. Gruber and Litovitz (4) and Irish and Young (12) have suggested that much of this structure persists in the melt as "polynuclear aggregates" or "polymers." Figure 1 illustrates a portion of this structure. The circles represent chlorine atoms lying in the plane of the paper. Triangles represent zinc atoms, those with apices pointing up lie above the plane of the paper at a distance of +1/3 of *d* and have Cl atoms above them at distance *d* above the plane of the paper. Triangles with apices pointing down lie below the plane of the paper, at —1/3 of *d*, and have Cl atoms below them in the next lower Cl plane. Circles marked with an X lie in the plane of the paper and have Zn atoms above and below them at ±2/3 of *d*. Lines of Cl atoms such as those marked A-A lie in Cl planes tilted 60° to the plane of the paper. Thus, each Zn atom is tetrahedrally coordinated to four Cl atoms and each Cl atom has two Zn neighbors. The array may be formed by fitting together

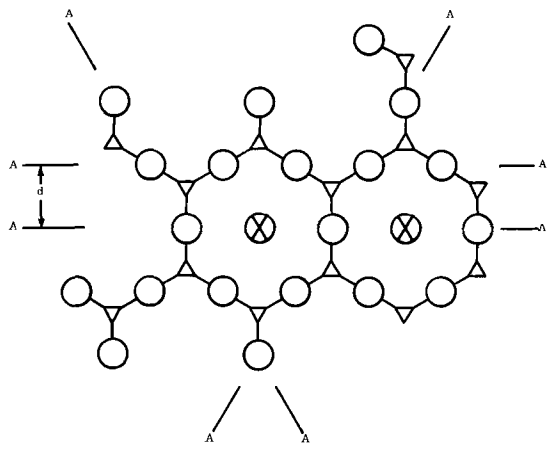

Fig. 1. Structure of crystalline $ZnCl_2$: △ Zn 1/3 of *d* above plane of paper; ▽ Zn 1/3*d* below plane of paper; ○ chlorine.

$ZnCl_2$ molecules, with the four bonds to the Zn atoms becoming equivalent by sp^3 hybridization.

These polynuclear aggregates will have a totally symmetric "breathing" vibration that will give rise to a strong, polarized Raman band. This band has been observed at 230 cm^{-1} in the $ZnCl_2$ crystal, in melts, and in very concentrated aqueous solutions, as given in Table II. There will also be peripheral groups that will vibrate independently of the fully coordinated body of the aggregate. These groups will include $ZnCl_4^{2-}$, $ZnCl_3^-$, and $ZnCl_2$ groups attached through a chlorine. A $ZnCl_4^{2-}$ group will probably be only slightly distorted from the normal tetrahedral symmetry by its attachment, so that the frequency of its symmetrical breathing vibration will not be much different from that of a completely separated $ZnCl_4^{2-}$ ion. Considered as fragments of a tetrahedral structure, a $ZnCl_3^-$ group would be pyramidal and a $ZnCl_2$ would be bent. However, Cl-Cl repulsion would tend to make these structures planar and linear, respectively. In either case, attachment to the aggregate will not change the group frequency greatly.

Just above the melting point, the aggregates will be large, and the number of small groups, both peripheral and free, will be relatively small. Increasing temperature will break the aggregates into smaller units, each of which will still have the characteristic breathing vibration so that the associated Raman band will not change much in intensity until the dissociation is essentially complete. However, the intensities of the bands representing the smaller units should increase. The presence of excess chloride ion from an added alkali metal halide would promote splitting off of peripheral groups and, hence, reduction of the aggregates.

The Raman spectrum of pure molten $ZnCl_2$ is dominated by the strong 230 cm^{-1} band characteristic of the polynuclear aggregate. A band at 305 cm^{-1} is weak at low temperatures and becomes stronger with increasing temperature so that it must be associated with a fragment. Since in aqueous solutions a 305 cm^{-1} band has been assigned to the $ZnCl_2$ molecule and since this unit is one of the most likely peripheral groups or fragments in the melt, it is reasonable to assign the 305 cm^{-1} band to the $ZnCl_2$ molecule in the melt also. There is a still weaker band in the 250-270 cm^{-1} range; Moyer, Evans, and Lo found it at 250 cm^{-1}, Irish and Young at 266 cm^{-1}, and this work at 260-270 cm^{-1}. The intensity of this band decreases with increasing temperature, and so it cannot be associated with a fragment that increases in concentration with temperature, such as $ZnCl_4^{2-}$ or $ZnCl_3^-$. Irish and Young assign it to a fragment that is thermally unstable. If it were associated with the aggregate, it would probably represent an unsymmetric stretching vibration, but our observations indicate that

it is polarized, which means that it arises from a symmetric vibration. The fragment may be a ring of six $ZnCl_4$ tetrahedra or a group containing only one Zn-Cl-Zn linkage. The observation that it is also unstable toward excess Cl^- ion is further evidence against the $ZnCl_4^{2-}$ or $ZnCl_3^-$ groups, but in favor of a species containing at least one Zn-Cl-Zn link. We observed a very weak band at 350 cm^{-1} in pure $ZnCl_2$. Because of its weakness we were unable to establish its state of polarization. However Moyer, Evans, and Lo claim that it is polarized. If the band is polarized, it must belong to a ZnCl vibration of higher energy than that in $ZnCl_2$. The only likely species of this description is the $ZnCl^+$ ion. This assignment is consistent with the behavior on addition of excess Cl^- ion observed by Moyer, Evans, and Lo and by us; namely, that it increased in intensity somewhat in the composition range around 25 mole % added chloride, then decreased until it disappeared at compositions containing more than 50 mole % alkali metal chloride.

At compositions containing 33 mole % alkali metal chloride or more, a band appears at 290 cm^{-1} and, at still higher concentrations of added chloride, another at about 275 cm^{-1}. These bands are definitely different from the 305 cm^{-1} band assigned to $ZnCl_2$ molecules. Since they are associated with successively higher ratios of Cl to Zn, it is assumed that they represent species containing more than two chlorines per zinc, namely, $ZnCl_3^-$ and $ZnCl_4^{2-}$. In Table I, the wave numbers 286 cm^{-1} and 275-280 cm^{-1} are assigned to $ZnCl_3^-$ and $ZnCl_4^{2-}$, respectively, in aqueous solutions. The appearance of the same bands in the aqueous and molten systems implies that the same species are present. However, in aqueous solution, the positions in the coordination sphere of the zinc atom not occupied by chlorine atoms can be filled with water molecules. In the melt the only ligand available is the chloride ion, so that the $ZnCl_3^-$ species, with its incomplete coordination sphere, appears unlikely. Moyer, Evans, and Lo found only one Raman band at 290 cm^{-1}. Bues recorded two bands, 292 cm^{-1} and 280 cm^{-1}, but not at the same composition, and Bredig and Van Artsdalen argue that they were probably the same band. This work confirms Bues' observations of 290 cm^{-1} at the $ZnCl_2$-KCl composition and 280 cm^{-1} at $ZnCl_2 \cdot 3KCl$. The shapes of the bands and the precision of locating their centers indicate the presence of two different bands even though the two have not been observed together in the same spectrum. Therefore, we conclude that both $ZnCl_3^-$ and $ZnCl_4^{2-}$ do exist in melts.

Cation effect.—Two effects of the size of the alkali metal cation might be expected. The presence of the cation might distort the symmetry of the vibrating species and change the frequency somewhat. Janz and James (24) reported this effect on the nitrate ion in melts. We did not find any systematic change in frequency with changing cation for any of the bands. Since we are concerned here with equilibria among several chemical species of different degrees of complexity, a change in cation might affect the equilibria to shift the relative concentrations of the species involved. The high polarizing power of the smaller cations might have a disruptive effect on the more highly complexed species. This effect is observed to a minor extent on the un-ionized species, namely, the $(ZnCl_2)_n$ polymer and $ZnCl_2$ monomer. At the equimolar composition, the relative intensities of the 230 and 305 cm^{-1} bands are somewhat greater for Cs and Rb than for K and Li. No consistent trend is observed for the 280, 290, and 350 cm^{-1} bands.

Zinc bromide system.—The Raman spectra of compositions in the $ZnBr_2$-KBr system show many of the same characteristics of those in the chloride system. There is a group of weak, depolarized bands below 100 cm^{-1} that are presumably related to bending vibrations. There are several strong, polarized bands in the 100-200 cm^{-1} region that are typical of symmetric stretching vibrations and thus represent several chemical species. The spectrum of pure $ZnBr_2$ is dominated by a strong band at 150 cm^{-1}. This band was reported by Salstrom and Harris (15) for a melt, but does not appear in aqueous solutions (of 1M concentration) (10). This band is unstable with respect to increasing temperature and increasing Br^- ion concentration. By analogy with $ZnCl_2$, this band may be assigned to a polymeric complex, $(ZnBr_2)_n$. At higher temperatures and with added Br^- ion, new bands appear at 170 and 180 cm^{-1}, which are identical with the bands assigned to $ZnBr_4^{2-}$ and $ZnBr_3^-$, respectively, in aqueous solutions. Consistent with this assignment, the species associated with the 170 cm^{-1} band increases in stability with increasing Br^-:Zn ratio, but tends to be less stable at higher temperatures than the species represented by the 180 cm^{-1} band. Yellin and Plane (13) assigned the 180 cm^{-1} band in aqueous solution to $ZnBr_2$ instead of $ZnBr_3^-$. In view of the persistence of this band to high concentrations of excess Br^- ion, the $ZnBr_3^-$ assignment seems preferable. A weak 200 cm^{-1} band at 80 $ZnBr_2$-20KBr probably corresponds to the $ZnBr_2$ monomer.

The weak, depolarized bands at 225 and 260 cm^{-1} are assumed to arise from asymmetric stretching vibrations of the $ZnBr_4^{2-}$ and $ZnBr_3^-$ complexes.

Acknowledgment

The experimental work was performed by Mr. A. C. Freeman, Associate Chemist. The very valuable discussions and assistance in interpretation of the spectra of Dr. W. C. Coburn, Jr., is gratefully acknowledged. This work was supported by the U. S. Atomic Energy Commission under Contract No. AT-(40-1)-2073.

Manuscript received Dec. 20, 1965. This paper was presented at the San Francisco Meeting, May 9-13, 1965.

Any discussion of this paper will appear in a Discussion Section to be published in the December 1966 JOURNAL.

REFERENCES

1. J. D. Mackenzie and W. K. Murphy, *J. Chem. Phys.*, **33**, 366 (1960).
2. G. Bruni and A. Ferrari, *Rend. Accad. Nazl. Lincei*, **4**, 10 (1926).
3. B. Brehler, *Z. Krist.*, **115**, 375 (1961).
4. G. J. Gruber and T. A. Litovitz, *J. Chem. Phys.*, **40**, 13 (1964).
5. H. I. Moss, "Vapor Pressures, Vapor Compositions, and Derived Thermodynamic Information of the KCl-$CdCl_2$ and KCl-$ZnCl_2$ Molten Salt Systems," Thesis, Indiana University, Bloomington, 1960; University Microfilms, Inc., Ann Arbor, Michigan, Mic 60-6310.
6. M. F. Lantratov and A. F. Alabyshev, *J. Appl. Chem. USSR*, **27**, 685 (1954).
7. E. R. Van Artsdalen, *J. Phys. Chem.*, **60**, 172 (1956).
8. M. L. Delwaulle, *Comp. rend.*, **240**, 2132 (1955); *Bull. Soc. Chim. France*, **1955**, 1294.
9. Z. Kecki and J. Mankowski, *Rozcnicki Chem.*, **36**, 375 (1962).
10. D. F. C. Morris, E. L. Short, and D. N. Waters, *J. Inorg. Nucl. Chem.*, **25**, 975 (1963).
11. D. E. Irish, P. McCarroll, and T. F. Young, *J. Chem. Phys.*, **39**, 3436 (1963).
12. D. E. Irish and T. F. Young, *J. Chem. Phys.*, **43**, 1765 (1965).
13. W. Yellin and R. A. Plane, *J. Am. Chem. Soc.*, **83**, 2448 (1961).
14. W. Bues, *Z. anorg. u. allgem. Chem.*, **279**, 104 (1955).
15. E. J. Salstrom and L. Harris, *J. Chem. Phys.*, **3**, 241 (1935).
16. J. R. Moyer, J. C. Evans, and G. Y-S. Lo, paper presented at the San Francisco Meeting of the Society, May 9-13, 1965, Extended Abstracts of Electrothermics and Metallurgy Division, **3** (1), 140 (1965).
17. J. K. Wilmshurst, *J. Chem. Phys.*, **39**, 1779 (1963).
18. M. A. Bredig and E. R. Van Artsdalen, *ibid.*, **24**, 478 (1956).
19. J. D. Corbett, in "Techniques of Inorganic Chem-

istry," H. B. Jonassen and A. Weissberger, vol. 1, Interscience Publishers. New York (1963); Also *idem., Inorg. Chem.*, **1**, 700 (1962).
20. P. Bender and P. A. Lyons, *J. Chem. Phys.*, **18**, 438 (1950).
21. I. N. Nikonowa, S. P. Pavlenko, and A. G. Bergman, *Bull. Acad. Sci. USSR, sev. Chim.*, **1941**, 391; Ya. A. Ugai and V. A. Shatillo, *Zh. Fiz. Khim*, **23**, 744 (1949). However, R. A. Fleming and F. R. Duke, *This Journal*, **104**, 251 (1957) did not find 2 $ZnCl_2 \cdot KCl$.
22. E. Korreng, *N. Jb. Min. Beil*, **37**, 94 (1914); I. P. Palyura and A. P. Palkin, *Zh. Neorg. Khim*, **4**, 2715 (1959).
23. K. Itachmeister, *Z. anorg. u. allgem. Chem.*, **109**, 145 (1919).
24. G. J. Janz and D. W. James, *J. Chem. Phys.*, **35**, 739 (1961).

Adsorption and Electrooxidation of Butane on Platinum Black in H_2SO_4

Joseph A. Shropshire and Hugh H. Horowitz

Process Research Division, Esso Research and Engineering Company, Linden, New Jersey

ABSTRACT

Rates of butane adsorption on platinum black in sulfuric acid have been measured at 95°C using voltammetry in a flow-through electrode system. Initial adsorption rates showed a strong dependence on potential in the range 100-300 mv *vs.* the reversible hydrogen electrode. This effect was shown to arise from blockage of butane adsorption sites by adsorbed hydrogen atoms. The data strongly indicate that butane adsorbs only on Type II (most anodic) H· sites.

Although a significant research effort has been devoted in recent years to the determination of the mechanism of electrooxidation of saturate hydrocarbon fuels, particularly those potentially useful in fuel cell systems, no clear picture of the rate limiting steps involved in such an oxidation is as yet available (1-7). While it is generally conceded that the adsorption or adsorption-cracking of saturate fuels on noble metal catalysts of the type generally used can constitute a significantly slow step in the over-all reaction, and has been suggested as the factor determining limiting current in some cases (5-7), no meaningful measurements of adsorption rates on practical catalysts, free of solubility and diffusion effects, have been made.

Progress has been restricted by the fact that useful fuel cell electrocatalysts are prepared as chemically precipitated high surface powders or highly dispersed on conductive substrates. Catalyst materials of this type may be fabricated into porous electrodes which avoid diffusion limits because they are covered by very thin electrolyte films. However, such electrodes are not well suited to the fast electrochemical transient techniques such as high speed voltammetry and high current chronopotentiometry (8, 9). Smooth microelectrodes, which are suitable for fast techniques, are operated under electrolyte, where they would be subject to diffusion limitations with sparingly soluble hydrocarbon fuels.

Another possible drawback of smooth electrodes is that they may be chemically different from high surface area electrodes, perhaps having different crystal planes exposed and different types of lattice defects. Smooth platinum electrodes consistently appear to oxidize hydrocarbons at more anodic potentials than platinum black. By the same token, adsorption studies from the gas phase on dry catalyst leave open the question of the effect of large quantities of water and other components adsorbable in the aqueous solutions to be used in actual practice and effect of electrode potential on the processes.

This paper describes the results of a study of the adsorption of butane on a commercially available high surface platinum black (Engelhard) in H_2SO_4. In addition to electrochemical measurements of the equilibrium butane adsorption on this catalyst, voltammetric measurements on the catalyst in a rapidly moving stream of butane-saturated electrolyte have been used to determine maximum adsorption rates at low polarization. The flowing electrolyte technique, used previously in studies on highly soluble fuels and oxidants (10), appears to overcome the objections discussed previously and thus sheds considerable light on the over-all question of hydrocarbon adsorption-reaction.

Experimental Technique and Equipment

Two types of electrode were used in this study. In experiments involving measurement of the equilibrium adsorption of butane and its desorption with potential, the (Engelhard) platinum black in 10:1 mixture with Teflon 41BX (du Pont) was pressed on simple platinum flag electrodes.

The apparatus used to obtain measurements on butane adsorption rates in the flowing electrolyte system is shown in Fig. 1. The platinum black powder, generally 10 mg/cm^2 (on a total of 3.8 cm^2) was held at the upper face of an 18 mil porous tantalum sheet (courtesy of Kennametal) by the downward flow of electrolyte. Maximum flow rates obtainable with a 6-in. electrolyte head at 95°C were of the order of 70-80 cc/min (~20 cm/min) with lower values regulated by a stopcock on the exit line at the bottom. The two-liter flask containing 3.7M H_2SO_4 at 95°C was stirred briskly by a stream of Instrument Grade butane. Make-up electrolyte was added as necessary from addition bottle "N" at as near to the equilibrium conditions in the flask as was possible. Electrical connections were made to the tantalum plate via a gold current collector, a platinum auxilliary electrode in the flask, and a saturated calomel electrode with Luggin capillary tip about ¼ in. above the surface of the porous tantalum plate. The Luggin capillary itself was filled with 3.7M H_2SO_4 and changed frequently to prevent chloride contamination of the electrolyte. As a result of the minimum time actually required in measurement and the high butane sparge rates, no effect of the slight amount of hydrogen or oxygen evolved at the counter electrode was ever noticed.

Prior to the individual runs, the piece of porous tantalum plate to be used was abraded lightly on its upper surface with a steel wire brush and cleaned with a once-through application of aqueous HF to remove any oxide film and subsequently rinsed with deionized water at room temperature.

Potentiostatted triangular or sawtooth voltage signals could be applied to the electrode from a modified

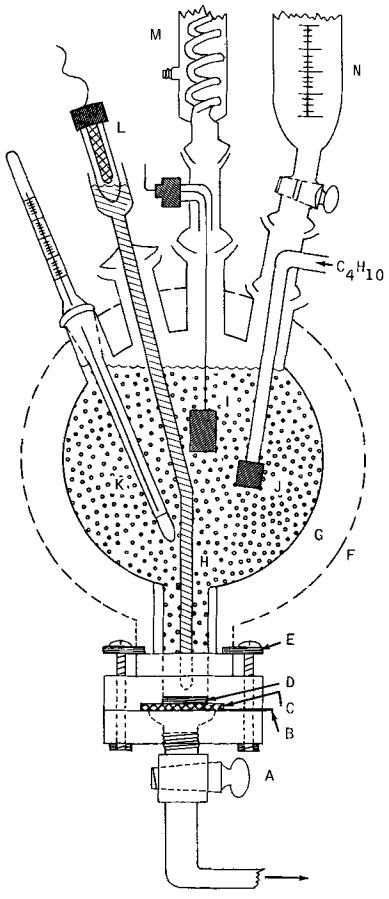

Fig. 1. Equipment for flowing electrolyte measurements: A, Teflon stopcock; B, gold current collector; C, porous tantalum plate; D, powdered platinum black; E, clamp; F, insulation over tape heaters; G, 2-liter flask; H, Luggin capillary; I, counter electrode; J, butane sparger; K, thermometer with Therm-o-watch relay; L, saturated calomel electrode; M, condenser; N, make-up addition bottle.

Anotrol Model 4100 Research Controller fed by the output of a Servomex LF 51 function generator. Resultant I-V (or t) functions were recorded on a Moseley Model 135 X-Y plotter and coulombic quantities obtained by integration of the desired peaks using a planimeter. For the scan speeds used with these active platinum catalysts all the adsorbed fuel was oxidized from the electrode, and the current equalled the blank values by the time the positive voltage limit of the scan was reached. No remaining fuel was detected in repeat scans on the electrode under quiescent conditions. (Due to the irreversibility of hydrocarbon fuel oxidation, high speed voltammetry and high current chronopotentiometry generally do not fulfill this condition until considerably more positive voltage levels are reached.) Fractional coverages referred to in this paper are derived from measured coulombic values referred to saturation or maximum levels. Thus, for want of precise measurements of true surface area, all coverages refer to the electrochemically active surface.

All solutions were prepared using reagent grade concentrated H_2SO_4 and deionized water of conductivity less than 10^{-6} mho/cm. Previous experiments have shown that further purification of the acid solution by preelectrolysis does not affect the adsorption results. In the measurement times involved trace impurities would not be expected to affect these high area catalysts significantly. Potentials are reported *vs.* the saturated calomel electrode (S.C.E.) the measured voltage of which, as a result of liquid junction and thermal potentials, is 0.138v *vs.* a hydrogen electrode in these acid solutions at 95°C.

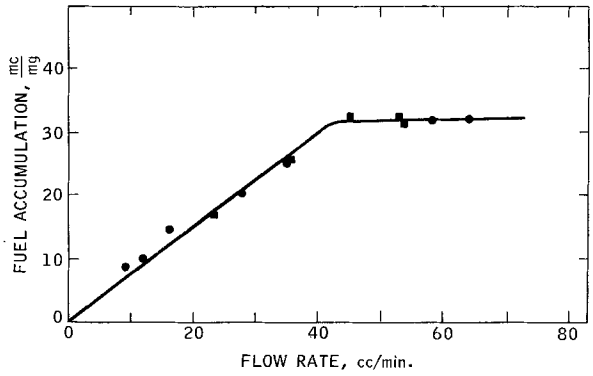

Fig. 2. Relative rate of butane accumulation as a function of flow rate. Continuous voltage scan 0-1.1v *vs.* S.C.E., 22 mv/sec, 3.7M H_2SO_4, butane saturated, 95°C; •, 10 mg Pt/cm^2; ■, 25 mg Pt/cm^2.

Experimental Results and Discussion

Applicability of the flow system concept.—In order to determine the feasibility of determining adsorption rates in a flowing fuel-saturated electrolyte system, a series of screening experiments were carried out to define the response of the system to electrolyte flow rate and catalyst loading changes. For this purpose the quantity of coulombs in the butane oxidation peak during a continuous triangular voltage scan from 0.0 to 1.1v *vs.* S.C.E. at 22 mv/sec was taken as a relative measure of the fuel accumulation rate (6, 11). Measurement of a meaningful adsorption rate requires that the fuel accumulation rate must become independent of the flow rate, *i.e.*, bulk mass transfer, in the region of measurement. Confidence is added to the measurement if the relative rate in the flow independent region is insensitive to catalyst amount.

Results of these initial tests, shown in Fig. 2, for flow rates to 65 cc/min and two catalyst loadings, show that a maximum in fuel accumulation rate, presumed to be an adsorption rate limit, is reached at levels above ~40 cc/min. Excellent agreement in the normalized relative rates for two widely differing catalyst loadings indicates that the method provides a sound basis for further studies. Due to the desire to obtain maximum flow rates in all subsequent experiments of this type, catalyst loading was thereafter maintained at the 10 mg/cm^2 level.

A further confirmation of the limitation of fuel accumulation by adsorption rather than mass transport was obtained from the temperature dependence of fuel accumulation. Thus, in the interval from 80° to 100°C the increase in coulombs accumulated during the fixed scan period indicated an apparent activation energy of 11 kcal/mole. This value, much too high for transport limitation, is in good agreement with that obtained as the temperature dependence of the limiting current for butane electrodes in 3.7M H_2SO_4 at 100°C (6, 11).

Characterization of the platinum substrate.—In order to establish a firm basis for the comparison of further data and subsequent interpretation of effects, voltage scan measurements were carried out to characterize electrochemically the Engelhard platinum black. These measurements were made using the pressed electrodes described previously immersed in argon-sparged 3.7M H_2SO_4 at 80°C. Adsorption-discharge of protons to form H· in the region negative to +0.2v *vs.* S.C.E. was defined as a function of potential, and total coulombs of chemisorbed hydrogen atoms were related to the coulombs for oxide formation and reduction during a fixed scanning procedure. In this way it was possible to relate subsequent measurements to one another, through known relationships.

A summary of this data is contained in Table I and a plot of the hydrogen atom coverage with potential is shown in Fig. 3. The inflection in the coverage curve reflects the existence of two peaks in the anodic volt-

Table I. Hydrogen deposition on platinum as a function of potential

48 mg sample of Engelhard Pt black; total oxide reduction from 1.3 v *vs.* S.C.E., Q_o (1.3), = 100 mc/mg.

Equilibration potential, v *vs.* S.C.E.	Total H·, mc	Total H·, mc/mg	Fraction of maximum H·
+0.05	314	6.54	0.14
+0.02	577	12.0	0.25
0.0	738	15.4	0.32
−0.02	825	17.2	0.36
−0.04	943	19.7	0.41
−0.06	1095	22.8	0.48
−0.08	1395	29.1	0.61
−0.10	1787	37.2	0.78
−0.12	2045	42.6	0.89
−0.144	2295	47.8	1.00

age scan through the hydrogen region on platinum. The presence of two distinct peaks, generally taken to indicate the existence of two "types" of H·, adsorbed under differing energy considerations, is well known and has been the topic of many recent investigations (12-14). Attention is drawn to this point for later reference in the discussion of results.

As a general reference point in this, as well as other previous studies (6), voltage scans on the platinum black electrodes were extended to +1.30v *vs.* S.C.E. Under those conditions, at 0.026 v/sec, Table I indicates that the quantity of coulombs for oxide formation (or reduction) to that potential is, within a few per cent, twice that for the total H· accumulation. Thus, on the usual assumption of one H· per Pt atom, the surface at +1.30v *vs.* S.C.E. is believed to consist essentially of a completed layer of PtO (15).

The value of millicoulombs passed during hydrogen atom chemisorption prior to H_2 evolution was used to calculate a rough value for the electrochemical surface area of the catalyst. Using a value of 210 μcoul/cm^2 as the value for H· deposition on one true square centimeter (8, 14), a total surface area of about 23 m^2/g is calculated. This value is in fairly good agreement with the 28 m^2/g found by the (nitrogen) B.E.T. method.

Technique for measurement of adsorption rates.— Actual voltammetric measurement of adsorption rates was made using a 1.1v single pulse sawtooth potentiostatted signal in conjunction with the flowing electrolyte system described previously. Application of a sawtooth signal enabled the use of the linearly increasing portion of the potential signal (55 mv/sec) for integration and calculation of coulombic quantities of fuel present, while the step function collapse to the preset potential level minimized the time necessary for oxide reduction on the electrode and return to a zero current condition. This return to zero current was accomplished in about 3-5 sec for a total of 38 mg of platinum black in the presence of butane fuel. Using a manual pulse initiating switch, a series of traces was obtained for various adsorption times at a given preset potential in the time interval generally not exceeding 40 sec from the time of return to zero current after the

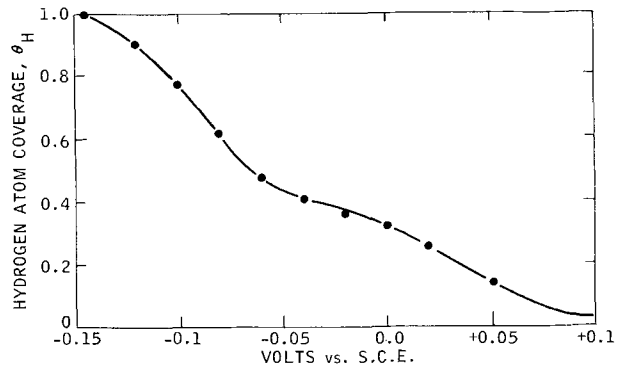

Fig. 3. Relative hydrogen atom coverage *vs.* potential

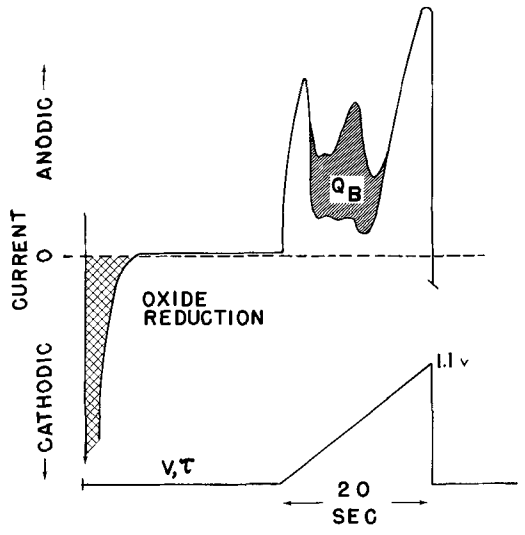

Fig. 4. Diagram of sawtooth scan sequence and typical response

preceding pulse. Normally six to eight scans were enough to clearly define the required coulombs of fuel *vs.* time slope. Accumulation of fuel in this time period represents the initial adsorption rate on the freshly reduced surface and was found to be quite linear up to about 50-60 sec. In the time periods employed maximum butane coverages are less than one third the saturation values. A typical scan sequence is shown in Fig. 4.

Since the oxidation of adsorbed fuel was carried out during a 20 sec scan period, a certain definite quantity of additional fuel was adsorbed and oxidized during the scan period. This fixed contribution, plus any contribution during the few second reduction period was evidenced as an intercept on the Q *vs.* t plot. A typical set of curves obtained at three different potentials is shown in Fig. 5. Constancy of the intercept affirms the fact that the total of these contributions remained essentially constant in the potential range studied.

During the time period while fuel accumulates at the platinum electrode, even in very low polarization regions, these active platinum catalysts do not remain inert. Thus, during the wait period at a given potential, a steady state current of fuel oxidation flows in the circuit. It was necessary, therefore, to measure this current during the wait period for each preset potential and correct the observed slope of the coulombs *vs.* time curve for the appropriate fuel loss. This correction becomes greater as the potential moves positively and soon becomes large enough to render the observed coulombs-time slope unreliable. For this reason adsorption rate measurements were

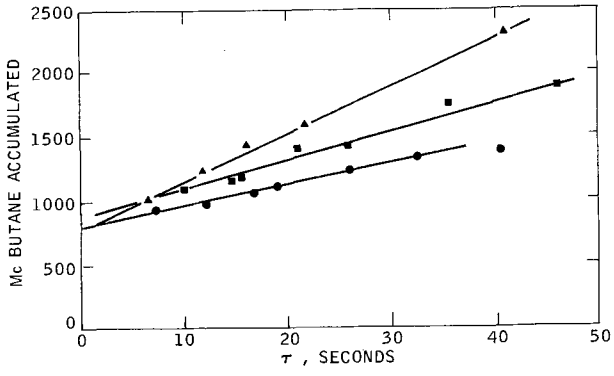

Fig. 5. Typical plot of millicoulombs butane adsorbed *vs.* wait time (from switching); 3.7M H_2SO_4, 95°C, 55 mv/sec sawtooth scan; ■, +0.15v S.C.E.; ▲, 0.05v S.C.E.; ●, 0.0v S.C.E.

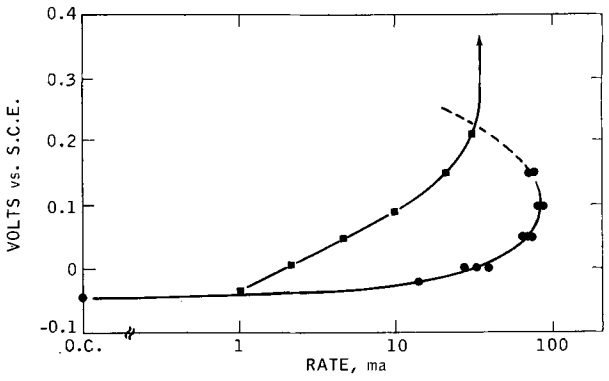

Fig. 6. Butane adsorption rates vs. potential, compared to steady-state performance in H_2SO_4 from ref. (11); 3.7M H_2SO_4, 95°C; ■, steady-state performance; ●, adsorption rates. Rate adjusted to 50 mg Pt.

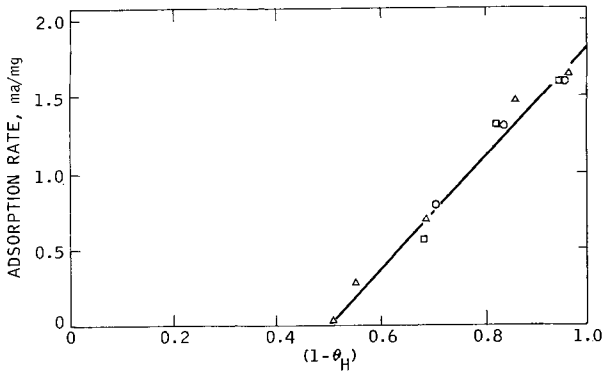

Fig. 7. Butane adsorption rates plotted against relative "free" surface, $1-\theta_H$; △, series III; □, series II; ○, series I.

restricted to the potential range —0.05 to +0.15 *vs.* S.C.E. Measurements positive to this potential are not considered meaningful since the steady state current becomes excessively large. Argon blanks were obtained for each "preset" potential just prior to commencing the butane adsorption studies.

Rates of Butane adsorption vs. potential and initial hydrogen coverage.—Adsorption rates determined from the coulombs *vs.* time slopes as a function of electrode potential are shown in Fig. 6 for three series of measurements involving separate systems. Corrections applied to compensate for steady state currents are noted in Table II. For reference, Fig. 6 includes a typical curve of butane steady state performance (galvanostatic) on a platinum-Teflon electrode at 95°C in 3.7M H_2SO_4 (11). It is apparent that adsorption rates here are adequately high to easily support the required steady state currents. Although the adsorption for +0.15v *vs.* S.C.E. is subject to the highest probable error, the evidence of a decrease in adsorption rate is believed to be adequately reliable. Thus, adsorption rate is essentially nil at —0.05v and appears to reach a maximum at about +0.10v *vs.* S.C.E. with subsequent decline with more positive potentials, possibly as water or sulfate ions become strongly oriented at the surface and occupy fuel sites.

One further piece of indirect evidence for this decline in rate was obtained from measurement of the maximum butane adsorption on the platinum surface under flow conditions. Thus, the maximum observed (saturation) quantity of butane measured with a 26 mv/sec, 1.3v scan in the flowing fuel-electrolyte system, $Q_B^s/Q_o(1.3) = 1.61$, was about equal to that observed in a stagnant system where fuel accumulation by diffusion is very slow (6). Since, under flow conditions a significant contribution to the observed coulombs is expected as oxidized fuel is replaced during the time of the scan (estimated 10-15% additional total coulombs) this observation suggests that fuel adsorption rates are low in the middle potential region prior to the onset of oxide formation. Details of the estimation of expected fuel adsorption during the scan duration are given in the Appendix.

An explanation of the previous adsorption behavior is obtained from a knowledge of the initial condition of the surface with respect to hydrogen atoms.

Table II. Corrections for butane steady state oxidation during adsorption measurement

Measurement potential, v *vs.* S.C.E.	Current, ma/mg	Measurement potential, v *vs.* S.C.E.	Current, ma/mg
−0.050	0	+0.050	0.33
−0.025	0	+0.100	0.58
0.00	0.13	+0.150	0.82

Thus, from the argon blanks obtained prior to each series of butane measurements, it was possible to obtain the initial fractional coverage of the surface with hydrogen atoms for each potential in the absence of butane. This parameter was used to derive the function $(1-\theta_H)$, shown in Fig. 7 plotted against rate of butane adsorption for the three series of experiments. Several features are evident: (*i*) initial rate of butane adsorption is linear with $1-\theta_H$, reaching the observed maximum rate at $\theta_H = 0$ (value for +0.15v *vs.* S.C.E. is not on the plot since θ_H goes to zero just prior to that potential); (*ii*) the intercept of zero rate at $1-\theta_H = 0.5$, coupled with further evidence to be presented next, strongly suggests that the adsorption of this fuel occurs only on the Type II (more anodic) H· sites. Thus, as shown in Fig. 3 the potential of —0.05 *vs.* S.C.E. corresponds closely to the inflection in the curve defining H· coverage and also defines the point in Fig. 6 at essentially zero rate of adsorption. The linearity with $1-\theta_H$ further implies that the initial adsorption rate per exposed site probably does not vary appreciably in the potential region wherein Type II H· is present. As mentioned previously, the observed rate of adsorption beyond about +0.15v *vs.* S.C.E., however, does appear to actually decline.

Additional evidence in support of Type II site adsorption.—With indications that butane adsorption occurred only on that type of site occupied by Type II H·, further evidence was sought in measurement of the equilibrium adsorption of the fuel on platinum. In a previous paper (6) the ratio of coulombs of butane fuel at saturation, Q_B^s, to the coulombs required for reduction of PtO on the electrode, Q_o, from 1.3v *vs.* S.C.E. at 80°C, was established for eight platinum catalysts, including Engelhard platinum black, to be 1.58 ± 0.13. On the basis of the oxide-hydrogen atom coulombic ratios in Table I, this ratio calculated on total H· would be, $Q_B^s/Q_H^s = 3.3$. If, however, adsorption of butane fuel occurs only on Type II H· sites, then saturation of these sites, about 50% of the total H·, would lead to a value of $Q_B^s/Q_{H(II)}^s = 6.6$. This value corresponds closely to the expected 6.5 electrons per site for the complete oxidation of butane to CO_2 (3, 6) if a four-point Pt-C_4H_{10} attachment occurs, and thus adds some strength to the postulated attachment on one type of site.

An additional series of studies was carried out to define the relationship between fuel and H· coverage in potential regions near H_2 evolution. The technique used here was identical to that used previously to obtain equilibrium coverage of butane on platinum (6).

Electrodes were of the pressed platinum-Teflon on platinum flag type described previously and data was obtained in simple butane sparged cells at 80°C in 3.7M H_2SO_4 for comparison with the earlier experiments. Coulombic quantities were determined from triangular voltage scans.

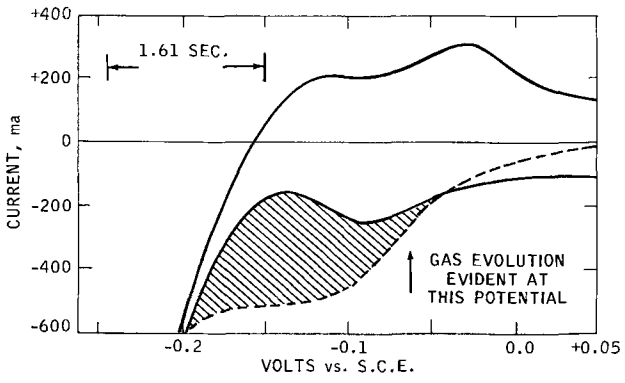

Fig. 8. Typical scan toward H_2 evolution as adsorbed butane desorbs. Dotted line is curve with desorbing butane. Solid line is blank. Integration of hatched area indicates 4 electrons per initial butane molecule.

Saturation of the catalyst surface with butane with the electrode potentiostatted at 0.0v *vs.* S.C.E. gave the expected $Q_B^s/Q_o(1.3v) = 1.6$. Moreover, no trace of Type II hydrogen remained in the anodic scan from 0.0 *vs.* S.C.E. In order to ensure that only Type II sites were involved, however, a similar butane saturated electrode was subjected to a cathodic scan to H_2 evolution potentials. Surprisingly at potentials of —0.02v *vs.* S.C.E., an obvious evolution of gas occurred from the electrode together with a significant increase of scan current in the region of the Type I hydrogen peak as shown in Fig. 8. Integration of the excess coulombs over and above the normal Type I H· coulombs indicated, for two such cases, values equivalent to 3.87 and 3.94 electrons respectively per molecule of butane known to exist on the saturated catalyst. Thus, it is believed that the butane is desorbed rapidly as Type I hydrogen begins to form on the surface and that, subsequent to fuel desorption from the initially saturated Type II sites, the four missing hydrogen atoms are rapidly replaced on the surface with the passage of four electrons per original butane molecule.

Verification that the preponderance of desorbed gas was actually butane was obtained by vapor phase chromatography. A few tenths of a cubic centimeter of desorbed gas trapped in a small sampling apparatus indicated essentially 100% butane with traces of propane, ethane, and methane. Some small amount of cracking of the hydrocarbon fuel apparently takes place as has been reported previously (5, 7).

Desorption of fuel during a cathodic sweep can pose problems for the investigator interested in fuel surface coverages. Although admittedly the cathodic scan here is carried out at a relatively slow speed, 31 mv/sec, it is obvious that the use of the decrease in total H· as a measure of adsorbate coverage, a technique enjoying wide popularity recently, must

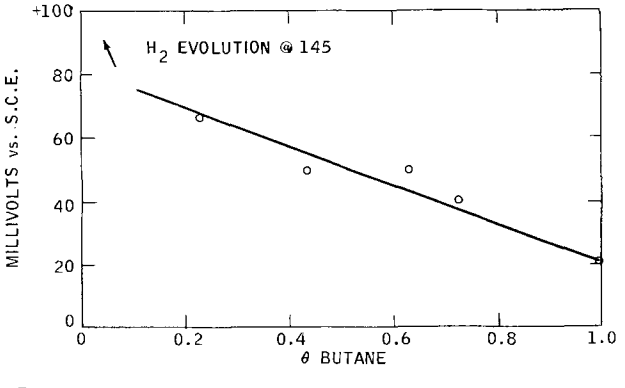

Fig. 9. Potential of initial (desorbing) gas evolution as a function of relative coverage derived from Q_B/Q_B (maximum).

be exercised with caution and with strict attention to scan speed, etc., if misleading effects are to be avoided. If fuel desorption occurs rapidly, surface coverages inferred from adsorbed hydrogen measurements could indicate much lower fuel coverages than actually exist.

A series of experiments was carried out to define roughly the desorption potential as a function of butane coverage, θ, derived from Q_B/Q_B (saturation). For this purpose a visual estimation of the potential of initial observable gas bubble formation was used. A plot of the observed desorption potentials as a function of approximate coverage is shown in Fig. 9. The potential of obvious desorption varies about linearly with coverage over a range from —0.065 *vs.* S.C.E. for the lowest coverage studied, to —0.02 for saturation. Thus, even minimum quantities of butane are desorbed at —0.065, *i.e.*, in the potential range where significant quantities of Type I H· exist. Data on the H· coverage is not sufficiently precise to tell if the anodic end of the range, —0.02v *vs.* S.C.E., is the potential at which first minute quantities of Type I H· are formed. No obvious explanation is at hand to explain this complete incompatibility of adsorbed butane with formation of Type I H·. An answer to this question, however, would undoubtedly require a detailed knowledge of the platinum surface species and the precise nature of the difference in Type I and Type II H· sites.

Discussion and Conclusions

Based on the preceding data, a fairly complete summary of butane adsorption behavior on electroactive Pt can be made. The fuel molecule appears to adsorb only on that type of site normally occupied by Type II (more anodic) H·. The initial observed rate of adsorption is a linear function of the number of such sites empty of H·, although eventually, as saturation fuel coverage is approached all Type II H· is replaced by fuel. Combination of the known coulombs involved in Type II H· deposition with the coulombs obtained from oxidation of an equilibrium (saturated) quantity of butane on the platinum leads to a value of 6.6 electrons/H· site. In view of the 26 electron complete oxidation of the four carbon molecule to CO_2, this value is consistent with a four-site attachment of butane to platinum, *i.e.*, the molecule lying down on the surface. It must be cautioned, however, that this is not a necessary conclusion since an end-on adsorption of the fuel molecule could also result in loss of 4H· if the local energy or space considerations on the surface are significantly affected by the fuel molecule adsorption.

Depending slightly on the surface coverage, adsorbed fuel begins to desorb in the potential range —0.02 to —0.06v *vs.* S.C.E. in this system as the region of Type I H· formation is reached. Traces of lower carbon number saturates indicate some slight cracking of the adsorbed fuel.

Positive to the region of significant Type II H· existence, *i.e.*, positive to ~+0.10v *vs.* S.C.E. in this system, initial rates of fuel adsorption are difficult to measure on the active electrocatalyst since steady state current flow becomes a significant fraction of the adsorption rate. Indications are present, however, that the observed adsorption rate begins to decrease in the region positive to +0.10v *vs.* S.C.E. This might very well be due to loss of fuel adsorption sites again as water begins to strongly orient at the surface. At any rate it seems quite reasonable that the over-all situation is as originally depicted in Fig. 6, with the intersection of the decreasing adsorption rate curve (dotted line) with the $2RT/F$ electron transfer limited Tafel line dictating the limiting current capability of the system.

The knowledge that fuel adsorption can occupy only Type II H· sites in the region from about —0.05 to +0.15v vs. S.C.E. in this system leads to an obvious question as to the occupancy of Type I sites in this

potential range. Since it is probable that Type I sites contain adsorbed water or hydronium ions in this region, is it too bold to suggest that fuel electrooxidation is accomplished by interaction of the fuel molecules adsorbed on Type II sites with water molecules on another, possibly Type I, site? In the absence of a physical picture of the exact nature of these so-called "sites" it is difficult to say. For instance, are the "sites" not really physical but a differentiation in the binding energy for two successive hydrogen atoms? Is one set of hydrogen atoms dissolved in the lattice and the second adsorbed at the external sites? In view of the previous data, the recent suggestion by Will (14) that Type I and II merely represent the H+ discharge-adsorption on two different crystal faces of platinum (the 110 and 100) does not seem too appealing. Thus H· adsorption on one crystal face would not be expected to produce such a significant electronic effect as to cause desorption of butane from an entirely different face on which it is preferentially adsorbed.

The extended implications of the possibility of two-site interaction in the over-all mechanism of hydrocarbon oxidation are too broad, however, to be discussed as a part of this study. Further discussion will be reserved until additional evidence is available to support these preliminary findings. The ramifications of a two-site surface will then be discussed not only with respect to the reaction of saturate hydrocarbons, but also for low molecular weight oxygenated species (CH_3OH, HCHO, etc.) and for olefins.

Acknowledgments

The work reported in this paper was made possible by the support of the Advanced Research Projects Agency under Order No. 247 through the U.S. Army Electronics Laboratories, Contract No. DA 36-039 AMC-03743 (E). Permission to publish is gratefully acknowledged. The authors wish to thank H. E. Frew for carrying out much of the experimental work.

Manuscript received Aug. 10, 1965.

Any discussion of this paper will appear in a Discussion Section to be published in the December 1966 JOURNAL.

REFERENCES

1. M. J. Schlatter, Preprints Am. Chem. Soc. Mtg., Chicago, 1961, **6**, (4-B) 149, also in "Fuel Cell Systems" "Advances in Chemistry No. 47," ACS, Washington (1965) p. 292.
2. W. T. Grubb, Proc. 16th Annual Power Sources Conference, 34 (1962).
3. H. Binder, A. Kohling, H. Krupp, K. Richter, and G. Sandstede, *This Journal*, **112**, 355 (1965).
4. H. Wroblowa, B. J. Piersma, and J. O'M. Bockris, *J. Electroanal. Chem.*, **6**, 401 (1963).
5. L. W. Niedrach, *This Journal*, **111**, 1309 (1964).
6. J. Shropshire, E. H. Okrent, and H. H. Horowitz, Presentation at Symposium on Fuel Cells, Div. of Fuel. Chemistry, 149th Mtg. ACS, Atlantic City, September 1965.
7. W. T. Grubb and L. W. Niedrach, *This Journal*, **110**, 1086 (1963).
8. S. B. Brummer and J. I. Ford, *J. Phys. Chem.*, **69**, 1355 (1965).
9. S. Gilman, Report No. 6, Contract DA 44-009 ENG 4909, General Electric Co., July 1, 1964-December 31, 1964.
10. L. C. Austin, P. Palasi, and R. R. Klimpel in "Fuel Cell Systems," p. 35, R. F. Gould, Editor, "Advances in Chemistry No. 47," ACS (1965).
11. C. E. Heath, *et al.*, Report No. 5, Contract DA 36-039 AMC-03743(E), Esso Research and Engineering Co., (Jan. 1, 1964-June 30, 1964).
12. C. H. Presbey, Jr. and S. Schuldiner, *This Journal*, **108**, 985 (1961).
13. T. C. Franklin and D. H. McClelland, *J. Phys. Chem.*, **67**, 2436 (1963).
14. F. G. Will, *This Journal*. **112**, 451 (1965).
15. J. S. Mayell and S. H. Langer, *ibid.*, **111**, 438 (1964).

APPENDIX

Estimation of Expected Butane Adsorption During Scan on Initially Saturated Surface

As discussed previously, the saturation adsorption of butane measured under flowing conditions did not differ significantly from that measured under stagnant conditions, during which accumulation of fuel by diffusion is negligible.

If adsorption of butane on free area occurred in the potential region positive to +0.15v *vs.* S.C.E. at the maximum rates observed previously, a significant number of coulombs would be expected to accumulate during the course of the burn-off scan on the previously saturated electrode.

This accumulation in coulombs, ΔQ, would be

$$\Delta Q = \int_{t_1(V_1)}^{t_2(V_2)} R_o(1 - \theta_b)(1 - \theta_{ox})\,dt$$

where θ_b represents the coverage with adsorbed butane at any time (voltage) in the scan, and a term in θ_{ox}, the surface oxide coverage, has been inserted to accommodate the fact that surface oxide formation will undoubtedly interfere with butane adsorption at some voltage level. Two functions for θ_{ox} were considered: (I) A term where $\theta_{ox} = 1$ at one half the total coulombs for total 2 electron oxide formation. This would be the case if PtO formation occurred on a single type of site first. (II) A term with $\theta_{ox} = 1$ at the full oxide level, *i.e.*, when Q_{ox} equalled twice $Q_H{}^s$, the total saturation H· coverage. The θ terms were evaluated over the time interval of the scan by stepwise integration of the respective fuel and oxide formation peaks on the platinum.

Evaluation of the integral for ΔQ indicates that during the course of the scan in the flowing electrolyte system an additional contribution of a minimum of 10-15% would be expected in the observed $Q_B{}^s$ value depending on which θ_{ox} function is assumed. If no $(1 - \theta_{ox})$ diminishing function is applied, this increase would be expected to be about 22%. Thus, it is inferred that the rate of butane adsorption decreases rapidly in the region beyond +0.15v *vs.* S.C.E. and accordingly the rate in this region in Fig. 5 (dotted line) is shown decreasing to intersect the Tafel line.

Faradaic Impedance of Polarized Porous Electrodes

II. Nonlinear Kinetics

R. Darby[1]

LTV Research Center, Ling-Temco-Vought, Inc., Dallas, Texas

ABSTRACT

A previous analysis of the Faradaic impedance of polarized porous gas diffusion electrodes has been extended to include kinetic rate expressions which are other than first order. An approximate analysis reveals impedance characteristics which are qualitatively similar to those for first order kinetics for reaction orders greater than unity and less than ½. However for orders between one and ½, the Argand diagram exhibits two semicircular regions instead of one, as well as the inductive characteristic at sufficiently high frequency. These curves are compared with the data of Brodd on Leclanché cells which exhibit similar characteristics.

The a-c impedance characteristics of electrochemical systems are important as a possible indication of reaction and transport mechanisms [*e.g.*, (1) — (11)], as well as an indication of the response to varying load conditions of such power sources as fuel cells and batteries. Both capacitive and inductive characteristics have been experimentally observed, as discussed by Gutman (12) and have also been predicted for a polarized porous dual-layer gas diffusion electrode for the case in which the electrode kinetics are first order, as shown in a previous paper (13). The object of the present paper is to extend the previous results to include electrode reactions which are not first order, and hence attempt to shed some light upon certain experimentally observed impedance characteristics (7).

In (13), the Faradaic impedance characteristics of a polarized gas diffusion electrode were determined by assuming a small amplitude a-c signal superimposed on a larger polarizing d-c current. The formulation of the problem was in terms of a general electrode reaction, represented by

$$gG + lL + ne^- \rightarrow pP \qquad [1]$$

the kinetics of which was assumed to follow the generalized rate expression

$$I = I_o \left(\frac{G}{G_o}\right)^{g'} \left(\frac{L}{L_o}\right)^{l'} \exp\left(\frac{\alpha n' F}{RT} E\right) \qquad [2]$$

Although [2] is written in terms of a general reaction order, the results given in (13) were for a first order reaction only. The present analysis will be for reaction orders other than unity, including both integral and fractional orders. In this regard, it should be pointed out that [2] is assumed to be simply a rate expression representing the net rate of the overall reaction [1], but not necessarily indicative of the reaction mechanism. Many complicated reactions involving several steps such as the heterogeneous catalytic reaction in a porous medium with which we are concerned can be adequately represented by a nonlinear rate equation such as [2], particularly when adsorption or desorption steps are significant, and where the reaction orders may be nonintegral [see *e.g.* (14)].

The Model

The dual-layer model mechanism was described in detail in (13) and will be reviewed briefly. A schematic of the model, Fig. 1, shows three regions for consideration. Region I is a porous layer containing a gas phase only within the pores (reactant plus inert); region II is a porous layer containing the liquid electrolyte phase (also assumed to consist of a reactant plus inert); and region III is a (narrow) region of the liquid filled layer, adjacent to the interface of the two porous layers, wherein reaction [1] is assumed to take place. The gaseous reactant diffuses through the pores in region I in the presence of the inert component, as does the liquid reactant in region II. At the gas-liquid interface the gaseous reactant dissolves in the liquid phase, the resulting concentration of dissolved gas being determined by Henry's law. As the dissolved gas diffuses through the liquid filled pores in region III, it is simultaneously consumed by reaction at catalytic sites on the pore walls. Region III is assumed to be small compared with region II, so that semi-infinite boundary conditions apply to the dissolved gas reactant. Further, since the concentration of dissolved gas is small compared with the liquid reactant concentration, the latter can be taken as essentially constant over region III (the reaction zone).

The additional assumptions of (13) with regard to the use of a pseudodiffusion coefficient for the porous medium, the influence of migration, and uniform matrix potential apply as before. Also, as concluded in (13), there is no loss in generality for this model by setting the liquid reactant order (l') equal to zero since the effect of liquid reactant concentration on impedance is simply to add an additional term which is similar in form to the contribution from diffusion of the gaseous reactant in region I.

D-C Analysis

The flux of the gaseous reactant, and hence the total electrode current, is governed by the diffusion equation (Fick's second law) in region I, and by this equation including a reaction term, r, in region III

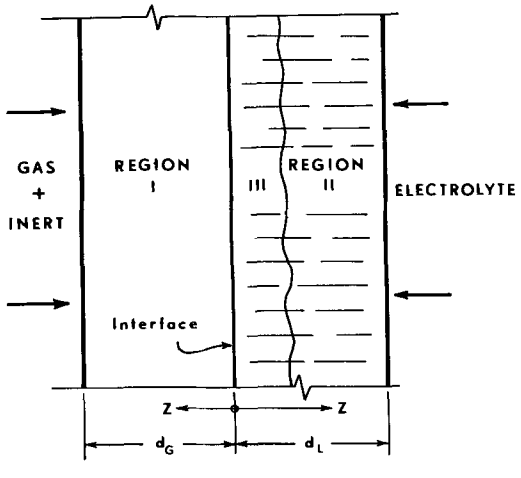

Fig. 1. Schematic diagram of dual-layer model

[1] Present address: Chemical Engineering Department, Texas A & M University, College Station, Texas.

$$\frac{\partial C}{\partial t} = D_{GL}\frac{\partial^2 C}{\partial z^2} - r = D_{GL}\frac{\partial^2 C}{\partial z^2} - I\left(\frac{ag}{nF}\right) \quad [3]$$

Here, Ia represents the local specific current resulting from the electrochemical reaction in region III, in amp/cm^3.

For a steady state, the combination of Eq. [3] and [2] (without the liquid reactant term) for region III results in

$$\frac{d^2C}{dz^2} = KC^{g'} \quad [4]$$

where

$$K = \frac{I_o\, ag}{nF\, D_{GL}\, C_o^{g'}} \exp\left(\frac{\alpha n'F}{RT}E\right) \quad [5]$$

The solution to [4] subject to the following boundary conditions

$$\begin{array}{ll}(a) & C = C_i \text{ at } z = 0\\ (b) & C \to 0 \text{ as } z \to \infty\end{array} \quad [6]$$

is (14, 15)

$$C = C_i\left[(g'-1)\sqrt{\frac{KC_i^{(g'-1)}}{2(g'+1)}}z + 1\right]^{2/(1-g')} \quad [7]$$

The total d-c electrode current is given by

$$I_t = -\frac{nF\, D_{GL}}{g}\left(\frac{dC}{dz}\right)_{z=0} = \frac{nF\, D_{GL}\, C_i}{g}\sqrt{\frac{2KC_i^{(g'-1)}}{g'+1}} \quad [8]$$

from which K can be evaluated in terms of the total current density, I_t, and the concentration of dissolved gaseous reactant at the interface C_i. The latter is determined by the diffusional flux of the gaseous reactant through region I, together with the assumption of equilibrium at the interface as represented by Henry's law. The result, including the effect of the inert component, has been previously derived (13, 15) and is

$$C_i = \frac{cP_o}{H}\left[1 - (1 - G_o/P_o)\exp\left(I_t/A_2\right)\right] \quad [9]$$

where

$$A_2 = (nF\, P_o\, D_{GG})/(g\, RT\, d_G) \quad [10]$$

An inspection of the concentration profile [7] reveals the following characteristics (14). For $g' > 1$, the concentration remains finite for all z, asymptotically approaching zero. However, for $g' > 1$, the concentration falls to zero at a finite value of z equal to $[2(g'+1)/(KC_i^{g'-1})]^{1/2}/(1-g')$.

Equations [5], [7], [8], and [9] define the relation between the steady-state concentration gradient within the reaction zone (region III), the total current density, and the total electrode polarization.

Impedance Analysis

As in (13), the electrode impedance is defined by the ratio of a small amplitude alternating component of polarization (η) to the corresponding alternating component of current (i), which are superimposed upon the steady d-c values.

The assumption of small amplitudes allows linearization of the equations, as follows. Rewriting [2] for region III in terms of total (a-c plus d-c) quantities, gives

$$I + i = I_o\left(\frac{C+\gamma}{C_o}\right)^{g'}\left(\frac{L+\lambda}{L_o}\right)^{l'} \exp\left[\frac{\alpha n'F}{RT}(E+\eta)\right] \quad [11]$$

The small amplitude assumption for the a-c quantities means that

$$\left(\frac{\gamma}{c}, \frac{\lambda}{L}, \frac{n'F}{RT}\eta\right) << 1$$

so that terms of second order in these quantities can be neglected. Thus [11] can be linearized as follows

$$i = I\left[g'\left(\frac{\gamma}{C}\right) + l'\left(\frac{\lambda}{L}\right) + \frac{\alpha n'F}{RT}\eta\right] \quad [12]$$

Combining Eq. [2], [3], and [12] (again omitting the l' term) results in the following equation for γ

$$\frac{\partial \gamma}{\partial t} = D_{GL}\left[\frac{\partial^2 \gamma}{\partial z^2} - KC^{g'}\left(g'\frac{\gamma}{C} + \frac{\alpha n'F}{RT}\eta\right)\right] \quad [13]$$

where C is a function of z, as given by [7].

In order to determine the a-c impedance of the electrode to a sinusoidally varying current, we must solve [13] for the ratio of the LaPlace transforms of the a-c components of polarization and total current, and replace the transform variable s by $j\omega$. The total a-c current density is given by

$$i_t = -\frac{nF\, D_{GL}}{g}\left(\frac{d\gamma}{dz}\right)_{z=0} \quad [14]$$

Combining [13] and [7] and transforming the result gives

$$\frac{d^2\,\bar{\gamma}(s)}{dz^2} - K\bar{\gamma}(s)\left[\frac{s}{KD_{GL}} + \frac{f}{(ez+1)^2}\right] = h\,\bar{\eta}\,(ez+1)^{2g'/(1-g')} \quad [15]$$

where

$$e = (g'-1)\sqrt{\frac{K\,C_i^{(g'-1)}}{2(g'+1)}} \quad [16]$$

$$f = g'\,C_i^{(g'-1)} \quad [17]$$

$$h = (\alpha n'F\, C_i^{g'}\, K)/(RT) \quad [18]$$

The boundary conditions which accompany [15] are

$$\begin{array}{ll}(a) & \bar{\gamma}(s) = \bar{\gamma}_i(s) \text{ at } z = 0\\ (b) & \bar{\gamma}(s) = 0 \text{ at } z = -e \text{ for } g' < 1\\ (b') & \bar{\gamma}(s) \to 0 \text{ as } z \to \infty \text{ for } g' > 1\end{array} \quad [19]$$

Here $\bar{\gamma}_i(s)$ is determined from the diffusion flux (Fick's law) for region I, the total a-c current, and Henry's law in a manner analogous to the derivation of [9]. The result is

$$\bar{\gamma}_i(s) = \bar{i}_t(s)\frac{A_4}{d_G\sqrt{s/D_{GG}}}\left[\frac{1 - \exp\left(d_G\sqrt{s/D_{GG}}\right)}{1 + \exp\left(d_G\sqrt{s/D_{GG}}\right)}\right] = \bar{i}_t\, A_4\, \Gamma(s) \quad [20]$$

where

$$A_4 = (gc\, RTd_G)/(nFHD_{GG}) \quad [21]$$

A general solution to [15] is possible in terms of a finite series or hypergeometric functions, but the resulting expressions are such that boundary conditions [19] cannot be readily applied. However, all that we require from the solution to [15] is an expression for the first derivative of $\bar{\gamma}$ which is valid near $z = 0$, from which $\bar{i}_t$ can be evaluated by means of [14]; hence an approximate solution valid near $z = 0$ should be adequate for this purpose. This is not to imply that the result is valid only for a very narrow reaction zone, as such is not the case, although in practice this zone should be small compared with region II under polarized conditions, as shown previously (13). Thus for sufficiently small z, the following approximations may be made

$$(ez+1)^{-2} \approx 1 - 2\,ez$$

$$(ez+1)^{2g'/(1-g')} \approx 1 + \frac{2g'\,ez}{(1-g')} \quad [22]$$

If we make the additional substitution of $\bar{\gamma}_i(s)z$ for $\bar{\gamma}(s)z$, which is also valid for sufficiently small z. Eq. [15] becomes

$$\frac{d^2\bar{\gamma}(s)}{dz^2} - \bar{\gamma}(s)K\beta_1 = h\bar{\eta}(s)\left[1 + \frac{2g'ez}{(1-g')}\right] + 2eKf\bar{\gamma}_i(s)z \quad [23]$$

where

$$\beta_1 = f + s/(KD_{GL}) \quad [24]$$

The similarity between [23] and Eq. [18] of ref. (13) for first order kinetics is apparent. The appropriate solution for $g' > 1$ is

$$\bar{\gamma}(s) = [\bar{\gamma}_i(s) - h\bar{\eta}(s)/\delta]\exp(-z\sqrt{\delta}) - [h\bar{\eta}(s) + ze\alpha_1]/\delta \quad [25]$$

where

$$\alpha_1 = 2g'h\bar{\eta}(s)/(1-g') - 2fK\bar{\gamma}_i(s) \quad [26]$$

and

$$\delta = K\beta_1 \quad [27]$$

For $g' < 1$, the solution is

$$\bar{\gamma}(s) = \frac{\sinh(z\sqrt{\delta})}{\sinh(\sqrt{\delta}/e)}\left\{[\bar{\gamma}_i(s) + h\bar{\eta}(s)/\delta]\exp(\sqrt{\delta}/e) + \frac{\alpha_1 - h\bar{\eta}(s)}{\delta}\right\} + [\bar{\gamma}_i(s) + h\bar{\eta}(s)/\delta]\exp(-z\sqrt{\delta}) - [h\bar{\eta}(s) + e\alpha_1 z]/\delta \quad [28]$$

Using [25] or [28] to calculate $\bar{i}_t(s)$ (Eq. [14], substituting for $\bar{\gamma}_i(s)$ from [20], and solving the result for $\bar{\eta}(s)/\bar{i}_t(s)$ gives, for $g' > 1$

$$\frac{\bar{\eta}(s)}{i_t(s)} = \frac{(\beta_1 Kg)/(nFD_{GL}) + A_4K\Gamma(2ef - \beta_1\sqrt{\delta})}{h[\sqrt{\delta} + eg'/(1-g')]} \quad [29]$$

and for $g' < 1$

$$\frac{\bar{\eta}(s)}{i_t(s)} = \left\{\sinh(\sqrt{\delta}/e)\left[\frac{g\delta}{nFD_{GL}} - A_4\Gamma(\delta^{3/2} - 2efK)\right] - KA_4\sqrt{\delta}\Gamma[2f - \beta_1\exp(\sqrt{\delta}/e)]\right\} \Big/ \{h\sinh(\sqrt{\delta}/e)[\delta + eg'/(1-g')] - h\sqrt{\delta}[\exp(\sqrt{\delta}/e) - 1/(1-g')]\} \quad [30]$$

The complex impedance, $Z(j\omega)$, is given by [29] or [30] when the transform variable s is replaced by $j\omega$. The result can be separated into frequency dependent real (resistive) and imaginary (reactive) components

$$Z(j\omega) = R(\omega) - jX_c(\omega) \quad [31]$$

or into magnitude and phase angle components. The latter can be represented as the impedance attenuation, $(DB)_z$, and capacitive phase angle, θ, defined as

$$(DB)_z = 20\log(|Z|/|Z_o|) \quad [32]$$

$$\theta = \tan^{-1}(X_c/R) \quad [33]$$

The complex impedance components, attenuation, and phase angle were determined for various values of reaction order g' from 0.25 to 3.0, as a function of the dimensionless frequency parameter ξ,

$$\xi = d_G\sqrt{\omega/2D_{GG}} \quad [34]$$

which enters through Eq. [20]. A family of curves was obtained for each case, each curve corresponding to a given value of ϕ, the ratio of d-c current density to limiting current density

$$\phi = I_t/I_{lim};\ I_{lim} = A_2/(1 - X_o) \quad [35]$$

Results

Impedance characteristics were calculated with the aid of a computer, using representative values of parameters which are listed in Table I. These results fall into three separate groups each showing similar characteristics, depending on the magnitude of g'. These correspond to the following values of g': less than 0.5, 0.5 to 1.0, and greater than 1.0; and are typified by the curves for $g' = 1/3$, $2/3$, and 2.0. Figures 2-7 show the impedance attenuation and phase angle curves for these three reaction orders, and Fig. 8-10 show the corresponding Argand diagrams, or reactance *vs.* resistance components. The curves for g' of 1/3 and 2 appear similar. However, the Argand diagram for $g' = 2$ shows that the diameter of the semicircular region goes through a minimum at a ϕ of about 0.5, then increases with decreasing ϕ, whereas for $g' = 1/3$ this diameter decreases continuously as ϕ decreases. For values of g' between 0.5 and 1.0, two semicircular regions appear on the Argand diagram which appear at least qualitatively to be a combination of the other two cases. That is, the circular region on the left grows as ϕ decreases, whereas the one on the right shrinks and eventually disappears at small values of ϕ.

Figure 9 may be compared with data given by Brodd (7) for the impedance of Leclanché cells at various stages of discharge. Although Leclanché cells do not contain porous gas diffusion electrodes and

Table I. Parameter values used in calculations

Gas phase: $x_o = 0.21$ mole fraction, $P_o = 1$ atm
Henry's law constant: $H = 3.95 \times 10^4$ atm/mole fraction
Porous medium: $\Phi = 0.5$, $\tau = 15$, $d_G = d_L = 0.1$ cm
Diffusivities: $D_{GG} = 0.2$ cm²/sec, $D_{LL} = 2 \times 10^{-5}$ cm²/sec
$D_{GL} = 1 \times 10^{-5}$ cm²/sec
Kinetic parameters: $I_o = 10^{-5}$ amp/cm², $n = n' = 4$, $\alpha = 1/2$
$(aI_o) = 5 \times 10^{-5}$ amp/cm³, $T = 25°C$

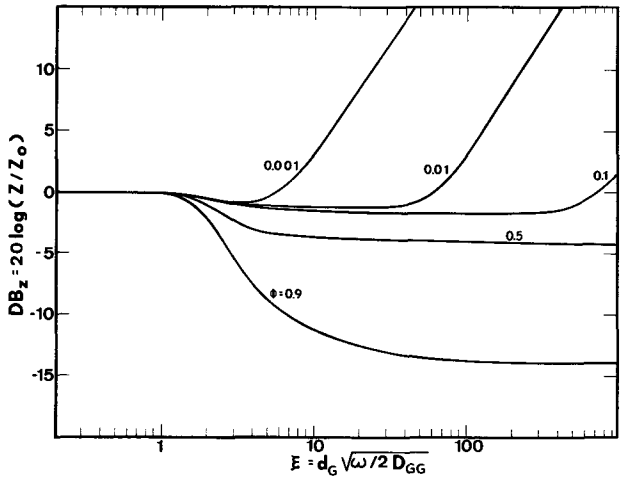

Fig. 2. Impedance attenuation, second order reaction, as a function of frequency and current density.

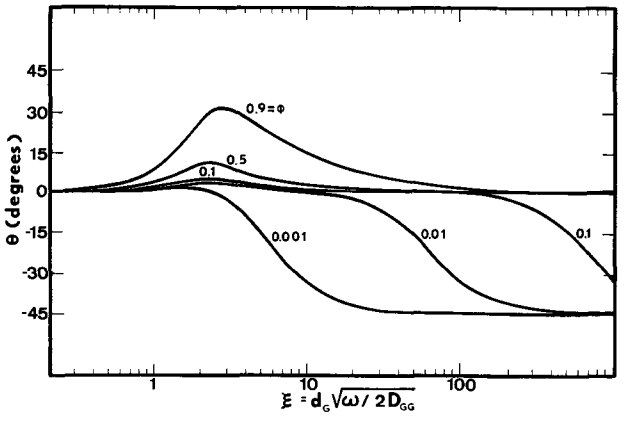

Fig. 3. Capacitive phase angle, second order reaction, as a function of frequency and current density.

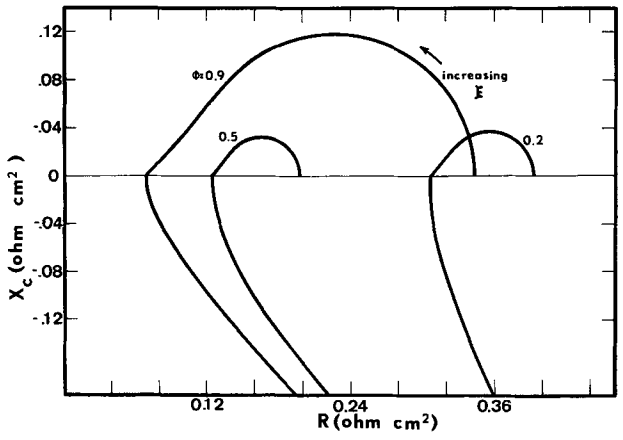

Fig. 4. Argand diagram, second order reaction

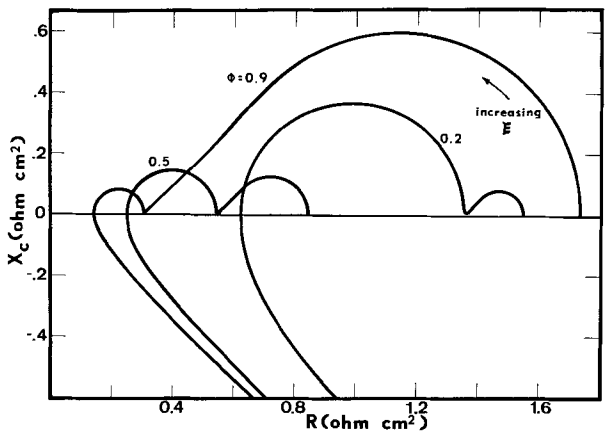

Fig. 7. Argand diagram, reaction order = 2/3

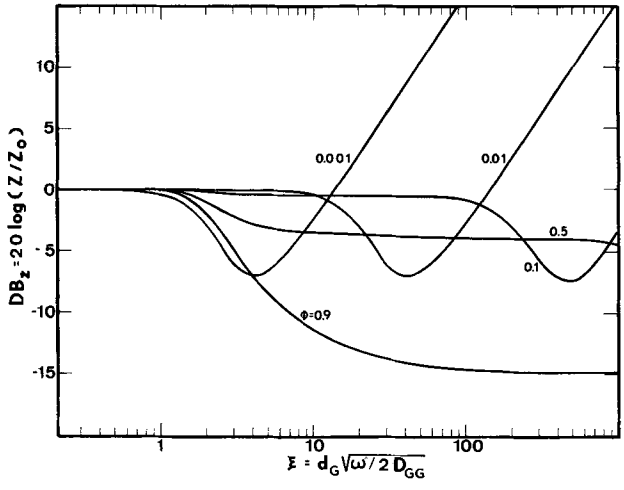

Fig. 5. Impedance attenuation, reaction order = 2/3, as a function of frequency and current density.

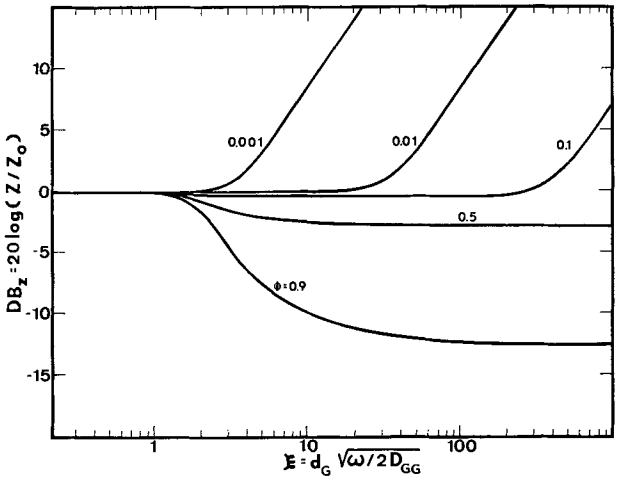

Fig. 8. Impedance attenuation, reaction order = 1/3, as a function of frequency and current density.

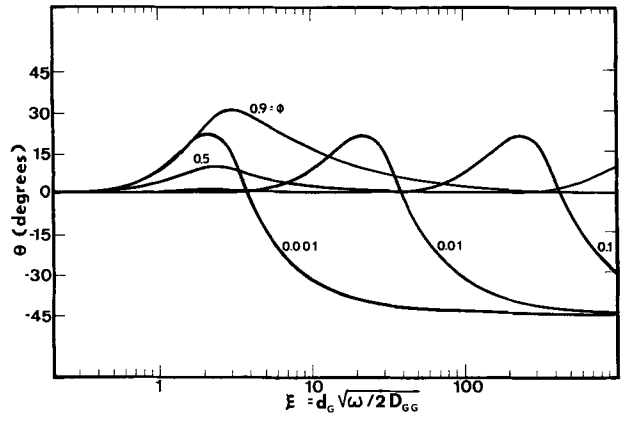

Fig. 6. Capacitive phase angle, reaction order = 2/3, as a function of frequency and current density.

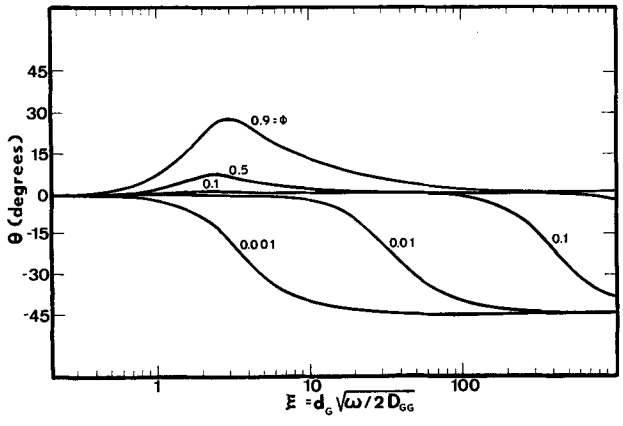

Fig. 9. Capacitive phase angle, reaction order = 1/3, as a function of frequency and current density.

would not normally be thought to correspond to the model of Fig. 1, the porous manganese dioxide-carbon black mixture would comprise a region of simultaneous diffusion and reaction analogous to region III of the model. Indeed, it is possible that a similar region might exist adjacent to the zinc electrode after discharge, resulting from the increased surface roughness and/or accumulation of reaction products. Furthermore, although Brodd's data were apparently taken under open-circuit conditions, the various states of discharge of the cells might be considered to correspond to various degrees of polarization. His Argand diagrams are a combination of at least two semicircular regions (he concludes the existence of three from trial and error curve fitting), the relative sizes of which depend on the state of discharge of the cell. His data do not show any region of inductive reactance, although the highest frequency employed was 50 kc and the inductive region would generally be expected to appear at frequencies higher than this. However, in another reference (16), he has indicated the observation of inductive reactances under certain circumstances. Brodd attributes the existence of the several separate semicircular regions to separate electrode rate processes, while the present results show

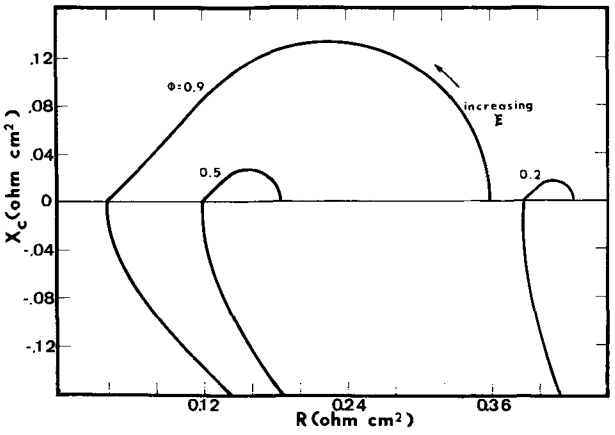

Fig. 10. Argand diagram, reaction order = 1/3

them to result from a single fractional order rate expression. However, these results are not incompatible inasmuch as a fractional order rate expression is most likely to result from a complex heterogeneous catalytic reaction involving several steps, such as that occurring in a porous electrode [*e.g.*, (17), (18)].

As in the previous analysis for first order kinetics (13), the effects of the non-Faradaic ohmic resistance and double layer capacitance have not been included in the calculation of electrode impedance. These effects have been considered by a number of authors, notably Ksenzhek and Stender (19), Winsel (20), deLevie (21), and Feuillade (22). The inclusion of distributed resistive and capacitive circuit elements representing these non-Faradaic effects in a porous electrode is frequently treated in a manner analogous to an R-C transmission line. These contributions can, at least in principle, be separated from impedance data, but while the experimental elimination of ohmic resistance is common practice, the isolation of the combination of distributed resistance and capacitance is not a simple matter. However, these effects would have to be included in a quantitative comparison of data and theory.

Manuscript received June 16, 1965; revised manuscript received Jan. 10, 1966.

Any discussion of this paper will appear in a Discussion Section to be published in the December 1966 JOURNAL.

REFERENCES

1. R. deLevie, *Electrochemica Acta*, **9**, 1231 (1964).
2. J. Euler and W. Nonnenmacher, *ibid.*, **2**, 268 (1960).
3. D. C. Smith, *Analyt. Chem.*, **36**, 962 (1964).
4. J. E. B. Randles, *Discussion Faraday Soc.*, **1**, 11 (1947).
5. J. E. B. Randles and K. W. Sommerton, *Trans. Faraday Soc.*, **48**, 937 (1952).
6. R. J. Brodd, *J. Research National Bureau Standards*, **65A**, 275 (1961).
7. R. J. Brodd and H. J. DeWane, *This Journal*, **110**, 1091 (1963).
8. D. C. Grahame, *ibid.*, **99**, 370C (1952).
9. D. C. Grahame, *J. Phys. Chem.*, **57**, 257 (1953).
10. P. Delahay, "New Instrumental Methods in Electrochemistry," Interscience, New York (1954).
11. K. J. Vetter, "Elektrochemische Kinetic," Springer-Verlag, Berlin (1961).
12. F. Gutman, *This Journal*, **112**, 94 (1965).
13. R. Darby, *ibid.*, **113**, 392 (1966).
14. D. A. Frank-Kamenetskii, "Diffusion and Heat Exchange in Chemical Kinetics," Princeton (1955).
15. R. Darby, *Advanced Energy Conversion*, **5**, (1965).
16. R. J. Brodd, Paper presented at the New York Meeting of the Society, Sept.-Oct. 1963.
17. K. J. Laidler, "Chemical Kinetics," McGraw-Hill Book Co., New York (1950).
18. P. H. Emmett, Editor, "Catalysis, V.II.," Reinhold Publishing Co., New York (1955).
19. O. S. Ksenzhek and V. V. Stender, *Zhur. Phiz. Khim.*, **31**, 117 (1957).
20. A. W. Winsel, *Z. Elektrochem.*, **66**, 287 (1962).
21. R. deLevie, *Electrochemica Acta*, **8**, 751 (1963).
22. G. Feuillade, *Compt. rend.*, **256**, 2786 (1963).

SYMBOLS

a_1	specific catalytically active area, cm²/cm³
A_2	term defined by Eq. [10]
A_4	term defined by Eq. [21]
c	total concentration of liquid phase, mole/cm³
C	concentration of dissolved gaseous reactant, mole/cm³
d_G	width of gas-filled pore layer, cm
d_L	width of liquid filled pore layer, cm
$\mathcal{D}_{AB}$	binary molecular diffusion coefficient of phase A reactant in phase B, cm²/sec
D_{AB}	pseudodiffusion coefficient for porous medium, cm²/sec
e	term defined by Eq. [16]
E	d-c polarization (deviation from open-circuit potential), v
f	term defined by Eq. [17]
g	stoichiometric coefficient for gas phase reactant
g'	reaction order with respect to gas phase reactant
G	gas phase reactant, concentration, mole/cm³
h	term defined by Eq. [18]
H	Henry's law constant, atm/mole fraction
i	alternating component of current density, amp/cm²
I	d-c current density, amp/cm²
I_o	exchange current density, amp/cm²
j	$=\sqrt{-1}$
K	term defined by Eq. [5]
l	stoichiometric coefficient of liquid phase reactant
l'	reaction order with respect to liquid phase reactant
L	liquid phase reactant, concentration, mole/cm³
n	number of electrons involved in over-all electrode reaction
n'	equivalent electron change in rate equation
P_o	gas pressure, atm
R	resistance, ohm-cm²
s	transform variable, sec^{-1}
X_c	capacitive reactance, ohm-cm²
x_o	mole fraction of reactant in gas phase
Z	impedance, ohm-cm²
z	distance from gas-liquid interface, cm

Greek

α	transfer coefficient
α_1	term defined by Eq. [26]
β_1	term defined by Eq. [24]
δ	term defined by Eq. [27]
γ	alternating component of dissolved gas phase reactant concentration, mole/cm³
ζ	alternating component of gas phase reactant concentration, mole/cm³
η	alternating component of polarization, v
θ	capacitive (lagging) phase angle, degrees
λ	alternating component of liquid phase reactant concentration, mole/cm³
ξ	dimensionless term defined by Eq. [25]
τ	tortuosity
ϕ	ratio of d-c current density to gas diffusion limited current density
ω	angular frequency, sec^{-1}
Γ	term defined by Eq. [20]

Subscripts

i	gas-liquid interface
o	bulk phase, external to electrode
t	total value

Technical Notes

Resistance for Flow of Current to a Disk

John Newman

Inorganic Materials Research Division, Lawrence Radiation Laboratory, and

Department of Chemical Engineering, University of California, Berkeley, California

In order to obtain the concentration and activation overpotential for a rotating disk electrode it is necessary to subtract from the measured overpotential the ohmic potential drop between the reference electrode probe and the disk. The ohmic drop for a small disk is concentrated in the solution near the disk (Fig. 1). Rather than try to put the probe from a reference electrode very near the surface and thus distort the potential and velocity distributions, one can estimate the ohmic drop from the resistance between a disk imbedded in the surface of an insulator and a counter electrode at infinity. This procedure does not account for deviations from the primary current distribution.

For the purpose of calculating the potential distribution from Laplace's equation, we use rotational elliptic coordinates[1] ξ and η related to cylindrical coördinates by

$$z = a\xi\eta$$
$$r = a\sqrt{(1+\xi^2)(1-\eta^2)} \qquad [1]$$

where a is the radius of the disk, z is the normal distance from the disk, and r is the distance from the axis of symmetry (see Fig. 1, where lines of constant Φ are also lines of constant ξ). In this coördinate system Laplace's equation is

$$\frac{\partial}{\partial\xi}\left[(1+\xi^2)\frac{\partial\Phi}{\partial\xi}\right] + \frac{\partial}{\partial\eta}\left[(1-\eta^2)\frac{\partial\Phi}{\partial\eta}\right] = 0 \qquad [2]$$

and the boundary conditions are

[1] These are related to "oblate spheroidal coördinates" by $\xi = \sinh\mu$ and $\eta = \cos\theta$.

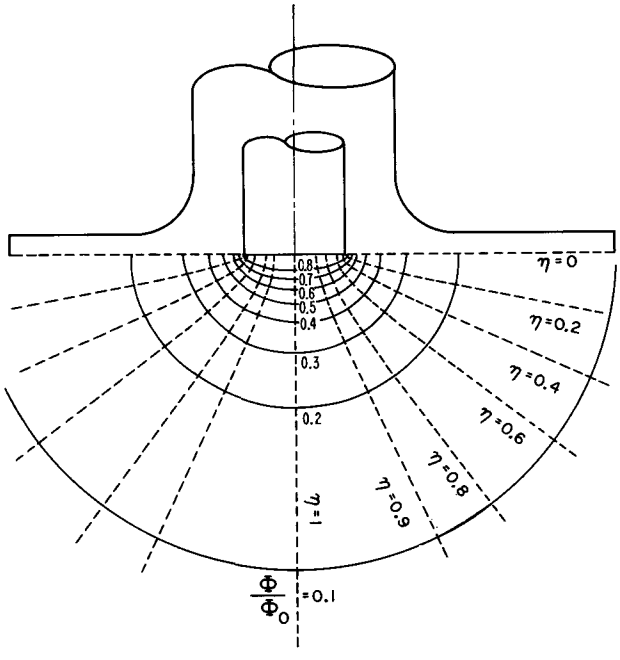

Fig. 1. Current and potential lines for a disk electrode

$$\left.\begin{array}{l}\Phi = \Phi_0 \text{ at } \xi = 0 \text{ (on the disk electrode)}\\ \partial\Phi/\partial\eta = 0 \text{ at } \eta = 0 \text{ (on the insulating annulus)}\\ \Phi = 0 \text{ at } \xi = \infty \text{ (far from the disk)}\\ \Phi \text{ well behaved at } \eta = 1 \text{ (on the axis of the disk)}\end{array}\right\} \qquad [3]$$

To obtain a solution by the method of separation of variables we set

$$\Phi = P(\eta)Q(\xi) \qquad [4]$$

The differential equations for P and Q are

$$\frac{d}{d\eta}\left[(1-\eta^2)\frac{dP}{d\eta}\right] + nP = 0,$$
$$\frac{d}{d\xi}\left[(1+\xi^2)\frac{dQ}{d\xi}\right] - nQ = 0 \qquad [5]$$

where n is the separation constant. The solutions of these equations are Legendre functions. In order to have well behaved solutions, n is restricted to values $n = l(l+1)$ where $l = 0, 1, 2, \ldots$. In order to satisfy the condition on the insulating surface, l must be even. It turns out that the condition $\Phi = \Phi_0$ on the disk can be satisfied simply with the solution for $n = 0$. Integration thus yields

$$\Phi/\Phi_0 = 1 - (2/\pi)\tan^{-1}\xi \qquad [6]$$

Equipotential lines are shown on Fig. 1.

The current density at the disk surface can then be evaluated as follows

$$i = -\kappa\left.\frac{\partial\Phi}{\partial z}\right|_{z=0} = \frac{-\kappa}{a\eta}\left.\frac{\partial\Phi}{\partial\xi}\right|_{\xi=0}$$
$$= \frac{2}{\pi}\frac{\kappa\Phi_0}{a\eta} = \frac{2\kappa\Phi_0}{\pi\sqrt{a^2-r^2}} \qquad [7]$$

Hence the total current to the disk is

$$I = 2\pi\int_0^a i\,r\,dr = 4\kappa a\Phi_0 \qquad [8]$$

and the resistance is

$$R = \Phi_0/I = 1/4\kappa a \qquad [9]$$

This result agrees satisfactorily with that of Gröber (1) for the analogous heat conduction problem. The resistance of a hemisphere of radius a mounted on an insulating plane is easily calculated to be $1/2\pi\kappa a$. Hence the resistance of the disk is greater than that of a hemisphere by a factor of $\pi/2 = 1.5708$.

Table I. Apparent resistance for various probe positions

$a = 0.25$ cm, $\kappa = 0.00872$ (ohm-cm)$^{-1}$

r, cm	z, cm	R, ohm	Probe position
0	0.05	14.48	Below the disk
0	0.1	27.78	Below the disk
0	2.5	107.43	Below the disk
2.5	0	107.39	Beside the disk
2.7	0	107.93	Beside the disk
∞	∞	114.7	At infinity

For a 0.1M copper sulfate solution and a 0.5 cm (diameter) disk the above formula gives $R = 114.7$ ohms since $\kappa = 0.00872$ (ohm-cm)$^{-1}$ for this solution at 25°C (2).

Far from the disk the potential approaches

$$\Phi \rightarrow 2\Phi_0 a/\pi\rho \text{ as } \rho \rightarrow \infty \qquad [10]$$

where ρ is the distance from the center of the disk in spherical coördinates. This formula can be used to estimate the error for the situation where the reference electrode is not at infinity and the potential field is distorted by the walls of the cell.

The ohmic resistance of the solution is tabulated in Table I for several possible locations of the probe from the reference electrode. These show that even with the probe only half a millimeter from the surface, the resistance is by no means negligible. Far from the disk the resistance is not very sensitive to small uncertainties in the location of the probe. These considerations suggest that it is better to put the probe some distance from the disk.

Equation [7] shows that the current density becomes infinite at the edge of the disk, a general characteristic of the primary current distribution where electrode polarization is ignored. This is in marked contrast to the uniform current density predicted by Levich (3) on the basis of mass transfer limitations. At currents below the limiting current both factors, ohmic drop in the solution and mass transfer limitations near the disk, influence the current distribution, which will then finally neither be uniform on the disk nor infinite at the edge of the disk. We have formulated this more general problem and expect to report results for the rotating disk in the near future.

Acknowledgment

This work was supported by the United States Atomic Energy Commission, under Contract W-7405-eng-48.

Manuscript received Dec. 6, 1965; revised manuscript received Jan. 31, 1966.

Any discussion of this paper will appear in a Discussion Section to be published in the December 1966 JOURNAL.

REFERENCES

1. Heinrich Gröber, "Die Grundgesetze der Wärmeleitung und des Wärmeüberganges," Julius Springer Verlag, Berlin (1921).
2. B. Fedoroff, *Annal. Chim.*, **16**, 154 (1941).
3. B. Levich, *Acta Physicochim. U.R.S.S.*, **17**, 257 (1942).

Preliminary Evaluation of Ceria-Lanthana as a Solid Electrolyte for Fuel Cells

David Singman

Power Supply Branch, Harry Diamond Laboratories, Washington, D. C.

Solid electrolytes which are oxygen-ion conducting offer attractive possibilities for the construction of fuel cells capable of electrochemical oxidation of hydrogen and various hydrocarbons. Aqueous electrolyte fuel cells are limited to low current densities by activation polarization. The life of fused salt electrolyte cells is limited by corrosion. A solid electrolyte fuel cell utilizing a mixture of 85 mole % ZrO_2 and 15 mole % CaO was reported by Weissbart and Ruka (1). Although this cell is relatively unaffected by activation polarization, its output is resistance limited to operation near 1000°C because the specific conductance of the solid solution is 0.02 ohm^{-1} cm^{-1} at 1000°C and 0.002 ohm^{-1} cm^{-1} at 800°C (2).

A solid solution of 85 mole % ceria-15 mole % lanthana having higher conductivity has been reported by Croatto and Mayer (3). As is shown in Fig. 1, curves I and II, the conductivity of ceria-lanthana at 800°C is approximately equal to calcia-zirconia's conductivity at 1000°C. Oxygen ion conductance should occur in ceria-lanthana solid solution according to the concepts of Wagner (4) and Kingery (5) because fluorite lattice having anion vacancies exists (6). If the conduction is 95% or more ionic, this electrolyte may be suitable for fuel cell use because as much as 5% electronic conduction may be tolerated (7). Consequently, preliminary investigations were made of this electrolyte to determine its suitability in fuel cells.

Experimental

Initially, 99.9% pure (minimum) cerium oxide and a purified grade of lanthanum nitrate hexahydrate, 98% pure, were used as starting materials. A higher grade of purity of nitrate, 99.997% pure, was later used.

The mixed oxide was prepared by conversion of ceric oxide to an aqueous solution of the nitrate, addition of lanthanum nitrate solution, evaporation to dryness, and ignition of the residue. X-ray intensity measurements indicated that the solid solution had fluorite structure (8). Wafers were molded from the fine powder. After being hydraulically pressed at 10,000 lb/in. and ignited for several hours at 1000°C, the disks had the following dimensions: 2 cm diameter and 0.1 cm thickness. Porous platinum electrodes, 1.4 cm in diameter, were formed on the faces which had been ground smooth and parallel.

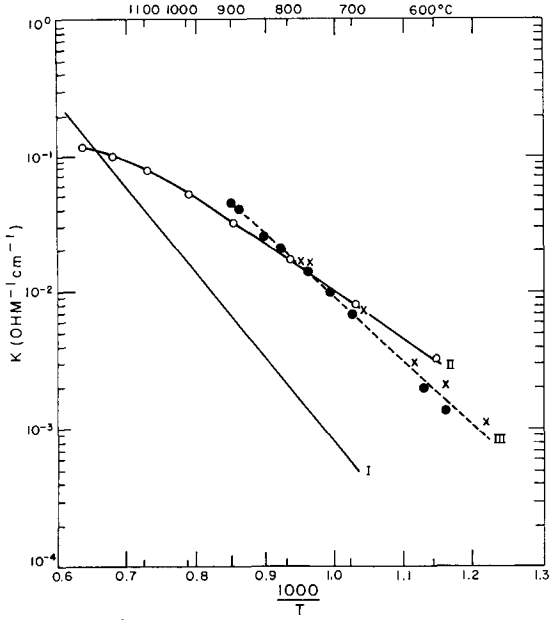

Fig. 1. Comparison of electrical conductivity of calcia-zirconia and ceria-lanthana.

Curves	Electrolyte	Workers
I	Calcia-zirconia	Kingery *et al.* (12)
II	Ceria-lanthana	Croatto and Mayer (3)
III	Ceria-lanthana	This laboratory

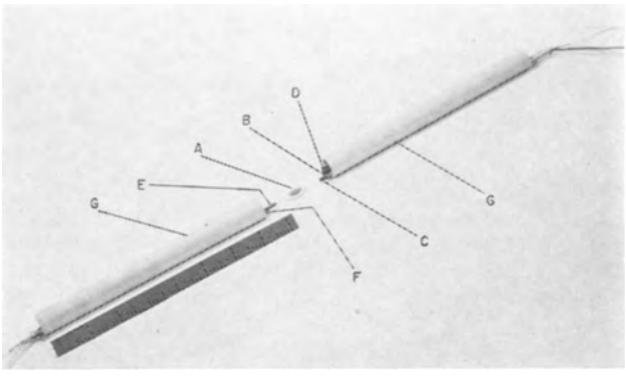

Fig. 2. Experimental cell: A, electrolyte disk; B, thermocouple protection tube; C and E, insulated probe leads; D and F, gas inlet tubes; G, mullite tubes forming half cell compartments.

The experimental cell is shown in Fig. 2. The mullite tubes forming the anode and cathode compartments were held against the electrolyte wafer by spring tension applied by an end plate-bolt assembly external to the furnace. Platinum wire probes encased in thin ceramic tubing were pressed against the platinum coated areas of the disk so as to maintain electrical contact. Thin ceramic tubing was used to feed oxygen into the cathode chamber and 10% hydrogen-90% nitrogen mixture into the anode chamber. Temperatures were measured by a potentiometer and a chromel-alumel thermocouple placed approximately 1 cm from the electrolyte disk. Voltage was determined by use of a potentiometer and current by a milliameter. Electrical resistance was measured by a Wheatstone Bridge at 1000 cycles.

Results and Discussion

The experimental method for evaluating small disks of mixed oxide as electrolyte was tested by the use of commercially available wafers of calcia-zirconia. An open-circuit voltage of 1.05v was obtained at 1010°C for oxygen at the cathode and nitrogen-hydrogen mixture at the anode. The discharge curves obtained at 900° and 1000°C, curves II and III, Fig. 3, are similar to those obtained by Binder *et al.* (9).

Figure 1, curves III and II, compares the experimental results obtained for conductivity as a function of temperature of 85 mole % of ceria and 15 mole % of lanthana with those obtained by Croatto and Mayer (3). The two sets of points in curve III represent separate runs on two samples prepared similarly from the same batch of mixed oxide obtained from the purer grade of lanthanum nitrate hexahydrate. The dependence of conductivity on temperature may be expressed by the equation, $K = Ae^{-Q/RT}$ where K is the electrical conductivity in ohm^{-1} cm^{-1}, A is a constant, Q is the activation energy in calories, and e, R, and T have their usual significance. A value of 21 kcal was calculated for Q. Croatto and Mayer (3) report a value of 14.7 kcal.

The difference in slopes of the conductivity-reciprocal temperature curves, II and III, Fig. 1, was probably caused by differences in purity and porosity of the electrolytes and by contact resistance effects. Croatto and Mayer used nitrates of "special purity" as starting materials. Their electrolyte may have been more porous as their pellets were pressed at a lower pressure, 85 lb/in.^{2}, and were fired at a lower temperature, 1400°C.

Open-circuit voltage obtained with ceria lanthana mixed oxide, prepared from 98% pure lanthanum nitrate hexahydrate, was 0.67v at 800°C and increased only to 0.68v at 850°C. The same open-circuit voltage was observed at 800°C with electrolyte prepared from 99.99% pure lanthanum nitrate hexahydrate thus indicating that the low open-circuit voltage was not caused by impurities contributed by the 98% pure lanthanum nitrate.

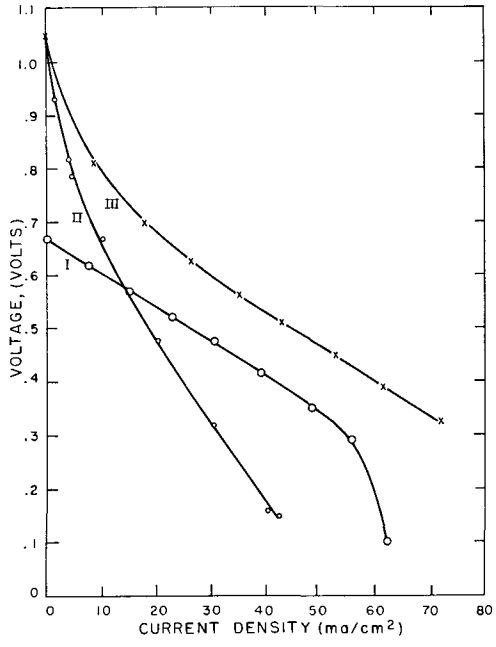

Fig. 3. Comparison of cell voltage-current curves obtained with different electrolytes: curve I for $(CeO_2)_{0.85}$ $(La_2O_3)_{0.15}$ at 800°C; curve II for $(ZrO_2)_{0.85}$ $(CaO)_{0.15}$ at 900°C; curve III for $(ZrO_2)_{0.85}$ $(CaO)_{0.15}$ at 1000°C.

Open-circuit voltages were measured before and immediately after several discharges at constant load. The open-circuit voltage after discharge was 6 to 51 mv lower than before discharge depending on the number of coulombs passing through the disk. Open-circuit voltage obtained with calcia-zirconia electrolyte returned immediately to its initial value when the circuit was opened. The drop in open-circuit voltage observed with ceria-lanthana electrolyte was probably caused by composition changes.

Variation in conductivity with oxygen pressure was observed with electrolyte prepared from both grades of lanthanum nitrate hexahydrate. At 800°C, specific conductivity values of 6.4 x 10^{-2} and 1.1 x 10^{-1} ohm^{-1} cm^{-1} were observed in air and in nitrogen-hydrogen mixture, respectively, for the less pure electrolyte. With electrolyte prepared from the 99.99% pure lanthanum nitrate hexahydrate, lower values were obtained. These values were 2.2 x 10^{-2} and 5.8 x 10^{-2} ohm^{-1} cm^{-1} at 800°C in air and in nitrogen-hydrogen mixture, respectively. In oxygen, 1.4 x 10^{-2} ohm^{-1} cm^{-1} was obtained.

This variance in conductivity with oxygen pressure indicates the presence of electronic conductance (10) which probably contributed to the low open-circuit voltage. Although it was realized that high-purity starting materials were essential to avoid electronic conduction, the finest grade of ceric oxide which was commercially available to this laboratory was 99.9% pure; 0.1% of other rare earths were detected spectrographically (11). Since the further purification of this oxide is especially difficult (11), additional purification was not attempted in this preliminary investigation.

A representative voltage-current curve obtained with electrolyte prepared from the purer grade of lanthanum nitrate hexahydrate is shown by curve I, Fig. 3. The linear portion of the curve from 0 to 50 ma/cm^2 shows that resistance polarization is predominant within this current range. The abrupt change in slope at 50 ma/cm^2 indicates concentration polarization resulting possibly from cation transport.

Conclusion

Change in open-circuit voltage after current is drawn indicates a change in electrolyte composition.

Hence, ceria-lanthana solid solution is probably not suitable for use as solid electrolyte in fuel cells.

Acknowledgments

The author is indebted to C. W. H. Barnett for molding, pressing and igniting the electrolyte disks. Helpful discussions with A. F. Forziati and C. W. H. Barnett and critical review of the manuscript by G. B. Wood are greatly appreciated.

Manuscript received March 24, 1965; revised manuscript received Jan. 3, 1966.

Any discussion of this paper will appear in a Discussion Section to be published in the December 1966 JOURNAL.

REFERENCES

1. J. Weissbart and R. Ruka, *This Journal*, **109**, 723 (1962).
2. Calculated from data of W. D. Kingery, J. Pappis, M. E. Doty, and D. C. Hill, *J. Am. Ceram. Soc.*, **42**, 393 (1959).
3. U. Croatto and E. Mayer, *Gaz. chim. ital.*, **73**, 199 (1953).
4. C. Wagner, *Naturwissenschaften*, **31**, 265 (1943).
5. W. D. Kingery, "Introduction to Ceramics," p. 657, John Wiley & Sons, Inc., New York (1960).
6. E. Zintl and U. Croatto, *Z. anorg. u. allgem. Chem.*, **242**, 79 (1939).
7. H. H. Mobius, Diss. Rostock 1958 cited in *Z. Chem.*, **2**, 100 (1962).
8. F. L. Roth and S. Schneider, National Bureau of Standards, Wash., D. C., Private communication.
9. H. Binder, A. Kohling, H. Krupp, K. Richter, and G. Sanstede, *Electrochim. Acta*, **8** (10), 781 (1963).
10. K. Kiukkola and C. Wagner, *This Journal*, **104**, 379 (1957).
11. H. Kremers, American Potash and Chemical Corporation, New York, N. Y. Private communication.
12. W. D. Kingery, J. Pappis, M. E. Doty, and D. C. Hill, *J. Am. Ceram. Soc.*, **42**, 393 (1959).

Optical Absorption in Chromium Doped, High Resistivity GaAs in the 0.6 to 1.5 ev Range

Charlie E. Jones, Jr., and A. Ray Hilton

Central Analytical Chemistry Facility, Texas Instruments Incorporated, Dallas, Texas

Optical absorptions, in high resistivity gallium arsenide, on the long wavelength side of the main absorption edge have been previously reported (1, 2, 3). Sturge (1) reported thresholds of 0.70, 0.49, and 0.27 ev, from the main absorption edge, for some unknown impurities. Bube (2) recorded three unidentified impurity absorptions at about 0.5, 0.6, and 0.7 ev below the conduction band. Holeman and Hilsum (3), studying photoconductivity in high resistivity GaAs, observed a deep lying level with a threshold energy of 0.63 ev. The electrical properties of doped, high resistivity, GaAs are still not thoroughly understood. Investigators are not in agreement as to whether a deep donor or a deep acceptor is responsible for the high resistivity. These difficulties are discussed by Cronin and Haisty (4) and by Sturge (1). We have noted an energy level common to all chromium doped samples. The accurate location of this level and its behavior at reduced temperature adds to the present knowledge of high resistivity GaAs.

Experimental

The measurements were made using a Perkin-Elmer Model 350 spectrophotometer. The 350 is a double beam recording instrument covering the range 0.46-7.1 ev. The energy passes through the monochromator prior to entering the sample chamber. The instrument scans from low energy to high with a resolution at 1.5 ev of better than 0.002 ev. The output is a linear plot of transmittance or absorbance against wavelength.

The measurements were performed with the sample located in a Dewar capable of maintaining the specimen at the temperature of the inner chamber. The sample holder is a large mass of copper attached directly to the bottom of the Dewar. Samples are attached to this holder with Dow Corning silicone vacuum grease. Measurements using a gold-cobalt *vs.* copper thermocouple, as described by Powell *et al.* (5), show that samples properly mounted on this sample holder reach a temperature of about 80°K when the inner chamber contains liquid nitrogen. Samples reach an equilibrium temperature about 1 hr after the 1-liter Dewar is filled and hold constant for about 3 hr. All measurements, carried out at reduced temperature, were performed at this stable temperature. Quartz windows were used and the base of the system was designed to fit directly into the raceways of the sampling compartment.

Material

The slices studied were sawed from a high resistivity (10^8 ohm-cm) crystal of GaAs. The crystal was pulled from an alumina boat on the (111) direction from a melt compounded in the crystal puller. The technique used was previously described (4). The crystal was doped with radiotracer Cr^{51}. The chromium was added to the gallium metal. Chromium content of each slice was accurately known from a knowledge of the activity of the slice.

The slices were mechanically polished, to a mirror finish, with 0.05μ alumina and then briefly etched in a $H_2SO_4 \cdot H_2O_2 \cdot H_2O$ etchant. We have previously shown (6) that a GaAs surface treated in this manner has the optical properties of the bulk.

Results and Conclusions

Five samples were measured in this investigation. The chromium content of each sample was as follows:

Sample	Cr atoms/cc
A	5.9×10^{15}
B	1.9×10^{16}
C	2.1×10^{16}
D	2.5×10^{16}
E	3.2×10^{16}

Each sample was scanned through the 0.6 to 1.5 ev range at 295° and 80°K. A common absorption which increased as the chromium content increased, was noted. Figure 1 shows a spectrophotometer trace of one of the samples at each temperature. An absorption is evident at a wavelength slightly larger than the band edge. As the temperature decreases to 80°K the absorption is stronger and the absorption edge moves to shorter wavelength. The absorption coefficients for each sample were calculated from the simplified expression

$$T = (1 - R)^2 e^{-\alpha x}$$

where T = transmission, R = reflectivity (0.296 for GaAs), x = sample thickness (cm), and α = absorption coefficient. Since there is a theoretical relationship between the absorption coefficient and energy squared (1) and in order to define the threshold energy more carefully, the square root of the absorption coefficient

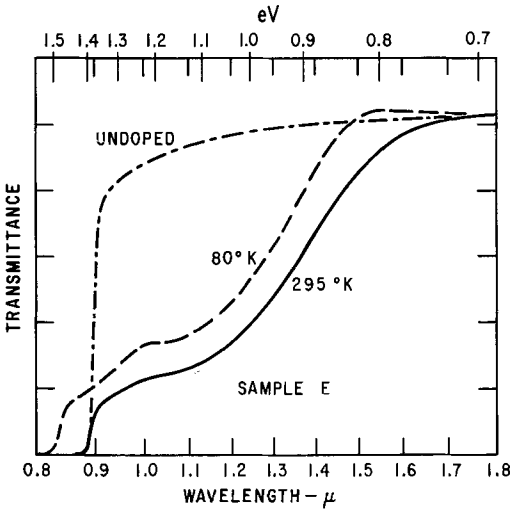

Fig. 1. Transmittance of chromium doped GaAs

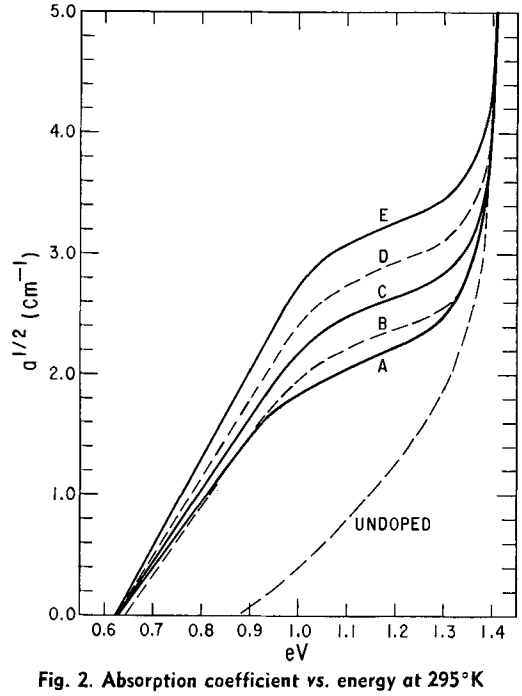

Fig. 2. Absorption coefficient vs. energy at 295°K

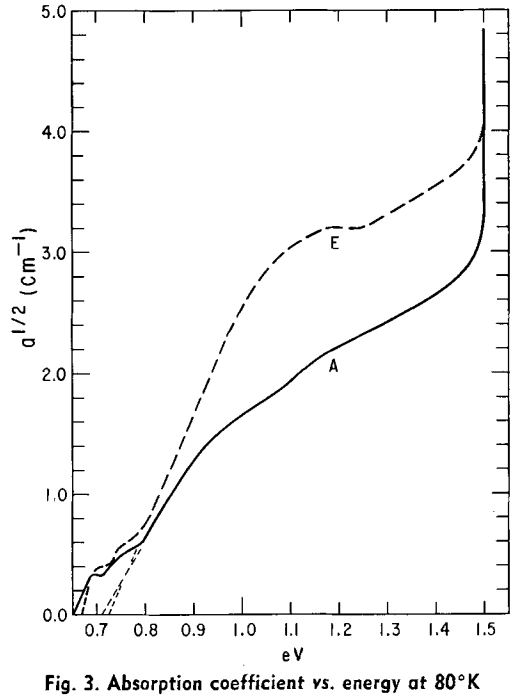

Fig. 3. Absorption coefficient vs. energy at 80°K

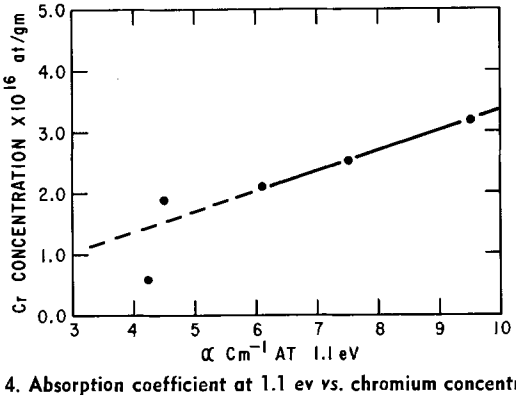

Fig. 4. Absorption coefficient at 1.1 ev vs. chromium concentration

was plotted against energy. This plot, for the 295°K measurements, is shown in Fig. 2. The threshold was determined by extrapolating the linear part of the absorption curves to zero absorption. The extrapolated energy values for all samples are the same within the experimental errors of the measurements. The threshold is at 0.63 ± 0.02 ev. Following Sturge's connotations and band gap value (1.43 ev) this level is 0.80 ev from the main absorption edge. Similar data for two samples from the 80°K measurements are shown in Fig. 3. The level at 80°K is 0.79 ev from the absorption edge. Apparently, the energy level is attached to either the valence or conduction bands and does not change its position relative to the appropriate band as the temperature is lowered. Other levels also begin to appear at the lower temperature. This is consistent with Sturge's (1) work. Figure 4 is a plot of the absorption coefficient (295°K) at 1.1 ev, the approximate maximum, *vs.* the chromium concentration. There is a linear relationship between absorption and chromium content for all except sample A, the lightest doped sample. The nonlinearity of the curve in the lowest doping region could be due to difficulties in the measurement technique or partial compensation in the sample with a small chromium content. An optical absorption was found to occur at the same wavelength, in more than 15 different samples, grown in our laboratory, of chromium doped high resistivity GaAs. This absorption measurement alone is insufficient evidence to determine whether the level is a deep acceptor state. The energy level observed does agree with the value found by Cronin and Haisty (4) by plotting the $RT^{3/2}$ *vs.* $1/T$ and the photoluminescence peak of Turner *et al.* (7) if the transition observed is from the valence band to the chromium state.

Acknowledgments

The authors wish to thank G. Larrabee for supplying the samples used in this study and G. R. Cronin, R. W. Haisty, and R. Conrad for helpful discussions. Jim Parker made the transmission measurements.

Manuscript received Jan. 13, 1966.

Any discussion of this paper will appear in a Discussion Section to be published in the December 1966 JOURNAL.

REFERENCES

1. M. D. Sturge, *Phys. Rev.*, **127**, 768 (1961).
2. R. H. Bube, *J. Appl. Phys.*, **31**, 315 (1960).
3. B. R. Holeman and C. Hilsum, *J. Phys. Chem. Solids*, **22**, 19 (1961).
4. G. R. Cronin and R. W. Haisty, *This Journal*, **111**, 874 (1964).
5. R. L. Powell, M. D. Bunch, and R. J. Corruccini, *Cryogenics*, **1** (1961).
6. C. E. Jones and A. R. Hilton, *This Journal*, **112**, 908 (1965).
7. W. J. Turner and G. D. Pettit, *Bull. Am. Phys. Soc. Series*, **9**, 269 (1964).

Vapor-Deposited Microcrystalline Silicon

E. Sirtl and H. Seiter

Forschungslaboratorium, Siemens & Halske AG, München, Deutschland

For some years thin films of semiconductors have been of growing interest for device technology. On the one hand there are papers on polycrystalline films of II-VI compounds (1), III-V compounds (2), and silicon (3); on the other hand some authors obtained an oriented growth of thin silicon layers on an insulating substrate (4-6). Since only a few single crystal substances are suitable for this purpose, we therefore have examined, along with our own work on oriented silicon layers (7), the growth and the properties of polycrystalline silicon films.

In the material normally resulting from uncontrolled growth the crystal shapes and sizes widely differ and depend on the nature of the substrate. A silicon film of uniform and small grain size requires a sufficient number of nuclei for its growth; this is attainable by simultaneous deposition of a second phase which favors nucleation. In this paper we discuss the growth and properties of shiny microcrystalline layers of silicon formed during the thermal decomposition of organosilicon compounds. It was found that in this case simultaneously deposited silicon carbide caused the continuous formation of nuclei of arbitrarily oriented silicon crystallites of uniform grain size.

Preparation and Structure of Silicon Layers

If organosilicon compounds, such as CH_3SiCl_3, CH_3SiHCl_2, or $(CH_3)_2SiCl_2$, are decomposed below 1300°C, the reaction results primarily in deposits of silicon, in contrast to investigations at higher temperatures (8). The same phenomenon can be observed when mixtures of chlorosilanes and simple hydrocarbon derivatives, such as CH_2Cl_2, near the stoichiometric ratio required for the formation of SiC are thermally decomposed in the presence of hydrogen or an inert gas. Most of our experiments were carried out under the following conditions: temperature (uncorrected), 1100°C; molar ratio CH_3SiHCl_2: $SiHCl_3$: H_2, 1:2:60; gas flow rate in the reaction zone, 3 cm/sec; deposition rate, 10μ /min.

The layers in this study were produced in a quartz reactor, the schematic layout of which is shown by Fig. 1. The samples were placed on a gas-tight graphite heater which is brought to the desired temperature by passing a current directly through it. The pyrometrically measured temperatures are given without corrections. All gas reactions took place in a flowing system (approximately 1-2 l/min).

If a material of this type is deposited on smooth surfaces, shiny layers will be obtained at certain temperatures and concentrations. If the layers are made thicker, even rough substrate surfaces will yield the same result. The grain size of this microcrystalline deposit is often below the resolution limit of light microscopes. Figure 2 shows the fracture of such a layer, the plane of the fracture being perpendicular to the surface of a silicon monocrystal disk which was used as the substrate in this case. This picture already shows the uniform structure and the low degree of roughness on the surface of the relatively thick growth layer. Figure 3 enables comparison of the photos taken of a typical surface structure through a light microscope and through an interference mi-

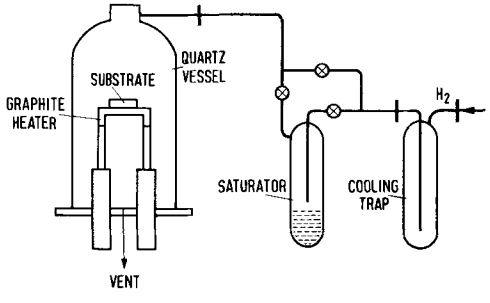

Fig. 1. Schematic diagram of deposition apparatus

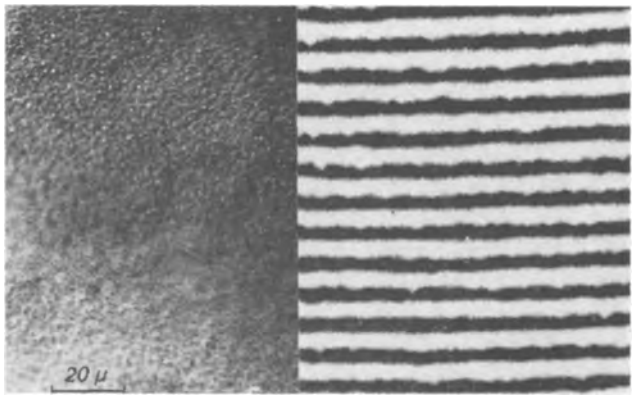

Fig. 3. Surface of microcrystalline silicon layer: left side; normal photomicrograph, phase-contrast; right side, with interference fringes.

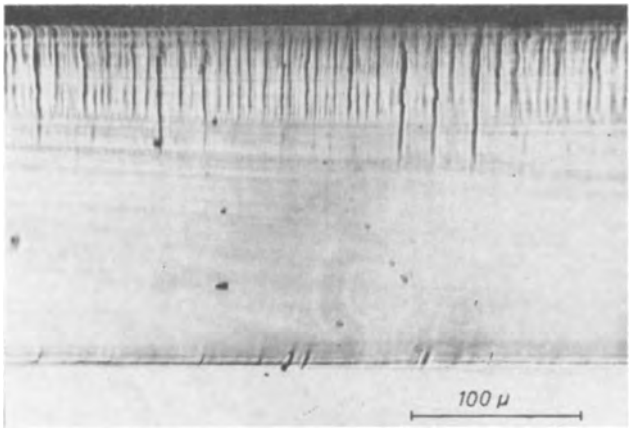

Fig. 2. Cross section of microcrystalline silicon layer (fractured)

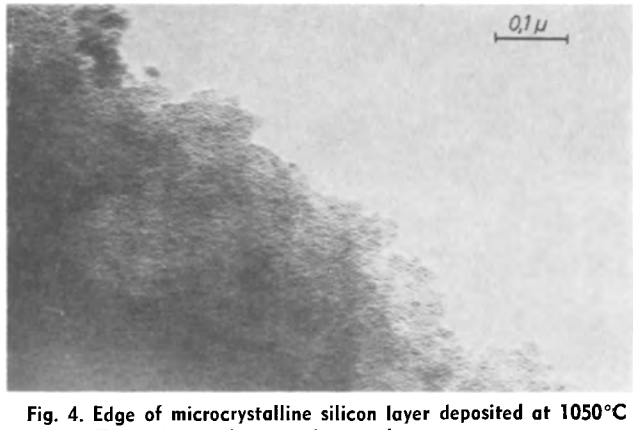

Fig. 4. Edge of microcrystalline silicon layer deposited at 1050°C (uncorr.). Transmission electron micrograph.

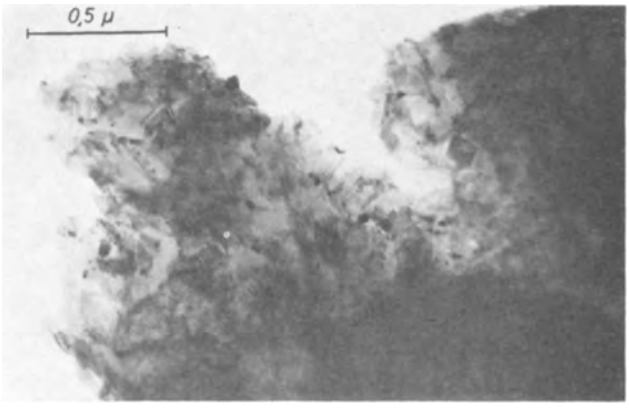

Fig. 5. Edge of microcrystalline silicon layer deposited at 1200°C (uncorr.). Transmission electron micrograph.

croscope. A deflection of the interference lines by an amount corresponding to the distance between two lines would indicate a difference in thickness of 0.27μ.

Electron micrographs of thin etched layers showed the high degree of dependence of the grain size on the deposition temperature. Thus the dimensions of the crystallites discernible in Fig. 4 are very near the limit of the resolution power of the electron microscope (1050°C), while Fig. 5 already shows larger uniform areas (1200°C).

X-ray and electron diffraction patterns confirmed that silicon carbide in measurable quantities is present in such layers. The presence of carbon was also proved by chemical and spectrometric methods. A quantitative determination of the total carbon content was made possible by burning the silicon samples in an oxygen current and coulometric determination of the CO_2 produced in this way.[1] However, there could be made only semiquantitative comparisons between the chemical total carbon values and the x-ray or electron diffraction data. Surprisingly, analytical values of samples deposited at temperatures between 1000° and 1150°C did not display any significant differences. In all cases the carbon content amounted to about 2 g-a/o. This result might be explained by the fact that both the tendency to form SiC precipitates and the silicon yield increased considerably in this temperature range. The better crystallinity of SiC at higher temperatures would then result in a coarsening of the grain structure of the silicon because of the reduced rate of nucleus formation.

Chemical Behavior

Since the grain size of microcrystalline silicon depends practically only on the conditions prevailing during the gas reaction, it is possible to get shiny layers on a wide variety of substrates. Such production is dependent on good adherence of the films to the substrates, an inert behavior of the substrate under deposition conditions, and a minimum difference between the thermal expansion coefficients of the two substances.

The following substances have been found suitable for use as substrate material: silicon(with and without oxide layer), porcelain, sintered corundum, molybdenum, and graphite (roughened). Only thin layers (10-30μ) can be deposited if there is a noticeable difference in the expansion behavior of the substances, since otherwise the layers would tend to crack and chip. A certain extent of p-type doping (by diffusion of aluminum from the interface) will be found in most cases where porcelain or sintered corundum is used for the substrate.

The carbon content of microcrystalline silicon apparently does not affect the latter's behavior during oxidation. The oxidation rates agree with those measured in the case of monocrystalline samples. The same applies to the porosity of the oxide layers. No grain growth could be observed during any of the oxidation or annealing processes.

Depending on the carbon (carbide) content, etching of the surfaces is rendered more or less difficult. At higher carbon concentration, an oxidizing fused salt bath (*e.g.*, KOH-KNO_3-KF mixture at 400°C) proved helpful.

[1] Analyzed by K. H. Neeb, Siemens-Schuckert-Werke, Erlangen.

Table I.

	n cm^{-3}	ρ ohm-cm	μ cm^2/vsec
as grown	$4.5 \cdot 10^{15}$	60	23
4 hr in O_2 1200°	$2.1 \cdot 10^{16}$	8.6	34
8 hr in O_2 1200°	$7.4 \cdot 10^{16}$	5.8	15

Electrical Properties

Doping of the growing silicon by adding volatile arsenic or boron compounds to the reaction gas does not yet result in reproducible electrical properties. Thus the carrier concentration of otherwise unprocessed samples is much lower than that measured in monocrystalline growth layers with a comparable history. Definite p-type doping by the vapor phase seems to be altogether impossible.

However, if such layers are subsequently annealed in nitrogen or oxygen, the carrier concentration calculated from Hall measurements will correspond approximately to that originally expected. This means that the doping agents which are concentrated primarily in the grain boundaries will be homogeneously distributed by a diffusion process. The carrier mobility measured in subsequently annealed layers was between 10 and 50 cm^2 volt^{-1} sec^{-1}. Typical results are shown in Table I. The layers had a thickness of 150μ and were gas doped by a molar ratio of PCl_3 : Si-compounds = 10^{-5}.

In the growth direction, the electrical properties varied greatly since different zones had formed, probably as a result of heater temperature fluctuations. It was possible to make these zones visible by etching the surface of oblique cuts. The diffusion rate of boron (B_2O_3-SiO_2 source, "box method") is greatly reduced in samples with a higher SiC content. The diffusion front is wavy, and the corresponding p-n junctions display almost no barrier effect, mostly because of the very high series resistances, the magnitude of which depends on geometric factors and on the carbon content.

Discussion

It is not yet known if it is possible to increase the mobility in the system silicon-silicon carbide. Irrespective of the electrical properties, the silicon "modification" here described should be suitable wherever components technology calls for polycrystalline material with maximum uniformity in grain size. A typical field for its appliance could be the method of "dielectric isolation" (9, 10). This method of growing microcrystalline silicon layers may be transferred to other systems; this means that one may insert any other additional phase of low solubility instead of SiC into silicon or other semiconductors.

Acknowledgments

The authors wish to express their gratitude to Mr. G. Prätzel for the great care with which he prepared the silicon layers, Mrs. Ch. Raetzel for the performance of the electrical measurements, and Dr. E. Fuchs for the electron-microscope photographs. The authors gratefully acknowledge the support of this work by the Federal Ministry of Defense.

Manuscript received Nov. 1, 1965; revised manuscript received Jan. 31, 1966. This paper was presented at the Buffalo Meeting, Oct. 10-14, 1965.

Any discussion of this paper will appear in a Discussion Section to be published in the December 1966 JOURNAL.

REFERENCES

1. P. K. Weimer, *Proc. IRE*, **50**, 1462 (1962).
2. K. G. Günther in "Compound Semiconductors," Vol. 1, p. 313, R. K. Willardson and H. L. Goering, Editors, Reinhold Publishing Corp., New York (1962).
3. J. D. Heaps, O. N. Tufte, and A. Nussbaum, *IRE Trans. Electron Devices*, **8**, 560 (1961).
4. H. M. Manasevit and W. I. Simpson, *J. Appl. Phys.*, **35**, 1349 (1964).
5. R. W. Bicknell, J. M. Charig, B. A. Joyce, and D. J. Stirland, *Philos. Mag.*, **9**, 965 (1964).
6. C. W. Mueller and P. H. Robinson, *Proc. IEEE*, **52**, 1487 (1964).
7. H. Seiter and C. Zaminer, *Z. Angew. Phys.*, **20**, 158 (1965).
8. K. M. Merz in "Silicon Carbide," p. 73, J. R. O'Connor and J. Smiltens, Editors, Pergamon Press, New York (1960).
9. J. G. F. Bouchard and F. W. Hammond, Paper presented at the Washington Meeting of the Society, Oct. 11-15, 1964.
10. D. F. Allison, *Solid State Design*, **6**, 29 (1965).

A Point Contact Method of Evaluating Epitaxial Layer Resistivity

C. C. Allen, L. H. Clevenger, and D. C. Gupta[1]

Semiconductor Research and Development Laboratory, Texas Instruments Incorporated, Dallas, Texas

Various methods (1-5) have been devised for measuring the resistivity of epitaxial layers of silicon or germanium on substrates of the same conductivity type and lower resistivity. The point contact breakdown voltage method gives a nondestructive and a quick measurement. The purpose of this report is to present a semiautomatic pulsed current technique which (*a*) reduces the error in determining when breakdown has occurred, and thus allow better reproducibility, and (*b*) reduces power dissipation in the sample during measurement.

Pulse Technique and Apparatus

The apparatus uses a current regulated square wave pulse which increases until breakdown is reached. Figure 1 shows a block diagram of the set. A square wave of 500 μsec pulse duration and repetition rate of 80 pulses/sec is generated by the blocking oscillator. Risetime of the pulse varies between 20 and 200 μsec, depending on the load. The pulse is fed to a ramp generator which, on command, produces a series of progressively increasing voltage pulses. These voltage pulses are used to control the current output from a constant current generator. The current generator has a maximum capability of about 600v, with a current of 0 to 125 ma.

The voltage probe is connected through a voltage divider to a high input impedance amplifier. A diode detector is used to charge a capacitor to the peak voltage. The breakdown point is detected by means of a slope detector. This detector turns the ramp generator off when the rate of change of voltage becomes zero or negative. Reset and timing are handled by means of a monostable flip flop with a 10-sec time constant. The breakdown voltage is read on a peak reading voltmeter which has a risetime of 150 μsec.

Osmium-tipped probe having a tip radius of 2.5 mils is used. The weight on the probe is adjusted to 20g in normal use.

[1] Present address: General Electric Company, SPD Electronics Park, Syracuse, New York.

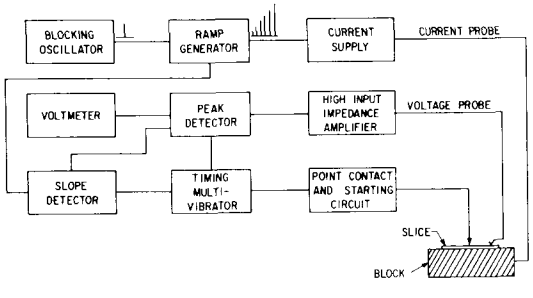

Fig. 1. Block diagram of the semiautomatic measuring circuit

Experimental Techniques

Since the point contact method of measuring epitaxial layer resistivity is empirical, a calibration curve for point contact breakdown voltage *vs.* resistivity was developed as follows. Slices of 30 mils thickness or more were cut from melt grown bulk material. The resistivity of these slices was measured on a four-point probe resistivity meter (6) and the avalanche breakdown voltage was measured on point contact resistivity set several times. Impurity concentrations were determined from the measured resistivity and Irvin's curve (7). The avalanche breakdown voltage is plotted as a function of impurity concentration in Fig. 2.

Whenever the layer thickness is greater than or equal to the depletion layer thickness, the breakdown voltage can be represented as a function of concentration only. However, for smaller layer thickness, the breakdown is limited by the width of the epitaxial layer as well as its impurity concentration. Total breakdown voltage for this epitaxial layer can be calculated by assuming the relationship of ionization rate per unit path length as a function of electric field (8) and is given by (see Appendix)

$$V_T = \left(\frac{2qK}{3\epsilon\epsilon_0} N^{p+1}\right)^{1/2} \cdot t - \frac{q}{6\epsilon\epsilon_0} N t^2 \qquad (0 \leq t \leq t_{\min}) \qquad [1]$$

$$V_T = V_{B^\infty} \quad (t \geq t_{\min}) \qquad [2]$$

where t is the epitaxial layer thickness, N is the impurity concentration in the layer, $t_{\min}$ is the minimum

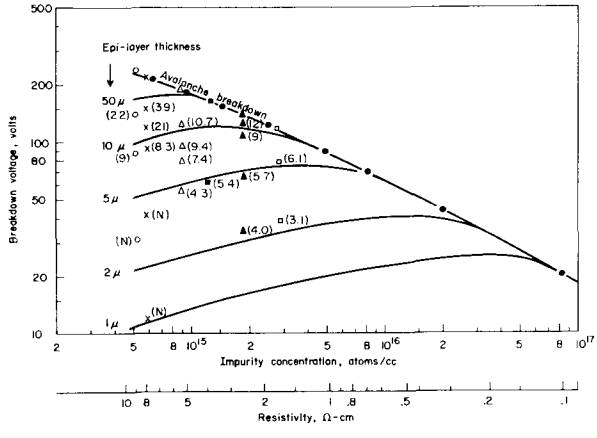

Fig. 2. Point contact breakdown voltage for n-type silicon. •, melt grown bulk material; other symbols, epitaxial wafers etched successively several times; ( ), thickness of the epitaxial layer in microns; (N), epitaxial layer thickness not available.

thickness required to obtain avalanche breakdown V_{Boo} and K and p are constants given in Table II.

The breakdown voltage is calculated using Eq. [1] in the region where it is limited by the width of the layer as well as its impurity concentration and is plotted in Fig. 2 for epitaxial layer thicknesses of 1, 2, 5, 10, and 50μ.

To verify the theoretical curves for epitaxial layer width limited samples experimentally, n-type silicon epitaxial slices sufficiently thick to provide avalanche breakdown were taken and were etched several times. The breakdown voltage was measured on the point contact breakdown set and the epitaxial layer thickness was measured on a Beckman IR-5A Spectrophotometer each time. Results are plotted in Fig. 2. A fair correlation exists between the experimental results and the theoretical calibration.

Effects of Duty Cycle, Probe Pressure, and Surface Quality

Figure 3 shows the breakdown voltage obtained for samples of n-type silicon when 60 cps half-wave rectified current and a 500 μsec current pulse are used. Due to a reduction of power dissipation heating, pulse technique yields a higher breakdown voltage for the same resistivity sample. However, for a given per cent error in a voltage measurement the range of corresponding resistivities is equal for both methods.

The point contact breakdown voltage is dependent on the probe pressure. An increase in weight on the probe decreases the avalanche breakdown voltage as shown in Fig. 4. The effect of pressure has been noted to be generally less on low resistivity material than on high resistivity material. Data published by Gardner and Schumann (5) on pressure effects on n-type bulk silicon have been compared (Fig. 4) by calculating V_{BO} by $V_{BO} = V_B/0.955$ where V_B = 45v taken from Fig. 2 for 0.33 ohm-cm. It was observed that the effect of probe pressure is different on avalanche and punch through voltages above 25g on the probe, however, below this value, both voltages were affected in the same manner by the probe pressure. Weights below 10g were not sufficient to provide desired repeatability in the measurements. Therefore, a weight of 20g was used on the probe in normal use. Figure 5 shows the change in avalanche breakdown voltage

Table I. Resistivity comparison of p/p$^+$ epitaxial silicon
(Epitaxial film thickness = 16.0μ)

Resistivity ohm-cm			% Error with respect to diode V-C	
Diode V-C	Point contact probe	Pilot slice	Point contact probe	Pilot slice
0.29	0.19	0.45	−34.5	+55.1
0.30	0.24	0.36	−2.0	+2.0
0.30	0.28	0.42	−6.7	+40.0
0.34	0.40	0.50	+17.6	+47.1
0.44	0.48	0.69	+9.0	+56.8
0.50	0.43	0.88	−14.0	+76.0
0.58	0.56	0.10	−3.5	+89.7
0.65	0.80	1.75	+23.0	+169.2
1.53	1.50	2.10	−2.0	+37.3
10.8	13.0	14.0	+20.3	+30.5

Table II. Constants K and P
Typical values

Material	K	p	Region*
Silicon (n-type)	2.20×10^8	−0.406	$5 \times 10^{14} \leq N < 2 \times 10^{15}$
	4.56×10^9	−0.492	$2 \times 10^{15} \leq N < 2 \times 10^{16}$
	3.73×10^{10}	−0.548	$2 \times 10^{16} \leq N < 1 \times 10^{17}$
Silicon (p-type)	1.22×10^{10}	−0.509	$1 \times 10^{15} \leq N < 1 \times 10^{16}$
	4.30×10^{12}	−0.668	$1 \times 10^{16} \leq N < 2 \times 10^{17}$
Germanium (p-type)	8.93×10^4	−0.20	$1 \times 10^{14} \leq N < 6 \times 10^{14}$
	1.89×10^6	−0.306	$6 \times 10^{14} \leq N < 5 \times 10^{15}$
Germanium (n-type)	1.75×10^8	−0.436	$1 \times 10^{14} \leq N < 6 \times 10^{14}$
	1.54×10^9	−0.50	$6 \times 10^{14} \leq N < 2 \times 10^{15}$

* Since the calibration curves were not linear on the log-log scale, the curves were divided in different regions to obtain best fit. Note that these constants should be determined each time the calibration curve is changed.

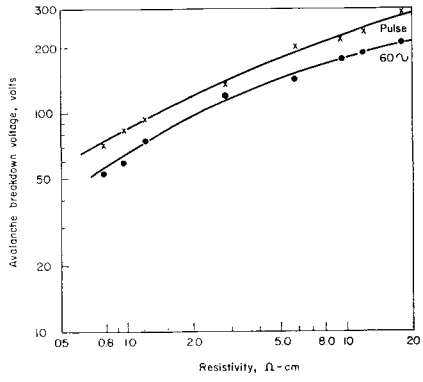

Fig. 3. Effect of duty cycle on avalanche breakdown voltage of n-type silicon.

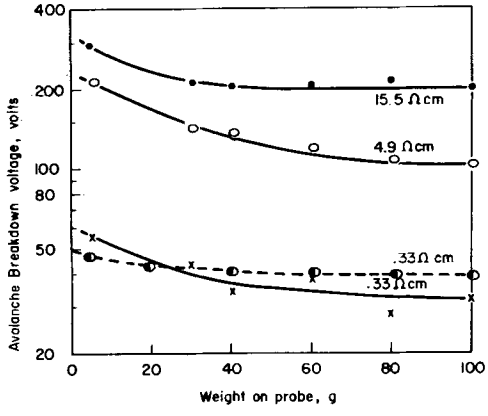

Fig. 4. Breakdown voltage *vs.* gram weight on probe for n-type silicon. — — — half dark circle — — —, results of Gardner and Schumann (5).

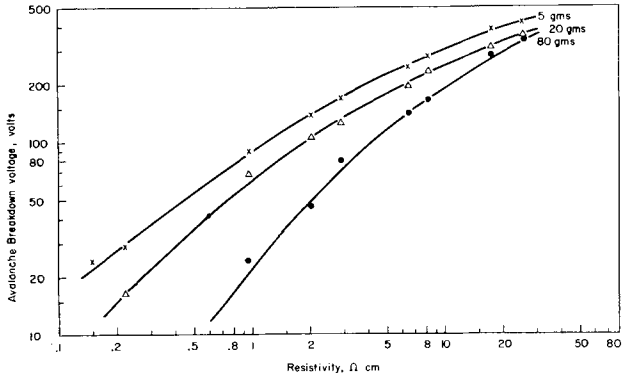

Fig. 5. Probe pressure dependence on point contact breakdown voltage for p-type silicon. Weight on probe in grams: X, 5; △, 20; •, 80.

with respect to resistivity of p-type silicon for different weights on the probe.

To determine the effects of surface quality on breakdown voltage, three silicon slices of different resistivities having a mechanical polish on one side and a lapped surface on the other side were measured. The slices were then chemically polished, and the breakdown voltage was measured on the lapped side several times as the etching progressed. Figure 6 shows the results. It is seen that the breakdown voltage increases as the chemical etching progresses, finally approaching a limiting value as the material damaged by the lapping operation is removed.

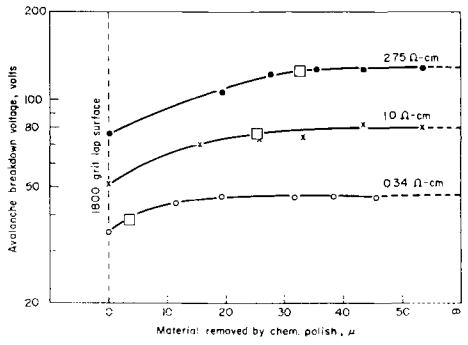

Fig. 6. Effect of surface quality on avalanche breakdown voltage of n-type silicon. □ Represents mechanically polished mirrorlike surface.

Accuracy

To compare the accuracy of the pilot slice method (3) and the point contact method, the resistivities of ten p/p^+ epitaxial slices were determined by the pilot slice method and by the point contact method. Diodes were then constructed from these slices, and the resistivity of the epitaxial layer was found by the diode voltage capacitance technique. Results are shown in Table I. Using the resistivity as determined by the diode voltage capacitance technique as the actual resistivity of the epitaxial layer, only 10% of the resistivities as found by the pilot slice method agreed to within 20% of the value as found by the diode V-C technique, whereas 70% of the values found by the point contact method agreed to within 20% of the resistivity as found by the diode V-C technique.

Conclusion

In conclusion, the point contact breakdown voltage method for measuring resistivity has been shown to be more accurate than the pilot slice method by comparing the two with the diode voltage capacitance technique. An automatic test set using the pulsed current supply gives a fast read out and eliminates the operator judgment. A method for obtaining the calibration for epitaxial layers of thickness greater than or less than the depletion layer thickness has been discussed. This calibration, however, is dependent on the probe pressure. A weight of 20g on the probe was found to be most suitable. To obtain a consistent breakdown voltage, a damage-free chemically polished surface should be used.

Acknowledgment

The authors wish to acknowledge help from several colleagues in the Materials Branch of the Semiconductor Research and Development Laboratory, in particular to W. R. Runyan and S. B. Watelski for their encouragement and suggestions.

Manuscript received May 19, 1965; revised manuscript received Jan. 29, 1966. This paper was presented at the San Francisco Meeting, 9-13, 1965.

Any discussion of this paper will appear in a Discussion Section to be published in the December 1966 JOURNAL.

REFERENCES

1. J. R. Biard and S. B. Watelski, *This Journal*, **109**, 705 (1962).
2. C. O. Thomas, D. Kahng, and R. C. Manz, *ibid.*, **109**, 1055 (1962).
3. H. C. Theuerer, *ibid.*, **108**, 649 (1961).
4. J. Brownson, Paper presented at the Los Angeles Meeting of the Society, May 6-10, 1962; *ibid.*, **111**, 919 (1964).
5. E. E. Gardner, J. F. Hallenback, Jr., and P. A. Schumann, Jr., *Solid-State Electronics*, **6**, 311 (1963).
6. C. C. Allen and W. R. Runyan, *Rev. Sci. Instr.*, **32**, 824 (1961).
7. J. C. Irvin, *B. S. T. J.*, **41**, 388 (1962) (Fig. 1).
8. J. Shields, *J. Electronics and Control*, **6**, 130 (1959).
9. K. G. McKay, *Phys. Rev.*, **94**, 877 (1954).

APPENDIX

The differential equation describing the growth of current density for spherical geometry can be written as

$$\frac{dj_n}{dr} = J\alpha(E) \qquad [3]$$

where, $J = j_n + j_p$ and $\alpha(E)$ is the ionization rate of electrons and holes. Integrating Eq. [3] and assuming, multiplication factor, M to be much greater than one (9) and $\alpha(E) = CE^n$ where C and n are constants (8), one can write for avalanche breakdown, *i.e.*, where the depletion layer is confined to a single resistivity region.

$$E_{B\infty} = \left(\frac{q}{3\epsilon\epsilon_0} \cdot \frac{n+1}{C} \cdot N\right)^{1/n+1} \qquad [4]$$

Using Poisson's equation, the breakdown field, $E_{B\infty}$ can be calculated in terms of the breakdown voltage $V_{B\infty}$ as

$$E_{B\infty} = \left(\frac{2q}{3\epsilon\epsilon_0} NV_{B\infty}\right)^{1/2} \qquad [5]$$

From the curve of avalanche breakdown, Fig. 2, one can write

$$V_{B\infty} = KN^p \qquad [6]$$

The values of constants K and p are given in Table II. Equations [4], [5], and [6] give the values of n and C in terms of K and p.

As the voltage across the thin epitaxial layer is increased above the punch-through voltage, V_p, the space charge region extends to a region of the different resistivity material, *i.e.*, substrate. If E_{add} is the additional field after punch-through necessary to cause breakdown, the condition for breakdown is written as

$$\int_{E_{add}}^{E_p+E_{add}} \alpha(E)\,dE = \frac{qN}{3\epsilon\epsilon_0} \qquad [7]$$

Integrating Eq. [7] and assuming

$$E_p + E_{add} >> E_{add} \qquad [8]$$

the expression for total breakdown voltage $V_T = V_p + V_{add}$ is given by Eq. [1] for $0 \leq t \leq t_{min}$ where t_{min} is the minimum thickness required to obtain avalanche breakdown $V_{B\infty}$ and is given by

$$t_{min} = \left(\frac{6K\epsilon\epsilon_0}{q} N^{p-1}\right)^{1/2} \qquad [9]$$

for $t \geq t_{min}$

$$V_T = V_{B\infty} \qquad [10]$$

The Preparation of Ultrahigh-Purity Nickel Single Crystals

V. J. Albano and R. R. Soden

Bell Telephone Laboratories, Incorporated, Murray Hill, New Jersey

Ultrahigh-purity nickel single crystals are required for experimental studies of their intrinsic electrical properties. The presence of certain impurities, even in the extremely low ppm range, may completely obscure such phenomena as magnetoresistance and cyclotron resonance which are used to explore electronic structure. The suitability of a metal for these studies is conveniently judged by its resistance ratio ($R_{273°K}/R_{4.2°K}$). The room temperature resistance ($R_{273°K}$) is mainly a measure of the thermal contribution to the resistance, and the liquid helium temperature resistance ($R_{4.2°K}$) is dominated by the contribution of chemical impurities in solid solution. This ratio is a relative measure of the impurity content. In general purer materials will have higher resistance ratios. Values for nickel up to 1000 have been reported heretofore (1). Reed and Fawcett of these laboratories (2) in their studies of the Fermi surface of nickel by means of magnetoresistance measurements used single crystal nickel obtained in the early stages of the present work which had a ratio of 2200. Nickel having a resistance ratio of 3500 has been produced by the present technique.

Electrochemical deposition from rigorously purified nickel chloride was used as the primary means of winning the metal. This method produces the nickel directly in massive form and avoids high-temperature reduction operations which could be serious sources of contamination. Further refinement of the plated nickel and consolidation into single crystal form was accomplished by zone melting individual bars of the material after a surface oxidation treatment.

Purification of $NiCl_2$ *solution.*—The nickel chloride used as the starting material was Baker and Adamson's special reagent grade which is low in cobalt. A spectrographic analysis of one lot of this material is given in Table I. Its purification was accomplished principally by the ion exchange technique. Extensive studies by Kraus and Nelson (3) showed that strong-base anion exchange resins of the type Dowex I are capable of removing the anionic chlorocomplexes of about 30 elements from solutions of HCl of appropriate concentrations, but will not remove nickel since it does not form a chlorocomplex. Our studies showed that the use of HCl is unnecessary when purifying $NiCl_2$ since the salt itself provides the high concentration of chloride ions needed to form anionic chlorocomplexes. A high-purity analytical grade Dowex I anion exchange resin designated AGI-XIO, 50-100 mesh, chloride form was used in these studies. It is obtainable from Bio-Rad Laboratories of Richmond, California.

Table I. Emission spectrographic analyses

Element	$NiCl_2 \cdot 6H_2O$, Lot 151 ppm	Ni-XVI, As plated, ppm
Na	12 *vs.* Ni	<0.1
K	<1.0 N.D.	<0.5
Li	<0.5 N.D.	<<0.1
Fe	16	1.3
Cu	2.7	0.5
Mn	2.5	N.D.
Co	<1.0 N.D.	N.D.
Pb	<1.0 N.D.	N.D.
Al	2.4	N.D.
Ca	8.2	N.D.
Mg	4.6	0.9
Si	<0.5	0.9

N.D. — Not detected.

The efficacy of the anion exchange method for removing iron and cobalt, two elements which may have a particularly adverse effect on the resistance ratio of nickel, was tested by radioisotope tracer techniques. A 10*N* $NiCl_2$ solution was treated with H_2O_2 to convert iron to the ferric state and was then passed once through a 12 in. column of clean anion exchange resin. By this treatment the iron is decreased by a factor of better than 1/500 and the cobalt by a factor of 1/1000. After two passes through the resin, both the iron and the cobalt are unmeasurable.

Other possible impurities in nickel chloride that are of considerable concern in this work and which are removable by ion exchange treatment of the 10*N* chloride solution are copper, zinc, and all the platinum metals except rhodium. Lead, silver, and rhodium, which also may be contaminants, are not removed from the 10*N* solution by ion exchange, but can be removed from a solution in which the chloride concentration is 2.5*N*. The ion exchange technique will not eliminate aluminum or silicon which may be present in the nickel chloride solution. These may be removed by precipitation as $Al(OH)_3$ and silica by using a specially prepared slurry of $Ni(OH)_2$ in dilute $NiCl_2$ as the precipitant.

The anion exchange treatment does introduce into the nickel chloride solution traces of organic material which apparently manifests itself as carbon impurity in the finished nickel. The AGl-XlO resin used in this work was chosen because it contributed less organic contamination than other resins which were explored. It was possible to effect an appreciable lowering of the organic content of the treated nickel chloride solution by prolonged degradative oxidation with H_2O_2 at 80°C.

The sequence of operations and the quantitative details for the preparation of about four liters of plating solution are shown in the flow sheet in Fig. 1. This chart also outlines the plating and zone refining steps.

Plating operations.—The plating procedure used for winning the nickel is essentially that reported by Wesley (4) in 1956. The plating bath contains nominally 300 g/l of the purified $NiCl_2 \cdot 6H_2O$ and 17 g/l of a special high-purity B_2O_3 for *p*H buffering pur-

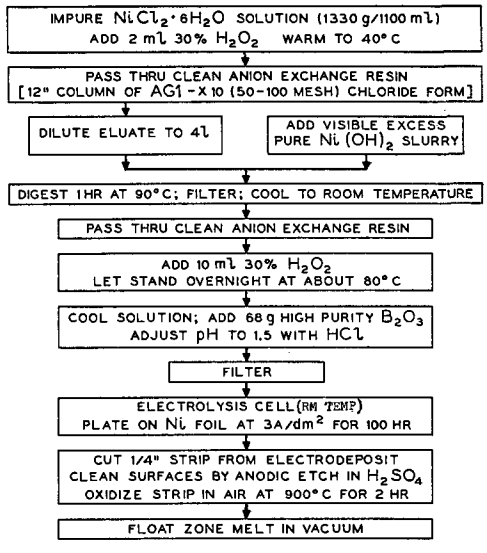

Fig. 1. Flow sheet for production of ultrahigh-purity nickel

poses. The bath is adjusted to a *p*H of about 1.5 by a small addition of HCl and is filtered through an 0.8μ "Micropore" filter to remove any particulate matter which may be present. Plating was carried out initially from 3 liters of solution contained in a 4-liter Pyrex beaker. The volume of plating solution increases progressively during a plating run as appropriate additions of concentrated pure $NiCl_2$ and HCl are made periodically to compensate for nickel depletion and to maintain the *p*H at about 1.5. The cathode on which the nickel was plated is an etched foil 1 mil x 2.5 cm x 13 cm prepared from highest purity nickel available. Twin anodes of 10% iridium-platinum were used to plate both sides of the foil. The purest nickel thus obtained was plated at room temperature, without agitation, at a cathode current density of about 3 amp/dm^2. Plating must be carried out in a fume hood since chlorine is evolved during the operation.

The nickel thus deposited was satiny in appearance. It was nominally flat over the area corresponding to the original foil, but extending beyond this it was roughly cylindrical at the sides and bottom and nodular at the corners. The spectrographic analysis of a section of a flat portion is given in Table I.

Zone melting.—The electrodeposited nickel is polycrystalline and, although very pure in terms of metallic impurities, it does contain occluded nickel chloride and traces of organic matter which are probably adsorbed on the crystal faces of the nickel. Zone melting will remove the nickel chloride by volatilization and will convert the metal to single crystal form. At the same time the organic matter will be degraded to carbon which dissolves in the nickel and is not removed by zoning. Simple float-zone-melting of the plated nickel results in a product containing about 20 ppm of carbon and having a resistance ratio of the order of 2000.

The lowering of the carbon content is accomplished by first oxidizing a strip of the nickel in air at 900°C for 2 hr. This results in a thin green coating of NiO on its surface. The sample is then suspended in the vacuum floatzone melting apparatus (6) and given 4 to 6 passes at 0.001 ips. Apparently the carbon in the nickel reacts in the molten zone with the oxygen from the NiO to form CO and/or CO_2 which are then removed by volatilization along with excess oxygen. Typical vacuums run between 2×10^{-5} to 5×10^{-7} mm of mercury during zone melting. The removal of total oxygen to less than 2 ppm can be observed by noting when the surface of the rod becomes smooth. At this point zone melting should be stopped since carbon recontamination can occur from back-streaming of vapors from the oil used in the diffusion pumps of the zone melting apparatus even though extensive liquid nitrogen traps are present. Nickel having a resistance ratio of 3500 has been obtained by this treatment.

Discussion

The absolute chemical purity of nickel made by this process is very difficult to assess since the usual analytical techniques are not precise enough for determining impurities in the very low or fractional ppm range. Emission spectrographic analysis using specially refined techniques was used as the principal means of evaluation because of its broad capabilities. Experience has shown that no significant change in the metal impurity content of the plated nickel occurs after it has been zone melted. Consequently the spectrographic analysis given in Table I is applicable to the oxidized and zone melted nickel having a resistance ratio of 3500. Mass spectrographic analysis of a sample of Ni-XVI which had been float-zone melted without prior oxidation agreed in essence with the emission spectrographic findings and indicated that other metallic impurities, if present at all, were there in fractional ppm. Very slight traces of cobalt cannot be determined by either of these methods, but in view of the fact that it was so thoroughly removed from the $NiCl_2$ by the ion exchange treatment, its presence in the nickel is highly improbable.

Table II. Analysis for H, N, O, and C

Element	Ni-XVI, Before zone melting	Ni-XVI, After zone melting
H	0.5	0.2
N	2.0	2.0
O	4.6	2.0
C	29	<5*

* Estimated.

Reliable values for its carbon content are not available since the precision of the analytical method is low at carbon levels as low as they are in this nickel. The purification technique used for removing carbon is basically the same as the combustion method used for its analytical determination, and since this method is only sensitive to about 5 ppm, the probable carbon content of the nickel is less than 5 ppm. The H,N,O contents of this Ni-XVI before and after zone melting were determined by the vacuum fusion method and are reported in Table II.

Efforts are being directed at lowering the impurity levels still further by prepurification of the materials and reagents used in the procedures and, in general, by more diligent attention to cleanliness to avoid contamination during processing. Lowering the impurity levels should result in nickel having resistance ratios higher than the 3500 which has been achieved to date. It is not possible to predict what the ultimate ratio should be since the exact contribution of each impurity to the resistivity of Ni at liquid helium temperature is not known and may be vastly different for each element (5). Work in progress indicates that iron and carbon have very serious effects on the resistivity of nickel at 4.2°K (6). Other impurities which are not being detected by the present analytical methods possibly may have even more adverse effects on the resistance ratio than the iron or carbon. If all the impurities were removed, the resistance ratio would probably approach some high but limiting value since structural defects in the crystal lattice would then be the controlling factor. It is evident that an urgent need exists for more sensitive methods of analysis in order to recognize and evaluate the effects of these ultra trace impurities so that appropriate procedures can be developed to improve the nickel further by removing the remaining significant contaminants.

Manuscript received Oct. 25, 1965; revised manuscript received Feb. 10, 1966.

Any discussion of this paper will appear in a Discussion Section to be published in the December 1966 JOURNAL.

REFERENCES

1. J. H. Wernick, D. Dorsi, and J. J. Byrnes, *This Journal*, **106**, 245 (1959).
2. W. A. Reed and E. Fawcett, *Phys. Rev. Letters*, **9**, 336 (1962).
3. K. A. Kraus and F. Nelson, *Proc. Intern. Conf. Peaceful Uses Atomic Energy, Geneva*, **7**, 113 (1956).
4. W. A. Wesley, *This Journal*, **103**, 296 (1956).
5. J. E. Kunzler, "Ultra-High-Purity Metals," American Society for Metals, Cleveland, p. 173.
6. R. R. Soden, To be published.

Electrolytic Reduction of Amides

II. p-Aminobenzanilide and Anisamide

Sherlock Swann, Jr., J. C. Bresee,[1] and R. A. Strehlow[1]

Department of Chemistry and Chemical Engineering, University of Illinois, Urbana, Illinois

This communication is the final part of a study of the influence of the cathode material on the electrolytic reduction of amides in sulfuric acid solution. In the first part (1) the compounds studied were N-substituted aliphatic amides, N-dimethylvaleramide and acetanilide. An attempt was made later (2) to reduce N, N-dimethylvaleramide at a carbon cathode. The present study is on aromatic amides. The amino substituted benzanilide was chosen in preference to the unsubstituted compound on account of its greater solubility in the electrolyte and anisamide because it is less easily hydrolyzed than benzamide itself.

There appears to have been no previous study of the electrolytic reduction of p-amino or any benzanilide in an aqueous or aqueous alcoholic catholyte.

The reduction of anisamide to p-methoxybenzylamine has been carried out by Kindler (3) at a lead cathode, but the reduction at a carbon cathode was unsuccessful (2).

Apparatus and Procedure

The apparatus and general procedure was the same as that in the first part of the investigation (1, 5).

Reduction of p-Aminobenzanilide.—The procedure for recovery of the products of the reduction of p-aminobenzanilide used in most of the runs was as follows: The catholyte was diluted with water and neutralized with sodium carbonate. Any p-aminobenzylaniline should float to the surface yellow oil (4). It was found that large amounts of the starting material appeared as a white crystalline solid as soon as the catholyte was diluted. After some runs, therefore, the crystals were filtered off before neutralization. In no case was any oil found; there was, at best, a small amount of semi-solid after some runs with a lead cathode.

p-Methoxybenzylamine.— The procedure for the recovery of the products of the reduction of anisamide has already been described (2). In the last part of the work sodium hydroxide was used for the neutralization. Any amine formed was extracted with ether. The extract was dried with solid sodium hydroxide, the ether removed by distillation, and the remaining amine heated in a small distillation flask until the temperature of the thermometer reached 200°C. The residue was then weighed.

Discussion of Results

Electrolytic reduction of p-aminobenzanilide.— Anode, lead cylinder; anolyte, 10% sulfuric acid; catholyte, 10g of p-aminobenzanilide in 90-110 cc of a solution of 50 cc of water, 110 cc of ethyl alcohol, and 60g of sulfuric acid; cathode area, 100 cm²; amp 5; current density 0.05 amp/cm²; temperature about 30°C; duration of run, 1 hr (theoretical for reduction to p-aminobenzylaniline).

The following cathodes were used: copper, zinc, cadmium, mercury, aluminum, lead, tin, bismuth, iron, cobalt, and nickel. Only traces of product were found even with a lead cathode after double the theoretical amount of current had been allowed to pass. Between 5 and 8½g of starting material remained after each run.

Electrolytic reduction of anisamide.—Anode, lead cylinder; anolyte, 10% sulfuric acid; catholyte, 20g of anisamide in 90-100 cc of a solution of 50 cc of water, 110 cc of ethyl alcohol, and 60g of sulfuric acid; amp, 5; area of cathode, 100 cm²; current density, 0.05 amp/cm²; temp, about 30°-37°C; duration of run, 2 hr and 50 min (theoretical for reduction to p-methoxybenzylamine).

Other cathodes tried were: iron sheets, copper rods, nickel sheets, electroplated cobalt, electroplated bismuth, aluminum, tin, and mercury. Before use they were prepared in the usual manner (5). The only active cathodes were zinc, cadmium, and lead. Other methods of treament before reduction led in all cases to lower yields than those obtained when the cathode was etched.

The product was converted to the hydrochloride, which was recrystallized from n-butyl alcohol after the solution had been decolorized by activated charcoal. The mp of the hydrochloride was 235°-238°C (unc.). The mp of the pure hydrochloride is 240°C.

Optimum temperature, and current density were not studied with the lead cathodes shown in Table I but other studies showed 0.05 amp/cm² to be the limiting current density. Poor results were obtained at room temperature.

[1] Present address: Oak Ridge National Laboratory, Oak Ridge, Tennessee.

Table I

Cathode material	Grams of p-methoxybenzylamine	% Yield of p-methoxybenzylamine	Treatment of cathode
Zinc RT	7.6	47	Etched in 1:4 HCl 5 min at 10°-15°C
Same	7.4	40	
Cadmium RT	7.6	40	Etched in 1:6 HNO_3
Same	5.6	30	3 min at 10°-20°C
Lead RT	11.1	59	Etched in conc. HNO_3
Same	11.3	61	at 60°C

RT, Cast in a mold at room temperature.

Conclusions

Attempts to carry out the electrolytic reduction of p-aminobenzanilide were unsuccessful.

Anisamide was found to be reduced to p-methoxybenzylamine only at cathodes of zinc, cadmium, and lead. The best results were obtained at lead. Etched cathodes were far more active than those which had been anodized, as had been found in certain previous studies.

Manuscript received Dec. 20, 1965. This paper was presented at the Pittsburgh Meeting, Oct. 9-13, 1955.

Any discussion of this paper will appear in a Discussion Section to be published in the December 1966 JOURNAL.

REFERENCES

1. S. Swann, Jr., *Trans. Electrochem. Soc.*, **84**, 165 (1943).
2. S. Swann, Jr., and H. D. Kerfman, *ibid.*, **92**, 427 (1947).
3. K. Kindler, *Arch. Pharm.*, **265**, 390 (1927).
4. C. Paal and H. Sprenger, *Ber.*, **30**, 69 (1897).
5. S. Swann, Jr., "Electrolytic Reactions" in "Techniques of Organic Chemistry," Vol. II. 2nd ed., A. Weissberger, Editor, Interscience Publishers, Inc., New York (1956).

Anodic Tafel Slopes for N-Type Germanium

C. Gordon Peattie

Texas Instruments Incorporated, Dallas, Texas

As a preliminary part of another study, reproducibility of the Tafel slope of the n-type germanium anode and its sensitivity to electrolyte type and temperature have been measured.

Experimental Procedure

The cylindrical, single-crystal germanium anode used throughout these measurements was n-type, with a resistivity of 12-18 ohm-cm. The crystal had been grown by pulling along the (111) axis. Ohmic contact to the germanium was made by doping one surface with a 99% Au-1% Sb alloy in a dry helium atmosphere at 570°C for 2 hr and then by soldering a lead to that surface. The lead and the area where it joined the germanium were then covered with Apiezon W wax.

A schematic diagram of the experimental system is shown in Fig. 1. Current measurements were made with a Model 425A Hewlett-Packard DC microvolt ammeter and voltage measurements with a Model 801B John Fluke potentiometric-type voltmeter. Current adjustments were made with a series combination of four Model AR Beckman Helipots (100K, 200K, 300K, and 400K ohms), two Model IN-11 Heathkit decade resistance boxes, and four coarse rheostats that had a total resistance of 7 megohms. Temperature for any one run was held constant to ±0.5°C or better by a water bath and an E. H. Sargent "Thermonitor." Four 45v dry cell batteries in parallel were used as the current source.

Two different electrolytes were used: (*i*) 0.2M KCl, buffered at *p*H 5.0 with potassium hydroxide and potassium acid phthalate and (*ii*) 0.1*N* H_2SO_4 containing 0.1M K_2SO_4. The nominal electrolyte volume used was one liter. Finely ground semiconductor grade germanium was added to the electrolyte. Measurements in 0.2M KCl were made in the range 20.2°-20.6°C and 50°-55°C; in 0.1M K_2SO_4-0.1*N* H_2SO_4, at 0°C and in the 50°-55°C range.

The following etch technique was used: CP-4A for 20 sec, deionized water rinse, 48% HF for 30 sec, deionized water rinse. The sample was then moved quickly into the electrolyte and an anodic voltage applied to it.

The germanium electrode was held in the electrolyte with the (111) face (5.1 cm^2) completely immersed. The sides of the cylindrical electrode were also wet with electrolyte to a height varying between 1/16 and 1/8 in. Considering the area wet on the sides by the electrolyte to lie between 1.3 and 2.6 mm and disregarding any surface roughness factor, the total geometrical anodization area lay somewhere between 6.4 and 7.7 cm^2. The end of the agar bridge that led to the reference electrode, a saturated calomel electrode held at room temperature, was positioned about 1/8 in. from the center of the immersed germanium face. The cathode was a platinum cylinder having an effective area of 56 cm^2. The electrolyte was deaerated by cylinder CO_2 that had been first passed sequentially through an Engelhard Deoxo Model D purifier, Linde molecular sieves, and "Drierite," and then bubbled through water before passing into the electrolyte. The electrolyte was deaerated for at least an hour before starting a run. Deaeration was continued throughout the experiment.

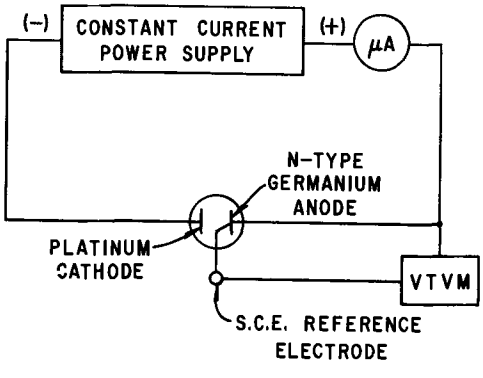

Fig. 1. Schematic diagram of experimental system

Anodic Tafel data were obtained under two conditions:

1. The current-voltage curve was begun within a minute of etching of the sample;
2. The current-voltage curve was preceded by anodization at 100 μa for a measured period of time, equal to or greater than 30 min.

After each current change, at least one minute was allowed to elapse before the voltage was measured. Over the anodic current range studied, 2.3-3000 μa, no correction of voltage was made for IR drop.

Experimental Results

The average value of the Tafel slopes in 24 sets of current-voltage curves, made by starting the measurements within a minute of etching the sample and without any pre-anodization, was 0.087 ±0.004 (std. devn.). Twenty of these curves were measured in 0.2M KCl, buffered to *p*H 5.0. Of these 20 runs, 16 were at 20.2°-20.6°C and four at 50°-55°C. The four remaining curves were measured in 0.1M K_2SO_4-0.1*N* H_2SO_4 electrolyte. Three of these were run at 0°C, the fourth, at 51.6°C. This last curve is shown by curve A in Fig. 2. Curves obtained in the *p*H 5-buffered 0.2M KCl electrolyte were parallel to curve A but displaced from it along the voltage axis because of the difference in *p*H of the two electrolytes.

The average value of the Tafel slopes in 12 sets of current-voltage curves, each preceded by a pre-anodization of at least 100 μa for 0.5 hr, was 0.106 ±0.010 (std. devn.). Five of these runs were made in the temperature range, 19.3°-21.1°C, seven in the 50°-55°C range. A Tafel curve obtained under these conditions at 51.8°C is shown by curve B in Fig. 2.

Analysis of variance (F-test) showed that with 99% confidence these two average Tafel slopes, 0.087 ±0.004 and 0.106 ±0.010, were significantly different.

Discussion

Relation of Tafel slope to pre-anodization.—The slope of 0.087, obtained without pre-anodization, agrees with the value, 0.08, reported by Lovrecek and Moslavac (1) for n-type germanium, etched with CP-4 and anodized in 0.5*N* NaOH to 1.6 ma/cm^2. Gerischer (2) reported slopes in the range 0.073-0.082 for p-type germanium, dissolved anodically in 0.01*N* NaOH/0.9*N* $NaClO_4$ and 0.1*N* NaOH/0.9*N* $NaClO_4$ over the current density range, 10-1000 μa/cm^2, presumably without pre-anodization following a CP-4 etch.

Without pre-anodization, there was some voltage instability in the current range, 1-10 μa. Brattain and Boddy (3) have commented on this voltage instability, presumably etch-derived. To counteract it, they applied pre-anodization currents of 100-200 μa/cm^2 for around 5 min, together with illumination of the n-type germanium electrodes, before taking current-voltage data. The slope of the Tafel curve for 25.5 ohm-cm,

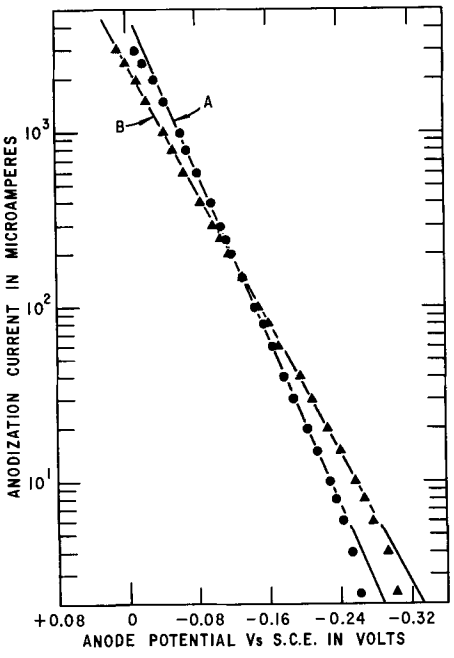

Fig. 2. Tafel curves for 6-18 ohm-cm, n-type germanium electrode, run with and without pre-anodization following etch. Electrolyte, 0.1M K_2SO_4-0.1*N* H_2SO_4; curve A (51.6°C), no pre-anodization; curve B (51.8°C), with pre-anodization.

p-type germanium, shown in Fig. 5 of their paper, is 0.11. Turner (4) cites 0.12 as the approximate Tafel slope obtained with either n-type or p-type germanium anodes in either 0.1*N* H_2SO_4 or 0.1*N* NaOH, but he does not state whether or not pre-anodization was used. Anodic dissolution data in the 1-100 $\mu a/cm^2$ range, reported by Boddy (5) for 38.65 ohm-cm, p-type germanium, polished in CP-4 and then pre-anodized at the (111) face in *p*H 7-buffered 0.1M K_2SO_4 electrolyte, show Tafel slopes of 0.10-0.11. Boddy stated that the dissolution curves for n-type electrodes were very similar.

It is felt that the two significantly different Tafel slopes measured in this work reflect two different compositions of the germanium anode surface. The surface of germanium, freshly etched with CP-4 or CP-4A, is probably covered with adsorbed HF molecules (6). Pre-anodization presumably brings about replacement of these with hydroxyl groups. The hydroxyl-saturated germanium surface is the one assumed in mechanisms proposed to explain the anodic dissolution (4, 7).

The relatively significant role of the initial surface composition in determining the anodic Tafel slope is interesting. Over the current range, 2.3-1000 μa, and under the measurement conditions used, no change of slope was observed during the course of a single run to denote a shifting of the surface composition from that characteristic of the freshly etched surface to that typical of the pre-anodized surface. This apparent retention of initial surface condition may be similar to the effect of specific anion adsorption on the kinetics of chemical (not anodic) dissolution of germanium observed by Harvey and Gatos (6). However, either prolonged anodization at relatively low currents (100 μa for 30 min) or short anodization at relatively high currents (1000-3000 μa) will suffice to change the Tafel slope from the 0.087 ±0.004 range to the 0.106 ±0.010 region. For example, the effect of the higher currents was shown by the fact that, on repeating a series of Tafel measurements without removing the sample from the electrolyte, the slope of the second curve would be that characteristic of the pre-anodized electrode.

Lack of effect of electrolyte type on anodic Tafel slope.—The Tafel slopes obtained without pre-anodization were measured in two different electrolytes, 0.2M KCl, buffered to *p*H 5.0, and 0.1M K_2SO_4-0.1*N* H_2SO_4. No measurable effect of electrolyte on slope was observed, nor did the widely differing *p*H values of the two electrolytes change the Tafel slope. This lack of effect of *p*H on slope agrees with the constant slopes reported by Beck and Gerischer (7) for electrolytes with different hydroxyl ion concentrations.

Lack of effect of temperature on anodic Tafel slope.—All Tafel slopes measured in this work were free from any observable temperature effect at the three nominal temperatures 0°, 20°, and 55°C. Young (8) has discussed the expected temperature dependence of the anodic Tafel slope. The value, $dE/d \log i$, where E is the measured anode potential and i is the anodic current should increase directly with absolute temperature. With such a temperature dependence, there should be a 20% increase in the slope of the anodic Tafel curve for germanium on going from 0°C (273°K) to 55°C (328°K). Such a change in slope would have been seen in measurements made at 0° and 55°C without pre-anodization because the standard deviation for such measurements was ±4.6%. In the case of measurements made with pre-anodization, the standard deviation of ±9.4% would still not have obscured the change in slope on going from 0° to 55°C.

Temperature independence of anodic Tafel slopes has been reported by other investigators for several metals. Vermilyea (9) has reported that the anodic Tafel slope of tantalum showed no temperature dependence at 0.5°, 19°, 40.5°, 60.5°, and 79°C. His observations were confirmed by Young (10) at 20° and 60°C and by Bray, Jacobs, and Young (11), working from 0° to 100°C. Young (12) observed a similar independence of anodic Tafel slope from 0° to 100°C for niobium. He (13) also reported that measurements by Adams, van Rysselberghe, and Willis on zirconium from 6° to 55°C gave indications of the same temperature independence of anodic Tafel slope. Dewald (14) proposed that this temperature-independent Tafel slope results from cancellation, under appropriate conditions, of the temperature effect which theory predicts by space charge in the oxide film.

However, Adams and Koo (15), working at intervals of 10°C over the temperature range —10° to 70°C, found that the measured temperature dependence of the Tafel slope for very thin anodic oxide films on niobium agreed with that predicted by the single-barrier theory of Mott and Cabrera, which assumed that no space charge is established in very thin films (<100Å). Adams and Koo pointed out that Vermilyea (9) and Young (10), who had observed no temperature dependence, had worked with oxide films ranging in thickness from several hundreds to several thousands of angstroms and that, under these conditions, it was probable that a space charge was established in the steady state.

In the work reported here, the temperature independence of the anodic Tafel slope over the temperature range 0° to 55°C indicates an oxide film thick enough for the existence of one or more factors, presumably space-charge-derived, that act to cancel the direct variation of the anodic Tafel slope with temperature. On the other hand, the solubility of the GeO_2 would tend to limit this film thickness. For example, Zwerdling and Sheff (16), who formed anodic oxide films 730-1240Å in thickness on germanium in 0.25*N* sodium acetate dissolved in glacial acetic acid, had initially failed to grow satisfactory oxide films on germanium in aqueous electrolytes because of the appreciable water solubility of the formed GeO_2.

The total charge passing through the germanium anode in a typical Tafel measurement like that shown in Fig. 2 would nominally be 784,500 μcoulomb. Assuming a 100% current efficiency, this would correspond to 850 μg GeO_2. Using a density of 4.703g GeO_2/cm^3 GeO_2 and an anodization area of 6.4-7.7 cm^2, the corresponding oxide thickness would be 2400-2800Å.

However, the solubility of GeO_2 in water at 20°C is 0.405g per 100g H_2O. Its solubility in either of the two electrolytes used in this work is not known. Judging from the experience of Zwerdling and Sheff (16) mentioned above, this solubility should be relatively high. However, it is apparently not high enough to result in the existence of a space charge-free oxide film.

Manuscript received Nov. 12, 1965.

Any discussion of this paper will appear in a Discussion Section to be published in the December 1966 JOURNAL.

REFERENCES

1. B. Lovrecek and K. Moslavac, *Electrochim. Acta*, **10**, 627 (1965).
2. H. Gerischer in "Semiconductor Electrode Reactions," Chap. 4 of "Advances in Electrochemistry and Electrochemical Engineering," Vol. I, p. 181, P. Delahay, Editor, Interscience Publishers, Inc., New York (1961).
3. W. H. Brattain and P. J. Boddy, *This Journal*, **109**, 574 (1962).
4. D. R. Turner, *ibid.*, **103**, 252 (1956).
5. P. J. Boddy, *ibid.*, **111**, 1136 (1964).
6. W. W. Harvey and H. C. Gatos, *ibid.*, **107**, 65 (1960).
7. F. Beck and H. Gerischer, *Z. Elektrochem.*, **63**, 500 (1959).
8. L. Young in "Anodic Oxide Films," Chap. 2 and 3, pp. 12 and 19, especially, Academic Press Inc., New York (1961).
9. D. A. Vermilyea, *Acta. Metall.*, **1**, 282 (1953).
10. L. Young, *Trans. Faraday Soc.*, **50**, 153 (1954).
11. A. R. Bray, P. W. M. Jacobs, and L. Young, *Proc. Phys. Soc.*, **71**, 405 (1958).
12. L. Young, *Trans. Faraday Soc.*, **52**, 502, 515 (1956).
13. L. Young in "Anodic Oxide Films," pp. 261-262, Academic Press, Inc. New York (1961).
14. J. F. Dewald, *This Journal*, **102**, 1 (1955).
15. G. B. Adams, Jr., and T. Koo, *ibid.*, **107**, 640 (1960).
16. S. Zwerdling and S. Sheff, *ibid.*, **107**, 338 (1960).
17. N. A. Lange, "Handbook of Chemistry," pp. 254-255, McGraw-Hill Book Co., Inc., New York (1961).

The Effects of Gravity on the Electromotive Force of Thermogalvanic Cells

Minas Ensanian

Physical Chemistry Group, Bell Aerosystems Company, Buffalo, New York

What may be termed a "zero gravity effect" has been discovered on the potential of a partially frozen thermogalvanic cell under conditions approaching nearly free fall. In a series of drops in air from a 17-ft tower, iron, copper, and aluminum thermocells all exhibited an oscillation in potential of 0.4 sec maximum duration, followed by a sharp decrease in potential and a subsequent recovery prior to impact. The results indicate a possible cross-phenomenon or coupling between a gravitational field and chemical reaction of interest in the theory of coupled transport processes.

Des Coudres (1) and Tolman (2), respectively, have studied the effects of gravity and centrifugal force on the emf of galvanic cells. Des Coudres, *e.g.*, simply connected two reversible calomel electrodes by means of a rubber tube filled with 2.71*M* KCl and by variations in their respective heights obtained a value of 0.510×10^{-8} v/cm for the (potential/height) ratio.

Tolman, whose apparatus attained speeds of 80 rps, found that the cell emf varied directly with the square of the number of revolutions per second. MacInnes (3) has given a theoretical discussion of these effects.

To the author's best knowledge the literature with respect to the effects of reduced gravity on the operation of a thermogalvanic cell is nonexistent, and the general question of a "gravitational effect" on the rate of a chemical reaction, although academic, would in its most profound philosophical aspects entail Einstein's famous "clock paradox" (4-6) especially if a terrestrial observer were following the kinetics of an electrochemical process in an orbiting satellite.

Generales (7) has defined zero-gravity as that particular point, never fixed, at which two or more gravitational fields become neutralized so that we have a physical situation, mathematically supported, where there is no gravitational attraction of an object, however big or small, that would cause it to accelerate beyond the momentum originally imparted to it within the confines of the universe.

The principal effect of zero-gravity is the absence of body forces, *i.e.*, a body in zero-gravity retains its mass but does not exert any weight on its environment. The behavior of liquids in free fall has given considerable insight into the behavior of liquids in space and is now established on a theoretical and experimental basis (8-10). The problem of heat transfer in boiling liquids in a zero-gravity environment has been considered by Zuber and Kutateladze-Borishanskii (11).

In practice, a thermogalvanic cell or thermocell is the simplest battery that can be made, consisting merely of a glass tube filled with a solution of a metal salt at whose opposite ends are electrodes of the same metal but at different temperatures. In the present work, and as previously reported by the author (12), iron, copper, and aluminum thermogalvanic cells in which the electrolyte surrounding one of the electrodes was frozen by means of dry ice while the other remained at ambient temperature, were dropped in air (without the use of guide wire) from a 17-ft tower. The cells were made from 10 mm ID Pyrex tubing, 33 cm long and mounted in a vertical position in the drop capsule. The total weight of the test capsule was 5 lb and consisted of a 15 in. by 4 in. ID plastic pipe with a steel weight attached. For practical reasons no attempts were made to measure the respective electrode temperatures.

To reduce induction effects resulting from the 26-ft lead wires crossing the earth's magnetic field, the wires were given about 5 twists per inch to reduce surface area. Variations in the output potentials, which could vary between 0-500 mv, with the cells operating under equilibrium (temperature of the cold electrode constant) or nonequilibrium conditions during the free fall period (1 sec), were observed in different experiments by means of recorders, VTVM, microammeters, and potentiometers. With minor modifications a millivolt recorder with a balancing speed of 1 sec was found satisfactory.

Figure 1 represents a typical (time/potential) curve from data obtained from over 80 drops with the thermocells mentioned. There is an initial oscillation in potential lasting up to a maximum of 0.4 sec, then

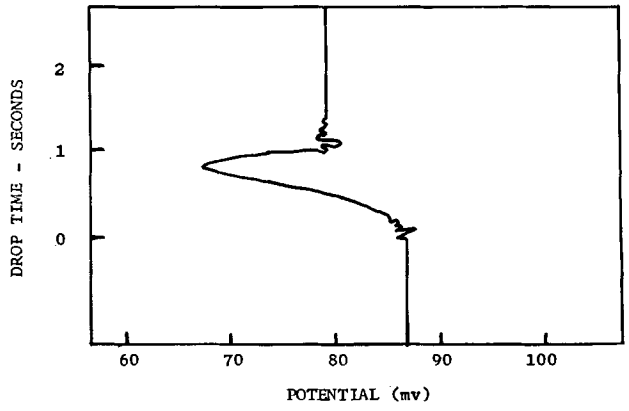

Fig. 1. A typical (time/potential) curve for a partially frozen aluminum thermogalvanic cell (0.1M sulfate solution) representative of the type of curves observed in this study. The electrodes (coiled wire 4 cm in length) were mounted in a vertical glass tube and 21 cm apart, and the upper electrode was frozen. Although these same cells frozen and dropped in a horizontal position exhibited the same general type of curve, the initial perturbations at the beginning of the postdrop period were more erratic and voltage stabilization took longer. The recorder chart speed was 24 in./min.

a sharp decrease followed by a buildup just prior to impact, whereupon voltage is soon stabilized and generally at a lower value, provided the system was not damaged.

Each experiment may be considered as having three phases, *viz.*, a predrop, drop, and postdrop period. The iron copper, and aluminum thermogalvanic cells were studied when their predrop potentials varied between their maximum and minimum value, the only criterion being, however, that the cell be hermetically sealed as a result of the frozen upper electrode, thus eliminating any possibility of spillage or bubbles.

On the average a predrop potential below 10 mv (during the freezing cycle) would diminish by 20-50% during the dropphase; however if it were above 10 mv, the decrease would range from 10-20%.

Below a 5 mv predrop potential there was no observable recovery prior to impact. In the initial phases of this work two cell geometries were considered, *viz.*, a U-tube and a straight tube (mounted in a vertical position); because of its general stability with regard to handling, the straight tube was preferred. The latter were often mounted, frozen, and tested in the horizontal position.

Although the electrolyte concentration was generally 0.1M, some tests were made with 1 and 0.01M sulfate solutions; however, the data were insufficient and comparison difficult, although there is a semblance of a more pronounced effect at the higher concentration where the predrop potentials permit a reasonable comparison.

It is a characteristic of newly constructed thermogalvanic cells to exhibit a high output potential (short lived) when no temperature differential exists between the electrodes. These may arise from differences in the elastic strain energy between the supposed identical electrodes or from local effects associated with microscopic bubbles. For nonfrozen systems when negligible current is drawn, the total voltage produced by a thermocell is approximately the product of the thermogalvanic coefficient (dE/dT) and ($T_2 - T_1$).

There are two possible explanations for the observed potential recovery just prior to impact, *viz.*, that the nearly free fall condition does not exist near the end of the drop due to air resistance, or the inability to resolve the exact impact time, since in the attempt to eliminate all electromagnetic effects which could in any way interfere with the measurements, the test capsule was released manually by means of a mechanical device. However, after numerous calibration drops in which this factor was studied, it appears that the effect is genuine.

Preliminary tests were made with hermetically sealed standard Weston cells and, although perturbations were noted during the drop phase, instrumentation difficulties do not permit any conclusions to be made at this time.

It is of interest to note (13) that a silver-cadmium cell aboard the Explorer XIV satellite for a period of 10 months, during which the g-level decreased from 5×10^{-2} to about 10^{-7}g, showed no adverse effects in the low g environment; however, this may have been due to the particular construction which limited discontinuities in the liquid phase. However, there may have been an influence on the separation of the evolved gases at the electrodes.

In the present work, in order to substantiate and isolate this observed gravity effect, numerous tests were made to ascertain role and magnitude of the following factors, *viz.*, induction effects due to the earth's magnetic field, effects due to the twisting of lead wires as well as frictional effects due to slip between metal wire and plastic insulation, effects due to stray electromagnetic radiation, effects of handling, shaking, vibration and rotation of the weighted test capsule, the role of entrapped microscopic gas bubbles and metallic thermocouple effects.

In addition to these considerations, iron, copper, and aluminum wire and plate were used to short-circuit the cell leads; with and without controlled current running through them, the drop phases were studied, and it became evident that it was possible under the experimental conditions of the reported work to resolve the effect.

It is of interest to consider the nature of the observed effect in terms of the phenomenological theory of irreversible thermodynamic processes (14) particularly with respect to cross-phenomena between the scalar gravitational potential and scalar chemical reaction.

For example, with respect to cross phenomena, ordinary stress corrosion not only reflects the principle of Le Chatelier (15), but also the coupling between two scalar transport processes, *viz.*, relaxation and chemical reaction. In a more complicated situation involving coupling between physical and chemical scalar transport processes reported by Croatto (16) where stress corrosion proceeds in the presence of a magnetic field, it was shown that the reaction rate depends jointly on the stress and the intensity of the magnetic field.

Coupling phenomenon are governed by Curie's theorem, which forbids the coupling of transport processes of different tensor rank, *i.e.*, a vectorial flow cannot be combined with a scalar force nor a scalar flow with a vectorial force. Although the flow of a scalar quantity constitutes a vector flux, nevertheless the theorem is still valid under special circumstances with respect to coupling between scalar chemical reaction and vector heat flow, provided the chemical reaction is spatially variable, *i.e.*, proceeding at different rates in different regions of space.

In a thermogalvanic cell the imposed thermal gradient gives rise to a concentration gradient (Soret effect); in a similar manner an electrical potential gradient may produce a concentration gradient and may be expressed in terms of the so-called diffusion potential (17).

In electrochemical phenomena, since mass and electric charge are carried together as a result of ion movement, the two forces may be coupled and thus may be represented by a single function, *viz.*, the electrochemical potential difference. In this same vein deBethune (18) has considered the total entropy transferred during the operation of a galvanic cell in terms of two quantities, *viz.*, the entropy of electrochemical transport and entropy associated with electrolytic migration.

The well-known Nernst and Ettinghausen effects reflect crossflow between a magnetic field and a spatially variable thermal field.

Finally, with respect to the nature of the potential decrease, several explanations may be possible since the physical system (cell) is experiencing a reduction in the force of gravity, *viz.*, a certain amount of unmixing either at the electrode/electrolyte interface or in the bulk of the solution in the absence of convective forces. One can never rule out the possibility of gas films although controlled experiments with small bubbles present in the solution displayed (time/potential) curves of a different character than that shown in Fig. 1.

If the weak assumption is made that the nearly free fall state does not give rise to changes in the thermal and concentration gradients, then the remote possibility exists that the reduction of the gravitational field has somehow reduced the collision frequency of the reactants perhaps via viscosity changes as a result of changes in liquid order in the immediate vicinity of the reacting species since there is no evidence for a remaining possibility, *i.e.*, a gravitational field effect on electron transport in the solid state.

In conclusion, aside from the necessity for additional experimental facts, a theoretical treatment of possible crossflow between a gravitational field and thermogalvanic phenomena might be resolved within the present framework of the theory of nonequilibrium thermodynamic processes.

Acknowledgment

The author wishes to thank the Engineering Laboratories and the members of the Chemistry Section for their generous cooperation and B. N. Ensanian and A. O. Ensanian for the tedious task of constructing numerous cells. He also thanks Dr. W. G. Amey and W. McAdam of the Leeds & Northrup Company for their interest and comments as well as for the loan of a recorder, and James W. Useller and D. A. Petrash of NASA-Lewis for a helpful discussion.

Manuscript received Oct. 11, 1965.

Any discussion of this paper will appear in a Discussion Section to be published in the December 1966 JOURNAL.

REFERENCES

1. Th. Des Coudres, *Ann. Physik Chem.*, **49**, 284 (1892); **57**, 232 (1896).
2. R. C. Tolman, *Proc. Am. Acad. Arts Sci.*, **46**, 109 (1910); *J. Am. Chem. Soc.*, **33**, 121 (1911).
3. D. A. MacInnes, "The Principles of Electrochemistry," p. 174, Reinhold Publishing Corp., New York (1935); see also F. D. Rossini, "Chemical Thermodynamics," p. 414, John Wiley & Sons, Inc., New York (1950).
4. E. M. McMillan, *Science*, **126**, 3270 (1957).
5. C. N. Gordon, *Proc. Phys. Soc.*, **80**, 569 (1962).
6. E. T. Benedikt, "Advances in the Astronautical Sciences," vol. 8, p. 488, Western Periodicals Co., North Hollywood, Calif. (1963).
7. C. D. J. Generales, Jr., "Medical and Biological Problems of Space Flight," G. H. Bourne, Editor, p. 124, Academic Press, New York (1963).
8. E. T. Benedikt, *J. Amer. Rocket Soc.*, **29**, 150 (1959).
9. W. C. Reynolds, *J. Aero/Space Sciences*, **26**, 12 (1959).
10. D. A. Petrash, R. C. Nussle, and E. W. Otto, "Effect of Contact Angle and Tank Geometry on the Configuration of the Liquid-Vapor Interface During Weightlessness," NASA TN D-2075. Oct. (1963); C. E. Siegert, D. A. Petrash, and E. W. Otto, "Time Response of Liquid-Vapor Interface after Entering Weightlessness," NASA TN D-2458, Aug. (1964).
11. N. Zuber, *Trans. ASME*, **80**, 3 (1958).
12. M. Ensanian, *This Journal*, **112**, 6 (1965).
13. T. J. Hennigan, "Proceedings of the Zero-Gravity Fluid Behavior Review and Planning Meeting," held at NASA Headquarters, Oct. 8-9 (1963), Washington, D. C.
14. S. R. de Groot, "The Thermodynamics of Irreversible Processes," North Holland Publishing Co., Amsterdam (1951).
15. A. Le Chatelier, *Ann. Mines*, **13**, 200 (1888).
16. U. Croatto, *Rec. Sci.*, **18**, 1573 (1948).
17. K. G. Denbigh, *Nature*, **165**, 199 (1950).
18. A. J. de Bethune, *This Journal*, **107**, 829 (1960).

Brief Communication

Explosion of a Chemical Polishing Solution

S. F. Bubar and D. A. Vermilyea

General Electric Company, Research and Development Center, Schenectady, New York

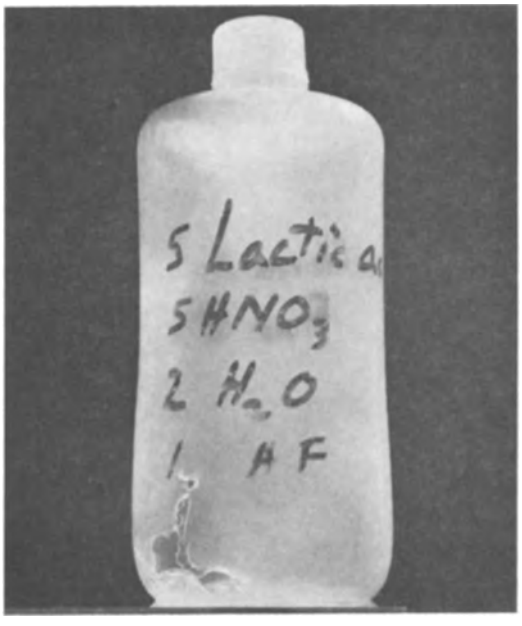

Caution should be exercised in the use of the chemical polishing solution described by Banter in his article "Determination of the Refractive Index and Thickness of Oxide Films on Anodized Zirconium From Transmission Interference Measurements" (1). The solution in question consists of (by volume) 5 parts lactic acid, 5 parts nitric acid, 2 parts water, and 1 part hydrofluoric acid. This solution is unstable and should not be stored after mixing.

Lactic acid and nitric acid react autocatalytically, so that while there is no apparent reaction for the first few hours, there is a very rapid rise in temperature (to ~90°C) and extremely vigorous gas evolution approximately 12 hr after mixing.

In our experience, this gas evolution was sufficient to rupture the plastic container we had used because of the HF content of the solution. Fortunately in our case, the solution was stored in a fume hood and no one was standing nearby when the explosion occurred. It may be worth noting that if a sealed glass bottle had been used, a much higher pressure would have been present at rupture, possibly sufficient to blow a few more bottles of various concentrated acids off the shelf. The enclosed photo shows the container used. A similar incident was recently reported by Green (1). Other dangerous etching and polishing solutions have been mentioned (3).

Manuscript received Feb. 9, 1966.

Any discussion of this paper will appear in a Discussion Section to be published in the December 1966 JOURNAL.

REFERENCES

1. J. C. Banter, *This Journal*, **112**, 388 (1965).
2. W. V. Green, *J. Less-Common Metals*, **9**, 155 (1965).
3. Jack Lowen, *This Journal*, **112**, 1057 (1965); C. V. King, *ibid.* **112**, 251C (1965).

A Stable High-Valency Nickel Oxide

P. Bro and D. Cogley

Laboratory for Physical Science, P. R. Mallory & Co., Inc., Burlington, Massachusetts

ABSTRACT

A high-valency amorphous nickel oxide prepared by the hypochlorite oxidation of nickel nitrate exhibited a mixture of oxidation states characterized by a mean nickel valency of approximately 3.5. The high-valency amorphous oxide was stable in strongly alkaline solutions, but it decomposed rapidly below pH 9. The oxide discharged efficiently when used as a cathode in an alkaline primary cell.

The existence of high-valency amorphous nickel oxides is well established (1), but there has been some discussion regarding the nature of the excess nickel valency in such oxides. The high valency has been attributed to the presence of a tetravalent nickel ion (2) and to superficial oxygen (3). The recent magnetic studies of Labat (4) provide convincing evidence for the existence of a tetravalent nickel.

Data in the literature (5, 6) indicate that high-valency nickel oxides decompose readily, but recent work of Tuomi (7) shows that it is not necessarily so. The data given by Tuomi imply a reasonable stability of tetravalent nickel prepared electrochemically under suitable conditions.

We were interested in exploring the use of a high-valency amorphous nickel oxide as a cathode material for primary cells, but before such use could be considered, it would be necessary to establish whether the high valence state could be stabilized and whether it could be exploited faradaically. Both of these questions can be answered affirmatively, and we report here the work which led to these conclusions.

Experimental Techniques

A laboratory evaluation was conducted of the various methods for preparing high-valency nickel oxide. First among them was the anodic oxidation of mixtures of divalent nickel hydroxide and carbon with a CMC binder in concentrated base at room temperature on a nickel screen. The electrochemical method was unsatisfactory because of the poor adhesion of the oxide to the conductor and because of analytical complications due to the oxides of carbon and the presence of nickel. These considerations notwithstanding, Tuomi (7) obtained satisfactory results with the electrochemical method. Among the chemical methods, the hypochlorite oxidation was found to be most convenient and we used it. It is interesting to note that, although this method has been known for many years (8), it apparently was not recognized that it could yield a stable high-valency oxide.

Preparative procedures.—All the reagents, except the technical grade hypochlorite, were analytical grade chemicals, and the specific preparative conditions were varied as shown in Table I. The sequence of the operations was the same in all cases. The solution of nickel nitrate was added dropwise to the solution of the alkaline hypochlorite during approximately ½ hr. When the nickel oxide precipitate had settled the supernatant liquid was removed by siphoning, and the precipitate was washed twice with fresh base. The oxide was stored under base in a polyethylene container at 25.0°C.

No interferences would be expected by the nitrate shuttle discussed by Casey *et al.* (9), since no reducing agents were present. The anion effects would have to be considered in assembled cells.

The possibility was considered that the oxidative capacity of the nickel oxide might be caused, at least in part, by hypochlorite inclusions in the precipitate. Analyses of the dissolved precipitate for chloride ions showed any such inclusions to be negligible.

In order to evaluate the variability of the entire sequence of the preparative operations and the analyses, a set of three oxides were prepared separately under identical conditions similar to those used in run 4 with the results shown below:

Preparation	Oxidation state
a	3.49
b	3.50
c	3.48

It may be seen that the oxides could be prepared reproducibly with a variability of ±0.01 in the average nickel valency.

The results shown in Table I indicated that the oxidation state of the nickel did not change markedly with the preparative conditions. The values were all within the range of 3.33-3.61. Attempts to prepare higher valency oxides with an oxidation state approaching four were successful in a restricted sense. In the presence of an excess oxidant, under conditions similar to those of run 4, oxidation states between 3.95 and 4.00 were obtained. However, these high valency oxides decomposed rapidly to the lower valency compounds (*ca.* 3.5 oxidation state) as the hypochlorite concentration decreased. The hypochlorite concentration decreased due to the decomposition of hypochlorite in the presence of high-valency nickel oxide. The decomposition of the oxide and the hypo-

Table I. Preparative conditions

Run	Temperature, °C	Oxidant	$Ni(NO_3)_2$ solution	Valency
1	−5	800 ml 0.67M NaOCl 1.0M KOH	200 ml 0.67M	3.54
2	−5	600 ml 0.40M NaOCl 10M KOH	200 ml 0.52M	3.5
3	0	800 ml 0.34M NaOCl 6.45M KOH	200 ml 0.17M	3.52
4	25	800 ml 0.34M NaOCl 6.45M KOH	200 ml 0.17M	3.49
5	40	800 ml 0.34M NaOCl 6.45M KOH	200 ml 0.17M	3.45
6	25	800 ml 0.34M NaOCl 4.0M LiOH	200 ml 0.17M	3.46
7	25	800 ml 0.25M NaOCl sat'd KOH	200 ml 0.17M	3.60
8*	40	800 ml 0.34M NaOCl 6.45M KOH	200 ml 0.17M	3.61
10**	25	200 ml 2.2M Br_2 sat'd KOH	15 ml 2.26M	3.33
11	25	200 ml 6M KOCl 6M KOH 1M KCl	15 ml 2.26M	3.43
12	25	10400 ml 0.34M NaOCl 6.5M KOH	2600 ml 0.17M	3.46

* Product reoxidized repeatedly with 1M $K_2S_2O_8$ at 25°C.
** Product reoxidized with 0.9M Br_2 in 500 ml 5M KOH at 25°C.

chlorite was accompanied by a noticeable gas evolution. The decomposition reaction between the valence states of approximately 4.0 and 3.5 was not investigated beyond these summary observations.

Chemical analyses.—The oxidation state of the nickel was obtained by iodometric titrations and concurrent polarographic analyses for nickel (Metrohm, Polarecord Model E261). Since the procedures deviated from conventional practice, they will be given in some detail. Two to ten milliliters of slurried nickel oxide in base were added to 35 ml 20% KI with stirring. The *p*H of the solution was adjusted by the slow addition of 2M H_2SO_4 to bring the solution to *p*H 3 and to hold it there for *ca.* 3 min. Then, more H_2SO_4 was added to give a solution of *p*H 1.5, and within 1 min 25 or 50 ml of the solution was transferred to a beaker containing 15 ml H_2O, 5 ml 2M H_2SO_4, and thyodene indicator. The free iodine was titrated with 0.1*N* $Na_2S_2O_3$ to a colorless end point.

The preceding steps were selected from several alternate schemes which were evaluated. The nickel oxide had to be added to an alkaline KI solution, contrary to standard iodometric practice, to avoid losses due to the escape of oxygen which occurs in acid solutions. Calibration tests showed that the results were unaffected by the initial alkalinity provided the titrations were conducted in acid solutions under conditions which prevented air oxidation of iodide. At *p*H values above 2, the nickel oxide was incompletely reduced, and at *p*H values less than 1, air oxidation became noticeable. Therefore, the titrations were done at *p*H 1.5. The iodometric calibration runs agreed with one another within 0.3%.

The nickel content of the oxide was determined by analyzing 1-5 ml of the *p*H 1.5 solution polarographically in 20 ml 1M NH_4Cl, 1M NH_4OH at 40°C. A 0.008% solution of CMC was found to be a satisfactory suppressor. The use of the elevated temperature was dictated by the suppressor requirements. The polarographic method was calibrated against a standard nickel solution prepared from the pure metal, and the calibration runs were reproducible within 0.5%. All of the analytical results reported in this paper represent average values obtained from four determinations for each set of conditions, except for the values given in Fig. 1 where single determinations were made.

Stability of the Oxide

The preparative work had established that a high-valency nickel oxide could be prepared reproducibly. Accordingly, a series of experiments was initiated to investigate the relative stability of the oxide under various conditions.

Sample No. 1, Table I, which had been prepared and stored at —5°C in 1M KOH was analyzed periodically. No change was observed in the oxidation state of the nickel; it remained at a value of 3.54 during the period of observation, 105 days. Thus, the high-valency oxide was stable at —5°C in 1M KOH. Sample No. 7, prepared at 25°C, showed no decomposition during the two days it was examined at 25°C, and sample No. 8, prepared at 40°C, showed no decomposition during the three days it was tested at 40°C. These and similar tests on the other specimens indicated that the high-valency oxides were stable at room temperature in 1M or more concentrated, strong base.

A large batch of high valency oxide, run 12, Table I, was prepared to provide a single source of specimens for a study of the effect of solution *p*H on the stability of the oxide. The oxide was prepared at 25°C and stored at the same temperature under 10^{-3}M KOH. Small portions of nickel oxide suspensions were introduced with stirring into large volumes of buffers with *p*H values down to *p*H 6.0 at 25°C, and samples were withdrawn after a period of three days for analyses. Results are shown in Fig. 1. It may be seen that the oxide had decomposed appreciably in the solutions with a *p*H less than *p*H 9 and that it was relatively stable in the high *p*H solutions. Some decomposition had occurred in the high *p*H solutions, since the nickel valency had decreased from 3.46 for the freshly prepared oxide to a value of 3.34 for the three day old sample in dilute base.

Decomposition of the Oxide

The existence of a *p*H range in which the high-valency oxide decomposed at an appreciable rate allowed measurements to be made of the influence of temperature and *p*H on the rate of the decomposition reaction. The rate measurements were made, using the procedures already described, and the time intervals between the *p*H adjustment of the suspensions and the addition of the suspensions to the iodide solutions were taken to be the reaction intervals. The nickel oxide suspensions were taken from the same master batch to insure an identical starting material for comparison purposes.

The decomposition rates of the high-valency oxide in a *p*H 6.0, 2M phosphate buffer are shown in Fig. 2 for three different temperatures between —1° and 55°C. The results are again expressed in terms of the mean oxidation state of the nickel. It may be seen that the decomposition curves exhibited an induction period at —1° and 15°C, but not at 55°C. Furthermore, the reaction rates increased markedly with the temperature.

The influence of the *p*H of the solutions on the rate of the decomposition reaction was investigated at 25°C in MacIlvaine buffers between *p*H 4.0 and *p*H 6.0. Results are shown in Fig. 3. The rate of the reaction increased markedly as the acidity of the solutions increased, and the reactions proceeded practically to the divalent nickel state. The *p*H effect was studied on a fresh batch of high-valency oxide, and the data indicated that the fresh oxide was more reactive than the aged oxide. In the *p*H 6 phosphate

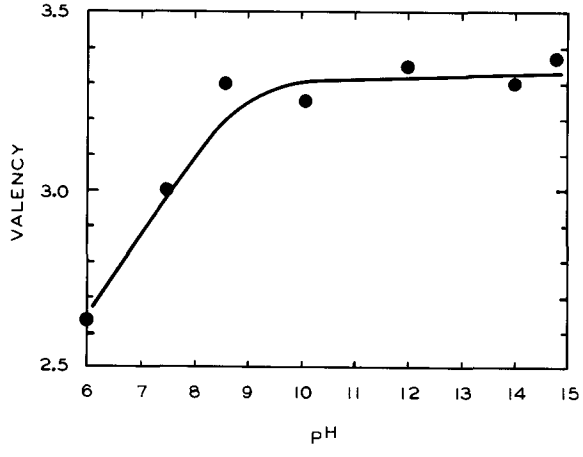

Fig. 1. The *p*H effect on the stability of high-valency nickel oxide

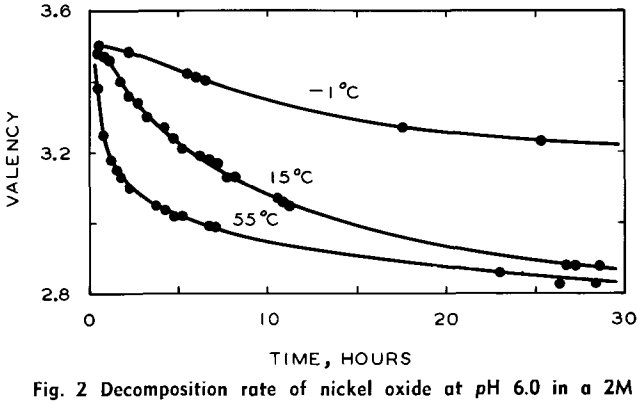

Fig. 2 Decomposition rate of nickel oxide at *p*H 6.0 in a 2M phosphate buffer, aged oxide.

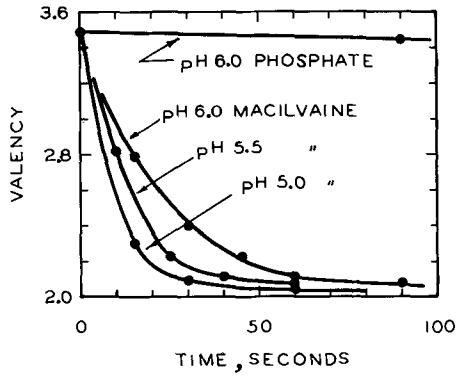

Fig. 3. Influence of pH and buffer type on the decomposition rate of nickel oxide, fresh oxide.

buffer, the valency of the fresh oxide changed by 0.78 units at 25°C during the first 3.9 hr of reaction time, whereas the valency of the aged oxide changed by only 0.53 units at 55°C during the same period, the higher temperature of the latter notwithstanding. A comparison of the pH 6 phosphate and pH 6 MacIlvaine data in Fig. 3 shows the decomposition reaction to be much faster in the MacIlvaine buffer, which indicates a specific buffer effect.

Cathodic Utilization of the Oxide

Some of the electrochemical characteristics of the high-valency oxide were evaluated by discharging the oxide in conventional primary cell configurations *vs.* zinc anodes in 40% KOH containing 6% ZnO. The desiccated oxide was blended with 5 w/o graphite and pressed into circular pellets approximately 0.25 cm thick with a diameter of 1.3 cm under a pressure of 30,000 psi. The discharge curve of such a cell is shown in Fig. 4. It had an open-circuit voltage of 1.75v, and it exhibited a fairly flat discharge curve. The cell voltage remained at an average value of 1.5v for drain rates in the range of 5-7 ma/cm^2. Polarization characteristics of the cell are shown in Fig. 5 for various discharge levels. It polarized severely at deep discharge levels for current densities in excess of 10 ma/cm^2. However, the cell was not optimized to give a good discharge behavior.

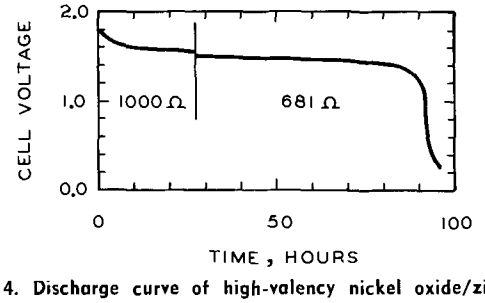

Fig. 4. Discharge curve of high-valency nickel oxide/zinc cell, two load conditions.

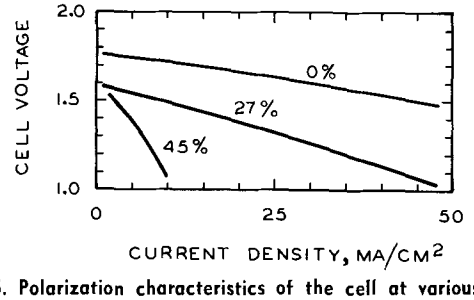

Fig. 5. Polarization characteristics of the cell at various depths of discharge.

An analysis of the discharged cathode showed that the nickel had been reduced to an oxidation state of 2.41. The failure of the cathode to discharge to a valence state of 2.0 may be attributed to an excessive polarization under the conditions of the experiment. The charge withdrawn from the cell was equivalent to a valence change of 0.91, which corresponded to an initial oxidation state of 3.32. The nickel in the wet starting material had a valency of 3.49, but experiments had shown that drying of the high-valency oxide tended to decrease its oxidation state. The dried, charged cathodes had not been analyzed.

Discussion of the Results

The high-valency nickel oxide has been described in terms of the mean oxidation state of the nickel. In an attempt to define the chemical species more precisely, we examined the x-ray diffraction patterns of the oxides in various valence states between 2.2 and 3.5 (Norelco X-Ray Diffraction Unit). In no case did we observe any lines except those due to the cellophane tape used to mount the sample, which prevented a comparison on a structural basis of our material with that of other investigators. Electron microscopic observations (Hitachi HU-11) of the oxide after it had been washed in water and ethanol failed to disclose any discrete crystals at a magnification of 30,000X. The alcohol rinse was used to prevent the introduction of any water into the electron microscope, and it was accompanied by the decomposition of the oxide to the divalent state. Distinct electron diffraction patterns were obtained of the decomposed oxide, which showed it to be a crystalline material. There is a possibility that the material may be composed of very thin crystalline flakes, less than 30Å thick and as large as 1000Å in diameter, which would be transparent to the electron beam except when viewed on edge. It would appear, therefore, that no definitive statements can be made on the basis of our data regarding the exact chemical nature and physical structure of the reaction products resulting from either the oxidation or the reduction reactions.

The highest mean oxidation state obtained in reproducible experiments was 3.6 (except as noted below), and there is a question whether or not this state represented an equilibrium composition of the oxide. It is conceivable that the solid phase contained tri- and tetravalent nickel in equilibrium proportions. However, large surface area states do not normally represent equilibrium states. They may be expected to undergo morphological changes to reduce their surface free energy. Thus, we are led to consider the oxidation product as a metastable entity, and there are no apparent reasons why a mean nickel valency of 3.6 should represent the highest attainable oxidation state for the oxide. We did obtain specimens with mean oxidation states between 3.95 and 4.00, but they could not be maintained in these high valence states unless an excess of the oxidant was present. There are reasons for believing, therefore, that higher valency oxides may be synthesized and stabilized.

No stable tri- or tetravalent nickel ions have been reported in aqueous media; the only stable aqueous nickel ion being divalent (10). It would seem, therefore, that the oxidation reaction must be a heterogeneous reaction, and two requirements must be met for the successful synthesis of very high-valency oxides: (*i*) an adequate concentration of the oxidant must be maintained at the reaction site, and (*ii*) the oxidized surface must be protected from reaction with water by the further precipitation and concomitant oxidation of nickel hydroxide on top of previously oxidized nickel. Thus, there would seem to be a need for detailed investigations of the precipitation kinetics and the morphology of nickel oxides to provide a basis for the selection of the best conditions for the synthesis of high valency nickel oxides. The observations of Okada *et al.* (11) on the

formation of amorphous divalent nickel hydroxide provide a useful basis for further studies.

The observed stability of the high-valency oxide in strongly alkaline solutions agreed with the results obtained by Tuomi (7) who found that the high-valency alpha nickel oxide could be formed readily in concentrated KOH or NaOH but not in dilute alkali solutions and with the results of Conway and Bourgault (12) on a series of oxides having a lower valency than the oxides studied by us.

An analysis of the kinetic form of our rate data was precluded by the inadequacy of the available information. In addition to the absence of an identification of the reaction species, the surface area of the oxides and the concentration of the nickelous ions in solution in the electrolyte occluded in the amorphous precipitate were unknown. The two latter quantities are experimentally inaccessible. Surface areas measured by gas adsorption techniques would be invalid because area changes take place during the dehydration of the specimens. The use of solution adsorption isotherms (13) may prove useful for these materials in the future. Insofar as the analysis of the residual valence state of the oxide is concerned, there is no chemical method available for distinguishing between the nickel in solution in the occluded electrolyte and the nickel in the solid oxide which is sufficiently rapid to be used for kinetic measurements. To the extent that it is possible to determine the true composition of the solid phase and the adjacent solution, it should be possible to obtain mechanistically meaningful data on the decomposition reaction. A detailed analysis of the reaction mechanism using the methodology of Conway and Bourgault (14) would be valuable.

The coincidence of the *p*H range of oxide instability with the *p*H range of solubility of divalent nickel in equilibrium with solid $Ni(OH)_2$ (10) suggested that the decomposition reaction proceeded *via* a dissolution step. Supporting evidence for such a conjecture comes from the observation that the MacIlvaine buffer enhanced the decomposition rate significantly. This buffer contains citrate ions, which are known to complex with divalent nickel (15). Therefore, the solubility of $Ni(OH)_2$ would be greater in citrate buffers than in pure phosphate buffers, and an enhanced decomposition rate would be expected in the citrate buffer, if the mechanism involved the reaction between a high-valency surface ion and a solution species to give a low-valency surface oxide. The transport of reagents and/or products through the divalent surface oxide would control the rate of the reaction, and the removal of the divalent oxide by means of complexation would lead to an increase in the decomposition rate.

The explanation for the differences observed in the reaction rates of fresh (fast) and aged (slow) oxides under comparable conditions must remain conjectural in the absence of a defined morphology of the oxide. An assumption which appears reasonable is that the aged oxide had rearranged to provide a smaller exposed surface area, or that the oxide had rearranged on aging to a configuration with an increased activation energy for one of the solid-state reaction steps involved in the decomposition process. It is also possible that the aged oxide had acquired a thicker surface layer of divalent oxide. However, if this were the case, an accompanying substantial decrease should have been observed in the mean nickel valency, which was not the case.

The rate curves obtained on the aged oxide in the *p*H 6 phosphate buffer at the low temperatures exhibited an initial induction period, an intermediate fast reaction period, and a final slow reaction period. This behavior is consistent with the conjecture that the oxides had acquired an inhibiting surface film. While still present, the film would prevent the decomposition reaction from proceeding very rapidly. Its dissolution would lead to an acceleration in the rate of the reaction because of the increase in the reactive surface area. As the reaction products would accumulate in the interior of the porous structures, the rates would decrease and become mass transfer controlled. The differences in the reaction rates during the intermediate reaction period at the various temperatures would, therefore, be due to the influence of the temperature on the rate of dissolution of low-valency surface oxide. The mass transfer controlled rates would be expected to be relatively insensitive to temperature, as observed. The fresh oxides did not exhibit any induction periods probably because of their larger surface areas, or because of the absence of an effective low-valency surface layer.

The cathodic behavior of the high-valency oxide showed that the high oxidation state of the chemically prepared material was available for electrochemical reduction. This agrees with observations on nickel-cadmium cells where some excess capacity can be obtained by discharging the cells immediately after charging. In the case of secondary cells, however, the excess capacity disappears in a few hours.

The open-circuit potential of the high-valency oxide-zinc primary cell corresponded to that expected for the system in concentrated KOH on the basis of the values given by Latimer (16). Since the high-valency oxide did discharge and since no significant potential arrests were observed above the trivalent nickel potential, it would appear that the high valence state did have a potential close to that of trivalent nickel. However, the assignment of an exact and a thermodynamically meaningful potential to the high-valency material must await the required definitive studies.

If the closeness of the discharge potentials of the trivalent and the higher valency oxides holds for their reversible half-cell potentials as well, the equilibrium constants of the reactions leading to the formation of trivalent and tetravalent nickel would be correspondingly close. Therefore, since the formation of trivalent oxide is thermodynamically favored, so would be the formation of tetravalent nickel. The observed, apparent limitations in the value of the mean valence state of nickel suggest that the reaction of tetravalent nickel with water is kinetically favored over that of trivalent nickel. This is in agreement with our conjecture that the synthesis of the high-valency oxide is limited by kinetic rather than thermodynamic factors. Therefore, it is to be expected that nickel oxides with valencies above 3.6 may be prepared provided the proper oxidation conditions can be established based on detailed information on the kinetics of the precipitation and decomposition reactions of the nickel oxides.

Conclusions

Investigations of the high-valency amorphous nickel oxides showed that they could be prepared reproducibly at room temperature with a mean oxidation state of 3.6 for the nickel. The oxides were stable at room temperature and at lower temperatures in strongly alkaline solutions but decomposed at *p*H values below *p*H 14. Between *p*H 9 and *p*H 14 the decomposition reaction was very slow; below *p*H 9 it became very fast.

The results indicated that the degree of oxidation of the nickel was kinetically as well as thermodynamically controlled, and it is believed that it may be possible to prepare nickel oxides with mean valencies in excess of 3.6.

Primary cell cathodes prepared from the high-valency material exhibited a good utilization of the high oxidation state of nickel.

Acknowledgment

The authors are indebted to J. Epstein for the electrochemical measurements; they wish to express their appreciation to the management of P. R. Mallory & Co., Inc., for permission to publish this report.

Manuscript received Nov. 22, 1965; revised manuscript received Feb. 21, 1966.

Any discussion of this paper will appear in a Discussion Section to be published in the December 1966 JOURNAL.

REFERENCES

1. J. Labat, *J. Chim. Phys.*, **60**, 1253 (1963).
2. O. Glemser and J. Einerhand, *Z. anorg. u. allgem. Chem.*, **261**, 26 (1950).
3. L. Dede and H. Zieriacks, *Z. Anal. Chem.*, **124**, 25 (1942). Quoted by (1).
4. J. Labat, *Ann. Chim.*, **9**, 400 (1964).
5. O. R. Howell, *J. Chem. Soc.*, **123**, 1772 (1923).
6. E. Jones and W. F. K. Wynne-Jones, *Trans. Faraday Soc.*, **52**, 1260 (1956).
7. D. Tuomi, *This Journal*, **112**, 1 (1965).
8. J. Besson in P. Pascal, "Nouveau Traite de Chimie Minerale," Vol. 17, p. 742-59, Masson & Cie, Paris (1963).
9. E. J. Casey, A. R. Dubois, P. E. Lake, and W. J. Moroz, *This Journal*, **112**, 371 (1965).
10. M. Pourbaix, "Atlas D'Équilibres Electrochimiques," Gauthier-Villars & Cie., Paris (1963).
11. T. Okada, T. Shiraishi, and K. Watanabe, *J. Chem. Soc. Jap. Ind. Chem. Soc.*, **51**, 129 (1948).
12. B. E. Conway and P. L. Bourgault, *Can. J. Chem.*, **40**, 1690 (1962).
13. D. H. Everett, *Trans. Faraday Soc.*, **60**, 1803 (1964).
14. B. E. Conway and P. L. Bourgault, *Can. J. Chem.*, **37**, 292 (1959).
15. L. G. Sillen and A. E. Martell, "Stability Constants of Metal-Ion Complexes," The Chemical Society, London (1964).
16. W. M. Latimer, "The Oxidation States of the Elements and Their Potentials in Aqueous Solutions," Prentice-Hall, Inc., New York (1952).

Equilibrium Pressures of Oxygen over Oxides of Lead at Various Temperatures

Earl M. Otto

National Bureau of Standards, Washington, D. C.

ABSTRACT

PbO_2 apparently requires four stages of decomposition to reach PbO. Based on thermogravimetric studies the intermediate products appear to be $5PbO_2 \cdot 4PbO$, $4PbO_2 \cdot 5PbO$, and Pb_3O_4. Although the first three stages seem irreversible, they too come to a steady state in decomposition, but no recombination takes place. $\Delta H°$ and $\Delta S°$ values have been calculated for the four stages.

Thermal decomposition of lead dioxide has been studied by a number of investigators with the emphasis being placed on the composition and the crystal structure of the dioxide and the lower oxides that were formed. Earliest work indicated that an intermediate product of Pb_2O_3 is formed (1) (1878). Later, Moles and Vitoria (2) (1929), Renker (3) (1936), and Baroni (4) (1938) agreed that no other substance than Pb_2O_3 is formed before Pb_3O_4 appears. When the mathematical error of Baroni was corrected showing the formula of the oxide to be $PbO_{1.6}$, more investigation and speculation began. Clark and Rowan (5) (1941) refer to the oxide as Pb_5O_8. Holtermann and Laffitte (6) (1937) ascribed the formula Pb_7O_{11}. However, LeBlanc and Eberius (7) (1932) had stated that the structure of PbO_2 persists to $PbO_{1.66}$ and had ascribed the formula Pb_3O_5 to an intermediate product. They also reasoned that Pb_2O_3 is formed. A few years later Bystrom (8) (1945) and Katz (9) (1950) showed that two intermediate oxides were indicated and these were termed $\alpha\ PbO_x$ and $\beta\ PbO_y$, the former having a monoclinic crystal structure of nonstoichiometric composition where x is somewhat more than 1.5 and the latter having an orthorhombic crystal structure of nonstoichiometric composition where y is less than 1.5 and approximating 1.4. Recently Butler and Copp (10) (1956), and Anderson and Sterns (11) (1959) have confirmed the existence of two intermediate oxides, the latter authors proposing the formulas $Pb_{12}O_{19}$ and $Pb_{12}O_{17}$.

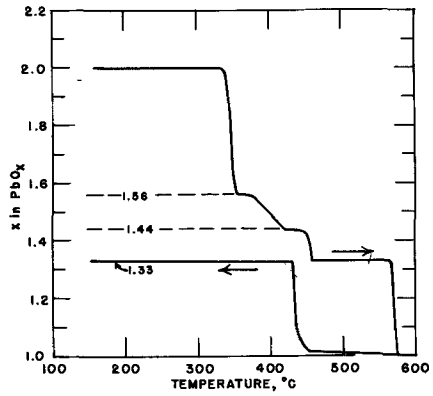

Fig. 1. Thermal balance study of the dissociation of PbO_2 to PbO and reoxidation to Pb_3O_4. Influence of temperature on the value of x in PbO_x, calculated from weight loss.

Very little study has been made of the equilibrium pressures of oxygen over the various oxides of lead. LeChatelier (12) (1897) Reinders and Hamburger (13) (1914) separately determined oxygen pressures over $PbO\text{-}Pb_3O_4$; the two sets of data did not show much agreement.

In view of the lack of pO_2-oxide temperature equilibrium data for the oxides of lead it was thought desirable to conduct the present investigation.

Experimental

Preliminary to the study of oxygen pressures over the PbO_2 and the lower oxides a thermal balance was constructed and used to get indications as to the approximate temperatures at which decompositions in air could be expected. Figure 1 shows that weight loss began before a temperature of 330° was reached and that at about 360° the weight became constant and the formula of the oxide was calculated to be approximately $PbO_{1.56}$. At 420° another level was reached, and calculations indicated the oxide to be approximately $PbO_{1.44}$. At 450° further decomposition began and continued to 460°, at which stage the oxide was $PbO_{1.33}$. (This material is the well-known "red lead," Pb_3O_4.) The final decomposition was reached at 570°, and the product was $PbO_{1.00}$. On cooling the PbO slowly in air, oxygen was consumed starting at about 450° and forming $PbO_{1.33}$. No further reoxidation was observed. The time of decomposition, from PbO_2 to PbO was seven days. This whole experiment was repeated twice, and the results were essentially the

same. Anderson and Sterns suggested that the formation of lower oxides is a result of nucleation and growth. The above mentioned values of x in PbO_x appear to indicate that nine molecules of PbO_2 are involved in the formation of each unit. Thus the products formed are postulated to be $5PbO_2 \cdot 4PbO$, $4PbO_2 \cdot 5PbO$, and $3PbO_2 \cdot 6PbO$. (The last substance may break down forming $PbO_2 \cdot 2PbO$, which is the same as Pb_3O_4.) Further evidence of a nine molecule unit is supplied by Anderson and Sterns for they say that acid leaching of one intermediate oxide gave $PbO_{1.886} \cdot 0.16H_2O$. The product in this case could be represented by $8PbO_2 \cdot PbO$.

The apparatus used for the pressure studies was similar to that previously employed by the author (14, 15) in studies of the Mn_2O_3-Mn_3O_4 and MnO_2-Mn_2O_3 equilibria. Both Fisher, and Baker and Adamson analytical grades of PbO_2 were used in the investigations. Five furnaces, four sets of manometers, and one 300-psi gauge were involved. Each furnace had its own constant temperature cabinet. Essentially the procedure consisted in heating *in vacuo* a sample of PbO_2 in a bulb contained in a crucible furnace until the evolved oxygen, having passed through the silica gel desiccant, began to change the mercury levels in the manometers. The temperature was stabilized and the pO_2 was allowed to become steady. Time for reaching a steady pressure sometimes was hundreds of hours and sometimes less than 5 hr, depending on the stage of dissociation. In one instance in the last stage the build-up in pO_2 from near vacuum to one third equilibrium pressure required less than 2 min. After a steady state was established the temperature or pressure or both were altered and a new steady state sought. After the first stage of dissociation was satisfactorily studied the investigation was extended to the second and third stages. Only one sample of PbO_2 was carried to the fourth stage because the equilibria of the last stage were so quickly attained and because commercially produced (analytical reagent grade) Pb_3O_4 could be used.

Except for the last stage of decomposition no recombination was ever observed when a somewhat higher than steady-state pressure of oxygen was provided to the partially dissociated oxides. The Pb_3O_4-PbO-O_2 reaction was readily reversible and equilibrium attainable in either direction.

The data obtained are shown in Table I and Fig. 2 to 5. The only available data from the literature are included in Fig. 4. The present data on Pb_3O_4-PbO are in good agreement with those of Reinders and Hamburger.

Table I. Dissociation of PbO_2 temperature-pressure steady-state data

Steady state hr to:	hr at:	Temperature, °C	Pressure, atm
		First stage	
168	144	254.2	0.0787
120	120	258.6	0.1467
1960	270	267.2	0.4600
360	144	269.7	0.5256
1632	120	277.4	1.1910
2300	300	285.2	2.258
168	24	286.2	3.401
288	144	287.2	3.016
96	72	287.9	4.238
48	24	298.8	10.88
		Second stage	
360	240	318.5	0.1521
120	48	335.8	0.4369
120	64	357.1	1.4067
360	120	363.4	2.186
		Third stage	
72	24	348.1	0.2174
264	24	354.0	0.3299
240	66	364.0	0.5339
360	480	382.3	1.2593
*		Fourth stage	
16	0	484.1	0.0416
60	0	487.2	0.0474
24	0	524.5	0.1395
19	24	538.8	0.2250
60	0	547.2	0.2938
24	24	547.5	0.2984
5	4	561.2	0.4127
16	96	563.6	0.4277
10	15	564.5	0.4669
16	0	569.2	0.5195
22	48	601.9	1.2466
24	0	603.6	1.2785
40	0	606.2	1.3321
7	16	609.6	1.4522
12	10	627.5	2.3511
8	0	632.0	2.5355
24	0	632.9	2.6376
48	72	634.8	2.6505
20	0	638.4	2.8176

* Minimum time to steady state was not observed. These were the periods that were convenient to the investigator.

Treatment of Data

The straight lines shown in Fig. 2, 3, and 4, drawn for the new experimental data, form the basis for determining values for the thermodynamic functions ΔH° and ΔS°, on the assumption that steady pressures were true equilibrium pressures. The equations for the straight lines, fitted to the experimental point by sight, were put in the form of

$$\Delta H^\circ/T - \Delta S^\circ = \Delta G^\circ/T = -4.5756 \log pO_2$$

The resolved values for the four stages of dissociation are, precisely applicable only for the mean temperatures, as follows:[1]

Proposed equation	Temperature range, °C	ΔH° kcal mol^{-1} O_2	ΔS° cal deg^{-1} mol^{-1} O_2
$9/2PbO_2 \rightarrow 1/2(5PbO_2 \cdot 4PbO) + O_2$	270 ± 30	66.4	121.0
$2(5PbO_2 \cdot 4PbO) \rightarrow 2(4PbO_2 \cdot 5PbO) + O_2$	345 ± 25	44.2	70.9
$2(4PbO_2 \cdot 5PbO) \rightarrow 6Pb_3O_4 + O_2$	367 ± 17	39.9	61.4
$2Pb_3O_4 \rightarrow 6PbO$ (yellow) $+ O_2$	560 ± 80	37.5	43.2

Excepting for the Pb_3O_4-PbO stage these values cannot be converted from the experimental temperatures to 298°K, since heat capacities, heat contents, and entropy changes are unknown for the intermediate oxides and are estimated or partially known for PbO_2 and Pb_3O_4. Considering the first three stages as one, the equation becomes $3PbO_2 \rightarrow Pb_3O_4 + O_2$. Using the

[1] One thermochemical calorie = 4.1840 joules.

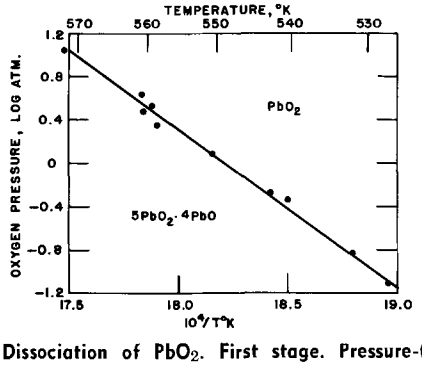

Fig. 2. Dissociation of PbO_2. First stage. Pressure-temperature relationship at steady state.

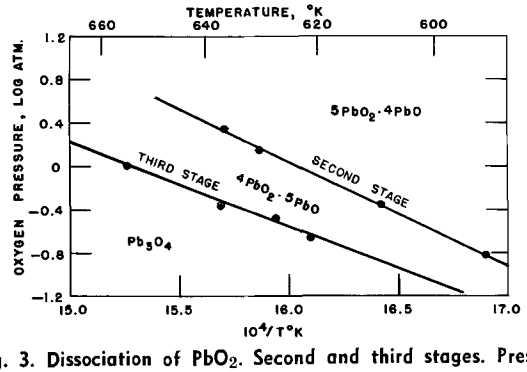

Fig. 3. Dissociation of PbO_2. Second and third stages. Pressure-temperature relationship at steady state.

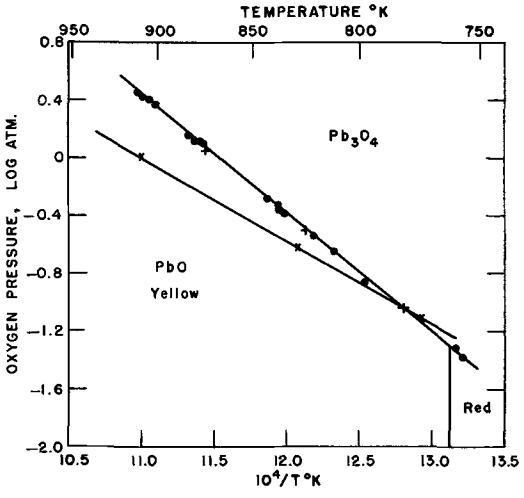

Fig. 4. Dissociation of PbO_2. Fourth stage. (Identical with first stage of dissociation of Pb_3O_4.) Half of the equilibrium points obtained in forward direction and half in the reverse. ● Present work; × LeChatelier; + Reinders and Hamburger.

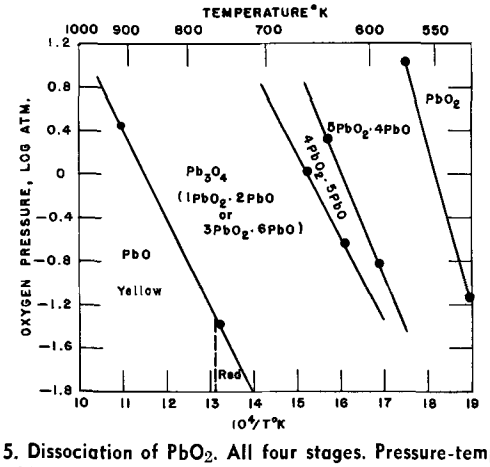

Fig. 5. Dissociation of PbO_2. All four stages. Pressure-temperature relationship at equilibrium. Dots mark the limits of experimental investigation.

Cp values given by Kelley (16) the $\Delta(H_T-H_{298})$ and $\Delta(S_T-S_{298})$ were obtained, where T = 585°K (a rough average of the temperatures of the first three reactions). These are −1.7 kcal/mol O_2 and −2.7 cal/deg, respectively. When these are added to the ΔH° and ΔS° values for the sum of the three reactions, one obtains ΔH°_{298} = 56.6 kcal and ΔS°_{298} = 100 cal/deg. From these ΔG° is calculated to be +26.8 kcal. Taking ΔG°_f of PbO_2 to be −52.0 kcal the ΔG°_f of Pb_3O_4 becomes −129.2 kcal.

The Pb_3O_4-PbO-O_2 system was readily brought to equilibrium and the Cp equation for PbO is well established. It does have to be assumed that the Cp value for Pb_3O_4 at 298°K is usable up to 1000°K. For the reaction $2Pb_3O_4 \rightarrow 6PbO + O_2$ at the mean temperature of 833°K ΔH°_{833} = 37.5 kcal/mol O_2 and ΔS°_{833} = 43.2 cal/deg.

From the Cp equations the calculated value of $\Delta(H_{833}-H_{298})$ becomes +7.1 and $\Delta(S_{833}-S_{298})$ becomes +21.1, thus making ΔH°_{298} = 44.6 kcal/mol and ΔS°_{298} = 64.3 cal/deg. From these two figures ΔG°_{298} is found to be 25.4 kcal. On the selection of ΔG°_f of PbO as −45.2 kcal ΔG°_f of Pb_3O_4 then becomes −148.3 kcal.

The resulting values for Pb_3O_4 may now be compared with those from the literature.

	$\Delta G^\circ_f Pb_3O_4$ kcal
From cell data for $Pb_3O_4 + 2HgO = 3PbO_2 + 2Hg$	
Chartier (17)	−148.4
Andrews and Brown (18)	−146.0
From cell data for $3PbO + HgO = Pb_3O_4 + Hg$	
Andrews and Brown (18)	−142.5
From present work $3PbO_2 = Pb_3O_4 + O_2$	−129.2
From present work $2Pb_3O_4 = 6PbO + O_2$	−148.3

Note: In the above considerations selected values were

$$\Delta G^\circ_f PbO_2 = -52.0 \text{ kcal and } \Delta G^\circ_f PbO = -45.2 \text{ kcal}$$

The results are surprisingly good, considering the lack of precise thermodynamic data for some of the oxides of lead and considering the fact that steady-state pressures were obtained in only one direction for the first three stages of dissociation.

Manuscript received Nov. 9, 1965; revised manuscript received Feb. 11, 1966. This paper was presented at the Buffalo Meeting, Oct. 10-14, 1965.

Any discussion of this paper will appear in a Discussion Section to be published in the December 1966 JOURNAL.

REFERENCES

1. Debray, *Compt. rend. Paris*, **86**, 813 (1878).
2. Moles and Vitoria, *An. Fis. Quim.*, **27**, 52 (1929).
3. Renker, *Bull. Soc. Chim. France*, **3**, 981 (1936).
4. Baroni, *Gazz. Chim. Ital.*, **68**, 387 (1938).
5. Clark and Rowan, *J. Am. Chem. Soc.*, **63**, 1305 (1941).
6. Holtermann and Laffitte, *Compt. rend. Paris*, **204**, 1813 (1937). Also Holtermann, *Ann. Chim. Paris*, **14**, 121 (1940).
7. LeBlanc and Eberius, *Z. Physik. Chem.*, **A160**, 69 (1932).
8. Bystrom, *Ark. Kemi. Mineralog. Geol.*, **20A**, No. 11 (1945).
9. Katz, *Ann. Chim. Paris*, **5**, 5 (1950).
10. Butler and Copp, *J. Chem. Soc.*, 725 (**1956**).
11. Anderson and Sterns, *J. Inorg. Nucl. Chem.*, **11**, 272 (1959).
12. LeChatelier, *Bull. Soc. Chim. France*, **17**, 791 (1897).
13. Reinders and Hamburger, *Z. Anorg. Chem.*, **89**, 71 (1914).
14. E. M. Otto, *This Journal*, **111**, 88 (1964).
15. E. M. Otto, *ibid.*, **112**, 367 (1965).
16. K. K. Kelley, *U. S. Bur. Mines Bull. 584* (1960).
17. Chartier, *Compt. rend. Paris*, **256**, 1976 (1963).
18. Andrews and Brown, *J. Am. Chem. Soc.*, **56**, 388 (1934).

Oxidation of Copper Single Crystals in Aqueous Solutions of Inorganic Salts

III. Kinetics of Oxidation in $Cu(OAc)_2$ Solution

W. W. Porterfield and G. T. Miller, Jr.[1]

Department of Chemistry, Hampden-Sydney College, Hampden-Sydney, Virginia

ABSTRACT

The kinetics of formation of Cu_2O on the three principal (low-index) faces of Cu metal monocrystals are reported and correlated with the surface microtopography. A novel technique is described for the determination of surface areas of small metal samples. Over extended periods of time the relative rates of oxide formation are found to be: (100)>(111)>(110); the forms of the rate curves, however, differ markedly. The specific forms of the rate curves on the three faces are accounted for by a proposed mechanism in which the rate-controlling step is the drift velocity of positive holes through the Cu_2O film. This mechanism also correctly indicates the microtopography on the basis of the previously observed epitaxial relationships.

This is the third in a series of papers describing the oxidation of copper metal in solutions of copper(II) salts. The first two papers (1, 2) dealt with the topography of the copper(I) oxide film formed in such oxidations and are indispensable to an understanding of the data reported here. The present work attempts to describe the kinetics of the oxide growth and to begin, at least, the inference of a mechanism for the oxidation process.

Benard (3) has an excellent summary, with critical comments, of experimental techniques for the determination of oxide film thickness on metal surfaces. Of the methods he describes, the coulometric was chosen because of its experimental simplicity. This method is well established (4-8) but requires some comment in two respects. First, even though the electropolishing technique enables the worker to assume that the metal surface area is equal to the gross area of the specimen, the measurement of area continues to be a problem with this method; in this case, the problem was accentuated by the small areas available when using monocrystalline specimens. A procedure was devised, which is described below, that enabled the measurement of surface areas within an error of 1%; in this work the error was on the order of 0.1 mm^2. It is felt that this may be of use to other workers using coulometric techniques on small specimens. Second, as Evans (9) has made clear, the phenomenon of metal corrosion is, to a substantial extent, inherently irreproducible. It is therefore necessary to indicate clearly the extent to which irreproducibility affects conclusions to be drawn from irreproducible data. Unfortunately, many previous workers have not made such an indication. It should be noted, then, that the error bars shown in Fig. 2, 3, and 4 represent 2σ, the standard deviation for measurements displaying Gaussian scatter about an unknown true value.

The previous studies, in parts I and II of this series, of the topography of oxide films as a function of the anion and as a function of time show clearly that in this system, as in others, there is a marked difference in the behavior of the three principal crystal faces. It seemed likely, then, that the coulometric study of oxide formation, performed on individual crystal faces and interpreted in conjunction with the known variations of topography with time, would yield important evidence bearing on the mechanism of the oxide growth. This appears to be true, although much further experimentation will be required to conclusively demonstrate a detailed mechanism.

Experimental

99.999% copper monocrystals were used throughout this series of experiments (Virginia Institute for Scientific Research, Richmond, Virginia). Flats were cut on these crystals to expose the (100), (110), and (111) faces individually. The orientation of these faces was maintained within 2° [1° for the (100) face] by Laue back-reflection x-ray photography after every fourth mechanical polishing [every second mechanical polishing for the (100) face]. The crystals were mechanically polished through 4/0 Buehler paper, then electropolished in an unstirred phosphoric acid bath and washed, finally, in water of approximately 1.2 x 10^6 ohms resistivity. The flats were dried in a stream of Seaford grade nitrogen (Southern Oxygen Company, Washington, D.C.; maximum impurity limits 30 ppm total) before immersion in the corroding solution. The only solutions used in this study were 0.0500*N* $Cu(C_2H_3O_2)_2$, made up from Fisher copper(II) acetate dihydrate, used as received from lot number 731759. Oxidation patterns from this lot were found to remain unchanged upon repeated recrystallization, whereas other lot numbers gave patterns which only approached that from this lot after two or three recrystallizations. Solutions were adjusted to a *pH* of 4.300 ± 0.005 before each oxidation. All solutions were thermostatted at 30.0°C before and during the corrosion process, since a study of the effect of temperature on the corrosion process, to be undertaken shortly, is expected to reveal marked temperature dependence. After oxidation for stipulated times, each crystal was dried and the spherical sides of the crystal, together with the edges of the flat face, were masked by painting with the electrically insulating lacquer Miccrostop (Michigan Chrome and Chemical Company, Detroit, Michigan). Coulometric measurement of the oxide on the area remaining was made in the apparatus shown in Fig. 1, after appropriate deaeration. The electrical potential of the crystal against an Ag/AgCl electrode was recorded on a Bausch and Lomb VOM-5 recorder. The exposed area of the flat was calculated by stripping the masking lacquer from the crystal, photographing the flat by using a Polaroid film pack at 6X on a Reichert metallurgical microscope, and measuring the photographed area with a planimeter. Equivalent copper(I) oxide film thickness could then be calculated on the assumptions that: (*i*) film density was equal to that of the bulk oxide; (*ii*) current efficiency was 1.000; and (*iii*) the oxide formed a film of uniform thickness. A discussion of the influence of departures from these assumptions upon reproducibility follows below; here it might be noted that the error bars in Fig. 2, 3, and 4 are roughly between 5 and 10% of the indicated mean.

With respect to the first assumption, lattice parameter measurements for films on the major faces of copper [(10) and references therein] indicate a linear expansion of 1-2% normal to the surface, but an offsetting compression in the surface plane. The unit cell volume is that of the bulk oxide, and the density

[1] Present address: Department of Chemistry, St. Andrews Presbyterian College, Laurinburg, North Carolina.

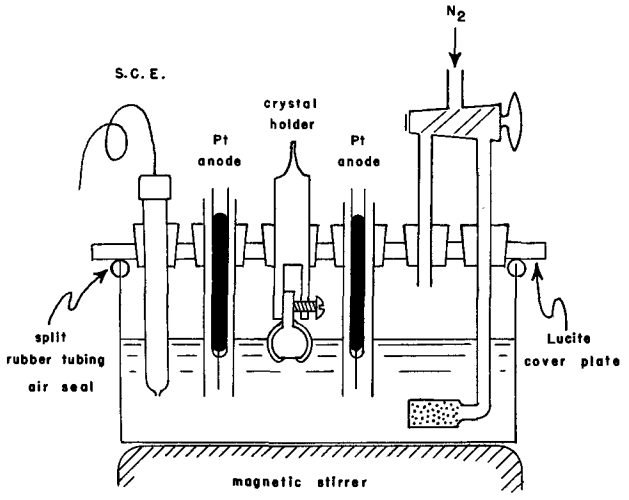

Fig. 1. Apparatus for coulometric oxide determination. Crystal holder is shown with a masked crystal in place.

will thus be unaffected. The validity of the second assumption is more difficult to establish. Studies comparing oxygen uptake (in gaseous oxidation) with coulometric values suggest an efficiency of at least 0.90 (11), and studies of current efficiency as a function of current density (micro-amperes/cm^2) for the Fe-Fe_3O_4-Fe_2O_3 system (7) suggest the same approximate figure under our experimental conditions. Of course, this is not a comparable system, but the order of magnitude of current density is perhaps suggestive. In any event, only the absolute determination of deposited oxide mass would suffer from this type of error; the rate curves would retain their general form and relative magnitudes. However, substantial scatter could arise from this source. Finally, the assumption of a uniform oxide film requires severe qualification. The rather rugged microtopography revealed in the electron micrographs (1, 2) indicates that interpretation of the coulometric data as thicknesses of oxide films is illusory. Clearly, the only appropriate interpretation is that of a gross average, that is, deposited oxide mass per unit area. This figure is used in each case.

Results and Discussion

Figures 2, 3, and 4 show the oxide growth rates on the three low-index faces of copper metal crystals, as determined in this study. Figure 5 indicates the marked differences between the faces. In Fig. 2, 3, and 4 the notation is as follows: (*i*) The error bars, as previously stated, are 2σ long. (*ii*) The arithmetic mean of all determinations is indicated by a crossbar. It must be remembered, however, that the arithmetic mean is the most probable value only for a Gaussian error distribution. It is not certain that this is the true distribution in corrosion measurements. (*iii*) The mode

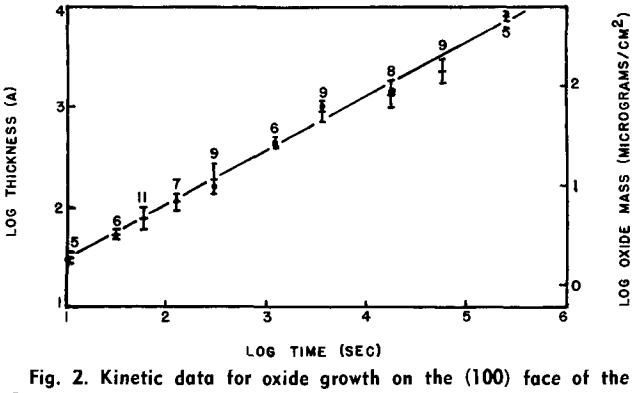

Fig. 2. Kinetic data for oxide growth on the (100) face of the Cu metal crystal. Reciprocal slope is 1.86.

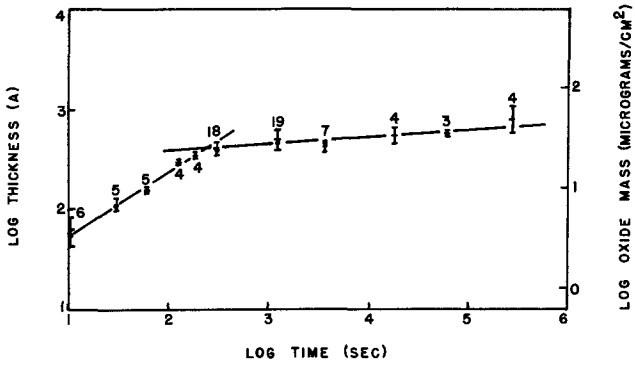

Fig. 3. Kinetic data for oxide growth on the (110) face of the Cu metal crystal. Reciprocal slope of initial rise is 1.57.

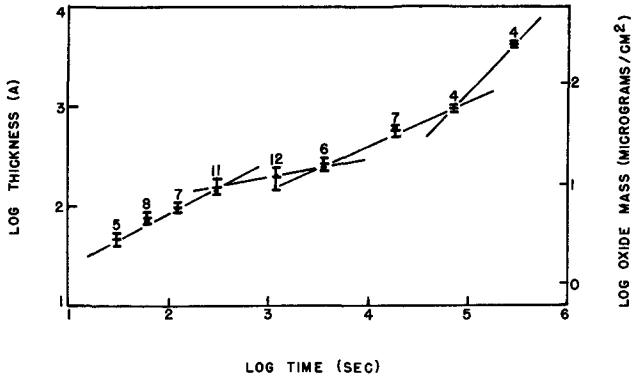

Fig. 4. Kinetic data for oxide growth on the (111) face of the Cu metal crystal. Reciprocal slope of initial rise is 1.99.

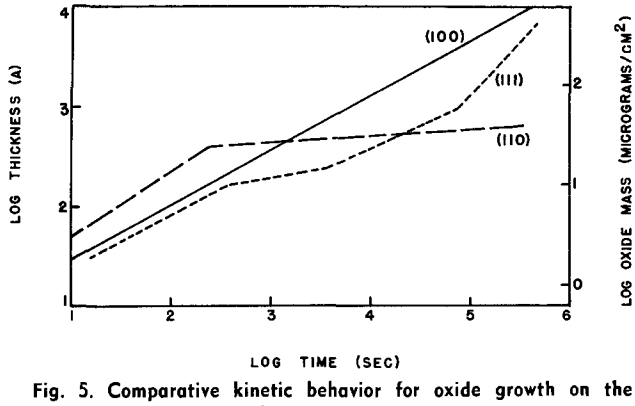

Fig. 5. Comparative kinetic behavior for oxide growth on the three principal metal crystal faces.

is indicated by a heavy dot. Evans (9) has suggested that, given the irreproducible nature of the measurements, the mode may be the most significant quantity. (*iv*) The number of measurements at a given time of immersion is indicated over the error bar. (*v*) To provide a more meaningful interpretation, the right-hand scale in these figures is given as deposited copper(I) oxide mass per unit area (micrograms per square centimeter). However, the convenient comparison of this work with other film-thickness studies requires that the data also be presented as equivalent average thickness in Angstrom units. It must be remembered that these thicknesses are rather fictional; that both vertical and lateral growth are occurring, and to different extents on different crystal faces of the metal.

It was anticipated from preliminary experiments that the oxide growth would be quite rapid; Fig. 2, 3, and 4 confirm this. Indeed, the growth on all three faces is so fast that it does not seem possible for the

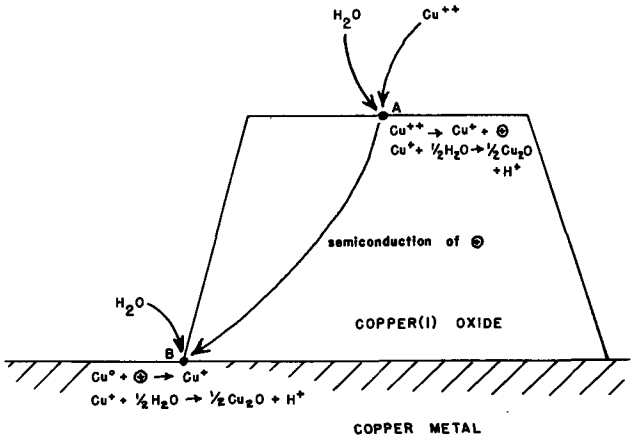

Fig. 6. Schematic representation of proposed mechanism

rate-determining step to be the diffusion of copper atoms through the oxide film, which is almost immeasurably slow at 30°C, the temperature of the reaction. Thus it seems likely that a significant amount of Cu(I) in the oxide film must originate from the Cu(II) in solution. Furthermore, if atomic (or ionic) diffusion is ruled out, any Cu(I) in the oxide originating from the metal must be obtained from a location where the oxide is either quite thin or nonexistent.

Figure 6 diagrammatically indicates a mechanism which appears to satisfy these requirements. Copper(II) ions from solution are adsorbed onto existing copper(I) oxide nuclei which are in contact with bulk copper metal. This adsorption may be assumed to occur preferentially on the close-packed faces of the oxide (not necessarily on the close-packed faces of the metal). After adsorption each ion donates a positive charge to the copper(I) oxide, becoming a Cu(I) ion. This ion may react immediately with the solution's oxygen-supplying species (at point A) or may migrate some distance across the surface of the Cu_2O polyhedron before reacting to form additional Cu_2O. The mean migration distance will be governed by the ratio of the migration velocity to the rate of reaction with the oxygen-supplying species in solution. The copper(I) oxide, functioning as a p-type semiconductor, conducts the positive hole to a point at which the three phases Cu_2O, Cu°, and solution are all present (such as point B in Fig. 6). Here a copper atom acquires the positive charge, becoming a copper(I) ion, and reacts with the solution to form more Cu_2O. The same migration considerations apply at point B as at point A. The mechanism may be summarized as follows:

(*i*) diffusion of Cu(II) species and adsorption on the oxide surface

(*ii*) $Cu^{2+} \rightarrow Cu^+ + \oplus$ (cathodic reaction at A)
(*iii*) $Cu^+ + \frac{1}{2}H_2O \rightarrow \frac{1}{2}\underline{Cu_2O} + H^+$
(*iv*) movement of $\oplus$ from A to B
(*v*) $\oplus + Cu^\circ \rightarrow Cu^+$ (anodic reaction at B)
(*vi*) $Cu^+ + \frac{1}{2}H_2O \rightarrow \frac{1}{2}\underline{Cu_2O} + H^+$

The net cathodic and anodic processes are, respectively the sum of (*ii*), (*iii*) and (*v*), (*vi*):

$$Cu^{2+} + \tfrac{1}{2}H_2O \rightarrow \tfrac{1}{2}\underline{Cu_2O} + H^+ + \oplus \qquad (E_c)$$

$$Cu^\circ + \tfrac{1}{2}H_2O + \oplus \rightarrow \tfrac{1}{2}\underline{Cu_2O} + H^+ \qquad (E_a)$$

$$Cu^{2+} + Cu^\circ + H_2O \rightarrow \underline{Cu_2O} + 2H^+ \qquad (E_{net})$$

It must be noted that steps (*v*) and (*vi*) of such a mechanism require that the oxidizing solution be in contact with the oxide-metal interface for growth to occur, since the solution must provide the oxygen for the lattice, otherwise the oxide cannot continue to remove positive holes from its surface. The crevices visible in the earlier electron micrographs (1) would appear to provide just such a solution contact. Possible sources of oxygen would be free H_2O, the aquo complex of Cu(II), CH_3COO^-, or dissolved O_2. (H_2O is used as an example in the equations above.) Exploratory experiments using BF_4^- anion and dissolved O_2 removal indicate that probably neither the anion nor dissolved O_2 provides the oxygen.

In examining the rate curves it will be shown below that the adequacy of the proposed mechanism depends on the assumption that adsorption of the copper(II) species on the Cu_2O surface occurs preferentially on the most closely packed surface of the oxide. This is intuitively reasonable but by no means necessary. It may be that another mechanism could be devised which would not require this feature, but its nature is not immediately obvious.

The forms of the three rate curves (Fig. 2, 3, and 4) must be examined separately with respect to the proposed mechanism because of their strikingly different natures (Fig. 5).

Oxide growth on the (100) face occurs by an apparently uniform mechanism over an extended period of time (Fig. 2). It might be noted in passing that on the logarithmic scale employed here the age of the universe would not fill a double-page spread of this Journal! The mathematical form of the growth law, as determined from the inverse slope of the log-log plot, is very roughly parabolic (exponent 1.86). The parabolic law might be expected if the positive hole draft velocity were the rate-determining step: $d(Th)/dt = K\mu$, where Th represents oxide thickness and μ the drift velocity. Drift velocity is proportional to electric field strength, which in this case is decreasing with increasing thickness, so that

$$\mu = K'/Th$$

Then

$$d(Th)/dt = KK'/Th, \text{ and } (Th)^2 = K''t$$

The steady growth is also consistent with the topography of the oxide on the (100) face (polyhedra), since the crevices between the polyhedra would permit the necessary uninterrupted solution contact with the metal-oxide interface.

The (110) face is quite different. Oxide grows on it somewhat faster than on the (100) face initially (exponent 1.57), but only for the first three or four minutes. Growth then stops almost completely. Some justification for this may be found in the electron micrographs of the (110) face, which reveal an unusually smooth oxide film (1). Apparently lateral growth fills the crevices between oxide nuclei in this orientation, thereby preventing solution contact with the oxide-metal interface and providing effective protection for the metal. The very slow growth which continues to occur may be due to a few unfilled crevices or to positive hole conduction to exposed oxide-metal interfaces on adjacent faces of different orientation. It is interesting to observe that the initial growth on this face is faster than that on the (100) face; one would not expect this either from metal-atom packing considerations or by analogy with the high-temperature dry oxidation of copper (12).

Upon consideration of the probable modes of deposition of the copper(II) ions, however, the relative rates may be rationalized. The epitaxial relationships displayed in this system are as follows (13): the (100) copper face requires the growth of the (111) Cu_2O face parallel to it; the (110) metal face, the (110) oxide face; the (111) metal face, the (111) oxide face. Then, following the assumption of preferential adsorption on the close-packed face, the (100) and (111) metal faces will both tend to adsorb copper(II) ions on the top of the nuclei, thereby producing the vertical growth governed by the parabolic law; but the (110) metal face, having the thermodynamically more stable (close-packed) (111) faces on the slant sides of the nuclei, will tend to adsorb on the sides. In this case the growth will be predominantly lateral, with

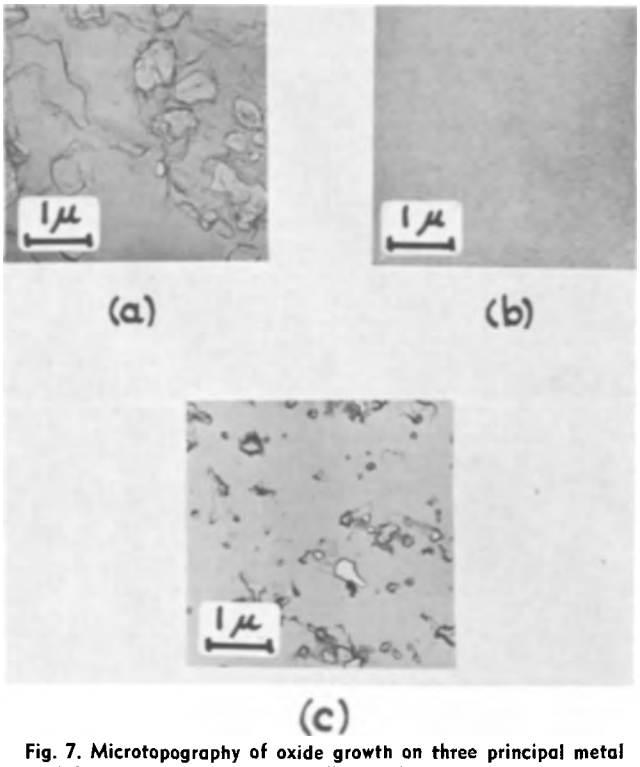

Fig. 7. Microtopography of oxide growth on three principal metal crystal faces after 72 hr (2.6 x 10^5 sec). (a) (100); (b) (110); (c) (111).

the vertical thickness changing only rather slowly. The drift velocity, μ, will be essentially constant, and the oxide growth will occur by a linear law. To the extent, then, that lateral growth predominates over vertical growth, the exponent in the growth law will be reduced from 2 toward 1. The faster growth on the (110) face, characterized by the lower exponent, is thus consistent with the orientation of close-packed faces produced by epitaxy, as is the almost complete cessation of growth after complete coverage has been achieved. The slight lowering of the exponent for the (100) face (from the hypothetical 2.00 to the observed 1.86) is perhaps also due to appreciable lateral growth.

Growth of oxide on the (111) face is also, initially, approximately parabolic (exponent 1.99). After five to ten minutes, however, a slackening of rate occurs like that on the (110) face. The electron micrographs at this time (1) corroborate this, since the surface appears to be reasonably uniformly covered, with few crevices to allow solution access to the positive hole sink. The rate soon increases again to approximately the parabolic value, and after quite a long time increases to nearly a linear rate (exponent 1.0). The increase appears to be due to etching of the oxide film, which would provide renewed solution access to the metal.

Etching is indicated by the electron micrographs shown in Fig. 7 for the three faces after 72 hr. These electron micrographs were obtained as part of the series described in part I (1). The conditions of polishing, washing, and microscopy are described therein. Note that the etching appears to be more pronounced on the (100) and (111) faces than on the more or less permanently protected (110) face. Photomicrographs (a) and (c) of Fig. 7 indicate that etching probably occurs to roughly the same extent for the oxide on the 100 and 111 metal faces. However, the patterns of etching are not at all similar and it is difficult to compare the two faces' kinetic behavior on this basis. Close examination of Fig. 2 suggests that there may be a slackening of oxidation rate (around 10^4 sec) like that seen clearly in Fig. 4, but the reproducibility of the data is simply inadequate to allow a confident interpretation in this way. After a crevice had opened by etching it would presumably remain open, since further nucleation on the bare metal could not occur due to the surface tension differential between a new nucleus and the large polyhedra.

A consideration of etching brings up the question of the importance of the effect of *p*H on the growth process proposed in the mechanism outlined above, which produces H^+ at localized sites. Although the bulk *p*H remained essentially constant during each experiment, local *p*H changes could profoundly affect the topography. Careful observations of the *p*H changes during the reaction and its *p*H dependence are presently being made and will be reported on in a subsequent part of this series.

The present measurements provide only a possible interpretation of the growth laws and topography of the principal faces; the proposed mechanism assumes existing nuclei and does not suggest any features of the nucleation process. Preliminary results from the *p*H study which is underway indicate that the nucleation is quite sensitive to small *p*H changes. Other studies are contemplated which might yield more information on nucleation and confirm or reject the proposed growth mechanism. It must also be pointed out that this study does not account for the persistence of well-defined oxide polyhedra on the (100) face and their merging on the other two faces (1). It is felt that this is a feature more of the nucleation process than of the growth process, and may be due to the symmetry mismatching in epitaxy.

Acknowledgments

The authors are deeply indebted to Dr. K. R. Lawless of the Department of Materials Science of the University of Virginia for the generous use of specialized equipment, and to Dr. Lawless and Dr. J. W. Mitchell of the Department of Physics of the University of Virginia for helpful discussions. Students at this college who participated in this project and to whom a great deal of credit is due are: P. R. Anderson, A. T. Elliott, L. E. Hightower, D. W. Mason, D. J. McKittrick, E. B. Noland, L. F. Towers, and W. F. Wright. This research was supported by National Science Foundation Undergraduate Science Education grants and by PHS Research grants DE-01893-02 and DE-01893-03, National Institute of Dental Research, Public Health Service.

Manuscript received Nov. 29, 1965; revised manuscript received March 3, 1966.

Any discussion of this paper will appear in a Discussion Section to be published in the December 1966 JOURNAL.

REFERENCES

1. C. E. Guthrow, Jr., and G. T. Miller, Jr., *This Journal*, **113**, 415 (1966).
2. R. W. Topham and G. T. Miller, Jr., *ibid.*, **113**, 421 (1966).
3. J. Benard, "L'Oxydation des Metaux," pp. 97 ff, Gauthier-Villars et Cie., Paris (1962).
4. U. R. Evans and H. A. Miley, *Nature*, **139**, 283 (1937).
5. J. A. Allen, *Trans. Faraday Soc.*, **48**, 273 (1952).
6. G. R. Hill, *This Journal*, **100**, 345 (1953).
7. H. G. Oswin and M. Cohen, *ibid.*, **104**, 9 (1957).
8. R. H. Lambert and D. J. Trevoy, *ibid.*, **105**, 18 (1958).
9. U. R. Evans, "The Corrosion and Oxidation of Metals," Chap. XXII, Edward Arnold Ltd., London (1960).
10. J. V. Cathcart and G. F. Petersen, "Studies of Thin Oxide Films on Copper Crystals with an Ellipsometer," Proc. Symp. on Ellipsometry in Measurement of Surfaces and Thin Films, Washington (1963).
11. K. R. Lawless, Private commmunication.
12. F. W. Young, J. V. Cathcart, and A. T. Gwathmey, *Acta Met.*, **4**, 145 (1956).
13. K. R. Lawless and G. Tyler Miller, Jr., *Acta Cryst.*, **12**, 594 (1959).

Effect of Plastic Deformation on the Anodic Dissolution of Iron in Acids

Z. A. Foroulis

Esso Research and Engineering Company, Florham Park, New Jersey

ABSTRACT

The effect of plastic deformation, introduced by cold-rolling, on the anodic dissolution of iron was investigated using short-time galvanostatic transients in deaerated HCl, H_2SO_4, and $HClO_4$ at 25°C. Cold-rolling was found to have no effect on the anodic Tafel polarization parameters of iron. Anodic Tafel lines in 1*N* HCl have slopes of about 60 mv; the slope is reduced at higher polarizing potentials. For 1*N* H_2SO_4 and 1*N* $HClO_4$ the slopes were about 40 mv and 35 mv, respectively. The results indicate that the dissolution kinetics of iron is controlled by charge transfer, and any effect on the kinetics of iron dissolution, due to surface topography, is not observed. The variation of the anodic Tafel polarization parameters with the nature of the acid anion is explained by specific adsorption of anions on the iron surface in competition with OH^-. The decrease in polarization of iron in HCl solutions at higher polarizing currents ($i > 10^{-2}$ amp cm^{-2}) indicates that adsorbed Cl^- may directly participate in the dissolution process depending on the potential region of polarization.

The published work relating to the influence of mechanical stress on the electrode behavior of metals in aqueous media is contradictory. It is well established that stresses within the elastic range change the potential reversibly by less than 1 mv (1, 2). It is in the range of plastic deformation and its effect on the anodic polarization and corrosion that many investigators have reported conflicting results and interpretations (3-10). It is clear, then, that this problem should be reexamined. This paper reports the results of a laboratory study on the effect of cold-rolling on the anodic polarization behavior of iron in acidic environments, using short-time galvanostatic transients.

Experimental

The cell used for electrochemical measurements consists basically of three compartments; the inner two compartments each approximately 100 ml in volume are removable and fitted through ground glass joints to the center compartment; these compartments contain one auxiliary platinum electrode each and could be deaerated in the same manner as the large center compartment. Electrical communication is achieved by means of fine glass fritted discs. The test electrode was introduced through the center compartment by means of two eccentric joints so that the distance between the test electrode and the top of the Luggin capillary could be adjusted. The tip of the Luggin capillary, about 1 mm OD, was placed about 1 to 2 mm from the electrode, so that screening effects and IR corrections were negligible (11). Additional features of the cell include a capillary stopcock for withdrawing known quantities of solution for analysis, a hydrogen bypass arrangement, and a salt bridge with a Luggin capillary filled with same solution as the cell. Greaseless ground glass joints were used to avoid possible contamination from lubricant.

The electrodes about 2-3 cm^2 total exposed area were cut from remelted (in a helium atmosphere) electrolytic iron castings. The analysis of the iron was 0.009%C, 0.003% N, < 0.003% S, < 0.004% O, < 0.001% Cu, < 0.001% Ni. The castings were cold-rolled in the direction of the long axis by successive passes to a final reduction in thicknesses 20, 40, 50, 60, and 70%. After cold-rolling the specimens were aged at R.T. for about two years. Before cold-rolling, the castings were homogenized in a purified helium atmosphere at 1050°C for about 48 hr. All the reported results were obtained with electrodes made from the above remelted electrolytic iron. The electrode assembly was similar to the one described earlier (12). Surfaces were abraded through 4-0 emery paper, pickled in same solution as the test solution to remove effects of abrading, rinsed thoroughly in double distilled water, and immediately placed in the solution.

Solutions were prepared using reagent grade acids and double distilled water, one distillation of the latter being carried out in dilute alkaline potassium permanganate. The following test solutions were used, 1*N* HCl, 1*N* H_2SO_4, and 1*N* $HClO_4$. Solutions were deaerated by bubbling prepurified hydrogen through the solution for at least 24 hr prior to a run and over the solution during the run. Additional purification of the high-purity commercial hydrogen was done by passing it successively through copper turnings heated at 500°C, ruthenium catalyst at 350°C, and palladium catalyst at R. T. The solutions were preelectrolyzed between platinum electrodes for about 24 hr at about 1.5 ma. Preelectrolyses were carried out at a potential below that corresponding to appreciable evolution of H_2 to avoid significant change of *p*H in the solution. Potentials were measured against a SCE using a vacuum tube millivoltmeter (high impedance). Constant current was obtained through an appropriate assembly of decay resistance units from a high d-c voltage source ($R_{ext} >> R_{cell}$). Figure 1 shows

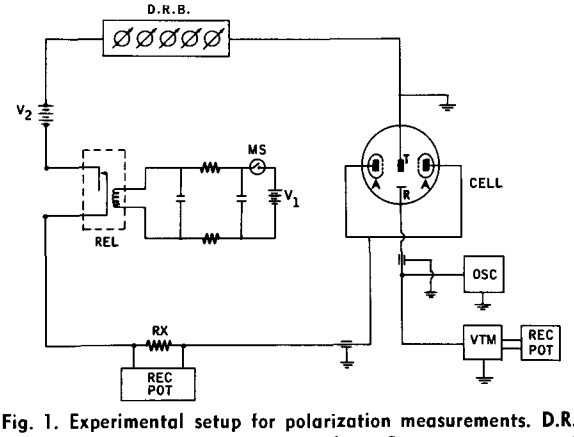

Fig. 1. Experimental setup for polarization measurements. D.R.B., current controlling decay-resistance box; R_x, current measuring resistance; MS, microswitch activating the relay; VTM, high impedance vacuum tube voltmeter; REC. POT., recording potentiometer; REL, relay; V_1, relay driving voltage; V_2, applied d-c voltage; T, test electrode; R, reference electrode; A, auxiliary electrodes (Pt), enclosed in removable compartments fitted with fritted glass disks.

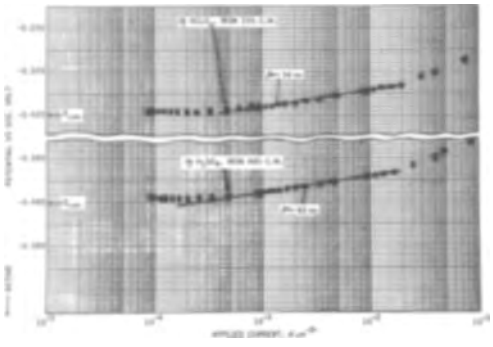

Fig. 2. Anodic polarization of iron in acids (H_2 sat'd), 25°C

the experimental arrangement which is similar to the one reported earlier (13).

In making a run, each electrode was immersed in solution and after a stable corrosion potential was measured, solution samples were withdrawn for Fe^{++} analysis, and immediately after that anodic polarizations were conducted by applying short-time galvanostatic transients. The electrode was subjected to a series of short-time anodic pulses (from 10 to 15 sec in duration) at various increasing current densities. In a few instances, the potential/time transients were recorded photographically on the oscilloscope screen and enlarged several times. The polarization curves were established by plotting the steady-state potential *vs.* the applied current density. Similar polarization curves were established at various decreasing current densities.

Results

The time of sweep for the anodic galvanostatic transients was determined by the time necessary to reach steady-state and was about 10-15 sec. The analysis of galvanostatic transients and their advantages for polarization studies were discussed earlier in the literature (13-15). The applied current density range was about 5×10^{-5} to 1×10^{-1} amp cm^{-2}.

In H_2SO_4 and $HClO_4$ solutions after each pulse the electrode potential returned to the steady-state corrosion potential usually within a few seconds so that further pulses were applied almost continuously ("continuous" polarization). The polarization curves traced with increasing and decreasing current density coincide (Fig. 2). In this figure are shown anodic polarization curves for iron in deaerated sulfuric and perchloric acids. The upper curve is for iron (cold-rolled to 20% reduction in thickness) in 1*N* $HClO_4$. The lower curve is for iron (cold-rolled to 40% reduction in thickness) in 1*N* H_2SO_4.

In the HCl solutions a much longer time of recovery was necessary after each pulse before the electrode potential returned to the steady-state corrosion potential so that further pulses were applied only after sufficient time had elapsed for the electrode potential to return to the steady-state corrosion potential ("interrupted" polarization). When "continuous" polarization was applied in HCl solutions, hysteresis was observed between the ascending and the descending polarization curves (lower curve in Fig. 3). In Fig. 3 are shown anodic polarization curves of iron (cold-rolled to 20% reduction in thickness) in 1*N* HCl. The upper curve was determined by interrupted polarization. The lower curve was determined by continuous polarization, and a hysteresis was observed between the ascending and descending polarization curves.

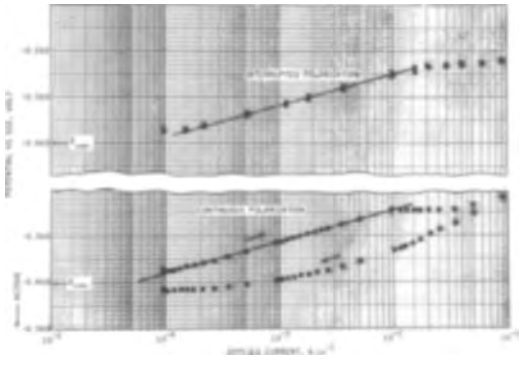

Fig. 3. Anodic polarization of iron, 20% C.W., in 1*N* HCl (H_2 sat'd), 25°C.

Cold-rolling was found to have no effect on the anodic Tafel polarization parameters of iron. The anodic Tafel lines in 1*N* HCl have slopes β_{Fe} of about 60 ± 8 mv at c.d. 10^{-4} to 10^{-2} amp cm^{-2}, and are the same for both the annealed and cold-rolled iron as shown in Fig. 4. Tafel slopes in HCl solutions were determined from the ascending polarization curves established by continuous polarization. Interrupted polarization gave identical Tafel slopes.

Figure 5 shows the dependence of the anodic Tafel slopes at c.d. 6×10^{-4} to 2×10^{-2} amp cm^{-2} for iron dissolution on the degree of cold-rolling for H_2SO_4, $HClO_4$ acids. A slope of about 40 ± 10 mv was found for 1*N* H_2SO_4 and about 35 ± 8 mv for 1*N* $HClO_4$. In both acids the slopes were the same for the annealed as well as the cold-rolled specimens.

At current densities higher than 10^{-2} amp cm^{-2}, the Tafel slope in HCl is reduced to about 40 mv or lower, but the reproducibility of the slope in this region of polarization was poor and in many runs a slope of zero was observed. As can be seen from Fig. 3 in HCl, iron does not polarize significantly at anodic current higher than 10^{-2} amp cm^{-2}. In $HClO_4$ and H_2SO_4, at c.d. 2×10^{-2} to 10^{-1} amp cm^{-2} or higher, polarization of iron deviates from the Tafel line and increases appreciably. This deviation is probably due to IR contribution and in particular to concentration polarization due to diffusion limited mass transport

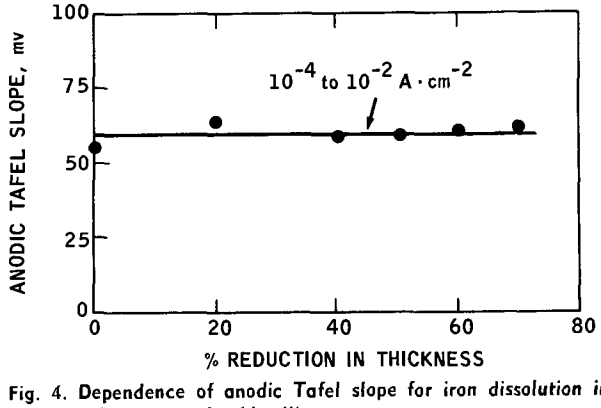

Fig. 4. Dependence of anodic Tafel slope for iron dissolution in 1*N* HCl on the degree of cold-rolling.

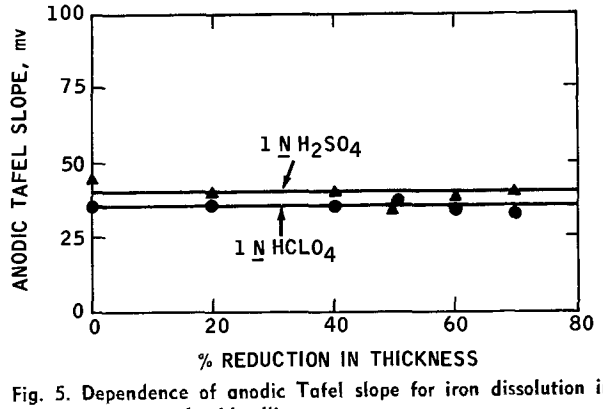

Fig. 5. Dependence of anodic Tafel slope for iron dissolution in acids on the degree of cold-rolling.

of OH^- at the iron surface sites. It is, therefore, rather apparent that the significant decrease in polarizability of iron in HCl at c.d. higher than 10^{-2} amp cm^{-2} is associated with chloride ions which directly participate in the dissolution process by adsorption and eventual complex formation with the iron surface atoms.

Exchange current densities for the anodic dissolution of iron ($i_{o,Fe}$) were determined by extrapolation of the Tafel lines to the reversible potential of iron in each solution tested. The concentration of Fe^{++} in each solution was determined by colorimetric analysis prior to each polarization using the orthophenanthroline colorimetric method (16). Reversible potentials were calculated using the Nernst equation and the activity of Fe^{++} in solution. Activity coefficients were calculated from the Debye-Hückel theory using equation (17)

$$\log f = -\frac{0.358\, Z^2\, \Gamma^{1/2}}{1 + 10^8\, \alpha\, 0.2325\, \Gamma^{1/2}} \qquad [1]$$

where f is the rational activity coefficient for Fe^{2+}, α is the effective diameter of the hydrated Fe^{2+} ($\alpha = 6 \times 10^{-8}$ cm), Z is the charge on each Fe^{2+} in solution, and $\Gamma = 2\, I(m)$ where $I(m) = \sum_i m_i Z^2_i$ is the ionic strength of the solution taking into consideration all the ionic components of the solution. The activity coefficients were calculated because of the lack of experimental data on activity coefficients of Fe^{2+} in HCl solutions. The error in $i_{o,Fe}$ introduced by calculating the activity coefficients by use of Eq. [1] is small in comparison with that produced by small errors in the experimentally determined Tafel slopes.

As can be seen from Table I, for any particular acid solution the $i_{o,Fe}$ was found to be independent of the degree of cold-rolling. However, it varied substantially with the nature of the acid anion and was of the order of 10^{-11} amp cm^{-2} for 1*N* HCl, 10^{-13} for 1*N* H_2SO_4, and 10^{-16} for 1*N* $HClO_4$. The experimental analyses for Fe^{2+} in solution for a typical set of runs, together with the calculated activities and reversible potentials ($E_{Fe,Fe2+}$) are given in Table I.

Anodic polarization ($E_{meas'd} - E_{corr}$) at 10 ma cm^{-2} determined for iron in various solutions from the polarization curves as a function of per cent reduction in thickness by cold-rolling is given in Fig. 6. Figure 6 shows that the anodic polarization at 10 ma cm^{-2} is the same for the annealed iron as well as iron cold-rolled down to 70% reduction in thickness. However, the anodic polarization depends on the acid anion and is about 145 mv in 1*N* HCl, about 65 mv in 1*N* H_2SO_4, and about 52 mv in 1*N* $HClO_4$. Similar independence of the anodic polarization on the degree of cold-rolling was observed at an applied current of 2 ma cm^{-2}.

Table I. Dependence of exchange current for iron dissolution in acids on the degree of cold-rolling

Acid	% Thickness reduction by cold-rolling	Exchange current $i_{o,Fe}$, amp/cm²	Fe^{2+} Concentration M	Fe^{2+} Activity M	$E_{rever.}$, calc, V
1*N* HCl	Annealed	7.9×10^{-12}	198×10^{-5}	4.1×10^{-6}	−0.600
1*N* HCl	20	6.3×10^{-11}	1.5×10^{-5}	3.1×10^{-6}	−0.603
1*N* HCl	40	1×10^{-11}	3.5×10^{-5}	7.3×10^{-6}	−0.592
1*N* HCl	50	5×10^{-12}	2.37×10^{-5}	4.9×10^{-6}	−0.597
1*N* HCl	60	1.6×10^{-11}	2.67×10^{-5}	5.5×10^{-6}	−0.595
1*N* HCl	70	7.9×10^{-11}	1.98×10^{-5}	4.1×10^{-6}	−0.599
1*N* H_2SO_4	Annealed	1.2×10^{-13}	2.04×10^{-5}	3.8×10^{-6}	−0.600
1*N* H_2SO_4	20	2.5×10^{-13}	1.35×10^{-5}	2.5×10^{-6}	−0.606
1*N* H_2SO_4	40	2.5×10^{-13}	3.27×10^{-5}	6.08×10^{-6}	−0.594
1*N* H_2SO_4	50	1×10^{-13}	1.26×10^{-5}	2.34×10^{-6}	−0.607
1*N* H_2SO_4	60	1.2×10^{-14}	2.0×10^{-5}	3.7×10^{-6}	−0.601
1*N* H_2SO_4	70	6.3×10^{-14}	1.84×10^{-5}	3.42×10^{-6}	−0.602
1*N* $HClO_4$	Annealed	3.1×10^{-16}	2.2×10^{-5}	4.6×10^{-6}	−0.599
1*N* $HClO_4$	20	7.9×10^{-16}	1.9×10^{-5}	3.9×10^{-6}	−0.600
1*N* $HClO_4$	40	6.3×10^{-17}	2.03×10^{-5}	4.2×10^{-6}	−0.598
1*N* $HClO_4$	50	1.6×10^{-16}	1.55×10^{-5}	3.21×10^{-6}	−0.603
1*N* $HClO_4$	60	5×10^{-17}	3.45×10^{-5}	7.13×10^{-6}	−0.592
1*N* $HClO_4$	70	1×10^{-16}	2.51×10^{-5}	5.2×10^{-6}	−0.596

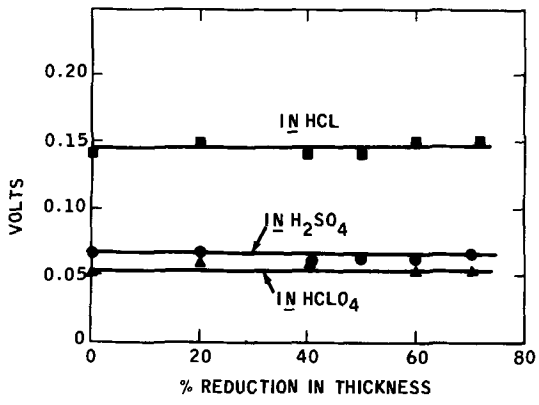

Fig. 6. Dependence of anodic polarization ($E_{meas'd} - E_{corr}$) at 10 ma/cm² for iron dissolution in acids on the degree of cold-rolling, 25°C.

Discussion

It is well known that an equilibrium metal surface is characterized by a distribution of steps each having a large population of kinks. The nonequilibrium metal surface has, in addition, a large distribution of steps arising from dislocations having a component of the Burger's vector normal to the surface and numerous other steps arising from the mechanism of growth of that particular surface.

An annealed polycrystalline iron specimen is bounded by numerous such surfaces of various crystallographic orientations, which are separated by ordinary high angle grain boundaries of rather high surface energy. Cold-rolling such an iron specimen introduces numerous dislocation loops which are arrayed in their slip planes. They are prevented from retreating into their sources when the deforming force is no longer applied by formation of jogs as a result of intersection with other dislocations, by becoming "locked" by interaction with other dislocations, because their source may have moved out of the slip plane in which the loops have originated, or because parts of the loops may have emerged at a free surface or into a grain boundary. During severe deformation, arrays of dislocations are produced on several intersecting sets of slip planes, so that numerous parts of dislocation loops are emerging at a free surface. Severe cold-working is known to increase the density of dislocations from perhaps 10^8 for annealed iron to 10^{12} dislocations/cm² (18).

Another major effect of deformation is on the orientations of the grains. It is known that the deformation of a randomly oriented polycrystalline specimen results in material with a preferred orientation, the grains tending to approximate progressively to one or more well-defined orientations. Cold-rolling of iron produces a preferred orientation of the (001) crystal face parallel to the rolling plane (19). In addition to a high content of dislocations, cold-rolling produces a considerable excess of vacancies as a result of the movement of jogs in directions that do not correspond to slip. However, it is expected the excess vacancies anneal during the long R.T. aging of our specimens after cold-rolling.

Let us now consider the dissolution of a specimen bounded by such surfaces in contact with an electrolyte. At temperatures below the critical temperature of surface roughening (20) such surfaces are expected to be characterized by large numbers of equilibrium and nonequilibrium steps and kinks. Consequently, such surfaces have been considered (7) to be able to dissolve at least initially by the lateral motion of such steps in accordance with the crystal growth and dissolution theories (21-23). Jenkins (24) found that under certain conditions the dislocations played a role in the dissolution process of the (100) copper surface at low current densities in deaerated

solutions of acidified $CuSO_4$. He showed that at current densities of about 2 $\mu a/cm^2$ dissolution occurred only from the steps on the surface that result because of the difficulty of preparing a perfect crystal face. At current densities of about 10 $\mu a/cm^2$, pitting attack was observed at dislocations until finally the pits grew in size and a faceted surface resulted. The above experiments were carried out under low overpotential, to which crystal growth and dissolution theories might be applicable. However, during anodic dissolution of iron in acid solutions, the anodic overpotential is much higher, and it probably plays a dominant role in determining the kinetically slow step in the over-all reaction path of anodic iron dissolution.

It is more likely that at the high overpotentials (large driving free energy) necessary to establish the anodic polarization curve for iron homogeneous dissolution occurs anywhere on the surface, and any effect due to surface topography is lost. This is in accord with the present data indicating that, in the three acid solutions used, cold-rolling was found to have no effect on the Tafel parameters ($i_{o,Fe}$, β_{Fe}) for anodic dissolution of iron (Fig. 4 and 5 and Table I), or the anodic polarization (Fig. 6).

In sulfuric acid solution the observed Tafel slope of 40 mv/decade, *i.e.*, $2/3(2.303RT/F)$ in the region of current density 6×10^{-4} to 1.5×10^{-2} amp cm^{-2} is in agreement with results obtained by Bockris *et al.* (13) and more recently by Kelly (25) for iron in acidic sulfate solutions. For the anodic dissolution of iron in sulfuric acid solutions, the mechanism proposed by Bockris *et al.* (13) can be expressed in terms of the following equations.

$$Fe + OH^- \rightleftarrows Fe(OH)_{ads} + e^- \quad [2]$$

$$Fe(OH)_{ads} \rightarrow (FeOH)^+ + e^- \text{ (rate determining)} \quad [3]$$

$$(FeOH)^+ = Fe^{++} + OH^- \quad [4]$$

in which the surface species $Fe(OH)_{ads}$ act as a reaction intermediate.

In 1*N* HCl solution the observed Tafel slope of 60 mv/decade, *i.e.*, $(2.303RT/F)$ during interrupted polarization experiments or during continuous polarization from the ascending curve, in the region of current density 10^{-4} to 10^{-2} amp cm^{-2} is consistent with the following mechanism

$$Fe + OH^- \rightarrow Fe(OH)_{ads} + e^- \text{ (rate-determining)} \quad [5]$$

$$Fe(OH)_{ads} \rightarrow Fe(OH)^+ + e^- \text{ (rate-determining)} \quad [6]$$

$$Fe(OH)^+ \rightleftarrows Fe^{++} + OH^- \quad [7]$$

in which the OH^- competes with the Cl^- for the metal surface sites.

Tafel slopes of 54 mv/decade in chloride solutions were reported by Makrides *et al.* (26), 68 mv/decade by Stern and Roth (27), and 30 mv/decade in HCl (pH > 1.5) by Lorenz *et al.* (28). The difference in Tafel slopes obtained by the various investigators can be attributed to the various chloride anion concentrations and the experimental techniques used. Recently, it has been recognized (29) that short-time galvanostatic transients offer many advantages over conventional polarization techniques which often give rise to complex results difficult to interpret.

In 1*N* $HClO_4$ solution the observed Tafel slope of 35 mv/decade, *i.e.*, $(2.303RT/2F)$ is consistent with the following mechanism:

$$Fe + OH^- \rightleftarrows Fe(OH)_{ads} + e \quad [8]$$

$$Fe(OH)_{ads} \rightarrow Fe^{++} + OH^- + e \text{ (rate-determining)} \quad [9]$$

The observed Tafel slope is in agreement with the results of Bonhoeffer and Heusler (30) who found for iron in perchlorate solutions at 20°C a slope of 30 mv/decade.

The observed hysteresis in the anodic polarization of iron in HCl during continuous polarization (Fig. 3)

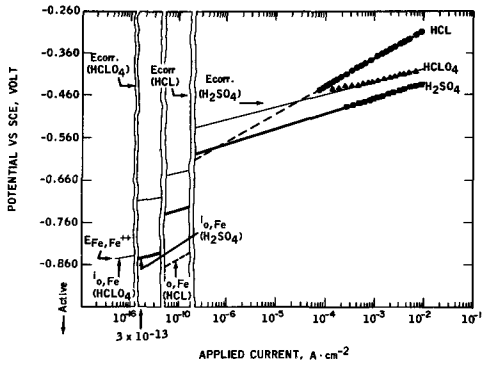

Fig. 7. Anodic polarization curves for iron illustrating the influence of the Tafel slope, β, and the ferrous ions activity in solution, a_{Fe++}, on the exchange current, $i_{o,Fe}$, in three acids.

is probably due to adsorption of Cl^- and the eventual complex formation with the iron surface atoms at higher polarizing potentials. This phenomenon will be discussed in more detail in another paper (31). Participation of anions such as Cl^-, Br^-, I^- in the dissolution of cadmium and indium amalgams was proposed by Kolotyrkin (32). Heusler and Cartledge (33) also suggested that the iodide ion participates in the anodic reaction of iron dissolution.

The large variation of the exchange currents for anodic dissolution of iron ($i_{o,Fe}$) with the nature of the acid anion shown in Table I can be realized if one considers the difference in the Tafel slopes for the various acids and the low activity of Fe^{++} in solution, necessitating extrapolation of the Tafel slopes to the fairly active potential of the reversible iron electrode in these solutions ($E_{Fe,Fe++}$) in order to establish the $i_{o,Fe}$. This is shown in Fig. 7. It is also obvious that a small error in the experimentally determined Tafel slopes produces a large error in $i_{o,Fe}$. This explains the large scatter in $i_{o,Fe}$ values observed (Table I) for the same acid.

In determining the reversible electrode potential $E_{Fe,Fe++}$ using the Nernst equation, the same value of the standard electrode potential $E^o_{Fe,Fe++} = -0.440$v *vs.* SHE was used for both cold-rolled and annealed iron electrodes. This is justified because of the lack of precise data on the effect of cold-rolling on the reversible standard electrode potential of iron, which in any case is very small.[1]

The lack of any effect of cold-rolling on the Tafel polarization parameters of iron dissolution in acids and also the acid anion dependence of this reaction suggest that at high polarizing potentials necessary to establish the anodic polarization curves (large driving free energy) homogeneous dissolution takes place directly from the surface and it is independent of the number of kink sites on the iron surface. The rate of anodic dissolution is kinetically controlled by the charge transfer step. The nature of the rate-determining charge transfer step depends on the nature of the acid anion as can be seen from Eq. [3], [5], [6], and [9].

Recently, Greene and Saltzman (8) reported an increase, with plastic deformation, of the exchange current density for anodic dissolution of iron and steel in 1*N* H_2SO_4. They interpreted their results to indicate that iron dissolves during anodic polarization, preferentially from dislocation sites because of the lower bonding energy of iron atoms at such sites. This explanation, however, is not compatible with the small increase in residual energy (approximately 5 cal/g) of severely cold-worked iron (34), and in

[1] For iron the increase in internal energy by severe cold-working was measured calorimetrically to be about 5 cal/g (34). Neglecting entropy effects, this value of enthalpy change corresponds to a change of potential of about 6 mv (35). However, as shown by Titchener and Bever (34) the change in entropy by cold-working a metal is positive and thus the change of potential due to cold-working, corrected for entropy effects, should be less than 6 mv.

particular with the high overpotentials involved during anodic polarization of iron in 1*N* H_2SO_4. Our own work, on the other hand, has not shown an effect of plastic deformation on the anodic Tafel polarization parameters. The increase noted by Greene and Saltzman must, therefore, have another explanation. The above authors reported that the specimens (wires) after torsional deformation, by twisting them a number of times, were degreased in benzene, rinsed in water, and dried before testing without additional polishing of the twisted wire surface. It is possible, therefore, that the torsional straining produced an increase of true surface area with accompanying higher exchange current densities.

It remains our conclusion, therefore, that at high overpotentials the anodic iron dissolution is kinetically controlled by the charge transfer step, and it is independent of the number of kink sites introduced by cold work on the iron surface.

Details on the kinetics of anodic dissolution of iron in various acidic environments are not given in the present paper since the purpose of this report is to discuss the effect of cold-rolling on the anodic polarization behavior of iron. However, the kinetics of anodic dissolution of iron will be discussed in detail in another report.

Acknowledgment

The author is grateful to Esso Research and Engineering Company for permission to publish the work. He also acknowledges the skillful assistance of Mr. A. W. Putnoky who conducted the experimental measurements.

Manuscript received Nov. 17, 1965; revised manuscript received March 10, 1966. This paper was presented at the Buffalo Meeting, Oct. 10-14, 1965.

Any discussion of this paper will appear in a Discussion Section to be published in the December 1966 JOURNAL.

REFERENCES

1. G. T. Yang Ling Horne and C. M. Pound, "Physical Metallurgy of Stress-Corrosion Fracture," p. 29, Interscience Publishers Inc., New York (1959).
2. K. Nobe, E. Baum, and F. W. Sayer, *This Journal*, **108**, 97 (1961).
3. H. Gerischer and H. Rickert, *Z. Metallk.*, **46**, 681 (1955).
4. Z. A. Foroulis and H. H. Uhlig, *This Journal*, **111**, 522 (1964).
5. M. T. Simnad and U. R. Evans, *Trans. Faraday Soc.*, **46**, 176 (1950).
6. I. Sekerka and O. Vanicek, *Coll. Czech. Chem. Comm.*, **22**, 705 (1957).
7. T. Hurlen, *Electrochim. Acta*, **7**, 653 (1962).
8. N. D. Greene and G. A. Saltzman, *Corrosion*, **20**, 293t (1964).
9. H. E. Bühler and W. Schwenk, *Z. Metallk.*, **56**, 24 (1965).
10. A. Windfeldt, *Electrochim. Acta*, **9**, 1139 (1964).
11. S. Barnartt, *This Journal*, **99**, 549 (1952); *ibid.*, **106**, 722 (1959).
12. M. Stern and A. C. Makrides, *ibid.*, **107**, 782 (1960).
13. J. O'M. Bockris, D. Drazic, and A. R. Despic, *Electroch. Acta*, **4**, 325 (1961).
14. W. Mehl and J. O'M. Bockris, *J. Chem. Phys.*, **27**, 818 (1957); *Can. J. Chem.*, **37**, 190 (1959).
15. H. Gerischer, *This Journal*, **62**, 256 (1958).
16. E. B. Sandell, "Colorimetric Determination of Traces of Metals," p. 271, Interscience Publishers Inc., New York (1944).
17. B. E. Conway, "Electrochemical Data," p. 102, Elsevier Publishing Co., Amsterdam (1952).
18. L. Darken in "The Physical Chemistry of Metallic Solutions and Intermetallic Compounds," Vol. II. 4G, Nat. Phys. Lab. Symp. No. 9 (London) (1959).
19. "Structure of Metals," C. Barrett, 2nd Ed, p. 446, McGraw-Hill Book Co. (1952).
20. N. Cabrera, The Structure of Crystal Surfaces. *Discussion Faraday Soc.*, **28**, 16 (1959).
21. W. K. Burton, N. Cabrera, and F. C. Frank, *Proc. Roy. Soc.*, **A243**, 299 (1951).
22. M. Fleischmann and H. R. Thirsk, *Electrochim. Acta*, **2**, 22 (1960).
23. T. Hurley, *ibid.*, **8**, 609 (1963).
24. L. H. Jenkins and J. O. Stiegler, *This Journal*, **109**, 467 (1962).
25. E. J. Kelly, *ibid.*, **112**, 124 (1965).
26. A. C. Makrides, N. W. Komodromos, and N. Hackerman, *ibid.*, **102**, 363 (1955).
27. M. Stern and R. M. Roth, *ibid.*, **104**, 390 (1957).
28. W. Lorenz, H. Yamaoka, and H. Fisher, *Ber. Bunsenges. Physik. Chem.*, **67**, 932 (1963).
29. W. Mehl and J. O'M. Bockris, *J. Chem. Phys.*, **27**, 818 (1957); *Can. J. Chem.*, **37**, 190 (1959); H. Gerischer, *This Journal*, **62**, 256 (1958).
30. K. F. Bonhoeffer and K. E. Heusler, *Z. Physik. Chem.*, **8**, 390 (1956).
31. Z. A. Foroulis, *This Journal*, To be submitted for publication.
32. J. M. Kolotyrkin, *ibid.*, **108**, 209 (1961).
33. K. E. Heusler and G. H. Cartledge, *ibid.*, **108**, 731 (1961).
34. A. Titchener and M. Bever, *Prog. in Metal Phys.*, **7**, 247 (1958).
35. Z. A. Foroulis and H. H. Uhlig, *This Journal*, **112**, 1177 (1965).

The Role of the Anion in the Anodic Dissolution of Magnesium

P. F. King[1]

Metallurgical Laboratory, The Dow Metal Products Company, Division of The Dow Chemical Company, Midland, Michigan

ABSTRACT

In a number of aqueous environments the increase in the corrosion rate (i_c) of magnesium with an increase in impressed anodic current (i) is expressed by

$$\frac{d\,i_c}{di} = \tau_a$$

where τ_a is the transport number of the anions of the electrolyte. This adds confirmation to the viewpoint that film damage by anions rather than metal spalling or the production of monovalent magnesium ions is the chief contributor to the current inefficiency observed with magnesium anodes. The same equation holds for the decrease in corrosion rate of magnesium with applied cathodic current in acids, indicating that anion supply to the metal surface is controlling that process, also.

Because of its low equivalent weight and its active potential under load, magnesium has become important as an anode for cathodic protection and in primary cells. However, the full benefit of magnesium's low equivalent weight is not realized. Instead, the anode consumption is substantially greater than that

[1] Present address: Parker Rust Proof Division, Hooker Chemical Corporation, Detroit, Michigan.

calculated from Faraday's law and the formation of divalent magnesium ions as the sole electrode process. This excess metal loss results in an increase in the amount of hydrogen at the anode above that evolved on open circuit in contrast to the decrease observed on other, less active metals. Since the decrease has been known historically as the difference effect (1), the increase as observed with magnesium has long been known as the negative difference effect.

The causes for the coulombic inefficiency of the magnesium anode have been the basis for much research and conjecture. Explanations that have been offered for the inefficiency include: (*a*) the formation of metastable, monovalent magnesium ions as well as the divalent ions (2-5); (*b*) the loss of metal by spalling (6-8); and (*c*) corrosion that is accelerated through damage to the protective film by the impressed current (9, 10).

In an earlier publication, Robinson and King (10) expressed the view that the film damage explanation offered a reasonable and sufficient description of the excess consumption, the steady-state potential, and the transient potential behavior of the magnesium anode. According to this view, the consumption of the anode (i_t) can be represented as the sum of the applied and local action currents (i and i_c^o, respectively) and the excess weight loss caused by the applied current [$f(i)$]

$$i_t = i + f(i) + i_c^o \qquad [1]$$

In many environments, as discussed previously (10), $f(i)$ has been shown to be directly proportional to i, so that for these environments Eq. [1] can be rewritten

$$i_t = i + ki + i_c^o \qquad [2]$$

If we define the excess corrosion rate i_c as

$$i_c = i_t - i \qquad [3]$$

from Eq. [2] we have

$$i_c = ki + i_c^o \qquad [4]$$

and differentiation gives

$$\frac{di_c}{di} = k \qquad [5]$$

We suggested previously that this is true because the number of anions transported to the anode and, therefore, the amount of film damaging soluble magnesium salts at the anode increases linearly with current. Thus, a logical extension of the above reasoning is that k in Eq. [2], [4], and [5] and the anion transport number τ_a should be simply related. Indeed since both are dimensionless numbers, they might be equal. The work to be described here was planned to test this hypothesis.

Experimental Details

The experiments were carried out in the following manner. Primary magnesium was chosen for study because of its relative purity (98.5%), availability, and the unlikelihood, as deduced from the work reported by Robinson and George (11), that impurities have much effect on the efficiency of the magnesium anode at high enough current densities. A 2.5 × 0.5 cm cylindrical primary magnesium anode was mounted in a glass holder as previously described (10) and immersed in a round bottom flask containing additional openings for platinum working electrodes and a capillary reference probe. The latter was used only to insure that the anode had not become passive during the measurements.

The experiments were run at room temperature (20° ± 2°C) in stagnant solutions made from chemically pure salts and distilled water. The experiments in acidic environments were usually of 5-min duration. In salt solutions under anodic drain, times were adjusted to give weight losses of the order of 50 mg. Where currents greater than 100 ma/cm² were required, the anode area was reduced by the use of electroplater's tape. Before use, the specimens were pickled for 1 min in the so-called acetic-nitrate pickle (5% $NaNO_3$, 40% acetic acid, remainder distilled water), thoroughly rinsed and dried before weighing. At the conclusion of electrolysis they were rinsed with distilled water, cleaned until cleaning action stopped at 90°C in 20% chromic acid containing a pinch of $AgNO_3$, rinsed, and once again dried thoroughly before weighing. Where electroplater's tape was used, this final drying took considerable time.

Results and Discussion

In order to test the hypothesis that the constant k in Eq. [2], [4], and [5] is equivalent to the transport number of the anion of the electrolyte under study, the anodic dissolution rate of magnesium was tested at a number of current densities in six electrolytes selected for wide variation in transport properties. The results of these tests are shown in Fig. 1-5. In Fig. 6 results are summarized with the anion transport numbers from the literature (12) compared with the constant k as calculated from Eq. [2]; it should be pointed out that in some cases the literature transport numbers are extrapolated ones. The agreement, while not perfect, is good enough and covers a wide enough range of values to suggest that Eq. [5] may be rewritten

$$\frac{di_c}{di} = \tau_a \qquad [6]$$

a strikingly simple expression, and one which adds additional credence to the theory developed in the earlier publication.

It now becomes apparent why the observed anode efficiency of magnesium almost always lies between 50 and 100% if measurements are made at high enough current densities that the open-circuit corrosion is a trivial portion of the total anode consumption. The efficiency under these conditions is defined as

$$\% \text{ eff} = \frac{i}{i + i_c} \times 100 \qquad [7]$$

or, substituting τ_a for k in Eq. [4] and then combining Eq. [4] and [7] (continuing to neglect i_c^o)

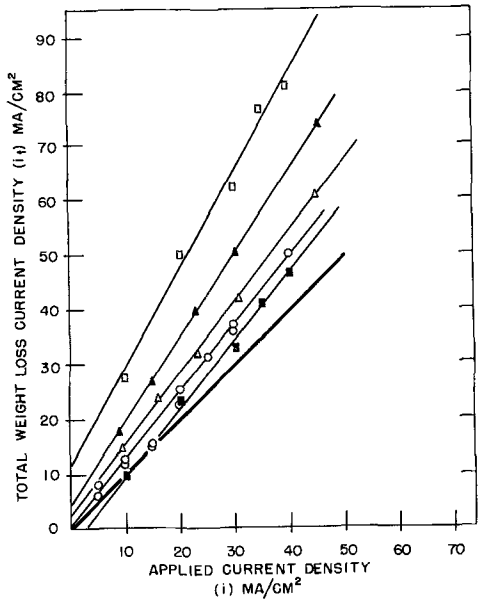

Fig. 1. Weight loss current density as a function of applied anodic current density for primary magnesium in 1*N* potassium malonate (○); 0.1*N* LiCl (□); 0.1*N* $KC_2H_3O_2$ (■); 1*N* $KCHO_2$ (△); and 2*N* $MgCl_2$ (▲). The heavy line represents Faraday's law.

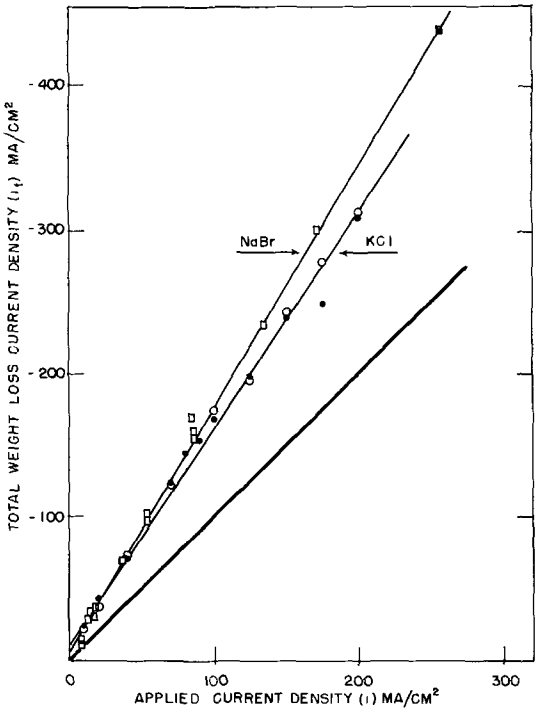

Fig. 2. Weight loss current density as a function of applied anodic current density for primary magnesium in 1*N* NaBr (□); 1*N* KCl (○); and 0.1*N* KCl (●). The heavy line represents Faraday's law.

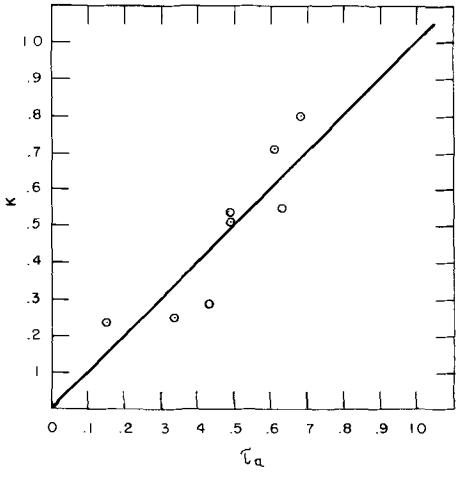

Fig. 3. Comparison of the constant *k* from Eq. [5] with literature τ_a values. The line is theoretical; that is, it assumes $k = \tau_a$.

$$\% \text{ eff} = \frac{i}{i + \tau_a i} \times 100 = \frac{100}{1 + \tau_a} \qquad [8]$$

and since τ_a is bounded by 0 and 1, the efficiency must be bounded by 100 and 50%.

Table I shows a test of Eq. [8] as a method for predicting the limiting efficiencies. The agreement between the measured and the predicted efficiencies suggests that Eq. [8] will be of practical value in the selection of electrolytes.

The results suggest that each anion equivalent which reaches the magnesium surface removes, in some manner, an equivalent of magnesium over and above that which is put into solution by the external anodic current. The exact mechanism by which this occurs is still unclear. However, since the limiting anodic efficiency of magnesium thus appears to bear a quantitative relationship to the electrochemical properties of

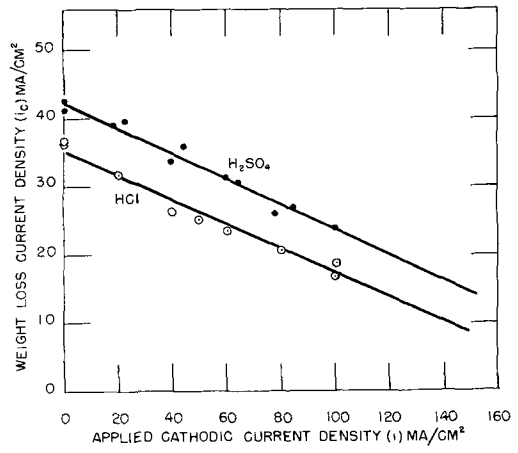

Fig. 4. Weight loss current density as a function of applied cathodic current density for primary magnesium in H_2SO_4 at pH 1.1 and in HCl at pH 1.1. The lines are drawn with slopes corresponding to τ_a in $H_2SO_4 = 0.18$; τ_a in HCl = 0.17.

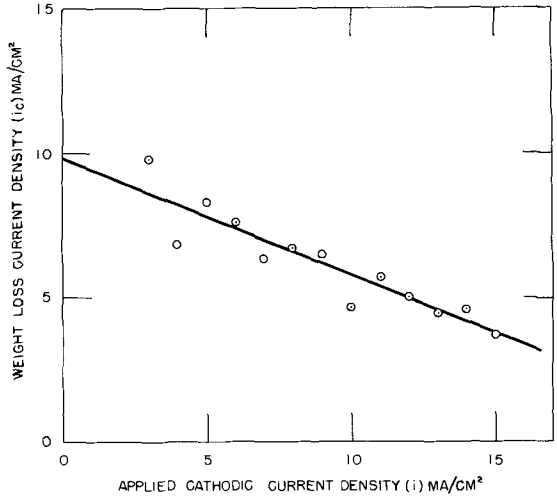

Fig. 5. Weight loss current density as a function of applied cathodic current density for primary magnesium in 1*N* $NaC_2H_3O_2$ containing 0.1*N* $HC_2H_3O_2$.

the environment, it seems unlikely that Mg^+ formation and metal spalling can be an important part of the process. It should be pointed out that there is no doubt that some magnesium spalling does occur. One can sometimes see metal in the anodic corrosion products. If one tries to liberate hydrogen from this corrosion product with acid in these cases, however, one can account for at most only a few per cent of the wasteful corrosion. In addition, only a few per cent of the corrosion product appears to be solid metal by x-ray diffraction examination.

It also appears that τ_a is the appropriate coefficient for the linear reduction of the corrosion rate of magnesium in acids with applied cathodic current which was observed by Coates (13) and Roald and Beck (14). These authors did not attempt to explain this linearity beyond Roald and Beck's comment that

Table I. Comparison of experimental and theoretical efficiency values

Salt	Efficiency calculated from: Concentration, *N*	Literature transport numbers, %	Experimental efficiency, %
$MgCl_2$	2	61	65
$KCHO_2$	1	70	78
$KC_2H_3O_2$	0.1	75	80
LiCl	0.1	60	56
Potassium malonate	2	87	81
NaBr	1	62	59
KCl	1	67	66
KCl	0.1	67	65

transport within the diffusion layer might be responsible. In contrast to the anodic case where the detailed mechanism remains obscure to the author, a reasonable physical picture of this situation can be proposed.

It is generally agreed (13-16) that on open circuit the dissolution of magnesium is controlled by the diffusion of acid to its surface. The over-all reaction is

$$Mg + 2HA \rightarrow H_2\uparrow + MgA_2$$

where A stands for the anion of a magnesium salt which must be soluble to prevent film growth with concomitant stifling of the reaction. Because preservation of charge requires that both protons and anions diffuse to the surface at the same rate, protons to provide the cathodic reaction and anions to sustain the solubility of magnesium are equally available to sustain dissolution.

If now magnesium reacting with pure aqueous acid is made a cathode, the current carried by protons reaching the magnesium surface will be increased by $\tau_{H^+} i$. However, since the applied cathodic current must liberate hydrogen at the cathode at a rate equal to i, it follows that

$$i_c = i_c^o + \tau_{H^+} i - i = i_c^o - (1 - \tau_{H^+}) i \qquad [9]$$

Because $(1 - \tau_{H^+}) = \tau_a$ for the pure acid, Eq. [9] can be restated as

$$i_c = i_c^o - \tau_a i \qquad [10]$$

which is the same equation one would deduce if anion supply, being reduced by transport away from the surface by cathodic current, were controlling the dissolution rate. That these equations do apply to the present case is shown by Fig. 4, which compares the reduction of i_c by impressed cathodic current for magnesium in dilute H_2SO_4 and dilute HCl at pH 1.1 with lines having slopes of —0.18 and —0.17 corresponding to the respective τ_a values for each acid.

It appears that distinction can be made between the relative importance of proton transport and anion transport by using a buffer wherein the dissociation of the acid is greatly suppressed. Figure 5 shows the results for the dissolution of a magnesium cathode in 0.1*N* HOAc plus 1*N* NaOAc. In this system τ_{H^+} should be trivial. Thus, τ_a should be approximately 0.42, which is the transport number for acetate ions in 1*N* NaOAc, while $(1 - \tau_{H^+})$ should be very close to unity. The line in Fig. 5 has a slope of —0.41. Therefore, it appears that under impressed cathodic current

$$i_c = i_c^o - \tau_a i > i_c^o - (1 - \tau_{H^+}) i \qquad [11]$$

This suggests that the rate of supply of anions rather than the rate of supply of protons controls the rate of dissolution of magnesium in acids. A simple rationale for this result is that so long as film growth is thwarted by the formation of soluble reaction products, the reduction of water is able to sustain the rate.

Summary

The excess corrosion of the magnesium anode at currents high with respect to open-circuit corrosion currents appears to be related quantitatively to the rate of arrival of the anions of the electrolyte at the anode surface. That is, the excess corrosion is equal to $\tau_a i$, where τ_a is the transport number of the anion involved and i is the applied anodic current. Thus, the increase in the wasteful corrosion rate with increasing anodic current, di_c/di is simply τ_a.

Correspondingly, in acids the corrosion of magnesium is decreased by cathodic current since anions are thereby transported away from the magnesium surface. The proportionality constant between the applied current and the decrease in corrosion rate again is τ_a.

These observations support the view that anion promoted film-damage and a resultant more or less direct reaction of the underlying magnesium with water is responsible for the nonfaradaic corrosion of the magnesium anode in aqueous environments.

Manuscript received Aug. 20, 1965; revised manuscript received Feb. 20, 1966. This paper was presented at the Buffalo Meeting, Oct. 10-14, 1965.

Any discussion of this paper will appear in a Discussion Section to be published in the December 1966 JOURNAL.

REFERENCES

1. U. R. Evans, "The Corrosion and Oxidation of Metals," p. 321, Edward Arnold (Publishers) Ltd., London (1960).
2. R. L. Petty, A. W. Davidson, and J. Kleinberg, *J. Am. Chem. Soc.*, **76**, 363 (1954).
3. M. D. Rausch, W. E. McEwen, and J. Kleinberg, *Chem. Rev.*, **57**, 417 (1957).
4. A. W. Davidson in "The Encyclopedia of Electrochemistry," p. 49, C. E. Hempel, Editor, Reinhold Publishing Co., New York (1964).
5. W. E. McEwen, *ibid.*, p. 53.
6. M. E. Straumanis, *ibid.*, p. 44.
7. M. E. Straumanis and B. K. Bhatia, *This Journal*, **110**, 357 (1963).
8. W. J. James, M. E. Straumanis, B. K. Bhatia, and J. W. Johnson, *ibid.*, 1117.
9. H. A. Robinson, *Trans. Electrochemical Soc.*, **96**, 499 (1946).
10. J. L. Robinson and P. F. King, *This Journal*, **108**, 36 (1961).
11. H. A. Robinson and P. F. George, *Corrosion*, **10**, 182 (1954).
12. R. Parsons, "Handbook of Electrochemical Constants," Butterworth Scientific Publications, London (1959).
13. G. E. Coates, *J. Inst. Metals*, **71**, 457 (1945).
14. B. Roald and W. Beck, *This Journal*, **98**, 277 (1951).
15. C. V. King and M. M. Braverman, *J. Am. Chem. Soc.*, **54**, 1744 (1932).
16. C. V. King and W. H. Cathcart, *ibid.*, **59**, 63 (1937).

Correction

In the paper "Concentration Gradients at Horizontal Electrodes" by R. N. O'Brien which appeared in the April 1966 issue of the *Journal*, pp. 389-392, the principal formula was printed incorrectly. It should be

$$AC_{(x,t)} = \frac{2\sqrt{Dt/l^2}\, Ilt^-}{nFD} \text{ierfc} \frac{1 - x/l}{2\sqrt{Dt/l^2}}$$

The Oxidation of GaP and GaAs

M. Rubenstein

Westinghouse Research Laboratories, Pittsburgh, Pennsylvania

ABSTRACT

Thermal oxidation of GaP and GaAs by oxygen has been studied. GaP on oxidation undergoes a violent exothermic reaction at 1130° ± 20°C. The products of the oxidation of GaP are the christobalite form of $GaPO_4$ as a primary product and β-Ga_2O_3 as a secondary product (about 5 w/o). GaAs on oxidation undergoes a mild exothermic reaction at 840° ± 10°C. The products of this reaction are β-Ga_2O_3 as a primary product and the low quartz form of $GaAsO_4$ as a secondary product (about 10 w/o). The $GaAsO_4$ at temperatures higher than 1000°C decomposes to As_2O_5 + β-Ga_2O_3. The above statements are made on the basis of x-ray diffraction data, change in weight data, and wet chemical analyses. On the basis of this data, it is concluded that thermal oxide masking should be readily applicable to GaP and that thermal oxide masking should not be applicable to GaAs.

GaP and GaAs are usually considered very stable compounds, especially with respect to their reactivity toward oxygen. At temperatures less than 800°C this is more or less true. A film might form on the surface at temperatures less than 800°C, but the bulk of the material would not change with respect to weight, crystal structure, or other physical parameters. The thermal oxide masking of GaAs was investigated (1) but was found to be not readily applicable.

Experimental

Oxygen was passed over the sample to be oxidized at a flow rate of about 200 cc/min. A Pt-Pt 10% Rh thermocouple was tied to the quartz boat containing the sample, using a platinum wire insulated from the thermocouple. A hinged split furnace with a 1¼ in. bore accommodated the quartz tube. A variable autotransformer and a Wheelco Capacitrol Model 402 were used to control the temperature. The oxygen was dried using a P_2O_5 packed vertical tower and a CO_2-acetone cold trap.

Weight change determinations were made to the nearest tenth of a milligram. Sample sizes were usually about half a gram. Wet chemical analyses were made on some of the oxidized GaP and GaAs samples. Phosphorus was determined by the precipitation of magnesium ammonium phosphate in the presence of citric acid. This precipitate was ignited, thermally decomposed, and weighed as $Mg_2P_2O_7$. Arsenic was extracted from a 2*N* HCl solution with diethyl-ammonium diethyldithiocarbamate in chloroform. The extracted arsenic was oxidized and determined by the photometric molybdenum blue method.

X-ray diffraction studies were made using a 57.32 mm radius Straumanis-type camera with nickel filtered copper radiation.

Results

GaAs.—If GaAs, on being oxidized by oxygen, produced only β-Ga_2O_3, the weight loss would be 35.20%. If $GaAsO_4$ were the product, there would be a weight gain of 44.25%. When GaAs was heated above 700°C, a weight loss was observed which increased with temperature (see Fig. 1). In the range of temperature between 830°-850°C, an exothermic reaction took place. Between 850° and 965°C the weight loss was 30-32%. At a temperature of 1000°C and higher, there was a total weight loss of about 35.4%.[1] Samples heated for longer periods of time, at temperatures under 830°C, showed larger decreases in weight than samples heated for shorter periods of time, at the same temperature (see Fig. 1, samples heated at 760°C).

X-ray diffraction studies showed that the products of the oxidation of GaAs between 850° and 965°C were

[1] $2GaAsO_4 \rightarrow \beta$-$Ga_2O_3$ + As_2O_5 at 1000°C and at higher temperatures (2).

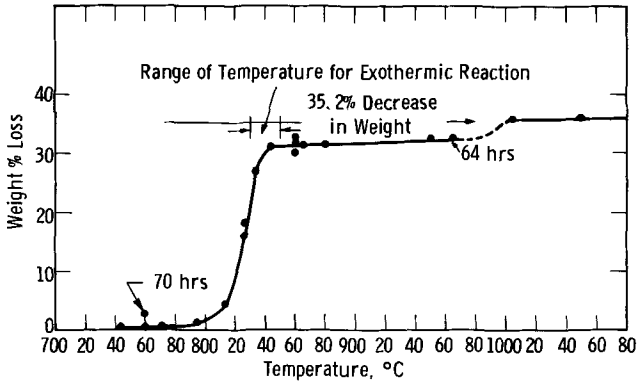

Fig. 1. Oxidation of GaAs in oxygen. Per cent weight loss vs. temperature. All points on this curve are for samples fired for 20 ± 2 hr, except 2 labeled points.

primarily β-Ga_2O_3 (3) with a minor constituent of the low quartz form of $GaAsO_4$ (2) (about 10%). Samples heated at temperatures of 1000°C and above showed only β-Ga_2O_3 as a product.

Wet chemical analyses of several samples of oxidized GaAs were performed and the total weight per cent arsenic in the samples was obtained. Assuming that the samples analyzed contained only $GaAsO_4$ and Ga_2O_3, weight per cent values for these two products were calculated from wet analysis data and from weight loss data. These values are presented in Table I-GaAs. The weight percentages of $GaAsO_4$ and Ga_2O_3 obtained from these two independent measurements agree quite well. The total weight loss of sample S14S (Table I) is 35.6%. The theoretical weight loss if all the GaAs were oxidized to β-Ga_2O_3 is 35.2%. Possibly some of the Ga_2O_3 and/or GaAs was vaporized during the oxidizing reaction.

Figure 2 shows photographs of the progressive oxidation with temperature of slices of GaAs. Figure 3 shows how the oxidation proceeds from the surface of a sample. The samples in Fig. 3 were cracked perpendicular to the plane of the plate, and lapped and polished on this cracked edge to give these cross-sectional views.

When a sample of GaAs was oxidized with oxygen to 965°C, there was a loss of volume of 0.66% and the bulk density is 3.58 g/cc. Since the density of GaAs is 5.3216 g/cc (4), the density of the low quartz form of $GaAsO_4$ is 4.20 g/cc (2), and the density of β-Ga_2O_3 is 5.88 g/cc (2), the product of the oxidation of GaAs showed a porosity of 35.6%.

GaP.—If GaP, on being oxidized by oxygen produced only β-Ga_2O_3, there would be a weight loss of

Table I

GaAs

Sample designation	Temperature, °C	Hr at temperature	Weight % loss	Weight per cent $GaAsO_4$ From weight loss	Weight per cent $GaAsO_4$ From wet analysis	Weight per cent Ga_2O_3 From weight loss	Weight per cent Ga_2O_3 From wet analysis
S14S	1050	20	35.6	0.0	0.1	100	99.9
S12N	950	19	32.2	7.8	9.8	92.2	90.2
S18J	860	22	32.4	7.7	8.1	92.3	91.9
S10F	850	22	29.8	13.9	15.3	86.1	84.7

GaP

Sample designation	Temperature, °C	Hr at temperature	Weight % gain	Weight per cent $GaPO_4$ From weight gain	Weight per cent $GaPO_4$ From wet analysis	Weight per cent Ga_2O_3 From weight gain	Weight per cent Ga_2O_3 From wet analysis
S24N	1110	20	63.2	(99.76)	92.13	(0.24)	7.87
S21H	1130	24	62.3	(99.08)	93.55	(0.92)	6.45
S21J	1150	22	62.5	(99.15)	95.4	(0.85)	4.6

6.92%. If $GaPO_4$ were the only product, then there would be a weight gain of 63.6%. When GaP was heated above 1000°C, a weight increase was observed, increasing slowly with temperature (see Fig. 4) until a range of 1110°-1150°C. In this range a very energetic exothermic reaction took place. The product of the reaction melted.[2] At the beginning of this exothermic reaction, the furnace was opened (for several experiments), and measurements as high as 1700°C were made with an optical pyrometer. It was noted at that time that a small amount of white powder was evolved during this reaction. This powder deposited on the quartz wall nearby which had a temperature in excess of 1100°C. Samples which had undergone the exothermic reaction experienced a weight gain of 62-63%. Heating at higher temperatures (as high as 1250°C) did not cause any further weight change. Samples heated for longer periods of time, at temperatures under 1110°C, showed larger increases in weight than samples heated for shorter periods of time, at the same temperatures (see Fig. 4, samples heated at 1100°C). Figure 5 photographically shows the progressive oxidation with temperature of slices of GaP. The 1120°C sample had gone through the exothermic reaction and the melted product is shown in its quartz boat. Figure 6 is a cross section of the "1100°C, 70 hour" sample of Fig. 5. This sample was cracked perpendicular to the plane of the plate and lapped and polished on this cracked edge to give a cross-section view.

X-ray diffraction studies showed that the products of the oxidation of GaP over the entire range of temperatures were the christobalite form of $GaPO_4$ (2) as a major phase and as a minor phase, β-Ga_2O_3 [5-10 w/o (weight per cent)].

Wet chemical analyses of several samples of oxidized GaP were performed and total weight per cent phosphate in the samples was obtained. Assuming that the samples analyzed contained only $GaPO_4$ and Ga_2O_3, weight per cent values for these two products were calculated from the wet analysis data and the weight gain data, and these values are given in Table I-GaP.

[2] The melting points of β-Ga_2O_3 and the christobalite form of $GaPO_4$ are 1715° ± 15°C (3) and 1670° ± 10°C (2), respectively.

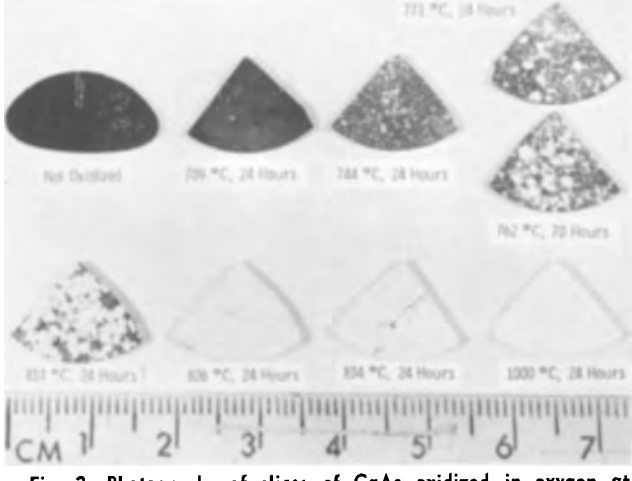

Fig. 2. Photographs of slices of GaAs oxidized in oxygen at various temperatures. Samples oxidized at 834° and 1000°C had undergone the exothermic reaction.

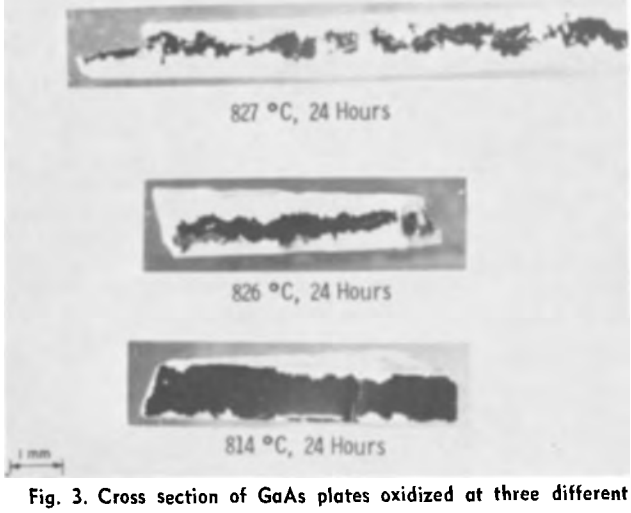

Fig. 3. Cross section of GaAs plates oxidized at three different temperatures.

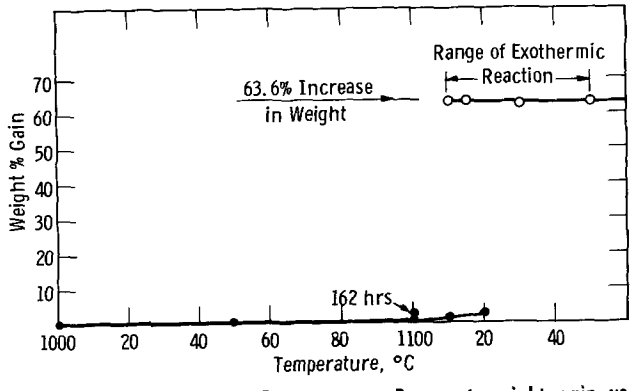

Fig. 4. Oxidation of GaP in oxygen. Per cent weight gain vs. temperature. All points on this curve are for samples fired for 22 ± 2 hr, except the labeled points.

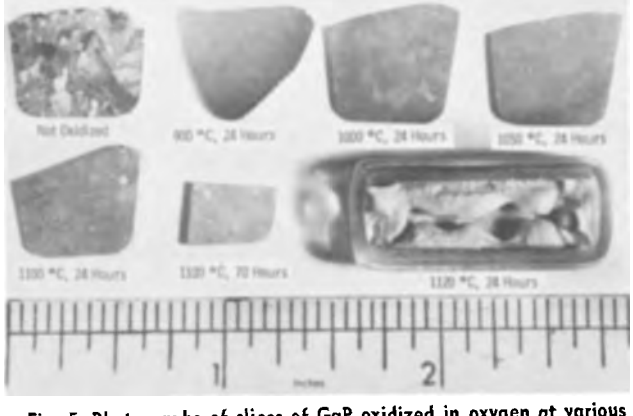

Fig. 5. Photographs of slices of GaP oxidized in oxygen at various temperatures. Sample fired at 1120°C for 24 hr had undergone the violent exothermic reaction.

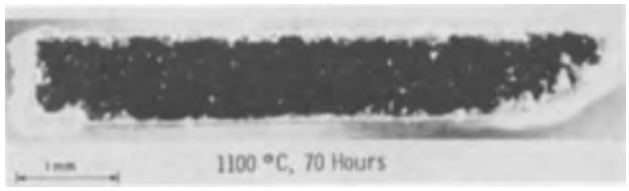

Fig. 6. Cross section of GaP plate oxidized in oxygen. Some sample as 1100°C, 70 hr in Fig. 6.

The values obtained for the weight per cent of $GaPO_4$ and Ga_2O_3 from wet analysis and weight gain data differ markedly. Since β-Ga_2O_3 was observed on the x-ray film for these samples, one can be sure that β-Ga_2O_3 was present in concentrations of at least a few per cent. It is felt that the weight gain measurements are all on the high side. Some of the powder deposited during the reaction was scraped off the wall of the quartz tube and examined by x-ray diffraction. Christobalite $GaPO_4$ with a small amount of β-Ga_2O_3 was identified. Therefore, the weight per cent $GaPO_4$ and β-Ga_2O_3 obtained by wet chemical analysis are considered quite reliable, and the quantitative data for Ga_2O_3 obtained from weight gain data are to be considered too low.

The densities of the christobalite form of $GaPO_4$, GaP, and β-Ga_2O_3 are 3.29 g/cc (2), 4.1304 g/cc (4), and 5.88 g/cc (3). The density of the oxidation product is certainly less than either GaP or β-Ga_2O_3.

Conclusion

The thermal oxidation of GaAs with oxygen produces β-Ga_2O_3 as a primary product and the low quartz form of $GaAsO_4$ as a secondary product. This was demonstrated by x-ray diffraction and quantitatively proved by weight loss determinations and wet chemical analysis. Minden observed that an oxide masking film was not formed when GaAs was thermally oxidized with oxygen. This paper has tried to prove that a low bulk density product composed primarily of β-Ga_2O_3 is formed, but the product is porous (about 35%), and As_2O_3 is driven from the area of the reaction.

The thermal oxidation of GaP with oxygen produced the christobalite form of $GaPO_4$ as a primary product with a secondary product of β-Ga_2O_3. This was demonstrated by x-ray diffraction, indicated by weight loss determinations, and proved by wet chemical analysis. When GaP is thermally oxidized by oxygen, the resulting product is primarily $GaPO_4$. Since this is a lower density material than GaP it spreads over the surface of the GaP and tends to cover the entire surface in much the same manner that an SiO_2 film covers a silicon surface. Only a small amount of a volatile product (P_2O_5) may be produced in this reaction since some β-Ga_2O_3 is formed.

Since this oxidation of GaP takes place slowly at temperatures below 1100°C the thickness of the oxide film can easily be controlled. This paper would like to suggest that thermal oxide masking may be applicable to GaP.

Manuscript received Dec. 23, 1965.

Any discussion of this paper will appear in a Discussion Section to be published in the December 1966 JOURNAL.

REFERENCES

1. H. T. Minden, *This Journal*, **109**, 733 (1962).
2. E. C. Shafer and R. Roy, *J. Am. Ceram. Soc.*, **39**, 330 (1956).
3. R. Roy, V. G. Hill, and E. F. Osborn, *J. Am. Chem. Soc.*, **74**, 719 (1952).
4. Von G. Giesecke and N. Pfister, *Acta Cryst.*, **11**, 369 (1958).

Properties of Anodic Films Formed on Reactively Sputtered Tantalum

D. Gerstenberg

Bell Telephone Laboratories, Incorporated, Murray Hill, New Jersey

ABSTRACT

The technique of reactive sputtering has been used for producing tantalum films with various concentrations of interstitial additives like oxygen, carbon, nitrogen, and hydrogen. A number of compounds between tantalum and these nonmetallic elements also have been deposited. The dielectric properties of anodic films on the tantalum formed in an aqueous solution of citric acid have been related to the composition of the tantalum. It was found that the capacitance density of 130v anodic films remains unaffected by the presence of oxygen and hydrogen, while it decreases as the atomic concentration of nitrogen and carbon in the tantalum increases. The dielectric constant, ϵ, of anodic films on Ta_2N is approximately 50% of the value of anodic Ta_2O_5 formed on pure tantalum.

The properties of sputtered refractory metal films like tantalum, niobium, and titanium are influenced greatly by deliberate addition of reactive gases to an argon sputtering atmosphere (1-4). Nonmetallic additives like oxygen, nitrogen, or carbon are incorporated in these films during the deposition process. At low concentrations, this incorporation takes the form of interstitial solution, and the solubility limits for all three additives appear to be much higher in tantalum and niobium films than in the bulk metals. At higher concentrations a number of compounds like oxides, nitrides, and carbides are formed. The resistivity and the temperature coefficient of resistivity of reactively sputtered refractory metal films depend strongly on the type of gas and the partial pressure at which the films are sputtered.

Reactively sputtered tantalum nitrides and carbides have a much higher resistivity than tantalum, a very low temperature coefficient, and a high thermal stability when deposited on heated substrates. In particular, tantalum nitride films have proven their usefulness as resistive components for integrated circuitry (5) and as individual components (6).

Preliminary results also indicated interesting dielectric properties of anodically formed films on tantalum sputtered with deliberately added nitrogen (7). These results were obtained on anodic films formed on tantalum which, initially, without deliberate addition of

nitrogen consisted of β-tantalum (8). As the atomic concentration of nitrogen is increased in the tantalum films the resulting anodic film has lower capacitance, but equivalent dielectric loss and leakage compared to anodic films formed on pure tantalum films (9). It was also demonstrated that the decrease in capacitance was caused by a change in dielectric constant due to the formation of a tantalum oxynitride. Associated with the decrease in capacitance is a large increase in the cathodic breakdown voltage. The purpose of the present investigation was to study the influence of other nonmetallic elements on the dielectric properties of anodic films formed on reactively sputtered tantalum films. The reactive gases used in this study include oxygen, methane, hydrogen, and nitrogen. Nitrogen has been added to this list because it was desirable to reinvestigate the properties of thin film capacitors fabricated from nitrogen containing tantalum sputtered under conditions which allow deposition of bcc α-tantalum reproducibly.

Experimental

As in the previous investigation (1) the tantalum films were sputtered from a high purity tantalum cathode through a mask on clean 2.5x7.5 cm barium alumina borosilicate glass substrates to a thickness of 4500Å. The distance between cathode and anode was 6.5 cm and the deposition rate about 130 Å/min for tantalum at 0.25 ma/cm^2, 4 kv and an argon pressure of $25\text{x}10^{-3}$ Torr. A removable shield between substrate and cathode allowed equilibrium to be reached in the sputtering atmosphere before starting deposition on the substrate. For outgassing, the mask and the substrate were maintained at 400°C during the presputtering and the subsequent sputtering run. The resistivity of the tantalum films was determined by a four point probe technique immediately after deposition.

The tantalum films were anodized at room temperature in an aqueous solution of 0.01% citric acid at a current density of $5\text{x}10^{-3}$ amp/cm^2. After reaching the desired voltage the anodization was continued for another 30 min allowing the current to decrease to $5\text{x}10^{-6}$ amp/cm^2 which is in the order of the electronic leakage current. The majority of the films were anodized to 130v resulting in oxide films on pure tantalum about 2000Å thick (10). In most cases, the anodization was interrupted to etch the tantalum films electrochemically at weak spots in the oxide in an aluminum chloride in methanol solution, which has proven beneficial in reducing anodic leakage or shorts (11). A number of films were anodized to voltages ranging from 75 to 250v for determining the amount of charge passed during anodization, and the dependence of the capacitance density on the forming voltage. The last step in the capacitor fabrication was the evaporation of the counter electrode structures from a tungsten filament at pressures of $1\text{x}10^{-4}$-$1\text{x}10^{-5}$ Torr. Gold counter electrodes, about 2000Å thick, were evaporated through mechanical masks yielding from 8 to 10 capacitors per substrate with an area of 0.35 cm^2 per capacitor. A General Radio Type 1620A Measuring Assembly was used for the determination of the capacitance and tan δ at 1 kc, and in a number of cases at frequencies ranging from 0.1 to 10 kc.

The structure of the tantalum films sputtered at different reactive gas pressures has been determined by x-ray diffraction analysis of processed slides after the capacitor properties had been evaluated. Since the anodic oxide is x-ray amorphous it does not generate a pattern interfering with the x-ray diffraction pattern obtained from the underlying tantalum film.

Experimental Results and Discussion

Resistivity.—Figure 1 shows how the resistivity of reactively sputtered tantalum films is affected by the type and the partial pressure of the reactive gases added to the argon atmosphere. The tantalum films

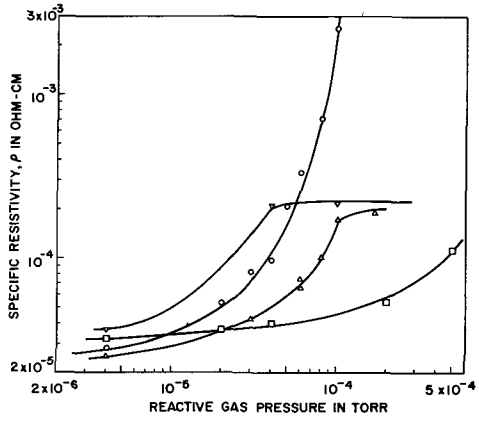

Fig. 1. Specific resistivity of 4500Å tantalum films as a function of the type and reactive gas pressure (measured by four-point probe). Sputtered films: ▽ N_2; △ CH_4; ○ O_2; □ H_2.

which were sputtered without deliberate addition of a reactive gas ($p = 3\text{x}10^{-6}$ Torr) have resistivities, ρ, ranging from 25 to 35 μohm-cm. These values are between 2 and $3\cdot\rho_B$, where ρ_B is the resistivity of pure bulk tantalum, indicating an impurity concentration of less than 3 a/o (atomic per cent) of interstitials like oxygen or nitrogen (1). The deliberate addition of reactive gases increases the resistivity until in the case of nitrogen and methane the curve reaches a plateau region at about 200-250 μohm-cm. These values agree very well with those reported for 1200Å films (1). The curve for tantalum sputtered in a partial oxygen atmosphere shows a sharp rise in resistivity above $6\text{x}10^{-5}$ Torr. The formation of insulating Ta_2O_5 occurs at partial pressures of oxygen of $1.7\text{x}10^{-4}$ Torr and above. The presence of hydrogen in the sputtering atmosphere does not seem to influence the resistivity of the tantalum films very much below 10^{-4} Torr, while in the 10^{-4} Torr range the values increase by about an order of magnitude.

Structure and composition.—The structure of the tantalum films sputtered with various additions of nitrogen, methane, oxygen, and hydrogen is indicated on the upper half of Fig. 2. The tantalum films deposited in a partial nitrogen atmosphere have the same phases Ta_2N and TaN which have been reported before (1). Sputtering of tantalum in a partial methane atmosphere results in the formation of Ta_2C and TaC (12). The phase Ta_2C had not been observed for reactively sputtered tantalum films before (1) either due to the small concentration range of this phase or due

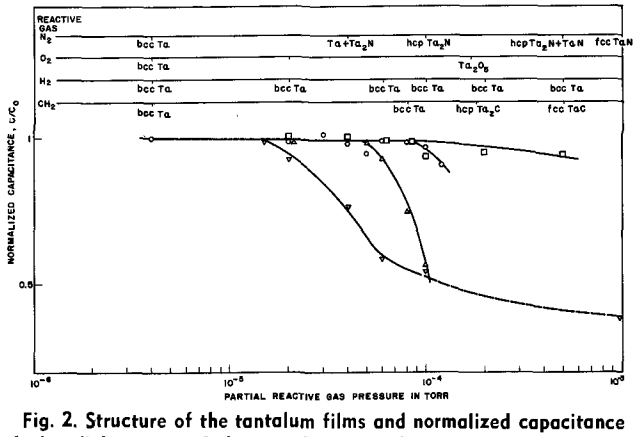

Fig. 2. Structure of the tantalum films and normalized capacitance of the dielectric at 1 kc vs. the type of gas and gas pressure. Capacitors were fabricated by anodization in 0.01% citric acid to 130v and have an area of 0.35 cm^2. C_0 is the capacitance of Ta_2O_5 on pure bcc tantalum films. C_0 = 0.031 uF. Sputtered films: same symbols as in Fig. 1.

Table I. Data on tantalum films sputtered in a partial oxygen atmosphere prior to anodization

Partial oxygen pressure P_{O_2} 10^5 Torr	Resistivity $\rho \times 10^6$ ohm-cm	Lattice constant a_o, in Å	Average crystallite diameter in Å*	Concentration** of oxygen in at. %
No O_2	27	3.327	94	—
2	52	3.360	64	3.6
4	97	3.405	52	11.4
6	340	3.430	17	—
8	720	3.46	16	29.5
10	2500	3.50	14	46

* The true average size of the crystallite is probably somewhat larger because of the x-ray line broadening on which this calculation was based might also be caused by strain in the tantalum films.
** Determined by anodization of films using Faraday's law.

to a higher solubility limit for carbon in tantalum at small film thicknesses. The films for the structural determination in the previous study by electron diffraction were only 300Å as compared to about 4000Å for the present films. Only preliminary data with respect to the composition of nitrogen and methane sputtered films are available. It has been established, however, that for both types of films (13, 14) the solubility limits are in the order of 10 to 15 a/o before the x-ray diffraction pattern of a second phase, Ta_2C or Ta_2N, can be observed.

The addition of oxygen to the sputtering atmosphere results in a drastic decrease of the crystallite size while the lattice constant increases as shown in Table I. The drop in crystallite size becomes particularly noticeable between $4x10^{-5}$ and $6x10^{-5}$ Torr probably indicating the formation of small Ta_2O_5 particles. These particles, however, are not large enough to contribute to the x-ray diffraction pattern. The tantalum films sputtered in a partial hydrogen atmosphere do not show a change in structure. This is reasonable in view of the fact the substrate temperature during deposition was about 400°C, too high a temperature for the formation of stable tantalum hydrides (15). It is likely, however, that there is interstitial solution of hydrogen which might occur during deposition or during the cooling period after sputtering.

Capacitance.—The lower half of Fig. 2 shows how the normalized capacitance of 130v anodic films on the reactively sputtered tantalum measured at 1 kc changes with increasing reactive gas pressure. The concentration of the gases in the tantalum is not known for all films, but the preliminary analytical results mentioned in the previous section indicate that the atomic concentration of the reactive gases is directly proportional to the reactive gas pressure in the sputtering atmosphere. The normalized capacitance of the dielectric on tantalum films sputtered with additions of oxygen and hydrogen appears to be affected the least. This result is to be expected for the anodic film formed on tantalum films sputtered in a partial oxygen atmosphere. The drop in capacitance for these films at $1x10^{-4}$ Torr is probably due to the presence of oxide particles prior to anodization resulting in an increased effective thickness for the anodic film. Films sputtered at this pressure contain about 45 a/o of oxygen. Anodic films formed on tantalum containing such high oxygen concentrations also tend to crystallize during anodization.

The incorporation of nitrogen and carbon in the tantalum films results in fairly large decreases in capacitance which are accompanied by a slow change of the interference color of the 130v anodic film. It will be shown in the next section that the lower capacitance for the capacitors formed on nitrogen sputtered films is not due to a variation in oxide thickness but rather due to a decrease in the dielectric constant with increasing nitrogen concentration in the films. The anodization of Ta_2N does not present difficulties; the voltage increases at a constant rate with time during the constant current period, and after reaching voltage the anodization current drops inversely with time (16). The films consisting solely of TaN exhibit gas evolution during the anodization process. They can be anodized to at least 130v but the resulting anodic film has a rather dull appearance. The finished capacitors also have low anodic and cathodic breakdown characteristics. In the case of the carbon containing tantalum, anodization of films sputtered at $1x10^{-4}$ Torr of methane consisting of a mixture of tantalum with a small amount of Ta_2C results in discoloration and low breakdown characteristics for the dielectric. For Ta_2C and TaC films citric and nitric acid act as etchants when a positive voltage is applied to these films.

Coulometric and other measurements.—A number of "pure"[1] tantalum films, and films sputtered at various reactive gas pressures were used for measuring the charge transfer during anodization. The theoretical values for the charge transfer per volt during the conversion of tantalum metal to Ta_2O_5 has been calculated on the basis of a reduction in thickness of the metallic film which is $k_3(Ta) = 6.63$ Å/v (10, 17). This value and the one obtained for converting metallic Ta_2N to the dielectric by anodization, $k_3(Ta_2N) = 4.8$ Å/v, (17, 18), had been determined previously from the increase in resistance of samples due to the reduction of the conducting film thickness by anodization. The number of electronic charges per volt of anodization and per square centimeter of film area, q_{th}, is then according to Faraday's law

for Ta:

$$q_{th} = n \cdot k_3(Ta) \cdot N_{Ta} \cdot e \quad [1]$$

and for Ta_2N:

$$q_{th} = n \cdot k_3(Ta_2N) \cdot N_{Ta_2N} \cdot e \quad [2]$$

where n is the number of charges per tantalum atom, N is the number of tantalum atoms per cubic centimeter of the original film of tantalum or Ta_2N which is equal to the inverse of the volume of the unit cell times the number of tantalum atoms per unit cell, and e is the electronic charge. The resulting q values for tantalum and Ta_2N are, respectively, $q_{th} = 0.287 \cdot 10^{-2}$ coulomb/v cm^2 [2] and $q_{th} = 0.194 \cdot 10^{-2}$ coulomb/v cm^2 for $n = 5$, assuming no changes in valency for the nitrogen atoms during anodization.

The experimental values for q were determined graphically from the plot of the anodizing current as a function of time. A comparison of the theoretical value with the experimental value for tantalum films sputtered without addition of a reactive gas which were anodized to 130 and 250v shows satisfactory agreement (see Table II) indicating about 100% efficiency for the anodization process. The oxygen containing tantalum films show the expected decrease in the q values. In Fig. 3 the resistivity of these films has been plotted as a function of the atomic concentration of oxygen calculated from the q values. Also shown are the resistivity values of 1200Å films *vs.* oxygen concentration de-

[1] Pure films are those sputtered without deliberate addition of a reactive gas.

[2] In a more refined treatment the change in cell parameter due to the presence of interstitial oxygen, etc. would have to be taken into consideration for the calculation of q_{th} of tantalum.

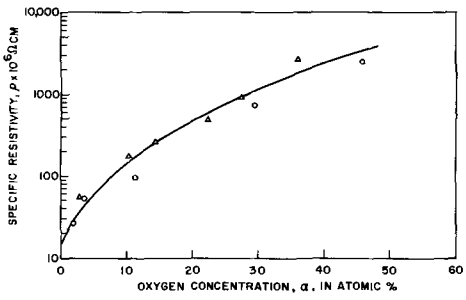

Fig. 3. Resistivity as a function of the atomic concentration of oxygen in reactively sputtered tantalum films: ○ based on the coulometric measurements, 4000Å; △ analyzed by inert gas fusion analysis, 1200Å.

Table II. Results of coulometry experiments on reactively sputtered tantalum films

Gas pressure $p \times 10^{-5}$ Torr	Reactive gas	No. of samples	Anodization voltage, V_A in V	Charge transfer $q \times 10^3$ coulomb/v-cm^2	Structure of the original film
—	None	4	130, 250	0.296 ± 0.012	bcc Ta
2×10^{-5}	O_2	6	130	0.301	bcc Ta + O
4×10^{-5}		4	130	0.258	bcc Ta + O
8×10^{-5}		6	130	0.179	bcc Ta + O
10×10^{-5}		2	130	0.118	bcc Ta + O
10×10^{-5}	N_2	4	100, 150, 200, 250	0.192 ± 0.014	Ta_2N
8×10^{-5}	CH_4	4	100, 150, 200, 250	0.293 ± 0.008	bcc Ta + C
35×10^{-6}	H_2	2	130	0.289	bcc Ta + H

termined by inert gas fusion analysis (1). Both sets of values agree very well suggesting that the coulometric experiments are a convenient method for oxygen analysis of tantalum films if the oxygen is uniformly distributed throughout the tantalum.

The experimentally determined value for the charge transfer during formation of the dielectric on Ta_2N, listed in Table II, is approximately equal to the theoretical value. The calculation of q_{th} for Ta_2N was based on the assumption that the tantalum atoms reacting with oxygen during anodization have five charges. The good agreement between the theoretical and the experimental value, therefore, seems to indicate five oxygen atoms react with each Ta_2N molecule during the formation of the anodic film. This has been confirmed by the gravimetric determination of the mass of the dielectric on Ta_2N formed during anodization. The conversion factor k_3 has not been determined for methane and hydrogen sputtered films. But if we assume that it is close to that of pure bcc tantalum which still is the structure of these reactively sputtered films it can be concluded from the q values that carbon and hydrogen do not participate in the charge transfer during anodization.

The results of capacitance measurements, plotted in Fig. 4 as a function of the anodization voltage, reveal that the inverse capacitance is not a linear function of the voltage which would be expected for a uniform composition of the dielectric. Especially the inverse capacitance of the dielectric film formed on Ta_2N films shows a large deviation from linearity at higher voltages. But the values for the dielectric formed on methane sputtered tantalum films also reveal a nonlinear dependence on voltage. Such a nonlinearity could be attributed to either a nonlinear dependence of the thickness of the dielectric with increasing voltage or a nonuniform distribution of the additives in the original film. Both possibilities have been investigated for the Ta_2N films and the results indicate that these two factors cannot be responsible for the nonlinearity of the inverse capacitance.

For all the Ta_2N films, anodized from 70 to 200v, the step height of the dielectric above the surface of the original Ta_2N film has been measured by Talysurf[3] and it was found to be a linear function of the anodization voltage. The factor for the increase in thickness was found to be $k_2(Ta_2N) = 11.9$ Å/v.

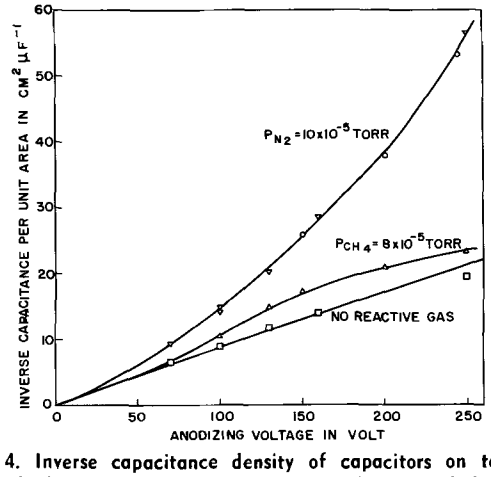

Fig. 4. Inverse capacitance density of capacitors on tantalum films with three different compositions as a function of the formation voltage.

Thus the total thickness of the dielectric formed on Ta_2N films per volt is then $k_3(Ta_2N) + k_2(Ta_2N) = k_1 = 16.7$ Å/v. Similar measurements for pure tantalum films yielded a value of $k_3(Ta) + k_2(Ta) = k_1 = 16.5$ Å/v. These values were used to determine the dielectric constant, ϵ, which is listed in Table III. The table also contains the film thickness of the original films before anodization. Since the anodic films formed on Ta_2N showed a systematic decrease in dielectric constant with increasing anodization voltage which might be due to a nonuniform composition of the Ta_2N, films with only half the original thickness have been anodized to intermediate voltages. The values of the dielectric constant of the anodic films formed on 2200Å Ta_2N films correspond closely with those found for the anodic films on thicker Ta_2N films. These results suggest that the decrease of the dielectric constant for the dielectric on Ta_2N films cannot be explained by a nonuniform distribution of nitrogen in the original film. It might be speculated, however, that the potential applied during anodization might cause migration of nitrogen ions. Such a migration might then result in a nonuniform distribution of the nitrogen in the dielectric.

It is not clear at present whether the increase of the dielectric constant with anodizing voltage obtained for anodic films on pure tantalum (Table III) is systematic and what its causes are. In addition, the average of the dielectric constant, 21.7, is considerably lower than the value reported by Young (19) which is widely used in the literature, but very close to the value recently obtained by Klerer (10).

Finally, the values for the decrease in thickness below the surface of the metallic film, k_2V_A, and the total thickness of the oxide, $(k_2 + k_3)V_A$, have been used for determining the density of the anodic films formed on pure tantalum and Ta_2N films. The density was calculated by combining Eq. [3] and [4]

$$\rho_{Ta_2O_5} = \frac{M_{Ta_2O_5}}{A \cdot (k_2 + k_3) \cdot V_A} \quad [3]$$

$$\rho_{Ta} = \frac{M_{Ta}}{A \cdot k_2 V_A} \quad [4]$$

[3] Taylor-Hobson, Ltd. Model 3 Talysurf with a straight line datum attachment.

Table III. Dielectric constant of anodic films

(a) On tantalum			(b) On Ta_2N		
Original film thickness, t[Å]	Anodization voltage, V_A[V]	Dielectric constant, ϵ	Original film thickness, t[Å]	Anodization voltage, V_A[V]	Dielectric constant, ϵ
4400	70	20.1	4400	70	13.7
4400	100	20.8	4400	100	12.7
4400	130	21.5	2200	100	13.7
4400	160	22.2	4400	130	12.15
4400	250	24.0	2200	150	10.97
	Average	21.7	4400	160	10.50
			2200	200	10.0
			2200	245	8.70
			4400	250	8.34

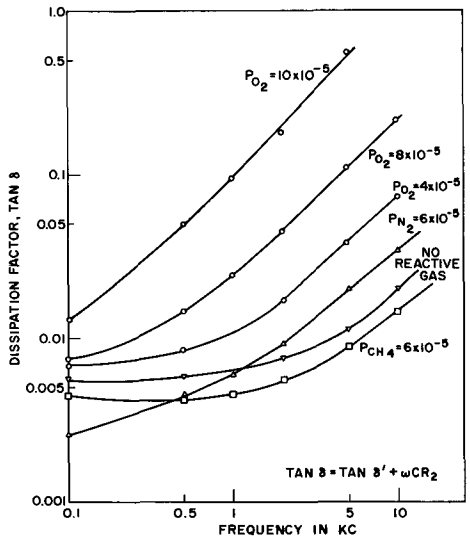

Fig. 5. Plot of the dissipation foctor vs. frequency for capacitors formed on reactively sputtered tantalum.

to Eq. [5]

$$\rho_{Ta_2O_5} = \frac{M_{Ta_2O_5} \cdot k_2}{M_{Ta} \cdot (k_2 + k_3)} \cdot \rho_{Ta} \qquad [5]$$

where ρ is the density, M is the mass (which can be replaced by the molecular weight in Eq. [5], V_A is the anodizing voltage, and A is the area of the anodized film which both can be eliminated. The resulting value of 8.12 g/cm³ for the density of the Ta_2O_5 formed on pure tantalum is in good agreement with those found by Young (19) and Klerer (10).

For the calculation of the density of the dielectric on Ta_2N films it has been assumed that the dielectric has the stoichiometric composition Ta_2O_5N yielding a density of 5.30 g/cm³. But even if the anodic film contains a nitrogen concentration which is larger or smaller, it would have only a small effect on the molecular weight and, therefore, would change the density of the dielectric very little. Thus the presence of nitrogen in the dielectric formed on Ta_2N appears to result in a structure considerably less dense than that of Ta_2O_5 formed on pure tantalum.

Frequency and temperature characteristics.—The capacitance and the dissipation factor of a number of typical capacitors have been measured at frequencies between 0.1 and 10 kc. The results are summarized in Fig. 5. Since tantalum oxide belongs to a category of dielectrics which show only a small dependence of the dielectric loss on frequency up to very high frequencies, the dissipation factor of the dielectric itself and the loss due to the series resistance of the tantalum film can be separated according to the following equation (20)

$$\tan \delta = \tan \delta' + \omega C R_2 \qquad [6]$$

Where tan δ' is the frequency independent dissipation factor of the dielectric, ω is the angular frequency, C is the capacitance, and R_2 is the series resistance of the tantalum film and the counter electrode.

If the dissipation factor, tan δ, obeys this equation, then when tan δ is plotted against frequency as shown in Fig. 5, tan δ' should predominate at low frequencies and tan δ will vary little with frequency. At higher frequencies ωCR_2 will predominate and the curve will approach a 45° slope. The capacitors made from pure tantalum films appear to fulfill this expectation. There is little change in tan δ from 0.1 to 1 kc, and above 5 kc the curve approaches a 45° slope indicating predomination of ωCR_2. With increasing oxygen concentration, this term predominates at lower and lower frequencies suggesting a steady increase of the R_2 values. An analysis of the data shows that R_2 increases from 8.5 to 810 ohms while tan δ' decreases from 0.0051 to 0.0030 as the partial oxygen pressure used in sputtering is increased to $1x10^{-4}$ Torr. The capacitors made from nitrogen sputtered tantalum films have the lowest tan δ' values.

The R_2 values of the methane sputtered film are even lower than the value of the pure tantalum film although its specific resistivity is six times higher, and the film thickness is the same. The low R_2 value and the initial decrease of tan δ (Fig. 5) probably indicate that tan δ' is dependent on frequency and that the present model is too simple for describing the frequency dependence of tan δ for these films. The capacitors made from carbon containing tantalum films are the only ones showing such a behavior.

The changes in capacitance in the frequency range are between 0.59 and 1.19%, except for the capacitors formed upon oxygen containing tantalum films. They reveal a larger decrease in capacitance at higher frequencies, especially those on films sputtered at $8x10^{-5}$ and $10x10^{-5}$ Torr of oxygen.

Figures 6 and 7 show how the reduced capacitance and dissipation factor of a number of capacitors change with temperature. The measurements were carried out in a dry atmosphere in order to eliminate the influence of moisture on these properties (11). For control purposes the measurements were made while increasing the temperature as well as while decreasing it.

The capacitors fabricated on pure tantalum films (sputtered without deliberate addition of a reactive gas) show the largest changes (Fig. 6). The temperature coefficient of capacitance for these capacitors in

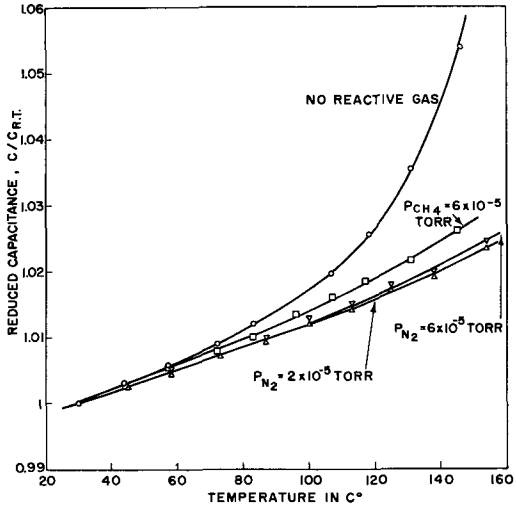

Fig. 6. Capacitance ratio as a function of temperature for capacitors formed on reactively sputtered tantalum.

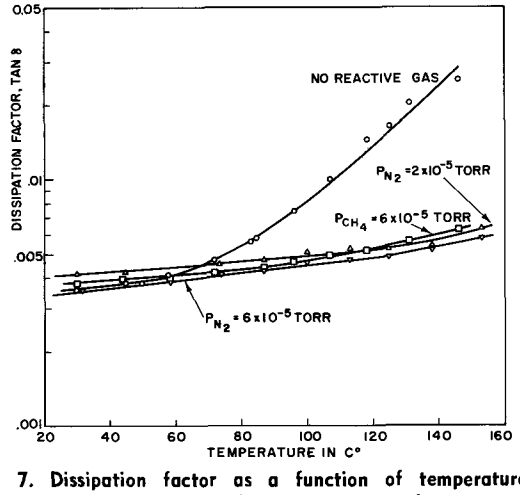

Fig. 7. Dissipation factor as a function of temperature for capacitors formed on reactively sputtered tantalum.

the range of a linear dependence of the capacitance on temperature, up to 60°C, is 220×10^{-6}/°C, below the value reported for tantalum thin film capacitors (8). Between 100° and 150°C these capacitors display a more rapid change with temperature. The capacitors made from reactively sputtered films (containing nitrogen and carbon) have smaller temperature coefficients, between 170×10^{-6} and 190×10^{-6}/°C, and the linear dependence of the capacitance on temperature holds up to higher temperatures. The capacitors made from pure tantalum films also show the largest change in the dissipation factor with temperature which is about an order of magnitude for the temperature range (Fig. 7). The temperature dependence of tan δ is much smaller for the capacitors made on reactively sputtered films.

Conclusions

One of the important results of the present investigation is the observation that the presence of interstitial oxygen, nitrogen, carbon, and hydrogen atoms does not interfere with the formation of anodic films on tantalum when it is deposited by reactive sputtering. The presence of Ta_2C in the tantalum film, however, results in a varied oxide growth so that the anodic film does not show a uniform interference color but rather displays a spectrum of interference colors. The dielectric strength of these anodic films is an order of magnitude lower. Further increase in carbon concentration, when the structure of the films is that of Ta_2C or TaC, inhibits the formation of anodic films in 0.01% citric or 0.01% nitric acid. In the case of the nitrogen containing tantalum the anodic films formed on Ta_2N still show uniform and bright interference colors and the dielectric strength remains high. It does not begin to decrease until the Ta_2N films become mixed with a considerable amount of TaN. There is an anodic reaction in citric acid even for TaN films but the resulting anodic film on TaN has very low dielectric strength. The capacitance density of the anodic films on carbon and nitrogen containing tantalum films decreases with increasing atomic concentration of these additives in the tantalum to less than 50% compared to that of anodic films on pure tantalum. The cause for this decrease in capacitance for nitrogen containing tantalum films could be attributed to a lower dielectric constant of the anodic film. The dielectric on tantalum nitride films also shows a much lower density than that of Ta_2O_5 and its stoichiometric composition can probably be best described as $Ta_2O_5N_x$ where the upper limit for x remains to be determined by analytical techniques. More experimental data are also required for the determination of the dielectric constant and the density of anodic films formed on carbon containing tantalum.

Acknowledgment

The x-ray diffraction analysis of the tantalum films by Mrs. M. H. Read and the Talysurf measurements of film thicknesses by R. Brown are greatly appreciated.

Manuscript received Dec. 30, 1965. This paper was delivered before the San Francisco Meeting, May 9-12, (1965).

Any discussion of this paper will appear in a Discussion Section to be published in the December 1966 JOURNAL.

REFERENCES

1. D. Gerstenberg and C. J. Calbick, *J. Appl. Phys.*, **35**, 402 (1964).
2. D. Gerstenberg and P. M. Hall, *This Journal*, **111**, 936 (1964).
3. D. Gerstenberg, *Ann. Phys.*, **11**, 354 (1963).
4. N. Schwartz, "Transactions of 10th National Vacuum Symposium 1963," p. 325, MacMillan Co., New York (1963).
5. D. Gerstenberg and E. H. Mayer, Proceedings of the 1962 Electronic Components Conference, p. 57.
6. R. W. Berry *et al.*, Proceedings of the 1964 Electronic Components Conference, p. 86.
7. (a) N. Schwartz, M. Gresh, and J. Deaderick, Abstr. No. 15, 1962 Meeting of the Electrochem. Soc., Los Angeles; (b) D. A. McLean, N. Schwartz, and E. D. Tidd, Proc. of the IEEE 52, 1450 (1964).
8. C. Altman and M. H. Read, *Appl. Physics Letters*, **7**, 51 (1965).
9. R. W. Berry and D. J. Sloan, *Proc. IRE*, **47**, 1070 (1959).
10. J. Klerer, *This Journal*, **112**, 896 (1965).
11. N. Schwartz and M. Gresh, *ibid.*, **112**, 295 (1965).
12. V. I. Smirnova and B. F. Ormont, *Dokl. Akad Nauk SSSR*, **96**, 557 (1954).
13. W. G. Guldner, Proceedings of the 1964 Electronic Components Conference, p. 9.
14. W. G. Guldner, Private communication.
15. M. Hansen and K. Andero, "Constitution of Binary Alloys," McGraw-Hill Book Co., New York (1958).
16. W. Ch. van Geel and H. Emmens, *Z. Phys.*, **87**, 220 (1933).
17. D. Gerstenberg, Unpublished results.
18. D. Mills, Private commmunication.
19. L. Young, "Anodic Oxide Films," p. 82, Academic Press, London and New York (1964).
20. D. A. McLean, *This Journal*, **108**, 48 (1961).

The Effect of the Concentration of Hypophosphite Ion on the Magnetic Properties of Chemically Deposited Co-P Films

J. S. Judge, J. R. Morrison, and D. E. Speliotis

Systems Development Division, International Business Machines Corporation, Poughkeepsie, New York

ABSTRACT

Samples of electroless cobalt phosphorus films of various thickness in the region less than 3000Å were prepared from solutions containing different concentrations of hypophosphite ion. These samples were analyzed by x-ray fluorescence and their magnetic characteristics were studied. The per cent phosphorus in the films was found to increase approximately logarithmically as the concentration of hypophosphite was increased. The plating rate increased concomitantly. The saturation magnetic moment and the coercivity were found to depend strongly on the phosphorus content of the films. The coercivities of these films also have a strong dependence on thickness. To a large extent the interaction of these two physical properties of the film determine the magnetic properties observed.

The magnetic properties of films of chemically deposited cobalt-phosphorus have been investigated several times in the past. Fisher and Chilton (1) have reported the preparation of high coercivity deposits as possible media for magnetic recording. The present authors have shown that somewhat thinner deposits exhibit superior recording performance and have reported on their magnetic properties (2, 3). Ransom

Table I. Composition of solution

$CoSO_4$	0.0855M
Na_3 citrate	0.183M
$(NH_4)_2$ H citrate	0.088M
$(NH_4)_2$ SO_4	0.307M

pH = 8.3 (at 85°C)—adjusted with NH_4OH
Temperature = 85°C

and Zentner (4) have shown that low coercivity uniaxial deposits of electroless cobalt can be prepared under somewhat different conditions of deposition. In short, the magnetic properties of chemically deposited cobalt-phosphorus films are critically dependent on the conditions of preparation. The magnetic properties of these deposits are a complicated function of the phosphorus content, crystallite size, and orientation of the deposits which in turn are controlled by the deposition variables, primarily solution composition, pH, and temperature. In this investigation we have restricted ourselves to a study in some detail of the effects of one of the more important variables in solution composition, the concentration of hypophosphite ion.

Preparation

The films were deposited on Mylar[1] substrates which were presensitized with the usual $SnCl_2$-$PdCl_2$ treatments (5). Prior to this, the Mylar substrates had been rendered hydrophilic by immersion into a hot chromic-sulfuric acid solution and then a hot sodium hydroxide solution (6). The composition and condition of the solution used for the deposition are shown in Table I. This solution is similar in composition to that used by Ransom and Zentner for the deposition of low coercivity uniaxial films, except that it is operated at a significantly higher pH. The agitation during deposition was kept at a minimum, merely sufficient to assure temperature and concentration uniformity.

The weight of cobalt and phosphorus deposited was determined by x-ray fluorescence analysis. The amount of phosphorus codeposited was found to be independent of deposit weight, as shown in Fig. 1. However,

[1] E. I. du Pont de Nemours & Co., (Inc.) registered trademark.

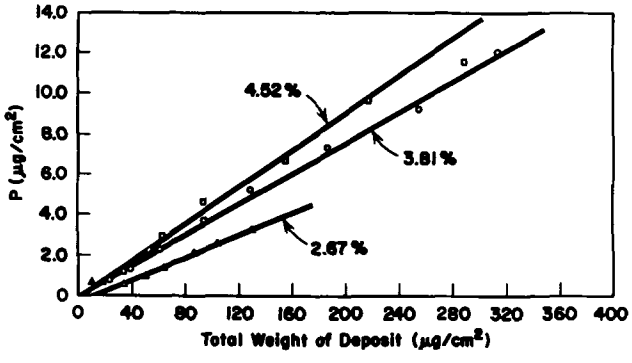

Fig. 1. Weight of phosphorus deposited vs. total deposit weight

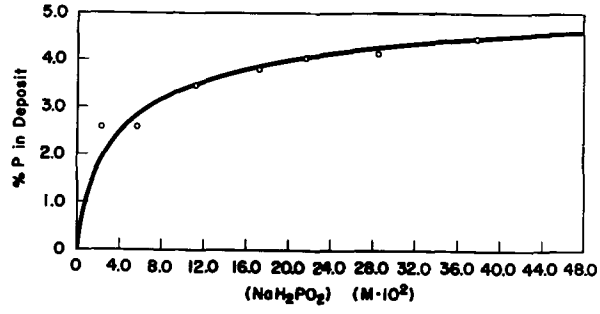

Fig. 2. Dependence of per cent P in deposit on the concentration of NaH_2PO_2.

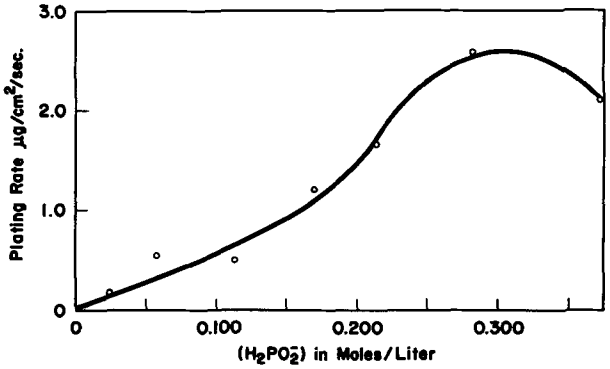

Fig. 3. Plating rate vs. $(H_2PO_2^-)$

above deposit weights of ~ 200 μg/cm², or approximately 2500Å in thickness, there was a tendency for the phosphorus content to decrease with increasing thickness. Since such deposits would tend to exhibit a trend in composition with thickness, these were not included in this study. Consequently only deposits of less than ~ 2500Å were considered. Fortunately it is in this thickness region that the most interesting magnetic behavior is exhibited.

The average phosphorus content for the deposits at each concentration of hypophosphite ion was determined from the slope of such plots as shown in Fig. 1. The dependence of the per cent phosphorus on the hypophosphite content of the solution is shown in Fig. 2. It is apparent that the phosphorus content of the deposits increases as the hypophosphite content of the solution increases. Moreover, there is apparently an approximately logarithmic relationship between the two. Figure 3 shows the dependence of the plating rate on the hypophosphite content of the solution. The rate increases monotonically to ~ 0.3M in hypophosphite and then exhibits a slight decrease as the hypophosphite concentration is further increased. This effect is similar to electroless nickel deposition where an optimum ratio of metal ion to hypophosphite ion exists for maximum deposition rate.

Crystallographic Properties

X-ray diffraction indicated that all deposits were predominantly hexagonal cobalt. The crystallite size of the deposits was estimated from x-ray line broadening. Such estimates gave values in the range 200-1000Å. However, the crystallite sizes so obtained showed no correlation with thickness, phosphorus content, or magnetic properties. In order to obtain significant peaks for x-ray diffraction, it was necessary to use several samples stacked together. This would be expected to produce additional line broadening. In addition, deposit stresses and stacking faults will contribute to the line broadening. Consequently these estimates of crystallite size are in reality the lower limit of the crystallite size in these deposits. All deposits exhibited a preferred orientation of the C-axis in the

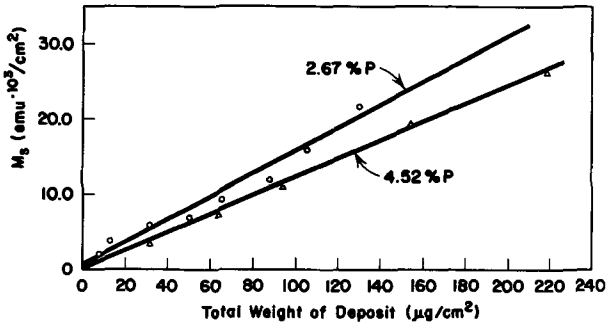

Fig. 4. Dependence of the saturation magnetic moment on deposit weight.

Table II. Values for various phosphorous contents

% P	σ_s emu/gram
2.67	156.0
2.62	147.5
3.45	114.0
3.81	118.0
4.06	120.5
4.22	127.5
4.52	122.5

plane of the substrate. However, a higher degree of orientation was exhibited by the higher phosphorus deposits. Unfortunately it was impossible to obtain an estimate of orientation on deposits of less than ~ 500Å in thickness.

Magnetic Properties

The saturation magnetic moment of the deposits was measured by a Faraday type magnetic balance in a field of 6000 oe. The moments so obtained were found to be independent of deposit thickness. This fact is illustrated by Fig. 4 which is a plot of the magnetic moment *vs.* deposit weight for the two extremes of phosphorus content. The saturation magnetic moment per gram (σ_s) of the material was calculated from the slopes of such plots. Table II illustrates the values so obtained for the various phosphorus contents. At the lowest per cent P the highest values of σ_s are observed. A decrease as the per cent P is increased would be expected whether the phosphorus merely acted at a dilutant or entered in chemical combination with some of the cobalt. However, the observed decrease is not monotonic with increasing per cent P, but exhibits a minimum at ~ 3.5% P.

Measurement of the hysteretic properties of the deposits were made in a vibrating sample magnetometer with a maximum field of approximately 10,000 oe. The squareness (*i.e.*, the ratio of the remanent magnetic moment to the saturation magnetic moment) showed no clear trends with thickness, but the average value decreased from 0.83 to 0.70 as the phosphorus was increased from 2.6 to 4.5%.

For the two lowest phosphorus contents the dependence of the coercivity of the deposits on deposit weight or thickness is shown in Fig. 5. Both of these series had very near the same per cent P, 2.62 and 2.67%. In both cases the coercivity drops as the weight increases from ~ 1100 oe at a deposit weight of ~ 15 $\mu g/cm^2$ approaching a constant value of ~ 300 oe for large deposit weight. Figure 6 is a similar plot for the remaining series of higher per cent P. At 3.45% P a slight maximum begins to appear in the coercivity at ~30 $\mu g/cm^2$. As the per cent P is increased beyond this, the maximum begins to shift out in thickness until at 4.5% P the coercivity appears to increase with increasing weight over the entire weight range. The heights of these maxima, however, are decreasing with increasing per cent P. These points are clarified in Fig. 7 where the value of H_c at the peak and the weight of deposit at which the peak in H_c occurs has been plotted against the per cent P. The value of (H_c) peak drops from ~ 1200 oe at 3.5% P to 650 oe at 4.5% P. Meanwhile, the deposit weight at which the maximum occurs increases from < 20 $\mu g/cm^2$ for the low P deposits to > 200 $\mu g/cm^2$ for the 4.5% P deposits. Since the deposits with the least phosphorus did not exhibit a maximum in H_c for even the thinnest deposits measured, the actual (H_c) peak and weight at the peak would probably be higher and lower respectively than those points entered which merely represent the highest H_c observed.

Figure 8 summarizes the effect of phosphorus content on H_c for constant deposit thickness. The thicknesses have been calculated assuming a density of 8.9 g/cm^3. For a given thickness the coercivity increases to a maximum and then falls as the % P increases. At a deposit thickness of 560Å a maximum coercivity of 1200 oe is reached at ~3.5% P whereas at 2250Å a maximum H_c of ~ 800 oe is reached at 4.2% P. The

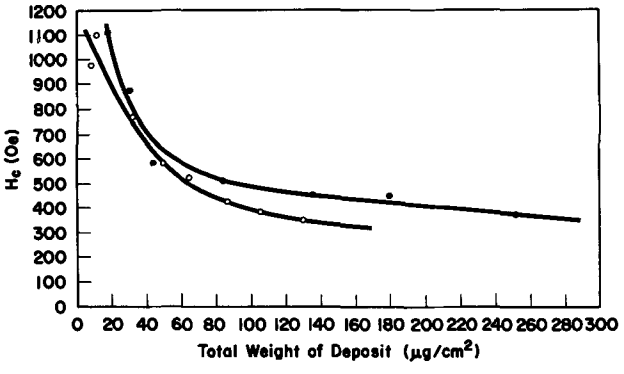

Fig. 5. H_c vs. deposit weight. ○ = 2.67% P; circle with x = 2.62% P.

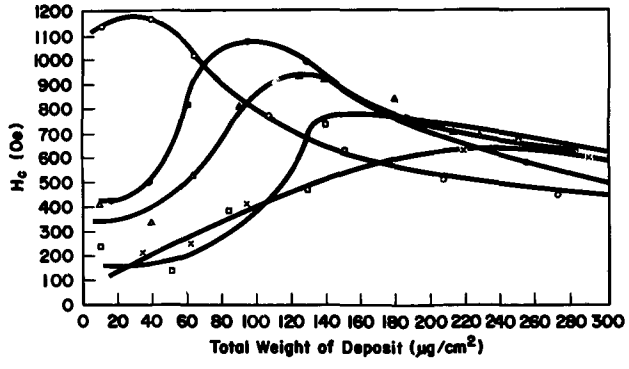

Fig. 6. H_c vs. deposit weight. ○ = 3.45% P; • = 3.81% P; △ = 4.06% P; □ = 4.22% P; X = 4.52% P.

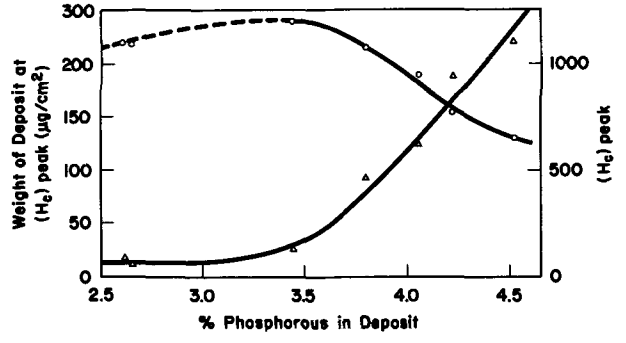

Fig. 7. Dependence of the maximum in H_c on per cent P. ○ = (H_c)p; △ = (wt)p.

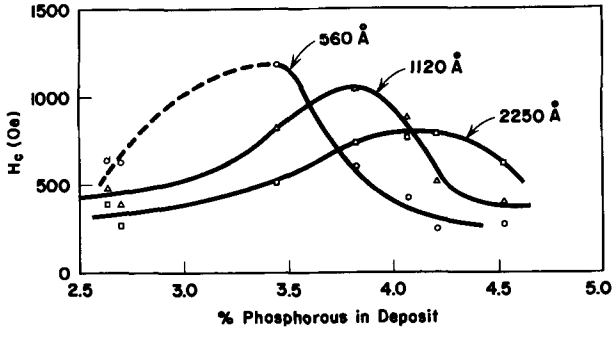

Fig. 8. Dependence of H_c on per cent P for three different thicknesses.

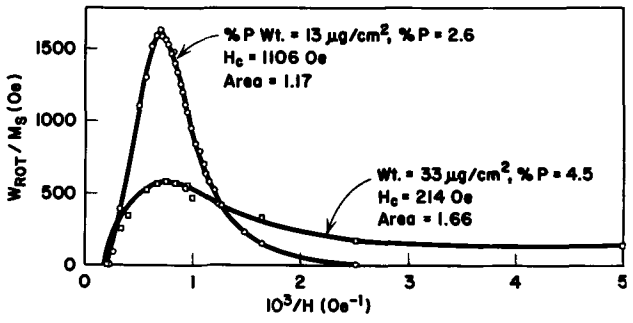

Fig. 9. Dependence of rotational hysteresis on field for two thinner samples of different per cent P.

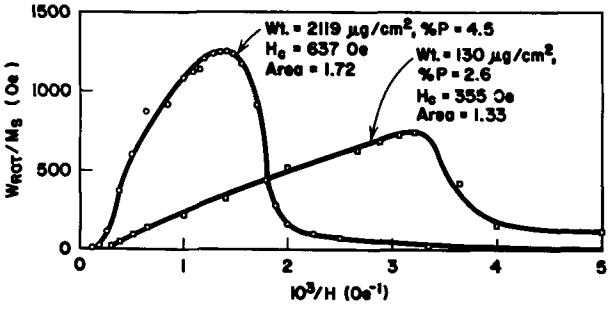

Fig. 10. Dependence of rotational hysteresis on field for two thicker samples of different per cent P.

intermediate thickness deposits of 1120Å reach an intermediate maximum of 1050 oe at an intermediate phosphorus content of 3.8%.

Discussion

The high coercivities observed for many of the samples of chemically deposited cobalt-phosphorus necessitate a single domain model to explain their magnetic properties. Assuming the phosphorus exists as the weakly magnetic Co_2P, 4% by weight of P would correspond to ~25% by volume of Co_2P. At any rate a significant proportion of the volume of these films consists of a nonmagnetic dilutant. A semi-particulate model is therefore reasonable for these films. The high magnetocrystalline anisotropy of cobalt, moreover, demands that these particles exhibit a strong uniaxial character. Consequently these films can be characterized qualitatively as a random (in the plane) assembly of interacting uniaxial particles. It has been shown by Reimer (7) that such a model leads to squarenesses higher than 0.64 (which would be expected for no interactions).

The energy loss in rotational hysteresis as a function of applied field was measured on a number of samples by means of a torque balance. Figure 9 is a plot of this energy, W_{Rot}, normalized for differences in magnetic moment *vs.* the reciprocal of the applied field. The values on the Y axis can be interpreted as the energy per magnetization jump times the number of particles involved. It is apparent that the low thickness low phosphorus sample shows a very narrow distribution of high field rotational processes consistent with its high coercivity. However, the low thickness, high phosphorus sample exhibits a large proportion of low field processes, again consistent with its low coercivity. Figure 10 shows the same results for much thicker films of low and high per cent P. With reference to the high phosphorus film, the distribution is now much sharper and apparently as the film has grown those particles exhibiting low field switching characteristics have disappeared. The low phosphorus film, on the other hand, now has its distribution shifted to much lower fields, indicating the appearance of low field processes as the film has grown.

Table III. Values for sample of three different per cent P

% P	Deposit wt (μg/cm²)	H_c (oe)	R	H_{pk} (oe)
2.67	13	1106	1.17	1390
	50	591	1.89	480
	87	432	2.21	365
	130	355	1.33	310
3.81	16	423	1.32	1670
	61	819	1.67	1350
	95	1069	1.68	1250
	187	774	2.19	750
4.52	33	214	1.66	1330
	63	246	1.89	1000
	94	405	1.23	960
	219	637	1.72	690

The value of the area under these curves has been shown to be characteristic of the mode of magnetization reversal. The theoretical values for the area (8) are (*a*) single-domain model, coherent rotation, 0.4; (*b*) single-domain model, incoherent rotation, 0.4 to 4.0; (*c*) domain wall, 4.0. In Table III the values of R, the area under the curve, are tabulated for samples of three different per cent P values. All values lie in the range 1.2-2.2 and exhibit no trends with thickness or per cent P. These values are consistent with a single domain model involving incoherent reversal, probably a magnetization buckling in the plane of the film. The value of the applied field at which the peak of the rotational hysteresis was observed is also tabulated in Table III. It can be seen that the value of this peak field decreases with increasing thickness in all cases. Figure 11 is a plot of the peak field *vs.* thickness for these samples. The peak field drops much more sharply as the thickness is increased for the low per cent P film than for those of higher phosphorus. Thus in the low per cent P films both the rapid decrease in peak field and especially the significant build up of low field processes as the thickness increases indicate a growth of particles out of the single domain size to particles large enough to support domain walls.

For the high per cent P films the peak field decreases and approaches the value of the coercivity as the thickness builds up and the low field processes disappear. This suggests that the thinner films have a significant portion of very small particles which exhibit a semi-superparamagnetic behavior. The particles grow as the film becomes thicker and enter the single domain size region. The greater the per cent P of the film, the greater is the thickness which must be reached before the contribution of these very small particles disappears. However, at the same time, because of the initial wide distribution of particle size in the higher per cent P films, some particles grow and enter the multidomain region causing a lowering of the maximum coercivity observed as the % P increases.

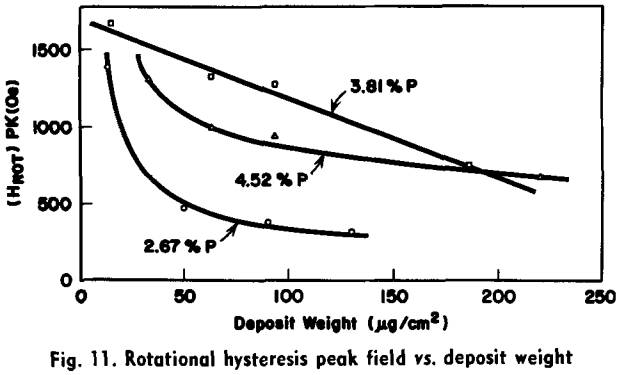

Fig. 11. Rotational hysteresis peak field *vs.* deposit weight

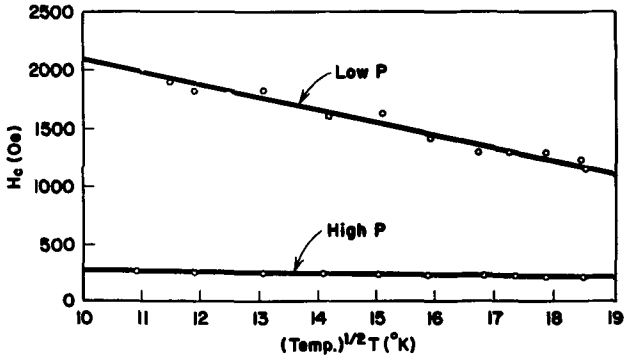

Fig. 12. Dependence of H_c on temperature for two thin deposits of different per cent P.

The temperature dependence of the coercivity of a selected number of these films was measured and the results for two of them are shown in Fig. 12. These particular samples are the thinnest samples of the low and high phosphorus films. The presence of near superparamagnetic particles should contribute a temperature dependence to the coercivity, such that H_c would be proportional to $-T^{1/2}$ if the anisotropy constants for the particles involved were independent of temperature (9). As shown in Fig. 12 the coercivity of these films is approximately proportional to $-T^{1/2}$. However, the low per cent P film shows by far the greatest temperature dependence.

Summary

Table IV summarizes the previous results for a selected number of samples. The temperature dependence of H_c is seen to be greatest for the low per cent P films. This appears to be in conflict with the postulate of less superparamagnetic behavior in these films. However, the uniaxial anisotropy constant for cobalt does increase ~50% in going to 77°K and this alone may be sufficient to account for the observed temperature dependence. All of the samples exhibit an orientation of the C-axis of cobalt in the plane of the film. The degree of orientation, however, is apparently greater for the higher per cent P films. In thin films in which the magnetization may be constrained, due to shape effects, to stay in the plane of the film, this orientation would lead to higher coercivity. However, the difference in orientations indicated here do not seem to play a large role.

Table IV. Summary of results for a selected number of samples

	Low P (2.6%)	Med P (3.8%)	High P (4.5%)
~t(Å)	150Å	180Å	350Å
$\frac{I(002)}{I(100)} \cdot N$	—	—	—
H_c	1000 oe	450 oe	200 oe
% increase of H_c at 77°K	70%	18%	22%
t(Å)	980Å	1070Å	1060Å
$\frac{I(002)}{I(100)} \cdot N$	0.54	0.23	~0
H_c	400 oe	1100 oe	400 oe
% increase of H_c at 77°K	53%	4%	14%
t(Å)	1460Å	2100Å	2460Å
$\frac{I(002)}{I(100)} \cdot N$	0.46	0.09	0.08
H_c	300 oe	700 oe	600 oe
% increase of H_c at 77°K	54%	24%	31%

In conclusion, we have shown that variation of the hypophosphite concentration of this plating solution causes concomitant variations in the plating rate and the per cent P of the resulting films. Below a thickness of ~2500Å the composition and magnetic moment density are independent of thickness. The hysteretic properties are a function of both thickness and per cent P. The study of the magnetic properties indicate that the high per cent P films have smaller particles at higher thicknesses than do the low per cent P films.

Manuscript received Dec. 17, 1965. This paper was presented at the Buffalo Meeting, Oct. 11-14, 1965.

Any discussion of this paper will appear in a Discussion Section to be published in the December 1966 JOURNAL.

REFERENCES

1. R. D. Fisher and W. H. Chilton, *This Journal*, **109**, 485 (1962).
2. J. S. Judge, J. R. Morrison, D. E. Speliotis, and G. Bate, *ibid.*, **112**, 681 (1965).
3. D. E. Speliotis, J. R. Morrison, and J. S. Judge, Proc. of the Intermag. Conf., p. 12.5 (1965).
4. L. D. Ransom and V. Zentner, *This Journal*, **111**, 1423 (1964).
5. E. A. Bergstrom, U. S. Patent #2,702,253.
6. H. Koretzky and B. Leland, U. S. Patent #3,142,582.
7. L. Reimer, *Z. Angew. Phys.*, **17**, 196 (1964).
8. W. D. Doyle, J. E. Rudisill, and S. Shtrikman, *J. Appl. Phys.*, **32**, 1785 (1961).
9. I. S. Jacobs and C. P. Bean, "Magnetism," Vol. 111, Chap. 6, p. 277, G. T. Rado and H. Suhl, Editors, Academic Press, New York (1963).

Gold Plating Directly on Molybdenum

R. M. Finne and W. R. Bracht

Bell Telephone Laboratories, Incorporated, Murray Hill, New Jersey

ABSTRACT

A technique has been developed to electrodeposit gold directly on a molybdenum substrate without prior deposition of other metals. The electrodeposited gold films are adherent and protective against highly corrosive ambients. The process involves the formation of a porous oxide on the molybdenum substrate, deposition of gold into this oxide, and hydrogen reduction of the oxide. During the reduction of the oxide, the gold is mechanically trapped and the substrate in the vicinity of the molybdenum surface is converted to a two-component gold-molybdenum layer. This layer provides a suitable surface for further deposition.

Prior to the development of the technique described in this paper, it had not been possible to electrodeposit gold on molybdenum or molybdenum-manganese substrates to produce an adherent and highly protective coating. Previous techniques have generally depended on the deposition of a more active metal such as copper, nickel, or chromium prior to deposition of gold (1). For many applications, particularly in the semiconductor field, such predepositions are undesirable since they may subsequently diffuse into the gold and degrade its alloying characteristics, or may diffuse into a semiconductor and perturb its electronic

properties. Alternatively, techniques have been proposed which involve the deposition of thin layers of gold followed by heat-treatment in non oxidizing ambients to form alloyed surface regions (2). Attempts to deposit gold directly on molybdenum by employing such standard electroplating techniques together with heat treating have not, in general, yielded acceptable results. This is because of the critical nature of certain preparatory steps in the process. By insuring the formation of a porous oxide on the molybdenum surface, depositing gold into this oxide and reducing the oxide to trap the gold, it has been possible to gold plate directly onto the molybdenum sample.

Apparatus and Materials

The electrodeposition apparatus and materials used were essentially standard in nature, and both still and barrel plating proved suitable. A typical bath construction was as follows: polypropylene tank, quartz immersion heaters, and gold anodes in an anode to cathode area ratio in excess of four to one. The acid citrate gold bath was prepared by mixing 20 ± 1g of sodium gold cyanide (71% gold) and 100 ± 1g of diammonium citrate and water to make one liter of solution. This was then boiled in a hood for 30 min to convert the cyanide gold complex to the citrate complex with the accompanying evolution of HCN. The bath was operated at a current density of 49 ma/in.^{2} at 60°C, and deposited 0.93 mg/cm^2/min. Both acid citrate and alkali cyanide solutions were used successfully.

Substrates used in the initial work were both machined molybdenum studs and molybdenum-manganese films which were silk-screened onto ceramic surfaces. Subsequent work has been done with a great variety of sample shapes and sizes.

Method

Figure 1 shows a schematic flow diagram for the plating method. The following is a description of the optimum procedure developed for our samples.

1. Initial degreasing of the substrates in trichloroethylene.
2. Fire in dry hydrogen (< 2 ppm H_2O) at 1000°C for approximately 10 min. (In no case were the samples passed through the flame curtain on the oven.)
3. Immerse in a solution of four parts NH_4OH (28%) to one part H_2O_2 (30%) for approximately 8 sec at room temperature.
4. Wash in deionized water.
5. Gold strike to deposit 0.15-0.62 mg/cm^2.
6. Wash in deionized water.
7. Fire in dry hydrogen (< 2 ppm H_2O) at 900°C for approximately 10 min.
8. Electrodeposit gold to the final desired thickness (~ 15 mg/cm^2).

Evaluation

The electrodeposited gold was tested for substrate protection against gaseous and liquid ambients, and for adherence to the substrate.

Protection against gaseous ambients was evaluated by exposure of the sample to wet hydrogen at 600°C for 1 hr. Protection against liquid ambients was evaluated by immersion of the sample in a 5 part HNO_3 (70%) —1 part HF (48%) solution at room temperature. The presence of blistering, peeling, or cracking on the sample when viewed under ten power magnification was considered evidence of unsatisfactory plating.

Nonadherence of an electrodeposited gold film would, in all probability, be made evident by a blistering of the coating during the testing described above. However, to test adherence further, a silicon wafer 30 mils in diameter was alloyed to the plated sample and the alloyed wafer was subjected to a shearing force of 9500 psi. If the wafer pulled gold from the substrate, the plate was considered unsatisfactory.

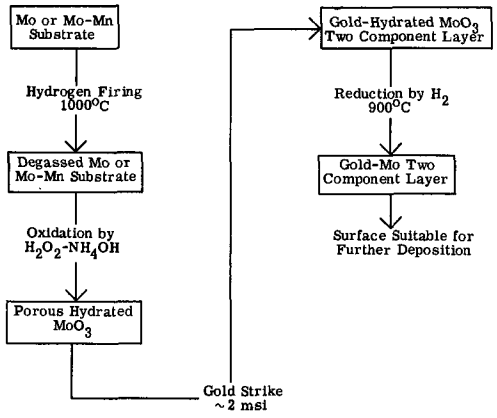

Fig. 1. Flow chart of the optimum processing steps

Discussion

Initial attempts to gold plate directly on molybdenum surfaces resulted in either nonadherent plates or plates which would not survive exposure to corrosive ambients. The substrates were carefully cleaned so that it was not a case of failure caused by surface contamination. These molybdenum samples (20 mils thick) were degassed at 1200°C for 1 hr in a vacuum of 10^{-6} Torr, but were unsatisfactory after plating. We therefore concluded that gassing was not the main problem. Since it is well known that molybdenum forms oxides such as MoO_3 which are stable at low temperatures, we postulated that such oxides were forming a barrier between the gold plate and the molybdenum surface.

Since gold and molybdenum form no alloys, and the solubility of each in the other is negligible (3), it is not possible to form a two-component phase by heating a gold plated molybdenum sample below its melting point. Since gold does not react with molybdenum oxide, chemical bonding cannot occur at the gold plate-substrate interface. Such mechanisms may be instrumental in the formation of satisfactory electrodepositions with metals such as copper, nickel, and chromium.

Instead of attempting to remove the nonporous oxide immediately prior to plating, the technique which was evolved makes use of a porous oxide which is generated on the molybdenum surface by aqueous oxidation. Plating solutions can permeate this type of molybdenum oxide and are deposited in the oxide during the strike. Reduction by hydrogen follows, which converts the molybdenum oxides to molybdenum, physically trapping the gold in a molybdenum matrix. This two-component layer is then suitable for further plating.

The postulated roles played by the significant processing steps are as follows:

1. The firing of dry hydrogen prior to plating serves two purposes: first, it reduces surface oxides; second, it degasses the surface. The temperature of this firing exceeds that of any subsequent processing step.
2. The treatment with ammoniacal peroxide solution forms a porous oxide on the substrate. The major reaction proceeds as in Eq. [1].

$$Mo + 3H_2O_2 \rightarrow MoO_3 \cdot xH_2O + (3-x)\ H_2O \qquad x = 1, 2 \qquad [1]$$

This oxide dissolves in the ammonium hydroxide forming ammonium molybdate as in Eq. [2].

$$MoO_3 \cdot xH_2O + 2NH_4OH \rightarrow (NH_4)_2MoO_4 + (x+1)H_2O \qquad x = 1, 2 \qquad [2]$$

This etching action forms a fresh surface which reacts to form a porous, hydrated oxide.

3. The gold strike solution permeates the oxide structure.

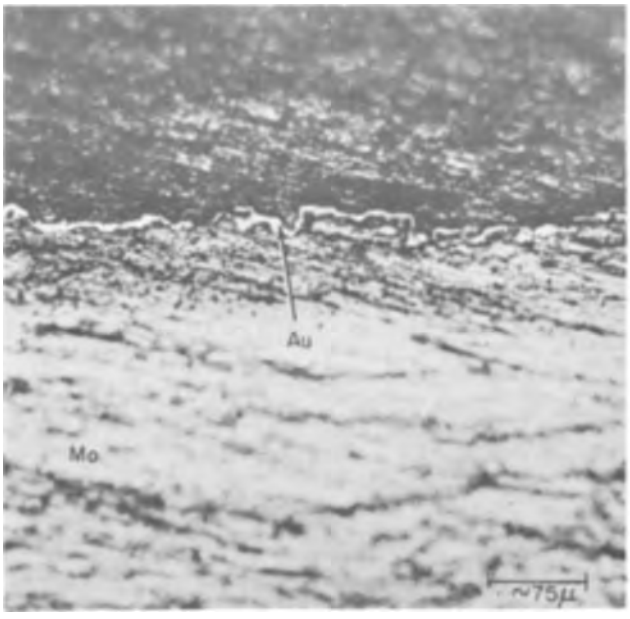

Fig. 2A. Thermally oxidized sample, angle lapped. Magnification *ca.* 170X.

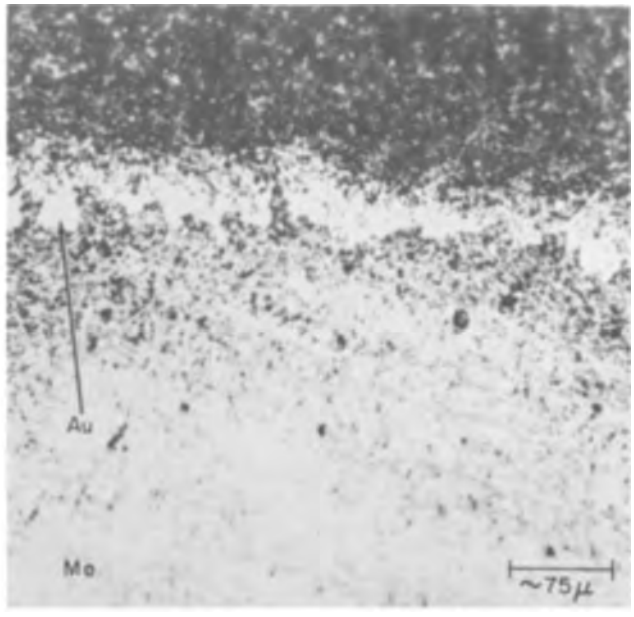

Fig. 3A. Chemically oxidized sample, angle lapped. Magnification *ca.* 170X.

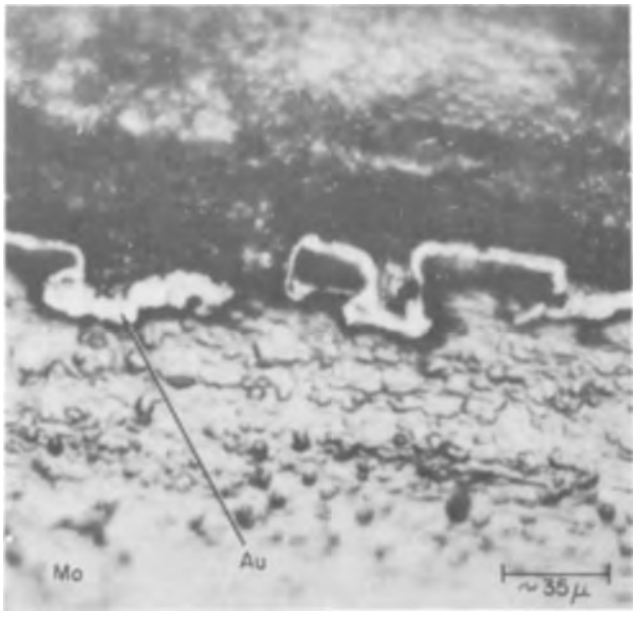

Fig. 2B. Thermally oxidized sample, angle lapped. Magnification *ca.* 670X.

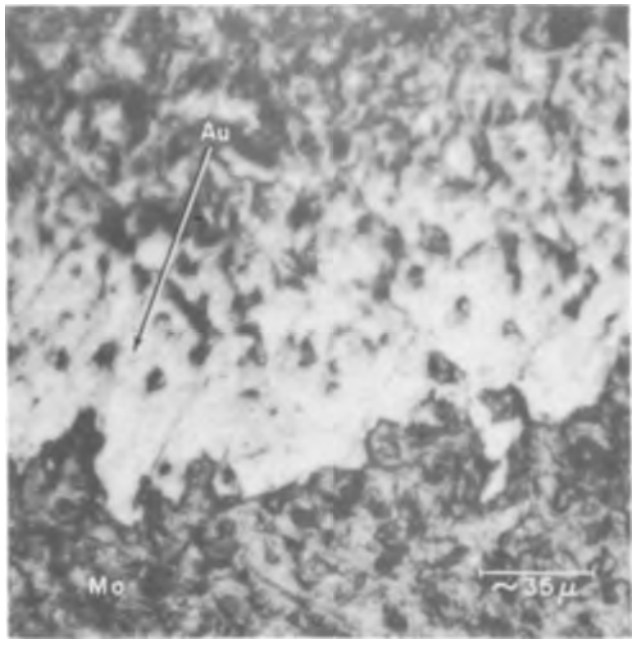

Fig. 3B. Chemically oxidized sample, angle lapped. Magnification *ca.* 670X.

4. The firing in dry hydrogen subsequent to the gold strike reduces the molybdenum oxide to molybdenum as in Eq. [3].

$$MoO_3 \cdot xH_2O + 3H_2 \rightarrow Mo + (3 + x)H_2O \qquad [3]$$
$$x = 1, 2$$

This creates a two-component region at the surface of the substrate which is suitable for further plating by routine techniques.

In order to verify the critical postulated roles, several experiments were performed.

Firing.—The initial hydrogen firing of step two was eliminated from the processing. The resulting samples blistered on heating, predominantly at the corners and edges. This is often characteristic of gassing. From this we may infer that step two is instrumental in degassing the substrate.

In addition, argon was substituted for hydrogen and the final results were satisfactory. This implies that the process is a thermal one and does not depend on the chemical nature of the heating ambient.

Oxidation.—A thermal oxidation was substituted for the ammoniacal peroxide treatment. All plated parts failed the tests. The results of metallographic sectioning and angle lapping are shown in Fig. 2 and 3. In the case of the thermal oxide, the electrodeposited gold appears to rest on the surface of a thin oxide layer. In the case of the chemically produced oxide, the electrodeposited gold appears to have penetrated into the oxide.

In addition, electron micrographs were taken of the oxide surfaces. Figures 4 and 5 show the results for the two types of oxide described. The chemical oxide appears to have a cellular, porous structure while the thermally grown oxide appears to be smooth and continuous.

Strike.—The gold strike was increased in thickness which resulted in an increased porosity of the electrodeposited film. This may be due to the formation of a relatively continuous layer of gold over the gold-permeated oxide. Such a continuous layer might inhibit the reduction of the oxide which takes place in

the following step. It appears desirable, therefore, not to provide complete surface coverage by the strike.

Reduction.—The hydrogen reduction after the strike was eliminated from the process. This resulted in non-adherent electrodepositions. Also, a lowering of the firing temperature produced an increase in the porosity of the gold plate. This step is essential to the process.

Variations in the processing are possible. For example, molybdenum samples which had a large surface to volume ratio and which appeared to be without surface oxide on delivery were processed successfully without the use of the hydrogen firing prior to the gold strike.

Fig. 4. Chemical oxide, electron micrograph, replica. Magnification *ca.* 23,330X.

Fig. 5. Thermal oxide, electron micrograph replica. Magnification *ca.* 23,330X.

Fig. 6. Oxide formed with NH_4OH, electron micrograph. Magnification *ca.* 6700X.

Fig. 7. Oxide formed with H_2O_2, electron micrograph. Magnification *ca.* 6700X.

Fig. 8. Oxide formed with H_2O, electron micrograph. Magnification *ca.* 6700X.

This same type of sample was also successfully processed with the substitution of water for the ammoniacal peroxide solution in step three. However, this can only be done with samples which do not require the removal of surface layers for cleaning. Attempts to use only NH_4OH (28%) were successful, but attempts to use H_2O_2 (30%) only were not. Figures 6, 7, and 8 show electron micrographs of the oxide surfaces of samples processed in NH_4OH (28%), H_2O_2 (28%), and water. It can be seen that the cellular structures formed by water, ammonium hydroxide, and the ammoniacal peroxide solution are similar whereas the hydrogen peroxide solution appears to attack the surface more vigorously and produces an extremely rough oxide. This rough surface is apparently not satisfactory for further plating.

This process has also been used on molybdenum-manganese films deposited on ceramics. In this case, the time of the oxide formation step is critical since excessive removal of the thin metal film is undesirable.

Conclusion

The process described can be used to electrodeposit gold on molybdenum and molybdenum-manganese substrates without the use of preplates of other metals. Essential steps in the process are:

1. Formation of a porous molybdenum oxide.
2. Permeation of the oxide with gold, without forming a continuous gold layer over the oxide surface.
3. Reduction of the oxide, which traps the gold in the molybdenum lattice and forms a two-component layer on the surface.

The electrodeposited gold films produced by this process are adherent and protective, and have been plated to thicknesses of over one mil using both still and barrel plating.

Acknowledgments

The authors thank Mrs. A. M. Hunt who performed the electron micrography, and Mr. A. A. Tartaglia who performed the metallurgical sectioning.

Manuscript received Jan. 13, 1966; revised manuscript received March 9, 1966. This paper was presented at the San Francisco Meeting, May 9-13, 1966.

Any discussion of this paper will appear in a Discussion Section to be published in the December 1966 JOURNAL.

REFERENCES

1. Schaer and Beach, U. S. Pat. 2,886,499, May 12, 1959.
2. A. G. Russel, U. S. Pat. 2,816,066, Dec. 10, 1957.
3. M. Hansen, "Constitution of Binary Alloys," p. 217, McGraw-Hill Book Co., Inc., New York (1958).

Protection of Steel from Hydrogen Cracking by Thin Metallic Coatings

I. Matsushima and H. H. Uhlig

Corrosion Laboratory, Massachusetts Institute of Technology, Cambridge, Massachusetts

ABSTRACT

Cold rolled and stress relieved 0.5% carbon steel specimens electroplated with Ni, 0.50-2.5μ thick and bent to the test span after plating are especially resistant to hydrogen cracking when polarized cathodically in dilute sulfuric acid saturated with As_2O_3. Arsenic or an As compound deposits cathodically on the Ni coating which supplements protection by Ni alone. The dual coating is also effective in the presence of additives to H_2SO_4, such as thiourea, which normally accelerate occlusion of hydrogen by steel. The critical hardness value of steel below which some degree of protection is achieved by Ni + As coatings is about Rockwell C 35. Ni coatings alone are protective against sulfide cracking when cathodically protected in 6% NaCl-0.5% acetic acid, saturated with H_2S. The mechanism of protection is apparently one of altering the kinetics of H^+ discharge, resulting in less occlusion of hydrogen by steel. Accordingly, such coatings to be protective need not be continuous.

Limited data have been reported previously on the protective quality of metallic coatings on steel exposed to environments which generate hydrogen by a corrosion reaction, thereby leading to hydrogen cracking (1,2). Still less information is available on the relative effect of such coatings under conditions of continuous polarization which provides cathodic protection to the coating and avoids damage to it by corrosive attack. This situation deserves study both because it leads to a better understanding of the mechanism of protection by coatings and also because it suggests practical means of protecting susceptible steels against damage. This is the subject of the present paper. The problem has become much more important in recent times be-

cause of increased use of high-strength steels which are exposed to many different environments, some of which induce hydrogen cracking.

Probably the most significant data bearing on this problem were presented by Freiman and Titov (3). They measured diffusion rates of hydrogen through Armco iron sheets 0.17 mm thick, cathodically polarized in H_2SO_4 to which $NaAsO_2$ was added. A thin coating of Cu, Sn, Pb, or Ni applied to one side of the sheet effectively slowed down entrance of hydrogen into the iron when H^+ discharged on the coating. Nickel coatings only 0.1-2.5μ (0.004-0.1 mil) thick were especially effective whereas Pb coatings to be similarly effective had to be 10μ (0.4 mil) thick. There was little or no difference in diffusion rates for any of the coatings when H^+ discharged on the iron surface and occluded hydrogen diffused subsequently through the metallic coating.

Tardif and Marquis (4) cathodically charged 0.06% C steel sheet 0.38 mm thick in 2% NaOH at 40°C. They measured diffusion rates of hydrogen through the coated steel and also measured the fracture tendency of the steel after it had been polarized, employing a special deformation test. All coatings, *e.g.*, Cr, Au, Au-Ni, Ni, Cu, Pb, Cd, and Al, except for Zn and Mg, were beneficial to some extent in retarding entry of hydrogen into the steel.

Experimental

The base steel on which coatings were applied was a commercial 1055 steel (0.52% C, 0.81% Mn, 0.01% P, 0.01% S) cold reduced 50% and stress relieved in a salt bath at 400°C for 3 hr. The rolling direction was parallel to the longest dimension. Stress relief heat-treatment was chosen to prolong normal cracking time and thereby improve reproducibility of the present tests from an average of 6 min for the cold-rolled steel to 42 min for the stress-relieved steel. For some experiments, the steel specimens were quenched from 925°C and tempered at various temperatures up to 500°C in a salt bath for 1 hr. Above 500°C specimens were sealed in evacuated Vycor capsules and heated in a furnace for 1 hr. Specimens, as sheared to size, measured 1¾ x 3/16 x 0.041 in. (4.5 x 0.48 x 0.10 cm). After shearing they were abraded to a final No. 0 emery paper which removed approximately 1 mil of all 6 surfaces. They were then degreased in boiling benzene, pickled in 5 v/o HNO_3, 95°C for 1 min, washed, immersed in acetone, and dried in a warm air blast. Specimens were subsequently plated and then bent to the proper span for testing.

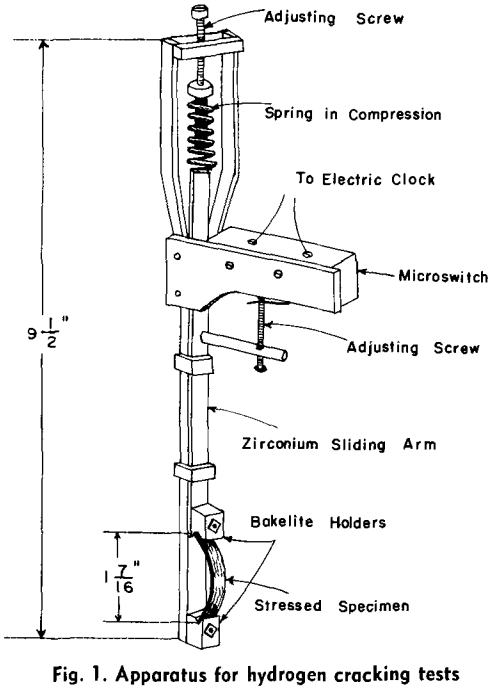

Fig. 1. Apparatus for hydrogen cracking tests

The test apparatus depicted in Fig. 1 was arranged so that specimens under constant spring load were polarized cathodically at 24 ma/cm^2 in 5% H_2SO_4 saturated in most cases with As_2O_3 at room temperature. Failure by cracking tripped a switch connected to an electric clock. That portion of the test apparatus in contact with the electrolyte was constructed of commercial Zr[1] to avoid corrosion. The insulated specimen itself was cathodically protected by the prevailing cathodic current. Specimens were bent beyond the elastic limit to an initial span of 1⅝ in. (4.1 cm), then transferred by means of a metal holder to the notched Bakelite insulators of the test apparatus. A compression spring was adjusted until the final span of the specimen was 1-7/16 in. (3.65 cm), carefully avoiding springback. A nickel wire, previously spot welded to one end of the test specimen, was attached to the negative terminal of a rectifier; the positive terminal was connected to an auxiliary Pt electrode immersed in the electrolyte contained in a 250-ml beaker. Tests were carried out a maximum of 200 hr, lack of failure within this time representing appreciable resistance to hydrogen cracking. Susceptible specimens commonly cracked within a fraction of an hour. For long runs, distilled water and As_2O_3 were added to the electrolyte every 24 hr.

Some tests were carried out in 6% NaCl-0.5% acetic acid saturated with H_2S at room temperature. For those tests, specimens were bent to the usual span and mounted in simple holders of Bakelite. They were placed in a 5-liter glass desiccator vessel and totally immersed in the test solution. Specimens were examined visually for cracks without removing them from the container.

Coatings, when applied, were electrodeposited to a thickness of 0.01-0.5 mil (0.25-12.7μ) as determined by weight gain. Nickel electrodeposits employed a $NiSO_4$-NH_4Cl-boric acid bath, lead coatings a fluoride-boric acid bath, copper coatings a cyanide bath, iron coatings a ferrous sulfate bath, cobalt coatings a cobalt sulfate-boric acid bath, and arsenic coatings a sodium cyanide-As_2O_3 bath. A few specimens were coated with electroless Ni (5).

Results

Cracking times of coated steel specimens are summarized in Table I. Lead coatings were relatively effective if the thickness was at least 0.1 mil, and copper coatings were similarly effective at 0.5 mil. Nickel coatings of 0.5 mil thickness, on the other hand, cracked when the specimen was bent preparatory to testing; such specimens subsequently failed in the H_2-cracking tests. Surprisingly, however, thinner Ni coatings which did not visibly crack afforded protection for a thickness of only 0.02 mil. This thickness seems also to coincide with marked reduction in porosity of the coating as shown by data of Fig. 2. A measure of

[1] Supplied by courtesy of Carborundum Metals Climax, Inc.

Table I. Effect of electrodeposited coatings on H_2 cracking of 1055 steel, cold rolled 50%, annealed 400°C, 3 hr, cathodically polarized in 5% H_2SO_4 + As_2O_3, 24 ma/cm^2 (minimum of 2 specimens for each run)

Coating	Thickness of coating, mils					
	0.00	0.01	0.02	0.05	0.1	0.5
	Avg cracking time, hr					
None	0.7					
Ni		2.4	NC	NC	NC	1.0
Pb		3.3	—	23	NC	NC
Cu		2.5	—	—	1.7	NC
Co		—	—	51	72	10
Fe		—	—	2.3	0.6	—

NC = no cracking in >200 hr.

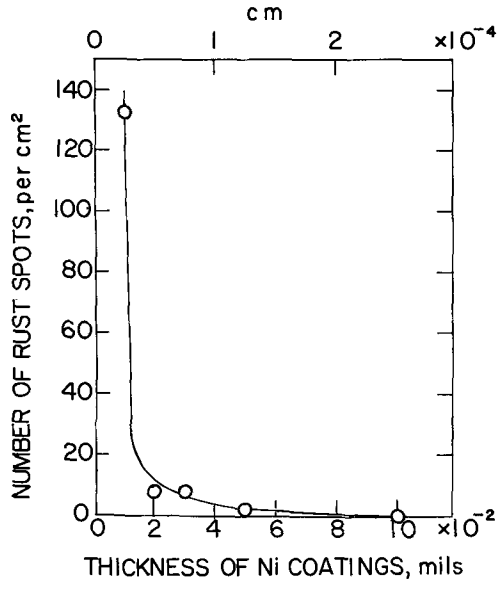

Fig. 2. Porosity of nickel coatings as a function of thickness

porosity was obtained by counting under the microscope the number of rust spots per unit area after immersing specimens horizontally for 10 min in 3% NaCl + 1.5% by volume of 30% H_2O_2. It is unlikely that any of the Ni coatings were truly pore free, so that the protective mechanism of thin Ni coatings probably depends on a critical area ratio of Ni to exposed Fe at pores. This unusual protective quality of Ni coatings prompted a more detailed study of their properties.

The next attempt was to protect a quenched martensitic 1055 steel (Rockwell hardness = C 64), which, compared to the stress relieved cold-rolled material (C 31), is much more sensitive to hydrogen cracking. Uncoated quenched specimens cracked prematurely on bending; tempered at 300°C for 1 hr (C 51) they could be bent but, subsequent to bending, they suffered H_2 cracking within 1/3 min. Data for various tempering temperatures are summarized in Fig. 3. Here it is noted that the quenched steel, tempered subsequently at 300° or 400°C, cracked in very short time whether or not a thin coating of nickel covered the surface. However, at higher tempering temperatures, beginning at 450°C (Rockwell hardness = C 35), the nickel-coated specimens were appreciably more resistant than the uncoated specimens. Since hardness of the steel decreases with increasing tempering temperatures accompanied by decrease in susceptibility to hydrogen

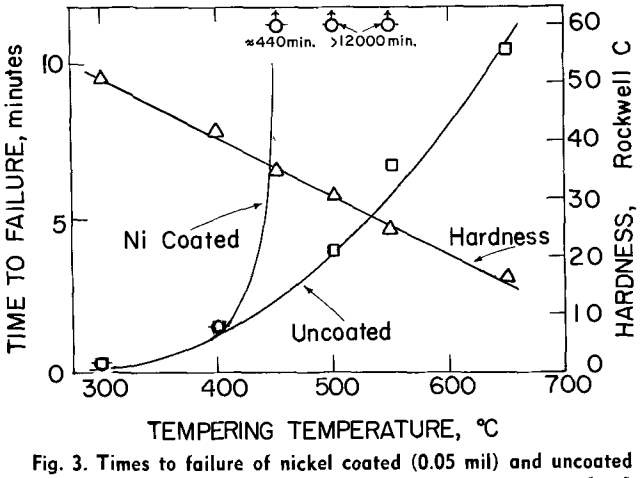

Fig. 3. Times to failure of nickel coated (0.05 mil) and uncoated quenched AISI 1055 steel tempered at various temperatures for 1 hr, 5% H_2SO_4 + As_2O_3 (saturated), 24 ma/cm², room temperature.

Table II. Effect of various catalyst poisons in 5% H_2SO_4 on H_2 cracking of 1055 steel, cold rolled 50%, annealed 400°C, 3 hr, coated with Ni, cathodically polarized 24 ma/cm²

Poison	Avg cracking time
0.05 mil Electrodeposited Ni	
As_2O_3 (sat'd)	>200 hr (3 spec.)
Sb_2O_3 (1.6 g/l)	163 hr (3 spec.)
Thiourea (0.2 g/l)	26 hr (7 spec.)
H_2SeO_3 (0.3 g/l)	14 hr (4 spec.)
0.1 mil Electroless Ni	
As_2O_3 (sat'd)	>200 hr (2 spec.)
Thiourea (0.2 g/l)	2 hr, 169 hr

cracking, it is presumably only below a critical susceptibility (Rockwell hardness <C 35) that the thin Ni coating provides an advantage. It is possible, of course, that Ni coatings would extend their range of effectiveness for more susceptible specimens under less severe conditions of H_2 charging.

Of interest to the mechanism were experiments carried out on Ni-coated specimens using catalyst poisons in H_2SO_4 solution other than As_2O_3. Data are summarized in Table II. Results are also included for 2.5μ (0.1 mil) electroless Ni coatings which were found to behave in much the same manner as electrodeposited coatings. Electroless Ni coatings 3.8μ (0.15 mil) thick were similar in behavior to the thinner coatings. It is obvious that thin Ni coatings are effective in presence of As_2O_3, but less so in presence of other poisons.

Experiments were next carried out to determine whether Ni-coated specimens prepolarized in 5% H_2SO_4 + As_2O_3 afford subsequent protection when cathodically polarized in 5% H_2SO_4 containing other type poisons, *e.g.*, thiourea. The thought behind this experiment was to learn whether protection was supplemented by arsenic deposited on a Ni surface. Also, if arsenic is effective, would it be similarly effective if predeposited from a cyanide bath, or if codeposited along with nickel by adding As_2O_3 to a nickel plating bath. Results are summarized in Table III. Prepolarization in H_2SO_4 + As_2O_3 for 15 hr is effective, the time for which can be shortened by prepolarizing at the boiling temperature of the H_2SO_4 electrolyte. None of the other pretreatments comparatively was as effective. This is a preliminary conclusion which should be substantiated by further tests accompanied by analyses of the electrodeposits. Probably the main reason for lack of protection is that specimens were bent for testing after deposition of As or As + Ni coatings, thereby producing cracks in the coating which allowed hydrogen penetration to the base steel. Ni-plated specimens

Table III. Effect of arsenic plus Ni coatings on H_2 cracking of 1055 steel, cold rolled 50%, annealed 400°C, 3 hr, cathodically polarized in 5% H_2SO_4 + 0.2 g/l thiourea, 24 ma/cm², room temperature

Treatment	Avg cracking time
1. Deposition of As on 0.05 mil Ni from cyanide bath, 5 ma/cm², 0.5 hr.	
Room temperature	55 hr (2 spec.)
Arsenic-coated specimen heated in H_2O, 100°C ½ hr	53 hr (2 spec.)
2. Codeposition of Ni and As, 10 ma/cm², 4 min	
Room temperature	34 hr (6 spec.)
Coated spec. heated 400°C, 3 hr	9 hr (3 spec.)
3. Prepolarization of 0.05 mil Ni in 5% H_2SO_4 + As_2O_3, 24 ma/cm²	
Room temp, 2.5 hr	2.7 hr (2 spec.)
5.0 hr	56 hr (2 spec.)
15.0 hr	NC (2 spec.)
Boiling point, 2.5 hr	77 hr (2 spec.)
5.0 hr	NC (2 spec.)*

NC = no cracking in >200 hr.
* A third spec. failed in 112 hr.

Table IV. Hydrogen cracking of stressed cold rolled 1055 steel, previously cold rolled 50%, annealed 400°C, 3 hr, immersed in 6% NaCl, 0.5% acetic acid saturated with H_2S; with and without cathodic polarization, room temperature

Specimen	Cracking time, days		
Cath. current density →	0	0.05	0.5 ma/cm²
Uncoated	<2	<2	<2
Coated with 0.05 mil Ni	<2	<1	7, NC
The same prepolarized 15 hr in 5% H_2SO_4 + As_2O_3	<2	4-5	NC
Coated with 0.1 mil Ni	<2	<2	NC
The same prepolarized 15 hr in 5% H_2SO_4 + As_2O_3	<2	2-3	NC

NC = no cracking in >8 days.

of Table III prepolarized in H_2SO_4 + As_2O_3 were already stressed to the test span during pretreatment and were then transferred to the H_2SO_4 + thiourea electrolyte without changing the span.

The next series of experiments was conducted to determine to what extent Ni plus As coatings are effective in total immersion tests in 6% NaCl-0.5% acetic acid periodically saturated with H_2S. This test is commonly employed to determine susceptibility of stressed steels to hydrogen cracking or sensitivity to so-called sulfide cracking. The base steel was again 1055 steel, cold rolled and annealed at 400°C, with the thickness of nickel coating being either 0.05 or 0.1 mil. Data are summarized in Table IV. Since all specimens failed within 2 days whether coated with Ni or with Ni plus As, additional tests were carried out with continuous cathodic polarization of the specimens in the same test medium. At 0.05 ma/cm², failure times for some specimens coated with Ni + As were extended, but all specimens failed nevertheless. At a higher current density of 0.5 ma/cm², Ni-coated specimens, except one, survived the maximum test period of 8 days. Protection was obtained whether or not the specimens were prepolarized in the H_2SO_4-As_2O_3 electrolyte. In other words, thin Ni coatings are effective in diminishing H_2 cracking of steel for H_2S-type exposures, but only if the coated steel is cathodically protected. Unlike the polarization experiments in H_2SO_4 previously reported, presence of As on the nickel surface does not seem to be essential, although results at 0.05 ma/cm² suggest that some small advantage results.

Discussion

Although metal coatings conceivably protect against hydrogen penetration into steel by acting as a diffusion barrier, it is not likely that this particular mechanism operates for the thin films now under study. Instead, the coatings apparently act mainly to alter kinetics of hydrogen ion discharge, resulting in less occlusion of hydrogen by the metal electrode. The specific surface properties of the metal are more important, in other words, than its diffusivity for hydrogen. This was demonstrated by results of Freiman and Titov (3) who also proposed that the surface electrochemical factor in their experiments accounted largely for the protective effect of thin metal coatings on diffusion of hydrogen into steel.

The important effect of the electrode surface is also apparent from the large effect on cracking produced by small additions of catalyst poisons, *e.g.*, arsenic compounds, thiourea, sulfur ions, etc., to the electrolyte. In absence of $NaAsO_2$ in their sulfuric acid electrolyte, Freiman and Titov (3) found no hydrogen to diffuse through uncoated steel after cathodic polarization for 2 hr, whereas in the presence of $NaAsO_2$ hydrogen appeared after 1 or 1½ min. Schuetz and Robertson (6) found that CS_2 additions to H_2SO_4 electrolyte increased hydrogen absorption of a cathodically polarized 10% Ni-Fe alloy by a factor of 15. It is known, moreover, that often a highly stressed steel exposed to an acid environment will not hydrogen crack except in presence of compounds like H_2S or As_2O_3.

The present results are the more surprising in view of the beneficial effect of thin Ni coatings associated with As where the latter element instead of increasing hydrogen occlusion by the underlying steel, decreases it. The arsenic retains its beneficial influence even in presence of other poisons such as thiourea (Table III). One exception is in the acetic acid-H_2S test (Table IV) where Ni coatings alone are effective, and As is not required to supplement protection against failure. Addition of As_2O_3 to H_2SO_4 leads to visible cathodic deposition of elemental As or an As compound on the cathode surface, and, as Freiman and Titov (3) showed, if the film is not too thick, occlusion of hydrogen by uncoated steel is increased by its presence. Elemental As has a high value of hydrogen overvoltage apparently leading to increased thermodynamic activity of adsorbed atomic hydrogen on the steel surface and hence to a greater tendency for hydrogen to enter the metal lattice.

Accordingly, the beneficial effect of As associated with a Ni coating can be ascribed to the possibly low hydrogen overvoltage of a chemical compound formed between As and Ni. This hypothesis is supported by the reduced time necessary to achieve protection by the duplex coating when the electrolyte is heated during As deposition which probably favors compound formation (Table III). Raub *et al.* (7) found that when As is codeposited with Ni on an electrode at which H^+ discharges simultaneously, the potential becomes more noble, corresponding to a decrease in hydrogen overvoltage. This shift of potential is in the right direction to explain the effect of the present Ni-As coatings. The Ni coatings containing As by codeposition, on the other hand, were not found to be especially effective, but, as described earlier, this is probably because of the brittle nature of coatings containing arsenic, allowing formation of cracks during bending through which hydrogen can enter the steel. Preliminary potential measurements on the present protective Ni-As coatings confirmed that a lower hydrogen overvoltage results when As is deposited on Ni. The observed difference of 40 mv at 24 ma/cm² (changing with time), was not large, however; hence there is the possibility that factors enter in addition to overvoltage effects. Even for metals like Pb with high H_2 overvoltage, there is apparently little tendency for cathodic hydrogen either to enter the Pb lattice or to transfer occluded H to the underlying steel.

Assuming that a compound is formed between Ni and As, the next step was to identify it by x-ray. The thin black surface layers of several Ni-As coated electrodes were carefully removed and examined in a Debye-Scherrer camera, but only lines of Ni appeared. Patterns were repeated several times with the same results. A black residue which collected on the bottom of the H_2SO_4-As_2O_3 electrolyte after a long period of electrolysis, and which is presumably elemental arsenic, gave an amorphous pattern. Hence it is concluded that if a surface compound of Ni and As forms, it is either amorphous or the layer is too thin for x-ray diffraction. The inability of the Ni-As coatings to protect quenched 1055 steel suggests that the amount of hydrogen necessary to cause failure of the martensitic steel is so small that the present thicknesses of coatings are not sufficiently protective. For tempered martensite, or for cold rolled steel, on the other hand, the apparent required amount of hydrogen is greater, and for this situation the coatings adequately reduce occlusion of hydrogen by steel to a value below that required for failure. The present investigation demonstrates that metal coatings need not be continuous in order to protect steel against hydrogen cracking and that their porosity need only fall below a critical value.

Acknowledgment

This research was supported by the U.S. Army Research Office-Durham, on Contract DA-31-124-

ARO(D)-47 to whom the authors express their appreciation.

Manuscript received Dec. 13, 1965; revised manuscript received March 7, 1966.

Any discussion of this paper will appear in a Discussion Section to be published in the December 1966 JOURNAL.

REFERENCES

1. M. Bartz and C. Rawlins, *Corrosion*, **4**, 205 (1948).
2. D. Warren and G. Beckman, *ibid.*, **13**, 631t (1957).
3. L. Freiman and V. Titov, *Zhur. Fiz. Khim.*, **30**, 882 (1956).
4. H. Tardif and H. Marquis, *Can. Met. Quart.*, **1**, 153 (1962).
5. In accord with No. 1 bath, "Modern Electroplating," Fred Lowenheim, Editor, 2nd ed., p. 700, John Wiley & Sons, Inc., New York (1963).
6. A. Schuetz and W. Robertson, *Corrosion*, **13**, 437t (1957).
7. E. Raub, M. Wittum and S. Gmünd, *Korros. u. Metallschutz*, **15**, 127 (1939).

Impurity Segregation in Binary Compounds

M. R. Lorenz and S. E. Blum

Watson Research Center, International Business Machines Corporation, Yorktown Heights, New York

ABSTRACT

The effect of the pressure of the constituents of a binary compound on the segregation coefficient (k_o) of a substitutional impurity is considered. The theory concerning the incorporation of an impurity is briefly reviewed, and the dependence of k_o on P_M is given for various combinations of electrical character of an impurity and the site the impurity occupies. The impurities In and Sb were studied in CdTe. k_o(In) is inversely proportional to P_{Cd} and k_o(Sb) directly proportional to P_{Cd}. The results are in quantitative agreement with the theoretical prediction if it is assumed that native defects play a negligible role as a source of free carriers or charge compensation. The donor Te, the acceptor Zn, and the amphoteric impurity Sn were studied in InAs by pulling crystals by the Czochralski method at various arsenic pressures. The k_o's follow the predicted behavior. The practical significance of the dependence of k_o on the pressure of compound constituents in relation to materials preparation is discussed briefly.

Research on semiconductor systems has brought about a good understanding of segregation processes and of the factors governing distribution coefficients in binary systems (1). The knowledge acquired in such two-component systems has also been applied to the more complex ternary systems. There have been a number of investigations concerned with various aspects of the segregation of an impurity in a binary compound. Most of this work was done on III-V compounds and much of it has been recently reviewed (2). In many of these studies the segregation coefficients were determined by assuming a pseudobinary system, *i.e.*, an impurity (one component) and a binary compound (the second component). In general the investigations were concerned with segregation in liquid-solid phase equilibria. More recently Chang and Pearson (3) studied solubilities and distribution coefficients of Zn in GaAs and GaP from vapor-solid equilibria while McCaldin (4) studied the Zn-GaAs system as a true three-component system. The behavior of Ge in GaAs was investigated in liquid-solid phase equilibria (5). Segregation of Zn between solid InSb and In-Sb melts of various compositions has also been investigated (6). The solubility of group II, IV, and VI elements in GaP was studied by Trumbore *et al.* (7, 8).

The major aim of this study was to examine the dependence of the distribution coefficient on the site the impurity occupies, the effects of the electrical characteristics of the impurity, and the role of the chemical potential of the component that normally occupies the site. For our experimental investigation we chose the In-As system as a representative of the III-V compounds and the Cd-Te system as a representative of the II-VI compound family. Both compounds are low melting and therefore presented the least difficulty experimentally. Three impurities were studied in InAs, and two impurities were investigated in CdTe.

Theory

We wish to review briefly the theory concerning the incorporation of an impurity atom X in the compound MN. We will use the mass action approach of Kroeger and Vink (9) and follow approaches similar to those used by Thomas (10), McCaldin (4), and Kroeger (11). We confine our attention to impurities which sit on normally occupied lattice sites. Let us assume first that X is a donor which resides on an M site (X_M^D). The equilibrium of X in the solid MN and some external phase (X_l) can be illustrated by the reaction.

$$V_M + X_l = X_{MD}^+ + e^- \qquad (I)$$

where V_M is a neutral M vacancy, X_{MD}^+ is the ionized donor, and e^- is a free electron. Making the usual assumption of ideal solution behavior, we write the equation which governs reaction (I) as follows

$$\frac{[X_{MD}^+]\, n}{[V_M][X_l]} = K_1(T) \qquad [1]$$

where $K_1(T)$ is the temperature dependent equilibrium constant. Since all K's are temperature dependent, the bracketed T will hereafter be dropped for simplicity. In general, we are concerned with impurity states which lie close to their respective bands. For such states we can assume that at or near the melting temperature of the compound they are sufficiently ionized that the concentration of the ionized impurity is equal to the total concentration of that impurity, *i.e.*, $[X_M^D] = [X_{MD}^+] + [X_{MD}^0] \cong [X_{MD}^+]$. With this assumption we may write the equilibrium segregation coefficient for a donor impurity substituted on an M site, $k_o(X_M^D)$

$$k_o(X_M^D) \simeq k_o(X_{MD}^+) = \frac{[X_{MD}^+]}{[X_l]} = \frac{V_M K_1}{n} \qquad [2]$$

where k_o describes the solid-liquid equilibrium. Since $[V_M]$ is inversely proportional to the pressure of M. as $P_{M_y}^{1/y}$ where y is the number of atoms in the given vapor specie, we can write Eq. [2] as

$$k_o(X_M^D) = \frac{K_3}{n\, P_{M_y}^{1/y}} \qquad [3]$$

Table I. Dependence of the impurity segregation coefficient, k_o, on lattice sites, P_M, and carrier type and concentration
The K's are temperature dependent constants with subscripts omitted for simplicity. For the definition of k_o see Eq. [2]

Impurity character site	X_M^D	X_N^D	X_M^A	X_N^A	$X_{M,N}^{A,D}$
Segregation coefficient	$\frac{K}{n P_{M_y}^{1/y}}$	$\frac{K P_{M_y}^{1/y}}{n}$	$\frac{K}{p P_{M_y}^{1/y}}$	$\frac{K P_{M_y}^{1/y}}{p}$	$\frac{K}{n P_{M_y}^{1/y}} + \frac{K' P_{M_y}^{1/y}}{p}$

Inherent in the above and subsequent treatment are the assumptions that solid MN has a narrow homogeneity range, the impurity concentration is small, the system is nondegenerate, and that Schottky disorder prevails.

If we now consider the same case but let X occupy N sites, we find that

$$k_o(X_N^D) = \frac{K_4}{n P_{N_y}^{1/y}} = \frac{P_{M_y}^{1/y} K_5}{n} \quad [4]$$

From Eq. [3] and [4] we note that the segregation coefficient for an impurity is either directly or inversely proportional to the pressure of M in the system. Similar equations govern the segregation coefficients of acceptors at substitutional sites. There are also a limited number of impurities which can occupy either site readily. If a mass action law is valid for the impurity on each type of site, then

$$k_o(X_{M,N}^{A,D}) = \frac{[X_M^A] + [X_N^D]}{[X_i]} = \frac{K_6}{p P_{M_y}^{1/y}} + \frac{P_{M_y}^{1/y} K_5}{n} \quad [5]$$

where p is the hole concentration. A summary of the dependencies of segregation coefficients on the site the impurities occupy and on the electrical characteristics they have is given in Table I.

Experimental

Cadmium telluride.—The CdTe ingots used in these studies were prepared from high-purity, 6-9's, elements in vacuum-sealed quartz tubes by the Bridgman Drop procedure. Ingots weighed typically about 80g and occupied about 60% of the tube volume. The dopant, In or Sb, was added directly to the Bridgman tube. The cadmium pressure in the system was initially controlled by the excess Cd used. However, it is apparent that the P_{Cd} in the system is changing throughout the freezing period because the composition of the melt is changing. We analyzed only the first 15% of the ingot to freeze and assumed a P_{Cd} corresponding to the initial condition (12-14). This leads to an uncertainty of about 10% in P_{Cd}. The distribution coefficients of indium and antimony were determined at cadmium pressures of 5.3 and 0.08 atm.

Indium arsenide.—The indium arsenide crystals used in these studies were prepared from high purity, 6-9's, elements. The sealed magnetic Czochralski crystal puller used was previously described (15). InAs was synthesized *in situ* and grown in the <111> direction. The solid-liquid interface was always flat and perpendicular to the pull direction. The rotation rate was in all cases 8 rpm. Hall measurements taken on wafers cut perpendicular to the growth axis showed no appreciable variation in carrier concentration within a wafer. Therefore inhomogeneous segregation of the impurities due to faceting effects (26, 27) was assumed to be negligible. The dopants were added directly to the indium charge. The arsenic pressure in the system was maintained at the desired value by the temperature control of condensed arsenic at the coldest portion of the puller tube. Crystal growth was obtained in the usual way. To study the influence of arsenic pressure, the pulling was interrupted and the arsenic reservoir temperature was increased. After arsenic pressure equilibrium was established, the pull was resumed.

Tellurium and tin in InAs were treated as nonvolatile dopants. The initial dopant composition of the melt was therefore known. The dopant concentration in the melt after the pressure change was calculated from the InAs phase diagram (16). The quantity of Te already incorporated in the pulled crystal was taken into account. Our justification for treating Te as a nonvolatile dopant is based on the fact that for our experimental temperature conditions Te is a noncondensable impurity and the gas volume is sufficiently small to make the quantity of Te in the gas phase negligible compared to the total Te in the system.

As in the above case, the dopant zinc was added directly to the melt. However, the zinc concentration in the melt must be calculated differently from the Te or Sn case. When the InAs-zinc melt is in equilibrium with arsenic at a vapor pressure of 0.17 atm, the zinc concentration in the melt is dependent on the vapor pressure of condensed Zn_3As_2 at the arsenic reservoir temperature where solid Zn_3As_2 coexists with solid As. Using Silvestri's data (17), the zinc pressure in the system was calculated. The corresponding concentration of Zn in the melt was calculated from Raoult's law and the vapor pressure of pure Zn at the melt temperature (18). When the minimum temperature in the system was increased to 623°C (P_{As_4}= 1.45 atm), condensed Zn_3As_2 still controlled the Zn vapor pressure and condensed arsenic controlled the arsenic pressure. The Zn concentration in the melt was recalculated as above.

Measurements.—The cadmium telluride crystals were analyzed for the dopants by emission spectrochemical analysis. The indium arsenide crystals used were similarly analyzed for the dopants Te and Sn. In addition, the InAs crystals were investigated by measurements of their Hall coefficients. When possible we used Hall bridges; otherwise Van der Pauw samples had to suffice.

Results and Analysis

CdTe.—The results of segregation of In and Sb in CdTe under high and low P_{Cd} are shown in Table II. The first column gives the initial composition and the second column the cadmium pressure associated with the initial composition (12-14). The third column gives the corresponding liquidus temperatures (T_l) (12, 14). C_l is the initial solute concentration in the liquid and C_s is the measured impurity concentration in the solid. The segregation coefficients are shown in the last column. We note that the k_o's for In differ for the two P_{Cd}'s by about a factor of 6. Similarly for Sb the k_o's show a variation by a factor of about 17. The dependence of k_o on P_{Cd} is significant.

Because the k_o's above were not determined at the same temperature, we must rule out the possibility that the variation in k_o is due to the temperature difference. It has been shown empirically for a number of impurities in Si and Ge with k_o's much less than unity that the temperature dependence of the distribution coefficient can be approximated by the expression (19)

$$k = (k_m)^{T_m/T} \quad [6]$$

Here k_m is the segregation coefficient of the solute at infinite dilution; this occurs at the maximum melting point (T_m) of the solvent; k is the segregation coefficient at any temperature, T. Trumbore *et al.* (20)

Table II. Segregation coefficient of In and Sb in CdTe
The k_o for each impurity is given for each of two initial melt compositions. The calculated P_{Cd}, melting point, impurity concentration in the melt C_l, and in the solid C_s are listed.

Atom fraction Cd	Cd pressure atm	T, °K	Solute	C_l *	C_s * ‡	C_s** at./cm³	$k_o = \frac{C_s}{C_l}$
0.555	5.3	1308	In	4.45×10^{-4}	3.8×10^{-5}	1.18×10^{18}	8.5×10^{-2}
0.445	0.081	1328	In	4.45×10^{-4}	2.2×10^{-4}	6.84×10^{18}	49×10^{-2}
0.555	5.3	1308	Sb	4.45×10^{-4}	87×10^{-6}	2.7×10^{18}	20×10^{-3}
0.445	0.081	1328	Sb	4.45×10^{-4}	5.2×10^{-6}	1.62×10^{17}	1.2×10^{-2}

* In units of gram atoms solute per gram atoms of solvent (Cd plus Te).
‡ Three separate determinations were made in the first 15% of the solid that froze. The average is shown.
** The intrinsic electron concentration at the above temperatures are, respectively, $n_i(1308°K) = 3.9 \times 10^{17}/cm^3$; $n_i(1328°K) = 4.3 \times 10^{17}/cm^3$.

have shown that Eq. [6] is not applicable over large temperature ranges. For the relatively small temperature differences near the maximum melting point in question here Eq. [6] may serve as a useful estimate. Applying this equation to CdTe (treating the system as a pseudobinary for determining the "pure" temperature dependence), we calculate a change in k_o of about 5% for the 20°K difference shown in Table II. This is a negligible change compared to the experimental observation.

Let us now consider the influence of P_{Cd} and n on the segregation coefficient for the shallow donor In in CdTe (14, 21). We assume substitutional occupation of Cd sites. According to Eq. [3]

$$k_o(In_{Cd}) = \frac{K}{n P_{Cd}}$$

We need to determine the carrier concentration n at the high temperature equilibrium condition. If we assume that the deviation from stoichiometry contributes a negligible number of carriers and that self compensation itself is negligible, then the charge neutrality equation becomes $n - p = [In_{Cd}{}^{D+}]$. Furthermore, the carrier concentration due to the intrinsic process is governed by the relation

$$np = K_i = N_c N_v \exp(E_v - E_c)/kT \qquad [7]$$

where N_c and N_v are the density of states in the conduction and valence band, respectively, E_v and E_c the relative energies of the valence and conduction band edges, k is the Boltzman constant, and T the absolute temperature. Combining Eq. [7] with the charge neutrality equation leads to

$$n^2 - n[In_{Cd}{}^{D+}] = K_i \qquad [8]$$

We evaluate K_i as follows. For the density of states, we have used an effective electron mass (21) of 0.1 m_o and a hole mass of 0.6 m_o (22, 23). The term $E_v - E_c$ is equal to the negative of the band gap energy E_g, which has also been reported as a function of temperature (14). The calculated K_i for 1308°K is 1.52×10^{35} ($E_g = 0.96$ ev) and 1.85×10^{35} ($E_g = 0.95$ ev) at 1328°K. The intrinsic carrier concentrations corresponding to these values are shown at the bottom of Table II. The value of n at 1328°K deduced from Eq. [8] is equal to $[In_{Cd}{}^{D+}] = C_s$. The same holds for n at 1308°K. Therefore

$$k_o(In_{Cd}{}^{D}) = \frac{K}{C_s P_{Cd}}$$

Using the experimental results for $P_{Cd} = 0.081$ atm, we find the temperature dependent constant K_{In} (1328°K) $= 2.7 \times 10^{17}$ atoms atm cm^{-3}. We can now compute the segregation coefficient for $P_{Cd} = 5.3$ atm utilizing the experimentally determined $C_s = 1.2 \times 10^{18}$. The calculated value for k_o is 4.3×10^{-2} which is to be compared with the experimental value of 8.5×10^{-2}. The agreement is good for measurements and analyses of this type. This also gives some justification for our assumption of negligible self-compensation. If appreciable self-compensation occurred, then our results would be in variance with the predicted behavior.

A similar analysis can be made for the impurity Sb which acts as an acceptor and is assumed to be a substitutional impurity residing on the Te site. Again we compute the temperature dependent constant using the data, $P_{Cd} = 5.3$ atm, $p = C_s = 2.7 \times 10^{18}$ and $k_o(Sb_{Te}{}^{A}) = 20 \times 10^{-2}$, and obtain for $K_{Sb}(1308°K)$ a value of 1.02×10^{17}. In calculating the segregation coefficient for $P_{Cd} = 0.081$ atm, we determine p from the neutrality condition and note that $p = 5.2 \times 10^{17} \neq C_s$. The calculated value for $k_o(Sb_{Te}{}^{A}) = 1.6 \times 10^{-2}$ which compares very well with the experimental value of 1.2×10^{-2}. We note that segregation coefficients can change significantly with a change of component pressure. Moreover the analysis shows that there is a near quantitative agreement between experiment and theoretical prediction.

InAs-Te.—The impurity segregation in the InAs system was investigated at constant chemical potentials of the constituents, *i.e.*, crystals of InAs were pulled from the melt at constant As pressure. The ingot was characterized along the growth axis by measuring the carrier concentration (Hall measurements) and by spectrochemical analysis. For Hall measurements, the constant r in the relation $n = r(R_H ec)^{-1}$ was taken as unity. We found that n from electrical measurements was consistently higher than the corresponding [Te] deduced from chemical analysis. This was observed only for Te. We have arbitrarily made the two sets of data coincident by applying a constant multiplying factor of 1.45 to the chemical data (the accuracy of the chemical analysis for Te was ±20% and therefore does not explain the observed difference). The results are shown in Fig. 1.

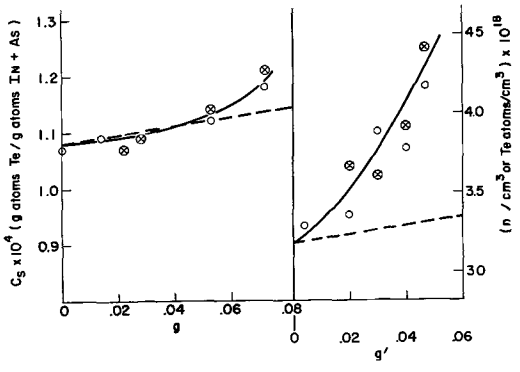

Fig. 1. Tellurium concentration in InAs as a function of the fraction of the melt grown. The data for $P_{As4} = 0.53$ atm and for 1.1 atm are shown. The dotted lines represent the theoretical curves for normal freeze of the off-stoichiometric melts for $k_o = 0.311$ and $C_o = 3.48 \times 10^{-4}$ for the g curve ($T_M = 942°C$) and for $k_o = 0.290$ and $C_o = 3.11 \times 10^{-4}$ for the g' curve ($T_M = 931°C$). ○ represents electrical data and circle with x chemical data. The chemical data was multiplied by a constant factor of 1.45 to bring it into coincidence with the electrical data.

The concentration profile of Te in the solid phase is given by the solid lines. The curve is extrapolated to obtain C_s at $g = 0$ where g is the fraction of melt solidified. Since the initial Te concentration (C_o) in the liquid is known, we can compute the segregation coefficient for the initial P_{As}. After the As pressure change, C_o' was recalculated as described previously, C_s' at $g' = 0$ is obtained as before and k_o' is calculated. All the pertinent data are given in Fig. 1. It is to be noted that the dotted lines correspond to the theoretically predicted modified normal freeze curves which take into account the off-stoichiometry in the liquid phase (24). A strong positive deviation of the experimental data at the higher P_{As} is noted. This is believed to be caused by a too rapid rate of growth. We used the same pulling speed of 12 mm/hr for both arsenic pressures. Although the rate was sufficiently slow for the lower P_{As} which corresponded to a near stoichiometric melt, it was too rapid for the higher P_{As}. For the latter case slower rates are necessary to allow for the diffusion of the excess component As away from the growing interface. It is also suspected that the extrapolation of C_s' to $g' = 0$ leads to a value which is higher than the equilibrium value.

The effect of changing the As pressure during crystal growth is well demonstrated in Fig. 1. The discontinuity at the point of ΔP_{As} is clear. The change in the amount of Te incorporated in the solid is due to two effects. First there is a dilution effect which occurs when additional As is transferred from the reservoir to the melt as a result of increasing P_{As} (24). The second effect, of course, is the one we are mainly concerned with in this investigation. We have sufficient knowledge of the InAs phase equilibria (16) to take into account the dilution effect. Therefore, using $k_o = 0.311$ for $P_{As4} = 0.53$ atm as a standard we can calculate k_o' for $P_{As4}' = 1.1$ atm from the relation

$$k_o' = k_o \frac{n}{n'} \left[\frac{P_{As4}}{P_{As4}'} \right]^{1/4}$$

We assume that the temperature dependence of k is negligible for the small difference in liquidus temperatures, *i.e.*, 942°C *vs.* 931°C. Again, as in the case of CdTe, we assume the simple charge neutrality condition: $n - p = Te_{As}^{D+}$. We have calculated K_i for InAs at 930°C using the following data: $E_G = 0.415$ ev at 2°K (25), $dE_G/dT \simeq 3 \times 10^{-4}$ ev/deg., $m_h = 0.3\ m_o$ (25), and $m_e = 0.03\ m_o$ (25). The assumptions include a constant temperature dependence of E_G and that only the conduction and valence band near $k = 0$ are involved in the intrinsic ionization process. The intrinsic electron concentration was found to be 4.5×10^{18} cm^{-3} which makes $K_i = 2.0 \times 10^{37}$. We calculate the appropriate n's from an equation similar to Eq. [8] and determine $k_o' = 0.28$. This compares favorably with the observed value of 0.29.

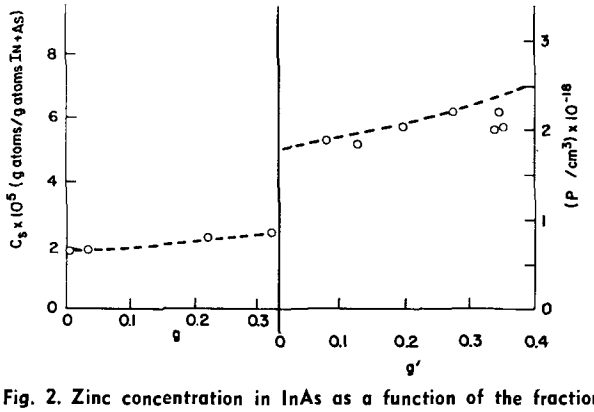

Fig. 2. Zinc concentration in InAs as a function of the fraction of the melt grown. The data are for $P_{As4} = 0.165$ atm and 1.45 atm. The data were obtained from electrical measurements. The dotted lines represent theoretical curves for normal freeze of the off-stoichiometric melts for $k_o = 0.324$ and $C_o = 5.65 \times 10^{-5}$ and for $k_o = 0.421$ and $C_o = 1.2 \times 10^{-4}$ for g ($T_M = 937°$) and g' ($T_M = 920$°C), respectively.

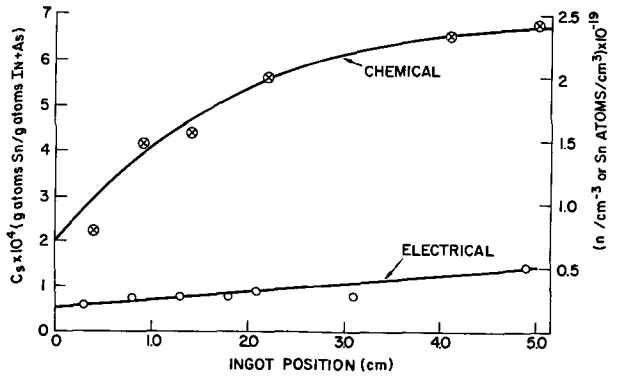

Fig. 3. Concentration of tin and free charge carriers in InAs as a function of length and ingot grown for $P_{As4} = 0.17$ atm; $C_o = 1.226 \times 10^{-3}$; $T_M = 937$°C; $k_o = 1.63 \times 10^{-1}$.

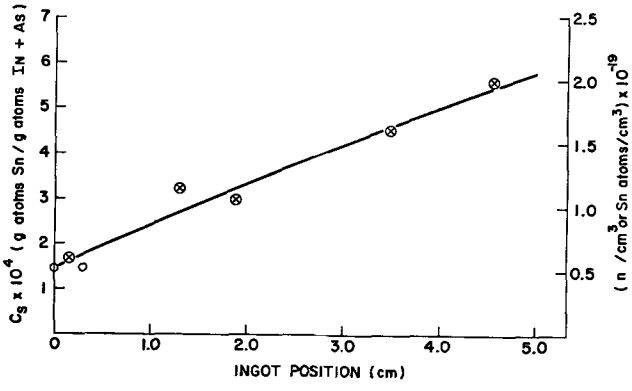

Fig. 4. Concentration of tin and free charge carriers in InAs as a function of length of ingot grown for $C_o = 2.75 \times 10^{-3}$; $T_M = 885$°C; $k_o = 5.34 \times 10^{-2}$; $P_{As4} = 3.5$ atm; ○ electrical data; circle with x chemical data.

InAs-Zn.—The impurity Zn in InAs occupies In sites and is an acceptor. Essentially the InAs-Zn system was treated like the InAs-Te one. The zinc concentration in the melt, however, was calculated as described in the experimental section.

In characterizing the pulled ingot only electrical measurements were used. The results of this study are shown in Fig. 2. Again, one notes the discontinuity at the point where P_{As} was increased. The theoretical normal freeze curves (24) are much more closely approximated by the data. This is undoubtedly due to the reduction of the pulling rate to 6 mm/hr.

We have analyzed our results along the same line as before. We assume that [Zn] = p, where the latter is the measured hole concentration. We again calculate p at the high-temperature equilibrium from our neutrality condition and K_i. If we use $k_o = 0.32$ for $P_{As4} = 0.165$ atm as a standard, then we would predict k_o for $P_{As4} = 1.45$ atm to be 0.49. This compares favorably with the measured value of 0.42.

InAs-Sn.—Impurities of group IV A of the periodic table have been observed to act both as donors and acceptors in III-V compounds depending on the site they occupy. Tin is this type of amphoteric impurity in InAs. We have grown two ingots of InAs doped with Sn at two different As pressures. The impurity and carrier concentration profiles of the ingots were obtained from chemical analysis, and electrical measurements and are shown in Fig. 3 and 4. The chemical analyses (emission spectroscopy) are precise to ± 20% at the 90% confidence level. The crystal pulled

at 0.17 atm As pressure was mainly single, and electrical measurements were made along most of the ingot. It should be noted in Fig. 3 that the chemical analyses indicate considerably larger concentrations of Sn than found by electrical measurements. We interpret these results as follows. Sn is basically a donor in InAs and therefore at low Sn concentration it prefers the In sites. However, at low P_{As_4} as the total Sn concentration increases, the probability of occupation tends to the same value for both sites. Therefore. the free electron concentration stays essentially constant for high concentrations of Sn as is shown in Fig. 3.

At P_{As_4} of 3.5 atm it was quite difficult to pull single crystals. Even at the slowest pull speeds attainable with our equipment (3 mm/hr) the ingot was polycrystalline except for the first few mm near the seed, which was single and free of gross defects. After the first centimeter of ingot, void inclusions were observed. These were characteristic of trapped arsenic gas bubbles. It was therefore possible to make electrical measurements only in the first few millimeters of the ingot. The rest of the ingot was characterized by chemical analysis. Results are shown in Fig. 4. We note that for this case the carrier concentration is equal to the concentration of Sn in the initial part of the ingot. We cannot say whether this holds true for the higher concentration of Sn, *i.e.*, for every part of the ingot. Nevertheless, the results indicate that under the higher As pressure the Sn atoms favor the In sites. The results follow the prediction that as the As pressure increases the occupation of As sites by Sn decreases relative to similar occupation of In sites. Along with the decrease of Sn solubility on As sites, there is a decrease in the total distribution coefficient. This is not unexpected. A more quantitative analysis and comparison of the Sn segregation coefficient is unfortunately not possible.

Discussion

We have reviewed the theoretical aspects of impurity incorporation in binary compounds. The primary variables affecting k_o are the temperature, the pressure of the compound constituents, the concentration of the impurity, and the free carrier concentration. Of these variables we have been concerned mainly with the pressure of the compound constituents and how the variation of P_M or P_N affects the segregation coefficient of various impurities. Of primary importance are the sites the impurities occupy. The theoretical predictions were tested experimentally for several impurities in CdTe and InAs. In no cases were the experimental observations in conflict with the theory; moreover, in most cases there was good quantitative agreement. One assumption inherent throughout is that the impurity activity in the liquid phase is not strongly dependent on the composition of the liquid phase. The agreement between theory and experiment indicates that our assumption was justified. It should be noted, however, that the impurity concentration was always dilute. When the liquid phase is appreciably off stoichiometry, *i.e.*, when $M >> N$ or $M << N$ then the assumption of composition independence may no longer be valid.

The dependence of k_o on the chemical potential of the constituents is of practical importance. k_o is a parameter that is useful in either minimizing or maximizing the incorporation of impurities into the host crystal. In addition there is another aspect that is of particular importance with high vapor pressure compounds, *e.g.*, GaAs, InP, etc., where one must maintain good control of P_M usually by temperature control of a reservoir. A fluctuation of P_M may induce temperature fluctuations in the melt, due to the solution or evaporation of the reservoir component. These fluctuations result in variations of k_o, and this may yield inhomogeneities in the growing crystal.

Special consideration must be given to the phase diagram of the binary compound under investigation. In the II-VI systems, either constituent can be used to control the composition of the vapor phase and hence the other phases. Large variations in the component pressure lead to only small variations in the liquid composition as seen in Table II. The III-V compounds on the other hand are generally controlled by the pressure of the group V elements only. In the III-V system the liquidus curves near the binary compound composition are quite flat, and therefore a variation in the component pressure is reflected more strongly in a variation of the liquid composition. The determination of the most suitable conditions must thus take into account the phase diagram of the system.

Acknowledgments

The authors wish to express their appreciation to R. C. Chicotka for growing the InAs crystals, to J. A. Kucza for growing the CdTe crystals, and to W. Reuter for performing the chemical analyses.

Manuscript received Dec. 3, 1965; revised manuscript received March 10, 1966. This paper was presented at the San Francisco Meeting, May 9-13, 1965.

Any discussion of this paper will appear in a Discussion Section to be published in the December 1966 JOURNAL.

REFERENCES

1. See for instance C. D. Thurmond and J. D. Struthers, *J. Phys. Chem.*, **57**, 831 (1953); K. Lehovec, *J. Phys. Chem. Solids*, **23**, 695 (1962).
2. "Compound Semiconductors," Vol. 1, "Preparation of III-V Compounds," R. K. Willardson and H. L. Goering, Editors, Reinhold Publishing Corp., New York (1962); O. Madelung, "Physics of III-V Compounds," Chap. 5, John Wiley & Sons, Inc., New York (1964).
3. L. L. Chang and G. L. Pearson, *J. Phys. Chem. Solids*, **25**, 23 (1964).
4. J. O. McCaldin, *J. Appl. Phys.*, **34**, 1748 (1963).
5. L. J. Vieland and T. Seidel, *ibid.*, **33**, 2414 (1962).
6. U. Merten and A. P. Hatcher, *J. Phys. Chem. Solids*, **23**, 533 (1962).
7. F. A. Trumbore, H. G. White, M. Kowalchik, R. A. Logan, and C. L. Luke, *This Journal*, **112**, 782 (1965).
8. F. A. Trumbore, H. G. White, M. Kowalchik, C. L. Luke, and D. L. Nash, *ibid.*, **112**, 1208 (1965).
9. F. A. Kroeger and H. J. Vink, "Solid State Physics," **3**, pp. 307-435, F. Seitz and D. Turnbull, Editors, Academic Press, New York (1956).
10. D. G. Thomas, "Semiconductors," Chap. 7, N. B. Hannary, Editor, Rheinhold Publishing Corp., New York (1959).
11. F. A. Kroeger, "The Chemistry of Imperfect Crystals, North-Holland Publishing Co., Amsterdam (1964).
12. M. R. Lorenz, *J. Phys. Chem. Solids*, **23**, 939 (1962).
13. M. R. Lorenz, *ibid.*, **23**, 1449 (1962).
14. D. de Nobel, *Philips Research Repts.*, **14**, 361-399 and 430-492 (1959).
15. K. Weiser and S. E. Blum, *This Journal*, **107**, 189C (1960).
16. J. van den Boomgaard and K. Schol, *Philips Research Repts.*, **12**, 127 (1957).
17. V. J. Silvestri, Unpublished results.
18. R. E. Honig, *RCA Rev.*, **23**, 567 (1962).
19. R. N. Hall, *J. Phys. Chem. Solids*, **3**, 63 (1957).
20. F. A. Trumbore, C. R. Isenberg, and E. M. Porbansky, *ibid.*, **9**, 60 (1958).
21. B. Segall, M. R. Lorenz, and R. E. Halsted, *Phys. Rev.*, **129**, 2471 (1963); D. T. F. Marple, **129**, 2466 (1963).
22. S. Yamada, *J. Phys. Soc. Japan*, **15**, 1940 (1960).
23. M. R. Lorenz and B. Segall, *Phys. Lett.*, **7**, 18 (1963).
24. M. R. Lorenz, *J. Appl. Phys.*, **36**, 2908 (1965).
25. A Mooradian and H. Y. Fan, Seventh International Conference on the Physics of Semiconductors, 4 Radiative Recombination in Semiconductors, Paris, p. 39-45 (1964).
26. J. B. Mullin and K. F. Hulme, *Phys. Chem. Solids*, **17**, 1 (1960).
27. J. A. M. Dikhoff, *Solid State Electronics*, **1**, 202 (1960).

Anomalous Behavior of Copper during Acceptor Diffusions into Gallium Arsenide

G. B. Larrabee and J. F. Osborne

Texas Instruments Incorporated, Dallas, Texas

ABSTRACT

A radioactive tracer study of the behavior of copper during acceptor diffusions into gallium arsenide has clearly shown anomalous copper concentration profiles. A pronounced minimum in the copper diffusion profile was found in the vicinity of the electrical p-n junction. The shape and position of this minimum was dependent only on those diffusion conditions (time and temperature) which affected the indiffusing acceptor. Crystal origin, crystal orientation, and annealing had no effect on the copper diffusion profile. It is felt that the minimum or dip in the profile is caused by the large built-in field of the p-n junction which sweeps out the singly charged copper interstitials in the vicinity of the junction.

The diffusion, solubility, and electrical activity of copper in gallium arsenide have been carefully studied (1-3) and with the excellent work of Hall and Racette (4) is now better understood. The behavior of copper in all semiconductors is considerably complicated by the existence of the two copper species, interstitial Cu_i, and substitutional Cu_s. These two species exist together in gallium arsenide and their ratio (Cu_s to Cu_i) is controlled by several factors including the doping of the gallium arsenide. In intrinsic gallium arsenide, this ratio was found to be around 30 (4). This ratio is upset if the material is doped greater than the intrinsic carrier content of the copper content. If the semiconductor is n-type, the ratio is shifted in favor of the substitutional species. Similarly, p-type material shifts the ratio to favor interstitial species. The properties of these two copper species are radically different both during and after diffusion.

Interstitial copper (Cu_i) diffuses very rapidly into gallium arsenide (effective $D \sim 10^{-6}$ cm^2-sec^{-1} at 800°C). Electrically, interstitial copper is a singly charged donor. However, in the crystal the interstitial species reacts with vacancies to produce copper in substitutional sites

$$Cu_i + V = Cu_s$$

Substitutional copper is relatively immobile and appears to be a double acceptor in gallium arsenide (4). Furukawa *et al.* (6, 7) observed only the 0.145 ev copper level but their work did not preclude the presence of the deep level at 0.47 ev. Fuller *et al.* (5) and Allison *et al.* (13) carefully investigated the behavior of copper diffused into n-type gallium arsenide and demonstrated the double acceptor behavior of copper.

The effective diffusion coefficient for copper is a function of the relative abundance of the two copper species which in turn is determined by the dopant. In the formation of a p-n junction, by diffusing an acceptor into n-type material, it is not at all clear how copper will behave. Hall (4) showed that the diffusion coefficient for interstitial copper was independent of the acceptor concentration. However, diffusion into extrinsic n-type gallium arsenide material is complicated by the fact that the copper interstitial solubility is greatly reduced.

This work was initiated to determine the behavior of copper during acceptor diffusions into n-type gallium arsenide.

Experimental Procedure

Each gallium arsenide sample was sawed to a thickness of 30 mils and then lapped and polished until optically flat. The sample was etched in 8:1:1 etch (8 parts H_2SO_4, 1 part 30% H_2O_2, and 1 part H_2O), and rinsed in running deionized water. The radiocopper-64[1] was introduced onto the crystal wafer by equilibrating the crystal in a 1*N* nitric acid solution containing 4 to 5 ppm copper ion (labeled with copper-64) for 30 min. The copper was thereby electrochemically deposited on the gallium arsenide (8). The wafer was then carefully rinsed in deionized water and allowed to dry. The slice was sealed into a 10 cm^3 volume quartz tube[2] with other acceptor diffusants at a pressure of less than 1μ. Unless otherwise stated, all diffusions were carried out at 815°C for 6 hr in a furnace with a 10-in. zone that was flat to ± 1°C. After diffusion, the quartz diffusion ampoules were air quenched, and the diffused gallium arsenide slice was removed. The edges were lapped with a coarse grit on a lapping plate to a depth of at least 500μ. The face of the diffused slice was then incrementally lapped and each lapping was gamma counted using a sodium iodide scintillation detector. Both gamma-ray spectroscopy and half-life studies showed only the presence of copper-64 activity.

Experimental Results

The initial acceptor diffusion studied was manganese into a copper-64 labeled wafer as described in the Experimental Procedure. Figure 1 shows the copper concentration profile as a function of depth into the crystal. As can be seen, a pronounced dip or minimum was obtained that looked much like that reported by Cun-

[1] Copper-64 was obtained and assayed from Oak Ridge National Laboratories, Oak Ridge, Tennessee. An average specific activity of 60,000 to 80,000 mc/g was used.

[2] All quartz used was G.E. 204.

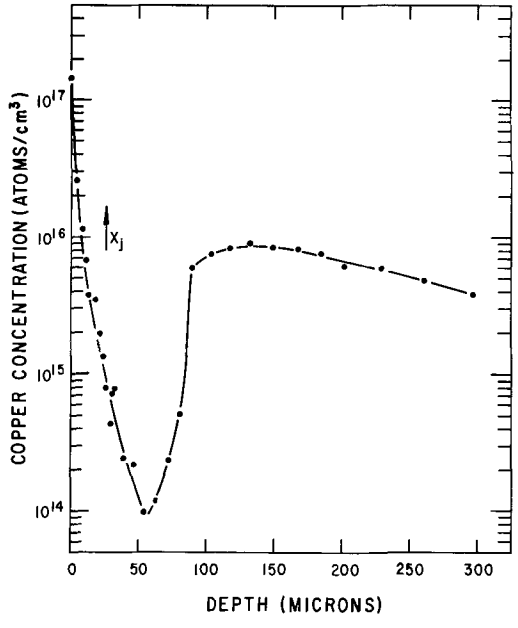

Fig. 1. Typical distribution of copper in n-type gallium arsenide when diffused with manganese at 815°C for 6 hr.

nell and Gooch (9). The surface concentrations of manganese, observed using radiomanganese-54, were of the order of 10^{19} atoms/cc. The diffusion conditions were repeated several times and shown to reproducibly yield this anomaly. It was decided to vary carefully only one experimental parameter at a time in an effort to understand this phenomenon.

Material origin and crystallography.—Several different Texas Instruments n-type pulled gallium arsenide crystals (lightly doped tin and tellurium and undoped, but not intrinsic) as well as some undoped, but not intrinsic Bell and Howell horizontal Bridgeman material were shown to behave in the same manner. This dip in the copper diffusion profile was not peculiar to any one melt grown n-type gallium arsenide crystal. The gallium arsenide material used in the acceptor diffusion reported in this work was tin doped to 4 to 6 x 10^{16} at./cm^3. Heavily doped material as discussed by Schockley and Moll (14) was not investigated as n-type substrates in this study.

Similarly, efforts to show a dependence on crystallographic orientations was not successful. Manganese diffusions into <311>, <111>, and <115> material all yielded copper profiles with a pronounced dip or minimum.

Since most of the diffusion work in this study was carried out on <111> oriented crystals, the effect of the gallium rich (A) face *vs.* the arsenic rich (B) face was investigated. No differences in the copper diffusion profiles were observed. This was not unexpected since <311> and <115> oriented wafers have only very slight A and B face characteristics.

The one material or slice parameter that had the most pronounced effect on the over-all shape of the dip in the copper profile was positioning in the diffusion tube. That is, the face laying up in the diffusion tube consistently showed more pronounced or sharper dips in the profiles than the down face. This observation has added significance when it is coupled with some radiomanganese-54 and -56 work (10) which clearly shows the upper diffusion face to have higher manganese surface concentrations and deeper p-n junction depths. This would imply that the anomalous dip in the copper profile was intimately connected with the indiffusing acceptor and is not dependent on the host crystal.

Diffusion conditions.—On the premise that the dip in the copper profile was caused by the manganese; several diffusion conditions were studied.

Diffusion time.—A manganese diffusion into a copper-64 labeled wafer was carried out as described in the Experimental Procedure except the diffusion time was reduced from 6 to 0.6 hr. The copper diffusion profile is shown in Fig. 2. The depth of the minimum (12μ) is significantly less than in comparable 6 hr diffusions

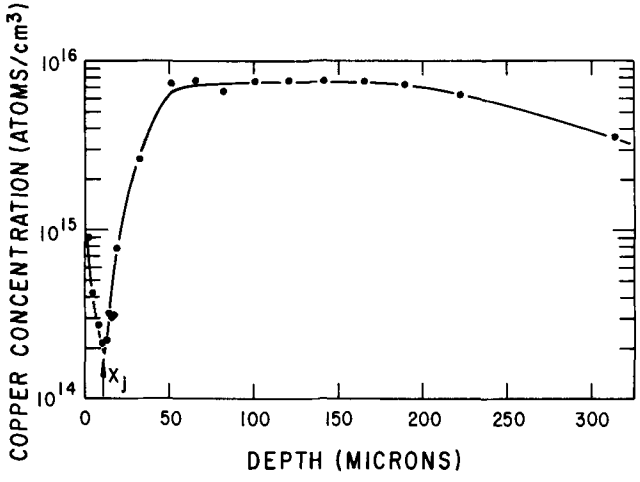

Fig. 2. Effect of diffusion time on the copper distribution during manganese diffusion into n-type gallium arsenide. Diffusion carried out at 815°C for 0.6 hr.

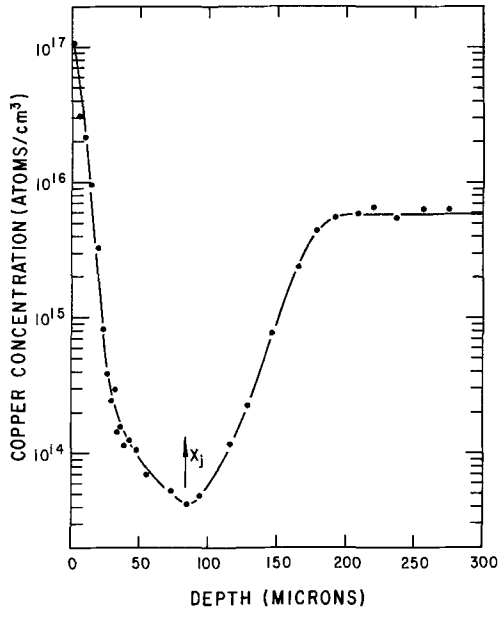

Fig. 3. Effect of increased temperature on the copper concentration profile during the diffusion of manganese into n-type gallium arsenide. Diffusion carried out at 915°C for 6 hr.

which average around 55μ. Since the acceptor diffusion depth would vary with the square root of the diffusion time, one would expect the minimum to be about 1/3 the depth of a comparable 6-hr diffusion. An average of two 0.6-hr diffusions was 15μ which is in good agreement with the time dependent diffusion laws.

Temperature.—A manganese diffusion was carried out as described in the Experimental Procedure but increasing the diffusion temperature to 915°C. As can be seen in Fig. 3, the dip in the copper profile was much wider and the minimum was deeper into the crystal (87μ) than the 815°C diffusions. A diffusion at 1000°C produced a much broader dip with a minimum around 150μ. This change in the shape of dip in the copper profile along with the change in the position of the minimum again strongly suggest a dependence on acceptor behavior and movement.

Annealing.—Two diffusions were carried out under the standard diffusion conditions described earlier. At the end of the 6-hr diffusion one tube was removed and water quenched while the other tube was removed inside a larger Inconel block which took approximately 3 hr to reach room temperature. There was no difference in the shape of the copper diffusion profiles. The anomalous dips occurred at the same depth in the crystal. It appears that the effects of annealing after diffusion are very small.

Other Acceptor diffusants—zinc.—All of the copper-acceptor diffusions reported in this work were carried out using manganese with the exception of two zinc diffusions. In these zinc diffusions all diffusion conditions were as described earlier except that the amount of zinc was chosen to yield a p-n junction at a depth of 20 to 30μ. The copper profile is shown in Fig. 4, and it is apparent that an extremely sharp dip is obtained using zinc.

Here again, the anomalous distribution of copper appears to be closely related to the indiffusing acceptor. It should be noted that the width of the minimum is considerably more narrow than in comparable manganese diffusions.

Absence of acceptor.—To gain some insight into the mechanism of the interaction between the copper and the indiffusing acceptor, a series of diffusions was carried out with copper-64 labeled wafers in the absence of an acceptor. The gallium arsenide used was horizontal Bridgeman grown, undoped, but not intrinsic, with a carrier concentration of 1.2 x 10^{16} electrons/cm^3. The first series of diffusions was run with

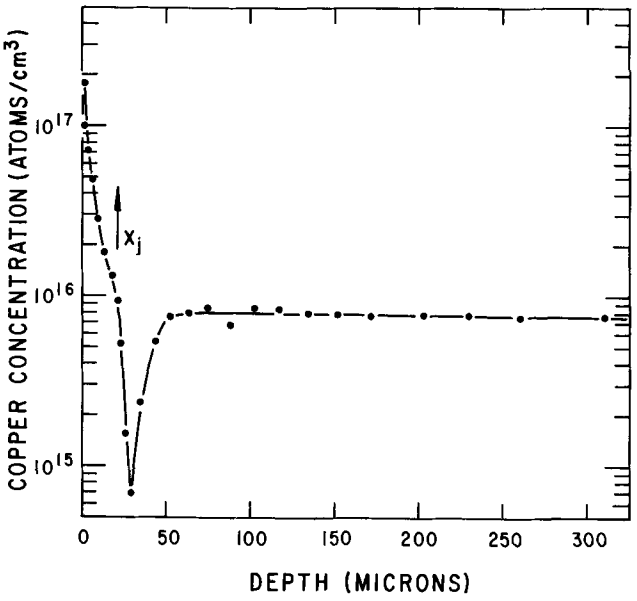

Fig. 4. Copper distribution oberved during zinc diffusion into n-type gallium arsenide at 815°C for 6 hr.

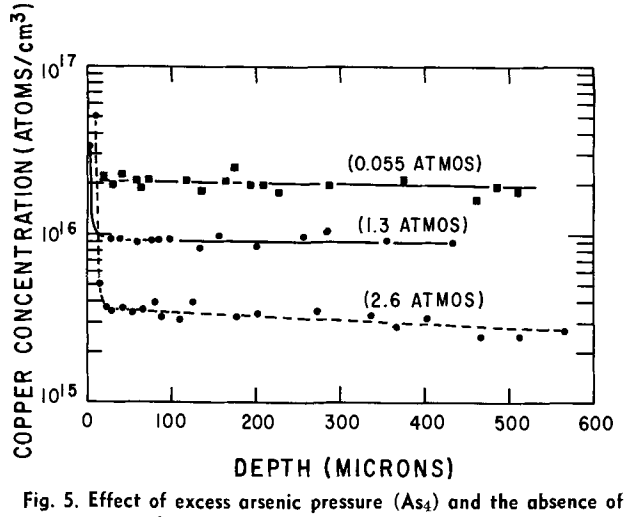

Fig. 5. Effect of excess arsenic pressure (As_4) and the absence of an acceptor on the copper distribution during a 6-hr diffusion into n-type gallium arsenide at 815°C.

varying amounts of excess arsenic in the diffusion ampoule. The excess arsenic would prevent dissociation of the gallium arsenide and would generate gallium vacancies in the crystal near the surface.

The results of three diffusions with varying amounts of excess arsenic in the diffusion tube are shown in Fig. 5. The apparent inhibition of the copper diffusion by the excess arsenic suggests interaction of the copper with gallium vacancies to form immobile substitutional copper. Hall and Racette (4) report reduced solubility of copper in n-type (5×10^{15} electrons/cm^3) gallium arsenide and suggest that this reduced solubility is due to the presence of an arsenic-rich phase at the surface. This suggestion of precipitation of copper arsenide at the surface does not seem to fit the experimental data since in all three cases the amount of arsenic added to the diffusion tube was far in excess of that necessary to react with the small amount of copper on the surface.

Furukawa and Thurmond (6) report a similar decrease in copper solubility with increasing arsenic pressure and explain the dependence by assuming that copper on arsenic sites is singly ionized Cu_{As}^-. It should be noted that the larger dips or minima observed in the copper diffusion profiles during acceptor diffusions were not obtained here.

Discussion

A simple straight forward explanation of the behavior of copper during acceptor diffusions does not appear possible. From the experimental data it is apparent that the minimum or dip in the copper diffusion profile is closely associated with the acceptor and, by implication, the formation of a p-n junction. Any changes made in the diffusion parameters which affect the acceptor impurity are reflected in the copper diffusion concentration profile by changes in the position and shape of the dip.

Kendall (11) has reported a similar phenomenon when indium was diffused into gallium arsenide in the presence of cadmium. Kendall attributes the "uphill" branch to an interaction between interstitial indium (In^{3+}) and gallium vacancies with the vacancies diffusing out of the interior toward the acceptor diffusion zone. The "downhill" side of the dip in the indium profile was attributed to a retardation of the incoming interstitials by the built in field of the acceptors.

Cunnell and Gooch (9) reported a similar anomaly in their investigation of the diffusion of cadmium into gallium arsenide using cadmium-115. Kendall (11) feels that the anomaly observed was due to the rapidly diffusing interstitial indium-115 daughter. Kendall was able to duplicate their results using indium-114 diffusing simultaneously with nonradioactive cadmium.

The electrical p-n junction in all the manganese and zinc-copper diffusions in this work were found to occur just at the minimum or slightly to the left of the minimum. In no case was the junction found to the right or deeper than the minimum of the dip in the copper diffusion profile.

In any explanation or interpretation of the behavior of copper during acceptor diffusions, the solubility data of Hall and Racette (4) must be carefully examined. Hall and Racette clearly showed that copper had high solubility in extrinsic p-type gallium arsenide because of enhanced interstitial solubility. This enhanced solubility of an impurity as a function of doping in a semiconductor is the same as that explained by Riess, Fuller, and Morin (15) using chemical interactions in silicon and germanium. Shockley and Moll (14) explained this same enhanced solubility of a charged impurity in a semiconductor using band theory by using the Fermi level as a measure of the dopant concentration. None of these workers predict the depressed solubility for copper in the vicinity of the pn junction that was observed in this work. At the temperatures used in these diffusions (815°C) and the low copper concentrations used, there is no question of solubility limitations. At 815°C the n-type substrates used in this work are intrinsic (E_F near mid gap) and Hall (4) observed no distinguishable difference between the copper solubility in semi-insulating (E_F mid gap) and extrinsic n-type material. On the basis of these solubility considerations, one would expect enhanced copper solubility in the p-region and a flat distribution in the n-region. But there should be no pronounced minimum or anomaly in the copper diffusion profile. For the Shockley-Moll model (14) to explain the concentration difference observed in Fig. 3, for example, it would be necessary for $e^{\Delta E_F/kT} = 3 \times 10^2$ on the n side of the p-n junction. That is the Fermi level would have to move about 0.57 ev which is not reasonable because at 815°C the band gap has decreased to around 1.0 ev ($\beta_G = -4.9 \times 10^{-4}$ ev/°K). The Fermi level for 1×10^{19} Mn/cm^3 in 1×10^{16} electrons/cm^3 material is 0.24 ev above the valence band edge and the n-type substrate Fermi level is mid gap ($E_F \sim 0.5$ ev) at 815°C.

Copper is known to diffuse by the dissociative mechanism (1) and has an effective D of approximately 5×10^{-6} cm^2/sec (1) at 815°C. The time required for the interstitial copper to saturate the 30 mil wafers used in this work would be in the order of 10 min which is small compared to the total 6-hr diffusion time used. We feel that the copper rapidly diffuses

throughout the wafer during the first 10 min of the 360-min diffusion cycle and then redistributes as the slower acceptor diffusion proceeds. This is supported by our experimental data on the 0.6-hr diffusion where the copper was profiled for 350μ (half-way through 30 mil wafer) (Fig. 2) into the crystal and found to be more or less uniformly distributed past the usual minimum.

Hall and Racette (4) showed that the mobile copper interstitial species was a singly charged donor by using drift measurements in an electric field. The drift field used was small (2 v/cm) compared to the built in field caused by acceptor gradients and p-n junctions ($\sim$ 600 v/cm) (12). It would be reasonable to expect this large built-in field to sweep the singly charged copper interstitials out of the region of the p-n junction. The enhanced interstitial solubility in the p-type region would not adversely affect this movement and would lead to the formation of a sharp minimum in the copper diffusion profile because of the solubility minimum observed by Hall (4) in slightly extrinsic p-type material. The copper concentration after the junction would then rise to an equilibrium level and be flat in the n-type bulk region of the crystal.

Acknowledgment

The authors wish to thank R. W. Haisty and P. Hoyt for their helpful discussions and for supplying some of the gallium arsenide samples used in this work. Their grateful acknowledgment is due to R. A. Reynolds for his discussions.

Manuscript received Jan. 31, 1966.

Any discussion of this paper will appear in a Discussion Section to be published in the December 1966 JOURNAL.

REFERENCES

1. C. S. Fuller and J. M. Whelan, *J. Phys. Chem. Solids*, **6**, 173 (1958).
2. J. Blanc and L. R. Weisburg, *ibid.*, **25**, 221 (1964).
3. D. F. Rose, D. Meyerhofer, and R. V. Jensen, *J. Appl. Phys.*, **31**, 1105 (1960).
4. R. N. Hall and J. H. Racette, *ibid.*, **35**, 379 (1964).
5. C. S. Fuller, H. W. Allison, and K. B. Walfstirn, *J. Phys. Chem. Solids*, **25**, 1329 (1964).
6. Y. Furukawa and C. D. Thurmond, *ibid.*, **26**, 1535 (1965).
7. Y. Furukawa, *ibid.*, **26**, 1869 (1965).
8. G. B. Larrabee, *This Journal*, **108**, 1130 (1961).
9. F. A. Cunnell and C. H. Gooch, *Nature*, **188**, 1096 (1960).
10. G. B. Larrabee, Unpublished work.
11. D. L. Kendall, *Appl. Phys. Letters*, **4**, 67 (1964).
12. F. M. Smits, *Ergeb. Exak. Naturwiss.*, **31**, 167 (1959).
13. H. W. Allison and C. S. Fuller, *J. Appl. Phys.*, **36**, 2519 (1965).
14. W. Shockley and J. L. Moll, *Phys. Rev.*, **119**, 1480 (1960).
15. H. Riess, C. S. Fuller, and F. J. Morin, *Bell Sys. Tech. J.*, **35**, 535 (1956).

Compositional X-Ray Topography

J. K. Howard[1] and R. D. Dobrott

Texas Instruments Incorporated, Dallas, Texas

ABSTRACT

The advent of new semiconductor materials frequently demands new methods of investigating and defining those growth flaws which can degrade device performance. A new x-ray topographic method and concept were developed to study the defect structures in the heteroepitaxial systems. Compositional x-ray topography is an extension of the scanning-reflection method, which permits a nondestructive evaluation of the perfection in the substrate, deposit, and heterojunction. The theory and limitations of this method are discussed. Compositional x-ray topography was applied to the study of homogeneity and perfection in various heteroepitaxial systems, *i.e.*, GaAs-GaP, GaAs-InAs.

Heteroepitaxial systems have become the focus of many new device concepts (1, 2). Epitaxial deposition of pseudobinary alloys such as Ga(As, P) onto GaAs substrates has received considerable attention in the semiconductor industry (3-9). Layers of (Ga, In)As have also been deposited on single crystal GaAs substrates yielding material from which light-emitting diodes, mixer diodes, and varactor diodes can be fabricated (2). The crystalline perfection and homogeneity of these deposits is of importance in fabricating devices from this material. Since imperfections reflect the growth process, a knowledge of their concentration and type will permit a better understanding of the deposition parameters and clarify their effect on the deposit quality. Previous investigators have utilized back-reflection Laue methods and powder diffraction techniques to ascertain information on the structural quality and homogeneity of their deposits (4, 6). These methods are time consuming and yield results which may not be characteristic of the bulk deposit.

X-ray topography is a nondestructive method of evaluating the defect structure of many monocrystalline materials (10-18). The extinction contrast transmission method was developed by Lang (10) and modified by Schwuttke (13-15) for the study of semiconductor grade silicon. Defects in GaAs have been investigated by the anomalous transmission topographic method (16). The scanning-reflection x-ray topographic method (17) was developed to map imperfections over large area crystal surfaces (18). Compositional x-ray topography introduces a new concept to the field of x-ray topography. This method is capable of nondestructively examining the defects created at the heterojunction and "tracking" them through the deposit.

[1] Present address: IBM Systems Development Division, Fishkill, New York.

Scanning-Reflection X-Ray Topography (SRT)

Using the transmission arrangement, Schwuttke (15) was able to study dislocation arrays in silicon epitaxial deposits. The dislocation density of the silicon substrates was nearly zero in most cases; the superposition of the substrate flaws on the topographic image did not prevent the imperfections in the deposit from being discerned. The dislocation density of GaAs is usually $> 5 \times 10^3$ cm^{-2} which prevents exact identification of deposit flaws in the transmission topographs. Since the total thickness of the GaAs deposit and substrate produced a value of $\mu t >> 1$, anomalous transmission must be used if a nondestructive analysis is required (16).

The scanning-reflection method was designed to inspect the active growth surface of the GaAs substrate for mechanically induced damage and grown-in de-

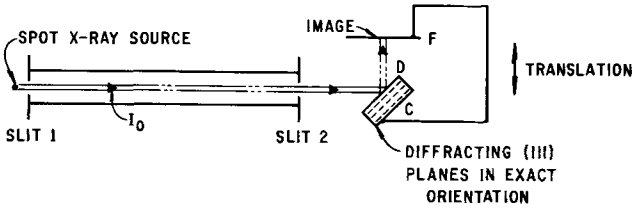

Fig. 1. Experimental arrangement for scanning-reflection x-ray topography.

fects. After deposition, another topograph revealed only the defect array in the GaAs deposit (17, 18); an attempt was made to relate the deposit flaws to either the substrate preparation and/or perfection, or the deposition parameter.

The experimental arrangement is depicted in Fig. 1. The substrate crystal (C) in diffracting position is coupled to a film holder (F) mounted perpendicular to the diffracted beam (D). The incident beam (I_0) is restricted by slits (S_1) and (S_2); slit (S_2) is adjusted until only the $K\alpha_1$ component of the characteristic radiation can diffract. The ribbon-shaped incident beam (25 x 0.05 mm) impinges on the crystal at the proper angle, and a projected image of the flaws in the irradiated material is formed on the photographic plate. An image of the entire slice is obtained by translating the coupled film-sample unit perpendicular to the incident beam or parallel to the slice surface. The sequence of examination (substrate topograph-deposition-deposit topograph) is tedious and can introduce a contamination and/or strain problem because of handling. A more desirable method of inspection would permit *in situ* examination of the substrate and epitaxial film perfection after deposition.

Principle of Compositional X-ray Topography

Compositional x-ray topography is an application of the scanning-reflection x-ray topographic method. The perfection, homogeneity, and single crystallinity of many heteroepitaxial systems can be investigated with this method. The diffraction angle depends on the lattice parameter (which can be calculated or experimentally determined); the substrate and film can be examined separately by the employment of the proper diffraction angle. Only that volume element in the irradiated material which has the desired lattice parameter will diffract to form the topographic image. This method of examination is effective to the depth of penetration of the incident x-ray beam. The maximum penetration depth, D (microns), can be expressed by the relation

$$D = -\ln A \cdot 10^4 / \left(\frac{\mu}{\rho} \cdot \rho \left[\csc(\theta - \psi) + \csc(\theta + \psi) \right] \right) \quad [1]$$

μ/ρ (cm^2/g) is the mass absorption coefficient, ρ (g/cm^3) is the density, θ the diffraction angle, ψ the angle between the slice surface and the diffracting planes, and A is the fractional attenuation of the incident beam.

A plot of the penetration depth as a function of $\theta - \psi$ (angle between the incident beam and the slice surface) is shown in Fig. 2. For a given radiation, crystal growth axis, and reflecting plane, the $\theta - \psi$ value can be calculated and the penetration depth determined. The graph depicts D in GaAs for various wavelengths of radiation ($A = 0.1$); this plot is a good approximation for Ga(As, P).[2]

[2] Experimental verification of $\theta - \psi = 45°$ (copper radiation) consists of determining the Ga(As, P) thickness which completely attenuates the (333) reflection of the substrate. The composition measurement developed by Miller (19) and employed by Dobrott (20) indicated that a 25μ Ga(As, P) deposit eliminated the (333) GaAs reflection ($\theta - \psi = 45°$) as compared to 21.8μ calculated from Eq. [1].

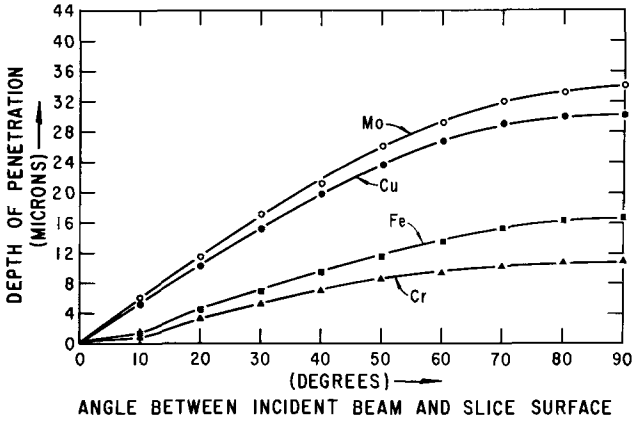

Fig. 2. X-ray penetration depth in GaAs

The principles of compositional x-ray topography are only satisfied under certain conditions: (*a*) the total film thickness is less than the penetration depth of the incident x-ray beam; (*b*) the diffraction angles of the film and substrate are sufficiently separated to insure exact angular selection; (*c*) the absorption coefficient is constant for each compositional layer. These restrictions, however, can be utilized to gauge the quality of the deposit.

Compositional x-ray topography applied to the GaAs-GaP *and* GaAs-InAs *heteroepitaxial systems.*— The variation of lattice parameter and composition has been shown to be linear in the GaAs-GaP and GaAs-InAs alloy systems (5, 21). Since the difference between the diffraction angles for GaAs and GaP (or GaAs and InAs) is small compared to θ, then θ_x (where x is the mole fraction of GaP) has been shown to vary directly with composition (20). A plot of these variables is depicted in Fig. 3 for the case of a Ga(As, P) film deposited on a (111) GaAs substrate. The Δ 2θ value changes from the (333) reflection of GaAs to the (333) reflection of GaP (copper Kα radiation). Because of this linearity, the mole fraction of GaP, x, can be related to the diffraction angle by the expression

$$2\theta\,[GaAs_{1-x}P_x] = x \cdot 2\theta\,[GaP] + (1-x) \cdot 2\theta\,[GaAs] \quad [2]$$

Similar relationships exist for other reflections, *i.e.*, the {440} reflections of GaAs and GaP. The composi-

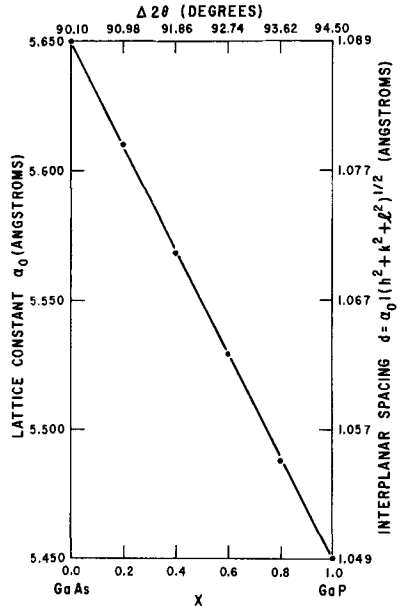

Fig. 3. Plot showing the linear relationship between the mole fraction of GaP and the diffraction angle; •, Rubenstein.

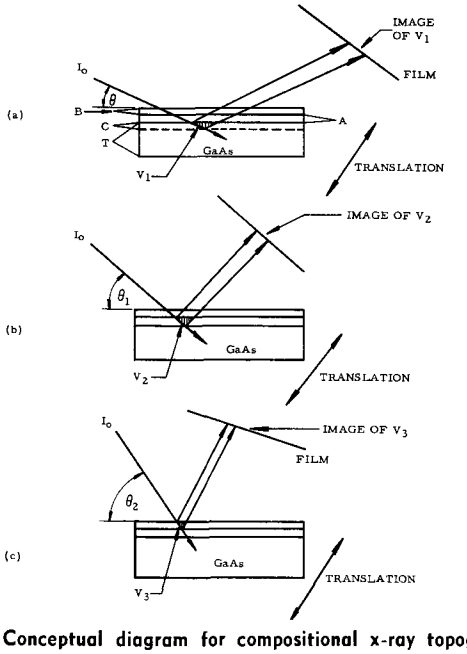

Fig. 4. Conceptual diagram for compositional x-ray topography. Each layer can be diffracted separately by utilizing the diffraction angle which corresponds to the lattice parameter (composition) of that layer.

tion of the alloy deposit determines the diffraction angle.

Figure 4 depicts an idealized case of the GaAs-GaP heteroepitaxial system. Epitaxial layers A and B have been sequentially deposited on a GaAs substrate. Assume that the A layer has a composition $GaAs_{1-x_1}P_{x_1}$ and diffraction occurs when the incident beam impinges at an angle θ_1 with respect to the diffracting planes which are parallel to the slice plane. The B layer has a GaP concentration x_2, $GaAs_{1-x_2}P_{x_2}$, where $x_1 << x_2$. This layer is in diffraction position when the incident beam impinges at an angle θ_2 where θ (GaAs) $< \theta_1 < \theta_2$. In Fig. 4(*a*) the incident beam I_0 strikes the crystal at the angle θ, and only the GaAs substrate is properly oriented. The beam penetrates to a depth C below the substrate surface; a volume element, V_1, diffracts coherently to form the topographic image. The image of the defects in V_1 is registered on the film plate placed perpendicular to the diffracted beam. As the crystal-film unit is translated perpendicular to the incident beam, the diffracting volume V_1 is "swept" parallel to the diffracting planes. This total image displays the perfection of the substrate in the C layer. If the crystal is rotated about an axis perpendicular to the plane of Fig. 4, the incident beam now impinges at an angle θ_1. The A layer is now in diffracting position [Fig. 4(b)]. The volume element V_2 bounded by the incident and diffracted beams diffracts to form an image of the flaws in V_2. Subsequent translation permits the A layer to be examined independent of the B layer and the substrate. The perfection of the B layer can be determined in a similar manner [Fig. 4(c)]. If Fig. 4 represents a cleaved {110} surface perpendicular to the plane of the slice, then (SRT) topographs of this surface would reveal compositional changes in the growth direction.

Experimental

Materials.—Single crystals of GaAs were grown using the Czochralski method; the growth axis was parallel to either the [111] or [100]. In the case of the crystals grown on the (111) plane, slices were cut 5° off (111) toward <100>. The slice thickness after sawing with an ID saw was approximately 0.030 in. The slices were then chemically polished on the (111)-B [or the (100)] face with a solution of NaOCl: H_2O (22). These slices were employed as substrate material following a brief etch ($8H_2SO_4$:H_2O:H_2O_2).

An open-tube vapor transport system was used to deposit epitaxially the Ga(As, P) or (Ga, In)As alloy on the GaAs substrate (1-3).

Composition measurement and x-ray procedure.—The sample (film/substrate) was clip-mounted on a goniometer head which was at the end of a shaft. The shaft was inserted into a standard Norelco diffractometer. Characteristic copper radiation was employed in the measurement; the diffracted radiation was rendered monochromatic with a focusing monochromator. The substrate was then aligned to diffract the (333) reflection in the case of a (111) sample. The (400) reflection was utilized if the substrate was (100). However, asymmetric reflections have been employed for specific applications. The sample was scanned between the angular limits of the alloy, *i.e.*, 2θ [GaAs] to 2θ [GaP]. The Ga(As, P) reflection occurs between these angles. Since the diffraction angle of the GaAs substrate was known, the substrate reflection acts as an internal standard. Since Vegard's laws hold in the GaAs-GaP alloy system and the interplanar spacing, d, can be determined from the alloy peak position, then the mole fraction of GaP can be calculated from the expression

$$x = (d\,\mathrm{Ga(As,P)} - d\,\mathrm{GaAs}) / (d\,\mathrm{GaP} - d\,\mathrm{GaAs}) \quad [3]$$

x can also be calculated from Eq. [2] as θ_x is linear with d in the alloy range.

The composition measurement uniquely determined the diffraction angles of the compositional layers in the deposit. These angles are used to align each layer for (SRT) topographs. An open-tube detector was used to establish the diffraction peaks; receiving slits were employed to culminate the alignment. Previous investigators have employed the standard powder diffraction methods to determine composition; this method is destructive and time consuming (4, 6).

The sample was mounted on a standard goniometer head in the (SRT) camera. The GaAs substrate was oriented with a scintillation detector-ratemeter circuit. The diffraction angles of the deposit are found by rotating the sample about the ω axis. The topographs were obtained with copper radiation. The effective size of the focus was 100μ (Jarrell-Ash microfocus generator). Nickel foil (0.002 in.) was placed over the film holder to filter the radiation diffracted from the sample. Kodak type A plates were utilized; the average exposure time was 1½ hr.

Results and Discussion

Inhomogeneity.—A composition measurement performed on a (100) deposit of (Ga,In)As yielded the (400) diffraction angle of 64.2°; the GaAs reflection was registered at 66.2° (Fig. 5). This angular separa-

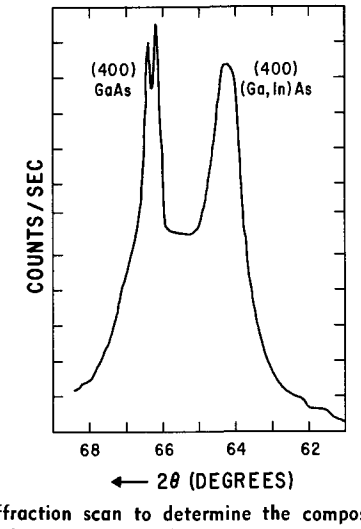

Fig. 5. Diffraction scan to determine the composition of an inhomogeneous deposit of (Ga,In)As.

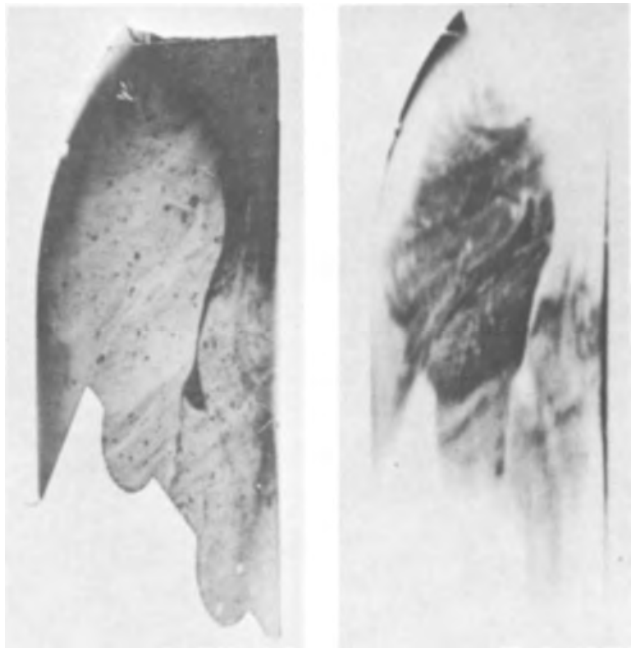

Fig. 6(a). (left). (400) topograph reveals inhomogeneous regions in the (100) deposit of (Ga,In)As; the alloy reflection was used to form the topographic image: (b) (right) the relative contrast was reversed when the GaAs diffraction angle was employed to obtain the (400) topograph.

tion corresponds to a 50% InAs alloy. The (400) topograph of the alloy layer reveals an image which exhibits nonuniform darkening (Fig. 6a). The central region of the image is of lower contrast than the periphery. The relative contrast was reversed by the employment of the GaAs diffraction angle to form the topographic image (Fig. 6b). The GaAs layer is coherently incorporated into the alloy matrix. This layer acts as an absorber, which attenuates the intensity diffracted from this region. These topographs map the spatial position of the compositional variations in the deposit.

A (111)-B (Ga, In)As deposit was also evaluated for composition (Fig. 7). The (333) alloy peak was displaced 2.5° from the (333) GaAs reflection. The (333) topograph of the 35% InAs layer revealed large areas of null contrast in the matrix (Fig. 8). The inhomogeneous region was shown to be GaAs rich in the same manner as Fig. 6a and Fig. 6b.

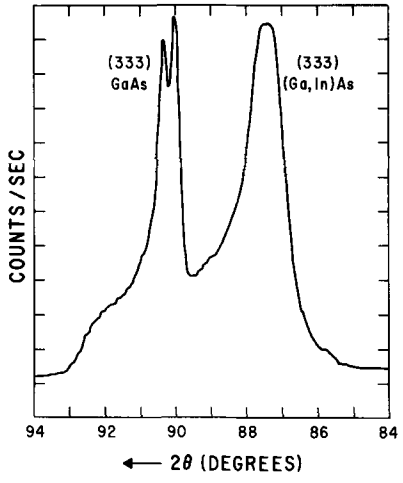

Fig. 7. Diffraction scan of an inhomogeneous (111) deposit of (Ga,In)As. The alloy composition was 35% InAs.

The scanning-reflection x-ray topographic method was employed to investigate planar variations in composition over large area deposits of (Ga, In)As. This type of analysis has certain advantages in the detection of gross inhomogeneity in the alloy deposits: (*a*) the scanning and /or counting time which would be involved in an electron microprobe analysis of these large area deposits would be impractical; (*b*) the shape of the alloy peak (composition measurement) has been shown to be sensitive to inhomogeneity, but no inference can be made to the spatial distribution of the inhomogeneous regions; (c) the reflectivity method (20) could not detect small variations in composition across the surface. X-ray topography clearly differentiated two regions in a Ga(As,P) deposit which differed by only 3% GaP (18). The topographic method is a fast, semiquantitative, and nondestructive technique to evaluate homogeneity.

Reflectivity measurements have been employed to determine axial changes in composition of Ga(As,P) epitaxial deposits (20). Homogeneity can be evaluated by incrementally etching the deposit, in conjunction with compositional determinations by reflectivity; the reflectivity measurements determine the composition at the surface only. This measurement can be quantitative (x-ray standards), but is a destructive process which involves a long evaluation time.

Compositional x-ray topography can also be applied to the evaluation of axial changes in composition. The method is simple, nondestructive, and yields a very sensitive qualitative display of the compositional changes encountered during epitaxial growth. A (111)-B Ga(As,P) deposit (0.002 in. thickness) was

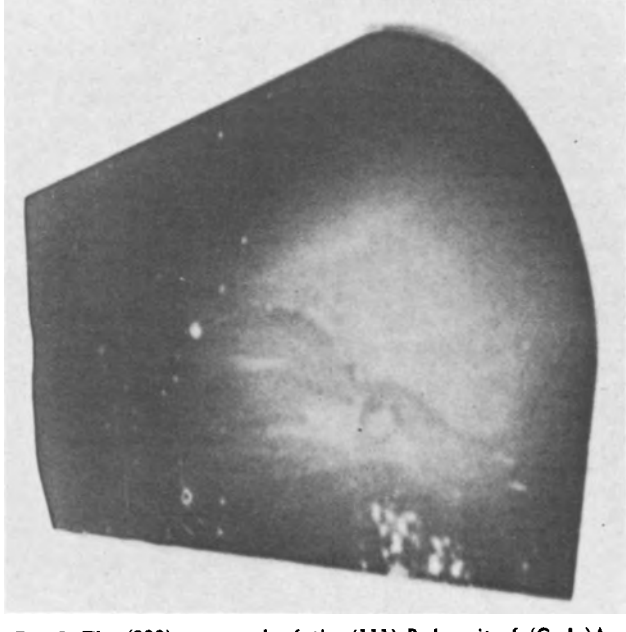

Fig. 8. The (333) topograph of the (111)-B deposit of (Ga,In)As which reveals a compositional gradient across the slice.

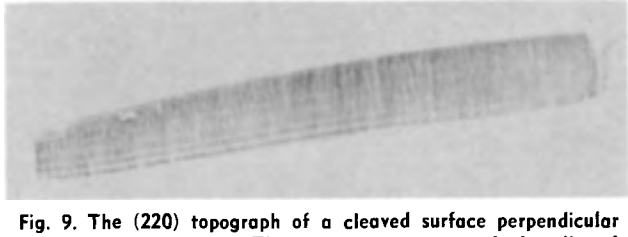

Fig. 9. The (220) topograph of a cleaved surface perpendicular to the (111) slice plane. The deposit image reveals lamella of different composition.

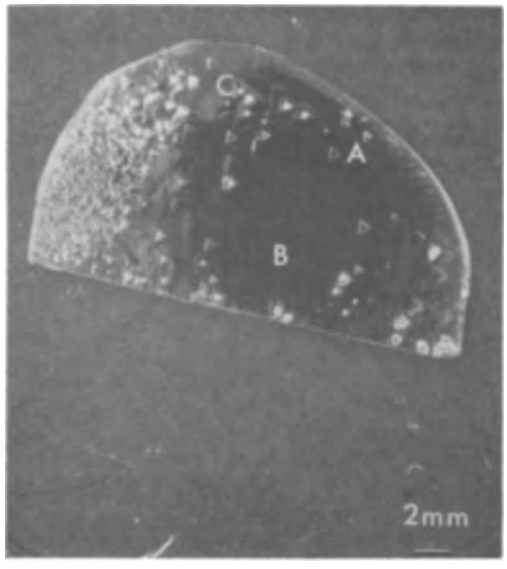

Fig. 10. Numerous hillocks on a (111)-B Ga(As,P) epitaxial film

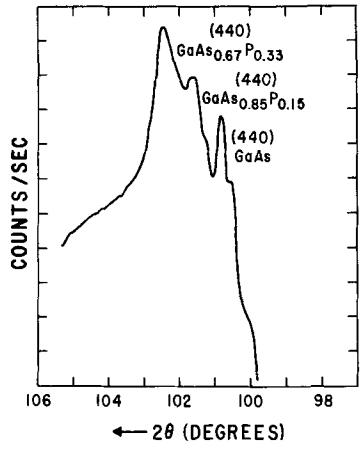

Fig. 11. Composition scan of Ga(As,P) deposit with hillocks

cleaved to expose a {110} cleavage plane normal to the plane of the slice. This is a standard technique to determine film thickness by interferiometric methods. A $(2\bar{2}0)$ topograph of the cleaved surface is shown in Fig. 9. The image consists of a series of alternating light and dark lines.

Since the sample was aligned to diffract Ga(As,P), the substrate image was not observed. The deposit image revealed dark lines traversing the width of the film. These lines correspond to regions of fixed composition, whereas the light lines (no contrast) represent lamella of different composition. The spacing between the lines decreases during growth which indicates that the deposit was approaching a constant composition. This effect has been observed in many alloy deposits and could degrade the efficiency of light-emitters fabricated from this material (23).

Hillocks.—Hillocks (localized surface protrusions) have been observed on epitaxial deposits of silicon (24-26), germanium (27-28), and GaAs (29). More recently, these (or similar) defects were detected in epitaxial deposits of Ga(As,P) and (Ga,In)As. Compositional x-ray topography was used to study the morphology of these flaws in Ga(As,P).

Numerous hillocks were obtained in a (111)-B deposit of Ga(As,P) (Fig. 10). The thickness of the film was determined to be 14μ. A composition measurement was obtained by the employment of the asymmetric (440) reflection. The diffraction scan is shown in Fig. 11. The (440) GaAs reflection was registered at 100.8°; the (440) $GaAs_{0.85}P_{0.15}$ layer and the (440) $GaAs_{0.67}P_{0.33}$ layer yielded diffraction angles of 101.6° and 102.5°, respectively. The relative peak heights indicate that the 15% GaP layer was the initial deposit, *i.e.*, this reflection was attenuated by absorption more than the 33% GaP layer. The diffraction angles were then used to align each layer for (SRT) topographs.

The (440) topograph of the GaAs substrate (Fig. 12a) reveals the hillocks as triangular regions of null contrast. The image shapes are either sharp (arrow A), diffuse (arrow B), or diffuse with a definite triangular center (C). The lack of contrast observed in the hillock images indicated that they are misoriented with respect to the substrate which corresponds, in this case, to a difference in composition. The (440) topograph of the $GaAs_{0.67}P_{0.33}$ layer also displayed the hillocks as regions of reduced contrast (Fig. 12b). The intense darkening in this image was the result of local cracks in the deposit which indicates the effect that hillock formation can have on the deposit quality. The sample was then oriented to diffract the $GaAs_{0.85}P_{0.15}$ layer; the (440) topograph exhibits only the hillock images (Fig. 12c). The matrix was misoriented for diffraction.

The hillocks are probably generated at the substrate interface since their composition corresponds to the 15% GaP layer. The final compositional layer (33% GaP) forms around the hillocks and frequently overgrows these defects. A diffuse image was observed in Fig. 12a (arrow B), and no image was registered in

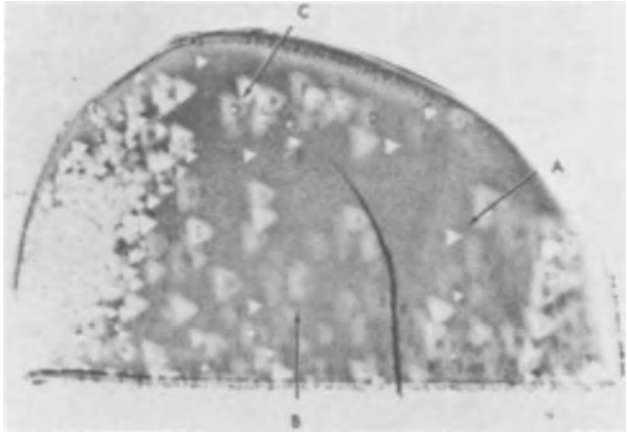

Fig. 12(a). The (440) topograph of the GaAs substrate which reveals the hillocks as triangular regions of null contrast. The dark line traversing the image is a spurious reflection.

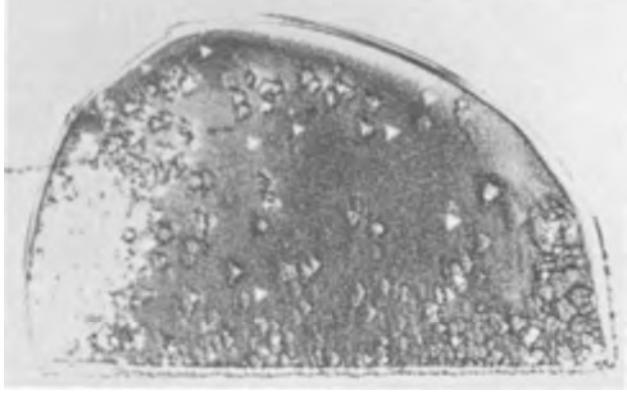

Fig. 12(b). The (440) topograph of the $GaAs_{0.67}P_{0.33}$ layer; the dark contrast results from local cracks in the deposit.

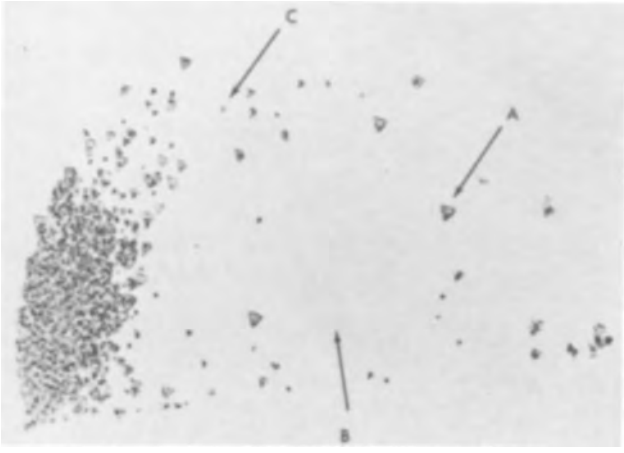

Fig. 12(c). The (440) topograph of the $GaAs_{0.85}P_{0.15}$ layer, only the hillocks are in diffracting position.

Fig. 12c. However, other hillocks protrude through the top layer (arrow A). The hillocks which protruded through the surface layer are revealed as triangles in Fig. 12c (arrow A). The partially overgrown hillocks (C) produce the diffuse images with null contrast centers (Fig. 12a, arrow C); only the triangular center can be seen in Fig. 12c.

The sample was angle-lapped and stained (Fe-HNO_3) on a 5° bevel to reveal the cross section of a hillock (Fig. 13). The dark irregular line, A, is the substrate and $GaAs_{0.85}P_{0.15}$ layer interface. The line at B is the junction between the $GaAs_{0.85}P_{0.15}$ and $GaAs_{0.67}P_{0.33}$ layers. The hillock, C, has the same stain as the $GaAs_{0.85}P_{0.15}$ layer which confirms the x-ray results. This hillock was determined to be 7μ above the $GaAs_{0.85}P_{0.15}$ layer.

Summary and Conclusions

The joint application of x-ray topography (SRT) and a diffractometer method to determine composition (compositional x-ray topography) has been shown to be an effective method to study the structural perfection and homogeneity of epitaxial Ga(As,P) and (Ga, In)As. Some results of this investigation are: (*a*) a planar compositional gradient was observed in (Ga,In)As deposits; the inhomogeneous regions were spatially located, and their composition was shown to be GaAs rich; (*b*) axial changes in composition were detected in a Ga(As,P) deposit (presumed to be constant composition); (*c*) the composition of hillocks generated at the substrate-$GaAs_{0.85}P_{0.15}$ layer interface was determined to be 15% GaP; (*d*) the hillocks (15% GaP) were frequently overgrown by a 33% GaP layer, and local cracking of this layer appeared to be related to the existence of hillocks.

Although this investigation was restricted to the GaAs-GaP and GaAs-InAs heteroepitaxial systems, this method has been successfully used to study stress relief mechanisms in deposits of germanium on silicon substrates (30). Another application concerns the perfection of (Ga, In)As which was deposited in holes that were cut (etched) into heavily dislocated monocrystals of GaAs (31). The dislocation density at the GaAs-(Ga,In)As heterojunction has also been compared to the dislocation density characteristic of the deposit (32). This type of examination is of interest in the determination of structural flaws created by lattice mismatch.

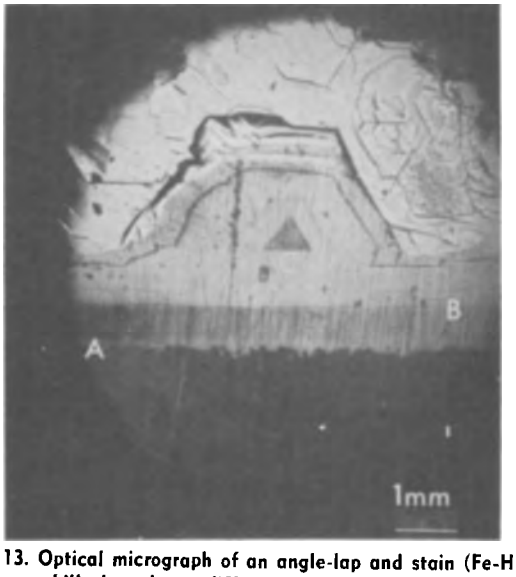

Fig. 13. Optical micrograph of an angle-lap and stain (Fe-HNO_3) junction; a hillock and two different compositional layers are displayed. Magnification, approximately 100X.

Acknowledgments

The authors gratefully acknowledge the interest and cooperation of the Materials Science Research Laboratory. In particular, Dr. R. W. Conrad supplied the (Ga,In)As samples; the Ga(As,P) sample was grown by Dr. R. H. Cox. Dr. D. W. Shaw is to be thanked for helpful discussions on hillocks. Mr. James A. Arnold performed the x-ray composition measurements.

Manuscript received Dec. 9, 1965; revised manuscript received Feb. 17, 1966. This paper was presented at the Buffalo Meeting, Oct. 10-14, 1965.

Any discussion of this paper will appear in a Discussion Section to be published in the December 1966 JOURNAL.

REFERENCES

1. "Development of Gallium Arsenide-Phosphide Graded Band-GaP Base Transistor Structures," Contract No. NObsr 91238, Final Report 1964.
2. "Research and Investigation of Gallium Arsenide-Indium Arsenide Alloy System," Contract No. AF 33(615)-1272, Final Report 1965.
3. W. F. Finch and E. W. Mehal, *This Journal*, **111**, 815 (1964).
4. G. E. Gottlieb, *ibid.*, **112**, 192 (1965).
5. M. Rubenstein, *ibid.*, **112**, 426 (1965).
6. San-Mei Ku, *ibid.*, **110**, 991 (1963).
7. E. M. Hull, *ibid.*, **111**, 1295 (1964).
8. G. R. Antell, *J. Appl. Phys.*, **31**, 1686 (1960).
9. Papers Presented on Technical Conference on Solid/Solid Interfaces, Electronic Properties, Boston, Mass., Aug. 31-Sept. 2, 1964, Trans. AIME, March 1965.
10. A. R. Lang, *J. Appl. Phys.*, **30**, 1748 (1958).
11. U. Bonse, *Z. Physik*, **153**, 278 (1958).
12. J. B. Newkirk, *Trans. AIME*, **215**, 483 (1959).
13. G. H. Schwuttke, *J. Appl. Phys.*, **33**, 2760 (1962).
14. G. H. Schwuttke, *ibid.*, **36**, 2712 (1965).
15. G. H. Schwuttke and V. Sils, *Bull. Amer. Phys. Soc.*, **2**, 48 (1964).
16. E. D. Jungbluth, *This Journal*, **112**, 580 (1965).
17. J. K. Howard and R. D. Dobrott, *Appl. Phys. Letters*, **7**, 101 (1965).
18. J. K. Howard and R. H. Cox, In press.
19. D. P. Miller, Unpublished results.
20. E. W. Williams, R. H. Cox, and R. D. Dobrott, To be published.
21. J. C. Woolley and K. W. Blazey, *J. Phys. Chem. Solids*, **25**, 713 (1964).

22. A. Reisman and R. Rohr, *This Journal*, **111**, 1425 (1964).
23. D. Kendall, Private communication.
24. S. Mendelson in *Single Crystal Films* (Conference at Blue Bell, Pa., May 1963), p. 251, M. H. Francombe and H. Sato, Editors, Pergamon Press Inc., New York (1964).
25. D. P. Miller, S. B. Watelski, and C. R. Moore, *J. Appl. Phys.*, **34**, 2813 (1963).
26. S. Mendelson, *ibid.*, **36**, 2525 (1965).
27. M. Takabayashi, *J. Appl. Phys. Japan*, **1**, 22 (1962).
28. T. Arizumi and T. Akasaki, *ibid.*, **2**, 143 (1963).
29. J. A. Amick in "Single Crystal Films" (Conference at Blue Bell, Pa., May 1963), p. 283, M. H. Francombe and H. Sato, Editors, Pergamon Press Inc., New York (1964).
30. J. K. Howard, Unpublished results.
31. J. K. Howard, R. W. Conrad, and D. W. Shaw, To be published.
32. J. K. Howard, To be published.

Potential of a Platinum Electrode at Low Partial Pressures of Hydrogen and Oxygen

II. An Improved Gas-Tight System with a Negligible Oxygen Leak

Sigmund Schuldiner, Bernard J. Piersma,[1] and Theodore B. Warner

United States Naval Research Laboratory, Washington, D. C.

ABSTRACT

A tight electrochemical system was constructed in which the P_{O_2} above the cell solution was $<10^{-9}$ atm. Comparing potentials with data from a previous paper (1) showed that very small amounts of O_2 leaking into a closed system can have marked effects on potential behavior at low P_{H_2}. Reduction of the oxygen leak to negligible proportions showed that: (*a*) the Nernst equilibrium relation for the H^+/H_2 couple holds only for P_{H_2} in excess of 10^{-6} atm; (*b*) at low P_{H_2}, trace amounts of O_2, even in the presence of several orders of magnitude more hydrogen, acted as an electrode poison causing a positive deviation from the theoretical Nernst behavior; (*c*) in O_2-free solution, at P_{H_2} below 10^{-6} atm, the potential remained at 0.18v positive to NHE and was independent of P_{H_2}. The potential-determining reaction in this region may be an exchange of H^+ in solution with H atoms dermasorbed in the Pt. The potential *vs.* oxygen partial pressure relation was essentially the same as found in previous work from this laboratory. Residual hydrogen associated with Pt at potentials from 0.18 to 0.2v did not react with oxygen.

In the first paper of this series, Warner and Schuldiner (1) determined open-circuit rest potentials on bright platinum as a function of oxygen or hydrogen partial pressures from 10^{-2} to 10^{-7} atm. The oxygen leakage (from air) into the cell was estimated to give a partial pressure of about 10^{-7} atm. The Nernst equilibrium relation for the H^+/H_2 couple held only at hydrogen partial pressures in excess of 1×10^{-4} atm. At hydrogen pressures smaller than this value the measured potentials were positive to the theoretical Nernst values. No satisfactory explanation could be given for this deviation, but it was felt that the trace of oxygen leaking into the system might be the cause. Even though a correction for the oxygen leak, assuming complete reaction with hydrogen at the Pt surface, was made, trace amounts of oxygen could possibly have remained on the surface when the hydrogen partial pressure was below 10^{-4} atm. This oxygen might then act as a poison for the H^+/H_2 exchange (even though the hydrogen partial pressure was several orders of magnitude higher) and give potentials positive to the theoretical equilibrium values. To determine if such traces of oxygen could affect the potential at low hydrogen pressures it was necessary to improve our gas-tight system to reduce further the leakage of oxygen into the cell. This was done in three ways: (*a*) improved purification of the helium carrier gas (Fig. 1) using two Meyer-Ronge (2) columns instead of one; (*b*) construction of a more compact gas purification and cell system; (*c*) installation of the critical part of the gas purification system, the gas generator, and the cell in a controlled environment box under an atmosphere of nitrogen (Fig. 2). Thus the outside of the system was exposed to nitrogen rather than air. The partial pressure of O_2 in the environment box was maintained at $5 \pm 2 \times 10^{-4}$ atm. This meant that at the outside of the system the O_2 pressure was reduced by 1/400 of the value in air.

[1] National Academy of Sciences, National Research Council Postdoctoral Research Associate.

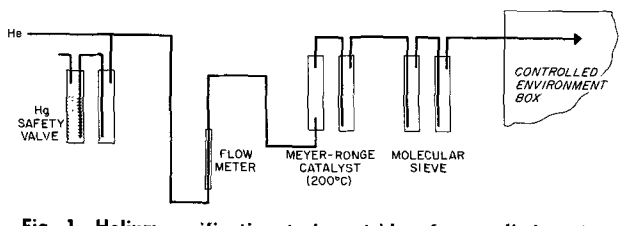

Fig. 1. Helium purification train outside of controlled environment box.

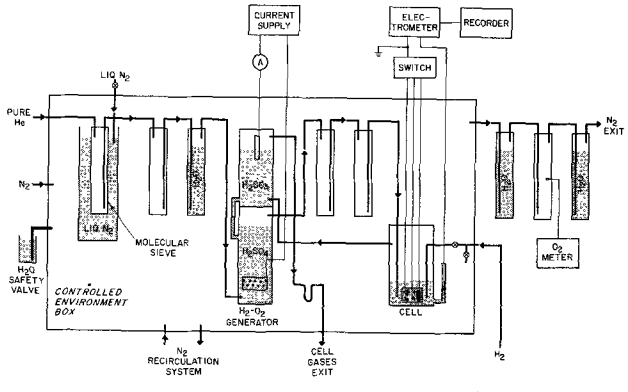

Fig. 2. Electrochemical system inside of controlled environment box and associated equipment.

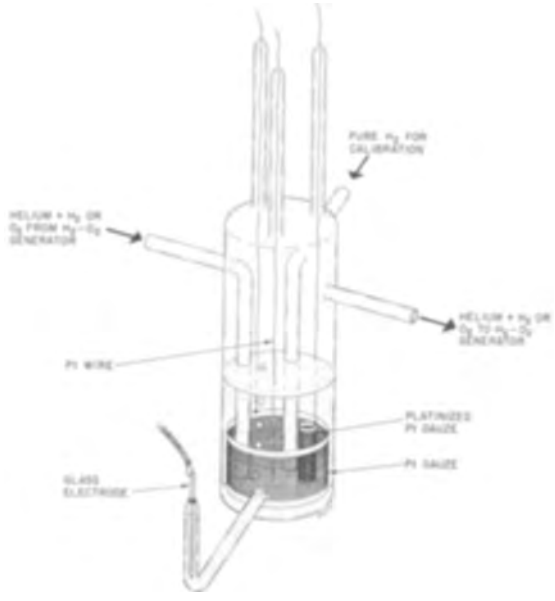

Fig. 3. Schematic of electrolytic cell. Glass pipe connections were actually used for electrode and gas connections and to connect upper and lower section of cell compartment. [See Fig. 1, p. 1143 of ref. (3) for illustration showing construction of cell.]

This improved gas-tight system reduced the oxygen leak into the cell to immeasurable proportions and, as the data will show, strongly affected the hydrogen pressure *vs.* potential relation.

Experimental

Apparatus.—The electrochemical cell (3) (Fig. 3) contained a miniature glass electrode, a Pt wire electrode 5 cm long with a 0.064 cm diameter, a large Pt gauze electrode (~100 cm^2), and a large tightly rolled cylinder of Pt gauze platinized in lead-free platinic acid (total geometric area about 30 cm^2). The electrolyte was 1M H_2SO_4 maintained at 25° ± 2°C. The helium purification train, electrolytic H_2 or O_2 generator (1), cell, and controlled environment system are shown in Fig. 1 and 2. The two stopcocks leading to the cell (Fig. 2) were Kern high-vacuum greaseless stopcocks with Viton A diaphragms. The controlled environment box was manufactured by Vacuum/Atmospheres Corporation and was 45 in. long by 30 in. deep by 33 in. high. The liquid nitrogen cold trap consisted of a molecular sieve (Linde 5A) column in a Linde LD 10 liter Dewar. This Dewar flask was filled *via* an insulated copper pipe which led outside the box where it was shut off with a valve. Copper tubing connected the helium tank to the flow meter. From this point the system was glass with one Viton A O-ring connection between the two Meyer-Ronge catalyst columns. At the end of the second molecular sieve column a gold-plated (to prevent diffusion of hydrogen in from the room atmosphere) copper tube was connected with a second Viton A O-ring. This gold-plated copper tube conducted the purified helium into the environment box to the cold trap. Therefore, even though two Viton A seals were used outside the box, one seal was between the two Meyer-Ronge columns so any trace of O_2 which diffused through it was removed by the second Meyer-Ronge column. The second seal outside the box was in front of the molecular sieve-liquid N_2 cold trap so that any O_2 which diffused through this O-ring would be frozen out. Since the liquid N_2 cold trap was inside the environment box, diffusion of O_2 through any of the other seals was minimized. The manufacturer of the Viton-A O-rings claims a seal good to 10^{-6} Torr, and previous work (1) indicated an oxygen leak in the entire system equivalent to about 10^{-7} atm, so with the new system used we feel that the oxygen leak within the cell should not exceed 10^{-9} atm. In any case, attempts to determine the amount of oxygen leaking into the cell from the atmosphere were fruitless because of its extremely low concentration.

An N_2 atmosphere inside the environment box was obtained by passing tank N_2 into the box for several days until O_2 partial pressure inside the box dropped to about 10^{-3} atm. The flow of N_2 was then reduced, and the gas inside the box was recirculated through a bed of copper turnings at 450°C to remove oxygen. Recirculation was *via* a high-speed gas pump with a flow of about 1.5 l/min. It was soon discovered that the evaporation of liquid N_2 maintained a sufficient gas flow through the environment box and the tank N_2 was eliminated. Once the O_2 pressure dropped to 5 x 10^{-4} atm, as determined on the outlet side with a Beckman, Model E2 oxygen analyzer, recirculating N_2 was no longer helpful in reducing the O_2 partial pressure. From that point on the only sources of N_2 needed were from the evaporation of liquid N_2 and from the tank N_2 used to pump liquid N_2 into the Dewar. It was necessary to fill the Dewar every two weeks. This operation resulted in a large influx of N_2 into the box so that a large outlet valve from the box had to be kept open to keep the internal pressure below 5 in. of water in excess of atmospheric pressure. In addition a water-filled safety valve was attached to the box. This valve would release N_2 when the pressure inside of the box exceeded 5 in. of water above normal atmospheric pressure.

Electrical connections were made as shown in Fig. 2. A system of rotary switches was used to alternate every 5 min from one Pt electrode in the cell to another. The potential between each Pt electrode and the glass reference electrode was measured with a Keithley 610A electrometer and displayed alternately on a Varian recorder.

Procedure.—Glassware was cleaned with boiling nitric acid and rinsed 12 to 15 times with triply distilled water (one stage of distillation from alkaline permanganate solution, another from water containing fumed phosphoric acid, the final two stages being from a quartz still). The sulfuric acid solution was preelectrolyzed for three days at 50 ma. This was followed by calibration of the glass electrode against the platinum electrodes in H_2 saturated solution at 1 atm pressure. Hydrogen flow was then replaced with a flow of pure helium always maintained at 40 std ml/min. Pressure within the cell was about 10 Torr above atmospheric. The hydrogen line was disconnected, flushed, and filled with helium. The environment box was then sealed and air was replaced with N_2 by the procedure described above. Either hydrogen or oxygen was introduced into the helium carrier gas by the special electrolytic H_2 or O_2 generator (1) designed at this laboratory. Gas generation rates were calculated from constant electrolysis currents. The partial pressures were calculated from the rate of flow of helium (known to 5%) and the rates of H_2 or O_2 generation (known to 1%).

The rate of attainment of steady-state potentials was very dependent on electrode area, especially at partial pressures below 10^{-6} atm. The platinized Pt electrode area was so large that at low partial pressures this electrode lagged far behind the other two Pt electrodes. All three electrodes would come to the same potential given sufficient time, but the platinized Pt electrode required such a long time (months) at very low partial pressures that in most measurements only enough time was allowed for the Pt wire and gauze to come to the same steady-state values. The experiments which gave the data recorded in this paper took about 11 months. Several runs up and down the pressure scale were taken.

When pure helium or helium mixtures with low hydrogen partial pressures flowed through the cell, the addition of liquid N_2 to the cold trap caused the Pt

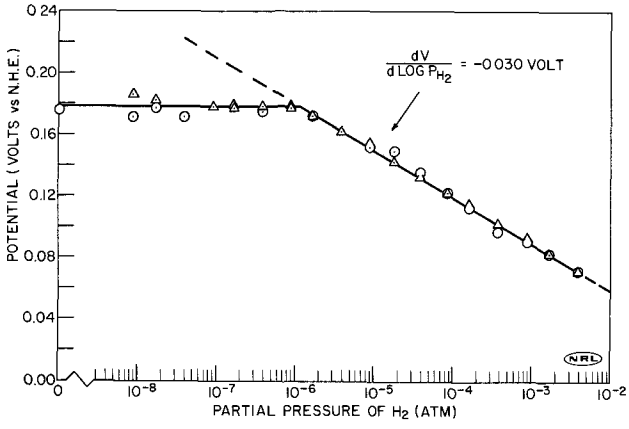

Fig. 4. Relation between hydrogen partial pressure and rest potentials. Dashed line shows normal Nernst potential relation for H^+/H_2 exchange; ○ decreasing H_2 pressure; △ increasing H_2 pressure.

wire and gauze electrode potentials to deviate in a positive direction. Several hours were required for these electrodes to recover their original potentials. We attribute this effect to a trace of O_2 which was introduced during the cooling of the environment box (its temperature usually decreased to about 17°C during the filling of the Dewar). This cooling caused a decrease in pressure in two arms of the cell, and the space above the solution in these compartments decreased as the cell solution rose slightly in them. This may have caused a trace of oxygen trapped in these side arms or in the counter electrode side of the gas generator to go into solution and/or caused a further removal of traces of oxygen associated with the interior walls of the glass system. The rise of solution in these side arms showed that leaks did not exist. In any case liquid N_2 was added only once every 14 days so that this effect was minimized.

Results and Discussion

Experimental results.—The experimental results are shown in Fig. 4 for the hydrogen electrode and in Fig. 5 for the oxygen electrode. Values were obtained with both increasing and decreasing gas partial pressures and were taken only after steady-state potentials were reached. For hydrogen partial pressures below 10^{-5} atm, steady-state meant no significant change in potential (values constant within ± 3 mv, and no monotonic trend within this uncertainty) on the Pt wire and gauze for at least several days. Their potentials generally agreed to 2 mv, with occasional differences of 5-7 mv. For the platinized platinum gauze at the lowest partial pressures, the electrode continually changed in the expected direction, but at such a slow rate that we did not normally wait for this electrode to reach the steady-state value of the other two electrodes.

For oxygen partial pressures, the rate of attainment of steady-state potentials for decreasing oxygen pressures was very slow, even for the Pt wire. Here also the potentials shown in Fig. 5 represent values that were unchanged for at least several days, but because of extreme system sluggishness, agreement between electrodes was poorer (5-30 mv) and random variations with time larger. Experiments were conducted also in which the gas flow was changed from helium containing first hydrogen and then oxygen and *vice versa*. This made no difference in the final rest potential providing one waited long enough for the rest potential to be attained.

In one experiment, after the electrodes were exposed to oxygen-containing helium for over two months, the oxygen flow was cut off. The rest potential on the Pt wire was reached in about one week (0.2v). Then, to test the purity of the solution, the cleanliness of the electrodes, and the tightness of the entire system, a single constant current pulse was applied to the Pt wire in the helium-saturated solution. This test took place six months after cleaning and closing the system. An anodic charging curve of the first applied current pulse gave an oscilloscopic trace which showed a small hydrogen region from 0.2 to 0.4v followed by double layer and linear oxygen regions. The shape of the charging curve met our published (4) requirements for a clean Pt surface free of detectable amounts of either oxidizable or unoxidizable organic contaminants or of electrode poisons. The fact that hydrogen was still associated with the Pt surface after such a long exposure to oxygen was unexpected, but it does account for the relatively low positive potentials of Pt observed in helium-saturated solution.

Effect of oxygen leak.—In order to estimate the maximum possible amount of oxygen which leaked into the cell, the following experiment was carried out. After passing pure helium through the cell for five days, the average potential of the three Pt electrodes was 0.175v. The sequence of changing the partial pressure of either oxygen or hydrogen in the cell to the values shown in Fig. 6 was then carried out. At the end of each time noted for the given partial pressure shown in Fig. 6 the potential of the Pt wire, the electrode with the fastest response, is shown. It should be noted that these are not the final rest potentials at these partial pressures. These results are for the purpose of demonstrating the effects of small alternate additions of oxygen and hydrogen on the potential. As the data show, potentials are sensitive to oxygen partial pressures as low as 4.4×10^{-9} atm and hydrogen partial pressures as low as 8.7×10^{-9} atm. From this we can conclude that the oxygen leak into the system cannot be, at most, more than enough to give a partial pressure of 10^{-9} atm. In fact, from the relatively fast response times shown in Fig. 6, one can conclude

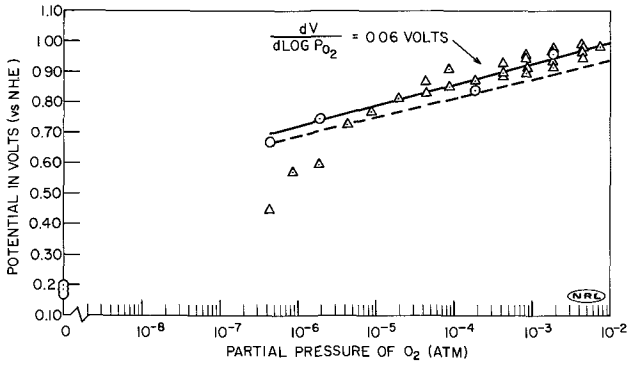

Fig. 5. Relation between oxygen partial pressure and rest potentials. Dashed line indicates average values previously obtained at this laboratory (1, 3); ○ decreasing O_2 pressure; △, increasing O_2 pressure.

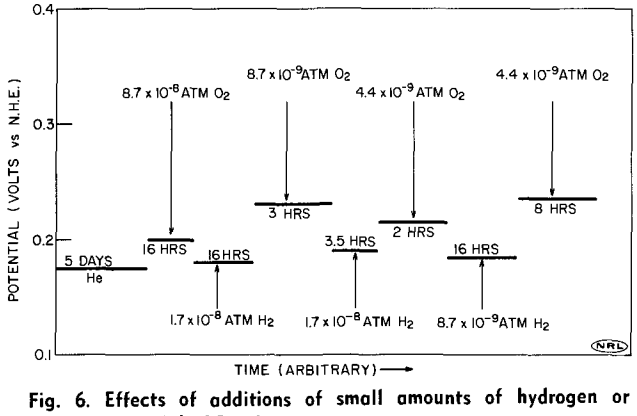

Fig. 6. Effects of additions of small amounts of hydrogen or oxygen on potential of Pt wire.

that the oxygen leak, expressed in terms of resulting partial pressure, was likely under 10^{-10} atm.

Platinum rest potentials vs. P_{H_2} or P_{O_2}.—The data in Fig. 4 demonstrate that a normal Nernst equilibrium relation between potential and log P_{H_2} exists down to 1 x 10^{-6} atm of hydrogen. At lower hydrogen pressures the potential is independent of P_{H_2}, this implies that the exchange current density of the H^+/H_2 exchange at P_{H_2} below 10^{-6} atm is so low [$\approx$1.4 x 10^{-9} amp/cm^2 (5)] that another potential-determining reaction takes over. Such a reaction could be

$$Pt\text{-}H \rightleftarrows Pt + H^+ + e$$

where Pt-H either represents hydrogen atoms dermasorbed in the Pt skin or an alloy of Pt and H atoms. Schuldiner, Castellan, and Hoare (6) concluded that a similar potential-determining reaction took place on α Pd-H alloys.

Luk'yanycheva and Bagotskii (7) determined the initial open-circuit potentials of carefully degassed platinum in 1*N* H_2SO_4 degassed under vacuum. These potentials were 0.210 and 0.215v. They observed that these rest potentials are close to the point of zero charge of platinum.

Our measurements in helium-saturated solution gave rest potentials 15-50 mv more negative than those of Luk'yanycheva and Bagotskii. In addition, the fact that we were able to find a small amount of hydrogen associated with the electrode after prolonged exposure to oxygen showed that the rest potentials we found in helium-saturated solutions and the plateau at 0.178v shown in Fig. 4 are influenced by hydrogen.

Since the potential plateau in Fig. 4 is below the theoretical Nernst line, oxygen is not a factor as it was in the first paper of this series (1). The stability of Pt-H in this region is demonstrated by the rest potential in pure helium-saturated solution. The experiments which showed that after an electrode has been in oxygen-rich helium the rest potential in pure helium is about the same indicate that this residual hydrogen does not react with oxygen. In addition, it shows that sorbed oxygen is in equilibrium with O_2 gas because when the O_2 pressure drops to zero the oxygen coverage of the surface appears to drop to zero. The stability of this residual hydrogen indicates that it is irreversibly sorbed with respect to H_2 and supports the repeatedly stated view from this laboratory that this hydrogen is dermasorbed in the Pt skin and may be alloyed with Pt. The hydrogen content of the Pt electrode apparently did not change with H_2 partial pressures below 10^{-6} atm, as indicated by the unchanging electrode potential in this region. This may be contrasted with the dependence of hydrogen content of α Pd-H on H_2 partial pressure as shown by Moon (8). However, much smaller amounts of H are involved than in the case of α Pd-H alloys.

One may argue that the plateau shown in Fig. 4 is due to an organic or other trace material in solution. However, the cleanliness test made after the system was used for six months shows that this possibility is unlikely. In addition, finding hydrogen associated with the platinum after long exposure to oxygen indicates that hydrogen determines the potential. Another experiment to show the effects of hydrogen on potential was made by determining the rest potential in pure helium followed by addition of oxygen to give a more positive rest potential followed by the addition of less than 10^{-6} atm H_2 which then gave the same rest potentials shown in Fig. 4. Furthermore, the total area of Pt in solution was so large that impurity levels, which were below the detectable limit of our cleanliness test (4), would be so minute that even the traces of oxygen or hydrogen used would overcome their effects (as was demonstrated by the reported tests).

The possibility must also be considered that the 0.2v open-circuit potentials under pure helium could be due to leakage of hydrogen into the gas stream from the Pd-tube counter electrode in the electrolytic gas generator. The design of the gas generator made this improbable. Additional evidence that this did not occur came from the following experiment: after the electrodes were exposed to a He + O_2 mixture, pure helium was substituted. While the potentials were changing to less positive values the electrolyte contact with the Pd counter electrode in the gas generator was broken. The rate of potential change on the Pt electrodes in the cell did not change significantly, and final rest potentials were the same as previously found.

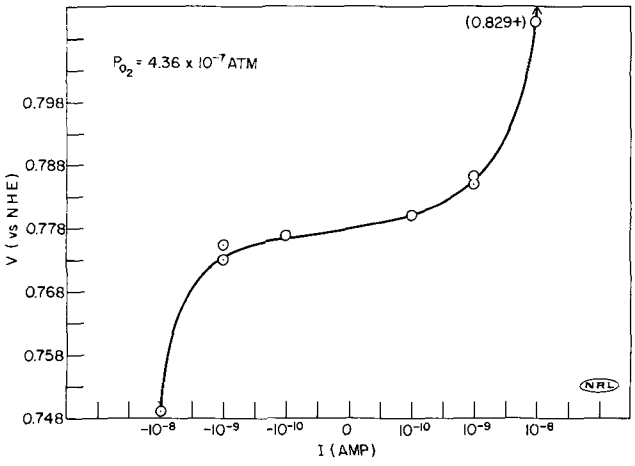

Fig. 7. Anodic and cathodic polarization of Pt wire electrode

The rest potentials shown in Fig. 5 give essentially the same dependence of potential on oxygen partial pressure as was previously determined (1, 3). There was, however, a significant difference. The broken line in Fig. 5 represents the average data previously found (1, 3) and as can be seen the data from this investigation indicated the same slope but an upward displacement of the average curve by about 40 mv. The reason for this difference is unknown. Stirring effects, effect of platinized Pt, effects of light, etc., were all checked and none seemed to be important. It also should be noted that the low potential values found at increasing very low oxygen partial pressures is most likely due to the very long times required to attain steady state. Decreasing values of oxygen partial pressures fell on the straight line shown in Fig. 5. A current-voltage relation was determined at P_{O_2} = 4.36 x 10^{-7} atm and is shown in Fig. 7. The open-circuit potential was a little above the rest potential later found. The data in this curve indicate that the potential is determined by a reversible reaction involving oxygen.

In previous work (1, 3) it was suggested that the potential was determined by an O_2/HO_2 exchange. The results found in this work confirm this.

Conclusions

1. True steady-state open-circuit potentials can be obtained and maintained when sufficient steps are taken to insure solution and gas purity and electrode cleanliness.

2. Considerable periods of time (up to a month or more) are required to establish steady-state potentials with low partial pressures (below 10^{-4} atm) of H_2 or O_2. Response times are faster with hydrogen.

3. At low partial pressures, the surface area becomes dominating in the time for establishment of steady-state potentials. At higher partial pressures, the surface/volume ratio of the electrode is the determining factor.

4. The oxygen background in this improved system is less than 10^{-9} atm.

5. The deviation from Nernst behavior previously reported (1) for the hydrogen electrode was due to the effects of small amounts of oxygen poisoning the hydrogen equilibrium.

6. Below hydrogen partial pressures of 10^{-6} atm, the steady-state potential is independent of P_{H_2}, *i.e.*, the Nernst potential relation for the H^+/H_2 equilibrium is not valid below 10^{-6} atm.

7. The potential plateau observed at 0.18v for hydrogen partial pressures below 10^{-6} atm is not due to an organic impurity.

8. The 0.18v potential is believed to be established by an equilibrium involving hydrogen ions in solution and hydrogen atoms dermasorbed in the electrode (or alloyed with the Pt). This reaction has an exchange current density on the order of 10^{-9} amp/cm^2.

9. The residual hydrogen associated with Pt at potentials from 0.18 to 0.2v did not react with oxygen.

10. The potential-oxygen partial pressure relation found had the same slope as previously reported (1, 3) although potentials at the same partial pressures ran about 40 mv higher.

Manuscript received Feb. 16, 1966.

Any discussion of this paper will appear in a Discussion Section to be published in the December 1966 JOURNAL.

REFERENCES

1. T. B. Warner and S. Schuldiner, *This Journal*, **112**, 853 (1965).
2. F. R. Meyer and G. Ronge, *Angew. Chem.*, **52**, 637 (1939).
3. S. Schuldiner and R. M. Roe, *This Journal*, **110**, 332, 1142, (1963).
4. S. Schuldiner and T. B. Warner, *J. Phys. Chem.*, **68**, 1223 (1964).
5. S. Schuldiner, *This Journal*, **106**, 891 (1959).
6. S. Schuldiner, G. W. Castellan, and J. P. Hoare. *J. Chem. Phys.*, **28**, 16 (1958).
7. V. I. Luk'yanycheva and V. S. Bagotskii, *Dokl. Akad. Nauk, SSSR*, **155**, 160 (1964).
8. K. A. Moon, *J. Phys. Chem.*, **60**, 502 (1956).

Electrochemical Measurement of the Available Surface Area of Carbon-Supported Platinum

J. F. Connolly, R. J. Flannery, and G. Aronowitz

Research and Development Department, American Oil Company, Whiting, Indiana

ABSTRACT

The measurement of charge consumed in the galvanostatic stripping of adsorbed oxygen or hydrogen from carbon-supported platinum surfaces gave a measure of the area of platinum in contact with solution. A combination of the two methods proved superior to either used alone. The combination compensated for the charge consumed on the carbon with sufficient accuracy to permit measurements down to the region where the platinum area is 1/100 of the support area. Comparison with x-ray diffraction measurements suggests that, with high platinum concentrations on low area carbons, standard platinum deposition techniques yield electrodes in which much of the platinum surface is not in contact with solution.

When platinized porous-carbon electrodes are used in fuel cells, some of the platinum may be unavailable because it is physically inaccessible to the solution or because of adsorbed material on its surface. Knowledge of the available area of the platinum is useful for optimizing cell performance. X-ray diffraction does not exclude unavailable platinum area and may miss very small crystallites. However, electrochemical methods can be expected to measure only platinum which is in contact with solution, and there should be no lower limit on the size of platinum crystallites which can be detected.

The areas of unsupported metals can, in principle, be measured by four electrochemical techniques: measurements of capacitance (1), measurement of exchange currents (2), stripping or deposition of oxygen (3), and stripping or deposition of hydrogen (4). The first technique has been applied to a number of unsupported metals (1), while the other three would be useful only in special cases.

For platinum supported by a porous-carbon electrode, capacitance measurement may be ruled out because the capacitance of the platinum will not differ enough from that of the support, and because pore resistance makes capacitance difficult to measure. Likewise, measurements of exchange currents will in general be thwarted by mass transfer limitations in a porous electrode and where this is not the case, as in hydrogen evolution, by excessive pore resistance.

However, the oxygen and hydrogen stripping methods are probably unaffected by mass transfer in a porous electrode although nonuniform current distribution due to pore resistance has some effect on the form of the "arrest" (a region of minimal slope in the potential *vs.* charge curve). Therefore, these two methods were investigated, singly and in combination, with a series of platinized porous-carbon electrodes having a broad range of surface areas and platinum loadings. The major difficulty encountered was in correcting for the charge consumed on the carbon support, the area of which was many times the platinum area. This problem was solved to the extent that cases in which the platinum area is as small as 1/100 of the support area can be handled.

Experimental

The measurements were carried out in an H-cell, connected to a mercurous sulfate-mercury reference electrode through a Luggin capillary. Carbon-supported platinum electrodes were held between tantalum screens mounted in a tantalum holder. Potential was controlled by a Wenking potentiostat, and mercury wetted relays were used for switching to a galvanostat which consisted of resistors and a 90v battery. Voltage variations were followed on a Tektronix oscilloscope and recorded with a Polaroid camera.

The arms of the H-cell were separated by a medium glass frit and could be flushed with helium to remove oxygen. Preelectrolyzed 1M H_2SO_4, prepared from permanganate-distilled conductivity water, was the electrolyte in the cell, in the bridge to the reference electrode, and in the reference electrode compartment. For comparison with the mercurous sulfate-mercury reference electrode, the working compartment was frequently converted to a hydrogen reference electrode. This was done by inserting a platinized platinum electrode into the compartment and changing the flushing gas from helium to hydrogen. All voltages are given with reference to this "hydrogen electrode in the same solution." Ohmic voltage drops not

Table I. Electrode properties

Carbon	Area of block carbon, m^2/g	w/o Pt	Carbon[a] charge ratio, $Q_{C,O}/Q_{C,H}$	Carbon charge, % of O arrest, $100Q_{C,O}/Q_{T,O}$	Carbon charge, % of H arrest, $100Q_{C,H}/Q_{T,H}$
NC60	0.4[b]	4.2	6.9	0	0
NC60	0.4[b]	0.9	6.9	55	30
NC60	0.4[b]	1.0	6.9	55	30
FC11	3.0	4.4	6.4	5	0
FC21	1.0	1.0	6.5	30	15
PC59H	5.4	4.9	7.0	15	5
PC139	1.6	1.0	6.3	40	20
PC57H	1.3	0.8	6.6	50	35
FC14	10	5.2	6.4	10	5
FC11	3.0	1.1	6.4	15	5
PC59H	5.4	1.1	7.0	45	25
AC[c]	11[c]	4.8	5.6	45	25
FC14	10	1.1	6.4	35	15
PC62	200	20.4	6.8	55	30
PC62	200	7.2	6.8	60	30
PC64	700	27.7	5.1	70	50
PC62	200	4.8	6.8	75	50

[a] Charge consumed by blank powdered carbon from 1.1 to 0.35v divided by charge consumed from 0.05 to 0.30v.
[b] Estimated from apparent integral capacitance and gas chromatography.
[c] Powder. Courtesy sample from R. G. Haldeman (8).
Weight per cent = w/o.

eliminated by the Luggin capillary were corrected for by noting the gap in the oscilloscope trace at the beginning of a galvanostatic pulse.

The carbons, in block form, were platinized by impregnating with a solution containing chloroplatinic and oxalic acids, and then heating to 160°-180°C in an inert atmosphere for 8 hr. The reduction was completed by adding hydrazine and excess reagents were leached out in distilled water. In a few cases hydrogen of hydrazine alone was used as the reducing agent. Because these procedures did not give uniform platinum loadings, the platinized carbons were powdered before samples were taken for platinum analysis, x-ray diffraction, and electrochemical area measurements.

Carbon supports were obtained from National Carbon (NC), Pure Carbon (FC), Stackpole (PC), and American Cyanamid (AC). The manufacturer's designations and areas of the block form are listed in Table I. When powdered, the carbons having low surface areas all increased in area, as indicated by apparent integral capacitance in the 0.05-0.30v range. This is reflected in the large carbon charge consumptions listed in the last two columns of Table I. The surface areas of the high-area carbons were relatively little affected by powdering.

To form the electrodes, platinized-carbon powders were mixed with Teflon suspension, dried at room temperature, and pressed at 50,000 psi. The finished electrodes contained 3% Teflon and were strong enough to hold together in solution as long as they were supported between tantalum screens. Because the Teflon bonding procedure often made platinized carbons electrochemically inactive the electrodes were anodized at 1.2-1.4v for 10 to 30 min. However, care had to be used to obtain the mildest possible activating conditions in each case because anodizing roughens the carbons.

The affect of grinding and Teflon bonding on the platinum area measurements was ascertained as follows: Electrochemical measurements were made on several chips of solid platinized carbon. The chips were then processed into Teflon-bonded electrodes and the electrochemical measurements were repeated. The results showed that apparent losses in platinum area caused by the electrode-forming procedure were less than 10% as long as the Teflon-bonded electrodes were sufficiently anodized.

Immediately prior to oxygen stripping, the electrodes were pretreated by holding at 1.4v for 1 min. Before hydrogen stripping they were held at 1.2-1.4v for 1 min and then at 0.05v for 1 min. After

[1] This behavior and the comparison with x-rays to be made later indicate that the surface migration of hydrogen from platinum to carbon observed for gas-solid systems at high temperatures (5) is not a problem in the present case.

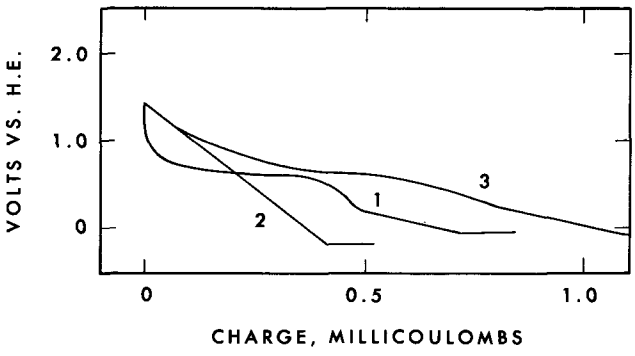

Fig. 1. Oxygen reduction: curve 1, 1 cm^2 Pt; curve 2, 15 cm^2 carbon; curve 3, Pt on carbon.

the first 30 sec there was very little change of arrest length with time at 0.05v,[1] unless the solution contained oxidizable impurities. These treatments were in addition to any necessary to cure poisoning of the Teflon-bonded electrodes.

The current densities during the galvanostatic strippings were adjusted to give an over-all voltage change rate of about 0.05v/sec. This required current densities of 0.5 to 1.0 $\mu a/cm^2$ of true area for the blank carbon electrodes, and higher values for the platinum loaded electrodes. Under these conditions 5-10 mg electrodes required total currents ranging from 0.1 to 25 ma. For any particular blank carbon sample the charge consumption in the 1.1 to 0.35 or 0.05 to 0.30 voltage intervals usually decreased or increased by about 10% for a fivefold increase or decrease in current density. The platinum loaded carbons were less affected by changes in current density. The current necessary for holding a sample at a particular voltage before switching to the galvanostat was less than 5% of the stripping current.

Oxygen Arrest

The arrest formed when adsorbed oxygen is stripped galvanostatically from a pure platinum electrode is illustrated by curve 1 in Fig. 1. The arrest starts near 1.1v and is complete at 0.35v. A potential *vs.* charge curve for a blank carbon electrode of moderate area is nearly linear as shown by curve 2. The effects of using carbon-supported platinum, rather than solid platinum, are to lengthen the oxygen arrest and to make its end points less distinct. These effects are illustrated in Fig. 1 by curve 3, in which 40% of the charge is being consumed on the carbon support. Because of the lack of distinctness in the arrest end points, measurements were made by using the end points which were consistently observed for those cases where the end points were distinct, *i.e.*, 1.1 and 0.35v.

For electrodes which have all been anodized in the same way, the charge consumed on platinum in the oxygen arrest is proportional to the platinum area, *i.e.*

$$A_{Pt} = Q_{Pt,O}/k_O = (Q_{T,O} - Q_{C,O})/k_O \qquad [1]$$

where A_{Pt} is the available platinum area, $Q_{Pt,O}$ is the charge consumed on the platinum in the oxygen arrest, k_O is a proportionality constant, $Q_{T,O}$ is the total charge consumed in the electrode in the oxygen arrest, and $Q_{C,O}$ is the charge consumed on the carbon support.

Because we did not have a platinum sample of known roughness, the results of Laitinen and Enke (3), corrected for the difference between H_2SO_4 and $HClO_4$ electrolytes (6), were used to estimate the proportionality constant k_O. This procedure gave 0.45 mc/cm^2 of true platinum area, for the charge consumed between 1.1 and 0.35v after pretreatment at 1.4v for 1 min.

$Q_{C,O}$, the charge consumed on the support, can be assigned in part to double layer capacitance and probably even in greater measure to oxygen adsorbed on

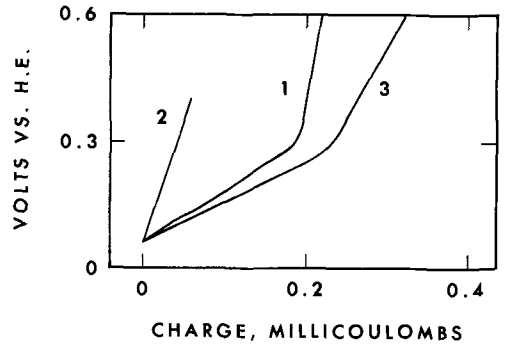

Fig. 2. Hydrogen oxidation: curve 1, 1 cm² Pt; curve 2, 15 cm² carbon; curve 3, Pt on carbon.

the carbon. This effect was small per unit area (an apparent integral capacitance of about 20 μf/cm² over the interval 1.1 to 0.35v) but, because the carbon area ranged up to 100 times that of the platinum, a major correction was necessary in most cases. It was evaluated by making a separate stripping measurement on an electrode formed from a nonplatinized sample of the same support. This procedure involved considerable uncertainty because of possible differences between the carbon supports of the platinized and nonplatinized electrodes. These differences could be expected to occur because of: nonuniform carbons, differences in grinding during the electrode preparation procedure, effect on the carbon of the chemicals used for platinizing, blockage of pores by platinum, and small differences in the stripping measurements.

Hydrogen Arrest

The arrest formed when adsorbed hydrogen is stripped galvanostatically from a pure platinum electrode is illustrated by curve 1 of Fig. 2. In the illustration the arrest commences at 0.05v and is complete near 0.30v. The hydrogen arrest for carbon-supported platinum differs from that of solid platinum in three aspects. It is longer, the faint fine structure is lost, and the change in slope near 0.30v is less sharp. These effects are illustrated by curve 3 in Fig. 3 in which 20% of the charge is being consumed on the carbon support.

The hydrogen arrest is analogous to the oxygen arrest in that the platinum areas of electrodes which have had like pretreatment will be proportional to the charge consumed on the platinum, *i.e.*

$$A_{Pt} = Q_{Pt,H}/k_H = (Q_{T,H} - Q_{C,H})/k_H \qquad [2]$$

where $Q_{Pt,H}$ is the charge consumed on the platinum in the hydrogen arrest, k_H is a proportionality constant, $Q_{T,H}$ is the total charge consumed in the electrode in the hydrogen arrest, and $Q_{C,H}$ is the charge consumed on the carbon support.

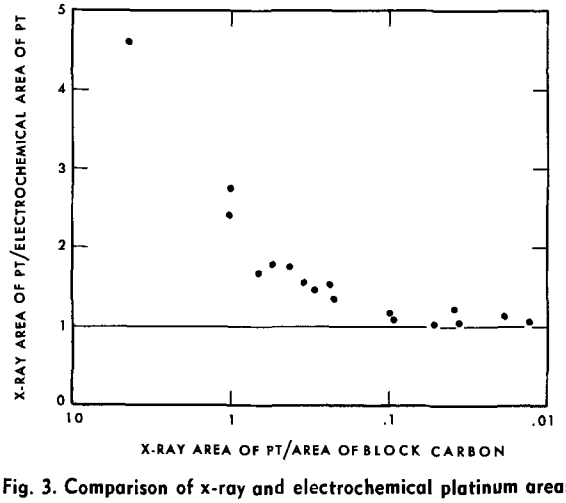

Fig. 3. Comparison of x-ray and electrochemical platinum areas

The proportionality constant k_H was determined by using pure platinum electrodes whose areas had been determined from the length of the oxygen arrest. This gave 0.19 mc/cm² of platinum for the charge consumed between 0.05 and 0.30v on bright platinum and platinized platinum electrodes which had been exposed to the atmosphere for several days. Freshly prepared electrodes gave a value 20% higher. The lower value was adopted because the aged electrodes should be a better approximation to the situation encountered with carbon-supported platinum. The carbon charge consumptions $Q_{C,H}$ were measured on nonplatinized carbon electrodes and are subject to the uncertainties listed in the oxygen arrest section.

Because $Q_{C,H} < Q_{C,O}$, the accuracies of the hydrogen arrest and oxygen arrest methods differ. To evaluate the relative uncertainty we will assume that the main error in an area measurement is due to the uncertainty in determining the charge consumed on the support. If this charge consumption is uncertain by some value e in per cent, then the percentage errors in the area determination by the oxygen and hydrogen arrest methods are

$$\Delta_O = eQ_{C,O}/Q_{Pt,O} \qquad [3]$$

and

$$\Delta_H = eQ_{C,H}/Q_{Pt,H} \qquad [4]$$

Now $Q_{Pt,H}/Q_{Pt,O} = k_H/k_O = 0.19/0.45$ and, as shown in Table I, $Q_{C,O}/Q_{C,H}$ is about 6.5. Thus, measurements of carbon-supported platinum areas, made using the oxygen arrest, should contain an error 2.7 times larger than those made using the hydrogen arrest.

Therefore, where the ratio of platinum area to support area is low, the hydrogen arrest method should give the better result. However, when this ratio is large, greater ease of activation (leading to earlier achievement of a reproducible state) and insensitivity to solution impurities (which do not adsorb as readily in the surface oxide formation region) favor using the oxygen arrest.

Oxygen and Hydrogen Arrests Used in Combination

As the platinum to carbon area ratio approaches 0.01 the fraction of the charge consumed in the carbon in the oxygen arrest reaches 75% and the fraction consumed in the hydrogen arrest reaches 50%. Thus, unless the carbon charge consumption is accurately known these methods become useless.

For reasons discussed in the oxygen arrest section, a separate measurement on the nonplatinized carbon does not give an accurate value for the charge consumption of the carbon in a platinized carbon. To get reasonable accuracy a method which uses direct measurements on the platinized carbon, with minimal dependence on blank carbon measurements, is desirable. Such a method is obtained by combining the oxygen-arrest and hydrogen-arrest charge consumptions as measured on the platinized-carbon electrode, with the ratio of the charges consumed by the support in the same regions as measured on a blank-carbon electrode, *i.e.*, from Eq. [1], [2], and

$$r = Q_{C,O}/Q_{C,H} \qquad [5]$$

we obtain

$$A_{Pt} = (rQ_{T,H} - Q_{T,O})/(rk_H - k_O) \qquad [6]$$

Thus the measured area of platinum becomes dependent on a ratio of carbon charge consumptions rather than on their absolute values.

The superiority of this combination method lies in its minimizing of dependence on blank carbon electrode measurements. Thus r should, as measured on the blank carbon electrode, apply to the platinized electrode with much greater accuracy than similarly measured absolute values of carbon charge consumption; *e.g.*, the plugging of carbon pores by platinum

Table II. Comparison of measurements of the area of carbon-supported platinum

Carbon area, m^2/g	w/o Pt	Area[a] ratio, Pt to carbon	Pt area, m^2/g Pt			
			O Arrest[b]	H Arrest	Combination	X-ray[c]
0.4	4.2	4.5	4	7	9	38,44
0.4	0.9	1.0		16	16	41,48
0.4	1.0	1.0		18	18	38,45
3.0	4.4	0.60	23	24	25	39,46
1.0	1.0	0.55	26	29	31	52,59
5.4	4.9	0.45	24	25	25	40,48
1.6	1.0	0.35	31	34	36	52,59
1.3	0.8	0.30	44	36	32	43,51
10	5.2	0.20	27	28	28	39,46
3.0	1.1	0.20	38	41	44	55,62
5.4	1.1	0.10	44	41	40	43,51
11	4.8	0.10	26	22	19	17,25
10	1.1	0.05	44	46	46	43,51
200	20.4	0.04		25	25	27,34
200	7.2	0.04		109	95	89,96
700	27.7	0.02		43	30	30,38
200	4.8	0.01		44	47	47,53

[a] X-ray area of Pt divided by area of block carbon.
[b] Values are omitted where charge consumption of the carbon support (Table I) is greater than 50% of the total.
[c] The two areas listed are from the calculation methods of Jones (7) and Warren (7), respectively.

of the platinized-carbon electrodes causes major reductions in the absolute values of the carbon charge consumptions in the oxygen and hydrogen arrests. However, their ratio, r, should not be appreciably affected.

Results

The platinum areas of carbon-supported platinum electrodes were measured for a variety of carbon supports and platinum loadings. Table II compares the results for carbons having areas from 0.4 to 700 m^2/g and for platinum loadings from 1 to 28%. The reproducibility of these measurements was about 10% for the oxygen-arrest method and the hydrogen-arrest method, as long as the charge consumption on the carbon supports did not exceed 25% of the total charge consumed in the arrest. The combination method (Eq. [6]) gave a reproducibility of 10% or better for all of the electrodes.

If numerator and denominator of Eq. [3] are each divided by $Q_{T,O}$, the total charge in the oxygen arrest, we see that the uncertainty in the platinum area increases in proportion to $P/(100\text{-}P)$, where $P = 100Q_{C,O}/Q_{T,O}$ is taken from Table I. Thus when the percentage of the charge consumed on the support is 75%, the error is three times as large as when this consumption is 50%.

Expressions for the charge consumed on the supports in carbon-supported platinum electrodes can be derived from Eq. [1], [2], and [5], *i.e.*

$$\frac{Q_{C,O}}{Q_{T,O}} = r\left(1 - \frac{k_O}{k_H}\frac{Q_{T,H}}{Q_{T,O}}\ r - \frac{k_O}{k_H}\right)$$

$$\frac{Q_{C,H}}{Q_{T,H}} = \left(\frac{Q_{T,O}}{Q_{T,H}} - \frac{k_O}{k_H}\ r - \frac{k_O}{k_H}\right)$$

Calculated fractions of total charge consumption due to carbon are listed in Table I.

The platinum areas in the last column of Table II were obtained from crystallite sizes measured by x-ray diffraction. The average crystallite sizes derived from x-ray spectra depend on the calculation method because assumptions about particle size distribution differ. The two areas listed are from crystallite sizes calculated by the method of Jones (7) and Warren's method (7), respectively. The model for calculating platinum areas from crystallite sizes was that of cubes with one face obscured by contact with the support surface.

Figure 3 compares the electrochemical platinum area values, obtained by combining the oxygen and hydrogen arrests (Eq. [6]), with the averaged x-ray results. The agreement between the electrochemical and x-ray surface areas gets progressively better, as evidenced by the x-ray to electrochemical area ratio approaching 1, as the platinum to carbon area ratio decreases. After the latter ratio reaches 0.10 the agreement stays within experimental error.[2] This behavior suggests that the crystallites are crowded at high platinum to carbon area ratios (at least in the case of the preparation methods used here) and hence much of the platinum surface does not contact the solution. Thus, while the x-ray method sometimes gives areas which are "truer" they are not always "available."

Conclusion

Carbon-supported platinum surface area measurements, using a combination of the arrests due to adsorbed oxygen reduction and adsorbed hydrogen oxidation, are feasible at least down to a platinum to carbon area ratio of 0.01, and are much more accurate than values obtained from either method alone. When the charge consumption on the carbon support is very small, one method is sufficient, adsorbed oxygen reduction probably being more reliable.

Comparison of the electrochemical method with x-rays shows good agreement for high area carbons, but when platinum is crowded onto a low area support agreement with x-rays is poor; probably because much of the platinum area is inaccessible to wetting. In the latter case, the electrochemical area measurement is to be preferred for predicting the performance of fuel cell electrodes.

Acknowledgments

The authors thank B. L. Meyers for making the x-ray measurements and R. F. Waters for platinizing the electrodes.

Manuscript received Feb. 7, 1966.

Any discussion of this paper will appear in a Discussion Section to be published in the December 1966 JOURNAL.

REFERENCES

1. R. J. Brodd and N. Hackerman, *This Journal*, **104**, 704 (1957).
2. B. E. Conway, "Electrode Processes," p. 105, Ronald Press, New York (1965).
3. H. A. Laitinen and C. G. Enke, *This Journal*, **107**, 773 (1960).
4. F. G. Will, *ibid.*, **112**, 451 (1965).
5. A. J. Robell, E. V. Ballou, and M. Boudart, *J. Phys. Chem.*, **68**, 2748 (1964).
6. J. S. Mayell and S. H. Langer, *This Journal*, **111**, 438 (1964).
7. H. P. Klug and L. E. Alexander, "X-ray Diffraction Procedures," p. 506, John Wiley & Sons, Inc., New York (1954).
8. R. G. Haldeman, W. P. Colman, S. H. Langer, and W. A. Barber, "Fuel Cell Systems," p. 106, American Chemical Society, Washington, D. C. (1965).

[2] In view of the arbitrary assumptions made in obtaining crystallite sizes and then in choosing a model to calculate areas, the consistency deserves more note than the absolute agreement.

The Electrochemical Reduction of Oxygen on Electrodes Partially Immersed in Phosphoric Acid

R. J. Roethlein and H. J. R. Maget

Direct Energy Conversion Operation, General Electric Company, Lynn, Massachusetts

ABSTRACT

Diffusion-controlled currents for the reduction of oxygen in phosphoric acid for partially immersed electrode structures which have an intrinsic meniscus and thin film extending over their surface can be predicted from a general rate equation. For platinum black electrodes, and temperatures ranging from 25° to 170°C, the limiting current varies linearly with the square root of electrolyte conductivity, electrode polarization, and oxygen partial pressure. The increased current obtained on partially immersed electrodes has been shown to be associated with a very narrow region starting approximately 0.28 cm (the height of the meniscus) above the bulk of the electrolyte solution. Approximate calculations of the activation energy of diffusion using parameters from the rate equation give values which are close to those expected for a diffusional process. Good agreement is obtained between theoretical and experimentally determined values of the limiting current at 25°C. Equations have been derived to describe the interfacial liquid-gas geometry of the intrinsic meniscus and film formed by contact of the electrolyte with the electrode.

The purpose of this work was the development of an analytical model needed to interpret the behavior of oxygen (air) electrodes operating at high temperatures (less than about 170°C), in concentrated phosphoric acid [greater than 85 w/o (weight per cent)]. Since practical electrode structures frequently display rather complex interfacial geometries and geometric characteristics, investigations of transport phenomena were carried out on a simplified model of an oxygen cathode, *i.e.*, a single pore.

The reported experimental work was conducted to determine the rate-controlling reactions associated with the electrochemical reduction of oxygen. Earlier work conducted in presence of sulfuric acid (1) had shown the importance of the liquid electrolyte film and electrode surface roughness on local and total currents observed on simulated single macropores. This paper presents some results obtained at higher temperatures.

Experimental

Apparatus.—The experiments were carried out in a Pyrex cell consisting of a large central compartment and two smaller sections separated from the main section by fine pore fritted glass disks. The middle compartment which served as the test electrode section also contained a thermometer well and a gas bubbler which was capable of keeping a steady gaseous flow over the electrolyte solution. One of the side compartments contained a platinum black mesh electrode which served as the counter electrode. The other section served as a reference cell and had a Luggin capillary extending into the main compartment. The reference consisted of two platinum black electrodes with a constant current of 1.0 ma flowing between them. The electrode which evolved hydrogen gas came to a steady overpotential within a few minutes; this then served as the reference potential.

The test electrode consisted of a cylindrical piece of platinum tubing (99.99%) pure, 1.0 cm long, 1.5 cm in diameter, and 0.2 cm in wall thickness. The electrode assembly was essentially the same as that described in a previous paper (1) except that only one cylindrical section was employed as the test electrode. A modified 10/30 Teflon gland provided a closed system and still enabled the electrode structure to be raised or lowered into solution without allowing the system to be open to the atmosphere. Measurements of electrode height above the solution were made by means of a specially modified L. S. Starret Vernier height gauge with an accuracy of $\pm$ 1.2 x 10^{-3} cm.

The height and shape of meniscus and film were determined by electrical methods. The resistance measurements were obtained by means of a semicircular platinum foil 1.0 cm in diameter and 1.27 x 10^{-2} cm thick, sealed between two cylindrical glass tubes and finely polished to form a continuous smooth surface. Electrical contact was made by spot-welding a platinum wire to the foil inside the glass cylinder. The Starret Vernier height gauge could raise or lower the glass tube into the electrolyte. Resistance measurements were obtained by means of an a-c resistance bridge operating at 1000 cps.

The electrode surface was pretreated by electrodeposition of platinum from a 3 w/o chloroplatinic acid solution (with traces of lead acetate) at 10 ma/cm^2 for 12, 60, and 240 sec.

Procedure.—Polarization measurements were made with a "fast rise" Wenking potentiostat (Model 61 TR) which has an operating potential source of $\pm$ 2v, a current measurement accuracy of 1.5% full scale, and a zero point stability of 5 mv/day. All gases used in these experiments were of a high grade prepurified quality. A silicone oil constant temperature bath maintained the desired study temperature within $\pm$ 1°C.

All reactant gases were preheated and humidified by passing through a gas bubbler which contained electrolyte at the same temperatures and concentration as that in the test cell.

The various phosphoric acid concentrations used in these experiments were prepared from C.P. Reagent Grade stock solution using doubly distilled water containing less than 0.4 ppm impurities.

Experimental Results and Discussion

Interfacial liquid-gas geometry.—Resistance measurements can be used to determine the liquid-gas interfacial geometry at the meniscus-film boundary. Figure 1 presents a plot of ohmic resistance divided by the electrolyte resistivity *vs.* x/h, the relative position in the meniscus (h = total intrinsic meniscus height, x = variable distance above the electrolyte level). Only a gradual resistance increase with height is observed in the meniscus region. However, on entering the thin film region, the resistance increases rapidly. The slope of this linear increase can be used to calculate the electrolyte film thickness.

The interfacial liquid-gas geometry of the intrinsic meniscus and film can be approximated by the expression

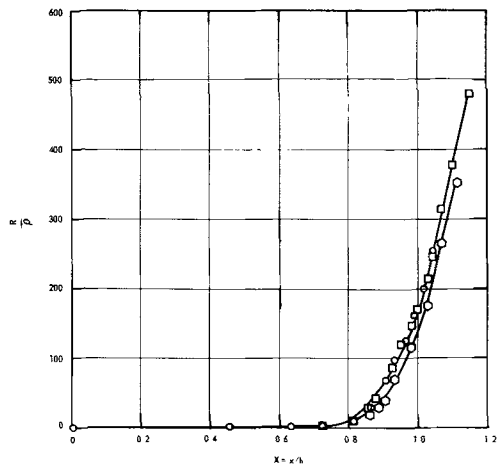

Fig. 1. Normalized ohmic resistance vs. relative position in the meniscus. R, measured resistance; ρ, electrolyte resistance; x, height above electrolyte level; h, height of meniscus, 0.28 cm; □, ○, 95.8 w/o H_3PO_4, 130°C; ○, 96.5 w/o H_3PO_4, 140°C.

$$\delta = \delta_h + A(1-X)^2 \text{ for } X \leq 1 \qquad [1]$$

where δ = meniscus thickness, cm; δ_h = film thickness, cm; $X = x/h$ represents the relative position in the meniscus; A can be theoretically evaluated from properties of the electrolyte, as presented by Landau and Lifshitz (2). However, since the surface tension of phosphoric acid at these temperatures is not known, it is better to evaluate A from resistance measurements.

It can be shown (1) that, near the meniscus-film interface, the ionic resistance is expressed by

$$R(x) = \frac{\rho h}{2b\pi} \frac{1}{(A\,\delta_h)^{1/2}} \left\{ \frac{\pi}{2} - \tan^{-1}\left(\frac{A}{\delta_h}\right)^{1/2}(1-X) \right\} \qquad [2]$$

where ρ = electrolyte resistivity, ohm-cm and b = electrode radius, cm. The film thickness δ_h can be determined from the slope of the linear section of the resistance plot

$$\left(\frac{dR}{dX}\right)_f = \frac{\rho h}{2\pi b\,\delta_h} \qquad [3]$$

The constant (A) can be evaluated from the total meniscus resistance, R_m at $X = 1$, for which

$$R_m = \frac{\rho h}{4b\,(A\,\delta_h)^{1/2}} \qquad [4]$$

For the experimental results presented in Fig. 1, the film thickness is calculated to be 0.5μ. The resistance can be represented by

$$R = 253\left\{ \frac{\pi}{2} - \tan^{-1} 16\,(1-X) \right\} \qquad [5]$$

and the meniscus-film geometry by

$$\delta = [0.5 + 130\,(1-X)^2]\,10^{-4} \qquad [6]$$

for values of $X \geq 0.9$, *i.e.*, at a level in the meniscus and film where the largest contribution to the total current is observed.

Current-potential behavior.—Current voltage curves taken on platinum black electrodes at elevated temperatures for the reduction of oxygen in phosphoric acid are similar to those obtained at lower temperatures in sulfuric acid (1). Raising the electrode out of solution causes an increase in current up to a maximum value obtained when the full meniscus and film are formed on the electrode surface. This behavior is represented in Fig. 2. For overvoltages greater than

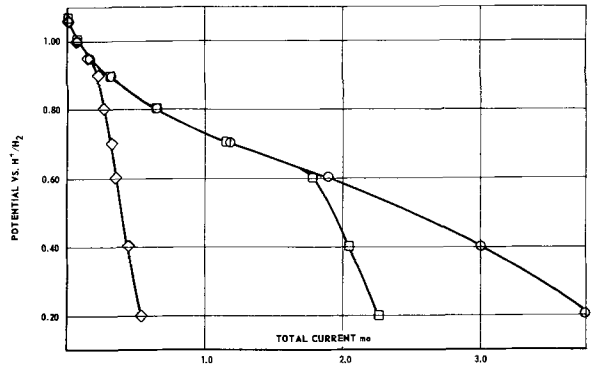

Fig. 2. Current-potential behavior as a function of electrode position. 97.8 w/o H_3PO_4, 150°C, pure O_2. Electrode position: ○, full meniscus and film; □, partial meniscus; ◇, submerged.

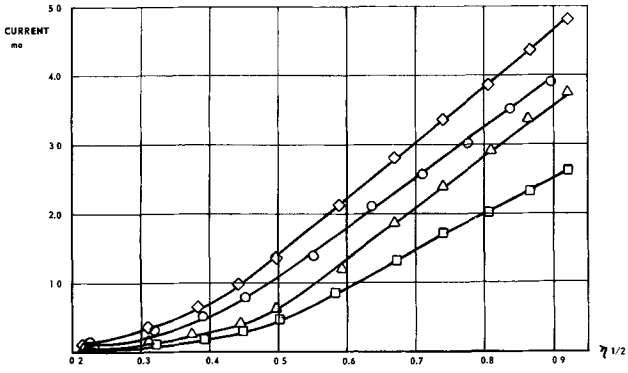

Fig. 3. Total current vs. square root of electrode polarization

	w/o H_3PO_4	Temp, °C	Deposition time, sec.
○	93.7	144	12
□	93.7	115	12
◇	92.6	144	240
△	97.8	144	60

about 0.25v (*vs.* electrode rest potential) *i.e.*, at potentials outside the region of activation overvoltage, the current follows a square-root relationship with overvoltage. This experimental result is presented in Fig. 3 for various electrolyte concentrations, temperatures, and surface roughnesses.

The variation of the current with position, above the electrolyte level, obtained at constant potential is also similar to that observed in sulfuric acid. The electrode current rises sharply in a narrow region which coincides with the boundary between upper meniscus and thin film which are formed on the electrode surface above the level of the bulk electrolyte. Figure 4 represents a typical variation of the current

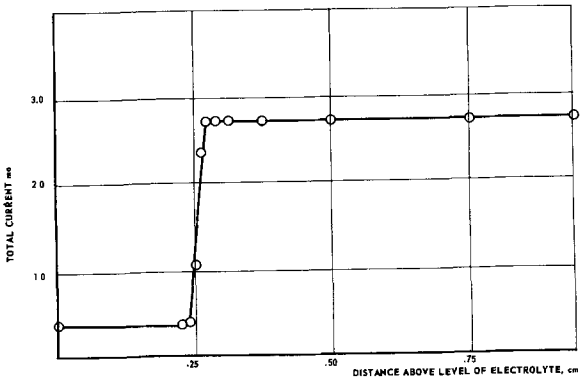

Fig. 4. Current vs. height behavior of a platinum black electrode at a constant potential of +0.400v vs. H^+/H_2. 93.7 w/o H_3PO_4, 150°C, pure O_2.

Table I. Dependence of electrode current on oxygen partial pressure (total pressure: 1 atm)

Partial pressure of oxygen, P_{O_2}, atm	Total current, i_L ma	$i_L/P_{O_2}^{1/2}$	Electrolyte concentration, w/o	Temp, °C
1.00	2.95	2.95	97.8	144
0.50*	2.05	2.90	97.8	144
0.21*	1.30	2.84	97.8	144
1.00	1.85	1.85	100	120
0.50	1.20	1.70	100	120
0.21	0.84	1.88	100	120
1.00	3.20	3.20	51.1	25
0.50	2.30	3.25	51.1	25
0.21	1.50	3.28	51.1	25
1.00	0.35	0.35	92.5	25
0.50	0.25	0.36	92.5	25
0.21	0.16	0.35	92.5	25

* All data obtained for binary mixtures O_2-N_2.

with electrode position; the height of the meniscus is approximately 0.28 cm (identical to the value observed in 1*N* and 10*N* H_2SO_4). Further withdrawal of the electrode from the electrolyte does not produce additional variations in current once the full meniscus and film have been formed.

On a partially immersed platinum black electrode the limiting current shows a linear variation with the square-root of the oxygen partial pressure. This relationship is valid for varying concentrations of H_3PO_4 (5-100 w/o) and over the complete temperature range of this study, *i.e.*, 25°-170°C. Characteristic values are reported in Table I.

Relationship between limiting current and conductivity.—Extensive studies were conducted to determine the current on partially immersed platinum black electrodes in the high phosphoric acid concentration range, from 80 to 100 w/o. It was found that the currents obtained at a constant potential of 0.400v *vs.* H^+/H_2 varied in a monotonic manner with the square root of the conductivity, Fig. 5. Two slopes were obtained: one in the low conductivity region which extrapolates to zero, as expected, and another in the higher conductivity range where the linear dependence is mantained over a large conductivity range from 0.36 to 0.64 (ohm-cm)$^{-1}$. Since the conductivity varies nearly linearly with temperature (3), it is not possible to explain the monotonic variation of the current, as presented in Fig. 5, on the basis of abrupt variations in conductivity in the temperature range between 110° and 170°C. (The measured currents were divided by the square root of the oxygen partial pressure to correct for water vapor pressure above the electrolyte since under experimental conditions the vapor pressure of water could be as high as 410 mm Hg.) Experimental results are presented in Fig. 5 as a function of the square root of electrolyte conductivity, since the correlation of the result was based on the assumption that currents on partially immersed electrodes can be predicted from the following general equation (4, 5) derived for hydrogen oxidation

$$i_L = \pi D\ (n\mathbf{F}C\mathcal{D}\mathcal{H}\eta)^{1/2} \qquad [7]$$

where D = diameter of the cylinder, 1.5 cm; n = number of electrons; $\mathbf{F}$ = Faraday's constant; $\mathcal{H}$ = electrolyte conductivity (ohm-cm)$^{-1}$; C = concentration of oxygen in phosphoric acid, mole/cm^3; $\mathcal{D}$ = diffusion coefficient, cm^2/sec.; η = polarization from open circuit, volts. Verification of the above equation will be shown for a region where limited values for solubilities and diffusion coefficients are either available or can be reasonably estimated.

A possible explanation for the increased slope at higher electrolyte conductivities and temperatures may be based on the change of oxygen solubility and diffusion coefficient in phosphoric acid at elevated temperatures. The combination of these parameters plays an important role in determining the limiting current.

The dependence of current on conductivity was further verified by adding $NaH_2PO_4 \cdot H_2O$ to a H_3PO_4 solution in order to decrease the electrolyte conductivity. [400g of $NaH_2PO_4 \cdot H_2O$ added to a liter of 85% H_3PO_4 yielded a conductivity of 0.33 (ohm-cm)$^{-1}$ at 130°C as compared to 0.49 (ohm-cm)$^{-1}$ for a salt-free identical acid concentration.] The current obtained from the lowered conductivity fell within the predicted value for the current at this conductivity (see Fig. 5).

Variation of electrode surface roughness did show some effect on current behavior. Platinum black was electrodeposited on the cylindrical electrode for 12, 60, and 240 sec at 10 ma/cm^2. Several concentrations were investigated for each roughness, and the currents were observed to increase with increasing surface roughness. Variations, however, were not large, *i.e.*, a current increase of 30% was observed for the highest as compared to the lowest surface roughness.

Current-temperature relationship.—Temperature effects on the currents, measured at 0.4v *vs.* H^+/H_2, are appreciable, as can be observed from Fig. 6 for various electrolyte concentrations, once corrected for oxygen partial pressure and electrolyte conductivity.

Since the conductivity does not vary appreciably with temperature for concentrated solutions (3), the slopes of $i_L/(\mathcal{H}P_{O_2})^{1/2}$ *vs.* $1/T$, at constant potential, represent the contribution of solubility and diffusivity to an activation energy. Solubility measurements reported in the literature (6, 8) for high concentrations

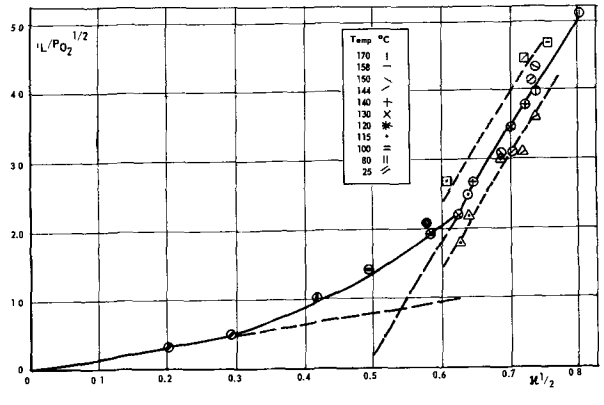

Fig. 5. $i_L/P_{O_2}^{1/2}$ vs. $\mathcal{H}^{1/2}$ for the reduction of O_2 in concentrated H_3PO_4 solutions from 25° to 170°C. Deposition time at 10 ma/cm^2: □, 240 sec; ○, 60 sec; △, 12 sec; •, addition of $NaH_2PO_4 \cdot H_2O$.

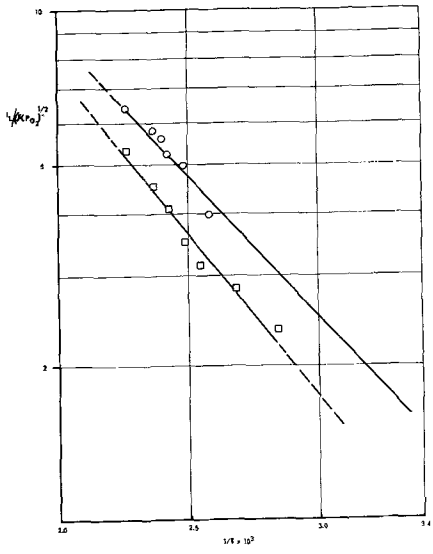

Fig. 6. Variation of limiting current as a function of temperature. Weight per cent H_3PO_4: □, 100; ○, 85.8-92.5.

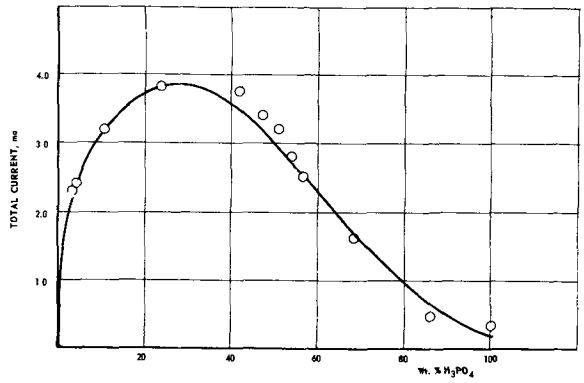

Fig. 7. Values of the limiting current on a partially immersed platinum black electrode for O_2 reduction in various concentrations of H_3PO_4 at 25°C; ———, calculated from equation $i_L = \pi D \{nFC\mathcal{D}\ \mathcal{H}\eta\}^{1/2}$; ○, experimental points.

of H_3PO_4 between 25° and 170°C allow one to estimate a heat of dissolution of 1 kcal/mole. The slopes of Fig. 6, once corrected for this heat of dissolution, yield activation energies of 4.1 and 4.3 kcal/mole, which are within the range of values expected for diffusion-controlled processes.

Variation of limiting current with phosphoric acid concentration.—Currents for the reduction of oxygen on a partially immersed platinum black electrode were obtained potentiostatically at an applied potential of 0.400v *vs.* H^+/H_2 as a function of phosphoric acid concentration at 25°C. Results plotted in Fig. 7 show good agreement with the theoretical values calculated from the general equation assuming a mass transport-controlled process on a partially immersed electrode displaying a full meniscus and thin film on its extended surface, Eq. [7]. Data for the electrolyte conductivity and oxygen solubility is available in the literature (3, 6, 8). Since no data are available for the diffusion coefficient of oxygen in phosphoric acid at 25°C values were estimated from the equation of Wilke and Chang (7). Table II presents the values for the conductivity, oxygen solubility, and diffusivity in phosphoric acid at 25°C as a function of acid concentration, used to calculate the current reported in Fig. 7.

Lack of data concerning the diffusivity of oxygen in concentrated phosphoric acid does not allow to prove the application of Eq. [7] to currents measured at higher temperatures. However, on the assumption that Eq. [7] is applicable, it is possible from available data on oxygen solubility, electrolyte conductivity, and measured limiting currents to estimate diffusion coefficients. From the computed values presented in Fig. 8 for the temperature range from 25° to 170°C good agreement is obtained between the calculated values and two experimental results measured in 85.5 w/o H_3PO_4 (8). These results suggest that this method may be used to determine rapidly the product of solubility and diffusivity.

Conclusions

The electrochemical reduction of oxygen on partially immersed platinum black electrodes in phosphoric acid, from room temperature to 170°C, occurs mainly

Table II. Variation of electrolyte conductivity, oxygen solubility, and diffusivity for various phosphoric acid concentrations at 25°C

H_3PO_4 w/o	Conductivity (ohm-cm)$^{-1}$	Solubility moles/cm^3 × 10^6	Diffusion coefficient cm^2/sec × 10^5
0	—	1.26	2.60
5	0.040	1.18	2.42
10	0.070	1.10	2.20
20	0.123	0.96	2.00
40	0.222	0.73	1.40
60	0.213	0.52	0.87
80	0.117	0.32	0.42
100	0.030	0.13	0.10

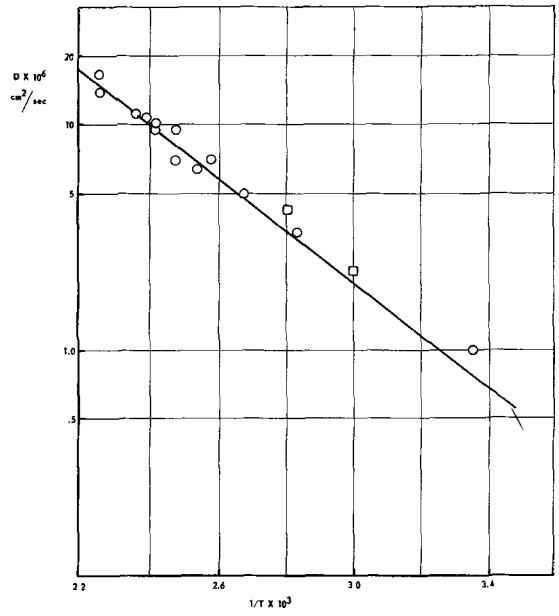

Fig. 8. Variation of O_2 diffusion coefficient in concentrated phosphoric acid as a function of temperature: ○, calculated; □, measured.

in the upper meniscus and thin film region of the electrode surface. This was shown by the increased current associated with the gradual withdrawal of a submerged electrode, potentiostatically polarized, into a condition of partial immersion. The height of the meniscus in phosphoric acid even at elevated temperatures is the same as that found for sulfuric acid at room temperature, *i.e.*, approximately 0.28 cm.

Using a general equation which describes diffusion-controlled limiting currents for an electrode having a meniscus and film, good agreement has been obtained between the observed currents and those predicted from the equation over the entire concentration range of phosphoric acid at 25°C. For higher temperatures, results obtained show that the limiting currents also depend on the square root of electrolyte conductivity, polarization, and oxygen partial pressure. In addition, diffusion coefficients obtained by the use of this equation show good agreement with experimentally measured values of this parameter. This suggests that this general equation is also applicable to temperatures up to 170°C.

Further proof of the validity of this equation is exemplified by the approximate values obtained for the activation energy of diffusion for two different acid concentrations. The values obtained are in the approximate range of energies associated with diffusional processes. This same equation may be able to predict currents at other temperatures once sufficient data are obtained for oxygen solubility and diffusivity in phosphoric acid.

From the resistance measurements, equations have been derived to describe the interfacial liquid-gas geometry of the intrinsic meniscus and film formed by contact of the electrolyte with the electrode. These measurements have also provided an approximate value of the film thickness immediately above the intrinsic meniscus, 0.5μ.

Manuscript received Aug. 2, 1965; revised manuscript received Feb. 21, 1966. This paper was presented at the San Francisco Meeting, May 9-13, 1965.

Any discussion of this paper will appear in a Discussion Section to be published in the December 1966 JOURNAL.

REFERENCES

1. H. J. R. Maget and R. J. Roethlein, *This Journal*, 112, 1034 (1965).

2. L. D. Landau and E. M. Lifshitz, "Fluid Mechanics," p. 235, Pergamon Press, New York (1959).
3. Monsanto, Phosphoric Acid, Technical Bulletin 1-239. Also D. Macdonald, Technical Summary Report No. 4, Dec. 1963; Contract Da-44-00-ENG-4909, USERDL, Ft. Belvoir, Va.
4. F. Will, *This Journal*, **110**, 145 (1963).
5. Carl Wagner, Unpublished results.
6. D. Macdonald, Technical Summary Report No. 6, 1 July '64-31 Dec. '64, Contract DA-44-009-ENG-4909, USERDL, Ft. Belvoir, Va.
7. Reid and Sherwood, "The Properties of Gases and Liquids," McGraw Publishing Co., New York.
8. K. E. Gubbins and R. D. Walker, Solubility and Diffusivity of Hydrocarbons and Oxygen in Fuel Cell Electrolytes, Contract No. DA-49-186-AMC-45(X), Harry Diamond Laboratories, Final Report, June 30, 1965.

The Electrochemical Oxidation of Ethylene

Comparison of Results by the Potential Sweep and Steady-State Methods

E. Gileadi,[1] G. Stoner, and J. O'M. Bockris

Electrochemistry Laboratory, John Harrison Laboratory of Chemistry,

University of Pennsylvania, Philadelphia, Pennsylvania

ABSTRACT

The electrochemical oxidation of ethylene on platinum electrodes in 1*N* sulfuric acid at 80°C was studied by the potential sweep method over a wide range of sweep rates (10^{-5} — 2 v/sec). The results were compared with those obtained previously under steady-state conditions. Over three decades of sweep rate (2×10^{-3} — 2 v/sec) an apparent Tafel slope of approximately $2.3 \times 3\ RT/\mathbf{F}$ was observed. This was shown to be consistent with the behavior for a totally irreversible diffusion-controlled reaction. In the same region the peak potential V_M was found to shift 65 mv/decade increase in sweep rate and the peak current i_M was proportional to the square root of the sweep rate with a proportionality constant in agreement with the calculated value.

It is shown that the application of the potential sweep may change the mechanism of the process taking place (in the present case the change is from activation control in steady state to diffusion control during potential sweep). During potential sweep a totally irreversible, diffusion-controlled reaction will give rise to a linear Tafel plot with a slope about 35% higher than the mechanistically significant slope of $2.3\ RT/\alpha\mathbf{F}$. Further, an apparent passivation region can be observed, due to depletion of the solution near the electrolyte from reactant molecules and quite independent of the nature of the electrode surface. During potential sweep measurements the partial coverages θ by various species on the surface cannot reach their steady-state value. The kinetic parameters derived from such measurement, therefore, cannot be used to represent the results under steady-state conditions, unless the sweep rate is made sufficiently slow to correspond in practice to steady state.

The anodic oxidation of ethylene on platinum electrodes in 1*N* H_2SO_4 at 80°C has been studied recently (1). From the kinetic parameters obtained under steady-state condition a mechanism has been suggested, with water discharge as the rate-determining step, preceded by equilibrium adsorption of ethylene (1). This mechanism was further confirmed by a comparative study of the electrochemical oxidation of a number of unsaturated hydrocarbons under identical conditions (2) and by recent tracer studies (3). Independent electrosorption measurements for ethylene (4) and benzene (5) in the same system by a radiotracer technique yielded further support for the above mechanism. Thus, for the rate-determining step

$$H_2O \rightarrow OH_{ads} + H^+ + e \qquad [1]$$

the rate equation was given as

$$i = i_o\,(1 - \theta)\exp(\beta V\mathbf{F}/RT) \qquad [2]$$

where θ represent the total surface coverage which in the linear Tafel region (0.4 — 0.8v RHE) is essentially equal to the coverage by unreacted adsorbed organic molecules. Under the conditions studied [*i.e.*, with ethylene bubbled through the solution or with liquid benzene at equilibrium with the solution (1, 2)] the surface coverage by organic is in the saturation region (4, 5), and hence θ may be considered independent of potential, giving rise to

$$b = \left(\frac{\partial V}{\partial \log i}\right)_{T,C_i} = \frac{2.3\ RT}{\beta\mathbf{F}} \sim 2.3 \times (2RT/\mathbf{F}) \qquad [3]$$

The negative reaction order observed is also consistent with the adsorption data for this mechanism since, while θ remains essentially constant in the saturation region, the term $(1 - \theta)$ can vary substantially and give rise to a decreased reaction rate with increasing bulk concentration of the organic.

Most recent studies of electrochemical oxidation of potential fuels have relied on nonsteady-state techniques, in particular the potential sweep method (6, 7) and cyclic voltametry (8). The results of such measurements have not usually been interpreted in terms of a molecular mechanism.

In the present work the electrochemical oxidation of ethylene on bright and platinized platinum electrodes in 1*N* H_2SO_4 at 80°C was studied as a function of sweep rate over a wide range (1×10^{-5} — 2v/sec). The results obtained in this manner are compared with previous results of steady-state measurements in the same system, and the limitations of the application of potential sweep techniques for the study of the kinetics of complex electrode reactions are brought out. The potential sweep technique has been applied previously to the oxidation of ethylene on rotating disk platinum electrodes (9), but the effect of sweep rate has not been considered.

Experimental

Cell, electrodes, and solution.—A standard three-compartment all-glass cell was employed with glass frits separating the compartments. A bright platinum wire of 1 cm^2 served as working electrode and was treated anodically and cathodically as described pre-

[1] Present address: Chemistry Department, Tel-Aviv University, Tel-Aviv, Israel.

viously (1). For lower sweep rates a 50 cm^2 planar bright platinum electrode was used, and for comparison a small 1 cm^2 planar platinized Pt electrode was employed. A Hg/Hg_2SO_4 reference electrode in the same solution was used and a large platinized platinum gauze served as the counter electrode.

Solutions were made up from Baker Analyzed sulfuric acid in distilled water. C. P. grade ethylene (99.5% purity) and prepurified nitrogen (99.996% purity) were employed.

Electrical circuit.—The potential between the working and reference electrode was controlled by a Wenking potentiostat, and the current between the working and counter electrode was recorded on a Moseley "Autograph" recorder model 680 in parallel with a variable shunt resistance. For slow potental sweeps the reference potential fed into the potentiostat was varied with motor drive potentiometers connected to a battery. For faster sweep rates a transistorized triangular sweep generator constructed in this laboratory was employed (10), which could supply a symmetrical triangular wave form with sweep rates in the range of 10^{-3} — 10^3 v/sec. During measurements at higher sweep rates the current was recorded as a function of potential on a Tektronix model 564 memory oscilloscope used as an X — Y recorder (with the time base replaced by a differential amplifier type 2A63 plug-in unit). The oscillographic traces were photographed with a model C-12 oscilloscope poloroid camera.

Procedure.—Electrodes prepared in the manner described elsewhere (1) were introduced into the sulfuric acid solution, and prepurified nitrogen was bubbled through until the rest potential of approximately 0.25v NHE was reached. Ethylene was then introduced into the cell, and sufficient time was allowed for adsorption equilibrium at this potential to be reached (15-30 min). All data reported here refer to a single anodic sweep. Good reproducibility between different runs in the same solution and runs on different days in different solutions was obtained.

Results

Current-potential relationship.—The current-potential relationships obtained at three sweep rates are represented in Fig. 1 as a plot of current density *vs.* potential. The same results are shown in semilogarithmic form in Fig. 2 as V *vs.* log i. The variation of b, the apparent Tafel slope observed experimentally with sweep rate, is shown in Fig. 3. A constant value of $b = 2.3 \times (3\ RT/F)$ is observed for sweep rates of 2×10^{-3} up to 2 v/sec. The steady-state value of $b = 2.3 \times (2\ RT/F)$ is approached only at very slow sweep rates of the order of 10^{-5} v/sec.

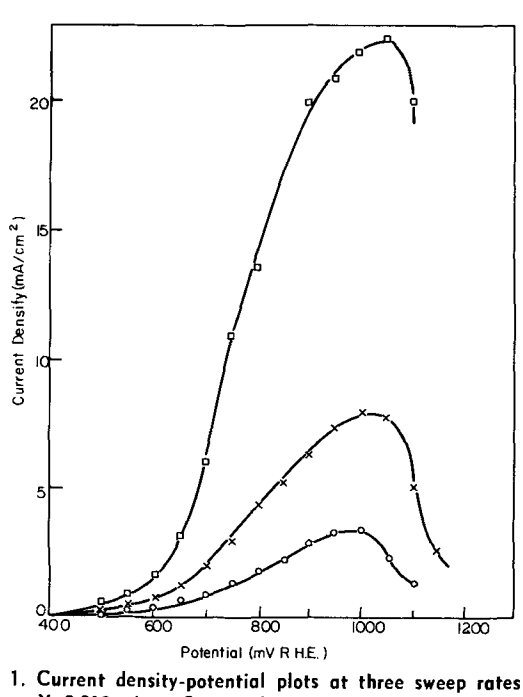

Fig. 1. Current density-potential plots at three sweep rates: □, 0.1 v/sec; X, 0.013 v/sec; ○, 0.0022 v/sec.

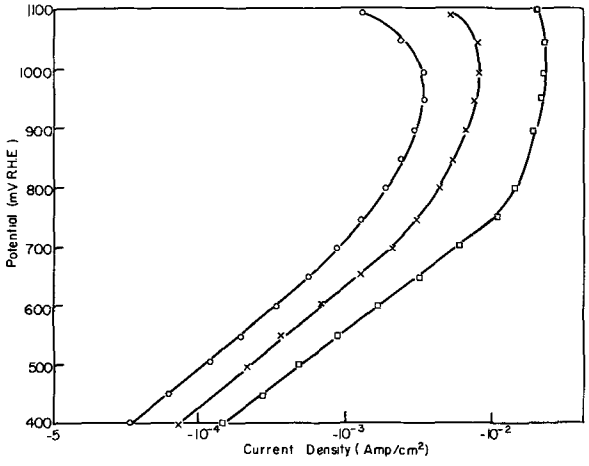

Fig. 2. Results of Fig. 1 plotted on a semilogarithmic scale

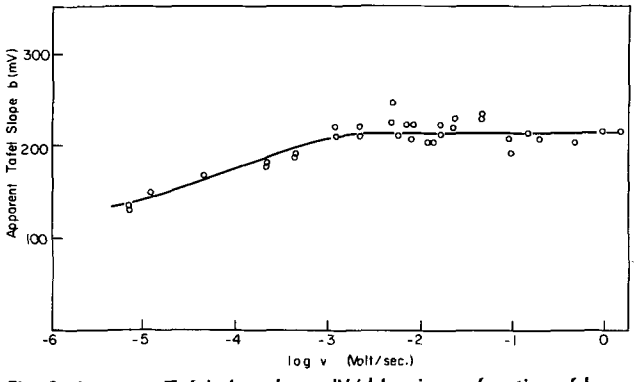

Fig. 3. Apparent Tafel slope $b = dV/d \log i$ as a function of log v

Peak current and potential.—Figure 4 shows a plot of the peak current i_M as a function of the sweep rate v on a log-log scale. A linear plot results for sweep rates above a few mv/sec, with a slope of approximately 0.5. At lower sweep rates the peak currents are much smaller and depend only to a very small extent on sweep rate. Results obtained for a platinized Pt electrode are shown for comparison.

The potential V_M at which the current reaches a maximum is plotted in Fig. 5 as a function of log v. A

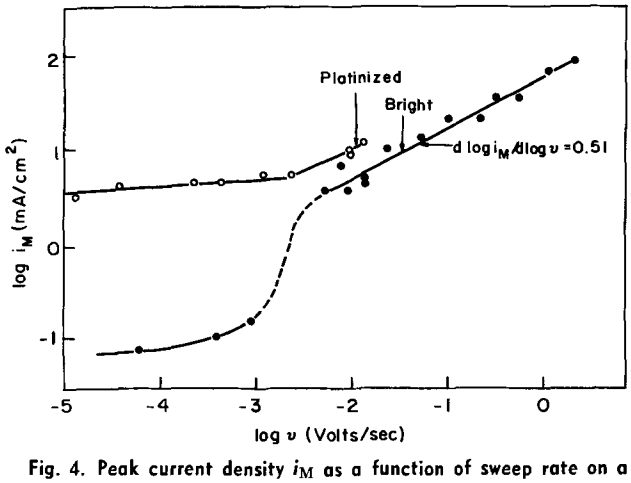

Fig. 4. Peak current density i_M as a function of sweep rate on a log-log scale; ○, platinized Pt; •, bright Pt.

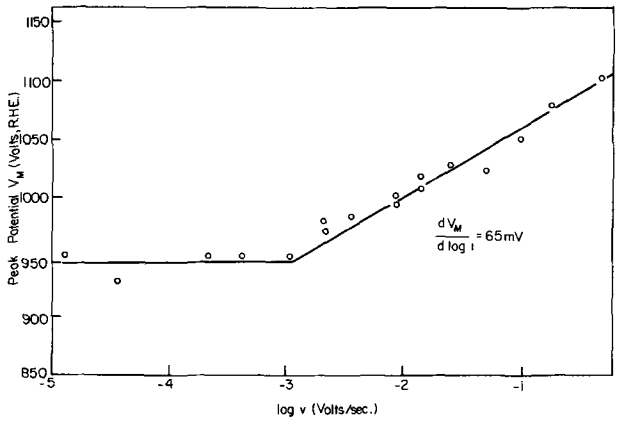

Fig. 5. Peak potential V_M as a function of log v

slope of $dV_M/d \log v \sim 2.3 \times (RT/\mathbf{F})$ is obtained for sweep rates higher than a few mv/sec. At lower sweep rates V_M is essentially independent of sweep rate and the same for bright and platinized electrodes. It should be noted that the break in the lines in Fig. 3, 4, and 5 occur at the same sweep rate, within experimental error.

Discussion

The peak current.—For a totally irreversible, diffusion-controlled reaction the current density during potential sweep has been shown (11, 12) to be given by an equation of the following form

$$i = \pi^{1/2} n\mathbf{F}\beta^{1/2} D^{1/2} C^o \chi(\beta t) \quad [4]$$

where (utilizing for this equation Delahay's symbol)

$$\beta = \frac{\alpha n_a \mathbf{F}}{RT} v \quad [5]$$

n and n_a are the number of electrons transferred in the over-all reaction and in the rate-determining step, respectively; α is the transfer coefficient, D the diffusion constant, C^o the bulk concentration of reactant, and $\chi(\beta t)$ is a complex function of (βt) which has been given numerically as a function of (βt). It is noted that during a linear potential sweep

$$V = V_i + vt \quad [6]$$

where V_i is the initial value of the potential at the $t = 0$. Hence from Eq. [5] and [6]

$$\beta t = \frac{\alpha n_a \mathbf{F}}{RT} (V - V_i) \quad [7]$$

and the function $\chi(\beta t)$ may be regarded as dependent on potential. The variation of $\chi(\beta t)$ with (βt) has been calculated by Delahay (11). In view of relationships [4] and [7] this also reflects the variation of the current density with potential.

At the peak potential $\chi(\beta t)$ has a value of 0.282. With $D = 1.7 \times 10^{-5}$ cm²/sec (9), $C^o = 2.2 \times 10^{-6}$ mole/cm³ (9), $n_a\alpha = 0.5$ and $n = 12$, Eq. [4] yields

$$i_M = 23v^{1/2} \text{ ma/cm}^2 \text{ (real area)} \quad [8]$$

The experimental relationship obtained from Fig. 4 is

$$i_M = 60\, v^{1/2} \text{ ma/cm}^2 \text{ (apparent area)} \quad [8a]$$

The discrepancy between calculated and observed results may be due in part to the uncertainty in the values of D and C^o used, and in part to departure from semi-infinite linear diffusion in the experimental set-up. Below a sweep rate of a few millivolts per second the peak current on bright platinum drops drastically to lower values corresponding to the activation-controlled process taking place at steady state with a much smaller dependence on sweep rate, which can probably be associated with the slow "time effects" observed in steady-state measurements. A comparison of results on bright and platinized Pt lends further support for the diffusion-controlled behavior postulated here for the higher sweep rate region. At low sweep rates the current density on platinized Pt is found to be about 40-50 times higher than on bright Pt. Taking a roughness factor of 2 for the bright surface this gives rise to a reasonable value of 80-100 for the roughness factor on the platinized surface. At higher sweep rates the line for platinized Pt parallels that for bright Pt, but the ratio of current densities is only approximately 2.0. For a diffusion-controlled process the current is determined largely by the apparent surface area. The slightly larger current densities observed on platinized Pt are probably due to surface irregularities of dimensions similar to or larger than the diffusion layer thickness.

Variation of peak potential with sweep rate.—The relationship between peak potential and sweep rate has been given by Delahay (11, 12) as

$$V_M = V_i + \frac{RT}{\alpha n_a \mathbf{F}}\left[0.77 - \ln(k/D^{1/2}) + \tfrac{1}{2} \ln\left(\frac{\alpha n_a \mathbf{F}}{RT} v\right)\right] \quad [9]$$

where k is the (potential dependent) specific rate constant at the potential V_i. Thus

$$\frac{\partial V_M}{\partial \log v} = \frac{2.3\, RT}{2\alpha n_a \mathbf{F}} = 2.3 \times (RT/\mathbf{F}) \text{ for } \alpha n_a = 0.5 \quad [10]$$

In Fig. 5 a slope of $\partial V_M/\partial \log v = 65$ mv is obtained, in agreement with Eq. [10] ($2.3 \times RT/\mathbf{F} = 70$ mv at 80°C).

It is important to note the fact that a peak in the $i - V$ relationship is obtained here for a diffusion-controlled reaction, independent of the state of the electrode surface. This may account for some of the apparent passivation regions which have been reported in studies of the anodic oxidation of organic fuels by the potential sweep method. The position of the peak depends, among other things, on the specific rate constant of the reaction studied, but not on the bulk concentration of reactant (cf. Eq. [9]). When stable intermediates are formed in the reaction sequence in concentrations not negligible with respect to the concentration of the reactants several "diffusion peaks" of this kind could be observed on the polarogram. This has already been pointed out by Delahay (12), but has apparently been disregarded in subsequent work.

Observed Tafel slope.—Figure 3 shows the variation of Tafel slope with sweep rate. The steady-state value of $2.3 \times 2\ RT/\mathbf{F}$ is only approached at very low sweep rates $V < 10^{-5}$ v/sec in this system. As the sweep rate is increased above 10^{-5} v/sec, the observed Tafel slope increases steadily toward a value of $2.3 \times 3\ RT/\mathbf{F}$. Above approximately 2×10^{-3} v/sec the Tafel slope remains constant independent of sweep rate over three decades of sweep rate up to $v = 2$ v/sec. The region of constant Tafel slope of $2.3 \times 3\ RT/\mathbf{F}$ coincides with the upper regions of Fig. 4 and 5 where $d \log i_M/d \log v = 0.5$ and $dV_M/d \log v = 2.3\ RT/\mathbf{F}$, respectively, corresponding to diffusion-controlled kinetics.

The existence of a linear Tafel region for a diffusion-controlled reaction is only due to the particular method of measurement (*i.e.*, the potential sweep method), and the observed slope of $2.3 \times 3\ RT/\mathbf{F}$ (which is not normally encountered in kinetic studies of activation controlled reactions) can be shown to be consistent with the water discharge mechanism postulated earlier as the rate-determining step under steady-state conditions.

Figure 6 gives a plot of (βt) *vs.* $\log \chi(\beta t)$ which was constructed from the plot of $\chi(\beta t)$ *vs.* (βt) given by Delahay (11, 12). From this plot one finds numerically

$$\partial(\beta t)/\partial \log \chi(\beta t) = 3.1 \quad [11]$$

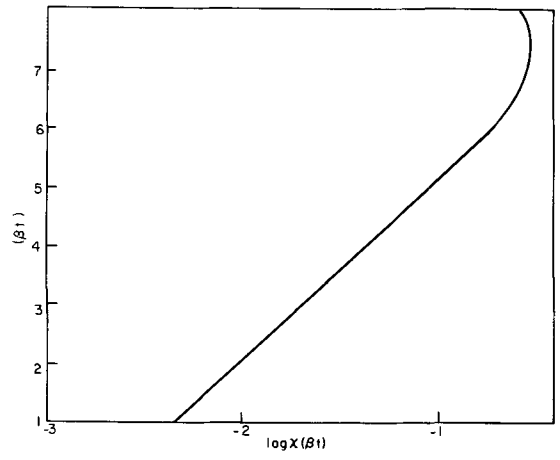

Fig. 6. (βt) plotted vs. the function log $\chi(\beta t)$

and

$$\frac{\partial V}{\partial \log i} = \frac{\partial V}{\partial \log \chi(\beta t)} \times \frac{\partial \log \chi(\beta t)}{\partial \log i} \quad [12]$$

From Eq. [4]

$$\partial \log \chi(\beta t)/\partial \log i = 1 \quad [13]$$

and from Eq. [7]

$$\partial V = \frac{RT}{\alpha n_a \mathbf{F}} \partial(\beta t) \quad [14]$$

Combining Eq. [12]-[14] one has

$$\frac{\partial V}{\partial \log i} = \frac{RT}{\alpha n_a \mathbf{F}} \frac{\partial(\beta t)}{\partial \log \chi(\beta t)} = \frac{3.1\,RT}{\alpha n_a \mathbf{F}} = \left(\frac{3.1}{2.3}\right) \times \frac{2.3\,RT}{\alpha n_a \mathbf{F}} \quad [15]$$

Thus a linear Tafel relation with a slope 35% higher than the mechanistically significant slope of 2.3 $RT/\alpha n_a \mathbf{F}$ can result due to diffusion control during the potential sweep. In the case studied here, the observed Tafel slope of b = 210 mv is consistent (at 80°C) with the above interpretation if αn_a = 0.45. This is in agreement with the steady-state value of α = 0.46-0.50 reported for this system.

Limitations of the potential sweep method.—The mechanism of the anodic oxidation of ethylene on Pt electrodes has been established previously on the basis of kinetic parameters obtained under steady-state conditions (1), as discussed in the introduction. The critical question to be answered here is what type of mechanistic information could have been derived from the potential sweep data presented in this paper alone. The answer to this question will then bear relevance to the limited applicability of the slow potential sweep technique for the study of mechanisms of anodic oxidation of organic fuels. Typical sweep rates used by various authors for mechanistic studies are in the range of 10-100 mv/sec (*e.g.*, Griffith and Rhodes (9) used v = 26 mv/sec, Breiter (6) used v = 35 mv/sec), and thus the behavior observed here in the upper sweep rate region (2 x 10^{-3} — 2 v/sec) will be discussed below.

As has been shown above, the relationship between peak current, peak potential, and sweep rate satisfies Eq. [4] and [9] which have been derived (11, 12) for a totally irreversible diffusion-controlled reaction. This should be contrasted with the activation-controlled kinetics established at steady state. Further, a positive pressure effect is observed during the sweep measurement while at steady-state negative reaction orders were observed for ethylene (1) and several other unsaturated hydrocarbons (2). Thus, the results of potential sweep measurements would indicate that the reaction is diffusion controlled. This, however, will have little effect on the operation of a fuel cell, the characteristics of which will be determined by the steady-state activation-controlled kinetics.

The transition from activation control at steady state to diffusion control during the transient is unusual and arises due to the time dependence of the partial coverage θ during the transient. It will be remembered that the steady-state current is proportional to the term $(1 - \theta)$ (Eq. [2]). Also direct adsorption measurements show (4) that θ must be very high and $(1 - \theta)$ is probably of the order of 10^{-2} or less. During the potential sweep transient the reactant at and near the electrode is used up and θ decreases. Under these conditions the water discharge step can occur a hundred times or more faster and, it is no longer rate limiting for the over-all process.

The observed Tafel slope can be discussed next. If measurements at a single sweep rate were performed, any slope between 2.3 x 2 $RT/\mathbf{F}$ and 2.3 x 3 $RT/\mathbf{F}$ could be obtained, depending on the sweep rate chosen. The observation that the Tafel slope is independent of sweep rate over a wide range is no indication that it is also equal to the value which would be obtained at steady state, as shown above. If it is established that the system is a totally irreversible, diffusion-controlled reaction (as is the case in the present study), the mechanistically significant Tafel line can be calculated from the observed value (Eq. [15]). This again will only be relevant, however, to the kinetic behavior during the transient which may be entirely different from that observed at steady state.

In conclusion, the potential sweep technique is not generally applicable to kinetic studies because the system is altered by the measurement. In a proper study, when correction for sweep rate and diffusion effects are made, the kinetic behavior of the system during the sweep may be evaluated. This, however, may be quite different from the steady-state behavior which is the only one relevant for the continuous operation of electrochemical energy converters.

Conclusions

The kinetic parameters calculated from measurements employing the potential sweep or cyclic voltametry technique cannot be used directly as diagnostic criteria for mechanistic determinations. In general three regions of potential sweep rate may be expected to occur. At sufficiently low sweep rates (region A) the steady state of the system is not significantly disturbed by the sweep, and the kinetic parameters observed are independent of sweep rate. At intermediate sweep rates (region B) the reaction can be diffusion controlled. This region is characterized by a linear dependence of peak current i_M on the square root of the sweep rate and (for totally irreversible reactions) a linear dependence of the peak potential V_M or log v, with a slope of $\partial V_M/\partial \log v$ = 2.3 $RT/2\alpha n_a \mathbf{F}$ (11, 12). In this region a linear Tafel behavior can also be observed with a slope which is about 35% higher than the mechanistically significant slope of 2.3 $RT/\alpha n_a \mathbf{F}$. Finally, at very high sweep rates (region C) most of the Faradaic current is associated with oxidation of reactants which have been adsorbed on the surface before application of the sweep; or with adsorption or desorption of intermediates formed in the reaction sequence. Region C is characterized by a linear dependence of the current on sweep rate [the current may be regarded as pseudocapacitative in this region in that it obeys the simple relationship $i = Cv$ where C is the effective pseudocapacity of the system under a given set of conditions (13)]. A linear plot of V_M *vs.* log v will result in this region. The slope, however, will be 2.3 $RT/\alpha \mathbf{F}$, *i.e.*, twice that observed in the diffusion controlled region (14).

The sweep rate corresponding to the three regions discussed above will depend on the specific rate con-

stants of the reactions studied, the concentration of reactants in the bulk of the solution and other factors. In the case of ethylene oxidation on platinum electrodes at 80°C studied here, region A corresponds to $v < 10^{-5}$ v/sec. Region B spreads from $v = 2 \times 10^{-3}$ up to 2 v/sec, and region C probably starts at $v > 100$ v/sec. In certain cases these regions may tend to overlap, and in particular diffusion controlled conditions may not be observed experimentally at high reactant concentration and for systems where steady state can be reached rapidly.

The peak current and subsequent decrease in current with increasing potential (quasi-passivation region) observed in steady-state and slow sweep measurements (region A) have been associated with formation of oxide layers on the surface. In contrast, the apparent passivation in regions B and C are due to a depletion of the electrolyte near the electrode from reactant molecules and to a decrease of the combustible adsorbed reactant on the surface, respectively, and are independent of the state of the electrode surface. Several such peaks may occur in region B if stable intermediates are formed in substantial amounts in the reaction sequence, or due to impurities in the fuel or in the electrolyte.

Acknowledgment

Financial support for this work by U.S. Engineers Research and Development Laboratory, Fort Belvoir, Va., under Contract No. DA44-009-AMC-469(7) is gratefully acknowledged.

Manuscript received Oct. 8, 1965.

Any discussion of this paper will appear in a Discussion Section to be published in the December 1966 JOURNAL.

REFERENCES

1. H. Wroblowa, B. J. Piersma, and J. O'M. Bockris, *J. Electroanal. Chem.*, **6**, 401 (1963).
2. J. O'M. Bockris, H. Wroblowa, E. Gileadi, and B. J. Piersma, *Trans. Faraday Soc.*, **61**, 2531 (1965).
3. H. Wroblowa, A. T. Kuhn, and J. O'M. Bockris, In preparation.
4. E. Gileadi, B. T. Rubin, and J. O'M. Bockris, *J. Phys. Chem.*, **69**, 3335 (1965).
5. W. Heiland, E. Gileadi, and J. O'M. Bockris, *J. Phys. Chem.*, **70** (1966).
6. M. W. Breiter, *Electrochim. Acta*, **8**, 973 (1963).
7. S. Gilman and M. W. Breiter, *This Journal*, **109**, 1099 (1962).
8. A. L. Juliard and H. Shalit, *ibid.*, **110**, 1002 (1963).
9. L. R. Griffith and D. R. Rhodes, Fuel Cells and CEP Technical Manual 32 (1963).
10. B. D. Cahan, To be published.
11. P. Delahay, *J. Am. Chem. Soc.*, **75**, 1190 (1953).
12. P. Delahay, "New Instrumental Methods in Electrochemistry," Interscience Publishers, Inc., New York (1954).
13. B. E. Conway, E. Gileadi, and H. Kozlowska-Angerstein, *This Journal*, **112**, 341 (1965).
14. S. Srinivasan and E. Gileadi, *Electrochim. Acta*, **11**, 321 (1966).

Current Distribution at a Gas-Electrode-Electrolyte Interface

I. Experimental Observations

Douglas N. Bennion[1] and Charles W. Tobias

Department of Chemical Engineering, University of California, Berkeley, California

ABSTRACT

The variation of current density along a cylindrical, partially immersed electrode relative to the position of the apparent or intrinsic meniscus has been measured as a function of total applied current. Measurements of current distribution are reported for the cathodic reduction of O_2 gas in aqueous KOH electrolyte on sectioned Ni and Ag electrodes. A thin film of electrolyte was observed to exist above the intrinsic meniscus. It was found that the charge transfer which takes place at the electrode-electrolyte surface occurs almost totally above the bottom of the intrinsic meniscus, and that a large portion of this charge transfer occurs in the thin film as high as 1-5 mm above the top of the intrinsic meniscus. However, as the total current is increased, the charge transfer reaction is gradually crowded closer to the top of the intrinsic meniscus, and a smaller fraction of current passes up into the film. On nickel the current is more uniformly distributed in the upper areas of the thin film than on silver.

Many of the possible fuels and oxidants proposed for use in fuel cells are gases. To gain an understanding of the dynamic behavior of electrodes involving gaseous reactants, analysis of transport phenomena at gas electrode-electrolyte interfaces is necessary. Various studies of porous media involving only electrode-electrolyte interfaces have been presented recently (1-4). The presence of a gas phase provides additional problems which are to be considered here.

Porous electrodes are used to increase the reaction area per unit volume and, in the case of gaseous reactants, to provide separation between gas and electrolyte. In such electrodes, many simultaneous and consecutive processes occur, and the nature and extent of the actual reaction area within the pores is not well defined or understood. A plane electrode partially immersed in an electrolytic solution offers a simpler system for studying the behavior of gas electrode-electrolyte interfaces.

[1] Present address: Department of Engineering, University of California, Los Angeles, California.

In 1957 Wagner (5) postulated that a thin film of electrolyte exists above the visible meniscus on the surface of a partially immersed electrode and that the electrode surface in contact with this thin film should contribute appreciably to the charge transfer reaction.

In their study of current density distribution of oxygen reduction on copper, Weber, Meissner, and Sama (6) did not consider the possibility of the existence of a thin electrolyte film above the intrinsic or readily visible meniscus. Will (7, 8), in experiments involving oxidation of hydrogen in sulfuric acid on platinum, observed the variation of the total current with the length of platinum extending above the liquid level of the electrolytic solution at a constant applied overpotential. Will concluded that a thin film did exist above the intrinsic meniscus and that most of the charge transfer reaction occurred in a narrow region adjacent to the upper edge of the meniscus. He also showed that surface migration of hydrogen along the platinum was not a significant mode of mass transfer.

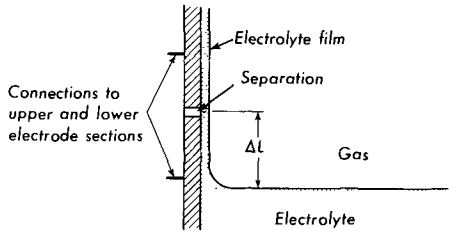

Fig. 1. Schematic representation of gas electrolyte interface showing the insulating separator. ΔL could be changed by raising or lowering the electrolyte level.

Diffusion of hydrogen through the film was determined to be the rate-controlling step. This was the first really definitive experiment to show the role of thin electrolyte films. However, as the platinum electrode was extended further and further out of the electrolyte, new area on which an electrolyte film could exist was produced. Thus, the film geometry and resulting current distribution changed during the course of an experiment.

The present work was undertaken to investigate the role of the thin film during oxygen reduction, and to obtain a quantitative description of the transport processes involved. For experimental work, oxygen gas, aqueous 3.5M KOH, and either nickel or silver electrodes were chosen.

Experimental Equipment and Procedures

The objective was to measure the variation of current density along a partially immersed electrode relative to the position of the bulk electrolyte surface. In order to accomplish this, sectioned electrodes (9) were employed. The sections must be insulated electrically from one another, and the insulating separators should not significantly disturb the geometry of the thin liquid film on the surface of the electrode. Also, the sections of the metal electrode must be at the same potential.

In order to satisfy these requirements as closely as possible, only two sections and a single separation were used (see Fig. 1). With this approach, the variation in the current from each section could be measured as a function of the distance, ΔL, of the bulk electrolyte level below the separation (see Fig. 1). The sum of the two currents equals the total; therefore, only one of the currents is independent. In order to compare the results of different total currents more easily, the per cent current out of the top section, defined as %C.O.T. = (Current out top section) (100)/(Total Current), was used as the independent variable.

The experimental procedure involved determination of the %C.O.T. as a function of ΔL at various total currents on nickel and silver electrodes. To determine the actual current density variation, one plots the %C.O.T. *vs.* ΔL and takes the slope of this curve. The slope at a given value of ΔL, in cm^{-1}, times the applied current, I, in microamperes per centimeter of electrode circumference, gives the transfer current density at a height ΔL above the electrolyte level. The readings were consistent to within 3% for a single run except at the lowest current levels when variations up to 10% of the measured current were inherent in the circuit design.

To avoid edge effects cylindrical electrodes were used. Electrodes of both 0.8045 and 1.465 in. in diameter were used. The current, I, in microamperes per centimeter times the electrode diameter, gives the total current. The working length of the electrode was approximately 12 cm; this was found to be long enough to avoid appreciable end effects at the top and bottom. The electrode was constructed using a cylindrical plexiglass spindle over which two cylinders of nickel[2] (or silver[3]) were slipped (see Fig. 2.). These were

[2] The nickel was 99.5% pure. The principal impurities were Mn and Fe.

[3] The silver was 99.95% pure.

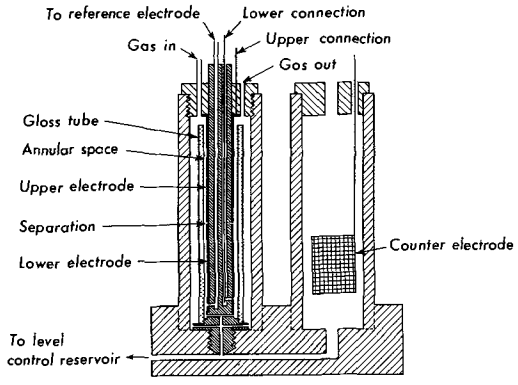

Fig. 2. Cross-sectional view of cell used for measurement of distribution of current relative to position of meniscus.

separated by a thin "gasket" made from a sheet of oriented polystyrene 25μ thick. This thickness was necessary to insure that no metallic electrical connection occurred between the two sections.

In order to avoid the possibility of systematic errors and to confirm the reproducibility of the data, 2 different silver cells and 5 separate nickel cells were built. The procedures in constructing the separations in the working electrodes (such as rounding the corners of the electrode where it contacts the insulating jacket) were modified slightly to see if the results were affected. No effects on the results were noted from these changes. For one of the silver electrodes, runs were also made with the 25μ thick polystyrene gasket replaced by a separator made from filter paper approximately 70 microns thick. This was done to check the results for any dependence on the nature of the material used as the separator.

The cell consisted of two cylindrical compartments as shown in Fig. 2. The cylindrical electrode spindle described above was screwed into the left-hand compartment. In the right-hand compartment, nickel screens served as the counter electrode. The over-all reaction at the working electrode was

$$O_2 + 2H_2O + 4e^- = 4\,OH^-$$

The reaction at the counter electrode was the reverse of the above reaction. The reactions were driven externally by a constant current power supply.[4]

The two compartments mentioned above were connected to a storage reservoir, not shown in Fig. 2. By carefully adjusting the height of the reservoir, the liquid level in the cell compartments could be accurately adjusted. The value of ΔL was determined by measuring the height of the bulk liquid and the height of the separation, to ± 0.05 mm, using a cathetometer.

The electrolyte entered the working electrode compartment through radial holes drilled in the lower part of the plexiglass spindle. This provided for an axially symmetric electric field. To align the electric field more nearly parallel to the electrode and to reduce convection effects, a precision-bore glass tube was placed over the electrode as shown in Fig. 2. The bulk electrolyte was confined in an annular space about 1 mm wide. The bottom of the meniscus was used as the reference level for measuring ΔL. The distance from the bottom of the meniscus to the top of the apparent or "intrinsic" meniscus was in the range of 0.6-1.1 mm. The electrolyte in the cell outside the jacket did not participate in the reaction and need not be considered.

Convection currents in the electrolyte below the meniscus would tend to give abnormally high currents from the bottom section. The precision-bore glass jacket which confined the electrolyte next to the electrode in an annular region reduced this effect. Smaller

[4] Electronics Measurements, Inc., Constant Current Power Supply, Model C612.

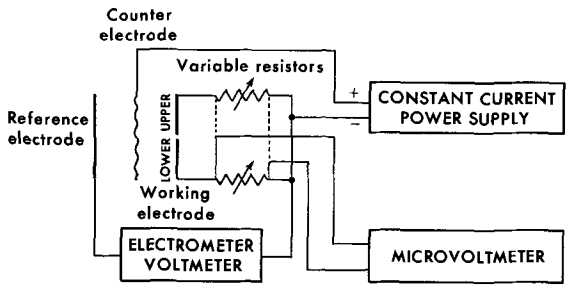

Fig. 3. Power and measurement circuit for sectioned electrode cell.

spacing would have reduced the probability of convection further (10), but this would have caused more severe relative variations in the annular space. The value chosen was considered to be a suitable compromise.

The readings were sensitive to the surface conditions of the electrodes. If any oxide formed on either the nickel or silver electrodes, the results were not reproducible. Care was always taken that, following polishing,[5] the electrode was immediately placed in the cell and cathodically polarized to prevent oxide formation. The current was increased to approximately 200 ma yielding vigorous hydrogen evolution. During the 24-48 hr cleaning period, the electrolyte was changed each 2-5 hr The cleanliness of the surface was considered satisfactory when, on lowering the electrolytic level, the surface remained uniformly wetted.

Electrolytic contact was made to a Hg, HgO reference electrode through a hole drilled lengthwise down the spindle and out through a small hole at the bottom of the metal electrode (11). Electrical connection to the bottom section of the electrode was made with a nickel rod down a hole in the spindle. A stainless steel screw went through the electrode and was threaded into the nickel rod. The electrical connection to the top section was made by a nickel plate in the bottom of the cap. When the cap was screwed down, the nickel plate pressed down on the upper electrode section and completed the contact. The resistances due to these connections were less than 0.1 ohm.

Figure 3 shows a schematic drawing of the electrical circuit. Before the measurements were started, the variable resistors[6] were set at zero; the two electrode sections were then shorted together and thus were at the same potential. When measurements were to be made, the resistances were increased until a measurable voltage drop[7] was obtained. When properly adjusted, the potential drop across each resistor was equal. As small a voltage drop as practical was used so that errors in balancing would be negligible. These potential differences varied between 10 and 1000 μv for the lowest and highest total applied currents. From the voltage drop and the known resistance, the current from each section could be calculated. The potential of the working electrode with respect to the Hg, HgO reference cell was measured with an electrometer.[8]

The start-up procedure was to refill the cell with 3.5M KOH, begin bleeding in O_2 saturated with water with respect to 3.5M KOH, and to set the total current at a fixed level. The liquid level was then lowered to near the bottom of the electrode, corresponding to a large value of ΔL. The cell was left for about 15 hr to allow the liquid film to drain and reach an equilibrium thickness. The level was next raised a small distance and a set of readings were taken. After each set of readings, the level was raised again and in this manner a series of readings for different values of ΔL were obtained. Observations were made at 30-min intervals to allow steady-state conditions to prevail during readings. At each electrolyte level the value of %C.O.T. could easily be calculated.

[5] Of the various polishing compounds, "Flow-five" aluminum oxide proved to be the most satisfactory. Although the roughness of surfaces was different depending on the polishing compounds used, no significant differences in the pattern of current distribution resulted.

[6] General Radio type 1432-U or 1432-K decade resistance boxes were used.

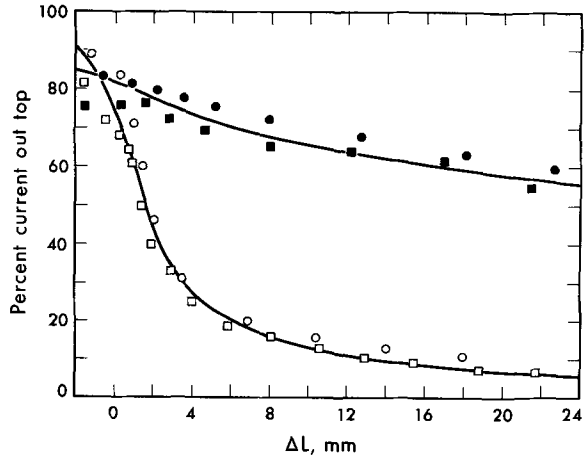

Fig. 4. Penetration of current in the electrolyte film. I = 4.84 μa/cm. Upper curve: nickel cathode, cells No. 2 and 3, runs 6 and 6'; lower curve: silver cathode, cell No. 4, runs No. 6 and 15.

Experimental Results

Exploratory experiments showed (12) that after the electrolyte level was lowered, a thin electrolyte film was left behind on the exposed electrode. The fraction of current from the upper section was very high but it dropped off with time. This decrease with time continued for up to 90 hours, after which a steady-state value remained as long as the run was continued, for several more days in some cases. This behavior was attributed to the draining of the electrolytic film which was initially thick but became thinner as draining progressed. Thicker films have a small resistance and thus tend to allow penetration of the current higher into the film.

Simple optical observations were made in an attempt to observe the film and determine its thickness by light interference techniques. The existence of the film was confirmed by the observation of weak interference colors when white incident light was used and by the observation of a "wake" when a small corner of tissue paper was drawn over the surface. Quantitative measurements of the film thickness were beyond the scope of this work. Müller (13) has made a detailed investigation of the optical properties of thin electrolytic films on nickel electrodes and found that in the range of 2-5 mm above the meniscus the film thickness is in the order of 1μ for 3.5M KOH.

Plots showing %C.O.T. as a function of ΔL are shown in Fig. 4, 5, and 6 for 4.84, 15.4, and 48.4 μa/cm applied current, respectively. Figure 7 shows the observed dependence of the electrode potential on the applied current.

A feature to be noted is that at higher currents the reaction tends to be concentrated nearer the top of the intrinsic meniscus. A comparison of the results for equal applied currents shows that the reaction on nickel spreads significantly more into the film than on silver.

One of the requirements of the sectioned electrode was that the separation should not disrupt the film. This becomes especially important when it is realized that the electrolyte film is about 1μ thick and the separation is 25μ wide. Such a wide gasket obviously causes some distortion. The possible distortion effects can be broken down into three categories as follows:

[7] This voltage drop was measured using a Keithly model 149 millimicrovoltmeter.

[8] Keithly Model 610R electrometer was used here. Its internal resistance is rated at 10^{14} ohms or greater.

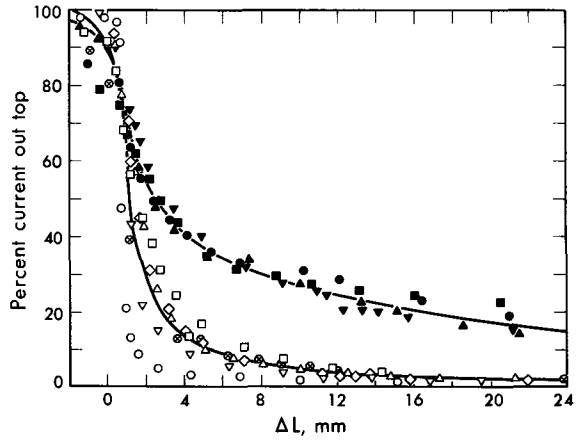

Fig. 5. Penetration of current in the electrolyte film. $I = 15.4$ μa/cm. Upper curve: solid symbols, experimental points, nickel cathode, cells No. 2 and 3, runs 5 and 5'; lower curve: open symbols, experimental points, silver cathode, cell No. 4, runs 5, 11, and 14.

1. Assume that the insulating gasket is perfectly flush with the metal surface and that the film thickness does not vary. The only error from such an ideal situation results from no electrode reaction occurring along the insulating section. This inactive length of the film will act as an "unnatural" resistance. If this occurs near the bottom of the film where the current might reach 100 μa/cm as a maximum and if the film is 1μ thick, the "unnatural" resistance will cause a potential drop of 4.2 mv. This compares to a total potential drop in the film of about 140 mv.

2. Referring to case 1, the net effect of the separation might be such that the film appears to be thicker as it passes the separation. For this situation, the "unnatural" resistance will be lowered, and the error will be less than for case 1.

3. The situation might also be an effective thinning of the film as it passes the separation. At worst, this thinning will occur along the full length of the separation. A thinning of this type, for example, to one-fourth of the normal thickness, will increase the "unnatural" resistance so that, using the example of case 1, the added potential drop would be 19 mv. Such an added potential drop would cause a shift in the results, such that less current would pass to the upper section than on an uninterrupted surface.

The reproducibility of the data was confirmed by using different cells of slightly modified design. Similarly, no change in the results was detected by replacing the 25μ thick polystyrene separator with a 70μ thick separator made from filter paper (see Fig. 5 and 6).

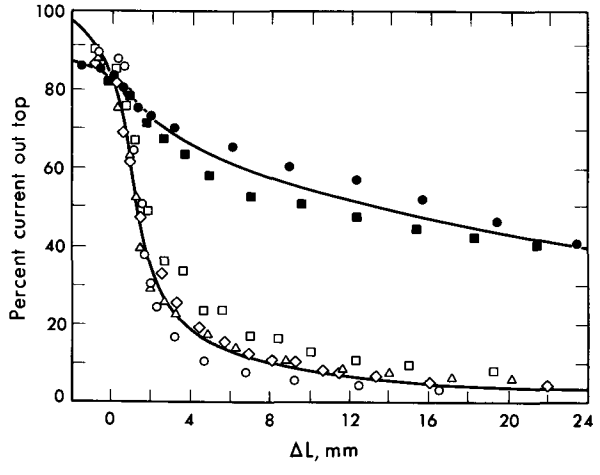

Fig. 6. Penetration of current in the electrolyte film. $I = 48.4$ μa/cm. Upper curve: solid symbols, experimental points, nickel cathode, cells No. 2, 3, and 7; runs 4, 4', 19, 20; lower curve: open symbols, experimental points, silver cathode, cells No. 4 and 6, runs 4, 10, 13, 19, 20.

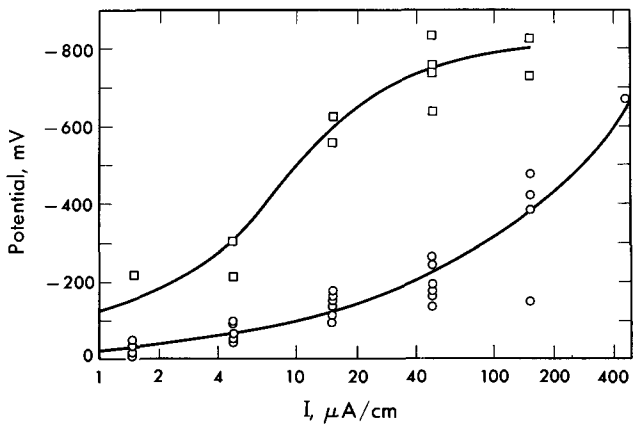

Fig. 7. Potential of the oxygen cathode (not corrected for ohmic drop) relative to the Hg/HgO reference electrode. Upper curve, nickel cathode; lower curve, silver cathode.

From these observations it is concluded that the film on the separator was not significantly thinner than on the adjacent metal surfaces. The maximum error in the current out the top, due to the presence of the separator, is estimated to be 3%.

Discussion

These experiments have confirmed that a stable, thin film of electrolyte adheres to the electrode surface above the top of the intrinsic meniscus. A large part of the reaction takes place on the surface of the electrode exposed to this film. The reaction rate drops off very rapidly within the visible meniscus and is very small along the electrode area exposed to the bulk electrolyte. The obvious reason for the abrupt decrease in reaction rate on the electrode surface below the intrinsic meniscus is mass transport limitation of the molecular oxygen. However, the controlling factors in the film region can arise from other sources.

Will (7, 8) concluded that the rate-limiting step was the mass transfer of gaseous reactant, hydrogen in this case, through the film to the electrode surface. He also found that the reaction rate dropped off very rapidly above the "top of the intrinsic meniscus." The observations with the oxygen-KOH system show that the reaction rate remains appreciable for several millimeters above the "top of the intrinsic meniscus." In addition, it is observed that the reaction extends further up the film for nickel than for silver.

It is also possible that the limiting step can be charge transfer at the electrode surface. It is known that silver is a better catalyst for the reduction of oxygen than is nickel (14). Thus one would expect that if the dependence of charge transfer "overpotential" on current density were higher for nickel than for silver, the reaction would tend to "spread out" or be distributed over a wider area, thus further up into the film.

Both the charge transfer and mass transfer overpotential tend to cause the reaction to spread out farther. It is the potential drop in the film which limits the extension of the reaction up into the film. From either standpoint, if the film were thicker, the reaction would tend to extend further into the film. Observations made during the initial stages when the film was draining confirm this argument.[9]

[9] A greater penetration of current up into the film on nickel relative to silver could be explained qualitatively by a significantly larger film thickness on nickel. Although precise observations regarding the film thickness on nickel were not available at the time this work was concluded, preliminary data by Müller (13) indicated that the film thickness on silver is actually somewhat greater than on nickel.

Conclusions[10]

1. The existence of a thin film of electrolyte above the intrinsic meniscus on clean nickel and silver has been confirmed. The thickness of this film is established as being in the order of magnitude of wave length of visible light.

2. For the cathodic oxygen electrode, current density distribution measurements on cylindrical nickel and silver electrodes established that a large portion of the current arises in the thin electrolytic film above the intrinsic meniscus. The fraction of current transferred as much as 10-20 mm above the bottom of the intrinsic meniscus is not negligible.

3. The thicker the film and the smaller the applied current, the further the current spreads over the electrode surface covered by the film. At a given value of applied current, the reaction is concentrated nearer the intrinsic meniscus on silver than on nickel surfaces.

Acknowledgment

This work was supported by the Advanced Research Project Agency through the U.S. Army Electronic Laboratory.

Manuscript received June 2, 1965. Revised manuscript received Jan. 10, 1966.

[10] After the completion of this manuscript, an account of the work of Yu A. Mazitov *et al.* (15) has come to the authors' attention. Current distribution along a silver wire in the reduction of oxygen in 10.6*N* KOH was measured by the method originally used by Will (7, 8). Although their experimental observations are in qualitative agreement with the results presented above, the reader's attention is called to the use of an uninterrupted cathode and the much shorter draining times (3-4 min) reported by Mazitov *et al.*

Any discussion of this paper will appear in a Discussion Section to be published in the December 1966 JOURNAL.

REFERENCES

1. J. S. Newman and C. W. Tobias, *This Journal*, **109**, 1183 (1962).
2. E. A. Grens, II, and C. W. Tobias, *Ber. Bunsen Ges. Physik. Chem.*, **3**, 236 (1964).
3. J. L. Bomben, Master's Thesis, University of California, Department of Chemical Engineering, September 1963.
4. J. Euler and W. Nonnenmacher, *Electrochim. Acta*, **2**, 268 (1960).
5. Carl Wagner, Private communication.
6. H. C. Weber, H. P. Meissner, and D. A. Sama, *This Journal*, **109**, 884 (1962).
7. F. G. Will, *ibid.*, **110**, 145 (1963).
8. F. G. Will, *ibid.*, **110**, 152 (1963).
9. E. Mantzell, *Z. Elektrochem.*, **42**, 303 (1936).
10. U. Böhm, N. Ibl, and A. M. Frei, Paper presented at the 13th CITCE Meeting in Rome, Sept. 24-29, 1962; in press *Electrochim. Acta*.
11. M. Eisenberg, C. W. Tobias, and C. R. Wilke, *This Journal*, **102**, 415 (1955).
12. D. N. Bennion, Dissertation, University of California, Berkeley, June 1964.
13. R. H. Müller, Extended Abstracts of Theoretical Division, **2**, 19, The Electrochemical Society, New York.
14. H. M. Dittman, E. W. Justi, and A. W. Winsel, "DSK Electrodes for the Cathodic Reduction of Oxygen," in "Fuel Cells," Vol. II, G. J. Young, Editor, Reinhold Publishing Corp., New York (1963).
15. Yu A. Mazitov, K. I. Rosenthal, and V. I. Vesilowskii, *Zhur. Fis. Khim.*, **38**, 449 (1964).

Current Distribution at a Gas-Electrode-Electrolyte Interface

II. Theoretical Treatment

Douglas N. Bennion[1] and Charles W. Tobias

Department of Chemical Engineering, University of California, Berkeley, California

ABSTRACT

The dynamic behavior of a cathodic oxygen electrode is critically dependent on charge and mass transport preceding and following the charge transfer recation at the electrolyte-electrode interface. A mathematical model is presented which takes into account diffusion and migration of relevant substances and the solubility of oxygen in the electrolyte. The model accounts for the concentration dependence of transport properties. A comparison of the theoretical and experimental results indicates that the current density distribution is controlled by a balance between charge transfer overpotential and ohmic resistance drop in the electrolyte film. Because of the much greater length of diffusion paths, and consequent slowness of oxygen transport, a relatively small fraction of the charge transfer reaction occurs on the electrode area below the top of the intrinsic meniscus.

An experimental study (1) in this laboratory has shown that on partially immersed gas electrodes a thin film of electrolyte may exist on the electrode above the bulk electrolyte, and when this film exists the electrochemical reaction takes place primarily on the surface of the electrode which contacts the thin film.

By considering several possible physical models Wagner (2), in 1957, demonstrated the likelihood of the importance of thin electrolyte films in actual gas electrodes. Since then, various models have been proposed which attempt to duplicate more closely actual physical conditions. Will (3, 4) was able to explain his experimental results obtained on partially immersed, plane electrodes in terms of a theoretical model. His model did not include consideration of charge transfer overpotential, and the only transport property of the electrolyte employed was the conductivity which he assumed to be invariant. Grens *et al.* (5) in a model geometrically similar to the one by Will included an Erdey-Gruz-Volmer-type charge transfer overpotential expression. Transport of ions by both diffusion and migration is accounted for, and the movement of water is assumed to occur only in the electrolyte phase. Grens *et al.* were able to show how systems can become charge transfer or mass transfer limited depending on the magnitude of the physical parameters involved. Although variations of transport properties were not considered, their model predicts large concentration gradients in the thin film. It should be noted that, of these models, only that of Will has been compared directly to experiments, and that his model incorporated features characteristic of the hydrogen, sulfuric acid, platinum system.

The above theories provide primarily a guide to understanding the detailed behavior of the electrode reaction within and near a thin electrolyte film which

[1] Present address: Department of Engineering, University of California, Los Angeles, California.

may exist on plane, metal electrodes. Other models have been proposed which attempt to explain the behavior of porous electrodes in terms of certain assumed microstructures of the porous matrix. Some recent models by Gurevich (6), Rockett (7), Iczkowski (8), and Burshtein *et al.* (9), have incorporated the possibility of a thin film existing on the walls of the gas filled pores or cavities within the electrode. Of these, the one by Burshtein *et al.* is of particular interest, since it includes a transformation of a rather sophisticated model into one where equations developed for two-phase porous electrodes can be applied (10-12). In Burshtein *et al.'s* model, a detailed description of what is taking place within the thin film is not undertaken, and a simple, linear relation between the local overpotential and the current being transferred is assumed.

The theoretical model to be presented here is one in which the details of the film behavior are described. Our model is to be for the oxygen, KOH, silver system and is to include a realistic charge transfer overpotential relation. It also allows for variation of electrolyte composition and consequent changes in the solubility of oxygen and in the transport properties of oxygen and KOH. Consideration is given to whether water transport occurs in the gas phase or the liquid phase. Direct comparison of the theoretical model and experimental results is designed to further our understanding of the system and its controlling features.

The Mathematical Model

Geometric considerations.—The model describes an oxygen half-cell operating cathodically in aqueous KOH electrolyte. From the analysis of experimental results (1) it has been concluded that a large portion of the reaction takes place in a thin film which extends above the bulk electrolyte on the surface of the electrode. Measurements of the film thickness by Müller (13) show that the thickness of this film decreases with height above the bulk liquid. However, the per cent change in thickness is small compared to the observed per cent changes in the reaction rate over comparable distances (15). In our model, to avoid unnecessary mathematical difficulties, the thin film is assumed to have a constant thickness, δ.

Since the current density was observed to spread out over a comparatively large area, the charge transferred in the vicinity of the curved meniscus is small compared to the total current. This suggests that the precise geometry of the meniscus is not important (1, 3, 4). Consequently, in our model (see Fig. 1) the thin film is assumed to change its thickness abruptly.

Mass transport considerations.—Mathematically, the model is one dimensional. No variations in concentration, c, or current density, i, across the width of the film are considered. Oxygen is assumed to reach the electrode by diffusion in the x direction through the upper film (see Fig. 1). In the lower (bulk) electrolyte region oxygen is assumed to move only in the negative y direction. The consumption of oxygen through reaction at the electrode is treated as a homogeneous sink term (see Eq. [10]).

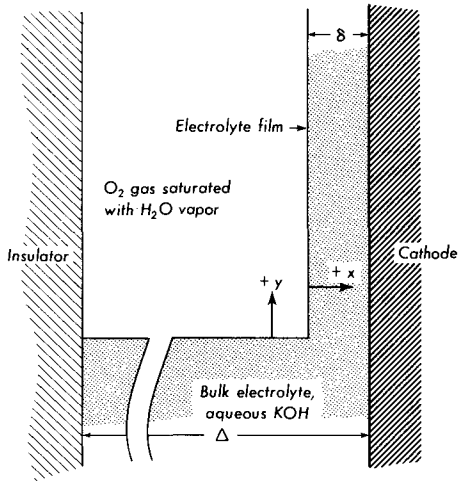

Fig. 1. Mathematical model of the gas-electrolyte-electrode interface.

The system is assumed to be at steady state. The over-all electrode reaction is

$$O_2 + 2H_2O + 4e^- = 4\,OH^-$$

The rate of reaction at the electrode is proportional to the transfer current density, J. J is taken as positive when the reaction proceeds from left to right as written. In the thin film, O_2 migrates toward the electrode in the x direction, OH^- ions move down the film, and the K^+ ions remain stationary at steady state. The water can reach a reaction site by two mechanisms or combinations thereof. It can diffuse up into the film countercurrently to the OH^- ions or condense from the gas phase onto the film surface and diffuse cocurrently with the oxygen. Convection is assumed to be negligible.

Equations for electrolytic transport.—Algebraically, the ionic fluxes and the water flux can be written as

$$N_+ = 0$$

$$N_- = -i/F$$

$$N_o = -\tfrac{1}{2}\,Q\,N_-$$

$$v^\star = \frac{1}{c_T}(N_+ + N_- + N_o) = \frac{-i}{c_T F}\left(1 - \frac{Q}{2}\right) \qquad [1]$$

By electroneutrality

$$c_+ = c_- = c \qquad [2]$$

Q is equal to unity if the water is supplied wholly by diffusion up the film, and it is equal to zero if supplied totally by condensation from the gas phase. It seems reasonable that one mechanism or the other will be controlling so that Q will be assumed to equal either one or zero. The model is not suitable for fractional values of Q.

The equations representing the flow of current and movement of the K^+ and OH^- ions have been discussed elsewhere (14, 15). Incorporating the concentration dependence of the transport properties, and assuming use of a Hg/HgO reference electrode, we obtain

$$i = \kappa\nabla\Phi - \frac{\kappa}{F}RT\,\nabla \ln a\left[\frac{2B}{A+B} + \frac{c}{c_o}\right] \qquad [3]$$

$$N_+ = \frac{-\mathcal{D}}{RT}\frac{\nu_+}{\nu}c\nabla\mu_e + \frac{t_+^\star\, i}{Fz_+} + c_+ v^\star \qquad [4]$$

$$N_- = \frac{-\mathcal{D}}{RT}\frac{\nu_-}{\nu}c\nabla\mu_e + \frac{t_-^\star\, i}{Fz_-} + c_- v^\star \qquad [5]$$

$$\frac{-z_+ z_- eF\sqrt{\nu c c_T}}{\kappa\mu} = G + \frac{AB}{\nu_+ A + \nu_- B}\frac{\sqrt{\nu c_o}}{\sqrt{c c_T}} \qquad [6]$$

$$\mathcal{D} = \frac{\nu kT/\mu}{\nu_+ A + \nu_- B} \qquad [7]$$

$$t_+^\star = 1 - t_-^\star = \frac{c_-}{c_T} + \frac{c_o}{c_T}\frac{B}{A+B} \qquad [8]$$

Values of A, B, and G for KOH are (14, 15): $A = 28.89 \times 10^{-8}$ cm; $B = 8.63 \times 10^{-8}$ cm; $G = 9.63 \times 10^{-8}$ cm.

Equations for oxygen transport.—In the thin film, oxygen diffusion can be represented by

$$J = \frac{FD_1[(p/p^o)c_1^o - c_1]}{\delta}, \quad (y \geqq 0) \qquad [9]$$

The transfer current density, J, is equal to the oxygen flux times $4F$. It is assumed that Henry's law holds and that p is the partial pressure of oxygen in atmospheres. D_1 is the diffusion coefficient of oxygen at the concentration of KOH existing at the point under consideration in the film. The numerical calculations were easily adapted to allow for the variation of D_1 as a function of the KOH concentration (16) at different positions in the film.

In the lower or bulk electrolyte region the following equation applies to steady-state oxygen transport.

$$D_1 \frac{d^2c_1}{dy^2} = \frac{J}{4F\Delta}, \quad (y \leqq 0) \qquad [10]$$

Equations relating current and overpotential[2].—A relationship between local overpotential and local transfer current density, J, is still needed. A review of the literature on the kinetics of the oxygen electrode (15, 36) indicates that a generally accepted kinetic description for the oxygen electrode is not yet available (17-19). Based on work by Krasilshchikov, Nefodova, Belina, and Andreeva (20-25) and by Bagotskii and Yablokova (26), a sequence of elementary steps emerges which seems to be satisfactory for use with Ag, Au, and Hg electrodes. From this reaction sequence, summarized by Vetter (36), the following kinetic expression can be developed (15)

$$J = k[O_2]^{\alpha}[OH^-]^{\lambda}[H_2O]^{\gamma} \left\{ e^{\frac{4(\alpha-1)F\eta}{RT}} - e^{\frac{4\alpha F\eta}{RT}} \right\} \qquad [11]$$

where k is a constant, square brackets indicate the activity of the enclosed species, and η is the overpotential defined as the potential of the working electrode compared to a reversible oxygen electrode located just outside the double layer. For a silver electrode in alkaline solution

$$\alpha = 0.625, \lambda = 0.5, \gamma = 0.5 \qquad [12]$$

Work on carbon electrodes (27-30) also seems to support the above mentioned reaction sequence. As mentioned in the Appendix, the kinetics of oxygen reduction on nickel seems more complex. For the case of silver it is assumed that Eq. [11] is applicable at any point on the electrode, *i.e.*, k and α are true constants without any dependence on η or position on the surface. For nickel electrodes Eq. [11] would have to be replaced by an expression of a probably more complex nature, accounting for the dependence of the rate-controlling step (or steps) with η. A generally applicable reaction sequence or kinetic rate expression for the reduction of oxygen on nickel does not appear available (17, 18, 31, 32). For this reason no attempt is made to apply the present mathematical model to the nickel electrode.

Equations relating charge transfer current density and current density in the solution.—Two relations are needed in addition to the equations already mentioned. Since charge must be conserved, the transfer current density, J, and the current density in the solution, i, which is assumed to vary only in the y direction, are related by

$$J = -\delta \frac{di}{dy}, \quad (y \geqq 0); \quad J = -\Delta \frac{di}{dy}, \quad (y \leqq 0) \qquad [13]$$

It is convenient to replace the potential of the reversible oxygen electrode by that of a Hg/HgO reference electrode

$$\eta = -\Phi - \frac{RT}{4F} \ln \{[O_2]/p\} \qquad [14]$$

Here Φ is the potential of the Hg/HgO reference electrode with respect to the working electrode.

[2] A more detailed discussion is given in the Appendix.

Activities used in kinetic equation.—The activities of the reacting species are assumed to be represented by the following:

$[O_2]$ is assumed to be the concentration of oxygen with unit activity being the concentration of oxygen in equilibrium with gaseous oxygen at a partial pressure of one atmosphere. In the numerical work it was possible to allow the solubility of the oxygen to depend on the concentration of KOH.[3]

$[OH^-]$ is assumed to be the same as the mean ionic activity, a, of the KOH. The activity coefficients were taken from Robinson and Stokes (33). The activity at a KOH concentration of 3.866M is taken to be unity.

$[c_o]$ is assumed to be the concentration of free water. This is determined by subtracting from the total water concentration the concentration of water that is associated with the KOH ions (14, 15). Unit activity is assumed to be the activity of water in 3.866M KOH solution.

Numerical solution.—There are 5 dependent variables, c, c_1, J, η, and i. These are related by Eq. [3], [4], [9] or [10], [11], and [13]. Equation [9] is used in the upper film and Eq. [10] in the lower region. Equation [14] allows one to convert from η to Φ when desirable. The equations are slightly different for the upper and lower sections. The two sections are solved for separately and their boundary conditions matched, since the potential and current are continuous in the electrolyte.

The boundary conditions at the top of the upper film are $y \to +\infty$, $\eta \to 0$, and $i \to 0$.

The boundary conditions at the bottom of electrode are: at y = bottom of electrode, $\eta = \eta_o$ or $i = i_o$.

The equations are nonlinear, 1st, and 2nd order differential equations. They were transformed into finite difference form and solved numerically using an IBM 7090 digital computer. In a numerical sense, it was possible to solve the equations for the thin film region exactly. That is, no iterations were necessary. This was accomplished through an appropriate change of variables. In the lower section, it was necessary to linearize the equations, put them in matrix form, and solve the matrix (15). The nonlinearities were mild, and only three or four iterations were necessary. The method appeared to be stable and to converge rapidly to the correct answer.

Theoretical Results and Comparison with Experimental Observations

Explanation of figures.—Experimental results are summarized in Fig. 2 through 6. A comparison between the calculated variation of current above a

[3] The solubility of oxygen at 25°C in aqueous KOH and for a total pressure of 1 atm as determined in this laboratory (16) may be represented by

$$c_1 = (1.18 \times 10^{-3} \text{ mole/liter}) \exp(-0.405c)$$

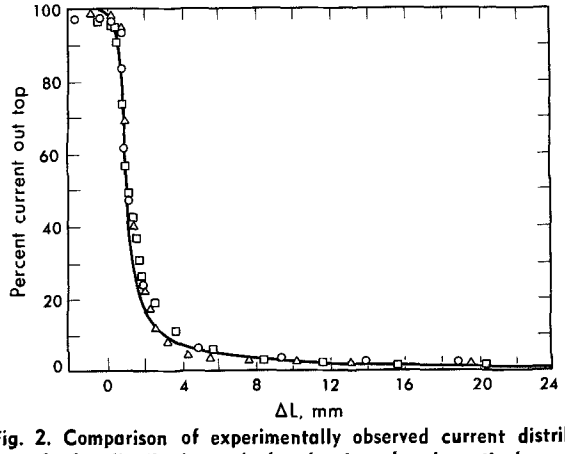

Fig. 2. Comparison of experimentally observed current distribution with the distribution calculated using the theoretical model. Nickel cathode, I = 154 μa/cm. Cell No. 4, runs 7, 9, and 12. Numerical solution with $\delta = 2.25\mu$, $i_o = 1.76 \times 10^{-9}$ amp/cm². Open symbols, experimental points, silver.

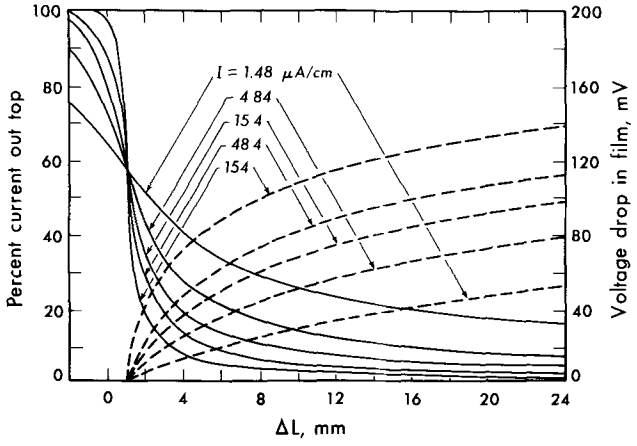

Fig. 3. Theoretical variation of potential and per cent current relative to the meniscus level as a function of applied current.

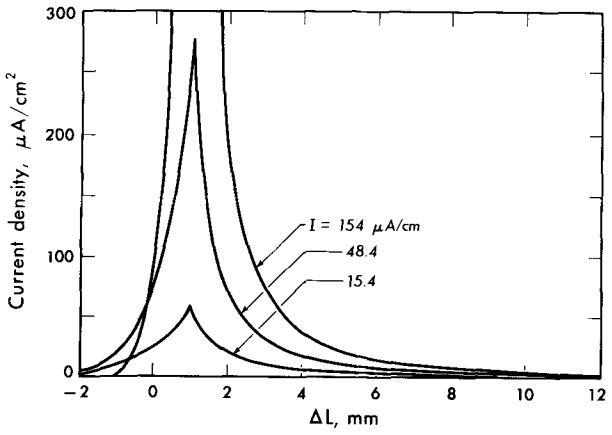

Fig. 5. Theoretical current density distribution relative to the position of the meniscus. High current range.

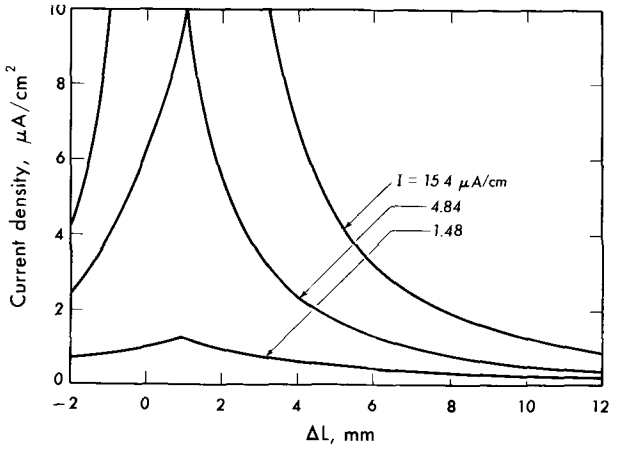

Fig. 4. Theoretical current density distribution relative to the position of the meniscus. Low current range.

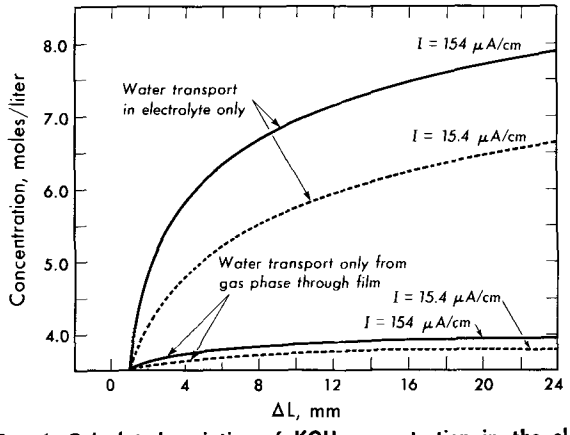

Fig. 6. Calculated variation of KOH concentration in the electrolyte film.

fixed point on the electrode, ΔL, and the experimental observations corresponding to similar conditions is given in Fig. 2. Experimental observations at 48.4, 15.4, and 1.48 μa/cm were presented in Part I, Fig. 4-6. In these figures the curves referring to the silver electrode are those calculated by using parameters as described below, while those for nickel represent a qualitative fitting of the data. No experimental data are available for the voltage variation in the film.

Figure 3 shows the theoretical variation of potential and the per cent current above a fixed point on the electrode as a function of applied current. Figures 4 and 5 present the calculated current density variation along the electrode. The curves in Fig. 3 are the integrals of the curves in Fig. 4 and 5 for corresponding total applied currents. Figure 6 shows computed examples of variation in the concentration of KOH in the film as a function of electrode height. A comparison is made between the concentration variations for both modes of water transport to the reaction sites.

Current distribution and the square meniscus assumption.—ΔL is the independent variable used in the experimental work which indicates position on the electrode relative to the bottom of the intrinsic or visible meniscus. The variable y is used in the theoretical work to indicate position along the electrode relative to the sudden, right-angle widening of the thin film. In order to make direct comparison between the two approaches, y and ΔL must be properly related.

The distance from the top of the intrinsic meniscus over which the current density remains appreciable is to be noted. Even at the lowest currents observed (1.45 μa/cm), the area lying under the level of the bottom of the intrinsic meniscus contributes less than a third to the total current. At the highest currents observed (154 μa/cm) this fraction falls to below a hundredth. The discontinuity of the current density distribution curves at ΔL of 1 mm (see Fig. 4 and 5) results from the square shaped meniscus used in the model. In reality, the transition from the charge transfer and conductance controlled region in the film to the oxygen mass transport controlled area below the top of the intrinsic meniscus occurs over a finite length near the top of the intrinsic meniscus. However, the current density drops off rapidly as the film begins to thicken from approximately 1μ to a thickness in the order of 1 mm at the bottom of the intrinsic meniscus, over a vertical distance of approximately 1 mm. The region of high current density at the bottom of the thin film contributes a large portion of the total current. However, the reaction remains appreciable for several millimeters above the intrinsic meniscus. Due to the large area available in the upper film, the contribution to the total current from that region is appreciable.

In matching the theoretical and experimental current distribution curves, it was found that $y = 0$ corresponded to a ΔL of 1 mm. This implies that below the level of 1 mm above the bottom of the intrinsic meniscus the film thickness is sufficient to cause oxygen transport to become controlling.

A theoretical treatment using a curved meniscus and a tapered film is possible. However, it appears this would greatly increase the numerical complexity due to a second geometric dimension. Such a modification is not expected to yield significant further information or insight. It is established by experimental evi-

dence (1) and a reasonably realistic, theoretical model that an overwhelming proportion of the current originates well above the bottom of the intrinsic meniscus. The changes in the pattern of the current density distribution that can be expected if one substitutes a smoothly curving meniscus for the square meniscus are not expected to be appreciable.

Effect of i_o.—Of the parameters which appear in the numerical calculations, several can be calculated from independent experimental data. Where values are not available, reasonable estimates have to be made.

The shape and position of the theoretical current distribution curves depends on the reaction orders, α, λ, and γ. These appear as the exponents of the OH^-, H_2O, and O_2 activities, respectively, in Eq. [11].[4] The values of α, λ, γ given in Eq. [12] were based on the reaction sequence, rate-controlling step, ($HO_2 + e^- = HO_2^-$), and the value of the transfer coefficient recommended by Krasilshchikov (18). There are, of course, a very large number of reaction sequences and rate-controlling steps which might be chosen. Calculations involving another rate-controlling step ($O_2 + e^- = O_2^-$) yielded a good fit of the experimental data only when unrealistic values of δ were employed.

The parameter known with the least certainty is k in Eq. [11]. When multiplied by the concentration terms raised to the appropriate power in Eq. [11], k can be identified with an exchange current density, i_o. A value for i_o in the order of 10^{-9} amp/cm^2 was found to "fit" the data best. However, this could be varied by plus or minus three orders of magnitude with little effect on the position or shape of the theoretical curve. Although literature reports on measurements of i_o for the oxygen electrode vary widely, a comparison to the Tafel lines shown by Belina and Krasilshchikov (25) indicate that the value used is not unreasonable. The relatively insignificant changes in distribution calculated for i_o's ranging from 10^{-6} to 10^{-12} amp/cm^2 are to be expected, since in the current density ranges used in the computations, except for large values of ΔL, the electrode operated in the Tafel region. Thus a change in i_o results in shifting the potential of the electrode by a constant value, not affecting the distribution of current at a fixed value of total current.

Effect of the film thickness parameter, δ.—The theoretical results were very sensitive to changes in the film thickness parameter, δ. It should be remembered that in reality the film tapers while the model assumed δ to be constant. Since the current extends further up the film at low currents, it is to be expected that the effective average film thickness will decrease with decreasing total current. For the indicated total applied currents, the following values of δ yielded good agreement between the experimental data and our model

I	1.48 μa/cm	4.84 μa/cm	15.4 μa/cm	48.4 μa/cm	154 μa/cm
δ	0.33μ	0.43μ	0.75μ	1.50μ	2.25μ

The values of δ used in the numerical solutions are in reasonable agreement with the average film thicknesses obtained by Müller (13, 15), who noted that the average film thickness increases significantly with increasing cathodic current.

As confirmed by our model, experimental observations have shown that the current density distribution varies a great deal while the film is draining, *i.e.*, while the film thickness is diminishing with time. In thinning films, the over-all overpotential increases and the reaction spreads less and less into the film.

Consideration of the tapering of the film may be justified after sufficient data on film thickness variations with position and current density become available. Otherwise, the introduction of a second geometric variable would require another adjustable parameter (the slope or curvature of the film) without appreciably contributing to the physical understanding of the phenomena observed.

Influence of variable transport parameters and water transport.—In the present work, current distributions were calculated both with constant and variable transport properties. Although the assumption of constant (average) properties did not yield significantly different distributions, this finding should be regarded as valid only under the specific experimental conditions employed. By providing water to the reaction sites through the film from the vapor phase, the steady-state concentration gradient in the film is quite mild compared to the case when water transport occurs by diffusion from the bulk electrolyte in the liquid phase (see Fig. 6).

The high concentration gradients which are predicted when water is assumed to be transported only within the film cause the KOH concentration to exceed the saturation limit. It is suggested that in actual porous gas electrodes water is supplied to the reaction site, at least in part, by condensation from the vapor phase.

Oxygen transport.—Except for the region below the meniscus, oxygen transport should not be a limiting factor. The numerical results show that throughout and across the entire length of the film, the activity of oxygen is very close to unity,[5] *i.e.*, nearly identical to the activity at the electrolyte-gas interface. However, once one moves below the meniscus where the diffusion path for the oxygen becomes large, the oxygen activity drops quickly resulting in the rapid decrease in current density below the top of the intrinsic meniscus.

Rate-controlling process.—Since our model shows that the oxygen activity does not vary noticeably in the thin film, it follows that the penetration of the reaction into the film depends on a balance between the charge transfer overpotential and resistance drop in the electrolyte. As stated in Part I, the significant differences between behavior of the nickel and silver electrodes suggest this to be the case.

Will (3) in his work with the hydrogen electrode on platinum found that the transport of hydrogen gas to the electrode surface through the thin film was controlling, along with ohmic resistance drop, except at very low currents. This is not in contradiction with the results found for the oxygen electrode. The hydrogen electrode on platinum is much more reversible than is oxygen on silver. Consequently, the concentration of current in the immediate vicinity of the intrinsic meniscus is rendered less possible in the case of oxygen, and charge transfer overpotential along with the ohmic drop in the film can be expected to control the current distribution.

Conclusion

In the foregoing treatment it is shown that the current distribution under an electrolyte film above the intrinsic meniscus of an oxygen cathode on silver may be quite successfully described by a rational theoretical model. Realistic geometric and kinetic parameters yield a good agreement between the calculated distributions and those observed experimentally.

Oxygen transport is not limiting in the thin upper film. The current density distribution in this region arises from a balance between charge transfer overpotential and resistance drop in the film. Below the intrinsic meniscus, the bulk electrolyte region, the oxygen activity decreases rapidly due to the mass transport limitations of dissolved oxygen. Thus, the current density is small in this region. The high con-

[4] Note that the parameter α is related to (but not the same as) the transfer coefficient.

[5] It should be remembered that, although the activity remains constant, the concentration of oxygen varies along the length of the film due to the decreasing solubility with increasing KOH concentration.

centration gradients which result when water is not supplied from the gas phase point to the desirability of supplying water as vapor in the oxygen gas.

Acknowledgment

This work was supported by the Advanced Research Project Agency through the U.S. Army Electronic Laboratory.

Manuscript received June 2, 1965; revised manuscript received Jan. 10, 1966.

Any discussion of this paper will appear in a Discussion Section to be published in the December 1966 JOURNAL.

NOMENCLATURE

A, B, C	subsidiary transport properties defined so as to reduce the concentration dependence, Å
a	mean molar activity of KOH $= f_{\pm}c$
c	$c_+/\nu_+ = c_-/\nu_-$ — concentration of KOH, mole/cm^3
c_1	concentration of oxygen, mole/cm^3
c_1^o	saturation concentration of oxygen under a partial pressure of 1 atm, mole/cm^3-atm
c_+	concentration of K^+, mole/cm^3
c_-	concentration of OH^-, mole/cm^3
c_o	concentration of water, mole/cm^3
c_T	$= c_+ + c_- + c_o$ — total concentration, including solvent
D_1	diffusion coefficient of oxygen in aqueous KOH, cm^2/sec
$\mathcal{D}$	molecular diffusion coefficient of KOH based on activity gradients, cm^2/sec
e	electronic charge, coulombs
e^-	symbol for an electron
$f_{\pm}$	mean molar activity coefficient. [Values from ref. (33) were used.]
F	Faraday's constant, coulombs/equivalent
i	current density in the solution, amp/cm^2
i_o	exchange current density, amp/cm^2
J	transfer current density, amp/cm^2
k	kinetic parameter related to exchange current density, amp/cm^2
N_+	flux of K^+, mole/cm^2-sec
N_-	flux of OH^-, mole/cm^2-sec
N_o	flux of H_2O, mole/cm^2-sec
p	partial pressure of oxygen, atm
p^o	reference pressure, 1 atm.
Q	one when H_2O is transferred in liquid phase; zero when H_2O transferred in the gas phase
R	universal gas constant, joule/mole-°K
t_i^*	transference number of species i with respect to molar average velocity
T	absolute temperature, °K
v^*	molar average velocity, cm/sec
x	coordinate perpendicular to the plane of the electrode, cm
y	coordinate parallel to the electrode in the vertical direction, the independent variable, cm
z_i	valence or charge number of species i, negative for anions
α	kinetic parameter related to reaction order of oxygen and to the transfer coefficient
γ	kinetic parameter indicating reaction order of H_2O
δ	film thickness, μ
Δ	width of annular electrolyte region below meniscus, cm
η	overpotential referred to a reversible oxygen electrode, volts
κ	conductivity, mho/cm
λ	kinetic parameter indicating reaction order of OH^-
μ_e	chemical potential of KOH, joule/mole. (RT ln $f_{\pm}$ c)
μ	viscosity, poise
ν_+	number of cations per molecule of electrolyte
ν_-	number of anions per molecule of electrolyte
ν	$= \nu_+ + \nu_-$
Φ	overpotential referred to a reversible Hg/HgO electrode, volts

APPENDIX

Notes of the Kinetics of the Oxygen Electrode

There has been accumulated a body of information which suggests that hydrogen peroxide is an intermediate in oxygen reduction (19-31, 34-36). Although the evidence is fairly conclusive for such electrodes as Ag, Hg, C, and Au, it appears that there may be competing sequences of steps on such electrodes as Pt and Ni (17, 18, 31, 34). At this point only the former category of electrodes appears amenable to a simple kinetic analysis.

A review of the above mentioned references indicates that the assumption of the following sequence of elementary kinetic steps is reasonable on Ag, Hg, C and Au electrodes.

1. $O_2 + M = MO_2$
2. $MO_2 + e^- = MO_2^-$
3. $MO_2^- + H_2O = MHO_2 + OH^-$
4. $MHO_2 + e^- = MHO_2^-$
5. $MHO_2^- + H_2O = MH_2O_2 + OH^-$
6. $MH_2O_2 + e^- = MOH + OH^-$
7. $MOH + e^- = M + OH^-$

The M represents an adsorption site and, when associated with a molecular symbol, implies that the molecule is adsorbed. It is possible for any adsorbed molecule on the right side of an equation to desorb before reacting in the next step. The O_2^- and HO_2 are so reactive that this is unlikely. The desorption of HO_2^- or H_2O_2 (depending on the pH) could occur. However, there is evidence (20, 25) which indicates that on silver and in alkaline solution the rate of desorption is small compared to reaction by steps 6 and 7. It should be noted that, because the O_2^- and HO_2 radicals are very reactive, they have not been positively identified.

It appears that the adsorption step is not rate controlling and that either step 2 or 4 is rate determining. The choice appears to depend on pH and on the electrode material. For silver in alkaline solution step 4 appears to be rate controlling. With these assumptions, the kinetic expression can be written as

$$J = k[O_2]^{\frac{\alpha_4 + 2}{4}} [H_2O]^{\alpha_4} [OH^-]^{(1-\alpha_4)} \left\{ e^{\frac{(\alpha_4 - 2)F\eta}{RT}} - e^{\frac{(\alpha_4 + 2)F\eta}{RT}} \right\}$$

where J is the local transfer current density, α_4 is the transfer coefficient for step 4, η is the local overpotential, and k is a kinetic rate constant. Brackets signify the activity of the enclosed species.

On electrode surfaces such as nickel and platinum it appears that other sequences of elementary steps may compete with those outlined above (17-19, 31, 34, 37). On such materials, metal oxides may appear in some of the elementary steps. It is likely that the rate-controlling step and indeed the whole rate-controlling sequence of steps may depend on the local potential. Until more precise information is available on the kinetic parameters the distribution of oxygen reduction on such a surface cannot be predicted.

REFERENCES

1. D. N. Bennion and C. W. Tobias, *This Journal*, **113**, 589 (1966).
2. Carl Wagner, Private communication dated June 13, 1957.
3. F. G. Will, *This Journal*, **110**, 145 (1963).
4. F. G. Will, *ibid.*, **110**, 152 (1963).
5. E. A. Grens, II, R. M. Turner, and T. Katan, *Advanced Energy Conversion*, **4**, 109 (1964).
6. I. G. Gurevich, *Inzhener, Fiz. Zhur., Akad. Nauk Belorus, SSR*, **2**, 78 (1959).
7. J. A. Rockett, Extended Abstracts of Battery Division, Vol. 8, New York Meeting of The Electrochemical Society, 1963.
8. R. P. Iczkowski, *This Journal*, **111**, 605 (1964).
9. R. Chs. Burshtein, V. S. Markin, A. G. Pshenichnikov, V. A. Chismadgev, and Y. G. Chirkov, *Electrochim. Acta*, **9**, 773 (1964).
10. J. S. Newman and C. W. Tobias, *This Journal*, **109**, 1183 (1962).
11. E. A. Grens, II, and C. W. Tobias, *Ber. Bunsen Ges., Phys. Chem.*, **68**, 236 (1964).
12. J. Euler and W. Nonnenmacher, *Electrochim. Acta*, **2**, 268 ((1960).
13. R. H. Müller, Extended Abstracts of the Theoretical Electrochemistry Division, Vol. 2, p. 19, Toronto Meeting of The Electrochemical Society (1964).

14. J. S. Newman, D. N. Bennion, and C. W. Tobias, *Ber. Bunsen Ges. Phy. Chem.*, **69**, 608 (1965).
15. D. N. Bennion, "Phenomena at a Gas-Electrode-Electrolyte Interface," Dissertation, University of California, Berkeley, June 1964.
16. R. Davis, G. L. Horvath, and C. W. Tobias, *Electrochim. Acta*, in press.
17. D. T. Sawyer and L. V. Interrante, *J. Electroanal. Chem.*, **2**, 310 (1961).
18. A. I. Krasilshchikov, "Electrochemical Reactions of Oxygen," Soviet Electrochemistry, *Trudy 4-go Soveshchaniya Po Elektrokhimi*, II (1956). (English translation, *Soviet Electrochemistry*, Vol. II, Consultants Bureau, New York (1961).
19. J. O'M. Bockris and A. K. M. Huq, *Proc. Roy. Soc. London*, **A237**, 277 (1956).
20. A. I. Krasilshchikov, *Zhur. Fiz. Khim.*, **26**, 216 (1952).
21. A. I. Krasilshchikov, *ibid.*, **21**, 849 (1947).
22. I. D. Nefedova and A. I. Krasilshchikov, *ibid.*, **21**, 855 (1947).
23. A. I. Krasilshchikov, *ibid.*, **23**, 332 (1949).
24. A. I. Krasilshchikov and V. A. Andreeva, *ibid.*, **27**, 389 (1953).
25. T. N. Belina and A. I. Krasilshchikov, *ibid.*, **28**, 1286 (1954).
26. V. S. Bagotskii and I. E. Yablokova, *ibid.*, **27**, 1663 (1953).
27. W. G. Berl, *J. (and Trans.) Electrochem. Soc.*, **93**, 128 (1948).
28. R. S. Weizz and S. S. Jaffe, *ibid.*, **93**, 128 (1948).
29. M. O. Davis, M. Clark, E. Yeager, and F. Hovorka, *This Journal*, **106**, 56 (1959).
30. Ernest Yeager and Akiya Kozawa, "Kinetic Factors in Fuel Cell Systems: The Oxygen Electrode," paper presented before the Sixth AGARD Combustion and Propulsion Colloqium on "Energy Sources and Energy Conversion," sponsored by NATO, Cannes, France, March 16-20, 1964.
31. J. J. Lingane, *J. Electroanal. Chem.*, **2**, 296 (1961).
32. L. N. Nekrasov and L. Muller, *Akad. Nauk SSSR*, **149**, 5 (Physical Chemistry Section) 1107 (1963).
33. R. A. Robinson and R. H. Stokes, *Ind. Eng. Chem.*, **4**, 461 (1935).
34. W. G. Berl, *This Journal*, **83**, 253 (1943).
35. A. Frumkin, L. Nekrasov, B. Levich, and Ju. Ivanov, *J. Electroanal. Chem.*, **1**, 84 (1959).
36. K. J. Vetter, "Electrochemische Kinetik," Springer-Verlag, Berlin (1961).
37. D. Bianchi and T. Mussini, *Electrochim. Acta*, **10**, 445 (1965).

Tracer Diffusion Measurements in Mixtures of Molten Alkali Carbonates

P. L. Spedding and R. Mills

Diffusion Research Unit, Research School of Physical Sciences,

Australian National University, Canberra, Australia

ABSTRACT

Tracer diffusion[1] coefficients have been measured for Na^+ ion in Li_2CO_3, for Na^+ and $CO_3^=$ ions in the binary eutectic $Li/NaCO_3$, for K^+ and $CO_3^=$ ions in the binary eutectic Li/KCO_3, and for Na^+, K^+, and $CO_3^=$ ions in the binary eutectic Na/KCO_3. The magnitudes of the diffusion coefficients and the derived experimental activation energies are discussed in relation to previous studies. Preliminary work designed to test the Lumsden model for interaction in binary mixtures is also presented.

We have recently reported (1) tracer diffusion measurements for the pure Na_2CO_3 melt and for various ions in the eutectic mixture $Li/Na/KCO_3$. As a result of this study, interesting comparisons became available of the experimental activation energies for the transport processes of conductance, viscous flow, and diffusion. This led us to believe that an extension of these studies to binary mixtures would be profitable. The work has now been extended to include Li_2CO_3 and the binary $Li/NaCO_3$, Li/KCO_3, and Na/KCO_3 eutectics.

A recent publication by Moynihan and Laity (2) uses the Lumsden (3) model to explain the change in mobility of ions in binary mixtures. In addition, we have, therefore, made some preliminary tracer diffusion measurements in certain binary systems with a view to being able to test this model further. As stated in the first paper of the series, we believe also that transport studies in the general area of molten alkali carbonates will be of value in high-temperature fuel cell work.

Experimental

Apparatus and materials.—Full details of the apparatus and materials used were given in a previous paper (1).

Procedure.—The major portion of the procedure used has also been reported previously (1). However, several modifications and refinements of this procedure have now been made. For example, originally the diffusion tubes were held vertically in a small auxiliary furnace and filled by manual placement of a charged filling capillary. Successful location of the capillary was difficult, and so the method was modified. The charged capillary was momentarily removed from the auxiliary furnace and placed in the diffusion tube. The capillary and attached tube were then placed in the furnace in an almost horizontal position for temperature equilibration. The tube was then brought to a vertical position on the top of an inclined plane (leading to a locating hole) and filled by a combination of manual manipulation and capillary air pressure. Occasionally bubbles were formed in the diffusion tube with this method (about 12% of tubes filled), but its rapidity made it more attractive than the more reliable vacuum filling technique.

Difficulty was experienced with the lithium carbonate experiments in removing the solid salt from the diffusion tubes due to binding of the vibratory drill bit. Consequently the salt was drilled out manually. To minimize this tedious procedure the initial activity was, in this case, determined by a weighing-counting method similar to that used by Angell and Tomlinson (4).

Problems arose in the counting analyses due to drift in the counting rates arising from various causes. Procedures have been developed in this laboratory which minimize this source of error, in particular a rotational counting technique due to Albright (5). With this technique the initial (C_o) and final (C_{av}) radio-

[1] In a previous study on the alkali carbonates (1) the term "trace-ion diffusion" has been used. However, it has been inferred from the measurements in that study that the unit involved in tracer diffusion is not necessarily a single ion so that the more general term is now preferred.

active solutions were counted alternatively in two separate counting trains, 1 and 2. The two counting containers, a and b, were then interchanged and the alternate counting procedure repeated. The count rate, in such a case, would be equal to the sum of products of the radioactive solution concentration, the container counting efficiency, α, and the equipment counting efficiency, β. The counts are then grouped so as to eliminate the long term drift

$$\text{Count ratio} = \frac{C_{av}\,(\alpha_a\beta_1 + \alpha_b\beta_2)}{C_o\,(\alpha_b\beta_1 + \alpha_a\beta_2)}$$

Assuming that $\alpha_b = (1 + x)\,\alpha_a$ and $\beta_2 = (1 + y)\beta_1$ where x and y are very small and also constant, then by substitution

$$\text{Count ratio} = \frac{C_{av}}{C_o}\,\frac{\alpha_a\beta_1\,[1 + (1 + x)\,(1 + y)]}{\alpha_a\beta_1\,[(1 + y) + (1 + x)]} \simeq \frac{C_{av}}{C_o}$$

With a sufficient number of counts, a counting reproducibility of better than ± 0.1% has been achieved using this method which is more than sufficient counting accuracy for the open-ended capillary.

Auxiliary Measurements

End Effects.—Errors due to the end effects associated with the open-ended capillary method were discussed in a preliminary way in the previous study (1), and it was concluded that an experimentally derived flow region existed in which the Δl effect was negligible. However, as there has been a certain amount of controversy in the literature concerning the effect, we have now made a more detailed analysis using boundary layer theory (6, 7).

The boundary layer refers to the region of progressive reduction of velocity from the main stream value to zero at the adhering molecular layer on the solid surface. When a liquid flows past an open-ended capillary at stream-lined velocities (Fig. 1), a boundary layer is formed at the leading edge and a point of three-way separation at the trailing edge of the capillary. This latter would cause a trailing turbulent region to be set up in the form of Karman's vortex streets. This latter condition occurs at $Re_0 \geq 1$ for a cylinder in cross flow (7), where Re_0 is the Reynolds number referred to the external capillary diameter. The boundary layer increases in thickness across the capillary tube face until it meets the turbulent front set up by the trailing edge. With increased flow velocity a turbulent profile would occur at a steadily decreasing critical distance from the leading edge. The lower point of this turbulent profile would sweep down through the boundary layer disturbing the liquid in the vicinity of the capillary face and result in high diffusion coefficients being recorded. Calculation shows that this turbulent front begins to remove radioactivity from the bore of the capillary at high velocities (Re_0 = 1,484) *i.e.*, well beyond the range normally considered in relation to the Δl effect.

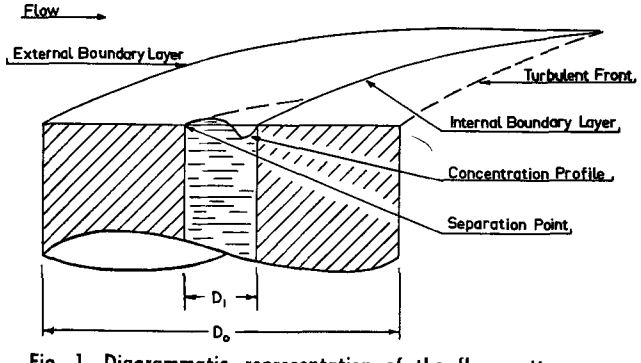

Fig. 1. Diagrammatic representation of the flow patterns over a capillary face.

Further, the measured diffusion coefficients for aqueous solution (Fig. 2) show an initial sharp rise and then a steady increase up to about Re_0 = 190 whereafter the rise is increasingly rapid. It is obvious, therefore, that the Δl effect is not primarily caused by the external boundary layer, but must be due to phenomena within its precincts. This conclusion is reinforced by consideration of plots of measured diffusion coefficients in various media against Re_0 (Fig. 3). These graphs exhibit no similarity among different media such as aqueous solutions and molten metals and salts; an occurrence which would be expected had the Δl effect depended primarily on the external boundary layer. The fact is that the dense molten media consistently show a more pronounced effect.

At first sight, it would seem more realistic to plot the measured diffusion data against Re_1, the Reynolds number determined by using the diameter of the capillary bore, since the phenomena causing the Δl effect are in the vicinity of the capillary bore and encompassed by the external boundary layer. Such plots do materially change the relative order among the different media shown in the lower part of Fig. 3, but reasonable agreement is still lacking. This helps

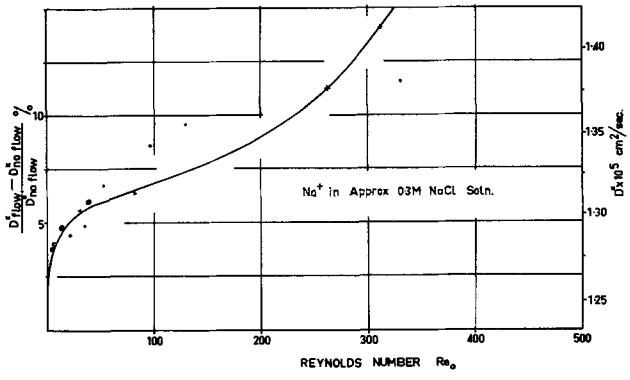

Fig. 2. Variation in measured diffusion coefficient with increasing flow over the capillary face. X, Mills (8); •, Rastas and Kivalo (9).

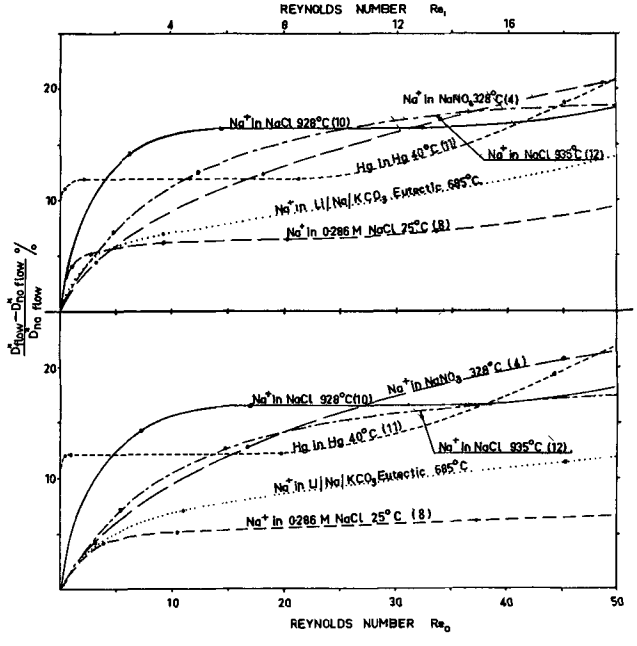

Fig. 3. Effect of flow conditions on the measured diffusion coefficients in various liquid media. In the upper section the flow is referred to the capillary bore and in the lower section to the external capillary diameter.

to confirm our conclusion that the flow phenomena causing the Δl effect are unconnected with the external boundary layer. Reference to Fig. 1 shows how we envisage the flow disturbance. The leading edge of the capillary bore constitutes a point of separation while another internal boundary layer is set up at its trailing edge. This latter formation would be very disturbed because of the concave nature of the surface of the bore wall presented to the flow. The total effect of these inner disturbances is that a wave-shaped profile is established over the mouth of the bore, rising above the datum of the capillary face at the leading edge and sweeping down into the capillary bore just prior to the trailing edge. Within a certain limited flow region these two effects would cancel (within experimental error), and the Δl effect would in essence be eliminated which is in line with the experimental findings of Mills (8). Dye experiments in aqueous solution have visually confirmed that these two opposing effects are, in fact, present.

The lack of similarity of the Re_1 plots of measured diffusion coefficients for the different media illustrated in the upper part of Fig. 3 could well be caused by the differing experimental conditions involved. A temperature gradient is imposed purposely in dense media to prevent the occurrence of thermal mixing. No such provision was made in the aqueous solution measurements where apparently the much narrower capillary diameter employed effectively suppressed thermal mixing. The imposed temperature gradient also would stabilize the no flow condition in the molten salts resulting in the much greater flow influence shown in the lower part of Fig. 3. The intermediate position of the alkali metal carbonate eutectic results substantiates this view as the temperature gradient employed was considerably smaller than that normally used for molten salts. The difference between the no flow and imposed flow conditions is affected also by the temperature of the bath. For example in Fig. 4 the diffusion coefficients determined for the no flow and $Re_0 = 12$ flow conditions are plotted as a function of temperature. It should be noted in passing that, due to the relatively large viscosity change involved, flow rates were altered with temperature to ensure a constant Reynolds number and consequently comparable flow conditions. The difference between the two values is observed to diminish with increased temperature as thermal movement in the main salt bath increasingly affects the conditions at the capillary mouth.

Effect of CO_2.—Certain $CO_3^=$ anion diffusion experiments in the Li/KCO_3 eutectic were conducted under conditions of excessive CO_2 pressure to ascertain if dissolved CO_2 in the melt would materially affect the results. Normally the apparatus was maintained under a CO_2 pressure well in excess of the respective dissociation pressures of the melts in order to ensure constant composition. With double the normal CO_2 pressure, no observable variation was detected in the measured diffusion coefficients so the possibility of a CO_2 effect could be discounted.

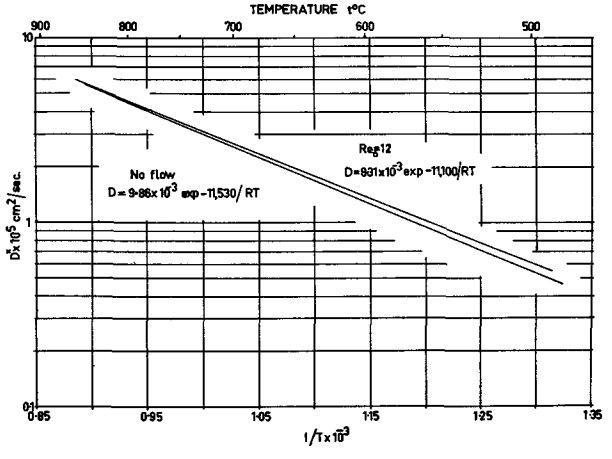

Fig. 4. Measured diffusion coefficients of Na^+ ion in $Li/Na/KCO_3$ ternary eutectic for the no flow and corrected flow conditions.

Results

The data for tracer diffusion of the various ions in the melts investigated are detailed in Tables I to IV.

Table I. Tracer diffusion in $Li/NaCO_3$ eutectic melt (53.3/46.7 mole %)

Temp, °C	$D^*_{Na^+} \times 10^5$, cm²/sec	Temp, °C	$D^*_{CO_3^=} \times 10^5$, cm²/sec
580	1.47	569	0.70
	1.49		0.72
	1.49		0.73
632	2.24	622	1.08
	2.19		1.08
	2.28		1.06
671	2.75	680	1.73
	2.70		1.68
	2.81		1.69
768	4.78	720	2.24
	4.82		2.18
	4.89		2.19
811	5.99	789	3.03
	5.86		3.03
853	7.09		3.03
	7.43	842	3.87
	7.23		3.82
			3.83

$D^*_{Na^+} = (9.81 \pm 0.14) \times 10^{-3} \exp - (10{,}990 \pm 140)/RT$
$D^*_{CO_3^=} = (7.36 \pm 0.32) \times 10^{-3} \exp - (11{,}560 \pm 120)/RT$

Table II. Tracer diffusion in Li/KCO_3 eutectic melt (42.7/57.3 mole %)

Temp, °C	$D^*_{K^+} \times 10^5$, cm²/sec	Temp, °C	$D^*_{CO_3^=} \times 10^5$, cm²/sec
614	1.07	575	0.69
	1.11		0.72
650	1.35		0.71
	1.36		0.69
	1.42	645	1.20
	1.37		1.20
698	1.84		1.19
	1.84	694	1.59
	1.83		1.67
	1.90		1.62
761	2.68	750	2.29
	2.68		2.30
	2.60		2.35
814	3.50	789	2.92
	3.51		2.93
	3.54		2.88
860	4.24		2.88
	4.29	862	4.13
	4.48		4.17
	4.19		4.10

$D^*_{K^+} = (7.26 \pm 0.43) \times 10^{-3} \exp - (11{,}490 \pm 120)/RT$
$D^*_{CO_3^=} = (7.94 \pm 0.41) \times 10^{-3} \exp - (11{,}860 \pm 100)/RT$

Table III. Tracer diffusion in Na/KCO_3 eutectic melt (58.0/42.0 mole %)

Temp, °C	$D^*_{Na^+} \times 10^5$, cm²/sec	Temp, °C	$D^*_{K^+} \times 10^5$, cm²/sec	Temp, °C	$D^*_{CO_3^=} \times 10^5$, cm²/sec
810	3.32	793	2.86	756	1.22
	3.34		2.91		1.18
840	3.97	850	3.60		1.28
	3.80		3.77	797	1.53
	3.87		3.76		1.49
862	4.35	872	4.18		1.52
	4.31		4.20	819	1.79
	4.43	904	4.94		1.65
904	5.36		4.94		1.72
	5.30		4.96	855	1.94
932	6.07		4.82		2.01
	5.96	912	4.89		1.95
965	6.60		4.91		1.88
	6.33		5.01	891	2.22
			5.01		2.21
		963	6.04		2.36
			6.12	919	2.68
			6.26		2.60

$D^*_{Na^+} = (8.18 \pm 0.74) \times 10^{-3} \exp - (11{,}820 \pm 220)/RT$
$D^*_{K^+} = (7.61 \pm 0.52) \times 10^{-3} \exp - (11{,}840 \pm 170)/RT$
$D^*_{CO_3^=} = (2.71 \pm 0.30) \times 10^{-3} \exp - (11{,}030 \pm 120)/RT$

Table IV. Tracer diffusion in Li_2CO_3 melt

Temp, °C	$D^*_{Na^+} \times 10^5$, cm²/sec
809	1.46
	1.51
858	1.70
	1.78
871	1.80
905	2.12
	2.25

$$D^*_{Na^+} = (1.32 \pm 0.44) \times 10^{-3} \quad \exp - (9{,}630 \pm 370)/RT$$

The constants in the equations were calculated by the method of least squares.

Discussion

The diffusion data from this study together with those from our previous paper, are represented in Fig. 5 in the form of Arrhenius graphs (log D *vs.* $1/T$). Comparing first the magnitudes of the various diffusion coefficients it can be seen that for any given medium, the diffusion mobility varies inversely with the ionic radius. For ions isotopic to a species in the medium similar trends have been observed in alkali metal nitrates (13) and in their binary mixtures (14). It should be noted, however, that this type of dependence does not necessarily hold for nonisotopic trace species as has been shown by Ketelaar and Honig (15).

Another feature which is brought out by Fig. 5 is the marked change in diffusion mobility which is shown by both Na^+ and $CO_3^=$ ions in different media. The Na^+ ion, for instance, has a high coefficient in all the eutectics and in pure Na_2CO_3, but a much lower value in pure Li_2CO_3. This is contrary to what might have been expected if certain aspects of the Lumsden model (3) had been considered to apply. These aspects concern the preferential polarization of anions by the smaller cations in a binary melt. On this model, in Li_2CO_3 the $CO_3^=$ anions would presumably be strongly polarized thus leaving the Na^+ ions with more freedom of movement compared to that

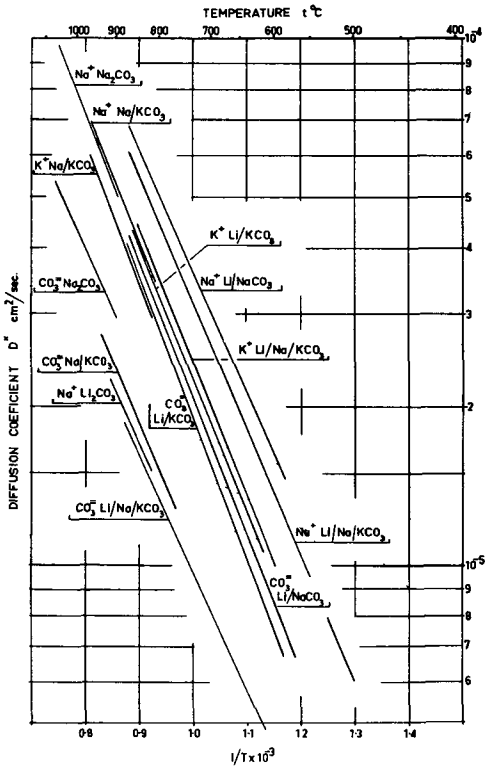

Fig. 5. Arrhenius graphs of the measured diffusion coefficients of various ions in pure alkali metal carbonates and their binary and ternary eutectics.

in the pure Na_2CO_3 melt. An explanation for the low Na^+ ion mobility can, however, be given if we accept a lattice picture for molten carbonates. The pure Li_2CO_3 melt can then be visualized as a fairly close-packed anion-type lattice, with the small Li^+ ions fitting into the interstices. The trace sodium ions introduced would slightly expand the lattice in their neighborhood, but basically it would remain as in the pure salt. Under these conditions a low diffusion mobility would be expected. As a cooperative act is probably involved, the $CO_3^=$ ion might be expected to have a fairly low mobility in this melt also, but further experiments will be made shortly to check this prediction.

The $CO_3^=$ ion has a low mobility in the Na/K and Li/Na/K eutectics and pure Na_2CO_3, but it almost exactly doubles in the Li/K and Li/Na eutectics. There is no obvious explanation for the marked change in diffusion mobility between the two groups of melts. One cannot attribute it solely to greater distortion arising from difference in ion size in the binary eutectics containing lithium because this factor would also operate in the ternary eutectic. The measurement of tracer-diffusion coefficients of the Li^+ ion may help to resolve this problem.

The slopes of the curves in Fig. 5 give the "Arrhenius activation energy" for tracer-diffusion. As stated in our previous paper (1) the exact significance of these energies and their relation to theory are not known. However, it is generally agreed that they have qualitative value in the interpretation of the mode of diffusion in molten salts. In Table V we have tabulated these experimental activation energies together with those available for other transport processes.

The differences between the experimental activation energies for conductance, viscous flow, and tracer diffusion, and possible qualitative explanations of these differences have been discussed in our first paper. In brief, the high activation energy for viscous flow in the pure melt was attributed in part to the necessity to shear a lattice which derives its stability from the coulombic forces between the ions. The low value for conductance was explained by the ability of cations to migrate through the lattice without appreciable disturbance whereas the constancy of the diffusion activation energies suggested some kind of cooperative act between anion and cation. The new data which have been added reinforce these conclusions. In particular the similarity between the diffusional activation energies for all ions studied in the six media is again most striking. The inference that diffusional movement in these melts proceeds by some cooperative act, which may be a coupled vacancy mechanism, ion-pair motion, or cluster movement, seems inescapable. At the moment evidence from other fields as summarized by Janz and co-workers (16) favors the ion-pair concept of the form $(M^+CO_3^=)^-$.

The appearance of a recent paper by Moynihan and Laity (2) in which they predicted that tracer diffusion coefficients in binary melts might be expected to show a closer linear dependence with composition than the

Table V. Experimental activation energies of transport in alkali carbonate melts

Medium	E_Λ, kcal/eq.	E_{vis}, kcal/mole	E_{D^*}, kcal/mole
Na_2CO_3	4.23 (16a)	25.7 (16b)	12.2 (Na^+)
			10.6 ($CO_3^=$)
Li_2CO_3	4.60 (16d)		9.6 (Na^+)
$Li/NaCO_3$ eutectic	4.53 (16d)		11.0 (Na^+)
			11.6 ($CO_3^=$)
Li/KCO_3 eutectic	4.49 (16d)		11.5 (K^+)
			11.9 ($CO_3^=$)
Na/KCO_3 eutectic	3.96 (16d)		11.8 (Na^+)
			11.8 (K^+)
			11.0 ($CO_3^=$)
$Li/Na/KCO_3$ eutectic	6.46 (16c)	10.7 (16b)	11.1 (Na^+)
			11.9 (K^+)
			10.1 ($CO_3^=$)

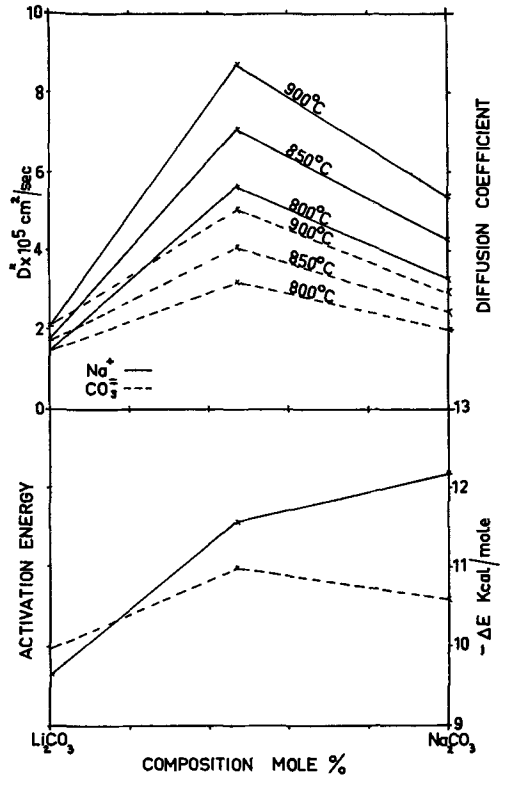

Fig. 6. Activation energies and tracer-diffusion coefficients of Na^+ cation and $CO_3^=$ anion in Li_2CO_3/Na_2CO_3 mixtures.

ionic conductances, prompted us to make preliminary measurements of this kind. These measurements are for Na^+ and $CO_3^=$ ions at the eutectic composition of the $Li/NaCO_3$ binary mixture, Na^+ in Li_2CO_3 and Na_2CO_3 and $CO_3^=$ in Na_2CO_3. The results are shown in graphical form in Fig. 6. For the reasons outlined earlier, we have tentatively assigned a value for $CO_3^=$ ion in Li_2CO_3 equivalent to that for Na^+ ion. It is evident that the tracer diffusion coefficients for Na^+ and $CO_3^=$ at the indicated temperatures are by no means linear with composition, but instead show a marked positive deviation from the additivity line. This is to be compared with the results of Lantelme and Chemla (14) in the alkali nitrates who have reported a positive deviation for K^+ in $KNO_3/LiNO_3$ mixtures. Other cations, however, exhibit a near linear dependence. Further points of interest are that the Na^+ ion diffusion mobility is lower in Li_2CO_3 than in Na_2CO_3 which is in contrast to cation diffusion in the alkali nitrates. Lantelme and Chemla (14) have shown that Li^+, Na^+, and K^+ ions diffuse faster when going over a composition range from KNO_3 to $LiNO_3$. However they have reported more recently (17) that for NO_3^- ion the values diminish as the mixtures are enriched in $LiNO_3$. The high values of the coefficients at the eutectic point are also noteworthy, and these may well represent maxima on the curves. As our measurements were made at a series of temperatures, we have also been able to determine experimental activation energies and these are shown in the lower part of Fig. 6. The values for Na^+ ion rise fairly steadily, and those for $CO_3^=$ ion indicate a maximum. Such trends are not readily explained, and we therefore propose to make measurements to explore this type of behavior further.

We have also made a detailed study of the conductance for this binary system and obtained a negative deviation from the addition line for two of the binary systems. These differences between the two processes serve to reemphasize that the mechanisms of conduction and tracer diffusion in molten salts may differ considerably. (The reservation should be made that the tracer diffusion of Li^+ ion would also need to be measured in order to say definitely that the processes are different in character.) This fact of course has previously been inferred from attempts to apply the Nernst-Einstein equation and from the marked difference between the Arrhenius activation energies for the two processes.

In the context of the fuel cell electrolyte problem, it may be noted that, although $CO_3^=$ ion diffusion is considerably faster in the binary than the ternary eutectics, this seems to have little or no effect in reducing polarization in molten salt cells. Both the binary $Li/NaCO_3$ and the ternary $Li/Na/KCO_3$ eutectics have been used as fuel cell electrolytes and the voltage losses are very comparable in each case (18).

Acknowledgment

Grateful acknowledgment is made to the Reserve Bank of Australia for a grant for fuel cell research, part of which has been used to finance the above study.

Manuscript received Nov. 29, 1965.

Any discussion of this paper will appear in a Discussion Section to be published in the December 1966 JOURNAL.

REFERENCES

1. P. L. Spedding and R. Mills, *This Journal*, **112**, 594 (1965).
2. C. T. Moynihan and R. W. Laity, *J. Phys. Chem.*, **68**, 3312 (1964).
3. J. Lumsden, *Discussions Faraday Soc.*, **32**, 138 (1961).
4. C. A. Angell and J. W. Tomlinson, *ibid.*, **32**, 237 (1961).
5. J. G. Albright, Unpublished work.
6. H. Schlichting, "Boundary Layer Theory," McGraw-Hill Book Co., New York (1955).
7. E. R. G. Eckert and R. M. Drake, "Heat and Mass Transfer," McGraw-Hill Book Co., New York (1959).
8. R. Mills, *J. Am. Chem. Soc.*, **77**, 6116 (1955).
9. J. Rastas and P. Kivalo, *Acta Polytechnica Scandinavica*, **C35** (1964).
10. J. O'M. Bockris and G. W. Hooper, *Discussion Faraday Soc.*, **32**, 218 (1961).
11. J. F. Kasener, R. J. Russel, and R. C. Grace, *Trans. Am. Soc. Metals*, **55**, 858 (1962).
12. A. Z. Borucka, J. O'M. Bockris, and J. A. Kitchener, *Proc. Roy. Soc.*, **A241**, 554 (1957).
13. A. S. Dworkin, R. B. Escue, and E. R. Van Artsdalen, *J. Phys. Chem.*, **64**, 872 (1960).
14. F. Lantelme and M. Chemla, *C. R. Acad. Sci., Paris*, **258**, 1484 (1964).
15. J. A. A. Ketelaar and E. P. Honig, *J. Phys. Chem.*, **68**, 1596 (1964).
16. (a) G. J. Janz and M. R. Lorenz, *This Journal*, **108**, 1052 (1961); (b) G. J. Janz and F. Saegusa, *ibid.*, **110**, 452 (1963); (c) Ward and G. J. Janz, *Electrochim. Acta*, **10**, 849 (1965); (d) Unpublished work.
17. F. Lantelme and M. Chemla, Abstracts, 16th C.I.T.C.E. Meeting, Budapest, 217 (Sept. 1965).
18. G. J. Young, "Fuel Cells," Chap. 6, 8, Reinhold Publishing Co. New York (1960).

The Role of Crystalline Orientation on the Behavior of Copper as Electrode in Chloride Solutions[1]

Ugo Bertocci

Solid State Division, Oak Ridge National Laboratory, Oak Ridge, Tennessee

ABSTRACT

Single crystal copper electrodes having (100), (110), (111), and (321) orientations, as well as polycrystalline specimens, have been used as electrodes in chloride solutions containing cuprous ions, previously equilibrated with copper metal under a hydrogen atmosphere. Anodic and cathodic overvoltages as a function of current density have been recorded in the range from 10^{-7} to 10^{-3} amp/cm^2. Faceting patterns formed by electrolysis at various current densities, as well as those formed by corrosion in nonequilibrated solutions, have been examined, using both the optical microscope and the double-circle reflection goniometer. In all instances, it has been found that the behavior of (100) oriented surfaces was quite different from that of all other orientations investigated. The overvoltages recorded for (100) electrodes were considerably higher, exhibiting an extremely high $(d\eta/di)_{i=0}$ of the order of 10^5 ohm-cm^2. Lower overvoltages were found on the other close-packed orientations, differences between them being only minor, and the lowest values were exhibited by (321) oriented electrodes.

The faceting behavior of (100) surfaces was also different from that of all other orientations: whereas (100) developed only facets vicinal to {100}, the other surfaces formed a completely different set of facets, including {111} and {110}. By correlating the overvoltage data and the faceting structure, some suggestions are made concerning the relative influence of elementary processes, such as nucleation of new steps and their motion across the surfaces on the kinetic behavior. The most likely conclusion at this stage seems to be that the rate-determining step is linked to the removal or addition of atoms to the surface steps.

The study of the electrochemical behavior of copper in halide solutions presents the possibility of examining the electrode reaction between copper metal and cuprous ions, since divalent copper plays only a minor role. In addition, in such solutions the etching pattern can be made very sensitive to the structure of the crystalline phase, as evidenced by the formation of pits at dislocations (1). Overvoltage data for copper in chloride solutions being relatively scarce, it was interesting to collect information on the kinetic behavior in such systems as a function of crystal orientation, particularly in the low current density range, where the properties of the metal surface can be rate determining.

In this paper the results of some experiments showing the influence of crystal orientation on the electrochemical behavior of copper are described and discussed.

Experimental Methods

The copper crystals used for the experiments were disk-shaped slices cut from 99.999% Cu single crystal slugs. The dislocation density was of the order of 10^5/cm^2. The cutting method has already been described (2). In order to obtain orientations as close as possible to the desired ones (usually within one half of a degree or less), before polishing the surfaces on the lapping wheel, the etched crystals were positioned on an adjustable holder, using a microscope fitted with the Nomarski interference contrast attachment to control their orientation. The technique employed to measure the orientation of etching facets, as well as the modifications to the microscope, are described elsewhere (3).

After a final electropolishing in a phosphoric acid bath, the crystals were mounted in the electrolysis cell against glass tubings, having beveled Teflon gaskets at their ends, so that the electrodes exposed only one orientation to the solution. Three crystals were mounted in the same cell. A more detailed description of the cell has been given in a previous paper (4). The cell was evacuated and filled with purified hydrogen several times, and then the solution, which had been equilibrated with copper metal, was transferred in the cell under hydrogen pressure.

Overvoltage measurements were carried out by passing a constant current pulse between the electrode under investigation and an auxiliary electrode by means of a group of dry cells and a large resistance in series. The voltage *vs.* time curves were recorded on a strip chart recorder coupled to a high-impedance amplifier. In most experiments the reference electrode was a saturated calomel electrode. Sometimes the curves were recorded on a cathode-ray oscilloscope, a suitable timing device giving the required synchronization to display the signal on the scope screen.

Because of the small currents employed and the high conductivity of the solution, no device for minimizing the errors due to ohmic drop was used; checks carried out comparing data taken from reference electrodes positioned at different distances from the electrode under study, as well as inspection of the voltage-time curves on the cathode ray oscilloscope, showed that the ohmic drops included in the readings were always negligible.

For qualitative information on the relative rate of attack of different orientations, some etching experiments were also carried out on spherical single crystals; their surfaces were prepared by electropolishing in a phosphoric acid bath.

After the experiments the copper electrodes were examined under the optical microscope, and the orientation of the faceting pattern obtained was studied by means of a double circle reflection goniometer.

Experimental Results

Preliminary investigations were directed to finding whether specimens having different surface orientation exhibited different equilibrium potentials. It was soon realized, however, that the solutions always contained cupric ions in excess of the equilibrium concentration and therefore the electrodes were corroding. The corrosion rate, due to oxygen leakage into the cell, was estimated to be of the order of 20-50 μa/cm^2,

[1] Research sponsored by the U. S. Atomic Energy Commission under contract with Union Carbide Corporation.

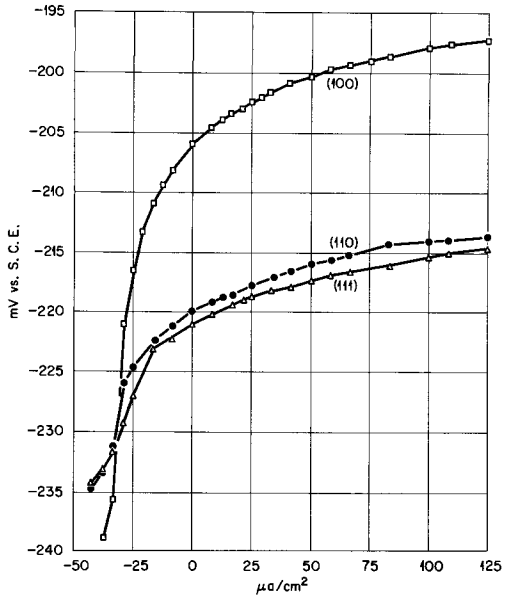

Fig. 1. Overvoltages of Cu single crystals in 0.03M Cu, 2.7M HCl under slow corrosion; temperature 23.5°C.

as calculated from the increase of Cu concentration in solution.

Further improvements in the experimental setup reduced the corrosion rate below any detectable value; accordingly, the former experiments will be referred to as experiments under corrosion, and the latter ones as experiments in absence of detectable corrosion. Even in the latter case, however, it is believed that the solution composition was not that corresponding to equilibrium, and the experimental results are interpreted according to this assumption.

Experiments under corrosion.—The potential differences between different surface orientations under slow corrosion conditions showed that after a very short period of time a steady state was reached in which the (100) orientation was nobler than (110) and (111) by about 15 mv. This potential difference could be maintained within 3 to 5 mv for periods of time as long as 16 days, after which the experiment was stopped. (111) crystals were slightly more negative than (110). Potential *vs.* current density curves recorded on these slowly corroding specimens are shown in Fig. 1. The overvoltage curves for the various orientations intersect at a certain value of cathodic current density. This value is approximately equal to the corrosion rate determined from the increase with time in copper concentration in solution.

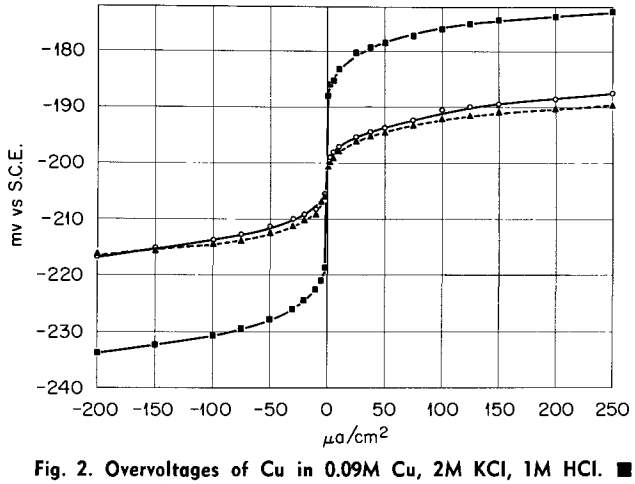

Fig. 2. Overvoltages of Cu in 0.09M Cu, 2M KCl, 1M HCl. ■ (100), ▲ (111), ○ (321); temperature 23.5°C.

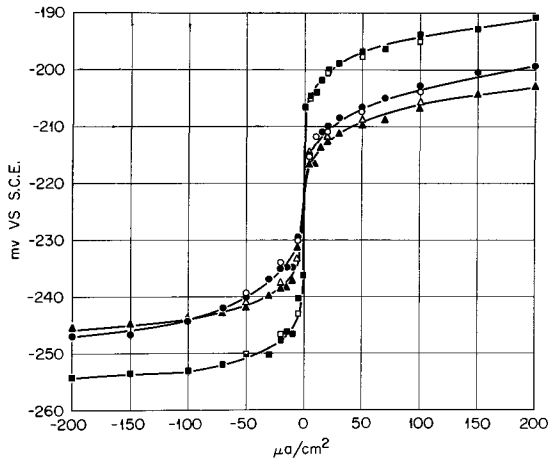

Fig. 3. Overvoltages of Cu in 0.04M Cu, 2.7M HCl. Decreasing CD, □ (100); △ (321); ○ polycrystalline; increasing CD, ■ (100); ▲ (321); ●, polycrystalline; temperature 23.5°C.

Inspection of the surfaces after the test showed extensive faceting on all orientations. On (100) crystals shallow square pits were formed at an early stage, and they subsequently grew to cover the whole surface, leaving it uniformly faceted. The (111) crystals had large plateaus of the original (111) orientation, bounded by steep walls; (110) surfaces were covered by grooves oriented toward <110>. Examination with the reflection goniometer revealed that the original (100) orientation had disappeared completely, and the facets formed lay in a region between 2° and 4° from (100), producing a square reflection pattern with corners toward <100>. The reflection patterns for (110), (111), and (321) orientations were remarkably similar to each other: sharp reflections were found at {111} and {110}, and also there was a diffuse reflection around {100} approximately square-shaped with corners about 15° from {100} toward <100>.

Experiments in absence of detectable corrosion.—The overvoltage *vs.* current density curves obtained in absence of detectable corrosion are given in Fig. 2 and 3. In order to determine the point where the curves relative to different surface orientations intersect and where they exhibit the maximum slope, the extremely low anodic and cathodic current density range was examined in detail (Fig. 4 and 5). The results show that the cathodic and anodic branches of

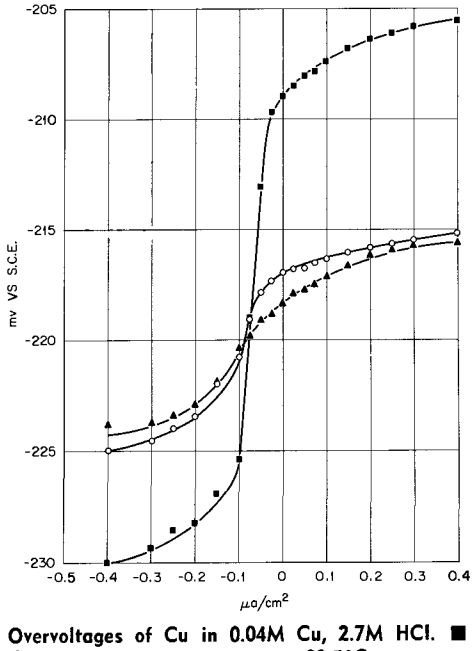

Fig. 4. Overvoltages of Cu in 0.04M Cu, 2.7M HCl. ■ (100), ▲ (321), ○ polycrystalline; temperature 23.5°C.

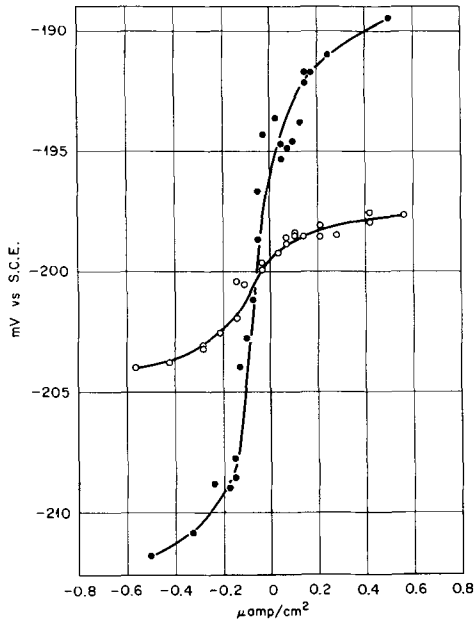

Fig. 5. Overvoltages of Cu in 0.09M Cu, 2M KCl, 1M HCl. ● (100), ○ (111); temperature 23.5°C.

the overvoltage curves are symmetric with respect to a middle point which, within the accuracy of the experimental method, is common to all crystal orientations. The point of intersection corresponds to a cathodic current density, whose value tended to become smaller with time: typically it was about 0.8-0.5 $\mu a/cm^2$ on the first few days after introduction of the solution and then decreased to less than 0.1 $\mu a/cm^2$. During this period the overvoltage curves did not vary except for a translation along the current density axis.

Evaluation of the maximum slope of the overvoltage curves is rather inaccurate: for (100) crystals the value ranges from 10^5 to 4.10^5 ohm-cm^2, whereas the other orientations give values from 10^4 to 7.10^4 ohm-cm^2.

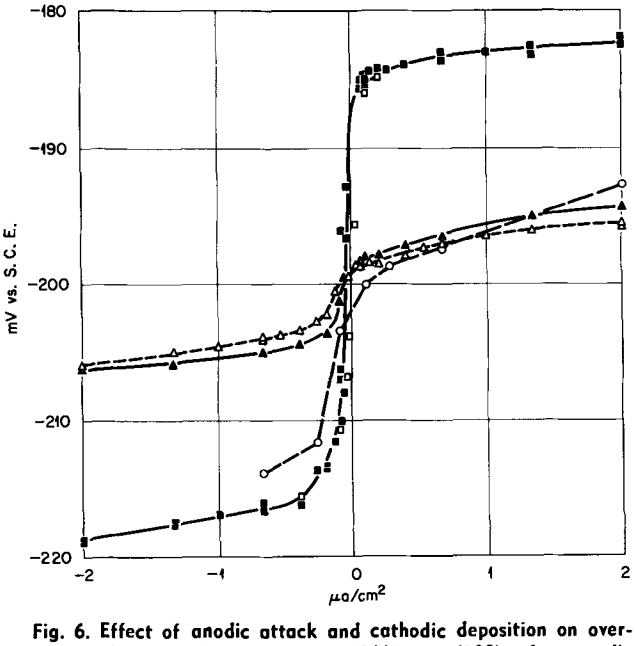

Fig. 6. Effect of anodic attack and cathodic deposition on overvoltages of Cu single crystals. ■ (100); □ (100) after anodic attack at 3.3 $\mu a/cm^2$ (12.8 mcoul/cm^2); ○ (100) after cathodic deposition at 3.3 $\mu a/cm^2$ (13.4 mcoul/cm^2); ▲ (111); △ (111) after anodic attack at 3.3 $\mu a/cm^2$ (0.298 coul/cm^2). Solution: 0.09M Cu, 2M KCl, 1M HCl; temperature 23.5°C.

The effect of extensive electrolysis on the overvoltage curves was investigated, and some of the results are given in Fig. 6. For (111) orientations and also for all orientations other than (100), anodic attack tends to lower slightly the overvoltage curves, whereas (100) surfaces are hardly affected. Extended cathodic deposition on (100) crystals greatly affects the anodic branch of the overvoltage curve, which becomes similar to that found for other orientations, but has a much smaller effect on the cathodic values. An anodic attack approximately equal to one-half of the preceding cathodic pulse is generally sufficient for restoring the usual overvoltage curve.

After a cathodic current pulse the electrode potential decayed to its open-circuit value in two stages, separated by an inflection point of minimum slope; the potential value of the inflection point was found to be very close to that of the middle point about which the overvoltage *vs.* current density curves are symmetric. The decay time was longer the greater the quantity of electricity of the preceding cathodic pulse, the inflection point becoming a plateau of almost constant potential. The phenomenon is similar to that observed on polycrystalline zinc in acidic solutions (5).

After a sufficiently long anodic attack the faceting pattern could be observed. It was found that the surface structure as well as the reflection pattern was the same as that observed under corrosion conditions, provided that the current density chosen was of the same order of magnitude. Some changes were detected in the faceting pattern for dissolution at higher current densities; for instance, a reflection spot corresponding to {47,20,0} was quite clearly observed on (111) and (321) crystals attacked at 1 ma/cm^2, whereas at the same current density (100) surfaces developed, besides the usual pattern, facets very close to the {100} orientations at 90° from the original one. On the whole, however, the etching pattern was found to be rather insensitive to anodic current density in the range studied.

After etching spherical single crystals, small bright areas were found at {111} and {110}, as well as a square-shaped area around {100}, with corners about 15° from [100] toward <100>. The remainder of the sphere was heavily faceted, but no attempt was made to measure the orientations of the facets formed.

Discussion

The high resistance for the electrode reaction in the low current density range as deduced by the slope of the overvoltage curves places such stringent requirements on the magnitude of the rate of spontaneous processes, (for example, corrosion caused by an excess of cupric ions over the equilibrium concentration), which can be allowed without significant departure of the electrodes from the equilibrium potential, that it is impossible to attach thermodynamic significance to the open-circuit potentials. The fact, however, that the curves relative to different orientations as measured in the same solution intersect for the same value of potential and current density, plus the fact that the overvoltage curves are symmetric with respect to the intersection point, which lies on the point of maximum slope, lend support to the conclusion that the potential associated with the intersection point is the equilibrium potential for all copper electrodes investigated. If the validity of this criterion for determining the equilibrium potential is accepted, it can be concluded that single crystals of different orientation, as well as polycrystalline electrodes, have the same equilibrium potential, or at least that the differences are smaller than 1 to 2 mv. Analogous conclusions had been previously reached for copper single crystals in sulfate solutions (4). All the differences recorded between rest potentials can be easily accounted for in terms of differences in their kinetic behavior.

If the point where the various curves intersect can be assumed to correspond to the equilibrium potential,

the cathodic current density necessary to maintain such a potential will correspond to the reduction of cupric ions diffusing from the bulk of the solution to the electrode

$$(i)_{\eta=0} = \frac{FD_{Cu^{++}}}{\delta}\left[Cu^{++}_{eq} \exp\left(\frac{\mathbf{F}}{RT}\eta'\right) - Cu^{++}_{bulk} \right] \quad [1]$$

where δ is the thickness of the diffusion layer, Cu^{++}_{eq} and Cu^{++}_{bulk} are total concentrations of Cu^{++} ions, whether free or as chloride complexes, at equilibrium and in the bulk, $D_{Cu^{++}}$ is the diffusion coefficient valid for the solution composition in which the experiment is carried out, and η' is the overvoltage for the reaction

$$Cu^{+} \rightleftarrows Cu^{++} + \theta \quad [2]$$

Here the assumption is made that homogeneous equilibria are fast and that transference numbers for copper ions are negligibly small, because of the large excess of indifferent electrolyte. The results shown in Fig. 1, where even for relatively large values for $(i)_{\eta=0}$ ($\sim$ 30 μa/cm^2) the point of maximum slope in the overvoltage curves corresponds to the same current density for (100), (110), and (111) crystals, indicate either that η' is relatively insensitive to orientation or that it is negligibly small. The second alternative can be reasonably accepted when the current density is of the order of 10^{-7} amp/cm^2. In this case formula [1] can be employed to estimate the excess of Cu^{++} in the bulk over the equilibrium concentration. The evaluation of the product $D_{Cu^{++}}(Cu^{++})$ is unfortunately very difficult, since the values of the stability constants for cupric chloride complexes, as quoted in the literature, vary considerably from author to author (6). The diffusion coefficient is probably abnormally large, as shown by the negative transference number of copper in complex cupric chloride solutions (7). By assuming a value of 100 amp cm/mole for $FD_{Cu^{++}}/\delta$ and considering that Cu^{++}_{eq} should be of the order of 10^{-11} mole/cm^3, a current density of 10^{-7} amp/cm^2 would indicate that the concentration in the bulk of the solution was from 20 to 100 times greater than the equilibrium value.

Because of the extreme steepness of the overvoltage curve at very low current densities, particularly in the case of (100) surfaces, the question can be raised as to whether any process involving dissolution or deposition actually takes place in this range, or only the redox reaction [2], which does not involve any alteration of the metal surface, occurs at the electrode. If one assumes that reaction [2] occurs without appreciable overvoltage, around the equilibrium potential the slope of the overvoltage curve as given by reaction [2] alone is (8)

$$\left(\frac{d\eta}{di}\right)_{\eta=0} = \frac{RT\,\delta}{F^2 D_{Cu^{++}}(Cu^{++}_{eq})}$$

Again the calculation entails the knowledge of the product $D_{Cu^{++}}$ (Cu^{++}_{eq}), and it is subject to the uncertainties already mentioned. Using the most reliable data, the reaction resistance due only to reaction [2] should be about 10 megaohms-cm^2, that is, more than a factor of ten higher than the value measured on (100) surfaces. This would support the conclusion that deposition or dissolution occur at a nonzero rate for every overvoltage value.

The homogeneous reaction

$$CuCl'_2 \rightleftarrows Cu^{+} + 2Cl' \quad [3]$$

which in chloride solution is coupled to the electrode reaction, was not found to have any effect on the over-all reaction rate in the range of current densities investigated. Since the equilibrium potential of Cu with respect to SCE is about —0.2v, the Cu^{+} ion activity is of the order of 10^{-8} mole/liter. If reaction [3] were slow, a small limiting current for the cathodic discharge should be found. The experimental results, however, have shown that no limiting current phenomena can be detected.

The shape of the decay curves after short cathodic pulses, as well as the effect of extensive deposition on (100) crystals on the subsequent anodic overvoltages can be explained by assuming that the surface structure of the deposits is different from that formed by anodic attack. Therefore, after a cathodic pulse under conditions of slight corrosion, the freshly deposited copper will exhibit a low anodic overvoltage, giving rise to an inflection in the decay curve. Accordingly, the potential of the inflection was the closer to the point of maximum slope of the overvoltage curve, the smaller was the departure from equilibrium in solution, and it was found to be in general more positive, by a few millivolts, than the equilibrium value as determined in the way outlined in the first part of this discussion. After extensive deposition on a (100) surface, anodic overvoltages similar to those on the other orientations could be measured, until dissolution eliminated the surfaces having low overvoltage. Although no systematic examination of the surface structure of cathodic deposits has been made, some instances of formation of facets never observed after anodic attack on (100) crystals were found.

Conclusions

Examination of the experimental results does not indicate that on any orientation the nucleation of new steps is rate determining, since extensive anodic attack leading to a faceted surface has little influence on the overvoltage values. Comparison of the overvoltage curves of (111) and (321) crystals supports the same conclusion. On (321) surfaces no nucleation is theoretically required for the dissolution or crystallization process; nevertheless, the overvoltages are very close to those measured on a close-packed surface like the (111). The facets formed on (111) and (321) have the same orientation, but on the latter the number of edges is significantly greater, which would account for the slightly lower reaction resistance, but fails to single out the formation of new steps as the kinetically decisive phenomenon.

It is therefore likely that the motion of steps is rate controlling; on (100) crystals such a motion is very slow and difficult, so that the surface is left covered by steps giving the characteristic faceting pattern slightly misoriented from (100); on the other orientations, steps move at a much higher speed, and this accounts for the lower overvoltages as well as for the faceting pattern: smooth (111) facets are formed, and the steps interact easily forming orientations at large angles from the original surfaces. Not all difficulties in interpreting the results are eliminated by such a conclusion; one would expect a greater influence of the number of steps on the surface if their motion were the slowest process. Above a relatively low current density, however, the overvoltage curve flattens out considerably, so that an increase in number of steps will cause a small decrease in overvoltage. Moreover. microscopic observation shows that on (111), (110), and (321) crystals a large part of the new surface area created by faceting is oriented about 15° from (100), an orientation having rather high reaction resistance, as evidenced by the etching pattern on spherical single crystals.

On the cathodic side, the remarkable influence of extended deposition on the subsequent anodic overvoltages of (100) orientations indicated that the deposit does not have the same surface structure as the substrate. Incorporation of the deposited copper into the lattice occurs slowly, as indicated by the inflection points in the decay curve after short cathodic pulses.

The shape of the overvoltage curves, however, suggests the hypothesis that a nucleation process is necessary to initiate the removal of copper from the steps or its addition to them.

Manuscript received Nov. 1, 1965.

Any discussion of this paper will appear in a Discussion Section to be published in the December 1966 JOURNAL.

REFERENCES

1. U. Bertocci, L. D. Hulett, and L. H. Jenkins, *This Journal*, **110**, 1190 (1963).
2. F. W. Young, Jr., and T. R. Wilson, *Rev. Sci. Inst.*, **32**, 559 (1961).
3. U. Bertocci and T. S. Noggle, In press.
4. L. H. Jenkins and U. Bertocci, *This Journal*, **112**, 517 (1965).
5. U. Bertocci, *Rend. Ist. Lombardo Sci. e. Lett.*, **91**, 39 (1957).
6. L. G. Sillén and A. E. Martell, "Stability Constants of Metal Ion Complexes," The Chemical Society, London (1964).
7. J. Bjerrum, *Kem. Maanedsblad*, **26**, 24 (1945); V. Kohlschütter, *Ber. deutsch. chem. Ges.*, **37**, 1153 (1904); S. B. Watkins and H. G. Denham, *J. Chem. Soc.*, **115**, 1269 (1919).
8. U. Bertocci, *Electrochim, Acta*, In press.

Induced Polarization of Porous and Tubular Electrodes[1]

F. A. Posey and S. S. Misra

Chemistry Division, Oak Ridge National Laboratory, Oak Ridge, Tennessee

ABSTRACT

The apparent resistance of solutions contained in porous or tubular electrodes is affected by the presence of oxidizable and reducible substances in solution. Passage of current is accompanied by a gradient of potential in the solution phase so that a gradient of the interfacial potential difference is induced throughout the length of the electrode. As a consequence of the induced polarization, anodic and cathodic reactions occur near opposite ends of the electrode. A number of boundary value problems corresponding to this physical situation have been solved. The relations suggest that induced polarization measurements can be used to determine the concentration of oxidizable and reducible substances in flowing streams, to measure corrosion rates of pipes or porous metals, and to estimate transfer coefficients and exchange current densities of electrochemical reactions.

The conductivity of electrolytes in porous nonconducting materials is not difficult to measure in principle, and measurements of this type have been made for various purposes. As noted by Ksenzhek, Kalinovskii, and Baskin (1), it is more difficult to measure the conductivity of solutions inside porous or tubular metallic electrodes. This is particularly true when oxidation reduction reactions can occur at the metal-solution interface. Passage of current through the solution phase induces a gradient of the interfacial potential difference throughout the length of the electrode. As a consequence of this gradient, anodic reactions occur at the pore walls near one end of the electrode, and cathodic reactions take place near the other end. A fraction of the total current is conducted by ions in the solution phase, and the rest of the current is conducted by electrons in the metallic phase; this fraction depends on the geometrical properties of the electrode, the characteristics of the electrolyte and the electrochemical reactions, and the position inside the electrode. A number of boundary value problems corresponding to this physical situation have been solved by use of methods for the calculation of polarization in porous electrodes (2). The results are presented below together with some experimental measurements which support the theory. The relations obtained suggest that induced polarization of porous and tubular electrodes can be used to determine the concentration of oxidizable and reducible substances in flowing streams, to measure corrosion rates of pipes or porous metals, and to estimate certain parameters of electrochemical reactions.

Experimental Configuration

A schematic diagram of the experimental arrangement for measurement of induced polarization of porous or tubular electrodes is shown in Fig. 1. The total current (i) is passed from the front side ($x = 0$) to the back side ($x = l$) of the electrode by use of auxiliary polarizing electrodes. No current lead is attached to the porous electrode itself; potential changes which occur in this electrode are induced by passage of current between the polarizing electrodes. The potential of the front or back sides and the total potential drop through the electrode may be measured by use of reference electrodes situated at $x = 0$ and $x = l$. Passage of current in the direction shown in Fig. 1 induces a negative change in interfacial potential difference (negative polarization) near $x = 0$ and a positive polarization near $x = l$. When oxidizable and reducible substances are present in solution, cathodic reactions can occur near $x = 0$ as a consequence of the induced negative polarization and, correspondingly, anodic reactions can occur near $x = l$. This electrode configuration is essentially the same as the bipolar electrode studied by Tomassi and co-workers (3-6) as a means of coupling electrochemical processes.

Induced Polarization with Linear Rate Law

The solution resistance in porous or tubular electrodes, measured in the absence of oxidizable and reducible substances by use of the configuration of Fig. 1, is given simply by Eq. [1], where R_o is the resistance of electrolyte

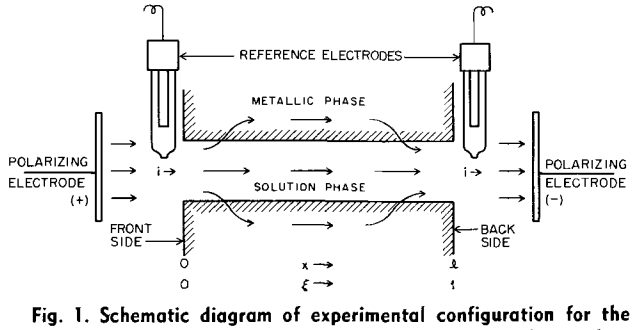

Fig. 1. Schematic diagram of experimental configuration for the measurement of induced polarization of porous and tubular electrodes.

[1] Research sponsored by The Office of Saline Water, U. S. Department of the Interior, under Union Carbide Corporation's contract with the U. S. Atomic Energy Commission.

$$R_o = \frac{\phi_s(0) - \phi_s(l)}{i} = \frac{l}{\sigma A} \quad [1]$$

in the pores (ohm), $\phi_s(0)$ and $\phi_s(l)$ are potentials in the solution phase at $x = 0$ and $x = l$ (volt), i is total current (amp), l is pore length (cm), σ is specific conductance of the electrolyte (ohm^{-1}cm^{-1}), and A is total cross-sectional area of electrolyte (cm^2). In the presence of oxidation reduction reactions the measured or apparent resistance, R_{app}, is less than R_o because of the shunting effect of the current carried by the metallic phase, which is assumed to have negligible resistivity (see below, however). The apparent resistance may be calculated in certain cases by solution of Eq. [2], which is the fundamental differential equation for potential

$$\frac{d^2\eta(x)}{dx^2} = \frac{S}{\sigma A} j(x) \quad [2]$$

distributions in one-dimensional porous electrodes (2, 7-9). In Eq. [2], $\eta(x)$ is the polarization or change in interfacial potential difference at the point x induced by passage of current (i), S is interfacial surface area per unit length of electrode (cm^2/cm), and $j(x)$ is the current density of the interfacial reaction (amp/cm^2). Boundary conditions corresponding to the configuration of Fig. 1 are given by Eq. [3]. For the case of a simple

$$\left(\frac{d\eta(x)}{dx}\right)_{x=0} = \left(\frac{d\eta(x)}{dx}\right)_{x=l} = \frac{i}{\sigma A} \quad [3]$$

oxidation reduction reaction, the rate law may be assumed to be of the conventional form given by Eq. [4], where j_o is the exchange current density

$$j(x) = j_o\{\exp[\beta n F\eta(x)/RT] - \exp[-(1-\beta)nF\eta(x)/RT]\} \quad [4]$$

(amp/cm^2), n is the electron number, β is the (anodic) transfer coefficient, and RT/F is the thermal volt equivalent. We assume that non-Faradaic currents and changes of reactant concentrations because of the electrochemical reaction are negligible as well as effects due to diffusion, migration, and convection of reactants and to the structure of the double layer.[2]

For sufficiently small values of polarization, Eq. [4] may be linearized to give the rate law of Eq. [5]. Substitution of Eq. [5] into Eq. [2]

$$j(x) = \frac{nj_oF\eta(x)}{RT} \quad [5]$$

and integration of the resulting expression with use of the conditions of Eq. [3] lead to the potential distribution of Eq. [6] in terms of the

$$\frac{\eta(\xi)}{i\,R_o} = \frac{\cosh[\sqrt{\kappa}\cdot\xi] - \cosh[\sqrt{\kappa}(1-\xi)]}{\sqrt{\kappa}\cdot\sinh(\sqrt{\kappa})} \quad [6]$$

dimensionless parameters $\xi = x/l$ and $\kappa = Sj_ol^2nF/\sigma ART$. The parameter κ is essentially a ratio of solution impedance to interfacial impedance. Relative potential distributions calculated from Eq. [6] are shown in Fig. 2 as a function of the parameter κ. When κ is less than unity, no appreciable interfacial reaction occurs and the measured resistance should be essentially that given by Eq. [1]. For values of κ large with respect to unity, an appreciable fraction of the current is carried by the metallic phase and R_{app} is less than R_o.

Equation [7] gives the ratio of the apparent resistance to the resistance

$$\frac{R_{app}}{R_o} = 2\frac{\cosh(\sqrt{\kappa}) - 1}{\sqrt{\kappa}\cdot\sinh(\sqrt{\kappa})} \quad [7]$$

[2] Concentration effects may be minimized experimentally by use of flowing solutions. Some of the restrictions cited above are relaxed later in considering transient effects.

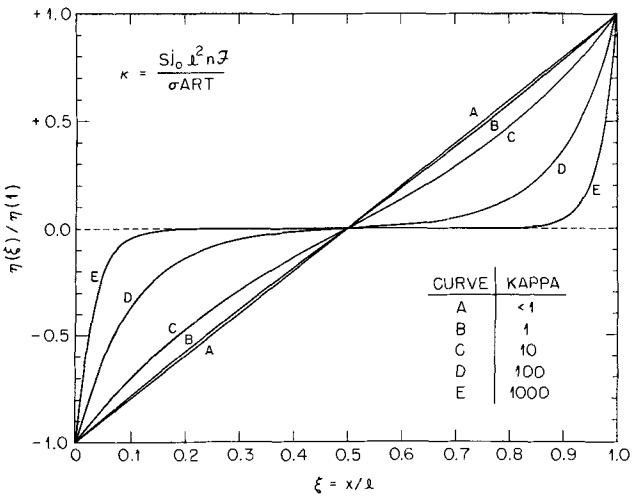

Fig. 2. Relative potential distribution in porous or tubular electrodes as a function of the dimensionless parameter κ.

of the electrolyte (cf. Eq. [1]). The fraction of the total current which is carried by the metallic phase is given by Eq. [8]. For large values of κ,

$$\text{Current fraction} = \frac{\cosh\left(\frac{1}{2}\sqrt{\kappa}\right) - 1}{\cosh\left(\frac{1}{2}\sqrt{\kappa}\right)} \quad [8]$$

an appreciable region exists inside the electrode where essentially no polarization occurs on passage of current (cf. curve E of Fig. 2). This behavior resembles the phenomenon of the Faraday shield. Variation of the apparent resistance with the parameter κ as predicted by Eq. [7] is shown in Fig. 3. For large values of κ the apparent resistance is inversely proportional to $\sqrt{\kappa}$. The curve in Fig. 3 may be used to estimate κ from measurements of R_{app} if R_o is known. The quotient $1/\sqrt{\kappa}$ is a measure of the degree of penetration of an electrochemical process into a porous electrode (2). Since κ is proportional to j_o, and j_o depends on the concentrations of oxidizable and reducible species (cf. Eq. [10]), Eq. [7] should be applicable to analysis of concentrations of oxidation reduction couples in flowing streams. The relation given by Eq. [7] and shown in Fig. 3 may also be used to estimate corrosion rates of pipes or porous metals from measurements of the apparent resistance. In this case κ is replaced by κ_{corr} of Eq. [9], where j_{corr} is

$$\kappa_{corr} = \frac{S\,j_{corr}\,l^2\,(\beta_a n_a + \beta_c n_c)F}{\sigma ART} \quad [9]$$

the current density of the corrosion reaction in the absence of external polarization (amp/cm^2), β_a and β_c are transfer coefficients of the anodic and cathodic

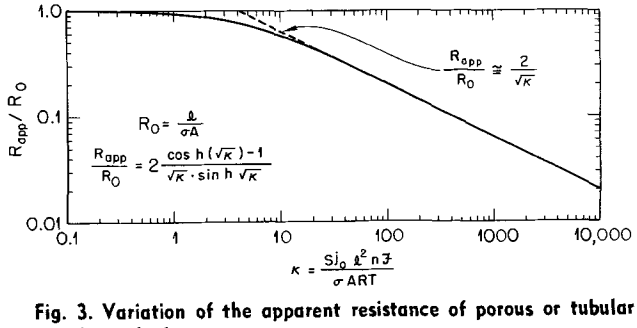

Fig. 3. Variation of the apparent resistance of porous or tubular electrodes with the parameter κ.

processes, and n_a and n_c are the corresponding electron numbers.

Determination of the Transfer Coefficient by Induced Polarization

The transfer coefficient of oxidation reduction reactions may be determined by measurement of induced polarization when the linear rate of law of Eq. [5] is a good approximation. The exchange current density may be expressed by Eq. [10] where j_o^o is the standard exchange current density including

$$j_o = j_o^o C_R^{(1-\beta)} C_o^{\beta} \qquad [10]$$

activity coefficients (amp-cm/mole) and C_R and C_o (mole/cm^3) are concentrations of anodic and cathodic reactants, respectively (10). When C_R and C_o are large enough so that R_{app}/R_o is less than about 0.5 (cf. Fig. 3), Eq. [7] reduces to $R_{app}/R_o = 2/\sqrt{\kappa}$ and substitution of the relation for κ leads to Eq. [11]. In Eq. [11], $\kappa_o = S\, j_o^o\, l^2\, nF/\sigma ART$. Combination of Eq. [10]

$$\frac{j_o}{j_o^o} = \frac{4}{\kappa_o}\left(\frac{R_o}{R_{app}}\right)^2 \qquad [11]$$

and [11] leads to Eq. [12] which shows that a log-log plot of $C_R(R_{app}/R_o)^2$

$$C_R\left(\frac{R_{app}}{R_o}\right)^2 = \frac{4}{\kappa_o}\left(\frac{C_R}{C_o}\right)^{\beta} \qquad [12]$$

against (C_o/C_R) should be linear with a slope of $-\beta$.

Figure 4 shows a plot of the type suggested by Eq. [12] for induced polarization of the ferrocyanide-ferricyanide couple in 0.5M K_2SO_4 at 25°C in a gold tube. The apparent resistance was measured as a function of the ratio of concentrations of oxidized and reduced species (ferricyanide and ferrocyanide concentrations varied in the range 10^{-3} to $10^{-2}M$). The line shown in Fig. 4 corresponds to a transfer coefficient of 1/2. Our data seem to support this value of the transfer coefficient, which was also reported by others (11). The data of Fig. 4 correspond to $R_{app}/R_o \cong 0.15$ so that $\kappa \cong 2 \times 10^2$.

Induced Polarization Curves

Solution of Eq. [2] for the more general rate law of Eq. [4] cannot be accomplished explicitly for arbitrary values of the transfer coefficient. However, numerical methods of solution may be used and Fig. 5

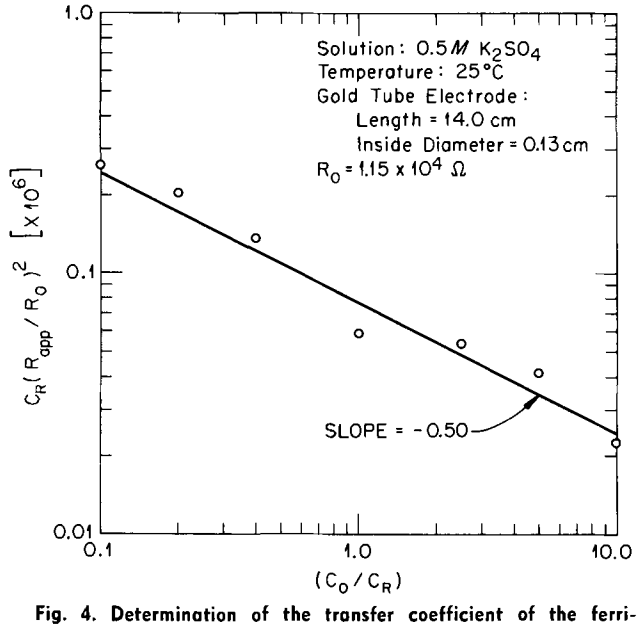

Fig. 4. Determination of the transfer coefficient of the ferricyanide-ferrocyanide couple by induced polarization of a tubular gold electrode.

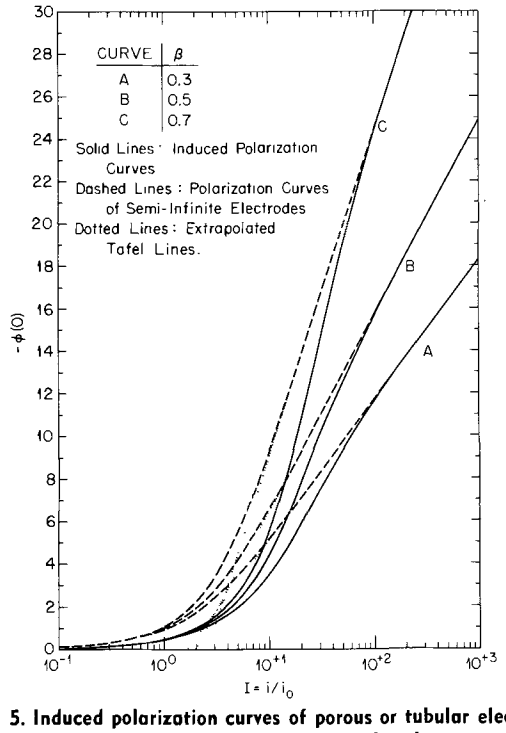

Fig. 5. Induced polarization curves of porous or tubular electrodes as a function of the transfer coefficient, β, for the case $\kappa = 1$.

shows a set of induced polarization curves calculated by use of a high-speed digital computer[3] as a function of the transfer coefficient (β) for the case, $\kappa = 1$. Combination of Eq. [2] and [4] leads to Eq. [13] in which $\phi(\xi) = nF\eta(\xi)/RT$.

$$\frac{d^2\phi(\xi)}{d\xi^2} = \kappa\{\exp[\beta\phi(\xi)] - \exp[-(1-\beta)\phi(\xi)]\} \qquad [13]$$

The sigmoid solid curves in Fig. 5 are solutions of Eq. [13]; $\phi(0)$ is the (reduced) polarization at $\xi = 0$ and $I = i/i_o = i/Slj_o$ is a dimensionless current variable [i_o is the total exchange current (amp)]. At high currents ($i >> i_o$), the induced polarization curve approaches that of a semi-infinite porous or tubular electrode (2). Equation [14] gives the Tafel line

$$I = \left(\frac{2}{\beta\kappa}\right)^{1/2} \exp[-\beta\phi(0)/2] \qquad [14]$$

for this region. At low currents ($i << i_o$), the linear rate law of Eq. [5] is a good approximation and the polarization curve may be calculated from Eq. [6]; this result is given by Eq. [15]. No simple relation can be derived

$$\frac{\phi(0)}{I} = -\sqrt{\kappa}\,\frac{\cosh(\sqrt{\kappa}) - 1}{\sinh(\sqrt{\kappa})} \qquad [15]$$

for the transition region between low and high currents.

Dissymmetry Potentials

One of the unique aspects of induced polarization measurements is the fact that the magnitude of the

[3] Equation [13] was integrated numerically on a computer (Control Data Corporation Model 1604-A) with boundary conditions analogous to those of Eq. [3] by use of a Runge-Kutta method. An initial value of $\phi(0)$ was assumed and the corresponding potential distribution computed from an explicit difference scheme. The interfacial reaction rate distribution was then computed and tested for equality of total anodic and cathodic currents. The sign and magnitude of any difference determined a new value for $\phi(0)$ and the computation cycle was repeated until successive iterations showed little improvement. A similar procedure was used to compute the initial potential distribution in the solution of Eq. [19] and [20]. Concentration changes in successive time intervals were determined by Eq. [20] in difference form; substitution of new concentrations into Eq. [18] then allowed computation of a new potential distribution by solution of Eq. [19] using the iterative procedure noted above.

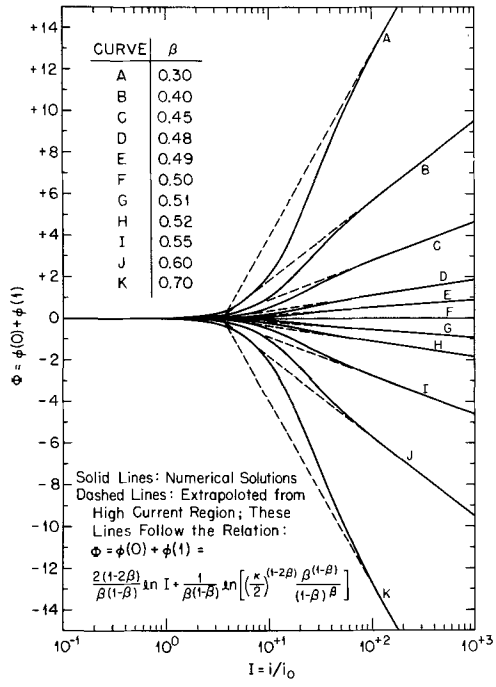

Fig. 6. Dissymmetry potential as a function of applied current and of the transfer coefficient, β, for induced polarization of porous or tubular electrodes ($\kappa = 1$).

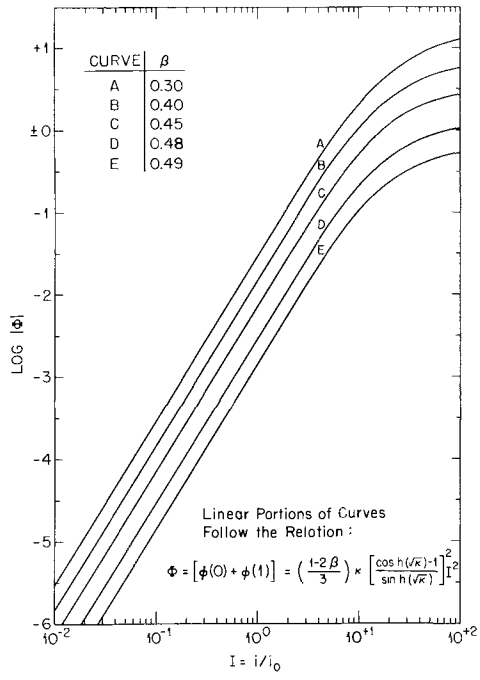

Fig. 7. Dissymmetry potential of porous or tubular electrodes in the region of small currents as a function of the transfer coefficient, β, for the case $\kappa = 1$.

observed polarization of the front side ($x = 0$) may be different from that of the back side ($x = l$). This occurs when $\beta \neq 1/2$ in Eq. [4] so that the rate law is not symmetrical. The sum $\Phi = \phi(0) + \phi(1)$ may be defined as the dissymmetry potential. It is positive or negative depending on whether β is less than or greater than 1/2, respectively. Measurements of the dissymmetry potential (Φ) may be used to determine both β and κ for an oxidation reduction reaction in a porous or tubular electrode.

Figure 6 shows dissymmetry potentials for induced polarization as a function of the reduced current ($I = i/i_o$) and of the (anodic) transfer coefficient (β) for the case, $\kappa = 1$. A Tafel region is observed at sufficiently high currents and the relation for the Tafel line is given by Eq. [16] which was derived by combination of Tafel expressions like Eq. [14]

$$\Phi = \frac{2(1-2\beta)}{\beta(1-\beta)} \ln I + \frac{1}{\beta(1-\beta)} \ln \left[\left(\frac{\kappa}{2}\right)^{(1-2\beta)} \frac{\beta^{(1-\beta)}}{(1-\beta)^{\beta}} \right] \quad [16]$$

for $\phi(0)$ and $\phi(1)$. The slope of the Tafel line depends only on β, and the intercept at $\Phi = 0$ depends on both κ and β. The parameter $\kappa(Sj_o l^2 nF/\sigma ART)$ may be expressed as $\kappa = i_o R_o f$, where $f = nF/RT$ (volt^{-1}), so that the total exchange current of the oxidation reduction reaction (i_o) may be determined easily if R_o is known.

The dissymmetry potential remains finite even at very low currents. Figure 7 shows Φ plotted as a function of current (log-log plot) for a number of values of β when $\kappa = 1$. This type of plot should be useful in detecting small deviations of β from the value 1/2. Expansion of Eq. [4] to quadratic terms and substitution into Eq. [2] yield an expression which can be solved to give Φ in the region of low currents; this relation is given by Eq. [17]

$$\Phi = \left(\frac{1-2\beta}{3}\right)\kappa \left[\frac{\cosh(\sqrt{\kappa}) - 1}{\sinh(\sqrt{\kappa})}\right]^2 I^2 \quad [17]$$

Figure 7 shows that Eq. [17] holds up to $I \cong 5$. The dissymmetry potential varies with the square of the applied current for $I < 5$. If $\kappa = i_o R_o f$ is known, β may be calculated by use of Eq. [17].

Concentration Transients

The solutions for induced polarization effects discussed above apply only when reactant concentrations are essentially constant during a measurement both with respect to time and with respect to position inside the electrode. In the absence of solution flow through the electrode, however, reactant concentrations will change as a result of the Faradaic reactions at the metal-solution interface. The reaction rate at the interface for a simple oxidation-reduction reaction can be expressed as usual (10) by Eq. [18], where $\rho(\xi, t)$ is the reduced reaction rate, $C_R(\xi, t)$ and $C_o(\xi, t)$

$$\rho(\xi,t) = \frac{j(\xi,t)}{j_o} = \frac{C_R(\xi,t)}{C^o} \exp[\beta\phi(\xi,t)] - \frac{C_o(\xi,t)}{C^o} \exp[-(1-\beta)\phi(\xi,t)] \quad [18]$$

are concentrations of reduced and oxidized species, respectively (mole/cm^3), C^o is the initial concentration (we assume for simplicity that $C_R(\xi,0) = C_o(\xi,0) = C^o$), and j_o is the initial exchange current density. The potential distribution obeys Eq. [19], which is a form of Eq. [2], providing excess

$$\frac{\partial^2\phi(\xi,t)}{\partial\xi^2} = \kappa \cdot \rho(\xi,t) \quad [19]$$

inert electrolyte is present or reactant and product have the same conductivity contribution. The concentrations may be assumed to change with time approximately according to Eq. [20], where $\theta = nFC^oAl/i_o$ is a time constant

$$\frac{\partial[C_o(\xi,t)/C^o]}{\partial t} = -\frac{\partial[C_R(\xi,t)/C^o]}{\partial t} = \frac{\rho(\xi,t)}{\theta} \quad [20]$$

(sec). We assume that tube or pore sizes are small compared with distances over which appreciable concentration changes occur. The time constant θ is the ratio of the total coulombs available from complete

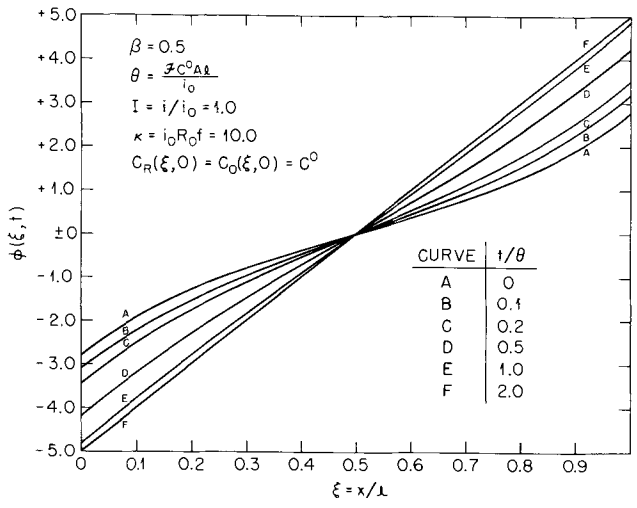

Fig. 8. Variation of induced polarization with time due to oxidation reduction reactions in the interior of a porous or tubular electrode.

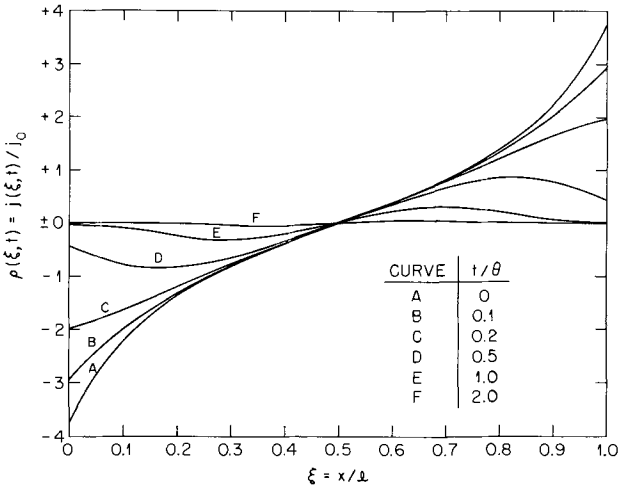

Fig. 10. Variation of current density profile with time due to oxidation reduction reactions in the interior of a porous or tubular electrode ($\beta = 0.5$; $\kappa = 10.0$; $I = 1.0$).

reaction of either the oxidized or reduced species to the initial exchange current of the reaction. Potential and concentration transients are obtained by simultaneous solution of Eq. [19] and [20] with use of the boundary conditions of Eq. [21].

$$\left(\frac{\partial\phi(\xi,t)}{\partial\xi}\right)_{\xi=0} = \left(\frac{\partial\phi(\xi,t)}{\partial\xi}\right)_{\xi=1} = \kappa I \qquad [21]$$

Although general solutions of this system of equations are not obtainable in terms of explicit functions, numerical methods may be used to find solutions for particular values of the parameters, β, κ, and I.

Figures 8, 9, and 10 show how the polarization, the reactant concentrations, and the reaction rate change with time and with position in the electrode during the course of a transient. These results were obtained by use of a high-speed digital computer;[3] parameters used were $\beta = 1/2$, $I = 1.0$, and $\kappa = 10.0$. Initially most of the reaction occurs near the ends of the electrode (cf. Fig. 10). With time a reaction "wave" is propagated toward the center of the electrode. Oxidized species react to form reduced species near $\xi = 0$, and the reverse reaction occurs near $\xi = 1$ (cf. Fig. 9). In the new steady state the gradient of the polarization is constant throughout the length of the electrode so that $\phi(1) - \phi(0) = \kappa I$ (cf. curve F of Fig. 8), interfacial reactions no longer occur anywhere in

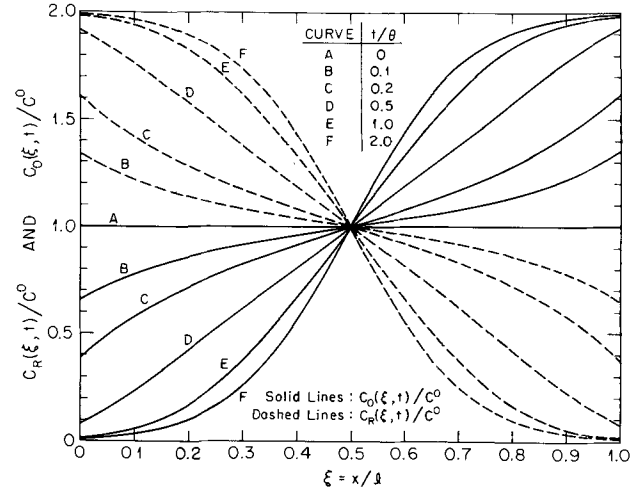

Fig. 9. Variation of reactant concentration profiles with time due to oxidation reduction reactions in the interior of a porous or tubular electrode ($\beta = 0.5$; $\kappa = 10.0$; $I = 1.0$).

the electrode, and concentrations of oxidized and reduced species are related by the Nernst equation, $C_O(\xi,\infty)/C_R(\xi,\infty) = \exp[\phi(\xi,\infty)]$. During the concentration transient the apparent resistance increases from its initial value up to the limit R_o, the electrolyte resistance which would be observed if no oxidation reduction couple were present in the solution. The time constant θ may be useful as a semi-quantitative measure of the time required for concentration transients in induced polarization measurements. If measurements of apparent resistance are made within about 0.01 θ, no significant concentration changes should occur.

Induced Charging of the Double Layer

Induced charging of the double layer in porous or tubular electrodes in which no Faradaic reactions can occur produces charging transients similar to those obtained by direct galvanostatic charging of porous electrodes. The induced double layer charging transient may be obtained by solution of Eq. [22] (12, 13). The time constant τ is equal to $SCl^2/\sigma A$ where C is the

$$\frac{\partial^2\phi(\xi,t)}{\partial\xi^2} = \tau\frac{\partial\phi(\xi,t)}{\partial\tau} \qquad [22]$$

differential capacity per unit area (farad/cm²). Alternatively, $\tau = R_oC_T$ where $R_o = l/\sigma A$ is the resistance of the electrolyte as before and $C_T = SCl$ is the total differential capacity (farad). The initial condition is given by $\phi(\xi,0) = 0$ and the boundary conditions are the same as those of Eq. [21]. The induced double layer charging transient is given by Eq. [23] and Fig. 11

$$\frac{\phi(\xi,t)}{\kappa I} = \frac{2}{\pi^2}\sum_{k=1}^{\infty}\frac{(-1)^k}{k^2}\{\cos[\pi k\xi] - \cos[\pi k(1-\xi]\}\{1-\exp[-\pi^2k^2t/\tau]\} \qquad [23]$$

shows a plot of the measurable potential transients against t/τ and against $(t/\tau)^{1/2}$. During the initial moments the potentials $\phi(0,t)$ and $\phi(1,t)$ follow the $\sqrt{t}$ law of Eq. [24]. In a plot of $\phi(0,t)$ or $\phi(1,t)$ against $\sqrt{t}$, the

$$\lim_{t\to0} -\frac{\phi(0,t)}{\kappa I} = \lim_{t\to0}\frac{\phi(1,t)}{\kappa I} = 2\left(\frac{t}{\pi\tau}\right)^{1/2} \qquad [24]$$

initial slope of the charging transient is inversely proportional to $(R_oC_T)^{1/2}$. The final steady state is given by $\phi(\xi,\infty)/\kappa I = \xi - (1/2)$ so that $\phi(1,\infty) - \phi(0,\infty) = \kappa I$, which is equivalent to Eq. [1]. Both R_o

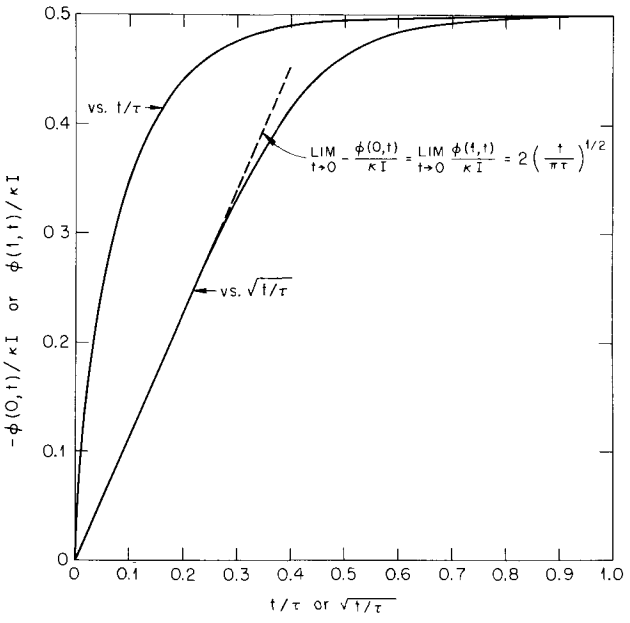

Fig. 11. Induced charging of the double layer in porous or tubular electrodes in the absence of faradaic reactions.

and C_T may be determined from induced charging transients by use of these relations.

Effect of Conductance of Metallic Phase

The relations derived above for induced polarization and charging transients may be corrected for situations where the conductivity of the metallic phase is comparable to that of the liquid phase. When potential gradients can occur in the metallic (electron conducting) phase, Eq. [2] may be replaced by Eq. [25], where σ_s and σ_m are specific conductances of solution and metal

$$\frac{d^2\eta(x)}{dx^2} = S\left(\frac{1}{\sigma_s A_s} + \frac{1}{\sigma_m A_m}\right) j(x) \qquad [25]$$

phases, respectively, and A_s and A_m are the corresponding cross-sectional areas. The net result of this correction is that κ must be replaced by

$$\kappa' = \frac{Sj_o \ln F}{RT}\left(\frac{l}{\sigma_s A_s} + \frac{l}{\sigma_m A_m}\right) = i_o\,(R_o + R_m) f$$

where $R_m = l/\sigma_m A_m$ is the resistance of the metallic phase (ohm). In a similar manner the time constant for charging of the double layer (τ) must be replaced by $\tau' = C_T(R_o + R_m)$. The forms of all equations in which κ and τ appear (*e.g.*, Eq. [6] and [22]) are left unchanged by this substitution.

Summary

Solutions are presented above to several one-dimensional boundary value problems which occur in the theory of induced polarization of porous or tubular electrodes. Measurements of induced polarization may find application in analysis of flowing streams because the apparent resistance is sensitive to the presence of oxidation reduction reactions which can occur at the interface. Induced polarization may also prove to be useful as a monitor of corrosion rates of pipes or porous metals. In addition, certain parameters of importance in electrode kinetics (transfer coefficient and exchange current density) may be estimated in a unique manner from measurements of the dissymmetry potential or the apparent resistance. More elaborate models which include factors not treated here (diffusion and convection of reactants, reactions with consecutive charge-transfer steps, etc.) may be devised which might suggest other possibilities for the utilization of induced polarization measurements on porous and tubular electrodes.

Manuscript received Sept. 7, 1965; revised manuscript received Feb. 24, 1966. This paper was presented at the Cleveland Meeting, May 1-6, 1966.

Any discussion of this paper will appear in a Discussion Section to be published in the December 1966 JOURNAL.

REFERENCES

1. O. S. Ksenzhek, E. A. Kalinovskii, and E. L. Baskin, *Zhur. Priklad. Khim.*, **37**, 1045 (1964); *Russian J. Appl. Chem.*, **37**, 1048 (1964).
2. F. A. Posey, *This Journal*, **111**, 1173 (1964).
3. W. Tomassi, *Compt rend.*, **256**, 3093 (1963).
4. W. Tomassi, *Przemysl Chem.*, **42**, 345, 410 (1963).
5. W. Tomassi, H. Jankowska, and R. Milek, *ibid.*, **43**, 6 (1964).
6. W. Tomassi, H. Jankowska, S. Pietrzyk, and J. Brylka, *Electrochim. Acta*, **10**, 605 (1964).
7. V. S. Daniel'-Bek, *Zhur. Fiz Khim.*, **22**, 697 (1948).
8. J. S. Newman and C. W. Tobias, *This Journal*, **109**, 1183 (1962).
9. E. A. Grens, II, and C. W. Tobias, *Ber Bunsenges. physik. Chem.*, **68**, 236 (1964).
10. P. Delahay, "Double Layer and Electrode Kinetics," Interscience, New York (1965).
11. N. Tanaka and R. Tamamushi, *Electrochim. Acta*, **9**, 963 (1964).
12. R. de Levie, *ibid.*, **8**, 751 (1963).
13. F. A. Posey and T. Morozumi, *This Journal*, **113**, 176 (1966).

SYMBOLS

A, A_s	cross-sectional area of electrolyte in porous or tubular electrode, cm^2
A_m	cross-sectional area of metallic phase in porous or tubular electrode, cm^2
C	differential capacity per unit area, farad/cm^2
C_T	total differential capacity, farad.
$C_R, C_R(\xi,t)$	concentration of reduced species in solution, mole/cm^3
$C_o, C_o(\xi,t)$	concentration of oxidized species in solution, mole/cm^3
C^o	$=C_R(\xi,0) = C_o(\xi,0)$; initial concentration of oxidized and reduced species, mole/cm^3
f	$= nF/RT$, reciprocal thermal volt equivalent, volt^{-1}
F	Faraday constant, coulomb/equivalent
i	total current passed through porous or tubular electrode, amp
i_o	$= Sj_o l$; total exchange current, amp
I	$= i/i_o$; dimensionless reduced total current
$j(x), j(\xi,t)$	current density of interfacial reaction, amp/cm^2
j_o	exchange current density, amp/cm^2
j_o^o	standard exchange current density, amp-cm/mole
j_{corr}	corrosion current density, amp/cm^2
k	summation index
l	length of porous or tubular electrode, cm
n	electron number of oxidation reduction reaction
n_a, n_c	electron numbers of anodic and cathodic reactions, respectively
RT/F	thermal volt equivalent, v
R_o	$= l/\sigma A = l/\sigma_s A_s$; resistance of solution phase in absence of oxidation reduction reactions, ohm
R_m	$= l/\sigma_m A_m$; resistance of metallic phase, ohm
R_{app}	$= [\eta(l) - \eta(0)]/i$; apparent resistance of porous or tubular electrode, ohm
S	interfacial area of porous or tubular electrode per unit length, cm^2/cm
t	time, sec
x	distance coordinate, cm
β, β_a	anodic transfer coefficient.
β_c	cathodic transfer coefficient
$\eta(x)$	change of interfacial potential difference by induced polarization, volt
θ	$= nFC^oAl/i_o$; time constant for concentration transients, sec

κ = $Sj_0l^2n\ F/\sigma ART = i_oR_of$; dimensionless resistance parameter, a ratio of solution impedance to interfacial impedance

κ_O = $\kappa j_o^o/j_o$

κ' = $i_o(R_o + R_m)f = \kappa(R_o + R_M)/R_o$

κ_{corr} = $Sj_{corr}l^2(\beta_an_a + \beta_cn_c)\ F/\sigma ART$; dimensionless resistance parameter useful for estimating corrosion rates of pipes or porous metals

ξ = x/l; dimensionless distance coordinate

$\rho(\xi,t)$ = $j(\xi,t)/j_o$; dimensionless reduced reaction rate.

σ,σ_s specific conductance of solution phase, $ohm^{-1}cm^{-1}$

σ_m specific conductance of metallic phase, $ohm^{-1}cm^{-1}$

τ = $SCl^2/\sigma A = R_oC_T$; time constant for charging of double layer, sec

τ' = $C_T(R_o + R_M)$

$\phi_s(x)$ potential of solution phase, volt

$\phi(\xi),\phi(\xi,t)$ = $f\cdot\eta(\xi,t)$; dimensionless reduced change in interfacial potential difference induced by passage of current

Φ = $\phi(0) + \phi(1)$; dimensionless dissymmetry potential.

Electrochemical Processes in Thin Films

1. Preliminary Survey of the Roles of Convection and Concentration Polarization

E. N. Lightfoot

Department of Chemical Engineering, University of Wisconsin, Madison, Wisconsin

ABSTRACT

An analysis is made of the roles of convection and concentration polarization during oxidation of hydrogen in acidic supermeniscus films. In this preliminary analysis activation overvoltage is assumed constant throughout the reaction zone. It is concluded that both convection and concentration polarization are important, and that they are in part responsible for formation of films above the normal meniscus. It is postulated that concentration polarization induces water recirculation, up in the surrounding vapor phase, and down as a gravity-driven falling film on the anode surface. Calculated film heights and thicknesses are in agreement with published observations.

Recently there has been considerable interest in electrochemical processes taking place at the wetted surfaces of metallic rods partially immersed in electrolyte solutions. This interest stems in large part from the outstanding work of Will (1) and from the belief that studies in such systems will give improved insight into the behavior of porous electrodes.

Up to the present, however, analysis of the diffusional processes contributing to the electrolytic current have been incomplete, and the postulated presence of very thin films above the equilibrium meniscus has not been adequately explained. It is felt by the author that more thorough study of these factors is in order, and, indeed, that electrode behavior cannot be adequately understood until these uncertainties are resolved.

The present paper reports a preliminary analysis of convection and concentration polarization relative to immobilization of electrochemically inactive solutes. In spite of the approximations introduced, this development indicates that both convection and concentration polarization are important and that their effects should be further studied. Of particular importance is the strong probability that systems of this type can be influenced by gravitational forces and hence both by configuration and orientation of the electrode.

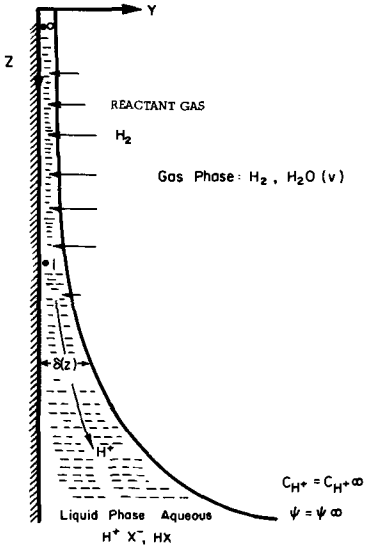

Fig. 1. System considered

The system considered is pictured in Fig. 1. It consists of an electrolyte meniscus adjacent to a vertical electrode surface and quite possibly distorted from normal meniscus shape in its upper regions. This distortion may be due to hydrodynamic effects, as discussed below, or to the presence of a liquid film of as yet undetermined origin. In any event, it is assumed that the gas-diffusion path is short compared to that for the discharging ions, so that migration of the two will be one-dimensional in each case, and mutually perpendicular.

Behavior of the system can be described in terms of conservation relations for the diffusing species, and of electric charge, the Nernst equation, and Kirchoff's voltage law. Where convection is to be considered the equation of fluid motion must also be used, with possible serious complication of the problem at hand. Only simple falling films will be considered in this initial development, but a more thorough analysis is planned in which natural convection and the effects of surface-tension forces will be taken into account.

Continuity Relations

For our present purposes we shall consider the solution to contain only hydrogen ions, one unspecified anion X^-, a very small amount of dissolved hydrogen, and water.[1] It will be further assumed that diffusion coefficients are concentration independent throughout the reaction zone and that diffusional coupling between species is unimportant. Finally, it will be assumed that water is the major constituent so that the

[1] Partially dissociated electrolytes can be handled by an extension of the development presented here, but in this case both the dissociation equilibrium and rate constants must be known.

divergences of both the mass-average and molar-average velocities are zero. We then need explicit continuity equations only for hydrogen and the two ionic species.

The continuity equation for hydrogen is particularly simple and may be written directly in integral form as

$$N_{H_2} = \frac{\mathcal{D}H_2 m}{\delta(z)} [c_{H_2}{}^{o} - c_{H_2}(0,z)] \quad [1]$$

where $c_{H_2}{}^{o}$ is the solubility of hydrogen in the electrolyte. This equation may be rewritten in terms of the rate of increase of electrolytic current in the z-direction, since this current is produced solely by oxidation of hydrogen. We thus obtain

$$\boxed{dI/dz = [2PF\mathcal{D}_{H_2 m}/\delta(z)][c_{H_2}{}^{o} - c_{H_2}(0,z)]} \quad [2]$$

Since the entire electrolytic current is carried by the hydrogen ions, we may write the continuity equations for the ionic species as

$$H^+: \; I_z = -FP\delta(z)\left\{\mathcal{D}_{H^+ m}\left(\frac{dc_{H^+}}{dz} + c_{H^+}\frac{d\Psi}{dz}\right) - c_{H^+}v_z^*\right\} \text{ (hydrogen ion)} \quad [3]$$

$$X^-: \; 0 = -\mathcal{D}_{x-m}\left(\frac{dc_{H^+}}{dz} - c_H + \frac{d\Psi}{dz}\right) + c_{H^+}v_z^* \text{ (anion, } X^-) \quad [4]$$

Use of these pseudobinary diffusion expressions has been amply justified for reasonably dilute electrolytes and should be satisfactory for our limited present purposes. The assumptions of uniform electrolytic current density and negligible curvature of the electrode perimeter are consistent with the assumption of thin films underlying the entire development.

Equation [4] states the requirements for immobilization of the anion: a balance between concentration-diffusion, forced-diffusion, and convective fluxes. Simultaneous consideration of all three fluxes is difficult because it requires detailed knowledge of water transport across the gas-liquid interface. For the present, when it is only desired to obtain a semi-quantitative understanding of system behavior, a simpler approach seems in order, and two limiting cases are considered for this purpose:

1. No water transport across the liquid-gas interface: $v_w = v_{x-} = 0$; $v^* - x_H + v_{H^+}$. Under these conditions convection is of minor importance, and the primary mechanism of immobilization is concentration polarization.

2. No resistance to water transport: $dc_{H^+}/dz = dc_{H^+}/dy = 0$. Under these conditions anion immobilization is entirely by convection. Since this requires a very substantial solution velocity, large amounts of water will have to condense into the liquid film and be transported downward by gravitational action, or else there will have to be very substantial spontaneous mixing. Real behavior should be intermediate between predictions for these two limiting situations.

For the case of no water transport across the gas-liquid interface and no spontaneous mixing, *i.e.*, negligible convection, Eq. [3] and [4] reduce to

$$I_z = -2FP\delta(z)\mathcal{D}_{H^+ m}c_{H^+}\frac{d\Psi}{dz} \text{ (negligible convection)} \quad [5]$$

$$\frac{dc_{H^+}}{dz} = c_{H^+}\frac{d\Psi}{dz} \text{ (negligible convection)} \quad [6]$$

Equation [6] may be readily integrated and the result substituted into Eq. [5] to obtain[2]

[2] Other available analyses taking concentration polarization into account include (2-4).

$$I_z = -2FP\delta(z)\, c_{H^+\infty}\mathcal{D}_{H^+ m}\, e^{(\Psi-\Psi_\infty)}\frac{d\Psi}{dz} \text{ (negligible convection)} \quad [7]$$

Then, for conditions of negligible convection the effective conductivity of the film is a function of applied voltage, through the dependence on Ψ_∞, the potential at large z.

When fluid convection prevents the development of appreciable concentration gradients, Eq. [4] reduces to

$$v^* = -\mathcal{D}_{x-m}\frac{d\Psi}{dz} \text{ (convection dominant)} \quad [8]$$

This may be put into Eq. [3] to obtain

$$I = -P\delta(z)\{Fc_{H^+}(\mathcal{D}_{H^+ m} + \mathcal{D}_{x-m})\}\frac{d\Psi}{dz} \text{ (convection dominant)} \quad [9]$$

The expression in braces is defined as $\kappa = KRT/F$ where K is the conductance of the electrolyte, mhos/cm. We may then write

$$I = -P\delta(z)\,\kappa\frac{d\Psi}{dz} \text{ (convection dominant)} \quad [10]$$

This is the expression used by Will, and it is, therefore, important to recognize both the restrictions on it and its physical significance:

(*i*) *Restrictions.*—Equation [10] is valid only when concentration gradients are substantially eliminated by convective mechanisms. This implies a substantial flow of solvent down the film, either because of effective equilibriation with the gas phase, natural convection, or the action of surface forces. These requirements clearly imply a sensitivity to geometry, scale factors, and orientation with respect to gravitational fields.

(*ii*) *Physical significance.*—The effect of convection is to oppose electrodiffusion of X^- and to reinforce that of H^+, in each case by exactly the same amount. Since its effect on X^- must exactly cancel out the corresponding electrodiffusion, its contribution to H^+ movement, *i.e.*, to the electrolytic current, is exactly that of electrodiffusion of X^- in an alternating voltage field.

It should also be noted that $\mathcal{D}_{X-m}$ is always much smaller than $\mathcal{D}_{H+m}$. It follows that effective electrolyte resistance for conditions of negligible convection is only about half that for conditions of negligible concentration polarization, even at quite low applied voltages. At higher voltages the differences are even larger.

Then for the one-one electrolyte considered here, it should not be hard to determine from experimental data whether convection or concentration polarization is primarily responsible for immobilization of electrochemically inactive ions. This can be seen rather clearly by rewriting Eq. [7] and [10] in the common form

$$\boxed{I = -P\delta(z)\,\kappa_\infty\alpha\frac{d\Psi}{dz}} \quad [11]$$

with

$$\alpha = 1 \text{ (convection dominant)} \quad [12]$$

$$\alpha = 2\exp[\Psi(z) - \Psi(\infty)]/\left(1 + \frac{\mathcal{D}_{x-m}}{\mathcal{D}_{H+m}}\right) \text{ (convection negligible)} \quad [13]$$

Equations [2] and [11] through [13] summarize the useful continuity relations for this system. It should be kept in mind, however, that the situation is much more complicated for partially dissociated electrolytes.

Development of Current-Voltage Relations for Thin Films

Here, the hydrogen concentration $c_{H_2}(0, z)$ will be eliminated from Eq. [2] through use of Kirchoff's law and a modification of the Nernst equation, in a manner similar to that used by Will. In this way it may be shown that

$$\Psi_0 - \Psi_1 \doteq \ln \left[\frac{(c_{H^+})_1}{(c_{H^+})_0} \sqrt{\frac{(c_{H_2})_0}{(c_{H_2})_1}} \right] + \frac{F}{RT} (\eta_1 - \eta_0) \quad [14]$$

In the present analysis overvoltage η will be assumed constant. This is a major assumption which may result in serious error for many electrochemical reactions of practical interest. It should however be acceptable for our present limited purposes, for hydrogen oxidation. Variation in overvoltage, but not hydrodynamic flow, is treated by Grens, Turner, and Katan (4). We may thus rewrite Eq. [14] as

$$\frac{(c_{H_2})_1}{(c_{H_2})_0} = e^{-\beta(\Psi_0 - \Psi_1)} \quad [15]$$

with

$$\beta = 2 \text{ (convection dominant)} \quad [16]$$

$$\beta = 4 \text{ (convection negligible)} \quad [17]$$

Equation [15] may be rewritten more conveniently as

$$\boxed{c_{H_2}/c_{H_2}^{\circ} = \exp [-\beta\psi + (\beta - 2)\psi_\infty]} \quad [18]$$

with

$$\psi = \Psi_e - \Psi \quad [19]$$

Here Ψ_e is the solution potential for $c_{H_2} = c_{H_2}^{\circ}$ and $c_{H^+} = (c_{H^+})_\infty$. Equations [2] and [18] can now be combined to eliminate concentration and the result put in dimensionless form for convenience. The result is

$$\frac{dH}{d\zeta} = 1 - e^{-\beta\psi + (\beta - 2)\psi_\infty} \quad [20]$$

where the dimensionless current H and position ζ are defined as in the nomenclature list. The corresponding form of Eq. [11] is

$$H = \frac{1}{2} \epsilon\alpha \frac{d\psi}{d\zeta} \quad [21]$$

where ϵ is also defined in the nomenclature list. These two equations may now be combined and integrated to yield the desired current-voltage relations

$$H = \sqrt{\epsilon} \sqrt{\psi - \frac{1}{2}(1 - e^{-2\psi})} \quad \text{(convection dominant)} \quad [22]$$

$$H = \sqrt{\frac{2\epsilon}{1 + (\mathcal{D}_{x-m}/\mathcal{D}_{H+m})}} \sqrt{\frac{4}{5} e^{\psi_\infty/2} + \frac{1}{5} e^{-5\psi + 3\psi_\infty} - e^{-\psi + \psi_\infty}} \quad [23]$$

convection negligible

To evaluate the integration constants in these two expressions use was made of the fact that $H = 0$ when $c_{H_2} = c_{H_2}^{\circ}$. Note that the total applied voltage can be defined as ψ_∞ and that the total current is H_∞. Therefore, to obtain an expression for total electrode performance from Eq. [22] or [23], it is only necessary to replace ψ by ψ_∞ and H by H_∞.

It may be noted that:

1. Both relations are completely independent of film shape, provided only that the film is thin enough to provide mutually perpendicular gas and ion diffusion, and, of course, that $\gamma(\eta_0 - \eta_1)$ be zero.
2. The current-voltage relation at intermediate points in the film is dependent on total applied voltage when concentration polarization is appreciable, but not otherwise.
3. Current-voltage characteristics are quite different for the two limiting cases considered, so that it may be possible to determine the relative importance of convection and concentration polarization from experimental measurements. For acid hydrogen anodes, as considered here, greater currents are obtained when concentration polarization is appreciable. For alkaline hydrogen anodes or acid oxygen cathodes the reverse should, of course, be true.

The last of these points is the most important for our present purposes, and is worth considering in more detail.

To facilitate comparison of Eq. [22] and [23] we define r as the ratio of potentials for convection negligible and dominant

$$r \doteq 2/[1 + (\mathcal{D}_{x-m}/\mathcal{D}_{H+m})]^{1/2} \qquad (\text{Limit}, \psi_\infty \to 0)$$

For a rather typical value of 0.2 for $(\mathcal{D}_{X-m}/\mathcal{D}_{H+m})$ one thus obtains a value of the order of 2 for r, at low applied voltages. Since $RT/F \doteq 0.025$v at normal temperature, this expression would only be expected to be valid for applied potentials of about 10 mv or lower. At very high applied voltages

$$r \doteq \sqrt{\frac{8}{5} \frac{\exp(\psi_\infty/2)}{\left(1 + \frac{\mathcal{D}_{x-m}}{\mathcal{D}_{H^+}}\right)\left(\psi_\infty - \frac{1}{2}\right)}} \quad [25]$$

so that r rapidly becomes large.

Comparison of Predicted Behavior with Available Data

The most complete available data directly applicable to the above analysis appear to be the experimental results of Will for cylindrical platinum electrodes immersed in 1*N* and 8*N* H_2SO_4 at 25°C. Representative results are reproduced in Fig. 2 and 3, along with predictions for the assumption of convection dominant in immobilization of the anions. Calculated results for the assumption of concentration polarization dominance are not shown because they are not directly applicable to a partially dissociated dibasic acid such as H_2SO_4.

At very low applied voltages (see Fig. 2) experimental results are in fair agreement with the assumption of convection dominance, although the experimental currents are slightly lower than predicted for the case of 8*N* acid. This result may be a consequence of activation polarization or inaccuracies in the assumed values of physical properties. The dif-

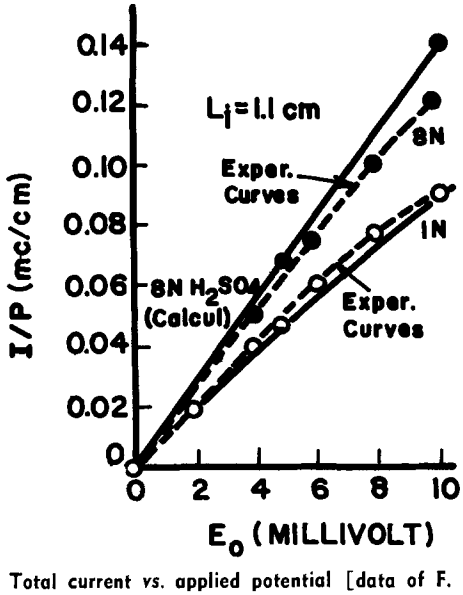

Fig. 2. Total current vs. applied potential [data of F. G. Will, ref. (1)].

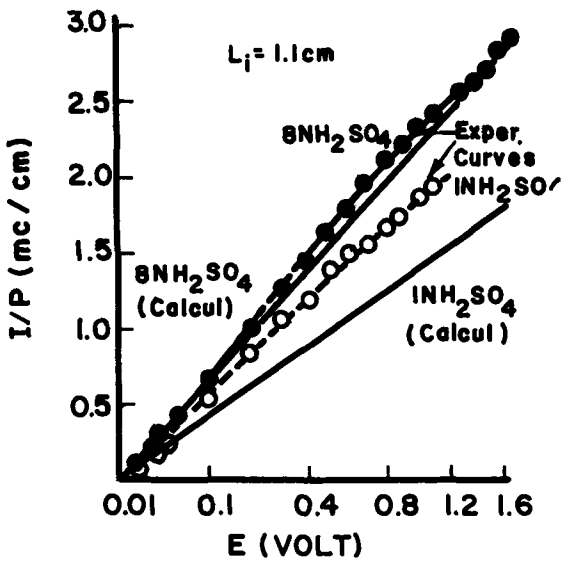

Fig. 3. Total current vs. applied potential [data of F. G. Will, ref. (1)].

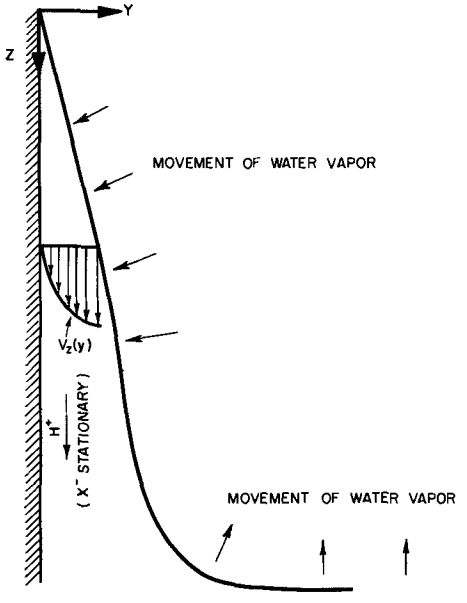

Fig. 4. Convection in film by vapor recirculation mechanism

fusivity of dissolved hydrogen, for example, is not accurately known. However, it may also be a result of concentration polarization superimposed on convection since 8*N* is very nearly the concentration of maximum sulfuric acid conductivity.

At higher applied voltages experimental currents for 1*N* acid are about 1/3 higher than those predicted, and, as previously stated by Will, this is an indication of concentration polarization. The magnitude of this effect is, however, far lower than can be explained by the above analysis for a 1-1 electrolyte with negligible convection. It would appear then, either that convection is important here, or that the effect of concentration polarization is markedly reduced, either by the partial dissociation of the acid, or by kinetic limitations. It is the opinion of the author that convection is important, but the complexities of sulfuric acid dissociation make a convincing analysis impossible at present. For 8*N* acid there is almost complete agreement with the assumption of convection dominance, but once again caution is indicated. At this rather high acid concentration diffusional interaction between the ions and between these and the undissociated acid must also be considered. This is impossible at present, and it is clear that sulfuric acid is too complex an electrolyte to permit meaningful interpretation of experimental results.

In summary then it appears reasonable to agree with Will that concentration polarization plays only a minor role in these experiments, but this is by no means certain.

It is also important to note that Will found strong indirect evidence of a liquid film, approximately 1μ in thickness, above the equilibrium meniscus, and that an appreciable fraction of the hydrogen oxidation took place in this super-meniscus region. The existence of such films has since been demonstrated experimentally by Muller (5, 6), using interferometric techniques, during reduction of oxygen on nickel cathodes partially immersed in aqueous sodium hydroxide. Muller found his films to be stable during the passage of the current, and that they increased in thickness with current density. The existence of such a film during this reaction was later used by Bennion and Tobias (2, 3) in their analysis of electrode behavior.

To date no convincing explanation for stable supermeniscus films with thickness of the order of microns has been offered for equilibrium conditions, *i.e.*, in the absence of a current. Their presence requires an appreciable charge density in the bulk of liquid in the film, or other equivalent repulsive force. Such forces have been observed, for example, in soap films (7), but it is easily shown (8) that they are not large enough to stabilize 1μ films under conditions being considered here.

Such films can be explained qualitatively in the presence of a current by water-condensation and gravitational flow, as explained above for hydrogen oxidation in an acid electrolyte. This is also true for oxygen reduction in a basic reaction, in spite of water consumption in the electrochemical reaction, and for the same reasons. It remains to determine if such an explanation is quantitatively appealing. This is the purpose of the next section.

Tentative Analysis of Convection

From the above analysis and the experimental observations of Will (1) and of Muller (5, 6) substantial fluid motion in the film-meniscus system appears quite possible. There are at least three possible causes of such motion, each basically dependent on the concentration polarization which must accompany a direct electrolyte current. These are: (*a*) surface-tension gradients, which must be considered in combination with density gradients; (*b*) natural convection; and (*c*) recirculation of water through the gas phase driven by differences in equilibrium water vapor pressure.

All of these should be considered, and it is planned ultimately to do so, but only the third is treated here. This is in part because it produces the simplest and most believable type of fluid motion, closely analogous to the classic Nusselt condensed-steam film. Natural convection or surface-tension driven flows, on the other hand, require both rising and descending currents in the same thin film.

The goal of the following analysis is then a simple and restricted one: to determine whether the falling film required to immobilize anions at an acid hydrogen anode has characteristics consistent with our knowledge of electrode reactions in film-meniscus systems. The acid hydrogen anode is used not only because it is the best understood, but also because convection is downward. Thus, a first approximate description can be attempted without detailed knowledge of surface forces. The procedure then will be first to relate film thickness to the mass average velocity in the film and then to relate this velocity to the total current.

Since the film will be thin and the Reynolds number of the flow in it extremely small the integrated equation of motion may be written down directly in the form

$$v = \rho g \delta^2 / 3\mu \quad [26]$$

where v is the flow-average value of the mass-average velocity in the axial direction. Next Eq. [3] is rewritten in the form

$$I = P \delta c_{H+} v_{H+} \quad [27]$$

where v_{H+} is the flow-average velocity of the hydrogen ion. Next the velocity of water in the film is related to that of hydrogen through combination of Eq. [8], [9], and [27].

$$v^* = x_{H+} v_{H+} + x_w v_w = v_{H+} \Big/ \left[1 + \frac{\mathcal{D}_{H+m}}{\mathcal{D}_{X-m}} \right] \quad [28]$$

where v^* is again a flow-average value. Note that to write Eq. [28] in flow-average terms it is necessary to neglect changes in species velocity ratios across the film. Since $x_w = 1 - 2x_{H+}$ it follows that

$$v_w = v_{H+} \left[\frac{1 - \left(1 + \dfrac{\mathcal{D}_{H+m}}{\mathcal{D}_{x-m}} \right) x_{H+}}{(1 - 2x_{H+}) \left(1 + \dfrac{\mathcal{D}_{H+m}}{\mathcal{D}_{x-m}} \right)} \right] \quad [29]$$

and, therefore, that the mass-average velocity

$$v = w_{H+} v_{H+} + w_w v_w = A v_{H+} \quad [30]$$

with

$$A = w_{H+} + w_w \left[\frac{1 - \left(1 + \dfrac{\mathcal{D}_{H+m}}{\mathcal{D}_{x-m}} \right) x_{H+}}{(1 - 2x_{H+}) \left(1 + \dfrac{\mathcal{D}_{H+m}}{\mathcal{D}_{x-m}} \right)} \right] \quad [31]$$

Equations [27] and [31] may now be combined to yield

$$I = P \delta c_{H+} v / A \quad [32]$$

or, introducing Eq. [26]

$$I = \frac{F P \rho g c_{H+} \delta^3}{3\mu A}; \quad H = \left(\frac{\rho g \delta^3}{6\mu A \mathcal{D}_{H2m}} \frac{c_{H+\infty}}{c_{H_2}^{\circ}} \right) \quad [33\text{-a, b}]$$

Then, within the limits of this development, film thickness is simply related to local current in a way strongly reminiscent of the Nusselt condensate films. This expression is, however, only useful in the upper region of the meniscus, and there only if the calculated δ is much greater than the film thickness in absence of a current. It is not applicable at all to systems in which ion flow is upward. With all these limitations, however, Eq. [33] does permit an estimate of the contribution of convection to film thickness.

Consider then as an illustrative example the following hypothetical, but reasonable, conditions

$$I/P = 0.05 \text{ ma/cm}$$
$$c_{H+} = 10^{-3} \text{ eqts/cm}^3$$
$$\mu/\rho = 10^{-2} \text{ cm}^2/\text{sec}$$
$$\mathcal{D}_{H+m}/\mathcal{D}_{x-m} = 4.5$$

Then

$$A \doteq 0.001 + 0.999 \left[\frac{1 - \dfrac{(1 + 4.5)}{55}}{\left(1 - \dfrac{2}{55} \right)(1 + 4.5)} \right] \quad [34]$$

$$= 0.17$$

$$\delta = \left[\frac{(0.17) \left(5 \times 10^{-5} \dfrac{\text{coulombs}}{\text{sec cm}} \right) (3) \left(10^{-2} \dfrac{\text{cm}^2}{\text{sec}} \right)}{\left(980 \dfrac{\text{cm}}{\text{sec}^2} \right) \left(9.65 \times 10^4 \dfrac{\text{coulombs}}{\text{equivalent}} \right) \left(10^{-3} \dfrac{\text{eqts}}{\text{cm}^3} \right)} \right]^{1/3} = 1.4\mu \quad [35]$$

This corresponds remarkably well with the estimated thickness of 1.5μ suggested by Will for very similar conditions but a somewhat different physical model. While this degree of agreement must be considered coincidental, it is nevertheless encouraging.

Film height can also be determined readily. For the low current of the above numerical example acceptable results may be obtained quite readily. Here

$$H \doteq \sqrt{\epsilon}\, \psi \quad [36]$$

and

$$\frac{dH}{d\zeta} = \delta \frac{dH}{dz} \doteq 2\psi$$

$$\doteq 2H/\sqrt{\epsilon} \quad [37]$$

Combining this result with Eq. [33] yields the desired relation for film shape

$$\frac{d\delta}{dz} = \frac{2}{3\sqrt{\epsilon}} \quad [38]$$

Then $L/\delta = 3/2\sqrt{\epsilon}$ where L is distance from top of film to level at which thickness is δ. For sulfuric acid at 25°C

$$F/RT = 39.0 \text{ volt}^{-1}$$

$$c_{H_2}^{\circ} = 7.67 \times 10^{-7} \frac{\text{moles}}{\text{cm}^3} \; (1N \; H_2SO_4); \quad 7.17 \times 10^{-7} \; (8N)$$

$$\mathcal{D}_{H2m} = 3.1 \times 10^{-5} \frac{\text{cm}^2}{\text{sec}} \; (1N); \quad 2.2 \times 10^{-5} \; (8N)$$

$$K = 0.215 \text{ mhos/cm } (1N); \quad 0.826 \; (8N)$$

Then for these conditions $\epsilon = 2.40 \times 10^3$ and $(L/\delta) = 73.5$ ($1N$ H_2SO_4) or 118 ($8N$ H_2SO_4).

By way of contrast, Will found the electrochemically active region to extend about 100 to 200 film thickness above the visible meniscus. In view of the uncertainties, both in analysis and experiment, these predictions are in reasonable agreement with Will's data.

The only experimental evidence of meniscus thickening to date appears to be that of Muller for reduction of oxygen on a nickel tube in 3.5N KOH. Film thickness was found to increase with current density for this system, for example, thickening from about 0.3 to about 0.5μ at 15 mm above bulk liquid level, when the current was raised from 0.0047 to 0.047 ma/cm. This thickening was ascribed to electrocapillary effects, but without proof. It is not possible at present to say more than that this degree of thickening is of the order predicted by the above convective development. It is also important to note that Muller's films were thinner at higher elevations, and, in fact, that available data as reported in ref. (3) indicate the triangular cross section predicted by Eq. [38].

In summary then, both the thickness and height of the falling film required to immobilize the anions are consistent with experimental observation. In fact, the agreement between prediction and experiment is much better than would be expected in view of the many approximations made in this development. It would be unwise to neglect other mechanisms of diffusional stabilization or other sources of thin liquid films on the metal electrode surface. It is also too early to speculate on the specific effects of geometry and orienation on electrode performance.

Nevertheless, two facts seem to be demonstrated by this analysis:

1. Superficial treatment of the current-carrying diffusional and convective processes in meniscus-film systems preclude thorough understanding of electrode performance.
2. Convective processes are likely to prove important in many practical situations.

Failure to consider these points would make full practical utilization of Dr. Will's outstanding work on thin films very unlikely.

Manuscript received Jan. 7, 1965; revised manuscript received Jan. 8, 1966.

Any discussion of this paper will appear in a Discussion Section to be published in the December 1966 JOURNAL.

REFERENCES

1. F. G. Will, *This Journal*, **110**, 152 (1963).
2. D. N. Bennion and C. W. Tobias, Paper presented at the Washington, D. C. Meeting of the Society, October 1964
3. D. N. Bennion, "Phenomena at a Gas-Electrode-Electrolyte Interface," Ph.D. Thesis, Dept. of Chemical Engineering, University of California, Berkeley, California, June 1, 1964.
4. E. A. Grens, R. M. Turner, and T. Katan, *Advanced Energy Conversion*, **4**, 109 (1964).
5. R. H. Muller, Paper presented at the Toronto Meeting of the Society, May 1964.
6. R. H. Muller, Paper presented at the Washington Meeting of the Society, October 1964.
7. J. T. Davies and E. K. Rideal, "Interfacial Phenomena," Academic Press, New York (1961).
8. V. H. Ludviksson and E. N. Lightfoot, Unpublished calculations.

NOMENCLATURE

$$A = w_{H+} + w_w \left[\frac{1 - \left(1 + \frac{\mathcal{D}_{H+m}}{\mathcal{D}_{x-m}}\right) x_{H+}}{(1 - 2x_{H+})\left(1 + \frac{\mathcal{D}_{H+m}}{\mathcal{D}_{x-m}}\right)} \right]$$

c	total molar concentration
c_i	molar concentration of species i
$\mathcal{D}_{im}$	effective binary diffusivity of species i
E_o	standard electrode potential = 96,500 coulombs/equivalent, Faraday's constant
g	980 cm/sec^2, gravitational acceleration
H	$I/2PFc_{H_2}{}^{o}\mathcal{D}_{H2m}$, dimensionless (axial) current
I	(axial) current, amp
K	specific conductivity, mhos/cm
L	(total) film length
N_i	molar flux of species i relative to stationary coordinates, moles/area, time
P	electrode perimeter, normal to electrolytic current flow
R	international gas constant
T	absolute temperature
v	axial mass-average velocity, flow average value for film
v^*	(axial) molar average velocity, flow average for film
v_i	(axial) species velocity, flow average for film
x_i	mole fraction of species i
z	axial distance
α	dimensionless factor defined by Eq. [11]-[13]
β	dimensionless factor defined by Eq. [15]-[17]
γ	dimensionless factor defined by Eq. [15], [18], [19]
δ	film thickness in direction of dissolved hydrogen diffusion
ϵ	$= \kappa_x/c_{H_2}{}^{o}\mathcal{D}_{H2m}F$ (dimensionless)
ζ	$= z/\delta$
η	overvoltage
κ	$= KRT/F$
μ	viscosity
ρ	density
ϕ	electrostatic potential, volts
Ψ	$= \phi F/RT$, dimensionless potential
ψ	$= (\phi^o - \phi)F/RT$, dimensionless local applied potential relative to top of film
w_i	mass fraction of species i

Superscript

o	conditions at top of film

Subscripts

e	conditions for which $c_{H+} = (c_{H+})_\infty$ and $c_{H_2}(o,z) = c_{H_2}{}^{o}$
w	water
H^+	hydrogen ion
x^-	(unspecified) anion
∞	conditions at lower end of film-meniscus system

Technical Notes

Studies on the Oxygen Gradients in Oxidizing Metals

IV. Kinetics of the Oxidation of Hafnium at High Temperatures

J. P. Pemsler

Ledgemont Laboratory, Kennecott Copper Corporation, Lexington, Massachusetts

Like zirconium, hafnium dissolves significant quantities of oxygen during oxidation so that a metal zone rich in oxygen forms beneath the oxide layer. In a previous paper the author has shown that the oxygen gradient beneath the oxide film may be calculated with an appropriate diffusion equation and that the experimentally determined gradient is in good agreement with the theoretical expression (1). In addition, it was found that a remarkable anisotropy of the oxidation film growth occurred which persisted to the thick film region and that the effect was associated with a variation in the stoichiometry of the oxide film covering differently oriented grains (1). In previous studies of zirconium it has been shown that, while the oxygen solution obeys diffusion kinetics and remains parabolic for sufficiently thick samples, film growth does not obey normal rate laws (2).

It is the purpose of this paper to attempt to separate quantitatively the film growth and oxygen dissolution processes and to attempt to gain insight into the film growth mechanism.

Experimental

Hafnium in the form of ¾-in. rod was obtained from the Carborundum Metals Climax Company. The vendor's analysis lists Zr as 2.5 w/o and the following in ppm: Al < 80, Cu < 40, Nb < 50, Ta < 100, Ti < 20, Fe-475, and N-33. The purity of the oxygen used has been reported previously (3). Experimental details concerning the preparation of spherical sam-

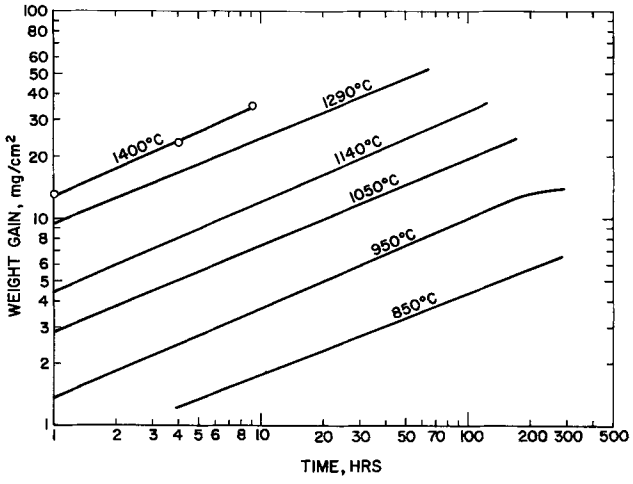

Fig. 1. Total weight gain of hafnium oxidized between 850° and 1400°C.

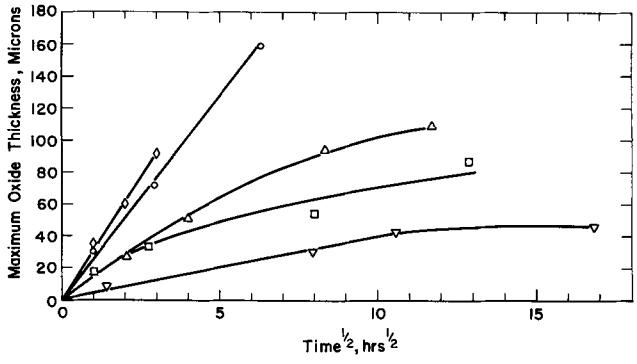

Fig. 2. Maximum oxide film thickness on oxidized hafnium. ○, 1293°C; △, 1140°C; □, 1050°C; ▽, 950°C; ◇, 1400°C.

ples, oxidation, and weight gain and film thickness measurements are similar to those used for zirconium (3).

Results

Total weight gain.—Data for the total weight gain between 850° and 1400°C are given in Fig. 1 in the form of a logarithmic plot. With the exception of the data at 1400°C where the separate data points are indicated, the results were obtained as a continuous weight gain record. The slopes of the log-log plots are about 0.42 and indicate a kinetic behavior between cubic and parabolic. Since the total weight gain is the sum of the film growth and oxygen solution and the latter two do not conform to the same kinetic behavior, no mechanistic interpretation of the total weight gain data can be made at this time.

Film thickness.—Examination of cross sections of the oxidized spheres indicate that at all times and temperatures there is a high degree of irregularity of the film thickness. This may be presumed to be associated with the high degree of anisotropy of oxide film formation on hafnium (1). In order to present the data it was found desirable to plot maximum, minimum, and average thicknesses of the film, and a parabolic plot of these data is shown in Fig. 2, 3, and 4. Data at the lowest temperature may be approximated as parabolic. At the intermediate temperatures the film growth is characterized by a continuously decreasing rate of higher power than parabolic. At the highest temperatures the film growth rate may again be approximated as parabolic.

During film formation grain growth occurs in the metal and becomes pronounced at high temperatures and long times. Oxygen in high concentration retards grain growth so that metal grains within the oxygen gradient may be smaller than those beyond the depth

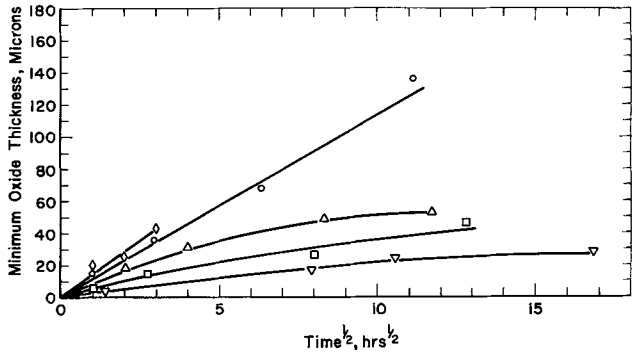

Fig. 3. Minimum oxide film thickness on oxidized hafnium. Symbols are the same as in Fig. 2.

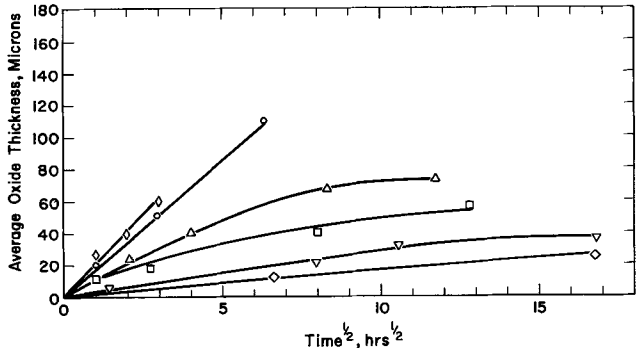

Fig. 4. Average oxide film thickness on oxidized hafnium. ○, 1293°C; △, 1140°C; □, 1050°C; ◇, 850°C; ▽, 950°C; ◇, 1400°C.

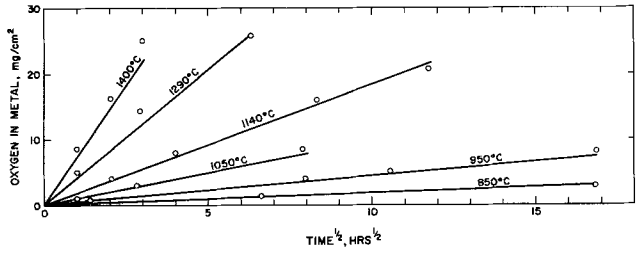

Fig. 5. Oxygen in solution in oxidized hafnium

of appreciable oxygen penetration. Since grain growth is apt to result in a preferred orientation, it is likely that grain growth coupled with the anisotropy of film formation might alter the film growth process. Thus, at the lowest temperatures grain growth is sufficiently slow so that the orientation of the different oxidizing grains is roughly constant. At intermediate temperatures grain growth becomes more pronounced, and the degree of preferred orientation is consequently altered, thereby altering the film growth. At the highest temperatures grain growth is exceedingly rapid, and the retarding effect of the oxygen gradient is absent, so that after a short time the characteristic grains develop which will be present for the remainder of the oxidation.

Oxygen in the metal.—A knowledge of the total weight gain and the measurement of the oxide film thickness enables computation of the quantity of oxygen dissolved in the metal substrate beneath the oxide film. Furthermore, the latter quantity can be calculated by equations previously given (3). Calculated and experimental data for oxygen dissolved in the metal are plotted as a function of a square root of time in Fig. 5. Here, the solid line represents calculated values, and the separate experimental points are indicated in the figure. Good agreement exists between calculated and observed oxygen content of

the metal and the data are parabolic as demanded by diffusion theory.

Discussion

During an investigation of the high-temperature oxidation of zirconium, it was postulated that there exists easy diffusion paths through the oxide which are not interconnected laterally (2). An hypothesis was also presented for the stabilization of the high-temperature tetragonal phase of zirconia at temperatures far below the normal transformation temperature and of different transport rates through the monoclinic and tetragonal oxides. It is possible that similar situations exist during the oxidation of hafnium. In order to understand the mechanism of film formation on hafnium, it is desirable to determine the contribution of nonlattice diffusion and tetragonal oxide to the film growth process. It is also necessary to determine the kinetics of film formation on single crystal material of well-defined orientations. This should give insight into the mechanism causing the pronounced anisotropy of film growth and yield meaningful film growth rates which are not affected by grain growth in the sample. The aforementioned investigations are being pursued in this laboratory.

Acknowledgment

It is a pleasure to acknowledge the valuable assistance and suggestions of J. K. Litchfield.

Manuscript received Dec. 2, 1965.

Any discussion of this paper will appear in a Discussion Section to be published in the December 1966 JOURNAL.

REFERENCES

1. J. P. Pemsler, *This Journal*, **111**, 1339 (1964).
2. J. P. Pemsler, *Electrochem. Technol.*, **4**, 128 (1966).
3. J. P. Pemsler, *This Journal* **112**, 477 (1965).

A Chemical Polish for Tin Telluride

Marriner K. Norr

United States Naval Ordnance Laboratory, White Oak, Silver Spring, Maryland

Until now there has been only one satisfactory method for chemically polishing SnTe (1, 2). It has had the disadvantage of frequently leaving a whitish haze (and sometimes dark stains) on the samples when they were polished for a long enough time (3-5 min) to remove the scratches formed by previous mechanical polishing (2).

This note describes a method of chemically polishing SnTe that gives a clean, somewhat flatter surface than (1, 2).

Procedure

The sample is mounted in a stainless steel jig assembly and ground flat on No. 600 grit SiC paper. It is then transferred to a polycarbonate jig assembly (to which it is attached with paraffin) and polished with Carborundum No. 50 grit Al_2O_3 optical finishing powder on a paraffin lap. Finally, it is polished with Linde A abrasive on a paraffin lap. Each of the abrasives is lubricated with a 1:1 solution of Joy detergent in ethanol. The sample, jig assembly, and hands should be thoroughly cleaned after each step of grinding and polishing.

The solution for chemical polishing is prepared by dissolving 0.35g I_2 in 40 ml ethanol (or methanol) and then adding 10 ml dist. H_2O and 4.0 ml 49% HF. A polyethylene beaker is used to avoid contamination from the container.

A piece of twill jean cloth[1] is stretched over a smooth Teflon plate and saturated with the solution at 25°C. It is recommended that the hands be protected from the solution with polyethylene gloves. The sample (still mounted in the polycarbonate jig assembly) is polished by lightly rubbing it over the wet twill jean cloth, using a figure eight motion, for 15-20 min. Periodically, additional solution must be added to keep the cloth saturated. The sample is then rinsed in a stream of methanol, followed by a stream of distilled water, and dried on lens paper. After demounting, it is soaked 2-3 times in fresh benzene to remove any adhering paraffin and dried on lens paper.

The SnTe crystals used in this work were grown by the Czochralski method. The polish produced a mirrorlike surface which has been used successfully for reflectivity measurements (3). Back-reflection Laue photographs, diffractometer measurements, and a Kossel photograph indicated that the surface was free of major strains.

[1] K. S. 2423 twill jean cloth, Exeter Manufacturing Company, Inc., Exeter, New Hampshire.

Acknowledgments

The author is indebted to Dr. Bland Houston for supplying the SnTe crystals and for helpful advice, to John V. Gilfrich for taking the Laue photographs and diffractometer measurements, and to Harvey Yakowitz for taking the Kossel photograph. The use of a cloth saturated with a chemical polishing solution was suggested to the author by a publication of Schmidt (4).

Manuscript received Feb. 28, 1966.

Any discussion of this paper will appear in a Discussion Section to be published in the December 1966 JOURNAL.

REFERENCES

1. J. W. Faust, Jr., and A. Sagar, Private communication through C. R. Martin.
2. M. K. Norr, "Polishes and Etches for Tin Telluride, Lead Sulfide, Lead Selenide, and Lead Telluride," NOLTR 63-156, U. S. Naval Ordnance Laboratory, White Oak, Maryland (1963).
3. R. F. Bis, *Solid State Commun.*, **2**, 161 (1964).
4. P. H. Schmidt, *This Journal*, **109**, 879 (1962).

Segregation Coefficients of Some Rare Earth Niobates in $SrMoO_4$

L. H. Brixner

Pigments Department, Experimental Station

E. I. du Pont de Nemours & Company, Incorporated, Wilmington, Delaware

The original laser experiments employing scheelite-type hosts were carried out with $CaWO_4$ (1). Other scheelites such as $SrMoO_4$ (2, 3), $CaMoO_4$ (4, 5), $PbMoO_4$ (4), and $SrWO_4$ (2) also have been used as host materials for lasers employing rare earth ions. Because low thresholds and ease of excitation, rods containing Nd^{+3} have been studied most intensively. However, rods containing other infrared emitting rare

Table I. Segregation coefficients for some $LnNbO_4$-type niobates in $SrMoO_4$

	% Deviation from Sr^{+2}	% Deviation from Ca^{+2}	Crystal color	k	c_s/c_n	Ln_2O_3: Nb_2O_5
Sc^{+3}	−27.7	−18.2	—	—	—	—
Y^{+3}	−17.8	−7.1	Colorless*	0.67	0.60	1:1.17 (T)
						1:1.05 (B)
La^{+3}	+1.8	+15.2	Colorless	1.04	1.01	1:0.91
						1:0.90
Ce^{+3}	−4.5	+8.1	Yellow	0.91	0.90	1:1.00
						1:0.97
Pr^{+3}	−5.3	+7.1	Green	0.96	0.97	1:0.95
						1:0.94
Nd^{+3}	−7.1	+5.1	Blue	0.93	0.95	1:0.90
						1:0.89
Sm^{+3}	−10.7	−1.0	Amber	0.88	0.83	1:1.07
						1:1.06
Eu^{+3}	−12.5	−1.0	Deep Red	0.93	0.89	1:0.88
						1:0.85
Gd^{+3}	−13.4	−2.0	Colorless	0.79	0.76	1:1.01
						1:0.99
Tb^{+3}	−16.9	−6.1	Colorless*	0.71	0.70	1:1.06
						1:1.05
Dy^{+3}	−17.8	−7.1	Light Yellow*	0.66	0.63	1:1.12
						1:1.04
Ho^{+3}	−18.7	−8.1	Light Brown*	0.62	0.59	1:1.00
						1:0.99
Er^{+3}	−20.5	−10.0	Pink*	0.48	0.50	1:1.11
						1:1.04
Tm^{+3}	−22.3	−12.1	—	—	—	—
Yb^{+3}	−23.2	−13.1	—	—	—	—
Lu^{+3}	−24.1	−14.1	—	—	—	—

* These crystals cracked on cooling.

earth ions such as Ho^{+3} and Tm^{+3} (4) also have been studied. The above papers describe mostly laser experiments; there have been few comprehensive studies of all rare earths in a given host with details on preparative and analytical procedures, as for instance in (5) and (6). Even here, no attempts have been made to correlate the observed segregation (or distribution) coefficients with the structural fit of the rare earth into the cation site of a scheelite.

In this note, we should like to point out some relationships between the ionic radii and the segregation coefficients for the $LnNbO_4$-type rare earth niobates in $SrMoO_4$. All single crystals were grown by the Czochralski technique as previously described (5). Conditions were maintained as uniform as possible with respect to pulling speed, rotation, shape, and weight of crystal. The starting mixture of all compositions was prepared according to the following stoichiometry:

$$0.99SrMoO_4 + 0.005Ln_2O_3 + 0.005Nb_2O_5 \rightarrow Sr_{0.99}Ln_{0.01}Mo_{0.99}Nb_{0.01}O_4,$$

where Ln = Y^{+3}, La^{+3}, Ce^{+3}, Pr^{+3}, Nd^{+3}, Sm^{+3}, Eu^{+3}, Gd^{+3}, Tb^{+3}, Dy^{+3}, Ho^{+3}, and Er^{+3}. This resulted in an activator concentration of 1% in the melt for all rare earth niobates, and it should be remembered at this point that k can also be a function of the concentration of the dopant.

Analysis and computation of k was done as described in (5). Table I summarizes the results. Crystals with Sc^{+3}, Tm^{+3}, Yb^{+3}, and Lu^{+3} were not grown, and the ionic radii deviations are merely included for completeness. For the purpose of a comparison we have also given the ionic radii deviation for Ca^{+2}. The most striking result is the fact that the segregation coefficient varies directly with the deviation of the rare earth ion size from that of Sr^{+2} as is evident in Fig. 1.

In the case of the examples marked with an asterisk no crack-free crystal could be grown on repeated attempts. It is particularly interesting to note that this transition from sound to cracked crystals occurred for a cation size difference of around 15%, the amount of deviation generally accepted as the limit of isomorphous substitution. That this is observable in single crystals at such low concentration is interesting; in the case of Y, six crystals grown from the melt cracked while being cooled to room temperature,

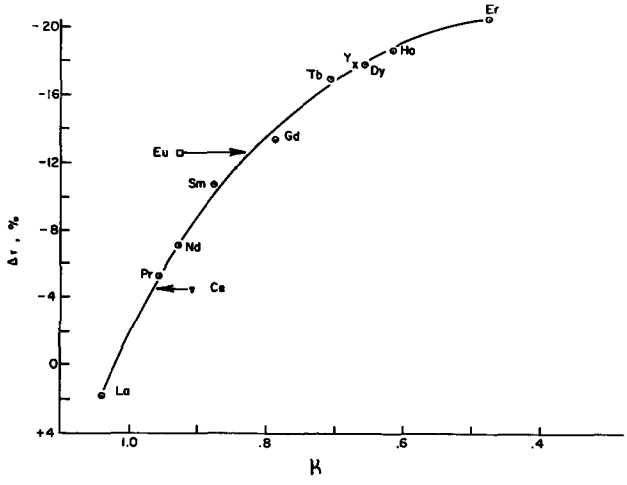

Fig. 1. Segregation coefficient k for $LnNbO_4$ in $SrMoO_4$ as a function of differential ionic radii ($r_{Ln+3} - r_{Sr+2}$).

indicating that true single crystalline solid solution are only stable at high temperature. There are two exceptions to the normal relationship, Ce^{+3} and Eu^{+3}; k for Ce seems too small and k for Eu^{+3}, too big. In the first case, we can only postulate that perhaps a small amount of Ce^{+4} causes this deviation as indicated by the intense yellow color, whereas in the Eu case we know that some Eu^{+2} enters the crystal, which has a deep red color. The better structural fit of Eu^{+2} in the Sr^{+2} site would account for the segregation coefficient nearer to unity. It is interesting to note that, contrary to the $CaMoO_4/EuNbO_4$ case, it was impossible to oxidize Eu^{+2} in $SrMoO_4$. After 100 hr under pure oxygen at 1400°C, the crystal was still deep red. A similar observation was made for $CaWO_4/Eu$ (6).

The column marked c_s/c_n gives the ratio of the concentration in the top of the crystal to the nominally charged concentration and in each case comes very close to k determined from analyses of top and bottom of the crystal. In the last column are the ratios of rare earth oxide to niobium pentoxide in top (T) and bottom (B) of crystal. Since the stoichiometric deviation is generally very small, it appears justified to treat the rare earth niobate in its entirety as we did for all computations. The general tendency is for this ratio to become smaller as the crystal grows, indicating somewhat stronger segregation of Nb_2O_5, but the change is certainly in no proportion to the change experienced by k itself. With the exception of Eu and Ce, a straightforward relationship between segregation coefficients and ionic radii has been established which permits the prediction of distribution coefficients from knowledge of the deviation of the substituted ion's size from that of the host ion. Failure to grow sound crystals with rare earths deviating more than 15% in size from that of Sr^{+2} indicates that these cannot be incorporated into the single crystalline $SrMoO_4$ lattice, at least not at this concentration and at room temperature. Compared to $SrMoO_4$, $CaMoO_4$ should be the better host for Nd^{+3}, although ultimately an appropriate solid solution of the two host compositions may be the best material, with essentially no segregation of the active constituent. This should also be possible for Ce and Pr, where the deviation of ionic radii in $CaMoO_4$ is opposite to the one in $SrMoO_4$.

Manuscript received Feb. 8, 1966.

Any discussion of this paper will appear in a Discussion Section to be published in the December 1966 JOURNAL.

REFERENCES

1. L. F. Johnson and K. Nassau, *Proc. IRE*, **49**, 1704 (1961).

2. L. F. Johnson and R. R. Soden, *J. Appl. Phys.*, **33**, 757 (1962).
3. P. A. Flournoy and L. H. Brixner, *This Journal*, **112**, 779 (1965).
4. L. F. Johnson, *J. Appl. Phys.*, **34**, 897 (1963).
5. L. H. Brixner, *This Journal*, **111**, 690 (1964).
6. K. Nassau and A. M. Broyer, *J. Appl. Phys.*, **33**, 3064 (1962).

Solubilities of Some II-VI Compounds in Bismuth

M. Rubenstein

Research Laboratories, Westinghouse Electric Corporation, Pittsburgh, Pennsylvania

Attention was first focussed on some of the larger band gap II-VI compounds, *i.e.*, ZnS, CdS, ZnSe, and CdSe, because of the interest in various optical properties such as luminescence. Much effort was and is still being expended to prepare powders of such materials in doped and undoped states. More recently other II-VI compounds (ZnTe and CdTe) have been studied because of possible uses in electroluminescence and in solar battery materials.

Since more attention is now being centered on trying to understand the observed phenomena exhibited by these materials and since some of the devices cannot utilize powders, there has been a greater effort in preparing single crystals in pure and doped states. Such single crystals have been grown from a vapor state and from a melt state. It is also possible to grow these II-VI compounds from a solution having an excess amount of the II or VI element, *i.e.*, one can grow single crystals of ZnTe by cooling a solution in which the initial charge is ZnTe and an excess of zinc. In order to grow such crystals a knowledge of the phase diagrams is of importance. Liquidus phase diagrams of ZnSe (1), ZnTe (2), CdS (3), CdSe (4, 5), and CdTe (6, 7) are already in the literature.

Solution growth must involve a solute and a solvent. A solution of a II-VI compound as the solute and the II element as the solvent has just been mentioned. ZnTe can also be grown by cooling a solution in which the initial charge is ZnTe and an excess of tellurium. One may also use solvents other than one of the constituent elements. For example, although GaP and GaAs crystals may be grown from solutions of gallium, they can also be grown from lead, bismuth, tin, indium, selenium, tellurium, and germanium (8, 9). BP can be grown from a solution of BP dissolved in nickel (10).

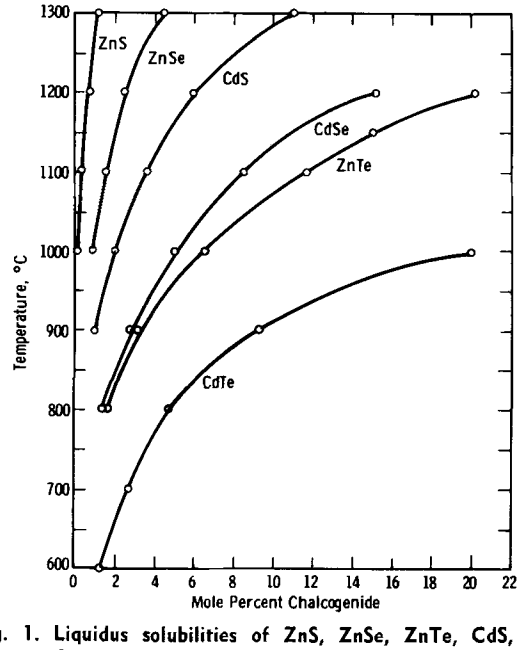

Fig. 1. Liquidus solubilities of ZnS, ZnSe, ZnTe, CdS, CdSe, CdTe as a function of temperature.

Data presented in this paper concern the liquidus solubilities of solutes ZnS, ZnSe, ZnTe, CdS, CdSe, and CdTe in a bismuth solvent.

The method used to obtain this data is the high-temperature filtration technique previously described (8). Temperature measurements were made using Pt-Pt 10% Rh thermocouples calibrated with the melting point of gold.

The bismuth used as the solvent was 99.999+% from ASARCO. The ZnS was RCA 33-Z-19 fired in H_2S at 1100°C, pressed into pellets, and fired in an evacuated tube (sealed off at a pressure less than 10^{-5} Torr) at 1100°-1200°C for 16 hr. The ZnSe was G.E. 118-8-3 purified by repeated sublimations in argon at 1300°C followed by a vapor transport (11) to produce either single crystals or masses with, at most, several crystals. The ZnTe was prepared from heating 99.999+% zinc and tellurium in argon to 500°C, and then the temperature was allowed to rise to 800°C. This material was heated in hydrogen at 600°C to remove excess tellurium. Single crystals were prepared using a vapor transport method (11). CdS was G.E. 118-8-2 material which was fired in H_2S at 1000°C followed by a vapor transport technique (11) to produce a sound mass of CdS. CdSe was prepared by sealing G.E. 118-8-4 material in a quartz tube at a pressure of less than 10^{-5} Torr and heating for several days at 950°C. The sintered material was removed from the tube and resealed at the same pressure and reheated for several days at 950°C. This yielded a hard sintered CdSe. The CdTe was prepared by heating 99.999+% cadmium and tellurium from ASARCO, sealed in a graphitized quartz ampule at a pressure less than 10^{-5} Torr, slowly to 1135°C and then slowly cooling this melt. Large single crystals were often prepared in this manner.

The mixtures of chalcogenide and bismuth were sealed in quartz tubes, maintained at temperature for 16 hr (the 1300°C experiments were maintained at temperature for 6 hr), filtered, and cooled. The filtrates and residues were separately weighed to the nearest 0.1 mg and treated with an excess of mercury at 150°C to remove the bismuth. The mercury-bismuth liquid solution was sucked off at 150°C using a small diameter tube, and finally small amounts of mercury were removed by heating the chalcogenide samples under vacuum. The chalcogenide samples were then separately weighed to the nearest 0.1 mg. Solubility measurements had a precision and accuracy of better than ±0.1 mole per cent for measurements in excess of 3 mole per cent chalcogenide and better than ±0.05 mole per cent for measurements less than 3 mole per cent chalcogenide.

The data obtained using this high-temperature filtration technique are shown in Fig. 1. It can easily be demonstrated, for the six chalcogenides, that solubility decreases as the molecular weight of the solute decreases and that solubility decreases as the sum of the tetrahedral covalent radii ($R^{II} + R^{VI}$) decreases. Needles of ZnS and platelets of the other five compounds were obtained from the filtrates.

Acknowledgments

The author would like to thank Dr. Willi Lehmann for preparing the samples of CdS, ZnSe, and ZnTe used in this paper. Also, thanks are extended to John

Burger for his assistance in the experimental phase of this work.

Manuscript received Feb. 15, 1966.

Any discussion of this paper will appear in a Discussion Section to be published in the December 1966 JOURNAL.

REFERENCES

1. A. G. Fischer, AFCRL-65-524, May 31, 1965, p. 16.
2. J. Carides and A. G. Fischer, *Solid State Communications*, **2**, 217 (1964).
3. H. H. Woodbury, *J. Phys. Chem. Solids*, **24**, 88 (1963).
4. M. Chikashige and R. Hitosaka, *Mem. Coll. Sci., Univ. Kyoto*, **2**, 239 (1917).
5. A. Reisman, M. Berkenblit, and M. Witzen, *J. Phys. Chem.*, **66**, 2210 (1962).
6. D. DeNobel, *Philips Research Repts.*, **14**, 488 (1959).
7. M. R. Lorenz, *J. Phys. Cehm. Solids*, **23**, 939 (1962).
8. M. Rubenstein, Extended Abstracts of the Electronics Div., **11**, 129, The Electrochemical Society Los Angeles Meeting, May 6-10, 1962.
9. M. Rubenstein, Extended Abstracts of the Electronics Div., **13**, 240, The Electrochemical Society Toronto Meeting, May 3-7, 1964.
10. B. Stone and D. Hill, *Phys. Rev. Letters*, **4**, 282 (1960).
11. W. W. Piper and S. J. Polich, *J. Appl. Phys.*, **32**, 1278 (1961).

Reaction Rates on Partially Blocked Rotating Disks–Effect of Chemical Kinetic Limitations

Daniel E. Rosner

AeroChem Research Laboratories, Inc., Subsidiary of Ritter Pfaudler Corporation, Princeton, New Jersey

Gregory and Riddiford (1) noticed that a chemically inert center stud failed to appreciably alter the rate of dissolution of a zinc disk rotating in iodine solutions, despite the fact that the inert area comprised some 4% of the working surface of the disk. Pursuing this further, these authors reported data (2) on the effect of progressively blocking off the center of rotating copper disks in H_2SO_4 solutions. In a discussion of this work, Ibl (3) correctly pointed out that, if the reaction on the unblocked disk was completely diffusion controlled, then the relation between the fractional reduction in reaction rate, J/J_0, and the fractional area blockage, $f \equiv (r_0/R)^2$ (see Fig. 1), would be

$$(J/J_0)_{\text{diff}} = (1 - f^{3/2})^{2/3} \qquad [1]$$

This relation is a straightforward consequence of Levich's result for species transport to a rotating disk (4, 5), as generalized by Zaidel (4) to include the effect of an inert central region ("patch"). The resulting blockage effect is considerably different from the simple result

$$(J/J_0)_{\text{chem}} = 1 - f \qquad [2]$$

(expected if the reaction were chemically controlled) since in the partially blocked diffusion-controlled case the reduction of active area is partially compensated for by greatly improved local conditions of convective diffusion (initially thin diffusion boundary layer) in the active region.

Objective.—Clearly, Eq. [1] and [2] represent two limiting cases of a more general relation governing reactions which (in the unblocked case) are neither reaction rate controlled nor diffusion controlled. Indeed, if this more general relation were known, such measurements could offer an attractive new method for inferring the extent of diffusion control, and hence true rate constants for rapid heterogeneous reactions. The purpose of this note is to outline how this more general relation can be obtained exactly[1] and to present graphically the pertinent results. For a detailed account of the theory of partially blocked rotating disks and their interesting relation to short tubular reactors, the reader is referred to ref. (6). An excellent critical review of the now extensive use of the rotating disk system in electrochemical investigations is provided in ref. (7).

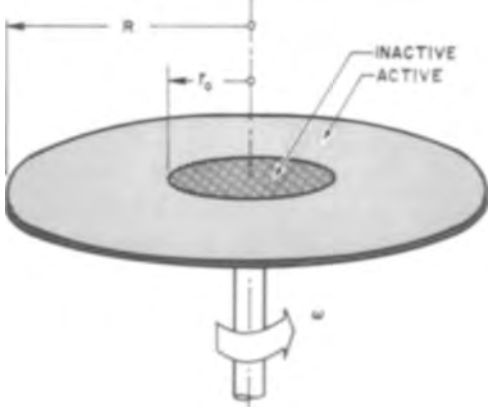

Fig. 1. Partially blocked rotating disk configuration

Outline of the analysis.—In the general case of species diffusion to a partially blocked reactive surface, outside of the nonreactive region a steady-state distribution of reactant concentration is established such that the local rate of diffusional transfer to the active disk surface is everywhere equal to that demanded by the concentration dependence of the surface reaction. While the reactant concentration (mass fraction) far from the surface, c_e, is uniform, a radial distribution of reactant concentration $c_w(r)$ is established along the surface in the region $R \geqq r \geqq r_0$. Both the local rate of convective diffusion and the local reaction rate depend on $c_w(r)$; hence, equating these two rates provides an equation for $c_w(r)$, from which all other quantities of interest can be obtained.

If δ_0 is the effective diffusion layer thickness as obtained from the Levich solution for the unblocked case,[2] then it can be shown (6) that the local mass rate of diffusional transport $-j''(r)$ to the active surface is related to the (as yet unknown) concentration distribution $c_w(r)$ by

$$-j''(r) = \frac{-D\rho}{\delta_0} \int_{\xi=r_0}^{\xi=r} \left[1 - \left(\frac{\xi}{r}\right)^3\right]^{-1/3} d[c_e - c_w(\xi)] \qquad [3]$$

At every $r > r_0$ this flux must be identically equal to the kinetic consumption rate, $-\mathcal{R}''$ independently expressible in terms of the local reactant concentration at the interface. In the special case of a first-order heterogeneous reaction $-\mathcal{R}''$ is given by $k_w \rho c_w$; hence, the reactant conservation equation at the interface

[1] *i.e.*, making no approximations other than those underlying the original Levich-Zaidel relation; *viz.* steady, laminar flow; constant physical properties (density, ρ, kinematic viscosity, ν, and Fick diffusivity, D); diffusional Prandtl (Schmidt) number $Pr (\equiv \nu/D) >> 1$; and negligible interfacial velocity.

[2] *i.e.*, $\delta_0 = [0.62048(Pr)^{1/3}(\omega/\nu)^{1/2}]^{-1}$, where ω is the disk speed.

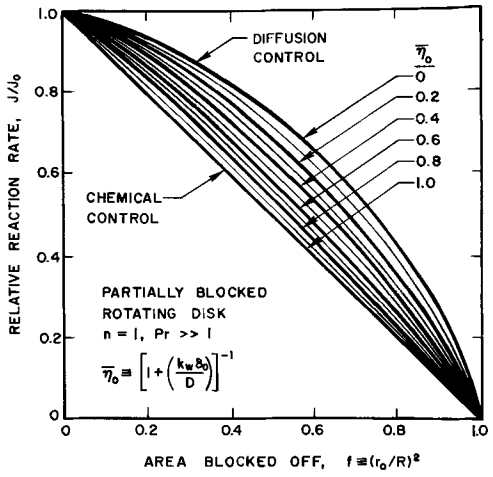

Fig. 2. Normalized reaction rate *vs.* fractional area blocked; first-order heterogeneous reaction.

takes the form of a linear, singular integral equation of the Volterra type[3]

$$k_w c_w(r) = \frac{-D}{\delta_0} \cdot \int_{\xi=r_0}^{\xi=r} \left[1-\left(\frac{\xi}{r}\right)^3 \right]^{-1/3} \frac{dc_w}{d\xi} \cdot d\xi \qquad [4]$$

Results

While local solutions to the dimensionless form of this equation can be obtained analytically, results over the entire $(k_w\delta_0/D)\,[(r/r_0)^3 - 1]^{1/3}$ range of interest are most readily obtained by numerical means on a digital computer. This has been done (6) and the results used to obtain the total reaction rate

$$-J \equiv k_w \rho \int_{r_0}^{R} c_w(r)\; 2\pi r\, dr \qquad [5]$$

from which the effects of partial blockage follow immediately. As expected, it is found that the reduction in reaction rate, J/J_0, depends not only on the fractional area blocked, $f \equiv (r_0/R)^2$ but also on the dimensionless chemical kinetic parameter $k_w\delta_0/D$. Equation [1] is recovered only when the unblocked reaction is diffusion controlled (*i.e.*, when $k_w\delta_0/D \to \infty$). Alternatively, Eq. [2] is recovered only when the unblocked reaction is chemically controlled (*i.e.*, when $k_w\delta_0/D \to 0$). Hence, by comparing the experimentally observed (J/J_0) *vs.* f relation with that predicted from Eq. [4], [5] (see Fig. 2),[4] one can infer the value of $k_w\delta_0/D$. However, rather than $k_w\delta_0/D$, we have chosen $\bar{\eta}_0$ as the parameter in Fig. 2, where

$$\bar{\eta}_0 \equiv [1 + (k_w\delta_0/D)]^{-1} \qquad (0 \leq \bar{\eta}_0 \leq 1) \qquad [6]$$

since this is the ratio of the actual reaction rate on the unblocked disk to the chemically controlled reaction rate on the same disk (5). Equivalently, $\bar{\eta}_0$ is the ratio of the apparent rate constant, $k_{w,a}$, to the true rate constant k_w. Thus, it now appears that diffusion corrections to apparent rate constants can be obtained directly[5] from careful reaction rate measurements on partially blocked disks.

It should be remarked that near the extreme of complete blockage (f near 1)[6] simple rational approximations can be obtained.[7] Thus, provided $\bar{\eta}_0$ is not too small, a first approximation to $\bar{\eta}_0$ (written $\bar{\eta}_0^{(0)}$) can be computed from

$$\bar{\eta}_0^{(0)} = (1-f)/(J/J_0)_{\text{observed}} \qquad [7]$$

which overestimates the true value of $\bar{\eta}_0$ with a relative error of about

$$\tfrac{3}{4}\,(0.8269934)\,[(1-\bar{\eta}_0^{(0)})/\bar{\eta}_0^{(0)}]\,(1-f)^{1/3} \qquad [8]$$

It is hoped that the present results, and similar exact "blockage effect" calculations under way for other flow reactor configurations, will provide the basis for a useful approach to the experimental inference of diffusion corrections and kinetic constants for rapid heterogeneous reactions.

Acknowledgments

It is a pleasure to acknowledge G. D. Bleich for programming the solution of Eq. [4] and A. Crossley for her assistance in presenting the results.

Manuscript received Feb. 10, 1966. The work on this paper was supported by the U. S. Air Force Office of Scientific Research, Propulsion Division, under Contract No. AF 49(638)1654.

Any discussion of this paper will appear in a Discussion Section to be published in the December 1966 JOURNAL.

REFERENCES

1. D. P. Gregory and A. C. Riddiford, *J. Chem. Soc.* **731**, 3756 (1956).
2. D. P. Gregory and A. C. Riddiford, *This Journal*, **107**, 950 (1960).
3. N. Ibl, *This Journal*, **108**, 610 (1961).
4. V. G. Levich, "Physicochemical Hydrodynamics," 2nd ed., Prentice Hall, New Jersey (1962).
5. D. E. Rosner, *AIAA J.*, **2**, 593 (1964).
6. D. E. Rosner, In preparation.
7. A. C. Riddiford, "The Rotating Disk System," in "Advances in Electrochemistry and Electrochemical Engineering," Vol. 4 (in press).
8. D. E. Rosner, *Int. J. Heat Mass Transfer*, In press.

[3] An identical equation governs the finite rate dissolution problem. In that case the local dissolution rate, $\mathcal{R}''$, is expressible in the form $k_w\rho \cdot (c_{w,eq} - c_w)$, where $c_{w,eq}$ is the equilibrium (or "saturation") value of the transferred species mass fraction at the wall. The equation governing the ratio $(c_{w,eq} - c_w)/(c_{w,eq} - c_e)$ is the same as Eq. [4], and the results presented below for the total normalized reaction rate, J/J_0, therefore apply to the case of dissolution as well. It should be reiterated that the present results are exact only in the absence of appreciable interfacial velocities. As discussed in ref. (8), this implies that the condition $(c_{w,eq} - c_e) \ll (1 - c_{w,eq})$ must be satisfied.

[4] A full-scale plot of these results is available from the author on request.

[5] Incidentally, on treating the 25°C data of ref. (2) in this way (allowing for some experimental scatter) we estimate that $\bar{\eta}_0$ was between 0.1 and 0.2, corresponding to a nearly diffusion-controlled dissolution.

[6] This corresponds to the use of a "ring" (electrode or active surface) of width $\Delta r \ll r_0$ in which case $1 - f$ may be identified with $2(\Delta r/r_0)$.

[7] Perhaps the simplest function that can be constructed to approximate the exact J/J_0 *vs.* f relation over the entire range of f and $\bar{\eta}_0$ is

$$J/J_0 \approx \{[\bar{\eta}_0/(J/J_0)_{\text{chem}}] + [(1-\bar{\eta}_0)/(J/J_0)_{\text{diff}}]\}^{-1}$$

However, this relation is found to be inadequate for inferring accurate values of $\bar{\eta}_0$ from experimental rate *vs.* area blockage data.

Brief Communications

The Pseudobinary System Ge-GaAs

M. B. Panish

Bell Telephone Laboratories, Incorporated, Murray Hill, New Jersey

Recently, several papers in which the liquid-solid equilibria in the Ge-GaAs pseudobinary system was discussed have appeared in the literature (1-3). Although there is agreement that the system is essentially simple binary eutectic in nature, there is considerable disagreement as to the position of the liquidus curve and the temperature and composition of the eutectic.

During studies of the Ga-As-Ge ternary system (4), this author determined the liquidus and eutectic temperatures at several compositions along the Ge-GaAs pseudobinary. These data, along with the previously reported data, are shown in Fig. 1.

It should be noted that Glazov and Malyutina (1), Takeda *et al.* (2), and this author agree quite well as to the eutectic composition (~ 16 mole % GaAs), while Lieth and Heyligers (3), Takeda *et al.* and this author agree very well on the eutectic temperature (663° ± 3°C). The major discrepancies are the liquidus and eutectic temperatures of Glazov and Malyutina, and the liquidus curve and eutectic composition of Lieth and Heyligers (3). The liquidus and eutectic temperatures of Takeda and this author are in fair agreement.

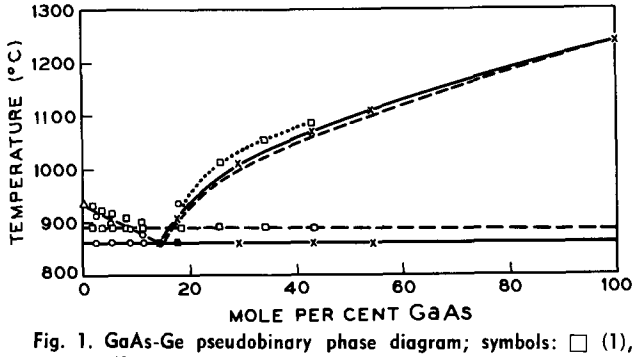

Fig. 1. GaAs-Ge pseudobinary phase diagram; symbols: □ (1), — — — (2), X this work, ○ (5), △ (6).

If the latter data are taken as essentially correct, the higher temperatures of Glazov and Malyutina may be ascribed to a thermometric discrepancy. It is more difficult to account for the data of Leith and Heyligers. The agreement between the eutectic temperatures eliminates any serious thermometric error or the possibility of serious component contamination by impurities. It is possible that the discrepancy between their data and that of Takeda and this author arises from an error in the way composition was reported. The assumption can be made that Lieth and Heyligers reported as mole per cent GaAs a quantity which was actually weight per cent GaAs. Their revised data (5) are shown in Fig. 1 and, except for one point, are in good agreement with the data of Takeda and this author.

Acknowledgment

Helpful discussions with C. D. Thurmond are gratefully acknowledged.

Manuscript received March 10, 1966.

Any discussion of this paper will appear in a Discussion Section to be published in the December 1966 JOURNAL.

REFERENCES

1. V. M. Glazov and G. L. Malyutina, *Russ. J. Inorg. Chem.*, **8**, 1000 (1963).
2. Y. Takeda, H. Hirai, and H. Hirao, *This Journal*, **112**, 363 (1965).
3. R. M. A. Lieth and H. J. M. Heyligers, *ibid.*, **113**, 96 (1966).
4. M. B. Panish, *J. Less Common Metals*, **10**, 416 (1966).
5. R. M. A. Lieth and H. J. M. Heyligers, Private communication.
6. F. X. Hassion, C. D. Thurmond, and F. A. Trumbore, *J. Phys. Chem.*, **59**, 1076 (1955).

Adsorption of Perchlorate Ions on Gold

J. D. Goodrich and G. M. Schmid

Department of Chemistry, University of Florida, Gainesville, Florida

In the course of a previous study of the differential capacity of the electrical double layer on a gold electrode in 1.0-0.01M perchloric acid solution (1) a hump in the capacity-potential curve at 0.4-0.8v *vs.* a standard hydrogen electrode (SHE) was ascribed to the adsorption of perchlorate ions on the electrode. To obtain experimental support for this assumption we attempted to measure the depletion of perchlorate ions from a very dilute solution in contact with gold foil polarized to various points in the indicated potential range.

Gold foil (fine gold, Engelhard Industries, Inc.) of 40 cm^2 apparent area was shaped into a tube and embedded at the bottom into Kel F-100 wax in a Pyrex cell. Electrical contact was provided by a gold wire welded to the foil. This test electrode was concentric to a polarizing electrode made of gold wire of about 1 cm^2 area. The reference electrode was a hydrogen saturated palladium wire (+ 50 mv *vs* SHE) (2). The volume of the cell was approximately 10 ml.

The test electrode was etched in aqua regia, cleaned in sulfuric acid-dichromate solution, and soaked in triple distilled water for several days. Helium, saturated with water vapor, was passed over the system for several hours prior to and during a run. The cell was polarized with a Sensitive Research Instrument model PV potentiometer; the potential was monitored with a Keithley model 610B electrometer.

Perchlorate ions, in 10 ml of solution, before and after a run, were determined spectrophotometrically after extraction with methylene blue according to Iwaski, Utsumi, and Kang (3) in the range 0.04-1.00

Table I. Polarization data: gold in perchloric acid

Concentration, M x 10^6	Potential, v *vs.* SHE	Time polarized, hr
2.072	0.50	2.5
2.072	0.25	6
1.036	0.30	3

ppm. By weighing all solutions to 0.01 mg and keeping the ambient temperature to 23° ± 1° the average deviation of the method could be kept to ±0.01 ppm (28 determinations).

Table I gives a sample of the perchloric acid concentrations used, the polarizing potentials, and the duration of polarization. No concentration change was noted in any of the experiments. With the method of determination used a concentration change of 0.01 ppm in 10 ml, or 6 x 10^{14} perchlorate ions, should have been detected. The coverage of the test electrode under the conditions employed here is therefore less than about 10^{13} perchlorate ions/cm^2 of apparent area, or less than about 1 % of a monolayer, not taking into account a roughness factor which is certainly greater than unity.

It should be pointed out that these results do not invalidate the assumption of perchlorate adsorption on gold made previously (1). The perchlorate ion adsorption we failed to detect here would be for a system in equilibrium with 10^{-6}M perchloric acid, whereas the assumption was originally based on work with 1.0-0.01M solutions.

Acknowledgment

Thanks are due to the National Science Foundation for financial support of this work under Grant No. 4228, and for a Summer Research Fellowship for one of us (J.D.G.).

Manuscript received Dec. 30, 1965.

Any discussion of this paper will appear in a Discussion Section to be published in the December 1966 JOURNAL.

REFERENCES

1. G. M. Schmid and Norman Hackerman, *This Journal*, **109**, 243 (1962).
2. D. Ives and G. Janz, "Reference Electrodes," Academic Press, New York (1961).
3. I. Iwasaki, S. Utsumi, and C. Kang, *Bull. Chem. Soc. Japan*, **36**, 325 (1963).

Discussion Section

This Discussion Section includes discussion of papers appearing in the JOURNAL of the Electrochemical Society, Vol. 112, No. 1, 6, 7, 8, 9, 10, 11, and 12 (January and June to December 1965). Discussion not available for this issue will appear in the Discussion Section of the December 1966 JOURNAL.

Catalytic Decomposition of Aqueous Formic Acid on Platinum Electrodes

D. R. Rhodes and E. F. Steigelmann (pp. 16-21, Vol. 112, No. 1)

W. Vielstich and U. Vogel[1]: In a series of publications it has been shown by different investigators that during the anodic oxidation of formic acid in acid electrolytes an intermediate product is formed which blocks the surface in a certain potential region. Anodic potential scans show three current peaks (at 0.5, 0.8, and 1.3v *vs.* H_2 electrode). In the region of the first peak the intermediate is formed; at the potential of the second peak the intermediate is oxidized to CO_2.

Rhodes and Steigelmann assume that the intermediate product is carbon monoxide formed by catalytic decomposition of HCOOH into CO and H_2O. Potential scan diagrams with HCOOH and CO are performed in order to prove this hypothesis.

In their experiments the authors observe a small difference (30 mv at a sweep rate of 1.2 v/sec, see their Table I) between the potential of the peak for CO and the potential of the second formic acid peak, especially during the first sweep, their Fig. 1 and 3. Nevertheless Rhodes and Steigelmann suggest that two peaks are caused by the oxidation of the same species.

In our laboratory we have repeated the above mentioned experiment,[2] recording the current/potential diagrams (corresponding to their Fig. 1 and 3) on the same figure. This diagram (our Fig. 1) clearly shows:

[1] Institut fuer Physikalische Chemie der Universitaet Bonn, Wegelerstrasse 12, Bonn, Germany.

[2] W. Vielstich and U. Vogel, Unpublished results.

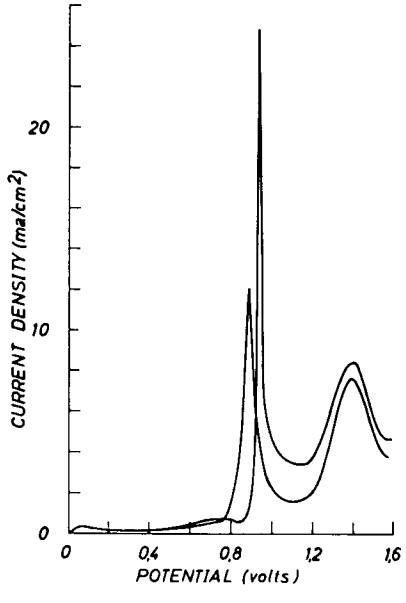

Fig. 1. First sweep of 0.085M HCOOH in 1*N* H_2SO_4 at 30°C on 1 cm^2 smooth Pt, sweep rate of 260 mv/sec; (*a*) N_2 stirring; (*b*) CO stirring.

(*a*) the difference in potential between the two peaks is very pronounced and amounts to about 60 mv; (*b*) the rising part of the CO peak is so sharp that due to adsorbed carbon monoxide only a very small current should be possible in the region of the formic acid peak.

In addition to the different shape of the current/potential diagrams there exists another strong argument against the assumption of carbon monoxide as intermediate product. Johnson and Kuhn[3] have made a simultaneous determination of the number of coulombs and the number of chemical equivalents of reduced CO_2; these species are identical with the intermediate product of formic acid oxidation.[4,5] Instead of the number of 2 electrons per particle stated in the paper[3] one of the authors recently informed us that, due to an error in calculation, the true number is one electron per particle.[5a]

Therefore, the results of Johnson and Kuhn[3, 5a] are in agreement with our own conclusion[4,5] that the intermediate product should be a formate radical, prob-

ably of the form 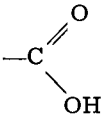

.

D. R. Rhodes and E. F. Steigelmann: The figure presented by Vielstich and Vogel does clearly show a

[3] P. R. Johnson and A. T. Kuhn, *This Journal*, **112**, 599 (1965).

[4] W. Vielstich and U. Vogel, *Ber. Bunsen Ges. Physikal. Chem.*, **68**, 688 (1964).

[5] W. Vielstich, "Brennstoffelemente—Moderne Verfahren zur elektrochemischen Energiegewinnung," Verl. Chemie, Weinheim 1965.

[5a] A. T. Kuhn, private communication.

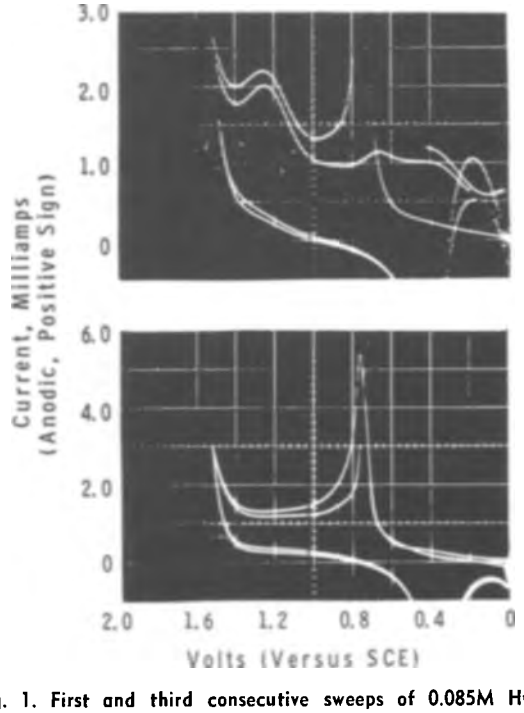

Fig. 1. First and third consecutive sweeps of 0.085M HCO_2H (top) and saturated CO (bottom) in 1*N* H_2SO_4 at 30°C on a platinum disk electrode rotating at 600 rpm; 0.97 cm^2 real surface area; sweep rate of 1.2 v/sec.

difference of 60 mv between the peaks for the first sweep of formic acid and carbon monoxide. Therefore, we have reexamined our curves from similar experiments.

One set of such curves is given in this discussion. These were used to sketch the figures given in our original article. They were obtained at a sweep rate of 1.2 v/sec and at a starting potential of 0.0v *vs.* SCE. The first sweep in each photograph is represented by the tallest peak at about +0.7v. The third sweep in each photograph, which was obtained by closing the camera shutter during the second sweep, shows that the peaks at about +0.7v have shifted slightly in the negative direction for both formic acid and CO. This effect was discussed in the original article.

Our figures show that we obtained a difference of 30 ± 10 mv between the formic acid and CO peak at about 0.7v during the first sweep. A check of the rest of our original data given in the article in Table I for the various sweep rates showed that the differences listed were accurate to ± 10 mv. Because we might have made some error during this series of experiments, we examined another set of similar data taken several days earlier. Once again the data fit to within ± 10 mv. We had also recorded sweeps of CO and formic acid oxidation on a recorder at sweep rates equal to 0.13 v/sec and lower. In each case the corresponding *dv/dt* curve had been recorded. At 0.13 v/sec the difference between the two peaks during the first sweeps was 20 ± 10 mv.

From the above discussion we conclude that the difference in peak voltages listed in Table I of the original article is a real effect and not an experimental error. Therefore, the difference between our results and that by Vielstich and Vogel must be a difference in experimental parameters. One obvious difference is that we started our sweeps at 0.0v *vs.* SCE (0.245v *vs.* NHE); whereas, they started their sweeps at 0.0v *vs.* NHE, which is well within the hydrogen region. It is known that the type of adsorption of CO affects the potential where it is oxidized [our figure here and Ref. (6)]. Perhaps the results by Vielstich and Vogel reflect the effect of hydrogen on CO oxidation and/or formic acid adsorption.

Perhaps the most important point brought out by Vielstich and Vogel is that Johnson and Kuhn[7] have changed from two electrons per particle to one electron per particle for the intermediate product of formic acid oxidation. We do not feel like making any comment on this change until it is made public.

On the Potential/*p*H Diagrams of the Cu-NH_3-H_2O and Zn-NH_3-H_2O Systems

H. E. Johnson and J. Leja (pp. 638-641, Vol. 112, No. 6)

F. Letowski and J. Niemiec[8]: The potential/*p*H diagrams given by Johnson and Leja as well as the potential/*p*H diagrams discussed by them and developed by Mattsson[9] enabled the authors to interpret the results of studies on the corrosion of brass in aqueous ammonia and ammonium salts solutions. Johnson and Leja disputed in their paper the correctness of the position of the stability ranges of Cu_2O and CuO oxides as well as those of the basic cupric sulfate $Cu(SO_4)_{0.25}(OH)_{1.5}$ on the potential/*p*H diagrams given by Mattsson. According to Johnson and Leja the oxides CuO_2 and CuO are stable, in 0.05M solution of Cu and 1.0M of NH_3 and NH_4^+ at *p*H values exceeding 11, but these compounds are not stable in the *p*H range 3-7.5 determined by Mattsson. In the discussion below it is shown, on the basis of the equilibria determined by Johnson and Leja and Mattsson,[9] that the solid phases in question are also stable in both of the *p*H ranges discussed.

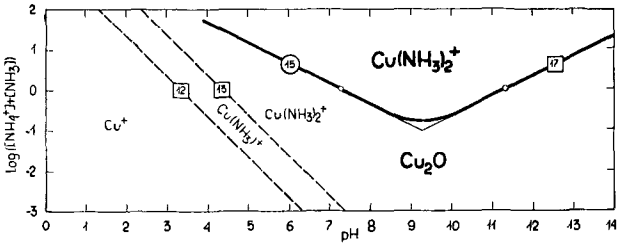

Fig. 1. Influence of pH and total NH_3 + NH_4^+ activities on the solubility ranges of Cu_2O at 25°C (total dissolved Cu =0.05M; □—equilibria according to Johnson and Leja; ○—according to Mattsson).

According to Johnson and Leja the equilibrium of their reaction [17], dissolution of Cu_2O in ammonia solution,

$$Cu_2O + 4NH_3 + 2H^+ = 2Cu(NH_3)_2^+ + H_2O \quad [17]$$

is described by

$$pH = 9.99 + 2\log[NH_3] - \log[Cu(NH_3)_2^+]$$

The equilibrium [17] is shown in the plot of log ($[NH_3 + NH_4^+]$) *vs.* pH at Cu activity 0.05M in Fig. 1. It is valid merely within the range of NH_3 predominance, *i.e.*, at *p*H values higher than 9.26. At *p*H values lower than 9.26 the NH_4^+ ions prevail and equilibrium [17] (Johnson and Leja) becomes senseless. As determined by Mattsson for the reaction

$$0.5Cu_2O + 2NH_4^+ = Cu(NH_3)_2^+ + H^+ + 0.5H_2O$$

the equilibrium

$$pH \quad 8.56 - 2\log[NH_4^+] + \log[Cu(NH_3)_2^+] \quad [15]$$

becomes valid in this region. A plot of this equilibrium is shown in Fig. 1 at Cu activity 0.05M. Near *p*H 9.26 the NH_3 and NH_4^+ concentration (or activities) change with *p*H logarithmically; in Eq. [17] and our [15] their sum $[NH_3]$ + $[NH_4^+]$ should be taken into account instead of the individual $[NH_3]$ and $[NH_4^+]$ activities. A gently transition of equilibrium [17] into [15] is thus obtained and, for *p*H 9.26, the logarithm of the sum of activities at which the solution over Cu_2O is saturated with $Cu(NH_3)_2^+$ is equal to —0.7. The ordinate values of the points situated in equilibrium curves [17] and [15] (Fig. 1) at a total $[NH_3]$ + $[NH_4^+]$ = 1.0M should define the positions of these equilibria on the potential/*p*H diagrams of a Cu-NH_3-H_2O system; the first one extends toward the right from *p*H 11.29 (Johnson and Leja) and the second one toward the left from *p*H 7.26 (Mattsson).

By plotting the CuO and $Cu(SO_4)_{0.25}(OH)_{1.5}$ dissolution equilibria as log ($[NH_3]$ + $[NH_4^+]$) against *p*H (Fig. 2) one obtains evidence that the stability

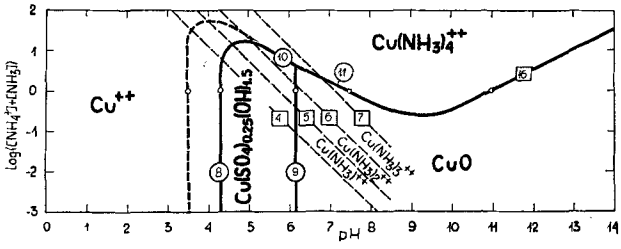

Fig. 2. Influence of pH and total NH_3 + HN_4^+ activities on the solubility ranges of CuO and $Cu(SO_4)_{0.25}(OH)_{1.5}$ at 25°C (total dissolved Cu = 0.05M; □—equilibria according to Johnson and Leja; ○—according to Mattsson; --- according to Bustorff and Muylder, and Letowski and Niemiec).

[6] S. Gilman, *J. Phys. Chem.*, 66, 2657 (1962).

[7] P. R. Johnson and A. T. Kuhn, *This Journal*, 112, 599 (1965).

[8] Institute of Inorganic Chemistry and Metallurgy of Rare Elements, Technical University, Wroclaw, Wybrzeze Wyspianskiego 27, Poland.

[9] E. Mattsson, *Electrochim. Acta*, 3, 279 (1961).

ranges of these solid phases were correctly placed by Johnson and Leja in the range of pH values higher than 10.95 and by Mattsson in the pH range 4.28-7.46. In conclusion, a correct image of the Cu-NH_3-H_2O system equilibria, based on thermodynamic data used by Johnson and Leja, and Mattsson, is obtained by superimposing their potential/pH diagrams [*This Journal*, **112**, 629, Fig. 2a and 2b]. The solubility limits of the basic cupric sulfate $Cu(SO_4)_{0.25}(OH)_{1.5}$ also seem to be controversial. Therefore, these limits in a 0.05M copper solution and 1.0M total ammonia and ammonium ions solution were also indicated in Fig. 2 by a dotted line, according to the potential/pH equilibria of the Cu-H_2O-H_2SO_4 system developed by Bustorff and Van Muylder[10] as well as the Cu-H_2O-NH_3-H_2SO_4 system developed by Letowski and Niemiec.[11] These differences in the solubility ranges of the basic cupric sulfate result from differences between the thermodynamic data used for elaboration of these systems.

Johnson and Leja have also argued the occurrence of the $Zn(OH)_2$ stability range in the potential/pH diagram of the Zn-NH_3-H_2O system made by Mattsson.[9] It follows, however, from the dissolution equilibria of zinc hydroxide shown in Fig. 3 that the presence of the $Zn(OH)_2$ stability range in the potential/pH diagram of the Zn-NH_3-H_2O system made by Mattsson is not in contradiction with the equilibria given by Johnson and Leja [*This Journal*, **112**, 640, Fig. 3a and 3b], as these diagrams are made for different zinc activities in solution (Mattsson, 0.01M; Johnson and Leja, 0.001M). The positions of the equilibria in Fig. 3 at $[NH_3] + [NH_4^+] = 1.0M$ are denoted by the points. The ordinate values of these points define the pH values at which the ZnO hydrat dissolution equilibria should be placed in the potential/pH diagram. For Zn activity = 0.01M (Mattsson), two stability ranges of zinc hydroxide should appear; the first one is comprised of the pH range 6.54-7.48 defined by equilibria [18] and [19] according to Mattsson[9]; the second one should be in the pH range from 11.19 to 13.89 limited by the equilibria of the reactions

$$Zn(NH_3)_4^{++} + H_2O = ZnO + 4NH_3 + 2H^+$$

$$pH = 10.19 + 2 \log [NH_3] - 0.5 \log [Zn(NH_3)_4^{++}]$$

according to the authors of the present discussion and

$$ZnO + H_2O = ZnO_2^{--} + 2H^+$$

$$pH = 14.89 + 0.5 \log [ZnO_2^{--}]$$

according to Pourbaix.[12] For Zn activity = 0.001M (Johnson and Leja) there should be only one ZnO hydrat stability region in the pH range from 11.69 to 13.39 which is determined by the above two equilibria.

Plotting of equilibria [21] and [22] in the potential/pH diagram of the Zn-NH_3-H_2O system of Johnson and Leja [*This Journal*, **112**, 640, Fig. 3b] does not seem to be justified. According to the Pourbaix's definition[12] these equilibria should separate the relative predominance ranges of Zn^{++} from those of $Zn(NH_3)_3^{++}$ and $Zn(NH_3)_3^{++}$ from $Zn(NH_3)_4^{++}$. However, because of the close positions of these equilibria such a situation never occurs. In Fig. 3 a dependence of pH and percentage contents of a more basic form in 1.0M total $NH_3 + NH_4^+$ solution is shown. The $Zn(NH_3)_3^{++}$ ions will never occur in concentrations equal to those of the neighboring ions. The maximum contents of the $Zn(NH_3)_3^{++}$ ions do not exceed 14%, so in the whole pH range in question the Zn^{++} or $Zn(NH_3)_4^{++}$ ions prevail.

The argument for the localization of oxide phases made by Johnson and Leja on the basis of ΔG° values as well as their questioning of the stability ranges of solid phases defined by Mattsson, seem to be unnecessary; ΔG° depends on the stability constants according to $\Delta G^\circ = -RT \ln K$, and the effect of the thermodynamic potential on equilibria is manifested in the equilibrium constants themselves which, on the other hand, determine the position of equilibria on the potential/pH diagram.

H. E. Johnson and J. Leja: We are grateful to Messrs. Letowski and Niemiec for their contribution which helped us to pin-point the source of error in the issue under discussion.

The attempt of theirs to strike a compromise between Mattsson's and our evaluation does not agree with our limited evidence that the system copper-ammonia does not show the development of Cu_2O tarnish in the pH range indicated by Mattsson (if precautions are taken to eliminate CO_2). Secondly, it seems inconceivable that the domains of stability of $Cu(NH_3)_2^+$ and Cu_2O, Fig. 1 of Letowski and Niemiec, can be separated by two lines thus endowing the same two species with an alternately reversed acid-basic characteristics.

We cannot agree that reaction [17] "becomes senseless" at pH values below 9.26 where NH_4^+ ions outnumber NH_3 groups; analogous reasoning would lead to the conclusion that reactions involving hydrogen ions are senseless at pH values above 7.0 where they are outnumbered by their hydroxyl ion counterparts. The crux of the present problem is the seeming inconsistency of Eq. [17] and [15]. Letowski and Niemiec have suggested a compromise which involves the sum of the $[NH_3]$ and $[NH_4^+]$ activities; it is interesting to note that a third modification of equations [17] and [15] can be written to express the dissolution of Cu_2O in terms of both NH_3 and NH_4^+ as follows

$$Cu_2O + 2NH_4^+ + 2NH_3 = 2\,Cu(NH_3)_2^+ + H_2O$$

Note that since this equation involves neither redox reactions no hydrogen ions it cannot be represented on a potential/pH diagram. Equation [17], on the other hand, considers the ligand rather than the undissociated ion, NH_4^+, and seems to represent the actual experimental observations.

[10] A. Bustorff and J. Van Muylder, *Electrochim. Acta*, 9, 607 (1964).

[11] F. Letowski and J. Niemiec, *Roczniki Chem.*, 40, [7-8] (1966).

[12] M. Pourbaix, "Atlas d'Equilibres Electrochimiques a 25°C," Gauthier-Villars, Paris (1963).

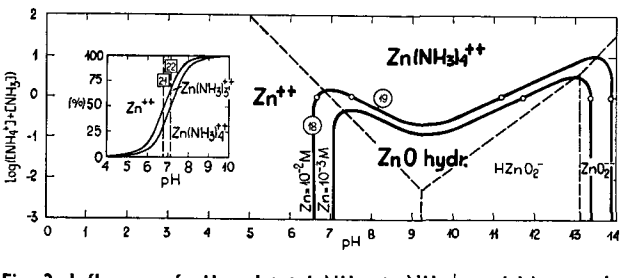

Fig. 3. Influence of pH and total $NH_3 + NH_4^+$ activities on the solubility of ZnO hydr. and the influence of pH on the percentage contents of Zn^{++}, $Zn(NH_3)_3^{++}$ and $Zn(NH_3)_4^{++}$ in 1.0M solution of $NH_3 + NH_4^+$ (□—equilibria according to Johnson and Leja; ○—according to Mattsson).

Hydrogen Peroxide Reactions on Gold Electrodes

A. K. M. S. Huq and A. C. Makrides (pp. 756-757, Vol. 112, No.7)

G. Bianchi, F. Mazza, and T. Mussini[13]: As far as gold in acid solutions of hydrogen peroxide is concerned, the reaction which determines the rest potential and the reaction which gives support to significant currents should be taken into account distinctly. In fact,

[13] Laboratory of Electrochemistry and Metallurgy, University of Milan, Milan, Italy.

the reaction which determines the rest potential of gold has a very low exchange current, and cannot support currents significant and constant in the time.[14]

In our papers cited by Huq and Makrides, in a prior one,[15] and in a subsequent one[16] dealing explicitly with the process of oxygen and hydrogen peroxide on gold electrodes, we proposed the mechanism

$$H_2O_2 + 2H_{ads} \rightarrow 2H_2O$$

to explain the cathodic process at current densities ranging from 5×10^{-5} to 10^{-3} amp/cm^2. The range of electrode potentials corresponding to this range of current densities is + 0.4 to — 0.1v (NHE) and is not incompatible with the mechanism cited above, if the preceding reaction is rapid and no H_{ads} accumulation on the gold surface takes place.

As for the slope of the Tafel's line, the values one can draw from the Huq and Makrides' graph in the case of 10^{-3} m H_2O_2 solutions are 0.18 for increasing current densities and 0.30 for decreasing ones, respectively. Within the same range of current densities as above, we found a 0.18 slope in agreement with the previous results of Akopyan[17] who also made a distinction of processes occurring at currents either higher or lower than 5×10^{-5} amp/cm^2. Setting aside the question of the reaction which determines the rest potential of gold, as it is the subject of a next paper, we think that at present there is no argument to make inapplicable the mechanism we proposed for the cathodic reduction of hydrogen peroxide on gold at significant currents ranging from $5 \cdot 10^{-5}$ to 10^{-3} amp/cm^2.

As concerns the anodic reaction, we proposed a mechanism involving an adsorbed surface oxide and not the gold bulk oxide, the reactivity of the latter besides being the lower as the nobler is its anodic potential of formation.[17] The fact that at the + 1.4v (NHE) potential an anodic inhibition takes place, due to a beginning occurrence of the gold bulk oxide,[18] is not an argument against that mechanism since we proposed it in terms of a H_2O_2 anodic oxidation by reaction with an adsorbed surface oxide which forms within + 1.0 and + 1.4v (NHE), in the case of gold.

The Absorption of Electrolytically Generated Hydrogen

F. Matsuda and T. C. Franklin (pp. 767-771, Vol. 112, No. 8)

G. Dubpernell[19]: It is not believed that hydrogen can diffuse through solid iron at room temperature,[20] but rather that any diffusion is associated with pores or defects in the structure of the metal. It is noted that the iron membranes were prepared by etching shim steel sheet with 1M nitric acid, and that the membrane in Fig. 12 was 3.0×10^{-3} cm thick (0.0012 in.) and in Fig. 13, 2.5×10^{-3} (0.001 in.) thick.

It would be of interest to know how long the membranes were etched, and what was their original thickness. Was the loss in weight determined? How was the final thickness measured? Was any effort made to check whether or not the membranes had any pores or holes in them?

F. Matsuda and T. C. Franklin: The two membranes studied in this article were prepared from commercially available shim steel. The 3×10^{-3} cm membrane was prepared by severe etching of a sheet 0.003 in. thick in 1M nitric acid, while the 2.5×10^{-3} cm membrane was obtained by dipping a 0.001 in. sheet briefly in acid and immediately removing and rinsing. Thus the thinnest membrane was (as indicated by a micrometer caliper) essentially unetched 0.001 in. shim steel. In view of the fact that the results on the two membranes (prepared from different samples of starting material, etched in one case severely and in the other case negligibly, and having different final thickness) gave, when corrected for thickness, almost identical rate constants (4.3×10^{-5} and 4.8×10^{-5} cm/min) strongly indicates that migration could not have occurred by something so haphazard as holes.

In addition it should be pointed out that an iron membrane with a thickness of 0.003 in. (7.5×10^{-3} cm) (after degreasing and dipping briefly in nitric acid) was used in some early experiments. The results obtained were qualitatively the same as those indicated in the paper. This membrane was not used for quantitative runs because the increased thickness extended the time for a complete run beyond a convenient value. It is difficult to imagine pores in a membrane this thick.

In order to further check on this question two other experiments were run: (A) A new iron crucible with a wall thickness of 0.08 cm, after degreasing and a momentary dip in 1M nitric acid, was filled with 2*N* sodium hydroxide containing some potassium permanganate. Hydrogen was generated electrolytically on the exterior of the crucible immersed in 2*N* sodium hydroxide solution. The color of the permanganate solution was compared with that of a blank run, identical in every respect, except for the fact that hydrogen was not generated on the exterior wall of the crucible. Although the permanganate undergoes some decomposition on its own and there is some reduction by the iron, it was obvious after 1 hr, even to the naked eye, that the rate of reduction in the crucible acting as a hydrogen membrane was much greater than the rate of reaction in the blank. This increased reduction rate could only be caused by hydrogen passing through the iron crucible. Again, it is difficult to visualize the presence of pores in a new iron crucible. (B) Some measurements were made on the amount of hydrogen codeposited in the electrolytic deposition of iron. The plating bath consisted of 213g of ferrous sulfate ($FeSO_4 \cdot 7H_2O$) in one liter of solution with the pH maintained at 2.8-3.5 with sulfuric acid. The bath temperature was 45°C and the current density was 17.3 ma/cm^2. The cathode and the anode were prepared from Baker Analyzed Reagent Grade iron wire. The cathodes (21 cm long) were degreased in kerosine, rinsed in distilled water, dipped in 1-1 nitric acid and rinsed in distilled water. After plating, the amount of hydrogen codeposited with the iron was measured by the coulometric technique described in this paper and in the paper by Franklin and Goodwin.[21]

The amount of hydrogen found codeposited in iron by the coulometric method should increase linearly with increasing thickness of the deposit. However, at some thickness this increase should begin to depart from linearity because the method can only analyze for the amount of hydrogen that can diffuse to the surface during the time that the voltage sweeps through the hydrogen region. (Approximately 3 min.) Figure 1 shows the results obtained in a series of runs. It can be seen that the data is linear throughout the range covered by these experiments. Using the density of iron the largest deposit was calculated to be 2.3×10^{-3} cm thick. To explain this linear graph by migration only through pores or defects would require that such pores or defects be continuous throughout the deposit. Although possible, this does not seem probable. Migration along grain boundaries seems to

[14] J. P. Hoare, *This Journal*, **110**, 245 (1963).

[15] G. Bianchi, *Corrosion et Anticorrosion*, **5**, 146 (1957).

[16] G. Bianchi, F. Mazza, and T. Mussini, "Oxygen and Hydrogen Peroxide Electrochemical Behavior on Gold Electrodes," AFOSR-TN 2054, December 1961.

[17] A. U. Akopyan, *Zhur. Fiz. Khim.*, 33, 1625 (1959).

[18] S. B. Brummer and A. C. Makrides, *This Journal*, **111**, 1122 (1964).

[19] M&T Chemicals Inc., Detroit 20, Michigan.

[20] G. Dubpernell, *This Journal*, **112**, 646 (1965).

[21] T. C. Franklin and J. R. Goodwyn, *This Journal*, **109**, 288 (1962).

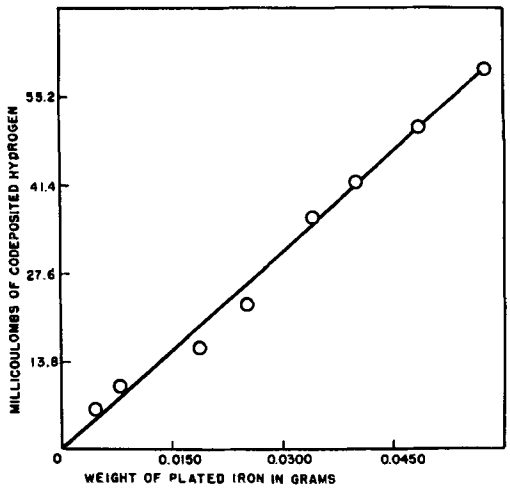

Fig. 1. The amount of hydrogen codeposited with iron

best explain the majority of data taken in our laboratory.

We wish to thank the Robert A. Welch Foundation of Houston for their support of this study.

Oxygen Overvoltage Measurements on Bright Pt in Acid Solutions, III. Nitric Acid Passivated Bright Platinum

J. P. Hoare (pp. 849-853, Vol. 112, No. 8)

J. A. Shropshire[22]: In reading the author's analysis of the effect of concentrated HNO_3 on the oxygen reduction in acid solution, I was disappointed that he failed to mention possible effects other than formation of a complex oxide structure. It is well known, for instance, that a platinum electrode in H_2SO_4 solution containing HNO_3 can exhibit extremely noble potentials, comparable to those for reversible oxygen, as a result of the complex NO, HNO_2, *etc.*, equilibrium.[23,24] It would appear that much of the transient behavior reported in this work, both cathodic and anodic to the reversible oxygen potential could be explained in terms of strongly adsorbed NO, HNO_2, species which can be removed by severe cathodization or anodization. The reduction of adsorbed HNO_2 coupled with an oxygen regeneration of the reduced product *in situ* might well support the observed cathodic currents. The efficient function of an adsorbed molybdate species in just this fashion is known in the oxidation of HCHO and CH_3OH at a platinum electrode in H_2SO_4.[25]

Although no coulombic data are available from the paper it would be interesting to see if the quantity of anodic coulombs consumed in the initial anodic transition shown in, *e.g.*, Fig. 4 in the paper corresponds to oxidation of monolayer quantities of material. As mentioned previously, I think it would be desirable to have the author recognize and comment on these possibilities.

J. P. Hoare: The comments of Dr. Shropshire are well taken and were a source of some concern as pointed out earlier.[26] However, it was noted that the high anodic potentials (about 1.28v) were observed by Vetter[27] when the nitric acid concentration ranged from 7 to 14.5N. Nitric acid concentrations studied by Shropshire and Tarmy[28] extended from 0.2 to 1M. Since the nitric acid treated electrodes used in these polarization studies[29] and referred to as Pt-O-alloy electrodes[30] were soaked in triply distilled water for at least one-half hour with at least five changes of water before being plunged into O_2-saturated, H_2O_2-free, 2N H_2SO_4 solution, it was considered safe to assume that a NO_2/NO couple was not potential-determining.[26] The concentration of HNO_3 in this case is minuscule.

In some recent studies,[31] treated and untreated samples of Pt were examined with x-ray diffraction techniques. The results show that only Pt diffraction lines were obtained in both cases except that the lines were slightly shifted in the treated case. From the results of vacuum fusion studies, the treated samples in every case not only contained more oxygen but also contained the same or even less nitrogen than the untreated samples.

It is concluded[31] that the treatment of Pt with HNO_3[26] permits more oxygen to be dissolved in the surface layers of the metal. This oxygen exists as an alloy of Pt and O atoms in these surface layers. Finally, this skin of Pt-O alloy is a better catalyst for many electrode reactions[29,32] than bare Pt. It must be remembered that the presence of adsorbed oxygen on the metal surface may inhibit the reduction of oxygen[33,34] but oxygen dissolved in the metal accelerates the reduction of oxygen.[29]

Consequently, explanations for the electrochemical behavior of the Pt-O-alloy electrode involving adsorbed NO, HNO_2, and the like must be rejected.

Electrochemical Studies of NO^+ and NO_2^+ in Concentrated H_2SO_4

L. E. Topol, R. A. Osteryoung, and J. H. Christie (pp. 861-864, Vol. 112, No. 8)

G. Bianchi and T. Mussini[35]: As concerns reaction [i] $NO^+ + e \rightarrow NO$ with subsequent stage [ii] $2NO + 2H^+ + 2e \rightarrow H_2N_2O_2$ or the possible alternative stage [iii] $NO + 3e + 4H^+ \rightarrow NH_2OH_2^+$ depending on the appearance of hydroxylamine as a final product of reaction, it is to be pointed out that results obtained with mercury electrodes cannot apply validly to the case of platinum, apart from the fact that platinum can exert a catalytic intervention[36,37] in the reaction [iv] $4NH_2OH_2^+ \rightarrow 2NH_4^+ + H_2N_2O_2 + 2H_2O + 2H^+$. Moreover, reaction [v] $NH_2OH + NO^+ \rightarrow H_2N_2O_2 + H^+$ (or else $NH_2OH + HNO_2 \rightarrow N_2O + 2H_2O$) can take place[38,39]; this is very rapid in the intermediate concentration range of H_2SO_4 (from 4 to 14M). The results obtained by Masek and Przewlocka[40] working with a platinum vibration electrode show a wave at the + 0.43v (SCE) half-wave potential, very near the + 0.70v (NHE) potential we proposed for reaction [i].[41] On mercury the half-wave

[22] Esso Research & Engineering Company, P. O. Box 121, Linden, New Jersey 07036.

[23] J. A. Shropshire and B. L. Tarmy, "The Nitric Acid-Oxygen Redox Electrode in Acid Electrolyte" in "Advances in Chemistry," No. 47, p. 153, ACS (1965).

[24] K. Vetter, *Z. Physik. Chem.*, 194, 199 (1950).

[25] J. A. Shropshire, *This Journal*, 112, 465 (1965).

[26] J. P. Hoare, *This Journal*, 110, 1091 (1963).

[27] K. J. Vetter, *Z. Anorg. Chem.*, 260, 242 (1949).

[28] J. A. Shropshire and B. L. Tarmy, "Advances in Chemistry," No. 47, p. 153, ACS (1965).

[29] J. P. Hoare, *This Journal*, 112, 849 (1965).

[30] J. P. Hoare, *Nature*, 204, 71 (1964).

[31] J. P. Hoare, S. G. Meibuhr, and R. Thacker, *This Journal*, To be submitted.

[32] J. P. Hoare, *J. Electroanal. Chem.*, In Press.

[33] M. W. Breiter, *Electrochim. Acta.*, 9, 441 (1965).

[34] W. Vielstich, *Z. Instrumkde.*, 71, 29 (1963).

[35] Laboratory of Electrochemistry and Metallurgy of the University of Milan, Milan, Italy.

[36] P. Pascal, "Nouveau Traité de Chimie Minérale," Vol. X, p. 277, Masson, Paris (1956).

[37] J. W. Mellor, "A Comprehensive Treatise on Inorganic and Theoretical Chemistry," Vol. VIII, pp. 286-287, Longmans & Green, London (1928).

[38] J. W. Mellor, cited p. 283.

[39] J. Masek and H. Przewlocka, *Coll. Czech. Chem. Commun.*, 28, 682 (1963).

[40] J. Masek and H. Przewlocka, *Coll. Czech. Chem. Commun.*, 28, 677 (1963).

[41] G. Bianchi, T. Mussini, and C. Traini, *Chem. e Ind.*, 45, 1333 (1963).

potentials are[42] about 0.0v (SCE) for reaction [i] and about —1.0v (SCE) for reaction [iii].

As for the anodic process of NO^+ oxidation to N_2O_4 and the rapid disproportionation of N_2O_4 in 96% w/w H_2SO_4, it is to be pointed out that the N_2O_4 disproportionation is very rapid at low H_2SO_4 concentrations (< 58% w/w): $N_2O_4 + H_2O \rightarrow HNO_3 + HNO_2$; and also at higher H_2SO_4 concentrations (> 85% w/w): $N_2O_4 + H_2SO_4 \rightarrow HO{\cdot}SO_2{\cdot}NO_2 + HNO_3$. At intermediate concentrations of H_2SO_4, corresponding to the field where we observed the anodic wave of NO^+ oxidation to N_2O_4, the velocity of N_2O_4 disproportionation may verify a minimum.[43] In a recent paper[44] the results obtained with the rotating-disk electrode method proved that the process $2NO^+ + 2H_2O - 2e \rightarrow N_2O_4 + 4H^+$ is a first-order reaction, whose standard potential is $E^\circ = +1.25$v (NHE).

In our opinion platinum exerts a catalytic action on the processes of nitrogen oxides. The results, particularly anodic curves, may be really affected by the surface state of the electrode, as it has been shown also in the work under discussion. For analogy with order cases[45] we consider the degassing of platinum electrodes *in vacuo* at 500°C to be essential. No direct comparison is possible with results obtained working with different metals, like gold or mercury.

L. E. Topol, R. A. Osteryoung, and J. H. Christie: In regard to Bianchi and Mussini's comment on the formation of $H_2N_2O_2$ or $NH_2OH_2^+$ we would like to point out that the dispute actually concerns them and Masek[46,47] and Przewlocka.[47] We did not work in the acid concentration range where the occurrence of the above electrode reaction products were reported.

As for the oxidation of NO^+ to N_2O_4, even if the disproportionation of N_2O_4 is slow in intermediate acid concentrations as claimed, we did not see any sign of NO_2^+ in the 96% solution. The reported formation[48] of N_2O_4 in this solution with its rapid subsequent disproportionation would yield NO_2^+ as well as NO^+ and the NO_2^+ should be detected in our studies.

Preferential Vaporization of Carbon from Hafnium Carbide

R. L. Hansler (p. 881, Vol. 112, No. 8)

Charles P. Kempter[49]: Dr. Hansler has cited only one reference relating the lattice parameter of hafnium carbide to composition and no references relating the electrical resistivity to lattice parameter and/or composition. In addition to Avarbe *et al.*, Cotter and Kohn,[50] Krikorian, Witteman, and Bowman,[51] Goretzki,[52] Bittner and Goretzki,[53] Nowotny, Benesovsky, and Rudy,[54] Krikorian, Wallace, and Anderson,[55] Adams and Beall,[56] Zhelankin and Kutsev,[57] Houska,[58] and Sara[59] have studied the lattice parameters of known compositions of hafnium carbide. A plot of all of these data indicates that the lattice parameter of stoichiometric HfC, if it exists, is ~4.641Å. The value of 4.6450 ± 0.0005Å reported by Hansler is very high and might be explained by the presence of a significant percentage of zirconium carbide in solid solution with the hafnium monocarbide. A spectrographic analysis of the filament would have been advisable. The room temperature specific electrical resistivities, lattice parameters, and combined carbon contents reported by Goretzki[52] are 172, 200, 230, 242, 245 microohm-cm, 4.638, 4.637, 4.634, 4.632, 4.625Å, and 47.4, 46.5, 45.1, 43.8, 41.3 a/o, respectively. $Hf_{0.901}$ corresponds to 47.4 a/o combined carbon. According to Paderno[60] the specific electrical resistivity of $HfC_{0.999}$ is 45.0 microohm-cm at room temperature. Other resistivity values have been reported for "HfC," but the stoichiometry was not stated.

According to Lyon,[61] "hafnium carbide has a congruently vaporizing composition at a carbon concentration slightly less than stoichiometric." Since Goretzki's measurements show that the specific electrical resistivity increases markedly with decreasing carbon content, Hansler's results are not in disagreement with those reported by Lyon.

R. L. Hansler: I wish to thank Dr. Kempter for his discussion.

Theory of Organic Corrosion Inhibitors—Adsorption and Linear Free Energy Relationships

F. M. Donahue and K. Nobe (pp. 886-891, Vol. 112, No. 9)

R. R. Annand[62]: When I first saw this paper I enthusiastically thought that now we might have a workable relationship to use for seeking inhibitor structure correlations. I was particularly favorably impressed with the arguments and derivations which tend toward developments of a specific set of sigma values for inhibitor or adsorption situations. On further study, however, it seems to me that before a reliable set of specialized sigma values can be developed it will be necessary to establish better experimentally a point that is assumed by the authors.

Usual LFER theory applies to organic reactions in which the mesomeric demands during the course of the reaction result in a highly localized electron distribution at the reaction center [for a brief but lucid discussion see ref. (63)]. Indeed, from his data showing a linear relationship between substituent constants and the energy of adsorption (reproduced in Fig. 1 of Donahue and Nobe's paper), Snyder concluded that he was observing charge localization at the nitrogen atom in his compounds during adsorption onto alumina from a highly nonpolar solvent.[64]

Donahue and Nobe have taken charge localization at a specific atom as an assumption, and as a necessary part of their theory. It seems to me that this

[42] J. Masek and H. Przewlocka, *Coll. Czech. Chem. Commun.*, 28, 673, 680 (1963).

[43] J. W. Mellor, cited, p. 701.

[44] T. Mussini and G. Casarini, *Chem. e Ind.*, 47, 600 (1965).

[45] G. Bianchi and T. Mussini, *Electrochim. Acta.*, 10, 445 (1965).

[46] J. Masek, "Advances in Polarography," I. S. Longmuir, Editor, Vol. I, p. 340, Pergamon Press, New York (1960).

[47] J. Masek and H. Przewlocka, *Coll. Czech. Chem. Commun.*, 28, 670 (1963).

[48] G. Bianchi, T. Mussini, and C. Traini, *Chim. Ind.*, 45, 1333 (1963).

[49] Los Alamos Scientific Laboratory, University of California, Los Alamos, New Mexico.

[50] P. G. Cotter and J. A. Kohn, *J. Am. Ceram. Soc.*, 37, 415 (1954).

[51] N. H. Krikorian, W. G. Witteman, and M. G. Bowman, *This Journal*, 110, 560 (1963).

[52] H. Goretzki, Doctoral dissertation, University of Vienna, 1963.

[53] H. Bittner and H. Goretzki, *Monatsh. Chem.*, 93, 1000 (1962).

[54] H. Nowotny, F. Benesovsky, and E. Rudy, *Monatsh. Chem.*, 91, 348 (1960).

[55] N. H. Krikorian, T. C. Wallace, and J. L. Anderson, *This Journal*, 110, 587 (1963).

[56] R. P. Adams and R. A. Beall, U. S. Bureau of Mine Rpt. Invest. 6304, 1963.

[57] V. I. Zhelankin and V. S. Kutsev, *Zhur. Strukt. Khim.*, 4, 865 (1963).

[58] C. R. Houska, *J. Amer. Ceram. Soc.*, 47, 310 (1964).

[59] R. V. Sara, Tech. Doc. Rpt. WADD TDR-60-143, Part V, 1964.

[60] V. N. Paderno, Izv. Akad. Nauk SSSR, Otd. Tekhn. Nauk, Met. i Toplivo, p. 176, 1962.

[61] T. F. Lyon, "Condensat. and Evap. of Solids," E. Rutner, P. Goldfinger, and J. P. Hirth, Editors, Gordon and Breach, New York (1964).

[62] Petrolite Corporation, 369 Marshall Avenue, St. Louis, Missouri 63119.

[63] J. F. Bunnett, "Technique of Organic Chemistry," Vol. 8, S. L. Friess, E. S. Luwis, and A. Weissberger, Editors, pp. 210-220, Interscience Publishers, Inc., New York, (1961).

[64] L. R. Snyder, *J. Phys. Chem.*, 67, 2344 (1963).

assumption is sufficiently challenged by previously reported work that its validity will have to be solidly confirmed before reliable substituent constants can be developed for inhibitor situations. In adsorption (particularly at metal surfaces where proton acidity is not possible) or in inhibition, there is no *a priori* reason why electron localization should occur at a specific atom in an aromatic molecule.

Among the literature references which challenge the charge-localization assumption, the following are typical: Bockris and co-workers have found that when aromatic molecules adsorb to metal surfaces from solutions of electrolytes, the electrons in the conjugated system participate in the bonding.[65] Furthermore, they have found that the contribution to the free energy of adsorption of a hydrocarbon radical is greater by about 6 kcal/mole for the naphthyl radical than for the butyl radical.[66] Indeed, they have found that naphthalene itself will adsorb to metal surfaces in the flat position.[67] Finally, in every adsorption investigation of which I am aware where the configuration of the aromatic amine was examined critically, it was found that the aromatic molecules preferentially adsorbed parallel to the plane of the metal surface.[68-70] All of this body of evidence supports the thesis that participation is predominantly by the electron cloud of the conjugated system, not by electron localization at an individual atom.

In fact, interaction of the electron cloud of double bonds (without localization at one of the atoms connected by the bond) is observed in a rather wide range of circumstances including: olefins with metal ions[71]; olefins with metal surfaces from the gas phase[72]; and even with an acidic hydrogen as in hydrogen bonding.[73,74]

In view of this background, indicating that the electron cloud of the conjugate bonds of an aromatic system also participate in the adsorption of molecules at metal surfaces, it is disappointing when a large portion of the author's data points do not fall on the theoretical line supporting the single atom anchoring group hypothesis, and when in large measure the arguments revolve around reasons why the anomalous points do not fit the theoretical line. For example, in Fig. 2 it is argued that only four out of the eight points should fall on the theoretical line. It seems to me certainly possible that the theoretical line is not correct either when one can draw a straight line through six out of eight of the points, if the last six points are used instead of the first four.

To put this theory into a category worthy of working into inhibitor function correlations, or other aspects of inhibitor research, a carefully selected group of compounds should be critically examined to establish the statistical fit of the points to a line. Ideally there should be the widest spread possible, both on the inhibition axis and on the substituent constant axis. It should be possible to take these data relatively simply under controlled conditions of concentration, volume of acid, temperature and corroding time so that (*a*) the rate of corrosion is constant throughout the corroding period; (*b*) reproducibility is at least ± 10%; and (c) the effects from the poorer compounds are sufficiently different from the better ones that they can be reliably differentiated. Complex equipment and procedures are not necessary for this purpose; a judicious choice of compounds which are then reliably examined under identical experimental conditions is necessary.

I think this attempt to formalize the general approach to the structure-inhibition problem is possibly a useful one. It would be a great deal more useful if a reasonable amount of confidence could be found in experimental support for the approach. I hope this support will be put forth in the near future and that it will bear out the reliability of the theory.

Francis M. Donahue[75] and Ken Nobe: The authors wish to express their gratitude for Dr. Annand's interest in our work and his comments. However, we feel that he has not completely understood our intent.

We are not attempting to develop "a specific set of sigma values for inhibitor or adsorption situations." On the contrary, it is our intent to utilize the existing sigma values which are found in the literature (we cited four such references in the paper under discussion).

It appears that Dr. Annand has misread Snyder's[76] and our work concerning the correlation of the free energy of adsorption (Snyder's data) and substituent constants. The $\Delta\Delta G_{ads}$ data plotted in Fig. 1 of our paper were the differences between the "ΔF_p average" values of the substituted pyridine compounds and the ΔF_p average value of pyridine in Snyder's Table III.[76] On the other hand, in his LFER correlation, Snyder[76] plotted the $\Delta\Delta F_p$ values tabulated in his Table III. These values were the differences in the ΔF_p average (experimental results) and the ΔF_p calculated from his Eq. [5].[76] According to Snyder,[76] this equation accounts for contributions to the free energy of adsorption from all adsorbate groups within the molecule as well as the strongly adsorbing groups, but does not account for the electronic effects of the substituent on the strongly adsorbing groups (*e.g.*, the nitrogen in pyridine). Thus, the $\Delta\Delta F_p$ values in Snyder's Table III are a measure of the latter effects. He achieved a correlation for all his adsorbates (excluding the O-substituents).

Although Snyder's results showed that the nitrogen atom of the pyridines, pyrroles and anilines was strongly adsorbed, thus substantiating the anchoring group concept, he concluded that these compounds were all adsorbed parallel to the adsorbent surface. It is evident that adsorption at the anchoring group and parallel adsorption are not as mutually exclusive as Dr. Annand seems to imply.

Dr. Snyder[77] has pointed out that the method of plotting Fig. 1 in our paper assumes there is no contribution to the adsorption energy from the substituent group; results of other types of compounds show that the substituent groups could contribute to the adsorption energy. Therefore, according to Snyder,[77] our interpretation of the points in group B of Fig. 1 in our paper appears incorrect since the adsorption energies due to the substituents were not considered.

The concept of charge localization has indeed been utilized in the initial developments of LFER theory by organic chemists studying homogeneous reaction kinetics. However, in the opening paragraph we state "the assumption that the electron density at the 'anchoring group' uniquely determines the adsorbability still allows the possibility of π-interactions *provided* (emphasis added) that such interactions are assumed to vary in the same qualitative manner as the electron density at the functional group under consideration." Since the function group (nitrogen) in the pyridines is part of the conjugated system, it is not an outland-

[65] E. Blomgren and J. O'M. Bockris, *J. Phys. Chem.*, **63**, 1475 (1959).

[66] E. Blomgren, J. O'M. Bockris, and C. Jesch, *J. Phys. Chem.*, **65**, 2000 (1961).

[67] J. O'M. Bockris, M. Green, and D. A. J. Swinkels, *This Journal*, **111**, 743 (1964).

[68] Yu Yao Yung-Fang, *J. Phys. Chem.*, **68**, 101 (1964).

[69] B. H. Claussen, *This Journal*, **111**, 646 (1964).

[70] R. R. Annand, R. M. Hurd, and N. Hackerman, *This Journal*, **112**, 138 (1965).

[71] R. G. Guy and B. L. Shaw, "Advances in Inorganic Chemistry and Radio Chemistry," H. J. Emeléus and A. G. Sharpe, Editors, pp. 79-81, Academic Press, Inc., New York (1960).

[72] L. H. Little, N. Sheppard, and D. J. C. Yates, *Proc. Roy. Soc.*, **A-259**, 242 (1960).

[73] A. W. Baker and A. T. Shulgin, *J. Am. Chem. Soc.*, **80**, 5358 (1958).

[74] M. R. Basila, E. L. Saier, and L. R. Cousins, *J. Am. Chem. Soc.*, **87**, 1665 (1965).

[75] Present address: Department of Chemical and Metallurgical Engineering, University of Michigan, Ann Arbor, Michigan.

[76] L. R. Snyder, *J. Phys. Chem.*, **67**, 2344 (1963).

[77] L. R. Snyder, Private communication.

ish assumption to suggest that the electron densities in the conjugated system are coupled to that at the nitrogen.

Annand's allegation notwithstanding, there is an *a priori* reason why there should be electron localization at specific atoms in an aromatic molecule provided that one defines electron localization in terms of the electronic charge densities which may be calculated based on Molecular Orbital Theory.[78,79]

Correlations have been obtained by us[80-82] utilizing the data of Blomgren and Bockris.[83] The latter showed rather conclusively, as Annand has pointed out, that the orientation is parallel to the surface. Such a correlation by us merely underlines the validity of the proviso which we added to the original premise and have enumerated above.

Annand suggests that Fig. 2 is a rather weak argument for the correlation since he feels that more collinear points are obtained by ignoring, among other things, the parent compound. Such an attempt is justified only if one is attempting to fit data. It was our intent that we test the extent of the theory. On the basis of the theory, four of the points were required to fall on the line. The others were not. We frankly admitted, however, that one of those points did and we likewise surmised that, on the basis of Fig. 2, we could not make a firm statement concerning the orientation of the pyridines on iron. It should be noted that Hackerman and Ayers[84] were likewise at a loss to choose whether the orientation was parallel or not on the basis of their data.

As Annand has pointed out, to verify the suggested relationships it will be necessary to study systems where the extent of inhibition is large as well as the range of sigma values. We have addressed ourselves to this problem in the past[80-82] and are currently extending the initial studies.[85]

It was not our intent in the paper under discussion to present a panacea to the problem of the structure-inhibition relationship. It was instead an attempt at formalizing an approach to inhibition in a manner which has been hinted by previous authors, but which has not been structured such that it could be tested quantitatively. We feel that this paper was, at best, a first approximation, but it is felt that it is a significant starting place.

The Effect of Electrode Pretreatment on the Oxygen Reduction on Platinum in Perchloric Acid

Y. L. Sandler and E. A. Pantier (pp. 928-931, Vol. 112, No. 9)

G. Bianchi and T. Mussini[86]: In a recent paper on cathodic reduction of oxygen on smooth platinum electrodes in acid solutions,[87] phenomena of platinum poisoning during the cathodic reduction of oxygen in acid solution (0.5M H_2SO_4) have been put in evidence. Such a poisoning can be destroyed either by a cathodic polarization at potentials lower than + 0.2v, NHE, or by an anodic polarization at potentials higher than + 1.2v, NHE. In our opinion, such a poisoning is not due merely to oxygen strongly embedded in the surface, but to an intermediate species reducible or oxidizable which we deduced to be the HO_2 radical stabilized on the platinum surface. In a previous paper on catalytic decomposition of acid hydrogen peroxide solutions on platinum, iridium, palladium, and gold surfaces,[88] of which the authors seem to be unaware, we showed that an anodic or a cathodic treatment of the platinum surface does not change the catalytic activity of platinum for the decomposition of hydrogen peroxide, provided such treatments (anodic or cathodic) are made for short times and with moderate overpotentials, so that significant amounts of hydrogen or oxygen are neither evolved nor absorbed on platinum. On the contrary, an increasing catalytic activity of platinum treated with hydrogen may result from the destruction of the oxygen embedded in the surface (or better, in our opinion, of the adsorbed HO_2 radical) by hydrogen diffusing from the bulk of platinum. For this reason we thing it is necessary to degas platinum *in vacuo* at 500°C in order to obtain reproducible and reliable results when studying the cathodic reduction of oxygen. Another important point to be taken into due account is that some impurities, like chloride ions (and halide ions in general), can poison the platinum surface and strongly affect the catalytic decomposition of hydrogen peroxide.

Y. L. Sandler and E. A. Pantier: We cannot express a definite opinion as to the reason for the very strong poisoning observed by Bianchi and Mussini in their experiments. It may be connected with the particular experimental methods used.

The main point in our paper was the demonstration of the effect of the existence of different modes of oxygen chemisorption on the characteristics of the platinum oxygen electrode. This possibility is not considered and no evidence for it is found in Bianchi's work. In our experiments, the very strongly bound oxygen was formed either by thermal pretreatment of the electrode with oxygen at a high-temperature (and transfer to the cell in a closed system) or by pretreatment *in situ* at a high anodic potential.

Bianchi and Mussini's argument that short term variations in potential (between +0.6 and 1.1v, Bianchi and Mussini's Ref. 88) do not essentially influence the catalytic activity, is not in disagreement with our results and presumably means that the strong oxygen chemisorption is not affected under these conditions.

Our samples, after hydrogen pretreatment, were flushed with pure helium at 600°C for about 10 min before cooling very slowly in helium. It is unlikely that this treatment is less effective in removing the hydrogen than Bianchi and Mussini's treatment *in vacuo* at 500°C for 3 hr; it is also unlikely that any remaining hydrogen could support a sufficient flux to the surface at room temperature for continuous removal of HO_2 radicals which Bianchi and Mussini consider to be the poisoning species.

Any difference in the results must be due to differences in the purity of the system and electrode pretreatment. Bianchi and Mussini's standard pretreatment consists of grinding the electrode with quartz powder while exposed to laboratory air. No sensitivity to oxygen pretreatment is found by these authors. They come to the conclusion that their pretreatment simply makes the platinum surface really bare (Bianchi and Mussini's ref. 87, p. 447). We find this hard to believe and suggest that this result merely emphasizes again the need for very careful control of purity in this type of research.

[78] "Molecular Orbital Calculations," by J. D. Roberts, Benjamin, New York (1962).

[79] A. Streitwieser, "Molecular Orbital Theory for Organic Chemists," John Wiley & Sons, Inc., New York (1962).

[80] F. M. Donahue, Ph.D. Thesis, University of California (1965).

[81] F. M. Donahue, A. Akiyama, and K. Nobe, To be published.

[82] F. M. Donahue and K. Nobe, Paper presented at the Buffalo Meeting of The Electrochemical Society, October 10-14, 1965. Abstract 57.

[83] E. Blomgren and J. O'M. Bockris, *J. Phys. Chem.*, 63, 1475 (1959).

[84] R. C. Ayers, Jr., and N. Hackerman, *This Journal*, 110, 507 (1963).

[85] A. Akiyama and K. Nobe, Unpublished results.

[86] Laboratory of Electrochemistry and Metallurgy, University of Milan, Milan, Italy.

[87] G. Bianchi and T. Mussini, *Electrochim. Acta.*, 10, 445 (1965).

[88] G. Bianchi and T. Mussini, *Electrochim. Acta.*, 7, 457 (1962).

The Indous Ion: an Intermediate in the Electrochemical Oxidation of Indium Metal

R. E. Visco (pp. 932-937, Vol. 112, No. 9)

M. E. Straumanis[89]: Although it is known that In(I) ions exist even in aqueous solutions, nevertheless, there are observations which are not in accord with the electrochemical mechanism proposed, postulating that the irreversible electrochemical step is associated with the further oxidation of In(I) to In(III).

Davidson and Jiric[90] could not prove the presence of In^+ ions during the dissolution of the metal in acids; therefore they assumed, in order to explain the deviation from Faraday's law, that a secondary reaction occurs in acidic solutions with high speed

$$In^+ + 2H^+ \rightarrow In^{3+} + H_2 \qquad [1]$$

Stubbs[91] doubts whether there are In^+ and In^{2+} at all in form of oxides.

Straumanis and Martin[92] concluded from coulometric measurements that In (from an amalgam) goes into solution quantitatively (within the limits of error) only in the form of In^{3+}. Therefore, the first step is

$$In^o \rightarrow In^{3+} + 3e \qquad [2]$$

and there seems to be no justification for step 3:

$$In^o \rightarrow In^+ + e \qquad [3]$$

What might have happened in the experiments of Dr. Visco was the anodic partial disintegration of In. Already Davidson and Jirik[90] saw that, while the current was flowing, fine particles separated from the In anode and accumulated at the bottom of the vessel. This observation could be confirmed later.[92] Figure 1 shows such metallic In particles.

That the particles could not originate in a disproportionation process

$$3In^+ \rightarrow 2In + In^{3+} \qquad [4]$$

follows from the coulometric measurements, as no In^+ ions were formed.

Therefore, what is swept away from the In anode are not In^+ ions but very fine metallic In particles originating from the partially disintegrating anode. However, since small amounts of In^+ were detected polarographically, it might be that reaction [4] is slightly reversible: some In^{3+} are reduced by the fine

[89] University of Missouri at Rolla, Graduate Center for Materials Research, Rolla, Missouri.

[90] A. W. Davidson and F. Jirik, *J. Am. Chem. Soc.*, 72, 1700 (1950).

[91] M. F. Stubbs, *J. Am. Chem. Soc.*, 74, 6201 (1952).

[92] M. E. Straumanis and R. L. Martin, *Z. anorg. u. allgem. Chem.*, 334, 321 (1964).

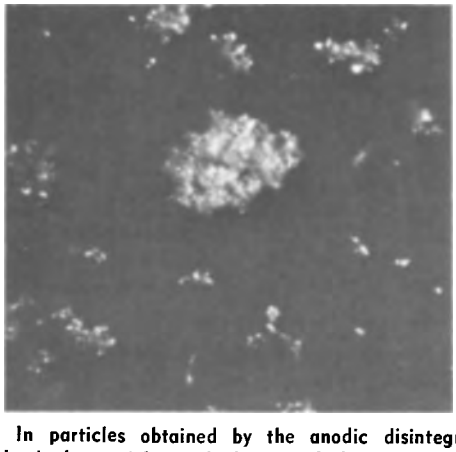

Fig. 1. In particles obtained by the anodic disintegration of the metal; single particles and clusters of them; current density, 70 ma/cm^2. 1430X, oil immersion.

In^o particles to In^+. The In-amalgam may act in the same manner. In fact the reducing ability of In metal or particles was even used by Dr. Visco to have In(I) in solution[93]:

$$In(III) + 2In(0) \rightleftharpoons 3In(I) \qquad [5]$$

Naturally, In(I) must then be found polarographically, if In(0) is present. Since finest In particles are formed continuously during anodic dissolution (at 70 ma/cm^{-2} streams of them can be detected already with the bare eye), a large surface of In metal is available for reaction [5]. Now the necessity of stirring becomes evident: it increases the outcome of In(I). This outcome also depends on the current density (see abstract) because the degree of surface disintegration of the anode changes with it.

Thus, Dr. Visco showed only that unstable In(I) is formed (in a secondary reaction) but not at all that the formation of In(I) is the first step in the dissolution of In(0) which also would be in contradiction to the coulometric measurements.[92]

Robert E. Visco: The observation by Professor Straumanis that an indium anode disintegrates when it is shorted to a large platinum cathode is doubtless quite real; but under these conditions, the initial current density is large (easily the order of 1A/cm^2) and it seems likely that preferential attack along grain boundaries could occur, thereby altering the anode surface and providing a mechanism for easy particle formation. One of the points of my paper was to investigate in a controlled way the low current density region in the anodic dissolution of indium metal where gross attack is less likely. I wished to determine (*a*) If measurable quantities of In^+ can be detected, and (*b*) if In^+ is formed, does it account for the apparent deviations from Faraday's law (based on an assumed 3 equivalents/mole for the oxidation of In). The answer to both questions is yes; In^+ can be found by polarography in the anolyte, and the quantity of In^+ formed as determined either independently by polarography or coulometry agree and they show that sufficient In^+ is formed to explain the apparent deviations from Faraday's law.

Further, I went on to point out in this and an earlier paper[93] that since indium electrodes do not corrode at an appreciable rate in In^{+++} solutions containing only $HClO_4$, the equilibrium:

$$In^{+++} + 2In \rightleftharpoons 3In^+$$

is difficult to achieve in acid solution containing no complexing anions and, further, it must lie far to the left. How then does one explain large quantities of In^+ observed on anodic dissolution? The simplest and I think the most rational explanation is to say that In oxidation occurs in unit steps to give In^+, then In^{+2}, and finally In^{+3} and that the reason In^+ can be observed in the dissolution is because the rate-determining step in the above sequence is after In^+ formation. Thus, In^+ can be transported away from the anode. Recently Losev[94] has reached the same conclusions, based on an entirely different set of experiments and procedures. These experiments, in effect, measured the same quantities which I have reported.

The above results were confirmed by studies of the anodic dissolution of dilute amalgams. Recent unpublished calculations indicate that the quantity of In^+ formed from metal and amalgam anodes seems to be dependent only on the activity of indium in the amalgam relative to that in the metal. This suggests that the initial unit step in the anodic dissolution, that is

$$In \rightleftharpoons In^+ + e^-$$

[93] R. E. Visco, *J. Phys. Chem.*, 69, 202 (1965).

[94] A. P. Pchelnikov and V. V. Losev, *Protection of Metals*, 1, 482 (1965).

is at equilibrium for both liquid and solid indium electrodes and that the rate-determining step is later in the sequence of unit steps which lead to In^{+++}.

The Hydrogen Evolution Kinetics and Hydrogen Entry into α-Iron

J. O'M. Bockris, J. McBreen, and L. Nanis (pp. 1025-1030, Vol. 112, No. 10)

F. E. DeBoer[95]: In the first part of the discussion section, the authors say that two simultaneous reactions are occurring: reaction A (the hydrogen evolution reaction), and reaction B (hydrogen permeation). According to the data, reaction B is 1% of the total. It seems unreasonable that from the characteristics of this very minor reaction one can make definite conclusions about the mechanism of the major reaction, as the authors have done.

Complicating matters is the fact that they have taken no account of the complex nature of their membrane; that is, α-iron was treated as a perfect membrane for hydrogen permeation. It is the hydrogen that has permeated the iron that is measured, and these measurements are used to make conclusions about the hydrogen that has not even entered the iron; no account at all is taken of the hydrogen that has entered the iron and has not come out (*i.e.*, the hydrogen atoms might combine at internal discontinuities, and so forth). It is feasible that the amount of internal hydrogen is far greater than that which is measured.

The fact that the single crystal data are similar to the polycrystalline data does not invalidate this criticism, since atoms can be rendered immobile inside the iron at sites other than crystal boundaries.

J. O'M. Bockris, J. McBreen, and L. Nanis: In Eq. [3] and [9] of our paper, we give the relationship between the H permeation rate, the coverage (θ), and the rate of H evolution. The only major assumption here is that the adsorbed H intermediate is the same for H entry into the metal and for H gas evolution. The fraction of H which passes through the metal is related to the diffusion coefficient, the membrane thickness, and the ratio of the rate constants of the surface to bulk reactions. For the membrane thickness used, the potential range covered, and the temperature of the investigation, it turns out that the rates are such that the H which permeates the metal is of the order 1% of the total H which is discharged per unit time. Variation in the permeation rate with potential for constant inhibitor concentration reflects changes in θ, *i.e.*, of the adsorbed intermediate concentration. However, $\partial\theta/\partial\eta$ is a function if the mechanism assumed for the evolution reaction and theoretical relations are known which principal mechanisms. Hence the permeation-potential relation gives evidence concerning the mechanism of the evolution reaction which runs parallel to the permeation.

The consistence of our results support the assumption of identical intermediates for both reactions. The fact that the permeation rate happens to be about 1% of the total discharge rate in our system is not directly relevant to a discussion of mechanism.

The matters concerning H in the metal are dealt with in detail in a paper by Beck, Bockris, McBreen, and Nanis* which will be published shortly. In the potential region referred to for mechanism indications, it was found that no trapping of H occurred in the metal. Such trapping did occur if the potential was made more negative than a certain value. Data obtained in this region were not used to deduce mechanism: hence the termination of the permeation potential plots at about −0.5v with respect to NHE.

U. R. Evans[97]: The research provides valuable information about the entry and movement of hydrogen, and is greatly to be welcomed. The picture of the mechanism in absence of "poisons" appears acceptable, particularly the idea that the adsorbed state assumed before entry into metal as atoms is the same as that assumed before evolution as molecular gas (p. 1027). I am not equally happy about the idea (p. 1030) that poisons directly favor entry by loosening the H-metal bond; most earlier theories have pictured the poison as interfering with H_2 gas formation, and thus indirectly favoring the alternative reaction, the entry into the metal as atoms. Such a view appears to me more probable.

If adsorbed anions loosen the $M\text{-}H_{ads}$ bond, then doubtless, provided that nothing else happens, the number of H atoms passing from an external (adsorbed) site to an internal (absorbed) site will be increased, say from n to $n + \Delta n$, so that the proportionate increase in hydrogen entry would be $\Delta n/n$. But the same loosening will surely increase the number of hydrogen pairs joining to form molecular (gaseous) H_2, say from N to $N + \Delta N$; since we are now dealing with pairs, the difference between squares must be taken and, if nothing else happens, the proportionate outward movement as H_2 gas will be

$$\frac{(N + \Delta N)^2 - N^2}{N^2} = \frac{2\Delta N}{N}, \text{ approximately}$$

Unless there is reason to think that $\Delta n/n$ is greater than $2\Delta N/N$, there is no reason to expect, on these grounds, that adsorption of CN or I will increase the entry of atomic hydrogen into the metal.

A more probable explanation, involving no *ad hoc* assumptions about bond loosening, is based on the fact that where a process involves two adjacent atoms, it will be more affected by coverage with a poison than a process involving only one atom. If α is the fraction of the surface not covered with poison (CN or I), then the rate of entry of atomic hydrogen (in absence of rival process) would be $k_1\alpha$, where k_1 is a constant, but the rate of evolution of *molecular* hydrogen would be

$$k_2\alpha p_{\alpha c}$$

where $p_{\alpha c}$ is the probability that a neighboring site is uncovered with a poison atom, which depends, not only on α, but also on c, the coordination number defining the number of "neighbors." Since two sites are involved in the H_2-evolution, it may be expected that

$$\frac{\text{Entry of atomic H}}{\text{Evolution of molecular } H_2} = \frac{k_1\alpha}{\frac{1}{2}k_2\alpha p_{\alpha c}} = \frac{2k_1/k_2}{p_{\alpha c}}$$

If c were known, $p_{\alpha c}$ could be calculated from simple probability theory. However, whatever the value of c, $p_{\alpha c}$ must decline as α declines, and immediately we reach the conclusion that, in absence of further complications, an increase of contamination with CN or I will diminish the fraction of hydrogen evolved as gas and increase that entering the metal as atoms.

This is only true of substances adsorbed as small ions or atomic groups. If the substance adsorbed consists of large molecules of irregular shape, there will be irregular gaps between the covered areas which, being left uncovered, will offer the same facilities for H-entry and H_2-evolution as a surface which is completely uncontaminated. Since the coverage of a large fraction of the area will, at constant potential, reduce the total current flowing, it follows that both H-entry and H_2-evolution will be reduced.

This seems to explain why CN and I favor the entry of hydrogen into metal, while organic nitriles diminish it. The effect of naphthalene is not so easily explained. It may be that single H atoms can enter the metal

[95] Corrosion Research Laboratory, Continental Can Company, Incorporated, 7622 South Racine Avenue, Chicago, Illinois.

[96] W. Beck, J. O'M. Bockris, J. McBreen, and L. Nanis, *Proc. Roy. Soc.*, in press.

[97] 19 Manor Court, Grange Road, Cambridge, England.

through the centers of the hexagonal rings, but that the points of entry are too much isolated from one another to allow union as H_2; this picture may seem rather fanciful, but it is difficult to think of an alternative.

J. O'M. Bockris, J. McBreen, and L. Nanis: Dr. Evans' view that additives effect the permeation rate of H through Fe by reduction of the rate of combination of H to H_2 is certainly a possible suggestion for such phenomena. However, it would only be tenable if the rate-detemining step (r. d. s.) in the hydrogen evolution reaction were combination; or is, in the sequence $2H^+ + 2e \rightarrow 2H_{ads} \rightarrow H_2$, the latter step were in equilibrium. In fact, the relation of the permeation rate to current density on the polarization side of the membrane

$$\partial P/\partial \ln J = 4\,RT/F$$

suggests strongly that $H^+ + e \rightarrow H_{ads}$ is the r. d. s. and is coupled to the following H combination reaction, with the reaction velocity $H_2 \rightarrow 2H_{ads}$ being negligible.

The most important of the points of experimental evidence in favor of this concerns the change of reaction rate associated with a change of permeation rate. As the r. d. s. for the over-all evolution reaction is not combination, the change reaction rate following additive additions (with constant mechanism) must arise from the effect of the adsorbed additive on bond strength. Thus, a decrease of the M-H bond strength would be consistent with an increase in overpotential for the same total current density,† but this would also lead to a corresponding increase of the permeation rate, as observed with CN^- and I^-.

We do not think that Dr. Evans' hypothesis is consistent with both the linked increase of over-potential and permeation and with the r. d. s. consistent with the $V/\log J$ relation.

In addition, the observations on the change of β with additions of additives has to be interpreted. Qualitatively, this arises from our model, for β depends on $\partial U/\partial x$, the slope of the potential energy-distance relation in stretching of the metal-hydrogen bond. It is easy to show that this coefficient is proportional to the bond strength. Finally, it may be noted that the interpretation given here to the permeation results in not a special theory but an application of independent interpretations previously made in respect to so-called "poisons" on the velocity of the hydrogen evolution reaction.

Electrode Potentials in Fused Systems, IX. Liquid Junction Potentials in the AgCl-AgBr System

K. Stern (pp. 1049-1050, Vol. 112, No. 10)

A. J. Easteal[98]: For the experimental cell

$$\mathrm{Ag}\,|\,\underset{\text{(electrolyte I)}}{\mathrm{AgCl(x_1),\ AgBr(x_2)}}\,\|\,\underset{\text{(electrolyte II)}}{\mathrm{AgCl(x_1'),\ AgBr(x_2')}}\,|\,\mathrm{Ag}$$

where ‖ represents a liquid junction, Stern states: "In this cell any nonzero emf is a liquid junction potential and must arise from differences in the anion mobilities and transport numbers."

It is not true however that $(E_t - \epsilon) = 0$, where E_t is the cell emf and ϵ the liquid junction potential, except in certain limiting conditions. Assuming that the electrolytes I and II are completely dissociated into the simple ions Ag^+, Cl^-, and Br^-, and setting z_i equal to the electrovalency of the ions ($z_i > 0$ for cations, $z_i < 0$ for anions), the emf of the cell is given by the relationship[99]

$$E_t = -(RT/F)\int_{\mathrm{I}}^{\mathrm{II}} \sum_i t_i \left(-\frac{1}{z_i} d\ln a_i + \frac{1}{z_{Ag^+}} d\ln a_{Ag^+} \right) \quad [1]$$

and the liquid junction potential by

$$\epsilon = -(RT/F)\int_{\mathrm{I}}^{\mathrm{II}} \sum_i t_i \left(-\frac{1}{z_i} d\ln a_i \right) \quad [2]$$

By Eq. [1] and [2]

$$E_t - \epsilon = -(RT/F)\int_{\mathrm{I}}^{\mathrm{II}} d\ln a_{Ag^+} = -(RT/F)\ln(a_{Ag^+}{}^{\mathrm{II}}/a_{Ag^+}{}^{\mathrm{I}}) \quad [3]$$

where $a_{Ag^+}{}^{\mathrm{I}}$ and $a_{Ag^+}{}^{\mathrm{II}}$ denote the activities of Ag^+ ions in electrolytes I and II, respectively. According to Eq. [3], $E_t = \epsilon$ only if the activity of Ag^+ ions is the same in the two electrolytes. The fact that the concentration of Ag^+ is the same in the two electrolytes does not necessarily imply that no difference in a_{Ag^+} exists. If the system AgCl + AgBr were thermodynamically ideal in the sense

$$\left.\begin{array}{l}\gamma_{AgCl} = \gamma_{AgBr} = 1, \text{ for all values of } x \\ \text{such that } x_1 \geq x_{AgCl} \geq x_1'\end{array}\right\} \quad [4]$$

(where γ denotes activity coefficient) then it would be reasonable to assume that

$$\left.\begin{array}{l}\gamma_{Ag^+} = 1 \\ x_1 \geq x_{AgCl} \geq x_1'\end{array}\right\} \quad [5]$$

However proposition [4] is not valid,[100] at least for mixtures whose composition is such that

$$0.60 \geq x_{AgCl} \geq 0.30$$

It is therefore not possible to assess the difference in the activity of Ag^+ ions in the two electrolytes. Consequently it may not be true that the whole of the cell emf arises from the liquid junction potential.

Stern also states that the cell emf can be zero only if $t_{Cl^-} = x_1$, $t_{Br^-} = x_2$. That this is not a necessary condition for vanishing cell emf, is shown by the following considerations: E_t is zero if and only if

$$-(RT/F)\int_{\mathrm{I}}^{\mathrm{II}} \{(t_{Cl^-}\cdot x_{AgBr} - t_{Br^-}\cdot x_{AgCl})/x_{AgBr}\}\, d\ln a_{AgCl} = 0 \quad [6]$$

Since $d\ln a_{AgCl} \neq 0$, a sufficient condition for $E_t = 0$ is, therefore

$$\left.\begin{array}{l}t_{Cl^-}/t_{Br^-} = x_{AgCl}/x_{AgBr} \\ \text{for all values of } x \text{ such that} \\ x_1 \geq x_{AgCl} \geq x_1'\end{array}\right\} \quad [7]$$

A particular circumstance for which this condition is fulfilled is

$$\left.\begin{array}{l}t_{Cl^-} = x_{AgCl} \\ t_{Br^-} = x_{AgBr} \\ x_1 \geq x_{AgCl} \geq x_1'\end{array}\right\} \quad [8]$$

The conditions expressed by Eq. [7] (and its special case, Eq. [8]), are not however, necessary conditions for $E_t = 0$.

K. H. Stern: Dr. Easteal has raised two points. The first of these is the old question of single-ion activity again. In essence the question is: "what is the single ion activity of Ag^+ in a AgCl-AgBr mixture," or "is the activity of Ag^+ in AgCl and AgBr the same?"

Now we certainly know the activities of the thermodynamic components AgCl and AgBr in AgCl-AgBr

† We refer to "the same" current density for hydrogen evolution because the fraction of H which passes through the membrane is about 1% of the total H discharged, so that, if the total current density is constant, the current used by hydrogen evolution is constant to better than 1%.

[98] Chemistry Department, University of Auckland, Auckland, New Zealand.

[99] This equation is readily derived by the method of E. A. Guggenheim, "Thermodynamics," p. 396 *et seq.*, North-Holland Publishing Co., Amsterdam (1959).

[100] I. G. Murgulescu and D. I. Marchidan, *Zh. Fiz. Khim*, 34, 2534 (1960).

mixtures. The activities of the pure components are unity if a Raoult's law standard state is used. But the difficulty is that we do not know how to split up $a_{AgCl} = a_{Ag^+} a_{Cl^-}$ into single ion activities either for the pure compound or for AgCl in the mixture.

For example, Dr. Easteal's Eq. [3] contains two unknowns, the liquid junction potential ϵ and the ratio $(a_{Ag^+}{}^{II}/a_{Ag^+}{}^{I})$. In order to evaluate one we must make some assumption about the other. The usual way out of this dilemma is to assign a value of unity to the activity ratio and to interpret the cell emf only in terms of events at the liquid junctions.[101] If Dr. Easteal has a better suggestion it does not appear in his comments.

His second point concerns Eq. [6]. Since $d \ln a_{AgCl} \neq 0$ and $X_{AgBr} \neq 0$ $E_t = 0$ if and only if $t_{Cl^-} - X_{AgBr} - t_{Br^-} X_{AgCl} = 0$.

Now, since t_{Cl^-} and t_{Br^-} are transport numbers relative to t_{Ag^+}, $(t_{Cl^-} + t_{Br^-}) = 1$ and also $X_{AgBr} + X_{AgCl} = 1$ from which his Eq. [7] and [8] follow immediately. Thus these equations are not only sufficient but also necessary.

The Voltage Sweep Method—Electronic Device for Producing Triangle Pulse and Ramps

F. G. Will (pp. 1157-1159, Vol. 112, No. 11)

N. S. Clayton[102]: The paper by Will deals with a circuit to produce a slow linear voltage sweep. A solid-state circuit Fig. 1, which has identical functions is in

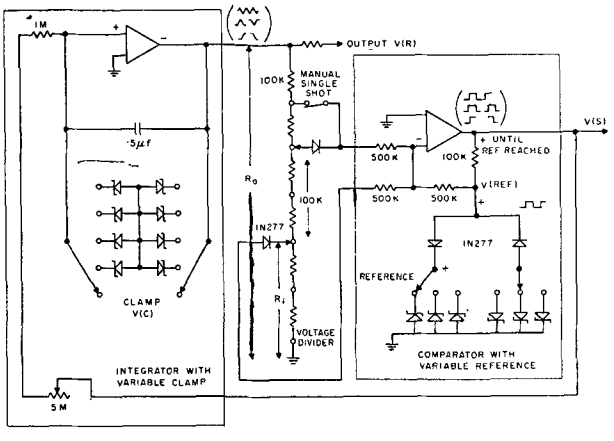

use here in conjunction with work on metal-oxide-silicon capacitors. Two operational amplifiers are used for integration and comparison, respectively. This allows the circuit to be constructed and modified simply and quickly.

Consider first the case with clamp switch open circuited. When the constant input to the integrator is positive, the output $V(R)$ ramps negative at a rate varied by the 5MΩ pot. R_1/R_0 of $V(R)$ is fed to the comparator.

The comparator operates in the noninverting mode in the sense that when the reference voltage V(ref) is reached the comparator switches to the same polarity as the input.[103] The sign of the feedback to the integrator $V(S)$ changes polarity causing the ramp to change direction. Note, $V(S)$ is always locked in positive or negative saturation due to positive feedback and thus provides a well-regulated input voltage to the integrator, while V(ref) is always clamped at the appropriate reference voltage.

$V(R)_m = (R_0/R_1)\ V$(ref), the height of wave form, is independently variable in each direction, provided the back biased diode on R_0 does not have significant leakage to the summing point.

It is now a simple matter to obtain single pulses or ramps starting from a prefixed voltage. A selection of back to back reference diodes may be switched in across the integrating capacitor which will clamp $V(R)$, *i.e.*, if $V(C) < (R_0/R_1)\ V$(ref). To unclamp or commence, a push button switch momentarily increases R_1 to change the state of the comparator.

The system is relatively insensitive to modifications: for example, the integrator feedback and interconnecting network have been varied by one or more orders of magnitude with no noticeable deterioration in performance. The integrating amplifier should be high quality, and the feedback network should allow little leakage current. The comparator amplifier is less critical. A high current amplifier (10 ma) is used to signal a stepping relay which automatically selects the next sample after one or half a cycle, as required.

F. G. Will: It is readily agreed that there are alternate methods of producing triangle pulses and ramps. It is the purpose of the original note to show how this can be done by a simple modification of commercial function generators that produce periodic waveforms. Dr. Clayton describes how operational amplifiers can be used to build a function generator as outlined in Textronix Manual 070-323. The addition of the back-to-back Zener diodes to clamp the integrator to several selected voltage levels is indeed a simple way of producing single pulses and ramps. It can be applied in cases where a continuous variation of clamping voltage levels is not required.

Logarithmic Oxidation Kinetics of Zinc

V. O. Nwoko and H. H. Uhlig (pp. 1181-1185, Vol. 112, No. 12)

F. E. DeBoer[104]: At the beginning of the paper, the authors say that the kinetics of this reaction have been described as parabolic as well as logarithmic. However, subsequently, they do not again refer to the possibility of parabolic behavior. On the contrary, they assert positively that they have proved that a two-stage logarithmic equation is obeyed. This is faulty on two counts: (*i*) the fact that a few points on semilog paper fit reasonably well on a straight line does not prove a logarithmic kinetic law. This is especially true when these points are closely bunched. Further, when it takes two straight lines to describe the form of these points, the possibility that this is indeed not a logarithmic relationship is high. (*ii*) The authors apparently did not test the parabolic law. In order to try this roughly, I used the curve labeled 206° of Fig. 2 and found that there was almost a perfect fit to a straight line described by $d = 2.35\ t^{1/2}$ (where d is oxide thickness in angstroms and t is time in minutes). Admittedly, it is difficult to determine data from a plot of the size presented (the other curves of Fig. 2 would be even harder to work with), but the fit was very good. Before assuming a two-stage logarithmic process, the authors should, at the least, show how well their original data fit when plotted in other ways, especially parabolically in this case.

A. Winterbottom in a discussion following Vernon's paper[105] pointed out that some of his low-temperature data would fit well on a parabolic plot. These were in the lower half of the temperature range discussed in the present paper. In view of this and the distinct possibility that the data discussed here conform to a parabolic law, it is probable that the oxidation is parabolic below 225° and logarithmic above 225° (see Vernon).

U. R. Evans[106]: The authors have done a service in showing that the oxidation of zinc shows the same

[101] K. H. Stern, *J. Phys. Chem.*, **63**, 741 (1959).

[102] Molecular Electronics, Research and Development Laboratories, Canadian Westinghouse Company, Limited, P.O. Box 510, Hamilton, Ontario, Canada.

[103] Operational Amplifiers and Their Applications, Tetronix Manual.

[104] Corrosion Research Laboratory, Continental Can Company, Incorporated, 7622 S. Racine Avenue, Chicago, Illinois 60620.

[105] W. Vernon, E. Akeroyd, and E. Stroud, *J. Inst. Metals*, **65**, 301 (1939).

[106] 19 Manor Court, Grange Road, Cambridge, England.

sudden breaks as does that of copper, nickel, cobalt, and iron. If the activation energy is almost the same for the two stages, that would suggest that the oxidation-mechanism is similar.

Figure 3 and Table I may convey the idea that oxidation is more rapid in the second stage than in the first. This is due to the fact that the time-scale in Fig. 3 is much more "open" for the first stage than for the second. The following table gives rough measurements of the time t_1 needed to produce the thickness L at which the second stage starts, and the additional time t_2 needed to produce an additional thickness equal to L (making $2L$ in all). Accurate measurements are impossible on any small-scale diagram, and the authors may care to provide a more accurate table. If they confirm that t_2 is greater than t_1, the conclusion will be that the second stage is the slower.*

Temperature, °C	L	t_1	t_2
125	4.5	95	245
157 (0.763 mm)	11	105	290
175	12	95	145
206	24	130	275

"Breakdowns," leading to spurts of renewed oxidation, are not confined to metal obeying the logarithmic law. Often there are several successive breakdowns; about 40 years ago, Pilling and Bedworth,[107] studying copper, published curves with about four breakdowns. Curves showing repeated breakdowns have also been published by Vernon,[108] by Tylecote,[109] and by Caplan and Cohen,[110] studying aluminum, copper, and iron-chromium alloys, respectively.

The rational explanation of breakdown is springing a leak of the film where it has become unsupported through the outward movement of cations, leaving vacancies. The same outward movement provides a simple explanation of the logarithmic growth law. At high temperature, these vacancies generally coalesce to form cavities, which are visible under the microscope, so that their existence is not in doubt. That, however, involves diffusion of vacancies over considerable distances; Dunnington, Beck, and Fontana[111] record cases where vacancies have diffused right through a sheet, so that its scale has become loose on one side while remaining adherent to the other side. Where there is coalescence of many vacancies into a few big cavities, the area where oxide is out of contact with metal is small, and the oxidation-rate will not be greatly effected. At low temperatures, diffusion of vacancies can only occur over small distances; some vacancies are doubtless annihilated at dislocations or other "sinks," others by atoms subsiding into them from the film, but some will remain at the interface. The effect will be to impede movement across the interface. When the gap between metal and oxide becomes at some places sufficiently broad to prevent crossing altogether, the area available for the passage of metal into oxide will diminish with time.† It has been shown[112] that this leads, according to the assumption made regarding the growth law which would be obeyed if the whole area remained available for passage, either to the classical logarithmic equation

$$W = k \log (at + 1)$$

or to a "new" logarithmic equation

$$W = k \log (at^{1/2} + 1)$$

There are, of course, numerous examples of conformity to the classical equation, but when first I arrived at the "new" equation,[113] no experimentally established example was available. Shortly afterwards, T. Mills, studying the oxidation of copper, brought me results which failed to accord with the classical equation. I suggested that he tried the new equation, with which he was then unacquainted; the results fitted.[114]

If the falling off, much faster than the parabolic law would predict, is due to an increasing area of "no contact" between metal and oxide, a time will come when the "roof" will collapse or start to leak, and oxidation will be resumed, over the areas in question, at roughly the original pace. If the breakdown does not occur until conditions of "no contact" have spread over the whole area, the scale will flake off intact. If it remains adherent (as on zinc), that is proof that the "no contact" condition has not been established everywhere, and the renewed oxidation-rate of the specimen as a whole will be less than at the start of the first stage—which appears to be the case.

The discussion between the authors and Fromhold shows that they are strongly attached to interpretations based on space charges. This comment is addressed to those who prefer an explanation which, without *ad hoc* assumptions, offers an interpretation of the known facts up to the breakdown; after the breakdown, the geometry becomes complicated and the kinetics difficult. The simplicity of the interpretation may be an advantage, since, if there is a flaw in the argument, no reader can fail to detect it.

H. H. Uhlig: To prove whether a single equation fits a given set of data requires experimental points over a sufficient time interval; otherwise more than one equation may fit the points. One of the traditional difficulties of treating thin film oxidation data is that the time interval over which thin films exist is relatively limited. Therefore, the suggestion has sometimes been made, as F. De Boer mentions, that the parabolic as well as the logarithmic equation applies. If still fewer points than those presented in our Fig. 2 had been taken, it could also be demonstrated that the linear equation fits the data. However, several investigators have previously demonstrated that the logarithmic equation is commonly the only equation which fits thin film oxidation data when the data are carried out over a sufficient length of time so as to leave no doubt about the matter. Lustman and Mehl[116] showed that the data they obtained on oxidation of copper single crystals could be represented only by the logarithmic equation and the same conclusion is reached from low-temperature data by Tylcote,[117] and from our own measurements on copper. Kubaschewski and Hopkins[118] conclude that most thin film oxidation data for metals conform to the logarithmic equation or inverse logarithmic equation, with distinction between the two being difficult.

* The reason why Table I shows a higher value for the rate constant (k'_1) of the second stage than for that of the fast stage (k_1) is that τ' is much larger (110-140 min) than τ (5.5-7 min). The equations are $y = k_1 \log (t/\tau + 1)$ and $y = k'_1 \log (t/\tau' + 1)$. Clearly a time of, say, 10 min will only slightly increase $(t/\tau' + 1)$ above unity, but will greatly increase $(t/\tau + 1)$. Thus, even supposing that the oxidation rates were the same in both stages, k'_1 would need to be much larger than k_1, if the same value of t (10 min) is to produce the same increase of thickness, y.

† A small amount of oxidation can develop gradually even at the areas of "no contact" by the mechanism proposed by Dravnieks and McDonald.[115]

[107] N. B. Pilling and R. E. Bedworth, *J. Inst. Metals*, 29, 529 (1923).

[108] W. H. J. Vernon, *Trans. Faraday Soc.*, 23, 152 (1927).

[109] R. F. Tylecote, *J. Inst. Metals*, 81, 681 (1952).

[110] D. Caplan and M. Cohen, *J. Metals*, 4, 1057 (1952); *Corrosion*, 15, 141 (1959).

[111] B. W. Dunnington, F. H. Beck, and M. G. Fontana, *Corrosion*, 8, 2 (1952).

[112] U. R. Evans, "Introduction to Metallic Corrosion," 2nd Ed., pp. 192-195. Arnold (1963).

[113] U. R. Evans, "Reviews of Pure and Applied Chemistry," 5, 1 (1955).

[114] T. Mills and U. R. Evans, *J. Chem. Soc.*, p. 2182 (1956).

[115] A. Dravnieks and H. J. McDonald, *This Journal*, 94, 139 (1948).

[116] B. Lustman and R. Mehl, *Trans. AIME*, 143, 246 (1941).

[117] R. Tylecote, *J. Inst. Metals*, 78, 327 (1950-1951).

[118] O. Kubaschewski and B. Hopkins, "Oxidation of Metals and Alloys," p. 37-39, Academic Press, New York (1962).

It was our intent, therefore, to show that our data for zinc obtained over a limited time interval are consistent with the logarithmic equation in accord with most thin film oxidation data. This we have done. In particular, our data are consistent with two-stage logarithmic kinetics, also found by other investigators, the theoretical significance of which is outlined.

Dr. Evans' comments deal first with the characteristics of any logarithmic relation. It is, of course, true that growth of oxides following the logarithmic equation decreases markedly as time proceeds. In fact, early investigators suggested that the oxide completely stopped growing after a given time, whereas it is now considered more likely that the oxide continues growing and that it is only the peculiar relation of oxide thickness to logarithm of time which makes it appear as if oxide growth ceases. In the two-stage logarithmic oxidation process, the important consideration is that the value of the reaction rate constant k'_1 in the relation $y - L = k'_1 \log(t/\tau' + 1)$ for second-stage oxidation is demonstrably greater than the corresponding value of k_1 during first-stage oxidation. The greater value of k'_1 compared to k_1 means that the corresponding thickness of oxide at any time beyond L is greater than it would otherwise have been had oxidation continued in accord with first-stage kinetics. This conclusion is clearly evident by examining our Fig. 3.

Dr. Evans is correct, of course, in pointing out that discontinuities in the oxidation rate have various causes. Most of the instances he cites are for relatively thick films where spalling and cracking of the oxide is the common cause. An example of discontinuous oxidation rate can also be seen in the data of Heindlhofer and Larsen for oxidation of iron at 700°C reproduced in the "Corrosion Handbook" on p. 633. However, spalling, blistering and cracking are not as likely to occur in thin film oxidation (100-10,000Å), and in fact we have never observed evidence for it in any of our numerous experiments on oxidation of copper, nickel, and chromium-iron alloys. Consideration should also be given to the fact that the beginning of second-stage logarithmic oxidation tends to be more reproducible than one would expect if accidental spalling and cracking, caused in part by thermal fluctuations, were the cause. The fact that second-stage logarithmic oxidation begins at about the same time and thickness for a given temperature of oxidation suggests that its cause lies in a different source. Our work on Volta potentials of growing thin oxide films suggested to us that space charge may enter as the important factor, and subsequent exploration of this possibility led to the conclusions that are outlined in our present and previous papers.

It is of some interest that Tylecote's data on oxidation of copper, cited as reference by Dr. Evans, lends support to our viewpoint. Tylecote found that the parabolic equation fitted his data only at high temperatures (615°-908°C) whereas the logarithmic equation fitted his data in the lower temperature range (350°-550°C) especially during the first stages of oxidation (thin films). The transition between logarithmic and parabolic kinetics is not sharply defined, but significantly Tylecote points out that the thickness at which the transition occurs is in the order of 10^5Å which he states is "the same order as the 'barrier layer' on copper/copper oxide rectifiers as determined by measurements of electrical capacity; this correspondence appears to support the contention of Campbell and Thomas[119] that the departure from the parabolic relationship at low temperatures is a consequence of the peculiar electrical conditions in these thin films." The maximum thickness of oxide, equal to 10^5Å, for which logarithmic oxidation kinetics apply, corresponds to our maximum thickness of space charge including both the constant density and diffuse space charge layers. Tylecote goes on to say that "the logarithmic curve appears to be in two portions" corresponding, of course, to our described first- and second-stage logarithmic kinetics.

I think it unlikely that any model of thin film oxidation based on movement of atoms or ions through an oxide lattice as the controlling mechanism can hope for much success in describing the facts as we now know them. For example, there is a marked effect of Curie temperature, crystal face and lattice type on the thin film oxidation rate. In general, any of these factors within the metal would not be expected to have an effect on rate of migration of species such as ions or vacancies in the oxide phase. For this reason, I believe that the work function of the metal which is affected by Curie temperature, crystal face and lattice type, plus a growing space charge in the thickening oxide (confirmed by Volta potential measurements) enter as the more important determining factors accounting for observed logarithmic oxidation kinetics.

[119] W. Campbell and U. Thomas, *Trans. Electrochem. Soc.*, 91, 623 (1947).

On the Use of Galvanostatic Transients for the Study of Fuel Adsorption on Platinum

M. W. Breiter (pp. 1244-1245, Vol. 112, No. 12)

S. B. Brummer[120]: In a previous paper[121] a novel current-reversal method of estimating fuel adsorption on Pt was described. In this method, which was used both for HCOOH adsorption[121] and CO adsorption,[122] an anodic pulse is applied to strip the adsorbate partially (charge Q). Then a cathodic pulse is applied to determine how much of Q has gone toward electrode oxidation ($Q_{o,cath}$ in Breiter's terminology) and how much has gone toward cleaning the adsorbate off the electrode. The latter is determined as the fraction of the electrode available for H-atom deposition (θ_H). In the paper under discussion, the general point about this method is made that it has rarely been found that $Q_{o,an}$ (charge in oxidizing Pt) is the same as the charge found in reducing the oxide ($Q_{o,cath}$). This point was appreciated in the application of the current-reversal method and was fully discussed both for HCOOH[123] and for CO.[122] In the latter case, $Q_{o,cath}/Q_{o,an}$ ($= \theta_H$) was found to be unity. This would remove the substance of the objection. For HCOOH, as indicated by Breiter, the extent of electrode oxidation is small until almost all the adsorbate has been oxidized. (However it is not zero; the importance of which will be shown later.)

In the case of other adsorbates, one would certainly have to know the value of θ_o. In this connection, one may note that in two rather careful recent studies by Bold and Breiter[124] and Gilman[125] θ_o has been found to be unity although the reduction of the Pt(O) is rather irreversible.[125] This irreversibility could pose a problem since it might mean that some oxide reduction is pushed into the H-atom deposition region. Since the oxide reduction is much more reversible when electrode oxidation is small, as it is in the application of the current-reversal technique, there is no interference due to oxide reduction in the H-atom deposition region. It is very likely that the reason θ_o is often found as < 1[126,127] is due to the presence of impurities in the solution. These impurities would adsorb on the Pt and their oxidation during the anodic pulse makes

[120] Tyco Laboratories, Incorporated, Bear Hill, Waltham, Massachusetts.

[121] S. B. Brummer, *J. Phys. Chem.*, 69, 562 (1965).

[122] S. B. Brummer and J. I. Ford, *J. Phys. Chem.*, 69, 1355 (1965).

[123] Tech. memo. no. 13 on Contract Nonr-3765(00), Aug. 1964.

[124] W. Bold and M. Breiter, *Electrochim. Acta*, 5, 145 (1961).

[125] S. Gilman, *Electrochim. Acta*, 9, 1025 (1964).

[126] K. J. Vetter and D. Berndt, *Z. Electrochem.*, 62, 378 (1958).

[127] S. W. Feldberg, C. G. Enke, and C. E. Bricker, *This Journal*, 110, 826 (1963).

an additional contribution to $Q_{o,an}$. If this were so, θ_o would always be unity when a strongly adsorbing fuel is available to adsorb on the electrode since this would prevent the adsorption of the impurities. This was found for CO adsorption.[122]

The paper also makes a number of specific points about the comparison between earlier results for HCOOH adsorption[128] and those obtained with the current-reversal method. It was reported[128] that θ_H decreases linearly with increase of θ_F during adsorption of HCOOH up to about 0.5 in θ_F (θ_F = $HCOOH_{ads}$ coverage/maximum $HCOOH_{ads}$ coverage). Thereafter, a curvature convex to the θ_F axis (curve b of Fig. 1) was found. Using the current-reversal method, θ_H and θ_F were found to be completely linear (curve a of Fig. 1). Breiter claims that there is in fact curvature at high θ_H in Fig. 5 and 6 of ref. (121). This is most evident he says in Fig. 6. No curvature, within the significance of the data, is evident to me in Fig. 5 of ref. (121). In Fig. 6, it should be noted that the data is uncorrected for electrode oxidation and for oxidation of material in the solution during the anodic transient. Both of these are discussed in ref. (121) (p. 569). The former is the more important in this case, and the dotted region of curve a at high θ_H in Fig. 1 is just the region when electrode oxidation is not zero. When this correction is made, the points at high θ_H of Fig. 6 of ref. (121) fall right on the line and θ_H is completely linear in θ_F over the whole range of coverage. There is another important point in this connection. Breiter appears to assume that curvature at high θ_H in Fig. 5 and 6 of ref. (121) would improve the agreement between curves a and b of Fig. 1. This is not so. If this curvature were real, it would lead to curve c in Fig. 1. This is concave to the θ_F axis and curved at the low θ_F end.

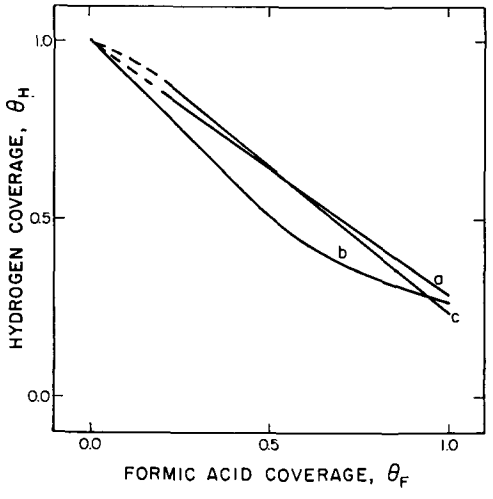

Fig. 1. Curve a, based on data of ref. (121) such that Q_{HCOOH}^{max} = 285 μcoul/real cm² and θ_H goes from 1.0 to ~0.28. Dotted region at low θ_H is omitted as described in ref. (121). Curve b, from paper under discussion, based on ref. (128). Curve c, based on ref. (1). Includes curvature suggested in paper under discussion, Q_{HCOOH}^{max} is taken as 356 μcoul/real cm².

The paper attempts to show that the estimate of Q_{HCOOH}^{max} in ref. (121) is too low, to improve agreement with data of ref. (128). Actually this would lead to further disagreement since the value of ref. (121) (285 μcoul/210 μcoul of H-atom charge, *i.e.*, per real cm²) is already higher than that of (128) (260 μcoul/real cm²). The agreement between these two values determined by two methods (10%) is already excellent considering that the comparison is based on 4 or 3 separate charge determinations, respectively, none of which is better than ± 1-2%.

The disagreement between curves a and b of Fig. 1 could arise as follows: Curve a represents the desorption of material adsorbed at a single potential: the slope gives the number of electrons released per site on oxidation of the adsorbate [~ 2, see ref (121)]. Curve b, on the other hand, represents the relationship between θ_F and θ_H when the HCOOH is adsorbed at various potentials. Specifically, the high θ_F end refers to material adsorbed at the lowest potentials. There is a considerable view growing that $HCOOH_{ads}$ is not HCOOH itself but some other species.[121,129,130,131] If this were so, we might not be surprised to find a more reduced species tending to accumulate on Pt during the last stages of HCOOH adsorption at low potentials. The slope of curve b at low θ_H is about 4 electrons per site, and this may represent evidence that some of the adsorbate at low potentials differs from that at higher potentials.[132]

M. W. Breiter: As stated in my paper, it was not mentioned in the fundamental paper[133] that the applicability of the technique depends upon the fulfillment of the condition $Q_{o,an}/Q_{o,cath}$ = 1. After this requirement was pointed out by me in the oral discussions at the Washington Meeting of the Electrochemical Society, it was dealt with in a subsequent paper[134] sent in for publication after the meeting. Reference (123) in Brummer's comments is not a publication. It is not clear why the above condition which represents a restriction of the technique was not discussed in the first paper[133] if it was known to its author. In the absence of fuel, the experimental result $Q_{o,an}/Q_{o,cath} \geq 1$ is due to a superposition of several effects: oxidation of adsorbed organic impurities, diffusion of oxygen atoms into the platinum, and O_2 evolution. It is not possible at present to separate the contributions of these processes.

With respect to the shape of the curves a and b in Fig. 1 of my paper, it should be pointed out that a straight curve implies that all the sites used for adsorption of H atoms are also used for the adsorption of HCOOH molecules or intermediates (COOH for instance). This assumption is not very likely. The specific points raised in Brummer's comments involve small corrections and extrapolations. The validity of the arguments falls in the realm of subjective judgment. The question of the nature of the adsorbed species has not been settled.

[128] M. W. Breiter, *Electrochim. Acta*, **8**, 447 (1963).

[129] S. B. Brummer and A. C. Makrides, *J. Phys. Chem.*, **68**, 1448 (1964).

[130] J. Giner, *Electrochim. Acta*, **8**, 857 (1963).

[131] J. Giner, *Electrochim. Acta*, **9**, 63 (1964).

[132] Data presented for adsorption of HCOOH at 0.2v [M. W. Breiter, *Electrochim. Acta*, **10**, 503 (1965)] show a higher value for Q_{HCOOH} than that found in ref. (128). This may also be evidence for this point.

[133] S. B. Brummer, *J. Phys. Chem.*, **69**, 562 (1965).

[134] S. B. Brummer and J. I. Ford, *J. Phys. Chem.*, **69**, 1355 (1965).

Equilibrium Pressures of Oxygen over Ag_2O-Ag at Various Temperatures

Earl M. Otto

National Bureau of Standards, Washington, D.C.

ABSTRACT

Although earlier investigators showed the dissociation of Ag_2O to be reversible and equilibrium points had been obtained, there was a range from 191° to 203°C that had not been studied. This region has now been studied. From all the data available and heat capacity data $\Delta H°_{298}$, $\Delta S°_{298}$, and $\Delta G°_{298}$ have been calculated to be 14.69 kcal, 31.92 kcal, and 5.17 kcal per mol O_2, respectively, for the dissociation reaction $2Ag_2O \rightarrow 4Ag + O_2$.

As early as 1887 LeChatelier (1) showed that the dissociation of Ag_2O into Ag and O_2 is reversible. Lewis (2) obtained three equilibrium points in the temperature range of 302°-445°C. Keyes and Hara (3) working in the range of 374°-500°C determined six equilibrium values, five of which were approached both by decomposition and by combination. Not until 1932 was this reversible reaction studied at 1 atm and lower. Benton and Drake (4) established equilibrium values at five temperatures from 173° to 191°C, similarly by combination as well as decomposition.

Since there was an intermediate range of 110°C that remained uninvestigated, and since there had been no overlapping of investigations at the lower temperatures, it seemed advisable to make a further study of the reaction. An examination of all the data of all four investigations should result in better calculated values for $\Delta H°$, $\Delta S°$, and $\Delta G°$.

Experimental

The apparatus used was essentially that described previously by the author (5). Silica gel desiccant was included in the system, located in the horizontal glass section between the reaction bulb and the first manometer. When the oxygen pressure was between 2 and 3 atm it was necessary to employ two manometers in series, outside the constant temperature cabinet. At higher pressures a nickel bomb with a Vycor insert was used to contain the sample, and the pressure was measured by a gauge, connections thereto having been made by means of stainless steel capillary tubing.

The experimental work consisted essentially in maintaining a sample of Merck's reagent grade Ag_2O at a constant temperature until the pO_2 ceased to increase, or in maintaining a more or less dissociated Ag_2O at a constant temperature while a small quantity of oxygen from an outside source was being consumed by the silver and was reaching a steady pressure. Temperatures were kept constant for 100 hr or more. Approximately four days were required for equilibrium pressures to be established from points 2 to 5% away from the equilibrium pressures and, in each case, both temperature and pressure had to be steady for about three days before equilibrium was as-

Table I. Dissociation of Ag_2O data and calculated results

Temperature, °K	Observed pressure, atm*	Compressibility factor	$R\ln$ Fugacity	$-R\ln \frac{a^4_{Ag}}{a^2_{Ag_2O}}$	$\frac{\Delta G°_T}{T}$	$\frac{\Delta Y°}{T}$		$\Delta H°_{298}$, kcal
			Present investigation					
554.15	13.33	1.0032	−5.1532	+0.0122	−5.1410	−5.1667		14.537
524.15	7.007	1.0017	−3.8722	+0.0063	−3.8659	−3.9365		14.479
494.15	2.767	1.0006	−2.0236	+0.0020	−2.0217	−2.1630		14.648
476.15	1.566	1.0003	−0.8918	+0.0006	−0.8911	−1.0886		14.667
474.15	1.526	1.0003	−0.8404	+0.0006	−0.8398	−1.0428		14.639
471.15	1.305	1.0002	−0.5294	+0.0004	−0.5291	−0.7441		14.683
469.65	1.318	1.0002	−0.5492	+0.0004	−0.5488	−0.7693		14.628
453.35	0.717	1.0001	+0.6608	−0.0003	+0.6605	+0.3754		14.676
447.15	0.596	1.0001	+1.0280	−0.0005	+1.0276	+0.7152		14.650
							Average	14.623
			Lewis investigation					
718.15	207.0	1.0650	−10.7221	+0.1570	−10.5652	−10.6888		14.483
598.15	31.8**	1.0097	−6.8936	+0.0282	−6.8655	−6.8656		14.601
575.15	20.5	1.0060	−6.0137	+0.0186	−5.9951	−6.0030		14.509
							Average	14.532
			Keyes and Hara investigation					
773.35	388.3	1.1274	−12.0853	+0.2741	−11.8112	−12.0660		14.532
757.15	323.5	1.1072	−11.6865	+0.2331	−11.4535	−11.6657		14.626
740.85	257.8	1.0854	−11.1959	+0.1897	−11.0062	−11.1790		14.615
725.15	213.5	1.0707	−10.7942	+0.1604	−10.6338	−10.7719		14.668
676.15	114.5	1.0376	−9.4930	+0.0918	−9.4012	−9.4538		14.603
647.15	74.3	1.0240	−8.6080	+0.0620	−8.5460	−8.5661		14.589
							Average	14.606
			Benton and Drake investigation					
464.35	1.039	1.0002	−0.0764	0.0000	−0.0764	−0.3168		14.686
461.35	0.943	1.0002	+0.1164	−0.0001	+0.1163	−0.1358		14.681
456.25	0.796	1.0001	+0.4531	−0.0002	+0.4529	+0.1800		14.669
451.15	0.670	1.0001	+0.7955	−0.0004	+0.7951	+0.5005		14.672
446.15	0.555	1.0001	+1.1700	−0.0006	+1.1695	+0.8526		14.669
							Average	14.675
							Grand average of 23 values	14.618

* 1 atm = 101325 newtons/square meter (N/m^2).
** From Lewis's dissociation data. Better to disregard his short duration slow recombination attempt.

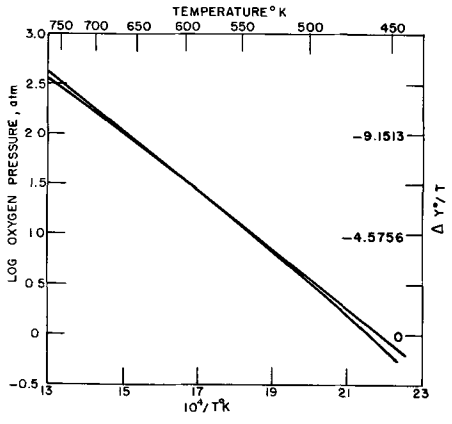

Fig. 1. Dissociation of Ag_2O. The curve (lower line) is a graph of all available data, given in Table I, columns 1 and 2. The straight line (upper) is obtained by application of the method of least squares to the data in Table I, columns 1 and 7.

sumed. (Since the decomposition of Ag_2O is hard to initiate, it was found most satisfactory to preheat each new sample to about 325°C until 5 to 10% decomposed and then to reduce the temperature to that at which equilibrium was to be sought.)

Treatment of Data

The data obtained are presented in columns 1 and 2 of Table I and on Fig. 1 along with the data reported by the three previous investigators. It is to be noted that the line drawn through the equilibrium points is not straight. The treatment of data is, in part, similar to that used by the author for the study of Mn_2O_3 (5) and MnO_2 (6), with the addition that molar volumes of Ag_2O and Ag were taken into consideration.

For the reaction $2Ag_2O \rightleftarrows 4Ag + O_2$

$$K = \frac{a^4\text{Ag} \times a\ O_2}{a^2Ag_2O}$$

where K is the equilibrium constant and a represents activity.

$$R\ln a\ O_2 = R\ln(p\ O_2 \times Z)$$

where $Z = pv/RT$. The values for Z, the compressibility factor, were obtained from NBS Circular 564 (7) by interpolations and by log log extrapolations (straight lines) for pressures in excess of 100 atm. These values, shown in column 3 of Table I, are multiplied by the corresponding pressures (column 2) to get the fugacities.

The method used by Pitzer and Smith (8) for calculating $R\ln(a_{Ag_2O}/a^2_{Ag})$ was adopted.

$$R\ln a_{Ag_2O}/a^2_{Ag} = 1/T \int_1^P (V_{Ag_2O} - 2V_{Ag})\,dp$$

$V_{Ag_2O} - 2V_{Ag}$ is considered constant and equal to 11.3 cm^3. By integration between P and 1 atm one obtains

$$R\ln(a_{Ag_2O}/a^2_{Ag}) = 1/T \times \frac{1.98717\ \text{cal/mol}}{82.056\ \text{cm}^3\ \text{atm}} \times 11.3\ \text{cm}^3\ (p-1)$$

The resulting values, multiplied by −2, give $R\ln(a^4_{Ag}/a^2_{Ag_2O})$ and these are shown in column 5.

The calculated $\Delta G°/T$ values gotten by adding columns 4 and 5 appear in column 6. By the use of the Cp equations given by Kelley (9) for Ag_2O, Ag, and O_2 the values in column 6 were projected to points (column 7) which would determine a straight line at 600°K, approximately the midpoint of the range of temperature over which the Ag_2O-Ag-O_2 system has been studied. (The heat capacity of Ag_2O has been determined only up to 500°K, but it is assumed here that the equation applies to 773°K.)

This portion of the method of treatment of the data has previously been given in detail by the author (5). The T_{AV} in the present case is 600°K and for the reaction $2Ag_2O \rightarrow 4Ag + O_2$

$$\Delta C_p° = 5.26 - 21.80 \times 10^{-3}T + 1.04 \times 10^5 T^{-2}$$

From the relations

$$\Delta Y°/T = (\Delta H°_{600}/T) - \Delta S°_{600}$$

and

$$\Delta Y°/T = \Delta G°_{600}/T + C$$

where the correction

$$C = -\Delta(H°_T - H°_{600})/T + \Delta(S°_T - S°_{600})$$
$$= -1/T\int \Delta C°_p\,dT + \int (\Delta C°_p/T)\,dT$$

one can obtain the correction to obtain $\Delta Y°/T$ for each temperature in column 1 of Table I.

The straight line obtained by the method of least squares for the data in Table I, columns 1 and 7, is shown in Fig. 1, and it has the following characteristics $\Delta H°_{600}$ (the slope) = 13.524 kcal;[1]

s.d. = 0.042 kcal

$\Delta S°_{600}$ (the intercept) = 29.502 cal/deg;

s.d. = 0.080 cal/deg

Standard deviation for the fit of the $\Delta Y°/T$ points to the equation

$$\Delta G°_{600} = \Delta H°_{600} - T\Delta S°_{600} \text{ is } 0.06994.$$

Again using the $Cp°$ equations of Kelley

$$\Delta H°_{298.15} = 14.69 \text{ kcal/mol } O_2$$
$$\Delta S°_{298.15} = 31.92 \text{ cal/deg mol } O_2$$
$$\text{Then } \Delta G°_{298.15} = 5.17 \text{ kcal/mol } O_2$$

In another treatment of the combined sets of data the heat of dissociation ($\Delta H°_{298}$) of $2Ag_2O$ (numerically equal to the heat of formation, but with opposite sign) is calculated from the equilibrium temperature-pressure data, the entropy ($\Delta S°_{298}$), the $\Delta(S°_T - S°_{298})$ and the $\Delta(H°_T - H°_{298})$, using the equation

$$\Delta H°_{298} = \Delta G°_T - \Delta(H°_T - H°_{298}) + T\Delta S°_{298} + T\Delta(S°_T - S°_{298})$$

$\Delta G°_T$ is gotten by multiplying the values given in column 6 of Table I by the corresponding temperatures of column 1. The heat content and entropy changes are based on data given by Kelley for Ag_2O up to 500°K, Ag and O_2. For Ag_2O above 500°K the equations of Kobayashi (10) are used, adjusting the results so that the data of Kobayashi agreed with the Kelley data at 500°K. The entropy of formation at 298°K of Ag_2O is taken as −15.9 cal/deg (11). For all of the 23 equilibrium points the $\Delta H°_{298}$ values are calculated and they appear in the last column of Table I. The average values of $\Delta H°_{298}$ shown for the four investigations are in good agreement. The grand average value of 14.62 kcal of the second method compares very favorably with the 14.69 kcal obtained by the first method. It is safe to assume that true equilibria were obtained in the experimental work. A word of caution should be given here. Although a plot of the $(H_T - H_{298})$ for Ag_2O looks much like a straight line, a straight line extrapolation to high temperatures results in $\Delta H°_{298}$ values in the neighborhood of 13.6 kcal. The curvature of the line has to be maintained above 500°K just like it obviously has to be for $(S_T - S_{298})$.

For calculation of the dependence of pO_2 on the temperature of the sample, without regard to the compressibility of the oxygen and the activities of the substances, the following empirical equations have been derived. Standard deviations are given for the fit of actually observed points to the equations. It

[1] One calorie = 4.1840 joules.

would appear that Eq. [3] or [4] may be used to give fairly precise pressures for given temperatures

$$\log pO_2 = 6.48773 - 2996.83/T; \quad \text{s.d.} = 0.02731 \quad [1]$$

$$\log pO_2 = -2493.13/T + 2.02688 \log T; \quad \text{s.d.} = 0.03709 \quad [2]$$

$$\log pO_2 = 94.6148 - 7438.44/T + 0.00991043T - 31.1855 \log T; \quad \text{s.d.} = 0.01281 \quad [3]$$

$$\log pO_2 = -292.9857 + 5301.69/T - 0.102885T + 120.944 \log T + 0.000031697T^2; \quad \text{s.d.} = 0.01278 \quad [4]$$

The least squares analyses in this paper were carried out on the National Bureau of Standards electronic computer, using the appropriate OMNITAB Program (12).

Conclusions

A study of the Ag_2O-Ag-O_2 system has been completed, overlapping the work of Benton and Drake, and closing the gap which existed between the temperature ranges used by Benton and Drake, and Lewis. It can now be said that the system has been studied from 446°K, the lowest temperature used by Benton and Drake, to 773°K, the highest temperature used by Keyes and Hara. All data have been included in the present determination of the thermodynamic constants.

Acknowledgment

The author wishes to express his gratitude to Dr. W. J. Hamer for his continued interest in the investigation.

Manuscript received Feb. 8, 1966. This paper was presented at the Buffalo Meeting, Oct. 10-14, 1965.

Any discussion of this paper will appear in a Discussion Section to be published in the June 1967 JOURNAL.

REFERENCES

1. H. LeChatelier, *Z. physik. Chem.*, **1**, 516 (1887).
2. G. N. Lewis, *J. Am. Chem. Soc.*, **28**, 139 (1906).
3. F. G. Keyes and H. Hara, *ibid.*, **44**, 479 (1922).
4. A. F. Benton and L. C. Drake, *ibid.*, **54**, 2186 (1932).
5. E. M. Otto, *This Journal*, **111**, 88 (1964).
6. E. M. Otto, *ibid.*, **112**, 367 (1965).
7. J. Hilsenrath, U. S. Nat'l. Bur. Standards Circular 564 (1955).
8. K. S. Pitzer and W. V. Smith, *J. Am. Chem. Soc.*, **59**, 2633 (1937).
9. K. K. Kelley, U. S. Bur. Mines Bull., 584 (1960).
10. K. Kobayashi, *Sci. Rep. Tohoku Univ.*, (I) **35**, 173 (1951).
11. D. D. Wagman, U. S. Nat'l Bur. Standards Technical Note, 270-1 (1965).
12. J. Hilsenrath, G. G. Ziegler, C. G. Messina, P. J. Walsh, and R. J. Herbold, U. S. Nat'l Bur. Standards Handbook 101 (in press).

Studies of Hydrocarbon Fuel Cell Anodes by the Multipulse Potentiodynamic Method

II. Behavior of Methane on Conducting Porous Teflon Electrodes

L. W. Niedrach

General Electric Company, Research and Development Center, Schenectady, New York

ABSTRACT

Rates of adsorption of methane on semimicro Teflon-bonded, platinum black fuel cell electrodes in the presence of a perchloric acid electrolyte are about an order of magnitude lower than those previously observed with ethane. At 65°C the measured rate of adsorption on a clean surface correlates well with the maximum anodic current that can be drawn from the electrode. The ad-layer on the surface of the electrode consists of C_1 species, some of which are partially oxidized. Similar C_1 species which form upon the adsorption of higher molecular weight hydrocarbons appear to play an important role in the over-all anodic oxidation of hydrocarbons. This implies that an efficient catalyst for hydrocarbon anodes should promote the cracking of higher molecular weight hydrocarbons to form C_1 radicals and also promote the reaction of these fragments with water.

The behavior of ethane and related hydrocarbons on smooth platinum electrodes in the presence of a perchloric acid electrolyte has been investigated with the multipulse potentiodynamic (MPP) method in this laboratory (1, 2). Recently the method has been extended to porous fuel cell anodes of more complex structure with which the behavior of ethane was examined in detail; a few preliminary experiments were performed with methane and propane (3). For this purpose a miniature version of a previously described (4) conducting-porous-Teflon fuel cell electrode (containing platinum black as catalyst) was employed.

This work showed that the behavior of ethane on the Teflon-bonded electrodes is both mechanistically and kinetically similar to that on smooth platinum (3). It also indicated that ethane and propane are similar in that their ad-layers on the electrode surface show two oxidation waves when a linear anodic sweep (l.a.s.) is applied. The first wave occurs at potentials below which (approximately 0.8v) the electrode surface is itself oxidized. This first wave generally exhibits a well-defined peak. The second wave is more diffuse and extends all the way from approximately 0.8v to oxygen-evolution potentials. Methane was found to differ markedly, however, in that only one wave could be detected during oxidation of its ad-layer. Because this wave corresponded to that of the more readily oxidized species from ethane and propane, it was felt desirable to investigate the behavior of methane in greater detail.

As in the previous study of ethane, a perchloric acid electrolyte was employed over a range of temperatures. Particular attention was given to the rates of adsorption and the nature of the species that form on the surface of the electrode. In addition data were again obtained to relate these properties to the over-all polarization curve for the fuel electrode.

Experimental

The equipment and general procedures utilized in these investigations have been described previously (3). In brief, the 0.2-cm diameter Teflon-bonded, platinum black electrode was mounted in a three-compartment, Teflon cell. Platinized platinum flags served as the hydrogen reference and counter electrodes. The former communicated with the working anode through

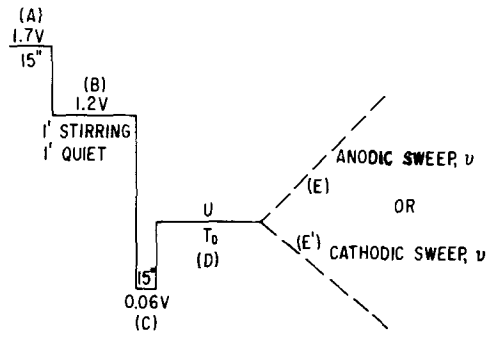

Fig. 1. Potential sequences applied to the test electrode

a Luggin capillary. The cell was operated in an air thermostat enabling control of the temperature to within 0.1°C.

The 4.3*N* perchloric acid electrolyte solution used for this work was prepared from reagent grade perchloric acid and quartz distilled water. Electrolytic grade hydrogen was used in the reference electrode chamber, and Phillips research grade methane was used as the fuel. Tank argon, deoxygenated by passage over heated copper turnings, was used as the "fuel" for obtaining solvent blanks. Tank argon was also used for degassing the solution.

The electronic instrumentation and circuit have been described previously (5).

The potential-time sequence applied to the anode for adsorption studies at constant potential is shown in Fig. 1. The rationale behind the various steps has been discussed in detail elsewhere (1-3, 5). Briefly, however, steps A through C serve to precondition the electrode and return it to a reproducible state before each equilibration. Following oxidation of impurities during step A, the electrode is taken to step B to allow the system to become quiescent while adsorption of fuel is prevented by an "adsorbed oxygen" layer on the electrode. In step C the oxygen layer is reduced at a potential sufficiently low that fuel adsorption is still prevented. Upon shifting to the potential of step D fuel adsorption occurs for the allotted time, T_D. Anodic sweep E is then applied to determine the charge required for the oxidation of the fuel ad-layer. The alternative cathodic sweep E' is used to determine the "real" surface area of the electrode from the charge corresponding to hydrogen deposition. In this case, argon is substituted for the fuel.

For the present electrode the useful range of sweep speed v for oxidation of the ad-layer was previously established by adsorbing a fixed amount of ethane (corresponding to T_D = 600 sec) and measuring the charge required for its oxidation over a range of sweep speeds (3). The useful range was found to extend from approximately 0.1 to 0.4 v/sec. Lower sweep rates resulted in additional charge from the oxidation of fuel that adsorbed during the sweep. At higher sweep rates the traces tended to lose definition, because of the diffuse structure of the electrode. A sweep speed of v = 0.1 v/sec was used routinely in the present work.

Steady-state polarization curves such as that in Fig. 7 were obtained in two ways. The first method involved application of steps (A-D) of Fig. 1 before each measurement of current at a particular potential U. Ten-minute equilibrations were allowed on each point before the final value of current was recorded. In the second method, steps (A-D) of Fig. 1 were applied only once, at the lowest value of U. The potential was then changed in increments and the current recorded for each potential after an apparent constant value was established. The two methods gave essentially identical results.

Results

The general form of the current-voltage trace obtained during oxidation of adsorbed methane with a linear anodic sweep is shown for a range of equilibration times, potentials, and temperatures in Fig. 2-4. For each experimental condition a trace corresponding to the background solvent blank is also presented. Figure 2 shows a series of traces for adsorbed methane at 65°C for various equilibration times at a potential of 0.3v. The effect of the equilibration potential at 65°C appears in Fig. 3. Similar data showing the effect of temperature appear in Fig. 4. In obtaining the data for the latter two figures 10-min equilibrations were used throughout.

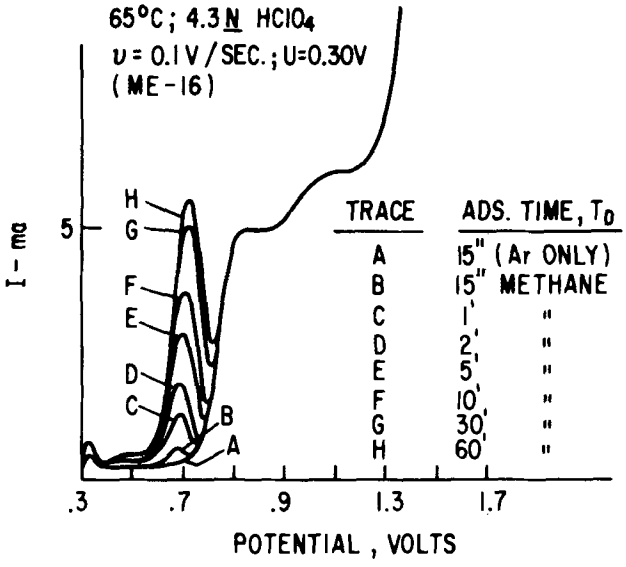

Fig. 2. Current-potential (time) traces for methane after different adsorption times.

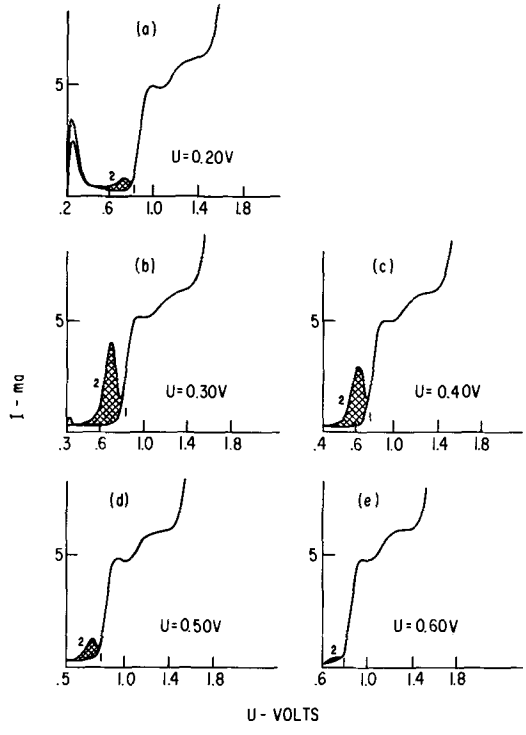

Fig. 3. Current-potential (time) traces for methane adsorbed at several potentials. 4.3*N* $HClO_4$; 65°C; V = 0.1 v/sec; T_D = 10 min; 1, Ar blank; 2, methane; ME-16.

It is clear from Fig. 2-4 that the amount of methane adsorbed is a strong function of the time, potential, and temperature. However, for all conditions of potential and temperature and for equilibration times as long as an hour only the single wave is obtained during oxidation of the ad-layer. This wave, like wave 1 for ethane (3), becomes more prominent as the tem-

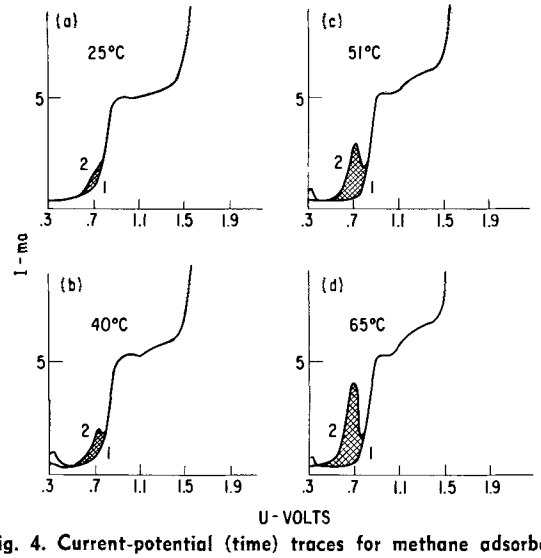

Fig. 4. Current-potential (time) traces for methane adsorbed at several temperatures. 4.3*N* $HClO_4$; *V* = 0.1 v/sec; T_D = 10 min; *U* = 0.3v; 1, Ar blank; 2, methane; ME-16.

perature is increased. Because the material is so readily oxidized it is no longer seen when equilibrations are performed as potentials greater than 0.5v.

The magnitude of the charge, Q_{E_1},[1] associated with the oxidation of the material adsorbed after any time, T_D, was obtained by integrating the area enclosed by the solvent (blank) curve and the methane curve. This is indicated by the shaded areas in the figures. It is to be noted that hydrogen formed by dissociation during the initial adsorption step is not included in these measurements.

Variations in Q_{E_1} with time at different potentials are shown in Fig. 5 for equilibrations performed at 65°C. The data have been normalized to charge per unit of "real" surface area as determined by cathodic deposition of hydrogen on the electrode. A conversion factor of 0.21 mcoul/cm² was used in calculating the "real" area (6).

As in the case of ethane (3) the rate of adsorption is initially constant and then follows an empirical Elovich relationship over a moderate range. Ultimately a steady-state coverage is achieved when the rate of adsorption equilibrates with the rate of oxidation. At 65°C the maximum (initial) adsorption rate for methane in terms of $\Delta Q_{E_1}/\Delta t$ is approximately 0.00030 mcoul/sec/cm² of real area.

[1] Q_{E_1} is used to designate this charge because the oxidation occurs in the same potential region as that of wave 1 for ethane and propane. In contrast to ethane and propane, however, $Q_{E_1} = Q_{E_{tot}}$ for methane; here $Q_{E_{tot}}$ is the charge required to oxidize all of the adsorbed surface species derived from the hydrocarbon fuel.

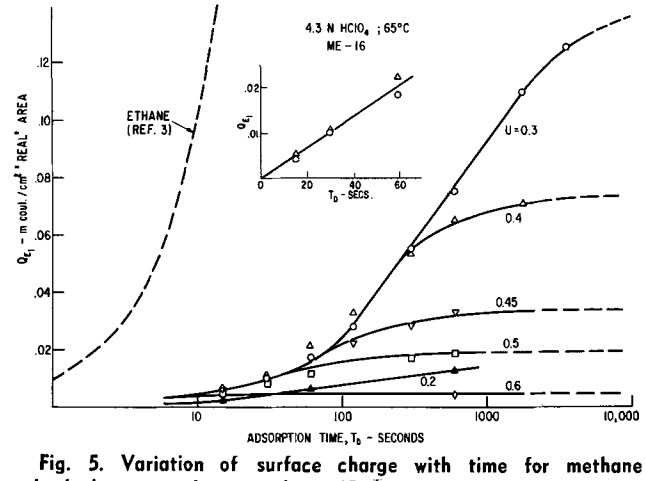

Fig. 5. Variation of surface charge with time for methane adsorbed at several potentials at 65°C.

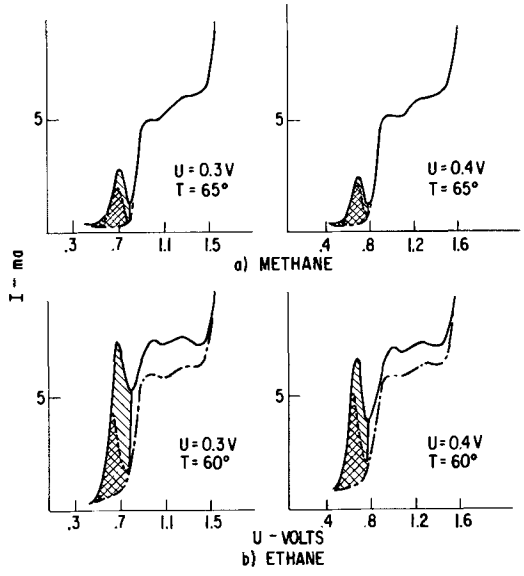

Fig. 6. Effect of cathodic hydrogenation on the current-potential (time) traces for adsorbed methane and ethane. 4.3*N* $HClO_4$; ——— initial; --- after hydrogenation; —·— argon blank; T_D = 5 min.

Because of the low rate, even at 65°C, detailed measurements of this type were not made at other temperatures. However, at 25°C Q_{E_1} = 0.0088 mcoul/cm² of real area after a 10-min equilibration. At this low coverage it is to be expected that the adsorption would still be in the linear region. Using such an assumption one calculates a rate of 0.000015 mcoul/sec/cm² of real area, or a magnitude less than that at 65°C. This corresponds to an activation energy of about 15 kcal/mole. For ethane a similar temperature effect was found by direct measurement of the initial rates at 25° and 60°C (3). The observed rates at the two temperatures, which were 0.0010 and 0.010 mcoul/sec/cm² of real area, respectively, correspond to an activation energy of 13 kcal/mole.

The single wave for methane occurs in the same potential range as wave 1 for ethane and propane, as well as such partially oxygenated species as CO, formic acid and "reduced CO_2" (3). It therefore appears that similar surface species are involved in these cases. To determine whether some of the species of this wave for methane are removable by cathodic hydrogenation and therefore probably unoxygenated, cathodic hydrogenations were performed after equilibrations of the electrode with methane at 0.3 and 0.4v. In these experiments, sequence A-D of Fig. 1 was first followed. After adsorption for time, T_D, the potential was again stepped down to 0.06v for 2 to 5 min before application of the linear anodic sweep. Similar experiments were also performed with ethane for comparison. The results of these experiments are summarized in Fig. 6 and Table I. It is clear that in each case a portion of the surface species was removed by this treatment. The amount removed decreased with increasing equilibration potential. In the case of ethane all of wave 2 was removed by the hydrogenation treatment. The present results for ethane differ

Table I. Effect of cathodic hydrogenation on wave 1 (T_D = 5 min; T_{Hyd} = 5 min)

	Methane 65°C		Ethane 60°C	
	0.3v	0.4v	0.3v	0.4v
Q_{E_1} = initial; mcoul	4.0	2.8	10.1	8.0
Q_{E_1} = after hydrogenation: mcoul	2.5	2.3	3.8	5.5
ΔQ_{E_1} mcoul	1.5	0.5	6.3	2.5
Per cent removed	38	18	62	31

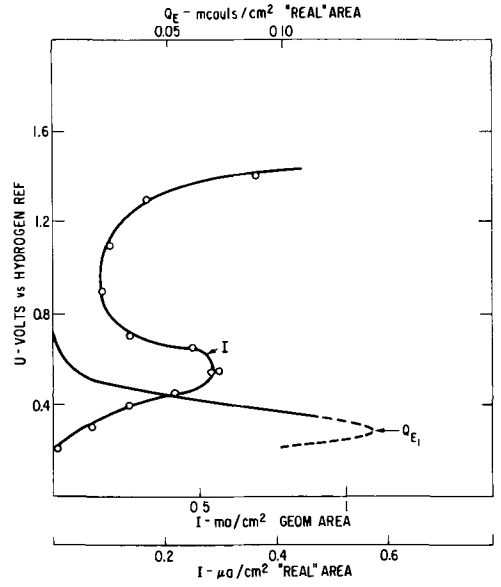

Fig. 7. Polarization and surface charge curves for methane. 4.3*N* $HClO_4$; T =65°C; ME-16.

from those of Gilman (1) who performed similar hydrogenations with the wire microelectrode after equilibrations at 0.4v. In that case no desorption of wave 1 species was observed after hydrogenation at 0.06v. The diffuse structure of the Teflon electrode as well as small differences in the catalytic behavior may account for the observed differences.

One additional point for consideration is the relationship between the adsorption data and the polarization curve for the electrode operating on methane. Such a polarization curve obtained at 65°C is shown in Fig. 7. The abscissa is expressed in terms of the current density per unit of real and geometrical area of the electrode. Therefore the data may be related to the adsorption studies as well as performance curves for fuel cells. Also shown in the figure is the measured surface coverage, Q_{E_1} as determined from linear anodic sweep measurements. The forms of the polarization and surface coverage curves are similar to those previously reported for ethane (3); however, the amplitudes of both are considerably less than for ethane.

Similar bell shaped curves relating surface coverage to potential have also been observed by others with platinum electrodes and a variety of fuels and electrolytes. For example such curves have been obtained electrochemically for ethane (1), ethylene (2) and acetylene (2) with a perchloric acid electrolyte, for methane (7), ethane (7), propane (7, 8) and butane (7) with a phosphoric acid electrolyte, and for ethane with a hydrofluoric acid electrolyte (7). Radiochemical tracer techniques have also given similar results for ethylene with a sodium hydroxide electrolyte (9) and a sulfuric acid electrolyte (10) and for butane with a sulfuric acid electrolyte (11).

Discussion

In considering the results for methane, it will be most useful to relate them to the previous observations with other fuels. As already noted, a most significant difference lies in the fact that but a single oxidation wave is obtained for the ad-layer from methane in contrast to the two waves from the ethane and propane. Gilman, after studies of ethane (1), ethylene (2), and acetylene (2) has concluded that wave 2 from ethane is associated with the oxidation of partially dehydrogenated C_2 species on the electrode surface. It is reasonable to conclude that similar multiple carbon species are associated with the second wave from propane and that a corresponding analogy will hold for higher hydrocarbons. With these higher molecular weight materials it is likely that a variety of species of different chain length will be present and contribute to the second wave. These would result from cracking and polymerization reactions which have been demonstrated to occur even at 25°C (12).

It has also been noted in past work that C_1 species are among the cracking products obtained from the higher hydrocarbons at 25° (12) and at 65°C (13). Furthermore, the cracking of propane on platinum in the absence of electrolyte has been observed to form methane and ethane and to have a pronounced temperature coefficient (14). In view of these observations and the fact that only wave 1 is observed with methane, it seems clear that the more readily oxidized surface material corresponds to C_1 species. Previous observations (1, 12) as well as the data in Table I and Fig. 6 indicate further that these species are partially oxygenated.

The adsorption rates and steady-state coverages for methane are considerably lower than those previously observed with ethane; however the variation in coverage with potential parallels that for ethane. With regard to the lower rate of adsorption for methane, this may relate to the somewhat higher dissociation energy required to break the first C-H bond than is required for ethane, 101-102 kcal *vs.* 97 kcal, respectively (15). Alternatively, it may reflect a weaker physical adsorption prior to dissociation on the surface to form the chemisorbed species. Sufficient detailed data are, however, unavailable at the present time to reach a definitive conclusion concerning the reason for the pronounced differences.

The shape of the curve relating surface coverage to potential reflects the influence of competing reactions. At low potentials (< 0.3v) adsorption is hindered because the required dissociation of the adsorbing hydrocarbon is repressed by the presence of atomic hydrogen on the electrode surface. At potentials above 0.3v the surface coverage again declines in order to permit the rate of adsorption to keep pace with the increasing rate of oxidation of the ad-layer. It is possible that the shape of the curve is further influenced by a potential-dependent, competitive adsorption with water which has been used in the interpretation of the effect of potential on the adsorption of ethylene (10).

The low adsorption rates for methane are reflected in the low current densities obtained with methane as seen in the polarization curve of Fig. 7. The maximum current density, at 0.5v, is about one tenth that obtained with ethane. In this connection it is of interest to relate the maximum current density to the adsorption rates on the clean surface, *e.g.* the initial rates at 0.3 and 0.4v.

To convert the adsorption rates to equivalent current densities, it must be recalled that the former are expressed in terms of the change in surface charge with time, $\Delta Q_{E_1}/\Delta t$. Allowance must therefore be made for any oxidation that occurred during the adsorption step itself, *e.g.*, immediate oxidation of dissociated hydrogen. This may be done by multiplying $\Delta Q_{E_1}/\Delta t$ by the ratio of the charge associated with oxidation of the hydrocarbon fuel molecule to that required for oxidation of the adsorbed species.

While the precise composition of the ad-layer has not been established for either methane or ethane, especially after short equilibrations, it is possible to calculate a range of limiting currents from the initial adsorption data at 0.3 and 0.4v. In the case of methane, depending on whether the ad-layer is assumed to have an average composition approaching that of methyl radicals or that of a highly oxygenated species, such as CO, the observed rate of adsorption would be equivalent to a steady state current density of from 0.30 to 1.2 $\mu a/cm^2$ of real area. The observed value of 0.3 $\mu a/cm^2$ is in good agreement in view of the evidence for a mixture of C_1 radicals and partially oxygenated species.

A similar calculation has been made for ethane (3). In this case the calculated maximum current density fell in a range from 14 to 35 $\mu a/cm^2$ and the ob-

served value was 2.5 μa/cm^2 of real area. For comparison, Rhodes (16) obtained adsorption rates equivalent to 22 μa/cm^2 (10^{13} molecules/cm^2/sec) for ethane on a rotated platinum electrode (600 rpm) at 80°C with a 1*N* H_2SO_4 electrolyte. While this value is in excellent agreement with the results with the Teflon bonded electrode, no data were obtained for the steady-state maximum current obtainable with the rotating electrode.

The discrepancy between the calculated and observed maximum current densities for ethane on the Teflon-bonded electrode undoubtedly reflects the fact that at the potential of the maximum steady-state current some of the more refractory species are present on the surface and lower the adsorption rate relative to that on the "clean" surface at 0.3v. The decline in the current density that occurs at higher potentials appears to reflect further reductions in adsorption rate as a result of such processes as surface oxidation, anion adsorption, and stronger bonding of water to the surface. These processes would also contribute to the similar decline in methane performance at potentials above 0.5v.

At low potentials, the effect of the adsorption rate on the polarization curve is minimal. Here it is clear that the overvoltage required for the further oxidation of surface intermediates to CO_2 is limiting. This is true, of course, under potentiostatic conditions as well as with the resistive loads of practical fuel cells.

The pronounced temperature coefficients for both the methane and ethane adsorptions (activation energy of about 14 kcal/mole) are reflected in the observed improvement in the performance of hydrocarbon fuel cells with increasing temperature. In particular, they relate to the regions of "unstable" performance observed with saturated hydrocarbon fuel cells operating on resistive load (17-19). Under these conditions, it will be recalled that at low current densities steady performance is obtained while at higher current densities the performance decays with time or, under certain conditions, oscillations set in (19, 20). As a result of the increasing adsorption rates with increasing temperature, the region of instability occurs at continuously higher current densities as the operating temperature is increased. When polarization curves are obtained potentiostatically, as in the present work, maximum currents are observed in place of the instability associated with resistive loads.

While it would be premature to discuss the mechanisms of the electrode reactions in any detail at this time, it is appropriate to consider briefly some of the possible paths suggested by the available information. In particular it is pertinent to speculate about the meaning of the two separate l.a.s. waves seen with ethane and propane, the single wave seen with methane, and the evidence for the partially oxidized surface species. In the discussion that follows, ethane will be used as the model with the expectation that higher molecular weight hydrocarbons will behave similarly. The behavior of methane, in turn, will be somewhat simpler.

The initial step must certainly involve adsorption of the fuel on the electrode surface. On the basis of careful kinetic studies with ethane on wire microelectrodes, Gilman has concluded (1, 2) that this primary adsorption step corresponds to the formation of an ethyl radical on the surface. This may be represented by

$$C_2H_6\ (\text{gas})^2 + S \rightarrow S - C_2H_5 + H^+ + e \qquad [2]$$

at potentials at which appreciable currents are drawn from the electrode. He points out that an equivalent route is given by

$$C_2H_6\ (\text{gas}) + 2S \rightarrow S - C_2H_5 + S - H \qquad [2a]$$

[2] More precisely, the gas will first dissolve in the electrolyte and be transported by diffusional processes to the electrode where it will adsorb from solution. While mass transport processes are not limiting in the work under discussion, it is obvious that they can become important under some conditions of operation. For practical fuel cell electrodes it is important that mass transport limitations be minimized.

in which case the adsorbed hydrogen is rapidly consumed by the Volmer reaction:

$$S - H \rightarrow S + H^+ + e \qquad [2b]$$

At low potentials, of course, some of the hydrogen will remain adsorbed on the surface.

Gilman then reasons that the ethyl radical follows two paths. The first results in the formation of four surface bonds to the surface without rupture of the C-C linkage

$$S - C_2H_5 + 3S \rightarrow S_4 - C_2H_2 + 3H^+ + 3e \qquad [3]$$

This species is associated with wave 2 obtained with a l.a.s. and is identical with the single adsorbed species obtained when ethylene and acetylene are adsorbed (2). The present work is in accord with this interpretation, and cathodic hydrogenations of adsorbed ethane at 25°C have shown that the major material on the surface at that temperature corresponds to C_2 species while that for propane corresponds to C_3 species (12).

The second reaction path of the ethyl radical results in the formation of the material associated with wave 1, which Gilman also obtained for ethane on the platinum wire microelectrode. In the absence of detailed kinetic data for the species associated with wave 1 Gilman did not speculate in detail on its identity.

The new data obtained with the Teflon-bonded electrodes are helpful in this area. The similarities between the single wave for methane and wave 1 for ethane, as well as other evidence noted above, strongly suggest that the second reaction path of the ethyl radical involves C-C bond fission as indicated in the following general equation

$$S - C_2H_5 + S \rightarrow 2S - CH_a + (5 - 2a)\ H^+ + (5 - 2a)\ e \qquad [4]$$

(The methylene radical with two carbon bonds to the surface may represent the principal species in parallel with the C_2H_2 of wave 2 which also has two surface bonds per carbon atom.)

The C_1 species in turn appear to react readily with water to form a partially oxygenated material which corresponds to the previously proposed "CO-like" species of Niedrach (12) and the "reduced CO_2" of Giner (21), and which Giner has also more recently found to be formed during the oxidation of hydrocarbons in the presence of a sulfuric acid electrolyte (22). Brummer and Turner (8) have also obtained evidence for the presence of partially oxygenated surface species in their studies of propane at higher temperatures with a phosphoric acid electrolyte, as have Niedrach and Tochner (7).

The specific identity of the oxygenated species is as yet unknown and the reaction can therefore best be represented by

$$S - CH_a + b\,H_2O + cS \rightarrow S_{(c+1)} - CH_dO_b + (a + 2b - d)\ H^+ + (a + 2b - d)\ e \qquad [5]$$

That both the C_1 species and the partially oxygenated species are present on the surface and oxidize over the same potential range is indicated by the new hydrogenation experiments with methane and ethane. Since Eq. [4] represents a "cracking" reaction and Eq. [5] a "reforming" reaction, these observations suggest that it would be profitable to direct attention toward the study of the behavior of alternative catalysts in promoting such reactions.

With regard to the more refractory species of wave 2, which oxidize only at higher potentials, it is likely that an entirely different mechanism of oxidation prevails. This conclusion is based on Gilman's observation that conversion to the species of wave 1 is slow (2). It is therefore likely that oxidative attack occurs before the C-C bonds are ruptured. This could result in the formation of alcohol-like species as intermediates. It should be emphasized, however, that such intermediates will undoubtedly be quite distinct from those involved in the direct oxidation of alcohol-

type fuels at moderate temperatures. The alcohol-like species derived from hydrocarbons would be strongly bound to the surface by multiple carbon-metal linkages, and hence complete oxidation to CO_2 would be assured. With alcohol fuels it is more likely that weaker bonds between the oxygen and the metal are involved. This is suggested by the incomplete oxidation to organic acids that is often observed with alcohols (23) at moderate temperatures. It is further supported by the behavior of alcohols towards deuterium exchange, where it is found that the hydroxylic hydrogen undergoes exchange most readily (24).

Relating to the oxidation of these multiple-carbon species is the work of Bockris and co-workers (25-27) dealing with the oxidation of ethylene and acetylene. They interpret Tafel plots and other evidence in terms of a slow step involving the production of hydroxyl radicals from water. Such a route would not be in conflict with the present results.

Summary and Conclusions

The behavior of methane on Teflon-bonded fuel cell electrodes parallels that of ethane in that adsorption at intermediate potentials varies linearly with time at low coverages, and a semilogarithmic relationship applies at higher coverages. Rates of adsorption of methane are, however, over an order of magnitude lower than those previously observed with ethane. At 65°C the measured rate of adsorption of methane on a "clean" surface correlates well with the maximum anodic current that can be drawn from the electrode. This is in marked contrast to the behavior of ethane where the observed maximum current is almost an order of magnitude lower than that calculated from the adsorption rate. The difference in behavior of the two fuels is related to the ad-layers formed during adsorption. In the case of methane only readily oxidized C_1 species, some of which are partially oxygenated, form. The ad-layer from ethane also contains relatively refractory C_2 species which block the surface and limit the adsorption rate at the potential of the maximum current.

On the basis of the behavior of methane and ethane it is possible to construct a tentative picture of the steps involved in the anodic oxidation of hydrocarbons on platinum catalyzed fuel cell electrodes. After a primary adsorption step, at least two distinct reaction paths are followed by ethane and higher hydrocarbons. One path results in the formation of the relatively refractory species. The most desirable path results in "cracking" of the carbon chain to form the more reactive C_1 radicals and the partially oxygenated species. At low current densities the overvoltage associated with oxidation of the ad-species to CO_2 limits performance. As the current density is increased the adsorption rate eventually becomes the limiting factor.

In view of the many species present on the electrode surface and the changes in coverage and composition with temperature, potential, and time, much attention to analytic detail will be required before a definitive mechanism can be derived. It seems unlikely that electrochemical measurements alone will be sufficient to unravel all of the steps. Instead, much supplementary information must be sought, particularly with regard to the identification of surface species and their roles as active intermediates or passive by-products. Radiotracer, infrared, chromatographic, and other related techniques should prove invaluable in identifying such species, in measuring "turnover" rates on the electrode surface, and in providing additional supporting information.

Acknowledgments

The author is indebted to S. Gilman for many helpful discussions.

This work is a part of the program under contracts DA-44-009-AMC-479(T) and DA-44-009-ENG-4909, ARPA Order No. 247 with the U. S. Army Engineer Research and Development Laboratories, Ft. Belvoir, Virginia, to develop a technology which will facilitate the design and fabrication of practical military fuel cell power plants for operation on ambient air and hydrocarbon fuels.

Manuscript received Nov. 18, 1965; revised manuscript received April 6, 1966.

Any discussion of this paper will appear in a Discussion Section to be published in the June 1967 JOURNAL.

REFERENCES

1. S. Gilman, *Trans. Faraday Soc.*, **61**, 2546, 2561 (1965); **62**, 466, 481 (1966).
2. S. Gilman, in "Hydrocarbon Fuel Cell Technology," p. 349, B. S. Baker, Editor Academic Press, New York (1965).
3. L. W. Niedrach, S. Gilman, and I. Weinstock, *This Journal*, **112**, 1161 (1965).
4. L. W. Niedrach and H. R. Alford, *ibid.*, **112**, 117 (1965).
5. S. Gilman, *J. Phys. Chem.*, **67**, 78 (1963).
6. F. G. Will and C. A. Knorr, *Z. Elektrochem.*, **64**, 258 (1960).
7. L. W. Niedrach and M. Tochner, To be published.
8. S. B. Brummer and M. J. Turner, in "Hydrocarbon Fuel Cell Technology," p. 409, B. S. Baker, Editor, Academic Press, New York (1965).
9. H. Dahms, M. Green, and J. Weber, *Nature*, **195**, 1310 (1962).
10. E. Gileadi, B. T. Rubin, and J. O'M. Bockris, *J. Phys. Chem.*, **69**, 3335 (1965).
11. R. J. Flannery and D. C. Walker, in "Hydrocarbon Fuel Cell Technology," p. 335, B. S. Baker, Editor, Academic Press, New York (1965).
12. L. W. Niedrach, *This Journal*, **111**, 1309 (1964).
13. W. T. Grubb, *ibid.*, **111**, 1086 (1964).
14. D. W. McKee, *J. Phys. Chem.*, **67**, 841 (1963).
15. B. E. Knox and H. B. Palmer, *Chem. Rev.*, **61**, 247 (1961).
16. D. R. Rhodes, Paper presented at the Washington Meeting of the Society, October 1964, Extended Abstracts of the Battery Division, p. 36.
17. W. T. Grubb, Proc. 16th Annual Power Sources Conference, Atlantic City, N. J., p. 31 (1962).
18. L. W. Niedrach, *This Journal*, **109**, 1092 (1962).
19. M. J. Schlatter, *Advan. Chem. Ser.*, **47**, 292 (1965).
20. H. Binder, A. Köhling, H. Krupp, K. Richter, and G. Sandstede, *This Journal*, **112**, 355 (1965).
21. J. Giner, *Electrochim. Acta*, **8**, 857 (1963).
22. J. Giner, 15th Meeting CITCE, London and Cambridge, September 21-26, 1964, summaries of papers, p. xxix.
23. H. Binder, A. Köhling, and G. Sandstede, *Advan. Chem. Ser.*, **47**, 283 (1965).
24. G. C. Bond, "Catalysis by Metals," p. 220, Academic Press, New York (1963).
25. M. Green, J. Weber, and V. Drazic, *This Journal*, **111**, 721 (1964).
26. J. W. Johnson, H. Wroblowa, and J. O'M. Bockris, *ibid.*, **111**, 863 (1964).
27. H. Wroblowa, B. J. Piersma, and J. O'M. Bockris, *J. Electroanal. Chem.*, **6**, 401 (1963).

Anodic Oxidation of Cadmium and Reduction of Cadmium Hydroxide and Oxide in Alkaline Solutions

M. W. Breiter and J. L. Weininger

General Electric Company, Research and Development Center, Schenectady, New York

ABSTRACT

The anodic oxidation of smooth cadmium and the subsequent reduction of cadmium hydroxide and oxide were studied by voltammetric methods with and without superimposed a-c voltage. Under voltammetric conditions a layer of $Cd(OH)_2$ appears to be formed at potentials below the passivation potential. Passivation results from a continuous thin film which forms at potentials between 0.05 and 0.1v. The small capacitance and the large resistance of the interface electrode/solution are due to this film. On reduction the thin film is reduced first. A pseudocapacitance which is attributed to the adsorption of OH radicals is observed during the anodic sweep in a potential range where formation of $Cd(OH)_2$ or CdO is not yet possible.

The study of the electrochemical oxidation of cadmium and reduction of cadmium hydroxide and oxide in alkaline electrolytes has been of interest because of the use of Cd-electrodes as the negative plates in Ni-Cd batteries. Casey and Lake (1, 2) concluded that the anodic oxidation occurs by a two-step mechanism in the absence of carbonate

$$Cd \xrightarrow{\text{electrochemical}} CdO \xrightarrow{\text{chemical}} Cd(OH)_2 \qquad [1]$$

The primary reaction product, CdO, is converted to $Cd(OH)_2$ through a soluble intermediate. The conversion product, $Cd(OH)_2$, is porous. A film consisting of a dark, tightly adherent layer next to the metal and an outer layer of a loose, scaly or powdery yellow material was produced anodically. X-ray diffraction patterns showed the presence of crystalline $Cd(OH)_2$. The inner layer was assumed to be CdO since it has the dark color of CdO and since the observations of the composition of the outer layer were parallel to those of Huber (3). Huber had stated (3) that electron diffraction photographs of very thin coatings formed anodically on cadmium appeared to indicate that the initial oxidation product is CdO. Conclusions on the electrical properties of the film were drawn on the basis of potential decay curves after current interruption and of capacity measurements (2). The work of Huber (3) and Casey and Lake (1, 2) has received general recognition because it pointed out the importance of a soluble intermediate in the formation of $Cd(OH)_2$. However, the sequence of the two reactions in Eq. [1] has been open to question.

No evidence of CdO was found by Croft (4) who studied the oxidation of cadmium by cyclic voltammetry and by oxidation at constant potential. Again the existence of crystalline $Cd(OH)_2$ was established by x-ray diffraction. However, it should be pointed out that the absence of CdO-lines in the diffraction pattern excludes only the presence of crystalline CdO, not of amorphous CdO. The oxidation was attributed (4) to the reaction

$$Cd + 2\,OH^- = Cd(OH)_2 + 2e^- \qquad [2]$$

The rate depended in a similar way on the potential for both techniques. It has maxima at two potentials differing by 22 mv. After sufficient time had elapsed the rate of oxidation at constant potential followed a parabolic growth law. It was suggested that the growth of a film is controlled by the transport of mass and charge through the layer and that the process in the electrolyte is not relevant. A general formulation of this concept was given by Croft and Tuomi (5). The passivation of reaction [2] at more anodic potentials was attributed to properties of the semiconducting $Cd(OH)_2$ film.

Lange and Ohse (6, 7) pointed out that the primary formation of CdO is improbable on thermodynamic grounds. The standard affinity of reaction [2] is less negative with −1.04 kcal than that of the reaction

$$Cd + 2\,OH^- = CdO + H_2O + 2e^- \qquad [3]$$

with −2.9 kcal. Their reasoning involves the assumption that with anodic polarization the overvoltages of reactions [2] and [3] are such that reaction [3] is not favored. The close agreement between experimental and theoretical values of the potentials for each of the two plateaus which appeared after current interruption during intermittent anodic charging curves seems to confirm this assumption. However, it is not quite sure from the figures in ref. (7) that the potentials measured at a certain time after current interruption represent equilibrium values corresponding to reaction [2] or [3], respectively. It was suggested (7) that cadmium hydroxide which is formed initially dehydrates partially on the metal surface

$$Cd(OH)_2 = CdO + H_2O \qquad [4]$$

Thus the local arrangement $Cd/CdO/Cd(OH)_2/OH$ is produced in agreement with the results on the composition of the films. The occurrence of reaction [4] is attributed to a local decrease of the chemical potential of water toward the metal inside the $Cd(OH)_2$ film.

Other contributions to the elucidation of the mechanism of the cadmium oxidation either generally follow (8-10) the reaction scheme of Eq. [1] or assume (11, 12) that $Cd(OH)_2$ is the primary reaction product.

Thus the proposed mechanisms of the anodization of Cd either include or exclude CdO as primary reaction product. Each of the above interpretations explains certain experimental observations of the electrode reactions. It is the purpose of this communication to supply new experimental evidence which allows a more detailed description of the mechanism. The experiments were performed to investigate especially the possible role of CdO. Voltammetric measurements had proved useful in previous studies (13) of the anodic oxidation of nickel electrodes in alkaline solutions. Similar techniques were applied to examine the anodic oxidation of cadmium.

Experimental

Measurements were made in a Teflon vessel of standard design at room temperature in solutions bubbled vigorously with purified hydrogen. The solutions (0.2*N* KOH, 1*N* KOH, 5*N* KOH) were prepared from AR reagent chemicals and double-distilled water. Preelectrolysis of the electrolyte had no effect on the ex-

perimental results. This may be due to the removal of impurities by adsorption on the large platinized counter electrode (about 20 cm^2 geometric area) in a small volume (about 100 cm^3) of electrolyte. The potential U was measured *vs.* a hydrogen electrode in the same electrolyte as the test electrode. All potential measurements are referred to this reference electrode.

The Cd electrodes were prepared as follows. Pieces with a length of about 1 cm were cut from a rod (diameter 1 cm) of high purity (99.99%) supplied by Belmont Smelting and Refining Company. The cylindrical walls of these pieces were masked with Teflon sleeves which fitted tightly. Pt-wires were spot-welded as leads to the one end of the short Cd-rod inside the hollow Teflon rod. The other end was machined such that it formed a flat surface with the Teflon sleeve. It served as a test electrode.

The following pretreatment gave reproducible results. The new Cd-electrode was etched in concentrated nitric acid (50%) at room temperature. In preparation for each experiment the Cd electrode was chemically polished in a solution consisting of equal parts of glacial acetic acid and 30% H_2O_2 at room temperature. The electrode was washed thoroughly in distilled water saturated with hydrogen. The electrical connections were made before inserting the electrode at a potential of —0.8v in the vessel. The contact with air was minimized by the short duration of the insertion (2 sec) and by the water film on the electrode. The electrode was kept for 5 min at —0.8v to reduce cathodically traces of oxide or hydroxide. The reduction of traces of oxide is indicated by the decrease of the current with time. The cathodic current approaches a constant value within 5 min after the insertion. It was found that the shape of I-U curves is practically independent of the time of cathodic polarization after 5 min. Then the potential was rapidly changed potentiostatically to a less cathodic value (between —0.5 and —0.25v), and a periodic sweep of triangular shape was started by triggering manually the function generator. The capacity C_s measured by voltammetry with superimposed a-c current at 10,000 cps had values which are attributed to the capacitance of the Helmholtz layer at the starting potential of the sweeps (see subsequent discussion). Thus the surface is essentially free of oxides. The anodic sweep extended to a given potential; the subsequent cathodic sweep was reversed at about —0.7v. Measurements were made at sweep rates of 3 and 30 mv/sec. Results obtained at the slower sweep rate will be discussed here since certain features of the oxidation are more clearly observed at these slow rates. Measurements of the current I and the ohmic (R_s) and capacitive component ($1/\omega C_s$) of the impedance of the interface electrode/solution at a given frequency were made only during the first cycle. Before further measurements, the above procedure starting with chemical polishing was repeated. It was found that the electrode could be polished about 70 times before any deformation due to repeated use became noticeable. Then the electrode was machined and etched in nitric acid before continuing the experiments in the above way.

The experimental setup for the measurement of I-U curves, R_s-U curves, and $1/\omega C_s$-U curves was described previously (14). The large counter electrode was not appreciably polarized by cathodic currents up to several hundred ma and anodic currents up to 20 ma. The function generator type 250 of Exact Electronics was used. Data were recorded by the analog to digital recording equipment (14), and processed by the G. E. 235 computer in conjunction with the G. E. paper tape reader. During the a-c measurements the I-U curves were simultaneously recorded by the X-Y recorder F 80 Varian Associates. This served as a check of the reproducibility which was good. Impedance measurements were made and are subsequently discussed in a series analog circuit at 10,000, 1000, and 100 cps.

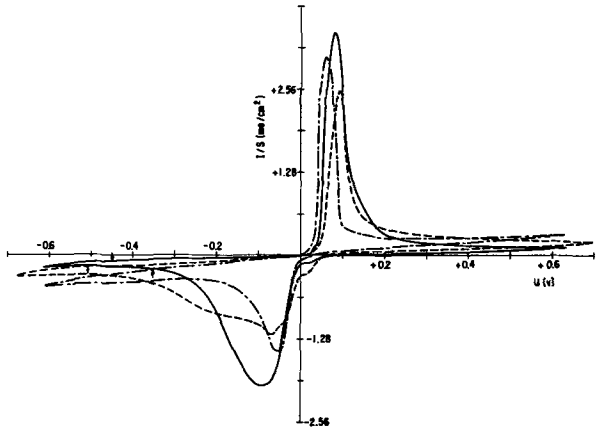

Fig. 1. Current-potential curves at 3 mv/sec on smooth Cd-electrodes. - - 0.2*N* KOH $S = 0.2$; ——— 1*N* KOH $S = 1$; -.-.- 5*N* KOH $S = 2$.

Some experiments were carried out in the assembly described in ref. (13) to study the oxidation of cadmium at constant potential in KOH by following the d-c current and the ohmic and capacitive component of the interfacial impedance at 1000 cps as functions of time. Again the freshly polished electrode was maintained for 5 min at —0.8v. Then the potential was switched rapidly by the Wenking potentiostat to a desired value in the vicinity of the reversible potential of reaction [2]. Readings were taken between 10 sec and 10 min after the change of potential.

Results

Typical I-U curves are shown in Fig. 1. The curves are reproductions of the actual traces on the chart of the X-Y recorder. The start of the cycle (anodic sweep) is marked by vertical arrows. In order to accommodate current densities obtained in three different solutions the ordinate has different units for each curve. The curves are self-explanatory except for the following points: The large anodic peak was observed by Croft (4). With increasing concentration of KOH, its voltage at maximum current shifts toward less positive potentials, and the maximum anodic current increases. At potentials above about 0.3v, the current is nearly independent of potential during the anodic sweep. A small wave appears between 0.1v and 0 in 0.2*N* KOH and 1*N* KOH at $U < 0.1$v. The height of the small wave decreases with the KOH concentration. It is absent in 5*N* KOH. The width of the big reduction wave between 0 and about —0.4v increases with decreasing KOH concentration. Simultaneously its height becomes smaller.

The I-U curves in Fig. 2 were measured in 1*N* KOH. Curves a and b demonstrate the effect of different po-

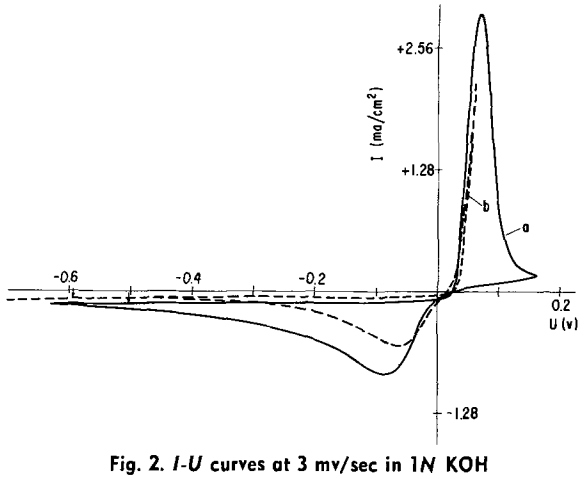

Fig. 2. I-U curves at 3 mv/sec in 1*N* KOH

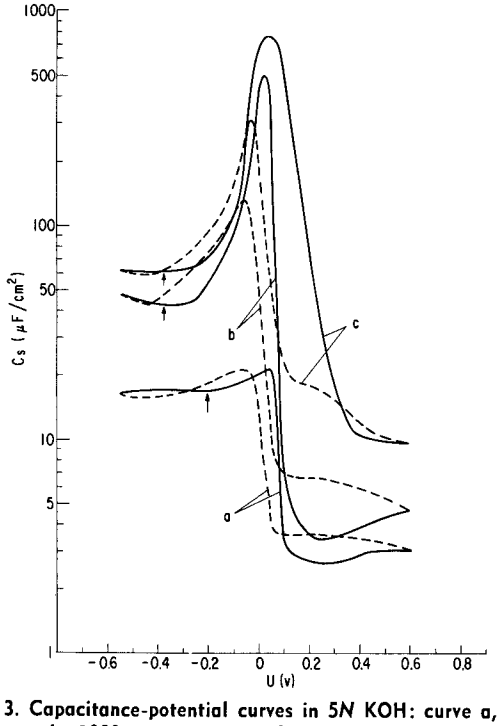

Fig. 3. Capacitance-potential curves in 5*N* KOH: curve a, 10,000 cps; curve b, 1000 cps; curve c, 100 cps; ——— anodic sweep; --- cathodic sweep.

tentials of reversal at the end of the anodic sweep on the shape of current-potential curves. Similar results were obtained in 0.2*N* and 5*N* KOH. The reduction of the layer formed during the preceding anodic sweep occurs at $U < 0.02$v. The cathodic wave is always wider than the main anodic wave which appears between 0.02 and 0.15v. The rate of layer formation is nearly the same at a given potential during the anodic and cathodic sweep for curve b. The *I-U* curves at 30 mv/sec are not shown here. They exhibit the same waves as the corresponding curves in Fig. 1 and 2. However, the waves are wider at larger currents. The details of the passivation of the layer formation during the anodic sweep above $U > 0.1$v and of the layer reduction during the cathodic sweep are better pronounced at the small sweep rate of 3 mv/sec.

The results of the impedance measurements in 5*N* KOH by voltammetry with superimposed a-c voltage are plotted in Fig. 3 and 4. The sweep rate was 3 mv/sec. The start of the measurements is marked by vertical arrows. A semilogarithmic plot was used to accommodate the curves measured at 10,000, 1000, and 100 cps. The general shape of the C_s-*U* curves and R_s-*U* curves of the anodic sweeps at $U > 0$ is similar to those of L'vova and Fortunatov (10) obtained under conditions of quasi-equilibrium. The remarkable feature of the C_s-*U* curves a and b in Fig. 3 is the rapid decrease of C_s with potential between 0.05 and 0.1v during the anodic sweep and the increase of C_s between 0.05 and —0.05v during the cathodic sweep. The potential range of the rapid decrease of C_s (10,000 cps) coincides with that of the decrease of *I* (Fig. 1 and 2) for each of the three solutions. The same behavior is reflected by the rapid increase of R_s between 0.05 and 0.1v during the anodic sweep and the decrease between 0.05 and —0.05v during the cathodic sweep (see curves a and b in Fig. 4). The C_s-*U* curves and R_s-*U* curves in 0.2*N* and 1*N* KOH look similar to the corresponding curves in Fig. 3 and 4.

The influence of the concentration of KOH is shown by the C_s-*U* curves of Fig. 5. These curves were obtained in 0.2*N* KOH. They differ only slightly from the corresponding curves in 1*N* KOH. Generally the capacitance is larger at a given potential and frequency in 5*N* KOH than in 0.2*N* KOH and 1*N* KOH at potentials $U < 0$v. At the smaller frequencies of 1000 and 100 cps the C_s-*U* curves exhibit an increase of C_s with *U* between about —0.3 and about 0v. This increase occurs for the three solutions in a potential range where layers of phase cadmium hydroxide or oxide cannot yet be formed on thermodynamic grounds.

If the sweep is reversed at the end of the anodic cycle at potentials smaller than the potential of the peak of the respective *I-U* curve, C_s-*U* curves of the type in Fig. 6 are obtained. The curve which is represented in a linear plot of C_s *vs.* *U* was measured at 1000 cps in 0.2*N* KOH. The C_s values nearly coincide during the anodic and cathodic sweep. The increase of C_s with *U*, starting at about —0.3v, is clearly pronounced.

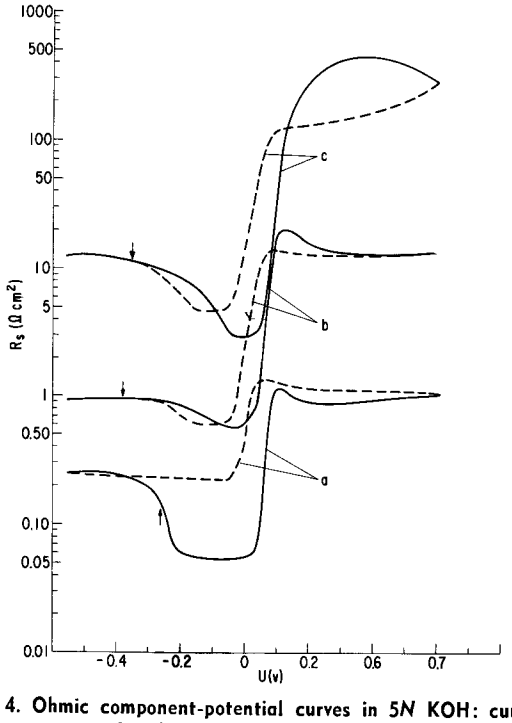

Fig. 4. Ohmic component-potential curves in 5*N* KOH: curve a, 10,000 cps; curve b, 1000 cps; curve c, 100 cps; ——— anodic sweep; --- cathodic sweep.

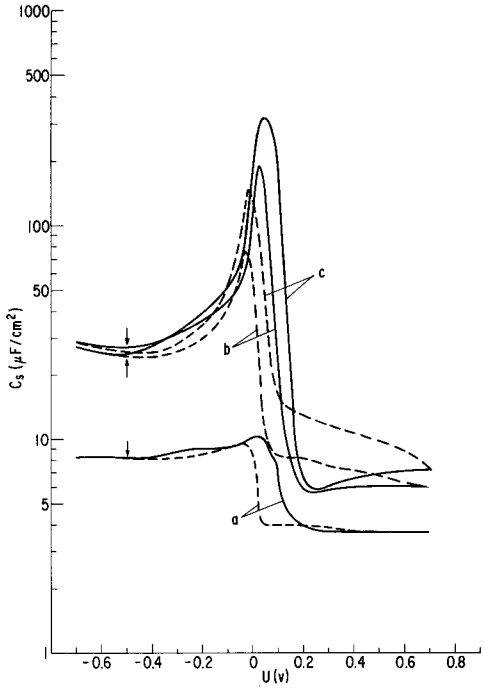

Fig. 5. Capacitance-potential curves in 0.2*N* KOH: curve a, 10,000 cps; curve b, 1000 cps; curve c, 100 cps; ——— anodic sweep; --- cathodic sweep.

Some of the results on the oxidation of cadmium at constant potential in 1*N* KOH are shown in Fig. 7. The capacity and the current density are plotted *vs.* the logarithm of time. At 0.02v the oxidation is very slow. At potentials between 0.02 and 0.1v, the *I*-log *t* curves have a maximum which is shifted toward shorter times with potential. A trace on the Varian F80 X-Y recorder showed that the maximum appeared after about 0.5 sec at 0.1v. The current decrease is linear with log *t* after 10 sec at 0.1v. The value of C_s after 10 sec is 550 μF/cm^2 during the oxidation at 0.02v. Then C_s decreases slowly with time. The C_s values at 10 sec become smaller with increasing potential. A marked decrease of C_s with time is observable between 10 and 500 sec for $U \leq 0.1$v. Above 0.1v the capacitance has values below 10 μF/cm^2 already after 10 sec. The subsequent decrease of C_s with time is small.

Discussion

Oxidation and reduction mechanism on the basis of I-U curves.—From the results shown in Fig. 1 and 2, it is suggested that cadmium hydroxide is formed under the present experimental conditions as the primary product, followed by the formation of a thin film with different physical properties at more anodic potentials. This conclusion is based on the following reasons:

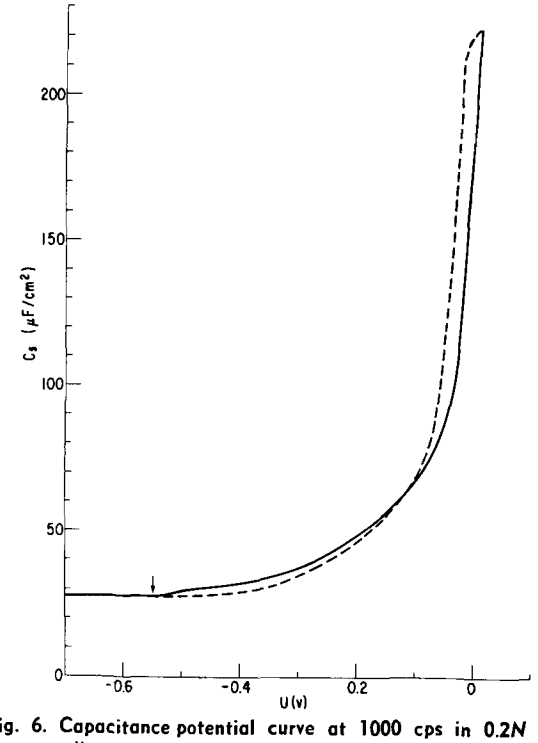

Fig. 6. Capacitance potential curve at 1000 cps in 0.2*N* KOH; ——— anodic sweep; --- cathodic sweep.

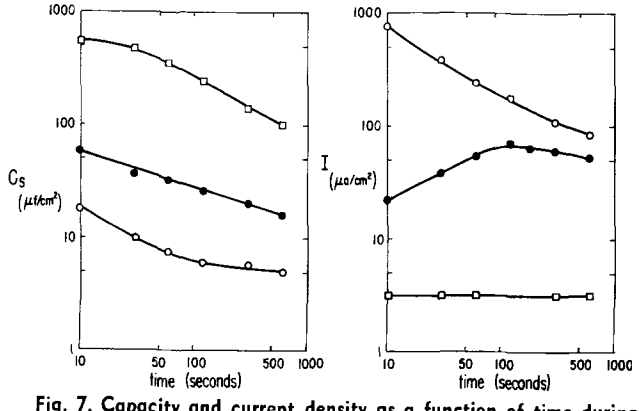

Fig. 7. Capacity and current density as a function of time during the oxidation at constant potential: □, 0.02v; ●, 0.035v; ○, 0.1v.

1. During the anodic sweep the current which is initially cathodic becomes anodic at potentials which are close to the theoretical value (0.019v) of reaction [2]. Reaction [3] cannot occur (6, 7) at these small potentials since the equilibrium potential of the respective reaction is slowly approached from the cathodic direction.

2. The rate of layer formation increases with potential, passes through a maximum, and then decreases. It is suggested that the passivation is due to the thin film located probably between the metal and the thick layer.

A distinction is made between a thick and a thin layer of oxidation products. It is suggested that the thick layer which begins to form below the passivation potential consists of $Cd(OH)_2$. Strong passivation is due to a continuous thin layer, probably CdO. The thick layer which continues to grow on top of the thin layer at more anodic potential need not have the same composition as the layer below the passivation potential. The integration of the *I-U* curves in 0.2*N*, 1*N*, and 5*N* KOH yields 2.2, 16, and 40 mC/cm^2, respectively, at 0.065v. This represents a substantial coverage of the Cd electrode with $Cd(OH)_2$ or CdO in concentrated solutions.

The thick layer continues to grow on top of the thin film. The driving force for the layer formation remains nearly constant during the anodic sweep above 0.3v. During the subsequent cathodic sweep the current decreases nearly linearly between 0.7 and 0.1v. This suggests that the rate of layer formation on top of the thin film is largely controlled by the resistance of this layer which remains nearly constant. The small cathodic waves at the foot of the big reduction wave (Fig. 1) appear in 1*N* KOH at potentials which are too anodic (6,7) for the reduction of $Cd(OH)_2$. The small waves are attributed to the cathodic reduction of the thin layer. Ohse (7) similarly concluded on the basis of three potential plateaus during intermittent cathodic charging curves that CdO is reduced. The reduction of the thin film and the anodic formation of the thick layer overlap between 0.065 and 0.02v during the cathodic sweep. The height of the small wave decreases with increasing KOH concentration because the production of the thick layer becomes more favorable. The small wave is absent in the *I-U* curve of Fig. 2 because the thickness of the layer was not yet close to the limiting thickness at the moment of the sweep reversal. Finally the thick layer is reduced in the range 0 to —0.4v during the cathodic sweep.

The anodic charge Q_{an} for the formation of the thick layer was obtained by integration of the *I-U* curves between about 0.02v and the potential of reversal during the anodic sweep and between the potential of reversal and about 0.1v during the cathodic sweep. The charge Q_s for the reduction of the CdO film was determined approximately by integrating the *I-U* curves in 0.2*N* and 1*N* KOH between about 0.07 and 0v. The overlapping of the reduction of the thin film and of the thick layer at $U < 0$ prevents an exact determination of Q_s. It is difficult to find the charge Q_{cath} corresponding to the reduction of the thick layer during the cathodic sweep. The upper limit of the integration is uncertain because of a residual cathodic current of H_2 evolution. The presence of the latter is apparent from the anodic sweep between —0.6 and 0v. The integrations were done by the computer. The values of Q_{an} and Q_s are compiled for the same potential of reversal at the end of the anodic sweep in Table I.

The data in Table I demonstrate an increase of Q_{an} with the KOH concentration. The increase from 0.2*N*

Table 1. Charges Q_{an} and Q_s for a potential of reversal of 0.6v

		0.2*N* KOH	1*N* KOH	5*N* KOH
Q_{an} in	mC/cm^2	44.10	156	215
Q_s in	mC/cm^2	0.88	0.91	—

to 1*N* KOH is larger than that from 1*N* to 5*N* KOH. It is not proportional to the solubility (15) of $Cd(OH)_2$ in KOH. The dependence of Q_{an} on the KOH concentration is in agreement with the general assumption that a soluble intermediate is involved in the formation of the thick layer. The charge equivalent Q_s is relatively small and nearly the same in 0.2*N* and 1*N* KOH. It is estimated on the assumption of a small wave with symmetry to the *I*-axis that the actual Q_s values may be up to twice as large as those in Table I. The assumption of the symmetry is supported by the C_s-*U* curves a in Fig. 3 and 5 (see next section). The Q_s values correspond to CdO films which consist of only a few atomic layers.

Properties of films on the basis of impedance measurements at 10,000 cps.—The mechanism which was proposed on the basis of *I-U* curves in the preceding section is substantiated by the results of the impedance measurements which give information on the semiconducting properties of the films and the potential range of formation and reduction of the CdO layer. The capacitance C_s (10,000 cps) in Fig. 3 is nearly independent of potential between —0.55 and —0.2v. It is attributed to the Helmholtz double layer in the solution. During the anodic sweep the capacitance decreases in 5*N* KOH from about 20 to about 3 $\mu F/cm^2$ between 0.06 and 0.1v. This rapid decrease is due to the formation of the thin film whose capacitance is in series with and smaller than the capacitance of the Helmholtz layer. Since the capacitance does not change much during both the anodic and cathodic sweep, it is concluded that the thin film does not grow at $U > 0.2$v anymore. The *I-U* curves demonstrate a considerable increase of the thickness of the total layer in the same potential range. This increase is not reflected by the C_s (10,000 cps)-*U* curve. During the cathodic sweep the capacitance C_s (10,000 cps) increases rapidly between 0.05 and —0.05v in Fig. 3 and 5. This is in the potential range where the thin film is reduced. The C_s values between —0.05 and —0.3v differ only slightly from those between —0.3 and —0.7v (curve a in Fig. 3 and 5). It may be concluded again that the thick layer does not affect C_s (10,000 cps) much since its reduction occurs between 0 and —0.3v during the cathodic sweep. This can be explained by a porous or more highly conducting structure. Similar conclusions follow from curve a in Fig. 4. The formation of the thin layer is reflected by a tenfold increase of R_s between 0.05 and 0.1v during the anodic sweep, resulting from its semiconducting properties. The continued formation of the thick layer between 0.1 and 0.6v has only a slight influence on R_s (10,000 cps). The ohmic component drops to a small value between 0.05 and —0.05v where the thin film is reduced during the cathodic sweep. The reduction of the thick layer between 0 and —0.3v during the cathodic sweep does not affect R_s (10,000 cps). The flat minimum of curve a between —0.4v and 0 is attributed to an additional effect discussed below.

Faradaic pseudocapacitance.—The conclusions in the preceding section were drawn on the basis of impedance measurements at 10,000 cps. The C_s-*U* curves at 1000 and 100 cps in Fig. 3 and 5 and the corresponding R_s-*U* curves in Fig. 4 confirm the previous deductions in general. However, they do not allow the determination of the potential ranges of formation and reduction of the thin layer because of the presence of pseudocapacitances originating from electrochemical processes.

The C_s-*U* curves b and c in Fig. 3 and 5 and the curve in Fig. 6 demonstrate an increase of C_s with *U* between about —0.3v and 0 during the anodic sweep. This increase is too large to result from changes in the structure of the Helmholtz layer. It becomes larger with the KOH concentration and depends on frequency. Since the formation of phase hydroxide or oxide is not possible in the said potential range, the capacitance increase is attributed to the reaction:

$$OH^- = OH_{ad} + e \qquad [5]$$

Here OH_{ad} represents adsorbed OH radicals. The adsorption of OH radicals was postulated in the oxidation mechanism given in ref. (10). It had been assumed (16) to be the primary process in the oxidation of several metals.

It is conceivable that the pseudocapacitance between 0 and 0.7v during the anodic sweep (curves c in Fig. 3 and 5) is also due to reaction [5] which may constitute the first step in the $Cd(OH)_2$ formation. Reaction [5] may be responsible for the arrest observed by Ohse (7) in potential decay curves after cathodic polarization. A more detailed study of the frequency dependence of reaction [5] is planned.

Oxidation at constant potential.—The large value of C_s after 10 sec during the oxidation at 0.02v in Fig. 7 is attributed to the faradaic pseudocapacitance of reaction [5]. The pseudocapacitance decreases slowly with time because parts of the surface become blocked with patches of $Cd(OH)_2$. The inhomogeneous growth of the layer formed at $U < 0.1$v could be confirmed by visual observations of the surface of electrodes which were removed from the electrolyte at constant potentials after some time of oxidation. The latter observation is in agreement with the corresponding results in ref. (9). The C_s values after 10 sec of oxidation become smaller with increasing potential because the initial rate of oxidation at constant potential increases, leading to a rapid blocking of the surface. At $U \geqq 0.1$v, the values of C_s after 10 sec are close to those of the thin layer observed during the anodic sweep (see Fig. 3 and 5). The above results are in agreement with the preceding results obtained by voltammetric measurements.

Acknowledgment

The authors acknowledge gratefully discussions with Dr. D. A. Vermilyea, General Electric Research and Development Center.

Manuscript received Dec. 20, 1965; revised manuscript received March 18, 1966.

Any discussion of this paper will appear in a Discussion Section to be published in the June 1967 JOURNAL.

REFERENCES

1. P. E. Lake and E. J. Casey, *This Journal*, **105**, 52 (1958).
2. P. E. Lake and E. J. Casey, *ibid.*, **106**, 913 (1959).
3. K. Huber, *ibid.*, **100**, 376 (1953).
4. G. T. Croft, *ibid.*, **106**, 278 (1959).
5. G. T. Croft and D. Tuomi, *ibid.*, **108**, 915 (1961).
6. E. Lange and R. Ohse, *Naturwiss.*, **45**, 437 (1958).
7. R. W. Ohse, *Z. Elektrochem.*, **64**, 1171 (1960).
8. I. Sanghi, S. Visvanathan, and S. Ananthanarayanan, *Electrochim. Acta*, **3**, 65 (1960).
9. S. Yoshizawa and Z. Takehara, *ibid.*, **5**, 240 (1961).
10. L. A. L'vova and A. V. Fortunatov, *Zhur. fiz. Khim.*, **37**, 1708 (1963); **37**, 1712 (1963).
11. S. U. Falk, *This Journal*, **107**, 661 (1960).
12. M. Fleischman, K. S. Rajagopalan, and H. R. Thirsk, *Trans. Faraday Soc.*, **59**, 741 (1963).
13. J. L. Weininger and M. W. Breiter, *This Journal*, **110**, 484 (1963); **111**, 707 (1964).
14. M. W. Breiter, *ibid.*, **112**, 845 (1965).
15. D. E. Ryan, J. R. Dean, and R. M. Cassidy, *Can. J. Chem.*, **43**, 999 (1965).
16. See Proceedings of the 4th Conference on Electrochemistry, Moscow, 1956, Academy of Sciences, Moscow, 1959, pp. 577-646.

The Kinetics and Mechanism of Oxidation of Superpurity Aluminum in Dry Oxygen

I. Apparatus Description and the Growth of "Amorphous" Oxide

M. J. Dignam, W. R. Fawcett,[1] and H. Böhni[2]

Department of Chemistry, University of Toronto, Toronto, Ontario, Canada

ABSTRACT

A vacuum microbalance and furnace assembly was constructed and employed to determine the growth kinetics of oxide films on aluminum. Using electropolished foil samples of geometric area 80 cm^2, and making corrections for spurious weight changes arising from thermal diffusion effects, film thickness changes as small as 0.3Å could be reliably detected. In addition to kinetic data, the structure of representative oxide films was examined by electron microscopy. It was found that only "amorphous" oxide grew for about the first 10 hr at 454°C and for shorter periods at 478° and 505°C, the weight gain data being in good accord with an equation similar to that proposed by Mott and Cabrera for the growth of very thin oxide films, an approximate integrated form of which is sometimes referred to as the inverse logarithmic equation. The data could not be represented satisfactorily by either a parabolic oxidation law or a direct logarithmic law.

The kinetics of the oxidation of aluminum at high temperatures has been the subject of a number of experimental investigations in the past twenty years (1-6). In these experiments it has been common to follow the reaction kinetics by measuring the weight gain of a superpurity metal sample. The relevance of this type of data depends on the method of surface preparation (6), and indeed, mechanical surface preparations have been shown to lead to anomalous results in the case of aluminum (5). Other investigators have studied the morphology of the growing oxide (6-11), the main observation being that crystalline γ-alumina (defect spinel structure) nucleates beneath the continuous "amorphous" film at oxidation temperature in excess of about 450°C.

In the present investigation weight gain data were obtained in the temperature range 454°-601°C for superpurity aluminum samples whose surfaces had been prepared by electropolishing. This technique, rather than chemical polishing, was selected because of the excellent success obtained with it in this laboratory, both in the fields of anodic and thermal oxidation. In addition, representative oxide films were removed from oxidized samples and examined by electron microscopy. In the present paper the apparatus and experimental technique are described. Results for the growth of the continuous amorphous oxide film which forms exclusively for a period of about 10 hr at 454°C and for shorter periods at 478° and 505°C are presented.

The mechanism and kinetics of growth of the γ-alumina crystallites are considered in detail in Part II of this paper.

Experimental

Apparatus.—The apparatus used consisted principally of a recording vacuum microbalance, Sartorius Model Electrono I, in conjunction with a metal high vacuum system and quartz tubular furnace (see Fig. 1). The quartz tube was sealed into the system with O'rings housed in the metal heads H_2 and H_3. The sample, initially suspended from the end of rod R in a cooled section of the apparatus below the furnace, could be transferred into the furnace by raising R. The rod was sealed into the system by a double O'ring seal effected with specially constructed Teflon O'rings in housing H_1, and thus the transfer operation could be carried out either under vacuum or controlled atmosphere conditions.

Two metal bellows, B_1 and B_2, were incorporated to help isolate the balance from vibrations and to facilitate horizontal movement of the balance, necessary in order to transfer the sample from the rod to the balance arm. This operation was viewed through a glass window incorporated in the metal connector C. The sample was introduced by removing plate P_2, which was normally sealed to plate P_1 by an O'ring seal. Gases could be introduced through valves V_2, V_3, and V_4. The pumping system consisted of a three-stage oil diffusion pump backed by a rotary pump. With this system an ultimate vacuum of 1×10^{-6} Torr could be obtained. The section of metal tubing parallel to the furnace was included in the system to provide a convective cycling path in which gases could be rapidly mixed during addition of one gas to another. Valve V_1 provided a means of closing this path during oxida-

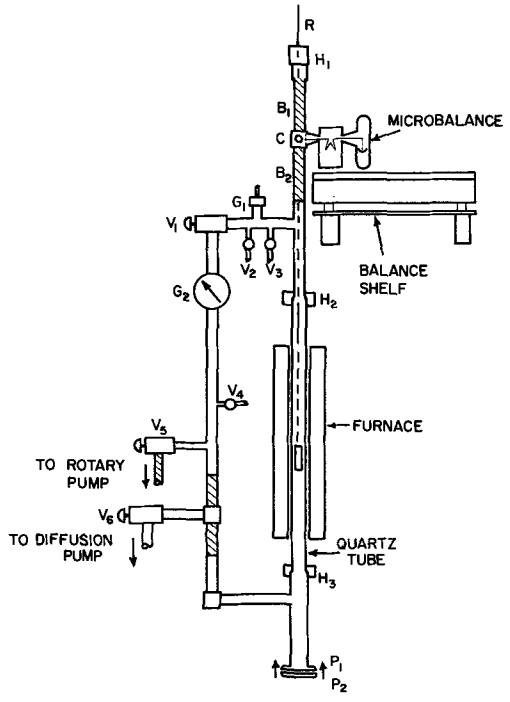

Fig. 1. Schematic diagram of vacuum microbalance and furnace assembly.

[1] Present address: Department of Chemistry, University of Bristol, Bristol, England.

[2] Present address: Eidgenössische Technische Hochscule, Zürich, Switzerland.

tion experiments. An ionization gauge with a cold cathode head (G_1) was used to measure pressures in the range $1x10^{-7}$ to $2.5x10^{-2}$ Torr. Pressures in the range 0-22 Torr were measured on gauge G_2.

The electrical tubular furnace, about 2 ft long and 2 in. ID, contained three windings; a central winding 16 in. long and two end windings, each 4 in. long. The power input to each was delivered by a separate controller in order to minimize thermal end effects. The central controller was a thyratron proportional controller similar to one described by Benedict (12), but modified to deliver larger currents. The sensing element was a 100 ohms (0°C) platinum resistance. The end windings were controlled by two "Acro-Relays" (Model 301 by Acromag Inc.), also employing a platinum resistance as sensing element. Each relay controlled only a portion of the power, this portion being adjusted to minimize temperature fluctuations. With the above system, the temperature in the sample region, about 6 in. long, was uniform to within ± 0.1°C, contained no measurable ripple, ($\lesssim$ 0.01°C), and was constant to a fraction of a degree for long periods of time. The temperature controllers have been described in detail elsewhere (13). A resistance thermometer, mounted in a hollow tube which could replace the rod R, allowed the temperature of the furnace to be measured at various positions under controlled atmosphere conditions. The optimum control conditions for each temperature and the resulting temperature profile were thus obtained.

The automatic microbalance when operated on its most sensitive scale had a sensitivity of better than 1 μg and a full-scale deflection of 100 μg. Differences in weight of up to 5 mg between the two balance arms could be compensated by changing the tension on the torsion wire on which the balance beam was suspended. Thus, during an experiment, changes in weight could be followed continuously on the most sensitive scale.

Materials.—Specimens were prepared from 99.996% aluminum foil (Republic Aluminum Foil Company) of thickness 7.6×10^{-3} cm. Strips of foil 33 x 1.6 cm were electropolished in one part by volume of 70% perchloric acid to five parts of ethanol. The electropolishing cell was designed so that, when the foil sample was clamped into position, its surfaces were parallel to those of two nickel cathodes. The electrolyte was circulated through the cell and a heat exchanger in series, the latter maintaining the electrolyte temperature between 18° and 22°C. The specimens were electropolished for 3 min at 23v, the current density being initially 1.5 amp cm^{-2} but falling to about 0.6 amp cm^{-2} within a minute. After polishing, the sample was given an immediate preliminary rinse in absolute ethanol, then rinsed thoroughly under a stream of distilled water for 3 min, and finally dried in a blast of air. It was then removed from the cell clamping device, and the several centimeters at each end where it had been clamped were cut off, leaving a specimen with a geometric surface area of about 80 cm^2. The polished samples were stored in a desiccator over anhydrous calcium sulfate.

Commercial tank grade oxygen (99.6% purity) was purified by distillation from a liquid nitrogen trap, the initial and final fractions being discarded. The middle fraction was stored in a glass bulb connected to the high vacuum system.

Argon (99.998% pure, from Matheson Company of Canada) which was used to inhibit oxidation of the specimen as it was being heated to the desired oxidation temperature was further purified by bubbling it through molten sodium and was stored as above.

Experimental procedure.—An electropolished sample was placed on a platinum frame suspended by a platinum wire from the end of rod R and then drawn into the water-cooled compartment below the furnace. The system was evacuated for about 8 hr with the furnace at the desired temperature, the ultimate vacuum achieved being better than 10^{-5} Torr. Purified argon was then introduced to a pressure of 9 Torr, the specimen was raised into the furnace, and the sample suspension system was transferred to the arm of the microbalance. The balance was then turned on, and the torsion wire adjusted to give a small displacement from zero on the most sensitive scale. After allowing 10 min for the sample to achieve thermal equilibrium, oxygen was introduced until the total pressure was 10 Torr. During this operation, valve V_1 was opened in order to guarantee thorough mixing of the gases. After closing valve V_1, about 30 sec were required for the balance to settle down. A continuous record of weight was then obtained. The weight changes were read from the recorder chart to the nearest 0.2 μg.

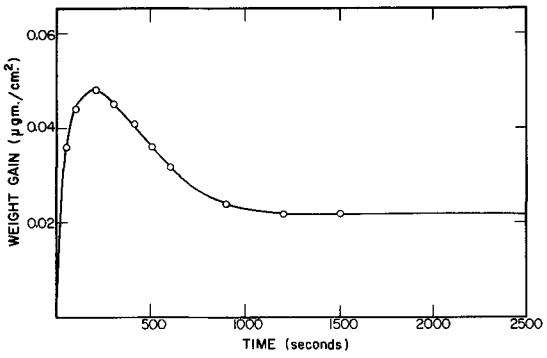

Fig. 2. Apparent weight gain data for "blank" oxidation run at 454°C.

When the rate of weight gain had fallen to a negligibly small value, the system was evacuated and argon and oxygen introduced as before. Such "blank" oxidation runs provided the data necessary to correct for changes in convective and buoyancy forces arising in the first instance when oxygen was introduced, and then as a result of the diffusive separation of the gases in the thermal gradients at the furnace ends (Soret effect). At 454°C (see Fig. 2) the blank runs indicate an apparent weight increase of 0.036 μg cm^{-2} at 50 sec, increasing to a maximum of 0.048 μg cm^{-2} at 200 sec, and then falling to a limiting value of 0.022 μg cm^{-2} for times of 1200 sec or greater. The effect, although similar at the other temperatures, differed in detail, the maximum apparent weight increase occurring at 601°C, where it reached a value of 0.077 μg cm^{-2}. Preliminary runs using helium as the inert gas gave rise to very much larger apparent weight increases, as expected, since the difference in diffusion rate between helium and oxygen is very much larger than that between argon and oxygen. To keep this apparent weight effect small and reproducible it was necessary to have a very uniform temperature zone in the neighborhood of the specimen, work at low total pressures, use an inert gas close in molecular weight to that of oxygen, and have one of the component gases present in considerable excess. On the other hand, too low a total pressure leads to insufficient damping of the pendulum motion of the specimen suspension system and hence to erratic balance performance. The procedure described was evolved with these considerations in mind.

The question arises as to whether or not the procedure outlined above represents a satisfactory one in relation to sorbed impurities present prior to initiating oxidation. The surface was, of course, far from clean, in that at the very least there was an oxide film some 25Å in thickness. In a number of previous studies, however, extensive outgassing of the sample at the oxidation temperature was carried out before initiating oxidation. It is in this connection that we raise the issue.

The outgassing of the sample at room temperature should remove loosely bound or physically adsorbed

surface impurities, the most important of these being water. On bringing the sample to temperature, the remaining sorbed water and oxygen will either desorb from the surface or react with the metal to form new film. This process will probably be completed within a few seconds, and certainly in far less than 10 min. Clearly no amount of vacuum outgassing will remove this newly formed film. Prolonged treatment *in vacuo* at high temperatures would therefore appear to be ineffective against reactive contaminants. On the other hand, such treatment will provide ample opportunity for extensive reaction with residual gases, and at a temperature where the reaction rates will be high. To be effective, therefore, outgassing must be carried out in ultrahigh vacuum ($\sim 10^{-10}$ Torr). The present procedure of introducing the sample into the hot furnace in purified argon, rather than *in vacuo*, was used in order to minimize surface contamination by reducing the rate of diffusion of the residual gases to the sample. Using this procedure, there was no observable change in weight during the several minutes prior to introducing oxygen.

The extensive outgassing observed in the case of metallographically polished metal (2) is to be expected since the mechanical polishing action is bound to lead to the formation of pockets of air and/or polishing lubricant in the surface region of the metal.

An electron micrographic examination of the oxide films formed was undertaken for selected specimens. The films were isolated by dissolving the metal in a solution of 2% bromine in methanol.

Experimental results.—The apparent weight of a superpurity aluminum specimen as a function of time was read from the recorder chart, the initial weight being taken as the recorded weight in argon prior to introducing the oxygen. Then the correction due to thermal diffusion and change in buoyancy was subtracted from the apparent weight gain readings. The resulting corrected weight gain data for typical runs at 454°, 478°, 505°, and 530°C are presented in Fig. 3. The geometric area was used in calculating the weight gain per unit area.

Typical electron micrographs and diffraction patterns for films formed at different temperatures and after different periods of time are shown in Fig. 4. The results, which are in accord with previous studies, may be summarized as follows. At 454°C for oxidation periods below about 10 hr the film consists primarily of amorphous alumina, the diffraction pattern being similar to that found for anodically formed oxide on aluminum. After prolonged oxidation at 454°C and following relatively short oxidation periods at the higher temperatures, a diffraction pattern characteristic of a cubic structure of lattice constant 7.9Å is evident, presumably indicating the presence of crystalline γ-alumina. At the same time, the transmission micrographs show dark areas of the order of a few thousand angstroms across, presumably crystallites of γ-alumina much thicker than the background amorphous film, very similar to that reported previously by one of us (6). The diameter of the crystallites is observed to increase with oxidation period until the entire film consists of close packed crystallites. Although dependent on metal grain orientation, the number density of these crystallites does not appear to change appreciably either with oxidation temperature or oxidation period.

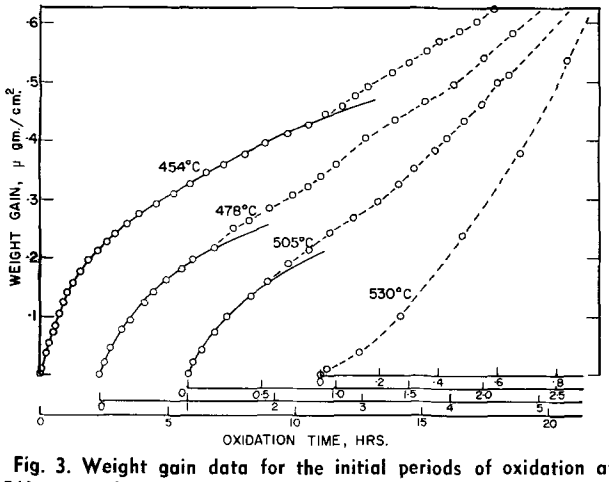

Fig. 3. Weight gain data for the initial periods of oxidation at 454°, 478°, 505°, and 530°C.

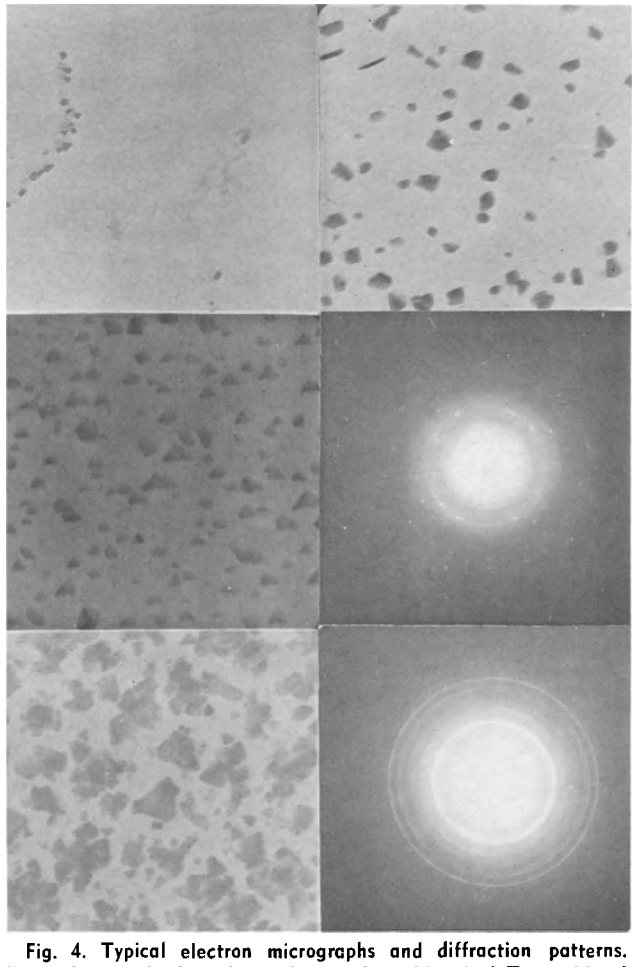

Fig. 4. Typical electron micrographs and diffraction patterns. (Magnification 24500 before reduction for publication) Top, oxidized at 454°C for 6 and 16 hr, respectively; center, oxidized at 454°C for 24 hr; bottom, oxidized at 601°C for about 2 hr.

Discussion of Results

From Fig. 3 it is seen that the kinetic characteristics of the oxidation process at 454°C change at about 10.5 hr. In the initial period the rate of weight gain steadily decreases with time, whereas in the second period it begins to increase slowly. The kinetic data in the initial period are characteristic of the growth of a protective oxide film and correspond to the thickening of the initially present "amorphous" film. The point of inflection is no doubt related to the onset of appreciable growth of crystalline oxide. Doherty and Davis (11) observed that crystallites of γ-alumina were nucleated at the surface between metal and amorphous oxide and grew down into the metal by diffusion of oxygen from the oxide-oxygen interface. Thus the onset of this process should be accompanied by an increase in the rate of oxidation over that due to the growth of the amorphous film alone, as observed.

The weight gain data for 478° and 505°C (Fig. 3) show the same features as those for 454°C, the onset

of growth of crystalline oxide, however, occurring very much sooner. At 530°C and above, the growth of crystalline oxide appears to commence at essentially time zero. An analysis of the kinetics of the growth of the amorphous film by the method of weight gain is therefore not possible for temperatures much in excess of 500°C. Data for the growth of the amorphous film at temperatures of 450°C and below have been presented previously (6) and will ultimately be discussed with the present data.

The growth of crystalline oxide commences at a lower value for the total weight gain as the temperature is increased above 450°C. The data at 450°C accordingly represents the most extensive data insofar as the growth of the amorphous film is concerned. These data were therefore used to determine the functional form of the kinetics, *i.e.*, parabolic, logarithmic, etc. The data for the higher temperatures enable an activation energy to be calculated once the functional form is known, and provide a somewhat insensitive test of the functional form itself. We shall proceed first with an analysis of the data for 454°C.

Data for 454°C.—As electron micrographic data indicate that the amorphous film grows as a compact, adherent film of uniform thickness, we shall limit our consideration to the following rate laws: the parabolic law; the direct logarithmic law; and the Mott-Cabrera rate law for the growth of thin oxide films (14), an approximate integrated form of which is commonly referred to as the inverse logarithmic law.

Although other forms of rate law have been justified on theoretical grounds, they are for one reason or another clearly not relevant to the present case and hence will not be considered. As the data are ultimately shown to be in accord with an equation of the form of that proposed by Mott and Cabrera, their theory and the resulting rate law will be considered first.

Mott and Cabrera assumed that, for oxide films of thickness substantially less than the characteristic space charge length for the oxide, the rate would be controlled by ion transport across the film under the influence of a homogeneous field established by the equilibration of electrons between the metal and surface levels associated with chemisorbed oxygen molcules or atoms. They further assumed that the potential, V, across the film, giving rise to the homogeneous field, was independent of both film thickness and temperature. Although Grimley's (15) theoretical treatment does indicate an insignificant dependence of V on film thickness, the validity of the assumption regarding the temperature dependence is somewhat less certain. We shall proceed, nevertheless, on this assumption. Mott and Cabrera further assumed that the rate-controlling process for very thin films, for which the homogeneous field would be very large, was the transport of cations across the metal-oxide interface. However, the same form of equation is obtained regardless of where the rate-controlling ion transport step occurs. As the thickness of the amorphous oxide film on alumina has been shown previously to be independent of the crystalographic orientation of the metal surface (6), we shall assume, in the present instance, the rate-controlling ion transport process to be transport within the film. This assumption has the further advantage that a single equation will represent both the "thin film," and the "very thin film" cases discussed by Mott and Cabrera (14).

Employing the above assumptions, the rate equation is derived in the following manner. According to Mott and Gurney's theory of conduction in solids (16) the most general expression for the velocity, v, of a charged mobile point defect due to an electrostatic field, E, is the following

$$v = 2\nu\alpha \exp(-U/kT) \sinh\left(\frac{\mu^* E}{kT}\right) \qquad [1]$$

where U is the zero field activation energy associated with movement of the species, μ^* the corresponding activation distance times the effective charge on the species, or the activation dipole, ν is the usual frequency term, and α the distance travelled per activation or the jump distance. Assuming that the field strength is sufficiently large that the contribution to ion flux arising from concentration gradients may be neglected, the rate of growth of a film is given by

$$\frac{dX}{dt} = 2A \sinh(B/X) \qquad [2]$$

$$A = \Omega\nu\alpha n \exp(-U/kT),\ B = (\mu^* EX/kT) = (\mu^* V/kT)$$

where X is the film thickness at time t, n the concentration of the mobile species, Ω the volume of oxide per cation or anion (depending on whether transport is cationic or anionic), and V the potential drop across the film. For films sufficiently thin such that $X<<B$, 2 sinh (B/X) may be replaced by exp (B/X) leading to an equation identical in form to that proposed by Mott and Cabrera for "very thin films." For somewhat thicker films such that $X>>B$, but still thinner than the characteristic space charge length, sinh (B/X) may be replaced by B/X leading to an equation identical to that proposed by Mott and Cabrera for "thin films."

To convert weight gain data per unit area to change in film thickness, Bernard and Cook's (17) value for the density of anodically grown amorphous oxide, 3.17 g cm^{-2} was used and the surface roughness factor assumed to be unity. On this basis a weight gain of 1 μg cm^{-2} corresponds to a film thickness increase of 66.4Å.

In order to illustrate the calculation procedure used to determine the values of A and B in Eq. [2] which give the best fit to the data, Eq. [2] is rewritten below in integrated form

$$\int_{B/X}^{B/X_0} \frac{\tfrac{1}{2}\,\mathrm{csch}\,u}{u^2}\,du = \frac{A}{B}\,t \qquad [3]$$

where X_0 is the film thickness at time zero, that is the thickness of the film initially present prior to oxidation. As the precise value of the initial film thickness is unknown, trial values for X_0 were assumed. Having chosen X_0, the data were fitted to Eq. [3] by a 7094 IBM computer using a nonlinear least squares program. For each trial value of X_0, values of A and B which minimized S (the root mean square deviation of the experimental points from the calculated curve) and the value of S itself were determined.

Values for parameters A and B were determined in this way for three values of X_0, 20, 25, and 30Å. These values were chosen in consideration of experimental studies of the room temperature oxidation of aluminum (8, 18-20) where it has been found that the limiting film thickness achieved in about a day is less than 50Å and probably lies within the range 20-30Å. These values, averaged for 5 runs, are given in Table I.

It can be seen that B and A vary considerably more rapidly with X_0 than does S; that is the agreement between the theory and the data is rather insensitive to the choice of X_0. Since a reliable experimental value of X_0 is not available, the parameters calculated assuming an initial thickness of 25Å are accepted as this value of X_0 minimizes S. The choice of this value

Table I. Kinetic parameters for oxidation of aluminum at 454°C

X_0, Å	B, Å	$-\log_{10} A$, A in Å-sec^{-1}	S, Å
20	95.2 ± 3.4	4.310 ± 0.034	0.27 ± 0.08
25	129.4 ± 4.4	4.509 ± 0.045	0.24 ± 0.04
30	167.4 ± 5.9	4.702 ± 0.049	0.27 ± 0.07

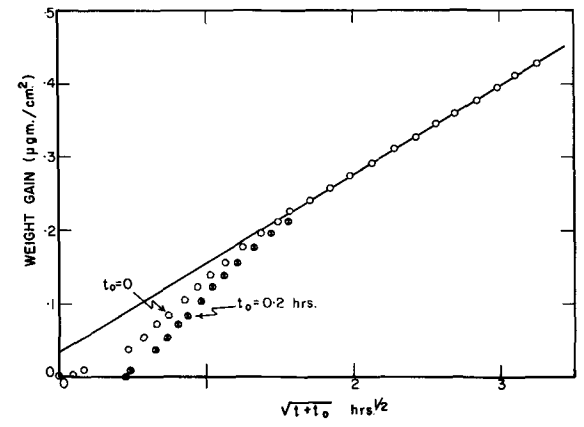

Fig. 5. Weight gain data at 450°C plotted according to the parabolic oxidation law for two choices of the parameter t_o.

for X_o is, however, further justified later. The solid curve shown in Fig. 3 was calculated using this set of parameters. As can be seen the agreement between the data and calculated curve is excellent. In fact, the average standard deviation of the experimental data from the calculated curve, 0.2$_4$Å, corresponds to a standard deviation in the weight measurements of only 0.3 μg for a sample with an area of 80 cm^2. Since this is of the order of the sensitivity of the balance, we may conclude that no detectable discrepancy exists between the data at 454°C and Eq. [2].

In Fig. 5, the data for 454°C have been plotted in accord with the most general form of the parabolic oxidation law [weight gain *vs.* $(t + t_o)^{1/2}$] for two values of the parameter t_o. It is apparent that no value for t_o will lead to a linear relationship over the entire range of the data. It is interesting to note, that for $t_o = 0.2$ hr, the data fall very nearly on two intersecting straight lines. An attempt to explain the kinetic data in this manner (*i.e.*, by two independent rate laws with a total of five disposable constants) is clearly far less satisfactory than that based on Eq. [2] and illustrates the danger of applying more than one rate equation to a single set of data. The linear region for large oxidation periods is expected, since Eq. [2] reduces to a parabolic law for sufficiently large film thickness.

In Fig. 6, the data for 454°C have been plotted in accord with the direct logarithmic oxidation law (curve a). Choosing the optimum value for the parameter t_o, the data fall on a good straight line over about ¾ of the full range of weight increments. As it stands, this fit is substantially inferior to that obtained with Eq. [2]. The question remains, however, as to

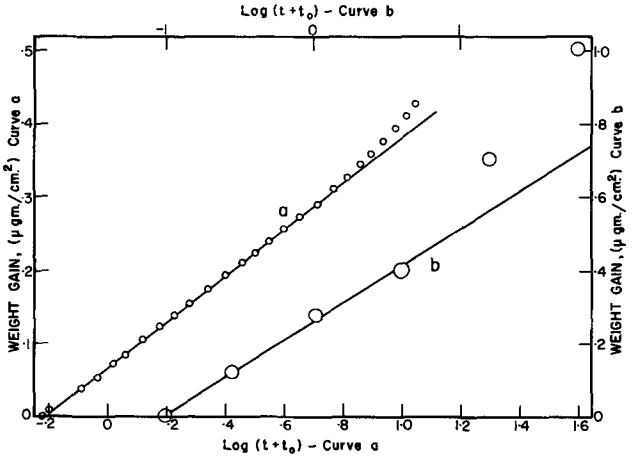

Fig. 6. Weight gain data plotted in accord with direct logarithmic law: curve a, present data for 454°C; curve b, previous data (6) for the oxidation of Al + 0.24% Si at 450°C.

whether the deviation from linearity apparent for high oxidation times (Fig. 6, curve a) might not possibly arise as a result of initiation of growth of crystallites of γ-alumina. To test this possibility, weight gain data published previously (6) for the oxidation at 450°C of aluminum with 0.24% Si added have also been plotted according to the direct logarithmic equation (Fig. 6, curve b). These data were selected since little or no crystalline oxide was found on this alloy following oxidation for 64 hr at 450°C (6). Furthermore, data for this alloy were indistinguishable from those for superpurity aluminum in so far as the kinetics of growth of the amorphous film were concerned (6). We see that these data as well deviate from the direct logarithmic law, the deviation commencing at about the same value for $(t + t_o)$ and becoming very large indeed at 64 hr. It should be noted that Eq. [2] predicts adherence to a direct logarithmic law to a good approximation for a range of data corresponding to an increase of about a factor of two in the film thickness.

It appears that the failure of the direct logarithmic law to represent the full range of the data cannot be attributed to growth of crystalline film so that we may conclude not only that Eq. [2] fits the data at 454°C with no deviation beyond experimental scatter, but that no other single rate law yet formulated does.

Data for 478° and 505°C.—At these temperatures, the following procedure was adopted in analyzing the data for the growth of the amorphous film. Equation [3] may be written in the form

$$f(B/X) = (A/B)(t + t_o) \qquad [4]$$

where

$$t_o = (B/A)\, f(B/X_o) \qquad [5]$$

and

$$f(z) = \int_z^\infty \frac{\frac{1}{2}\,\mathrm{csch}\, u}{u^2}\, du \qquad [6]$$

or alternatively as

$$\log[f(B/X)] = \log(t + t_o) + \log(A/B) \qquad [7]$$

If the data are in accord with Eq. [2], then B at 478° and 505°C (or for that matter any other temperature) may be calculated given B at 454°C and assuming $\mu^* V$ independent of temperature. Thus B/X may be calculated as a function of time, and the results plotted in accord with Eq. [7], *i.e.*, log $[f(B/X)]$ *vs.* log $(t + t_o)$. If the data are in accord with [2], then the resulting graph will be linear and of unit slope. The intercept will yield an experimental value for A. In plotting the data according to Eq. [7], an estimate of t_o is used initially, ultimately being adjusted in accord with Eq. [5] so that the final plot represents a single parameter fit, A being the only unknown parameter. Despite the inconvenience associated with Eq. [7] arising from the necessity for trial and error adjustment of t_o, it is preferable to plot the data according to this equation rather than [4], as the latter leads to crowding of most of the points close to the time zero intercept.

The relation between Eq. [7] and the so-called inverse logarithmic law can easily be found for the case $B/X >> 1$, since for $z >> 1$, $f(z) \simeq [\exp(-z)]/z^2$ so that Eq. [7] becomes

$$\frac{-B}{2.303\, X} + \log X^2 \simeq \log(t + t_o) + \log(A \cdot B)$$

For the present results, however, this equation represents a poor approximation to Eq. [7]. Accordingly, tables of values of log $[f(z)]$ were calculated as follows. Noting that $\frac{1}{2}\,\mathrm{csch}\, u = e^{-u}[1-e^{-2u}]^{-1} = (e^{-u} + e^{-3u} + e^{-5u} \ldots .)$ for $u > 0$, the expression for $f(z)$ may be written

$$f(z) = (1/z)\,[E_2(z) + E_2(3z) + E_2(5z) + \ldots\ldots] \qquad [8]$$

where $E_2(y)$ is the second degree exponential integral, tabulated values for which are available (21), and is defined as follows

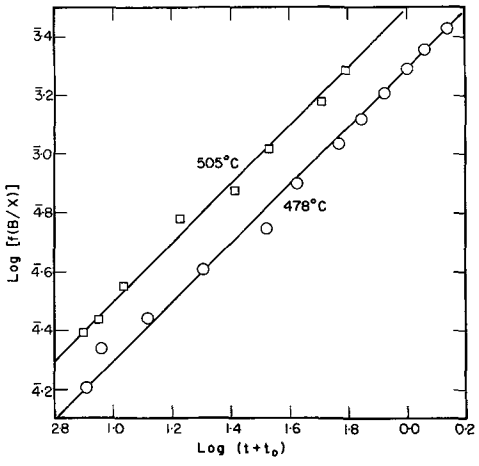

Fig. 7. Weight gain data for 478° and 505°C plotted according to Eq. [7], *i.e.*, according to the generalized Mott-Cabrera law.

$$E_2(y) = \int_1^\infty \frac{e^{-yu}}{u^2}\,du = y\int_y^\infty \frac{e^{-u}}{u^2}\,du$$

For $z > 1$, the series representation for $f(z)$ converges very rapidly, no more than the first few terms being required. Thus tables of the function log $[f(z)]$ may be readily calculated using [8].

The data for the initial period of oxidation at 478° and 505°C are plotted in Fig. 7 according to [7] using the values of X_o and $B(454°)$ giving the best fit at 454°C (*i.e.*, X_o = 25Å, B = 129.4 x 727/T). The straight lines on the graph are drawn with slope unity. It is clear that all the points shown fall on these lines well within experimental scatter. As one goes to oxidation periods greater than those shown in Fig. 7, however, the points lie increasingly above the line, a result expected following the onset of growth of crystalline oxide.

Analysis of previous data for 250°, 350°, and 450°C. —In order to test further the validity of Eq. [2] with regard to the growth of amorphous oxide on aluminum, previous data (6) covering the temperature range 250°-450°C was analyzed in the same manner as the data at 478° and 505°C. Before proceeding with the analysis, however, a brief discussion of the experimental method used to obtain these data is in order. Aluminum samples were electropolished, using essentially the same procedure as that employed for this investigation, oxidized for the desired period of time, then removed from the furnace and their film thickness determined by an electrometric method. The method involved placing the sample in an electrolytic cell and determining the minimum cell overpotential, V_b, required to cause significant ion current to flow through the oxide film. Provided that the conduction properties of all the films are the same, this potential, frequently referred to as the "barrier voltage," should be a linear function of the film thickness. In the previous paper, evidence was presented which showed that films formed in oxygen at 450°, 350°, and 250°C all had the same conduction properties. A re-examination of the data has indicated, however, that this conclusion should be qualified in that it only applies to samples which have been oxidized for a sufficient period of time at the temperature in question. Specifically, it appears that the oxidation period must be greater than approximately t_o before the conduction properties become independent of temperature and time, where t_o is given by [5] and is the time required to form a film of the initial thickness at the oxidation temperature in question. This is an interesting, although not entirely surprising, observation which we shall pursue no further as a discussion of the effect does not bear directly on the subject matter of this paper.

For the present analysis, values of V_b were obtained from Table I of (6) by averaging the results of superpurity aluminum and superpurity aluminum containing respectively 0.2% Ga, 0.01% Fe, 0.53% Mn, 0.011% Cu, as these alloys gave results indistinguishable from those of superpurity. Since all the alloys studied previously, except the superpurity plus 0.24% Si alloy, had formed γ-alumina crystallites following 16 hr oxidation at 450°C, only the data for this alloy were used for 16 and 64 hr at 450°C. Except for oxidation periods $< t_o$, this alloy also appears to give values of V_b indistinguishable from those for the above mentioned alloys.

In Fig. 8, values for V_b for oxidation at 450°C are plotted against film thickness values calculated from the values for A and B for X_o = 25Å deduced from the present results. The data fall within experimental error on a straight line, the equation for which is given by

$$X = 15.6\,V_b - 6.9\text{Å} \qquad [9]$$

The value of the conversion factor, 15.6 Å/v, is substantially larger than that used previously (6). For the most recent data relating to the anodic oxidation of aluminum (22) and an analysis of the shape of the polarization curves used to obtain V_b, a conversion factor of about 14.4 Å/v may be estimated. This would be in accord with the above value if the electropolished samples used for the present study had a roughness factor of (15.6/14.4) = 1.08, which is indeed about the expected roughness factor.

Using Eq. [9], the barrier voltage data for 350°C were converted to film thickness values and the results plotted in accord with Eq. [7], using precisely the same procedure as was used in processing the data for 478° and 505°C. As can be seen in Fig. 9, the points lie almost precisely on the straight line of unit slope. It should be emphasized again that this represents a one parameter fit. If the entire calculation involved in Fig. 8 and 9 is repeated assuming X_o = 20 or 30Å, rather than 25Å, a significantly poorer fit is obtained, lending further support to the choice X_o = 25Å.

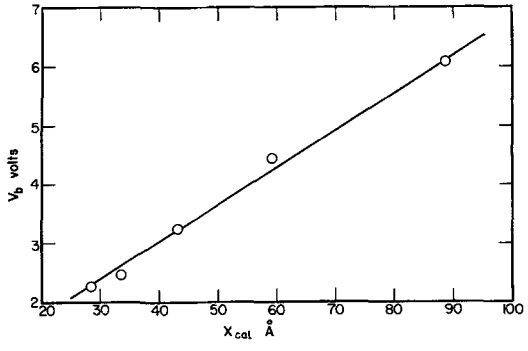

Fig. 8. Barrier voltage data for oxidation at 450°C, reported previously (6), plotted against film thickness calculated using the oxidation parameters determined in the present investigation.

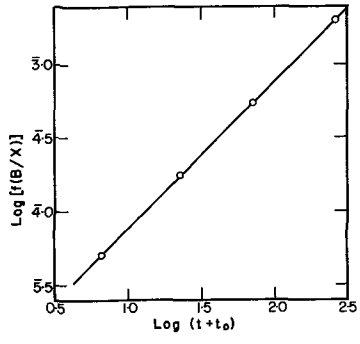

Fig. 9. Data reported previously (6) for oxidation at 350°C plotted according to Eq. [7], *i.e.*, according to the generalized Mott-Cabrera law.

Table II. Previously published barrier voltage data (6) converted to film thickness using [9]

	t, hr	$(t + t_o)$ hr	V_b, v	X, A
450°C	0	0.18_2		25.0
	0.25	0.43_2	2.27	28.3
	1	1.18_2	2.46	31.3
	4	4.18	3.25	43.8
	16	16.18	4.44	62.3
	64	64.18	6.09	88.1
350°C	0	6.6		25.0
	16	22.6	2.03	29.6
	64	70.6	2.70	35.3
	256	262.6	3.31	44.6
250°C	0	181		25.0
	600	781	2.35	29.7

Unfortunately, at 250°C only a single barrier voltage value corresponds to an oxidation period in excess of t_o, namely that for 600 hr. A value for A can nevertheless be determined from this single thickness (in addition to the time zero thickness of 25Å) using Eq. [7] or [4] as before. The value so determined cannot be considered very accurate, however, as the increase in film thickness from time zero amounts to only about 5Å.

The relevant barrier voltage values and film thicknesses calculated from [9] are presented in Table II along with the actual oxidation period, t, and the oxidation period from bare metal, $t + t_o$.

Values of log A obtained from Fig. 7 and 9 are plotted against reciprocal absolute temperature in Fig. 10, along with the value obtained at 454°C and the somewhat questionable value for 250°C. The points appear to be colinear within experimental error, the equation for the line being represented by

$$A = 2.5\text{x}10^6 \exp(-1.60/kT) \text{ Å/sec} \quad [10]$$

Summary

A careful analysis of precise weight gain data for the oxidation of electropolished aluminum foil at 454°C in dry oxygen shows that the growth of the continuous amorphous oxide film may be represented accurately (*i.e.*, within a standard deviation of 1/4Å) by an equation of the form $dX/dt = 2A \sinh(B/X)$ where A and B are constants under isothermal conditions. The same data cannot be represented even approximately by a parabolic law except in the final stages of growth when the above equation reduces approximately to parabolic form. A direct logarithmic equation represents the data well for the initial period of oxidation, but for long oxidation periods significant deviation from this law is apparent. Once again such behavior is expected for data in accord with the above equation since for a limited range of film thickness, and for $B/X >> 1$, it reduces approximately to a direct logarithmic equation.

Analysis of data for 478° and 505°C, along with previously published data for 250° and 350°C, showed agreement with the above equation with the temperature dependence of A and B given by

$$B = \mu^* V/kT, \quad \mu^* V = 8.2\, e\text{Å}V$$

$$A = A_o \exp(-Q/kT), \quad A_o = 2.5 \times 10^6 \text{ Å}\cdot\text{sec}^{-1}, \quad Q = 1.6 \text{ ev}$$

The extent of the data at temperatures other than 454°C was insufficient to verify the inverse temperature dependence of B.

Significant growth of crystallites of γ-alumina oxide, as evidenced by the initial inflection point in the weight gain curve, began after oxidation periods of about 12 hr at 454°C, 2 hr at 478°C, 1 hr at 505°C, and within less than 0.1 hr at 530°C. The induction period for growth of crystalline oxide is undoubtedly a function of the initial film thickness, X_o, as well as oxidation temperature (1).

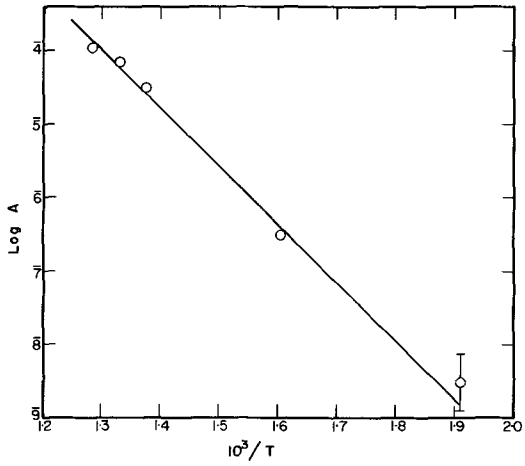

Fig. 10. Temperature dependence of the parameter A

Manuscript received Nov. 12, 1965; revised manuscript received April 18, 1966.

Any discussion of this paper will appear in a Discussion Section to be published in the June 1967 JOURNAL.

REFERENCES

1. E. A. Gulbransen and W. S. Wysong, *J. Phys. Colloid. Chem.*, **51**, 1087 (1947).
2. W. W. Smeltzer, *This Journal*, **103**, 209 (1956).
3. D. W. Aylmore, S. J. Gregg, and W. B. Jepson, *J. Inst. Metals*, **88**, 205 (1959-60).
4. P. E. Blackburn and E. A. Gulbransen, *This Journal*, **107**, 944 (1960).
5. C. N. Cochran and W. C. Sleppy, *ibid.*, **108**, 322 (1961).
6. M. J. Dignam, *ibid.*, **109**, 192 (1962); **109**, 184 (1962).
7. L. deBrouckere, *J. Inst. Metals*, **71**, 131 (1945).
8. G. Hass, *Z. anorg. Chem.*, **254**, 96 (1947).
9. G. D. Preston and L. L. Bircumshaw, *Phil. Mag.*, **22**, 654 (1936).
10. K. Thomas and M. W. Roberts, *J. Appl. Phys.*, **32**, 70 (1961).
11. P. E. Doherty and R. S. Davis, *ibid.*, **34**, 619 (1963).
12. M. Benedict, *Rev. Sci. Instrum.*, **8**, 252 (1937).
13. W. R. Fawcett, Ph.D. Thesis, University of Toronto, 1964.
14. N. Cabrera and N. F. Mott, *Repts. Progr. Phys.*, **12**, 163 (1948-49).
15. T. B. Grimley, *Discussions Faraday Soc.*, **28**, 223 (1959).
16. N. F. Mott and R. W. Gurney, "Electronic Processes in Ionic Crystals," pp. 34-45, Oxford University Press (1940).
17. W. J. Bernard and J. W. Cook, *This Journal*, **106**, 643 (1959).
18. N. Cabrera and J. Hamon, *C. R. Acad. Sci. (Paris)*, **224**, 1713 (1947).
19. V. V. Andreeva and N. A. Shishakov, *Zhur. Fiz. Khim.*, **32**, 1671 (1958).
20. R. K. Hart, *Proc. Roy. Soc. (London)*, **A236**, 68 (1956).
21. V. I. Pagurova, Tables of the Exponential Integral, Pergamon Press (1961).
22. M. J. Dignam, D. Goad, and M. Sole, *Can. J. Chem.*, **43**, 800 (1965).

The Kinetics and Mechanism of Oxidation of Superpurity Aluminum in Dry Oxygen

II. The Growth of Crystallites of γ-Alumina

M. J. Dignam and W. R. Fawcett[1]

Department of Chemistry, University of Toronto, Toronto, Ontario, Canada

ABSTRACT

Weight gain data for the oxidation of electropolished aluminum in the temperature range 475° to 600°C are presented and analyzed in terms of the following model. The γ-alumina crystallites, which nucleate beneath the amorphous oxide film, are assumed to achieve a terminal thickness rapidly, following which only radial growth takes place. This growth proceeds at a constant velocity, until the crystallites impinge on one another. The negative temperature coefficient, observed for the terminal thickness, and the terminal thickness itself follow from the proposed growth mechanism for the crystallites, which is given in sufficient detail to permit comparison of values of the experimental and theoretical pre-exponential factors. The proposed model is in complete accord with electron micrographic and other data for the system, the kinetic parameters also being in agreement with independent estimates.

Although a very considerable amount of information has been published on the high-temperature oxidation of aluminum in dry oxygen (1-8), only one quantitative treatment (9) of the oxidation kinetics in the temperature range 450°-600°C has been given which is reasonably consistent with the known morphology of the growing oxide (10, 7, 6).

In connection with the morphological features, the excellent data of Doherty and Davis (10) deserve special mention. The principal observations of these authors are that the crystallites of γ-alumina (spinel structure) nucleate beneath the amorphous film above 450°C and grow down into the metal substrate, and that the growth of the crystallites occurs by oxygen migration through the amorphous film.

The purpose of the present investigation was first to obtain weight gain data relating to the growth of the crystalline oxide for aluminum samples prepared by electropolishing, and second to provide a quantitative analysis of the data so obtained. Mechanical surface preparations were not used since such treatments are likely to lead to anomalous results, as pointed out previously by one of us (8).

The picture which emerges from the present study is that of oxygen species diffusing along a boundary between crystalline and amorphous oxides, the growth kinetics being controlled by the diffusion rate and the oxide "recrystallization" rate. Activation energies for both the diffusion and recrystallization processes are obtained, with the pre-exponential factors in excellent accord with those predicated on the basis of the model.

The kinetics of growth of the amorphous film have been treated in Part I of this paper (11).

Experimental

The apparatus and procedure used have been described previously (11).

The weight gain data for typical oxidation runs at 478°, 505°, 530°, 549°, and 601°C are illustrated in Fig. 1 to 5. Reproducibility from run to run was about ± 3%. It is interesting to observe that the limiting film thickness decreases with increasing temperature from 478° to 601°C, a result which has been noted by others (2-5).

The results of the present electron micrographic study are in accord with previous studies, with the main observations being presented in Part I of this paper (11). The pertinent points are summarized in the development of the model.

Discussion of Results

At 454°C for oxidation periods less than about 10 hr and for shorter periods at 478° and 505°C, the growth of the amorphous film has been shown previously (11) to be in accord with an equation of the form of that proposed on theoretical grounds by Mott

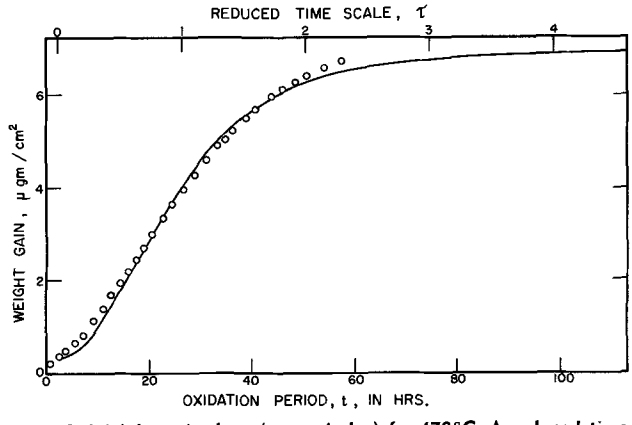

Fig. 1. Weight gain data (open circles) for 478°C. A reduced time scale, $\tau = \bar{\beta}^{-1/2}\ (t - t_0)$, is included for future reference, as is the calculated solid line.

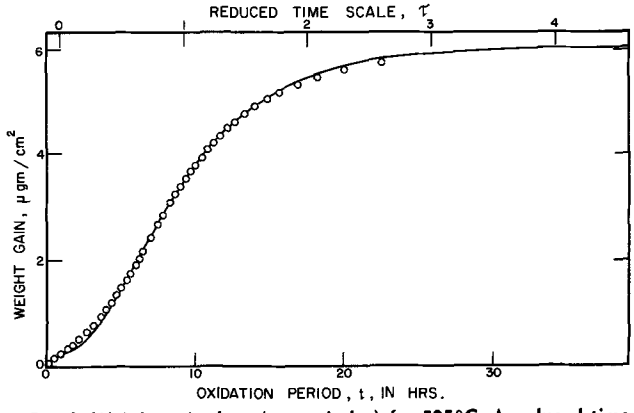

Fig. 2. Weight gain data (open circles) for 505°C. A reduced time scale, $\tau = \bar{\beta}^{-1/2}\ (t - t_0)$, is included for future reference, as is the calculated solid line.

[1] Present address: Department of Chemistry, University of Bristol, Bristol, England.

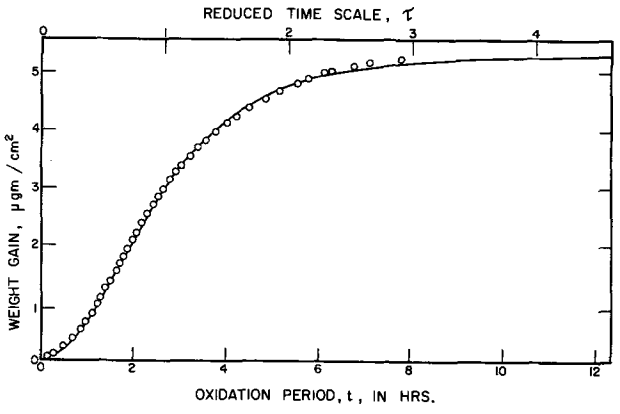

Fig. 3. Weight gain data (open circles) for 530°C. A reduced time scale, $\tau = \bar{\beta}^{-1/2}(t - t_0)$, is included for future reference, as is the calculated solid line.

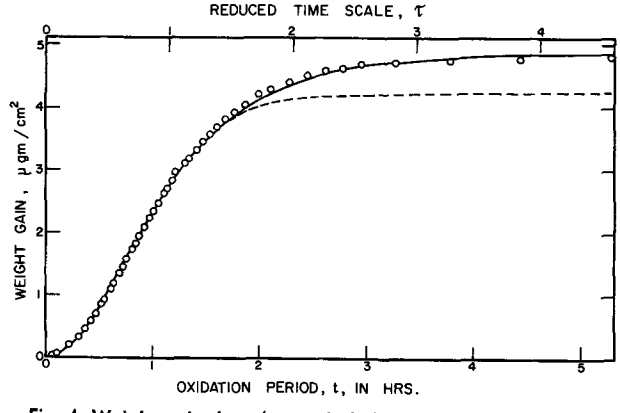

Fig. 4. Weight gain data (open circles) for 549°C. A reduced time scale, $\tau = \bar{\beta}^{-1/2}(t - t_0)$, is included for future reference, as are the calculated lines.

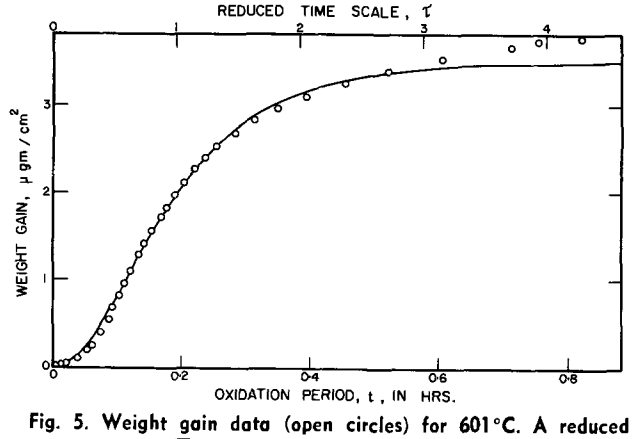

Fig. 5. Weight gain data (open circles) for 601°C. A reduced time scale, $\tau = \bar{\beta}^{-1/2}(t - t_0)$, is included for future reference, as is the calculated solid line.

and Cabrera (12), an approximate integrated form of which is generally referred to as the inverse logarithmic law. The present analysis is concerned solely with the mechanism and kinetics of the formation and growth of the crystallites of γ-alumina.

Model

The model proposed in this section is based in large measure on the results reported by Doherty and Davis (10) from their excellent electron micrographic study of the formation of crystallites of γ-alumina on aluminum. The independent experimental results, *i.e.*, results apart from the kinetic data reported herein, on which the present model is to be based are summarized below.

1. The crystallites grow down into the metal rather than protrude from the surface and do not extend to the surface.
2. The crystallites grow as a result of transport of oxygen species, rather than metal species, through the amorphous film.
3. The crystallites form over a short period of time relative to their period of growth, in that the number density of crystallites, once formed, is independent of oxidation time within the limits of observation. It is also independent of oxidation temperature in the range 450°-600°C.
4. The local number density of crystallites varies somewhat within the boundaries of a single metal grain and very significantly from grain to grain.
5. As far as it is possible to tell by examination of the micrographs, the breadth of a crystallite increases approximately linearly with time, until coalescence occurs. The variation in shape of crystallites from one metal grain to another, however, makes size comparison difficult.
6. The amorphous film lying between the crystallites continues to grow. Thus contact between the amorphous film and the metal in these regions is maintained.
7. The amorphous film lying on top of the crystallites does not continue to grow.

Points 1 and 2 result from the work of Doherty and Davis, points 3 to 5 from the present and a previous electron micrographic examination (11, 7) and points 6 to 7 from data published previously by one of us (7, 8). Discussion of these latter two points follows.

In one of the previous papers (8) data for the oxidation of aluminum and aluminum containing 0.24% Si are presented. Of significance to the present paper are the following points. The growth of the oxide film on the two alloys was indistinguishable at temperatures of 350°C and below, and for oxidation periods less than about 7 hr at 450°C. For oxidation periods greater than about 7 hr at 450°C, crystallites of γ-alumina formed on superpurity aluminum, but did not form on the alloy doped with silicon even after 64-hr oxidation. Film conductance measurements were obtained for samples of the two alloys oxidized various lengths of time at 450°C, by applying to the specimens immersed in an aqueous borate electrolyte an anodic potential which increased linearly with time. The resulting polarization curve (current density *vs.* anodic overpotential) for superpurity aluminum oxidized 16 hr at 450°C is shown in Fig. 6 as the solid line. This

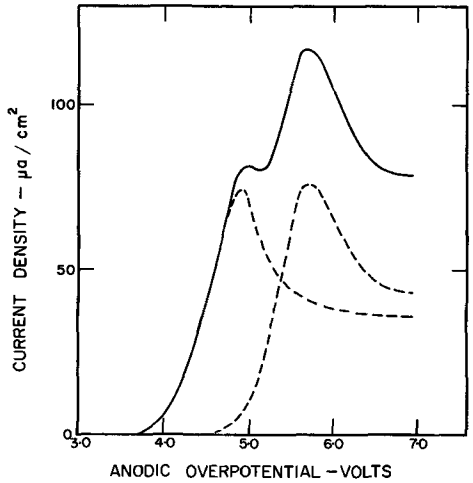

Fig. 6. Polarization curve for superpurity aluminum oxidized 16 hr at 450°C (solid line) (7). The polarization curve may be resolved into the sum of the two curves shown as broken lines.

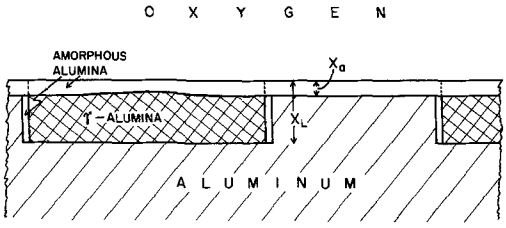

Fig. 7. Schematic representation of cross section of growing crystallite.

curve may be resolved into the sum of two curves (shown as broken lines) which resemble remarkably closely polarization curves for samples of the silicon doped alloy oxidized for about 9 and 16 hr, respectively (7), the current density values, however, being in both cases reduced by about a factor of 2. In other words, as far as the polarization measurement is concerned, the superpurity sample oxidized 16 hr at 450°C behaved as if half of its surface were covered with amorphous film of one thickness (corresponding to ~9 hr oxidation at 450°C) and the other half of another thickness (corresponding to ~16 hr oxidation at 450°C). As electron micrographs for such a sample indicated that roughly half of the surface was covered with crystallites of γ-alumina, the conclusion that the amorphous film lying on top of the crystallites does not continue to grow is strongly indicated. The same evidence, of course, indicates the continued growth of the amorphous film lying between the crystallites. Further discussion of these rather interesting conduction data is presented later.

Before proceeding with a development of the model we note that the above interpretation implies that the amorphous oxide between the crystallites remains in contact with the underlying metal. Since the growth of the crystallites into the metal is accompanied by about a 40% increase in volume, we must conclude that the stresses set up in the metal phase are relieved by the diffusion of metal from the regions of compressional stress to those of tensional stress. As the temperatures in question are close to the melting point of aluminum, rapid diffusion of aluminum along the phase boundary between the metal and the oxide is to be expected. Furthermore, as the number density of crystallites is about 10^9 cm^{-2}, the maximum diffusion length will be no more than a few thousand angstroms. The above mechanism for the relief of strain within the metal therefore appears entirely reasonable.

A cross section of a growing crystallite is represented schematically in Fig. 7. Certain detailed features of this diagram must await discussion until completion of the analysis; some, however, may be mentioned now. The variation of the thickness of the amorphous film on top of the crystallite from the central to peripheral regions follows from points 5, 6, and 7 above. Since the weight gain virtually ceases once the surface of the sample is completely covered with crystalline oxide, we conclude that, once formed, the crystalline oxide does not thicken appreciably. The picture which emerges, therefore, is that of nucleation of crystallites which rapidly achieve a limiting thickness and subsequently grow only laterally across the surface until they impinge on adjacent crystallites. Such a growth law would be expected if a growing crystallite is fed with oxygen at the periphery, the limiting thickness of the crystallite being determined by the rate at which oxygen can be supplied. A thin layer of amorphous film is shown on the peripheral surface of the schematic diagram of the growing crystallites (Fig. 3), the argument for this being that the initial product formed on contact of oxygen with bare metal is, in all probability, amorphous oxide. Since rapid migration of oxygen through the amorphous film is necessary for the growth of the crystallites, we are obliged to assume the existence of some sort of fault boundary through the amorphous oxide close to the periphery of the crystallites. Such faults might well be generated as a result of the volume expansion during formation of the crystalline oxide.

The picture which emerges, therefore, is one in which oxygen diffuses along the fault boundary in the amorphous film and the phase boundary between the amorphous and crystalline oxides. The lateral growth rate of the crystallites is controlled by the rate of recrystallization of the amorphous film to form the crystalline film, a steady-state thickness of amorphous film being maintained between the metal and the crystallite. The thickness of the crystallite is determined in part by the rate of oxygen diffusion along the fault and phase boundaries.

The detailed analysis of the model follows: In a region of the phase boundary where free oxygen is available, the advance of the crystalline boundary will be accompanied by consumption of the oxygen to form more amorphous film. The rate of consumption of oxygen will therefore be controlled by the "recrystallization" rate, a steady-state thickness of amorphous oxide being established between the metal and the growing faces of the crystalline oxide. At $x = X_L$, the concentration of oxygen species per unit area, n, will be zero, the thickness of the crystalline oxide therefore being controlled by the diffusion rate of the oxygen species and the recrystallization rate. For the diffusion process, the flux per unit length at position x, $J(x)$, is related to the diffusion constant, D, and the interfacial concentration gradient by the following equation

$$J(x) = -D dn/dx \qquad [1]$$

Since the oxygen species are being consumed at a rate controlled by the rate of recrystallization, K_2 units of length per unit time, the variation of $J(x)$ with x is given by

$$\begin{aligned} dJ(x)/dx &= -K_2/\Omega \quad \text{for } n > 0, x > X_a \\ &= 0 \quad \text{for } n = 0 \\ &= 0 \quad \text{for } X_a \geqq x \geqq 0 \end{aligned} \qquad [2]$$

where Ω is the volume per oxygen species in the crystalline oxide. For $X_L > x > X_a$, the equation to be solved is therefore

$$d^2n/dx^2 = K_2/\Omega D \qquad [3]$$

Applying the boundary conditions $dn/dx = 0 = n$ at $x = X_L$, the solution of [3] becomes

$$n = (K_2/2\Omega D)\ (X_L - x)^2 \qquad [4]$$

so that at $x = X_a$, where $n = n'$

$$n' = (K_2/2\Omega D)\ (X_L - X_a)^2 \qquad [5]$$

For $X_a > x > 0$, the equation to be solved is

$$d^2n/dx^2 = 0 \qquad [6]$$

Applying the boundary conditions that $J(x)$ is continuous at $x = X_a$, and $n = n_o$ at $x = 0$, the solution of [6] becomes

$$n = n_o - (K_2/\Omega D)\ (X_L - X_a)x \qquad [7]$$

so that at $x = X_a$

$$n' = n_o - (K_2/\Omega D)\ (X_L - X_a)\ X_a \qquad [8]$$

In deriving [7] and [8] it is assumed that to a satisfactory approximation the same value for the diffusion constant may be used in the two regions, $(0, X_a)$ and (X_a, X_L).

Eliminating n' from [5] and [8] leads to the following equation

$$X_L^2 - X_a^2 = 2\Omega D n_o/K_2 \qquad [9]$$

As the transformation of Al to its oxide takes place with an increase in volume, there should exist no actual crack at the crystalline oxide-amorphous oxide phase boundary, so that oxygen would not likely diffuse as molecular oxygen but rather as chemisorbed oxygen atoms or possibly ions. As the heat of chemisorption of oxygen at the phase boundary will almost certainly be large compared with kT, n_o should correspond very nearly to saturation conditions and hence be essentially independent of temperature and pressure and of the order of $\Omega^{-2/3}$. In accord with elementary kinetic theory, the expressions for D and K_2 are given below

$$D = \nu_D a^2 \exp(-U_D/kT) \quad [10]$$

$$K_2 = \nu_2 n_s \Omega \exp(-U_2/kT) \quad [11]$$

where a is the diffusion on "jump" distance, U_D the activation energy for diffusion, n_s the surface concentration of oxygen ions at the phase boundary, U_2 the activation energy for recrystallization, ν_D the vibrational frequency associated with a diffusing oxygen species, and ν_2 that associated with an oxygen ion in the amorphous oxide at the interface. In writing the expression for K_2 it has been assumed that the transport of oxygen ions, rather than metal ions, across the phase boundary is the rate-controlling step for the recrystallization process. No significant change in the present treatment is required, however, if metal ions are involved.

Proceeding now with Eq. [9], on substituting for K_2 and D, one obtains

$$X_L^2 - X_a^2 = 2(\nu_D/\nu_2)\ (n_o/n_s)\ a^2 \exp[(U_2 - U_D)/kT] \quad [12]$$

or since $\nu_D \simeq \nu_2$, $n_o \simeq n_s$, and from the experimental results $X_L >> X_a$, this becomes

$$X_L \simeq \sqrt{2}\, a \exp[(U_2 - U_D)/2kT] \quad [13]$$

In relation to the schematic diagram of Fig. 7, two points should be mentioned. Within the approximations made in obtaining [13], the total limiting film thickness, X_L, is a constant, as shown in Fig. 7. From [12], however, it is clear that some variation of X_L with X_a is to be expected. Examining a typical case in which $X_L \simeq$ 300Å and X_a varies from say 25 to 100Å as one moves from the central to peripheral regions of a crystallite, from [12] the corresponding change in X_L would be only 14Å, or less than 5% of X_L. On this basis, the approximation of constant limiting film thickness is seen to be a satisfactory one.

The second point concerns the shape of the growing face of a crystallite. In Fig. 7, the face is shown normal to the surface of the specimen. One would expect instead a variation of this angle with the crystallographic orientation of the substrate metal grain. In itself, this would not alter the lateral growth rate, but would lead to a range of values of X_L. Thus interpreting X_L as the mean limiting film thickness, the right hand side of [13] should be multiplied by the mean value of $|\sin\phi|$, where ϕ is the angle between the growing crystallite face and the surface of the specimen. Taking as one extreme the case where all angles are equally probable, we conclude that this correction factor should lie between 0.64 (*i.e.*, $2/\pi$) and unity. Again, neglect of this factor, whose value is unknown, lies within the approximation contained in the pre-exponential factor of [13].

In summary, for this model, apart from the nucleation and initial stages of growth of a crystallite, where a more detailed analysis than that given here is required, we see that within the approximations contained in [13], the film thickness X_L does not vary with time. The sign of the temperature coefficient of the limiting film thickness will be determined by the relative magnitudes of U_2 and U_D. As U_D corresponds to the activation energy for transport of oxygen along the phase boundary, and U_2 that for oxygen transport across the phase boundary, U_2 should be somewhat greater than U_D so that the limiting film thickness, X_L, is predicted to have a negative temperature coefficient, which is in agreement with the experimental observations (Fig. 1 to 5).

From the above model, we see that the oxidation kinetics (weight gain as a function of time) will be determined by the number density of crystal nucleation sites N, the nucleation probability K_1, the lateral growth rate K_2, and the limiting film thickness X_L. The analysis of the present nucleation problem differs only in a rather minor way from that presented by Avrami (13) for the kinetics of random volume nucleation associated with the thermal decomposition of a solid. The mathematical development of the following equation will therefore not be given. The result is recorded below.

$$-\ln(1-\alpha) = 2\pi N\,(K_2^2/K_1^2)\,[1 - \exp(-K_1 t') - K_1 t' + K_1^2 t'^2/2] \quad [14]$$

where α is the fraction of the surface covered with crystalline oxide and t' the time elapsed from the onset of the nucleation process. Equation [14] is derived by assuming the nucleation sites to be completely randomly distributed and their concentration independent of their position on the surface. Furthermore, the crystallites are assumed to be disk-shaped. Choosing a different crystallite shape will merely replace 2π by a constant of the same order. From the electron micrographs, all of the nuclei appear to form over a time period short compared with that required for the lateral growth of the crystallites. For such conditions we may set $K_1 t' >> 1$ for t' not too small. Equation [14] then becomes

$$-\ln(1-\alpha) \simeq N\pi K_2^2\,(t - t_o)^2 \text{ for } t > t_o \quad [15]$$

where t' has been replaced by $t - t_o$, t being the oxidation period and t_o the induction period for formation of crystal nuclei. Equation [15] may be written alternatively as

$$\alpha = 1 - \exp[-\beta(t - t_o)^2], \quad t > t_o \quad [16]$$

where

$$\beta = N\pi K_2^2$$

Equation [16] is only valid, as mentioned previously, if N is independent of position on the surface. By direct electron micrographic observation, N was found to vary considerably from one region of the surface of a sample to another. If we assume N, and hence β, to be distributed according to a distribution function, $P(\beta)$, then α will be given not by [16] but instead by the following equation

$$\alpha = 1 - [\int_o^\infty [\exp(-\beta[t - t_o]^2)]P(\beta)\,d\beta]/[\int_o^\infty P(\beta)\,d\beta] \quad [17]$$

Although one might assume the nuclei number density, N, to be distributed according to a Gaussian distribution, a Pearson type III distribution law (14) is preferable from the physical standpoint, as the probability density for this distribution goes to zero at $N = 0$. Furthermore, this law leads to a mathematically more tractable result. The most general form of the Pearson type III distribution law can be written

$$P(\beta) = K\beta^p \exp(-p\beta/a') \quad [18]$$

where $P(\beta)$ is the probability density for a given value of β, and K, p, and a' are constants which can readily be related to more familiar parameters.

From [17] and [18] above, we obtain the following expression for α (see Appendix).

$$\alpha = 1 - [1 + \bar{\beta}\epsilon^2(t - t_o)^2]^{-1/\epsilon^2}, \quad t > t_o \quad [19]$$

where $\bar{\beta}$ is the mean value of β (and is simply related to the mean value of N, $\bar{N}$; $\bar{\beta} = \bar{N}\pi K_2^2$) and ϵ is the standard deviation of the distribution of β (or N) expressed as a fraction of $\bar{\beta}$ (or $\bar{N}$).

We may relate the weight gain to α as follows. The total oxide weight per unit area associated with crystalline regions of the specimen, $g_c(t)$, and that associated with intercrystalline regions, $g_a(t)$, are given by

$$g_c(t) = \rho X_L \alpha$$

$$g_a(t) = \rho X_a(t)\ (1 - \alpha) \qquad [20]$$

where ρ is the crystalline oxide density and X_L and $X_a(t)$ the limiting and amorphous film thickness respectively, as defined previously (Fig. 7).

For simplicity, the density of the amorphous oxide has been set equal to that for the crystalline oxide. The error introduced by this approximation is small and such as to compensate for the approximation made in obtaining [13] from [12].

The weight gain per unit area at time t, $W(t)$, is given by

$$W(t) = (M_o/M_{ox})\,\rho[\alpha X_L + (1 - \alpha)X_a(t) - X_a(0)] \qquad [21]$$

where M_{ox} and M_o are the formula weight of oxide and the weight of oxygen per formula weight of oxide, respectively. From [21], the weight gain at $t = t_o$, corresponding to the initiation of nucleation, W_o, is given by

$$W_o = (M_o/M_{ox})\rho[X_a(t_o) - X_a(0)\ ] \qquad [22]$$

and the limiting weight gain, W_L, achieved after complete coverage of the surface with crystallites, by

$$W_L = (M_o/M_{ox})\rho[X_L - X_a(0)\,] \qquad [23]$$

Eliminating X_L and $X_a(0)$ from [21], [22], and [23] we obtain

$$W(t) = W_o + \alpha(W_L - W_o) + (M_o/M_{ox})\rho(1 - \alpha)\,[X_a(t) - X_a(t_o)] \qquad [24]$$

The final term in [24] represents the contribution to the weight gain made by the continued growth of the amorphous film following crystal nucleation. It is evident from the data, say for 504°C, that the contribution made by this final term is small, partly because $X_a(t)$ is small compared with X_L, and partly because of the factor $(1 - \alpha)$ which approaches zero for large times.

Before proceeding with an analysis of the data, equations for X_L and $\bar{\beta}$ are given below. They were obtained from [23], and from [11] and $\bar{\beta} = \bar{N}\pi K_2^2$, respectively.

$$X_L = X_a(0) + (M_{ox}/M_{o\rho})\,W_L \qquad [25]$$

$$\bar{\beta} = (\bar{N}\pi v_2^2 n_s^2 \Omega^2) \exp\,[-2U_2/kT] \qquad [26]$$

Since, as mentioned previously, the evidence indicates no appreciable temperature dependence of the number density of nuclei, we may presume that both $\bar{N}$ and ϵ are essentially independent of temperature, although they might vary somewhat from sample to sample.

Comparison of Data with Model

In Fig. 1-5 the weight gain data have been plotted on a reduced time scale $\tau = (t - t_o)\bar{\beta}^{1/2}$, in order to illustrate clearly the fact that the limiting weight gain per unit area decreases with increasing temperature. The solid lines represent curves calculated in the manner outlined below.

Combining Eq. [19] and [24], neglecting the final term in [24], we obtain

$$W(t) = W_L - (W_L - W_o)\,[1 + \bar{\beta}\epsilon^2(t - t_o)^2]^{-1/\epsilon^2},\ t > t_o \qquad [27]$$

Setting aside for the moment the small correction terms W_o and t_o, the principle parameters to be determined are W_L, $\bar{\beta}$, and ϵ. Using a digital computer, the most probable values of W_L and β were determined independently for each oxidation run, calculations being repeated for a number of trial values for ϵ. It was found that a value for ϵ of 0.7 ± 0.1 gave the best fit with the data at all temperatures, indicating that ϵ is independent of temperature, as it should be.

The pair of parameters (t_o, W_o) correspond to the time of crystal nucleation and the corresponding weight gain at that time. For the runs at temperatures of 530°C and above, the induction period for crystal nucleation appears to be very nearly zero (*i.e.*, $t_o \simeq 0$) so that for these runs t_o, W_o were set equal to zero. At 478° and 505°C, however, the induction period is appreciable (11) and may not be neglected. For runs at these temperatures, therefore, t_o was chosen to give the best fit with the data, the corresponding value of W_o being read from the oxidation curve.

An examination of Fig. 1 to 5 will show that the agreement between the curves calculated in the above manner and the experimental data is extremely good at 505°, 530°, and 549°C. At 601°C, a significant deviation for large times is apparent, a point we shall return to later. The agreement at 478°C, although not excellent, is quite good. The assumption of "instant nucleation" (*i.e.*, $K_1 t' >> 1$) is perhaps only a fair approximation at this temperature, the small discrepancy arising therefore as a result of formation of the crystal nuclei over an appreciable period of time. On the whole, the agreement must be regarded as quite satisfactory.

In Fig. 4, the best fit with the data which can be obtained neglecting the variation of the number density of crystal nucleation sites with position, is shown as a broken line. The broken line was calculated as before, but using [16] rather than [19] for α (*i.e.*, setting $\epsilon = 0$). The importance of allowing for the distribution is evident.

Table I gives the values of the parameters calculated for the various runs along with the standard deviations of the experimental points from the computed curves. In the worst case, the standard deviation amounts to only 2.3% of the limiting weight gain.

Before proceeding with an analysis of the temperature dependents of $\bar{\beta}$ and W_L, independent experimental justification for the choice of the distribution function and for the value of the distribution parameter, $\epsilon = 0.7 \pm 0.1$, will be given. Seventeen micrographs, obtained by random sampling of specimens oxidized at 601°C, and ten micrographs of specimens oxidized at 549°C, were analyzed in the following manner. A circular area, corresponding to about 10^{-8} cm² in the original sample, was selected at random within each micrograph and the number of crystallites lying in this area noted. From these measurements, the values of $\bar{N}$ and ϵ were calculated to be 1.27×10^9 cm^{-2} and 0.7_9, respectively, at 549°C, and 1.43×10^9 cm^{-2} and 0.6_0, respectively, at 601°C. Since neither the mean value of the number density of nuclei, $\bar{N}$,

Table I. Parameters obtained by computer fit of the data to Eq. [28], for $\epsilon = 0.7$

Temp, °C	$\bar{\beta}$, hr^{-2}	W_f, μg/cm²	Std. deviation, μg/cm²	W_o, μg/cm²	t_o, hr
478	1.72×10^{-3}	6.96	0.16	0.32	2.28
505	1.45×10^{-2}	6.05	0.065	0.24	0.94
	1.31×10^{-2}	5.80	0.056	0.42	1.92
	1.65×10^{-2}	6.00	0.083	0.30	1.07
530	1.39×10^{-1}	5.35	0.039	0	0
	1.54×10^{-1}	5.60	0.040	0	0
549	10.1×10^{-1}	5.00	0.043	0	0
	7.50×10^{-1}	4.93	0.035	0	0
601	23.1	3.96	0.070	0	0
	23.4	3.50	0.055	0	0
	27.1	3.52	0.045	0	0

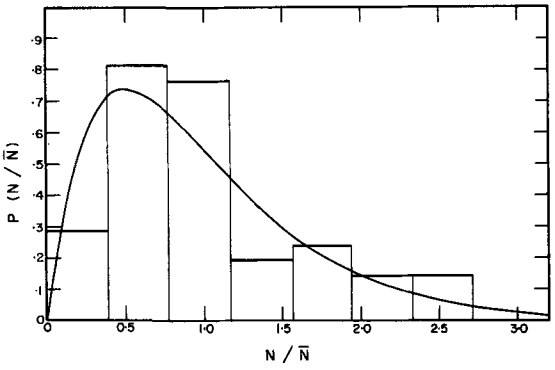

Fig. 8. Comparison of the histogram for the measurements of the number of crystallites per 10^{-8} cm^2, with the Pearson type III distribution curve, $P(N/\bar{N})$, for $\epsilon = 0.7$. (N and $\bar{N}$ are the local and mean number density of crystallites, respectively.)

nor the relative standard deviation, ϵ, show any significant temperature dependence, the data for 549° and 601°C were combined and a histogram constructed for comparison with the Pearson type III distribution curve. Both the histogram, and the Pearson type III distribution function for $\epsilon = 0.7$, are plotted in Fig. 8. The rectangular area at the extreme left-hand end has a height proportional to the number of samples having between 0 and 5 crystallites within the chosen area; the next rectangular area has a height proportional to the number of samples having between 5 and 10 crystallites within the chosen area, etc. To facilitate comparison with the distribution curve, the histogram has been plotted against $N/\bar{N}$ and a scaling factor applied to the height of the rectangles so that the total area under the histogram would be unity. The mean and the standard deviation for the entire 27 samples are given by $\bar{N} = 1.3 \times 10^9$ cm^{-2}, $\epsilon = 0.6_6$.

From the above we see that the value of the relative standard deviation, ϵ, deduced from the kinetic analysis is in excellent agreement with that measured by direct electron micrographic observation. Furthermore, the histogram obtained from the direct observation is in good accord with the Pearson type III distribution curve. This being the case, ϵ need not be regarded as a parameter adjusted to give agreement with the kinetic data, but rather as one determined by direct electron micrographic examination.

Thus the calculated curves for the oxidation runs at 530°C and above involve only two disposable constants, $\bar{\beta}$ and W_L. At the lower temperatures an additional parameter t_o is required.

At a sufficiently high temperature, we might expect that following complete coverage of the surface with crystallites, further oxidation could proceed by oxygen migration along the surfaces of impingement of the individual crystallites. Examination of Fig. 4 shows that, if such an effect exists, it makes a negligible contribution during oxidation at 549°C. The data of Fig. 5, however, indicate that such a contribution might be important during the final stages of oxidation at 601°C. If oxidation were taking place by oxygen diffusion along the surfaces of impingement of the crystallites, we would expect a direct logarithmic oxidation law in accord with the mechanism proposed by Evans (15, 16) in which it is assumed that a decrease in the number of diffusion paths with time results from blockage of paths due both to oxide growth at the bottom and also to compressional forces rising from the volume increase accompanying oxidation. To test this postulate, the experimental weight increase less the calculated weight increase for a typical run at 601°C is plotted against the logarithm of the oxidation period in Fig. 9. The majority of the points lie on a straight line, lending support to this hypothesis. Presumably a similar effect would be observed for oxidation at 549°C if the run were continued for a sufficiently long period of time.

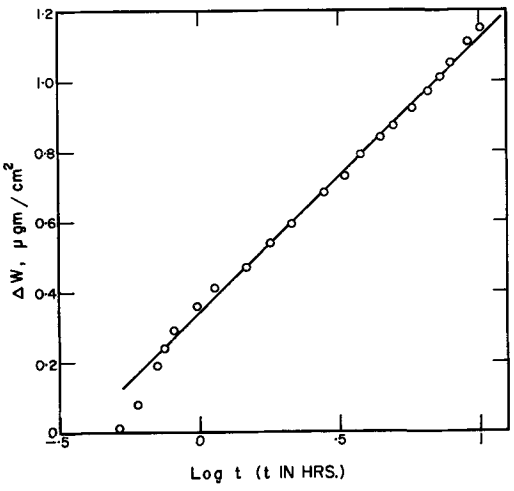

Fig. 9. Excess weight gain ΔW (experimental less calculated weight gain) plotted against the logarithm of the oxidation period, for oxidation data at 601°C.

Temperature Dependence of K_2 and X_L

In Fig. 10, the values of $\bar{\beta}$ given in Table I are plotted in the form log $\bar{\beta}$ against $1/kT$. The results lie on a straight line, in accord with [26], the equation for the least squares regression line being represented by

$$\bar{\beta} = 10^{27.1_6} \exp(-4.46/kT) \text{ hr}^{-2} \qquad [28]$$

when kT is expressed in electron volts. Comparing Eq. [28] and [26], and setting $\Omega = 1.56 \times 10^{-23}$ cm^3 for γ-Al_2O_3 of density 3.6 g cm^{-3}, $n_s \simeq \Omega^{-2/3}$ and $\bar{N} = 1.3 \times 10^9$ cm^{-2}, we obtain $U_2 = 2.2_3$ ev, $\nu_2 \simeq 6.7 \times 10^{12}$ sec^{-1}. The calculated value for ν_2 is clearly of the correct magnitude, indicating that the pre-exponential factor is in accord with that predicted on the basis of the proposed mechanism. It is not really possible to predict the value of U_2. However, we note that U_2, the activation energy for ion transfer across the amorphous oxide-crystalline oxide phase boundary, is very nearly equal to the activation energy for the steady-state anodic oxidation of aluminum in a glycol-borate electrolyte, 2.1_7 ev (17). According to a

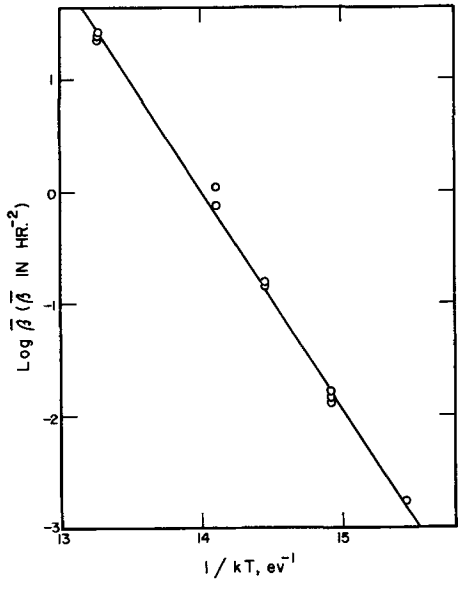

Fig. 10. Temperature dependence of the kinetic parameter, $\bar{\beta}$

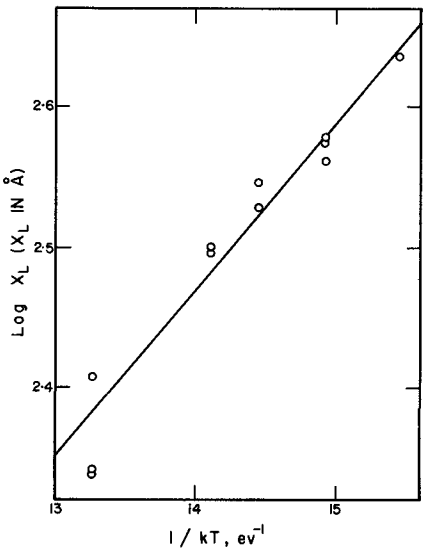

Fig. 11. Temperature dependence of the limiting film thickness, X_L

recent theory for the anodic oxidation of aluminum and tantalum (18, 19), the amorphous oxide film is assumed to consist of a mosaic of microcrystallites, or polymeric units, the activation energy being associated with ion transfer across the boundaries. On the basis of these two theories, therefore, the activation energies should in fact be the same, or very nearly the same.

Again, from the values of W_L in Table I and using Eq. [25], values of X_L have been calculated and plotted in the form log X_L against $1/kT$ in Fig. 11. A value of 25Å was used for $X_a(0)$, in accord with the results presented in Part I of this paper (11). The results presented in Fig. 11 lie on a straight line, within experimental scatter, in accord with [13]. The equation for the least squares regression line is represented by

$$X_L = 6.6 \exp (0.27/kT) \text{ Å} \qquad [29]$$

when kT is expressed in electron volts. Comparing Eq. [29] and [13], we have

$$(U_2 - U_D) = 0.54 \text{ ev}, \; a \simeq 4.7 \text{ Å}$$

Once again we see that the value for a, the "jump distance," is of the correct magnitude, the value of $U_2 - U_D$ also being reasonable. Combining the above value for $U_2 - U_D$ with the value for U_2 gives $U_D = 1.69$ ev.

General Discussion

Before summarizing the results, there remain several points, each of some importance, to discuss. The first concerns the well-known fact that amorphous oxide formed on aluminum by anodic oxidation or air oxidation at low temperature, will not "crystallize" to form γ-alumina in the absence of either oxygen or metal except at very high temperatures ($\gtrsim$ 1000°C). In the presence of oxygen and metal, γ-alumina does, of course, form, but at the expense of metal, not by transformation of the amorphous film present.

Contrasting these findings with the postulated model, according to which the thin layer of amorphous film which separates the growing faces of the crystallites of γ-alumina from the metal is continuously being transformed to γ-alumina, we see that an objection to the present interpretation arises which must be resolved in some fashion. Although a fully satisfactory justification is not possible at present, it appears to the authors not unreasonable that transformation of amorphous to crystalline oxide could occur under the extraordinary conditions which obtain according to the proposed model. It will be recalled that this very thin layer of amorphous oxide, in addition to transforming to crystalline oxide, is also continuously growing at the expense of the metal phase, the net effect being the maintenance of a constant thickness of amorphous film. Thus the oxide transformation is assumed to occur under extreme nonequilibrium conditions in which very high electrochemical potential gradients ($\sim 10^7$ ev/cm molecule) are present in the amorphous film. Such conditions are very likely to assist any sort of atomic reorganization.

A second point concerns the detailed interpretation of the conduction measurements presented in Fig. 6. We shall examine various possible explanations for these data, and compare the consequences of each with other data, and with the model. Because of the remarkable similarity between the resolved polarization curves of Fig. 6 and curves obtained in a similar manner for samples covered solely with amorphous oxide (7), it is assumed that the conduction processes involved are the same in all kinetically important aspects as those occurring during measurements involving only amorphous oxide. That such an assumption may not be valid need hardly be stated. With the information available, however, it appears to be the only assumption justifiable at present.

The immediate consequence of the above assumption is that during this polarization measurement, the crystalline oxide must have been acting as an ionic conductor of substantially lower resistance than the amorphous film. If the crystallites had been acting as good electronic conductors, there would have been no mechanism for increasing the thickness of the amorphous film lying on top of the crystallite, and hence nothing to check the increase in the current with increasing potential. The resulting polarization curve would therefore have been very different from that observed. Furthermore, oxygen evolution would have occurred, whereas the absence of such was specifically noted (7).[2]

We now examine the question of whether, during the polarization measurement, conduction through the crystallites was predominantly anionic or cationic. If anionic, the anodizing current would lead to the formation of new amorphous oxide beneath the crystallites, rather than to thickening of the thermally formed amorphous film lying on top of the crystallites. Transport through this thermally formed amorphous film would therefore take place only through the thinnest portions of it, with the new amorphous oxide being formed, however, under the entire crystallite. The resulting polarization curve would therefore resemble closely that for an aluminum sample covered with an amorphous film of thickness approximately equal to that of the thinnest regions on top of the crystallites, and of area approximately equal to that covered by the crystallites. Such a conclusion is not only in agreement with the conduction data (Fig. 6), but also consistent with the model proposed herein. It should perhaps be noted that "effective transport" of oxygen ions through the amorphous film can take place by high field ionic conduction regardless of the conduction mechanism, in that per Faraday of charge passed one electrochemical equivalent of oxygen will be removed from the electrolyte, and the same quantity of oxygen ions made available at the amorphous oxide-crystalline oxide interface.

If, during the polarization measurement, ionic conduction through the crystallites were cationic, the oxide formed during polarization would lead to thickening of the thermally formed amorphous film lying on top of the crystallites. According to the model presented herein (Fig. 7), the amorphous film lying on top of a crystallite is thinnest in the central region and increases steadily as one proceeds toward

[2] The statement appearing in ref. (7) "Electronic contribution to the measured current was shown experimentally to be small" refers mainly to the fact that no oxygen was evolved even after prolonged anodic oxidation.

the periphery, until at the periphery it is equal in thickness to the film lying between the crystallites. Such a distribution of film thickness would definitely not give rise to a polarization curve in accord with Fig. 6. The polarization curve, although broadened compared with that for a sample of nearly uniform oxide thickness, would not show two distinct peaks. Thus either the model must be incorrect, or the crystallites were acting as anionic rather than cationic conductors during the conduction measurement.

Assuming, tentatively, that the model is incorrect and that conduction through the crystallites is cationic, it follows from the polarization measurement that the crystallites are covered with an amorphous film of approximately uniform thickness somewhat less than that of the film between the crystallites. Revising the analytical treatment presented herein in accord with such a modified model in fact leads to no change in any of the final expressions, the minor alteration in the model being in effect eliminated in the approximations made in obtaining Eq. [13]. However, a serious objection to this revised model exists. If the amorphous film on top of the crystallites is uniform in thickness and thinner than that lying between the crystallites, then, as the crystallites grow laterally during thermal oxidation, they must also grow into the amorphous film above the crystallites by recrystallization. However, once one accepts this proposition, there appears to be no reason for the process to stop until the crystallites emerge at the oxygen-oxide interface. This, however, is contrary to the observations of Doherty and Davis (10).

On the basis of the assumption stated at the outset of this discussion, we conclude, therefore, that during the polarization measurement the crystallites acted as good anionic conductors, and further that the conduction data are consistent with the model illustrated in Fig. 7. The question arises, however, as to whether or not these crystallites act as good ionic conductors during thermal oxidation. If they do, then it is difficult to understand why the crystallites would not continue to increase in thickness once formed. The present kinetic evidence indicates that they do not. More direct evidence in this regard is provided, however, by the data of Hunter and Fowle (20). These authors studied the growth of oxide films on aluminum by measuring "barrier voltages" for oxide covered specimens prepared by thermal oxidation in dry oxygen. The barrier voltages were measured at room temperature by polarizing the specimens anodically in an electrolyte and noting the minimum voltage required to cause significant ion current to flow. The feature of these results to which we wish to refer is that as a specimen approaches complete coverage with crystallites of γ-alumina, the barrier voltage increases rapidly by a factor of three to four and then remains constant. Thus, for example, at 475°C, the barrier voltage remains constant at about 4v for oxidation periods varying from 1 to 9 hr. Following 21 hr oxidation, however, the barrier voltage value is nearly 12v. A similar rapid increase in the barrier voltage occurs for oxidation at 500°C. At higher temperatures, the first readings taken correspond already to high barrier voltage values.

Hunter and Fowle's results, coupled with the present weight gain data, indicate that the crystallites do not have a high conductivity, but instead a specific conductivity rather close to that for the amorphous film. We are faced, therefore, with an apparent contradiction, since the data of Fig. 6 indicate otherwise. There is, however, a fairly obvious explanation for these results. The coefficient of thermal expansion of aluminum is much larger than that for alumina. On quenching a thermally oxidized sample from 450°C or above to room temperature, compressional stresses will be applied to the crystallites, particularly since these are imbedded in the metal matrix. In addition, a shear stress will develop in the plane defined by the base of the crystallites. For specimens in which most of the surface is covered with crystallites, one would expect the stress to be relieved primarily by slippage in this shear plane. If, on the other hand, only a portion of the surface is so covered, the compressional stress could easily lead to structural damage of the crystallites. The high anionic conductivity of the crystallites, evidenced in the results of Fig. 6, could have arisen, therefore, as a result of thermal quenching, the compressional stresses leading to the formation of "short circuit" diffusion paths in the crystallites. Indeed, we have been unable to reconcile these data with those of Hunter and Fowle on any other satisfactory basis.

Before leaving this question, it is important to point out that the oxidation mechanism proposed herein is not dependent on the validity of the foregoing conclusion concerning the conduction properties of the crystallites. It is entirely possible that other interpretations of the conduction data can be found which are consistent with all available data. The interpretation given, however, is internally consistent, and consistent with available data, in addition to being in accord with the proposed oxidation mechanism.

Finally, the model presented herein, while somewhat similar to that proposed by Bartlett (9), differs from it considerably in detail. The present treatment provides very substantially better agreement with the data, while employing essentially the same number of disposable constants. Furthermore, the present treatment is more specific in its predictions, giving as it does theoretical values for the pre-exponential factor for $\bar{\beta}$ and X_L in agreement with the experimentally deduced values, as well as predicting a negative temperature coefficient for the limiting film thickness.

Summary and Conclusions

Data for the growth of crystalline γ-alumina have been obtained for the oxidation of electropolished superpurity aluminum in the temperature range 475°-600°C. These data have been quantitatively interpreted in terms of a model in which the γ-alumina crystallites nucleate beneath the amorphous film, rapidly achieve a terminal thickness, and grow radially at a linear velocity until they impinge on adjacent crystallites. The terminal thickness of the crystallites arises as a consequence of the mechanism by which oxygen is fed to the growing faces of the crystallites. It is proposed that this occurs by oxygen diffusion along the phase boundary at the periphery of the growing crystallite formed by the crystallite and a thin amorphous oxide layer next to the metal phase. The radial growth constant is determined by the rate of transformation of the thin amorphous oxide layer to crystalline oxide. The values for the pre-exponential factors and activation energies obtained from the analyses are in complete accord with the model.

The expressions for both the diffusion constant, D, for the diffusion of oxygen along the inter-oxide phase boundary, and the radial growth constant, K_2, for the transformation of the amorphous oxide layer to crystalline oxide, are given below

$$D = 2 \times 10^5 \exp(-1.6_9/kT) \text{ cm}^2/\text{sec} \quad [31]$$

$$K_2 = 1.5 \times 10^{-2} \exp(-2.2_3/kT) \text{ cm/sec} \quad [32]$$

when kT is expressed in electron volts. Equations [31] and [32] were obtained from [10] and [11] and the experimentally determined parameters, assuming as before

$$n_s \simeq \Omega^{-2/3} \text{ and } \nu_D \simeq \nu_2$$

Acknowledgments

The authors are grateful to The National Research Council of Canada for supporting this research and for a scholarship (W.R.F.).

Manuscript received Jan. 12, 1966; revised manuscript received April 18, 1966. Part of this paper was presented at the 14th Canadian Chemical Engineering Conference, Hamilton, Ont., October 1964.

Any discussion of this paper will appear in a Discussion Section to be published in the June 1967 JOURNAL.

REFERENCES

1. E. A. Gulbransen and W. S. Wysong, *J. Phys. Colloid Chem.*, **51**, 1087 (1947).
2. W. W. Smeltzer, *This Journal*, **103**, 209 (1956).
3. D. W. Aylmore, S. J. Gregg, and W. B. Jepson, *J. Inst. Metals*, **88**, 205 (1959-60).
4. P. E. Blackburn and E. A. Gulbransen, *This Journal*, **107**, 944 (1960).
5. C. N. Cochran and W. C. Sleppy, *ibid.*, **108**, 322 (1961).
6. K. Thomas and M. W. Roberts, *J. Appl. Phys.*, **32** (1961).
7. M. J. Dignam, *This Journal*, **109**, 184 (1962).
8. M. J. Dignam, *ibid.*, **109**, 192 (1962).
9. R. W. Bartlett, *ibid.*, **111**, 903 (1964).
10. P. E. Doherty and R. S. Davis, *J. Appl. Phys.*, **34**, 619 (1963).
11. M. J. Dignam, W. R. Fawcett, and H. Böhni, *This Journal*, **113**, 656 (1966).
12. N. Cabrera and N. F. Mott, *Prog. Phys.*, **12**, 163 (1949).
13. M. Avrami, *J. Chem. Phys.*, **7**, 1103 (1939); **8**, 212 (1940); **9**, 177 (1941).
14. M. A. Kendall, "The Advanced Theory of Statistics," 3rd ed., Vol. 1, Chap. 6, Griffin and Co. Ltd., (1947).
15. U. R. Evans, *Trans. Electrochem. Soc.*, **91**, 547 (1947).
16. U. R. Evans, *Rev. Pure Appl. Chem.*, **5**, 1 (1955).
17. M. J. Dignam, *Can. J. Chem.*, **42**, 1155 (1964).
18. M. J. Dignam, *This Journal*, **112**, 722 (1965).
19. M. J. Dignam, *ibid.*, **112**, 729 (1965).
20. M. S. Hunter and P. Fowle, *ibid.*, **103**, 482 (1956).

APPENDIX

Modification of Law of Expanding Cylinders to Allow for a Nonuniform Distribution of Sites

The law of expanding cylinders, assuming a uniform number per unit area of cylinders, takes the form given in [16], *viz*,

$$\alpha = 1 - \exp[-\beta(t - t_o)^2], \quad t > t_o \qquad [A1]$$

where α is the fraction of the surface covered by the cylinders, t_o the time of commencement of their lateral growth, and $\beta = \pi N K_2^2$ where N is the number density or surface concentration of the cylinders, and K_2 their radial growth rate, assumed independent of time and radius. If N (and hence β) is not a constant, independent of position on the surface, but instead varies in accord with a Pearson type III distribution law (14)

$$P(\beta) = K\beta^p \exp(-p\beta/a') \qquad [A2]$$

(where K, p, and a' are constants of the distribution) then α is not given by [A1] but instead by

$$\alpha = 1 - \int_o^\infty [\exp(-\beta[t - t_o]^2)]P(\beta)\,d\beta \qquad [A3]$$

for $P(\beta)$ normalized. The normalization condition gives

$$\int_o^\infty K\beta^p \exp(-p\beta/a')\,d\beta = K[\Gamma(p+1)]/(p/a')^{p+1} = 1 \qquad [A4]$$

where Γ represents the usual gamma function (generalized factorial function). The mean value of β, $\bar{\beta}$, is given by the following integral

$$\bar{\beta} = \int_o^\infty K\beta^{p+1} \exp(-p\beta/a')\,d\beta = K[\Gamma(p+2)]/(p/a')^{p+2} \qquad [A5]$$

so that from [A4] and [A5] $K = (p/a')^{p+1}/\Gamma(p+1)$ and $\bar{\beta} = (a'/p)(p+1)$.

The standard deviation for the distribution of β values, σ, is given by

$$\sigma^2 = \int_o^\infty (\beta - \bar{\beta})^2 K\beta^p \exp(-p\beta/a')\,d\beta = (a'/p)^2(p+1) \qquad [A6]$$

Thus

$$\epsilon^2 \equiv \sigma^2/\bar{\beta}^2 = 1/(p+1)$$

so that

$$p = \epsilon^{-2} - 1, \quad a' = (1 - \epsilon^2)\bar{\beta}$$

The distribution function can now be rewritten

$$P(\beta) = \frac{(1/\epsilon^2\bar{\beta})\epsilon^{-2}}{\Gamma(\epsilon^{-2})} \beta^{\epsilon^{-2}-1} \exp(-\beta/\bar{\beta}\epsilon^2) \qquad [A7]$$

Substituting [A7] in [A3] gives the following expression for α

$$\alpha = 1 - [1 + \bar{\beta}\epsilon^2(t - t_o)^2]^{-1/\epsilon^2}, \quad t > t_o \qquad [A7]$$

which is identical to [19] in the body of the paper. Since ϵ represents the standard deviation of the distribution of N, expressed as a fraction of $\bar{N}$, Eq. [A7] should reduce to [A1] in the limit as $\epsilon \to 0$. It is readily shown that this is the case.

The Oxidation of Oxygen-Deficient Zirconia and Its Relationship to the Oxidation of Zirconium

D. L. Douglass

Vallecitos Atomic Laboratory, General Electric Company, Pleasanton, California

and Carl Wagner

Max-Planck-Institut für physikalische Chemie, Göttingen, Germany

ABSTRACT

Upon heating black oxygen-deficient zirconia in oxygen of atmospheric pressure to 450° to 900°C, oxygen is taken up. The increase in the thickness $\Delta\xi_w$ of a white layer of virtually ideal composition with time t follows a parabolic rate law, $\Delta\xi_w^2/2t = k_p$. The rate constant k_p is about two orders of magnitude higher than Tammann's rate constant $k_T = (\Delta\xi_{oxide})^2/2t$ for the increase in thickness $\Delta\xi_{oxide}$ of a ZrO_2 layer during the oxidation of zirconium metal. Equations for the concentrations of ionic and electronic defects in zirconia as functions of the oxygen partial pressure are presented in order to derive theoretical equations for the rates of oxidation of oxygen-deficient zirconia and of zirconium metal.

According to various investigators (1-12) the oxidation of unalloyed zirconium conforms only in part to the parabolic rate law. It must be noticed that the weight gain of a sample is determined by two processes, *viz.*, formation of a ZrO_2 layer and diffusion of oxygen dissolved in the metal. Even under these conditions, however, the parabolic rate first deduced by Tammann (13) for diffusion as the rate-deter-

mining step should apply (8, 11, 12) if the oxide layer is dense, local equilibrium at the phase boundaries gas/oxide and oxide/metal is established, the thickness of the electrical double layers is small in comparison to the thickness of the ZrO_2 layer, and the oxygen concentration at the center of the metal is much less than the oxygen concentration in the metal in equilibrium with the oxide. Hussey and Smeltzer (9) have observed that the rate of oxidation depends on the kind of surface preparation. Chemically polished samples were found to oxidize more slowly than abraded samples. Moreover, it was observed that the oxidation rate is affected by a previous anneal of the sample. In view of these observations it is not surprising that results obtained in different laboratories differ to some extent. Some investigators (3, 6) have reported that their results conform to a cubic rather than a parabolic rate law. The dependence on surface preparation and deviations from the parabolic rate law indicate that in addition to diffusion there must be other factors which determine the rate of oxidation. In particular, local detachment of the scale from the metal may be an important factor. Thus diffusion studies in ZrO_2 free of complications due to processes occurring at the oxide/metal interface, especially spalling off of the oxide, are desirable. For this reason, in what follows results for the diffusion of oxygen into oxygen-deficient zirconia are reported and analyzed.

Experimental

Oxygen-deficient zirconia is black, whereas ZrO_2 of virtually ideal composition is white. Upon heating black oxygen-deficient zirconia in oxygen of atmospheric pressure, one observes the formation of a white zone which thickens in accord with the parabolic law

$$\Delta\xi_w^2/2t = k_p \qquad [1]$$

where $\Delta\xi_w$ is the thickness of the white zone at time t, and k_p is a constant. Details of the experimental technique and the determination of the extent of oxygen deficiency of the starting material with the help of gravimetric and manometric measurements have been described previously (14, 15). Measurements have been made with both samples free of foreign cations and samples containing additions such as Y_2O_3, Cr_2O_3, NiO, and Fe_3O_4. Data for oxygen diffusion into $ZrO_{1.994}$ between 450° and 900°C are represented by the Arrhenius equation

$$k_p = 0.055 \cdot \exp(-33{,}400/RT)\ \mathrm{cm^2/sec}$$

and data for oxygen diffusion into $Zr_{0.981}Y_{0.019}O_{1.980}$ by

$$k_p = 0.27 \cdot \exp(-27{,}200/RT)\ \mathrm{cm^2/sec}$$

Theoretical Analysis

The following analysis aims at an understanding of the salient features. Numerous approximations are introduced and, therefore, the final equations have only semi-quantitative significance. The finite thickness of space charge regions is neglected since the concentration of charged defects in black zirconia $ZrO_{2\text{-}0.006}$ is fairly high and, therefore, the effective thickness of a space charge layer is only about three times the diameter of an oxygen ion. The ideal law of mass action is used as an approximation, *i.e.*, interaction among charged defects is neglected.

Defect equilibria.—The electrical conductivity κ of zirconia without foreign cations has been measured as a function of oxygen partial pressure p_{O_2} by Rudolph (16), by Kofstad and Ruzicka (17), and most recently by Vest, Tallan, and Tripp (18). At 990°C κ rises with increasing values of p_{O_2} if $p_{O_2} > 10^{-6}$ atm in accord with prevailing p-type electronic conduction. In CO_2-CO and H_2O-H_2 mixtures involving values of p_{O_2} less than 10^{-20} atm, κ rises with decreasing values of p_{O_2} in accord with prevailing n-type electronic conduction. In an intermediate range of p_{O_2} with very small deviations from the ideal stoichiometry, ionic conduction prevails according to results of emf measurements on the cell $Zr|ZrO_2|Pt,O_2$ conducted by Dalgaard (19).

Since the lattice of ZrO_2 is a distorted CaF_2 lattice, one may assume the same type of ionic defects in ZrO_2 as in CaF_2 found by Ure (20), *i.e.*, interstitial anions and anion vacancies. Thus the following lattice defects in zirconia are considered: interstitial oxygen ions, oxygen ion vacancies, excess electrons, and electron holes, whose concentrations expressed as ratios of the number of defects to the number of Zr atoms are denoted by $x_{\circ}$, $x_{\square}$, x_n and x_p, respectively.

The oxygen deficiency δ in a sample represented by the formula $ZrO_{2-\delta}$ is equal to the difference $x_{\square} - x_{\circ}$

$$\delta = x_{\square} - x_{\circ} \qquad [2]$$

In order to satisfy the condition of electrical neutrality, the number of positive excess charges must equal the number of negative excess charges. Thus

$$2x_{\square} + x_p = 2x_{\circ} + x_n \qquad [3]$$

From Eq. [2] and [3] it follows that

$$\delta = \frac{1}{2}(x_n - x_p) \qquad [4]$$

For the internal reaction

$$\text{oxygen anion on a regular lattice site} = \text{interstitial oxygen ion} + \text{anion vacancy} \qquad [5]$$

one has the equilibrium condition

$$x_{\circ}x_{\square} = K_1 \qquad [6]$$

Similarly, for the internal reaction

$$\text{valence electron} = \text{excess electron} + \text{electron hole} \qquad [7]$$

one has the equilibrium condition

$$x_n x_p = K_2 \qquad [8]$$

For the oxygen uptake from the gas phase

$$\frac{1}{2}O_2(g) + 2\ \text{excess electrons} = \text{interstitial oxygen ion} \qquad [9]$$

one has the equilibrium condition

$$\frac{x_{\circ}}{p_{O_2}^{1/2}x_n^2} = K_3 \qquad [10]$$

Defect concentrations as functions of oxygen partial pressure.—Equations [2], [4], [6], [8], and [10] are sufficient in order to calculate the defect concentrations $x_{\circ}$, $x_{\square}$, x_n, and x_p and further the oxygen deficit δ as functions of p_{O_2} provided the constants K_1, K_2, and K_3 are known.

The following limiting cases involving two majority defects each are noted.

1. For nearly ideal stoichiometric composition

$$x_{\circ} \cong x_{\square} >> \delta \qquad [11]$$

one has in view of Eq. [6]

$$x_{\circ} \cong x_{\square} \cong K_1^{1/2} \qquad [12]$$

(a) If

$$x_p >> x_n \qquad [13]$$

one has in view of Eq. [4]

$$-\delta \cong \frac{1}{2}x_p \qquad [14]$$

where a negative value of δ indicates an excess of oxygen with respect to the ideal formula ZrO_2.

From Eq. [8], [10], [12], and [14] it follows that

$$x_p \cong -2\delta \cong \frac{K_2K_3^{1/2}}{K_1^{1/4}} p_{O_2}^{1/4} \quad [15]$$

(b) If

$$x_n >> x_p \quad [16]$$

one has in view of Eq. [4]

$$\delta \cong \frac{1}{2} x_n \quad [17]$$

From Eq. [10], [12], and [17] it follows that

$$x_n \cong 2\delta \cong \frac{K_1^{1/4}}{K_3^{1/2}} p_{O_2}^{-1/4} \quad [18]$$

2. For zirconia with a substantial excess of oxygen

$$-\delta \cong x_{\circ} \cong \frac{1}{2} x_p >> x_{\square} \quad [19]$$

it follows from Eq. [8], [10], and [19] that

$$x_{\circ} \cong \frac{1}{2} x_p \cong \left(\frac{1}{4} K_2^2K_3\right)^{1/3} p_{O_2}^{1/6} \quad [20]$$

Substituting Eq. [20] in Eq. [6], one obtains

$$x_{\square} = \frac{K_1}{x_{\circ}} = \frac{K_1}{\left(\frac{1}{4} K_2^2K_3\right)^{1/3}} p_{O_2}^{-1/6} \quad [21]$$

In view of Eq. [20] and [21], one may replace condition [19] by

$$p_{O_2} >> \frac{16K_1^3}{K_2^4K_3^2} = p_{O_2}^{I} \quad [22]$$

where $p_{O_2}^{I}$ is amid the oxygen partial pressure range in which the transition from limiting case 1 to limiting case 2 takes place.

3. For zirconia with a substantial deficiency of oxygen

$$\delta \cong x_{\square} \cong \frac{1}{2} x_n >> x_{\circ} \quad [23]$$

it follows from Eq. [6], [10], and [23]

$$x_{\square} \cong \frac{1}{2} x_n \cong \left(\frac{K_1}{4K_3}\right)^{1/3} p_{O_2}^{-1/6} \quad [24]$$

Substituting Eq. [24] in Eq. [6], one obtains

$$x_{\circ} = \frac{K_1}{x_{\square}} = (4K_1^2K_3)^{1/3} p_{O_2}^{1/6} \quad [25]$$

In view of Eq. [24] and [25], one may replace condition [23] by

$$p_{O_2} << \frac{1}{16K_1K_3^2} \equiv p_{O_2}^{V} \quad [26]$$

where $p_{O_2}^{V}$ is amid the oxygen partial pressure range in which the transition from limiting case 1 to limiting case 3 takes place.

Figure 1 shows schematically the various defect concentrations as functions of the oxygen partial pressures in accord with analogous diagrams presented by Kröger and Vink (21) for other systems. The pressures $p_{O_2}^{I}$ and $p_{O_2}^{V}$ differ by many orders of magnitude, whereas the corresponding change in δ is much less than unity.

Ionic and electronic conductivity of zirconia.— The partial electrical conductivity, κ_{ion}, due to the motion of oxygen ions either as interstitial ions or via vacancies may be written as

$$\kappa_{ion} = 2F(u_{\circ}x_{\circ} + u_{\square}x_{\square})/V_m \quad [27]$$

where $u_{\circ}$ and $u_{\square}$ are the electrochemical mobilities of interstitial oxygen ions and anion vacancies, respectively, F is the Faraday constant, and V_m is the molar volume.

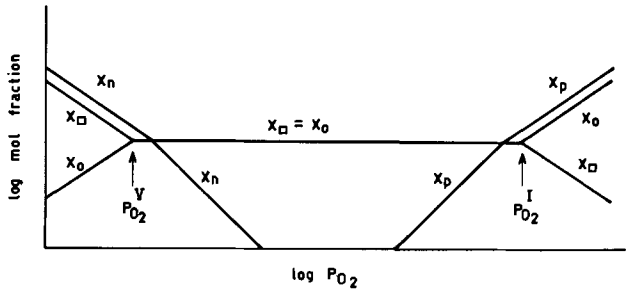

Fig. 1. Dependence of defect concentrations on oxygen partial pressure p_{O_2}.

Similarly, the partial electronic conductivity, κ_e is

$$\kappa_e = F(u_n x_n + u_p x_p)/V_m \quad [28]$$

where u_n and u_p are the mobilities of excess electrons and electron holes, respectively.

The mobility of an electron is in general much greater than that of an ion. Furthermore, in view of results obtained for CaF_2 (20) one may assume that the mobility of anion vacancies in zirconia is much greater than that of interstitial anions. Thus

$$u_n >> u_{\square} >> u_{\circ} \quad [29]$$

For the three limiting cases involving different majority defects, one obtains the following special relations.

1. If $x_{\circ} \cong x_{\square}$ and according to Eq. [22] and [26]

$$p_{O_2}^{V} << p_{O_2} << p_{O_2}^{I} \quad [30]$$

it follows on substitution of Eq. [12] in Eq. [27] that

$$\kappa_{ion} \cong 2F(u_{\circ} + u_{\square})K_1^{1/2}/V_m \quad [31]$$

(a) If $u_p x_p >> u_n x_n$, one obtains from Eq. [15] and [28]

$$\kappa_e \cong \frac{Fu_p}{V_m} \frac{K_2K_3^{1/2}}{K_1^{1/4}} p_{O_2}^{1/4} \quad [32]$$

(b) If conversely $u_n x_n >> u_p x_p$, one obtains from Eq. [18] and [28]

$$\kappa_e \cong \frac{Fu_n}{V_m} \frac{K_1^{1/4}}{K_3^{1/2}} p_{O_2}^{-1/4} \quad [33]$$

2. For zirconia with a substantial excess of oxygen

$$p_{O_2} >> p_{O_2}^{I} \quad [34]$$

it follows from Eq. [19], [20], [21], [27], and [28] that

$$\kappa_{ion} \cong \frac{2F}{V_m}\left[u_{\circ}\left(\frac{1}{4} K_2^2K_3\right)^{1/3} p_{O_2}^{1/6} + u_{\square} \frac{K_1}{\left(\frac{1}{4} K_2^2K_3\right)^{1/3}} p_{O_2}^{-1/6}\right] \quad [35]$$

$$\kappa_e \cong \frac{2Fu_p}{V_m}\left(\frac{1}{4} K_2^2K_3\right)^{1/3} p_{O_2}^{1/6} \text{ if } u_p x_p >> u_n x_n \quad [36]$$

3. For zirconia with a substantial deficiency of oxygen

$$p_{O_2} << p_{O_2}^{V} \quad [37]$$

it follows from Eq. [23], [24], [25], [27], [28], and [29] that

$$\kappa_{ion} \cong \frac{2Fu_{\square}}{V_m}\left(\frac{K_1}{4K_3}\right)^{1/3} p_{O_2}^{-1/6} \quad [38]$$

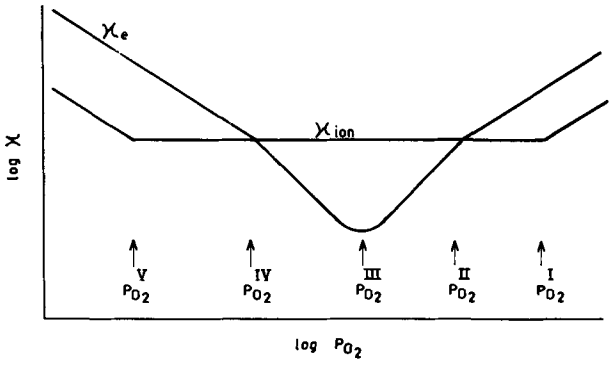

Fig. 2. Dependence of partial ionic and electronic conductivities on oxygen partial pressure p_{O_2}.

$$\kappa_e \cong \frac{2Fu_n}{V_m}\left(\frac{K_1}{4K_3}\right)^{1/3} p_{O_2}{}^{-1/6}, \text{ if } u_n x_n >> u_p x_p \quad [39]$$

Variations of the partial conductivities for ions and electrons are schematically shown in Fig. 2. The following characteristic oxygen partial pressure are marked: (*a*) $p_{O_2}{}^{II}$ at which the ionic conductivity equals the p-type electronic conductivity [$\sim 10^{-7}$ atm at 990°C (18)]; (*b*) $p_{O_2}{}^{III}$ for equal partial n-type and p-type conductivities corresponding to a minimum of the partial electronic conductivity κ_e; (c) $p_{O_2}{}^{IV}$ at which the ionic conductivity equals the n-type electronic conductivity [$\sim 10^{-21}$ atm at 990°C (18)].

Equations for oxygen diffusion.—Assuming ambipolar diffusion of oxygen ions and electrons for diffusion of oxygen in zirconia, one may write for the inward flux, j, of oxygen in equivalents per unit area per unit time for one-dimensional conditions (22)

$$j = -\frac{RT}{4F^2}\frac{\kappa_{ion}\kappa_e}{\kappa_{ion}+\kappa_e}\frac{d\ln p_{O_2}}{d\xi} \quad [40]$$

where κ_{ion} and κ_e are the partial conductivities for oxygen ions and electrons, respectively, p_{O_2} is the local oxygen equilibrium partial pressure, and ξ is the distance from the outer surface.

On the other hand, according to Fick's first law

$$j = Dd(2\delta/V_m)/d\xi \quad [41]$$

where D is the phenomenological diffusion coefficient, δ is the local oxygen deficit, V_m is the molar volume of ZrO_2, and accordingly, $2\delta/V_m$ is the local oxygen deficit in equivalents of oxygen per unit volume. From Eq. [40] and [41] it follows that

$$D = \frac{V_m RT}{8F^2\delta}\frac{\kappa_{ion}\kappa_e}{\kappa_{ion}+\kappa_e}\left(-\frac{d\ln p_{O_2}}{d\ln\delta}\right) \quad [42]$$

The dependence of D on p_{O_2} calculated from Eq. [42] and the foregoing equations for κ_{ion}, κ_e, and δ as functions of p_{O_2} is shown schematically in Fig. 3. The diffusion coefficient is high if ionic conduction prevails and low if electronic conduction prevails because the defect with the lower mobility determines the ambipolar diffusion coefficient D as is shown in what follows for special situations.

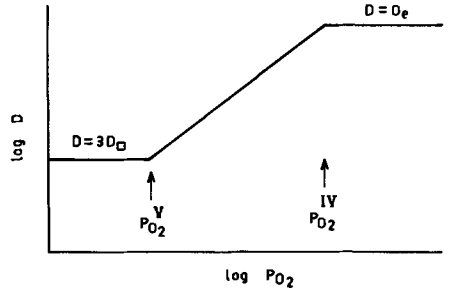

Fig. 3. Dependence of diffusion coefficient D on oxygen partial pressure p_{O_2}.

If

$$p_{O_2}{}^{III} << p_{O_2} << p_{O_2}{}^{II} \quad [43]$$

one has in view of Eq. [28]

$$\kappa_e \cong Fu_p x_p/V_m << \kappa_{ion}$$

The mobility u_p of defect electrons is related to their diffusivity D_p by the Nernst-Einstein equation

$$D_p = u_p RT/F$$

whereupon in view of Eq. [14], [15], and [42] for $\kappa_e >> \kappa_{ion}$

$$D = D_p \quad [44]$$

If

$$p_{O_2}{}^{IV} << p_{O_2} << p_{O_2}{}^{III} \quad [45]$$

one obtains similarly

$$D = D_n \quad [46]$$

If

$$p_{O_2} < p_{O_2}{}^{V} \quad [47]$$

one has in view of Eq. [23] and [27]

$$\kappa_{ion} = 2Fu_{□}x_{□}/V_m << \kappa_e \quad [48]$$

The diffusion coefficient of anion vacancies with a double change is according to the Nernst-Einstein equation

$$D_{□} = u_{□}RT/2F \quad [49]$$

Upon substitution of Eq. [23], [24], [48], and [49] in Eq. [42], it follows that

$$D = 3D_{□} \quad [50]$$

In this case the ambipolar diffusion coefficient D is three times the diffusion coefficient $D_{□}$ of anion vacancies because the movement of the anions is supported by a diffusion potential due to the tendency of the faster electrons to move ahead.

In the intermediate range

$$p_{O_2}{}^{V} << p_{O_2} << p_{O_2}{}^{IV} \quad [51]$$

zirconia has a slight oxygen deficiency with prevailing n-type electronic conduction, ($\kappa_{ion} << \kappa_e$). Upon substitution of Eq. [12] [17], [18], [29], [31], and [49] in Eq. [42] it follows that

$$D = 4D_{□}K_1{}^{1/4}K_3{}^{1/2}p_{O_2}{}^{1/4} \quad [52]$$

Diffusion of oxygen into oxygen-deficient zirconia without dope.—Let us now consider diffusion of oxygen into zirconia which has initially a uniform oxygen deficit δ_o, *e.g.*, $\delta_o = 0.006$. When the thickness of the diffusion zone represents a small fraction of the whole sample, one may use the conditions for one-dimensional diffusion into semi-infinite space.

Fick's second law reads

$$\frac{\partial\delta}{\partial t} = \frac{\partial j}{\partial\xi} = \frac{\partial}{\partial\xi}\left(D\frac{\partial\delta}{\partial\xi}\right) \quad [53]$$

The initial condition is

$$\delta = \delta_o \text{ at } \xi > 0,\ t = 0 \quad [54]$$

The deviation from the ideal stoichiometric composition at the outer surface in oxygen is denoted by δ_s. Thus

$$\delta = \delta_s \text{ at } \xi = 0,\ t > 0 \quad [55]$$

As an approximation let us use the relations for the four above limiting cases and let us disregard transient conditions. Denoting the oxygen deficit at the oxygen partial pressures $p_{O_2}{}^{I}$, $p_{O_2}{}^{II}$, etc., by δ^{I}, δ^{II}, etc., respectively, one has in view of Eq. [44], [46], [50], and [52]

$$D = D_p \text{ if } \delta^{II} \leqq \delta \leqq \delta^{III}$$

$$D = D_n \text{ if } \delta^{III} \leqq \delta \leqq \delta^{IV}$$

$$D \propto p_{O_2}^{1/4} \propto \delta^{-1} \text{ if } \delta^{IV} \leqq \delta \leqq \delta^{V}$$

$$D = 3\,D_{\square} \text{ if } \delta^{V} \leqq \delta$$

Writing all expressions in terms of that for the range $\delta^V \leqq \delta$, one obtains

$$D = 3(D_p/D_n)D_{\square}(\delta^V/\delta^{IV}) \text{ if } \delta^{II} \leqq \delta \leqq \delta^{III} \quad [56a]$$

$$D = 3D_{\square}(\delta^V/\delta^{IV}) \text{ if } \delta^{III} \leqq \delta \leqq \delta^{IV} \quad [56b]$$

$$D = 3D_{\square}(\delta^V/\delta) \text{ if } \delta^{IV} \leqq \delta \leqq \delta^{V} \quad [56c]$$

$$D = 3D_{\square} \text{ if } \delta^{V} \leqq \delta \quad [56d]$$

If $\delta_o >> \delta^V$, the dependence of D on δ has to be considered only if $\delta << \delta_o$. Under these conditions the flux is virtually independent of ξ. Thus

$$D\frac{\partial\delta}{\partial\xi} \cong \text{constant if } \delta << \delta_o \quad [57]$$

Integration of Eq. [67] yields

$$\xi(\delta) = A\int_{\delta_s}^{\delta} D(\delta)\cdot d\delta \text{ if } \delta << \delta_o \quad [58]$$

where A is a parameter which is proportional to $t^{1/2}$ as is calculated below in Eq. [62].

Conductivity data (16, 18) indicate that $p_{O_2} = 1$ atm is in the range between $p_{O_2}^{II}$ and $p_{O_2}^{III}$. Substituting Eq. [56a] to [56c] in Eq. [58], one obtains

$$\xi(\delta) = 3AD_{\square}\left\{\delta_V\left[\frac{\delta^{III}-\delta_s}{\delta^{IV}}\frac{D_p}{D_n} - \frac{\delta_{III}}{\delta_{IV}} + \ln(\delta^V/\delta^{IV})\right] + \delta\right\} \text{ if } \delta^V \leqq \delta << \delta_o \quad [59a]$$

The mobility of a defect electron is in general less than that of an excess electron and, therefore, $D_p < D_n$. Moreover, it can be assumed that δ^{III} and $\delta^{III} - \delta_s << \delta^{IV}$. Then the first and the second term in brackets may be neglected and Eq. [59a] becomes

$$\xi(\delta) = 3AD_{\square}[\delta^V \ln(\delta^V/\delta^{IV}) + \delta] \text{ if } \delta^V < \delta << \delta_o \quad [59b]$$

On the other hand, if $\delta > \delta^V$ and $D = 3D_{\square}$, differential Eq. [53] with the initial condition in Eq. [54] has the solution

$$\delta = \delta_o\{B \operatorname{erf}[\xi/2(3D_{\square}t)^{1/2}] - (B-1)\} \quad [60]$$

where B is a constant.

Using the first term of a series expansion for small values of the error function, one obtains

$$\delta = \delta_o\left[B\frac{\xi}{(3\pi D_{\square}t)^{1/2}} - (B-1)\right] \text{ if } \delta^V < \delta << \delta_o \quad [61]$$

Equating the expressions for δ and the fluxes, *i.e.*, $D(\partial\delta/\partial\xi)$ at $\delta = \delta^V$ according to Eq. [59] and [61], one obtains two equations from which the parameters A and B may be calculated. Thus

$$A = \frac{(3\pi D_{\square}t)^{1/2}}{3D_{\square}[\delta_o + \delta^V \ln(\delta^V/\delta^{IV})]} \quad [62]$$

$$B = 1 + [(\delta^V/\delta_o)\ln(\delta^V/\delta^{IV})] \quad [63]$$

Substitution of Eq. [62] in Eq. [59] yields for the distance at which $\delta = \delta^V$

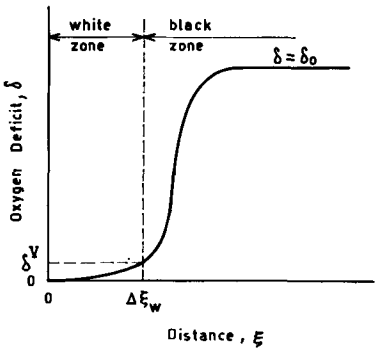

Fig. 4. Oxygen deficit *vs.* distance ξ during oxidation of oxygen-deficient zirconia.

$$\xi(\delta = \delta^V) = \frac{\delta^V[1 + \ln(\delta^V/\delta^{IV})]}{\delta_o + \delta^V \ln(\delta^V/\delta^{IV})}(3\pi D_{\square}t)^{1/2}$$

$$\cong \frac{\delta^V}{\delta_o}\left[1 + \ln\frac{\delta^V}{\delta^{IV}}\right](3\pi D_{\square}t)^{1/2} \text{ if } \delta^V << \delta^o \quad [64]$$

The variation of δ with ξ according to Eq. [58] and [60] is shown schematically in Fig. 4. A rapid change in composition occurs if $\xi \gtrsim \xi(\delta = \delta^V)$. This may account for the observation of the sharp boundary between the white and the black zone of oxygen-deficient samples oxidized in oxygen. Consequently, for the sake of an approximation, one may equate $\xi(\delta = \delta^V)$ to the observed thickness $\Delta\xi w$ of the white zone. Thus, on combining Eq. [1] and [64] the parabolic rate constant for the oxidation of oxygen-deficient zirconia is found to be

$$k_p = \frac{(\Delta\xi w)^2}{2t} \cong \ldots \frac{3\pi D_{\square}}{2}\left[\frac{\delta^V}{\delta_o}\left(1 + \ln\frac{\delta^V}{\delta^{IV}}\right)\right]^2 \quad [65]$$

Discussion

The rate of diffusion of oxygen into oxygen-deficient zirconia may be compared with the rate of oxidation of zirconium. For this purpose, it is especially appropriate to use the rate constant k_T introduced by Tammann (13), which has the same dimension as k_p (cm²/sec)

$$\frac{1}{2}\frac{(\Delta\xi_{oxide})^2}{t} = k_T \quad [66]$$

where $\Delta\xi_{oxide}$ is the thickness of the oxide layer at time t. From the foregoing analysis especially Eq. [56a] to [56c] and [57] it can be concluded that during the oxidation of zirconium most of the oxide layer is oxygen-deficient zirconia with virtually equivalent concentrations of anion vacancies and excess electrons in accord with Eq. [23]. Under these conditions the rate of oxygen diffusion is determined by $D = 3D_{\square}$ according to Eq. [50]. Accordingly, the rational rate k_r constant defined by Wagner (22) as the flux of equivalents of oxygen per unit area and unit time for unit thickness of the oxygen layer is

$$k_r = 3D_{\square}\cdot\frac{2(\delta_{eq} - \delta_s)}{V_m} \cong \frac{6D_{\square}\delta_{eq}}{V_m} \quad [67]$$

where δ_{eq} is the equilibrium oxygen deficit of zirconia coexisting with the metal, $\delta_s \cong 0$ is the oxygen deficit at the surface, and $2(\delta_{eq} - \delta_s)/V_m$ is the concentration difference in terms of equivalents per unit volume.

For the sake of an approximation, diffusion of oxygen into zirconium may be disregarded. Then the constants k_T and k_r are interrelated by the formula (22)

$$k_r = 4k_T/V_m \quad [68]$$

Table I. Comparison of rate constants k_p for the diffusion of oxygen into oxygen-deficient zirconia with $\delta_o = 0.006$ according to Douglass (14, 15) and rate constants k_T for the oxidation of zirconium metal according to Hussey and Smeltzer (9) for chemically polished samples with anneal

Temp, °C	k_p Eq. [1], cm²/sec	k_T Eq. [69], cm²/sec
400	0.7×10^{-13}	0.6×10^{-14}
450	4.4×10^{-13}	4.0×10^{-14}
500	18×10^{-13}	11×10^{-14}
550	70×10^{-13}	37×10^{-14}
600	230×10^{-13}	160×10^{-14}

and the rate constant k_T may be calculated from measurements of the weight gain per unit area ($\Delta m/A$) with the help of the formula (22)

$$k_T = \frac{1}{2} \frac{(\Delta m/A)^2}{t} \left(\frac{V_m}{2 \cdot 16} \right)^2 \qquad [69]$$

On combining Eq. [67] and [68], one obtains

$$k_T = \frac{3}{2} D_{\square} \delta_{eq} \qquad [70]$$

According to Eq. [65] and [70] the ratio of the rate constants k_p and k_T is found to be

$$\frac{k_p}{k_T} = \frac{\pi}{\delta_{eq}} \left[\frac{\delta^V}{\delta_o} \left(1 + \ln \frac{\delta^V}{\delta^{IV}} \right) \right]^2 \qquad [71]$$

These equations can be applied only to data which conform approximately to the parabolic rate law, *e.g.*, data reported by Hussey and Smeltzer (9). Numerical values for k_p and k_T are compiled in Table I. The ratio k_p/k_T is of the order of 10^2. Since in Eq. [71] only $\delta_o = 0.006$ is known but numerical values of δ^{IV}, δ^V, and δ_{eq} are lacking, it is not possible to check Eq. [71] and the underlying assumptions at the present. Data for the oxygen deficit δ_{eq} in zirconia coexisting with zirconium have been reported (23) only for temperatures above 800°C and cannot be extrapolated to lower temperatures with sufficient confidence. Future research is desirable especially in order to obtain reliable values for δ^{IV}, δ^V, and δ_{eq} and to check whether the rate constant k_p is inversely proportional to the initial oxygen deficit as predicted by Eq. [65].

Analogous calculations can be made for diffusion in zirconia doped with CaO or Y_2O_3 where the anion vacancy concentration at $p_{O_2} = 1$ atm is much greater than in ZrO_2 without dope. Thus in ZrO_2 doped with CaO or Y_2O_3, the characteristic values δ^{IV} and δ^V are greater than in ZrO_2 without dope, where in this context δ^V is the oxygen deficit at which the excess electron concentration is equivalent to the anion vacancy concentration at $p_{O_2} = 1$ atm, which is in essence given by the concentration of the dope. If the oxygen deficit characteristic of the boundary between the white and the black zone in a sample subject to diffusion, is greater than δ^V in doped ZrO_2, it follows from Eq. [65] that the parabolic rate constant k_p defined in Eq. [1] in doped ZrO_2 is greater than in ZrO_2 without dope. This is in accord with observations.

Manuscript received June 21, 1965; revised manuscript received March 16, 1966. This work was performed under the Joint USAC-EURATOM Research Development Program, Contract AT (04-3)-189, Project Agreement 24.

Any discussion of this paper will appear in a Discussion Section to be published in the June 1967 JOURNAL.

REFERENCES

1. E. A. Gulbransen and K. F. Andrew, *Trans. AIME*, **185**, 515 (1949).
2. D. Cubicciotti, *J. Am. Chem. Soc.*, **72**, 4138 (1950).
3. J. Belle and M. W. Mallett, *This Journal*, **101**, 339 (1954).
4. E. A. Gulbransen and K. F. Andrew, *Trans. AIME*, **209**, 394 (1957).
5. G. R. Wallwork and A. E. Jenkins, *This Journal*, **106**, 10 (1959).
6. H. A. Porte, J. G. Schnizlein, R. C. Vogel, and D. F. Fisher, *ibid.*, **107**, 506 (1960).
7. J. Debuigne and P. Lehr, *Corrosion of Reactor Materials*, **II**, 105, IAEA Vienna (1962).
8. G. R. Wallwork, W. W. Smeltzer, and C. J. Rosa, *Acta Met.*, **12**, 409 (1964).
9. R. J. Hussey and W. W. Smeltzer, *This Journal*, **111**, 564, 1221 (1964).
10. J. Staab, *Z. physik. Chem. N. F.*, **43**, 371 (1964).
11. C. J. Rosa and W. W. Smeltzer, *Acta Met*, **13**, 55 (1965).
12. J. P. Pemsler, *This Journal*, **112**, 477 (1965).
13. G. Tammann, *Z. anorg. u. allg. Chem.*, **111**, 78 (1920).
14. D. L. Douglass, *Corrosion of Reactor Materials*, **II**, 223, IAEA, Vienna (1962).
15. D. L. Douglass, Report GEAP-4473 (1964).
16. J. Rudolph, *Z. Naturforsch.*, **14a**, 727 (1959).
17. P. Kofstad and J. D. Ruzicka, *This Journal*, **110**, 181 (1963).
18. R. W. Vest, N. M. Tallan, and W. C. Tripp, *J. Am. Ceram. Soc.*, **47**, 635 (1964).
19. S. B. Dalgaard, Atomic Energy of Canada Limited Report AECL-2066 (1964).
20. R. W. Ure, *J. Chem. Phys.*, **26**, 1363 (1957).
21. F. A. Kröger and H. J. Vink, "Solid State Physics," Vol. 3, p. 310, F. Seitz and D. Turnbull, Editors, Academic Press, New York (1956).
22. C. Wagner, *Z. physik. Chem. (B)*, **21**, 25 (1933).
23. R. F. Domagala and D. J. McPherson, *Trans. AIME*, **200**, 238 (1954).

Effects of Anions on Corrosion Inhibition by Organic Compounds

Norman Hackerman

The University of Texas, Austin, Texas

and E. S. Snavely, Jr., and J. S. Payne, Jr.

TRACOR, Incorporated, Austin, Texas

ABSTRACT

The effects of inorganic anions, organic compounds, and combinations of the two on corrosion of mild steel in various acids were determined. From corrosion rates of steel in acids the order of the degree of adsorption of anions was concluded to be

$$I^- > Br^- > Cl^- > SO_4^= > ClO_4^-$$

The largest effects on corrosion mitigation were observed for I^- and I^- in combination with amines. The specificity of effects attributable to I^- suggests a strong interaction with the steel surface possibly through chemisorption. The enhancement of inhibitor efficiency by I^- is dependent on molecular structure of the inhibitor. The extent of synergism between I^- and organic amines was observed to be in the order: octamethyleneimine> di-n-butylamine>n-octylamine. Synergistic effects of anions and organic cations is greater than can be expected by a shift in the metal surface potential by anion adsorption and must be attributed in part to stabilization of the adsorbed anion layer by organic cations, possibly by covalent bonding.

Isolated examples of corrosion inhibition by simple anions have been noted for some time. In 1930, Walpert (1) showed that the addition of HCl slowed the corrosion rate of mild steel in H_2SO_4 by 78%. Putilova (2) gives numerous examples of corrosion inhibition by anions, *e.g.*, 90% inhibition efficiency of the corrosion of mild steel in *N* nitric acid by addition of KI, KBr, or KCl. The presence of certain anionic species often complements the efficiency of an organic inhibitor resulting in greater inhibition than achieved by either additive alone, *e.g.*, Malowan (3) patented the use of mixtures of iodide ion and organic amines for inhibition of the corrosion of steel in phosphoric acid.

Inhibition by anions and the synergistic effect of some anions and organic compounds (there is also an antagonistic effect) is a complex phenomena, and it is doubtful if one mechanism accounts for all the observations. Passivating potentials imposed by redox couples (4) accounts for the mechanism of ions in some systems. Mixed oxide formation (5) also is a plausible mechanism for other systems. A third mechanism is the strong adsorption of anions on metal surfaces; this is the one which best explains synergistic effects between anions and organic inhibitors and inhibition in the absence of alternate redox couples and/or bulk oxide formation.

The adsorption of anions on metal surfaces has been investigated by Conway (6), Hackerman (7), Schmid (8), Frumkin (9), and Kolotyrkin (10) by electrical double layer capacity measurements using a-c bridges and single-pulse techniques. For example, Murakawa and Hackerman (7) show the relative degree of adsorption of Cl^- and ClO_4^- ions by means of capacity-potential curves. The capacity-potential curve for zone-refined iron in $HClO_4$ alone shows a peak due to adsorption of ClO_4^-. As Cl^- is added to $HClO_4$, the ClO_4^- peak disappears, and a decrease in capacity occurs over the entire potential range investigated. These results indicate that Cl^- is more strongly adsorbed than is ClO_4^- on steel and can displace the latter. From similar work it is seen that the order of adsorption of anions on steel is shown as follows

$$\begin{matrix} & & F^- & & \\ I^- & > & Br^- & > & Cl^- > RCO_2^- > ClO_4^- \\ & & SO_4^= & & \end{matrix}$$

The relationship of the type of ion adsorbed to the zero point of charge and corrosion potentials of metal has been developed to a high degree by Antropov (11). From the above, one would expect the order of inhibition to be in the same order as the order of adsorption; however, no systematic survey of a wide range of anions in a single system is available. The purpose of this paper was to determine the inhibitor efficiencies of anions in various acids and the synergistic effects with organic cations in relation to the order of adsorption predicted by electrochemical methods.

Experimental

Mild steel coupons, ½ x 2 in., were cut from the same cold rolled sheet 0.065 in. thick. The coupons were abraided, polished, and degreased immediately before use. The steel analysis gave 0.09C, 0.40Mn, 0.02P, 0.037S, 0.03Si, and remainder Fe.

All solutions were made from reagent-grade chemicals used as-received, except for the HI which was distilled under inert atmosphere to remove preservative. Solutions containing I^- were stored for only short periods, under N_2, and in the dark.

Corrosion rates were calculated from slopes of curves giving total hydrogen evolved as a function of time. The data were programmed for a CDC 3200 computer which corrected hydrogen volume to standard temperature and pressure and calculated corrosion rates from root mean square fit of the data. Weight losses of the coupons were also measured, and these were used to check stoichiometry of the corrosion reaction and to validate the total volume of hydrogen observed. Duplicate runs were made of all experiments; reproducibility was within 4% for low rates of attack, but at high rates (<50% inhibition), results were only within 10%. Inhibitor efficiencies were calculated as follows

$$\% \text{ Inhibition} = \frac{R_o - R}{R_o} \times 100$$

where R_o is the corrosion rate in the absence of inhibitor and R is the corrosion rate in the presence of inhibitor.

Results

Uninhibited corrosion rates of mild steel were obtained in 3M solutions of HI, HBr, HCl, $HClO_4$, H_2SO_4,

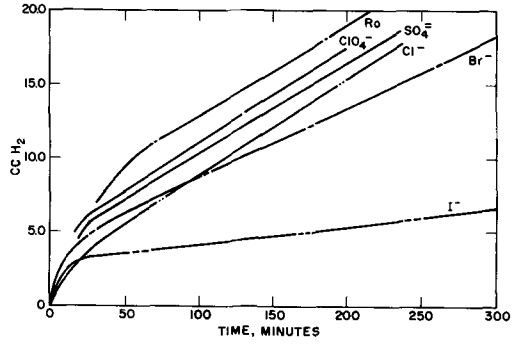

Fig. 1. Corrosion of mild steel in 3.0M H_3PO_4 containing 6.4 × 10^{-2}M of various anions; coupon area, 14.2 cm^2; temperature, 35°C.

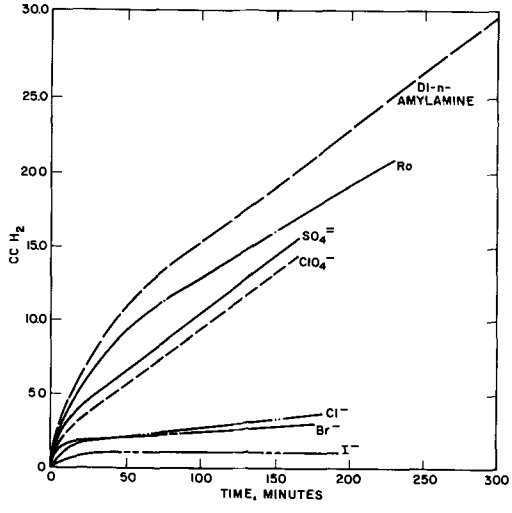

Fig. 2. Corrosion of mild steel in 3.0M H_3PO_4 containing 6.4 × 10^{-3}M di-n-amylamine and 6.4 × 10^{-2}M of various anions; coupon area, 14.2 cm^2; temperature, 35°C.

and H_3PO_4. These experiments were repeated using 3M acids containing 6.4 x 10^{-3}M diamylamine, n-decylamine, and propargyl alcohol. The effects of added anions were determined by adding sufficient quantities of acid to five of the above 3M acids, both with and without the organic inhibitor, to make solutions 6.4 x 10^{-2}M in the desired anion.

Hydrogen evolution as a function of time is given in Fig. 1 for the corrosion of mild steel in 3.0M H_3PO_4 and 3.0M H_3PO_4 + 6.4 x 10^{-2}M additions of various anions. Note that in the absence of organic additives, bromide ion has only a small effect on the corrosion reaction, and the slope for chloride ion is the same as for the pure acid. The addition of 6.4 x 10^{-3}M (1000 ppm) di-n-amylamine to 3.0M H_3PO_4 has no effect on the corrosion of mild steel as shown in Fig. 2. In this system, however, chloride and bromide ions show a strong synergism with di-n-amylamine in mitigating the corrosion of steel. The same strong inhibition effect of I^-, Br^-, and Cl^- is evident in solutions of n-decylamine and propargyl alcohol in 3.0M H_3PO_4 as shown in Fig. 3 and 4.

Data for the corrosion of mild steel in 3.0M solutions of pure acids containing 6.4 x 10^{-2}M additions of various inorganic anions are summarized in Table I. In general, the only effects on corrosion by added anions occur in halogen-containing acids or by addition of halogen ions to other acids which may or may not be halogen acids. More specifically, all the anions studied inhibited corrosion of steel in 3.0M HI, and the addition of HI inhibited corrosion in all the acids studied. The dissolution rate of mild steel in 3.0M HI without the additives is about the same as in HCl, *i.e.*, 3700 mdd. Bromide ion has the next most frequent effect, showing some inhibition effect in all the acids except HCl. It is significant to note

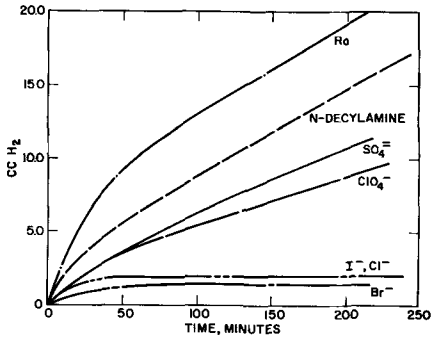

Fig. 3. Corrosion of mild steel in 3.0M H_3PO_4 containing 6.4 × 10^{-3}M n-decylamine and 6.4 × 10^{-2}M of various anions; coupon area, 14.2 cm^2; temperature, 35°C.

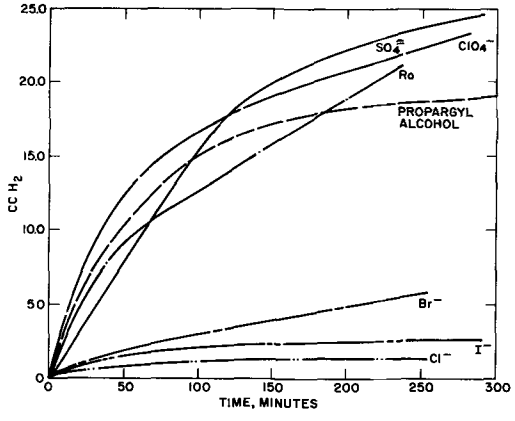

Fig. 4. Corrosion of mild steel in 3.0M H_3PO_4 containing 6.4 × 10^{-3}M propargyl alcohol and 6.4 × 10^{-2}M of various anions; coupon area, 14.2 cm^2; temperature, 35°C.

that the order of inhibition of the halogen anions concurs with the observed order of adsorption, *viz.*, $I^->Br^->Cl^-$, except in HI where the order is reversed. The absence of inhibition by Cl^- in 3.0M H_2SO_4 does not contradict the results of Walpert (1) since he used much higher concentrations of HCl in H_2SO_4. Also HI is the only acid in which inhibiting effects of Cl^-, ClO_4^-, $SO_4^=$, and $PO_4^=$ were noted at the concentrations employed.

Results obtained in solutions containing 6.4 x 10^{-3}M di-n-amylamine and inorganic anions are shown in Table II. Di-n-amylamine is a corrosion inhibitor

Table I. Per cent corrosion inhibition by added anions
Acid concentration, 3.0M; anion concentration, 6.4 × 10^{-2}M; temperature, 35°C

	Anions					
Acids	I^-	Br^-	Cl^-	ClO_4^-	$SO_4^=$	$PO_4^=$
HI		67	78	85	16	68
HBr	39		0	0	0	0
HCl	81	0		0	0	0
$HClO_4$	89	55	0		0	0
H_2SO_4	82	70	0	0		0
H_3PO_4	80	23	0	0	0	

Table II. Per cent corrosion inhibition by di-n-amylamine plus various anions
Acid concentration, 3.0M; anion concentration, 6.4 × 10^{-2}M; di-n-amylamine concentration, 6.4 × 10^{-3}M; temperature, 35°C

	Anions					
Acids	I^-	Br^-	Cl^-	ClO_4^-	$SO_4^=$	$PO_4^=$
HI	95	97	97	99	67	95
HBr	70	0	0	0	0	0
HCl	93	29	0	50	34	17
$HClO_4$	100	82	41	0	62	72
H_2SO_4	99	90	71	43	−65	40
H_3PO_4	94	85	77	0	0	−35

Table III. Per cent corrosion inhibition by n-decylamine plus various anions

Acid concentration, 3.0M; anion concentration, 6.4 × 10^{-2}M; n-decylamine concentration, 6.4 × 10^{-3}M; temperature, 35°C

Acids	Anions					
	I^-	Br^-	Cl^-	ClO_4^-	$SO_4^=$	$PO_4^{\equiv}$
HI	100	99	99	98	94	98
HBr	93	94	94	96	99	97
HCl	96	92	92	95	92	97
$HClO_4$	99	93	91	71	89	84
H_2SO_4	99	96	95	72	96	58
H_3PO_4	98	96	98	61	53	0

Table IV. Per cent corrosion inhibition by propargyl alcohol plus various anions

Acid concentration, 3.0M; anion concentration, 6.4 × 10^{-2}M; propargyl alcohol concentration, 6.4 × 10^{-3}M; temperature, 35°C

Acids	Anions					
	I^-	Br	Cl^-	ClO_4^-	$SO_4^=$	$PO_4^{\equiv}$
HI	99	99	98	100	97	99
HBr	98	95	98	98	98	94
HCl	98	98	99	96	98	95
$HClO_4$	97	98	100	94	92	83
H_2SO_4	99	97	97	45	97	94
H_3PO_4	99	86	98	39	0	0

only in 3.0M HI at the concentration employed. No significant effect was noted in 3.0M HBr, HCl, or $HClO_4$, and an accelerating effect occurred in 3.0M H_2SO_4 and H_3PO_4. In these experiments all the added ions had an inhibiting effect in the presence of di-n-amylamine, and numerous examples of synergism were observed. Notable examples are inhibition by Br^- and Cl^- in H_3PO_4, $PO_4^{\equiv}$, and $SO_4^=$ in $HClO_4$, and Br^- and $SO_4^=$ in HI where little, if any, effects were obtained in the absence of di-n-amylamine.

Inhibition by n-decylamine was greater than 90% in all the acids investigated except $HClO_4$ (71%) and H_3PO_4 (0). In these two acids inhibition was increased to over 90% by added halogen ions and was increased to a lesser degree by addition of ClO_4^-, $SO_4^=$, and $PO_4^{\equiv}$. Instances of antagonism are also evident in Table III; inhibition of 96% by n-decylamine in H_2SO_4 was decreased to 72% and 58% by ClO_4^- and $PO_4^{\equiv}$ ions, respectively.

Propargyl alcohol inhibited all acids greater than 90%, except for H_3PO_4 in which it had no effect as shown in Table IV. The high inhibition achieved by propargyl alcohol alone makes the effects of added anions less evident. The only anion effects are the increased inhibition by Cl^- and Br^- in H_3PO_4 solutions containing propargyl alcohol and the antagonism of ClO_4^- ion in H_2SO_4 which was also evident in the presence of n-decylamine as shown previously in Table III.

Structural Effects of Amines

Comparisons were made of the effects of various concentrations of I^- (as HI) on enhancing corrosion inhibition of mild steel in 3.0M HCl by octamethyleneimine, di-n-butylamine, and n-octylamine. The octamethyleneimine was synthesized here. The starting material, cyclooctanone, was converted to the lactam by the Schmidt reaction (12). The lactam was reduced to the cyclic imine by reduction with lithium aluminum hydride. The resulting impure imine was purified by gas chromatographic trapping. Its structure and purity were verified by nuclear magnetic resonance spectra. Di-n-butylamine was purchased and purified by recrystallization as the hydrochloride; n-octylamine was also purchased, but required no purification as shown by gas chromatographic analysis.

The greatest synergistic effect between I^- and the organics was observed for octamethyleneimine as shown in Fig. 5. This chart shows the observed inhibitor efficiencies (in parentheses) of various concentrations of I^- and octamethyleneimine alone and in mixtures of concentrations up to 1000 ppm. The results are also given as isocorrosion curves which were plotted by interpolation of the experimental data. The molecular weight of octamethyleneimine and the atomic weight of iodine are approximately equal, therefore equal ppm's of the two also correspond to equal molar concentrations. This is approximately true for the other two amines. The enhancing effect of I^- is shown by noting that the inhibitor efficiency of 1000 ppm I^- alone is 86%, 1000 ppm octamethyleneimine alone is 89%, and a mixture of only 10 ppm of each is 85%.

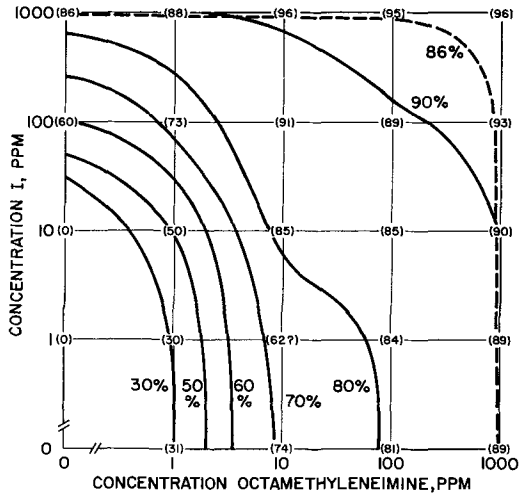

Fig. 5. Isocorrosion curves of mild steel in 3N HCl at 35°C; iodide and octamethyleneimine inhibitors. (Figures in parentheses are observed per cent inhibition.)

The synergism of octamethyleneimine and iodide ion is shown more clearly by the isocorrosion curves in Fig. 5. The dashed curve represents the shape of curve one would expect in the absence of synergistic effects between the iodide and octamethyleneimine. For example, the intersection of the dashed curve and the 100 ppm octamethyleneimine line represents the concentration of iodide required to give 86% inhibitor efficiency if the mixture behaved as either iodide or octamethyleneimine alone. The observed 90% curve occurs at concentrations far less than one would expect if iodide and octamethyleneimine behaved independently.

The cooperative effects of iodide and di-n-butylamine occur mostly at lower concentrations, at 100 ppm and below, and are negligible or entirely absent at higher concentrations as shown by the observed

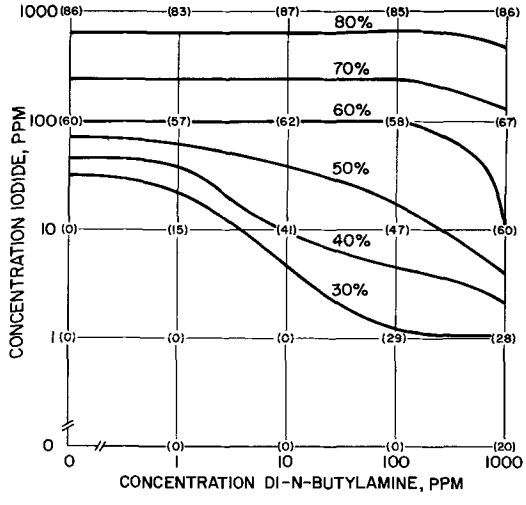

Fig. 6. Isocorrosion curves of mild steel in 3N HCl at 35°C; iodide and di-n-butylamine inhibitors. (Figures in parentheses are observed per cent inhibition.)

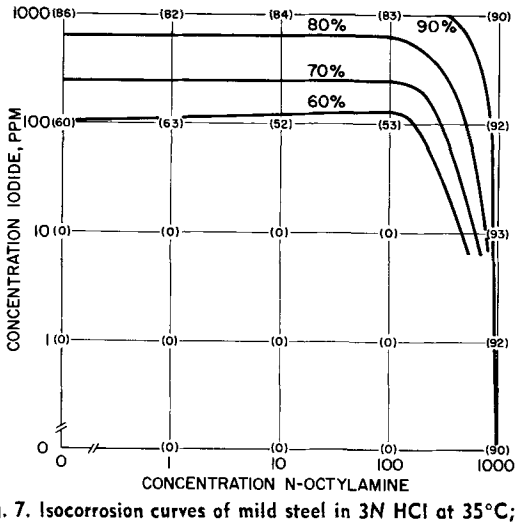

Fig. 7. Isocorrosion curves of mild steel in 3N HCl at 35°C; iodide and n-octylamine inhibitors. (Figures in parentheses are observed per cent inhibition.)

inhibitor efficiencies in Fig. 6. Corrosion inhibition by 1000 ppm iodide is not improved by the addition of 1000 ppm di-n-butylamine; however, 41% inhibitor efficiency is obtained by a mixture of 10 ppm of each additive although no inhibition occurs on the addition of 20 ppm of either species alone. The absence of synergistic effects at higher concentrations is also reflected in the isocorrosion curves of Fig. 6. The slopes of the isocorrosion curves become negative at increasingly lower amine concentrations as the concentration of iodide is decreased.

Little or no synergism is observed in the n-octylamine-iodide system. Both additives are essentially inert in combination or alone for concentrations of up to 100 ppm n-octylamine and 10 ppm I^- as shown in Fig. 7. The isocorrosion curves for this system (Fig. 7) have essentially the shape one would expect for a nonsynergistic system as shown previously in Fig. 5.

Discussion

In the absence of organic additives anionic effects were noted only in halogen acids or by the addition of halogen ions to other acids. The anionic effects in all acids except HI are in the order $I^->Br^->Cl^-$ as predicted from electrochemical methods. The effects of ClO_4^-, $SO_4^=$, and $PO_4^{\equiv}$ were small and within experimental error so that no conclusion can be drawn concerning their order of adsorption under the conditions employed. The only instances of inhibition by the latter ions are noted in HI, where one would not expect any effects by other ions in the presence of 3.0M strongly adsorbed I^-.

In the absence of a preservative, solutions of HI are unstable so traces of free iodine are inevitable. It is likely that results in 3.0M HI are influenced by the presence of the $I_3^- \rightleftarrows 3I^-$ couple. In this case a shift of the corrosion potential to more positive values with respect to the zero point of charge must be assumed to account for inhibition by foreign anions. This can be accomplished by depolarization of the cathode reaction or increased polarization of the anode reaction. These effects appear reasonable for all the added anions including Cl^- which is usually considered an anodic depolarizer, but has been shown by Lorenz (13) to polarize the anodic reaction of steel in H_2SO_4 solutions. The specificity of halogen ions in general, and especially iodide, suggests chemisorption as the means of inhibition of steel.

The effects of all the anions studied are amplified by the addition of organic amines. Synergism of amine and foreign anions is noted most in acids containing di-n-amylamine which does not have much effect alone. Iofa (14) shows that iodide and sulfide

Table V. Effect of iodide and octamethyleneimine on the corrosion potential of mild steel in 3N HCl (Figures are mV negative with respect to SCE)

Ppm I⁻					
1000	475	477	475	474	467
100	475	476	471	467	461
10	476	475	474	471	469
1	478	471	471	469	463
0	476	473	467	464	463
	0	1	10	100	1000

Ppm octamethyleneimine

ions increase the polarization of both the anodic and cathodic reactions on corroding steel in the presence of tribenzylammonium ion. This effect is attributed to an increased negative charge on the metal surface caused by adsorption of anions which then promote the adsorption of organic cations. If anions are adsorbed sufficiently to promote the adsorption of cations, one would expect the anions themselves to exhibit a partial inhibiting effect. This is not the case, however, as shown by the increase in inhibition from 0 to 70% for Cl^- in H_2SO_4 and H_3PO_4 in the presence of di-n-amylamine. The adsorption of the organic cation appears to stabilize the anion layer on the metal, possibly by displacement of the equilibrium between solution and adsorbed ions toward surface positions on the metal.

Simple measurements of the corrosion potential of steel in 3.0M HCl were made to aid in interpreting the mechanism of synergism by iodide with amines. Potentials were measured with respect to a saturated calomel electrode in nitrogen-stirred solutions.

Results of the measurements for additions of iodide and octamethyleneimine and combinations of the two are given in Table V. The corrosion potential of mild steel in 3.0M HCl shifts in a positive direction with additions of octamethyleneimine; however, the magnitude of the changes are small being only 13 mv for addition of 100 ppm of imine. These observations are in accord with those observed previously (15) for steel in HCl containing nonamethyleneimine. In this work it was observed that both the anodic and cathodic reactions are polarized by the addition of nonamethyleneimine. Additions of iodide have little, if any, effect on the corrosion potential as shown in Table V. This result is attributed also to polarization of both the anodic and cathodic reactions as observed by Iofa (14) for corrosion inhibition by KI in H_2SO_4.

The shift in corrosion potential to a more positive value affords a greater tendency for the metal to absorb anions. However, the additional observations in Table V that mixtures of iodide and octamethyleneimine, *e.g.*, 10 ppm of each, do not shift the corrosion potential yet inhibit corrosion to a greater extent than either additive alone indicate that covalent bonding of the halide also plays a part in the mechanism of synergistic inhibition.

Solution chemistry of the organic additive is, of course, a factor as shown by a comparison of results for di-n-amylamine, n-decylamine, and propargyl alcohol. Acetylenic compounds like propargyl alcohol form cationic complexes. Thus, in this respect, they are similar to nitrogen compounds (16). Mechanisms to account for the antagonism of ClO_4^- in the latter systems are not known. It is not feasible to assume that ClO_4^- would be adsorbed sufficiently to displace adsorbed amine or alcohol because ClO_4^- has no effect on the corrosion of steel in the absence of the organics. A complete explanation of the results must take into account the chemistry of the systems involved. For example, propargyl alcohol may undergo reduction or addition of halogen acids across the triple bond.

Molecular structure of the organic compounds is important in synergistic inhibition as shown by the results for octamethyleneimine, di-n-butylamine, and n-octylamine in HCl containing additions of iodide ion. It has been shown that, in the absence of foreign

anions, those organic cations that have the greatest tendency toward covalent bonding give the best corrosion inhibition. Covalent bonding of organic nitrogen compounds to iron has been discussed previously (15). Specifically, it was shown that, of the amines investigated, nonamethyleneimine had both the highest p character of the electron pair on N and the highest inhibition (15). Iofa (14) has shown that I^- alone polarizes both the anodic and cathodic reaction of iron over a wide potential range. It is apparent then that the effects of I^- are not due to electrostatic effects alone, but some covalent bonding to the metal must be involved. The large size and ease of polarizability of I^- facilitate electron pair bonding. The greatest synergistic inhibition is to be expected for an anion-cation pair, in which both ions have an appreciable tendency toward covalent bonding. For example, in the case of octamethyleneimine and I^- in HCl, the chemisorbed iodine serves as a link, or bridge, between the metal surface and the imine, as would an anion associated with the surface by purely electrostatic forces. However, the former is more effective, for reasons not yet fully apparent.

Conclusions

Of the ions studied, I^-, Br^-, Cl^-, ClO_4^-, $SO_4^=$, and $PO_4^{\equiv}$, the order of adsorption based on corrosion inhibition efficiency is $I^->Br^->Cl^-$, while insufficient effects were noted for the others on which to base an order of adsorption. The specificity of effects attributable to I^- suggests a strong interaction with the steel surface possibly through chemisorption.

Synergism of inhibitor efficiency between anions and organic cations is greater than can be expected by a shift in the metal surface potential by anion adsorption and must be attributed in part to stabilization of the adsorbed anion layer by organic cations.

Molecular structure of the organic compound may play a dominant role in the degree of enhancement of inhibition by a foreign anion, with the greatest enhancement occurring when both the anion and cation show a tendency toward electron pair bonding.

Acknowledgment

One of the authors (N. H.) takes this opportunity to express his thanks to the Robert A. Welch Foundation and the Office of Naval Research for their support of the work in his laboratory which led in part to this work.

Manuscript received Feb. 11, 1966; revised manuscript received March 30, 1966.

Any discussion of this paper will appear in a Discussion Section to be published in the June 1967 JOURNAL.

REFERENCES

1. G. Walpert, *Z. Phys. Chem.*, **A151**, 219 (1930).
2. I. N. Putilova, S. A. Balezin, and V. P. Barannick, "Metallic Corrosion Inhibitors," Pergamon Press, New York (1960).
3. J. E. Malowan, U. S. Pat. 2,567,156, Sept. 4, 1951.
4. A. C. Makrides and Milton Stern, *This Journal*, **107**, 877 (1960).
5. U. R. Evans, "An Introduction to Metallic Corrosion," Edward Arnold, Ltd., London (1948).
6. B. E. Conway, "Transaction of the Symposium on Electrode Processes," John Wiley & Sons, New York (1961).
7. Takao Murakawa and N. Hackerman, *Corrosion Sci.*, **4**, 387 (1964).
8. G. M. Schmid and N. Hackerman, *This Journal*, **109**, 243 (1962).
9. A. N. Frumkin and B. B. Damaskin, *J. Electroanal. Chem.*, **3**, 36 (1962).
10. Ja. M. Kolotyrkin, *This Journal*, **108**, 209 (1961).
11. L. I. Antropov, "Kinetics of Electrode Processes and Null Points of Metals," Catholic Press, Ranchi, India (1960).
12. L. F. Fieser and M. Fieser, "Advanced Organic Chemistry," p. 521, Reinhold Publishing Corp., New York (1961).
13. W. J. Lorenz, *Corrosion Sci.*, **5**, 121 (1965).
14. Z. A. Iofa, V. V. Batrakov, and Cho-Ngok-Ba, *Electrochim. Acta*, **9**, 1645 (1964).
15. N. Hackerman, R. M. Hurd, and R. R. Annand, *Corrosion*, **18**, 37t (1962).
16. J. D. Roberts and M. J. Caserio, "Basic Principles of Organic Chemistry," p. 217, W. A. Benjamin, Inc., New York (1965).

Some Aspects of the Mechanism of Hydrogen Evolution at a Mild Steel Electrode

J. S. Ll. Leach and S. R. J. Saunders

Department of Metallurgy, Imperial College of Science & Technology, London, England

ABSTRACT

The hydrogen evolution reaction on mild steel has been studied in both acid and alkaline solutions. The associated overvoltage at constant current increased under some conditions during the hydrogen permeation process through a foil electrode. This increase has been interpreted as resulting from an increase in the hydrogen content of the metal. The results suggest that the hydrogen evolution reaction in acid solution takes place on the surface of the electrode, whereas in alkaline solutions the evolution process involves dissolution of hydrogen in the metal.

The hydrogen evolution overvoltage at an iron electrode being cathodically charged under galvanostatic conditions has been observed to increase with time. The following interpretations have been proposed to account for this effect: (*a*) The adsorption of impurities in the system which may poison the electrode for the recombination of hydrogen atoms (1); (*b*) the adsorption of hydrogen atoms on the electrode surface (2); (*c*), the formation of iron hydride (3); (*d*) an increase in the hydrogen content of the metal (4). This last explanation is perhaps the most generally favored.

The nature of the electrode interface is important in determining both the hydrogen adsorption and desorption rates on a metal. The rate of adsorption of electrolytic hydrogen at an iron electrode is dependent on the pH and the imposed current density. Berg (5) has shown that the rate of hydrogen desorption in the presence of water is greater than the corresponding rate in air.

In view of the importance of hydrogen in corrosion processes (6-8), it was decided to re-examine, as a function of the environment, the hydrogen overvoltage at a mild steel electrode during the permeation process.

The observations reported here appear to lend support to the idea that the overvoltage increase arises from a change in hydrogen content of the electrode

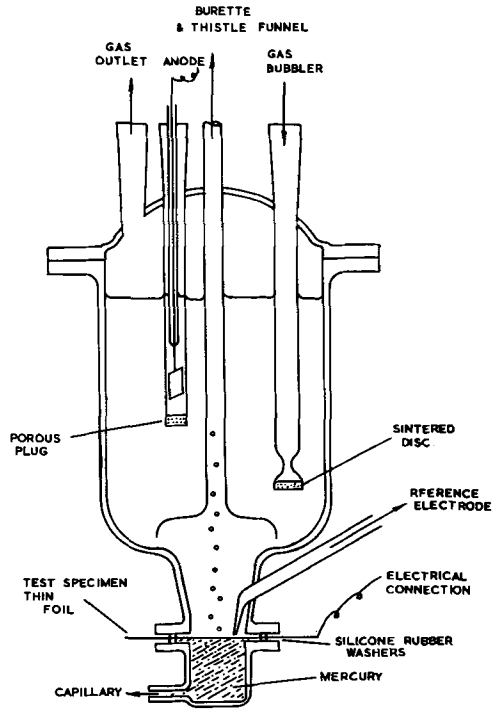

Fig. 1. Hydrogen pick-up test cell

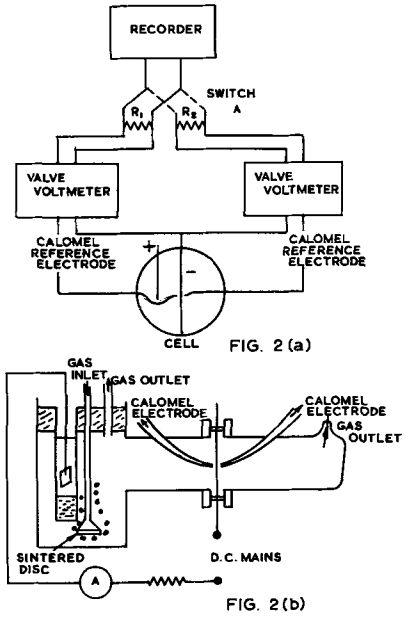

Fig. 2. Apparatus for measurement of transferred overvoltage. Fig. 2a. Electrical circuit; Fig. 2b. cell (diagrammatically).

and that under certain circumstances dissolution in the electrode may be a necessary step in the hydrogen evolution process.

Experimental Procedure

Simultaneous measurement was made of the hydrogen overvoltage, the hydrogen permeation rate through the foil, and the hydrogen evolution rate. The presence of an oxide on the surface of the electrode would be expected to produce complications; in the present work the *p*H of the solutions and the potential of the electrodes were such that oxides of iron were thermodynamically unstable and that no corrosion of the electrode occurred.

The cells employed for this work are shown diagrammatically in Fig. 1 and 2. Figure 1 illustrates the cell used to measure the hydrogen permeation rate. The position of the gas bubbler was chosen to minimize the diffusion of oxygen from the anode compartment to the cathode compartment. The permeation rate was measured by observing the movement of a mercury column in a capillary of known bore. The mercury was displaced from behind the electrode at the nonpolarized interface by the hydrogen permeating through the electrode. The capillary was placed at the same level as the electrode so that the permeating gas had only to overcome atmospheric pressure before moving the mercury. It was difficult to be certain exactly how much hydrogen must leave the electrode before the mercury begins to move; provided that the system is clean it is thought to be only a very small amount. However, the discussion is primarily concerned with steady-state conditions, and therefore this uncertainty becomes relatively unimportant. By changing the size of capillary, permeation rates from 0.0001 to 0.01 cc/cm^2/min could be measured. The hydrogen evolution rate was measured by placing a thistle funnel above the cathode and collecting the gas in a graduated buret by displacement of the solution inside. The volume was corrected to S.T.P. The potential of the electrode was measured with respect to a calomel half cell. A Luggin capillary was placed approximately ⅛ in. from the specimens, connection being made to the half cell by means of a polythene tube containing the solution. All potentials quoted in this paper are expressed on the standard hydrogen scale and are designated E_H.

Figure 2 illustrates the cell used to investigate the permeation-potential characteristics of the electrode when the nonpolarized interface was solid/aqueous. The permeation rate was not measured in this case, but an estimate of the time taken for hydrogen to reach the nonpolarized interface could be obtained from an observation of the potential at this interface. A change in potential toward more negative values at this interface can be associated with the arrival of hydrogen.

The solutions used were made from Analar reagents and distilled water. The distilled water was "equilibrium water" with a conductivity of 10^{-6} mho/cm. The *p*H of the water was 6.5 which was due to the presence of a low concentration of sulfurous impurities. The solutions used, which were degassed both before and during the experiments with oxygen-free nitrogen to reduce the oxygen concentration, had the following compositions: (*i*) carbonate/bicarbonate buffer (0.2*N* $NaHCO_3$ + 0.2*N* Na_2CO_3) *p*H 9.7; (*ii*) sodium sulfate of variable *p*H. (The *p*H was adjusted with sodium hydroxide or sulfuric acid.)

The presence of sulfurous impurities in the system was desirable since these increased the hydrogen permeation rate which otherwise would have been very slow under the experimental conditions. To confirm that these impurities only increased the permeation rate and did not change the mechanism of the process, some experiments were repeated with solutions prepared from the distilled water purified by a further distillation in the presence of alkaline permanganate. In order to prevent possible contamination of the solutions by impurities from the electrode, high-purity iron (analysis below) was used in these tests.

The electrode materials used in this investigation were cold rolled and wet ground with successively finer carborundum papers up to 600 grade and then carefully washed in distilled water. This treatment was chosen because it has been shown (9) that both cold rolling and a rough surface increase the permeation rate. The foil thickness was 0.0127 cm unless otherwise stated. The analysis of the electrode materials is as follows:

Mild steel: (w/o, weight per cent) carbon 0.15-0.25 w/o; manganese 0.4-0.9 w/o; sulfur 0.06 w/o; phosphorus 0.06 w/o; silicon 0.05 w/o; remainder iron.

Pure iron: carbon 0.00034 w/o; manganese 0.005 w/o; sulfur 0.004 w/o; phosphorus 0.01 w/o; silicon

0.006 w/o; oxygen 0.0006 w/o; nitrogen 0.0001 w/o; remainder iron.

The glass cells were cleaned with chromic acid, concentrated nitric acid, distilled water, and finally absolute alcohol. The silicone rubber washers were degreased with acetone and absolute alcohol.

Various constant current values were obtained by placing suitably large resistors in series with the d-c mains. The current was monitored and found to be constant within ± 1%.

The valve voltmeter (E.I.L. Model 23A) used for the potential measurements was of the differential amplifier design with high input impedance and high stability over long time periods. The electrode potential and polarizing current were automatically recorded.

The system was tested by measuring the current efficiency for the hydrogen evolution reaction. The number of coulombs passed agreed to within 1% with the number required to liberate the amount of hydrogen evolved plus that which permeated through the foil.

Results

The effect of current density and pH on the hydrogen permeation rate is shown in Fig. 3 and 4. Figure 3 shows that in acid solution the permeation rate is independent of the imposed current density, while in alkaline solution at high current density change in the imposed current changes the permeation rate. The low current density range shows a threshold effect which has been interpreted (10) in terms of the need for a minimum current density before permeation begins.

Further experiments were conducted in solutions of selected pH so that the transition between these two types of behavior could be observed (Fig. 4). At low

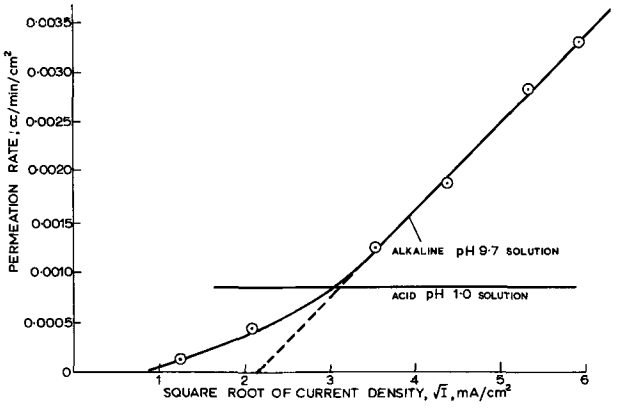

Fig. 3. Effect of current density on the permeation rate through mild steel in acid and alkaline solution.

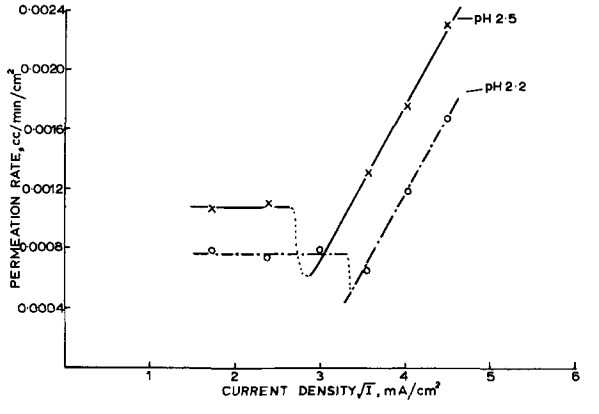

Fig. 4. Effect of current density on the permeation rate through mild steel showing regions of transition.

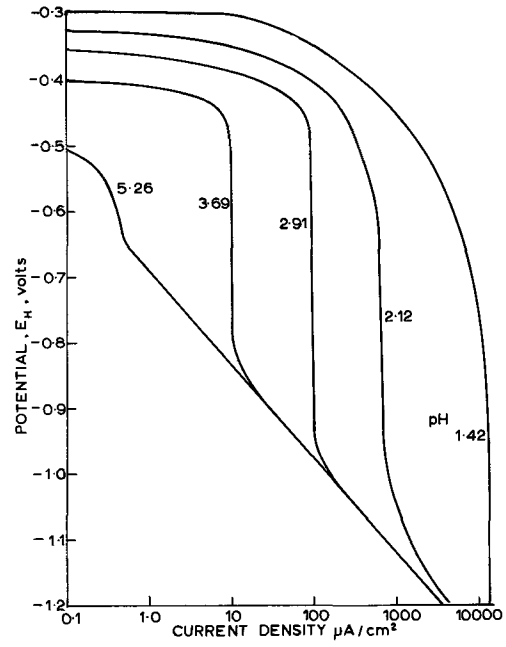

Fig. 5. Current-voltage relationship on iron in solutions of different pH [after Stern (11)].

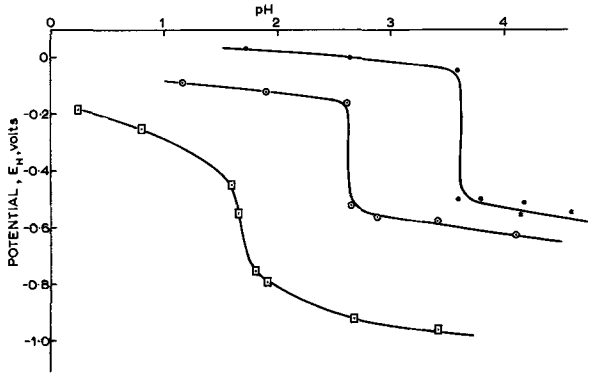

Fig. 6. Effect of pH on the current-voltage relationship on mild steel: • 0.64 ma/cm²; ○ 6.4 ma/cm²; □ 64.0 ma/cm².

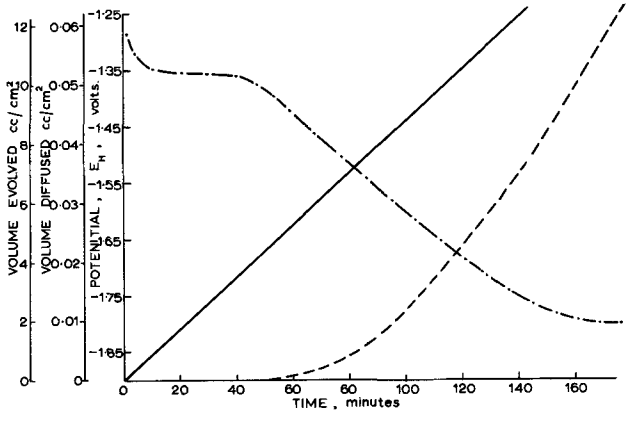

Fig. 7. Overvoltage changes in pH 9.7 solution at a mild steel electrode during hydrogen permeation into an inert environment; current density 12.8 ma/cm². ——— Evolved; — — — diffused; —·—·— potential.

current densities the permeation rate is independent of the imposed current, but at higher currents, the permeation rate becomes dependent on the current density. In these experiments foil thickness of 0.0076 and 0.01 cm were used.

A change in the hydrogen evolution kinetics in acid solutions takes place on increasing the current den-

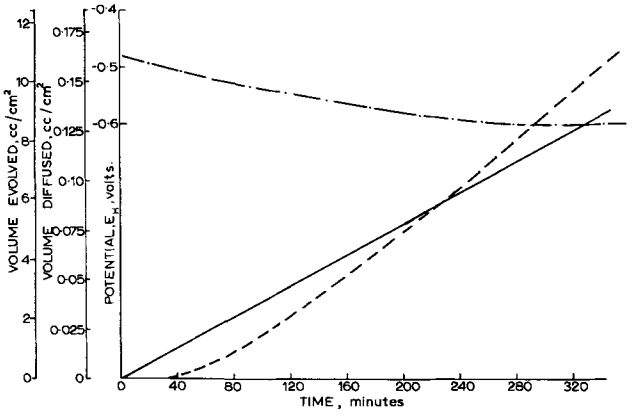

Fig. 8. Overvoltage changes in pH 1.2 solution at a mild steel electrode during hydrogen permeation into an inert environment; current density 4.23 ma/cm². ——— Evolved; — — — diffused; — . — . potential.

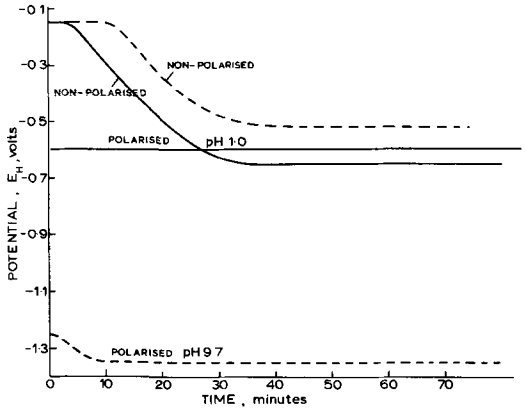

Fig. 9. Overvoltage changes at the polarized and nonpolarized interfaces during hydrogen permeation through mild steel into an aqueous environment (solution pH 9.7); current density 12.8 ma/cm². Full lines polarized interface pH 1.0; broken lines polarized interface pH 9.7.

sity, which is illustrated by the Tafel curves obtained by Stern (11) for mild steel (Fig. 5). In Fig. 6 results obtained in the present work show the same effect. These results are plotted in a different way to show that a change of one pH unit results in a tenfold change in the current density at which a transition in the hydrogen evolution mechanism takes place.

Overvoltage changes observed at the polarized interface during the permeation of hydrogen through the mild steel foils under various conditions are shown in Fig. 7, 8, and 9. For the case of a mild steel electrode in alkaline solution with mercury initially making contact with the nonpolarized interface the results are shown in Fig. 7. The overvoltage increases during the first 10 min of the experiment; having changed by 0.1v, it then remains constant for approximately an hour. After this the overvoltage again increases and becomes constant when the permeation rate has attained a steady value. This second increase in the overvoltage appears to coincide with the evolution of hydrogen from the back of the foil. However, in acid solutions under otherwise similar conditions, the overvoltage increases gradually from the start of the experiment (Fig. 8), the total increase being smaller than the corresponding case in alkaline solution. The evolution of the hydrogen from the back of the foil starts about 40 min from the beginning of the experiment.

Using doubly distilled water for solutions and the pure iron electrode the same general trends are observed as in the impure system, but on a reduced scale and at longer times. These results suggest that

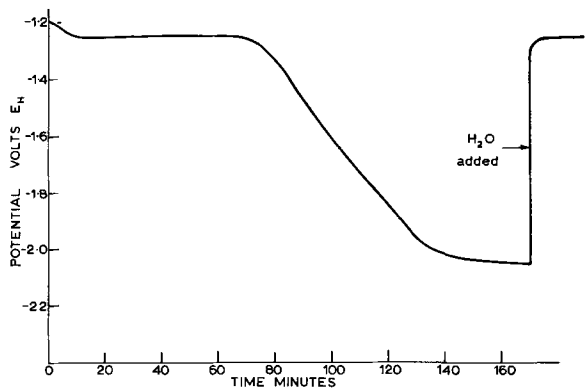

Fig. 10. Overvoltage changes at a mild steel electrode in pH 9.7 solution during permeation into an environment initially inert subsequently changed to aqueous.

the additional impurities do not change the mechanism but only the rate of the permeation process.

Results of overvoltage measurements made during the permeation of hydrogen into an aqueous environment (solution pH 9.7) appear in Fig. 9. Changes in potential at the nonpolarized interface are interpreted as corresponding to changes in the hydrogen permeation rate. The exact origin of these potential changes is considered in more detail in the discussion. With an alkaline solution at the polarized interface the overvoltage there increased by 0.1v in the first 10 min of the experiment (compare with Fig. 7); thereafter it remains constant. The overvoltage at the nonpolarized interface also increases but only after the overvoltage at the polarized interface has reached a constant value. With an acid solution at the polarized interface, the overvoltage there remains constant throughout the experiment while that at the nonpolarized interface increases soon after the experiment has commenced.

It will be noticed from Fig. 7, 8, and 9 that the environment of the nonpolarized interface influences both the time for breakthrough of hydrogen and the overvoltage at the polarized interface. This suggested an experiment in which an aqueous environment could be substituted for an inert environment at the nonpolarized interface. Results are shown in Fig. 10 where it will be seen that changing the environment after the second overvoltage change has occurred at the polarized interface causes the potential to rise rapidly to the value obtained after the first overvoltage increase.

This large increase in overvoltage in alkaline solutions was investigated further by measuring the Tafel slopes for mild steel during the permeation process with an inert environment behind the electrode. The results illustrated in Fig. 11 were obtained at various stages in the experiment as the overvoltage increases, and indicate that the slope remains approximately at 0.2 in all the overvoltage ranges.

Discussion

The mechanism of the hydrogen evolution reaction is believed (12) to be governed by the pH of the solution and the imposed current density. At low current densities in acid solution the reaction takes place by the reduction of hydronium ions. Increasing the pH causes the concentration of hydronium ions to decrease. For any given pH there is a maximum current which can be carried by the reduction of hydronium ions; imposing greater currents than this limiting value results in an increase in the overvoltage sufficient to allow the reduction of water by the following reaction

$$H_2O + e \rightarrow OH^- + M{-}H \qquad [1]$$

where M—H represents a hydrogen atom adsorbed on the metal surface. The adsorbed hydrogen atoms

may then recombine to form a molecule. Hydroxyl ions are produced at the electrode as a by-product of this reaction causing a local increase in the pH of the solution. It has been suggested (2, 12) that under these conditions the local pH near the electrode is constant regardless of the pH in the bulk solution. This may provide an explanation of the effect seen in Fig. 5 where the overvoltage-current relation is the same for solutions of different pH once the transition in the evolution kinetics has occurred. In the remainder of the discussion the differences observed between the evolution behavior in acid and in alkaline solution are interpreted as being associated with the change in the discharging species.

From Fig. 3 and 4 it may be seen that the permeation rate is independent of the imposed current density in acid solutions. In alkaline solutions, however, the permeation rate varies with the current density, and this has been plotted as a square root dependence after the work of Barrer (10). No significance is attached to the square root relation as an equally good line may be obtained for the present results by plotting a linear dependence on the current density. The exact form of the relationship is not considered in the subsequent discussion; only the fact that there is a change from current independent permeation rates

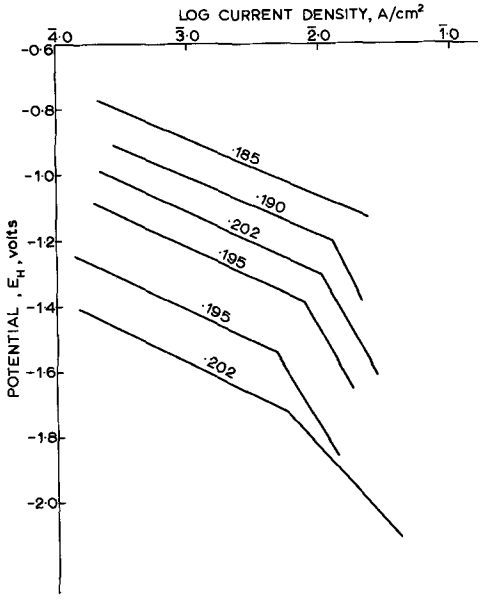

Fig. 11. Current-voltage relationship on mild steel in pH 9.7 solution at different overvoltages during hydrogen permeation into an inert environment.

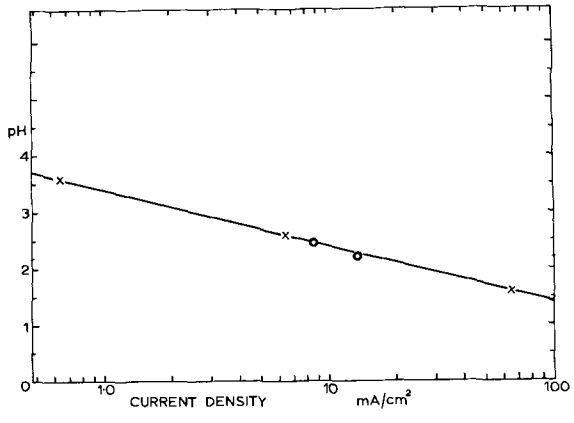

Fig. 12. Critical current density vs. pH for changes in the hydrogen evolution kinetics at a mild steel electrode: O changes in permeation kinetics derived from Fig. 4; x changes in evolution kinetics derived from Fig. 6.

in acid solutions to rates dependent on current density in alkaline solutions.

The values of pH and current density at which the hydrogen permeation kinetics change may be derived from Fig. 4. The relation between the current density and the solution pH at which the hydrogen evolution kinetics change may be deduced from Fig. 6. All these values are shown in Fig. 12, and it will be seen that the transitions in both processes show the same current density/pH relationship.

Before examining the way in which the hydrogen permeation and hydrogen evolution processes may be related it is relevant to consider the experimental observations shown in Fig. 7-10. These are concerned with the effects on the overvoltage for hydrogen evolution of the nature of the unpolarized interface of the electrode.

The overvoltage changes shown in Fig. 7 and 8, with the exception of the first change in the alkaline solutions (Fig. 7), do not arise from the presence of impurities. This is deduced from results shown in Fig. 9 where no such changes occur when an aqueous environment is at the back of the foil. This deduction is also supported by results shown in Fig. 10. Here the experimental conditions were similar to those pertaining to the results shown in Fig. 7, but after a steady state had been achieved at about —2.0v E_H an aqueous environment was substituted for the inert environment at the back of the foil electrode. The potential rose rapidly without further change in the conditions. These changes in overvoltage might arise from changes in the hydrogen evolution mechanism, but in general this should result in changes in the Tafel slope such as those seen in Fig. 5. Measurements made during the observed overvoltage increase in alkaline solution show the Tafel slope to be essentially constant (Fig. 11) suggesting that no change in the mechanism occurs.

If it can be shown that the large overvoltage increase is associated with increased hydrogen content of the electrode, then a satisfactory explanation for both the overvoltage behavior and the permeation kinetics may be proposed.

An aqueous environment has been shown (5) to assist the removal of hydrogen from the metal to a greater extent than an inert environment such as nitrogen or hydrogen. For a given rate of hydrogen removal from the metal at the nonpolarized interface, the concentration of hydrogen in the metal would be higher when the surface of the metal forms an interface with an inert environment rather than an aqueous environment. This increased concentration at the nonpolarized interface results in an increased concentration in the metal at the polarized interface.

Consider the effect on the hydrogen evolution reaction of the permeation process into an inert environment. Under these conditions it has been shown that an increased hydrogen concentration in the metal may be expected when compared with the permeation process into an aqueous environment. Figures 7 and 8 illustrate the overvoltage changes that occur at the polarized interface during the hydrogen evolution process when hydrogen is being generated from acid and from alkaline solutions, respectively. It can be seen that the overvoltage change at the polarized interface is considerably greater for alkaline solutions than for acid solutions.

Any mechanism proposed for the hydrogen evolution reaction should take into account the following observations: (*A*) In acid solution (i) the permeation rate is independent of the imposed current density, and (ii) the hydrogen evolution process is not markedly dependent on the hydrogen content of the electrode, as reflected by a small change in the overvoltage during the permeation process into an inert environment. (*B*) In alkaline solution (i) the permeation rate is dependent on the current density, and (ii) the evolution process is dependent on the hydrogen con-

tent of the metal, as reflected by a substantial change in the overvoltage during the permeation process into an inert environment.

The suggested differences between the mechanisms for hydrogen evolution in acid and in alkaline solutions which are described below afford an explanation of the experimental observations.

In acid solutions it is proposed that the evolution process takes place entirely on the surface of the electrode. Electrons would be removed from the metal by the field arising from the positively charged ionic species H_3O^+ adjacent to the metal surface so discharging the hydronium ion to form a water molecule and a hydrogen atom which may then combine with another. Any hydrogen entering the metal does so under existing potential and concentration gradients and not as a necessary step in the evolution reaction.

In alkaline solutions, on the other hand, it is proposed that the evolution reaction takes place *via* hydrogen dissolution in the metal. Due to the high concentration of hydroxyl ions at the electrode surface created as a by-product in the reduction of water, some hydroxyl ions should be adsorbed on the electrode. The hydroxyl ion is polar and would align itself with the hydrogen closer to the electrode. Since the net charge on the electrode is negative the removal of an electron from the metal would not be favored. It is suggested, therefore, that the following reaction may take place

$$[OH]_{ads} + H_2O \rightarrow 2\,OH^- + [H^+]_{in\ Fe} \qquad [2]$$

The undoubtedly large energy required to remove H^+ from OH^- might be supplied in part by the heat of solution of the proton in iron. This is of the order of −40 kcal/g atom for atomic hydrogen (13). The proton in metallic solution loses its charge and may either diffuse into the metal under a concentration gradient or recross the phase boundary, combine with another atom, and finally be evolved as molecular hydrogen. It is difficult to see how a reaction which takes place entirely on the surface of the electrode, as in the acid case, could explain both the dependence of the permeation rate on the current density and the dependence of the evolution reaction on the hydrogen content of the electrode.

There are some aspects of these results which, although not directly related to the hydrogen evolution process, require an explanation: (*a*) the nature of the first increase in overvoltage at the polarized interface during permeation from an alkaline solution into an inert environment (Fig. 7); (*b*) the time taken for hydrogen permeation into the different environments.

The first increase in the overvoltage at the polarized interface is believed to be associated with the cathodic reduction of an oxygen-containing species adsorbed on the electrode in alkaline solutions. Preliminary impedance measurements support this interpretation.

The time taken initially for hydrogen permeation through the foil apparently varies for different environments. However the time taken for hydrogen to diffuse through the metal is relatively short as shown by measurements in which a steady-state permeation process into an aqueous environment is distributed by changing the current density at the polarized interface. The resulting change in the potential at the nonpolarized interface occurs within one minute (see Table I). Further evidence for rapid diffusion appears in Fig. 10 where the recovery of overvoltage also occurs in about 1 min.

At the start of an experiment the drop in potential at the nonpolarized interface, in the presence of an aqueous solution which indicates the arrival of hydrogen at this interface, can occur in about 10 min or less. Evidence of the permeation of hydrogen into a gaseous environment as shown by the movement of the mercury takes under otherwise similar conditions approximately 1 hr. These differences in the time taken for hydrogen to be observed at the nonpolarized interface may be related to the presence of an oxygen containing layer. In the case of an inert environment, the reduction of this layer may be favored compared with diffusion out of the interface. For an aqueous environment, however, the potential which is reached at the nonpolarized interface is such that the reduction process would not occur and therefore the hydrogen leaves the surface immediately.

Table I. Time required for hydrogen to diffuse through the metal foil

Current density changes, ma/cm²	pH polarized interface	Time for change in potential for foil 0.0127 cm thick, sec
10 → 30	1.0	62
30 → 90	1.0	57
10 → 30	9.7	65
30 → 90	9.7	53

Summary

Of the mechanisms put forward to explain the increase in hydrogen overvoltage, the adsorption of impurities (1) or of hydrogen atoms (2) is not in itself sufficient to account for all the effects observed in the present experiments. The most probable cause appears to be the increase in the hydrogen content of the metal. Other measurements to be reported in a later paper indicate that a reversible reaction which might involve the formation of a hydride may be occurring at the most negative potentials. It is believed, however, that this is the result of the high concentration of hydrogen in the metal and is not in itself the cause of the increase in overvoltage. The observations support the mechanism for the hydrogen evolution reaction proposed by McGraw and co-workers (14).

The hydrogen permeation process has been shown to be related to the hydrogen evolution mechanism. In alkaline solutions the permeation rate depends on the evolution rate whereas in acid solution no such dependence is observed. This is interpreted in terms of a change in the evolution mechanism; it is suggested that in alkaline solutions this takes place *via* hydrogen dissolution in the metal whereas in acid solution the reaction occurs in the metal surface.

A possible consequence of the concepts developed in the present work lies in the field of hydrogen pick-up. The absorption of hydrogen by a specimen depends on the mechanisms of proton discharge. In particular, the ease with which the electrons can be transferred across the phase boundary to permit discharge of protons without their entry into the surface layers of the material implies a dependence on such parameters as the work function of the interface as well as the availability of electrons in the electrode surface layers.

Acknowledgments

The authors wish to acknowledge the support of the United Kingdom Atomic Energy Authority for financing the project and providing the stipend of one of them (S.R.J.S.). The National Physical Laboratory kindly supplied the pure iron and their cooperation is greatly appreciated. Finally the authors are indebted to Professor J. G. Ball in whose department the work was carried out.

Manuscript received Jan. 18, 1965; revised manuscript received March 22, 1966.

Any discussion of this paper will appear in a Discussion Section to be published in the June 1967 JOURNAL.

REFERENCES

1. Y. E. Past and Z. A. Zofa, *Doklady Akad. Nauk. SSR.*, **106**, 1050 (1956).
2. J. O'M. Bockris and E. C. Potter, *J. Chem. Phys.*, **20**, 614 (1952).
3. G. P. Lochchinina, B. N. Kabanov, and A. M. Murtozaev, *Doklady Akad. Nauk. Uzbek, SSR*, **8**, 17 (1956).

4. I. A. Bagotskaya, *Doklady Akad. Nauk. SSR*, **110**, 397 (1960).
5. T. G. Owe Berg, *Corrosion*, **14**, 562 (1958).
6. M. W. Burkart, U.S.A.E.C. Rept. Westinghouse Electric Corp., W.A.P.D. 127 (1956).
7. J. E. Draley and W. F. Ruther, *This Journal*, **104**, 329 (1957).
8. J. S. Ll. Leach and A. Y. Nehru, "Corrosion of Reactor Materials," Vol. I, p. 58, I.A.E.A. Vienna (1962).
9. W. Raczynski and S. Stelmach, *Bull. Acad. Polon. Sci. Ser. Sci. Chem.*, **9**, 633 (1961).
10. R. Barrer, "Diffusion in and through Solids," p. 201, University Press (1941).
11. M. Stern, *This Journal*, **102**, 609 (1955).
12. P. Delahay, *J. Am. Chem. Soc.*, **74**, 3497 (1952).
13. G. Borelius, *Ann. Phys.*, **83**, 121 (1927).
14. L. D. McGraw, W. E. Ditmars, C. A. Snavely, and C. L. Faust, Rept. Battelle Memorial Institute B.M.I. N.A.C.A. 3164 (1954).

Effect of NH_3 on Deposition from Alkaline Electroless Nickel and Cobalt Plating Baths

G. S. Alberts, R. H. Wright, and C. C. Parker

Systems Development Division, International Business Machines Corporation, Poughkeepsie, New York

ABSTRACT

The ammonia generally used as a buffer in alkaline electroless nickel and cobalt plating baths has been shown to have a significant effect on both the rate of deposition of thin metal films and the magnetic and physical properties of such films. These effects have been studied on both metallic and nonmetallic substrates, using both ammonia and nonammine buffer systems, and attempts have been made to correlate them with spectral and polarographic observations.

Generally, ammonia is used as the buffer (1, 2) in alkaline electroless nickel and cobalt plating. However, from a control and reproducibility standpoint, the use of ammonia has several disadvantages. Among these are its volatility and, especially in the cobalt system, the formation of very stable cobalt(III) compounds, at least at room temperature. Furthermore, the effect of ammonia on the plating rate of alkaline cobalt and nickel electroless baths has not been defined clearly in the literature, and some disagreement exists. For instance, Brenner (3) states that "Ammonium salts increase the rate of deposition of nickel from the alkaline baths," but that "In the cobalt solution ammonium salts decrease the rate of deposition to a considerable extent . . ." (4). However, various Russian authors (5, 6) state that in alkaline cobalt solutions the rate increases slightly between 0 and 75 g/l NH_4Cl and then decreases rapidly, while in alkaline nickel solutions the rate increases between 0 and 50 g/l NH_4Cl and is level thereafter.

For the purpose of control and reproducibility the use of a different buffer system, sodium tetraborate, was investigated. In so doing, it was observed that there were some startling changes in the rate and deposit characteristics which appeared inconsistent with previous observations. This resulted in a more careful study of the effect of ammonia on the plating rate of baths of certain compositions and in the collection of spectral and polarographic data to try to explain these results.

The experiment.—Plating samples for all of the work to be reported were prepared on polyethylene terephthalate or copper substrates. The polyethylene terephthalate was prepared for plating by treatment in the normal caustic etch, tin presensitization, palladium sensitization sequence described by numerous authors (7, 8) to produce the initial catalytic surface. The copper substrate was simply cleaned in potassium dichromate-sulfuric acid solution and then treated in the palladium solution. All of the data to be presented on rate, magnetics, etc., are the average or range obtained from at least six samples plated for at least three different times, normally with a thickness of deposit between 300 and 10,000Å. When ammonia was present in the plating baths, the samples were plated from a semiclosed system, open to the atmosphere only through a reflux condenser. Ammonia analyses were run before and after the plates were made. In general, the total ammonia in the bath varied less than 3% over a 2-hr period. The metal and phosphorous content of the deposited films were measured by x-ray emission spectroscopy. A vibrating sample magnetometer was used to measure the magnetic characteristics of the films.

Table I. Effect of ammonia on the rate of electroless deposition of cobalt on polyethylene terephthalate

Bath: 35 g/l $CoSO_4 \cdot 7H_2O$ (0.12*M*); 35 g/l $Na_3C_6H_5O_7 \cdot 2H_2O$ (0.12*M*); 20 g/l $NaH_2PO_2 \cdot H_2O$ (0.19*M*); X g/l $(NH_4)_2SO_4$; *p*H adjusted with NaOH

g/l $(NH_4)_2SO_4$	Average plating rate, μg cobalt/cm²/min *p*H 8.0	*p*H 8.5	*p*H 9	Temp, °F
100	150	157	162	180
50	123	107	105	180
25	67	58	23	160
	(135)	(116)	(46)	
0	29	32	25	180

Results and Discussion

Table I shows some of the results of the electroless deposition of cobalt on polyethylene terephthalate, both as a function of *p*H and ammonia concentration. The composition of the bath is similar to baths reported in the literature (1-6). The plating rate is calculated by taking the amount of metal plated per unit area and dividing this by the plating time. The rate is reported as micrograms of metal deposited per square centimeter per minute. The data at 25 g/l $(NH_4)_2SO_4$ were taken at a different temperature, 160°F, because bath stability appeared to be an overriding problem at this concentration, even worse here apparently than at 0 g/l $(NH_4)_2SO_4$. The numbers in parentheses shown at this ammonia concentration are calculated to give a rough approximation of the rate at 180°F, assuming a doubling of rate for a 20° temperature change.

The important fact to be obtained from Table I is the relatively large increase in rate as the ammonia concentration is increased, even up to 100 g/l $(NH_4)_2SO_4$. It should also be pointed out that for the points on this matrix that were checked using copper

Table II. Effect of ammonia on the rate of electroless deposition of nickel on polyethylene terephthalate

Bath: 33 g/l $NiSO_4 \cdot 6H_2O$ (0.12*M*); 35 g/l $Na_3C_6H_5O_7 \cdot 2H_2O$ (0.12*M*); 20 g/l $NaH_2PO_2 \cdot H_2O$ (0.19*M*); X g/l $(NH_4)_2SO_4$; pH adjusted with NaOH, 160°F

g/l $(NH_4)_2SO_4$	Average plating rate, μg nickel/cm²/min pH 8.0	pH 8.5	pH 9
100	237	250	286
50	268	340	305
25	272	279	202
0	225	224	182

as the substrate the rates were almost identical to that on the plastic substrate. For example, at *p*H 9.0 and 100 g/l $(NH_4)_2SO_4$, the rate was 170 μg/min on copper as compared to 162 on polyethylene terephthalate. At *p*H 8.0 and 0 g/l $(NH_4)_2SO_4$ it was 33 compared to 29.

Table II shows the results of nickel plated from an electroless bath of the same composition as that used for the cobalt except that for this study, the temperature was kept at 160°F. In spite of this lower temperature, the rate is consistently higher than with cobalt and does not show any drastic change with ammonia concentration. It is possible that, if infinite accuracy is assigned to the data presented, one could see a change in rate with ammonia and might even predict maximum rates at different *p*H values as a function of ammonia concentration. However, the important point is that certainly the ammonia does not affect the rate of nickel plating as much as it did the cobalt.

Using copper substrates for the nickel deposition, the rate decreased somewhat, being about 2/3 of that observed with polyethylene terephthalate substrates.

Table III shows the range of coercivities obtained on the samples used to measure the plating rates of the electroless cobalt and nickel baths. As might be expected, the coercivities at a given bath composition are not constant, but appear to vary with the per cent phosphorus and/or thickness of the films. No real correlation with either of these variables could be made, however, from the data taken.

For all the cobalt samples, the amount of phosphorus was in the range 1-6%, even with those samples which show very low coercivities. In general, especially at *p*H 8.5 and 9.0, the coercivities of the films tend toward lower values as the ammonia concentration is decreased through 25 g/l $(NH_4)_2SO_4$. However, at 0 g/l $(NH_4)_2SO_4$ the coercivities are again as high as at 100 g/l. This is an unexplained and unexpected result which warrants further investigation.

For the alkaline electroless nickel samples, the coercivities at all of the ammonia concentrations except 0 g/l are in the range of 10-80 oe, and the per cent phosphorus in the films varies between 3 and 6%. However, as seen from Table III, at 0 g/l $(NH_4)_2SO_4$ the coercivity dropped to zero and, as might be expected from the low magnetics (9), the per cent phosphorus increased to between 10 and 17%.

Table III. Range of H_c observed on samples used in the plating rate studies (Tables I and II)

g/l $(NH_4)_2SO_4$	pH 8.0	pH 8.5	pH 9.0	Temp, °F
	E/L cobalt on polyethylene terephthalate			
100	300-900	400-800	400-700	180
50	450-1100	400-600	50-200	180
25	300-1000	50-70	30-50	160
0	400-1100	500-800	500-1000	180
	E/L nickel on polyethylene terephthalate			
100	10-20	30-80	30-50	160
50	10-20	30-70	40-60	160
25	10-20	10-40	50-80	160
0	0	0	0	160

Table IV. Plating rate and coercivity range of borate-buffered electroless cobalt bath

Bath: 10 g/l $CoSO_4 \cdot 7H_2O$; 150 g/l $Na_3C_6H_5O_7 \cdot 2H_2O$; 10 g/l $NaH_2PO_2 \cdot H_2O$; 150 g/l $Na_2B_4O_7 \cdot 10H_2O$; *p*H adjusted with H_2SO_4, 180°F

pH 8.7 Rate	pH 8.7 H_c	pH 9.2 Rate	pH 9.2 H_c
2	70-180	2	60-150

Another interesting point observed from the magnetics measurements, especially with the cobalt samples, was that the range of coercivities obtained from a given bath using the copper substrate was much smaller than observed with the polyethylene terephthalate substrate, even though approximately the same variations in thickness, per cent phosphorus, etc., existed on both substrates. For example, at 100 g/l $(NH_4)_2SO_4$ and *p*H 8.0, where a range of 300-900 oe was observed on polyethylene terephthalate, a range of only 500-550 oe was observed on copper.

As mentioned previously, attempts were made to use a buffer system other than ammonia for the alkaline electroless nickel or cobalt plating. However, it was found that one could not simply replace the $(NH_4)_2SO_4$ with sodium tetraborate and obtain a stable bath. Several adjustments had to be made in the bath to make it useful. For example, metal ion solubility in the presence of borate appeared to be a problem, and the concentration of citrate had to be increased. However, a bath buffered with borate and with some of the other parameters adjusted can be used for electroless deposition.

Table IV shows the composition of the borate-buffered cobalt bath used in this investigation and some of the results obtained. Again, the rates are in micrograms of metal per square centimeter per minute. From the data in Table IV one can see that the rate of deposition from the borate baths is considerably less than even that for the 0 g/l $(NH_4)_2SO_4$ baths. Although some of this difference may be ascribed to the different bath composition (owing to different amounts of citrate, cobalt, hypophosphite, etc.), some of it probably is also due to the different buffer system. It is also noticeable that the magnetics from the borate-buffered cobalt bath are relatively low.

However, a more interesting result was obtained when the per cent phosphorus was measured on some of these samples. For samples prepared at *p*H 8.7 in the borate-buffered cobalt bath, the amount of phosphorus varied around a rather normal 4%. In the bath at *p*H 9.2, the amount of phosphorus varied up to an astonishing and almost unbelievable 60 w/o (weight per cent). Results on some of these films are suspect because of the thinness of the films and associated analysis problems, but quite definitely the films from some of these borate-buffered baths have exceedingly high phosphorus contents.

Table V shows the results obtained in the electroless nickel deposition from borate-buffered baths. The bath composition is the same as that used for cobalt. Once again, the plating rate for the borate-buffered bath is considerably less than that observed in even the 0 g/l $(NH_4)_2SO_4$ bath. Furthermore, the films are paramagnetic, and the amount of phosphorus was in the range of 15-18%. The magnetics and per

Table V. Plating rate and coercivity range of borate-buffered nickel bath

Bath: 9.3 g/l $NiSO_4 \cdot 6H_2O$; 150 g/l $Na_3C_6H_5O_7 \cdot 2H_2O$; 10 g/l $NaH_2PO_2 \cdot H_2O$; 150 g/l $Na_2B_4O_7 \cdot 10H_2O$; *p*H adjusted with H_2SO_4, 180°F

pH 8.7 Rate	pH 8.7 H_c	pH 9.2 Rate	pH 9.2 H_c
42	0	45	0

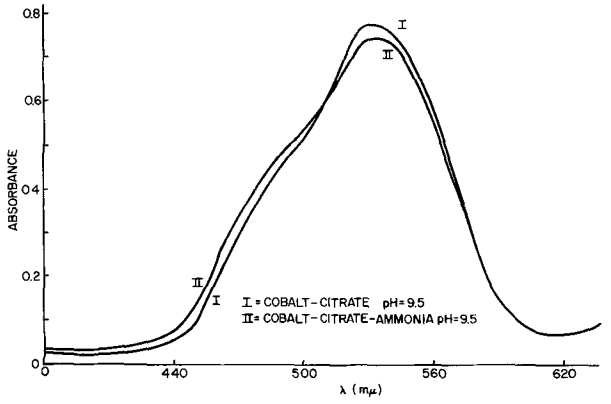

Fig. 1. Visible spectra of the cobalt-citrate and cobalt-citrate-ammonia (air-free) systems.

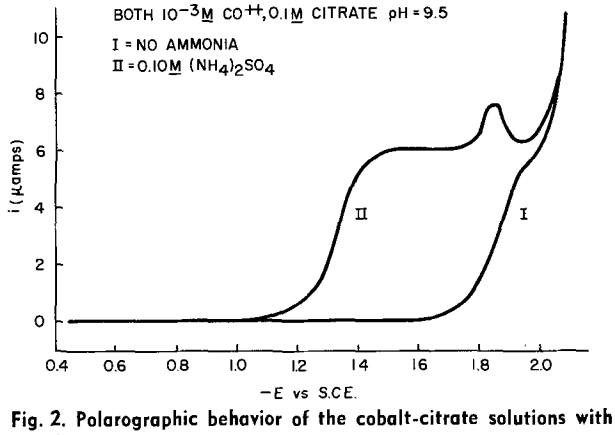

Fig. 2. Polarographic behavior of the cobalt-citrate solutions with and without ammonia present.

cent of phosphorus are similar to those in the 0 g/l $(NH_4)_2SO_4$ bath.

A further experiment with some of the borate-buffered cobalt baths involved adding $(NH_4)_2SO_4$ to them and again checking their rate and magnetics. It was found that even with relatively small amounts of added ammonia, 10 g/l or less, the rate of deposition increased markedly, and the magnetics went up to the range observed in ammine-buffered baths.

From the data presented, one can see that the effect of ammonia in the electroless deposition of cobalt is somewhat different from that in nickel deposition. The data indicate that ammonia increases the rate of cobalt deposition with a somewhat inconsistent effect on the magnetic characteristics of the film. On the other hand, ammonia does not affect the rate of nickel deposition as greatly and only affects the magnetics by its absence; that is to say, one observes paramagnetic films with no ammonia. In order to try to explain some of these results, spectral and polarographic studies of these baths were undertaken.

Based on the effect of ammonia on the cobalt rate, one might expect to see a large interaction of ammonia with the cobalt-citrate complexes using spectral measurements. However, such is not the case, as shown in Fig. 1.

Curve I in Fig. 1 shows the visible spectra of cobalt-citrate, and curve II is that of cobalt-citrate-ammonia. Of course, the samples with ammonia present were run under air-free conditions in order to prevent the formation of Co(III). Figure 1 shows that the spectra with and without ammonia are quite similar and no great spectral changes can be ascribed to ammonia in the visible region. This result is somewhat discouraging if one is to try to study the effect of ammonia on the electroless plating rate. However, on further consideration, this lack of spectral change due to ammonia can be rationalized by the fact that a small interaction of ammonia with a cobalt-citrate complex, such as occupying one or two of the cobalt coordination positions with NH_3 groups, might not affect the spectra greatly. This is made even more plausible when one realizes that the Co(II) ammonia complex has about the same extinction coefficient as the cobalt-citrate, and absorbs in the same region, having its absorption maximum at about 490 mμ.

Predicting from the apparent small effect of ammonia on the plating rate of the alkaline electroless nickel solutions, one might also expect to see little, if any, effect on the spectra of the nickel solutions. However, this is not the case; large shifts in the spectra can be observed even with the naked eye. With no ammonia in the solution, the nickel-citrate is a bright green. When ammonia is added, however, the solution changes to the typical deep blue nickel-ammonia color.

Thus, the spectral effects of ammonia on the cobalt and nickel solutions appear to be the opposite of the effects observed on the plating rates. That is, little spectral variation due to ammonia is observed for cobalt, while a large rate change is observed. On the other hand, a large spectral effect is observed with nickel, which does not show a large rate change. For this reason, another technique, polarography, was used to look at the systems involved.

The qualitative polarographic behavior of the electroless cobalt bath under different conditions is shown in Fig. 2. Curve I is typical of the behavior without ammonia present, and it can be seen that the normal cobalt wave expected around —1v has shifted cathodically until it can just be seen before the hydrogen wave. In fact, under some conditions, this wave shifts beyond hydrogen reduction and can no longer be seen. However, when ammonia is added to these solutions, the cobalt wave is again observed at about —1.3v as shown by curve II. Furthermore, at very low ammonia concentrations, the height of this wave is a function of time after the ammonia addition. Here, at last, would appear to be an independent measurement of the effect of ammonia on the electroless cobalt plating rate if it were not for the following observations.

Figure 3 shows the qualitative polarographic behavior of the nickel system. Again, one observes that without ammonia present (curve 1) the wave has shifted beyond the hydrogen reduction wave. However, when ammonia is added to the system (curve II) one observes the same sort of shift as is seen in the cobalt system. That is, the ammonia appears to affect the nickel wave in the same manner it did the cobalt wave, and it is apparent that the simple polaro-

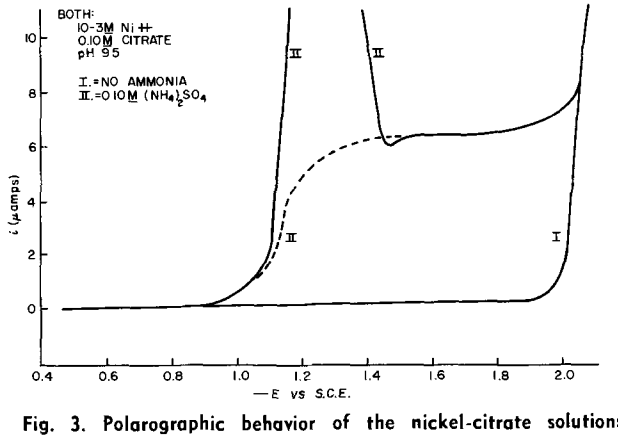

Fig. 3. Polarographic behavior of the nickel-citrate solutions with and without ammonia present.

graphic behavior cannot be used to explain the difference in plating rate of the two solutions.

Conclusions

In summary, several facts appear evident for the bath compositions and conditions used for these studies.

1. Ammonia increases the rate of alkaline electroless cobalt deposition.
2. Ammonia has little effect on the rate of alkaline electroless nickel deposition.
3. Relatively hard magnetic films are produced in alkaline electroless cobalt deposition and ammonia does not seem to be the primary variable influencing these magnetics.
4. In alkaline electroless nickel deposition, the absence of ammonia produces paramagnetic films and the presence of ammonia gives a soft magnetic material.
5. Spectral observations cannot be used at this time to explain the different effects of ammonia on alkaline electroless cobalt and nickel deposition.
6. The polarographic behavior of the cobalt and nickel systems is similar and to date has offered no evidence to explain the rate and magnetic differences observed.
7. New or modified techniques will have to be used to study the rate and magnetic variations caused by ammonia and to improve the understanding of the deposition processes.

Acknowledgment

The authors are indebted to Mr. A. Arcus and Miss B. J. Kriscka for the composition measurements of the films, and to Mr. A. Grady for the magnetics measurements.

Manuscript received Jan. 12, 1966; revised manuscript received March 24, 1966. This paper was presented at the Buffalo Meeting, Oct. 10-14, 1965.

Any discussion of this paper will appear in a Discussion Section to be published in the June 1967 JOURNAL.

REFERENCES

1. S. Wein, *The Glass Industry*, **40**, 532 (1959).
2. E. B. Saubestre, *Metal Finishing*, **60**, 49 (July 1962).
3. A. Brenner, *ibid.*, **52**, 61 (December 1954).
4. A. Brenner and G. Riddell, *Plating*, **34**, 156 (1957).
5. A. I. Lipon and E. V. Masyutin, *Zh. Prikl. Khim.*, **37**, 1188 (1964).
6. K. M. Gorbunova and A. A. Nikiforova, "Physicochemical Principles of Nickel Plating," Academy of Sciences of the USSR, 1960 (from the Office of Technical Services, U. S. Dept. of Commerce, Washington, D. C., publication #OTS 63-11003).
7. E. A. Bergstrom, U. S. Pat. No. 2,702,253.
8. H. Koretzky and B. Leland, U.S. Pat. No. 3,132,582.
9. E. B. Saubestre, *Metal Finishing*, **60**, 45 (August 1962).

Ohmic Electrical Contacts to High-Resistivity ZnS Crystals

George H. Blount, Mark W. Fisher, Robert G. Morrison, and Richard H. Bube

Department of Materials Science, Stanford University, Stanford, California

ABSTRACT

Ohmic electrical contacts to high-resistivity ZnS single crystals can be made by annealing crystals at 400°-475°C with In-Ga contacts in an inert atmosphere. Optimum contacts are obtained by annealing first at about 475°C and then at 400°C. The following four stages are indicated in contact formation through annealing at progressively higher temperatures: (*i*) poor quality contact determined primarily by the properties of an impurity transition layer on the surface, insensitive to temperature to 300°C; (*ii*) a deterioration in contact quality as this impurity layer is penetrated by the electrode metal and before diffusion of the metal into ZnS; (*iii*) a rapid improvement in the contact properties with increasing temperature as electrode metal diffuses into existing zinc vacancies in the crystal, terminated by an independence of electrode quality on increasing temperature when all zinc vacancies are occupied near the metal-semiconductor interface; and (*iv*) deterioration in contact quality as more vacancies are thermally formed and the electrode metal diffuses extensively into the crystal.

An ohmic contact is one that is able to provide a reservoir of carriers in an insulator or semiconductor sufficient to supply carriers as needed to maintain charge neutrality. In seeking to provide ohmic contacts for II-VI materials in general, the following three guidelines have been helpful. (*i*) Choose a metal for the contact electrode that has a smaller work function than the electron affinity of the semiconductor. If there are no surface layer or surface state effects of importance, then this criterion should be both necessary and sufficient for an ohmic contact. (*ii*) Within the requirements of the first guideline, choose a metal that, if diffused into the semiconductor, will provide majority carriers, *i.e.*, as an impurity in the semiconductor, the metal should be a donor if the conductivity is n-type, or an acceptor if it is p-type. (*iii*) Use some method of heating the contact-semiconductor interface to allow the metal to diffuse into the semiconductor.

In the case of CdS, satisfactory ohmic contacts can be produced following these guidelines, using In or Ga as the contact metal (1), and with only moderate heat-treatment, usually no more than that required to melt the metal in forming the contact. Mead (2) has shown that metal-semiconductor barriers for nonohmic contact vary with the work function of the metal on CdS, thus indicating that the work function criterion is meaningful. In addition it is a simple matter to produce high-conductivity CdS by diffusion of In or Ga, both of which are donors in n-type CdS. The work of Kröger *et al.* (3) has shown that diffusion of donor impurity from the electrode metal can play an important role in achieving ohmic contacts to n-type crystals.

Ohmic contacts to ZnS crystals, on the other hand, have been more difficult to obtain. ZnS has at least two distinctive properties that make ohmic contact formation difficult. First, it has a low electron affinity, about 1 ev less than that of CdS (4). Second, unless special precautions are taken, self-compensation of donor and acceptor imperfections is thermodynamically favored (5) so that high-conductivity ZnS is not easily prepared by simple impurity diffusion. The first property of ZnS suggests that metals like In and Ga with sufficiently low work function to provide ohmic contacts on CdS may not meet the requirement that the work function be less than the electron affinity in ZnS. The use of these metals, then, re-

quires that their diffusion into ZnS be the dominant factor in determining the nature of the contact, and the second property of ZnS indicates that self-compensation phenomena will act to prevent the easy formation of a region of graded conductivity.

Recently, Aven and Mead (4) have succeeded in making good, but not quite ohmic, contacts to highly conducting ZnS crystals. In general, the more insulating the crystal the more difficult is the forming of ohmic contacts, in spite of the fact that the density of carriers required of the contact is lower for insulating than for conducting crystals. Williams (6) has described a method for making useful transparent electrical contacts to ZnS crystals using In_2O_3 with Sn impurity.

It is the purpose of this paper to offer an explanation for some of the common problems encountered in making ohmic contacts to high-resistivity ZnS crystals, based on an investigation of contact quality control by annealing in an inert atmosphere. It is found that ohmic contacts can be produced in high-resistivity photosensitive ZnS crystals with proper annealing of the electrode-semiconductor interface.

Experimental

A simple strip-heater furnace with a flat molybdenum ribbon heater element was used for temperature annealing of contacts. Cooling from a higher to a lower kinetically stable temperature could be accomplished in a period of about a second, and the temperature could be maintained for hours to within less than a degree of a specified value. For the study of contact formation, crystals with their contacts were annealed at successively increasing temperatures, with quenching to room temperature and measurement of contact quality after each annealing. For such measurements, the annealing time was held fixed for each treatment at 3 or 4 min.

The contact alloy used was a mixture of In and Ga in the proportions of 50-50% or 25-75%. These mixtures are liquid at room temperature and show good wetting of the ZnS crystal, thus making a mechanical bond between electrode and crystal relatively easy to achieve.

Air was excluded during the annealing, and an atmosphere of dry hydrogen or nitrogen was maintained. No differences were observed between the two atmospheres, indicating that the possible formation of nitrides had no detectable effect. Because of the massive nature of the metal contacts it would be expected that any nitride formation would be restricted to the outer surfaces and would not affect the metal-semiconductor interface.

The crystals of ZnS used were grown by a chemical transport method with HCl as the transport agent. In the dark they had very high resistivity greater than 10^{10} ohm-cm, and they showed considerable photosensitivity.

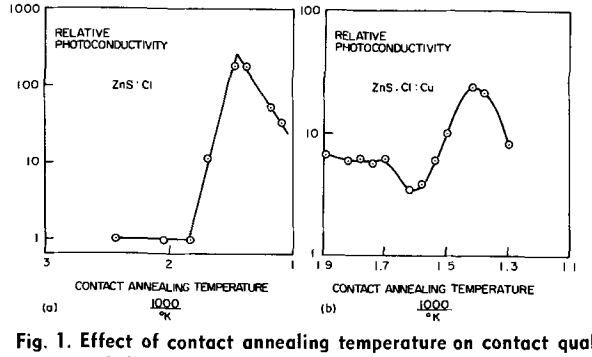

Fig. 1. Effect of contact annealing temperature on contact quality as measured by the room temperature photoconductivity of the crystal and contacts. The photosensitivity of the crystal in (a) is larger than that of the crystal in (b). The relationship between the scales in (a) and (b) is arbitrary.

Contact quality was judged in three ways. (*i*) The potential drop at each contact was measured when current was flowing in the crystal. (*ii*) The current *vs.* voltage characteristic of the crystal and its contacts was measured. (*iii*) The absolute magnitude of the photocurrent passed through the crystal for a fixed light intensity was measured. In every case where all three types of measurements were made, it was found that the lowest potential drops at the electrodes and the most nearly linear current-voltage curves were always accompanied by the highest photocurrents. Because of its simplicity, the magnitude of the photocurrent was therefore frequently used as a measure of the contact quality.[1] Other tests for ohmic contacts, such as the absence of photovoltaic effects and noise instabilities, were made only qualitatively.

Results

Typical dependence of photocurrent, measured at room temperature for fixed excitation intensity, on annealing temperature for two ZnS crystals is given in Fig. 1. The results on many such crystals can be described in terms of four temperature ranges for annealing. (*A*) Contacts applied at room temperature and subjected to no annealing are found to be grossly nonohmic. No improvement in contact quality is obtained by annealing below 300°C. (*B*) Annealing just below the temperature threshold at which contact quality improves generally causes a small decrease in contact quality below that found for no annealing at all. This proved to be the case for every measurement of sufficient detail to reveal the effect. (*C*) Beyond the temperature threshold, contact quality increases as the temperature of annealing is increased, until a maximum is reached. Typically contact quality, as measured quantitatively by the magnitude of the photocurrent, increases exponentially with $1/T$ in this range. (*D*) Annealing at still higher temperatures beyond the maximum results in poorer contact properties. The basic features of the dependence of contact quality on annealing temperature are summarized in Fig. 2.

A potential distribution typical of an unannealed contact is shown in Fig. 3a. 90% of the applied voltage is found across the metal-semiconductor cathode junction. The corresponding variation of current with voltage is shown in Fig. 3b. The potential profile of a crystal subjected to optimum annealing is shown in Fig. 3c. Small inhomogeneities in the crystal are

[1] This is clearly not an absolute measure, since its sensitivity, *i.e.*, the magnitude of the increase in photocurrent accompanying proper annealing, is governed by the photosensitivity of the crystal. The photocurrent obtained with unannealed contacts is determined primarily by the contact resistance. But when the contacts are nearly ohmic, the photocurrent is determined by the crystal resistance, which is a function of its photosensitivity and its geometry. Thus the difference between the photocurrents obtained without annealing and those obtained with proper annealing will vary from crystal to crystal.

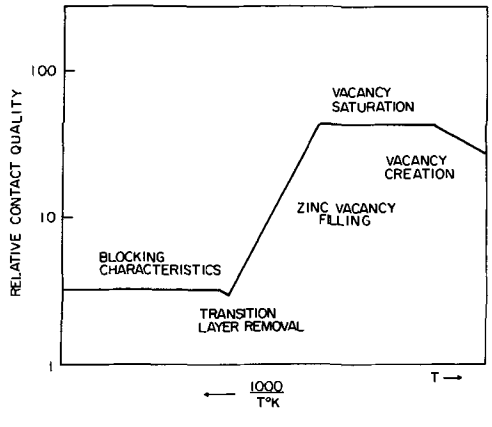

Fig. 2. Summary of the dependence of contact quality on annealing temperature.

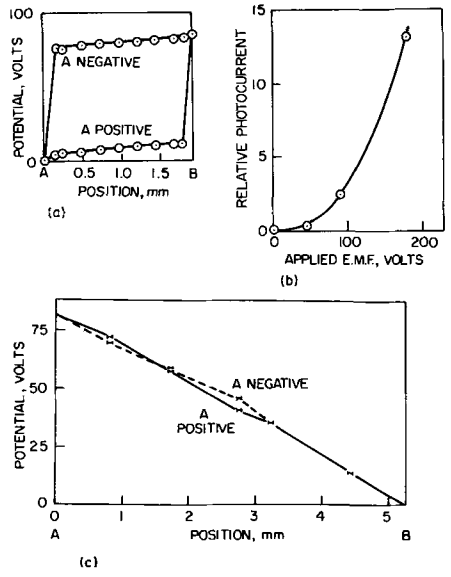

Fig. 3. Comparison of the quality of unannealed contacts, (a) and (b), and properly annealed contacts, (c), on ZnS:Cl:Ag crystals. The data of (a) and (b) are for the same crystal, and the data of (c) are for a similar crystal.

probably responsible for the departures from linearity in the potential profile of this crystal.

A comparison of contact quality for optimum and above optimum annealing is given in Fig. 4. It is evident that the contact quality is degraded by the higher temperature annealing. There is some disagreement here with the report of Alfrey and Cooke (7) that annealing contacts to 600°C was necessary for making ohmic contacts to high-resistivity ZnS crystals.

The dynamics of the annealing effects on contact quality are quite different at temperatures above and below the optimum temperature. For lower temperatures the changes produced by annealing are irreversible, whereas for higher temperatures the changes produced are reversible. At the optimum temperature or above, the properties of the contact are established by the final annealing regardless of the previous history. A convenient operating procedure for obtaining optimum contacts has been to anneal first for a period at about 475°C, followed by annealing at about 400°C.

Measurements of dark conductivity reveal no effect of annealing except for long annealing times at high annealing temperatures. In the dark the resistance of the crystal is much greater than the resistance of even poor contacts, and the quality of the contacts does not introduce significant effects.

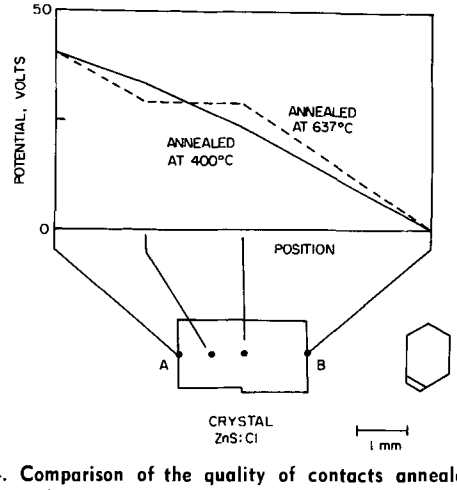

Fig. 4. Comparison of the quality of contacts annealed at optimum and above optimum temperature.

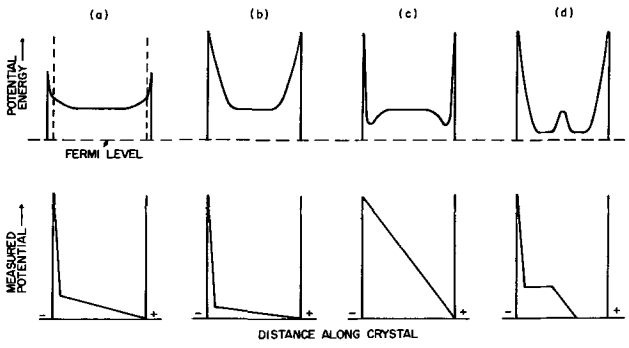

Fig. 5. Contact potential energy diagrams and typical measured potential profiles for the four principal regions found in annealing contacts. (a) Contact to the crystal through a surface layer transition region at low temperatures; (b) penetration of the electrode metal through the surface layer but without diffusion into the crystal, just below the threshold temperature for contact improvement; (c) ohmic contacts obtained by diffusion of metal donors without formation of new zinc vacancies; (d) result of annealing at a temperature above the optimum, showing wider barrier at the contact because of vacancy compensation of diffused metal donors near the surface, with high conductivity region due to uncompensated metal donors which have diffused further into the crystal.

Cooling to liquid nitrogen temperature does not greatly affect the contact quality provided that the contacts have been annealed to provide good ohmic contacts at room temperature. The greater the departure from ohmic behavior at room temperature, the greater is the deterioration of contact quality caused by cooling.

Discussion

The four temperature ranges for annealing effects summarized at the beginning of the previous section and illustrated in Fig. 2 may be correlated with the nature of the electrode-semiconductor barrier and with measured potential profiles along the crystal, as indicated in Fig. 5.

In the low-temperature annealing range, the contacts between metal and semiconductor can be considered as simply the junction of different materials. An explanation for the nonohmic character of this junction can be sought either in the presence of an insulating surface layer on the ZnS that is penetrated only after the temperature is made sufficiently high, or in an intrinsic mismatch of metal work function and ZnS electron affinity that prevents an approach to ohmic behavior unless the crystal becomes highly doped with the electrode material. That the latter condition exists is indicated by the work of Aven and Mead (4). Neither of these possibilities by itself, however, explains the decrease in contact quality just below the threshold temperature for contact improvement.

The observed decrease can be explained in terms of both a mismatch of work functions and a surface layer. If a surface layer exists on the ZnS crystal with a larger electron affinity than ZnS, the junction barrier height between metal and surface layer will be less than between metal and ZnS. The surface layer can therefore provide a transition region between metal and ZnS, giving a slightly better contact than would be obtained by metal-ZnS contact directly. At the threshold temperature, the surface layer is penetrated or removed, and therefore the contact quality deteriorates until the electrode metal can diffuse into the ZnS at higher annealing temperatures. The transition at the threshold is between the situation pictured in Fig. 5a and that in 5b.

The increase in contact quality beyond the threshold temperature can be explained in terms of diffusion of the electrode metal into the ZnS where it acts as a donor impurity, thus increasing the conductivity of the ZnS and creating a bulk transition re-

gion. The situation is pictured in Fig. 5c; the remaining barrier at the surface has been reduced to a sufficiently narrow width to permit tunneling. The importance of tunneling through such a barrier at the surface is probably the reason that it is easier to make ohmic contacts to high-conductivity ZnS than to high-resistivity ZnS crystals.

As long as the annealing temperature is sufficiently low, zinc vacancies present in the crystal are immobile and new zinc vacancies cannot be thermally created. Since the vacancies present are immobile, diffusion of the metal donors will be restricted to a narrow region near the contact interface. The quality of contact formation should not increase with lengthy annealing, and this is found to be the case. Since new zinc vacancies cannot be thermally created, the diffusing metal ions occupy those vacancies already present and compensated by donors in the crystal. The occupation of such zinc vacancies by metal donors frees electrons to increase the conductivity of the transition region. Since new vacancies cannot be formed, the self-compensation tendency in ZnS is inhibited.

The importance of existing zinc vacancies is indicated by the experimental observation that the optimum annealing temperature is a function of the history of the crystal, as well as of the composition of the electrode material. If zinc is added to the contact alloy, the optimum temperature is reduced, but the ohmic character of this contact is not as good as that made with the zinc-free alloy. It is reasonable to propose that the zinc diffuses into the crystal to occupy zinc vacancies, thus decreasing the density of vacancies available for occupancy by metal donors.

Contacts that are annealed above about 480°C are generally not as good as those annealed at a lower temperature. When the temperature exceeds 480°C it is proposed both that vacancies present in the ZnS become mobile and that new vacancies are thermally created. The increased mobility of vacancies present in the crystal makes it possible for uncompensated metal donors to diffuse further into the crystal, thus creating a high-conductivity region well removed from the contact interface. The creation of new vacancies begins at the surface of the crystal. The result is that between the contact interface and the high-conductivity region in the volume of the crystal there is a region where newly created zinc vacancies have compensated diffusing metal donors. The contact is now no longer between the electrode metal and a high-conductivity transition region in the ZnS, but between the electrode metal and a high-resistivity region in the ZnS. The result is the observed deterioration in contact quality as pictured in Fig. 5d.

The experimental observations are in agreement with the proposals just made. Crystals whose contacts are annealed above 480°C show changes in electronic properties in macroscopic regions near, but separate from, the contacts. In such regions the crystals become visibly cloudy, fluorescence becomes green, and electrical conductivity becomes very high. There is still a large potential drop at the contact interface, however, which indicates the inferior nature of these high-temperature annealed electrodes.

Independent confirmation of the probability of zinc vacancy mobility and creation at these temperatures may be obtained from the work of Mandel (5), and of Aven and Halsted (8), who noted that heating ZnSe to about 600°C produces rapid changes in stoichiometry.

Acknowledgment

This work was partially supported by the Army Research Office (Durham), and by the Advanced Research Projects Agency through the Center for Materials Research at Stanford University. Two of the authors (M. W. F. and R. G. M.) were supported by the National Science Foundation.

Manuscript received Jan. 28, 1966, revised manuscript received March 24, 1966.

Any discussion of this paper will appear in a Discussion Section to be published in the June 1967 JOURNAL.

REFERENCES

1. R. W. Smith, *Phys. Rev.*, **97**, 1525 (1955).
2. C. A. Mead, *Appl. Phys. Letters*, **6**, 103 (1965).
3. F. A. Kröger, G. Diemer, and H. A. Klasens, *Phys. Rev.*, **103**, 279 (1956).
4. M. Aven and C. A. Mead, *Appl. Phys. Letters*, **7**, 8 (1965).
5. G. Mandel, F. F. Morehead, and P. R. Wagner, *Phys. Rev.*, **136**, A826 (1964).
6. V. A. Williams, *This Journal*, **113**, 234 (1966).
7. G. F. Alfrey and I. Cooke, *Proc. Phys. Soc.*, **B70**, 1096 (1957)
8. M. Aven and R. E. Halsted, *Phys. Rev.*, **137**, A228 (1965).

Properties of Amorphous Silicon Nitride Films

S. M. Hu

Systems Development Division, East Fishkill Facility, International Business Machines Corporation, Hopewell Junction, New York

ABSTRACT

This paper describes insulating films of silicon nitride as deposited on silicon substrates by pyrolytic reaction and reactive sputtering. The following physical properties were investigated: amorphism, surface electron micrography, Si-N atomic distance, infrared adsorption spectrum, index of refraction, dielectric constant, electrical resistivity, ionic conductivity and polarization, breakdown voltage, MIS CV characteristics and silicon surface charge, and related phenomena.

Surface films of silicon dioxide have been a convenient and excellent material for passivating silicon electronic devices. Nevertheless, there is room for improvement, such as increased resistance to impurity diffusion, *e.g.*, sodium ions, and more inertness to electrode reaction. Materials such as silicon nitride therefore deserve some attention as a substitute for silicon dioxide under certain specific or stringent conditions. Some physical properties of crystalline silicon nitride have been compiled by Popper and Ruddlesdon (1) and Rabenau (2). There are recent publications concerning silicon nitride films. However, close examination of these published data, as compared to data obtained in this laboratory, indicates that these films reported are really something other than silicon nitride. It appears that the first published successful attempt to prepare films of silicon-nitride is the recent work of Sterling and Swann (3). Silicon nitride films have also been prepared in the laboratories of Doo (4), Pennebaker (5), and the author. This work

summarizes the preliminary results of extensive evaluations of a wide range of physical and electrical properties of silicon nitride films and a discussion of their implications. Emphasis of the silicon nitride studies is made from the point of view of its application to the semiconductor device industry.

The films studied were prepared by the pyrolytic deposition method from a reaction of anhydrous NH_3 and SiH_4 and by r.f. and d-c reactive sputtering of a silicon cathode in pure nitrogen, respectively. Evaluations discussed pertain to films formed on silicon substrates with resistivity of 2-5 ohm-cm, both p- and n-type, although films have also been prepared on quartz and on vitreous silica substrates.

Structure of Films of Silicon Nitride

Amorphism.—In most applications for electrical insulation, surface passivation, and masking, it is generally better to have the film in an amorphous form because of the reduced interfacial strain and greater continuity. There are exceptions as in the case of semiconductor device isolation where an epitaxial growth of another layer of single-crystalline semiconductor on the insulating film is desired. All silicon nitride films studied in this work are essentially amorphous. This is not surprising when one considers the complexity of the crystalline structure of both the α- and the β-silicon nitride, and the relatively low temperatures, 20°-900°C, at which the films were prepared. Attempts have been made in our laboratories to prepare films of silicon nitride at higher temperatures. Direct nitridation of substrate silicon wafers at 1300°-1400° and pyrolytic decomposition at 1100°C invariably yielded crystalline silicon nitride in the form of either small crystals or microcrystallites rather than a continuous film. Besides the reason of relatively high vapor pressure of silicon nitride at these temperatures to facilitate the growth in the third dimension, one has to consider the characteristic difference between the crystal structure of silicon and that of silicon nitride. Assuming the [0001] direction of silicon nitride crystal is parallel to the [111] direction of the substrate silicon, one may note that the lattice parameter of the former, $a = b = 7.75$Å (α-Si_3N_4), is approximately equal to the face-diagonal period [$1\bar{1}0$] of a unit cell of the latter (7.67Å). Unfortunately, although both are axes of threefold symmetry, there are screw axes in the silicon nitride which causes an elevation mismatch of silicon atoms in one-half of the unit cell in the basal plane. The actual atomic positions are also different. Thus, the feasibility of epitaxial growth is doubtful, unless a new phase of crystalline silicon nitride could be formed.

X-ray diffraction patterns were made of the silicon nitride films by first etching a hole in the silicon substrate, leaving the film over the window. X-ray diffraction did not reveal any pattern and exhibits only a uniformly dark exposure, indicating a completely amorphous structure. However, electron diffraction did show patterns of diffused rings, indicating the existence of extremely short range order, Fig. 1. The electron beam wavelength was 0.0385Å. The outer ring corresponds to a spacing of approximately 1.4-1.5Å. It is considered to be the distance between neighboring silicon and nitrogen atoms. It is interesting to compare this bond length of 1.4-1.5Å with the published values of 1.72-1.75Å (6). If the published structure is correct, the α-silicon nitride should have a density of 7.18 g cm^{-3}. The actual density of α-silicon nitride is 3.44 g cm^{-3}. Of course, one must note the flexibility of an amorphous structure as compared to the rigid structure of a crystalline phase. A high degree of covalent nature is indicated here. The ill-defined inner ring may actually be a mixture of a large variety of spacings, ranging from 2.2 to 4.7Å.

Surface topography of films.—The surface texture of films of silicon nitride varies greatly according to the method and the conditions of preparation. Figures 2-4 show various surface topographies on the electron microscopic scale. The electron micrographs were taken of collodion surface replicas shadowed with a carbon-platinum mixture. The magnification is 54,000X for all pictures.

Figure 2 shows the surface topography of a film formed by the pyrolitic deposition method at 800°C. The surface texture is seen to be featureless down to the limit of resolution of the collodion replica. Although microscopic variation of film thickness over the entire wafer were observed, there was no observable electron microscopic variation. Figure 3 shows the surface texture of a film prepared by r.f. sputtering. Blisterlike spots, about 500Å in diameter, are seen over the entire wafer. This type of surface roughness, however, is not peculiar to sputtered films of silicon nitride. Occasionally, it is observed in other types of sputtered films, such as silicon dioxide, although the degree of roughness varies (18). The origin of these raised spots is not understood, but it is doubtful that they are blisters in the usual sense because of the small size of the spots ($\sim 0.05\mu$) compared to the thickness of the film ($\sim 1.4\mu$). If these were real blisters, there would exist a tremendous amount of vertical slippage of the film, because it is impossible for

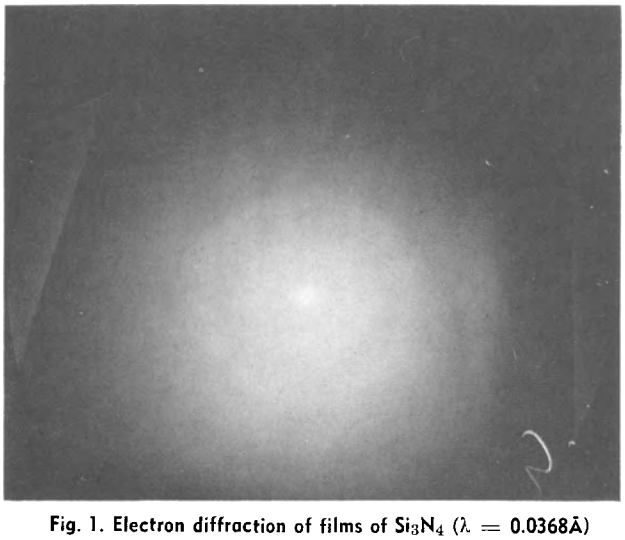

Fig. 1. Electron diffraction of films of Si_3N_4 ($\lambda = 0.0368$Å)

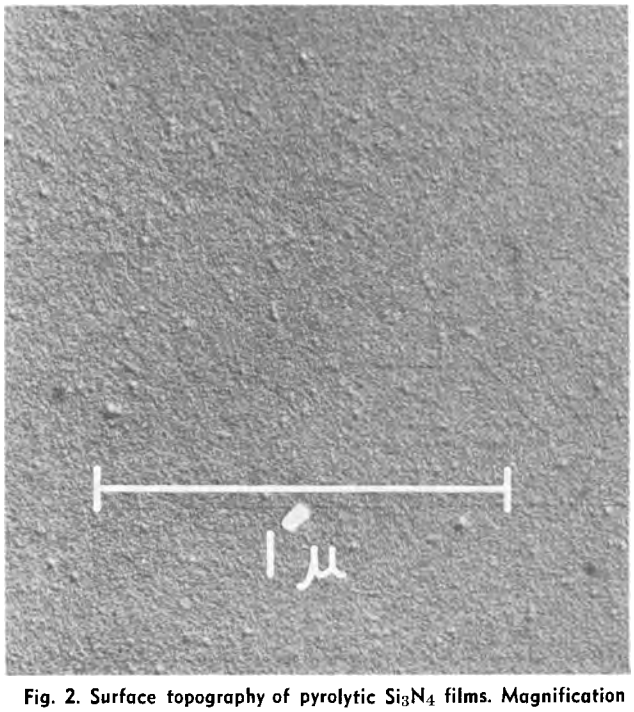

Fig. 2. Surface topography of pyrolytic Si_3N_4 films. Magnification 54,000X.

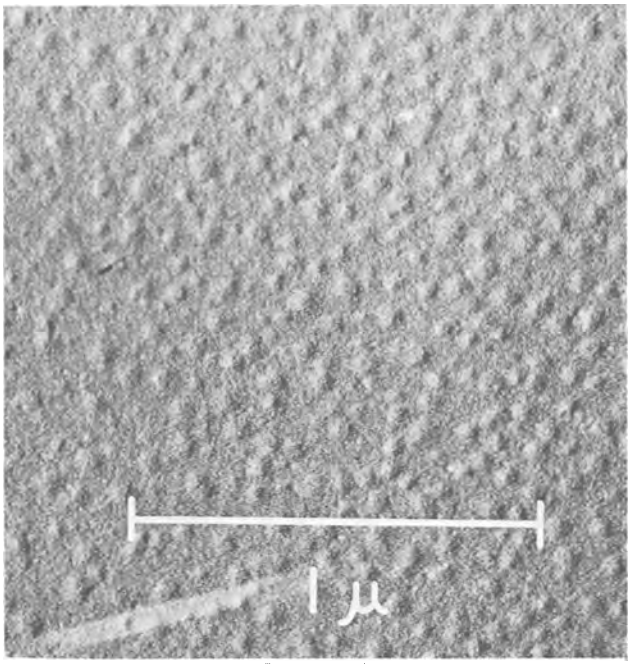

Fig. 3. Surface topography of a sputtered Si_3N_4 film. Magnification 54,000X.

a rigid beam with such a thickness to undergo a deflection of such magnitude of curvature without breaking. Frequently, one also obtains r.f. reactively sputtered films with surface smoothness comparable to pyrolytic films (see Fig. 4). Typical films prepared by means of d-c reactive sputtering are usually rougher. Since films with this type of surface texture were found to be leaky in moderate electric field, it is assumed that submicroscopic cracks exist in these d-c sputtered films. The grain texture became finer and less pronounced as the d-c voltage decreased. Thus, it is thought that high intensity electron and perhaps negative ion bombardment together with the evolution of gases are the causes of this surface roughness. The surface topography of the silicon substrate after the formation of the sputtered film is revealed in an electron micrograph taken after the silicon nitride

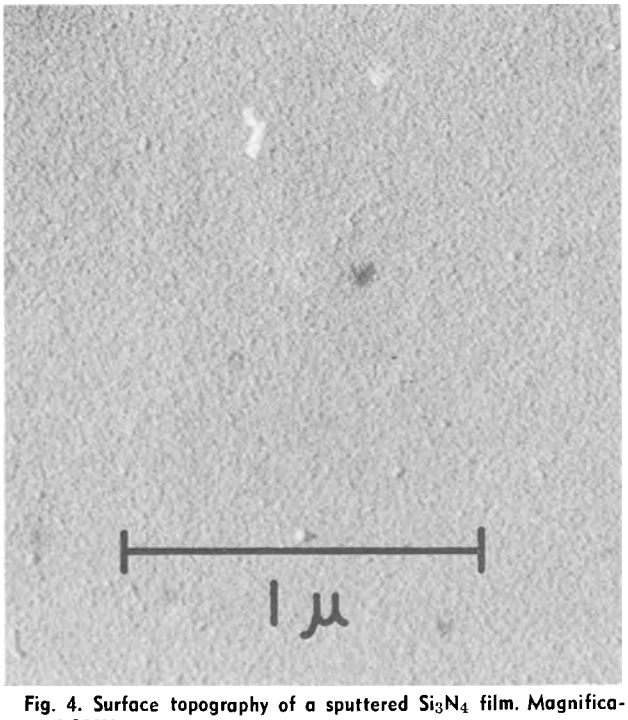

Fig. 4. Surface topography of a sputtered Si_3N_4 film. Magnification 50,000X.

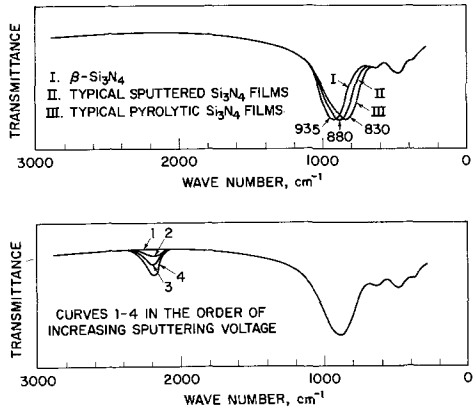

Fig. 5. 5a (top) and b (bottom). Infrared spectra of various films of silicon nitride.

film has just been removed by dissolution in hydrofluoric acid. The silicon substrate surface underneath the nitride film appeared to be smooth down to the resolution of collodion replica. Electron bombardment was minimized by confining the plasma in a magnetic field and placing the substrate outside the plasma confinement. Relatively pin-hole-free films were obtained this way. It is not certain whether an appreciable concentration of negative ions could exist in the plasma because of the small probability of electron attachment. It was found that the deposition rate was an order of magnitude greater when the substrate was outside than when it was inside the plasma.

Infrared spectra of films of silicon nitride.—Infrared spectra were taken for all samples prepared. For the purpose of comparison, an infrared spectrum of β-Si_3N_4 is included here. This spectrum was taken with potassium bromide disk method by Pliskin (7). Finely divided β-silicon nitride powder was dispersed in the KBr disk. The absorption peak occurs at 10.7μ in the KBr disk sample. This is identified as the Si-N stretching band, see curve I in Fig. 5a. Amorphous films of silicon nitride deposited on silicon by both methods mentioned show a considerable amount of shift toward longer wavelength of the Si-N stretching band. This is expected because of the looser structure of the amorphous film. Pliskin has observed similar phenomenon in the case of films of silicon dioxide (8). Curve III of Fig. 5a is a typical spectrum for a film prepared by the pyrolytic process. The Si-N stretching band has been shifted to a wave length of 12.0μ, and has been considerably broadened. The broadening is not unexpected because of the distribution of the interatomic distances. This is consistent with the decrease of the density and of the index of refraction. A typical reactively sputtered silicon film has an I.R. spectrum as shown in curve II of Fig. 5a.

The Si-N stretching band is seen to be shifted to ~11.3μ, an intermediate position between the crystalline phase and pyrolytic films. Curves 1-4 in Fig. 5b are arbitrarily selected infrared spectra taken of films prepared by d-c reactive sputtering. In addition, under certain conditions there exists an absorption peak at 4.7μ, which is absent in films of crystalline phase as well as films from the pyrolytic process. The peak at 4.7μ is seen to increase with the d-c voltage in the sputtering process and may become very pronounced when the d-c voltage is 3-4 kv. It is thought that this peak is probably due to triply bonded Si≡N. This occurs when the sputtering rate is high and the diffusion time is short for the sputtered ions and atoms, causing insufficient chemical reaction with the excited nitrogen and leading to the formation of unsaturated bonds. Thus, a slow rate is preferred for closer stoichiometry to the normal silicon nitride. Oxidation at 1100°C for 30 min in an oxygen stream did not change the characteristics of the infrared spectrum. This may not necessarily indicate the resistance of the Si≡N group toward oxidation, for one

must note that diffusion of oxygen through films of silicon nitride will encounter far greater resistance than the chemical reaction, and becomes the controlling step. Absorption bands corresponding to either Si-O (9.4μ) or N-H (2.9μ) were not observed.

Index of Refraction, Dielectric Constant, and Electric Resistivity of Amorphous Films of Silicon Nitride

The index of refraction of these nitride films were determined both by multiple-beam interferometry and by the Vamfo technique (9, 10). The Vamfo technique is believed to give more accurate results. Both methods, however, agree quite well. At $\lambda = 5460$Å, the index of refraction is 1.98-2.05, with small variations from film to film. The value 2.05 is for reactively sputtered films. Published value for α-Si_3N_4 is 2.1. The dielectric constant was measured using an MIS (Metal-Insulator-Semiconductor) varactor structure. The details of the structure and its measurement are described below. When the nitride films are formed on n-type silicon substrate, the dielectric constant can be measured directly. When the films are formed on p-type substrates, there will be an n-type inversion layer on the surface of the substrate which is removed by applying a small negative bias voltage (a negative bias is defined as one under which the metal electrode is negative with respect to the semiconductor electrode). For reactively sputtered silicon nitride films, the average dielectric constant measured at 10 kc is 6.5; for pyrolytic films, the average value is 6.2. Deviations from these values were observed, but were very small.

The electrical resistivity was determined from an analysis of I-V loop characteristics. Details of this experiment are also described below. Electrical resistivity data for crystalline silicon nitride reported in the literature are quite inconsistent and may differ by several orders of magnitude from each other. This is probably due to impurity incorporation in the materials. A value of 10^{13}-10^{14} ohm-cm as reported by Samsonov and Tsekulya (11) is perhaps closer to the intrinsic resistivity of silicon nitride, although it still may be somewhat low. Amorphous films studied show the resistivity to be too high at room temperature to be measured accurately as reported in the section on ion migration. At 400°C, the film resistivity was $\sim 1 \times 10^{15}$ ohm-cm. At 500°C, the resistivity decreased to 2×10^{13} ohm-cm. It should be noted that the I-V characteristic is nonohmic and depends greatly on the nature and condition of preparation. The breakdown voltage is $\sim 1 \times 10^7$ v cm^{-1}.

Interfacial Properties of Silicon Nitride Films on Silicon Substrates

The effect of a silicon nitride film on surface properties of silicon substrates is of prime significance to semiconductor devices, as the word passivation implies. Since most semiconductor devices are based on a potential barrier configuration, it is important that the potential near the surface not be altered or become unstable due to various surface processes. The surface potential is always altered when there are trapped charges or adsorbed dipoles or pile-up of ions at or near the interface. The surface potential, which is defined as the difference in potential between the surface and the bulk, can be determined in terms of charge removal from the surface to bring about a zero surface potential. An MOS, or more pertinently here MIS, varactor device is convenient for this measurement.

Aluminum of better than 99.999% purity was vacuum deposited on the silicon nitride film at room temperature through a tantalum mask, giving circular disk electrodes 20 mils in diameter and between 2500 to 3000Å in thickness. The C-V (capacitance *vs.* voltage) characteristics were traced out by applying a small a-c signal of 10 kc frequency for capacitance measurement, and a slow triangular wave of 2 v/sec

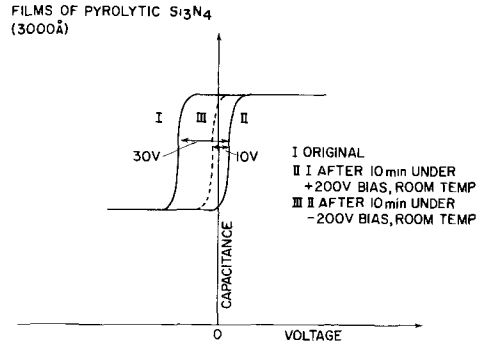

Fig. 6. Room temperature drifting of the surface potential at the Si_3N_4 interface.

for d-c bias. The analysis of the C-V characteristics has been described in the literature (13, 14) for this type of surface varactor. The term surface charge or trapped charge used here refers to the amount of charge (either positive or negative) removed to bring about a zero surface potential. A surface charge density of 1.2-1.4 x 10^{12} cm^{-2} was found for r.f. reactively sputtered films; a more uncertain value was found for d-c reactively sputtered films. Pyrolytic films of silicon nitride seem to have a higher surface charge density (15) of 3-5 x 10^{12} cm^{-2} (see Fig. 6).

The surface charge densities mentioned above were original values for fresh samples. The sign of the charge indicates an n-shift of the silicon surface under the silicon nitride film. The surface n-shift is defined as the increase of potential in the positive direction at the surface with respect to the bulk. Under continued application of a positive bias, the n-shift of the silicon surface continued to decrease, until finally the surface potential became slightly positive. It is interesting to note that the direction in which the surface potential shifted is opposite to that observed in the Si-SiO_2 interfacial system where the n-shift of the surface potential can be explained in terms of ion migration through the SiO_2 film in the applied field resulting in positive ion pile-up at the Si-SiO_2 interface. Thus, the drifting of the surface potential under a silicon nitride film must be explained as something other than ion migration. The drifting occurred at room temperature and appeared to require a threshold field. For pyrolytic silicon nitride films, a threshold field of about 2-4 x 10^6 v cm^{-1} was required (15). It may be noted that this is a rather high field and close to the breakdown field of a typical thermal SiO_2 film.

The surface potential drift at room temperature appeared to be largely irreversible. A continued negative bias caused a small amount of n-shift of the surface potential from that after positive bias. However, the "recovery" was less than one-third the magnitude of the p-shift under positive bias. The term recovery is

Table I. Physical properties of films of silicon nitride

Form	Films	Crystallites
Structure	Amorphous with extremely short range order	β-Si_3N_4
Si-N atomic distance	1.4-1.5Å (elec. diffr.)	
Si-N IR band	11.3μ (sputtered) 12.0μ (pyrolytic)	10.7μ
Index of refraction	2.05	2.1
Dielectric constant	6.5 (sputtered) 6.2 (pyrolytic)	9.4
Breakdown voltage	$\sim 10^7$ v cm^{-1}	
Electric resistivity	$\sim 1 \times 10^{15}$ ohm-cm (400°C) $\sim 2 \times 10^{13}$ ohm-cm (500°C)	10^{13}-10^{14} ohm-cm (?) (room temp.)
Ionic conductivity	Not detectable below 400°C	
Surface charge	1.2-1.4 x 10^{12} cm^{-2} (sputtered) 3-5 x 10^{12} cm^{-2} (pyrolytic)	
Threshold for room temp. drifting	2-4 x 10^6 v cm^{-1}	
Polarization ion concentration	3 x 10^{16} cm^{-3} (500°C)	

rather arbitrary since it is thought that the original surface potential of the fresh sample was not really the equilibrium value. Thus, the positive and negative bias cycle is merely a process of an electric stress annealing. Since, as discussed before, and as is to be elaborated on later, the ion migration process must be ruled out, it is proposed that two processes may occur during the electrical bias, *i.e.*, the reduction of hole traps inside the silicon nitride phase close to the interface via minor structural change or the high field annealing of the surface states at the silicon-silicon nitride interface.

The postulate of hole traps to account for this peculiar phenomenon in silicon nitride film necessitates models that can explain minor structural changes in a high electrical field. One interesting postulate speculated is as follows: normally, three silicon atoms are hinged together with a nitrogen atom. If there is a nitrogen atom vacancy, then the three unpaired electrons might become quite unstable and a three-centered two-electron bond could be formed to bridge the three silicon atoms together directly. The extra electron would then be expelled; in other words, the unit trapped a hole. If this occurred in the vicinity of the Si_3N_4-Si interface, it would cause a surface N-shift. When a sufficiently high electrical field of the order of 2-4 x 10^6 v-cm^{-1} is applied, irreversible polarization takes place through minor structural change, and the three-centered electron pair is shifted to two of the silicon atoms to make a regular bond bridging the two atoms. The remaining silicon atom could now regain an unpaired electron, or it could serve as an electron trap for an extra electron. This would cause the surface to become neutral or negative.

This is only one of the possible mechanisms. There are insufficient data at present for any definite assertion of a particular model.

If the postulated annealing process was fully irreversible, one would expect the surface to be stable under voltage stress at elevated temperatures up to at least 400°-500°C, since the usual cause of an unstable surface of the system Si-SiO_2 is regarded as ion migration and is excluded in this case. It appeared that, after initial room temperature bias treatment, the surface became more stable and drifted only a small amount under later voltage stress treatment at elevated temperatures. This observation is only exploratory, and more extensive investigation of this subject is being carried out (15). Some preliminary

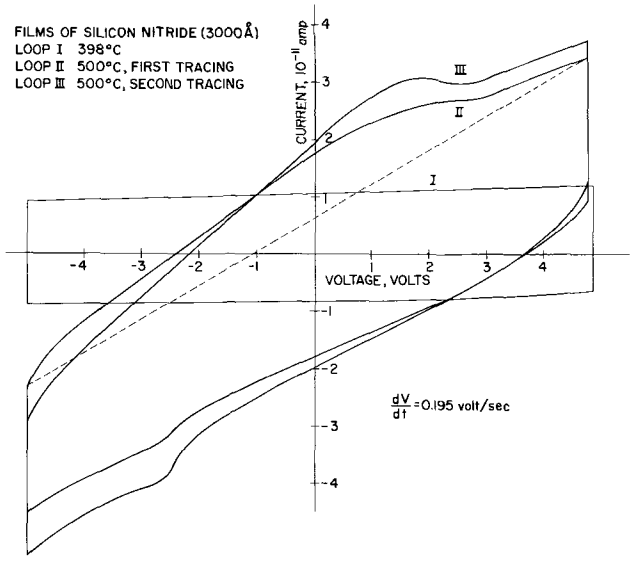

Fig. 7. I-V loop for a pyrolytic silicon nitride film at elevated temperatures.

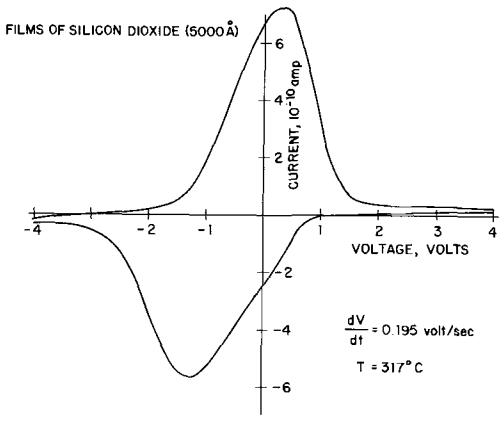

Fig. 8. I-V loop of an ordinary thermal SiO_2 film

results show that under a voltage stress of 1 x 10^6 v cm^{-1} at a temperature of 500°C, a surface p-shift of +10v (for the film thickness of 3000-3600Å) was produced, apparently as a result of further annealing. Compared to the far larger n-shift (opposite direction) at lower temperatures in a slightly lower field usually observed in SiO_2 passivated silicon surface, the results are remarkable.

Ion Migration and Polarization

Since ion migration and related polarization are two important causes affecting surface stability, preliminary experiments have been done on the nitride film. The I-V loop method employed by Yamin (16, 17) for the study of SiO_2 films was used for this investigation. The method consisted of placing an MIS type of device, similar to that used in the surface varactor measurement, in a thermostat chamber, and applying a slow d-c triangular wave at a speed of 0.195 v/sec. The current flux to the electrodes was recorded against voltage. One or more complete loops were traced for each sample at each temperature level; a typical result is shown in Fig. 7.

Loop I is essentially a rectangle, indicating that the MIS structure with silicon nitride film is a simple capacitive element. At a constant rate of voltage change, dv/dt, the electrode current is simply $i = c(dv/dt)$. This loop was traced at 398°C. No detectable amount of ionic polarization was observed. However, precise analysis could separate a conductive element also in the MIS structure, which is the slope of the slight inclination, giving an electrode current of

$$i = \pm 0.195\ C + GV \text{ amp}$$

where C is the capacitance in farad, G the conductance in mho, and V the voltage in volt. At 500°C, ionic migration and polarization became appreciable. This is seen in loop II and III of Fig. 7.

The humps in both the upper part ($dv/dt > 0$) and the lower part ($dv/dt < 0$) of the loop represent the polarization of some unknown species of ions in the film. Each hump consists of a depolarization and polarization of half the complete cycle, and the area bounded by the hump and the dotted line, multiplied by a factor converting voltage to time scale (the voltage used was a linear function of time), gives the total amount of ions polarizable at the temperature. Thus, the polarizable ions at 500°C is about 3 x 10^{16} charges/cm^3. It was also observed that the conductivity of the film seemed to be modified under the voltage stress at the relatively high temperature of 500°C. Sufficient data have not been obtained as to whether there exists any correlation between this conductivity modification and trap reduction.

For comparison, an I-V loop of a typical thermal SiO_2 is shown in Fig. 8. Notice that the current scale has been increased 20 times in this case, and that the temperature is 317°C.

Barrier vs. Diffusion Impurities

A silicon nitride film of 1000Å was shown to block completely diffusion of gallium, oxygen, steam, and phosphorus into the underlying silicon substrate, at a temperature of 1050°C for 40 min. However, quantitative data regarding diffusivity are not available at this time.

Conclusion

From the evaluated characteristics, silicon nitride appears to be an excellent material for semiconductor surface passivation, especially for its resistance to ion migration. Improvements remain to be made in the direction of reducing the surface charge density in the silicon-silicon nitride system.

Acknowledgment

The author wishes to thank L. V. Gregor for his various suggestions and encouragement, D. R. Young who initiated the project, and V. Y. Doo and W. Pennebaker who supplied a number of their samples for comparison with the author's work; he is thankful for the many helpful discussions and experimental assistance received from D. Cameron, D. Kerr, J. Logan, C. Ma, and W. Pliskin; R. Marvel and J. Petrak did a large portion of the experimental work.

Manuscript received Dec. 14, 1965; revised manuscript received March 7, 1966. This paper was presented at the Buffalo Meeting, Oct. 10-14, 1965.

Any discussion of this paper will appear in a Discussion Section to be published in the June 1967 JOURNAL.

REFERENCES

1. P. Popper and S. N. Ruddlesden, *Trans. Brit. Ceram. Soc.*, **60**, 603 (1961).
2. A. Rabenau, *Ber. Dtsch. Keram, Ges.*, **41**, 6 (1963).
3. H. F. Sterling and R. C. G. Swann, *Solid-State Electronics*, **8**, 653 (1965).
4. V. Doo, Paper presented at the Buffalo Meeting of the Society, Oct. 10-14, 1965.
5. W. Pennebaker, Private communication.
6. D. Hardie and K. H. Jack, *Nature*, **180**, 332 (1957).
7. W. Pliskin, Private communication.
8. W. Pliskin and H. Lehman, *This Journal*, **112**, 1013 (1965).
9. W. Pliskin and E. Conrad, *IBM J. Res. & Dev.*, **8**, 43 (1964).
10. W. Pliskin and R. Esch, *J. Appl. Phys.*, **36**, 2011 (1965).
11. G. B. Samsonov and G. G. Tsekulya, *Ukr. Fiz. Zh.*, **5**, 615 (1960).
12. G. B. Samsonov, Proroshkovaya, *Met. Akad. Nauk Ukr. S.S.R.*, **1**, 53 (1961).
13. D. Frankl, Solid-State Electronics, **2**, 71 (1961).
14. R. Lindner, *Bell Syst. Tech. J.*, **41**, 803 (1962).
15. D. Kerr, Private communication.
16. M. Yamin and F. L. Worthing, Paper presented at the Toronto Meeting, May 3-7, 1964.
17. M. Yamin, *IEEE Trans. Electron Devices*, **ED 12**, 88 (1965).
18. P. Davidse, Private communication.

Diffusion of Arsenic in Germanium from a Germanium Arsenide Source

Prediffusion and Diffusion

G. F. Foxhall and L. E. Miller

Bell Telephone Laboratories, Incorporated, Laureldale, Pennsylvania

ABSTRACT

This paper reports on the diffusion of arsenic in germanium from a germanium arsenide source. This versatile source is suitable for prediffusion over a temperature range of 475° to 725°C, and produces sheet resistances varying from 3000 to 0.5 ohms/□. Techniques for diffusion at temperatures up to 900°C have also been developed. Loss of dopant through outdiffusion has been eliminated even for high-resistivity layers. Background resistivity is maintained by rigorous cleaning prior to diffusion and annealing after diffusion. The closed box technique is used in both cases.

This paper presents results of an investigation of diffusion of arsenic in germanium. The closed box technique is used for both prediffusion and diffusion.

A germanium arsenide alloy (1) is used as a diffusant source for prediffusion. This compound has proved to be quite versatile in that it is suitable for use over a temperature range of 475° to 725°C. Layers varying in sheet resistance from 3000 to 0.5 ohms/□ are obtained.

Techniques have been developed for diffusion at temperatures as high as 900°C. Loss of dopant through outdiffusion, even in high-resistivity layers, has been eliminated by the use of a tightly closed diffusion boat. Background resistivity is controlled by rigorous cleaning prior to diffusion and an annealing process after diffusion.

Prediffusion

The diffusion boat assembly, shown in Fig. 1, is of high-purity, optical grade quartz. The mating surfaces between boat and lid are ground flat to effect a tight seal. Three shelves are fitted into the boat to provide space for 18 slices. The source lies in the bottom of the boat.

To minimize thermal conversion effects (2), a rigorous cleaning procedure is followed. Purified hydrogen is used for the diffusion ambient.

The variation of prediffusion sheet resistance with time and temperature is shown in Fig. 2. Control is good as indicated by the 3σ limits shown for the 1-hr runs. These vary from 30% at 500°C to 2% at 725°C. At a given temperature, the sheet resistance varies reasonably in accordance with the inverse square root of time except at the lower temperatures. Also in this low-temperature region, the sheet resistance begins to increase rapidly as temperature is decreased. Several effects combine to cause this divergence from square law dependence. First, the thermal inertia of the diffusion assembly is sufficient to introduce uncertainty into the diffusion times; second, at these low temperatures, temperature dependent surface rate limitation may be expected. Berman, for example, has reported a surface rate limitation on the diffusion of antimony into germanium in this temperature range.

The dependence of junction depth on temperature and time is shown in Fig. 3. These curves exhibit two distinctive slopes, the smaller of which is associated

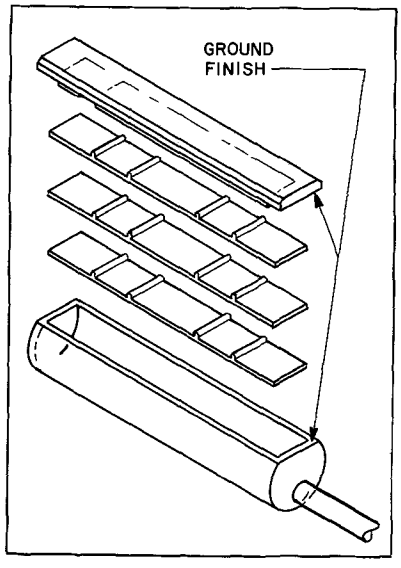

Fig. 1. Diffusion assembly

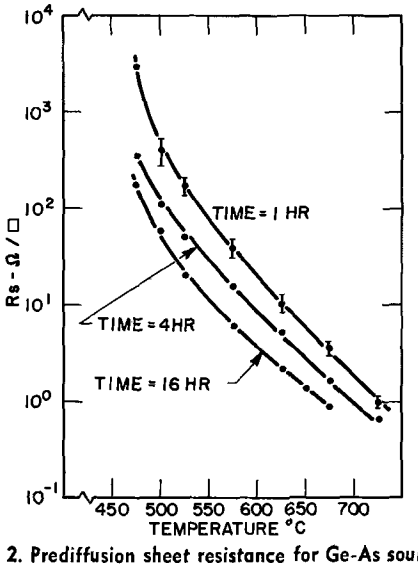

Fig. 2. Prediffusion sheet resistance for Ge-As source

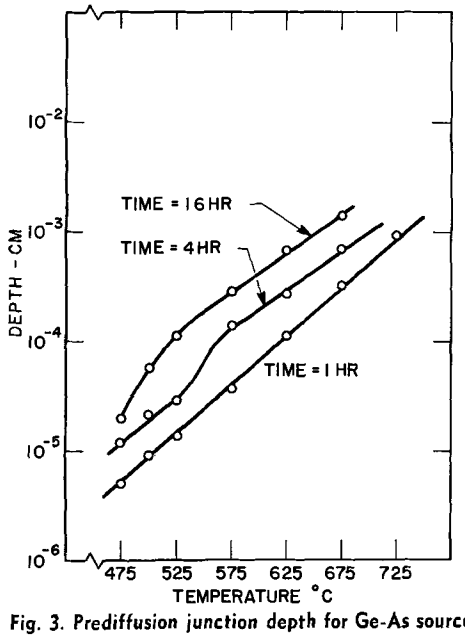

Fig. 3. Prediffusion junction depth for Ge-As source

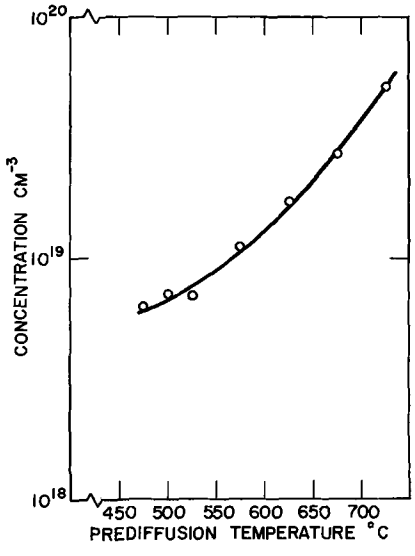

Fig. 4. Dependence of surface concentration on prediffusion temperature for Ge-As source.

with long time and high temperature, and the larger with short time and low temperatures. One notes that in the former region the depth varies nicely with the square root of time, whereas in the latter region it does not. Again one can explain this behavior by thermal inertia and surface rate limitation, which tend to reduce junction depth disproportionately for short times and low temperatures.

Variation of surface carrier concentration with prediffusion temperature is shown in Fig. 4. These values were measured by successively etching and measuring sheet resistance to give a differential conductance and subsequently the effective resistivity of the layer which had been removed. It will be seen later that the actual concentration of arsenic atoms may be considerably in excess of the values shown here.

In connection with this, a typical profile for a prediffused layer is shown in Fig. 5. The distribution is non-Fickian in a manner typical of prediffused layers as has been reported elsewhere (4). The dip in measured concentration adjacent to the surface is common to these prediffused layers over the whole temperature range. This cannot be due to outdiffusion and rather is believed to be due to the formation of a germanium arsenic compound at the surface. The values of surface concentration are taken by extrapolating the profile to the surface as indicated by the dashed line.

Diffusion

Prior to diffusion, the slices are cleaned again. Here the procedure serves to remove a small amount of arsenic which condenses on the surface during the cooling cycle of the prediffusion. Failure to remove this condensate will result in uncontrollably low sheet resistance. At the end of the designated diffusion time, the furnace is reset to progressively lower temperatures without removing the boat from the furnace. This process has been named step annealing.

Success of these diffusions depends on the control of two fundamental factors. The first of these is outdiffusion. For high-resistivity diffused layers, unlimited outdiffusion as in the case of open tube diffusion, for example, would result in an unconverted surface with perhaps a band of n-type in the bulk.

The closely fitted lid traps arsenic which outdiffuses initially in the box. When the surface concentration is high from the prediffused layer, the arsenic outdiffuses until its vapor pressure rises to the point where it is in equilibrium with the concentration of arsenic in the slice. Data by Lee and Speeney (5) indicate that this is on the order of 10^{-6} mm Hg. A simple calculation shows that there is abundant arsenic in the prediffused slice to provide this pressure.

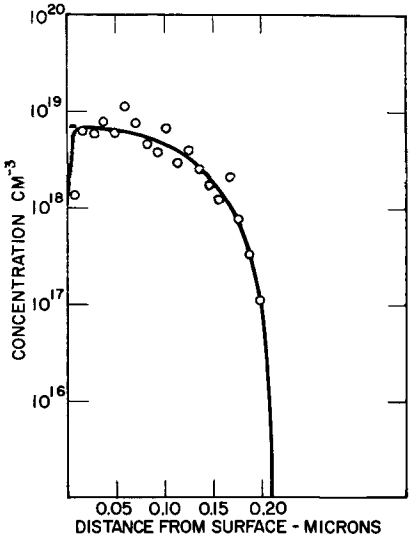

Fig. 5. Impurity profile for prediffused layer 16 hr at 475°C with Ge-As source.

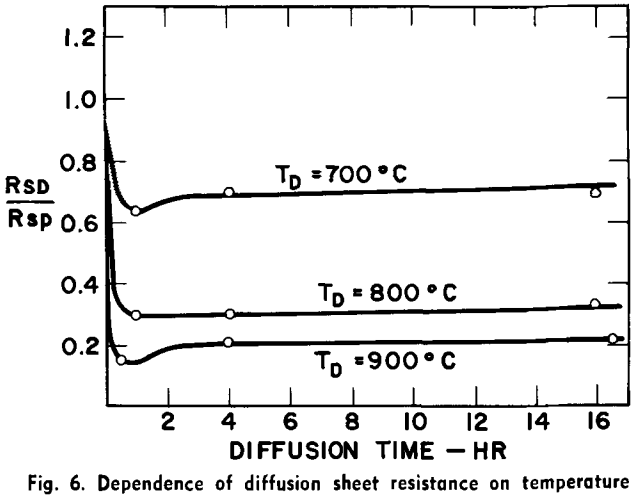

Fig. 6. Dependence of diffusion sheet resistance on temperature and time. R_{SP} = 170 ohms/□.

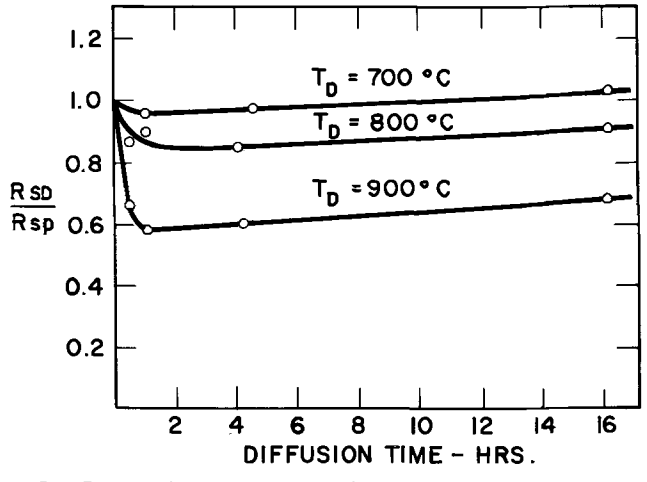

Fig. 7. Dependence of diffusion sheet resistance on temperature and time. R_{SP} = 10 ohms/□.

As the arsenic in the bulk diffuses into the slice, thereby dropping the surface concentration, arsenic in the gaseous state is taken back into the slice to maintain equilibrium between gaseous and solid phases. Prediffusion sheet resistance of 3000 ohms/□ has been observed to drop to about 100 ohms/□ during a 22-hr diffusion at 900°C. This indicates that: (*A*) Loss of dopant through outdiffusion has been significantly

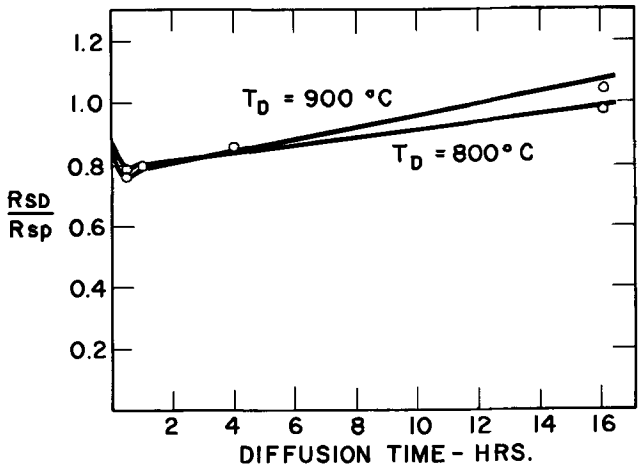

Fig. 8. Dependence of diffusion sheet resistance on temperature and time. R_{SP} = 1.0 ohm/□.

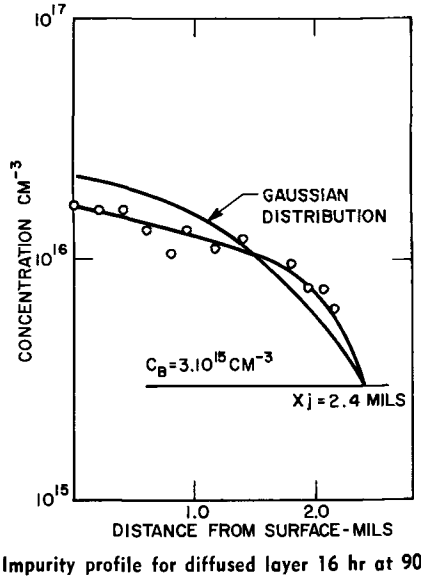

Fig. 9. Impurity profile for diffused layer 16 hr at 900°C. R_{SP} = 170 ohms/□; R_{SD} = 35.8 ohms/□.

limited. (*B*) There is a large amount of arsenic in or on the prediffused slice which is not ionized. This is indicated by the fact that, when the prediffused samples are diffused, a significant reduction in sheet resistance occurs. A factor of eight reduction in sheet resistance is predicted as a result of drive-in diffusion because of the change in mobility which results from a decrease in impurity concentration (6). The observed reduction is significantly greater than that predicted, equaling as much as thirty. This effect is typical of non-Fickian diffusions, and has been reported for the silicon-phosphorus system (4).

The ratio of diffusion sheet resistance, R_{SD}, to prediffusion sheet resistance, R_{SP}, is shown in Fig. 6 as a function of time with temperature as a parameter. All prediffusion sheet resistances were 170 ohms/□. An initial rapid drop in sheet resistance, representing the effects of redistribution of the impurities, is followed by a gradual increase in sheet resistance. This increase represents a loss of impurity atoms from the diffusion boat assembly and is seen to be independent of temperature, being limited, apparently, by the leakage rate from the diffusion boat. This being so, one would expect that at the higher diffusion temperatures, where diffusion into the slice is more rapid, a lower net loss of impurity, and consequently lower sheet resistance, would result. The curves verify this temperature dependence of diffusion sheet resistance.

A similar system of curves is shown in Fig. 7, the difference being that all prediffusions were in this

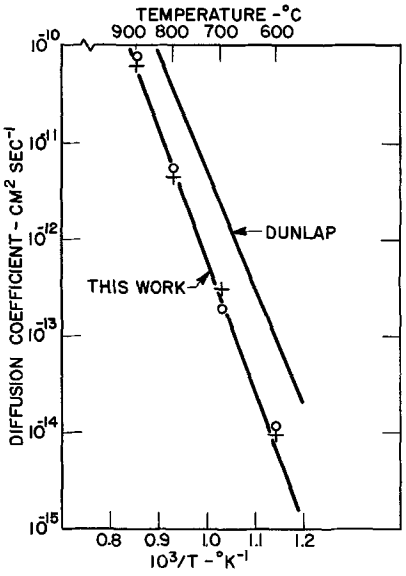

Fig. 10. Diffusion coefficient of arsenic in germanium: + 4-hr runs; ○ 16-hr runs.

case 10 ohms/□. In the presence of the higher concentrations, the rate of loss of impurities is more rapid. It is still independent of temperature, however. Sheet resistance also decreases with diffusion temperature as before.

In Fig. 8 the same type of curves is shown with prediffusion sheet resistance now down to 1.0 ohm/□. Under the influence of these very high concentrations, the rate of loss is now temperature dependent and considerably greater. The behavior of sheet resistance with temperature is also changed.

A profile typical of the diffused layers is shown in Fig. 9. Of particular note is the absence of a dip in concentration at the surface, indicating that outdiffusion has been reduced significantly. Also of importance is the fact that the profile very nearly matches the Gaussian distribution drawn for the same junction depth and sheet resistance.

In calculating the diffusion coefficient, the diffused layers were assumed to be Gaussian. Values are shown in Fig. 10. On all the samples measured, prediffused layers had sheet resistance of 170 ohms/□ and junction depth of about 1300Å. Diffusion times of four and sixteen hours were used at each temperature. The results obtained are seen to be considerably smaller than those of Dunlap (7). The values from this work are believed to represent the concentration independent diffusion coefficient, while the values given by Dunlap are in the concentration dependent range. Diffusion coefficients calculated from the prediffusion data do, in fact, agree generally with Dunlap's work. This work may represent the first data on the diffusion coefficient of arsenic in germanium without concentration enhancement effects.

The second factor which must be controlled is thermal conversion. This is achieved by the step annealing process described above. In spite of rigorous cleaning, some thermal conversion appears to be inevitable. Tweet (8) showed that copper precipitates from the germanium lattice on dislocations according to the relationship

$$\psi = e^{-t/\tau_p(T)}$$

where ψ is the fraction of copper remaining after time t and τ_p is the temperature (T) dependent relaxation time for precipitation. Since τ_p decreases with increasing temperature, it is possible to remove most of the added acceptors at a rapid rate at the higher temperatures of the annealing cycle, while only small amounts are left to be removed at the lower temperatures where the precipitation rate is low. The step anneal reduces the added acceptor level to less than 2×10^{14} cm^{-3} after diffusion at 900°C.

Conclusion

A closed box, two-step system for the diffusion of arsenic into germanium has been developed. Prediffusions have been done over a temperature range of 475°-725°C producing sheet resistances from 3000 to 0.5 ohms/□. Prediffused slices can be diffused at temperatures as high as 900°C with layer depths of 2.5 mils and surface concentrations of 2×10^{16} cm^{-3}. The system offers the advantages of simplicity, flexibility, and controllability.

This work was motivated by demand in the Bell System for high breakdown voltage germanium diodes. The diffusion assembly is currently being used by the Western Electric Company for routine diffusion at 900°C. This produces diodes having breakdown voltages of 350-400v.

Acknowledgments

The authors wish to thank Messrs. T. R. Robillard and W. J. Frankfort for suggesting the use of the germanium arsenide source. They are also indebted to Mr. R. A. Kiehl for assistance in implementing the diffusion.

Manuscript received Oct. 5, 1965; revised manuscript received March 24, 1966. This paper was presented at the San Francisco Meeting, May 10-14, 1965.

Any discussion of this paper will appear in a Discussion Section to be published in the June 1967 JOURNAL.

REFERENCES

1. M. Kowalchik, Unpublished paper.
2. F. vander Maesen, P. Penning, and A. van Wiergien, *Philips Research Repts.*, **8**, 241 (1953).
3. R. Berman, Paper presented at the Buffalo Meeting of the Society. Abstract No. 117, October 1965.
4. E. T. (Tannenbaum) Handelman, *Solid State Electronics*, **2**, 123 (1961).
5. C. H. Lee and D. V. Speeney, Unpublished data.
6. A. B. Phillips, "Transistor Engineering," pp. 65-71, 76, McGraw Hill Book Co., Inc., New York (1962).
7. W. C. Dunlap, Jr., *Phys. Rev.*, **94**, 1531 (1954).
8. A. G. Tweet, *ibid.*, **106**, 221 (1957).

The Effect of Ion Bombardment on the Photoelectric Threshold of Single Crystal Cuprous Oxide

Richard J. Komp

Research Division, Xerox Corporation, Webster, New York

and Dan Trivich

Department of Chemistry, Wayne State University, Detroit, Michigan

ABSTRACT

Samples of single crystal cuprous oxide prepared by quenching after equilibration at various oxygen pressures at high temperature were subjected to bombardment by argon ions and hydrogen ions, and the photoelectric emission was then measured. The curves for the photoelectric quantum yield Y *vs.* the photon energy E were characterized by the presence of a double shoulder indicating the presence of two thresholds. The data could be fitted to the equation $Y^{1/n} = k\ (E-E_0)$ with n usually having the value of 2, and this was used to evaluate the threshold energy E_0. The high energy threshold was relatively constant at 5.1 ev regardless of the amount of ion bombardment, but the low energy threshold was much more variable, often starting at ~4.0 ev and increasing to 4.6 ev with bombardment. It is proposed that the high energy threshold represents the process of direct excitation with scattering from the valence band. The lower values of the low energy threshold are presumed to represent excitation from surface impurities which are gradually removed by bombardment. The limiting value of the low energy threshold is assigned to excitation from states similar to the bulk acceptor states usually found in Cu_2O at 0.4 ev above the valence band.

The semiconducting properties of cuprous oxide have been known and studied for several decades, notably by Wagner and co-workers (1). Recently with the development of methods in this laboratory (2) and elsewhere (3) for the production of single crystals of the material, it has been possible to provide more definitive information on the electrical properties. Recent investigations on the high temperature (600°-1100°C) thermoelectric effect (4) and the low temperature Hall effect (5) have confirmed that cuprous oxide is a p-type semiconductor under all attainable conditions of temperature and environmental oxygen pressure. The results of these experiments together with measurements of the electrical conductivity at high temperatures (6, 7) and a study of the weight variation (8) with changes in the environmental oxygen pressure have substantiated a modified Wagner model in which an excess of oxygen in the crystal lattice produces copper atom vacancies which can act as electron acceptors. The excess oxygen is in equilibrium at high temperature with the oxygen gas surrounding the crystal.

However the results of measurements on quenched samples at low temperatures are rather complex (5) so that the Wagner model can be applied only in a grossly qualitative fashion. Also in the vicinity of room temperature, one can observe progressive changes in the electrical conductivity and Hall effect if the samples are allowed to stand at slightly elevated temperatures (40°-100°C). These changes may be due to changes in the character of certain bulk acceptor states or may be due to changes in surface states. One possible approach to the study of states at or near the surface is by means of photoelectric emission, and this paper is an initial report of such measurements on cuprous oxide.

The photoelectric emission from compound semiconductors has been measured by several workers. Apker and Taft (9) have carried out an extensive series of investigations on alkali halides. The work by Smith and Dutton (10) on lead sulfide and that by Spicer (11) on alkali antimonides indicate that the majority of photoemitted electrons comes from the valence band of the material. Using a set of theoretical predictions by Kane (12) on the nature of the quantum yield relation as a guide, Allen and Gobeli (13) have made a detailed study of the excitation mechanisms and surface states present in clean silicon.

Allen and Gobeli have also studied the effects of positive ion bombardment and subsequent annealing on silicon surfaces (14). These treatments were developed by Farnsworth (15) and others as a cleaning technique and have been extensively employed to produce clean, well ordered surfaces, notably on silicon and germanium. Although sufficient ion bombardment will remove adsorbed impurity atoms, the treatment leaves a large amount of disarray and some implanted bombardment atoms which may be removed by heating the sample. Cuprous oxide cannot be heated to high temperatures without changing the amount of excess oxygen present in the crystal, so that annealing cannot be used in this case. However, the changes in the photoelectric emission of surfaces upon annealing are not usually found to be as large as those produced by bombardment of a contaminated surface.

In the present investigation most of the ion bombardment was done using argon, but the work was extended to bombardment by hydrogen ions since some interesting special effects might be expected. Muller (16) sputtered copper onto cuprous oxide in a hydrogen atmosphere and produced rectifying and photovoltaic junctions on the top surface of the sample. Waibel (17) also subjected cuprous oxide to a hydrogen glow discharge and produced similar effects. Some preliminary work in our laboratory indicated that proton bombardment causes reduction of the top surface of the cuprous oxide to copper.

Experimental

Sample preparation.—Polycrystalline cuprous oxide sheets were prepared by the oxidation of 99.999+% pure copper plates (purchased from Johnson Matthey and Company Ltd., England) at 1020°C in air. Large crystals of cuprous oxide were then produced in the plates by a grain growth method developed in this laboratory (2).

Portions of the Cu_2O plates were equilibrated at high temperatures and known oxygen pressures to es-

Table I. Summary of values of photoelectric threshold obtained for various cuprous oxide samples and equilibration conditions used to prepare samples.

Sample No.	Equilibration conditions: Temperature (°C)	Time (hr)	Oxygen pressure (Torr)	Photoelectric thresholds (ev): High energy	Low energy[d]	Limiting[e]
D	1020	1.9	120[a]	5.12	4.66	4.33
G	1020	2.2	15.3[a]	5.01	4.65	4.05
H	1020	7.0	1.04[b]	5.15	4.63	4.08
I	1020	15.0	0.11[b]	5.13	4.66	3.95
Ia	Cut from same sample plate as I			5.03	4.25	3.95
E	1020	4.0	9.48×10^{-3}[a]	5.01	4.55	4.22
J	750	18.0	0.12[b]	5.13	4.63	4.42
K	750	19.0	9.12×10^{-3}[a]	5.10	4.57	4.18
L	750	47.0	6.3×10^{-6}[b]	5.06	4.67	4.31
N	750	71.0	2.4×10^{-7}[c]	5.14	4.46	4.10

[a] Flowing gas mixture at atmospheric pressure.
[b] Flowing gas mixture at low pressure.
[c] Pumped closed system.
[d] Highest value observed for sample.
[e] Lowest value observed for sample.

tablish the equilibrium concentration of copper atom vacancies in the crystal. This process was carried out in an apparatus designed by Wright (5). The samples were hung in the center of a 12 in. long tube furnace by a long platinum wire. The desired partial pressures of oxygen were obtained by flowing calibrated mixtures of oxygen and nitrogen through the system, usually at atmospheric pressure, but sometimes at moderately reduced pressures. The lowest oxygen pressure used, 2.4×10^{-7} Torr, was obtained by pumping the closed system and assuming that oxygen comprised 20% of the ultimate pressure. Table I gives a summary of the equilibration conditions for the samples studied.

After the sample had come to equilibrium with the surrounding atmosphere and temperature, the composition was frozen by dropping the sample out of the furnace and quickly cooling the sample with a stream of helium at liquid nitrogen temperature. The resulting samples showed no trace of cupric oxide on their surfaces.

The crystals were then ground on one side using No. 400 alundum abrasive until one half of the thickness was removed, assuring that the disordered region in the center of the crystal was not present in the final sample. The other side was ground lightly to remove the top surface and both sides were then ground using No. 305 emery to remove pits and scratches. The samples were then cut into squares 1 cm on a side, etched in 0.5*N* sodium cyanide for 5 min, washed in distilled water, and air dried. A gold contact was applied on the back of the sample by vacuum evaporation and the sample was left in the metallizing chamber under vacuum until it was to be placed into the measuring system.

Measurement system.—During the bombardment of the sample and the measurement of the photoemission the sample was kept in a bakable, ultrahigh vacuum system, capable of reaching 5×10^{-10} Torr. During most of the photoemission measurements the pressure was maintained below 10^{-8} Torr. Because cuprous oxide cannot be heated much above room temperature without causing changes in its properties, the system could not be baked with the sample in place. To avoid this difficulty, the clean system was backfilled with purified helium and quickly opened. The sample was inserted into the holder while a slight positive pressure in the system kept helium streaming out the open flange. After the system was once more sealed tight and pumped down, the molecular sieve trap was baked. This procedure usually resulted in the attainment of a pressure of 10^{-9} Torr after pumping overnight.

The samples were bombarded with positive ions from an ion source similar to that designed by Moak, Reese, and Good (18). The ion source was separated from the main system by a small capillary tube, and this arrangement allowed the pressure around the sample to remain at 10^{-5} Torr during the bombardment in addition to producing a controllable low current density. The gas used for bombardment was fed into the ion gun by means of a bakable variable leak and was ionized by a 25 mc rf field produced by an external coil. An accelerating voltage of 1500v was applied between a tungsten rear electrode and the source exit nozzle, which was grounded. The sample was kept at ground potential. The ion currents used were usually 0.07 μa/cm^2 for argon and 2 μa/cm^2 for hydrogen.

The light source used for the photoemission experiments was a Hanovia Model 7606 medium high pressure mercury lamp illuminating a Bausch and Lomb 250 mm effective focal length monochromator with entrance and exit slits set at 0.5 mm. An image of the square ruled portion of the monochromator grating was focused by means of an auxiliary quartz lens through a 4 mm square hole in the collecting anode to illuminate the sample. The spectral output of the entire optical system was measured using a sodium salicylate fluorescent plate and a 1P28 photomultiplier detector (19). An absolute calibration of the output of the system was performed using an Eppley thermopile and National Bureau of Standards standard lamp, and the absolute output of the optical system is estimated to be known to ±10%. A quartz window in the vacuum system allowed measurements to be made down to 2000Å.

The photoemitted electrons escaping from the sample were collected by a platinum plate anode placed parallel to the sample and 3 mm from its front surface. The current produced was measured with a Beckman Instruments RXG-2 Micromicroammeter. To reduce electron emission from sources other than the sample, only the sample and sample holder were biased (at —90v with respect to the anode). All other parts of the vacuum system were grounded. All measurements were made at room temperature.

The photoemission from the samples was measured before any bombardment and remeasured after each bombardment period. These periods ranged from 1 min to 1 hr with most samples being subjected to a series of bombardments of 15 min duration. After

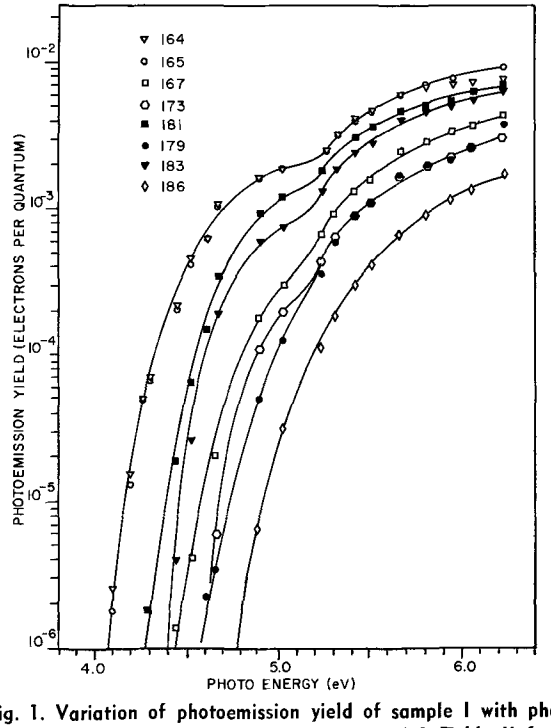

Fig. 1. Variation of photoemission yield of sample I with photon energy after various bombardment treatments (cf. Table II for experimental conditions).

Table II. Experimental conditions used to obtain results in Fig. 1 and volues of photoelectric thresholds obtained from these results.

Run number	Bombard-ment gas	Time of bombard-ment (min)	Time after bom-bardment	Yield at 2100Å (× 10^{-3})	Thresholds (ev) High	Low
164	—	—	—	7.0	5.13	3.95
165	Ar	1	5m	7.8	5.14	3.96
166	Ar	5	2.5m	6.3	5.13	4.25
167	Ar	15	4m	3.3	5.12	4.40
168	—	—	1d	5.9	5.14	4.25
169	Ar	20	2m	3.3	5.14	4.40
170	Ar	30	4m	3.5	5.15	4.45
171	—	—	10m	2.4	5.14	4.55
172	—	—	16m	2.3	5.14	4.41
173*	—	—	23m	2.25	5.14	4.50
174	—	—	8.5h	3.1	5.14	4.40
175	H_2	15	5.5m	4.3	5.14	4.18
176	H_2	15	2m	4.2	5.11	4.41
177	—	—	8m	4.6	5.11	4.25
178	H_2	15	3m	3.2	5.14	4.39
179	H_2	15	1.5m	2.4	5.13	4.55
180	—	—	7.5m	2.9	5.13	4.40
181	—	—	5d	5.9	5.11	4.38
182	H_2	15	3m	4.9	5.10	4.40
183	H_2	15	5h	1.17	4.87	4.66
186	H_2	15	2d	1.7	4.83	4.64 (?)

* Argon gas was introduced at 10^{-3} Torr for 30 sec before 173.

several periods of argon ion bombardment produced no further change in the photoemission spectral response, the sample was bombarded with protons for several periods.

Experimental results.—Typical results of photoemission quantum yield (electrons per incident photon) *vs.* photon energy are shown in Fig. 1. The experimental conditions used to obtain these results are given in Table II. The various curves are for measurements on a single sample after different amounts of ion bombardment and various times between bombardment and measurement. A prominent feature of the results is the presence of a double shoulder in the photoemission yield curves thus indicating the existence of two energy thresholds. Figure 2, which is a collection of curves from several samples after similar treatments, indicates that these features are a normal result for such samples of cuprous oxide.

The dependence of the yield on photon energy above the high energy threshold obeys a relation of the form

$$Y = k(E - E_o)^n$$

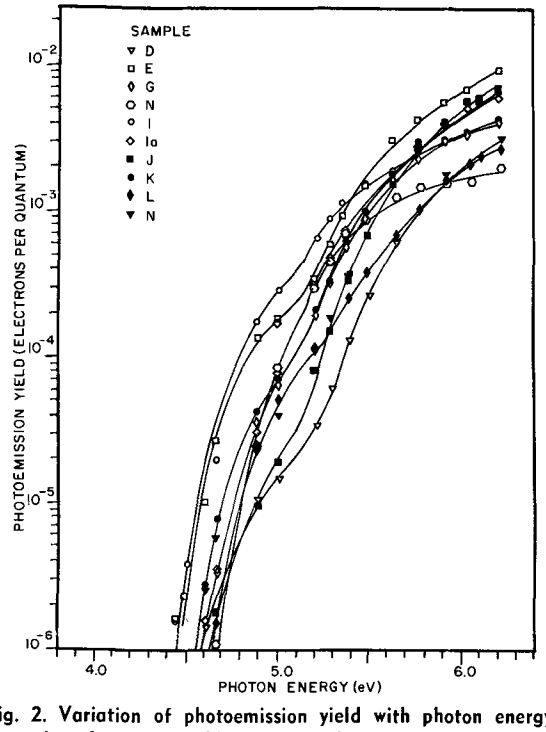

Fig. 2. Variation of photoemission yield with photon energy for all samples after comparable amounts of argon ion bombardment.

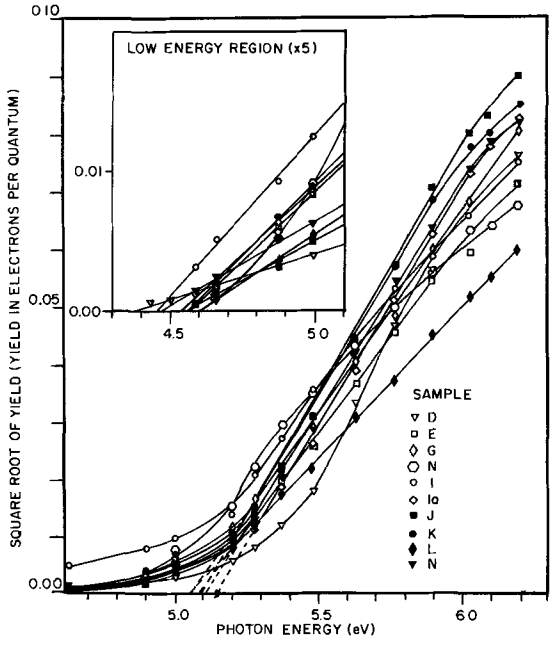

Fig. 3. Plots of the squore root of the photoemission yield vs. photon energy for all samples treated with argon.

where Y is the yield, E is the photon energy, E_o is the threshold energy, and k is a constant. The exponent, n, was found to have a value of 2 for almost all of the samples tested as can be seen in the plots of the square root of the yield *vs.* photon energy shown in Fig. 3. These curves are for all the samples under equivalent conditions and are representative of those used in the extrapolations to determine the threshold energies. The data for two of the samples could be fitted with yield relations with $n = 1$ while a third is best represented by $n = 3/2$, but for all other samples n is very close to 2. The high energy threshold was normally calculated by plotting the square root of the photoelectric yield *vs.* the photon energy and extrapolating to zero yield to obtain the threshold.

The high energy threshold values were remarkably stable for any particular sample and could be reproduced to within 0.02 ev even after treatment of the sample had greatly modified the apparent form of the yield curves. For the various samples measured, these values for the high energy threshold ranged from 5.01 to 5.15 ev. The absolute magnitude of the yield at energies above the high energy threshold varied by as much as a factor of three with changes in the surface condition of the sample, even when the contribution due to the low energy shoulder was subtracted. The yield decreased as a result of bombardment and increased slowly with time of standing after bombardment.

In contrast to the behavior above the high energy threshold, the results in the low energy region varied widely both in the value of the threshold and in the absolute yield. The variation in results from one sample to another was large but also the change in the behavior of any one sample with even a slight amount of treatment was great. However, the samples showed a characteristic general behavior. In spite of the large variation in the results of the measurements on the samples before any bombardment, the curves for the different samples had the same general appearance after only 15 microcoulombs of argon bombardment. As can be seen in Fig. 1, additional bombardment raised the low-energy threshold and decreased the yield until with sufficient argon bombardment the portion of the yield due to the low energy shoulder almost completely disappeared and a limit was reached in the threshold. This limiting value of the low energy threshold was approximately 0.4 ev below

the high energy threshold and was the same for all samples. If the samples were allowed to stand undisturbed in the vacuum system, the low energy threshold slowly decreased and the yield increased correspondingly. The same effect was observed but after a much shorter time if hydrogen gas was introduced into the system to raise the pressure to approximately 10^{-4} Torr. From this evidence it was concluded that the variation in low energy threshold was an effect associated with surface impurity atoms.

Proton bombardment had a much greater effect on cuprous oxide than did argon bombardment, but this effect was not apparent until after considerable total bombardment. At first, as can be seen from Table II and Fig. 1, the low energy threshold behaved as it did for argon and the high energy threshold remained unchanged; but, after approximately 0.015 coulombs of proton bombardment, a sudden change occurred in the yield relation. The low energy threshold usually disappeared completely and the high energy threshold shifted to 4.85 ev.

Argon bombardment had no apparent effect on the appearance of the sample surface, but proton bombardment produced a gold sheen on the sample which further bombardment developed into a definite copper color. After removal from the vacuum system, the samples were found to have what appeared to be a thin deposit of copper on the bombarded surface.

Neither the temperature nor the oxygen pressure surrounding the sample during the high temperature equilibration had any obvious effect on the observed threshold values. If an effect does in fact exist, the variations in the thresholds and yields due to other factors make it impossible at the present time to discuss its nature.

Discussion

The experimental results show the presence of two thresholds, a relatively constant one lying at about 5.1 ev and another one at lower energy which can vary from 3.95 to 4.66 ev depending on the initial conditions and the amount of bombardment. While the present measurements are apparently the first to be done on single crystal cuprous oxide, even the literature on polycrystalline Cu_2O is relatively scanty in regard to photoemission measurements and most of the studies precede the time of a clear understanding of the difference between work function and photoelectric threshold for semiconductors. These earlier studies deal with only a single threshold which is the more obvious higher energy threshold. Ioffe (20) quotes without reference a value of 5.15 ev, which may have been derived from the data of Fleischmann (21). A more recent substantial work by Wasser (22) yields a value of 4.80 ev. A brief communication by Cashman (23) gives a value of 5.34 ev and mentions the existence of a small "tail" in the results at low energies, which was assigned to impurity levels. Other earlier literature is reviewed in Gmelin (24).

The simplest way to explain several features of the present results is with a model having at least two simultaneous but independent mechanisms producing the photoemission and yielding the two thresholds observed experimentally. Because of the large yield associated with the high energy threshold and because of its relative constancy, this threshold most likely represents excitation of electrons from the valence band. According to the general theoretical treatment by Kane (12), the possible mechanisms for the escape of an electron from the valence band are direct excitation, direct excitation with scattering, and indirect excitation. Direct excitation either with or without scattering apparently is the most likely mechanism in the case of cuprous oxide because of the magnitude of the yield, but also because the yield varies as the first or second power of the photon energy above the threshold in accordance with the relations derived by Kane. Since for most of our samples the yield relation has a value of $n = 2$, it is likely that the usual process responsible for the high energy threshold in Cu_2O is one of direct excitation with scattering. Sample H which obeys a yield relation with $n = 1$ may represent the case of direct excitation with no scattering. Sample I, for which $n = 3/2$, may represent an intermediate case with some scattering of the excited electrons so that the total process in the case of this sample is a composite of the two mechanisms. The threshold energy for a direct excitation process without scattering should be greater than that for the process with scattering. Sample H does have the largest value observed, 5.15 ev, in a comparison of all samples under similar conditions. The thresholds for the remaining samples tend to be somewhat lower, averaging 5.05 ev. Taking the value for the band gap in Cu_2O to be 2.3 ev, it is estimated that the electron affinity of Cu_2O is about 2.8 ev. If band bending due to surface states is present, this may affect the high energy to a certain extent. However, in view of the relative constancy of the high energy threshold, at least as compared with the large variations in the low energy threshold, it has been assumed in the preceding discussion that the electrons emitted after excitation from the valence band come from depths below the surface which are small compared with the space charge region.

In the case of the low energy threshold, it becomes necessary to deal with surface states more explicitly. Because of the large variation in the low energy threshold and its dependence on surface conditions as affected by ion bombardment, it is probable that the low energy threshold is strongly affected by the presence of surface states. The fact that the experimental value for the exponent n in the yield relation is normally 2 indicates a mechanism similar to Kane's case of surface imperfections with a continuous distribution in energy in the vicinity of the Fermi level. The variation of the threshold energy with surface conditions indicates that the Fermi level at the surface can vary relative to the vacuum level and thus lead to bending of the bands at the surface as illustrated in Fig. 4. It is assumed that when band bending occurs the bands are bent downward at the surface as shown.

From the model, one can infer that the effect of ion bombardment is to remove gradually some of the surface impurity species and that this causes the drastic lowering of the yield with increased amounts of ion bombardment. As the surface species are removed, the amount of the band bending decreases so that the value of the low energy threshold increases.

With large amounts of bombardment, the energy threshold increases to a limiting value of 4.66 ev, which differs from the high energy threshold by

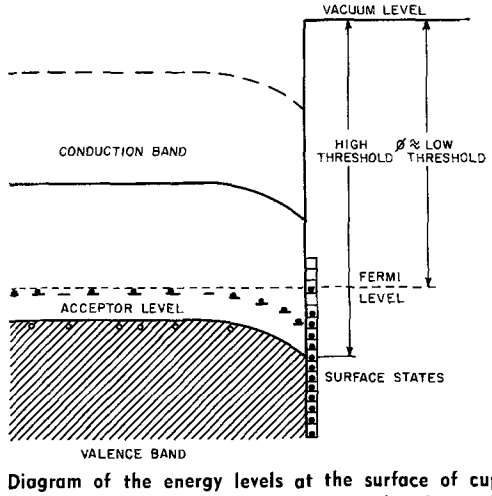

Fig. 4. Diagram of the energy levels at the surface of cuprous oxide indicating the effects of band bending on the photoemission threshold.

about 0.45 ev. This approaches the value of 0.4 ev observed from the temperature coefficient of the Hall effect (5) and which can be assigned to the energy separation between the valence band and the bulk acceptor levels. The photoemission for this limiting case can be assigned to excitation from bulk acceptor levels under conditions where very little band bending is present.

Manuscript received Jan. 31, 1966.

Any discussion of this paper will appear in a Discussion Section to be published in the June 1967 JOURNAL.

REFERENCES

1. C. Wagner and H. Hammen, *Z. physik. Chem, (Leipzig)*, **B40**, 197 (1938).
2. R. S. Toth, R. Kilkson, and D. Trivich, *J. Appl. Phys.*, **31**, 1117 (1960).
3. Y. Ebisuzaki, *ibid.*, **32**, 2027 (1961).
4. M. H. Zirin and D. Trivich, *J. Chem. Phys.*, **39**, 870 (1963).
5. M. R. Wright, Ph.D. Dissertation, Wayne State University, Detroit, Michigan (1962); (cf. *This Journal*, **109**, 208C (1962).
6. R. S. Toth, R. Kilkson, and D. Trivich, *Phys. Rev.*, **122**, 482 (1961).
7. M. O'Keeffe and W. J. Moore, *J. Chem. Phys.*, **35**, 1324 (1961).
8. M. O'Keeffe and W. J. Moore, *ibid.*, **36**, 3009 (1962).
9. L. Apker and E. Taft, *Phys. Rev.*, **79**, 964 (1950); **81**, 698 (1951); **82**, 814 (1951).
10. A. Smith and D. Dutton, *J. Phys. Chem. Solids*, **22**, 351 (1961).
11. W. E. Spicer, *Phys. Rev.*, **112**, 114 (1958).
12. E. O. Kane, *ibid.*, **127**, 131 (1962).
13. G. W. Gobeli and F. G. Allen, *ibid.*, **127**, 141 (1962).
14. F. G. Allen and G. W. Gobeli, *J. Appl. Phys.*, **35**, 597 (1964).
15. R. E. Schlier and H. E. Farnsworth, "Semiconductor Surface Physics," R. H. Kingston, Editor, Chap. 1, University of Pennsylvania Press, Philadelphia (1957).
16. R. H. Muller and W. O. Teeters, *Trans. Electrochem. Soc.*, **64**, 457 (1936).
17. F. Waibel and W. Schottky, *Physik Z.*, **33**, 583 (1932).
18. C. D. Moak, H. Reese, Jr., and W. M. Good, *Nucleonics*, **9**, 18 (1951).
19. K. Watanabe and E. C. Y. Inn, *J. Optical Soc. Am.*, **43**, 32 (1953).
20. A. F. Ioffe, "Physics of Semiconductors," p. 230, Infosearch Ltd., London (1960).
21. R. Fleischmann, *Ann. Phys.*, **5**, 73 (1930).
22. E. Wasser, *Physik. Z. Sowjetunion*, **6**, 351 (1934).
23. R. J. Cashman, *Phys. Rev.*, **57**, 1090 (1940).
24. Gmelin, "Handbuch der Anorganischen Chemie," Kupfer Teil D. Elecktrische Eigenschaften der Kupferoxide. System-Nummer 60. 8th edition, p. 163, Weinheim: Verlag Chemie (1963).

Kinetics of Thermal Growth of Silicon Dioxide Films in Water Vapor-Oxygen-Argon Mixtures

Takashi Nakayama and F. C. Collins

Department of Chemistry, Polytechnic Institute of Brooklyn, Brooklyn, New York

ABSTRACT

The kinetics of growth of silicon dioxide films in mixtures of water vapor, oxygen, and argon have been studied in the range of water partial pressures from 4.6 to 355 Torr and the temperature range 850° to 1217°C. A combined linear-parabolic law of growth adequately represents the data over the complete region of temperatures and partial pressures studied. In the absence of oxygen, the linear and parabolic growth constants have first order dependence on the water vapor pressure at low pressures. In the case of the parabolic constant a saturation effect is evidenced by strong negative deviations from the first order law at higher water vapor pressures. This deviation is explained in terms of an adsorption isotherm at the oxide surface. The adsorption calculated from the growth behavior accurately fits the Langmuir adsorption isotherm. The apparent activation enthalpies of the parabolic and linear rate constants are 1.1 ev and approximately 3.3 ev, respectively, over the region of linear dependence upon the water vapor pressure. The enthalpy change calculated from the temperature dependence of the Langmuir adsorption isotherm is near zero. The measured enthalpies correspond to a superposition of the enthalpies of adsorption, desorption, generation of active sites for adsorption, and diffusion through the oxide film. The data do not enable the resolution of these several enthalpies. In the mixed water, oxygen argon ambient, the effect of introducing small vapor pressures of water at fixed oxygen partial pressure is to catalyze that part of the total growth rate due to the presence of oxygen. Higher vapor pressures of water repress the oxygen contribution to the growth rate at 850°. The latter effect was not observed at 1000°C over the partial pressure range investigated.

The kinetics of growth of thermally grown silicon dioxide films on silicon in both dry and wet oxygen and in steam ambients have been intensively investigated (1-24). The process is, at least in part, diffusion controlled as is shown by the generally parabolic form of the law of growth. Departures from the parabolic law which have been observed at temperatures below 1000°C have been interpreted on the basis of the Wagner (25) and Mott (26, 27) theories which predict linear or logarithmic behavior in the initial stage of oxide film growth depending on conditions. The observed values of the activation energy for growth quoted in the cited literature vary widely. There is a small trend in the literature to lower values in the case of wet oxygen as has been pointed out by Lieberman and Averkion (22), but it is not conclusive in view of the large discrepancies in the published values. Because of the fairly high permeability (28) and solubility (29) of water in fused quartz, the existence of a water catalyzed growth process in the case of growth in oxygen presumed dry can not be ruled out where growth is carried out by conventional techniques in a fused quartz furnace tube.

The present detailed investigation of the kinetics of the thermal oxidation of silicon in water-oxygen-argon ambients was undertaken in order to assess the separate roles of water and of oxygen in the oxidation process.

Experimental

The oxidations were carried out on a quartz boat in a 2.6 cm ID quartz tube with 2 mm wall thickness in a three zone diffusion type furnace with the central

zone temperature maintained within ±1°C. The fixed water vapor pressures were provided by a quartz humidiostat using deionized water maintained at a constant temperature. The argon gas used as the inert diluent was 99.998% pure. Tank oxygen of a purity of 99.60% was used in those runs in which oxidation in water-oxygen ambients was studied. The ambient flow rate was maintained at a constant rate of 150 ml/min corresponding to a linear velocity of 1.25 cm/sec within the furnace tube. The exit port of the furnace tube was closed by a silicone oil bubbler to prevent entrance of atmospheric moisture in the runs at low humidities.

The oxide films were grown on single crystal silicon slices doped to $5x10^{13}/cm^3$ with phosphorus. The oxidation studies of Deal and Sklar (21) indicate that phosphorus doping below $10^{19}/cm^3$ has no effect on the oxidation rate. The ingots were grown by the Czochralski method, sliced along the (111) planes, lapped, and polished to mirror smoothness by a vapor etching method (31). Immediately before being placed in the furnace, the slices were treated with HF to remove any oxide film and then successively rinsed in deionized water and methyl alcohol.

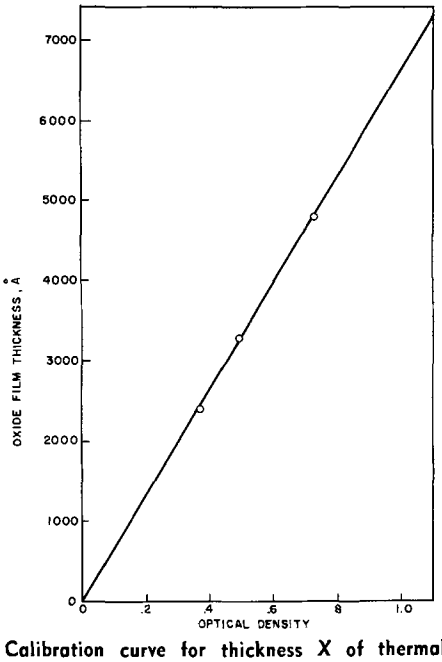

Fig. 1. Calibration curve for thickness X of thermally grown silicon dioxide films relative to optical density at 9.25μ.

The determinations of oxide film thickness were made by infrared absorbance measurements, a method suggested by Pliskin (30). The measurements were made at 9.25μ, the absorbance peak of the Si-O bond in thermally grown amorphous silica. A Perkin-Elmer Model 21 double beam recording spectrophotometer was used with two sample holders exposing equal 0.197 cm^2 areas to the two beams. An unoxidized portion of the same silicon slice which had received the same preliminary treatments was used as a blank in the reference beam. The optical density measurements of film thickness were found to be rapid and quite reproducible. They were calibrated against the Vamfo interference method (32). A linear interpolation was employed between 2400Å and zero. The validity of the interpolation was investigated by comparing the optical density at 9.25μ of a slice thinly oxidized on both sides with the optical density of the slice having the oxide from one side removed. Lambert's law was obeyed down to at least 400Å within an error of ±30Å. The calibration curve for optical density *vs.* oxide film thickness is shown in Fig. 1. At the humidity levels studied in the present investigation, there were no significant differences in the structure of the band in the 9.25μ region from that obtained for specimens thermally grown in pure oxygen. The same calibration curve was found to hold for the lowest and highest humidities studied here.

Data and Discussion

The primary data obtained for growth in water vapor and argon are presented in Fig. 2, 3, and 4. It will be observed that the data fit the purely parabolic law of growth only at temperatures of 1000°C and above. At the lower temperatures the data are consistent with a combined linear-parabolic law of the form

$$AX + BX^2 = t \qquad [1]$$

where X is the thickness of the oxide film at the time t and A and B are constants. The combined linear-parabolic law of the growth of silicon dioxide on silicon has been previously observed (17, 18, 24). The use

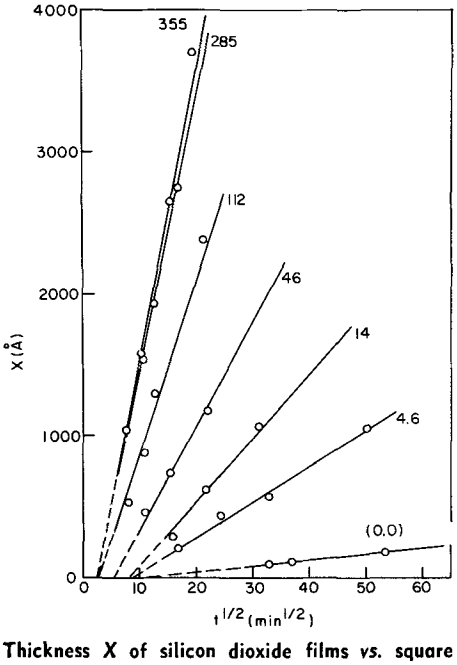

Fig. 2. Thickness X of silicon dioxide films *vs.* square root of the growth time $t^{1/2}$ at 850°C at various pressures of water vapor as indicated in Torr.

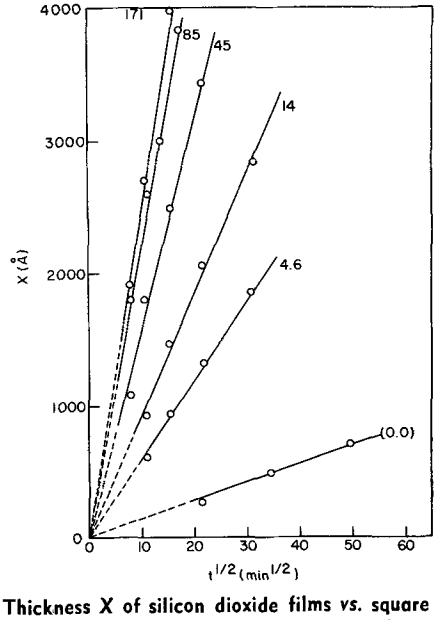

Fig. 3. Thickness X of silicon dioxide films *vs.* square root of the growth time $t^{1/2}$ at 1000°C at various pressures of water vapor as indicated in Torr.

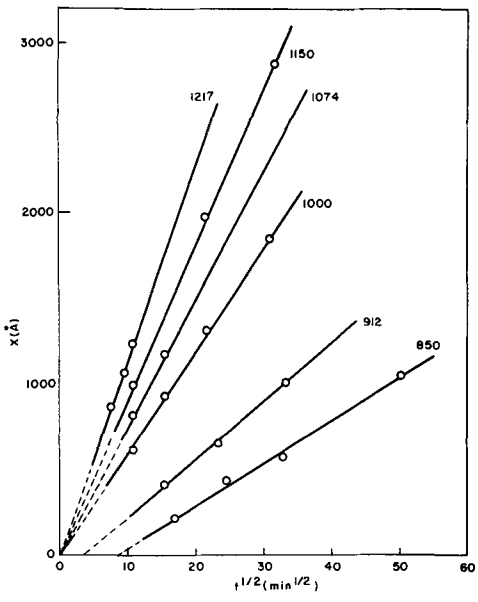

Fig. 4. Thickness X of silicon dioxide films vs. square root of the growth time $t^{1/2}$ at a water vapor pressure of 4.6 Torr at various temperatures as indicated in °C.

of this growth law is discussed theoretically in a subsequent section of this paper where it is shown that A and B are the reciprocals of rate constants for surface controlled and diffusion controlled reactions. Numerical values of these constants are found from the intercept and slopes of linear plots of t/X *vs.* X, as in Fig. 5.

The data illustrating the dependence of the parabolic rate constant k_2 on the partial pressure of water vapor at 850° and 1000°C are shown in Fig. 6. The rate law is first order in water vapor pressure, as expected, over the lower vapor pressure range but displays a marked departure from law at higher water vapor pressures.[1] This saturation effect is to be explained by existence of an equilibrium for the adsorption of water vapor on the surface of the growing oxide. The adsorption isotherm is clearly of the Langmuir type as shown in Fig. 7 in which the experimental points P_{H_2O}/k_2 are well represented by a curve linear in P_{H_2O}.

[1] This observation is not in agreement with the conclusions drawn by Deal and Grove (23) from the data of Flint (11) that the rate law is first order in partial pressure of water vapor up to 760 Torr. However, examination of the experimental points given in their Fig. 8 indicates a systematic negative deviation at higher partial pressures from a straight line drawn through the points at low vapor pressures.

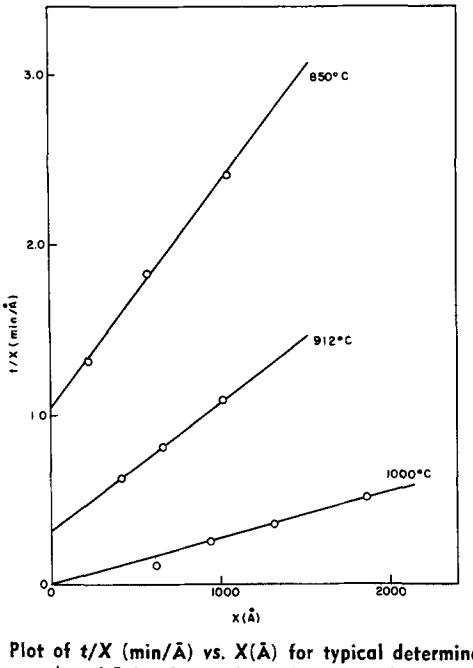

Fig. 5. Plot of t/X (min/Å) vs. X(Å) for typical determination of the constants A and B for the combined linear-parabolic law.

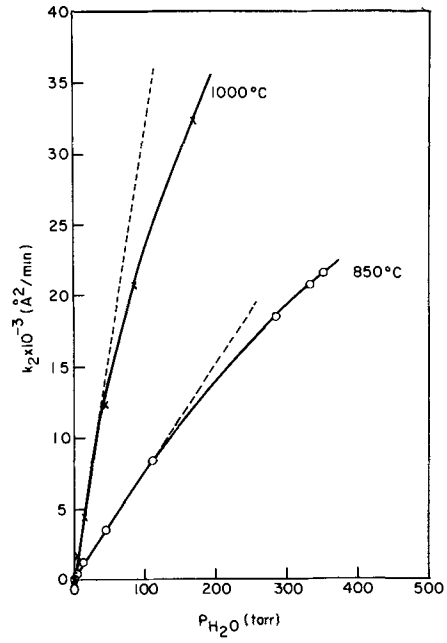

Fig. 6. Dependence of the calculated parabolic rate constant k_2(Å^2/min) on the partial pressure of water vapor P_{H_2O} at 850° and 1000°C.

The linear rate constant k_1 is first order in the water vapor pressure P_{H_2O} over the full range of water vapor pressures studied as is shown in Fig. 8. This is an expected result from the Langmuir adsorption behavior as will be later shown in detail.

Figure 9 presents a plot of the logarithm of the parabolic rate constant k_2 at water vapor pressure of 4.6 Torr against the reciprocal of the absolute temperature $1/T$. The activation enthalpy for the diffusion process calculated by least squares from the plot is 1.14 ev (26.3 kcal). It will be later shown that the activation enthalpy is necessarily independent of the water vapor pressure over the range in which the parabolic rate constant is first order in the water vapor pressure. In the region in which the parabolic

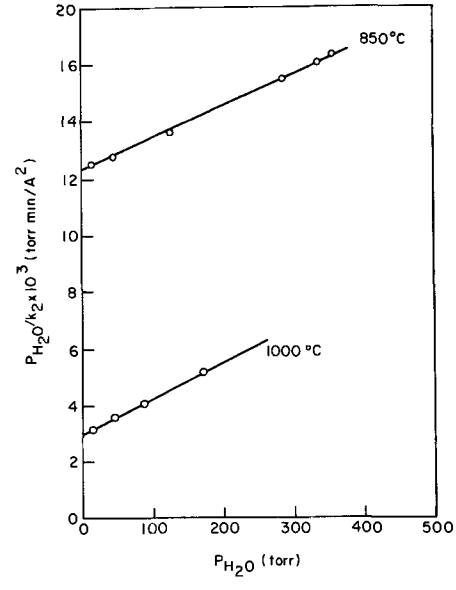

Fig. 7. Plot of k_2/P_{H_2O} vs. P_{H_2O} confirming Langmuir-type adsorption of water in growth mechanism.

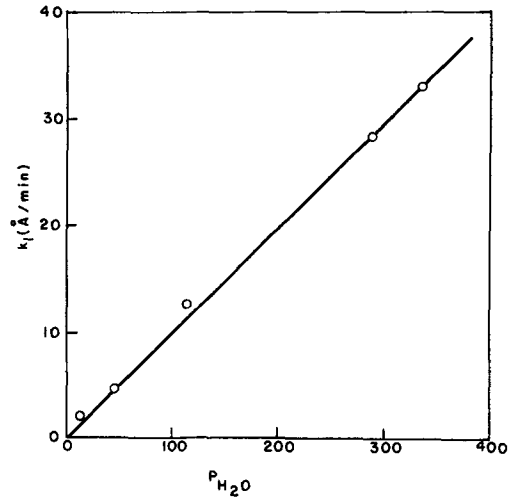

Fig. 8. Dependence of the calculated linear rate constant k_1 (Å/min) on the partial pressure of water vapor P_{H_2O} at 850°C.

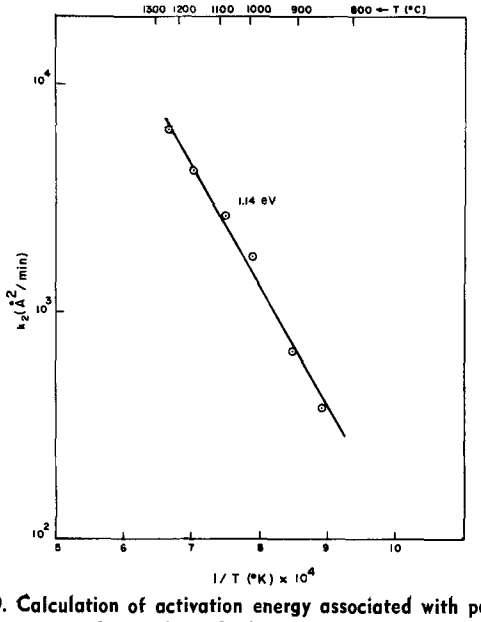

Fig. 9. Calculation of activation energy associated with parabolic growth pressure from plot of the logarithm of the parabolic growth rate constant k_2 vs $1/T$.

rate constant departs from this law, it is apparent from Fig. 6 that the calculated variable activation enthalpy will be lower than that in the linear region of the curves of Fig. 6. The numerical values of the varying activation enthalpy which might be calculated in the nonlinear region of the water vapor pressure dependence are not particularly revealing of the underlying processes. A more definitive quantity is the over-all enthalpy change involved in the Langmuir adsorption process. This is found from Fig. 7 and is zero within the precision of the measurements.

The activation enthalpy for the linear growth rate constant calculated from the linear growth rate constants at 850° and 912°C is 3.3 ev. As this value rests upon only two points, it is probably not of high accuracy, but it is apparently much larger than that for the parabolic rate constant.

The dependence of the parabolic growth rate constants on the partial pressure of water vapor for three oxygen isobars are given in Fig. 10 and 11 at temperatures of 850° and 1000°C. The behavior is obviously quite complex. For the purpose of detailed study, we shall here assume that the gross parabolic rate constant may be written as a superposition of two terms

$$k_2 = k'_2 P_{H_2O} + k''_2 (P_{O_2}; P_{H_2O}) \qquad [2]$$

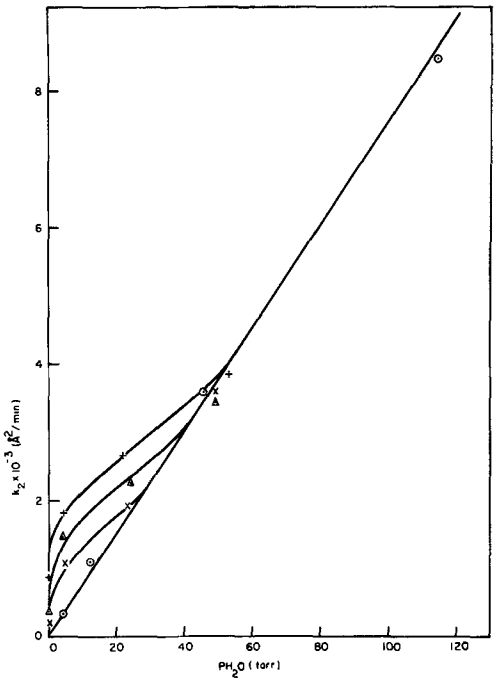

Fig. 10. Dependence of the calculated parabolic growth rate constant k_2 at 850°C on the water vapor pressure P_{H_2O} at various fixed oxygen partial pressures as indicated in Torr in water-oxygen-argon ambients. + P_{O_2} = 500 Torr; △ P_{O_2} = 200 Torr; × P_{O_2} = 100 Torr; ⊙ P_{O_2} = 0 Torr.

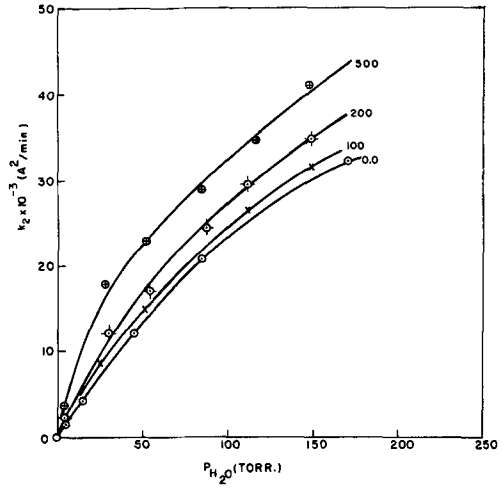

Fig. 11. Dependence of the calculated parabolic growth rate constant k_2 at 1000°C on the water vapor pressure P_{H_2O} at various fixed oxygen partial pressures as indicated in Torr in water-oxygen-argon ambients.

where k'_2 is the parabolic rate constant in the absence of oxygen and k''_2 is a new parabolic rate constant which depends on both the partial pressure of oxygen and that of the water vapor. The behavior of the incremental rate constant k''_2 with respect to the partial pressures of oxygen and water is quite different at 850° and 1000°C.

Figures 12 and 13 show the dependence of the incremental parabolic rate constant k''_2 on the water vapor pressure at fixed oxygen partial pressure at 850° and 1000°C. It will be seen from these figures at both these temperatures that the presence of small amounts of water vapor strongly catalyzes the oxidation of silicon by oxygen. This effect is well known in the oxidation of certain metals. At 850°C, however, additional partial pressure of water vapor, beyond a certain point, inhibits the contribution of oxygen to the oxidation of silicon. This inhibition at higher water vapor

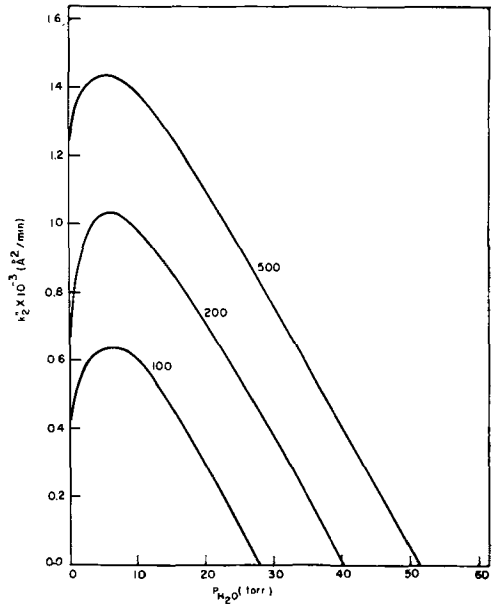

Fig. 12. Dependence of the incremental parabolic rate constant k''_2 at 850°C on the water vapor pressure P_{H_2O} at various fixed oxygen pressures as indicated in Torr.

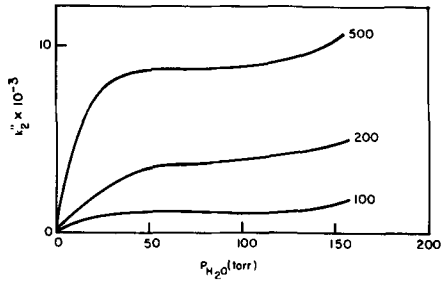

Fig. 13. Dependence of the incremental parabolic rate constant k''_2 at 1000°C on the water vapor pressure P_{H_2O} at various fixed oxygen partial pressures as indicated in Torr.

pressures is not apparent at 1000°C, at least over the range of vapor pressures investigated in this research.

Chemisorption of Oxidants

The saturation effect at high water vapor partial pressures suggests that the water vapor is taken up only at certain active sites at the surface of the growing oxide film. Applying the reasoning of the Langmuir adsorption isotherm, we have

$$c = c_0\theta \qquad [3]$$

where c_0 is the concentration of active sites at the surface and θ is the fraction of these sites which are occupied by adsorbate. For convenience c_0 is here expressed as a volume concentration. The fraction of occupancy is given by the well-known equation

$$\theta = \frac{K P_{H_2O}}{1 + K P_{H_2O}} \qquad [4]$$

where K is the equilibrium constant for the adsorption process. As will be later discussed in more detail, the parabolic rate constant may be assumed to be proportional to the concentration of the adsorbed oxidant species

$$k_2 = mc \qquad [5]$$

where the proportionality constant m contains the mobility of the diffusing species. Combining the last three equations, we have

$$k_2 = mc_0 \frac{KP_{H_2O}}{1 + KP_{H_2O}} \qquad [6]$$

Table I. Graphical values of mc_0 and adsorption equilibrium constant K

Temperature, °C	mc_0, Å²/sec	K, Torr⁻¹
850	8.3×10^4	0.93×10^{-3}
1000	7.7×10^4	4.3×10^{-3}

which may be put into the form

$$\frac{P_{H_2O}}{k_2} = \frac{1}{mc_0K} + \frac{P_{H_2O}}{mc_0} \qquad [7]$$

The last equation is the basis of the linear plots of Fig. 7 and establishes the observed adsorption process to be of the Langmuir type. The quantities mc_0 and K may be evaluated from Fig. 7 and are given in Table I.

The increase with temperature of the adsorption equilibrium constant per site corresponds to an endothermic process with $\Delta H^0 = 0.78$ ev. This is rather unexpected, but it does not necessarily lead to the conclusion that the total adsorption process is endothermic. The adsorption equilibrium also involves the formation of active sites. The lack of temperature dependence of the quantity mc_0 indicates that the formation of active sites is an exothermic process in view of the certainly endothermic activation energy of the diffusion coefficient contained in the constant m. The present data are not sufficient to calculate separately the latter two energies. Two firm conclusions which can be drawn from the region in which the parabolic rate constant is linear in the water vapor pressure.

1. The activation energy for film growth must be independent of the water vapor pressure in this linear region. In this region, the parabolic rate constant assumes the limiting form

$$k_2 = m(T)c_0(T)K(T)P_{H_2O} \qquad [6a]$$

so that at any two temperatures

$$\frac{k_2(T_2)}{k_2(T_1)} = \frac{m(T_2)c_0(T_2)K(T_2)}{m(T_1)c_0(T_1)K(T_1)} \qquad [8]$$

which is independent of the water vapor pressure. It follows that the activation energy must likewise be independent of the water vapor pressure in the linear region. The product mc_0K at 850° and 1000°C may be determined from the slopes of the linear portions of the curves in Fig. 6. The activation energy calculated from the ratio of Eq. [8] is 1.12 ev in close agreement with that calculated from Fig. 9.

2. The activation energy for growth is not uniquely determined by the activation energy for diffusion of the migrating species although the growth process is clearly diffusion-controlled in the parabolic growth law region. The temperature dependence of the parabolic rate constant and its apparent activation energy is determined by the separate temperature dependencies of the three quantities in Eq. [6a]. It may be remarked that the separate factors tabulated in Table I enable a third independent determination of the activation energy connected with the parabolic rate constant k_2. The activation energy so determined from the ratio mc_0K at 850° and 1000°C calculated from Table I is 1.15 ev in agreement with the values more directly obtained from the growth data in the foregoing. It provides a further indication of the general consistency of the data with the interpretation in terms of the Langmuir adsorption isotherm.

The growth rate data at 1000°C do not indicate any inhibition of the oxygen contribution to the parabolic growth rate constant by higher water vapor pressures. It is likely that an inhibition effect would have become evident if the present investigation had been extended to still higher water vapor pressures. Deal and Grove (23) find that the substitution of oxygen by argon produces no change in the growth rate when the partial pressure of the water vapor is *ca.* 640 Torr.

Table II. Representative values of activation energy in ev for parabolic rate growth constant calculated between 850° and 1000°C in water-oxygen-argon mixtures at various partial pressures of water vapor and oxygen

Water, Torr / Oxygen, Torr	4.6	10	25	50	100	150
0	1.12	1.12	1.12	1.12	0.93	0.86
100	0.57	0.93	1.23	1.12	0.97	0.87
200	0.41	0.74	1.13	1.24	1.05	0.92
500	0.86	1.11	1.39	1.44	1.20	1.08

The upward trend of the incremental parabolic rate constant k''_2 in the higher water vapor pressure region of Fig. 13 may be due to enhancement of the water contribution to the parabolic rate constant. This would be contrary to the assumption embodied in Eq. [2] which states that the water vapor contribution is quite independent of the oxygen partial pressure. The possible enhancement of the water vapor contribution by oxygen has some plausibility as indicated in the next section of this paper.

The irregular behavior of the incremental rate constant k''_2 at 850° and 1000°C prevents the calculation of significant activation energies connected with the variation of this rate constant between these two temperatures. Table II gives a few representative values of the activation energy for the combined parabolic rate constant at various partial pressure of water vapor and oxygen. The calculated values of the activation energy are possibly not of high accuracy but there do appear to be significant trends with respect to the ratios of water vapor to oxygen.

Chemical Species Involved in Film Growth

The Wagner-Mott electrochemical theory of oxide film growth (25-27) implies an ionic diffusing species. Jorgensen (14) has demonstrated that this is indeed the case by showing that the growth could be stopped by applying an external electrical potential counter to that of the postulated electrochemical cell. Marker experiments (7, 14, 33) show that the oxidant is the diffusing species. Jorgensen (14) concluded that the diffusing species is an oxygen anion. Seraphim and co-workers (34) have suggested that the oxide ion vacancies could be mobile species in amorphous silicon dioxide films.

The data existing at the present time do not enable a firm conclusion to be reached as to the identity of the diffusing species. However, all of the data are consistent with the hypothesis that the diffusing species is hydroxyl ion. If this hypothesis is correct, the following reactions presumably take place on the opposite sides of the film: At the outer surface

$$2H_2O \rightleftarrows 2\ OH^- + 2H^+ \qquad [R\text{-}1]$$

and at the $Si\text{-}SiO_2$ interface

$$2\ OH^- + Si \rightleftarrows SiO_2 + 2H^+ + 4e \qquad [R\text{-}2]$$

The protons and electrons could combine either at both faces or at the outer surface only. This process may be represented by

$$4H^+ + 4e \rightleftarrows 2H_2 \qquad [R\text{-}3]$$

In any event, the transport of an equivalent number of electrons across the oxide film is required in order to balance the charge carried by the diffusing anions. The mechanism of the electron transport across the silicon dioxide film is not known at present.

The strong catalysis by water of the oxygen oxidation of silicon as evident from Fig. 10, 11, 12, and 13 lends support to the hypothesis that the hydroxyl ion is also the diffusing species in the oxidation by oxygen. This suggests that the adsorption of oxygen is attended by the reaction

$$O_2 + 2H^+ + 4e \rightleftarrows 2\ OH^- \qquad [R\text{-}4]$$

the protons being furnished by the adsorbed water. As the reaction at the silicon-silicon interface [R-2] will remain unchanged, it provides a source of protons for the reaction [R-4] thus establishing a chain process. Accordingly, the presence of only a very small amount of water may be sufficient to set up the hydroxyl ion diffusion mechanism.

Christie (28) has found appreciable amounts of water in the gas efflux from conventional fused quartz furnace tubes under ordinary operating conditions. In the present investigation, a non-zero growth rate was found in pure argon which had been dried by passage through a cold trap refrigerated with dry ice and acetone, see Fig. 2 and 3. The growth rate under these conditions implies the presence of 0.22 Torr of water vapor at 850°C and 0.35 Torr at 1000°C. For the oxidation behavior of silicon in very dry oxygen, reference may be had to the forthcoming paper of Burkhardt and Gregor (24).

The suggested role of protons in facilitating the adsorption of oxygen and catalyzing the oxidation of silicon by oxygen also provides a possibility that it also facilitates the adsorption of water in that it removes one of the products of the latter adsorption, *i.e.*, protons. This could account for the anomalies in the behavior of the incremental parabolic constant k''_2 at 1000°C as it would invalidate the superposition relation, Eq. [2], upon which the significance of the k''_2 depends.

Electrochemistry of Film Growth

In a companion paper (36), the basic electrochemistry of film growth is formulated in a way somewhat different from that originally presented by Wagner (25). The effective electrostatic potential difference ΔV across the film is given by

$$\Delta V = -E^\circ + \Delta\phi \qquad [9]$$

where E° is the potential of the electrochemical cell representing the oxidation process, and $\Delta\phi$ is the Fermi potential difference across the film. The latter quantity is shown to be[2]

$$\Delta\phi = \frac{4q\rho}{M}\frac{k_2}{\sigma_e} \qquad [10]$$

where $M/4$ is the equivalent weight of SiO_2, ρ its density, σ_e the purely electronic (or hole) conductivity of the oxide, k_2 the parabolic rate constant, and N_o Avogadro's number.

Where space charge is absent from the film, the ionic flux J may be put into the form

$$J = -\frac{Dq\Delta V}{kTX}\frac{[c(X)e^{-q\Delta V/kT} - c(O)]}{[e^{-q\Delta V/kT} - 1]} \qquad [11]$$

The value of the electrostatic potential difference ΔV depends on the value of the electronic conductivity σ_e in Eq. [10] and the electrochemical cell potential E°.

Table III gives the calculated cell potentials for the two oxidation reactions relevant to the present work

$$Si + O_2 \rightarrow SiO_2 \qquad [R\text{-}5]$$

$$Si + 2H_2O \rightarrow SiO_2 + 2H_2 \qquad [R\text{-}6]$$

The data for the free energies of formation of quartz silicon dioxide and water were taken from the JANAF

[2] The derivations of Eq. [10] and [11] are given in the companion paper (36).

Table III. Standard free energy changes and cell potentials for oxidation of silicon by oxygen and by water at various temperatures

Temperature, °C	Oxygen ΔG°, kcal	Oxygen E°, V	Oxygen qE°/kT	Water ΔG°, kcal	Water E°, V	Water qE°/kT
850	−169.35	1.84	19.0	−88.81	0.37	9.0
1000	−163.15	1.77	16.1	−84.77	0.85	7.7
1150	−156.99	1.70	13.9	−80.70	0.82	6.7

Tables (35). The free energy changes so calculated are probably somewhat greater than those actually taking place in the above reactions in the present study as amorphous silica rather than quartz is produced. The difference however, should not be large. The standard cell potentials E° are obtained by use of the well-known equation

$$E^\circ = -\Delta G^\circ/nF \qquad [12]$$

where $n = 4$ is the number of electrons transferred in the cell reaction and F is the Faraday.

Where $q\Delta V >> kT$, Eq. [11] assumes the limiting form

$$J = \frac{Dq}{kT} c(X) \frac{\Delta V}{X} \qquad [13]$$

where the concentration of the diffusing species $c(X)$ is proportional to the concentration of the ions adsorbed at the outer surface. The growth rate may then be cast into the form

$$\frac{dx}{dt} = \frac{M}{\rho} J = \frac{k' c}{X} \qquad [14]$$

where c is the concentration of the adsorbed ions. Equation [14] is applicable in both the linear and the parabolic regions of film growth as may be readily demonstrated by combining the adsorption and diffusion equations.

The time dependence of the concentration c in the zone of thickness δ at the surface of the oxide film is

$$\delta \frac{dc}{dt} = k_a(c_o - c)P - k_d c - \frac{k'}{X} c \qquad [15]$$

where k_a and k_d are the specific rate constants for adsorption and desorption, respectively, c_o is the concentration of active sites, and P is the partial pressure of the oxidizing species. We now introduce the usual steady state hypothesis of chemical reaction kinetics

$$\frac{dc}{dt} = 0 \qquad [16]$$

Upon solving Eq. [19] for c and introducing it into Eq. [14] we obtain

$$\left(\frac{k_a P}{k'} + \frac{k_d}{k'}\right) X \frac{dX}{dt} + \frac{dX}{dt} = k_a c_o P \qquad [17]$$

Introducing the boundary condition $X = X_o$ at $t = 0$ and integrating lends to

$$\frac{1}{2}\left(\frac{k_a P}{k'} + \frac{k_d}{k'}\right)(X^2 - X_o^2) + (X - X_o) = k_a c_o P t \qquad [18]$$

The thickness of native oxide X_o at the commencement of the thermal oxidation is small, generally of the order of 20Å for a surface which has been freshly treated with HF. As $X_o << X$ for the region of the measurements of this investigation, it has been dropped in the present analysis.

The linear rate constant may now be identified as

$$k_l = k_a c_o P \qquad [19]$$

corresponding to adsorption rate control of the growth process at small values of X.

The parabolic rate constant is given by

$$k_2 = k' \left(\frac{k_a}{k_a P + k_d}\right) c_o P \qquad [20]$$

in the linear region of dependence upon the pressure P. Thus comparison with Eq. [6] provides

$$m = k' \qquad [21]$$

$$K = \frac{k_a}{k_d + k_a} \qquad [22]$$

Acknowledgments

The participation of one of the authors (T. N.) in this research was made possible by a Fellowship under NSF Grant No. GP 1246. L. V. Gregor, D.P. Seraphim, P. J. Burkhardt, K. J. Zaininger, and A. Revesz are to be thanked for a number of very helpful discussions concerning the research. L. V. Gregor furnished the vapor polished silicon slices. The authors are particularly indebted to W. A. Pliskin for the suggestion of infrared absorbance for the determination of silicon dioxide film thickness and for making the determinations of the thickness of reference samples by the Vamfo technique for the calibration of the infra-red absorbance method.

Manuscript received Feb. 15, 1966. This paper is taken from the dissertation of one of the authors (T. N.) submitted to the Faculty of the Polytechnic Institute of Brooklyn in partial fulfillment for the Ph.D. degree, 1966.

Any discussion of this paper will appear in a Discussion Section to be published in the June 1967 JOURNAL.

REFERENCES

1. M. B. Brodsky and D. Cubicciotti, *J. Am. Chem. Soc.*, **73**, 3497 (1951).
2. J. T. Law, *J. Phys. Chem.*, **61**, 1200 (1957).
3. J. W. Evans and S. K. Chatterji, *ibid.*, **62**, 1064 (1958).
4. C. T. Sah, H. Sello, and D. A. Traymore, *J. Phys. Chem. Solids*, **11**, 288 (1959).
5. J. R. Ligenza, quoted in M. M. Atalla, E. Tannenbaum, and E. J. Scheibner, *Bell System Tech. J.*, **38**, 749 (1959).
6. M. M. Atalla, "Properties of Elemental and Compound Semiconductors," H. Gatos, Editor, vol. 5, pp. 163-181, Interscience Publishers, New York (1960).
7. J. R. Ligenza and W. G. Spitzer, *J. Phys. Chem. Solids*, **14**, 131 (1960).
8. J. R. Ligenza, *J. Phys. Chem.*, **65**, 2011 (1961).
9. W. G. Spitzer and J. R. Ligenza, *J. Phys. Chem. Solids*, **17**, 196 (1961).
10. J. R. Ligenza, *This Journal*, **109**, 73 (1962).
11. P. S. Flint, Paper presented at the Los Angeles Meeting of the Society, May 6-10, 1962, Abstract No. 94.
12. M. O. Thurston and K. O. Kang, U. S. Govt. Report AD 294657 (1962).
13. T. H. Yeh, *J. Appl. Phys.*, **33**, 2849 (1962).
14. P. J. Jorgensen, *J. Chem. Phys.*, **37**, 874 (1962).
15. N. Karube, K. Yamamoto, and M. Kamiyama, *J. Appl. Phys. (Japan)*, **2**, 11 (1963).
16. H. Edagawa, Y. Morita, S. Maekawa, and Y. Iniushi, *ibid.*, **2**, 765 (1963).
17. B. E. Deal, *This Journal*, **110**, 527, 1292 (1963).
18. A. Revesz and K. H. Zaininger, *J. Phys.*, **25**, 66 (1964).
19. H. C. Evitts, H. W. Cooper, and S. S. Flaschen, *This Journal*, **111**, 698 (1964).
20. C. R. Fuller and F. J. Strieter, Paper presented at Toronto Meeting of the Society, May 3-7, 1964, Abstract No. 74.
21. B. E. Deal and M. Sklar, *This Journal*, **112**, 430 (1965).
22. M. A. Lieberman and G. Averkion, Paper presented at San Francisco Meeting of the Society, May 9-13, 1965, Abstract No. 91.
23. B. E. Deal and A. S. Grove, *J. Appl. Phys.*, **36**, 3770 (1965).
24. P. J. Burkhardt and L V. Gregor, *Trans. Met. Soc. AIME* (to appear March 1966).
25. C. Wagner, *Z. Phys. Chem.*, **B21**, 25 (1933); **B32**, 447 (1936); *Trans. Faraday Soc.*, **34**, 851 (1938); C. Wagner and K. Grunewald, *Z. Phys. Chem.*, **B40**, 455 (1938).
26. N. F. Mott, *Trans. Faraday Soc.*, **36**, 472 (1940); **43**, 429 (1947).
27. N. Cabrera and N. E. Mott, *Rept. Progr. Phys.*, **12**, 163 (1948).
28. G. L. Christie, NASA Accession No. N65-15208, Contract No. DCBRL-TN-64-7 30 pp (1964), Sai. Tech. Aerospace Rept. **3**(s) 725 (1965).

29. A. J. Moulson and J. P. Roberts, *Trans. Faraday Soc.*, **57**, 1208 (1961); G. J. Roberts and J. P. Roberts, *Phys. Chem. Glasses*, **5**, 26 (1964).
30. W. A. Pliskin, Private communication.
31. L. V. Gregor, P. Balk, and F. J. Campagna, *IBM J. Res. and Dev.*, **9**, 327 (1965).
32. W. A. Pliskin and E. E. Conrad, *ibid.*, **8**, 43 (1964); W. A. Pliskin and R. P. Esch, *J. Appl. Phys.*, **36**, 2011 (1965).
33. W. A. Pliskin and R. P. Gnall, *This Journal*, **111**, 872 (1964).
34. D. P. Seraphim, A. E. Brenneman, F. M. d'Heure, and H. L. Friedman, *IBM J. Res. and Dev.*, **8**, 400 (1964).
35. JANAF Thermochemical Tables, Clearing House for Federal Scientific and Technical Information, U. S. Dept. of Commerce.
36. F. C. Collins and T. Nakayama, Submitted to *This Journal*.

GaSb Prepared from Nonstoichiometric Melts

F. J. Reid, R. D. Baxter, and S. E. Miller

Columbus Laboratories, Battelle Memorial Institute, Columbus, Ohio

ABSTRACT

Gallium antimonide single crystals have been prepared from melts ranging in composition from nearly stoichiometric to Sb/Ga atom ratios of about 3/1. P-type GaSb and, by suitable impurity additions, n-type GaSb have been produced with superior electrical properties. The residual acceptor concentration has been reduced to the order of $2 \times 10^{16}/cm^3$ by the growth of crystals from antimony-rich melts. Hole mobilities at 78°K of 6000 cm^2/volt-sec and electron mobilities of over 10,000 cm^2/volt-sec have been realized.

Gallium antimonide is a III-V compound semiconductor with a melting point of 706°C and a forbidden band gap of about 0.7 ev at 300°K. The compound is not difficult to prepare in single-crystal form, but it has been a particularly trying material from the standpoint of obtaining low carrier concentrations. Studies on GaSb (1-5) had revealed the highest purity material to be p-type, containing 1 to 2×10^{17} free holes/cm^3. Analysis for chemical impurities (6) indicated that there were none present, with the possible exception of carbon and oxygen, in sufficiently high concentrations to account for the residual acceptor concentration. In addition, studies by the authors (7), using lithium additions to produce ion pairs between lithium and the residual acceptor and also using additions of donor impurities to produce compensated p-type GaSb, have fairly well established the residual acceptor to be at least a doubly ionizable defect. Therefore, many possible chemical impurities, including carbon and oxygen, can be ruled out as the troublesome residual acceptor, leaving only elements, such as copper, silver, and gold and the alkali metals, which, with the possible exception of sodium, would readily be detected by spark-source mass spectrographic analysis. Thus, the possibility of the residual acceptor in GaSb being a stoichiometric or lattice defect received substantial support. In view of Effer and Etter's first report (5) of success in reducing the residual acceptor concentration in GaSb by a preparation from an antimony-rich melt, the investigation which forms the basis of this paper was undertaken.

Experimental Techniques

Crystals of GaSb were grown from melts ranging in composition from nearly stoichiometric to Sb/Ga atom ratios of about 3/1. High-purity gallium (99.9999%) and antimony (99.9999%) or zone refined GaSb were used as the starting materials. Two crystal growing techniques were used: zone freezing in which the molten zone contained the excess antimony, and crystal-pulling in which a GaSb seed was dipped into a nonstoichiometric, antimony-rich melt. In the first case (zone freezing) the composition of the antimony-rich melt remained constant because nearly stoichiometric GaSb was added by the melting of the crystal at one end of the zone and was removed at the same rate at the other end of the zone by crystallization. In the crystal pulling case, the melt composition changed as the nearly stoichiometric crystal of GaSb grew; however, crystal pulls were concluded after only a small portion of the melt was crystallized, corresponding to about 1/3 of the gallium content. The calculated maximum gradient of hole concentration along the length of our pulled crystals is about ¼ of 1% per mm of crystal pulled. Most of the electrical data pertain to the pulled single-crystal samples.

The electrical properties of interest are the Hall coefficient R and the conductivity σ. The carrier density n was calculated from the equation $R = \pm \gamma/ne$, where e is the electronic charge and $\pm$ indicates the presence of positive carriers (holes) or negative carriers (electrons). The factor γ was taken to be unity; however, the magnitude of the error introduced by this procedure at 78°K will be discussed for p-type GaSb in the section on "Results and Discussion." Another property of interest is the mobility of the charged carriers, which can be specified as a conductivity mobility μ [$\equiv \sigma_o/ne = R_{H\to\infty}\ \sigma_o$] or as a Hall mobility μ^H [$\equiv R_o\ \sigma_o$] (8), where σ_o is the zero magnetic field conductivity and R_o and $R_{H\to\infty}$ are, respectively, the weak- and strong-field Hall coefficients.

Current and potential leads were attached to the Hall samples with indium solder after the surfaces had been etched in a 10:1:90 mixture of HNO_3:HF:H_2O. The samples were placed in a Pyrex tube and measured in an ambient of helium gas or a vacuum. Hall coefficient and conductivity measurements were made at temperatures in the range 25°-400°K, using a L&N type K-3 potentiometer. In making electrical measurements, the sample current and magnetic field were reversed independently and voltage readings averaged to eliminate thermomagnetic and thermoelectric voltages.

Results and Discussion

Figure 1 shows the hole concentrations at 298° and 78°K for GaSb samples prepared from antimony-rich melts. The melt compositions are shown on the abscissa in terms of the antimony content in atomic per cent. The circles represent data for GaSb prepared by zone freezing and crystal pulling techniques in which the freezing rate was 0.16 cm/hr. The triangles represent data for crystals pulled at a rate of 0.72 cm/hr. For all pulling experiments the seed and melt were rotated in opposite directions, giving a net rotation rate of 12 rpm.

In the case of the growth of GaSb from antimony-rich melts, the controlling feature regulating the melt composition at the freezing solid/liquid interface is the segregation of excess antimony at this interface. In most elementary treatments of segregation in a freez-

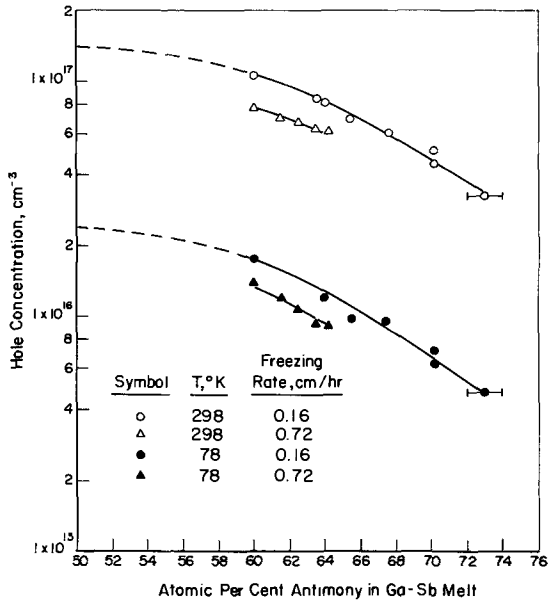

Fig. 1. Hole concentration in GaSb as a function of gallium-antimony melt composition.

ing process, it is assumed that no diffusion occurs in the solid and that the liquid remains completely mixed. Although solid-state diffusion generally can be neglected, complete mixing in the liquid is an idealized condition that is attained only in the limit as a zero freezing rate is approached or as an infinitely rapid rotation rate, and hence thorough stirring, is realized. The boundary-layer treatment of Burton *et al.* (9) for prediction of segregation in crystal growth from the melt has been extended recently by Wilcox (10). Our results are in qualitative agreement with this work, *i.e.*, a finite boundary layer having a larger antimony content than the average of the melt appears to be present particularly at the larger freezing rate. Hence, the data for samples prepared at the two freezing rates could be made to coincide if one assumed the hole concentration to be determined by the composition of a boundary layer, which is more antimony rich than the bulk of the melt.

The dashed portion of the curves in Fig. 1 represent extrapolations between nominal values of hole concentrations for GaSb prepared from nearly stoichiometric melts and data for melts containing greater than 60 a/o antimony. It is to be noted that it is not worthwhile to make a "half-hearted" attempt in investigating antimony-rich melts because even at 60% antimony only a small reduction in hole concentration is observed. This small reduction could easily be overlooked without the supporting data at larger Sb/Ga ratios.

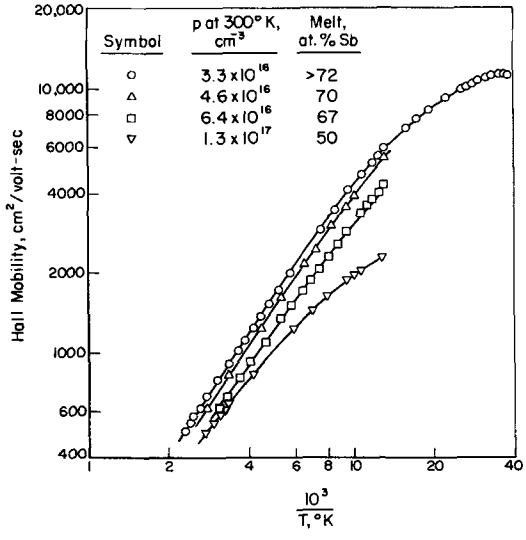

Fig. 2. Hall mobility as a function of temperature for several specimens of p-type GaSb.

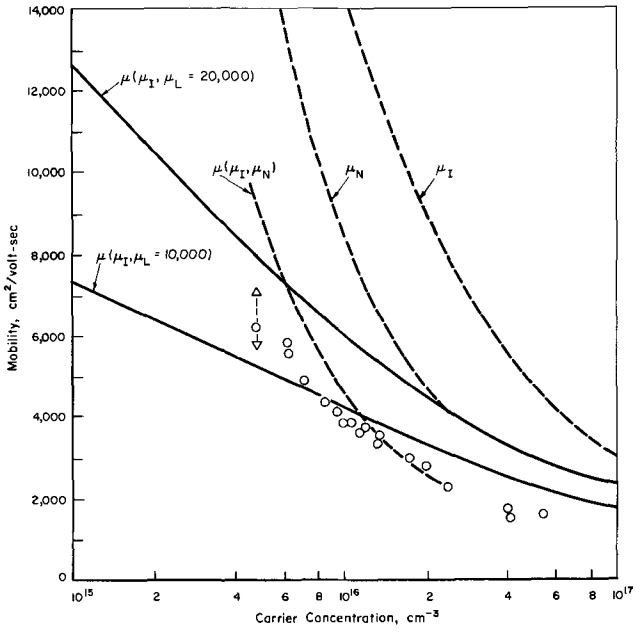

Fig. 3. Mobility at 78°K as a function of carrier concentration for p-type GaSb. △, $\mu^H[\equiv \sigma_0 R_0]$; ▽, $\mu[\equiv \sigma_0 R_{H\to\infty}]$; ○, $\sigma_0 R_{H=5.7kg}$.

Figure 2 shows the hole mobility of four p-type GaSb samples as a function of temperature. The hole concentration, p, and melt composition from which the crystal was prepared are shown. It is noted that the mobility, which is sensitive to the density of ionized defects, becomes progressively larger as hole concentration is reduced by growing from melts containing progressively larger antimony excesses. These data verify that the reduction which has been achieved in hole concentration is truly a decrease in ionized defect concentration and not the result of increased compensation. Hole mobilities reported for GaSb prepared from nearly stoichiometric melts have been in the range 2000-4000 cm²/v-sec at 78°K. Effer and Etter (5) obtained mobilities of about 5000 cm²/v-sec, and the present work has realized mobilities of about 6000 cm²/v-sec at 78°K with a value of about 12,000 cm²/v-sec at 30°K.

Figure 3 presents some data on the hole mobility in p-type GaSb as a function of the hole concentration at 78°K. Some idea of the magnetic field dependence of the Hall coefficient in p-type GaSb is revealed from the points indicative of the lowest carrier concentration sample. It is seen that μ^H/μ is about 1.2 for this sample, which is much the same as for p-type germanium (11). The open circles represent mobilities from Hall measurements done at 5700 gauss and are about 7% higher than the strong field limit (H > 15 kilogauss) in the worst case. Theoretical curves were obtained, using appropriate equations in the references cited, for an ionized-impurity scattering mobility μ_I (12, 13), a neutral-impurity scattering mobility μ_N (14), a combination of μ_I and μ_N (15), and a combination of μ_I and μ_L (16), the acoustic mode lattice scattering mobility. A dielectric constant of 15 and a hole effective mass m^* of 0.5 m_o were assumed for all cases. Values in the literature for m^* range from 0.23 to 0.5 m_o. Use of the smaller effective mass increases the theoretical mobility for the combination of μ_I and μ_L and decreases it slightly for the combination of μ_I and μ_N.

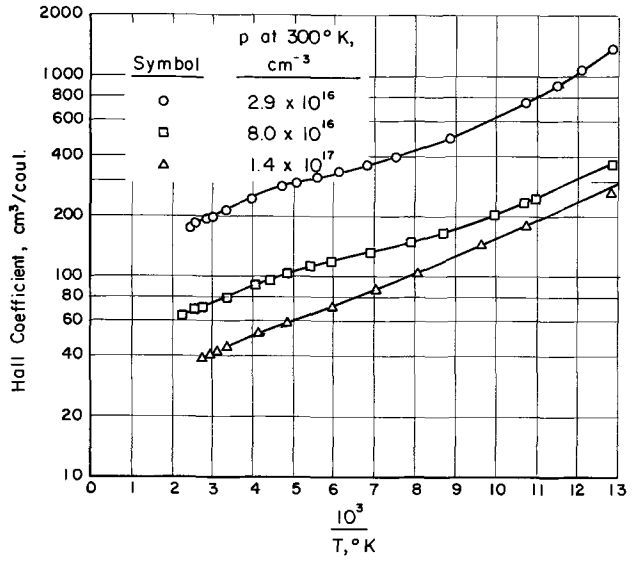

Fig. 4. Hall coefficient as a function of temperature for three different specimens of p-type GaSb.

It appears that neutral-impurity effects are significant, particularly at large carrier concentrations, because the combination of μ_I and μ_L predicts much larger mobilities than are observed at large carrier concentrations. Introducing polar mode lattice scattering only makes this situation worse. The neutral impurities are seen to arise from the deionization of acceptors as the temperature is lowered. One may appreciate this by considering the temperature dependence of the Hall effect as shown in Fig. 4. Of course, the combination of μ_I and μ_N becomes unrealistic at the smaller carrier concentrations because lattice scattering becomes controlling in this range. An integral form to combine all three scattering processes is available; however, the effort to evaluate this integral is hardly justified for present purposes.

Figure 5a shows the phase diagram for the gallium-antimony system after Greenfield and Smith (17). The solidus is, of course, so narrow in this illustration that it appears as a solid line. What one accomplishes by using nonstoichiometric melts is to lower the freezing point of GaSb by going out on the liquidus to high antimony concentrations. Hence, since the reduction in the residual acceptor concentration was shown to result from a reduction in a lattice defect concentration, it follows that the defect in question is characteristic of gallium-rich material as shown in Fig. 5b, where the abscissa scale is greatly magnified and the solidus curve was obtained from a detailed analysis of Hall effect as a function of temperature on the basis of a doubly ionizable defect model (7).

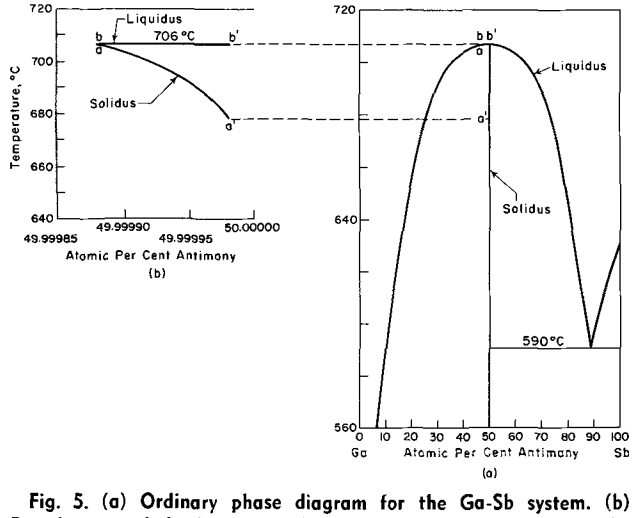

Fig. 5. (a) Ordinary phase diagram for the Ga-Sb system. (b) Greatly expanded abscissa scale revealing fine structure in the solidus aa'. Due to the narrowness in over-all composition now covered by the expanded abscissa, the deviations in the liquidus from horizontal are too small to be seen. The data sensitive enough to delineate the fine structure were obtained by analysis of electrical measurements.

Now, with the maximum melting point of GaSb lying on the gallium-rich side, and because of the existence of at least a doubly ionizable type of lattice defect, it appears likely that the nature of the defect is a gallium atom substituted on an antimony site. This follows, inasmuch as a gallium interstitial would be expected to be a donor. Also, it is unlikely that a simple antimony vacancy could act as an acceptor, especially one capable of double ionization. Actually the antistructure defect mentioned above might involve other rearrangements of the lattice in the vicinity of the suggested antistructure defect and be quite complex in reality.

One of the more interesting avenues that this investigation has opened is the possibility of obtaining relatively low carrier concentration n-type GaSb that does not contain a large concentration of compensating acceptors, particularly doubly ionized acceptors. Theoretical predictions (18) indicate that the electron mobility should be considerably higher than has thus far been realized experimentally. Figure 6 shows the electron mobility of some Te-doped samples of GaSb prepared from antimony-rich melts. The lowest curve (inverted triangular data points) is for a sample from a melt containing 68% antimony and the open-circle data points for a sample, from the same melt, when it contained 73% antimony. The increase in carrier concentration from 2.0 to 3.7 x 10^{17} per cm^3 results partly from an increase in tellurium content and partly from a reduced concentration of the doubly ionized acceptor defect. The observed increase in mobility is considerably greater than has been observed for samples of comparable carrier concentrations but with no reduction in the concentration of compensating defects.[1]

The two curves with triangular data points are illustrative of results before (inverted triangles) and after lithium diffusion into a sample of n-type GaSb. The higher carrier concentration, higher mobility sample contains lithium, which apparently pairs with acceptor defects, resulting in reduced compensation and less ionized impurity scattering (7, 20-22). Finally, the top curve is for a lithium-diffused sample which was prepared from a melt containing about 66% antimony with a smaller addition of tellurium than was used for doping the other crystals.

[1] For n-type GaSb in this carrier concentration range, the electron mobility is observed to increase with increasing carrier concentration (19).

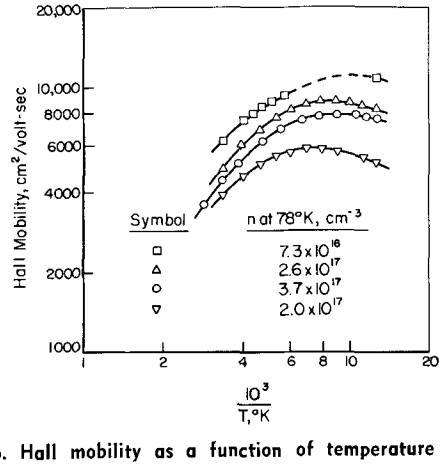

Fig. 6. Hall mobility as a function of temperature for several specimens of n-type GaSb.

Summary

It has been shown that a reduction in the residual acceptor concentration, with a corresponding increase in the hole mobility, can be effected by growing GaSb crystals from antimony-rich melts. In the improved material, with carrier densities of 2 x $10^{16}/cm^3$, it appears that the residual acceptor is still the dominant source of free carriers. Further reduction by the present techniques will be hampered by the existence of a gallium-antimony eutectic which has a Sb/Ga atom ratio composition of about 87/13. The maximum melting point of GaSb has been found to be on the gallium-rich side of the exact 1 to 1 composition. It appears that the dominant stoichiometric defect present in material prepared at the maximum melting point is not a simple vacancy defect. The most straightforward model suggested for the defect consists of gallium atoms substituted for antimony atoms on the antimony sublattice. The actual defect may be considerably more complicated involving other rearrangements of the lattice in the vicinity of the antistructure defect. However, the antistructure defect model is in good agreement with experimental observations.

The findings of this work have made it possible to produce p- and n-type GaSb with electrical properties superior to those previously attainable. The availability of such materials should permit investigations in the areas of fundamental transport properties under conditions of decreased impurity scattering, and studies of impurity behavior and device feasibility under conditions of decreased contributions from residual acceptors. An important feature of the work in growing GaSb from nonstoichiometric melts is that this is the first III-V compound in which fairly complete and convincing evidence of the importance of stoichiometric defects has been developed. It is interesting to note that, because of the very narrow width of the apparent solidus region of GaSb, analyses of electrical properties is the only method sensitive enough to delineate this region.

Acknowledgment

The authors wish to thank Dr. A. C. Beer and Dr. H. L. Goering for helpful suggestions and discussions. This paper is based on the results of research supported by the Air Force Office of Scientific Research under Grant No. 525-64 and Grant No. 525-66.

Manuscript received Jan. 5, 1966; revised manuscript received March 23, 1966. This paper was presented at the San Francisco Meeting of the Society, May 9-13, 1965.

Any discussion of this paper will appear in a Discussion Section to be published in the June 1967 JOURNAL.

REFERENCES

1. H. N. Leifer and W. C. Dunlap, Jr., *Phys. Rev.*, **95**, 51 (1954).
2. D. P. Detwiler, *ibid.*, **97**, 1575 (1955).
3. D. F. Edwards and G. S. Hayne, *J. Opt. Soc. Am.*, **49**, 414 (1959).
4. B. Boltaks and Yu. A. Guterov, *Soviet Phys.-Solid State*, **1**, 930 (1960).
5. D. Effer and P. J. Etter, *J. Phys. Chem. Solids*, **25**, 451 (1964).
6. E. B. Owens and A. J. Strauss, "Ultrapurification of Semiconductor Materials," p. 340, M. S. Brooks and J. K. Kennedy, Editors, MacMillan Co., New York (1962).
7. R. D. Baxter, R. T. Bate, and F. J. Reid, *J. Phys. Chem. Solids*, **26**, 41 (1965).
8. *See*, for example, A. C. Beer, "Galvanomagnetic Effects in Semiconductors," Supplement 4 to "Solid State Physics," pp. 98-100, Academic Press, New York (1963).
9. J. A. Burton, R. C. Prim, and W. P. Slichte, *J. Chem. Phys.*, **21**, 1987 (1953).
10. W. R. Wilcox, *J. Appl. Phys.*, **35**, 636 (1964).
11. A. C. Beer and R. K Willardson, *Phys. Rev.*, **110**, 1286 (1958).
12. H. Brooks, *ibid.*, **83**, 879 (1951) and *Advances in Electronics*, **7**, 128 (1955).
13. R. B. Dingle, *Phil. Mag.*, **46**, 831 (1955).
14. C. Erginsoy, *Phys. Rev.*, **79**, 1013 (1950).
15. T. Fukuroi and C. Yamanouchi, *Sci. Repts. Research Insts. Tohoku Univ.*, **A9**, 267 (1957).
16. See ref. 8, pp. 116-120.
17. I. G. Greenfield and R. L. Smith, *J. Metals*, **7**, 351 (1955).
18. C. Hilsum, *Proc. Phys. Soc. (London)*, **76**, 414 (1960).
19. A. J. Strauss, *Phys. Rev.*, **121**, 1087 (1961).
20. R. D. Baxter and F. J. Reid, To be published.
21. M. H. van Maaren, "The Behavior of Lithium in GaSb Single Crystals," Thesis, Ryks-Universiteit te Utrecht, The Netherlands (1965).
22. T. O. Yep and W. M. Becker, To be published in *J. Appl. Phys.*

The Epitaxial Growth of Silicon on Silicon Webs and Silicon Slices

T. L. Chu

Research Laboratories, Westinghouse Electric Corporation, Pittsburgh, Pennsylvania

ABSTRACT

Silicon webs with flat principal faces of {111} orientation are ideal substrates for the epitaxial growth of silicon, and this growth has been carried out by the pyrolysis of silane and the thermal reduction of trichlorosilane in a flow system. Epitaxial layers of good structural perfection have been grown on web substrates and accurately oriented {111} substrates at relatively low temperatures (1080°C) and high growth rates (1.5 μ/min). The exact {111} surface of the substrate has no effect on the macroscopic perfection of the epitaxial layer, in contrast with the commonly observed growth pyramids. The thermal reduction of trichlorosilane has been used for the epitaxial growth of silicon on individual silicon slices with main faces of various crystallographic orientations. The growth rate has been found to be independent of the crystallographic orientation of the substrate surface, due to the fact that the diffusion of reactants to the substrate surface is the rate-determining step of the growth process. However, when a substrate has two or more adjacent faces of different crystallographic orientations, the growth rate on these faces becomes orientation-dependent.

Silicon web consists of an extended sheet with flat faces of {111} orientation bounded by two dendrites; the sheet portion is usually much wider and thinner than the supporting dendrites (1-3). The web grows along a <211> direction, and the sheet and dendrites are of the same crystallographic orientation. Although the presence of twin planes in dendrites is essential for their growth, the twin structure of dendrites may or may not continue through the sheet. Twin planes in the sheet do not impair its usefulness for device purposes since {111} twin boundaries in silicon have been shown to have no unusual diffusion properties and no influence on p-n junction characteristics (4), and twin structures in germanium have been shown to have no detectable effects on the recombination of minority charge carriers (5). Furthermore, in contrast to dendrites, microsegregation of dopants is not observed in the sheet even in highly doped materials. Both n- and p-type webs of good crystalline perfection and of resistivities over a wide range have been prepared in long lengths. When desirable, the supporting dendrites in the web can be removed readily by using aqueous sodium hydroxide as a preferential etchant (6) or by mechanical stripping processes (7). These facts indicate that silicon webs are ideal substrates for the preparation of epitaxial devices, offering many advantages. For example, the mechanical and chemical operations involved in the preparation of substrates from conventional ingots are eliminated, and the preparation of very large area devices or continuous processing is also possible. Large area solar cells have been prepared by the epitaxial growth technique using web substrates (8).

The epitaxial growth of silicon on web substrates has been carried out to study the structural perfection and morphology of these epitaxial layers. Silicon slices with main faces of various low-index orientations, prepared from conventional crystals, were also used as substrates for comparison. The use of the thermal reduction of trichlorosilane or the pyrolysis of silane in a flow system has produced epitaxial layers of good crystalline perfection at rates of 0.5-1.5μ/min on silicon webs, the same as the growth of silicon on conventional substrates. The fact that the surface of the silicon sheet is of exactly {111} orientation has no observable influence on the structural perfection of the grown layer. Furthermore, the growth rate has been found to be independent of the crystallographic orientation of the substrate surface under conditions used in this work. These results are discussed in this paper.

Experimental

The epitaxial growth of silicon was carried out in a flow system using the thermal reduction of trichlorosilane with hydrogen or the pyrolysis of silane in a hydrogen atmosphere. Doping of the grown layer was accomplished by using diborane or phosphine as a dopant. Semiconductor grade trichlorosilane, purchased from the Union Carbide Corporation, was purified by fractional distillation through a quartz column. Semiconductor grade silane, purchased from Gray Chemical Company, was used without further purification. Commercial grade hydrogen was purified by diffusion through a palladium-silver alloy.

Silicon webs used in this work, grown at the Westinghouse Research Laboratories and the Westinghouse Semiconductor Division (1,2), had dislocation densities of 0-10^2 cm^{-2} and 10^2-10^4 cm^{-2} on the main faces and across sections, respectively. When the webs had been exposed to the laboratory atmosphere over a period of time, they were cleaned successfully with organic solvents, hydrofluoric acid, and deionized water, or etched briefly in a hydrofluoric acid-nitric acid mixture. In some cases, the dendrites were removed by using a 30% sodium hydroxide solution at 95°C as a preferential etchant (6) in which the dendrites exhibited considerably faster dissolution rate than the sheet portion. The silicon substrates prepared from Czochralski crystals were of {111}, {110}, {100}, and {211} orientations; x-ray goniometric measurements indicated that the surfaces of {111} oriented substrates deviated no more than 15 min from a {111} orientation. They were mechanically lapped with American Optical Company No. 305 abrasive and chemically polished with CP_4. To minimize foreign contaminants on the substrate surface, the subsequent operations such as rinsing, drying, assembly, etc., were carried out in a laminar flow ultraclean bench where the air was filtered with Cambridge absolute filters.

The growth process was carried out in a horizontal fused silica tube, and the substrates were placed on a silicon or silicon-coated graphite heater in this tube. To determine the dependence of growth rate on the crystallographic orientation of substrate surfaces, silicon webs and conventional substrates of various orientations were used in the same experiment so that the growth on each substrate proceeded under almost

identical conditions of temperature, reactant composition, etc. The temperature variation among all substrates in a given experiment was less than 10°C. Prior to the growth process, the substrates were further etched in the reaction tube with anhydrous hydrogen chloride (9) or water vapor (10). Both techniques were found to yield the same results. During the growth process, the substrate temperature was varied from 1050° to 1180°C, and the reactant contained 0.07-0.5% silane or 0.5-2% trichlorosilane. The deposition rate was 0.5-1.5 μ/min. The thickness variation of the epitaxial layer among substrates in a run was usually less than 10%.

The structural perfection of epitaxial silicon layers was evaluated by chemical etching using the Sirtl etch[1] (11). The thickness of the grown layer was determined either by cross-sectioning technique or from the dimensions of the etch figures of stacking faults on the as-grown surface (12). The growth thicknesses determined by these techniques were in good agreement.

Results and Discussion

Growth on silicon webs.—Epitaxial silicon layers were deposited on silicon webs at 1080°C by the pyrolysis of silane in a flow system using hydrogen as a diluent. The reactant mixture contained 0.07-0.5% silane, yielding deposition rates in the range of 0.5-1.5 μ/min. Similar deposition rates were obtained by the thermal reduction of trichlorosilane on silicon webs at 1170°-1180°C. In these experiments, accurately oriented {111} silicon slices were also used as substrates for comparison. The as-grown surfaces of all epitaxial layers prepared under proper cleanness conditions were planar and followed the topography of the substrate.

The absence of triangular pyramidal defects on these epitaxial layers is in contrast with the commonly observed effects of accurately oriented {111} substrates on the surface morphology of epitaxial germanium and silicon. For example, triangular growth pyramids were observed invariably on epitaxial germanium deposited on accurately oriented {111} substrates by the transport technique in a closed or an open system (13, 14). However, the growth on substrates misoriented from a <111> direction appeared to be free of pyramids. Pyramids were also observed frequently on {111} oriented epitaxial silicon layers prepared by the thermal reduction of silicon tetrachloride, depending on the deposition rate and the degree of misorientation of the substrate surface (15). At a given temperature, pyramids were found to form when the deposition rate for a particular substrate orientation exceeded a certain value, about 1 μ/min at 1200°C for a substrate with a 0.5° misorientation from the <111> direction. Thus, the pyramidal growth has been attributed to the effects of the substrate orientation, and the use of substrates misoriented 0.5° or more from a <111> direction has long been a general practice. On the other hand, it was found in this work that the grown layer on webs or on {111} oriented substrates always had high concentrations of growth pyramids over the entire surface when foreign impurities were present on the substrate surface or in the growth system. Since planar growth was achieved at relatively low temperature (1080°C) and high growth rates (1.5 μ/min) by using proper *in situ* etching and growth techniques, foreign impurities must be one of the factors governing the pyramidal growth. Other growth parameters such as the substrate temperature and the nature of the chemical reaction also play important roles. It is believed, however, that the growth on webs and accurately oriented {111} substrates is more susceptible to the effect of impurities than that on substrates slightly off from a {111} orientation. A misoriented {111} plane may be considered as consisting of many steps with nominal {111} faces, and the region along these steps will facilitate the nucleation process thus minimizing the effects of impurities.

[1] 100g anhydrous CrO_3, 200 ml H_2O, and 200 ml 49% HF.

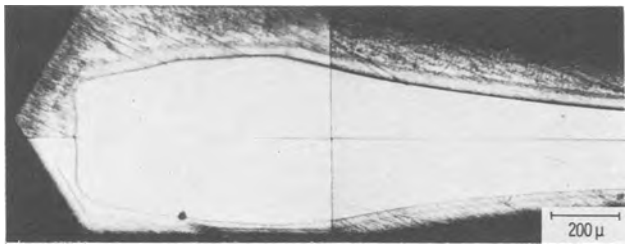

Fig. 1. Portion of the cross section of a specimen perpendicular to the long dimension of the silicon web showing the epitaxial growth of silicon on the web, Sirtl etch, 1 min.

The morphology of the cross section of epitaxial silicon deposited on silicon webs is of interest. Figure 1 shows a portion of the cross section of a specimen with an epitaxial layer of approximately 120μ in thickness prepared by the thermal reduction of trichlorosilane. This cross section was made perpendicular to the long dimension of the web; its surface is therefore of {211} orientation. The substrate-deposit interface and the twin plane in the web and supporting dendrite were brought out by chemical etching. The growth on the bottom surface of the web was due mainly to the transfer of silicon from the heater surface. It is noted that the grown material has a hexagonal cross section. This hexagonal geometry is a result of the dependence of growth rate on the crystallographic orientation of the substrate surface. Since, on the vertically cross-sectioned surface, the side faces make an angle of approximately 118° and the angle between a side face and a grown surface is approximately 121°, these side faces are therefore of {311} orientation. The {311} side faces were also found in the silicon ribbon prepared by the iodine transport of silicon in a closed tube containing impurities (16). Furthermore, when a single crystal silicon filament with its axis oriented in a <211> direction was used as the substrate, the crystal developed to a slightly irregular hexagon with two sets of adjacent {311} faces separated by {111} faces (17, 18). The development of the {311} faces presumably arises from the fact that the {311} planes are the lowest energy planes perpendicular to the {211}.

Epitaxial silicon was also grown on silicon sheets after the supporting dendrites were removed from the web. Figure 2 shows the cross section of a specimen consisting of four epitaxial layers of different resistivities deposited on a silicon sheet by the thermal reduction of trichlorosilane. The left-hand photograph shows the growth near the edge of the sheet, and the right-hand photograph shows the growth at the center of the sheet. Although the cross section of the specimen still has a hexagonal geometry, the growth thickness along the thickness direction of the sheet is highly uniform.

Structural imperfections in epitaxial silicon layers on silicon webs were mostly inherited from the web. The imperfections in the web are mainly the twin lamella and dislocations. The twin lamella have no effect on the perfection of the epitaxial layer except

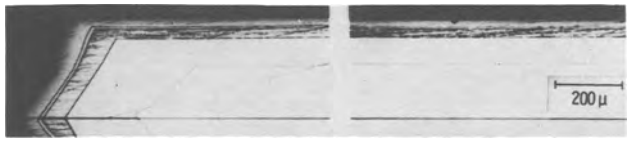

Fig. 2. Two regions of the cross section of a specimen perpendicular to the long dimension of the silicon sheet, showing the uniform growth of silicon on the sheet, Sirtl etch, 30 sec. The regions of different resistivity in the grown layer are delineated by chemical etching.

when the twin plane terminates at the principal surface of the web. Under this condition, random growth always occurred at this region. Silicon webs may have dislocations with axes perpendicular and parallel to the main face; only the former propagated into the epitaxial layer. Under proper growth conditions, the epitaxial layers were essentially free from process-induced imperfections such as stacking faults, growth pyramids, polycrystalline inclusions, etc. Results indicate that p-n junctions prepared by depositing n- or p-type silicon on webs of opposite conductivity type exhibited good electrical characteristics (19).

Dependence of growth rate on crystallographic orientations of substrates.—The dependence of the growth rate of epitaxial germanium and silicon on the crystallographic orientation of the substrate surface has been of general interest. In the epitaxial growth of germanium on a {110} oriented germanium substrate by the closed-tube transport technique, the variation in the growth thickness around the periphery of the substrate indicated that the growth rate increased with crystallographic direction in the following order <100>, <111>, <110> (20). During the epitaxial growth of silicon on a silicon rod with its axis in a <111> direction, {$\bar{1}$10} and {$\bar{2}$11} faces were developed initially (17, 18). A nearly regular hexagonal habit with six {$\bar{2}$11} faces resulted after prolonged growth, indicating a higher growth rate along the <$\bar{1}$10> directions. When individual silicon slices of various crystallographic orientations were used as substrates for the growth of silicon by the thermal reduction of silicon tetrachloride at 1200°C, the deposition rate was found to increase as the substrate surface deviated from the {111} orientation, and the growth rate on the {110} oriented substrates, about 1.3 μ/min, was more than twice of that on the {111} oriented substrates (15).

In this work, the growth rate of silicon on individual slices with main faces of {111}, {110}, {100}, and {211} orientations and on silicon webs was compared using the thermal reduction of trichlorosilane at 1170°C. The growth rate was in the range of 0.5-1.5 μ/min, and the duration of each experiment was adjusted to yield epitaxial layers of approximately 100μ in thickness to minimize measurement errors. The results of many experiments under these conditions indicated that the growth rate was independent of the crystallographic orientation of the substrate surface. These results are in contrast to those obtained by the tetrachloride process (15) and will be discussed in relation with the growth process.

In the growth process under consideration, the formation of silicon by the chemical reaction takes place predominately on the heated substrate surface since no silicon is deposited on the cooler walls of the reaction tube. Most probably, the growth process involves the following consecutive steps: the diffusion of reactant molecules to the substrate surface, the adsorption of one or more reactant species on the surface, the chemical reaction on the surface and the incorporation of silicon atoms into the crystal lattice, the desorption of by-products and their diffusion away from the surface. The over-all rate of the growth process is controlled by the slowest of these steps. If epitaxial layers of good perfection are to be obtained, the rate of chemical reaction must be equal to or slower than the rate of incorporation of silicon atoms into the crystal lattice. Otherwise, silicon atoms not incorporated into the crystal would yield polycrystalline deposits since they cannot evaporate at appreciable rates at temperatures used in the growth process. Thus, the addition of silicon atoms to the crystal lattice is not the rate-determining step of the growth process. Furthermore, under growth conditions used in this work, the growth rate was found to be independent of substrate temperature in the temperature range 1150°-1220°C, similar to the findings of Glang and Wajda concerning the trichlorosilane process (21). Since the chemisorption of reactants on the substrate surface and their subsequent reaction have appreciable activation energies, these processes cannot, therefore, be the rate-determining steps of the growth process. Thus, the rate of the growth process must be limited by the rate of diffusion of the reactant molecules to the substrate surface, and the diffusional resistance is concentrated predominately in a laminar layer in the immediate vicinity of the substrate surface. When individual silicon slices are used as substrates in the epitaxial growth process, each substrate has a main face of one crystallographic orientation exposed to the reactant mixture. All substrate surfaces are maintained at the same temperature and are subjected to the same flux of reactants. Since the diffusion of reactants is the rate-determining step in the trichlorosilane process, the diffusion, adsorption, and chemical reaction at all substrate surfaces takes place at the same rate irrespective of the crystallographic orientation of the substrate surface. Consequently, the same number of silicon atoms deposit on a unit area of each substrate surface, and the growth thickness or growth rate is the same. It should be noted that, although the number of atomic layers grown on substrate surfaces of various orientations and the density of atoms on these crystallographic planes are different, their product is a constant. For example, the average spacings of atomic layers parallel to {111}, {110}, {100}, and {211} planes are of the ratio $1 : \sqrt{\frac{3}{2}} : \frac{\sqrt{3}}{2} : \frac{3\sqrt{2}}{4}$, and the average density of atoms on these planes also have the same ratio.

The kinetics of the epitaxial growth of silicon by the tetrachloride process has been studied by several authors; however, their results on the variation of growth rate with substrate temperature have not been consistent. While a linear relation between the logarithm of the growth rate and the reciprocal of the absolute temperature was observed over the temperature range 900°-1300°C by Theuerer (22), the growth rate was found by Bylander to be relatively temperature-independent at substrate temperatures higher than 1100°C (23). When the growth rate is temperature-dependent, the surface processes, chemisorption, and chemical reaction, become the rate-determining steps of the growth process. Since substrate surfaces of various crystallographic orientations possess different structure and consequently different chemical reactivity, the growth rate may depend on the orientation of the individual substrate as reported by Tung (15).

When a substrate with two or more adjacent faces of different crystallographic orientations is used for epitaxial growth, the growth rate could become orientation-dependent even when the growth process is governed by the diffusion process. The difference in the growth rate of silicon on adjacent {111} and {311} planes of the web by the trichlorosilane process is shown in Fig. 1 and 2. This is again related to the different chemical reactivity associated with surfaces of different orientation. After the reactant molecules diffused through the laminar layer, the various faces of the substrate compete for these molecules resulting in the orientation dependence of the growth rate.

Summary and Conclusions

Epitaxial silicon layers of good structural perfection have been deposited, at rates of 0.5-1.5 μ/min, on silicon webs at 1080°-1180°C by the pyrolysis of silane and the thermal reduction of trichlorosilane in a flow system. Contrary to the common belief, the use of substrates of exactly {111} orientation, such as the main faces of the web, had no observable influence on the structural perfection of the epitaxial layer when the layer was grown at relatively low temperatures (1080°C) and high deposition rates (1.5 μ/min). How-

ever, good *in situ* etching and growth techniques were found to be necessary for obtaining planar surfaces. Dislocations with axes perpendicular to the main face of the web were continued into the web, and twin planes terminating at the principal face of the web promoted the random growth. However, these imperfections in the web are easily eliminated, and silicon webs are ideal substrates for the preparation of epitaxial devices.

When individual silicon slices of various low-index orientations were used as substrates, the growth rate of silicon at 1170°C, obtained by the thermal reduction of trichlorosilane at rates up to 1.5 μ/min, was found to be independent of the crystallographic orientation of the substrate surface. This is due to the fact that the diffusion of reactant molecules to the substrate surface rather than the incorporation of silicon atoms into the crystal lattice is the rate-determining step of the growth process. However, when a substrate has two or more adjacent faces of different crystallographic orientations, the growth rate on these faces is orientation-dependent because of their difference in structure and bonding requirements.

Acknowledgment

The author wishes to thank J. R. Gavaler, G. A. Gruber, R. L. Tallman, and S. Wickersham for their contributions in various phases of experimental work.

Manuscript received Jan. 10, 1966; revised manuscript received March 14, 1966.

Any discussion of this paper will appear in a Discussion Section to be published in the June 1967 JOURNAL.

REFERENCES

1a. S. N. Dermatis and J. W. Faust, Jr., Electrochem. Soc. Electronics Div. Abstracts, **11** [1], 123 (1962).
1b. S. N. Dermatis and J. W. Faust, Jr., *IEEE Trans. Comm. and Elect.*, **65**, 194 (1963).
2. S. O'Hara and A. I. Bennett, *J. Appl. Phys.*, **35**, 686 (1964).
3. T. N. Tucker, Electrochem. Soc., Electronics Div. Abstracts, **14** [1], 157 (1965).
4. H. J. Queisser, *This Journal*, **110**, 51 (1963).
5. J. P. McKelvey, *J. Appl. Phys.*, **32**, 442 (1961).
6. D. W. Ing, *This Journal*, **112**, 1251 (1965).
7. R. K. Riel, Westinghouse Semiconductor Division, Private communication.
8. K. S. Tarneja and R. K. Riel, "Drift-Field Silicon Solar Cell," paper presented at the 1965 Photovoltaic Specialist Conference, NASA Goddard Space Flight Center, Greenbelt, Md., Oct. 18-20, 1965.
9. K. E. Bean and P. S. Gleim, *This Journal*, **110**, 265C (1963).
10. T. L. Chu and R. L. Tallman, *ibid.*, **111**, 1306 (1964).
11. E. Sirtl and A. Adler, *Z. Metalk.*, **52**, 529 (1961).
12. T. L. Chu and J. R. Gavaler, *This Journal*, **110**, 388 (1963)
13. H. S. Ingham, Jr., P. J. McDade, and D. M. J. Compton, in "Metallurgy of Elemental and Compound Semiconductors," R. O. Grubel, Editor, Metallurgical Soc. Conferences, Vol. 12, p. 285, Interscience Publishing Co., New York (1961).
14. A. Reisman and M. Berkenblit, *This Journal*, **112**, 315 (1965).
15. S. K. Tung, *ibid.*, **112**, 436 (1965).
16. E. S. Greiner, J. A. Gutowski, and W. C. Ellis, *J. Appl. Phys.*, **32**, 2489 (1961); R. S. Wagner and R. C. Trenting, *ibid.*, **32**, 2490 (1961).
17. E. Sirtl and K. Reuschel, *Z. anorg. u. allgem. Chem.*, **332**, 113 (1964).
18. J. E. Allegretti, D. J. Shombert, E. Schaarschmidt, and J. Waldman, in "Metallurgy and Elemental and Compound Semiconductors," R. O. Grubel, Editor, Metallurgical Soc. Conferences, Vol. 12, p. 255, Interscience Publishing Co., New York (1961).
19. J. Philips and D. Walczak, Westinghouse Semiconductor Division, Private communication.
20. J. C. Marinace, *IBM Journal*, **4**, 248 (1960).
21. R. Glang and E. S. Wajda, in "Metallurgy of Semiconductor Materials," J. B. Schroeder, Editor, Metallurgical Society Conferences, Vol. 15, p. 27, Interscience Publishing Co., New York (1962).
22. H. C. Theuerer, *This Journal*, **108**, 649 (1961).
23. E. G. Bylander, *ibid.*, **109**, 1171 (1962).

Effect of Dry Oxygen on Conductivity of Fluoridated Silicon Surfaces

M. Yamin and R. Lieberman

Bell Telephone Laboratories, Incorporated, Murray Hill, New Jersey

ABSTRACT

When high resistivity silicon surfaces are heated in dry nitrogen at temperatures below 350°C, a marked rise in surface conductivity may occur. When the surface is subsequently exposed to dry oxygen at room temperature, a rapid decrease in surface conductivity occurs. The magnitude of the effect was found to depend on the chemical treatment of the surface prior to heating and on the subsequent thermal history of the surface. The greatest effect was found on surfaces which had been exposed to HF vapor. Exposure of the surface to water tended to decrease the magnitude of the conductivity changes.

This paper describes a study of changes in surface conductivity which occur on gas baking of unpassivated silicon surfaces. The material used was 700 ohm-cm n-type silicon, cut into bars about 0.015 x 0.060 x ¾ in. Ohmic gold-antimony contacts were alloyed to either end, and the bars were etched bright in 10 HNO_3:1 HF. The resistance of the bars was about 10^5 ohms and was essentially constant at measuring voltages from −10 to +10v. The samples were mounted by their gold leads in a glass cell through which dry gases could be passed. The cell, which also contained an iron-constantan thermocouple, could be surrounded by either a small resistance furnace for heating or a thermostated water jacket for measurement. All resistance measurements were taken in this cell at 30° ± 0.1°C in the dark, using a General Radio No. 650A impedance bridge, the measuring voltage being 1v d.c. The gases used were dry nitrogen and dry oxygen. The oxygen was passed through a freshly regenerated Lectrodryer; the nitrogen came from a dry nitrogen line whose moisture content was generally less than 5 ppm. The gas handling system was all metal, except for a short length of polyethylene tubing. A flow rate of 0.5 to 1.0 l/min was used through the 150 ml glass cell.

The fundamental effect with which this paper is concerned will be referred to as the "oxygen effect." The oxygen effect of a typical specimen is illustrated

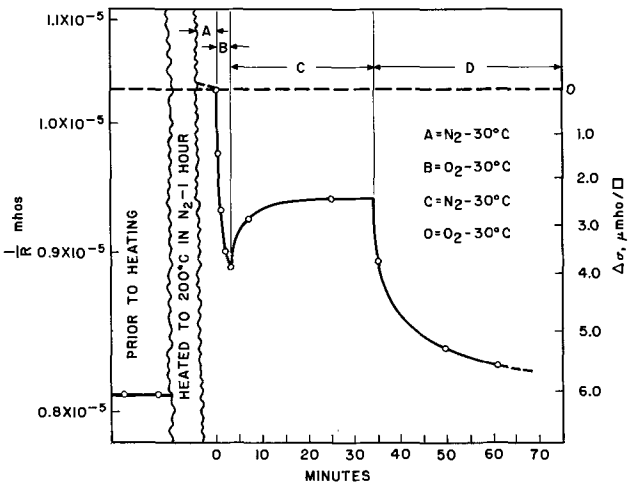

Fig. 1. Oxygen effect. Conductance (1/R) is initially 0.81×10^{-5} mho. After heating in dry nitrogen and cooling to 30°C, the conductance is 1.03×10^{-5} mho. Exposure to dry oxygen causes a rapid decrease in conductance. Changing of the gas back to nitrogen halts this decrease, but it resumes on restoring oxygen. This cycle can be repeated by reheating the specimen in dry nitrogen. The values of $\Delta\sigma$ (decrease in surface conductivity) are referred to the value immediately before the exposure to oxygen.

in Fig. 1. The scale at the left is measured 1/R; that on the right is the surface conductivity relative to that when the oxygen was first applied to the specimen. The conductance 1/R of the specimen is measured at 30°C in dry nitrogen. The specimen is then heated in dry nitrogen in the 150°-300°C range. On cooling to 30°C, a significantly higher value of conductance than that prior to the heating cycle may be observed. This value of conductance will show only a slow downward drift in nitrogen. If the ambient is now changed to oxygen, a rapid decrease in conductance will occur. If, while the conductance is decreasing in oxygen, the ambient is switched back to dry nitrogen, the rapid drop in conductance will be interrupted, and the conductance may even rise a little. Restoring oxygen will cause the drop in conductance to resume, eventually leveling off, usually at a value slightly lower than that before the hot nitrogen-cold oxygen cycle. Reheating the sample in dry nitrogen will restore the high conductance value, and the oxygen effect can then be repeated. No such effect is observed if the heating phase is conducted in oxygen; in fact, this treatment destroys the subsequent reactivity of the sample. The conductance changes can correspond to a rise in surface conductivity after nitrogen baking, and a subsequent drop on exposure to cold oxygen, as high as 20 μmho/□; the measured resistance of the specimens used can actually double in a few minutes on exposure to oxygen.

This effect is not obtained invariably on a given silicon surface, and its magnitude is subject to considerable variation. In this work, the magnitude of the oxygen effect is used to measure the reactivity of the surface to the hot nitrogen-cold oxygen cycle after various chemical and thermal treatments. A standard measurement routine was used. The sample was dried at room temperature for 30 min in flowing dry nitrogen after a chemical treatment, then heated in dry nitrogen for 30 min at the desired temperature. The cycling cell was next surrounded by the 30°C water jacket and let stand with nitrogen flowing for 20 min. At this point the resistance was measured, giving a value R_1, and the gas flow was changed to dry oxygen. Resistance measurements were made for 30 min, at which time the resistance had virtually ceased to rise. This final resistance was R_2. Resistance measurements were related to the surface conductivity change, on the assumption that the bulk resistivity remained unchanged, by the following equation

$$\Delta\sigma = \frac{L}{P}\left(\frac{1}{R_1} - \frac{1}{R_2}\right) \qquad [1]$$

where L is the distance between the gold contacts and $P = 2t + 2w$, where t is the thickness of the sample and w its width.

Effect of Surface Fluoridation

The first requirement for investigation of the effect was to determine a chemical treatment which would invariably produce a reactive surface as a starting point for further investigations. It was observed that re-etching an unreactive surface in HNO_3-HF mixtures restored its reactivity, but considerable variation was introduced as a result of the necessary rinsing operations which followed etching. Eventually it was found that exposure of the specimen for 15 min to the vapor over 48% aqueous HF solution at room temperature would produce surfaces which were most reactive to the hot nitrogen-cold oxygen cycle, and that this treatment would regenerate the reactivity of a surface whose reactivity had been destroyed as described below. For example, one specimen showed a value of $\Delta\sigma$ (determined as defined in Eq. [1], following nitrogen baking at 267°C) of 5.22 μmho/□ when freshly etched; subsequently, its $\Delta\sigma$ was reduced to 0.20 μmho/□ by thermal treatment as described below, but exposure to HF vapor restored a $\Delta\sigma$ of 5.89 μmho/□.

Effect of Temperature of Heating

The oxygen effect obtained is a function of the temperature at which the hot nitrogen phase of the cycle is carried out, and also of the thermal history of the sample. The behavior of a specimen on many repetitions of the hot nitrogen-cold oxygen cycle is illustrated in Fig. 2, in which $\Delta\sigma$ for each of 26 consecutive hot nitrogen-cold oxygen cycles is represented by a vertical line. The initial $\Delta\sigma$ for this specimen after HF activation was 8.3 μmho/□ with a heating temperature, T_H, of 150°C. On subsequent cycles, with T_H = 150°C, $\Delta\sigma$ declined to about 4 to 5 μmho/□, but after the 5th cycle remained relatively constant. Increasing T_H to 200°C again produced a $\Delta\sigma$ in this range, and so did going to 250°C (cycle 15) and to 300°C (cycle 18). Cycle 19, with T_H = 200°C, however, produced a much lower $\Delta\sigma$ of 1.1, and cycle 21, with T_H = 250°C, produced a $\Delta\sigma$ of 2.0. The interspersed cycles, 20 and 22, with T_H = 300°C nevertheless produced $\Delta\sigma$'s of 3.7 and 3.6, nearly as high as the

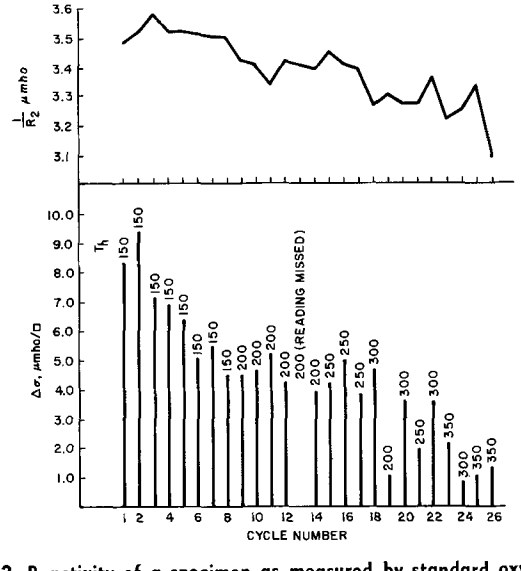

Fig. 2. Reactivity of a specimen as measured by standard oxygen effect $\Delta\sigma$ on many repetitions of the hot N_2-cold O_2 cycle. Upper diagram shows that final conductance, $(1/R_2)$, in oxygen tends to decrease with many repetitions of the cycle.

previous 200° and 250°C results. Going to $T_H = 350°C$ on cycle 23, we see that we destroy the subsequent reactivity of the specimen at 300° and also at 350°C. Some apparent increase in the reactivity on 400°C cycling is observed, but since this is above the eutectic temperature of the gold-silicon alloy contact, other influences than that of temperature on the silicon surface may be present.

This pattern of behavior, which is typical of that observed with a number of specimens, seems to lead to the following generalization. After the initial decline of $\Delta\sigma$ on the first few cycles, a relatively constant value will be observed for T_H between 150° and 300°C, so long as any cycle is performed at a temperature equal to or greater than all previous T_H. However, heating to any temperature in this range destroys reactivity at any lower temperature. Heating at 350°C destroys reactivity at any temperature including 350°C.

Also plotted in Fig. 2 is $1/R_2$ for the specimen, that is, its final stable value of conductance in dry oxygen subsequent to each cycle. It will be observed that this value creeps slowly downward during the experiment.

As mentioned earlier, the reactivity of this specimen is entirely restored by exposure to HF vapor.

Effect of Water Soaking

In order to investigate the effects of chemical treatments on the reactivity of silicon surfaces to the hot nitrogen-cold oxygen cycle, the values of $\Delta\sigma$ were compared for two silicon specimens which were given identical treatment except for the chemical process under investigation. The two specimens were mounted together in the glass cycling cell, activated together by exposure to HF vapor, heated together to a standard temperature (which was fixed at 250°C for such investigations), and exposed to dry oxygen after cooling to 30°C. The chemical treatment being investigated was applied to one of the specimens prior to the heating cycle. As Fig. 2 shows, the magnitude of $\Delta\sigma$ changes from one heating cycle to the next, presumably as a result of variations in temperature and time of heating as well as of changes in the silicon surface. It is assumed that for two similarly treated specimens essentially the same cycle-to-cycle variation of $\Delta\sigma$ will occur, and that therefore the ratio of $\Delta\sigma_t$ (for the treated specimen) to $\Delta\sigma_c$ (for the control specimen) will be constant. If one of the specimens is subjected to a chemical treatment, any change in the ratio $Y = \Delta\sigma_t/\Delta\sigma_c$ must reflect this treatment; even if random variations of Y occur, repeated chemical treatment of one specimen should produce a constant variation in Y which is distinguishable from random change.

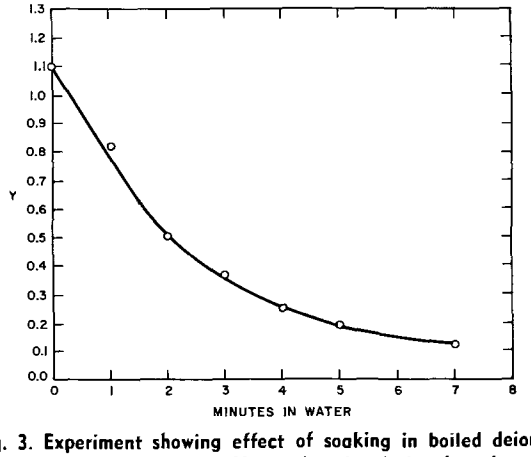

Fig. 3. Experiment showing effect of soaking in boiled deionized water at room temperature. $Y = (\Delta\sigma_t/\Delta\sigma_c)$ is plotted against total time of soaking of the test specimen in water; test and control specimens are subjected to identical hot N_2-cold O_2 cycle after each period of water treatment.

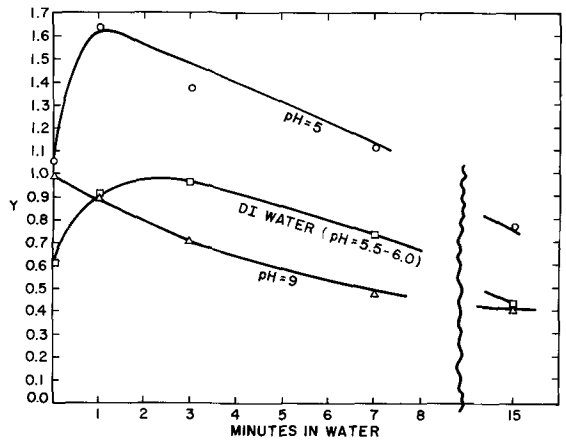

Fig. 4. Effect of soaking in water at three pH levels

The particular treatment investigated was water soaking at 30°C. The test specimen would be immersed in water for a measured interval, usually 1 or 2 min, and dried; the hot nitrogen-cold oxygen cycle would then be performed on both test and control specimens; then the water treatment would be repeated. Figures 3 and 4 show the results of such an experiment. In Fig. 3, the ratio Y is plotted against total minutes of soaking of the test specimen at room temperature in deionized water which had been boiled and cooled in flowing nitrogen to remove dissolved oxygen and carbon dioxide. It is seen that the effect of water is to reduce the reactivity of the treated specimen far below that of the control specimen; after about 7 min, the ratio Y has been found to level off at some value generally between 0.1 and 0.4. (In some cases, the initial value of Y is not 1.0, as a result, presumably, of variations in the HF activation procedures.) The presence or absence of oxygen in the water does not seem to be significant. In Fig. 4, similar plots are shown for three samples of water: one, as obtained from the deionizing system, whose *p*H was measured with a Beckman *p*H meter as 5.5-6.0 (this acidity probably resulting from dissolved carbon dioxide); one whose *p*H had been adjusted to 5.0 with HCl; and one whose *p*H had been adjusted to 9.0 with NaOH. The basic solution is seen to have a different initial effect on the reactivity of the silicon surface than the acidic ones.

Discussion

It appears from the experimental results described above that five reactions occur on silicon surfaces, all of which affect the surface conductivity. They are:

1. The reaction of HF with the surface (activation reaction).
2. The reaction of the activated surface on heating in nitrogen, which produces a large increase in surface conductivity.
3. The reaction of the above conductive surface with oxygen at room temperature.
4. The reaction that causes the activated surface to lose its reactivity on heating to elevated temperatures in nitrogen.
5. The reaction that causes the activated surface to lose its reactivity on exposure to water at room temperature.

Buck and McKim (1) have studied the effects of chemical treatments on the surface conductivity of silicon. Figure 5, in which surface conductivity is plotted against the position of the Fermi level at the surface, U_s, for 425 ohm-cm n-type silicon, is adapted from their Fig. 1. This figure was constructed using the data of Kingston and Neustadter (2). The curve for 700 ohm-cm material would not be significantly different for the purposes of this discussion. Buck

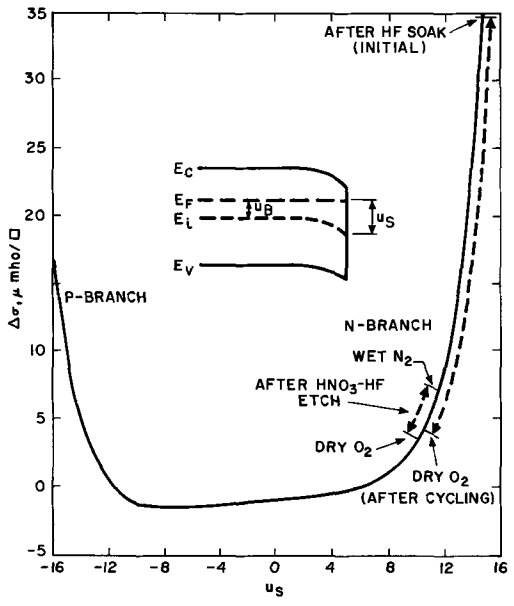

Fig. 5. Surface conductivity (referred to flat band condition) of 425 ohm-cm n-type silicon vs. surface potential. Adapted from ref. 1, Fig. 1 by courtesy of the authors.

and McKim (1) found that soaking in HF produced a very strong n-shift; Brattain-Bardeen cycling of this surface resulted in a decrease in surface conductivity in dry oxygen and an increase in wet nitrogen, but this was superimposed on a steady downward trend in surface conductivity. Etching in HNO_3-HF also produced an n-type surface as shown. It is likely that reaction 1 in our listing above produces a surface similar to that resulting from HF soaking; we may assume that the effect of HF treatment is to remove any oxide present and to produce a surface on which many of the free valence bonds of surface silicon atoms are satisfied with fluorine. It is also likely that reaction 5 is the hydrolysis of Si-F surface groups to Si-OH by water; this would be similar to the irreversible decrease in surface conductivity found by Buck and McKim on repeated wet-dry cycling. We may further speculate that reaction 4 also results in the elimination of fluoride from the silicon surface, in this case perhaps by the condensation of a number of surface fluorine atoms on a single silicon atom causing eventual bond rupture and volatilization as silicon tetrafluoride. It is seen from Fig. 2 that this reaction also causes an irreversible decrease in surface conductivity. Thus, our hypothesis is that the activation reaction is fluoridation; the deactivation reactions result from the removal of fluoride and the conversion of the silicon surface to its normal oxidized (or hydroxylated) condition.

This leaves reactions 2 and 3: those which constitute the oxygen effect. Reaction 2, which occurs on nitrogen baking, raises the surface conductivity; we may assume that this treatment produces an n-shift in surface potential, and that reaction 3, on exposure to dry oxygen, reduces the potential in the p-direction. (If the effect of nitrogen baking were to transfer the potential to the p-branch, we might expect a minimum in conductivity with time during exposure to oxygen; this is not observed.) The simplest way to discuss these reactions is to assume that a fluoridated silicon surface which has been exposed to air is covered with a layer of adsorbed oxygen; reaction 2 would then be the desorption of the oxygen layer and reaction 3 its readsorption. Hall, Baird, and Williams (3) have observed, by gas chromatography, an enhancement of oxygen adsorption on an HF treated surface.

It is interesting that a fluoridated silicon surface reversibly adsorbs oxygen; if the surface were not fluoridated, it would of course immediately and irreversibly react with the oxygen to form the first layer of oxide; in fact, part of the loss of reactivity to the hot nitrogen-cold oxygen cycle on repeated cycling may result from some of the adsorbed oxygen penetrating the fluoride layer to form such oxide. The ease of desorption probably indicates that the adsorbed species is molecular oxygen. The binding force may be of a van der Waals type, but it is interesting to speculate whether there may be some sharing of electrons in the conduction band of the n-type silicon with orbital levels in the oxygen molecule, producing a weak binding. Such a mechanism would help to account for the p-type shift of the surface potential on adsorption of oxygen.

The effects observed have important implications regarding the stability of silicon semiconductor devices which have not been passivated by the growth or deposition of insulating films. Many devices receive, in the final stages of manufacture, an etch which leaves their surfaces partly fluoridated; they are subsequently baked and encapsulated in vacuum or in dry inert gas. This work shows that the bakeout may result in a shift of surface potential comparable with that observed on wet-dry cycling, and that subsequently the surface will be sensitive to traces of oxygen. Such instabilities could easily be eliminated (*a*) by assuring that the device surface is effectively freed of fluoride, prior to encapsulation, by water soaking or by baking at a temperature of 350°C, and (*b*) by encapsulation in an ambient containing sufficient oxygen that the desorption leading to n-type surface potential shifts cannot occur. The latter technique was successfully used by Buck *et al.* for surface stabilization of p-n junction radiation detectors (4).

Manuscript received Nov. 29, 1965; revised manuscript received March 25, 1966.

Any discussion of this paper will appear in a Discussion Section to be published in the June 1967 JOURNAL.

REFERENCES

1. T. M. Buck and F. S. McKim, *This Journal*, **105**, 709 (1958).
2. R. H. Kingston and S. F. Neustadter, *J. Appl. Phys.*, **26**, 718 (1955).
3. J. Hall, S. S. Baird, and R. P. Williams, Paper presented at the Los Angeles Meeting of the Society, Electronic Division Abstracts, **11**, Abstract 60, p. 114 (1962).
4. T. M. Buck, G. H. Wheatley, and J. W. Rodgers: *IEEE Trans. on Nuclear Science*, **NS11**, 294 (1964).

The Preparation and Properties of Vapor-Deposited Epitaxial $GaAs_{1-x}P_x$ Using Arsine and Phosphine

James J. Tietjen and James A. Amick

RCA Laboratories, Radio Corporation of America, Princeton, New Jersey

ABSTRACT

Single crystal $GaAs_{1-x}P_x$ layers have been grown epitaxially from the vapor phase in a novel apparatus, using gaseous arsine and phosphine as sources of arsenic and phosphorus. These layers exhibit the highest quality, and the widest range of controlled resistivity yet reported for solid solutions in this system. Vegard's law is obeyed over the entire composition range. At room temperature, the change from a direct to an indirect transition across the band gap occurs at the value, $x = 0.44$. Electron mobilities in these layers are high; a sample containing 27% GaP, for instance, had a room temperature mobility of 4900 cm^2/v-sec, and a 69% gallium phosphide alloy had a mobility of 700 cm^2/v-sec at room temperature. Both n- and p-type doping have been obtained, with hydrogen selenide gas and zinc vapor as the sources of donor and acceptor impurities, respectively. In this apparatus it is also easy to prepare multilayered structures incorporating layers of different resistivity and/or composition.

The preparation of homogeneous solid solutions of gallium arsenide-gallium phosphide, $GaAs_{1-x}P_x$, is of both fundamental and practical importance. Throughout most of the composition range, the band gap for this system corresponds to energies associated with the visible region of the spectrum. These materials are therefore potentially useful for the fabrication of luminescent devices, such as electroluminescent diodes and injection lasers. This system also affords opportunity to study changes in band structure with composition, especially in the region of the cross-over from a direct to an indirect (phonon-assisted) band-gap transition. Further, it is desirable to control the electrical characteristics of these crystals by the controlled addition of donor or acceptor impurities. Although it is possible to prepare these compositions from the melt (1), vapor deposition techniques have been more commonly employed (2-6). In both sealed tube and continuous gas flow apparatus, epitaxial growth has been obtained by means of a single transporting agent, such as water vapor or a hydrogen halide. Such techniques, however, do not allow for the independent, precise control of the partial pressure of two volatile species, such as arsenic and phosphorus. Furthermore, if one provides liquid or solid sources of arsenic and phosphorus, their vapor pressures are exponentially dependent on the temperature of the reservoirs. While this dependence may not be critical for the growth of the pure compounds, it becomes extremely critical for the preparation of homogeneous solid solutions.

The epitaxial growth of gallium arsenide layers by direct synthesis from arsenic vapor and gallium chloride was recently reported (7). The apparatus has been redesigned to permit the introduction of arsenic and phosphorus independently in the form of their gaseous hydrides, arsine (AsH_3) and phosphine (PH_3). On heating, these hydrides decompose to form the respective elements, with hydrogen as a by-product. As in the earlier apparatus, gallium is transported as its subchloride, prepared by passing hydrogen chloride over gallium. Since the epitaxial growth is carried out in an excess of hydrogen, the substitution of arsine and phosphine for the elements does not substantially alter the chemistry of the growth. This substitution offers the following advantages, however: (*i*) The partial pressure of arsenic and of phosphorus in the growth region is determined by the rate of introduction of arsine and phosphine, respectively. Since both of these compounds are gases at room temperature, their vapor pressure is not a strong function of the temperature. (*ii*) These gases can conveniently be obtained commercially, diluted in hydrogen to any desired concentration, and stored in pressurized cylinders for indefinite periods of time. (*iii*) They can be metered into the apparatus through flowmeters, allowing the introduction rate to be held constant and measured with precision. (*iv*) The rates of introduction of arsine and phosphine can be changed independently, permitting gradual or rapid changes in the composition of the growing layer. (*v*) Since no temperature control of these gases is necessary, the apparatus is simplified; only three critically controlled temperature zones are required.

Still another feature of the new apparatus is that n- and p-type doping over a wide range of resistivities can be obtained easily. Selenium is added as the n-type dopant by introducing gaseous hydrogen selenide; zinc is introduced directly in the vapor form to provide p-type doping. Because of the characteristics of the flow apparatus, doping can be initiated and discontinued at any time, at almost any rate, and during any stage of the crystal growth.

These features have made possible the epitaxial growth of single crystal $GaAs_{1-x}P_x$ solid solution layers of unusually high purity and homogeneity over the entire compositional range. In addition, crystals having a wide variety of resistivities, both p- and n-type, have been prepared. Finally, multilayer structures have been prepared sequentially within the growth apparatus, the samples not being removed from the apparatus until all growth operations are completed.

Experimental

Apparatus.—The apparatus consists principally of a single 2.5 cm ID quartz tube 80 cm long; it is shown schematically in Fig. 1. The three heated zones are surrounded by conventional temperature controlled, resistance heated furnaces. A large bore (35 mm) stopcock separates the growth portion of the apparatus from a forechamber. As described previously (7), substrates mounted at the end of a precision ground (Trubore) rod can be inserted into the forechamber. This chamber can then be purged with hydrogen before the samples are inserted through the stopcock into the growth portion of the apparatus. In this manner, contamination of the growth region during insertion and withdrawal of the samples is minimized. Furthermore, the substrates may be etched or heat-treated in this forechamber prior to their insertion into the growth region. Finally, following

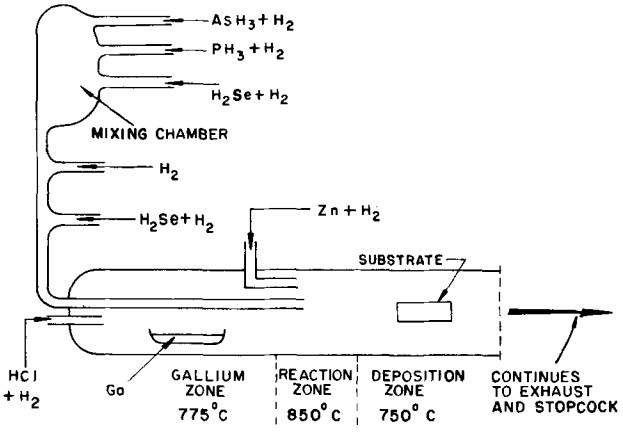

Fig. 1. Schematic representation of vapor-deposition apparatus

deposition, the substrates can cool to room temperature in this chamber in a controlled atmosphere before being withdrawn into the laboratory.

Arsine, phosphine, and hydrogen selenide are introduced through flow meters into a 2-liter ballast vessel which empties into the hydrogen carrier gas stream. This permits these reagents to be thoroughly mixed before they enter the reaction zone, and helps to smooth out small sporadic fluctuations in the individual gas flows. If desired, the hydrogen selenide can be made to by-pass the mixing bulb if abrupt gradients in donor impurity concentrations are required. As shown in Fig. 1, the arsine-phosphine-hydrogen mixture is introduced into the reaction zone through a long quartz tube which extends beyond the gallium. Through a shorter quartz tube a mixture of hydrogen chloride and hydrogen is injected. This mixture, passing over gallium in a quartz boat, provides the gallium subchloride. It is a significant feature of this method of introducing the different vapor phase constituents that at the gas stream velocities used in this investigation only the hydrogen chloride and hydrogen come into contact with the gallium. Since the equilibrium for the reaction between gallium and hydrogen chloride is rapidly attained, and since the contents of the boat are essentially pure gallium throughout the entire deposition, the composition of the gas phase components can be maintained constant during the entire growth cycle. In addition, abrupt changes in the crystal composition can be introduced during the growth period, since the crystal growth at any time does not depend on the previous history of the growth apparatus. In contrast, when arsenic trichloride and phosphorus trichloride are used as transport agents, the contents of the gallium boat change as the run proceeds. As a result, it is difficult, with these transport agents, to start and stop the growth abruptly. P-type doping is obtained from a small amount of metallic zinc held in a quartz "bucket" attached to a Trubore rod. This zinc can be inserted into a heated side arm adjacent to the growth region of the apparatus, and the zinc is transported into the growth region in hydrogen carrier gas. The temperatures of the three zones shown in Fig. 1 are selected so that deposition is emphasized in the vicinity of the substrate and minimized on the long quartz tube through which the arsine-phosphine mixture passes. The concentrations of the reactant species are controlled by adjusting the flow rates of the gaseous species entering the apparatus.

Materials.—The gases employed in this work were obtained commercially and used without further purification. Typically the arsine is obtained diluted in H_2 to a concentration of 10%,[1] the PH_3 as a 5% dilution in H_2,[1] and the H_2Se diluted to 500 ppm in H_2.[1] A typical mass spectrometric analysis of the impurities present in the arsine is presented in Table I. It should be noted that, at the levels present here, the three primary impurities apparently do not affect the growth characteristics or electrical properties of the layers. The hydrogen chloride is obtained in standard cylinders.[2] The hydrogen employed as the carrier gas is purified by passage through a standard palladium-alloy diffuser. The manufacturers reported purity for the gallium[3] and zinc[4] is 99.9999 and 99.9998%, respectively.

Table I. Mass spectrometric analysis of arsine impurities
Average of five analyses

Element detected	Concentration, ppm
Nitrogen	46
Argon	36
Carbon dioxide	15
Oxygen	6

Both germanium and gallium arsenide substrates were employed in this study. Germanium substrates nominally had {111} surfaces, while gallium arsenide wafers having {111}, {110}, and {100} surfaces were used. Although it was demonstrated that epitaxial layers of $GaAs_{1-x}P_x$ can be successfully deposited on {111} germanium surfaces or on gallium arsenide surfaces oriented normal to the <110> and <111> directions, gallium arsenide wafers having {100} surfaces, about 1 cm^2 in area and 0.5 mm thick, were almost exclusively used in this work. These were mechanically polished to a flat, mirror-smooth finish and then chemically polished in a mixture of sulfuric acid, hydrogen peroxide, and water in the ratio, 4:1:1 (Caro's acid). As substrates, a wide variety of n-type, gallium arsenide wafers oriented normal to the <100> direction were employed, having electron carrier concentrations in the range, 1×10^{16} to $2 \times 10^{18}/cm^3$, with the major impurities including silicon, selenium, tellurium, and tin.

Procedure.—Freshly etched substrates are first mounted on the substrate support. Since growth is usually required on only one surface of a substrate wafer, two wafers are usually mounted in a common slot, back to back. In this manner, two substrates having essentially identical growth history can be obtained in one run. When inserted into the apparatus, the surfaces of these substrates are parallel to the direction of gas flow. With no further treatment, the substrates are introduced into the growth region of the apparatus, the entire apparatus being at room temperature. After purging the system with hydrogen, the furnaces are turned on, and the temperature rises at about 20°C per minute. When the substrate temperature reaches 600°C, the arsine flow is started in order to establish an arsenic atmosphere in the deposition zone and to prevent decomposition of the substrate. When all three zones have reached the operating temperature, the hydrogen chloride flow over the gallium is started; at this time, gallium arsenide begins to deposit epitaxially on the substrate. The phosphine flow is then initiated to produce a gas phase mixture of arsine and phosphine appropriate to the desired gallium arsenide-phosphide composition. Because of the 2-liter ballast vessel in the gas introduction system, the composition of the epitaxial growth on the substrate changes slowly from pure gallium arsenide to the selected alloy composition. It is believed that this gradual transition aids in minimizing strain arising from differences between the lattice constants of the substrate and of the deposited alloy.

Typically, the sum of the flow rates of pure arsine and pure phosphine are about 15 cc/min. The hydrogen chloride flow rate is approximately 5 cc/min. An additional 2.5 liters/min of hydrogen is employed as a

[1] Matheson Company, Rutherford, New Jersey.

[2] Frontier Chemical Company, Wichita, Kansas.

[3] AIAG Metals, New Nork, N. Y.

[4] United Mineral and Chemical Corporation, New York, N. Y.

carrier. With these flow rates, with a substrate temperature in the range 725°-775°C, a reaction zone temperature of 850°-875°C, and a gallium zone temperature of 775°-800°C, growth rates of approximately ½ μ/min are obtained under steady-state conditions. With these growth conditions, the contents of any of the gas cylinders permits at least 60 hr of continuous crystal growth.

To determine the electron carrier concentrations and mobilities in the deposited layers, a technique was developed which permits Hall coefficient and resistivity measurements to be made on layers as thin as 50μ. Indium contacts are alloyed to the grown layer in a hydrogen atmosphere. The temperature required to alloy ohmic contacts ranges from 450°C for GaAs to 850°C for GaP. The sample is then fastened to a quartz lapping plate with glycolphthalate and the substrate is lapped off. Final contacts and measurements are made while the sample remains supported on the quartz lapping plate. In this way the measurements are made on layers that have been completely removed from the substrate but are otherwise unaltered. To test this procedure, several bulk samples of gallium arsenide were measured first by conventional techniques and then, using this procedure, after being lapped to about 100μ thickness. In all cases, the second set of measurements produced identical results to the first.

Results and Discussion

Crystallinity and Homogeneity

X-ray analysis by the Debye-Scherrer technique shows that these layers are single phase, cubic, solid solutions which have a very high degree of homogeneity, as revealed by the sharpness of the diffraction lines. The width of the diffraction lines, for 15 specimens of different alloy compositions, is identical to those for pure gallium arsenide and pure gallium phosphide. Thus, any variation in composition was below the detection limit. This result is in agreement with electroluminescent data obtained from diodes fabricated from selenium-doped alloys containing up to 30% gallium phosphide. For these diodes, the width of the incoherent emission peak at 77°K is equal to that of pure gallium arsenide. Since the maximum experimental error associated with this measurement is approximately 5%, this result indicates that compositional variations are less than 0.1 mole %. Also, the threshold current densities of laser diodes fabricated from specimens containing as much as 20% gallium phosphide is the same as that for pure gallium arsenide (8). In addition, there is no drop in electron mobility with alloying up to 30% gallium phosphide (9). Moreover, the room temperature electron mobilities of undoped layers, presented in Table II, are high for all alloy compositions. Note especially the values of 4900 and 700 cm^2/v-sec for alloys containing 27 and 69% gallium phosphide, respectively. These results are also attributed to the high degree of homogeneity of these materials.

X-ray analysis by the Laue back-reflection technique reveals that the layers are epitaxial. In Fig. 2 the lattice constant is presented as a function of alloy composition showing that Vegard's law of solid solutions is obeyed in this system. This result is in agreement with those of Pizzarello (4) and Rubenstein (6). The compositions were determined by chemical analysis (10) with an accuracy of ±0.5%. It was also demonstrated by chemical analysis that compositions can be reproduced in sequential runs to within ±1%.

Table II. Room temperature electron mobility of $GaAs_{1-x}P_x$ alloys having electron carrier concentrations in the range, 5×10^{15} to 1×10^{16} cm^{-3} (9)

x	μ, cm^2/v-sec
0	5100
0.06	5000
0.09	5000
0.12	5200
0.22	4800
0.27	4900
0.37	3800
0.42	1400
0.69	700
1	120

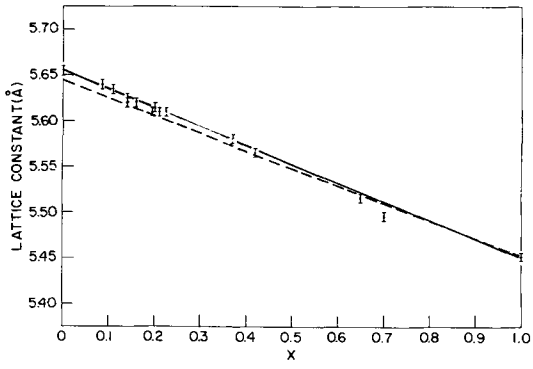

Fig. 2. Dependence of the lattice constant on alloy composition in the system, $GaAs_{1-x}P_x$. The dependence observed by Rubenstein (6) and Pizzarello (4) is also included: ——— Rubenstein; — — — Pizzarello; I this paper.

Growth Morphology

As a result of a novel etchant (11) developed by Abrahams and Buiocchi of the RCA Laboratories, it is now possible to observe dislocation densities on the major low index faces of $GaAs_{1-x}P_x$ alloys. Etch pit densities were obtained (12) using this etchant, which reveal that the density of dislocations in the grown layers are determined almost exclusively by the dislocation densities of the substrates. Practically all dislocations which lie in the substrate, and intersect the plane of the substrate-grown-layer interface, propagate into the grown layer. The additional dislocations which originate in the grown layer are much smaller in number by at least an order of magnitude than those originating in the substrate. Typical dislocation densities for the substrates employed in this study, and therefore for the grown layers, are usually of the order of 10^3/cm^2, but have ranged up to 10^6/cm^2.

Electrical Properties

The epitaxial layers were examined by Hall coefficient measurements. Typical electron carrier concentrations for undoped specimens are in the range, 5×10^{15} to 1×10^{16}/cm^3. The high values of the electron mobility at 77°K of alloys containing up to 20% gallium phosphide, as shown in Fig. 3, attest to the high quality of the undoped samples and demonstrate that this material is noncompensated.

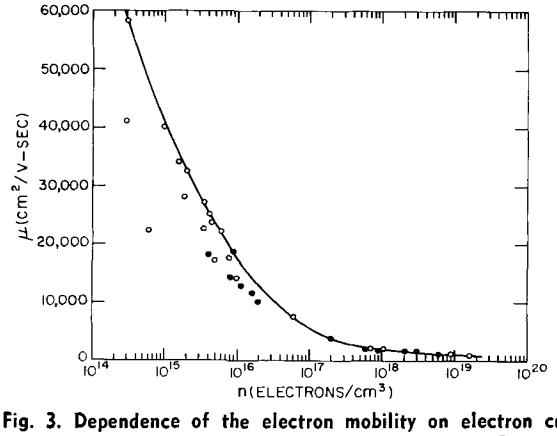

Fig. 3. Dependence of the electron mobility on electron carrier concentration in selenium-doped $GaAs_{1-x}P_x$ at 77°K: ○, X = 0; ●, 0 < X < 0.2.

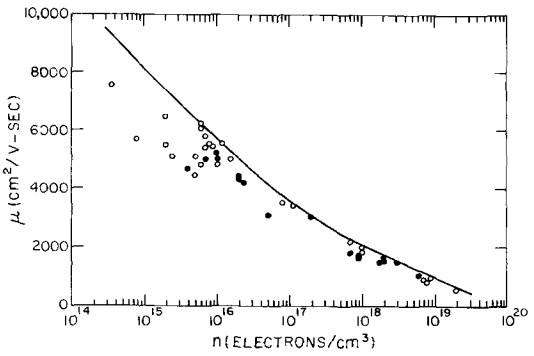

Fig. 4. Dependence of the electron mobility on electron carrier concentration in selenium-doped $GaAs_{1-x}P_x$ at 300°K; symbols are the same as in Fig. 3.

Doping

Attempts were made to dope the layers using hydrides of various donor impurities as the source of the n-type dopant. These included hydrogen sulfide, hydrogen selenide, germane, and silane. However, it was found that the best results were obtained with hydrogen selenide, and it was, therefore, used almost exclusively. The primary advantage of hydrogen selenide is that a lower gas phase concentration of this hydride is required. Apparently, selenium is incorporated into the growing layer much more efficiently than the other doping agents. As compared with the other hydrides, as much as 100 times less hydrogen selenide is needed to produce a given electron carrier concentration in the deposited crystal. This has the inherent advantage of introducing less unknown contamination to the growth system. Using hydrogen selenide diluted in hydrogen in the concentration range 5-5000 ppm allows for doping from 5×10^{16} to 2×10^{19} electrons/cm^3 with a reproducibility of ±25%.

Selenium-doped samples containing up to 20% gallium phosphide were prepared having electron carrier concentrations as high as 2×10^{19}/cm^3. The dependence of the electron mobility on the carrier concentration is shown in Fig. 3 and 4 for 77°K and room temperature, respectively. The relatively high values for the electron mobility of heavily doped samples imply that the crystals are extremely homogeneous and contain few defects. In addition, the dependence of the mobility on electron carrier concentration is the same for the alloy specimens as for pure gallium arsenide. It is concluded that doping to these high donor levels does not interfere with the preparation of homogeneous material.

The investigation of acceptor doping with zinc has been carried out to a lesser extent. However, it has been demonstrated that hole concentrations in the range 2×10^{18} to 4×10^{19}/cm^3 can easily be attained with mobilities varying from 120 to 60 cm^2/v-sec for this doping range.

In addition to the preparation of single epitaxial layers doped with donor or acceptor impurities, multilayered structures have been fabricated by varying the introduction of the doping agents at different times during crystal growth. Figure 5 shows a section of a gallium arsenide multilayered structure in which an N^+, N, P^+ arrangement has been grown on a {100} surface of a gallium arsenide substrate. The P^+ region has a hole concentration of about 2×10^{19}/cm^3 while the N^+ and N regions have electron concentrations of about 4×10^{18} and 5×10^{15}/cm^3, respectively. Because of the low growth rates that can be realized in this system, the thickness of the individual layers can be controlled to about 1μ. This method of preparing multilayered structures during the growth of the alloy crystal has been used to fabricate several types of semiconductor devices having superior electrical characteristics (13).

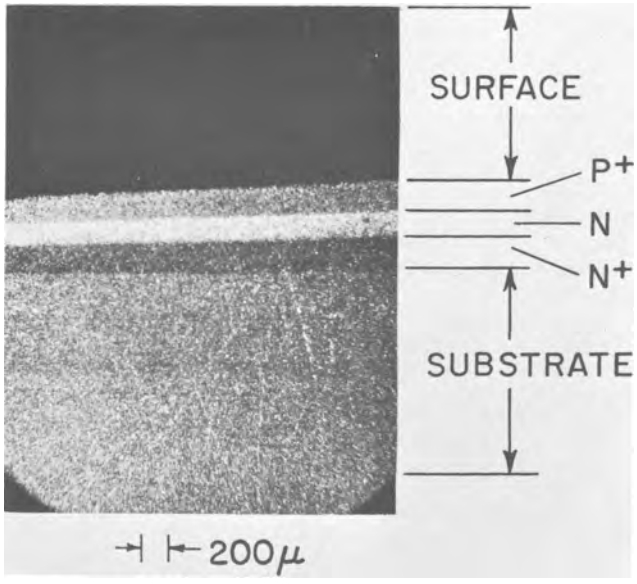

Fig. 5. Cross section of a P^+, N, N^+ GaAs structure, angle-lapped at 3° and chemically stained to reveal the individual regions. The geometric magnification introduced by angle-lapping increases the vertical dimension by a factor of approximately 20. Therefore, the actual thickness of each layer is about 10μ.

Optical Band Gaps

Optical absorption measurements were made in a Cary model 14R spectrophotometer on the same epitaxial films used for the Hall coefficient measurements. These measurements revealed that, on the high energy side of the absorption edge the absorption coefficient, α, obeys the relationship

$$\alpha = \alpha_o (E - E_o)^n$$

where E is the photon energy and E_o is the energy of the band gap (14). For alloys containing greater than 50% gallium phosphide n is equal to 2, while for alloys containing less than 45% gallium phosphide n is approximately unity. A value of n equal to 2 is indicative of an indirect (phonon assisted) band gap transition while values of n less than unity have been associated with a direct band gap transition (15). The dependence of E_o on alloy composition at room temperature and 77°K is presented in Fig. 6. It is apparent that a distinct transition occurs at $x = 0.44$ (at room temperature) as the slope of the curve changes abruptly. This is undoubtedly due to the change from a direct to an indirect band gap transition. These data are in excellent agreement with the results of Pilkuhn and Rupprecht (16), Fenner (17) and Cusano, Fenner, and Carlson (18), but are in par-

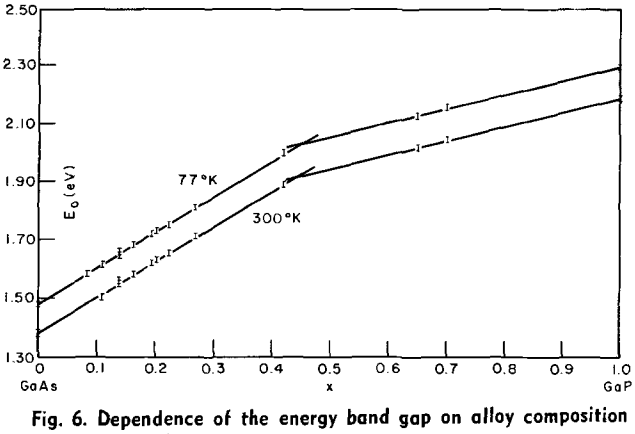

Fig. 6. Dependence of the energy band gap on alloy composition in the system, $GaAs_{1-x}P_x$.

tial disagreement with the results of Pizzarello (4) and Ku (3).

Conclusions

The superiority of this vapor-growth method for the preparation of homogeneous $GaAs_{1-x}P_x$ alloys has been demonstrated. Furthermore, very homogeneous alloys are obtained for a wide range of doping concentrations as both p- and n-type material. In addition, the versatility of this method has been explored in terms of growing a multilayer structure incorporating this high-quality material.

Measurements on the material prepared by this technique reveals that very high mobilities can be attained in this alloy system. It is especially striking that an alloy containing 27% gallium phosphide had a room temperature mobility of 4900 cm^2/v-sec, while a 69% gallium phosphide alloy had a mobility of 700 cm^2/v-sec at room temperature. Vegard's law of solid solutions was found to be obeyed, and optical absorption data showed that the change from a direct to indirect band gap transition occurs at $x = 0.44$ at room temperature.

This technique should also be useful for the preparation of any semiconducting compound or alloy system where volatile halides and/or hydrides occur.

Acknowledgments

The authors wish to express their sincere appreciation to H. F. Gossenberger for his valuable assistance throughout the course of this study, and to D. Richman and L. R. Weisberg for many very helpful suggestions and discussions. Thanks are extended to G. W. Neighbor, R. Paff, and R. Smith for performing the x-ray analysis, to S. Ochs for measuring the electroluminescent spectra, and to I. J. Hegyi and A. Salerno for mobility data. The research reported in this paper was sponsored by the Advanced Research Projects Agency, Materials Sciences Office, under Contract No. SD-182.

Manuscript received Jan. 17, 1966; revised manuscript, received March 21, 1966.

Any discussion of this paper will appear in a Discussion Section to be published in the June 1967 JOURNAL.

REFERENCES

1. H. Flicker and P. G. Herkart, *Bull. Am. Phys. Soc.*, **5**, II, 407 (1960).
2. N. Holonyak, Jr., D. C. Jillson, and S. F. Bevacqua, "Metallurgy of Semiconducting Materials," p. 49, Interscience Publishers, Inc., New York (1962).
3. S. Ku, *This Journal*, **110**, 991 (1963).
4. F. A. Pizzarello, *ibid.*, **109**, 226 (1962).
5. G. E. Gottlieb, *ibid.*, **112**, 192 (1965).
6. M. Rubenstein, *ibid.*, **112**, 426 (1965).
7. J. A. Amick, *RCA Review*, **24**, 555 (1963).
8. J. J. Tietjen and S. A. Ochs, *Proc. IEEE (Correspondence)*, **53**, 180 (1965).
9. J. J. Tietjen and L. R. Weisberg, *Appl. Phys. Letters*, **7**, 261 (1965).
10. B. L. Goydish, To be published.
11. M. S. Abrahams and C. J. Buiocchi, *J. Appl. Phys.*, **36**, 2855 (1965).
12. M. S. Abrahams and J. J. Tietjen, To be published.
13. J. J. Tietjen, To be published.
14. R. A. Smith, "Semiconductors," Cambridge University Press, 193 (1959).
15. C. Hilsum and A. C. Rose-Innes, "Semiconducting III-V Compounds," pp. 167-171, Pergamon Press, New York (1961).
16. M. Pilkuhn and H. Rupprecht, *J. Appl. Phys.*, **36**, 684 (1965).
17. G. E. Fenner, *Phys. Rev.*, **134**, A1113 (1964).
18. D. A. Cusano, G. E. Fenner, and R. O. Carlson, *Appl. Phys. Letters*, **5**, 144 (1964).

The Epitaxial Growth of Silicon Carbide

V. J. Jennings,[1] A. Sommer,[2] and H. C. Chang

Research Laboratories, Westinghouse Electric Corporation, Pittsburgh, Pennsylvania

ABSTRACT

A method for growing SiC epitaxially on the (0001) plane of 6H SiC is described. The SiC is grown from the vapor phase by the reaction of hydrogen with silicon and carbon tetrachlorides. Cubic SiC grows at temperatures between 1600° and 1775°C. In order to grow hexagonal SiC, the substrate surface must be polished mechanically and the temperature must be greater than 1725°C.

This work was undertaken as part of a program for the development of a SiC active device. Hexagonal SiC crystals in the form of platelets, with basal plane areas up to 1 cm^2, may be prepared by the sublimation of polycrystalline SiC. However, it is dfficult to control the purity of the crystals obtained by this method. An epitaxial growth technique, where SiC is formed by the hydrogen reduction of silicon and carbon containing gases, would permit a greater control of purity. In the present work, an epitaxial layer was grown by the hydrogen reduction of silicon and carbon tetrachlorides.

Apparatus and Substrate Preparation

Apparatus.—Figure 1 shows a schematic diagram of the epitaxial growth reactor. This was a water-cooled 1-in. ID quartz tube. The heater was a graphite pedestal, which was heated with a 450 k/c generator.

The brightness temperature of the SiC substrate was measured with a "Pyro" micro-optical pyrometer. The true crystal temperature is estimated to be 100°-150°C higher than the brightness temperature, by making corrections for the absorption of radiation by the quartz water jacket and the emissivity of SiC.

Tank hydrogen (Ultrapure-Matheson Company, East Rutherford, New Jersey) was purified by passing it through a liquid nitrogen cold trap containing Linde 5A molecular sieves, and was filtered through a 0.22μ millipore filter. The purified hydrogen was metered into two saturators held at 0°C which contained silicon tetrachloride (Electronic Grade, Anderson Chemical Division, Stauffer Chemical Company) and carbon tetrachloride (Analyzed Reagent, Baker Chemical Company), respectively. The saturation obtained was 30% at 0°C. In experiments, the normal hydrogen flow through each saturator was fixed to give a 0.1% mole concentration of both silicon and carbon tetrachlorides to the hydrogen. The total hydrogen flow was 4×10^{-2} g moles/min.

Substrate preparation.—The substrates were 6H SiC and were grown in these laboratories. Prior to growth, most substrates were etched for 2 min in a 3:1 mixture

[1] Present address: Lanchester College of Technology, Coventry, Warwickshire, England.

[2] Present address: State University College at Brockport, Brockport, New York.

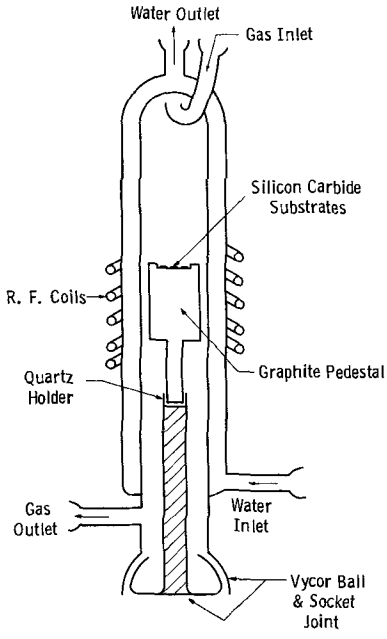

Fig. 1. Schematic diagram of epitaxial growth reactor

of sodium hydroxide to sodium peroxide at 700°C. After etching, one basal plane face of the substrate was shiny [the (0001) face], and the other was dull [the (000$\bar{1}$) face] (1, 2). Sometimes after the (0001) face was identified, it was then mechanically lapped successively on 600, 800, and 1000 grit boron carbide and polished with 1 and 0.25μ diamond paste.

All substrates were cleaned by immersion for 15 min in 48% hydrofluoric acid and washed in deionized water. They were then washed ultrasonically in trichloroethylene followed by methanol and dried.

Experimental Results

Figures 2 and 3 are the surfaces of layers grown at 1650°C on natural[3] (0001) and (000$\bar{1}$) faces of SiC substrates. A similar result was obtained for each face in the temperature range 1600°C to 1775°C. Below 1600°C, growth on the (0001) face became polycrystalline. Above 1775°C, the growth rate was much reduced and by 1800°C the substrate was etched. There was no significant difference in the type of mosaic line patterned growth obtained on either a natural or an etched natural (0001) surface. When the mole ratio of tetrachloride gases to hydrogen was increased from 0.1 to 0.3% the layer consisted of many intergrown yellow crystals, frequently with triangular facets growing parallel to the (0001) face of the substrate, as may be seen in Fig. 4. When growth occurred on a mechanically polished substrate at a temperature between 1725° and 1775°C the layer was colorless and showed no mosaic lines. Below 1725°C, the layer was yellow in color.

[3] A natural crystal face is defined here as the condition of the crystal face after growth in the sublimation furnace.

Fig. 3. Growth at 1650°C on natural (000$\bar{1}$) SiC surface

Layer Evaluation

Temperature dependence of growth rate.—The growth rate was determined by growing a layer for a period of 1 hr at a known temperature. The thickness of the layer was obtained by cross-sectioning the specimen either by scribing and breaking or by bevelling at an angle of a few degrees. The growth rate as a function of temperature is plotted in Fig. 5. The reaction to produce SiC was too complex to per-

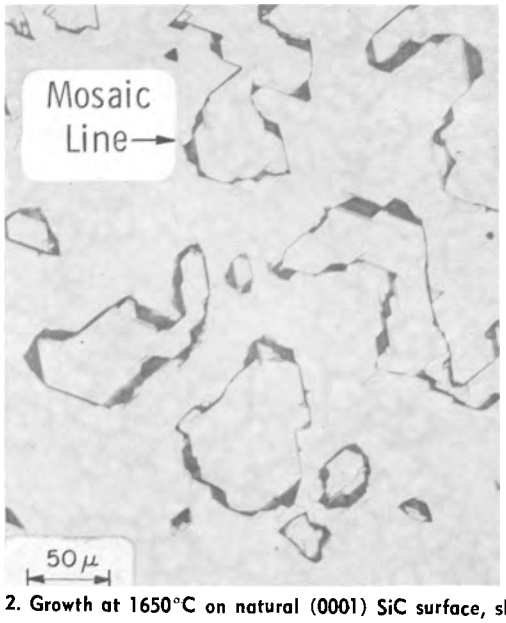

Fig. 2. Growth at 1650°C on natural (0001) SiC surface, showing mosaic.

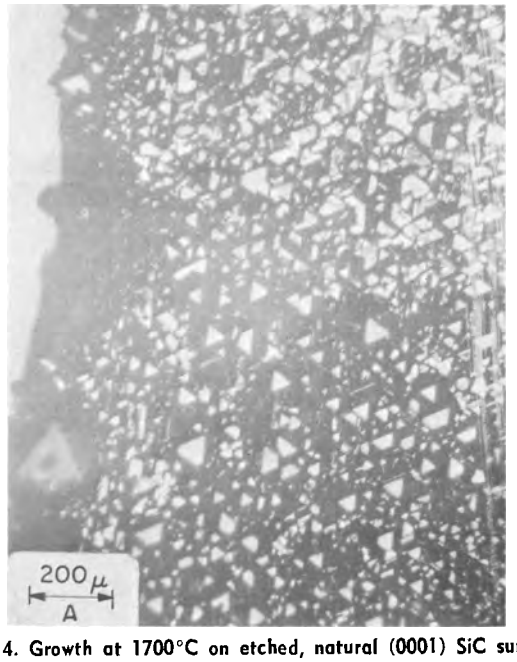

Fig. 4. Growth at 1700°C on etched, natural (0001) SiC surface when mole ratio was 0.3%.

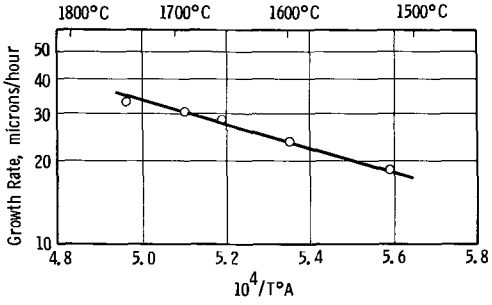

Fig. 5. Temperature dependence of SiC growth rate

mit the determination of its true activation energy. The apparent value was 20 kcal/mole.

Structure of SiC *layer.*—The structure of the layer was examined by molten salt etching. All yellow colored layers gave triangular shaped etch pits. Although these layers seemed homogeneous, after etching, colorless lamellae could be seen intergrown with the yellow material. Figure 6 shows the etched surface of the yellow material. It may be seen that there was a twin relationship between the orientation of the etch pits on each side of the mosaic line. Colorless layers, after etching gave a surface showing hexagonal etch pits (see Fig. 7).

Some substrate 6H crystals were subjected to Laue transmission x-ray analysis in order to confirm the polytype (3, 4). Transmission photographs of colorless layers after growth were found to be identical with those before growth, thus showing that the layer was also of the 6H polytype.

Purity of the SiC *layer.*—The purity of the colorless layers was evaluated by the capacitance method in which the room temperature capacity of a tantalum-SiC epitaxial layer rectifier was measured as a function of d-c voltage. It was found that the layer was not doped uniformly. The method of Anderson and O'Rourke (5) was used to calculate the impurity density distribution in the layer. The results showed that the purest SiC layers contained 10^{14} to 10^{15} ionized acceptors per cubic centimeter at room temperature.

Discussion

The yellow colored layer grown on the (0001) face of a 6H SiC substrate was predominantly cubic SiC, since triangular etch pits were obtained on etching.

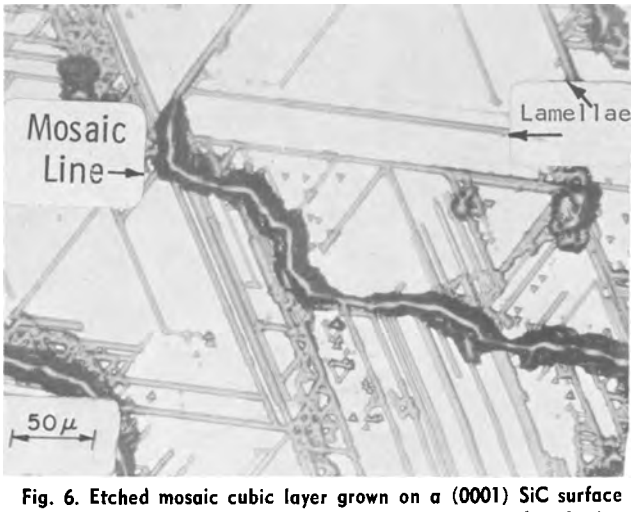

Fig. 6. Etched mosaic cubic layer grown on a (0001) SiC surface showing twinning by means of the orientation of trigonal etch pits.

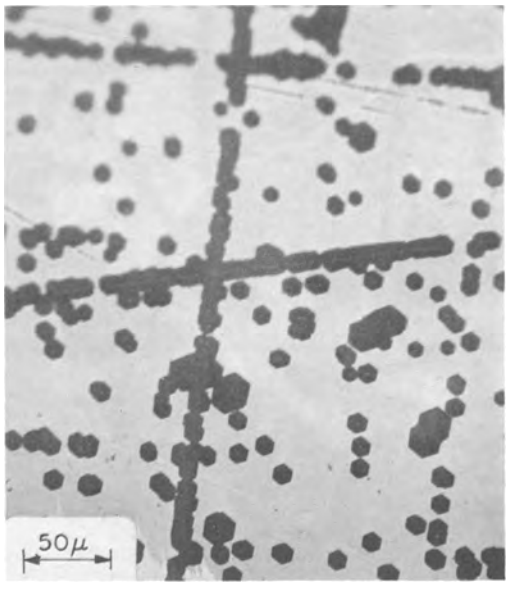

Fig. 7. Etched hexagonal layer grown on 0.25μ diamond polished (0001) SiC surface.

However, the colorless lamellae revealed by etching suggested that a mixed cubic and hexagonal layer had been grown, similar to those grown by Knippenberg using a sublimation process (6). Such yellow layers could be grown at temperatures between 1600° and 1775°C. At temperatures higher than 1800°C, the substrate was etched. At the latter temperature, SiC has an appreciable dissociation pressure (7), and the hydrogen gas used may act as an etchant.

An epitaxial 6H SiC layer could be grown on a mechanically polished substrate at temperatures between 1725° and 1775°C. The layer was p-type in conductivity when grown on a p-type substrate. Electrical measurements of the layer showed it to be of high purity although inhomogeneously doped. The inhomogeneity was due probably to diffusion and/or vapor transport of impurities from the substrate into the growing layer.

The fact that cubic SiC grows over a wide range of temperatures and substrate conditions, whereas hexagonal SiC does not, may be explained by Knippenberg's theory on the stability of SiC polytypes (8). According to this theory, cubic SiC is an unstable modification at all temperatures and not just at low temperatures. Thus, random crystallographic imperfections on natural and etched natural substrates could act as favored nucleation sites for initial deposition of cubic SiC.

Acknowledgment

The authors would like to thank Dr. R. Armstrong for his evaluation of the x-ray data, Mr. R. Yut for able assistance in the laboratory, and Dr. G. Della Pergola for his evaluation of the purity of the hexagonal layers. They also thank Dr. D. R. Hamilton and Mr. J. C. Castle for helpful discussions.

This work was supported in part by the Electronic Research Directorate of the Air Force, Cambridge Research Laboratories, Office of Aerospace Research, Contract AF 19 (604)-8499.

Manuscript received July 22, 1965; revised manuscript received March 25, 1966. This paper was presented the Boston Meeting, Sept. 16-20, 1962.

Any discussion of this paper will appear in a Discussion Section to be published in the June 1967 JOURNAL.

REFERENCES

1. J. W. Faust, Jr., "Silicon Carbide, A High Temperature Semiconductor," J. R. O'Connor and J. Smil-

tens, Editors, p. 403, Pergamon Press, New York (1960).
2. S. Amelinckx, G. Strumane, and W. W. Webb, *J. Appl. Phys.* **31**, 1359 (1960).
3. N. W. Thibault, *Amer. Minerologist*, **29**, 327 (1944).
4. R. S. Mitchell, *ibid.*, **38**, 60 (1953).
5. R. L. Anderson and M. J. O'Rourke, *I.B.M. J. Res. Dev.*, **4**, 264 (1960).
6. W. F. Knippenberg, *Phillips Research Repts.*, **18**, 264 (1963).
7. J. Drowart and G. DeMaria, "Silicon Carbide, A High Temperature Semiconductor," J. R. O'Connor and J. Smiltens, Editors, p. 16, Pergamon Press, New York (1960).
8. W. F. Knippenberg, *Phillips Research Repts.*, **18**, 270 (1963).

Absorption, Degassing, and Solution Equilibrium in the Nitrogen-Niobium System at Ultrahigh Vacuum and High Temperature

R. A. Pasternak, B. Evans, and B. Bergsnov-Hansen
Stanford Research Institute, Menlo Park, California

ABSTRACT

In the nitrogen-niobium system, sorption at high constant temperature and low pressure follows approximately the parabolic rate law

$$\frac{S}{S_o} = 1 - \left(\frac{c}{c_e}\right)^2$$

where S is the sticking probability at the nitrogen concentration c in the metal, S_o the initial sticking probability, and c_e the saturation concentration. This rate law can be explained by a reversible reaction mechanism: Nitrogen is adsorbed atomically on the essentially clean metal surface at a rate which is proportional to pressure but independent of temperature; it then transfers rapidly into the bulk and distributes itself uniformly by fast diffusion. In the reverse reaction nitrogen recombines on the surface at a rate which is proportional to the square of the nitrogen atom concentration in the bulk. The observed degassing rates at both constant and variable pressure can be explained by the same mechanism.

The refractory metals of group 5a and 6a of the periodic table show low resistance to corrosion and embrittlement at elevated temperatures because they dissolve oxygen, nitrogen, and hydrogen easily. Extensive research has been carried out to elucidate the solution mechanisms involving oxygen. In most of these studies the pressures and temperatures employed were such that oxide layers were formed on the metal surface; only rarely were experimental conditions approached which permitted studying the primary reaction step between the gas and the essentially clean metal surface (1-3). The kinetics of solution of nitrogen in refractory metals has been studied less extensively; again, data on the primary surface reaction are meager (4, 5).

In a recent paper the mechanisms of adsorption and of the early stages of absorption at very low pressures were discussed for the nitrogen-niobium system (6). The present investigation, which extends that study, is concerned with the solution equilibrium and with the kinetics of absorption and of degassing at such low pressures and high temperatures that only the primary reaction between the gas and the essentially clean metal surface occurs. A similar study of the low pressure interaction of nitrogen with niobium-1% zirconium alloy is in progress elsewhere (7). (7).

Experimental

The sorption kinetics was investigated in an ultrahigh vacuum flow system by a constant pressure technique which has been described in detail elsewhere (6, 8). In this approach, the pressure in the sorption cell is kept constant by varying the gas flow into the cell; the flow rate is adjusted by means of a servo-controlled, motor-driven valve to compensate for gas pumping or release by the sample. This flow rate, which is recorded continuously, is a measure of the sorption rate and can be converted to the latter by simple arithmetic manipulations.

The solubility of nitrogen in niobium was determined by a modification of this approach: Nitrogen was dissolved in amounts well defined by absorption runs; then, at a controlled pressure in the cell the sample temperature was adjusted to a value at which gas was neither absorbed nor released. Such steady-state points in the solubility diagram were determined over a wide range of the three parameters, pressure, temperature, and concentration. The relative change in solute concentration during the adjustment of pressure and temperature was negligible, since steady state was established virtually instantaneously. Also, the same steady-state temperature-pressure pair was observed, within the precision of the measurements, from whichever direction it was approached. Since throughout this study the gas phase was at ambient temperature (300°K), the measured pressures p were multiplied by the factor $\sqrt{T/300}$; the resulting equivalent pressures P at temperature T of the sample are assumed to be equal to the true equilibrium pressure (9).

Information on the sorption mechanism was also obtained by degassing the sample without admitting gas; the pressure p in the system then decreased with time t. If the volume term $V(dp/dt)$ is small compared with the gas flow out of the cell, the degassing rate is given by $(dM/dt) = -f_o v p$, where f_o is the effective area of the valve opening to the pump.

The samples used were ribbons, about 0.004 x 0.1 x 25 cm, rolled from a zone-melted ingot with a total impurity level of less than 50 ppm. The samples were chemically cleaned and, after mounting in the unit, degassed thoroughly in ultrahigh vacuum at about 2200°K. At these temperatures, dissolved oxygen is removed as a volatile unsaturated oxide (10). A more detailed description of the preparation and properties of such samples has been given elsewhere (6). The gas used was Research Grade nitrogen (total impurity less than 50 ppm) which was dried over liquid nitrogen.

The ribbons were heated electrically using lead storage batteries and high-wattage resistors in series. Brightness temperatures were measured with an optical micropyrometer; they were corrected for absorption by the walls, and for emissivity which has been shown to be independent of solute concentration (11). No correction was applied for the temperature variation along the sample (about ±50°C at the highest temperatures), or for end effects, which are, however, rather small because of the length of the sample. Approximately constant temperature was maintained during sorption runs by applying a constant voltage. A small temperature correction, required when a run covered a wide concentration range, was derived from the correlation between resistivity, temperature, and nitrogen concentration established previously in calibration runs (12).

The data presented here were obtained mainly with two samples; less extensive measurements with additional samples agreed with the over-all pattern.

Results

Equilibrium measurements.—A series of equilibrium curves at concentrations between 0.05 and 0.5 a/o (atom per cent) are shown in Fig. 1; log P is plotted *vs.* $1/T$. The data cover a pressure range of about 10^{-5} to 10^{-8} Torr and a temperature range of 1900°-1400°K. The experimental points define a series of parallel straight lines. The heat of solution ΔH_{sol}, calculated by a least-squares treatment of the data for each concentration, is 53.5 ± 1.5 kcal/g atom. No systematic variation in ΔH_{sol} with concentration was found.

Figure 2 is a plot of log P *vs.* log c_e at 1600°K, derived from the curves in Fig. 1. The points lie, within the precision of the measurements, on a straight line drawn with the slope 2; thus, Sieverts' law is obeyed, and the solution equilibrium can be described by the equation

$$c_e = 1.2 \times 10^{-5} \exp [53{,}500/RT] P^{1/2} \text{ a/o}$$

The pre-exponential factor was derived from the plot in Fig. 2. Equilibrium runs with other samples resulted in heats of adsorption agreeing within 2 kcal/g atom with the value given here. However, variations by a factor of about three in the pre-exponential factor were found which undoubtedly arise from the systematic errors in pressure and temperature measurements.

Absorption and degassing at constant pressure.—In the preceding low-pressure study of nitrogen adsorption by niobium (6), the initial sticking probability S_o of nitrogen on a thoroughly degassed sample was found to be approximately constant over a wide range of high temperatures and low pressures; however, S_o varied for different samples between 0.05 and 0.09. In the present study the kinetics of solution of nitrogen beyond this initial adsorption state was investigated in detail. The rates of solution were measured at temperatures from 1650° to 2000°K and pressures from 6×10^{-7} to 6×10^{-6} Torr. They all exhibit the same dependence on the nitrogen concentration in the sample, as illustrated by the curves in Fig. 3 and 4(a). These plots of sticking probability S *vs.* nitrogen concentration c in the sample have an initial slope close to zero, then bend over and exhibit an approximately linear approach to the saturation concentration c_e. The rate curves for all the experiments when normalized in terms of S/S_o and c/c_e coincide within the precision of the measurements.

Rates of degassing were determined at pressures of 9×10^{-7} and 2×10^{-6} Torr, and temperatures of 1640° to 1830°K; (a wider range of the parameters was inaccessible for experimental reasons). Figure 4 shows the method used and the internal consistency of the measurements. After the sample absorbed nitrogen at 2×10^{-6} Torr almost to saturation (a), a pressure increase to 4×10^{-6} Torr led to additional gas uptake (b); reduction in pressure to 2×10^{-6} Torr resulted in degassing (c) which returned the sample to the same equilibrium concentration origi-

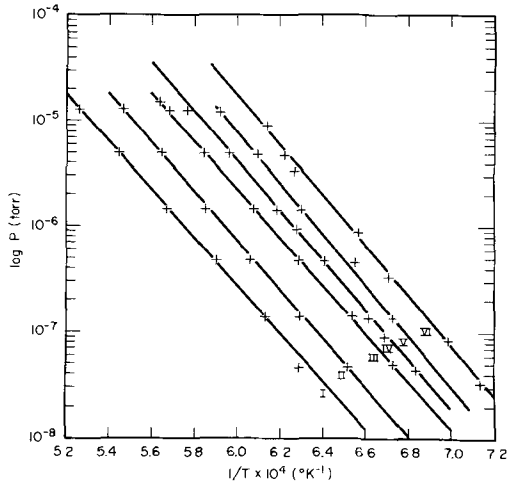

Fig. 1. Solution equilibrium of nitrogen in niobium; log P *vs.* $1/T$ for six nitrogen concentrations c_e

Curve No.	I	II	III	IV	V	VI
c_e (at. %)	0.050	0.092	0.175	0.225	0.36	0.445

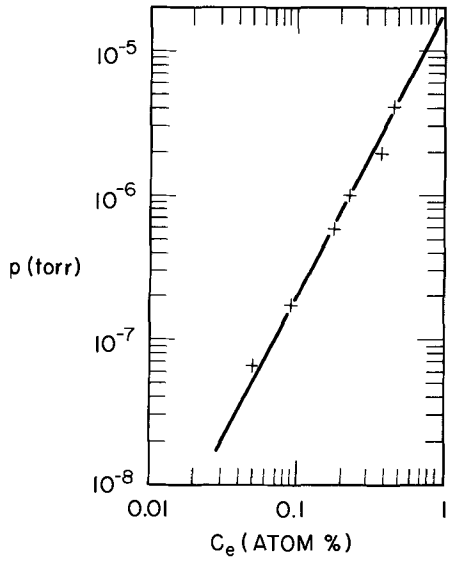

Fig. 2. Solution equilibrium of nitrogen in niobium; log P *vs.* log c_e at $T = 1600$°K. A straight line with slope 2 is drawn through the points. At $c_e = 1$, log $P = -4.68$.

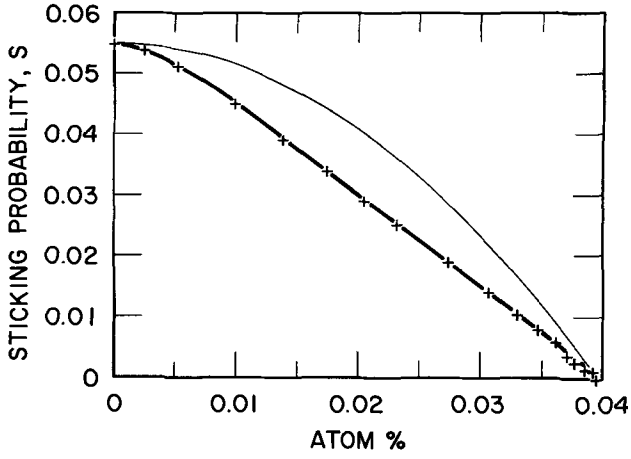

Fig. 3. Absorption at constant pressure and temperature; Nitrogen concentration in atom per cent. The heavy line represents the experimental sticking probability curve; the thin line is a parabola; $T = 1950$°K, $p = 2 \times 10^{-6}$ Torr.

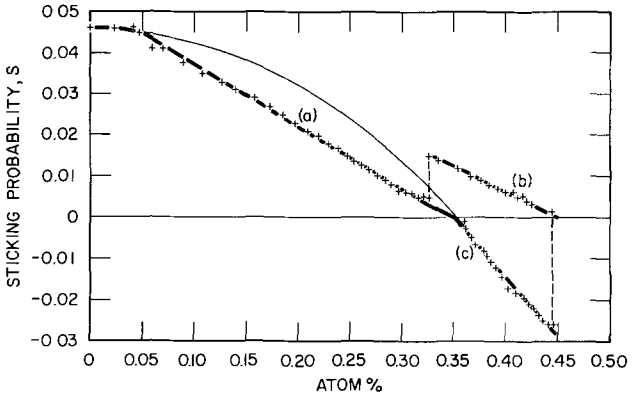

Fig. 4. Absorption and degassing at constant pressure and temperature. Nitrogen concentration in atom per cent. (a) Absorption at 2 x 10^{-6} Torr; (b) absorption at 4 x 10^{-6} Torr; (c) degassing at 2 x 10^{-6} Torr; T = 1640°K. The thin line is a parabola.

nally approached by absorption at this pressure. The experimental conditions for other degassing runs and the slopes of the rate curves expressed as S/S_o *vs.* c/c_e are listed in Table I.

The data presented so far cover only homogeneous solutions of nitrogen in niobium. When the solubility limit is exceeded, the sorption pattern is modified. This is illustrated by the absorption run at 2 x 10^{-6} Torr and 1470°K in Fig. 5. Both the sticking probability and the sample resistance are plotted *vs.* total concentration in the sample. During the earlier stages of sorption, the sticking probability exhibits a similar concentration dependence as in runs at higher temperatures; however, at about 0.8 a/o it approaches a constant value insensitive to further uptake of nitrogen. Similarly, the linear resistance curve changes its slope at about the same concentration. Both curves indicate formation of a new phase. This is suggested also by the equilibrium pressure over the sample which was measured at the end of the absorption run; this pressure was equal to that over a homogeneous solution at a concentration of about 0.6 a/o, although the over-all total concentration was 1.6 a/o.

Degassing at variable pressure.—Degassing rates were measured as a function of temperature and of conductance f_o to the pump when no gas was leaked into the cell. In such degassing runs the pressure p decreased with time according to the equation $p^{-1/2} = a + bt$, as illustrated in Fig. 6. It will be shown in the Discussion that this relationship is equivalent to a second order rate law in respect to nitrogen concentration, and the slope b is a rate constant of degassing. The Arrhenius plot of the rate constants measured at different temperatures results in a straight line as shown in Fig. 7. Curve (a) represents the data of Fig. 6 for a conductance f_o = 0.1 cm², curve (b) data of another series for f_o = 0.18 cm². From the slopes and intercepts of these plots, activation energies ΔH_a of 56 and 54 kcal/g atom and pre-exponential factors of 7 x 10^5 and 1.2 x 10^6 Torr$^{-1/2}$ sec^{-1} are derived.

Table I. Degassing at constant pressure and temperature concentration range and slopes of degassing curves

p x 10^6, Torr	T°K	c, a/o initial	c, a/o equil.*	c/c_e	$-\left[d\left(\frac{S}{S_o}\right)/d\left(\frac{c}{c_e}\right)\right]$** expt.	calc.
2.0	1640	0.46	0.37	1.24	2.28	2.24
0.9	1670	0.20	0.17	1.18	2.26	2.18
2.0	1760	0.18	0.13	1.38	2.36	2.38
0.9	1760	0.13	0.10	1.30	2.32	2.30
2.0	1830	0.11	0.07	1.57	2.46	2.57
0.9	1830	0.071	0.05	1.30	2.34	2.30

* By extrapolation to S = 0.
** S_o = 0.05.

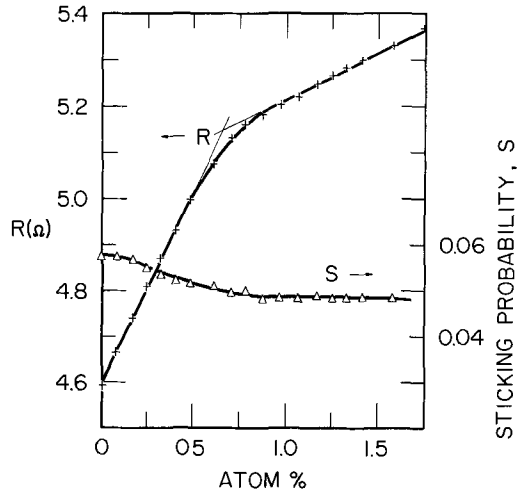

Fig. 5. Absorption at constant pressure and temperature. Resistance and sticking probability as function of nitrogen concentration. The change in slope of the curves at about 0.7 a/o indicates the appearance of a second solid phase. T = 1470°K, p = 2 x 10^{-6} Torr.

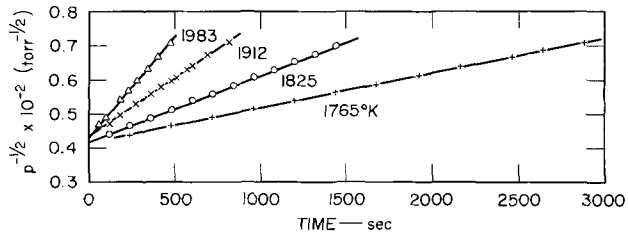

Fig. 6. Degassing at variable pressure as function of temperature. Plots of $p^{-1/2}$ *vs.* time. Conductance to the pump f_o = 0.1 cm².

Finally, the dependence of the degassing rates on conductance is shown in Table II.

Discussion

Solution equilibrium.—The close fit of the experimental equilibrium data to the equation

$$c_e = KP^{1/2} = K_o \cdot \exp\left[\Delta H_{sol}/RT\right] \cdot P^{1/2} \qquad [1]$$

is convincing evidence that within the temperature and concentration range of this study (1400 < T < 1900°K, c_e < 0.5 a/o) nitrogen dissolves atomically

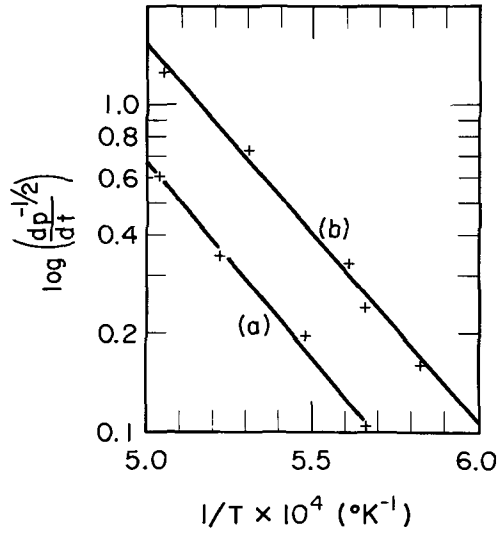

Fig. 7. Activation energy for degassing at variable pressure. Plots of log $[d(p^{-1/2})/dt]$ *vs.* $1/T$. (a) Conductance f_o = 0.1 cm²; (b) f_o = 0.18 cm².

Table II. Experimental slopes $d\,(p^{-1/2})/dt$ ($Torr^{-1/2}$ sec^{-1}) for degassing curves at variable pressure as function of conductance. $T = 1685°K$

f_o, cm^2	0.22	0.15	0.10	0.05
$\frac{d\,(p^{-1/2})}{dt}$	0.14	0.11	0.08	0.04(5)
$\frac{1}{f_o}\cdot\frac{d\,(p^{-1/2})}{dt}$	0.64	0.73	0.80	0.90

in niobium to form a homogeneous, regular solution. This result is in agreement with two earlier studies (11, 12) of the nitrogen-niobium system; close adherence to the same functional relationship had been found in a temperature range between 1800° and 2500°K. The constants fitting these earlier data were $K_o = 6.2 \times 10^{-4}$ and 7.7×10^{-4} a/o $Torr^{-1/2}$ and $\Delta H_{sol} = 46.0$, and 42.4 kcal/g atom (11, 13). A heat of solution of 51 kcal/g atom has been observed by Inouye (7) for low concentrations of nitrogen in niobium 1% zirconium alloy. The values derived in the present study are 1.2×10^{-5} a/o $Torr^{-1/2}$ and 53.5 kcal/g atom. Although the reported entropies and enthalpies found in these studies differ considerably, the free energies are rather close. It is not possible to ascertain on the basis of the present data whether the observed differences have thermodynamic significance or are artifacts due to systematic errors, particularly in the determination of absolute temperature. The tantalum-nitrogen solution equilibrium also obeys Sieverts' law (4) as would be expected in view of the general similarity of the two metals.

Absorption and degassing at constant pressure.—The over-all sorption process can be logically separated into three reversible, sequential processes: dissociative adsorption, transfer of adsorbed atoms from surface to bulk, and diffusion of atoms in the bulk.[1]

A clean surface is maintained at least during the earlier stages of absorption; this is indicated by the approximate constancy of the sticking probability over a wide pressure and temperature range and a significant concentration range. Thus, transfer of the adsorbate into the bulk must be a much faster process than adsorption. Furthermore, an estimate based on the known diffusion coefficient of nitrogen in niobium (15) showed that for our experimental conditions the diffusion rates are sufficiently high to distribute the dissolving nitrogen virtually instantaneously and uniformly throughout the bulk (6). Finally, high rates of transfer and diffusion relative to the rate of desorption are suggested by this observation: on flash-heating a well-degassed sample which is covered with a monolayer of nitrogen, no gas burst is observed; nevertheless the sample, after cooling, again adsorbs a monolayer of nitrogen.

For the formulation of a quantitative rate law we assume that the opposing surface reactions

$$(N_2)_{gas} + 2\ \text{sites} \rightleftarrows 2\,(N)_{ad} \qquad [2]$$

are the rate-determining steps, since diffusion is so fast that surface and bulk are at all times in virtual equilibrium with each other. If we in addition assume that the surface concentration is small as is the bulk concentration, the two concentrations are proportional to each other

$$(N)_{ad} = K_D c \qquad [3]$$

and K_D, the distribution constant, is of the order of unity or smaller, when both concentrations are expressed in comparable units.[2] Consequently, the rate of adsorption is at all times proportional to the impingement rate of molecules on the surface, *i.e.*, to the pressure, since the impinging molecules see always an essentially clean surface; and the rate of desorption is proportional to the square of the bulk concentration.

The resulting over-all rate of sorption, per unit area, is given by

$$\frac{1}{a}\left(\frac{dM}{dt}\right)_{p,T} \equiv Svp = S_o vp - k\,(N)^2_{ad} = S_o vp - k'c^2 \qquad [4]$$

where S is the normalized net rate of sorption, and S_o the constant rate of adsorption; a is the sample area and v the incidence rate per unit area at unit pressure. Since the net sorption rate becomes zero at equilibrium, the constant k' can be expressed in terms of S_o and the equilibrium concentration c_e, and one obtains the simple parabolic rate law, after dividing by vp

$$\frac{S}{S_o} = 1 - \left(\frac{c}{c_e}\right)^2 \qquad [5]$$

The observed sorption kinetics is described reasonably well by this rate law. In particular, the rate curves expressed as S/S_o *vs.* c/c_e are found to be independent of pressure and temperature, and their slopes at $c/c_e = 0$ are approximately zero (Fig. 3, 4, 5). Moreover the degassing curves fit the parabola well, as illustrated in Fig. 4c. (The precision of the measurements is not sufficient to detect the predicted slight curvature.) This good fit is also shown in Table I; the slopes of the experimental degassing curves agree closely with the calculated slopes of the parabola at the mid-point of the concentration range of each degassing run. However, the sticking probabilities for adsorption deviate significantly from the parabola (Fig. 3, 4a). We suspect that this deviation is an experimental artifact; this is suggested by the discontinuity in the slope of the experimental rate curves at saturation concentration (Fig. 4a and c).

The kinetics of gas uptake extending beyond the solubility limit (Fig. 5) can be explained by the same basic mechanism. In the one-phase region the sticking probability curve again may be fitted approximately by a parabola which now passes through the hypothetical equilibrium point for a homogeneous solution at the pressure and temperature of the particular experiment. In the two-phase region, where the concentration of the solute in the metallic phase remains constant, the sticking probability is constant also; apparently the new phase, probably Nb_2N (11) does not segregate as a surface layer.

Degassing at variable pressure.—When no gas is admitted into the cell, the rate of degassing is equal to the rate at which the gas is leaving the cell, and the pressure is now a function of time; moreover, if we assume that rate Eq. [5] also applies in this case, the conditions hold

$$-\left(\frac{dM}{dt}\right)_{T,f_o} = -\alpha\left(\frac{dc}{dt}\right)_{T,f_o} = f_o vp \qquad [6a]$$

and

$$-\alpha\left(\frac{dc}{dt}\right)_{T,f_o} = avpS_o\left[\left(\frac{c}{c_e}\right)^2 - 1\right] \qquad [6b]$$

where α is a conversion factor proportional to the sample volume, a the area of the sample, and f_o the conductance to the pump; c is the concentration and p the pressure at time t, and c_e is the concentration if the sample was in equilibrium with the gas phase at pressure p. At any time during degassing $c_e < c$.

Equation [6b] can be expressed in terms of the experimental parameters c and p by the substitution

[1] Physisorption has been proposed as the step preceding chemisorption even at high temperatures (3): it has little physical meaning in the temperature range of interest here for the following reason. An adsorbed molecule has a residence time on the surface of about 10^{-13} exp $[\Delta H_d/RT]$ sec, where ΔH_d is the heat of desorption, and the associated jump frequency for surface diffusion is about 10^{13} exp $-[\frac{1}{4}\Delta H_d/RT]$ sec^{-1} (14). For example, a rather high heat of physisorption of 5 kcal and a temperature of 1500°K result in a residence time of about 10^{-12} sec, and the molecular undergoes only 3 surface jumps in this time interval.

[2] A large value of K_D implies the existence of an energy barrier for the transfer of adsorbate into the bulk. This important case will not be treated here, since the formalism given appears to be sufficient for the interpretation of the data.

$$c_e = KP^{1/2} = K\left(\frac{T}{300}\right)^{1/4} p^{1/2}$$

By elimination of p from Eq. [6a] and [6b] the second order rate law is obtained

$$-\left(\frac{dc}{dt}\right)_{f_o,T} = k'_2 c^2 \qquad [7a]$$

The time dependence of the pressure is derived from Eq. [7a] and [6a] by elimination of c and dc/dt, and integration

$$p^{-1/2} = p_o{}^{-1/2} + k_2 t \qquad [7b]$$

where

$$k_2 = \frac{\nu}{\alpha}\left(\frac{300}{T}\right)^{1/4} f_o\left(\frac{S_o a}{f_o + S_o a}\right)^{1/2} K^{-1} = \beta K^{-1} \qquad [8]$$

and $K = K_o \exp[\Delta H_{sol}/RT]$ is the solubility constant.

A second order rate law would have been arrived at simply by assuming that the rate of degassing was proportional to the square of the solute concentration in the bulk. Our treatment, however, correlates the degassing process with the solution equilibrium and with the mechanism of sorption: The rate constant is inversely proportional to the solubility constant K, and thus the activation energy of degassing is equal to the heat of solution (if one disregards the factor $T^{-1/4}$). For $S_o a >> f_o$, degassing takes place at quasi-equilibrium, and

$$\beta = \frac{\nu}{\alpha}\left(\frac{300}{T}\right)^{1/4} f_o$$

the rate constant is proportional to f_o, and is independent of S_o. For $S_o a << f_o$, only an insignificant fraction of the gas released in readsorbed, and

$$\beta = \frac{\nu}{\alpha}\left(\frac{300}{T}\right)^{1/4} a^{1/2} S_o{}^{1/2} f_o{}^{1/2}$$

the rate is now proportional to the square root of both f_o and of S_o.

The derivation of the rate law for sorption contains the assumption that no significant energy barrier exists for the transfer of adsorbate from the bulk to the surface. If, however, the energy barrier is significant, the observed activation energy of degassing becomes a function of f_o: for small values of f_o (*i.e.*, for degassing at quasi-equilibrium), it is equal to the heat of solution, whereas for large value of f_o (*i.e.*, for rapid degassing), it approaches the true activation energy.

The experimental degassing data support the simple model. The linear dependence of $p^{-1/2}$ on time is closely obeyed over a reasonably wide temperature and pressure range (Fig. 6). Also, the experimental slopes of the curves increase less than linearly with the conductance f_o (Table II); however, the limited range of conductance values achievable in these experiments does not permit a quantitative test of the relationship given. Finally, the activation energies of degassing, 56 and 54 kcal/g atom found for the two series at conductances of 0.1 and 0.18 cm^2 (Fig. 7) are, within the uncertainty of the measurements, equal to the heat of solution (53.5 kcal). Also, the pre-exponential factors K_o of 3.4 and 3.2 x 10^{-5} a/o Torr$^{-1/2}$ calculated from the degassing experiments and from the parameters of the sample (α = 2.0 x 10^{18} molecules, a = 4.6 cm^2, S_o = 0.05) are close to the value of 1.2 x 10^{-5} obtained directly from equilibrium measurements. As satisfactory as this agreement is, it does not rule out an energy barrier for transport of solute from surface to bulk, since the accessible pumping speeds were too small to displace the system far from equilibrium; only 30 and 44% of the released gas were removed in these runs. The data, however, show that the solubility of gases in metals can be determined from degassing experiments alone, without information about the actual solute concentration in the sample.

Manuscript received Jan. 10, 1966; revised manuscript received March 21, 1966. This research was supported by the Fuels and Materials Development Branch Division of Reactor Development and by the Research Division of the United States Atomic Energy Commission.

Any discussion of this paper will appear in a Discussion Section to be published in the June 1967 JOURNAL.

REFERENCES

1. H. Inouye, in "Columbium Metallurgy," p. 649, Interscience Publishers, New York (1960).
2. E. Gebhardt and R. Rothenbacher, *Z. Metallk.*, **54**, 689 (1963).
3. P. Kofstad and S. Espevik, *This Journal*, **112**, 153 (1965).
4. E. Gebhardt, E. Fromm, and D. Jakob, Metals for the Space Age, Proceedings, 5. Plansee Seminar, 1964, p. 421, Springer-Verlag (1965).
5. K. Osterhagen and P. Kofstad, *J. Less-Common Metals*, **5**, 7 (1963).
6. R. A. Pasternak and R. Gibson, *Acta Met*, **13**, 1031 (1965)
7. H. Inouye, Private communication.
8. R. A. Gibson, B. Bergsnov-Hansen, N. Endow, and R. Pasternak, "Sorption Measurements in Ultra-high Vacuum at Constant Pressure," the Tenth National Vacuum Symposium, American Vacuum Society, p. 88 (1963).
9. P. Kisliuk, *J. Chem. Phys.*, **30**, 174 (1959).
10. R. A. Pasternak and B. Evans, To be published.
11. J. R. Cost and C. A. Wert, *Acta Met.*, **11**, 231 (1963).
12. R. A. Pasternak and B. Evans, *Trans. AIME*, **233**, 1194 (1965).
13. E. Gebhardt, E. Fromm, and D. Jakob, *Z. Metallk.*, **55**, 423 (1964).
14. G. Ehrlich, in "Structure and Properties of Thin Films," p. 423, John Wiley & Sons, New York (1959).
15. R. W. Powers and M. V. Doyle, *J. Appl. Phys.*, **30**, 514 (1959).

Liquidus Curves for Aluminum Cell Electrolyte

IV. Systems NA_3AlF_6 and Na_3AlF_6-Al_2O_3 with MgF_2, Li_3AlF_3, and K_6AlF_6

David A. Chin and E. A. Hollingshead

Aluminium Laboratories Limited, Arvida, Quebec, Canada

ABSTRACT

Liquidus curves have been determined from cooling curves and by sampling melts saturated with alumina. The latter technique was used to redetermine the alumina-rich liquidus of the binary Na_3AlF_6-Al_2O_3 system and yielded a eutectic point at 10.0% Al_2O_3 and 962°C. The binary systems of Na_3AlF_6 with Li_3AlF_6, MgF_2, and K_3AlF_6 gave respectively: eutectic point at 62.0% Li_3AlF_6 and 716°C; pseudobinary eutectic point at 18.0% MgF_2 and 924°C; and a minimum melting point at 40% K_3AlF_6 and 945°C. (Compositions are given in weight per cent). Diagrams are given for Na_3AlF_6-Li_3AlF_6, Na_3AlF_6-K_3AlF_6, and the Na_3AlF_6-rich side of the systems Na_3AlF_6-Al_2O_3, Na_3AlF_6-MgF_2, Na_3AlF_6-Al_2O_3-MgF_2, Na_3AlF_6-Al_2O_3-Li_3AlF_6, and Na_3AlF_6-Al_2O_3-K_3AlF_6.

Previous reports (1-3) from this laboratory have given liquidus curves for aluminum cell electrolytes now employed industrially. This paper gives similar data for Na_3AlF_6-Al_2O_3 with MgF_2, Li_3AlF_6, or K_3AlF_6, which are considered to be possible alternate electrolytes.

The only previously reported liquidus diagram of the ternary Na_3AlF_6-Al_2O_3-MgF_2 system is that by Vatslavik and Belyaev (4). The ternary systems with Li_3AlF_6 and K_3AlF_6 were reported in the book by Belyaev *et al.* (5). Rolin and Muhlethaler (6) more recently reported on the solubility of Al_2O_3 in Na_3AlF_6-Li_3AlF_6 melts and Mashovets and Petrov (7) on the Na_3AlF_6-Li_3AlF_6-Al_2O_3 system. Since other results by cooling curves for melts in the alumina phase field have been proven (1-3) to be in error, these ternary systems were redetermined.

Materials

Sodium cryolite was specially hand picked natural cryolite. The freezing point by cooling curves was 1009±1°C. Aluminum fluoride (99+% by difference) was the product of vacuum distillation of commercial grade (90%) AlF_3. The major impurities were Al_2O_3 (0.12%), Fe (0.06%), and Si(0.05%). Alumina was a special low-soda product produced experimentally, and the impurities detected were 0.01% Na, 0.03% Fe, and 0.01% Si. Lithium fluoride was reagent grade from J. T. Baker Chemical Company. Potassium fluoride (dried at 105°C before use) was reagent grade from General Chemical Division of Allied Chemical and Dye Corporation. Magnesium fluoride (99%) was spectroscopic grade from A.D. MacKay Inc.

Method

Primary freezing points were determined by cooling curves on melts from which the cryolites were the primary crystalline phase. Cooling curves were determined on 150g samples weighed out, mixed, and heated to 1060°C. The stirred melts were held until clear and then cooled at 1-3°C/min until the primary freezing point was registered.

The visual method (1), which consisted essentially of determining the temperature at which crystals could be first seen to separate from a slowly cooling melt, formerly used for the points in the alumina phase field has been replaced by a saturation method. For saturation measurements, melts containing an excess of alumina were stirred at the saturation temperature for 20 min, the alumina was allowed to settle out, and the supernatant melt was sampled with a preheated rhodium spoon. The quenched samples were analyzed for free Al_2O_3 by the $AlCl_3$ method (8).

The Pt, 10% Rh-Pt thermocouples were guaranteed by the manufacturers (Johnson Matthey and Mallory Ltd.) to be within 1°C. They were checked periodically at the freezing point of reagent grade NaCl, 801°±0.5°C.

Accuracy

The error in the cooling curve determinations was not greater than 3°C (2). The analysis for free Al_2O_3 was found to be accurate to ± 0.3% Al_2O_3, compared with ±0.25% reported by Henry and Lafky (8) for values in the range of 0 to 12% alumina. The presence of MgF_2 or Li_3AlF_6 did not affect the accuracy of the determinations. However, in the presence of K_3AlF_6 or KF, the $AlCl_3$ method yielded very low values for the alumina content of the melts. In this case, analysis of the quenched melt was made for total aluminum and the alumina content calculated after correcting the total aluminum figure for the weighed-in K_3AlF_6 and Na_3AlF_6 proportions. The standard error of the mean of duplicate analyses was calculated to be 0.5% Al_2O_3.

Results and Discussion

The eutectic point in the binary Na_3AlF_6-Al_2O_3 system has been determined by the saturation method to be at 10.0% alumina and 962°C. (Compositions are given in weight per cent.) The values by Fenerty and Hollingshead (3) for primary freezing points on the cryolite side of the eutectic were employed. The binary diagram together with previous results (1, 3, 9) is given in Fig. 1. The results of the present work for the solubility of Al_2O_3 agree with those at 975° and 1000°C reported by Henry and Lafky (7). They are as much as 1.0% lower than found previously by the visual method (1). Above 1030°C, good agreement was obtained with Foster's results (9) by the quenching method; below this temperature, alumina solubilities lower by 0.3-0.6% were detected.

The liquidus diagram of the Na_3AlF_6-MgF_2 system which was determined up to 45% MgF_2 is shown in Fig. 2 together with the reproduced diagram of previous workers (5). It was found that this is not a true binary system. X-ray diffraction analysis of crystals from a partially crystallized melt originally containing 26% MgF_2 yielded patterns for both $2NaF \cdot MgF_2 \cdot AlF_3$ (weberite) and $NaF \cdot MgF_2$. It was not determined which of these two compounds was the primary phase.

In the Na_3AlF_6-Al_2O_3-MgF_2 system, sections were determined at 2, 5, 10, 14, 15, 16, and 20% MgF_2 (compositions expressed on Al_2O_3-free basis), and the results are shown in Fig. 3. (To avoid confusion in the diagram, the results for 14, 16, and 20% MgF_2

were not plotted). The cryolite corner of the diagram (Fig. 4) is based on these results (Fig. 3) and on the revised diagrams for Na_3AlF_6-MgF_2 and Na_3AlF_6-Al_2O_3. A pseudoternary eutectic point was found at 3.0% Al_2O_3, 14.5% MgF_2, 82.5% Na_3AlF_6, and 912°C. Previously a ternary eutectic at 4.5% Al_2O_3, 15.5%

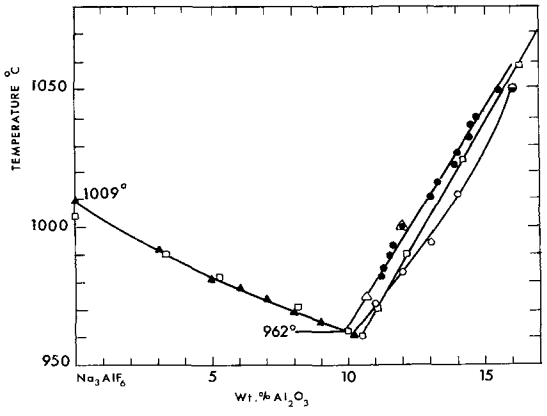

Fig. 1. Liquidus diagrams for sodium cryolite-alumina.

Investigators	Method
▲ Fenerty and Hollingshead	Cooling Curve
○ Fenerty and Hollingshead	Visual
◒ Singleton *et al.*	Visual
□ Foster	Quenching
△ Henry and Lafky	Saturation
● This work	Saturation

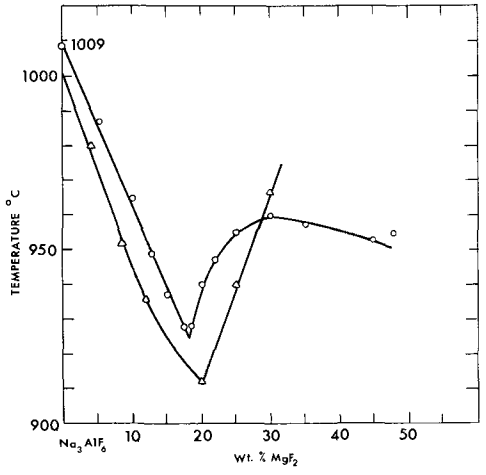

Fig. 2. Liquidus diagrams for sodium cryolite-magnesium fluoride: ○ this work; △ Belyaev *et al.*

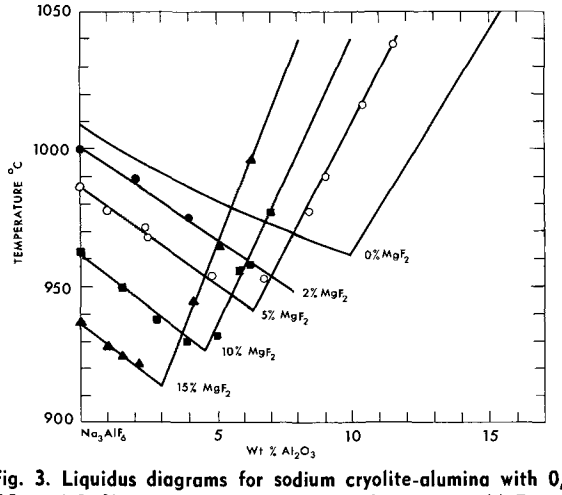

Fig. 3. Liquidus diagrams for sodium cryolite-alumina with 0, 2, 5, 10, and 15% magnesium fluoride. Weight per cent MgF_2 given on alumina-free basis.

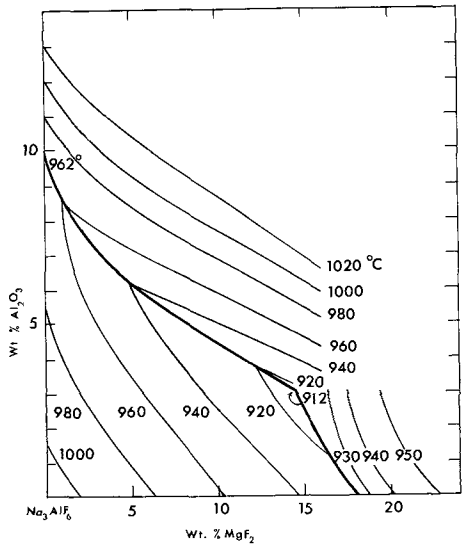

Fig. 4. Liquidus diagram for sodium cryolite-alumina-magnesium fluoride: % Na_3AlF_6 + % Al_2O_3 + % MgF_2 = 100.

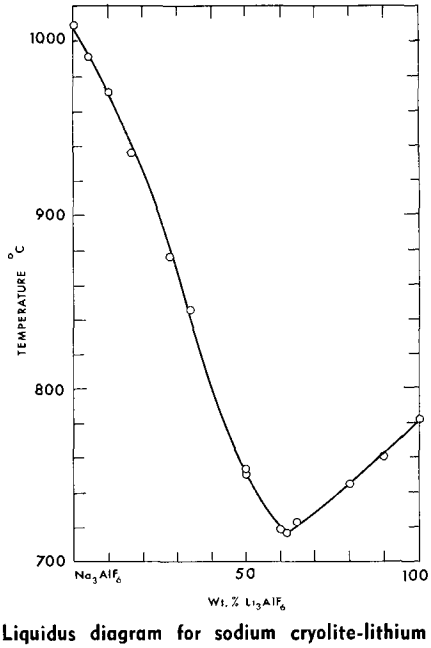

Fig. 5. Liquidus diagram for sodium cryolite-lithium cryolite

MgF_2, 80.0% Na_3AlF_6, and 919°C was reported by Vatslavik and Belyaev (4).

The eutectic line separating the crystallization fields of cryolite and alumina and the isothermal contour indicating the alumina solubility (Fig. 4) show a fairly steep drop for the addition of the first 5% MgF_2 and then a gradual decrease up to 14.5% MgF_2. The eutectic line from 18% MgF_2 in Na_3AlF_6 to the pseudoternary eutectic point separates the Na_3AlF_6 field from a $2NaF \cdot MgF_2 \cdot AlF_3$ (or $NaF \cdot MgF_2$) field. No attempt has been made to determine the extent of this field.

The binary system Na_3AlF_6-Li_3AlF_6 (Fig. 5) has a eutectic point at 62.0% Li_3AlF_6 and 716°C. This agrees with the work of Mashovets and Petrov (7).

In the ternary Na_3AlF_6-Al_2O_3-Li_3AlF_6 system, sections were determined at 5, 10, 15, 20, 25, and 30% Li_3AlF_6 (compositions expressed on Al_2O_3-free basis) and are shown in Fig. 6. The ternary diagram based on these and the present diagrams for the two binary systems Na_3AlF_6-Li_3AlF_6 and Na_3AlF_6-Al_2O_3 is plotted in Fig. 7. The eutectic line separating the fields of crystallization of sodium cryolite and alumina shows a fairly steep decrease for up to 10% Li_3AlF_6, but on

the other hand the isothermal contours indicating the alumina solubilities show a gradual reduction in alumina content. Rolin and Muhlethaler (6) reported larger Al_2O_3 solubilities in Na_3AlF_6-Li_3AlF_6 melts, but it must be noted that their binary eutectic for Na_3AlF_6-Al_2O_3 at 11.2% Al_2O_3 is also high (see Fig. 1).

The liquidus diagram for Na_3AlF_6-K_3AlF_6 is depicted in Fig. 8. With addition of increasing amounts of K_3AlF_6, the primary freezing points decrease to 945°C at 40% K_3AlF_6 and then rise to 955°C at 60-70%. This is interpreted as the tendency toward the formation of the compound elpasolite ($2KF \cdot NaF \cdot AlF_3$) which can be shown by x-ray diffraction analysis to be present in frozen Na_3AlF_6-K_3AlF_6 melts. The present liquidus diagram does not agree with that of Belyaev and Studenzov (10) in the range 30-70% K_3AlF_6; there is good agreement with the form of the liquidus diagram, *i.e.*, a somewhat flat portion between 50 and 75% K_3AlF_6, attributed to Lundina (11).

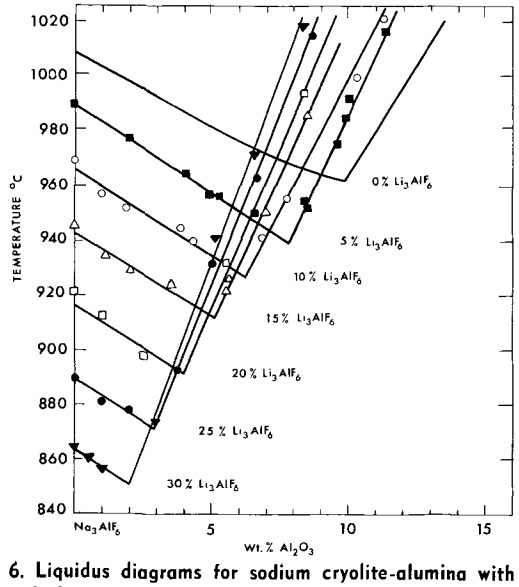

Fig. 6. Liquidus diagrams for sodium cryolite-alumina with 0, 5, 10, 15, 20, 25, and 30% lithium cryolite; weight per cent Li_3AlF_6 given on alumina-free basis.

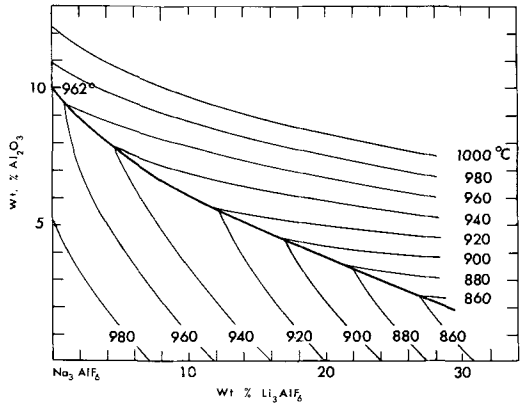

Fig. 7. Liquidus diagram for sodium cryolite-alumina-lithium cryolite: % Na_3AlF_6 + % Al_2O_3 + % Li_3AlF_6 = 100.

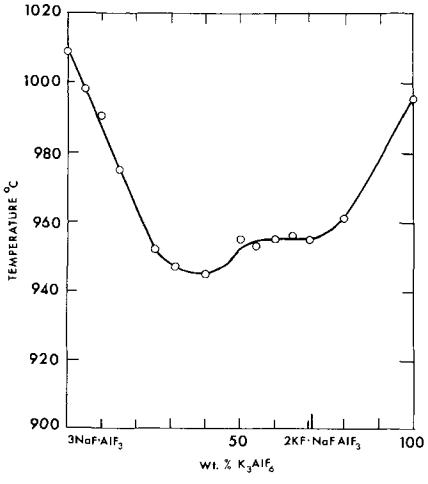

Fig. 8. Liquidus diagram for sodium cryolite-potassium cryolite

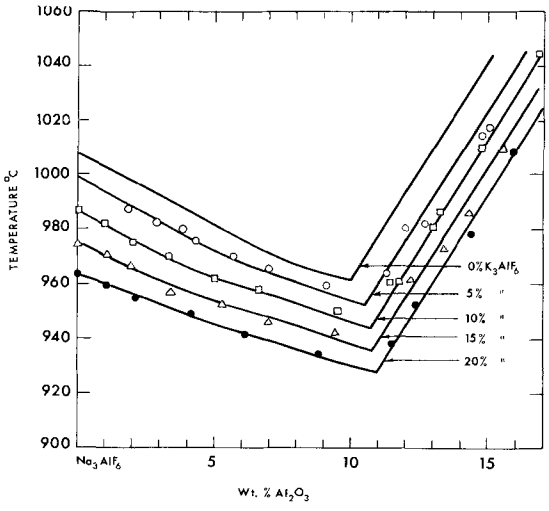

Fig. 9. Liquidus diagrams for sodium cryolite-alumina with 0, 5, 10, 15, and 20% potassium cryolite; weight per cent K_3AlF_6 given on alumina-free basis.

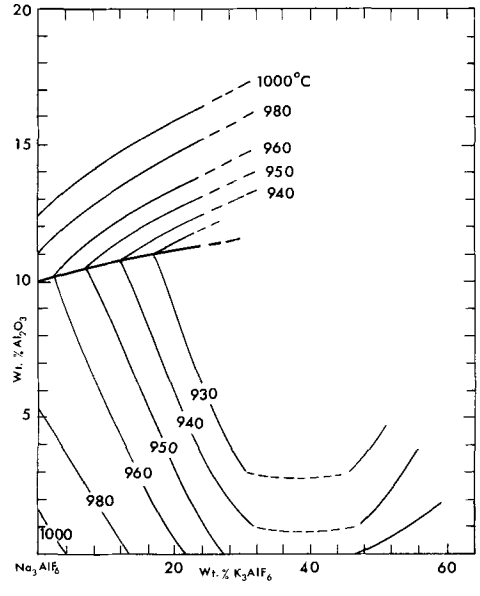

Fig. 10. Liquidus diagram for sodium cryolite-alumina-potassium cryolite: % Na_3AlF_6 + % Al_2O_3 + % K_3AlF_6 = 100.

Figure 9 shows sections across the Na_3AlF_6-Al_2O_3-K_3AlF_6 system, and the ternary diagram (Fig. 10) was constructed from these and other sections determined at 1, 2, and 3% Al_2O_3 (not shown). Addition of K_3AlF_6 increases the Al_2O_3 solubility, as reported by Baimakov and Batashev (12).

It is not clear why the Al_2O_3 in quenched melts containing potassium cryolite should be soluble in $AlCl_3$ solutions; possibly it is present as some kind of oxyfluoride. Leach water is not alkaline to phenolphthalein, showing the absence of aluminate, and no unusual x-ray diffraction pattern was obtained from a quenched melt containing 10.5% Al_2O_3 in K_3AlF_6 even though only 3.7% Al_2O_3 was insoluble in $AlCl_3$ solution. Possibly there is a connection between the change in form of the Al_2O_3 and the substantially higher solubility in K_3AlF_6.

Manuscript received Dec. 20, 1965.

Any discussion of this paper will appear in a Discussion Section to be published in the June 1967 JOURNAL.

REFERENCES

1. N. W. F. Phillips, R. H. Singleton, and E. A. Hollingshead, *This Journal*, **102**, 648 (1955).
2. N. W. F. Phillips, R. H. Singleton, and E. A. Hollingshead, *ibid.*, **102**, 690 (1955).
3. Anne Fenerty and E. A. Hollingshead, *ibid.*, **107**, 993 (1960).
4. E. Vatslavik and A. I. Belyaev, *J. Inorg. Chem. (U.S.S.R.)*, **3**, 1044 (1958).
5. A. I. Belyaev, M. B. Rapoport, and L. A. Firsanova, "Metallurgie des Aluminiums," Vol. 1., Berlin, VEB Verlag Technik, 1956. (Russian Edition, Moscow 1953). Translated from Russian by H. Frahn.
6. M. Rolin and R. Muhlethaler, *Bull. Soc. Chim. France*, **10**, 2593 (1964).
7. V. P. Mashovets and V. I. Petrov, *Zhur. Priklad. Khim.*, **30**, 1695 (1957).
8. J. L. Henry and W. M. Lafky, *Ind. Eng. Chem.*, **48**, 126 (1956).
9. P. A. Foster, Jr., *J. Am. Ceram. Soc.*, **43**, 66 (1960).
10. A. I. Belyaev and J. E. Studenzov, see ref. (5), p. 61.
11. S. F. Lundina, see ref. (5), p. 61.
12. J. W. Baimakov and P. P. Batashev, see ref. (5), p. 81.

Electrode Kinetics of Oxygen Evolution and Dissolution on Rh, Ir, and Pt-Rh Alloy Electrodes

A. Damjanovic, A. Dey,[1] and J. O'M. Bockris

John Harrison Laboratory of Chemistry, Electrochemistry Laboratory, University of Pennsylvania, Philadelphia, Pennsylvania

ABSTRACT

Cathodic and anodic Tafel parameters, stoichiometric numbers, and decay kinetics have been determined on rhodium, iridium, and platinum-rhodium alloy electrodes. Two regions of constant $\partial \ln i_{anodic}/\partial V$ for a given substrate were observed. The catalytic activity of the substrates in acid solution above about 1.4v (*vs.* N.H.E.) was $i_{Pt} < i_{Pt\text{-}Rh} < i_{Rh} < i_{Ir}$. On the anodic side, the alloy substrate tends to behave as Rh, on the cathodic side as Pt. Time decay behavior was conventional except for the alloy surface, where the decay from the anodic side behavior resembled that on Pt. The stoichiometric number on Rh, Ir, and Pt-Rh was about 2. Rate-determining steps have been determined unambiguously by the criteria mentioned because of the existence and helpful diagnostic nature of two distinct values for $\partial \ln i/\partial V$ on the anodic side, and because of the availability of stoichiometric numbers. After anodic polarization, Pt-Rh electrodes behave as if the substrate were an individual area of Pt and Rh oxides. A model which rationalizes this deduction is suggested.

Recently, the situation concerning the mechanism of oxygen dissolution and evolution on platinum electrodes has been the subject of increased study (1-30). The desire for enhanced electrocatalysis, and hence efficiency and power in electrochemical converters, is the origin of much of this work, but it cannot be fulfilled easily if there is not comprehensive knowledge of the mechanism of the reaction on a sufficient number of electrode catalysts. Consequently, in this paper, a study is reported of the oxygen electrode reactions on rhodium, iridium, and on a platinum-rhodium alloy in acid and in alkaline solutions. Data on the kinetics of O_2 reaction on these electrodes are scarce (30-32).

Experimental

Experiments were carried out in highly purified acid and alkaline solutions. Since the experimental procedure in this work was basically the same as described in a previous publication (10), it is given here only briefly.

Cell, solution, and chemicals.—An all-glass cell with three compartments separated by stopcocks used in these experiments was previously described (1, 9, 10).

Oxygen, which was bubbled through the test and the counter electrode compartments of the cell, was purified by passing through a purification train (10).

Solutions were prepared from conductivity water directly redistilled into the cell which had already been cleaned by acids and rinsed with conductivity water (see below). A known amount of perchloric acid, which was twice recrystallized in an auxiliary vessel (10), was introduced along the closed glass tubing system (including the measuring buret) into the cell. Concentration of the solution was adjusted to 1*N* $HClO_4$ by redistilling more conductivity water into the cell. The solution was further purified by anodic pre-electrolysis for about 20 hr or more at a c.d. (current density) of 1 ma/cm^2 on an auxiliary electrode of 4 cm^2.

Alkaline solutions were made from Baker Analyzed Reagent Grade potassium hydroxide. Concentration was adjusted to 1*N* KOH. Alkaline solutions were anodically pre-electrolyzed longer than the acid.

Rh and Ir, and Pt-Rh alloy in the form of wires were obtained from A. D. Mackay, Inc. Alloy composition was 40 at. % Rh.

Electrode treatment.—Wire electrodes (diameter 0.5 mm) of known geometrical area (~0.50 cm^2) were sealed to a true bore ground glass tubing fitting the bore on the cap of the test electrode compartment of the cell. In order to ensure a leak-proof seal, one end of the test wire is spot welded to a narrow (~1 mm), thin (0.001 mm) platinum foil (length about 5 mm), the other end of which was spot welded to a piece of platinum wire (d $\approx$ 0.5 mm or less) serving for contact. The platinum foil with the welded portions of the test electrode and of the contact wire are sealed into a glass bead which is then joined to a true bore ground glass tube.

Electrode pretreatment includes washing with organic solvents, chromic-sulfuric, and nitric sulfuric acid, and finally thoroughly with conductivity water.[2] After the electrode was introduced into the test electrode compartment which itself was washed with acids and conductivity water, it was washed once again inside the cell in freshly redistilled conductivity water. The cell was all the time under slight (~5 -10 mm of H_2O) overpressure of purified O_2

[1] Present address: Hooker Chemical Corporation, Niagara Falls, New York.

[2] Electrodes treated in different ways (10) yielded the same results.

Measurements.—The electrical circuits were described elsewhere (33).

After an electrode had been anodized with 10^{-3} amp/cm^2 for 20 min, anodic Tafel lines were taken by reducing c.d. in steps of half decade. Once the lowest c.d. was reached, anodic lines were retraced by increasing c.d. In the range of the c.d. usually studied (10^{-8} to 10^{-2} amp/cm^2), bubbling of oxygen through the test electrode compartment had no effect on potential. Bubbling caused the potential to decrease (10) only at current densities less than 10^{-8} amp/cm^2, and for that reason oxygen bubbling was disconnected for measurements at lower ($<10^{-8}$ amp/cm^2) c.d. Cathodic lines were obtained on electrodes which had been first anodized, and then a constant cathodic current was applied. Steady state was observed as a plateau on a recorder. At current density of 10^{-4} amp/cm^2, the plateau established in about 1 sec, after which time the potential changed less than 10 mv/min in the next few minutes. Readings were taken at the initial part of the plateau (*e.g.*, for this c.d. after about 5 sec). At lower c.d., steady-state potentials are more stable, and readings are taken at correspondingly longer times. This change of the potential with time at high cathodic c.d. was interpreted as being due to the gradual (but far from complete) reduction of oxides. It is now established (34) that when a Pt electrode, for instance, is reduced, reduction of O_2 proceeds along a path different from that on the oxide covered electrode. Fast measurements at the highest cathodic c.d. used in the present work ($\sim 10^{-4}$ amp/cm^2) are taken so that the effect of the gradual reduction of oxide (which at the potential of the measurements proceeds at a far lesser rate than the reduction of O_2) is minimized.

Coverage with oxygen-containing films on potentiostated electrodes was determined by cathodic reduction with a constant current. Electrodes were potentiostated for 1 min at a given potential after which the potentiostating circuit was broken and a constant ($\sim$30 ma/cm^2) cathodic current was applied immediately (33) ($\sim 10^{-5}$ sec). The change of potential with time during the cathodic pulse was followed on an oscilloscope. All experiments were carried out in the oxygen saturated solutions (10).

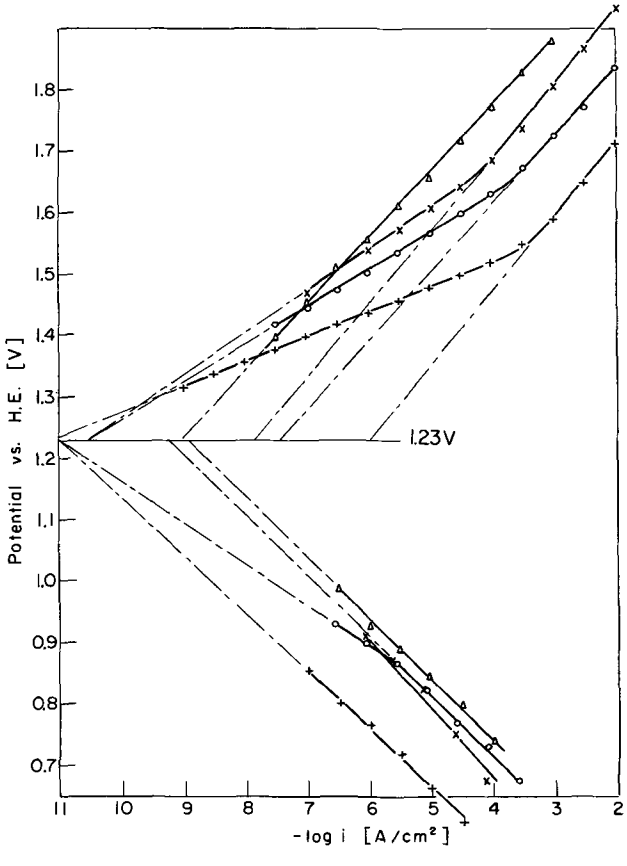

Fig. 1. *V*-log *i* plots for Rh (○), Ir (+), and Pt-(40 at. %) Rh (x) alloy electrodes in 1N $HClO_4$. Data (10) on Pt (△) are included.

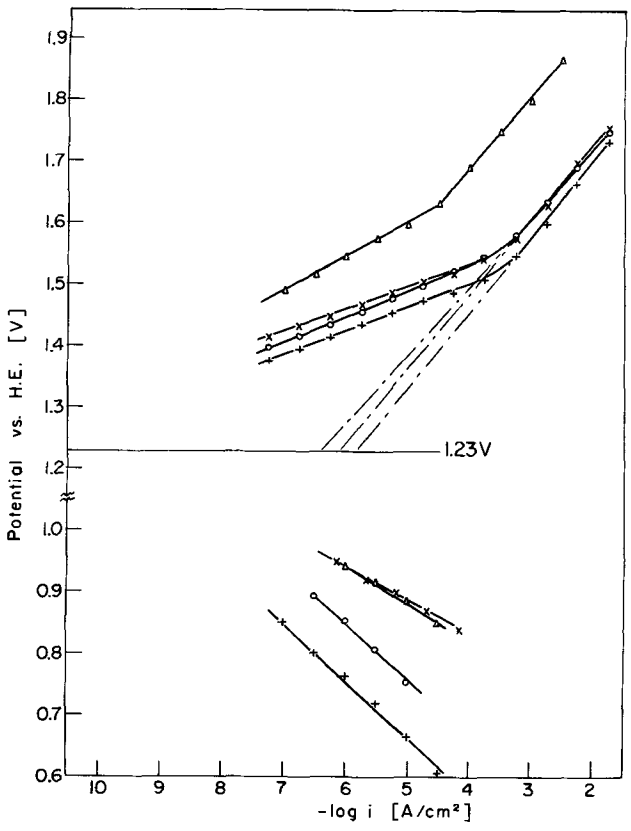

Fig. 2. *V*-log *i* plots for Rh(○), Ir (+), and Pt-(40 at. %) Rh (x) alloy electrodes in 1*N* KOH. Data (10) on Pt (△) are included.

Results

Potential current density relations.—Rh and Ir, and Pt-Rh alloy electrodes, in acid and in alkaline solutions, show two distinct linear *V*-log *i* anodic regions with different slopes. Transition from one region to another is rather sharp; it occurs in less than 1 unit of log *i*. On the cathodic side, only one linear region on each of these electrodes was observed, except for Rh in acid solution where, at lower c.d., another linear region appears to exist. In Fig. 1 and 2, these relations are shown for 1*N* $HClO_4$ and 1*N* KOH solutions, respectively; data are summarized in Table I. In these figures and in Table I data (10) for Pt are included for comparison.

At high anodic η, both in acid and in alkaline, $\partial V/\partial \ln i \simeq 2RT/\mathbf{F}$ for all electrodes. At low η, it is either close to $2RT/3\mathbf{F}$, as for Ir in both solutions and for Rh and Pt-Rh in alkaline, or to $RT/\mathbf{F}$, as for Rh and for Pt-Rh in acid (and for Pt in alkaline) solutions. On the cathodic side, $\partial V/\partial \ln i$ approach the ideal $2RT/\mathbf{F}$ on all electrodes except for Pt-Rh, and Pt in alkaline solution ($\sim RT/\mathbf{F}$). On Rh in acid solution, in addition to the $2RT/\mathbf{F}$ slope, a second slope close to the ideal $RT/\mathbf{F}$ appears at lower cathodic η.

The change of anodic slopes in acid solution[3] occurs at a constant current density ($\sim 10^{-4}$ amp/cm^{-2}) rather than at a constant η. In alkaline, in contrast to the acid case, *V*-ln *i* curves (almost) overlap for all electrodes except for Pt, which behaves more like Rh or Pt-Rh in acid solution. Ir in acid and in alkaline solution has the same η-ln *i* relation in contrast to all other electrodes.

[3] Including also Pt in KOH.

Table I. Observed diagnostic criteria

Electrode	$\frac{\partial\eta \text{ anodic}}{\partial \ln i}$ low η, mv	$\frac{\partial\eta \text{ anodic}}{\partial \ln i}$ high η, mv	$\frac{\partial\eta \text{ cathodic}}{\partial \ln i}$ low η, mv	$\frac{\partial\eta \text{ cathodic}}{\partial \ln i}$ high η, mv	$\left(\frac{\partial\eta \text{ anodic}}{\partial \ln t}\right)$ $t > 1$ sec, mv	$i_o \cdot 10^{11}$ (amp/cm^{-2}) Anodic low η	Anodic high η	Cathodic	ν
					1N $HClO_4$				
Rh	~60	125	(65)	~100	62	3	3.10^3	60(1)**	(2.08)** 2.5***
Ir	~40	120	~105	—	37	1	10^5	1	1.9
Pr-Rh	65-70(125)*	120	~110	—	95 average	$3(10^2)$*	10^3	10^2	2.7
Pt	110	—	~105	—	115 at $\eta < 1.5$v	~10^3	—	~10^2	3.6
					1N KOH				
Rh	~42	115	~100	—	43	6.10^{-1}	~10^5	3	1.9
Ir	~40	~120	~100	—	35	1	~10^5	~1	1.9
Pt-Rh	~40	~120	~55	—	40	10^{-1}	~10^5	3.10^{-1}	1.5
Pt	~60	115	~60	—	—	3.10^{-1}	~10^3	3.10^{-1}	2

* At current densities below 10^{-7} amp/cm^2.
** From cathodic Tafel slope at low η.
*** Calculated with the cathodic slope at high η.

At any given potential above about 1.4v (*vs.* H.E.), the activity in acid solution is in the order

$$i_{Pt} < i_{Pt\text{-}Rh} < i_{Rh} < i_{Ir} \qquad [1]$$

Similar trend holds also in alkaline, although, at higher η, alloy electrodes almost overlap with Rh.

At low c.d. ($<10^{-8}$ amp/cm^2), Tafel lines of Rh and Ir electrodes often tend to deviate from linearity, and η approaches[4] (not shown in Fig. 1 and 2) a rest potential between 1.25 and 1.45v (*vs.* H.E.). These potentials probably correspond to the mixed potential of an oxide reaction with the reversible oxygen reaction.

When the experiments were carried out on Pt-Rh alloy electrodes in highly purified acid solution below about 10^{-7} amp/cm^2, the Tafel line appears to reassume the slope of $2RT/F$ (Fig. 3).

Reproducibility of results.—Anodic V-ln i curves are well reproduced at current densities above about 10^{-7} amp/cm^2. Positions and slopes of anodic Tafel lines above 10^{-7} amp/cm^2 were not affected by the rest potentials established at zero c.d. At lower c.d. ($<10^{-8}$ amp/cm^2) it was often difficult to reproduce results. Cathodic lines are, in general, less reproducible than anodic lines. The degree of reproducibility depends on the time an electrode was kept at a potential below about 1v (*vs.* H.E.). The longer the time and the lower the potential, the poorer was the reproducibility. This is attributed to the change on the electrode surface due to the partial reduction of the surface oxides below certain potential. On an oxide free electrode surface, the mechanism and rates for O_2 reduction are, in general, different than on oxide covered electrode surface (34). This is illustrated in the case of prereduced and preanodized Rh electrodes in Fig. 4. With the present technique of measurement [fast measurement on preanodized electrodes (10)] dissolution was certain to occur on the same type of electrode surface as the evolution, namely, on oxide covered electrodes. For this reason, current density range on the cathodic side over which a linear relation was established is shorter than on the anodic side.

Exchange current densities.—For Ir (and Pt), both in acid and in alkaline solution, and for Rh and Pt-Rh alloy in alkaline solutions, cathodic and anodic (at low c.d.) Tafel lines when extrapolated intercept close to 1.23v *vs.* H.E. (±0.035v). For Rh and Pt-Rh alloy in acid, however, cathodic line with $\partial V/\partial \ln i \approx 2RT/F$ intercepts $\eta = 0$ axis at $i_o \approx 6 \cdot 10^{-10}$ and 10^{-9} amp/cm^2, respectively, while the anodic lines (at low η) intercepts this axis at about $3 \cdot 10^{-11}$ amp/cm^2 for both electrodes. If experimental points on Rh at low cathodic η are considered only, cathodic line with slope corresponding to RT/F extrapolates to $\eta = 0$ at $i_o = 10^{-11}$ amp/cm^2, hence close to the point where the anodic branch intercepts the axis (3.10^{-11} amp/cm^2). This appears to justify the interpretation of the experimental points on Rh in acid at low cathodic η in terms of a linear V-log i with $\partial V/\partial \ln i \approx RT/F$. Similarly, in acid solution extrapolation of the anodic Tafel line of Pt-Rh alloy electrode from the lowest

[4] This is particularly so if an electrode was anodized for longer (30 min) time at high (10^{-2} amp/cm^2) c.d.

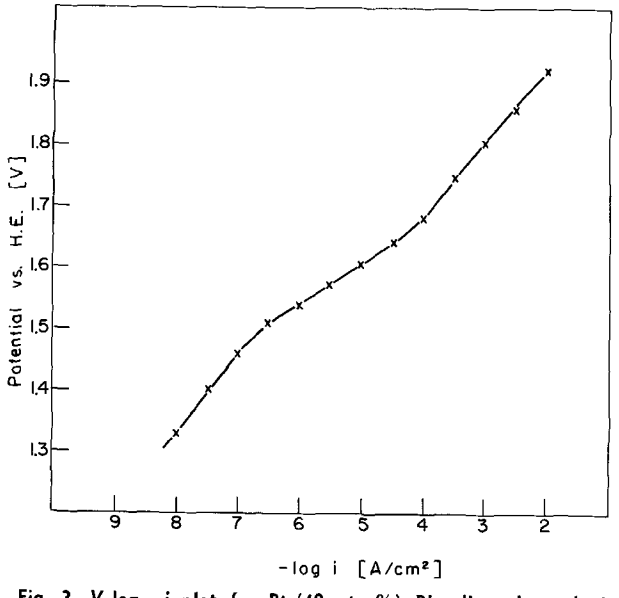

Fig. 3. V-log i plot for Pt-(40 at. %) Rh alloy electrode in highly purified acid (1N $HClO_4$) solution. At lowest current density additional linear relationship appears with the slope close to $2RT/F$ (compare with Fig. 1).

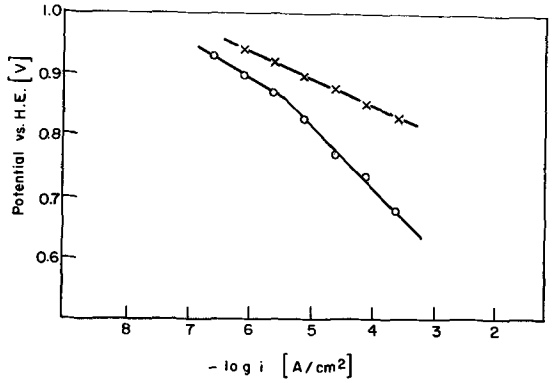

Fig. 4. V-log i plot for O_2 dissolution on Rh electrodes in 1N $HClO_4$. (○): preanodized electrode; (x) prereduced electrode by potentiostating at 0.2v (*vs.* H.E.) for 20 sec. Different mechanisms are operative on these electrodes.

Table II. Idealized stoichiometric numbers and Tafel slopes

Electrode		Anodic		Cathodic		Stoichiometric number	
		low η	high η	low η	high η		
Rh	Acid	RT/F	$2RT/F$	(RT/F)	$2RT/F$	(2)**	2.5***
	Alkaline	$2RT/3F$	$2RT/F$	$2RT/F$	—	2	
Ir	Acid	$2RT/3F$	$2RT/F$	$2RT/F$	—	2	
	Alkaline	$2RT/3F$	$2RT/F$	$2RT/F$	—	2	
Pt-Rh	Acid RT/F	$(2RT/F)$*	$2RT/F$	$2RT/F$	—	3	
	Alkaline	$2RT/3F$	$2RT/F$	RT/F	—	1-2	
Pt	Acid	$2RT/F$	—	$2RT/F$	—	4	
	Alkaline	RT/F	$2RT/F$	RT/F	—	2	

* At the lowest measured current densities.
** On the basis of cathodic slope at low η (RT/F).
*** On the basis of cathodic slope at high η ($2RT/F$).

current densities (Fig. 3) leads to the exchange c.d. of 10^{-9} amp/cm^2, in agreement with that extrapolated from the cathodic side.

The exchange c.d. obtained by extrapolation of linear Tafel regions both at low and at high η's are given in Table I.

Open-circuit potential decay.—Plots of potential decay after anodic polarization in acid solution are shown in Fig. 5 for times longer than 1 sec.[5] Similar plots were obtained for alkaline. Data on $\partial\eta/\partial \ln t$ are summarized in Table I. Decay potential data agree with $\partial V/\partial \ln i$ data, except for Pt-Rh alloy in acid solution with $\partial V/\partial \ln t$ being higher (average 95 mv) than $\partial V/\partial \ln i$ ($\simeq RT/F$). However, at the lowest potentials, $dV/d \ln t$ for the alloy corresponds closely to $2RT/F$.

Using these potential decay data and those from V-ln i curves, idealized diagnostic criteria are summarized in Table II.

Stoichiometric number.—The stoichiometric numbers, calculated by the equation (35)

$$\nu = \frac{n\mathbf{F}}{RT}\left[\frac{1}{b_a} - \frac{1}{b_c}\right]^{-1} \qquad [2]$$

[5] Because of the low exchange c.d., the electrodes are still in the linear region.

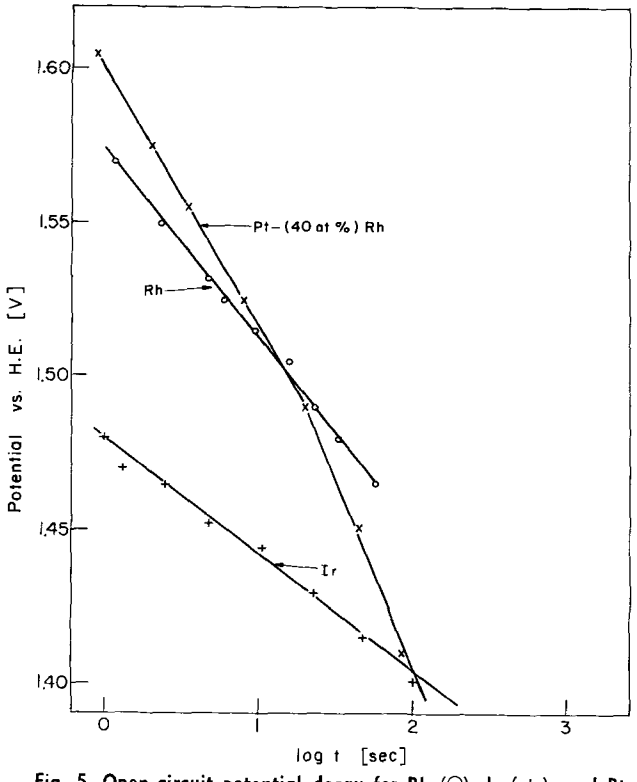

Fig. 5. Open-circuit potential decay for Rh (○), Ir (+), and Pt-(40 at. %) Rh alloy (x) electrodes in 1N $HClO_4$. On the Pt-Rh alloy electrode at low potentials slope increases to about 115 mv.

where b_a and b_c are anodic and cathodic Tafel slopes, respectively, are given in Table I. Only b_a's at low anodic η were used. For Rh in acid, η was calculated with both cathodic slopes ($RT/\mathbf{F}$ at low, and $2RT/\mathbf{F}$ at high η).

Coverage by oxygen-containing film.—Galvanostatic cathodic transients of Rh and Ir electrodes, after potentiostating in acid solution at a potential above 1v (*vs.* H.E.), differ significantly between themselves (Fig. 6). Ir electrode shows a prominent "flat" region in the V-t transients at relatively high potentials. In alkaline solutions, transients on Rh and Ir are much alike and are similar to that of Ir in acid solution.

A similar dependence exists of coverage by oxygen containing species on the potential (at which electrodes were potentiostated for 2 min) for both Rh and

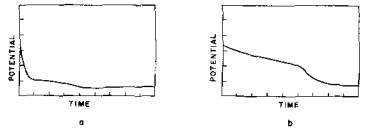

Fig. 6. Typical constant current transients in reduction of oxides on Rh (a) and on Ir (b) electrodes. Electrodes were potentiostated at 1.4v (vs. H.E.) in 1N $HClO_4$. Reduction current density 30 ma/cm^2; time scale 20 ms/cm; potential scale 0.5 v/cm.

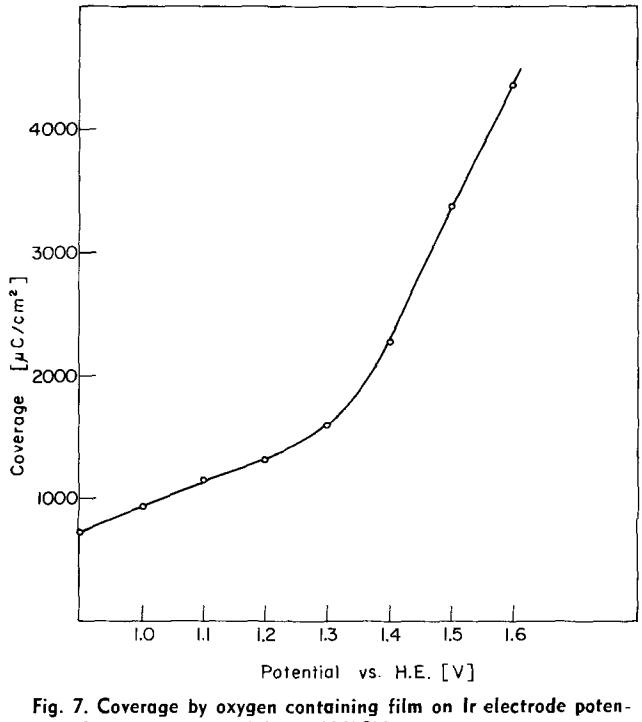

Fig. 7. Coverage by oxygen containing film on Ir electrode potentiostated at various potentials in 1N $HClO_4$.

Table III. Selected paths with diagnostic criteria

	$\partial V/\partial \ln i$ Anodic low η	$\partial V/\partial \ln i$ Anodic high η	Cathodic	ν	$\partial\eta/\partial$ pH Low η acid	Low η alk.	High η acid	High η alk.
A. "Electrochemical oxide" path (36)								
$S + H_2O \rightarrow SOH + H^+ + e^-$	$2RT/F$		$2RT/3F$	2	RT/F	$-RT/F$		
$SOH + S + H_2O \rightarrow SO + SH_2O + H^+ + e^-$	$2RT/3F$	$2RT/F$	$2RT/F$	2	$RT/3F$	$-RT/3F$	RT/F	$-RT/F$
$2SO \rightarrow O_2 + 2S$	$RT/4F$		∞	1				
B. (10)								
$S + H_2O \rightarrow SOH + H^+ + e^-$	$2RT/F$		$2RT/3F$	2	RT/F	$-RT/F$		
$SOH + H_2O \rightarrow SO - - H - - OH^- + H^+$	RT/F		RT/F	2	0	$-RT/F$		
$SO - - - H - - - OH^- \rightarrow SO - - H - - OH + e^-$	$2RT/3F$	$2RT/F$	$2RT/F$	2	$-RT/3F$	$-RT/3F$	$-RT/F$	$-RT/F$
$SO - - H - - OH \rightarrow SO + H_2O$	$RT/2F$	RT/F	∞	2	0			
$2SO \rightarrow 2S + O_2$	$RT/4F$		∞	1				
C. Krasilshchikov (37)								
$S + H_2O \rightarrow SOH + H^+ + e^-$	$2RT/F$		$2RT/3F$	2	RT/F	$-RT/F$		
$SOH \rightarrow SO^- + H^+$	RT/F		RT/F	2	0	$-RT/F$		
$SO \rightarrow SO + e^-$	$2RT/3F$	$2RT/F$	$2RT/F$	2	$-RT/3F$	$-RT/3F$	$-RT/F$	$-RT/F$
$2SO \rightarrow O_2 + 2S$	$RT/4F$		∞	1				
D.								
$S + H_2O \rightarrow SOH + H^+ + e^-$	$2RT/F$		$2RT/3F$	2	RT/F	$-RT/F$		
$SOH + H_2O \rightarrow SH_2O_2^- + H^+$	RT/F		RT/F	2	0	$-RT/F$		
$2SH_2O_2^- \rightarrow S + SO_2^{2-} + 2H_2O$	$RT/2F$	RT/F	$RT/2F$	1	$-RT/F$	$-RT/F$	$-RT/F$	0
$SO_2^{2-} \rightarrow S + O_2 + 2e^-$	$RT/3F$		RT/F	1	$-RT/3F$	$-RT/3F$		
E.								
$S + H_2O \rightarrow SOH + H^+ + e^-$	$2RT/F$		$2RT/7F$	1	RT/F	$-RT/F$		
$SOH + H_2O \rightarrow SO_2H_2^- + H^+$	RT/F		$RT/3F$	1	0	$-RT/F$		
$SO_2H_2^- \rightarrow SO_2H_2 + e^-$	$2RT/3F$	$2RT/F$	$2RT/5F$	1	$RT/3F$	$-RT/3F$	$-RT/F$	$-RT/F$
$SO_2H_2 \rightarrow SO + H_2O$	$RT/2F$	RT/F	$RT/2F$	1	0			
$SO + H_2O \rightarrow SHO_2 + e^-$	$2RT/5F$	$2RT/3F$	$2RT/3F$	1				
$SHO_2 \rightarrow S + O_2 + H^+ + e^-$	$2RT/7F$		$2RT/F$	1				

Ir electrodes in acid or in alkaline solutions. In Fig. 7, the relation for Ir electrode in $HClO_4$ is shown. Two distinct and to a first approximation linear regions are apparent. They intercept at about 1.3v (*vs.* H.E.).

Some irreproducibility in coverage measurements was observed, particularly if an electrode was used for some time, in which case, the electrode, for the same potential, has a higher coverage than it had initially. This was attributed to gradual roughening of the electrodes in successive anodic and cathodic pulsing. New electrodes were used for these measurements.

Discussion

Mechanism on Ir *in acid and alkaline solutions.*— The intercepts of the extrapolated cathodic and anodic Tafel line at low η, which are close to 1.23v (*vs.* H.E.), show that the mechanisms for the over-all reaction

$$2H_2O \rightarrow O_2 + 4H^+ + 4e^- \quad [3a]$$

for acid, or

$$4\,OH^- \rightarrow O_2 + 2H_2O + 4e^- \quad [3b]$$

for alkaline solution, are the same both in evolution and in dissolution. $\partial V/\partial \ln i$ of $2RT/3F$ at low anodic, and $2RT/F$ at cathodic η's, imply[6] that the rate of the over-all reaction (3) is controlled by an electrochemical step which occurs twice ($\nu = 2$) while the over-all reaction occurs once.[7] For the anodic direction of the reaction, two charge transfers precede the rate-controlling step.[7] Three reaction paths, which satisfy this requirement are given in Table III. They are paths A, B, and C. Path A is the "electrochemical oxide" path of Bockris (36), path B was recently suggested by the present authors as a possible path for O_2 reaction on Pt electrodes in alkaline solutions (10), and path C is that given by Krasilshchikov (37) for the same reaction on Ni electrodes. For path A, the second step, and for paths B and C, the third step in the anodic direction would be rate-controlling.

High value of $\partial V/\partial \ln i$ at high anodic η's ($\sim 2RT/F$) can be explained by either of these three paths. Two possibilities exist. First, at high anodic η, coverage by intermediates becomes high, the result of which is that for the same path and the rate-controlling step potential current density relationship changes and second, higher slope, appears at higher η's. This case was discussed first by Bockris (36) and more recently by the present authors (10). The second possibility is that for the same path the rate-controlling step at high anodic η's changes, and the first step (in either of these paths) becomes rate-controlling (10).

*p*H dependence of overpotential in acid solution could discriminate between the electrochemical path (A) and the other two (B and C). $\partial\eta/\partial$ *p*H at low and at high η's is positive for the former and negative for the latter two (see Table III). No such distinctions could be made in alkaline solution. For the electrochemical oxide path, the *p*H dependence of η for each step reverses its sign when the solution changes from acid to alkaline. This, and the fact that for Ir,

[6] Langmuirian type of adsorption assumed [cf. ref. (10)].

[7] This can be shown using Eq. [4].

Table IV. Summary of the mechanisms of O_2 reaction on various electrodes

		Anodic low η	Anodic high η	Cathodic low η	Cathodic high η
Rh	Acid	B(2)	B(1)	B(2)	B(3)
	Alkaline	A(2)	A(2) or A(1)	A(2)	—
Ir	Acid	A(2)	A(2) or A(1)	A(2)	—
	Alkaline	A(2)	A(2) or A(1)	A(2)	—
Pt-Rh	Acid	B(2)	B(1)*	B(2) and/or 1(1) 3(1) or 4(1)**	—
	Alkaline	A(2)	A(2) or A(1)	B(2) or D(2)	—
Pt (10)	Acid	1(1), 3(1) or 4(1)**	—	1(1), 3(1) or 4(1)**	—
	Alkaline	B(2) or D(2)	B(1) or D(1)	B(2) or D(2)	—

* At lowest overpotential the mechanism is 1(1), 3(1) or 4(1).
** These are the "oxide" path, "hydrogen peroxide" path, or "metal peroxide" path, respectively. Symbolism here corresponds to that in ref. (10).

V-log i curves overlap in acid and in alkaline solutions (and, hence, over-all $\partial\eta/\partial$ pH = 0) would favor the electrochemical oxide path over the other two. However, it is possible that the path in acid is different from the path in alkaline solution.[8]

Mechanism on Rh *in alkaline solution.*—Rh in alkaline solution behaves in the same way as the Ir electrode. Correspondingly, the discussion for Ir holds also for Rh. In Table IV, mechanisms for each electrode are tabulated.

Mechanisms on Rh *electrode in acid solution.*—Observed $\partial V/\partial \ln i$ close to $RT/\mathbf{F}$ at low anodic η's required a chemical rate-controlling step which follows an electrochemical step(s). This can be shown with the Eq. [4] (10, 18, 39, 40).

$$\frac{\partial V}{\partial \ln i} = \frac{RT}{\mathbf{F}} \left[\beta_k n_k + \sum_{i=1}^{k-1} \frac{\nu_i n_i}{\nu_k} \right]^{-1} \qquad [4]$$

where ν_i and ν_k are "stoichiometric numbers" (11),[9] and n_i and n_k are the numbers of electrons transferred in the single step i, and in the rate-controlling step k, respectively. Thus,[10] is $n_k = 1$ (a rate-controlling step involving charge transfer), and to satisfy the condition $\partial V/\partial \ln i = RT/\mathbf{F}$ at low anodic η's, Σ is ½. Two possibilities might be thought to satisfy this requirement: $\nu_i = 2$ and $\nu_k = 4$; or $\nu_i = 1$ and $\nu_k = 2$. If $\nu_i = 1$ and $\nu_k = 2$, only one electron is transferred before the rate-controlling step, but two are needed to form (at least) two identical intermediates required as reactants for the rate-controlling step ($\nu_k = 2$). If $\nu_i = 2$ and $\nu_k = 4$, then six electrons would be transferred in the over-all reaction. In general, an electrochemical rate-controlling step in O_2 evolution with the parameters given is therefore not possible.

With $n_k = 0$ (a chemical rate-controlling step), ν_k could be any integer from 1 to 4, but must be equal to the total number of electrons transferred before the rate-controlling step ($= \sum_{i=1}^{k-1} \nu_i n_i$). Four paths which satisfy this condition, B, C, D, and E, are given in Table III. Path D is the alkaline path of Hoar (2), and E was introduced by the present authors in a previous publication (10). The second step in this anodic direction in all these paths would be rate-controlling for the reaction.

With the anodic $\partial V/\partial \ln i$ of $RT/\mathbf{F}$ (and, hence, $n_k = 0$, and $\sum_{i=1}^{k-1} \nu_i n_i = \nu_k$), and, since in this case (see above) $\sum_{i=1}^{k-1} \nu_i n_i$ is equal to the number of electrons transferred before the (chemical) rate-controlling step, the number of electrons transferred before the (same) rate-controlling step in O_2 dissolution is $n - \nu_k$, where n is the number of electrons for the over-all reaction. It follows from Eq. [4] that, for this cathodic reaction, $n - \nu_k = \nu_k\, \alpha_{\text{cath.}}$, where $\alpha_{\text{cath.}}$ is the transfer coefficient for the cathodic direction of the reaction. $\alpha_{\text{cath.}}$ in this relationship cannot have value of ½, and, hence, (for the given conditions: anodic $\partial V/\partial \ln i = RT/\mathbf{F}$) cathodic slope of $2RT/\mathbf{F}$ at low η's must be excluded.

The observed value of $2RT/\mathbf{F}$ on the cathodic side must, therefore, reflect the change of the Tafel slope in the cathodic direction with increased η. This is supported by the fact that the observed Tafel line with $2RT/\mathbf{F}$ intercepts the $\eta = 0$ axis at c.d. higher than does the anodic Tafel line. Short and apparently linear range of V *vs.* ln i observed on the cathodic V-log i curves at low η's does intercept in extrapolation the anodic branch close to $\eta = 0$ axis. Hence, this short region of V-ln i at low η's represents a true linear relation of V *vs.* log i. Its slope is close to $RT/\mathbf{F}$. This is a permissible cathodic slope for the condition $(\partial V/\partial \ln i)_{\text{anodic}} \simeq RT/\mathbf{F}$, the only other permissible slope being $RT/3\mathbf{F}$. With the latter slope, the extrapolated exchange c.d. would be far less than that obtained from the anodic extrapolation, and, hence, this slope is impossible.

With the cathodic slope at low η's of $RT/\mathbf{F}$, the stoichiometric number $\nu_k = 2$ and the possible paths reduce to B, C, and D. It remains, however, to explain the appearance of the $2RT/\mathbf{F}$ slope of high cathodic η. The change of the slope from $RT/\mathbf{F}$ at low η's, to $2RT/\mathbf{F}$ at high cathodic η's, is most probably due to the change in the rate-controlling step with potential. Path D can now be eliminated, as there is no $2RT/\mathbf{F}$ cathodic slope required for high η (cf. Table III). For the remaining two paths, B and C, the third steps (in the anodic direction) are the only possible rate-controlling steps at high cathodic η. (The first three steps in these two paths differ only in the "hydration" of intermediates and are indistinguishable by present electrochemical criteria.)

Finally, the change of slope in the anodic V-ln i from approximately $RT/\mathbf{F}$ at low η, to $2RT/\mathbf{F}$ at high η, is due either to a change in mechanism from B(2)[11] to B(3), or from B(2) to B(1)[12] (see Table III). One point here favors the change in mechanism from the second to the first step. Extrapolation of the anodic Tafel line at high η gives the exchange current density of $3 \cdot 10^{-8}$ amp/cm^2. Extrapolation for the cathodic side at high η gives to the exchange current density of $6 \cdot 10^{-10}$ amp/cm^2. This shows different mechanisms at high anodic and at high cathodic η. Since on the cathodic side at high η the mechanism can be only B(3), at high anodic η it is B(1).

Mechanism on Pt-Rh *alloy electrodes.*—Pt-Rh alloy electrodes behave in a peculiar way. In acid solution, $\partial V/\partial \ln i$ of $RT/\mathbf{F}$ at low anodic η excludes $2RT/\mathbf{F}$ as a slope on the cathodic side. The reasoning for this conclusion is given in the discussion of Rh in acid solutions. However, in contrast to the behavior for Rh, plot of V-log i of the alloy does not show or indicate another cathodic slope at low η. The cathodic Tafel line intersects the $\eta = 0$ axis at higher values of (exchange) current density than does the anodic branch, and so it is possible that the linear V-ln i relationship with a slope of $RT/\mathbf{F}$ exists at still lower cathodic current densities. If so, the arguments advanced for the case of Rh in acid solution would hold here, too, and the mechanism would be (see Table III) either B(2) [or C(2)], at low anodic, or cathodic η, B(1) [or C(1)] at high anodic η, and B(3) [or C(3)] at high cathodic η.

In alkaline solution, the anodic slope at low η of $2RT/3\mathbf{F}$ excludes (the observed) cathodic slope of $RT/\mathbf{F}$. The only acceptable slopes are $2RT/5\mathbf{F}$ and $2RT/\mathbf{F}$. Almost the same exchange current densities are extrapolated from the anodic (10^{-12} amp/cm^2) and the cathodic ($3 \cdot 10^{-12}$ amp/cm^2) side. Were the cathodic slopes to be $2RT/5\mathbf{F}$ or $2RT/\mathbf{F}$, the extrapolated exchange current density from the cathodic side would be either lower or higher, respectively, than that extrapolated from the anodic side and, consequently, the latter two slopes are also impossible. This apparent inconsistency of the experimental results may be rationalized in the following way.

From Fig. 1 and 2, it can be seen that the reaction, both the oxidation to O_2 and the reduction to H_2O, follows the kinetic characteristics corresponding to the individual metals, whichever has the faster

[8] Recently, Wong (38) has shown that for O_2 evolution on Ir electrodes in acid solution $(\partial\eta/\partial \text{pH})_i \approx +20$ mv at low η's, and about +40 mv at high η's. These results are consistent with the electrochemical path.

[9] ν_i is the number of times the step i occurs for one act of the over-all reaction; it is here called a stoichiometric number although, formally, this term applies only to the rate-controlling step.

[10] In this analysis, it is taken that no more than one charge can be transferred in any single reaction step.

[11] B(2) means the second step in the anodic direction of the path B is rate-controlling.

[12] Since the first three steps in paths B and C are indistinguishable by electrochemical means only path B is considered here.

rate. The likely interpretation of this is that the homogeneous alloy substrate has become a heterogeneous mixture of a platinum oxide and a rhodium oxide.[13] Although the reaction takes place on both oxides, the over-all rate is determined by the rate for that oxide on which the reaction at the given potential proceeds faster. Thus, on the anodic side, the reaction at higher potentials occurs predominantly on rhodium oxides. At lowest anodic η's in acid solution, Tafel line of the alloy (Fig. 3) deviates toward lower potentials. This is exactly what would be expected on the basis of the proposed hypothesis: the rate of the over-all reaction at these lowest overpotentials is determined by the rate on platinum oxides (cf. Fig. 1, 2, and 3). The cathodic reaction occurs in alkaline solution (Fig. 2) predominantly on Pt oxides, on which the rate is faster than on Rh oxides. In acid, in the potential range examined, both oxides are equally active, and the reaction occurs on both of them. At the lowest cathodic η (in acid solution), Tafel line for alloy does not show additional slope as does the line for Rh. This additional slope on alloy electrodes is not expected since, according to the advanced hypothesis, the rate of the reaction at low cathodic η (in acid solutions) would be controlled by the rate with which the reaction occurs on a Pt electrode.

A reason for this situation may be suggested tentatively as follows. When a platinum-rhodium alloy surface undergoes anodic oxidation, it is probable that the platinum and the rhodium atoms alternatively (since there is almost an equal atomic composition of the alloy) leave the kink sites and diffuse across the surface of the metal. Nucleation at individual patches containing platinum and oxygen and those containing rhodium and oxygen must occur, respectively, on the surface, to form platinum oxides and rhodium oxides effectively. On each of these oxides, the reaction mechanism and the rates of the reaction may be different. Such an electrode would behave as a mixed electrode,[14] and the over-all rate of the reaction would be given by

$$i_a = F_A i_o^A \exp\left[\frac{\alpha_a{}^A F\eta}{RT}\right] + F_B i_o^B \exp\left[\frac{\alpha_a{}^B F\eta}{RT}\right] \quad [5]$$

where i_o^A and i_o^B are the exchange current densities for the corresponding oxide. F_A and F_B are the fractional surface areas of these oxides. Subscript a stands for anodic. Similar equation would hold for the cathodic reaction. If $\alpha_a{}^A = \alpha_a{}^B = \alpha_a$, the same linear dependence of V on ln i holds for both oxide phases, and the over-all reaction proceeds with the rate

$$i_a = [F_A i_o^A + F_B i_o^B] \exp\left[\frac{\alpha_a F\eta}{RT}\right] = (i_o)_{Ap} \exp\left[\frac{\alpha_a F\eta}{RT}\right] \quad [6]$$

where

$$(i_o)_{Ap} = F_A i_o^A + F_B i_o^B \quad [7]$$

is the apparent exchange current density. In general, one term in the sum (7) would be expected to be larger than the other, and the over-all rate of the reaction will be controlled by the rate of the reaction corresponding to one oxide. If $\alpha_a{}^A \neq \alpha_a{}^B$, the rate of the over-all reaction in different potential range may be controlled by the rate of different oxides. In general, if

$$i_o^A \exp\left[\frac{\alpha^A F\eta}{RT}\right] > i_o^B \exp\left[\frac{\alpha^B F\eta}{RT}\right] \quad [8]$$

the rate is controlled by the phase A.

Additional support for the hypothesis advanced to account for the behavior of Pt-Rh alloy electrode comes from the analysis of the open-circuit potential decay curve for the alloy. At lowest potentials, this curve for acid solution has a slope corresponding to $2RT/\mathbf{F}$ (cf. Fig. 5), as expected for a pure Pt electrode.

Hence, the behavior of Pt-Rh alloy electrodes, both in acid and in alkaline solutions, is fully accounted for by the advanced hypothesis. Appropriate mechanisms are given in Table IV.

Nature of electrode surfaces.—Cathodic transients on an Ir electrode after it was potentiostated at 1.4v for 2 min in acid solution show prominent "flat" region between two inflections at relatively high potentials. On Rh electrodes (acid solution) this region is far less prominent and the reduction occurs at higher overpotential than on Ir (Fig. 6). In alkaline solutions, transients of both Rh and Ir are almost identical and are similar to that of Ir in acid solution. If the potential at which an oxide is reduced is a measure of the exchange current density for oxide formation (or reduction), it appears that the oxides on Rh in alkaline and on Ir both in acid and in alkaline solutions behave similarly, but are different from that on Rh in acid solution. There is, hence, a correlation between the "type" of oxides on an electrode surface and the reaction mechanism for the oxygen evolution reaction.

High coverage values (Fig. 7) on all these electrodes at potentials above about 1v can only be accounted for if phase oxides form. The existence of phase oxides has been proved unambiguously by the ellipsometric technique on Pt electrodes potentiostated above 1v (*vs.* H.E. in the same solution) in acid solution (11). Phase oxide also forms in alkaline solution (41). It is expected, on this basis, that on an alloy electrode oxides also form.

At potentials below about 1v (*vs.* H.E.) oxides reduce and, hence, O_2 dissolution, in contrast to the evolution which always occurs on oxide covered electrodes, may occur either on oxide covered or oxide free electrode surfaces. Mechanisms, and hence activity at a given potential, may differ on oxide covered and on oxide free electrodes. This was already shown for Pt electrodes (34), and here it is illustrated on Rh electrodes in acid solutions (Fig. 4). In the present experiments, measurements have been conducted so that electrodes remained oxide covered in O_2 dissolution also.

In contrast to Pt electrodes, where oxide coverage increases linearly with potential up to about 1.7v with no change of slope (5, 10, 11) on Rh, and on Ir electrodes (Fig. 7), initially (from 1 to about 1.35v) oxide coverages increase slower with potential, but above about 1.35v, the coverage increases sharply with potential. The change in the slope is not, however, related to the change in the slope of V-ln i curves. The latter change occurs at potentials above 1.5v (at about 1.6v).

Conclusions

The present paper is an example of a situation in which the mechanism criteria of the steady-state Tafel line slope may be applied to give mechanism information. The effectiveness of the criteria in this instance is associated with the presence of knowledge of the stoichiometric number and the existence in the experimental data of changes of slope at certain potentials. The slope values are in all cases (*a*) constant and (*b*) simply related to $RT/\mathbf{F}$.

The mechanisms discussed in this paper (summarized in Table IV) are derived largely from the criteria: Tafel slopes in cathodic and anodic direction; stoichiometric numbers; pH dependence of rate; and some knowledge concerning the nature of the substrate. Mechanism deductions in this manner can be made only when the exchange current densities are sufficiently low and when the change of the substrate with potential and time is negligible in the potential region of the kinetic analysis.

[13] The electrodes under conditions at which the reactions occur are covered with a layer of a few angstroms of oxides (10).

[14] Mixed electrodes here should not be confused with polyelectrodes at which two or more different reactions occur simultaneously to establish a mixed potential.

Some recent papers use the term "mechanism" to apply to knowledge of the number of electrons used in the over-all reaction. It is desired to stress that this is only a preliminary stage of a mechanism analysis; the path and rate-determining step are the goal. In so far as they can be known, or at least number of alternative paths and rate-determining steps reduced, so is the contribution of the work to the electrocatalysis situation for the reaction increased.

Acknowledgment

The authors wish to thank the United States Air Force Materials Laboratory, Air Force Systems Command, Wright-Patterson Air Force Base, Ohio, for the financial support of this work under Contract No. AF 33(616)-8150.

Manuscript received Sept. 17, 1965; revised manuscript received March 17, 1966.

Any discussion of this paper will appear in a Discussion Section to be published in the June 1967 JOURNAL.

REFERENCES

1. J. O'M. Bockris and A. K. M. S. Huq, *Proc. Roy. Soc.*, **A237**, 271 (1956).
2. T. P. Hoar, "Proc. 8th Meeting CITCE," p. 439, Butterworths, London (1956).
3. E. A. Efimov and N. A. Izgayshev, *Zhur. fiz. Khim.*, **30**, 1606 (1956).
4. N. A. Izgayshev and E. A. Efimov, *ibid.*, **30**, 1807 (1956).
5. W. Visscher and M. A. V. Devanathan, *J. Electroanal. Chem.*, **8**, 127 (1964).
6. L. N. Nekrassov and L. Müller, *Electrochim. Acta*, **9**, 1015 (1964).
7. B. E. Conway and E. Gileadi, *Can. J. Chem.*, **40**, 1933 (1962).
8. D. T. Sawyer and R. J. Day, *Electrochim. Acta*, **8**, 589 (1963).
9. N. Watanabe and M. A. V. Devanathan, *This Journal*, **111**, 615 (1964).
10. A. Damjanovic, A. Dey, and J. O'M. Bockris, To be published.
11. M. Genshaw, A. K. N. Reddy, and J. O'M. Bockris, *J. Electroanal. Chem.*, **8**, 406 (1964).
12. H. Wroblowa, M. L. B. Rao, A. Damjanovic, and J. O'M. Bockris, In course of publication.
13. M. W. Breiter, *Electrochim. Acta*, **9**, 441 (1964).
14. B. E. Conway and E. Gileadi, *Trans. Faraday Soc.*, **58**, 2493 (1962).
15. J. Giner, *Z. Elektrochem.*, **64**, 491 (1960).
16. H. A. Laitinen and C. G. Enke, *This Journal*, **107**, 773 (1960).
17. T. N. Belina and A. I. Krasilshchikov, *Zhur. fiz. Khim.*, **28**, 1286 (1954).
18. A. C. Riddiford, *Electrochim. Acta*, **4**, 170 (1961).
19. Yu. A. Masitov, K. I. Rosental, and V. J. Veselowsky, *Zhur. fiz. Khim.*, **38**, 449 (1964).
20. J. Jacq and O. Bloch, *Electrochim. Acta*, **9**, 551 (1964).
21. E. E. Criddle, *ibid.*, **9**, 853 (1964).
22. J. P. Hoare, *This Journal*, **110**, 1019 (1963).
23. J. P. Hoare, *ibid.*, **109**, 858 (1962).
24. J. P. Hoare, *ibid.*, **111**, 968 (1964).
25. A. Hickling and J. Hill, *Trans. Faraday Soc.*, **46**, 550 (1950).
26. A. V. Pamtilov and A. I. Tsinman, *Ukrain. khim. Zhurn.*, **23**, 579 (1957).
27. S. Schuldiner and T. Warner, *This Journal*, **112**, 212 (1965).
28. W. Vielstich, *Z. physik. Chem.*, **15**, 409 (1958).
29. D. Winkelmann, *Z. Elektrochem.*, **60**, 731 (1956).
30. J. B. Westhaver, *Z. physik. Chem.*, **51**, 65 (1905).
31. J. P. Hoare, *This Journal*, **111**, 232 (1964).
32. G. Bianchi, S. Mazza, and T. Mussini, U. S. Dept. Commerce, Office Tech. Service, AD *277,394*, 34 pp (1961).
33. W. Mehl, M.A.V. Devanathan, and J. O'M. Bockris, *Rev. Sci. Instr.*, **29**, 180 (1958).
34. A. Damjanovic and J. O'M. Bockris, *Electrochim. Acta*, **11**, 376 (1966).
35. R. Parsons, *Trans. Faraday Soc.*, **47**, 1332 (1951).
36. J. O'M. Bockris, *J. Chem. Phys.*, **24**, 817 (1956).
37. A. I. Krasilshchikov, *Zhur. Fiz. Khim.*, **37**, 531 (1963).
38. M. Wong, Private communication.
39. R. Parsons in T. P. Hoar, "Proc. 8th Meeting CITCE," p. 439 Butterworths London (1956).
40. H. Mauser, *Z. Elektrochem.*, **62**, 419 (1958).
41. V. Brusic, Private communication.

The Application of Irreversible Thermodynamics to the Thermogalvanic Behavior of Copper-Copper Sulfate Systems

Paul D. Miller, Arch B. Tripler, Jr., and J. J. Ward

Battelle Memorial Institute, Columbus, Ohio

ABSTRACT

Experiments with the thermocells $Cu(T_2)/CuSO_4(T_2)/CuSO_4$ Bridge/ $CuSO_4$ (25°C)/Cu (25°C) are described. The cell potentials were quite dependent on the *p*H of the 0.01*M* solution. Experimental results were in fairly good agreement with data obtained from a physicochemical model using procedures of irreversible thermodynamics. Procedures used to calculate ionic entropy values for copper are described.

Thermogalvanic corrosion is one form of metal deterioration of great practical importance which has not been extensively studied experimentally. The action is one in which an area of a metal surface wet by an electrolyte becomes anodic (corrodes) while another becomes cathodic as a result of a temperature difference. Thus, the different electrode reactions result in a potential difference which can be measured.

It is possible to treat such nonequilibrium systems by the techniques of the Onsager thermodynamics of irreversible processes. The present paper illustrates the use of irreversible thermodynamics to interpret the experimental data obtained from a thermogalvanic cell (thermocell) composed of copper immersed in 0.01*M* copper sulfate. The treatment relies quite strongly on the theoretical approach suggested by two fairly recent papers by de Bethune (1, 2).

The cold copper electrode is anodic in the cell being discussed while the hot one is cathodic. On the other hand, copper, as well as most other metals studied, is anodic when it forms the hot section of a thermocell with sodium chloride as electrolyte. Thus, it can be seen that metal dissolution can occur at

either hot or cold areas depending on the system. The treatment which follows, however, is devoted entirely to the copper sulfate thermocell.

Experimental Work

Thermogalvanic cells and circuitry.—Figure 1 is a schematic diagram of the apparatus and circuitry used in this study. The basic portion of the experimental setup consists of two individually isothermal electrolytic half-cells operating at different temperatures and connected by a liquid bridge to form a thermal cell. Each half-cell consists of copper dipping into a copper sulfate solution. The cells are kept at the desired temperatures (left cell 25°-100°C, right cell 25°C) by suitable thermostatic equipment. The Pyrex containers hold about 750 ml of solution and are flanged at the top to fit covers containing four 24/40 standard taper openings. Electrodes, gas sparge tubes, connecting bridge, and thermometers are introduced through these openings. The connecting bridge is made from 14 mm diameter Pyrex tubing.

The metal specimens are solid cylinders about 25 cm^2 in area which have been drilled out and tapped on the upper end. A threaded rod of the same material is screwed into the specimen and is protected from contact with the solution by a glass tube surrounding it. Leakage of the solution is prevented by a Teflon washer placed between the glass tube and the top of the metal cylinder. Pressure is applied on the seal by means of a nut at the top end of the metal rod which extends beyond the glass tube. Copper wires were used in all connections and circuitry.

High-purity copper, 99.999+, was used in most of the experiments. Oxygen-free high-conductivity (OFHC), 99.96% copper was used in some instances. Reagent grade copper sulfate was used for preparing the solutions.

Cell potentials were read primarily with a L&N type K-2 potentiometer using an electronic ammeter-voltmeter having a high input resistance as a null indicator. Some readings were made with an electrometer with an input impedance of 10^{13} ohms. The zero resistance ammeter was not used when thermogalvanic potentials were being read. That is, cell currents were measured in separate experiments.

Hg-Hg_2SO_4 reference electrodes were prepared from triply distilled mercury and mercurous sulfate. Hg_2SO_4 was wetted with the $CuSO_4$ solution. The readings with reference electrodes were made primarily to furnish data under isothermal conditions.

Thermogalvanic potential measurements.—Thermogalvanic potentials of copper in 0.01, 0.1, and 1.0*M* copper sulfate solutions were measured over a ΔT of 70°C. It was found that in the most dilute solution the potentials were dependent on the solution *p*H. Results

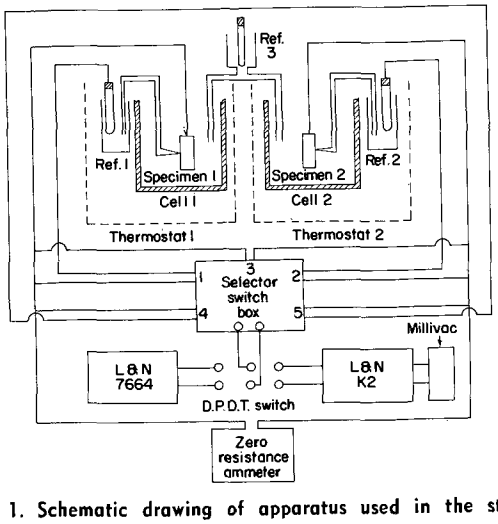

Fig. 1. Schematic drawing of apparatus used in the study of thermogalvanic potentials and currents.

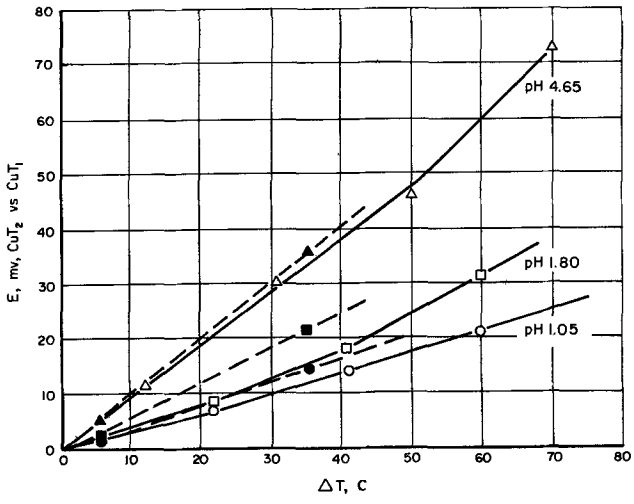

Fig. 2. Effect of *p*H on the thermogalvanic potentials of copper in 0.01M $CuSO_4$. ——— and open points, experimental values; — — — and solid points, calculated values.

at three *p*H levels reached by additions of H_2SO_4 are illustrated in Fig. 2 for 0.01*M* solutions. Note that the slope of the line decreases with decreasing *p*H. The data obtained in 0.1 and 1.0*M* solutions at all *p*H values could be expressed by lines somewhere in the area near the line for *p*H 4.65 in Fig. 2.

In all instances the cold electrode was negative (anodic) in these thermal cells. The reproducibility of voltage readings was sometimes good to only ±5 mv although frequently it was better than ±1 mv. Accordingly, it was assumed that the Soret effect in these cells was small.

Application of irreversible thermodynamics to copper-copper sulfate thermal cells.—A mathematical treatment for interpreting the data obtained from the experiments with thermogalvanic cells is given in the following paragraphs. The development is based largely on that presented by deBethune (1, 2). The thermal cell can be expressed by:

$$M(T_1)/\text{Electrode}(T_1)/\text{Electrolyte}(T_1)/$$
$$\text{Electrolyte}(T_2)/\text{Electrode}(T_2)/\text{Electrode}(T_1)/M(T_1) \quad [1]$$

The thermogalvanic potential of such a cell can be expressed by

$$\left(\frac{dE^*}{dT}\right)_{th} = \frac{S^*}{nF} \quad [2]$$

where $nF = 46.12$ mv/deg.

According to de Bethune, the transported entropy can be considered to be moved by a threefold mechanism according to the following equation

$$S^* = S^*_E + S^*_M - nS^*_{(\text{electrons})} \quad [3]$$

where the three terms on the right are defined as follows: (*i*) $S^*_E = Q^*_E/T$, called the entropy of electrochemical transport, results from the electrode reactions. (*ii*) $S^*_M = Q^*_M/T$, called the entropy of migration transport. This entropy comes from the migration of non-reversible ions which carry heat. A consideration of this term leads to the conclusion that it is required to satisfy the Onsager principle of microscopic reversibility (6). (*iii*) $nS^*_{(\text{electrons})}$, called the entropy of electron transfer. This entropy comes from the migration of electrons from the anode to the

cathode in the external circuit. Since this term is small it is neglected in all calculations.

The thermal temperature coefficient $(dE/dT)_{th}$ is defined as positive when the hot electrode is the (+) terminal of the cell.

Equation [2] was then used to calculate the thermal temperature coefficients so that a comparison could be made with experimental values derived from the slopes of the lines in Fig. 2 in the following manner.

The term S^*_E, entropy of electrochemical transport, in Eq. [3] depends basically on the reaction which takes place at the hot electrode. The experiments in the copper-copper sulfate system showed that copper was plated out on the hot electrode and that this electrode reads (+) on the electrometer. Accordingly the hot-electrode reaction can be expressed as

$$Cu^{++} + 2e \rightarrow Cu^{\circ} \qquad [4]$$

the reverse reaction takes place at the cold electrode. The entropy of electrochemical transport can then be expressed as

$$S^*_E = S^{\circ}_{Cu^{\circ}} - (\bar{S}_{Cu^{++}} + 2S^{\circ *}_{H^+}) \qquad [5]$$

where $S^{\circ}_{Cu^{\circ}}$ = entropy of metallic copper, $\bar{S}^{\circ}_{Cu^{++}}$ = partial molal entropy of transport for Cu^{++} ion, $2S^{\circ *}_{H^+}$ = standard ionic entropy of H^+ ion (introduced to correct term to standard state).

It can be seen that the proper placing (in hot or cold compartments) of reaction [4] is quite important since it helps to determine the sign of S^*.

The second term S^*_M, entropy of migration transport, is sometimes related to transference numbers for the ions involved as in

$$S^*_M = t_- S^*_M (SO_{4^=}) - t_+ S^*_M (Cu^{++}) \qquad [6]$$

However, in the system under discussion it was found experimentally that the H^+ was quite important in the cell potentials. Furthermore the ionic mobility of this ion is much greater than for the sulfate ion. The proposed model therefore was selected to permit the transfer of entropy by the H^+ moving in the opposite direction as the copper ion. It should be noted that this transfer also satisfies the principle of microscopic reversibility. The equation expressing this concept is

$$S^*_M = 2S^*_{H^+} \qquad [7]$$

Three other possible explanations for the large effect of pH on thermogalvanic potential were also considered. These were: (*i*) ratio of HSO_4^-/SO_4^{--}, (*ii*) effect of Cu^+; (*iii*) the reaction of the copper ion with water to form a cupric oxide film and hydrogen ions.

Calculations showed that none of these explained the effect of pH on the potential. Therefore, the assumption that the hydrogen ion migration accounted for the change of thermogalvanic potential as the pH varied is quite reasonable.

It should also be mentioned that a model assuming transference of the sulfate ion to satisfy microscopic reversibility does not provide agreement between calculated and experimental values.

The over-all entropy summations can then be expressed as

$$S^* = S^{\circ}_{Cu^{\circ}} - (\bar{S}_{Cu^{++}} + 2S^{\circ *}_{H^+}) + 2S^*_{H^+} - 2S^*_{(electron)} \qquad [8]$$

As was mentioned before, the entropy contribution from the electron flow is small and is considered zero.

In Tables I and II the individual entropy contributions in Eq. [8] are listed separately for the systems at 30° and 60°C, respectively. Note in particular the large entropy contribution furnished by the H^+ ion. From these individual entropy contributions, the Peltier heat transferred from one compartment to the other can be calculated. This calculation was made by multiplying the temperature of the compartment by the entropy transferred to it, and the product is listed as TS^* in the table. The pH values and temperature are chosen to agree with experiments so that a direct comparison can be made between calculated and experimental results.

The entropy values for metallic copper (Cu°) were taken from Kelley (7). The tables also include the temperature coefficients $(dE/dT)_{th}$.

The calculated results required an entropy value for the partial molal entropy of the copper ion at 30° and 60°C. The values used are presented in Table III and are based on experimental results from Wetmore and Gordon (3). Their data were confirmed in this laboratory by isothermal cell measurements. In these experiments the potentials between copper and a $Hg\text{-}Hg_2SO_4$ reference electrode were measured under reversible conditions at 25° and 60°C in 0.01, 0.05, 0.1, and 1.0*M* solutions.

The model also requires the entropy of transport of H^+ at various pH values in 0.01*M* copper sulfate solution. These data were not available. An approximation of these values was obtained by calculating the entropy of transfer of the H^+ ion by a method similar to

Table I. Entropy and thermal temperature coefficient values for the copper-0.01 *M* copper sulfate thermogalvanic cell at 30°C

		Solution pH 4.65 (initial)			Solution pH 1.80 (initial)			Solution pH 1.05 (initial)		
S^*, entropy terms	Contributing reaction	S^*, entropy, cal/g ion/K	$(dE/dT)_{th}$, mv/deg	TS^*, Peltier heat, cal/g ion	S^*, cal/g ion/K	$(dE/dT)_{th}$, mv/deg	TS^*, cal/g ion	S^*, cal/g ion/K	$(dE/dT)_{th}$, mv/deg	TS^*, cal/g ion
S^*_E	$Cu^{\circ} \rightarrow Cu^{\circ}$ $T_1 \rightarrow T_2$	+8.1	+0.18	+2,450	+8.1	+0.18	+2,450	+8.1	+0.18	+2,450
S^*_E	$Cu^{++} \rightarrow Cu^{++}$ $T_2 \rightarrow T_1$	+5.8	+0.13	+1,760	+5.6	+0.12	+1,700	+5.5	+0.12	+1,670
S^*_M	$2H^+ \rightarrow 2H^+$ $T_1 \rightarrow T_2$	+32.9	+0.71	+9,970	+7.7	+0.16	+2,330	+1.2	+0.03	+360
$S^*_{(electron)}$	$2e \rightarrow 2e$ $T_1 \rightarrow T_2$	Assumed zero			0	0	0	0	0	0
S^*	Net (calculated)	+46.8	+1.01	+14,180	+21.4	+0.46	+6,480	+14.8	+0.32	+4,480
S^*	Experimental	+47.3 (Between 25°-36°C)	+1.00	+14,330	+18.6 (Between 25°-47°C)	+0.40	+5,640	+14.8 (Between 25°-47°C)	+0.32	+4,480

Table II. Entropy and thermal temperature coefficient values for the copper-0.01*M* copper sulfate thermogalvanic cell at 60°C

		Solution pH 4.65 (initial) 3.85 (final)			Solution pH 1.80 (initial)			Solution pH 1.05 (initial)		
S^*, entropy terms	Contributing reaction	S^*, entropy, cal/g ion/K	$(dE/dT)_{th}$, mv/deg	TS^*, Peltier heat, cal/g ion	S^*, cal/g ion/K	$(dE/dT)_{th}$, mv/deg	TS^*, cal/g ion	S^*, cal/g ion/K	$(dE/dT)_{th}$, mv/deg	TS^*, cal/g ion
S^*_E	$Cu^{\circ} \rightarrow Cu^{\circ}$ $T_1 \rightarrow T_2$	+8.6	+0.19	+2,860	+8.6	+0.19	+2,860	+8.6	+0.19	+2,860
S^*_E	$Cu^{++} \rightarrow Cu^{++}$ $T_2 \rightarrow T_1$	+13.5	+0.29	+4,500	+12.8	+0.28	+4,260	+12.5	+0.27	+4,160
S^*_M	$2H^+ \rightarrow 2H^+$ $T_1 \rightarrow T_2$	+25.0	+0.54	+8,320	+6.2	+0.13	+2,065	−0.6	−0.01	−200
$S^*_{(electron)}$	$2e \rightarrow 2e$ $T_1 \rightarrow T_2$	Assumed zero			0	0	0	0	0	0
S^*	Net (calculated)	+47.1	+1.02	+15,680	+27.6	+0.60	+9,185	+20.5	+0.44	+6,820
S^*	Experimental	+43.8 (Between 56°-75°C)	+0.95	+14,585	+23.1 (Between 47°-65°C)	+0.50	+7,690	+18.0 (Between 47°-65°C)	+0.39	+5,990

Table III. Values of partial molal entropy $\bar{S}_{Cu^{++}}$ for nominal concentrations as estimated from the work of Wetmore and Gordon (3)

Molality	$\bar{S}_{Cu^{++}}$, e.u. 30°C	60°C
0.01	+3.3	−2.75
0.05	+2.1	−3.95
0.10	+0.9	−4.80
1.00	−2.75	−7.30

Table IV. Ionic entropy of electrochemical transport of hydrogen ion vs. pH of solution

pH	$S^*_{EH^+}$, cal/g ion/K 25°C	30°C	40°C	60°C
0	−4.48	+4.60	−4.89	−5.38
1.0	+0.48	+0.36	0.00	−0.45
1.5	+2.60	+2.46	+2.30	+1.75
2.0	+4.80	+4.67	+4.50	+4.00
2.5	+7.35	+6.89	+6.70	+6.37
3.0	+9.32	+9.19	+8.90	+8.68
5.0	+18.43	+18.32	+18.00	+17.58

one described by de Bethune and co-workers (1). The results of these calculations for the entropy transfer of H^+ in the absence of Cu^{++} are given in Table IV. Results are based on the data presented by Bates and Bower (4) and Fales and Mudge (5).

Discussion of Results

The implications of the results of the research just described are brought out by a comparison of values calculated from theory with those obtained from experiment. The individual entropy terms, S^*, $(dE/dT)_{th}$, and TS^* can be compared in Tables I and II and also in Fig. 2. The solid points and dotted lines in this figure were obtained by calculating the thermogalvanic potentials assuming the hot electrode was at 30° or 60°C while the cold one was at 25°C and using Eq. [2]. The agreement between calculated and experimental values is very good over a range of temperature and at several pH values. Thus, the results confirm that the coupling of entropy terms as suggested by theory in Eq. [8]

$$S^* = S^\circ_{Cu^\circ} - (\bar{S}_{Cu^{++}} + 2S^\circ_{H^{+*}}) + 2S^*_{H^+} - 2S^*_{(electron)}$$

is reasonable. It is significant that this agreement has been reached for solutions greatly removed from ideality and that both cell polarity as defined by de Bethune and cell potential are essentially correct. Continuing studies have shown a similar agreement between theory and experiment for 0.1 and 1.0*M* copper sulfate solutions. The hydrogen ion plays a much less significant role in these more concentrated solutions.

The electrochemical model on which Eq. [8] is based predicts that copper is reduced at the hot electrode and oxidized at the cold one. Experiments carried out separately under conditions to permit large thermogalvanic currents to develop showed that metallic crystals of copper were indeed deposited at the hot electrode.

The work has also been carried over to the nickel-nickel sulfate system where the proper cell polarity was predicted by theory and fair agreement was obtained for the value of the thermogalvanic temperature coefficient for pure nickel electrodes in 0.1*M* nickel sulfate.

Attempts are currently being made to carry this type of analysis to the zinc-zinc sulfate system as well as to thermal cells in high conductivity water. Some progress has been made along these lines and final results could be the subject of a future paper.

Acknowledgment

The work described was sponsored by the Department of the Interior, Office of Saline Water, and their assistance is gratefully acknowledged.

Manuscript received Jan. 20, 1965; revised manuscript received Nov. 30, 1965.

Any discussion of this paper will appear in a Discussion Section to be published in the June 1967 JOURNAL.

REFERENCES

1. A. J. de Bethune, T. S. Licht, and N. Swendeman, *This Journal*, **106**, 616 (1959).
2. A. J. de Bethune, *ibid.*, **107**, 829 (1960).
3. F. E. W. Wetmore and A. R. Gordon, *J. Chem. Phys.*, **5**, 60 (1937).
4. R. G. Bates and V. E. Bower, *J. Research Nat. Bur. Standards*, **53**, 283 (1954).
5. H. A. Fales and W. A. Mudge, *J. Am. Chem. Soc.*, **42**, 2434 (1920).
6. Lars, Onsager, *Phys. Rev.*, **37**, 405 (1931); **38**, 2265 (1931).
7. K. K. Kelley and E. G. King, *Bur. of Mines Bull. 584* (1960), and *592* (1962).

Technical Notes

Charge-Discharge Mechanisms in Electrolytic Capacitors

Walter J. Bernard

Research and Development Center, Sprague Electric Company, North Adams, Massachusetts

The use of aluminum wet electrolytic capacitors as energy storage devices, as in the "photoflash" application, is dependent on the ability of the capacitor to tolerate a very large number of charge-discharge cycles without damage to its physical and electrical properties. Since the current within the capacitor is carried by an electrolyte subject to the laws of electrochemical change at the electrodes, some questions may be raised concerning the physical and chemical mechanisms operating within the capacitor.

The circuit shown in Fig. 1 is applicable to the process under discussion. The capacitor C is charged from the d-c source by closing S_1; S_1 is then opened and the capacitor is discharged through R by closing S_2. It is an observed fact that, for capacitors subject to this type of cycling, one must use etched aluminum cathode foil of large effective surface area or suffer loss of capacitance in the capacitor as a consequence of oxide formation at the cathode. Evolution of gas, as evidenced by pressure increase, may be encountered as well.

If one considers the electrochemical reactions which must occur on charge-discharge cycling, the consequences of nonetched foil use should be anticipated.

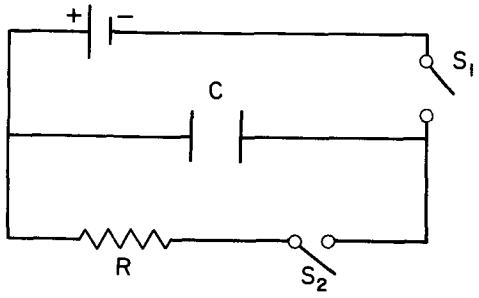

Fig. 1. Circuit for capacitor energy storage applications

During charging, a charge q, equal to C_AV, where C_A is the anode capacitance and V the voltage, is built up on the anode; an equivalent charge migrates to the cathode and brings about an electrochemical change. If the cathodic reaction is the expected one of reduction of hydrogen ion, then C_AV/F (F = 96,500 coulombs) equivalents of hydrogen must be generated at the cathode surface. On discharge of the anode, electron transfer from the solution to the aluminum cathode, and thence to the external circuit, can be achieved by the discharge of hydroxyl ion to produce either molecular oxygen or anodic aluminum oxide.[1]

These observations suggest that, under any circumstance, one would observe excessive gas evolution, cathode formation, and eventual electrolyte depletion. However, it is a fact that with a well-constructed capacitor of etched cathode design, it is possible to get in excess of 10^6 cycles of service without the occurrence of these predicted modes of failure. The following explanation is advanced to account for this behavior.

On charging the anode, hydrogen ions are first discharged on the cathode surface as hydrogen atoms, and then undergo combination to form molecular hydrogen. Each hydrogen atom is bound to the metal by surface valence forces and only combines with another hydrogen atom when its concentration becomes too large for a given metal surface. Although it is not known what the maximum concentration of atomic hydrogen would be on aluminum under any given set of conditions, it is not difficult to imagine that incomplete coverage could result since a relatively small amount of electrochemical change occurs during a single charging cycle of a capacitor. (For example, under the conditions described in the experimental part of this paper, it may be calculated that a full charge on the anode corresponds to the deposition of 2.3 x 10^{-8} equivalents of hydrogen at the negative electrode. For smooth foil cathodes the average surface density of hydrogen would then be approximately one atom for each seventy square angstroms, but for etched foil the density would be at least one order of magnitude less than this.) Therefore, if a capacitor plate is charged and hydrogen ions are discharged at the cathode to form only hydrogen atoms, with little or no combination to give rise to molecular hydrogen, then on capacitor discharge the anions impinging on the aluminum surface will have available two modes of discharge: the usual anodic reaction which, for convenience and simplicity, may be written:

$$6\,OH^- + 2Al \rightarrow Al_2O_3 + 3H_2O + 6e^- \qquad [1]$$

leaving the previously adsorbed H undisturbed; or

$$OH^- + H_{Adsorbed} \rightarrow H_2O + e^- \qquad [2]$$

Reaction [2] would be expected to be favored over [1] since [1] requires that aluminum atoms overcome barrier effects at the interface in order to react, whereas in [2] the hydrogen atoms are already on the surface of the metal and available for combination with OH^-.

This approach would suggest that all that is required for successful energy storage operation is an aluminum cathode, but in fact plane foil (nonetched) does not behave ideally, whereas etched foil does. Apparently then, the etched surface enhances the effect of hydrogen adsorption, but the question which is raised is whether it is due to the greater surface area or to some induced surface activity brought about by the etching process.

[1] The electrolyte must obviously contain not only OH^- but other anions as well. However, with conventional electrolytes, the only important anodic reaction is the production of oxygen.

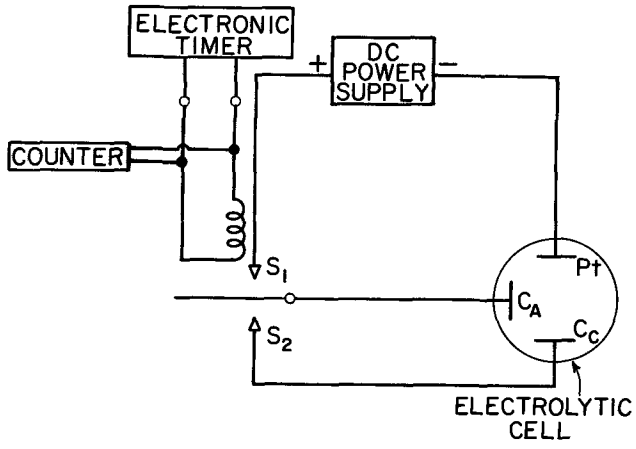

Fig. 2. Experimental circuit to separate the electrochemical reaction occurring at the cathode of an electrolytic capacitor during charging and discharging.

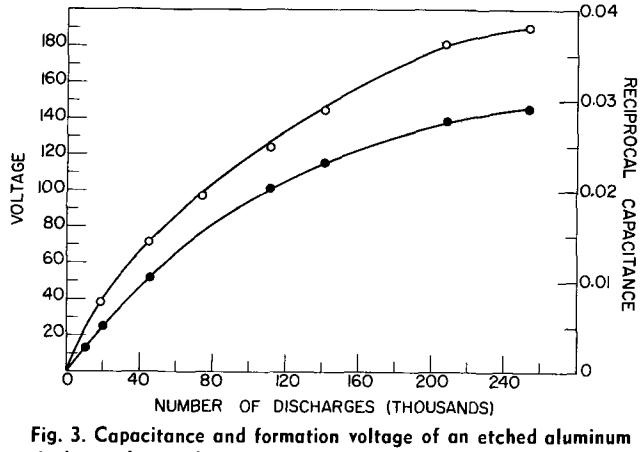

Fig. 3. Capacitance and formation voltage of an etched aluminum cathode vs. the number of capacitor discharges. Platinum electrode used as cathode during charging. ○ Reciprocal capacitance; ● voltage.

Experimental

In order to choose between these alternatives, the experimental arrangement shown in Fig. 2 was devised. The d-c source is a well-regulated constant voltage power supply. Switching is controlled by means of a relay connected to a variable electronic timer, permitting between 30 and 200 charge-discharge cycles/min; an electric counter is connected in parallel with the relay. During charging S_1 is closed and S_2 is open; cathodic discharge of hydrogen occurs at the platinum electrode and the aluminum anode, C_A, is charged. S_1 is then opened and S_2 is closed, discharging C_A through C_C, the aluminum cathode. Since there is no hydrogen at the aluminum cathode under these conditions, the only reactions which can occur there are the evolution of oxygen and the formation of Al_2O_3. Oxygen is not expected to be a product since the electrolyte used was a borate-glycol solution known to have a high current efficiency of oxide formation (1). This arrangement effectively separates the two electrochemical reactions which occur at the

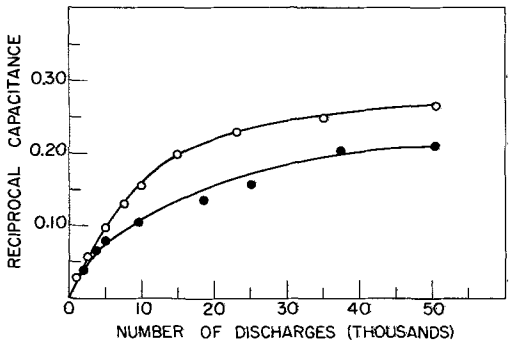

Fig. 4. Capacitance of nonetched aluminum cathodes vs. number of capacitor discharges. ○ Pt cathode in circuit; ● Al cathode only.

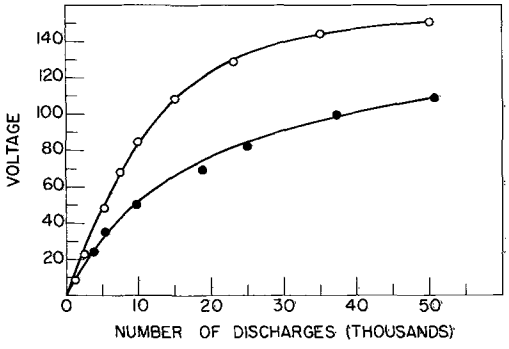

Fig. 5. Formation voltage of nonetched aluminum cathodes vs. number of capacitor discharges. ○ Pt cathode in circuit; ● Al cathode only.

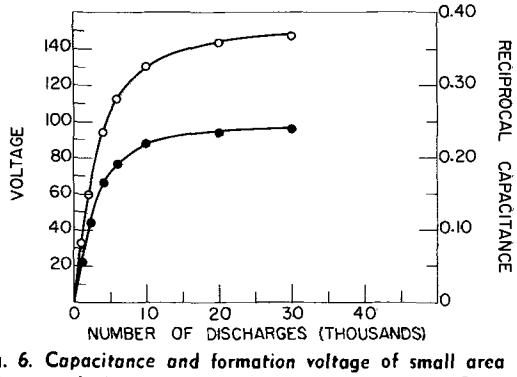

Fig. 6. Capacitance and formation voltage of small area etched aluminum cathode vs. number of capacitor discharges. ○ Reciprocal capacitance; ● voltage.

cathode during the charge-discharge cycles and enables one to determine the true effect of etched surfaces.

During discharge the two aluminum surfaces, C_A and C_C, act as parallel capacitors; when no hydrogen is on the surface we expect C_C to become charged to the maximum voltage which may be impressed before ionic current can flow. Charge from C_A will continue to flow to C_C until the voltages across the two capacitors are equal. If there is an oxide film on C_C, a residual charge will remain on C_A and thus, during subsequent charging of C_A, something less than the charge q ($= C_A V_C$) will be required for each cycle. As the cycling continues, the oxide film on C_C will continue to grow and its thickness will approach a limiting value, at which point the two capacitors will be permanently charged to V_C. Thereafter no further current will flow, assuming that the leakage currents are negligible. This effect should occur for both plain and etched foil; the only difference expected would be the time required to bring this about because of the greater surface area of the etched metal.

For the experiments described here, etched foil anodes of 100 cm² area and anodized to 200v were used. The capacitance was 14.8 mfd and the charging voltage was 150v. The course of reaction was followed both by measuring the cathode capacitance and by measuring the d-c voltage which could be impressed on the cathode before causing a rapid rise in current (2).

Results

Figure 3 shows the increase in reciprocal capacitance and voltage on an etched aluminum specimen of 100 cm² (geometrical) area used as the "cathode" during the discharge portion of the cycle. These curves clearly demonstrate that the oxide film on this electrode increases to a thickness that will eventually accommodate the charging voltage on the anode.[2] Gas was also observed at the platinum electrode during the experiment, in accord with prediction.

The aluminum cathode was then replaced with a fresh etched specimen and the platinum electrode was removed from the circuit, giving essentially the circuit of Fig. 1 (the energy storage application). There was no discernible increase in the oxide film on the cathode by either of the two methods of measurement, even after 280,000 cycles. This effect is the same as that observed in capacitor use, and corresponds to the explanation advanced above, *i.e.*, hydrogen adsorption on the aluminum surface and subsequent reaction with hydroxyl ion.

Some experiments with smooth aluminum foil also serve to demonstrate this effect in a slightly different manner. Figures 4 and 5 show the change in reciprocal capacitance and formation voltage, respectively, of specimens with and without the presence of the platinum electrode. Because of the much smaller surface area, as compared to etched foil, oxidation of the aluminum cathode occurs in both instances, but is markedly faster when a platinum electrode is available for the discharge of hydrogen. It should also be noted that in the absence of the platinum electrode, formation of oxide on the cathode ceases well below the total charging voltage. For the specimens in Fig. 4 and 5 no further growth in oxide thickness was observed by increasing the total number of discharges to 160,000. The reason for this behavior is simply that, as the oxide layer increases on the cathode, the amount of charge transferred from the anode continually decreases, until the point is reached where even a nonetched aluminum surface can accommodate the hydrogen atoms deposited during the charging part of the cycle. Subsequent discharge of the anode then results in the usual depolarizing reaction observed on etched cathodes.

One additional experiment was run to show that the total surface area (and not the nature of the etched surface) is responsible for the difference in behavior between etched and nonetched cathodes. A specimen of etched aluminum with a geometrical area of 5.0 cm² was used for the cathode. Even though this foil was etched it would be expected to form an oxide film since the charge density during cycling would be approximately the same as smooth foil of 100 cm² area. Figure 6 shows that, as expected, oxide formation occurred, gas evolution at the cathode was also observed and, as in the case of smooth foil, a limiting thickness of oxide is reached.

Manuscript received March 21, 1966.

Any discussion of this paper will appear in a Discussion Section to be published in the June 1967 JOURNAL.

REFERENCES

1. W. J. Bernard and J. W. Cook, *This Journal*, **106**, 643 (1959).
2. M. S. Hunter and P. Fowle, *ibid.*, **101**, 481 (1954).

[2] Continued cycling is equivalent to prolonged aging of the electrode at constant applied voltage, and therefore the so-called formation voltage, since it is measured effectively at constant field, will tend to exceed the charging voltage.

Solubilities of GaAs in Metallic Solvents

M. Rubenstein

Research Laboratories, Westinghouse Electric Corporation, Pittsburgh, Pennsylvania

Liquidus solubilities of GaAs in gallium have been reported for temperatures from 1237° down to 450°C (1-3). The phase diagram for the GaAs-Ge system has also been reported (4). Liquidus solubilities are reported here for GaAs in solvents gallium, tin, bismuth, and lead. The liquidus solubility data reported here were obtained using a high-temperature filtration technique (5).

This technique involves a quartz tube which is divided into two compartments by a quartz disk which has 1 mm diameter holes. GaAs fragments and the metal in question are placed in the bottom compartment; the ampoule is sealed under a pressure of less than 10^{-5} Torr. A quartz rod is attached to the top of the ampoule. The ampoule is placed in a furnace with the quartz rod projecting out of the furnace. The temperature of the furnace is raised to the desired temperature and maintained at temperature for 16 hr. By means of the quartz rod the ampoule is turned 180°C about the axis of the quartz rod, and, by gentle tapping, the solution is filtered so that the solution of GaAs in a metal is separated from the undissolved GaAs.

The furnace is then cut off so that the ampoule and contents are cooled to room temperature. In some cases the ampoules are air quenched after filtration.

The ampoule is then opened and the filtrate and residue are quantitatively analyzed to ascertain how much GaAs and metal are in the filtrate and the residue. All of the solution (at the elevated temperature) does not have to enter the filtrate. If one can assume that the solution of GaAs in the metallic solvent is at equilibrium after 16 hr at the elevated temperature, any portion of this solution which enters the filtrate is representative of the entire solution. The size of the solution should be large enough so that weighing errors become unimportant to the calculation of the solubility measurement.

In the systems reported here, gallium, tin, bismuth, and lead were separated from GaAs using three different techniques. Gallium metal was separated from GaAs by using concentrated hydrochloric acid. Tin was separated from GaAs by using concentrated hydrochloric acid with a platinum wire in contact with the tin. Bismuth and lead were dissolved using 30% H_2O_2 and glacial acetic acid in the ratio of 1:1. If the high-temperature filtration samples were cooled slowly from the elevated temperatures, the crystallite size of the GaAs was much larger than if the samples were air quenched. The larger crystallite size allowed one to have a more quantitative recovery of GaAs when the metal was being dissolved.

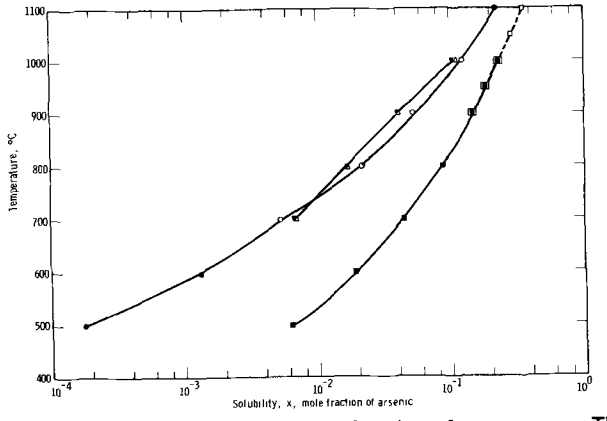

Fig. 1. Solubilities of GaAs as a function of temperature. The solvents are gallium, tin, bismuth, lead and germanium. ○ Gallium as solvent; ● gallium as solvent (3); ■ tin as solvent; ▼ bismuth as solvent; △ lead as solvent; □ germanium as solvent (4).

X-ray diffraction studies on the GaAs recovered from the filtrates showed no change in lattice constants (no change in the fourth significant figure of the lattice constant of GaAs) when the solvent was gallium, tin, bismuth, or lead. Figure 1 shows the solubility data of GaAs in the four solvent systems: gallium, tin, bismuth, and lead. This figure also shows the solubility data of GaAs in germanium recalculated from ref. (4). The curves for lead and bismuth are virtually superimposable. The precision of the solubility measurements presented in this note is ± 0.001 for solubility measurements for $x > 0.010$ and ± 0.0005 for $x < 0.0100$. Table I presents the solubility data from ref. (1) and (3), together with data presented in this paper. The comparison demonstrates the reliability of the data obtained by the high-temperature filtration technique.

Similar measurements were made on the systems GaAs-In, GaAs-Te, and GaAs-Se. These three systems are not pseudobinaries. They have been investigated in ref. (6-9): GaAs-InAs (6, 7), GaAs-Ga_2Te_3 (8), and GaAs-Ga_2Se_3 (8, 9).

In the case of GaAs-In, the solid recovered from the filtrates indicated the formation of GaAs-InAs solid solutions from 22 mole % indium for the filtrations at 500°C to 7 mole % indium for the filtrations at 1200°C. The GaAs-Te system is also not a pseudobinary one, and there is evidence to believe that some Ga_2Te_3 was formed. The same is true of the GaAs-Se system (some Ga_2Se_3 was formed). When filtrations were performed on the GaAs-Se system at 650°C, crystals were left behind with the undissolved GaAs which were analyzed as Ga_2Se_3 (by x-ray fluorescence analysis). Of two samples investigated, one had an arsenic concentration less than 0.1 mole % and the other 2 mole %. These crystals were red-brown in color and tetragonal with $a = 5.47$Å, $c = 5.41$Å ($c/a = 0.989$). X-ray diffraction showed the same tetragonal dimensions for these two samples and other samples. Ga_2Se_3 is reported in the literature (10) as being reddish-black in color and cubic, with $a = 5.418$Å.

Manuscript received Jan. 21, 1966; revised manuscript received March 28, 1966. Portions of this paper were presented at the Toronto Meeting, May 3-7, 1964.

Any discussion of this paper will appear in a Discussion Section to be published in the June 1967 JOURNAL.

REFERENCES

1. W. Köster and B. Thoma, *Z. Metallk.*, **46**, 291 (1955).

Table I. Mole fraction arsenic

Temperature, °C	Köster & Thoma (1)	Hall (3)	This paper
1200	3.5×10^{-1}	3.6×10^{-1}	3.77×10^{-1}
1100	2.2×10^{-1}	2.3×10^{-1}	—
1000	1.45×10^{-1}	1.3×10^{-1}	1.24×10^{-1}
900	1.0×10^{-1}	6.1×10^{-2}	5.3×10^{-2}
800	7.5×10^{-2}	2.3×10^{-2}	2.2×10^{-2}
700	5.5×10^{-2}	6.5×10^{-3}	5.3×10^{-3}
600	4.5×10^{-2}	1.3×10^{-3}	—
500	3.0×10^{-2}	1.8×10^{-4}	—

2. J. van der Boomgaard and K. Schol, *Philips Research Repts.*, **12**, 127 (1957).
3. R. N. Hall, *This Journal*, **110**, 385 (1963).
4. Y. Takeda, T. Hirai, and M. Hirao, *ibid.*, **112**, 363 (1965).
5. M. Rubenstein, Electrochemical Society Electronics Division Abstracts, **11**, 129 (1962).
6. J. C. Woolley and B. A. Smith, *Proc. Phys. Soc. (London)*, **72**, 214 (1958).
7. J. C. Woolley, C. M. Gillett, and J. A. Evans, *ibid.*, **77**, 700 (1961).
8. J. C. Woolley and B. A. Smith, *ibid.*, **72**, 867 (1958).
9. N. A. Goryunova and V. S. Grigoréva, *Zhur. Tekh. Fiz.*, **26**, 2157 (1956).
10. H. Hahn and W. Klingler, *Z. Anorg. Chem.*, **259**, 139 (1949).

Microplasma Observations in Silicon Junctions Using a Scanning Electron Beam

John W. Gaylord

RCA Laboratories, Radio Corporation of America, Princeton, New Jersey

It has been shown (1-2) that signals induced in junctions by a scanning electron beam can be helpful in device failure analysis. This technique has now been used to locate and study certain microplasma sites (areas which emit visible light) in an effort to determine the cause of low collector-base breakdown voltage in silicon junctions. A scanning electron beam microscope was used to produce micrographs of p-type base regions diffused into an n-type substrate. N-type spikes were observed extending from the substrate up into the p-base region at locations corresponding to areas of optical light emission. In addition, these areas were shown to be the avalanche sites which limit the collector-base breakdown voltage characteristic of the junction.

An optical micrograph of a typical junction is shown in Fig. 1. The junction was formed by diffusing boron in a teardrop pattern into n-type silicon. A round hole has been etched in the oxide over the center of the junction to permit contact by a probe as shown. External bias was applied to the junction by means of this probe and a conducting support for the wafer. Figure 2 illustrates the circuit used. The junction region was scanned by an 18 kv, 0.4 na electron beam approximately 5μ in diameter. Electron-hole pairs generated by this scan were collected at the junction producing a reverse current that modulated the beam current of a cathode ray tube. The cathode-ray tube was made to scan in synchronism with the electron beam. Typical micrographs obtained by photographing the screen of the cathode ray tube

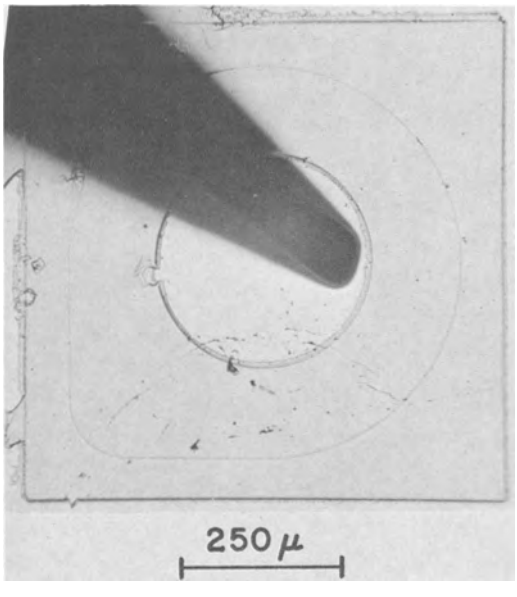

Fig. 1. Optical micrograph of junction

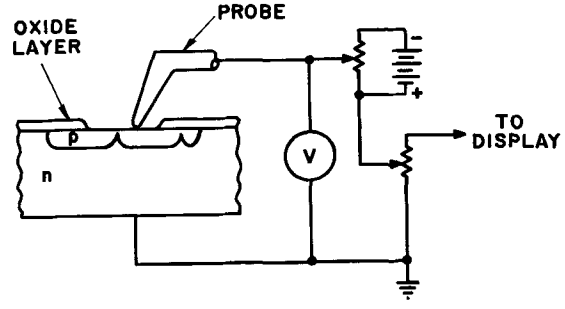

Fig. 2. Video signal sensing circuit

are shown in Fig. 3 and 4. Current flow is such that enhanced reverse current either from electron-hole pairs or from an avalanche induced by the beam appears as bright areas in the micrographs. Streaks in these pictures running from right to left after an abrupt change in brightness are caused by the recovery characteristics of the electronics and are not related to physical properties of the junction. The center area where oxide has been removed is brighter than the surrounding junction region because the electron beam intensity has not been reduced during travel through the oxide layer prior to reaching the junction region.

Figure 3 is made without any external reverse bias ($V = 0$). The area around the bottom edge of the oxide hole shows several bright spots, labeled A, B, and C. These areas constitute sites in the junction where increased currents are generated during scanning. It was deduced that this increase in current is caused by the junction coming closer to the surface as illus-

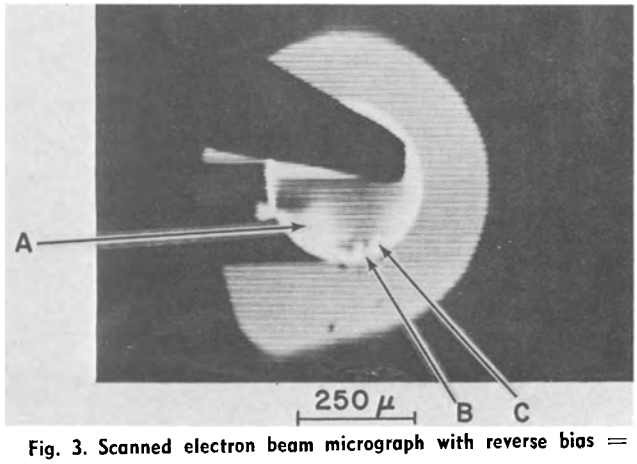

Fig. 3. Scanned electron beam micrograph with reverse bias = 0v.

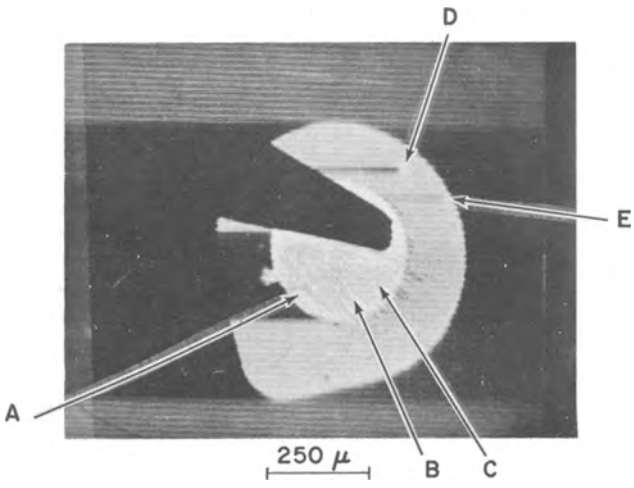

Fig. 4. Scanned electron beam micrograph with reverse bias = 20v.

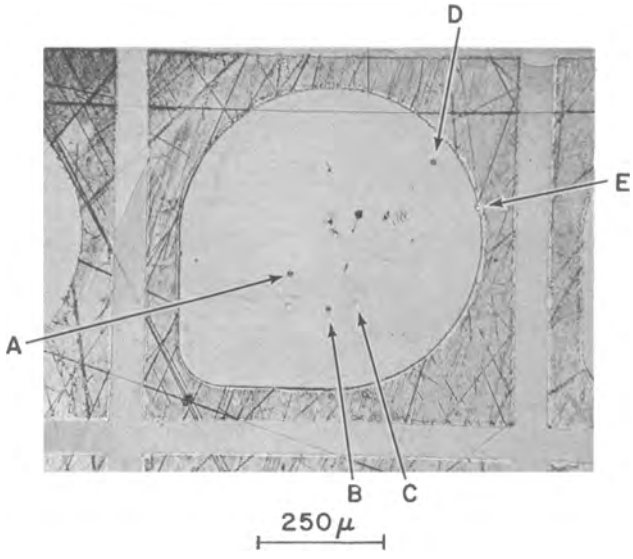

Fig. 5. Optical micrograph of lapped and stained junction

trated in Fig. 2 where the flux of electrons from the beam is greater because of reduced scattering and absorption in the silicon. Figure 4 shows the effect of applying a reverse bias of $V = 20$v to the junction. Two additional bright spots now appear labeled D and E as well as enhanced brightness from spots A, B, and C. These spots indicate that a localized avalanche (multiplication) is being excited by the electron beam as it injects carriers in regions of high field. Such high fields would be expected from the geometry of the junctions as seen in Fig. 2. As the bias increases, the avalanche effect increases at each of the sites until complete breakdown can be initiated by scanning a single site at a reverse bias slightly less than the static breakdown limit. It was thus deduced from the micrographs that the cause of low collector-base breakdown voltage is the presence of these avalanche sites and that the sites are spikes or columns of n-doped material extending through the p base region to or near the silicon surface.

The most pronounced avalanche sites, A, D, and E are sources of relatively strong "microplasma" light emission as can be observed optically when a reverse bias greater than breakdown is applied. This phenomenon is also to be expected for the enhanced field produced at the tips of n-type spikes extending into the p-region.

To verify completely the junction model deduced from electron beam scanning the sample was successively lapped and stained. Figure 5 is a micrograph of the sample taken during this operation. The oxide has been removed and enough of the surface lapped away to reveal the spikes by conventional copper staining techniques. Continued lapping revealed the spikes to be quite narrow, and it was observed that they coincide with the avalanche sites shown by electron beam scanning and by light emission.

Conclusion

The scanning electron beam technique combined with conventional electrical tests provides a means of nondestructively locating and analyzing a source of low breakdown voltage in semiconductor junctions. The possibility now exists of coupling this technique with conventional microprobe analysis to locate and determine the presence of foreign impurities in a manner heretofore impossible.

Acknowledgments

The author is indebted to Mr. H. R. Meisel of RCA EC&D Division, Somerville, for supplying the samples analyzed, A. W. Fisher for staining and lapping the junctions, and F. E. Heiselmann for assisting in the operation of the scanning electron microscope.

Manuscript received Feb. 9, 1966.

Any discussion of this paper will appear in a Discussion Section to be published in the June 1967 JOURNAL.

REFERENCES

1. T. E. Everhart, O. C. Wells, and R. K. Matta, *This Journal*, **111**, 929 (1964).
2. W. Czaja and J. R. Patel, *J. Appl. Phys.*, **36**, 1476 (1965).

A Reference Electrode for Use in Dimethyl Sulfoxide: Thallium Amalgam–Thallous Chloride

William H. Smyrl and Charles W. Tobias

Inorganic Materials Research Division, Lawrence Radiation Laboratory, and Department of Chemical Engineering, University of California, Berkeley, California

The measurement of thermodynamic properties of electrolytes and the study of electrode processes in dimethyl sulfoxide (DMSO) requires a suitable reference electrode of the second kind. Solubility studies (1-4) have shown the chlorides, bromides, iodides, nitrates, and perchlorates to be the most soluble salts in DMSO. Sulfates, fluorides, and carbonates were found to be generally insoluble. For practical reasons the choice of a halide couple would be most advantageous since it affords the establishment of con-

centration cells without transference.

The silver-silver chloride electrode was explored for use in DMSO by Kolthoff and Reddy (5), who found that silver chloride is quite soluble in excess chlorides. In this laboratory silver iodide and silver bromide were found to dissolve in excess iodide and bromide, respectively, thereby eliminating the silver-silver halide electrodes from consideration as reference electrodes.

The other obvious choices, the analogues of the calomel electrode, were shown to be unsuitable because mercurous chloride, bromide, and iodide each disproportionate in DMSO. After the salts have been in contact with the solvent for a short time, small droplets of mercury appear in the bottom of the vessel. Analysis of the solution has not been made to confirm the presence of the Hg^{+2} ion. However, since $HgCl_2$, $HgBr_2$, and HgI_2 are highly soluble in DMSO, these products of disproportionation would promise to be quite stable in solution.

Among the metals which form amalgams and are stable with respect to the solvent, thallium appeared promising. Hills (6) discussed the use of the thallium amalgam-thallous chloride reference electrode in liquid ammonia. Since the thermodynamic properties of thallium amalgams are well known (7), this electrode couple looked promising. Solubility studies were initiated, and thallous iodide and chloride were found to be sparingly soluble in dimethyl sulfoxide. Excess iodide precipitates thallous iodide from solution. From visual observations, excess chloride does not precipitate TlCl, nor does any more solid TlCl dissolve. Further, experiments have shown the solubility product of TlCl in DMSO to be of the order of 10^{-6}.

On the basis of this information exploratory measurements were initiated with a thallium amalgam-thallous chloride reference electrode. Manipulations were carried out in a dry box. The liquid amalgam, containing approximately 10^{-2} mole fraction thallium, was introduced into each one of three special cups, to which electrical contact was made by platinum wires isolated from contact with the electrolyte solution by glass tubes. A 1-2 mm layer of thallous chloride was sprinkled on the amalgam surfaces, the three electrodes were placed into the cell, and the electrolyte was introduced. In the tightly sealed cell an argon atmosphere of 1 atm pressure was maintained over the solution throughout the measurements. The cell was thermostated at 25° ± 0.01°C.

The solvent, purified by distillation, contained less than 50 ppm moisture as determined by Karl Fischer titration. Measurements were made with four different 10^{-2}M solutions, containing one of LiCl, RbCl, $MgCl_2$, $InCl_3$. [Mercury, Baker's Analyzed "reagent"; thallium, Cominco "69's Grade"; thallous chloride, Electronic Space Products "Analytical Grade"; lithium chloride, Baker and Adamson "Reagent Grade", dehydrated by treatment with thionyl chloride (8); rubidium chloride, City Chemical Corporation "Reagent Grade"; magnesium chloride, K & K Laboratories "99.9% Purity"; indium chloride, Indium Corporation of America "99.99% Purity".]

The bias potential between the electrodes was measured by a L&N K-3 potentiometer, using a galvanometer of 4.5 x 10^{-10} amp/mm sensitivity to determine balance. The difference in potential between any two of the three electrodes was always found to be less than 0.03 mv, and less than 0.01 mv in the case of solutions containing LiCl. Equilibrium was established rapidly and maintained for at least one week, after which a particular test run was discontinued.

The equilibrium was offset by the application of 0-10 mv potential between electrode pairs, also with reversed polarity. The current passed in either direction ranged up to 2 x 10^{-7} amp. This was repeated for all combinations of the three electrodes. The current was always found proportional to the applied potential, and on no occasion was a hysteresis effect observed. The current was applied by an Electronic Measurements Model C 612 constant current power supply, and was measured by a Sargent Model MR Recorder. The voltage was measured by a Keithley Model 610R electrometer.

On the basis of these findings, the thallium amalgam-thallous chloride electrode appears suitable for thermodynamic measurements in DMSO solutions, and may be recommended for a practical reference electrode. Care must be taken to protect the amalgam from oxidation, and workers should be aware of the toxicity of thallium and its compounds.

(Editor's Note: Dimethyl sulfoxide is readily absorbed through the skin and has certain physiologic effects on the body. While it has shown promise as a therapeutic agent, tests on humans have been discontinued for the present because of possible undesirable side effects.)

Acknowledgment

This work was supported in part by the Electrochemistry Branch of the Naval Ordnance Laboratory, Corona, California, and by the United States Atomic Energy Commission.

Manuscript received Feb. 7, 1966.

Any discussion of this paper will appear in a Discussion Section to be published in the June 1967 JOURNAL.

REFERENCES

1. Jouko Kenttämä, *Suomen Khemistilehti,* **B33**, 180 (1960).
2. H. L. Schläfer and W. Schaffernicht, *Angew. Chem.*, **72**, 618 (1960).
3. *Dimethyl Sulfoxide Technical Bulletin,* Crown Zellerbach Corporation, Camas, Washington.
4. C. A. Melendres, M.S. Thesis, University of California, Berkeley, September 1965.
5. I. M. Koltoff and T. B. Reddy, *Inorg. Chem.*, **1**, 189 (1962).
6. G. J. Hills, in "Reference Electrodes," p. 455, D. J. G. Ives and G. J. Janz, Editors, Academic Press, New York (1961).
7. T. W. Richards and F. Daniels, *J. Am. Chem. Soc.*, **41**, 1732 (1919).
8. Therald Moeller, Editor, "Inorganic Syntheses," Vol. 5, p. 153, McGraw-Hill Book Co., New York (1957).

Brief Communication

Hydrothermal Attack of Silver and the Formation of Silver Crystals

Solomon Levinson and Forrest Lee Carter

United States Naval Research Laboratory, Washington, D. C.

Silver has been found to be unattacked by NaOH at 538°C under a dry forming gas atmosphere (1). Under hydrothermal conditions (temperature unspecified) Laudise and Nielsen (2) have found silver to be inert to a 4-5*M* alkaline solution while Lux and Niedermaier (3) have found enhanced silver corrosion with NaOH at 410°C in the presence of oxygen (and water) above the melt. In the course of a program to grow ruby for laser use hydrothermally, we first studied the growth of α-Al_2O_3 without Cr addition. Small crystals of silver were observed when a heliarc-welded fine silver liner containing α-Al_2O_3 nutrient and seeds in a 4*M* NaOH solution was employed at 46% fill. With the exception of copper (4), we have found no previous reference to the growth of other metal crystals by this technique. The autoclave containing the liner was pressure balanced with water. It had been maintained for three weeks at a bottom temperature of 500°C. The top of the liner was cooler by about 50°C.

Two liquid layers were observed after opening the liner; the lower was considerably more viscous. The largest crystals of silver had formed in the vicinity of the two-liquid interface although smaller ones could be found higher up on the seed rack. The sum total of impurities as determined by spectrographic analysis was found to be about 0.003%.

The deposited silver was in intimate contact with a mass of transparent material (not identified). The very soft and fragile nature of the deposited silver necessitated the removal of the imbedding matrix by means of a 6*N* HCl solution. The deposited silver occurred predominantly in the form of very thin platelets, the largest of which was 5 mm across and 0.01 mm thick and also in the form of fine three-dimensional filigree. In addition a few thicker rhombus shaped crystals were observed, unusual examples of which are indicated by the two spears in Fig. 1.

An isolated rhombus (hollow)) was examined by x-rays using a G. E. single crystal orienter (CuK_α radiation) and a precession camera (MoK_α radiation). The rhombus face of the single crystal was the (111) plane and was related to the cubic axes as indicated in Fig. 2a. The majority of the thin platelets had forms as in Fig. 2b and 2c. It appears that most of the silver was epitaxially deposited on substrate crystals subsequently removed by the HCl treatment. The unit cell edge was 4.086 ± 0.001Å.

Manuscript received March 5, 1966.

Any discussion of this paper will appear in a Discussion Section to be published in the June 1967 JOURNAL.

REFERENCES

1. C. M. Craigshead, L. A. Smith, and R. I. Jaffee, Screening Tests on Metals and Alloys in Contact with Sodium Hydroxide at 1000° and 1500°F, Battelle Memorial Institute Report No. 706, November, 1961.
2. R. A. Laudise and J. W. Nielsen, "Solid State Physics," Vol. 12, pp. 160-1, Academic Press, New York (1961).
3. H. Lux and T. Niedermaier, *Z. anorg. u. allgem. Chem.*, **282**, 196 (1955).
4. J. Wyart, *Discussions Faraday Soc.*, **5**, 323 (1949).

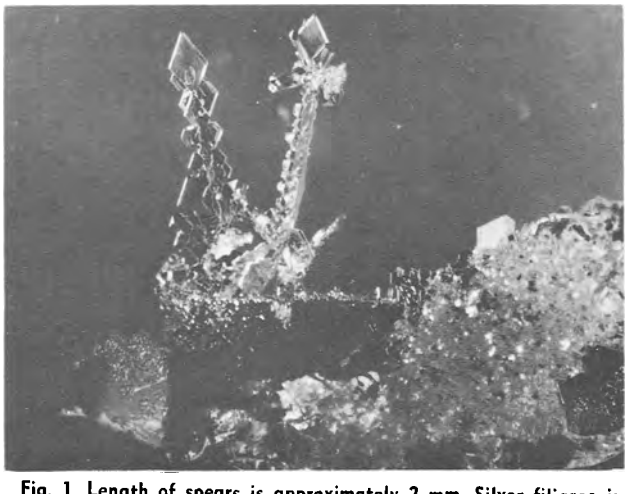

Fig. 1. Length of spears is approximately 2 mm. Silver filigree is shown on lower right. Less obvious are a few platelets.

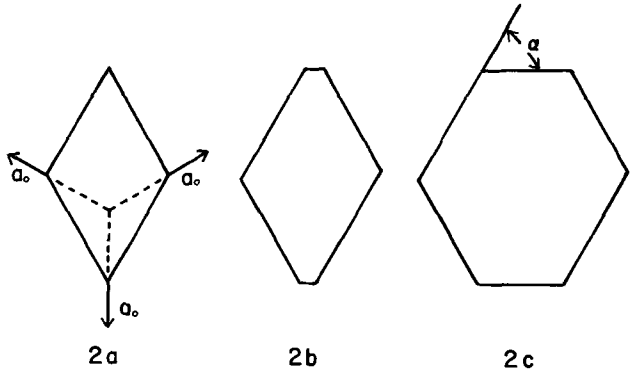

Fig. 2. Unit cell and directions are indicated by a_0 vectors in Fig. 2a. The single crystal examined by x-rays consisted of two parallel thin rhombus plates (111) joined at two edges. Figures 2b and 2c indicate the general shapes of the majority of the platelets. The sides are in general unequal in length although the external angles, α, are within one-half degree of 60°.

Charging the Silver Oxide Electrode with Periodically Varying Current

II. Repeated Open-Circuit Periods

Charles P. Wales

United States Naval Research Laboratory, Washington, D. C.

ABSTRACT

Sintered silver electrodes were oxidized anodically in 35-50% KOH at 25°C, usually at the 20-hr rate, sometimes at faster rates. Length of charge plus open-circuit periods varied from 8 hr to 1/60 sec. A particular charge length and open-circuit length was repeated until oxygen evolution occurred. In 50 or 45% KOH this charge method gave either the same capacity as a constant d-c charge or less capacity, but in 35% KOH the improvements averaged as high as 40% under certain conditions. Best results were obtained when the preceding discharges were at low rates.

The discharge capacity of AgO electrodes is strongly influenced by conditions of the preceding charge (anodic oxidation). It has been shown that capacity of AgO electrodes can be increased by charging with a periodically varying current if pulses of charge current are added to the normal charging current using the proper conditions (1). Polarization decreases during a short pulse of increased current, perhaps as a result of breaking or roughening the oxide film which covers the electrode. Thus the surface area increases, and a larger amount of oxide can form before oxygen evolution begins. There may also be an increase in conductivity during a pulse if there is appreciable activation of the semiconductors Ag_2O or AgO (2, 3). Pulses of increased charging current must be short or else concentration gradients become so large that polarization increases greatly and resultant capacity is less than normal.

In general, both the total amount of AgO that forms on a silver electrode and the AgO crystal size vary inversely with the charging current density that is used (4). When charging storage batteries that contain silver electrodes it is often impractical to use rates requiring a day or more for completion, even though these low rates give a high capacity. As a compromise, sometimes a high charging current is used at first, followed by a lower current after potential begins to rise to the oxygen evolution value. This usually gives less capacity than if a lower current had been used for the entire charge, because the fine AgO crystals that form when using high current densities may make a tight coating on the electrode surface and limit further oxidation (4).

Capacity can be increased somewhat by putting a silver oxide electrode on open circuit for a time, when charging potential approaches the gassing value. The present work was undertaken because it was believed that there may be benefit from periodically interrupting the charge current throughout a charge.

Experimental Procedure

The test cells contained sintered silver plaques that had been manufactured for use in commercial silver-zinc storage batteries. The silver plaques were 30.5 x 63.5 x 0.8 mm or 41.5 x 38.0 x 0.8 mm. Neglecting the grid of expanded silver metal, the plaques had an average weight of 7.9 or 5.8g, respectively, for a theoretical capacity of 3.9 or 2.9 amp-hr. Porosity of unused electrodes, as determined by liquid absorption, was 50-56%. The silver plaques were wrapped in cellulosic separator material of a type normally used in commercial silver-zinc cells. Similar silver electrodes were used for both the cathode and anode. The test cells contained an excess of 35 or 50% KOH.

A constant current which gave an average discharge length on the order of 20 hr following a charge using this same current was defined as the 20-hr rate of charge and discharge. This 20-hr rate was taken as the standard or "normal" charge current. Charges were continued until potential stopped changing rapidly after reaching oxygen evolution (about 510 to 530 mv positive to the Ag/Ag_2O reference electrode). This resulted in a charge input which was usually 101-102% of the following discharge. Discharges were done with a controlled constant current and ended at a final potential 300 mv negative to the Ag/Ag_2O reference. Normal charges (as defined above) alternated with charges using interrupted current. All discharges used the 20-hr rate except where noted otherwise. The work was done at 25° ± 1°C.

Some charges by interrupted current were repeated with commercial silver-zinc secondary cells using 35 or 45% KOH. These cells were rated at 5 amp-hr, and each cell contained four silver electrodes. These electrodes were the same size as the test electrodes which had a theoretical capacity of 2.9 amp-hr. The test electrodes had been manufactured for use in this size of silver-zinc cell. The silver-zinc cells were charged to 2.05v and discharged to 1.10v using the 20-hr rate of constant current (as defined above). The electrolyte supplied with these cells was analyzed and found to be 45.0% KOH and 0.6% K_2CO_3. The "35%" KOH was prepared from reagent grade KOH. Analysis of this solution gave 34.7% KOH and 0.9% K_2CO_3. When the electrolyte was used in the cells the carbonate concentration probably increased from degradation of the cellulosic separators.

There were four types of charge regime using interrupted current. In each of the four a particular length of charge and open circuit was repeated until strong oxygen evolution occurred. In one type, a cell was charged for 3 hr at the normal (20-hr) rate of constant current. This was followed by a stand period ranging from 12 min to 5 hr before resuming the charge. In the second type the charge periods began every 60 min, with the cell being charged at the normal (20-hr) rate for periods ranging from 59 to 45 min and the remaining 1-15 min being the stand period. In the third type the charge periods began every 10 min, with the cell being charged at the normal (20-hr) rate for periods ranging from 9.5 to 4 min and the remaining 0.5-6 min being the stand period. The fourth type of charge was derived from rectified 60-cycle alternating current, using unidirectional currents that were equivalent in coulombs per unit time to either the 20-hr or 6-hr charge rate.

Several sources of controlled d.c. were used. When stand times were under 1 min, a power source was

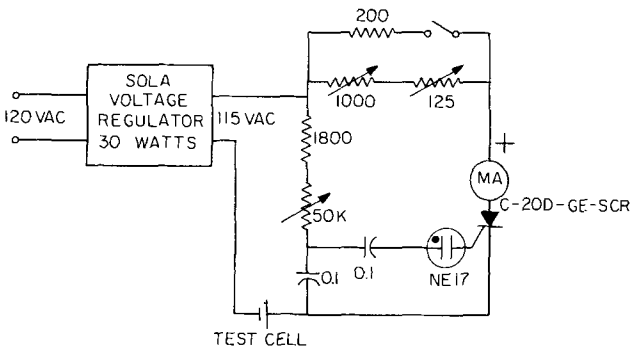

Fig. 1. Circuit for obtaining rectified a.c. with current interrupted for more than half of the a-c cycle.

used that had a recovery time of less than 50 μsec for reaching the preset current value. For longer stand times, a d-c source having a recovery time of several seconds was used also. Half-wave and full-wave rectified a.c. were obtained from 60-cycle a.c. by typical rectifier circuits. Rectified a.c. in which the current flowed less than half of the a.c. cycle was obtained by using a silicon-controlled rectifier (Fig. 1). These forms of current were used rather than the customary square wave, because they were easily obtained and seemed more practical for possible widespread use.

Rectified a.c. which consisted of approximately the last half of an a-c half-wave was called "quarter-wave rectified a.c." for simplicity. Current rose rapidly to a maximum value and then fell more slowly to zero, with no current flowing for ¾ of the time (upper part of Fig. 2). Similarly the last quarter of an a-c half-wave was called "eighth-wave rectified a.c." (Fig. 2). Average current in these examples was 80 ma including the time in which no current flowed.

Results

Each new test cell was charged and discharged at the 20-hr rate of constant current several times until capacity stopped changing rapidly, before charging with periodically interrupted current. The initial or second cycle often gave as much as 70-80% of theoretical capacity for the sintered silver. Capacity dropped in the next few cycles. After about 12 cycles

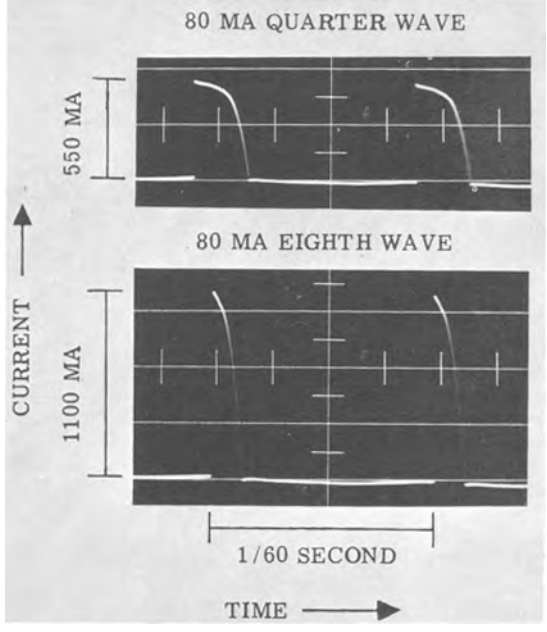

Fig. 2. Oscilloscope traces showing wave form of quarter-wave and eighth-wave rectified a.c. with approximate current calibration. Average current was 80 ma.

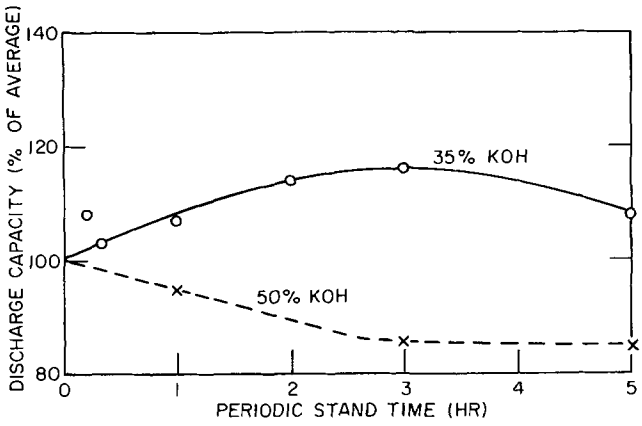

Fig. 3. Change in discharge capacity following charges at 20-hr rate with stand periods after each 3 hr of charge. Plotted points are averages of several discharges.

capacity showed no further loss but varied irregularly, with the capacity of normal cycles in 35% KOH usually falling in the range 44-57% of theoretical capacity and averaging 50-55% of theoretical. In 50% KOH the capacity was usually in the range 36-48% of theoretical.

Variations in cell capacity were minimized by calculating the average discharge capacity of the four normal cycles (20-hr constant current charge and discharge) nearest to each discharge. This average was then taken as the "normal" capacity at that point in the cycle life of the cell. Capacity of each discharge was expressed as a per cent of this normal capacity. These calculations also improved comparison between cells having different capacities. Throughout this paper the results are presented as being a certain per cent of normal capacity. Normal capacity always means the average discharge capacity that was measured when using a constant current at the 20-hr rate for both charge and the following discharge.

Although capacity of individual normal cycles varied irregularly, 135 normal cycles in 35% KOH that alternated between the charges with repeated stands had a discharge capacity which averaged 100.1% of normal capacity and had a standard deviation of 7.1. The center half of these normal capacities fell in the range 96.1-103.4%. In 50% KOH there was less variation, the average of the discharge capacities of 27 normal cycles being 99.6% of normal capacity (standard deviation = 2.4) and the center half falling in the range 98.2-100.8%.

When stand periods followed each 3 hr of charge, most charge-stand combinations gave increased capacity in 35% KOH, and decreased capacity in 50% KOH (Fig. 3). The plotted points for 50% KOH were the average of two discharges and were very reproducible. In 35% KOH the plotted points were averages of 3 to 7 discharges with individual capacities varying widely. For example, the 115.7% shown for 3-hr stands repeated every 3 hr in 35% KOH is the average of 5 discharges, divided between two cells, with individual capacities varying from 99.7 to 131.8% of normal capacity. Potentials of a charge having stand periods of 1 hr alternating with charge periods of 3 hr are given in Fig. 4.

Higher charge currents in 35% KOH also could give beneficial results. When there were 3-hr stands after every 3 hr of charge at the 6-hr rate, the capacity averaged 90% of the normal 20-hr value and about 9 hr (total of charge time + stand time) was required. This should be compared to the 83% of normal capacity that was obtained when using uninterrupted constant current at the 6-hr rate. When using 1-hr stands repeated after every 1 hr of charge at the 6-hr rate, a charge required about 13 hr (total) and 5 of these cycles gave an average 110.3% of normal capacity. When 1-hr charges at the 3-hr rate alternated

Table I. Effect on commercial silver-zinc cells of stands after each 3 hr of charge using 20-hr charging current

Periodic stand time, hr	Average discharge capacity, %	
	35% KOH	45% KOH
1	97.8[4]	96.3 [3]
3	114.2 [3]	99.8 [2]
5	105.8 [3]	95.9 [2]

Values in brackets give the number of measurements made.

with 1-hr stands, there was 83-93% of normal capacity obtained in about 6 hr.

This charging method was tried at the 20-hr charge rate with commercial silver-zinc cells (Table I). Although results were not identical with test cell results, trends were similar.

Stand periods of 1-15 min repeated every 60 min during a charge gave discharge capacities that differed little from capacities following an uninterrupted charge at the 20-hr rate (Fig. 5). This type of charge was not tried in 50% KOH.

Stands repeated every 10 min during a charge could be beneficial or harmful, depending on conditions (Fig. 6). Although the averages fell close to a smooth curve, individual charges in 35% KOH gave widely varying capacity, particularly when using stands of 2, 3, or 4 min. There were 6 to 9 charges for these three times and at least one of the following discharges varied more than 36% from each of these three averages (Fig. 6).

Selected portions of potentials that were measured during a charge having 2-min stands repeated every 10 min are given in Fig. 7. The first excerpt is at hour 4.33 as potential rose to the peak value that started the Ag_2O/AgO plateau. Potentials rose to a maximum value in 0.4-0.8 min after the charge was resumed following most of the 2-min stands at the

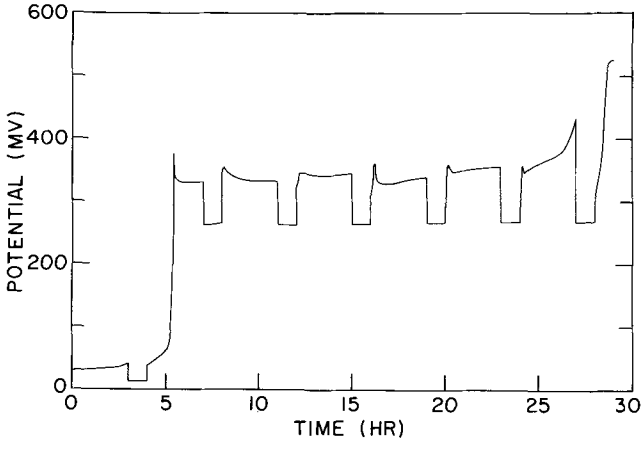

Fig. 4. Potentials during charge at 20-hr rate in 35% KOH with 1-hr stands after each 3 hr of charge. Potentials are given with respect to Ag/Ag_2O reference electrode.

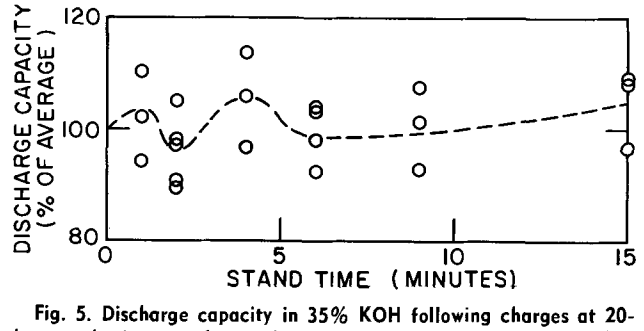

Fig. 5. Discharge capacity in 35% KOH following charges at 20-hr rate having stand periods repeated every 60 min. Dashed line connects averages of plotted values.

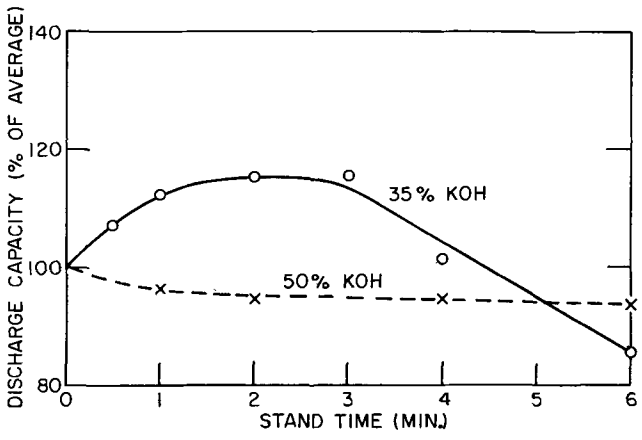

Fig. 6. Discharge capacity following charges at 20-hr rate having stand periods repeated every 10 min. Plotted points are averages.

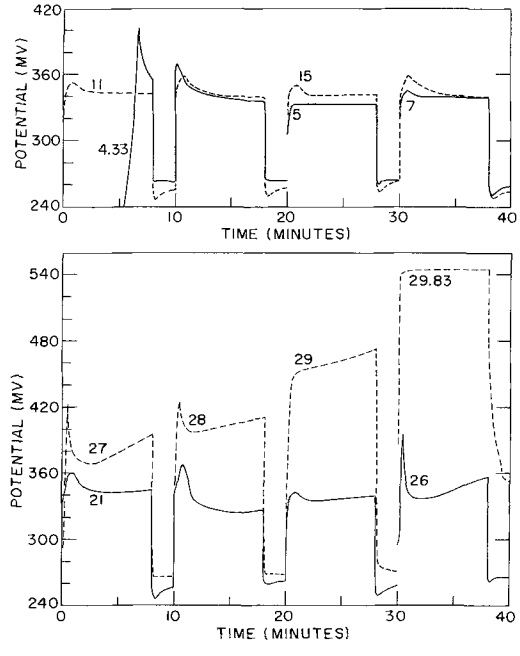

Fig. 7. Some brief excerpts taken from charge in 35% KOH having stand periods of 2 min every 10 min. Numbers indicate total elapsed time in hours at beginning of the particular 8-min charge excerpt that is shown. Lack of number indicates charge was continuous from previous stand shown. Potentials are given with respect to Ag/Ag_2O electrode.

Ag_2O/AgO plateau. After the third 8-min charge period at this plateau, stand potential fell to a minimum value in 0.2-0.3 min and then rose more slowly. This behavior continued throughout most of the charge after hour 5 (Fig. 7 and 8). There was a marked tendency for the charge and stand potentials to be relatively low during one 10-min period but higher the next, beginning about hour 11. This is shown more clearly in the 20-min excerpt at hour 15 (Fig. 7). After the electrode was two-thirds charged the potential patterns usually repeated themselves every 30 min instead of 20 min (hour 21 Fig. 7 and 8).

The same type of charge in 50% KOH gave potentials that were more steady. Until the electrode was half charged, potentials in 50% KOH lacked a maximum when charge was resumed following the brief stands. After the electrode was half charged there was a small maximum in charge potential following the brief stands but this maximum was usually less than 10 mv. Stand potentials did not show a minimum in 50% KOH, but did fall to increasingly lower values as

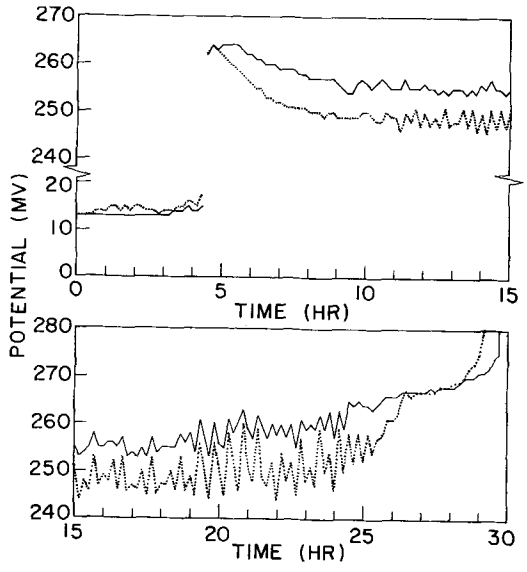

Fig. 8. Open-circuit potentials after standing 0.25 min (dotted line) and 2.0 min (solid line) during charge shown in Fig. 7.

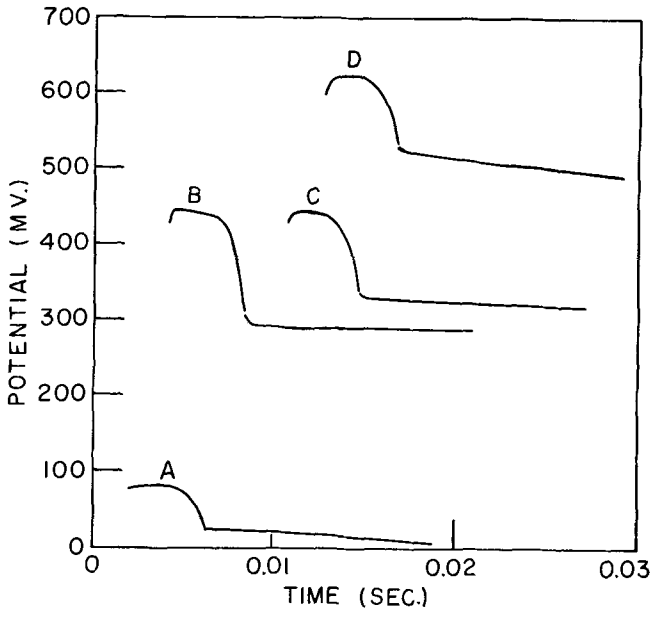

Fig. 9. Some potentials during quarter-wave charge at 20-hr average current in 35% KOH. Potentials are given with respect to Ag/Ag_2O electrode. A, half charged at Ag/Ag_2O potential plateau; B, ⅛ charged at Ag_2O/Ag plateau; C, ⅞ charged at Ag_2O/AgO plateau; D, while strong oxygen evolution occurred.

the charge progressed until the electrode was 80% charged. This charge in 50% KOH gave a capacity slightly below normal. Six-minute stands repeated every 10 min in 35% KOH, a charge that gave relatively low capacity, had similar weak maxima in the charging potentials.

Two-minute stands every 10 min were also tried when using the 6-hr charge rate in 35% KOH. Two cycles gave an average 98% of normal (20-hr rate) capacity, instead of the 83% average obtained using constant current at the 6-hr rate. This charge was tried with the commercial silver-zinc cells at the 20-hr rate, but it gave no significant change in capacity.

A charge current that was interrupted 60 times a sec resulted in improved capacity when using 35% KOH, but had no particular effect in 50% KOH (Table II). Included in Table II are normal constant current cycles which alternated with the cycles using rapidly pulsating charge current that was derived from 60-cycle a.c. Although there was variation in capacity during the life of the cells, the variation did not conceal the beneficial effects that could be obtained, even when actual discharge capacity was considered. This is shown in Table II where discharge capacity is given both in terms of average normal capacity at a particular point in the cycle life of the cells and also as a per cent of capacity that was theoretically possible for the sintered silver of the six test electrodes that were used here.

A few typical potentials drawn from oscilloscope photographs of a quarter-wave charge are given in Fig. 9. The average current was the 20-hr rate, but peak current was about 7 times larger. This current wave-form was shown in the upper part of Fig. 2. The same types of charge current were used at the 6-hr rate (Table III) and using commercial silver-zinc cells (Table IV).

During a discharge following a normal charge at the 20-hr rate, 26-32% of the capacity was obtained before reaching the Ag_2O/Ag potential plateau. The same proportion was obtained after a charge with repeated stand periods, with but few exceptions. The proportion of discharge at the upper potential plateau was often 5-10% longer than normal following charges having stands of 2 or more hours after each 3 hr of charge. After charging with the various forms of rectified 60-cycle a.c. at the 20-hr rate, the dis-

Table II. Effect of 20-hr charges using current pulsating 60 cps

Type of charge current	35% KOH			50% KOH		
	Normal	Theor.	No.	Normal	Theor.	No.
Constant d.c.	99.8	48.6	22	100.1	41.4	12
75% constant d.c. with 25% superimposed half-wave rectified a.c.	108.4	54.7	3			
50% constant d.c. with 50% superimposed half-wave rectified a.c.	140.2	65.8	3	103.2	43.8	2
Full-wave rectified a.c.	123.2	57.3	6	99.1	40.9	2
Half-wave rectified a.c.	128.9	59.0	3	100.8	41.2	2
Quarter-wave rectified a.c.	131.0	65.9	4	95.0	40.1	2
Eighth-wave rectified a.c.	125.9	64.8	5	101.4	42.6	2

Normal means average discharge capacity given as a per cent of normal capacity. Theor. means average discharge capacity given as a per cent of theoretical capacity. No. means the number of measurements made.

Table III. Capacity following charges at 6-hr rate using current pulsating 60 cps compared to capacity following constant current charges at 20-hr rate

Type of charge current	Average discharge capacity, %	
	35% KOH	50% KOH
Constant d.c. at 6-hr rate	83.3 [4]	67.9 [6]
50% constant d.c. with 50% superimposed half-wave rectified a.c.	95.1 [3]	58.6 [2]
Full-wave rectified a.c.	83.0 [3]	57.8 [2]
Half-wave rectified a.c.	82.4 [3]	66.3 [2]
Quarter-wave rectified a.c.	99.0 [3]	53.7 [2]
Eighth-wave rectified a.c.	97.2 [3]	55.8 [2]

Values in brackets give the number of measurements made.

Table IV. Effect on commercial 5 amp-hr silver-zinc cells of 20-hr charges using current pulsating 60 cps

Type of charge current	Average discharge capacity, %	
	35% KOH	45% KOH
Constant d.c.	101.6 [6]	100.4 [5]
50% constant d.c. with 50% superimposed half-wave rectified a.c.	107.0 [2]	98.9 [2]
Full-wave rectified a.c.	96.6 [2]	103.9 [2]
Half-wave rectified a.c.	102.3 [2]	99.1 [2]
Quarter-wave rectified a.c.	108.0 [2]	104.0 [2]

Values in brackets give the number of measurements made.

charge at the upper plateau was at a lower potential and the proportion was usually 5-10% shorter than normal. Capacity obtained at this plateau had not increased as much as total capacity had increased. The discharge capacity at this plateau was practically unchanged following a charge of 50% constant current with 50% superimposed a.c., although total discharge capacity was considerably increased. This resulted in the proportion of discharge being about 20-25% less than the normal proportion.

For one series of cycles a cell was charged at the 20-hr rate and was then discharged at the 1-hr rate, instead of the 20-hr rate. The initial discharge at the 1-hr rate gave a capacity that was about the same as normal capacity, but on repetition the capacity of discharges at the 1-hr rate was increased by an average of 10%. Under these conditions full-wave rectified a.c. or repeated 8-min charges followed by 2-min stands gave about the same capacity at the 1-hr discharge rate as did constant current charges. Quarter-wave rectified a.c. gave about 5% additional improvement in discharge capacity.

Discussion

The experimental results showed that significant improvements in capacity were possible through the use of repeated open-circuit periods during charge when using 35% KOH as the electrolyte. The largest capacity increases were obtained by using a rapidly fluctuating current, with or without stand periods (Table II). All of these rapidly pulsating currents that were tried at the 20-hr rate improved capacity in 35% KOH. There was no marked change in capacity when stand length and pulse current both increased, with net current remaining equivalent to the 20-hr rate (Table II). Superimposing a charge current that was pulsating 60 times per second onto a constant charge current, the smoothest type of current used except for constant current, could give a large improvement. This type of current is related to that used earlier, in which current was increased for a few seconds every 10-60 min and an increase in capacity up to 30-40% was obtained (1). Lack of improvement in 50% KOH was also noted in this earlier work.

Constant current at the 6-hr rate gave only about 5/6 of normal capacity in 35% KOH but close to normal capacity could be obtained by using rapidly pulsating currents (Table III). Here again a relatively large improvement resulted from superimposing a charge current that was half-wave rectified a.c. onto a steady charge current. Benefits at the 6-hr rate of charge were less in proportion than they were at the 20-hr rate.

Comparison of Fig. 3, 5, and 6 showed that neither stand length nor charge length nor ratio of these lengths determined whether or not a particular charge-stand combination was beneficial. A disadvantage to some of these types of charge with repeated stands was that total charge time increased greatly. Higher capacity was not just an effect of this increase in total charge time. Charging at the 6-hr rate with 1-hr stands after every hour of charge required only two-thirds of normal charge time but gave 10% more capacity than a normal charge. Charging at the 20-hr rate with charge periods of 3 hr alternating with stands of 3 hr required approximately the same total time as the 40-hr rate of uninterrupted constant current but averaged about twice as much capacity improvement, comparing both types of charge to a normal charge. The use of low charging currents may be preferable for some applications, however, because the following discharge will have a shorter AgO/Ag_2O potential plateau and thus give a more constant discharge potential. Although more AgO is present after charging with a low current than is present after using a high current, the surface area is smaller when the oxide is formed slowly, and this smaller surface is covered more rapidly with Ag_2O during a discharge (4). Therefore the discharge shows less capacity at the AgO/Ag_2O potential level even though total discharge capacity has increased. This initial potential plateau lasted 17-25% of the total time for a discharge immediately following a 40-hr charge, and 7-16% when discharged immediately following an 80-hr charge. As mentioned earlier, 26-32% was obtained following a 20-hr charge or most charges using stand periods.

The wide scatter of individual measurements in 35% KOH that were averaged for the points shown in Fig. 3 and 6 indicated that all factors were not under control. If all factors could be controlled consistently, there is possibility of an improvement larger than that shown by these figures because many individual measurements were much better than the averages. The scatter could not be attributed to different cells nor to whether a measurement was made early or late in the cycle life of a cell.

Potentials gave an indication of electrode conditions. When using stands repeated after 3 hr of charge or stands repeated every 10 min, the largest capacity followed a charge showing strong potential maxima soon after many of the open-circuit periods at the Ag_2O/AgO plateau. A charge lacking these maxima, or having but slight maxima, gave only normal capacity. When a silver electrode is oxidized anodically with constant current, the potential rises sharply to a maximum value after the silver surface is covered with Ag_2O. The first reaction following this potential peak or maximum is Ag_2O oxidizing to AgO. Little or no additional silver oxidizes until a large part of the Ag_2O has oxidized (4, 5). With some charge-stand combinations the open-circuit potentials began to have a minimum value as the charge continued to form more AgO (Fig. 7, 8). The potential minimum tended to reach increasingly lower values as the AgO layer thickened, for approximately the first half of this type of charge (Fig. 8). The potential minima were probably the result of nonuniform distribution of oxygen and silver in the oxide layer (6).

When the electrode was about one-third charged using 2-min stands every 10 min, potential patterns began to be repeated every 20 min (hour 11 Fig. 7, 8). The low stand potential and the following high charging potential both indicated that ion movements were retarded under these conditions. Then a change must have occurred that decreased concentration gradients in the electrode. It is believed that the oxide coating cracked, allowing electrolyte to penetrate nearer to the silver, and this decreased the concentration gradients in the oxide layer. Decreased concentration gradients were indicated both by the lowered charge potentials and by the potentials of the next stand being nearer to equilibrium values, close to values measured earlier when only a small amount of AgO was present. The process was repeated as the film built up again. It is likely that development and removal of concentration gradients in the electrode were also at least partly responsible for the potential maxima observed after stands of 1-5 hr. These comparatively slow changes within the electrode probably did not take place to any great extent when using current pulsating 60 times per second because of the short time between successive current pulses.

An additional factor during the long stands was formation of a thin Ag_2O film on the silver as a result of the reaction between silver and AgO (3). During short stands the formation of Ag_2O was not appreciable. When charge was resumed after 1-hr stands, potential often did not rise to a peak immediately (Fig. 4) as it should have done if the maximum were caused entirely by Ag_2O resistance. The reaction between silver and AgO can result in slightly deeper oxidation and slightly increased capacity. Benefit would be limited because the reaction rate probably decreased as the Ag_2O film thickened and separated the reactants. In earlier work Ag_2O was not definitely

visible to x-ray diffraction even after 2½ days stand of a charged electrode, although x-ray diffraction patterns of AgO had weakened in this time (4). It should be noted that Ag_2O was more likely to form deep in the electrode where silver was available than at the electrode surface where Ag_2O could be detected more readily by x-ray diffraction.

It is unlikely that enough Ag_2O was formed in the longer stand times used in these charging methods for the Ag_2O to cause sufficient resistance to account for the entire potential rise. If there were a high internal resistance due to Ag_2O, there would be a large potential gradient in the electrode as current passed. Although grid or terminal potential could be quite high the surface potential would not be expected to rise beyond the potential necessary for oxidation of Ag_2O to AgO. But potentials rising to the oxygen evolution value have been observed after long stands (2). It may be that as conducting paths to the surface are formed, when a charge is resumed after very long stands, concentration of charge current along these conducting paths allows the surface to reach the gas evolution potential. Oxidation of Ag_2O and oxygen evolution could then take place simultaneously until potential fell as more or better paths to the surface are formed.

A more important factor to be considered is changes in AgO crystallinity under the different charge conditions. It has been established that there is an exchange of oxygen between a KOH solution and AgO (7). It would not be surprising if there is also an exchange between dissolved silver and AgO. These exchange reactions would allow perfection of the AgO crystallinity and smoothing of the surface when time was sufficient, such as during long stand periods or during low-rate charges. Thus true current density following a long stand would be higher at the surface of the electrode and the increased current density could account for high charge potentials as well as the low discharge potentials that have been observed at the AgO/Ag_2O level after very long stands. Results in 50% KOH, although not improved by a charge with repeated stands, usually were much more reproducible than in 35% KOH. This was probably at least partly caused by physical differences between the AgO coatings that formed on silver in 35% KOH and the coating in 50% KOH. Perhaps AgO crystallizes in a physical form in 50% KOH that retarded passage of oxygen through the AgO. There is no reason to assume that a cubic AgO forms initially and that this AgO converts to monoclinic AgO at low current or during long stands as has been suggested (2). Monoclinic AgO can actually be detected quite soon after anodic potential reaches the Ag_2O/AgO plateau (4) and the compound originally reported as cubic AgO has since been shown to be a different material (5).

The most important cause of increased capacity in the charges that were beneficial was believed to be an increased surface area. Increased surface area allowed more AgO to be formed during a charge before slow diffusion through the AgO caused sufficient polarization that potential rose to the oxygen evolution value. When the charging potential increased to a relatively high value after a stand, oxygen from the surface layers could penetrate deeper into the oxide layer under the influence of the high charging potential, thus oxidizing silver that was under the oxide coating.

There is a large expansion when a certain quantity of silver is oxidized to an equivalent amount of Ag_2O. There is only a slight additional increase in volume when Ag_2O is oxidized to an equivalent amount of AgO. If the reactions take place entirely in the solid state, with each single crystal of Ag_2O changing into a single crystal of AgO, then an oxide film may also be broken by distortion of the crystal lattice. Two cell dimensions expand, one contracts and one angle changes as a face-centered cubic crystal of Ag_2O is oxidized to monoclinic AgO. Expansion of the crystal lattice as AgO formed from Ag, most likely through Ag_2O as an intermediate, probably cracked the oxide coating which covered the electrode and allowed electrolyte to penetrate nearer to the silver under these conditions. The increased porosity resulted in decreasing current density and decreasing concentration gradients within the oxide layer. For this reason the charge potential fell to its lowest value in the same 8-min period that had the highest potential (for example see curve at 21 hr 10 min in Fig. 7).

Thus the potential drop after the maximum was probably caused by breaking of the smooth oxide layer and, after long stands, also partly caused by oxidation of resistive Ag_2O to AgO. If the drop in potential were merely the result of activation of the semiconductors Ag_2O (3) or AgO (2), conditions after activation would be the same as they were before interrupting the current, and there would be no reason to expect increased capacity after a series of potential maxima, but the best discharge capacity usually followed charges that showed irregular potentials. It is proposed here that the capacity increase was mainly the result of deeper oxidation of the silver, caused by breaking of the surface as AgO formed below the electrode surface.

The increased amount of oxide that formed when using current pulsating 60 times per second in 35% KOH was probably also the result of surface area increasing as the oxide film on the electrode broke or roughened when current was high. Stresses may be set up as a result of fast formation of the oxide film or layer and then be relieved by cracking. Stand time was not important or even necessary when using these rapidly pulsating currents (Tables II, III). Current being high for only a brief time prevented harmful formation of large concentration gradients, such as would have occurred if curernt had remained high for longer times. Charges at the 6-hr rate were less beneficial than charges at the 20-hr rate because the faster charge resulted in larger concentration gradients in the electrolyte and smaller crystals of AgO were formed (4). Both of these effects could limit further oxidation.

The mobility of the hydroxyl ion is an important factor in the oxidation process (8). Lack of hydroxyl ion at the electrode can seriously impair charges. This can occur in concentrated KOH solution, or when using high current densities, or at low temperatures. A combination of these is more harmful than any one singly. For example, capacity decreased more rapidly with increasing charge current in 50% KOH than it did in 35% KOH (9). Thus one would expect that a current pulsating 60 times per second (and momentarily reaching higher current densities than a normal charge) would not necessarily give as good results in 50% KOH as it does in 35% KOH, especially when using faster charges (Tables II, III). The limited amount of free electrolyte in the commercial silver-zinc cells, due to tight packing in the cell cases, probably resulted in increased concentration gradients in the electrolyte near the electrode surface compared to test cell conditions. This may be the reason for the commercial cells usually not showing the improvement that test cells showed, but no experimental work was done to prove this.

As mentioned earlier, the rate at which a cell was discharged in 35% KOH had a large effect on the results of a charge using pulsating current. It has been shown that a charge following a high-rate discharge gave more capacity than a charge following a low-rate discharge because of differences in chargeability of the forms of silver that resulted under these conditions (4). Therefore when a cell was given a series of complete discharges at low current density, capacity tended to decrease at least to a point. If a cell was then given a series of complete high-rate discharges, capacity tended to increase back toward the original value. As a result of this, although a single

discharge at the 1-hr rate might give less capacity than the preceding discharge at the 20-hr rate, after several discharges at the 1-hr rate (and recharges at the 20-hr rate) the capacity increased to a value larger than it was after a series of discharges at the 20-hr rate. Charge acceptance at the Ag/Ag_2O plateau had doubled, but charge at the Ag_2O/AgO plateau was only 90% of its normal length. Under these conditions, where the capacity was high already, a constant current charge gave about the same capacity as the pulsating charges.

Several phenomena were involved in the results reported here and no single explanation will adequately cover them all. Further work is obviously necessary for a more definitive explanation and will be undertaken after determining the effect on capacity of current reversals during a charge. In particular a microscopic examination of the electrodes at various steps in the different types of charge is expected to be useful.

Conclusions

The charge methods described can be beneficial or harmful, depending on specific conditions. Faster charges or greater capacity after slow charges could be obtained by these charging methods. Results in 35% KOH were always better than in 45 or 50% KOH. The charge methods worked best when a cell had previously been discharged at low currents.

Acknowledgment

The author wishes to thank Mr. C. H. Presbrey, Jr., for technical advice and assistance in adapting and setting up the circuitry used in part of this investigation.

Manuscript received Dec. 22, 1965; revised manuscript received April 29, 1966. This paper was presented at the Buffalo Meeting, Oct. 10-14, 1965.

Any discussion of this paper will appear in a Discussion Section to be published in the June 1967 JOURNAL.

REFERENCES

1. C. P. Wales, *This Journal*, **111**, 131 (1964).
2. V. N. Flerov, *Zh. Prikl. Khim.*, **36**, 1980 (1963).
3. G. Dalin and Z. Stachurski, Paper presented at the New York Meeting of the Society, Sept. 29-Oct. 3, 1963.
4. C. P. Wales and J. Burbank, *This Journal*, **112**, 13 (1965).
5. C. P. Wales and J. Burbank, *ibid.*, **106**, 885 (1959).
6. S. Yoshizawa and Z. Takehara, *J. Electrochem. Soc. Japan*, **31**, 91 (1963).
7. K. I. Rozental and V. I. Veselovskii, *Zh. Fiz. Khim.*, **35**, 2670 (1961).
8. T. P. Dirkse, *This Journal*, **106**, 920 (1959).
9. C. P. Wales, *ibid.*, **108**, 395 (1961).

The Photogalvanic Disruption of Cuprous Oxide Films on Copper

E. J. Duwell

Minnesota Mining and Manufacturing Company, St. Paul, Minnesota

ABSTRACT

The cuprous oxide film normally present on copper is disrupted by photogalvanic action. Partial illumination of an oxidized copper surface in an electrolyte results in reduction of the cuprous oxide to metallic copper in the illuminated areas and oxidation and dissolution of the cuprous oxide in the unilluminated areas. The disrupted film is believed to lead to an observed increase in corrosion rate of copper in an illuminated salt-spray cabinet.

It is well known that a photovoltaic effect characteristic of a p-type semiconductor can be observed on cuprous oxide (1-5). Since the oxide layer on mildly oxidized copper consists essentially of cuprous oxide, it is not surprising that there have been numerous reports of the effect of light on the corrosion of copper (6-10). In general, light has been found to accelerate the corrosion of copper, although it has been shown recently that the rate of initial growth of the oxide film is decreased by light under certain conditions (11), while the dissolution of cuprous oxide to cupric ions is promoted by light.

When the oxide film becomes relatively thick (200Å), it serves to some extent as a protective film against further corrosion. We have found that the effectiveness of this film is greatly decreased by light if the oxide coated surface is covered by a conducting solution. The purpose of this paper is to describe the photogalvanic reactions which take place on oxidized copper surfaces to disrupt the continuity of the oxide film. Using a simple salt-spray corrosion test, the effect of light on the oxidation rate of copper was also evaluated.

Experimental

Because copper is a relatively noble metal, the oxide can be removed from the surface by acid dissolution without appreciable attack of the metal. If a dilute acid such as 2M H_2SO_4 is used, only half of the copper in the cuprous oxide film is dissolved as a result of disproportionation

$$Cu_2O + H_2SO_4 \rightarrow Cu^o + Cu^{++} + SO_4^{=} + H_2O$$

Although this method has been used for oxide film analysis by previous investigators (12), it was felt that total dissolution of the oxide film with concentrated hydrochloric acid would be more suitable for our purposes. In this case the acid dissolves all of the cuprous oxide with formation of the anionic chloride complex

$$Cu_2O + 4HCl \rightarrow 2CuCl_2^{-} + 2H^{+} + H_2O$$

In either case, care must be taken to exclude atmospheric oxygen which would cause further oxidation and dissolution of the metal. Cupric oxide is dissolved by either method, and, therefore, the latter method can be considered an analysis for total oxidized copper, while the former method would result in an ambiguity if the oxide film contained an unknown amount of cupric oxide. The oxide film on copper treated at 300°C for about 10 min has been shown to be essentially all cuprous oxide (13). Analysis of equal areas of an oxide film prepared under these conditions by both the dilute sulfuric acid and concentrated hydrochloric acid dissolution methods resulted in twice the concentration of copper in the hydrochloric acid solutions, thus verifying the self-consistency of the two methods.

Analysis for copper in solution was done spectrophotometrically after formation of the tetraethylene pentamine complex as outlined in the literature (14).

The copper corrosion samples were ASTM B-133 pure copper (99.9+%). Other chemicals used were all reagent grade. Ordinary household tungsten filament incandescent lamps were used for illumination.

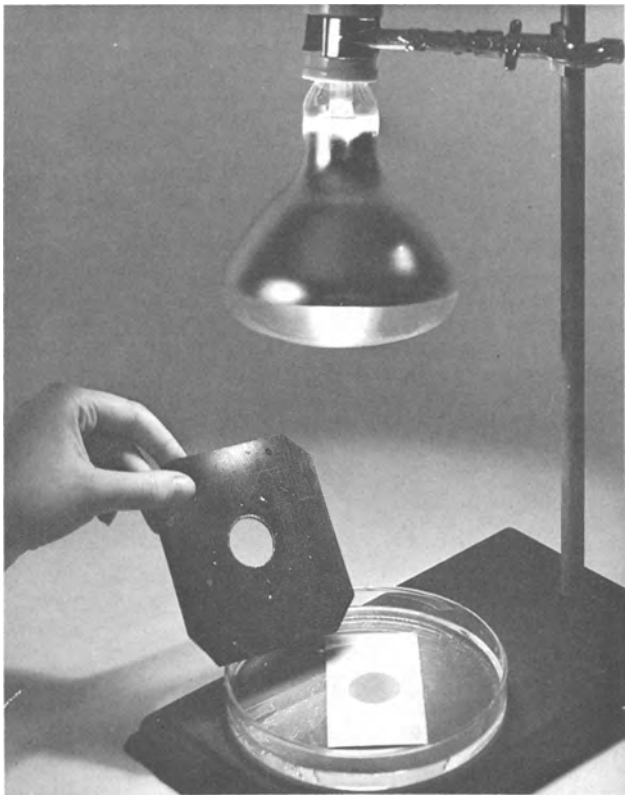

Fig. 1. Photogalvanic action on an oxidized copper panel immersed in saturated KCl solution. The exposed area became black after illumination for 10-15 min at a light intensity of 5000 ft-c.

Experimental Results

A photogalvanic cell reaction on oxidized copper is easily demonstrated. The copper may be heated at 300°-400°C for 30 min or may be simply held in a Bunsen flame until the reddish brown cuprous oxide coating develops but not until an incoherent cupric oxide film is formed. If the copper panel is then immersed in a salt solution and partially illuminated, the illuminated portion of the surface eventually becomes black (Fig. 1). At a light intensity of 5000 ft-c, the discoloration on the illuminated surface just becomes discernible in 1 min. The same area is quite black after 10 min. The blackening is greatest at the periphery of the spot. These areas are, of course, closest to the unilluminated area, and the resistance through the solution is a minimum. Apparently any soluble salt which does not attack the oxide surface will serve as an electrolyte and will permit the photogalvanic reaction to take place. There is no evidence of a surface reaction if the surface is dry or is covered with distilled water. Also, simple qualitative experiments revealed that the rate of blackening depends on salt concentration.

The change in potential of the illuminated surface can be compared through an external circuit with the electrode potential of a similar panel kept in the dark or more simply with a calomel reference cell. In either case, light is noted to make the oxidized copper more positive by a potential as high as 0.12v (Fig. 2). The magnitude of the effect apparently depends on the manner in which the oxide layer is formed. If the oxide layer is grown in a salt-spray cabinet for several days, the change in potential is from 10-25 mv. Short exposures of the copper to higher temperatures generally appears to produce a more photosensitive surface than slow oxide growth at lower temperatures.

A copper cylinder, ⅜ in. in diameter, was oxidized at about 300°C, immersed in saturated KCl solution, and a small portion of the surface illuminated with a tungsten lamp. The illuminated portion of the surface

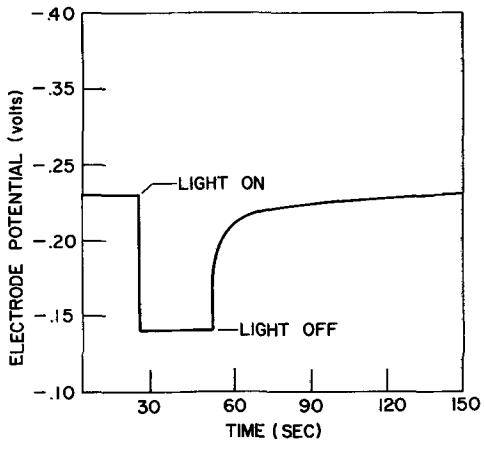

Fig. 2. Photogalvanic response of an oxidized copper panel relative to a saturated calomel electrode. The light intensity was 3000 ft-c.

which became black was compared with the original surface by grazing angle electron diffraction. The original surface gave a diffraction pattern characteristic of cupric oxide, while the illuminated surface gave a diffraction pattern of metallic copper. No diffraction pattern was observed on surfaces adjacent to the illuminated area indicating the formation of an amorphous surface layer. It is not surprising that a cupric oxide rather than cuprous oxide pattern was obtained on the original surface since a thin layer of cupric oxide always appears to form over the cuprous oxide. The same result was obtained by Beck and Pryor (13) who also identified the cuprous oxide layer using a stripping technique and diffraction patterns obtained by electron transmission.

In a photogalvanic cell (Fig. 3) constructed of two copper electrodes oxidized at 360°C for 1 hr, the illuminated electrode was also observed to become blackened with time. Immersion of both electrodes in concentrated hydrochloric acid resulted in complete cleaning of the unilluminated electrode, but an insoluble black sludge consisting of finely divided metallic copper clung to the illuminated electrode. This sludge was easily removed with a rubber policeman and dissolved in dilute nitric acid. Initially, the conversion of the oxide coating appears to proceed linearly with time (Fig. 4). Approximately 0.01 mg Cu/cm^2 is removed without illumination. This is probably a result of air oxidation and mechanical removal of the oxide film. The total amount of oxidized copper available for reduction was about 0.30 mg/cm^2.

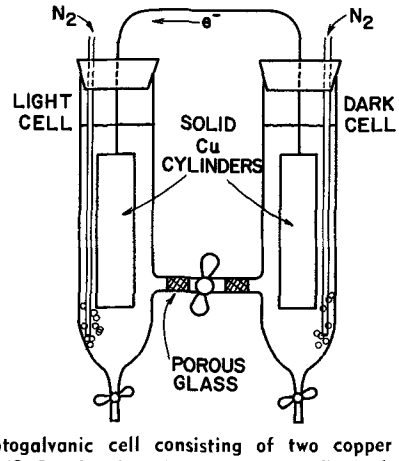

Fig. 3. Photogalvanic cell consisting of two copper electrodes oxidized at 360°C. The direction of electron flow when the left cell is illuminated is from right to left. The cells are kept free of oxygen through the use of nitrogen bubblers.

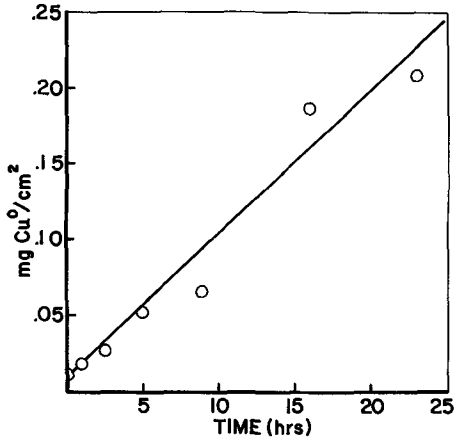

Fig. 4. Reduction of Cu_2O to copper metal as a function of time at a light intensity of 500 ft-c (light cell, Fig. 3).

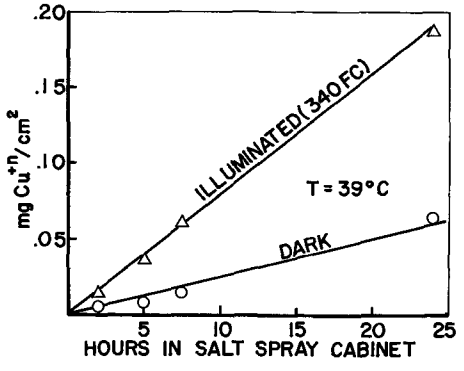

Fig. 5. Corrosion rate of copper as a function of time in a dark and illuminated salt-spray cabinet. Temperature was constant at 39°C.

If the external circuit of the photogalvanic cell (Fig. 3) is opened, reduction of the oxide on the illuminated electrode still takes place but at a slower rate. Despite careful cleaning and uniform illumination, both cathodic and anodic sites must, therefore, be present on the illuminated electrode. Closing the circuit results in dissolution of the oxide film on the unilluminated electrode as evidenced by analysis of the cell solutions after 7 hr of illumination (Table I).

The rate of corrosion of copper in a salt-spray cabinet was increased by a factor of 3.2 when the panels were illuminated on one side with a light intensity of 340 ft-c (Fig. 5). The panels were abraded clean and washed in acetone prior to being placed in the salt-spray cabinet. A further increase in corrosion rate was noted at higher light intensities (Fig. 6). The lamp was kept in an air-cooled container to avoid a temperature increase in the chamber.

Discussion

Although the kinetics of some electrode processes may be affected by photosensitive reaction steps or by photosensitive products of the electrode reaction, the reactions which have been described appear simply to be generated by the photovoltaic effect commonly observed in cuprous oxide. Accordingly, the electrode reactions do not appear to depend on the composition of the electrolyte but only require the presence of a neutral conductive solution. For example, since no electrode reactions occur in distilled water, it can be concluded that light does not directly cause disproportionation of the oxide film. Rather, the illuminated surface undergoes reduction

$$2e^- + Cu_2O + HOH \rightarrow 2Cu^\circ + 2\,OH^-$$

while anodic oxidation of the oxide film takes place on the unilluminated surface

$$4H_2O + Cu_2O \rightarrow 2Cu(OH)_2 + H_2O + 2H^+ + 2e^-$$

The copper initially goes into solution, but prolonged operation of the cell shown in Fig. 3 eventually results in the appearance of gelatinous cupric hydroxide in the dark chamber. The observed polarity can be correlated with the effect of light on the current carrying mechanism in p-type semiconductors (5), of which cuprous oxide is an example.

It is apparent that the introduction of oxygen to the system presents a complex chemical situation. It can probably be assumed that photogalvanic reactions make the surface more susceptible to further oxidation, thus increasing the corrosion rate under conditions such as those encountered in a salt-spray cabinet. To determine if such reactions occur more readily at anodic or cathodic sites and if the subsequently formed oxide surface is also photosensitive, the anodic and cathodic reactions must be isolated in a system in which the oxygen concentration is carefully regulated.

Table I. Effect of illumination on surface and solution composition of photogalvanic cell

A: External circuit open; B: external circuit closed

	Light Chamber		Dark Chamber	
	$Cu_{electrode}$,* mg	$Cu_{solution}$	$Cu_{electrode}$,* mg	$Cu_{solution}$
(A)	35.5	0.01	34.2	0.01
(B)	36.7	0.07	27.2	7.40

* Includes Cu^{+n} and reduced metal removed by wiping.

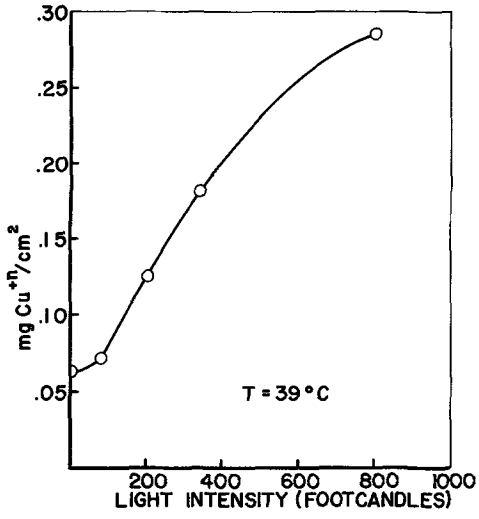

Fig. 6. Amount of copper corrosion after 24 hr in a salt spray cabinet as a function of light intensity.

Acknowledgments

The author wishes to thank Mr. J. H. Herschleb and Dr. W. E. Thatcher for the preparation and interpretation of the electron diffraction data.

Manuscript received Jan. 19, 1966; revised manuscript received May 16, 1966.

Any discussion of this paper will appear in a Discussion Section to be published in the June 1967 JOURNAL.

REFERENCES

1. A. D. Garrison, *J. Phys. Chem.*, **27**, 601 (1923).
2. R. Audubert, *Compt. Rend.*, **196**, 475 (1933).
3. V. P. Barton, *Phys. Rev.*, **23**, 337 (1924).
4. J. Bloem, *Philips Research Repts.*, **13**, 167 (1958).
5. R. Williams, *J. Chem. Phys.*, **32**, 1505 (1960).
6. G. D. Bengough and O. F. Hudson, *J. Inst. Metals*, **21**, 37 (1919).

7. C. C. Palit and N. L. Dhar, *J. Phys. Chem.*, **30**, 1125 (1926).
8. F. Goldman and E. Rupp, *ibid.*, **38**, 180 (1930).
9. T. Marhovic and O. Jaric, *Werstoffe u. Korrosion*, **6**, 535 (1955).
10. D. J. G. Ives and A. E. Rawson, *This Journal*, **109**, 447 (1962).
11. J. Kruger and J. P. Calvert, *ibid.*, **111**, 1038 (1964).
12. V. A. Pyankov and A. P. Kostyuk, *Ukrain. Khem. Zhur*, **38**, 138 (1960).
13. A. F. Beck and M. J. Pryor, *This Journal*, **108**, 417 (1961).
14. F. D. Snell and C. T. Snell, "Colorimetric Methods of Analysis," Vol. II, p. 120 (1949).

The Effect of Oxide Volatilization on the Oxidation Kinetics of Cr and Fe-Cr Alloys

C. S. Tedmon, Jr.

General Electric Company, Research and Development Center, Schenectady, New York

ABSTRACT

The oxidation of Cr and Fe-Cr alloys which form Cr_2O_3 scales involves at least two processes: (*i*) the solid-state, diffusive transport of ionic species, with parabolic kinetics, and (*ii*) the oxidation of Cr_2O_3 to a volatile species, probably CrO_3, with linear kinetics. The effects of this second reaction cannot be neglected, either in interpretation of short-term oxidation results, or in predicting long-term oxidation behavior. In this paper equations are derived which describe the oxidation behavior of a system in which both diffusive and gas/oxide interface processes occur simultaneously. According to the model, the oxide scale grows to a limiting thickness which is determined by the parabolic rate constant and the surface-reaction rate constant; as the limiting thickness is approached, a transition from parabolic to linear kinetics takes place. The model is applied to the oxidation of Cr and Fe-Cr alloys, and good agreement with experimental data is found.

When Cr_2O_3 is heated to above 1000°C in an oxidizing atmosphere, it loses weight (1-6). This weight loss cannot be accounted for simply by vaporization of the oxide, since it occurs only when the specimen is exposed to an oxidizing atmosphere (3-5); furthermore, the reported values of the vapor pressure of Cr_2O_3 (4, 7) are too low to account for the observed rates of weight loss. The chemical reaction involved in the Cr_2O_3 weight loss has not been completely identified, but is probably (3, 7)

$$Cr_2O_3(s) + 3/2\ O_2(g) \rightarrow 2CrO_3(g) \qquad [1]$$

Reduction of CrO_3 back to Cr_2O_3 subsequently occurs in cooler parts of the system.

Hagel (4) measured the rate of weight loss of Cr_2O_3 samples exposed to oxygen and found that the weight loss could be expressed by

$$\frac{\Delta M}{A}\left(\frac{g}{cm^2}\right) = -k_v t \qquad [2]$$

where the "volatilization rate constant," k_v, has the temperature dependence

$$k_v = 0.214 \exp(-48{,}000 \pm 3000/RT)\ g\ cm^{-2}\ sec^{-1} \qquad [3]$$

Although Hagel (4) corrected his highest temperature (1350°C) Cr oxidation data for such weight loss, the large effect that this surface reaction has on the parabolic oxidation kinetics of Cr and alloys which form Cr_2O_3 scales has not been generally recognized. It will be seen in the following discussion that unless this surface reaction is taken into account in oxidation studies, two significant effects can appear: (*i*) short-time oxidation kinetic data may be incorrectly interpreted, and (*ii*) estimates of service life will be in error.

That a surface-controlled reaction could alter parabolic oxidation kinetics was pointed out by Loriers (8). Subsequently, Webb, Norton, and Wagner (9) derived more general equations in order to explain their tungsten oxidation data. More recently, Birchenall (10) has discussed various factors which could alter parabolic oxidation kinetics, including the effect of a gas/oxide interface reaction.

Derivation of Rate Equations

Rate of scale-growth.—Consider the case of a metal having an adherent, dense, external scale, of thickness x at some time t. The instantaneous rate of growth of the scale is given by

$$\frac{dx}{dt} = \frac{k_d}{x} \qquad [4]$$

where k_d is equal to one-half of the usual parabolic rate constant, k_p. Because of the oxide-gas interface reaction, the scale will tend to get thinner, and the kinetics for this process are described by

$$\frac{dx}{dt} = -k_s \qquad [5]$$

where k_s is proportional to k_v. Combining Eq. [4] and [5] gives

$$\frac{dx}{dt} = \frac{k_d}{x} - k_s \qquad [6]$$

Integration of Eq. [6] yields

$$\frac{-x}{k_s} - \frac{k_d}{k_s^2}\ln(k_d - k_s x) + C = t \qquad [7]$$

where C is the integration constant. The integration constant may be evaluated applying the boundary condition that $x = 0$ at $t = 0$. Solving for C and rearranging terms gives

$$t = \frac{k_d}{k_s^2}\left[-\frac{k_s}{k_d}x - \ln\left(1 - \frac{k_s}{k_d}x\right)\right] \qquad [8]$$

Since the rate of scale growth decreases with increasing thickness, eventually the rate of growth of the scale will become zero, and a limiting scale thickness is reached. For Cr oxidation, this means that the rate of supply of Cr^{+3} cations to the gas/oxide interface from diffusion through the scale is balanced by the rate of loss of Cr ions, presumably due to reaction [1] or some similar process. The limiting scale thickness may be determined by setting Eq. [6] equal to zero, yielding

$$x_f = \frac{k_d}{k_s} \quad [9]$$

If c.g.s. units are employed then the dimensions of k_d and k_s are $cm^2\ sec^{-1}$ and $cm\ sec^{-1}$, respectively. Obviously Eq. [8] is valid only for $0 \leq x < x_f$.

The logarithm term in Eq. [8] may be expanded in a Taylor series, whereby Eq. [8] becomes

$$t = \frac{1}{2}\frac{x^2}{k_d} + \frac{1}{3}\frac{k_s}{k_d^2}x^3 + \ldots + \frac{1}{n}\frac{k_s^{n-2}}{k_d^{n-1}}x^n + \ldots \quad [10]$$

Equation [10] is useful when either x or k_s is small. It is seen from Eq. [10] that when $k_s = 0$, parabolic kinetics obtain, and $k_d = \frac{1}{2}k_p$.

If the activation energies for the parabolic and linear reactions are Q_d and Q_s, respectively, then the limiting scale thickness x_f will be temperature dependent if $Q_d \neq Q_s$. When the limiting scale thickness is reached, the oxidation reaction is no longer diffusion-limited, and oxidation proceeds with a linear rate.

Rate of metal recession.—It is also of interest to determine the effect of a surface reaction such as that described above on the rate of metal recession, since it is this quantity that is of most interest to the corrosion engineer. Let y be the extent of metal recession at some time t ($y = 0$ is the original metal/gas interface at $t = 0$); the differential equations describing the parabolic and linear contributions to the metal recession rate are then

$$\frac{dy}{dt} = \frac{k_d'}{y} \quad [11]$$

and

$$\frac{dy}{dt} = k_s' \quad [12]$$

respectively. Combining these equations yields

$$\frac{dy}{dt} = \frac{k_d'}{y} + k_s' \quad [13]$$

which is of the same form as Eq. [6]. Integrating and solving with the boundary condition above gives

$$t = \frac{k_d'}{(k_s')^2}\left[\frac{k_s'}{k_d'}y - \ln\left(1 + \frac{k_s'}{k_d'}y\right)\right] \quad [14]$$

The logarithmic term in Eq. [14] may be expanded to give an equation analogous to [10].

Kinetic measurements.—A common method of determining the oxidation kinetics of a metal is to measure the weight-change that occurs when a sample is exposed to an oxidizing atmosphere. Clearly, if two reactions are taking place, such as described above, then the weight-change measured is the difference between the gain due to oxygen pick-up and the loss due to metal escaping in the volatile oxide. The weight change may be predicted by utilizing Eq. [5] and [8]. With Eq. [8], the weight-gain arising from oxygen in the oxide can be accounted for, since the oxide thickness at a given time can be calculated. The weight loss, due to the metal contained in the volatile oxide, can be determined as a function of time, by integration of Eq. [5]. The difference between these quantities, that is, oxygen pick-up in Cr_2O_3 and Cr loss in CrO_3, is what is actually measured in a gravimetric experiment.

Application to Cr, Fe-Cr *Alloys, and Other Alloys Which Form* Cr_2O_3 *Scales*

Since the rate of loss of Cr_2O_3 by reaction [1] ought to be essentially independent of the source of Cr_2O_3, the oxidation kinetics of any alloy which forms an adherent, protective Cr_2O_3 scale will be influenced by the loss. This would include such alloys as the ferritic stainless steels which contain more than about 13% Cr (11, 12). Since both oxidation data (4, 13) and Cr_2O_3 evaporation data (3, 4) are available, the constants k_d, k_s, k_d', and k_s' may be evaluated as a function of temperature.

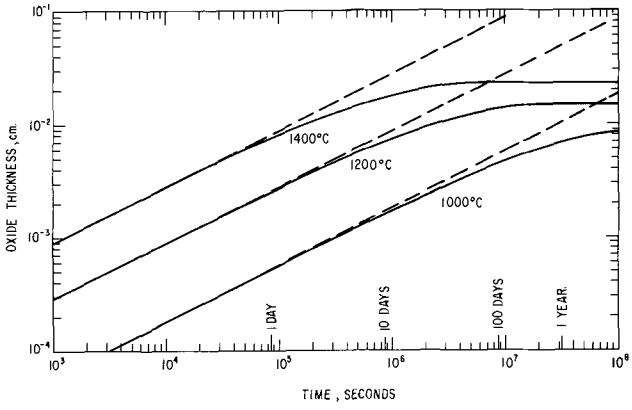

Fig. 1. Calculated oxide thickness as a function of time. The solid curves were calculated from Eq. [8]. — — — Parabolic kinetics.

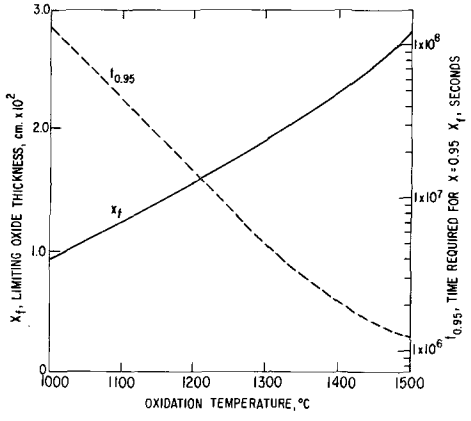

Fig. 2. Temperature dependence of the limiting oxide thickness and the time required for the scale to grow to 95% of its limiting thickness.

Rate of Growth of Cr_2O_3 *Scale.*—Using the data of Hagel (4) to determine the rate constants, Eq. [8] has been evaluated for various temperatures and is plotted in Fig. 1. The dashed lines show the expected growth assuming only parabolic kinetics. For short times, *e.g.*, $t < 10^5$ sec, the growth rate appears to be nearly parabolic. By 10^6 sec, however, significant departures from parabolic behavior are seen at all three temperatures. It is seen that the limiting oxide thickness increases with increasing temperature; however, with increasing temperature, shorter times are required to reach that limiting thickness. The temperature dependence of the limiting oxide thickness is shown in Fig. 2 which also shows the time required for the oxide scale to grow to 95% of its final value, as a function of temperature. By the time the thickness of the scale has reached this value, it is much less than the thickness expected from parabolic kinetics alone.

Metal recession rate.—Metal recession values as a function of time are presented in Fig. 3 for three temperatures. After about 10^7 sec at 1200°C, it is seen that the transformation to linear kinetics is essentially complete. Note that at 10^6 sec, or about 116 hr, the estimated metal-recession is about 20% greater than that expected from parabolic kinetics alone.

Weight-gain rate.—With Eq. [5] and [8], using the data from ref. (4), the net weight-gain (or loss) has been calculated as a function of time for a given temperature. The results of this calculation at 1200° and 1300°C are shown as solid lines in Fig. 4. The dashed curves indicate the weight gain that would be ex-

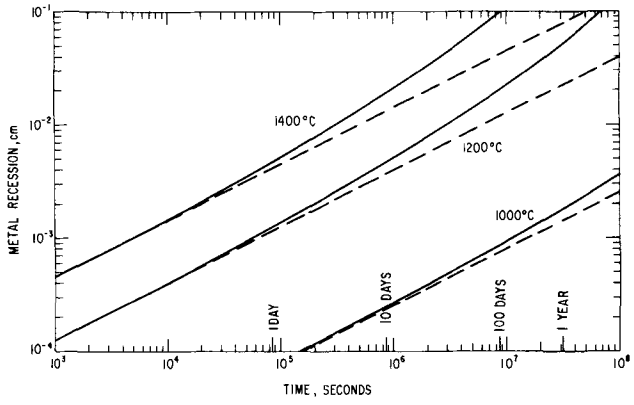

Fig. 3. Calculated metal-recession as a function of time. The solid curves were obtained from Eq. [14]. — — — Parabolic kinetics.

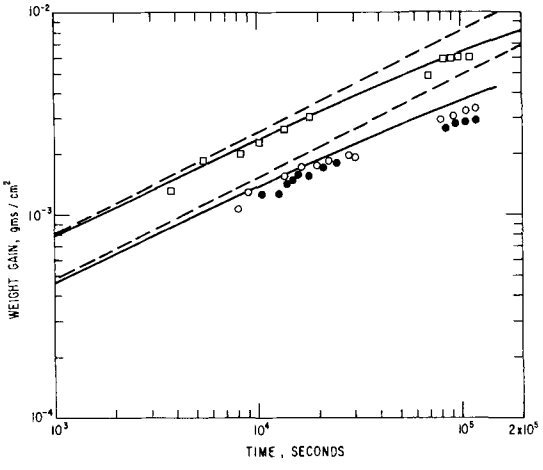

Fig. 4. Calculated and experimental values of weight-gain as a function of time, for short times. P_{O_2} = 100 Torr. □ Fe-70 w/o Cr, 1300°C; ○ Fe-45 w/o Cr, 1200°C; ● iodide Cr, 1200°C. — — — Parabolic kinetics; ——— corrected for loss.

pected from parabolic kinetics alone. Also presented in this figure are some oxidation data for three different alloys which form Cr_2O_3 scales, *viz*, Fe-70 w/o Cr, Fe-45 w/o Cr, and iodide-grade Cr. In spite of the scatter, the data are in good agreement with the calculated curves obtained from Eq. [5] and [8]. The departure from parabolic kinetics for these experiments is not large, because relatively short times are involved. If the data were interpreted in terms of parabolic behavior, the parabolic rate constants thus obtained would be essentially valid when interpreted in terms of ionic transport mechanisms (14, 15). Such data, however, are insufficient to describe the oxidation process fully, especially for extended times. This is shown in Fig. 5, which presents weight-change data for Cr which contained 0.2 w/o Y. This sample was oxidized at 1200°C for almost two weeks. The solid curve is the calculated weight-change evaluated from Eq. [5] and [8]. The dashed curve is the weight change expected from parabolic oxidation kinetics. The circles are experimental gravimetric data; the agreement between calculated values and experimental data may be considered to be quite good.

Summary

The oxidation behavior of Cr and alloys which form Cr_2O_3 scales cannot be accurately described by a parabolic rate law; the effects of a gas/oxide interface reaction, probably $Cr_2O_3(s) + 3/2\ O_2(g) \rightarrow 2CrO_3(g)$ must be recognized and taken into account.

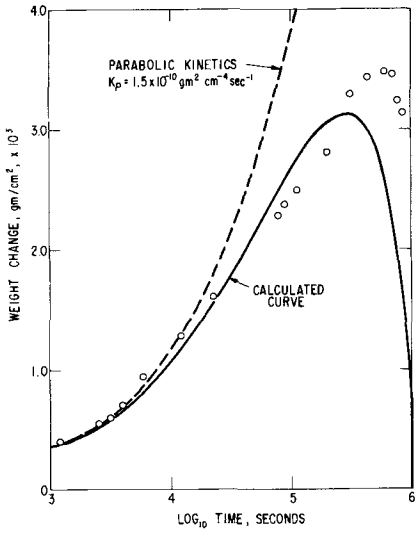

Fig. 5. Calculated and experimental values of weight-gain for extended oxidation. ○ Cr + 0.2Y alloy, 1200°C.

The effect of this surface reaction is to cause a transition from parabolic to linear oxidation kinetics. The oxide scale will grow to a limiting thickness; thereafter, metal-recession will proceed at a linear rate. Also, as the limiting value of oxide thickness is approached, gravimetric data will show departure from parabolic kinetics, and eventually weight loss will ensue at a linear rate. The interpretation of short-time oxidation data and estimated long-term oxidation performance will therefore be in error if based only on a parabolic rate law.

The equations presented herein, while applied to the specific cases of Cr and Cr-alloy oxidation, have completely general applicability to any scaling reactions involving processes possessing parabolic and linear kinetics.

Acknowledgment

Appreciation is extended to Mr. D. E. Broecker, who made the kinetic measurements and to many colleagues who contributed valuable discussion.

Manuscript received Feb. 8, 1966.

Any discussion of this paper will appear in a Discussion Section to be published in the June 1967 JOURNAL.

REFERENCES

1. D. Caplan and M. Cohen, *J. Metals*, **4**, 1057 (1952).
2. G. R. Wilms and Rea, *J. Less-Common Metals*, **1**, 411 (1959).
3. D. Caplan and M. Cohen, *This Journal*, **108**, 438 (1961).
4. W. C. Hagel, *Trans. ASM*, **56**, 583 (1963).
5. A. U. Seybolt, Private communication in ref. (3).
6. K. Hauffe and K. Pschera, *Z. Anorg. Chem.*, **262**, 147 (1950).
7. R. T. Grimley, R. P. Burns, and Mark G. Inghram, *J. Chem. Phys.*, **34**, 664 (1961).
8. J. Loriers, *Compt. rend.*, **231**, 522 (1950).
9. W. W. Webb, J. T. Norton, and C. Wagner, *This Journal*, **103**, 107 (1956).
10. C. E. Birchenall, "Metal-Gas Reactions," in "Kinetics of High-Temperature Processes," p. 277, W. D. Kingery, Editor, Technology Press/Wiley, New York (1959).
11. A. U. Seybolt, *This Journal*, **107**, 147 (1960).
12. E. J. Felten, *ibid.*, **108**, 490 (1961).
13. E. A. Gulbransen and K. F. Andrew, *ibid.*, **99**, 402 (1952).
14. N. F. Mott and R. W. Gurney, "Electronic Processes in Crystals," Clarendon Press, Oxford, (1955).
15. C. Wagner, "Diffusion and High-Temperature Oxidation of Metals," in "Atom Movements," ASM, Cleveland, Ohio (1951).

The High-Temperature Oxidation of Ductile Cr-Re Alloys

C. S. Tedmon, Jr.

General Electric Company, Research and Development Center, Schenectady, New York

ABSTRACT

The high-temperature oxidation behavior of ductile Cr-Re alloys containing 32 and 44 a/o (atomic per cent) Re has been investigated using thermogravimetric, metallographic, electron microbeam probe, and x-ray analytical techniques. The oxidation reactions taking place include the formation of a Cr_2O_3 external scale, a subscale, and volatile Re oxides. The Cr_2O_3 scale which forms on the Cr-32 a/o Re alloy is an effective barrier to loss of Re; on the Cr-44 a/o Re alloy, the Cr_2O_3 scale is quite porous, and Re loss as volatile oxide ensues, giving rise to linear kinetics. Air-oxidized samples showed essentially the same kinetics as samples exposed to oxygen; Cr_2N did not form.

Cr-Re alloys with Re concentrations near the bcc α-phase solubility limit possess good ductility and high strength (1-3). Since the use of Cr as a structural material has been limited historically by its lack of ductility at low temperature ($T<300°C$) (4-7), the discovery of the Re ductilizing effect has aroused increased interest in ductile Cr-base alloys. Although there is considerable interest in potential applications of Cr-Re alloys at elevated temperatures, an understanding of their oxidation behavior has been lacking.

Over the temperature range of 700°-1300°C, unalloyed Cr oxidizes with parabolic kinetics (8-11). The rate is primarily controlled by Cr^{+3} cation diffusion (8, 12, 13) although other factors such as surface preparation (11), oxide blistering (8, 11) and oxide evaporation (8, 11, 14) can alter the kinetics significantly. Caplan *et al.* have suggested that anion diffusion could also affect the kinetics (11).

The oxidation of Re has been studied by several investigators (15-17). Above about 600°C, linear rates of weight loss are observed due to the formation of volatile Re oxides, probably ReO_3 or Re_2O_7 (17).

The objectives of this investigation were to determine the oxidation behavior of ductile Cr-Re alloys and to identify the factors controlling the kinetics.

Experimental Procedure

Sample preparation.—The melt stock used for the alloys was iodide Cr (99.99%) and Re powder (Chase Brass, 99.99%). The Re powder was vacuum sintered in an electron-beam furnace prior to melting in order to reduce surface oxide and surface area.

The ductility of Cr-Re alloys increases with increasing Re content (3, 18), including Cr supersaturated with Re. Two compositions were studied, *viz.*, Cr-32 a/o Re and Cr-44 a/o Re. Both alloys were prepared by nonconsumable electrode arc-melting under purified argon. Chemical analyses of the alloys are presented in Table I. As prepared, both alloys were single phase, α-bcc structures. The solubility limit of Re in Cr, below about 1400°C, is 36 a/o; above this temperature the solubility increases to 50 a/o at 2280°C (19). The Cr-44 a/o Re alloy, as cast, was supersaturated with respect to Re. Metallographic examination and electron microbeam probe scans showed the alloys to be homogeneous. During oxidation runs at 1100°C and above, the Cr-44 a/o Re alloy transformed to a two-phase $\alpha+\sigma$ structure.

Kinetic measurements.—Samples for kinetic oxidation runs were prepared by cutting slices from the cast ingot, followed by polishing through No. 400 grit SiC paper. Specimens were typically about 4 cm^2 in surface area and about 0.01 cm thick. All samples were degreased and cleaned in toluene and acetone immediately before insertion into the spring-balance furnace.

Isothermal weight-change data were obtained using a quartz helical spring; the sample was hung on a sapphire rod which was connected to the spring. The system was evacuated and the furnace brought to temperature. The desired atmosphere was introduced and the run was commenced. All runs were carried out in a static atmosphere, either dry O_2 at a pressure of 100 mm Hg, or in dry air at 760 mm Hg. Specimen temperature was measured with a Pt/Pt-10 Rh thermocouple located in an Alundum tube, with its junction about ¼ in. from the center of the sample. Temperature control was about ±5°C at the highest temperature (1400°C) and ±2°C in the lower temperature range (1000°C and below). Weight change was determined by following a fiducial mark on the sapphire rod with a cathetometer. Conversion factors for the quartz springs were about 10^5 $\mu g/cm$. Readings were reproducible to about ±0.0005 cm giving a sensitivity of ±50 μg, or for a typical specimen, about ±15 $\mu g/cm^2$. After completing a run, the furnace was shut off and the system was evacuated.

As another means of following oxidation kinetics, isothermal metal-recession measurements were made on the Cr-44 a/o Re alloy as a function of time at 1300°C. The change in sample thickness was determined metallographically.

Auxiliary measurements.—The oxide scales were identified from Debye-Scherrer diffraction patterns. Electron microbeam probe studies of oxidized samples were carried out using a Cambridge Mark II unit.

Following the kinetic runs, oxidized samples were mounted and polished using standard metallographic procedures. Specimens which were to be examined in the microprobe were mounted in an electrically conducting base of copper-filled diallyl phthalate.

Experimental Results

The kinetic data for the Cr-32 a/o Re alloy are summarized in Fig. 1. The data from the 900°C run were quite erratic during the first few hundred minutes. At 1000°C, very little change in weight was observed. Samples run at 1200°, 1300°, and 1390°C exhibited weight gains, with rates decreasing with time, although not in a parabolic manner. The results from two runs at 1300°C are shown; the data represented

Table I. Chemical analyses of Cr-Re alloys
Spectrographic Analysis, w/o

	Bi	Sb	Mg	Al	Cu	Si	Fe	Ni	Ti	Co
Cr-32 a/o Re	0.0010	0.0070	0.0030	0.002	0.0015	0.020	0.040	0.025	0.010	0.0025
Cr-44 a/o Re	0.0006	0.0060	0.0050	0.0030	0.0015	0.0020	0.020	0.0035	0.0015	0.0020

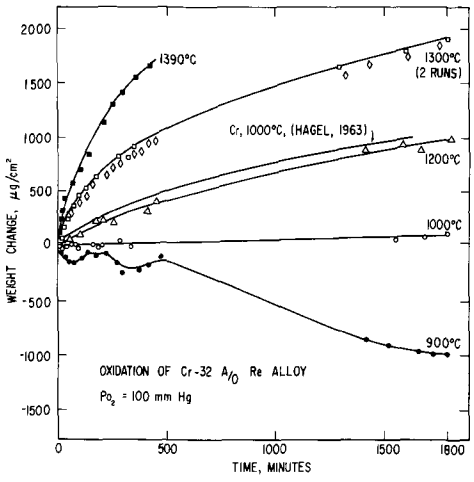

Fig. 1. Gravimetric oxidation data for Cr-32 a/o Re alloy at various temperatures.

by open squares are from a sample exposed to oxygen at 100 mm Hg pressure, and those shown by the open diamonds are from a sample exposed to air at a pressure of 760 mm Hg. Also included in this figure, for comparison, is a plot for pure Cr at 1000°C (8). From the weight-gain data, it would appear that at 1000° and 1200°C, the Cr-32 a/o Re alloy oxidized slower than pure Cr. As a check on this, metal recession measurements were made on these samples. Results are presented in Table II. The last column gives figures for the metal recession that would have occurred on pure Cr during oxidation under the conditions given in the first two columns. These values were calculated from the parabolic rate constant equation for Cr given in ref. (8), and converting weight-gain to metal recession. The metal recession values for the alloy were obtained by comparing the thickness of oxidized samples, as determined by photomicrographs of cross sections, with the original thickness. This is a rather inaccurate measurement, and it is further complicated by the presence of a subscale, as shown in Fig. 2. In determining metal recession, the presence of the subscale was ignored, and the sample thickness was measured from the metal/oxide interface. This means the values in the third column of Table II are somewhat optimistic in describing the extent of oxidation. In any case, it is clear from Table II that the gravimetric data presented in Fig. 1 do not fully describe the oxidation behavior of the Cr-32 a/o Re alloy.

Diffraction analyses of oxide scales from samples run at 1300°C and below showed only Cr_2O_3 to be present. No extra lines were observed, and the lattice parameters of the scales agreed with handbook values (20), within experimental error (±0.001Å).

For the sample oxidized at 1390°C, however, an expansion in lattice parameters was observed, with the a_o and c_o values increasing from 4.954 to 4.960Å, and 13.584 to 13.589Å, respectively.

Scans across oxidized samples with the electron microbeam probe showed a region of Re enrichment and Cr depletion in the metal adjacent to the metal/oxide interface. Figures 3a and 3b present schematically the intensity data for a sample oxidized at 1300°C for 30 hr. The amount of Re enrichment and

Table II. Metal recession on Cr-32 a/o Re samples

Oxidation temp, °C	Time of exposure, min	Observed metal recession, cm	Metal recession for Cr, cm
1000	1875	1×10^{-3}	0.3×10^{-3}
1200	1820	3×10^{-3}	1.4×10^{-3}
1300	1955	5×10^{-3}	2.7×10^{-3}
1300 (air)	1800	6×10^{-3}	2.6×10^{-3}

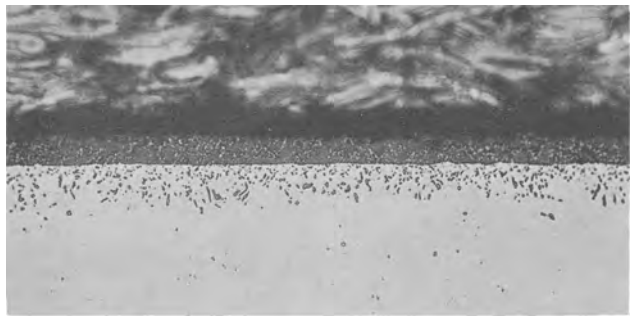

Fig. 2. Micrograph of Cr-32 a/o Re alloy after oxidation at 1300°C. Unetched. Magnification 500X.

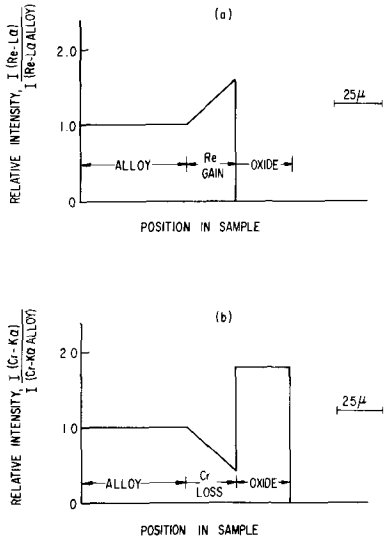

Fig. 3. Schematic presentation of electron microbeam probe scans on Cr-32 a/o Re alloy. (a) Re-Lα radiation; (b) Cr-Kα radiation.

Cr depletion increased with increasing temperature. For exposure at 900°C, for 30 hr, the Re-Lα intensity increased about 15% above the bulk value, with a corresponding decrease in Cr-Kα intensity.

Figure 2 is a photomicrograph of a cross section of a sample of the Cr-32 a/o Re alloy oxidized at 1300°C. The external Cr_2O_3 scale is quite dense and well-bonded to the metal. Adjacent to the external scale is a region containing a subscale; intermixed with the subscale are σ-phase particles, which precipitated out of the α-phase as the latter became depleted in Cr. X-ray diffraction results from samples taken near the surface showed only lines characteristic of the metal phases and Cr_2O_3. Therefore, it appears that the subscale is probably Cr_2O_3.

Cr-*44* a/o Re *Alloy*.—The gravimetric oxidation data for the Cr-44 a/o Re alloy are presented in Fig. 4 and 5. Figure 4 shows the weight changes that occurred during the first few hours of oxidation at various temperatures; behavior for extended periods of oxidation is shown in Fig. 5. The data are characterized by a period of rapid weight loss, which may tend to level out with time, depending on the temperature. The data for the 1200°C run, for example, appeared to level out after 300 min of oxidation (Fig. 4), but after 1200 min, there was further loss (Fig. 5).

The results of the isothermal metal-recession experiment are shown in Fig. 6. The open circles are measured values of metal-recession; the dashed line is the metal-recession extrapolated from the 1300°C gravimetric data. In making the calculation, a value of −100 $\mu g/cm^2/min$ was taken for the slope of the weight-change curve (Fig. 5). It was assumed that the weight-change was due only to Re loss; both

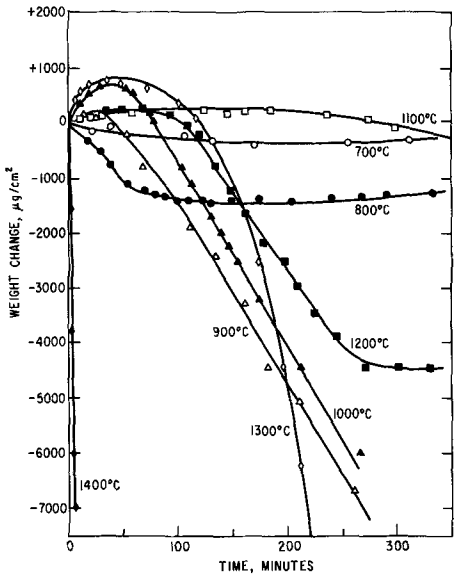

Fig. 4. Short-time oxidation behavior of Cr-44 a/o Re alloy at various temperatures: P_{O_2} = 100 mm Hg.

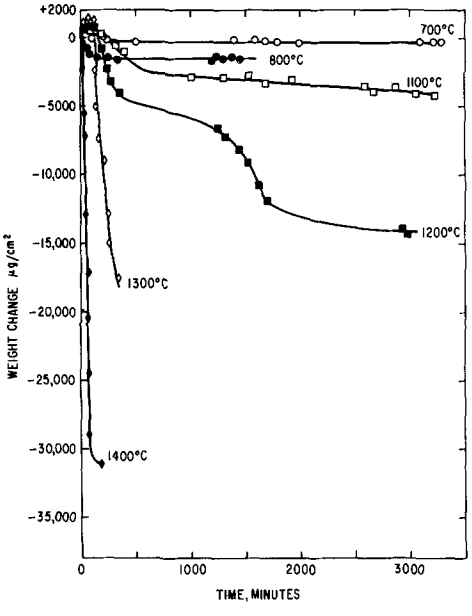

Fig. 5. Extended oxidation of Cr-44 a/o Re alloy at various temperatures. P_{O_2} = 100 mm Hg.

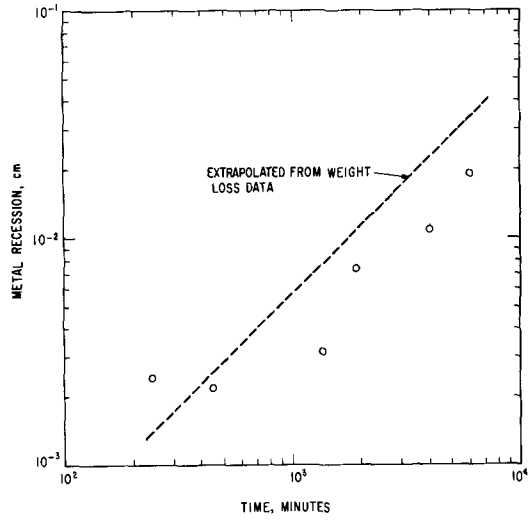

Fig. 6. Isothermal metal recession data for Cr-44 a/o Re alloy. Open circles are experimentally determined data; the dashed line is the extrapolated recession based on a linear rate of weight-loss of 100 μg/cm²min.

weight gain due to oxygen pick-up in Cr_2O_3, and weight losses due to Cr_2O_3 volatilization (8, 14) and metal vaporization were neglected. The density of the alloy is about 13.5 g/cm³. The largest error is in the first assumption; there is of course Cr_2O_3 formation which would tend to offset the weight loss from Re oxide volatilization. The extent of this error is about 20%. At 1300°C, the rate of Cr_2O_3 vaporization is about 2.2 μg/cm²/min (8). The vapor pressure of the alloy is not known. However, since the metal recession data lie within about a factor of two from the calculated curve, certainly the dominant factor influencing the gravimetric data is the rate of loss of Re from the alloy.

It is of interest to compare the rate of weight-loss of this alloy to that of pure Re. At 1300°C, the maximum rate of weight-loss of the Cr-44 a/o Re alloy is about 10^2 μg/cm²/min; pure Re at the same temperature oxidizes to give a linear rate of weight-loss of about 10^5 μg/cm²/min (17).

A few oxidation runs were made in air at atmospheric pressure. The weight-change kinetics were essentially the same as for specimens oxidized in pure oxygen at 100 mm Hg pressure.

X-ray diffraction analysis showed Cr_2O_3 to be the primary oxide product in the external scale. Diffraction results from a sample oxidized at 1400°C indicated that the presence of a small amount of another phase in addition to Cr_2O_3; its Debye-Scherrer pattern could not be indexed.

Electron microbeam probe scans were made on oxidized samples of the Cr-44 a/o Re alloy. The results were qualitatively similar to those obtained from the Cr-32 a/o Re alloy; that is, Cr depletion and Re enrichment occurred in the region adjacent to the metal/oxide interface.

The oxide scale which formed on the Cr-44 a/o Re alloy was adherent and did not spall. The scale was quite porous, as can be seen in Fig. 7(a) and 7(b), taken from a sample oxidized at 1300°C. This porous structure was typical for samples of this composition. The amount of porosity in the scale was somewhat temperature-dependent; at lower temperatures, the scale tended to be more dense. In addition to the porous Cr_2O_3 scale, there is a region of internal oxidation. The morphology of the internal oxide has been strongly influenced by the σ-phase which precipitated from the supersaturated α-solid solution. Metallograpic and x-ray data showed Cr_2N to be absent in samples oxidized in air.

Discussion

Comparison of the gravimetric data with observed metal-recession indicates that with both alloys there are two concurrent processes taking place: (*i*) oxidation of Cr to Cr_2O_3, and (*ii*) oxidation of Re to ReO_3 or Re_2O_7, both of which are volatile at the oxidation temperature (15-17). Since the Cr-32 a/o Re alloy showed weight gains in the gravimetric experiments at 1200°C and above, it appears that in this temperature range the external Cr_2O_3 scale acts as a barrier to further oxidation, and hence linear kinetics do not obtain. The scale is not fully protective, in the usual sense, since some Re loss occurs, as shown by the data in Table II. The formation of the volatile Re oxides could occur by Re diffusing through the Cr_2O_3 scale and reacting with oxygen at the oxide/gas interface, or by reaction with oxygen at the metal/oxide interface, where cracks and similar defects in the scale existed. Since no expansion in lattice parameter was observed, except at 1390°C, and since x-ray fluores-

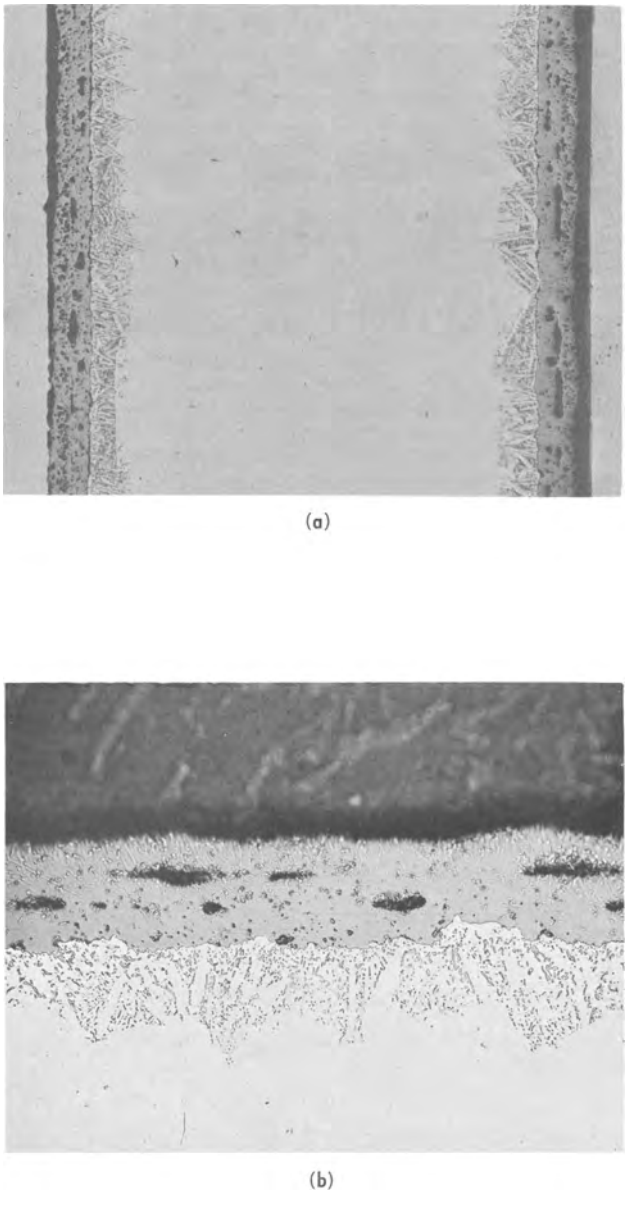

Fig. 7. Micrograph of Cr-44 a/o Re alloy, oxidized at 1300°C. Unetched. (a) Magnification 150X; (b) Magnification 500X.

cence analyses and microprobe scans showed no indication of Re in the Cr_2O_3 scale, there is very little evidence to support the first mechanism. More likely, it would appear that as the external scale grows, mechanical defects form, providing oxygen access to the Re-rich alloy at the metal/oxide interface.

When the Re content is increased to 44 a/o, the Cr_2O_3 scale becomes quite porous, as shown in Fig. 7. Although the scale thickens with time, Re loss continues, and the gravimetric data show weight-loss. The weight-change data indicate that at 1100°C and below, the oxidation rate decreased after several hundred minutes. At 1200°C, the sample showed an increase in rate after about 1000 min of oxidation, apparently due to a mechanical failure in the oxide. At 1300° and 1400°C, the rate of weight-loss was so rapid that the capacity of the spring-balance system was exceeded, after only a few hundred minutes of exposure. The metal-recession data presented in Fig. 6 show that at 1300°C, essentially linear kinetics prevail even after several thousand minutes of oxidation, and at about the same rate indicated from the gravimetric results. Again, as with the Cr-32 a/o Re alloy, the oxidation kinetics appear to be governed by the accessibility of oxygen to the metal/oxide interface.

The subscale which forms on both alloys is apparently Cr_2O_3. It has been suggested that the subscale first forms as a Cr-Re mixed oxide or suboxide, which is stable only in low oxygen partial pressures, converting to Cr_2O_3 and ReO_3 or Re_2O_7 on exposure to oxygen at higher pressures (21). There are however, no x-ray data to support this hypothesis.

The absence of Cr_2N is of interest. It has been postulated that the Re ductilizing effect is a consequence of reduced interstitial solubility (1, 22, 23). In further pursuit of this point, vacuum fusion analyses for total nitrogen content was performed on oxidized and unoxidized samples of the Cr-44 a/o Re alloy. The as-cast, unoxidized sample contained 11 ppm N_2. After oxidation for 28 hr at 1100°C in air, the N_2 content was 28 ppm. This latter figure includes the nitrogen content of the external Cr_2O_3 scale. The inability of Cr_2N to form is probably due to the reduced Cr activity in the Cr-Re alloys (21).

The identity of the volatile Re oxide was not established. During oxidation runs with the Cr-44 a/o Re alloy, a blue condensate formed in cool regions of the furnace, where the temperature was below about 200°C. Opening the system to the laboratory air after a run caused the condensate to become grey-brown. Attempts to identify this were unsuccessful. A blue modification of ReO_3 has been reported in the literature (24).

Conclusions

The oxidation kinetics of ductile Cr-Re alloys containing 32 and 44 a/o Re have been investigated. The oxidation reactions taking place include the formation of a Cr_2O_3 external scale, a subscale, and volatile Re oxides, probably ReO_3 or Re_2O_7.

The Cr-32 a/o Re alloy forms a Cr_2O_3 scale which is compact and adherent. Re loss, as a volatile oxide, takes place by mechanical defects in the scale, such as cracks. The 44 a/o Re alloy forms a porous external scale, which allows direct access of oxygen, resulting in essentially linear kinetics, at least at 1300° and 1400°C.

Air-oxidized samples showed essentially the same kinetics as samples exposed to oxygen; Cr_2N did not form.

Acknowledgments

Appreciation is extended to D. E. Broecker, who carried out a large part of the experimental work. Dr. W. C. Hagel provided much help and advice throughout the experimental program. The author also wishes to thank Dr. C. S. Wukusick, who supplied the Cr-32 a/o Re alloy, and Dr. D. H. Wilkins, who performed the chemical analyses of the alloys.

Manuscript received Feb. 18, 1966; revised manuscript received May 13, 1966.

Any discussion of this paper will appear in a Discussion Section to be published in the June 1967 JOURNAL.

REFERENCES

1. G. T. Hahn, A. Gilbert, and R. I. Jaffee, "Refractory Metals and Alloys II," p. 23. Interscience, New York (1963).
2. J. G. Booth, R. I. Jaffee, and E. I. Salkovitz, "Plansee Proceedings 1964," p. 547, Metallwerk Plansee AG., Reutte/Tyrol (1964).
3. C. S. Wukusick, General Electric Co., NMPO Report No. GEMP-314 (Nov. 1964).
4. A. Gilbert, C. N. Reid, and G. T. Hahn, *J. Inst. Metals*, **92**, 351 (1964).
5. R. E. Hook and A. M. Adair, *Trans. Met. Soc. AIME*, 227, 151 (1963).
6. K. E. Solie and O. N. Carlson, *ibid.*, **230**, 480 (1964).
7. A. H. Sully, E. A. Brandes, and K. W. Mitchell, *J. Inst. Metals*, **81**, 585 (1953).
8. W. C. Hagel, *Trans. ASM*, **56**, 583 (1963).
9. E. A. Gulbransen and K. F. Andrew, *This Journal*, **99**, 402 ((1952).

10. E. A. Gulbransen and K. F. Andrew, *ibid.*, **104**, 334 (1957).
11. D. Caplan, A. Harvey, and M. Cohen, *Corr. Sci.*, **3**, 161 (1963).
12. A. U. Seybolt, *This Journal*, **107**, 147 (1960).
13. W. C. Hagel and A. U. Seybolt, *ibid.*, **108**, 1146 (1961).
14. D. Caplan and M. Cohen, *ibid.*, **108**, 438 (1961).
15. C. Agte, H. Alkethum, K. Becker, C. Hegne, and K. Moers, *Z. anorg. u. allgem. Chem.*, **196**, 129 (1931).
16. C. T. Sims, C. M. Craighead, and R. I. Jaffee, *Trans. AIME*, **203**, 168 (1955).
17. W. L. Phillips, Jr., *J. Less-Common Metals*, **5**, 97 (1963).
18. C. S. Wukusick, AIME Conference on the Physical Metallurgy of Refractory Metals, French Lick, Indiana, Oct. 3-5, 1965, Proceedings in press.
19. E. M. Savitskii, M. A. Tylkins, and K. B. Pavarova, *Russ. J. Inorg. Chem.*, **4**, 873 (1959).
20. ASTM X-ray Powder Data File.
21. A. U. Seybolt, Private communication.
22. R. I. Jaffee, C. T. Sims, and J. J. Harwood, "Plansee Proceedings 1958," p. 380, Metallwerk Plansee A.G., Reutte/Tyrol (1958).
23. D. A. Robins, *Trans. ASM*, **52**, 943 (1958). (Discussion to paper of Sims and Jaffee).
24. K. B. Lebedev, "Rhenium," English translation: OTS Translation T.T. 64-31632, p. 38 (1964).

Microsegregation and the Tendency for Pitting Corrosion in High-Purity Aluminum

A. P. Bond,[1] G. F. Bolling, and H. A. Domian[2]

Scientific Laboratory, Ford Motor Company, Dearborn, Michigan

and H. Biloni[3]

Harvard University, Cambridge, Massachusetts

ABSTRACT

Single crystals of 99.99%, 99.999%, and 99.9999% Al have been grown from the melt under conditions controlled to produce either homogeneous solute distributions, or microsegregation (on the scale ~100μ) of the dominant residual impurities Fe, Cu, and Si. Exposure of samples to NaCl + H_2O_2 resulted in a fine-scale pitting of segregated specimens while homogeneous specimens remained free of such pits. Various mechanical and annealing treatments did not disturb this contrast and, in general, the pitting could be quantitatively related to a previous segregation study in these metals. Polarization measurements showed that the main effect of segregation is to produce a decrease in the cathodic overvoltage which shifts the corrosion potential into a range where pitting occurs. Since the two less pure grades exhibited segregation in the same size scale, and were relatively indistinguishable, it seems that the distribution, rather than the total amount of residual impurity, is more important in producing a tendency for pitting.

Severe microsegregation achieved under conditions of normal solidification in several grades of "pure" aluminum has recently been examined in detail by a combination of an anodic film technique used to locate areas of segregation, and the electron microprobe (1). With the results of this study in hand, it is possible to search for correlation between fine segregation and the initiation of pitting corrosion in purer metals. Although several types of segregation are possible as a consequence of solidification at high impurity levels, in the range of 10 ppm, the cellular substructure is most important. Since much original work and several reviews of the genesis and characteristics of this substructure are available [for example, Chalmers (2)], the following description can be taken as a brief review to accompany Fig. 1 and Eq. [1]

$$\frac{G_L}{V} < \frac{-m_L C_\infty (1-k_o)}{D_L k_o} = \beta \qquad [1]$$

Whenever solidification occurs with solute of concentration C_∞ in the liquid in a binary system of liquidus slope m_L, distribution coefficient k_o, and solute diffusivity in the liquid D_L, such that Eq. [1] holds in unidirectional solidification for growth velocity V, and temperature gradient in the melt G_L, a planar solid-liquid interface is unstable. Equation [1] has been termed the condition for constitutional supercooling; when it is exceeded in progressive degree, various kinetic substructures develop. Extreme conditions lead to dendritic growth but over quite a large

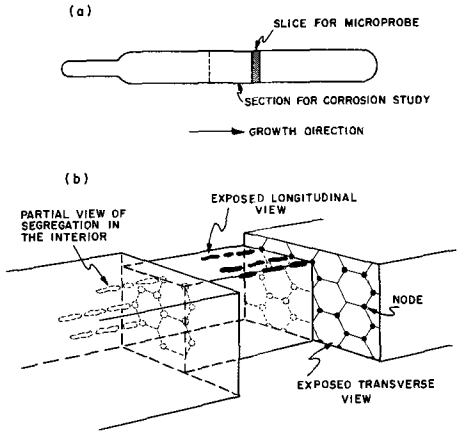

Fig. 1. Schematic diagram showing (a) the location of the samples studied in the as grown crystal and (b) an enlarged (about 100 times) representation of the segregation developed in the cellular substructure. Note that since the regions of high impurity concentrations are discontinuous, a transverse section will not intersect a highly segregated area at every junction of cell walls.

[1] Present address: Climax Molybdenum Company of Michigan, Ann Arbor, Michigan.

[2] Present address: Babcock and Wilcox, Alliance, Ohio.

[3] On leave from and now at Comision National de Energia Atomica, Buenos Aires, Argentina.

Table I. Suppliers impurity analyses

Element	Impurities ppm Al 493		Al 593	ZR
Fe	20		2	~0.3
Cu	30		1.5	0.2
Si	<10		4	~0.3
Mg	10		<1	0.2
Zn	10		<1	—
Al	—	Balance	—	—

range (3-6) of imposed growth conditions the segregated structure is as depicted in Fig. 1. After solidification is complete there may be a hexagonal net of segregation extending in the direction of crystal growth but it only appears certain that pronounced segregation occurs at nodes, as the junctions of three cell boundaries have been called. The exact configuration of solute in the nodes depends on the solute concentration level and other parameters contained in β; comparative studies have been made in the system Sn-Pb (7-9). At the low concentration levels, which are the most critical test, the nodes display extended, but noncontinuous regions (prolate spheroids), that may be enhanced in concentration by orders of magnitude above C_x. As a result, for many systems such an enhancement must lead to a second phase, that may be quite complex if several residual solutes are concerned in a pure metal, and as solubilities decrease nearer to room temperature, these segregated areas can prove to be indefinitely stable.

Aluminum single crystals already examined quantitatively for the segregation of Fe, Cu, and Si were available for corrosion studies (1). The average quoted purities of the aluminum used are given in Table I. Except for the ultra-pure, zone-refined aluminum, it turns out that segregation can be induced or inhibited at will by manipulation of the growth conditions in Eq. [1]. Thus the zone-refined aluminum which is pure enough to be beyond the range of cellular segregation under normal crystal growth provides an important control and contrast.

Experimental Procedure

In the preceding study, ⅛-in. thick slices were removed approximately halfway along the length of 5 in. crystals of half-inch-square cross section for microprobe study (1). Specimens for corrosion study were taken immediately adjacent to these slices from the single crystals of the two purity levels grown at 1 and 60 cm/hr. The following designation is used: 493-1, 593-1, 493-60, 593-60, and ZR for the 99.993% Al grown at 1 cm/hr, etc., and for the zone-refined aluminum. Investigation of Eq. [1] and Table I shows that the cellular substructure should not appear at the slow growth rate for 493 and 593 nor at all in ZR, but should be present in the other two samples. This was indeed the case (1).

Thus, two sets of samples were available of identical impurity content, differing only in the distribution of impurities. This difference in distribution was revealed by anodizing in sulfuric acid for a short time producing an oxide film whose thickness varied with the nature of the underlying metal, thus giving rise to interference colors that revealed the nodes in the cellular sample (10, 11, 1). Figure 2 shows monochrome prints made from photomicrographs obtained from cellular and noncellular samples of the same composition.

Samples for corrosion study were prepared for all tests by electropolishing in a mixture of two parts acetic anhydride and one part perchloric acid, cooled below 20°C. Several hours at an applied potential of 30v was required for a satisfactory polish, free of pits.

All pitting measurements were carried out by exposing the polished aluminum to 0.5M NaCl containing 0.3% H_2O_2 for 200 min. The *p*H of this solution ranged from 5.6 to 6.0. Cathodic polarization measurements were made galvanostatically in the same solutions. Potential readings were made 1 min after switching on the desired current. Potentiostatic anodic polarization measurements were made in 0.5M NaCl deaerated with nitrogen. Current readings were made 5 min after setting the desired potential.

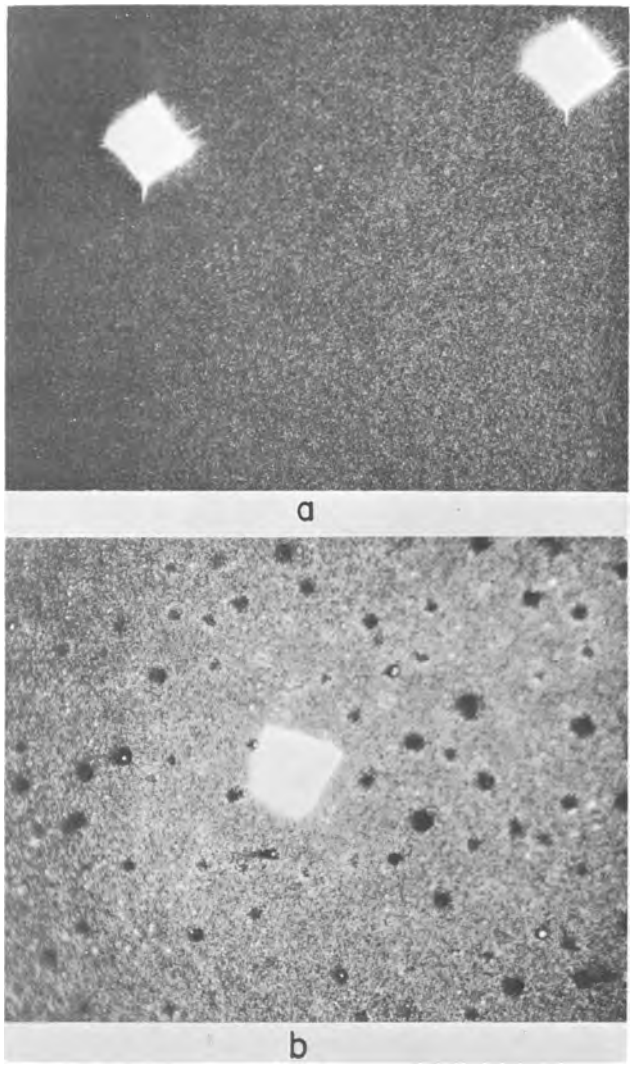

Fig. 2. Anodically filmed aluminum (a) 493-1 (noncellular) and (b) 493-60 (cellular); fiducial marks are visible. Magnification 120X.

Results

Pitting tests.—Exposure of the as-grown specimens in the NaCl-H_2O_2 pitting solution produced pronounced fine-scale pitting in the cellular samples, as shown in Fig. 3, but had little or no effect on the specimens having the more homogenous distribution of impurities (*i.e.*, noncellular). It appears that there is little difference apart from pit size, when pits are visible, in the behavior of the 493 and the 593 samples. This indicates by comparison for the two ranges of impurity levels that the total amount of impurity is less important than the impurity distribution. The ZR aluminum, which has too low an impurity content for development of the cellular structure was not detectably affected by exposure to the pitting solution for periods up to 260 hr.

In order to examine the effect of mechanical and thermal treatments on the behavior of these specimens, samples were cold rolled parallel to the crystal growth direction to 75% reduction in thickness and examined in the as-rolled condition as well as after annealing 1 hr at 200°C or 25 hr at 600°C. Both the as-rolled specimens and the specimens annealed at 200°C retained the pitting characteristics and pit density of

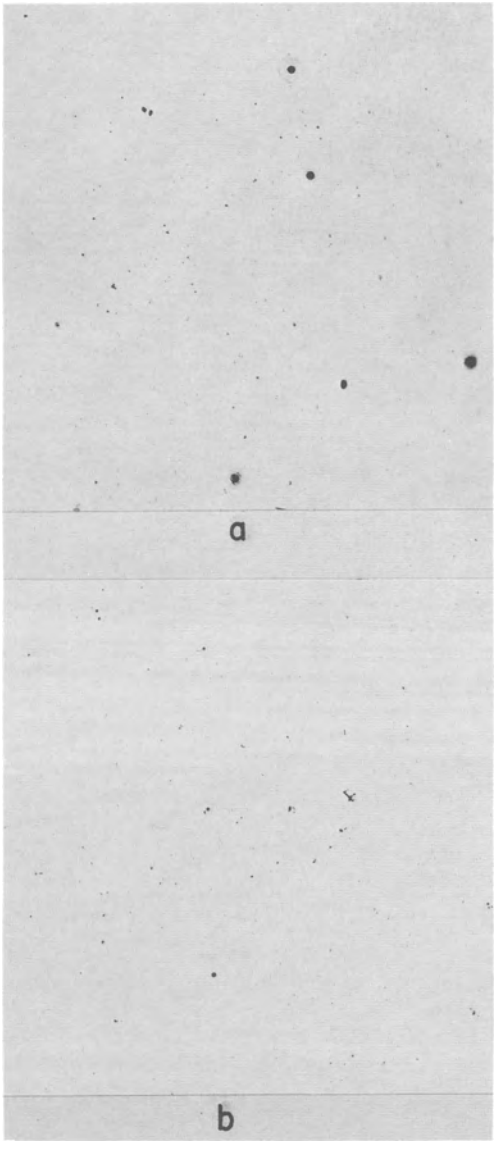

Fig. 3. As-grown aluminum samples exposed to 0.5M NaCl + 0.3% H_2O_2 for 200 min. (a) 493-60; (b) 593-60. Magnification 120X.

the original crystals while the originally noncellular Al remained free of pits after these treatments. This result is not surprising since at these low temperatures diffusion of the principal impurities, iron or copper, over appreciable distances is not possible. The 24-hr anneal at 600°C did affect the behavior somewhat. The pits on the cellular samples became smaller, but more numerous, while very small pits were apparent on the less pure noncellular sample, 493-1. At this temperature there is appreciable solubility of iron and copper in aluminum, and during the anneal sufficient diffusion apparently could take place to redistribute the impurities; however, no pronounced pitting was noted for sample 593-1 after 24 hr at 600°C, indicating that at this low impurity level the driving force for redistribution was too small to produce a noticeable effect in the time allowed.

Finally an attempt was made to extend this examination of the initiation of pitting to the stage of more well developed pits. Samples of 493-1 and 493-60, cold rolled, and cold rolled and aged at 200°C, were exposed for 260 hr to the pitting solution. The over-all contrast between the cellular and noncellular specimens was preserved, although all the specimens exhibited two or three small isolated areas of severe attack (per square centimeter). The pits observed in the 493-60 were generally distributed about as shown in Fig. 3, but were increased nearly five times in diameter after this longer exposure. In contrast, the 493-1 remained free of pits except in the isolated areas mentioned. Since these tests of the worked single crystals and the low temperature recrystallized polycrystals are closer to corrosion practice than those possible on single crystals, there seems to be a basis for attributing a tendency for pitting corrosion to microsegregation.

Electron microprobe results.—Although the preceding results are indicative, they do not establish that the fine-scale pits are definitely associated with the cellular nodes. To do this, two tests were undertaken in 493-60. First a simple counting technique with about 90% reliability showed a density of 165 pits/mm^2 after corrosion compared to 150 nodes/mm^2 before corrosion. Even though this difference is within the experimental error of the pit density determination, a higher number could be expected after pitting since progressive corrosion might reveal regions unaffected previously.

The second test consisted of a microprobe analysis undertaken on 493-60 after pitting. The same technique reported previously (1) was used here, with the exceptions, that an electron beam of 25μ diameter was necessary because of the pitted surface, and that the analysis was limited to the most important element, iron. As a further step, the pitted sample was reanodized to aid in the location of segregated areas and reanalyzed with the electron microprobe. The three analyses are given in Table II. The correlation is better than it appears. The fact that about half the pits as corroded, no longer exhibit high impurity concentration does not necessarily mean that they are not located at or adjacent to node sites. It is quite likely that in the corrosion process the local high impurity concentrations are being destroyed. This is indicated by the increased significance in locating high iron concentration after reanodization.

Polarization measurements.—The results of anodic polarization measurements on these samples, given in Fig. 4, do not show any significant differences for all the samples investigated, but do show a sharp change in anodic current as the potential is shifted from —0.75 to —0.70v *vs.* SCE. A similar result has been

Table II. Microprobe analysis for Fe on sample Al 493-60

Beam‡ diam, μ	Highest conc observed	Avg node conc	Avg cell conc	Avg diff.	Supplier's analysis	Null sig. of difference	Population p, %
			ppm				
Previous results [ref (1)]							
Anodic film on 20	1720	490	−60	550	20	0.1	70
Anodic film off 20	1790	540	30	510	20	1.8	30
As corroded, on pits 25	1220	170	0	170	20	4	60
Corroded and reanodized 25	2440	150	20*	130	20	0.1	75

* 20 ppm is about the detection limit; thus a value, −60, is not surprising.
‡ The results for a 25μ beam must be lower than for a 20μ beam.

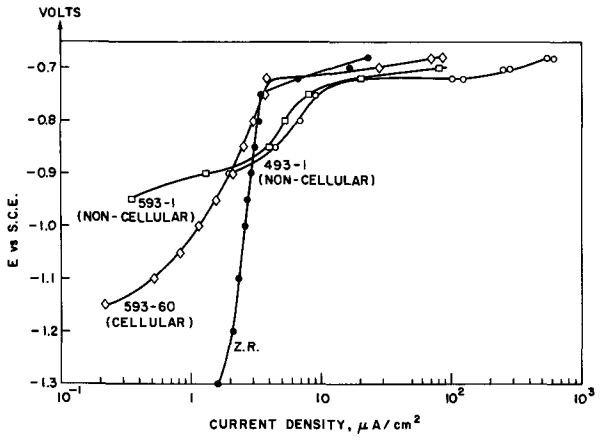

Fig. 4. Anodic polarization curves obtained in deaerated 0.5M NaCl.

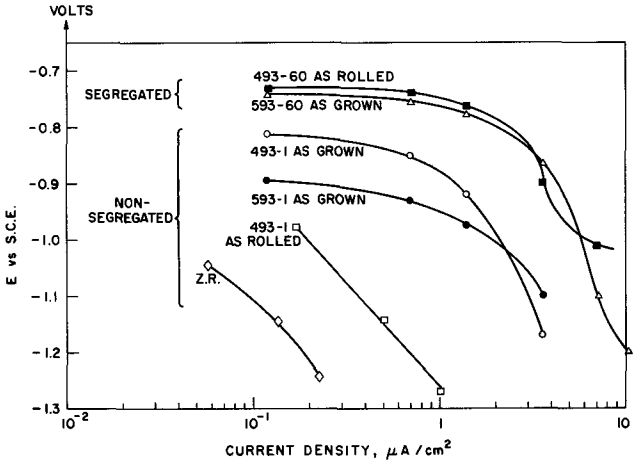

Fig. 5. Cathodic polarization in 0.5M NaCl + 0.3% H_2O_2

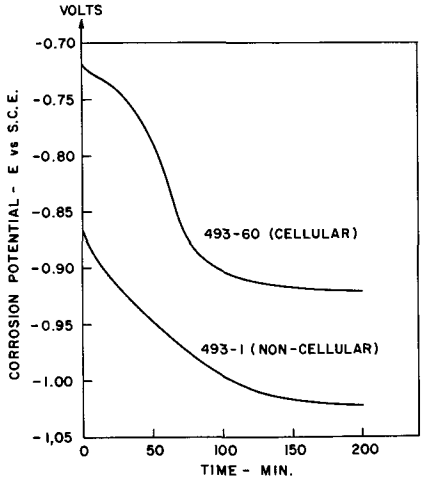

Fig. 6. Typical corrosion potential-time plots for cellular and noncellular samples.

reported by Kaesche (12). The current fluctuates at potential more noble than about —0.72v. This rise in anodic current corresponds to the onset of pitting as can be demonstrated by holding electrodes of zone-refined aluminum in nitrogen saturated 0.5M NaCl at —0.75 and at —0.73v for 90 min; no pitting occurred at —0.75v while definite pitting was observed after holding at —0.73v.

The potential at which pitting first occurred was quite reproducible, but the magnitude of the anodic current at potentials more active than the pitting potential was variable and time dependent, so that no great significance can be attached to the current variation from sample to sample below the pitting potentials. However, it is not surprising that at the more active potentials the zone-refined sample shows the highest anodic currents since the current plotted is the applied current and does not include the contribution of local action corrosion currents. This local action current would be expected to be smallest on the highest purity aluminum while making an important addition to the true anodic current on the less pure samples at the most active potentials investigated.

In the absence of chloride, no pitting occurred in 0.5M Na_2SO_4 even at potentials much more noble than —0.73. This is in accord with the known anodizing characteristics of aluminum in sulfates.

On the other hand, the cathodic polarization characteristics of these samples were strongly affected by impurity content and distribution. Figure 5 gives results of cathodic polarization in 0.5M NaCl + 0.3% H_2O_2. It can be seen that the cellular samples have the lowest cathodic overvoltage at all current densities while the zone-refined aluminum has the highest. From this it must be concluded that the impurity concentrations at nodes provide very favorable sites for the cathodic reaction, presumably reduction of H_2O_2.

It must be noted for strictness, that these results presented in Fig. 5 are not steady-state measurements. In fact, a steady state would require days for establishment. However, it was found that reproducible measurements could be made by placing the electrode in the electrolyte, waiting 5 min on open circuit, then applying the lowest desired current for 1 min, proceeding to the next current, and so on. In this way the measurement can be made before pitting alters the surface of the cellular samples a great deal. Exposure of the cellular sample for long periods led to an increase in the cathodic overvoltage, most probably due to the destruction by pitting of the most active cathodic sites.

Corrosion potential measurements were also made on these samples as a function of time. Figure 6 shows typical results for a cellular and a noncellular aluminum. The potential of the cellular sample starts out near the region indicated by the anodic data to be the area where pitting occurs. The drift of the corrosion potential in the active direction can easily be explained by supposing the destruction of some of the active cathodic node sites as pitting proceeds. (This is consistent with a decreased number of iron rich pits or nodes as shown in Table II.) The corrosion potential of the nonsegregated aluminum remains considerably more active than the pitting potential right from the start of the run. Table III shows the corrosion potential measured 5 min after immersion of the specimen for the types of samples investigated. It can be seen that all the cellular specimens exhibit potentials close to the pitting potential while all the noncellular samples, except 493-1 annealed at 600°C, have potentials much more active than the corrosion potential. The noncellular sample 493-1 annealed at 600°C did pit to some extent so it appears that the

Table III. Corrosion potential vs. SCE 5 min after immersion in 0.5M NaCl + 0.3% H_2O_2

Sample	Condition			
	As grown	As rolled	1 hr 200°C	24 hr 600°C
493-1	−0.86	−0.99	−0.88	−0.75
493-60 (cells)	−0.73	−0.74		−0.74
593-1	−0.88	−0.85		−0.84
593-60 (cells)	−0.74	−0.75	−0.74	−0.75
ZR	−0.96			

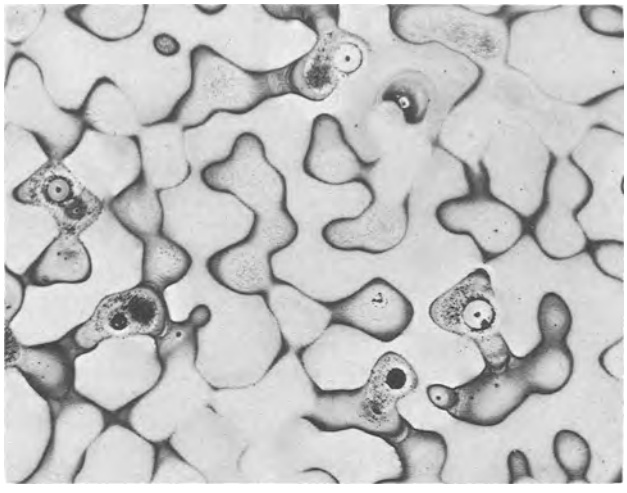

Fig. 7. Specimen from a crystal exhibiting cellular substructure taken just behind a decanted interface and exposed 200 min in 0.5M NaCl + 0.3% H_2O_2.

corrosion potential is a reliable indicator of the pitting tendencies of these materials.

Discussion

It is useful to point out that most solidification studies of the cellular substructure have involved observations of the decanted (13) solid-liquid interface. However, as often pointed out, the segregation at a decanted solid-liquid interface is not representative of the steady-state segregation created in a completely solidified crystal. That is, a remnant liquid clings to the decanted interface and freezes rapidly, leading to a more extreme segregation. Therefore, although such studies have been useful in generating an understanding of cellular segregation, a study of decanted interfaces is not germane here. This is emphasized by comparing Fig. 7, a decanted interface of 99.99% Al grown cellularly and corroded similarly to Al 493-60, with Fig. 2 and 3. Indications of cell walls as well as nodes and a more extreme and complex pitting is clearly evident in the singular case of Fig. 7.

The present study of microsegregation and the initiation of pitting corrosion has thus been limited to prepared sections of completely grown crystals. It is possible to conclude that preparation techniques such as cutting and polishing must have had little effect, when it is considered for example, that rolling and lower temperature anneals did not alter the contrasts between cellular and noncellular specimens.

At another point it is possible to question the preparation procedure. The anodic film on aluminum is not homogeneous; otherwise, the location of excess impurity would not be possible. The following observation has been made many times: at the beginning of anodization, a surface viewed under white light first appears to exhibit a blue color, whereas those regions eventually to be recognized as nodes are still colorless. As anodization proceeds, node-free areas progress in the sequence blue-green-red-blue while nodes lag behind as colorless-blue-green-red. A closer investigation might reveal interposing colors elsewhere in the spectrum, but this general observation indicates that the oxide film is thinner in a region of impurity segregation (14). For completeness, we note that the samples examined here were not controlled to have standard oxide films. This must be especially true since materials of two purities were used, and from observation it was noted that more than one sequence of passage through the color spectrum could sometimes be observed.

It is possible to speculate on the effect of impurity concentration on the properties of the protective oxide film. The thinner film near nodes could be an indication that incorporation of the impurity metals in the aluminum oxide leads to a decrease in electronic resistivity. If this effect is carried over in the film formed in the corrosion environment, it is reasonable to correlate improved electronic conductivity with an increase in the cathodic reduction reaction velocity. It is also possible that the oxide film in the regions of high impurity concentration remains thin enough for electron tunneling to occur, thus facilitating the electron transfer involved in the cathodic reaction.

Previous studies have shown that impurities affect corrosion (15-18). However, there is no apparent prior indication that a distribution of impurities in single crystals at such minor levels as those investigated here can be important. An elementary knowledge of solidification processes forces the conclusion that cast materials of the purity level 99.99% or less must all be subject to the same segregation as studied here, unless uncommon precautions are taken. Moreover, since the mechanical and lower thermal treatments undertaken were of no appreciable affect in altering corrosion characteristics, the dominant segregation of iron must be expected to persist in these metals even after treatments subsequent to casting. The correlation with solidification characteristics is emphasized by the unchanged nature of pitting corrosion even as purity level is changed after short-time exposures to the pitting reagent. However, since the 260 hr exposures can also be argued to be "short-time," a correlation between the fine scale and massive pitting must really be deduced not concluded. This is nevertheless reasonable if the observations of Edeleanu and Evans (19) are accepted, *i.e.*, small pits tend to grow, or the pitting corrosion in aluminum is autocatalytic.

The experimental results of the exposure to a corrosive environment are at least a confirmation of the existence of severe microsegregation in aluminum of purity as high as 99.999% after certain growth conditions, and do show a correlation between this segregation and the tendency for pitting corrosion in aluminum. In particular, concentration of iron and copper at nodes in the cellular substructure reduces cathodic overvoltage sufficiently to bring the corrosion potential to the critical value at which chlorides lead to pitting corrosion. That these impurities exert a strong effect on cathodic overvoltage is not unexpected since Hansen and Wetmore (15) have interpreted their work on the hydrogen overpotential on aluminum on this basis. However, the present work does demonstrate that the distribution, rather than the total amount of residual impurity seems more important at very low impurity levels.

Manuscript received Aug. 9, 1965; revised manuscript received Feb. 14, 1966. This paper was presented at the Buffalo Meeting, Oct. 10-14, 1966.

Any discussion of this paper will appear in a Discussion Section to be published in the June 1967 JOURNAL.

REFERENCES

1. H. Biloni, G. F. Bolling, and H. A. Domian, *Trans. AIME*, **233**, 1926 (1965).
2. B. Chalmers, "Principles of Solidification," John Wiley & Sons, New York (1964).
3. W. A. Tiller and J. W. Rutter, *Can. J. Phys.*, **34**, 96 (1956).
4. T. S. Plaskett and W. C. Winegard, *ibid.*, **38**, 1077 (1960).
5. F. Weinberg, *Trans. AIME*, **227**, 223 (1963).
6. J. Bartel, J. Kunge, and R. Scharfenberg, *Phys. Stat. Sol.*, **6**, 529 (1964).
7. J. J. Kramer, G. F. Bolling, and W. A. Tiller, *Trans. AIME*, **227** (1963).
8. H. Biloni and G. F. Bolling, *ibid.*, **227**, 1351 (1963).
9. H. Biloni, G. F. Bolling, and G. S. Cole, *ibid.*, **233**, 251 (1965).
10. P. Lacombe and M. Mouflard, *Metaux* (Corrosion-Ind.), **34**, 471 (1953).
11. H. Biloni, *Can. J. Phys.*, **39**, 1501 (1961).

12. H. Kaesche, *Z. Phys. Chem. F. F.*, **26**, 138 (1960).
13. C. Elbaum and B. Chalmers, *Can. J. Phys.*, **33**, 196 (1955).
14. B. Chalmers, "The Physical Examination of Metals," E. Arnold and Co., London (1939).
15. D. J. Hansen and F. E. W. Wetmore, *Can. J. Chem.*, **34**, 659 (1956).
16. G. Wyon and P. Lacomb, Defects in Crystalline Solids—Report of 1954 Bristol Conference, The Physical Society, London, p. 187.
17. F. Montariol, *Corrosion Anticorrosion*, **6**, 101 (1958).
18. R. Bakish, R. J. Kornhaas, and E. Z. Borders, *Electrochem. Technol.*, **1**, 358 (1963).
19. C. Edeleanu and U. R. Evans, *Trans. Faraday Soc.*, **47**, 1121 (1951).

Chemical Nickel-Iron Films

A. F. Schmeckenbecher

Systems Development Division, International Business Machines Corporation, Poughkeepsie, New York

ABSTRACT

Ferromagnetic films, useful for computer applications, have been deposited from a modified Brenner bath by chemical reduction using hypophosphite. The deposits contain about 25% iron, 1-0.5% phosphorus, small amounts of oxygen, carbon, etc. The balance is nickel. The films are well suited for memory applications because of their high creeping threshold and their fast coherent rotational switching. The effects of certain plating parameters on the properties, in particular on the magnetic properties, are discussed.

Nickel films have been deposited on active surfaces by reduction with hypophosphite (1, 2). The technique is widely used mainly because films of uniform thickness and special properties can be deposited on intricately shaped surfaces. Adding an iron salt to the alkaline nickel plating bath under certain conditions results in a nickel-iron alloy deposit. Electroless deposition of nickel-iron alloys seems to have been investigated to a relatively small extent (3-5). Little is known about the properties, in particular the magnetic properties, of such films.

The mechanism of reduction of nickel alone has been discussed in detail (6-8). When plating a nickel-iron alloy, the situation is complicated by the fact that different types of complexes are involved. The nickel ions are mainly bound to nitrogen in an ammonia complex while the iron mainly is bound to oxygen in a chelate (tartrate, citrate, etc.). Also, while the iron is reduced directly from its bivalent state (ferrous ion) to the metal, it can be introduced into the bath in its trivalent state. Therefore, equilibria between both the ferrous, ferric, and nickelous ions and their complexes would have to be considered. Also insoluble compounds such as nickel hydroxide and basic tartrate, etc., may form at *p*H values between 8.5 and about 7 in the deposition zone and might be incorporated in the film. Plating parameters such as temperature, pressure, *p*H value of the plating solution and concentration of bath constituents affect the deposition mechanism and as a consequence the composition and properties of the deposits. For instance, when the *p*H value of the bath is increased from 8 to 11 by adding ammonia, less nickel ions become available for reduction. The iron content of the deposit increases. Similarly, at high *p*H values the deposition of phosphorus, which has hydroxyl ions as a by-product, is slowed down. The phosphorus content decreases.

For the purpose of this discussion we consider the effect of the thickness of the deposit, of the ratio of nickel to ferrous ions, and of the metal and hypophosphite ion concentrations on the composition and properties of the deposits.

Plating Technique and Effect of Plating Time on Film Properties

We plated on beryllium-copper sheets, which had been activated by dipping in a 0.1% palladium chloride solution. The surface being plated was between 2 and 12 in.^{2}/liter of plating bath. The plating bath was newly made up and heated in a water bath to 75°C. The bath was not agitated during plating. A typical plating bath contains 56 mM/liter Ni^{++} as nickelous chloride, 20 mM/liter Fe^{++} as ferrous ammonium sulfate, 100-350 mM/liter sodium potassium tartrate, 10 g/l or 94 mM/liter sodium hypophosphite, and 3.6 mols/liter ammonia.

The potential during plating measured against a saturated calomel electrode was —1.01v. Taking the calomel electrode potential at 75°C as —0.211v, the deposition potential was —0.799v. The potential was measured on a relatively large substrate. If the area being plated is smaller than about 0.1 mm^2, fluctuations of the potential by about 10-15 mv are observed, which occur with a frequency of about 3 per min. Agitation of the bath lowers both the potential and the plating rate: while in baths containing nickel only, agitation increases the potential and plating rate.

The deposits were analyzed for iron and nickel by dissolving them in hydrochloric acid and comparing the intensity of x-ray fluorescence of the solution with standard nickel and iron solutions. The accuracy of the method is within ±3% of the values.

The phosphorus content was determined colorimetrically by the "Heteropoly method," with a precision of ± 15%. Also, radioactive hypophosphite was used in one experiment, with P^{32}, giving a phosphorus content about 30% higher than the colorimetric method. In the charts the colorimetric figures are given. Samples of the deposits were flash heated to 5000° in vacuum; gases set free were qualitatively identified in a mass spectrograph.

For thickness determination, the deposits on a known area were weighed directly, or the weight was determined by the x-ray fluorescence method, and using a density figure of 8.4 g/cm^3 the thickness was calculated. Also, microsection techniques were used to check the thicknesses. The thickness is 10-15% higher with the microsections. In the charts the data obtained with the x-ray fluorescence method are given.

The deposits contain 25% iron, 0.5-1% phosphorus, small amounts of hydrogen, carbon monoxide, oxygen, water, and nickel. Within the first 25 min of plating, in a newly made up bath, very little change of potential, plating rate, or iron content beyond the precision of the analysis was observed. The absorption of the bath of ultraviolet and visible light (at 285 mμ and 575 mμ) did not change within the first 30 min. Changes beyond a plating time of 30 min depend on the ratio of surface being plated to the bath volume and are probably due to consumption of hypophosphite, oxidation of ferrous to ferric ion, and other changes in the bath.

After plating, the films were kept at room temperature for at least 24 hr, without further treatment. Changes occurring with time and temperature are not being discussed here.

The deposits up to about 1000Å thickness are silvery in appearance with a high reflectance (as measured on a Bausch and Lomb "Spectronic 20" spectrophotometer at 525 mμ with a reflectance attachment). When the deposits become heavier, they get a golden brown tinge. On rolled beryllium-copper the thinnest deposits (500-100Å) had a reflectance of about 45% of the magnesium carbonate standard. With increasing thickness of the deposits, the reflectance decreased to level off at 10,000Å to a value of about 30% of the magnesium carbonate standard. Electromicrographs of the surface of deposits of various thickness show an agglomeration of balls, the size of which increases with increasing thickness up to 10,000Å, then levels off to a constant value of about 1000Å diameter (Fig. 1 and 2). Micro-cross-sections of the films show both a columnar and laminar structure similar to the structure known for chemical nickel deposits (1, 10). X-ray data (line broadening technique) indicated a crystallite size in the order of 200-300Å. The sheet resistance of 10,000Å thick films plated on glass and measured using spring loaded metal contacts is about 50 μohms-cm as compared to about 18 μohms-cm for bulk nickel-iron alloy (11). When plated, the films are under considerable tensile stress, which at 10,000Å reaches a value of about 30,000 psi.

For the magnetic measurements, the films were deposited on 3-in. long beryllium copper strips of about 4 mils by 2.5 mils cross section. The strips were photoetched out of beryllium-copper sheet of 2.8 mils thickness. An orienting field of 40 oe was applied along the long axis of the strips during deposition.

The coercive force (H_c) and anisotropy field (H_k) were measured on a 60 cycle BH loop tester, by the usual methods. It is understood that the anisotropy field is a function of the shape of the material. The data are given for the described configuration.

Figure 3 shows that above 10,000Å thickness, the coercive force (H_c) and anisotropy field (H_k) are fairly constant; going below 10,000Å, the coercive force increases rapidly.

Fig. 1. Nickel-iron film 4000Å-thick. Magnification ca 49,000X

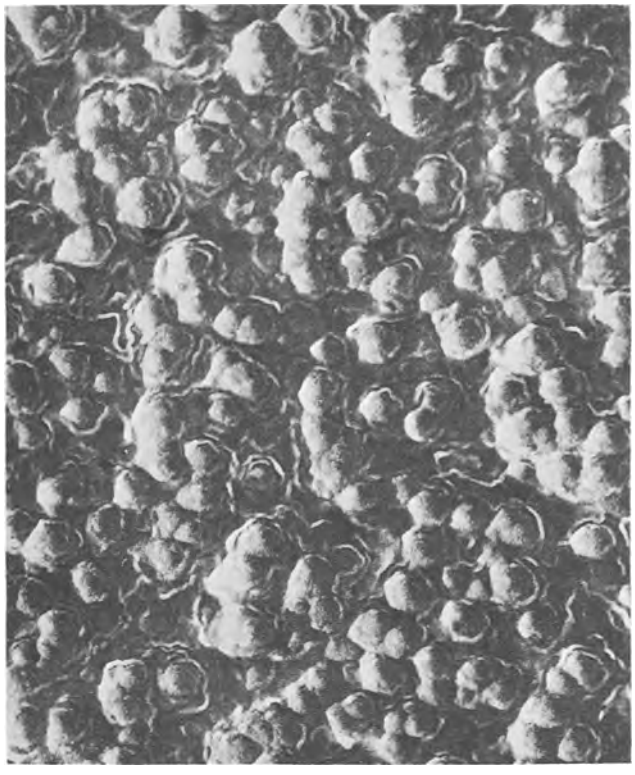

Fig. 2. Nickel-iron film 20,000Å-thick. Magnification ca 49,000X

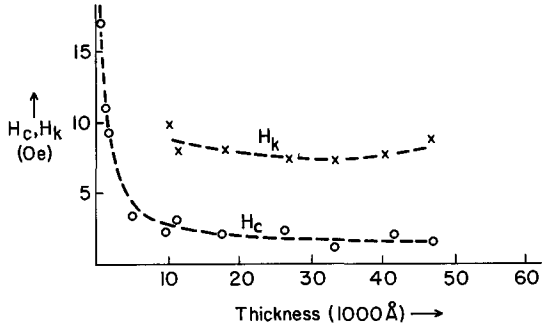

Fig. 3. Coercive force (H_c) and anisotropy field (H_k) vs. thickness of deposit.

Ni^{++}/Fe^{++} *ratio.*—Deposits of 10,000Å thickness were plated from baths with constant nickel content (56 mM/liter) and iron content varying from 0-30%. The plating rate drops almost linearly from 1700Å/min at 0% Fe, to 900 Å/min at 30% Fe. The coercive force (Fig. 4) follows the pattern observed in nickel-iron alloys deposited by other techniques (13). However, the minimum normally observed at 18% iron has been shifted to about 10% iron. The magnetostriction constant is positive in deposits containing considerably less than 19% iron, while in nickel-iron alloys deposited by other techniques it becomes negative at about 19% iron (14). X-ray diagrams show the presence of nickel phosphides and nickel oxide (NiO) and iron oxide (FeO). H_k increases with decreased iron content.

Metal concentration in bath.—The concentration of the heavy metals in the bath (Ni and Fe), with the ratios of nickel to iron and of iron to tartrate kept constant, was varied next. Figure 5, top section, shows that with increasing metal concentration the iron content of the film goes up to a constant level. The plating rate also increases up to a certain point, and then levels

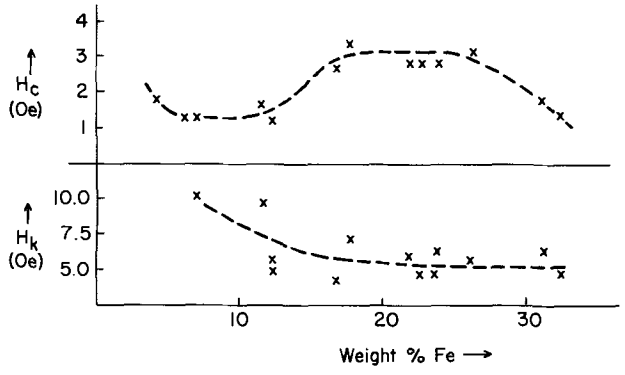

Fig. 4. Coercive force (H_c) and anisotropy field (H_k) vs. Ni^{++}/Fe^{++} ratio.

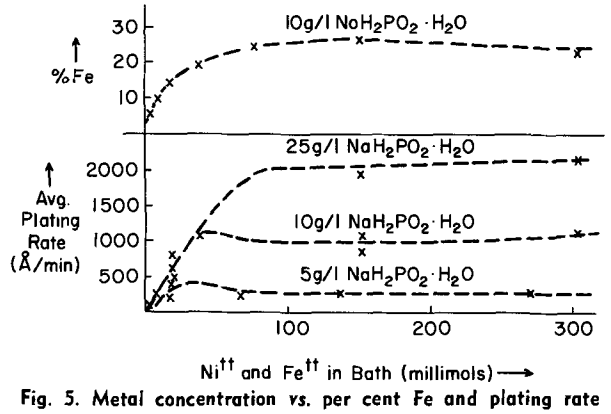

Fig. 5. Metal concentration vs. per cent Fe and plating rate

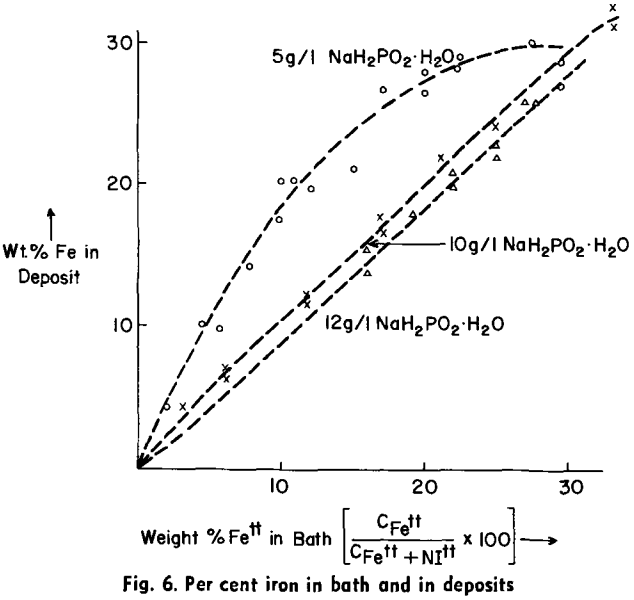

Fig. 6. Per cent iron in bath and in deposits

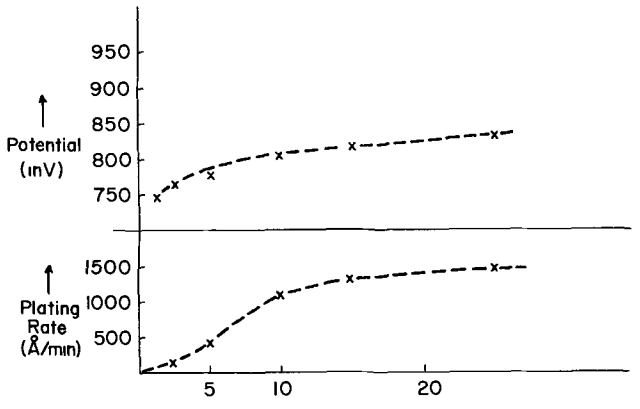

Fig. 7. Plating potential and plating rate

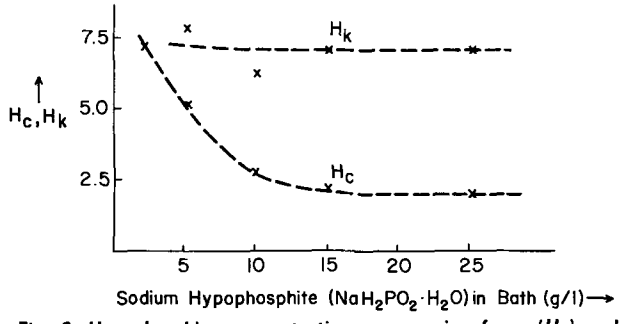

Fig. 8. Hypophosphite concentration vs. coercive force (H_c) and anisotropy field (H_k).

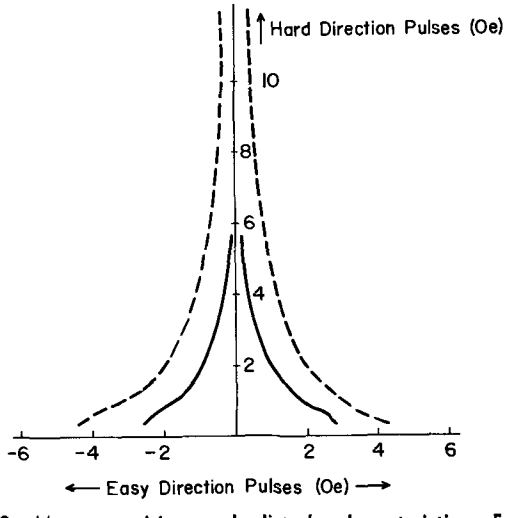

Fig. 9. Memory writing and disturb characteristics, 5 g/l $NaH_2PO_2 \cdot H_2O$.

out, at levels depending on the amount of hypophosphite in the bath (Fig. 5, bottom section).

Effect of hypophosphite concentration.—The hypophosphite concentration in the bath affects the composition of the films, as well as the magnetic properties.

In Fig. 6 the percentage of iron in the bath (from the sum of Ni^{++} and Fe^{++} concentration in the range of 0-30% Fe) is plotted against the percentage of iron in the film for various hypophosphite contents.

Above 10 g/l sodium hypophosphite the codeposition is normal (15); *i.e.*, the less noble iron deposits more slowly than the more noble nickel. Below 10 g/l sodium hypophosphite the codeposition is anomalous, while at 10 g/l sodium hypophosphite the codeposition is close to equilibrium over a relatively wide range.

At a given iron content in the bath (such as 25% Fe^{++}) the deposition potential and the deposition rate increase with increased hypophosphite content (Fig. 7).

Figure 8 shows, against the hypophosphite content in the bath, the coercive force (H_c) and the anisotropy field (H_k) of deposits which were 10,000Å thick, and which had 25% iron obtained by adjusting the Ni^{++}/Fe^{++} ratio in the bath with the other parameters kept constant. The phosphorus content of the films increased almost linearly with increased hypophosphite content (from 0.5 to 1.5% P for 2-25 g/l $NaH_2PO \cdot H_2O$).

With lower hypophosphite content the coercive force increases while the anisotropy field stays low.

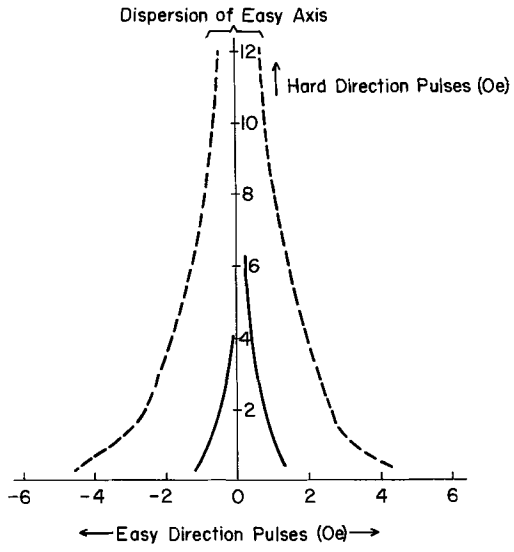

Fig. 10. Memory writing and disturb characteristics, 15 g/l $NaH_2PO_2 \cdot H_2O$.

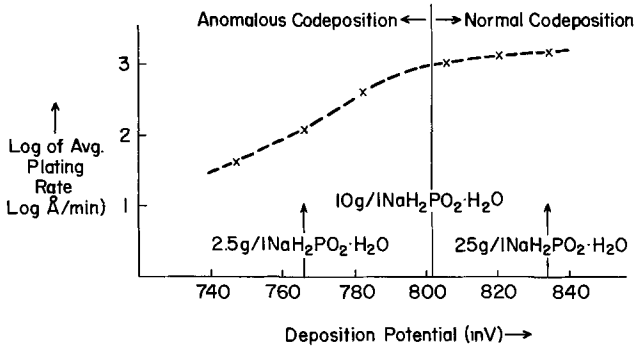

Fig. 11. Deposition potential vs. plating rate

Chemical nickel-iron deposits were tested for use in memory applications, in particular in the orthogonal mode (12), with pulses both in the hard and easy directions.

Figure 9 shows how a deposit of 9000Å thickness performs under such conditions, plated from a bath containing 5 g/l $NaH_2PO_2 \cdot H_2O$ with a H_k/H_c ratio of 1.3.

The dotted lines of the asteroid show the combinations of pulses in the easy and hard directions needed to switch 90% of the deposit; the inner lines show the combinations of a large number of pulses needed to start switching the magnetization (creeping threshold). The pulses used had a rise time of 15 nanosec, duration of 80-160 nanosec. The usual techniques *i.e.*, setting the magnetization of the material by a large number of overlapping easy and hard direction pulses and for the creeping threshold a large number of disturb pulses simulating the conditions in the memory application, have been used (12). The distance between the dotted lines at the top of the asteroid is a measure of the dispersion of the easy axis (12).

There is a wide range of combinations of the easy and hard direction pulses which switch the film, but for which the individual pulses stay below the creeping threshold.

Figure 10 shows similar plots for a deposit from a bath containing 15 g/l $NaH_2PO_2 \cdot H_2O$. The H_k/H_c ratio in this case is 3.5. The creeping threshold is too low for memory applications.

Discussion

A look at Fig. 5, bottom section, shows that the deposition rate appears to be controlled either by the concentration of the metal ions, or if the concentration of the metal ions surpasses a certain value, by the concentration of the hypophosphite ions in the bath.

If we plot the deposition potential at various hypophosphite concentrations against the logarithm of the deposition rate (Fig. 11), we see that at 10 g/l sodium hypophosphite, *i.e.*, at equilibrium codeposition, the curve has a break. At the lower potentials (low hypophosphite concentrations) the deposition rate is controlled by the hypophosphite concentration, at the higher potentials the metal concentration controls the deposition rate. The temperature dependence of the plating rate shows that the logarithm of the deposition rate is inversely proportional to the absolute temperature in the range of 35°-75°C. At the lower deposition potentials (in hypophosphite controlled deposition) the activation energy is smaller than at the higher deposition potentials. Not considering the mechanisms involving the oxidation of the hypophosphite ions (6-8), a number of rate controlling steps involving the metal ions are possible: the diffusion of metal ions or complexes, the dissociation rate of metal complexes, formation of precipitates affecting the catalytic surface, adsorption of metal ions on the surface and re-dissolution of metal. Figure 5 shows that with low metal concentrations, the iron content of the deposit is lower. It is believed that this is caused by different rates of diffusion or dissociation of the iron tartrate complex from that of the hexammine nickel complex.

It is in the hypophosphite controlled baths that we observe the unusual magnetic properties in the nickel-iron films.

Recent investigations (16) indicate that a nonmagnetic layer of about 20Å thickness between two layers of about 250Å of permalloy tends to increase the coercive force and the creeping threshold of the magnetic layers, provided the nonmagnetic layer has irregular phase boundaries. The minimum of the coercive force at 10% Fe, rather than 18%, points to the presence of nonmagnetic material in the deposits. The laminar structure of the deposits possibly consists of magnetic layers of 80-20 nickel-iron alloy interspaced between relatively nonmagnetic layers of nickel phosphide, and/or oxide of the appropriate thickness to raise the creeping threshold of the deposits.

Conclusion

The deposition of chemical nickel-iron films containing up to 30% iron by reduction with hypophosphite is controlled either by the metal ion concentration or, above a certain metal content, by the hypophosphite concentration. The codeposition may be normal or anomalous, depending on the hypophosphite concentration.

Properties, in particular certain magnetic properties, have been discussed. The chemical reduction with hypophosphite offers a simple, internally controlled method to prepare a useful magnetic material for computer memories.

Acknowledgments

The author is grateful to D. W. Hall, J. A. Lindholm, and H. E. Towner for carrying out the plating experiments; Dr. H. O. Leilich, T. R. Scott, H. H. Zappe and others for evaluating the films magnetically; Mary E. Fritsch and R. Flitsch for the chemical analysis; D. P. Cameron for the electron micrographs; Dr. C. L. Masters for P^{32} tracer analysis; and to P. Geldermans, Drs. G. Kahan, K. L. Romankiw, and N. W. Silcox, and many others for helpful discussions.

Manuscript received Jan. 26, 1966; revised manuscript received April 27, 1966. This paper was presented at the Buffalo Meeting, Oct. 10-14, 1965.

Any discussion of this paper will appear in a Discussion Section to be published in the June 1967 JOURNAL.

REFERENCES

1. A. Brenner and G. E. Riddell, *J. Research, Nat. Bur. Standards*, **39**, 385 (Nov. 1947).
2. G. Gutzeit, *Corrosion Technology*, **3**, 331 (1956).
3. P. H. Eisenberg, U.S. Pat. 2,837,399 (March 1958).
4. A. F. Schmeckenbecher, Belg. Pat. No. 626,491 (April 1963).
5. Thompson-Ramo-Woolridge, Inc., Brit. Pat. No. 955,782 (April 1964).
6. G. Gutzeit, ASTM Special Technical Publication No. 256, p. 8 (1959).
7. S. Ishibashi, Himeji Kogyo Daigaku Kenkyu Hokoku, No. 13, 68-76 (1961).
8. R. M. Lukes, *Plating*, **51**, 969 (1964).
9. W. J. Hamer, *This Journal*, **72**, 45 (1937).
10. A. W. Goldenstein, W. Rostoker, F. Schoosberger, and G. Gutzeit, *ibid.*, **104**, 104 (1957).
11. R. M. Bozorth, "Ferromagnetism," p. 107, D. Van Nostrand & Co., New York (1951).
12. E. W. Pugh, "Physics of Thin Films," p. 277, J. Hass, Editor, Academic Press Inc., New York (1963); and R. F. Soohoo, "Magnetic Thin Films," p. 246, Harper & Row, New York (1965).
13. R. M. Bozorth, "Ferromagnetism," p. 115, D. Van Nostrand & Co., New York (1951).
14. R. M. Bozorth, *ibid.*, p. 649.
15. A. Brenner, "Electrodeposition of Alloys," Vol. 1, p. 80 ff, Academic Press Inc., New York (1963).
16. E. Feldtkeller, K. J. Stein, and H. Harmus, *1965 Proc. the Intermag. Conference*, Section 8.4.

Transport Processes in the Thermal Oxidation of Silicon

Douglas O. Raleigh

North American Aviation Science Center, Thousand Oaks, California

ABSTRACT

Previous experiments on the effect of an electric field on the oxidation rate of silicon are reconsidered. It is shown that such experiments do not in themselves prove that oxidation occurs by the diffusion of a charged species through the reaction layer, but may be analyzed in terms of an electrolytic process being superposed on the normal oxidation process. Supplementary data present in the literature are also insufficient to conclude whether a charged species is involved. A theoretical analysis of the transport processes to be expected when oxidation involves a charged diffusant shows that the rate of such a process may be predicted if the electronic conductivity of SiO_2 under the conditions of oxidation is known. Suitable experiments for determining this quantity are suggested.

The kinetics of oxidation of silicon has in recent years become of interest in the fabrication of semiconductor devices (1). Air oxidation of silicon at elevated temperatures yields uniform, compact, adherent films of vitreous silica which are the basis of the well-known MOS structures. Accordingly, there has been considerable effort devoted to elucidating the oxidation mechanism under various experimental conditions and its relation to the characteristics of the resultant devices. Although largely outside this area, in the last few years there has also been considerable study of the electrochemical and transport properties of solids, principally by Wagner and co-workers (2). It is felt by the author that insights from this work, together with Wagner's earlier studies on metallic oxidation (3), can be used to bring into better focus some basic considerations on the mechanism of silicon oxidation. Specifically, it is intended to reexamine the question of the diffusing species involved in the high-temperature oxidation of silicon by dry oxygen.

A large number of investigators (4-10) have found that the rate of oxidative growth of a silica film on Si obeys the parabolic law characteristic of a diffusion-controlled process; that is, $dx/dt = k/x$, where x is the film thickness and k the rate constant. Law (5) has pointed out that a parabolic rate dependence does not necessarily prove diffusion control unless a linear plot of x^2 *vs.* t back-extrapolates through the origin, and found evidence of partial rate control by a phase boundary process for films 100-500Å thick. Deal *et al.* (11) found evidence of partial phase boundary control under some experimental conditions from studies on the oxidation of heavily doped silicon. Deal and Grove (12) recently provided an excellent analysis of the general situation where both diffusion and phase boundary processes are involved. In general, however, oxidation does appear to be diffusion-controlled for film thicknesses in excess of 1000Å under a wide variety of conditions. Jorgenson (8), for instance, obtained a plot of x^2 *vs.* t that was linear through the origin for 2000-5000Å films in normal oxidation at 850°C. Since, at any rate, the question of what is the diffusing species is best examined under conditions of diffusion control, the considerations in this paper relate to experiments carried out under these conditions. Moreover, the discussion is limited to dry oxidation, since the diffusing species involved in wet oxidation is manifestly another question.

In further studies, marker experiments by Jorgenson (8) at 850° and by Karube *et al.* (13) at 1250°C indicated that the oxidation process involves the diffusion of oxygen rather than silicon through the SiO_2 reaction layer, so that oxidation occurs at the $Si|SiO_2$ interface. Karube's studies at 1250° included infrared absorption measurements to show that a 2000Å reaction layer was essentially all SiO_2 rather than other oxides of Si. Motzfeldt (14) has recently compared a wide variety of data on the oxidation of Si and SiC with data on the rate of permeation of oxygen through vitreous silica membranes to show that all three processes follow the same rate kinetics. A master plot of the collective data shows an activation energy of 26.3 kcal/mole for the above rate constant k, in excellent agreement with subsequent data by Deal and Grove (12) in which phase boundary effects were corrected for. Motzfeldt's comparison thus appears to show that the oxygen transport properties of thermally grown SiO_2 and silica glass are the same. In consequence, available measurements (15, 16) of the diffusion coefficient of oxygen ions in silica glass should be applicable to the oxidation process.

There appears to be a fairly widespread conviction (12, 14, 17-22) that the oxygen diffusing through SiO_2 in the oxidation process has been demonstrated to be in the form of oxygen ions. This conclusion rests on experiments by Jorgenson (8) which intended to show that the oxidation rate is influenced by the application of an electric field across the reaction layer. Jorgenson subsequently employed similar experiments to show that oxygen ions are likewise involved in the oxidation of zinc (23). It is felt by the author, however, that there are serious conceptual errors in the interpreta-

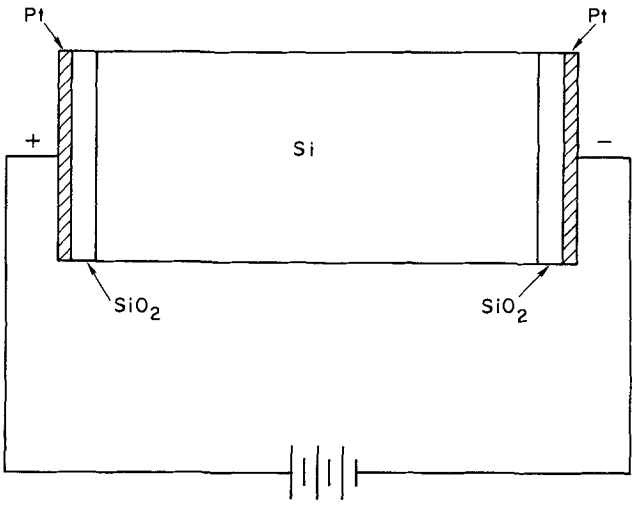

Fig. 1. Jorgenson's apparatus for studying the effect of an electric field on the oxidation of silicon.

tion of these experiments, so it is well to consider the experiments in some detail for the case of silicon oxidation.

Effect of an Electric Field on Silicon Oxidation

In Jorgenson's experiments, porous platinum electrodes were affixed to the opposite sides of a partially oxidized silicon single crystal. The experimental arrangement is shown in Fig. 1. The assembly was heated at 850° in the presence of oxygen, and the SiO_2 film thickness on each side was monitored as a function of time interferometrically. Experiments were carried out in the presence and absence of an applied voltage on the assembly, where the voltage corresponded to an electric field of about 10^4 v/cm across each SiO_2 layer. It was reasoned that, if the oxygen diffusing through the SiO_2 film in normal oxidation possessed a negative charge, the applied field shown would accelerate the process at the film on the right and retard film growth on the left. Plots of x^2 *vs.* t appeared to indicate this was the case. Linear plots were obtained for both the field-free and "accelerated" film growths, the slope being considerably greater for the accelerated case. At the "retarded" side, film growth proceeded at an initially smaller rate than in the absence of a field and came to a halt at about 3000Å in 50 hr, there being no further thickness increase observed in 120 hr.

In subsequent experiments, constant currents in the range 1-4 μa were applied to the assembly and the voltage across each film measured as a function of time. For the accelerated case, a parabolic voltage-time plot was obtained. In the case of the retarded film, the voltage rose to a constant value, corresponding to the halted film growth, which was independent of the current, although achievement of the halt voltage took longer at lower currents. The above experiments were taken as evidence that the oxygen involved in the oxidation possessed a negative charge. The constant voltage obtained across the retarded film was said to correspond to the free energy of formation of SiO_2 at 850°, although a somewhat lower than theoretical value was obtained.

In reinterpreting these experiments, one must begin by asserting that the external application of an electric field *per se* cannot provide a steady-state driving force for a diffusion-controlled process such as the thermal oxidation of silicon. This is because, in any such oxidation, the net process must be the transport of an electroneutral species (elemental oxygen in this instance) through the reaction layer. Regardless of the details of the diffusion mechanism, the transport of elemental oxygen across the film can occur only in response to a gradient in its chemical potential. Since the chemical potential of oxygen is chemically fixed on both sides of the film (by the ambient oxygen pressure on the gas side and by the presence of the phases Si, SiO_2 on the silicon side), its gradient is not accessible to influence by an externally applied electric field.

Microscopically, we may see this as follows. Suppose the transported oxygen were in the form of oxygen ions. Then, to correspond to the transport of electroneutral oxygen, a flow of oxygen ions across the film would have to be accomplished by an equal flow of electronic charge in the opposite direction (3). In consequence, any applied field which accelerated the ionic flow would retard the electronic flow. If the flows were thus unbalanced, the net result would be the transport of uncompensated charge across the film. The steady-state result would inevitably be the accumulation of opposite charges on the two sides of the film until the field generated by them cancelled out the externally applied field. Thereafter, oxygen transport would proceed as in the field-free case.

A sample calculation shows the field-free condition would be reestablished quite rapidly on the time scale of the oxide film growth. Let us consider the field generated by the build-up of one monolayer of uncompensated charge on each side of the oxide film. One monolayer of Si^{+4} or $O^{=}$ ions in SiO_2 corresponds to about 5×10^{-4} coul/cm^2. If we consider the oxide layer as a capacitor with a dielectric constant of 4, such a surface charge density would result in a field of $\sim 10^9$ v/cm within the layer. Thus, the charge accumulation due to a temporary unbalancing of the ion and electron flows in the presence of an applied electric field would be sufficient to cancel out most fields of interest when only a fractional monolayer of mass transport had occurred.

It should be remarked that the term "field-free," as used here, refers only to the absence of an externally imposed field. There are, to be sure, internal fields associated with such oxide films, but, as we shall see later, such fields are uniquely determined by the parameters of the system and are thus inaccessible to external influence. In another point of interest, it is possible at least in principle that the application of an external field, while not changing the gradient of oxygen chemical potential, can alter the basic transport properties of the diffusing entities. If, for instance, an externally applied field exceeded the electronic breakdown voltage of the oxide, the mechanism of electronic transport would be changed. Such effects, however, are in general only relevant to much thinner films than those we are considering in the present study.

The most likely reason why Jorgenson found an apparent effect of an applied field involves the manner in which such a field *per se* can be legitimately applied in a system of this nature. Jorgenson noted that Uhlig and Brenner (24) and, more recently, Cismaru and Cismaru (25) were unable to influence the oxidation rates of copper and zinc, respectively, with an electric field. He attributed this to their use of a condenser to impose the electric field, which he maintained resulted in virtually no field across the oxide. Jorgenson, however, in his use of a battery circuit, not only applied an electric field, but also provided an external circuit for electronic flow. As we have noted above, diffusive transport of oxygen through the reaction layer as oxygen ions would require both ionic and electronic flows, so would depend on both the ionic and electronic conductivities of SiO_2. If an external circuit, however, were provided for the electronic flow, oxygen ion transport would then require only ionic conductivity, so that what may have been only a minor transport mechanism because of a low electronic conductivity might then assume larger significance. In fact, Jorgenson appears to have carried out an electrolysis. The fact that ionic transport can occur under these conditions is no more indicative of ionic transport in the absence of a field than is the

anodic oxidation of a metal in an aqueous solution a proof that normal corrosion of the metal in the solution involves transport of dissolved atmospheric oxygen through the solution as oxygen ions. In fact, as we shall discuss, there is at least some evidence to the contrary for silicon oxidation. Experiments by Schmalzried (26), for instance, have indicated that vitreous silica at 1000°C is a pure ionic conductor. Pressure dependence data on the silicon oxidation rate (12) and on the permeability of vitreous silica to oxygen (27) tend to favor molecular oxygen as the transported species. While none of this data may yet be considered a proof, it does at least show that the question of the nature of the oxygen diffusant in silicon oxidation must be regarded as still unsettled.

Let us now consider the details of Jorgenson's experimental results in terms of an electrolytic process, since it will be seen that we may obtain a reasonable picture of their significance. In view of the fact that electrolytic conduction must occur in the reaction films to account for the effect of an electric field, we may consider Jorgenson's experimental assembly to consist of two electrolytic cells, $O_2(g)$,Pt $SiO_2(s)|Si(s)$, placed back-to-back. Reversible oxygen electrodes of the type $Pt,O_2|$(solid oxide) are well known in the literature of solid-state electrochemistry (2) and reversible $SiO_2|Si$ electrodes have been suggested both explicitly (28) and as an implicit consequence of observed galvanic emfs (21) in MOS structures. If ionic conduction in the SiO_2 is by oxygen ions, the following half-cell reactions may be postulated

$$O_2(g) + 4e \rightleftharpoons 2\,O^=$$

$$2\,O^= + Si \rightleftharpoons SiO_2 + 4e$$

and the total cell reaction will be $Si + O_2 \rightleftharpoons SiO_2$, the direction of the arrow in each case depending on the direction of the cell current. If conduction is partially or entirely by silicon ions, somewhat different half-cell reactions would apply, but the net cell reaction would still be the same. In the experimental assembly shown in Fig. 1, application of the voltage shown would form SiO_2 electrolytically from its elements at the reaction layer on the right and decompose it into its elements on the left. Since passing a particular amount of current would, in accordance with Faraday's law, form the same amount of SiO_2 on the right as is decomposed on the left, there will be zero free energy change in the over-all system and hence no galvanic emf to be surmounted in order for the electrolysis to occur.

Consider now the processes that occur in the assembly at elevated temperatures in the presence of the applied voltage. The normal diffusive or thermal oxidation process must occur on both sides at a rate unaffected by the presence of an electric field, but is augmented on the right side by electrolytic SiO_2 formation and opposed on the left by electrolytic decomposition. The net rate of oxide film growth will be given by

$$\frac{dx}{dt} = \frac{k}{x} \pm \frac{M}{4\rho\mathbf{F}}\, i_{\text{ionic}} \qquad [1]$$

where M is the molecular weight of SiO_2, ρ is its density, $\mathbf{F}$ is Faraday's constant, i_{ionic} is the ionic current density, and the plus and minus signs refer to the right and left sides of the assembly, respectively. In the early stages, the growth process will be dominated by the thermal oxidation process because of the inverse dependence of its rate on the film thickness, apparently being retarded on the left by the electrolytic process and accelerated on the right. Since Jorgenson's data for the accelerated growth showed only a 20% rate increase due to the field, it is not surprising that an apparent parabolic growth rate was observed for it. At the retarded side, however, the oxide film apparently grew sufficiently to reduce the thermal oxidation rate to that of the electrolytic decomposition, resulting in the observed "halt." At this point, where $dx/dt = 0$, one would have under constant-current conditions no further film growth. The differing extents to which the field affected thermal oxidation at the two electrodes may be accounted for by different effective electrode areas, since this would result in different current densities and hence different rates per unit area of the electrolytic processes at the two electrodes.

It must be emphasized that such a balance between thermal growth and electrolytic decomposition would not be a precarious or fortuitously achieved one, but rather a self-perpetuating, dynamic steady state that would inevitably be achieved in such a system at any particular level of current density. This is because the current density defines a particular decomposition rate per unit area toward which the initially faster thermal oxidation rate must approach as film growth proceeds. When a film thickness is reached at which the rates of the opposing processes are equal, there will no longer be any net driving force toward further film growth, and hence the constant film thickness will define a constant thermal oxidation rate equal to the electrolytic dissociation rate. The effect of lowering the electrolysis current will merely be to increase the film thickness required to achieve this balance, so that longer oxidation times will be required, as was found experimentally (8).

It is of interest to consider the significance of the voltage across the retarded film in the experiments where various currents were passed through the assembly and this quantity was measured. It is to be recalled that a halt point voltage was obtained which was the same at each current level. At the halt point, where the rates of oxidative formation and electrolytic decomposition become equal, one may write from Eq. [1]

$$\frac{k}{x} = \frac{M}{4\rho\mathbf{F}}\, i_{\text{ionic}} = \frac{MI_{\text{ionic}}}{4\rho\mathbf{F}A} = \frac{t_{\text{ions}}IM}{4\rho\mathbf{F}A} \qquad [2]$$

where I_{ionic} and I are the ionic and total currents (taking into account the possibility of partial electronic conduction in the SiO_2), t_{ionic} is the transference number for ionic conduction, and A the effective electrode area. In the most general case, the voltage across the film will be given by $V = \epsilon_0 + IR$, where ϵ_0 accounts for any galvanic emf between the voltage-measuring leads and R is the film resistance. If the voltage-measuring leads were made to the Pt electrode and Si crystal, the occurrence of a finite ϵ_0, corresponding to the galvanic couple $Si|SiO_2|O_2$, would depend on whether the contact to the Si crystal was made in the absence of any SiO_2 film and maintained in an oxygen-free environment. Otherwise, an oxygen electrode similar to the one on the gas side would result at this contact and one would have $\epsilon_0 \approx 0$. Since the description of the experiment does not indicate this precaution was taken, it seems likely that there was no galvanic emf involved. Further evidence for this is in the voltage-time data itself, which appears to extrapolate to zero at the start of the experiment (*i.e.*, as $R \to 0$) rather than to some finite voltage.

One has, then, for the voltage across the layer at the halt point

$$V_{\text{halt}} = IR_{\text{halt}} = I\frac{x_{\text{halt}}}{\sigma A} \qquad [3]$$

where σ is the total conductivity of SiO_2. Solving Eq. [2] for I and substituting in Eq. [3], one obtains

$$V_{\text{halt}} = \frac{4\rho\mathbf{F}k}{Mt_{\text{ions}}\sigma} = \frac{4\rho\mathbf{F}k}{M\sigma_{\text{ionic}}} \qquad [4]$$

One sees that a value of the halt voltage is obtained which depends only on transport properties of the SiO_2, being independent of the cell current and unrelated to the free energy of formation of SiO_2. V_{halt} is current-independent because it is the IR drop at the

halt point. When I is lowered, R (which is proportional to x_{halt}) is correspondingly raised, since a thicker film is required at the lower current to reduce the rate of the thermal oxidation to that of the electrolytic dissociation.

A rough estimate of this voltage may be made for comparison with the experimental value. As Motzfeldt (14) has noted, one may derive from Jorgenson's normal oxidation curve a rate constant $k = 1.25 \times 10^{-11}$ cm²/hr, in good agreement with data from other sources. For σ_{ionic}, one notes that Jorgenson's accelerated oxidation curve shows a thickness augmentation of 1.0×10^{-5} cm above that obtained by normal oxidation at the end of 100 hr. It may be calculated from Eq. [1] that this would require an average electrolytic current density of 0.37 μa/cm². With a stated electric field of approximately 10^4 v/cm, this would imply an ionic conductivity of about 3.7×10^{-11} ohm^{-1} cm^{-1}. Using these values for k and σ_{ionic}, one obtains $V_{halt} = 1.25$v. This is within 25% of the value experimentally obtained (1.62v), which is satisfactory agreement considering the approximateness of the calculation. Because of the relation of V_{halt} to k and σ_{ionic}, it would seem that halt voltages such as these would provide useful supplementary data in conjunction with studies on ionic conductivity and oxidation rates.

Oxygen Ions, Atoms, or Molecules? Relevant Data and Experiments

The considerations thus far have had mostly the negative objective of showing that experiments on the effect of an applied electric field on metallic oxidation do not in themselves offer a valid means of determining whether diffusion of a charged species is involved. Rather, no effect of a field *per se* is to be expected, and the use of a field in conjunction with an external circuit yields effects which should properly be considered in the framework of electrochemistry. These latter effects, however, may be of interest in themselves in studying various aspects of transport in reaction films, provided their electrochemical nature is recognized. Jorgenson's experiments, for instance, showed the existence of at least one precondition for oxidative transport by ions, namely, that SiO_2 possesses a measurable ionic conductivity. We ask now whether other information from elsewhere in the literature may offer further insights on this question.

We have noted previously that Motzfeldt's comparison of data on the oxidation rate of Si and SiC and the permeation rate of oxygen through silica glass shows all three processes are apparently rate-determined by the same transport phenomenon, that of oxygen through vitreous silica. The permeability of silica glass to oxygen, as measured by Norton (27) in the range 950°-1100°C, was in fact directly converted to an equivalent oxidation rate constant k, by essentially no more than a change to the units appropriate for k, and showed excellent agreement with values of k obtained from oxidation rate data. Thus, it would appear that not only does this provide further evidence for diffusion control in the oxidation process, but indicates that there is nothing unusual in the oxygen transport properties of "grown" SiO_2, as compared to silica glass.

Norton's experiments included a determination of the diffusion coefficient of oxygen in silica glass by a "lag time" method. A log D *vs.* $1/T$ plot gives an activation energy for diffusion of 27 kcal/mole and an extrapolated value of about 1.6×10^{-9} cm²/sec for D at 850°C. By contrast, Sucov (16) measured the diffusion coefficient of oxygen ions in silica glass in the range 925°-1225°C, using a tracer method, and found an activation energy of 71.2 kcal/mole. The extrapolated D at 850° is about 2.1×10^{-16} cm²/sec. Similar values are indicated in the earlier work of Haul and Dumbgen (15). The expected conclusion, however, cannot be drawn since, as Shewmon (29) has pointed out, the chemical diffusion coefficient, as measured by Norton in a transport experiment, is the diffusion coefficient of the defects responsible for the transport, where tracer experiments would measure the diffusion coefficient of the average oxygen ion in silica glass. Since the latter would be immobile except for the brief periods when it exists in a defect configuration, a much smaller value would be expected than for defects, and the activation energy associated with its diffusion would involve both the activation energy for diffusion and the formation energy of the defect involved. The available D values from tracer studies, however, permit an interesting supplementary calculation. If this D is that of the average oxygen ion in silica, then the ionic conductivity of silica due to oxygen ions should be approximately given by

$$\sigma = 2N\mathbf{F}\mu = \frac{4N\mathbf{F}\mathbf{F}'D}{RT} \qquad [5]$$

where N is the oxygen-ion concentration in silica in moles/cm³, μ is the oxygen-ion mobility, $\mathbf{F}$ and $\mathbf{F}'$ are Faraday's constant in units of coul/eqvt and kcal/volt-eqvt, respectively, and the Nernst-Einstein diffusion-mobility relation has been employed. Using $N = 0.069$, calculated from Jorgenson's reported average density of 2.08 g/cm³ for his silica films, and an average value from the two available references (15, 16) for D at 850°, one obtains $\sigma = 3.5 \times 10^{-11}$ ohm^{-1} cm^{-1}, in fortuitously good agreement with the value previously calculated from Jorgenson's data, considering the possible sources of error. It would appear, however, that we have further evidence for the essentially similar nature of "grown" SiO_2 and silica glass.

More direct evidence regarding the nature of the diffusing oxygen in silicon oxidation could be derived from the oxygen pressure dependence of the oxidation rate. In accordance with the considerations of Motzfeldt and Norton, the flow rate of dissolved oxygen through the reaction film, when this is the rate-determining process for oxidation, will be given by

$$J = \frac{2\rho}{nM}\frac{dx}{dt} = D_c\frac{\Delta C}{x} \qquad [6]$$

where J is in moles oxygen solute/cm²-sec, n is the number of oxygen atoms in the solute species, D_c is the chemical diffusion coefficient as previously discussed, and ΔC is the difference in concentration of dissolved oxygen at the two sides of the reaction film. Since the phase boundary $SiO_2|Si$ defines an extremely low chemical potential of oxygen on this side, we may replace ΔC with C_s, the solubility of oxygen in SiO_2 on the gas side in moles solute per cubic centimeter SiO_2. Comparison with $dx/dt = k/x$ yields from the above expression

$$k = \frac{nMD_cC_s}{2\rho} \qquad [7]$$

Since k should thus vary linearly with C_s, it is apparent from Henry's law that a linear dependence of k on p_{O_2}, the partial pressure of oxygen in the gas phase, would be the case if the dissolved species were O_2, where a $(p_{O_2})^{1/2}$ dependence would imply O as the dissolved species.

In the case where gaseous oxygen would dissolve to form oxygen ions, say, by the formation of an equivalent number of electronic holes

$$O_2(g) \rightleftharpoons 2\,O^{=}(\text{in defect sites}) + 4\oplus$$

the p_{O_2} dependence would be less certain. If SiO_2, however, were a predominant or even an appreciable ionic conductor, as data by Schmalzried (26) indicate, one would expect the hole concentration to be small compared with the total oxygen-ion defect concentration. In this event, mass action considerations would predict a $(p_{O_2})^{1/2}$ dependence. In fact, a vari-

ety of pressure dependence have been noted (5, 7, 27, 30, 31). Data by Norton indicate a linear dependence of the permeation rate on p_{O_2} at 1100°, but data on SiC oxidation at higher temperatures show a square root dependence and, as Motzfeldt has noted, there appears to be little by way of reliable data on the pressure dependence of silicon oxidation under diffusion-controlled conditions. Deal and Grove (12) have recently analyzed unpublished oxidation rate data by Flint (31) to assert that, when correction is made for phase boundary effects, the data show a linear dependence on p_{O_2}. These authors suggested that in view of Jorgenson's conclusions, the diffusing species may be the superoxide ion, O_2^-. In view of the above discussion, however, it would seem that molecular O_2 is also a likely possibility, assuming that a linear pressure dependence has been demonstrated. In the latter respect, it may still be desirable to obtain pressure dependence data under explicitly diffusion-controlled conditions.

Finally, we consider the important question of electronic transport in SiO_2 and its relation to an oxidation process involving oxygen ions. The kinetics of processes of this type have been treated in the metal oxidation theory of Wagner (3). An account of the forms of this theory and its success in matching experimentally observed oxidation rates in various systems has recently been given by Kubaschewski and Hopkins (32). It is felt, however, that previous expositions of the theory, especially in its more exact forms, have been heavily thermodynamic in nature, with resultant difficulties in visualizing the physical processes involved. In what follows, a somewhat different approach has been taken, a suitable kinetic expression being derived for the case of Si oxidation on the basis of essentially flow rate and electroneutrality requirements.

Let us suppose that oxygen is introduced into vitreous silica as oxygen ions and electronic holes, in accordance with the above oxide-gas equilibrium, which then diffuse across the reaction layer to react with the silicon

$$2\,O^{=} + 4\oplus + Si = SiO_2$$

The fluxes of oxygen ions and holes at any point within the SiO_2 in response to their respective concentration gradients dN_O/dx and $dN_\oplus/dx$ and whatever electrostatic field $d\phi/dx$ arises from spacecharge effects should be given by

$$-J_O = D_O \frac{dN_O}{dx} - \frac{\sigma_O}{2\mathbf{F}} \frac{d\phi}{dx} \qquad [8]$$

$$-J_\oplus = D_\oplus \frac{dN_\oplus}{dx} + \frac{\sigma_\oplus}{\mathbf{F}} \frac{d\phi}{dx} \qquad [9]$$

in accordance with Fick's and Ohm's laws. Here, the fluxes are in moles/cm²-sec and σ_O and $\sigma_\oplus$ are the partial specific electrical conductivities in SiO_2 due to oxygen ions and holes, respectively, it being assumed that each migrating oxygen ion possesses two negative charges regardless of its defect configuration. D_O is the average diffusion coefficient of whatever defects are responsible for the oxygen-ion migration. As we have noted previously, fluxes such as the above must be intimately coupled to preserve bulk electroneutrality. Since holes and oxygen ions are being introduced at the gas phase side of the reaction layer on a 2-for-1 basis and being removed on the Si side on the same basis at essentially the same rate,[1] one may define an effective flux J of electroneutral oxygen such that at steady state $J \equiv J_O = \frac{1}{2}J_\oplus$ at any point within the film. Moreover, if holes are the only electronic defects in the film, one must have matching charge gradients due to oxygen ions and holes to preserve bulk electroneutrality, so that we may also define an effective oxygen concentration gradient by $dN/dx \equiv dN_O/dx = \frac{1}{2}dN_\oplus/dx$. Introducing the quantities J and N in the above equations, we now have

$$-J = D_O \frac{dN}{dx} - \frac{\sigma_O}{2\mathbf{F}} \frac{d\phi}{dx} \qquad [10]$$

$$-2J = 2D_\oplus \frac{dN}{dx} + \frac{\sigma_\oplus}{\mathbf{F}} \frac{d\phi}{dx} \qquad [11]$$

If we now eliminate $d\phi/dx$ by multiplying Eq. [10] by $\sigma_\oplus/\sigma_O$, dividing Eq. [11] by 2, and adding, we obtain

$$-\left(1 + \frac{\sigma_\oplus}{\sigma_O}\right) J = \left(D_\oplus + \frac{\sigma_\oplus}{\sigma_O} D_O\right) \frac{dN}{dx} \qquad [12]$$

for the oxygen flux within the film as a function of the local concentration gradient. The special significance of this result is that, in consequence of the coupled ionic and electronic flows, the steady-state oxygen flux depends only on transport parameters of the diffusing entities and on the average value of the oxygen concentration gradient, as established across the film by the chemically fixed oxygen potentials at its boundaries. Thus, as we asserted earlier, no effect of an externally imposed electric field is to be expected. Alternatively, Eq. [10] and [11] could have been solved for the local internal field $d\phi/dx$ to show that it is uniquely established by transport parameters of the diffusants and by the externally imposed oxygen concentration gradient. Again, we are assuming the transport parameters are field-independent, which is believed to be the case for oxide films sufficiently thick to exhibit parabolic growth behavior.

A special case of Eq. [12] is of interest. Since one expects $D_O << D_\oplus$ in view of the generally much larger electronic than ionic mobility in solids, the second term in brackets on the right may be neglected if the electronic conductivity is small compared to the ionic conductivity or even comparable to it. Moreover, if the ionic conductivity is due only to oxygen ions, as we have been assuming implicitly, we may equate the bracket on the left to $1/t_{ions}$, so that we obtain

$$-J = t_{ions} D_\oplus \frac{dN}{dx} = \frac{1}{2} t_{ions} D_\oplus \frac{dN_\oplus}{dx} \qquad [13]$$

This result is quite general, since the same expression with $D_\oplus$ and $N_\oplus$ replaced by $D_\ominus$ and $N_\ominus$ may be derived in like manner if the electronic defects are assumed to be conduction band electrons. In this case, one would be dealing with an oxygen-ion deficient structure, in which diffusion would involve countercurrent flows of oxygen ions and electrons. One further special case of interest is that in which the reaction layer is a strongly predominant ionic conductor. In this case, Eq. [13] becomes

$$-J \approx D_\oplus \frac{dN}{dx} = \frac{1}{2} D_\oplus \frac{dN_\oplus}{dx} \qquad [14]$$

and one has the expected result that the oxygen transport is strictly limited by the field-free diffusion of the electronic carriers. Equation [14] is, in fact, an upper bound to the size of the oxygen-ion flux in relation to the electronic diffusion current, a result which is of interest since, as we shall see later, we may determine the latter directly by a well-known experimental arrangement in solid-state electrochemistry.

We may now evaluate the oxidative rate constant k to be expected when diffusion proceeds by oxygen-ion

[1] There will be a very small divergence of the effective oxygen flux due to solution of oxygen in the growing reaction layer, but this may be ignored for our purposes.

migration. For the relation of k to oxygen flux J, we have, from Eq. [6], $J = (2\rho/nM)(dx/dt) = 2k\rho/Mx$, where we have used $n = 1$ for oxygen ions. Since J is essentially constant across the reaction layer, we may write as an integrated form of Eq. [13], $J = \frac{1}{2}\overline{t_{ions}}\,D_{\oplus}\,\overline{(dN_{\oplus}/dx)} = \frac{1}{2}\overline{t_{ions}}\,D_{\oplus}N_{\oplus}^{\circ}/x$, where the bars represent average values across the film, $N_{\oplus}^{\circ}$ is the equilibrium hole concentration in SiO_2 in contact with the ambient gas phase, and we have assumed negligible hole concentration on the Si side in accord with previous considerations of low oxygen solubility on this side. Comparing these expressions for J gives

$$k = \frac{M\overline{t_{ions}}D_{\oplus}N_{\oplus}^{\circ}}{4\rho} \qquad [15]$$

Then, employing the Nernst-Einstein expression, $D_{\oplus} = \mu_{\oplus}RT/\mathbf{F}'$ and defining the specific hole conductivity of SiO_2 in equilibrium with the ambient gas phase by $\sigma_{\oplus}^{\circ} = N_{\oplus}^{\circ}\mathbf{F}\mu_{\oplus}$, we obtain

$$k = \frac{M\overline{t_{ions}}\sigma_{\oplus}^{\circ}RT}{4\rho\mathbf{F}\mathbf{F}'} \qquad [16]$$

This expression for k is more accurate than a somewhat different one suggested by Motzfeldt (14) on the basis of the Wagner oxidation theory, in that it takes into account the expected variation in electronic carrier concentration across the film, but is arrived at without the rather complex thermodynamic considerations attendant in previous treatments with this refinement. It is still approximate in that an average value of t_{ions} is involved, but the use of such an average should not introduce too much error if ionic conduction in the film predominates or is at least comparable with electronic conduction. In the case of predominant electronic conduction, other forms of the Wagner theory (32) would be more appropriate.

In all the above, the central role of electronic conductivity in oxygen transport by ions is to be noted. We consider now what relevant information is available in the literature or accessible through experimentation. As noted earlier, experiments by Schmalzried have indicated that vitreous silica is a pure ionic conductor. Conduction by impurities, however, could not be ruled out in this work and, at any rate, a quantitative estimate of the electronic transference number, however small, is not available from the data. Moreover, measurements on grown films of SiO_2 on Si would undoubtedly be more convincing, despite the apparent similarity of grown SiO_2 and vitreous silica. Jorgenson suggested $t_{ions} = 0.4$ on the basis of a single voltage measurement, but, by his own admission, the accuracy of the measurement was questionable and may reflect some of the contact problems discussed earlier in connection with measuring the halt voltage.

In recent years there has been considerable success in measuring electronic conductivity in predominant ionic conductors by the use of so-called "polarization cells," first suggested by Wagner (2a). Cells of this type employ an electrochemical arrangement in which ionic conduction is "blocked" and the electronic conductivity is measured from a residual electronic diffusion current. In analogy with previous cell arrangements (33-35), the cell

$$(-)\mathrm{Si}|\mathrm{SiO_2}|\mathrm{Pt},\ \text{inert gas}\ (+)$$

is in principle capable of determining the electronic conductivity of grown SiO_2 films atop silicon. Since the electronic conductivities of such compounds are in general a function of the chemical activities of their elemental components, valuable complementary information could be obtained from the cell arrangement

$$(+)\mathrm{O_2(g)},\mathrm{Pt}|\mathrm{SiO_2}|\mathrm{Pt}(-)$$

with various oxygen pressures. Since, in this cell, the electronic diffusion current (36) existing just below the SiO_2 decomposition potential would be precisely the same as that represented in Eq. [14], its measurement would provide a direct determination of the upper limit of permissible oxygen transport in SiO_2 by oxygen ion diffusion. A similar arrangement has been used by the author (37) to measure bromine-induced hole conductivity in AgBr. Cells such as the above provide data not only on the degree of electronic conduction, but on the electronic carrier involved, and would be of great intrinsic value for an understanding of SiO_2 in addition to the question of the oxidation mechanism.

Conclusion

The question of whether an ionic species is involved in diffusion-controlled oxidation of metals is not directly answerable by experiments on the effect of an electric field *per se*, although associated electrochemical experiments may be of great interest if their electrochemical nature is realized. Ionic oxidation mechanisms have been quite successful in interpreting experimental results in a number of systems, but the open, disordered structure of vitreous silica could also conceivably permit the diffusion of an electroneutral entity such as O_2. Conclusion as to which type of transport process predominates does not appear possible on the basis of data available now. Suggested future experiments include better determination of the pressure dependence of the oxidation rate under conditions where the rate is known to be diffusion-controlled and measurements of the electronic conductivity in such films for use with oxidation rate theory. Studies of this type should be of broader interest than the question of the oxidation mechanism because of the apparent similarity of transport processes in grown SiO_2 and silica glass.

Manuscript received Feb. 16, 1966; revised manuscript received April 26, 1966.

Any discussion of this paper will appear in a Discussion Section to be published in the June 1967 JOURNAL.

REFERENCES

1. See, for instance, *IEEE Trans. Electron Devices*, **12** [3] (1965).
2. See, for instance: (a) C. Wagner, *Proc. Int. Comm. Electrochem. Thermo. Kinetics (CITCE)*, **7**, 361 (1957); (b) D. O. Raleigh, "Progress in Solid State Chemistry," Vol. 3, p. 83, H. Reiss, Editor, Macmillan, New York (1966).
3. C. Wagner, *Z. Physik. Chem.*, **B21**, 25 (1933).
4. D. J. McAdam and G. W. Geil, *J. Research Natl. Bur. Standards*, **28**, 593 (1942).
5. J. T. Law, *J. Phys. Chem.*, **61**, 1200 (1957).
6. J. W. Evans and S. K. Chatterji, *ibid.*, **62**, 1064 (1958).
7. J. R. Lizenga and W. G. Spitzer, *Phys. & Chem. Solids*, **14**, 131 (1960).
8. P. J. Jorgenson, *J. Chem. Phys.*, **37**, 874 (1962).
9. B. E. Deal, *This Journal*, **110**, 527 (1963).
10. B. H. Claussen and M. Flower, *ibid.*, p. 983.
11. B. E. Deal and M. Sklar, *ibid.*, **112**, 430 (1965); B. E. Deal, A. S. Grove, E. H. Snow, and C. T. Sah, *Trans. AIME*, **233**, 524 (1965).
12. B. E. Deal and A. S. Grove, *J. Appl. Phys.*, **36**, 3770 (1965).
13. K. N. Karube, K. Yamamoto, and M. Kamiyama, *Japan. J. Appl. Phys.*, **2**, 11 (1963).
14. K. Motzfeldt, *Acta Chem. Scand.*, **18**, 1596 (1964).
15. R. Haul and G. Dumbgen, *Z. Elektrochem.*, **66**, 636 (1962).
16. E. W. Sucov, *J. Am. Ceram. Soc.*, **46**, 14 (1963).
17. P. Siffert and A. Coche, *IEEE Trans. on Nuclear Science*, **11** [3], 244 (1964).
18. J. E. Thomas and D. R. Young, *IBM J. Res. Dev.*, **8**, 368 (1964).
19. M. Waldner, *J. Appl. Phys.*, **36**, 188 (1965).
20. A. G. Revesz, *IEEE Trans. on Electron Devices*, **12**, 97 (1965).

21. M. Yamin, ibid., p. 88.
22. P. F. Schmidt and J. E. Sandor, *Trans. AIME*, **233**, 517 (1965).
23. P. J. Jorgenson, *This Journal*, **110**, 461 (1963).
24. H. H. Uhlig and A. E. Brenner, *Acta Met.*, **3**, 108 (1955).
25. D. Cismaru and G. D. Cismaru, "1st. International Congress on Metallic Corrosion," p. 237, Butterworths', London (1961).
26. H. Schmalzried, *Z. Physik. Chem. N.F.*, **38**, 87 (1963).
27. F. J. Norton, *Nature*, **191**, 701 (1961); "Transactions of the 8th Vacuum Symposium and 2nd International Congress," pp. 8-16, Pergamon Press, New York (1962).
28. D. P. Seraphim, A. E. Brennemann, F. M. d'Heurle, and H. L. Friedman, *IBM J. Res. Dev.*, **8**, 400 (1964).
29. P. G. Shewmon, "Diffusion in Solids," Chap. 5, McGraw-Hill Book Co., New York (1963).
30. M. O. Thurston and K. D. Kang, U.S. Gov't. Report AD 294657 (1962).
31. P. S. Flint, Paper presented at the Los Angeles Meeting of the Society, Abstract No. 94, May 6-10, 1962.
32. O. Kubaschewski and B. E. Hopkins, "Oxidation of Metals and Alloys," 2nd ed., pp. 82-96, Butterworths', London (1962).
33. J. B. Wagner and C. Wagner, *J. Chem. Phys.*, **26**, 1597 (1957).
34. B. Ilschner, *ibid.*, **28**, 1109 (1958).
35. A. Morkel and H. Schmalzried, *ibid.*, **36**, 3101 (1962).
36. Ref. 2b, pp. 104-107.
37. D. O. Raleigh, *J. Phys. Chem. Solids*, **26**, 329 (1965).

Emission Spectra of Impurity Activated (Zn,Cd)(S,Se,Te) Phosphors

II. Silver Activated Phosphors

W. Lehmann

Research Laboratories, Westinghouse Electric Corporation, Pittsburgh, Pennsylvania

ABSTRACT

Silver activated (Zn,Cd)S and (Zn,Cd)Se phosphors are essentially single band emitters. The emission band shifts monotonically to lower quantum energies with increasing replacement of Zn by Cd. In contrast, gradual replacement of sulfur in ZnS or CdS by selenium, or of selenium in ZnSe by tellurium, causes little or no shift of the emission band but gradual replacement by a new band. Silver is a two-band emitter in all intermediate Zn(S,Se), Cd(S,Se), and (to some extent) Zn(Se,Te) phosphors. The dependences are demonstrated in recombination term schemes assuming predominantly ionic crystal bonding and validity of the Schön-Klasens model of luminescence.

Emission spectra due to copper in (Zn,Cd) (S,Se, Te) phosphors as a function of the composition of the binary or ternary host material were reported in a previous paper (1). This present paper deals with a similar investigation on silver activated phosphors. Copper and silver are both well known activator impurities in the II-VI compounds, and a fair amount of knowledge has accumulated in the literature especially on the emission due to silver in ZnS and in (Zn,Cd)S phosphors. However, and also similar to the case of copper, little is known yet on the question of how the Ag-emission depends on the composition of the host material within the rest of the II-VI compounds.

The experimental work was limited to powder phosphors containing Ag in the order of 10^{-4} g-mole/g-mole of Zn and/or Cd. The conditions of preparation, excitation (by ultraviolet, at 77°K) and measurement were identical to those described in ref. (1).

Two complications arose which have to be taken into account when the measured emission spectra are identified. First, all ZnSe and ZnTe used contained copper in the order of 1 to 10 ppm (determined by spectroscopic analysis). This contamination is enough to create also a weak copper emission, besides the stronger silver emission, in all samples containing either ZnSe or ZnTe. Second, silver activated II-VI compound phosphors fairly persistently also show an emission band [called SAL emission by Rotschild (2)] at a relatively high quantum energy (*e.g.*, in the near ultraviolet in ZnS:Ag). This emission was actually assumed to be due to silver by van Gool (3), but it can be observed also in phosphors containing no silver (*e.g.*, in self-activated ZnS:Cl) so that van Gool's assumption probably is in error. Both the weak copper emission and the also relatively weak SAL emission sometimes are hard to differentiate from the silver emission. Nevertheless, a clear correlation between activation and at least the strong emission bands can be observed in the case of silver as well as in the case of copper activation, and questionable identifications will be especially mentioned as such.

Zinc Sulfide

The best known and usually best developed emission band of silver in cubic or hexagonal zinc sulfide consists of a single, structureless band in the blue (4-6). A green emission band (corresponding to the green emission of ZnS:Cu) has also been reported (7, 8) but, if it is real, it is always weak compared to the blue band. The following observations on the blue emission band of ZnS:Ag were made within these investigations:

(*a*) Position and shape of the blue Ag-emission band do not noticeably depend on the quantum energy of the exciting ultraviolet. However, the peak position is slightly uncertain and may vary from sample to sample over a range of approximately 0.03 ev even within phosphors made of identical compositions. Also the width is somewhat uncertain and may vary between about 0.23 to 0.28 ev (measured at half-maximum) at 77°K, analogous to corresponding observations on Cu-activated ZnS (1).

(*b*) The mean peak position of the blue emission band of ZnS:Ag depends on structure, and on the kind of the co-activator used, roughly in the same way as observed for the blue band of ZnS:Cu. The following peak positions were measured (at 77°K) as averages over many samples:

cubic ZnS:Ag, (Cl, Br, or I)	2.78 ev
cubic ZnS:Ag, (Al, Ga, or In)	2.81 ev
hexagonal ZnS:Ag, (Cl, Br, or I)	2.85 ev
hexagonal ZnS:Ag, (Al, Ga, or In)	2.81 ev

Some typical spectra are shown in Fig. 1. It will especially be noted that, on the average, hexagonal

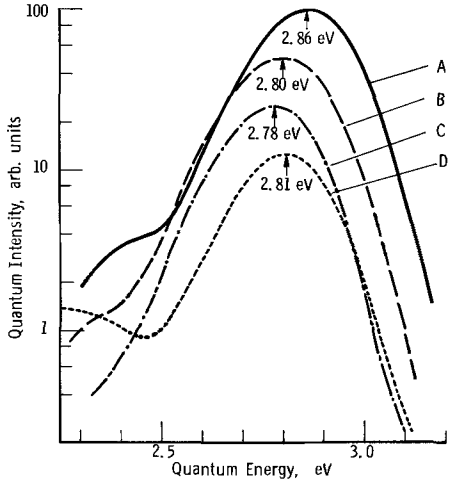

Fig. 1. Emission spectra of four different ZnS:Ag phosphors, all excited by ultraviolet of 3.40 ev (λ = 365 nm) at 77°K. A: Hex. ZnS:Ag(0.01%),Cl(0.1%), 1100°C, S_2 + argon. B: Hex. ZnS:Ag (0.01%), Al(0.03%), 1100°C, H_2S. C: Cub. ZnS:Ag(0.01%), Br(0.1%), 800°C, S_2 + argon. D: Cub. ZnS:Ag(0.01%),Ga(0.01%), 800°C, H_2S.

ZnS:Ag gives a peak position at roughly 0.07 ev higher quantum energy only in case of halide co-activation, while no such difference exists in cases of co-activation with Al, Ga, or In, and that the blue band of cubic and of hexagonal ZnS:Ag, halide is virtually indistinguishable from the blue band of corresponding copper activated phosphors (1).

(c) A weak green emission band (peak near 2.35 to 2.40 ev) could be observed in several samples of ZnS:Ag (examples Fig. 1). The question whether this green band is due to an accidental contamination with copper (present in the order of 1 ppm) or whether it is the reported green band of silver (7, 8) is as yet undecided.

Hexagonal Zinc-Cadmium Sulfide

Gradual replacement of ZnS by CdS causes the well known gradual shift of the blue emission band of ZnS:Ag toward red and into the near infrared (3, 4, 9-13). Thus, the emission of hexagonal ZnS:Ag,Cl (peak ~2.85 ev at 77°K) corresponds directly to an emission band of similar width and shape with the peak near 1.69 ev (λ = 734 nm) in hexagonal CdS:Ag,Cl. Measured spectra are shown in Fig. 2 and 3. Consideration of the II-VI compounds to be predominantly ionic compounds, so that a variation of the cation means a variation of the conduction band, and application of the Schön-Klasens model of luminescence, yields the recombination term scheme of Fig. 4 where the quantum energies of the peaks of the emission bands are plotted downward from the edge of the conduction band. The resulting points can be connected by a curve approaching a horizontal straight

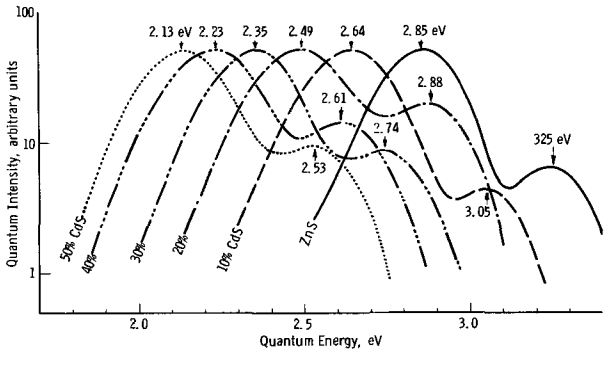

Fig. 2. Emission spectra of hexagonal (Zn,Cd)S:Ag(0.01%),Cl phosphors excited by band gap radiation at 77°K.

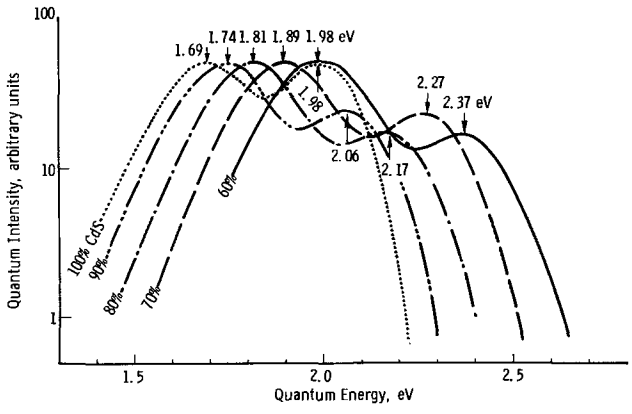

Fig. 3. Emission spectra of hexagonal (Zn,Cd)S:Ag(0.01%),Cl phosphors excited by ultraviolet of 3.40 ev (λ = 365 nm) at 77°K.

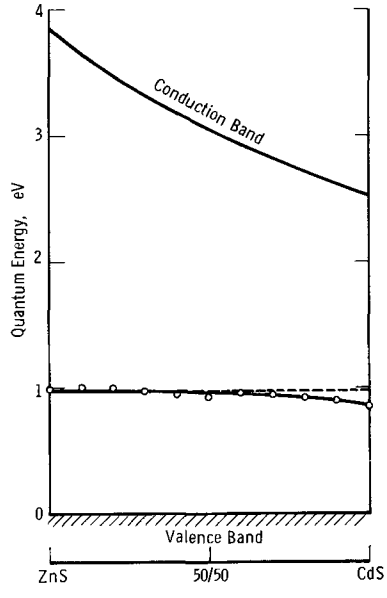

Fig. 4. Recombination term scheme of hexagonal (Zn,Cd)S:Ag at 77°K.

line at the Zn-rich side but slightly deviating downward at the Cd-rich side [in contrast to the corresponding curves derived for copper which are horizontal straight lines over the whole range (1)].

Cubic Zinc Sulfo-Selenides

Emission spectra of Zn(S,Se):Ag phosphors are published by Leverenz (4) and by Klasens (14). Both agree in the observation that a few per cent of S in ZnS:Ag phosphors replaced by Se causes a strong green emission band, in addition to the common blue band of ZnS:Ag, to appear. Our observations are essentially in agreement with this statement although a closer inspection reveals that the matter is somewhat more complicated. Some spectra are shown in Fig. 5 and 6.

Cubic ZnS:Ag,Cl phosphors emit practically only in a blue band at ~2.78 ev. Replacement of only 1% of ZnS by ZnSe causes a strong green band at ~2.47 ev to appear (Fig. 5) in agreement with Leverenz (4) and Klasens (14). Simultaneously, the peak position of the blue band seems rather abruptly to change from ~2.78 to ~2.73 ev. This "jump" of the peak position is hard to observe because of a too strong overlap of the two emission bands [it was not noted in a previous publication (15)], but it is in accord with a similar, but much stronger, jump observed in corresponding copper activated phosphors (1). Further increase of the ZnSe concentration above 1% then causes only a comparatively weak shift of both emission bands and a gradual increase of the low-energy

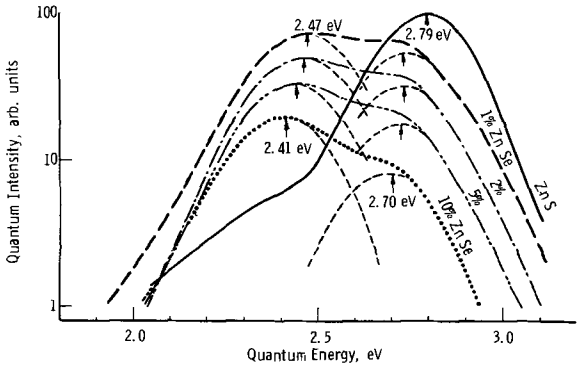

Fig. 5. Emission spectra of cubic Zn(S,Se):Ag(0.01%),Cl phosphors excited by ultraviolet of 3.40 ev (λ = 365 nm) at 77°K.

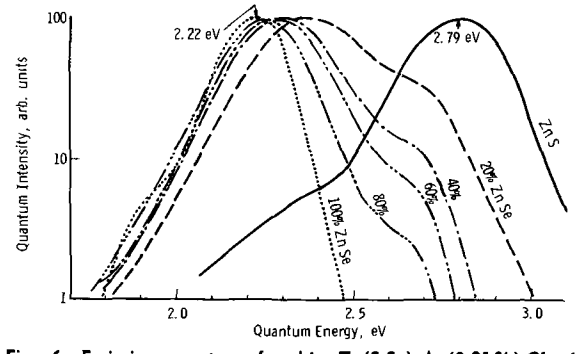

Fig. 6. Emission spectra of cubic Zn(S,Se):Ag(0.01%),Cl phosphors excited by ultraviolet of 3.40 ev (λ = 365 nm) at 77°K.

band at the expense of the high-energy band until in 100% ZnSe only the former, which is then shifted to ~2.20 ev (yellow) is observed (Fig. 6). The yellow Ag-emission in ZnSe can ordinarily be observed in full intensity only at low temperature, it is more or less thermally quenched at room temperature.

All ZnSe:Ag phosphors made and examined to date showed, in addition to the strong yellow band, also two weak emission bands at ~1.95 ev (red) and at ~2.6 ev (blue-green), respectively. The former most likely is not due to Ag but to unavoidable contaminations with copper. The latter was originally believed (15) to be the remnant of the blue band of ZnS:Ag which, in ZnSe, would be shifted just approximately to that position. However, it might also be the emission band corresponding to the near-ultraviolet SAL-emission frequently observed in ZnS:Ag phosphors. In any case, the questionable emission is weak so that ZnSe:Ag is essentially a single band emitter just as well as ZnS:Ag.

In the ionic picture, a variation of the composition of the host material from ZnS to ZnSe means a variation of the valence band while the conduction band remains unchanged. Using the Schön-Klasens model of luminescence, the measured peak positions are plotted downward from the edge of the conduction band in Fig. 7, and the resulting points are connected by two curves. Neither curve is a perfectly horizontal line, but the deviation from the horizontal is much less than the strong variation of the edge of the valence band observed over the same range. No unsteadiness comparable to the small jump in the lower curve near 100% ZnS is to be observed in the upper curve near 100% ZnSe.

Cubic Zinz Seleno-Tellurides

Replacement of a small amount of Se in ZnSe:Ag phosphors by Te causes little or no change on the position of the yellow emission band at ~2.2 ev but causes a new band at ~1.8 ev (deep red) to build up at the expense of the yellow band, which disappears

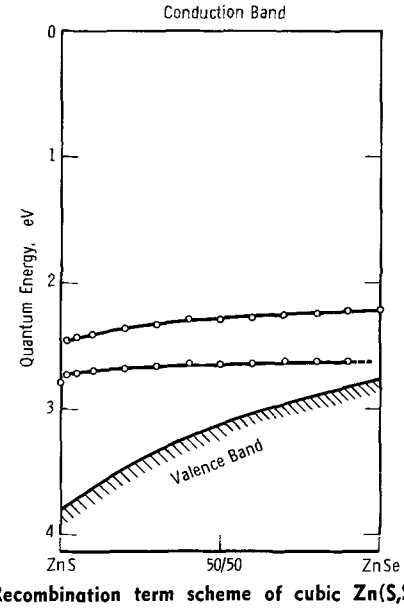

Fig. 7. Recombination term scheme of cubic Zn(S,Se):Ag,Cl at 77°K.

at about 30% Te. The intensity of the red band goes through a maximum and disappears at ~50% ZnTe (Fig. 8). The writer was unable to detect any emission in Zn(Se,Te):Ag containing more than about 50% of ZnTe which unambiguously could be ascribed to be due to silver. If the observed peak positions are plotted downward from the horizontal edge of the conduction band, one obtains the recombination term scheme of Fig. 9. Two points corresponding to an

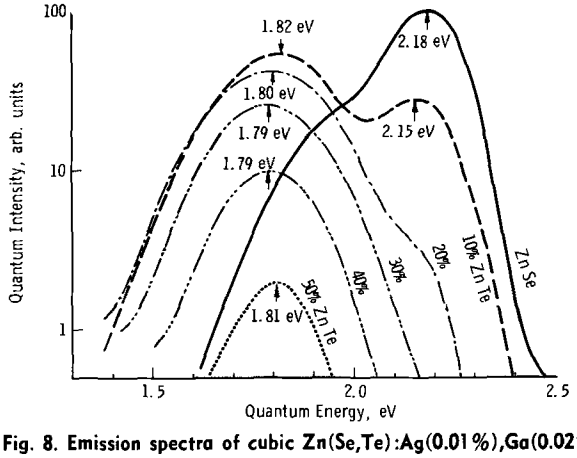

Fig. 8. Emission spectra of cubic Zn(Se,Te):Ag(0.01%),Ga(0.02%) excited by ultraviolet of 3.40 ev (λ = 365 nm) at 77°K.

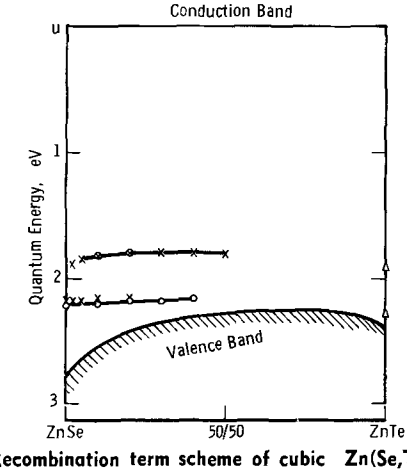

Fig. 9. Recombination term scheme of cubic Zn(Se,Te):Ag,(Cl or Ga). ○ = Cl, X = Ga, △ from ref. (16).

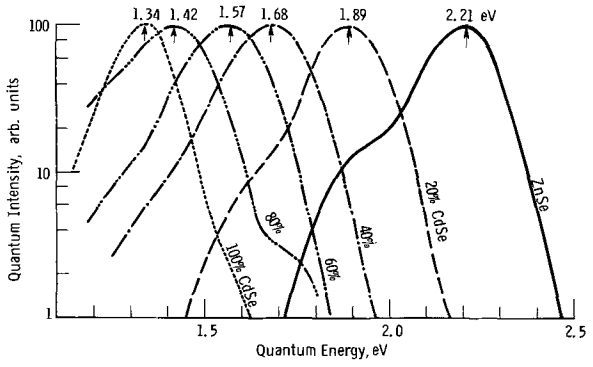

Fig. 10. Emission spectra of cubic or hexagonal (Zn,Cd)Se:Ag (0.02%),I excited by ultraviolet of 3.40 ev (λ = 365 nm) at 77°K.

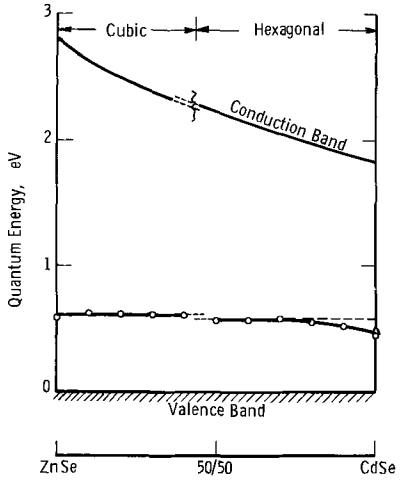

Fig. 11. Recombination term scheme of cubic or hexagonal (Zn,Cd)Se:Ag at 77°K.

emission in ZnTe:Ag reported by Halsted, Aven, and Coghill (16) are also shown in Fig. 9, but their correlation to the curves on the ZnSe-side of the diagram is not clear.

Zinc-Cadmium Selenides

Silver activated ZnSe (cubic) emits, predominantly or only, in a single band at ~2.2 ev. The emission spectrum of CdSe:Ag (hexagonal) is reported (17) to consist of a single band at 920 nm (1.35 ev), measured at 77°K. Some emission spectra of (Zn,Cd)Se:Ag phosphors prepared and measured within these investigations are shown in Fig. 10. All consist of a single strong band accompanied by one or two weaker side bands at lower or higher quantum energies, *i.e.*, left or right of the main band in Fig. 10. The left side band most likely is due to unavoidable copper contamination. The right side band probably is the analog of the SAL emission frequently observed in ZnS:Ag phosphors. Only the strong center emission band can be attributed to silver with a reasonable degree of certainty. The band moves steadily to lower quantum energies with increasing concentration of CdSe, completely similar to the shift observed in corresponding sulfide phosphors, so that the 2.2 ev band of ZnSe:Ag corresponds directly to the 1.34 ev band of CdSe:Ag. If the Schön-Klasens model of luminescence is used and the quantum energies corresponding to the peaks of the measured emission bands are plotted downward from the curved edge of the conduction band, one obtains the recombination term scheme of Fig. 11, where all points scatter closely around a horizontal straight line. The slight discontinuity between 40 and 50% of CdSe may be due to the transition of the crystal structure from cubic to hexagonal. Similar to the case of corresponding sulfides (Fig. 2), the points deviate slightly but distinctly from the horizontal

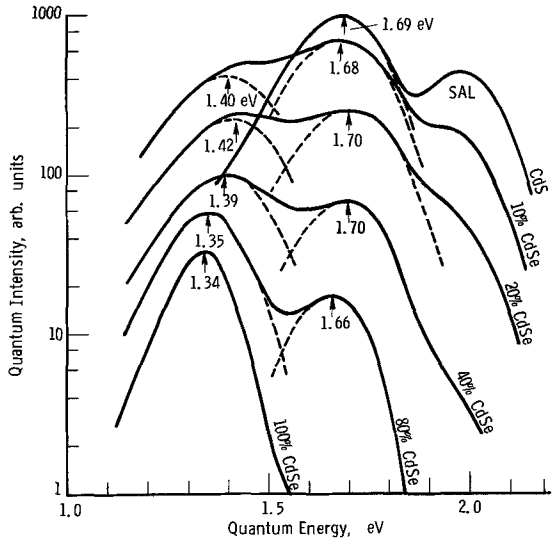

Fig. 12. Emission spectra of hexagonal Cd(S,Se):Ag(0.03%) excited by ultraviolet of 3.40 ev (λ = 365 nm) at 77°K.

straight line only near the cadmium-rich side of the diagram.

Hexagonal Cadmium Sulfo-Selenides

Emission spectra of intermediate Cd(S,Se):Ag phosphors, except those of the two end-members CdS:Ag and CdSe:Ag, do not seem to be reported before. Some spectra measured within these investigations are shown in Fig. 12.

The emission spectrum of CdS:Ag frequently consists of two bands at approximately 1.98 ev and at about 1.70 ev, respectively. The writer believes the former to be the SAL emission; only the 1.70 ev band can be attributed fairly certainly to silver. Gradual replacement of CdS by CdSe causes a new emission band near 1.40 ev to appear and develop. The new band requires about 10 mole % of sulfur to be replaced by selenium to be fairly fully developed, and no unsteadiness is observed in the peak position of the 1.70 ev band near the 100% CdS composition, all in contrast to corresponding zinc compounds (Fig. 5). Further increase of the CdSe concentration causes only very little shift of both emission bands, but a gradual increase of the intensity of the 1.40 ev band at the expense of the 1.70 ev band until, in CdSe:Ag, only the former is still present and moved to ~1.34 ev. Hence, CdS:Ag and CdSe:Ag are both essentially single-band emitters (the SAL-emission disregarded) but the 1.70 ev band of CdS:Ag does not directly correspond to the 1.34 ev band of CdSe:Ag.

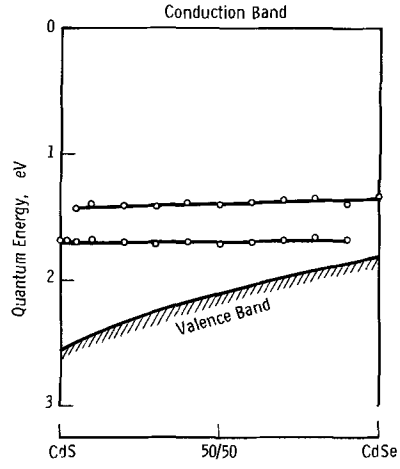

Fig. 13. Recombination term scheme of hexagonal Cd(S,Se):Ag at 77°K.

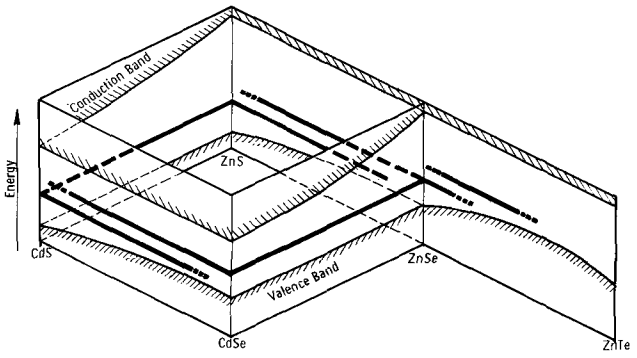

Fig. 14. Simplified recombination term scheme of silver in the binary and ternary (Zn,Cd)(S,Se,Te) phosphors covered in these investigations.

If the quantum energies corresponding to the peaks of the emission bands are plotted downward from the horizontal edge of the conduction band, one obtains the recombination term scheme of Fig. 13, where all points are connected by two curves both almost (not quite) horizontal straight lines, quite in contrast to the pronounced variation of the valence band.

Discussion

The main observations on the emission spectra due to silver in the II-VI compound phosphors can be summarized as follows:

The emission in the binary compounds ZnS, ZnSe, CdS, and CdSe consists essentially of only one band. The exact peak position depends not only on the host material but also on a number of other parameters some of which are still unknown. Gradual replacement of zinc by cadmium either in the sulfides or in the selenides causes a steady shift of the emission band toward lower quantum energies so that the difference between the band gap and the emission peak remains approximately constant. By contrast, gradual replacement of sulfur in ZnS or CdS by selenium, or of selenium in ZnSe by tellurium, causes little or no shift of the emission but the gradual replacement of the one emission band by another one. The consequence is that silver in Zn(S,Se), in Cd(S,Se), and (at least to some extent) also in Zn(Se,Te) is just as much a two-band emitter as copper is (1), and that altogether in the whole system three different emission bands appear to be due to silver. One band requires the presence of sulfur, another the presence of selenium, and the third that of tellurium. The positions of the three recombination terms in the band diagram of the entire system are, highly schematically and neglecting all details, shown in Fig. 14. It is tempting to assume that each one of the three emission bands belongs to a particular recombination center involving, besides silver, either sulfur or selenium or tellurium. This assumption is probably wrong, however, for two reasons.

First, an activator can be considered as a localized center consisting of an impurity cation (silver in this case) surrounded by four anions as next neighbors. Hence, if the compositions of the material varies from ZnS to ZnSe, for instance, there should be some kind of a statistical distribution of impurity cations surrounded by X sulfur and 4-X selenium ions where X = 0,1,2,3,4. Hence, a variation from ZnS to ZnSe should produce a more gradual change of the emission involving five (possibly closely overlapping) emission bands, but not only two bands. The theory of this variation is discussed by Fonger (18) for the case of Zn(S,Se), and probably it holds essentially also for Cd(S,Se) and Zn(Se,Te).

Second, it would certainly be rather arbitrary to restrict a model which correlates the three observed emission bands to three assumed kinds of recombination centers (each containing an impurity ion and either sulfur or selenium or tellurium) to the case of silver activated phosphors only. However, there is open disagreement between the model and the cases of phosphors activated by copper and, as far as known, by gold since copper and gold both produce two emission bands even in the sulfides containing no selenide, and copper also in selenide phosphors containing no sulfide and no telluride.

The only conclusion to be drawn at the moment is that our knowledge of the true mechanism of luminescence in copper or silver activated II-VI compound phosphors is still incomplete. A consideration of the II-VI compounds as predominantly ionic compounds and an assumption of validity of the Schön-Klasens model of luminescence are able to explain the experimentally observed behavior only to some extent, and a considerable amount of it is still open for interpretation.

Acknowledgment

The author wishes to express his thanks to H.F. Ivey and to W. A. Thornton for proof-reading and helpful suggestions, and to H. H. Dorman for much careful work in preparation and measurement.

Manuscript received Feb. 25, 1966; revised manuscript received May 5, 1966.

Any discussion of this paper will appear in a Discussion Section to be published in the June 1967 JOURNAL.

REFERENCES

1. W. Lehmann, *This Journal*, **113**, 449 (1966).
2. S. Rotschild, *ibid.*, **110**, 28 (1963).
3. W. van Gool, "Semiconductors and Phosphors," Proc. Int'l. Coll. Garmisch-Partenkirchen, Germany, 1956 [Interscience Publishers Inc., New York (1958)].
4. H. W. Leverenz, "An Introduction to Luminescence of Solids," John Wiley & Sons, Inc., New York (1950).
5. W. van Gool, A. P. Cleiren, and J. H. M. Heijligers, *Philips Research Repts.*, **15**, 254 (1960).
6. F. A. Kröger and J. Dickhoff, *Physica*, **16**, 297 (1950).
7. M. H. Payen de la Garanderie, *J. Phys. Rad.*, **22**, 423 (1961).
8. H. Treptow, *Czech. J. Phys.*, **13**, 115 (1963).
9. W. van Gool, *Philips Research Repts.*, **13**, 157 (1958).
10. K. Kamm, *Ann. Phys.*, **30**, 333 (1937).
11. S. Rotschild, Z. *Phys.*, **108**, 24 (1938).
12. W. Lehmann, *This Journal*, **110**, 754 (1963).
13. G. E. Gross, *Phys. Rev.*, **116**, 1478 (1959).
14. H. A. Klasens, *This Journal*, **100**, 72 (1953).
15. W. Lehmann, *ibid.*, **112**, 1256 (1965).
16. R. E. Halsted, M. Aven, and H. D. Coghill, *ibid.*, **112**, 177 (1965).
17. M. Avinor and G. Meijer, *J. Chem. Phys.*, **32**, 1456 (1960).
18. W. H. Fonger, *Phys. Rev.*, **137**, A-1038 (1965).

The Basic Significance of Oxygen Chemisorption on the Photoelectronic Properties of CdS and CdSe

Richard H. Bube

Department of Materials Science, Stanford University, Stanford, California

ABSTRACT

The long-known phenomenon of oxygen chemisorption on CdS and CdSe, more intensively studied recently, is shown to have a basic significance for the photoelectronic properties of thin crystals or layers. It is proposed that every "pure" crystal of CdS or CdSe is of relatively high conductivity [$\geq 10^{-6}$ (ohm cm)$^{-1}$] and high photosensitivity (electron lifetime of 10^{-3} sec) as prepared by standard techniques. If the crystal or layer is thin enough, oxygen adsorption obscures these properties and gives the appearance of a highly insulating insensitive material. Smaller effects are found in crystals containing deliberately incorporated impurities as long as the Fermi level at room temperature lies above the level associated with the surface state for chemisorbed oxygen. Because of the universal presence of oxygen chemisorption effects, every experiment in which the effect of heat, vacuum, or photoexcitation are investigated toward understanding the nature of photochemical changes, must be interpreted in the light of the significant effects associated with the simple desorption of oxygen.

The effect of oxygen on the photoelectronic properties of CdS and CdSe has been known from the early days of research in this area. A common prescription for improving the light-to-dark resistance ratio of photoconducting cells was to bake the cells in air to increase the dark resistance (1). The importance of adsorbed oxygen in determining measured values of dark resistance and photosensitivity in CdS (2, 3) and CdSe (4) was investigated a number of years ago, but it is only in recent years that the general importance of these effects has been realized. The effect of adsorbed oxygen on the photovoltaic effect of CdS has been studied by Williams (5) and by Haas, Fox, and Katz (6), on the lifetime and response time for strongly absorbed light in CdS by Mark (7-9), on the conductivity of CdSe layers by Somorjai (10), on the photoelectronic properties of sintered layers of CdS-CdSe and CdSe by Shear, Hilton, and Bube (11), and on the photo-Hall effect of sintered layers by Robinson and Bube (12). The importance of oxygen chemisorption phenomena in simulating other types of photochemical changes has also been discussed for CdS-CdSe crystals (13), for which the electron lifetime at room temperature could be varied by a factor of 20 by varying the amount of adsorbed oxygen.

It now appears that what was originally believed to be an appreciable effect of importance for only a few specially prepared crystals or for particular excitation conditions is in fact a quite general effect that can have a profound influence on the photoelectronic properties of CdS and CdSe. The effects would be expected to be the most pronounced for thin crystals or layers of these materials for which surface chemisorption of oxygen could have electrical effects extending throughout the volume of the material.

Mark has given a thorough report on the phenomenon of oxygen chemisorption on CdS crystals, both as to its kinetics and its energetics. He has worked with strongly absorbed photoexcitation of CdS crystals without photosensitivity in the red portion of the spectrum and has located the surface level associated with chemisorbed oxygen at 0.91 ev below the conduction band. The largest change in electron lifetime reported by Mark is an increase by a factor of 35; he reports that changes in lifetime of less than 20% are found in all red-sensitive crystals.

It is the purpose of the present paper to indicate that the changes in photoelectronic properties of "pure" crystals (*i.e.*, relatively red-insensitive) due to oxygen adsorption can be surprisingly large, amounting to seven to ten orders of magnitude in dark conductivity and to three to four orders of magnitude in electron lifetime. Effects involving several orders of magnitude in dark conductivity and one order of magnitude in electron lifetime are found even in thin crystals with red sensitivity. Only in crystals in which the Fermi level at room temperature lies at or below the level of the surface state of chemisorbed oxygen does the effect become very small. The realization of the importance that chemisorbed oxygen effects can have on all thin crystals and layers of CdS and CdSe provides the basis for explaining a number of previous observations.

Experimental

Four different types of crystals were used in the present investigation: (*i*) pure crystals of CdS prepared with extreme caution to eliminate impurities, particularly oxygen during the crystal growth, in thin platelet form (14); (*ii*) thin platelet crystals of CdS:Cl:Cu which had been grown with an excess of chlorine and then had been compensated by diffused copper (15); (*iii*) crystals of CdS:Cu grown by sublimation from an initial charge of CdS and Cu_2S (16); and (*iv*) crystals of pure CdSe, used in a previous investigation of the effect of vacuum annealing (17). All these crystals were available through the courtesy of RCA Laboratories.

Ohmic contacts were applied to the crystals by melted indium electrodes applied in air. That the properties of the crystals were not altered by this electrode application process was demonstrated by measuring the properties of crystals with gallium contacts applied without heating at room temperature.

Measurements of dark conductivity and photoconductivity were made in a special cryostat in which flowing atmospheres of helium, oxygen, or air could be maintained. The temperature range covered was from 80°K to the melting point of indium at about 430°K. Photoexcitation was by a Bausch and Lomb monochromator. All currents were directly recorded on a L&N X-Y recorder through a L&N micromicroammeter.

Results

Measurements made on 5 crystals of pure CdS, 2 crystals of CdS:Cl:Cu, and 2 crystals of CdS:Cu are summarized in Table I. In addition to the atmosphere present during the measurement, Table I gives the

Table I. Summary of oxygen desorption effects on CdS

Crystal	Run	Heating atmosphere	E, ev	Dark σ 300°K, (ohm cm)$^{-1}$	τ, sec
CdS-A-1	Initial				2×10^{-6}
(1.3 × 0.7 × 0.05)	1	He	5.7	$<4 \times 10^{-10}$	
mm^3	2	He	0.42	10^{-8}	
	3	He	0.35	10^{-7}	2×10^{-3}
CdS-A-2	Initial				6×10^{-7}
(1.3 × 3.2 × 0.025)	1	Air	3.1	$<2 \times 10^{-10}$	
mm^3	2	Air	0.42	8×10^{-8}	2×10^{-4}
	3	He	0.57	3×10^{-7}	3×10^{-4}
	Initial*				7×10^{-7}
	4	He	2.3	$<2 \times 10^{-10}$	
	5	He	0.32	10^{-7}	5×10^{-5}
CdS-A-3	Initial				10^{-7}
(1.5 × 1.5 × 0.020)	1	He	4.3	$<5 \times 10^{-10}$	
mm^3	2	He	0.38	3×10^{-7}	4×10^{-4}
	3	O_2	0.71	7×10^{-10}	
	4	He	0.53	9×10^{-9}	
	5	He	0.42	5×10^{-7}	
	6	O_2	—	7×10^{-9}	
	7	O_2	0.98	$<5 \times 10^{-10}$	
CdS-B-1	Initial				2×10^{-6}
(2.0 × 3.5 × 0.025)	1	O_2	5.5	$<2 \times 10^{-10}$	
mm^3	2	He	0.47	4×10^{-7}	5×10^{-4}
CdS-B-2	Initial				2×10^{-6}
(2.2 × 3.0 × 0.012)	1	He	3.4	$<6 \times 10^{-10}$	
mm^3	2	He	0.43	2×10^{-6}	10^{-3}
CdS:Cl:Cu-1	Initial				10^{-4}
(1.0 × 1.7 × 0.05)	1	He	1.6	$<10^{-10}$	
mm^3	2	He	0.41	3×10^{-9}	10^{-3}
CdS:Cl:Cu-2	Initial				2×10^{-4}
(1.0 × 1.0 × 0.060)	1	He	2.6	2×10^{-10}	
mm^3	2	He	0.40	3×10^{-8}	7×10^{-4}
CdS:Cu(1.2%)	Initial				3×10^{-4}
(2.1 × 2.3 × 1.0)	1	He	0.99	$<10^{-11}$	
mm^3	2	He	0.86	$<10^{-11}$	
	3	He	0.81	$<10^{-11}$	2×10^{-3}
CdS:Cu(3.3%)	Initial				8×10^{-5}
(3.0 × 2.7 × 1.0)	1	He	1.15	$<10^{-11}$	
mm^3	2	He	0.90	$<10^{-11}$	
	3	He	0.80	$<10^{-11}$	2×10^{-4}

* Exposed to room air for 5 days between runs 3 and 4.

activation energy associated with the dark conductivity, the actual value of the dark conductivity at room temperature measured during the run for which it is listed, the initial electron lifetime determined from the steady-state photoconductivity, and the electron lifetime measured after the run for which it is listed.

Similar measurements on 3 crystals of pure CdSe are listed in Table II; all of these measurements were done in a helium atmosphere.

Although in our experience it is only the rare crystal that shows appreciable oxygen desorption upon heating in even a nonoxygen atmosphere to 100°C, a wide variety of crystals show oxygen desorption effects on heating to 125°-150°C regardless of the atmosphere. Insofar as most measurements reported in the literature usually do not involve heating appreciably above 100°C, the purpose of the heating being to eliminate water vapor from the Dewar system, such measurements deal with crystals with chemisorbed oxygen.

Dark conductivity.—Only one of the twelve crystals in this investigation had a measurable dark conductivity at room temperature, the limitation of the instrumentation being about 10^{-10} (ohm cm)$^{-1}$ depending on the exact geometry of the crystal. The initial heating almost always gave an apparent activation energy for all but the CdS:Cu crystals, which was too large to have physical significance as a simple conductivity process (1.6-5.7 ev), but requires interpretation as due to oxygen desorption as well. In the oxygen-free state, the dark conductivity of all 5 pure CdS crystals is between 10^{-7} and 2×10^{-6} (ohm cm)$^{-1}$ (see Table III for summary of parameters from Table I).

Dark conductivity data for the CdS-A-1 crystal are given in Fig. 1. The initial heating has a very steep slope with apparent activation energy of 5.7 ev. The dark conductivity at the upper temperatures was also time dependent, again indicating the importance of thermal desorption of oxygen in the flowing helium atmosphere. Curve 2 in Fig. 1 shows the results of partial

Table II. Summary of oxygen desorption effects on CdSe in helium

Crystal	Run	E, ev	Dark σ 300°K, (ohm cm)$^{-1}$	τ, sec
CdSe-1	Initial			2×10^{-8}
(1.5 × 1.0 × 0.1)	1	0.90	$<10^{-10}$	
mm^3	2	0.14	2×10^{-6}	2×10^{-5}
CdSe-2	Initial			5×10^{-8}
(2.3 × 1.5 × 0.050)	1	2.7	$<3 \times 10^{-10}$	
mm^3	2	0.064	10^{-3}	2×10^{-3}
CdSe-3	Initial			10^{-7}
(1.6 × 1.1 × 0.3)	1	2.9	$<5 \times 10^{-11}$	
mm^3	2	0.014	7×10^{-4}	2×10^{-3}

Table III. Summary of parameters from Table I on CdS

Crystal	Lifetime ratio	Max. dark σ 300°K, (ohm cm)$^{-1}$	Max. τ, sec	Avg E in He, ev,* after heating in He
CdS-A-1	1000	10^{-7}	2×10^{-3}	0.38
CdS-A-2	500	3×10^{-7}	3×10^{-4}	0.32
CdS-A-3	4000	3×10^{-7}	4×10^{-4}	0.40
CdS-B-1	250	4×10^{-7}	5×10^{-4}	0.47
CdS-B-2	500	2×10^{-6}	10^{-3}	0.43
CdS:Cl:Cu-1	10	3×10^{-9}	10^{-3}	0.41
CdS:Cl:Cu-2	3.5	3×10^{-8}	7×10^{-4}	0.40
CdS:Cu(1.2%)	6	$\approx 2 \times 10^{-13}$	2×10^{-3}	0.89
CdS:Cu(3.3%)	3	$\approx 10^{-13}$	2×10^{-4}	0.95

* The average value of E for the first 7 crystals of the above table in all those cases where a measurement in He follows a measurement in He is 0.40 ± 0.03 ev.

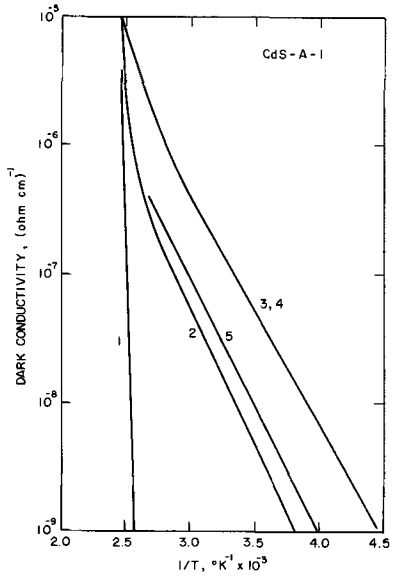

Fig. 1. Dark conductivity of pure CdS-A-1 in flowing helium as a function of temperature 1. Initial heating after long period of exposure to air; 2. second heating after reaching maximum temperature of 127°C; 3, 4, third and fourth heatings after reaching maximum temperature of 146°C; 5, fifth heating after the measurement of photoconductivity and thermally stimulated conductivity vs. temperature.

desorption of oxygen, and curves 3 and 4 indicate the reversible state arrived at by heating to 146°C. Curve 5 was measured later, after the measurement of photoconductivity and thermally stimulated conductivity as a function of temperature, during which time some readsorption of oxygen had apparently occurred. The activation energy for dark conductivity for curves 2 through 5 is between 0.35 and 0.42 ev.

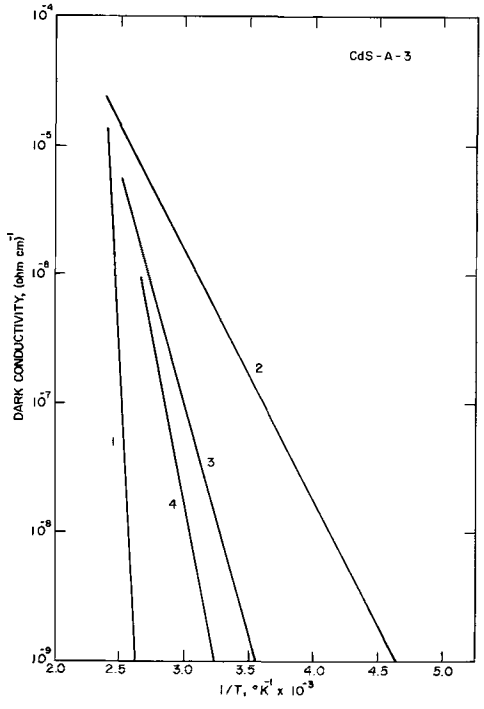

Fig. 2. Dark conductivity of pure CdS-A-3 as a function of temperature. 1, Initial heating in flowing helium after long period of exposure to air; 2, second heating in flowing helium after heating to 144°C; 3, heating in flowing oxygen; 4, heating in flowing oxygen after photoexcitation at elevated temperature and while cooling.

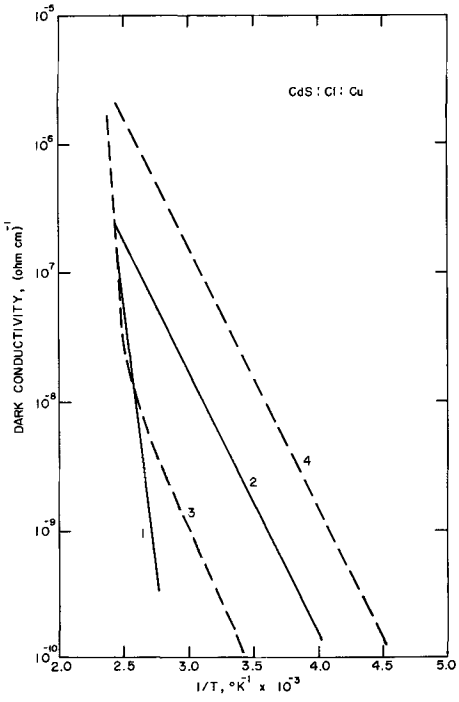

Fig. 3. Dark conductivity of two CdS:Cl:Cu crystals in flowing helium as a function of temperature. 1, Initial heating of CdS:Cl:Cu-1 after long period of exposure to air; 2, second heating of CdS:Cl:Cu-1 after reaching maximum temperature of 144°C; 3, initial heating of CdS:Cl:Cu-2 after long period of exposure to air; 4, second heating of CdS:Cl:Cu-2 after reaching maximum temperature of 147°C.

Similar data for CdS-A-3 are shown in Fig. 2. Curve 2, which represents the dark conductivity in the oxygen-free state, has an activation energy of 0.38 ev. Curve 3 represents the reasonably reversible variation of dark conductivity for this crystal if oxygen is used to replace the helium after the run shown in curve 2. If, in addition, the crystal is photoexcited at the highest temperature reached in curve 3 and is then cooled rapidly continuing photoexcitation, subsequent heating yields curve 4, indicating still greater oxygen adsorption as a result of the photoexcitation.

Such results are not confined to pure CdS crystals. Data for the two crystals of CdS:Cl:Cu are given in Fig. 3. The initial heating is given in curves 1 and 3 and the properties of the oxygen-free surfaces in curves 2 and 4. Once again the activation energy for the dark conductivity in the oxygen-free state is about 0.40 ev. Crystal CdS:Cl:Cu-2 shows a low-temperature conductivity slope of 0.44 ev on the initial heating, indicating the presence of these centers even with adsorbed oxygen.

Values of the dark conductivity activation energy are summarized in the last column of Table III for all measurements made in helium, following a heating in helium to eliminate oxygen adsorption effects. An average value of activation energy of 0.40 ± 0.03 ev is obtained for 9 measurements on the 7 pure CdS or CdS:Cl:Cu crystals.

Very large increases in apparent dark conductivity are found also for the pure CdSe crystals tested, as shown in Table II. The activation energies for the oxygen-free crystals are much lower than in CdS crystals and do not show such constancy from crystal to crystal.

Strikingly different is the behavior of the two CdS:Cu crystals. The activation energy on the initial heating is only slightly larger than on subsequent heatings in helium, and the dark conductivity in the oxygen-free state is probably about 10^{-13} (ohm

Table IV. Ratio of the photoconductivity in the oxygen-free state for several CdS crystals to that with adsorbed oxygen for various wavelengths of photoexcitation

Crystal	Photoconductivity ratio at 4000Å	Photoconductivity ratio at λ_{max}	Photoconductivity ratio for long λ
CdS-A-1	7000	1000	17,000 (5400Å)
CdS-A-2	3000	500	4,500 (5400Å)
CdS-A-3	18,000	4000	10,000 (5300Å)
CdS:Cl:Cu-1	95	10	300 (7500Å)
CdS:Cl:Cu-2	20	3.5	6 (8000Å)
CdS:Cu(3.3%)	25	3	3 (7500Å)

cm)$^{-1}$, the estimated dark conductivity in the initial state being about 10^{-14} (ohm cm)$^{-1}$.

Electron lifetime.—Although the initial electron lifetimes for the 12 crystals measured varies from 2×10^{-8} to 3×10^{-4} sec, the lifetime in the oxygen-free state for all crystals except one lies in the range of 2×10^{-4} to 2×10^{-3} sec. In other words, removing the adsorbed oxygen increases the electron lifetime by a maximum factor of 4×10^4 (CdSe-2) and by a minimum factor of 3 [CdS:Cu(3.3%)], but the final electron lifetime in all cases is essentially of the order of 1 millisec. These results indicate that CdS and CdSe crystals as prepared by a variety of standard methods and, regardless of the kind of impurity incorporation over a wide range, are all highly photosensitive in the absence of adsorbed oxygen.

Spectral dependence of photoconductivity.—The values of electron lifetime used in the previous section and in Table I-III are the values calculated for excitation at the maximum of the photoconductivity spectrum. The change in photoconductivity with oxygen desorption is a minimum for this wavelength, often being appreciably larger for both shorter and longer wavelengths. Results for several of the CdS crystals are summarized in Table IV.

Thermally stimulated conductivity and electron lifetime.—Earlier investigations (7, 8, 18) have reported a much larger increase in response time or in thermally stimulated conductivity on oxygen desorption from CdS crystals than in electron lifetime. Mark, for example, cites an increase in electron lifetime of 35 being accompanied by an increase in thermally stimulated conductivity by a factor of 10^5.

Measurements were made on the temperature dependence of electron lifetime and of thermally stimulated conductivity both with adsorbed oxygen and in the oxygen-free state for crystals CdS-A-2 and CdS-B-2. Results are summarized in Table V. Although attempts to compare these figures in any exact quantitative way are unjustified because of the differences in current levels involved, it does appear that they are of comparable magnitude and that a large discrepancy between changes in free electron lifetime and in thermally stimulated conductivity is not found.

Dynamic behavior.—Some of the changes accompanying oxygen desorption reported above are so large, particularly for the pure crystals, that it may be wondered whether oxygen desorption is indeed the only process involved. In order to provide evidence that the effects are indeed reversible oxygen chemisorption effects, several measurements were made of the dynamic behavior of dark conductivity and photoconductivity with changes of atmosphere.

Table V. Comparison of changes in electron lifetime and thermally stimulated conductivity with oxygen desorption

Crystal	T, °C	Ratio of electron lifetime	Ratio of thermally stimulated conductivity
CdS-A-2	−150	100	250
	−100	60	200
	−50		300
	0		
	25	60	
CdS-B-2	−150	400	10,000
	−100	1200	20,000
	−50	2000	2,000
	0	2500	1,000
	25	8000	700

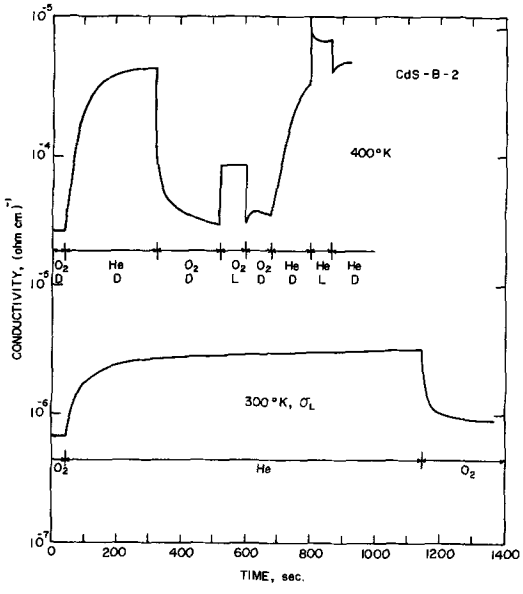

Fig. 4. Dynamic behavior of conductivity in CdS-B-2 crystal. Lower curve shows variation in photoconductivity at room temperature with variation between oxygen and helium atmosphere. Upper curve shows variation in dark conductivity and in photoconductivity with variation between oxygen and helium atmosphere. D represents "dark," and L represents "light."

Figure 4 shows a series of dynamic measurements for the pure CdS-B-2 crystal. The lower curve shows the effect on the photocurrent at 300°K of replacing the oxygen atmosphere around the crystal by a helium atmosphere, and then returning to the oxygen. The upper curve shows a series of measurements at 400°K, demonstrating the reversibility of atmosphere effects on the dark conductivity and on the photoconductivity.

Figure 5 shows the dynamic behavior of CdS-A-3 at room temperature after having been heated in helium to desorb oxygen. Even in helium in the dark there is a slow decay of dark conductivity, evidently associated with readsorption of oxygen present in trace amounts, as mentioned previously. A decrease in lifetime by a factor of about 1000 is observed directly from the data of Fig. 5 on replacement of helium by oxygen, as well as a decrease in dark conductivity.

Reversibility in the oxygen chemisorption effects is also demonstrated by the data given in Table I for CdS-A-2. After desorption of oxygen had increased the dark conductivity and the electron lifetime, the crystal was simply exposed to air at room temperature for 5 days. Subsequent measurements showed that the initial dark conductivity and electron lifetime values were restored.

Discussion

"Pure" crystals.—The results indicate that every "pure" crystal of CdS and CdSe has a relatively low resistivity and a high photosensitivity as prepared by any one of the standard techniques. If the crystal is thin enough, oxygen adsorption obscures these properties and gives the appearance of a highly insulating insensitive crystal.

An immediate explanation is hereby offered for the observation that large crystals of pure CdS invariably have high dark conductivity, whereas thin crystals of pure CdS can be prepared easily with low dark conductivity. How thin a crystal must be for the effect of oxygen adsorption at room temperature to be domi-

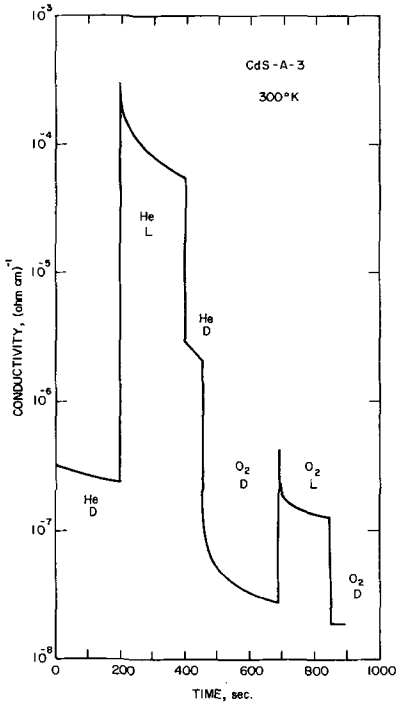

Fig. 5. Dynamic behavior of conductivity at room temperature for crystal CdS-A-3. D represents "dark," and L represents "light."

nant can be estimated from the thickness of the barrier layer associated with chemisorbed oxygen

$$d = \left[\frac{\epsilon\phi_0}{2\pi eN}\right]^{1/2} \qquad [1]$$

If we set $\epsilon = 10$, $\phi_0 = (0.9\text{-}0.4) = 0.5$v, we can calculate d if the value of N, the density of ionized donors, is known. Since the room temperature conductivity of such pure crystals in the oxygen-desorbed state is of the order of 10^{-6} (ohm cm)$^{-1}$, the corresponding value of N is about 2×10^{10} cm^{-3} for an assumed electron mobility of 300 cm^2/v-sec. Under such conditions, $d = 240\mu$. This means that high-resistivity, pure CdS crystals should in general have a thickness of less than a few hundred microns. The thicknesses of the 5 pure crystals used in this investigation were between 12 and 50μ.

Pure, thin crystals of CdS have been generally found to have poor photosensitivity. It has been conventional (19) to ascribe this lack of sensitivity to the absence of compensated sensitizing centers, *i.e.*, particular compensated acceptors with a much smaller capture cross section for free electrons than for free holes. The fact that photosensitive crystals can be produced by the incorporation of trace amounts of halogen impurities (14) has been attributed either to the creation of sensitizing-type defects or to compensation of existing sensitizing-type defects by the incorporated halogen. It now appears probable that the principal effect of the halogen is to supply electrons to reduce the effects of adsorbed oxygen. The fact that pure crystals are highly photosensitive in the oxygen-free state is additional evidence that the sensitizing-type defects are indeed intrinsic crystal defects such as cadmium vacancies.

The dominant donor in the pure CdS crystals in the oxygen-free state appears to have an ionization energy of about 0.40 ev. Since the ionization energy of the donors in highly nonstoichiometric CdS is of the order of 0.03 ev, it is possible that the 0.40 ev activation energy is associated with the second ionization level of an anion vacancy. The fact that the same activation energy of 0.40 ev is found in the CdS:Cl:Cu crystals is additional evidence of its identification with an intrinsic crystal defect. It is possible that the activation energy of 0.40 ev corresponds only to a particular value in a relative continuous distribution of donor levels, this particular value being fixed by the degree of oxygen desorption associated with the experimental conditions that prevented heating above 156°C in order not to melt the indium electrodes. The similarity of activation energy between curves 2 through 5 in Fig. 1, and between curves 2 through 4 in Fig. 3, argues against this possibility.

In the case of CdSe-1, an activation energy of 0.14 ev was found for the dark conductivity in the oxygen-free state. When crystals of this same type are annealed above 500°C in vacuum, dark conductivity with an activation energy of 0.14 ev is found (17). This result indicates that the density of 0.14 ev donors is increased by the vacuum anealing to the point where the effects of oxygen adsorption can be overcome.

Impure crystals.—Oxygen adsorption effects will of necessity be minimized in crystals in which the Fermi level lies near or below the level of the surface state corresponding to adsorbed oxygen. A Fermi level lying 0.91 ev below the conduction band at room temperature in CdS corresponds to a dark conductivity of about 10^{-13} (ohm cm)$^{-1}$, again using an electron mobility of 300 cm^2/v-sec and an electron effective mass ratio of 0.2.

The thin CdS:Cl:Cu crystals have a dark conductivity of about 10^{-8} (ohm cm)$^{-1}$ in the oxygen-free state, and oxygen adsorption effects on dark conductivity and electron lifetime are measurable, although they are not as large as in the pure crystals.

The CdS:Cu crystals, on the other hand, have a dark conductivity at room temperature of about 10^{-13} (ohm cm)$^{-1}$, estimated by extrapolation of dark conductivity data above room temperature. It would be expected that the effects of oxygen adsorption on these crystals would be small. Such is found to be the case.

Thermally stimulated conductivity.—The apparent occurrence of a much larger increase in thermally stimulated conductivity than in electron lifetime with oxygen desorption led Mark (8) to propose that a high density of surface electron traps was compensated by an equally high density of surface hole traps, in order to avoid a barrier field at the surface much larger than the breakdown field of CdS.

Measurements in the present investigation, summarized in Table V, indicate that to a first approximation the increase in thermally stimulated conductivity can be interpreted as a direct result of an equal increase in electron lifetime with no appreciable change in actual trap density. Since this indicates that a high density of electron surface traps is not a necessary part of the oxygen-free surface condition, it suggests that the earlier results (7, 8, 18) may involve an incorrect assessment of the actual trap density in the oxygen-free state. Such an error could result if the electron lifetime in the thermally stimulated conductivity or response time measurements were actually much larger than the electron lifetime for steady-state excitation (20). Mark has also pointed out this possibility (21), but has argued that the increased effective lifetime found for electrons released during a TSC measurement is the result of their having been released from surface traps, recombination becoming possible only after a compensating hole is released into the bulk from a surface trap. Experiments on the effects of adsorbed oxygen on electron lifetime and thermally stimulated conductivity in the carefully studied CdS-CdSe single crystal system indicated a direct correspondence between changes in electron lifetime and in thermally stimulated conductivity (13).

General consequences.—Since the properties of CdS and CdSe crystals and layers can be changed by such large factors by the simple alteration of the amount of adsorbed oxygen, other experiments in which desorption of oxygen may occur must be carefully inter-

preted. This would apply in particular to experiments in which the effect of heat, vacuum, or photoexcitation is investigated to understand the nature of photochemical changes.

Acknowledgments

Helpful discussions in the course of this work were held with G. A. Dussel and with Dr. Guy Marlor and Dr. Victor Serdyuk.

Work on this paper was supported partially by the Army Research Office (Durham) and partially by the Advanced Research Projects Agency through the Center for Materials Research at Stanford University.

Manuscript received March 25, 1966.

Any discussion of this paper will appear in a Discussion Section to be published in the June 1967 JOURNAL.

REFERENCES

1. S. V. Forgue, R. R. Goodrich, and A. D. Cope, *RCA Rev.*, **12**, 335 (1951).
2. R. H. Bube, *Phys. Rev.*, **83**, 393 (1951).
3. S. H. Liebson, *J. Chem. Phys.*, **23**, 1732 (1955).
4. R. H. Bube, *ibid.*, **27**, 496 (1957).
5. R. Williams, *J. Phys. Chem. Solids*, **23**, 1057 (1962).
6. K. J. Haas, D. C. Fox, and M. J. Katz, *ibid.*, **26**, 1779 (1965).
7. P. Mark, *ibid.*, **25**, 911 (1964).
8. P. Mark, *ibid.*, **26**, 959 (1965).
9. P. Mark, *ibid.*, **26**, 1767 (1965).
10. G. A. Somorjai, *ibid.*, **24**, 175 (1963).
11. H. Shear, E. A. Hilton, and R. H. Bube, *This Journal*, **112**, 997 (1965).
12. A. L. Robinson and R. H. Bube, *ibid.*, **112**, 1002 (1965).
13. R. H. Bube, G. A. Dussel, C.-T. Ho, and L. D. Miller, *J. Appl. Phys.*, **37**, 21 (1966).
14. R. H. Bube and L. A. Barton, *RCA Rev.*, **20**, 564 (1959).
15. R. H. Bube and S. M. Thomsen, *J. Chem. Phys.*, **23**, 15 (1955).
16. A. B. Dreeben and R. H. Bube, *This Journal*, **110**, 456 (1963).
17. R. H. Bube and L. A. Barton, **29**, 128 (1958).
18. R. H. Bube, *J. Appl. Phys.*, **34**, 3309 (1963).
19. R. H. Bube, "Photoconductivity of Solids," p. 172, John Wiley & Sons, Inc., New York (1960).
20. G. A. Dussel and R. H. Bube, *J. Appl. Phys.*, **37**, 934 (1966).
21. P. Mark, *RCA Rev.*, **26**, 461 (1965).

The P-T-X Phase Diagram of the System Ga-S

R. M. A. Lieth, H. J. M. Heijligers, and C. W. M. v.d. Heijden

Solid State Physics Group, Department of Technical Physics, Technical University, Eindhoven, The Netherlands

ABSTRACT

The phase diagram of the system Ga-S has been determined. Two maxima are found in the T-X diagram, one at the composition of GaS, the other at the composition of Ga_2S_3. The compound GaS has a maximum melting point of 962° ± 4°C at a sulfur pressure of $0.9 \cdot 10^{-4}$ mm Hg Ga_2S_3 has a maximum melting point of about 1090°C at a sulfur pressure of 1.3 mm Hg. A range of liquid immiscibility exists between about 10 and 48 a/o (atom per cent) S and possibly also between about 65 and >90 a/o S.

Investigations on GaS have revealed that this compound has interesting semiconducting properties (1, 2). In order to grow single crystals of this layer compound under controlled conditions we found it useful to know more about the P-T-X diagram of the system Ga-S.

While the solid-liquid phase equilibria of the system Ga-Te, In-Te, In-S, and In-Se are fully described (3-6), there seems to be no report on a phase diagram of the system Ga-S. Klemm and von Vogel (7) synthesized GaS from the elements and Ga_2S_3 by passing a stream of H_2S over Ga_2O_3 at 1250°C. They report melting points of 965° and 1250°C for GaS and Ga_2S_3, respectively.

Spandau and Klanberg (8) reported the decomposition of GaS when heated at temperatures between 970°-1200°C. Ga_2S, one of the decomposition products, was used in a vapor pressure experiment, and above 950°C Spandau and Klanberg found an inhomogeneous melt containing Ga and GaS, while complete miscibility was found above 1150°C.

On the basis of a comparison of Debye-Scherrer powder photographs Spandau and Klanberg suggested a hexagonal structure for Ga_2S which was almost the same as that of GaS. These authors reported a melting point for GaS of 970° ± 3°C which is in accordance with the work of Brukl and Ortner (9). The same authors also synthesized Ga_2S_3 from the elements. Above 950°C, Ga_2S_3 started to loose sulfur and decomposed into Ga_4S_5 and S_2.

Experimental Procedures

To obtain the phase relations as a function of temperature and composition, use was made of thermal analysis (10) carried out on samples sealed under a vacuum of 10^{-3} mm Hg in vitreous silica tubes which had an axial thermocouple well. As the closed silica tubes were almost completely filled with the substance under investigation and because the equilibrium sulfur pressures at the temperatures involved are low, as discussed later, the uncertainties introduced by evaporation of sulfur from the melt are negligible.

The samples used in these experiments were synthesized by heating the elements[1] for several hours in an electrically heated furnace. Samples with a sulfur content up to 50 a/o were kept at a temperature of 1100°C, those with a sulfur content higher than 50 a/o were heated at 1300°C.

Afterwards, cooling curves as function of time t were taken, the melting points being shown by a change in the slope, or by a horizontal portion of the temperature-time curve.[2] In order to get an indication of the form of the diagram, in the first series of cooling experiments the samples were cooled down from 1100° and 1300°C, respectively. This was repeated several times, and with the information gained a second series of cooling and heating measurements was made on the same samples.

In these experiments the melt was maintained for several hours at a few degrees above its liquidus temperature and then cooled down at a rate of 10°C/min. These measurements were repeated until a difference of less than 2.5°C was obtained between the thermal arrests of the cooling and heating curves of each sample. The Pt-Pt 10% Rh thermocouples were calibrated under identical experimental conditions by cooling curves taken on pure silver and sodium chloride. No supercooling occurred during these experiments.

[1] From Johnson Matthey and Co. Ltd., spectrographically pure.

[2] This was done with a Philips automatic measuring bridge.

Preliminary work had shown that GaS had a maximum sulfur pressure at its melting point of less than 10^{-6} atm. In the case of Ga_2S_3 this was less than 10^{-2} atm.

To obtain the phase relations as a function of pressure and temperature, the following method was used: accurately weighed samples were heated for several hours at various temperatures in sealed silica tubes together with a known volume of hydrogen. This hydrogen had a pressure of 1 atm at room temperature. At the temperatures involved, equilibrium is attained according to the equation

$$H_2 + \frac{1}{2}S_2 \leftrightarrows H_2S \qquad [1]$$

in which the sulfur pressure is the equilibrium sulfur pressure over the sulfide. The values of

$$K_{H_2S} = \frac{p_{H_2S}}{p_{H_2} \cdot p_{S_2}^{1/2}} \qquad [2]$$

at the various temperatures can be obtained from literature (11). Cooling the quartz tubes rapidly to room temperature, the equilibrium is frozen in. After opening the tube the H_2S content can be determined by iodometric titration (12), the hydrogen pressure under equilibrium conditions can be calculated, and this together with the determined H_2S content enables one to calculate the sulfur pressure by using Eq. [2].

In the case of Ga_2S_3 a second method was used as a check on the above mentioned experiments, although it is a time consuming method. Sulfur and Ga_2S_3 were placed in separate quartz bulbs connected by a smaller tube. Both bulbs were equipped with thermocouple holes. The whole system was sealed under a vacuum of 10^{-3} mm Hg and placed in a two-section electrically heated furnace in which each section could be heated independently.

A definite sulfur vapor pressure was created by heating the sulfur-containing part of the system to the appropriate temperature (T_1). The other bulb was maintained at a temperature somewhat higher than the melting point of Ga_2S_3 (T_2). As P_{Ga} and $P_{Ga_2S_3}$ are very low at the temperature T_2,[3] the liquid Ga_2S_3 comes into equilibrium with the sulfur vapor pressure established at T_1. The melting point of Ga_2S_3 was then repeatedly determined by thermal analysis until no change could be detected in this melting point and the corresponding sulfur pressure established at T_1 could be regarded as the equilibrium pressure over Ga_2S_3. These values were in good agreement with those obtained by the first method.

Results

The T-X projection.—In Table I the results of the thermal analysis for the various Ga-S mixtures are given. In column 1 the sulfur contents of the samples are listed; column 2 gives the appearance of these samples. In columns 3, 4, and 5 the temperatures of the first, second, and third thermal arrest points are indicated. Column 2 shows the change in color in going from the Ga-rich side of the system to the S-rich side. Alloys rich in gallium contained inclusions of metallic gallium, which could be seen without breaking the regulus into pieces. The majority of Ga_2S_3 synthesized in the course of our experiments exhibited a dark-red color. It happened occasionally that a batch was ivory colored with a mother of pearl shine on its outer surface. In the literature Ga_2S_3 is reported to be ivory or white (7, 8). Debye-Scherrer photographs showed no difference between the different colored substances. Thermal analysis on the other hand revealed a difference in the melting points. Compared with the yellow and white substances which contain, respectively, 63 and ≈ 65 a/o S, we therefore consider the ivory colored compound with "60" a/o S to be sulfur rich Ga_2S_3. The determined phase diagram is shown in Fig. 1.

[3] P_{Ga} is less than 10^{-5} atm according to the work of Speiser and Johnston and Cochran and Foster (13, 14). $P_{Ga_2S_3}$ is assumed to be very low, since even after several days no sublimation occurred under the above mentioned sulfur pressures.

Table I. Melting points in the system gallium-sulfur

Sulfur content, a/o	Sample appearance	1st Thermal arrest, °C	2nd Thermal arrest, °C	3rd Thermal arrest, °C
10	Dark green with metallic Ga	959	—	—
33.5	Dark green with metallic Ga	958	—	—
45	Dark green with metallic Ga	958	—	—
47	Dark green with less Ga	958	—	—
47.5	Dark green with less Ga	958	—	—
48.5	Dark green with less Ga	958.5	—	—
50	Greenish-yellow	962	—	—
51.5	Greenish-yellow	953	900	—
52	Yellow	947	898	—
53.5	Yellow	922	902	—
55.5	Canary-yellow	900	—	—
56	Canary-yellow changing to yellow red	941	899	833
57		977	896	836
58		1007	892	828
59		1055	886	828
60	Dark red	1090	—	—
„60"	Ivory colored	1088	985	—
63	Yellow-white	1080	989	—
~65	White	1085	980	—
99.5		119	—	—

The compounds GaS and Ga_2S_3 melt at temperatures lying considerably above the melting points of the components. On the gallium-rich side, near pure Ga, no thermal arrest above the melting point of Ga could be detected. The first detectable melting point was at a sulfur content of 10 a/o.

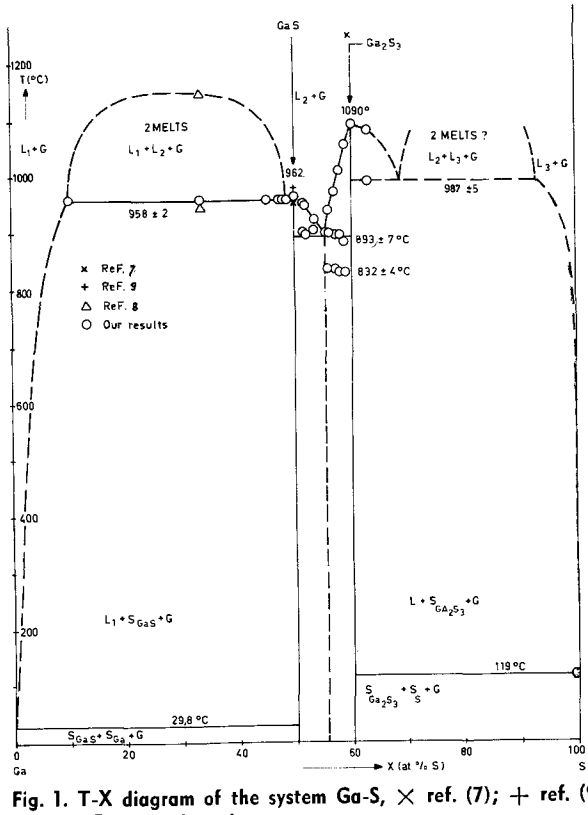

Fig. 1. T-X diagram of the system Ga-S, × ref. (7); + ref. (9); △ ref (8); ○ authors' results.

Between about 10 and 48 a/o S the monotectic at 958°C indicates the existence of a range of liquid immiscibility in good agreement with the work of Spandau and Klanberg (8). Analogous regions of liquid immiscibility are found in the systems Ga-Te (3), In-Te (4), In-S (5), In-Se (6), and Sn-S (15). It is therefore reasonable to suppose that the composition of the eutectic point on the gallium-rich side must be very close to that of pure Ga.

Between GaS and Ga_2S_3 there is a eutectic point at 893° ± 7°C at a composition of about 55 a/o S. Analysis of x-ray powder patterns on samples at 56 a/o S showed lines characteristic of GaS with 4 extra lines and some GaS lines missing. There was no indication of the existence of a compound Ga_4S_5. The effects found at 832° ± 4°C indicate the possibility of a phase transition in the solid state. On the sulfur-rich side of the diagram, thermal analysis, as mentioned above, could not be done on samples with a sulfur content from 65% to about 99.5%. Efforts to synthesize small samples containing more than 65 a/o S at temperatures around 1200°C, in large sealed quartz vessels[4] always resulted in a mixture of Ga_2S_3 and free sulfur, which would have too high a pressure (16) for the silica tubes used in thermal analysis.

The P-T projection.—In Table II the values of the sulfur vapor pressure above various Ga-S samples, as determined by the method described above, are listed. The S_2-vapor pressure values of samples with a sulfur content of 50 a/o were determined at temperatures ranging from 798° to 978°C, and the value P_{S_2} at 962°C as shown in Fig. 2 was obtained from these values by graphic interpolation. The same procedure was followed for samples with a sulfur content of 60 a/o S to determine the pressure at 1090°C. For samples with a sulfur content between 50 and 60 a/o the vapor pressure was determined at the melting points. Every value given in Table II is an average of at least two determinations.

In the P_{S_2} *vs.* 1/*T* projection as shown in Fig. 2, the values of P_{S_2} at the melting points of the various samples are plotted. The line AB presents the vapor pressure of pure sulfur as a function of the temperature (16).

Marked sublimation of GaS at temperatures around 920°C was observed when we tried to grow single crystals. In these experiments GaS powder was sealed in a silica tube under vacuum of 10^{-3} mm Hg and placed in a temperature gradient. After 24 hr sublimed crystals could be seen at the cold end of the tube (850°C). These platelike crystals had the greenish-yellow color of GaS. In the foregoing discussion it was shown that the P_{S_2} at temperatures around 920°C is very low. This fact together with the observed sublimation indicates that the equilibria in the dissociation reactions

[4] These vessels were so large that the total amount of free sulfur could not create a pressure of more than 20 atm.

Table II. Sulfur vapor pressures in the system gallium-sulfur

Sulfur-content of substance, a/o	Heated with hydrogen, temperature, °C	S_2-vapor pressure, mm Hg
50	798	1.0×10^{-6}
50	810	1.3×10^{-6}
50	858	3.2×10^{-6}
50	920	2.3×10^{-5}
50	978	1.5×10^{-4}
55	897	4.5×10^{-4}
57	980	4.0×10^{-3}
58½	1035	4.9×10^{-2}
60	1080	1.0
60	1135	3.8
		3.8

The S_2-vapor pressure values of samples with a sulfur content of 50 a/o were determined at temperatures ranging from 798° to 978°C. The value of P_{S_2} at 962°C as shown in Fig. 3 was obtained by graphic interpolation of these values. This was also done for the samples with 60 a/o S. The samples with 55, 57, and 58.5 a/o S were only heated at their melting points and the P_{S_2} corresponding to these temperatures are given in this table and in Fig. 3.

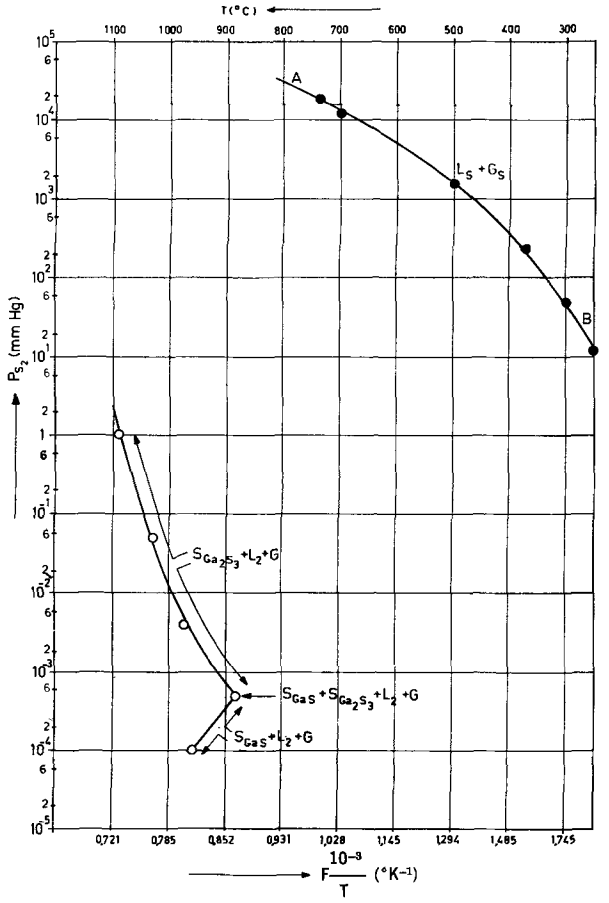

Fig. 2. P_{S_2} *vs.* 1/T diagram of the system Ga-S. The line AB presents the vapor pressure of pure sulfur as function of the temperature.

$$2GaS_{(g)} \leftrightarrows 2Ga_{(l)} + S_2 \qquad [3]$$

and

$$2GaS_{(g)} \leftrightarrows Ga_2S + \tfrac{1}{2}S_2 \qquad [4]$$

lies strongly to the left and sublimation is carried by GaS molecules.

The P-X projection.—From the data of the T-X projection and the P_{S_2} *vs.* 1/*T* projection given in Fig. 1 and 2, the P-X projection of the three-phase lines $S_{GaS} + L + G$ and $S_{Ga_2S_3} + L + G$ can be deduced (see Fig. 3).

This figure shows the steep increase of the sulfur vapor pressure of substances with a sulfur content between 0 and about 10 a/o and between 50 and 60 a/o. Only a very small increase of the sulfur pressure is required to increase the S-content of the substance from 10 to 50 a/o; this results in a horizontal line connecting the regions between 10 and 50 a/o S. With the estimation of a second range of liquid immiscibility for substances with a sulfur content > 65 a/o in the T-X projection, one must assume a continued rise in the sulfur pressure beyond Ga_2S_3 with an increasing sulfur content until a second liquid phase appears. This is the liquid immiscibility region. From here on the P_{S_2} remains constant with increasing sulfur content until the Ga_2S_3 rich liquid (L_2 see Fig. 1) has disappeared. Adding more sulfur will lower the melting point and also the vapor pressure until at 100 a/o S the melting point will be 119°C and the pressure around $3 \cdot 10^{-2}$ mm Hg (16).

Crystal structures.—The crystal structure of GaS has been determined by Hahn and Frank (17). It has a hexagonal layer structure, each layer consists of 4-sublayers in the sequence S-Ga-Ga-S in which every Ga-atom is surrounded tetrahedrally by one gallium and three sulfur atoms. There are three structures for Ga_2S_3 as determined by Hahn and Frank

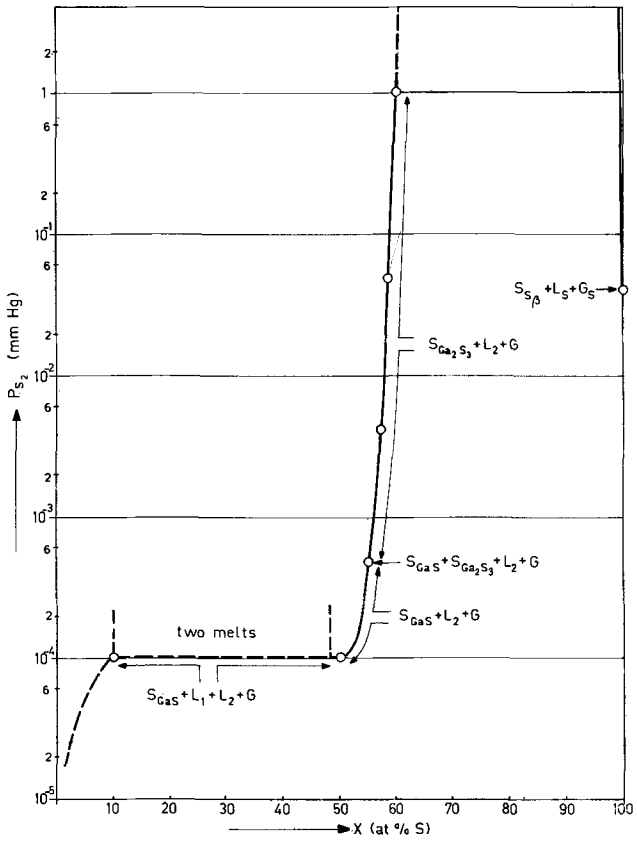

Fig. 3. P_{S_2} vs. X diagram of the system Ga-S. S_β is monoclinic sulfur.

(17), Hahn and Klingler (18), and Goodyear, Duffin, and Steigman (19). These are called α-Ga_2S_3, β-Ga_2S_3, γ-Ga_2S_3. According to Hahn and Klingler Ga_2S_3 can crystallize in one of two modifications, a low-temperature form (the γ-form) or a high-temperature form (the β-form). The inversion temperature is thought to be between 550° and 600°C, and these authors found that the low- and high-temperature phases have structures which are related to the zinc blende and wurtzite structures, respectively, each having a random distribution of vacancies in the sites normally occupied by Zn in the model structures, while α-Ga_2S_3, the ordered low-temperature phase, has a monoclinic symmetry according to Goodyear *et al.* (19).

Acknowledgment

The authors thank Professor F. van der Maesen for his stimulating discussions and his continuous interest in this work.

Manuscript received Feb. 9, 1966; revised manuscript received May 4, 1966.

Any discussion of this paper will appear in a Discussion Section to be published in the June 1967 JOURNAL.

REFERENCES

1. M. Bassani, D. L. Greenway, and G. Fischer, The Physics of Semiconductors, Paris 1964, Proceedings of the 7th international conference, M. Hulin, Editor.
2. G. Fischer and J. L. Brebner, *J. Phys. Chem. Solids*, **23**, 1363 (1962).
3. P. C. Newman, J. C. Brice, and H. C. Wright, *Philips Research Repts.*, **16**, 41 (1961).
4. E. G. Grochowski, D. R. Mason, G. A. Schmitt, and P. H. Smith, *J. Phys. Chem. Solids*, **25**, 551 (1964).
5. M. Hansen, Metallurgy and Metallurgical Engineering Series, "Constitution of Binary Alloys," McGraw-Hill Book Co., New York-Toronto-London (1958).
6. G. K. Slavnova, N. P. Luzhnaya, and Z. S. Medvedeva, *Zhur. Neorganicheskoi Khim.*, **8**, 1199 (1963).
7. W. Klemm and H. U. von Vogel, *Z. anorg. u. allgem. Chem. Bd.*, **219**, 45 (1934).
8. N. Spandau and F. Klanberg, *Z. anorg. u. allgem. Chem.*, **295**, 300 (1958).
9. A. Brukl and G. Ortner, *Naturwissenschaften*, **18**, 393 (1930).
10. W. Hume-Rothery, J. W. Christian, and W. B. Pearson, "Metallurgical Equilibrium Diagrams," Chapman and Hall, London (1953).
11. M. Randall and F. R. von Bichowsky, *J. Am. Chem. Soc.*, **40**, 368 (1918).
12. K. Jellinek and A. Deubel, *Z. Elektrochem. u. angew. phys. Chem.*, **35**, 451 (1929).
13. R. Speiser and H. L. Johnston, *J. Am. Chem. Soc.*, **75**, 1469 (1953).
14. C. N. Cochran and L. M. Foster, *This Journal*, **109**, 144 (1962).
15. W. Albers and K. Schol, *Philips Research Repts.*, **16**, 329 (1961).
16. Landolt-Börnstein, "Zahlenwerte und Funktionen aus Physik, Chemie, Astronomie, Geophysik, Technik," Springer-Verlag, Berlin-Göttingen, Heidelberg (1960).
17. H. Hahn and G. Frank, *Z. anorg. u. allgem. Chem.*, **278**, 340 (1955).
18. H. Hahn and W. Klingler, *Z. anorg. Chem.*, **259**, 135 (1949).
19. J. Goodyear, W. J. Duffin, and G. A. Steigmann, *Acta. Cryst.*, **14**, 1168 (1961).

Growth Studies of Silicon Carbide Crystals

L. J. Kroko

Research Laboratories, Westinghouse Electric Corporation, Pittsburgh, Pennsylvania

ABSTRACT

Silicon carbide crystals are commonly grown from the vapor at a temperature of about 2600°C in so called "sublimation" furnaces wherein crystals are grown on the inside walls of a cavity formed within a large porous block of silicon carbide. A model for growth in this system is postulated and growth rate as a function of temperature is calculated. Growth in argon with pulses of nitrogen introduced at regular (7½ min) intervals is shown to produce sharp green lines that define the successive crystal sizes during the entire growth period (~8 hr). Temperature changes are made during growth and the growth rates are measured during successive temperature cycles. Considerable fluctuation in growth rate is revealed by this new measuring procedure. Theory and experiment are in qualitative agreement.

Although single crystals of silicon carbide obtained as an accidental by-product in commercial abrasive production have been known since the early nineteen twenties, it is only since about 1954 (1) that practical methods for producing crystals in the laboratory have been available.

The basic structure used for this purpose is a sintered block of silicon carbide, *ca.* 40% density, with

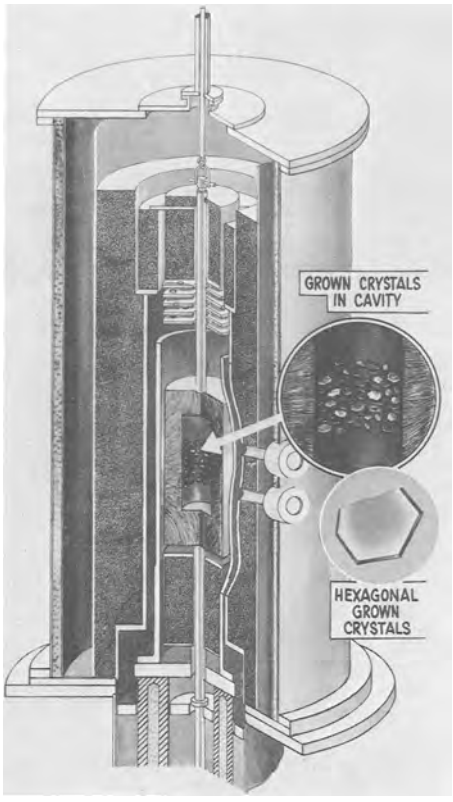

Fig. 1. Schematic drawing of 2600°C silicon carbide crystal growth furnace showing water-cooled envelope, powdered graphite insulation, and crucible with crystals attached to cavity wall.

an internal void or cavity. Crystals grow from the walls of such cavities when certain thermal conditions to be described later are met. In furnaces used for abrasive production, cavities form when the starting mixture of coal, sand, and sawdust shift during combustion; in laboratory furnaces the cavities are formed by deliberate stacking of chunks of pre-reacted silicon carbide or through the use of thin-walled graphite tubes (2). An electrically heated furnace of a type commonly used in the laboratory for this purpose is shown in Fig. 1. The outer container is made of stainless steel and is water cooled. The heating element is a graphite cylinder so slotted that current flows up one half of the cylinder and down the other. Insulation is provided by combinations of graphite powder and machined solid shapes. (No known metals or ceramics can be used in the hot zones because of the extreme temperatures and reactive vapors, particularly silicon vapor.)

The "charge" for the furnace is a circular graphite crucible, in this case 4 in. diameter by 8 in. long overall, filled with silicon carbide grain or with a near stoichiometric mixture of finely divided silicon and carbon. The loose bulk material is kept out of the central portion of the charge by a hollow right circular cylinder made from a graphite tube 2 in. diameter, 3 in. long, 0.004-0.008 in. thick, and 1/16 in. thick end-caps.

Inside the furnace the "charge" is suspended from above by a graphite rod threaded into the lid of the crucible. Usually the crucible is rotated to provide better thermal symmetry. In a typical run, the charge just described is heated to about 2600°C and held there for 5-20 hr, depending on the result desired. In an average run about 10-20% of the silicon carbide mass put inside the charge is lost; the remainder fuses to form a coarse grained porous mass whose structural features will be considered in detail later. Crystals nucleate and grow from the walls of the central cavity in the manner depicted in Fig. 1. Approximately 10% of the runs produce no crystals, 20% produce exceptionally fine large (up to ½ in.) ones, and 70% of the runs produce reasonable yields (>100) of crystals of the order of ¼-⅜ in.

As a basis for the study of this growth process, the following observations may be made:

(*A*) Crystals appear in a zone on the cavity wall. Near the zone center the hexagonal platelets have nearly plane parallel faces and intersect the substrate at right angles; at the zone extremities crystals often have one flat side and one "staircase" side, are usually relatively thick and comparatively small.

(*B*) Cross sections of the furnace charge disclose "lines" of crystallization in the bulk material which closely resemble a trace of what one might expect as heat flow paths in an orthogonal system of flow and isothermal lines.

(*C*) Most crystals, especially the largest, are oriented so that normals to their flat faces are nearly parallel to the long axis of the growth cavity (Fig. 1).

(*D*) Crystals tend to have a thickness-to-width ratio of the order of ⅛, but ratios as large as ½ and as small as 1/100 are not uncommon. Crystals often grow at vastly different rates in the "a" directions on the basal plane as evidenced by the unequal lengths of the hexagonal sides. The perfection of crystals depends strongly on the substrate character and the number of interfering crystals. The best crystals are those which grow with few neighbors. Even these, however, show surface spirals and other physical evidence of dislocations (3).

(*E*) P-type crystals (aluminum doped) are blue in color, n-type (nitrogen doped) green, and pure or compensated crystals are colorless. The greater the impurity concentration, the greater the color density. Degenerate crystals are nearly opaque.

By the study of these features and others, such as growth rates as functions of temperature, considerable progress can be made in understanding silicon carbide growth processes.

Discussion of Growth Features

"Crystallization" lines.—Perhaps the most important clue to the working of this system is the set of curved crystallization lines which form in the bulk material surrounding the cavity. By experience it has been found that the best crystals are grown when conditions are adjusted so that horizontal or vertical planes through the cavity center are mirror planes for the crystallization lines. Some typical forms observed and the resulting crystals are shown in Fig. 2. In Fig. 2a the horizontal crystallization lines intersect the substrate at 90° in the central region of the cavity and deviate from 90° above and below. Only when this pattern is observed are good crystals obtained.

In Fig. 2b the entire line structure is shifted downward and the horizontal crystallization lines intersect

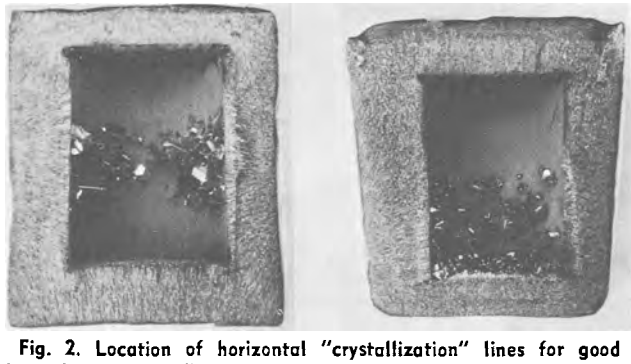

Fig. 2. Location of horizontal "crystallization" lines for good thermal symmetry "a" (left) and poor thermal symmetry "b" (right).

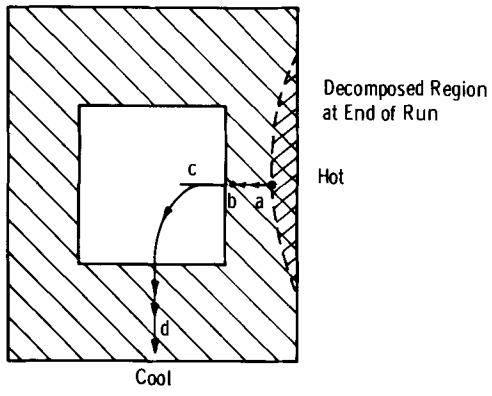

Fig. 3. Transport paths which give rise to "crystallization lines" in a silicon carbide charge.

the end cap. In this case crystals grow from the wall as well as from the end cap and the perfection is very poor.

In searching for an explanation of this structure one is quickly led to a "flow" theory because of the strong resemblance these lines bear to graphical solutions of Laplace's equation. One can easily imagine heat flow in from the right and left and out through the top and bottom in Fig. 2a. This pattern is entirely consistent with the heater geometry, and measurements confirm that the sides of the container (Fig. 2a) are hotter than the top and bottom. With these boundary conditions the origin of the lines follows immediately.

As the furnace is heated, point "a" (see Fig. 3) reaches a temperature T_a where material begins to decompose appreciably (SiC has no liquid phase at reasonable pressures), and the vapors diffuse in all directions. There is some vapor which travels toward "b" where it condenses as a result of the lower temperature T_b there. This results in a concentration gradient which enhances diffusion of the silicon carbide species toward the cavity. At growth temperature material is steadily transported from a to b to c to d along the typical path shown. This steady decomposition and condensation along the temperature gradient results in grain-like patterns which accurately define the flow path (and the associated orthogonal isothermal lines). For very long or very high temperature runs, a realm of decomposition progresses from a along the path shown and after some time there will be silicon carbide only at d; the rest having been decomposed to graphite-like pseudomorphs.

Temperature environment of growing crystals.—In view of the heat flow path and temperature gradient just established, it is apparent that the root of a growing crystal must be at least as hot as the growing faces. Therefore the heat of solidification of the incoming molecules must be discharged somehow into the cavity proper; it cannot be conducted to the substrate. This of course, could be accomplished through conduction by the ambient gas or by radiation. In a later section it will be apparent that conduction is negligible compared with radiation because of the high absolute temperature and the small temperature difference.

Crystal size variations.—The first widely accepted theory for the enormous range of sizes, >100:1, observed in a typical furnace run was based on the notion that the nucleation of crystals was a continuous process. Those crystals which grew to large size were assumed to have nucleated early in the run while those which were small were assumed to have nucleated late. In 1956 this notion was invalidated by unpublished work of the author who showed, by pulse nitrogen doping experiments similar to ones described in the section on Observation of Growth Rates, that all crystals which grew to significant size were nucleated during a short period of about 10 min duration at the beginning of a run. This discovery was quite surprising and gave impetus to studies of temperature and vapor supply as possible causes of growth rate variations.

Temperature differences at least on the scale of physical observations with an optical pyrometer could normally be held to a few degrees and were constant for any given run. Furthermore the location of large and small crystals was completely random. Small crystals sometimes grew alone and sometimes adjacent to very large crystals. It seemed that these conditions required variations in the controlling parameter which were large compared to crystal spacing and therefore the small area properties of vapor supply and temperature variations were considered.

If vapor supply were the controlling factor then one should expect to find no preferred crystal orientation, however such ordering is one of the dominant growth features. The source orientation effects appear also when graphite cloth is substituted for the thin graphite cylinder. The structure of graphite cloth is such that the point-to-point variations in vapor supply are highly improbable. These arguments make it unlikely that vapor supply can be made to account for crystal to crystal size variations.

There is still the matter of growth rate differences along the various "a" directions in any one crystal. With negligible exception crystals have faces flat to within small integral multiples of the basic polytype unit cell. (For the commonest forms, 4H, 6H, 15R, this amounts to several hundreds of angstroms at most.) This flatness can occur only if the surface mobility of the absorbed species is very high. This suggests that the actual source of the vapor must be unimportant and that directional rate variations must be due to something else.

For temperature variations between crystals to be responsible for the observed growth rate differences, one must find a heat transfer mechanism which can support temperature differences of a large enough value. Because conduction to the substrate is ruled out by the direction of the thermal gradient, and differences in conduction through the gas for adjacent crystals are unlikely to be adequate quantitatively, it appears necessary to consider the possibility that radiative effects are the cause of the growth rate differences.

Actually strong evidence for the dominance of radiation comes from many observations and experiments. The most obvious of these is the unfailing habit of grown crystals to be oriented with their largest faces subtending what is known to be the coldest area of the cavity (top and bottom). This is clearly evident in Fig. 2a. When there are massive clusters of intergrown crystals, crystal orientation is less obvious but this is easily accounted for by multiple reflection radiation paths.

A direct measure of the importance of orientation has been obtained by planting fully grown crystals in the thin graphite wall prior to a growth run. In all cases it is found, when the experiment is not complicated by wild profuse cluster growth, that growth is maximum on those samples oriented as in Fig. 1 and minimum (indeed, usually negative) when normal to this direction. For angles between the extremes a smooth progression in rate occurs.

In a variation of the latter experiment a series of crystals all parallel to one another and in a line between top and bottom of the cavity has been used. In this arrangement the crystals on the end subtend the cold sink while each successive crystal is blocked there from by one or more crystals. In these experiments the end crystals grow most on the side toward the end caps. Each succeeding crystal grows less and usually the crystal in the middle of the line decomposes. In these structures the only difference in environment for the separate crystals is their relative radiative shielding from the ultimate sink.

The shielding effect can in fact be carried to the extreme in another experiment. If one considers lines from the vertical midpoint of the cavity wall to the center of the top and bottom of the cavity in Fig. 2a it is possible to visualize 3 or 4 shields evenly spaced between the center and each end such that each shield extends from the substrate to the line so that any point on the substrate sees at least one shield between it and the end cap. When this is done it is found that not only is crystal growth eliminated but nucleation as well. This shows that the supersaturation of vapor required for nucleation as well as for growth is controlled completely by heat radiation to the cold portions of the cavity.

Nuclei formation.—The radiation hypothesis explains the fact that useful nuclei form only during some short interval at the beginning of a furnace run. As the furnace is heated up the thermal capacity of the charge gives rise to larger gradients than those which exist in the steady state. Therefore on the cavity walls supersaturation is highest early in the run, and nuclei of all orientations may form. Once formed they radiate heat and grow. After a short time the gradient becomes less, the supersaturation is reduced, and the probability of forming new nuclei becomes small. The nucleation process is also retarded by the fact that after the initial nuclei grow beyond a certain size they screen the wall from the sink and reduce the supersaturation still further.

Before summarizing the pertinent deductions it is worthwhile to consider temperature profiles within the cavity. A quick glance would tempt one to extend the crystallization lines of the bulk into the cavity and thereby deduce that crystals grow along the gradient so defined. This construction is, however, fallacious since the emissivity of a crystal and of a gas are different and hence the temperature at any point depends heavily on whether or not there is a crystal there. In short, the crystal determines the temperature at its faces by virtue of its radiative surroundings. Its physical location, relative to the extended crystallization lines, is not of fundamental importance.

One other point is worthy of comment here. It is not uncommon for authors to speak of silicon carbide crystals as growing in isothermal cavities. Such a condition is truly impossible since condensation of material on a crystal face requires the rejection of a positive quantity of heat. Indeed the basis of this work is that it is the existence of small but positive temperature gradients which completely governs growth rate.

Summary of observations.—As a result of the preceding discussion, the following qualitative picture of growth can be put forth. Thermal gradients imposed on the growth structure from outside, cause silicon carbide transport through the bulk charge by an evaporation condensation cycle which produces characteristic lines of crystallization. When these vapors enter the cavity, they condense on nuclei in amounts determined by the relative ability of the individual nuclei to radiate away the energy of condensation. Although nuclei of all orientations are originally available only those favorably oriented for heat radiation grow, the others disappear so that in the final system certain orientations are prominent. A fundamental part of the model proposed is that the rate limiting step is heat transfer by radiation. Vapor supply and the nucleation of growth ledges, etc., are found to be of second order importance. The model is developed quantitatively in the section that follows.

Growth Model and Growth Rate Calculations

Figure 4 represents a crystal located in a cavity within a mass of loosely packed silicon carbide. The temperature configuration is such that $T_1 > T_2 > T_3$. T_2 is controlled by radiation to the sink T_3 and hence bears some definite relation to T_1 and T_3. The crystal

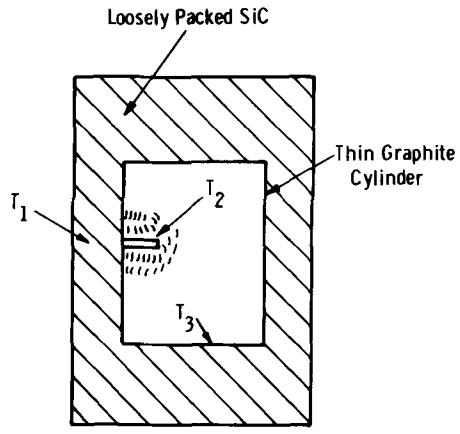

Fig. 4. Model for growth of silicon carbide crystals by the sublimation method.

is assumed to be surrounded by vapor at a temperature T_1. It is further assumed that the processes of condensation and evaporation at the crystal faces do not couple, *i.e.*, are independent of one another.

From kinetic theory the mass of molecules arriving at the crystal surface from the T_1 source is

$$G_i = C_0 T_1^{-1/2} \exp\left[\frac{-\Delta E}{RT_1}\right] \quad [1]$$

where G_i is in g/cm²/sec, T in °K, R is the gas constant, kcal/mole/°K, and ΔE is activation energy for dissociation, kcal/mole. A similar expression for molecules arriving from T_3 should also be written, but it will be seen later that this complication adds little to the results obtainable from the analysis. Similarly an expression for the mass of molecules leaving the crystal surface is

$$G_v = C_0 T_2^{-1/2} \exp\left[\frac{-\Delta E}{RT_2}\right] \quad [2]$$

The net rate is

$$G_i - G_v = C_0 T_1^{-1/2} \exp\left[\frac{-\Delta E}{RT_1}\right] - C_0 T_2^{-1/2} \exp\left[\frac{-\Delta E}{RT_2}\right] \quad [3]$$

It is quite likely that C_0 and ΔE of Eq. [1] are not equal respectively to C_0 and ΔE of Eq. [2] and it would be useful to have separate values appropriate to the two processes. Unfortunately such a determination is very difficult to execute and for the purposes of this study the aforementioned assumptions were made. As will be seen later the temperatures T_1 and T_2 differ by the order of 1°C and $T_1^{1/2}$ and $T_2^{1/2}$ therefore differ by less than 1%. Hence Eq. [3] may be simplified to yield for the net growth rate

$$G = C_1\left[\left(\exp\frac{-\Delta E}{RT_1}\right) - \left(\exp\frac{-\Delta E}{RT_2}\right)\right] \quad [4]$$

C_1 and ΔE in this expression can be determined by direct measurement of the rate of decomposition of crystals. This is presented in the Appendix where the values obtained for 1 atm argon pressure are $C_1 = 3.08 \times 10^7$ g/cm²/sec and $\Delta E = 148$ kcal/mole. However before calculations of growth rate can be made representative values for T_1 and T_2 or more specifically for T_1-T_2 must be known.

Direct experiments to determine T_1 and T_2 by optical pyrometry have shown that any opening big enough to permit visual sighting causes heat leaks sufficient to change the entire heat pattern as evidenced by the altered crystallization pattern of the bulk charge. Even under such extreme conditions temperature differences are less than the resolving capability of optical pyrometers (*ca.* 5°C).

For purposes of defining the range of computation an approximate value for T_1-T_2 may be obtained by making use of the heat of condensation of silicon carbide as follows. Assume that the crystal in Fig. 4 must dissipate heat by radiation at a rate sufficient to dispose of the heat of condensation of incoming molecules only. (For typical size crystals and temperature differences deduced, heat conducted via the ambient gas is small compared with heat lost by radiation.)

The heat per unit area transferred between the crystal at T_2 and the sink at T_3 is

$$P = \epsilon\sigma\,[T_2^4 - T_3^4]\ \frac{\text{watts}}{\text{cm}^2} \qquad [5]$$

where ϵ = effective emissivity of the growing crystal and its sink, and σ = Stephan Boltzmann constant (5.67×10^{-2} w/cm^2/°K^4). Now experiment shows that a typical crystal in a growth run of 6 hr at ~2500°C may have an area of 0.1 cm^2 (*ca.* 0.3 x 0.3 cm), a thickness of 0.025 cm, and a weight of 0.0077g. From the value for ΔE of the Appendix (148 kcal/mole) a crystal of this weight requires 28.5 cal to be dissipated in the 6 hr. Hence from Eq. [5], it is readily shown that for $\epsilon = 1$ T_2-T_3 needs to be only of the order of 0.1°C while for $\epsilon = 0.1$ T_2-T_3 needs to be about 1°C.

It may be further shown that T_1-T_2 is within 10% of T_2-T_3 by assuming an equilibrium situation where the power transfer is constant.

On the basis of these arguments it is reasonable to evaluate Eq. [4] for temperature differences in the range of 1°C for purposes of comparison with experiment. It is possible to argue that it is unrealistic to assume T_1-T_2 is not a function of temperature; however simple computations show that it is not a steep function of temperature and in addition the over-all assumptions are too severe to make this refinement meaningful.

Theoretical curves of growth rate from Eq. [4] are given in Fig. 5 for argon at atmospheric pressure. Roughly a 100°C change in temperature produces a 2.5:1 change in growth rate for a constant ΔT. The effect of ΔT is also seen to be considerable, for example a change of ΔT from 1° to 2°C approximately doubles the growth rate. In view of the absolute growth temperature ~2600°C it may be concluded that the control of growth rate presents serious problems. Furthermore, measurements of growth rate are likewise difficult and a method for doing this is developed in the remainder of this paper. The results of such measurements are rationalized with the discussion of growth already presented.

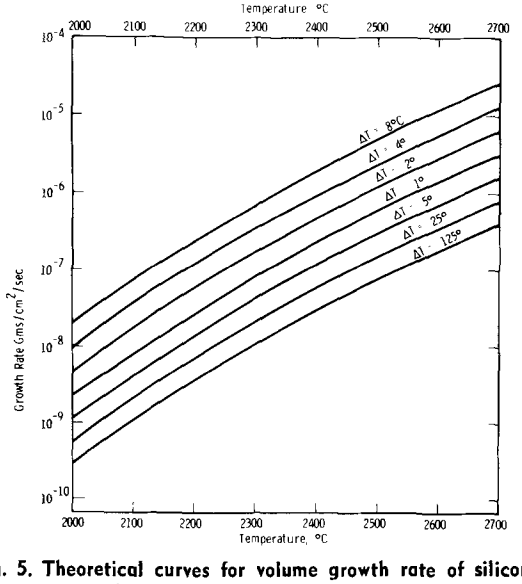

Fig. 5. Theoretical curves for volume growth rate of silicon carbide crystals in "sublimation" furnace.

Observation of Growth Rates

Prior attempts to relate growth rate and temperature compared rates measured in separate experiments in each of which large numbers of crystals of all sizes were produced. From statistical treatment of such data Hamilton (4) concluded that rate increased with temperature but the actual rate was not obtainable from the data.

In this work the growth rate at a minimum of two temperatures was measured in each of the many crystals of a single run. To accomplish this the temperature was alternated between two different values for several cycles during the growth run. Each crystal thus contained several regions grown at each temperature. The different regions were outlined by admitting small quantities of nitrogen each time the temperature was changed. The dark green color thus imparted by nitrogen was limited to small areas by a constant flow of argon which served to purge the furnace and return the atmosphere to one which produced very light green material before temperature was changed again.

Some crystals grown in variations of this experiment are shown in Fig. 6, 7, and 8. These figures show only selected samples from a wide range of the sizes and shapes obtained in each actual run (*ca.* 1000 crystals total). There were many crystals too small to be seen with the unaided eye as well as one or two much larger than those shown. All but the largest show a distribution of band patterns similar to those illustrated. The very largest have bands whose spacing show no effect of temperature. These will not be discussed here, since they represent a negligible fraction of the total and are very imperfect and probably grew fast for this reason.

Fig. 6. Crystals from growth rate experiment. The bands defined by nitrogen doping each represent 1 hr of growth (the temperature schedule is given in Table I).

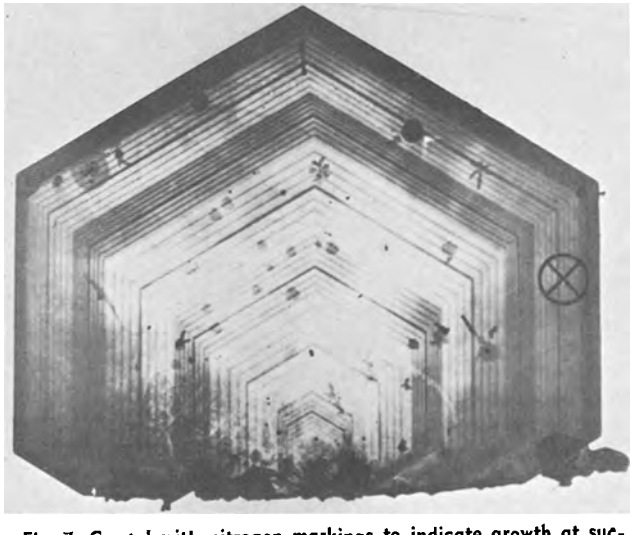

Fig. 7. Crystal with nitrogen markings to indicate growth at successive time intervals, see Table I for details of temperature changes, and the text for particulars of the nitrogen doping. The fine lines occur at 7½ min intervals.

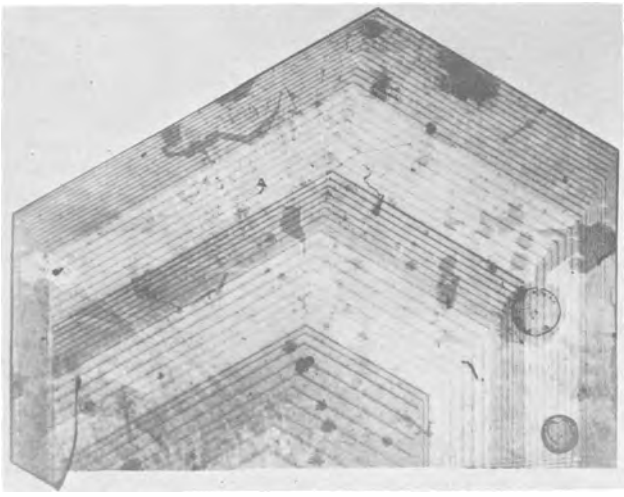

Fig. 8. Silicon carbide crystals with nitrogen markings showing growth rate fluctuations in various directions on the basal plane. Fine lines occur at 7½ min intervals.

Figure 6 was the first experiment of this sort and each band represents 1 hr of growth for the temperature schedule of Table I. Figures 7 and 8 are typical of refinements in the procedure in that each hour period is divided into 8 parts with a fine mark each 7½ min. In the crystal of Fig. 7 the half hour marks were intensified by tripling the nitrogen volume introduced. In Fig. 8 another variation of marking was used. For the outer band (~1½ hr, 12 marks) all marks were of the same density but for the other bands the quantity of nitrogen was varied in equal steps from the first to the eighth band. This was done to disclose any effect of nitrogen on growth rate. The temperatures for the three samples are given in Table I where the first entry is for the last band (*i.e.*, the edge of the crystal).

The crystal of Fig. 7 represents one of the better examples of good hexagonal symmetry to be found among crystals produced by this process. This sample is of uniform thickness, *0.006* in., perpendicular to the illustration, and measures 0.270 in. across from left to right. (Crystals approaching 1 in. across have been grown in other experiments.) Growth rates in all directions tend to be very nearly equal, except for those which intersect the ragged edge where the platelet was attached to the substrate. There is however some asymmetry in the region of small hexagons (early growth).

Comparison of this crystal with that of Fig. 8 shows some important effects. To begin with the extremes of the crystal of Fig. 8 show an asymmetry, but more than that it can be seen that while growth rate was reasonable during the last period along the left side it was near zero for the three preceding periods and normal before that. This has been found to be a rather common occurrence in crystals and can be attributed to a change in the thermal environment of an edge brought about by other crystals and/or changes in the heat input pattern from the heater.

Table I. Time temperature schedule for growth rate experiments

Fig. 6		Fig. 7		Fig. 8	
Time	Temp, °C	Time, hr	Temp, °C	Time, hr	Temp, °C**
35 min	2620	1	2490	1½	2540
1 hr	2515	1	2590	1	2640
1 hr	2620	1	2490	1	2540
1 hr	2515	1	2590*	1	2640
1 hr	2620	1	2490	1	2540
		1	2590		
		1	2490		
		1	2590		

* Note: fourth band has triple quantity of nitrogen.
** Note: all but the outer band have graduated marks.

Another characteristic obvious in Fig. 7 and 8 is the apparent difference in background color density (related to the N_2 content) for the alternate high and low temperature regions. During the growth of the region between marks nitrogen put in to make the mark is depleted to some level which is the same for low and for high temperature regions. Nevertheless the color shows that the amount of nitrogen incorporated is greater in the low temperature regions. This supports the notion that the rate of incorporation of nitrogen increases with decreasing temperature as proposed by Hamilton (4).

Also of interest are the terraces or rings of Fig. 6. It can be seen on crystals B and C that there would appear to be growth ledges spreading out from the faster moving, shorter, edges. This pattern is consistent with the explanations given earlier where it is proposed that the ability of a surface to dissipate heat governs the volume grown. In this instance the limit of progress of a growth ledge defines the extent of the cooled region of the crystal.

Interpretation of Results

As pointed out earlier, crystals from microscopic size to those of Fig. 6, 7, and 8 were obtained in these experiments. All grew for the same length of time and hence there is a tremendous variation in growth rate. As a result one is immediately faced with the problem of deciding which, if any, crystals can be compared with the preceding theory. This question is easily resolved by recalling the assumptions of the theoretical model. Reference to Fig. 4 shows that the crystal considered enjoyed direct radiative access to the heat sink and by the arguments given so far is therefore set to grow at the maximum possible rate. Therefore crystals to be measured should be the largest found in any specific case. The crystals of Fig. 6, 7, and 8 are such samples.

Having chosen the largest crystals there is still a problem associated with crystals like that of Fig. 8 where the growth rate was obviously interrupted along the left side. Here one wonders whether the material not deposited along that direction is to be found elsewhere on the crystal or whether it is lost to the crystal. This cannot be determined directly and therefore growth rate will be presented in two approximate forms, linear rates and volume rates.

In some crystals, such as B in Fig. 6, the growth rates perpendicular to the sample bear the same ratio to the corresponding widths as the final thickness bears to the final width. In others, the crystal of Fig. 7, for example, special account must be made for fluctuations in rate. A schematic of the latter crystal section is shown in Fig. 9. The extra growth in the cross-hatched section occurred in the second band from the outer edge marked X in Fig. 7. It is seen that the linear rate is not unusual although the crystal approximately doubled its thickness in this period. This type of short-term accelerated growth seems to be very common, and there is some evidence for thinking that unbalanced growth rates exist somewhere in every crystal. It is believed that such growth results from temporary increases in thermal gradient for the subject crystal since others in the same run have accelerated growth in different periods. When large seed crystals, properly oriented, are planted in a growth structure they have unobstructed access to

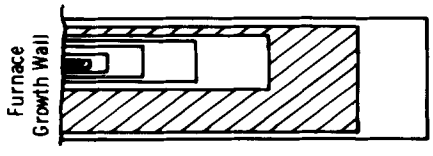

Fig. 9. Schematic cross section of a crystal with thickness growth rate variations. The illustration is representative although not to scale of fluctuations seen in the crystal of Fig. 7.

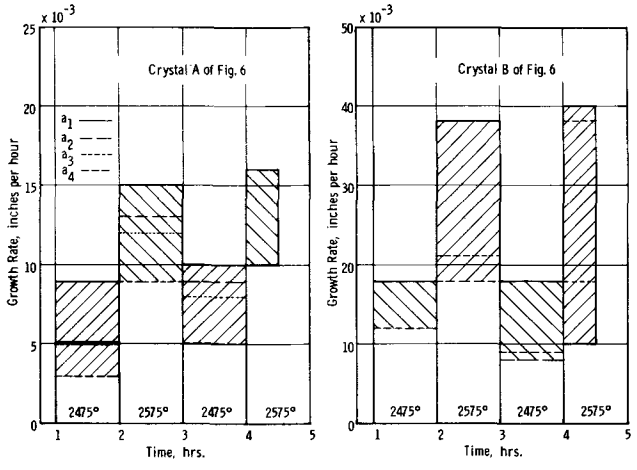

Fig. 10. Silicon carbide linear growth rates vs. temperature (measured).

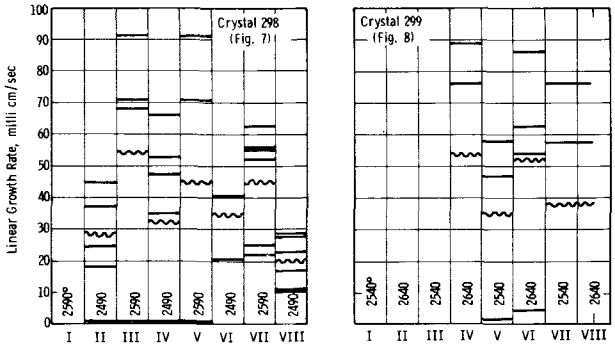

Fig. 11. Linear growth rates for various axes in the crystals of Fig. 7 and 8. Average values are represented by wavy lines.

the col sinks at least for a while and in every case extreme thickness to width ratios are observed. This is taken as evidence that growth in the C direction, as in Fig. 9 cross-hatched, arises from temporary abnormal gradients.

In an aggregation of crystals (Fig. 1, for example) it is unlikely that any one crystal, unless planted as a large seed, ever sees the full gradient of the cavity and therefore it may be impossible to associate a predicted growth rate with any given crystal. In Fig. 10 and 11 linear growth rates for the various "a" directions are presented for the crystals of Fig. 6(A + B), 7, and 8. The growth rates depend on the axes considered. Average values (of all axes measured) are given as wavy lines in Fig. 11. A systematic variation of growth rate with temperature can be seen in this figure. Volume rates are given in Fig. 12 for crystal 298 (shown in Fig. 7). During the seventh growth period abnormal thickening occurred (as discussed with reference to Fig. 9) and this increase is shown separately in the diagram.

Figure 12 shows, during the initial cycles at least, a fall off of growth rate with time. The volume growth rates (not shown here) for the crystal of Fig. 8 show a similar decrease. Although the reason is not known with certainty a consistent explanation for the decrease in rate at the same apparent temperature can be obtained from the radiation hypothesis. For region I in Fig. 12, the crystal was small, the shielding effect of neighbors is correspondingly small, and the sample grew as though it were exposed to nearly the full cavity gradient. As it and its associates grew, shielding became important and the rate at both temperatures decreased until reaching an apparent steady state in periods V, VI, VII, and VIII. During period VII the thickening increment makes the total growth almost equal to that of period I, suggesting that somehow the full gradient was again operative. Figure 13

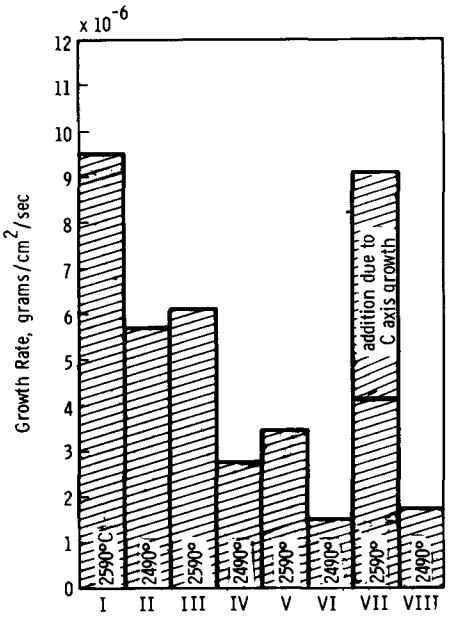

Fig. 12. Measured volume growth for crystal 298 (Fig. 7) each period 1 hr.

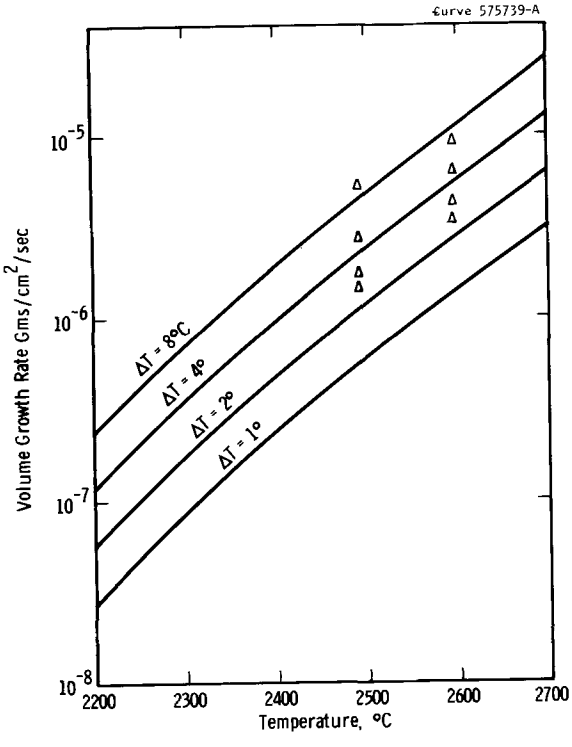

Fig 13. Theoretical volume growth rate (curves) and actual growth rate (triangles) for SiC crystals vs. temperature for crystal to sink ΔT of 1.0°, 2.0°, 4.0°, and 8°C.

presents theoretical lines of growth rate *vs.* temperature from Eq. [4] for temperature differentials of 1°-8°C and measured volume rates of growth for the crystals of Fig. 7.

It is concluded that the theoretical model predicts both the absolute growth rate and its variation with temperature to an accuracy consistent with the resolving power of growth experiments. Furthermore all growth habits are readily explained by the model and none are in conflict with it. Further progress in this work requires better control of experimental conditions and higher accuracy for measurement of local temperature.

Acknowledgment

The author wishes to acknowledge the assistance of D. R. Thornburg and D. L. Barrett in the execution of growth rate experiments.

This work was supported in part by the Aeronautical Systems Division of Wright-Patterson Air Force Base, Dayton, Ohio, under Contracts AF 33(657)-7027 and AF 33(657)-8719.

Manuscript received Jan. 7, 1966; revised manuscript received April 19, 1966.

Any discussion of this paper will appear in a Discussion Section to be published in the June 1967 JOURNAL.

REFERENCES

1. J. A. Lely, *Ber. deut. keram. Ges.*, **32**, 229 (1955).
2. H. C. Chang and L. J. Kroko, AIEE Conference Paper 57-1131 (1956).
3. A. R. Verma, " Silicon Carbide," p. 202, Pergamon Press, Inc., New York (1960).
4. D. R. Hamilton, *ibid.*, p. 43.

APPENDIX

Decomposition Rate for Silicon Carbide

The activation energy for decomposition of silicon carbide was measured by weight loss in argon under conditions simulating the sublimation furnace in which crystals are grown. In the actual arrangement crystals of known area, weight, etc., were mounted in a graphite block (previously outgassed) and surrounded with a graphite enclosure. At least two crystals were used in each measurement; one was a high purity clear crystal and the other was doped to the levels encountered in grown PN junctions ($\sim 10^{19}$ cm^{-3}). Furnace runs varied from ½ to 3 hr and weight losses were measureable to about 3%. After a run, crystals typically had a graphite-like surface which was removed by burning before weighing. The weight of this layer was very low, about 5% of the total weight loss. The existence of this layer did not seem to inhibit decomposition to any observable degree.

The losses exhibited by all crystals, pure and impure alike, were the same within experimental error. The spread in data points is attributed mainly to variations in the decomposition rate of the part of the crystal embedded in the graphite block. The little tab provided for this purpose decomposed at different rates in the different runs presumably depending on the tightness of the fit.

The data was plotted and a mean square line fitted thereto. Calculation of the intercept and slopes of the line yielded $3.08 \times 10^7/cm^2/sec$ and $\Delta E = 148$ kcal/mole.

Impurity Distribution in Single Crystals

II. Impurity Striations in InSb as Revealed by Interference Contrast Microscopy

August F. Witt and Harry C. Gatos

Department of Metallurgy, Massachusetts Institute of Technology, Cambridge, Massachusetts

ABSTRACT

The nature of impurity striations in InSb grown in the <111> direction was investigated by interference contrast microscopy. Six different types of impurity striations were revealed in the {211} planes parallel to the growth axis. The impurity concentration in the melt, size of the crystal, rate of rotation, pulling rate, temperature gradients, and growth direction were found to affect the density, intensity, and other characteristics of the striations.

The existing uncertainty on the nature and origin of impurity striations in crystals (1-3) can be attributed largely to the fact that their detailed structure cannot be sharply revealed by conventional optical techniques because of lack of contrast. Similarly radiotracer techniques and standard resistivity microprofiles suffer from insufficient resolution. Interference contrast microscopy combined with properly prepared surfaces provided high resolution as well as high contrast and led to the identification of six different types of striations.

Experimental Procedure

Single crystals of InSb containing tellurium as impurity (2-50 mg Te per 50g InSb melt) were grown in a Czochralski-type apparatus. Purified hydrogen was passed over the melt at an approximate rate of 10 cc/min. The melt temperature was controlled to within 0.1°C.

The single crystals grown in the <111> B[1] direction were cut along the growth axis to expose a (211) plane which was subsequently polished with a Linde B abrasive (particle size 0.05μ). For best results in our optical investigation the final polishing was done in a direction perpendicular to that of the striations of interest. In this way any scratch marks could be clearly differentiated from striations. After polishing the specimens were rinsed with distilled water and the still wet samples etched with modified CP4 ($5HNO_3$, $3CH_3COOH$, 3HF, $11H_2O$). The etchant was applied with a piece of cotton so that the formation of gas bubbles on the reacting surfaces could be prevented by rubbing them gently with the cotton. After etching the specimens were again rinsed with distilled water and subsequently dried with hot filtered air after treating them with a mild detergent to prevent stain formation. By properly positioning the specimens under the interference contrast attachment the visibility of scratch marks could be minimized while the striations could be observed with optimum contrast.

Etching characteristics of {211} planes.—By cutting the crystals along the <111> growth direction and parallel to one of the three commonly present peripheral flat regions the (211) and $(\bar{2}\bar{1}\bar{1})$ planes are exposed. If the facet at the crystal-melt interface is indexed as the $(\bar{1}\bar{1}\bar{1})$ plane, then the surface exhibiting optimum etching characteristics is found on the section containing the peripheral flat region parallel to the cut, i.e., $(\bar{2}\bar{1}\bar{1})$. The corresponding (211) plane exhibits etching characteristics which are not suitable for the investigation of impurity striations. The noncentrosymmetric nature of the <211> direction is clearly reflected in the behavior of the {211} planes shown in Fig. 1. Here rotational twinning of the crystal has exposed simultaneously the (211) and $(\bar{2}\bar{1}\bar{1})$ planes.

Results and Discussion

Single crystals grown in a <111> direction exhibit more or less extensive "coring" as well as impurity

[1] It is common practice to denote the {111} surfaces of III-V compounds terminating with group V atoms as {111}B surfaces or simply B surfaces and those terminating with group III atoms as {111}A or just A surfaces.

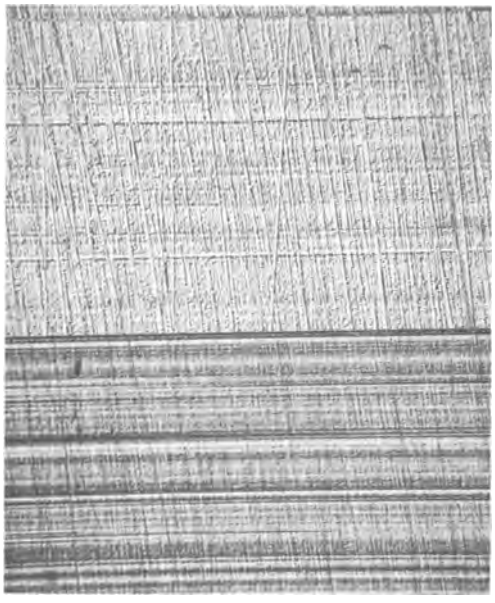

Fig. 1. Impurity striations on a rotational twin; the upper part is a (211) and the lower part a $(\bar{2}1\bar{1})$ plane. The latter one is employed throughout this study for revealing the various types of striations. Magnification 95X.

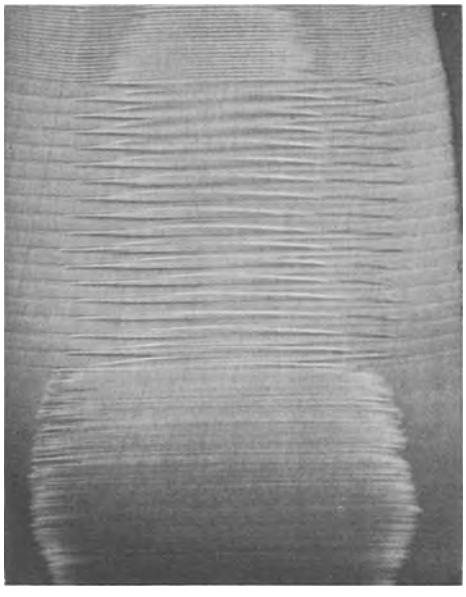

Fig. 2. Rotational impurity striations in InSb (8 mg Te in 50g melt). The upper part was pulled at 18 rpm, the middle part at 4 rpm, and the lower at 45 rpm."On core" and "off core" regions can be observed. Magnification 7X.

striations if impurities are present in the melt as shown in Fig. 2. The core results from the presence of the well-known (111) facet at the solid-melt interface and is revealed through its impurity concentration which is significantly different from that of the off core region. The extent of coring (laterally) can vary between zero and 100% depending on the prevailing thermal conditions in the crystal-melt system.

Hulme and Mullin's findings (4) that the extent of coring increases with increasing impurity concentration could not be confirmed in the present experiments. In intrinsic crystals the presence of a core could not be revealed by etching techniques. Its presence can only be presumed from the existence of the (111) facet at the crystal-melt interface. Depending on the specific experimental conditions prevailing during growth, several different types of striations were encountered. Since all of these striations may coexist

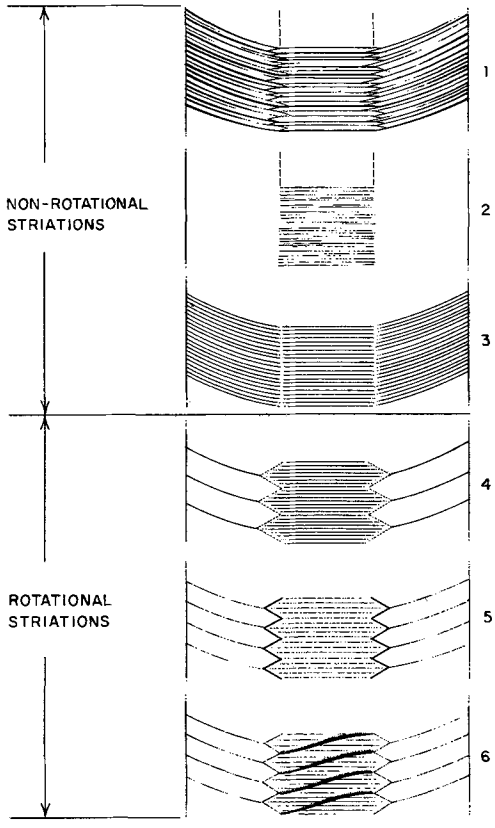

Fig. 3. Schematic diagram of impurity striations encountered in InSb single crystals.

very complex patterns were frequently observed which are extremely difficult to analyze.

For convenience and clarity the different striations will be discussed individually with the aid of the schematic diagram shown in Fig. 3.

Nonrotational striations.—Striations observed in crystals without rotation are generally attributed to growth rate variations caused either by temperature fluctuations occurring at the solid-melt interface during growth or by irregular variations of the pulling

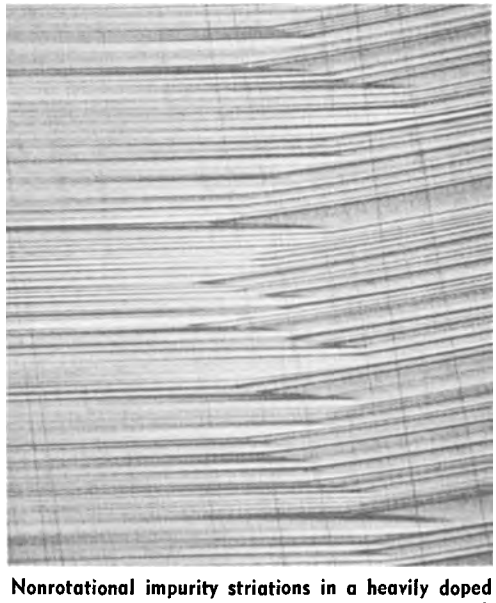

Fig. 4. Nonrotational impurity striations in a heavily doped crystal (60 mg Te in 50g melt). The striations are straight in the "on core" region on the left and exhibit curvature in the "off core" region on the right hand side of the photograph. The on core-off core interface is corrugated in appearance. Compare with striations No. 1 in Fig. 3. Magnification 95X.

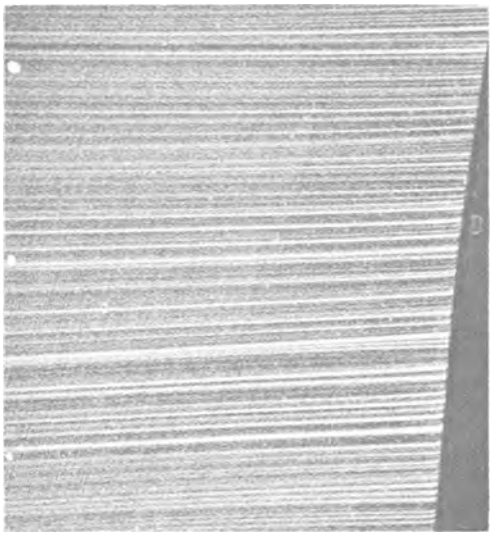

Fig. 5. Nonrotational striations as observed in the off core region of a single crystal. Notice the decrease of intensity of the striations in the direction of the center of the crystal, from right to left in the photograph. Magnification 95X.

rate originating in the mechanical arrangement (5). This type of striations is very common in crystals grown with Czochralski type techniques and can be observed in various forms under virtually any experimental conditions.

Striations of type 1 in Fig. 3 exhibit several distinctive features (see Fig. 4). Their shape always reflects the configuration of the crystal-melt interface at the time of their formation. The width, density (frequency), and intensity (sharpness) as revealed by etching were found to vary, generally increasing, with increasing impurity concentration. Their intensity frequently decreases toward the center of crystal. Accordingly, faint striations near the periphery of the crystal often become completely invisible toward the center of the crystal as shown in Fig. 5. This change in intensity of striations most likely reflects corresponding changes in impurity concentration in the melt.

These striations do not exhibit a long-range periodicity although short-range periodicity can frequently be observed. They are continuous through the core of the crystal at high impurity concentrations. This type of striations is invisible in dark field illumination because of their diffuse nature.

Striations of type 2 in Fig. 3 are much less common and differ significantly from the previously discussed nonrotational striations (see Fig. 6a). They appear only in the core region, and apparently their formation is associated with the (111) growth facet which is responsible for the crystal core. Being extremely sharp they can be individually investigated in dark field illumination in which standard nonrotational striations are invisible (see Fig. 6b). In this way it was observed that the striations are of limited and varying length, usually terminating somewhere within the core. Their intensity is not significantly sensitive to variations in impurity concentration. The fact that these striations can still be observed after successive polishings to a depth of several millimeters indicates that they are planar in nature and not line defects. The frequency of their appearance is a function of the growth direction and increases sharply with deviation from the <111> direction. On the basis of all aspects considered it is concluded that the mechanism of their formation is basically different from that of all other striations. They are tentatively considered as a planar defect structure associated with slip planes or stacking faults.

Striations of type 3 in Fig. 3 can only be observed under high magnification following highly controlled

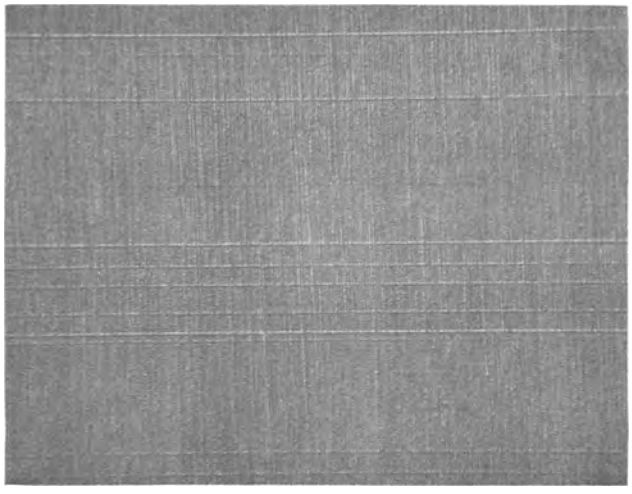

Fig. 6a. Sharp on core striations in bright field illumination. Compare with striations No. 2 in Fig. 3. Magnification 390X.

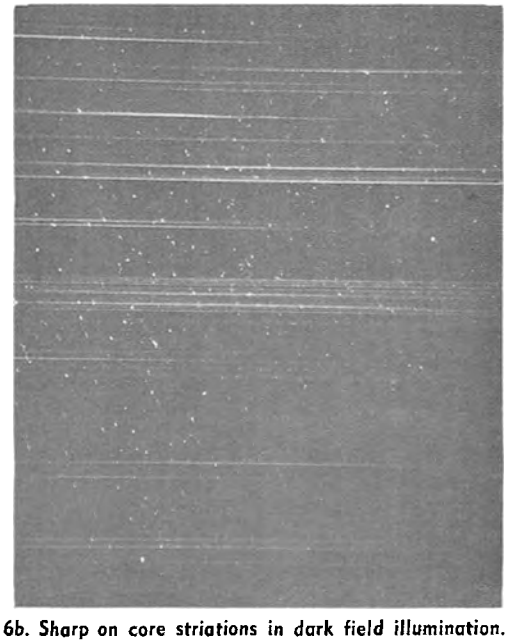

Fig. 6b. Sharp on core striations in dark field illumination. Magnification 275X.

polishing and etching (see Fig. 7). The spacing of these rather faint striations is around 1μ and their frequency of formation is between 1 and 20 per sec. They were observed on core and off core with a discontinuity at the core boundary. The fact that they were found throughout the crystal suggests that their formation is associated with the over-all solidification process rather than with some specific aspect of solidification kinetics; the solidification kinetics is presumed to be significantly different for the core and the off core region. The observed high frequency of formation on the other hand makes it rather difficult to associate their origin with temperature fluctuations due to convection as was the case with the striations of type 1 and 2.

These striations are most likely associated with pulling rate fluctuations or vibrations of the melt surface. Indeed precise measurements of the pulling rate by means of a velocity transducer (sensitivity 500 mv/in./sec) revealed pulling rate fluctuations having frequencies between 1 and 10 per sec. (see Fig. 8). These values are in the range of the observed striations. Furthermore, low-frequency vibrations were observed on the surface of the melt.

The close spacing of these striations delineates short time changes of the crystal-melt interface. Such

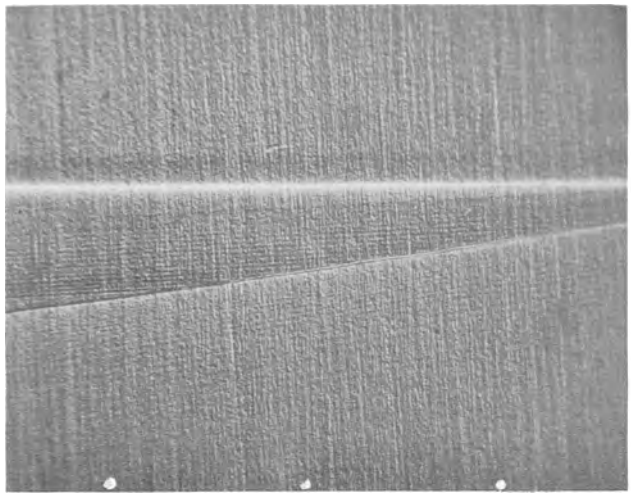

Fig. 7. Close spaced impurity striations observed in the absence of regular nonrotational striations after extremely careful polishing and etching. Compare with striations No. 3 in Fig. 3. Magnification 390X.

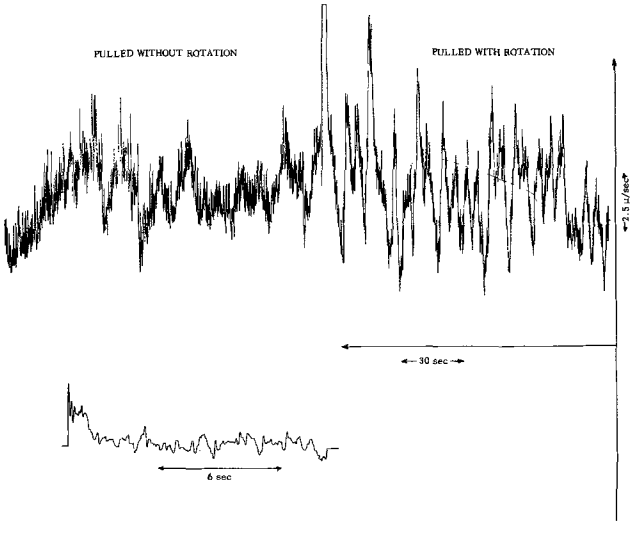

Fig. 8. Pulling rate variations as determined by means of a velocity transducer (sensitivity 500 mv/in./sec).

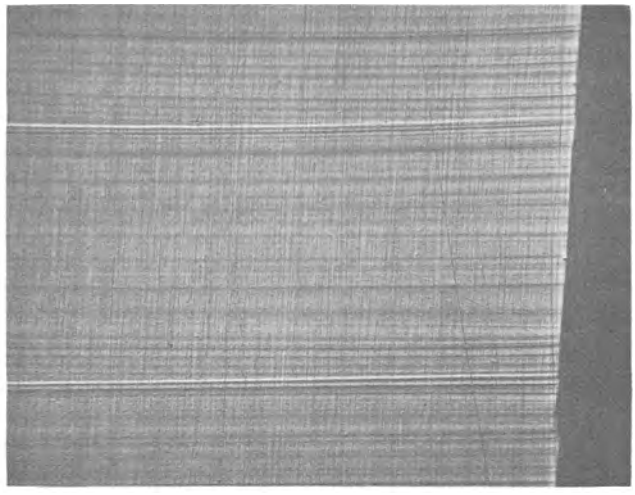

Fig. 9. Section of the off core region of a crystal showing rotational striations of high intensity (the two sharp white lines) superimposed to low intensity nonrotational striations. Compare with striations No. 4 in Fig. 3. Magnification 95X.

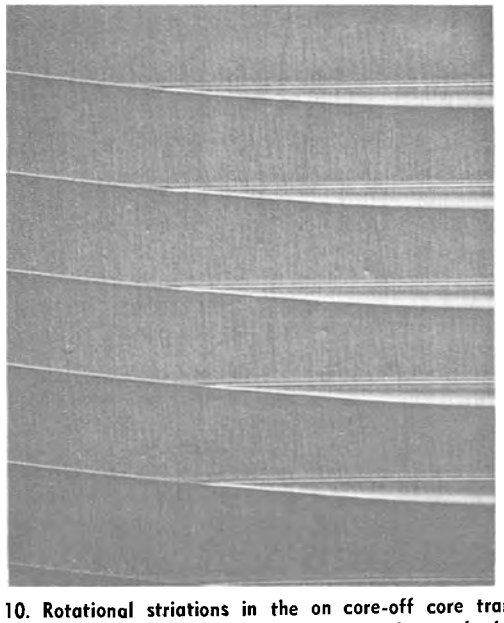

Fig. 10. Rotational striations in the on core-off core transition region. The absence of nonrotational striations is due to the low impurity concentration (6 mg Te in 50g melt). Magnification 95X.

changes could be valuable in investigating crystal growth kinetics.

Rotational striations.—All crystals pulled under rotation exhibit the so-called "rotational" striations in addition to the previously discussed nonrotational striations (see Fig. 9). Since they are more pronounced than the nonrotational striations they can be observed at lower impurity concentrations where the previously discussed types of striations are absent (see Fig. 2).

Striations of type 4 in Fig. 3 are intense and in crystals of constant diameter exhibit short- as well as long-range periodicity (see Fig. 10). The long-range periodicity can be calculated from the pulling and rotation rates after correcting for the continuous change of the melt level. In crystals of varying diameter the short-range periodicity was not observed. An increasing crystal diameter resulting from a decrease in the melt temperature is associated with an increased growth rate which at constant pulling rate is accommodated by a shift of the solidification front into the melt. Conversely an increase in the melt temperature results in a decreasing rate of solidification (or even back melting) and thus in a rise of the crystal-melt interface.

Rotational striations in the off core region differ only by their increased intensity from nonrotational striations. Their penetration into the core region is complex and very difficult to analyze. Thus, each striation appears to split and to develop a substructure which changes continuously across the core region (see Fig. 11 and 12). The component striations of the substructure are straight and reflect the (111) facet growth. The complexity of the substructure increases with increasing deviation of crystal growth from the <111> direction (see Fig. 13).

Striations of type 5 in Fig. 3 delineate the off core-on core interface and reflect the sudden change of impurity concentration in this transition region (see Fig. 14). The corrugated nature of this interface and therefore of the core is believed to be caused by the fact that the rotation and thermal axis of the growing crystal do not coincide. Under such conditions the (111) facet is being continuously relocated with respect to the over-all crystal in order to conform with the solidification isotherm. The extent of relocation depends on the rate of rotation and the separation of the rotation and the thermal axis. Thus, the extent of penetration of the off core region into the core reflects the lack of thermal and rotational symmetry of the growth system. The irregularities observed within

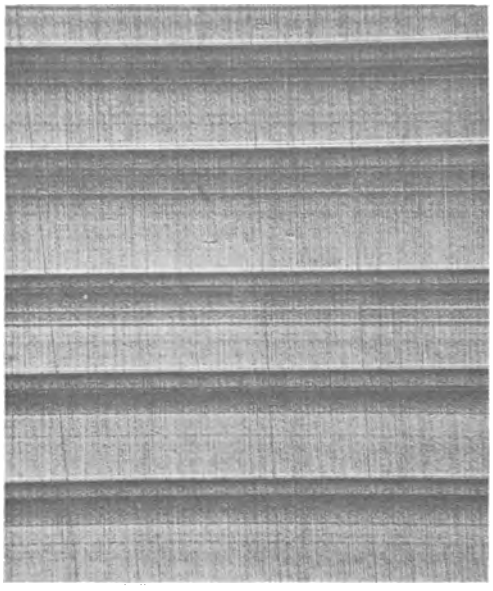

Fig. 11. Substructure of rotational striations in the on core region grown in the <111> direction. Magnification 95X.

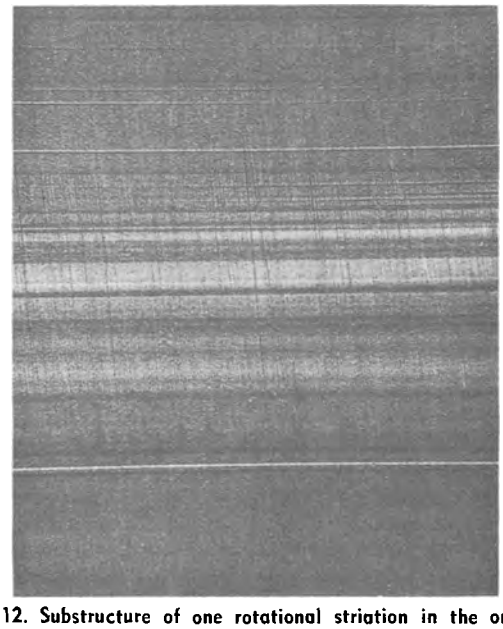

Fig. 12. Substructure of one rotational striation in the on core region of a crystal grown several degrees off the <111> direction. Compare with Fig. 11. Magnification 275X.

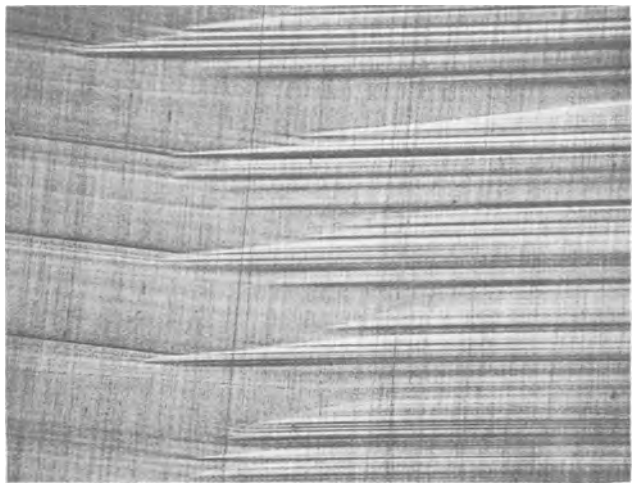

Fig. 13. Rotational striations in the off core-on core transition region of a crystal grown 9° off the <111> direction (impurity concentration 6 mg in 50g melt). Compare with Fig. 10. Magnification 95X.

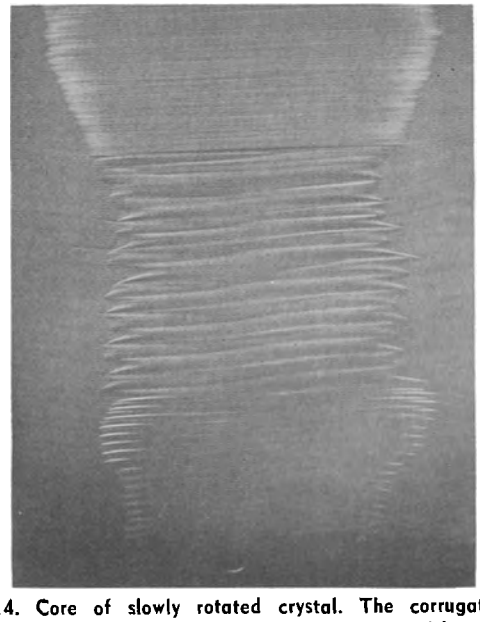

Fig. 14. Core of slowly rotated crystal. The corrugated off core-on core interface is clearly visible. Compare with striations No. 5 in Fig. 3. In addition we observe helical striations which are not parallel to the (111) facet. Compare with striations No. 6 in Fig. 3. Magnification 7X.

the corrugated structure are believed to result from the irregular (noncircular) shape of the (111) growth facet.

Striations of type 6 in Fig. 3 are directly associated with rotation and consequently have a helical structure as seen in Fig. 14. They are encountered in the on core region of crystals pulled under slow rotation. Their intensity decreases with increasing rotation rate, and they could not be observed in crystals rotated at rates greater than 5 rpm. These striations do not lie in the (111) growth facet. In most instances they were found to cross the on core striations at varying angles. Accordingly they are not considered to be regular (111) facet growth striations.

If we assume that a striation of a given intensity reflects a constant impurity concentration, then the formation of these striations can be explained on the basis of varying impurity concentration on the (111) growth facet as follows. The (111) facet moves laterally when the thermal and rotation axes do not coincide (see above) so that the region of a given concentration on the facet forms a helical pattern resulting from the combined lateral and vertical motion. Thus, these striations are essentially the locus of points of the same concentration in consecutive growth layers. A decrease in impurity concentration in the direction of the center of the core was indeed measured in nonrotated and slowly rotated crystals by resistivity measurements using a four point microprobe.

Although the various types of impurity striations have been discussed individually, they are often encountered simultaneously developing rather complex striated structures which cannot be fully analyzed.

Summary

Interference contrast microscopy in conjunction with special polishing and etching techniques was employed for the investigation of impurity striations under conditions of high optical contrast. Individual striations were studied with a spacing of less than 1μ. Six different types of impurity striations were identified. It was furthermore observed that under conditions of incomplete stirring, the crystal core generally exhibits a concentration gradient along the (111) growth facet which is reflected in the apperance of

helical striations. Impurity striations and the associated defect structure are believed to be powerful tools in studying crystal growth kinetics.

Acknowledgment

This work was supported by the Atomic Energy Commission under Contract AT(30-1)-3208. The authors wish to express their appreciation to Mrs. Mary C. Lavine for her valuable suggestions and discussions, to Mr. K. Morizane for his constructive criticism, and to Mr. C. J. Herman for his skillful laboratory assistance.

Manuscript received March 7, 1966.

Any discussion of this paper will appear in a Discussion Section to be published in the June 1967 JOURNAL.

REFERENCES

1. A. Mueller and M. Wilhelm, *Z. Naturforsch.*, **19a**, 254 (1964).
2. H. Ueda, *J. Phys. Soc. Japan*, **16**, 61 (1961).
3. P. R. Camp, *J. Appl. Phys.*, **25**, 459 (1954).
4. K. F. Hulme and J. B. Mullin, *Solid State Electronics*, **5**, 211 (1962).
5. K. Morizane, A. F. Witt, and H. C. Gatos, *This Journal*, **113**, 51 (1966).

Preparation and Properties of Boron Arsenides and Boron Arsenide-Gallium Arsenide Mixed Crystals

S. M. Ku

General Telephone and Electronics Laboratories Incorporated, Bayside, New York

ABSTRACT

Both cubic and rhombohedral forms of boron arsenides were made by the vapor-phase technique. Energy gaps of the cubic and rhombohedral forms were estimated to be 1.46 and 1.51 ev, respectively, by the optical transmission technique of powdered samples. Mixed crystals of boron arsenide-gallium arsenide were also prepared by vapor-transport reaction. Variation of energy gaps from 1.36 to 1.27 ev was observed within the mixed crystal composition range containing 0.8 to 2.8 w/o (weight per cent) of boron. Measurements of effects of temperature and injection level on the emission of diodes prepared from these mixed crystals indicate that all compositions up to 2.8 w/o of boron are direct semiconductors.

The advent of injection-luminescent diodes and lasers and of Gunn effect devices has prompted extensive studies of the composition ranges available in mixed crystals produced by solid solution of two III-V compounds and of the resulting variation in semiconducting properties. In spite of the potentially attractive properties of III-V boron compounds, such as relatively high energy gaps and high mobilities (1-3), these materials remain relatively unexplored because of the formidable difficulties involved in the synthesis of reasonably pure and large single crystals (4). It is the purpose of this paper to report on an investigation of a new III-V mixed crystal system, BAs-GaAs. This work was primarily concerned with preparation of boron arsenide-gallium arsenide mixed crystals and the determination of their electrical and optical properties. It also included preparation of boron arsenides by various techniques, and measurements of some of their optical properties.

Preparation and Properties of Boron Arsenides

Preparation methods.—The boron arsenides were prepared by a method similar to that described by Williams and Ruehrwein (5). A weighed amount of finely powdered amorphous boron of 99.99% purity was placed at one end of a quartz capsule, and an amount of 99.9999% pure arsenic in excess of that required to react with the boron was inserted at the other end of the capsule. The entire ampoule was evacuated to 10^{-5} Torr and then baked at 250°C for at least 4-6 hr to remove any residual gases that were adsorbed on the surface of the micron-size boron powder. After the baking cycle, the capsule was sealed off and inserted into a two-zone resistance furnace, where the boron was kept at a temperature in the range of 850°-1100°C and the arsenic was held at 640°C in order to maintain 1 atm arsenic pressure in the capsule. Since the equilibrium vapor pressure of solid arsenic has an exponential dependence on temperature, precise temperature control is required to obtain the stability required for vapor synthesis. The arsenic cold-sink temperature was usually controlled within ±1°C during the entire operation. At 1 atm arsenic pressure over 100 hr were usually required to complete the reaction.

Boron arsenide was also prepared by reacting finely powdered AlAs with BI_3. Hydrogen was bubbled at a rate of 0.5 liter/min through BI_3 held between 120°-150°C and was then carried over AlAs powder which was held at 750°C. Boron arsenide was deposited downstream in the cooler parts of the furnace tube. Boron arsenides prepared by the double displacement reaction of AlAs and BI_3 were found to be a mixture of boron monoarsenide, subarsenides, residual AlAs, aluminum silicate, and other compounds. Layers deposited on the wall of the quartz tube were less than 1μ in thickness after 6 hr of reaction, and the color of these layers varied from deep amber to dark black. No further attempt was made to characterize these layers.

Structure.—Two distinct microcrystalline forms of boron arsenide were prepared by the direct vapor synthesis technique described above. With the arsenic pressure in the range of 1-2 atm, the product at a reaction temperature of 875° ± 25°C was of dark brownish color; at 1000°C or above, the product was of amber color. X-ray powder diffraction pattern analysis identified the lower temperature product as cubic boron monoarsenide BAs, and the high-temperature material as rhombohedral boron subarsenide with lattice parameters of 4.7778 and 5.3177Å ($\alpha = 70° 32'$), respectively. The compositions of the synthesized materials were determined by both chemical and x-ray fluorescence analysis. The structures and compositions confirm those assigned by Matkovich (6) and LaPlaca and Post (7). When the boron monoarsenide was heated above 1000°C under arsenic pressures varying from a few tenths of an atmosphere to 3 atm, the BAs transformed into the subarsenide. However, the reverse transformation of the rhombohedral form to the cubic structure did not take place at 850°C even under arsenic pressures as high as 5 atm.

Impurity content.—Spectrographic analysis indicated that the boron compounds synthesized by direct

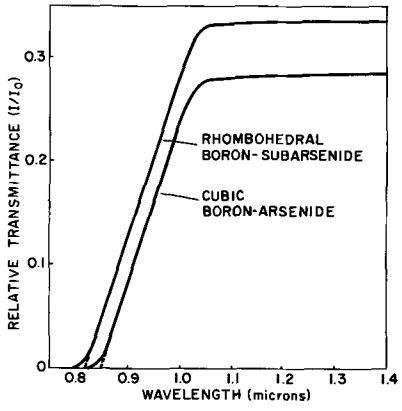

Fig. 1. Comparison of optical transmission vs. wavelength (300°K) of rhombohedral and cubic forms of boron arsenides.

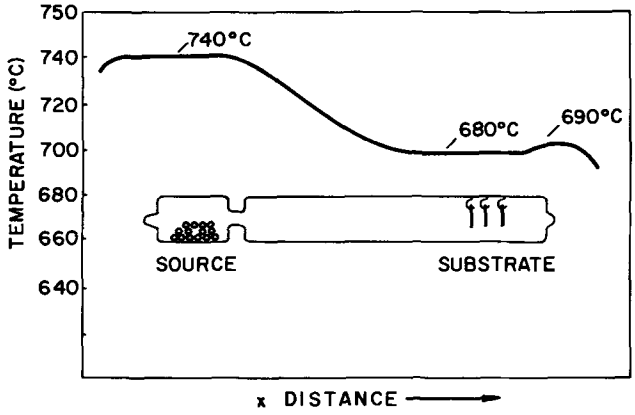

Fig. 2. Furnace temperature profile for epitaxial growth and relative position of the reaction tube in the furnace.

vapor reaction contained impurities such as Mg, Ag, Al, and Pb at levels below 50 ppm. These impurities can be traced to the starting materials used in the preparation. Copper and silicon were the only two impurities detected in more than 50 ppm concentration in the boron arsenides. The silicon content increased with the duration and temperature of the run and presumably came mainly from the quartz tube. In subarsenides (synthesized near 1100°C) silicon concentrations as high as 1% were observed. In monoarsenides (synthesized near 870°C) the silicon content was usually less than 100 ppm. The fact that the copper concentration (50-100 ppm) was independent of the synthesis conditions indicates that the boron arsenides do not effectively leach copper from quartz within the temperature range used for synthesis.

Optical energy gaps.—Transmission *vs.* wavelength measurements were made to estimate the optical energy gaps for the monoarsenides and subarsenides. Since large specimens of these two compounds were not available, the transmission samples were prepared in the following manner. Boron monoarsenide and subarsenide microcrystallines were ground to —300 mesh, mixed with KBr powder of the same particle size, and pressed into 0.025 in. thick pellets ½ in. in diameter. These pellets were then lapped and polished down to 0.007-0.010 in. wafers in a dry nitrogen atmosphere to prevent absorption of moisture by the KBr. The optical absorption of the specimen was measured in the wavelength range 0.55-1.50μ using a DF-2 prism spectrometer (Perkin-Elmer 112). Figure 1 is a plot of the optical transmission *vs.* wavelength measurement at room temperature. The optical energy gaps estimated from the extrapolation of the slope of these curves to zero transmission were 1.46 ev for monoarsenide and 1.51 ev for subarsenide. However, the 1.51 ev value might be considerably less than the actual optical gap of subarsenide since the subarsenide samples were heavily contaminated with Si and the absorption coefficient of Si is extremely high in this region.

Boron Arsenide-Gallium Arsenide Mixed Crystals

Preparation.—The apparatus for growing monocrystalline boron arsenide-gallium arsenide mixed crystals from the vapor phase consisted essentially of a 2 in.-diameter quartz tube extending through two separately controlled constant-temperature regions, the lower-temperature region for the substrate and higher temperature zone for the source. The temperature profile and the capsule placement in the furnace is illustrated in Fig. 2. Oriented gallium arsenide single crystals cut perpendicular to the <110> or <111> direction and etched in sulfuric acid-H_2O_2 solution were used as substrate. The transporting agents were either BI_3 + H_2 or I_2 + H_2. The BI_3 was presynthesized by reacting amorphous boron under I_2 vapor at 1000°C; the white BI_3 was collected in a side tube which was controlled at a temperature of 200° ± 1°C. Crushed gallium arsenide pieces and free arsenic were used as source materials when the transport agents were BI_3 and H_2; otherwise, vapor synthesized microcrystalline boron monoarsenide and gallium arsenide were the source materials. If n-type doping was desired in the epitaxy, SnI_4 was added to the transport agents.

Composition and structure.—Mixed crystals were prepared by the iodide vapor transport reaction with various predetermined source compositions ranging from 10 to 75 mole % of cubic boron-monoarsenide. The compositions of the mixed crystals were determined by several analytical methods: x-ray fluorescence, electron-beam (E-B) probe, "wet" chemical, and lattice-constant determination. The first two methods give the boron composition only indirectly by measuring the gallium-to-arsenic intensity ratio of the sample. Although the third method gives an independent direct measurement of the weight per cent of each of the three elements, B, Ga, and As in the mixture, the inherent disadvantages of this technique are: first, it is destructive analysis, and second, large samples are needed in order to achieve a high degree of accuracy (within ±0.25 w/o). The fourth method relies on the assumption that Vegards' law of solid solution holds for this mixed system; thus with the known lattice constants of the two terminal compounds one can determine the composition.

The analytical results of the boron arsenide-gallium arsenide mixed crystals obtained by the last three methods were found to be in good agreement (see Table I). They indicate that the compositions of all these vapor-transported epitaxies contained less than 3 w/o of boron. For instance, a predetermined source of 75 mole % of boron monoarsenide (which is equivalent to 8 w/o of boron) yielded a sample containing only 2.8 w/o of boron. Evidently a one-to-one transport of boron and gallium from the source to the substrate does not follow in this III-V mixed crystal, but the relative rates of transport of Ga and B seemed to be fairly uniform since in each case the layer was found to be homogeneous. The variation of composition along the parallel and vertical plane of the epitaxy-substrate interface was measured to be less than ±0.1 w/o of boron (by E-B probe analysis).

Table I. Analytical results

Sample No.	E-B probe analysis, w/o		"Wet" chemical analysis, w/o			$B_{substituted}$ / $Ga_{replaced}$	Lattice constant, Å
	B & As	Ga	B	Ga	As		
122	Balance	46.50	0.78	46.6	52.65	2.0	5.648
129	—	—	1.51	46.8	51.70	7.5	—
126	Balance	46.60	2.80	45.2	52.30	5.2	5.638

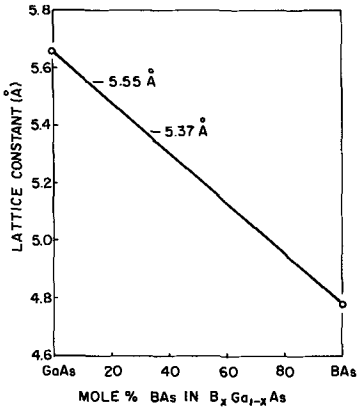

Fig. 3. Variation of lattice constant with composition in an idealized solid solution of $B_xGa_{1-x}As$ system.

The lattice constants of the mixed crystals were measured by the Laue back-reflection technique at room temperature. Both the chemical analyses and the lattice constants given in Table I indicate that the epitaxial layers do not consist of simple solid solutions of BAs and GaAs. The analytical data show that substitution occurs with more than one boron atom per gallium atom replaced. The ratio of boron atoms substituted to gallium atoms replaced is quite variable, ranging from about two for sample 122, to 5.2 for sample 126, and 7.5 for sample 129. These ratios are only approximate because of their sensitivity to small errors in the analytical results for gallium and arsenic. A similar conclusion is reached on consideration of the lattice-parameter values. Application of Vegards' law to BAs-GaAs solid solutions would predict a much larger contraction of the lattice with increasing boron concentration than that observed. Thus the 2.82 w/o boron of sample 126 corresponds to approximately 32 mole % BAs in a BAs-GaAs solid solution and would, by Vegards' law, be expected to have a lattice constant of 5.37Å (Fig. 3) instead of the measured value of 5.638Å. A similar discrepancy exists for sample 122. These discrepancies are too large to be accounted for by usually encountered deviations from Vegards' law and, together with the analytical results, indicate that the boron is present in a form other than that of a BAs-GaAs solid solution.

In order to determine whether the excess numbers of boron atoms existed in a second phase or whether the layers were mixed crystals of boron subarsenide-gallium arsenide, both x-ray powder pattern determinations and high-magnification microscopic examinations were made. The x-ray patterns showed neither broadening of the back-reflection peaks nor the presence of additional peaks, indicating a high degree of crystalline perfection in these layers and the absence of a second phase. High-magnification microscopic examination of the polished and etched layers also revealed no evidence of any second-phase precipitate. It appears therefore that the excess boron atoms were in solid solution, even in samples of the highest boron concentration. Although our experiments could not determine directly whether the excess boron atoms are present in the lattice substitutionally, interstitially, or both, the chemical and x-ray data suggest that the resulting epitaxies were homogeneous mixed crystals of boron subarsenide and gallium arsenide. Analytical evidence for this is afforded by the fact that the ratios of the boron substituted to the arsenic replaced in the layers of boron content greater than 1.5 w/o are compatible with the value 6.0 to be expected for GaAs-B_6As solid solutions. One discrepancy (in sample 122) may reflect experimental inaccuracy, as the determination of this ratio is less accurate at low boron concentrations, or it may represent a small content of BAs.

Table II. Electrical properties of boron arsenide-gallium arsenide mixed crystals

Sample No.	Boron composition, w/o	Free carrier conc., atoms/cm³	Hall mobility cm²/volt-sec	Resistivity, ohm-cm
122	0.78	$n = 1.6 \times 10^{18}$	515	7.3×10^{-3}
126	2.8	$n = 7.3 \times 10^{17}$	280	3.1×10^{-2}

In addition, it should be noted that the lattice parameter for the rhombohedral boron subarsenide equivalent to that of a cubic structure is 5.3177Å, which is a closer match to that of GaAs (5.6533Å) than the 4.7778Å of cubic boron monoarsenide. The rhombohedral structure may be considered a cubic form which has been elongated or compressed along a body diagonal axis and the angle θ of rhombohedral boron subarsenide is 70° 32′, which is identical to the angle between the two (111) faces of the cubic structure. It is structurally quite conceivable for solid solutions of boron subarsenide-gallium arsenide to form. The values of the lattice constant of our mixed crystal layers given in Table I are in close agreement with those resulting from application of Vegards' law to such solid solutions.

Electrical properties.—Specimens used for electrical measurements were cut from the center portion of the epitaxial layer to avoid any unnecessary variation of homogeneity from either the surface or the epitaxy-substrate interface. They were in the form of rectangular blocks of 16 x 11 x 19 mils. The Hall mobilities and free carrier concentrations of these epitaxies were calculated and are listed in Table II.

Although many factors may contribute to the electrical properties of these mixed crystals, it should be noted that a significantly lower Hall mobility is observed in these epitaxial mixed crystals than in gallium arsenide of comparable free carrier concentrations, *e.g.*, in sample No. 122 for a free carrier concentration of $1.6 \times 10^{18}/cm^3$ the Hall mobility is almost five times lower than that for GaAs having the same free carrier concentration. Furthermore, the Hall mobility of the higher boron composition sample (No. 126) decreased by a factor approaching two, where the free carrier concentration is approximately two times lower than the lower boron composition sample (No. 122). Similar behavior has also been observed in other mixed crystals such as GaAs-GaP (8), InSb-GaSb (9), InAs-InP (10), etc., where a pronounced decrease in mobility was found with increasing content of the lower mobility component. This is further indirect evidence that the epitaxial layers are crystals of mixed boron and gallium arsenide since a decrease of Hall mobility accompanies an increase in boron

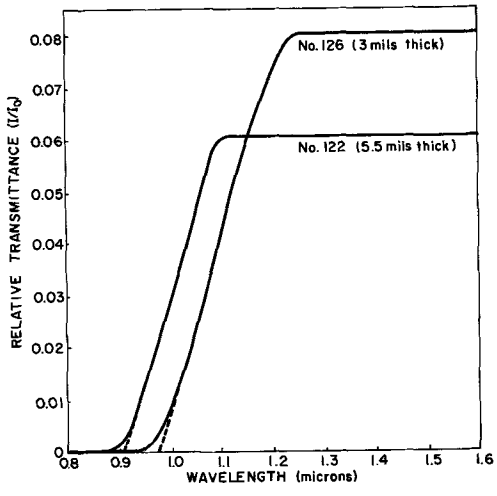

Fig. 4. Variation in optical transmission (300°K) of two different mixed crystal compositions.

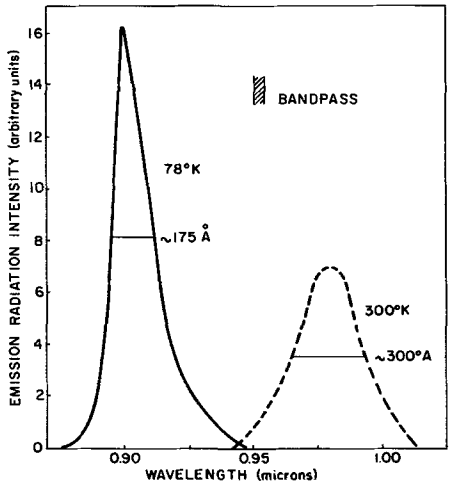

Fig. 5. Comparison of emission spectra at same current level for a mixed crystal diode at 300° and 78°K. Current level, 1.0-A peak current, 2-μsec pulse width, 1000 pulses/sec.

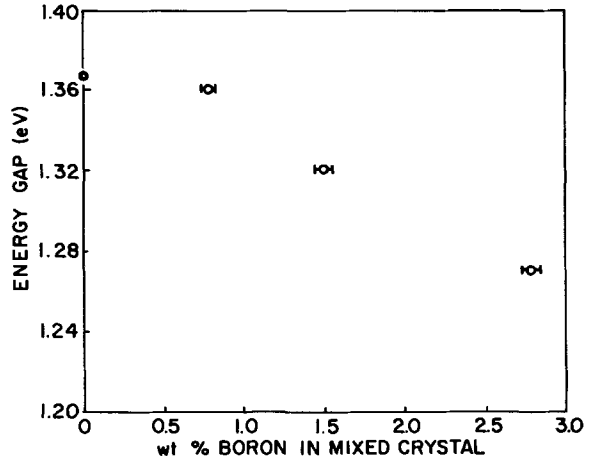

Fig. 6. Emission energy gap (300°K) vs. variation of boron concentration in mixed crystal system.

concentration. Of particular interest is the question of whether the mobility of the carriers is decreased in this mixed crystal by alloy scattering, *i.e.*, by virtue of a statistical distribution of the atoms of the components. At this stage of the investigation, however, the mobilities of boron arsenides and the parameters governing the mobility are not sufficiently known to permit discussion of the scattering mechanism.

Optical properties.—Absorption properties of these epitaxial mixed crystals were measured in the wavelength range of 0.6-1.6μ using a Perkin-Elmer Spectrophotometer Model No. 350. These specimens were first lapped and polished with diamond grit to a mirror-finish surface. Figure 4 shows curves of optical transmittance *vs.* wavelength of both the 0.8 and 2.8 w/o samples at room temperature. Their respective optical energy gaps, extrapolated from the slope of these curves to zero transmission, are 1.36 ev (0.91μ) and 1.27 ev (0.98μ).

Since all the epitaxial mixed crystals made in this investigation were n-type, p-n junctions were fabricated by the standard closed-tube zinc diffusion technique, using zinc arsenide as diffusant to give a surface concentration of $N_A \sim 10^{19}/cm^3$.

Diode emission was measured with a Perkin-Elmer Model No. 112 spectrometer and an RCA 7102 detector. Within the spectrometer scanning range of 0.65-1.52μ, only one radiation peak was observed from each diode at both 300° and 78°K. Since these radiative peaks vary with the square of the pulse current of the diode (*i.e.*, as i^2), and their intensity rises as the temperature decreases (Fig. 5), it is reasonable to assume that they are due to transitions across the energy gaps. These measured emission peaks agree fairly well with the values obtained from the transmission data, since by definition, the energy gaps obtained from the diode-emission data are always lower than those from the optical transmission measurements (11). The absence of impurity emission in these diodes made it impossible in this experiment to determine whether the material has a direct or indirect band gap.

Figure 6 shows that there is a systematic decrease of emission-energy gap with increasing boron composition in the mixed crystal diodes. Previous investigators have shown that GaAs diodes of n- and p-type impurity levels comparable to the present diodes show no decrease in band-edge emission energy. Thus the present decrease is evidently due to the increased concentration of the boron-containing constituent of the solid solutions. This is similar to the decrease of the energy gap with increase in composition of the second terminal compound found in other III-V mixed crystals of comparable terminal energy gap values, *e.g.*, InSb-GaSb (12).

Another feature of interest is the narrowing of the bandwidth of these diode emission peaks from about 300Å at room temperature to 175Å at 78°K (Fig. 5). This shows that the composition along the p-n junction is fairly homogeneous and that the broadening of the bandwidth at higher temperature is due mostly to thermal smearing.

Acknowledgment

The author would like to express her gratitude to R. Weberling, W. Sutkowski, J. Cosgrove, and their associates for providing, the "wet" chemical, E-B probe, x-ray and spectrophotometric analysis which were indispensable in interpreting the results. Technical assistance in the experimental work was skillfully supplied by A. Marx. The author is indebted to Dr. B. Smith whose interest and encouragement made possible this work, and to Dr. D. Baird for carefully reviewing the manuscript and giving valuable comments.

Manuscript received March 4, 1966.

Any discussion of this paper will appear in a Discussion Section to be published in the June 1967 JOURNAL.

REFERENCES

1. B. Stone and D. Hill, *Phys. Rev. Letters*, **4**, 6, 282 (1960).
2. C. C. Wang, M. Cardona, and A. G. Fischer, *RCA Rev.*, 159 (1964).
3. R. J. Archer, R. Y. Koyama, E. E. Loebner, and R. C. Lucas, *Phys. Rev. Letters*, **12**, 19, 538 (1964).
4. D. E. Hill and R. I. Stearns, U.S. Air Force Contract AF 19(628)-500; Subcontract 297, Final Report, June 30 (1964).
5. F. V. Williams and R. A. Ruehrwein, *J. Am. Chem. Soc.*, **82**, 1330 (1960).
6. V. I. Matkovich, *ibid.*, **83**, 1804 (1961).
7. S. La Placa and B. Post, *Planseeber. Pulvermet.*, **9**, 109 (1961).
8. S. M. Ku, *This Journal*, **110**, 991 (1963).
9. J. C. Woolley and C. M. Gillett, *J. Phys. Chem. Solids*, **17**, 34 (1960).
10. H. Weiss, *Ann. Phys.*, **4**, 121 (1959).
11. S. M. Ku and J. Black, *Solid-State Electronics*, **6**, 505 (1963).
12. V. I. Ivanov-Omskii and B. T. Kolomiets, *Doklady Akad. Nauk S.S.S.R.*, **127**, 135 (1959). J. C. Woolley, S. A. Evans, and C. M. Gillett, *Proc. Phys. Soc.*, **74**, 244 (1959).

Optical Study of $GeCl_4$ Ge, He, and H_2 Systems

K. E. Haq[1]

International Business Machines Corporation Watson Research Center, Yorktown Heights, New York

ABSTRACT

The optical absorption characteristics of $GeCl_4$, Ge, He, and H_2 systems have been studied at elevated temperatures under flow conditions for the wavelength region between 2300-5000Å. It is found that at all temperatures the behavior of $GeCl_4$, Ge, and He systems is very similar to that of the $GeCl_4$, Ge system in a sealed tube. However, in the case of $GeCl_4$-H_2 system, hydrogen reacts with $GeCl_4$ at temperatures of 500°C and above and gives rise to $GeCl_2$. In addition, when $GeCl_4$ carried by hydrogen is passed through a germanium bed, it is found that at 350°C $GeCl_4$ reacts with Ge to give rise to $GeCl_2$, and at 450°C hydrogen reacts with $GeCl_2$ with precipitation of free germanium.

In an earlier paper (1), the results of optical absorption studies of $GeCl_4$, with and without solid germanium present in the system, were reported. As the data were acquired in a sealed system, the results were indicative of the species formed at elevated temperatures in the absence of any carrier gas. Since most methods for deposition of epitaxial Ge films utilize carrier gases, it is of practical importance to know the vapor phase species in a $GeCl_4$ system at elevated temperatures under dynamic conditions, particularly in the presence of carrier gases, such as helium, hydrogen, etc. Hence, the measurements have been extended to flow systems. In the present paper the results of studies of the following systems are reported: (*i*) $GeCl_4$-He, (*ii*) $GeCl_4$-He-Ge, (*iii*) $GeCl_4$-H_2, and (*iv*) $GeCl_4$-H_2-Ge.

Experimental

Apparatus.—A detailed description of the optical arrangement used for measurements was given in the earlier report (1). The arrangement shown in Fig. 1 was used for introducing the $GeCl_4$ and carrier gas mixture into the sample cell. The carrier gas, high-purity helium, or hydrogen, as the case might be, first passed through a molecular sieve and then through a flow meter before entering the bubbler. To ensure proper saturation of the gas, the bubbler was provided with a glass frit for dispersing the gas. It was also provided with a by-pass line so that the whole system could be flushed out by passing pure helium through it whenever necessary. The temperature of the bubbler was held constant by means of a suitable temperature bath, in order to maintain a constant concentration of $GeCl_4$ in the gas stream. The exit end of the absorption cell was connected to a long glass tube with a tapered end to prevent back diffusion of air and moisture. On the entrance side of the cell, a section, approximately 9 in. in length, of the quartz tube which connected the cell with the rest of the apparatus was inside the furnace and was maintained at the same temperature as the cell itself. This section of the tube served two purposes: (*a*) it enabled the gas to come to temperature equilibrium before entering the cell; and (*b*) whenever necessary it could be filled with crushed germanium and used as a germanium bed.

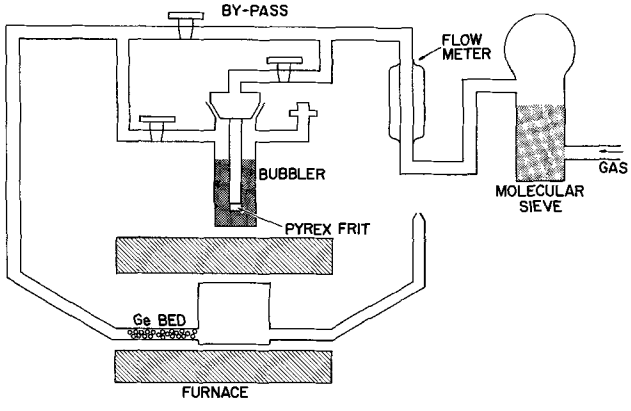

Fig. 1. Experimental arrangement for introducing the $GeCl_4$ and carrier gas mixture into the sample cell.

In the present case the furnace consisted of a single winding so that the cell and the germanium bed could be maintained at the same temperature. Further, to produce a uniform temperature over the entire length of the furnace a copper liner was inserted inside the furnace tube.

Procedure.—The system was first flushed with helium by using the by-pass line in the bubbler; then it was heated to the temperature at which the absorption measurement was to be made. The intensity of the light beam transmitted through the cell was then measured over the whole spectral range to get the I_o values at different wavelengths. If hydrogen was used as the carrier gas, the initial intensity I_o of the light beam was measured with hydrogen flowing through the system. This was a great improvement over the previous sealed tube system in that the initial intensity of the beam could be measured at all temperatures with only the carrier gas present in the cell; thus the effect of the instrumental distortion due to heating could be avoided. Further, the absorption measurements at different concentrations of $GeCl_4$ could be made merely by maintaining the $GeCl_4$ bubbler at different temperatures.

After the measurement of I_o the by-pass line was closed and the carrier gas was allowed to pass through the bubbler. When the cell was completely filled with the mixture of $GeCl_4$ and carrier gas emerging from the bubbler, the final intensity I of the light beam transmitted through the cell was measured. Whether or not the carrier gas in the cell was completely replaced by the mixture was determined by observing the absorption at a suitable wavelength in the region of the absorption continuum of $GeCl_4$. In cases where a germanium bed was used in the path of the gas stream, it was determined by observing the intensity of the transmitted beam at 3150Å, which is believed to be the peak of the $GeCl_2$ absorption band.

Results and Discussion

In order to facilitate discussion, the results of the sealed system are briefly reviewed: Pure $GeCl_4$ exhibited no absorption band within the wavelength range in which the investigation was made. However, it had an absorption edge which begins at 2300Å at 150°C. With increase in temperature the edge extended into longer wavelength regions. This absorption edge was shown to be part of a dissociation continuum of $GeCl_4$. When solid germanium in molar

[1] Present address: Electronics Research Center, NASA, Cambridge, Massachusetts.

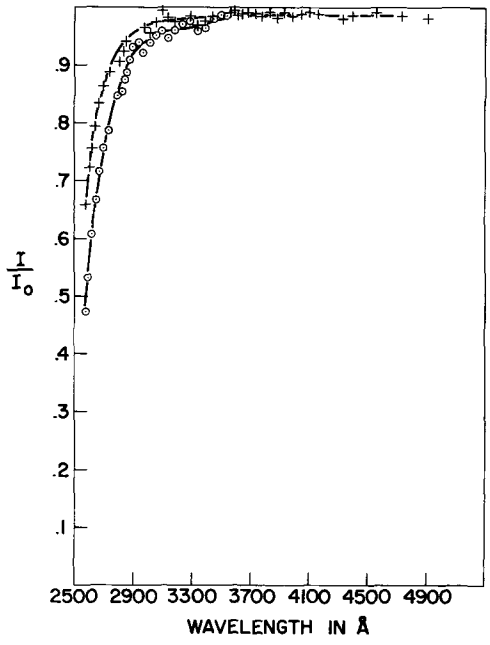

Fig. 2. Transmittance of $GeCl_4$ and He system, $GeCl_4$ at 22°C, flow rate < 10 cc/min; + 500°C; ⊙ 600°C.

quantity less than that of $GeCl_4$ was added to the system, an absorption band with a peak at 3150Å was observed. This was interpreted to be due to $GeCl_2$. If the molar quantity of solid germanium was more than that of the tetrahalide, an additional band with a peak at 4120Å was also observed. In both cases there was an enhancement of absorption in the region of the dissociation continuum of $GeCl_4$. The above results were observed for a wide range of $GeCl_4$ pressures, including those at which the measurements in the open tube systems reported below were made.

The $GeCl_4$-He *system.*—The transmission characteristics of the $GeCl_4$-He open tube system are shown in Fig. 2. The results are very similar to those obtained with pure $GeCl_4$ in a sealed tube. However, in the present case, the increase in absorption with temperature rise at a given wavelength within the absorption continuum was found to be much less than the corresponding increase observed for a closed tube. This difference between the two systems can be explained in the following way. In the case of the open tube system, the total pressure was constant at all temperatures, and hence the density of $GeCl_4$ decreased as the temperature was raised. Thus the increase in the $GeCl_4$ absorption due to temperature rise was largely compensated for by the corresponding decrease in density of the material. As a result, the enhancement in the total absorption was not as great as in the case of the closed tube system, where the density remained constant.

The $GeCl_4$-He-Ge *system.*—The transmittance of the $GeCl_4$-He-Ge system is shown in Fig. 3. The characteristic absorption band with a peak at 3150Å believed to be due to $GeCl_2$ is readily observed. In a manner analogous to the behavior observed in the sealed system, an additional increase in absorption within the continuum region of $GeCl_4$ absorption was observed with temperature increase on introduction of a source of Ge. Thus, in the case of the $GeCl_4$-He system with the partial pressure of $GeCl_4$ at 78 mm, the absorption at 2600Å at 500°C was found to be 27.5% whereas in the case of the $GeCl_4$-He-Ge system with the partial pressure of $GeCl_4$ at 6 mm the absorption was 55%. The above observation lends credence to the earlier conclusion that the species formed as a result of the reaction between $GeCl_4$ and Ge absorbs in the region of the dissociation continuum of $GeCl_4$.

It should be pointed out that, in addition to the 3150Å absorption band, there is a smaller band with the peak at 4120Å which was observed also in the case of the "germanium excess system" in a sealed tube. This result is not unexpected since the present situation represents a germanium excess system. Thus the behavior of the above two systems, namely, $GeCl_4$-He and $GeCl_4$-He-Ge was quite analogous to that of their respective analogs in a sealed tube, *i.e.*, the $GeCl_4$ and $GeCl_4$-Ge systems.

The $GeCl_4$-H_2 *system.*—The transmittance of the $GeCl_4$-H_2 system shown in Fig. 4 indicates that up to 500°C no reaction occurs between hydrogen and $GeCl_4$. At temperatures of 500°C and above, it appears that hydrogen does react with $GeCl_4$ as is evident from the appearance of the absorption band at 3150Å which is attributed to $GeCl_2$.

The $GeCl_4$-H_2-Ge *system.*—Figure 5 shows the transmittance of the $GeCl_4$-H_2-Ge system. In this case the reaction appears to proceed in two steps. At temperatures below 450°C the system behaves in the same way as the $GeCl_4$-He-Ge system. In this temperature

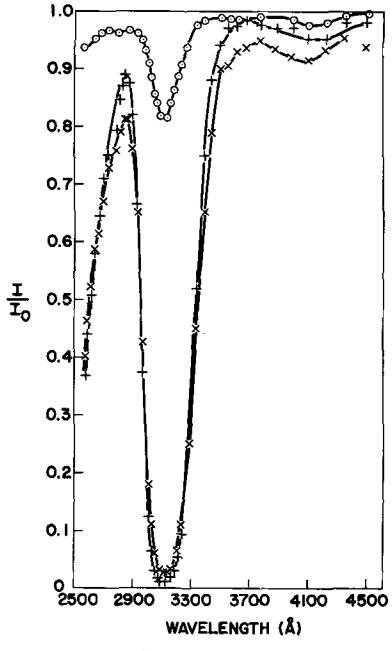

Fig. 3. Transmittance of $GeCl_4$, Ge, and He system. $GeCl_4$ at −20°C; flow < 10 cc/min; ⊙ 350°C; + 500°C; × 600°C.

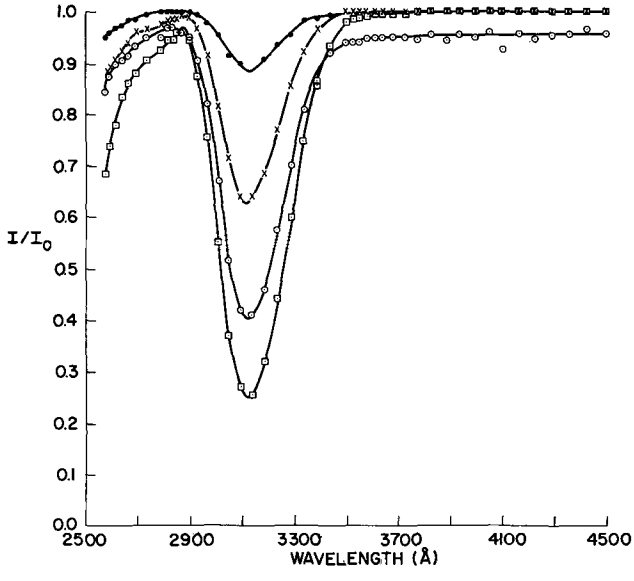

Fig. 4. Transmittance of $GeCl_4$ and H_2 system. $GeCl_4$ at −20°C; ● 500°C; × 550°C; ⊙ 575°C; □ 600°C.

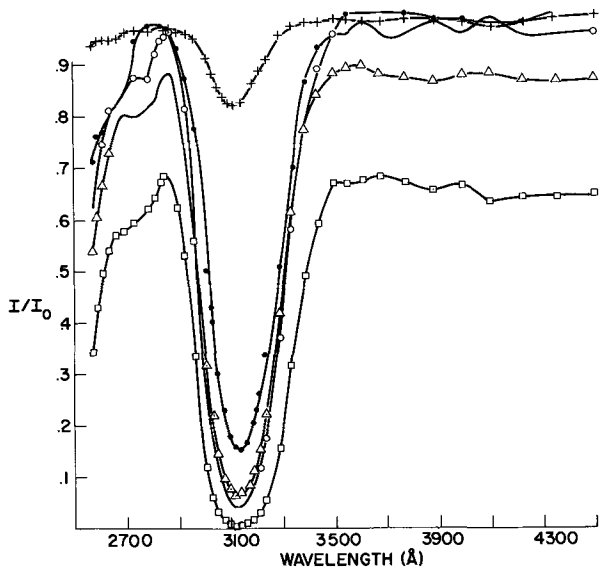

Fig. 5. Transmittance of $GeCl_4$, Ge, and H_2 system. $GeCl_4$ at —20°C; + 350°C; ● 450°C; ⊙ 475°C; △ 496°C; □ 509°C.

range, hydrogen appears to act only as a carrier gas, without participating in the reaction. At temperatures of 450°C and above, the effect of hydrogen as a reactant becomes apparent in the form of absorption over a wide spectral range. When the cell was visually examined at the conclusion of a run, elemental germanium was found to be deposited on the walls and the windows of the cell. The absorption over the wide spectral range might be due either to the coating of the cell windows by germanium film alone or to some unknown species plus a germanium film. By the present technique alone no simple means could be devised to determine if any other species were formed.

It may be contended that the deposition of germanium took place by disproportionation rather than by a reaction between hydrogen and $GeCl_2$. However, the following arguments mitigate against this contention: (*A*) The absorption cell was located near the center of the furnace, whereas the germanium bed extended from the entrance end of the cell to the furnace opening. In this geometrical configuration, the temperature of the cell was equal to or higher than that of the germanium bed. Thus the deposition of germanium on the cell windows by disproportionation is unlikely in view of the fact that in the temperature range under consideration transport by this process takes place from hot to cold. (*B*) If the germanium were deposited by disproportionation, then the same result would have been observed in the case of the $GeCl_4$-He-Ge system.

The above results suggest that, in the deposition of germanium films by hydrogen reduction of $GeCl_4$ an intermediate process is involved in which the formation of $GeCl_2$ and HCl precedes the actual precipitation of germanium. If this is indeed the case, the epitaxial film growth occurs in the presence of $GeCl_2$ and HCl from the beginning. Therefore, this suggests further that in the epitaxial growth process significant etching of the seed wafer attends the phenomenon of an over-all net deposition of Ge. Such an occurrence provides an explanation for the impurity gradient observed across a grown junction.

Acknowledgments

The author is indebted to Dr. A. Reisman for helpful discussions and to W. Lee for untiring assistance with the experiments.

Manuscript received Feb. 28, 1966. This paper was presented in part at the Washington Meeting, Oct. 11-15, 1964. This work was supported by A.F.C.R.L. Contract No. AF19(628)-2468.

Any discussion of this paper will appear in a Discussion Section to be published in the June 1967 JOURNAL.

REFERENCE

1. K. E. Haq and W. von Muench, *This Journal*, **113**, 260 (1966).

Diffusion-Induced Stress and Lattice Disorders in Silicon

J. E. Lawrence

Fairchild Semiconductor, Division of Fairchild Camera & Instrument Corporation, Palo Alto, California

ABSTRACT

The planar diffusion of boron or phosphorus into silicon can create stresses sufficient to form dislocations within the diffused region and contribute to dislocation formation near the crystal surface outside the diffused region. The effects of two dislocation networks which form within a diffused region are investigated: one network consists of a planar array of concentric loops (Frank-Read source) while the other network consists of a grid of edge dislocations terminating at nodes. The dislocations comprising the concentric loop network can relieve essentially all of the stress created by the diffused impurities. The edge dislocations comprising the grid network do not relieve a large amount of the lattice stress, thus causing the nondiffused silicon lattice surrounding the diffused region to become strained. This strain often extends over 100μ from the diffused region within zones bound by the $\langle\bar{1}10\rangle$ tangents of the diffused region. Dislocations which form in these nondiffused zones as a result of the diffused impurity stress appear as either intersecting lines or periodically spaced parallel dislocations which terminate at the crystal surface. The impurity-induced lattice strain near the crystal surface outside the diffused region contributes to excessive recombination currents in p^+n junctions.

One of the initial steps in forming a planar p-n junction consists of depositing a controlled amount of a dopant impurity such as boron or phosphorus on a silicon surface through a window in a silicon dioxide film. This process creates a shallow diffused region, normally 2μ deep, with a dopant impurity concentration near the solubility limit of the solute in the silicon lattice. Since both boron and phosphorus atoms have smaller ionic radii than silicon (1) and since they occupy substitutional sites in the silicon matrix, a net

contraction of the silicon lattice occurs in the region of impurity diffusion (2). This contraction leads to the formation of dislocations within the diffused region. Prussin (3) and others (1, 4-6) have observed such dislocations to form during uniform sheet diffusion processes. This contraction in planar diffused structures often contributes to the formation of lattice imperfections outside the diffused region as well as dislocations within the diffused region as reported by Ino *et al.* (7).

The present work was undertaken to determine the significance of the dopant impurity concentration and residual strain (due to stresses other than diffused impurities) in the formation of crystal disorder during an impurity diffusion. The electrical behavior of crystal disorder generated during an impurity diffusion was investigated by determining the reverse bias characteristics of selected p^+n junctions. This analysis extends the scope of the work of Rindner and Braun (8) who reported a recombination current dependence on lattice strain.

Experimental

The investigation in general was conducted by systematically varying the concentration of diffused impurities while performing diffusion tests in crystals containing lattice strain from stresses other than that associated with the diffusion process. The amount of stress associated with the minimum concentration of diffused impurities required to noticeably influence the strain in the nondiffused lattice outside a diffused region was determined by comparing the effects of the diffused impurity stress and the effects of stress from an external force. The manner in which a silicon crystal adjusts to accommodate diffused impurities was investigated by determining the configuration and density of crystal disorder formed during an impurity diffusion.

Silicon wafers cut to the (111) surface, lapped to 400μ thick, and chemically polished to a final thickness of 200μ comprised the starting material for this investigation. The freshly polished wafers were oxidized at 1200°C in a steam ambient for periods up to 2 hr to grow a silicon dioxide film thick enough to restrict adequately the penetration of dopant impurities from the silicon lattice. Windows were then opened in the protective film by the photoresist process to allow the selective diffusion of dopant impurities.

The oxidized wafers were deformed by different means to introduce varying amounts and distributions of strain in the crystals prior to the dopant impurity diffusion. This was accomplished by bending, depressing, impulse stressing in the $<\bar{1}10>$ and $<\bar{2}11>$ directions, or combinations of the above. The deformed wafers were then cleaved into large chips to enable the effects of several different concentrations of diffused impurities to be analyzed on wafer sections which contain essentially the same amount and crystallographic distribution of strain prior to the diffusion process. (Care was continuously taken to minimize a variation in strain between different chips.)

The dopant impurities were planar diffused into the test wafer chips from a constant near-solubility limit surface concentration of dopant impurities. The concentration of dopant impurities that passed into the silicon lattice through oxide windows was controlled by varying the duration of the deposition process. Boron deposition was performed at 1200°C in a furnace containing a constant concentration boron tribromide source. The phosphorus deposition was performed at 1070°C in a furnace containing a constant phosphorus oxychloride source. The influence of the concentration of diffused impurities on the manner in which the lattice adjusts was investigated by systematically increasing the periods of deposition from 3 to 10 min for boron, providing $Q = 1.1 \times 10^{16}$ atoms/cm^2 to 4.8×10^{16} atoms/cm^2, and 5 to 30 min for phosphorus, providing $Q = 3.2 \times 10^{16}$ atoms/cm^2 to 4.7×10^{16} atoms/cm^2, assuming a complementary error function distribution. The time required for the silicon lattice to stabilize after the impurity deposition was investigated by diffusion-annealing tests at 1200°C in a dry oxygen ambient for periods of 5 min to 6 hr.

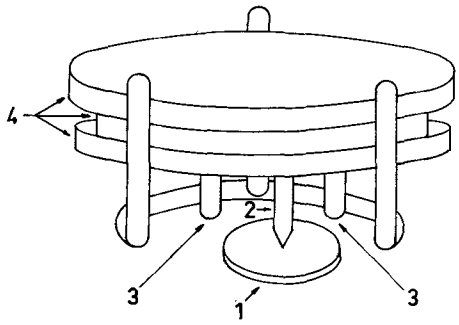

Fig. 1. High-temperature loading apparatus used to simulate surface component of lattice stress generated by diffused impurities: 1, silicon specimen; 2, silicon pin (contract area $A_S = 2 \times 10^3$ μ^2); 3, quartz weight stabilizers; and 4, silicon weights; size: 2 x 2 x 3 cm.

Several wafers prepared for impurity deposition tests were physically deformed by a weighted pin to approximate the stress created outside the diffused region by the diffusion of boron. These loading tests were conducted on wafer chips at 1200°C for a period identical to that in which matching wafer chips were boron diffused. The surface component of stress generated by the weighted pin was systematically varied from 10^7 dynes/cm^2 to 10^{10} dynes/cm^2 during a series of tests using the high-temperature stress apparatus shown in Fig. 1. The application of stress by this apparatus was found to create no plastic deformation at room temperature; however, when it was used to apply the same stress at 1200°C, essentially all of the lattice deformation occurred within the first minute of thermal treatment.

The manner in which the silicon lattice adjusts to accommodate diffused impurities and the adjustment during loading tests was determined by analyzing the type, density, and distribution of lattice disorders created during the respective tests. These structural disorders were delineated by a copper decoration and preferential chemical etching technique (9), by electron transmission microscopy, and by surface x-ray topography. Dislocations, faults, and voids which are copper decorated resist 30 sec of Sirtl (10) etching to create topographic irregularities on the silicon surface that can be analyzed on a conventional optical microscope. The electron transmission microscopy technique was applied to the analysis of copper-decorated and copper-free crystal disorders. Such analysis was aided by the development of a quick and reliable technique for preparing uniform films 1000Å thick and greater than 2 mm in diameter (11). Verification of the copper decoration-preferential etching and electron transmission observations was provided by an x-ray topograph of the diffused surface.

Results

The amount of lattice stress created during an impurity deposition process was found to depend on the total concentration of diffused impurities and not the surface concentration of diffused impurities. This stress is relieved by the generation of dislocations within the diffused region and often by the deformation of the nondiffused lattice surrounding the diffused region. The lowest concentration of diffused boron that is necessary to create a stress sufficient to alter the position of a pre-existing dislocation in the nondiffused lattice adjoining the diffused region is Q min. = 2.6×10^{16} boron/cm^2 with a junction depth of 1.5μ. Above this value of Q min. the stress associated with the diffused impurities is sufficient to deform the non-

diffused lattice surrounding the diffused region and thus alter the position of pre-existing dislocations in the nondiffused lattice. Below this value of Q min. the lattice within the diffused region appears to compensate, through dislocation generation, for all except a nondetectable amount of the stress created by the diffused boron. The total diffused impurity concentration, Q max, that is necessary to generate a stress sufficient to create a dislocation in the "strain-free" nondiffused lattice surrounding a diffused region is greater than $Q = 4.8 \times 10^{16}$ boron/cm^2 with $x_j = 2.2\mu$ or 4.7×10^{16} phosphorus/cm^2, the highest doping levels achieved in this study. The concentration of diffused impurities necessary to generate a stress sufficient to form a dislocation in the nondiffused lattice surrounding a diffused region decreases as the amount of nonimpurity strain in the surrounding lattice increases. Ino *et al.* (7) have reported the concentration of diffused impurities sufficient to cause plastic deformation in the surrounding nondiffused lattice as being less than the maximum values achieved in this study. It is possible that they did not perform their tests using samples with very low background lattice strain. The impurity content required to form a dislocation within a diffused region is less than the quantity required to form a dislocation outside the diffused region. Shockley (1) identifies $Q = 3 \times 10^{15}$ boron/cm^2 as the theoretical minimum dopant concentration necessary for generating dislocations within the diffused region of an ideal silicon lattice.

Lattice strain from nonimpurity stresses was essential in this investigation for our method of determining the manner in which the lattice adjusts during an impurity diffusion was based on analyzing the nature of the dislocations which form during the deposition process. As mentioned above, the Q max obtained in this investigation was not sufficient to cause plastic deformation in the "strain-free" nondiffused lattice surrounding a diffused region. The surrounding nondiffused lattice was made to deform plastically in the presence of an elastic strain induced by diffused impurities by maintaining the amount of nonimpurity lattice deformation slightly below the elastic limit of the silicon lattice. In so doing, the amount and distribution of any elastic strain caused by the diffused impurities would be recorded by an array of newly formed dislocations. No quantitative measure of the magnitude of lattice strain from bending, depressing, or impulse stressing was obtained. Comparative tests were performed which allowed the nonimpurity induced strain to be distinguished from the diffused impurity stress's contribution to defect formation during the impurity deposition process. Wafer bending did not induce sufficient strain prior to impurity deposition noticeably to influence the adjustment of the lattice during an impurity deposition.

The degree to which the lattice surrounding the diffused region must deform during an impurity deposition is very greatly influenced by the structure of the lattice disorder which forms in the diffused region to alleviate the stress generated by the diffused impurities. Two configurations of dislocation networks which commonly form within a diffused region are schematically illustrated in Fig. 2A. One network, "A" in Fig. 2A, generally lies in a subsurface (111) plane near the penetration front of the diffused region and thus does not intersect the crystal surface except when it climbs to the surface near the surface periphery of the diffused region. The stress vector associated with the diffused region is in the direction of impurity diffusion, *viz.*, the $\langle\bar{1}\bar{1}\bar{1}\rangle$ direction in the center of planar diffused regions of (111) wafers. The individual dislocations comprising this subsurface network terminate at nodes, thus forming a flat grid-like array. This network is very likely formed by a dislocation reaction between pairs of dislocations gliding in the same (111) plane. These dislocations are probably edge in character for they lie in a (111) slip plane perpendicular to the $[\bar{1}\bar{1}\bar{1}]$ applied stress. Dislocations which form within the diffused region during a uniform sheet diffusion process and possess similar characteristics have been identified as edge dislocations earlier (4). The other network, "B" in Fig. 2A, consists of an array of concentric loops lying in a plane inclined to the crystal surface. The inclined plane intersects the crystal surface at a $\langle\bar{1}10\rangle$ direction, very likely a $\{\bar{1}11\}$ plane. Figure 2B illustrates the distribution of individual dislocations comprising this dislocation network at a deflection $\vec{g} \cdot \vec{b} \neq 0$. A single reflection was found, but not identified, such that $\vec{g} \cdot \vec{b} = 0$ for all dislocations comprising this network. This observation identified all of the composite dislocations as having the same Burgers vector and that the concentric loop network was very likely formed by the Frank-Read mechanism (12). Formation conditions leading to the generation of this dislocation network within a diffused region are provided by a $\langle\bar{2}11\rangle$ directed impulse stress and a $[\bar{1}\bar{1}\bar{1}]$ directed impurity stress. The exact interaction between these two stress fields is complex and difficult to analyze experimentally.

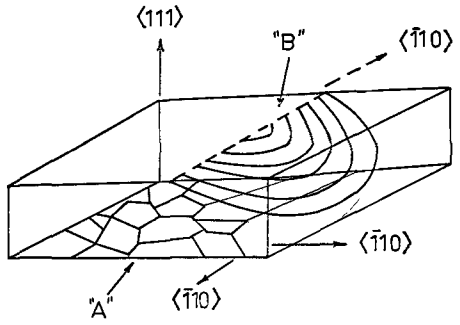

Fig. 2A. Two dislocation networks that form within a diffused region: network "A" is a (111) grid of edge dislocation lying near the subsurface diffusion front, network "B" consists of concentric loops of the Frank-Read formation type.

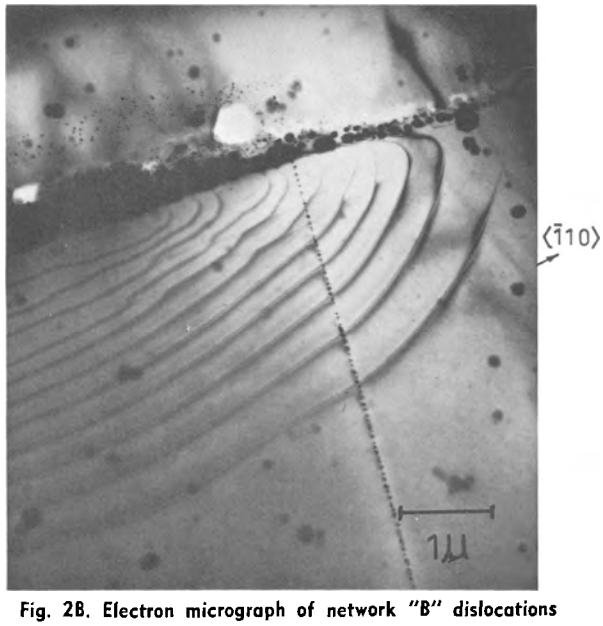

Fig. 2B. Electron micrograph of network "B" dislocations

These two dislocation networks were analyzed in this investigation, not to resolve their exact formation mechanism, but to understand their relationship to the manner in which the lattice adjusts during an impurity deposition process. The great amount of lattice stress generated during the deposition process is reduced by the formation of either network configuration. The (111) grid network, however, has been found

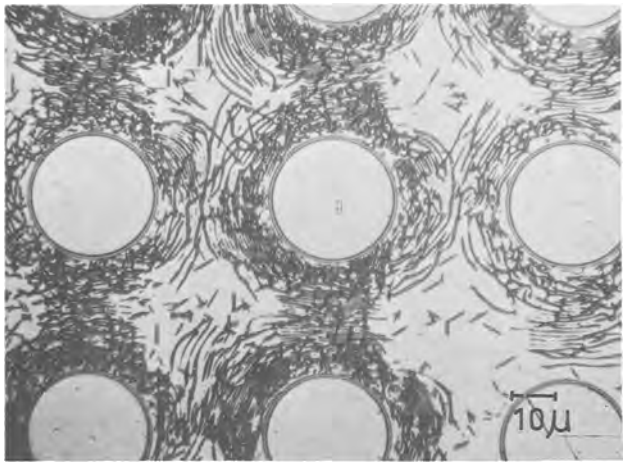

Fig. 3A. Dislocation (dark curved line) in the nondiffused lattice surrounding a planar diffused region delineated by copper decoration and preferential etching.

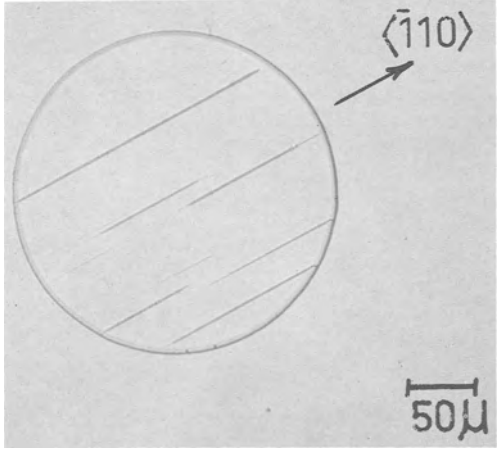

Fig. 3B. No dislocations (absence of dark lines)) in the nondiffused lattice surrounding a planar diffused region delineated by copper decoration and preferential etching. Parallel lines within diffused region are network "B" dislocations.

to relieve much less of the stress generated by the diffused impurities than concentric loop network. This was determined by analyzing the dislocation network configuration within a diffused region and the lines of plastic deformation in the nondiffused lattice surrounding the diffused region which formed during the deposition process. The dark lines surrounding the circular diffused regions in Fig. 3A are delineated dislocations which formed in the nondiffused lattice due to the inability of the (111) grid network dislocations within the diffused region to relieve the lattice stress created by the diffused impurities. In contrast, the absence of dark lines in the nondiffused lattice surrounding the diffused region in Fig. 3B identified the concentric loop network dislocations within the diffused region as relieving essentially all of the stress created by the diffused impurities.

The nondiffused lattice surrounding the diffused region prefers to deform within particular zones to relieve the impurity-induced stress remaining after the formation of the (111) grid network dislocations within the diffused region. These zones are bound by the $\langle\bar{1}10\rangle$ tangents of the diffused region as schematically represented in Fig. 4A and shows in the micrograph in Fig. 4B.

The lines of plastic deformation which form in the surrounding nondiffused lattice as a combination of the elastic strain fields associated with the diffused impurity and the nonimpurity induced deformation are dislocations as determined by $\vec{g} \cdot \vec{b} = 0$ contrast ex-

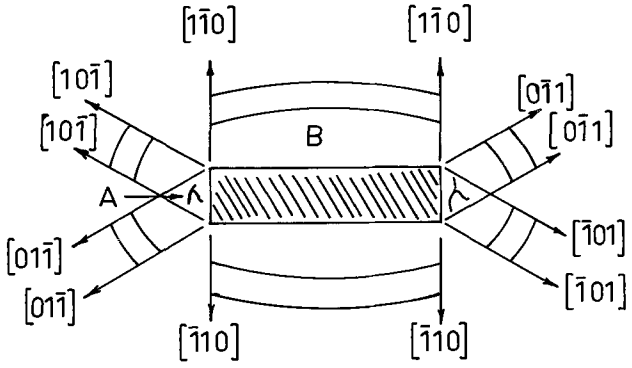

Fig. 4A. A schematic illustration of the $\langle\bar{1}10\rangle$ tangents of a diffused region. "Intersecting line dislocations" develop in the nondiffused lattice at zones "A" while "periodic dislocations" develop in zones "B".

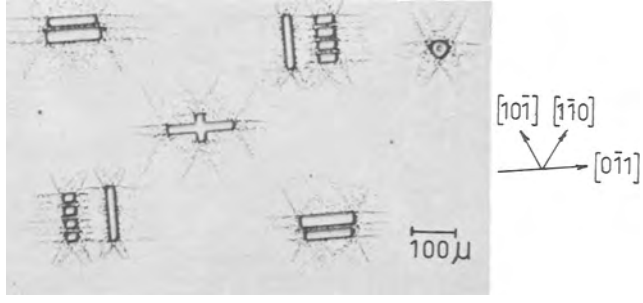

Fig. 4B. Sirtl etch generated pits (dark dots) identify surface intersection of dislocations within $\langle\bar{1}10\rangle$ tangents of the diffused regions.

periments on the electron microscope. These dislocations appear in two general configurations: "random intersecting lines" and "periodic lines" generally perpendicular to the $\langle\bar{1}10\rangle$ projection of the diffused region. The intersecting line configuration of dislocations, shown in Fig. 3A and 5A and graphically at "A" in Fig. 4A, develops in a region near the diffused region where nonparallel stresses from several portions of a diffused region intersect. The dislocations comprising this network configuration are neither pure edge nor screw. They do, however, generally lie in a (111) plane below the crystal surface. Most of the dislocations comprising the intersecting line configuration terminate at nodes with other dislocations gliding in the same (111) plane. The "periodic line" configuration, shown in Fig. 3A and 5B and graphically at "B" in Fig. 4A, develops when a near-unidirectional strain field exists. Each dislocation in a "periodic line" network is a shallow loop aligned to a general $\langle\bar{2}11\rangle$ direction. They terminate on the crystal surface at a $\langle\bar{1}10\rangle$ tangent of the diffused region. The etch pits which define the $\langle\bar{1}10\rangle$ tangents of the diffused regions in Fig. 4B are at the surface intersections of $\langle\bar{2}11\rangle$ oriented dislocation loops comprising "parallel line" networks. These dislocations are primarily edge in character for they lie in the (111) slip plane perpendicular to the direction of the stress vector, *viz.*, $\langle\bar{1}10\rangle$. The portion of these dislocations near their ends are not edge in character for they leave the (111) slip plane and climb to the crystal surface. These dislocations are often several hundred microns long and lie less than 2μ below the crystal surface.

The dislocations which develop in the nondiffused lattice surrounding a diffused region during the deposition process were found to be initiated by a flow of the surface lattice by comparing the structure and distribution of these disorders with those created by

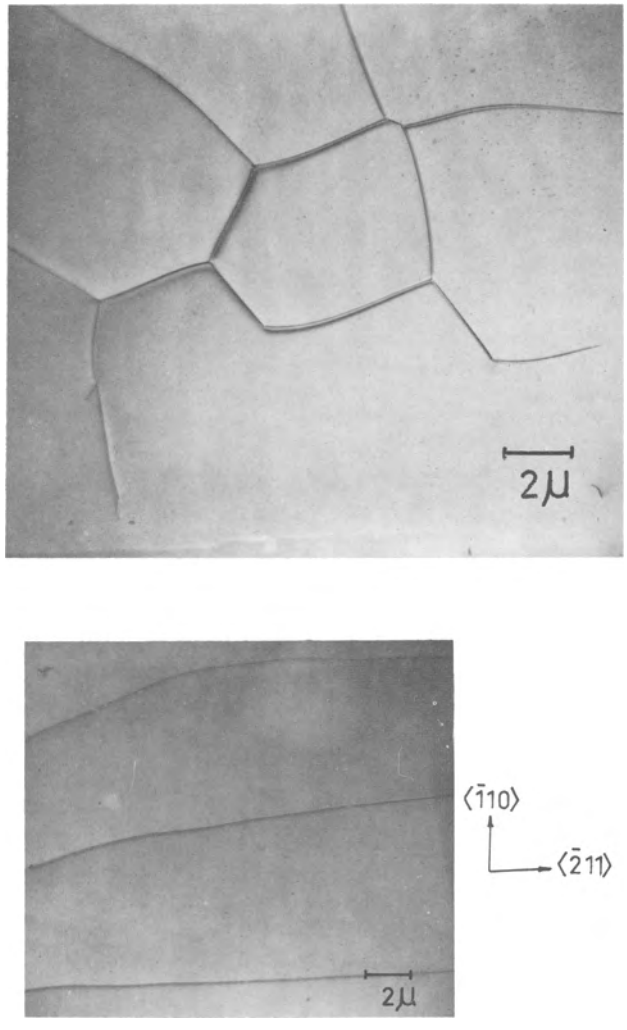

Fig. 5A (top). Dislocation networks created in the nondiffused lattice surrounding a diffused region to relieve the stress induced by diffused impurities; "Intersecting Line Network" Fig. 5B (bottom) "Periodic Line Network." Electron micrographs.

physically deforming the crystal surface. Weighted-pin tests conducted at 1200°C (the boron deposition temperature) produced a distribution of lines identical to those caused by the diffusion of dopant impurities illustrated in Fig. 5. An electron transmission analysis of the lines created by both sources confirmed their structural similarity. The magnitude of the impurity-induced stress at the surface periphery of a diffused region was identified by associating the lowest Q required to form dislocations in the surrounding lattice with the lowest surface component of loading stress required to form similar dislocations. Comparative tests were conducted on the same wafers to normalize the contribution of nonimpurity lattice strain. The loading tests identified $\sigma_1 = 2.5 \pm 2 \times 10^9$ dynes/cm^2 as being the magnitude of the peripheral surface stress created in the nondiffused lattice surrounding a region where boron of $Q_1 = 2.6 \times 10^{16}$ atoms/cm^2 had been planar diffused and (111) grid network dislocations had formed within the diffused region.

Calculated Stress

The magnitude of the stress generated within a diffused region by the diffused impurities can be calculated using an expression formulated by Prussin (3). He adjusted Timoshenko's expression (13) for mechanical stresses in a thin plate to comply with a complementary error-function distribution of diffused atoms as the deformation source, assuming the impurity stress-mechanical stress relationship identified in this work. The Prussin expression for the maximum impurity-induced stress along the crystal surface inside the diffused region is

$$(\sigma x)_{\max} = \frac{\beta C_S E}{(1-\nu)}$$

where β is the solute lattice contraction coefficient, C_S is the solute surface concentration, E is Young's modulus, and ν is Poisson's ratio. Using this expression Prussin calculated $(\sigma x) = 6.0 \times 10^9$ dynes/cm^2 for boron. Since the publication of Prussin's work, improved values of these factors have been reported. Wortman and Evans (14) identifies Young's modulus and Poisson's ratio as $E = 1.7 \times 10^{12}$ dynes/cm^2 and $\nu = 0.33$ for the [1̄10] direction of the (110) plane. The value of the solubility limit of boron in silicon has remained at $C_S = 5 \times 10^{22}$ (15). β can be calculated using the following general expression

$$\beta = \left[1 - \left(\frac{r_{sol}}{r_{Si}}\right)^3\right] N^{-1}$$

where r_{Si} is the covalent radius of silicon, $r_{Si} = 1.17$Å (16), $r_{sol} = 0.98$Å for boron (1), and N is the concentration of silicon atom sites, $N = 5 \times 10^{22}$/cm^3. These values in the above expression provide $\beta = 8.2 \times 10^{-24}$ cm^3/atom. This value lies between the values of β calculated from the contracted lattice parameters reported by Horn (17), 16×10^{-24} cm^3/atom, and Pearson *et al.* (2), 6.6×10^{-24} cm^3/atom. Applying these improved values to Prussin's expression provides (σx) max $= 1.0 \times 10^{10}$ dynes/cm^2 as the maximum internal stress created by the diffusion of boron into silicon. A further refinement of these values or the above expressions at this time would have little justification for the magnitude of the impurity-induced stress in the surrounding nondiffused lattice is greatly influenced by the noncontrolled formation of lattice disorder within the diffused region. The stress required to cause yield in highly boron doped silicon whiskers was obtained by extrapolating the data of Pearson *et al.* (18) to 1200°C, σ(yield limit) $= 1.0 \times 10^9$ dynes/cm^2. The first approximation values obtained from Prussin's expression identify the stress generated within the diffused region as exceeding the amount required to cause yield, as it should since lines of plastic deformation are created within the diffused region.

Results—Electrical

The strain in the nondiffused lattice surrounding a diffused region resulting from the diffused boron stress contributes directly to excessive currents in reverse biased p^+n junctions as Fig. 6 indicates. Curve A identifies the log I *vs.* log V trace of a diode with no associated dislocations in the nondiffused lattice surrounding the deposited region, similar to that shown in Fig. 3B. Curves B and C identify the electrical

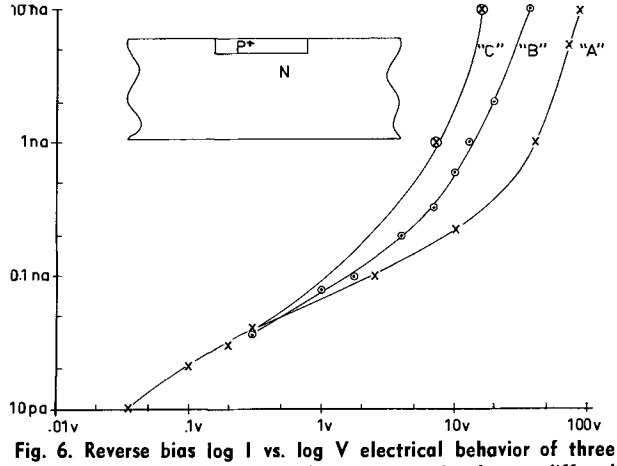

Fig. 6. Reverse bias log I vs. log V electrical behavior of three diodes with varying amounts of lattice strain in the nondiffused lattice surrounding the diffused region. "A" very little strain; "B" moderate strain; and "C" very great strain.

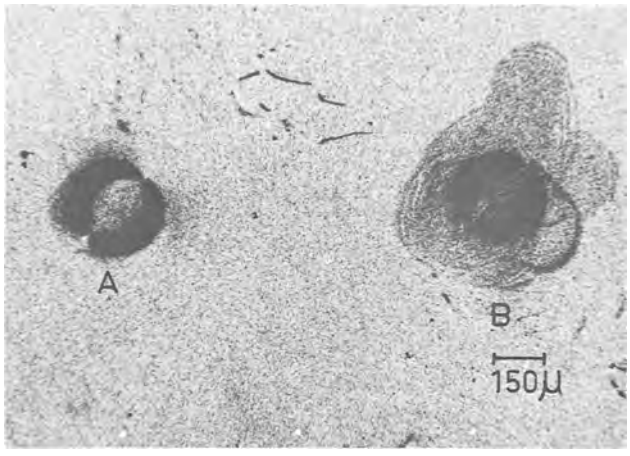

Fig. 7A. Negligible strain in the nondiffused lattice associated with network "B" dislocations within diffused region; (B) great lattice deformation in the nondiffused lattice associated with network "A" dislocations within the diffused region. X-ray topographs.

characteristics of two diodes, one with a moderately large density of associated dislocations in the nondiffused lattice, curve B, and the other with an extremely large quantity of associated dislocations in the nondiffused lattice, curve C, similar to those shown in Fig. 3A. The density of associated dislocations in the nondiffused lattice corresponds to the strength of the impurity-induced strain observed in the nondiffused lattice surrounding a diffused region.

Summary

The manner in which the silicon lattice adjusts to accommodate a large quantity of small diffused impurities has been investigated. The results of this investigation can be incorporated into a model which describes the behavior of the silicon lattice during an impurity deposition process.

The planar diffusion of boron during a 1200°C deposition process creates a maximum calculated stress near 1.0×10^{10} dynes/cm^2 within the diffused region. The silicon lattice in deforming to relieve this stress forms either of two different dislocation networks within the diffused region. The two dislocation networks relieve different amounts of the impurity-induced stress as identified earlier and verified in the x-ray topograph in Fig. 7. One of the dislocation networks (Frank-Read source) consists of a family of concentric dislocation loops which lie in a plane inclined to the crystal surface. The dislocations in this network relieve essentially all of the lattice stress created by the planar deposition process as shown at (A) in Fig. 7. This is very likely due to the size of the individual dislocations and their possessing significant screw as well as edge dislocation components. A different dislocation network commonly develops within the diffused region near the diffusion front of shallow diffused structures. The dislocations comprising this network are generally edge in character, but acquire dominant screw character near the periphery of the diffused region where the network leaves the (111) slip plane. The formation of these dislocations tends to lower the stress within the diffused region by only one order of magnitude, thus causing the nondiffused lattice surrounding the diffused region to deform to relieve the impurity induced strain as shown at (B) in Fig. 7. The nondiffused lattice surrounding the diffused region deforms within highly restricted zones when the lattice within the diffused region is unable to relieve the diffused impurity stress. These zones are bound by the $<\bar{1}10>$ tangents of the diffused region and extend to the depth of the region created by the planar deposition process, normally two microns. Portions of the nondiffused lattice a distance greater than 100μ from a diffused region are often deformed due to an impurity deposition.

The electrical characteristics of the p^+n junction created during the planar deposition of boron are influenced by the deformation of the nondiffused lattice surrounding the diffused region. Reverse currents in the nanoampere range have been associated with the above lattice deformation source.

Acknowledgments

The author wishes to thank Dr. R. N. Tucker for his stimulating discussions throughout the development of the study summarized in this paper. The electron transmission specimen preparation and analysis was performed with the skillful assistance of H. Koehler and D. Mattern. The author is also grateful to Dr. E. Meieran for the x-ray surface topograph and interesting discussions. Part of this work was supported by R.A.D.C., Contract number AF 30(602)-3776.

Manuscript received Jan. 17, 1966; revised manuscript received May 3, 1966.

Any discussion of this paper will appear in a Discussion Section to be published in the June 1967 JOURNAL.

REFERENCES

1. H. J. Queisser, *J. Appl. Phys.*, **32**, 1776 (1961).
2. G. L. Pearson and J. Bardeen, *Phys. Rev.*, **75**, 865 (1949).
3. S. Prussin, *J. Appl. Phys.*, **32**, 1876 (1961).
4. J. Washburn, G. Thomas, and H. J. Queisser, *ibid.*, **35**, 1909 (1964).
5. M. L. Joshi and F. Wilhelm, *This Journal*, **112**, 185 (1965).
6. G. H. Schwuttke and H. J. Queisser, *J. Appl. Phys.*, **33**, 1540 (1962).
7. H. Ino, T. Kawamura, and M. Yasufuku, *Japan. J. Appl. Phys.*, **3**, 692 (1964).
8. W. Rindner and I. Braun, *J. Appl. Phys.*, **34**, 1958 (1963).
9. J. E. Lawrence, *This Journal*, **112**, 796 (1965).
10. E. Sirtl and A. Adler, *Z. Metallkde.*, **52**, 529 (1961).
11. J. E. Lawrence and H. Koehler, *J. Sci. Instr.*, **42**, 270 (1965).
12. F. C. Frank and W. T. Read, Jr., *Phys. Rev.*, **79**, 722 (1950).
13. S. Timoshenko, "Theory of Elasticity," 1st. ed., p. 203, McGraw-Hill Book Co., Inc., New York (1934).
14. J. J. Wortman and R. A. Evans, *J. Appl. Phys.*, **36**, 153 (1965).
15. F. A. Trumbore, *Bell System Tech. J.*, **39**, 205 (1960).
16. L. Pauling, "The Nature of the Chemical Bond," 3rd. ed., p. 246, Cornell University Press, Ithaca, N. Y. (1960).
17. F. H. Horn, *Phys. Rev.*, **97**, 1521 (1955).
18. G. L. Pearson, W. T. Read, Jr., and W. L. Feldmann, *Acta Met.*, **5**, 181 (1957).

Epitaxial Growth of Silicon Carbide by the Thermal Reduction Technique

R. B. Campbell and T. L. Chu

Research Laboratories, Westinghouse Electric Corporation, Pittsburgh, Pennsylvania

ABSTRACT

The epitaxial growth of silicon carbide on the basal plane of hexagonal silicon carbide substrates has been accomplished by the thermal reduction of carbon and silicon tetrachlorides, and experimental parameters of the growth process have been studied. Using good *in situ* etching techniques and inert susceptor materials, epitaxial silicon carbide layers with structural perfection similar to that of the substrate were grown at a substrate temperature of 1700°C and a deposition rate of 0.5 μ/min. Doped silicon carbide layers were prepared using nitrogen, arsine, or phosphine as n-type dopants and diborane as a p-type dopant, and the electrical properties of these layers were evaluated by Hall measurements in the temperature range 78°-900°K. Preliminary junction structures prepared by doping techniques were found to be capable of supporting up to 50v at 500°C.

Silicon carbide devices, such as rectifiers (1), charged particle detectors (2), and unipolar transistors (3) are capable of operation at high temperatures, 500°C or above. Because of its refractory nature, the fabrication of silicon carbide junctions is difficult and involved. The epitaxial growth technique appears to be a promising junction formation method since epitaxial silicon carbide layers of controlled dopant distribution can be deposited on silicon carbide substrates at relatively low temperatures compared to the sublimation process (4).

The feasibility of using the thermal reduction of mixtures of carbon and silicon tetrachlorides with hydrogen for the isoepitaxial growth of silicon carbide, in a manner similar to the epitaxial growth of silicon by the hydrogen reduction of silicon tetrachloride, has been reported (5). The epitaxial growth of silicon carbide, however, poses the complicating problem in that it exists in cubic and hexagonal phases with the latter possessing a variety of polytypes. It was found in the early work (5) that either phase could be deposited on the basal planes of hexagonal silicon carbide substrates, depending on experimental conditions. Furthermore, the cubic phase was grown at substrate temperatures (brightness) of 1660°-1775°C, and the hexagonal phase was grown on mechanically polished substrates at brightness temperatures higher than 1725°C.

In this work, the epitaxial growth of silicon carbide on the basal planes of hexagonal silicon carbide substrates by the thermal reduction technique has been further studied with the aim of preparing rectifying junctions. To achieve this, new experimental techniques were devised to prepare epitaxial silicon carbide layers with structural perfection similar to that of the substrate. Doping techniques were also developed to control the conductivity type and carrier concentration of the epitaxial layer. Using these techniques, preliminary work on the preparation of silicon carbide p-n junctions was carried out. Various aspects of the isoepitaxial growth of silicon carbide are discussed in this paper.

Structural Perfection of Epitaxial Silicon Carbide

The structural perfection of the epitaxial layer is an important factor determining its usefulness for device purposes. It has been well established in the epitaxial silicon technology that the structural perfection of the epitaxial layer prepared under proper conditions of substrate temperature and growth rate is determined predominately by the purity of the growth apparatus and reactants, and the surface conditions of the substrate. Contaminants from the growth apparatus and foreign impurities on the substrate surface are the principal causes of imperfections in the epitaxial layer. Because of the temperatures required for the epitaxial growth of hexagonal silicon carbide, the purity of the growth apparatus is more difficult to maintain than in the silicon process. For example, the rf susceptor for the support and heating of silicon carbide substrates must be stable and inert toward silicon carbide and the reactants under the conditions used in the growth process. The choice of susceptor material therefore is limited. Refractory metals react with silicon carbide at high temperatures, and graphite and refractory carbides, including silicon carbide, react with hydrogen to form hydrocarbons. Refractory silicides were found to be more stable under conditions used for the epitaxial growth of silicon carbide. Tantalum silicide-coated tantalum was used as the susceptor in this work with satisfactory results.

The substrate surface should be free from foreign impurities and mechanical damage. While the usual etching and cleaning operations remove residual abrasives, dust, etc., they do not provide clean substrate surfaces required for the epitaxial growth process. The *in situ* etching of substrates has been shown to be useful for producing epitaxial silicon layers of good perfection (6). Chlorine-oxygen mixtures (7) or hydrogen (8) can be used as etchants. The hydrogen etch provides a clean and microscopically smooth surface and is particularly convenient to use in this process.

Experimental.—Electronic grade silicon tetrachloride and carbon tetrachloride were used for the epitaxial growth of silicon carbide. They were introduced into the reaction tube by using a measured amount of hydrogen as a carrier gas. The hydrogen was purified by diffusion through a palladium-silver alloy. Since nitrogen is electrically active in silicon carbide, the silicon and carbon tetrachlorides were thoroughly outgassed to remove dissolved air and the growth system was made gas-tight to minimize any undesirable doping.

Hexagonal silicon carbide platelets with main faces of (0001) orientation grown by the sublimation technique (4) were used as substrates for the epitaxial growth process. They were selected on the basis of optical examination and were etched in a molten 1:3 sodium peroxide-sodium hydroxide mixture to determine the polarity of faces (10).[1] The face of the sub-

[1] The (0001) and (000$\bar{1}$) faces of hexagonal silicon carbide exhibit different etching behaviors toward molten sodium peroxide. One face remains smooth and the other becomes rough in appearance. The former has been shown in a recent work to be the silicon face (10).

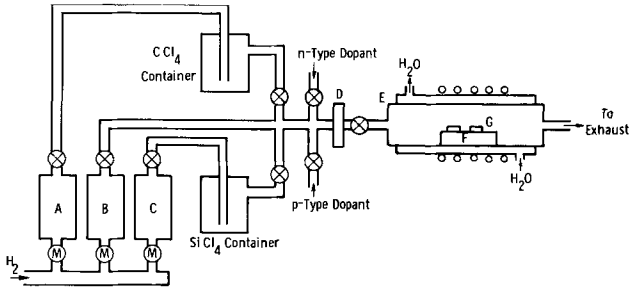

Fig. 1. Schematic diagram of the apparatus for the epitaxial growth of silicon carbide by the thermal reduction technique. Ⓜ metering valve; ⊗ shut-off valve; A, B, C flowmeters; D filter; E water-cooled reaction tube; F tantalum silicide coated susceptor; G SiC substrates.

strates with the desired polarity was then successively lapped with boron carbide and polished with diamond paste. The substrates were subsequently cleaned ultrasonically in hydrofluoric acid and water.

The growth experiments were carried out in a gas flow system, using a horizontal, water cooled quartz tube of 2.5 cm ID with gas inlet and exhaust tubes. The silicon carbide substrates were supported on a tantalum silicide-coated tantalum susceptor in the reaction tube, and the susceptor heated externally by an rf generator. Prior to the growth process, the substrates were etched with hydrogen at 1650°-1700°C[2] to remove about 10μ of silicon carbide from the substrate. A schematic of the apparatus is shown in Fig. 1.

During the growth process, the substrates were maintained at 1700°-1715°C. The flow rate of hydrogen was 2.5 l/min, and the concentration of silicon and carbon tetrachlorides in the reactant mixture was 0.04-0.1%. Under these conditions, the linear velocity of the reactant over the substrate surface in our apparatus at room temperature was about 12 cm/sec, and this high linear velocity was essential to provide a uniform flux of the reactant over the substrates.

The structural perfection of deposited silicon carbide layers was evaluated principally by chemical etching technique and optical microscopy. Imperfections in these layers were readily revealed by etching the specimen with a 3:1 $NaOH$-Na_2O_2 mixture at 700°C for 5-15 sec.

Results and discussion.—Under proper conditions of cleanness, the structural perfection of epitaxial silicon carbide layers is affected by the substrate temperature, growth rate, imperfections in substrates, etc. Using a given hydrogen flow rate at a given substrate temperature, the growth rate of silicon carbide depends on the concentrations of silicon and carbon tetrachlorides in the reactant mixture. In this work, equal concentrations of carbon and silicon tetrachlorides were used. Table I summarizes the growth rate of silicon carbide layers on the silicon face of the substrate as a function of the reactant composition; the substrate temperature was 1700°C and the hydrogen flow rate was 2.5 l/min. (The growth rate was found to be approximately 50% greater on the carbon face of the substrate.) The observed growth rate is the net result of the deposition of silicon carbide by thermal reduction and the etching of silicon carbide by hydrogen. Since the etch rate of silicon carbide by hydrogen is considerable at the temperature used for the deposition process, approximately 2 μ/min, the composition of the reactant mixture becomes very critical. Under a given set of growth conditions, there exists a definite reactant composition at which no net deposition of silicon carbide occurs, and any deviation from this composition results in the etching of the substrate or the deposition of silicon carbide. As indicated in Table I, the silicon carbide substrates were found to be etched when the concentration of carbon and silicon tetrachlorides was 0.055% or less. As the concentration of the tetrachlorides was gradually increased, the growth rate of silicon carbide increased rapidly. However, at tetrachloride concentrations of 0.08% or higher, the grown layer had large areas of apparently polycrystalline material.

Chemical etching and optical microscope examinations indicated that epitaxial layers grown at rates of about 0.5 μ/min were similar to the substrate in structural perfection and that defects in the grown layer were usually propagated from the substrate. An example is given in Fig. 2 where a noted defect in a grown layer is correlated, after the removal of this layer, with defects in the substrate. The apparent unevenness of the substrate surface was due to the higher etch rate in the defect areas.

The epitaxial growth of hexagonal silicon carbide layers of good structural perfection was achieved only over a limited temperature range. Using a reactant mixture containing 0.06-0.065% of carbon and silicon tetrachlorides, the grown layer was of cubic phase at temperatures below 1700°C. These layers were characterized by high concentrations of linear etch figures

[2] All temperatures reported here were brightness temperatures measured with a micro-optical pyrometer. These temperatures are about 100°C lower than the true temperature because of the emissivity correction of silicon carbide and the reflection loss at the wall of the reaction tube.

Table I. Growth rate of epitaxial silicon carbide layers as a function of reactant composition

(Brightness temperature of substrate = 1700°C., H_2 flow rate = 2.5 l/min)

Mole % of CCl_4 and $SiCl_4$	Growth rate, μ/min
0.055	Etching
0.060	0.4
0.075	0.7
0.090	Polycrystalline growth

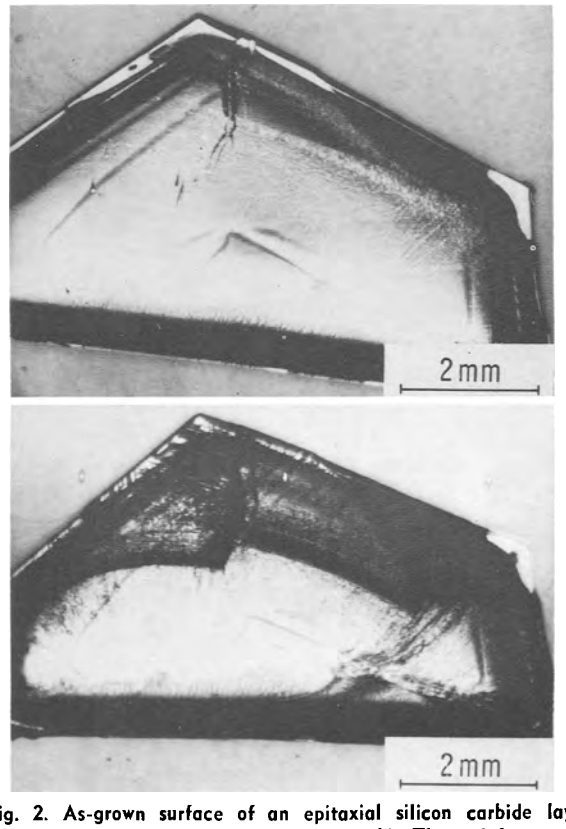

Fig. 2. As-grown surface of an epitaxial silicon carbide layer showing structural defects (upper photograph). These defects were correlated with those in the substrate after the removal of the epitaxial layer (lower photograph).

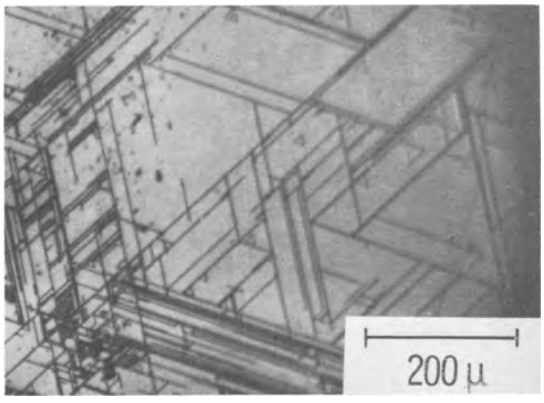

Fig. 3. Linear etch figures associated with stacking faults in a cubic silicon carbide layer deposited on a hexagonal substrate.

at 60° or 120° to each other (Fig. 3), and these etch figures are presumably stacking fault traces (11). Hexagonal silicon carbide layers were grown from 1700° to 1730°C, and no growth occurred at higher temperatures due to the increased etching rate of silicon carbide by hydrogen. Even when the concentrations of carbon and silicon tetrachlorides in the reactant mixture were increased by a factor of four, no growth was observed at substrate temperatures above 1750°C.

Epitaxial Growth of Doped Silicon Carbide Layers and Formation of Epitaxial Junctions

The electrical properties of epitaxial silicon carbide layers obtained by the thermal reduction technique without intentional doping are determined predominately by impurities in the reactant mixture and in the growth apparatus. When these impurity effects are known, controlled addition of dopants into the reactant can yield epitaxial layers of desired conductivity type and carrier concentrations. Junction structures can be prepared accordingly by programming the type and concentration of the dopant during the growth process.

Experimental.—The electrical properties of epitaxial silicon carbide layers deposited on substrates of opposite conductivity type were evaluated by resistivity and Hall in the temperature range 78°-900°K, using the van der Pauw technique (12). The specimen was ultrasonically cut into a disk form, 1.5-6.5 mm in diameter. Four contacts were then applied to the epitaxial layer. Using gold wires of 25μ diameter, the disk was attached to a ceramic plate having gold contacts, and these contacts served as voltage and current leads for the measurement. From the resistivity and Hall constant the carrier concentration and carrier mobility can be determined. The carrier mobility is independent of the thickness of the layer.

The control of carrier concentration in epitaxial silicon carbide layers was achieved by using diborane as a p-type dopant and nitrogen, arsine, or phosphine as n-type dopants. A series of growth experiments were carried out using varied amounts of each dopant to determine the relation between the electrical properties of the epitaxial layer and the composition of the reactant.

Subsequent to the control of the carrier concentration in the epitaxial layer, rectifying junctions were prepared by two principal approaches. In the first, an n- or p-type epitaxial layer was deposited on substrates of opposite conductivity type, and a p-n junction was formed near the growth interface. The second approach was aimed at the preparation of p^+ n^+-type structures by depositing an undoped silicon carbide layer onto a highly doped n-type substrate followed by the deposition of a highly doped p-type layer. The junctions were usually 25 mm^2 in area. To determine the electrical properties of epitaxial junctions, ohmic contacts were alloyed to the n-type and p-type regions, using Au-Ta and Au-Ta-Al alloys respectively, at 1225°C. The units were then etched in molten sodium peroxide and tested for electrical tests.

Table II. Electrical properties of doped silicon carbide Layers measured at room temperature

Flow rate of dopant, mole/min	Resistivity, ohm-cm	Mobility, cm^2/v-sec	Carrier conc, cm^{-3}
N_2 6×10^{-3}	0.053	48	2.8×10^{18}
N_2 2×10^{-4}	0.023	52	6.0×10^{18}
PH_3 0.5×10^{-6}	0.07	155	5.6×10^{17}
PH_3 2.2×10^{-6}	0.02	109	2.6×10^{18}
AsH_3 0.5×10^{-6}	0.32	37	5×10^{17}
B_2H_6 2.2×10^{-5}	90.4	2	4×10^{16}

Results and discussion.—Epitaxial silicon carbide layers grown by the thermal reduction technique without intentional doping were n-type, with representative room temperature resistivity of 0.07 ohm-cm, mobility of 290 cm^2/v-sec, and net carrier concentration of 3×10^{17} cm^{-3}. It is believed that these carriers were due to residual nitrogen in the reactants and in the apparatus.

When dopants were introduced into the reactant mixture under conditions yielding epitaxial silicon carbide layers of good perfection, the growth rate was found to increase more than 50%, with degradation in the quality of the layer. To obtain doped layers of good perfection, the concentrations of carbon and silicon tetrachlorides in the reactant were reduced to 0.04% to achieve a growth rate of 0.5 μ/min. The electrical properties of several representative doped layers, measured at room temperature, are summarized in Table II. The phosphorus doped layers showed a significantly higher mobility than similarly doped nitrogen or arsenic doped layers. Figure 4 shows the resistivity and carrier concentration of a phosphorus doped epitaxial silicon carbide layer in the temperature range 78°-900°K. The temperature dependence of the carrier concentration exhibits two distinct slopes corresponding to activation energies of 0.03 and 0.10 ev. It cannot be stated with certainty if both donor levels are associated with phosphorus or if an unknown impurity is present.

Many diodes were made by depositing n-type epitaxial layers on p-type substrates. The resistivity and mobility of representative substrate crystals were 0.01

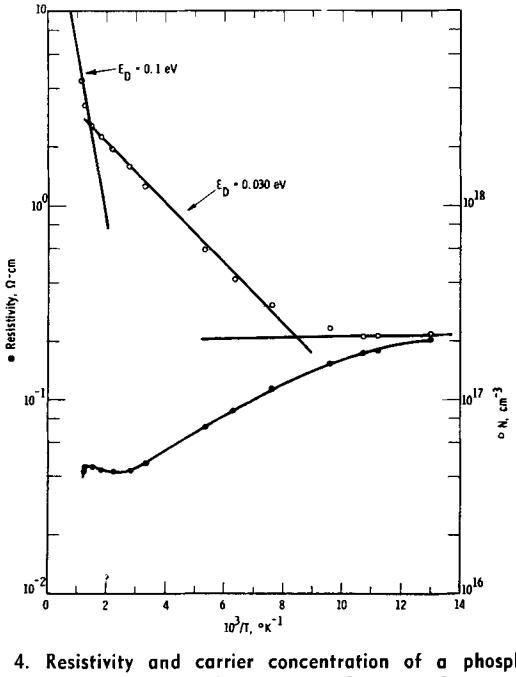

Fig. 4. Resistivity and carrier concentration of a phosphorus-doped epitaxial silicon carbide layer as a function of temperature.

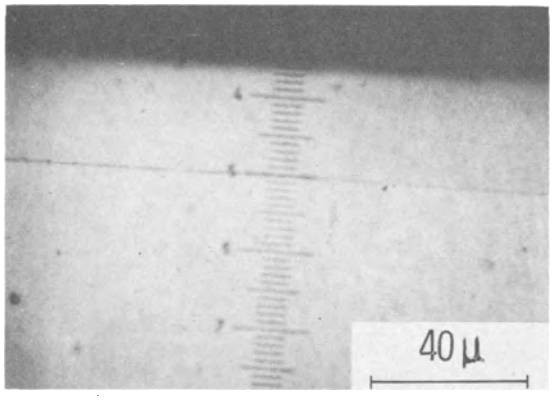

Fig. 5. An epitaxial p-n junction in silicon carbide delineated by electrolytic etching of a vertically cross-sectioned surface.

ohm-cm and 30 cm^2/v-sec, respectively. The epitaxial layers were usually 15 to 30μ in thickness, with properties as given in Table II. Figure 5 shows a p-n junction delineated by electrolytic etching of vertically cross-sectioned surface in a 75:1 methanol: HF mixture. These epitaxial junctions generally exhibited a low forward voltage (1.5-2.5v at 1-5A) with a reverse capability of 50v at 500°C. Several p^+ n^+-type structures were made and the reverse characteristics were similar.

Summary and Conclusions

Epitaxial silicon carbide layers of good structural perfection have been deposited on the basal plane of hexagonal silicon carbide substrates at temperatures considerably below its sublimation temperature by a thermal reduction technique. The substrate temperature, the concentrations of carbon and silicon tetrachlorides in the reactant mixture, the surface condition of the substrate, and the purity of the growth apparatus are important factors affecting the quality of the grown layer. The conductivity type of, and carrier concentration in, the grown layer have been controlled to a reasonable degree by using diborane as a p-type dopant and nitrogen, arsine, or phosphine as n-type dopants. Epitaxial junction structures have been prepared by varying the dopant concentration in the reactant mixture during the growth process. Although the preliminary structures could not support high voltages, the epitaxial growth technique is believed to be a practical method for preparing junction structures in silicon carbide and is worthy of further investigations.

Acknowledgment

This work was supported by the Air Force Avionics Laboratory, Wright-Patterson Air Force Base, Ohio, under Contracts AF 33(615)-1440 and AF 33(615)-2363. The authors also wish to thank K. C. Liang, E. H. Myers, R. John, R. Pfeil, and R. Yut for their assistance in experimental work.

Manuscript received Jan. 26, 1966; revised manuscript received May 16, 1966. This paper was presented at the Buffalo Meeting, Oct. 10-14, 1965.

Any discussion of this paper will appear in a Discussion Section to be published in the June 1967 JOURNAL.

REFERENCES

1. C. Goldberg and J. W. Ostroski, in "Silicon Carbide," Pergamon Press, New York (1960).
2. P. C. Canepa, P. J. Malinaric, R. B. Campbell, and J. W. Ostroski, *Trans. IEEE*, NS-11 No. 3, 262 (1964).
3. H. C. Chang, C. Z. LeMay, and L. F. Wallace in "Silicon Carbide," Pergamon Press, New York (1960).
4. D. R. Hamilton, *This Journal*, **105**, 735 (1958).
5. V. J. Jennings, A. Sommer, and H. C. Chang, *ibid.*, **113**, 728 (1966).
6. K. Bean and P. Gleim, *ibid.*, **110**, 265C (1963).
7. R. C. Smith, Electrochem. Soc., Electronics Div. Abstracts **12**, No. 2, 15 (1963).
8. T. L. Chu and R. B. Campbell, *This Journal*, **112**, 955 (1965).
9. J. W. Faust, Jr., in "Silicon Carbide," J. R. O'Connor and J. Smiltens, Editors, p. 403, Pergamon Press, New York (1960).
10. Karl Brack, *J. Appl. Phys.*, **36**, 3560 (1965).
11. W. K. Liebmann, *This Journal*, **110**, 475 (1963).
12. L. J. van der Pauw, *Philips Research Repts.*, **13**, 1 (1958).

The Growth of $FeSn_2$ Layers on Specifically Oriented Iron Single Crystals

H. E. Biber and W. T. Harter

Applied Research Laboratory, United States Steel Corporation, Monroeville, Pennsylvania

ABSTRACT

$FeSn_2$ layers on tinplate exhibit three different types of structure, the primary forms of which occur on the {100}, {110}, and {111} faces of iron. The rate and manner of growth of the alloy layer on each of these three faces have been studied for a heating rate that simulated commercial flow brighening of tinplate. Results show that the alloy layer grows at a different rate on each face. The alloy growth on both the {100} and {110} faces exhibits arrests that are associated with completion of base-metal coverage by the alloy layer. Results provide a reasonably clear understanding of the manner in which alloy layers grow on tinplate during commercial flow brightening.

Electrolytic tinplate, as it emerges from a plating bath, has a dull surface quite different from the highly reflective surface traditionally associated with tinplate. To impart high reflectivity to the surface, the matte tinplate is briefly heated above 232°C, the melting point of tin, and then quenched. This heating operation, known as flow brightening, also promotes a reaction between the iron and the tin, which results in the formation of a thin layer of $FeSn_2$ at the interface between the steel base and the protective tin coating.

The structure of this alloy layer has been a subject of considerable interest in the tinplate industry. Stoll (1), Ebben and Lawson (2), and Gabe and Mort (3) have shown by electron microscopy that alloy layers on commercial tinplate consist of numerous small crystallites of $FeSn_2$. The arrangement of these crystallites and their coverage of the steel base were

Table I. Results of chemical analysis of vacuum-melted iron from which single crystals were grown

	Weight per cent
Carbon	0.002
Oxygen	0.006
Nitrogen	0.0001
Manganese	<0.01
Phosphorus	0.001
Sulfur	0.003
Silicon	0.010
Nickel	0.025
Chromium	0.005

shown to vary from one small area to the next. These variations were thought to be caused by the varying orientation of the grains in the surface of the steel base. To obtain a better understanding of the influence of substrate orientation on alloy-layer structure and of the manner in which alloy layers grow during commercial flow brightening, our laboratory undertook a detailed study with specifically oriented iron single crystals.

Experimental

The single crystals were prepared by the strain-anneal technique developed by Stein and Low (4). Vacuum-melted iron of 99.9% purity was used, and single-crystal strips 0.04 x 1 x about 4 in. were obtained in approximately half of the trials. Results of chemical analyses of the starting materials are given in Table I, and the orientations of those single crystals used in this study are plotted on the unit stereographic triangle shown in Fig. 1.

For convenience the single-crystal strips were divided into half-inch squares. One large face of each square was polished with 0.3μ alumina on a wheel covered with kittenear broadcloth. After a 10-sec etch in 2% nital, the polished surface was coated with a nominal 60 μin. layer of tin in a PSA-DDS electrolyte at 110°F at a current density of 25 amp/ft^2. The electrolyte contained, per liter, 55g of stannous sulfate, 57 ml of 65% phenolsulfonic acid, and 6g of dihydroxydiphenylsulfone.

The matte tinplate squares were heated from the unplated side by a 500-w projection lamp. The lamp voltage was adjusted for each square before heating so that the tin coating melted 7.0 ± 0.2 sec from the start of heating. The amount of alloy layer on a ¼-in. diameter circular area of the heated specimens was determined by the coulometric method of Kunze and Willey (5).

To prepare the specimens for electron microscopy, the free tin on the surface was removed by anodic dissolution in 5% sodium hydroxide solution. Specimens were carefully washed in flowing water, rinsed with methanol, and dried in a draft of warm air. Replicas of the alloy layer were prepared by a technique developed by Ebben and Lawson (2). The shadowing angle was about 45°. The replicas were examined in a Hitachi HU-10 electron microscope.

For comparison, alloy-layer growth rates on polycrystalline steel were determined for these same heating conditions with ½-in. squares of matte tinplate prepared in a circulation cell. In addition some tinplated single crystal squares were heated in a 240°C oil bath and the resulting alloy layer examined by electron microscopy.

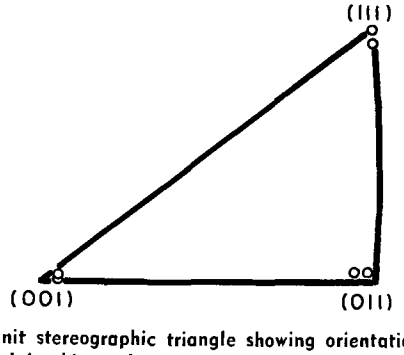

Fig. 1. Unit stereographic triangle showing orientations of single crystals used in this study.

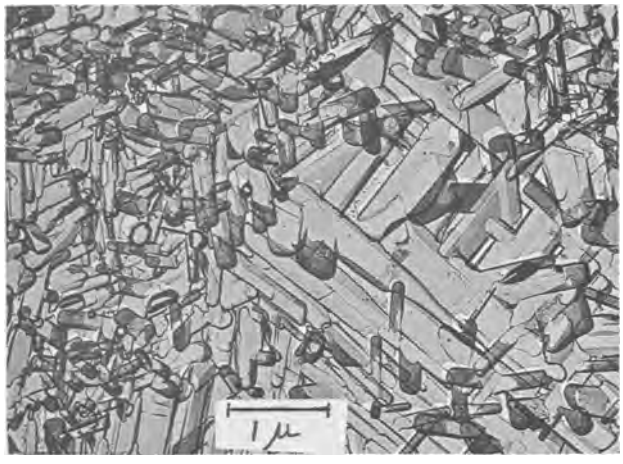

Fig. 2. Typical iron-tin alloy layer on steel

Results

On commercial flow-brightened tinplate the amount of alloyed tin is normally between 0.05 and 0.10 lb/bb (pounds per base box: 0.056 and 0.112 mg/cm^2, respectively). In electron micrographs of typical alloy layers on steel, Fig. 2, there appear to be many different alloy-layer structures. However, a study of the alloy layers formed on iron single crystals shows

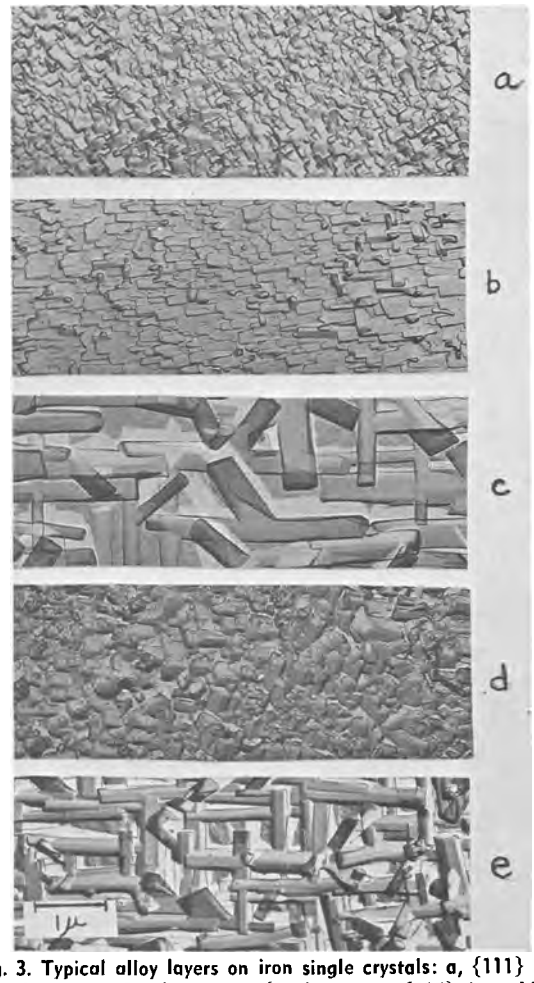

Fig. 3. Typical alloy layers on iron single crystals: a, {111} face; b, {110} face; c, {100} face; d, {112} face; e, {115} face. Identical magnification for each micrograph.

that there are actually only three basic alloy-layer structures. These occur on the {111}, {110}, and {100} faces of the iron crystal, Fig. 3a-c. On the {111} face the alloy layer consists of small columnar crystallites that project from the surface at various angles, Fig. 3a; on the {110} face the crystallites lie parallel to one another on the surface, Fig. 3b; and on the {100} face the crystallites are arranged in an approximately orthogonal array on the substrate surface, Fig. 3c. Alloy-layer structures on other faces of the iron crystal are simply variations of these three basic forms and resemble most closely the basic form on the primary face that is closest in orientation to the face in question. For example, the {112} face lies closest to the {111} face, forming angles of 19.5, 30.0, and 35.3° with the {111}, {110}, and {100} faces, respectively, and the alloy layer on this face has a {111}-like structure, Fig. 3d. The {115} face lies closest to the {100} face, forming angles of 38.9, 35.3, and 15.8° with the {111}, {110}, and {100} faces, respectively, and the alloy layer on this face has a {100}-like structure, Fig. 3e. Close inspection of Fig. 2 will show that each of the structures present can be placed in one of the three general classifications, "{111}", "{110}", or "{100}." It follows then that, with respect to alloy layer formation, the grains of steel in the surface of the substrate can also be grouped into these three general types, according to the structure of the alloy layer formed on them.

Thus, to obtain an understanding of the manner in which the alloy layer grows on commercial tinplate during flow brightening, it was sufficient to study alloy-layer growth on just the three principal faces of iron. The heating conditions were intended to simulate actual heating during flow brightening on an electrolytic tinning line. The melting time of 7 sec was within the range of commercial melting times, yet long enough to give a growth rate sufficiently slow that brief changes in the alloy-layer growth process might be observed. The heating curve obtained with the projection lamp, Fig. 4, did not differ greatly from estimates of the commercial heating curve.

Data for the growth of alloy layers on the {100}, {110}, and {111} faces of iron with these heating conditions are presented in Fig. 5. On the {100} face the alloy layer formed very slowly before the tin coating melted; less than 0.01 lb/bb of alloyed tin was formed in the first 7 sec of heating. After the tin coating melted, the alloy layer grew very rapidly for about 3.5 sec (to 10.5 sec), then the growth rate abruptly

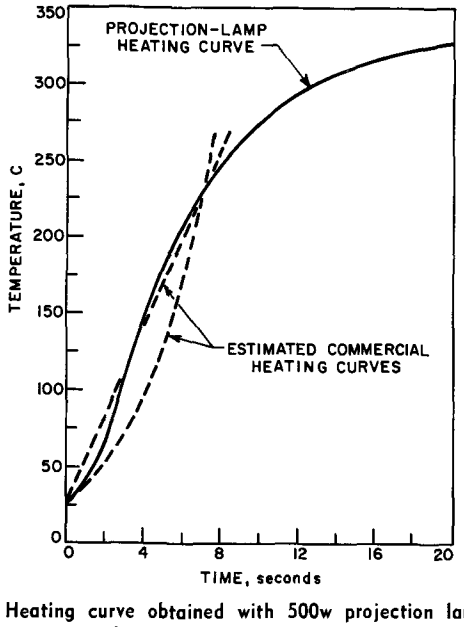

Fig. 4. Heating curve obtained with 500w projection lamp and estimated commercial heating curves.

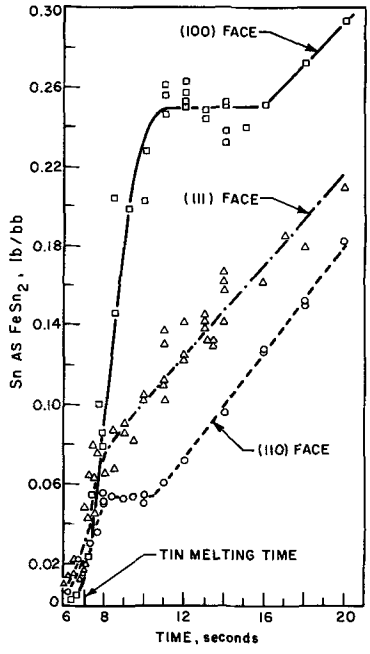

Fig. 5. Alloy-layer growth curves for each of the three principal faces of iron.

decreased, and from about 11 to 16 sec there was no additional alloy-layer growth. Following this arrest, the alloy layer resumed its growth, and from 16 to 20 sec (the extent of the measurements on the single crystals) grew at a uniform rate of about 0.011 lb/bb-sec.

On the {110} face the amount of alloy layer that formed before the tin coating melted was about twice that on the {100} face. However, after the tin coating melted, the {110} face exhibited the smallest over-all growth rate of the three faces. A growth arrest occurred for this face also, but lasted only from 8 to about 11 sec after start of heating. From 12 to 20 sec the alloy layer grew at a uniform rate of about 0.014 lb/bb-sec.

The amount of alloy layer formed on the {111} face before the coating melted was about the same as that on the {110} face. After the tin coating melted, the alloy layer on this face initially grew at a rate intermediate to the rates on the {110} and {100} faces for the same period. There was no growth arrest on this face, although after 8 sec the growth rate decreased. This decrease may have been at least partly due to the general decrease in heating rate after 8 sec. From 9 to 20 sec the alloy layer grew at a uniform rate of about 0.011 lb/bb-sec.

In order to relate changes in the growth rates to changes in the alloy-layer structures, electron micrographs were made of alloy layers at different stages of growth on the three crystal faces. Micrographs for the {100} face are shown in Fig. 6. Before the tin coating melted there were only a few small crystallites on the surface. Obviously the nucleation rate was low on this face. In addition, the nucleation must have occurred within a brief interval because all the crystallites were about the same size and shape. Most of them were arranged at approximately right angles to one another; however, a few were skewed at angles of about 45°. After the tin coating melted, the crystallites at right angles grew rapidly over the surface and produced the approximately orthogonal network that is characteristic of the alloy layer on the {100} face. Meanwhile, the skewed crystallites grew upward at various angles to the surface. Because they projected from the surface, the carbon replica film formed on their undersides as well as on their topsides. Thus, these secondary crystallites can be distinguished easily from the base crystallites in the micrographs because

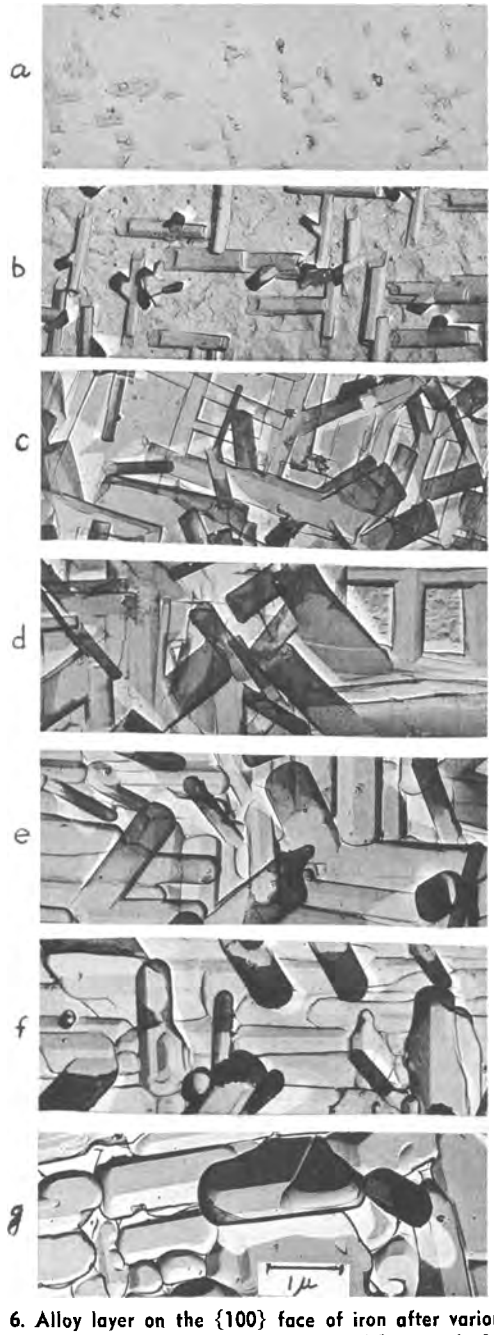

Fig. 6. Alloy layer on the {100} face of iron after various heating times: a, 6.75 sec; b, 7.75 sec; c, 10.0 sec; d, 11.0 sec; e, 13.5 sec; f, 15.0 sec; g, 18.0 sec. Indentical magnification for each micrograph.

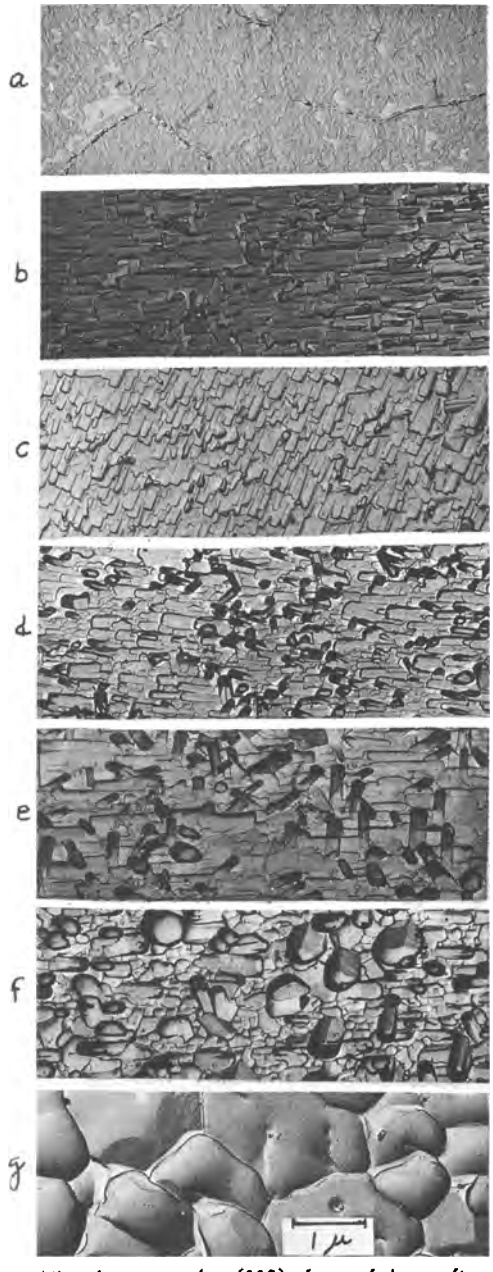

Fig. 7. Alloy layer on the {110} face of iron after various heating times: a, 6.75 sec; b, 7.75 sec; c, 9.5 sec; d, 11.5 sec; e, 13.5 sec; f, 15.0 sec; g, 18.0 sec. Identical magnification for each micrograph.

their ends are darker. The base crystallites gradually impinged upon one another, but even after 10 sec heating, considerable areas of substrate were still exposed. However, shortly afterward numerous small crystallites suddenly formed on these previously unalloyed areas and completed the coverage of the substrate by the alloy layer. This event coincided with the beginning of the growth arrest. During the growth arrest the ends and edges of the crystallites became rounded, but no new alloy was observed. Electron diffraction analysis revealed only $FeSn_2$ before, during, and after the growth arrest. When growth resumed the crystallites coalesced and formed massive particles, some faces of which were flat, while others were rounded. The secondary crystallites were no longer obvious, and the orthogonal relationship of the base crystallites was not as pronounced as it was in the early stages of growth.

The micrographs of the alloy layers on the {110} face are shown in Fig. 7. The nucleation rate on this face was much higher than that on the {100} face. Before the tin coating melted, there were many small crystallites of $FeSn_2$ on the surface; however, they did not cover the substrate completely. After the tin coating melted, the small crystallites formed larger columnar crystallites that were, in general, parallel to one another on the surface. In addition, secondary crystallites started to form on the base crystallites. Small areas of substrate remained exposed until the growth arrest began, but they were not observed thereafter. Thus, it appears that on the {110} face, as on the {100} face, the start of the growth arrest coincides with the disappearance of exposed substrate. During the growth arrest there was no appreciable change in the alloy-layer structure. Again electron-diffraction analysis showed only $FeSn_2$ before, during, and after the arrest. For a short while after the arrest, the secondary crystallites increased appreciably in size and thereby became the prominent feature of the

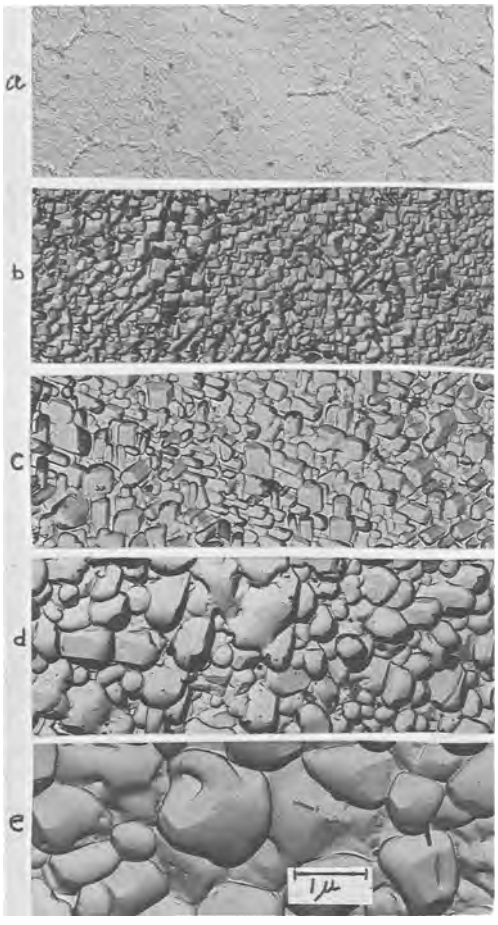

Fig. 8. Alloy layer on the {111} face of iron after various heating times: a, 6.75 sec; b, 8.0 sec; c, 11.0 sec; d, 14.0 sec; e, 18.0 sec. Identical magnification for each micrograph.

layer. However, with further heating the crystallites coalesced and formed massive rounded particles.

The electron micrographs of the alloy layers formed on the {111} face are shown in Fig. 8. Before the tin coating melted the base metal was completely covered with small crystallites of $FeSn_2$. After the coating melted, the small crystallites formed columnar crystallites that protruded from the surface at various angles. They grew together continuously and eventually formed massive rounded particles. In the later portion of the heating period the structure of the alloy layer on the {111} face was similar to that on the {110} face.

Discussion

The reader's attention is directed to the micrographs of the alloy layers on the {110} and {111} faces prior to melting of the tin coating, Fig. 7a and 8a. Certain of the crystallites in these micrographs are raised appreciably above the other crystallites on the surface. These crystallites, some of which are marked by arrows, delineate the grain boundaries of the matte tin deposit.[1] The grain boundaries of the matte tin deposit extended upward, away from the surface of the iron single crystal. The alloy crystallites grew upward along these grain boundaries. Because of the more favorable diffusion conditions at the grain boundaries, these crystallites were able to grow faster than those on other parts of the substrate surface. It is reasonable to expect that this upward growth of the alloy crystallites resulted from the combination of tin atoms at the upper extremities of the crystallites with iron atoms that had diffused upward from the substrate. Thus, the presence of these "grain boundaries" in the alloy layer is evidence that alloy-layer growth depends mainly on diffusion of the iron atoms.

In the early stages of growth, shortly after nucleation, both slow and rapid diffusion paths should be available for this iron-atom movement. The slow diffusion paths will be through the lattices of the crystallites, and the rapid diffusion paths will be along the surfaces of the substrate and the crystallites. When the crystallites impinge and completely cover the iron substrate, the paths of rapid diffusion between the substrate and the growing alloy surface(s) are closed off. This causes the growth rate to decrease to a value indicative of the lattice diffusion alone. But the results for the {100} and {110} faces show that when the coverage is completed the growth rate drops to zero. Thus it must be concluded that lattice diffusion did not contribute significantly to the alloy-layer growth. If lattice diffusion had contributed significantly, it would have continued to do so after surface diffusion ceased and the decreased growth rate would have been greater than zero. [A similar situation has been observed in the oxidation of magnesium where the initial layer of oxide apparently forms only by surface diffusion (6)].

A further indication of the insignificance of lattice diffusion is given by the fact that in the later portion of the heating period each crystal face exhibited the same alloy-layer growth rate even though the amount of alloy on each face was substantially different. If lattice diffusion were significant, the instantaneous growth rate on the {100} face would have been much smaller than that on the {110} face because the iron atoms would have had to diffuse through a much greater thickness of alloy to reach the growing surface.

The results of this study provide a reasonably clear understanding of the growth of the alloy layer during rapid heating as in commercial flow brightening. The alloy crystallites are nucleated at specific sites on the steel surface. The nature of these sites is unknown, but it is obvious that they differ in number for the different crystal faces of iron. When the nucleation rate is low, as on those faces that form a "{100}"-like alloy-layer structure, the individual crystallites are widely separated and must grow considerable distances over the surface before they can impinge. Because the crystallites thicken as they grow laterally, a relatively large amount of alloy has been formed when the crystallites finally impinge and completely cover the substrate. The elimination of the surface diffusion paths as a result of the impingement causes the growth to cease. In order for the alloy layer to resume its growth, the iron atoms must find new paths to the extremities of the crystallites. The growth arrest that follows completion of coverage of the substrate is believed to represent the time required to establish these new paths. Because lattice diffusion is apparently insignificant, these new paths are probably formed at "grain" boundaries in the alloy layer. The rounding of the edges of the crystallites during the arrest could be part of the process of establishing these new paths. The flow of atoms along these new diffusion paths should be slower than along the surface diffusion paths. Thus the growth rate after the arrest will be slower than that prior to the arrest.

When the nucleation rate is high, as on the {110} face, the crystallites have a shorter distance to grow laterally before they impinge. Thus the completion of coverage of the substrate, and therefore the growth arrest, occurs sooner than on the {100} face. Furthermore the total amount of alloy layer at the time of the growth arrest will be less than that on the {100} face.

When the nucleation rate is very high, as on the {111} face, the alloy crystallites completely cover the substrate shortly after nucleation, early in the heating period. Presumably a growth arrest occurs at this time, but is not observable because the amount of alloy

[1] The electrodeposited tin coatings were polycrystalline despite the single crystal substrates. No epitaxy was observed between the tin deposit and the substrate.

layer is below the limit of detection of the analytical method. This is in accord with the trend shown by the {100} and {110} faces where with increasing nucleation rate, the time of heating before the arrest and the amount of alloy formed at the time of the arrest decrease. After the tin coating melts, the alloy layer grows without interruption presumably by diffusion along paths established after the arrest.

Some investigators have been interested in studying the effects of processing variations on iron-tin alloy layer structure with the goal of increasing the coverage of the steel base and thereby possibly increasing the corrosion resistance of the tinplate. These studies are usually made with polycrystalline steel substrates. Thus all three types of alloy layer structure ({100}, {110}, and {111}) are likely to be encountered. Care must be taken in drawing conclusions from such studies so that changes in alloy layer structure due to differences in the underlying steel grain orientations are not incorrectly attributed to processing changes. It should also be noted that with normal processing, complete coverage of the {100}-type steel grains can be achieved if the heating during flow brightening is continued until the onset of the {100} growth arrest.

In a recent paper (7) it was shown that the growth rates of iron-tin alloy layers on polycrystalline substrates are greatly affected by the heating rate. With rapid heating rates (room temperature to 232°C in 10 sec or less) there is a marked growth arrest; with slow heating rates (room temperature to 232°C in about 50 sec) the arrest is not observed. These observations can now be explained in terms of the results of the present study. Alloy-layer growth curves were determined for two different lots of matte tinplate with the same heating conditions as those used for the single crystals, Fig. 9. For these particular steels two growth arrests were observed. The first arrest occurred after about 8 sec of heating and the second occurred after about 10 sec of heating. Comparison with the growth curves for single crystals shows that the first arrest was obviously due to the {110}-type grains on the steel surface and the second arrest was obviously due to the {100}-type steel grains. It will be noted that the amount of alloy layer at any given time of heating was somewhat different for the two tinplates. This is not surprising when one considers the markedly different growth rates on the {100}, {110}, and {111} faces and the fact that different steels will have somewhat different ratios of {100}, {110}, and {111}-type grains on their surfaces. The {110} arrest is not always observed. It will be absent from the growth curve if the time interval between measurements is too long or if the steel has a small number of {110}-type grains. Thus in the previously reported growth curves for rapid heating rates, only one arrest, that due to the {100}-type steel grains was observed.

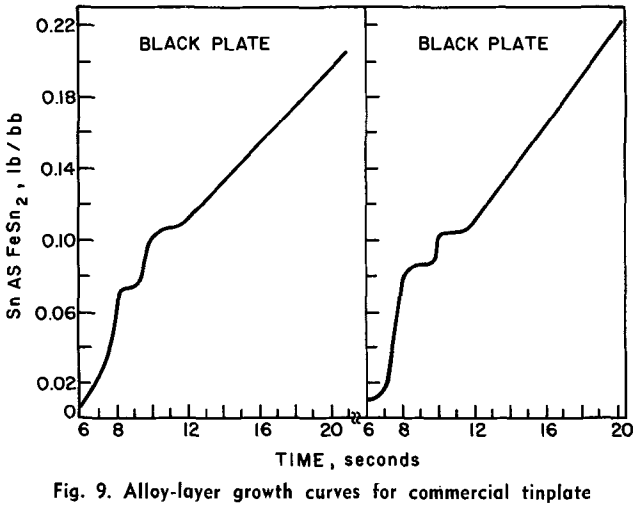

Fig. 9. Alloy-layer growth curves for commercial tinplate

The disappearance of this {100} growth arrest was due to a change in the growth behavior on the {100} grains as the heating rate was reduced. To understand how this change was effected, it is necessary to consider the alloy-layer growth on these grains in greater detail. Close examination of the sizes of the crystallites in Fig. 6a and b will show that before the tin coating melts lateral growth of the crystallites is favored over outward growth, but after the coating melts the reverse is true. With a rapid heating rate the coating melts before there is much lateral growth. Because there are relatively few crystallites on the {100} face they make considerable outward growth before their lateral growth causes them to impinge. Therefore the alloy layer on the {100}-type steel grains is relatively thick when it completes coverage of the base metal. The completion of base metal coverage marks the onset of the growth arrest. Because, as the single crystal data of Fig. 5 show, the amount of alloy on these grains is much greater than that on the {110}- and {111}-type steel grains, the alloy-layer growth curve for the tinplate for this period in the heating mainly reflects the growth on the {100}-type grains. Thus the {100} growth arrest is very pronounced in the alloy-layer growth curve for the tinplate.

As the heating rate is decreased there is an increase in the amount of lateral growth that occurs before the coating melts. When the heating rate is decreased sufficiently the {100}-type grains are completely covered by the alloy layer when the coating melts or shortly thereafter. However, the amount of alloy is relatively small because the outward growth of the crystallites was not favored and because, as the single crystal data show, the growth rate on the {100} face before the coating melts is less than that on the {110} and {111} faces. These considerations are illustrated by Fig. 10. This alloy layer was formed by slowly heating a {100} single crystal for 60 sec. The tin coating melted just at the end of the heating period. The substrate is almost completely covered, but the amount of alloy is only 0.025 lb/bb. (This alloy layer should be compared to that in Fig. 6c which was formed by rapid heating. The latter alloy layer provides much less substrate coverage even though the amount of alloy is about 0.23 lb/bb.) Thus with a slow heating rate the contribution of the {100}-type grains to the alloy layer growth data is much less than that when the tinplate is rapidly heated. Therefore, with a slow heating rate, the {100} growth arrest is not observed in the alloy-layer growth curve for tinplate.

An interesting observation concerning substrate surface preparation was made in the course of this study. We wanted to determine whether the same alloy-layer structures would result when a method of surface preparation other than mechanical polishing and etching was used. The single crystal sections were electropolished in a mixture of 15% perchloric acid and 85% acetic acid, rinsed with methanol, and electroplated with tin. Extensive rinsing with methanol prior to plating was necessary to obtain uniform matte deposits. The alloy layers that were subsequently formed had the same general morphologies as those observed

Fig. 10. Alloy layer on the {100} face of iron formed by slowly heating the single crystal for 60 sec.

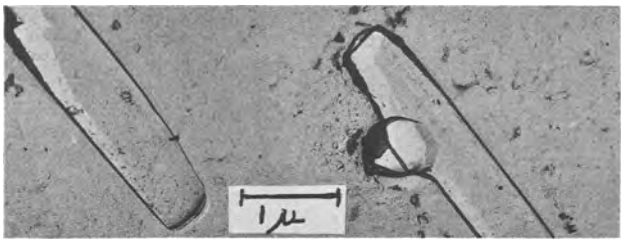

Fig. 11. Alloy layer on electropolished {100} face of iron

on the mechanically polished and etched surfaces; however, the alloy layer on the {100} face was always much less continuous. Even though the surface was rinsed sufficiently to give a uniform matte deposit, something remained on the surface and acted as a barrier to the nucleation of alloy crystallites. This effect was only observed for the {100} face. An example is shown in Fig. 11. (This micrograph was made with a different replication technique and for this reason is not of the same quality as the other micrographs.) A similar obstruction of $FeSn_2$ crystallite growth on the {100} face was observed by Luner and Murray for vacuum-deposited tin coatings (8).

Summary

It has been shown that the iron-tin alloy layers on commercial tinplate have three basic structures. These occur on the {100}, {110}, and {111} faces of iron. The rate and manner of growth of the alloy layer on each of these faces has been studied for a heating rate that simulated commercial flow brightening. The results of this study provide an understanding of the manner in which the alloy layer grows on tinplate. With this heating rate, before the tin coating melts, the alloy layer completely covers the {111} face, and almost completely covers the {110} face, but provides very little coverage on the {100} face. At the time of melting the amount of alloy on the {111} and {110} faces is about twice that on the {100} face. Immediately after melting the alloy layer on the {111} face grows at a rate which is faster than that on the {110} face, but slower than that on the {100} face. The {110} and {100} faces both exhibit growth arrests; that on the {100} face occurs later and lasts longer than that on the {110} face. The growth arrest on each face coincides with completion of base-metal coverage by the alloy layer on that face. It is believed that the duration of the growth arrest represents the time necessary to establish new diffusion paths for continued growth of the alloy layer.

Evidence is presented which shows that the alloy-layer growth depends on the diffusion of iron atoms from the substrate.

Manuscript received Dec. 3, 1965; revised manuscript received May 13, 1966.

Any discussion of this paper will appear in a Discussion Section to be published in the June 1967 JOURNAL.

REFERENCES

1. P. A. Stoll, "Electron Microscopy of Tin Plate," ASTM Special Technical Publication No. 262, p. 73 (1959).
2. G. J. Ebben and G. J. Lawson, *J. Appl. Phys.*, **34**, 1825 (1963).
3. D. R. Gabe and R. J. Mort, *J. Iron Steel Inst. London*, **203**, 64 (1965).
4. D. E. Stein and J. R. Low, Jr., *Trans. AIME*, **221**, 744 (1961).
5. C. T. Kunze and A. R. Willey, *This Journal*, **99**, 354 (1952).
6. W. H. Orr, "Oxide Nucleation and Growth," Cornell University Dept. of Engineering, Physics Technical Report No. 5, Project No. NR 036-035, April 1, 1962. See also T. N. Rhoden and D. Walton, "Metal Surfaces," ASM Publication p. 282 (1963).
7. H. E. Biber, *This Journal*, **113**, 362 (1966).
8. Charles Luner and M. V. Murray, *ibid.*, **111**, 407 (1964).

Oxidation of Silicon at High Temperatures and Low Pressure under Flow Conditions and the Vapor Pressure of Silicon

Earl A. Gulbransen, Kenneth F. Andrew, and Fred A. Brassart

Research Laboratories, Westinghouse Electric Corporation, Pittsburgh, Pennsylvania

ABSTRACT

Wagner has predicted from thermochemical and diffusion theory analyses that silicon may react actively or passively with oxygen at high temperature depending on the oxygen pressure. To determine the characteristics of the oxidation reaction for these reaction conditions, a kinetic study was made at temperatures between 1100° and 1300°C and pressures of 9×10^{-3}, 4×10^{-2}, and 1×10^{-1} Torr using a dynamic reaction system. Very fast reactions were found where predicted. The results were also related to (*i*) kinetic theory reaction efficiencies and (*ii*) gas flow efficiencies. Vapor pressure studies were made using the Langmuir method.

The oxidation behavior of high-purity silicon has been studied extensively under conditions where protective oxides are formed (1-7). In low-pressure oxygen atmospheres, silicon can form a volatile oxide above 1000°C. For these conditions, silicon may oxidize at a rapid rate. Wagner (8) has discussed the transition from active to passive oxidation for oxidation of silicon in inert gas atmospheres containing low partial pressures of oxygen.

This paper reports a kinetic study on the oxidation of silicon in low-pressure pure oxygen atmospheres under flow conditions in the temperature range of 1100°-1300°C.

Thermochemical Analyses

Table I shows the four reactions which occur in the silicon-oxygen system and the values of the equilibrium constants for the reactions. Both SiO(g) and SiO_2(s) can form. SiO_2(s) does not appreciably dissociate to SiO(g) in oxygen atmospheres of 9×10^{-3} Torr at temperatures below the mp of silicon, 1420°C. The solid phase reaction of Si(s) with SiO_2(s) can proceed in atmospheres of low pressures of SiO(g). The reverse reaction can proceed in high-pressure atmospheres of SiO(g).

Silicon is especially sensitive to reactions with gases containing carbon under conditions where a SiO_2(s) film is absent.

Experimental

The apparatus and method have been described (10). A Cahn type of microbalance (11) was used to follow the rate of oxidation in a dynamic type of reaction system. The rate of oxidation was followed

Table I. Thermochemical analyses of reactions in silicon-oxygen system

Reactions	Equilibrium constants (log K_p) (9) 927°-1527°C			
	927°	1127°	1327°	1527°
[1] $Si(s) + \frac{1}{2}O_2(g) \rightleftarrows SiO(g)$	8.397	8.222	7.707	7.201
[2] $Si(s) + O_2(g) \rightleftarrows SiO_2(s)$	30.26	24.65	20.45	17.10
[3] $\frac{1}{2}Si(s) + \frac{1}{2}SiO_2(s) \rightleftarrows SiO(g)$	−6.333	−4.106	−2.520	−1.347
[4] $SiO_2(s) \rightleftarrows SiO(g) + \frac{1}{2}O_2(g)$	−21.37	−16.43	−12.75	−9.90

continuously at constant pressure and temperature under controlled gas flow conditions. Gas flow velocities up to 53.5 meters/sec were used.

The reaction system consisted of a high-density alumina furnace tube 2 cm in diameter attached to the system by a Viton O-ring. The furnace tube was pretreated by baking in oxygen at 1500°C to remove any residual carbon gases and carbonaceous material so as to prevent the formation of SiC films on the silicon surface.

P-type semiconductor grade of silicon having a resistivity of 425 ohm-cm and a boron content of 10^{16} atoms/cm^3 was used. The single crystal silicon strip was 0.025-0.030 cm thick and 1 cm wide and had the (111) crystal plane in the surface. Pieces 0.5 cm wide were prepared by scribing and cracking, and a 0.075 cm diameter hole was drilled by cavitation to support the specimen. A 0.06 cm quartz fiber was used to support the specimen from the balance.

Reagent grade oxygen was used. The incoming and exit gases were checked by a mass spectrometer to aid in detecting contaminants which could form SiC(s) films.

Results and Discussion

The experimental work was divided in three sections: (*a*) the weight losses of silicon in vacuum at temperatures of 1100°-1350°C; (*b*) the reaction of silicon with low-pressure high-purity oxygen under flow conditions; and (*c*) the effect of contaminating gases on the oxidation of silicon in flow environments.

Vapor pressure of silicon.—To test the cleanliness of our silicon surfaces we have made vapor pressure measurements. If the surfaces are free from $SiO_2(s)$ and SiC(s) films, reasonable vapor pressure data should be measured.

The specimens were cleaned and pretreated at 1300°C in vacuum before starting the vaporization experiments. Several series of weight loss curves were made at temperatures of 1100°-1350°C. Typical weight loss data are given in Table II in units of g/cm^2-sec. Assuming the weight loss curves are due to the volatilization of silicon, the vapor pressures can be evaluated from the Langmuir equation (12)

$$\frac{dw'}{dt} = \alpha P \left(\frac{M}{2\pi RT} \right)^{1/2} \qquad [5]$$

Here M is the molecular weight of the evaporating species, T is the absolute temperature, dw'/dt is the rate of evaporation in g/cm^2-sec, and α is the condensation coefficient.

Table II. Rate of vaporization, vapor pressure, and heats of sublimation

Temp, °C	Rate, g/cm^2-sec × 10^7	−log P, atm	$\Delta H°_{298.15}$, kcal/mole
1100	3.76 × 10^{-2}	−9.20	106.15
1150	9.86 × 10^{-2}	−8.80	107.39
1150	9.63 × 10^{-2}	−8.81	107.46
1200	4.34 × 10^{-1}	−8.15	106.73
1200	4.36 × 10^{-1}	−8.15	106.73
1250	1.10	−7.74	107.46
1250	1.15	−7.72	107.32
1300	2.76	−7.33	107.96
1300	3.36	−7.24	107.32
1350	14.1	−6.61	105.98

Mean $\Delta H°_{298.15} = 107.1 \pm 0.6$

Table II and Fig. 1 show the calculated vapor pressure values assuming monatomic silicon and $\alpha = 1$. Figure 1 also includes the values given by the JANAF tables (9). An evaluation is made in these tables of the earlier data.

Table II shows the calculated values for the heats of sublimation $\Delta H°_{298.15}$ using the equation.

$$\frac{\Delta H°_{298.15}}{T} = -R \ln p - \left(\frac{F° - H°_{298.15}}{T} \right)_{gas} + \left(\frac{F° - H°_{298.15}}{T} \right)_{solid} \qquad [6]$$

where $(F° - H°_{298.15}/T)_{gas}$ and $(F° - H°_{298.15}/T)_{solid}$ are the free energy functions of the gas and solid, respectively. The mean value of $\Delta H°_{298.15}$ is 107.1 ± 0.6 kcal/mole and may be compared with an averaged value of 106.0 kcal/mole given in the JANAF tables (9).

The vapor pressure data given in Fig. 1 suggests that silicon is volatilizing from clean surfaces.

Low-pressure oxidation studies.—Rates of oxidation were determined on cleaned samples of silicon. All samples were pretreated at 1300°C for 15 min at 5 x 10^{-6} Torr. Three pressures 9 x 10^{-3}, 4 x 10^{-2}, and 1 x 10^{-1} Torr and three temperatures 1100°, 1200°, and 1300°C were used. The oxygen flow rates varied due to experimental difficulties in controlling the reaction pressure manually.

Linear weight loss curves were obtained in all of the experiments except in the 1100°C and 0.1 Torr experiment. The experimental weight change *vs.* time curves for 1100°C are shown in Fig. 2. At 1 x 10^{-1} Torr pressure, a small weight gain was found indicating a protective oxide was formed. At 9 x 10^{-3} and 4 x 10^{-2} Torr, weight loss curves were found indicating SiO(g) was formed. The experimental weight

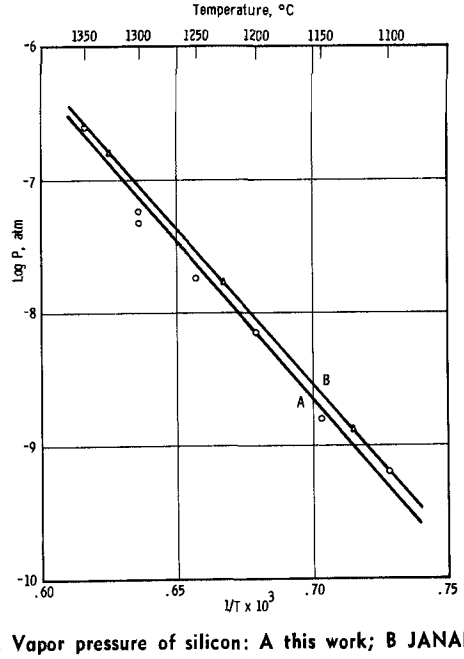

Fig. 1. Vapor pressure of silicon: A this work; B JANAF tables; December 31, 1962.

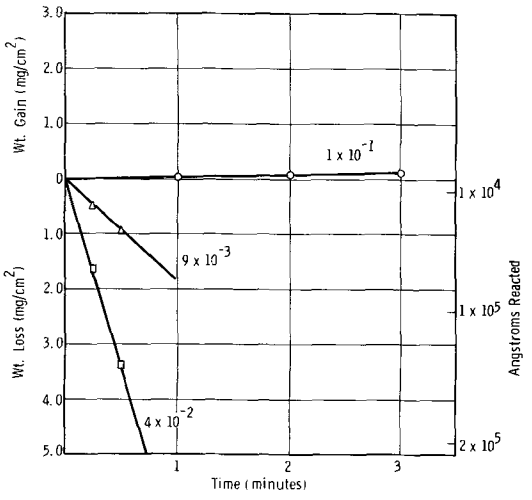

Fig. 2. Weight *vs.* time, oxidation of high-purity silicon, 1100°C, 9 x 10^{-3}, 4 x 10^{-2}, 1 x 10^{-1} Torr, flow conditions.

change *vs.* time curves at 1200° and 1300°C showed weight losses for the three pressures.

Table III shows the rates of oxidation in units of grams per second, atoms of Si reacted per second, and atoms of Si reacted per cm²-sec. Temperature was found to have no important effect on the observed rates of oxidation at a given pressure. Pressure and gas flow were the important factors in the determination of the rates of oxidation.

Figure 3 shows a log rate of oxidation *vs.* log flow rate plot of all of the data. The rate data at 9 x 10^{-3} Torr and 4 x 10^{-2} Torr show the rates of oxidation to be a nearly linear function of the flow rate and independent of temperature. Above 4 x 10^{-2} Torr pressure, the rate data fall from the linear dependence relation.

A plot of the log rate of oxidation *vs.* log of pressure also shows a nearly linear dependence. Since the flow rate is also a function of the pressure, it is difficult to separate the flow and pressure variables.

We conclude that the observed rates of oxidation, in our experiments, are a function mainly of the pressure and gas flow. This suggests that the access of oxygen to the surface is the rate-limiting factor in the reaction for these conditions.

We have evaluated the kinetic theory efficiencies using the collision rate of oxygen molecules, n, with a surface given by the equation

$$n = 3.5 \times 10^{22} \frac{P}{(MT)^{1/2}} \qquad [7]$$

Here P is the pressure in Torr and M is the molecular weight of oxygen molecules. Assuming 2 silicon atoms are reacted for each oxygen molecule, we calculate a kinetic theory efficiency of 8.7, 9.1, and 10.3% for the 9 x 10^{-3}, 4 x 10^{-2}, and 1 x 10^{-1} Torr experiments at 1300°C. These are very large numbers considering

Table III. Rates of oxidation of high-purity silicon 1100°-1300°C, 9 x 10^{-3}, 4 x 10^{-2}, and 1 x 10^{-1} Torr pressure

P, Torr	Temp, °C	Flow, atoms O/sec	Wt loss, g/sec	dn/dt, atoms Si/sec	dn'/dt, atoms Si/cm²-sec
9 x 10^{-3}	1100	8.6 x 10^{17}	1.41 x 10^{-5}	3.02 x 10^{17}	2.96 x 10^{17}
9 x 10^{-3}	1200	4.3 x 10^{17}	7.18 x 10^{-6}	1.54 x 10^{17}	1.56 x 10^{17}
9 x 10^{-3}	1200	1.0 x 10^{18}	1.70 x 10^{-5}	3.64 x 10^{17}	3.53 x 10^{17}
9 x 10^{-3}	1300	7.3 x 10^{17}	1.25 x 10^{-5}	2.68 x 10^{17}	2.45 x 10^{17}
4 x 10^{-2}	1100	3.9 x 10^{18}	5.67 x 10^{-5}	1.21 x 10^{18}	1.19 x 10^{18}
4 x 10^{-2}	1200	4.1 x 10^{18}	5.23 x 10^{-5}	1.12 x 10^{18}	1.09 x 10^{18}
4 x 10^{-2}	1300	3.9 x 10^{18}	5.34 x 10^{-5}	1.14 x 10^{18}	1.17 x 10^{18}
1 x 10^{-1}	1100	1.4 x 10^{19}	5.8 x 10^{-7}*	1.09 x 10^{16}	1.13 x 10^{16}
1 x 10^{-1}	1200	2.0 x 10^{19}	1.72 x 10^{-4}	3.68 x 10^{18}	3.51 x 10^{18}
1 x 10^{-1}	1300	2.0 x 10^{19}	1.65 x 10^{-4}	3.53 x 10^{18}	3.24 x 10^{18}

* Weight gain—O_2 pickup.

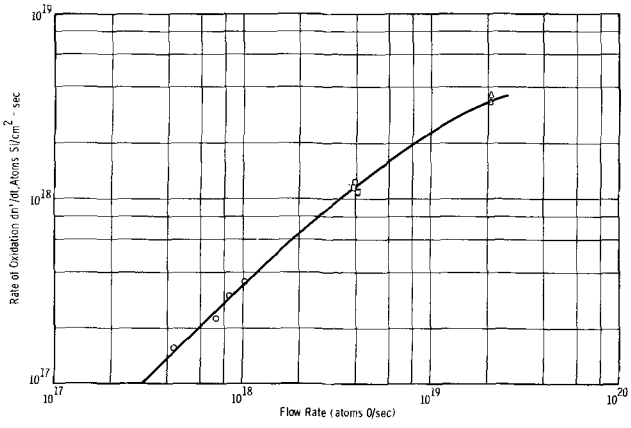

Fig. 3. Rate of oxidation *dn'/dt* vs. flow, 1100°-1300°C; ○ 9 x 10^{-3} Torr; □ 4 x 10^{-2} Torr; △ 1 x 10^{-1} Torr.

the fact that the rate of oxidation is still limited by gas flow. This suggests a very low heat of activation for the chemical processes involved in the reaction mechanism. These processes include adsorption, chemical reaction and desorption.

Table IV shows the results of calculations on the flow efficiencies, the actual gas flow in cubic centimeters per second, and the gas velocity at temperature. The flow efficiency, E, was given by the equation

$$E = \frac{2(dn/dt)}{F} \times 100 \qquad [8]$$

Here we assume SiO(g) was formed at the silicon surface and that SiO(g) was further oxidized in the gas phase or on the furnace tube surfaces to SiO_2(s). Two atoms of oxygen were required per silicon atom. dn/dt was the actual rate of silicon reacting per second and F was the flow rate in atoms of O per sec.

Table IV shows the flow efficiency calculations for the several temperatures and pressures. Flow efficiencies up to 73.8% were calculated. The gas velocities were calculated before reaching the reaction zone in the furnace tube.

We now need to explain why silicon reacts with oxygen at 1100°C and 4 x 10^{-2} Torr to lose weight while above 1 x 10^{-1} Torr, the sample gains weight. This is due to the formation of a SiO_2(s) film at the higher pressure which protects the surface from the fast type of reaction. SiO(g) formed by reaction [1] can act to reverse reaction [3] to form a SiO_2(s) film.

We suggest that the oxidation conditions of 1100°C and 1 x 10^{-1} Torr are conditions where a stable silica film can form.

Effect of contaminants.—The rates of oxidation of silicon at low oxygen pressures and at temperatures of 1100°-1300°C are very sensitive to the formation of silicon carbide films. This phenomenon was noticed when tank oxygen was used as the reaction gas and when the alumina furnace tubes were not sufficiently treated at high temperature with oxygen to remove

Table IV. Flow efficiencies and gas velocities, low-pressure oxidation of silicon

P, Torr	Temp, °C	Flow, atom O/sec	dn/dt, atoms Si/sec	Flow eff., %	Flow, cc/sec	Gas velocity, cm/sec
9 x 10^{-3}	1100	8.6 x 10^{17}	3.02 x 10^{17}	70.2	6800	2170
9 x 10^{-3}	1200	1.0 x 10^{18}	3.64 x 10^{17}	71.2	8500	2710
9 x 10^{-3}	1300	7.3 x 10^{17}	2.68 x 10^{17}	73.8	6590	2100
4 x 10^{-2}	1100	3.9 x 10^{18}	1.21 x 10^{18}	62.4	6890	2190
4 x 10^{-2}	1200	4.1 x 10^{18}	1.12 x 10^{18}	54.8	7840	2500
4 x 10^{-2}	1300	3.9 x 10^{18}	1.14 x 10^{18}	58.8	7840	2500
1 x 10^{-1}	1100	1.4 x 10^{19}	1.09 x 10^{19}*	0.16	9670	3080
1 x 10^{-1}	1200	2.0 x 10^{19}	3.68 x 10^{18}	36.4	16,800	5350
1 x 10^{-1}	1300	2.0 x 10^{19}	3.53 x 10^{18}	35.0	16,500	5260

* Weight gain.

gases containing carbon and contaminants. Transparent oxidation resistant films were formed on the silicon specimens.

Electron diffraction studies were made on films formed at 1100° and 1300°C, which were of the order of 1μ thick, using 250 kv electrons to penetrate the film. The electron diffraction patterns were compared to patterns from films formed on silicon when reacted with carbon dioxide, to patterns of crystals of synthetic α-SiC_{II}, and to x-ray diffraction data on α-SiC_{II}, 6 H Polytype. These studies showed that the film formed in tank oxygen using improperly pretreated furnace tubes at 1300°C was α-SiC_{II}.

We conclude that for certain low-pressure oxygen atmospheres at 1300°C, CO_2 and other contaminants form α-SiC_{II} on a silicon surface. The α-SiC_{II} reacts with oxygen but at a slower rate than the rate of formation of α-SiC_{II}. The net result is the formation of an α-SiC_{II} film.

Discussion.—Wagner (8) has treated the gas diffusion controlled oxidation process of silicon in an inert gas at low partial pressures of oxygen. Oxygen diffuses through the boundary layer to the silicon interface and SiO gas diffuses away from the surface through the same boundary layer. Wagner gives the following equation for the maximum oxygen pressure under which a bare silicon surface can exist.

$$p_{O_2(max)} = \frac{1}{2} (D_{SiO}/D_{O_2})^{1/2} p_{SiO(eq)} \qquad [9]$$

Here $p_{SiO(eq)}$ is the equilibrium pressure of SiO(g) from Eq. [3]. D_{SiO}/D_{O_2} is the ratio of diffusion constants for SiO(g) and O_2 in the boundary layer and depends on the characteristics of the boundary layer. Wagner estimates the ratio of D_{SiO}/D_{O_2} to be 0.64.

A similar analysis can be made for the reaction of silicon in low-pressure pure oxygen atmospheres under flow conditions. The thickness and the chemical composition of the boundary layer will be different. However, the ratio of diffusion coefficients can be assumed to be the same.

Assuming Wagner's equation can be applied to the transition conditions for active and passive oxidation, the following values of $p_{O_2(max)}$ were calculated from Eq. [9] and the equilibrium value of $p_{(SiO)}$. At 1100°C, $p_{O_2(max)} = 1.2 \times 10^{-2}$ Torr. At 1200°C, $p_{O_2(max)} = 8.8 \times 10^{-2}$ Torr and at 1300°C, $p_{O_2(max)} = 0.56$ Torr.

Experimentally we found that the maximum oxygen pressure at 1100°C for the formation of a silica film is between 4×10^{-2} and 1×10^{-1} Torr. This compares to a value of 1.2×10^{-2} Torr calculated from Eq. [9]. Gas flow may have an important effect in raising the maximum oxygen pressure to maintain fast oxidation reactions on bare silicon surfaces.

Summary and Conclusions

Kinetic studies show silicon loses weight when reacted with low-pressure oxygen environments of 9×10^{-3} and 4×10^{-2} Torr. For these conditions silicon reacted to form volatile silicon monoxide. Any silica which may form was reduced by silicon to form volatile silicon monoxide. Very fast oxidation rates were found. At 10^{-1} Torr and 1200°C, an oxidation rate of 3.7×10^{18} silicon atoms per cm^2-second was observed. This was 7100Å of silicon reacting per second. The rates of oxidation were nearly independent of temperature, but were a linear function of gas flow or pressure. Flow efficiencies of over 70% were found for the 9×10^{-3} Torr pressure runs.

Several conclusions were made from the kinetic studies. (*A*) Gas diffusion processes were rate controlling for the conditions of the reaction; (*B*) silicon reacted completely with oxygen under the conditions with only trace amounts of silica as residues; (*C*) Maximum oxygen pressure for maintaining oxide free surfaces were increased by the imposition of flow on the reaction; (*D*) Extreme care must be used to avoid contamination of the gas source or system with gases containing carbon; (*E*) the rate of oxidation was a direct function of flow or gas pressure.

Manuscript received July 2, 1965; revised manuscript received April 15, 1966. This paper was presented at the Buffalo Meeting, Oct. 10-14, 1965. The work described here was supported in part by the U. S. Army Research Office, Durham, North Carolina.

Any discussion of this paper will appear in a Discussion Section to be published in the June 1967 JOURNAL.

REFERENCES

1. J. T. Law, *J. Phys. Chem.*, **61**, 1200 (1957).
2. J. W. Evans and S. K. Chatterji, *ibid.*, **62**, 1064 (1958).
3. J. R. Ligenza and W. G. Spitzer, *J. Phys. & Chem. Solids*, **14**, 131 (1960).
4. B. E. Deal, *This Journal*, **110**, 527 (1963).
5. D. J. McAdam and G. W. Geil, *J. Research Natl. Bur. Standards*, **28**, 593 (1942).
6. M. B. Brodsky and D. Cubicciotti, *J. Am. Chem. Soc.*, **73**, 3497 (1951).
7. P. J. Jorgensen, *J. Chem. Phys.*, **37**, 874 (1962).
8. C. Wagner, *J. Appl. Phys.*, **29**, 1295 (1958).
9. JANAF Thermochemical Tables, The Dow Chemical Co., Midland, Michigan Si(s,l,g), SiO_2(s), SiC(s): Dec. 31, 1962; SiO(g): Sept. 30, 1963.
10. E. A. Gulbransen, K. F. Andrew, and F. A. Brassart, "Vacuum Microbalance Techniques," Vol. 4, p. 127, Paul Waters, Editor, Plenum Press (1965).
11. L. Cahn, *Instr. and Control Systems*, **35**, 107 (1962).
12. I. Langmuir, *Phys. Rev.*, **2**, 329 (1913).

Studies of the Electrochemical Kinetics of Indium

III. Systems In + $InCl_3$ and In + Combined Sulfate-Chloride Electrolyte

V. Markovac[1] and B. Lovrecek

Institute of Electrochemistry and Electrochemical Technology,

Faculty of Technology, University of Zagreb, Zagreb, Yugoslavia

ABSTRACT

In previous papers the kinetics of the deposition and dissolution of indium in indium sulfate solutions at *p*H 2.5 had been studied by a galvanostatic method of single current pulses. Continuing this work and using a similar experimental technique, kinetics of the deposition and dissolution of indium in indium chloride and combined indium sulfate-chloride solutions at *p*H 2.5 have been studied. The analysis of experimental data obtained by polarization in indium chloride solutions indicates that in the wide range of c.d.'s up to 1.0×10^{-1} amp/cm^2 the cathodic and anodic processes occur near the equilibrium potential. When the c.d.'s are higher, it was found that the first cathodic reaction step is rate-determining, and that during anodic polarization disproportionation reactions probably take place.

The curves η_A-$\log_{10} i$ obtained by cathodic polarization in the combined sulfate-chloride solutions show steep increases in the overvoltage of ca 400 mv, at certain characteristic c.d.'s, depending on the concentration of chloride in the solutions. It is concluded that in the range of c.d.'s before the steep increases, deposition of indium occurs by analogous mechanism as in the pure chloride medium. In the range after the steep increases, deposition of indium occurs as in the pure sulfate medium. The mechanism of this rapid change in the deposition of indium is discussed. From the analysis of the results of the anodic polarization in the combined electrolytes, it follows, that the third reaction step is rate-determining in accordance with the observations for the pure sulfate and chloride solutions.

This paper is a continuation of the study of electrochemical kinetics of indium in indium + indium sulfate system over a wide range of c.d.'s published in previous papers (1, 2). Now we have studied the mechanism of electrochemical deposition and dissolution of indium in pure chloride electrolyte and in combined sulfate-chloride electrolyte. For the analysis of the experimental data, the expressions for kinetics of "many step" electrode reactions were used (3).

Experimental

Apparatus for cathodic and anodic polarization of indium (as 0.3% indium analgam) consisting of an electrolytical cell with air thermostat, nitrogen purification unit and electrical device, was essentially the same as described (1, 2). The exception was an electrical device for supplying galvanostatic single pulses, used mostly in this work. In this case a rectangular wave pulse generator was used. The generator was constructed on the resistance basis, with a built-in Western Electric D171584 relay for triggering both the pulse and the time sweep of a cathode-ray oscilloscope. A Hewlett-Packard H15-130B oscilloscope with the bandwidth d.c. to 300 kc, and the sensitivity 1 mv/cm to 125 v/cm in 15 ranges, was used. On the oscilloscope a built in front panel switch permitted single sweep operation.

Polarization was carried out in the following electrolytes: 0.116*N* $InCl_3$ + 0.5*N* KCl, *p*H 2.5; 0.116*N* $In_2(SO_4)_3$ + 0.5*N* K_2SO_4 + 0.05*N* KCl, *p*H 2.5; 0.116*N* $In_2(SO_4)_3$ + 0.5*N* K_2SO_4 + 0.075*N* KCl *p*H 2.5. Chemicals used were of analytical reagent grade, and water was redistilled.

Experimental procedure and obtaining both the $\eta_t - t$ curves and the activation overpotentials η_A were carried out in the same way as previously described (1).

Results

Activation overpotential-current density relationship for chloride electrolytes.—When the values of activation overpotential η_A (obtained by subtraction of the ohmic overpotential from the experimental steady-state potential) were plotted against the logarithms of c.d. $\log_{10} i$, the curves for cathodic and anodic polarization in pure chloride solutions were obtained (Fig. 1). Both curves show linear relations in the range of the higher c.d.'s for the cathodic polarization at $1.7 \times 10^{-1} - 3.5 \times 10^{-1}$ amp/cm^2, and at $2.2 \times 10^{-1} - 4.5 \times 10^{-1}$ amp/cm^2 for the anodic one.

Double-wave $\eta_t - t$ curves at cathodic polarization in combined sulfate-chloride electrolytes.—As was shown in a previous paper (1) experimentally obtained $\eta_t - t$ curves for cathodic and anodic polarization reach the steady-state potentials and are represented with a single wave. That was at all measuring points in all electrolytes except at cathodic polarization in combined sulfate-chloride electrolytes. At cathodic polarization in solutions containing both sulfate and chloride the curves $\eta_t - t$ with two waves

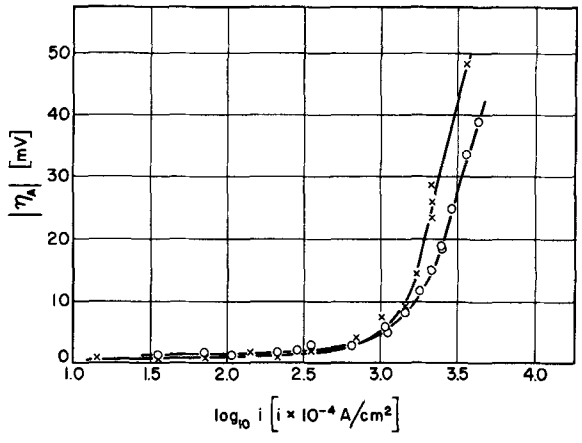

Fig. 1. η_A-$\log_{10} i$ curves for cathodic and anodic polarization. Electrolyte, 0.116*N* $InCl_3$ + 0.5*N* KCl; *p*H = 2:5; × cathodic; ○ anodic polarization.

[1] Present address: Scientific Research Staff, Ford Motor Company, Dearborn, Michigan.

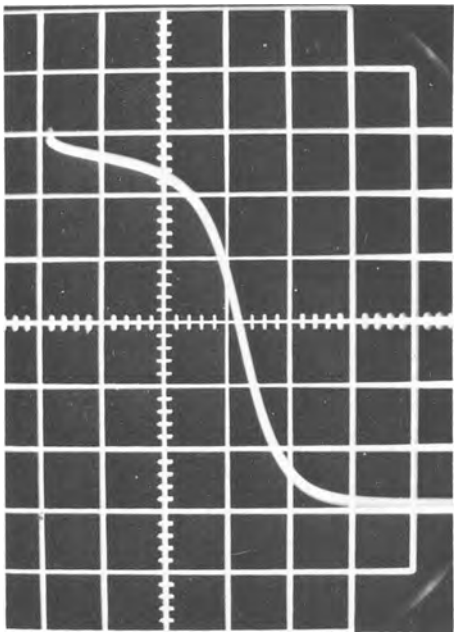

Fig. 2. Oscillogram of η_t-t double-wave curve for cathodic c.d. 5.97×10^{-3} amp/cm^2; sensitivity, 100 mv/cm; sweep time, 2 msec/cm; electrolyte, 0.116N $In_2(SO_4)_3$ + 0.5N K_2SO_4 + 0.075N KCl; pH = 2.5.

were observed on the screen of the oscilloscope (Fig. 2) in the very narrow regions of c.d.'s depending on the concentration of chloride in the solutions. With slightly lower c.d. only a single-wave $\eta_t - t$ curve was obtained, similar to those obtained in the pure chloride solutions. With slightly higher c.d. than that characteristic for the appearance of a double-wave curve, also a single-wave curve was observed, but similar to those from pure sulfate solutions. On changing the oscilloscope sweep rate it was possible to record the first and second wave just as the double-wave curve, only in the very narrow regions of c.d.'s.

Activation overpotential-current density relationship for combined sulfate-chloride electrolytes.—Experimentally obtained $\eta_A - \log_{10} i$ curves for cathodic polarization of indium in combined sulfate-chloride solutions show very rapid increases for about 400 mv (Fig. 3). For the electrolyte with 0.05N KCl, a rapid increase appears at c.d. of 3.0×10^{-3} amp/cm^2, but for the electrolyte with the higher concentration of chloride (0.075N KCl) the rapid increase is shifted to the region of higher c.d.'s and appears at 6.0×10^{-3} amp/cm^2. Before and after these rapid increases both curves show similar shapes forming the Tafel-linear relations.

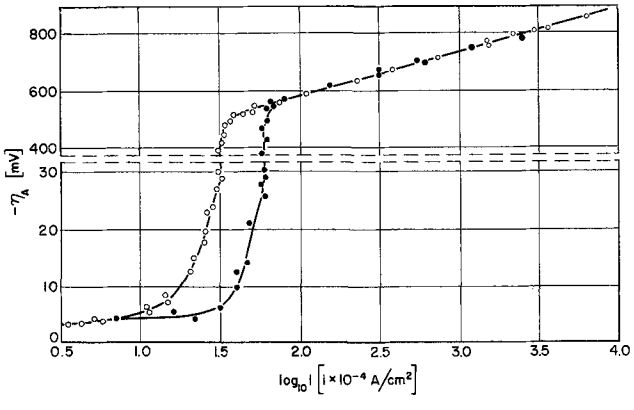

Fig. 3. η_A-$\log_{10} i$ curves for cathodic polarization. ○ electrolyte 0.116N $In_2(SO_4)_3$ + 0.5N K_2SO_4 + 0.05N KCl; pH = 2.5. ●, electrolyte: 0.116N $In_2(SO_4)_3$ + 0.5N K_2SO_4 + 0.075N KCl; pH = 2.5.

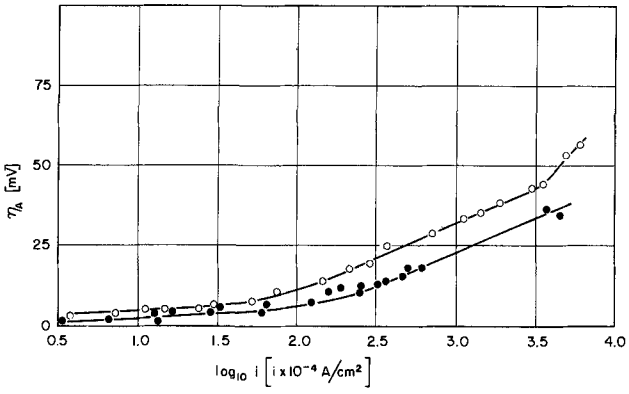

Fig. 4. η_A-$\log_{10} i$ curves for anodic polarization. ○ electrolyte: 0.116N $In_2(SO_4)_3$ + 0.5N K_2SO_4 + 0.05N KCl; pH = 2.5. ● electrolyte: 0.116N $In_2(SO_4)_3$ + 0.5N K_2SO_4 + 0.075N KCl; pH = 2.5.

Experimental curves $\eta_A - \log_{10} i$ for anodic polarization of indium in combined sulfate-chloride electrolytes also show linear relations (Fig. 4). For the electrolyte with 0.05N KCl, the linear part of the curve appears at $1.5 \times 10^{-2} - 3.0 \times 10^{-1}$ amp/cm^2, while for the electrolyte with the higher concentration of chloride (0.075N KCl) the linear part of the curve is shifted to a region of higher c.d.'s ($2.4 \times 10^{-2} - 3.3 \times 10^{-1}$ amp/cm^2).

The linear parts of the experimental $\eta_A - \log_{10} i$ curves, *i.e.*, Tafel lines, were treated with an earlier developed method (3) using expressions for the slowest reaction step, *i.e.*, the rate-determining step

$$\frac{\partial \log_{10} i_-}{\partial V} = -\frac{z\mathbf{F}}{2.303\,RT}(n_c^* - \alpha) \qquad [1]$$

$$\frac{\partial \log_{10} i_+}{\partial V} = \frac{z\mathbf{F}}{2.303\,RT}(n_a^* - 1 + \alpha) \qquad [2]$$

Since the left sides of Eq. [1] and [2] represent the slopes of the experimental Tafel lines, it was possible to calculate n_c^*, n_a^* and α from the experimental data. n_c^* and n_a^* are the ordinal numbers of the slowest reaction step for cathodic and anodic polarization (small integer), α the transfer coefficient ($0 < \alpha < 1$), and z the number of electrons involved in the slowest reaction step.

Results of the calculations are presented in Table I and Table II.

Table I. Kinetic parameters for cathodic polarization

Electrolyte	Range of c.d., amp/cm^2	$\frac{\partial \log_{10} i_- \#}{\partial V}$	$\alpha\#$	n_c^*	z
0.116N $InCl_3$ + 0.5N KCl, pH 2.5	1.7×10^{-1} to 3.5×10^{-1}	9.10	0.48	1	1
0.116N $In_2(SO_4)_3$ + 0.5N K_2SO_4	2.2×10^{-3} to 3.0×10^{-3}	10.18	0.41	1	1
+ 0.05N KCl, pH 2.5	5.0×10^{-3} to 6.5×10^{-1}	6.60	0.81	1	2
0.116N $In_2(SO_4)_3$ + 0.5N K_2SO_4	4.5×10^{-3} to 6.0×10^{-3}	8.91	0.48	1	1
+ 0.075N KCl, pH 2.5	7.0×10^{-3} to 2.5×10^{-1}	7.40	0.79	1	2

Mean values derived from 2-4 complete experimental curves.

Table II. Kinetic parameters for anodic polarization

Electrolyte	Range of c.d., amp/cm²	$\frac{\partial \log_{10} i_+ \#}{\partial V}$	$\alpha\#$	n_a*	z
0.116*N* $InCl_3$ + 0.5*N* KCl, pH 2.5	2.2×10^{-1} to 4.5×10^{-1}	11.95	0.69	1	1
0.116*N* $In_2(SO_4)_3$ + 0.05*N* K_2SO_4 + 0.05*N* KCl, pH 2.5	1.5×10^{-2} to 3.0×10^{-1}	48.5	0.81	3	1
0.116*N* $In_2(SO_4)_3$ + 0.5*N* K_2SO_4 + 0.075*N* KCl, pH 2.5	2.4×10^{-2} to 3.3×10^{-1}	49.2	0.86	3	1

Mean values derived from 2-4 complete experimental curves.

Discussion

Activation overpotential-logarithms of c.d. curves for chloride electrolytes.—Experimentally obtained $\eta_A - \log_{10} i$ curves show very low activation overpotentials for both cathodic and anodic polarization over a wide range of c.d.'s (Fig. 1), which is in agreement with other authors (4-6). In comparison with the results obtained in sulfate media (1), the exchange current i_o is now shifted to the region of significantly higher c.d.'s (three orders of magnitude). Losev and Molodov (7) do not indicate such a difference between the exchange currents in the sulfate and chloride electrolytes. The difference between our data and those found by Losev and Molodov is probably due to the fact that our data were obtained in the pure sulfate and chloride electrolytes, but their electrolytes almost always contained a large amount of perchlorate ion (7-10).

The shift of the exchange current to the higher values indicates that the processes of deposition and dissolution of indium in chloride media take place near the equilibrium potentials over a wide c.d. range. At higher c.d.'s the experimental $\eta_A - \log_{10} i$ curve for cathodic polarization (Fig. 1) also shows linear dependence, and the slope indicates using Eq. [1] that the first step is the slowest one.[2] The same was found in the case of electrochemical deposition of indium in sulfate solutions for lower c.d.'s (1).

$$In^{3+} \xrightarrow[\text{slowest}]{+e_o^-} In^{2+} \xrightarrow{+e_o^-} In^{1+} \xrightarrow{+e_o^-} In^{o} \qquad [3]$$

In the case of anodic polarization of indium in chloride solutions in the region of higher c.d.'s, the slope of the experimentally obtained η_A-$\log_{10} i$ curve according to Eq. [2] indicates that the first step is the slowest one, although it would be expected to be the third reaction step, by analogy with cathodic polarization.

$$In^{o} \xrightarrow[\text{slowest}]{-e_o^-} In^{1+} \xrightarrow{-e_o^-} In^{2+} \xrightarrow{-e_o^-} In^{3+} \qquad [4]$$

In the same way as for anodic polarization of indium in sulfate solutions (2), it can be assumed that the less stable ions, In^{2+} and In^{1+}, are accumulated because of the slow third reaction step. These ions permit and accelerate disproportionation reactions:

$$2In^{2+} \longrightarrow In^{3+} + In^{1+} \qquad [5]$$

$$3In^{1+} \longrightarrow In^{3+} + 2In^{o} \qquad [6]$$

The disproportionation reactions for the anodic dissolution of indium amalgam in chloride solutions are also proposed by other authors (11), and their observations are consistent with our explanations. With such disproportionation reactions it is easy to imagine that the second and third reaction steps of anodic dissolution of indium are less and less significant for the rate of over-all process of dissolution, especially in the region of higher c.d.'s. So, it is quite acceptable that the first step is controlling the over-all reaction in the region of higher c.d.'s.

Activation overpotential-logarithms of c.d. curves for combined sulfate-chloride electrolytes.—With the galvanostatic method of fast single pulses applied in this work for cathodic and anodic polarization of indium in sulfate and chloride solutions, the observations of other authors (4-6) are confirmed about the inhibition of sulfate ions and the activation of chloride ions. For better understanding of these effects, the polarization of indium was carried on in combined sulfate-chloride solutions.

The curves η_A-$\log_{10} i$ for cathodic polarization of indium in combined sulfate-chloride electrolytes (Fig. 3) show rapid increases[3] for about 400 mv at characteristic c.d.'s, depending on the concentration of chloride in the solutions.

Since with minimal increase or decrease of c.d. one can record only one wave, the second or first, respectively, it could be concluded that on increasing the c.d. the mechanism of deposition of indium rapidly changes. With lower c.d.'s (less than 3.0×10^{-3} amp/cm² for solution with 0.05*N* KCl and less than 6.0×10^{-3} amp/cm² for solution with 0.075N KCl) the deposition of indium is carried on under conditions characteristic for chloride media. By increasing the c.d.'s it is no longer possible to record the process characteristic for chloride media, but the process continues with remarkably higher overpotentials which suggests the existing conditions characteristic for sulfate media. This rapid change in the mechanism of deposition of indium in combined sulfate-chloride electrolytes can be explained by conceptions about the mechanism of the activating effect of chloride on the deposition of metals (4, 6), and the desorption of chloride by increasing the negative potential (13, 14).

We can presume that absorbed chloride ions or indium chloro-complexes enable easy discharge of indium (low overpotentials), probably because of their deformation ability. Increasing the c.d. over a characteristic value, which is dependent on the concentration of chloride in solution, increases the cathodic overpotential, so that we presume that desorption of chloride or chlorocomplexes takes place. So, the activating effect of chloride is lost, and the first process stipulated by indium chloride disappears. Furthermore, with galvanostatic conditions of the experiments, cathodic overpotential (*i.e.*, negative potential of electrode) simultaneously with desorption of chloride, necessarily increases until it attains the value adequate for the deposition of indium in sulfate media. Consequently at higher c.d., indium can only be deposited with the characteristics of sulfate media. In support of such a conception about the effect of chloride on the mechanism of deposition of indium, is also the fact that by increasing the concentration of chloride in combined sulfate-chloride solutions, the rapid change in mechanism of deposition of indium appears at a higher c.d., characteristic for a higher concentration of chloride.

The analysis of experimental curves η_A-$\log_{10} i$ (Fig. 3) shows in c.d. region, before the rapid increase, the analogy with the curve obtained in pure chloride media, and it is also calculated by Eq. [1], that the first cathodic reaction step is the rate-determining step. In the c.d. region after this change, the curves perfectly coincide with the curve obtained in pure sulfate media at the corresponding c.d. (2), so we may presume, following the explanations from previous paper (2) and Eq. [1] that here too, the reaction of In^{3+} with two electrons controls the over-all process of deposition of indium (Table I).

[2] In all equations comprising indium ions, we do not indicate the probable aqueous and/or chloro complexes, for the sake of simplicity.

[3] A similar "discontinuous jump in potential" was observed recently by polarographic studies, and was published as a short communication by R. E. Visco (12). The author described this phenomenon as "negative resistance" affected by anion adsorption.

The experimental curve η_A-$\log_{10} i$ for anodic polarization of indium in combined sulfate-chloride electrolytes (Fig. 4) indicates in a certain c.d. region that the third anodic reaction step is the rate-determining step (Table II). The same phenomenon has already been recorded in pure sulfate solutions, but in a lower c.d. region (1, 15). By increasing the concentration of chloride in combined sulfate-chloride electrolytes, a linear part of η_A-$\log_{10} i$ curve shifts to the higher c.d. region. These facts are also in accordance with the conception of the activating effect of chlorides and inhibiting effect of sulfates. Supporting this are observations in pure chloride solutions, where the process is carried on close to the equilibrium potential.

In the extremely high c.d. region, the slopes of the curves start to change, so here we can presume that disproportionation reactions take place.

Manuscript received Sept. 30, 1965; revised manuscript received May 9, 1966. Part of this work was presented at the 14th CITCE Meeting, Moscow, 1963.

Any discussion of this paper will appear in a Discussion Section to be published in the June 1967 JOURNAL.

REFERENCES

1. B. Lovrecek and V. Markovac, *This Journal*, **109**, 727 (1962).
2. V. Markovac and B. Lovrecek, *ibid.*, **112**, 520 (1965).
3. B. Lovrecek, *J. Phys. Chem.*, **63**, 1795 (1959).
4. J. Heyrovsky, *Discussion Faraday Soc.*, Electrode Processes, 212 (1947).
5. J. E. B. Randles, *ibid.*, 11 (1947).
6. R. Piontelli, *Z. Elektrochem.*, **57**, 387 (1953).
7. V. V. Losev and A. I. Molodov, *Doklady Akad. Nauk SSSR*, **130**, 111 (1960).
8. V. V. Losev and A. I. Molodov, *ibid.*, **135**, 1432 (1960).
9. V. V. Losev and A. I. Molodov, *ibid.*, **148**, 1114 (1963).
10. A. I. Molodov and V. V. Losev, *Elektrokhimiya*, **1**, 1253 (1965).
11. L. F. Kozin and E. E. Kobrand, *Zh. Prikladnoi Khim.*, **38**, 579 (1965).
12. R. E. Visco, *J. Electroanal. Chem.*, **10**, 82 (1965).
13. R. Parsons and M. A. V. Devanathan, *Trans. Faraday Soc.*, **49**, 673 (1953).
14. N. S. Polyanovskaya and A. N. Frumkin, *Elektrokhimiya*, **1**, 538 (1965).
15. R. E. Visco, *This Journal*, **112**, 932 (1965).

Interaction of Carbon Dioxide with Hydrogen Chemisorbed on a Platinum Electrode

Bernard J. Piersma,[1] Theodore B. Warner, and Sigmund Schuldiner

U. S. Naval Research Laboratory, Washington, D. C.

ABSTRACT

The effect of CO_2 on the oxidation of hydrogen atoms chemisorbed on a Pt electrode has been examined with potentiostatic and transient galvanostatic techniques. The results indicate that CO_2 is not reduced, but that H_{ad} oxidation is inhibited by CO_2, or possibly HCO_3^-. Under these conditions the inhibited or blocked H_{ad} is stable at potentials negative to 0.3v (*vs.* NHE). Dissociation of formic acid to H_{ad} and CO_2 may inhibit the further oxidation of HCOOH by a similar H_{ad}-CO_2 blocking mechanism.

The interaction of CO_2 with electrolytically generated hydrogen at platinum electrodes in acid solution has been reported by Giner (1), who demonstrated a difference between the anodic polarization behaviors of hydrogen-covered electrodes in CO_2 and in He saturated solutions. Giner concluded that CO_2 is reduced by reaction with electrochemically formed chemisorbed hydrogen, H_{ad}, between 0.0 and 0.25v (all potentials reported here are *vs* the NHE). The chemisorbed product, which he called "reduced CO_2," was oxidized at about 0.7v, at 25°C, during anodic galvanostatic polarization and oxidized in the potential region of 0.5-0.9v, during linear potential sweeps.

This study was initiated with the objectives: (*a*) to demonstrate that the experimental results observed by Giner were indeed due to his assumed interaction (or reaction) and not to an oxidizable impurity, (*b*) to investigate the nature of the adsorbed oxidizable species, and (c) to examine the implications of such an interaction on the interpretation of anodic organic reactions.

Experimental

Apparatus.—The electrolytic cell, purification of He and H_2, and general procedures were as previously described (2, 3). High current galvanostatic pulses (2.33 a/cm^2) were obtained with an Electro-Pulse Model 3450D generator. Low constant currents were applied either from an Electronic Measurements Company C-612 constant current supply (0.2 ma/cm^2-0.6 μa/cm^2) or a Keithley Model 600A electrometer (down to 0.05 μa/cm^2), both being switched manually. Cell polarization was either observed and photographed on a recalibrated Tektronix Type 547 oscilloscope or recorded on a Varian Associates Model G-11A strip chart recorder from the output of a Keithley Model 603 electrometer amplifier. Constant potentials were maintained with a Wenking Model 61-R fast rise potentiostat.

The Pd tube and miniature glass reference electrodes, large Pt gauze counter electrode, and 0.19 cm^2 true area Pt bead working electrode have been discussed previously (2, 3). All current densities are expressed in terms of true area as determined from the charge required to deposit one monolayer of oxygen atoms.[2] Baker Analyzed Reagent Grade CO_2 (purity 99.9992%; O_2 1.5 ppm; N_2 + CO, 6 ppm) was purified by passage through a trap containing, at different times, either palladium catalyst supported on alumina at −50°C, palladium oxide supported on alumina at 400°C, or Hopcalite followed by copper turnings (to remove possible traces of oxygen generated by the Hopcalite) both held at 350°C.

Galvanostatic technique.—Anodic charging curves were obtained in solutions saturated with purified He, CO_2, or a mixture of 22% H_2-78% CO_2. Prior to each charging curve, the electrode was either left at open circuit until the potential became stable or potentiostated at a given potential (the dependence of the charging curves on potential and time was examined). The open circuit potentials were 0.3v, or less, indicat-

[1] National Academy of Sciences Postdoctoral Resident Research Associate.

[2] The electrode area remained unchanged after 45 days of continuous use which included extended periods of anodization during pre-electrolysis. The constancy of areas of bright Pt beads is a general observation in this Laboratory. Barring failure in the mounting, an electrode area change has never been observed during normal use over periods as long as six months.

ing a low concentration of oxygen in the electrolyte as a result of gas purification, tightness of the closed system and the oxygen gettering of the Pd tube reference electrode (which contained enough dissolved hydrogen to maintain a stable α Pd-H potential of +0.055v). The working electrode was always anodized in a way such that dermasorbed oxygen, *i.e.*, oxygen dissolved into the skin of the Pt (2, 4), would not be formed. A convenient gas flow was established (experiments showed that the results were independent of flow rate) and the chosen sequence of currents and/or potentials were applied.

In all the low current experiments, the fixed current was switched from anodic to cathodic before a significant amount of oxygen could be generated. In high current experiments the electrode was cleaned with a 2.33 amp/cm^2 anodic pulse lasting less than 500 μsec (to avoid the formation of dermasorbed oxygen). Immediately after the cleaning pulse, the electrode potential was fixed with the potentiostat for a given time (to allow for interaction of CO_2 with H_{ad}) followed by another 2.33 amp/cm^2 anodic pulse, applied to determine the amounts of sorbed H, H_{ad}-CO_2 interaction (H_{ad}-CO_2 merely signifies the presence of both species on the surface), and O_{ad}. Switching between galvanostatic and potentiostatic control was manual with a switching time of less than 0.5 sec. The time of switching was not important since it was established that the amount of H_{ad}-CO_2 formed at a given potential for a set interaction time was unchanged at open circuit for at least 72 hr. The first pulse (or cleaning pulse) rapidly anodized the electrode to O_2 evolution, removed previously sorbed H_{ad}-CO_2 and provided a reproducible state. Thus, just prior to potentiostatic control, the electrode was free from dermasorbed oxygen and H_{ad}-CO_2. Each successive pulse not only gave the required charging curve, but stripped the surface of H_{ad}-CO_2, presenting a clean surface for the start of another experiment. The current pulses for a given current density were of the same duration.

Results

Low current galvanostatic charging curves.—After the cleanliness of the electrolyte and electrode surface had been established,[3] charging curves were obtained with He (flow rate of 88 std cc/min) (Fig. 1a) and then with CO_2 (flow rate of 4 std cc/min[4]) (Fig. 1b). In trace 1, Fig. 1a, the electrode was anodized from open circuit to 0.8v, and then cathodized to 0.0v. In trace 2, this procedure was preceded by cathodization for 10 sec to deposit chemisorbed hydrogen. In each case, the current was reversed at 0.8v, avoiding the deposition of oxygen as verified by the forms of the charging curves.

Analysis of these charging curves in He saturated solution showed that Q_a (the number of coulombs/square centimeter of anodic charge) required to polarize the electrode to 0.8v increased (*a*) as stirring rate decreased, (*b*) as the potential from which charging was started decreased, and (*c*) as the time of precathodization increased. These observations are attributed to the oxidation of hydrogen generated during precathodization which would contribute to Q_a. In solutions stirred with He flowed at 88 ml/min, Q_a varied from 600 μcoul/cm^2 when anodization was begun from the open circuit potential of 0.065v, to about 900 μcoul/cm^2 for 10 sec precathodization and about 1000 μcoul/cm^2 for 40 sec precathodization. Q_c (the number of coulombs/square centimeter of cathodic charge), required to polarize the electrode from 0.8 to 0.0v remained roughly constant at 520 ± 40 μcoul/cm^2. The variation between Q_a and Q_c noted here differs from Giner's results, where he found the anodic and cathodic branches roughly equal.

[3] The linearity of the voltage *vs.* time relation in the oxygen atom adsorption region has been found to be a reliable test of electrode cleanliness (5). Typical linear regions are seen, *e.g.*, in Fig. 3.

[4] A variation of the flow rates of CO_2 from 4 std cc/min to 250 std cc/min had no effect on the charging curves.

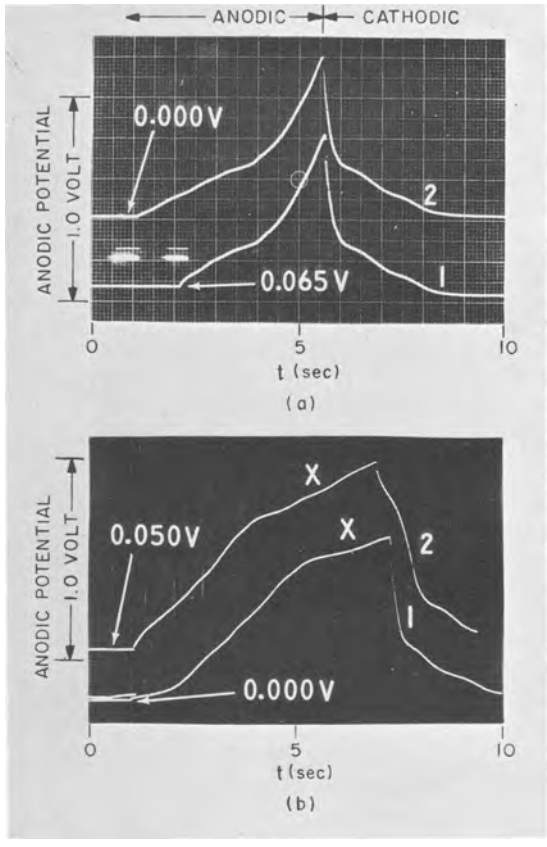

Fig. 1. Charging curves in 1M H_2SO_4 at 25°C. i = 0.2 ma/cm^2: (a) He flow 88 ml/min., trace 1 from open circuit potential of 0.065v, trace 2 immediately following cathodization to 0.00v. (b) CO_2 flow rate 4 ml/min, trace 1 immediately following cathodization to 0.00v, trace 2 following trace 1 after stable open circuit potential attained.

Figure 1b is typical of the charging curves obtained when CO_2 was substituted for He, where trace 1 was taken after 10 sec of precathodization and trace 2 taken from open circuit. The new plateau (designated region X by Giner) which appears at 0.69v was well below the potential of oxygen atom formation. Region X developed slowly, requiring about 15 min at open circuit to reach a maximum. Q_a was independent of the stirring rate with CO_2, indicating that the electrode surface had become passive to the oxidation of hydrogen formed in precathodization.

Purification of CO_2.—Slow adsorption of traces of an oxidizable impurity could affect both the appearance of the charging curves and the time required for the X region to develop. Carbon monoxide is one trace impurity possibly present in the CO_2 used and previous work (5, 6) has shown that extremely small amounts of CO will affect charging curves. Accordingly, the several purification techniques used were designed either to remove trace amounts of CO and organic compounds, or to oxidize them completely to CO_2. Since it is difficult to prove the absence of impurity, the criterion for acceptably pure CO_2 was that the X region develop identically after the CO_2 was purified in the several ways in separate experiments: *i.e.*, through Pd at −50°C, through PdO at 400°C, and through Hopcalite and copper at 350°C. The strong chemisorption of CO on Pd is well known (7); thus a Pd cold trap should be highly specific for CO and also very efficient for most organic impurities. PdO and Hopcalite were used to oxidize any organic impurity present completely to CO_2. In every experiment carried out, the X region developed identically.

CO_2 was replaced with He between each set of experiments and the electrode was tested for cleanliness. Figure 2 presents typical results, in this case obtained 65 min after starting the flow of He. The first trace

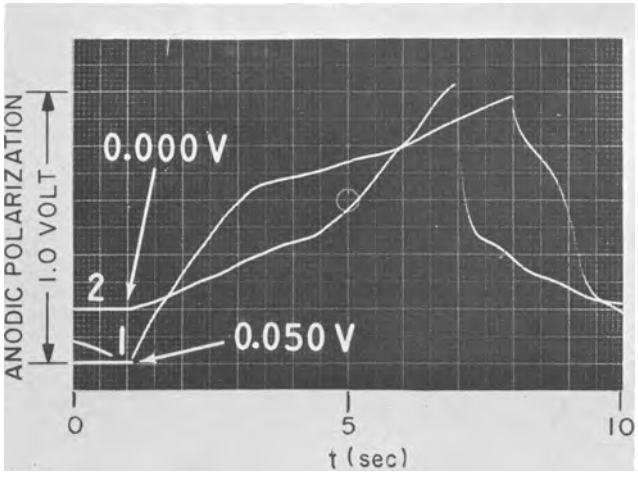

Fig. 2. Charging curves in 1M H_2SO_4 at 25°C. He flow 56 ml/min, i = 0.2 ma/cm^2. Effect of replacing CO_2 with He. Trace 1 first charging curve from open circuit; trace 2 second charging curve, precathodized 10 sec.

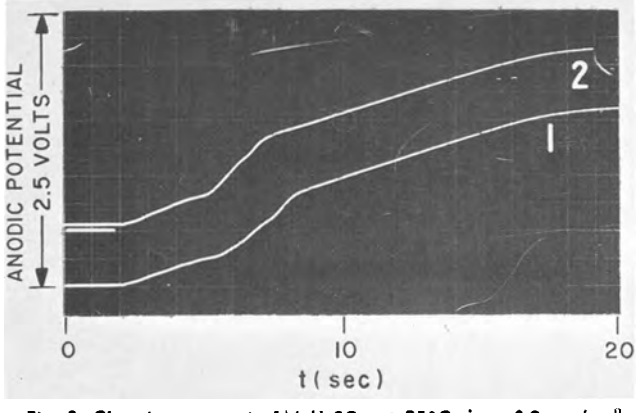

Fig. 3. Charging curves in 1M H_2SO_4 at 25°C. i = 0.2 ma/cm^2, He flow 56 ml/min. Electrode cleanliness tests. Trace 1 time since last polarization 2 min, precathodized 60 sec; trace 2 time since trace 1, 13 min, precathodized 10 sec.

shows that H_{ad}-CO_2 is adsorbed strongly enough to give the equivalent of a full monolayer, assuming a one electron discharge. Further experiments showed that even after 75 hr of He flow, a full monolayer is still present on the electrode. After the electrode surface was cleaned by the first pulse, the second trace (Fig. 2) shows that no oxidizable material is adsorbed from solution. Finally, to eliminate the possibility of slow adsorption of solution impurities, charging curves were taken after a waiting period at open circuit; *e.g.*, trace 2 of Fig. 3, which had a period of 13 min between pulses, shows no evidence of adsorption of oxidizable impurity.

High current charging curves.—The rate of formation of H_{ad}-CO_2 was examined both as a function of potential and of interaction time (c.f. Fig. 5). Figure 4 presents typical results of the influence of interaction time on the amount of H_{ad}-CO_2 formed at a

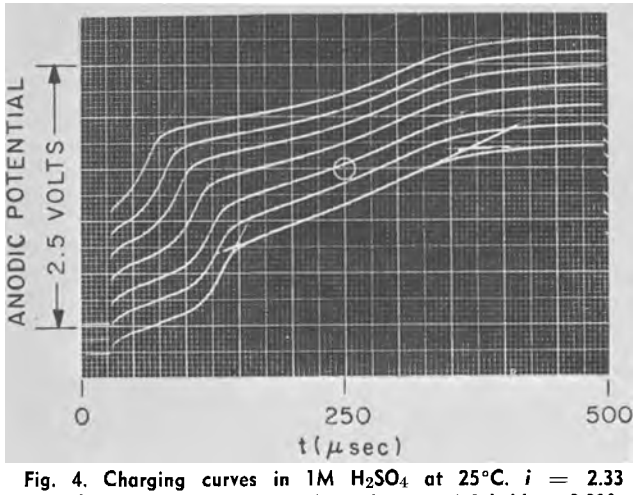

Fig. 4. Charging curves in 1M H_2SO_4 at 25°C. i = 2.33 amp/cm^2, CO_2 flow 2 ml/min, electrode potential held at 0.000v between pulses. Effect of time on X region: lowest pulse 1 sec after initial pulse, succeeding pulses reading upward were respectively 5, 10, 20, 40, 80, and 300 sec after preceding pulse.

given potential, in this case 0.00v. From this figure we see that as the interaction time increases, a dip, characteristic of the oxidation of many organic compounds, develops in the oxygen region at approximately 0.9v in the case of high-current pulses. Paralleling this oxidation plateau is the decrease in length of the usual hydrogen region.

The following quantities were determined from the oscillograms, in terms of microcoulombs/square centimeter: (*a*) Q_t, the total charge required to polarize the electrode to the potential at which O_2 evolution occurs, (*b*) (Q_H + Q_{Hdl}), the quantity of charge required to polarize the electrode to the potential at the start of the X region (H atom oxidation and double layer charging), and (c) (Q_O + Q_{Odl}), the quantity of charge required to polarize the electrode from the start of the X region to the potential of oxygen evolution (oxidation of adsorbed species, formation of a monolayer of O atoms and double layer charging). Thus

$$Q_t = Q_H + Q_{Hdl} + Q_O + Q_{Odl} \quad [1]$$

For a clean Pt electrode (3) in the absence of CO_2

$$Q_O^{CO_2\text{-free}} + Q_{Odl}^{CO_2\text{-free}} = 426\ \mu\text{coul/cm}^2 + 36\ \mu\text{coul/cm}^2 = 460 \pm 20\ \mu\text{coul/cm}^2 \quad [2]$$

Assuming that the charge required to form one monolayer of O atoms and to charge the double layer is identical for CO_2 and He saturated solutions, then

$$Q_X = Q_O + Q_{Odl} - 460\ \mu\text{coul/cm}^2 \quad [3]$$

where Q_X is the charge required to oxidize H_{ad}-CO_2.

When the electrode was potentiostated at 0.00v, Q_t reached a limiting value in less than 1 sec and remained constant as the interaction time increased, *i.e.*, as Q_H decreased, Q_O increased by an equivalent amount. As the electrode was held at successively more positive potentials, longer interaction times which, how-

Table I. Coulometric data obtained from high current charging curves*

Electrode interaction potential, v	$Q_t^{CO_2\text{-free}}$, μcoul/cm^2	Q_t observed after 1 sec interaction, μcoul/cm^2	Q_t observed limiting value, μcoul/cm^2	Q_X limiting value, μcoul/cm^2	$Q_t - Q_t^{CO_2\text{-free}}$ limiting value, μcoul/cm^2	Q_H limiting value, μcoul/cm^2
0.300	487 ± 25	489 ± 25	478 ± 25	0 ± 35	0 ± 35	0 ± 25
0.250	518	512	652	132	134	0
0.200	552	594	700	202	148	0
0.150	586	629	746	274	160	0
0.100	638	652	769	285	131	0
0.065	669	769	775	231	106	30
0.000	729	785	789	260	60	50

* For explanation of symbols, see text.

ever, were always less than 2400 sec, were required to reach a limiting value of Q_t. These data are collected in columns 3 and 4 of Table I. For comparison, the values of $Q_t^{CO_2\text{-free}}$ (Q_t in CO_2-free solution) are given in column 2. $Q_t^{CO_2\text{-free}}$ values were determined by addition of $Q_O^{CO_2\text{-free}} + Q_{Odl}^{CO_2\text{-free}}$, given above, with $Q_H^{CO_2\text{-free}} + Q_{Hdl}^{CO_2\text{-free}}$, derived from data obtained previously for hydrogen coverage of Pt electrodes as a function of open circuit potential and for double layer capacity as a function of potential [Fig. 10 and 5, ref. (3)]. The comparison of $Q_t^{CO_2\text{-free}}$, obtained in this way, with Q_t (cf. column 6, Table I) implicitly assumes that the coverage of a Pt electrode by hydrogen is the same when the electrode is at a given potential at open circuit and when it is maintained at this potential with a potentiostat. Limiting Q_X values, as determined using Eq. [3], are given in column 5. Q_H values, obtained from the anodic charging curves and corrected for double layer charging, are given in column 7.

The potential, V_p, at which oxidation of H_{ad}-CO_2 first occurs is a function of current density. Measurements of V_p (*i.e.*, the potential at the beginning of the X region) were made on charging curves obtained at different charging currents. The relationship is shown in Fig. 6.

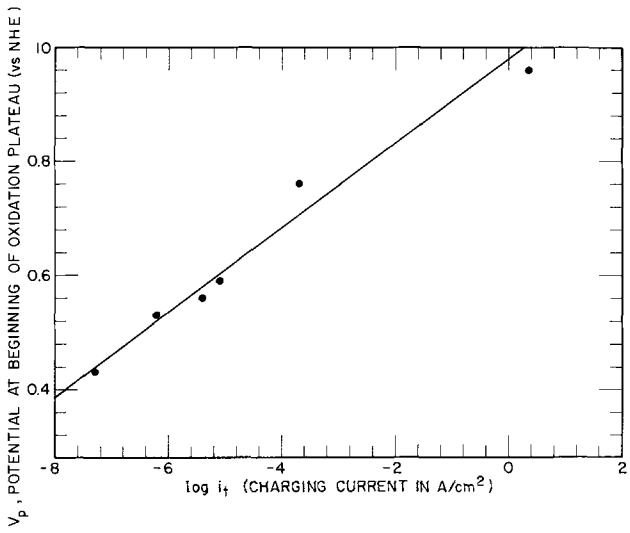

Fig. 6. Dependence of potential, V_p, at beginning of oxidation plateau on applied anodic charging current density, i_t.

Discussion

This work gives qualitative confirmation of the experimental observations of Giner (1) and gives additional information about the chemisorbed species. There is now concrete evidence that CO_2 is not reduced to CO. Under transient conditions (6, 8), the potential at which CO oxidation begins is in the range 0.9-1.3v, depending on the CO partial pressure. CO also does not appear to react when potentiostated below 0.9v (9). The initial potential of oxidation of the species resulting from the interaction of CO_2 with H_{ad} is dependent on the charging current (cf. Fig. 6), independent of the initial surface coverage, and in every case is below 1.0v. This chemisorbed species is completely oxidized at 0.3v under potentiostatic conditions. Furthermore, the shapes of the anodic charging curves for the "X region" resulting from the H_{ad}-CO_2 interaction are markedly different from those for the oxidation of CO, both in the presence and absence of hydrogen (6, 10).

In addition to establishing that CO_2 is not reduced by H_{ad} to CO, the results strongly indicate that CO_2 is not reduced at all. Limiting Q_x values found at interaction potentials below 0.250v (see Table I) show

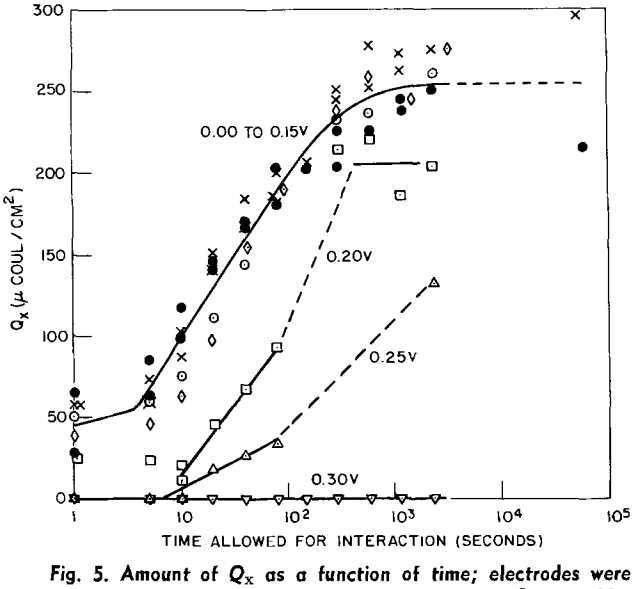

Fig. 5. Amount of Q_x as a function of time; electrodes were held at different potentials during interaction time: ○ = 0.00v, ● = 0.065v, X = 0.10v, ◇ = 0.15v, □ = 0.20v, △ = 0.25v, ▽ = 0.30v.

that the "X-region" is virtually saturated with an oxidizable species. On the other hand, V_p was found to depend only on charging current (Fig. 6). If a reduced CO_2 surface compound were formed, then V_p should depend on current density only if the oxidation rate depended on a slow charge transfer or chemical reaction step following change transfer. However, if the oxidation were dependent on a change transfer or chemical rate, then the degree of surface coverage of the reduced CO_2 should affect the initial oxidation potential. The results, as shown, *e.g.*, in Fig. 4, indicate that V_p is independent of the degree of coverage, strongly suggesting that no reduced CO_2 specie is oxidized, *i.e.*, that CO_2 is not reduced. Further evidence against the possibility of CO_2 reduction is seen in Fig. 5 which shows that Q_x is independent of the interaction potential and hence H_{ad} concentration from 0.00 to 0.15v.

The experimental results can be explained if there exists on the electrode surface only a small number of active sites at which oxidation can occur (*e.g.*, most of the sites could be blocked for oxidation by another species) and the process involves diffusion of the oxidizable species to these sites. It is well known that there are several types of sorbed atomic H. If the concentration of active H_{ad} were low, the rate of oxidation could be affected by the rate of diffusion of irreversibly held H atoms. At low current densities diffusion of H atoms to reactive sites would be fast enough to maintain a relatively constant coverage of these sites. At high current densities a diffusion overvoltage of H atoms would increase V_p. This mechanism is supported by the fact that V_p is independent of Q_x whereas in the "X region," the potential increases as the H coverage decreases.

Information concerning the nature of the sorbed H atoms in the presence of CO_2 is obtained from analysis of the data in Table I and Fig. 5 which show:

(*a*) At a given potential, hydrogen in excess of the amount formed in CO_2-free solution ($Q_t - Q_t^{CO_2\text{-free}}$) is generated on the electrode (column 6, Table I).

(*b*) At sufficiently long interaction times, the hydrogen ionization region normally associated with a Pt electrode in CO_2-free solution essentially disappears (column 7, Table I). The small values of Q_H at 0.00 and 0.065v are an indication that some active hydrogen is present at these potentials.

(*c*) Q_x remains essentially constant (260 ± 35 μcoul/cm^2) up to 0.15v (column 5, Table I), an amount of charge approximately equal to that required to oxidize the hydrogen normally adsorbed on

a clean Pt electrode at 0.00v (230 μcoul/cm^2). The rapid decrease in Q_x above 0.15v suggests that above this potential, there is insufficient hydrogen produced to form a monolayer. We infer from this that the excess hydrogen required to give the observed $Q_t - Q_t^{CO_2\text{-free}}$ is all strongly bonded to Pt since reversibly held H atoms cannot exist above about 0.15v and only strongly bound H atoms will be formed.[5] Since the sites available for the strongly bound H atoms will be limited, the equivalent of a full monolayer of H_{ad} cannot build up.

The fact that CO_2 can inhibit H_{ad} reactions on a Pt electrode is confirmed in Fig. 7, which compares the cathodic polarization behaviors in both 1M H_2SO_4 saturated with a CO_2 + He mixture and saturated with pure He. Behavior in pure CO_2 was found to be essentially the same as in CO_2 + He. Helium was added to increase gas stirring rates to establish a limit beyond which increased stirring did not increase current density. The decrease in current density at a given overpotential is indicative of a poisoned surface. It is difficult to see how CO_2 itself could act as an electrode poison. One possibility is that the HCO_3^- or $CO_3^=$ ions present in solution are the poisons. The formation of complexes having bicarbonate or carbonate structures in the gas phase adsorption of CO_2 has recently been suggested (11). The poisoning effect of these anions could then be similar to the effects of iodide ion on the rate of hydrogen ionization in H_2SO_4, reported by Shanina (12), who found the poisoning effect to occur slowly. Slygin and Frumkin (13) showed that the shapes of anodic charging curves for hydrogen ionization depend on the anion in solution. For example, several plateaus which were present for oxidation in H_2SO_4, could not be detected in HCl or HBr solutions. From arrests in the charging curves on platinized Pt in H_2SO_4 at about 0.7v, Slygin and Frumkin (13) suggested that some hydrogen could be so firmly bound as to require this higher potential for oxidation. The fact that they obtained a lengthening of this plateau with more intensive platinization, which presumably generated more sites at which H atoms could be strongly adsorbed, argues against a solution poison. Their results do suggest that under certain conditions, a much higher potential than expected is required to oxidize hydrogen.

The most probable effect of CO_2 on H_{ad} is one which shifts the equilibrium of the reaction

$$H_{ad} = H^+ + e^- \quad [4]$$

[5] Recent work (18) in this Laboratory has shown that the Nernst potential relation for a H^+/H_2 electrode on Pt (in a system for which the O_2 leakage is so low that the equivalent O_2 partial pressure above the solution is less than 10^{-9} atm) holds only to 0.18v (1×10^{-6} atm H_2). This 0.18v potential is independent of H_2 partial pressure below 1×10^{-6} atm. Hence at potentials of 0.18v and higher, the H^+/H_2 exchange is not potential-determining and the intermediate H_{ad} activity must be negligibly small. The conclusion that reversibly held H atoms cannot exist above about 0.18v thus appears valid.

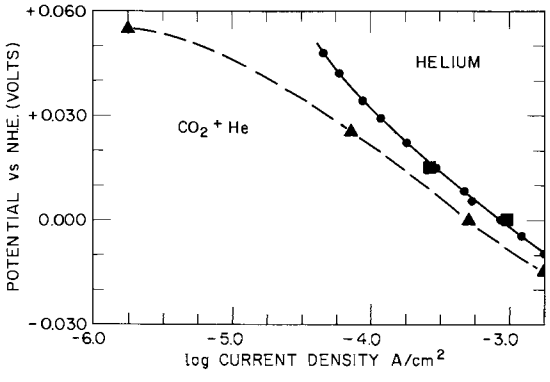

Fig. 7. Cathodic steady-state current density vs. potential in vigorously stirred solution (current density independent of higher gas flow rates). ○ Schuldiner (17); □ this work in solution stirred with helium at 690 std ml/min; △ this work in solution stirred with CO_2 + He at rates > 690 std ml/min.

such that at a given interaction potential the formation of additional H_{ad} is favored. Giner has previously inferred a similar shift in equilibrium. To examine further the question of reduced CO_2 compound formation, an intensive search was made (using charging curves after long periods at open circuit, cf. Fig. 2) to detect traces of a species in solution. None was ever found. In addition, Johnson and Kuhn (14) were unable by chemical analysis to detect a reduced CO_2 compound in solution after 24 hr of reaction.

Giner (15) came to the conclusion that upon anodic oxidation on Pt, and to some extent at open circuit, methanol and formic acid gave a product which was the same as that formed by reaction of CO_2 with atomic H. He considered that the CO_2 was reduced by atomic H. Vielstich and Vogel (19) concluded from their experiments on the anodic oxidation of formic acid that neither carbon monoxide nor oxalic acid are reaction products. We believe that in formic acid solution dissociation to H_{ad} and CO_2 takes place and that inhibition of H_{ad} or formic acid oxidation results. This interaction of the products of dissociative adsorption has several implications for the anodic oxidation of organic compounds and particularly for formic acid. The dissociative mechanism for formic acid oxidation;

$$HCOOH = HCOOH_{ad} \quad [5]$$

$$HCOOH_{ad} = H_{ad} + HCOO_{ad} \quad [6]$$

$$H_{ad} = H^+ + e^- \quad [4]$$

$$HCOO_{ad} = CO_2 + H^+ + e^- \quad [7]$$

has been generally accepted in the literature [cf. ref. (16)]. The present results indicate that such a mechanism cannot continue at potentials negative to 0.3v in H_2SO_4 at Pt electrodes at 25°C. After sufficient interaction of H_{ad} and CO_2 the formic acid dissociation could not proceed on a major fraction of the electrode surface, because of the blocking effect of CO_2.

A decrease in current with time is generally found for the potentiostated oxidation of organic compounds. Recently it has been suggested that this might be due to "reduced CO_2." However, this work shows that under steady state conditions CO_2 cannot block H_{ad} oxidation at/or above 0.3v. Hence a poisoning effect due to this at potentials above 0.3v is impossible. The present results also imply that the complete oxidation of organic compounds on Pt at potentials below 0.3v, *e.g.* to obtain higher cell voltages in electrochemical energy converters using organic fuels, may not be feasible.

Conclusions

1. CO_2 in solution, or possibly HCO_3^-, interacts strongly on Pt to affect subsequent oxidation of adsorbed hydrogen. The rate of this interaction is relatively slow; about 15 min are required to attain limiting conditions.

2. The interaction is apparently not simple physical adsorption of CO_2 on the metal substrate, nor is a reduced CO_2 surface compound nor a soluble species that is stable in solution formed. The H_{ad} blocked by CO_2 interaction is stable on the surface and irreversibly sorbed.

3. The oxidizable species is not CO.

4. Limiting coverage of H_{ad} blocked by CO_2 or HCO_3^- is ~260 μcoul/cm^2. This H_{ad} is stable at potentials negative to 0.3v. When potentiostated at 0.3v it is completely oxidized.

5. CO_2 or HCO_3^- inhibits the hydrogen evolution reaction on Pt.

6. Coulometric measurements strongly indicate that active (or weakly bound) hydrogen is present on the electrode below about 0.15v, but not above.

7. It is tentatively suggested that formic acid dissociates to H_{ad} and CO_2 and that CO_2 or HCO_3^- interacts on Pt to retard oxidation of HCOOH.

Acknowledgment

We are grateful to Dr. J. C. White for helpful suggestions concerning this work.

Manuscript received Dec. 6, 1965; revised manuscript received April 18, 1966. This paper was presented at the Cleveland Meeting, May 1-6, 1966.

Any discussion of this paper will appear in a Discussion Section to be published in the June 1967 JOURNAL.

REFERENCES

1. J. Giner, *Electrochim. Acta*, **8**, 857 (1963).
2. S. Schuldiner and T. B. Warner, *This Journal*, **112**, 212 (1965).
3. S. Schuldiner and R. M. Roe, *ibid.*, **110**, 332 (1963).
4. T. B. Warner and S. Shuldiner, *ibid.*, **112**, 853 (1965).
5. S. Schuldiner and T. B. Warner, *J. Phys. Chem.*, **68**, 1223 (1964).
6. T. B. Warner and S. Schuldiner, *This Journal*, **111**, 992 (1964).
7. D. O. Hayward and B. M. W. Trapnell, "Chemisorption," 2nd ed., p. 75, Butterworths, Washington (1964).
8. S. Gilman, *J. Phys. Chem.*, **66**, 2657 (1962).
9. B. J. Piersma, Unpublished results.
10. S. Schuldiner and T. B. Warner, *Electrochim. Acta*, **11**, 307 (1966).
11. V. R. Deitz, F. G. Carpenter, and R. G. Arnold, *Carbon*, **1**, 245 (1964).
12. L. Shanina, *Dokl. Akad. Nauk, S.S.S.R.*, **134**, 141 (1960).
13. A. Slygin and A. N. Frumkin, *Acta Physiochim. U.R.S.S.*, **3**, 791 (1935); A. N. Frumkin, "Advances in Electrochemistry and Electrochemical Engineering," vol. 3, p. 317, Interscience Publishers, New York (1963).
14. P. R. Johnson and A. T. Kuhn, *This Journal*, **112**, 599 (1965).
15. J. Giner, *Electrochim. Acta*, **9**, 63 (1964).
16. B. J. Piersma and E. Gileadi, "Modern Aspects of Electrochemistry," vol. 4, J. O'M. Bockris, Editor, In press.
17. S. Schuldiner, *This Journal*, **108**, 384 (1961).
18. S. Schuldiner, B. J. Piersma, and T. B. Warner, *ibid.*, **113**, 573 (1966).
19. W. Vielstich and U. Vogel, *Ber. Bunsengesellschaft*, **68**, 688 (1964).

Oxygen Overvoltage Measurements on Bright Platinum in Acid Solutions

IV. Methanol-Containing Solutions

James P. Hoare

Electrochemistry Department, Research Laboratories, General Motors Corporation, Warren, Michigan

ABSTRACT

Oxygen overvoltage measurements were made both galvanostatically and potentiostatically on bright Pt cathodes in O_2-saturated $2N$ H_2SO_4 solutions containing methanol. These curves were compared with those obtained in MeOH-free solutions. The rest potential was lowered by nearly 200 mv in an acid solution of 0.5M MeOH caused by a local cell set up between the $O_2 + 4H^+ + 4e \rightleftharpoons 2H_2O$ and the $(CH_3OH)_{ads} \rightarrow (CO)_{ads} + 4H^+ + 4e$ reactions. The presence of $(CO)_{ads}$ does not interfere with the over-all kinetics of the reduction of oxygen but, by a blocking action, reduces the number of active sites on the electrode surface available for the reduction of oxygen. This causes an increase in the overvoltage of about 40 to 60 mv. Although MeOH is oxidized at high current densities at the cathode, this current is not available to the external circuit since it is produced by a local cell mechanism. The equal number of coulombs of O_2 consumed in the local cell process also involves an additional loss of energy to the external circuit.

At first sight, methanol appears to be an ideal fuel for fuel cells (1, 2) since it is electrochemically active at low temperatures; it is inexpensive, and being a liquid it may be handled in the same way as gasoline. Because of the high solubility of MeOH in water solutions, MeOH may interact with the fuel cell cathode (3), producing intolerable polarization losses.

Studies of the anodic oxidation of MeOH at noble metal electrodes in acid and alkaline solutions (4-8) and of the adsorption of MeOH on the electrode surface as a function of potential (9-11) have been carried out. It appears that competition for surface sites from both H_2 adsorption at less noble potentials and oxygen adsorption at more noble potentials produces a maximum in the θ-potential curves at about 0.7v (9-11) on platinum in acid solutions. It is found that MeOH is oxidized all the way to CO_2 in acid solutions but stops at HCOOH in alkaline solutions.

To our knowledge, however, polarization curves for the reduction of oxygen in the presence of methanol-containing electrolytes cannot be found in the reviewed literature. In this report there is presented an account of the oxygen overvoltage measurements obtained on bright Pt electrodes galvanostatically and potentiostatically in oxygen saturated sulfuric acid solutions containing methanol. So that the effects of mass transfer may be more clearly separated from the effects of activation overvoltage on the polarization curves, these studies were carried out on the bright Pt electrodes instead of the porous diffusion electrodes required for fuel cell investigations.

Experimental

Test electrodes in the shape of small beads (0.02-0.03 cm^2 in area) melted at the end of pure (99.99%) Pt wires were mounted with Teflon spaghetti in a Teflon cell (12). The purification techniques and the cell and electrode preparation have been described before (12). Attention was paid to the rigorous control of impurities. The procedures for determining the galvanostatic (13) and the potentiostatic (14) data are the same as those recorded previously. Since the recorded data are steady state measurements, each potential (galvanostatic) and each current (potentiostatic) point was noted after the tested parameter had not changed sensibly in value for at least 60 sec. Under some circumstances, it required an hour or more to reach this steady value. Reagent grade absolute methanol was added to the electrolyte in the cell by means of a micropipette inserted through the gas exit tube in the cell top after the system had come to a steady rest potential in O_2-saturated, H_2O_2-free, $2N$

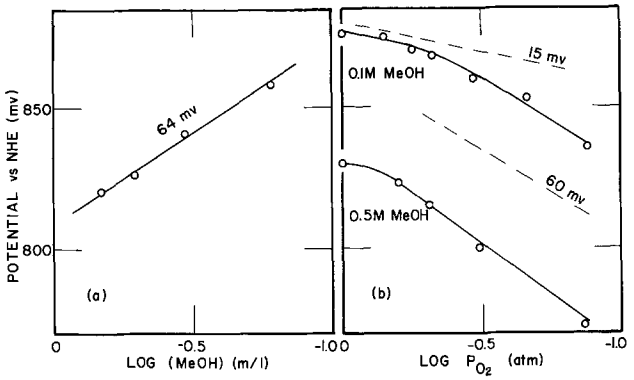

Fig. 1. Dependence of the rest potential on the bulk concentration of MeOH (a) and on the partial pressure of oxygen (b).

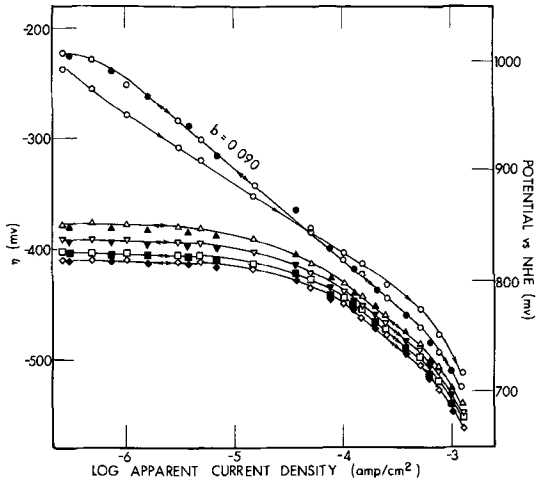

Fig. 2. O_2-η measurements on bright Pt obtained galvanostatically in MeOH containing acid solutions. Open symbols represent increasing current; filled, decreasing. MeOH concentrations are: ○, zero; △, 0.17; ▽, 0.34; □, 0.51; ◇, 0.68M.

H_2SO_4 solution. The studies were carried out over a range of concentrations of MeOH from 0.05 to 0.8 mole/liter. Unless otherwise stated, all potentials are recorded with respect to the normal hydrogen electrode (NHE), and the temperature at which this work was carried out was 25° ± 1°C. Partial pressure of oxygen measurements were obtained by diluting the O_2 stream with N_2 and monitoring the per cent of O_2 in the gas with a Beckman Oxygen Analyzer. To minimize mass transfer effects, the solutions were stirred with gas flows above 300 cc/min.

Results

The steady rest potential of a bright Pt bead in O_2-saturated 2*N* H_2SO_4 solution was 1048 mv, and when 0.1 cc of MeOH was added to the electrolyte (MeOH = 0.17M), the potential fell directly to 865 mv. After about 300 sec the potential was steady at 858 mv. Additional amounts of MeOH added to the solution produced further shifts of the potential toward less noble values. A plot of the rest potential as a function of the log of the MeOH concentration is given in Fig. 1a which gives a straight line with a slope of 64 mv. The rest potential also depended on the partial pressure of oxygen, P_{O_2}, and a plot of potential *vs.* log P_{O_2} is presented in Fig. 1b at two methanol concentrations. Lines with the indicated slopes were drawn as an aid in the analysis of the curves. In order to determine the effect of possible metal-metal oxide reactions on the rest potential, four noble-metal electrodes, Pt, Pd, Rh, Au, were placed in oxygen saturated 2*N* H_2SO_4 solution, and the open-circuit potential after 6 hr is recorded in the first line of Table I. In the next three lines of Table I, the rest potential is recorded just after, 1000 sec after, and 18 hr after adding MeOH to the system.

Table I. Rest potential of noble metal oxygen electrodes in oxygen saturated 2*N* H_2SO_4 solution containing 0.05M MeOH

	Pd (mv)	Pt (mv)	Rh (mv)	Au (mv)
In MeOH-free solution	925	1008	935	892
Made solution 0.005M in MeOH	922	920	931	888
After 1000 sec	928	928	929	885
After 18 hr	912	900	910	886

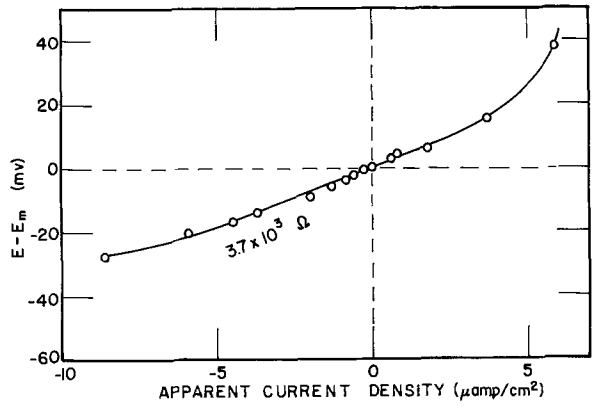

Fig. 3. Polarization of Pt electrode in O_2-saturated 2*N* H_2SO_4 solution 0.05 molar in MeOH at very low current densities.

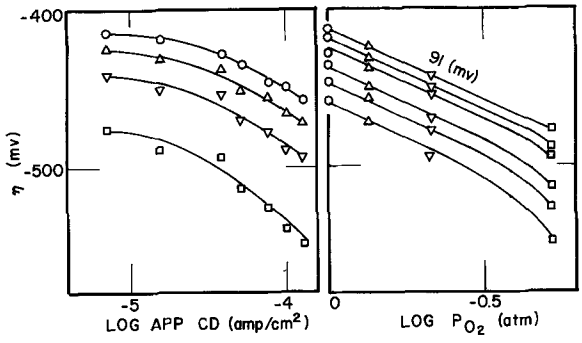

Fig. 4. Variation of overvoltage with partial pressure of oxygen. A plot of the overvoltage as a function of the log of the current density obtained galvanostatically is given on the left side for various values of P_{O_2}. P_{O_2} = 1, ○; 0.74, △; 0.46, ▽; 0.19 atm, □. These data were used to construct the plot of overvoltage as a function of log P_{O_2} on the right side. Curves for six different values of current density are shown. As the current density increases, the deviation from a 91-mv slope increases.

The top curve of Fig. 2 is the steady-state galvanostatic overvoltage curve for the reduction of oxygen in the absence of MeOH. The first cycle of increasing and decreasing current is shown, after which a reproducible curve with a slope of 0.09 is obtained from the average of three additional complete cycles of cathodic polarization (deviation from the mean within ±6 mv). Four additional polarization curves are given for increasing concentrations of MeOH, 0.17M, 0.34M, 0.51M, and 0.68M. These curves were very reproducible since the deviation from the mean value, averaged over three complete cycles of polarization, was within ±2 mv. The polarization of a Pt/O_2 electrode in O_2-saturated 2*N* H_2SO_4 solution containing 0.05M MeOH at low current densities is plotted in Fig. 3. In Fig. 4a, the influence of P_{O_2} on the η is shown for an acid solution 0.68M in MeOH, and in Fig. 4b the η-log P_{O_2} curves are plotted from the data in Fig. 4a.

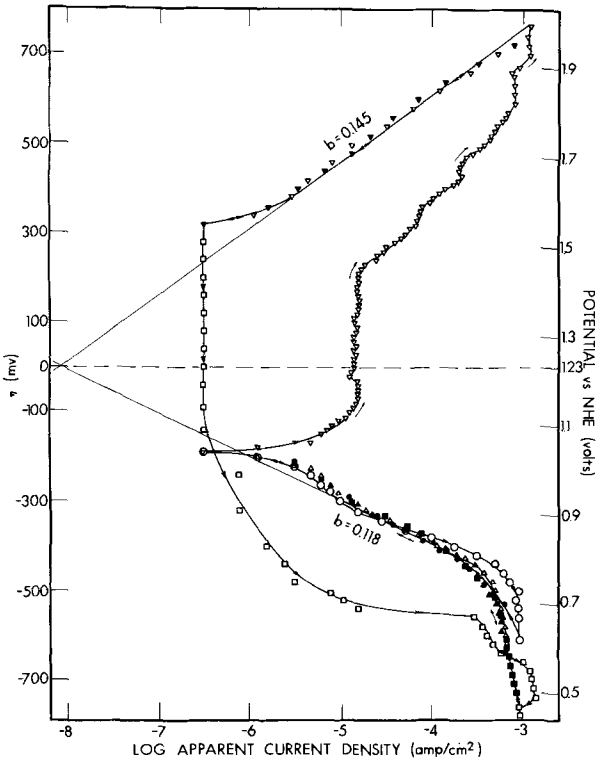

Fig. 5. Oxygen overvoltage curves obtained potentiostatically on Pt anodes and cathodes in O_2-saturated 2*N* H_2SO_4 free of MeOH. Open symbols represent increasing and filled decreasing polarization. ○, First cathodic curve; △, reproducible cathodic curve; ▽, anodic curves; □, cathodic curve of preanodized Pt. Tafel lines cross at zero η (1229 mv); i_o is 8.5 x 10^{-9} amp/cm².

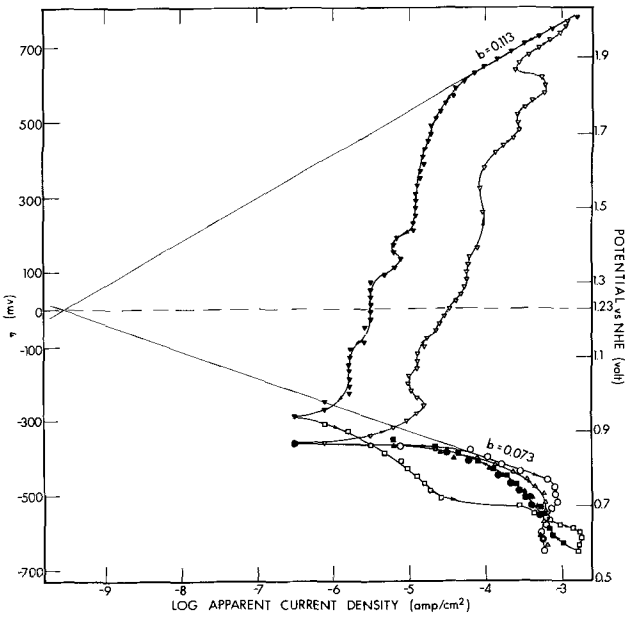

Fig. 6. Oxygen overvoltage curves obtained potentiostatically on Pt electrodes in O_2-saturated 2*N* H_2SO_4 solution containing 0.1M MeOH. Open symbols represent increasing and filled decreasing polarization. ○, First cathodic curve; △, second cathodic curve; ▽, first anodic curve; □, cathodic curve of preanodized Pt. Tafel lines of first polarization curves cross at zero η (1229 mv); i_o is 2.6 x 10^{-10} amp/cm².

Steady-state overvoltage curves for the anodic evolution and cathodic reduction of O_2 on bright Pt obtained potentiostatically in MeOH-free 2*N* H_2SO_4 solution are presented in Fig. 5. The points on the extreme left of the figure represent virtually zero current density. The same data for an acid solution which is 0.1M in MeOH is shown in Fig. 6.

Discussion

The rest potential.—As pointed out by Shlygin and Bogdanovskii (6), the shift of the rest potential of a Pt/O_2 electrode toward less noble values with the addition of MeOH cannot be caused by a purely double layer or specific adsorption effect because the magnitude of the shift is too great. Besides, the shift is in the wrong direction, and therefore, it is more likely produced by an electron transfer process. Since the standard potential, $E°$, of the O_2/H_2O reaction

$$O_2 + 4H^+ + 4e \rightleftharpoons 2H_2O \qquad [1]$$

is 1229 mv (15), and of the $MeOH/CO_2$ reaction

$$CH_3OH + H_2O \rightleftharpoons CO_2 + 6H^+ + 6e \qquad [2]$$

is 20 mv (8), the rest potential does not obey a Nernst relationship (see Fig. 1) and must be determined by a mixed potential mechanism. Giner (8) has also come to this conclusion.

Since the rest potential depends on P_{O_2} as seen in Fig. 1b and since the slope of the *E*-log P_{O_2} curve is low at high values of P_{O_2}, it is reasonable to assume that the O_2/H_2O reaction is one of the partial reactions making up the local cell. As shown in Fig. 1b, the rest potential also depends on the MeOH concentration in the bulk of the solution as has been recorded in the literature (4-11). Although Breiter (9, 10) concludes that MeOH is not adsorbed on Pt above 800 mv, Giner (8) and Bagotskii and co-workers (11) give evidence of MeOH adsorption above a volt. It therefore appears that the oxidation of MeOH could be the other half reaction of the local cell.

From studies of the oxidation of MeOH (8) and the reduction of CO_2 (16) at Pt electrodes, Giner has proposed that a stable intermediate, such as adsorbed CO or COOH, which inhibits the electrode reactions, is formed in these systems. It is possible (4-6) that the first step in the oxidation of MeOH is the oxidation of the hydroxyl hydrogen as

$$(CH_3OH)_{ads} \rightarrow (CH_3O)_{ads} + H^+ + e \qquad [3]$$

One may visualize further, with the discharge of three more electrons in acid solutions, the oxidation of the remaining three hydrogens of the methyl group giving successively $(H_2CO)_{ads}$, $(HCO)_{ads}$, and finally $(CO)_{ads}$. The over-all reaction would be

$$(CH_3OH)_{ads} \rightarrow (CO)_{ads} + 4H^+ + 4e \qquad [4]$$

Warner and Schuldiner (17) have shown that CO is strongly adsorbed on Pt. To remove the CO involves the discharge of a molecule of H_2O, and probably, as suggested by Warner and Schuldiner, the CO reacts rapidly with the adsorbed oxygen atoms produced by the discharge of H_2O.

Because the rest potential depends both on the MeOH concentration and on the P_{O_2} (Fig. 1), it is likely to be controlled by both half-reactions. A possible explanation for the observed behavior may be described in terms of a mixed potential composed of the O_2/H_2O, Eq. [1], and the MeOH/Pt-CO, Eq. [4], reactions. Sketches of the local cell polarization diagrams are given in Fig. 7 which show the influence of the concentration of O_2 and MeOH on the shape of the polarization curves. In these diagrams, the A-curves refer to the O_2/H_2O reaction and the B-curves to the MeOH/Pt-CO reaction. E_a is the standard potential, 1229 mv, and E_b is the $E°$ for the MeOH/Pt-O reaction which is unknown but which must be less noble than 800 mv according to mixed potential considerations (18).

The change in slope of the rest potential-log P_{O_2} curve (Fig. 1b) from 15 mv to 60 mv with decreasing

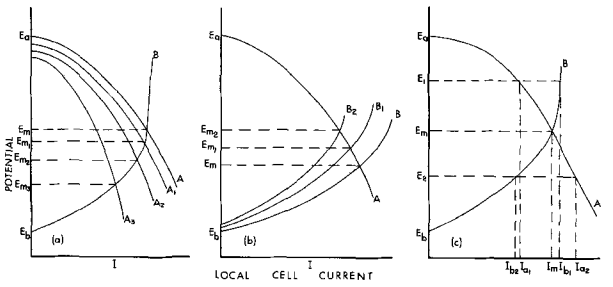

Fig. 7. Mixed potential diagrams. A-curves represent polarization of the O_2/H_2O reaction and B-curves the MeOH/Pt-CO reaction. The abscissa represents the absolute value of the local cell current, I. E_a and E_b are the $E°$ values for the respective partial reactions. (a) Curves A to A_3 represent the polarization curves for decreasing values of P_{O_2}, and the corresponding values of the mixed potential are shown as E_m to E_{m3}. (b) Curves B to B_2 represent the polarization curves for increasing concentrations of MeOH, and the corresponding mixed potential values are shown as E_m to E_{m2}. (c) When the potential is shifted anodically to E_1, the current in the external circuit is I_{b1}-I_{a1} and is positive; when shifted cathodically to E_2, external current is I_{b2}-I_{a2} and is negative.

values of P_{O_2} in MeOH-containing solutions may be interpreted in terms of the effect of adsorbed MeOH on the local cell polarization curve of the O_2/H_2O partial reaction (A-curves in Fig. 7a). At high values of P_{O_2}, the A-curve crosses the MeOH/Pt-CO polarization curve at a point, E_m, where the B-curve is at a limiting current. Consequently, the rest potential is determined by the O_2/H_2O reaction, and a value of 15 mv is expected for the slope of the E-log P_{O_2} curve. As the value of P_{O_2} decreases, the overvoltage for the reduction of O_2 increases as seen in Fig. 4, and hence, it is reasonable to suppose that the local cell polarization curves (A-curves of Fig. 7a) become more steep with decreasing P_{O_2}. Therefore, at lower P_{O_2} values, the A-curves cut the B-curve at points where the MeOH/Pt-CO polarization curve is no longer at a limiting current. Under these conditions, the rest potential is no longer controlled solely by the O_2/H_2O partial reaction but is also strongly influenced by the MeOH/Pt-CO reaction. This effect produces a larger change in rest potential, $E_{m3} - E_{m2}$, for a given change in P_{O_2} at low P_{O_2} than $E_{m1} - E_m$ for the same change in P_{O_2} at high P_{O_2}. This effect is reflected in the change to a higher slope (60 mv) in Fig. 1b.

As the methanol concentration is increased from 0.1 to 0.5M, the O_2/H_2O reaction becomes more inhibited, and the local cell polarization curves become steeper. From this viewpoint, the rest potential would be determined by the O_2/H_2O reaction over a shorter range of P_{O_2} values. As seen in Fig. 1b, the deviation from the 15-mv slope would occur at higher values of P_{O_2}.

According to the Nernst equation, the reversible methanol potential becomes more noble with decreasing MeOH concentrations. In Fig. 7b, the local cell polarization curves for the MeOH/Pt-CO reaction (B-curves) reach a limiting current at lower values of the current with decreasing MeOH concentrations. As a result, for a given change in MeOH concentration the change in E_m is much larger than the corresponding change in E_b, thus accounting for the apparent 1-electron dependency in Fig. 1a instead of the expected 4-electron dependency of Eq. [4].

Apparently, only the reduction of oxygen and the oxidation of methanol are involved in the mixed potential mechanism. Metal-metal oxide reactions do not seem to be important, because as shown in Table I, the rest potential is independent of the electrode material. The gold electrode may be somewhat out of line, but this may be caused by the observation (19) that gold slightly adsorbs MeOH. Current is not contributed to the external circuit by these local cell processes.

The mixed potential region.—If, however, the system is polarized from an external source, the observed current is the difference between the partial currents

$$I = I_a - I_b \qquad [5]$$

as pictured in Fig. 7c. It was shown (13) that an overvoltage, η_p, may be defined as $E - E_m$. A plot of $E - E_m$ as a function of the apparent current density obtained galvanostatically is presented in Fig. 3. In the vicinity of $E = E_m$, a linear curve passing through the mixed potential without a change in slope is obtained. The linear anodic branch is shorter than the cathodic which agrees with the mixed potential diagram in Fig. 7c. For relatively large values of η_p ($E_1 - E_m$ and $E_2 - E_m$ in Fig. 7c), the cathodic is larger than the anodic current for the same values of the anodic and cathodic overvoltage.

From the slope of the curve in Fig. 3, a value of 2.7 x 10^{-4} mho is obtained for $di/d\eta_p$; and it may be shown (13) that the local cell current at $E = E_m$ is given by

$$i_m = (di/d\eta_p)\frac{RT}{F} \qquad [6]$$

A value of 7.1 x 10^{-7} amp/cm^2 is obtained for i_m, the rate of oxidation of MeOH at a Pt surface in the presence of oxygen.

Galvanostatic reduction of oxygen.—For comparison, the galvanostatic cathodic overvoltage curve for the reduction of oxygen on a Pt electrode in MeOH-free, O_2-saturated 2N H_2SO_4 is plotted in Fig. 2. With MeOH present, the overvoltage is greatly increased at low current densities, but the curve is flat in this region due to the polarization of the mixed potential process. When the system is cathodized to higher currents, the mixed potential mechanism no longer controls the kinetics, and the reduction of oxygen contributes virtually all of the current to the external circuit. In this case the system is no longer a polyelectrode but a simple electrode, and a Tafel region with a slope equal to that on pure Pt in 2N H_2SO_4 solution is obtained. At current densities of about 10^{-3} amp/cm^2, the system reaches a limiting current leading to the reduction of H^+ ions.

Because the overvoltage is dependent on P_{O_2} (Fig. 4) and the presence of H_2O_2 may be detected with $TiSO_4$ reagent, it is concluded that O_2 is being reduced at the Pt cathode. Since the shape and slope of the overvoltage curves at high current densities are the same for H_2SO_4 solutions in the presence and in the absence of MeOH, the mechanism of O_2 reduction is likely to be the same in both cases. The observed effect, of course, is an increase in the overvoltage with increased MeOH concentration without a change in slope. It seems then that the presence of MeOH in the electrolyte only blocks some of the active sites for the reduction of oxygen with adsorbed CO. As a result, the electrode area available for O_2 reduction is reduced, and the system must go to a higher overvoltage to supply the same current that was obtained in the absence of MeOH. Methanol is oxidized at the high current densities by the mixed potential mechanism, but none of this current reaches the external circuit, since it appears entirely in the local cell circuit. Consequently the presence of MeOH does not interfere with the kinetics of the reduction of oxygen but only effectively increases the activation energy for the reduction-of-oxygen process by poisoning some of the surface reaction sites.

Potentiostatic data in the absence of MeOH.—To obtain additional evidence for these conclusions, potentiostatic polarization studies were made on Pt anodes and cathodes in O_2-saturated acid solutions both in the absence and in the presence of MeOH. Four complete cycles of polarization are shown in Fig. 5 for the reduction of oxygen on a Pt cathode in the absence of MeOH. The first cycle is shown by the circles (open for increasing and filled for decreasing polarization),

and the average of the next three cycles is shown by the triangles.

It is to be noted that the overvoltage for increasing polarization during the first cycle is greater than the average steady-state value (triangles) at low current densities but less at the high current densities. This effect was observed on the galvanostatic curves in Fig. 2 and Fig. 2 of ref. (13). Using triangular potential sweep techniques, Breiter (20) concluded that the presence of adsorbed oxygen on a Pt electrode inhibited the reduction of O_2 to H_2O_2. Bianchi and coworkers (21) found that the presence of adsorbed oxygen on a Pt electrode accelerated the reduction of H_2O_2 to H_2O. From a series of studies of the reduction of O_2 at a rotating ring electrode, Myuller and Nekrasov (22) observed that the reduction of oxygen to H_2O occurred in two stages: reduction of O_2 to H_2O_2 and reduction of H_2O_2 to H_2O. It is interesting to note that the specific rate, k_2, of the second stage was an order of magnitude larger than the specific rate k_1, of the first stage on oxidized Pt, but on reduced Pt, $k_1 > k_2$.

When a Pt electrode which is at a steady-state rest potential is first cathodized, the surface initially is partially covered with adsorbed oxygen. At low current densities where H_2O_2 concentrations are not built up in solution because the peroxide-decomposing capabilities of the electrode surface are adequate for the demanded current, the overvoltage is increased by the Pt-O layer since the rate of reduction of O_2 to H_2O_2 is inhibited. At high current densities, on the other hand, the rate of decomposition of H_2O_2 becomes important as the H_2O_2 concentration in solution builds up. In this case, the presence of the Pt-O layer enhances the rate of catalytic decomposition of H_2O_2, because, in agreement with Bianchi *et al.*, H_2O_2 is decomposed by reacting chemically with the Pt-O layer

$$H_2O_2 + Pt-O \rightarrow H_2O + O_2 + Pt \qquad [7]$$

Here the η is lowered by the Pt-O layer. Finally, at the high current densities where the limiting current for O_2 reduction is reached, the Pt-O layer is completely reduced, and now, the H_2O_2 is catalytically decomposed by an electrochemical process as suggested by Gerischer and Gerischer (23) and described by Fig. 5 of ref. (24). After the Pt-O layer is removed, the polarization curve follows the reproducible steady-state polarization curve (triangles) in Fig. 5. These data support the contention that O_2 is reduced at Pt cathodes in acid solutions in two 2-electron stages with H_2O_2 being formed as a stable intermediate. This is contrary to the conclusion arrived at by Liang and Juliard (25).

When a Pt/O_2 electrode is anodized from the steady-state rest potential, the initial part of the curve (open inverted triangles in Fig. 5) is the mixed potential region (13) in which a local cell mechanism composed of the O_2/H_2O and the Pt/Pt-O reactions (12) is kinetically controlling. As the potential is made more noble, a point is reached where the current no longer increases. Although a few wiggles are observed in this part of the curve, it is essentially a limiting current region. In this potential range, 1140 (η = —90 mv) to 1460 mv (η = 230 mv), it is believed that the surface becomes more covered with an electronically conducting monolayer of Pt-O. Since the surface coverage, θ, is potential-dependent (26, 27) and the layer is electronically conducting, the only change produced by an increase in potential is an increase in θ. At potentials above 1460 mv (η = 230 mv), oxygen is evolved on the conducting Pt-O layer. In the potential range between 1820 (η = 590 mv) and 1900 mv (η = 670), some Pt-O sites are converted to PtO_2 sites in a second limiting current region. Finally O_2 is evolved on a surface composed of Pt-O and PtO_2 sites. Once this surface is formed, a reproducible Tafel region with a slope of 0.145 is obtained over the current density range indicated in Fig. 5. The points in the Tafel region at the top of Fig. 5 are the average of three complete cycles of polarization with a deviation of ± 0.05 units of log i.

Apparently PtO_2 is unstable in the presence of Pt at potentials lower than about 1700 mv (η = 470 mv) because an oxide reduction curve such as that obtained in the Pd/O_2 case (14) was not observed when the anodized Pt electrode was cathodized. Instead, virtually zero current was obtained below 1500 mv (η = 270 mv) until a potential below 1100 mv (η = —130 mv) was reached. This behavior indicates that an oxide as such does not exist on a Pt surface in acid solutions below 1500 mv (η = 270 mv). In this region, it is believed that the surface is covered by a Pt-O layer (12, 13) with oxygen dissolved in surface layers of the Pt metal as suggested by Schuldiner and Warner (28).

Because the surface is strongly covered with adsorbed atomic oxygen, Pt-O, it would be expected from Myuller and Nekrasov's work that the reduction of O_2 to H_2O_2 would be greatly inhibited on such a surface. Indeed, as seen in Fig. 5 (open squares), the η is very large at low current densities as predicted. In addition, just as would be expected, the η is lower for the Pt-O surface than for the reduced surface in the high current density region where the catalytic decomposition of H_2O_2 is important. Once the Pt-O layer is removed in the high cathodic current density region, the overvoltage curve becomes identical with the original steady-state curve as shown by the filled squares in Fig. 5.

As a point of interest, the cathodic Tafel slope is about 0.09 for galvanostatic measurements but is very close (0.118) to 0.12, the value associated with an electron transfer controlled mechanism, for potentiostatic measurements. An explanation may be similar to that suggested in the Pd/O_2 case (14). In the galvanostatic case, the current or rate of reaction is fixed, and because of the activation energies involved, the concentration of a stable intermediate such as H_2O_2 may build up in solution. Such concentration changes may cause variations in potential [lower the potential (24) in the case of H_2O_2] which produce a flattening of the Tafel curve. The experimental conditions are fixed in the potentiostatic case, and the current or rate must adjust to this environment. Here, the effect of the intermediate, H_2O_2, is included in the kinetics, and a flattening of the curve does not occur. It has been suggested (13) that the rate-determining step is the discharge of the first electron

$$(O_2)_{ads} + e \rightarrow (O_2^-)_{ads}$$

so that a slope of 0.12 is expected.

Since the extrapolated anodic and cathodic Tafel lines cross at zero η, it is concluded that the over-all electrode reaction is the O_2/H_2O reaction, Eq. [1]. A value of 8.5×10^{-9} amp/cm^2 is obtained for i_o which is in good agreement with that, 1.3×10^{-9} amp/cm^2, found galvanostatically (13).

Potentiostatic data in the presence of MeOH.—In Fig. 6 the overvoltage curves obtained for an oxygen saturated acid solution containing MeOH on a Pt cathode are nearly the same as the galvanostatic curves in Fig. 2; the flat mixed potential region is followed by a Tafel region. Even in the high current density region there is lowering of the overvoltage caused by the Pt-O layer on the first half-cycle of polarization as discussed for Fig. 5. When this layer is removed, the η increases in the high current density region. The effect of the Pt-O layer is not observed at low current densities because the current is controlled by the MeOH mixed potential mechanism and not by the pure reduction of O_2 as shown in Fig. 5. These data show that virtually all of the external current goes into the reduction of oxygen.

When this system is anodized, a mixed potential region is observed initially, followed by a negative

resistance region at about 1000 mv (η = −230 mv). Another such negative resistance region is observed above 1800 mv (η = 570) where it is believed that PtO_2 is formed. Above 1860 mv (η = 630 mv), most of the current goes into the evolution of oxygen, because the overvoltage curves are the same whether the solution does (Fig. 6) or does not (Fig. 5) contain MeOH. Between the mixed potential and the oxygen evolution regions, a limiting region such as that observed in Fig. 5 is not observed because as the potential increases more MeOH is oxidized and hence the current increases. Both the evolution of oxygen and the oxidation of MeOH occur simultaneously between 1000 mv (η = −230 mv) and 1860 mv (η = 630 mv).

A Tafel region is observed above 1860 mv (η = 630 mv). It seems that in this region the presence of PtO_2 strongly inhibits the oxidation of MeOH, and nearly all of the current is used in evolving O_2 on the oxide covered Pt surface. With cathodic polarization below 1860 mv (filled, inverted triangles in Fig. 6) where the PtO_2 layer decomposes, the evolution of oxygen is overshadowed by the MeOH oxidation, and the η decreases rapidly compared with the corresponding curve in Fig. 5. Below 1500 mv (η = 270 mv) virtually all of the external current is contributed by the oxidation of MeOH. Finally, an open-circuit value of 940 mv is obtained which is more noble than the original value of 870 mv. This is to be expected because some of the MeOH has been oxidized, and as seen in Fig. 1a, the rest potential becomes more noble as the bulk concentration of MeOH decreases.

When this preanodized electrode is cathodized (open squares in Fig. 6), the polarization curve at low current densities falls to large values of the cathodic η just as in the case where MeOH is absent (Fig. 5). Similarly, the η is lower for the anodized surface than for the reduced surface at high current densities. As before, once the Pt-O layer is removed, the overvoltage curve becomes identical with the curve obtained for a reduced Pt surface (filled squares in Fig. 6).

Interestingly, the extrapolated Tafel lines from the first cycle of anodic and cathodic polarization cross at zero η. This is taken to be an indication that the overall electrode process at high anodic and high cathodic current densities is the O_2/H_2O reaction as in the MeOH-free case (Fig. 5). The i_o, 2.6 x 10^{-10}, is over a magnitude lower than the i_o value in the absence of MeOH. This behavior reflects the blocking action of the electrode reaction by the adsorbed CO, resulting in a poisoning of the catalytic Pt surface.

These data support the conclusion that the presence of MeOH at a Pt/O_2 cathode does not alter the kinetics of the O_2 reduction process but effectively reduces the available number of sites on which the electrode process can occur at high current densities. The visible effect is an increase in η for a given current density. A more drastic increase in η is observed at low current densities produced by the action of the MeOH mixed potential mechanism.

Manuscript received Dec. 8, 1965; revised manuscript received April 25, 1966. This paper was presented at the Cleveland Meeting, May 1-6, 1966.

Any discussion of this paper will appear in a Discussion Section to be published in the June 1967 JOURNAL.

REFERENCES

1. B. L. Tarmy, *Proc. Power Sources Conf.*, **16**, 29 (1962).
2. C. E. Heath, *ibid.*, **17**, 96 (1963).
3. C. E. Heath, *ibid.*, **18**, 33 (1964).
4. S. Tanaka, *Z. Elektrochem.*, **35**, 38 (1929).
5. T. O. Pavela, *Ann. Akad. Sci. Fennicae*, Ser. A II, **59**, (1954); *C.A.*, **49** 15559 (1955).
6. A. I. Shlygin and G. A. Bogdanovskii, Proc. 4th Conf. on Electrochemistry, Moscow (1956), Consultants Bureau, New York, Vol. II, (1961) p. 171; *Zhur. Fiz. Khim.*, **34**, 57 (1960).
7. R. P. Buck and L. R. Griffith, *This Journal*, **109**, 1005 (1962).
8. J. Giner, *Electrochim. Acta*, **9**, 63 (1964).
9. M. W. Breiter and S. Gilman, *This Journal*, **109**, 622, 1099 (1962).
10. M. W. Breiter, *Electrochim. Acta*, **7**, 533 (1962); **8**, 973 (1963); *This Journal*, **110**, 449 (1963).
11. O. A. Khazova, Yu. B. Vasil'ev and V. S. Bagotskii, *Electrokhim.*, **1**, 70 (1965).
12. J. P. Hoare, *This Journal*, **109**, 858 (1962).
13. J. P. Hoare, *ibid.*, **112**, 602 (1965).
14. J. P. Hoare, *ibid.*, **112**, 1129 (1965).
15. A. J. deBethune and N. A. S. Loud, "Standard Aqueous Electrode Potentials and Temperature Coefficients," Clifford A. Hempel, Skokie, Ill. (1964); W. H. Latimer, "Oxidation Potentials," Prentice-Hall, New York (1952).
16. J. Giner, *Electrochim. Acta*, **8**, 857 (1963).
17. T. B. Warner and S. Schuldiner, *ibid.*, **111**, 992 (1964).
18. C. Wagner and W. Traud, *Z. Elektrochem.*, **44**, 391 (1938).
19. M. W. Breiter, *Electrochim. Acta*, **8**, 973 (1963).
20. M. W. Breiter, *ibid.*, **9**, 441 (1964).
21. G. Bianchi, F. Mazza, and T. Muzzini, *ibid.*, **7**, 457 (1962); **10**, 445 (1965).
22. L. Myuller and L. N. Nekrasov, *Dok. Akad. Nauk SSSR*, **149**, 1107 (1963); **154**, 437, 2815 (1964); **157**, 416 (1964); *Electrochim. Acta*, **9**, 1015 (1964); *J. Electroanal. Chem.*, **9**, 282 (1965).
23. R. Gerischer and H. Gerischer, *Z. Physik. Chem. N.F.*, **6**, 178 (1956).
24. J. P. Hoare, *This Journal*, **112**, 608 (1965).
25. C. C. Liang and A. L. Juliard, *J. Electroanal. Chem.*, **9**, 390 (1965); *Nature*, **207**, 629 (1965).
26. J. A. V. Butler and G. Armstrong, *Proc. Roy. Soc.*, **A137**, 604 (1932).
27. W. Böld and M. W. Breiter, *Electrochim. Acta*, **5**, 145 (1961).
28. S. Schuldiner and T. B. Warner, *This Journal*, **112**, 212 (1965).

Kinetics of Electrode Reactions with Adsorbed Films

T. Biegler[1] and H. A. Laitinen

Noyes Chemical Laboratory, University of Illinois, Urbana, Illinois

ABSTRACT

The kinetics of reduction of cadmium ion on a mercury electrode partly covered by n-butanol, thymol, and leucoriboflavin and of plumbite ion in the presence of n-butanol was examined by the method of faradaic impedance with polarographic generation of reactants. Exchange currents and rate constants were lower than expected on the basis of a linear dependence on coverage. A small increase in the transfer coefficient for the reduction of cadmium was observed with partial coverage by leucoriboflavin. Slopes of the impedance plots were independent of coverage. Changes in polarographic log plots and $E_{1/2}$ values with decreasing rate constant were in line with the accepted criterion for polarographic reversibility.

Several authors have examined the kinetics of electrode reactions on surfaces partly covered by adsorbed films of uncharged electroinactive species (1-5). In most cases a linear relationship between exchange current or rate constant and fractional coverage has been demonstrated, a finding which tends to support a simple model for the influence of such adsorption on a reaction. Rek (4), working with the ferro-/ferri-oxalate system, reported a nonlinear dependence of exchange current on coverage by thymol, as well as by ionic surface-active species. Recently, Aramata and Delahay (5) showed that the effect of n-amyl alcohol on the zinc/zinc amalgam system was not simply a blocking of the reaction at covered portions of the surface, but that changes in double layer structure played a large part in the over-all effect. That this is true even at potentials near the electrocapillary maximum will be shown in the following communication in which results of a study undertaken to obtain kinetic data for several systems with clean and partly covered surfaces are presented.

Experimental

Electrode kinetic parameters were determined by measurement of faradaic impedance with polarographic generation of reactants; full experimental details have been described elsewhere (6). Briefly, the impedance of a dropping mercury electrode connected in a manual polarographic circuit was measured with a bridge technique at several frequencies in the range 100-2000 cps. The rate constant was obtained from the impedance at the half-wave potential of a reversible polarographic wave and the transfer coefficient from impedance data at several points on such a wave.

Surface coverages were obtained from the differential capacity of the electrode/solution interface, assuming linear dependence of capacity on coverage. This assumption is probably justified here since in all cases the potential was in the vicinity of the electrocapillary maximum and double layer capacities were independent of frequency (7). For leucoriboflavin, linearity between capacity and coverage in the potential range of interest has been fairly well established (8). Leucoriboflavin was generated at the electrode surface by diffusion-controlled reduction of riboflavin present in the solution in very small concentrations (0.4-2 x 10^{-5}M). Coverage was therefore a function of time and care was taken to obtain impedance measurements at approximately the same time during drop life for all the frequencies used. The same precaution was necessary with small concentrations of thymol where time dependent double layer capacities, indicating diffusion control of adsorption, were noted.

[1] Present address: Department of Physical Chemistry, University of Bristol, England.

Since a dropping mercury electrode was used no special purification procedures were deemed necessary. This attitude was justified by the good agreement with other workers on kinetic parameters for reactions at a clean mercury surface (6). Reagents used were of analytical grade. Solutions were prepared with water distilled from alkaline permanganate in an all-glass apparatus. General experimental procedure was as outlined previously (6). When a volatile surface active component was used the nitrogen for deaeration was first passed through a wash bottle containing a solution of the same composition as in the cell. All experiments were carried out in a water bath at 25°C.

Results and Discussion

Behavior of the Faradaic impedance.—In all cases examined the faradaic impedance behaved normally by the usual criteria (9); plots of the faradaic resistance AR_f (A is the electrode area) and reactance $A/\omega C_f$ against $\omega^{-1/2}$, where ω is the angular frequency of the alternating voltage, were parallel and the reactance plots passed through the origin. In a series of runs with increasing concentration of surface active material the reactance plots coincided, within experimental error, with that for discharge on a clean surface. The only effect of the adsorbed film was to move the resistance and reactance lines further apart as the process became slower (Fig. 1). This contrasts with the results of Laitinen *et al.* (3) in which the plots became steeper with increasing coverage.

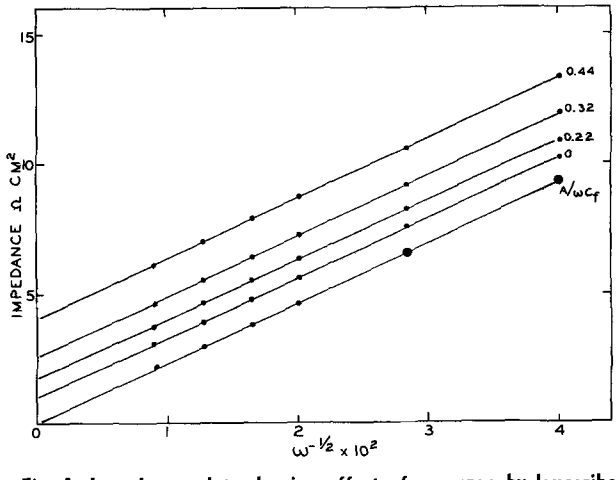

Fig. 1. Impedance plots showing effect of coverage by leucoriboflavin on discharge of 0.286 mM Cd^{++} in 0.1M $HClO_4$, 0.9M $NaClO_4$. Reactance plot (lower line) shows range of values at each frequency for the four runs. Numbers on resistance plots indicate coverage.

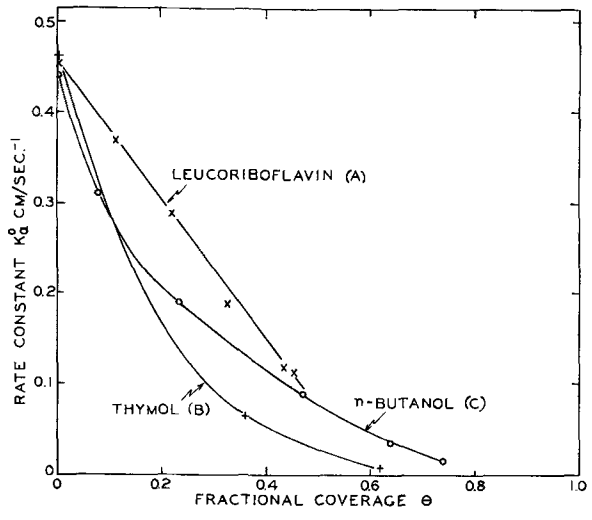

Fig. 2. Effect of surface coverage on apparent rate constant for discharge of cadmium ion. Adsorbed species indicated on diagram. Supporting electrolyte was 0.1M $HClO_4$, 0.9M $NaClO_4$. Cadmium concentrations were: A, 0.286 mM; B, 0.372 mM; C, 0.363 mM.

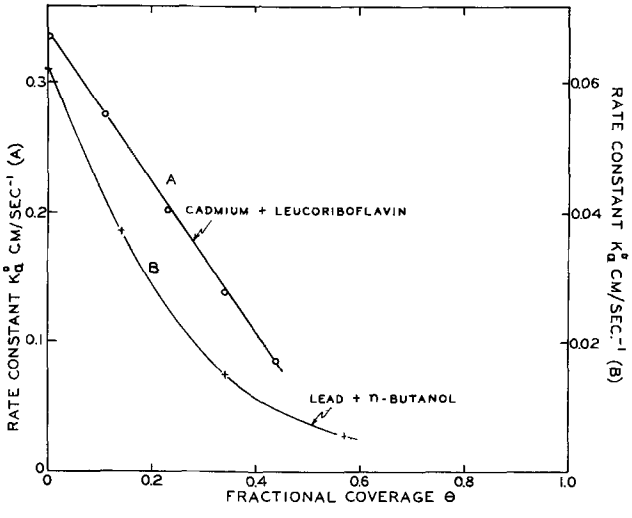

Fig. 3. Effect of coverage on apparent rate constant for: A, 0.280 mM Cd^{++} in 1.0M $HClO_4$; adsorbed species leucoriboflavin; B, 0.406 mM $HPbO_2^-$ in 0.1M NaOH, 0.9M $NaClO_4$; adsorbed species n-butanol.

Constancy of slope suggests at first that the adsorbed layer influences the reaction uniformly over the whole electrode surface rather than blocking it only at covered portions. However, at the frequencies used here (100-2000 cps) the diffusion layer for the a-c process ranges in thickness from about 2 x 10^{-4} to 2 x 10^{-3} cm which is very large compared with the dimensions of an adsorbed molecule or even of a relatively large island of such molecules. Under these circumstances the diffusion part of the faradaic impedance is unaffected by nonuniformity of reaction kinetics at the surface (10), and the electrode behaves with its total area.

Effect of coverage on rate constants.—Relationships between rate constants and fractional surface coverages (θ) for several systems are shown in Fig. 2 and 3. Coverage by leucoriboflavin appeared to affect the rate constant in a linear manner while for the other systems the plots were curved. In no case did the results show a linear dependence of rate on coverage of the type found previously (1-4) where k_a^0 approaches zero as θ approaches unity; all rate constants were smaller than predicted by such a dependence. Values of α needed to calculate k_a^0 (6) were assumed to be the same as for a clean surface although only minor changes would result if this assumption were not correct (see also below).

In a recent paper (5) it has been suggested that the over-all effect of a surface film can be accounted for by considering two factors, first a change in potential at the reaction site, assumed to be the outer Helmholtz plane, and second a linear decrease of current density with coverage. According to this view, correction of exchange current values for the potential drop across the diffuse double layer (Ψ) or, alternatively, normalization of exchange currents to a given potential of the outer Helmholtz plane, conveniently the value for the clean surface at the standard potential (Ψ_0), should give exchange currents and rate constants which depend linearly on coverage. We lack the necessary data to make such corrections, but nevertheless it is of interest to calculate the theoretical changes in Ψ which would cause the observed departures from linearity.

Thus, if I_θ is the measured exchange current density at coverage θ when the potential of the outer Helmholtz plane is Ψ_θ, then the exchange current I_θ^0 which would have been observed in the absence of any change in Ψ with adsorption, *i.e.* with $\Psi = \Psi_0$, is given by

$$\frac{I_\theta^0}{I_\theta} = \exp\left[\frac{(z - \alpha n)\mathbf{F}}{RT}(\Psi_\theta - \Psi_0)\right] \qquad [1]$$

where z is the charge on the reacting ion and n is the number of electrons involved in the reaction. I_θ^0 is estimated from the coverage by assuming that I_θ^0 changes linearly with θ and is zero when $\theta = 1$. Equation [1] is then used to calculate $\Psi_\theta - \Psi_0$, the change in potential of the outer Helmholtz plane needed to account for the observed difference between I_θ^0 and I_θ. Plots of $\Psi_\theta - \Psi_0$ (denoted in the following as $\Delta\Psi$) against θ are shown in Fig. 4.

As noted above, lack of knowledge of the double layer properties for these systems prevents a full analysis of the results, but it is possible to speculate on the likelihood of some of the $\Delta\Psi$ values of Fig. 4. The electrocapillary maximum (ecm) in 1M $NaClO_4$ is —0.493v *vs.* SCE (11) and is certainly close to this value in the supporting electrolyte used for A, B, and C of Fig. 4. Addition of 0.1M NaOH as in Fig. 4D also probably causes little change in the ecm in view of the minor specific adsorption of OH^- (12). The cadmium half-wave potential (—0.57v *vs.* SCE) is therefore some 75 mv cathodic to the ecm and, by analogy with data for perchloric acid (13), Ψ_0 is esti-

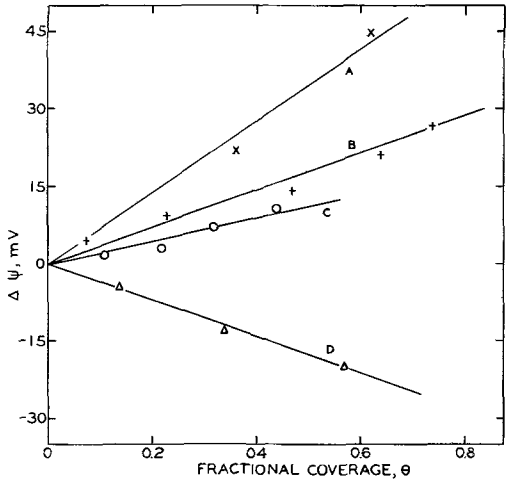

Fig. 4. Plots of $\Delta\psi$ (see text) as a function of fractional coverage θ for the following systems: A, 0.372 mM Cd^{++} in 0.1M $HClO_4$, 0.9M $NaClO_4$ plus thymol; B, 0.363 mM Cd^{++} in 0.1M $HClO_4$, 0.9M $NaClO_4$ plus n-butanol; C, 0.286 mM Cd^{++} in 0.1M $HClO_4$, 0.9M $NaClO_4$ plus leucoriboflavin; D, 0.406 mM $HPbO_2^-$ in 0.1M. NaOH, 0.9M $NaClO_4$ plus n-butanol.

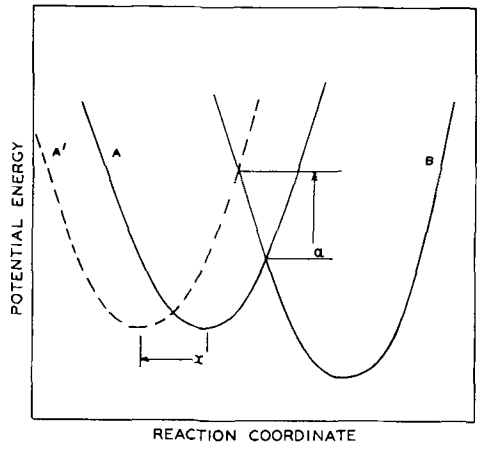

Fig. 5. Schematic energy diagram for electrode reaction. A and B are curves for reactants and products, respectively. A is shifted by a distance x along the reaction coordinate to A' and a is the increase in activation energy.

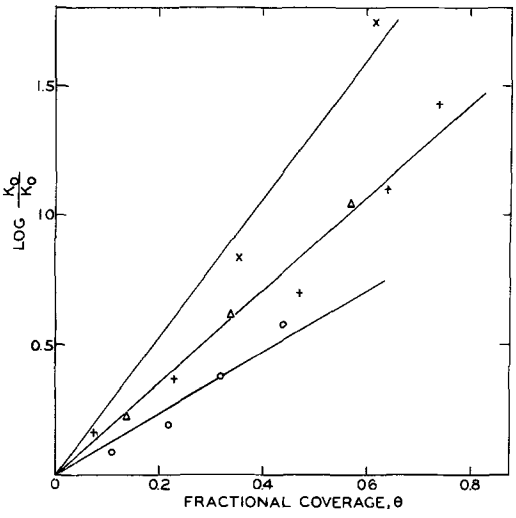

Fig. 6. Plots of log k_0/k_θ vs. θ for the systems of Fig. 4. X—A, +—B, O—C, Δ—D.

mated to be −23 mv. This relatively large value is due to the appreciable specific adsorption of perchlorate ion. Nothing is known of the effects of n-butanol on perchlorate adsorption, but even if such adsorption were markedly decreased $\Delta\Psi$ values of greater than about +20 mv seem unlikely in view of the fact that butanol shifts the ecm anodically. Thymol causes a cathodic shift of the ecm (15), but the large values of $\Delta\Psi$ required by Fig. 4A seem improbable. It is even harder to accept the negative values of $\Delta\Psi$ in Fig. 4D [Ψ_0 for this case is estimated from (13) to be −25 mv] and, if the model were correct the present behavior would provide evidence against the discharging species having a negative charge as was assumed in the calculation. It may be concluded that two of the systems studied here do not support the model proposed by Aramata and Delahay (5) while in the other systems the required changes in Ψ are feasible although not confirmed.

Another relatively simple model which has not been considered previously can be used to give a reasonable explanation of the present results. The assumptions made are: (a) The reaction is slowed down in the presence of adsorbed neutral molecules by virtue of the increased separation between the outer Helmholtz plane and the electrode surface; (b) this separation is a linear function of coverage; and (c) the effect of such increased separation may be represented by an increase in distance, along the reaction coordinate, between potential energy curves of the type conventionally used to represent the course of electrode reactions (Fig. 5). If the intersection of these curves occurs well above the energy minima, the increase in activation energy may be approximated to a linear function of the increased separation. By equating this energy to the heat of activation we can write

$$\Delta H_\theta^\ddagger = \Delta H_0^\ddagger + (\Delta H_1^\ddagger - \Delta H_0^\ddagger)\,\theta \qquad [2]$$

where the subscripts refer to the coverage. The rate constant is given by

$$k_\theta = A \exp\left(\frac{-\Delta H_\theta^\ddagger}{RT}\right) \qquad [3]$$

where A is a pre-exponential factor, assumed here to remain constant, *i.e.*, the entropy of activation is unchanged. It follows that

$$\log\frac{k_0}{k_\theta} = \theta\left(\frac{\Delta H_1^\ddagger - \Delta H_0^\ddagger}{2.3\,RT}\right) \qquad [4]$$

k_0 being the rate for the clean surface.

Plots of log k_0/k_θ *vs.* θ are shown in Fig. 6. Agreement with Eq. [4] is not entirely convincing, and it should be noted that extrapolation to $\theta = 1$ gives rate constants only about two orders of magnitude smaller than k_0 whereas it is well known that the rates of such reactions at high coverages are very much less than this. Another point is that "Frumkin" corrections of the type given by Eq. [1] have been neglected here and should be included in a complete treatment. However, as a first approximation the above model appears to account for the present results with reasonable success. Further development of this model would need to include a more thorough consideration of the shapes of the potential energy curves and the possibility that the slopes at the point of intersection vary with separation. Clearly, increased slopes on the upper branches of these curves would result in a faster change of a with x (Fig. 5) and could account for more rapid changes of k_θ with θ at higher coverages.

Effect of coverage on transfer coefficient.—Table I contains the results of α determinations for discharge of cadmium in presence and absence of surface films. In the case of butanol, coverage calculated from double layer capacities changed with potential, and the value given for α, which does not differ significantly from that for a clean surface, may be misleading. We have attempted to make approximate corrections to measured exchange currents by noting the rate of change of k_a° with θ for a similar system (cf. Fig. 2C) and calculating exchange currents for an arbitrarily selected coverage, in this case 0.35, which was the measured value of θ at $E_{1/2}$. This procedure gave $\alpha = 0.20$ so we must admit the possibility that α did in fact increase slightly.

Leucoriboflavin was chosen as an adsorbate for α determinations because coverage is essentially independent of potential (8). Experimentally, constant coverage is ensured by making all impedance measurements with a given bulk concentration of riboflavin at a fixed time, or within a small time range, during

Table I. Effect of surface films on α for discharge of Cd^{++}

Supporting electrolyte	Adsorbed species	Coverage	Rate constant cm sec^{-1}	α
1.0M $HClO_4$	None	0	0.35 ± 0.02	0.14 ± 0.01
	n-butanol	0.35*	0.075 ± 0.002	0.13 ± 0.02
0.1M $HClO_4$, 0.9M $NaClO_4$	None	0	0.45 ± 0.02	0.09 ± 0.01
	Leucoriboflavin	0.45	0.113 ± 0.005	0.14 ± 0.03

* Apparent coverage changed from 0.31 to 0.38 over potential range of measurements.

Table II. Effect of n-butanol on polarographic and kinetic data for discharge of plumbite ion (0.406 mM $HPbO_2^-$ in 0.1M NaOH, 0.9M $NaClO_4$)

Butanol concentration $\times 10^2$M	θ	I_a^o ma/cm²	$k_a^o \times 10^2$ cm sec^{-1}	$E_{1/2}$ *vs* SCE*	Log plot slope, mv
0	0	2.25	6.2	-0.680_2	30.1
1.42	0.14	1.34	3.7	-0.680_2	—
2.76	0.34	0.535	1.5	-0.682_6	30.5
4.05	0.57	0.204	0.56	-0.683_9	32.3
6.43	0.71	—	—	-0.688_1	35.5

* Saturated NaCl calomel electrode.

the life of a mercury drop. For example, the present impedance data were obtained at times varying from 9.36 to 9.78 sec from initiation of a drop, giving a variation in coverage (which depends on $t^{1/2}$) of $\pm 1.3\%$ about a mean value. This was quite satisfactory for the present purposes and the small increase in α shown in Table II is probably significant.

Low values of α connected with reduction of cadmium ion in several electrolytes have been attributed to a slow "chemical" step, possibly dehydration of the hydrated ion, preceding the electrochemical reaction (16, 17). In the systems studied here the exchange current was lowered by a factor of four or five with little effect on α. It is of course possible that both the chemical and charge transfer steps were equally affected and there is not enough information to decide whether these results provide evidence for or against the dehydration step hypothesis. It would seem important to examine these reactions at high coverages where the relative rates of chemical and electrochemical steps may be greatly altered with a concomitant change in the apparent value of α.

Relation between rate constant and polarographic reversibility.—Polarographic data for reduction of plumbite ion ($HPbO_2^-$) in presence of n-butanol are shown in Table II together with the measured exchange currents and rate constants. These results give direct evidence for the validity of the usually accepted criterion of polarographic reversibility, $k_a^o \geq 2 \times 10^{-2}$ cm sec^{-1} (18); a small but significant increase in $E_{1/2}$ and the slope of the conventional polarographic log plot (E *vs.* log $(i_d - i)/i$) occurred when the rate constant fell below this value. It should be noted that, because the method used here to measure k_a^o is strictly valid only for a reversible wave, values at the higher coverages must be taken as approximate.

Acknowledgment

The authors wish to acknowledge support of this work by the National Science Foundation under grant NSF G-21049.

Manuscript received Dec. 23, 1964; final revised manuscript received March 14, 1966.

Any discussion of this paper will appear in a Discussion Section to be published in the June 1967 JOURNAL.

REFERENCES

1. P. Delahay and I. Trachtenberg, *J. Am. Chem. Soc.*, **80**, 2094 (1958).
2. W. Müller and W. Lorenz, *Z. Phys. Chem.*, **27**, 23 (1960).
3. H. A. Laitinen, K. Eda, and M. Nakanishi, *Talanta*, **11**, 321 (1964).
4. J. H. M. Rek, Doctoral Thesis, State University, Utrecht (1963).
5. A. Aramata and P. Delahay, *J. Phys. Chem.*, **68**, 880 (1964).
6. T. Biegler and H. A. Laitinen, *Anal. Chem.*, **37**, 572 (1965).
7. R. Parsons, *J. Electroanal. Chem.*, **5**, 397 (1963).
8. T. Biegler and H. A. Laitinen, *J. Phys. Chem.*, **68**, 2374 (1964).
9. J. E. B. Randles, *Discussions Faraday Soc.*, **1**, 11 (1947).
10. K. J. Vetter, *Z. Physik. Chem.*, **199**, 300 (1952).
11. H. Wroblowa, Z. Kovac, and J. O'M. Bockris, *Trans. Faraday Soc.*, **61**, 1523 (1965).
12. R. Payne, *J. Electroanal. Chem.*, **7**, 343 (1964).
13. R. Parsons and R. Payne, Unpublished data.
14. E. Blomgren, J. O'M. Bockris, and C. Jesch, *J. Phys. Chem.*, **65**, 2000 (1961).
15. G. Gouy, *Ann. chim. phys.*, **8**, 291 (1906).
16. J. E. B. Randles in "Transactions of the Symposium on Electrode Processes," E. Yeager, Editor, Chap. 11, John Wiley & Sons, Inc., New York (1961).
17. G. C. Barker, *ibid.*, Chap. 18.
18. P. Delahay, *J. Am. Chem. Soc.*, **75**, 1430 (1953).

Technical Notes

Orthovanadate Phosphors with Zircon Structure

Frank J. Avella

General Telephone & Electronics Laboratories, Bayside, New York

The development by Levine and Palilla (1, 2) of europium-activated yttrium orthovanadate (YVO_4:Eu) as a highly efficient red-emitting cathodoluminescent phosphor and its recent adoption as a new primary for color television has aroused interest in other orthovanadates as potential hosts for lanthanide activators. Earlier, Van Uitert *et al.* (3) reported that YVO_4:Eu exhibits red fluorescence under ultraviolet excitation. Recently Brixner *et al.* (4) investigated $Ca_3(VO_4)_2$ and found it to be moderately efficient as a host for Eu; it is, however, substantially inferior to YVO_4. More efficient than $Ca_3(VO_4)_2$ are systems based on $M^{III}VO_4$, where M^{III} = Gd, Lu, and La. These have been described by Palilla, Levine, and Rinkevics (5) and Brixner and Abramson (6).

Several investigators have described the crystal structures of $M^{III}VO_4$ (7-11). When M^{III} has an ionic radius ranging approximately from 0.81 to 1.11Å (12), the material crystallizes with the tetragonal zircon-xenotime structure. This range includes the trivalent ions of Sc, Y and all the rare earth luminogens. Because trivalent La is a larger ion (1.15Å), its orthovanadate crystallizes in the monoclinic system with the monazite structure. However, $LaVO_4$ can accommodate small amounts of rare earths without serious lattice distortion. With Eu^{III} as the activator, the tetragonal vanadates have proved to be the better hosts (5). The crystal field of the monazite lattice favors the $^5D_0 \rightarrow {}^7F_1$ transition in Eu^{3+}, producing emission dominated by spectral lines between 558 and 595 nm.

In the zircon lattice with its D_{2d} site symmetry, the $^5D_0 \rightarrow {}^7F_2$ transition predominates and gives rise to the principal emission lines between 609 and 620 nm. Because of the greater intensity and more favorable color of the latter emission, YVO_4:Eu was recently adopted for use as the red-emitting primary in trichromatic cathode-ray tubes for television. This has led to further investigation of orthovanadate phosphors of the zircon type.

This paper presents data on a new series of Eu-activated phosphors derived from zircon-structured $M^{III}VO_4$ by substituting a divalent-tetravalent cation pair for two trivalent cations to form $M_{0.5}{}^{II}M_{0.5}{}^{IV}VO_4$. Activation with Eu^{III} is effected without need for charge compensation by partial replacement of both cations as represented by the formula $M_{0.5(1-x)}{}^{II}Eu_xM_{0.5(1-x)}{}^{IV}VO_4$. The choice of divalent and tetravalent cations is governed by their size, which should approximate that of the rare earth ions if the orthovanadates are to crystallize with the zircon structure. Some deviation from this size range may be possible on the part of one cation of the pair if the other stabilizes the zircon lattice.

Experimental

The following tetravalent ions were chosen for this investigation; their ionic crystal radii (12) are given in parentheses: Zr(0.80Å), Hf(0.81Å), Pb(0.84Å), Ce(1.01Å), Th(0.95Å) and U(0.89Å). The divalent ions were Mg(0.65Å), Ca(0.99Å), Sr(1.13Å), Ba(1.35Å), Zn(0.74Å), and Cd(0.97Å).

Preparation of powdered samples involved dry-blending appropriate reagent grade oxides, nitrates or carbonates in stoichiometric amounts, firing in open platinum crucibles at 500°-550°C for 5 hr, mortaring, and refiring between 600° and 900°C for upwards of 16 hr.

Synthesis results.—In the initial experiments Ca, which had been found capable of isostructural substitution for small amounts of Y in YVO_4, was paired with the tetravalent ions. Monophase products resulted when M^{IV} = Zr, Ce, and Th. X-ray diffraction data in Table I show by analogy that these compounds are isomorphs of the rare earth orthovanadates and, therefore, have the zircon structure. Hf, Pb, and U yielded multiphase products with indications of possible zircon-like phases. Of the three monophase materials, $Ca_{0.5}Ce_{0.5}VO_4$ had a body color too dark for consideration as a phosphor host, leaving Zr and Th for further evaluation.

When paired with the divalent ions, Zr formed the zircon structure only with Ca. Th was successfully paired with Sr and Cd in addition to Ca, while with Mg and Zn, zircon-like phases were major constituents of multiphase products. All of these materials were light tan or white in body color. Similar results have been reported by Schwartz for the zircon forms of $M_{0.5}{}^{II}Th_{0.5}VO_4$, where M^{II} = Ca, Sr, Cd, and Pb (13), and of $M_{0.5}{}^{II}Ce_{0.5}VO_4$, where M^{II} = Ca, Sr, and Cd (14).

The unactivated II-IV orthovanadates exhibit only feeble luminescence under ultraviolet excitation at room temperature, but the introduction of Eu^{3+} results in strong red photoluminescence. Maximum emission intensity is attained with an Eu concentration of approximately 15g a/o (atom per cent). Unlike $M^{III}VO_4$:Eu, the Eu-activated II-IV compounds respond only weakly to cathode-ray excitation. Activation with rare earths other than Eu produces very weak photoluminescence except for Sm which gives moderate emission. X-ray diffraction data verified that the introduction of rare earths into the II-IV lattices is actually isostructural. Furthermore, Eu stabilizes the Zn-Th compound and eliminates the nonzircon phase.

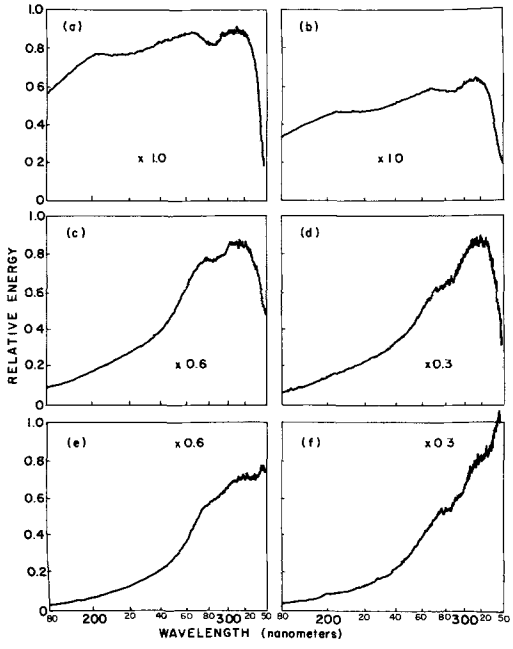

Fig. 1. Excitation spectra of Eu-activated orthovanadates: a, $Y_{0.95}Eu_{0.05}VO_4$; b, $Ca_{0.425}Eu_{0.150}Zr_{0.425}VO_4$; c, $Ca_{0.425}Eu_{0.150}Th_{0.425}VO_4$; d, $Sr_{0.425}Eu_{0.150}Th_{0.425}VO_4$; e, $Cd_{0.425}Eu_{0.150}Th_{0.425}VO_4$; f, $Zn_{0.425}Eu_{0.150}Th_{0.425}VO_4$.

Spectral measurements.—Excitation spectra presented in Fig. 1 were obtained by the method of Eby (15) where instrumental corrections are applied to produce spectra in terms of relative energy. Comparison of intensities is possible between phosphors when the ordinates are multiplied by the indicated factors. The emission spectra of Fig. 2 were determined by the method of Wiggins (16). A General Electric S-4 100w medium-pressure mercury vapor lamp was employed for excitation. The spectra were resolved with a ¾-meter Czerny-Turner Spectrometer (1200 line/mm grating and 50μ slit width) and detected with an ITT F4013 photomultiplier (S-20 response). In the Wiggins technique a correction function derived from the output of an NBS 1000w quartz-

Table I. X-ray diffraction data for monophase $M_{0.5}{}^{II}M_{0.5}{}^{IV}VO_4$

(Cu Radiation, Ni Filter, 1° 2θ/min)

interplanar d-spacings in angstroms

hkl	$Sr_{0.5}Th_{0.5}VO_4$	$CeVO_4$	$Ca_{0.5}Th_{0.5}VO_4$	$Cd_{0.5}Th_{0.5}VO_4$	$Ca_{0.5}Ce_{0.5}VO_4$	YVO_4	$Ca_{0.5}Zr_{0.5}VO_4$
101	4.93	4.88	4.81	4.85	4.77	4.74	4.64
200	3.70	3.70	3.63	3.62	3.58	3.57	3.48
211	2.96	2.95	2.91	2.89	2.87	—	2.84
112	2.78	2.76	2.73	2.74	2.70	2.67	2.63
220	2.62	2.62	2.57	2.55	2.54	2.52	2.47
202	2.46	2.44	2.41	2.41	2.39	2.36	2.33
301	2.31	2.30	2.27	2.25	2.24	2.23	2.18
103	2.10	2.08	2.06	2.07	2.04	2.02	1.99
231	1.96	1.96	1.923	1.909	1.902	1.888	1.848
132	1.906	1.90	1.871	1.863	1.850	1.836	1.801
400	1.853	1.85	1.816	1.799	1.796	1.783	1.746
123	1.825	1.81	1.792	—	—	1.754	1.692
411	—	1.73	1.697	—	1.68	—	1.65
420	1.655	1.65	1.625	—	1.607	1.596	1.562
004	—	1.63	1.612	1.610	1.596	1.575	—
332	—	1.54	1.512	—	1.495	1.484	1.459

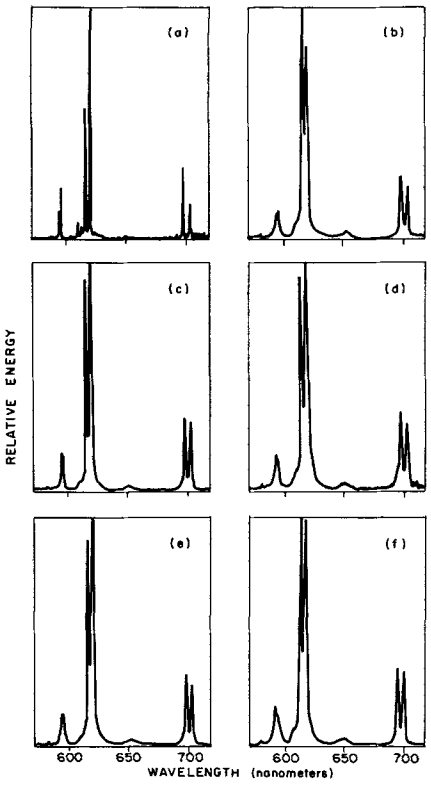

Fig. 2. Emission spectra of Eu-activated orthovanadates: a, $Y_{0.95}Eu_{0.05}VO_4$; b, $Ca_{0.425}Eu_{0.150}Zr_{0.425}VO_4$; c, $Ca_{0.425}Eu_{0.150}Th_{0.425}VO_4$; d, $Sr_{0.425}Eu_{0.150}Th_{0.425}VO_4$; e, $Cd_{0.425}Eu_{0.150}Th_{0.425}VO_4$; f, $Zn_{0.425}Eu_{0.150}Th_{0.425}VO_4$.

iodine standard lamp serves as an internal reference so that spectra appear directly in terms of relative energy. In this series of spectral determinations no provision was made for comparing the emission intensities of the several phosphors.

Discussion

Palilla *et al.* (5) have found that $M^{III}VO_4$:Eu compounds with either a zircon or monazite structure possess similar excitation spectra. They hypothesized that excitation occurs mainly through the orthovanadate ligand and is largely independent of the cation. The spectra of Fig. 1 show, however, that variations in the cationic species do alter the excitation characteristics of the II-IV orthovanadates. When compared with YVO_4:Eu, the CaZr compound is the most similar. Its excitation band is broad and has essentially the same character. The other II-IV phosphors exhibit relatively much less absorption at the shorter wavelengths. Absorption maxima between 260 and 280 nm and between 310 and 320 nm are common to each of these phosphors, including YVO_4:Eu. However, the Cd and Zn ions have introduced new primary excitations at longer wavelengths. These are near the instrumental limit of 350 nm and are not well defined in the figure.

Luminescence of the II-IV phosphors is dominated by emission from $^5D_0 \rightarrow {}^7F_2$ transitions, as expected from Eu^{3+} in the D_{2d} site of a zircon-type orthovanadate lattice. However, variations in spectral detail relative to YVO_4:Eu occur to different degrees in the emission resulting from transitions to the principal multiplets $^7F_{1,2,3}$. Most pronounced is line broadening, observed up to fivefold (width at half peak height) for the strong emission line lying near 619 nm. There also are small differences in the wavelengths and relative intensities of some emission lines. These effects indicate that substitution of $M^{II}M^{IV}$ for M^{III} has altered the crystal field influence on the Eu^{3+} ion, but that the lattice symmetry still governs the general character of the emission.

Another difference between the $M^{II}M^{IV}$ and M^{III} phosphors is seen in the reaction of their luminosity to increases in temperature up to 400°C. While little change is seen in the luminosity of YVO_4:Eu, the room temperature value for the CdTh and ZnTh compounds is reduced to about 75% at 200°C, 50% at 300°C, and 20% at 400°C.

Table II. Relative luminosity data

Formulation	Excitation at primary maxima	Excitation with S-4 mercury lamp
$Y_{0.95}Eu_{0.05}VO_4$	100	100
$Ca_{0.425}Eu_{0.150}Zr_{0.425}VO_4$	50	56
$Ca_{0.425}Eu_{0.150}Th_{0.425}VO_4$	57	54
$Sr_{0.425}Eu_{0.150}Th_{0.425}VO_4$	39	40
$Cd_{0.425}Eu_{0.150}Th_{0.425}VO_4$	39	80
$Zn_{0.425}Eu_{0.150}Th_{0.425}VO_4$	47	84

Because the emission spectra of these orthovanadates are similar, it is possible to approximate phosphor efficiency by comparing luminosity values obtained when the exciting radiation corresponds in wavelength to the primary excitation maximum for each sample. In the experimental arrangement the exciting wavelengths were selected from radiation of a Hanovia 901C-1 xenon lamp with the excitation monochromator of the Aminco-Bowman Spectrophotofluorometer. Visible harmonics were eliminated with a Corning 7-54 filter. Luminosity values measured with an RCA 1P21 photomultiplier fitted with a Kodak Wratten 106 filter were corrected for variations with wavelength of lamp output and 7-54 filter transmission characteristics by using sodium salicylate powder as a quantum counter (17). These data are presented in the first column of Table II. $Ca_{0.425}Eu_{0.150}Th_{0.425}VO_4$ was found to be the most luminous and, therefore, the most efficient of the II-IV phosphors. The luminosity value, however, is only 57% that of YVO_4:Eu.

A different situation exists when a medium-pressure mercury lamp is the excitation source. The data in the second column of Table II were obtained using General Electric S-4 lamp radiation filtered with the Corning 7-54 to eliminate the visible component which would be reflected by the sample. Again, detection was performed with the 1P21 photomultiplier and Wratten 106 combination. Under these conditions, the ZnTh and CdTh phosphors, having their principal excitation maxima closer to the dominant 3650-3654Å band of the mercury discharge, yield 84 and 80, respectively, on a luminosity scale where YVO_4:Eu is rated 100. Thus, two of the II-IV vanadates may possibly substitute for YVO_4:Eu in applications where excitation by medium- or high-pressure mercury discharge is required.

Summary

$M_{0.5}^{II}M_{0.5}^{IV}VO_4$:Eu analogues of zircon-structured $M^{III}VO_4$:Eu were synthesized. Luminescence spectra show the preferred electronic transitions in the Eu^{3+} activator to be characteristic of zircon symmetry in an orthovanadate lattice. The $M^{II}M^{IV}$ cation pair introduce variations in luminescence fine structure and in excitation characteristics. Luminosity approaches that of YVO_4:Eu under certain conditions of excitation.

Acknowledgments

The author is indebted to V. Qvistorff for assistance in sample preparation, to P. Lublin for x-ray diffraction data, and to J. Eby and C. S. Wiggins for spectral measurements. He also wishes to acknowledge helpful discussions with A. K. Levine and F. C. Palilla.

Manuscript received Jan. 17, 1966; revised manuscript received March 8, 1966.

Any discussion of this paper will appear in a Discussion Section to be published in the June 1967 JOURNAL.

REFERENCES

1. A. K. Levine and F. C. Palilla, *J. App. Phys. Letters*, **5**, 118 (1964).
2. A. K. Levine and F. C. Palilla, *Trans. N.Y. Acad. Sci.*, **27**, 517 (1965).
3. L. G. Van Uitert, R. C. Linares, R. R. Soden, and A. A. Ballman, *J. Chem. Phys.*, **36**, 702 (1962).
4. L. H. Brixner and P. A. Fluornoy, *ibid.*, **112**, 303 (1965).

5. F. C. Palilla, A. K. Levine, and M. Rinkevics, *This Journal*, **112**, 776 (1965).
6. L. H. Brixner and E. Abramson, *ibid.*, **112**, 70 (1965).
7. W. O. Milligan, L. M. Watt, and H. H. Rachford, Jr., *J. Phys. Chem.*, **53**, 227 (1949).
8. M. K. Carran, M. E. Mrose, and K. J. Murata, *Am. Mineral.*, **43**, 985 (1958).
9. V. S. Stubican and R. Roy, *J. Appl. Phys.*, **34**, 1888 (1963).
10. J. R. Gambino and C. J. Guare, *Nature*, **198**, 1084 (1963).
11. H. Schwarz, *Z. anorg. u. allgem. Chem.*, **323**, 44 (1963).
12. L. Pauling, "The Nature of the Chemical Band," 3rd ed., Cornell University, Ithaca, N. Y. (1960).
13. H. Schwarz, *Z. anorg. u. allgem. Chem.*, **334**, 261 (1965).
14. H. Schwarz, *ibid.*, **335**, 167 (1965).
15. J. E. Eby, Paper presented at the Toronto Meeting of the Society, Abstract No. 27, May 3-7, 1964.
16. C. S. Wiggins, To be published.
17. G. Dejardin and R. Schwegler, *Rev. Opt. (Theor. Instrum.)*, **13**, 313 (1934).

Current-Induced Oscillations in Liquid Ge

R. L. Anderson

Department of Electrical Engineering, Syracuse University, Syracuse, New York

During experiments on the Peltier effect at germanium solid-liquid interfaces, we have observed mechanical oscillations in the liquid Ge. It is the purpose of this note to describe some of the characteristics of these oscillations.

Bars of Ge were cut 10 cm long and from 0.2 to 1.0 cm^2 in cross-sectional area. The Ge was placed on a quartz boat in a quartz tube. Tungsten leads were attached to either end of the bar and were fed through stoppers at both ends of the tube. A molten zone 1-2 cm long was formed near the center of the bar by heating this region with two focused 1000w projector lamps (1). After the molten zone was formed, a direct current source was applied to the tungsten leads. Ambients of hydrogen, nitrogen, and argon were used at atmospheric pressure.

Germanium bars ranging in doping level from degenerate p-type to degenerate n-type (at room temperature) were used. Ga, In, and Sb were used as dopants. In all cases, with the application of current, the molten zone is displaced in the direction of current flow (2). The displacement is dependent on current density, being about ½ cm at the highest densities used.

In high-purity Ge an unexpected additional effect was observed. Tiny wavelets were seen to build up in the melt at the positive interface and gradually to propagate toward the negative interface. Concurrently, the liquid zone was observed to constrict near the positive interface and "bulge" near the negative interface. This is shown schematically in Fig. 1. The constriction and bulge become more pronounced with time until suddenly the liquid relaxes to its original (displaced) position and the process is repeated. The relaxation time is typically of the order of 40 sec.

The relaxation oscillation was clearly observable through the quartz tube; however, detail in the tiny wavelets was not. For closer observation, the wavelets were "frozen in" by shutting off the projection lamps while current continued to flow through the bar. We believe that the wavelets frozen into the bar are indicative of those in the melt before freezing, because wavelets are observed in the refreeze only in the area in which they were seen in the melt immediately before freezing. Further, wavelets are not seen, either in the melt or in the refreeze, in the absence of current.

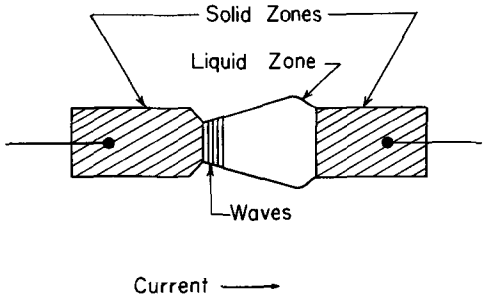

Fig. 1. Schematic representation showing constriction, bulge, and wavelets in liquid Ge.

In Fig. 2 and 3 are shown three representative patterns which were frozen into the melt. Figure 2 shows the region which before freezing was the positive solid-liquid interface. This sample was frozen at the beginning of a cycle, *i.e.*, little constriction had taken place. The portion on the right was liquid. The wavelets frozen into this portion appear as lines and the distance between crests, near the interface, is approximately 8μ. Figure 3a shows a region in the constricted area of another bar. Wavelets of approximately 20μ between crests are superimposed on a structured base. The direction of current is as shown. In Fig. 3b is shown a region taken at the bulge (but entirely in the melt) of another bar. Here the distance between crests is 60μ. A series of mounds is also visible; these mounds appear nearly regularly spaced in both directions. A crack which appeared on freezing is seen near the center of the picture.

The wavelet amplitude and the constriction are greatest for high-purity material and decrease rapidly

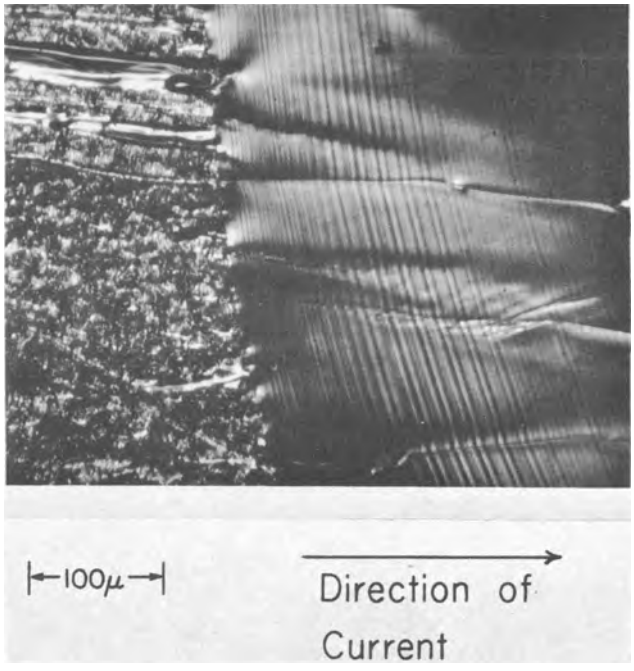

Fig. 2. Boundary between solid and refreeze. The waves are visible in the refrozen portion.

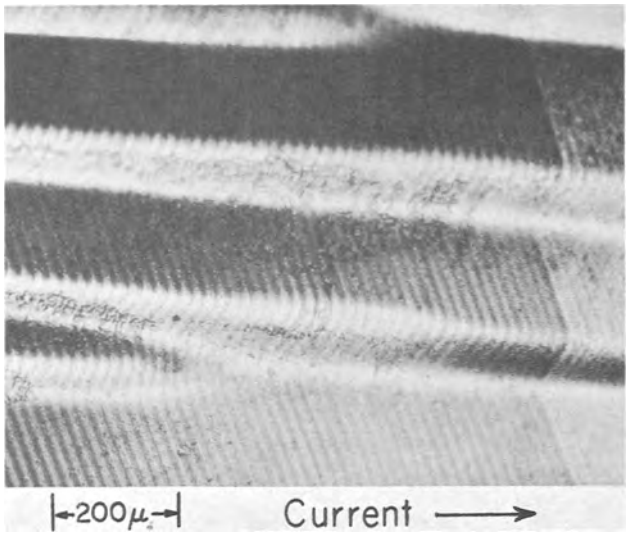

Fig. 3a. Wavelets on a structured base

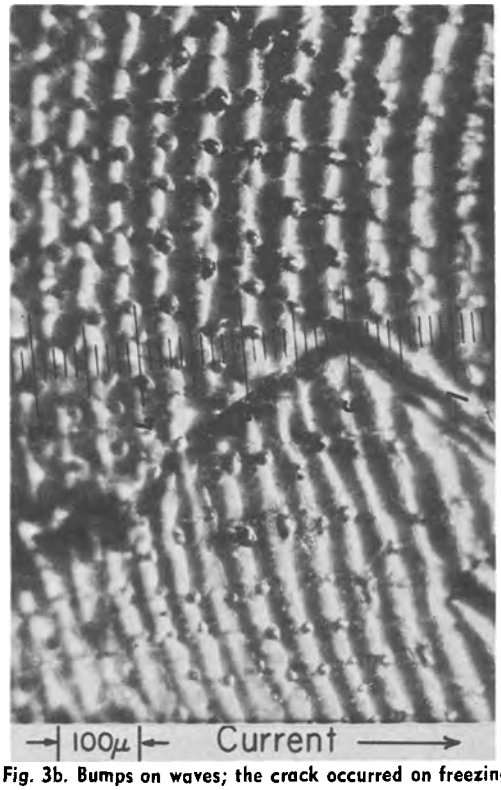

Fig. 3b. Bumps on waves; the crack occurred on freezing

as the impurity concentration is increased. Over a period of an hour the amplitude decreases substantially as the germanium becomes contaminated from the ambient. The impurity concentration above which oscillations are not observed is about 10^{15}-10^{16} cm^{-3}. No oscillations were observed in similar experiments involving tin.

It is found that increasing the current increases the amplitude of the wavelets but appears to have little influence on wavelengh. Although we were unable to observe wavelets at current densities below about 2 amp/cm^2, we believe that no current threshold for their formation exists, but merely that the amplitude was too small to see. The period of the relaxation oscillation seems little affected by current although maximum deformation of the melt increases with increasing current. At sufficiently high current (approximately 200 amp/cm^2 in the highest purity samples) the constriction is so great that it actually pinches the bar into two pieces.

There appears to be a relationship between the wavelets and the relaxation oscillation described here since both effects are always present simultaneously. Further, the degree of deformation (constriction and bulge) appears to depend on the area covered by wavelets. Immediately after a relaxation there is no deformation and no wavelets. As the wavelets begin to spread from the positive interface, the deformation also increases. It appears as though increased surface tension is associated with the wavelets resulting in constriction in this region and a corresponding bulge in the molten zone not covered with wavelets. We have never observed the molten zone to be totally covered with wavelets.

The displacement of the liquid zone on the application of current is thought to be primarily a result of Peltier heating at the positive interface and Peltier cooling at the negative interface (2), although the Thomson effect, electrolysis, and momentum transfer from current carriers to impurity ions (3-6) may affect the magnitude of the displacement.

Although oscillations at liquid-solid interfaces resulting from electric current flow have not been reported, Komarov and Regel (7) have observed oscillations in bismuth and in lead when the temperature gradient at an interface exceeds a threshold of 40°-60°C/cm. The impurity content is presumably not important in this effect since the addition of up to 2 a/o (atom per cent) of tin had no appreciable affect in the results. The oscillations are explained by the excitation of the surface by turbulent convection currents produced in the ambient by the high-temperature gradient. Cole and Winegard (8) have measured the temperature fluctuation in the melt near a solid-liquid interface for tin. The magnitude of the fluctuation increases with temperature gradient and is attributed to convection in the liquid. Mechanical oscillations were not reported.

It is believed that the current-induced oscillations reported here are not connected directly with the oscillations attributed to a large temperature gradient because our results are very sensitive to impurity content and because of the apparent absence of a threshold current. Although the temperature gradient at the interface would be expected to be altered by the Peltier effect on the application of current, if the effect depended on exceeding a temperature gradient threshold, this would be manifested by an apparent current threshold.

It is doubtful that the oscillations result from an electronic effect since the conduction in liquid Ge is thought to be metallic in nature (9), and it seems improbable that a small impurity content would affect the conduction appreciably. Likewise a plasma effect would appear to be ruled out because of the high concentration of electrons present in the liquid. It may be that these waves are associated with surface tension. It is known that a minute quantity of impurities changes surface tension in many materials. The current flow may move the impurities toward one end of the molten zone by electrolysis or by ion entrainment and thus create a gradient in surface tension in the liquid zone which might explain the pinch and bulge effects. It is not clear, however, how this would explain the wavelets or the relaxation. It is conceivable, however, that they might be associated with the change in surface tension at the positive interface due to charge accumulation, which in turn results from current flow across the discontinuity in electrical conductivity (10).

Acknowledgment

The assistance of W. Blake with the experiments and the comments of H. Gruenberg are acknowledged. This work was supported by the National Science Foundation.

Manuscript received Feb. 4, 1966.

Any discussion of this paper will appear in a Discussion Section to be published in the June 1967 JOURNAL.

REFERENCES

1. For a description of the apparatus, see E. H. Nicollian, G. R. Gunther-Mohr, and L. R. Weisberg, *IBM J. Res. Dev.*, **2**, 349 (1957).
2. W. G. Pfann, K. E. Benson, and J. H. Wernick, *J. Electronics*, Ser. 1, **2**, 597 (1957).
3. D. T. J. Hurle, J. B. Mullin, and E. R. Pike, *Phil. Mag.*, **9**, 423 (1964).
4. V. B. Fiks, *Phys. Letter*, **9**, 299 (1964).
5. W. A. Tiller, *J. Appl. Phys.*, **34**, 2757 (1963).
6. W. A. Tiller, *ibid.*, **34**, 2763 (1963).
7. G. V. Komarov and A. R. Regel, *Sov. Phys.-Solid State*, **5**, 563 (1963).
8. G. S. Cole and W. C. Winegard, *Can. Met. Quarterly*, **1**, 29 (1962).
9. R. W. Keyes, *Phys. Rev.*, **84**, 367 (1951).
10. See for example, R. F. Harrington, "Introduction to Electromagnetic Engineering," p. 200, McGraw-Hill, New York (1958).

Evaporated Ohmic Contacts on GaAs

W. A. Schmidt

United States Naval Research Laboratory, Washington, D. C.

Various schemes have been proposed for making ohmic contacts to GaAs (1-4). One of the common ones involves evaporation of a metal on the semiconductor surface, followed by alloying using conventional solders.

We have had considerable difficulties in making such evaporated contacts, and we therefore felt that a description of our technique may not be without general interest.

Contacts to both p and n material were made in the same manner. The GaAs material was first prepared by abrasive processes using either 25μ garnet or 600 grit silicon carbide; the surface to be metalized was etched in dilute nitric acid (4 pt. HNO_3:1 pt. H_2O) for 30 sec, then rinsed in water, acetone, and methanol. The sample was immediately mounted on a holder and placed in a vacuum evaporator. With the bell jar pumped down to 2 x 10^{-6}, the GaAs sample was heated to about 550°C to heat-clean the surface. After cleaning for a few minutes at the elevated temperature the power was turned off and the sample allowed to cool. When the sample cooled to about 200°C a 1μ thick film of silver was evaporated onto the surface. The temperature was again raised to 550°C and held there for a few minutes to heat treat the silver contact. After this the power was turned off and the wafer allowed to cool to room temperature, at which temperature a 0.3μ nickel film was deposited. The nickel film was not followed by a heat-treatment.

These contacts were tested for mechanical strength by pulling off small copper wires that had been soldered to the contact. (Fig. 1) It can be seen that some of the GaAs was pulled off along with the solder bead. The electrical nature of the contact was investigated using small area contacts that had been formed by masking small regions and abrading away the surrounding area.

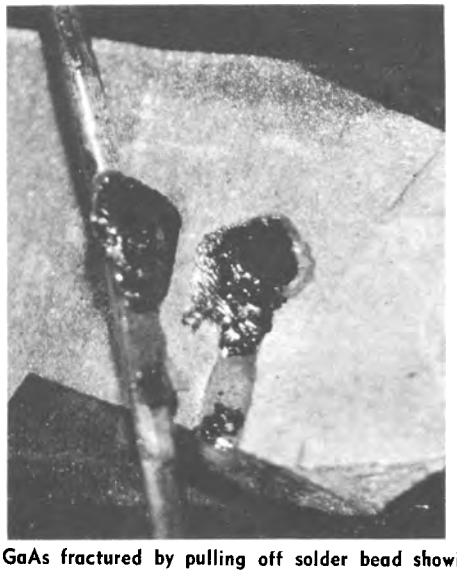

Fig. 1. GaAs fractured by pulling off solder bead showing both the piece removed and the crater in the GaAs.

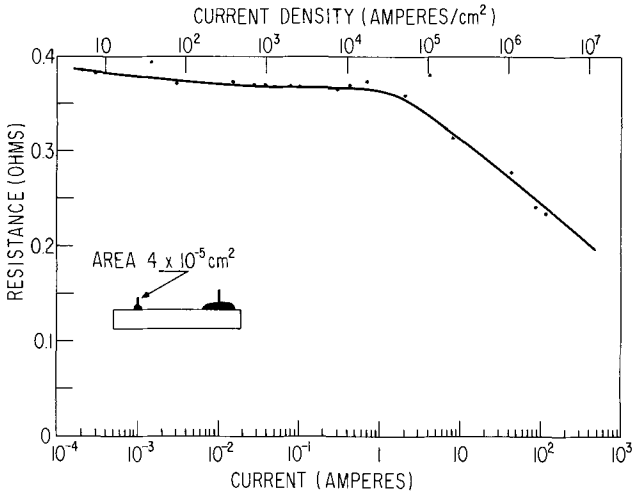

Fig. 2. Resistance between two contacts (see inset) as a function of current.

The I-V characteristic for a pair of contacts on 0.0033 ohm-cm material was measured with d.c. and with 1μ second pulses for currents above 100 ma. No significant deviations of this characteristic were noted when the current polarity was reversed. Figure 2 is a plot of the measured resistance up to a current density of 3 x 10^6 amp/cm^2. Taking the worst case, that all of the resistance is due to the contact, we find that the specific contact resistance is less than 2 x 10^{-5} ohm cm^2. (The total contact resistance $R_T = R_s/A$ where R_s is the specific contact resistance and A is the contact area.)

The same technique has been applied to polycrystalline n- and p-type GaAs with 10^{17} carriers/cm^3.

Manuscript received Feb. 4, 1966.

Any discussion of this paper will appear in a Discussion Section to be published in the June 1967 JOURNAL.

REFERENCES

1. R. Proebsting, *Solid State Technology*, **7**, 33 (1964).
2. J. R. Dale and R. G. Turner, *Solid State Electron.*, **6**, 388 (1963).
3. M. Pilkuhn, H. Rupprecht, and S. Blum, *ibid.*, **7**, 905 (1964).
4. R. Rediker and T. Quist, *ibid.*, **6**, 657 (1963).

The Arsenic-Rich Region of the Ga-As-Zn Ternary Phase System —Modification of the Ternary Diagram

M. B. Panish

Bell Telephone Laboratories, Incorporated, Murray Hill, New Jersey

In several recent papers (1, 2), the ternary phase diagrams of gallium and arsenic with Zn, Sn, and Ge have been presented. A striking feature of these phase diagrams is the extensive primary phase field of GaAs. In the case of the gallium-arsenide-zinc system (1) experimental data on the arsenic-rich side of the diagram were not obtained by this author. Instead, isotherms in the GaAs primary phase field were estimated by the use of a regular solution approximation. In order to more accurately present the Ga-As-Zn ternary phase diagram, phase transition data on the GaAs-Zn_3As_2 cut of the ternary system have been obtained by the differential thermal analysis procedure previously described (1). The only modification to the procedure was that the starting materials were GaAs and Zn_3As_2 rather than GaAs plus zinc and arsenic. This was necessary in order to prevent explosions which occur as a result of the reaction of zinc with arsenic in the restricted volume of the D.T.A. cell.

In Fig. 1 are presented the thermal effect data obtained when mixtures with over-all compositions along the GaAs-Zn_3As_2 cut were cooled. Also presented are the thermal effect data of Köster and Ulrich (3) for the same cut, and the melting point of GaAs obtained in this work. The latter value (1237° ± 2°C) is in excellent agreement with the value of 1238°C obtained by Köster and Thoma (4). T_1 represents the temperature at which the surface of primary crystallization is reached, T_2 represents the temperature of appearance of a second solid phase, and T_3 is the temperature at which a ternary eutectic between GaAs, Zn_3As_2, and $ZnAs_2$ precipitates.

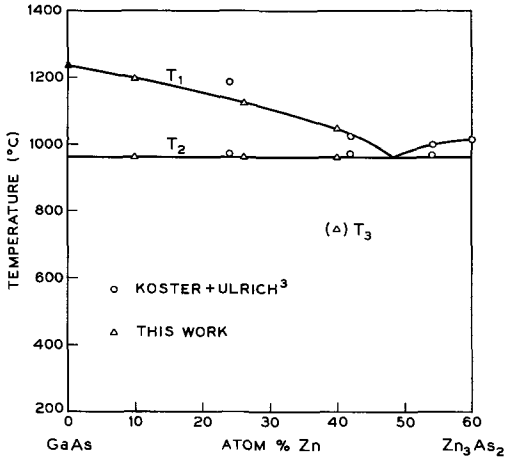

Fig. 1. Thermal effects in the GaAs-Zn_3As_2 pseudobinary system; ○ Köster and Ulrich (3); △ this work.

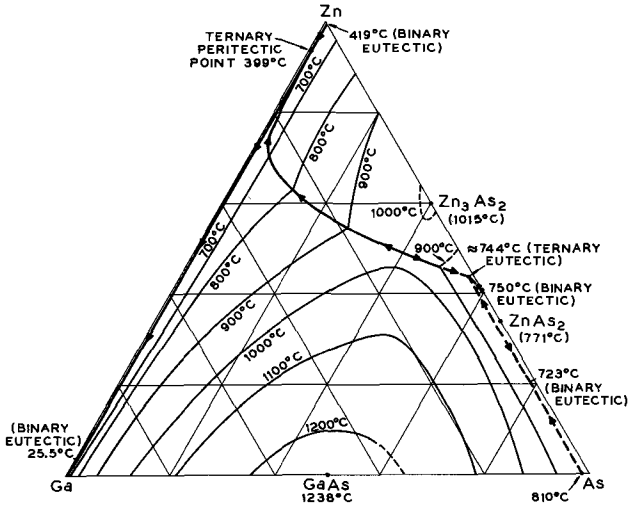

Fig. 2. The Ga-As-Zn ternary phase diagram

Some of the thermal effect data reported by Köster and Ulrich (3) on the GaAs-Zn_3As_2 cut and the GaAs-$ZnAs_2$ cut are consistent with the data reported earlier by this author (1) and that reported here. Their T_1 thermal effects in the vicinity of 1200°C are, however, in disagreement with the measurements reported here and with a reasonable extrapolation of our earlier data. A possible reason for this disagreement has already been presented (1).

The ternary Ga-As-Zn phase diagram based on our previous D.T.A. studies (1) and the data presented here is shown in Fig. 2. The method used for the construction of the diagram is similar to that employed for the Ga-As-Sn and Ga-As-Ge phase diagrams (2). This diagram is similar to that reported before except that the isotherms are all somewhat more distorted in the direction of the As-Zn binary axis.

Acknowledgment

The author would like to thank C. D. Thurmond for his advice during the course of this work, and S. Sumski for his help in the preparation of D.T.A. experiments.

Manuscript received Feb. 1, 1966.

Any discussion of this paper will appear in a Discussion Section to be published in the June 1967 JOURNAL.

REFERENCES

1. M. B. Panish, *J. Phys. Chem. Solids*, **27**, 291 (1966).
2. M. B. Panish, *J. Less Common Metals*, **10**, 416 (1966).
3. W. Köster and W. Ulrich, *Z. Metallkunde*, **49**, 361 (1958).
4. W. Köster and B. Thoma, *ibid.*, **40**, 291 (1955).

The Reversible Oxygen Potential in Phosphoric Acid Solutions

Raymond Thacker and James P. Hoare

Electrochemistry Department, Research Laboratories, General Motors Corporation, Warren, Michigan

It has been found that the potential of a bright platinum electrode which had been treated in concentrated nitric acid for 72 hr (1, 2) became steady at the normal oxygen potential, 1230 mv (3), for periods of time greater than 24 hr in O_2-saturated, H_2O_2-free $2N$ H_2SO_4 solutions. From rest potential studies (1), steady-state polarization measurements (2), and double layer capacity data (4), it was concluded that such a treatment produced a complete, electronically conducting film of adsorbed oxygen on the Pt surface which rendered the electrode surface inert to oxygen. Consequently, the mixed potential which was ordinarily observed (5) was suppressed, and the reversible oxygen potential was reached. Other investigators who have obtained this complete passivating film by anodization and exposure of the platinum to pure oxygen for long periods of time (6, 7) have also observed the reversible oxygen potential. This complete film is unstable in sulfuric acid solutions and eventually becomes incomplete, whereupon a mixed potential mechanism (5) sets in and the rest potential falls to less noble values.

In addition to forming the passivating film of adsorbed oxygen, it was concluded (2, 4) that the HNO_3 treatment also enabled a certain amount of oxygen to be dissolved in the surface layers of the Pt metal to form a Pt-O alloy. Recently, Warner and Schuldiner (8) referred to this absorbed oxygen as "dermasorbed oxygen" and found (9) that it was difficult to remove. X-ray analysis of the treated Pt (10) showed a shifting of the diffraction lines from those obtained on untreated Pt, and vacuum fusion analysis (10) showed that the treated samples contained more oxygen than the untreated samples. Nitric acid-treated Pt electrodes are called Pt-O-alloy electrodes (2, 4).

Since phosphoric acid is another good CO_2-rejecting electrolyte, it was considered important to look into the behavior of the rest potential of the Pt-O-alloy electrode in phosphoric acid solutions.

Test electrodes were made in the form of small beads melted at the end of bright Pt wires or in the form of squares of bright Pt gauze spot-welded to Pt wire leads. These electrodes were sealed into glass holders and mounted in a glass cell (11). The cell and electrode cleaning procedures were similar to those described before (4, 5, 11). The clean electrodes were soaked in concentrated HNO_3 for at least 72 hr, after which they were leached in triply distilled water for 2 hr with frequent changes of the water before being placed in the cell. Phosphoric acid solutions of 5, 3, 1, and 0.5M were made from reagent grade concentrated H_3PO_4 and were anodically preelectrolyzed in a separate vessel for 3 days followed by cathodic preelectrolysis for an additional 3 days. Any peroxide generated in the preelectrolysis procedure was removed by bubbling H_2 over Pt gauze in the solution until a negative test with $TiSO_4$ (12) was obtained. This purified solution was placed in the cell, and the rest potential was determined against a saturated calomel electrode (SCE). All potentials are reported with reference to a hydrogen electrode in the same solution, since in each solution the potential of a hydrogen electrode was determined against the SCE. The temperature was 25° ± 1°C. Duplicate runs on different electrodes were made in all solutions, and the spread of values of the steady potential (±0.5 mv) obtained from one electrode to another (±5 mv) is given in Tables I and II. All solutions were saturated with O_2. Similar measurements were made in 5, 1, 0.5, and 0.1M H_2SO_4 solutions.

Table I. Rest potentials of Pt-O-alloy electrodes in H_3PO_4 solution

Solution, M	Rest potential, mv	Activity of H_2O	Activity of H_3PO_4	1230—E, mv	0.03 log $a_{H_3PO_4}$, mv
5	1195 ± 5	0.87	9.72	35	30
3	1212 ± 5	0.93	4.05	18	18
1	1226 ± 5	0.98	0.96	4	−0.5
0.5	1230 ± 5	0.99	0.99	—	—

Table II. Rest potentials of Pt-O-alloy electrodes in H_2SO_4 solution

Solution, M	Rest potential, mv	Activity of H_2O
5	1226 ± 5	0.70
1	1227 ± 5	0.96
0.5	1225 ± 5	0.98
0.1	1225 ± 5	0.99

As pointed out by Bockris *et al.* (6, 13), rigorous control of impurities was required for reproducible results. In Table I are presented the steady-state rest potentials in various phosphoric acid solutions and in Table II those for sulfuric acid solutions. The rest potentials in H_3PO_4 solutions were steady for longer periods of time (about 72 hr) than those in H_2SO_4 solutions (about 24 hr). Such behavior may be interpreted to mean that the complete adsorbed oxygen film is more stable in H_3PO_4 solutions. Such behavior is not surprising because it is known (14) that Na_3PO_4 solutions are good inhibitors for the corrosion of iron. The presence of Na_3PO_4 assists in the formation of the protective film of cubic oxide on the iron surface. Possibly, the presence of phosphate ion stabilized the adsorbed oxygen film on the Pt-O-alloy electrodes.

An interesting point is the fact that the rest potential deviates from the normal oxygen potential, 1230 mv, at the higher H_3PO_4 concentrations, whereas this is not true in H_2SO_4 solutions. In both cases, the change in activity of water as seen in column 3 and taken from the literature (15, 16) cannot account for these observations since the water correction would be too small and, in any event, is in the wrong direction. The activity of phosphoric acid (15), recorded in column 4 of Table I, decreases with decreasing H_3PO_4 concentration in correlation with the decrease in the shift of the rest potential from the reversible potential recorded in column 5.

If the Nernst equation is written for the cell, one obtains

$$E = E^\circ_{O_2} - E^\circ_{H_2} - \frac{RT}{4\mathbf{F}} \ln \frac{a^2_{H_2O}}{P_{O_2} a^4_{H^+}} + \frac{RT}{\mathbf{F}} \ln \frac{P^{1/2}_{H_2}}{a_{H^+}} \quad [1]$$

or

$$E = 1230 - 0 - \left[\frac{0.06}{4} (2 \log a_{H_2O} - \log P_{O_2}) \right] + 0.03 \log P_{H_2} \quad [2]$$

Since the partial pressures of oxygen, P_{O_2}, and of hydrogen, P_{H_2}, are unity and the activity of water, a_{H_2O}, is approximately unity, the potential of the cell, E, is $E^\circ_{O_2} = 1230$ mv as found in the case of the sulfuric acid solutions in Table II. However, in solutions 1M or greater in phosphoric acid, the rest potential may be accounted for empirically by adding a term involving the activity of phosphoric acid, $a_{H_3PO_4}$,

$$-\frac{RT}{2\mathbf{F}} \ln a_{H_3PO_4} \quad [3]$$

to Eq. [1]. The value of this correction term is given in column 6 of Table I. This behavior indicates that anion adsorption of $H_2PO_4^-$ ions is important in solutions with concentrations greater than 1M H_3PO_4 and shifts the rest potential to less noble values. The effects of the adsorption of ions on electrode processes has been summarized by Frumkin (17) and Delahay (18). With acid solutions below 1M in H_3PO_4 and up to 5M in H_2SO_4, anion adsorption does not affect the rest potential significantly. From anion adsorption studies (17-19), one would expect a smaller effect with HSO_4^- than with $H_2PO_4^-$ ions.

As a check on the effect of the $H_2PO_4^-$ ion on the rest potential, the following experiment was performed. A Pt-O-alloy electrode was permitted to come to a steady open-circuit potential in 5M, H_2O_2-free, O_2-saturated H_3PO_4 solution. The potential came to the steady value of 1199 mv in agreement with the data in Table I. This electrode was removed from the 5M H_3PO_4 and washed with triply distilled water. After plunging the electrode in 1M H_2SO_4 solution, the rest potential rose to a steady value of 1227 mv. These results are offered in support of the conclusions reached concerning the effect of the adsorption of $H_2PO_4^-$ ions on the rest potential.

An important observation was the fact that several electrodes came to a steady rest potential in molar acid solutions at values between 1000 and 1100 mv. In each case it was found that the metal-to-glass seal was defective, and solution contact was made with the Pt wire lead which had not been exposed to HNO_3. The preferred explanation is the suggestion that a mixed potential is set up between sites on the electrode completely covered by the adsorbed oxygen film and uncovered Pt sites on the partially covered Pt lead wire. In this case a potential less noble than 1230 mv is to be expected as found on untreated Pt electrodes (5).

Manuscript received March 11, 1966.

Any discussion of this paper will appear in a Discussion Section to be published in the June 1967 JOURNAL.

REFERENCES

1. J. P. Hoare, *This Journal*, **110**, 1019 (1963).
2. J. P. Hoare, *ibid.*, **112**, 849 (1965).
3. W. M. Latimer, "Oxidation Potentials," 2nd ed., p. 39, Prentice-Hall, New York (1952); A. J. deBethune and N. A. S. Loud, "Standard Aqueous Electrode Potentials and Temperature Coefficients," Clifford Hempel, Skokie, Ill. (1964).
4. J. P. Hoare, *Nature*, **204**, 71 (1964).
5. J. P. Hoare, *This Journal*, **109**, 858 (1962).
6. J. O'M. Bockris and A. K. M. S. Huq, *Proc. Roy. Soc.*, **A237**, 277 (1956).
7. N. Watanabe and M. A. V. Devanathan, *This Journal*, **111**, 615 (1964).
8. T. B. Warner and S. Schuldiner, *ibid.*, **112**, 853 (1965).
9. S. Schuldiner and T. B. Warner, *ibid.*, **112**, 212 (1965).
10. J. P. Hoare, S. G. Meibuhr, and R. Thacker, To be submitted.
11. R. Thacker in "Hydrocarbon Fuel Cell Technology," B. S. Baker, Editor, Academic Press, New York (1966).
12. F. D. Snell and C. T. Snell, "Colorimetric Methods of Analysis," Vol. II, 3rd ed. (1949).
13. N. Pentland, J. O'M. Bockris, and E. Sheldon, *This Journal*, **104**, 182 (1957).
14. U. R. Evans, "The Corrosion and Oxidation of Metals," p. 136, St. Martin's Press, New York (1960).
15. K. L. Elmore, C. M. Mason, and J. H. Christensen, *J. Am. Chem. Soc.*, **68**, 2528 (1946).
16. H. S. Harned and W. J. Hamer, *ibid.*, **57**, 27 (1935).
17. A. N. Frumkin, *Proc. CITCE*, **9**, 396 (1959); *This Journal*, **107**, 461 (1960); *Electrochim. Acta*, **5**, 265 (1961).
18. P. Delahay, "Double Layer and Electrode Kinetics," Interscience Publishers, New York (1965).
19. D. C. Grahame, *Chem. Rev.*, **41**, 441 (1947).

The Performance of Flooded Porous Fuel Cell Electrodes

Ralph Brown and John A. Rockett

Pratt & Whitney Division, United Aircraft Corporation, East Hartford, Connecticut

ABSTRACT

The thin-meniscus model that is often applied to porous gas diffusion fuel cell electrodes has been found unsatisfactory for hydrogen reacting at nickel sinters in highly concentrated KOH electrolyte. The relative insensitivity of the performance to the gas-electrolyte pressure difference, which should have a strong influence on the active thin-meniscus area, requires the assumption that the flooded volume of the electrode is active. A model for a flooded pore is treated and the results of an approximate analytical solution compared with data.

The usual model for a biporous sintered electrode considers a thin liquid meniscus that covers the metal surface in that portion of the electrode from which liquid has been expelled (1-3). The typically low solubility-diffusivity products of gases in electrolytes causes those metal surfaces surrounded by any more liquid than a thin meniscus to be inactive, the transport rate of the reactant gas through the liquid being too small. We have applied this model to an oxygen electrode in alkaline electrolyte with a good deal of success. There are experimental indications, however, that suggest this model does not always apply when hydrogen reacts at a nickel sinter in alkaline electrolyte.

Part of a biporous electrode is the fine-pore region on the electrolyte side which acts as a gas barrier to prevent bubbling of the gas through the electrode. The pores are small enough that capillary forces are sufficient to maintain a specified gas-electrolyte pressure difference. The remaining portion of the electrode is the coarse pore region from which electrolyte has been expelled at operating gas-electrolyte pressure differences. Since the coarse pore contains a distribution of pore sizes, the gas-filled volume in which thin liquid meniscus covers the metal will increase with increasing pressure differences. The performance should then improve as pressure difference rises and more active meniscus area becomes available. This is the case for oxygen electrodes as illustrated in Fig. 1. The results were obtained from an experiment in which two 5-in. diameter electrodes were spaced about ¼ in. apart by a ring that was electrically insulated from the electrodes. The electrolyte contained between the electrodes and ring was connected by a nickel tube to a ¼ in. diameter Teflon tube which served as an electrolyte level indicator. As the electrode gas pressure was varied, the displacement of electrolyte in the electrode was determined by the electrolyte level in the calibrated Teflon tube. Hydrogen was bled through a silver palladium tube which was immersed in the electrolyte in the Teflon tube. This served as a reference electrode. The arrangement measured both the electrolyte displacement and potential as a function of gas to electrolyte pressure difference. Figure 1 shows that good performance on an oxygen electrode was obtained only after a considerable fraction of electrolyte was displaced. Below a gas to electrolyte pressure difference of 6 psi, where very little electrolyte was displaced by gas, the current at 0.2v polarization was very small. This behavior is not shown in Fig. 2, where a similar experiment was done on a hydrogen electrode. At 2 psi gas to electrolyte pressure difference, where the electrolyte displacement indicated the electrode was essentially flooded, the polarization was only slightly greater than pressure differences at which 30% of the void volume was displaced. This insensitivity of the hydrogen electrode to the gas-electrolyte pressure difference was observed for hydrogen electrodes at temperatures of 150°-250°C and KOH concentrations of 70-85%. Since gas displacement of electrolyte is unnecessary for good performance, the need for a large area of thin meniscus is not established. The only possible conclusion is that the flooded portion of the electrode is active. A means of transport for the hydrogen into the flooded region other than that limited by the low bulk solubility-diffusivity product must be assumed. Surface diffusion could account for the high effective hydrogen diffusivity if we assume enough thin meniscus is available to allow the hydrogen to get to the metal surface without causing a significant gas diffusion polarization.

The purpose of this paper is to describe the solution of the flooded electrode problem and determine if the results are consistent with hydrogen half cell data. The more complex problem of considering both gas-filled regions and flooded regions in one electrode

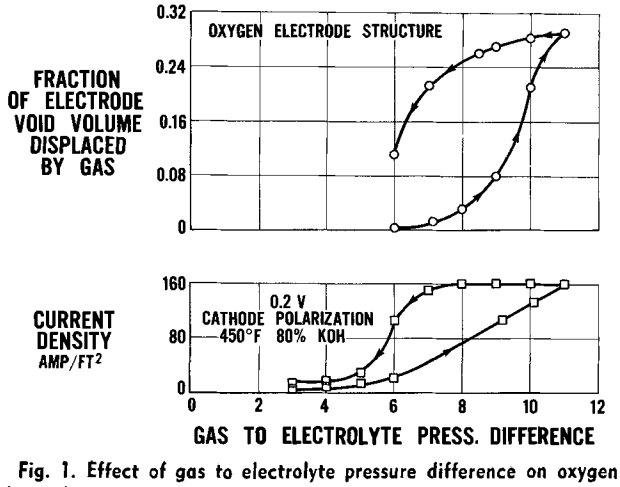

Fig. 1. Effect of gas to electrolyte pressure difference on oxygen electrode.

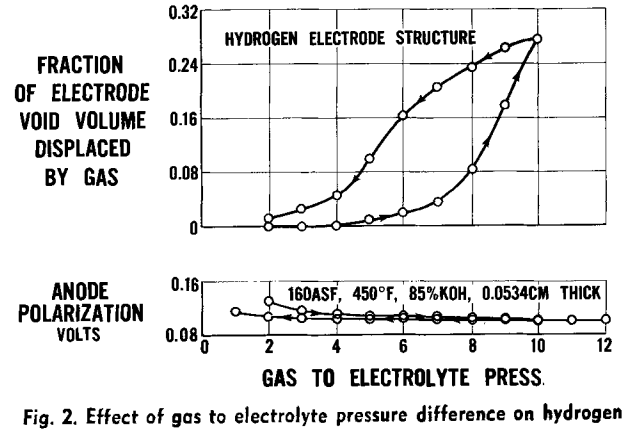

Fig. 2. Effect of gas to electrolyte pressure difference on hydrogen electrode.

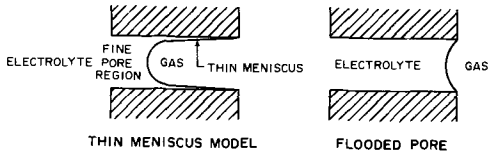

Fig. 3. Electrode models

is not discussed. This would involve a more sophisticated description of the electrode structure than the cylindrical pore model assumed here.

Theoretical Model

For purposes of comparison, both geometric models for the flooded electrode and the gas-filled electrode are shown in Fig. 3. The electrode is considered as an array of cylindrical pores whose diameter is that of the mean pore size of the structure. In the gas-filled model, the flooded portion represents the fine pore layer and the gas-filled coarse pore is coated with a thin liquid meniscus. The transport rate of gas through this thin liquid film is relatively high compared to what it would be in the flooded portion. In the flooded model, the entire cylinder is full of liquid, but gas can diffuse either along the surface or through the bulk metal. This effectively increases the diffusivity over what it would be in just the bulk liquid.

The next major assumption deals with the half-cell reaction. The over-all reaction for the oxidation of hydrogen in alkaline electrolyte is as follows

$$H_2 + 2\,OH^- \rightleftharpoons 2H_2O + 2e^- \qquad [1]$$

In order to write a precise kinetic expression for the net half-cell reaction, the sequence and relative rate constant for each reaction step must be known. For the case where the activity ratios of the electrolyte species are approximately unity, the following expression has been shown to be valid (4).

$$i = i_1 \left[\frac{\alpha_{H_2}}{\alpha_{H_2}^{\circ}} e^{\frac{F}{RT}\eta} - e^{-\frac{F}{RT}\eta} \right] \qquad [2]$$

In order to include the activity of the electrolyte species, the kinetic expression is written as follows

$$i = i_1 \left[\left(\frac{\alpha_{H_2}}{\alpha_{H_2}^{\circ}} \right) \left(\frac{\alpha_{KOH}}{\alpha_{KOH}^{\circ}} \right)^2 e^{\frac{F}{RT}\eta} - \left(\frac{\alpha_{H_2O}}{\alpha_{H_2O}^{\circ}} \right)^2 e^{-\frac{F}{RT}\eta} \right] \qquad [3]$$

The placement of these electrolyte species activity ratios with respect to the forward and reverse terms is arbitrary, but their exponents are consistent with the thermodynamics of the over-all reversible reaction. One of the most important assumptions regarding the choice of the kinetic expression is that the controlling step takes place either before or is the step during which the H-H bond is broken. This means that the hydrogen exchange current is directly proportional to hydrogen partial pressure.

Mathematical Formulation

The analysis considers a differential slice cut from the cylinder as shown in Fig. 4. The local current density on the metal surface is given by the kinetic expression. The potential, E, of the electrode is measured relative to a reference probe located in the bulk liquid to the left of the electrode fine pore. The ohmic potential in the electrolyte, ϕ, is chosen as zero at the left edge of the fine pore and chosen to have increasingly positive values in the positive x direction. The local metal-solution potential difference at any point in the pore is given by the difference between the electrode potential and the solution potential. The kinetic expression of Eq. [3] can then be

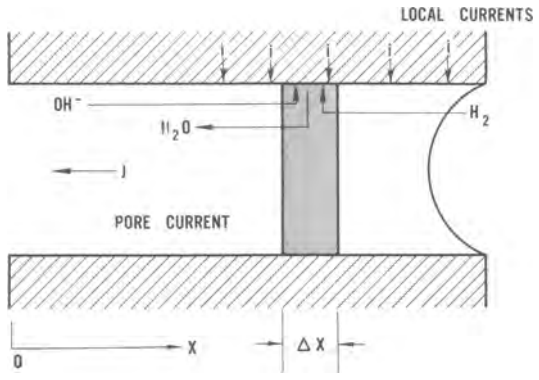

Fig. 4. Single pore

written with the driving potentials in terms of the solution potential.

$$i = i_1 \left[\left(\frac{\alpha_{H_2}}{\alpha_{H_2}^{\circ}} \right) \left(\frac{\alpha_{KOH}}{\alpha_{KOH}^{\circ}} \right)^2 e^{\frac{F}{RT}(E-\phi)} - \left(\frac{\alpha_{H_2O}}{\alpha_{H_2O}^{\circ}} \right)^2 e^{-\frac{F}{RT}(E-\phi)} \right] \qquad [4]$$

The local current density is related to the current in the axial direction of the pore by making a current balance on the differential wafer. Radial variations are neglected making the problem one-dimensional and the pore current goes in the negative x direction.

$$i = \frac{1}{2\pi R} \frac{dJ}{dx} \qquad [5]$$

The current in the axial direction of the pore is related to the ohmic potential in the electrolyte by Ohm's law.

$$J = -\pi R^2 \sigma \frac{d\phi}{dx} \qquad [6]$$

Substitution of Eq. [6] into Eq. [5] relates the ohmic potential in the electrolyte to the local current density.

$$i = -\frac{R\sigma}{2} \frac{d^2\phi}{dx^2} \qquad [7]$$

The current associated with the hydrogen flux in the axial direction of the pore can be related to the hydrogen activity by Fick's diffusion law.

$$J_{H_2} = -\pi R^2 n F D_{H_2} \alpha_{H_2}^{\circ} \frac{d(\alpha_{H_2}/\alpha_{H_2}^{\circ})}{dx} \qquad [8]$$

Substitution of Eq. [8] into Eq. [5] relates the hydrogen activity ratio to the local current density. The sign changes in this substitution to account for the fact that hydrogen moves to the surface in a direction opposite to that chosen for the local currents.

$$i = \frac{R}{2} n F D_{H_2} \alpha_{H_2}^{\circ} \frac{d^2(\alpha_{H_2}/\alpha_{H_2}^{\circ})}{dx^2} \qquad [9]$$

The water and KOH activity ratios can be related to the ohmic potential in the electrolyte as will be shown in a following section. This being the case, the local current density at any given electrode polarization is a function of only the ohmic potential in the electrolyte and the hydrogen activity ratio. Equations [7] and [9] are then the two equations in ϕ and $\alpha_{H_2}/\alpha_{H_2}^{\circ}$ that must be solved simultaneously in order to obtain $\alpha_{H_2}/\alpha_{H_2}^{\circ}$ as a function of x. The total pore current is then found by evaluating the first derivative of $\alpha_{H_2}/\alpha_{H_2}^{\circ}$ with respect to x at the point where all the hydrogen passes. The total current is

$$J = -\pi R^2 nF D_{H_2\alpha_{H_2}^o} \left.\frac{d(\alpha_{H_2}/\alpha_{H_2}^o)}{dx}\right|_{x=L} \quad [10]$$

Boundary conditions for Eq. [7] and [9] are defined at both ends of the pore. At the electrolyte side, the electrolyte potential is chosen at zero and no more hydrogen diffuses in the axial direction as none is consumed to the left of this point.

$$\text{at } x = 0: \quad \phi = 0 \quad [11a]$$

$$\frac{d(\alpha_{H_2}/\alpha_{H_2}^o)}{dx} = 0 \quad [11b]$$

At the gas side, the hydrogen activity is at its reference value and there is no ohmic gradient as no current is generated to the right of this point.

$$\text{at } x = L: \quad \alpha_{H_2}/\alpha_{H_2}^o = 1 \quad [12a]$$

$$\frac{d\phi}{dx} = 0 \quad [12b]$$

We have two simultaneous second-order equations to solve. The one in $\alpha_{H_2}/\alpha_{H_2}^o$ is linear, but the one in ϕ is nonlinear. If we neglect both the ohmic and the electrolyte concentration polarizations, both equations become linear and an analytical solution is readily obtained. The approximations are

$$E - \phi \cong E \quad [13]$$

$$\frac{\alpha_{H_2O}}{\alpha_{H_2O}^o} = \frac{\alpha_{KOH}}{\alpha_{KOH}^o} \cong 1 \quad [14]$$

The approximate differential equations become

$$-\frac{R\sigma}{2}\frac{d^2\phi}{dx^2} = i_1\left[\frac{\alpha_{H_2}}{\alpha_{H_2}^o}e^{FE/RT} - e^{-FE/RT}\right] \quad [15]$$

$$\frac{nFD_{H_2\alpha_{H_2}^o}}{2}\frac{d^2(\alpha_{H_2}/\alpha_{H_2}^o)}{dx^2} = i_1\left[\frac{\alpha_{H_2}}{\alpha_{H_2}^o}e^{FE/RT} - e^{-FE/RT}\right] \quad [16]$$

Equation [16] can be solved for the hydrogen activity ratio as a function of x by applying the boundary conditions of Eq. [11b] and [12a]

$$\frac{\alpha_{H_2}}{\alpha_{H_2}^o} = (1 - e^{-2FE/RT}) \frac{\cosh\left[\left(\frac{i_1}{RFD_{H_2\alpha_{H_2}^o}}\right)^{1/2} e^{FE/2RT}x\right]}{\cosh\left[\left(\frac{i_1}{RFD_{H_2\alpha_{H_2}^o}}\right)^{1/2} e^{FE/2RT}L\right]} + e^{-2FE/RT} \quad [17]$$

This is now differentiated with respect to x, evaluated at $X=L$, and substituted into Eq. [10] to obtain the total pore current.

$$J = 2\pi R\sqrt{RFD_{H_2\alpha_{H_2}^o}i_1}\,(e^{FE/2RT} - e^{-3FE/2RT}) \tanh\left[\sqrt{\frac{i_1}{RFD_{H_2\alpha_{H_2}^o}}}\,e^{FE/2RT}L\right] \quad [18]$$

The numerical solution of Eq. [7] and [9] was obtained by employing the method of quasilinearization. The solution of this system via quasilinearization entails expanding the expression for local current density into a truncated Taylor series. This reduces the nonlinear, two-point boundary value problem to the problem of solving a sequence of linear two-point problems. The sequence of linear two-point problems can then be solved in terms of initial value techniques through a numerical construction of Green's functions.

Transport of Electrolyte Species

The hydroxyl ion that is consumed in the reaction must diffuse axially through the pore from the bulk electrolyte to the reaction surface. If ideal solutions are assumed and bulk transport is neglected, the transport equations for both potassium and hydroxyl ions show a term proportional to KOH concentration gradient and a term proportional to ohmic potential.

$$J = \pi R^2\left[-FD_{OH}\frac{dC_{OH}}{dx} - \lambda_{OH}C_{KOH}\frac{d\phi}{dx}\right] \quad [19]$$

$$o = \pi R^2\left[-FD_K\frac{dC_K}{dx} + \lambda_K C_{KOH}\frac{d\phi}{dx}\right] \quad [20]$$

Equation [20] can be integrated using a reference concentration, C_{KOH}^o, as that in the bulk electrolyte where the reference electrolyte potential is zero. The variation of the diffusivity and ion equivalent conductance with concentration are neglected.

$$\frac{C_{KOH}}{C_{KOH}^o} = e^{-\frac{\lambda_K}{FD_K}\phi} \quad [21]$$

In extremely dilute solutions, the Nernst-Einstein relation could be applied to the coefficient of ϕ in Eq. [21] and the concentration variation as a function of ϕ would be known. In a nonideal electrolyte, however, the correct driving force for the diffusive transport is not the concentration gradient, but the gradient of chemical potential. Equation [21] can be corrected to the proper diffusive driving force by a simple adjustment to the diffusivity.

$$D_K = D_K^o\frac{\partial(\ln \alpha_{KOH})}{\partial(\ln C_{KOH})} \quad [22]$$

Application of the correction in Eq. [21] assumes the correction factor does not vary strongly with concentration. There are other correction factors for the diffusivity which are functions of the electrolyte fluid properties such as viscosity and density. These same corrections apply to the equivalent ion conductance so that the conductance to diffusivity ratio is assumed constant. With these assumptions, the Nernst-Einstein relation can be applied.

$$\frac{\lambda_K}{FD_K^o} = \frac{F}{RT} \quad [23]$$

The KOH concentration variation as a function of potential can now be written by substituting Eq. [22] and [23] into [21].

$$\frac{C_{KOH}}{C_{KOH}^o} = e^{-\frac{F\phi}{RT\frac{\partial(\ln \alpha_{KOH})}{\partial(\ln C_{KOH})}}} \quad [24]$$

It is necessary to relate the concentration changes to activity changes as are required in the kinetic equation. Activity coefficients for KOH have been measured but only to 50 w/o (weight per cent) (6). Water vapor pressures have been measured over highly concentrated KOH over a wide range of temperature (7). The solvent activity is defined as the ratio of electrolyte vapor pressure to pure solvent vapor pressure. The water vapor pressure data give us the water activity as a function of the solvent concentration. Specifically, the water vapor pressure data were related to the water concentration by the following empirical expression

$$p_{H_2O} = e^{(AF_{H_2O}^2 + BF_{H_2O} + C)} \quad [25]$$

where F_{H_2O} is the weight fraction water, $A = 34.135$; $B = 45.110\text{-}0.024055T$; $C = 0.021597\text{-}14.01648T$; and T is temperature, °F.

In order to calculate the water activity, the above expression is divided by the pure water vapor pressure which can be related to temperature by the Clausius-Clapyron equation. The water activity is

then known as a function of the water molar density or the KOH molar density from the following expressions

$$F_{H_2O} = C_{H_2O}M_{H_2O}/\rho \quad [26]$$

$$1 - F_{H_2O} = C_{KOH}M_{KOH}/\rho \quad [27]$$

The water activity ratio corresponding to the KOH molar density ratio of Eq. [24] is then given by substitution of Eq. [27] into Eq. [25] and taking water vapor pressure ratios

$$\ln \frac{\alpha_{H_2O}}{\alpha_{H_2O}^{\circ}} = A\left[\left(1 - \frac{C_{KOH}M_{KOH}}{\rho}\right)^2 - \left(1 - \frac{C_{KOH}^{\circ}M_{KOH}}{\rho}\right)^2\right] + B\frac{M_{KOH}}{\rho}(C_{KOH}^{\circ} - C_{KOH}) \quad [28]$$

The KOH activity ratio is related to the water activities by application of the Gibbs-Duhem expression

$$\ln \frac{\alpha_{KOH}}{\alpha_{KOH}^{\circ}} = -\int_{\ln \alpha_{H_2O}^{\circ}}^{\ln \alpha_{H_2O}} \frac{C_{H_2O}}{C_{KOH}} d(\ln \alpha_{H_2O}) \quad [29]$$

Application of the Gibbs-Duhem relation can also be employed to obtain the Onsager-Fuoss correction employed in Eq. [24]. Equation [29] is simply differentiated with respect to $\ln C_{KOH}$

$$\frac{\partial(\ln \alpha_{KOH})}{\partial(\ln C_{KOH})} = -C_{H_2O}\frac{\partial(\ln \alpha_{H_2O})}{\partial(\ln C_{KOH})} \quad [30]$$

The above relation is computed at the reference KOH concentration since, as previously indicated, it varies slightly with concentration.

It was assumed initially that bulk transport properties would be neglected. This is only precisely correct in a pore where the axial water diffusion molar flux is equal and opposite to the hydroxyl ion flux. Unless the product water of the total cell is allowed to evaporate into the hydrogen gas, the axial water diffusion flux does not balance the hydroxyl ion flux. It was found experimentally, however, that anode polarization was unaffected by wide variations in the flow rates of pure hydrogen over the electrode. These flow variations affect the water vapor pressure in the gas and so control the amounts of water transported through the working electrode. This experimental result indicates that the assumption of no bulk flow is a good one.

Comparison with Experiment

Hydrogen electrode half-cell data were measured for KOH concentrations ranging from 70 to 85 w/o and temperatures ranging from 300° to 500°F. The current-polarization measurements had been made on electrodes having essentially the same properties. These electrodes were 0.079 cm thick, had 70% porosity, and a 6μ mean pore diameter. The thickness of these electrodes was low enough that they exhibited little variation in performance over a range of gas-electrolyte pressure differences. The reason for this requirement will be amplified in the discussion.

The numerical solution of the equations proved quite time-consuming, requiring at least a minute on the IBM 7040 to make the computations required to define adequately one polarization curve. Considering the expense of the computation and the fact that electrolyte concentration and ohmic polarizations are a small portion of the total polarization at usual operating currents, the approximate solution given in Eq. [18] was employed to fit the data. This assumes that the polarization is controlled by gas diffusion and activation. The expression, written in terms of the current density in the electrode, is

$$I = 2P_{cp}\sqrt{\frac{FD_{H_2}\alpha_{H_2}^{\circ}i_1}{R}}\left(e^{FE/2RT} - e^{-3FE/2RT}\right)$$

$$\tanh\left[\frac{L}{R}e^{FE/2RT}\sqrt{\frac{i_1R}{FD_{H_2}\alpha_{H_2}^{\circ}}}\right] \quad [31]$$

There are two parameters that cannot be estimated and are employed as empirical factors in the theory-data fits. One is the exchange current, i_1, and the other is a characteristic hydrogen diffusion current, $FD_{H_2}\alpha_{H_2}^{\circ}/R$. No information on exchange currents in porous sinters is available. The diffusivity, being an "effective diffusivity" including metal surface and metal bulk diffusion, bears no relation to diffusivities in the electrolyte. All other terms in Eq. [31] are either sinter properties or physical constants. A typical theory-data fit is shown for data in 80% KOH in Fig. 5. Similar comparisons could be shown for data at other concentrations, but this comparison is sufficient to illustrate the point. The exchange currents employed for the fits in Fig. 5 and for fits with data from 75% and 83.5% KOH are plotted in Fig. 6 on a scale of logarithm current versus reciprocal temperature. The straight line is indicative of an Arrhenius law dependence on temperature as should be expected of a kinetic rate constant.

The fitted values of the solubility-diffusivity product were compared with hydrogen solubility measurements made in our laboratories which showed that $D_{H_2}\alpha_{H_2}^{\circ} = 10^{12}$ moles/cm-sec in 80% KOH at 450°F. The fitted values were about 10^4-10^5 greater than the measured values indicating that a means of diffusive transport other than diffusion through the liquid is a necessary assumption.

Discussion

The approximate solution given in Eq. [31] shows that the electrode current density at a given polarization is directly proportional to the geometric mean of the exchange current and the characteristic hydro-

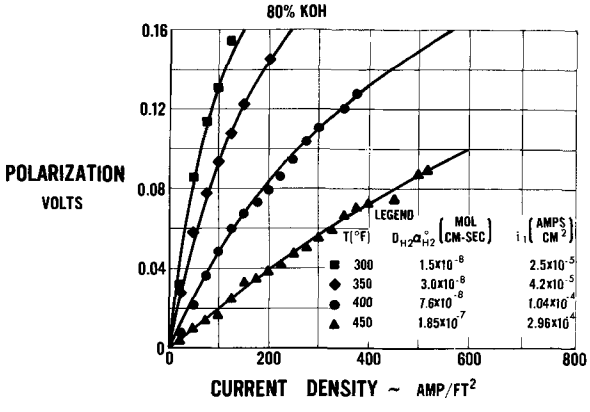

Fig. 5. Comparison of data and theory

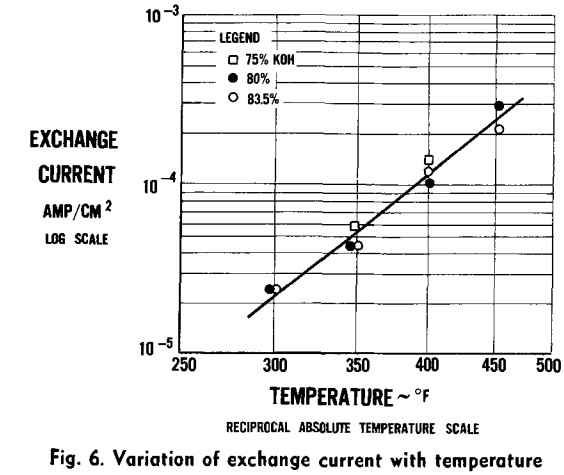

Fig. 6. Variation of exchange current with temperature

gen diffusion current. The fact that the pore current is a geometric mean of a diffusion property and a catalytic property illustrates a general feature of gas diffusion electrodes; their performance is not limited by one effect but by an interplay of several. Although electrolyte concentration and ohmic polarizations can be neglected, no useful approximation in which gas diffusion or activation polarization is eliminated can be made. The exchange current and diffusion current are both proportional to hydrogen partial pressure. The electrode current is then directly proportional to hydrogen partial pressure. Without going into too much detail, it is appropriate to point out a difference in this result and the result for the thin-meniscus model. The current in the thin-meniscus model is also proportional to the geometric mean of two properties, but only one of them is proportional to the gas partial pressure. The thin-meniscus model then predicts current is proportional to the square root of gas partial pressure.

The local current densities have their largest values at the gas side of the electrode where the gas concentration is at its highest. The current density decreases toward the electrolyte side of the electrode as consumption of gas lowers its concentration. The entire electrode produces current, but as the thickness is increased, the added electrode surface makes diminishingly small contributions to the current. This is illustrated in Fig. 7 where the fitted parameters for 75% KOH and 400°F were employed and the effect of varying electrode thickness is shown. Increasing the electrode thickness beyond 0.3 cm no longer produces any more improvement in the current.

Several comparisons were made between the approximate and rigorous solutions to determine the

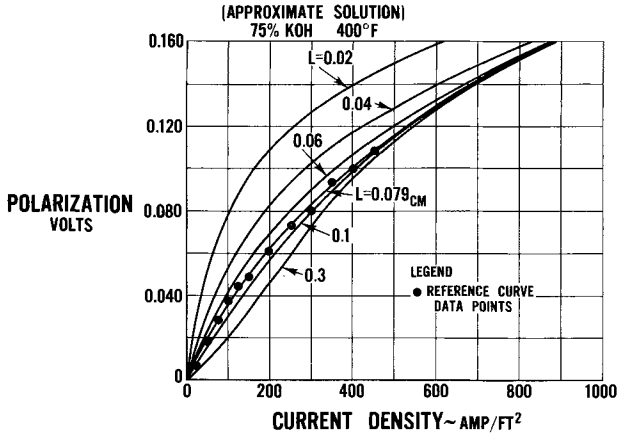

Fig. 7. Effect of electrode thickness on performance (approximate solution).

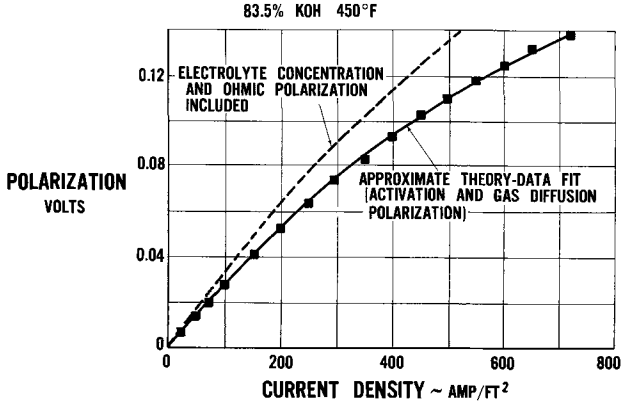

Fig. 8. Comparison of exact and approximate solutions

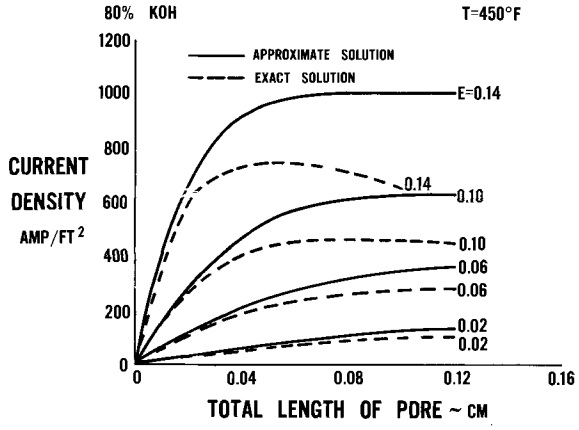

Fig. 9. Variation of cell performance with total pore length

validity of the assumption that there are negligible electrolyte concentration and ohmic polarizations. An example is shown in Fig. 8 where the constants from the approximate solution fit are employed in the nonlinear equations to calculate the polarization as a function of current. The rigorous solution shows a higher polarization as the ohmic and concentration polarizations are added. If the rigorous solution were fit to the data, an adjustment in the empirical constants would have to be made so that the total theoretical polarization would equal the experimental values. The purpose of Fig. 8, however, is to show that ohmic and electrolyte concentration polarizations account for about 15 to 20% of the total. This is not a negligible portion, but is small enough that its effect on the shape of the curve is small. This added portion is very close to linear with current density. The approximate solution, although not precisely correct, is still useful to fit data.

It was pointed out that increasing the electrode thickness increases the reactive surface and can help performance, but it also increases the electrolyte concentration and ohmic polarizations. This suggests that a flooded anode should have an optimum thickness for maximum performance. This is illustrated in Fig. 9 where the rigorous solution was made for several electrode thicknesses. The optimum thickness is lower at higher polarizations because the electrolyte concentration and ohmic polarizations are a higher portion of the total than at lower polarizations. Thicker anodes are found experimentally to be more sensitive to gas-electrolyte pressure difference than thin ones. This is because at the lower pressure differences the average position of the gas-electrolyte interface is close to the gas side. The effective flooded thickness is then too large. With increasing pressure differences, however, the flooded thickness is smaller. This line of argument suggests that there could be an optimum gas-electrolyte pressure difference for thick anodes, and this has been experimentally observed.

Having a theory that fits performance data taken over a wide range of electrolyte concentrations and temperatures leads us to a better understanding of the behavior of porous gas diffusion electrodes. The fact that a theory for a flooded electrode can be employed to fit hydrogen anode data helps explain their relative insensitivity to gas-electrolyte pressure difference. There are, however, certain limitations. Since certain empirical values of inestimable physical quantities are required in the fitting, the proof of the theory is, in part, circumstantial. Furthermore, the assumption of cylindrical pores of one size eliminates the possibility of estimating accurately the effects of both pore size distribution and the relative gas-filled to liquid-filled volumes in the electrode. The gas-filled volume should be considered, as there must be enough thin meniscus so that gas can diffuse to the metal surface if it is to take this route to the flooded part of

the sinter. Finally, perhaps the most difficult empirical result to accept is the fact that surface diffusion must explain a factor of 10^4-10^5 greater diffusion than that of hydrogen in the bulk electrolyte. The only reported determination of surface diffusion of hydrogen on nickel describes the results of field emission experiments (8). Extrapolating these measurements from 250° to 280°K to our experimental region of 500°K, the surface diffusivity is around 10^{-6} cm²/sec. Although this is about the same order of magnitude as the diffusivity in bulk electrolyte, another factor of 10^{+5} is required. We can argue, however, that the field emission results can be several orders of magnitude off when applied to these conditions. At the low pressures employed in field emission experiments, only the most tightly held molecules are held on the surface and are observed. At higher pressures, it would be expected that the less tightly held molecules would have considerably more mobility. Furthermore, the effect of the electrolyte could be very important. Measurements of hydrogen diffusion through porous nickel sinters at 500°K are being planned and the results may clear up the difficulty. In spite of these limitations, we have a model that seems to approximate the gross mechanisms in anodes and we can go on from this point to treat more sophisticated descriptions of the electrodes.

NOMENCLATURE

- a_{H2} solubility of hydrogen, moles/cm³
- A empirical constant
- B empirical constant which is a function of temperature
- C empirical constant which is a function of temperature
- C_j concentration of species j, moles/cm³
- C_j^o reference concentration of species j, moles/cm³
- D_j diffusivity of species j, cm²/sec
- D_j^o diffusivity of species j at infinite dilution, cm²/sec
- E electrode polarization, v
- F_{H2O} weight fraction of water
- F Faraday constant, 96500 coulombs/equivalent
- i local current density on surface of pore, amp/cm²
- i_1 exchange current, amp/cm²
- I electrode current density, amp/cm²
- J current generated in one pore, amp
- J_{H2} current associated with hydrogen flux, amp
- L thickness of electrode, cm
- n number of electrons transferred per mole of hydrogen reacted = (2)
- P_{cp} porosity of the electrode
- p_{H2O} water vapor pressure over electrolyte, atm.
- R gas constant, 8.314 joules/°C-mole
- R mean radius of electrode pores, cm
- T absolute temperature, °F
- x distance from electrolyte side of the electrolyte, cm
- α_j activity of species j
- α_j^o reference activity of species j
- η local metal-solution potential difference, v
- ρ density of electrolyte, gm/cm³
- σ conductivity of electrolyte, ohm-cm^{-1}
- λ_{OH} equivalent conductance of hydroxyl ions, ohm-cm^{-1}
- λ_K equivalent conductance of potassium ions, ohm-cm^{-1}
- ϕ ohmic potential in electrolyte, v

Manuscript received June 11, 1965; revised manuscript received Jan. 13, 1966. This paper was presented at the Buffalo Meeting, Oct. 10-14, 1965.

Any discussion of this paper will appear in a Discussion Section to be published in the June 1967 JOURNAL.

REFERENCES

1. C. Wagner, Unpublished work.
2. F. G. Will, *This Journal*, **110**, 152 (1963).
3. J. A. Rockett and Ralph Brown, *This Journal*, **113**, 207 (1966).
4. M. Breiter and R. Clamroth, *Z. Elektrochem.*, **58**, 493 (1954).
5. L. Onsager and R. M. Fuoss, *J. Phys. Chem.*, **36**, 2987 (1936).
6. G. C. Akerlof and P. Bender, *J. Am. Chem. Soc.*, **62**, 2366 (1948).
7. International Critical Tables.
8. R. Wortman, R. Gomer, and R. Lundy, *Chem. Phys.*, **27**, 1099 (1957).

The Manganese Dioxide Electrode in Alkaline Electrolyte; The Electron-Proton Mechanism for the Discharge Process from MnO_2 to $MnO_{1.5}$

A. Kozawa and R. A. Powers

Research Laboratory, Consumer Products Division, Union Carbide Corporation, Cleveland, Ohio

ABSTRACT

In the study of cathodic reduction of electrolytic manganese dioxide at constant-current discharge in alkaline electrolytes, effects of D_2O, Zn(II) ion added to the electrolyte, and of temperature on the discharge curves of the electrodeposited MnO_2 on a graphite rod were investigated. Results are discussed in view of the electron-proton mechanism. The potential *vs.* x value in MnO_x curve agrees in general with that calculated from

$$E = E^\circ - \frac{RT}{F} \ln \frac{[Mn^{3+}]_{solid}}{[Mn^{4+}]_{solid}}$$

corresponding to a reaction

$$MnO_2 + H_2O + e^- \rightarrow MnOOH + OH^-$$

which is assumed to take place in one phase of the oxide electrode system ($Mn^{3+} - Mn^{4+} - O^= - OH^-$). In 9M KOH prepared with KOH + D_2O, the polarization of the MnO_2 electrode was greater than that in electrolyte prepared with KOH + H_2O. Addition of zinc ion had no effect on the discharge curve from MnO_2 to $MnO_{1.5}$. A new definition of E° for a homogeneous redox solid system is proposed and the value for the $Mn^{4+} - Mn^{3+} - O^= - OH^-$ system compared to the conventional thermodynamic E° value. A few potential-controlling factors of the MnO_2 electrode are discussed.

The cathodic reduction of electrolytic manganese dioxide (γ-MnO_2) in alkaline electrolyte has been investigated by Cahoon and Korver (1), Bell and Huber (2), and Kozawa and Yeager (3). Those results have been compared and discussed in a previous publication (3). In the first two investigations (1,2) the manganese dioxide electrodes were constructed in a manner similar to that used in a battery (powdered electrolytic

MnO_2 and graphite mixed with KOH solution and pressed together), but in the third investigation (3) a much simpler electrode (MnO_2 electrodeposited on spectroscopic graphite rods) was used. Based on the discharge curves (potential *vs.* x in MnO_x) of the simpler electrode at constant current, Kozawa and Yeager found two steps in the electrochemical reduction of MnO_2 (refer to curve B in Fig. 4); the first step from MnO_2 to $MnO_{1.5}$ and the second step from $MnO_{1.5}$ to $MnO_{1.0}$, where there is a dip on the recorded potential-time curve at the end of the first step. In the first step the potential decreased continuously and therefore, during this period, the solid phase must be homogeneous according to the thermodynamic considerations presented by Vetter (4). In the second step a considerable portion of the discharge curve was flat; that is, it maintained a constant potential. This must mean that two solid phases are involved in the second step according to the thermodynamic consideration (4). Kozawa and Yeager proposed a new discharge mechanism (3) for the second step which has been further investigated. The results will be presented in a separate paper.

In the previous publication (3) the homogeneous phase discharge of the first step was discussed in accordance with the electron-proton mechanism, which has been proposed and investigated by Coleman (5), Vosburgh and co-workers (6, 7), Scott (8), Kornfeil (9), and Era, Takehara, and Yoshizawa (10). It was assumed in the electron-proton mechanism that MnO_2 was electrochemically reduced to MnOOH by receiving electrons and protons into the MnO_2 lattice without changing much of the original structure.

In this paper, attention will be focused on the first step of the discharge process. It was found that the two-step reduction which was observed in previous study (3) is also observed with a conventional cathode construction currently used in the alkaline MnO_2 cell. Effects of D_2O, zinc ion added to the electrolyte, and of temperature on the discharge curve of the electrodeposited MnO_2 on graphite rods will be presented and discussed from the point of view of the electron-proton mechanism.

Electron-Proton Mechanism

Since the purpose of this investigation is to test further the electron-proton mechanism in alkaline electrolyte, some details of the mechanism will be discussed here with the aid of Fig. 1. As we can see by Eq. [1] and in Fig. 1, in the cathodic reduction of MnO_2 (ionic crystal)

$$MnO_2 + H_2O + e^- \rightarrow MnOOH + OH^- \qquad [1]$$

electrons are introduced into the lattice and Mn^{4+} is reduced to Mn^{3+}. As a result of electron exchange between Mn^{4+} and Mn^{3+} in the lattice, the position of Mn^{3+} (not the manganese ion itself) moves around in the entire lattice. At the same time, H_2O molecules (an abundant source of protons under this condition) may be decomposed at the solid-solution interface, and protons are introduced into the lattice forming OH^-. Since the OH^- in the lattice is rotating and vibrating, the O-H bond is broken, and H^+ is transferred to the adjacent $O^=$ to form OH^- again. Thus, OH^- also moves around in the entire lattice by means of the proton jumping from one $O^=$ site to another.

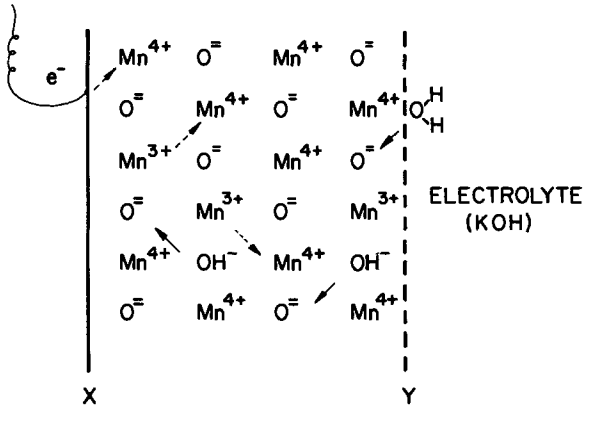

Fig. 1. Schematic presentation of the solid phase (Mn^{4+} — Mn^{3+} — $O^=$ — OH^-) during the discharge of MnO_2. The arrows show the directions of movement of the electrons and protons: ——— proton movement; - - - - electron movement; X, MnO_2-electronic conductor interface; Y, MnO_2-solution interface.

As the discharge proceeds, the concentrations of Mn^{3+} and OH^- in the lattice increase, and in an open-circuit condition, both of these species become distributed homogeneously throughout the oxide lattice. At equilibrium the electrode potential of the oxide having a homogeneous phase may be determined by the activity of the electron in the lattice, or by the ratio of $[Mn^{3+}]/[Mn^{4+}]$ in the solid, because of the relatively free electron exchange between Mn^{3+} and Mn^{4+}. As long as the lattice parameters (distance between two adjacent $O^=$ and that between two adjacent Mn^{4+}) permit fairly free movement of protons (through $O^=$ sites) and electrons (through Mn^{4+} sites) in the manner described above, the electrochemical reduction can take place in a homogeneous phase. However, as the discharge proceeds the original MnO_2 lattice expands, because the ionic radius of OH^- (1.53Å) (36) is greater than that of $O^=$ (1.40Å) (36), and Mn^{3+} (0.62Å) (37) is greater than Mn^{4+} (0.52 (38). Therefore, at a certain point, the crystal structure may be transformed to a new form in which such a free movement of the electron and proton may not be possible.

The potential-generating mechanism of the homogeneous $Mn^{3+} — Mn^{4+} — O^= — OH^-$ phase in contact with an electrolyte is somewhat analogous to an aqueous redox system; for example, an aqueous solution containing Fe^{2+} and Fe^{3+} ions which consists of a homogeneous phase and the potential can be expressed by Eq. [2].

$$E = E^\circ - \frac{RT}{F} \ln \frac{[Fe^{2+}]}{[Fe^{3+}]} \qquad [2]$$

In the $Mn^{3+} — Mn^{4+} — O^= — OH^-$ system, electrons and protons move around and the system is in an electrochemical equilibrium with species (OH^-, H_2O) in the electrolyte. The two systems may be considered similar in the relation of the electrode potentials to the variable activities of the oxidized and reduced forms present in a homogeneous phase. Therefore, the electrode potential of the oxide electrode system ($Mn^{4+} — Mn^{3+} — O^= — OH^-$) of a homogeneous phase may be expressed by Eq. [3], as a first approximation, with $[OH^-]$ and $[H_2O]$ assumed constant.

$$E = E^\circ - \frac{RT}{F} \ln \frac{[Mn^{3+}]_{\text{solid}}}{[Mn^{4+}]_{\text{solid}}} \qquad [3]$$

This can be tested experimentally by comparing the open-circuit potential of the MnO_2 electrode at various stages of the discharge to the calculated curve (Fig. 2, curve a) from Eq. [3]. If the discharge does not proceed through a homogeneous phase, but involves a conversion of one solid phase (MnO_2) to another separate solid phase (MnOOH or Mn_2O_3), the open-circuit potential must be constant in thermodynamic principle at any stage of the discharge, because in Eq. [4] the activities of those solid phases do not vary with the quantities present and must be constant in the entire range of the discharge as indicated by curve b in Fig. 2.

$$E = E' - \frac{RT}{F} \ln \frac{a_{MnOOH}}{a_{MnO_2}} \qquad [4]$$

An example of this kind of mechanism in which two solid phases are involved is the second step of the

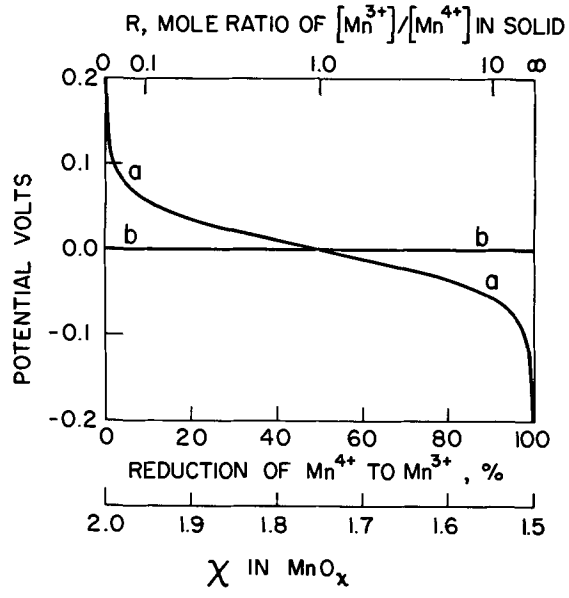

Fig. 2. Equilibrium potential curves for one-phase and two-phase reductions. Curve a, calculated from Eq. [3] for a one-phase (or homogeneous phase) reduction. Line b, for two-phase reduction (Eq. [4]). R and x in MnO_x are related by x = (2 + 1.5R)/(1 + R).

discharge, from MnOOH to $Mn(OH)_2$ in alkaline electrolyte, in which the open-circuit potential was constant (see Fig. 5). As a matter of fact, many of the electrode reactions in batteries currently in use seem to be heterogeneous phase (two-phase) reactions; $PbO_2 \rightarrow PbSO_4$, $NiOOH \rightarrow Ni(OH)_2$, $Zn \rightarrow ZnO \cdot x\,aq$, $Cd \rightarrow Cd(OH)_2$, etc., because the open-circuit potentials of these electrodes are almost unchanged at any stage of the discharge as has been well recognized. However, V_2O_5 (11) seems to be discharged in a homogeneous phase, although a homogeneous-phase reduction does not necessarily mean that the electron-proton mechanism is the only possibility. Cathodic reduction of PbO_2, TiO_2, Tl_2O_3 were studied and compared to that of MnO_2 by Mark and Vosburgh (46).

In this paper, the $E - x$ (in MnO_x) relation was obtained in 1M and 9M KOH and compared to the curve calculated from Eq. [3] (curve a in Fig. 2). Discharge curves at constant current were taken in KOH electrolyte prepared with both H_2O and D_2O, because if the discharge mechanism involves the proton migration in the oxide lattice, the deuterium ion, which is twice as heavy as a proton, should show more polarization. The effect of zinc ion added to 9M KOH was examined at constant current discharge, because this probably gives some indication whether or not a new solid phase is forming in the discharge process.

The electron-proton mechanism for the discharge process of manganese dioxide was proposed and investigated mainly in the Leclanché electrolyte (NH_4Cl-$ZnCl_2$-H_2O) (1, 2, 5-9). In this research alkaline electrolytes (1M NaOH and 9M KOH) were used in order to test some of the details of the electron-proton mechanism, because the concentration polarization (due to pH change) is practically negligible in these electrolytes, and most of the observed polarization during the discharge in alkaline electrolyte is attributed to the activation polarization which includes the slow diffusion process in the solid phase as well as the charge transfer process at the oxide-electrolyte interface.

Experimental

Preparation of MnO_2 electrodes.—Manganese dioxide was electrodeposited on spectroscopic graphite rods (AGKSP), 7.7 cm or 2.5 cm long and 4.5 mm in diameter, from 0.5M $MnSO_4$ + 0.5M H_2SO_4 or 1M $MnSO_4$ + 0.5M H_2SO_4 at 90° ± 1°C at a constant current of 20 ma for 5.0 min, or 5 ma for 20 min for the 2.5 cm rod. The electrode construction and the electrodeposition bath were described in the previous paper (3). After the electrodeposition the electrode with manganese dioxide was taken out of the Teflon holder, kept in a large amount of 0.1*N* H_2SO_4 with slow stirring for at least 24 hr, and then transferred into a large amount of distilled water. The electrode was washed for another 48 hr in distilled water, which was changed approximately every 12 hr, with slow stirring, and kept in distilled water until used.

In this study, the electrodes had much less MnO_2 [approximately 3.0 mg each instead of 10.6 mg as in previous experiments (3)], because the thinner the MnO_2 layer the faster the diffusion equilibrium in the solid should be, and the easier to replace H_2O by D_2O in the pores of the MnO_2 layer. Current efficiency of the electrodeposition was approximately 60-90% in the present experiments. The lower current efficiency than 100% was attributed to a side reaction (oxygen evolution) and varied depending on the current density and particularly on the kind of graphite rod. It was found by chemical analysis (7) the x value in MnO_x was 1.98-1.99 regardless of the current efficiency in the electrodeposition and that the amount of MnO_2 was almost constant (within 5%) among the electrodes prepared at the same time under the same conditions. It was also found that the discharge time to the dip (see Fig. 4) at the end of the first step of the discharge (around —0.40 to —0.45v *vs.* Hg/HgO [9M KOH] for the discharge in 9M KOH) is a good measure of the amount of MnO_2.

Discharge experiments.—All the discharges were carried out at constant current, continuously or intermittently, at room temperature (23° ± 0.5°C) or at higher temperature (65° and 95°C) in a polarographic H-cell (Fig. 3). Both arms of the H-cell were filled with electrolyte (1M NaOH or 9M KOH) and the solution levels were kept almost equal. The assembled electrode was placed in one arm and nitrogen gas bubbled through for 10 to 15 min to expel dissolved oxygen. The electrode was wrapped with a filter paper to avoid loss of dissolved Mn^{3+} ion, having a form $[Mn(OH)_4]^-$ and reddish color, from the electrode, particularly from 9M KOH at high temperature. During the discharge the solution was not stirred. The potential was measured against the Hg/HgO (1M NaOH or 9M KOH) reference electrode in

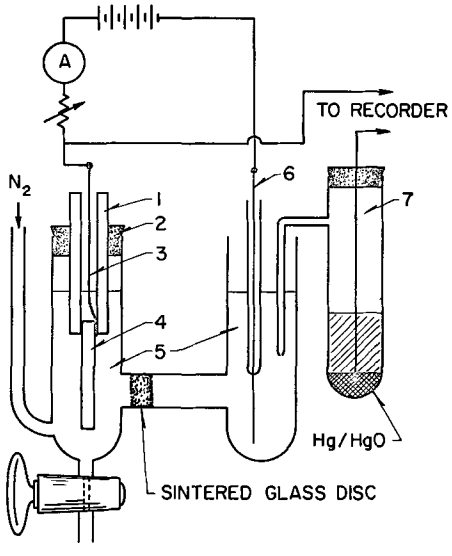

Fig. 3. Discharge cell and electrode construction: 1, Teflon tubing electrode holder; 2, Teflon stopper; 3, platinum lead wire, epoxy-coated except at the end contact; 4, graphite electrode with MnO_2 electrodeposited on it; 5, electrolyte; 6, counter electrode; 7, reference electrode.

the same solution. For the discharges at 65° and 95°C, the H-cell was placed in a thermostat, but the reference electrode was kept at room temperature.

Before the discharge the electrode was kept at room temperature for at least 48 hr in the electrolyte, which had the same concentration as that which was to be used in the discharge, but without the platinum lead (see Fig. 3) and the Teflon holder. It was checked and found that further immersion prior to the discharge, up to 10 days, did not show any change in the discharge behavior, including the experiments in D_2O solutions.

Discharge of the conventional MnO_2 *cathode.*—Powdered electrolytic manganese dioxide (32g), graphite, acetylene black, 9M KOH, and a small amount of binding material were mixed thoroughly. The mixture was molded in a D-size steel can by applying high pressure to form a cathode layer approximately 3.0 mm thick along the inside of the can. Then a paper separator, electrolyte (9M KOH), and a zinc anode (CMC-gelled zinc powder) were added in a manner which made it similar to a conventional cell. The cell was discharged at a constant current of 10 ma at room temperature, and the cathode potential was measured against a Hg/HgO (9M KOH) reference electrode. Provision was made to prevent loss of moisture from the cell and absorption of carbon dioxide into the electrolyte. After the zinc anode was exhausted an external constant current source was used to discharge the cathode completely. The net MnO_2 in the cathode was found to be 30.0g by chemical analysis of the electrolytic manganese dioxide.

Results and Discussion

Discharge curve of the molded cathode.—Bell and Huber (2) obtained a three step discharge curve (curve C in Fig. 4) in the discharge of a manganese dioxide cathode constructed with powdered electrolytic MnO_2 and graphite. Kozawa and Yeager (3) obtained a two-step discharge curve (curve B in Fig. 4) in the discharge of electrodeposited manganese dioxide on a porous graphite rod. It is suspected that this difference in the discharge behavior may be due to a difference in a physical factor, such as the contact between MnO_2 particles and graphite particles. In order to check this point, the present cathode was molded under high pressure and discharged at extremely low current density (10 ma per D-size cell or 0.33 ma/g of MnO_2) over a two-month period. Under such a low current density, conductivity of the oxide particles and the contact resistance between the oxide and graphite particles probably does not influence the discharge process. The present results are plotted on the basis of calculated x values (in MnO_x) from the electricity drawn. The curve is shown in Fig. 4 (curve A) where two steps are clearly seen corresponding to the two steps of curve B which was obtained with electrodeposited MnO_2 on a porous graphite rod. During the discharge of the cathode at 10 ma, practically no polarization (no potential difference between the closed circuit and the open circuit potentials) was observed in the first step and also in the beginning of the second step. The remaining part of the second step shows considerable polarization (dotted line ab shows open-circuit potential).

The present result (curve A in Fig. 4) proves that even with a powder electrode construction the two-step reduction of MnO_2 takes place in alkaline electrolyte under proper discharge conditions.

E-log $[Mn^{3+}]/[Mn^{4+}]$ *relation.*—Several electrodeposited electrodes were discharged at 250 μa, continuously and intermittently in 1M NaOH and 9M KOH. Typical results are shown in Fig. 5. Curve a shows the closed-circuit potential of the two discharges: one was discharged continuously and the other intermittently over a period of four days while the open-circuit potentials were taken at various stages of the discharge. The closed-circuit potentials of the two discharges are essentially the same. The recovery curves were taken at various stages of the discharge. Only three curves (curves c, d, and e) are shown here, which indicates that most of the polarization recovered within 60 min. The open-circuit potentials after a few hours were almost equal to those after an overnight period (about 15 hr).

At the end of the first step a dip was observed at 110 min as noted in Fig. 5. Therefore, 110 minutes was taken as a measure of the MnO_2 present in this electrode. The equilibrium potential observed experimentally (curve b in Fig. 5) was compared to the calculated curve from Eq. [3]. In this comparison, the middle point of the first step (that is, 110/2 = 55 min discharge) where $[Mn^{3+}]_{solid}/[Mn^{4+}]_{solid} = R = 1.0$ was chosen as a reference point. In other words, a curve obtained from $E = E^o - 0.059 \log R$ was superimposed on the curve b in Fig. 5 based on the reference point. This choice of the reference point seems to be reasonable since the initial open-circuit potential cannot be chosen for the reference point because a calculated potential for 100% MnO_2 is $+\infty$. Also, at the middle point, where $R = 1.0$, the potential is rather insensitive to the composition (R);

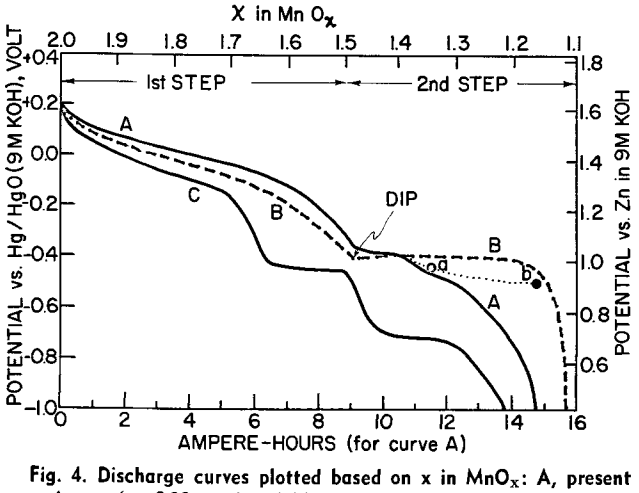

Fig. 4. Discharge curves plotted based on x in MnO_x: A, present experiment (at 0.33 ma/g of MnO_2); B, Kozawa and Yeager (3), electrodeposited MnO_2 on a graphite rod (at 11 ma/g of MnO_2); C, Bell and Huber (2), (at 0.5 ma/g of MnO_2).

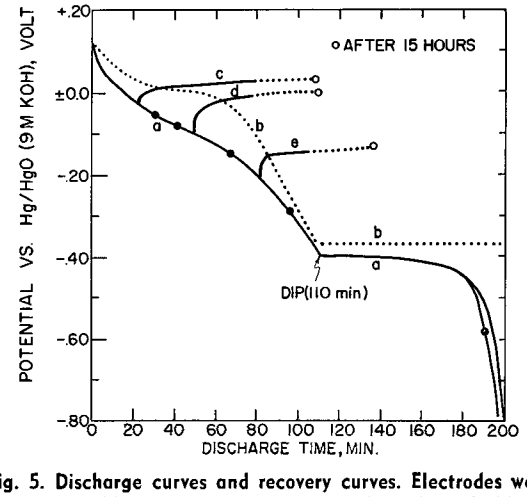

Fig. 5. Discharge curves and recovery curves. Electrodes were 7.7 cm long with MnO_2 electrodeposited on them from 0.5M $MnSO_4$ + 0.5M H_2SO_4 at 90°C at 20 ma for 5 min. They were discharged at 250 μa in 9M KOH at 23°C. Curve a, ——— closed circuit potential on intermittent discharge; —•— closed circuit potential on continuous discharge; curve b, open-circuit equilibrium potential; curves c, d, and e, recovery curves.

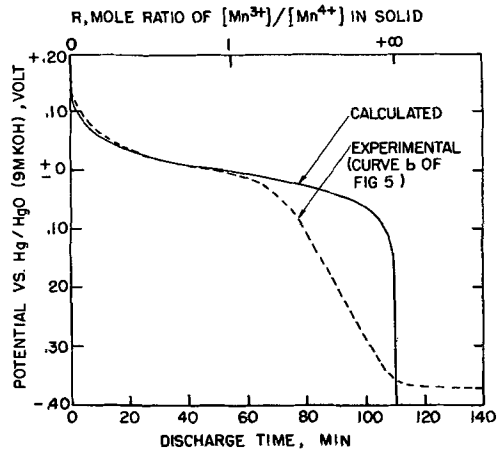

Fig. 6. Comparison of potential vs. log $[Mn^{3+}]/[Mn^{4+}]$ relation in 9M KOH at 23°C.

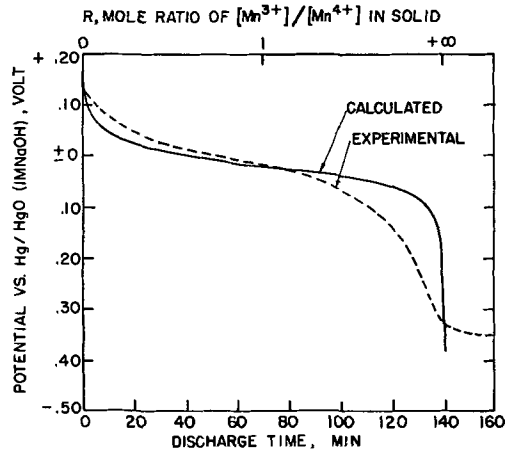

Fig. 7. Comparison of the potential vs. log $[Mn^{3+}]/[Mn^{4+}]$ relation for the equilibrium open circuit potential obtained in 1M NaOH at 23°C. The preparation of the electrode and the discharge conditions are the same as described in Fig. 5, excepting the electrolyte for discharge.

therefore, some experimental error in obtaining the middle point would not seriously influence the comparison. The comparisons are shown in Fig. 6 and 7 for the results obtained in 9M KOH and 1M NaOH, respectively. We can see that the agreement between the experimentally obtained and the calculated curves is not perfect in the entire range, but the general shape of the curve seems to agree with the original assumptions, a homogeneous phase discharge from MnO_2 to $MnO_{1.5}$.

The main disagreement between the observed and the calculated curves occurs at the later stage of the discharge. This can be well explained by assuming that at the later stage of the discharge a new lower oxide phase (Mn_2O_3) is formed on the surface of the original oxide ($Mn^{4+} - Mn^{3+} - O^{=} - OH^{-}$ system) and the potential is determined or largely controlled by the Mn_2O_3 phase on the surface. These assumptions are substantiated by the following facts and discussion. The x-ray study (2) in the course of discharge of electrolytic MnO_2 in alkaline electrolyte showed that at the beginning stage of the discharge ($MnO_2 \rightarrow MnO_{1.7}$) a lattice dilation of the original structure took place, rather than the formation of a new phase, indicating a homogeneous phase discharge, and in the subsequent stage of the discharge formation of lower oxide phases such as α-MnOOH and γ-Mn_2O_3 took place. It was previously demonstrated (12) that the formation of one or two layers of lower oxide on the surface of electrolytic MnO_2 brings the electrode potential of the MnO_2 to as low as that of Mn_2O_3 (in the experiment the lower-oxide film on the MnO_2 surface is formed by addition of Mn^{++} to a solution containing suspended MnO_2). We shall note here the important fact that when MnO_2 is reduced electrochemically even to a large extent (for example, 50% of the MnO_2 converted to lower oxide) the potential decrease is only 170 mv or so from its beginning value (see Fig. 4, 6, and 7), but when the MnO_2 is reduced chemically by adding Mn^{++} ($MnO_2 + Mn^{++} \rightarrow Mn_2O_3$ on the surface) only 15% reduction (150 mg of Mn^{++} added to 1.5g of MnO_2) (12) brought the potential decrease of 250 mv to roughly the potential of Mn_2O_3. This is evidence that the lower oxide phase formed chemically on the MnO_2 surface does not diffuse into the MnO_2 lattice, or at least cannot function as a homogeneous phase. Consequently the electrode potential under this condition is determined essentially by the surface oxide. Although the formation of the lower oxide depends on the discharge conditions, particularly on current density or surface area of the MnO_2, for the electrochemical reduction of MnO_2 at moderate or low-current discharge such a lower-oxide phase is not likely to be formed on the surface during the stage of the discharge from $MnO_{2.0}$ to $MnO_{1.75}$, and the potential is determined by the activity of the whole solid phase (a homogeneous $Mn^{4+} - Mn^{3+} - O^{=} - OH^{-}$ phase) as described earlier in this paper.

This viewpoint is also supported by the following experiment. In order to compare the potentials of MnO_2 which is partially reduced, the MnO_2 electrode was reduced by two different chemical methods: (*i*) addition of a calculated amount of Mn^{++} to reduce half of the MnO_2 to $MnO_{1.5}$ and (*ii*) addition of a calculated amount of Sb^{+++} to reduce half of the MnO_2 to $MnO_{1.5}$. The experiments were carried out in 9M KOH with the MnO_2 electrodeposited on a graphite rod. In these experiments Sb^{+++} or Mn^{++} ion was added to a N_2-saturated 9M KOH solution in which the MnO_2 electrode had been dipped in the same manner as in the discharge experiment in the H-cell. While stirring by means of bubbling N_2 gas, the potential was measured with time. It was assumed that the reaction of Mn^{++} or Sb^{+++} with MnO_2 was completed when the equilibrium potential was attained. In the case of Sb^{+++} addition, Sb^{+++} must be oxidized to Sb^{5+} in the potential range of the MnO_2-$MnO_{1.5}$ as seen from the polarographic behavior (see Fig. 8 and its legend), and the reaction product (Sb^{5+}) is a soluble form which does not form a new

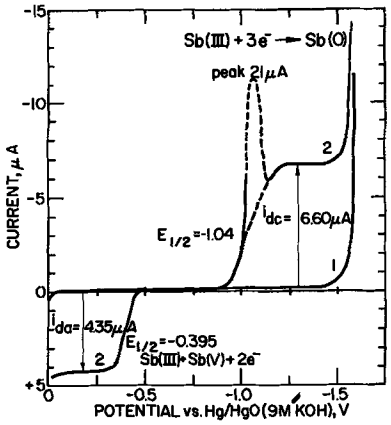

Fig. 8. Polarographic behavior of Sb^{+++} in 9M KOH at 23°C. The Sb^{+++} solution was prepared by dissolving Sb_2O_3 in 9M KOH. Curve 1, in 9M KOH; curve 2, in 9M KOH + 1 x 10^{-3}M Sb^{+++}. The ratio of the anodic limiting current (i_{da}) to the cathodic limiting current (i_{dc}) is 2:3 and the anodic and cathodic processes and their half-wave potentials are shown in the figure. The characteristics of the glass capillary were m = 1.42 mg/sec, t = 5.82 sec at open circuit in 9M KOH.

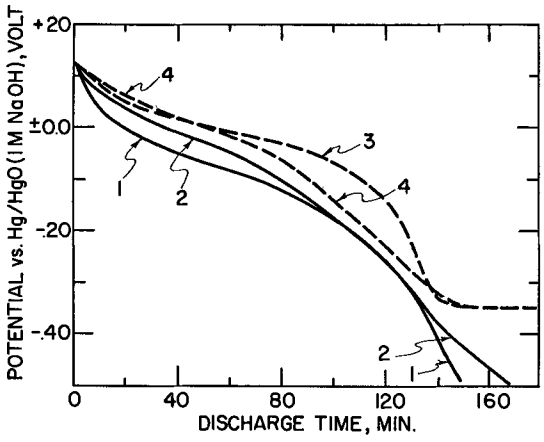

Fig. 9. Effect of temperature on the discharge of MnO_2 electrodes in 1M NaOH. The preparation conditions of the electrodes were the same as described in the caption of Fig. 5. They were discharged at 250 μa in 1M NaOH continuously and intermittently. Curve 1, closed-circuit potential at 23°C; curve 2, closed-circuit potential at 65°C; curve 3, open-circuit equilibrium potential at 23°C; curve 4, open-circuit equilibrium potential at 65°C.

lower oxide on the MnO_2 surface. In the case of Mn^{++} addition, Mn^{++} reacts with MnO_2 to form $MnO_{1.5}$ on the surface, although some of the Mn^{3+} can dissolve in the 9M KOH probably as $[Mn(OH)_4]^-$ (13).

The equilibrium potential attained in 10 hr in the Sb^{+++} addition was —0.01v *vs.* Hg/HgO (9M KOH) which is very close to the potential obtained at the discharge $R = 1.0$, but the equilibrium potential observed in the addition of Mn^{++} ion was much lower than that. The conclusion may be made here that the potential of partially reduced MnO_2 does not depend on the reduction method, chemical or electrochemical, as long as a new lower-oxide phase is not formed on the MnO_2 surface. Once a lower oxide is formed on the MnO_2 surface the potential is controlled largely by this lower oxide. The large disagreement between the observed and calculated curves at the later stage of the discharge, as shown in Fig. 6 and 7, can be understood on the basis of the lower oxide formation on the MnO_2 surface.

Effect of temperature.—The effect of temperature on the discharge curves is shown in Fig. 9. The discharges were carried out in 1M NaOH at 23°, 65°, and 95°C, but only the curves at 23° and 65°C are shown because those at 65°C or higher had very little difference. The temperature effect was examined only in 1M NaOH because Mn^{3+} and Mn^{2+} ions have fairly large solubilities in concentrated alkaline electrolyte, particularly at higher temperatures (13). The initial open-circuit potential of the MnO_2 electrode was practically constant in the temperature range (23°-95°C) when measured against the Hg/HgO (1M KOH) kept at 23°C. The main difference between the closed-circuit potentials at 23° and at 65°C occurs in the initial half of the discharge (compare curves 1 and 2 in Fig. 9). On the other hand the difference in the open-circuit potential occurs during the later half (compare curves 3 and 4).

Under the discharge conditions, ohmic drop and concentration polarization (due to the species in the solution) are negligible. Therefore, the polarization is mainly attributed to the slow diffusion of the proton and electron in the lattice and of the proton generation process at the solid solution interface ($H_2O \rightarrow H^+ + OH^-$). During the initial half of the discharge the original MnO_2 lattice may be well maintained, and polarization of this kind is expected to be much less at higher temperatures; therefore, the closed circuit potential should be kept higher at higher temperatures. However, during the later half of the discharge the potential is largely controlled by the formation of the lower oxide on the surface as mentioned above. The lower oxide formation is probably a chemical step following the primary electrochemical step and is probably taking place more rapidly at higher temperatures. On this basis the lower open-circuit potential at higher temperatures may be well interpreted.

Effect of D_2O.—A 9M KOH electrolyte was prepared by dissolving KOH pellets into 99.9 mole % D_2O. From the NMR study of the KOH-H_2O system (14), the proton exchange between H_2O (or D_2O) and OH^- is fast. Therefore, the average D_2O content in the KOH-D_2O electrolyte is approximately 85%. The discharge in the KOH-D_2O electrolyte was carried out at two current densities (250 μa or 1 ma per electrode) and the results were shown in Fig. 10 and 11, in which closed-circuit potentials on the continuous discharges are shown. At each condition (in electrolyte and current density) 3 to 5 electrodes were discharged to see the reproducibility of the experiment, and the highest and the lowest curves in each con-

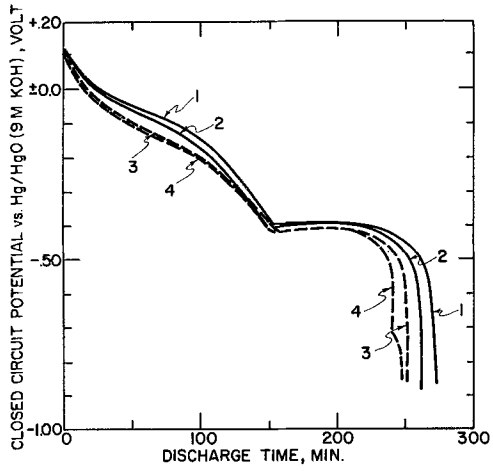

Fig. 10. Effect of D_2O at 250 μa discharges. Electrodes were 7.7 cm long with MnO_2 electrodeposited on them from 0.5M $MnSO_4$ + 0.5M H_2SO_4 at 90°C at 20 ma for 5 min. They were discharged at a constant current (250 μa) at 23°C. Curves 1 and 2, in 9M KOH in H_2O; curves 3 and 4, in 9M KOH in D_2O.

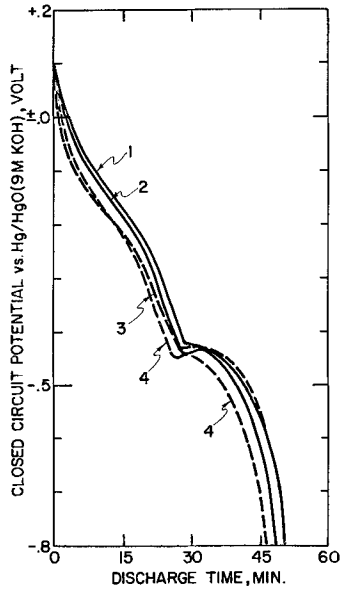

Fig. 11. Effect of D_2O at 1.0 ma discharge. Electrodes were prepared under the same conditions as described in the caption of Fig. 10. They were discharged at a constant current (1.0 ma) at 23°C. Curves 1 and 2, in 9M KOH in H_2O; curves 3 and 4, in 9M KOH in D_2O.

dition are shown in the figures to give the limit of the reproducibility. For the comparison and evaluation, the amount of MnO_2 present in the electrode must be taken into account, and the discharge time to the dip at the end of the first step should be considered as a measure of the MnO_2 present as mentioned previously. We can see in Fig. 10 and 11 that under these discharge conditions the polarization during the discharge of the first step is greater by approximately 60 mv in the KOH-D_2O electrolyte than in the KOH-H_2O electrolyte.

Effect of Zn(II) *ion.*—In previous publications concerned with the discharge reaction of manganese dioxide in the Leclanché cell, the formation of a lower oxide of manganese (hetaerolite) containing zinc, such as $ZnO \cdot Mn_2O_3$ or $ZnMn_2O_4$ has been shown (15-17). It was also shown that the formation of hetaerolite should give more energy output because of the difference in the ΔF from a thermodynamic calculation (18).

$$Zn + 2MnO_2 = ZnO + Mn_2O_3 \quad F = -66.5 \text{ kcal} \ (1.44\text{v})$$

$$Zn + 2MnO_2 = ZnMn_2O_4 \quad F = -72.8 \text{ kcal} \ (1.58\text{v})$$

If the discharge mechanism of the first step in alkaline electrolyte is not the electron-proton mechanism, but rather one involving a phase change from MnO_2 to a lower oxide phase containing zinc ion, then the zinc ion present in the electrolyte may be incorporated in the lower oxide phase as in the case of Leclanché electrolyte (NH_4Cl-$ZnCl_2$-H_2O), because the zinc-containing oxide is more favorable from the free energy value shown above.

This was tested by discharging the electrodes in 9M KOH and in 9M KOH saturated with ZnO, approximately 1M solution in ZnO (19). A typical result is shown in Fig. 12, in which we can see that the first step is not influenced by the presence of Zn(II) ion (the complex form is $[Zn(OH)_4]^=$ in the solution (20)). This result is in agreement with the proton-electron mechanism for the first step of the discharge.

Discussion

Reasons and results which substantiate the electron-proton mechanism for the first step of the discharge of MnO_2 are summarized below.

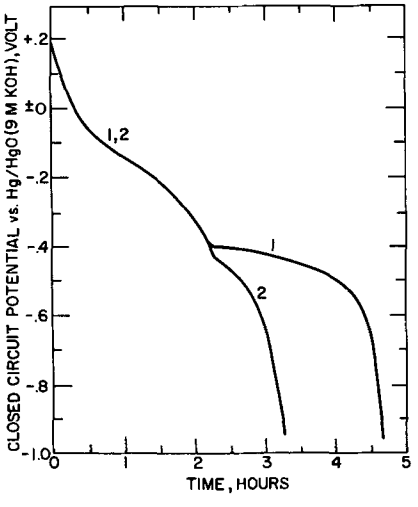

Fig. 12. Effect of zinc oxide on the discharge of MnO_2 in 9M KOH. Electrodes were 2.5 cm long with MnO_2 electrodeposited on them from 1M $MnSO_4$ + 0.5M H_2SO_4 at 5 ma for 20 min at 90°C. They were discharged at 250 μa (constant current) at 23°C. Curve 1, in 9M KOH; curve 2, in 9M KOH saturated with ZnO (approximately 1M).

1. During the electrochemical reduction of MnO_2, the potential (open-and closed-circuit potentials) decreases continuously and the $E - x$ (in MnO_x) curve agrees in general with the calculated curve by assuming a homogeneous phase reduction. The electron and proton movement in the solid phase can be fast compared to ions ($O^=$, OH^-, metal ions) and it seems reasonable to expect a homogeneous phase during the reduction.
2. The x-ray study by Bell and Huber (2) indicates that no new phase appeared at the beginning stage of the discharge of MnO_2, at least until $MnO_{1.7}$, substantiating a homogeneous phase discharge, although an amorphous phase cannot be detected by the x-ray method.
3. D_2O in place of H_2O in the KOH electrolyte increases the polarization.
4. Addition of a complexing agent (triethanolamine) has very little effect on the first-step discharge (3). This indicates that a phase change through dissolved species of manganese (II) is not likely to be involved in the discharge process, although Cahoon *et al.* (40, 41) described such a discharge mechanism in Leclanché electrolyte.
5. Addition of Zn^{++} ion in the electrolyte (KOH) has no effect.
6. The KOH concentration in a range of 0.1-9M KOH has very little influence on the discharge curve of the first step (3).

Based on the potential-generating mechanism in accordance with electron-proton movement in the Mn^{4+} — Mn^{3+} — $O^=$ — OH^- system, the following discussion is given in order to account for the potential of manganese dioxide.

$E - x$ in MnO_x relation.—Recently Vosburgh and DeLap (42), Bode *et al.* (43, 44) and Feitknecht *et al.* (45) examined the $E - x$ in MnO_x relation by reducing γ-MnO_2 chemically with hydrazine (43, 45) or electrochemically (42, 44). All of them found that the potential decreased almost linearly with decreasing x value for γ-MnO_2 between $MnO_{2.0}$ and $MnO_{1.5}$. We, however, plotted the potential against log R $\left(R = [Mn^{3+}]/[Mn^{4+}] \text{ in the solid, and } R \text{ and } x \text{ in } MnO_x \text{ are related by } x = \frac{2 + 1.5R}{1 + R} \right)$, since this plot gives a sharp increase and a sharp decrease in approaching to $x = 2.0$ and $x = 1.5$, respectively, and seems to give a better fitting to the data obtained in the present work. It should be noted, however, that the E — log R plot gives an almost straight line between $x = 1.9$ and 1.6 as shown in Fig. 2.

E^o of the MnO_x system.—In the past a number of attempts have been made to measure the correct potential of MnO_2 (21-29) and to understand the potential of the MnO_2-Zn cell on the basis of chemical thermodynamics (18). It seems that two factors disturbed the potential measurement. It has been recognized in recent years that ion-exchange properties (27-31) on the surface of MnO_2 play an important role in the potential measurement because the proton released to the solution by cation adsorption on the MnO_2 surface (30) acidifies the solution and the pH of the solution in the fine pores of the MnO_2 is considerably lower than that in the bulk solution. Now we know that a stable and reproducible potential can be obtained by using an electrolyte solution having a large pH buffer capacity or by digesting the manganese dioxide thoroughly in the solution.

Another factor which disturbed the previous investigators in obtaining a reproducible potential in neutral or alkaline solutions still seems to be unsettled. The potential value for the Pt/MnO_2, Mn^{++}, H^+ electrode in acid solution is in a range of 1.233 to 1.241v (28), and the values obtained by various workers agree with the value estimated from thermo-

dynamic data by Wadsley and Walkley (32). The potential of the so-called MnO_2-MnOOH system in neutral and alkaline solutions varied considerably. Various factors such as purity (MnO_2 content), crystal structure, (α-, β-, γ-MnO_2, etc.) heat-treatment (29), and the surface condition (12) of the oxide have been considered so far, but no satisfactory explanation has been given. According to the potential-generating mechanism of MnO_2 presented in this paper, the potential of pure MnO_2 has practically no meaning because the ratio $[Mn^{3+}]_{solid}/[Mn^{4+}]_{solid}$ is zero or a very low value; therefore, the potential is $+\infty$ (or a very high value from Eq. [3]). The ratio is also, in most cases, uncertain for a given sample. The practical potential value of pure MnO_2 in aqueous solutions may be limited to the redox potential of the O_2-H_2O system (O_2 evolution by H_2O decomposition). This is probably one important reason, in addition to the effect of the presence of the lower oxide on the surface which was discussed previously in this paper, why the potentials of MnO_2 so far obtained have been in poor agreement.

The E^o of the homogeneous solid having a redox couple like the Mn^{4+} — Mn^{3+} — $O^=$ — OH^- system has not been defined, but it seems reasonable to define the E^o as a potential at $[Mn^{3+}]_{solid}/[Mn^{4+}]_{solid} = 1.0$. The approximate standard potential thus defined of the Mn^{4+} — Mn^{3+} — $O^=$ — OH^- system is -0.01 ± 0.01v *vs.* Hg/HgO (1M NaOH) (or $+0.103$ *vs.* NHE).

In the construction of the *p*H-potential diagram which is based on chemical thermodynamics, the line for

$$2MnO_2 + 2H^+ + 2e^- = Mn_2O_3 + H_2O \qquad [5]$$

was found to be $E = 1.014 - 0.0591$ *p*H (33). This value was obtained from the ΔF when the β-MnO_2 phase is converted to the Mn_2O_3 phase; that is, the calculation is based on the hypothetical electrochemical reaction involving two solid phases. The activity of the solid does not depend on the quantity of the solid phase; and therefore, the potential should be constant while the ratio of the amount of β-MnO_2 and Mn_2O_3 changes during the hypothetical electrode reduction. The *p*H-potential diagram, therefore, has a single straight line for Eq. [5]. However, the true electrochemical reduction of MnO_2 seems to be a homogeneous phase reduction, regardless of the crystal structure (α-, β-, γ-MnO_2), although this has been examined only with γ-MnO_2 in this paper. Therefore, the *p*H-potential diagram for the homogeneous phase system (MnO_2-Mn_2O_3) is not a single straight line, but should be a zone for a range of the R value ($=[Mn^{3+}]/[Mn^{4+}]$). The E^o value for the hypothetical heterogeneous phase reaction in alkaline solution (Eq. [6]) is found to be $E = 1.014 - 0.059 \times 14 = +0.188$.

$$2MnO_2 + H_2O + 2e^- = Mn_2O_3 + 2OH^- \qquad [6]$$

This E^o value ($+0.188$ *vs.* NHE) for the hypothetical heterogeneous reaction, however, is not too far from the E^o value ($+0.103$ *vs.* NHE), which has been defined and found in this study for the homogeneous phase.

It is obvious in the discussion above that the previous effort (18) in understanding the open-circuit voltage of the MnO_2-Zn cell from the thermodynamic E^o value is not correct in principle because of the potential generating mechanism of the MnO_2 electrode.

Effect of lower oxide.—It was shown previously in this paper that a few layers of the lower oxide ($MnO_{1.5}$) present on the MnO_2 surface have a great influence on the potential of the MnO_2. This means that the lower oxide of manganese is a separate phase from the MnO_2 and the lower oxide phase does not diffuse into the MnO_2. In order to interpret or evaluate the potential of MnO_2, this fact must be taken into account in addition to the nature of the Mn^{4+} — Mn^{3+} — $O^=$ — OH^- system (curve a in Fig. 2 or Eq. [4]).

Deviation during the initial half.—In Fig. 6 and 7, the experimentally observed open-circuit potential deviates somewhat to higher potentials from the calculated curves, particularly in Fig. 7. This may be explained in one of the following factors or in both. The first is the activity of the Mn^{3+} and Mn^{4+} ions in the solid. In the calculation of the curve, no consideration was made on the activity coefficient of Mn^{3+} and Mn^{4+} ions in the solid, but simply the ratio of the concentrations $[Mn^{3+}]/[Mn^{4+}]$ was used. The deviation may be due to this. The second is the reference point in the comparison of the observed and the calculated curves. The reference point was taken as that at $[Mn^{3+}]/[Mn^{4+}] = 1.0$ by assuming that no lower oxide structure has begun to form on the surface of the original Mn^{4+} — Mn^{3+} — $O^=$ — OH^- structure. But the lower oxide may have started slightly at the point where $[Mn^{3+}]/[Mn^{4+}] = 1.0$. When such is found to be true, the reference point should be taken at a point where the ratio $[Mn^{3+}]/[Mn^{4+}]$ is less than 1.0 and the curve should be recompared.

Estimation of the D_2O *effect.*—In the electron-proton mechanism discussed earlier in this paper, the possible effect of D_2O in the electrolyte may be expected in two processes. One is in the dissociation of water molecules at the solid-solution interface and the other is in the proton diffusion process by jumping from one $O^=$ site to another within the MnO_2 lattice. However, the two processes may be considered the same for the purpose of estimation of the D_2O effect because the essential thing in those processes is a breakage of O-H bonds. Therefore, the difference which is expected in the polarization will be roughly estimated here on the basis of the difference in the bond energy between O-H and O-D.

The deuterium isotope effect in chemical kinetics has been widely studied and summarized in reviews (34, 35). Among the various factors (34) which contribute to the general lower reactivity of O-D bonds as compared to O-H bonds, only one, a difference in the activation energy in breaking the bond by $\frac{1}{2}h(\nu_D - \nu_H)$ which is derived from the lower zero point energy in O-D, was considered here. The difference in the energy is found to be 1400 cal (34) per mole from the stretching vibration. If the cathodic reduction current of MnO_2 is controlled by the rate of proton diffusion in the lattice, then the ratio of the current i_D/i_H at a given potential may be estimated as follows.

$$\frac{i_D}{i_H} = \frac{C_{D^+}}{C_{H^+}} \frac{K_D}{K_H} \exp \frac{\Delta G^*}{RT}$$

where ΔG^* is 1400 cal. By assuming that the concentrations (C's) at the interface and the K's are approximately equal, the ratio is found to be approximately 1/10 at room temperature. In this calculation, a possibility for penetration of the potential-energy barrier or tunneling was neglected. If the tunneling contributes to the process, the deuterium effect may be somewhat more pronounced. Therefore, we can expect at least 10 times higher current in H_2O electrolyte than in D_2O at a given potential.

Although the present results on the preliminary experiments (Fig. 10 and 11) demonstrate the D_2O effect qualitatively, they cannot be compared immediately to the estimated value, because the discharge was carried out at constant current in an 85% D_2O solution. However, the estimation indicates that the effect should be in a measurable range and a more refined experiment should be done to evaluate the D_2O effect in KOD + D_2O electrolyte by discharging at constant voltage.

Acknowledgment

The authors wish to thank Professor E. B. Yeager of Western Reserve University, Professor H. A. Laitinen of the University of Illinois and Professor W. C. Vosburgh of Duke University for their discussion and suggestions on this paper and also Mr. William Adams for his assistance in the preparation of this paper.

Manuscript received April 6, 1966; revised manuscript received June 3, 1966.

Any discussion of this paper will appear in a Discussion Section to be published in the June 1967 JOURNAL.

REFERENCES

1. N. C. Cahoon and M. P. Korver, *This Journal*, **106**, 745 (1959).
2. G. S. Bell and R. Huber, *ibid.*, **111**, 1 (1964).
3. A. Kozawa and J. F. Yeager, *ibid.*, **112**, 959 (1965).
4. K. J. Vetter, *ibid.*, **110**, 597 (1963).
5. J. J. Coleman, *Trans. Electrochem. Soc.*, **90**, 545 (1946).
6. D. T. Ferrell and W. C. Vosburgh, *This Journal*, **98**, 334 (1951).
7. W. C. Vosburgh, *ibid.*, **106**, 839 (1959).
8. A. B. Scott, *ibid.*, **107**, 941 (1960).
9. F. Kornfeil, *ibid.*, **109**, 349 (1962).
10. A. Era, Z. Takehara, and S. Yoshizawa, The 6th Battery Symposium, (Japan), Papers 3 and 4. Extended Abstract pp. 5 and 9 (1965).
11. N. V. Watson and A. B. Scott, *This Journal*, **112**, 883 (1965).
12. A. Kozawa, *ibid.*, **106**, 79 (1959).
13. A. Kozawa, T. Kalnoki-Kis, and J. F. Yeager, *ibid.*, **113**, in press (1966).
14. G. H. Newman and G. E. Blomgren, *J. Chem. Phys.*, **43**, 2744 (1965).
15. H. F. McMurdie *et al.*, *Trans. Electrochem. Soc.*, **90**, 509 (1946).
16. H. F. McMurdie *et al.*, *ibid.*, **86**, 313 (1944).
17. L. C. Copland and F. S. Griffith, *ibid.*, **89**, 495 (1946).
18. A. Walkley, *This Journal*, **97**, 209C (1952).
19. T. P. Dirkse, *ibid.*, **106**, 154 (1959).
20. J. S. Fordyce and R. L. Baum, *J. Chem. Phys.*, **43**, 843 (1965).
21. F. Daniels, *Trans. Electrochem. Soc.*, **53**, 45 (1928).
22. B. M. Thompson, *Ind. Eng. Chem.*, **20**, 1176 (1928).
23. H. D. Holler and L. M. Richie, *Trans. Electrochem. Soc.*, **37**, 607 (1920).
24. N. C. Cahoon, *ibid.*, **68**, 177 (1935).
25. R. S. Johnson and W. C. Vosburgh, *This Journal*, **99**, 317 (1952).
26. R. S. Johnson and W. C. Vosburgh, *ibid.*, **100**, 481 (1953).
27. K. Sasaki, Memoirs Faculty Eng. Nagoya Univ., **3**, 81 (1951).
28. A. K. Covington *et al.*, *Trans. Faraday Soc.*, **58**, 1975 (1962).
29. A. Kozawa and K. Sasaki, *J. Electrochem. Soc., Japan*, **22**, 569 (1954).
30. A. Kozawa, *ibid.*, **106**, 552 (1959).
31. J. P. Gabano *et al.*, *Electrochim. Acta*, **10**, 947 (1965).
32. A. D. Wadsley and Allan Walkley, *J.* (*and Trans.*) *Electrochem. Soc.*, **95**, 11 (1949).
33. A. M. Monssard, J. Brenet, *et al.*, International Committee of Electrochemical Thermodynamics and Kinetics (6th Meeting, Poitiers 1954), p. 190 (1955), Butterworth's Scientific Publications.
34. K. B. Wiberg, *Chem. Rev.*, **55**, 713 (1955).
35. F. H. Westheimer, *ibid.*, **61**, 265 (1961).
36. A. F. Wells, "Structural Inorganic Chemistry," 3rd ed., p. 71, Oxford University Press, Clarendon, England (1962).
37. L. Pauling, "The Nature of the Chemical Bond," 2nd ed., p. 350, Cornell University Press, Ithaca, N. Y. (1940).
38. T. Moeller, "Inorganic Chemistry," p. 140 (1952).
39. V. M. Goldschmidt, Geochemische Verteilungsgesetze der Elemente, **8**, 69 (1926); *Ber.*, **60**, 1263 (1927).
40. N. C. Cahoon, *This Journal*, **99**, 343 (1952).
41. N. C. Cahoon, R. S. Johnson, and M. P. Korver, *ibid.*, **105**, 296 (1958).
42. W. C. Vosburgh and J. H. Delap, *ibid.*, **107**, 255 (1960).
43. H. Bode and A. Schmier, "Batteries," D. H. Collins, Editor, p. 329, Pergamon Press, New York (1963).
44. H. Bode, A. Schmier, and D. Berndt, *Z. Elektrochem.*, **66**, 586 (1962).
45. W. Feitknecht, H. R. Oswald, and U. Feitknecht-Steinman, *Helvetica Chem. Acta*, **43**, 1947 (1960).
46. H. B. Mark and W. C. Vosburgh, *This Journal*, **108**, 615 (1961).

The Pitting Potential of Stainless Steels in Chloride Media

V. Hospadaruk and J. V. Petrocelli

Applied Research Laboratory, Ford Motor Company, Dearborn, Michigan

ABSTRACT

Anodic and cathodic potentiostatic polarization curves were obtained for various stainless steel alloys in sodium chloride and calcium chloride solutions. In the pH range 2 to 8 pitting occurs in the passive region. For a given chloride ion concentration pit initiation does not occur until a certain electrode potential, the pitting potential, is reached. The pitting potential is dependent on alloy composition and may be used as a relative measure of pitting tendency for various alloys. Calcium ion enobles the pitting potential when the chloride ion concentration is about 1*N* or less. The implications of a pitting potential on passivity theories is briefly discussed.

Stainless steel alloys are generally used in environments where they are in the passive state. Corrosion of the alloys in the passive state is usually localized and of the pitting type. Stainless steels are particularly susceptible to this type of corrosion when halide ions are present.

While several factors affecting pit growth have been described in the literature, the actual mechanism of pitting, especially pit initiation, is not known (1, 2). The first use of electrochemical methods in pitting corrosion studies of these alloys were aimed at accelerating the pitting by anodic polarization and measuring either the "break-through" potential or the density of pits formed in a given time.

The need for a satisfactory pit initiation test and the various attempts to devise one have been thoroughly reviewed by Streicher (2).

Streicher developed an electrolytic pitting test for stainless steels, the results of which showed some correlation with the known effect of alloy composition on service behavior (2). The specimen was anodically polarized and the current increased from zero to 3

ma/cm² and held at this value for 5 min. The number of pits formed per unit area was used as a measure of the relative resistance to pitting corrosion.

Rozenfeld *et al.* obtained galvanostatic anodic polarization curves for various alloys which showed that the curves may depend on alloy composition in dilute sodium chloride solutions (3).

These studies did not elucidate the mechanisms involved nor consider the role of the cathodic reactions in the actual corrosion process.

More recent papers, some of which appeared during the course of this work, began to shed more light on pit initiation. Kolotyrkin (4) and Schwenk (5) by using potentiostatic techniques have given strong evidence that the pitting of a given alloy at a given aggressive anion concentration can occur only within a definite potential range. Riggs (6) obtained potentiostatic anodic curves for AISI type 316 stainless steel in strong sulfuric acid solutions containing halide ions. The data also indicate the potential dependency of pitting for this alloy.

Since most of the electrochemical behavior of stainless steels described in the literature is for acid solutions, one objective of this study was to obtain information in weakly acid to alkaline media containing chloride ion. In particular the effects of calcium chloride versus sodium chloride were of interest. As a part of a broad program to obtain a better understanding of passivity and pitting attack by the aggressive anions it was desirable to explore the potentiostatic technique as a means of studying pit initiation and perhaps for the evaluation of the relative pitting tendency of various alloys.

Further experimental evidence that nucleation of pits on an otherwise passive surface is a function of the potential is important in the consideration of passivity theories. If this relationship is true, it must be accounted for in any acceptable theory of passivity.

The data presented describe the electrochemistry of several commercial alloys in solutions of sodium chloride and calcium chloride.

Experimental Procedure

The stainless steel alloys AISI 201, 301, 316, and 434 and a chromized steel were used. Compositions of the steel alloys are given in Table I. The chromized steel surface was prepared by a diffusion process, the coating was about 1.5 mils thick with a chromium content of about 35% at the surface.

Commercial steels were obtained in sheet form; they had been produced by conventional hot and cold rolling, annealed at 1700°-1800°F, slow cooled with a final 33% cold reduction. The surfaces were buffed to a bright finish. Specimens were thoroughly degreased and given a 30-sec treatment in 3.5*N* H_2SO_4.

Solutions were prepared with double-distilled water and reagent grade chemicals. The *p*H was adjusted with sodium hydroxide or sulfuric acid. Deaeration of solutions was accomplished by the use of pure nitrogen which was passed over hot copper turnings.

Electrode area was about 1 cm², and the potentiostatic polarization curves were obtained in the conventional manner. Prior to obtaining the anodic curves the specimens were cathodically polarized to about —1.00v, into the active state, in order to remove any film present on the surface.[1] The polarization curve

[1] Experiments conducted without precathodization showed that the general behavior and results would not be altered significantly.

Table I. Stainless steel composition, values in weight per cent

	AISI Types			
	434	201	301	316
Chromium	17.9%	17.3%	17.6%	17.0%
Nickel	0.18	4.6	7.7	13.0
Manganese	0.32	7.5	1.25	1.8
Silicon	0.46	0.53	0.50	0.35
Molybdenum	0.98	0.05	0.05	2.25
Sulfur	0.013	0.013	0.015	(0.03 max.)
Carbon	0.06	0.08	0.08	0.04

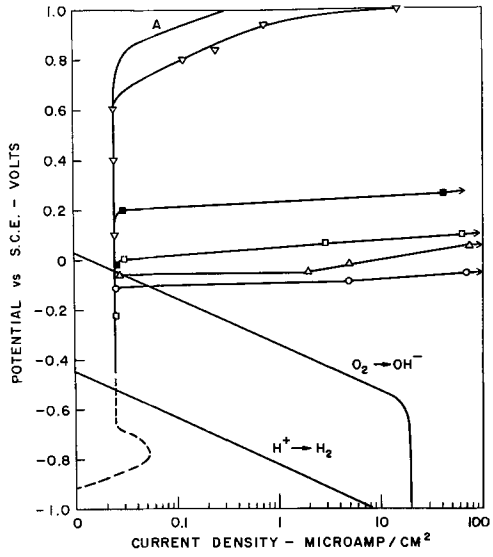

Fig. 1. Anodic polarization curves for several stainless steels in 0.5*N* NaCl, *p*H 6: ■ 316, □ 301, △ 201, ○ 434, ▽ a chromized steel with about 35% Cr at the surface. Curve A is the anodic curve for 301 in 0.5*N* Na_2SO_4, *p*H 6. The approximate positions of the cathodic reduction curves for hydrogen ions and oxygen are shown.

was then obtained by step-wise increase in the potential by about 25 mv; waiting for a fairly steady current value at each potential, this usually required about 20-30 min. For some special experiments here designated as "rapid polarizations" the rate was fixed at 10 mv/min. All potential values are given *vs.* the saturated calomel electrode.

Experimental Results

All of the steels exhibited stable passive behavior in neutral solutions which did not contain chloride ions. Curve A in Fig. 1 shows a typical anodic curve in sodium sulfate. The active and transition portions of the curve, shown dashed, is schematic. The very low value of the passivating current density in neutral solutions makes these portions difficult to obtain experimentally. It is significant to note that the cathodic curve for hydrogen ion reduction lies above the passive "peak" so that the steels are in the stable passive state in oxygen-free neutral solutions.

The other curves in Fig. 1 show typical results obtained in the presence of chloride ion. Any one steel assumes passive behavior until a certain potential is reached where the current begins to rise sharply and pits begin to form on the otherwise passive surface. The value ot this potential, designated here as the pitting potential, *Ep*, is dependent on the alloy composition and chloride ion concentration. For any given alloy and solution the *Ep* is fairly reproducible within about ±0.05v. The deviations may be due to variations in surface composition from one specimen to another, *i.e.*, chromium and/or nickel depleted areas would yield lower values.

The results are about the same in sodium chloride and calcium chloride at a given concentration of chloride ion and *p*H, except in solutions about 1.5*N* and less in chloride ion. At these lower concentrations there is a tendency for the calcium ion to increase the *Ep*.

Specimens held below the pitting potential for several days did not pit. On the other hand, if the potential of a pitting specimen was decreased below the pitting potential, the pitting would stop. The curves in Fig. 2 show a typical result. Curve 1 depicts the increase in current due to pitting, while curve 2 shows the decrease in current and final cessation of pitting. The amount of hysteresis depends on the time allowed for pitting. The greater the pit depth the

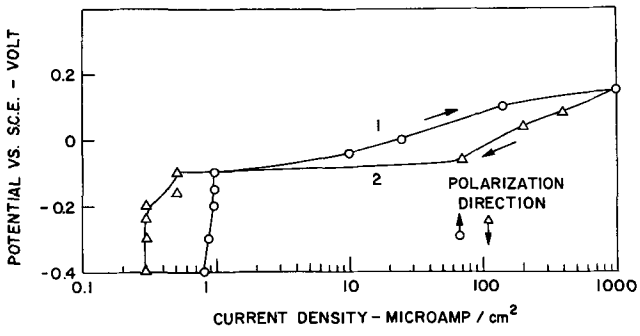

Fig. 2. Initiation and subsequent healing of pits on 434 in 0.5 NaCl pH 6. The specimen was potentiostatically polarized beyond the pitting potential and then back to potentials below Ep.

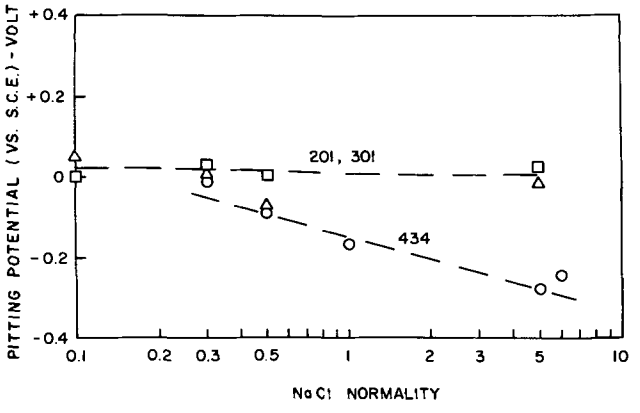

Fig. 3. Effect of chloride concentration on the pitting potential of the steels in sodium chloride solutions, pH 6: □ 301; △ 201; ○ 434.

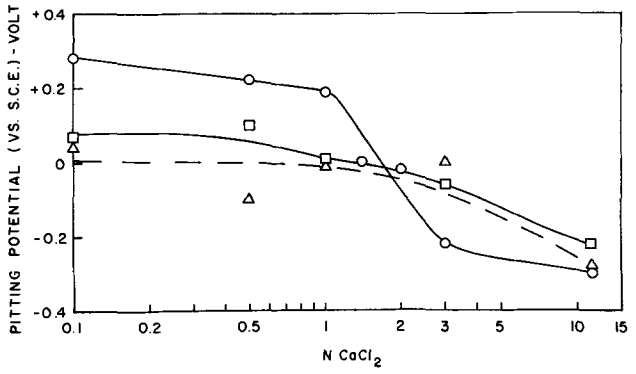

Fig. 4. Pitting potentials obtained in various concentrations of calcium chloride solutions, pH 6: □ 301; △ 201; ○ 434.

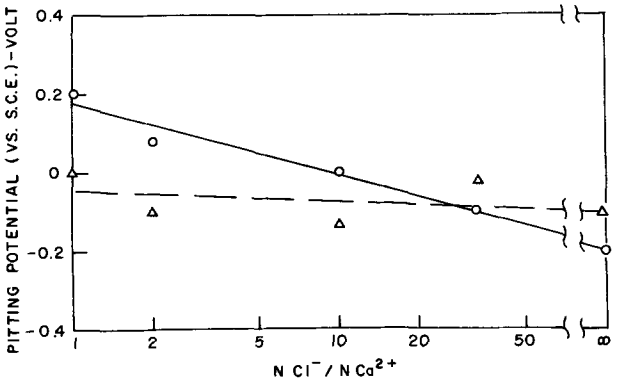

Fig. 5. Effect of the concentration ratio, N Cl^-/N Ca^{2+}, on the pitting potential of steels 434 and 201 for a constant 1N chloride ion concentration, pH 6: ○ 434; △ 201.

greater the hysteresis. This time effect may be due to the increase in metal ion concentration, hence lower pH, and chloride concentration at the bottom of deep pits.

Returning to Fig. 1, the potential required for the nucleation of pits on the various alloys increases in the order of 434 < 201 < 301 < 316 < chromized steel. This indicates that the inherent proneness to pitting corrosion should be in the reverse order.

The effect of chromium content on pitting tendency is shown by the anodic curve for the chromized steel given in Fig. 1. This steel showed no pitting and the behavior is almost identical to that of pure chromium. There is no rise in current prior to the transpassive region.

The effect of chloride concentration on the pitting potential in sodium chloride at pH 6 is shown in Fig. 3. The pitting potential of the austenitic steels is practically independent of concentration in the range 0.1-5.0*N* NaCl. In contrast, the pitting potential of the 434 steel decreased linearly with the decrease in log [Cl^-].

The pitting potential of these alloys was found to be practically independent of pH in the range pH 3-8 in sodium chloride.

As previously indicated, below about 1.5*N* chloride ion the *Ep* are somewhat greater in calcium chloride than in sodium chloride. The effect is quite pronounced with the 434 type steel, where there is an actual reversal in the relative order of *Ep*. In calcium chloride, below about 1.5*N* the *Ep* is greater than that of the austenitic steels. The pitting potential of 434 shows a sharp decrease between 1 and 3*N* calcium chloride and seems to reach a limiting value of about —0.3v with further increase in salt concentration, as shown in Fig. 4.

The specific effect of the calcium ion was also determined by obtaining the variations of *Ep* with the ratio of chloride ion concentration to calcium ion concentration at a constant (1.0*N*) chloride ion concentration at pH 6.0. The solutions were made by using the appropriate mixtures of calcium and sodium chloride. Results are shown in Fig. 5. The values for 301 are not shown since they are the same as those for 201. The pitting potential of 301 and 201 are practically independent of the chloride ion to calcium ion ratio, while that of 434 decreases almost linearly as the logarithm of the ratio increases.

The effect of pH on the pitting potential in 0.1 and 3.0*N* calcium chloride is shown in Fig. 6. In contrast to sodium chloride solutions the pH has a significant effect on the pitting potential, particularly in the more dilute calcium chloride solution. The pitting po-

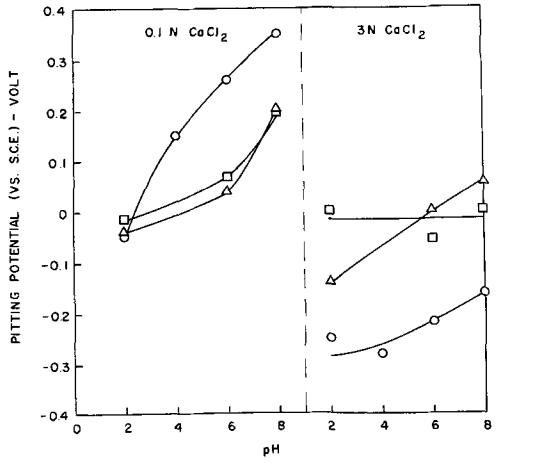

Fig. 6. Effect of pH on the pitting potential of 434, 201, and 301 steels on 0.1 and 3N calcium chloride: ○ 434; □ 301; △ 201.

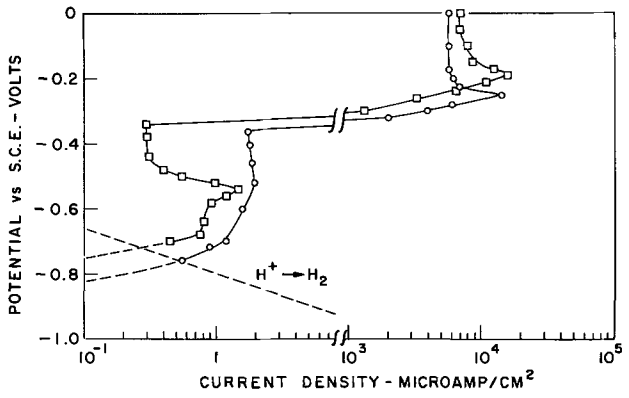

Fig. 7. Anodic polarization of 434, ○, and 301, □, in air-free 11.2N calcium chloride, pH 6. The hydrogen ion reduction curve is included.

tential increases as the *p*H increases, and the change is greater with 434 than the other steels.

As was the case in sodium chloride, the chromized steel was immune to pitting in the *p*H range 3-8 in calcium chloride, even in a 11.2*N* (saturated) solution.

Some rapid polarization curves[2] for the steels in viscous 11.2*N* calcium chloride, saturated solution at room temperature, are shown in Fig. 7. In this chloride concentration the behavior of the austenitic and ferritic steels are very similar. It is very interesting to note that the passivating current density is somewhat greater than in the more dilute solutions so that the active and transition portions of the curve may be obtained at *p*H 6.0.

At lower *p*H values the usual displacement of the passivating potential, hence transition portion, toward more noble potentials causes the *Ep* value to occur near the maximum of the passivity curve.

In these very concentrated solutions, 8.0-11.0*N* calcium chloride, the pit density is very high with probably rapid lateral pit growth so that the surface actually dissolves more or less uniformly as in active dissolution. The current density increases to very high values within a very small potential range until a limiting current density of about 10 ma/cm² is reached. The dissolution rate then remains practically constant with further increase in potential.

Immersion tests in the various solutions for periods of about three weeks confirmed the relative corrosion behavior predicted by the anodic and cathodic polarization curves.

In contrast to the pure metals, iron and nickel, the stainless steel alloys used in this work have a limiting potential below which they do not pit, even when chloride ion is 11*N*. This limiting value is about —0.3 to —0.35v on the saturated calomel scale. This, together with the observation that an occasional 434 specimen exhibited an abnormally high pitting potential and the oscillatory current behavior in some instances, strongly indicates that a healing process may occur at the lower end of the pitting potential zone.

In an attempt to detect a transient type of pitting, nucleation followed by healing, some rapid anodic polarizations were run. A rate of 10 mv/min was chosen. Some results obtained with 301 and 434 steels are given in Fig. 8. Curves A and C show the rapid steady increase in current at the same pitting potential as obtained in steady-state polarizations. The rapid curve B is representative of those occasionally obtained with some 434 specimens which have abnormally high steady-state pitting potentials. The curves B and C do show a "hump" which indicates that some pitting was initiated at about —0.20v, but that healing soon occurred; further pit initiation did not occur until about 0.0v.

Although, as previously indicated, the pitting potential for 434 steel increases as the chloride ion concentration decreases; the hump is apparently independent of chloride concentration and begins at about —0.25v.

Since, in all of the experiments reported above, the passive film was formed in the chloride medium, it was desirable to determine if this was a necessary criterion for pitting. Specimens of 434 steel were polarized in a chloride-free solution to +0.50v and held at this potential until "steady state" conditions were achieved. Chloride ion was then added to the solution to a final concentration of 0.2*N*. In about 5 min the current began to increase, indicating pitting. After a few more minutes the potential was reduced to —0.20v and the pitting stopped. A typical behavior is shown by curves A and B in Fig. 9. The potential was then increased again until pitting resumed, curve C. This time the specimen did not pit until +0.70v.

The results show that a passive film formed in a chloride-free medium is susceptible to chloride attack, and that pitting is potential dependent.

Some galvanostatic anodic charging experiments were performed in order to obtain the relationship between this type of data and the potentiostatic results. Specimens were polarized by imposing a constant current density of 7 μa/cm² until the pitting was well established. Results are shown in Fig. 10.

The potential rises rapidly until the onset of oscillations, when pitting begins. The potential then drops sharply, followed by a slow decay to a quasisteady state. The potential regions where oscillations of potential occur, the so-called break-through potentials, are about 400 to 500 mv more noble than the pitting potential obtained by the potentiostatic method. Values also vary with the magnitude of the current used.

The potential value obtained at the intersection of the extrapolated potential decay curves, marked E_c in Fig. 10, approximates closely the potentiostatic pitting potentials.

It will be noted that the specimens were in the active state (potential at about —1.00v) at the start of

[2] Steady-state polarizations did not shift the value of *Ep*.

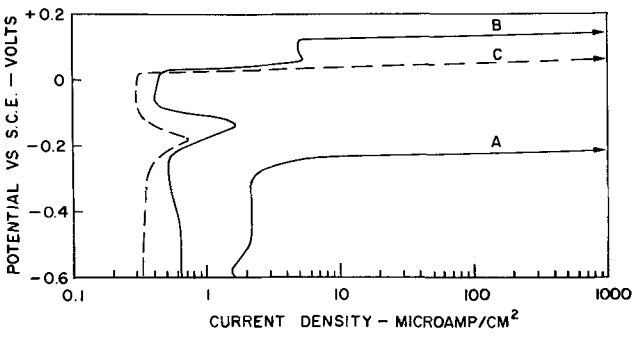

Fig. 8. Anodic polarization of 434 and 301 steels in air-free 6N NaCl, pH 6, at the rate of 10 mv/min in 20 mv steps. A and B, 434; C 301.

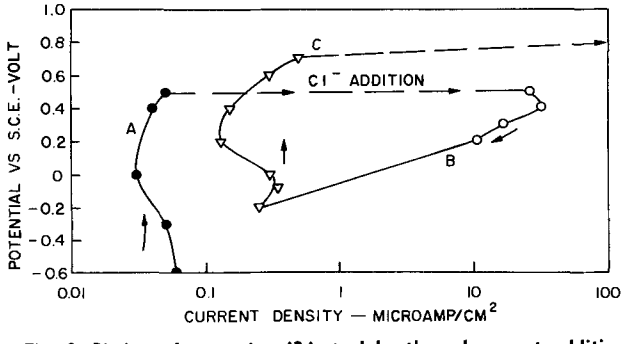

Fig. 9. Pitting of a passive 434 steel by the subsequent addition of sodium chloride to the 0.1N Na_2SO_4, pH 6. The repassivation and then reactivation of the pits are depicted by curve sections B and C.

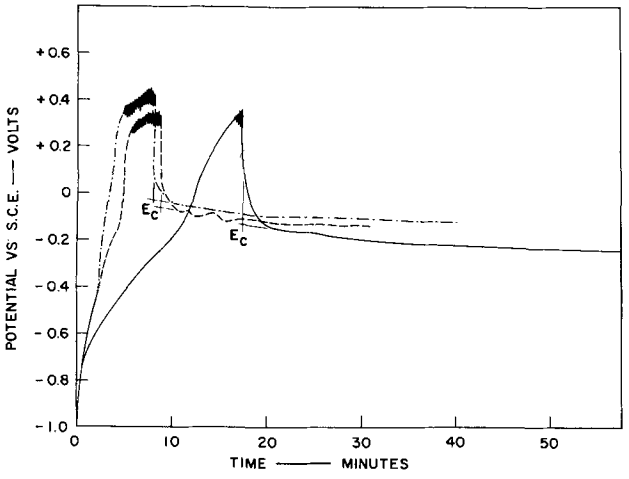

Fig. 10. Anodic changing curves for the steels in deaerated 1N NaCl, pH 6. Charging rate: 7 $\mu a/cm^2$: —— 434; - - - 201; — • — • 301.

the charging. The results show that the passive film is formed and then begins to pit. It is interesting to note that 434, which seems to have the greatest pitting tendency, has the shortest period of oscillations.

Discussion

The results show that the nucleation of pits on an otherwise passive surface is a function of the electrode potential. For a given chloride ion concentration and alloy composition, pitting does not occur until a certain potential is reached or exceeded. This pitting potential is characteristic of the alloy and may be used as a measure of the relative pitting tendency of various alloys. The potentiostatic technique is very promising as a pit initiation test.

The experimental data seem to indicate that all sites are not equally susceptible to pitting and that the nucleation of pits occurs over some broad potential range. Apparently, pit initiation at the measured *Ep* takes place at only the more susceptible sites. A special situation exists with highly concentrated chloride solutions such as 11.2*N* calcium chloride. Pit nucleation occurs so readily that the entire electrode surface is rapidly pitted at a potential not more than 50 mv above *Ep*.

In the use of *Ep* as a measure of pitting tendency it should be noted that service performance will also depend on the cathodic polarization curve. In order for pitting corrosion to occur in service the cathodic curve for the reduction of oxygen (or any other oxidant) must intersect the anodic curve at the pitting potential or more noble values. Thus, two alloys with significantly different *Ep* may both undergo pitting corrosion if the cathodic curve intersects the anodic curve at the *Ep* value on both alloys.

The oxygen reduction curve on the alloys used in this work does not vary appreciably with the alloy composition and as the curves in Fig. 1 indicate, all but AISI 316 of the stainless steels may be expected to undergo some pitting corrosion since the steady-state passive current, *i* pass., is slightly lower than the experimental value shown. The severity should decrease in the order 434 > 201 > 301 > 316.

It is interesting to note that the *Ep* of these alloys does not vary significantly with *p*H in the *p*H range 3-8. The decrease in pitting with increase in *p*H usually encountered in service is apparently due mostly to the shift of the cathodic curve to lower potentials as the *p*H increases. This exemplifies the important role of the cathodic curve.

The importance of the cathodic reaction is again demonstrated by the behavior of the stainless steel at open-circuit immersion in 11.2*N* calcium chloride solution. Although the pitting potential in this medium is at the minimum value of —0.30 to —0.35v the pitting attack after long-term immersion was not severe due to the low oxygen solubility and rate of diffusion in the viscous solution.

The role of chromium in increasing the pitting potential is especially noteworthy.

The specific effect of calcium ion and its dependency on *p*H is no doubt due to the adsorption of the ion or a basic calcium compound on the surface. It is not clear, however, why the effect is so pronounced on the 434 type steel.

The relationship between pit nucleation on the passive surface and electrode potential requires an explanation which is consistent with any acceptable theory of passivity. This aspect of the problem is under consideration, and we expect to offer suggestions at a future date.

Meanwhile, the following comments should be made. The important question is not why the chloride ion should cause a break-down of passivity, but rather why does it occur at potentials which may be significantly greater than the passivation potential. It is logical to assume that, if the chloride ion is adsorbed onto the surface at sufficient concentrations, it would prevent further film formation and/or create anion vacancies in the film so that it might collapse. The ability of chloride to become incorporated into a film lattice has been shown by Beck *et al.* in the case of aluminum (7).

An increase in the adsorption of chloride ion onto the passive surface with an increase in the measured electrode potential is not an obvious deduction. The potentiostatic anodic curve of the metals in question show a well defined constant current region. The "oxide" film theory is the most consistent theory with this experimental fact.

Accordingly the film thickens with an increase in the measured electrode potential along this current plateau. In the steady state the rate of film formation is equal to the rate of film dissolution. The potential distribution across the film has been discussed by Vetter (8) and Weil (9) and is shown schematically in Fig. 11. The increase in the measured electrode potential is predominantly if not entirely due to the increase in, V_{ox}, the potential difference across the film. The potential $e_{o/s}$, of the oxide-solution interface remains constant, in fact very close to the equilibrium potential for the reaction

$$[H_2O]_{ad} \rightleftarrows O_{ox} = +2H^+$$

Since the rate of chloride ion adsorption should be dependent on $e_{o/s}$, it is not clear how this rate or equilibrium concentration of adsorbed chloride ion increases with the measured potential.

One might possibly deduce that the chloride effect is a function of the film thickness and/or composition changes, which are dependent on the potential.

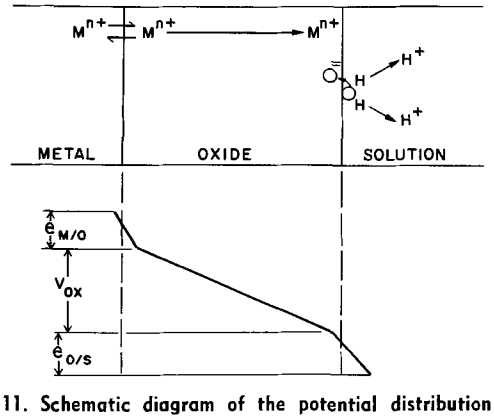

Fig. 11. Schematic diagram of the potential distribution across the oxide film.

One possible explanation which we suggest at this time is that during the dynamic situation where film growth and film dissolution are occurring at the same rate on the average there will be fluctuations so that certain areas become entirely free of film for brief periods of time. When the measured electrode potential is increased the potential difference at the "bare" metal-solution interface will become very high, with the promotion of very rapid adsorption of chloride ions.

The presence of a high concentration of adsorbed chloride ions at these sites will of course prevent further growth of the passive film and result in the establishment of active pits.

Such fluctuations in filmed-bare areas are likely because the emergence of metallic ions from the metal into the passive film, required for film growth, should occur at much greater rates at ledges, kinks, etc., than at the planar sites at the metal-oxide interface. At some critical "interledge" distance the film dissolution may momentarily exceed formation on a small planar site.

As previously indicated, we expect to treat this aspect of the aggressive anion effect in more detail at a future date.

Acknowledgments

The authors wish to express their appreciation to Ernest A. Styloglou for his experimental assistance and to the Ford Motor Company for permission to publish this work.

Manuscript received May 2, 1966. This paper was presented at the Buffalo Meeting, Oct. 10-14, 1965.

Any discussion of this paper will appear in a Discussion Section to be published in the June 1967 JOURNAL.

REFERENCES

1. L. L. Shreir, "Corrosion," vol. I, p. 1-108, L. L. Schreir, Editor, John Wiley & Sons, Inc., New York (1963); N. D. Greene and M. G. Fontana, *Corrosion*, **15**, 25t (1959).
2. M. A. Streicher, *This Journal*, **103**, 375 (1956).
3. I. L. Rozenfeld and V. P. Maksimchuk, *Russian J. Phys. Chem.*, **35**, 901 (1961).
4. Ja. M. Kolotyrkin, *This Journal*, **108**, 209 (1961); *Corrosion*, **19**, 261t (1963).
5. W. Schwenk, *Corrosion*, **20**, 129t (1964).
6. O. L. Riggs, Jr., *ibid.*, **19**, 180t (1963).
7. A. F. Beck *et al.*, *Corrosion Sci.*, **2**, 133 (1962).
8. K. J. Vetter, *Z. Elektrochem.*, **62**, 642 (1958); *ibid.*, **58**, 231 (1954).
9. K. G. Weil, *ibid.*, **59**, 711 (1955).

Oxidation of Copper Single Crystals in Aqueous Solutions of Inorganic Salts

IV. Effect of *p*H on Oxide Topography in $CuSO_4$ and $Cu(OAc)_2$ Solutions

D. B. Scott[1] and G. Tyler Miller, Jr.[2]

Department of Chemistry, Hampden-Sydney College, Hampden-Sydney, Virginia

ABSTRACT

Electron microscopic techniques were used to determine the effect of *p*H on the topography of Cu_2O formed on the (100), (110), and (111) faces of copper single crystals oxidized in aqueous solutions of $CuSO_4$ and $Cu(OAc)_2$. During reaction, changes in *p*H near the reacting metal surface were followed using a microprobe electrode. The *p*H near the metal surface dropped during reaction in $CuSO_4$ solutions, but remained constant in $Cu(OAc)_2$ solutions. Previous studies at constant initial bulk *p*H showed oxide polyhedra formation in $CuSO_4$ solutions and the formation of relatively smooth continuous films in $Cu(OAc)_2$ solutions. Comparison of oxide topography at the same surface *p*H rather than initial bulk *p*H revealed polyhedra formation in both systems, although polyhedra were more run together in the $Cu(OAc)_2$ system. Several other effects of anion were observed. Thus, *p*H appeared to be the major variable affecting oxide topography with the anion present acting as a second variable controlling the amount of surface covered by oxide. These results were shown to be consistent with a reaction mechanism proposed in an earlier paper in this series.

This is the fourth in a series of papers describing the oxidation of copper single crystals in solutions of copper(II) salts. The first two papers (1, 2) were concerned with the topography of the copper(I) oxide formed by oxidation in solutions of $CuSO_4$, $Cu(ClO_4)_2$, $Cu(OAc)_2$, and $Cu(CHO_2)_2$. The third paper (3) presented the relative rates of oxidation of the (100), (111), and (110) faces of Cu in 0.05*N* $Cu(OAc)_2$, described the kinetics involved, and proposed a reaction mechanism for copper(I) oxide formation.

These previous studies showed that at a constant initial bulk *p*H a relatively smooth film of oxide was formed in the $Cu(OAc)_2$ and $Cu(CHO_2)_2$ solutions, while well-defined oxide polyhedra formed in both the $CuSO_4$ and $Cu(ClO_4)_2$ solutions. The relative rates of oxide growth for the $Cu(OAc)_2$ system was shown to be: (100) > (111) > (110), but the shape of the rate curves differed considerably (3).

Although those previous studies demonstrated the important effect of the anion on oxide topography at a given initial *p*H, it did not provide any information on the effect of *p*H on oxide topography. It seemed probable that another major variable or perhaps the variable controlling polyhedra or smooth film formation could result from changes either in the bulk *p*H of the solution or local changes in *p*H near the reacting surface. The present paper reports results obtained in an attempt to check this hypothesis and to gain additional evidence as to the validity of the reaction mechanism previously proposed (3).

Experimental Procedure

Known crystallographic (111), (100), and (110) faces of carefully prepared copper single crystals were exposed for 10 min to 0.05*N* solutions of $Cu(OAc)_2$ and $CuSO_4$ maintained at 30° ± 0.05°C and with *p*H values ranging from 4.8 to 3.0 in increments of 0.1 *p*H unit. The *p*H of a given solution was adjusted to the desired value by the addition of small

[1] Present address: Institute of Molecular Biophysics, Florida State University, Tallahassee, Florida.

[2] Present address: Department of Chemistry, St. Andrews Presbyterian College, Laurinburg, North Carolina.

Table I. Values of initial and final bulk pH for the $CuSO_4$ system after immersion for 10 min

Initial bulk pH	Final bulk pH (111)	(100)	(110)
4.50	4.04	4.10	4.00
4.30	3.96	3.97	3.97
3.80	3.74	3.72	3.70
3.20	3.23	3.21	3.21
3.10	3.13	3.16	3.14

amounts of 0.05*N* $Cu(OAc)_2$ or 0.05*N* $CuSO_4$ solutions which had been adjusted to a *p*H of 2.0 by addition of reagent grade HOAc or H_2SO_4, respectively. After immersion, the crystal surfaces were washed and replicated, and the replicas were examined with an electron microscope. The detailed procedures used were the same as those described in the previous papers (1, 2).

A second series of experiments was run in order to determine whether small changes in *p*H were occurring near the surface of the crystal face during reaction. A small microprobe glass electrode was fixed at a distance of approximately 1 mm from the flat face of the metal. The *p*H changes in the solution were measured and recorded by following voltage change *vs.* a mercury-mercurous sulfate reference electrode. In order to minimize any effect of anions, the reference electrode was connected to the solution through a Luggin capillary.

Experimental Results

Experiments on the determination of *p*H changes approximately 1 mm from the surface of the crystal face yielded the very significant fact that for the $CuSO_4$ (initial *p*H 4.30) solution the *p*H dropped almost immediately on introduction of the crystal into the solution to a value of 4.00. This value remained relatively constant during the 10-min immersion period.

A similar series of experiments by Barker and Miller (4) in $Cu(OAc)_2$ showed that there was very little change in *p*H at a distance of approximately 1 mm from the surface. This was to be expected, since the $Cu(OAc)_2$-HOAc mixture served as a buffer system.

The final bulk *p*H values of the $Cu(OAc)_2$ solutions after 10 min of oxidation were essentially the same as the initial bulk values, while there was a considerable drop between the initial and final *p*H in the unbuffered $CuSO_4$ solutions. Results in $CuSO_4$ indicated that this final bulk *p*H was approximately equal to the value to which the surface *p*H fell when the crystal was first immersed in the solution.

A summary of the final bulk *p*H values for the $CuSO_4$ system is given in Table I.

The effect of *p*H on oxide topography on the (110) face oxidized in $CuSO_4$ solutions is shown in Fig. 1. It can be seen that as the bulk *p*H is lowered from 4.30 (Fig. 1b) to 3.10 (Fig. 1e) the amount of exposed metal surface area increased and the polyhedra became well defined with little running together. An analysis of shadow heights indicated that the polyhedra decreased in height as the *p*H was decreased. At *p*H values below 3.10 no oxide was formed on any of the three faces tested. It should be noted that the oxide formed on the (100) face seems to be more unstable than that formed on the (110) and (111) faces, since very little oxide remained even at a *p*H of 3.10. By comparing Fig. 1a to Fig. 1b it can be seen that the trend is reversed as the *p*H was raised from *p*H 4.30 to 4.50. This phenomenon was present on all three faces.

Figure 2 shows that this same general trend was observed on all three faces. Figure 1b, 2a, and 2b show, respectively, the oxide topography of the (110), (100), and (111) faces after 10 min in $CuSO_4$ solutions at constant *p*H. These photographs reveal that the

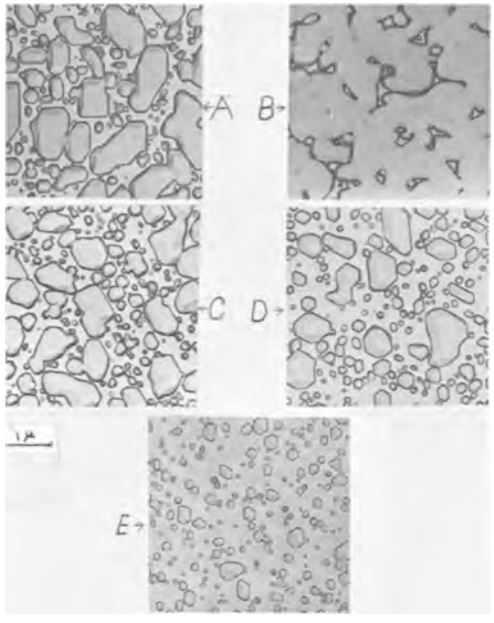

Fig. 1. Effect of pH on oxide growth on the (110) face of Cu after immersion in 0.05N $CuSO_4$ at 30.0°C for 10 min: a, pH = 4.50(4.00); b, pH = 4.30(3.97); c, pH = 3.80(3.70); d, pH = 3.20(3.20); e, pH = 3.10(3.14). pH values listed first are initial bulk values and values in parentheses are final bulk values. Magnification 15,000X before reduction for publication.

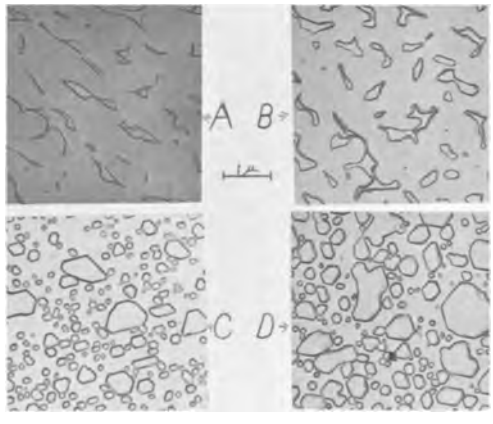

Fig. 2. Effect of pH on oxide growth on the (100) and (111) faces of Cu after immersion in 0.05N $CuSO_4$ at 30.0°C for 10 min: a, (100), pH = 4.30(3.97); b, (111), pH = 4.30(3.96); c, (100), pH = 3.20(3.20); d, (111), pH = 3.20(3.23). Values in parentheses are final bulk pH values. Magnification 15,000X before reduction for publication.

amount of bare metal surface present was approximately the same on all faces at the same *p*H. The same effect can be seen when the bulk *p*H is lowered to 3.20 by comparing Fig. 1d, 2c, and 2d. Thus, it appears that in the $CuSO_4$ system the area of exposed metal surface depends primarily on *p*H and does not vary significantly with face. As noted before, the (100) face at a *p*H of 3.10 represents an exception to this generalization, since very little oxide remains at this *p*H.

The effect of *p*H on oxide topography on the (110) face in $Cu(OAc)_2$ solutions is summarized in Fig. 3. Similar results were observed for the (100) and (111) faces. As the *p*H was lowered, the amount of bare metal surface area again increased. However, by comparing Fig. 3 with Fig. 1, it can be seen that the polyhedra were more run together in the $Cu(OAc)_2$ system than in the $CuSO_4$ system. Thus, although the primary variable affecting polyhedra formation and

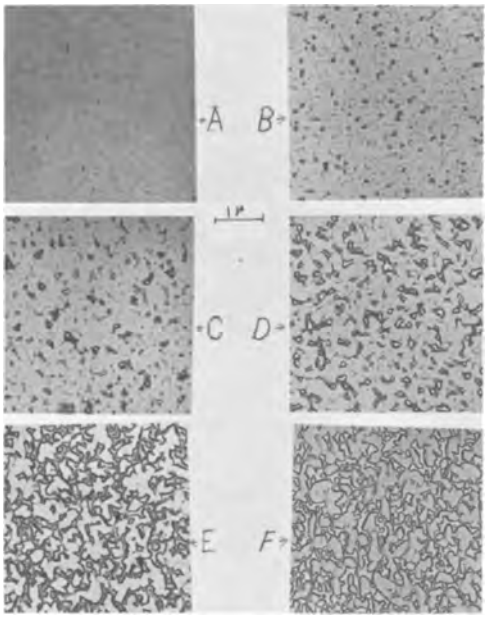

Fig. 3. Effect of pH on oxide growth on the (110) face of Cu after immersion in 0.05N $Cu(OAc)_2$ at 30.0°C for 10 min: a, pH = 4.30; b, pH = 4.20; c, pH= 4.10; d, pH = 4.00; e, pH = 3.90; f, pH = 3.80.

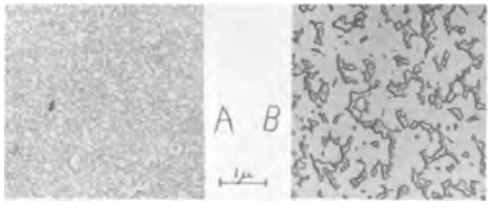

Fig. 4. Effect of pH on oxide growth on the (100) and (111) faces of Cu after immersion in 0.05N $Cu(OAc)_2$ at 30.0°C for 10 min: a, (100), pH = 4.10; b, (111), pH = 4.10.

surface coverage appears to be pH, the anion present is an additional variable that affects the degree of surface coverage.

The results shown in Fig. 1 and 2 revealed that at the same pH in the $CuSO_4$ system the amount of oxide coverage for the (100), (111), and the (110) faces was approximately the same. Figure 4, when compared with Fig. 3c, shows a similar comparison at the same pH in the $Cu(OAc)_2$ system. An examination of these photographs reveals that the amount of exposed metal surface area did vary with crystal face in this system in the order (100) > (111) > (110). The bulk pH at which no oxide remained on the surface was found to be in the same relative order (100) (pH 3.8) > (111) (pH 3.6) > (110) (pH ~ 3.5). Thus, the degree of surface coverage at the same bulk pH varied with face in the $Cu(OAc)_2$ system, but remained essentially constant with face in the $CuSO_4$ system.

Discussion

In the previous study (1), oxide formation in $CuSO_4$ (initial pH 4.30) was compared to that formed in $Cu(OAc)_2$ at the same initial bulk pH (4.30). It was found that, in general, oxide polyhedra formed in $CuSO_4$ solutions while relatively smooth continuous films formed in $Cu(OAc)_2$ solutions.

The present study revealed that in order to determine the effect of anion on oxide topography, the two systems should not be compared at the same initial value for the bulk pH. It was shown that a $CuSO_4$ solution with an initial bulk pH of 4.30 had a pH of approximately 4.0 near the surface during the immersion period, while there was no drop in pH near the surface in $Cu(OAc)_2$-HOAc solutions which act as a buffer system. Thus, in order to determine the effect of anion on topography, it is more meaningful to compare the oxidation in $CuSO_4$, having an initial bulk pH of 4.30, with oxidation in $Cu(OAc)_2$ with an initial bulk pH of 4.00. By comparing Fig. 1b with Fig. 3d, it can be seen that polyhedra tend to form in both systems when the pH near the surface is constant, although the polyhedra are more run together in the $Cu(OAc)_2$ system.

It is recognized that even this comparison might not be strictly valid, since the pH was measured at a distance of 1 mm from the surface and the pH nearer the surface would probably be lower than 4.00. The value of 4.00 is assumed to be reasonable, however, since at 1 mm from the surface the pH remained essentially constant during the reaction and since movement of the microprobe electrode closer to the surface gave no appreciable change in pH. In any case, since the pH near the surface in all of the $CuSO_4$ solutions tested was 4.00 or lower, the $CuSO_4$ system should be compared with a $Cu(OAc)_2$ solution in which the pH is 4.00 or lower. All such comparisons indicate polyhedra formation in both systems with the formation of more run together polyhedra in the $Cu(OAc)_2$ system.

Although polyhedra formation, and thus the degree of surface coverage, appear to depend primarily on pH, the degree of surface coverage was definitely affected by the anion present. At least three important effects of the anion were observed. First, as mentioned above, polyhedra formed in $Cu(OAc)_2$ solutions were more run together than those formed in $CuSO_4$ solutions. Second, the amount of surface covered at a given pH apparently did not vary significantly with crystal face in the $CuSO_4$ system, while the degree of surface coverage did vary with face in the $Cu(OAc)_2$ system. Finally, the pH value below which oxide did not form varied in the two systems [below 3.5-3.7 in $Cu(OAc)_2$ and below 3.1 in $CuSO_4$]. A more detailed interpretation of the effect of anion on oxidation was given in previous papers (2, 3).

It is felt that the results reported in this paper are consistent with the mechanism for oxidation of copper single crystals in solutions of $Cu(OAc)_2$ proposed in an earlier paper by Porterfield and Miller (3). The rate-determining step was postulated as the migration of "$\oplus$" (positive holes) through the oxide to specific reaction sites occurring at crevices or holes in the oxide. Continued or enhanced oxide growth of individual polyhedra was directly proportional to the amount of bare metal surface. The over-all net reaction was postulated as

$$Cu^{2+} + Cu + H_2O \rightleftarrows Cu_2O + 2H^+$$

Under a given set of reaction conditions, a balance between oxide formation and the reverse reaction of film dissolution would be achieved. The rate of the reverse dissolution reaction would also be directly proportional to the amount of bare metal surface present.

According to this mechanism, the pH near the surface should decrease during oxide formation, as was observed in the present study for the unbuffered $CuSO_4$ system. Furthermore, an examination of Fig. 3c 4a, and 4b shows that the amount of bare metal surface exposed in the $Cu(OAc)_2$ system follows the order (100) > (111) >(110), which is the same order as the oxidation rates determined in the previous study (3). The present study also demonstrated that, as pH decreased, the relative amount of metal surface exposed increased. This is also consistent with the proposed mechanism since an increase in H^+ would shift the equilibrium to the left due to the common ion effect and less Cu_2O would form on the surface. Further evidence was found in that the pH

below which no oxide formed in $Cu(OAc)_2$ is in the same order (100) (pH 3.8) > (111) (pH 3.6) > (110) (pH ~ 3.5). This mechanism would also account for the slight rise in pH found in the $CuSO_4$ system at low pH values (<3.2) as shown in Table I. The presence of a relatively high initial concentration of H^+ would tend to dissolve some or all of the thin film of Cu_2O formed during polishing and washing and thus yield a slight increase in pH.

Ives and Dawson (5) have given an excellent discussion of the electrochemical theory of oxidation of copper in aqueous solutions. Much of their discussion is consistent with the data obtained in the present work, although their duplex film model is not applicable to the present system, since it was proposed for systems containing very low concentrations of Cu(II) ion.

One additional result that needs to be discussed is the fact that although the amount of metal surface area exposed in the $CuSO_4$ system increased as the pH was lowered from 4.30 (Fig. 1b) to 3.10 (Fig. 1e), this trend was reversed when the pH was raised to 4.50 (Fig. 1a). One possible interpretation of this unexpected result can be offered in terms of the Pourbaix diagram for copper (6). According to the Pourbaix plot of potential *vs.* pH, Cu_2O is thermodynamically stable over a band of pH-potential values with Cu_2O dissolving to form Cu and Cu^{+2} at low pH values and with conversion to CuO at high pH values. Thus, either raising or lowering the pH eventually results in the thermodynamic instability of Cu_2O. It is recognized, however, that this line of reasoning may not be valid, since it consists of using a thermodynamic argument to account for a kinetic phenomenon in a system not at equilibrium. Additional experimentation will have to be carried out in order to obtain more information on this phenomenon.

Acknowledgments

The authors are deeply indebted to Dr. K. R. Lawless, Department of Materials Science, University of Virginia, for the use of an electron microscope. They would also like to thank the following students for their help in carrying out some of the experiments: L. E. Hightower, L. F. Towers, and E. B. Noland. This research was supported by a grant from the National Science Foundation Undergraduate Science Education Program and by PHS Research Grant DE-01893-03, National Institute of Dental Research, Public Health Service.

Manuscript received May 4, 1966.

Any discussion of this paper will appear in a Discussion Section to be published in the June 1967 JOURNAL.

REFERENCES

1. C. E. Guthrow, Jr., and G. T. Miller, Jr., *This Journal*, **113**, 415 (1966).
2. R. W. Topham and G. T. Miller, Jr., *ibid.*, **113**, 421 (1966).
3. W. W. Porterfield and G. T. Miller, Jr., *ibid.*, **113**, 528 (1966).
4. J. R. Barker and G. T. Miller, Jr., Unpublished results, Hampden-Sydney College.
5. D. J. G. Ives and A. E. Rawson, *This Journal*, **109**, 458 (1962).
6. M. J. N Pourbaix, "Thermodynamics of Dilute Aqueous Solutions," Edward Arnold and Co., London (1949).

Influence of Concentrated Neutral Salt Solutions on the Corrosion of Metals

K. Schwabe and Chr. Voigt

Technische Universität, Dresden, Germany

ABSTRACT

The H^+ activity of diluted strong acids, such as $HClO_4$ or HCl, rises by the addition of such neutral salts as $NaClO_4$, $Ba(ClO_4)_2$ from 10^{-1} to 10 at constant concentration of the acid. The effect of this increase of activity on the anodic dissolution of Fe, Co, and Ni has been investigated. Fe and Co show the order $z^+_{H+} = -2$ with respect to the H^+ activity, which was found by many other authors with respect to the H^+ concentration when stationary measurements were accomplished. In accordance with the Heusler mechanism the order changed to $z^+_{H+} = -1$ at unstationary measurements. The cathodic process has the order $z^-_{H+} = 0.5$ to 0.7 with respect to the H^+ concentration and 0.5 with regard to H^+ activity changed by addition of neutral salts. The anodic dissolution is influenced by the nature of the cations ($Na^+ < Ba^{++} < Li^+$).

On the contrary the order of anodic dissolution of Ni is $z^+_{H+} = -0.5$ with regard to H^+ concentration as well as to activity both at stationary and unstationary measurements. The cathodic process at Ni has the order $z^-_{H+} = +1$ with regard to H^+ concentration and 0.5 with regard to H^+ activity changed by addition of neutral salts. At the hydrogen ion discharge on the mercury electrode the order of reaction z^-_{H+} with regard to H^+ concentration rises from 0.5 to 1 with increasing ionic strength according to the theory of Frumkin. The dependence upon a_{H+} at constant H^+ concentration is complicated. The current density at constant potential passes through a maximum with increasing H^+ activity and content of neutral salt. Height and position of this maximum with regard to the neutral salt concentration depend on the potential. A qualitative interpretation of the experimental results is proposed.

When neutral salts such as $NaClO_4$ or $LiClO_4$ are added to dilute aqueous solutions of strong acids, a linear decrease of the pH value ($pH = -\log a_{H+}$) with salt concentration, m_{salt}, is observed, starting from about 1 mole/kg (1). The concentration of H^+ remains constant; therefore, the activity coefficient, f_{H+}, must grow exponentially with m_{salt}. The gradient $\Delta pH/\Delta m_{salt}$ depends on the ionic radius; the electrostatic interpretation of the pH shift is in sufficient agreement with the experimental results (2). The activity coefficients of the anions (f_{Cl-}, f_{Br-}, etc.) remain relatively constant (± 0.1) (2) over a concentration range of the salt which leads to an increase of f_{H+} by two orders of magnitude and more. Equi-

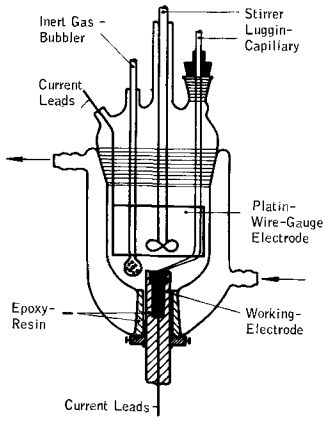

Fig. 1. Experimental procedure, the cell

libria in which H^+ take part are shifted by neutral salts according to the increase in their activity (2). The present work deals with the influence of the *p*H shift by neutral salts on the kinetics of electrode processes, in particular with the effect of neutral salts on the rate of anodic dissolution of Fe, Co, and Ni in the active region (at constant acid concentration) and on the kinetics of hydrogen ion discharge on these metals. Hydrogen ion discharge was also studied on the dropping mercury electrode, at constant H^+ concentration under variation of the H^+ activity by addition of salt as well as at high ionic strength under variation of the H^+ concentration.

Experimental Procedure

The electrodes were rods of metals such as Fe, Co, and Ni which had been molded into a special resin (EPOXID). On their front side, anodic and cathodic current-potential curves were measured galvanostatically in the cell shown in Fig. 1, according to a quasistationary method as used, for instance, by Heusler (3). The potentials were determined by a compensation method against a calomel electrode inside a Luggin capillary tube (Fig. 1). Before each measurement, the working electrode was resurfaced, polished, and degreased in the same manner. The salts were purified by repeated recrystallizations. Traces of impurities which would have disturbed especially the H^+ deposition were eliminated from the acid-salt solution by a preelectrolysis using an auxiliary electrode (4). From the various current-potential curves, the values of the current density, $(j)_\epsilon$, belonging to a certain constant potential ϵ, were read off, and from these the reaction order, z_{H+}, with respect to a_{H+} was found by plotting log j against *p*H.

Experiments on the dropping mercury electrode were made in an ordinary polarographic cell. The electrolyte solution was purified in an analogous way. Part of the values of the current density were measured at constant potential at a stationary mercury electrode (5) as a function of m_{H+} and of a_{H+}, respectively. So far, stationary measurements have been made predominantly on all electrodes; at the present time, we are working with a pulse method, and we shall report these results later.

Results

Armco iron.—According to the work of Heusler (6) and other authors, the current density of anodic dissolution of iron in the active region decreases with the square of the concentration of hydroxyl ions; the Tafel gradient $d\eta/d \log j$ is 30 mv. Other authors (7) have sometimes reported different (smaller) exponents, but they are in any case negative with respect to a_{H+}; that means the H^+ inhibit the anodic dissolution at higher concentration. When the *p*H value of sulfuric acid is varied by adding Na_2SO_4 at constant ionic strength j^+_{Fe} decreases with $a_{H+}{}^{-1.63}$. In Fig. 2,

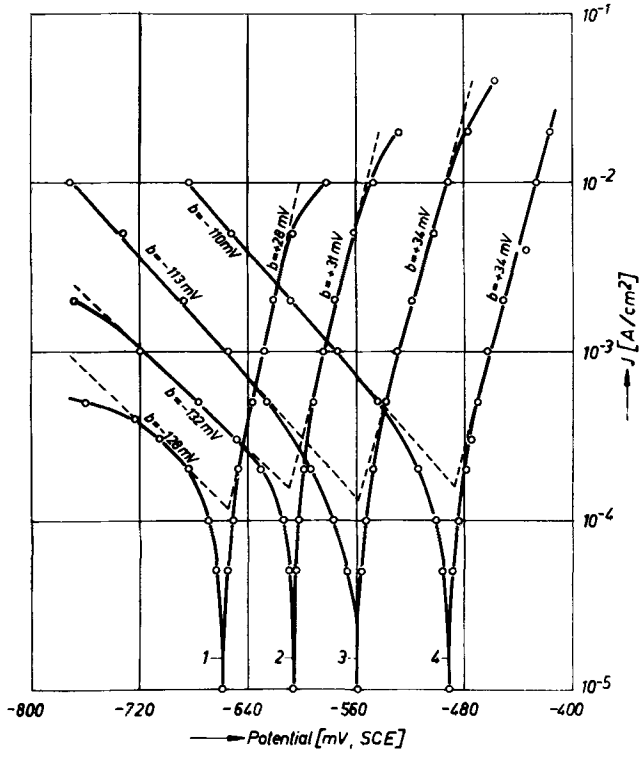

Fig. 2. Anodic and cathodic current-potential curves of the system Fe/H_2SO_4 + Na_2SO_4 (with stirring, t = 25°C, bubbling of H_2 galvanostatic, quasistationary). $c_{H_2SO_4}$ + $c_{Na_2SO_4}$ = 0.5N, except for curve 4. Curve 1, 0.001N H_2SO_4 + 0.499N Na_2SO_4, pH 3.66; curve 2, 0.01N H_2SO_4 + 0.49N Na_2SO_4, pH 2.62; curve 3, 0.1N H_2SO_4 + 0.4N Na_2SO_4, pH 1.51; curve 4, 1N H_2SO_4.

the current-potential curves are plotted semilogarithmically, and the anodic and cathodic gradients are listed.

In Fig. 3, (log J^+_{Fe}) and (log $j^-_{H+})^{Fe}$ are plotted against *p*H at constant potential, ϵ. Thus, the reaction order of active iron dissolution with respect to H^+ is, as mentioned above, $z^+_{H+} = -1.63$, and $b^{Fe} = 30$ mv; for the hydrogen reaction, we obtain $z^-_{H+} = +0.5$ and $b^{H_2} = 120$ mv (the Tafel slope of H^+ discharge). This value holds on iron up to high ionic strengths. We must point out that the addition of Na_2SO_4 to H_2SO_4 not only causes a change in the activity coefficient of H^+ but also a reduction in their number, according to the shift of the equilibrium: $H^+ + SO^{=}_4 \rightleftharpoons HSO^-_4$; it is for this reason that an increase in $pH = -\log m_{H+}f_{H+}$ can take place. But, when perchlorates are added to $HClO_4$, only the activity coefficient grows while m_{H+} remains constant.

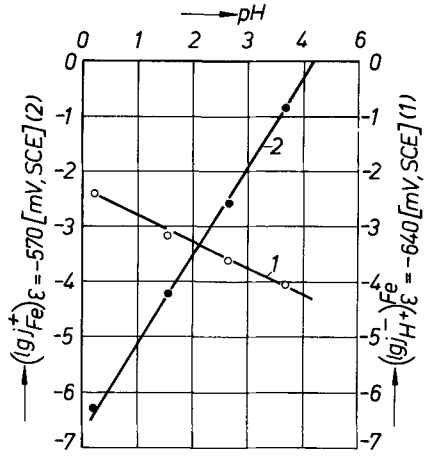

Fig. 3. Cathodic and anodic transfer current densities as a function of the *p*H value, at ϵ = const (taken from Fig. 2).

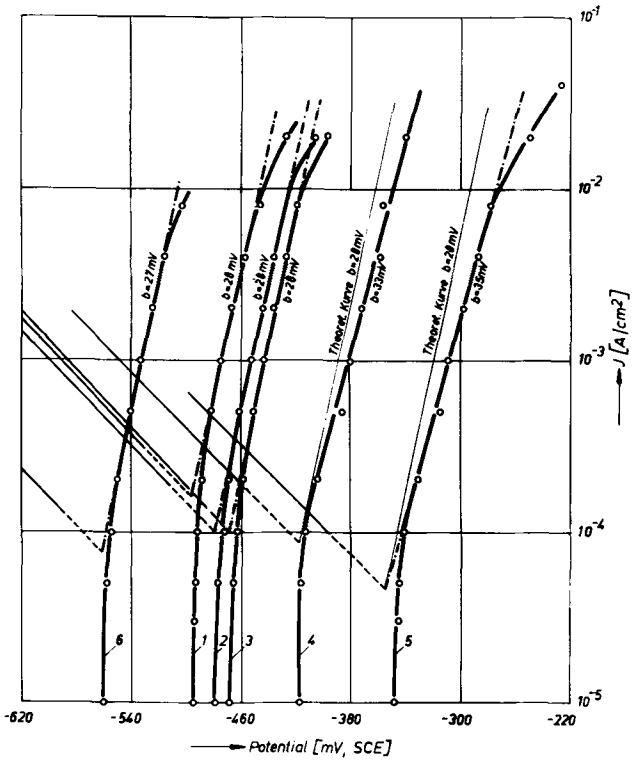

Fig. 4. Cathodic and anodic current-potential curves of the system Fe/0.1M $HClO_4$ + various amounts of $NaClO_4$, and also with addition of Na_2SO_4 (galvanostatic, quasistationary, bubbling of H_2, with stirring, t = 25°C). Curve 1, 0.1M $HClO_4$; curve 2, 0.1M $HClO_4$ + 1.06 mole/kg $NaClO_4$; curve 3, 0.1M $HClO_4$ + 2.85 mole/kg $NaClO_4$; curve 4, 0.1M $HClO_4$ + 6.72 mole/kg $NaClO_4$; curve 5, 0.1M $HClO_4$ + 1.85 mole/kg $NaClO_4$; curve 6, 0.1M $HClO_4$ + 1.5 mole/l Na_2SO_4.

In Fig. 4, the anodic and cathodic current-potential curves in 0.1M $HClO_4$ with additions of $NaClO_4$ are shown. It is seen that the Tafel slopes $d\eta/d \log j$ remain nearly constant, whereas the curves are shifted toward more positive values with increasing concentration of $NaClO_4$. If now for $\epsilon = -420$ mv (SCE) the logarithm of the anodic current density is plotted against the salt concentration, a straight line is found (Fig. 5) which has a slope of — 0.338 $(mole/kg)^{-1}$.

According to a pH shift of — 0.19 pH/mole $NaClO_4$, we may calculate from

$$j^+_{Fe} = K^+ \left[a^o \cdot 10^{K \cdot m_{salt}}\right] Z^+_{H^+} \cdot \exp\left[\frac{(\alpha \cdot n + \nu)F}{RT}\epsilon\right]$$

$$\log j^+_{Fe} = \log [K^+ \cdot a^o Z^+_{H^+}] + K \cdot m_{salt} \cdot Z^+_{H^+} + \frac{(\alpha \cdot n + \nu)F}{2.303RT} \cdot \epsilon$$

that

$$\left[\frac{d \log j^+_{Fe}}{d m_{salt}}\right]_\epsilon = K \cdot z^+_{H^+} = -0.338$$

and, using the value $K = 0.19$, we obtain $z^+_{H^+} \cong -1.8$. Therefore, the anodic current density of active dissolution of iron decreases at constant number of H^+ ions with their activity and at constant ionic strength with their concentration.

The cathodic curves (Fig. 6) are not so definite because the Tafel slope changes as shown. They give an order of H^+ discharge with respect to a_{H^+} of $z^-_{H^+} = +0.46$. At constant H^+ concentration, the current

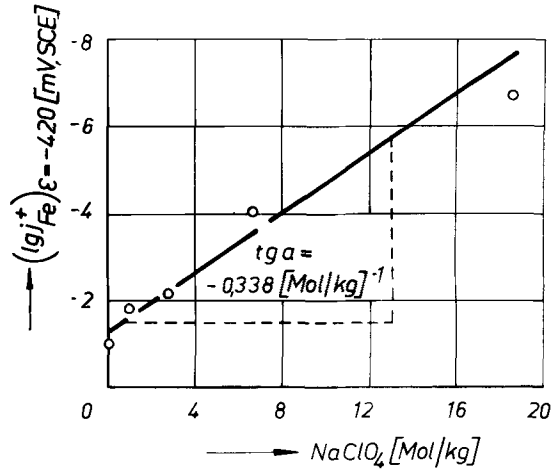

Fig. 5. (log $j^+_{Fe})_\epsilon$ as a function of the $NaClO_4$ concentration (from Fig. 4), at ϵ = const.

density also grows with the square root of the H^+ activity.

Analogous experiments were carried out with additions of $LiClO_4$ and $Ba(ClO_4)_2$ where the $\Delta pH/\Delta m_{salt}$ were, respectively, 0.26 and 0.42 $(mole/kg)^{-1}$. The order of active dissolution of iron was $(z^+_{H^+})^{Fe} = -2.7$ for $LiClO_4$ and $(z^+_{H^+})^{Fe} = -2.2$ for $Ba(ClO_4)_2$. In Fig. 7, log j^+_{Fe} at $\epsilon = -420$ mv (SCE) is plotted against the pH value as lowered by addition of neutral salts in 0.1M $HClO_4$. It shows that $LiClO_4$ gives the highest decrease, $NaClO_4$ the smallest. Evidently the

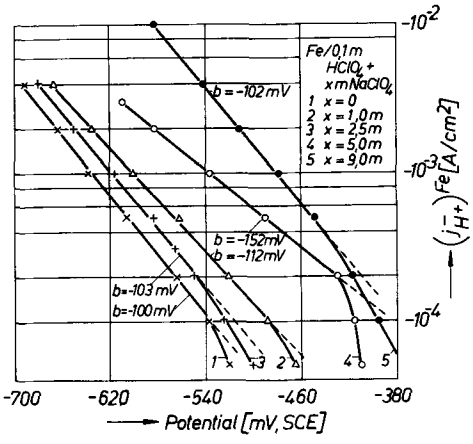

Fig. 6. Cathodic current-potential curves of the system Fe/0.1M $HClO_4$ + various amounts of $NaClO_4$ (mole/l) (galvanostatic, quasistationary, bubbling of H_2, with stirring, t = 25°C).

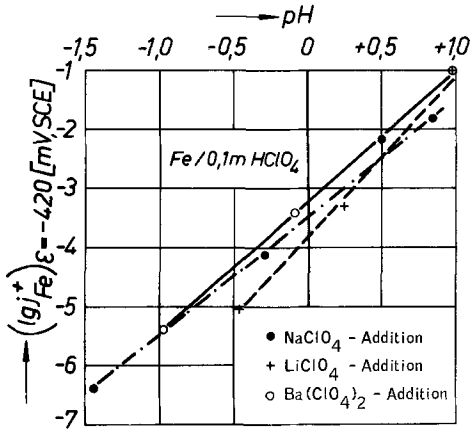

Fig. 7. (log $j^+_{Fe})_\epsilon$ as a function of the pH value (varied by addition of neutral salt) in 0.1M $HClO_4$ solution.

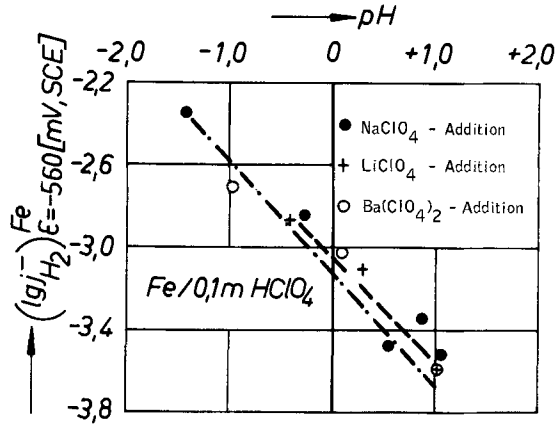

Fig. 8. (log $j^-_{H+})_\epsilon^{Fe}$ as a function of the pH value (varied by addition of neutral salt) in 0.1M $HClO_4$ solution.

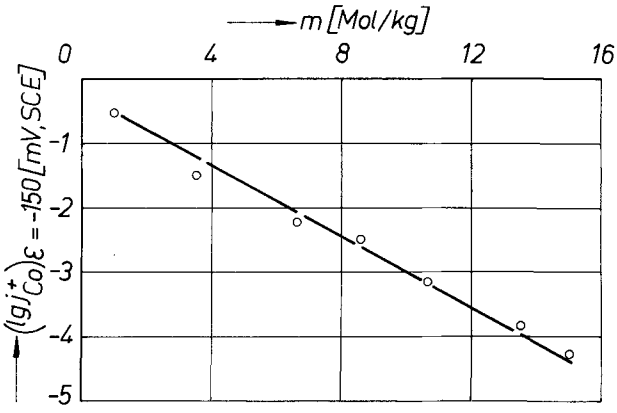

Fig. 10. (log $j^+_{Co})_\epsilon$ as a function of the $NaClO_4$ concentration (taken from Fig. 9).

cation is here of importance, too. The exponent z^+_{H+} increases nearly in the same way with decreasing ionic radius as the gradient $\Delta pH/\Delta m_{salt}$, if it is referred to equivalents. The b^{Fe} values, however, are independent of the cationic species, within the measuring accuracy.

In the case of hydrogen ion discharge, however, all these salts have about the same order as $NaClO_4$, that is 0.5. In Fig. 8, $(\log j^-_{H+})_\epsilon^{Fe}$ at $\epsilon = -560$ mv (SCE) is plotted against the pH value for increasing additions of perchlorates. For H^+ discharge, the effect of variation of the H^+ concentration at constant salt concentration has also been examined; in this case, too, the value of z^-_{H+} of about 0.5 was found. We may conclude from these results that both the anodic and the cathodic electrode reaction on iron are functions of a_{H+} and thus of $m_{H+}f_{H+}$, with $|z^+_{H+}| > 1$ and $z^-_{H+} = 0.5$.

Cobalt (99.9%).—The experiments (8) carried out so far on cobalt have shown the same reaction orders with respect to a_{H+} for the active anodic dissolution as well as H^+ discharge as those found on iron, when the H^+ activity was raised at constant H^+ concentration by addition of neutral salts. Here, too, the Tafel slope b^{Co} does not change when $NaClO_4$ is added to 0.1M $HClO_4$, as shown in Fig. 9, but its value (≅ 38 mv) is somewhat higher than on Fe. There is a linear decrease of log j^+_{Co} with salt concentration (Fig. 10); the result is: $j^+_{Co} \propto a^{-1.7}_{H+}$. Heusler (9) has found $b^{Co} = 29 \pm 5$ mv and $z_{H+} = -2 \pm 0.3$, similar results have been reported by Iofa and Vei Bao-min (10) and Kravtsov and Lokshtanova (11).

On cobalt, too, the Tafel slopes of H^+ discharge are not very constant when neutral salts are added. If, disregarding this, the reaction order with respect to a_{H+} is calculated, one finds also $z_{H+} = +0.5$, independent of the ionic strength.

Nickel (99.9%).—For the active anodic dissolution of nickel, we find no straight Tafel lines but S-shaped curves when making stationary measurements. This is in agreement with the findings of other authors (12). When we try, in spite of this, to calculate a reaction order with respect to a_{H+}, we find that it is smaller (in its absolute value) than −1 ($z^+_{H+} \cong -0.5$ to −0.6), both for an increase in a_{H+} at constant ionic strength when raising the acid concentration and for an increase in the activity coefficient at constant acid concentration by addition of neutral salt. Okamoto (12) reported $z^+_{H+} = -1$ with $b^{Ni} = 98$ −120 mv, but the uncertainty is rather great, not only on account of the insufficient linearity of log j but also on account of the pH dependence of the Tafel slopes.

For H^+ discharge on nickel, we find values for z^-_{H+} at constant ionic strength, J, which grow from +0.5 at $J = 1$ to +0.9 at $J = 10$ when the acid concentration is changed; the Tafel slope is about 110 mv. However, if $NaClO_4$ is added (up to 15 mole/kg) at constant acid concentration (0.1M $HClO_4$), the order remains almost constant; it changes with the addition of salt from 0.4 to 0.6 (Fig. 11). The Tafel lines are well defined and show a constant slope of 110 mv.

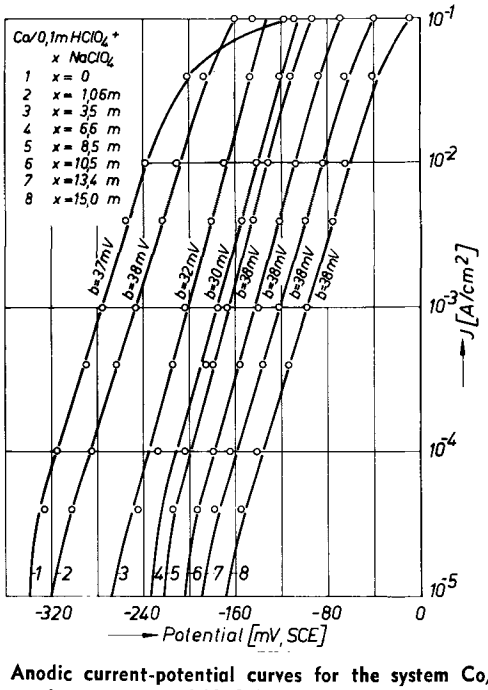

Fig. 9. Anodic current-potential curves for the system Co/0.1M $HClO_4$ + various amounts of $NaClO_4$ (galvanostatic, quasistationary, bubbling of N_2, with stirring, $t = 25°C$).

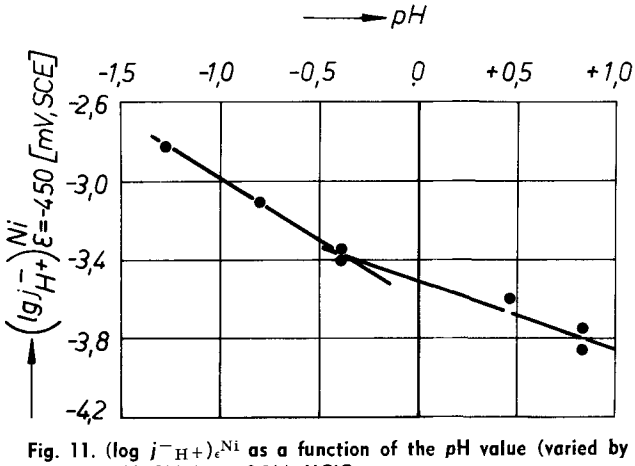

Fig. 11. (log $j^-_{H+})_\epsilon^{Ni}$ as a function of the pH value (varied by addition of $NaClO_4$) in 0.1M $HClO_4$.

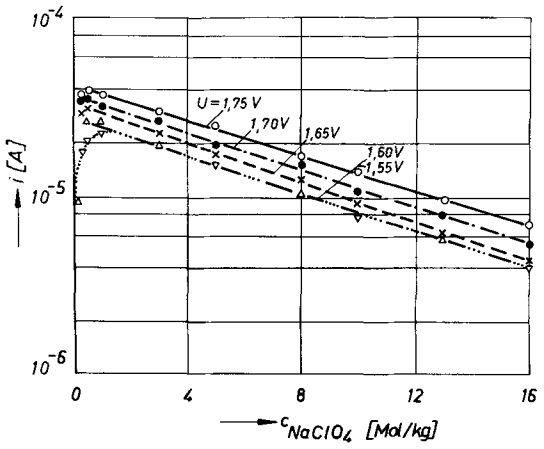

Fig. 12. Cathodic transfer current on a stationary mercury drop as a function of $NaClO_4$ concentration in 0.001M $HClO_4$ solution at ϵ = const (potentiostatic, bubbling of H_2, t = 25°C).

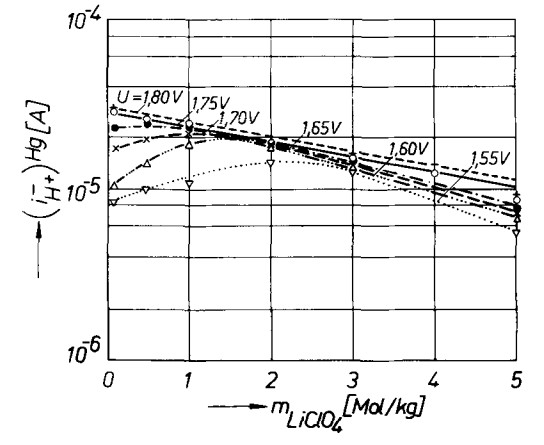

Fig. 13. Cathodic transfer current on a stationary mercury drop as a function of $LiClO_4$ concentration in 0.001M $HClO_4$ solution at ϵ = const (potentiostatic, bubbling of H_2, t = 25°C.

Nickel also differs from the two other metals with respect to the cathodic process.

Mercury (dropping electrode).—We have measured the effect of $NaClO_4$ and $LiClO_4$ on the transfer current (i^-_{H+}) on mercury in order to examine the conditions at a metal where the transfer reaction of hydrogen ion discharge is very strongly inhibited and has been studied extensively. We used a dropping electrode because eventually existing traces of impurities which may cause a drop in overvoltage cannot concentrate on the cathode. Part of the potentiostatic (cathodic) stationary current density-potential curves (Fig. 12, 13) have been obtained with a stationary mercury drop which had no effect on the results (5). For an increase in concentration of $HClO_4$ from $1 \cdot 10^{-3}$ to $50 \cdot 10^{-3}$ mole/kg, at constant concentration of $NaClO_4$ (0.1 mole/kg), the result was $(i^-_{H+})_\epsilon = k \cdot m^{1/2}{}_{H+}$. When the concentration of $HClO_4$ was varied over the same range for larger (constant) concentrations of $NaClO_4$, the exponent increased to a value of 1 (see Table I). If, at a concentration of $1 \cdot 10^{-3}$ mole/kg $HClO_4$, the $NaClO_4$ concentration is brought up to saturation, the dependence of i^-_{H+} on m_{NaClO_4} is also a function of the potential. At first, the transfer current increases, however, at higher concentrations it drops monotonously, see Fig. 12. The maximum becomes flatter as the potential increases and shifts to lower salt concentrations, as evidenced by measurements with $LiClO_4$ (Fig. 13). In the region of linear decrease, one has for i^-_{H+},

Table I. Electrochemical reaction order of the transfer reaction of H^+ discharge on Hg with respect to $[H^+]$ as a function of the ionic strength obtained by variation of $[H^+]$

c_{NaClO_4}, m/kg	$\frac{\partial \log i}{\partial \log m_{H^+}}$
0.1	0.45
0.5	0.46
1	0.61
5	0.73
10	0.97
16	1.04

$$\log (i^-_{H+})_\epsilon = \log k \cdot m^{z}{}_{H+} + K_H \cdot m$$

The value of z_{H+} increases with salt concentration from 0.5 to 1, as seen above, and K_H has a value of —0.048 for $NaClO_4$ and of —0.095 for $LiClO_4$. Here, too, the smaller cation has the greater influence.

Discussion

The influence of H^+ concentration on active iron dissolution has been known for a long time. It is usually referred, according to a suggestion by Frumkin (14), to the effect of OH^-; different reaction mechanisms are discussed, and Heusler maintains that the OH^- ions have a catalytic effect. Our experiments have shown that the current density $(j^+_{Me})_\epsilon$ at constant m_{H+} is proportional to $a_{H+}{}^{-p}$;[1] of course, a proportionality to the activity of OH^- ions, introduced by means of the ionic product of water, may also be considered. In this case, the shift in the activity of water caused by the high ionic strengths must be taken into account. We have been able to show (2) that a_{OH-} may increase as well as decrease by the addition of neutral salts. When $NaClO_4$ is added to alkaline solution, the *p*H value first decreases, and with it a_{OH-}, but later on, it increases (Fig. 14), and with it a_{OH-} increases, too. In $LiClO_4$ solutions, the *p*H value of alkaline solutions decreases monotonously as m_{LiClO_4} increases, but the behavior of $j_{Me}{}^+$ is almost the same in the two solutions. Further, the ionic product $m_{H+} \cdot m_{OH-}$ changes with growing additions of salt. It passes, for instance, through a maximum at 1 mole/kg $NaClO_4$ and reaches about 10^{-16} (mole/kg)[2] at 16 mole/kg $NaClO_4$ (13). This is the reason why the hydroxyl ion concentration decreases by about 2 powers of ten in acid solutions at these high salt concentrations. Consequently, we might write $(j^+_{Me})_\epsilon \propto m_{OH}{}^q$ or $(j^+_{Me})_\epsilon \propto a_{OH}{}^q$, respectively.[2] Since, however, the surface concentration of OH^- is extremely small (less than 1 ion/cm² in a film of 50Å), and a_{OH-} or m_{OH-} are, on the other hand, not linear functions of the salt concentration, we would prefer to assume that the equilibrium

[1] *p* represents the order of reaction with respect to H^+.

[2] *q* represents the order of reaction with respect to OH^-.

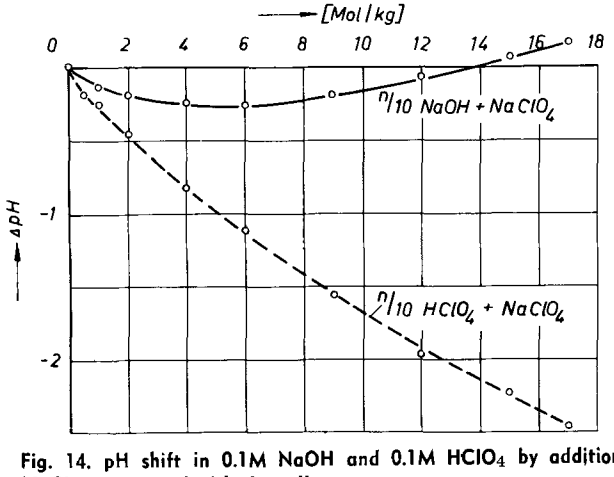

Fig. 14. pH shift in 0.1M NaOH and 0.1M $HClO_4$ by addition of $NaClO_4$, measured with the cells:
(Pt) H_2/$HClO_4$ (0.1M), $NaClO_4$//$NaCl_{sat.}$, Hg_2Cl_2 (s)/Hg
(Pt) H_2/NaOH (0.1M), $NaClO_4$//$NaCl_{sat.}$, Hg_2Cl_2 (s)/Hg

$$Me + OH_2 \rightleftharpoons MeOH_{ad} + e^- + H^+ \quad [1]$$

which precedes the transfer reaction brings about a dependence on $a_{H^+}{}^{-1}$. We have seen that, indeed, higher negative exponents are found on Fe and Co, although recently values of —1 have been reported (7). The assumption that a further proton equilibrium takes part in the electrode process is not very plausible. We can ascertain, on the other hand, that the exponents of a_{H^+} which are greater than unity are different from 2.0 at constant Tafel slope. Perhaps we may assume that the H^+ produce some kind of electrostatic inhibition. We know that these ions interchange very quickly with the H atoms of the water, and thus a mean positive charge density will be produced at the metal surface owing to the H_2O molecules present in the double layer, and this charge will increase with the number of H^+ and their excess power, $RT \ln f_{H^+}$. The metal ions going into solution have to pass through this positive potential barrier, and hence the anodic dissolution reaction is further inhibited. In this way, it is also possible to explain qualitatively the influence of the cations. The smaller their radius, the stronger their hydration and the more will they contribute to the structure of such a positive charge barrier with their own high charge density (when ion pairs are formed on the metal surface) and with that of the H^+ ions which alternate with the H atoms of their hydration water. At nickel, a different over-all mechanism of anodic dissolution must probably be assumed if the reaction [1] does not participate; however, at least the electrostatic inhibition by H^+ should be active, and this would agree with the exponents of 0.5-0.6.

Of course, this "electrostatic" inhibition effect of H^+ should, first of all, raise the anodic dissolution potential, and indeed the overvoltage increases remarkably with increasing a_{H^+} at constant current density.

In hydrogen ion discharge, the transfer current should increase with the square root of the H^+ concentration, according to the theory of Frumkin (14) which gives due regard to the ζ potential. If at high ionic strengths the influence of the ζ potential ceases, the value of the exponent should increase to 1, as verified by Frumkin on mercury. According to our results, even at high salt concentrations, a significant increase of the exponent with increasing H^+ concentration cannot be detected on Fe (and Co), but it is observed on Ni. The theory of Frumkin is confirmed in a particularly remarkable way on Hg where the exponent $z^-{}_{H^+}$ increases with growing ionic strength to 1 as m_{H^+} rises.

If, at $m_{H^+} = 0.1$ mole/kg, a_{H^+} is raised by addition of salt, the value of $z^-{}_{H^+}$ on Ni is found to be 0.4. According to Frumkin, $z^-{}_{H^+}$ is itself a function of the ionic strength; it should, therefore, increase to 1 with growing addition of salt. An inhibition is evidently in operation here which is especially significant on Hg. On this metal, $j^-{}_{H^+}$ decreases with increasing ionic strength and activity of H^+, even at m_{H^+} = constant. This dependence is, moreover, a function of the potential. Qualitatively, this may be explained as follows. At m_{H^+} = const and growing salt concentration in the double layer, the protons are displaced more the higher the concentration and the charge density of the cations and the more negative the potential. At very negative potentials, this may lead to a monotonous decrease of $j^-{}_{H^+}$ with a_{H^+} or with salt concentration, respectively. At high ionic strength, on the other hand, a growing quantity of H^+ will produce an increase of $j^-{}_{H^+}$. Of course, the question remains open as yet why we find a value of 0.5 for $z^-{}_{H^+}$ on Fe and Co, independent of the ionic strength when we vary m_{H^+} and a_{H^+}. We do not like to propose an explanation for it at this time because the measurements are not especially reproducible, the Tafel lines are not well defined, and the slopes are not constant so that the results do not seem to be certain enough.

Summary

The current densities of anodic dissolution of Fe, Co, and Ni are measured at constant hydrogen ion concentration with increasing additions of neutral salts which lead to a rapid increase of the activity of H^+. The anodic current density decreases with the activity of H^+, too, where $j^+{}_{Me} = K \cdot a_{H^+}{}^{-z^+}$, z_+ depends on the cation of the salt and is less than unity in the case of nickel. The current density of H^+ discharge is studied on the same metals as well as on Hg as a function of the addition of neutral salts. For the ferrous metals, an increase with $a_{H^+}{}^{+0.5}$ is found; on nickel, the exponent increases at high ionic strength to 0.9. On mercury, $j^-{}_{H^+} \propto m_{H^+}{}^{0.5}$ at small ionic strength; the dependence becomes $j^-{}_{H^+} \propto m_{H^+}{}^{1.0}$ at high ionic strength. The dependence on a_{H^+} at constant H^+ concentration is complicated. A qualitative interpretation of the experimental results is proposed.

Manuscript received Dec. 20, 1965; revised manuscript received May 20, 1966. This paper was presented at the Buffalo Meeting, Oct. 10-14, 1965.

Any discussion of this paper will appear in a Discussion Section to be published in the June 1967 JOURNAL.

SYMBOLS

$z^+{}_{H^+}$	Order of reaction with respect to H^+
α	Transfer coefficient
n	Transfer valence
ν	Number of equilibriums, preceding and potential dependent
K^+, K	Factors of proportionality
a^o	Activity of H^+ without salt addition
m_{salt}	Molality of added neutral salt

REFERENCES

1. see also K. Schwabe, *Z. Physik. Chem. (Frankfurt)*, **41**, 368 (1964); *Oesterr. Chemiker-Z.*, **11**, 339 (1964).
2. K. Schwabe, *Electrochim. Acta*, To be published.
3. K. E. Heusler, *Z. Elektrochem.*, **62**, 582 (1958).
4. For more details, see Chr. Voigt, *Dissertation*, Institut für Elektrochemie und physikalische Chemie, TU Dresden, to be published; and K. Schwabe and Chr. Voigt, *Werkstoffe und Korrosion*, **16**, 125 (1965).
5. For details about the experimental procedures, see K. Münnich, *Diplomarbeit*, Institute für Elektrochemie und physikalische Chemie, TU Dresden, 1965.
6. K. E. Heusler, *Z. Elektrochem.*, **62**, 582 (1958); B. Kabanow, Ch. Burstein, and A. N. Frumkin, *Discussions Faraday Soc.*, **1**, 259 (1947); L. A. Larin and Z. A. Iofa, *Z. Fiz. Khim.*, **34**, 1470 (1960); W. Lorenz, H. Yamaoka, and H. Fischer, *Ber. Bunsenges, Physik. Chem.*, **67**, 932 (1963); W. Lorenz, *Corrosion Sci.*, **2**, 121 (1965); H. Kaesche, *Z. Elektrochem.*, **63**, 492 (1959).
7. It cannot be seen in all cases whether the exponents are really integral values, mostly they are rounded off. Heusler, *e.g.*, has found experimentally—1.55, Kaesche found—1.75 with the same Tafel slope of 30 mv., T. Hurlen, *Acta Chem. Scand.*, **14**, 1533 (1960), reports, however, a value of $z_{H^+} = -1$, with a Tafel slope of $b^{Fe} = 29$ mv; also, J. O'M. Bockris and co-workers, *Electrochim. Acta*, **4**, 325 (1961); J. J. Podesta and A. J. Arvia, *Electrochim. Acta*, **10**, 171 (1965); and E. J. Kelly, *This Journal*, **112**, 124 (1965), but at $b^{Fe} = 40$ mv.
8. G. Wehle, *Diplomarbeit*, Institut für Elektrochemie und physikalische Chemie, TU Dresden, 1965.
9. K. E. Heusler, *Z. Elektrochem.*, **66**, 177 (1962).
10. Z. A. Iofa and Vei Bao-min, *Z. Fiz. Khim.*, **36**, 2558 (1962).
11. V. I. Kravtsov and O. G. Lokshtanova, *ibid.*, **36**, 2362 (1962).
12. G. Okamoto and S. Sato, *This Journal*, **111**, 897 (1964).
13. See also A. Ferse and K. Schwabe, *Z. Physik. Chem., (Leipzig)*, **230**, 20 (1965).
14. A. N. Frumkin, "Advances in Electrochemistry Electrochemical Engineer," p. 65, Interscience Publishers, New York and London (1961); *Z. Physik. Chem.*, **A164**, 121 (1933).

Deformation of Anodic Oxide Films

S. F. Bubar and D. A. Vermilyea

General Electric Research and Development Center, Schenectady, New York

ABSTRACT

Tantalum oxide films on smooth, pure substrates can be deformed as much as 50% before fracture. On surfaces containing impurity particles the films contain many flaws which nucleate cracks after relatively little deformation. Zirconium oxide films showed some evidence of deformation, but much less than tantalum oxide. Aluminum oxide films showed no evidence of deformation.

Protection against corrosion is usually afforded by a thin film of reaction product. The behavior of such a film during deformation of the underlying metal would be of great importance in determining corrosion under such conditions and may play a decisive role in stress corrosion cracking and corrosion fatigue. It is usually assumed that reaction films are brittle, and one currently popular theory of stress corrosion cracking asserts that repeated cracking of the passive film allows continued corrosion. Bradhurst and Leach (1) have shown that barrier-type anodic oxide films on aluminum are brittle, while Edeleanu and Law (2) have demonstrated that both porous anodic aluminum oxide films and the natural corrosion film on aluminum are brittle. Young (3), on the other hand, reported that anodic films on tantalum changed color during deformation of the metal indicating some deformation of the oxide, and Dunn (4) has told us that anodic films on tantalum deform along with the substrate when tantalum sheet is rolled. In this paper we report the use of a new technique to obtain quantitative information about the deformation of anodic films on aluminum, zirconium, and tantalum.

Experimental

Our technique relies on the fact that electrons can flow (presumably by tunneling) through very thin insulating oxide films to reduce ions in solution, while thicker films block such electronic currents. Figures 1 and 2 show typical results obtained with the materials and solutions used in this study. The data for tantalum show that the results are nearly independent of the nature of the test solution, but are strongly influenced by the purity of the tantalum. We found that the borate plus ferri-ferro cyanide solution was sufficiently stable for our purposes and that the attack on the aluminum oxide films during a test was negligible.

In order to detect film fracture anodized wire specimens were stretched in solutions with a potential applied such that the new film formed in any bare areas generated by fracture was 15-20Å thick. From the current flowing after straining and the data in Fig. 1 and 2 the amount of bare surface was calculated. Corrections were made for changes in specimen area as a result of the decrease in wire diameter and the fact that grease covered wire is drawn into the cell near the stationary grip; the latter correction was very small. The currents were time-dependent, since initially on any bare surface both anodization and reduction of ferric ions was occurring. Five minutes were allowed for the current to reach a reasonably steady value after each increment of strain. The apparatus used is shown in Fig. 3. The technique is capable of detecting a change in the bare surface of $3 \times 10^{-4}\%$.

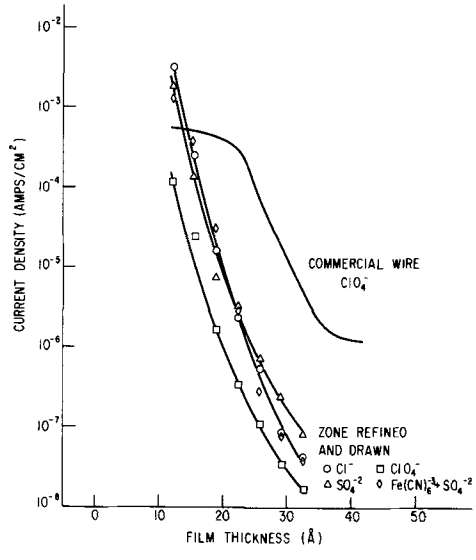

Fig. 1. Thickness dependence of electronic current through tantalum oxide films. All solutions were 1M in the acid of the anion shown and contained 0.1M each of aquo Fe^{+3} and Fe^{+2} ions except for one sulfate solution in which cyanide complexes were used. The test potential was about —0.1v on the hydrogen scale.

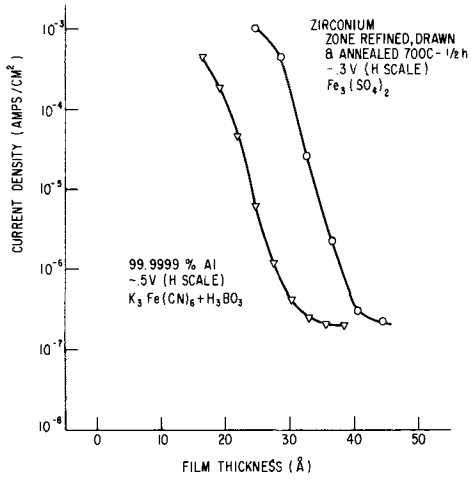

Fig. 2. Thickness dependence of electronic current through aluminum oxide and zirconium oxide films. For zirconium the solution contained 1M H_2SO_4 plus 0.1M each of Fe^{+3} and Fe^{+2}, while for aluminum the solution contained 1M H_3BO_3 plus 0.1M Fe^{+3} and Fe^{+2} as cyanide complexes.

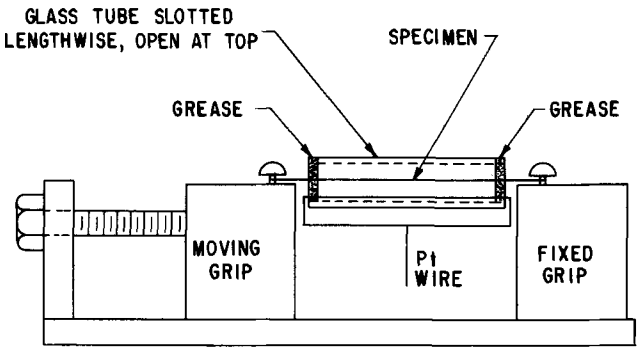

Fig. 3. Sketch of apparatus

Specimens were anodized at room temperature in 1 w/o (weight per cent) ammonium borate solution, and the film thicknesses were calculated from the applied potential using 17 Å/v for Ta_2O_5, 20 Å/v for ZrO_2, and 14 Å/v for Al_2O_3. The wires were chemically or electrochemically polished before anodizing. For tantalum, chemical polishing in (parts by volume) $5H_2SO_4$, $2HNO_3$, 2HF was followed by a 5-sec dip in concentrated HF. Aluminum was either electropolished in $5HClO_4$, 100 glacial acetic or chemically polished in a HNO_3-H_3PO_4 mixture, both treatments being followed by immersion in either HF or NaOH to remove the polishing residue. The results were the same after all treatments. Zirconium was chemically polished in a solution of 5 lactic acid, $5HNO_3$, $2H_2O$, 1HF, and the residue was not removed. This zirconium polishing solution is unstable (5, 6) and should not be stored.

Results and Discussion

Figure 4-8 give curves of per cent bare surface *vs.* per cent elongation of the wire for the metals studied. In the figures the "theoretical" curve was calculated from the relationship

$$\% \text{ Bare surface} = 100\left[1-\left(\frac{l_o}{l}\right)^{1/2}\right] \qquad [1]$$

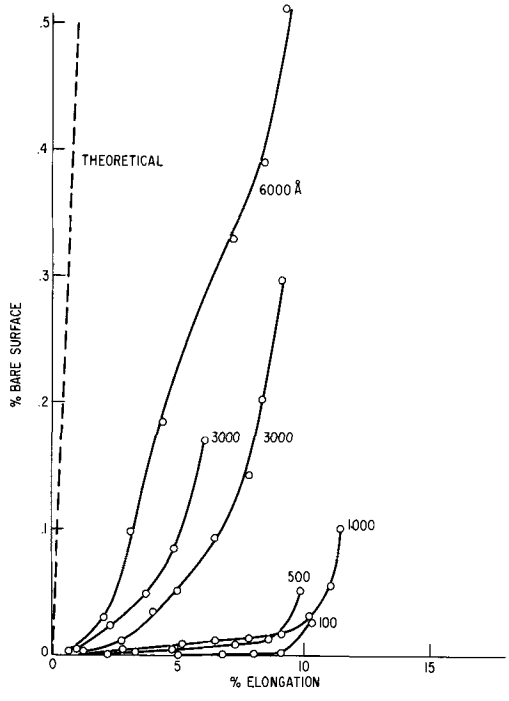

Fig. 4. Bare surface produced during straining of vacuum annealed tantalum wires covered with anodic films of the thicknesses shown. Perchlorate solution.

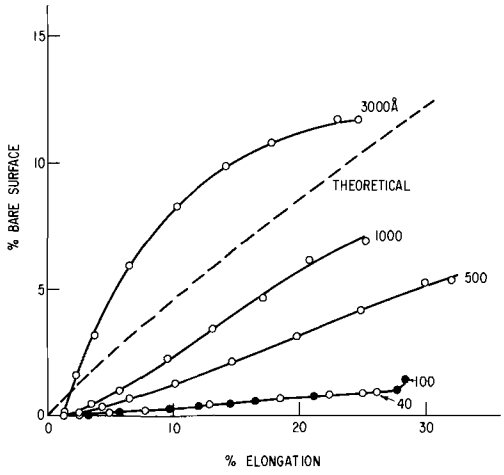

Fig. 5. Bare surface produced during straining of as received tantalum wire covered with anodic films of the thicknesses shown. Perchlorate solution.

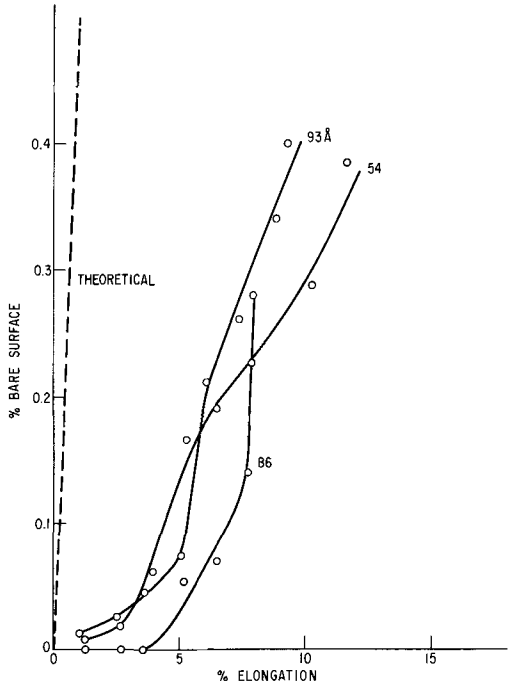

Fig. 6. Bare surface produced during straining of vacuum annealed tantalum wire covered with films formed in air at 300°C to the thicknesses shown. Perchlorate solution.

in which l_o is the initial specimen length and l is the length at any time. Equation [1] was derived on the assumptions that the volumes of metal and film are constant, that the film cracks at $l = l_o$, and that the film maintains contact with the metal while the diameter is reduced due to elongation. It should be noted that this last assumption requires some deformation of the film.

Figure 1 shows that Ta_2O_5 films formed on a very pure substrate can undergo extensive deformation before fracture. Films up to 1000Å showed essentially no evidence of fracture before the wire broke, and even then the crack area was small despite the very great deformation of the metal, which necked down to a chisel-shaped point. No evidence of loss of adhesion was observed. Thicker films also adhere perfectly, but show less capacity for deformation. On all of these specimens deformation was very nonuniform, some grains deforming much more than others with extensive local deformation markings visible. By

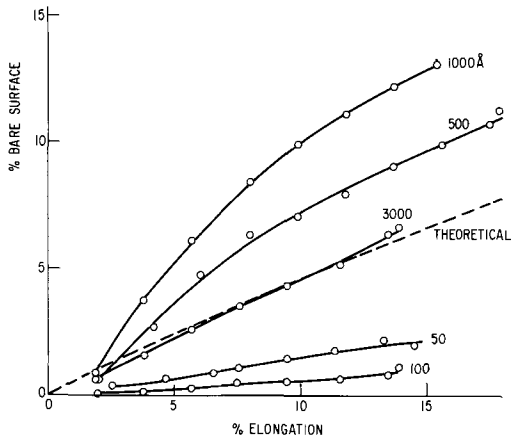

Fig. 7. Bare surface produced during straining of zirconium wire covered with anodic films of the thicknesses shown. Sulfate solution.

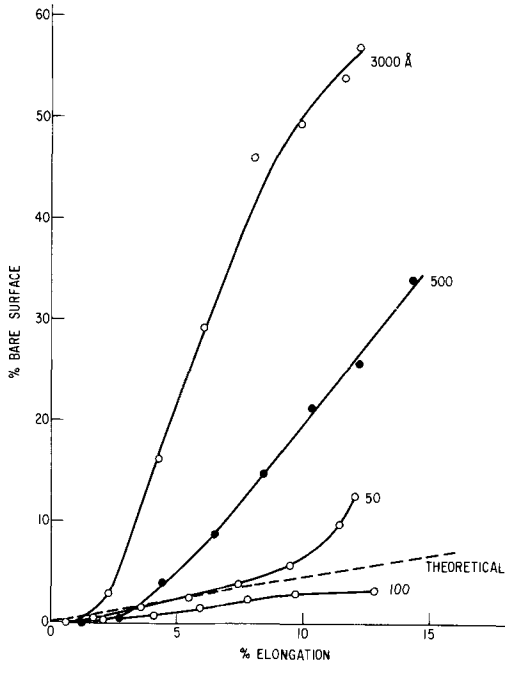

Fig. 8. Bare surface produced during straining of aluminum wire covered with anodic films of the thicknesses shown. Borate plus cyanide complex solution.

comparing colors after deformation it could be seen that reductions in film thickness as great as 20-30% occurred on some grains. From the relationship

$$t = \left(\frac{l_o}{l}\right)^{1/2} t_o \qquad [2]$$

where t and t_o are the final initial film thicknesses, it is deduced that the film must have elongated on some grains as much as about 50%. While these large deformations are probably plastic, this has not been proven. For one 1150Å film essentially identical results were obtained when the film was stretched in air instead of in the electrolytic solution.

When films less than 500Å thick fractured many small jagged cracks were seen in local regions of high strain while thicker films (1000-6000Å) cracked circumferentially. Examination of films during elongation showed that virtually all cracks which started prior to necking of the specimen nucleated at flaws in the film. It was also observed that cracks passed very close to other flaws with no obvious interaction.

When this same material was stretched without having been vacuum annealed the curves shown in Fig. 5 were obtained. For comparable elongations there is a many-fold increase in the amount of bare surface (or a many-fold decrease in film ductility). It is believed that the many flaws present in the films on the less pure material nucleated cracks at much smaller strains.

Films formed in air at 300°C gave the results shown in Fig. 6. It is evident that there is less ductility than for specimens having comparably thick anodic films. Thermal tantalum oxide films grown at <350°C are amorphous, as are the anodic films, but it is possible that there are crystal nuclei present and that these initiate cracks. This hypothesis is supported by the fact that a specimen which was anodized to form a 100Å film prior to heat treatment at 300°C for 2 hr gave no indication of film failure until the wire broke at ~9.5% elongation. Crystallization of anodic film does not occur at 300°C in such short times. A 100Å anodic film heat treated at 450°C for 2 hr was completely crystallized in a basket weave pattern similar to a Widmanstatten pattern and had grown to a thickness of perhaps 700Å. Such crystalline films cracked primarily at metal substrate grain boundaries, and the behavior in the test cell indicated that there was no appreciable ductility.

A few specimens were prepared from tantalum which was zone refined, drawn to 0.030 in. diameter, and vacuum annealed at 1400°C for 1 hr in this laboratory. The results of tests using such wire were essentially the same as those using vacuum annealed wire.

Figure 7 shows data obtained with films formed on a zone refined zirconium rod which was drawn to 0.030 in. diameter using three anneals at 700°C for ½ hr. The curves as a group show ~80 times as much bare surface for a given strain as the vacuum annealed tantalum, or slightly less ductility than the as-received tantalum. The decrease in ductility with film thickness is not as well ordered for zirconium as it is for tantalum. Some deformation of the zirconium oxide films is suggested by the fact that they did generally maintain contact with the substrate. It is possible

Fig. 9. Electron micrograph (indirect replica) of an aluminum wire surface after straining 14.7%. The wire was originally covered with a 500Å film.

that these zirconium wires contained particles of oxide which produced flaws in the oxide films, and that better films would deform more before fracture.

The cracks in the anodized zirconium films ran in all directions, each grain (~1/5 wire diameter) having a distinct set of cracks. Only on the 3000Å film was there some degree of crack continuity across grain boundaries. The multiple cracks broke the film into many tiny pieces which occasionally flaked off. There was no evidence of film color change due to elongation as was the case with tantalum.

Data obtained for films formed on aluminum specimens of 99.9999% purity are shown in Fig. 8. Examination after elongation revealed extensive loss of contact with the substrate as shown in Fig. 9. Evidently the anodic aluminum oxide film is not even sufficiently ductile to maintain contact with the wire as the diameter decreases. The greater than theoretical amount of bare surface is further evidence for this loss of contact.

Conclusions

Anodic tantalum oxide films exhibit great ductility, as much as 50%. Zirconium oxide films show some ductility, and possibly better specimens might show much more. Aluminum oxide films appear to be completely brittle. The technique is limited to the study of oxide films which are insulating, and thus we were not able to use it on stainless steel or nickel. We hope to use other techniques to measure the ductility of oxides on such metals.

Manuscript received June 9, 1966.

Any discussion of this paper will appear in a Discussion Section to be published in the June 1967 JOURNAL.

REFERENCES

1. D. H. Bradhurst and J. S. L. Leach, *Trans. Brit, Cer. Soc.*, **62**, 793 (1963).
2. C. Edeleanu and T. J. Law, *Phil. Mag.*, **7**, 573 (1962).
3. L. Young, *Trans. Faraday Soc.*, **53**, 841 (1957).
4. C. G. Dunn, Private communication.
5 W. V. Green, *J. Less-Common Metals*, **9**, 155 (1965).
6. S. F. Bubar and D. A. Vermilyea, *This Journal*, **113**, 519 (1966)

Dielectric Properties of Semiconducting Iron Phosphate Glasses

Kent W. Hansen and Mary T. Splann

Research and Development Laboratories, Corning Glass Works, Corning, New York

ABSTRACT

The dielectric constant and loss factor of glasses containing 55 mole % FeO_x-45 mole % P_2O_5 with varying Fe^{+3}/Fe_{total} ratios were measured as a function of temperature and frequency. An a-c dispersion was observed between 10^{-2} and 10^5 cps with a temperature dependence equivalent to the d-c conductivity temperature dependence. The dielectric constant was independent of frequency and temperature below the dispersion region. There was a distribution of relaxation times associated with the dispersion process.

In a previous paper it was suggested that electrical conduction in iron-phosphate glasses containing over 20 mole % FeO_x is an electronic process (1). The charge transfer results from holes (or electrons) migrating between Fe^{+3} and Fe^{+2} ions. In the proposed mechanism, the carrier concentration is essentially independent of temperature, whereas the carrier mobility is a thermally activated process. This conduction mechanism is similar to that proposed for $Li_xNi_{1-x}O$ and other transition metal oxides (2,3) and is often referred to as a "hopping" process. Munakata proposed a "hopping" model for electrical conduction in the vanadate glasses (4).

The dielectric loss and mechanical loss have been measured in $Li_xNi_{1-x}O$ (5) and $Li_xMn_{1-x}O$ (6). In each case the loss data were correlated with the hole movement around the lithium ion. Snowden and Saltsburg (7) measured the a-c conductivity of NiO at room temperature as a function of frequency. They observed a dispersion which they attribute to the hopping of the hole.

Dielectric loss measurements have been made on vanadium-phosphate and tungsten-phosphate glasses (8). The authors observed that the slope of the plot of the logarithm of d-c conductivity *vs.* reciprocal temperature was nearly equivalent to the slope of the logarithm of frequency *vs.* reciprocal of T_{max}, where T_{max} is the temperature at which tan δ was a maximum. Ioffe *et al.* suggested that conduction involves charge transfer between ions of different valencies.

The dielectric properties of glasses in the As-Te system have also been measured (9). The activation energies for conduction and dielectric relaxation were found to be nearly the same.

This paper contains work on the dielectric properties of glasses containing 55 mole % FeO_x-45 mole % P_2O_5 with different Fe^{+3}/Fe^{+2} ratios. The dielectric loss and constant were measured as a function of frequency and temperature. A correlation is made between the dielectric loss factor and d-c electrical conduction.

Experimental Procedure

The glasses included in this paper were studied previously (1). The preparation and characterization of these glasses are given there. Table I gives the composition, $Fe^{+3}/Fe^{+2} + Fe^{+3}$ ratio, and sign of the carrier determined from the thermoelectric power.

The samples were in the form of polished plates, 2 in. x 2 in. x 2 mm. Three-terminal electrodes were applied to the samples following ASTM specifications (10). Several electrode materials were used for comparison: Hanovia Liquid Gold Bright, vacuum evaporated gold, du Pont air-drying silver paint, and vacuum evaporated silver.

D-C conductivity, a-c conductivity and capacitance were measured as a function of temperature (from room temperature to ~100°C) and the latter two as a function of frequency (from 10^{-2} to 10^5 cps) in an air atmosphere. The accuracy of the electrical measurements was ± 10%. The d-c conductivity was measured with a Beckman Ultrohmeter at a potential of

Table I. Fe^{+3}/Fe_T ratio and sign of carrier for glasses containing 55 mole % FeO_x-45 mole % P_2O_5

Glass	$\frac{Fe^{+3}}{Fe^{+3} + Fe^{+2}}$	Conduction carrier
1	0.793	n
2	0.465	n
3	0.147	p

20v. The samples were ohmic up to at least 300 v/cm.

Between 10^{-2} and 10^{3} cps the a-c conductivity and capacitance were measured with a bridge designed by Weingarten (11). With this bridge the conductivity was determined from the following equation

$$\gamma_T = \frac{1}{R} \times \frac{t}{A} \text{ (ohm cm)}^{-1} \quad [1]$$

where R is resistance, t is sample thickness, and A is electrode area. The General Radio 1610A capacitance measuring assembly was used for the frequency range 10^2 to 10^5 cps. The conductivity was calculated from the measured values of loss tangent (tan δ) and relative dielectric constant (K') from the following relationship

$$\gamma_T = \frac{K' \times f \times \tan \delta}{1.8 \times 10^{12}} \text{ (ohm cm)}^{-1} \quad [2]$$

where f is frequency.

The measured conductivity (given in Eq. [1] and [2]) is the total conductivity (γ_T) which is a sum of the d-c conductivity ($\gamma_{d\text{-}c}$) and the a-c conductivity ($\gamma_{a\text{-}c}$). As the temperature increases and/or the frequency decreases, ($\gamma_{d\text{-}c}$) becomes a larger part of the total conductivity. In order to study the relaxation peaks, ($\gamma_{d\text{-}c}$) was subtracted from the measured conductivity, such that

$$\gamma_{a\text{-}c} = \gamma_T - \gamma_{d\text{-}c} \quad [3]$$

Using the adjusted conductivity ($\gamma_{a\text{-}c}$), the relative loss factor (K'') was calculated (12).

$$K'' = \frac{1.8 \times 10^{12} \times \gamma_{a\text{-}c}}{f} \quad [4]$$

This technique was used by Taylor (13) and Heroux (14) to investigate ionic conducting glasses.

The relative dielectric constant (K') was calculated from the following equation (12)

$$K' = C \times \frac{t}{0.0885 \times A} \quad [5]$$

where C is the measured capacitance in pica-farads, t is the sample thickness in cm, and A is the electrode area in cm^2.

Results and Discussion

Figures 1a and 1b contain plots of relative dielectric constant (K') and loss factor (K'') *vs.* the logarithm of the frequency for glasses 1 and 2, using gold electrodes. Only data for representative temperatures are shown. The upper temperature at which meaningful a-c loss data could be taken was limited by the d-c conduction loss. As can be seen in Fig. 1, the loss factor (K'') goes through a maximum as the frequency goes from 10^0 to 10^4 cps. This maximum shifts to higher frequencies as the temperature increases.

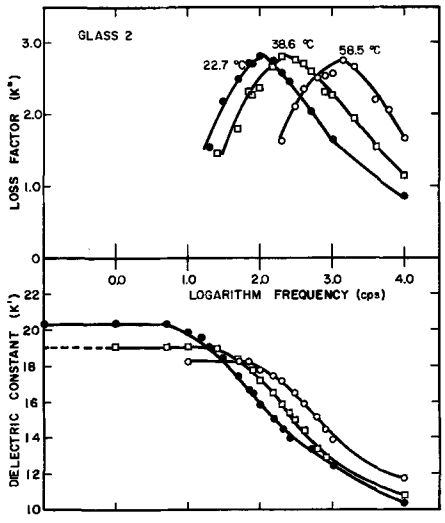

Fig. 1b. Dielectric constant and loss factor *vs.* logarithm of frequency for glass 2.

The dielectric constant (K') was found to be independent of frequency and temperature below the dispersion range. The leveling-off of the dielectric constant at low frequencies indicates the relaxation mechanism is one which does not lead to polarization, such as ionic migration. The dielectric constant of ionic conducting glasses increases rapidly as the frequency decreases in this region (14). The data in Fig. 1 are consistent with the electronic conduction mechanism proposed earlier (1).

Figure 2 contains a plot of K'' and K' *vs.* the logarithm of the frequency at representative temperatures for glasses 1 and 3 with silver electrodes. As in the case where gold electrodes were used, a loss peak was observed that shifted to higher frequencies as the temperature increased. The magnitude and temperature dependence (see Fig. 3) of the loss factor

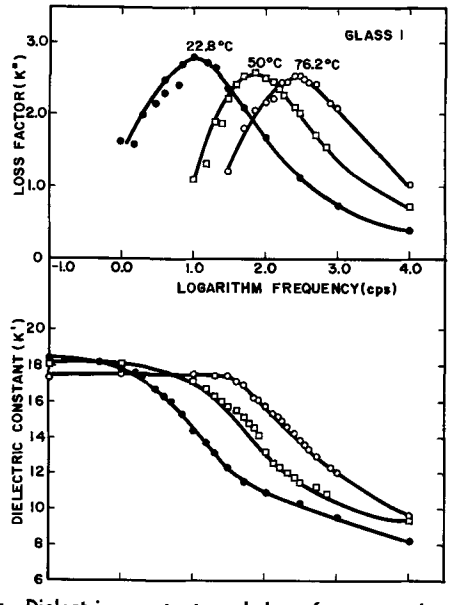

Fig. 1a. Dielectric constant and loss factor *vs.* logarithm of frequency for glass 1.

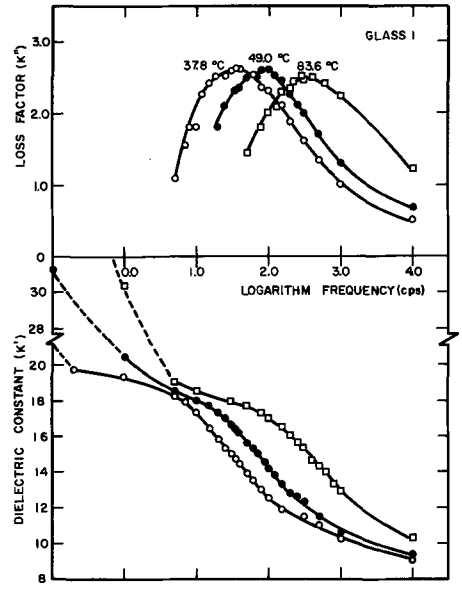

Fig. 2a. Dielectric constant and loss factor *vs.* logarithm of frequency for glass 1 with silver electrodes.

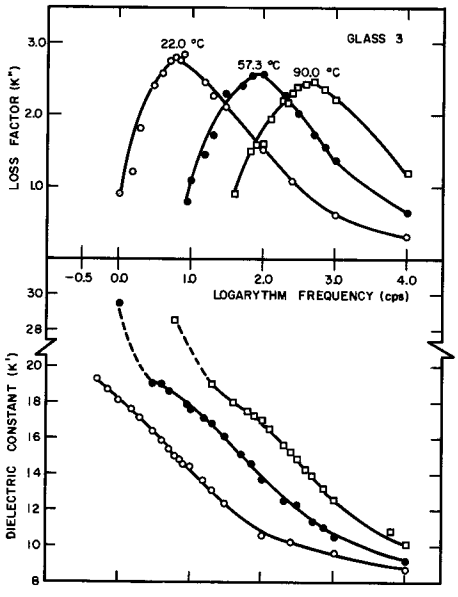

Fig. 2b. Dielectric constant and loss factor vs. logarithm of frequency for glass 3 with silver electrodes.

were the same for gold and silver electrodes. However, the dielectric constant increased rapidly with decreasing frequency at low frequencies. It is believed that this can be attributed to silver migration into the surface of the glass. After the silver electrodes were removed from glass 1 and gold electrodes reapplied, the dielectric constant did not completely level off as shown in Fig. 1. This is further evidence that silver had migrated into the glass surface.

The logarithm of the frequency (f_{max}) at which the loss factor is a maximum is plotted *vs.* $1/T$ in Fig. 3. Assuming the relaxation time (τ) is given by

$$\tau = \tau_0 e^{E/kT} \qquad [6]$$

where τ is $1/2\pi f_{max}$, τ_0 is a constant, and E is an activation energy; the activation energies given in Fig. 3 were calculated using the method of least squares.

If the conduction mobility (μ) is temperature dependent, such that $\mu T \alpha e^{-E/kT}$, the d-c conductivity can best be expressed by $\gamma_{d\text{-}c}T = \gamma_0 e^{-E/kT}$ rather than $\gamma_{d\text{-}c} = \gamma_0 e^{-E/kT}$. The logarithm of conductivity x temperature *vs.* $1/T$ is plotted in Fig. 4. The activation energies in the low-temperature region agree very well with the activation energies determined from a-c loss data in Fig. 3.

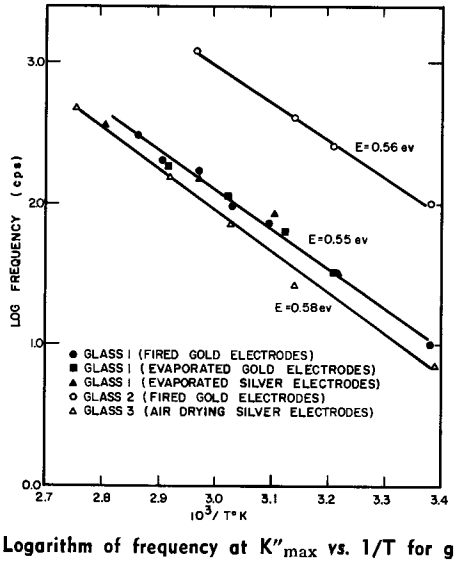

Fig. 3. Logarithm of frequency at K''_{max} vs. 1/T for glasses 1, 2, and 3.

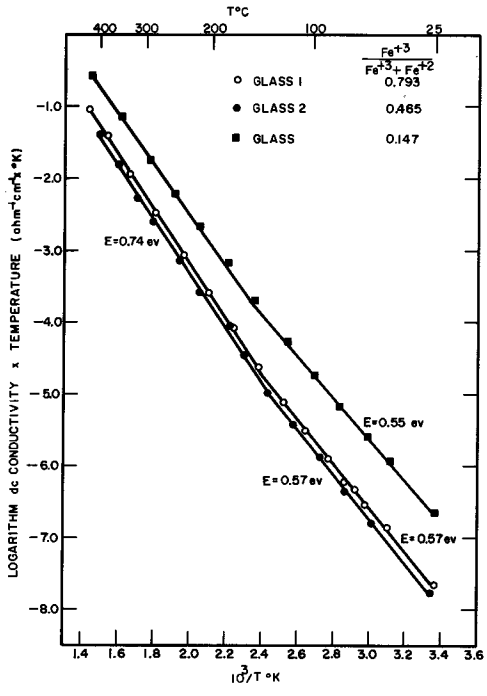

Fig. 4. Logarithm of d-c conductivity x temperature vs. 1/T

Killias (15) has suggested that the conduction activation energy is temperature dependent and is given by

$$E = \epsilon_0\left(1 - \frac{\theta_R}{T}\right) \qquad [7]$$

where ϵ_0 and θ_R are constants, and T is temperature. He suggests the temperature dependence is due to a distribution of jump distances. Figure 5 contains a plot of the logarithm of the d-c conductivity and frequency at which K'' is a maximum *vs.* $\left(\frac{1}{T} - \frac{\theta_R}{T^2}\right)$ for glass 1. θ_R was determined using the method of least squares. The conductivity data do give a straight line as predicted by Killias. It can be seen that the temperature dependence is the same for both the d-c conductivity and the loss factor data whether E is assumed to be temperature dependent or not. This suggests the relaxation time (τ) is associated with the

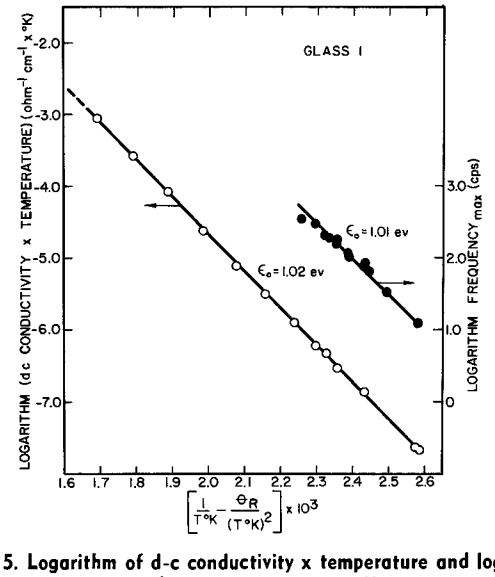

Fig. 5. Logarithm of d-c conductivity x temperature and logarithm f_{max} vs. $(1/T - \theta_R/T^2)$ where θ_R = 69.4°K.

conduction mechanism. It is believed the dielectric loss is due to electrons (or holes) hopping between Fe^{3+} and Fe^{+2} ions.

For a thermally activated diffusion process, the Nernst-Einstein equation relates the conductivity and relaxation time as follows

$$\gamma_{d\text{-}c} = \frac{ne^2d^2}{kT}\left(\frac{1}{\tau}\right) \quad [8]$$

where n is the carrier concentration, e is electronic charge, and d is the jump distance. For glass 3, n calculated from Eq. [8] was found to be 1.5 x 10^{20} cm^{-3} and 1.2 x 10^{20} cm^{-3} at 45.3° and 69.7°C, respectively. This compares with $n \approx 7 \times 10^{20}$ cm^{-3} at 200°C determined from

$$n = N_0 e \frac{-|Q|T}{kT} \quad [9]$$

where N_0 is total available sites, and Q is the thermoelectric power (1). Considering the accuracy of the measurements and the fact that two independent techniques were used, this is good agreement and indicates the carrier concentration is nearly independent of temperature. The d-c conductivity changed nearly three orders of magnitude over this temperature range. The agreement between n calculated from Eq. [8] and [9] is further evidence that the relaxation process and the conduction mechanism result from charge transfer between Fe^{+3} and Fe^{+2} ions.

Following the procedure of Yager (16) and Heroux (14), it was determined that there is a distribution of relaxation times rather than a single time. This is not surprising since the glass structure is amorphous. When a single relaxation process is in effect, the dielectric constant (K'_s) and loss factor (K''_s) are given by the following equations (12, 16)

$$K'_s = K_\infty + \frac{K_\infty k}{1+\omega^2\tau^2} \quad [10]$$

and

$$K''_s = \frac{K_\infty k\omega\tau}{1+\omega^2\tau^2} \quad [11]$$

where K_∞ is the dielectric constant at infinite frequency, k is a constant, and ω is 2π x frequency.

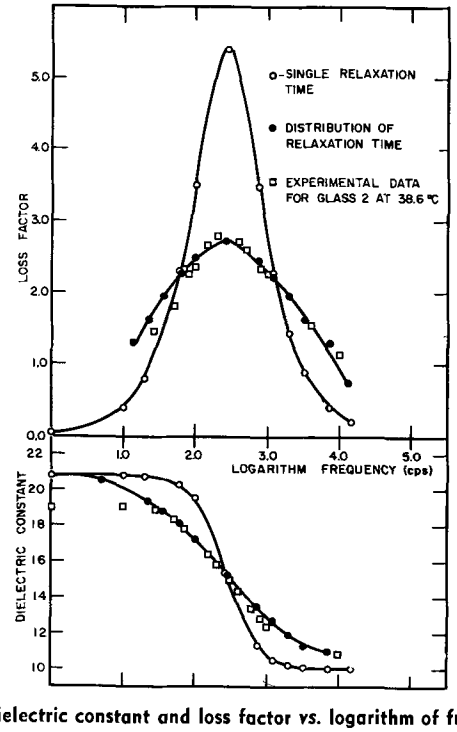

Fig. 6. Dielectric constant and loss factor vs. logarithm of frequency

Wagner (16, 17) proposed a Gaussian distribution of relaxation times which are spread logarithmically about a most probable relaxation time ($\bar{\tau}$). From expressions given by Yager for dielectric constant and loss, we have

$$K'_w = K_\infty + \frac{K_\infty bk \exp(-b^2Z_0^2)}{\sqrt{\pi}} \int_0^\infty \exp(-b^2u^2) \times \frac{\cosh u(2b^2Z_0-1)}{\cosh u} du \quad [12]$$

and

$$K''_w = \frac{K_\infty bk \exp(-b^2Z_0^2)}{\sqrt{\pi}} \int_0^\infty \exp(-b^2u^2) \times \frac{\cosh 2b^2Z_0u}{\cosh u} du \quad [13]$$

where $Z_0 = \ln \omega\bar{\tau}$, $Z = \ln \tau/\bar{\tau}$, and $u = Z + Z_0 = \ln \omega\tau$. Using a technique developed by Yager (16), Eq. [12] and [13] were evaluated. In Fig. 6 these results are compared with the experimental values of K'' and K' for glass 2 and K'_s and K''_s determined from Eq. [10] and [11]. The experimental data fit the Wagner curve reasonably well indicating there is a distribution of relaxation times rather than a single process. It can be seen that the experimental loss data fall below the theoretical curve at the low frequencies. This can be attributed to the fact that there is a greater error in determining K'' in this region than at higher frequencies because γ_T approaches $\gamma_{d\text{-}c}$ rapidly as the frequency decreases in this range.

Conclusions

1. The d-c conduction activation energy is equal to the activation energy of the dielectric relaxation process in the frequency range 10^{-2} to 10^5 cps.
2. The dielectric constant is independent of frequency and temperature below the dispersion region when gold electrodes are used.
3. There is a distribution of relaxation times rather than a single relaxation time associated with the dispersion process.
4. The a-c dispersion between 10^{-2} and 10^5 cps and the d-c conductivity are probably a result of charge carriers jumping between Fe^{+3} and Fe^{+2} ions.

Acknowledgment

The authors thank Mrs. M. Bentley and Mr. F. Voorhees for their experimental assistance.

Manuscript received March 14, 1966; revised manuscript received May 6, 1966.

Any discussion of this paper will appear in a Discussion Section to be published in the June 1967 JOURNAL.

REFERENCES

1. K. W. Hansen, *This Journal*, **112**, 994 (1965).
2. R. R. Heikes and W. D. Johnston, *J. Chem. Phys.*, **26**, 582 (1957).
3. S. van Houten, *J. Phys. Chem. Solids*, **17**, 7 (1960).
4. M. Munakata, *Solid-State Electronics*, **1**, 159 (1960).
5. S. van Houten and A. J. Bosman, in "Transition Metal Compounds," E. R. Schatz, Editor, Gordon and Breach Science Publishers (1964).
6. R. C. Miller and R. R. Heikes, *J. Chem. Phys.*, **28**, 348 (1958).
7. D. P. Snowden and H. Saltsburg, *Phys. Rev. Letters*, **14**, 497 (1965).
8. V. A. Ioffe, I. B. Patrina, and I. S. Poberovskaya, *Soviet Phys. Solid State*, **2**, 609 (1960).
9. S. Tsugane, M. Haradome, and R. Hioki, *Japan J. Appl. Phys.*, **4**, 77 (1965).
10a. ASTM Designation: D150-59T.
10b. ASTM Designation: D257-61.
11. I. R. Weingarten, *Annual Report of the Conference on Electrical Insulation* (National Academy of Science, National Research Council Publication *396*) (1955 meeting).

12. E. J. Murphy and S. O. Morgan, *Bell System Tech. J.*, **18**, 502 (1939).
13. H. E. Taylor, *J. Soc. Glass Technol.*, **41**, 350T (1957); H. E. Taylor, *ibid.*, **43**, 124T (1959).
14. L. Heroux, *J. Appl. Phys.*, **29**, 1639 (1958).
15. H. R. Killias, *Physics Letters*, **20**, 5 (1966).
16. W. A. Yager, *Physics*, **7**, 434 (1936).
17. K. W. Wagner, *Ann. d. Physik*, **40**, 817 (1913).

Some Cross-Substitutional Alloys of CdTe

J. C. Woolley and E. W. Williams[1]

Physics Department, University of Ottawa, Ottawa, Ontario, Canada

ABSTRACT

The alloys of CdTe with the cross-substitutionally derived ternary compounds $AgInTe_2$ and $CuGaTe_2$ are considered. It is found, in the case of the ternaries themselves, that neither is completely stable and that both tend to decompose under certain conditions of annealing. The alloys have been prepared by melt and anneal method, with due regard to the stability of the ternary concerned. By x-ray powder photograph techniques, the composition ranges for single phase zinc blende or chalcopyrite structure or for two-phase behavior have been determined and the lattice parameter data are given. For the single phase alloys, values of optical energy gap have been determined by the usual I. R. absorption method.

The development of ternary compounds from binaries by cross-substitution is well known (1-3). In the case of A^{II} C^{VI} compounds, it has been shown that many of the derived ternary A^{I} B^{III} C_2^{VI} compounds are stable and the crystallographic and semiconducting properties of these ternaries have been investigated (1, 4-6). The ternaries derived from zinc blende type A^{II} C^{VI} compounds show ordering of the A^{I} and B^{III} atoms and hence have a chalcopyrite structure rather than zinc blende. In the case of tellurides, the derived ternaries, *e.g.*, $AgInTe_2$, $CuInTe_2$, $CuGaTe_2$, etc., have received some attention (4, 8, 9).

A further step in the development of new materials is the consideration of solid solution between an A^{II} C^{VI} compound and a derived A^{I} B^{III} C_2^{VI} compound, where the particular C^{VI} element is common to both. The resulting alloys can be looked on as the results of partial cross-substitution in the binary compound. Such solid solutions which have already received attention are ZnS-$CuGaS_2$ and ZnS-$AgGaS_2$ [Apple (10)], $CdTe$-$CuInTe_2$ [Chernyavsky (11)], and $CdTe$-$AgInTe_2$ and $HgTe$-$AgInTe_2$ [Rodot (12)]. In these cases, complete solid solution was found for the ZnS-$CuGaS_2$ and $CdTe$-$CuInTe_2$ alloys, while the range of solid solution of $AgGaS_2$ in ZnS was found to be limited to 5 mole %. In the case of $CdTe$-$AgInTe_2$ and $HgTe$-$AgInTe_2$, Rodot (12) investigated thermoelectric properties, and the range of solid solution, etc., was not determined.

Here we consider certain alloys of CdTe, *viz.*, $CdTe$-$AgInTe_2$ and $CdTe$-$CuGaTe_2$. The ranges of solid solution have been found and the values of lattice parameters determined by x-ray powder photograph techniques. The room temperature optical energy gap has been obtained for the single phase samples by normal I.R. absorption measurements. The methods used are the same as those used in the investigation of the corresponding cross-substitutional alloys of InSb, etc., and which have been described in some detail previously (13).

Preparation and Problems of Stability of Compounds

The separate compounds were prepared by melting together the appropriate component elements. In the case of CdTe, the ingot was melted in a vertical furnace and then slowly cooled by lowering out of the furnace hot zone. The part of the ingot which solidified first was used to provide the CdTe required, this material being p-type with approximately 10^{15} carriers/cc.

The ternary compounds were produced by melting components and then quenching in water. With these quenched samples, $CuGaTe_2$ was found to have lattice parameter values of $a_0 = 6.025$Å and $c/a = 1.983$, while the optical energy gap E_g was 1.17 ev. The corresponding values for the quenched $AgInTe_2$ were $a_0 = 6.446$Å $c/a = 1.960$, and $E_g = 0.97$ ev. Previously reported values for these compounds are (1, 5): $CuGaTe_2$ $a = 6.006$Å, $c/a = 1.987$; $AgInTe_2$ $a = 6.419$Å; $c/a = 1.962$, $E_g = 0.96$ ev.

To check the behavior of these ternary compounds, they were annealed at various temperatures similar to those to be used when the alloys were annealed. It was found that when $CuGaTe_2$ (mp 870°C) was annealed at 750°C a second phase began to appear. Although it was difficult to detect the presence of this phase with the x-ray powder photographs, the results of both photomicrographic analysis and optical absorption measurements showed its presence. Even in the quenched state, a number of small needle-like inclusions were observed; on annealing at 750°C these inclusions grew, and then the second phase was observed to segregate out at the grain boundaries and to cause large cracks. Correspondingly, the quenched sample gave a normal absorption curve with an absorption edge at an energy of 1.17 ev, but after the sample was annealed at 750°C, a broad absorption peak appeared on the low energy side of the absorption edge at photon energies of about 0.7-0.9 ev, and the magnitude of this peak increased with continued annealing. When the $CuGaTe_2$ was annealed at lower temperatures (*e.g.*, 400°C), no growth of a second phase was observed in the photomicrographs beyond the small inclusions of the quenched state, and the optical absorption curve did not change with annealing from that for the quenched material.

The behavior of $CuGaTe_2$ appears similar to that observed for $AgSbTe_2$ which shows a precipitation of Sb_2Te_3 (14) on zone melting. However the precipitated phase in $CuGaTe_2$ would not appear to be Ga_2Te_3 as this has too high an energy gap to produce the observed I.R. absorption peak.

When $AgInTe_2$ (mp 680°C) was annealed at 600°C, no changes in behavior could be detected from that for the quenched material. However when samples were annealed at 400°C for 10 days, photomicrographs showed the appearance of a second phase (possibly tellurium) at the grain boundaries. In an x-ray photograph of this material the value of the lattice parameter a_0 (6.455Å) was found to be a little higher than that for the samples quenched and annealed at 600°C.

Thus neither of the ternary compounds were found to be stable over the whole temperature range from room temperature to melting point, $CuGaTe_2$ being

[1] Present address: Texas Instruments Inc., Dallas, Texas.

definitely unstable at 750°C and $AgInTe_2$ apparently showing a precipitated phase when annealed at 400°C. As the main interest of the work was in the semiconducting properties of the materials and not in phase diagram data, the ternary compounds were not investigated further. However, as is indicated in the next section, it was found that over a considerable range of composition, the solid solutions in CdTe could be retained in a homogeneous single phase condition. The properties of these alloys were therefore investigated further.

Properties of the Alloys

In all cases the alloys were prepared by melting together the appropriate amounts of CdTe and the ternary compound concerned, and then quenching in water. Such samples showed blurred x-ray lines, were generally in nonequilibrium condition and needed annealing to give equilibrium.

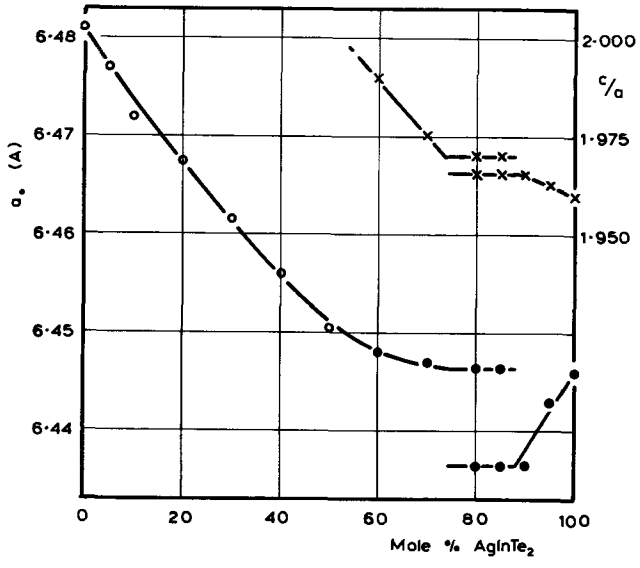

Fig. 1. Variation of lattice parameters with composition for CdTe-$AgInTe_2$ alloys: ○ zinc blende a_0; ● chalcopyrite a_0; X chalcopyrite c/a.

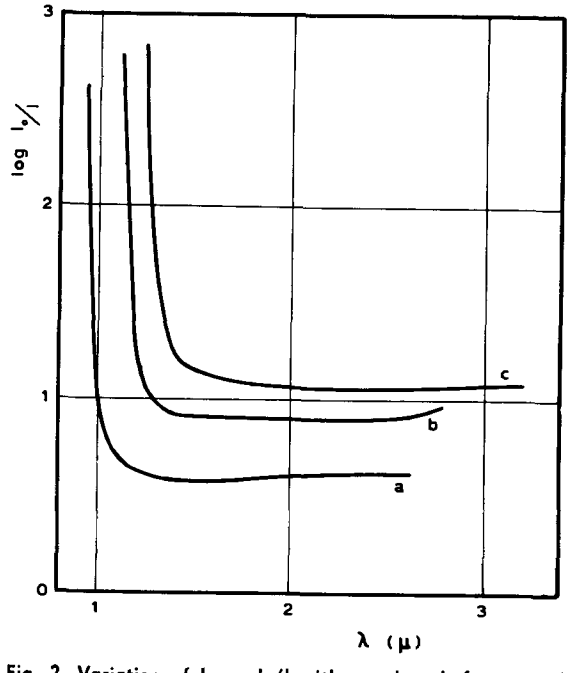

Fig. 2. Variation of $\log_{10} I_0/I$ with wavelength for transmission measurements on typical CdTe-$AgInTe_2$ alloys. Curve a, 90 mole % CdTe 10 mole % $AgInTe_2$; curve b, 60 mole % CdTe 40 mole % $AgInTe_2$; curve c, $AgInTe_2$.

CdTe-$AgInTe_2$.—Alloys were made up at 10 mole % intervals across the composition range plus extra specimens at 5, 85, and 95 mole % $AgInTe_2$.[2] All alloys were annealed initially at 600°C. Samples in the range 0-50 mole % $AgInTe_2$ were in good equilibrium condition after annealing for 30 days, but those in the range 60-95 mole % $AgInTe_2$ needed 60-90 days of annealing to obtain equilibrium. The values of lattice parameter for the alloys are shown in Fig. 1. From 0 to 50 mole % $AgInTe_2$, the alloys were single phase with zinc blende structure, while from 60 mole % onward the structures were chalcopyrite. The 60, 70, 90, and 95 mole % alloys were single phase, but the 80 and 85 mole % alloys were two phase, both phases having chalcopyrite structure. The 70 and 80 mole % alloys were then annealed for 30 days at 400°C. Both then showed the same two phase behavior. Thus the miscibility gap is wider at lower temperatures.

Optical absorption measurements were made on samples of all single phase alloys, samples of thickness in the range 100-200μ being used. Typical absorption curves are shown in Fig. 2, and the resulting values of the optical energy gap E_g are shown in Fig. 3. It is seen that the value of E_g varies smoothly with com-

[2] In calculating mole %, CdTe has been treated as Cd_2Te_2.

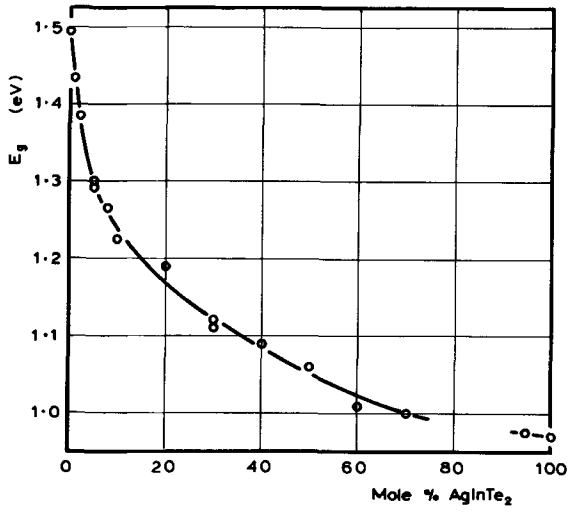

Fig. 3. Variation of optical energy gap E_g with composition for CdTe-$AgInTe_2$ alloys.

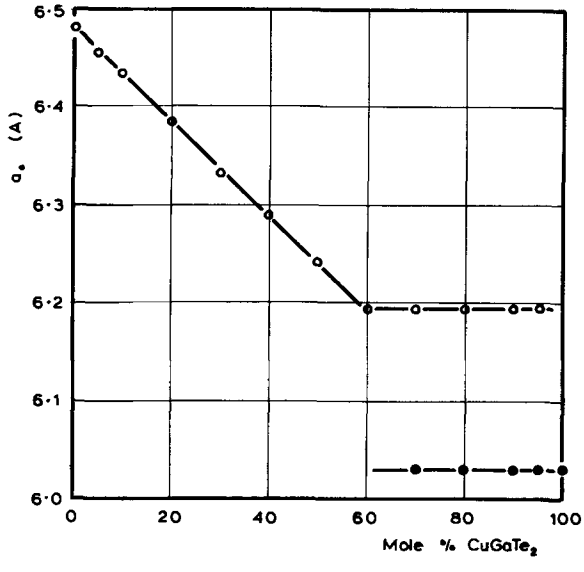

Fig. 4. Variation of lattice parameter a_0 with composition for CdTe-$CuGaTe_2$ alloys: ○ zinc blende; ● chalcopyrite.

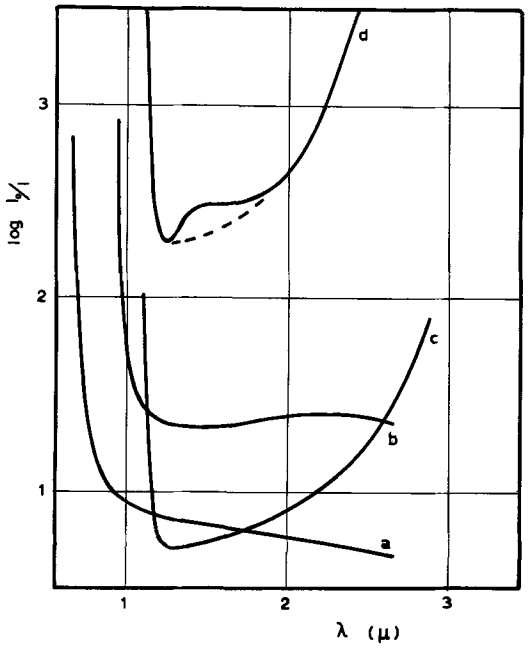

Fig. 5. Variation of $\log_{10} I_0/I$ with wavelength for transmission measurements on typical CdTe-$CuGaTe_2$ alloys. Curve a, CdTe; curve b, 90 mole % CdTe 10 mole % $CuGaTe_2$; curve c, 70 mole % CdTe 30 mole % $CuGaTe_2$; curve d, 50 mole % CdTe 50 mole % $CuGaTe_2$.

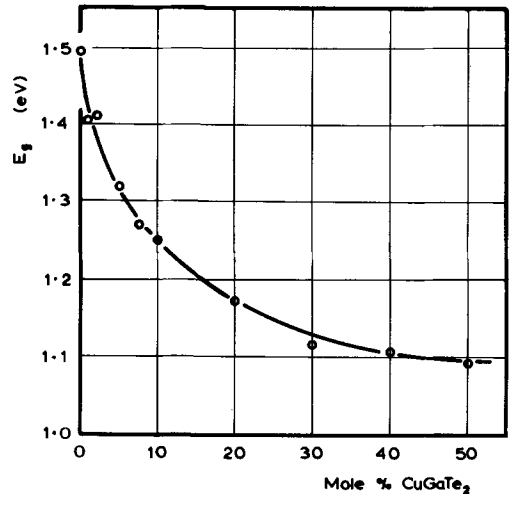

Fig. 6. Variation of optical energy gap E_g with composition for CdTe-$CuGaTe_2$ alloys.

position and that the onset of ordering in the chalcopyrite structure has little effect on the value of E_g.

CdTe-$CuGaTe_2$.—Again alloys were made up at 10 mole % intervals across the composition range plus alloys at 5 and 95 mole % $CuGaTe_2$. Samples of all alloys were annealed at 750°, 650°, and 350°C. The x-ray results obtained were the same for all three temperatures, and again annealing times of 30-60 days were needed at the higher temperatures to produce good equilibrium conditions. Values of lattice parameter are shown in Fig. 4. It is seen that single phase solid solution in the zinc blende phase occurs out to the 60 mole % $CuGaTe_2$ alloy, but that the 70, 80, 90, and 95 mole % alloys were two phase. The optical absorption curve of the 50 mole % alloy (Fig. 5) showed a small absorption peak on the low energy side of the absorption edge, indicating the presence of a small amount of second phase. Thus, despite the x-ray data shown in Fig. 4, this sample would not have been completely single phase, probably because of incomplete approach to equilibrium.

Because of the problems of stability in $CuGaTe_2$ described above, no attempt was made to investigate further the alloys containing more than 50 mole %. $CuGaTe_2$ or to determine any small range of solubility in the chalcopyrite structure, which would clearly be less than 5 mole %.

Optical absorption measurements were made on samples in the composition range 0-50 mole % $CuGaTe_2$, the samples again being of thickness in the range 100-200μ. Typical absorption curves are shown in Fig. 5, and the resulting variation of E_g is shown in Fig. 6.

Summary

1. As with other ternary chalcogenides (14, 15), complications are caused by the instability of the compounds. Thus, while $AgInTe_2$ is more stable than $CuGaTe_2$, even in the former there appears to be some segregation to grain boundaries with annealing at 400°C. Zalar (15) observed similar behavior in $CuInTe_2$.

2. In each case, a wide range of solid solution occurs in the relatively stable zinc blende type structure. The form of Fig. 1 and 4 indicates that pseudobinary conditions probably apply in the two sections investigated.

3. In the optical energy gap results, for both systems the value of E_g drops rapidly as ternary compound is added to CdTe, and then the E_g *vs.* composition curve levels out. Over the range 0-30 mole % ternary for the two cases, the curves of E_g *vs.* composition coincide within the limits of experimental error. This variation in E_g is very similar to that for the ZnS-$CuGaS_2$ system (10). The rapid fall in E_g is probably due to the weaker bonding in the ternary chalcogenides.

Acknowledgments

The authors wish to thank Dr. J. Warner for some preliminary x-ray investigations.

Manuscript received Feb. 25, 1966; revised manuscript received June 1, 1966.

Any discussion of this paper will appear in a Discussion Section to be published in the June 1967 JOURNAL.

REFERENCES

1. I. Austin, C. H. L. Goodman, and A. E. Pengelly, *This Journal*, **103**, 609 (1956).
2. C. H. L. Goodman, *J. Phys. Chem. Solids*, **6**, 305 (1958).
3. O. G. Folberth, *Z. Naturf.*, **149**, 94 (1959).
4. V. P. Zhuze, V. M. Sergeeva, and E. L. Shtrum, *Sov. Phys. Tech., Phys.*, **3**, 1925 (1958).
5. H. Hahn, G. Frank, W. Klingler, A. D. Meyer, and G. Stürger, *Z. Anorg. Chem.*, **271**, 153 (1953).
6. L. S. Palatnik, V. M. Koshkin, and Yu F. Komik, *Sov. Phys. Cryst.*, **7**, 99 (1962).
7. L. S. Lerner, *J. Phys. Chem. Solids*, **27**, 1 (1966).
8. A. V. Petrov and E. L. Shtrum, *Sov. Phys. Solid State*, **4**, 1061 (1962).
9. S. M. Zalar, *AIME Conf. Proc.*, (Interscience N. Y.) **15**, 263 (1962).
10. E. F. Apple, *This Journal*, **105**, 251 (1958).
11. V. P. Chernyavsky, *Fizika (Leningrad)*, 10 (1962).
12. H. Rodot, International Conf. on Semiconductor Physics, p. 1010, Prague (1960).
13. J. C. Woolley and E. W. Williams, *This Journal*, **111**, 210 (1964); J. C. Woolley, C. M. Gillett, and J. A. Evans, *J. Phys. Chem. Solids*, **16**, 138 (1960).
14. P. W. Armstrong, J. W. Faust, and W. A. Tiller, *J. Appl. Phys.*, **31**, 1954 (1960).
15. S. M. Zalar, Ratheon Tech. Memo. T-445 (1963).

Growth of Vanadium on Silicon Substrates

K. J. Miller, M. J. Grieco, and S. M. Sze

Bell Telephone Laboratories, Incorporated, Murray Hill, New Jersey

ABSTRACT

Vanadium has been grown on (111) oriented silicon substrates using the hydrogen reduction of VCl_4. The reaction kinetics related to the growth of the deposits has been investigated. V-Si diodes fabricated from the deposited vanadium on silicon samples were found to have a barrier height of 0.70 ± 0.04v in agreement with that theoretically predicted in other studies.

Recent interest in the chemical deposition of metals on semiconductor substrates has been stimulated by potential applications in the fabrication of diodes and metal-base transistors. Deposition of molybdenum on silicon has been reported by Casey *et al.* (1) and Lindmayer (2); the latter author reported that 100Å thick molybdenum layers on silicon were not single crystal. Crowell *et al.* (3) have reported deposition of polycrystalline tungsten films on silicon, germanium, and gallium arsenide substrates. The purpose of this paper is to present data on the growth of vanadium on silicon substrates and to study the feasibility of V-Si diode fabrication from these structures.

A schematic diagram of the deposition apparatus used is shown in Fig. 1. The deposition apparatus was the vertical reactor, RF-heated type, conventionally used for the hydrogen reduction of silicon tetrahalides (4). The VCl_4 was prepared by the reaction between vanadium and chlorine. The chlorine was passed over vanadium at 800°-1000°C. The chlorine was purified by passing it through graphite heated to 650°C. The VCl_4 was condensed at 0°C in a cold finger for subsequent controlled vaporization in a purified hydrogen flow. During deposition, hydrogen was passed over the VCl_4 at the rate of 0.5 l/min and another 4 l/min flow of hydrogen bypassed the cold finger and flowed into the reactor. The VCl_4 partial pressure was controlled by thermostating at temperatures from −15° to 25°C. The VCl_4 vapor pressure values used for calculating partial pressures of VCl_4 were obtained by extrapolating the data of Simons and Powell (5) below 39.5°C. It was assumed that the only significant compound formed from the V-Cl_2 reaction was VCl_4. The vanadium was obtained from Gallard-Schlesinger Chemical Corporation and was 99.9%. Silicon substrate samples were 1.5 ohm-cm, n-type single crystal wafers oriented in the (111) plane and were electrochemically polished. Over-all deposited thickness was determined by masking a portion of the substrate with a silicon chip and measuring the resulting step in the vanadium deposit with a Zeiss interference microscope. Vanadium was deposited with an over-all average thickness up to 10μ.

Variables affecting the deposition rate of vanadium which have been studied are the silicon substrate temperature and the partial pressure of VCl_4. The effect of temperature was studied between 1140° and 1300°C at a VCl_4 partial pressure of 0.2 Torr. For study of the variation of deposition rate with partial pressure variation, the VCl_4 was varied between 0.08 and 0.9 Torr, and silicon substrate samples were held at 1300°C. Figure 2 shows the variation of the vanadium deposition rate with temperature. The kinetic data for the deposition rate between 1140° and 1300°C could be fitted to an Arrhenius type equation

$$r = Ae^{-\Delta H_a/RT}$$

where ΔH_a, the apparent activation energy for the over-all reaction, was 72 ± 2 kcal/mole.

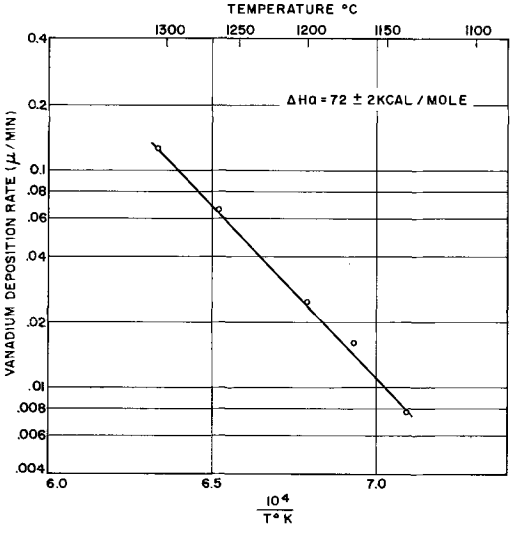

Fig. 2. Temperature dependence of vanadium deposition at 0.2 Torr VCl_4 pressure.

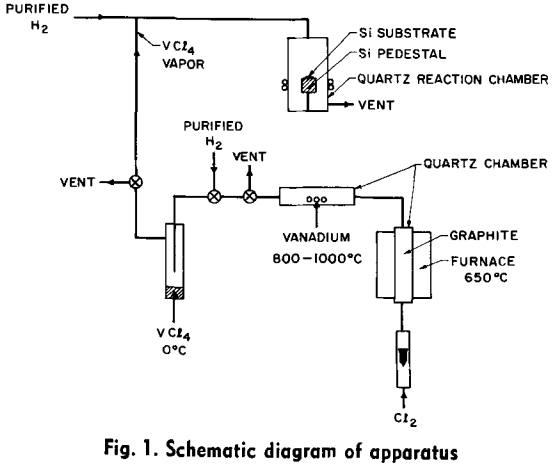

Fig. 1. Schematic diagram of apparatus

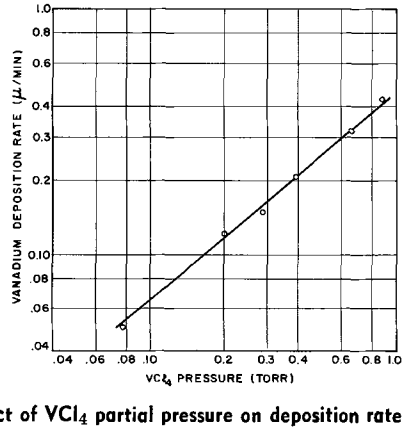

Fig. 3. Effect of VCl_4 partial pressure on deposition rate at 1300°C

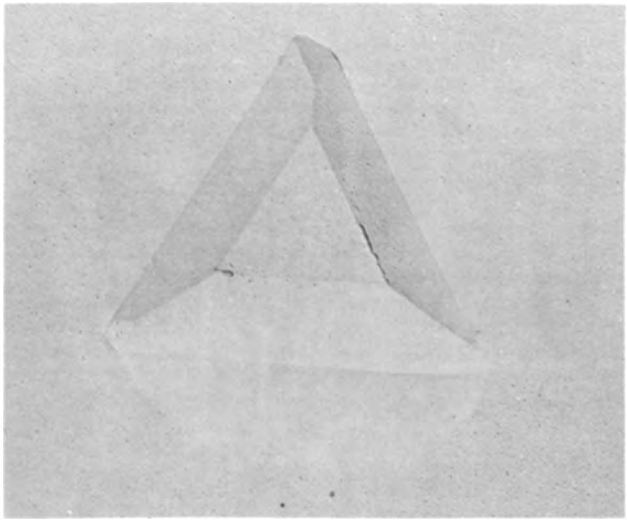

Fig. 4. Electron micrograph of deposited vanadium crystallite. Magnification 8000X.

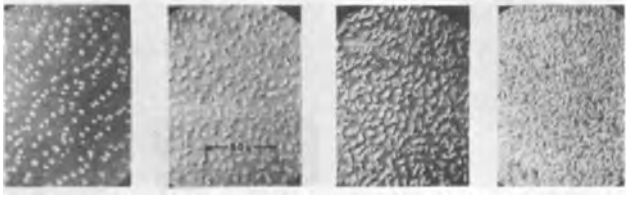

Fig. 5. Micrographs showing increasing density of deposited vanadium crystallites for average deposit thickness from 1 to 5μ (left to right).

Figure 3 shows the effect of the partial pressure of VCl_4 on the deposition rate of vanadium. Over the pressure range studied the deposition rate obeyed a relation of the type

$$r = kp^n_{VCl_4}$$

The slope of the deposition rate-pressure line in Fig. 3 gives a value of $n = 0.9$, indicating that the deposition reaction is close to first order. It can be assumed that the low partial pressures of VCl_4 used favor a heterogeneous reaction. Tyzack and England (7) have concluded that the following reduction reaction of VCl_2 to form vanadium is rate-controlling

$$VCl_2 + H_2 \rightarrow V + 2HCl$$

Their conclusion is apparently based on the increasing positive value of $\Delta G°$ with decreasing temperature below about 1250°C.

Vanadium crystal growth was observed to take place by island formation similar to that observed by Manasevit *et al.* (6) for epitaxial silicon growth on sapphire. The surface deposits were analyzed for vanadium by an electron probe microanalyzer. The electron probe used for these studies was a Microscan, manufactured by the Cambridge Instrument Company. This scanning type electron probe permitted two-dimension displays of the sample surface and showed the deposits to be vanadium particles or clusters. Transmission electron diffraction patterns obtained from vanadium deposited surfaces indicate that the vanadium crystallites are of the same (111) orientation as that of the silicon substrate and are single crystalline. No evidence of silicides was observed. Figure 4 shows a typical vanadium crystallite as viewed by electron microscopy. Optical microscopic examination of vanadium deposited surfaces showed that the deposits consisted of an array of discrete vanadium crystallites. Vanadium crystallite density varied with the over-all average depth of deposited vanadium. Figure 5 shows this density variation, for average depth of deposit from 1μ increasing to 5μ.

Vanadium-silicon diodes were made from vanadium which was deposited approximately 10μ thick and which covered approximately 80% of the silicon surfaces. The diodes were made using the procedure previously described for tungsten-silicon diodes (3): Au-Sb ohmic contacts were alloyed to the back surface of the silicon substrates at 370°C, 10 mil diameter gold dots were evaporated on the deposited vanadium surface, and samples were etched in 10:1 HNO_3:HF to remove vanadium from the unmasked areas. Because the substrate temperature during vanadium deposition is 100°C lower than the V-Si eutectic temperature, and diffraction studies did not show silicide formation, the junction is believed to be of the nonalloyed type. Current-voltage and capacitance-voltage measurements were used to investigate the V-Si diode characteristics. Typical forward current density-voltage plots are shown in Fig. 6. These curves can be fitted by the diode equation (8)

$$J = J_s[e^{(qV_a/nkT)} - 1]$$

where V_a is the voltage applied across the junction, n is an empirical constant, and J_s is the saturation current density. The value of n obtained from Fig. 6 is about 1.1 for current densities ranging from 10^{-4} to

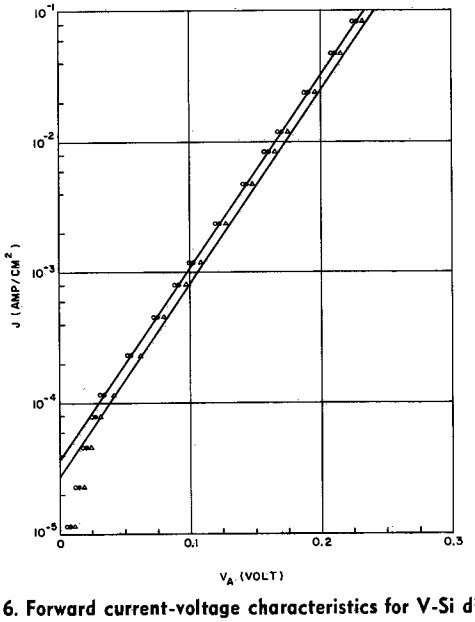

Fig. 6. Forward current-voltage characteristics for V-Si diodes

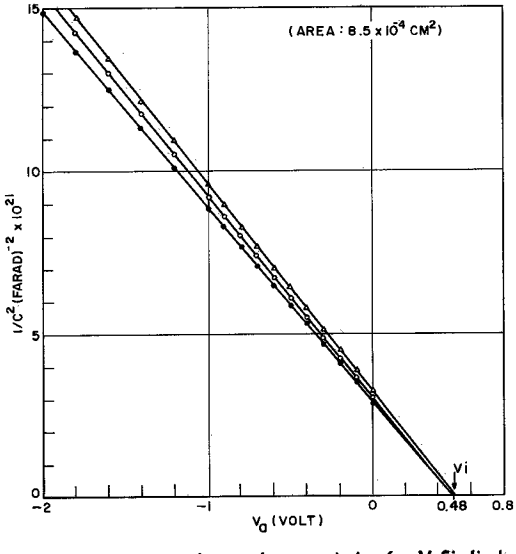

Fig. 7. Capacitance-voltage characteristics for V-Si diodes

10^{-1} amp/cm^2. The value of J_s is $(3.0\text{-}3.6)\times10^{-5}$ amp/cm^2. The barrier height, Φ_B, was found to be 0.70 ± 0.04v based on the assumption that the Richardson equation

$$J_s = A^*T^2e^{(-q\Phi_B/kT)}$$

can be used to relate the barrier height, Φ_B, and J_s (3). A theoretical value of A^*, 258 amp/cm^2/K^2, has been used (9). The J_s is the sum of the currents for V-Si and Au-Si diodes, because, as discussed above, approximately 80% of the areas are covered by vanadium and 20% covered by gold. However, the barrier height of Au-Si diode is about 0.80v (10) which is 0.1v higher than the presently measured barrier height. The correction in Φ_B of V-Si diode is less than 0.025v. The reverse characteristics of the diodes were qualitatively consistent with the diode equation with a reverse current density of the order of 10 ma/cm^2 at 10v.

Capacitance-voltage measurements on V-Si diodes are shown in Fig. 7. The doping level, N_D, determined from resistivity measurement, was 3.8×10^{15} cm^{-3}, and from the slope of the $1/C^2$ *vs.* V_a plot 4.3×10^{15} cm^{-3}. The barrier height can also be determined from the data in Fig. 7 by use of the equation (3, 11)

$$\Phi_B = V_i + V_f + kT/q - \Delta\Phi$$

where V_i is the voltage intercept, 0.48 ± 0.04v, V_f, the depth of the Fermi level below the conduction band, is 0.288v for 1.5 ohm-cm, n-type silicon, and $\Delta\Phi$ is the image force barrier lowering (12), approximately 15 mv for V-Si diodes. Thus Φ_B was found to be 0.71 ± 0.04v. Since the measured capacitance over the voltage range will only be affected by the combined diode system to less than 2%, the correction for Φ_B of V-Si diode is again of the order of 0.025v.

The consistency of the value of the barrier height obtained from the above measurements and the fact that n is close to unity and $1/C^2$ is linearly dependent on V_a indicate the existence of a Schottky junction. The barrier height obtained in this study has been found to be in reasonable agreement with that predicted theoretically by Cowley and Sze (13) based on the assumptions that the contact between the metal and the semiconductor has an interfacial layer of the order of atomic dimension and the surface state density at the interface is a property only of the semiconductor surface.

Acknowledgment

The authors are indebted to their associates at the Bell Telephone Laboratories for helpful comments on the manuscript.

Manuscript received March 30, 1966; revised manuscript received May 23, 1966. This paper was presented at the San Francisco Meeting, May 9-13, 1965.

Any discussion of this paper will appear in a Discussion Section to be published in the June 1967 JOURNAL.

REFERENCES

1. J. Casey, R. Garnache, J. Lindmayer, and J. L. Sprague, Paper presented at the "Characteristics of Metal Base Transistor Structures," Electrochemical Society Pittsburgh Meeting of the Society, April 15-18, 1963.
2. J. Lindmayer, *Proc. IEEE*, **52**, 1751 (1964).
3. C. R. Crowell, J. C. Sarace, and S. M. Sze, *AIME Trans.* **233**, 478 (1965).
4. H. C. Theuerer, *This Journal*, **108**, 649 (1961).
5. J. H. Simons and M. G. Powell, *J. Am. Chem. Soc.*, **67**, 75 (1945)
6. H. M. Manasevit, A. Miller, F. Morritz, and R. Nolder, *Trans. Met. Soc. AIME*, **233**, 540 (1965).
7. C. Tyzack and P. G. England, "Symposium on Extractive Metallurgy of Some Less Common Metals," Inst. Mining Met., London (1956).
8. H. K. Henisch, "Rectifying Semiconductor Contacts," Clarendon Press, Oxford (1957).
9. C. R. Crowell, *Solid State Electronics*, **8**, 395 (1965).
10. R. J. Archer and M. M. Atalla, *Am. Acad. Sci. N. Y.*, **101**, 697 (1963).
11. A. M. Goodman, *J. Appl. Phys.*, **34**, 329 (1963).
12. S. M. Sze, C. R. Crowell, and D. Kahng, *J. Appl. Phys.*, **35**, 2534 (1964).
13. A. M. Cowley and S. M. Sze, *ibid.*, **36**, 3212 (1965).

Selective Epitaxial Deposition of Gallium Arsenide in Holes

Don W. Shaw

Texas Instruments Incorporated, Dallas, Texas

ABSTRACT

Epitaxial deposition of gallium arsenide in holes etched into gallium arsenide substrates was investigated. Single crystal deposits with excellent surfaces were obtained. The effect of substrate orientation on the degree of lateral overgrowth above the substrate surface was studied. Depositions in {100} oriented substrates produce faceted deposits, whose upper surfaces are several microns above the substrate surface. Epitaxial hole deposits with surfaces level with or nearly level with the substrate surface are obtained with accurately oriented {111}-B substrates.

The importance of selective epitaxial deposition has long been realized in integrated circuit technology. Generally the technique involves epitaxial deposition onto the substrate only in certain areas which are exposed by windows in a protective film (*e.g.*, SiO_2). This technique has been investigated both for silicon (1) and gallium arsenide (2) substrates.

Extension of the technique to include selective depositions in substrate holes has not been widely reported. The investigations which have been reported, such as the recent studies by Jackson (3), have been directed toward the epitaxial deposition of silicon in holes etched into a silicon substrate. However, the selective deposition of gallium arsenide in substrate holes has been generally neglected.

Due to the availability of semi-insulating gallium arsenide, the three-dimensional integrated circuit or functional electronic block has become increasingly promising (4). In view of this as well as the accelerating importance of integrated circuits in general, an investigation of the nature of epitaxial deposition of GaAs in substrate holes was undertaken.

Experimental

Both semi-insulating (Cr doped) and n-type (Te doped) gallium arsenide substrates were employed. The crystals were x-ray oriented and cut into 25 mil thick slices, which were then polished with a sodium hypochlorite solution according to the method of Reisman and Rohr (5). Either {100} or {111}-B surfaces

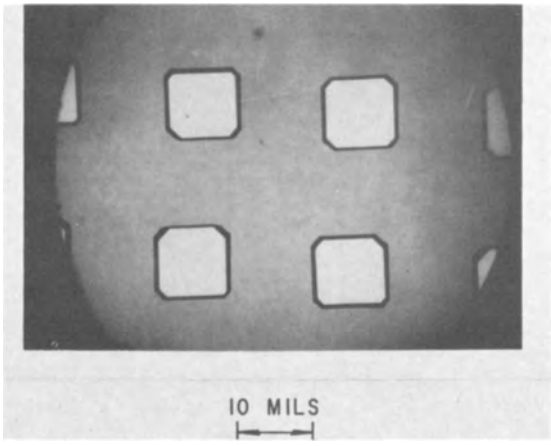

Fig. 1. Epitaxial deposits of GaAs in 8 x 10 mil holes etched ~ 15μ deep into a {100} GaAs substrate.

were utilized for all depositions. The slices were coated with protective SiO_2 layers by pyrolysis of tetraethyl orthosilicate in an evacuated system. Generally the SiO_2 thicknesses varied between 2500 and 4000Å.

Windows were formed in the SiO_2 films by masking with photoresist (Kodak Metal-Etch Resist) and etching away the unmasked areas. Then holes were formed in the substrate at the areas exposed by the windows. Three techniques were used to form the substrate holes: (*i*) etching with a Br_2:CH_3OH (1:1000) solution at room temperature; (*ii*) etching with a H_2SO_4:H_2O_2:H_2O (5:1:1) solution at 65°C; and (*iii*) vapor etching with HCl at 850°C in the epitaxial deposition reactor. The method of hole formation did not have a significant effect on the appearance of the final deposit.

The deposition process utilizes a vapor phase reaction of Ga and GaAs with $AsCl_3$ in an open flow system similar to that previously described (6, 7). The source temperature was maintained at 825°C, while the temperature of the substrate zone was varied between 750°-780°C. The substrate temperature was adjusted experimentally to the point that the deposition was so selective that no extraneous GaAs deposits were obtained on the reactor walls or the protective SiO_2 mask. The $AsCl_3$ flux was 1.0 x 10^{-4} mole/min, while the total gas flow ($AsCl_3$ + H_2) amounted to 380 ml/min. Under these conditions the {111}-B was found to be the slowest growing orientation.

Results and Discussion

Figure 1 illustrates typical deposits of epitaxial GaAs in holes etched into a {100} substrate. The upper {100} surfaces are very smooth, and the single crystal character of the deposits is indicated by the presence of facets. The deposits shown in Fig. 1 have an average height above the substrate surface of 27μ while the original hole depths averaged 15μ.

In order to investigate the crystallography of the {100} deposits, slices were cleaved along the {110} cleavage planes so that cross sections of the deposits were revealed (Fig. 2). Measurements of the interfacial angles between the {100} upper surface and the two side facets such as revealed in Fig. 2b yield values of 55° for each side. Although occasionally side facets which were perpendicular to the upper {100} surface were observed in the cleavage cross sections, by far the greatest majority of the side facets were inclined at an angle of 55° with the upper surface. Since the (111)-(100) interplanar angle is 54°44′, it indicates that four of the slow growing side facets (*i.e.*, the ones revealed by {110} cleavage cross sections) in {100} oriented deposits are {111} faces.

There are only two cleavage planes perpendicular to the surface of {100} oriented slices. Thus it is impossible to determine the angles between the remaining four side facets (the "corner" facets in Fig. 1 and 2) and the upper {100} surface by measurement of a cleavage cross section through them. The direction of the axes of intersections of the corner facets and the {100} upper surface is 45° from the axis of intersection of the {111} side facets and the upper surface.

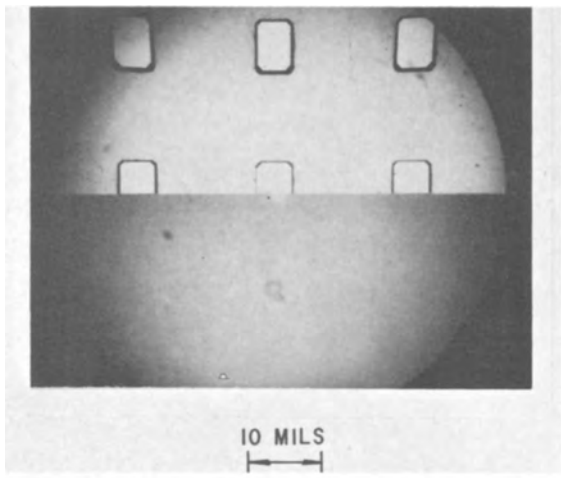

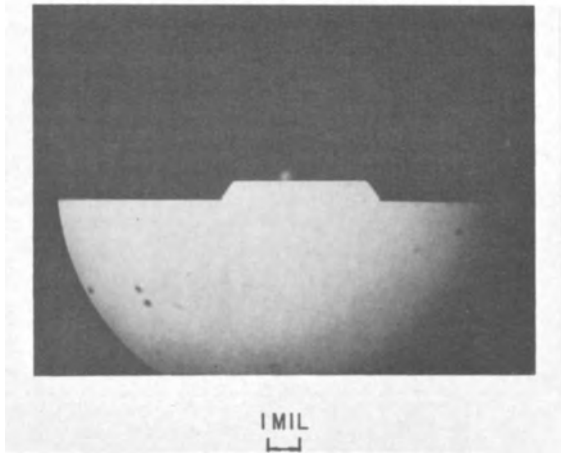

Fig. 2a (top). Epitaxial GaAs deposits in {100} GaAs substrate showing relative position of {110} cleavage plane.

Fig. 2b (bottom). Cross-sectional view along cleavage plane of center deposit shown in upper micrograph.

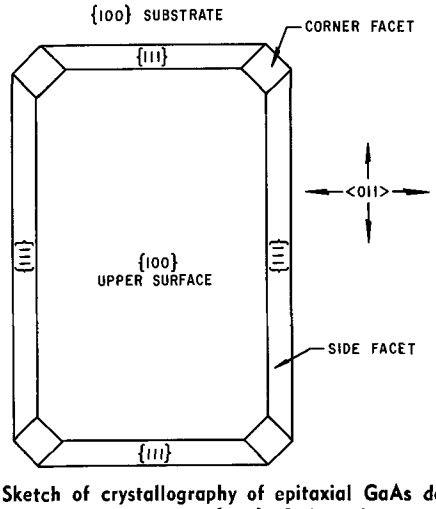

Fig. 3. Sketch of crystallography of epitaxial GaAs deposits obtained from holes etched into {100} GaAs substrates.

This indicates that {110} would be a likely orientation for the remaining four facets. Due to the inclined nature of the side and corner facets, prolonged deposition in holes etched in a {100} substrate should produce deposits with a pyramidal morphology. The crystallography of these deposits in {100} substrates is summarized by Fig. 3.

The tendency of {100} substrates to form deposits bounded on the sides by these well-defined facets results in a novel phenomenon if the hole walls are not oriented parallel to the {110} cleavage planes. This is illustrated by Fig. 4, where each of the deposits appears to have been rotated about an axis perpendicular to the {100} surface when compared with the shape of the original holes. However if the hole walls are oriented parallel with the {110} cleavage planes, no apparent rotation occurs (Fig. 3). The apparent rotation is due to the fact that the {100}-{111} zone axes (<110>) are in the same directions as the directions of the {110} cleavage planes. Thus if the hole walls are oriented at an angle with respect to the direction of the {110} cleavage planes, then the axes of intersection of the surface facet and the {111} side facets in {100} oriented substrates will be tilted at the same angle with respect to the hole walls and the deposit will appear to have "rotated" when compared with the original holes. In addition, misalignment of the hole walls from <110> directions will result in enhanced sizes of the corner facets relative to the sizes of the {111} side facets and an increased lateral overgrowth over the mask. Such a variation in the size ratios of the corner and side facets is evident from a comparison of Fig. 2 and 4.

Deposition in {111}-B substrates was investigated in an attempt to obtain deposits with upper surfaces level with or nearly level with the substrate surface by taking advantage of the slow growth characteristics of {111}-B faces. Initial deposits had excellent surfaces which were tilted from 3° to 6° with respect to the substrate surfaces (Fig. 5). Careful x-ray orientation studies revealed that the substrates themselves were slightly misoriented from the <111> direction by an amount equal to the surface tilt of the epitaxial deposit, indicating that the upper surface was indeed a {111}-B facet. In each deposit the lowest portion of the surface facet was flush with the substrate surface. This indicated that deposits with surfaces level with the substrate surface could be expected with accurately oriented {111}-B substrates.

Additional substrates were very precisely x-ray oriented in the <111> direction, and each slice was checked after polishing. The resulting substrates were oriented to <0.5° from the <111> direction. Deposits in holes etched into these substrates produced very flat deposits (Fig. 6) with heights above the substrate surface of $<2\mu$.

Comparison of the {111} deposits with the original holes revealed that some lateral overgrowth occurred. Since the upper {111}-B facet is a very slow growing surface in GaAs, prolonged deposition should result in overgrowth in a lateral direction over the SiO_2 film. Indeed considerable lateral overgrowth has been ob-

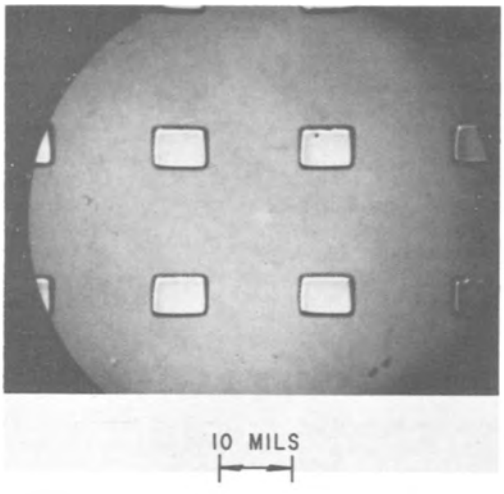

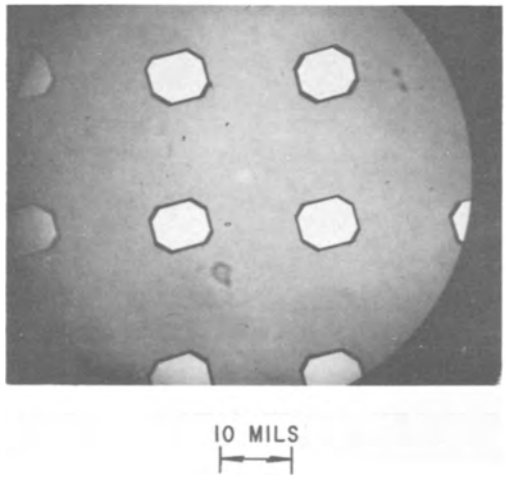

Fig. 4a (top). Holes etched into {100} GaAs substrate prior to deposition.

Fig. 4b (bottom). Epitaxial GaAs deposits obtained from above holes

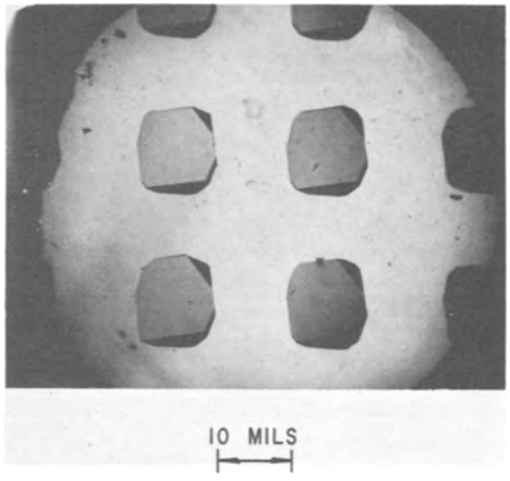

Fig. 5. Epitaxial GaAs deposits in holes etched into a slightly misoriented (~ 6°) {111}-B GaAs substrate.

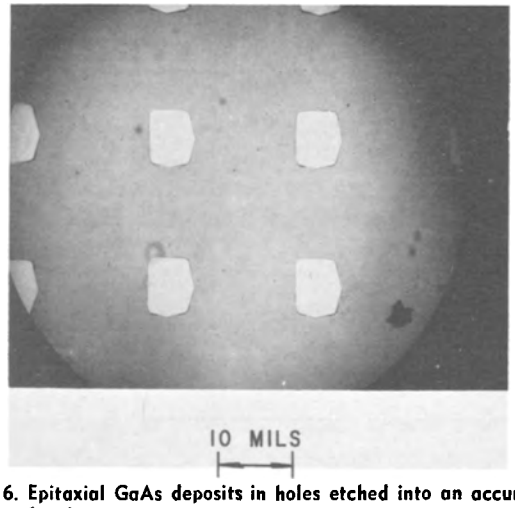

Fig. 6. Epitaxial GaAs deposits in holes etched into an accurately oriented {111}-B GaAs substrate.

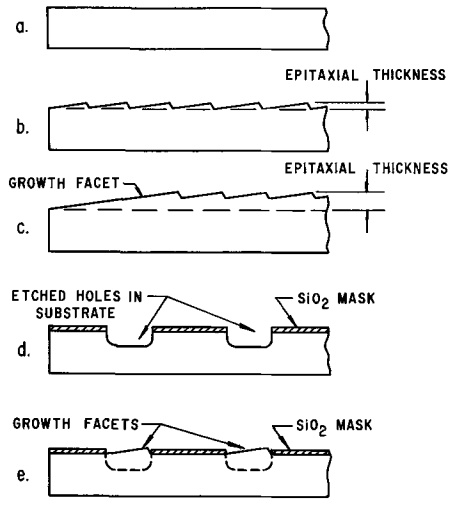

Fig. 7. Simplified sketches illustrating formation of growth facets with large area deposition (a, b, c) and with deposition in holes (d, e). Substrate slightly misoriented. a, Polished substrate prior to deposition; b, initial stage of deposition; c, later state of large area deposition; d, substrate with etched holes; e, after epitaxial deposition in substrate holes.

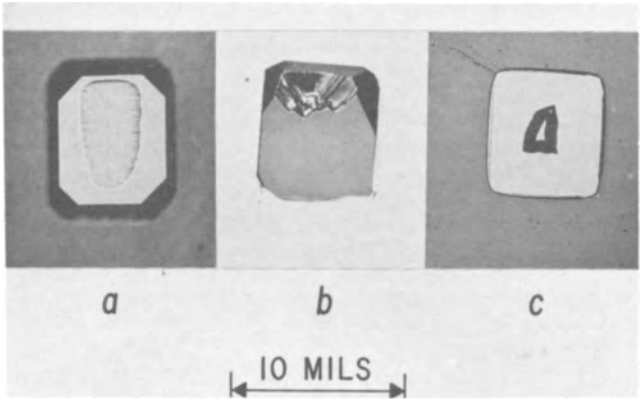

Fig. 8. Incomplete deposition of GaAs in holes etched into substrates of different orientations. a, {100}; b, misoriented (~ 6°) {111}-B; c, accurately oriented {111}-B.

served (2) on <111> oriented GaAs exposed in windows formed in a protective SiO_2 film.

The upper surfaces of the epitaxial hole deposits are highly reflective and are considerably smoother than the usual large area epitaxial deposits. Although the latter may appear smooth under ordinary microscopy conditions, they usually exhibit growth steps when examined with an interference contrast microscope. However, these steps are only rarely observed on the upper surfaces of the hole deposits. This surface quality difference may be explained in terms of the relative upper surface areas available for growth. As shown in Fig. 7b and 7c, as epitaxial growth proceeds over a large area, growth steps are formed whose propagation effectively results in growth perpendicular to the substrate surface. However the step at the extreme left edge in Fig. 7b increases in area as growth progresses (Fig. 7c), since no "macroscopic" steps are growing over it. This results in a small surface facet at one edge of the large area epitaxial deposit. Such facets are observed experimentally on large area deposits.

During deposition in holes, the upper surface areas are restricted by the sizes of the holes. Thus when the hole is filled a relatively small upper surface area (<100 sq mils) is available for growth. In this case the growth steps propagate across the entire upper surface of the hole deposit (Fig. 7d and 7e). This results in very smooth upper surfaces or facets. Since these growth facets correspond to low-index planes, the upper surfaces will be tilted with respect to the substrate surface by an amount equal to the degree of substrate misorientation (Fig. 5). In view of this it is not surprising that smooth and highly reflective upper surfaces are obtained independently of the roughness or irregularity of the hole bottoms or walls. The substrate holes formed by vapor etching quite often had very rough sides and bottoms, but the epitaxial deposits in these holes inevitably possessed excellent faceted surfaces. This is significantly different from the usual epitaxial deposition where the surface quality of the substrate is of extreme importance to the quality of the deposit. Of course such an independence between the appearance of the deposit surfaces and the original hole surfaces would be realized only when the growth conditions tended to produce faceted deposits.

Although accurate growth rate comparisons between growth in holes and ordinary surface growth were not made, in general, less time is required to fill a hole of a given depth than to grow an ordinary surface layer of the same thickness. This may be related to the fact that growth in holes proceeds from the walls inward as well as from the bottom upward. Due to this growth mechanism, "incomplete" depositions result in deposits with cavities or depressions in the upper surfaces such as shown in Fig. 8. As illustrated by Fig. 8, the shape of the depressions depends on the substrate orientation. For example, holes etched into {111}-B substrates (Fig. 8c) tend to fill primarily from the walls inward with relatively little growth from the bottom upward. A similar phenomenon was observed by Gabor (8) with deposition of GaAs in channels etched into Ge crystals. Although the interiors of the cavities in Fig. 8a and 8b are rough and irregular, the partially formed upper surface facets are very smooth. This illustrates the phenomenon of obtaining smooth upper surfaces regardless of the irregularity of the original hole surfaces.

The selection of the slowest growing orientation as the substrate orientation allows close control of the amount of deposition. Holes etched to a given depth in accurately oriented {111}-B GaAs substrates fill rapidly until the slow-growing {111}-B surface facet is formed, whereupon the deposition rate drops considerably. Such a phenomenon allows one to fill holes of different depths during the same deposition and obtain surfaces which are nearly even with the substrate surface for each of the deposits.

Summary

It has been shown that excellent epitaxial deposits can be obtained in holes etched into GaAs substrates. The growth proceeds from the walls inward and from the bottom upward so as to form a cavity in incompletely filled holes. Depositions in holes etched into {100} substrates produced deposits whose upper surfaces were somewhat above the substrate surface. However these deposits were bounded on the sides by well-defined facets which tended to prevent extensive lateral overgrowth. Epitaxial deposition in accurately oriented {111}-B substrates yielded deposits with very flat {111}-B upper surfaces which were nearly level with the substrate surface. Prolonged depositions in {111}-B holes did not produce deposits with significant heights above the substrate surface; although some lateral overgrowth was observed.

Acknowledgments

The author wishes to express grateful appreciation to Mr. E. W. Mehal of this laboratory for his helpful discussions and encouragement, and to Mr. I. A. Sessions for his assistance in the experimental work.

This work was supported by the Air Force Avionics Laboratory, Research and Technology Division, Air

Force Systems Command, Wright-Patterson Air Force Base, Ohio, under Contract AF 33(615)-1275.

Manuscript received Feb. 21, 1966; revised manuscript received May 23, 1966.

Any discussion of this paper will appear in a Discussion Section to be published in the June 1967 JOURNAL.

REFERENCES

1. (a) B. D. Joyce and J. A. Baldrey, *Nature*, **195**, 485 (1962); (b) J. M. Hirshon, *This Journal*, **109**, 72C (1963); (c) R. Glang and E. S. Wajda, "Metallurgy of Semiconductor Materials," Vol. 15, pp. 27-47, John Wiley & Sons, New York (1962); (d) G. L. Schnable, W. J. Hillega, Jr., and C. G. Thornton, *This Journal*, **110**, 185C (1963).
2. F. W. Tausch, Jr. and A. G. Lapierre, III, *This Journal*, **112**, 707 (1965).
3. D. M. Jackson, *Trans. Metallurgical Soc. AIME*, **233**, 596 (1965).
4. R. E. Johnson, R. C. Sangster, and W. J. Beyen, Proc. of 4th Annual Microelectronics Symposium, May 24-26, 1965, St. Louis.
5. A. Reisman and R. Rohr, *This Journal*, **111**, 1425 (1964).
6. W. F. Finch and E. W. Mehal, *ibid.*, **111**, 814 (1964).
7. R. R. Fergusson and T. Gabor, *ibid*, **111**, 585 (1964).
8. T. Gabor, *ibid.*, **111**, 825 (1964).

High-Temperature Oxidation

III. Zirconium and Hafnium Diborides

Joan B. Berkowitz-Mattuck

Arthur D. Little, Inc., Cambridge, Massachusetts

ABSTRACT

The oxidation of zone melted specimens of ZrB_2 and HfB_2 was studied at temperatures of 1200°-2000°K and at oxygen partial pressures of 1-700 Torr in helium. Parabolic rate behavior was observed. For ZrB_2 above 1400°K an activation energy of 77 ± 5 kcal/mole was determined. Below 1400°K the activation energy is much lower, and the mechanism of oxidation is different, probably because of the presence of boron oxide in the condensed phase. Below 1300°K, the parabolic rate constant appears to be directly proportional to oxygen partial pressure; at 1830°K, the rate constant is independent of oxygen pressure. For HfB_2 in the range 1480°-1870°K an activation energy of 47 ± 4 kcal/mole was observed. Around 1970°K, the transition temperature for the monoclinic to tetragonal phase change in HfO_2, there is a sharp increase in the rate of oxidation. The parabolic rate constant for total oxygen consumption increases as the 0.4 ± 0.1 power of the oxygen partial pressure at 1630° and 1760°K.

The oxidation of ZrB_2 was studied by Brown in the temperature range 649°-1315°C in pure oxygen and moist dry air (1). Since Brown worked with porous compacts of the diboride, his initial surface areas are unknown, and undoubtedly changed due to sintering during the course of exposure at high temperatures. He was able to conclude qualitatively that ZrB_2 is oxidized more rapidly in oxygen than in dry air in the range 650°-1100°C, and much more rapidly in moist air than in dry at 650°C.

Samsonov (2) oxidized ZrB_2 in air at 1000°C and measured a depth of corrosion of 0.45 mm after 150 hr. For material of theoretical density, this would correspond to stoichiometric oxidation of 0.274 g/cm² of the alloy, or to a total oxygen consumption of 0.0873 g/cm². The net weight change cannot be computed since an unknown portion of the $B_2O_3(l)$ must certainly have evaporated during the experiment. From metallographic examination of the oxide scale, Samsonov postulated the existence of ZrO(s) immediately adjacent to the alloy and a molten layer of B_2O_3 at the surface of the oxidized specimen. He assumed that, with increasing time of exposure, oxygen would diffuse through the $B_2O_3(l)$ to the alloy and react with ZrO(s) to form $ZrO_2(s)$, while at the same time B_2O_3 would vaporize gradually.

More recently, the oxidation of ZrB_2 was studied by Kuriakose and Margrave (3), who measured net weight change of fully dense samples with time, at temperatures of 1218°-1529°K and oxygen pressures between 100 and 760 Torr. They were able to fit their data to a parabolic rate law, with an activation energy for net weight gain of 19.8 ± 1.0 kcal/mole. The oxidation rate was independent of carrier gas flow rate and directly proportional to the oxygen partial pressure in helium.

No quantitative data have been reported in the literature for the oxidation of HfB_2. Samsonov exposed HfB_2 in air in a series of screening experiments and reported intensive oxidation above 600°-700°C and disintegrative oxidation at 1000°-1200°C (4).

The present work was undertaken to obtain data on the oxidation of ZrB_2 over a wider temperature and pressure range than that covered in previous studies, and to compare the oxidation of ZrB_2 and HfB_2 experimentally. In addition, in order to evaluate the effect of B_2O_3 volatility on the oxidation of ZrB_2, several measurements of total oxygen consumption were made under conditions for which Kuriakose and Margrave (3) had obtained net weight change data.

Experimental Method and Data Analysis

Samples of ZrB_2 were synthesized by the zone melting technique described by Westrum and Feick (5). Hafnium diboride was prepared by the same technique with a high-purity powdered starting material supplied by Wah Chang Corporation. The resultant zone refined bars contained less than 0.1% of zirconium.

The procedure for the oxidation experiments has been described in detail in earlier publications (6, 7). The only essential change necessitated in the work with borides was the substitution of platinum or rhodium support rods for the Al_2O_3 or ThO_2 fingers used previously. The B_2O_3 formed in the oxidation of diborides reacts with refractory oxides. Platinum was suitable for sample temperatures up to 1600°C; rhodium was required for higher temperature runs.

Specimens in the form of pellets, 0.3 cm long and 0.7 cm in diameter, were polished through diamond dust, cleaned, and degassed in helium prior to oxidation. A thermal conductivity apparatus was used both to monitor degassing and to measure the net oxygen consumed during the oxidation of inductively heated samples in a stream of helium and oxygen at a total pressure of one atmosphere.

A degassing temperature of about 1870°K was employed, and heating was continued until the signal from the monitoring thermal conductivity bridge in-

dicated a cessation of permanent gas evolution (approximately 30 min). Net weight changes during the degassing period were always less than 2 x 10^{-4} g. Temperatures were read with a Micro-Optical pyrometer, and were corrected for sample emissivity (assumed equal to 0.6) and the measured transmission characteristics of the optical system. A spectral emissivity of 0.6 ± 0.1 was measured early in the program both in inert and oxidizing atmospheres by comparing observed temperatures of diboride surfaces with observed temperatures of a black body cavity drilled ultrasonically in the samples. Within experimental error the measured emissivity did not vary enough during oxidation to affect the necessary correction factor appreciably. The variation in measured temperature during an experiment is about ±5°C. A carrier gas flow rate of 95 cc/min was used in most experiments, corresponding to a linear flow velocity in the neighborhood of the sample pellet of about 3.1 cm/sec.

In the oxidation experiments, a helium-oxygen stream is passed through the reference cell of a thermal conductivity bridge and over an inductively heated sample pellet which removes some of the oxygen by reaction. The gas stream, depleted in oxygen, is passed through the sampling cell of the thermal conductivity bridge. The reference and sampling cells form two arms of a Wheatstone bridge, whose output is continuously recorded. The signal obtained is proportional to the difference in oxygen partial pressure or gas density in the two cells. Since the measurements are carried out in an open flow system, the total pressure is everywhere close to 1 atm. Thus, when an experiment is run in pure oxygen, a zero signal is obtained, in spite of the fact that oxygen is consumed.

The output from the bridge, S, in millivolts is proportional to the difference in oxygen density in g/cc ($\rho_1 - \rho_2$) in the reference and sampling cells, respectively.

$$S = k\,(\rho_1 - \rho_2) \qquad [1]$$

where k is a proportionality constant. Since oxygen is consumed, the flow rates in the two cells must be different. If v_1 (cc/min) is the flow rate through the reference cell and v_2 is the flow rate through the sampling cell, then the desired rate of oxygen consumption by the sample under investigation, dm/dt (g/cm²-min) is given by

$$dm/dt = (\rho_1 v_1 - \rho_2 v_2) \qquad [2]$$

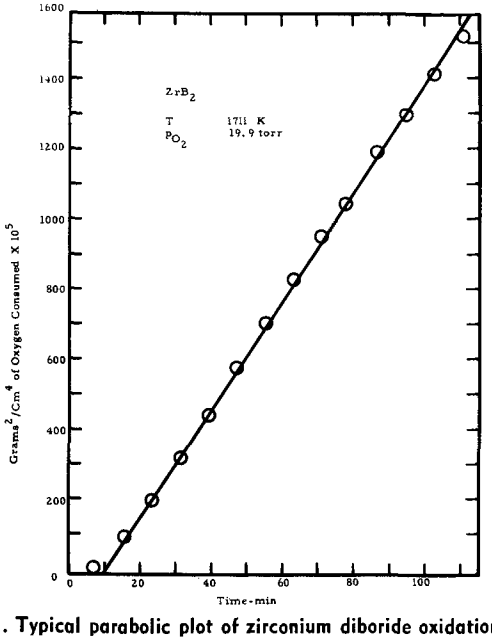

Fig. 1. Typical parabolic plot of zirconium diboride oxidation data

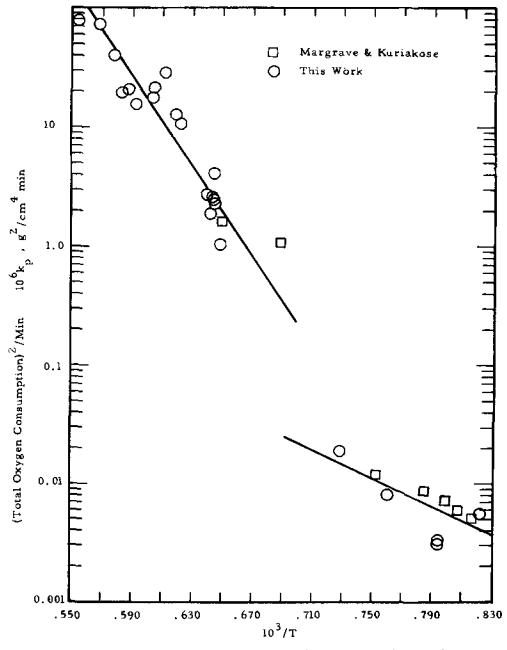

Fig. 2. Temperature dependence of the rate of total oxygen consumption for zirconium diboride-Arrhenius plot of parabolic rate constants, p_{O_2} = 37.5 Torr.

where m is total oxygen consumption in grams and t is time in minutes. The flow of helium must be constant throughout the system. Hence

$$\rho_{1,\mathrm{He}} v_1 = \rho_{2,\mathrm{He}} v_2 \qquad [3]$$

where $\rho_{1,\mathrm{He}}$ and $\rho_{2,\mathrm{He}}$ are the densities of helium in the reference and sampling cells, respectively. Solving [3] for v_2, and substituting in [2], one derives with the aid of [1] and the perfect gas laws an expression for the rate of oxygen consumption, dm/dt, in terms of measured quantities

$$dm/dt = v_1(S/k)/\{1 - p_1 + RT(S/k)/M\} \qquad [4]$$

where M is the molecular weight of oxygen, T is the temperature at which the flow rate v_1 is measured (298°K), R is the gas constant, and p_1 is the oxygen partial pressure in the initial gas stream in atmospheres. Since $\rho_2 \geq 0$, it follows that in [4] $RT(S/k)/M \leq p_1$. Therefore, if p_1 is a small fraction of an atmosphere, the rate of oxygen consumption, dm/dt, is directly proportional to the observed signal, apart from the previously discussed (6) effects introduced by the separation of reaction and detection sites. At high oxygen partial pressures, Eq. [4] must be used to interpret the results. In practice, the denominator in [4] is very nearly constant throughout any given experiment.

Results

Zirconium diboride.—The oxidation of zirconium diboride was studied in the temperature range 1200°-1820°K at oxygen partial pressures of 8-700 Torr. Parabolic rate behavior for total oxygen consumption was observed after an initial period of 10-30 min. The total oxygen consumed, m, represents the amount of oxygen in all of the product oxides, volatile or nonvolatile, formed during the oxidation experiment. A typical parabolic plot of m^2 *vs.* t, constructed from the corrected area under the experimental thermal conductivity curve according to Eq. [4] is shown in Fig. 1. The temperature dependence of the parabolic rate constants for total oxygen consumption is shown on a log k_p *vs.* $1/T$ plot in Fig. 2. Results were independent of carrier gas flow rate in the range 59-119 cc/min. Above 1400°K an activation energy of 77 ± 5 kcal/mole was calculated for the over-all oxidation process by the method of least squares. Below 1400°K, the activation

energy is clearly much less and will be discussed below in conjunction with the work of Kuriakose and Margrave (3).

The wide scatter of points about the least squares straight line in the high-temperature range is due to the high absolute value of the activation energy and to the presence of cracks in the as-prepared samples. Since the activation energy is high small errors in temperature measurement or small fluctuations in temperature during a run will result in large uncertainties in measured oxidation rates. For example, at 1500°K, an error or fluctuation of 10° in experimental temperature will be reflected in more than a 15% error in k_p. The presence of cracks, introduced in the zone-refining process, results in a difference between real and geometric surface areas. It will be shown below that the surface of a crack that extends into the bulk specimen is oxidized just as if it were external surface. Since the number of cracks is certainly not constant from one sample to another, the area used in computing k_p should really be the sum of gross geometric surface area and surface areas of cracks. The use of the former alone can introduce the observed scatter in the data.

The pressure dependence of oxidation rate was investigated briefly. The data suggest that rates increase linearly with pressure in the low-temperature range investigated, but become independent of pressure at higher temperatures. Kuriakose and Margrave (3) established that the rate of oxidation is linear at 1329°K over the oxygen pressure range 100-760 Torr. In reasonable agreement, we found an increase in parabolic rate constant of a factor of 13 (from 5.8 x 10^{-9} to 75.7 x 10^{-9} g^2/cm^4-min) with a pressure increase of a factor of 18 (from 37.5 to 694 Torr). On the other hand, we detected no change in oxidation rate with pressure at 1560°K over the range 8-40 Torr and at 1830°K over the range 20-700 Torr.

The data on both temperature and pressure dependence indicate that there is a fundamental difference in the mechanism of oxidation of ZrB_2 at low and high temperatures. Below 1330°K, oxidation proceeds with an activation energy of about 20 kcal/mole and seems to depend strongly on oxygen pressure. Above 1550°K, the activation energy is greater than 70 kcal/mole, and the rates become much less dependent on oxygen pressure.

Several samples were mounted and polished for metallographic examination of the oxide films. A typical specimen, oxidized for 114 min at a temperature of 1805°K and an oxygen partial pressure of 19.9 Torr, is shown in Fig. 3. The oxide in every photomicrograph shows considerable porosity, but we do not know whether it developed during oxidation at the high temperature, during cooling, or during polishing. Since ZrO_2 undergoes a phase transition with a change in density on cooling from 1805°K to room temperature, the physical properties of the oxide layer may be quite different during oxidation and after quenching. Hence, the microstructural observations must be interpreted with some caution. Figure 3a taken at a magnification of about 90X, shows clearly both the grain structure of the bulk material and the dense columnar oxide which forms on the surface during oxidation. Figure 3b is similar, but shows a region with an extensive crack running parallel to the ZrB_2 surface. Figure 3c at a magnification of about 450X focusses on the oxide within such a crack. The product is very similar to that on the surface of the refractory and appears to grow into the bulk material at certain preferred growth sites. Figures 3d, e, f, and g show the surface oxide once more at higher magnifications than Fig. 3a. The oxide is seen to be crystalline in nature, with the grains running for the most part perpendicular to the ZrB_2 surface. The oxide-metal interface is clearly not smooth, but the points of maximum growth rate do not seem to be related in an obvious way to the structure of the substrate. The interesting

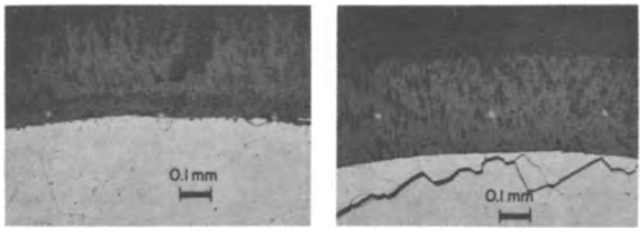

Fig. 3. Photomicrographs of oxidized ZrB_2. a (left) 90X; b (right) 90X before reduction for publication.

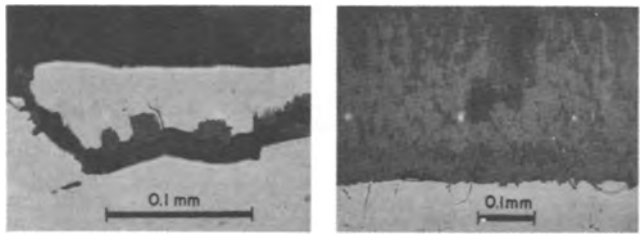

Fig. 3. Photomicrographs of oxidized ZrB_2. c (left) 450X; d (right) 170X before reduction for publication.

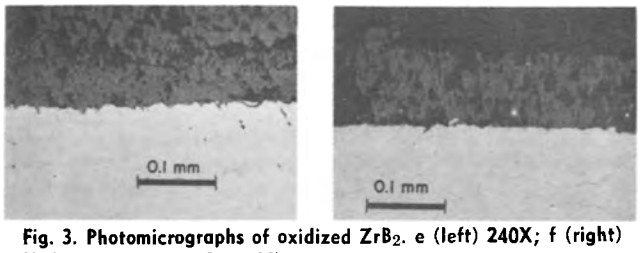

Fig. 3. Photomicrographs of oxidized ZrB_2. e (left) 240X; f (right) 240X before reduction for publication.

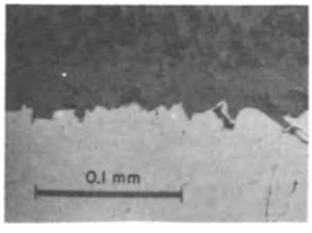

Fig. 3g: Photomicrograph of oxidized ZrB_2. 450X before reduction for publication.

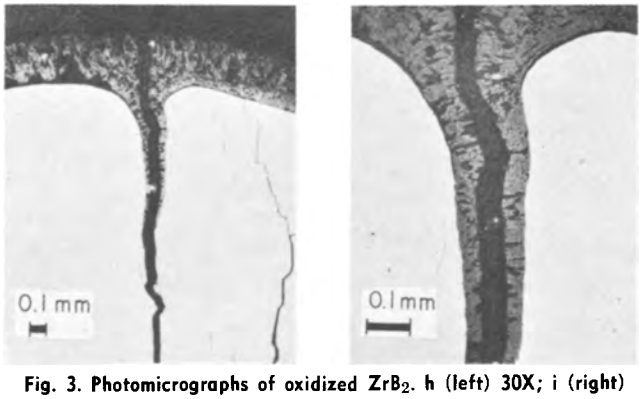

Fig. 3. Photomicrographs of oxidized ZrB_2. h (left) 30X; i (right) 90X before reduction for publication.

photomicrograph in Fig. 3h at a magnification of 30X (and the same area at 90X magnification in Fig. 3i) shows the oxidation behavior of ZrB_2 in the neighborhood of a crack that intersects the surface. The surface of the crack as seen in these pictures is almost certainly the surface of the original alloy. Therefore, the oxide must grow by inward diffusion of oxygen. The columns of oxide are seen to run perpendicular to the outer surface of ZrB_2, and in like manner, are seen to run perpendicular to the surface of the crack (parallel to the sample surface). A crack then effec-

tively increases the surface area of the alloy above that of the outer or geometric surface area.

X-ray analysis of the oxidized surfaces of all of the ZrB_2 samples showed lines for monoclinic ZrO_2, and no extraneous lines. Analysis was of course performed at room temperature on quenched samples and therefore does not necessarily reflect accurately the structure of the high-temperature oxide. Evidence was not found in either the photomicrographs or in x-ray for the existence of a lower oxide adjacent to the alloy substrate.

Gross oxidation behavior is typically monitored by net weight change or total oxygen consumption. In order to compare results obtained by the two methods, it is necessary to take into account any volatile oxides that may be formed. The oxidation of ZrB_2 is expected to yield the oxides ZrO_2 and B_2O_3. The latter has an appreciable vapor pressure, ranging from 2.3×10^{-6} atm at 1400°K to 5.4×10^{-2} atm at 2000°K (8). Thus the total oxygen consumption measurements reported above represent the sum of the amounts of oxygen in each of the product oxides. The net weight change measurements of Kuriakose and Margrave (3) represent the sum of a weight gain due to formation of condensed oxides and a weight loss due to vaporization of boron as $B_2O_3(g)$. The importance of oxide volatility in the over-all oxidation process must therefore be evaluated.

If it is assumed that the composition of the boride is not changed during oxidation, then the oxidation reaction may be considered in terms of two nonelementary steps as follows

$$ZrB_2(c) + (5/2)\ O_2(g) \rightarrow ZrO_2(c) + B_2O_3(l) \quad [5]$$

$$B_2O_3(l) \rightarrow B_2O_3(g) \quad [6]$$

The measured oxygen consumption, m, up to some time t, may be written as

$$m = \frac{2[O]}{[ZrO_2]} \cdot w_{ZrO_2(c)} + \frac{3[O]}{[B_2O_3]} \cdot w_{B_2O_3(l)} \quad [7]$$

where w_X is the number of grams of product X formed per unit boride surface area up to time t, and the symbols in brackets are molecular weights. Since the oxidation is supposed to be nonpreferential, the number of moles of $ZrO_2(c)$ formed must be equal to the number of moles of $B_2O_3(l)$ formed in the same time period. The measured oxygen consumption m and the net weight change w_{net} differ by the amount of B_2O_3 vaporized

$$w_{net} = m - w_{B_2O_3(g)} \quad [8]$$

If the amount of B_2O_3 that vaporizes is negligible, then

$$w_{net} = m \quad [9]$$

If B_2O_3 vaporizes as rapidly as it forms, then $w_{B_2O_3(g)} = w_{B_2O_3(l)}$, and

$$w_{net} = \left\{\frac{2}{5} - \frac{2[B]}{5[O]}\right\} m \quad [10]$$

The equilibrium rate of vaporization of B_2O_3 in vacuum is known. At a total pressure of 1 atm, the rate of vaporization is expected to be a factor of 10 to 1000 times less than the equilibrium rate (9). For the purposes of this discussion, it will be assumed that during the oxidation of ZrB_2, B_2O_3 vaporizes linearly at one one-hundredth of the equilibrium rate G as long as liquid B_2O_3 is present. If the rate of formation of $B_2O_3(l)$ is smaller than $0.01G$, the liquid will vaporize as rapidly as it forms.

Since the measured oxygen consumption was found to follow a parabolic rate law, it follows from [7] and from the assumption of stoichiometric oxidation that the condensed oxides $ZrO_2(c)$ and $B_2O_3(l)$ must also grow parabolically. Hence, at any temperature, there will be some time t_o after which the rate of vaporization of $B_2O_3(g)$ will exactly balance the rate of formation of $B_2O_3(l)$. At t_o

$$\frac{dw_{B_2O_3(g)}}{dt} = \frac{dw_{B_2O_3(l)}}{dt} \quad [11]$$

On the basis of the preceding discussion

$$\frac{dw_{B_2O_3(g)}}{dt} = 0.01G \quad [12]$$

$$\frac{dm}{dt} = \frac{k_p}{2m} \quad [13]$$

and hence

$$\frac{dw_{B_2O_3(l)}}{dt} = \frac{(k_p)^{1/2}[B_2O_3]}{(2)t^{1/2}(5)[O]} \quad [14]$$

where k_p is the parabolic rate constant for measured oxygen consumption. Equating [12] and [13], one can solve for the time t_o

$$t_o = \frac{0.19 \times 10^4 k_p}{G^2} \quad [15]$$

where k_p values can be taken from Fig. 2 and G values from the literature.

At 1330°K, t_o = 570 min, and the loss of $B_2O_3(g)$ over the 2-hr period of the present oxidation experiments is negligible. Therefore, to an excellent approximation, at all temperatures below 1330°K, weight gain and total oxygen consumption should be identical. At 1440°K and above, $t_o \leq 5$ min. Hence above 1440°K B_2O_3 should vaporize as rapidly as it forms, and the relationship between weight gain and total oxygen consumption should be given by Eq. [10]. Although we did not do chemical analysis on the oxides formed on the diboride surfaces, it may be noted that a dark gray glazed surface appeared below 1400°K, while a white crystalline oxide was formed at higher temperatures.

For purposes of comparison in Fig. 2, the weight change data of Margrave and Kuriakose (3) obtained at an oxygen pressure of 1 atm were converted to total oxygen consumption values at an oxygen pressure of 37.5 Torr by means of Eq. [9] below 1330°K and Eq. [10] above 1440°K, with the assumption of linear pressure dependence. On this basis, agreement between the two laboratories is good.

From thermodynamic considerations, one might also expect $BO_2(g)$ to be a significant volatile species formed on high-temperature oxidation. However, the relative amounts of $B_2O_3(g)$ and $BO_2(g)$ produced in the oxidation experiment would depend on kinetic factors and would have to be determined by independent measurement. Nonetheless, under our experimental conditions, any $BO_2(g)$ formed at the oxidizing surface would condense on the cool walls of the reaction chamber to $B_2O_3(c)$ with release of oxygen. Therefore, our measured oxygen consumption values would correspond to the stoichiometry of reactions [5] and [6].

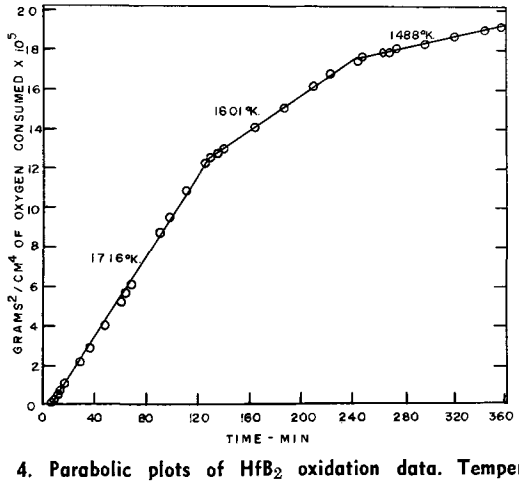

Fig. 4. Parabolic plots of HfB_2 oxidation data. Temperature 1720°, 1600°, and 1490°K, p_{O_2} = 19.9 Torr.

Hafnium diboride.—The oxidation of HfB_2 was studied at temperatures of 1480°-2000°K and oxygen partial pressures of 1-700 Torr. For all of the conditions investigated, the data could be fitted to a parabolic rate equation. Results of several experiments in which the temperature was varied during the run, are plotted parabolically in Fig. 4, 5, and 6, respectively.

The parabolic rate constants for total oxygen consumption are plotted in the form log k_p *vs.* $1/T$ in Fig. 7 at an oxygen pressure of 37.5 Torr. The activation energy for total oxygen consumption is 47 ± 4 kcal/mole in the range 1480°-1870°K. Around 1970°K, the transition temperature for the monoclinic to tetragonal phase change in HfO_2, there is a remarkably abrupt increase in the rate of oxidation. Following the analysis presented earlier for ZrB_2 it is found that at temperatures above 1488°K, the lowest temperature investigated, the rate of vaporization of B_2O_3 should be equal to its rate of formation, and HfO_2(c) should be the only condensed oxide on the surface of HfB_2. Therefore, the change in slope of the Arrhenius curve is not due to a change in the relative rates of formation of B_2O_3(l) and B_2O_3(g) as it might be in the ZrB_2 case, and it can be correlated directly with a phase change in the metal oxide. Measurements above the oxide transition temperature cover too small a range for a reliable numerical estimate of activation energy.

The data taken at 1630° and 1760°K for oxygen partial pressures between 1.4 and 694 Torr are plotted as a function of oxygen partial pressure on a log-log plot in Fig. 8. A least squares analysis of the data yields a pressure coefficient for total oxygen consumption of 0.4 ± 0.1, *i.e.*

$$k_p \propto p^{0.4\pm0.1}$$

Several samples were mounted and polished for metallographic examination after oxidation. Oxide was polished off one circular face revealing the alloy beneath and leaving the oxide at the outer rim. A photomicrograph of a pellet that had been oxidized for 2 hr at 1760°K and 26.8 Torr is shown in Fig. 9. The structure of the oxide is quite different from that shown in Fig. 3 on zirconium diboride. Two layers are clearly visible, a thin outer region and a thicker inner one. The patches of oxide at the left, apparently unconnected with the oxide at the outer rim, are probably areas of the surface which were oxidized more rapidly than the bulk alloy, and hence were not polished away during preparation of the sample. The oxidation rate may be a function of the crystalline orientation of the diboride. The crack in the right-hand quarter of the figure may be filled with oxide, suggesting that the oxide grows in part by outward diffusion of hafnium.

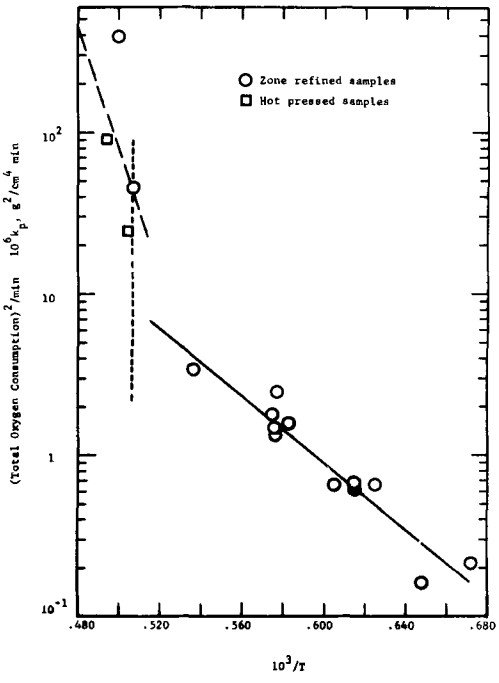

Fig. 7. Temperature dependence of the rate of total oxygen consumption for hafnium diboride-Arrhenius plot of parabolic rate constants.

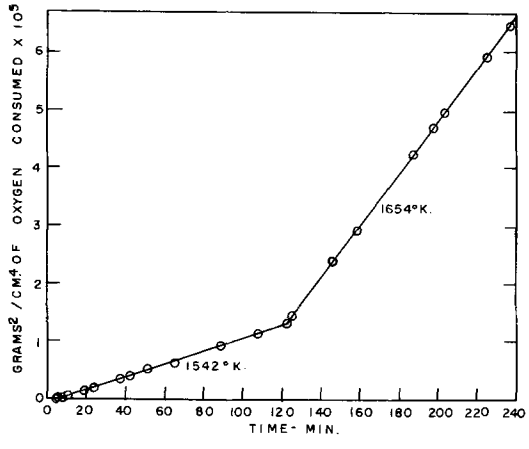

Fig. 5. Parabolic plots of HfB_2 oxidation data. Temperature 1650° and 1542°K, p_{O_2} = 19.9 Torr.

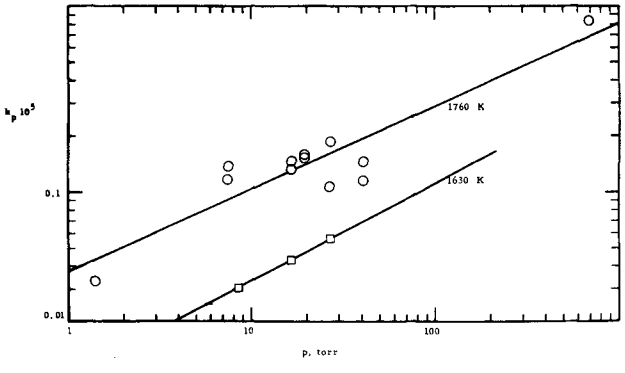

Fig. 8. Pressure dependence of the oxidation of hafnium diboride at 1760° and 1630°K.

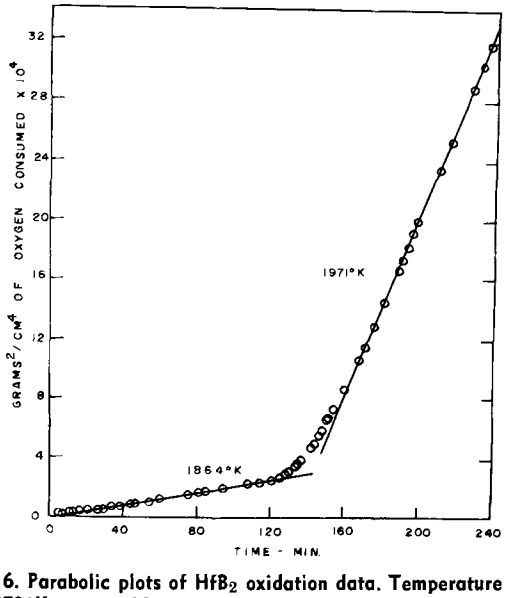

Fig. 6. Parabolic plots of HfB_2 oxidation data. Temperature 1860° and 1970°K, p_{O_2} = 18.5 Torr.

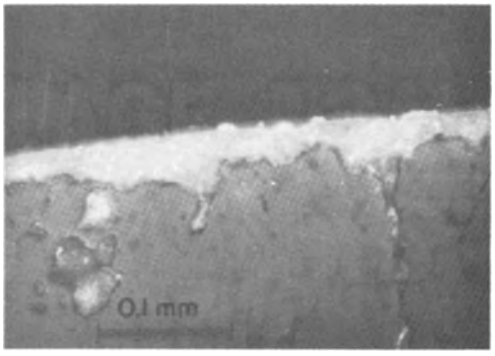

Fig. 9. Photomicrograph of oxidized hafnium diboride. Temperature 1760°K, p_{O_2} = 26.8 Torr.

Photomicrographs of the surface of a pellet that had been oxidized for 2 hr at 1864°K and for 2 hr at 1971°K at an oxygen partial pressure of 18.5 Torr are shown in Fig. 10. The thicker outer layer of oxide was probably formed at the higher temperature, the narrower inner layer at the lower, again suggesting motion of hafnium. In Fig. 11 a photomicrograph of a pellet that had been oxidized for 2 hr at 1654°K and for two hr at 1542°K at an oxygen pressure of 19.9 Torr is shown. The oxide is very similar to that shown in Fig. 9. A layered structure due to the change in temperature in the middle of the run could not be positively identified.

Discussion

In order to compare the zirconium diboride and hafnium diboride results in the 1400°-1900°K range, the parabolic rate constants for oxygen consumption were converted to an alloy consumption basis on the assumption of nonpreferential oxidation of the alloys to $B_2O_3(g)$ and metal dioxide. Results are compared in an Arrhenius plot in Fig. 12. In this temperature range, the parabolic rate constants for oxidation of HfB_2 are almost an order of magnitude less than the corresponding constants for ZrB_2. In Fig. 2 and 7 it is seen that the rate of oxidation of zirconium diboride increases sharply near 1400°K, while the rate of oxidation of hafnium diboride shows a similar increase around 1970°K. In the case of hafnium diboride, the jump in oxidation rate is clearly due to the monoclinic to tetragonal transition in the oxide. In the case of zirconium diboride, the phase transition in ZrO_2 does occur around 1400°K, but the increase in oxidation rate might also be due to the fact that $B_2O_3(l)$ is present on the surface of the alloy in the low-temperature range, but vaporized as rapidly as it is

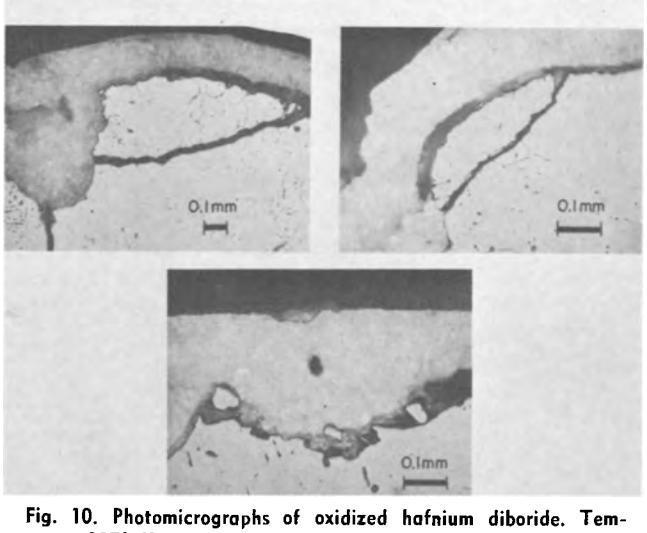

Fig. 10. Photomicrographs of oxidized hafnium diboride. Temperature 1970°K, p_{O_2} = 18.5 Torr. Top left, 65X; top right, 130X; center, 130X all before reduction for publication.

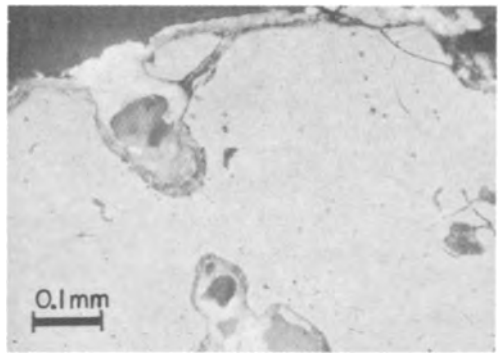

Fig. 11. Photomicrograph of oxidized hafnium diboride. Temperature 1650° and 1540°K, p_{O_2} = 19.9 Torr.

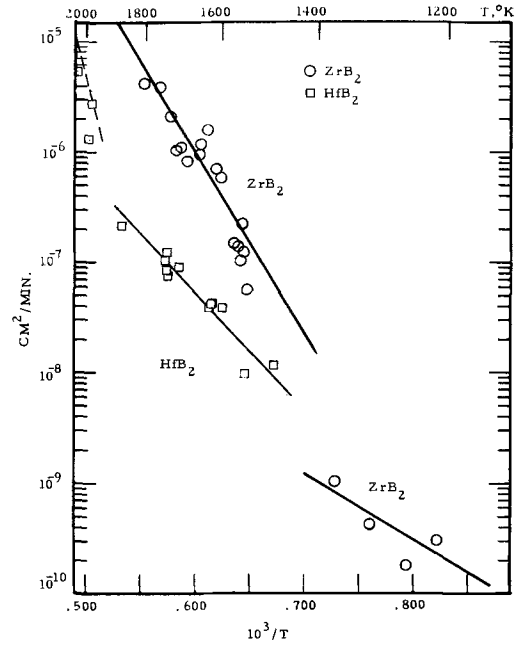

Fig. 12. Comparison of parabolic rate constants for oxidation of hafnium diboride and zirconium diboride as a function of temperature.

formed at higher temperatures. In any case, for both ZrB_2 and HfB_2 the monoclinic oxide appears to impart greater oxidation resistance than the tetragonal modification.

It has been suggested that the vaporization of $B_2O_3(g)$ during the oxidation of ZrB_2 and HfB_2 might influence the microstructure of the $ZrO_2(c)$ or $HfO_2(c)$, presumably formed simultaneously. If $B_2O_3(g)$ were produced at the boride/dioxide interface, it would be expected to cause rupture and/or porosity in the dioxide film and hence result in an enhanced net rate of oxidation. If on the other hand, the rate of diffusion of boron through the dioxide film were much more rapid than the rate of oxidation, gaseous $B_2O_3(g)$ would be formed at the dioxide/ambient interface, and the structure of the dioxide would be little affected. In the latter case, boron would have to be present in the dioxide film and should be detectable by appropriate techniques.

Although the experimental data for both zirconium diboride and hafnium were fitted to a parabolic rate equation, the mechanism of oxidation is not clear. ZrO_2 and HfO_2 are normally considered to be anion deficit semiconductors, and one might expect the oxidation of HfB_2 and ZrB_2 to be controlled by diffusion of oxygen ions via vacancies in the respective metal oxides. If this mechanism were valid, however, the activation energy for diffusion should be equal to the activation energy for oxidation, and the rate of oxi-

dation should be independent of oxygen partial pressure (10). The linear pressure dependence for oxidation of ZrB_2 found by Margrave and Kuriakose at 1329°K over the range 100-760 Torr and confirmed by us at 1200°K precludes a simple diffusion mechanism via anion vacancies in this temperature range. Above the phase transition temperature for ZrO_2, diffusion data is not available. However, the activation energy of 77 ± 5 kcal/mole found for oxidation is not an unreasonable energy for diffusion if one estimates the activation energy as the sum of the energy for formation of a vacancy plus that for motion of a vacancy (11). Furthermore, at 1830°K the parabolic rate constant for total oxygen consumption was found to be independent of oxygen pressure. Alternatively, one of the referees, in reviewing the manuscript, pointed out that the activation energy for oxidation corresponds very closely to the energy of formation of $BO_2(g)$ from $B_2O_3(l)$ and $O_2(g)$. The significance of gaseous $BO_2(g)$ in the oxidation of the borides obviously warrants additional experimental study.

The oxidation of HfB_2 to monoclinic $HfO_2(c)$ and gaseous $B_2O_3(g)$ was found to depend on the 0.4 ± 0.1 power of the oxygen pressure, which again is too high to be consistent with a diffusion mechanism via oxygen anion vacancies. In fact, the oxidation behavior in the neighborhood of a crack and the layered structure observed when the temperature was raised or lowered in the middle of a run suggested that hafnium is the major diffusing species during the oxidation of HfB_2.

Acknowledgment

The hot pressed samples of HfB_2 identified in Fig. 7 were supplied by ManLabs and were investigated under subcontract to AF 33(657)-8635. Able laboratory assistance in obtaining the oxidation measurements was given by Richard F. Quigley.

This research was supported by the United States Air Force under Contract No. AF 33(616)-6154, monitored by the Air Force Materials Laboratory, Research and Technology Division, Wright-Patterson Air Force Base, Ohio.

Manuscript received July 8, 1965; revised manuscript received May 16, 1966.

Any discussion of this paper will appear in a Discussion Section to be published in the June 1967 JOURNAL.

REFERENCES

1. F. H. Brown, Jr., Progress Report No. 20-252, Jet Propulsion Laboratory, California, Feb. 25, 1955.
2. G. A. Meyerson, G. V. Samsonov, R. B. Kotelnikov, M. S. Voyonova, I. P. Yerterjera, and S. D. Krasnenkova, *Akad. Nauk. SSSR Zh. Neorgancheskoy Khimii*, from *Konferenskiya Po Khimii Bora I Yego Soyedineii*, **1955**, 577 (1960).
3. A. K. Kuriakose and J. L. Margrave in L. A. McClaine *Thermodynamic and Kinetic Studies for a Refractory Materials Program*, ASD-TDR-62-204, Part II, Contract No. AF 33(616)-7472, May 1963, p. 98, published *J. Electrochem. Soc.* **111**, 827 (1964).
4. Ym. B. Paderno, T. I. Serebryakova, and G. V. Samsonov, *Tsvetnye Metally*, **11**, 48 (1959); D. S. I. Trans. No. 614.
5. E. F. Westrum, Jr. and G. Feick, *J. Chem. Eng. Data*, **8**, 193 (1963).
6. J. B. Berkowitz-Mattuck, *This Journal*, **111**, 908 (1964).
7. J. Berkowitz-Mattuck, Kinetics of Oxidation of Refractory Metals and Alloys at 1000°-2000°C, ASD-TDR-62-203, Part II, Contract No. AF 33(616)-6154, March 1963.
8. JANAF Tables of Thermodynamic Data, Dow Chemical Co., Midland, Mich.
9. Paul Blackburn, Oxidation of Tungsten and Tungsten Base Alloys, WADD-TR-59-575, Part II (1960).
10. O. Kubaschewski and B. E. Hopkins, "Oxidation of Metals and Alloys," Academic Press, New York, N. Y. (1963).
11. L. A. McClaine, Private communication.

Deposition of Silica Films by the Glow Discharge Technique

D. R. Secrist[1] and J. D. Mackenzie

Rensselaer Polytechnic Institute, Troy, New York

ABSTRACT

Noncrystalline SiO_2 films were deposited on various substrates at low temperatures and pressures by decomposing tetraethoxysilane by oxygen species from an R. F. induced oxygen plasma. The rate of deposition was controlled by physical adsorption; the apparent heats of adsorption of silica on NaCl, Pt, fused SiO_2, Al, and Al_2O_3 were determined. A mechanism for formation is presented. The decomposition of the tetraethoxysilane obeyed a first order rate law. The specific rate constant was calculated at 310°C and 250μ pressure.

Studies and utilization of thin films, both metallic and nonmetallic, have experienced considerable growth in the last decade. Silica films, in particular, have enjoyed a multitude of applications. For instance, masks for semiconductor devices or dielectric capacitors for miniaturized solid-state circuits are conveniently formed with glassy silica. Silica films can be formed by many techniques (1), most of which necessitate relatively high temperatures. The "glow discharge" method to be described facilitates the deposition of glassy silica films from the vapor phase at low temperatures and pressures by the decomposition of tetraethoxysilane with energized oxygen species from the discharge. Alt *et al.* (2) and Ing and Davern (3), for example, have prepared amorphous silicon oxide films of unknown stoichiometry in one form of the glow discharge technique. We have modified this technique by the use of a microwave glow-discharge. The effects of temperature, pressure, metal-organic flow (evaporation) rate, and nature of the substrate on the rate of film growth are reported in this paper.

[1] Present address: International Business Machines Corporation, Poughkeepsie, New York.

Experimental

Materials.—Tetraethoxysilane $(C_2H_5O)_4Si$, and tetraethysilane, $(C_2H_5)_4Si$, were obtained from Metallomer Laboratories, Maynard, Massachusetts, and were of >98% purity.

Apparatus.—The glow discharge apparatus consisted basically of a modified bell jar which could be maintained at low pressures under sustained gas flow. A schematic drawing of the flow system is illustrated in Fig. 1. Molecular oxygen was admitted to the system through a 0.003-in. precision bore capillary which was positioned between the legs of a mercury manometer. With a pressure differential of 770 mm, the in-

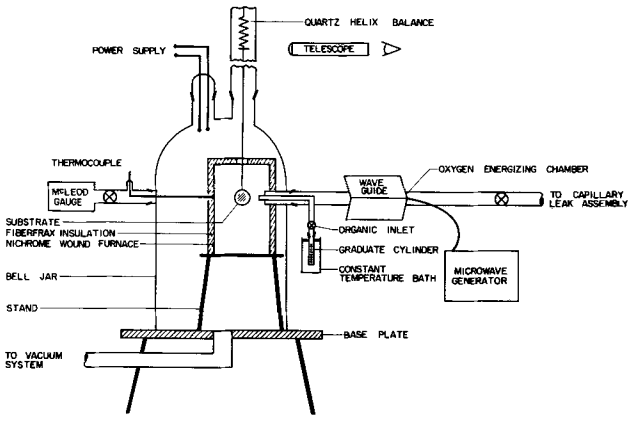

Fig. 1. Schematic drawing of glow discharge apparatus

coming gas flow rate was experimentally determined to be 1.76 ± 0.05 cm³/min at 25°C. A Pyrex tube, 2.54 cm in diameter, served as the glow discharge chamber. The electrodeless discharge was produced with a Raytheon PGM-10 Microwave Generator. This unit could supply 100w of microwave energy at a fixed frequency of 2,450 Mcps. The R.F. energy, as generated by a magnetron, was transferred by a coaxial cable to the antenna (labelled wave guide in Fig. 1) for dissipation.

The predominant excited product from a low-energy and low-pressure oxygen discharge has been identified as atomic oxygen in the ground state (4, 5). The atomic oxygen and other energized species thus formed were allowed to flow into the bell jar through a 0.5-in. diameter Pyrex tube. By the use of a nitrogen dioxide-titration technique (4), it was estimated that about 10% of the flowing molecular oxygen entered the bell jar as atomic oxygen. Tetraethoxysilane (as contained in a graduate cylinder immersed in a constant temperature bath) was introduced into the bell jar through a 5 mm diameter Pyrex tube under its own vapor pressure. The metal-organic evaporation rate (flow rate) at any particular bath temperature could be altered by adjusting a 1 mm bore Teflon stopcock, which served as the inlet valve into the bell jar. A constant temperature bath could be maintained inside an insulated two liter Dewar flask for long periods.

Initial experiments indicated that when the substrate was maintained at temperatures below 180°C, water was present in the films (6). Two nichrome-wound furnaces were therefore designed to "contain" the gas reaction. The majority of the studies were performed inside an aluminum furnace 2¼ in. in diameter and 4 in. long. A fused silica cylinder 1⅜ in. in diameter and 2½ in. long was used as the second furnace core. In each case, the top of the furnace was covered with a transite lid. The constant temperature zone for these furnaces extended 1 cm above and below the gas inlet port with a maximum radial temperature variation of ±5°C for points 1 cm from the cylinder axes. The substrate temperature was measured under deposition conditions with a calibrated chromel-alumel thermocouple. The corresponding furnace wall temperature was noted and used in subsequent experiments for temperature control.

The ultimate vacuum achieved in the glow discharge system was 240μ with an oxygen flow rate of 1.76 cm³/min. Periodic pressure measurements were made with a Stokes McLeod gauge and did not include the partial pressures of condensable gases such as water. Two liquid nitrogen cold traps were placed in the line leading to the vacuum pump to remove objectionable materials from the system. A thermocouple vacuum gauge was employed to monitor the exhaust pressure on a continuous basis.

Film deposition.—Depending on the nature of a particular experiment, the substrate on which a film was to be deposited was suspended from either a quartz helix balance or the furnace roof. Preliminary infrared transmission studies were conducted for the purpose of identifying the film deposited; wafers of NaCl and KBr were used as substrates. The substrates employed in the kinetic studies were hung from the fused silica balance and were limited in weight by the load capacity of the balance, which was 20 mg. For this work, the desirable weight of a specimen was arbitrarily set at 10 ± 1 mg. The fused silica substrates were of irregular shape and approximately 0.75 cm in diameter. Aluminum and platinum foils were available in the form of 1 cm diameter pans. To examine the effects of Al_2O_3 on the deposition rate, an alumina (Lucalox) substrate was prepared by grinding a wafer of the material to a thickness of 0.002 in. A sodium chloride disk 1 cm in diameter was formed by the compaction of NaCl powder in a die at 12,000 psi pressure.

With the exception of the sodium chloride substrate, the general cleaning procedure adopted consisted of the rapid dipping of the specimens into a 48% solution of hydrofluoric acid, followed by rinsing with distilled water. All substrates were positioned in the reaction vessel in the same manner, with their wide dimension perpendicular to the gas inlet tube. (The thin dimension is perpendicular to the inlet tube in Fig. 1.) Approximately 1 hr was required for the furnace to attain thermal equilibrium. During the period when the furnace temperature was increasing, the system was purged with tank purity oxygen gas supplied by the Linde Company (assay 99.7% oxygen). The average dew point of the gas was determined to be −56°F (0.071 mg water/liter) and was relatively constant from cylinder to cylinder. When the furnace had reached thermal equilibrium, the glow discharge was initiated with a Tesla coil and the substrate was bombarded with atomic and other excited oxygen species for 10-15 min as an additional cleaning procedure. In this work, the microwave generator was operated at 90% of its rated power output. On opening the metal-organic inlet valve, approximately 5 min were required for the system to return to thermal equilibrium. The temperature variation thereafter was limited to ±2°C. The total pressure of the glow discharge system (excluding condensable gases) increased by about 10% and was reproducible for specific organic evaporation rates.

The fused silica balance used in this study had a sensitivity of 1 cm/mg (Microchemical Specialties Company, Berkeley, California). A weight of 1 mg caused an extension of 10.1 mm from zero, and 98.6 mm after an appropriate load of 10 mg (approximate substrate weight). A typical weight gain experiment would extend the helix by 1-2 mm. Over this limited working range, the helix extension per unit weight gain was linear. A Bausch and Lomb optical reader was employed to determine the cumulative weight of the film deposited. The telescope combined a 5 mm diameter objective field with a filar micrometer eyepiece containing a cross-line divisible to 5000 parts. The minimum extension detectable with this arrangement was 0.005 mm, which corresponded to a weight gain of approximately 0.5 μg (or a 15Å layer of SiO_2 on a 1 cm diameter pan). Measurements were made every 5 or 10 min for the duration of the deposition period, which generally lasted from 1½ to 2 hr. The incoming gas flow rate was slow enough so that the substrate was stable in the position perpendicular to the flow inlet tube. The damping period of the helix was practically instantaneous; no oscillation was observed under equilibrium conditions. At the end of an experiment, the volume of the metal-organic evaporated was measured to ±0.025 cm³.

Table I. Gas analyses

Per cent	Gas Outlet Sample	Furnace Sample
O_2	12	7
CO_2	30	23
CO	38	52
H_2	20	18
H_2O	80μ/250μ*	Trace
$(C_2H_5O)_4Si$	Trace	Trace
CH_4	Trace	—
Alcohols	—	—

* Total gas sample pressure = 250μ; partial pressure of water = 80μ; partial pressure of noncondensable gases = 170μ.
$(C_2H_5O)_4Si$, density = 0.9356 g/cm^3 at 20°C; evaporation rate = 0.12 cm^3/hr at 25°C; oxygen flow rate = 1.76 cm^3/min at 25°C and 770 mm Hg; furnace temperature = 310°C.

Results and Discussion

Gas analysis.—A quantitative analysis of the gaseous reaction products was made by mass spectrometry. Results are shown in Table I. The decomposition is seen to produce extensive amounts of water. With a metal-organic evaporation rate of 0.12 cm^3/hr, the partial pressure of water for a gas sample collected from the outlet system was about 30% of the total pressure. The water produced in this manner could be chemically incorporated into the oxide films when the substrates were held below a certain temperature, which depended on the metal-organic flow rate (6). For example, with a $(C_2H_5O)_4Si$ evaporation rate of 0.015 cm^3/hr, silicic acid was observed to form below 180°C, as determined by infrared transmission studies. The acid exhibited a characteristic absorption band at approximately 11μ. In addition, the major Si-O absorption mode was modified by a "shoulder" at approximately 8.5μ. When the evaporation rate was increased to 0.15 cm^3/hr, the presence of acid was observed at temperatures as high as 290°C.

Film evaluation.—The refractive indices of the silica films were measured as 1.458 ± 0.002, by the "Becke Line" method. Specimens were obtained from the substrate and/or gas inlet tube. The index of refraction for high-purity silica glass (supplied by the General Electric Company) was measured as 1.458 ± 0.002, in good agreement with the film values. The films were isotropic when observed with polarized light and were amorphous by x-ray diffraction. A comparison of the infrared absorption spectrum of a silica film deposited on a NaCl substrate with that of fused silica glass is shown in Fig. 2. The infrared band at 1080 cm^{-1} has been identified as a definite Si-O-Si bond stretching vibration. The band at 800 cm^{-1} is not well understood, but has often been associated with the occurrence of ring groups in the glassy structure. The major Si-O stretching mode for the film has shifted to a somewhat lower frequency. A similar shift of the same absorption band has been reported for samples of silica glass which were highly stressed and densified by either the application of very high pressures or by neutron irradiation (7, 8). Pliskin and Lehman (9) have shown that porosity in the films and bond strain can affect the spectrum in the same manner. It is also possible that a variation of the Si-O-Si angle or a change in the orientation of silica tetrahedra could occur during the build-up of a silica network by vapor deposition and cause a shift.

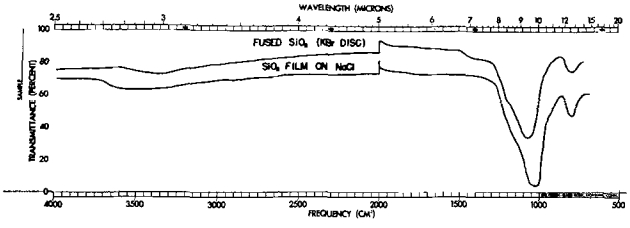

Fig. 2. Comparison of the infrared absorption spectra of a noncrystalline silica film prepared by vapor deposition, and fused silica glass.

The relative thickness of the films deposited on the front and back faces of a 1-in. diameter NaCl wafer was determined by measuring the area under the main infrared absorption band. The spectrum for both films was recorded and then re-examined after one film had been removed from the wafer. The area under the Si-O band for both films was approximately twice the area recorded for the single film. In this way, the films were determined to be of approximately the same thickness, which showed that the "silicon-oxygen specie" concentration in the gas phase immediately surrounding the substrate was relatively uniform. The thin silica films (5000Å) adhered well to all of the substrates. Films 3μ in thickness were readily deposited on the aluminum, fused silica, or alumina substrates, but spalled off from platinum foil when the thickness exceeded about 5000Å. This behavior could not be attributed to the differences in the thermal expansion coefficients of the substrates. Some of the films were re-examined after three weeks' exposure to the atmosphere. The refractive indices and infrared absorption spectra were unchanged.

Kinetics of deposition.—The decomposition of the $(C_2H_5O)_4Si$ was studied in a flowing system maintained at 250 ± 10μ pressure. By this method, the reaction products were removed from the system, and the secondary reactions were substantially reduced. The effect of temperature on the deposition rate of the glassy silica films was studied with a constant metal-organic evaporation rate of 0.15 ± 0.01 cm^3/hr. The effect of minor pressure variations was found to be negligible. For example when the total gas pressure was increased to 500μ (by the use of a valve leading to the vacuum pump), no change was detected in the rate of deposition. However, any further increase of the total pressure rapidly decreased the rate of deposition due to (*i*) poisoning effects from the reaction products and (*ii*) an increased recombination rate of the oxygen atoms in the gas phase. Under equilibrium conditions, the rate of deposition was constant, as shown in Fig. 3. The variation of the deposition rate with temperature could be described by the Arrhenius equation above 290°C.

$$r = A \exp(-H/RT) \quad [1]$$

where r is the deposition rate (mg/cm^2/min), A a constant, H the apparent heat of adsorption —(kcal/

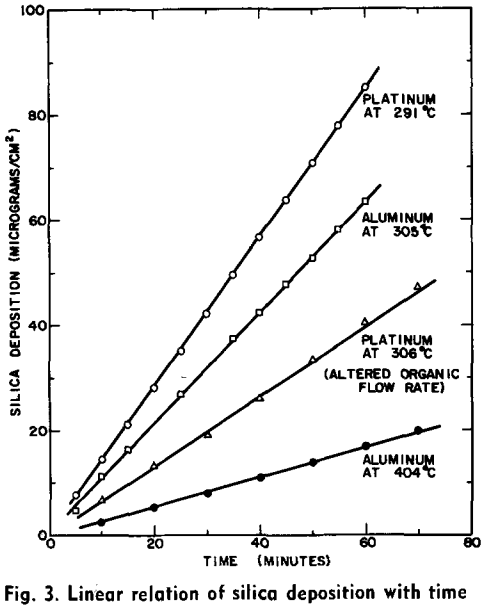

Fig. 3. Linear relation of silica deposition with time

mole), R gas constant (1.99 cal/degree/mole), and T substrate temperature (°K).

The relationship between logarithm r and reciprocal temperature is shown in Fig. 4. The data have been spread to show the temperature dependence of the deposition rate on each substrate. From Fig. 4, it is apparent that the deposition rate is relatively insensitive to temperature at least for platinum below about 290°C. Above this temperature, the rate decreases with increasing temperature. In addition, the rate of deposition on sodium chloride, fused silica, and platinum is equivalent, but different from the deposition rate on aluminum and alumina (for all practical purposes, the aluminum substrate, can be considered as alumina, since a surface layer of the oxide is always present). As previously mentioned, silicic acid was identified as a major constituent in the films formed below 290°C when the metal-organic evaporation rate was 0.15 cm³/hr. The relatively constant deposition rate noted in Fig. 4 below approximately 290°C can be associated with this acid formation. However, this does not imply that the acid is formed on the substrate surface. Brady (10) has stated that both $Si(OH)_4$ and $Si_2O(OH)_6$ probably exist in the vapor phase when steam is equilibrated with a siliceous molecule at relatively high pressures, and Straub (11) has suggested that silicic acid can be formed in the vapor phase. In addition, Brewer and Elliott (12) have proposed that $Si(OH)_2 \cdot 3H_2O$ can exist as a volatile specie. It is conceivable, therefore, that the silicic acid observed in the present study could be formed in the vapor phase. Since about 30% of the total gas pressure of the system was due to the water formed in the decomposition process, it was apparent that the mixture of "silicon-oxygen species" and water molecules or "hydrated silicon-oxygen species" bombarding the substrate surface was well in excess of the number which could be deposited. It is proposed that a maximum adsorption of the mixture occurs until a temperature is reached when the incorporation of water into the film is thermodynamically unfavorable, in this case, 290°C. Above this temperature, silica is deposited. Supporting evidence for this mechanism is offered by the work of Hockey and Pethica (13), who reported that the hydration of silica made by burning $SiCl_4$ in a hydrogen-oxygen mixture occurred as chemisorbed hydroxyl groups bonded to surface silicon atoms. In their studies, the surface hydroxyl groups could be removed from the silica surface by heating in the range 200°-400°C.

The decrease in the deposition rate above 290°C is characteristic of an adsorption-controlled process. In order for the free energy of the system to decrease, heat must be evolved, and the rate of an exothermic process will generally decrease with increasing temperature. From an atomistic viewpoint, in this study, the "silicon-oxygen specie" could be imagined to possess a mean lifetime in which to select a site on the substrate surface. As the temperature is raised, more kinetic energy would be imparted to the specie, and the mean lifetime for adsorption would be decreased. Klerer (14) has proposed a similar mechanism for the deposition of organic polymer films on silicon below 250°C.

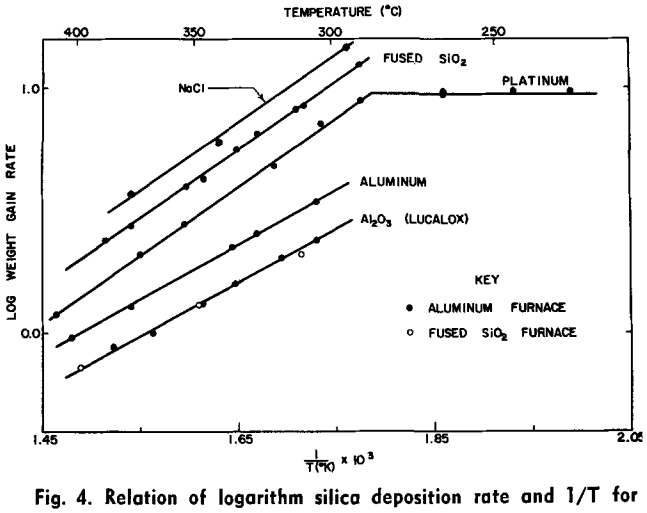

Fig. 4. Relation of logarithm silica deposition rate and 1/T for deposition on various substrates.

The apparent heats of adsorption of silica glass on the various substrates were calculated from the slopes of the lines in Fig. 4. A regression analysis of the data was made to determine the most probable slopes and the standard deviations. The apparent heat of adsorption of silica on the fused silica, NaCl, and platinum substrates was calculated to be 12.7 kcal/mole, with a standard deviation of 0.2 kcal/mole. For the aluminum or alumina substrates, the apparent heat of adsorption was calculated to be 9.5 kcal/mole, with a standard deviation of 0.3 kcal/mole. The magnitudes of the heats of adsorption are typical of those reported for physical adsorption processes, *e.g.*, the heat of adsorption of CO_2 on silica gel is approximately 7.1 kcal/mole; that of water on charcoal is about 10.0 kcal/mole (15).

In general, it may be stated that the heat of adsorption of the same adsorbate on different substrates is approximately the same (16). For multimolecular adsorption, the initial substrate surface is masked after several monolayers of adsorbate have been deposited. For example, in this study all subsequent condensate will fall on a SiO_2 layer rather than the original substrate surface. For this reason, the rate of deposition on all substrates should be similar. The difference in the apparent heat of adsorption of silica on the platinum, silica, or NaCl substrates and the alumina or aluminum substrates is real and much larger than the limit of error imposed by the standard deviations. It was concluded that the nature of the aluminum oxide surface was responsible for the difference in the apparent heats of adsorption observed. The reaction of alumina with silica to form a compound was not considered, since the rate of deposition of silica became constant soon after the metal-organic vapor was admitted to the reaction furnace. In addition, the rate of such a reaction would probably be quite slow at 300°-400°C.

The chemical nature of a substrate surface has been reported to influence a number of processes, even though the surface is covered with many molecular layers of adsorbate. For example, a mica substrate will affect the crystallization behavior of ammonium iodide through a film of cellulose acetate or rubber 1000Å in thickness (17). A similar observation was made in the present study when a potassium bromide substrate was used in place of a NaCl disk for the identification of silicic acid below 290°C. Silicic acid inclusions were not detected by infrared analysis when the films were formed on NaCl substrates held at 290°C (for metal-organic evaporation rates up to 1 cm³/hr). However, under similar conditions of temperature and pressure, but with an altered organic evaporation rate of 0.15 cm³/hr, silicic acid was observed to form in the film deposited on a KBr substrate. (The NaCl and KBr substrates were single crystals and showed no evidence of water by infrared analysis prior to these experiments.) From this experiment, it was concluded that the hydrophilic nature of the KBr surface could account for the selective absorption of water into the silica structure.

The adsorptive properties of an oxide surface are usually dependent on the degree of hydration and the chemical state of the hydrated surface (when the adsorbates can form hydrogen bonds). Peri and Hannon have reported that both hydroxyl groups and water molecules are held on the surfaces of γ-alumina (18). In their work, the water molecules were desorbed on

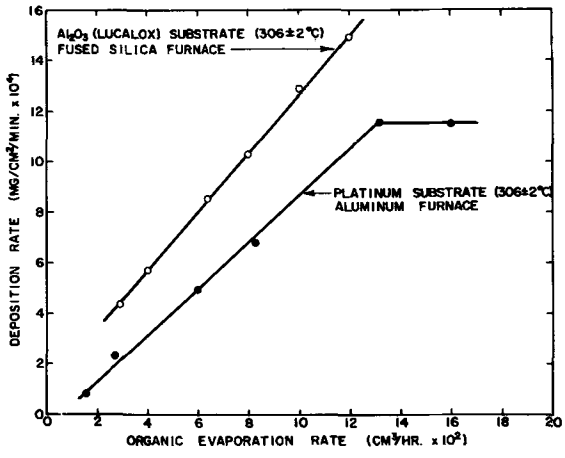

Fig. 5. Relation of silica deposition rate and tetraethoxysilane evaporation rate.

heating in a vacuum to 400°C, but about 40% of the surface area remained covered with hydroxyl groups. A similar state of hydration probably existed on the surface of the alumina disk used in this study. In the same way that the KBr substrate adsorbed water, it is proposed that a hydrated alumina surface would tend to incorporate further hydroxyl groups into the silica film. The adsorption of hydroxyl groups would account for the difference in the apparent heat of adsorption observed with the alumina surfaces.

Reaction order and specific rate constant.—The deposition rate of silica was directly proportional to the concentration (evaporation rate) of tetraethoxysilane for evaporation rates below 0.13 cm³/hr. This relationship is illustrated in Fig. 5 for silica glass deposited onto platinum and aluminum foil. For evaporation rates below 0.13 cm³/hr, it is evident that the decomposition of the metal-organic obeyed a first order rate law of the form

$$k = \frac{2.303}{t} \log \frac{a}{(a-x)} \qquad [2]$$

where k is the specific rate constant, sec^{-1}, t the reaction time, sec, a the metal-organic evaporation rate, cm³/hr, and x the metal-organic decomposition rate, cm³/hr. For evaporation rates in excess of 0.13 cm³/hr, the substrate area was rate limiting.

The maximum amount of tetraethoxysilane which could be decomposed in the oxygen plasma was not determined in this investigation, However, an indication of the amount of tetraethoxysilane decomposed could be obtained from the total pressure of the system. A slight, but progressive increase in pressure was noticed when the metal-organic evaporation rate was increased from 0.13 to 0.16 cm³/hr. Hence, the amount of silane decomposed was not rate limiting. The deposition rate on the alumina substrate was greater than that on the platinum substrate because of a variation in the "silicon-oxygen specie" concentration (the volume of the fused silica furnace was about one-third of that for the aluminum furnace with the same organic flow rate). The incorporation of hydroxyl groups into the silica film deposited on the alumina substrate would account for the difference in the slopes of the two lines in Fig. 5, as previously discussed.

In order to apply Eq. [2] to a flow system, Frost and Pearson (19) redefined the time variable as $t = V/u$, where V is the volume of the reaction chamber and u is the gas flow rate. The time variable V/u was a measure of the time that a gas reactant would spend in passing through the reaction vessel. In deriving this equation, it was assumed that the rate of the gas flow through the reaction furnace was constant and that the gases did not mix. An approximate value of the specific rate constant for the decomposition of tetraethoxysilane can be calculated from this latter equation. The following assumptions were made: (*a*) the rate of gas flow through the furnace was constant; (*b*) gas mixing did not occur; (*c*) the total reaction took place in the furnace; (*d*) the inlet gas temperature was similar to the furnace temperature; (*e*) the ideal gas law was applicable to both oxygen and tetraethoxysilane.

These assumptions are not unreasonable. The constant silica deposition rate would indicate that the flow rates were fairly constant. The reactant gases were fed into the furnace through individual inlet tubes and did not premix. The rate of deposition of silica decreased rapidly as the substrate was lowered in the reaction furnace, which showed that the reaction took place predominantly in the furnace vessel. The inlet gas temperature was similar to the furnace temperature because the radial temperature variation in the furnace was not appreciable under flow conditions. For the temperature and pressure conditions of the experiment, oxygen does not deviate appreciably from the ideal gas law. The oxygen flow rate was much larger than that of the metal-organic vapor, so that even if the ideal gas law were not obeyed by the latter, the effect on the calculations involved would be minor.

A calculation of the rate constant was made for the fused silica furnace (volume = 62.5 cm³) for a metal-organic evaporation rate of 0.12 cm³/hr. The amount of tetraethoxysilane decomposed was estimated from a knowledge of the reactant products and their respective concentrations. In view of the reaction products, it was evident that the oxidation of the tetraethoxysilane was quite complete. From Table I, the total number of moles of oxygen combined as either carbon monoxide or carbon dioxide is seen to be similar for the two gas samples; the amount of oxygen present in each case would be equivalent if the condensable water vapor pressure was taken into account (O_2 = 12% based on noncondensable gas pressure, O_2 = 8% including water pressure). By comparing the total number of moles of oxygen consumed (including oxygen available from the tetraethoxysilane) with the amount of oxygen required for the complete combustion of the tetraethoxysilane according to the analysis in Table I, it was estimated that 85% of the tetraethoxysilane was decomposed under equilibrium conditions. A 10% error in this estimate would cause a 37% error in the specific rate constant.

The total gas flow rate was calculated by assuming that the ideal gas law held for both the oxygen and tetraethoxysilane. The gas flow rate determined in this way was 1.96 cm³/min at 25°C and 1 atm pressure. This flow rate was corrected for a temperature of 310°C (furnace temperature) and 250μ pressure by the application of the ideal gas law. The values were then substituted into Eq. [2], and the specific rate constant was calculated to be 5.85 sec^{-1}. In view of the assumptions required for this calculation, the limits of error were estimated to be ±50%, or $k = 6 \pm 3$ sec^{-1} at 310°C and 250μ pressure.

Mechanism of film formation.—In this study, the energy necessary for the decomposition was supplied in the form of an oxygen plasma produced in a glow discharge. The predominant specie obtained from an oxygen discharge has been identified as atomic oxygen in the ground state (4, 5). The homogeneous recombination of atomic oxygen in the gas phase is accompanied by the release of 59.1 kcal/mole of atomic oxygen (20); it was presumed that the amount of energy liberated when the oxygen atoms interacted with the metal-organic molecules was of a similar order of magnitude.

A mechanism for the decomposition can be postulated from a consideration of the bond energies within

the molecule and the reaction products. The tetraethoxysilane molecule can be represented as

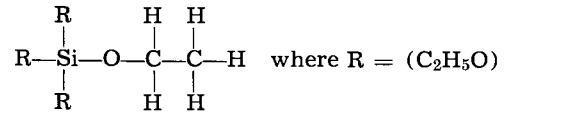

The bond energies involved are taken from Cottrell (20) and are as follows:

Si—O (108 kcal/mole)
C —O (86 kcal/mole)
C —H (96 kcal/mole)
C —C (83 kcal/mole)

From these data, it was apparent that the Si-O bond would be the least likely to rupture. The C-O bond is comparatively weaker, and rupture of this bond would free a C_2H_5 group. At the same time, hydrogen could be detached from the molecule. Although the subsequent reactions are too numerous to list, it is probable that the following preliminary reactions are among those which occurred

$$C_2H_5 \rightarrow C_xH_y \quad [3]$$

$$H + H \rightarrow H_2 \quad [4]$$

$$C_xH_y + O + O_2 \rightarrow CO_2 + H_2O \quad [5]$$

To determine whether the decomposition was influenced by the chemical nature of the furnace vessel, experiments were conducted in both a fused silica furnace (volume = 62.5 cm^3, surface = 81 cm^2) and an aluminum furnace (volume = 202 cm^3, surface = 181 cm^2). The apparent heats of adsorption of silica on an alumina substrate were found to be similar (see Fig. 4). This indicated that the mechanism of the decomposition was independent of the reaction chamber. In order to establish whether thermal energy contributed to the decomposition rate, two weight gain experiments were conducted at 400°C without a glow discharge and under both static and dynamic conditions. No decomposition or adsorption of the organic vapor occurred on a platinum substrate during an 8-hr period, which demonstrated that silica was not being deposited under these conditions.

Ing and Davern (3) have deposited silicon oxide films of unknown stoichiometry by decomposing tetraethoxysilane by a glow discharge operated at 0.5 megacycle. A mechanism for film growth was proposed, based on the high-energy particle bombardment decomposition of tetraethoxysilane in the gas phase to yield silicon oxide clusters. It was thought that the clusters were subsequently deposited on a substrate surface and that any attached organic groups were then further dissociated.

Glassy silica films were prepared in our studies by decomposing tetraethoxysilane in an argon plasma. The index of refraction of the films was measured as 1.458 ± 0.002, in agreement with the value for silica glass. The infrared adsorption spectra of these two monocrystalline solids were also similar, and exhibited absorption bands at 9.2 and 12.5μ. This experiment showed that the "silicon-oxygen specie" was available from the metal-organic molecule. Evidently the metal-organic molecule can absorb sufficient energy to cause bond rupture and a silicon-oxygen specie is formed. The rate of film growth in the argon plasma was exceedingly slow; a film of approximately 2000Å in thickness was deposited after 6 hr. This suggested that the rate of the decomposition was dependent on the simultaneous oxidation of the molecule. However, the amount of energy transferred in an argon plasma may be rate controlling and was not determined.

In order to ascertain whether the silicon oxygen specie could be formed entirely in the vapor phase, tetraethylsilane, $(C_2H_5)_4Si$, was decomposed in an oxygen plasma. It was found that the silica films deposited in this manner were indistinguishable from the silica films formed from $(C_2H_5O)_4Si$. The refractive indices and infrared adsorption spectra were similar; the apparent heats of adsorption on platinum were also the same, as determined from the temperature dependence of the deposition rate, which is shown in Fig. 6. With a $(C_2H_5)_4Si$ evaporation rate of 0.08 cm^3/hr, the deposition rate of silica on a platinum foil kept at 306°C was 4.15 x 10^{-4} mg/cm^2 min. Under similar conditions, the deposition rate with $(C_2H_5O)_4Si$ was 6.9 x 10^{-4} mg/cm^2 min. These deposition rates are not too different. It was concluded, therefore, that the silicon-oxygen specie which formed the Si-O-Si network could be synthesized directly in the vapor phase. Since the deposition of silica was possible in an argon plasma, it is reasonable to suspect that the main role of an oxidizing atmosphere was to remove the hydrocarbon portions of the metal-organic molecule.

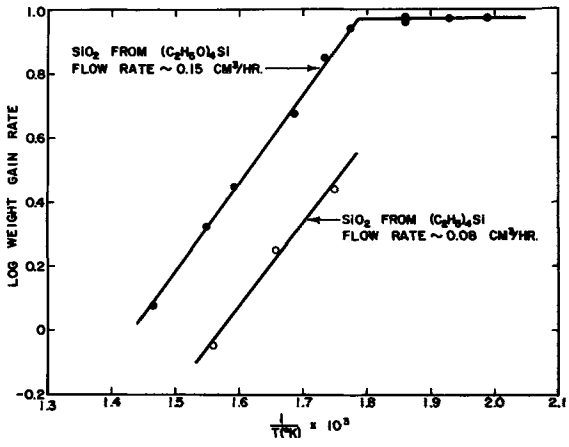

Fig. 6. Relation of logarithm silica deposition rate and 1/T for noncrystalline silica films prepared by the vapor phase decomposition of tetraethoxysilane and tetraethylsilane. (Deposition on platinum foil).

Based on the foregoing experiments, the following mechanism is proposed for the growth of a silicon dioxide film: The metal-organic molecules and energized oxygen species, predominantly atomic oxygen, enter the reaction furnace and collide. As a result, some of the metal-organic molecules absorb sufficient energy to cause bond rupture. A simultaneous oxidation of the hydrocarbon portions of the molecule assists the decomposition process and silicon-oxygen species are rapidly formed in the gas phase. Each specie is then imagined to possess a mean lifetime in which to select a site on the substrate and become physically adsorbed. The Si-O-Si network is formed when additional silicon-oxygen species are adsorbed. These species are not necessarily SiO_2 molecules, but may correspond to "free radicals" of the type SiO, SiO_3, or SiO_4, which are available from the metal-organic molecule. The adsorbed "radicals" may then crosslink to form a network of SiO_4 tetrahedra, and the over-all composition of the film deposited would correspond to SiO_2. As previously mentioned, the refractive indices and infrared adsorption spectra of all silica films deposited in this study were similar to the same properties of silica glass formed by fusion and subsequent cooling. Silicon dioxide always forms a network, whether it is crystalline quartz, cristobalite, tridymite, or a glass. It appears that the network is structurally the most stable form of the solid.

Conclusions

1. Noncrystalline SiO_2 films can be deposited at low temperatures by the decomposition of tetraethoxysilane by a gaseous plasma produced with a glow discharge. These films are structurally similar to silica

glass prepared by conventional fusion techniques, as evidenced by their infrared absorption spectra and refractive indices.

2. The decomposition of tetraethoxysilane by an oxygen plasma produces extensive water. This water can be chemically incorporated into the oxide films when the substrates are held below a certain temperature, which depends on the organic flow rate.

3. The decomposition of tetraethoxysilane by an oxygen plasma obeys a first order rate law at 250μ pressures and temperatures near 300°C.

4. The deposition rate of silica is directly proportional to the $(C_2H_5O)_4Si$ evaporation rate below a limiting value, which is dependent on the available surface area of the substrate and its temperature.

5. The silicon-oxygen species which form the silica network are physically adsorbed by the substrate below 410°C. The apparent heat of adsorption of silica on NaCl, Pt, or fused SiO_2 is 12.7 ± 0.2 kcal/mole. The apparent heat of adsorption on Al_2O_3 or Al is 9.5 ± 0.3 kcal/mole. The difference in the apparent heats of adsorption of silica is most likely due to the incorporation of hydroxyl groups into the silica film deposited on the alumina or aluminum substrates.

Acknowledgments

Dr. Francis Norton of the State University of New York at Albany generously donated his time to perform the gas analyses. The financial support of the National Aeronautic and Space Administration is gratefully acknowledged. One of the authors (D.R.S.) is also grateful to the Pittsburgh Plate Glass Company for the support of a fellowship.

Manuscript received Jan. 6, 1966; revised manuscript received May 23, 1966. This paper was presented at the Buffalo Meeting, October 10-14, 1965.

Any discussion of this paper will appear in a Discussion Section to be published in the June 1967 JOURNAL.

REFERENCES

1. D. R. Secrist and J. D. Mackenzie, *Glass Industry*, **45**, 408 (1964).
2. L. L. Alt, S. W. Ing, Jr., and K. W. Laendle, *This Journal*, **110**, 465 (1963).
3. S. W. Ing, Jr., and W. Davern, *ibid.*, **112**, 284 (1965).
4. "Progress in Reaction Kinetics," Chap. 1, p. 29, G. Porter, Editor, Pergamon Press, New York (1961).
5. S. Dondes, Private communication.
6. D. R. Secrist and J. D. Mackenzie, *Solid State Electronics*, **9**, 180 (1966).
7. J. D. Mackenzie, *J. Am. Ceram. Soc.*, **46**, 461 (1963).
8. I. Simon, Chap. 6 in "Modern Aspects of the Vitreous State," Vol. 1, J. D. Mackenzie, Editor, Butterworth & Co., Ltd., London (1960).
9. W. A. Pliskin and H. S. Lehman, *This Journal*, **112**, 1013 (1965).
10. E. L. Brady, *J. Phys. Chem.*, **57**, 706 (1953).
11. F. G. Straub, University of Illinois Engineering Experimental Station, Bull. Series 364 (1964).
12. L. Brewer and G. R. B. Elliott, Ph.D. Thesis, University of California, Berkeley, 1952.
13. J. A. Hockey and B. A. Pethica, *Trans. Faraday Soc.*, **57**, 2247 (1961).
14. J. Klerer, *This Journal*, **112**, 503 (1965).
15. S. Brunauer, "The Adsorption of Gases and Vapors," Vol. 1, "Physical Adsorption," p. 245, Princeton University Press.
16. See ref. (15), p. 244.
17. J. W. McBain, "Colloid Science," p. 76, D. C. Heath and Co., Boston (1950).
18. J. B. Peri and R. B. Hannan, *J. Phys. Chem.*, **64**, 1526 (1960).
19. A. A. Frost and R. G. Pearson, "Kinetics and Mechanism," 2nd ed., p. 262, John Wiley & Sons, Inc., New York (1961).
20. T. L. Cottrell, "The Strengths of Chemical Bonds," Chap. 8, p. 160, Academic Press, Inc., London (1958).

Electrical Conductance Study of Na^+ Ion Mobility in Silicogermanate, Aluminogermanate, and Aluminosilicate Melts

E. F. Riebling

Research and Development Laboratories, Corning Glass Works, Corning, New York

ABSTRACT

Correlations between Na^+ ion mobility, as determined by electrical conductance measurements, and structure changes were examined for ternary oxide melts between 1100° and 1700°C. Positive Λ and negative $\Delta H_K^{\neq}$ deviations for 25 mole % Na_2O silicogermanate melts, as well as negative Λ and positive $\Delta H_A^{\neq}$ deviations for high silica or germania content melts with Al/Na < 1.0, can be related to (*a*) the oxygen packing around the Na^+ ion, and (*b*) the local electroneutrality requirements (Na^+ remains near AlO_4^- portion of anions). Specific differences between the latter melts appear to be related to structural dissimilarities. The cation mobility increase that accompanies the gradual substitution of equimolar amounts of Al_2O_3 and Na_2O for either GeO_2 or SiO_2 suggests the formation of more open, cristobalite-like liquids as the 1/1/2 composition is approached in each system. Similarities between glass and melt conductance phenomena are also discussed.

Recent experimental studies have examined the temperature and compositional dependence of viscosity and density for ternary melts in the $Na_2O \cdot SiO_2 \cdot GeO_2$ (1), $Na_2O \cdot Al_2O_3 \cdot GeO_2$ (2, 3) and $Na_2O \cdot Al_2O_3 \cdot SiO_2$ (4) systems. Various partial molar volume models were developed to explain the observed molar volumes and other properties. Thus, GeO_6 octahedra were found to disappear by the time 50% of the GeO_2 is replaced in 25 mole % Na_2O melts in the first system. The GeO_6 octahedra stability limits in the second system apparently lie within the ternary compositions bounded by a 10 mole % semicircular sweep of the 23 mole % Na_2O point on the binary sodium germanate system. The aluminosilicate study revealed AlO_4 tetrahedra at all melt compositions with Al/Na $\leq$ 1.0.

A previous electrical conductance study of binary alkali germanate melts (5) showed that it was possible, to a limited degree, to correlate equivalent conductance (Λ) trends with both the cation field strength and the structure changes that were known to occur with the addition of alkali oxide to molten GeO_2. These findings prompted the attempt of a similar survey for selected series of related, but relatively more complicated ternary oxide melts that contained two network forming species.

This paper presents electrical conductance results for the following series of melts: (*a*) 25 mole % Na_2O silicogermanates, (*b*) Al/Na = 1.0 germanates, (*c*) 25 mole % Na_2O aluminogermanates, (*d*) 75 mole % GeO_2 sodium aluminogermanates, (*e*) Al/Na = 1.0 silicates, (*f*) 20 mole % Na_2O aluminosilicates, and (*g*) 75 mole % SiO_2 sodium aluminosilicates. The main objective was to search for possible correlations between sodium ion mobility and the previously postulated melt structure changes. The influence of anion variations on cation mobility was of specific interest.

Experimental

The individual glasses were prepared in Pt·20% Rh crucibles from Baker Reagent Grade analyzed Na_2CO_3 and Al_2O_3, Eagle Picher Electronic Grade GeO_2, and 200 mesh Pennsylvania Glass Sand Company ceramic Grade SiO_2. Preparative techniques and chemical analysis procedures, including spectrographic analysis of the GeO_2 and SiO_2 powders, have been described in detail elsewhere (1, 2, 4).

A dipping electrode arrangement (parallel Pt·40% Rh wires) was used to measure the melt resistances. Details of the instrument and its calibration procedures are described in greater detail elsewhere (6). Resistances were measured at 10 kc for an electrode immersion depth of 8 mm. Any contributions to the total impedance by capacitive reactances in the melt were negligible at that frequency. Capacitive effects were rather small between 1 kc ($\sim$ 0.02 μf) and 10 kc ($\sim$ 0.001 μf). While the normal resistance decrease amounted to 1-5% over the 1 to 10 kc range, less than a 1% decrease was generally observed between 5 and 10 kc. The capacitance level and frequency dependence of the sodium aluminosilicate melts were slightly larger than the above values.

Previous density and viscosity experiments (4) with sodium aluminosilicate melts had shown the need to use an argon atmosphere in order to eliminate reboil bubbles.[1] Consequently, the electrode arrangements were adapted to allow placement of an alumina argon inlet tube just above the radiation shield. The argon rate was approximately 1-1/3 l/hr. Argon was used only for the sodium alumino-silicate melts.[2]

The experimentally determined resistances, including a known temperature dependent contribution from the leads ($\sim$2.5 ohm), ranged from 3.5 to 5 ohms for the $Na_2O·SiO_2·GeO_2$ melts, from 3.5 to 30 ohms for the $Na_2O·Al_2O_3·GeO_2$ melts, and from 3.5 to 7 ohms for the $Na_2O·Al_2O_3·SiO_2$ melts.

Results

All of the specific conductance (κ) data observed the Arrhenius relationship with respect to temperature. Temperature cycling during each run produced no hysteresis effects. This allowed the use of a least squares treatment for the κ values. Table I gives the least squares constants of the log κ equations for each composition studied in the three systems to be discussed.

As before (5), the following equation was used to calculate equivalent conductances (Λ)

$$\Lambda = 100\,\kappa M/\rho m Z x \qquad [1]$$

where M is the molecular weight of M_xO_y, ρ is the melt density (g/cc), m the weight % M_xO_y, Z the charge on M, and x the number of M atoms per molecule of M_xO_y. The equivalent conductance so calculated is that due to one gram equivalent per cubic centimeter and is free of concentration effects. A composition dependent change of Λ can therefore be associated with a change of cation mobility.

The Λ isotherms are depicted as a function of composition for all of the melts studied in Fig. 1 through 7. Figure 1 shows Λ isotherms for 1100° and 1300°C

Table I. Specific conductance equations for ternary oxide melts

$\text{Log } \kappa = a - b \times 10^4/T(°K)$

$Na_2O·SiO_2·GeO_2$ System

Composition No.	Mole % Na_2O	% GeO_2 replaced by SiO_2	a	b	T, °C, range
1	23.7	5.04	2.3260	0.3340	1140-1350
2	23.9	10.7	1.9134	0.2872	1100-1330
2R	24.0[a]	9.4	1.1755	0.1872	1130-1360
3	24.4	21.3	2.0825	0.3082	1140-1360
4	25.3	28.2	1.5394	0.2358	1140-1310
4R	24.0[b]	29.2	1.6132	0.5218	1100-1310
5	25.4	33.1	2.0309	0.2982	1100-1320
5R	25.4[c]	33.1	1.6608	0.2503	1090-1330
6	24.0	40.1	1.6531	0.2643	1160-1350
6R	24.1[b]	41.2	1.8668	0.2832	1130-1350
7	23.9	52.1	1.8223	0.2734	1080-1300
8	23.1	59.0	1.8012	0.2727	1110-1340
9	24.3	69.6	1.7138	0.2684	1110-1330
10	24.6	80.0	1.7928	0.2815	1100-1350
11	24.7	89.8	1.9945	0.3103	1100-1340

$Na_2O·Al_2O_3·GeO_2$ System

Composition No.	Mole % Na_2O	Mole % GeO_2[d]	a	b	T, °C, range
12	24.4	71.7	2.0384	0.3153	1180-1330
13	24.4	65.4	2.1974	0.3516	1210-1360
14	24.3	58.4	2.5293	0.4313	1190-1370
15	24.4	54.9	1.8819	0.3338	1230-1360
16	22.1	74.5	2.2162	0.3500	1240-1360
17	19.4	74.6	1.9486	0.3354	1200-1360
18	16.8	75.7	2.1478	0.3927	1170-1350
19	14.4	76.1	2.6590	0.5065	1230-1370
20, 20R	4.51	90.3[e]	2.0933	0.5405	1270-1380
21	12.1	75.5	1.5913	0.3634	1180-1370
22	14.7	71.3	1.2875	0.2973	1200-1420
23	22.8	54.9	1.4349	0.2722	1260-1370

$Na_2O·Al_2O_3·SiO_2$ System

Composition No.	Mole % Na_2O	Mole % SiO_2[d]	a	b	T, °C, range
24	12.3	75.2	0.8785	0.2467	1460-1670
24R	12.3	75.2[e]	0.8085	0.2344	1510-1680
25	16.3	66.5	1.1073	0.2599	1500-1680
26	20.1	60.0	1.1810	0.2470	1380-1600
27	22.1	55.8	1.1650	0.2330	1480-1650
28, 28R	24.7	50.1[c]	1.8988	0.3721	1560-1700
29	19.9	74.7	2.0756	0.4030	1390-1600

[a] Same master sample, new analysis.
[b] New sample.
[c] Same master sample.
[d] Mole % Al_2O_3 can be obtained by difference.
[e] Rerun of same sample.

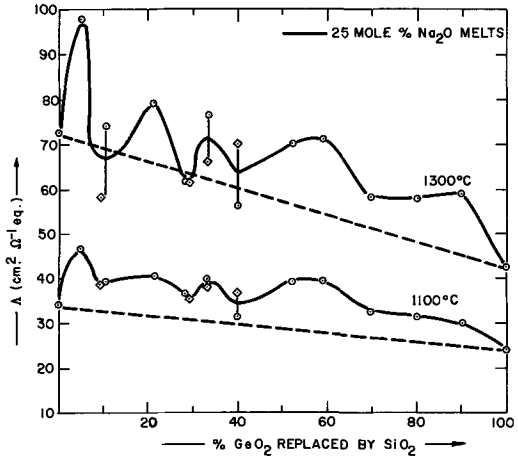

Fig. 1. Equivalent conductance isotherms *vs.* composition for $Na_2O·SiO_2·GeO_2$ melts.

[1] Oxygen reboil, which can occur at a platinum-oxide melt interface, results from the discharge of a concentration or thermal cell. For more details see J. H. Cowan, W. M. Buehl, and J. R. Hutchins, III, to be published in *J. Am. Ceram. Soc.*

[2] Experiments showed that an air or oxygen atmosphere causes about a 10% reduction of the specific conductance (κ) for these melts. Re-imposition of an argon atmosphere does not cause a complete return to the original κ level. Reboil bubble formation and only partial removal in these viscous silicate melts could explain this effect.

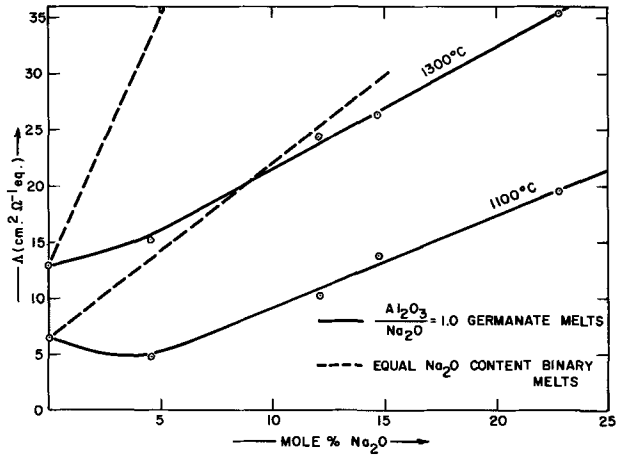

Fig. 2. Equivalent conductance isotherms vs. mole % Na_2O for equimolar sodium aluminate substituted germanate melts.

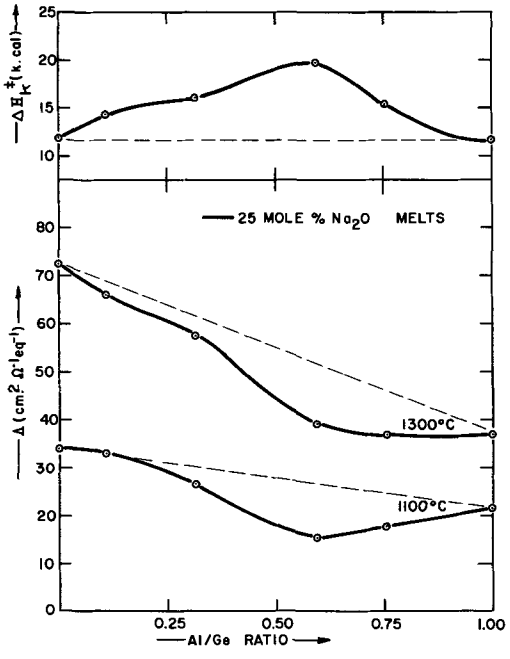

Fig. 3. Equivalent conductance isotherms and activation energy vs. Al/Ge ratio for 25 mole % Na_2O aluminogermanate melts.

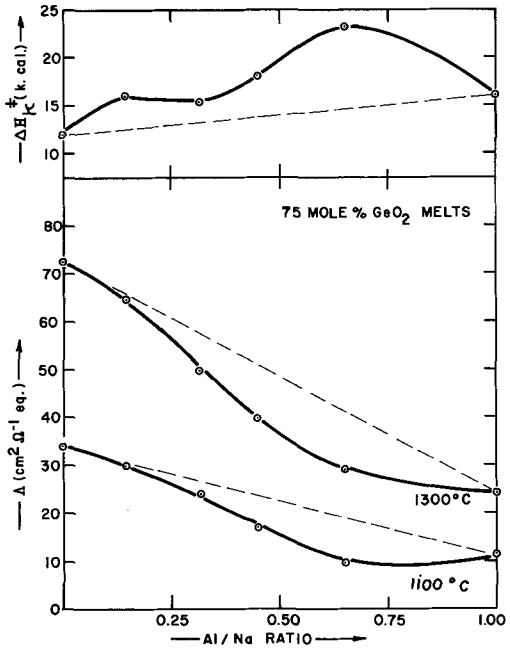

Fig. 4. Equivalent conductance isotherms and activation energy vs. Al/Na ratio for 75 mole % GeO_2 melts.

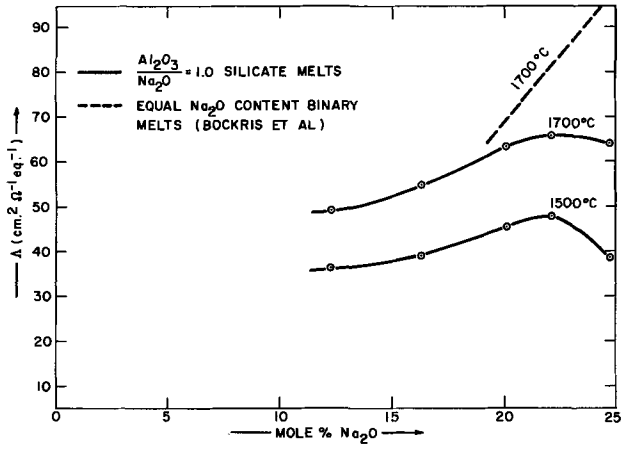

Fig. 5. Equivalent conductance isotherms vs. mole % Na_2O for equimolar sodium aluminate substituted silicate melts.

as a function of per cent GeO_2 replaced by SiO_2. Three of the four reruns produced differences at 1300°C that all but disappeared at 1100°C. These differences (15-20%) were larger than the usual level of reproducibility (< 5%). The reason for the better agreement at 1100°C is that the log κ *vs.* $1/T$(°K) plots for these six runs and reruns tend to intersect near the lower temperature. All four reruns were completed with the same electrode arrangement, which did not change calibration with use.

The 1100° and 1300°C equivalent conductance isotherms for the Al/Na = 1.0 germanate melts, the 25 mole % Na_2O aluminogermanate melts, and the 75 mole % GeO_2 sodium aluminogermanate melts are shown as functions of the mole % Na_2O in Fig. 2, of the Al/Ge ratio in Fig. 3, and of the Al/Na ratio in Fig. 4, respectively. A reproducibility check of one melt (composition No. 20) gave κ results that agreed to within 5%.

The 1500° and 1700°C equivalent conductance isotherms for the Al/Na = 1.0 silicate melts, the 20 mole % aluminosilicate melts, and the 75 mole % SiO_2 sodium aluminosilicate melts are shown as functions of the mole % Na_2O in Fig. 5, of the Al/Si ratio in Fig. 6, and of the Al/Na ratio in Fig. 7, respectively. A small amount of reaction was noted at the mullite tip for samples No. 27 and 28, primarily because of their higher Na_2O contents and the high temperatures. A fresh sample of No. 28 was rerun (No. 28R) at lower temperatures for shorter times. No mullite corrosion was observed and the κ points all agreed with the first few κ points from No. 28. Sample No. 24 was rerun as a check and showed a good level of reproducibility (Table I).

Discussion

The $Na_2O \cdot SiO_2 \cdot GeO_2$ *System*

The $\Lambda_{1300°C}$ fluctuations observed in the 0-50% GeO_2 replaced region (Fig. 1) could be associated with the previously suggested (1) structure change (disappearance of GeO_6 octahedra) for these melts. However, because of the lower net resistances at the higher temperatures and because of the lack of complete reproducibility, the above association is difficult to justify. Instead, the $\Lambda_{1100°C}$ isotherm (~ mp of GeO_2) will be assumed to more closely resemble reality for interpretive purposes.

The calculation of the Λ values was performed in such a fashion as to eliminate concentration or relative number of charge carriers as a factor. Thus, the fact that $\Lambda_{1100°C}$ exhibits positive deviations from ideality (or additivity) of up to 25% with the sub-

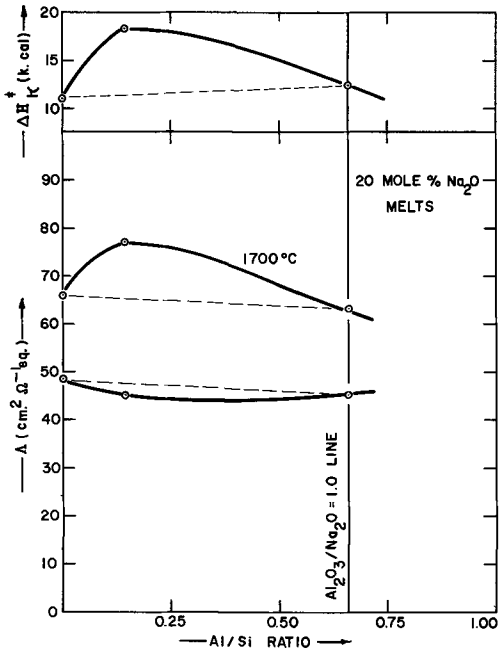

Fig. 6. Equivalent conductance isotherms and activation energy vs. Al/Si ratio for 20 mole % Na_2O aluminosilicate melts.

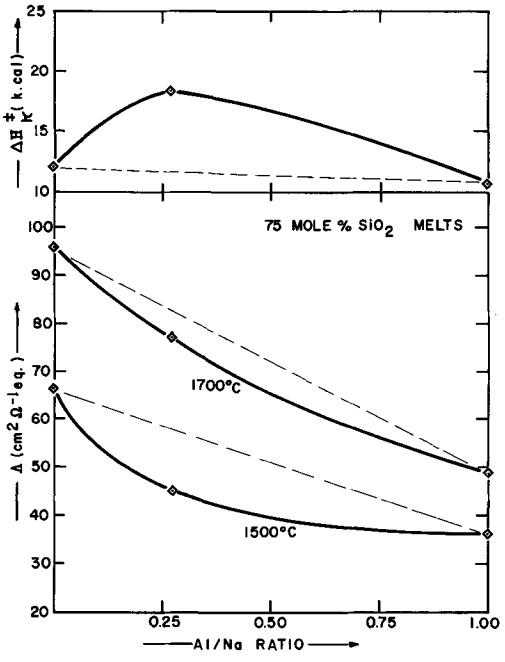

Fig. 7. Equivalent conductance isotherms and activation energy vs. Al/Na ratio for 75 mole % SiO_2 melts.

stitution of SiO_2 for GeO_2 is suggestive of an enhanced Na^+ ion mobility. The deviations from additivity are certainly greater than the normal experimental uncertainty associated with these measurements.

Of significance is the fact that cation mobility is enhanced for melts with greater than 50% GeO_2 replacement as well as for those melts with lesser GeO_2 replacements. The density and viscosity results indicated an absence of GeO_6 octahedra, with just GeO_4 and SiO_4 tetrahedra present, for the higher SiO_2 content melts. Thus, enhanced cation mobility does not appear to be directly related to the coordination number of germanium (IV).

One factor that can influence cation mobility is cation size or field strength. Thus, $\Lambda_{Li^+} > \Lambda_{Na^+} > \Lambda_{K^+}$ for the binary alkali germanates (5). Each Na^+ ion in these oxide melts can be thought of as possessing

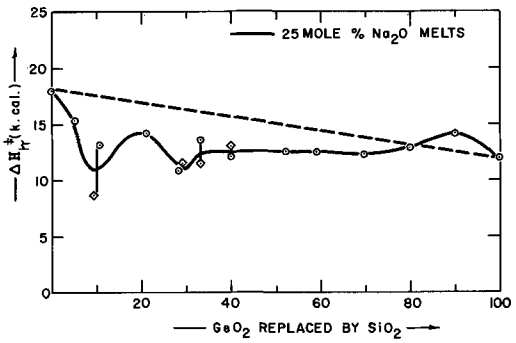

Fig. 8. Activation energy vs. composition for $Na_2O \cdot SiO_2 \cdot GeO_2$ melts

an oxygen polyhedron. The most plausible partial molar volume model for these 25 mole % Na_2O melts (1) involves smaller than ideal (~ 13%) partial molar volumes for Na_2O ($\bar{v}_{Na_2O}$). It is entirely possible that cation mobility could become enhanced if the oxygen packing of an NaO_4 or NaO_6 grouping were more efficient. This assumes that the entire cation-oxygen polyhedron is in some way involved in the activated process of ionic migration in a weak applied a-c electric field.

The above reasoning does not imply that the same oxygen environment moves with the cation (in this case, the Na^+ ion) during the process (mechanism) of activated complex formation. A simple cooperative positional adjustment of the surrounding oxygens could afford the Na^+ ion the opportunity to move a short distance. This cooperative rearrangement could be easier to accomplish, thereby increasing cation mobility (as observed), if the oxygen packing around the Na^+ ion were to become less voluminous (as seems to be the case). The negative $\Delta H^{\neq}_K$ departures from ideality (Fig. 8), which suggest a more favorable energy barrier, tend to support the above explanation of the enhanced cation mobility.

Bockris *et al.* (7) used Eyrings' theory of absolute reaction rates to develop an equation for the entropy of activation ($\Delta S^{\neq}_\Lambda$) for molten binary alkali silicate melts. That equation (5) was used to calculate $\Delta S^{\neq}_\Lambda$ values which are of the order of 0 to —3.0 e.u. for the present ternary oxide melts. This produces $\Delta H^{\neq}_\Lambda / T\Delta S^{\neq}_\Lambda$ ratios that lie between 3 and 20. Thus, as with the binary alkali germanates (5), $\Delta H^{\neq}_\Lambda$ appears to be the predominant and hence the significant term in the expression for $\Delta F^{\neq}_\Lambda$. This reinforces the relative role played by $\Delta H^{\neq}_\Lambda$ in the above analysis.

Another possibility is that the hole size and number distributions in the mixed anion melts are such that they enhance cation mobility to the extent of about 25%. Molar volume deviations can be associated in an approximate fashion with a change in the degree of openness in a liquid [melting point volume changes have been related to a change in the number of holes (8)]. However, the molar volume deviations from additivity, with respect to the experimentally determined end members of this system, amount to only about + 0.2% at the most (1).

The $Na_2O \cdot Al_2O_3 \cdot GeO_2$ *System*

Equimolar sodium aluminate melts.—The general trend of cation mobility is to increase with increase of alkali oxide content as the $Na_2O \cdot Al_2O_3 \cdot 2GeO_2$ (1/1/2) melt composition is approached (Fig. 2). This is an indication that the melt structure is being altered to the extent that the Na^+ ion mobility increases by a factor of four times. However, the cation mobility at 1100°C in the 1/1/2 ternary melt is still only 40% of the value obtained for a binary 25 mole % Na_2O germanate melt (dashed lines in Fig. 2). The same relationship holds for binary and ternary melts containing only 10 mole % Na_2O.

The above results suggest that the ternary melt structures are somewhat different from the previously postulated rather extensive network breakup associated with the formation of GeO_6 octahedra in binary alkali germanate melts (9). Thus, the lower cation mobilities support the density model of these ternary melts. That is, these equimolar sodium aluminate ternary melts tend to retain a three-dimensional type of liquid that gradually loosens as the 1/1/2 composition is approached.

Of significance is the fact that while the cation mobility increase is linearly related to the per cent Na_2O in the 5-25 mole % Na_2O region, mobility changes are small for the 0 to 5 mole % Na_2O region (Fig. 2). The $\Lambda_{1100°C}$ isotherm actually appears to go through a minimum when it is compared with the binary results. This phenomenon could be associated with the previously reported retention of a "random damaged network" to lower GeO_2 or SiO_2 contents in the presence of Al_2O_3 (2, 4, 10).

The activation energy dependence on composition for these Al/Na = 1.0 germanate melts (Fig. 9) is not as conclusive as the conductance trends. Although the $\Delta H^{\neq}_{\kappa}$ decrease is less pronounced for the 0 to 5 mole % ternary melts when it is compared to the binary melt trends, and hence agrees with the analysis of that conductance data, the slight $\Delta H^{\neq}_{\kappa}$ trend observed for larger Na_2O content ternary melts is unusual. It is possible that the slight change of mechanism suggested by the entropy of activation data for the 5 to 25 mole % Na_2O ternary melts does not show up in the $\Delta H^{\neq}_{\kappa}$ comparison ($\Delta H^{\neq}_{\Lambda} > T\Delta S^{\neq}_{\Lambda}$). The $\Delta S^{\neq}_{\Lambda}$ values are more negative (by about 2 to 3 e.u.) for these ternary melts. This suggests a slightly more restricted configuration for the activated complex in the ternary melts, which is in general agreement with their tighter three dimensional nature.

75 Mole % GeO_2 melts.—Two trends of the Λ *vs.* Al/Na ratio plots presented in Fig. 4 suggest melt structure changes, first, the Λ decrease that accompanies the substitution of Al_2O_3 for Na_2O. This agrees with the postulated extensive GeO_6 octahedra concentration that exists at the binary point and the three-dimensional nature of melts on the Al/Na = 1.0 line. Second, the negative departures from ideality (additivity) which can amount to as much as 25-50%. These deviations suggest that cation mobility is somehow retarded more than expected as AlO_4 tetrahedra substitute for the GeO_4 tetrahedra that link clusters of GeO_6 octahedra.

If one assumes that the $\bar{v}_{Na_2O}$ alone governs the Na^+ ion mobility, the results must be interpretable in terms of a relatively constant $\bar{v}_{Na_2O}$ of about 35 cc (3). Examination of Fig. 4 shows that this is not completely possible because the largest Λ deviations occur for Al/Na ratios > 0.5 and coincide with a pronounced $\Delta H^{\neq}_{\kappa}$ maximum at about Al/Na = 0.7. Clearly, cation mobility and the conductance mechanism in this case are influenced to a greater extent by the structure changes than by the packing of oxygens around the Na^+ ion. Cation location (near a charged AlO_4^- grouping)[3] could be more restricting for the intermediate compositions because of the limited positional possibilities for the AlO_4 tetrahedra, which appear to replace GeO_4 tetrahedra, not GeO_6 octahedra, at intermediate compositions.

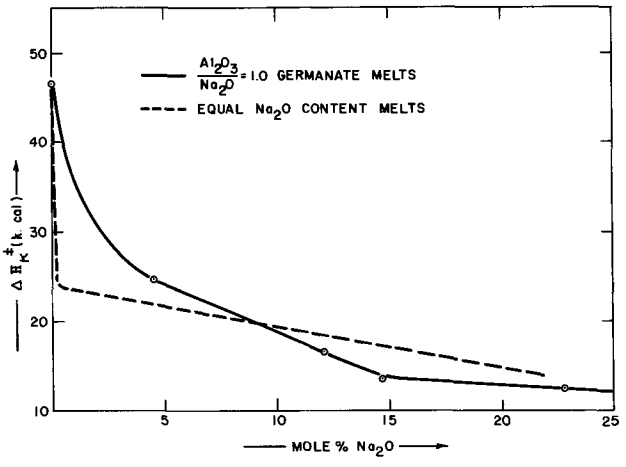

Fig. 9. Activation energy *vs.* mole % Na_2O for equimolar sodium aluminate substituted germanate melts.

25 Mole % Na_2O melts.—The Λ minima and the $\Delta H^{\neq}_{\kappa}$ maximum in Fig. 3 occur close to Al/Ge = 0.6, which corresponds to an Al/Na ratio of 0.7. This Al/Na ratio is close to the value at which similar phenomena occur for the 75 mole % GeO_2 melts (Fig. 4). It appears that a $\Delta H^{\neq}_{\kappa}$ ridge and a Λ valley occur along the Al/Na = 0.7 ternary line.

It was uncertain (3) as to whether the elimination of GeO_6 octahedra at the 25 mole % Na_2O level was (*a*) sudden or (*b*) gradual. The viscosity (2) and expansion coefficient results (3) favored the first possibility, which involved a sharp $\bar{v}_{Na_2O}$ minimum below Al/Ge $\cong$ 0.3 (as opposed to a gradual $\bar{v}_{Na_2O}$ change for the second model). Although the $\Delta H^{\neq}_{\kappa}$ increases slightly, the Λ deviations are minimal for these low alumina melts (Fig. 3).

Most of the conductance irregularities thus occur for alumina substitutions that are higher than anticipated from the molar volume models. It is difficult to say whether these Λ and $\Delta H^{\neq}_{\kappa}$ deviations are directly connected with the disappearance of GeO_6 octahedra or whether they simply reflect the gross structure change from a relatively fluid binary liquid to a ternary liquid that is three-dimensionally oriented. Either of these effects seems to outweigh the v_{Na_2O} factor for the series under discussion.

Certainly, the absolute value of cation mobility drops more sharply (with most of the concurrent $\Delta H^{\neq}_{\kappa}$ increase) below Al/Ge = 0.5 (Fig. 3). One could infer that most of the gross structure change does occur before the Al/Ge ratio exceeds 0.5. This conclusion would agree with the most likely molar volume model (3).

The $Na_2O \cdot Al_2O_3 \cdot SiO_2$ System

Equimolar sodium aluminate melts.—There is some degree of similarity between these conductance results (Fig. 5) and those just discussed for the analogous germanates (Fig. 2). Cation mobility appears to increase in the 10-20 mole % Na_2O region for both systems. This strengthens the conclusion that more open carnegieite-like network liquids are obtained as the 1/1/2 composition is approached.

However, there are specific cation mobility differences between the silicate and the germanates that outweigh the above similarity. First, the Na^+ ion mobility in the silicate melts can be about four times the value in the germanate melts. For example, $\Lambda_{1700°C} \sim 52.5$ in the silicate *vs.* $\Lambda_{1100°C} \sim 13.2$ in the germanate (both for the 15 mole % Na_2O composition).[4] Second, the Na^+ ion mobilities can be similar for the binary (7) and ternary silicate melts (Fig. 5). This is not the case for the germanates where the mobilities were considerably less in the ternary melts (Fig. 2). Third, the Na^+ ion mobility increases by a factor of 89% for the 10 and 20 mole % Na_2O ternary germanates compared to only a 31% increase for similar silicate melts. It appears that the relative structure change that accompanies substitution of Al_2O_3 and Na_2O is greater for the Al/Na = 1.0 germanate melts. This

[3] This factor does not exist for the substitution of SiO_4 tetrahedra for GeO_4 tetrahedra and GeO_6 octahedra.

[4] These reference temperatures are close to the melting points of the respective network forming oxides. A similar comparison between the binary alkali disilicate and digermanate melts revealed quite similar sodium ion mobilities (5).

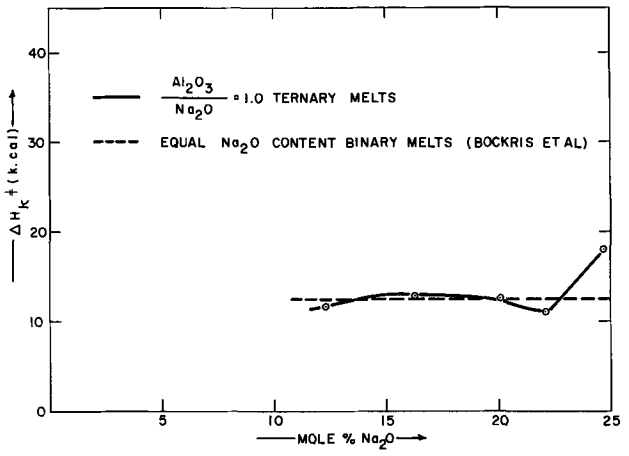

Fig. 10. Activation energy vs. mole % Na_2O for equimolar sodium aluminate substituted silicate melts.

conductance based conclusion agrees with the previous density and viscosity based conclusions.

The Na^+ ion mobility differences between these ternary silicate and germanate melts with an Al/Na ratio of 1.0 do not appear to be related to $\bar{v}_{Na_2O}$. That parameter takes a value of about 35 cc in the best partial molar volume models for the 1/1/2 melt composition in both series.

The $\Delta H^{\neq}_K$ plot shown for these melts in Fig. 10 is in agreement with most of the above discussion. Thus, the $\Delta H^{\neq}_K$ values in the 10 to 20 mole % Na_2O ternary region are similar to those reported by Bockris *et al.* (7) for the corresponding binary melts.[5] However, $\Delta H^{\neq}_K$ for molten carnegieite is about 50% greater than the value obtained for its germanate analogue (Fig. 9). This contrasts with much higher cation mobility (by a factor of three times) in the 1/1/2 silicate melt compared to the 1/1/2 germanate melt at the melting temperatures of the respective network forming oxides. A possible explanation of this paradox may be found in the fact that $\Delta H^{\neq}_K$ is strongly proportional to cation volume for low alkali content melts (< 10 mole % M_2O) that contain a high concentration of network forming tetrahedra (as per the melts under discussion). It was implied that hole size could thus play a significant role in the conductance mechanism (5). The present $\Delta H^{\neq}_K$ observations may be a manifestation of just such a parameter.

75 Mole % SiO_2 melts.—The Λ decrease that accompanies the substitution of Al_2O_3 for Na_2O (Fig. 7) is partially expected because the Na_2O content is reduced from 25 to 12.5 mole % in the process. A similar Λ decrease was observed by Bockris *et al.* for binary alkali silicates in the 25-19 mole % Na_2O region (7). Of more significance is the structure change later postulated for these particular binary melts by Bockris *et al.* (11). The decrease of alkali content was visualized as being accompanied by an increase of the size of silica-like "icebergs," with the alkali cations located between "icebergs." A random damaged silica network was supposed to be formed at about 12 mole % Na_2O. This phenomenon has recently been proposed for molar volume models of the ternary melt compositions under discussion (4). The now observed cation mobility trend agrees with this over-all picture.[6]

The Λ deviations from additivity are negative (Fig. 7), but do not exhibit the type of trend observed for similar 75 mole % GeO_2 melts (Fig. 4). The maximum Λ deviations appear to occur at lower Al/Na ratios in the silicates. The same might be said of the $\Delta H^{\neq}_K$ maximum (Fig. 7). Indeed, the fact that these maximum deviations occur at different Al/Na ratios in the two systems only serves to emphasize the structural differences. The fact that the trends are similar, in spite of the vastly different structures involved, could be due to coincidence or to an interplay of the parameters that influence cation mobility and the associated mechanism. As with the ternary aluminogermanates, one of the parameters influencing these Λ deviations could be the restriction that the Na^+ ion be near a charged AlO_4^- grouping.

20 Mole % Na_2O melts.—The electrical conductance results for the 20 mole % Na_2O series, although there is just one intermediate point close to the binary in composition, do suggest the presence of Λ_{1700} and $\Delta H^{\neq}_K$ maxima (Fig. 6). These observations differ from the previously discussed Λ minima (and $\Delta H^{\neq}_K$ maximum) that were found for the 25 mole % Na_2O aluminogermanate melts at a Al/Ge ratio of about 0.6 (Fig. 3).

The Λ_{1700} maximum is slight while the Λ_{1500} isotherm changes very little with composition (Fig. 6). Lower temperatures would probably produce a Λ minimum, thereby creating a Λ and $\Delta H^{\neq}_K$ situation below the melting point of SiO_2 that would be analogous to the germanate case for temperatures above the melting point of GeO_2. The lower temperature Λ minima, as well as the $\Delta H^{\neq}_K$ increase, can be rationalized in terms of the $\bar{v}_{Na_2O}$ increase that has been postulated for these particular silicate melts (4). The influence of this parameter could be more temperature dependent for this series than with the other melts studied. This might be associated with the postulated gradual change from a silica-like iceberg binary liquid to an open, cristobalite-like ternary liquid containing 60 mole % SiO_2 (4).

Comparison of Melts and Glasses

A recent electrical conductance and transport number study of several Al/Na < 1.0 sodium aluminosilicate glasses (12, 13) has confirmed the glasses to be essentially ionic conductors, with the Na^+ ion carrying most of the current. Similar results have been reported for binary alkali silicate melts (8). This suggests the possibility of a similarity between conductive processes in the glass and liquid states for a given sodium aluminosilicate composition. This correlation is known to exist for binary alkali germanate compositions (5) where for example, the ratio of $\Delta H^{\neq}_K$ melt/$\Delta H^{\neq}_K$ glass for a 25 mole % Na_2O germanate is about 0.67 in spite of a much greater cation mobility in the melt.

A comparison of the activation energies obtained by Isard (14) for Al/Na = 1.0 sodium aluminosilicate glasses with the present values for the corresponding high-temperature melts (Fig. 10) reveals a close similarity, again in spite of higher melt mobilities. Isard's $\Delta H^{\neq}_K$ values show a progressive decrease from about 17 to 13 kcal for ~ 20 mole % Na_2O glasses between the binary and the Al/Na = 1.0 line. These energies are similar in magnitude but different in trend to those reported for the corresponding melts in Fig. 6. It is interesting that Isard explained his glass state results in terms of an expansion of the coordination shell around sodium ions, but only for glasses with Al/Na < 1.0, that was caused by elimination of nonbridging oxygens with the addition of Al_2O_3.

The above electrical conductance similarities between the glass and liquid states for a given ternary oxide composition series are understandable in light of the recently discovered molar volume similarity for some of these sodium aluminosilicate glasses and liquids (4). The volume models for these liquids involved $\bar{v}_{Na_2O}$ values that increased with increase of Al_2O_3 content, regardless of the Al/Na ratio.

[5] The reason for the $\Delta H^{\neq}_K$ increase at the 1/1/2 composition is unclear. The K and $\Delta H^{\neq}_K$ data reproduced to within several per cent for runs with completely different carnegieite samples.

[6] The general Λ decrease observed for these 75 mole % SiO_2 melts could also be explained in terms of the $\bar{v}_{Na_2O}$ increase that occurs as the Al/Na = 1.0 line is approached (4).

Conclusions

In general, the equivalent conductance information obtained for these ternary oxide melts agrees with previously proposed molar volume structural models and data. In contrast to simple molten salt mixtures such as KI·KBr, where cation mobility deviations can be correlated with anion differences, no one particular factor seems to govern cation mobility in all of these ternary oxide melt systems. The gross melt structure changes are much more pronounced and are much more specific to each system for most of the molten oxide mixtures thus far studied. This situation serves to produce a somewhat incomplete unified interpretation of cation mobility for these ternary oxide melts.

Acknowledgment

The author would like to thank P. E. Blaszyk and P. C. Logel for assistance with experiments and Dr. S. D. Stookey for his encouragement.

Manuscript received Dec. 27, 1965. This paper was presented at the Cleveland Meeting, May 1-5, 1966.

Any discussion of this paper will appear in a Discussion Section to be published in the June 1967 JOURNAL.

REFERENCES

1. E. F. Riebling, *J. Chem. Phys.*, **41**, 451 (1964).
2. E. F. Riebling, *ibid.*, **43**, 499 (1965).
3. E. F. Riebling, *ibid.*, **43**, 1772 (1965).
4. E. F. Riebling, *ibid.*, **44**, 2857 (1966).
5. E. F. Riebling and S. D. Gabelnick, *This Journal*, **112**, 822 (1965)
6. E. F. Riebling and P. C. Logel, *Rev. Sci. Instr.*, **36**, 425 (1965).
7. J.O'M. Bockris, J. A. Kitchener, S. Ignatowiz, and J. W. Tomlinson, *Trans. Faraday Soc.*, **48**, 75 (1952).
8. H. Bloom and J. O'M. Bockris, "Molten Electrolytes," in "Modern Aspects of Electrochemistry," J. O'M. Bockris, Editor, Vol. 2, Academic Press Inc., New York (1959).
9. E. F. Riebling, *J. Chem. Phys.*, **39**, 3022 (1963).
10. E. F. Riebling, *Can. J. Chem.*, **42**, 2811 (1964).
11. J. W. Tomlinson, M. S. R. Heynes, and J. O'M. Bockris, *Trans. Faraday Soc.*, **52**, 1822 (1958).
12. R. L. Myuller and A. A Pronkin, *Zhur. Priklad. Khim.*, **36**, 1192 (1963).
13. A. A. Pronkin, *ibid.*, **37**, 887 (1964).
14. J. O. Isard, *J. Soc. Glass Technol.*, **43**, 113 (1959).

The Permeation of Electrolytic Hydrogen through Platinum

E. Gileadi,[1] M. A. Fullenwider, and J. O'M. Bockris

The Electrochemistry Laboratory, John Harrison Laboratory of Chemistry, University of Pennsylvania, Philadelphia, Pennsylvania

ABSTRACT

The absorption and permeation of electrolytically generated hydrogen through thin platinum foils have been observed directly by an electrochemical method. The diffusion coefficient and the associated apparent energy of activation were determined. The concentration of absorbed hydrogen was obtained, and it was shown that atomic hydrogen tends to concentrate in areas of high strain in the metal where it can be in a lower energy state. Hydrogen embrittlement phenomena similar to those found in iron and steel were observed. The variation of cathodic overpotential with time was explained in terms of the change in hydrogen concentration in the bulk of the metal near the cathodic surface.

The diffusion of hydrogen through platinum from the gas phase at high temperatures of 700°-1000°C was reported by Richardson *et al.* (1) in 1904. The diffusion coefficient was not obtained, but the apparent energy of activation for the over-all permeation process was calculated. It was also stated in this work that "it is a well-known fact that platinum through which hydrogen diffuses becomes brittle and will break under small stress." In 1956, Hoare and Schuldiner (2) used a membrane electrode (bi-electrode) to observe the variation of overpotential on one side of the membrane as a function of the applied cathodic current density on the other side. In the experimental setup used by these authors the cathodic and anodic sides were not connected to one another electrolytically, and the change in overpotential on the anodic side could only arise due to diffusion of atomic hydrogen from the cathodic side through the membrane. Hoare and Schuldiner used this method to study the kinetics of hydrogen evolution on Pd. They also observed a very small change (1 mv) in the potential of a platinum membrane only when the cathodic side was poisoned with a small amount of As_2O_3 added to the solution. Kheifetz and Krasikov (3) observed a change in the potential of zero charge of the anodic surface of a Pt membrane with time during constant current hydrogen evolution on the cathodic side. This was interpreted as due to the change in the concentration of absorbed hydrogen in the metal.

[1] Present address: Department of Chemistry Tel-Aviv University, Tel-Aviv, Israel.

Analysis of galvanostatic transients on Pt has recently (4) led to the conclusion that both hydrogen and oxygen are absorbed to an appreciable extent in Pt.

While the above evidence strongly implies that hydrogen can diffuse into platinum, there is no direct evidence so far for the permeation of electrolytic-hydrogen through platinum, and the diffusion coefficient for this process has not yet been reported.

In this paper the permeation of electrolytically produced hydrogen through Pt at relatively low temperatures (50°-80°C) has been observed directly. Further, the diffusion coefficient and its variation with temperature have been determined. The concentration of absorbed hydrogen is obtained and a model for the state of absorbed hydrogen in the metal is proposed.

Experimental

Method of measurement.—A simple, yet accurate and sensitive method for measuring the rate of hydrogen permeation through thin metal foils has been devised by Devanathan and Stachurski and described in detail elsewhere (5). In essence it consists of a bi-electrode (2) in the form of a thin foil which separates two identical electrochemical cells. On the cathodic side of the foil, hydrogen is evolved at a fixed rate, while the diffusion side is kept at an anodic potential such that the concentration of adsorbed atomic hydrogen on this surface is essentially zero. Thus, hydrogen which diffuses through the membrane and emerges on the anodic side is immediately ionized, and the current passed to maintain constant potential

on this surface is directly proportional to the hydrogen permeation rate.

Calculation of D and C_o.—Analysis of the diffusion problem with the boundary conditions imposed on the system, *i.e.*, $C(o,t) = C_o$; $C(L,t) = 0$ and $C(x,o) = 0$ allows one to calculate the diffusion coefficient from the form of the permeation transient as shown elsewhere (5, 6). Thus, the permeation rate J_t during the transient is given by

$$J_t/J_\infty = \frac{2}{\pi^{1/2}} \frac{1}{\tau^{1/2}} \exp(-1/4\tau) \quad [1]$$

where τ is a dimensionless parameter

$$\tau = Dt/L^2 \quad [2]$$

For $J_t/J_\infty = 0.50$, one finds $\tau = 0.138$, and thus by measuring the time required to reach this fractional permeation rate, the diffusion coefficient may be calculated. In general one can write Eq. [2] in the form

$$t_\gamma = \tau_\gamma L^2/D \quad [3]$$

where t_γ is the time required for the permeation rate J_t to reach a fraction γ of its steady-state value J_∞, L is the thickness of the membrane, and D is the diffusion coefficient. Under steady-state diffusion conditions Fick's first law applies giving

$$J_\infty = FD(C_o - C_L)/L = FDC_o/L \quad [4]$$

where J_∞ is the permeation rate in units of current density, $C_o \equiv C(o,t)$ = constant, and $C_L \equiv C(L,t) = 0$. From Eq. [3] and [4] both the diffusion coefficient and the concentration of hydrogen in the metal just under the cathodic surface can be calculated on the basis of a single permeation experiment.

Electrodes.—Platinum foils of thickness ranging from 2 to 5 x 10^{-3} cm were used in these experiments. The foils were first degreased by refluxing overnight in 1:1 methanol-benzene and then heated for 3 hr at 600°C in an atmosphere of argon to ensure zero hydrogen concentration in the metal. Calculated values of D and C_o are all based on the first transient. Only transients which have the theoretically expected shape were accepted for the calculation of D. This can be tested in a simple manner in that D should not vary systematically with γ. Cracks in the metal foil allowing contact between the electrolyte on the two sides of the membrane are easily detected. For such a membrane, turning on the cathodic current immediately affects the current recorded on the anodic side, while for an uncracked electrode a certain time elapses before the effect of a change on the cathodic surface is propagated through the membrane and can be observed on the anodic side.

Solution preparation.—A 0.1*N* sulfuric acid solution prepared from reagent grade H_2SO_4 and conductivity water was used on the cathodic side. The solution was preelectrolyzed externally in an auxiliary compartment and transferred to the cell with nitrogen pressure. Arsenic oxide was added in a concentration of 5 mg As_2O_3 per liter. No permeation current could be observed when hydrogen evolution occurred in unpoisoned solution (2).

On the anodic side a 0.2*N* NaOH solution was used. Analytical grade NaOH and conductivity water were used to make up this solution. The purity of the solution on the anodic side is important in that it determines largely the background current and hence limits the sensitivity of the measurement. Stable background currents of the order of 1 μa/cm^2 were observed and permeation rates as low as a few tenths of a microampere could be measured.

Results and Discussion

Shape of the permeation transient.—The shape of a typical set of permeation transients obtained at 70°C for a foil thickness of 3.8 x 10^{-3} cm is shown in Fig. 1. The diffusion coefficient was calculated from the shape of the first transient, obtained with a polarization current density of 0.5 ma/cm^2.

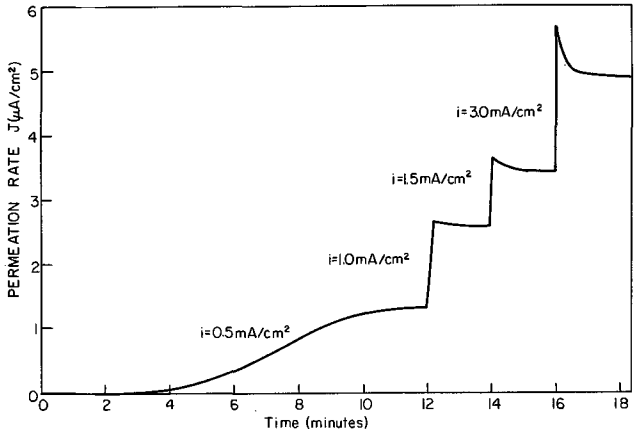

Fig. 1. Shape of successive permeation transients with increasing cathodic current density. L = 3.8 x 10^{-3} cm, 70°C.

At higher current densities the initial rise of the permeation rate is followed by a slower decrease towards a steady state. A similar behavior was observed by Bockris, McBreen, and Nanis (7, 8) for the permeation of hydrogen through iron and steel membranes and was associated there with the onset of hydrogen embrittlement. Thus, when the concentration of hydrogen in the metal exceeds its saturation value, corresponding to a critical cathodic current density i_{crit}, the hydrogen atoms diffuse to the surface of small crevices and voids in the metal and recombine there to form gaseous H_2, which can generate a high internal pressure, expand the crevices and voids, and cause further cracking. In view of the similarity in the form of the permeation transients at higher current density for Pt and Fe, and the early observation (1) that hydrogen embrittlement of Pt does indeed occur at high temperature, it may be concluded that the "overshoots" in the permeation transients for Pt are indicative of a similar embrittlement phenomenon.

At 70° the value of the critical current density according to Fig. 1 is just below 1.0 ma/cm^2. Qualitative evidence indicates that, unlike in the case of iron, $i_{crit.}$ decreases with increasing temperature.

Evidence for diffusion controlled permeation.—In Fig. 2 the steady-state permeation rate J_∞ is plotted as a function of $1/L$ for three thickness of Pt foil at 70°C. A linear plot is obtained going through the origin, as expected according to Eq. [4]. The slope of the straight line equals FDC_o. With D calculated independently from the shape of the transient (Eq. [3]), the concentration of hydrogen at $x = o$, namely, just below the cathodic surface, can be obtained.

A second test of the assumption of diffusion controlled permeation rate is based on Eq. [3]. Thus, a plot of t_γ *vs.* L^2 should be a straight line going through the origin. This is shown to be the case in Fig. 3 for $\gamma = 0.5$ at 70°C. Figures 2 and 3 show that the permeation of hydrogen through Pt is diffusion controlled both during the transient and at steady state. From the slopes of Fig. 2 and 3, one obtains

$$D_{70°C} = 3.4 \times 10^{-9} \text{ cm}^2/\text{sec}$$

$$C_{o_{70°C}} = 2.7 \times 10^{-5} \text{ gram atom/cm}^3$$

It should be noted that while both these quantities depend on the bulk properties of the metal, the concentration C_o is also a sensitive function of the state of the surface. It will depend on the applied cathodic current density and on the composition of the solu-

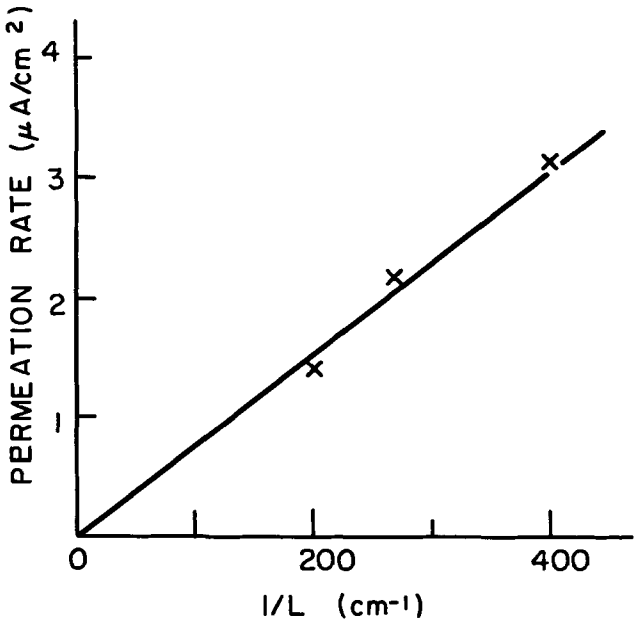

Fig. 2. Permeation rate as a function of 1/L. Cathodic current density 0.5 ma cm^{-2}, 70°C.

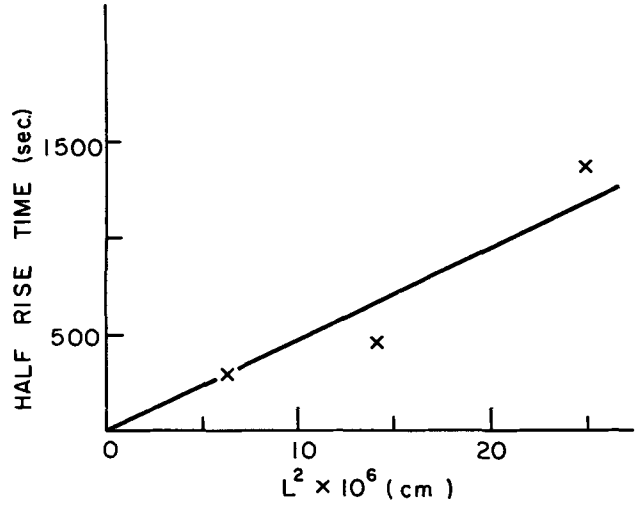

Fig. 3. Half rise time (t_γ for $\gamma = 0.5$) as a function of L^2. Cathodic current density 0.5 ma cm^{-2}, 70°C.

tion, in particular the amount and nature of surface poison added, while D is independent of these quantities.

Heat of activation for diffusion.—The diffusion coefficient was studied as a function of temperature over the range of 50°-80°C, using a polarization current density of 0.5 ma/cm^2. A straight semilogarithmic plot was obtained up to 70°C, giving an apparent energy of activation of 9.6 kcal/mole for the diffusion process (Fig. 4).

Above 70°C the value of D dropped sharply, as shown by the three lower points in Fig. 4, taken at 72.5°, 75°, and 80°C. However, when the polarizing current density was reduced to 0.2 ma/cm^2, higher diffusion coefficients were measured, which fall on a straight line with values obtained at lower temperatures, as shown in Fig. 4.

The interpretation of this phenomenon lies in the decrease of critical current density $i_{crit.}$ at which embrittlement occurs with increasing temperature. Thus, at 70°C or below, the cathodic current applied was less than $i_{crit.}$, and a regular transient resulted. Above 70°C $i_{crit.} < 0.5$ ma/cm^2 and the form of the transient is distorted, giving rise to an apparent low value of

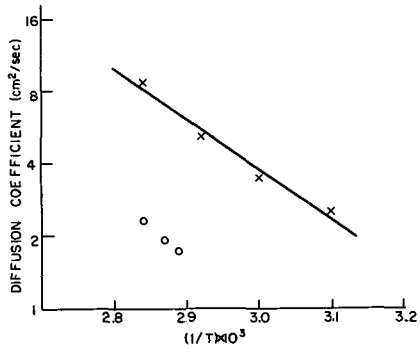

Fig. 4. Semilogarithmic plot of D vs. 1/T. L = 3.8 x 10^{-3} cm

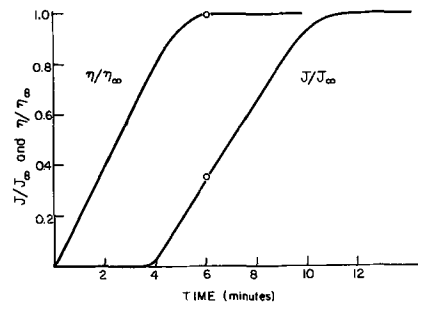

Fig. 5. Plots of (normalized) cathodic overpotential and permeation rate as a function of time. L = 3.8 x 10^{-3}, 70°C.

D. When the polarizing current is reduced to 0.2 ma/cm^{-2} (which is less than $i_{crit.}$ at 80°C) a value of D is obtained which is consistent with those at lower temperatures. It may be concluded, hence, that the diffusion coefficient is independent of the applied cathodic current density, as long as this is kept below a critical value. This may be regarded as further evidence that the permeation process is diffusion controlled in these systems, and that a critical change in the internal structure of the metal takes place at $i_{crit.}$.

Variation of overpotential with time.—Figure 5 shows the variation of cathodic overpotential with time during a permeation transient at 70°C. Both the overpotential η and the permeation rate J are plotted on a normalized scale as η/η_∞ and J/J_∞ in the same experiment. It may be seen that the overpotential reaches its steady-state value when $J/J_\infty = 0.35$, *i.e.*, at a time t_γ corresponding to $\gamma = 0.35$. Repeated experiments under a variety of conditions show that η/η_∞ approaches unity at times t_γ corresponding to $\gamma = 0.25$-0.50. The steady value of the overpotential reached after a relatively short time in these experiments is in contrast to the long time variation of η observed in hydrogen evolution studies on platinum (9).

The variation of η with time during the transient may be interpreted in terms of a change in the properties of the electrode due to hydrogen absorption. Thus, when steady-state permeation is attained the concentration of hydrogen at any point in the metal reaches a constant, time-independent value and no further change in overpotential will occur. The question still remains why the overpotential reaches a steady-state value when J_t/J_∞ is substantially smaller than unity. Figure 6 shows the calculated concentration profile of hydrogen in the metal at times t_γ corresponding to $\gamma = 1.0$; 0.5; 0.35; 0.25. At low values of x/L (*i.e.*, close to the cathodic surface) the concentration approaches its steady-state value when $\gamma > 0.25$. Figure 7 shows the variation of C with time at a distance x from the cathodic surface such that $x/L = 1/16$. The concentration of hydrogen inside the metal

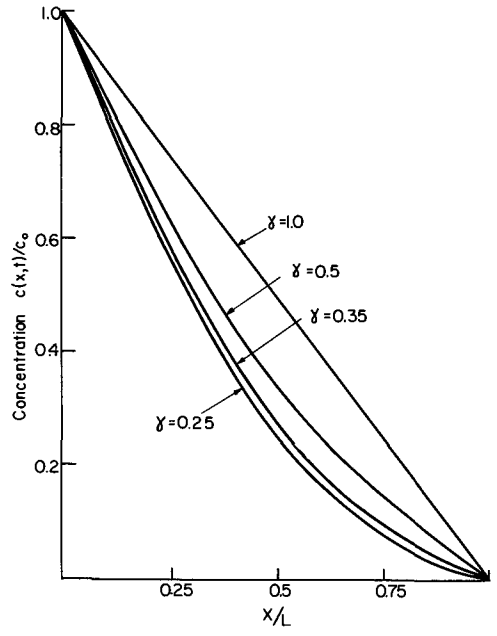

Fig. 6. Calculated concentration profiles of absorbed hydrogen in the metal foil at various times during the transient.

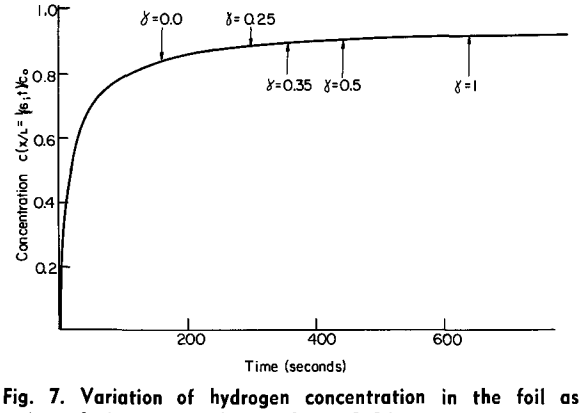

Fig. 7. Variation of hydrogen concentration in the foil as a function of time at a plane x/L = 1/16.

rises initially very rapidly and reaches 91% of its steady-state value at the break-through time.[2] At $\gamma = 0.25$ the concentration has reached 96% of its steady-state value and thereafter it changes very slowly with time. Since the cathodic overpotential depends on the state of the surface and perhaps a region in the bulk of the metal close to the surface ($x/L << 1$) it will not be expected to change much with time when γ has reached a value of 0.25-0.5, in agreement with experiment.

At room temperature D is about one order of magnitude smaller than at 70°. The time required for a wire electrode of 0.5 mm diameter to become saturated with hydrogen under these conditions is of the order of 50 hr, and the overpotential may hence be expected to change with time at constant current density for at least 10-20 hr.

Support for the view that hydrogen absorption in Pt can affect the kinetic parameters on the surface is found in recent studies of the potential of zero charge of Pt (10) which was found to depend critically on the presence of absorbed hydrogen. Also, time variation of the overpotential for hydrogen evolution on Pd cathodes was observed by Frumkin and Aladgalova (11) and interpreted similarly in terms of the changes in the metal structure caused by absorption of hydrogen.

[2] The break-through time has been defined (6) as the time elapsed between turning on the cathodic current and the emergence of the first measured amount of hydrogen on the anodic side.

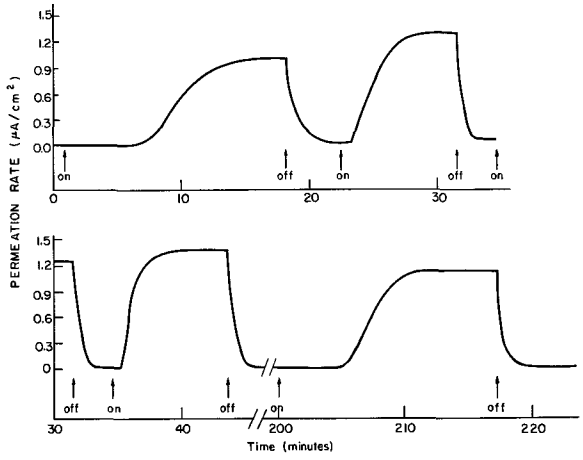

Fig. 8. Successive permeation transients through a foil. L = 2.5 x 10^{-3} cm, 70°C, cathodic current density = 0.1 ma cm^{-2}.

Stability of absorbed hydrogen in platinum.—Results of an experiment in which the cathodic polarization current density was switched on and off several times are shown in Fig. 8. The observations in this experiment may be summarized as follows: (*A*) The first transient differs substantially from following transients. The difference between the second and third transient, on the other hand, is small. (*B*) When the cathodic current is switched off the transient decays rapidly (the permeation current goes to zero within 3-4 min). (*C*) With the cathodic current switched off and the anodic potential maintained (*i.e.*, a condition where the hydrogen already in the metal is being "pulled out" while no new hydrogen is introduced) the membrane recovers very slowly to its original state. In the experiment shown in Fig. 8, 150 min were not quite enough to restore the original state of the membrane, even though the transient taken after this time resembles much closer the first transient than the second and third transients, which were taken a few minutes after the current was switched off (cf. Fig. 8).

In the case of hydrogen permeation through iron it has been shown (7, 8) that hydrogen diffuses through the lattice and not along grain boundaries. If this applies also to Pt, then hydrogen will move from one interstitial site to another, and in its interstitial position will cause a certain strain in the lattice structure. It can easily be shown (12) that under these conditions an uneven distribution of hydrogen in the metal will result, and points of local strain will constitute "islands" where the concentration of hydrogen will be larger than in the bulk.

A simple equilibrium of the type

$$H_b \underset{k_{-1}}{\overset{k_1}{\rightleftharpoons}} H_i \qquad [5]$$

may now be considered, where H_b is a hydrogen atom in a lattice site in the bulk of the metal and H_i is an atom of hydrogen in an island. If H_i represents a substantially more stable state than H_b, then the equilibrium constant $K = k_1/k_{-1}$ will be much larger than unity. Thus most atoms will reside on islands rather than in the bulk, and the rate of reaching an island will be much larger than the rate of escape from it.

Consider now the experimental evidence shown in Fig. 8 in the light of this model. During the first transient, hydrogen diffuses slowly through the metal because most of it is used to saturate the islands of high strain. When the cathodic current is switched off, hydrogen atoms from the bulk lattice diffuse out relatively quickly, but their escape from the islands of high strain is slow and does not occur to an appreciable extent within a few minutes. When the cathodic current is switched on again, diffusion occurs

through a hydrogen-loaded membrane, *i.e.*, one in which the islands of strain have already been saturated with hydrogen. Diffusion through such a membrane occurs much faster, as evidenced by the shorter transient (cf. the second and third transients in Fig. 8). When the cathodic current is switched off for several hours the hydrogen atoms absorbed in islands of high strain slowly diffuse out, and the initial state of the membrane can be restored.

An order of magnitude type calculation of the ratio of rate constants in Eq. [5] may be made on the basis of the data presented in Fig. 8.

From the shape of the second and third transients it may be inferred that saturation of the islands has almost, but not quite reached equilibrium during the first transient which lasted 18 min. On the other hand, the original state of the membrane was almost restored in 150 min between the third and the fourth transient. The amount of hydrogen taken out from the membrane after the current is switched off may be obtained from the area under the permeation decay transients in Fig. 8. The charge measured is $Q = (2\text{-}4) \times 10^{-4}$ coulombs. Thus

$$C_o = 2\overline{C} = 2Q/FV \qquad [6]$$

where $\overline{C}$ is the average concentration of free hydrogen in the metal, Q is the measured charge during decay, and V is the volume of the membrane. For a 1 cm^2 membrane having a thickness of 2.5×10^{-3} cm, this gives $C_o = (1.6\text{-}3.2) \times 10^{-6}$ gram atom/cm^3, as compared to a total concentration of 2.7×10^{-5} gram atom/cm^3 obtained above. Thus about 85-95% of all the hydrogen absorbed in Pt is concentrated in areas of high strain, and $K = 8\text{-}17$.

The diffusion coefficient calculated from the third transient is about 7 times that obtained from the first transient. It is this diffusion coefficient which should be used in Eq. [4] to obtain the concentration (C_o) of free hydrogen absorbed in the bulk of the metal. This gives rise to $C_o = 3.8 \times 10^{-6}$ gram atom/cm^3 and $K = 6$. It may thus be concluded that 85-95% of the hydrogen absorbed in Pt is concentrated in islands of local strain which are in slow equilibrium with hydrogen absorbed in the bulk. The equilibrium constant for the transfer of hydrogen atoms from the bulk to an island (Eq. [5]) is in the range of 6-17, and the time required to saturate an island is about ten times shorter than the time required to eliminate all the hydrogen from the metal under a given set of conditions.

Conclusions

The permeation of electrolytically generated hydrogen through Pt membranes has been observed directly in the temperature range of 50°-80°C. The process is shown to be diffusion controlled at steady state and during the transient. The diffusion coefficient at 70°C is 3.4×10^{-9} cm^2/sec, and the apparent energy of activation for the diffusion process is $\Delta H^{\neq}_D = 9.6$ kcal/gram atom. The total concentration of absorbed hydrogen just below the cathodic surface is $C_o = 2.7 \times 10^{-5}$ gram atom/cm^3. Most of the absorbed hydrogen is concentrated in regions of local strain in the crystal and only some 5-15% is free to move through the lattice. Hydrogen atoms absorbed in regions of local strain are relatively stable and take much longer to diffuse out than in.

Hydrogen permeation becomes detectable only when the cathodic surface of the membrane is poisoned, as others have found (2). Hydrogen embrittlement was found to occur, as in the case of iron and steel (7, 8). The overpotential for hydrogen evolution was shown to depend on the concentration of absorbed hydrogen just under the cathodic surface. Calculation using an experimental value of the diffusion coefficient shows that in a typical experiment at room temperature a variation of cathodic overpotential due to this effect could be observed for up to 10-20 hr.

Acknowledgment

The authors are grateful to the National Science Foundation for the support of this work under grant No. GK40.

Manuscript received Dec. 16, 1965; revised manuscript received June 10, 1966.

Any discussion of this paper will appear in a Discussion Section to be published in the June 1967 JOURNAL.

REFERENCES

1. O. W. Richardson, J. Nicol, and T. Parnell, *Phil. Mag.*, **8**, 1 (1904).
2. J. P. Hoare and S. Schuldiner, *This Journal*, **103**, 237 (1956).
3. V. L. Kheifets and B. S. Krasikov, *Doklady Acad. Nauk. SSSR*, **109**, 586 (1959).
4. S. Schuldiner and T. B. Warner, *This Journal*, **112**, 212 (1965).
5. M. A. V. Devanathan and Z. Stachurski, *Proc. Roy. Soc.*, **A270**, 90 (1962); *This Journal*, **111**, 619 (1964).
6. J. McBreen, L. Nanis, and W. Beck, In course of publication.
7. J. O'M. Bockris, J. McBreen, and L. Nanis, *This Journal*, **112**, 1025 (1965). cf. also W. Beck, J. O'M. Bockris, J. BcBreen, and L. Nanis, *Proc. Roy. Soc.*, **290A**, 220 (1966).
8. J. McBreen, Ph.D. Dissertation, University of Pennsylvania, 1965.
9. J. O'M. Bockris, I. A. Ammar, and A. K. M. S. Huq, *J. Phys. Chem.*, **61**, 879 (1957).
10. E. Gileadi, S. D. Argade, and J. O'M. Bockris, *J. Phys. Chem.*, **70**, 2044 (1966).
11. A. N. Frumkin and Aladjalova, *Acta. Physicochim. URSS*, **19**, 1 (1944).
12. J. O'M. Bockris and A. K. N. Reddy, "A Course in Modern Electrochemistry," Vol. II, Plenum Press (1967).

Electrochemistry of the Lithium Hydride Cell

James A. Plambeck,[1] John P. Elder,[2] and H. A. Laitinen[3]

Argonne National Laboratory, Argonne, Illinois

ABSTRACT

The hydrogen/lithium hydride electrode, which is of interest in thermally regenerative fuel cells, has been studied in fused LiCl-KCl eutectic at 375°C by voltammetric and chronopotentiometric techniques. The diffusion coefficient of LiH under these conditions is $1.67 \pm 0.04 \times 10^{-5}$ cm²/sec. Differences between anodic chronopotentiograms obtained using tungsten and iron flag electrodes are discussed.

Considerable attention has been directed toward thermally regenerative ionic hydride cells as direct energy conversion devices (1). As a consequence, a study of the electrochemistry involved in the operation of such cells is of potential interest. Such an investigation is described in this paper.

Lewis (2) initiated the electrochemical studies of saline hydrides when he showed that molten lithium hydride will conduct electricity. Moers (3), Peters (4), and Potter and Bockris (5) have studied the electrolysis of solid lithium hydride. In all cases, simultaneous cathodic deposition of lithium and anodic evolution of hydrogen were observed. Bardwell (6) dissolved calcium hydride in molten purified LiCl-KCl eutectic at about 365°C; electrolysis of these solutions evolved hydrogen at the iron anode in amounts calculated from Faraday's law for the discharge of hydride ion. This work has been questioned by Potter and Bockris (5) who were unable to detect any anodically evolved hydrogen from a solution of calcium hydride in this eutectic.

Johnson *et al.* (7) concluded from LiH-LiCl solid-liquid equilibrium studies that polymerization of lithium hydride in lithium chloride does not occur. Similar studies (8) of the LiH-NaCl reciprocal system yield evidence for the existence of unionized monomeric lithium hydride in dilute solutions in molten chlorides. Johnson and Heinrich (9) have made equilibrium potential measurements on cells of the type $H_2(g)/LiH(x)$, $LiCl(1-x)/Li^0(liq.)$ using iron as the inert electrode material. The concentration dependence of the potential corresponded to one electron/LiH and the pressure dependence to two electrons/hydrogen molecule. The electrochemical equilibrium was apparently established at the three-phase solid iron-fused salt electrolyte-hydrogen gas interface.

Qualitative data on thermally regenerative fuel cells using lithium hydride have been reported (10-13). Indig and Snyder (14) have studied the lithium hydride-hydrogen electrode in LiCl-KCl eutectic and have shown apparent one-electron Nernstian behavior in concentration cells. These authors interpreted their coulombic efficiency data on the basis of two competing reactions, $LiH \rightarrow Li^+ + \frac{1}{2}H_2 + e^-$ and $LiH \rightarrow Li^+ + H^+ + 2e^-$. Additional evidence cited for the occurrence of the latter was the evolution of hydrogen at the cathode, presumably from discharge of H^+. Inasmuch as the reaction $H^+ + LiH \rightarrow H_2 + Li^+$ can be expected to occur in any melt containing lithium hydride, the two-electron oxidation appears unlikely and the cathodic hydrogen evolution is probably due to some reaction involving impurities; such reactions have been studied in this solvent (15, 16).

[1] Present address: Department of Chemistry, University of Alberta, Edmonton, Alberta, Canada.

[2] Present address: Metals and Controls Division, Texas Instruments Inc., Attleboro, Massachusetts.

[3] Present address: Noyes Laboratory of Chemistry, University of Illinois, Urbana, Illinois.

Experimental

Apparatus.—Any investigation of a system involving molten alkali metals and their salts requires the maintenance of an inert atmosphere of high purity. These conditions have been achieved by the development (17) of a helium-atmosphere purification unit. In normal operation, the impurity levels in the inert-atmosphere box are less than 0.5 ppm water and less than 10 ppm total for oxygen and nitrogen.

The cell was operated in a furnace well attached to the base of such a box. The reactivity of molten lithium and molten salt solutions of this metal severely limits the cell design. Molten lithium has a finite solubility in LiCl-KCl eutectic. Up to the present time, no suitable electrical insulator has been found capable of withstanding prolonged attack by molten lithium or molten-salt solutions of this metal. Accordingly, all electrodes must be suspended from an insulator above the solution.

A diagram of the cell is shown in Fig. 1. All materials except the pin vise, which was nickel-plated steel, and where otherwise stated, was type 316 stainless steel. The two lithium cup electrodes and the two stainless steel-sheathed chromel-alumel thermocouples (Pyro Electric, Inc., Walkerton, Indiana) were symmetrically located with respect to the central indicating electrode, which was supported by the pin vise.

The inner crucible fitted into the furnace well. To reduce thermal gradients, the outer surface of the well was covered with ⅛ in. nickel-plated copper over a length 5 in. from the base. With an electrolyte depth of 1½ in., the electrolyte surface temperature was 371°-372°C when the bulk temperature was maintained at 375°C. The liquid lithium electrodes were held below the electrolyte surface on cylindrical metal sponges fitted into the stainless steel cups. The stainless steel sponge (Huyck Metals, Milford, Connecticut) was wetted by liquid lithium at 600°C and held it with great tenacity; the lithium did not detach from its support on immersion in the molten electrolyte. By placing a cap with a small central orifice on top of the cup, the rate of solution of lithium in the electrolyte was rendered negligible. The thermocouple sheaths and electrode leads passed through nylon-lined brass tubes which extended from the bottom of the cell head base into the box. At the head of each brass tube was a modified, nylon-lined brass vacuum coupling (Type C, Vacuum Electronics Corporation, Chicago, Illinois). The electrode leads were connected to micrometer depth gauges (No. 605, Brown and Sharpe Manufacturing Company, Providence, Rhode Island). A stepless temperature controller (JYSCR set point unit, PSCR-27-120 power unit; West Instrument Corporation, Schiller Park, Illinois) operated the furnace (Marshall Products Company, Columbus, Ohio). Tem-

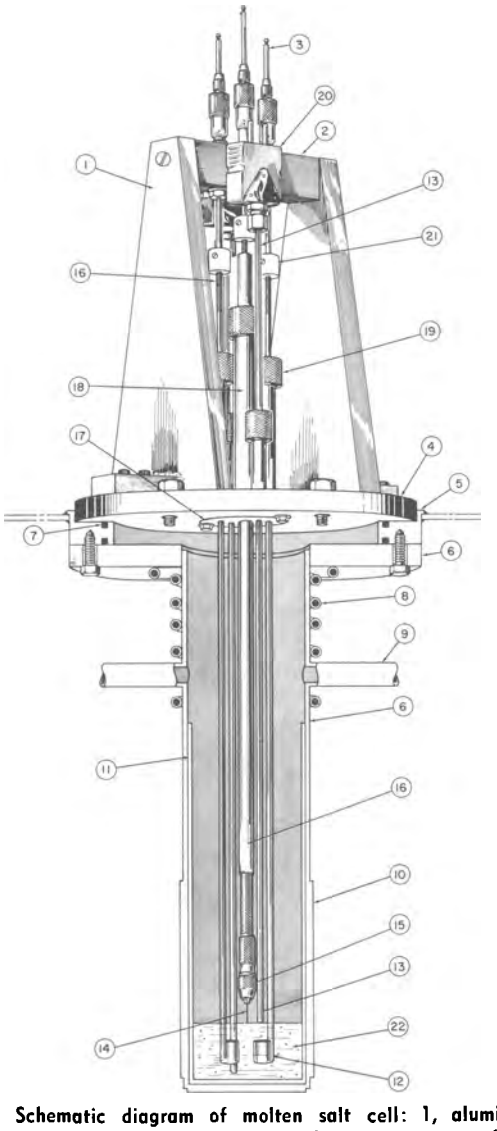

Fig. 1. Schematic diagram of molten salt cell: 1, aluminum depth gauge support; 2, Micarta insulating bar; 3, micrometer depth gauge; 4, cell head base; 5, base of box; 6, furnace well; 7, "O" ring seal; 8, water cooling coils; 9, gas inlet; 10, copper sheath; 11, crucible; 12, lithium cup electrode; 13, thermocouple; 14, wire microelectrode or flag electrode; 15, pin vise; 16, electrode lead rod; 17, insulating disk; 18, nylon-lined brass tube; 19, insulating vacuum coupling; 20, thermocouple connector block; 21, nylon insulating connector; 22, electrolyte.

peratures in the furnace were monitored with a recording potentiometer (Honeywell, Minneapolis, Minnesota). The bulk electrolyte temperature was controlled to ±0.5°C. The disparity in the areas of the microelectrode and the lithium cup electrode was such that, for the minute currents which passed through the cell, the latter electrode remained unpolarized.

A Model XV polarograph (E. H. Sargent and Company, Chicago, Illinois) was used to obtain the voltammetric data. Chronopotentiometric measurements were made using conventional solid-state circuits specifically designed for a low-impedance system; the current-time traces were displayed on a Model 7664 oscilloscope equipped with a Model 453-A1 Polaroid camera (Fairchild Dumont Laboratories, Clifton, New Jersey).

Materials.—Lithium hydride was prepared and analyzed as described by Johnson, Wood, and Crouthamel (7). Lithium metal (Foote Mineral Company, Philadelphia, Pennsylvania), supplied sealed under an argon atmosphere, had an impurity level less than 0.003% with respect to sodium, potassium, chlorine, and nitrogen. Prior to use in the cell, the requisite amount of lithium was taken and trimmed to a bright surface. The LiCl-KCl eutectic (59 mole % LiCl, mp 352°C (18); Anderson Physics Laboratories, Inc., Champaign, Illinois) had been purified with HCl (19) followed by displacement of heavy metal impurities with magnesium. Commercial hydrogen gas was purified by a silver-palladium alloy diffusion apparatus (Milton Roy Company, Park Ridge, Illinois). The voltammetric microelectrode was a 0.009 in. iron wire (B and A Reagent, Allied Chemical Company, New York). The chronopotentiometry flags were cut from 0.01 in. Armco ingot iron sheet or fabricated from 0.04 in. sheet tungsten flags welded to tungsten wires under helium.

The crucible, electrodes, and thermocouples which came in contact with the molten electrolyte were cleaned mechanically, rinsed in water and acetone, evacuated, and stored in the helium atmosphere box. These components were assembled to the cell head, heated in hydrogen at 900°C for 16 hr, and evacuated to remove any remaining oxide films prior to loading of the cell. All cell materials were weighed, trimmed, and loaded into the cell inside the high-purity helium atmosphere box. The time expended in these operations was kept to a minimum, and the furnace well containing the cell was sealed from box atmosphere with the gastight head. The well atmosphere was evacuated and the well refilled with hydrogen or helium before the cell was heated to 375°C.

Procedures.—The LiCl-KCl eutectic held at 375°C was saturated with lithium prior to studies of the lithium hydride system by immersing a fiber metal sponge soaked with lithium metal in the melt for several days. Displacement of potassium by lithium did not become noticeable as long as the temperature was kept below 450°C.

To obtain reproducible voltammetric data it was necessary to record the cell current at each potential until a steady-state condition (±0.1 μa) was attained; the time required varied from 3 to 30 min. Although the geometric area of the microelectrode could not be determined accurately since it was not defined by an insulating material, it was estimated to average 5×10^{-3} cm^2 by microscopic examination at the conclusion of several experiments. The geometric area of each flag electrode used in the chronopotentiometric studies was measured with a micrometer.

The currents applied to the chronopotentiometry cell were such that the transition times were one second or less. Five minutes were allowed to elapse between successive current pulses; delays of 5, 10, and 30 min between pulses produced identical chronopotentiograms, but delays of less than 5 min produced shorter transition times. Mechanical stirring of the cell between pulses was not feasible, and it was therefore necessary to rely on convective mixing in the cell.

Analyses of solutions of lithium and lithium hydride in the melt were carried out by acidimetric titration of hydrolyzed samples.

Results and Discussion

Curves A and B in Fig. 2 show the current-potential relationships for the electrolyte and lithium-saturated electrolyte respectively, both in a helium atmosphere. In the fused salt electrolyte alone the iron dissolution potential was +1.48v (all potentials are given with respect to the $Li^o(l)/Li^+$ reference electrode). In the lithium-saturated electrolyte, the iron dissolution potential is +2.13v. The discrepancy of +0.65v can be explained by assuming that on introduction of the lithium electrode into the unsaturated electrolyte a displacement reaction $2Li^o + Mg^{++} \rightarrow Mg^o + 2Li^+$ proceeds and magnesium is deposited on the surface of the electrode. This creates a Mg^o/Mg^{++} electrode system, whose standard potential (20) is +0.72v. The

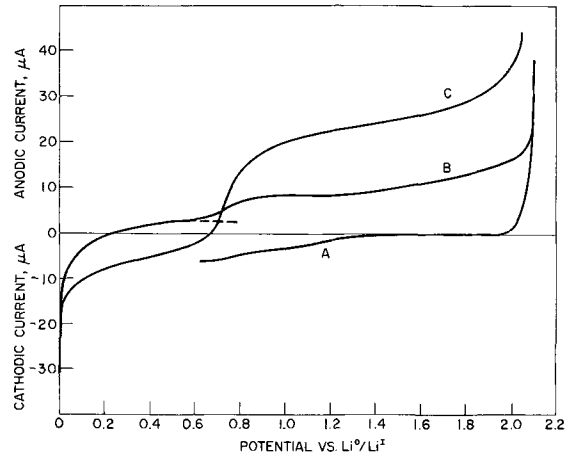

Fig. 2. Voltammetric data for the lithium hydride cell, LiCl-KCl eutectic, 375°C, iron microelectrode. (A) Electrolyte alone, helium atmosphere, 760 mm Hg; (B) lithium-saturated electrolyte, helium atmosphere, 760 mm Hg; (C) lithium-saturated electrolyte, hydrogen atmosphere, 760 mm Hg.

potential of this magnesium quasireference electrode is less positive than the standard potential due to the low concentration of magnesium ion in solution.

The section of curve B, Fig. 2, from 0 to +0.6v is characteristic of the oxidation of soluble lithium. The succeeding step can be analyzed using the Heyrovsky-Ilkovic equation (21) which gives $E_{1/2} = +0.74$v and $n = 1.1$. This step appears to be characteristic of lithium hydride oxidation. Although neither lithium hydride nor hydrogen was added to the cell, residual hydrogen from the preheating of the metallic parts in hydrogen could form lithium hydride by reaction with lithium metal dissolved in the fused salt. Since the stainless steel apparatus weighed several kilograms, it can be calculated (22) that more than enough hydrogen to produce the observed amount of LiH could have come from the stainless steel components. This amount of hydrogen would not, however, be sufficient to remove all lithium from solution, and thus the lithium oxidation wave should also be present.

Curve C, Fig. 2, was obtained for the same sample of lithium-saturated electrolyte, containing no added LiH, which had been held under 1 atm of hydrogen for two days. The shape and position of this curve, whose $E_{1/2}$ is the same as that of B, is characteristic of the lithium hydride-hydrogen system (compare with curve B, Fig. 3, which was obtained for the same electrolyte sample with solid LiH added). Between 0 and +0.66v activation effects appear to contribute toward the cathodic polarization inasmuch as the current is nowhere independent of the potential applied. A mass transfer-limited oxidation rate is attained at potentials more positive than +0.70v; this conclusion is supported by Fig. 4. The data of curve C, Fig. 2, are in accordance with the linear relationship shown in Fig. 4 on the assumption that all of the dissolved lithium was converted to lithium hydride by reaction with the hydrogen atmosphere over the two-day waiting period. Further evidence for this assumption is the fact that the blue color and anodic lithium wave characteristic of the lithium-saturated solvent disappeared during this time.

Curve B, Fig. 3, was observed for a dilute lithium hydride solution. As the microelectrode is made increasingly positive (forward polarization), at +0.40v the cathodic current approaches zero rapidly and becomes anodic (broken line). Between +0.48 and +0.52v, the anodic current becomes unstable, falls to zero, and finally attains a cathodic value commensurate with the extrapolation of the prepeak curve. Beyond this region steady currents are observed until the limiting anodic region is reached. In the limiting anodic region (+0.7 to +2.1v) the random current fluctuations observed are probably due to bubble formation during hydrogen gas evolution. The anodic limiting currents are directly proportional to the LiH concentration (Fig. 4). On reverse polarization, similar peaking behavior, but in a cathodic direction, is observed. If a steady-state condition is attained at each potential setting, this cathodic dip can be greatly minimized; such is not the case for the forward polarization anodic peak. Curve A, Fig. 3, is the current-voltage relationship for a saturated lithium hydride solution (*ca.* 5.0 mole % LiH). Stable currents are observed throughout except for random fluctuations in the anodic hydrogen evolution region. Curve B approaches A as the concentration of LiH increases. The peaking effect is observed until saturation is attained. For both forward and reverse polarization, the potential of maximum current increase in the unstable region is +0.42v. Similar peaking was observed when the iron microelectrode was replaced by a tungsten microelectrode of comparable size.

For a reversible electrochemical system containing soluble oxidized and reduced species and yielding composite anodic-cathodic polarization data, a form of the Heyrovsky-Ilkovic equation is valid (23). In Fig. 5, curve B of Fig. 3 is reproduced together with its analysis according to this equation. The value of the anodic limiting current $I_{L,A}$ was 73.0 μa. There is no well-defined cathodic plateau region, but the slope of the curve is minimal at +0.32v; the current at this potential was arbitrarily taken as the cathodic limiting current $I_{L,C}$. From eleven such plots obtained at different hydrogen pressures and hydride concentrations the mean n in the anodic region (line A) was 1.079, standard deviation, σ, 0.040, electrons/LiH. The

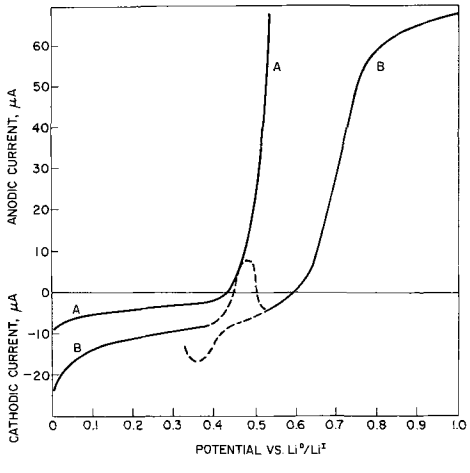

Fig. 3. Voltammetric data for the lithium hydride cell, LiCl-KCl eutectic, 375°C, iron microelectrode, hydrogen atmosphere, 760 mm Hg. (A) Lithium hydride-saturated electrolyte, *ca.* 5 mole % LiH; (B) unsaturated electrolyte, 8 x 10^{-2} mole % LiH.

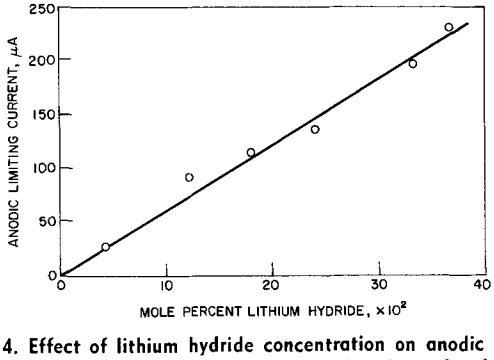

Fig. 4. Effect of lithium hydride concentration on anodic limiting current, LiCl-KCl eutectic, 375°C, iron microelectrode; hydrogen atmosphere, 760 mm Hg.

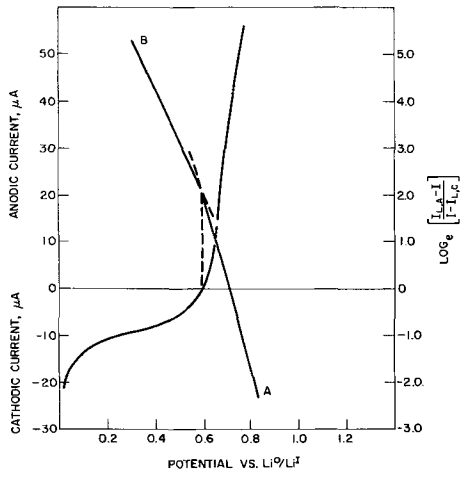

Fig. 5. Heyrovsky-Ilkovic analysis of voltammetric curve, LiCl-KCl eutectic, 375°C, iron microelectrode, 8 x 10^{-2} mole % LiH, hydrogen atmosphere, 760 mm Hg.

slope of the log plot line B varies in a random manner with the hydrogen pressure and amount of added hydride; in all cases, however, it is significantly less than that of A, as would be expected if the reduction occurring in this potential region involves at least one slow stage. The change of slope occurs at the zero current potential. Analysis of all the polarization data indicates that the cathodic reduction of hydrogen, but not the anodic oxidation of hydride, is characterized by an appreciable activation polarization under different experimental conditions.

If charge transfer processes are rate-determining, this rate can be expressed in terms of the equation below (24-26)

$$|\eta| = \frac{RT}{\beta\lambda F}\left[\ln I_C - \ln\left\{1 - \exp\left(\frac{-|\eta|\lambda F}{RT}\right)\right\}\right] - \frac{RT}{\beta\lambda F}\ln I_C^{\circ}$$

where I_C° is the exchange current, β the symmetry factor, η the cathodic overpotential, and λ the electron number. The electron number is n/ν where ν is the stoichiometric number (24).

Curve A, Fig. 6, is a graph of $|\eta|$ as a function of the cathodic current. It is difficult to be certain of the currents when the cathodic overpotential is much greater than 0.1v due to the proximity of the unstable peaking region. When $|\eta|$ is between 0 and 0.1v there is no linear (Tafel) region, which indicates that the data should be analyzed in terms of the equation given above.

A plot of $|\eta|$ *vs.* the logarithmic term in square brackets will be linear if and only if the correct value of λ is chosen. Examples of such plots are shown by curves B and C, Fig. 6. For $2 > \lambda > 1$, a family of curves intermediate between B and C is obtained; for $1 > \lambda > 0$ similar behavior is observed with curvature in the opposite sense. As can be seen, the correct choice is $\lambda = 1.0$. Similar analyses of data obtained at lower hydrogen pressures yield the same result. It is therefore concluded that the over-all kinetics of the electrochemical reduction reaction are governed by either a slow one-electron transfer step or a one-electron transfer step coupled with a slow chemical step. Although the uncertainty in the electrode area does not permit accurate determination of the exchange current density, it appears to be about 1 ma/cm². This is considerably lower than the exchange currents for metal-metal ion couples in LiCl-KCl eutectic at 450°C (27).

The time-current relationship at constant current for an electrode process under linear diffusion control (28) is $I\tau^{1/2} = 1/2\ nFAD^{1/2}\pi^{1/2}C$ where I is the current (amp), τ is the transition time (sec), C is the bulk concentration of the diffusing ion (moles cm^{-3}), D is the diffusion coefficient (cm^2sec^{-1}), A is the electrode area (cm^2), and the remaining terms have their usual significance. If the reaction is diffusion-controlled, $I\tau^{1/2}$ is independent of I for a given concentration of electroactive species. The amount of LiH present used in the calculation of the bulk concentration was the sum of the amount of LiH added and the amount formed from the lithium-saturated LiCl-KCl.

Chronopotentiometric measurements were made using tungsten flag electrodes. These anodic chronopotentiograms (Fig. 7) consistently contained four separate plateaus, A-D. Plateau D, due to chlorine evolution, occurs at +3.1v. A transition time could not be measured for plateau B, which appeared only as a change of slope in the potential-time curve and is probably due to the presence in the melt of an oxidizable impurity whose concentration is 10^{-4}M or less.

Plateau A is ascribed to the oxidation of lithium hydride since the transition time increased on the addition of lithium hydride to the cell. The potential of this plateau ranged from +0.5 to +0.7v, in agreement with the potential at which the voltammetric hydride wave was observed. The length and potential of this plateau appeared to be independent of hydrogen pressure. The value of $I\tau^{1/2}$ remained constant as the current density was varied from 0.1 to 4 amp/

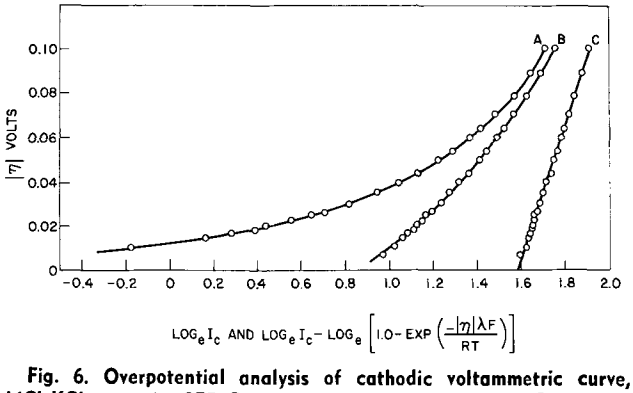

Fig. 6. Overpotential analysis of cathodic voltammetric curve, LiCl-KCl eutectic, 375°C, iron microelectrode, 8 x 10^{-2} mole % LiH; hydrogen atmosphere, 760 mm Hg. (A) $|\eta|$ *vs.* $\log_e I_C$; (B) $|\eta|$ *vs.* $\log_e I_C - \log_e\left[1.0 - \exp\left(\frac{-|\eta|\lambda F}{RT}\right)\right]$, $\lambda = 2.0$; (C) $|\eta|$ *vs.* $\log_e I_C - \log_e\left[1.0 - \exp\left(\frac{-|\eta|\lambda F}{RT}\right)\right]$, $\lambda = 1.0$.

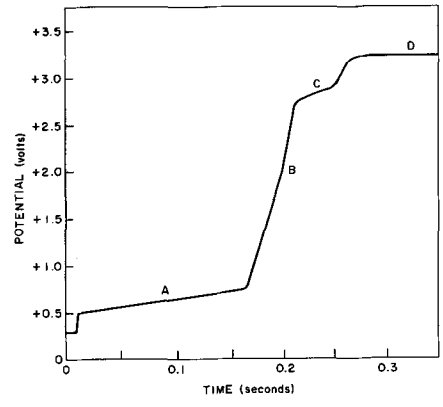

Fig. 7. Chronopotentiogram with tungsten electrode, LiCl-KCl eutectic, 375°C, electrode area 0.345 cm^2, current 129.7 ma, LiH 0.2568M.

Table I. Chronopotentiometric data, tungsten electrode*

Current, amp	Transition time A, sec	Transition time C, sec	$I_0\tau_A^{1/2}$, amp $sec^{1/2}$ cm^{-2}	$I_0\tau_C^{1/2}$ amp $sec^{1/2}$ cm^{-2}
0.0817	0.4110	0.0600	0.1525	0.0583
0.1297	0.1690	0.0260	0.1548	0.0580
0.1889	0.0795	0.0150	0.1545	0.0672
0.1889	0.0808	0.0138	0.1557	0.0643
0.2455	0.0480	0.0088	0.1565	0.0670
0.3049	0.0305	0.0046	0.1545	0.0600
0.3636	0.02025	0.00365	0.1501	0.0638
0.4241	0.0155	0.00265	0.1530	0.0632
0.4858	0.01195	0.0025	0.1539	0.0704
0.6093	0.00758	0.0017	0.1536	0.0728
0.7345	0.00526	0.0012	0.1545	0.0736
0.9877	0.00283	0.0008	0.1525	0.0812
1.2425	0.00180	0.00055	0.1528	0.0846

* Cell hydrogen pressure 760 mm Hg; temperature 375.0 ± 0.5°C; electrode area 0.345 cm^2; LiH concentration 0.2568M.

cm^2. Data from a representative run are given in Table I. It is assumed that the over-all reaction on tungsten must be the two-electron process $2LiH \rightarrow H_2 + 2Li^+ + 2e^-$, as indicated by potentiometric studies (9). The over-all reaction cannot be $LiH + M{\cdot}H \rightarrow H_2 + Li^+ + e^-$ because the solubility of hydrogen in tungsten is negligible (29) and the values of $I\tau$ are such that an adsorbed monolayer could not supply enough hydrogen. On this basis the mean value of D was 1.67 x 10^{-5} cm^2/sec, σ, 0.04 x 10^{-5} (2.2%), from 39 determinations at hydrogen pressures from 0.5 to 1.0 atm and lithium hydride concentrations from 0.1 to 0.3M, over the range of current densities given above. This is in good agreement with the range of 0.6 to 3.5 x 10^{-5} cm^2/sec and precision of 2.6% reported for the diffusion coefficients of several metal ions in this eutectic at 450°C (30).

Plateau C was less well-defined than A and the changeover from C to D was often indistinct. The length and potential of C were independent of the amount of lithium hydride added to the cell and the hydrogen pressure above it; plateaus B, C, and D, but not A, were observed even with no added lithium hydride. Under all conditions $I\tau^{1/2}$ remained approximately constant as the current was varied. The potential (at $\tau/4$) of this plateau was +2.6 to +2.8v. The mean value of $nCD^{1/2}$ calculated for this plateau on the basis of linear diffusion control is 8 ± 1 x 10^{-7} cm^{-2} equiv $sec^{-1/2}$ using data taken over the ranges of conditions given above.

This plateau is ascribed to the oxidation of hydrogen to hydrogen ion, the standard potential, $E_M°$, of which is +2.61v (31). Quantitative analysis of this plateau does not appear to be possible even though $I\tau^{1/2}$ is approximately constant with I, indicating a diffusion-controlled process. It has been shown (32) that for stepwise reduction of diffusing species $\tau_2 = 3\tau_1$ when $n_1 = n_2$; the calculation is equally applicable to stepwise oxidation. In every LiH cell experiment, τ_2 and τ_1 were nearly equal with τ_2 being, in most cases, less than τ_1. This behavior can be explained on the basis that much of the hydrogen produced electrochemically leaves the electrode other than by diffusion; since the melt is saturated with hydrogen, such an explanation does not appear unlikely. The concentration of H_2 in the melt calculated from the value of $nCD^{1/2}$ given above would be about 0.1M. This is about one order of magnitude greater than the solubility of HF in molten fluorides (33) and three orders of magnitude greater than that of the rare gases in the same solvent (34, 35); it cannot be considered a true measure of the solubility of hydrogen in the melt.

Armco iron has been studied as an anode material in lithium hydride cells (36). For this reason chronopotentiometric studies were made using Armco iron as the flag electrode. These chronopotentiograms (Fig. 8) consistently contained only two plateaus. The second plateau corresponds in potential (20) to the oxidation of iron to Fe(II), which would occur without transition at an iron electrode. The first plateau is ascribed to the oxidation of lithium hydride since the transition time increased on addition of lithium hydride to the cell. Both τ and $I\tau^{1/2}$ decreased with decreasing hydrogen pressure at all lithium hydride concentrations studied. The value of neither $I\tau$ nor $I\tau^{1/2}$ was constant when the current density was varied under otherwise constant conditions. At low concentrations of lithium hydride, $I\tau^{1/2}$ increased with increasing I; as the concentration of lithium hydride was increased, the relative increase in $I\tau^{1/2}$ with I became less. The values of D calculated using the equation for linear diffusion control ranged from 3 times to 4000 times those determined with the tungsten electrode; the lowest values were obtained at high lithium hydride concentrations. Data from a representative run are given in Table II.

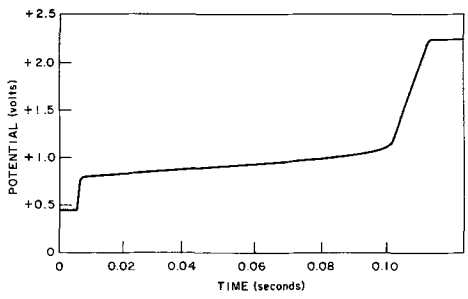

Fig. 8. Chronopotentiogram with iron electrode, LiCl-KCl eutectic, 375°C, electrode area 0.823 cm^2, current 860.2 ma, LiH 0.2662M.

Aqueous studies (37, 38) have shown that adsorption of the electroactive species causes the value of $I\tau^{1/2}$, and hence the calculated value of D, to increase with increasing current. Graphical attempts were made to fit all of the data taken using iron to each of the models discussed in these papers. Although no model could be successfully applied to all the data, the model in which an adsorbed layer is electrolyzed first followed by the diffusing species gave the best fit. These calculations are shown in Table III. The values of surface excess were calculated using the equation

$$I_0\tau = 1/2\, nFC\, \pi^{1/2}D^{1/2}\tau^{1/2} + nF\Gamma$$

for this model and the value of D calculated from the tungsten electrode studies. The slopes of the $I_0\tau - \tau^{1/2}$ plots were independent of hydrogen pressure while the surface excess calculated from the intercepts increased with hydrogen pressure. The surface excesses correspond to about 100 LiH monolayers, which is too thick a layer to be ascribed to an adsorption process. For this reason the adsorption models do not appear to explain these observations adequately.

These large surface excesses would be more reasonable if there were evidence for an increase in the

Table II. Chronopotentiometric data, iron electrode*

Current, amp	Transition time, sec	$I_0\tau^{1/2}$, amp $sec^{1/2}$ cm^{-2}
0.2455	0.5840	0.2279
0.3636	0.2200	0.2072
0.4858	0.1256	0.2092
0.6093	0.0820	0.2120
0.7345	0.0594	0.2175
0.8602	0.0457	0.2234
0.9877	0.0372	0.2315
1.1142	0.0313	0.2395
1.2425	0.0270	0.2481
1.3681	0.0237	0.2559
1.4974	0.0212	0.2649
1.6220	0.0186	0.2688
1.7486	0.0175	0.2811
1.8732	0.0155	0.2832
1.9978	0.0146	0.2934
2.1224	0.0135	0.2997

* Hydrogen pressure 760 mm Hg; temperature 375.0 ± 0.5°C; electrode area 0.823 cm^2; LiH concentration 0.2662M.

Table III. Diffusion-adsorption model calculations

Lithium hydride concentration, mole liter^{-1}	Hydrogen pressure, mm Hg	Surface excess, coul cm^{-2}
0.0208	760	0.0290*
0.0208	190	0.0094
0.0208	380	0.0120
0.0208	760	0.265*
0.0419	380	0.0150
0.0419	760	0.0202
0.0746	380	0.0119
0.0746	760	0.0229**
0.2662	380	0.0135
0.2662	760	0.0262
0.6349	380	0.0415*
0.6349	760	0.0200*
1.005	380	0.0130**
1.005	760	0.0130*

* Plot markedly nonlinear.
** Considerable scatter to the data.

true surface area of iron electrodes. Such evidence exists; in all experiments, only that part of the iron electrode in contact with the electrolyte appeared to be roughened, as indicated by a marked blackening of the surface. The remainder of the iron electrodes, and the entire surface of the tungsten electrodes, remained bright. The blackening did not appear to increase with successive runs, which is not unexpected as the surface was renewed for each pulse by going to iron dissolution.

When transition times were monitored repetitively at iron with decreasing time intervals between application of successive pulses and other conditions constant, the transition times decreased steadily for intervals of less than 5 min. They were constant when the intervals were longer than 5 min, suggesting some interaction that is slow but complete in about 5 min.

Both τ and $I\tau^{1/2}$ decreased with decreasing cell hydrogen pressure when iron electrodes were used (Fig. 9). The transition times observed for the first transition on tungsten were not affected by the hydrogen pressure. This observation, coupled with the longer transition times observed on iron and the dependence of surface excess on hydrogen pressure, cannot be explained except by the existence of some interaction, on iron, with the hydrogen gas above the melt. In this connection it should be noted that the solubility of hydrogen in iron, 0.34 cm^3 (STP)/100g at 375°C (39), is much greater than that in tungsten (29). There appears to be no significant difference in the potential at which the oxidation occurs on iron ($E_{\tau/4}$ = 0.7 — 0.8) and tungsten ($E_{\tau/4}$ = 0.6 — 0.7), implying that this interaction occurs before the current is applied and does not affect the oxidation potential.

The activation overpotential observed in the cathodic reduction of hydrogen may be involved with this slow interaction, and the interaction could give rise to the voltammetric anodic and cathodic peaks. An alternative explanation for the peaking consistent with the above discussion is given in the thesis of the first author.

In conclusion, the chronopotentiometric indication of a large value of surface excess on iron could be explained in part by a larger true surface area of the electrode and in part by the existence of some interaction between iron, lithium hydride in the melt, and hydrogen. A more quantitative understanding of these processes does not appear to be possible at this time. Quantitative analysis of the voltammetric work is difficult, since the meniscus region at which the microelectrode touches the melt can be quite complex as shown by aqueous work (40, 41). In the absence of suitable insulating materials this problem cannot be avoided. Quantitative analysis of the chronopotentiometric data for iron is difficult due

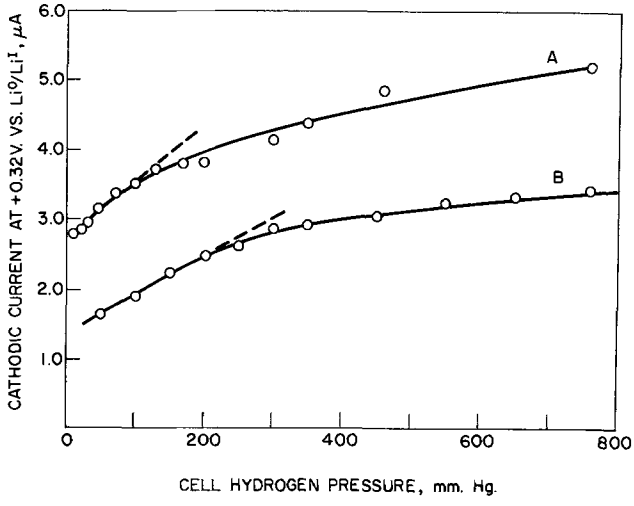

Fig. 9. Effect of hydrogen pressure on cathodic current at +0.32v, LiCl-KCl eutectic, 375°C, iron microelectrode. (A) Unsaturated electrolyte; (B) lithium hydride-saturated electrolyte.

to the complexity of the system, as well as a lack of general physical data related to hydride-melt systems.

Acknowledgment

Valuable discussions with Dr. C. E. Crouthamel and Dr. C. E. Johnson of Argonne National Laboratory are gratefully acknowledged.

Manuscript received October 28, 1965; revised manuscript received June 10, 1966. Work on this paper was performed under the auspices of the U.S.A.E.C. The paper was taken in part from the Ph.D. thesis of one of the authors (J.A.P.).

Any discussion of this paper will appear in a Discussion Section to be published in the June 1967 JOURNAL.

REFERENCES

1. R. C. Werner and T. A. Ciarlariello, U. N. Geneva Conference 35/GEN/14 (1961).
2. G. N. Lewis, *J. Am. Chem. Soc.*, **38**, 774 (footnote) (1916).
3. K. Moers, *Z. anorg. u. allgem. Chem.* **113**, 179 (1920.)
4. K. Peters, *ibid.*, **131**, 140 (1923).
5. E. C. Potter and J. O'M. Bockris. Colloques Intern. Centre Nat. Recherche Sci. (Paris), **39**, Electrolyse, C3-C6 (1952).
6. D. C. Bardwell, *J. Am. Chem. Soc.*, **44**, 2499 (1922).
7. C. E. Johnson, S. E. Wood, and C. E. Crouthamel, *Inorg. Chem.*, **3**, 1487 (1964).
8. C. E. Johnson, S. E. Wood, and C. E. Crouthamel, Private communication.
9. C. E. Johnson, R. R. Heinrich, and C. E. Crouthamel, Private communication.
10. R. E. Shearer and R. C. Werner, *This Journal*, **105**, 693 (1958).
11. R. C. Werner, R. E. Shearer, and T. A. Ciarlariello, Proc. Thirteenth Ann. Power Sources Conf., 122 (1959).
12. R. E. Shearer, J. W. Mausteller, T. A. Ciarlariello, and R. C. Werner, Proc. Fourteenth Ann. Power Sources Conf. (1960).
13. T. A. Ciarlariello and R. C. Werner, *Chem. Engr. Progr.*, **57**, 42 (1961).
14. M. E. Indig and R. N. Snyder, *This Journal*, **109**, 757 (1962).
15. J. Polart, P. Degobert, and O. Bloch, *Compt. rend.*, **255**, 515 (1962).
16. J. Polart and P. Degobert, *ibid.*, **255**, 2103 (1962).
17. M. S. Foster, C. E. Johnson, and C. E. Crouthamel, Report USAEC-ANL-6652 (December, 1962).
18. E. Elchardus and P. Laffite, *Bull. Soc. Chim. France*, **51**, 1572 (1932).
19. H. A. Laitinen, W. S. Ferguson, and R. A. Osteryoung, *This Journal*, **104**, 516 (1957).

20. H. A. Laitinen and C. H. Liu, *J. Am. Chem. Soc.*, **80**, 1015 (1958).
21. C. H. Liu, K. E. Johnson, and H. A. Laitinen, in "Molten Salt Chemistry," p. 695, M. Blander, Editor, Interscience, New York (1964).
22. Using data of ref. (39), p. 575.
23. J. J. Lingane, "Electroanalytical Chemistry," 2nd ed., pp. 260 *et seq.*, Interscience, New York (1958).
24. P. Delahay, in "Advances in Electrochemistry and Electrochemical Engineering," P. Delahay, Editor, Vol. 1, Chap. 5, p. 238.
25. J. O'M. Bockris, in "Modern Aspects of Electrochemistry," vol. 1, Chap. 4, pp. 180 *et seq.* J. O'M. Bockris, Editor, Butterworths, London (1954).
26. J. P. Elder and A. Hickling, *Trans. Faraday Soc.*, **58**, 1852 (1962).
27. H. A. Laitinen, R. P. Tischer, and D. K. Roe, *This Journal*, **107**, 546 (1960).
28. P. Delahay, "New Instrumental Methods in Electrochemistry," p. 184, Interscience, New York (1954).
29. A. Sieverts and E. Berger, *Ber. Deutsch. chem. Ges.*, **44**, 2394 (1911).
30. H. A. Laitinen and W. S. Ferguson, *Anal. Chem.*, **29**, 4 (1957).
31. H. A. Laitinen and J. A. Plambeck, *J. Am. Chem. Soc.*, **87**, 1202 (1965).
32. T. Berzins and P. Delahay, *ibid.*, **75**, 4205 (1953).
33. J. H. Shaffer, W. R. Grimes and G. M. Watson, *J. Phys. Chem.*, **63**, 1999 (1959).
34. M. Blander, W. R. Grimes, N. V. Smith, and G. M. Watson, *J. Phys. Chem.*, **63**, 1164 (1959).
35. W. R. Grimes, N. V. Smith and G. M. Watson, *ibid.*, **62**, 862 (1958).
36. R. R. Heinrich, C. E. Johnson, and C. E. Crouthamel, *This Journal*, **112**, 1067 (1965).
37. S. V. Tatwawadi and A. J. Bard, *Anal. Chem.*, **36**, 2 (1964).
38. H. A. Laitinen and L. M. Chambers, *ibid.*, **36**, 5 (1964).
39. Calculated from C. J. Smithells, "Metals Reference Book." p. 571, 3rd ed., Butterworths, Washington, D. C. (1962).
40. F. G. Will, *This Journal*, **110**, 145 (1963).
41. F. G. Will, *ibid.*, **110**, 152 (1963).

Thermopotential Measurements of Alkali Halides

Jacob Greenberg

National Aeronautics and Space Administration, Lewis Research Center, Cleveland, Ohio

ABSTRACT

Thermopotential measurements of NaCl, KCl, NaI, KI, and CsCl were made using inert (tungsten) electrodes. For NaCl and KCl, the maxima for the Seebeck coefficients were observed, one corresponding to a negative polarity at the hot junction and another corresponding to a positive polarity at the hot junction.

Experimental Procedure

Anhydrous salts were prepared by washing with liquid ammonia. The more conventional methods of purifying metal halides involve heating the salt and treating the melt to remove hydrolysis products. The heating of the salts in the presence of water produces hydrolysis products, which are then responsible in part for the corrosive action of the melts. By treating the solid with liquid ammonia at low temperatures, the introduction of hydrolysis products is limited. The water present in the halides becomes associated with the ammonia and is carried out in the diffusion stream (1).

The salts were purified in 300-ml round-bottom flasks. After the system was sealed off from the vacuum line, these halides were then transferred from the flasks to a quartz cell fitted with two tungsten electrodes by tilting the apparatus. The tungsten electrodes were initially beaded with a grading glass of slightly lower melting point than quartz. This was done in such a manner that the tungsten surface in contact with the graded glass was free of oxides. The seal was formed essentially by the compression of the metal in the glass. The tungsten electrodes that were beaded in this manner were then fused into the quartz container. A diagram of the cell used is shown in Fig. 1. In the cases of NaCl or KCl measurements were also made by filling the quartz cell directly and attaching the cell to a vacuum line. In such instances slowly raising the temperature of the solid while maintaining a pressure of less than 10^{-4} mm Hg gave satisfactory results.

The quartz cells were fitted with chromel-alumel thermocouples and covered with asbestos after having been suitably wrapped with high-temperature resistance wire. The heating wire was carefully wrapped to reduce the presence of temperature gradients, and the desired temperature differentials were imposed by use of a 10-ohm coil of resistance wire placed about one electrode. These heating units were supplied by two variable stepdown transformers and steady-state temperatures could be controlled to within 1%. Voltage measurements were made by means of a voltmeter with a high internal impedance and current-voltage plots were made with an X-Y recorder.

It was found that if a salt hydrate was submitted to the ammonia treatment (*e.g.*, $LiI \cdot 3H_2O$), a solution formed that persisted at room temperature. Pretreatment of the hydrate, which involved heating it in vacuum, was necessary in these cases. A volume expansion of the salt was observed in each system as a result of the ammonia treatment. In order that no residual ammonia would be present while measurements were being made, the cell was heated with a yellow flame until no pressure rise above 10^{-4} mm Hg

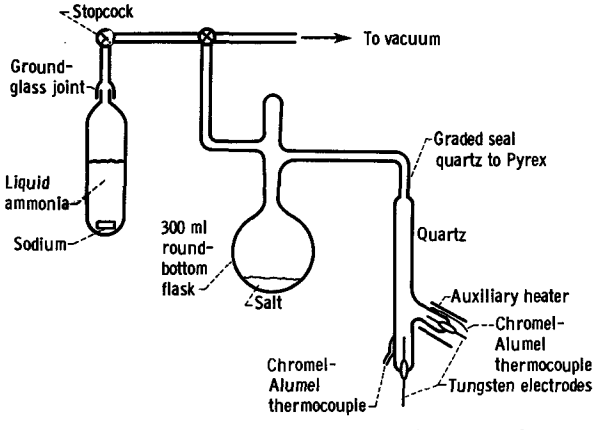

Fig. 1. Diagram of apparatus used to purify salts and measure thermopotentials.

was observed. The cell was then removed from the vacuum line.

Results

The use of inert electrodes implies that the electrode does not have an ion in common with the electrolyte as is the case with conventional thermocells. In measuring the potential some minimal current must flow with the consequent electrolysis of the electrolyte. In the case of NaCl this would result in the formation of decomposition products of sodium and chlorine at the electrodes interfaces. These elemental components with their corresponding ions in the electrolyte then constitute half-cell reactions that insure electrical contact to the electrolyte by providing a means for charge transfer. The presence of such half-cells constitutes a back-emf since the electrolysis of the salt will occur in such a manner as to negate the presence of the thermopotential. This would indicate that the observed voltage readings were somewhat lower than what would be expected if such half-cells did not exist. The observed voltage of the cell can then be considered to be analogous to a decomposition cell which was influenced by the preferential migration of ions in the thermal gradient.

The values of the Seebeck coefficient S observed are plotted in Fig. 2, and values for the discharge currents in CsCl are shown in Fig. 3. Temperature gradients of 10° to 50°C were maintained between the electrodes. All measurements were made when the voltage readings became reproducible after being at least 1 hr at the temperature of the measurement.

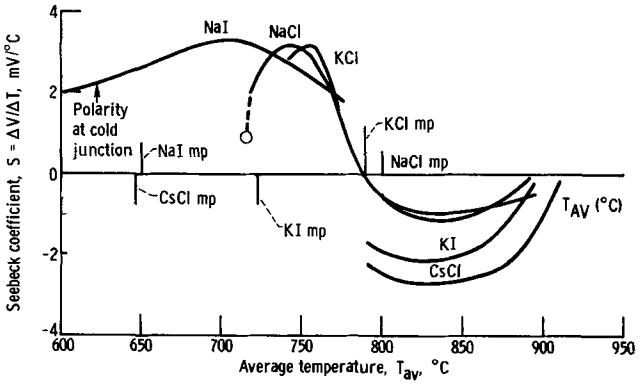

Fig. 2. Seebeck coefficients of alkali halides. ○, Value from ref. (4).

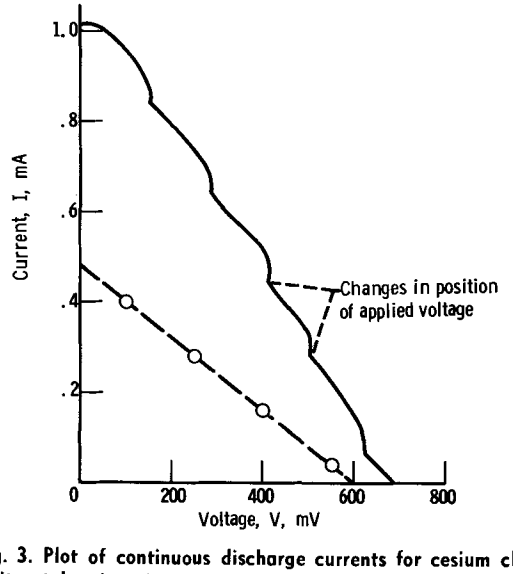

Fig. 3. Plot of continuous discharge currents for cesium chloride. Polarity at hot junction; temperature range, 720°-1002°C; average temperature, 852°C; Seebeck coefficients, 2.39 mv/°C. ——, Momentary fast-scan discharge; - - ○ - -, continuous discharge.

In order to obtain a possible indication of the number of mobile species present, the cells were allowed to discharge under their own thermopotential. The short-circuit currents observed were of the order of milliamperes; however, because of polarization by decomposition products these currents were short-lived. However, CsCl did maintain steady-state currents, possibly because of the increased solubility of decomposition products.

One of the principal sources of error in the measurements was introduced by too rapid a heating or cooling rate. In all cases, the salt was initially melted to ensure thermal equilibrium. To determine thermopotential values below the melting point, it was necessary to obtain as nearly a single crystal as possible. Too rapid a cooling rate would result in a polycrystalline material. Both of these conditions led to nonreproducible measurements of temperature and voltage. In addition, too rapid a cooling rate affected the quartz-tungsten seals. Since these seals are essentially of a compression type, they work well at high temperatures. When these seals were cooled to lower temperatures quickly, a crack would sometimes develop.

Although the lithium halide salts were run repeatedly no reproducible results were available. This may have been due to the failure to remove all impurities (H_2O, NH_3) as well as the accumulation of insoluble decomposition products at the electrodes.

Discussion

The thermopotential of the cell $\Delta\psi$ is a function of several terms (2).

$$\Delta\psi = \Delta\psi_{hom} + \Delta\psi_{het} + \Delta\psi_{el}$$

where $\Delta\psi_{hom}$ is the thermopotential evolved in salt as result of thermal gradient, $\Delta\psi_{het}$ is the potential due to reaction at electrodes, and $\Delta\psi_{el}$ is the potential due to having metal electrodes at two different temperatures.

Since $\Delta\psi_{el}$ is of the same order of magnitude as observed for metallic thermocouples and is of the order of microvolts, its effect can be considered as being negligible for these systems. Since there is a negligible current flowing through the cell and therefore there are minimal elemental components with which to constitute a half-cell at the electrodes, $\Delta\psi_{het}$ may be considered as being negligible (3). The observed thermopotentials are therefore a function of $\Delta\psi_{hom}$

$$\Delta\psi_{hom} \propto -\sum_R \left(\frac{t_R}{Z_R}\right)\frac{Q_R{}^{xx}}{T_{av}} \qquad [1]$$

where t_R = transference number of species R, Z_R = algebraic valence of species R, $Q_R{}^{xx}$ = reduced heat of transport, $T(S_R{}^x - S_R)$, $S_R{}^x$ = entropy of transport of species R, S_R = partial entropy of species R, and T_{av} = average temperature. The observed thermopotential, being a function of $\Delta\psi_{hom}$, can be written

$$\Delta\psi \propto -\sum_R \left(\frac{t_R}{Z_R}\right)\frac{Q_R{}^{xx}}{T_{av}} \qquad [2]$$

For NaCl this is

$$\Delta\psi \propto -t_{Na^+}\left(\frac{Q_{Na^+}{}^{xx}}{T_{av}}\right) + t_{Cl^-}\left(\frac{Q_{Cl^-}{}^{xx}}{T_{av}}\right) \qquad [3]$$

If the effects of temperature on the values of Eq. [3] are examined, a qualitative description of the ion processes involved when the NaCl system, for example, is heated from about 700° to 900°C can be evolved. It is known that the electrical conduction of solid alkali halides is a function of cation migration (4). The lower temperature values of the thermopotential are therefore due to cation migration from the hot to the cold zone. This results in a negative polarity at the hot junction. Since the values for the

reduced heats of transport Q_R^{xx} increase with temperature, the value of the thermopotential in the solid, where it is primarily a function of cation movement, can only go through a maximum if the transport number of the cation decreases. This would be due to the onset of anion conduction. A decrease in cation transport number with increasing temperature has also been observed in other systems (5). When the anion begins to contribute to the conduction of the system, it does so not only because of the influence of heat, but also because of the electrical potential established by the prior migration of cations. The rate of change of the entropy of transport for the anion as the temperature increases must therefore be large. The result of this is that, although the transport number of the anion is low, the product of the transport number and the reduced heat of transport of the anion is large and the value of the Seebeck coefficient goes to zero and then to a maximum of opposite polarity at the hot junction to the one initially observed at lower temperatures. As the temperature is raised further, the values of the transport numbers and associated ion entropies become nearly equal and the value of the Seebeck coefficient becomes minimal. In effect, therefore, in NaCl the transport number of Na^+ goes from 1.0 to ~0.5 and the transport number of Cl^- goes from 0 to ~0.5.

Since the value of the thermopotential in Eq. [3] is the result of the difference between two terms, it is possible to show this by graphically representing the terms themselves. This is shown in Fig. 4.

From the magnitude of the potentials measured it can be assumed that only a fraction of the ions present are actually mobile. An estimate of the number of mobile species can be made from the short-circuit currents observed when the cells were allowed to discharge under their own thermopotential. For a discharge time of 1 sec, the number of equivalents of salt which are dissociated to form mobile species are

$$\frac{10^{-3}\text{A} \times 1 \text{ sec}}{96\,500 \text{ C}} \cong 10^{-8} \text{ equivalents}$$

The discussion of transport phenomena concerns a relatively small fraction of dissociated species moving with respect to a much larger mass of undissociated species. The observed discharge currents were much higher (ma) than those observed for $ZnCl_2$ and $PbCl_2$ (μa) (6). This would indicate a larger degree of dissociation and consequently higher electrical conductivities observed in alkali halide melts.

It is interesting to note that the inflection points for the plot of Seebeck coefficients of NaCl and KCl as a function of temperature occur relatively close to the melting point. This is not the case for NaI. In the latter case it appears that the anion contribution to the thermopotential does not appear until about 50°C above the melting point. Thermopotential measurements of this kind can be used to make some inferences concerning the migration of the ion species as a function of temperature.

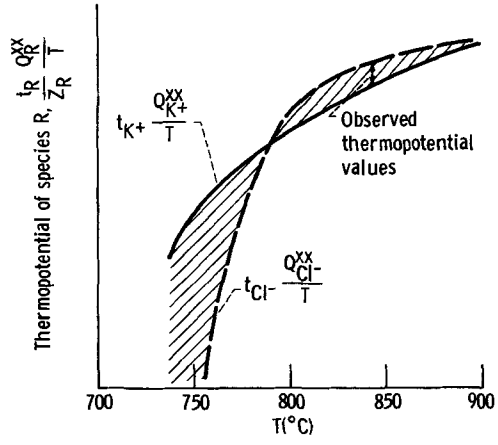

Fig. 4. Thermopotentials of potassium chloride plotted by difference of ion functions.

It should also be noted that, when the Seebeck coefficients from a thermocell with inert electrodes are subtracted from the Seebeck coefficients of thermocells with reversible electrodes, values of the single-ion entropies can be obtained. The thermopotential of a cell with inert electrodes is assumed to be a function primarily of the transference numbers and heats of transport of the ions constituting the electrolyte (Eq. [1]). However, in a classical thermocell with electrodes that are reversible to one of the ions of the electrolyte, the thermopotential is in addition a function of the change in entropy that occurs at the electrode with the passage of one Faraday.

$$F\frac{\Delta\phi}{\Delta T} \alpha -\sum_R \frac{t_R}{Z_R}\frac{Q_R^{xx}}{T_{av}} \quad \text{Inert electrodes}$$

$$F\frac{\Delta\phi}{\Delta T} \alpha -\sum_R \frac{t_R}{Z_R}\frac{Q_R^{xx}}{T_{av}} - \Delta S \quad \text{Reversible electrodes}$$

It is, therefore, possible to evaluate ΔS by subtraction when thermopotentials are available for both systems. Data are available on NaCl and KCl thermocells with chlorine electrodes (7). In this case ΔS may be defined as follows:

For the reaction $Cl^- \rightarrow \frac{1}{2}Cl_2 + e$

$$\Delta S = \tfrac{1}{2}S^\circ_{Cl_2} + S_e - S_{Cl^-}$$

where $S^\circ_{Cl_2}$ = molar entropy of chlorine gas at temperature; S_e = entropy of electron in electrode; and S_{Cl^-} = partial molar entropy of chloride ion in the electrolyte at temperature.

Since S_e will be of the order of 1% of $\frac{1}{2}S^\circ_{Cl_2}$ it can be neglected for a first approximation. The values of $S^\circ_{Cl_2}$ are listed; and we, therefore, can calculate the single-ion entropy of the chloride ion.

The lowest temperature for which reproducible results are reported for the Cl_2 — NaCl, Cl_2 — KCl thermocells is 927°C. At this temperature the Seebeck coefficient for the cell with inert electrodes is zero. This was explained as due to the fact that the transference numbers and reduced heats of transport for the cation and anion are equal. It was assumed that there are an equal number of dissociated, equally mobile ions of opposite charge so that a charge separation cannot be maintained. The Seebeck coefficient reported for the chlorine thermocell at this temperature is, therefore, directly proportional to the ΔS at the electrodes.

Chlorine thermocell at 927°C

$$F\left(\frac{\Delta\phi}{\Delta T}\right) = -\Delta S \alpha S_{Cl^-} - \frac{1}{2}S^\circ_{Cl_2}$$

$$\frac{\Delta\phi}{\Delta T} = -0.480 \times 10^{-3} \text{ v/°C [NaCl} - Cl_2 \text{ at 927°C]}$$

$$\frac{\Delta\phi}{\Delta T} = -0.475 \times 10^{-3} \text{ v/°C [KCl} - Cl_2 \text{ at 927°C]}$$

$F = 9.65 \times 10^4$ coulombs; 0.239 conv. to calories;

$$\frac{1}{2}S^\circ_{Cl_2} = 32.3 \text{ e.u.}$$

$S_{Cl^-} = 21.2$ e.u. (NaCl — Cl_2 at 927°C);

$S_{Cl^-} = 21.9$ e.u. (KCl — Cl_2 at 927°C)

These results, considering that we have neglected S_e, are in agreement with the approximation that the entropy of a system such as NaCl or KCl is equally

divided between cation and anion (8). Using this approximation with a small correction factor for the mass effect on diffusional entropy

$S_{Cl^-} = 21.9$ e.u. ($NaCl - Cl_2$ at 927°C);

$S_{Cl^-} = 22.12$ e.u. ($KCl - Cl_2$ at 927°C)

A deviation from this assumption is expected below 927°C since the maxima and minima observed are essentially due to the asymmetry in the number of allowable states (entropy) of the cation and anion.

Acknowledgment

The author wishes to express his appreciation to the reviewer for his diligence and suggestions.

Manuscript received Nov. 11, 1965; revised manuscript received June 10, 1966. This paper was presented at the San Francisco Meeting, May 9-14, 1965.

Any discussion of this paper will appear in a Discussion Section to be published in the June 1967 JOURNAL.

REFERENCES

1. J. Greenberg and I. Warshawsky, *J. Am. Chem. Soc.*, **86**, 3572 (1964).
2. H. Holtan, Jr., P. Mazur, and S. R. deGroot, *Physica*, **19**, 1109 (1953).
3. Jacob Greenberg, D. E. Weber, and L. H. Thaller, *J. Phys. Chem.*, **67**, 2488 (1963).
4. R. W. Christy, Y. W. Hsueh, and R. C. Mueller, *J. Chem. Phys.*, **38**, 1647 (1963).
5. P. F. Duby: A Contribution to the Study of Electrical Transport in Molten Salts. PhD Columbia University, Eng. Sc.d. (1962).
6. Jacob Greenberg, L. H. Thaller, and D. E. Weber, NASA TN D-2440.
7. G. D. Ulrich, "Studies of Molten Salt Thermocells," Ph.D. Thesis, Feb. 1964 M.I.T. Cambridge, Mass. Nonr-1841(78), NsG-496(N64-20647).
8. K. S. Pitzer, *J. Phys. Chem.*, **65**, 147 (1961).

Kinetics of Electrode Reactions

Mark Salomon

Wright Laboratory, Rutgers, The State University, New Brunswick, New Jersey

ABSTRACT

The use of absolute rate theory to predict rates of electrode reactions is discussed. It is shown that the rate of reaction at an electrode can be calculated from first principles if the absolute single electrode potential and its temperature coefficient are known. The single electrode potential can indeed be calculated and therefore used to predict the exchange current density for any electrode reaction. Exchange current densities calculated from first principles for various mechanisms in the oxygen and hydrogen evolution reactions are in good agreement with the presently accepted mechanisms.

The electrochemist has always maintained that the advantage of studying kinetics at electrodes is that the activation energy can be controlled simply by controlling the electrode potential. Despite this "advantage" the electrochemist cannot use absolute rate theory (1) to calculate reaction rates for single electrodes. Instead he is always left with at least one undefinable constant such as the "electrochemical" rate constant. If the rates at single electrodes could be calculated from first principles the electrochemist would have an additional method by which he could verify reaction mechanisms. It is the purpose of this paper to discuss and extend a new treatment of electrode kinetics in which absolute rate theory is used to predict the exchange current density. Calculations are based on the concept of single electrode potentials and the absolute entropies for half-cell reactions. Due to the importance of the single electrode potential and its temperature coefficient in the present calculations, a brief review is given on its evaluation, followed by exchange current density calculations for various mechanisms in the oxygen and hydrogen evolution reactions.

Kinetic principles.—For a rate-determining step involving a single electron transfer, the rate in amperes cm^{-2} is

$$i = kF\frac{\Pi c_i\gamma_i}{\gamma^{\neq}}$$

where k is the electrochemical rate constant, c_i is the concentration of the i-th species, and γ is the activity coefficient. For the activated complex, $\gamma^{\neq}$ will be assumed to be unity. The electrochemical rate constant differs from the familiar nonelectrochemical one in that in the former, the activation energy is a function of electrode potential according to ((2, 3)

$$k = A\ \exp -[E_o + \beta(\phi - \psi_1)zF]/RT \qquad [1]$$

Here E_o is the activation energy (including zero-point energies) which is modified by some fraction, β, of the electrode potential ϕ. The potential ψ_1 is that at the outer Helmholtz plane and can be calculated from Sterns theory of the double-layer (4). For unit charge transfer z is unity and denotes "direction" of the reaction, *i.e.*, whether an anion or a cation is the species being discharged. Hence for an anodic process involving such species as OH^-, Cl^-, CH_3COO^-, $z\mathbf{F}$ is negative, whereas for cathodic discharge of species such as H^+, Ag^+, Na^+, zF will be positive. Combining the above two equations and replacing the frequency factor A by its usual terms involving partition functions (1, 3) we have for the rate of discharge at the reversible potential, ϕ_r,

$$i_o = \tau F\frac{kT}{h}c_i\gamma_i \cdot \frac{Q^{\neq}/\sigma^{\neq}}{\Pi Q_i/\sigma_i} \cdot \exp -[E_o + \beta(\phi_r - \psi_1)zF]/RT \qquad [2]$$

where τ is the transmission coefficient which is unity (1), Q is the partition function per unit volume (q/v) or per unit area (q/A), and σ is a statistical factor denoting the number of reaction paths which is used instead of the symmetry number since use of the latter can lead to error (5, 6). For the case of proton discharge, Eq. [2] becomes

$$i_o = \frac{\sigma_{H_3O^+}}{\sigma^{\neq}}F\frac{kT}{h}C_M\,(1-\theta)\,a_{H_3O^+}\frac{q^{\neq}}{q_M\,Q_{H_3O^+}}$$

$$\exp -(1-\beta)\psi_1F/RT \cdot \exp -[E_o + \beta\phi_rF]/RT \qquad [3]$$

where the additional term in $-\psi_1F/RT$ arises from the use of bulk H_3O^+ activity instead of the surface activity (7). The reversible potential ϕ_r is that corresponding to the half-cell reaction

$$H_3O^+ + e_M \rightleftharpoons \frac{1}{2}H_2 + H_2O \qquad [4]$$

where the subscript in e_M indicates that ϕ_r is dependent on the metal which supplies the electrons. There are essentially two unknowns in Eq. [3], namely ϕ_r and E_o ($q^{\neq}$ is known if E_o is known). Hence if any one of these quantities is known, say E_o, we can use the experimental values of $Q_{H_3O^+}$, i_o, β, and ψ_1 to calculate ϕ_r. The problem involved in the calculation of ϕ_r therefore requires the evaluation of E_o. Placing all the constant terms in Eq. [3] in a constant A and from $-\phi F = \Delta H - T\Delta S$, we now have

$$i_o = F A C_M(1-\theta)\, a_{H_3O^+} \exp -(1-\beta)\psi_1 F/RT \cdot \exp -\beta\Delta S/R \cdot \exp -[E_o - \beta\Delta H]/RT \quad [5]$$

where ΔS and ΔH are, respectively, the entropy and enthalpy for the half-cell reaction [4]. The relation between the experimental energy of activation and frequency factor with the theoretical relations are (1, 3).

$$E_{exptl} = E_o + RT - \beta\Delta H \quad [6]$$

and

$$A_{exptl} = A \exp -\beta\Delta S/R \quad [7]$$

The absolute single electrode potential was calculated (3) by using a potential energy surface to fit E_o and A. We found ϕ_r for the h.e.r. at mercury to equal —0.225v at 25°C and —0.185v at 85°C (3). Having obtained ϕ_r for reaction [4] at a mercury electrode, it follows that the difference in ϕ_r for Hg and any other metal is simply equal to the difference in work functions of the two metals, *i.e.*

$$\phi_{r,M} - \phi_{r,Hg} = \Phi_M - \Phi_{Hg} \quad [8]$$

This result must be true if the measured p.d. between two reversible hydrogen electrodes at different metals is to be zero and can be confirmed by a simple consideration of the potentials of the various phases present [*e.g.* see (4), (10)]. From [8] it follows that ΔS is independent of the nature of the metal and that ΔH will vary accordingly. Applying this method now to predict i_o and E_{exptl} values for proton discharge at Ga and Cu cathodes, we found our calculated values of i_o and E_{exptl} to agree within 5% of the observed ones (3). The treatment can now be extended to other mechanisms in the oxygen and hydrogen evolution reactions.

Recombination rate of Pt *cathodes.*—It is generally believed (11-14) that the rate-determining step at Pt cathodes is the recombination of adsorbed H-atoms, *i.e.*

$$2MH \rightarrow 2M + H_2 \quad [9]$$

As further proof of this mechanism, the rate of recombination will now be calculated from first principles. Making the assumption that all pre-rate-determining steps are in quasi-equilibrium, the rate of recombination at the reversible potential is given by

$$i_o = \frac{2\sigma^2_{H_3O^+}}{\sigma^2_{H_2O}\sigma^{\neq}} \cdot \frac{FkT}{h} \left(\frac{a_{H_3O^+}}{a_{H_2O}}\right)^2 (1-\theta)^2 \frac{q^2_{H_2O} Q^{\neq}}{q^2_{H_3O^+}} \exp -E_o/RT \cdot \exp -2\phi_r F/RT \quad [10a]$$

In Eq. [10] we have treated the adsorbed H atoms as being mobile entities so that the concentration of metal sites does not enter into the rate equation (15, 16). We can simplify this equation slightly by taking the product of reaction paths and partition functions as being equal to unity (see appendix) and $a_{H_2O} = 1$ so that

$$i_o = 2F \frac{kT}{h} (a_{H_3O^+})^2 (1-\theta)^2 \exp \cdot -E_o/RT \cdot \exp -2\phi_r F/RT \quad [10b]$$

Using ϕ_r as calculated from Eq. [8], we could calculate i_o by varying the input parameters to a semi-empirical potential energy surface to fit E_{exptl} which is ~6 kcal mole^{-1} for the h.e.r. at platinum (17). However, this method gives rise to several problems. First, for the four-center activated complex, the semi-empirical method for evaluating E_o must be used and the author prefers, following the criticisms of Johnston (8, 9), not to commit himself to such a questionable method. The second difficulty involves the use of the tabulated value (18) of the metallic work function Φ_{Pt}. The work functions for randomly orientated metals do not exceed 5 ev with the exception of that for Pt (18). The value of $\Phi = 5.3$ ev for Pt appears to be much too high in comparison to the other metals, and this arises from the use of values varying from 6.3-6.4 ev in the averaging process. In fact if we omit all values of Φ in excess of 6 ev, then the average value is 4.94 ev which seems to be more reasonable.

In view of these difficulties, we could then proceed to calculate i_o in an alternative, but more valid, manner. By substituting Eq. [6] into [10b] noting that $-\phi_r F = \Delta H - T\Delta S$ we have

$$i_o = 2F \frac{ekT}{h} (a_{H_3O^+})^2 (1-\theta)^2 \exp -2\Delta S/R \cdot \exp -E_{exptl}/RT \quad [11]$$

and for 0.1N acid solution

$$i_o = 4.65 \cdot 10^{11} (1-\theta)^2 \cdot \exp -2\Delta S/R \cdot \exp -E_{exptl}/RT$$

Since $\Delta S = 15.48$ e.u. (3) and $E_{exptl} \doteq 6$ kcal mole^{-1} (17)

$$i_o = 0.12 (1-\theta)^2 \text{ amp cm}^{-2}$$

To arrive at a value for i_o, the coverage by adsorbed hydrogen, θ, must be known at the reversible potential. It is fairly well established that θ is large (19, 20), and from our own H/D-isotope work (14) we found that we could predict the experimental rate constant ratio, k_H/k_D, by fitting the coverage of H-atoms to 0.8-0.9. Hence taking $\phi_H \doteq 0.85$ we find that $i_o \doteq 2.7 \cdot 10^{-3}$ amp cm^{-2} which is in good agreement with the observed values (11, 12, 17, 21) which range from 10^{-4} to 5.10^{-3} amp cm^{-2}.

Rate of discharge in oxygen evolution.—One can now extend the above method to calculate the rate of discharge in the oxygen evolution reaction. The half-cell reaction in acid solution is written as

$$2H_3O^+ + \frac{1}{2}O_2 + 2e_M \rightleftharpoons 3H_2O \quad [12]$$

According to MacDonald and Conway (22), the discharge occurs from a water molecule in either acid or basic solution, and we can write the following discharge mechanism

$$M + H_2O \rightarrow M-OH^- + H^+ \quad \text{slow}$$
$$M-OH^- \rightarrow MOH + e_M \quad \text{fast}$$

so that, in effect, the OH^- species is involved in the rate-determining charge transfer step. The rate of discharge of OH^- at the reversible potential is then

$$i_o = \frac{\sigma_{H_2O}}{\sigma^{\neq}} F \frac{kT}{h} C_M (1-\theta)\, a_{H_2O} \frac{q^{\neq}}{q_M Q_{H_2O}} \exp -[E_o + \beta(\phi_r - \psi_1)zF]/RT \quad [13]$$

In Eq. [13] the concentration of metal sites must be considered because adsorbed oxide species are not mobile (15, 16). Also the ψ_1 potential can be calculated from Sterns theory [cf. (4)] taking the potential of zero charge for an oxide covered electrode to be about 0.5v *vs.* the normal hydrogen electrode (23). To evaluate i_o for the discharge of OH^- at a Pt anode in 0.1N acid solution, we shall proceed in a manner similar to that used above. We shall not attempt to calculate ϕ_r for reaction [12] but instead let us now simplify [13] as follows: taking $q^{\neq}/q_M = 1$ and

$Q_{H_2O} = 32.6$ (see appendix) and noting that $\sigma_{H_2O} = 2$ and $a_{H_2O} = 1$, we have

$$i_o = 2F \frac{ekT}{h} \frac{C_M (1-\theta)}{Q_{H_2O}} \exp -\beta\psi_1 F/RT \cdot \exp \beta\Delta S/R \cdot \exp -E_{exptl}/RT \quad [14]$$

The entropy change for the half-cell reaction [12] can be easily calculated as follows: combining the half-cell reactions in [4] and [12], the over-all entropy change is

$$\Delta S_{cell} = \Delta S_{O_2} + 2\Delta S_{H_2} \quad [15a]$$

where $\Delta S_{H_2} = -15.38$ e.u. as calculated previously (3) and described above. ΔS_{cell} can be calculated from standard entropy values such as those given by Latimer (24) from

$$\Delta S_{cell} = S_{H_2O} - \tfrac{1}{2} S_{O_2} - S_{H_2} \quad [15b]$$

From Latimer's tables $\Delta S_{cell} = -38.96$ e.u. and from [15a], $\Delta S_{O_2} = -8.21$ e.u. Taking $E_{exptl} = 22.1$ kcal mole^{-1} (25), $\beta = \tfrac{1}{2}$, $\psi_1 = 0.0950$v, and $C_{Pt} = 1.66 \cdot 10^{-9}$ mole cm^{-2}, Eq. 14 becomes

$$i_o = 2.11 \cdot 10^{-10} (1-\theta) \text{ amp cm}^{-2}$$

Since coverage by oxides is usually quite high (26) it follows that i_o is of the order of 10^{-11} amp cm^{-2} which is in satisfactory agreement with the experimental values which have been found to vary from 10^{-8} to 10^{-12} amp cm^{-2} (22, 25, 28).

Discussion

The method used here to predict i_o values is dependent on the knowledge of ϕ_r and E_{exptl}. The use of E_{exptl} rather than E_o to calculate i_o does not alter the reliability of the method because if E_o were used, one would have to vary the input parameters to the semi-empirical method and fit E_o to E_{exptl} by Eq. [6]. One major source of error is of course the experimental quantities since they have been found to vary considerably from one laboratory to another. For example, in the o.e.r., i_o values from 10^{-8} to 10^{-12} amp cm^{-2} have been reported, E_{exptl} values range from 18-25 kcal mole^{-1}, and values for β range from 0.4 to 0.65 (22, 25-29). Despite these variations, the i_o value calculated here agrees satisfactorily with the present assignment of a rate-determining OH^- discharge at platinum. Similar conclusions are reached concerning the calculated i_o values for atom recombination in the h.e.r. There is essentially no limit as to the type of electrode reaction for which we could calculate i_o values. The requirements are that we know the experimental E, i, and β values and that the reaction proceeds in a classical manner, *i.e.*, quantum mechanical tunneling contributions to the over-all rate of reaction are negligible. The calculation of ϕ_r for reaction [4] on Hg cathodes is based on a purely classical mechanism, and significant proton tunneling would therefore detract from the accuracy of this calculation. We have presented both theoretical and experimental evidence to show that tunneling of protons at Hg is negligible (2, 3, 30) and we feel our results are sufficient to counter the opinion that tunneling is significant (31, 32), in this reaction. There are several other metals which do appear to involve substantial tunneling of protons; *e.g.*, recent work on Ni indicates that tunneling effects are quite large (33). In fact, one can offer support of the tunneling mechanism indirectly by using the method present above. According to Bell (34) if we could calculate A and E from absolute rate theory (*i.e.*, corresponding to a classical mechanism), then both of these values should be larger than the experimental values if significant proton tunneling is involved. Preliminary calculations for the h.e.r. at Ni cathodes do in fact indicate that the calculated A and E values are too large (35) thereby indicating a tunneling mechanism according to Bell's criteria.

Acknowledgments

The author would like to thank the Chemistry Department and The Research Council of Rutgers, The State University, for financial support.

Manuscript received Nov. 22, 1965; revised manuscript received Feb. 23, 1966.

Any discussion of this paper will appear in a Discussion Section to be published in the June 1967 JOURNAL.

REFERENCES

1. S. Glasstone, K. J. Laidler, and H. Eyring, "Theory of Rate Processes," McGraw-Hill Publishing Co., New York, N. Y. (1941).
2. B. E. Conway and M. Salomon, *J. Chem. Phys.*, **41**, 3169 (1964).
3. M. Salomon, C. G. Enke, and B. E. Conway, *ibid.*, **43**, 3989 (1965).
4. R. Parsons, "Modern Aspects of Electrochemistry," Vol. 1, J. O'M. Bockris and B. E. Conway, Editors, Butterworths, London (1954).
5. E. W. Schlag, *J. Chem. Phys.*, **38**, 2480 (1963).
6. D. M. Bishop and K. J. Laidler, *ibid.*, **42**, 1688 (1965).
7. A. N. Frumkin, *Z. Physik. Chem.*, **A164**, 121 (1933); see also *Acta Physicochim. U.R.S.S.*, **6**, 502 (1937).
8. J. C. Davy, C. R. Guerra, H. S. Johnston, C. F. Weaver, and C. E Young, *J. Chem. Phys.*, **41**, 1517 (1964).
9. H. S. Johnston and C. Parr, *J. Am. Chem. Soc.*, **85**, 2544 (1963).
10. B. E. Conway, "Theory and Principles of Electrode Processes," Ronald Press, New York, N. Y. (1965).
11. J. O'M. Bockris and A. M. Azzam, *Trans. Faraday Soc.*, **48**, 145 (1952).
12. S. Schuldiner, *This Journal*, **101**, 426 (1954).
13. J. O'M. Bockris and S. Srinivasan, *ibid.*, **111**, 853 (1964).
14. M. Salomon and B. E. Conway, *Ber. Bunsenges, Physik, Chem.*, **69**, 669 (1965).
15. K. J. Laidler, "Catalysis," vol. 1, P. H. Emmett, Editor, Reinhold Publishing Co., New York, N. Y. (1955).
16. B. M. W. Trapnell, "Chemisorption," Butterworths, London (1955).
17. R. Parsons, *Trans. Faraday Soc.*, **56**, 1340 (1960).
18. A. Michaelson, *J. Appl. Phys.*, **21**, 536 (1950).
19. W. Böld and M. Breiter, *Z. Elektrochem.*, **64**, 897 (1960).
20. M. W. Breiter, *Trans. Faraday Soc.*, **60**, 1445 (1964).
21. J. O'M. Bockris, I. A. Ammar, and A. K. M. S. Huq, *J. Phys. Chem.*, **61**, 879 (1957)
22. J. J. MacDonald and B. E. Conway, *Proc. Roy. Soc., London*, **A269**, 419 (1962).
23. B. V. Ershler, *Uspekhi Khimi*, **21**, 237 (1952).
24. W. M. Latimer, "Oxidation Reduction Potentials," Prentice-Hall, New York, N. Y. (1952).
25. A. Rius, J. Llopis, and J. Giner, *An. real. Soc. espan. fis. quim.*, **49B**, 329 (1953) and other references quoted here.
26. See *e.g.*, W. Visscher and M. A. V. Devanathan, *J. Electroanal. Chem.*, **8**, 127 (1964).
27. J. O'M. Bockris, "Modern Aspects of Electrochemistry," J. O'M. Bockris and B. E. Conway, Editors, Butterworths, London (1954).
28. M. Breiter, "Advances in Electrochemistry," P. Delahay, Editor, John Wiley & Sons, Inc., New York, N. Y. (1961).
29. J. O'M. Bockris and A. K. M. S. Huq, *Proc. Roy. Soc., London*, **A237**, 277 (1956).
30. M. Salomon and B. F. Conway, *Discussions Faraday Soc.*, **39** (1965).
31. J. O'M. Bockris, S. Srinivasan, and D. B. Matthews, *ibid.*, **39** (1965).
32. St. von Christov, *ibid.*, **39** (1965).
33. B. E. Conway and D. McKinnon, To be published.
34. R. P. Bell, "The Proton in Chemistry," Cornell University Press, Ithaca, N. Y. (1959).
35. M. Salomon, To be published.
36. C. G. Swain and R. F. W. Bader, *Tetrahedron*, **10**, 182 (1960).

37. G. Nemethy and H. A. Scheraga, *J. Chem. Phys.*, **36**, 3382 (1962).

APPENDIX

In simplifying Eq. [10a] and [13], it was assumed that the ratio of partition functions is unity. The validity of this assumption can be demonstrated by evaluating the partition functions for translation, rotation, and vibration as follows:

The vibrational partition can be written as

$$q_{vib} = \prod^{3n-6} (1 - \exp - hc\nu/kT)^{-1} \qquad [16]$$

Providing ν(in cm^{-1}) is large, which is the usual case for real vibrations, q_{vib} is essentially unity.

For the rotational partition function, an equation similar to [16] was used because species in solution are subject to strong interactions by neighboring molecules or ions (*e.g.*, as in hydrogen bonding) and the molecule will not be free to rotate but will exhibit librational motion. Using the harmonic oscillator approximation [c.f. ref. (36)] q_{rot} can be calculated from [16] replacing $3n - 6$ by the degrees of rotational freedom. Since such librational frequencies have been observed to be around 650 cm^{-1} the assumption that $q_{rot} \to 1$ is a fairly good one. Ratios of q_{rot} approaching unity is even a better approximation.

The translational partition function for three degrees of freedom is

$$q_{tr} = 1.877 \cdot 10^{20} (MT)^{3/2} v_f \qquad [17]$$

where v_f is the free volume and M is the molecular weight in a.m.u. Taking $v_f = 4.4 \cdot 10^{-25}$ cm^3 for H_2O (38) and H_3O^+ (3), $q_{tr} = 32.6$ and 35.35, respectively. For two degrees of translational freedom

$$q_{tr} = 3.279 \cdot 10^{13} MT A_f \qquad [18]$$

where A_f is the free area. Since oxides are immobile, only the H_2 complex is considered to be mobile so that at 25°C

$$q_{tr} = 1.915 \times 10^{16} A_f$$

The activated complex possesses two degrees of translational freedom within the area A_f occupied by the site and this corresponds to $A_f \doteq 10^{-16} - 10^{-17}$ cm^2 so that $q_{tr} \doteq 1$ (16).

The rotational p.f. for two degrees of rotational freedom is given by

$$q_r = \frac{8\pi^2 IkT}{h^2} \qquad [19]$$

and taking $I = 4.6 \cdot 10^{-41}$ g cm^2 as an approximate value, $q_r \doteq 3$ at 25°C. Since the coverage by both adsorbed H and water dipoles is high, one would expect some type of restricted rotation and perhaps even a libration as in the case of water molecules. It is therefore reasonable to assume that q_{total} for H-atom recombination is unity so that from Eq. [10a], the ratio

$$\frac{\sigma^2_{H3O^+}}{\sigma^2_{H2O}\sigma^{\neq}} \cdot \frac{q^2_{H2O} Q^{\neq}}{q^2_{H3O}} \doteq 1$$

is a valid assumption for $\sigma_{H3O^+} = 3$, $\sigma_{H2O} = 2$, $\sigma^{\neq} = 2$.

However the ratio $q^{\neq}/q_M Q_{H2O}$ in Eq. [13], does not equal unity. For an immobile activated complex $q^{\neq}$ and $q_M \doteq 1$ (15, 16), but $Q_{H2O} = 32.6$, and this value was used in simplifying [13].

Optical Studies of Electrolyte Films on Gas Electrodes

Rolf H. Muller

Inorganic Materials Research Division, Lawrence Radiation Laboratory, University of California, Berkeley, California

ABSTRACT

The geometry of stable electrolyte films has been established on nickel and silver surfaces partially immersed in aqueous caustic solutions. Such films, which are very sensitive to factors affecting interfacial energies and may be useful for their determination, appear to be important for the mass transfer in certain gas diffusion electrodes.

The charge transfer at gas-consuming electrodes has long been assumed to occur at the top of the liquid meniscus where the gas, solid, and liquid phases, are in contact with each other. Although the concept of such a "line of reaction" leads one to postulate very large local current densities, and early observations by Grove (1) had indicated contributions of a finite electrode area, it was only recently that Wagner and Will called attention to the fact that neither gas diffusion through the bulk liquid near the meniscus nor surface diffusion of adsorbed gaseous species to the liquid phase, where reaction would take place as suggested by Schmid (3) and Justi (4), could account for many experimental results. Will (2) demonstrated that a relatively large electrode area participated in the electrode reaction. Similar conclusions can be drawn from computations by Iczkowski (5). The current distributions determined by Bennion and Tobias (6) and later by Maget and Roethlein (7) directly showed the spacial distribution of the electrochemical charge transfer reaction. Theoretical analysis of porous gas diffusion electrodes by Rockett (8) and Grens (9) and experiments by Katan *et al.* (10) have supported the concept of electrolyte films inside pores of some gas electrodes which are of practical interest.

Purpose of this study.—The finite current densities observed away from the apparent electrolyte meniscus suggested the existence of an electrolyte covering on the apparently dry metal surface, and it has been the purpose of this work to determine the extent of this electrolyte film on vertically oriented electrodes of simple geometry. In particular, the film thickness, which is an important parameter for the quantitative description of mass transfer on film-bearing gas electrodes, and the factors which affect it were to be studied. The rectangular and cylindrical electrodes employed may be regarded as highly idealized models of the capillaries in a porous body. The study was limited to mechanically polished nickel and silver electrode surfaces for reasons of optical reflection. Only cathodic polarization was employed in order to maintain the properties of the metal surface as much as possible.

Film interference.—Several techniques have been considered for the measurement of electrolyte film thickness as a function of position and time: Mechanical techniques, although independent of electrolyte and electrode materials, result in discontinuous, point-to-point measurements which may not be sensitive enough and also disturb the film. Electrical measurements could be made continuously; however, they depend on the electrolyte conductivity which is not well known and is a function of position. Electrical conductivity measurements also presuppose a uniform film over the test-distance and suffer from disturbance of the object by the probes. Of different optical techniques, light interference was finally chosen because

of the possibility of making continuous observations with a minimum of disturbance to the object, little requirement for uniform film geometry, and good sensitivity for the dimensions involved. A disadvantage of this technique is that it requires a knowledge of the refractive index of the film. The uncertainty of this quantity due to concentration variations, not *a priori* known, amounts, however, only to a few per cent. Light interference for the study of supported liquid films has recently been used by Bascom *et al.* (11) and Deryagin *et al.* (12).

Film interference, well known from the appearance of soap bubbles or oil spots on water, is due to partial reflection of an incident light wave on front and back sides of the film. The interference causes a tapered film to show, under monochromatic illumination, alternating bright and dark fringes which indicate contour lines spaced at distances corresponding to one wavelength optical path increment. The optical path difference ΔS in the film between interfering reflections depends on refractive index n, film thickness d and angle of refraction ϕ' as shown in Eq. [1]. It can also be expressed as a delay in phase, δ_{film}, given in Eq. [2] in radians where λ is the light wavelength in vacuum.

$$\Delta S = 2nd\cos\phi' \quad [1]$$

$$\delta_{film} = \Delta S\, 2\pi/\lambda \quad [2]$$

The use of white light results in interference colors which are often more sensitive to small film thickness variations than the corresponding monochromatic intensity variations, and which admit an easy distinction between the first few orders of interference. The colors can be calibrated by comparison with monochromatic patterns in a continuously tapered film; thus, the characteristics of the photographic color material do not affect the results. The observations on cylindrical electrodes are more difficult, but not basically different. A discussion of curved films has been given by Barakat (13).

As had been noted by Blodgett and Langmuir (14, 15), it is advantageous to use linearly polarized light to simplify the analysis of film interference. These authors also describe the improved contrast of an interference pattern when observed at a grazing angle of incidence. Similar observations are reported by Gaudin (16). A detailed analysis of interference in a transparent film on an absorbing substrate, which takes multiple reflections into account (17), shows that with light polarized parallel and normal to the plane of incidence (p and s polarization) "optimum angles of incidence" can be found for which the amplitudes of the interfering waves are equal, thus resulting in optimum interference contrast. The optimum angle of incidence is larger for p than for s polarization, it increases with increasing reflectivity of the metal substrate and decreases with increasing refractive index of the film. For many metal-film combinations 75° angle of incidence has been found to be a good intermediate value for observation with both s and p polarization.

For the quantitative interpretation of interference patterns in terms of film thickness, the phase change suffered by the light on reflection at the two film boundaries has to be taken into account as pointed out, *e.g.*, by Mayer (18), and discussed in a different context by Lindberg (19). The total phase difference δ between the interfering reflections is composed of a part δ_{film} due to the optical path in the film (taken negative as a relative delay in time) and the combined effect $\delta_{refl.}$ of the reflections as expressed in Eq. [3]. The latter quantity in turn represents the difference between the phase changes in dielectric and metallic reflections at the two film boundaries with respect to the incident wave (Eq. [4]).

$$\delta = \delta_{film} + \delta_{refl.} \quad [3]$$

$$\delta_{refl.} = \delta_{diel.} - \delta_{metal} \quad [4]$$

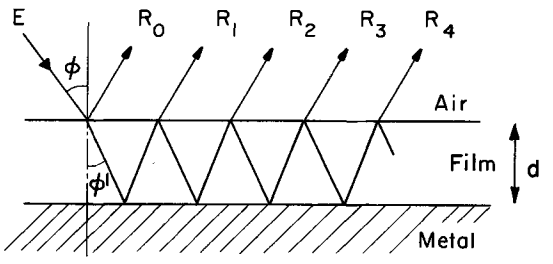

Fig. 1. Multiple beam interference from a transparent film on a metal substrate: E, incident wave; R, reflected waves; ϕ, angle of incidence on the film; ϕ', angle of refraction in the film.

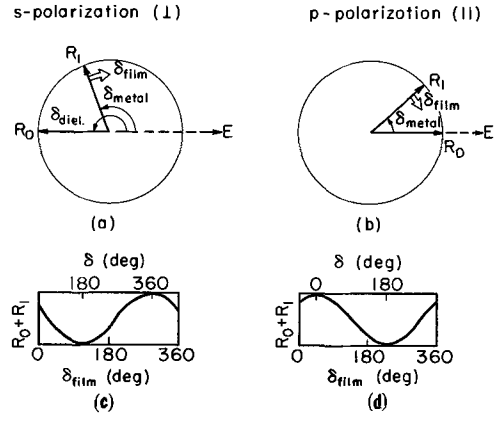

Fig. 2. Effect of phase changes in dielectric and metallic reflection on double beam film interference. (a), (b) vector representation of phase relationships between interfering waves R_0 and R_1 shown in Fig. 1; (c), (d) predicted interference intensity distribution in a wedge shaped film.

The phase changes in reflection affect the position of the origin of the film thickness scale deduced from the interference fringes and become particularly significant for film thicknesses of a wavelength of light or less. If only the first two of the multiple reflections in the film are considered for a moment (R_0 and R_1 in Fig. 1), the phase relationships can be visualized in a vector diagram illustrated in Fig. 2. This representation shows phase and amplitude as angular and radial coordinates, respectively, and takes the time-independent phase of the incident wave E at the gas-film interface as a reference. For an aqueous 3.4N KOH film (n = 1.365) on a nickel substrate and 75° angle of incidence ϕ on the film, for instance, (angle of incidence on the metal ϕ' = 45°) phase shifts δ_{metal} for the metallic reflection of 112° and 48° in the sense of a phase advance have been computed for s and p polarization, respectively, from the optical constants of the interface measured by ellipsometry (20). These values are indicated by the positions of the vectors R_1 in Fig. 2a and b. The vectors R_0 show a 180° or 0° phase change, with s and p polarization, respectively, characteristic of the dielectric reflection at the gas-film interface under angles of incidence larger than Brewster's angle. Since a film of increasing thickness increasingly delays reflection R_1 indicated by the double arrows in Fig. 2a and b, the sum of the two complex amplitudes R_0 and R_1, a measure of the observed interference intensity, as a function of film thickness goes first through a minimum for s polarization (Fig. 2c) but a maximum for p polarization (Fig. 2d). Thus, the interference patterns with the two polarizations are approximately complementary to each other. Because the characteristic interference fringes which can be used for a quantitative interpretation correspond to different film thicknesses in the two polarizations, the simultaneous use of both yields twice the number of measured contour lines.

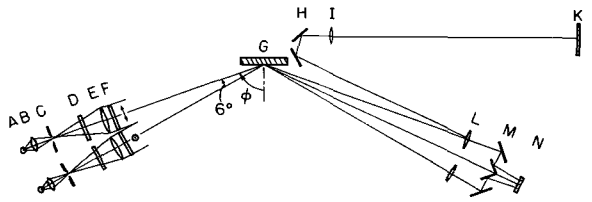

Fig. 3. Optical arrangement for slow motion movie photography of film formation. A, lamp; B. condenser; C, iris diaphragm; D, neutral density and color correction filters; E, collimator lens; F, polaroid filters with transmitted electric vector in and normal to the plane of the drawing; G, film covered surface; H, mirrors; I, objective; K, face of clock; L, objectives; M, mirrors; N, photographic film.

Experimental

The electrolytic cells employed contained optically polished[1] metal electrodes of rectangular (1.5×3 cm high) or cylindrical (2×13 cm high) geometry made of nickel or silver and inert counter electrodes of large surface area located in separate cell compartments (to avoid possible contamination of the electrode surface by corrosion products from the anode). Openings were provided to control the electrolyte level and to maintain atmospheres of known composition in the cell volume not occupied by the liquid. The nitrogen or oxygen gas was kept water-saturated with solution of the bulk concentration. After careful mechanical degreasing, the electrodes were electrolytically cleaned by hydrogen evolution. It is important that every trace of grease be excluded from the cell, particularly in working with dilute solutions, where even deposits from the laboratory atmosphere have been found to spread from the outside of the cell through open ports onto the electrode surface. Most experiments were initiated by rapidly lowering the liquid level in the cell to 5 mm above the lower electrode edge and observing the subsequent drainage of the film as a function of time. The optical arrangement used for this observation is given in Fig. 3 as a plan view diagram. Two collimated light beams A-F polarized parallel and normal to the plane of incidence are directed toward the film-covered surface G under an angle of incidence ϕ. The respective reflections are collected by two objectives L and placed by a set of first surface minors M side by side on the frame N of a 16 mm movie camera geared for single frame exposure. The image of a clock K was also placed on each frame by the objective I and the two mirrors H in order to record elapsed time. An automatic interval timer activated the camera shutter and turned the illumination off between exposures in order to avoid heating by light absorption.

[1] Microripple small compared to the wavelength of light.

Results

The evaluation of interference pictures from typical experiments along the vertical center line of the electrode results in film profiles given in Fig. 4a and b. After the initial drainage, a stationary film geometry is reached after a period in the order of 10 hr. This period is shorter and the resulting stationary film is thicker for an oxygen-consuming electrode as compared to the same metal-solution system not electrochemically polarized. The stationary film geometry has been asserted not to change in selected experiments over periods of several weeks.

If viscous and gravitational forces only are considered for the thinning of the electrolyte film, Eq. [5] can be derived (21) for the dependence of film thickness d on vertical coordinate z (measured from the upper electrode edge down) and time t

$$d = (\mu/\rho g)^{1/2} z^{1/2} t^{-1/2} \qquad [5]$$

where μ is the viscosity, ρ the density, and g the gravitational acceleration. Under these assumptions, a plot of film thickness *vs.* inverse square root of time would result in a straight line through the origin for a given electrolyte composition and electrode position. Such an analysis of the previously shown film profiles (Fig. 4) 1 cm above the liquid level results in the curves of Fig. 5. It can be seen that the expected relationship holds down to about 1μ film thickness. With no electrochemical polarization of the electrode (Fig. 5a), the rate of film thinning gradually deviates from that of a free-flowing liquid due to the effect of interfacial forces until a steady state value of 0.31μ is reached after 20 hr. The film thinning with concurrent cathodic oxygen consumption under constant current (Fig. 5b) exhibits an abnormally rapid thinning rate before reaching a steady state value of 0.39μ after 6 hr. The rapid film thinning may be due to electroosmotic ef-

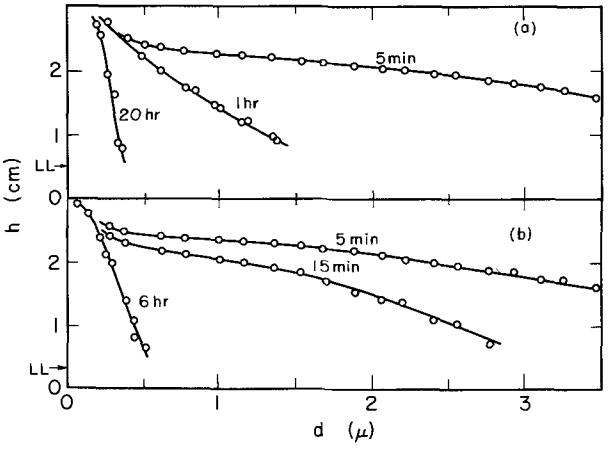

Fig. 4. Formation of electrolyte films on flat nickel plates after partial withdrawal from 3.4*N* KOH solution, selected film profiles; h, vertical dimension of electrode; d, film thickness, LL, position of liquid level after withdrawal. (a) Unpolarized electrode, nitrogen atmosphere; (b) cathodically polarized electrode (65 μa/cm), oxygen atmosphere.

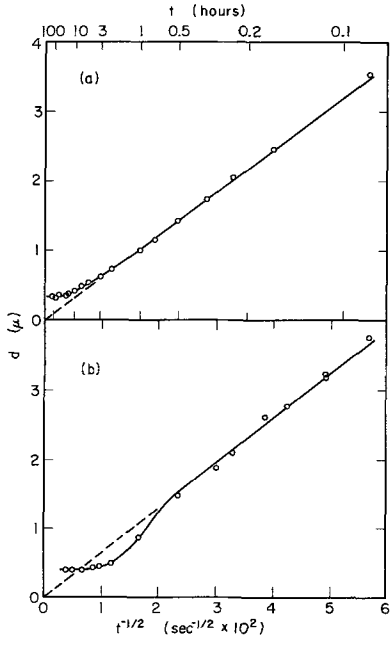

Fig. 5. Deviations from purely gravitation drainage of 3.4N KOH film on polished nickel surface at small film thickness observed 1 cm above the liquid level. (a) Unpolarized electrode, nitrogen atmosphere; (b) cathodically polarized electrode (65 μa/cm), oxygen atmosphere.

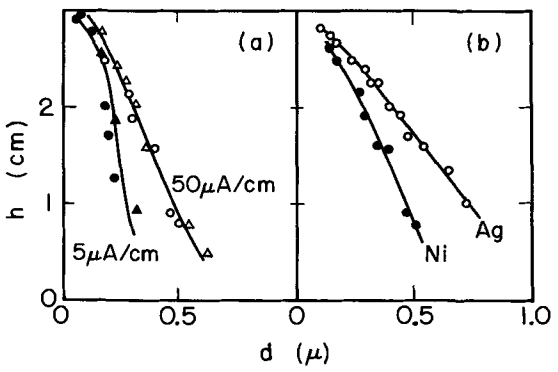

Fig. 6.(a) Stationary film profiles on flat (○) and cylindrical (△) nickel electrodes at different current densities, 3.5*N* KOH, O_2; (b) stationary film profiles on different metals. 3.5*N* KOH, O_2, 50 μa/cm.

fects, the establishment of a concentration profile, and the nonuniformity of electrochemical polarization. Two steady-state film profiles measured on the same electrodes under different load are shown in Fig. 6a. The response of film thickness to changes in cathodic polarization occurs with a transition time in the order of 10 hr. The same steady-state profiles are attained from previously higher or lower polarization. Such changes can be expected to take place in fuel cell electrodes under variable load.

Stationary film profiles of KOH solution on nickel and silver, two electrode materials of practical interest, are compared in Fig. 6b. They reflect the different surface properties and electrochemical polarization characteristics of the two metals.

The dependence of the steady-state film thickness on the liquid composition has been investigated with different potassium hydroxide concentrations; the film thickness has been found to increase with increasing concentration. For this reason, a 3.5*N* KOH film could be grown upward on a vertical nickel surface previously in equilibrium with distilled water, which forms a coverage just barely observable by the interference method. Such a film growth, measured 1 cm above the liquid level, is illustrated in Fig. 7. It can be seen that the transition, again, takes in the order of 10 hr.

Discussion

The experiments conducted have established the geometry of stable electrolyte films on polished nickel and silver surfaces partially immersed in aqueous caustic solutions. The film geometry reflects a balance of interfacial forces and therefore depends on the properties of the liquid, those of the solid and the electrical potential applied between the two phases. A satisfactory theory of film behavior will have to take into consideration that stable configurations are reached both with and without reaction occurring in the film. Gradients of concentration and other properties in the film can be expected to affect its geometry, but these do not seem to be the principal cause of film stability. The nature of the interfacial forces at play cannot be defined at present; however, it can be speculated on thermodynamic grounds for an equilibrium situation that with a typical heat of immersion of 100 erg/cm² for metals in water, considerable energy is available for film formation, practically all of which is used for establishing the film-gas interface that typically requires 75 erg/cm².

While the electrolyte films studied are of a much simpler nature than those presumably existing inside certain porous gas diffusion electrodes, where the presence of capillary and pressure forces may lead to different film geometries, the results obtained suggest further studies in this area. These include the practical significance of the unexpectedly long transition times to steady state, the effects of electrode surface pretreatments, and the complex interrelation of film geometry with the spatial distribution of current, potential, concentration and temperature in the film. Resulting changes in contact angle of the liquid meniscus inside capillary electrodes have been reported by Bonnemay *et al.* (22), and oscillating phenomena suggested for this area (23) have recently been reported by Bockris *et al.* (24).

The accuracy of the technique employed greatly depends on the optical properties of the substrate which determine the phase change in metallic reflection. These properties were computed from the complex refractive index of the solution-metal interface measured before and after each experiment. Various possibilities explored to check the phase relationships used in the evaluation of the interference fringes indicate a maximum error in film thickness of 0.1μ. The first such check is based on the dependence of the optical path ΔS in the film on the angle of refraction ϕ' expressed in Eq. [1]. This dependence should extrapolate to zero for a given film viewed under different angles, and thus ascertain the origin of the film thickness scale. According to Snell's law, there is only a limited range of values which the angle of refraction can assume for the maximum variation in angle of incidence. Therefore, this test requires a long extrapolation and can detect only gross errors in phase (Fig. 8). It is, however, sensitive enough to reveal an error of a full interference order possible by a misinterpretation of fringes in the data evaluation. Another test can be based on the wavelength dependence of the film interference seen in Eq. [2] and requires observation of the same film under a given angle of incidence with monochromatic light of different wavelengths. This presupposes a knowledge of the dispersion of the optical constants of metal and film. A third possibility consists in observing the sequence of interference colors as a film of a low solute content is rapidly evaporated to dryness by the introduction of a water-free gas phase. The variable refractive index of the film which represents another, although minor, source of error could possibly be determined by measuring Brewster's angle of incidence at which the

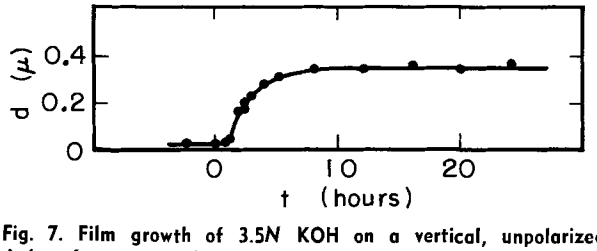

Fig. 7. Film growth of 3.5*N* KOH on a vertical, unpolarized nickel surface previously covered with a stationary distilled water film, observed 1 cm above the liquid level.

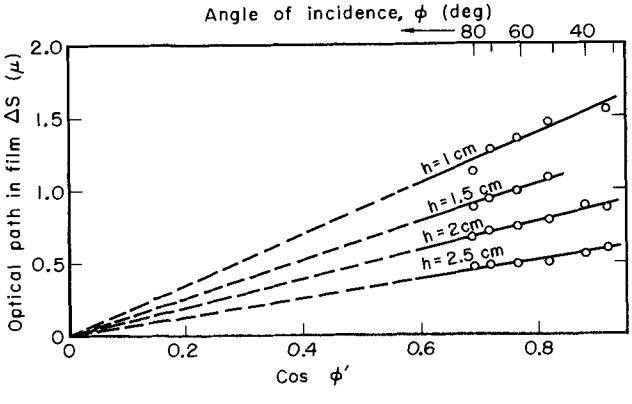

Fig. 8. Interference in the same film under different angles of incidence. Extrapolation of optical path length at different film levels h to check phase changes used in evaluation.

interference pattern completely disappears in p polarization (17). Finally, ellipsometry offers the possibility of simultaneously determining refractive index and thickness of the film provided that the optical constants of the film-metal interface and the approximate value of the film thickness are known. This check will have to be performed at a later time.

Experiments are in progress with larger flat electrodes in order to approach the behavior of an infinitely extended surface suitable for the analysis of surface forces and the derivation of interfacial thermodynamic data. A detailed understanding of electrolyte films on polarized electrodes may permit one to derive the electrocapillarity of solid electrodes.

Acknowledgment

This work was performed under the auspices of the United States Atomic Energy Commission.

Manuscript received Jan. 21, 1966; revised manuscript received May 27, 1966. This paper was presented in part at the Toronto Meeting, May 3-7, 1964 and at the Washington Meeting, Oct. 11-15, 1964.

Any discussion of this paper will appear in a Discussion Section to be published in the June 1967 JOURNAL.

REFERENCES

1. W. R. Grove, *Phil. Mag.*, **21**, 417 (1842).
2. F. G. Will, *This Journal*, **110**, 145 (1963).
3. A. Schmid, Diss. Basel 1922, Union Deutsche Verlagsgesellschaft, Stuttgart, 1923.
4. E. W. Justi and A. W. Winsel, "Kalte Verbrennung," "Fuel Cells," p. 89 ff, Steiner Verlag, Wiesbaden (1962).
5. R. P. Iczkowski, *This Journal*, **111**, 1078 (1964).
6. D. N. Bennion and C. W. Tobias, Paper presented at the Washington Meeting of the Society, Oct. 12, 1964.
7. H. J. R. Maget and R. Roethlein, *This Journal*, **112**, 1034 (1965).
8. J. A. Rockett, Paper presented at the New York Meeting of the Society, Oct. 2, 1963.
9. E. A. Grens, R. M. Turner, and T. Katan, *Advanced Energy Conversion*, **4**, 109 (1964).
10. T. Katan, S. Szpak, and E. A. Grens, *This Journal*, **112**, 1166 (1965).
11. W. D. Bascom, R. L. Cottington, and C. R. Singleterry, in "Contact Angle, Wettability and Adhesion," R. F. Gould, Editor, p. 355, American Chemical Society, Washington, D. C. (1964).
12. B. V. Deryagin, N. N. Zakhavaeva, S. V. Andreev, A. A. Milovidov, and A. M. Khomumov, in "Research in Surface Forces," B V. Deryagin, Editor, p. 110, Consultants Bureau, New York (1963).
13. N. Barakat, *J. Opt. Soc. Amer.*, **48**, 92 (1958).
14. K. B. Blodgett, *J. Phys. Chem.*, **41**, 975 (1937).
15. K. B. Blodgett and I. Langmuir, *Phys. Rev.*, **51**, 964 (1937).
16. A. M. Gaudin, *J. Phys. Chem.*, **41**, 811 (1937).
17. R. H. Muller, *J. Opt. Soc. Amer.*, **54**, 419 (1964), also Lawrence Radiation Laboratory Report UCRL-10963, July 1963.
18. H. Mayer, "Physik duenner Schichten," p. 54, Wiss. Verlagsges, Stuttgart (1950).
19. P. J. Lindberg, *Optica Acta*, **4**, 59 (1957).
20. W. Koenig in "Handbuch der Physik," H. Geiger and K. Scheel, Editors, Vol. 20, pp. 242, 243, Verlag Julius Springer, Berlin (1928); also R. H. Muller, J. R. Mowat, Lawrence Radiation Laboratory Report UCRL 11813, to be issued.
21. R. B. Bird, W. E. Stewart, and E. N. Lightfoot, "Transport Phenomena," J. Wiley & Sons, Inc., (1960); D. N. Bennion, Thesis, Dept. of Chem. Engr., University of California, June 1964.
22. M. Bonnemay, G. Bronoel, and E. Levant, *Electrochim. Acta*, **9**, 727 (1964).
23. R. H. Muller, Paper presented at the Washington Meeting of the Society, Oct. 12, 1964, Extended Abstract No. 4.
24. J. O'M. Bockris, L. Nanis, and B. D. Cahan, *J. Electroanal. Chem.*, **9**, 474 (1965).

Polarization Phenomena in Commercial Ion-Exchange Membranes

M. Block[1] and J. A. Kitchener

Department of Mining & Mineral Technology, Imperial College, London, England

ABSTRACT

Polarization phenomena occurring at ion-exchange membranes have been investigated with a number of commercial membranes of the type used in electrodialysis cells for desalting. Polarization is most marked with very dilute electrolyte solutions and with conditions favoring stagnation of the liquid films near the membrane; in particular, a horizontal membrane with upward direction of migration of counterions minimizes convection. Chronopotentiometric studies with this system have shown that the early stages of concentration polarization conform approximately to Sand's theory. Later, however, complicated phenomena are observed. At high current densities all of the cation-exchange membranes tested and certain of the anion-exchange membranes showed rapidly rising resistance, but certain other anion-exchangers were found capable of carrying high currents continuously, mainly in the form of hydroxyl ions. Experiments with radiotracers indicated that these differences did not arise from co-ion leakage or electroosmotic streaming. A possible explanation is that ease of passage of H^+ or OH^- ions through these membranes is dependent on the degree of microheterogeneity, which affects the possibility of transport by the Grotthus mechanism.

The permselectivity of most commercial ion-exchange membranes in dilute salt solutions is of the order of 90-100%, more or less, depending on the internal concentration of functional groups and the concentration of external electrolyte solution. In other words, when a direct current is passed through the system, about 90-100% of it is carried by migration of the counterions and the remainder by the movement of the co-ions of internal ("Donnan") electrolyte in the opposite direction. There is also some net transference of internal electrolyte solution by electroosmosis in the direction of migration of the counter ions. It is important to note, however, for the present problem, that these membranes are free from electronic conductivity, as shown by the fact that no evolution of oxygen or hydrogen gas is observed even when the membranes are subjected to very large potential gradients, *i.e.*, they do not behave as bipolar electrodes, but are purely electrolytic conductors.

Passage of current therefore leads to a reduction of concentration of electrolyte on the side which donates the counterions and an increase on the receiving side. Consequently, diffusion gradients are built up in the

[1] Present address: Vokes Ltd., Guildford, Surrey, England.

vicinity of the faces of the membrane and these constitute a type of concentration polarization, corresponding to the back emf that is detectable by means of Luggin capillary electrodes. Cooke (1) has made careful investigations of this type of membrane polarization. If the two solutions are stirred or otherwise renewed by flow, the extent of the diffusion regions is limited and a steady state is quickly reached in which diffusional transport up to and away from the membrane balances electrolytic transport through the membrane.

On the other hand, if convective transport is absent, or is inadequate in relation to the current passing, a more complicated sequence of events occurs. As extensive diffusion regions develop, the concentration of ions near the entry side of the membrane falls, and consequently an increasing potential gradient must be applied to maintain a given current density. The changes of density of the layers of solution and the differential heating may produce convection. Eventually, the local concentration of ions may become infinitesimal (*e.g.*, $<10^{-7}N$), and then an alternative process can take a significant part in carrying current, namely, the transport of one of the ionic species of water. With a cation-exchange membrane H^+ ions may be carried through, resulting in a rise of *p*H on the donating side and fall on the receiving side; with an anion-exchange membrane, transport of OH^- would produce the opposite *p*H changes. Such *p*H changes in electrodialysis have been known for many years and have been investigated by Bethe (2), Bethe and Toporoff (3), and more recently by Kressman and Tye (4), Frilette (5), Peers (6), Rosenberg and Tirrell (7), Uchino *et al.* (8), Cowan and Brown (9), Cooke (1), and Koblianski and Ulitin (10).

The conditions described in the preceding paragraph occur only at relatively high current densities and will be referred to as "high polarization" for brevity and to distinguish it from the simple steady-state concentration polarization. It is generally assumed that a certain critical current density is required to achieve high polarization, but the value necessary naturally depends on the set-up, the concentration and degree of agitation of the electrolyte, etc. The present work has shown that there is also considerable variation in polarization properties of different types of membrane.

It is generally accepted also that *p*H changes are more prominent with anion-exchange than with cation-exchange membranes, even above the supposed critical current density. For example, Cooke (1) found only 0.1% of the current to be carried by H^+ (from $0.05N$ solutions) whereas up to 60% transport by OH^- was found with anion-exchange membranes. (For this reason, in electrodialysis cells the diluate compartments generally become acidic and the concentrates alkaline.) These findings appear anomalous in relation to the theory of concentration polarization (see below).

In order to study the peculiarites of the high polarization regime, the conditions used in the present work were chosen to favor the onset of the condition, namely, high current densities, low electrolyte concentrations, absence of forced convection, and minimal natural convection. Under these conditions, not only is the permselectivity of the membranes practically unity, but also the diffusion zones approximate to the ideal plane-parallel layers required for Sand's well-known theory of concentration changes near an electrode to be applicable.

According to Sand's theory, which describes electrolysis at constant current under the influence of diffusion and electromigration and in absence of convection, the time required for the concentration of electrolyte to fall to zero at the plane of the electrode (membrane), the so-called "transition time," τ, is given by

$$\tau = \frac{\pi z^2 F^2 D C^2}{4I^2(1-T)^2}$$

where z is the valency of the current-carrying ion (*i.e.*, the counterion for a membrane), F is Faraday's constant, D and C the diffusion coefficient and bulk concentration of the electrolyte, I the current density, and T the transport number of the counterion in the solution. After the transition time has been passed, the current of counterions would fail to maintain I; if some other process takes over, a higher voltage will be required to maintain the current constant.

It follows that all membranes of a given ionic sign and with closely similar permselectivities should show the same transition time, irrespective of their chemical or physical structure. Similarly, if high polarization starts with depletion in the solution layers, the transition times for anion- and cation-exchange membranes should be in the inverse ratio of the squares of the transport numbers. The subsequent processes should depend on the mobilities of OH^- or H^+ in the membranes. As earlier published work had suggested that these ions would be especially mobile in the water-filled pores of strong-acid and strong-base ion-exchangers, a certain symmetry in the breakthrough of acid or alkali was to be expected, in contradiction to reported observations.

The experimental work described below was directed toward elucidation of these anomalies. Some unexpected results were obtained.

Experimental

Membranes.—The following membranes, kindly given by their manufacturers, were employed in the experiments (see Table I). Sometimes there were appreciable variations between replicate samples cut from different parts of the same sheet; furthermore certain membranes appeared to have asymmetric properties. However, only well-marked effects are reported here.

Methods.—The main technique employed was chronopotentiometry with horizontal membranes at a series of selected current densities, in absence of stirring. (Various auxiliary experiments are mentioned later.) The electrolyte was generally degassed $0.01N$ NaCl on both sides of the membrane, and the direction of applied potential was usually such that the counterions passed upward, thus causing dilution of the layer of solution below the membrane and concentration above it, the "stable" arrangement for minimizing convection.

Apparatus.—The cell shown in Fig. 1 is self-explanatory. The large silver-silver chloride electrodes could

Table I. List of commercial ion-exchange membranes investigated

Name of manufacturer	Trade name of membranes	Membrane designation: Cation-exchangers	Membrane designation: Anion-exchangers
Asahi Chemical Ind. Ltd. (Japan)	ACI	C; CK-1	A; CA-1
Asahi Glass Co. (Japan)	Selemion	—	AMG: AMT: AMP: ASG: AST: DMT*
American Machine and Foundry Co. (U.S.A.)	AMFion	C-60;	A-60
Ionac Chemical Co. (U.S.A.)	—	MC 3142	MA3148: MA3236
Ionics Inc. (U.S.A.)	Nepton	61 AZL	111 BZL
The Permutit Co. Ltd. (Gt. Britain)	Permaplex	C-20	A-20
Rohm and Haas Co. (U.S.A.)	Amberplex	C-1	A-1
Toyo Soda Mfg. Co. (Japan)	Toso	C	A

* In addition, the manufacturers kindly supplied specially prepared membranes, Selemion AM, AS, and CS, made without the usual reinforcing fibers.

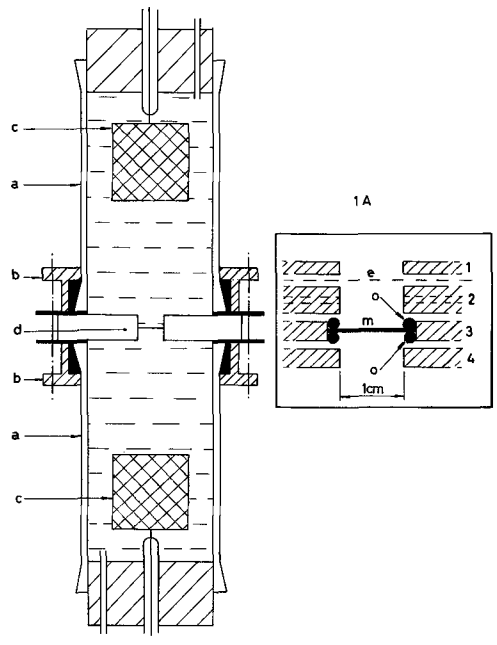

Fig. 1. Cell used for polarization measurements: a,a, glass flange joints; b,b, clamping brackets; c,c, silver/silver chloride gauze electrodes; d, membrane assembly. INSET (1A) exploded view of membrane mounting. 1, 2, 3, 4, "Perspex" plates (2 carries inlet and outlet channels); m membrane; 0,0 O-rings; e, cellophane sheet (when required).

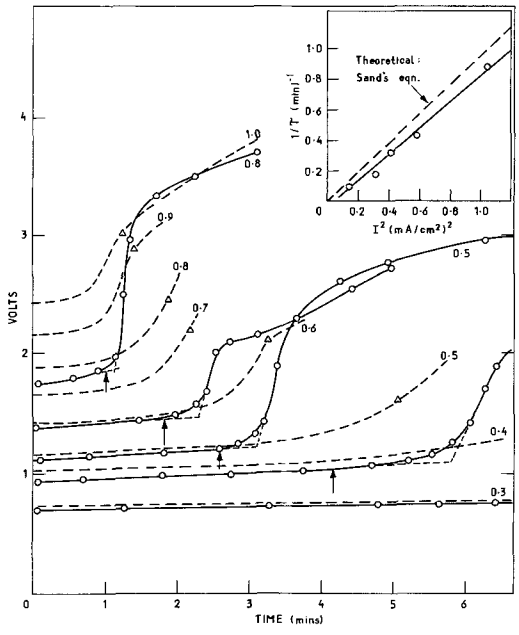

Fig. 2. Chronopotentiometric curves for anion-exchange membrane (ACI:A) at low current densities. △ point at which indicator color change was perceptible on the upper face. Figure beside lines is current in ma passing through disk of diameter 1 cm. Electrolyte: 0.01N NaCl; - - - - - - results obtained in normal laboratory; ——○—— results obtained with minimal disturbance. (Arrows indicate theoretical transition points). Inset: Graph of $1/\tau$ against I^2.

carry 50 ma for 30 min, or 200 ma for short periods, without gassing. For small currents a stabilized constant current supply built according to the design of Reilley (11) was used: when higher voltages were needed, a 0-750v stabilized voltage supply was dropped across a bank of 10 kohm, 25w resistors, and the current through the cell was kept steady by manual adjustment of rotary switches. The voltage, V, across the whole cell was recorded as a function of time at selected currents, both with and without the membrane. The voltage differences between the curves indicated the extra potential drop across the membrane and its adjacent liquid films produced by polarization (since the processes occurring around the electrodes and in the bulk solution were the same, at a given current, whether a membrane was present or not.)

Results of Chronopotentiometry

Low currents.—Figure 2 shows typical results for V as a function of t, for a series of low current densities through the membrane. The rise of voltage corresponding to complete depletion (of Cl^- ions) at the membrane is obvious, but under ordinary laboratory conditions the transition time was not sharply defined.

Conversely, when the counterions were made to pass downward, the current either remained constant (0.4-0.6 ma) or oscillated (0.8 ma). These effects are clearly due to convection arising from density changes.

In order to prove that beyond $t = \tau$ current was being carried by OH^- ions from water, some membranes impregnated with phenolphthalein were used in chronopotentiometric tests and the point at which alkalinity appeared, as indicated by a red color on the upper face of the membrane, was noted. These points are indicated by triangles in Fig. 2. The change in pH could not have been due to counter-current leakage of H^+ co-ions, as the change in color was seen first at the diluate side of the membrane and it then spread through it. Breakthrough of alkali is seen to occur shortly after the voltage has begun to rise, the delay presumably corresponding to penetration through, and saturation of, the anion-exchange membrane.

It was observed that the chronopotentiometric curves, such as those shown in Fig. 2, were sensitive to vibrations and thermal fluctuations. When the apparatus was transferred to a laboratory where vibrations and draughts were minimal, the rise of voltage was sharper, as indicated by the continuous lines in Fig. 2. The apparent transition times interpolated on the curves for 0.3, 0.4, 0.5, 0.6, and 0.8 ma are 11.2, 5.8, 3.1_3, 2.3_0, and 1.1_3 min, respectively, and the inset to Fig. 2 shows that these results are in rough agreement with Sand's equation, though the points correspond to somewhat larger values of τ than predicted theoretically. This is almost certainly due to some residual disturbance of the liquid layers, the discrepancy being relatively smaller at the higher current densities. As τ is inversely proportional to I^2, it was not practicable to obtain the necessary readings with the present apparatus at current densities much above 1 ma/cm^2; however, there is no reason to doubt that the theory is valid.

Chronopotentiometric curves obtained with cation-exchange membranes at low current densities were similar in form to those with anion-exchange membranes (Fig. 3). Again the rise in voltage was progressively closer to the theoretical value predicted by Sand's equation the higher the current density (see arrows). Apparently the diffusion layers did not remain undisturbed for more than about 1 min with either type of membrane; but, as τ was theoretically 63.2 sec for an anion-exchange membrane at 1 ma/cm^2 and 28.1 sec for a cation-exchange membrane, the rise of voltage appears sharper at a given current density with the latter membranes.

Although different manufacturers' membranes gave somewhat different values, and even specimens from the same sheet were not identical, it was generally observed (cf. Fig. 2 and 3) that the voltage rose to higher values with the cation-exchange than with the anion-exchange membranes, suggesting that an easier current-carrying mechanism was present in the latter rather than the former (after exhaustion of the diffusion of sodium chloride). The obvious possibility is that, after the transition has been reached, further current is carried by the ions of water.

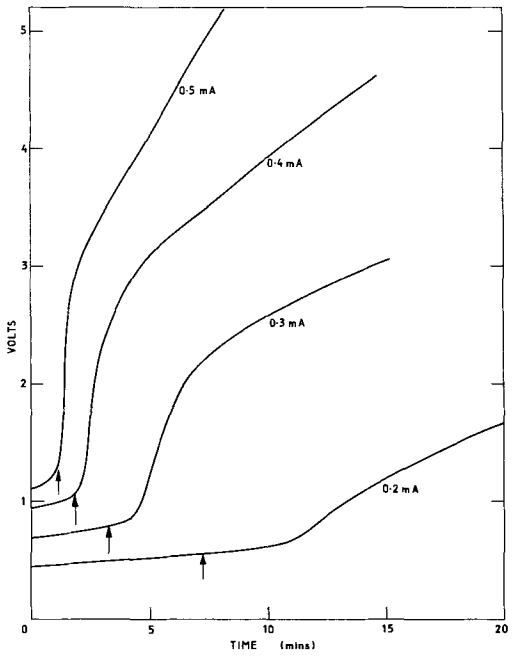

Fig. 3. Chronopotentiometric curves for cation-exchange membrane (ACI:C) at low current densities. (Arrows indicate theoretical transition points. Electrolyte: 0.01*N* NaCl.)

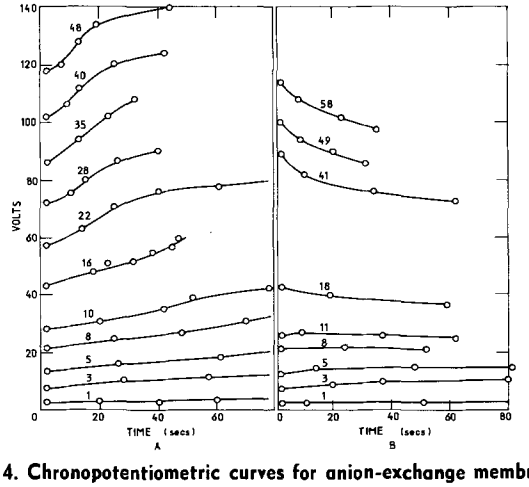

Fig. 4. Chronopotentiometric curves for anion-exchange membrane (Amberplex A1) at high current densities. (A, counter ions passing upward; B, counterions passing downward; numbers on curves are ma passing through disk of 1 cm diam. Electrolyte: 0.01*N* NaCl.)

At first sight this theory is contradicted by the apparently greater transport of OH^- by anion-exchangers than of H^+ by cation-exchangers. To check this important point, experiments were needed to determine the amounts of alkali and of acid transported respectively, and also the quantities of co-ion leaking through the membranes. However, to obtain measureable quantities for analytical determination, it was necessary to employ higher currents than those used in Fig. 2 and 3, and as certain other phenomena were then encountered, the chronopotentiometric data for higher currents will be considered next (Fig. 4 and 5).

High current densities.—With 5 ma/cm² or more, the theoretical transition time is 3 sec or less, and therefore too quick to be conveniently followed with the present apparatus. The first point recorded was arbitrarily taken immediately after the initial sharp movement of the voltmeter needle was complete. The phenomena responsible for the forms of Fig. 4 and 5 are, therefore, subsequent to the exhaustion of supply of diffusing counter ions from the solution, *i.e.*, they refer to events after the transition time.

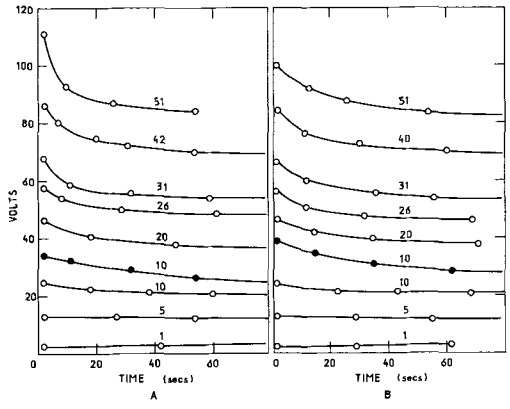

Fig. 5. Chronopotentiometric curves for anion-exchange membrane Toso A at high current densities. (A, counter ions passing upward; B, counter ions passing downward. ——●—— Measurements with agar gel disk below the membrane.) Electrolyte: 0.01*N* NaCl.

The voltage indicated in Fig. 4A and B refer to the total emf across the cell and therefore include the voltage drop across the electrolyte and polarization back emf's at the electrodes. It was not, however, necessary to determine these separately and subtract them from the total, as tests showed that, if just the membrane was omitted from the cell, the voltage required to pass a given current through the electrolyte plus reversible electrodes remained constant. Therefore, the significant feature is the change of voltage with time, corresponding to changes in effective resistance of the membrane and its adjacent layers of solution.

These experiments, unlike those at low c.d., revealed striking differences between different commercial membranes. All cation-exchange membranes, whether nominally "homogeneous" or "heterogeneous" in type, and certain anion-exchange membranes gave a set of curves similar to those of Fig. 4A, namely, with voltage rising with time, more and more steeply the higher the current passed. With the higher currents, the dissipation of power in the region of the membrane was so great (under static conditions) that eventually degassing and boiling brought the run to an end. (Temperature changes were checked by means of a small thermistor inserted below the membrane.) Application of the same power input in the form of a-c current produced no comparable local heating effects. Anion-exchange membranes falling in this class included ACI.A; ACI CA-1; Selemion AMT, AMP and DMT; AMFion A-60; Ionac MA 3236; Permaplex A-20; Amberplex A-1.

In contrast to the first type of membrane, certain other anion-exchange membranes yielded sets of curves of the kind shown in Fig. 5, the voltage decreasing with time and eventually levelling out to a constant value which could be maintained for long periods with only minor fluctuations. This class included TOSO A, Selemion AM, AS, AMG, ASG, AST and Nepton 111 BZL. The insertion of agar gel disks below the membrane increased the steepness of the curves similar to Fig. 4A but did not affect those similar to Fig. 5A.

For simplicity, the first type of membrane is referred to as "polarizing" and the second as "non-polarizing." The latter evidently possesses an adequate conduction mechanism to carry, for example, 50 ma/cm² continuously and even four times this value for short periods, whereas the former lacks such a mechanism.

It must be emphasized that these phenomena were observed only with arrangements conducive to stagnation of the solutions adjacent to the membrane (cf. Fig. 1). If the current was passed in the opposite direction (*i.e.*, counterions downward), curves of the

second type were obtained with all membranes; this is due, of course, to convection. The same applied to operation with the membrane vertical, or simply with reduction in thickness of the limiting orifice (1 cm thick) below the membrane. On the other hand, stirring of the solution above the membrane had no such effect. Therefore, the rising resistance of the polarizing membranes is associated with the membrane-diluate region.

Observations of the solution layers near the membrane were made during passage of current by means of the schlieren cell shown schematically in Fig. 6; the schlieren optical equipment was kindly made available by Sawistowski (Department of Chemical Engineering, Imperial College). Polarizing membranes at current densities of 14-66 ma/cm^2 showed violent turbulence in the diluate layer near the membrane, whereas nonpolarizing membranes showed no turbulence, even at 130 ma/cm^2. Instead, a thin layer of diluate just below the membrane appeared dark on the schlieren screen and gradually increased in depth. With a current density of 66 ma/cm^2 convectional circulation in the concentrate compartment commenced after about 10 sec.

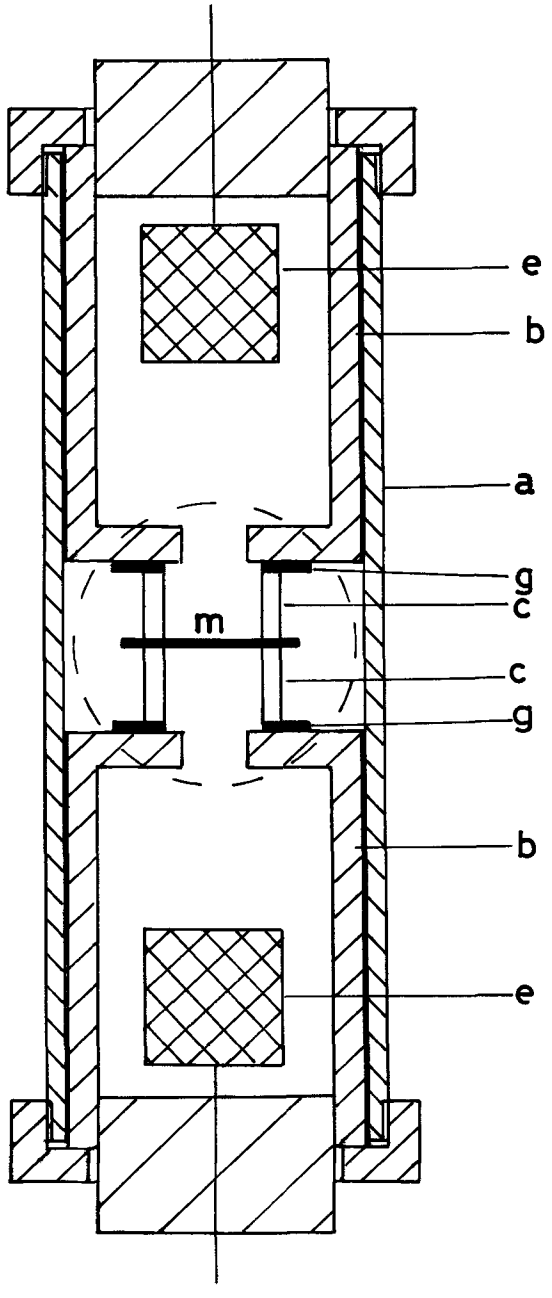

Fig. 6. Diagram of Schlieren cell: a; steel cylinder with screw ends and observation windows; b, b; "Perspex" electrode compartments; c, c; glass cylinders; m; membrane; g, g; gaskets; e, e; electrodes.

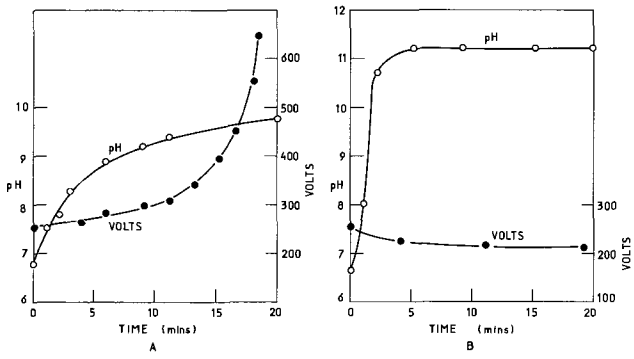

Fig. 7. Break-through of alkali with A. polarizing membrane (ACI A), and B. nonpolarizing membrane (Selemion ASG) at 66 ma/cm^2. Flow-rate across upper face of membrane: 24 ml/min. Electrolyte 0.01*N* NaCl.

pH changes during electrolysis.—To measure the amount of alkali generated during electrolysis with a nonpolarizing anion-exchange membrane, the cell was modified as in Fig. 1A so that a slow current of solution could be flowed across the top surface of the membrane and the *p*H of the effluent was determined. (To eliminate electrical disturbance of the pH-meter it was necessary to cause the effluent to fall as drops inside a polythene tube, thus electrically isolating the glass electrode vessel from the electrolysis cell.)

Results obtained with one polarizing and one nonpolarizing anion-exchange membrane at 66 ma/cm^2 are shown in Fig. 7. Both membranes passed considerable amounts of alkali, but the latter possessed a more facile conduction path and a steady state could be reached. In the steady state, the amount of alkali being released was sufficient to maintain the *p*H of the upper solution, flowing at 24 ml/min, at about 11.2; this corresponds to a transport number for OH^- of 0.93. It is certain, therefore, that practically all the current passing through the nonpolarizing membranes is carried by OH^- ions.

With the polarizing anion-exchange membrane of Fig. 7A, a steady state could not be reached, but, clearly, far less alkali had been generated for the same quantity of current passed. The *p*H was still rising after 19 min, but up to this time the bulk of the current must have been carried by other ions. Similar results were obtained with cation-exchange membranes (all polarizing): at most, only 6% of current was ever obtained in the form of H^+ transport, even at 66 ma/cm^2. The problem is therefore to account for the current that does pass in the highly polarized condition of the membrane. Several possible theories were tested by direct experiment (see below).

Leakage of co-ions.—The transport number for co-ions through commercial ion-exchange membranes is normally only a few per cent, but it seemed possible that under high polarization the value might increase. Measurements of transport of Na^+ and Cs^+ through four different anion-exchange membranes were therefore made, by means of ^{22}Na and ^{137}Cs, with 0.01*N* solutions of NaCl and CsCl as electrolytes and a current density of 66 ma/cm^2. The duration of the electrolysis ranged from 1.5 to 16 min.

The results showed co-ion transport numbers around 0.01 (ranging from 0.002 to 0.03, with results for Cs^+ being 2-3 times those for Na^+). Therefore, conductance by co-ions is a negligible factor in the polarization current.

These conclusions were supported by experiments in which a long-chain amine, "Hyamine 1622" (Rohm

and Haas Company), and a basic dye, methylene blue, both being cations too large to migrate through the membrane, were used as anolyte; the polarization response of the membranes was unaffected. These experiments show that the diluate side is rate-controlling.

Electroosmotic flow.—It seemed possible that nonpolarizing membranes might contain small pores through which solution streamed under high potentials, with consequent disturbance of the diffusion layers. Tests for electroosmotic flow were made by adding glucose, labelled with ^{14}C, to the catholyte and determining, by the method of Edwards and Kitchener (12), the amount of glucose transported into the anolyte. The assumption was made that glucose would diffuse through homogeneous membranes at a negligible rate, would be little adsorbed by the membrane, but would indicate any hydrodynamic streaming of catholyte through capillaries. The glucose tracer was at 10^{-5}M in 10^{-4}M inactive carrier; for analytical convenience, 0.01*N* NaOH was used as carrier electrolyte. A current of 66 ma/cm^2 was passed for 30 min. These experiments were done with a U-tube apparatus, with vertical membrane, in order to make it possible to continue electrolysis at high current density. It was argued that if pores were present in some but not other membranes, they should lead to differences of electroosmotic transport of glucose tracer.

The results showed transference of about 3×10^{-5} moles of glucose per Faraday, the values being of the same order for polarizing as for nonpolarizing membranes. Therefore, differences of electroosmotic flow could not be the explanation of the difference of polarization properties.

Stratified heterogeneity.—It seemed possible that the surface layer of a membrane might vary in properties, depending on whether it was cast on glass or exposed to air, as has been reported for cellulose acetate membranes by Sourirajan (13) and Keilin (14). Furthermore, membranes are known to be sensitive to surface contamination; therefore a membrane might behave in different ways when clean or when fouled during manufacture or handling. A further possibility with membranes made by introducing ionogenic groups into preformed hydrophobic plastic sheets is a chemical difference across the thickness of the sheet, if the reaction is not carried to completion (for example, to prevent the membrane becoming too brittle). The polarizing character of a membrane might be affected by such structural factors.

However, these expectations were not borne out by experiment, despite the fact that some of the membranes presented, surprisingly, a hydrophobic exterior, for neither abrasion of the surface with glass-paper nor creation of fresh surfaces by scraping with a scalpel changed the polarizing character.

Effect of hair-line cracks.—It was noticed that certain brittle membranes (containing reinforcing meshes), when subjected to gentle bending, developed microscopic cracks on the convex faces. These were practically invisible to the naked eye, but could be seen clearly under the microscope if the specimen was stained with a dye that did not diffuse into the resin matrix, for example, "Chlorazol Sky Blue" (I.C.I. Ltd.) for anion-exchange membranes. The cracks were seen to penetrate only as far as the reinforcement, the concave side being free from cracks.

A remarkable observation was made on the polarizing properties of these membranes, namely, that when a noncracked membrane or a cracked membrane with the cracked side uppermost (*i.e.*, facing the concentrate) was subjected to current, it polarized strongly. Correspondingly, in the schlieren cell violent convection was observed prior to boiling of the diluate. On the other hand, when the very same cracked specimens were tested with the cracks facing the diluate, nonpolarizing characteristics were observed; for example, a current of 66 ma/cm^2 could be passed for 30 min without marked heating or variation of voltage with time once the steady state had been reached. This behavior was reproducible with anion-exchange membranes made by different companies (*viz.*, Selemion AMG, ASG and AST: TOSO A; Ionics 111BZL).

The change from polarizing to nonpolarizing response could not be brought about by abrading the surface, by forming a fresh surface by means of a scalpel, by cutting vertical lines in the surface with a razor blade, or by applying wetting agents (anionic, cationic, or non-ionic) to generally hydrophobic membranes. A possible explanation of these phenomena is proposed later.

"Poisoning" by colloids.—"Orange G," an anionic dye of small molecular size, diffused into nonpolarizing membranes and had a small effect. But "Chlorazal Sky Blue," a larger dye that did not diffuse in, was found to restore the polarizing character of a deliberately microcracked brittle membrane. Apparently, the freshly formed surfaces within the microcracks were blocked as transport paths because of sorption of the dye. Similarly, treatment of inherently nonpolarizing membranes with an alkaline solution of an anionic polyelectrolyte (a high mol. wt vinyl acetate—maleic anhydride copolymer flocculant) converted them into polarizing membranes. As such polyelectrolytes certainly cannot penetrate into ion-exchange resins, their effects are confined to exposed functional groups. Not only are such groups eliminated as anion-exchangers, but the surface layer may be converted into a thin cation-exchanger which acts as a Donnan barrier to anions.

Discussion

The main facts requiring explanation are as follows: (*A*) Certain commercial anion-exchange membranes were found capable of carrying large currents (in the experimental set-up described) largely by means of OH^- ions, while others were not; (*B*) None of the cation-exchange membranes tested was found able to sustain substantial currents under comparable conditions.

These observations appear surprising only when considered in conjunction with the fact that all the membranes possessed high permselectivity and low resistivity in electrolyte solutions; therefore the development of concentration polarization should follow the same path, in all cases, as indicated by Sand's theory, as, indeed, it does, so far as transport of Cl^- or Na^+ ions is concerned. The auxiliary experiments reported show that the anomalies do not arise from differences of co-ion transport, leakage, or electroosmotic streaming. Furthermore, they appear to be confined to virtually salt-free membranes.

The only hypothesis that has been found to fit all the facts is the admittedly tentative suggestion that all the cation-exchanger membranes tested are relatively poor conductors of H^+ ions, that all the nonpolarizing anion-exchangers are good conductors of OH^-, and the polarizing anion-exchangers are relatively poor. As H^+ and OH^- are normally the most mobile cation and anion, respectively, this hypothesis seems, at first sight, improbable, but there is some evidence (discussed below) in favor of the idea. Furthermore, although the curves in Fig. 4A and 4B appear strikingly different, a quite small change of conditions (*e.g.*, the introduction of microcracks) sufficed to cause a switch from one class to another, and it is therefore likely that a delicate dynamic balance exists (under the test conditions) which requires only small differences of transport to upset it. Schlieren observations showed considerable convection in all the tests at high current density, and disturbances would presumably vary with transport rate.

It is generally accepted that the reason for the high mobility of H^+ and OH^- ions is their special transport mechanisms, the Grotthus chain, by which a charge is passed along a chain of hydrogen-bonded water molecules without actual migration of atoms. Now it has been found [Block (15)] by microscopic staining methods that all commercial membranes are highly heterogeneous and many are patchy and even partially hydrophobic. The manufacture of certain membranes by incomplete chemical attack on both sides of a sheet of polymer already introduces the probability of a greater concentration of exchange sites near the surfaces than at the center, where hydrophobic barriers might be present. Indeed, recent diffusion experiments have suggested the existence of such barriers [Crabtree and Glueckauf (16)]. Furthermore, the plastic sheets from which membranes of this type are made almost certainly contain amorphous and crystalline regions which would exhibit differential resistance to penetration of reagents. Therefore it seems very likely that the Grotthus chains are interrupted, more or less frequently, by hydrophobic barriers, through which ions have to migrate by a jump mechanism. Thus the advantage normally held by H^+ and OH^- would be reduced and might conceivably be reversed if these jumps required dehydration of the ions.

This theory cannot apply to truly homogeneous resins, and, indeed, conductance measurements on phenolsulfonic acid condensation resins show that H^+ retains its usual high mobility in highly swollen resins [Jakubovic, Hills and Kitchener (17)]. None of the commercial membranes available for test was homogeneous. However, Gregor and Peterson (18) have recently reported unique results obtained with a commercially obsolete membrane ("Nalfilm I", Nalco Chemical Company, Chicago). This membrane showed a transport number for H^+ ions above the initial current density of 0.4-0.7. The membrane is believed to have been of the polymer mixture type which are cast from a solution in dimethylformamide or dimethyl sulfoxide [Gregor (19)]; evaporation of solvent leaves the polyelectrolyte (polystyrenesulfonic acid) entangled with a water-insoluble plastic. These membranes were thin (96μ) and of low permeability, but it seems possible that continuous conduction paths for the Grotthus mechanism would be present.

Accurate conductance data for the various commercial membranes in counter-ion forms including H^+ (or OH^-), in absence of internal salt, would provide a check of the hypothesis that heterogeneity handicaps the ions of water by breaking Grotthus chain conduction paths; but unfortunately no suitable data are available at present. (Although the experiments reported here were in 0.01*N* NaCl, the membrane must presumably be virtually salt-free after a very short time.)

The influence of microcracks on the diluate side might also fit into the same model, as follows.

Application of Sand's equation for the concentration of electrolyte in the plane of electrolyte just above the membrane, namely, $c = c_o + 2F\sqrt{t/\pi D}$, shows an increase in salt concentration from 0.01 to 0.6*N* in 10 sec and 1.5*N* after 1 min at the current density of 66 ma/cm^2 generally used. The concentration of sodium hydroxide would be somewhat smaller, and would apply after exhaustion of the diluate layer adjacent to the membrane. Glueckauf and Watts (20) have shown that when an ACI A membrane sample was transferred from 0.01*N* sodium chloride to 0.4*N*, the equilibrium concentration of electrolyte within the membrane increased 160-fold and in the case of 1.0*N* solution increased 600-fold. It is therefore probable that the upper part of a polarized membrane has lost its permselectivity and that the critical zone is that part of the membrane adjacent to the diluate.

Therefore, if hydrophobic barriers are the limiting factor, microcracks through these barriers may be sufficient to maintain the current. When, however, such paths are poisoned, the membrane as a whole reverts to polarizing type.

Acknowledgments

This work was carried out in the Department of Mining and Mineral Technology, Imperial College, London, by kind permission of Professor M. G. Fleming. The authors thank G. and J. Weir Ltd., for a research studentship awarded to M.B. They are grateful to Professor R. S. Silver, Professor G. J. Hills, and Dr. H. C. Simpson for helpful discussions. They are also indebted to the many firms who freely supplied samples of membranes for examination.

Manuscript received March 24, 1966; revised manuscript received May 27, 1966.

Any discussion of this paper will appear in a Discussion Section to be published in the June 1967 JOURNAL.

REFERENCES

1. B. A. Cooke, *Electrochim. Acta*, **3**, 307 (1961); **4**, 179 (1961).
2. A. Bethe, *Muench. Med. Wochschft.*, **3**, 168 (1911).
3. A. Bethe and T. Toporoff, *Z. phys. Chem.*, **88**, 686 (1914).
4. T. R. E. Kressman and F. L. Tye, *Discussions Faraday Soc.*, **21**, 185 (1956).
5. V. J. Frilette, *J. Phys. Chem.*, **60**, 435 (1956); **61**, 168 (1957).
6. A. M. Peers, *Discussion Faraday Soc.*, **21**, 124 (1956).
7. N. W. Rosenberg and C. E. Tirrell, *Ind. Eng. Chem.*, **49**, 780 (1957).
8. T. Uchino, S. Nakaota, H. Hani, and T. Yawataya, *J. Electrochem. Soc. Japan*, **26**, E, 128 (1958).
9. D. A. Cowan and J. H. Brown, *Ind. Eng. Chem.*, **51**, 1445 (1959).
10. A. G. Koblianski and O. A. Ulitin, *Russ. J. Appl. Chem.*, **34**, 2553 (1961).
11. C. N. Reilley, W. D. Cooke, and N. H. Furman, *Anal. Chem.*, **23**, 1030 (1951).
12. B. Edwards and J. A. Kitchener, *Int. J. Appl. Rad. Isotopes*, **16**, 445 (1965).
13. S. Sourirajan, *Ind. Eng. Chem. Fundamentals*, **3**, 206 (1964).
14. B. Keilin, Office Saline Water R.D. (Washington) P.R. *84* (1963).
15. M. Block, Ph.D. thesis, University of London, 1964.
16. J. M. Crabtree and E. Glueckauf, *Trans. Faraday Soc.*, **59**, 2639 (1963).
17. O. Jakubovic, G. J. Hills, and J. A. Kitchener, *Trans. Faraday Soc.*, **55**, 1570 (1959); cf. G. Manecke and E. Otto-Laupenmühlen, *Z. physik. Chem. (Frankfurt)*, **2**, 336 (1954).
18. H. P. Gregor and M. A. Peterson, *J. Phys. Chem.*, **68**, 2201 (1964).
19. H. P. Gregor, *Symp. Saline Water Conversion*, (Washington, Natl. Acad. Sci.) Pub. *568*, 240 (1958).
20. E. Glueckauf and R. E. Watts, *Proc. Roy. Soc. (London), A*, **268**, 339 (1962).

Technical Notes

A Dynamic Method of Determining the Internal Resistance of Fuel Cells and Batteries

L. Reid, D. Cole, and I. Trachtenberg

Texas Instruments Incorporated, Dallas, Texas

Current interruption techniques (1, 2) have been used successfully to study fuel cells and batteries. One important parameter which can be measured by these techniques while the cell is on open circuit or under a steady d-c drain is the internal resistance. These interruption techniques permit use of reference electrodes without requiring a cumbersome Luggin capillary. However, all of these techniques are limited by the time required to interrupt the current and measure the voltage change. Errors as large as several tenths of a volt can occur if polarizations, other than ohmic polarization, have relatively short time constants compared with the time required for the measurement.

The previously reported single current interruption technique (1) utilized a mechanical relay which depended on mercury wetted contacts to give reproducible opening and closing without appreciable relay chatter. The make-before-break condition of this relay introduces an error in determining the exact current and voltage immediately prior to interruption. Also, some difficulty is always encountered in adjusting the oscilloscope delay circuits because of slight variations in the make-before-break time of the relay. One usually looks at only the voltage change at the break time on the shortest possible time scale. With the single current interruption methods, time scales shorter than 1 μsec/cm on an oscilloscope could not be used. Most internal resistance measurements with this technique can be made within 2-5 μsec after current interruption.

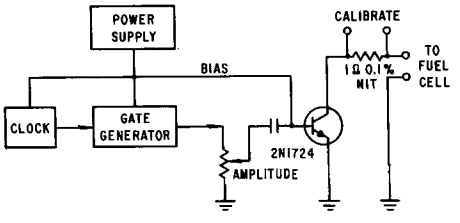

Fig. 1. Block diagram of circuit used for current interruption studies.

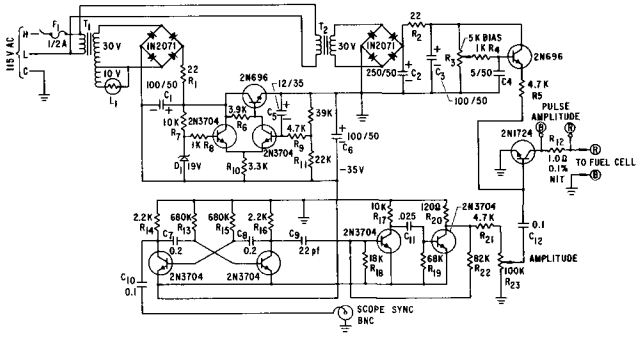

Fig. 2. Schematic diagram of circuit used for current interruption studies.

The method described here employs an electronic switch to interrupt a constant current which is imposed on the cell in its steady-state condition (open circuit or a steady d-c drain).

A block diagram of the circuit is shown in Fig. 1, and a detailed circuit diagram is given in Fig. 2. The power source is 115-v 60-cycle, and the only auxiliary piece of equipment is a fast rise oscilloscope such as the Tektronix 545B with a type W high gain differential plug-in preamplifier. This system has a rise time of 44 nsec on the most sensitive ranges. The clock circuit generates a 250 cps square wave pulse approximately 100 μsec long with a rise and fall time of less than 0.1 μsec. It also provides a trigger signal for the oscilloscope which allows the operator to view the leading edge of the pulse. By proper synchronization a fixed display on the scope is achieved. The clock frequency and pulse duration were arbitrarily chosen. No provisions were made in this design to vary these parameters; however, with suitable circuit modifications, they could be made variable without affecting the system performance.

The gate circuit amplifies and shapes the pulse, which is then coupled through an amplitude control potentiometer to the base of a passing transistor. This transistor is a high-frequency silicon power device in series with the fuel cell or battery. The electrochemical cell provides the collector voltage to the transistor. Bias is adjusted so some known direct current will flow. The magnitude of this current is determined by measuring the voltage drop across the 1-ohm precision resistor at the "calibrate" terminals.

Current levels as low as a few milliamperes and as high as several hundred milliamperes have been used with equally good results.

If polarizing the electrochemical cell to a greater extent by drawing larger currents is desired, a parallel external load may be connected. This allows a static load of any reasonable magnitude to be drawn from the electrochemical cell while only a hundred milliamperes or so is interrupted.

When the amount of d.c. flowing is set with the bias control, the oscilloscope is connected directly to the electrochemical cell terminals; and the pulse ampli-

Table I. Comparison of battery resistance measurement techniques

Battery	Current interruptor technique		A-C bridge technique
	Resistance in ohms	Current in ma	Resistance in ohms
No. 6 cell	0.030	80	0.026
	0.031	200	
	0.031	400	
D cell	0.18	80	0.20
	0.19	200	

tude is adjusted so during the 100-μsec pulse the passing transistor is driven to cut off. This interrupts current flow. By measuring the amplitude of this pulse at the "turn-off" time one can calculate the cell's internal resistance.

Corrections need not be made for lead resistance with this technique, an advantage not offered by the a-c bridge technique.

Table I lists typical examples of resistance measurements of Leclanché cells made by current interruptions and with a General Radio Type No. 1650-A Impedance Bridge. The test data in Table I were taken on used batteries.

Figure 3 illustrates a typical oscilloscope trace for a "D" size Leclanché cell. Preinterruption current was 80 ma, and the voltage change after 1 μsec was 15 mv.

This method has been applied to fuel cells containing a slurried molten carbonate electrolyte. One apparently typical group of five such fuel cells, in which the geometric areas of the anodes and cathodes were 8 in.^{2}, had minimum resistances of 0.012-0.014 ohm. The resistances of these cells varied between 0.012 and 0.025 ohm during operation.

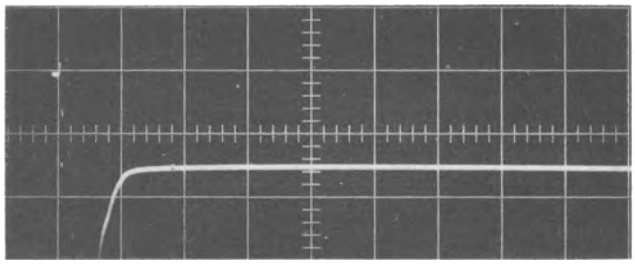

Fig. 3. Typical oscilloscope trace for "D" size Leclanché cell. Preinterruption current 80 ma; horizontal scale 1 x 10^{-6} sec/division; vertical scale 10 mv/division.

Manuscript received March 17, 1966; revised manuscript received May 23, 1966.

Any discussion of this paper will appear in a Discussion Section to be published in the June 1967 JOURNAL.

REFERENCES

1. I. Trachtenberg, *This Journal*, **111**, 110 (1964).
2. K. Kordesch and A. Marko, *ibid.*, **107**, 480 (1960).

Preparation of Homogeneous HgTe-ZnTe Alloys

E. Cruceanu and N. Nistor

The Institute of Physics, the Academy of the Socialist Republic of Romania, Bucharest, Romania

In view of the interesting properties of the mixed crystals of the $Cd_xHg_{1-x}Te$ system, and especially the extremely high mobility of the electrons observed in compositions with $x \approx 0.2$ (1, 2), particular attention has been focused on this system.

Although a number of similarities exist between the CdTe-HgTe and ZnTe-HgTe systems, the latter has been studied to a lesser extent. This may be due partly to the difficulties encountered in obtaining certain compact and homogeneous alloys suitable for electrical work. These difficulties are linked not only to the comparatively high temperatures of the liquidus curve of the system, but especially to the accentuated structural differences that exist between the substituting atoms (Hg-Zn), which lead to long homogenization periods and a marked tendency to the appearance of pseudo-eutectic structures.

The possibility of obtaining solid solutions in the whole range of HgTe-ZnTe compositions was demonstrated by Woolley and Ray (3), who also established the solidus curve of the system by the x-ray method. The liquidus curve of the system has recently been determined (4) by normal cooling-curve technique, checking at the same time the solidus temperatures of several of the compositions. The electrical properties of the system have been studied up to the present only for the compositions close to HgTe (5); variations in the optical energy gap with composition have been discussed in ref. (6) for thin layers.

Here the preparation of solid $Zn_xHg_{1-x}Te$ solutions, suitable for the determination of their semiconductor properties is discussed.

Preparation of solid specimens.—In the case of the two methods considered (*a*) the Bridgman-Stockbarger method, and (*b*) slow zone recrystallization, for the preparation of $Zn_xHg_{1-x}Te$ alloys, solid solutions in the form of powders, obtained in separate experiments after very prolonged heat-treatment of the appropriate amounts of HgTe and ZnTe (3), were used.

The Bridgman-Stockbarger method.—The vertical Bridgman-Stockbarger method can be successfully employed for the preparation of compact, monocrystalline alloy ingots, with $X \leq 0.12$, provided the rate of movement of the quartz ampoules is lower than 2 mm/hr and a small temperature gradient (5°-7°C/cm) is used. In order to obtain better homogeneity, the ingots are further annealed (400-500 hr) at temperatures immediately below the relevant solidus temperature and then studied from the microstructural and x-ray viewpoints. The ingots obtained were single phase along their whole length, and the high-angle x-ray reflections were clear-cut and intense, testifying to good equilibrium conditions.

All the samples for electrical determinations, cut perpendicular to the displacement direction of the ampoules, showed a p-type conductivity, without any special heat-treatment, with carrier concentrations at 77°K (ranging in terms of the composition) of from 6.10^{18}/cm^3 for $x = 0$ to $4.4 \cdot 10^{18}$ for $x = 0.08$. The fact that, after annealing in Hg vapor at temperatures close to 200°C, the concentration of acceptors falls to 8.10^{16} cm^{-3} would suggest that the nature of the acceptors is linked to the presence of mercury vacancies in the crystalline lattice of the alloys.

With increase in ZnTe concentrations, *i.e.*, $x > 0.12$, it is difficult to obtain solid solutions by the Bridgman-Stockbarger method, because of the high working temperatures and long periods in which the quartz ampoules must be kept at these temperatures.

Slow zone recrystallization has proved, in this instance, a good method. Quartz ampoules (140-160 mm long) were used in a set-up that permits slow movement of the ampoule along the three temperature zones used. The material was melted with high-frequency currents, inducing the necessary temperatures in graphite cylinders containing the quartz ampoules. The zonal temperature was determined with an optical pyrometer and its value fixed according to the liquidus curve established in (4) and shown in Fig. 1.

Temperature values in the two lateral background temperature zones were chosen in separate experiments carried out for the determination of the vapor pressure of solid solutions at various temperatures and were fixed at 500°C for $x = 0.6$ and 550°C for $x = 0.3$.

The velocity of the ampoule along the fixed zone was approximately 1.5 mm/hr, and the length of the molten zone was maintained between 10 and 20 mm.

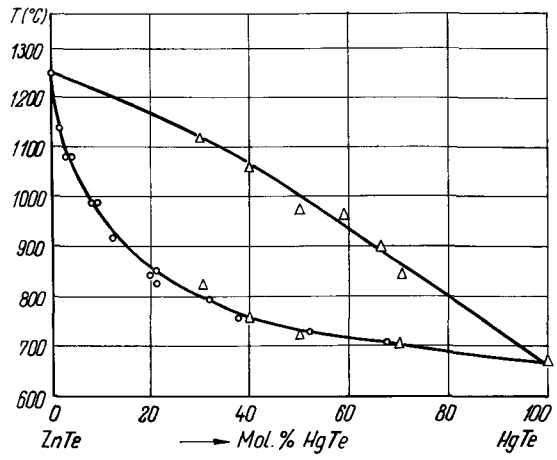

Fig. 1. Phase diagram of HgTe-ZnTe system. Liquidus curve, △-Cruceanu *et al.* (4); solidus curve, ○-Woolley and Ray (3).

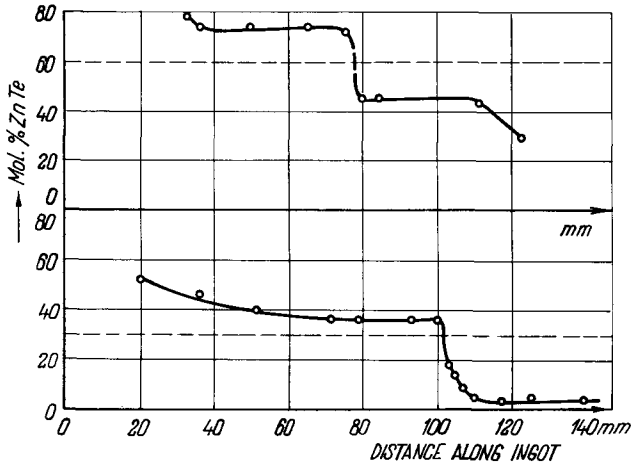

Fig. 2. Variation of composition of cross-sectional slice as a function of position in zone recrystallized ingots.

Two initial compositions were used, one with a higher molar HgTe ($Zn_{0.3}Hg_{0.7}Te$) composition, and the other with a higher molar ZnTe ($Zn_{0.6}Hg_{0.4}Te$) composition. In order to obtain better homogeneity, after moving the zone along their whole length, the ingots were annealed for approximately 300 hr at 650°C. The microstructural and x-ray analysis showed the ingots to be single phase in the center, over a length of 12-14 cm, the composition varying along the ingot according to the curves plotted in Fig. 2 [the composition was determined by the x-ray powder method in a ϕ 114 mm camera, using the data on the variation of the lattice constant with composition, obtained in (3) (4)].

It is of interest to note that although the aspect of the curves in Fig. 2 is, in general, similar to that of the InSb-InAs system curves (7), our results differ from those of Woolley and Warner in that we found one phase in the center of the ingot whereas they found the ingot to be homogeneous at the two ends. Moreover, our metallographic studies have demonstrated the existence of two phases at the ends of the ingot, over a distance of 1-2 cm, with a pseudo-eutectic structure, yielding either broader x-ray lines or two completely separate systems of lines. Hence, the composition could not be determined accurately, and in Fig. 2 the data for the ends of the ingot have been omitted.

Although the results on the electrical properties of alloys will be published elsewhere, we deem it of use to indicate that the solid solutions obtained by this method (with $0.35 \leq x \leq 0.74$) are all p-type and have extrinsic carrier concentrations of approximately 2.10^{16} cm^{-3} (at 77°K).

To conclude, zone recrystallization may be considered one of the most useful methods for obtaining massive and homogeneous HgTe-ZnTe alloys, with practically any composition, and will probably play an important role in the development of further studies on this system.

Acknowledgments

The authors wish to thank D. Niculescu and S. Ionescu-Bujor for many helpful discussions. Thanks are also due to E. Zamarca and R. Ilie for technical assistance.

Manuscript received April 25, 1966.

Any discussion of this paper will appear in a Discussion Section to be published in the June 1967 JOURNAL.

REFERENCES

1. T. C. Harman, A. J. Strauss, D. H. Dickey, M. S. Dresselhaus, G. B. Wright, and J. G. Mavroides, *Phys. Rev. Letters*, **7**, 403 (1961).
2. W. Giriat, Z. Dziuba, R. R. Galazka, L. Sosnouwski, and T. Zakrzewski, *Proc. Int. Conf. Phys. Semicond.*, (Dunod, Paris 1964), 1251.
3. J. C. Woolley and B. Ray, *J. Phys. Chem. Solids*, **13**, 151 (1960).
4. E. Cruceanu, D. Niculescu, N. Nistor, and A. Aldea, *Rev. R. Phys.*, **9**, 499 (1964).
5. E. Cruceanu, D. Niculescu, I. Stamatescu, N. Nistor, and S. Ionescu-Bujor, *Fiz. tverd. tela*, **7**, 2039 (1965).
6. S. A. Daniliuk and M. V. Kot; *Izv. Akad. Nauk, ser. fiz.*, **28**, 1071 (1964).
7. J. C. Woolley and J. Warner, *This Journal*, **111**, 1142 (1964).

Temporary Protection of Silicon Surfaces by Iodine Films

R. Lieberman and D. L. Klein

Bell Telephone Laboratories, Incorporated, Murray Hill, New Jersey

Silicon surfaces are normally covered with mixtures of oxide, hydroxide, and fluoride groups subsequent to chemical etching. This coverage results from the necessity of terminating the free or dangling bonds that are generated on new silicon surfaces. These terminations are responsible for the hydrophobic character observed on freshly etched silicon.

In an effort to eliminate this surface activity a barrier technique involving the formation of iodine films has been developed. The function of the iodine is to prevent formation of oxides and to displace fluoride and hydroxide terminations normally found on etched silicon. Atomically clean silicon surfaces can then be generated by removing these iodine films by sublimation.

Procedure

The procedure consists of quenching a freshly etched silicon surface in a saturated or concentrated solution of iodine in an anhydrous solvent. This quenching must immediately (~1-2 sec) follow the removal of the slice from the etchant. The anhydrous property of the solvent serves to prevent hydrolysis of the Si-I bonds formed during quenching. Several

solvents suitable for the iodine are chloroform, carbon tetrachloride, and methanol. After removing a silicon slice from the iodine solution, a gross iodine film can be observed on the surface for approximately 5 to 10 min in room ambient. A more tightly bound chemisorbed iodine layer is present on the surface and can be effectively removed by thermal treatment. In practice temperatures of about 500°-550°C have been employed to remove the chemisorbed iodine *in vacua* (*e.g.*, $\leq 10^{-6}$ Torr), or at atmospheric pressure in inert ambients. The removal of the iodine is accomplished in several minutes under these conditions.

Until the gross iodine film is removed by sublimation it is important to limit the temperature of treated surfaces to < 600°C. Otherwise, direct reaction of the silicon and iodine can occur and result in surface etching via the formation of SiI_4.

When slices must be stored subsequent to the iodine quench they can be left immersed in the iodine solution. Samples have been stored in this manner for extended periods (up to 72 hr) without loss of surface protection.

Discussion

The iodine treatment was found to produce atomically clean and well ordered silicon (111) surfaces as determined by low-energy electron diffraction studies.[1] The diffraction patterns were observed after removal of the iodine by heating the samples at pressures of $\sim 10^{-9}$ Torr. Results of the diffraction measurements indicate that the coverage of adsorbates (*e.g.*, oxygen) was less than a small fraction of a monolayer. The success of this technique may be due to several factors. These include the displacement reaction of fluorinated silicon surfaces directly with iodine as well as the physical adsorption of iodine on silicon surfaces.

The displacement of the fluorinated silicon surface probably results from the reaction of the iodine with the fluorine bonded to the silicon to form an interhalogen compound.[2] This type of reaction could account for the effective removal of fluorine from silicon surfaces. Hydroxyl groups can also be displaced, in this case, through the formation of HOI.

The physical adsorption of iodine on a freshly etched silicon surface results in the formation of a temporary barrier to other reactions.

Stronger van der Waals forces should exist between iodine and the silicon surface than between either fluorine or oxygen and the surface. The chemical formation, therefore, of Si-F and Si-O bonds will be inhibited since these reactions depend on preliminary physical adsorption of the reactants. The combination of a relatively large covalent radius (1.33Å), solubility in nonaqueous solvents and sublimation properties serve to make iodine an ideal material for a temporary barrier film.

The model that has been used to explain the effectiveness of the iodine treatment is a simplified description. A more detailed study of the interaction of silicon and iodine by means of low-energy electron diffraction has been reported by Lander and Morrison (1).

Applications

Oxide film prevention.—This process has been utilized to eliminate interfering surface oxides during closed vacuum system diffusion of arsenic into silicon. Oxide-free silicon surfaces are necessary for this type of diffusion in order that uniform junctions can be formed. Photomicrographs (Fig. 1) of angle lapped

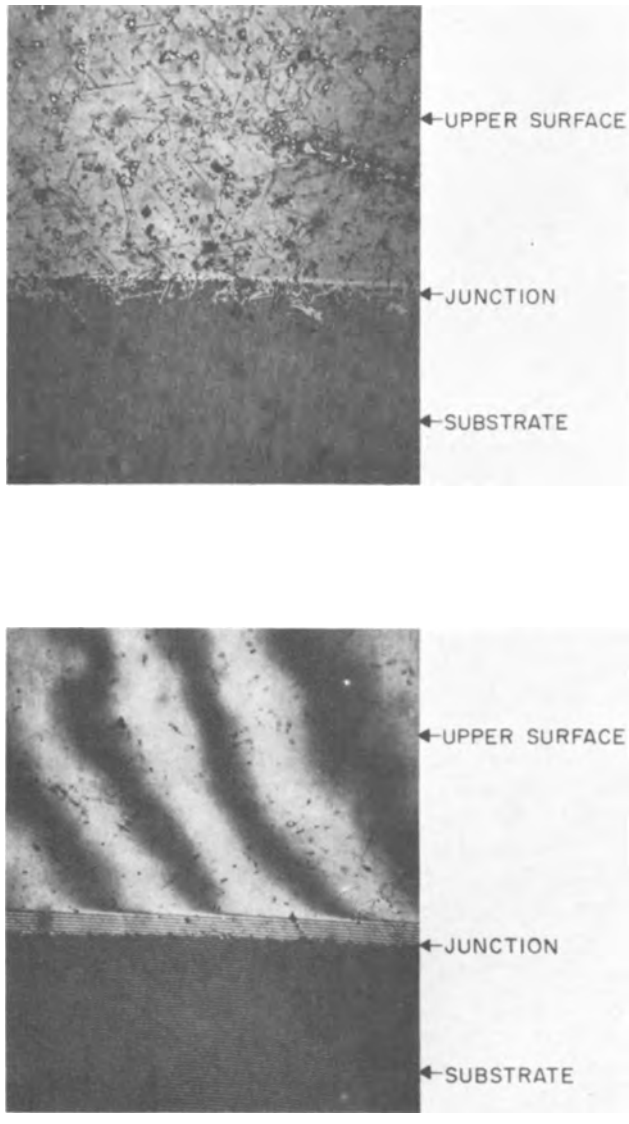

Fig. 1. Effect of I_2 quench on junction formation; double furnace diffusions, As at 600°C, Si at 1050°C. Top, without I_2 quench; bottom with I_2 quench. Angle lapped surfaces, 2° bevel. Magnification approximately 160X.

samples, with and without the use of the I_2-methanol quench, have demonstrated a marked difference in junction uniformity. The elimination of oxide on the iodine treated silicon surface prior to diffusion probably accounts for the improvement in the quality of the junction.

Control of defects in passivating films.—Normally, silicon surfaces etched in the presence of HF are initially hydrophobic. Silicon surfaces following iodine quenching and subsequent iodine removal are hydrophilic in character. The hydrophilic nature of the iodine quenched surface appears to influence the uniformity of surface oxide formation. Marked decreases of oxide defects, such as pinholes, have been demonstrated in oxide films formed by steam (1050°C, 1 atm) oxidation of silicon. Examinations of oxides on silicon surfaces subjected to the I_2-methanol quench have shown a significant decrease in the number of pinholes. These pinholes were exposed by a discriminatory water-amine-pyrocatechol etch.[2] Pinhole counts of steam oxidized (1 hr, 1 atm, 1050°C) silicon samples which were pretreated with I_2 quenches exhibited 230 pinholes/cm^2. The defect density of control samples prepared by quenching in water was found to be 900 pinholes/cm^2.

[1] The electron diffraction studies were performed by E. G. McRae and J. Morrison of these Laboratories who observed 7th order patterns.

[2] It is recognized that the Si-I bond energy (51 kcal) is considerably less than the energy of the Si-F bond (143 kcal). However, the displacement of the fluorine can probably be explained on the basis of mass action. The availability of large quantities of iodine in solution and the coordination of any labile fluorine entering the iodine solution could be expected to result in a high probability of fluorine replacement.

Influence on semiconductor junctions.—In order to investigate the possibility of deleterious effects caused by I_2-solvent quenches on devices, leakage currents of silicon detector diodes were measured following such treatment. These n-p diodes are large area, 10,000 ohm-cm resistivity mesa devices and as such are very sensitive to surface effects. Leakage currents of these diodes given either an I_2-methanol or an I_2-carbon tetrachloride quench following a 5-sec HNO_3-HF (40-1) etch displayed no degradation. Results after 10-min cycling in dry O_2 and wet N_2 did not differ from those obtained on control diodes. This would indicate that the iodine surface treatment did not degrade the electrical characteristics of these sensitive junctions.

Conclusions

The technique of I_2-nonaqueous solvent quenching has been investigated, and preliminary experiments indicate that it will temporarily prevent oxide, hydroxide, and fluoride formation normally experienced in silicon technology. This has been demonstrated by low-energy electron diffraction studies and by the application of the technique to several device processing procedures. Since the iodine films are readily removed, the procedure serves as a simple means of preparing atomically clean surfaces just prior to device processing.

Acknowledgment

The authors wish to thank R. W. MacDonald for his contributions to the diffusion experiment.

Manuscript received March 4, 1966; revised manuscript received May 23, 1966.

Any discussion of this paper will appear in a Discussion Section to be published in the June 1967 JOURNAL.

REFERENCES

1. J. J. Lander and J. Morrison, "Low Energy Diffraction Study of Silicon Surface Structures," Annals of the New York Academy of Sciences, **101**, 605 (1963).
2. R. M. Finne and D. L. Klein, *This Journal*, **111**, 63C (1964).

Enhanced GaAs Etch Rates Near the Edges of a Protective Mask

Don W. Shaw

Materials Science Research Laboratory, Texas Instruments Incorporated, Dallas, Texas

It has been observed in the author's laboratory that holes etched into gallium arsenide through windows in a protective silica etch mask are deeper near the edges of the mask than at the center of the hole. This phenomenon is illustrated by the angle-lapped section shown in Fig. 1. It is obvious from the morphology of the hole bottoms that the etch rate was greater near the mask edges than at the centers of the holes. This "edge effect" presents a severe problem to the fabrication of device structures by selective etch and deposition techniques.

The edge effect occurs when GaAs holes are etched with such etchants as bromine-methanol (1:1000), hydrogen peroxide-sulfuric acid-water (1:5:1), and 3% sodium hypochlorite solutions. It is also observed to a lesser degree with holes formed by HCl vapor etching at temperatures up to 800°C. The magnitude of the effect tends to decrease as the hole depths increase, *i.e.*, the deeper holes have flatter bottoms. The phenomenon is independent of the window dimensions with the exception that with very small windows the regions of enhanced etch rate near opposite walls may overlap.

The enhanced etch rates near the mask edges could be due either to localized stresses occurring at the mask-GaAs interface or to surface diffusion of adsorbed molecules along the protective mask which effectively results in a greater flux of etchant at the mask edges. As will be shown below, the experimental results provide strong support for the surface diffusion explanation.

Fig. 1. Micrograph showing 5° angle-lapped section through holes etched into GaAs with an unstirred bromine-methanol (1:1000) solution.

Stresses present at the mask-GaAs interface could be related to the differences in thermal coefficients of expansion between the silica film and GaAs. They would be imposed when the silica-coated GaAs crystal is cooled from the 450°C silica deposition temperature (oxidative tetraethyl orthosilicate process) to room temperature. To investigate further the effect of stress at the mask-GaAs interface, a polymerized KMER (Kodak Metal-Etch Resist) etch mask was employed. This mask was applied to the GaAs crystal at room temperature, but in this case also the edge effect was still present at the etched holes. Later a silica etch mask obtained by a room temperature, tetraethyl orthosilicate, glow discharge process was employed. Since the holes were then etched at room temperature, the effects of stress at the mask-GaAs interface should be minimized. However the etch rates were still greater near the mask edges than toward the center of the hole.

When a masked GaAs slice is placed in contact with the etchant, the etchant molecules are striking the protective mask as well as the GaAs exposed at the windows. Some of the molecules which strike the protective film are adsorbed and migrate across the surface for some distance before desorbing. A portion of these molecules will diffuse to the exposed GaAs and may react causing dissolution. Thus the exposed GaAs near the mask edge is receiving etchant molecules from surface diffusion as well as by "direct" diffusion. If the etch rate were limited by diffusion of etchant molecules to the reaction surface, then the above-mentioned process would result in an enhanced initial etch rate near the mask edge as compared with the etch rate near the center of the hole. This explanation is supported by the shapes of the hole bottoms shown in the angle-lapped section of Fig. 1. The holes on either side of the array have unsymmetrical edge effects, *i.e.*, the etch depth is greater near the edge having the largest adjacent area of protective mask. Since these edges have greater adjacent mask areas, they receive more etchant molecules from sur-

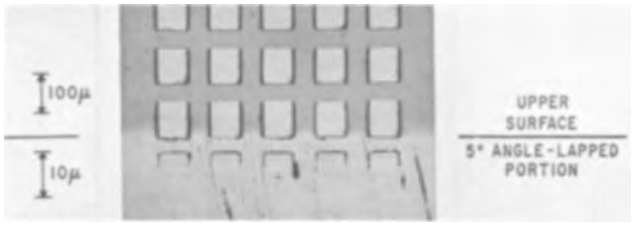

Fig. 2. Micrograph showing 5° angle-lapped section through holes etched into GaAs with a 0.7M H_2O_2-1M NaOH solution.

face diffusion. The three inner holes exhibit equal and symmetrical edge effects because they have equal adjacent mask areas. The exposed regions near the corners of the windows have the greatest adjacent mask areas and would be expected to exhibit the greatest edge effect. This is confirmed experimentally by observation of the hole bottom contours with an interferometer. It should be noted that the greatest contribution of etchant molecules due to surface diffusion would be realized at the initial stages of etching. This is in agreement with the experimental observation that the magnitude of the edge effect decreases with increasing hole depth.

It has been found that the etch rate of GaAs with a 0.7M hydrogen peroxide-1M sodium hydroxide solution is limited by the rate of chemical reaction rather than by the diffusion rate (1). If surface diffusion of adsorbed molecules along the protective mask is responsible for the enhanced GaAs etch rates near the mask edge, then the effect should be eliminated by etching with the above mentioned H_2O_2-NaOH solution. Figure 2 shows an angle-lapped section through GaAs holes formed by etching with this solution. The holes have flat bottoms, and no evidence of an enhanced etch rate near the mask edge is noted. These results provide strong support for the explanation of the edge effect based on surface diffusion of etchant molecules adsorbed on the protective mask.

Acknowledgments

The author wishes to express his appreciation to Dr. B. Carbajal for the glow discharge deposition of a silica film and to Mr. I. Sessions who assisted in the experimental work.

This work was supported by the Electronics Technology Division of the Air Force Avionics Laboratory in part under Contract No. AF 33(615)-1275 and in part under Contract No. AF 33(615)-2101.

Manuscript received March 31, 1966; revised manuscript received May 27, 1966.

Any discussion of this paper will appear in a Discussion Section to be published in the June 1967 JOURNAL.

REFERENCE

1. G. M. Orlova, S. K. Yerofeyev, and N. V. Romanova in "Khimiya Tverdogo Tela" (Chemistry of the Solid State), p. 218, Leningrad State University, Leningrad (1965).

Brief Communications

The Effect of Concentration on the Interdiffusion Coefficient of Chromium in Chromium-Iron Alloys

G. A. Davies, A. B. Ponter, G. C. Wood, and D. Whittle

The University of Manchester Institute of Science and Technology, Manchester, England

An investigation into the mechanism of oxide formation of chromium-iron alloys for a temperature range 800°-1200°C has resulted in determinations of the interdiffusion coefficients of chromium. The concentration profiles of chromium in the alloy were measured using an electron probe microanalyzer and metallographic techniques. The results which are presented in Fig. 1 exhibit a minimum value of diffusivity at 60% chromium concentration for a temperature of 1000°C. The values of Gorbunov *et al.* (1) for chromium concentrations of 84.5% and 29.4% Cr at 1000°C agree well with these data. Krwoglaz and Smernov (2) have indicated that the phenomenon of exhibiting minimum values is not common, but has been observed for diffusion in β-brass. Some anomalous predictions of chromium-iron behavior in their alloys may be attributed to the use of average values of interdiffusional coefficients over the range where a minimum exists. Here it is particularly important to use the discrete values reported.

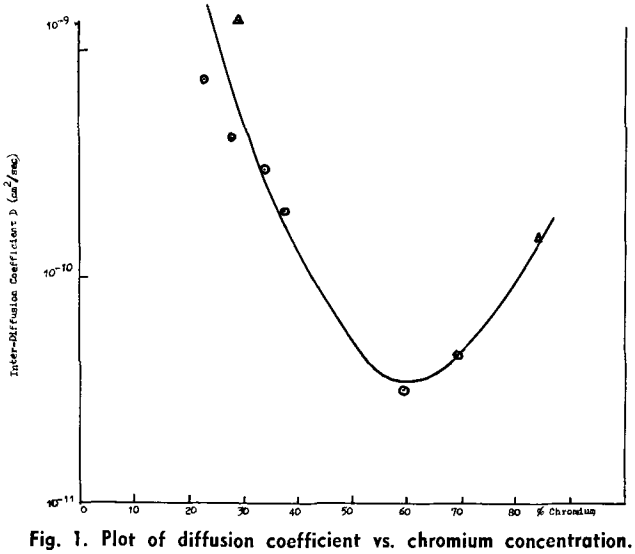

Fig. 1. Plot of diffusion coefficient vs. chromium concentration. △, Gorbunov; ⊙, authors.

Manuscript received June 6, 1966.

Any discussion of this paper will appear in a Discussion Section to be published in the June 1967 JOURNAL.

REFERENCES

1. N. S. Gorbunov, I. I. Arymaova, O. G. Selskaya, *Vosprosy Poroshkovoi Met. Sbornik*, **150**, 4 (1955).
2. M. A. Krwoglaz and A. A. Smernov, "Order and Disorder in Alloys," McDonald (1964).

Optical Phenomenon in $LiNbO_3$ Single Crystals

W. J. Croft and M. Kestigian

Sperry Rand Research Center, Sudbury, Massachusetts

Large, single crystals of $LiNbO_3$ are grown by the Czochralski technique and are oriented for physical measurements by the back-reflection Laue x-ray technique. The determination of the c-crystallographic direction presents somewhat of a problem in this rhombohedral crystal (1), as there are three pseudo-trigonal directions. It is the practice of this Laboratory to cut a slice perpendicular to the c-direction for microscopic confirmation of the axis using convergent polarized light. One crystal showed the presence of apparent oriented intergrowths with high-order interference colors (Fig. 1a), under low magnification in parallel polarized light (crossed nicols). Most of the area of the slice remains dark during rotation of the microscope stage except for the narrow bands. The bands make a triangular pattern and are perpendicular to the a-axis directions of the crystal. The dark areas of the crystal show a normal uniaxial interference figure. The bright bands in convergent polarized light show a "flash" phenomenon. A shadowy cross appears four times during complete rotation of the crystal slice. Examination of Fig. 1a and b, which are opposite sides of the same slice in parallel polarized light, show a peculiar phenomenon. On one side of the slice (Fig. 1a), the bands are sharp on the inside of the V and diffuse on the outside. On the other side of the slice (Fig. 1b), the opposite is true, and the bands are sharp on the outside of the V and diffuse on the inside.

A series of back-reflection Laue x-ray photographs were taken across one of these bands extending from one dark area to the other. All of the pictures gave the same c-axis orientation diagram.

The slices were cut from crystals which had been tightly bound with platinum wire during heat-treatment (1200°C). This phenomenon is caused by an apparent stress-induced incipient cleavage development.

From the measured thickness of the slice and the apparent width of the bands, as seen in the microscope, the plane of cleavage makes an angle of approximately 59° with the basal plane. This cleavage can be indexed to be along the {113} (hexagonal) planes.

Another phenomenon observed in Czochralski-grown $LiNbO_3$ single crystals is linear rows of fine

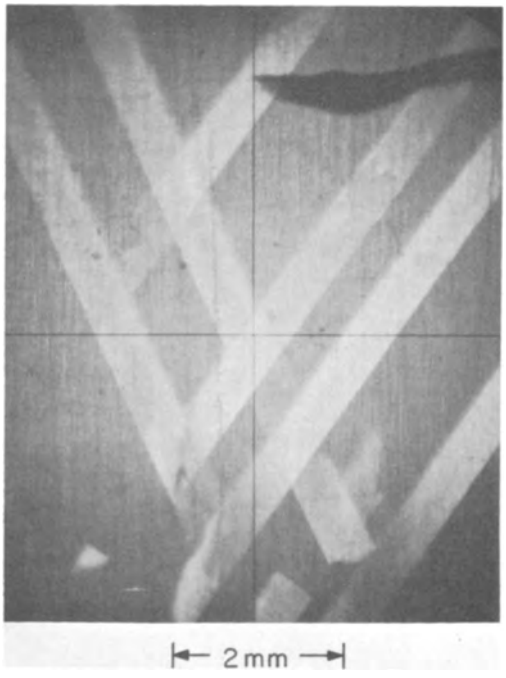

Fig. 1b. Same section viewed from the opposite surface.

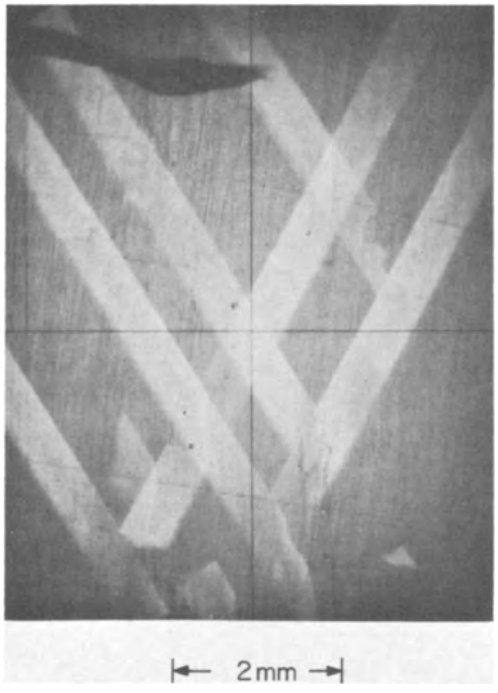

Fig. 1a. Section of $LiNbO_3$ crystal cut perpendicular to c axis and viewed in parallel polarized light.

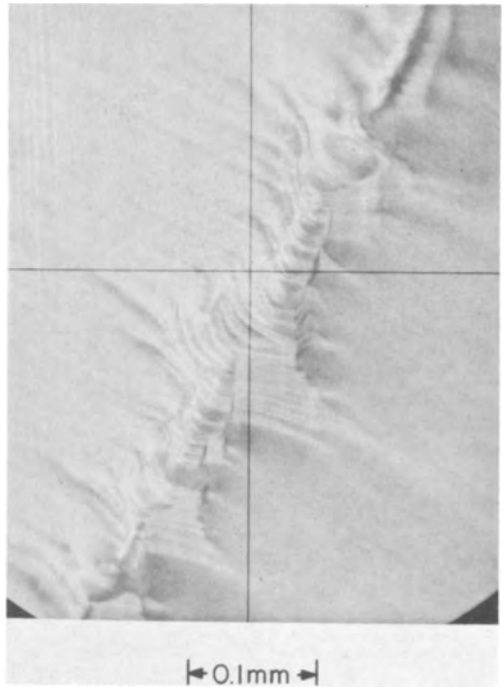

Fig. 2. $LiNbO_3$ single crystal boule showing row of growth notches

chips parallel to the growth direction of the boules (Fig. 2). These rows, to a degree, reflect the symmetry of the boule. When the growth axis is in a [0.001] direction, there are three equally spaced rows aligned with the lines joining the points at which the a axis intersects the surface of the crystal. In the case of a-axis grown crystals, there are usually four rows in sets of two and the boule forms in an orthogonal section rather than the round or trigonal section of c-axis crystals. Under the microscope these chips are curved rather than flat and probably represent some incipient face growth.

Manuscript received June 8, 1966.

Any discussion of this paper will appear in a Discussion Section to be published in the June 1967 JOURNAL.

REFERENCE

1. A. V. Lapitskii and Yu. P. Simanov, *Zhur. Fiz. Khim.*, **29**, 1201 (1955).

High-Speed Measurement of Reversible Electrode Potentials

T. Hagyard and K. M. Chapman

Department of Chemical Engineering, University of Canterbury, Christchurch, New Zealand

During measurements of the potential of aluminum electrodes in aqueous solutions (1), it was deduced that a quickly formed aluminum surface reached its equilibrium potential in microseconds and in ref. (2) anodic polarization curves were based on aluminum electrode potentials taken during the first 30μ. Using the same apparatus, it seemed desirable to determine if, indeed, a metal electrode could establish its usual equilibrium potential in so short a time. For this purpose a metal was needed in which hydrogen evolution would not occur at a perceptible rate at the equilibrium potential and whose rate of ionization was known to be fast. The work of Randles (3) indicated that the latter condition would be met by cadmium in equilibrium with the nitrate and, since cadmium also fulfills the first condition, metallic cadmium was tested.

Cadmium of analysis Zn 0.019, Pb 0.013, Cu 0.002, Fe 0.002% was used, but was too soft to be used exactly as described in ref. (2). The electrode used in the latter measurements was machined from ¼ in. diameter aluminum rod so that a thin insulated flange was formed and subsequently cut by impact of the ruby cutter, thereby exposing a new surface in about 6μ. For the present experiments it was not possible to use such an integral electrode. Instead, a thin cadmium disk was mounted on the end of a duralumin rod, the disk being backed by fused high-density polyethylene and the whole insulated with a fused layer of low-density polyethylene. Difficulty was still experienced due to deformation of the cadmium during cutting and lack of adhesion of the insulating layers. This resulted in most of the oscillograph traces showing irregularities ascribed to crack formation. Nevertheless, the more successful traces, such as that in Fig. 1, showed a rapid approach to a steady potential.

Figure 1 was obtained with cadmium in M/1000 $CaCl_2$ + M · KCl swept with purified hydrogen and shows at A the 10,000 cps time base and zero potential lines, at B the insulated electrode potential before cutting, at C the potential at the instant of cutting, and at D the very rapid rise to a more negative potential. This rise occurred in some 10μ, and thereafter the potential remained substantially constant except for the momentary deviation at E. The latter is characteristic of irregularities frequently met with in this work and is ascribed to defective adhesion of the insulation around the newly cut surface. In this figure, line F is the Weston cell potential calibration. Measurement of the potential of the electrode 10-30μ after cutting gives the value of —0.879v on the *N* calomel scale for this trace falling to —0.875v after 200μ and thereafter unchanged. Measurements on nine similar traces gave a mean value of —0.864 with standard deviation 0.062v.

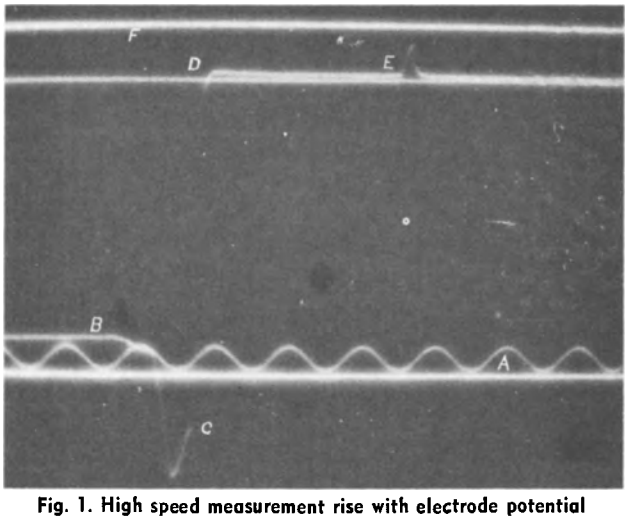

Fig. 1. High speed measurement rise with electrode potential

Static potential measurements with the same metal in massive form in the same solution swept with purified hydrogen, required about 1½ hr to reach equilibrium, presumably due to slow elimination of oxygen from the electrode surface and from the solution. Results depended somewhat on surface preparation:

Etched surface							
Time, min	20	40	60	80	95	120	140
Potential v N.C. scale	−0.817	0.842	0.854	0.852	0.864	0.865	0.865
Abraded with emery							
Time,	10	40	55	70	85	115	130
Potential	−0.843	0.849	0.850	0.850	0.851	0.850	0.851

It is considered that agreement between the 10-30μ oscillographic observations and the static observations is reasonably good.

With nitrate solutions the oscillograph traces for the fast measurements were much more irregular than for the chloride solutions, and a similar comparison with static measurements was less satisfactory possibly because of the metastability of nitrate solutions in the presence of hydrogen. Nevertheless, agreement was in general within some 20 mv [for details see Chapman (4)].

It is concluded that there is reasonable agreement between measurements of the equilibrium potentials of cadmium in chloride solutions by the present oscillographic technique and by the usual static method and that the methods used in ref. (1) and (2) are reasonable for fast electrode processes.

Manuscript received, May 4, 1966.

Any discussion of this paper will appear in a Discussion Section to be published in the June 1967 JOURNAL.

REFERENCES

1. T. Hagyard and J. R. Williams, *Trans. Faraday Soc.*, **57**, 2288 (1961).
2. T. Hagyard and W. B. Earl, To be published.
3. J. E. B. Randles, *Discussion Faraday Soc.*, **11**, (1947).
4. K. M. Chapman, The Potential of the Cadmium Electrode, B. E. project report, University of Canterbury, 1961.

The Electrode Potential of Evaporated Aluminum Films in Chloride Solution

T. Hagyard, W. B. Earl,[1] K. J. Kirkpatrick, and I. G. Watson[2]

Department of Chemical Engineering, University of Canterbury, Christchurch, New Zealand

Potential measurements as negative as -1.67 E_{H_2} volts in 1*N* KCl solution pH 3.2, have been measured on a freshly cut aluminum surface by a technique devised by Hagyard and co-workers (1, 2). A polythene-coated aluminum rod immersed in 1*N* KCl solution was cut by a ruby travelling at 1000 cm/sec. Potential measurements were made using a high-impedance cathode follower coupled to an oscilloscope. From the instant the cut was made into the aluminum, its potential was recorded by photographing a single traverse of the oscilloscope trace. A typical potential measurement is shown in Fig. 1.

The initial rapid potential rise to the peak was attributed to the dissolution of aluminum charging the double layer. After reaching the peak potential, only a small fraction of the electrode surface was thought to remain actively anodic while the slower hydrogen discharge process took place over most of the metal surface. The exponential fall in potential was attributed to the polarization of the anodic and cathodic processes. The information gained using this technique enabled the kinetics for aluminum dissolution and hydrogen discharge on aluminum to be studied.

The object of the present work was to confirm the validity of the measurements made by the above technique. The possible alternative explanations of the potential behavior of freshly cut aluminum that were considered by the authors were (*a*) that instantaneous high temperatures were generated at the cut surface by the shearing action of the ruby cutter; the high temperatures would be rapidly reduced by heat dissipation into the bulk of the metal, (*b*) severe stressing and dislocation of the aluminum electrode surface followed by relaxation of the surface structure; the peak in this case would be a stress potential.

Vacuum evaporated aluminum films were used in this work to obtain an uncontaminated oxide-free aluminum surface comparable with that exposed by the previous technique. The aluminum film was formed in an evacuated, degassed, Pyrex glass bulb by evaporating 99.99% aluminum from a stranded tungsten wire that was supported on tungsten leads. The target area was a smoothly ground glass button. Electrical contact with the aluminum film was made by a tungsten wire sealed through the center of the button. Figure 2 is a sectional drawing of the bulbs used. To limit the area on which the measurements were made, the shape of the button was designed so that with straight line evaporation only the front surface of the button was coated with aluminum.

The glass bulbs were evacuated to a vacuum better than 0.1μ by a two-stage G.E.C. mercury diffusion vacuum pump with liquid nitrogen trap. The bulbs were baked under vacuum for more than 2 hr at 400°C. After baking, the aluminum was evaporated rapidly (3-5 sec) to give a thick (2-10μ) nontransparent coating of aluminum over the interior of the bulb. Holland (3) recommends rapid evaporation for high quality films. At the start of evaporation aluminum vapor was relied on to act as a getter of any residual gases. Subsequent deposits of aluminum were assumed to be uncontaminated and oxide free. At the completion of the evaporation process, the bulb was sealed off from the vacuum pump.

[1] Present address: Shawinigan Chemicals Ltd., Montreal East, Quebec, Canada.

[2] Present address: Monsanto Chemicals Ltd., Acrefair, Denbighshire, North Wales.

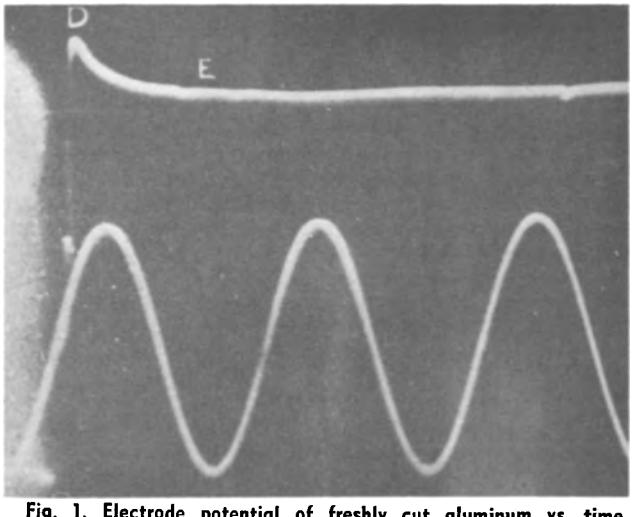

Fig. 1. Electrode potential of freshly cut aluminum vs. time. [From ref (1)]. IN KCl + HCl to pH 3.2, 300 cps sine wave has base at zero volts N calomel scale and is 1 S. Weston in amplitude, D peak potential, E mixed potential.

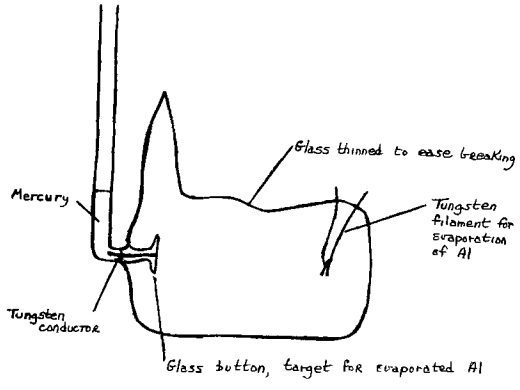

Fig. 2. Diagrammatic section of glass bulb

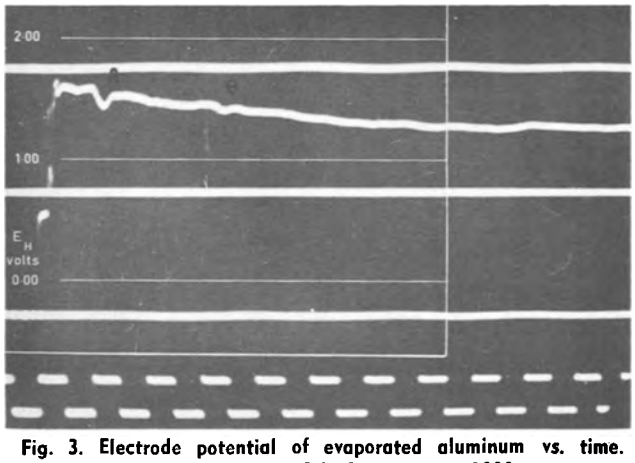

Fig. 3. Electrode potential of evaporated aluminum vs. time. Solution IN KCl + HCl to pH 3.2. Square wave 1000 cps.

Potential measurements were made in a 1*N* Analar KCl solution contained in a polythene beaker. The reference electrode was a normal calomel electrode. The electrical measuring circuit was a fast response (0.1 μsec) cathode follower, input impedance 10^7 ohms, coupled to a Cossor 1065 pulse oscilloscope. The potential of the evaporated aluminum film was measured by breaking the evacuated bulb under solution with a polythene-coated steel cutter. The cutter was driven through the bulb by a spring-loaded hammer device. A continuous photographic record of the potential change was obtained for the 10 msec following contact between the aluminum film and the KCl solution.

Figure 3 is an example of the potential-time trace obtained from evaporated films. Each trace reached a peak potential of -1.67 E_H volts then decayed in a similar but not entirely reproducible manner to the trace shown. The potential could be measured to better than ±0.05v. The authors believe that the difference in the potential decay characteristics between the two techniques is associated with the different mode of wetting the electrode surface. With the previous technique the electrode was a small v notch that was driven past the solution. The total time to cut and wet the electrode surface in this case was of the order of 10 μsec. The electrode area for the evaporated film method was approximately 1 cm^2. In this case the electrode was wet by the solution rushing into the evacuated glass bulb. It seems probable that the relatively large electrode area is wet progressively over possibly a millisecond or more. A peak potential was to be expected the instant the solution made electrical contact with the solution. Thereafter until the total electrode surface was wetted a mixed potential would result between that part of the electrode surface being wetted and that part already wet. The two jumps in potential at A and B, (shown in Fig. 3) were quite reproducible and could be associated with shock waves. A vigorous discharge of gas bubbles from the aluminum surface was observed immediately after the bulb was broken. It was strongly suspected that the gas discharged was hydrogen.

The conditions for the alternative explanation of the peak potentials obtained by the previous technique were absent from the evaporated aluminum films. When exposed to solution the films were neither at a high temperature nor in a severely stressed condition. The fact that the same peak potential has been obtained by two independent techniques is strong evidence that potential measurements by the earlier technique are valid.

Manuscript received May 4, 1966.

Any discussion of this paper will appear in a Discussion Section to be published in the June 1967 JOURNAL.

REFERENCES

1. T. Hagyard and J. R. Williams, *Trans. Faraday Soc.*, **57**, 2288 (1961).
2. W. B. Earl, B. E. Thesis, University of Canterbury (1961).
3. Holland, "Vacuum Deposition of Thin Films," John Wiley & Sons, Inc., New York, N. Y. (1956).

Double Layer Studies

Paul Delahay

Department of Chemistry, New York University, New York, New York

ABSTRACT

This paper covers four investigations dealing with hitherto neglected or hardly studied aspects of the electrical double layer. Topics are: (*a*) specific adsorption of inorganic cations; (*b*) resolution of simultaneous anion and cation specific adsorption; (*c*) double layer in media of low electrical conductivity; (*d*) interpretation of double layer capacity measurements for electrodes with a charge transfer reaction.

Double Layer with Specific Adsorption of an Inorganic Cation

This study was made for the particular case of thallium fluoride and followed the same general approach of similar work for inorganic anions exhibiting specific adsorption. No such detailed investigation has been made before to the writer's knowledge although the possibility of rather strong specific adsorption of some inorganic cations on mercury was conclusively shown some time ago (1). Details are given elsewhere (2), and only the essential points will be mentioned.

The TlF/Hg system was selected for the following reasons: specific adsorption of Tl^+ is quite pronounced even at potentials at which there is virtually no Tl deposition; specific adsorption of F^- can reasonably be neglected; complexation in solution does not interfere.

Electrocapillary curves and differential capacity data were interpreted in three steps: (*a*) thermodynamic calculation of the charge density q on the electrode and of the relative surface excesses Γ_+ and Γ_- of Tl^+ and F^-; (*b*) application of the Gouy-Chapman theory on the assumption of no F^- specific adsorption and calculation of the amount of specifically adsorbed Tl^+ and of the potentials in the outer plane of closest approach and across the compact double layer; (*c*) examination of isotherms.

Both Γ_+ and Γ_- were positive over the range af q being covered (2-12 microcoulombs · cm^{-2}) and varied linearly with q. Γ_+ reached up to 10 μcoul · cm^2. Such positive values of Γ_+ for markedly positive q's result from cation specific adsorption since Γ_+ for KF tends toward an asymptotic negative value (3) (little specific adsorption of K^+). The slope $-(\partial\Gamma_+/\partial q)$ at constant TlF chemical potential μ was equal to the slope of the Esin and Markov plot $(\partial E_-/\partial\mu)$ at constant q as expected.

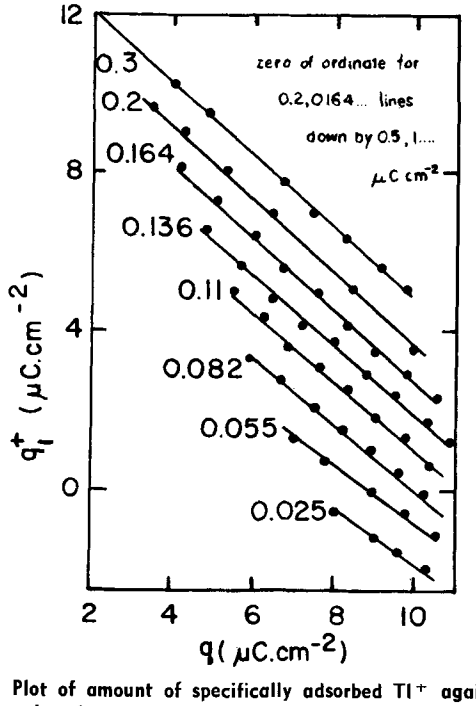

Fig. 1. Plot of amount of specifically adsorbed Tl^+ against the charge on the electrode for different concentrations of TlF (M). Vertical scale for 0.3M; all other curves equally spaced downward by 0.5 unit for 0.2M, by 1 unit for 0.164M, etc. (2).

The charge q_1^+ corresponding to specifically adsorbed Tl^+ was computed from the amount of Tl^+ in the diffuse double layer according to Grahame's method (3). The bulk dielectric constant was used for the diffuse double layer (not a source of serious error). Plots of q_1^+ against q are essentially linear (Fig. 1) much as for I^- specific adsorption (4). Note, however, that the highest q_1^+ (=12.3 μcoul · cm^{-2}) for Tl^+ was lower than $q_1^- \approx 40$ μcoul · cm^{-2} for I^-. Deposition of Tl prevented exploration at more negative q's where specific adsorption is enhanced.

The computation of q_1^+ involved as an intermediate step the calculation of the potential ϕ_2 in the outer plane of closest approach (from Γ_- and the Gouy-Chapman theory). The resulting ϕ_2's were all positive, and their dependence on E appeared quite normal. The difference of potential $\phi_M - \phi_2$ across the compact double layer could now be computed at constant charge in the scale of rational potentials. $\phi_M - \phi_2$ was then divided into two parts (5), $q_1^+/K_a + q/K_b$ where the K's are integral capacities. Thus $K_a \approx 16$ to 17 and $K_b \approx 32$ to 34 μf/cm^2. These values are about one-half those for (4, 5) Cl^- and I^-. It is believed that the formal division of $\phi_M - \phi_2$ into these two components, according to electrostatics, is open to question in this particular case. Using K_a and K_b for what they are worth one finds $(x_2 - x_1)/x_2 = K_b/K_a \approx 0.5$ to 0.6, where x_1 and x_2 are the distances of the inner and outer plane, respectively, to the electrode. Since this ratio equals 0.4 for I^- and 0.2 for Cl^- it would seem that Tl^+ approaches the electrode more closely than I^- and certainly more than Cl^-.

The last step in the interpretation dealt with the isotherm for Tl^+. If one assumes that this isotherm is of the form $f(q_1^+) = \beta a_+$ where a_+ is the activity of Tl^+ and β is solely a function of the charge on the electrode one can deduce the dependence of β on q. [See Parsons (6) for an approximate treatment and Parry and Parsons (7) for a more rigorous approach.] The corresponding plot of log β against q is linear (Fig. 2), and this seems to indicate that the standard free energy of adsorption $\overline{\Delta G}^\circ$ for Tl^+ varies linearly with q [$\beta = \exp(-\overline{\Delta G}^\circ/RT)$]. A similar dependence holds for other inorganic cations, *e.g.*, I^-. (The dependence for uncharged adsorbates is not the same and will not be discussed here.)

Among the various criteria which can be applied to isotherm assignment the one recently used by Parsons (8) was selected, namely, the plot of $(1/C) - (1/C_b)$ against log a_+ at constant q (C is the differential capacity of the compact double layer, C_b the same datum in the absence of specific adsorption; C_b can be computed from data on NaF.) This plot should

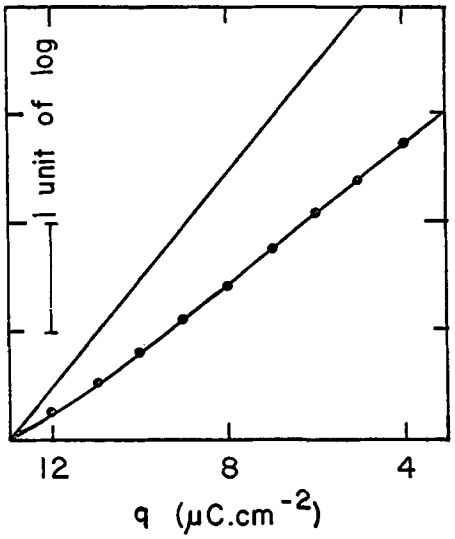

Fig. 2. Variation of the standard free energy of adsorption of Tl^+ with the charge on the electrode. Line with points corresponds to calculation with correction for diffuse double layer. Other line is without this correction (2).

be symmetrical for the Frumkin isotherm as was essentially the case. The Flory-Huggins isotherm (with a Frumkin interaction factor), also tested by Parsons (9), might provide a better approximation, but the data obtained here did not justify this approximation. The numerical value of the interaction parameter in the Frumkin isotherm ($A = 9.6$ for the isotherm written with $\log_{10}$) indicated a strong repulsion between Tl^+ ions.

The following conclusions can be drawn from this study: (*a*) Tl^+ specific adsorption can be described by the Frumkin isotherm; (*b*) the standard free energy of adsorption appears to vary linearly with the charge on the electrode; (c) Tl^+ ions approach the electrode more closely than Cl^- or I^-.

Double Layer with Simultaneous Specific Adsorption of Inorganic Anion and Cation

Analysis of simultaneous specific adsorption of anions and cations is the next logical step after the study of separate anion or cation specific adsorption. This problem has not received a detailed analysis to the writer's knowledge. Thallium nitrate was selected for this study because of available relevant information on Tl^+ (see above) and NO_3^- (10) [see also Frumkin (1)]. Complexation is minor ($pK_1 = 0.33$ for $TlNO_3$) and easily corrected for. Detailed results are available elsewhere (11), and only the essential points will be covered.

Thermodynamic analysis yielded Γ_+ and Γ_- for Tl^+ and NO_3^- and indicated the enhancement of Tl^+ adsorption by NO_3^- specific adsorption. This effect is shown in Fig. 3 in which the $\Delta\Gamma_+$ between the (Γ_+)'s for $TlNO_3$ and TlF for the same electrolyte concentration is plotted against q. Moreover, the plot of Γ_- for $TlNO_3$ against q exhibited a minimum (0.1 to 0.2M) caused by increased specific adsorption of Tl^+ as q decreased. [Γ_- in the absence of cation specific adsorption increases uniformly with q; see KNO_3 (3).]

The separation of $F\Gamma_+$ into the specifically adsorbed charge q_1^+ and the charge q_{2-s}^+ in the diffuse double layer and the similar separation of $F\Gamma_-$ into q_1^- and q_{2-s}^- is not possible by Grahame's method (3). We adopted the following approach based on the Gouy-Chapman theory and a simple electrostatic model, already used [*e.g.*, (12, 13)] in other problems. We write

$$\phi_M - \phi_1^+ = (4\pi/\epsilon)\, q x_1^+ \qquad [1]$$

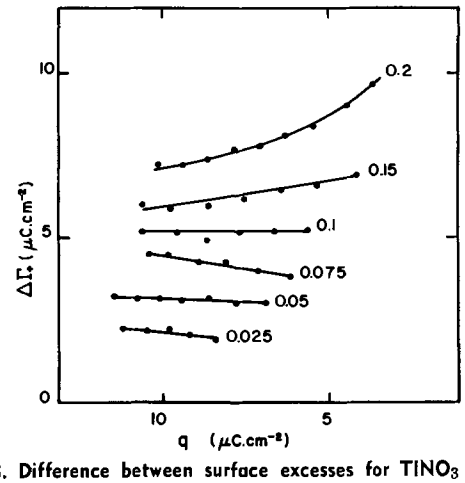

Fig. 3. Difference between surface excesses for $TlNO_3$ and TlF, at constant concentration of Tl(I) salt, against charge on the electrode.

$$\phi_1^+ - \phi_1^- = (4\pi/\epsilon)\,(q + q_1^+)\,(x_1^- - x_1^+) \qquad [2]$$

$$\phi_1^- - \phi_2 = -(4\pi/\epsilon)\, q_{2-s}\,(x_2 - x_1^-) \qquad [3]$$

where the superscript + corresponds to Tl^+, the superscript — to NO_3^- and ϵ pertains to the compact double layer. Note that we assume two inner planes at distance x_1^+ and x_1^- from the electrode ($x_1^+ < x_1^-$). We also write three other equations expressing the charge q_{2-s} as a function of ϕ_2 in the outer plane (Gouy-Chapman); the electroneutrality of the interface and the equality between $F\Gamma_+$ and $q_1^+ + q_{2-s}^+$. A system of six independent equations with the six unknowns is obtained: ϕ_1^+, ϕ_1^-, ϕ_2, q_1^+, q_1^-, and q_{2-s}. Resolution by interaction is possible provided x_1^+, x_1^-, and ϵ are known. An alternative approach would be to write three additional equations based on a more detailed model, *e.g.*, one taking into account discreteness effects. The method involving an *a priori* selection of x_1^+, x_1^-, and ϵ has the merit of simplicity and is not as arbitrary as might appear. (A more detailed model might not be free either of adjustable parameters.)

We selected $x_1^+ = 2A$, $x_1^- = 3.15A$, and $\epsilon = 6$, 8, or 9.6 for the compact double layer. (We used the bulk value of ϵ in the Gouy-Chapman theory.) It turned out that self-consistent results were obtained for $\epsilon = 6$ which is precisely the dielectric constant chosen by Macdonald and Barlow in a recent paper (14) on discreteness effects. The choice of x_1^+ was prompted by previous work of TlF, and we verified that this choice was not critical for $1.8 \leq x_1^+ \leq 2.2A$. The value of $x_1^- = 3.15A$ was selected on the basis of discreteness effect analysis (13) we made of Payne's results (10) for NO_3^- specific adsorption at low concentrations ($\leq 0.05M$). Variations of x_1^- from 3 to 3.5A did not affect the results considerably.

The charge q_1^+ at constant $TlNO_3$ concentration varied quite linearly with q except at the more positive q's (≈ 15 μcoul/cm^{-2}) where it tended to approach zero. The enhancement of Tl^+ specific adsorption caused by NO_3^- specific adsorption is shown in Fig. 4. (Negative Δq_1^+'s, which are small anyhow, probably result from the uncertainty of calculation.) The charge q_1^-, plotted against q, exhibited a minimum just as the comparable plot of Γ_- against q (see above).

Values of ϕ_2 were negative (between —0.045 and —0.075v) and showed qualitatively a normal dependence on q and $TlNO_3$ concentration. Negative ϕ_2's, instead of the positive ϕ_2's found for TlF, are to be expected since NO_3^- undergoes stronger specific adsorption than Tl^+ in the conditions prevailing in this work. It turned out that ϕ_2 (and also ϕ_1^+ and ϕ_1^-) was much more sensitive to the selection of ϵ than q_1^+ and q_1^-. In fact calculated ϕ_2's for $\epsilon = 8$ and $\epsilon = 9.6$

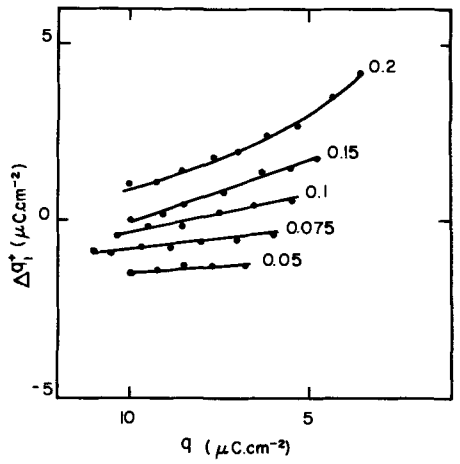

Fig. 4. Difference between the amounts of specifically adsorbed Tl^+ for $TlNO_3$ and TlF, at constant concentration of Tl(I) salt, against charge on the electrode.

were completely abnormal in their dependence on q and $TlNO_3$ concentration. This influence of the choice of ϵ is also evident for Fig. 5 showing ϕ_1^+ against q. The potential ϕ_1^+ appeared quite independent of $TlNO_3$ concentration for $\epsilon = 6$ and varied quite linearly with q_1. The same remark applied to the ϕ_1^- *vs.* q plot although there was some concentration dependence.

Adsorption was interpreted by means of two simultaneous Frumkin isotherms of the types proposed by Parry and Parsons (24). By using the $Tl^+ - Tl^+$ interaction parameter $A_{11} = 9.6$ from our TlF study, we found that the $NO_3^- - NO_3^-$ interaction parameter A_{22} varies from 2.0 to 5.5 for $4 \leq q \leq 10$ μcoul · cm^{-2} and that the $Tl^+ - NO_3^-$ interaction parameter A_{12} ($\equiv A_{21}$) varies from -6 to -9 for $4 \leq q \leq 10$ μcoul · cm^{-2}. The magnitude and sign of these parameters indicate repulsion between NO_3^- ions and strong association between Tl^+ and NO_3^-. The results cannot be regarded as quantitative, but they probably describe qualitatively interactions.

In conclusion, a relatively simple method is tentatively proposed for resolution of simultaneous cation and anion specific adsorption. This approach does depend on an *a priori* selection of parameters, but self-consistency of results imposes rather severe restrictions in the selection, particularly with respect to the dielectric constant in the compact double layer. A more detailed model analysis would be desirable, but might prove quite involved.

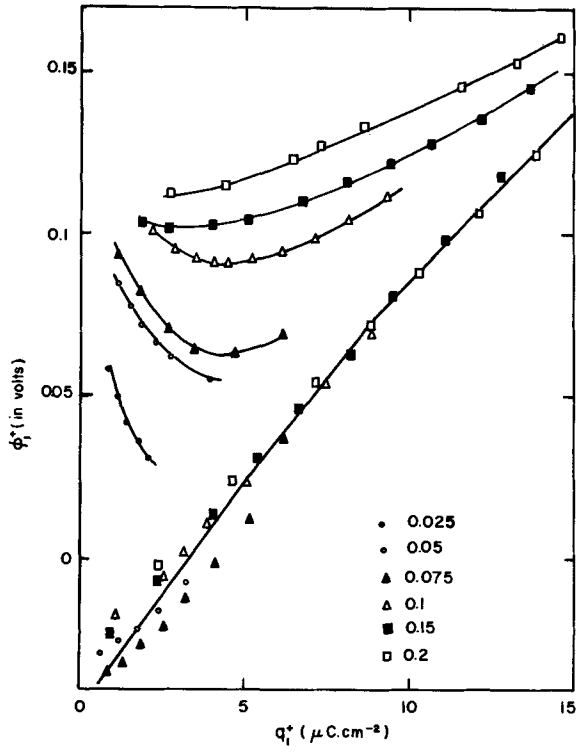

Fig. 5. Potential in the plane x_1 against charge on the electrode for different $TlNO_3$ concentrations (M). Lower curve calculated for $\epsilon = 6$; group of curves calculated for $\epsilon = 8$ (11).

Double Layer in Media of Low Electrical Conductivity

This phase of our work, in a very different vein from the previous two investigations, covers an aspect of the double layer which has not been touched on, namely, the electrical double layer for media of low conductivity, *e.g.*, for a metal in contact with very dilute (below 10^{-3}M) aqueous solution of strong electrolytes, electrolytes in nonaqueous solvents of low dielectric constant, solids with ionic conductivity (*e.g.*, ice), etc. The main problem, aside from theory, is the development of a suitable technique for the measurement of the double layer differential capacity. The conventional bridge fails, even at low frequencies, because the cell resistance is very much higher than the electrode impedance. This problem was solved by the following differential coulostatic method (15).

Two identical electrodes e_1 and e_2 (but not necessarily of the same area) are coupled with a reference electrode in a single cell. The potential of e_1 and e_2 is set at a known, identical value with a potentiometer. The potentiometer circuit is opened, and a small known charge is supplied to e_1 by discharge of a small capacitor ($|\Delta E| <$ 5-10 mv). The difference of potential across e_1 and e_2 is recorded (electrometer and oscilloscope or fast recorder) against time and extrapolated back to zero time. Extrapolation is necessary because small spurious faradaic processes cause a drift of potential at open circuit. This source of interference is minimized by the above differential technique.

Application was made to Hg/NaF system in the 10^{-3} to 10^{-5}M range. The electrodes were hanging mercury drops expelled from microsyringes. This system was selected because capacities can be computed from Grahame's data in the 1 to 10^{-3}M range on the basis of two reasonable assumptions: (*a*) the Gouy-Chapman theory is valid; (*b*) the differential capacity of the compact double layer at constant q is independent of the electrolyte concentration. Agreement between theory and experiment for 10^{-3}, 10^{-4}, and 10^{-5}M is good (Fig. 6). These are the first measurements of double layer capacity in very dilute solution of which we know.

Measurements at lower concentrations and with distilled water were still entirely feasible although the cell resistance reached several megohms, but two difficulties were encountered: lack of purity of water and drift of potential at the junction with the reference electrode. It is expected that these two difficulties will be eliminated.

This method is less accurate than the bridge method because it is direct reading, and faradaic processes (*e.g.*, reduction of residual oxygen) interfere more. (Interference by a fast process is also serious with the bridge because of the resulting pseudocapacity.) A detailed study of residual oxygen was also made (16) in this connection. Finally, electrodes of constant area are more easily contaminated than the dropping mercury electrode. Application of the latter type of electrode to the present method is complicated by the variation of potential resulting from variation of the electrode area at open circuit (17).

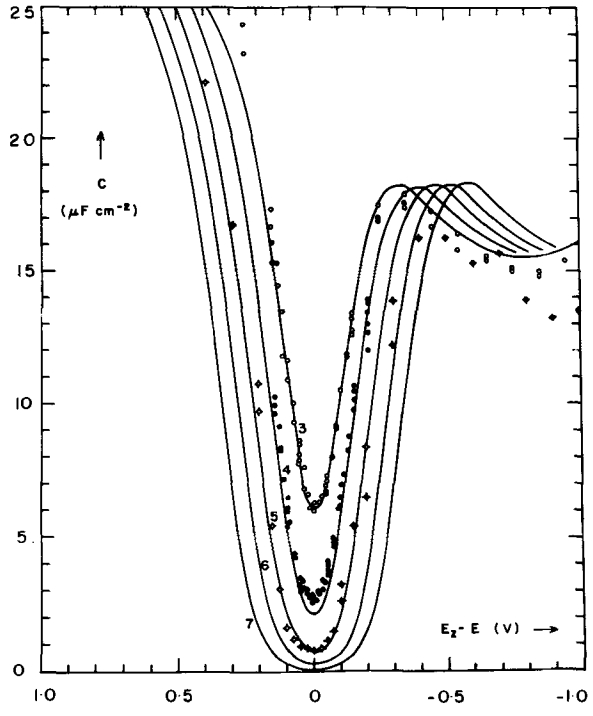

Fig. 6. Differential capacity of double layer for 10^{-n}M NaF in contact with Hg at 25°C. Values of n on each curve; points are experimental, curves are calculated (15).

In conclusion, a method is available for measuring double layer capacities with media of low conductivity. Further application is now being planned (distilled water, ice) or has actually been made [0.5 to 10^{-3}M potassium acetate in anhydrous acetic acid (18)]. Mass transfer generally poses no problem as an approximate treatment (unpublished) showed, but this aspect is now being reexamined more rigorously.

Double Layer for Electrodes with a Charge Transfer Reaction in Nonsteady-State Measurements

The double layer at an electrode on which a charge transfer reaction occurs has attracted little attention since emphasis has been placed over the last two decades on the ideal polarized electrode. Correction for charging of the double layer in kinetic measurements, *i.e.*, in presence of a large excess of supporting electrolyte, is generally made on the assumption that the double layer capacity is essentially unaffected by the presence of the reactants and products at low concentration. It is only recently that Sluyters and co-workers developed (19) a method for separating the double layer capacity from the electrode impedance in electrode impedance measurements. (See his series of papers in *Rec. trav. chim.* since 1960.) These workers showed that the foregoing empirical correction for double layer charging is not satisfactory in some cases because the double layer capacity is strongly affected by the reactants and/or products even with a large excess of supporting electrolyte. In view of this very interesting result, it seems necessary to question what is actually measured in charging of the double layer under such "dynamic" conditions as in impedance measurements or any other relaxation or perturbation method for fast processes (in contrast to the "static" conditions in electrocapillary curve measurements). This problem was recently examined by us (20), and our conclusions will be reviewed here.

There is no problem from the thermodynamic point of view since this question was settled long ago [see Grahame's review (21)] and was re-examined more recently (22, 23). Thus, the derivative or the interfacial tension with respect to potential, all other variables being kept constant, *e.g.*, for the reversible electrode $M^{+z} + ze = M$, is $q + zF\Gamma_+$ where Γ_+ is the relative surface excess of M^{+z}. This derivative is equal to q for an ideal polarized electrode. Interfacial tension measurements for a reversible electrode thus yield $q + zF\Gamma_+$. The question is whether this is also the case for dynamic measurements.

The essential idea is the recognition that *a priori* separation of faradaic and charging processes, as generally assumed [including Sluyters (19)], is not justified or physically conceivable for a nonideal polarized electrode under nonsteady-state conditions. Impossibility of *a priori* separation arises because there is, in addition to charging by ionic transfer of M^{+z}, charge separation or recombination at the interface without external current. The latter process occurs according to the reaction $M^{+z} + ze = M$ and depends on the kinetics of this reaction. If the exchange current i_o for this reaction is sufficiently low, charging occurs almost entirely by ionic transfer, just as for an ideal polarized electrode, and the differential capacity of the double layer is essentially dq/dE. Conversely, when i_o is sufficiently high, charging occurs almost entirely by charge separation or recombination, and the differential capacity is then that of a reversible electrode, namely, $d(q + zF\Gamma_+)/dE$ for a metal ion-pure metal electrode. [The expression is different for a metal ion-amalgam electrode (25).] Any capacity between these two values can be obtained for intermediate values of i_o and, furthermore, the capacity is then frequency- or time-dependent in nonsteady-state measurements. Correction for double layer charging, based on a constant capacity, is then in error to an extent that can be serious.

These ideas led (20) to three general equations which, after solution for any particular conditions, allow the detailed analysis of nonsteady-state and periodic electrode processes. The three equations are very general and apply to metal ion-pure metal electrodes, metal ion-amalgam electrodes, redox electrodes, etc. Detailed analysis has already been completed for impedance measurements (25) and for the usual relaxation methods and the interrupter method (26).

No *a priori* separation of faradaic and charging processes is postulated in the writing of the three general equations. *A posteriori* separation of the charging process is feasible by elimination of the faradaic component corresponding to the usual treatment (no double layer charging). This *a posteriori* separation is purely formal, but it has the advantage of explaining double layer charging in terms of a familiar model. It is found in this way that, at time zero, (or for infinite frequency) charging occurs as an ideal polarized electrode for any finite exchange current. (This is because there is no time for charge separation or recombination to occur.) Conversely, for time approaching infinity (or for zero frequency) charging occurs as an ideal reversible electrode for any finite exchange current. If the exchange current is supposed to be infinite, charging occurs always as an ideal reversible electrode. The transition from one behavior to the other occurs in a range of time or frequency which frequently corresponds to actual experimental conditions. Furthermore, the difference between the two limiting values of the capacity can be significant, even in the absence of specific adsorption. This may account, at least in part, for some discrepancies in kinetic parameters obtained by different methods. It is suggested some of the results obtained by different methods be re-examined and possibly revised in the light of the foregoing ideas and treatments derived from them. In some cases, correction will turn out to be negligible but in other cases the error resulting from *a priori* separation of faradaic and charging processes may be serious.

Acknowledgment

This work was supported by the National Research Foundation (all parts) and the Office of Naval

Research (the double layer studies in media of low conductivity). Part of the experimental work on thallium nitrate was done with support from the National Institute of Health.

SYMBOLS

a	activity of solute
A	interaction parameter in Frumkin isotherm
c	concentration, mole · cm^{-3} or mole · l^{-1} (specified)
c_s	bulk concentration, same units as c
C	differential capacity, μf · cm^{-2}
e	charge of the electron, cgs units
E	electrode potential, v
$E_\pm$	potential against a reference electrode reversible to cations (E_+) or anions (E_-), v
E_z	potential at zero charge, v
E_e	equilibrium potential, v
E_f	field in the compact double layer, cgs units
F	faraday, coulombs
ΔG^o	standard free energy of adsorption, cal · mole^{-1}
i_o	exchange current density, amp · cm^{-2}
K	integral capacity of double layer, μf · cm^{-2}
N	number of electrons corresponding to a given energy level
q	charge density on electrode, μcoul · cm^{-2}
$q_1^\pm$	charge density of specifically adsorbed cations (q_1^+) or anions (q_1^-), μcoul · cm^{-2}
q_{2-s}	charge density in diffuse double layer, μcoul cm^2
R	gas constant
t	time, sec
T	absolute temperature or transmission coefficient (no confusion)
x	distance from electrode, cm
x_1	distance from electrode to the inner plane of closest approach, cm
x_2	distance from electrode to the outer plane of closest approach, cm
W	energy, ergs
W_a	sum of the Fermi level energy and the work function, ergs
z	ionic valence on ion
β	defined by $\beta = \exp(-G^o/RT)$
γ	interfacial tension dynes · cm^{-1}
$\Gamma_\pm$	relative surface excess of cations (Γ_+) or anions (Γ_-), mole · cm^{-2}
ϵ	dielectric constant
η	overvoltage, v
μ	chemical potential, cal · mole^{-1}
ϕ_M	potential in metal, v
ϕ_1	potential in inner plane of closest approach, v
ϕ_2	potential in outer plane of closest approach, v

REFERENCES

1. A. N. Frumkin, "Transactions of the Symposium on Electrode Processes," pp. 1-12, E. Yeager, Editor, John Wiley & Sons., Inc., New York (1961).
2. P. Delahay and G. G. Susbielles, *J. Phys. Chem.*, **70**, 647 (1966).
3. D. C. Grahame and B. A. Soderberg, *J. Chem. Phys.*, **22**, 449 (1954).
4. D. C. Grahame, *J. Am. Chem. Soc.*, **80**, 4201 (1958).
5. D. C. Grahame and R. Parsons, *ibid.*, **83**, 1291 (1961).
6. R. Parsons, *Trans. Faraday Soc.*, **55**, 999 (1959).
7. J. M. Parry and R. Parsons, *ibid.*, **59**, 241 (1963).
8. R. Parsons, *J. Electroanal. Chem.*, **7**, 136 (1964).
9. R. Parsons, Personal communication.
10. R. Payne, *J. Phys. Chem.*, **69**, 4113 (1965).
11. G. G. Susbielles, P. Delahay, and E. Solon, *J. Phys. Chem.*, In press.
12. M. A. V. Devanathan, *Trans. Faraday Soc.*, **50**, 373 (1954).
13. S. Levine, G. M. Bell, and D. Calvert, *Can. J. Chem.*, **40**, 518 (1962).
14. J. R. Macdonald and C. A. Barlow, *J. Chem. Phys.*, **40**, 1535 (1964).
15. P. Delahay, R. de Levie, and A. M. Giuliani, *Electrochim. Acta*, In press.
16. F. R. Smith and P. Delahay, *J. Electroanal. Chem.*, In press.
17. P. Delahay, *Anal. Chem.*, **34**, 1267 (1962).
18. P. Delahay and H. Lauer, Unpublished investigation.
19. M. Sluyters-Rehbach and J. H. Sluyters, *Rec. trav. chim.*, **82**, 525 (1963).
20. P. Delahay, *J. Phys. Chem.*, submitted.
21. D. C. Grahame, *Chem. Revs.*, **41**, 441 (1947).
22. D. C. Grahame and R. W. Whitney, *J. Am. Chem. Soc.*, **64**, 1548 (1942).
23. D. M. Mohilner, *J. Phys. Chem.*, **66**, 724 (1962).
24. J. M. Parry and R. Parsons, *This Journal*, **113**, 992 (1966)
25. P. Delahay and G. G. Susbielles, *J. Phys. Chem.*, In press.
26. P. Delahay and G. G. Susbielles, Unpublished work.

Discussion

Roger Parsons: I would like to suggest that the assumed constancy of the distances x_1^+ and x_1^- and the dielectric constant of the inner region ϵ is only a first approximation. From the data we already have on systems involving only a single specifically adsorbed species it seems likely that these parameters are charge dependent.

Hence I believe it is important that the calculation of specific adsorption in a mixed system should be done without making such approximations. This can be done following the method proposed independently by Hurwitz[1] and by Dutkiewicz and myself[2] and used by us for the KI + KF system. For the $TlNO_3$ system this would involve measurements in two series.

(*a*) say $(1-x)MTlF + xMTlNO_3$

(*b*) say $(1-x)\ MKNO_3 + xMTlNO_3$

In (*a*) the appropriate form of the Gibbs equation at *T,p* constant is

$$-d\gamma = qdE^+ + \Gamma_{F^-}\,d\mu_{TlF} + \Gamma_{NO_3^-}\,d\mu_{TlNO_3}$$
$$= qdE^+ + RT\Gamma_{F^-}\,d\ln(1-x) + RT\Gamma_{NO_3^-}\,d\ln x$$

if activity coefficients may be assumed constant in a medium of constant ionic strength. Hurwitz treated a more elaborate situation. Hence

$$-d\gamma = qdE^+ + RT\left\{\Gamma_{NO_3^-} - \frac{x}{1-x}\Gamma_{F^-}\right\} d\ln x$$
$$= qdE^+ + RT\Gamma'_{NO_3^-}\,d\ln x$$

since the term $(x/1-x)\Gamma_{F^-}$ is just equal to the surface excess of NO_3^- in the diffuse layer only. Thus this experimental series gives the specifically adsorbed amount of NO_3^- subject to the approximation that F^- and NO_3^- have equal distances of closest approach to the electrode in the nonspecifically adsorbed state. This approximation may cause trouble if the diffuse layer is negatively charged but will be very good if it is positively charged.

Similarly in series (*b*) the Gibbs equation becomes

$$-d\gamma = qdE^- + \Gamma_{Tl^+}\,d\mu_{TlNO_3} + \Gamma_{K^+}\,d\mu_{KNO_3}$$
$$= qdE^- + RT\Gamma_{Tl^+}\,d\ln x + RT\Gamma_{K^+}\,d\ln(1-x)$$
$$= qdE^- + RT\left\{\Gamma_{Tl^+} - \frac{x}{1-x}\Gamma_{K^+}\right\} d\ln x$$
$$= qdE^- + RT\Gamma'_{Tl^+}\,d\ln x$$

It should now be possible to extrapolate the result in each series of experiments to $x = 1$ to obtain Γ'_{Tl^-} and $\Gamma'_{NO_3^-}$ in 1M $TlNO_3$, and other measurements would lead to similar results at other total ionic strengths.

[1] H. R. Hurwitz, *J. Electroanal. Chem.*, 10, 35 (1965).

[2] E. Dutkiewicz and R. Parsons, *ibid.*, 11, 100 (1966).

Also in connection with the results in $TlNO_3$ I would like to ask whether there is any evidence for $Tl^+NO_3^-$ ion-pair formation. This would be expected in the low dielectric constant medium of the inner layer since pK is 0.33 in bulk water.

Paul Delahay: Dr. Parsons' suggestion is a very good one. At first sight I have no objection to it except perhaps the possibility of difference in behavior similar to that found by Dr. Payne for adsorption of NO_3^- in pure KNO_3 solution and in mixtures of $NH_4NO_3 + NH_4F$. However, the experiments should be run.

With regard to your question about ion pairs, there is indeed strong association between Tl^+ and NO_3^-, as shown by the magnitude and sign of the corresponding interaction parameter for two simultaneous Frumkin isotherms of the type you advocated ($r = 1$ to simplify matters). I shall present some results on this point after presentation of your paper, and detailed data are given in ref. (11) of my paper.

B. E. Conway: In regard to your second charge-separation effect involving no transfer of electrons in the external circuit, would this not be equivalent to the reverse of what occurs on open-circuit decay of emf of electrodes which are not ideally polarizable, *e.g.*, as treated in the theory of Butler and Armstrong[3] for emf decay at Hg? If this is so, it may help to clarify the significance of the effect you propose.

Paul Delahay: Your comparison is interesting but I see there more an analogy than an equivalence. It is generally stated that, in open circuit decay, discharge of the double layer provides the faradaic current. You consider, I suppose, the opposite proposition, namely, that faradaic current charges the double layer. Actually, the situation is more complex because of the interplay of ionic fluxes, variations of the Γ's, and finally the faradaic current. One really should consider charge separation or recombination in the analysis of open potential decay (at least when the exchange current is high enough to warrant the analysis). This we have already done. This is why I think that your suggested equivalence is misleading.

F. C. Anson: I have not been able to follow all of Professor Delahay's very stimulating arguments and I hope to clarify my own thinking by asking him to comment on the following thought experiment.

Suppose one has a reversible, well-poised metal-metal ion electrode at equilibrium at potential E_1 in a sodium fluoride supporting solution. With an all but perfect potentiostat the electrode potential is stepped to a more cathodic potential, E_2. The charge-potential characteristic for the electrode in sodium fluoride is known so that the electronic charge on the metal electrode is known to be q_1 at E_1 and q_2 at E_2. Thus the total electronic charge that will have to be supplied to the electrode to change its potential from E_1 to E_2 will be $q_2 - q_1$.

I had thought that all of this charge, $q_2 - q_1$, would be supplied to the electrode from the potentiostat. However, as I understood Professor Delahay, he believes that some part of this charge may be supplied to the electrode by the faradaic reaction of the electrode itself according to

$$M \rightarrow M^{n+} + ne^- \qquad [1]$$

What I cannot understand is how such a net anodic reaction could have been induced to proceed by the application of a cathodic potential step. Furthermore, even if this reaction did somehow occur, the metal cations it produced would not help to satisfy the cationic charge required by the diffuse layer to match the negative electronic charge injected into the electrode by the potentiostat because each metal action produced by this reaction releases n electrons into the electrode so that the relative charges on the electrode and in the diffuse layer would remain unchanged.

Paul Delahay: First I must correct a statement made in Professor Anson's question, and then I shall answer his question.

If the potential of the electrode $M^{+z} + ze = M$ is changed from the equilibrium potential E_1 to some other value E_2 by an ideal potentiostat, one should not consider the charge density q on the electrode but some function of q and Γ_+ (of M^{+z}). Under ideal reversible behavior one has a variation of $(q + zF\Gamma_+)_{E_1}$ to $(q + zF\Gamma_+)_{E_2}$ where q and Γ_+ at E_2 correspond to the activity of M^{+z} just outside the diffuse double layer at E_2. This point, however, does not change the gist of Professor Anson's question.

The answer is a simple one: I always referred to charge separation or recombination, and by this meant that the reaction $M^{+z} + ze = M$ can occur in the forward (recombination) or backward (separation) directions.

When E varies from E_1 to E_2, q may either increase or decrease depending on the values of E_1 and E_2. Likewise Γ_+ can vary in either direction. Let us assume that

$$(\Gamma_+)_{E_1} > (\Gamma_+)_{E_2}$$

and that Γ_+ is positive at these two potentials (the situation Professor Anson wants, I believe). Variation from E_1 to E_2 causes recombination (and not separation), and consequently the ionic flux of M^{+z} at the electrode is greater than if recombination did not occur. Hence, recombination must be considered.

At $t = 0$, charging occurs as an ideal polarized electrode for a finite exchange current. Charge recombination comes into play for $t > 0$. If the exchange current is supposed to be infinite, charging occurs as an ideal reversible electrode for $t \geq 0$. This problem has already been worked out in collaboration with Mr. Susbielles (unpublished work).

In conclusion, I think that Professor Anson's question indicates that he considered only charge separation and not the opposite effect. I never made a suggestion along these lines.

F. C. Anson: Professor Delahay has stressed that the separation of a measured current into faradaic and nonfaradaic components cannot be made rigorously. I wonder if this difficulty could not be partially overcome if the total charge that passes, rather than the current, were the measured parameter. The total nonfaradaic charge which passes as a result of a potential step, for example, should be calculable *a priori* in favorable cases from a knowledge of the charge-potential characteristic of the pure supporting electrolyte.

Paul Delahay: The answer to Professor Anson's question is "No". Integration of the current is only a mathematical transformation of the signal which does not modify the basic premises on which theory is based. Integration (or differentiation, etc.), however, may facilitate analysis of results, minimize errors, etc.

It turns out that integration may minimize errors of results obtained by classical analysis based on *a priori* separation of faradaic and charging current. The reason is as follows.

The double layer charging contribution, as calculated by *a posteriori* separation, often depends on the derivatives, with respect to potential, of q and the Γ's. The Γ's in particular, can vary very rapidly with E over a narrow interval of potential. Hence, the derivatives can be high. Use of a technique in which

[3] J. A. V. Butler and G. Armstrong, *Proc. Roy. Soc. London*, 137A, 604 (1932).

the signal depends on the Γ's (and other factors) over a wide interval of E rather than on the $d\Gamma/dE$'s over a narrow interval of E may then be advantageous. In this sense, integration may help, but it does not remove the basic difficulty. I believe that the real answer is to solve a particular problem without assuming charge separation or recombination, and then compare the solution with the one obtained with *a priori* charge separation. The error can then be evaluated.

H. Gerischer: It is certainly very necessary to reconsider the basic concepts of our approaches to the study of electrode reaction kinetics as Professor Delahay has done in the fourth part of his paper. But to my regret, I have not yet understood why he assumes that the heretofore used concepts of discussing transients are not adequate. These concepts have been developed for describing nonequilibrium conditions. In principle the derivative of interfacial tension with respect to potential, all other variables being kept constant, cannot be measured for a reversible electrode since the potential in a reversible system can only be changed by variation of the composition of one of the two phases in contact (at constant T and p) without leaving equilibrium conditions. This derivative is therefore basically associated with the concept of the ideal polarized electrode. In kinetics, one studies the question of what goes on when we depart from equilibrium conditions? This is reached for electrode reactions by bringing additional electrical charges from an external current source to the electrode interface. This charging process can be done very fast (in principle with an infinitely high voltage source infinitely fast). If the reactants in the electrode process are ions, and this is always true for at least one of the reactants, the accumulation of charge in the double layer can be due partially to these ions themselves depending on their relative concentration and their specific charge, but I cannot see that this makes questionable the concept of distinguishing between faradaic and charging currents.

As a limiting case, the double layer can be charged by an extremely high external current pulse momentarily without noticeable faradaic discharge of the interface condenser. The deviation from this idealized charging behavior indicates to us the faradaic loss. The purely electrostatic part of such a charging process is defined by the assumption that the charge distribution is changed without chemical reaction; that means without any chemical change in the composition of the electrode half-cell as a whole. In this picture, the change in distribution of those ions which take part in the electrode reaction is assumed to occur by movement of ions already present in the electrolyte. It is further assumed that the distribution of charges in the double layer reaches equilibrium immediately.

All current flowing of a faradaic nature through the electrode interface is combined with changes in chemical composition. The products of the chemical reactions will change the composition of the electrolyte and (often of the electrode also) at and next to the phase boundary. We are accustomed to describe this as concentration polarization when we ask how this chemical change alters the driving force for the faradaic process. This change in composition includes also a change in the distribution of ionic charges in the double layer. But this means only, I believe, that the electrostatic capacity may vary somewhat. All this has to be included in the model as concentration polarization and this can be done by introducing into this model the kinetics of diffusion processes, adsorption, and formation of intermediates inside and outside the double layer. We all know that this can become extremely complicated.

It is obvious that this model of distinguishing between electrostatic and chemical effects can only be verified experimentally when the energy barriers for the transfer of charge through the double layer are essentially higher than those for the transport of ions in solution over the same distances. Only then do we have the chance to apply the electrostatic force at the electrode interface faster than the chemical reaction can follow. Otherwise we come immediately to a situation which is controlled only by the other rate processes which are involved, such as transport and chemical reactions. These cases will be found and are found, I think, but this is already included in the assumptions hitherto made.

I would like to add that this problem of distinguishing between the effects of electrical forces and chemical forces on the electrode reaction is closely related to the problem of distinguishing between electrical and chemical potentials for ionic species in electrolytes. We assume in our usual treatment that equilibrium is preserved in the double layer with respect to the electrostatic interaction in spite of nonequilibrium conditions with respect to the electrode reaction. This is certainly a somewhat dubious assumption when we discuss the influence of the concentration distribution in the double layer on kinetics. It seems to me that it is this problem which Professor Delahay tries to avoid. But at the moment I have not yet understood in what way this can be done without relying on any mechanistic interpretation of these indeed very complex processes.

Paul Delahay: To answer Professor Gerischer's question I shall consider two points: (*a*) Is the approach I suggest justified? (*b*) Does this approach lead to results that are significantly different from those obtained by the usual *a priori* separation of faradaic and charging processes.

I shall begin with the first question and try to answer it in two ways: (*i*) by introducing the concept of charge-separation or charge recombination without external current; (*ii*) by considering the three general equations I proposed (and without use of the charge-separation concept). The answer is the same by both methods. To simplify matters, I shall consider only a metal ion-pure metal electrode ($M^{+z} + ze = M$), but the analysis can be transposed to other types of electrodes. I hope to refute in this way, Professor Gerischer's arguments, inasmuch as I understand them. Further details can be found in a recent paper,[4] and application to electrode impedance measurements is made in another paper.[5]

Consider the electrode $M^{+z} + ze = M$ at equilibrium and assume that some perturbation is applied (current, potential, etc.). Further, assume that the double layer is at equilibrium with respect to the ionic concentrations (activities) just outside the diffuse double layer. (This is reasonable provided the time scale of measurements is large in comparison with the relaxation time of the double layer.) Finally, let us first suppose that all ions needed in the charging of the double layer are supplied (or removed) by ionic transfer. Then, the charging current is proportional to the charge density q on the electrode or the differential capacity dq/dE (E potential) depending on the charging conditions. (More complicated dependence need not be considered here.) This follows from the definition of q

$$q = -\Sigma z_j F \Gamma_j \qquad [1]$$

where z_j is the ionic valence of each ionic species with sign, Γ_j the corresponding surface excess (relative $\approx$ absolute; dilute solution) and F the faraday. This behavior is characteristic of an ideal polarized electrode and has been assumed in previous treatments of nonsteady-state processes. I believe there is no disagreement here.

[4] P. Delahay, *J. Phys. Chem.*, in press.

[5] P. Delahay and G. G. Susbielles, *J. Phys. Chem.*, in press.

Consider now the same electrode and assume that all ions but M^{+z} are supplied by ionic transfer. Let us leave for a moment the reason for making this assumption (see below), and let us proceed as before. The current for charging of the double layer is now proportional to $-\sum_{j \neq M^{+z}} z_j F_j \Gamma_j$ or to the derivative of this quantity with respect to E. One has by definition of q in Eq. [1]

$$-\sum_{j \neq M^{+z}} z_j F \Gamma_j = q + zF\Gamma_+ \qquad [2]$$

where z is the ionic valence of M^{+z} and Γ_+ is the surface excess of M^{+z}. We see that the charging current is now different from that of an ideal polarized electrode. Also note that the quantity $q + zF\Gamma_+$ is that appearing in the equation for the electrocapillary curve for an ideal reversible electrode (metal ion-pure metal). More about this point later.

I now return to the assumption I made, namely, that M^{+z} ions are not supplied (or removed) by ionic transfer. This assumption amounts to stating that there is charge separation or recombination by the reaction $M^{+z} + ze = M$ without external current. Thus a M^{+z} ion is supplied by this reaction, and the electronic charge $-|ze|$ is left on the electrode. This concept follows directly from the idea of exchange current. If we assume that the exchange current is infinite, any driving force, no matter how small it is, will cause some charge separation or recombination. When we disturb the system from equilibrium, some driving force is exerted, and the above mechanism must be considered. The contribution to charging by this mechanism, as compared to ionic transfer, depends on the exchange current and also on mass transfer characteristics. Hence, time or frequency must be considered.

I have used thermodynamics as guiding posts, but I like to stress that the problem is a kinetic one. This brings me to the second approach in which we simply consider balance conditions (1 equation for a metal ion-pure metal electrode; 2 equations for amalgam, redox electrodes, etc.). In writing the third equation I simply recognize that only ionic fluxes (converted to an electronic current at the counter electrode) can be measured. I make no assumption, in the writing of the first two equations, about the explicit form of the faradaic current. Of course, in applying these equations one needs some specific form for the faradaic current in terms of overvoltage, exchange current, concentrations, etc. Models then come into play, but only at that stage. No mention need be made of charge separation without external current, but the previous transition from ideal polarized to ideal reversible electrode follows naturally from the general equations.

One also finds from this treatment that at $t = 0$ (or at infinite frequency), charging occurs as an ideal polarized electrode provided the exchange current is finite. (If the exchange current is supposed to be infinite, the ideal reversible electrode behavior always prevails.) I agree with Professor Gerischer on this point, but I like to emphasize that behavior as an ideal polarized electrode prevails only for $t = 0$ (or infinite frequency). For $t > 0$ (or a finite frequency) there is a progressive transition toward ideal reversible electrode as t increases after the initial perturbation.

I hope these arguments are quite convincing, but anyhow let me now consider the second point, namely, is the effect significant? It turns out that it is more often than one might think, especially when the charging current is proportional to the potential derivatives of the quantities I mentioned. If one assumes no specific adsorption, one can show from diffuse double layer theory and the Nernst equation that $zF(d\Gamma_+/dE)$ can easily be larger than dq/dE. Specific adsorption may make the difference larger or smaller.

In conclusion, I shall restate what I said before: *a priori* separation of faradaic and charging processes is not justified in nonsteady-state electrode processes. Such a separation is not needed in the detailed treatment of nonsteady processes. The difference between the results obtained by the method I outlined and the classical one can be significant. Of course, there may be many cases (concentrated supporting electrolytes, *i.e.*, 1 M of 1-1 electrolytes) in which the difference is not particularly great. Finally, I might add that I explicitly separated the charging process in the discussion to express myself in terms of a familiar model.

I shall not discuss the separation of chemical and electrochemical forces, Professor Gerischer considered, as I do not see how it is directly relevant to the problem, at least as I treated it. However, I do not see there a refutation of the ideas I put forward.

G. C. Barker: I have a number of comments to make on Professor Delahay's interesting paper. First it should be mentioned that strong adsorption of metal on mercury ions often is observed with halide solutions, and there is now evidence in many cases that the adsorption is due either to the interaction of the metal ions with specifically adsorbed halide ions or to simple extraction by the interface of ion pairs or complex ions present in the solution. As it is known that Tl^+ is fairly readily complexed by NO_3^- is would seem likely that the enhanced adsorption for nitrate solution is partly if not entirely due to the presence of undissociated $TlNO_3$ in the interfacial region, and I wonder what the consequences of such adsorption may be when it comes to analyzing the data.

The adsorption which is observed with fluoride solutions seems more unexpected and may be connected with weak formation of an intermetallic compound between mercury and thallium. There is evidence for such compound formation in the case of platinum. It would be of interest to study the dependence of the adsorption on temperature in the mercury case to eliminate the slight possibility that the adsorption is connected with pair formation. Usually when there is strong adsorption arising from complex ion formation the surface excess falls rapidly as the temperature rises whereas there is some (not wholly conclusive) evidence[6] suggesting that the temperature coefficient, when the adsorption is due to the formation of intermetallic compounds, is relatively small.

My next point has to do with mass transport effects when double layer capacities are measured in solutions of low ionic strength by the coulostatic method described by Professor Delahay. Some studies of the mass transport problem made a few years ago led us to believe that the equivalent circuit for the double layer is not purely capacitative, but contains also a transmission line connected in series with the zero-frequency capacity.[7] Thus when charge is injected the potential should at first overshoot its final value and, provided the subsequent decay is small compared with the potential excursion, the amount by which the potential exceeds the equilibrium value should be inversely related to the elapsed time to the power 1/2. It would be of interest to know whether this theoretical expectation is realized, but even more important is the fact that the overshoot is dependent on the rate of change with potential of the surface excesses of anions and cations at the interface. Thus there is a slight possibility of using the dynamic technique developed by Professor Delahay to study surface excesses. This might provide a check on the data currently obtained by less direct methods.

Finally I would like to make a comment on the stimulating paper dealing with the influence of changes in reactant concentration caused by a faradaic

[6] G. C. Barker, Unpublished.

[7] G. C. Barker, "Transactions of the Symposium on Electrode Processes," E. Yeager, Editor, John Wiley & Sons, Inc., New York (1961).

process on the apparent double layer capacity of the interface. I understand the points that Professor Delahay is making, and I fully agree that changes in reactant concentration (regardless of whether the reactant is specifically or nonspecifically adsorbed) do influence the double layer charge and hence affect the apparent differential double layer capacity. My comment is that this effect has been taken account of in an earlier paper by myself and in one by Delahay and Senda,[8] although I would agree that the implications of interactions between faradaic and nonfaradaic phenomena have not been previously discussed adequately. I believe that it would be well to emphasize that generally errors resulting from neglect of the dependence of double layer charge on reactant concentration are small compared with the errors which occur when one neglects the influence of nonspecific or specific adsorption on the faradaic impedance or on the aperiodic equivalent circuit for the faradaic part of the interfacial impedance. Thus when studying the kinetics of fast or slow reactions by any linear or nonlinear relaxation technique one should always first give regard to the latter complication. To omit doing this and to apply only corrections for the dependence of double layer charge on reactant concentration would be disastrous in many instances, but I suspect that this is not what Professor Delahay is advocating in the paper which he has described briefly. One final point may be mentioned which I am sure Professor Delahay will agree with; this is that when one considers the aperiodic circuit for the interface, it is evident that the influence of changing reactant concentrations on double layer charge can be allowed for by a current generator shunting the differential double layer capacity for constant reactant concentration. Specific or nonspecific adsorption of the reactant in question can be allowed for with a high degree of accuracy, if the integral adsorption coefficient changes slowly with potential, by capacity shunting the diffusion impedance for the reactant in question. One can see intuitively that, when the surface excesses are small and the system at equilibrium is linear as regards reactant adsorption at constant potential, the current associated with the aforementioned current generator [see Fig. 8, ref. (2)] is linearly related to the current flowing through the capacity shunting the diffusion impedance. All therefore turns on the magnitude of the two currents, and I believe that in the majority of experimental systems the former current is much smaller than the latter largely because adsorption coefficients (nonspecific or specific) change only slowly with potential whereas the reactant concentration may change relatively rapidly with potential. However, there undoubtedly are exceptions (organic reactants), and in these cases due regard must be given to interaction between the faradaic and nonfaradaic parts of the interfacial impedance. Professor Delahay is to be congratulated on drawing attention to these involved matters.

Paul Delahay: I completely agree with your suggestion that $TlNO_3$ is formed, *i.e.*, that there is strong $Tl^+ - NO^-_3$ association between specifically adsorbed Tl^+ and NO^-_3. This is shown, at least qualitatively, by analysis on the basis of simultaneous isotherms. (Cf. my reply to Dr. Parsons' question.)

With respect to your comment on the coulostatic method, I believe that an answer is provided by analysis on the basis of the three general equations I gave in the discussion of my paper. This problem has now been solved, and one can show that there is a progressive transition from behavior as an ideal polarized electrode at $t = 0$ to an ideal reversible electrode at $t \to \infty$. The situation is similar to the one I discussed for impedance measurements. You are quite right in stating that one cannot regard the double layer as that of an ideal polarized electrode (except at $t = 0$, and there we disagree I believe), but I believe that we approach the problem in different ways. It would be of interest to see whether our conclusions are similar or identical.

I shall now take up your point about previous treatments of how to modify the equivalent circuit to account for adsorption (specific or not). These treatments have indeed been developed. My present position is that the problem can be attacked from a different point of view without *a priori* separation of double layer and faradaic processes. One can develop models for the writing of the faradaic current and solve the three general equations I presented. The effect of adsorption then comes out naturally from the treatment (frequency dependence) rather than from some modification of the equivalent circuit. On the basis of our calculation, I disagree with your statement that small effects can be expected in most cases. Detailed analysis of actual systems and measurements will provide the best answer.

D. M. Mohilner: Why is it that for the case of the reversible (very fast) charge transfer you attribute the entire change in the surface excess of the electroactive species to charge separation-recombination? I should have thought that even for this species a part of $zFd\Gamma_+$ required in time dt could be furnished by ion transport.

Paul Delahay: If we consider dynamic conditions, as prevailing in nonsteady state measurements, ideal reversible behavior implies an infinite exchange current. Hence, any driving force (*e.g.*, concentration gradient), no matter how small it is, causes charge separation or recombination. The contribution to charging, as far as M^{+z} is concerned, by ionic transfer in solution can then be neglected for a finite diffusion coefficient of M^{+z}.

I could also answer your question in another way by considering the charging process and showing that by assuming pure charge separation or recombination ($M^{+z} + ze = M$), one indeed finds that the charging current depends on $q + zF\Gamma_+$ (or the derivative of this quantity with respect to E depending on charging conditions) for a pure metal-metal ion electrode. Details are given in my paper [ref. (20)].

Richard Buck: The thermodynamic arguments for coupling of an exchange current-controlled Faradaic process and the double layer charging process in an over-all reversible process under nonsteady state conditions should be reinforced by an electrostatic treatment of this problem. The paper by Bass[9] may provide the necessary formalism although neither Bass nor Levich[10] treated the transient state. By combining Poisson's equation with the Nernst-Planck flux equations for each ion of a binary salt, Bass was able to give the potential distribution from the interior of the solution (where electroneutrality prevails) to the inner Helmholtz plane both for the case of zero current (Gouy-Chapman result) and for finite current. Presumably the potential distribution for the nonsteady state could be treated this way perhaps with the aid of a computer. From the potential distribution, the charge and capacitance can be found.

It would be surprising if this calculation gave anything different from the previously assumed result, *e.g.*, that charging occurs early in time and is not complicated by the faradaic process. It seems to me that Professor Delahay's suggestion implies that the divergence of the flux (divergence of the quantity-Dgrad$C$ $\pm zeuEC$ where D is the diffusion coefficient, C the

[8] M. Senda and P. Delahay, *J. Phys. Chem.*, 65, 1580 (1961).

[9] L. Bass, *Trans. Faraday Soc.*, 59, 1656 (1963).

[10] L. Bass and Levich, "Physicochemical Hydrodynamics," Chap. 6, Prentice Hall, New York (1962).

species concentration, z the ionic charge, e the electronic charge, u the mobility, and E the electric field strength) is not zero at the electrode surface (even for zero not current as was assumed by Bass) for an ion which can exchange electrons with the electrode. This means that a volume source of strength proportional to the exchange current density must be added.

It would be interesting to follow through with the above assumptions to see whether or not there is a verification of the coupling of faradaic and charging processes suggested by Professor Delahay. Would Professor Delahay care to comment on these points?

Paul Delahay: Dr. Buck may be quite right, and I only wish to correct a statement he made, namely that I developed the analysis by thermodynamic means. I did introduce thermodyanmic considerations to show the need for a transition from an ideal polarized electrode to an ideal reversible electrode. However, the three general equations I gave are of kinetic rather than thermodynamic character. This point is further discussed in my reply to Dr. Breiter.

James N. Butler: We have attempted, in our studies of gallium and gallium amalgam electrodes[11] (Cleveland Meeting) to measure the surface charge directly by observing current-time curves at a dropping electrode whose potential is held constant. Under the assumption that there is no interaction between the charging process and the faradaic process, a theoretical form of this dependence may be predicted, and this has been verified experimentally for double layer charging of gallium in the presence of hydrogen evolution, and on Ga-Hg alloys in the presence of gallium dissolution. These results are consistent with Professor Delahay's theoretical arguments in spite of his suggestion that for some situations there may be strong deviations from the approximation of independent double layer and faradaic currents.

In the case of simultaneous double layer charging and hydrogen evolution in 0.1M $HClO_4$ solutions, the faradaic process can contribute only a cathodic current. The reaction rate in the opposite direction is so slow that the electrode behaves as an ideally polarized electrode except for the discharge of hydrogn ions; and the charging current and faradaic current are strictly additive.

In the case of gallium dissolution, the time-dependence of the current indicates that the double layer charging current is independently additive to a diffusion-controlled anodic current. Because of the minute concentrations of Ga^{+3} in the solutions, the reverse reaction is probably very slow, and thus the currents are again independent.

The effects which Professor Delahay has predicted are important in systems where the reaction occurring at the electrode has approximately the same time scale as the transient measurement. We have observed deviations from strictly additive behavior under conditions where the concentration of gallium ions in the solutions becomes large enough so that the relaxation time of the $Ga \leftrightarrows Ga^{+3}$ reaction is probably comparable to the time scale of the measurements, about 0.01-1 sec. Such conclusions would have to be verified by direct measurements of the rate of this reaction, but could provide an important test of this theory.

Paul Delahay: There is no problem for the processes you refer to because the exchange current, under conditions of your measurements, is very low. I pointed this out precisely in my paper in some detail and showed a plot of the double layer capacity (*a posteriori* separation) as a function of frequency for different exchange currents. The same order magnitude for the time scale applies to other techniques than impedance measurements.

In your paper[12] you implicitly assumed algebraic additivity of the faradaic and charging currents at a dropping mercury electrode. You give no hint that this might not be the case. You may expect trouble in some of the applications you predict in your note, particularly for thallium amalgam, whenever the potential is such that the exchange current is high.

We independently developed the same technique, as you did, and made extensive measurements[13] on the $Hg^{+2} + 2e = Hg$ system while I was still at Louisiana State University (spring of 1965). It was this work (and also that of Sluyters) which led me to think about the whole problem of double layer charging with concomitant charge transfer reaction. The analysis of the type of analysis you used is now being worked out on the basis of the three general equations I presented.

Your last comment is in agreement with the views I expressed in the paper.

M. W. Breiter: It appears that the distinction resulting from the thermodynamic treatment of the "ideally polarizable electrode" and the "reversible electrode" is not useful here. In the absence of specific adsorption of ions a capacitance may be due to the amount of potential-determining ions in the diffuse double layer under certain experimental conditions. If adsorbed intermediates are formed in an adsorption reaction (for instance, H-atoms in the Volmer reaction), a large capacitance of up to several thousand $\mu F/cm^2$ may be measured at low frequencies. This capacitance has been designated as "faradaic capacitance," and the thermodynamics of this case is treated by Frumkin and co-workers in a paper which follows.

Paul Delahay: One can approach the problem in two ways (which I used): (*a*) Point out the difference between charging of an ideal polarized electrode and an ideal reversible electrode and then examine the transition from one case to the other for nonsteady-state measurements; (*b*) write the three general equations which I gave and deduce implications by solving the problem for the particular conditions prevailing in any given method.

The writing of the first two equations involves only balance considerations. The third equation, however, is a little more subtle and, to arrive at it, I found it useful to introduce the concept of charge separation or recombination without external current.

I agree with your comments on the hydrogen electrode, but I wish to point out that the three general equations also apply to this case. The treatment of this electrode for impedance measurements ought to be reexamined but the difference between the result and the one now used may not be significant (except for high exchange currents). We have plans for examining this and similar problems.

Finally, I believe the term "faradaic capacity" is misleading because of the impossibility of *a priori* separation of charging and faradaic processes. It is better to refer to electrode capacity, resistance, or impedance.

G. J. Hills: Professor Delahay's proposals, if correct, require the revision of many electroanalytical procedures. His faradaic charging term is written as

$$zF\Gamma_-$$

and the associated current as

$$zF\frac{d\Gamma_+}{dt}$$

[11] Abstract No. 171, Cleveland Meeting, May 1966.

[12] J. N. Butler and M. L. Meehan, *J. Phys. Chem.*, 69, 4051 (1965).

[13] G. Tessari, J. Murphy, R. de Levie, and P. Delahay, Unpublished work.

This can be equated to

$$zF\frac{d\Gamma_+}{d\mu_\pm}\cdot\frac{d\mu_i}{dE}\cdot\frac{dE}{dt}$$

where μ_i is the chemical potential of the potential-determining species. For a reversible electrode

$$\frac{\partial\mu_i}{\partial E}=\frac{zF}{RT}$$

and for a particular frequency or time-scale the significance of the faradaic charging current depends therefore on $\partial\Gamma_+/\partial\mu_+$ which will be small for nonspecifically adsorbed ions in the presence of excess supporting electrolyte. The faradaic admittance of adsorbable species is already taken care of.

Paul Delahay: First, I did not say or suggest that electroanalytical procedures ought to be modified as a result of my work. The difference between my approach and the classical one may be of no particular significance as far as analytical procedures are concerned. Further thought is required on that point. What I did say, however, was that the determination of kinetic parameters by nonsteady-state methods ought to be reexamined.

Now to your question. I am not sure I understand what you mean by "faradaic charging term," but anyhow your point is that $d\Gamma_+/d\mu_+$ is small in the absence of specific adsorption, *i.e.*, that the effect I discussed ought to be small. This conclusion is not correct as you can ascertain by calculating $zF\frac{d\Gamma_+}{d\mu_+}\frac{d\mu_+}{dE}$ $\left(\text{or more simply } zF\frac{d\Gamma_+}{dE}\right)$ from diffuse double layer theory and the Nernst equation. The calculation is given in the treatment of the faradaic impedance[14] based on the ideas I expressed. One easily reaches 100 $\mu f\cdot cm^{-2}$ for realistic conditions in 0.1M of a 1-1 electrolyte (no specific adsorption). Hence this term cannot be neglected in comparison with dq/dE or the capacity component of the usual faradaic impedance. I should add that in 1M supporting electrolyte, for the same conditions as above, the effect is less pronounced (about 7 $\mu f\cdot cm^{-2}$). This may explain why abnormal behavior has escaped attention in experimental work. Workers were simply not looking for it, and the temptation to ascribe abnormal behavior to kinetic complications (often real!) could not be resisted I suppose.

Finally, I do not understand what you mean by "The faradaic admittance of adsorbable species is already taken care of." I did not make any distinction between specifically and nonspecifically adsorbed ion in writing Γ's. These are surface excesses in the thermodynamic sense.

H. D. Hurwitz: It is interesting to note the importance of the influence of the diffuse layer composition (cf. the work of Dr. R. Payne). In this respect the method of mixed electrolytes at constant ionic strength[15,16] appears to be able to throw further light in this direction and to correct some earlier assumptions based upon the model of Gouy-Chapman.

It is also noteworthy that such results may be obtained from measurements of double layers in media of low electrical conductivity as shown by Professor Delahay in his paper. One must, however, stress the point that even at very low concentration the theory of Gouy-Chapman is inconsistent unless a linearization of Poisson-Boltzmann equation is performed, the solution of which does not yield a cosh behavior of the differential capacity. Nevertheless, some less rigorous approach [17] may lead to some stimulating results. For example, the smaller experimental values of C near the maximum on the cathodic side of Fig. 6 in Professor Delahay's work could be interpreted as resulting from electrostrictive effects of the adsorbed Na^+ in the diffuse layer.[17] In this respect, it is advisable to repeat such experiments with different cations.

[14] P. Delahay and G. G. Susbielles, *J. Phys. Chem.*, in press.

[15] E. Dutkiewicz and R. Parsons, *J. Electroanal. Chem.*, 11, 100 (1966).

[16] H. D. Hurwitz, *J. Electroanal. Chem.*, 10, 35 (1965).

[17] H. D. Hurwitz, A. Sanfelt, and A. Steinchen-Sanfelt, *Electrochim Acta*, 9, 929 (1964).

Discreteness-of-Charge Adsorption Micropotentials

III. Dielectric-Conductive Imaging

J. Ross Macdonald and C. A. Barlow, Jr.

Texas Instruments Incorporated, Dallas, Texas

ABSTRACT

A convenient general method for calculating potentials and fields arising from planar arrays of discrete adions under a variety of imaging conditions is described and illustrated. Adions are perfectly imaged by one conducting plane (single imaging) and are also imaged by a dielectric constant discontinuity at a plane on their other side. The method employs only solutions of the single imaging problem, is readily applied without a computer, and is pertinent to the usual electrolyte compact layer adjoining either an electrode or a dielectric material, which may be air. The single image solutions used in calculating more complex imaging results may be exact values obtained from a previous rather complicated approach, or for ease in calculation, may frequently be approximate but quite accurate values calculated by a simple method described herein. Using the exact approach, one can calculate, for the full range of the dielectric reflection parameter, fields and potentials along any line perpendicular to the conducting plane. Here we are primarily concerned with potentials and fields along the line through a removed adion, and the approximate single imaging solution is especially useful. Although we apply the method to regular hexagonal arrays, in the latter case it is equally applicable to arrays described by Grahame's partially smeared, cut-off model for single imaging. Some comparison with the results of this model is presented. In addition to calculating and illustrating the variation of field and potential within the compact layer and the adjoining dielectric medium, we have examined in detail the difference between the micropotential and the macropotential for many different imaging situations. The present study includes the previously treated single conductive plane imaging and also the (infinite) conductive-conductive imaging situations as special cases. It is found that special care is needed to describe the latter situation by the present model. Finally, the effect of possible conductive imaging by the electrolyte diffuse layer is considered qualitatively.

The system we shall consider in this paper is the electrolyte compact double layer (1). We shall assume it consists of a monolayer of ions (effective charge $z_v e$ and average surface charge density q_1) bounded on one side by a plane interface which we shall call the electrode-surface plane (ESP), generally (but not always) associated with an adsorbing conductor, and on the other side by an imaginary plane marking the points of closest approach of the charge centroids of ions in the electrolyte, or diffuse layer. The plane of closest approach is known as the outer Helmholtz plane (OHP), and the plane passing through the charge centroids of the adions in the monolayer is the inner Helmholtz plane (IHP). We shall define γ to be the distance between the OHP and the IHP and β to be the IHP-ESP separation; $d \equiv \beta + \gamma$ is therefore the total thickness of the compact layer.

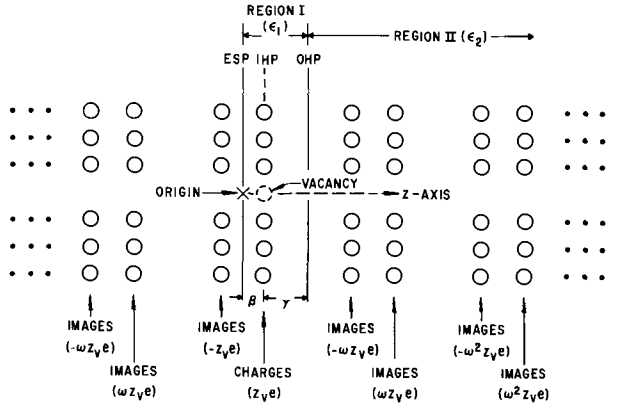

Fig. 1. Cross-sectional diagram of the double layer region showing charges, and some of their images applicable for calculating potential in region I, and the distances β, γ, and z.

The situation is illustrated in Fig. 1. The circle centers denote the positions of adion charge centroids. The diagram is not to scale since β is roughly equal to an ionic radius, and the minimum distance between spherical adions in the plane is thus approximately 2β. The present treatment of course applies for adsorption on a curved electrode surface such as a mercury drop provided, as is the case in practice, that the radius of curvature of the surface is much greater than the characteristic microscopic distances involved in the situation such as d and the effective Debye length in the diffuse layer.

The possibility immediately arises that other material besides the ions, such as adsorbed water molecules, may reside in the compact layer; to represent this possibility approximately as well as to take into account to the same degree of approximation the finite polarizability of the adions themselves, we regard these ions as point charges lying on the IHP and take the dielectric constant of the compact layer in which they reside to be ϵ_1. We have discussed the introduction of such an ϵ_1 in some detail elsewhere (1-4).

The present paper is concerned primarily with the determination of the electrical potential within the compact layer; this is because the potential's behavior is centrally related to virtually every measurable electrochemical property of the system (5). As it turns out, the potential within the system is sensitively dependent on certain structural aspects of the system; not only is it necessary to take the discreteness of the elements into account (6), but correspondingly one may only do so if reasonable models are used for the spatial distribution of the discrete adions within their plane (7). What is "reasonable" depends, it seems, on the temperature, the surface density of the monolayer, the quantities z_v, β, and γ, and other, more subtle, characteristics of the system. In the present work we shall usually assume that the ions form a perfect hexagonal array with lattice

constant r_1, although our general analysis is applicable even without this specific restriction. This is a popular model (3, 4, 7a, 8); and even though it is by no means applicable under all conditions (7), it seems to be a model which is approximately valid for many conditions of interest. As might be suspected, the hexagonal model begins to become inapplicable at low surface densities and/or high temperatures; further discussion of the applicability of this and other models appears elsewhere (7).

There is one other major consideration involved before one can determine the potential in the compact layer: What is the effect of those charges outside the compact layer on the potential? If one of the bounding planes is the surface of a conductor, the effect of those charges on and beyond this plane is straightforward; the conductor acts as an electrical imaging plane, and charges on the conductive surface in excess over those (proportional to q_1) involved in the imaging process set up an additional uniform electric field in the compact layer. If one or both of the bounding surfaces is that of a neutral dielectric insulator, then again a type of imaging is involved. A more difficult question, one which is responsible for much of the variety in the various theories of double layer structure and whose solution has significant impact on the expected properties of such systems, is the effect of the diffuse layer on the potential in the compact layer. One possible approximation is simply to neglect any variation in charge density or polarization within the diffuse layer along directions parallel to the OHP; that is, to assume that these quantities vary only in the direction perpendicular to the OHP. That this is not strictly true is a result of the discreteness-of-charge in the compact layer; that this assumption might still be a good approximation rests on the thermal motion of the ions in the diffuse layer, motion which tends to disrupt any "shadowing" within this layer of the charge density variations on the IHP through pairing of adions with counterions in the diffuse layer. If one makes this approximation, the explicit effect of the diffuse layer goes to nought, and the potential within the compact layer is determined completely by the monolayer ions and the boundary conditions at the other interface. Several more or less correct, exact or approximate, treatments of this model have appeared in print (4, 8c-f, 9, 10). The above situation, with a metal electrode, has been termed by the present authors the "single-imaging" case in a treatment (4) hereafter referred to as II.

At the extreme opposite end of things, another model of the diffuse layer's effect has been proposed and treated (3,7b, 8b-f, 11). This might be termed the "Ershler model" after its first proponent; the present authors have dealt with this model in some detail and have termed it the "infinite-imaging" case in a treatment (3) hereafter referred to as I. As the latter terminology implies to some of us, this model assumes that mobile diffuse-layer ions are capable of arranging themselves so as to make the OHP an equipotential surface. Effectively then, the OHP becomes a second conductive-imaging plane (exactly as though it were a metal surface) and the outcome of this is an infinite set of images, as in a hall of mirrors.

Unfortunately it has not been possible to establish unequivocally, either experimentally or theoretically, which of these two models more nearly represents the actual behavior of the diffuse-layer ions. An adequate treatment of the diffuse layer in the vicinity of the OHP, where the influence of the discrete compact-layer ions is greatest and the usual approximations most hazardous, may be as yet an unfinished assignment. The most promising approaches have been those of Stillinger and Kirkwood (12) and some of the Russian workers (13); however, even these treatments invoke expansions involving the ratio of electrical energy to thermal energy in the diffuse layer, and for concentrations of interest the validity of such theories is uncertain. The experimental problems are almost as sticky: The quantities actually measured are only related to local potentials after an "interpretive process" which is somewhat questionable; for example, isothermal measurements leading to adsorption coverages (q_1) only yield adsorption potentials *vs.* coverage if the form of the isotherm is known. Furthermore, it is possible that the state of ionization of the monolayer elements may change over certain ranges of surface coverages for some systems (2, 14, 15).

Returning to the refuge of our idealized situation, however, there is one diffuse-layer effect which should exist independent of the behavior of the diffuse-layer ions: In most situations there is a fairly abrupt change in the dielectric constant in going across the OHP. If we denote the dielectric constant of the bulk electrolyte, containing no excess ions, by ϵ_2, the difference $\epsilon_2 - \epsilon_1$ will induce dielectric imaging at the OHP. [We should note that the major dielectric constant change may not occur precisely at the OHP, so that the imaging plane may lie somewhat within the compact layer (16). This possibility will be neglected here.] When this imaging is accompanied by metallic imaging at the ESP, resulting in an infinite set of imperfect images, as though in a hall of imperfect mirrors, we have described this dielectric-conductive situation as the "partial-imaging" case. This case has the following features of particular interest. First, this type of imaging should be present in most systems, whatever additional effect may be present due to the diffuse-layer ions. The dielectric discontinuity, or an approximation thereto, would be expected in most cases, forming a "background effect" for any additional action by the diffuse-layer ions. In view of this effect, it is in fact difficult to construct an electrolytic system which displays "single imaging," and we now regard this case to be of interest only in reference to nonelectrolyte systems or as a least-imaging limiting case for electrolytes.

Since we plan to compare many of the theoretical single, partial, and infinite imaging discreteness-of-charge treatments mentioned above in a forthcoming review (17), we shall omit much of such cross-comparison from the present paper. It is perhaps worth mentioning that the present work contains in a certain sense all the results of the limiting cases I and II and also yields a continuous bridge between them. Although the present paper does not include a treatment of dielectric-dielectric imaging, a case treated to some extent by Levine *et al.* (7b), our present, easily applied methods require, as we shall show elsewhere, only simple modifications to apply to this situation as well.

General Analysis

In the remainder of this paper we shall be primarily concerned with the potential which results when a single vacancy is present in an otherwise perfect hexagonal array of adsorbed ions. As has been discussed in I and II, this leads to the interesting part of the micropotential; the effects of omitted self-images are independent of q and q_1 and may be subsumed into the "chemical" part of the adsorption potential. The potential ψ in our present work consists of two contributions: a discrete-charge contribution ψ_a which is always present whatever the charge on the ESP and a uniform-displacement component ψ_e which results from an additive constant D field normal to the ESP and vanishing when the ESP is grounded so its charge q becomes equal to $-q_1$ for dielectric-conductive imaging. We first determine the discrete-charge contribution ψ_a. The basic method is to replace the ESP and OHP interfaces with a system of fictitious "image charges;" the particular system depends on whether we seek the potential on the metal side or the solution side of the OHP. Thus, referring to Fig. 1, the potential between the metal and the OHP (region I) will derive from an infinite

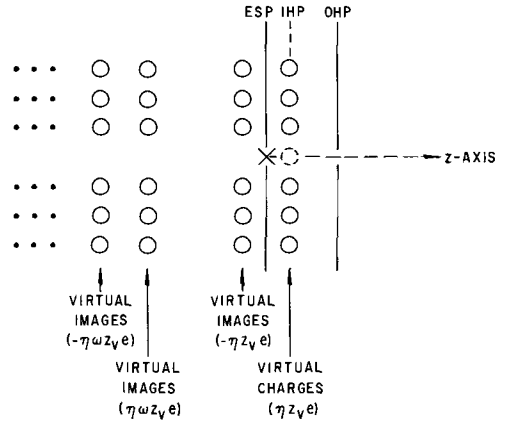

Fig. 2. Cross-sectional diagram of the double layer region showing effective charges and some of their virtual images applicable for calculating potential in region II.

set of images (for each charge on the IHP) as though the whole space were of dielectric constant ϵ_1; referring to Fig. 2, the potential on the solution side of the OHP (region II) will likewise involve an infinite set of images, and the whole space of region II is to be regarded as having dielectric constant ϵ_2. The sets of images for each charge on the IHP are chosen so that the resulting potentials satisfy the appropriate conditions on the ESP and OHP. In particular, the resulting potential should be zero on the ESP, continuous across the OHP, and result in a continuous variation in the normal component of electric displacement across the OHP. It may be verified by inspection that the set of images indicated in Fig. 1 and 2 lead to potentials satisfying these conditions.

We shall set up a coordinate system as follows: The positive z-axis is taken normal to the ESP, extending outwards towards the OHP. The x and y axes lie in the ESP, and the origin of coordinates is on the ESP and the normal line passing through the vacancy. Although the methods of the present paper may be readily extended to give potentials for positions other than $x = y = 0$, in the following we shall only be concerned with actually calculating the potential (and field) along this line.

Let us now define $\omega \equiv (\epsilon_2 - \epsilon_1)/(\epsilon_2 + \epsilon_1)$, and $\eta \equiv 1 + \omega = 2\epsilon_2/(\epsilon_1 + \epsilon_2)$. Referring to Fig. 1, we see that the array of adions and their images giving rise to ψ_a in region I form sheets of nonideal dipoles whose centers lie on the planes $z = z_n \equiv 2nd$ where n is an integer. The separation between the positive and negative charge of each nonideal dipole is 2β, and the strength of the dipole sheets drops off as $\omega^{|n|}$. Similarly, referring to Fig. 2, it may be seen that the potential ψ_a in region II derives from a set of nonideal dipoles similar to those pertaining to region I. The differences between the sets for the two regions are that the positive-n sheets are missing for the region II calculation and the dipole strengths are all multiplied by the factor η.

If we now define $\psi_{ao}(x,y,z)$ to be the potential produced at (x,y,z) by our array of adions in the single-image regime (the quantity known as ψ_a in II) we may take the foregoing into account and write

$$\psi_a(x,y,z) = \psi_{ao}(x,y,z) + \sum_{n=1}^{\infty} \omega^n \{\psi_{ao}(x,y,z + 2nd) - \psi_{ao}(x,y,2nd - z)\} \quad [1]$$

in region I, and in region II

$$\psi_a(x,y,z) = (\eta\epsilon_1/\epsilon_2) \sum_{n=0}^{\infty} \omega^n \psi_{ao}(x,y,z + 2nd) \quad [2]$$

where $\eta\epsilon_1/\epsilon_2 = 1 - \omega$. Thus, we have expressed the partial-image potential in terms of a single series (instead of the double or triple series used by others) involving the accurately known (4) single-image potentials. Levine *et al.* (7b, 11) have employed a similar approach (for the infinite imaging case), in which they used Grahame's cut-off model (8c) for the single image potential $\psi_{ao}(0,0,z)$. Similarly, defining $\mathcal{E}_a$ as the electric field associated with ψ_a in the present regime and $\mathcal{E}_{ao}$ as the field associated with the single-imaging potential ψ_{ao}, one obtains in regions I and II, respectively

$$\mathcal{E}_a(x,y,z) = \mathcal{E}_{ao}(x,y,z) + \sum_{n=1}^{\infty} \omega^n \{\mathcal{E}_{ao}(x,y,z + 2nd) + \mathcal{E}_{ao}(x,y,2nd - z)\} \quad [3]$$

$$\mathcal{E}_a(x,y,z) = (\eta\epsilon_1/\epsilon_2) \sum_{n=0}^{\infty} \omega^n \mathcal{E}_{ao}(x,y,z + 2nd) \quad [4]$$

These single-summation expressions for ψ_a and $\mathcal{E}_a$ converge quite rapidly; even for $\omega = 1$, the expression for potential in region I converges well. As ω approaches unity, the value of ψ_a in region II is bounded

$$\psi_a \leq (\eta\epsilon_1/\epsilon_2) \sum_{n=0}^{\infty} \omega^n \psi_\infty = \eta\epsilon_1\psi_\infty/\epsilon_2(1 - \omega) = \psi_\infty$$

where the upper bound, ψ_∞, is defined as in II; thus $\psi_\infty \equiv 4\pi\beta q_1/\epsilon_1$. In carrying out the sums for $\psi_a(0,0,z) \equiv \psi_a(z)$ it was usually found to be more convenient to use an approximate but highly accurate analytic expression for $\psi_{ao}(0,0,z) \equiv \psi_{ao}(z)$ than to use the exact results obtainable from II. The approximation used and its accuracy is discussed further in ref. (18) and in the Appendix. Calculation of $\psi_{ao}(z)$ by this approximation is far simpler than by the lengthy expressions given in II, yet yields adequate accuracy. The accuracy of the results in the present paper have, in fact, been checked by calculating many of them with both exact and approximate values for $\psi_{ao}(z)$.

To complete the potential, we must add the uniform D field part, ψ_e. The boundary conditions at the ESP require that, if the total surface charge density on the ESP is q, then the uniform field produced is simply $4\pi(q + q_1)$. Taking the zero of ψ_e to lie on the ESP, we obtain $\psi_e = -(4\pi/\epsilon_1)(q + q_1)z$ for region I and $\psi_e = -4\pi(q + q_1)[(d/\epsilon_1) + \{(z - d)/\epsilon_2\}]$ for region II. We note, incidentally, that if ψ_{aic} and $\mathcal{E}_{aic}$ (see II) are substituted for ψ_{ao} and $\mathcal{E}_{ao}$ in the foregoing equations, the resulting potentials and fields are the ones pertaining to a complete adion array.

Before presenting detailed results of our calculation of potentials, fields, and other quantities of interest, we point out an interesting feature pertaining to the limit $\omega \to 1$. Intuitively one might expect ψ_a (in region I) to approach the infinite-image (conductive-conductive) ψ_a as ω approaches unity. As it turns out, however, this preconceived notion is entirely wrong: The limiting behavior of the present ψ_a is distinctly different from the ψ_a determined in I, which we shall here denote as ψ_{acc}. Thus one cannot simply take $\omega = 1$ herein and directly obtain ψ_{acc}. What does occur for given q and q_1 is that the limiting value of the present $\psi = \psi_a + \psi_e$ is identical to the value of $\psi_{acc} + \psi_e$ obtained by redefining ψ_e (in I) so as to place its zero on the ESP (as has been done with our present partial-imaging ψ_e). In other words, the actual limiting behavior of the present ψ_a is given by $\lim_{\omega\to 1} \psi_a = \psi_{acc} + (4\pi q_1 z\beta/\epsilon_1 d)$. In particular, at the OHP where ψ_{acc} is zero, $\lim_{\omega\to 1} \psi_a = \psi_\infty$. This behavior represents a real physical effect and not just a trivial definition of the zero of potential. The physical origin of the effect lies in the fundamental difference between

a dielectric, no matter how "strong," and a conductor. Only the conductor allows charge to build up on its surface so as to render the field inside exactly zero.

Normalized Equations

For presentation and comparison purposes, it is convenient to deal with normalized equations whenever practical. We shall normalize potentials with the ψ_∞ introduced above and shall denote such quantities as ψ_{ao}/ψ_∞ and ψ_a/ψ_∞ as $\psi_{ao}{}^N$ and $\psi_a{}^N$, respectively. Note that since ϵ_1 occurs in ψ_∞, a potential such as ψ in region II, where $\epsilon = \epsilon_2$, is still normalized by a quantity involving ϵ_1, not ϵ_2, in this convention. It will prove convenient to normalize fields in an equivalent way, using $\mathcal{E}_\infty \equiv -4\pi q_1/\epsilon_1$. Finally, we will normalize electric displacements with $\mathcal{D}_\infty \equiv -4\pi q_1$.

From now on let us take $x = y = 0$ and define $Z \equiv z/\beta$ and $R_1 \equiv r_1/\beta$. Further, let $\gamma/\beta \equiv \Gamma$, $Z_o \equiv 1 + \Gamma \equiv d/\beta$, and $\rho \equiv 2Z_o$. Then the IHP occurs at $Z = 1$ and the OHP at $Z = Z_o$. For some purposes, as we shall see, it is useful also to use the normalized variable $\xi \equiv Z/R_1 \equiv z/r_1$.

We may now omit reference to x and y and write in place of [1] and [2]

$$\psi_a{}^N \equiv \psi_a{}^N(Z;R_1) = \psi_{ao}{}^N(Z;R_1) + \sum_{n=1}^{\infty} \omega^n\{\psi_{ao}{}^N(n\rho + Z;R_1) - \psi_{ao}{}^N(n\rho - Z;R_1)\} \quad [5]$$

(region I, $0 \leq Z \leq Z_o$)

$$\psi_a{}^N \equiv (1-\omega) \sum_{n=0}^{\infty} \omega^n \psi_{ao}{}^N(n\rho + Z;R_1) \quad [6]$$

(region II, $Z \geq Z_o$).

Equations following from [3] and [4] may be similarly written; instead, since it proves more convenient to plot displacements than fields, we give equations for $\mathcal{D}_a{}^N \equiv \mathcal{D}_a/\mathcal{D}_\infty$, equal to $\epsilon_1\mathcal{E}_a/\epsilon_1\mathcal{E}_\infty$ in region I and to $\epsilon_2\mathcal{E}_a/\epsilon_1\mathcal{E}_\infty$ in region II. To obtain $\mathcal{E}_a{}^N$ in region II, we need only multiply $\mathcal{D}_a{}^N$ in this region by $(\epsilon_1/\epsilon_2) = (1-\omega)/(1+\omega)$. The results for $\mathcal{D}_a{}^N$ are

$$\mathcal{D}_a{}^N = \mathcal{E}_{ao}{}^N(Z;R_1) + \sum_{n=1}^{\infty} \omega^n\{\mathcal{E}_{ao}{}^N(n\rho + Z;R_1) + \mathcal{E}_{ao}{}^N(n\rho - Z;R_1)\} \quad [7]$$

(region I)

$$\mathcal{D}_a{}^N = (1+\omega) \sum_{n=0}^{\infty} \omega^n \mathcal{E}_{ao}{}^N(n\rho + Z;R_1) \quad [8]$$

(region II)

For use in comparing with experimental results, it is frequently useful to have available complete potentials and fields which include the uniform D field contributions. We may write

$$\psi^N = \psi_a{}^N + \psi_e{}^N \quad [9]$$

$$\mathcal{E}^N = \mathcal{E}_a{}^N + \mathcal{E}_e{}^N \quad [10]$$

where $\epsilon_a{}^N = \mathcal{D}_a{}^N$ and $\{(1-\omega)/(1+\omega)\}\mathcal{D}_a{}^N$ in regions I and II, respectively, and

$$\psi_e{}^N = -\{1 + (q/q_1)\}Z \quad [11]$$

$$\mathcal{E}_e{}^N = -\{1 + (q/q_1)\} \quad [12]$$

$(0 \leq Z \leq Z_o)$

$$\psi_e{}^N = -\{1 + (q/q_1)\}[Z_o + \{(1-\omega)/(1+\omega)\}(Z - Z_o)] \quad [13]$$

$$\mathcal{E}_e{}^N = -\{1 + (q/q_1)\}[(1-\omega)/(1+\omega)] \quad [14]$$

$(Z \geq Z_o)$

There is, of course, no average D field contribution when $q = -q_1$ and the ESP is grounded.

The micropotential ψ_1 is related to the energy required to move an ion at the OHP to its adsorbed position at the IHP. This definition does not include the small p. d. V_2 in the diffuse layer between the OHP and the bulk of the solution. It is actually $\psi_1 + V_2$ which appears in an adsorption isotherm, but we shall neglect V_2 hereafter since it depends on q and q_1 and can be added in whenever pertinent. Remark, however, that unless the OHP is taken as an equipotential surface, which implies conductive imaging there, the usual one dimensional diffuse-layer theory is inconsistent with the requirement that the potential be continuous across the OHP. On the other hand, even when the OHP is not an equipotential, the value of V_2, now a function of x and y, will probably be quite close to that predicted by the usual one-dimensional theory.

From the above discussion, we have $\psi_1 \equiv \psi(\beta) - \psi(d)$. We wish to compare this p. d. to the average p. d., V_1, across the inner region. The average potential itself, $V(z)$, may be written in normalized form as (3)

$$V^N(Z) = -[Z(q/q_1) + (Z-1)] \quad [15]$$

for $Z \geq 1$. It is taken zero at $Z = 0$. $V_1{}^N$ is then $-V^N(Z_o)$. It will be convenient to introduce the normalized quantity $\lambda \equiv \gamma/d = \Gamma/(1+\Gamma) = \Gamma Z_o{}^{-1}$. For $\psi_1{}^N$ we readily obtain

$$\psi_1{}^N = \psi_a{}^N(1) - \psi_a{}^N(Z_o) + \Gamma\{1 + (q/q_1)\} \quad [16]$$

As in II, let us form the ratio (applicable for $Z_o \geq 1$)

$$\Lambda \equiv \psi_1/V_1 = -\psi_1{}^N/V^N(Z_o) \equiv \lambda(1+\Delta) = \frac{\Gamma\{1 + (q/q_1)\} + \Delta\psi_a{}^N}{\Gamma + (1+\Gamma)(q/q_1)} \quad [17]$$

where Δ is defined in [17] and $\Delta\psi_a{}^N \equiv \psi_a{}^N(1) - \psi_a{}^N(Z_o)$. The quantity Δ, which measures the deviation from linear proportionality of the micropotential to V_1, follows from [17] and may be written

$$\Delta = \frac{1 + \lambda^{-1}\Delta\psi_a{}^N}{\Gamma + (1+\Gamma)(q/q_1)} \quad [18]$$

When $q = 0$, we define $\Delta \equiv \Delta_o$, where

$$\Delta_o = \Gamma^{-1}[1 + \lambda^{-1}\Delta\psi_a{}^N] \quad [19]$$

Discussion of Results

Conducting ESP

In this section, we shall consider the usual electrolyte situation shown in Fig. 1 of a conducting electrode, a compact inner layer, and a diffuse layer extending beyond the OHP. We shall, for the time being, ignore effects arising from moveable ions in the diffuse layer and shall only be concerned with the effect of the $\epsilon_1 - \epsilon_2$ dielectric discontinuity at the OHP.

Suggested values of ϵ_1 in the compact layer have ranged from 6 to about 15 [see ref (1)]. The value of ϵ_2 for an aqueous electrolyte can be no greater than 81 at room temperature and will likely be appreciably reduced in the diffuse layer because of dielectric saturation arising from the average field there and the effects of closely neighboring ions (1, 19, 20). A reasonable approximate lower value for ϵ_2 might therefore be 50. Those combinations of the above values of ϵ_1 and ϵ_2 which give the smallest and largest ω's lead to $\omega_{min} \sim 0.54$ and $\omega_{max} \sim 0.86$. The smaller is ω, the less is dielectric imaging alone likely to approximate well to the actual electrolyte situation including diffuse layer conductive imaging. In the succeeding figures, however, we have shown results for a variety of values of ω between +1 and −1, for completeness, for comparison with the results of I and II, and because some of the negative values are pertinent to the situation discussed in the next section.

Figures 3 and 4 show the dependence of normalized potential and displacement on normalized distance from the ESP, ξ, for a number of ω values for the choice $R_1 = 5$ and several values of Γ. These values of Γ probably cover the experimentally likely possibilities for such electrolytes as KI. We have used

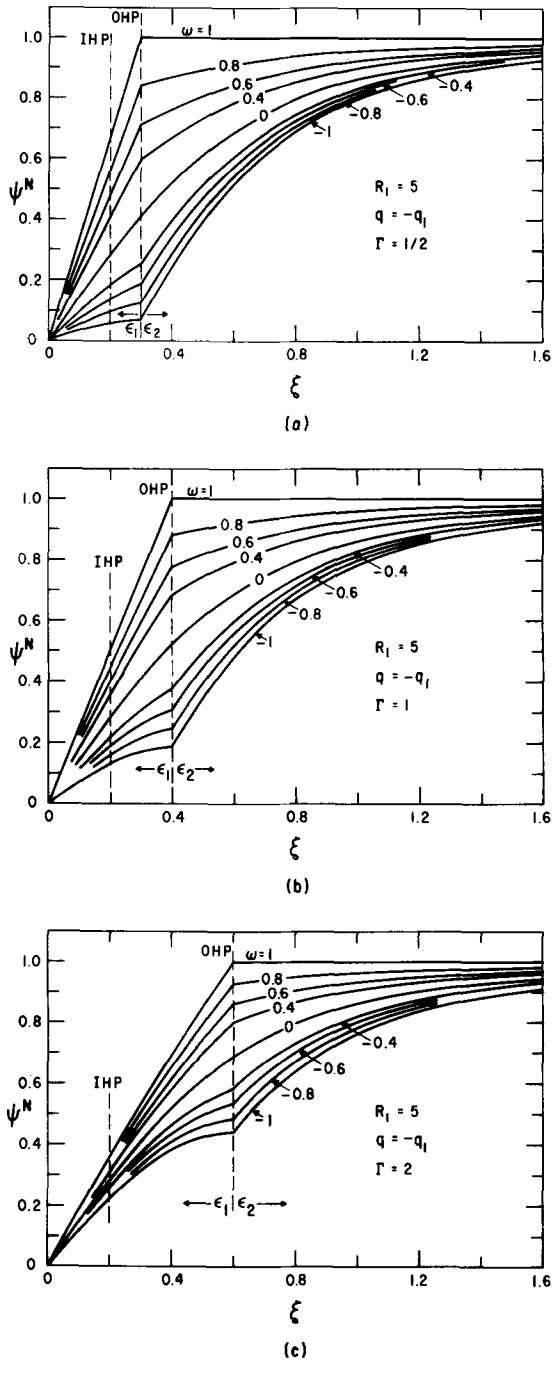

Fig. 3. Normalized discrete potential $\psi^N = \psi_a{}^N$ vs. normalized distance from ESP, $\xi \equiv Z/R_1$, for $R_1 = 5$ and $\Gamma \equiv \gamma/\beta$ equal to ½, 1, and 2. The parameter is $\omega \equiv (\epsilon_2 - \epsilon_1)/(\epsilon_2 + \epsilon_1)$.

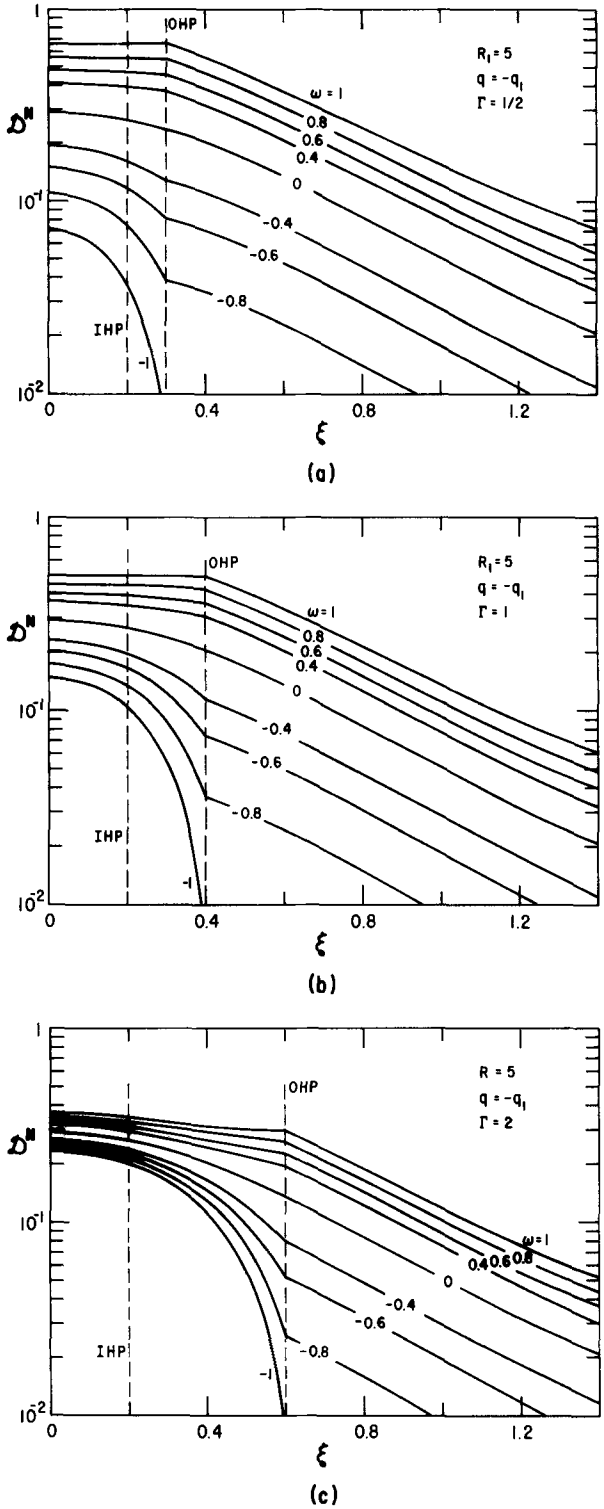

Fig. 4. Normalized discrete displacement $\mathcal{E}^N = \mathcal{E}_a{}^N$ vs. ξ for $R_1 = 5$, $\Gamma = ½, 1, 2$, and a variety of ω values.

the parameter ξ here instead of Z itself because we have found elsewhere (4, 18) that for single imaging ($\omega = 0$) $\psi_a{}^N = \psi_{ao}{}^N$ is a function primarily of ξ and depends only slightly on R_1 separately. The present curves may thus be compared directly with others plotted *vs.* ξ. Unfortunately, when $\omega \neq 0$, such virtual independence of R_1 is less marked, as we shall demonstrate elsewhere.

For greatest clarity and distinction between curves, we have taken $q = -q_1$ in Fig. 3 and 4. This choice has the effect of making $\psi^N = \psi_a{}^N$ and $\mathcal{D}^N = \mathcal{D}_a{}^N$. Although q seldom equals $-q_1$ in electrolyte situations of the kind discussed in the present section, ψ^N and $\mathcal{D}^N$ for $q \neq -q_1$ may be readily derived from the curves given through the use of Eq. [9] and [10], [11], and [12], and the known relations between $\mathcal{E}^N$ and $\mathcal{D}^N$. We have elected to plot $\mathcal{D}^N$ in Fig. 4 rather than $\mathcal{E}^N$ to avoid the discontinuities which would otherwise appear at the OHP. It is interesting to note that discontinuities still appear in the first derivative of $\mathcal{D}^N$ except when $\omega = 0$. Because of the infinite discontinuities which occur in some quantities at $\omega = 1$ and -1, our present results do not serve to yield $\mathcal{E}_a{}^N$ for $Z_o \geq 1$ when $\omega = -1$, but they do show that $\mathcal{E}_a{}^N = 0$ for $Z_o \geq 1$ when $\omega = 1$. The missing $\mathcal{E}_a{}^N$ portion for $\omega = -1$ can be readily calculated directly from Eq. [8], however, by first multiplying it by $(1 - \omega)/(1 + \omega)$ and then letting $\omega = -1$.

Although the present method of calculating ψ^N and $\mathcal{D}^N$ for any pertinent values of ω, Z, and R_1 is suffi-

ciently simple that no computer need be used to achieve 1% or better accuracy, we have required for this paper so many values of these and other related quantities that we have, in fact, used a computer for their calculation. We have made a careful comparison between the results of the approximate formulas for $\psi_{ao}{}^N$ and $\mathcal{E}_{ao}{}^N$ given in the Appendix and very accurate values of these quantities calculated as in II. This comparison shows, for example, that $R_1 = 5$ the use of the (3/3) approximant for $p(\xi)$ given as (a) in Table I of the Appendix yields values of $\psi_a{}^N$ for any reasonable Z, Γ, and ω choices which generally differ from the accurate ones by only a small amount in the fifth significant figure. The results for $\psi_a{}^N$ are thus at least as accurate as those for $p(\xi)$ itself and are usually more accurate. This approximant, or an even simpler one given in ref. (18), can be used in calculating results such as those shown in Fig. 3 and 4. An approximant such as the (2/3) one given for $F(\xi)$ in the Appendix is also required in calculating $\mathcal{D}_a{}^N$ by the modified cut-off method. When an approximant for $p(\xi)$ derived for $R_1 = 5$ is used to calculate values for $\psi_{ao}{}^N$ or $\mathcal{E}_{ao}{}^N$ when $R_1 \neq 5$, almost as high accuracy as with $R_1 = 5$ can be expected when $R_1 > 5$ since, as stated, $\psi_{ao}{}^N$ depends very little on R_1 alone but primarily on ξ. In particular, $R_1 = 5$ values are very close to $R_1 = \infty$ values of $\psi_a{}^N$ for a given ξ (18). When R_1 is < 5, there is somewhat more dependence on R_1, although the difference is still small even for $R_1 = 2$, the smallest value of R_1 that usually need be considered (18). For example, using the $R_1 = 5$ (3/3) $p(\xi)$ approximant to calculate values of $\psi_a{}^N$ for $R_1 = 4$ leads to deviations between accurate and approximate values of $\psi_a{}^N$ which usually occur in the fourth significant figure and rarely in the third. As discussed and listed in ref. (18), even simpler approximants than those given here in the Appendix may ordinarily be used to obtain adequate accuracy in calculated fields and potentials.

In order to achieve high accuracy in the present computer results, we summed such series as those of Eq. [5] to [8] to fairly high order and/or used the epsilon algorithm (21) to extrapolate to accurate final values when necessary. The series are all very rapidly convergent when $\omega << 1$. They are generally most slowly convergent when $\omega = 1$ so we examined this limit. When $\omega = 1$, the series of Eq. [5] is only conditionally convergent. Even so, it generally converges quite rapidly. Thus for $R_1 = 5$, $\Gamma = 1$, and $Z = 1$ we find that $\psi_a{}^N$ is within 1.7% of its final value when only three (accurate) terms of the series are used. With five terms the percentage is 0.71, and if the epsilon algorithm is used on these five terms, the percentage drops to 0.28.

Since [5] is only conditionally convergent when $\omega = 1$, rearrangement of its terms should change its value. We have found that this circumstance can be put to good use in calculating $\Delta\psi_a{}^N \equiv \psi_a{}^N(1) - \psi_a{}^N(Z_o)$ in the infinite imaging case where $\omega = 1$ and convergence is slowest. Ordinarily this quantity would have to be calculated by two separate evaluations of $\psi_a{}^N$ using [5]. After a slight rearrangement of the terms of [5], we find the surprising result, however, that

$$\Delta\psi_a{}^N = \psi_{ao}{}^N(1; R_1) - \psi_{ao}{}^N(\rho - 1; R_1) + \sum_{n=1}^{\infty} \{\psi_{ao}{}^N(n\rho + 1; R_1) - \psi_{ao}{}^N[(n+1)\rho - 1; R_1]\} \quad [20]$$

($\omega = 1$ only)

a series whose convergence is still generally good. The above is a lucky result; even it is unnecessary, however, if we note that when $\omega = 1$, $\psi_o{}^N(Z_o) \equiv 1$. Thus, when $\omega = 1$, $\Delta\psi_a{}^N$ can still be calculated using [5] only once to first obtain $\psi_a{}^N(1)$.

In II, we noted the extraordinary constancy of $\mathcal{E}(d)$ for $\beta = 3$Å, $\omega = 0$, and $\Gamma = 2/3$ over a wide range of q. There, Grahame's (22) values for q_1 as a function of q, determined from measurements on a 1N KI electrolyte at 25°C, were used in calculating $\mathcal{E}$. The above result suggested to us that it would be worthwhile to examine the field at the IHP, $\mathcal{E}(\beta)$, for several Γ and ω values. Results are shown in Fig. 5. We have chosen to look at the field at $Z = 1$ since its value at the site of a removed ion is pertinent to ionic polarization, dielectric saturation, and ionic compressibility

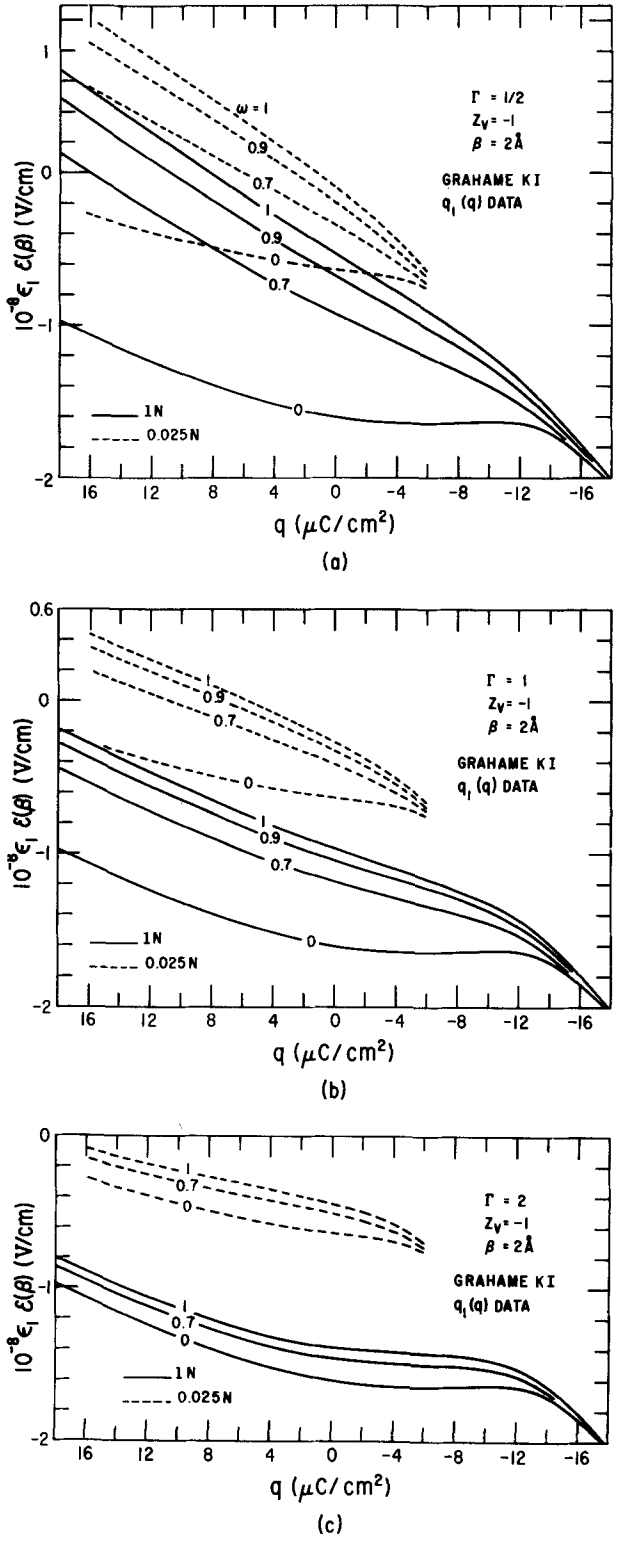

Fig. 5. Full electric field at the IHP, $\mathcal{E}(\beta)$, vs. average electrode charge density, q, using Grahame's KI $q_1(q)$ data for 1N and 0.025N concentrations; $\Gamma = \frac{1}{2}, 1, 2$; $\beta = 2$Å; and several values of ω.

effects (1). We show results in Fig. 5 using Grahame's $q_1(q)$ data for both $1N$ and $0.025N$ concentrations for the choice $\beta = 2$Å, which we now believe is a more likely value than the 3Å used in II. The results in Fig. 5 were calculated using the (b) and (c) approximants of Table I in the Appendix. The (b) approximant for $p(\xi)$ is particularly appropriate here since Z is fixed at one for these calculations and R_1 varies. The resulting approximant is therefore somewhat superior to that in (a) where R_1 is fixed at 5 and Z varies to produce changes in ξ. Since $F(\xi)$ is a small correction term, its $R_1 = 5$ approximant is quite adequate in the present case.

It will be seen from Fig. 5 that $\mathcal{G}(\beta)$ remains quite constant when $\omega = 0$ and remains so also even when $\omega \sim 1$ for $\Gamma = 2$. For $\Gamma = 1$, $\mathcal{G}(\beta)$ for the $0.025N$ concentration goes through zero in the experimental range of q when ω is about 0.4 or greater. Finally, when $\Gamma = \frac{1}{2}$, all of the curves shown change sign in the experimental range except those for $\omega = 0$. If we assume that the Γ appropriate to the actual experimental situation is 1 or less and that $0.7 < \omega \leq 1$, then it is evident that $\mathcal{G}(\beta)$ will vary sufficiently over the q range, for either $1N$ or $0.025N$ concentrations, that it will not be a good assumption to take ϵ_1 completely saturated and equal to 6 over the entire q range. For $\Gamma = 1$, $\omega = 0.9$, and this constant value of ϵ_1, the appropriate curve shows that $\mathcal{G}(\beta)$ varies from about 3.5×10^7 v/cm to 4×10^6 v/cm as q goes from -18 to $+18$ μC/cm^2. With ϵ_1 becoming less saturated and thus larger as $\mathcal{G}(\beta)$ decreases (20), $\mathcal{G}(\beta)$ at $q = 18$ μC/cm^2 might be as small as 2×10^6 v/cm. We remark again, however, that the introduction of an ϵ_1 at all in the present situation is a considerable approximation, making any conclusions about its variation uncertain.

Figure 6 shows the nonlinearity parameter Δ_0 for the usual values of Γ and many positive values of ω. These results form a bridge between the $\omega = 1$ results of I and the $\omega = 0$ results of II. Here and elsewhere in this paper all $\omega = 1$ and $\omega = 0$ results agree excellently with those previously given in I and II. We can now follow in detail the continuous change from one limiting case to the other, however. It should be noted that in the present paper the ω values 0 and 1 represent only limiting situations and are not examined in detail; more results for these specific values thus appear in I and II than are given here.

It will be noted from Fig. 6 that, except for ω values equal to or very near unity, Δ_0 is by no means negligible over most of the range of R_1 shown. At the top of Fig. 6a is shown a q_1 scale following from the R_1 scale when $\beta = 2$Å, probably a reasonable value for the KI system. The $R_1 = 2$ value, which is the smallest possible R_1 for close-packed spherical adions, corresponds to a q_1 of 115.6 μC/cm^2 for this choice of β. On the other hand, the largest value derived from Grahame's (22) experiments is about 43 μC/cm^2 (corresponding to $R_1 \simeq 3.3$ for $\beta = 2$Å), indicating a maximum adion surface coverage of about 37% for these experiments.

The dashed and dotted lines of Fig. 6b are calculated for the usual cut-off model of the inner region (8c, 18), not for a hexagonal array. They use values of $\psi_{a_0}{}^N$ obtained from Eq. [A-1] with constant p values, and [A-1] is applied for all Z and R_1 combinations since [A-4] is only applicable to the hexagonal array. The dotted-curve value $p = (\sqrt{3}/2\pi)^{1/2} \cong 0.5250376$ is Grahame's original figure. It is the value appropriate for a smeared array of charges and is thus also the value for the fixed hexagonal array when $\xi \to \infty$. It is the smallest value of p possible for such an array. The dashed-curve value $p = 4\pi/\sigma\sqrt{3} \cong 0.65752059$, where $\sigma \cong 11.034175$, is the value appropriate for an array of ideal dipoles when $\xi \to 0$ [see ref. (18)]. This p is thus the largest value possible with a hexagonal array. It is interesting that over much of the R_1 scale of interest, the accurate

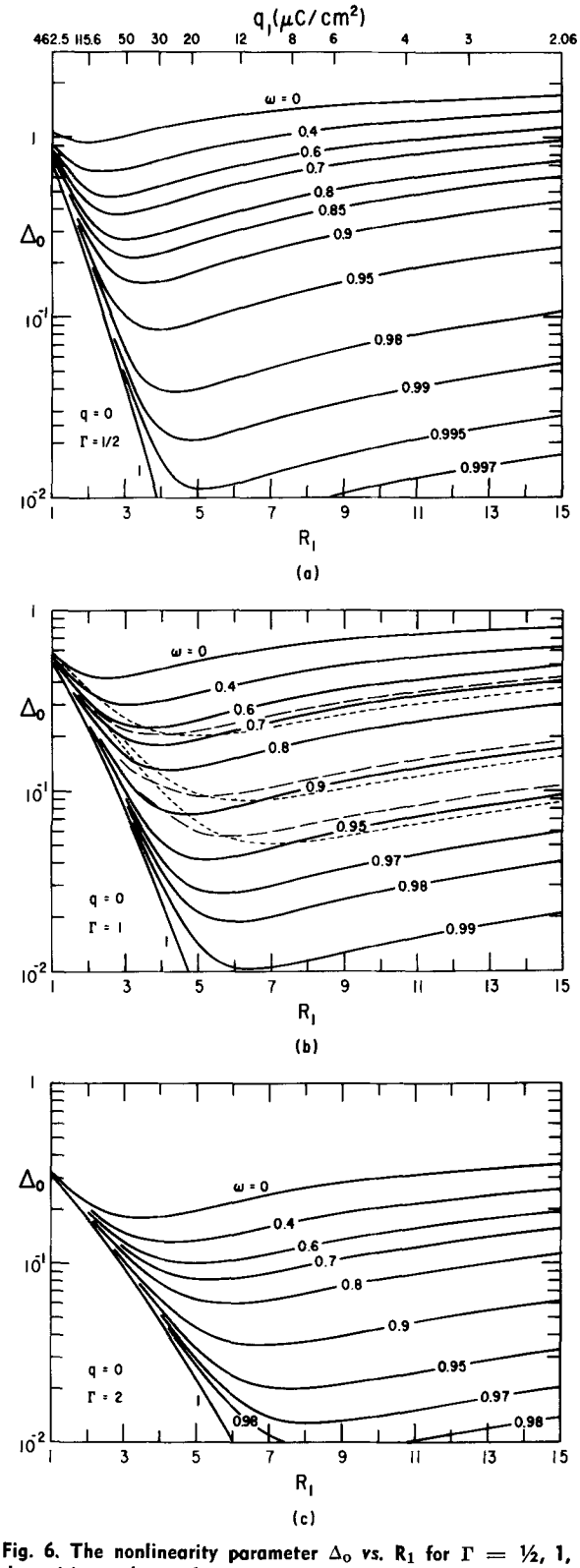

Fig. 6. The nonlinearity parameter Δ_0 vs. R_1 for $\Gamma = \frac{1}{2}$, 1, 2 and positive values of ω. Dotted lines were calculated using Grahame's cut-off model involving the constant value of p, $p_\infty \cong 0.5250376$. Dashed lines were calculated similarly with p again constant and equal to $p_0 \cong 0.65752059$. The nonlinear q_1 scale at the top of (a) is applicable for the choice $\beta = 2$Å only.

hexagonal-array results lie between those obtained with the above two limiting values of p. On the other hand, in the region of appreciable IHP charge density, say $2 \leq R_1 \lesssim 6$, where the fixed hexagonal array model is most appropriate at room temperature, we note regions of very appreciable deviation of the

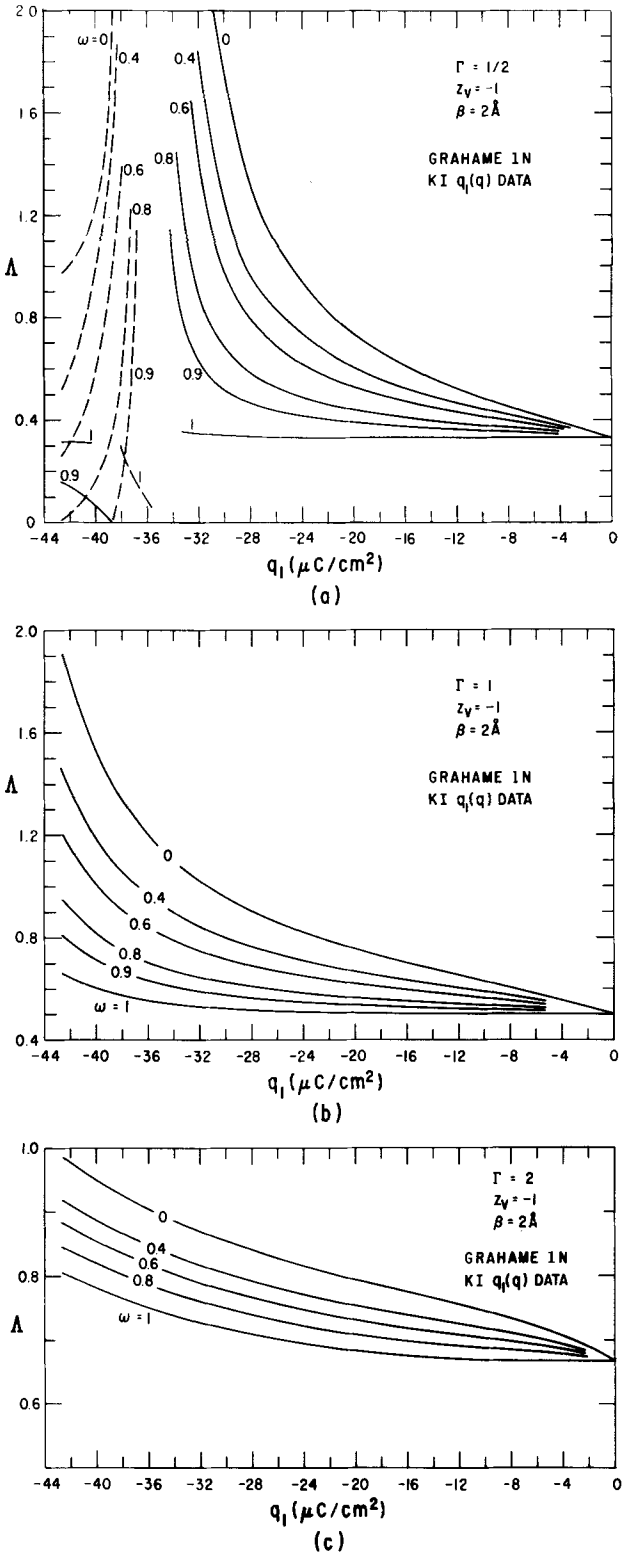

Fig. 7. Quantity $\Lambda \equiv \psi_1/V_1$ *vs.* Grahame's derived $q_1(q)$ for $\beta = 2$Å, $\Gamma = \frac{1}{2}$, 1, 2, and several positive values of ω. Dashed lines denote negative values.

fixed-p results from the hexagonal array results. In such a region, the hexagonal model is definitely preferable to a constant-p cut-off model. The exact charge density where the latter might be more preferable is difficult to determine [see (7, 17)], however.

Figure 7 shows the ratio of the micropotential to the macropotential, $\Lambda \equiv \psi_1/V_1$, *vs.* q_1 for $\Gamma = \frac{1}{2}$, 1, and 2, and several values of ω. Here again Grahame's (22) $q_1(q)$ values for 1N KI were employed in calculating Λ from Eq. [17]. For a given q, the corresponding q_1 was used to calculate R_1, using $\beta = 2$Å, then $\Delta\psi_a{}^N$ was calculated and was finally used in Eq. [17]. This calculation of $\Delta\psi_a{}^N$, and also most of those for Δ_o in Fig. 6, used the $R_1 = 5$ (3/3) approximant for $p(\xi)$ discussed in the Appendix together with Eq. [A-1] and [A-4]. We do not show Λ curves for the 0.025N concentration, but calculations for this case showed them to be quite similar to the 1N curves. We have elected to show Λ curves here instead of the corresponding Δ curves given in I and II because Δ turns out to be very appreciable for most of the curves (nonlinear distance dependence of ψ^N) and the ratio Λ is itself then of most direct interest.

Equation [17] shows that when $\Delta = 0$, $\Lambda = \lambda$. This is, of course, the case at the right of the Λ curves in Fig. 7 where $q_1 \approx 0$. Dashed lines are used in Fig. 7a to indicate negative values of Λ. These arise because V_1 may change sign, leading to a pole in Λ near $q_1 = -35$ μC/cm². Although both ψ_1 and V_1 are continuous, their ratio need not be. The peculiar behavior of the $\omega = 1$ curve in Fig. 7a is evidently produced by a zero in ψ_1 near but not at that of V_1.

The quantity of most interest for adsorption isotherms is ψ_1 itself. It can, of course, be readily obtained from the Λ values given here by multiplying by calculated values of V_1. In this paper, we shall not be directly concerned with adsorption isotherms and with the ψ_1 which enters them, reserving such discussion for another place (17). It is worthwhile to point out, however, that when Δ is neglected (often a good approximation for infinite imaging) and ψ_1 is then taken as λV_1, Grahame (22) and Grahame and Parsons (23) have found that the ψ_1 derived by using experimental results in a simple adsorption isotherm leads to a variable λ. Although this specific approach can probably be improved, it does lead to λ variation with q or q_1 of much the same form as that of Λ in Fig. 7b and c. In particular, λ is found to increase continuously for KI as q increases from −18 μC/cm² to 18 μC/cm². Reasonable values of Γ and ω can even be selected that lead to Λ variation quantitatively very similar to that found for λ, but we do not wish to stress this agreement even though the Grahame-Parsons $\lambda(=\psi_1/V_1)$ determined as above is formally fully equivalent to our Λ and they both equal the constant λ (a ratio of distances) of the present paper when $q_1 = 0$.

Dielectric ESP

While in the foregoing work metallic imaging is assumed to occur at a conducting electrode and dielectric imaging at the OHP, our mathematical model also pertains approximately to an entirely different system: At an electrolyte-dielectric interface, we may also have a surface phase in which ions are hexagonally arrayed on an "IHP." Separating this phase from the bulk electrolyte would be an "OHP;" separating it from the bulk dielectric would be an "ESP." While external charged electrodes might be present near the surface layer, producing a uniform field ψ_e, these electrodes need only be a microscopically large distance removed from the layer (a probable situation here) for their effect upon ψ_a to be negligible.

Our model in the present situation is that the OHP approximates to a metallic imaging plane and the ESP forms a dielectric imaging plane. Clearly, the OHP will approximate better and better to a conductive imaging plane the higher the concentration of ions in the diffuse layer. To maintain our previous equations with minimum change requires that we now define β as the IHP-OHP separation, γ as the IHP-ESP separation, q as the total surface charge density on the OHP, that we measure z from the OHP (thus $z = \beta + \gamma$ at the ESP), and that we define ϵ_1 and ϵ_2 to be the effective dielectric constants of the surface phase and bulk dielectric, respectively (see Fig. 8).

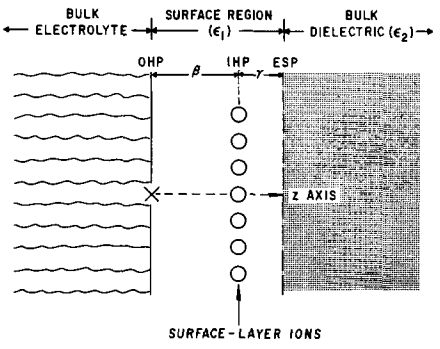

Fig. 8. Cross-sectional diagram showing appropriate situation and distances when the OHP is taken as a conducting plane.

There still remain certain differences between our system and the original compact layer for which our equations were derived. Most important of these is that the adion density on the IHP will now depend on the potential difference between the IHP and the conductive plane; thus, $\psi_1 \equiv \psi(\beta) - \psi(0) \equiv \psi(\beta)$, where "$\beta$" here is probably numerically equal to the "γ" of our original system. The reason for the present involvement of the conductive plane potential, which is of course zero, is that in this system the ions are presumed to originate (again neglecting V_2) from the conductive (outer Helmholtz) plane whereas earlier they originated from the dielectric imaging plane, and there the finite potential at the dielectric discontinuity had to be incorporated in the micropotential. Finally, apart from the numerical differences expected between new and old β's, γ's, q's, and so forth, we may now obtain with greater likelihood negative values for the parameter ω. Levine *et al.* (7b, 11) have discussed, to some extent, a situation where ϵ_2 is taken as 15, pertaining to silver chloride, and ϵ_1 taken as 10 or 15. In these cases, $\omega = 0.2$ and 0, respectively. On the other hand, the important air-electrolyte interface is a more common situation. For $\epsilon_1 = 10$ and 5, ω is about -0.82 and -0.67, respectively, for such a boundary.

We have already plotted in Fig. 3 and 4 normalized discrete potentials and displacements for $q = -q_1$ and negative values of ω. To make use of these curves in the present situation, however, we must interpret the plane marked OHP in those figures as being the ESP, and the plane $\xi = 0$, in the earlier case the ESP, as the OHP. The IHP is the same in both situations. The different interpretations now given to β and γ result in probable changes in the numerical values appropriate to these quantities; correspondingly, the numerical value of ψ_∞ is likely to be different. Note that if the numerical values of γ and β are simply interchanged in going from a conductive ESP to a dielectric ESP situation, then Γ in the dielectric situation has a magnitude which is just the reciprocal of that in the usual situation. Although we have only shown curves of potential and field applying when $q = -q_1$, the extension to the more general case is straightforward. The expression for ψ_e in the present situation is identical to that given for the case of a conducting electrode.

Finally, we wish to define and calculate a quantity Λ analogous to that defined for our original system. In the present situation, we shall again define

$$\Lambda \equiv \psi_1/V_1 = \psi(\beta)/V_1 = \psi^N(1)/V^N(Z_o) = \frac{[1 + (q/q_1)] - \psi_a{}^N(1)}{\Gamma + (1 + \Gamma)(q/q_1)} \quad [21]$$

This equation shows that when $q_1 \neq -q$ $\Lambda \to (1 + \Gamma)^{-1} = Z_o{}^{-1} = \Gamma^{-1}\lambda$ as $R_1 \to \infty$ for fixed q. Specializing now to the case most interesting and pertinent for the present situation, $q = -q_1$, we find $\Lambda = \psi_a{}^N(1)$, just the discrete-charge contribution to the normalized potential at the IHP. The choice $q = -q_1$ means that the charge on the IHP is entirely balanced by that in the diffuse layer, here taken to be on the (conducting) OHP. One would only expect $q \neq -q_1$ in the present situation when the inner layer was exposed to an externally applied field.

We have plotted curves for Λ *vs.* R_1 in Fig. 9. For completeness and because some authors have taken

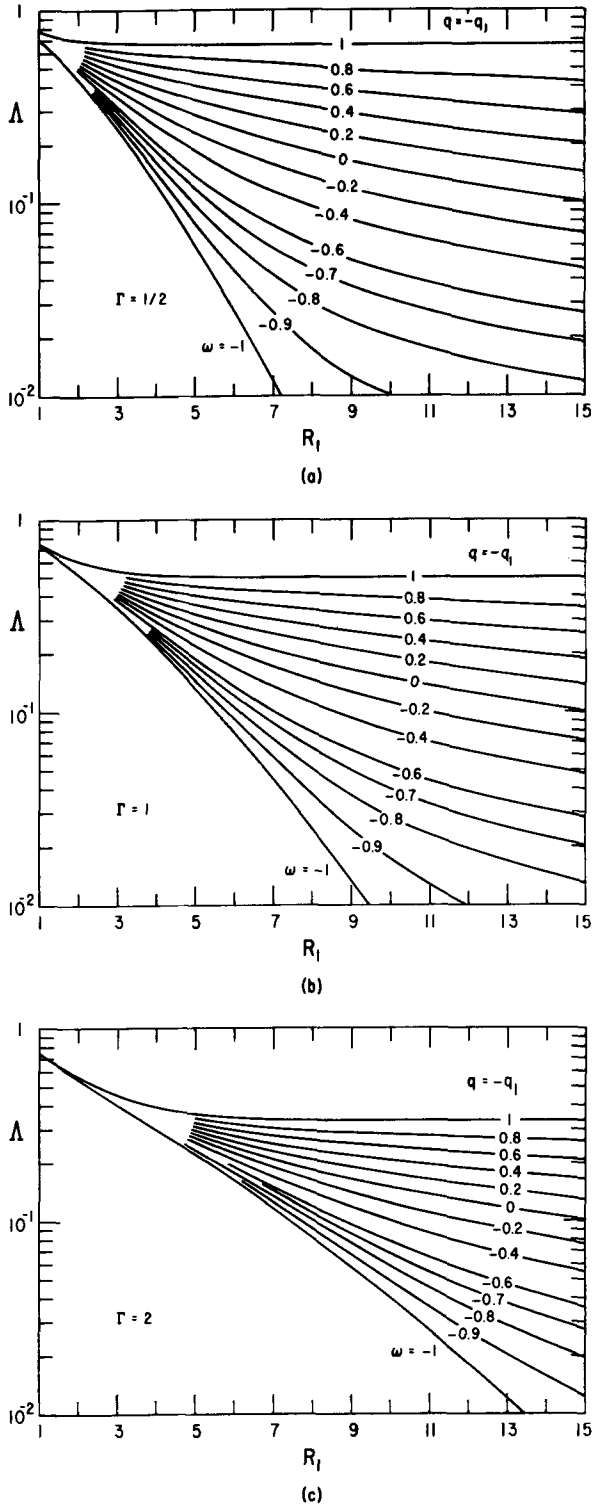

Fig. 9. Quantity $\Lambda \equiv \psi_1/V_1$ appropriate when the OHP is taken conducting *vs.* R_1 for $\Gamma = \frac{1}{2}$, 1, 2 for a full range of ω values. Here $q = -q_1$ and $\Lambda = \psi_a(\beta)/\psi_\infty$, pertinent to the conducting ESP case as well.

the OHP to be a metallic imaging plane in situations where the material beyond the ESP may lead to a positive value for ω, we show curves for positive ω values as well as negative ones. It will be noted that as R_1 increases all the $\omega = 1$ curves approach the limiting value $(1 + \Gamma)^{-1} = \beta/(\beta + \gamma)$. In this situation, $\psi_1 = \psi_a(\beta)$ is just the proper linear proportion, $\beta/(\beta + \gamma)$, of $V_1 = \psi_\infty$ and Δ, here defined through $\Lambda \equiv \Gamma^{-1}\lambda(1 + \Delta)$, would be zero as it should be. Again, we have presented curves of Λ rather than Δ since we believe Λ to be more significant in the present case.

The curves of Fig. 9 are particularly valuable since when $q = -q_1$, $\Lambda = \psi_a(\beta)/\psi_\infty$, and the curves show immediately how large the discrete-charge potential at the IHP is compared to the total potential (at large distances) set up by the array, ψ_∞. These results for $\psi_a{}^N(1)$ are, of course, just as appropriate for the situation of a conducting ESP discussed in the last section since they immediately give the relative ψ_a at the IHP in this case as well. Note further that since the average potential at the IHP, $V(\beta)$, is also ψ_∞ for $q = -q_1$, the curves show in addition how $\psi_a(\beta)$ differs from the average potential at the IHP.

In the present paper, we have made calculations based on a model in which there is one conductive imaging plane and one dielectric imaging plane (and have also included results appropriate for two conducting planes). These calculations were referred to two physical situations. In the first situation treated, the electrolyte was assumed to behave like a simple dielectric, mobile ions in the diffuse layer were not explicitly taken into account, and the OHP therefore was considered a dielectric imaging plane. In the second situation, the OHP was considered effectively to be a conductive imaging plane, and the dielectric imaging occurred elsewhere, at the surface of a true dielectric. How valid is our model for these two situations?

The theoretical difficulties associated with the first system have already been discussed somewhat and preclude a precise answer to this question for this case. However, we may make some reasonable guesses as follows. Inasmuch as the ions in the diffuse layer will cause the OHP to become to some extent a conductive imaging plane, we anticipate that the present model will not accurately portray the first system except possibly at ionic concentrations so low that the effective Debye lengths are larger than other characteristic dimensions of the system (*e.g.*, β and r_1), concentrations which are often lower than those of most interest. Note that the Debye length for $0.025N$ at 25°C is about 20Å. If $\beta = 2$Å, this corresponds to $R_1 = 10$, and complete neglect of any diffuse layer conductive imaging would probably then only be justified for R_1 values appreciably smaller than 10 for this bulk concentration. Although one might be tempted to apply the present model by using an effective ω, larger than that calculated on the basis of dielectric constants alone, which hopefully would approximately take into account the mobile ions, we do not here advocate this procedure as an entirely satisfactory solution to the problem for two reasons: Our own estimates of the importance of conductive imaging at the OHP for ionic concentrations such as $1N$ would imply effective ω values exceedingly close to unity, for which the Ershler model is appropriate. Furthermore, any actual small difference between the predictions of the Ershler model and those of the present model with $\omega \approx 1$ would probably be no larger than the errors introduced into the present treatment by the attempt to subsume the action of the diffuse-layer ions into an effective ω. Nevertheless, the present approach adequately illustrates for the first time the effects of the ever-present underlying dielectric imaging.

Concerning the second system considered, where the OHP is taken to be a conductive imaging plane, our evaluation of the model validity is accordingly considerably higher. The foregoing arguments which favor taking the OHP as just such an imaging plane are as encouraging in this situation as they were discouraging in the former one. We therefore feel that the present treatment pertains to a dielectric ESP (for the usual appreciable ionic concentrations) fairly well. If an accurate future theory should demonstrate that our present opinions are overestimates of conductive imaging at the OHP, then we would have to interchange our evaluations of the applicability of the present model to the two situations.

Acknowledgment

The authors greatly appreciate the help of Marilyn White and Charles Ratliff in writing the several computer programs used in this work.

APPENDIX

In another paper (18), we have discussed in some detail how Grahame's (8c) cut-off approximation for single imaging discreteness-of-charge potential calculations can be modified in a simple way to yield highly accurate results for hexagonal planar arrays of ideal or non-ideal dipoles. Here, we thus shall only quote results used in the present work.

For $\psi_{ao}{}^N$ and $\mathcal{E}_{ao}{}^N$ we may write

$$\psi_{ao}{}^N = \tfrac{1}{2}\{[(pR_1)^2 + (Z+1)^2]^{1/2} - [(pR_1)^2 + (Z-1)^2]^{1/2}\} \quad [A\text{-}1]$$

$$\mathcal{E}_{ao}{}^N = \tfrac{1}{2}\left\{\frac{Z+1-[(pR_1)^2/Z]F}{[(pR_1)^2+(Z+1)^2]^{1/2}} - \frac{Z-1-[(pR_1)^2/Z]F}{[(pR_1)^2+(Z-1)^2]^{1/2}}\right\} \quad [A\text{-}2]$$

In these equations, p and F (which are constant and zero, respectively in Grahame's work) are primarily functions of $\xi \equiv Z/R_1$ but depend slightly on R_1 as well (18). Here $F \equiv -d\ln p/d\ln\xi$. Using Chebychev rational function approximation methods, we obtained in ref. (18) very accurate, yet simple, approximations of the p and F functions which make [A-1] and [A-2] exact for hexagonal arrays. This method of approach was used because it was found that p changed only over a limited range for any fixed R_1 when ξ varied from 0 to ∞ and F was small over most of the range, reaching a maximum of about 0.14 near $\xi = 1$.

The rational function approximations for p and F are all of the type

$$f(\xi) = \sum_{i=0}^{n} a_i\xi^i \Big/ \sum_{i=0}^{m} b_i\xi^i \quad [A\text{-}3]$$

and may be termed (n/m) approximants. Note that $b_m \equiv 1$. In Table I we give the coefficients of (3/3) and (0/2) approximants for $p(\xi)$ and of a (2/3) approximant for $F(\xi)$. Coefficients of other simpler approximants are given in ref. (18). Here, we have used more complicated approximants than would normally be necessary in order to ensure accuracy of at least several decimal places in all the results calculated. In Table I, (a) values are for a fit which min-

Table I. Rational function coefficients for (a) $p(\xi)$ ($R_1 = 5$ fit), (b) $p(\xi)$ ($Z = 1$ fit) and (c) $F(\xi)$ ($R_1 = 5$ fit)

		(a) $\delta_R = 1.355 \times 10^{-4}$ (b) $\delta_A = 1.261 \times 10^{-3}$ (c) $\delta_A = 3.965 \times 10^{-3}$	
i		a_i	b_i
0	(a)	−41.607035	−63.857680
	(b)	6.2168220	9.4332222
	(c)	0	−3.3093430
1	(a)	27.059236	41.149777
	(b)	—	0.72151658
	(c)	−0.21067153	6.4039198
2	(a)	−33.039613	−59.285095
	(b)	—	1.0
	(c)	0.058259894	−5.2036756
3	(a)	0.75227306	1.0
	(b)	—	—
	(c)	—	1.0

imized the absolute value of the relative deviations, δ_R, while (b) and (c) values were for fits which minimized the absolute values of the absolute deviations, δ_A, between accurate values and approximate predictions. Values of the pertinent δ_R and δ_A's are shown in the table and illustrate the high accuracy of the approximants.

We have used the above expressions for $\psi_{ao}{}^N$ and $\mathcal{E}_{ao}{}^N$ for a hexagonal array for $Z < 1 + 3R_1$. When $Z \geq 1 + 3R_1$, however, the results of II reduce to

$$\psi_{ao}{}^N \cong 1 - (\sqrt{3}/4\pi)\,[R_1{}^2/(Z^2 - 1)] \qquad [A\text{-}4]$$

and

$$\mathcal{E}_{ao}{}^N \cong (\sqrt{3}/2\pi)\,[ZR_1{}^2/(Z^2 - 1)^2] \qquad [A\text{-}5]$$

accurate to about eight figures when $Z = 1 + 3R_1$ and becoming even more accurate as Z/R_1 increases further. Therefore, these simple expressions were employed in place of [A-1] or [A-2] when $Z \geq 1 + 3R_1$.

GLOSSARY

Basic Parameters of System

e	Charge of proton
q_1	Average surface charge density on IHP
q	Total surface charge density on conductive plane
z_v	Effective valence of surface-layer ions
ϵ_1	Effective dielectric constant of surface region
ϵ_2	Effective dielectric constant of dielectric region
β	Distance from IHP to conductive plane
γ	Distance from IHP to dielectric imaging plane
d	$\beta + \gamma$ = thickness of surface region
r_1	Lattice spacing of surface-layer ions
ω	$(\epsilon_2 - \epsilon_1)/(\epsilon_2 + \epsilon_1)$
η	$1 + \omega = 2\epsilon_2/(\epsilon_2 + \epsilon_1)$
λ	$\gamma/(\beta + \gamma)$
Γ	γ/β
ρ	$2d/\beta$
(x,y)	Coordinates in a plane parallel to IHP, generally set to zero here
z	Coordinate of position normal to ESP
Z	z/β
R_1	r_1/β
Z_o	$1 + \Gamma = d/\beta$
ξ	$Z/R_1 = z/r_1$

Unnormalized Potentials and Fields

ψ	$\psi_a + \psi_e \equiv$ actual potential at a point (x,y,z)
ψ_e	Portion of potential arising from a uniform electric displacement
ψ_a	Portion of potential arising from discrete system of charges and images
ψ_{ao}	Discrete potential in single image regime
ψ_{acc}	Discrete potential in infinite image regime
$\mathcal{E}$	Actual electric field, associated with ψ
$\mathcal{E}_a$	Field associated with ψ_a
$\mathcal{E}_{ao}$	Field associated with ψ_{ao}
$\mathcal{D}_a$	Displacement associated with ψ_a

Potential Differences, Average Quantities, and Normalizing Factors

ψ_1	Micropotential $\equiv \psi$(at IHP) $- \psi$(at OHP)
V_1	Average potential drop across surface layer
V_2	Potential drop across diffuse layer
$V(z)$	Average potential in a plane $z =$ constant
ψ_∞	$(4\pi\beta q_1/\epsilon_1)$ = average potential drop arising from discrete array of charges and images; used as a normalizing factor
ϵ_∞	Normalizing quantity for fields $\equiv -\psi_\infty/\beta$
ϕ_∞	Normalizing quantity for displacements $\equiv \epsilon_1\mathcal{E}_\infty$

Normalized Potentials and Fields

ψ^N	ψ/ψ_∞
$\psi_a{}^N$	ψ_a/ψ_∞
$\psi_{ao}{}^N$	ψ_{ao}/ψ_∞
$\psi_e{}^N$	ψ_e/ψ_∞
$\psi_1{}^N$	ψ_1/ψ_∞
$V_1{}^N$	V_1/ψ_∞
$V^N(Z)$	$V(z)/\psi_\infty$
$\Delta\psi_a{}^N$	$\psi_a{}^N(1) - \psi_a{}^N(Z_o)$
$\mathcal{E}^N$	$\mathcal{E}/\mathcal{E}_\infty$
$\mathcal{E}_a{}^N$	$\mathcal{E}_a/\mathcal{E}_\infty$
$\mathcal{E}_{ao}{}^N$	$\mathcal{E}_{ao}/\mathcal{E}_\infty$
$\mathcal{E}_e{}^N$	$\mathcal{E}_e/\mathcal{E}_\infty$
$\mathcal{D}_a{}^N$	$\mathcal{D}_a/\mathcal{D}_\infty$

Other Quantities

Λ	$\psi_1/V_1 \equiv$ a quantity measuring ratio of micropotential to full surface layer average p.d.
Δ	A quantity measuring departure from a strict proportionality between ψ_1 and V_1. When the ESP is conductive, $\Lambda \equiv \lambda(1 + \Delta)$; when the ESP is dielectric, $\Lambda \equiv \Gamma^{-1}\lambda(1 + \Delta)$
Δ_o	Value of Δ for $q = 0$
p,F	Quantities used in our modified cut-off approximation for ψ_a and $\mathcal{E}_a$

REFERENCES

1. J. R. Macdonald and C. A. Barlow, Jr., Proc. First Australian Conf. on Electrochemistry, Sydney, Australia, 15 February 1963, pp. 199-247, A. Friend and F. Gutmann, Editors, Pergamon Press, Oxford (1964).
2. J. R. Macdonald and C. A. Barlow, Jr., *J. Chem. Phys.*, **39**, 412 (1963); **40**, 237 (1964). An important correction to this paper is discussed in ref. (14) below.
3. C. A. Barlow, Jr., and J. R. Macdonald, *ibid.*, **40**, 1535 (1964). In Eq. [23]of this paper, the term in the square bracket should be in the denominator, not the numerator, of the equation. The term **h-h** which appears twice on p. 1543 should be $\mathbf{h}\text{-}\mathbf{h}_\lambda$.
4. C. A. Barlow, Jr., and J. R. Macdonald, *ibid.*, **43**, 2575 (1965). The colon in ref. (2) of this paper should be a semicolon; $\mathcal{E}$ in the Glossary should be $\mathcal{E}_a$; there should be a hyphen between "average" and "discrete" at the bottom of p. 2586; and Mignolet (28) on p. 2590 should be Mignolet (14).
5. For discussion of some of these relations see: (a) P. Delahay, "Double Layer and Electrode Kinetics," Interscience, New York (1965); (b) ref. (3) and (4) above; (c) A. N. Frumkin, *This Journal*, **107**, 461 (1960); and (d) A. Aramata and P. Delahay, *J. Phys. Chem.*, **68**, 880 (1964).
6. See ref. (5a) and (5b) and references therein. Also, J. R. Macdonald and C. A. Barlow, Jr., *J. Phys. Chem.*, **68**, 2737 (1964).
7. (a) J. R. Macdonald and C. A. Barlow, Jr., *Can. J. Chem.*, **43**, 2985 (1965); (b) S. Levine, J. Mingins, and G. M. Bell, *ibid.*, **43**, 2834 (1965).
8. (a) O. Esin and V. Shikov, *Zhur. Fiz. Khim.*, **17**, 236 (1943); (b) B. V. Ershler, *ibid.*, **20**, 679 (1946); (c) D. C. Grahame, *Z. Elektrochem.*, **62**, 264 (1958); (d) V. G. Levich, V. A. Kir'yanov, and V. S. Krylov, *Dokl. Akad. Nauk SSSR*, **135**, 1193 (1960); (e) V.S. Krylov, *ibid.*, **144**, 356 (1962); (f) V. S. Krylov, *Electrochim. Acta*, **9**, 1247 (1964).
9. N. F. Mott and R. J. Watts-Tobin, *Electrochim. Acta*, **4**, 79 (1961). Printing and other errors in this and some of the other papers referenced in the present work are listed in the references of the present ref. (1)
10. J. O'M. Bockris, M. A. Devanathan, and K. Müller, *Proc. Roy. Soc. (London)*, **A274**, 55 (1963). See also ref. (1), pp. 832-863.
11. S. Levine, G. M. Bell, and D. Calvert, *Can. J. Chem.*, **40**, 518 (1962).
12. F. H. Stillinger and J. G. Kirkwood, *J. Chem. Phys.*, **33**, 1282 (1960).
13. (a) V. S. Krylov and V. G. Levich, *Zhur. Fiz. Khim.*, **37**, 106 (1963); (b) *ibid.*, **37**, 2273 (1963).
14. (a) J. R. Macdonald and C. A. Barlow, Jr., *J. Chem. Phys.*, **44**, 202 (1966); (b) *ibid.*, *J. Appl. Phys.*, To be published.
15. L. Schmidt and R. Gomer, *J. Chem. Phys.*, **42**, 3573 (1965).
16. N. F. Mott, R. Parsons, and R. J. Watts-Tobin, *Phil. Mag.*, **7**, 483 (1962).
17. C. A. Barlow, Jr., and J. R. Macdonald, "Advances in Electrochemistry and Electrochemical Engineering," P. Delahay, Editor. To appear.
18. J. R. Macdonald and C. A. Barlow, Jr., *Surface Science*, **4**, 381 (1966).
19. J. R. Macdonald, *J. Chem. Phys.*, **22**, 1857 (1954).
20. J. R. Macdonald and C. A. Barlow, Jr., *ibid.*, **36**, 3062 (1962).
21. J. R. Macdonald, *J. Appl. Phys.*, **35**, 3034 (1964).
22. D. C. Grahame, *J. Am. Chem. Soc.*, **80**, 4201 (1958).
23. D. C. Grahame and R. Parsons, *ibid.*, **83**, 1291 (1961).

Discussion

H. D. Hurwitz: It must be stressed that the value of the micropotential is not sufficient to account for the total coulombic interaction among adsorbed particles. This is shown easily by deriving, as indicated next, the total coulombic energy of interaction for a set of charges of species α adsorbed at the inner Helmholtz plane (IHP), assuming as usual that: 1, the interaction α-solvent is implicitly stated in the definition of the local dielectric constant ϵ_0 and of the pair correlation function $g1,2$ introduced below; 2, the interaction α-diffuse layer charge is described by a simple average electrostatic effect in which the ionic distribution in the diffuse layer is smeared out over parallel planes to the electrode; 3, the dielectric discontinuity near the outer Helmholtz plane (OHP) leads to partial or total reflection of the charge e_α of α.

Under these conditions we assume that the surface density of α is p_α. Hence $p_\alpha 1$ gives the probability to find α at one given position, 1, of the IHP. The probability to encounter a neighbor to α at position 2 is then by definition $g1,2\ p2$ where $g1,2$ is the radial distribution function. The coulombic interaction between these two particles is $(e^2_\alpha/\epsilon_0)\gamma 1,2$ where $\gamma 1,2$ represents the reduced coulombic potential at 2 corresponding to an isolated charge located at the IHP at 1. The quantity $\gamma 1,2$ includes the effects of partial or total infinite reflections into the dielectric discontinuities of the model.

The probable pair interaction for positions 1 and 2 is

$$\frac{e^2_\alpha}{\epsilon_0}\gamma 1,2\, g1,2\, p_\alpha 1\, p_\alpha 2 \qquad [1]$$

Let us sum over all particles on the IHP considered to interact with α at 1 and over all central positions, 1, in order to get finally the total interaction energy

$$\frac{e^2_\alpha}{2\epsilon_0}\sum_1\sum_2 \gamma 1,2\, g1,2\, p_\alpha 1\, p_\alpha 2 \qquad [2]$$

(Because of symmetry of $\gamma 1,2\ g1,2$ the quadratic sum is divided by 2.) Instead of summing over all 1 and 2 we may integrate over-all distances s_{12} between 1 and 2 and over-all positions 1 in order to get finally

$$\Omega\frac{e^2_\alpha}{2\epsilon_0}\int g1,2\,\gamma 1,2\, p^2_\alpha\, ds_{12} \qquad [3]$$

where Ω is the total area of the IHP.

The change of interaction energy on introduction of one particle α is obtained through differentiation of [3]. Therefore

$$\frac{e^2_\alpha}{2\epsilon_0}\int \gamma(s_{12})\,\frac{\partial}{\partial p_\alpha}\,(g(s_{12})\,p^2_\alpha)\,ds_{12} \qquad [4]$$

It is clear that [4] is the contribution of coulombic interactions among specifically adsorbed charges to the change of potential energy of adsorption. A more convenient way to write [4] is to decompose this expression in the following manner

$$e_\alpha\left[p_\alpha\frac{e_\alpha}{\epsilon_0}\int\gamma(s_{12})ds_{12} + p_\alpha\frac{e_\alpha}{\epsilon_0}\int\gamma(s_{12})[g(s_{12})-1]ds_{12}\right] + \tfrac{1}{2}\,p^2_\alpha\frac{e^2_\alpha}{\epsilon_0}\int\gamma(s_{12})\,\frac{\partial}{\partial p_\alpha}\,g(s_{12})\,ds_{12} \qquad [5]$$

In view of the fact that the first term in [5] corresponds to the effect at [1] of charges uniformly distributed over the IHP, it is readily inferred that by definition this term pertains to the average electrostatic potential (macroscopic potential).

The second term is then a correction which results from discreteness-of-charge effects [$g(s_{12})$ is different from unity] and the first and second term together represent the so-called micropotential.

At this point we have to realize that whenever we introduce in our system at position 1 an ion α we do not alter only the local density p_α, but we modify simultaneously the radial distribution of particles. This in turn gives rise to some interaction energy. The last term of [5] reflects such an effect of radial redistribution. The contribution of this effect to the free energy of adsorption has yet been considered only from a qualitative viewpoint[1,2] and is generally neglected. However, a careful evaluation based on a simple model for $g1,2$ has led[3] to the conclusion that such work of redistribution is not negligible at all and may even be of the order of magnitude of the discreteness-of-charge correction as given by the second term in expression [5]. In the crude hexagonal lattice approximation of Ershler, in which no allowance is made for thermal motion, the $g1,2$ functions are represented by delta Dirac functions.

C. A. Barlow, Jr.: Three points seem to have been raised here. First, "that the value of the micropotential is not sufficient to account for the total coulombic interaction among adsorbed particles;" second, "that the work of redistribution is not negligible at all and may even be of the order of magnitude of the dicreteness-of-charge correction;" and third, that the hexagonal lattice approximation is crude, the use of exact two-particle correlation functions being preferable.

We disagree with the first point; however, the disagreement possibly stems merely from a different use of words: We assert[4] that the total coulombic energy $U(N)$ of a system of N charges is given by a sum over all particles of the local potential times one-half the charge; in other words, we agree entirely with Dr. Hurwitz's Eq. [2] within the approximation of the model. Now except for a contribution, V_2, from the diffuse layer, the "local potential" occurring above is just the micropotential. To equate the two involves the neglect of V_2 in the micropotential, to be sure, but this is discussed in our present paper just after Eq. [14], and this doesn't seem to be Dr. Hurwitz's objection. His objection, as seen from the second point raised, is that we are somehow neglecting rearrangement energy. This is not true; in the first place, in the present paper we did not need to calculate the energy of adsorbing one additional ion, $\Delta U \equiv U(N+1) - U(N)$. We have shown explicitly[4] that, having found the micropotential, we have a means of calculating the related quantity $U(N)$ in accordance with the foregoing. In the second place, our approach does lead to the redistribution energy in essentially the same way that it arises in Dr. Hurwitz's discussion when one finally gets down to the business of calculating ΔU, the energy of adsorption. The only difference in approach is that we initially calculate $U(N)$ and save the differencing with respect to N until the very last (as may be seen from our papers[5,6] where we determine the total energy for adsorbing an additional

[1] D. C. Grahame, *Z. Elektrochem.*, 62, 264 (1958).

[2] C. A. Barlow, Jr. and J. R. Macdonald, *J. Chem. Phys.*, 43, 2575 (1965).

[3] H. D. Hurwitz, *Z. physik. Chem.*, To be published.

[4] C. A. Barlow, Jr. and J. R. Macdonald, *J. Chem. Phys.*, 43, 2575 (1965).

[5] J. R. Macdonald and C. A. Barlow, Jr., "The Penetration Parameter for an Adsorbed Layer of Polarizable Ions," *J. Appl. Phys.*, To be published in 1966.

[6] J. R. Macdonald and C. A. Barlow, Jr., *Can. J. Chem.*, 43, 2985 (1965).

ion). We agree with Dr. Hurwitz's statement about orders of magnitude; we were, in fact, the first to make a correct quantitative study of redistribution energy in the present system. Indeed, although this question was considered quantitatively by us in the work cited by Dr. Hurwitz[4] and a curve plotted to show the numerical magnitude of the effect for a wide range of surface coverages, in his discussion Dr. Hurwitz only references his own unpublished work to support "the conclusion that such work of redistribution is not negligible at all and may even be of the order of magnitude of the discreteness-of-charge contribution." It is of interest to note that in our previously published work[4] we explicitly state that the work of redistribution is of the same order of magnitude as the full adsorption energy and is not at all negligible. Dr. Hurwitz seems to have missed noticing the significance of the quantity η in our paper,[4] since he refers to this paper as considering the question "only from a qualitative viewpoint." Further quantitative treatment of this matter will soon appear.[5]

Finally, that the hexagonal model may be "crude" cannot be denied. We have already presented a discussion of just how crude it may be under some conditions.[6] If the proper correlation functions were known, they would certainly be preferable to the δ-function lattice model. They are not known, however, so our approach has been to try to keep the following statement (concerning statistical physics) of Richard Feynman[7] in mind:

"Anyone who wants to analyze the properties of matter in a real problem might want to start by writing down the fundamental equations and then try to solve them mathematically. Although there are people who try to use such an approach, these people are the failures in this field; the real successes come to those who start from a physical point of view, people who have a rough idea where they are going and then begin by making the right kind of approximations, knowing what is big and what is small in a given complicated situation. These problems are so complicated that even an elementary understanding, although inaccurate and incomplete, is worth while having. . . ."

We believe the hexagonal array approach to be the "right kind of approximation" for a q_1 range of practical importance.[6]

Richard Payne: According to the results in Fig. 7, the ratio of ψ_1/V_1 is uniformly larger for the single imaging limit than for the infinite imaging limit. This does not seem consistent with the Esin and Shikov and Grahame calculations for the single imaging case which overexplained the Esin and Markov effect (*i.e.*, ψ_1/V_1 too small); whereas Ershler's treatment of the infinite imaging case gave larger values of ψ_1/V_1. It seems, therefore, that the trend in Fig. 7 as ω varies is inverted.

J. Ross Macdonald and *C. A. Barlow, Jr.*: The apparent discrepancy pointed out by Dr. Payne is not significant for several reasons. First, the single-imaging treatments of Esin and Shikov and Grahame not only treat a physically very different situation than the present single-imaging one but the situation treated is much less physically appropriate than is ours. Second, we properly include the uniform D field contribution to the single-imaging micropotential, omitted by other authors. The Esin-Shikov and Grahame treatments are not really single-image ones at all since they consider fixed arrays of adsorbed ions each with a rigidly paired counterion in the diffuse layer. The counterions are not taken as images of the adions but as real associated ions a fixed perpendicular distance from the adions. Ershler has modified this approach by considering single imaging of the adions in the diffuse layer, a preferable assumption. This is indeed a single-imaging treatment, but it necessarily still disagrees with our $\omega = 0$ results in Fig. 7 since there we take imaging in the electrode instead of the solution, take q variable, and include the D field contribution.

The significant point regarding Fig. 7 is that for reasonable Γ values the $\omega = 1$ curves generally yield micropotential values which are smaller than they should be to explain the Esin-Markov effect (Λ too small) while the $\omega = 0$ results yield micropotentials which are too large to explain it. For an appropriate value of Γ, it appears possible to pick a ω value near but less than unity which will lead to results which will explain the Esin-Markov effect (within the limitations of the present treatment) better than will results with either $\omega = 1$ or 0.

Richard Payne: It is not clear why grounding of the electrode should affect the charge on the metal since the whole system is electrically neutral. If the effect of grounding the electrode were to eliminate the uniform displacement component ψ_e, then it would be possible to determine the point of zero charge simply by measuring the potential of the grounded electrode with respect to a reference electrode.

J. Ross Macdonald and *C. A. Barlow, Jr.*: Actually one could not measure the ecm potential in this way without additional information about the system: The condition that the electrode is grounded is not the same as the condition of zero charge. The charge on the electrode which produces the ground condition depends on the imaging situation which applies, as well as the adsorbed surface charge density. Specifically, for single and for dielectric imaging the condition is that $q = -q_1$, whereas for infinite-conductive imaging we have $q = -\dfrac{\gamma}{\beta + \gamma} q_1$ at the ground condition. However, if one knew the physical (imaging) situation and measured q_1 with the electrode grounded, one might be able to infer from the average potential drop across the compact layer what the ecm potential is.

Richard Payne: I think it is important to point out that λ in the Grahame-Parsons analysis is not fully equivalent to ψ_1/V_1 in this treatment as stated by the author for the following reason. In the Grahame-Parsons analysis λ is obtained from the experimental results by investigating the concentration dependence of the adsorption energy at constant charge in the electrode. λ is therefore an average value over a range of concentrations and amounts adsorbed. In other words, the imaging conditions in the diffuse layer are not kept constant during the calculation whereas the calculations given here refer to definite imaging conditions in the solution.

J. Ross Macdonald: Our $\Lambda \equiv \psi_1/V_1$ is formally equivalent, as stated, to Grahame and Parson's $(\psi^i - \psi^o)/\psi^u$, which they set equal to λ on the basis of an approximate infinite-imaging treatment. Experimental results seem to indicate that the ratio $(\psi^i - \psi^o)/\psi^u$ depends only slightly, if at all, on the concentration. It therefore seems reasonable to compare our theoretical results, which assume a definite degree of dielectric imaging at the OHP, with experimentally derived results obtained using various concentrations. We do not expect much change of ω with concentration, and the change in the average charge density in the diffuse layer apparently does not affect the ratio with which we compare appreciably. The comparison thus appears useful even though there are approximations involved which preclude perfect agreement between theory and experiment.

[7] R. Feynman, R. B. Leighton, and M. Sands, "The Feynman Lectures on Physics," Vol. I, p. 39-2, Addison-Wesley, Reading, Mass. (1963).

Richard Payne: The authors have pointed out that the value of λ (and hence ψ_1) obtained in the Grahame-Parsons analysis is dependent on an assumed form of the isotherm which I think is an important point. Incidentally, I would also like to point out that λ also depends on whether the anion activity or the salt activity is used in the isotherm.

In this context, it seems to me that the Frumkin isotherm or better the Flory-Huggins modification of the Frumkin isotherm introduced by Parsons offers an excellent starting point for the experimental study of discreteness of charge effects for the following reasons. If we write down the Stern form of the isotherm,

$$\frac{\theta}{1-\theta} = a_{\pm} \exp\left[(\psi_1 + \Phi)F/RT\right] \qquad [1]$$

and compare this with the Frumkin isotherm in the form

$$\frac{\theta}{1-\theta} = \frac{a_{\pm}}{\Gamma_s} \exp\left[-\frac{\Delta G^{\circ}}{RT} + f(q) - A\theta\right] \qquad [2]$$

it seems reasonable to equate the specific adsorption potential Φ with the standard free energy of adsorption at zero coverage $-\Delta G^{\circ}$, *i.e.*

$$F\Phi = -\Delta G^{\circ} - \ln \Gamma_s \qquad [3]$$

and to write ψ_1 as

$$\frac{F\psi_1}{RT} = f(q) - A\theta \qquad [4]$$

where $f(q)$ is the form of the charge dependence of the standard free energy of adsorption at zero coverage and A is the lateral interaction coefficient of the adsorbed anions. I think it is clear from [4] that the Frumkin isotherm with a constant value of A represents the infinite imaging limit to a close approximation since the adsorption energy is linearly dependent on the amount adsorbed. Deviation from the linear θ dependence of the lateral interactions, *e.g.*, a $\theta^{3/2}$ dependence for single imaging should show up as variation in A when the Frumkin isotherm is applied. It is interesting to note that apparent variation of A is often found for adsorption of anions from solutions of a single salt.

A further point I would like to make here is that the infinite imaging case also leads to linear charge dependence of $-\Delta G^{\circ}$ providing the effect of replacement of oriented solvent dipoles is neglected and providing the dielectric constant is assumed constant:

$$\psi_1 = \frac{\gamma}{\beta+\gamma} V_1 = \frac{\gamma}{\beta+\gamma} \cdot \frac{4\pi}{\epsilon}\left[q + \frac{\gamma}{\beta+\gamma} \cdot q^1\right]\beta + \gamma$$

$$= \frac{\tau\pi\gamma}{\epsilon} q + \frac{4\pi}{\epsilon} \cdot \frac{\gamma^2}{\beta+\gamma} \cdot q^1$$

Deviations from the linear charge dependence of $-\Delta G^{\circ}$ can arise (*i*) from replacement of oriented dipoles which would contribute a term $4\pi n\bar{\mu}/\epsilon$ to V_1 where n is the number of dipoles replaced by each ion and $\bar{\mu}$ is the mean normal component of the dipole moment and (*ii*) through deviations of ψ_1/V_1 from constancy resulting from imperfect imaging in the solution.

J. Ross Macdonald and *C. A. Barlow, Jr.*: We do not agree that ψ_1 is given by $\frac{\gamma}{\beta+\gamma} V_1$ only that the uniform field part is given by this quantity in the infinite-conductive imaging situation. The linearity of ψ_1 with charge on the electrode, q, is independent of this, however, and in fact does not depend on the type of imaging present. We only refer to the explicit dependence of ψ_1 on q. Since evidently as q changes q_1 will generally change as well, we do not include all q-dependence in the present discussion. We are in fact referring to the linearity of ψ_1 with q under hypothetical circumstances where the constitution of the compact layer is held fixed and only q is allowed to change. Accordingly, we agree with the statement that ψ_1 will be explicitly linear with q, but disagree with the reasoning which led to this conclusion and with the comments concerning causes for "deviations from the linear charge dependence of $-\Delta G^{\circ}$." On the other hand, the remarks about "deviations . . . (etc.)" are interesting and pertinent if by "charge dependence" is meant "dependence on q_1." Note, however, that if one is concerned with the dependence of ψ_1 on q_1, he must include the contribution from the discrete ions and their images (ψ_a), and that such inclusion will itself destroy the linearity without the additional help of the two effects cited by Dr. Payne.

Roger Parsons: I think it is fair to say that the general idea of the discreteness of charge effect is widely accepted and is supported by several pieces of experimental evidence. However, it is much more difficult to demonstrate experimentally the fine details of the models proposed, *e.g.*, whether imaging is partial or infinite, whether the hexagonal lattice or the disordered models provide the closest approximation to reality. I should emphasize the importance of attempting to verify these models by experimental test. We have tried to examine imaging in the diffuse layer recently[8] and suggest that it is not complete. However, this work does not test the efficiency of imaging in the dielective jump.

In connection with the problem of thermal motion, is it correct to say that some of the difference between you and Levine *et al.* is due to the fact that you assume a lower dielective constant in the inner layer? A value of 6 or 7 seems more reasonable than 15.

I would like to point out that the variable λ obtained by Grahame and Parsons was further analyzed by Parry and Parsons[9] and an improved model suggested.

Finally, I think it is interesting to note that the elegant method of summation proposed in this paper has some relation to the intuitive way in which David Grahame discussed the potential drop in the inner layer[10].

J. Ross Macdonald and *C. A. Barlow*: We believe this difference of opinion as to the proper value of the dielectric constant to use in these circumstances is the only significant disagreement between Levine and his co-workers and ourselves although there are small perturbations on the final numbers for lattice stability coming from slight differences in stability criteria, etc. In a recent paper by Bell, Mingins, and Levine[11] the inner-layer dielectric constant is taken to be 10. As you have pointed out we have generally taken 5 or 6 to be more typical of the inner-layer dielectric constant, to the extent that one can define such an object. This choice was motivated by our prior work on differential capacitance in the electrical double layer. However, in later theoretical studies on electrode work function change, we calculate that the dielectric constant in some systems may be completely different from bulk values insofar as work function effects are concerned. The significant phrase is "insofar as work function effects are concerned." It turns out that the use of a single dielectric constant to characterize dielectric effects in the inner layer is incorrect, since this region is so completely different from three-dimensional bulk matter. We have re-

[8] E. Dutkiewicz and R. Parsons, *J. Electroanal. Chem.*, 11, 100 (1966).

[9] J. M. Parry and R. Parsons, *Trans. Faraday Soc.*, 59, 241 (1963).

[10] Fig. 5 in *Z. Elektrochem.*, 62, 264 (1958).

[11] Bell, Mingins, and Levine, *Trans. Faraday Soc.*, 62, 949 (1966).

cently estimated the dielectric constant effective in reducing the lateral interaction between adions and find that it is no greater than 2, and more likely to be closer to unity. So you see the question of the proper dielectric constant to use is a rather confused one. It seems to us that all previous estimates of lattice stability in the inner-layer (including our own) have employed a dielectric constant which is at least 3 times too large, and possibly much worse than that.

It is completely correct that our image summation method stems from that originally used (for $\omega \equiv 1$) by Grahame. We have generalized the approach to include the $|\omega| < 1$ case. In this connection, we think it is interesting to note a certain difficulty not fully appreciated by Grahame which troubled us for a while: Whereas the summation technique used here is absolutely convergent for all $|\omega| < 1$, the series is only conditionally convergent for $\omega = 1$. As it happens, the particular arrangement of terms employed by Grahame and ourselves in the $\omega = 1$ case leads to the potential appropriate for $q = -q_1$. Since this does not coincide with the condition $q = -\gamma q_1/(\beta + \gamma)$ obtaining when both imaging planes are at zero potential, this accounts for Grahame's conclusion that the infinite set of images and the adions contribute to the total p.d. across the inner layer, an incorrect conclusion for the model with conductive imaging at the OHP.

The Adsorption of Aromatic Sulfonates at a Mercury Electrode

II. Sodium p-Toluenesulfonate—An Example of Two-Position Adsorption

J. M. Parry[1] and R. Parsons

Department of Physical Chemistry, The University, Bristol England

ABSTRACT

The adsorption of the p-toluenesulfonate ion on a mercury surface from aqueous solution has been studied by measuring the interfacial tension and the capacity of the electrode as a function of concentration. An interpretation of the results is proposed in terms of two orientations of the adsorbed ion. A simple model of this type of system is proposed, at first neglecting interaction between adsorbed ions other than due to their space-filling properties. A very approximate allowance for interaction is introduced, and it is concluded that consideration of interaction is essential for a full description of the system.

In the previous paper of this series (1), we described the adsorption of the benzene m-disulfonate (BMDS) ion which may be treated by methods closely analogous to those used for simple ions such as the halides. This is essentially because adsorption of this ion occurs with the plane of the benzene ring oriented parallel to the plane of the mercury solution interface over the whole of the experimentally accessible range. As we mentioned previously, the behavior of the p-toluenesulfonate (PTS) ion is more complicated and, as we shall show in the present paper, it cannot be analyzed by using the surface pressure in a simple way. This is due to the existence of the adsorbed species in more than one orientation, and we believe that this system provides a clear-cut example of two position adsorption. This problem has been discussed in a qualitative way by Damaskin *et al.* (2); here a more quantitative description is attempted.

Experimental

Measurements of differential capacity and interfacial tension were carried out as described previously (1). Sodium p-toluenesulfonate was recrystallized three times from equilibrium water; it crystallizes as the hemihydrate from concentrated solutions. The water content was determined by heating and weighing and also volumetrically after exchanging the Na^+ for H^+ on an ion exchange resin.

Results

The concentration dependence of the capacity at constant temperature is shown in Fig. 1. It is evident from these data that the behavior of PTS is qualitatively different from that of BMDS as shown in Fig. 1 of ref. (1). At the lower concentrations up to 0.1M the capacity curves for both ions are similar in showing a marked peak at a potential of about −0.6v (SCE). However, as the concentration is increased above 0.1M this peak is lowered, eventually being replaced by a minimum, while a higher and narrower peak develops at more negative potentials (up to −1.4v *vs.* SCE). These results suggest that at low bulk concentrations the PTS ion is lying flat on the mercury surface like the BMDS ion while at higher concentrations re-orientation occurs to allow closer packing of the PTS ion.

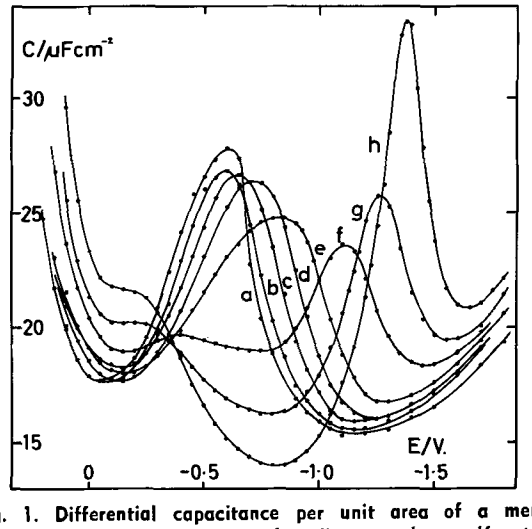

Fig. 1. Differential capacitance per unit area of a mercury electrode in aqueous solutions of sodium p-toluenesulfonate at 30°C plotted as a function of potential with respect to a saturated calomel electrode: a, 0.0113M; b, 0.0227M; c, 0.0567M; d, 0.113M; e, 0.227M; f, 0.567M; g, 1.134M; h, 2.268M.

The capacity curves were integrated numerically using a digital computer (Elliott 803) as described previously (3). The integration constants were obtained from the electrocapillary curves and are given in Table I. The potential of zero charge was found from the electrocapillary curve by extrapolating the

[1] Present address: Tyco Laboratories, Inc., Waltham, Massachusetts.

Table I. Coordinates of the electrocapillary maximum for aqueous sodium p-toluenesulfonate

	20°C		30°C		40°C		50°C	
10^3 c, mole/l	$-E^z$, mv	γ^z, dyne/cm	$-E^z$, mv	γ^z, dyne/cm	$-E^z$, mv	γ^z, dyne/cm	$-E^z$, mv	γ^z, dyne/cm
1.134	558	421.6	560	421.1	561	420.3	556	419.3
2.268	570	420.5	569	420.0	569	419.4	572	419.0
5.67	596	416.8	591	416.0	592	415.3	590	414.8
11.34	607	413.2	605	412.7	598	412.1	600	411.9
22.68	619	409.3	618	408.8	616	408.2	616	408.0
56.7	627	401.7	620	401.8	619	401.3	630	401.7
113.4	617	394.3	619	393.8	630	393.0	628	392.1
226.8	569	387.2	577	387.1	579	386.9	587	386.4

Potentials are measured with respect to the saturated calomel electrode at the temperature of the experiment.

diameter in the region of the maximum. The agreement between the integrated capacity curves and the experimental electrocapillary curves was within the experimental accuracy expected (approximately 0.5 dyne cm^{-1}) except at negative charges where the discrepancy rises to about 3.5 dynes in the most concentrated solution. This may be due to the measured capacity in the region of the cathodic peak being somewhat lower than the true equilibrium value, although no frequency dependence or increase of series resistance was observed. In this region, therefore, the electrocapillary measurements were used in preference to those derived from capacity curves.

The measured potentials were converted to an E^+ scale assuming that the liquid junction potential between the test solution and saturated potassium chloride is independent of the concentration of the test solution. Activity coefficients for sodium p-toluenesulfonate (4) were extended to concentrations below 0.1M using the values for KNO_3 as a guide (5). Values of the function (6) $\xi_+ = \gamma + qE^+$ were calculated and plotted against $(2RT/F) \ln a_\pm$ ($a_\pm$ is the mean activity of the salt) for integral values of q. These plots were differentiated graphically to obtain the component of charge (q_-) on the solution side of the double layer due to the anion. The cation was assumed not to be specifically adsorbed, and the surface charge contributed by it was used to calculate the charge due to anion in the diffuse layer. Classical diffuse layer theory (7) was used as it causes little error in this type of calculation (8). The resulting values of the charge due to the specifically adsorbed anions are shown in Fig. 2. It is not possible to obtain more accurate values by fitting the $\xi_+ - \log a_+$ curves with an integrated adsorption isotherm as described

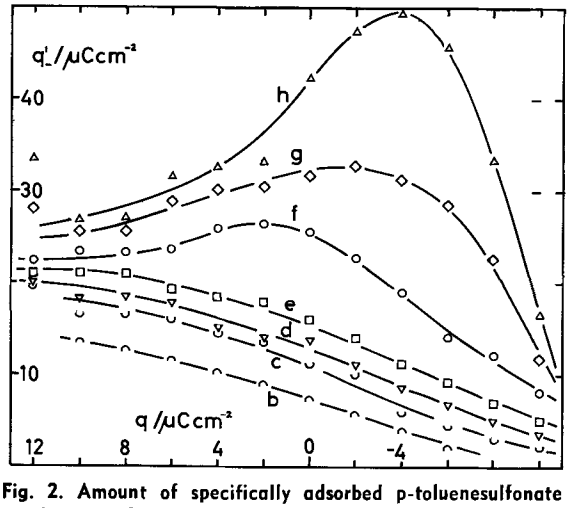

Fig. 2. Amount of specifically adsorbed p-toluenesulfonate ion per unit area of a mercury electrode expressed as charge plotted against the charge on the mercury electrode at 30°C. Letters have the same significance as those in Fig. 1.

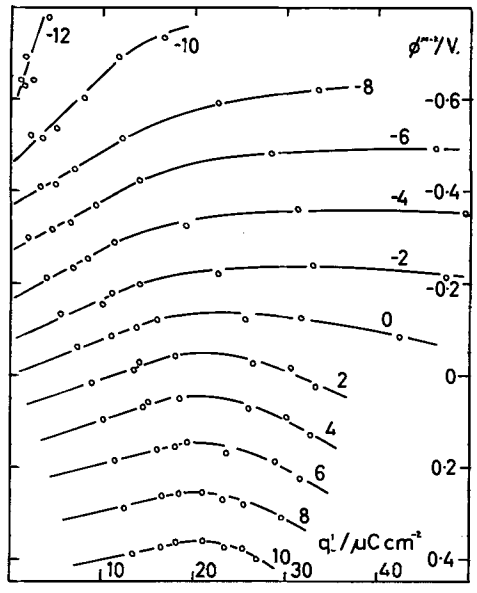

Fig. 3. Potential drop across the inner layer plotted against the amount of p-toluenesulfonate ion specifically adsorbed at constant values of the charge on the electrode indicated in $\mu C\ cm^{-2}$ by figure near each line; temperature 30°C.

previously because the adsorption isotherm for this system is too complex owing to the change in orientation of the adsorbed species.

We may note from Fig. 2 that at the lower concentrations the adsorption behavior is very similar to that of BMDS as noted above. As the charge on the metal becomes more positive, the amount adsorbed appears to approach a limit corresponding to complete coverage by flat adsorbed ions. The limiting charge of about 30 $\mu C\ cm^{-2}$ corresponds to an area per ion of 53 A^2, close to the calculated area of the flat ion. We may also note that the monotonic rise in the adsorption as q increases in this concentration range is consistent with a standard free energy of adsorption which is linearly dependent on the electrode charge. In contrast at the highest concentration studied the adsorption rises to 50 $\mu C\ cm^{-2}$ corresponding to an area per ion of 32 A^2 which is too small for ions lying flat, but is consistent with an orientation of the benzene ring with its plane perpendicular to that of the interface. Further, the existence of a maximum in the amount adsorbed in Fig. 2 is similar to the behavior of neutral molecules and suggests that the vertically oriented molecules have a standard free energy of adsorption which depends on the square of the charge.

Further evidence for the orientation of the adsorbed ion may be obtained from the relation between the potential drop across the inner layer (ϕ^{m-2}) and the amount of specifically adsorbed ion. ϕ^{m-2} was calculated in the usual way by subtracting from the measured potential difference the potential drop across the diffuse layer and a constant which is the potential of the point of zero charge in the absence of specific adsorption. The resulting plot is shown in Fig. 3. Two regions again may be distinguished: at low amounts adsorbed the lines are approximately parallel and the slope corresponds to a capacity $(\partial q_-^{-1}/\partial \phi^{m-2})_q$ which is several times the inner layer capacity. This is similar to the behavior of BMDS (and indeed to that of halides, etc.) and may be taken as characteristic of the flat orientation. At higher adsorbed concentrations the lines become much flatter and even begin to slope in the opposite direction when the electrode is positively charged. Thus the capacity $(\partial q_-^{-1}/\partial \phi^{m-2})_q$ becomes infinite or negative. An infinite value of this capacity would be expected if the distance $x_2 - x_1$ between the inner and outer Helmholtz planes became zero, *i.e.*, the charge on the spe-

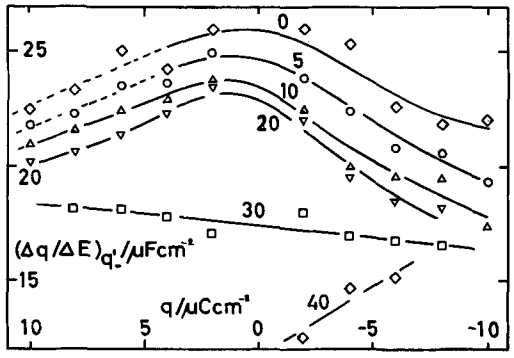

Fig. 4. Integral capacity of the inner layer at constant amount of specifically adsorbed p-toluenesulfonate ion at 30°C plotted against the charge on the mercury electrode. Amount of specifically adsorbed charge in μC cm^{-2} is indicated near each line.

cifically adsorbed ion was located on the outer Helmholtz plane or actually within the diffuse layer. This is consistent with orientation of PTS with the methyl group toward the electrode and the sulfonate group toward the bulk of the solution.

However, if the only change in structure of the double layer were the movement of the charge into the diffuse layer ($x_2 - x_1 \to 0$) the lines in Fig. 3 should become horizontal and remain parallel at high coverages. The actual divergence of these lines can best be understood in terms of the other component of the inner layer capacitance $(\partial q/\partial \phi^{m-2})_{q-1}$ which is inversely proportional to the vertical distance between adjoining lines in Fig. 3. With the charged head group of the molecule outside the inner layer this capacity is determined by the ratio of the average dielectric constant to the thickness of the inner region: ϵ^{m-2}/x_2 just as in a system in which neutral organic molecules are being adsorbed. The integral capacity at constant amount of adsorbed PTS ion is shown in Fig. 4, which shows that there is very little effect on this capacity up to a surface coverage of 20 μC cm^{-2} in which region the ion is lying flat. On the other hand, the lowering between 20 and 30 μC cm^{-2} is marked in agreement with the proposed reorientation of the adsorbed ion. Results for surface concentrations above this are very limited, and the lowering of capacity could be reasonably interpreted either as an increase in thickness, as a decrease in dielectric constant of the inner layer, or as a combination of both. Perhaps the predominant effect is the increase of thickness since the dielectric constant might tend to increase as the proportion of molecules oriented perpendicularly increases because the polarizability of the benzene ring is greater in directions parallel to the ring than in the perpendicular direction (9).

A simple two-position adsorption isotherm.—We have shown above that the experimental results on PTS require the assumption of at least two different orientations of the adsorbed species. We now investigate the properties of a simple model allowing for two orientations having different areas per molecule. It has become evident recently (10) that the most useful basis for an adsorption isotherm is the equation derived originally by Zhukovitskii (11) which is also known as the Flory-Huggins isotherm by analogy with the equations for polymer solutions: when the adsorbed species forms a monolayer at the electrode and replaces r molecules of the solvent the adsorption isotherm may be written

$$\frac{\theta}{r(1-\theta)^r} = \beta a \qquad [1]$$

where θ is the fraction of surface covered by the adsorbate, a is the latter's activity in the bulk of the solution, and β is the adsorption coefficient; $-RT \ln \beta = \Delta G^\circ$ the standard free energy of adsorption, the standard states being unity activity in the bulk of the solution and θ^* on the surface where $\theta^* = r(1-\theta^*)^r$ while the reference states are infinite dilution for both surface and bulk. Equation [1] assumes that the adsorbate and solvent are noninteracting, and a suggestion was made previously (12) of a way in which interaction could be introduced approximately.

The derivation of Eq. [1] may easily be extended to the adsorption of more than one species, for example by the quasi-chemical method (13). This leads to the expression for the fraction of surface covered by the i'th species

$$\frac{\theta_i}{r_i(1-\sum_i \theta_i)^{r_i}} = \beta_i a_i \qquad [2]$$

If the surface, in the absence of adsorbed species, is covered with N_s solvent molecules then the surface excess of the i'th species is

$$\Gamma_i = N_s\theta_i/r_i - (x_i/x_s)N_s(1-\Sigma\theta_i) \qquad [3]$$

from the usual definition of this quantity, where x_i and x_s are the mole fractions of i and of s, respectively, in the bulk of the solution.

We now consider a system in which one adsorbed species is present in the adsorbed state in two different orientations, flat in which it replaces r_1 solvent molecules and perpendicular in which it replaces r_2. Then we may write adsorption isotherms for the two forms

$$\frac{\theta_1}{r_1(1-\theta_1-\theta_2)^{r_1}} = \beta_1 a \qquad [4]$$

and

$$\frac{\theta_2}{r_2(1-\theta_1-\theta_2)^{r_2}} = \beta_2 a \qquad [5]$$

where β_1 and β_2 are the adsorption coefficients for the flat and perpendicular forms, respectively, and the bulk activity for both forms is of course identical. The total coverage due to adsorption of both forms is

$$\theta = \theta_1 + \theta_2 \qquad [6]$$

and the surface excess is

$$\Gamma = N_s\theta_1/r_1 + N_s\theta_2/r_2 - (x/x_s)N_s(1-\theta) \qquad [7]$$

where x is the mole fraction of the adsorbate in the bulk.

We now require to solve the adsorption isotherms [4] and [5] to obtain the surface excess. From Eq. [4], [5], and [6] we can obtain an equation for θ in the form

$$\theta = ar_1\beta_1(1-\theta)^{r_1}\left\{1 + \frac{r_2\beta_2}{r_1\beta_1}(1-\theta)^{r_2-r_1}\right\} \qquad [8]$$

To solve this equation for θ we must first describe the relation between β_1 and β_2.

We have suggested above that the PTS ion in its flat orientation behaves like the BMDS ion and therefore that the free energy of adsorption for this orientation, $-RT \ln \beta_1$, is approximately a linear function of the charge on the electrode. On the other hand, the perpendicularly oriented ion behaves like a neutral molecule and, therefore, $-RT \ln \beta_2$ may be taken to be quadratic in the charge on the electrode. Using the form of equations for these two cases derived previously (20) we write

$$-\ln\beta_1 = \frac{\Delta G_1^\circ}{RT} + aq \qquad [9]$$

and

$$-\ln\beta_2 = \frac{\Delta G_2^{max}}{RT} + b(q^{max} - q)^2 \qquad [10]$$

It is convenient to express β_2 in terms of β_1 which may then be used as the variable representing the charge dependence. Let

$$-\ln \beta_1^{max} = \frac{\Delta G_1^{o}}{RT} + aq^{max} \quad [11]$$

and

$$-\ln \beta_2^{max} = \frac{\Delta G_2^{max}}{RT} \quad [12]$$

so that Eq. [9] may be written

$$-\ln\left(\frac{\beta_2}{\beta_2^{max}}\right) = H\left(\ln\frac{\beta_1}{\beta_1^{max}}\right)^2 \quad [13]$$

where $H = b/a^2$. Equation [13] expresses the relationship between the adsorption coefficients of the two forms as they vary with the charge on the electrode. To substitute this relation into Eq. [8], we need the ratio of β_2/β_1, *i.e.*

$$\frac{\beta_2}{\beta_1} = \frac{\beta_2^{max}}{\beta_1}\exp\left\{-H\left(\ln\frac{\beta_1}{\beta_1^{max}}\right)^2\right\} = \frac{\beta_2^{max}}{\beta_1^{max}}\left(\frac{\beta_1^{max}}{\beta_1}\right)\exp\left\{-H\left(\ln\frac{\beta_1}{\beta_1^{max}}\right)^2\right\} \quad [14]$$

in terms of the ratio (β_1/β_1^{max}). The parameters which characterize the form of the relation between the two adsorption coefficients may thus most conveniently be taken as $\beta_2^{max}/\beta_1^{max} = S$ which represents the relative strength of adsorption of the two forms at the point where the perpendicular form is most strongly adsorbed and H which represents the rate at which the free energy of adsorption of this form falls off on either side of this point. Now Eq. [8] may be solved for θ as a function of log $(a r_1 \beta_1)$ with the given values of the parameter β_1^{max} r_1, r_2, S, and H. This is best done by iteration on a digital computer owing to the awkward form of Eq [8]. Once θ is obtained θ_1 is found from Eq. [4] in the form

$$\theta_1 = a r_1 \beta_1 (1-\theta)^{r_1}$$

and θ_2 from Eq. [6]. Finally Γ is calculated from Eq. [7], most simply by assuming dilute solutions, so that the last term may be neglected.

Some typical results are shown in Fig. 5 where Γ/N_s is plotted against $\log_{10}\beta_1$ for constant values of the activity of the adsorbate in the bulk of the solution. They were obtained with the aid of an IBM 1620 computer. It is clear from these results that, as the bulk activity increases, the shape of the curve changes from the monotonic rise with log β_1 characteristic of simple adsorption to one with a rapid rise to a high value of Γ followed by a fall to a lower limiting value.

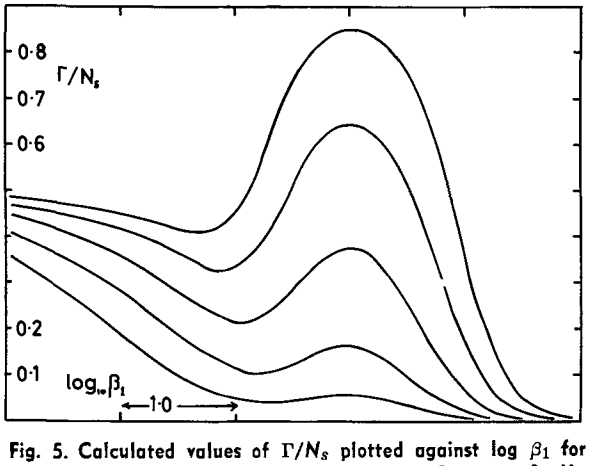

Fig. 5. Calculated values of Γ/N_s plotted against log β_1 for a two-position isotherm without interaction. $r_1 = 2$; $r_2 = 1$; H = 0.434; S = 12. The interval of $\log_{10}a$ between successive curves is 0.5.

In fact the general shape of the curves in Fig. 5 is quite similar to those in Fig. 2. However, there are quantitative differences which may be expressed by saying that the change in shape of the curves occurs over a narrower range of concentration than is found with the theoretical curves. This appears to be true over a wide range of parameters used for the calculated curves.

This discrepancy may be further explored by using the model to calculate the potential across the inner layer due to adsorption and thence the double layer capacity. In doing this, we must first note that the simple routes described previously (14) for this type of calculation cannot be used because this adsorption isotherm is not congruent, *i.e.*, it is not of the form $\Gamma = \Gamma(\beta a)$. Nevertheless, it is possible to start from the general relation [15]

$$\left(\frac{\partial E^+}{\partial \mu}\right)_q = -\left(\frac{\partial \Gamma_-}{\partial q}\right)_\mu \quad [15]$$

The potential of the mercury electrode with respect to a reference electrode reversible to the cation in solution may be expressed

$$E^+ = \phi^{m-2} + \phi_2 - \phi^{o}_{ref} - (RT/F)\ \ln a_+ \quad [16]$$

where ϕ^{m-2} is the potential across the inner layer and ϕ_2 that across the diffuse layer of the mercury electrode, ϕ^{o}_{ref} is the standard potential across the reference electrode and a_+ the activity of the cation in solution. If the variation of ϕ_2 is neglected and a_+ is put equal to the mean activitiy $a_\pm$, we may write Eq. [15] in the form

$$\frac{1}{RT}\left(\frac{\partial \phi^{m-2}}{\partial \ln a_s}\right)_q - \frac{1}{2F} = -\left(\frac{\partial \Gamma_-}{\partial \ln \beta_1}\right)_\mu \left(\frac{\partial \ln \beta_1}{\partial q}\right)_\mu = a\left(\frac{\partial \Gamma}{\partial \ln \beta_1}\right)_\mu$$

using Eq. [9] also,
thence

$$\phi^{m-2} - \phi^{m-2}\ (a_s = 0) = N_s RTa \int_0^{a_s} \frac{\partial(\Gamma/N_s)}{\partial \ln \beta} d\ln a_s + \frac{RT}{2F}\ln a_s \quad [17]$$

and the differential capacity of the inner layer can be found from

$$\frac{1}{C} - \frac{1}{C^b} = \left(\frac{\partial \phi^{m-2}}{\partial q}\right) - \left(\frac{\partial \phi^{m-2}}{\partial q}\{a_s = 0\}\right) = N_s RTa \frac{\partial}{\partial q}\int_0^{a_s} \frac{\partial(\Gamma/N_s)}{\partial \ln \beta_1} d\ln a_s = -N_s RTa^2 \frac{\partial}{\partial \ln \beta_1}\int_0^{a_s} \frac{\partial(\Gamma/N_s)}{\partial \ln \beta_1} d\ln a_s \quad [18]$$

Values of $\partial(\Gamma/N_s)/\partial \ln \beta_1$ were calculated from data like that shown in Fig. 5 and were then numerically integrated to obtain the reduced reciprocal capacity change, *i.e.*, $\{(1/C) - (1/C^b)\}/N_s RTa^2$ which is plotted in Fig. 6 against log β for various bulk concentrations. This theoretical calculation of the capacity curve is compared with the experimental results in the form of $1/C$ against q in Fig. 7. The comparison may be made directly since C^b does not vary much with q as seen in Fig. 4. Although some qualitative similarities can be seen it is again evident that the predictions of the simple theory show a less rapid change of the form of the curve with concentration than is found experimentally. There is also the important qualitative difference that the calculated capacity curve is more like that of a neutral compound than the experimental curves for PTS.

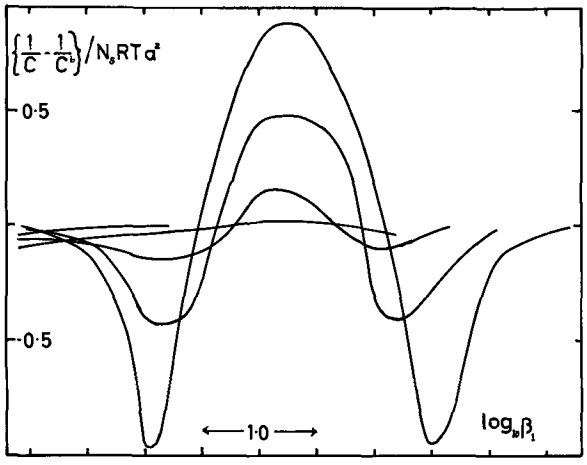

Fig. 6. Calculated reduced capacity curves for the two-position isotherm without interaction. The parameters have the same values as in Fig. 5, but the interval of $\log_{10}a$ between the successive curves is 1.0.

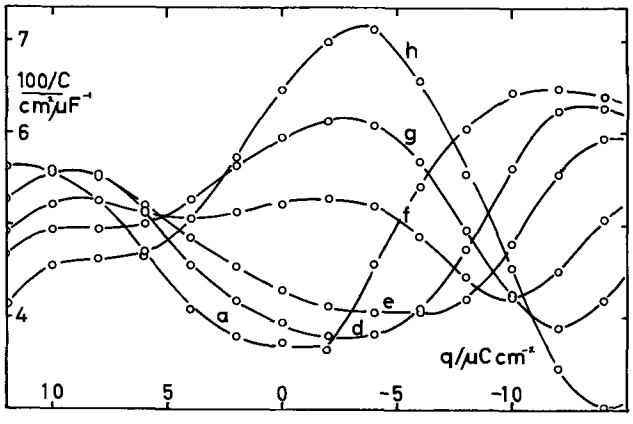

Fig. 7. Experimental curves of reciprocal capacity plotted against charge on the mercury electrode for aqueous sodium p-toluenesulfonate at 30°C. Letters on the curves have the same significance as those in Fig. 1.

A two-position adsorption isotherm with crude allowance for interaction.—The discrepancies between experiment and the simple theory described in the previous section cannot be overcome by variation of the parameters r_1, r_2, S, and H, so that it must be concluded that one of the postulates of this theory is incorrect. The one most likely to cause errors is the assumption that the adsorbed ions do not interact with one another. However, the difficulties in allowing for interaction in any realistic way are great. It has been suggested previously (12) that Eq. [1] could be modified to allow for interaction by introducing an exponential dependence on θ by analogy with Frumkin's modification (16) of Langmuir's isotherm

$$\frac{\theta}{r(1-\theta)^r}e^{A\theta} = \beta a$$

where A is a coefficient depending on interaction between adsorbed particles which may be interpreted as related to the two-dimensional second virial coefficient (17). The extension of such an equation to mixed adsorption would lead to [cf. Temkin (18)]

$$\frac{\theta_i}{r_i(1-\sum_i\theta_i)r_i}\exp\left(\sum_j A_{ij}\theta_j\right) = \beta_i a_i \qquad [19]$$

where A_{ij} expresses the interaction between adsorbed particles of the i'th and j'th type, and both summations are over all types of adsorbed particles except the solvent, although the effect of the latter must be included in the calculation of the A_{ij}. Even with the analogues of Eq. [4] and [5]

$$\frac{\theta_1}{r_1(1-\theta_1-\theta_2)^{r_1}}\exp\left(A_{11}\theta_1 + A_{12}\theta_2\right) = \beta_1 a \qquad [20]$$

and

$$\frac{\theta_2}{r_2(1-\theta_1-\theta_2)^{r}}\exp\left(A_{21}\theta_1 + A_{22}\theta_2\right) = \beta_2 a \qquad [21]$$

which might be applied to the present system the solution is difficult.

We have attempted to assess the effect of interaction on the two-position adsorption isotherm by simplifying [20] and [21]. It seems likely that the interaction between two PTS ions oriented flat will be repulsive, *i.e.*, A_{11} is positive, because the ionic groups are entirely within the inner layer, while the interaction between two vertically oriented ions will be attractive, *i.e.*, A_{22} is negative, since it is known that adsorbed hydrocarbon chains attract one another (19) and the ionic groups are in the diffuse layer where they are screened by the counter ions. The interaction between flat and vertically oriented ions may be weakly attractive due to polarization interactions; we shall assume that $|A_{21}| = |A_{12}| << |A_{22}|$ and $|A_{11}|$ and shall neglect their interactions. We also note that, owing to the opposite signs of A_{11} and A_{22}, the inclusion of both has the same qualitative effect of favoring the adsorption of the vertical form as its adsorption increases, while adsorption of the flat form is hindered. We shall, therefore, be able to investigate the effect of this interaction on the shape of the adsorption curves by introducing the coefficient A_{22} only, although its value will be larger (and negative) to allow for the other, neglected interaction coefficients. From Eq. [6], [20], and [21] $A_{11} = A_{12} = A_{21} = 0$, we obtain (20)

$$\theta = ar_1\beta_1(1-\theta)^{r_1}\left\{1 - \frac{r_2\beta_2}{r_1\beta_1}\exp^{-A_{22}\theta_2}(1-\theta)^{r_2-r_1}\right\} \qquad [22]$$

which differs from Eq. [8] only in the exponential factor in the last term. This equation may be solved using the results of the previous section and a simple graphical construction. Equation [8] is solved as described, for a series of values of S and θ_2, calculated. Log S is then plotted against θ_2. On this plot the value of θ_1 satisfying [22] is given by the intersection of this line with a straight line of slope $-A_{22}$. The position of this straight line can be characterized by the parameter S_o, *i.e.*, the value of S in the absence of interaction.

A set of curves of Γ_s/N against log β, calculated in this way with one set of parameters β_1^{max}, r_1, r_2, S_o,

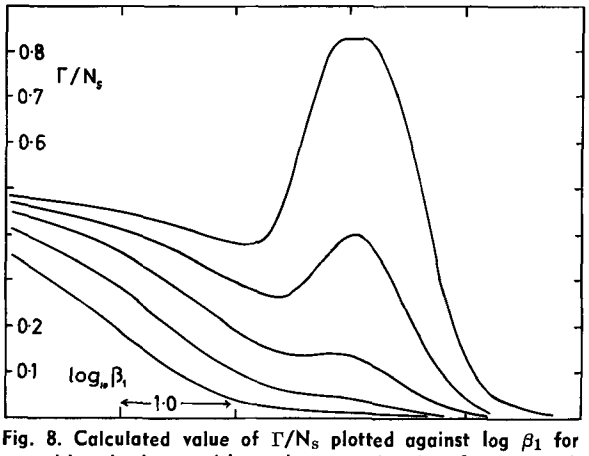

Fig. 8. Calculated value of Γ/N_s plotted against log β_1 for a two position isotherm with crude approximation for interaction. $r_1 = 2$; $r_2 = 1$; $H = 0.434$; $S_0 = 2$; $A_{22} = -2$. The interval of $\log_{10}a$ between successive curves is 0.5.

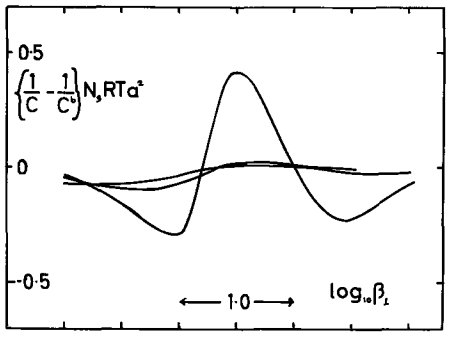

Fig. 9. Calculated reduced capacity curves for the two-position isotherm with crude approximation for interaction. The parameters have the same values as in Fig. 8, but the interval of $\log_{10}\alpha$ between the successive curves is 1.0.

H, and A_{22} is shown in Fig. 8. It is evident from this that the introduction of interaction in this way improves the agreement with experiment in that the change of shape of the curve occurs more rapidly with concentration. Capacity curves calculated by the route described in the previous section are shown in Fig. 9. Again there is some improvement in the agreement between the shape of these curves and those found experimentally as shown in Fig. 7. Nevertheless one major qualitative difference remains clearly expressed. This is the left-hand minimum in Fig. 9 at the highest concentration which would correspond to a marked peak at the left-hand side of Fig. 1. Comparing Fig. 8 and 2, we can see that this discrepancy is due to the fact that the displacement of the vertically oriented ions by flat ones at high concentrations occurs too rapidly. This may be ascribed to our neglect of the cross-coefficients $A_{12} = A_{21}$ which, as we suggested above, will correspond to an attractive force. This will act so as to stabilize the predominant form and will therefore lower the slope of the curve on the left-hand side of the maximum in Fig. 8. Little effect is to be expected on the right-hand side of the maximum owing to the fact that the concentration of the flat form is negligible in this region.

We therefore conclude that to account fully for the form of the experimental curves it is necessary to use the complete pair of Eq. [20] and [21].

Discussion

In this paper we have compared the predictions of a simplified model allowing adsorption of an ion in two-positions with experimental results for a system in which simple behavior of this type is observed. There seems little doubt that the general features of the model are correct and that proper allowance for interaction between the adsorbed ions would lead to a semiquantitative account of this system. However, apart from the practical difficulties of obtaining a solution for the simultaneous transcendental equations, it must be noted that the model based on Eq. [20] and [21] together with [9] and [10] would require at least 9 parameters to be fixed for a given set of curves even if no account is taken of deviations from [9] and [10] or variation of q^{max} with concentration. It therefore seems scarcely profitable to pursue the quantitative evaluation of the model further at present. Further experimental work on systems showing similar behavior may permit us to establish trends which may be correlated with the variation of individual parameters. The investigation of this type of model also provides a basis for the general problem of mixed adsorption which is of great importance in electrode kinetics.

Finally, we should note that this system provides a very clear example of an adsorption isotherm whose shape changes with change of the electrical parameter, *i.e.*, the isotherms at different charges are not congruent, because of the varying proportions of the two forms. Thus, the only satisfactory method for the calculation of surface concentrations is the direct use of the thermodynamic equations by graphical, or another type of, differentiation.

Acknowledgment

We should like to thank the Science Research Council (U.K.) for a maintenance grant (to J.M.P.) during the course of this work and also to thank the University of Bristol Computer Unit for facilities.

REFERENCES

1. J. M. Parry and R. Parsons, *Trans. Faraday Soc.*, **59**, 241 (1963).
2. B. B. Damaskin, I. P. Mishutushkina, V. M. Gerovich, and R. I. Kaganovich, *Zhur. Fiz. Khim.*, **38**, 1797 (1964).
3. R. Parsons and F. G. R. Zobel, *J. Electroanalyt. Chem.*, **9**, 333 (1965).
4. R. A. Robinson, *J. Am. Chem. Soc.*, **57**, 1165 (1935).
5. Landolt-Börnstein, Tabellen, 5th Ed., Vol. IIIc, 2148 (1936).
6. R. Parsons, *Trans. Faraday Soc.*, **51**, 1518 (1955).
7. D. C. Grahame, *Chem. Revs.*, **41**, 441 (1947).
8. H. R. Hurwitz, A. Sanfeld, and A. Steinchen-Sanfeld, *Electrochim. Acta*, **9**, 929 (1964).
9. cf. A. A. Bothner-By and J. A. Pople, *Ann. Rev. Phys. Chem.*, **16**, 43 (1965).
10. S. Levine, G. M. Bell, and D. Calvert, *Can. J. Chem.*, **40**, 518 (1962); J. O'M. Bockris and D. A. J. Swinkels, *This Journal*, **111**, 743 (1964).
11. A. A. Shukovitskii, *Acta Physicochim., U.R.S.S.*, **19**, 176 (1944).
12. R. Parsons, *J. Electroanalyt. Chem.*, **8**, 93 (1964).
13. D. H. Everett, *Trans. Faraday Soc.*, **61**, 2478 (1965).
14. R. Parsons, *J. Electroanalyt. Chem.*, **7**, 136 (1964).
15. R. Parsons, Proc. IInd Int. Congress Surface Activity III, 38 (1957).
16. A. N. Frumkin, *Z. physik. Chem.*, **116**, 466 (1925).
17. R. Payne, *J. Chem. Phys.*, **42**, 3371 (1965).
18. M. I. Temkin, *Zhur. Fiz. Khim.*, **15**, 296 (1941).
19. B. B. Damaskin and A. N. Frumkin, "Modern Aspects of Electrochemistry," 3rd ed., chap. 3, J. O'M. Bockris and B. E. Conway, Editors, Butterworths, London (1964).
20. R. Parsons, *J. Electroanalyt. Chem.*, **5**, 397 (1963).

Discussion

P. Delahay: My main comment on this paper pertains to the application of simultaneous isotherms (Eq. [19]) to the simultaneous adsorption of Tl^+ and NO_3^- in $TlNO_3$ solution in contact with mercury. The results, which are summarized in my paper at this meeting, will now be discussed more fully.

Calculations were made by assuming that the parameters r for Tl^+ and NO_3^- are equal to unity. An attempt to determine these parameters did not seem justified because of the uncertainty on the amounts of specifically adsorbed Tl^+ and NO_3^-. Furthermore, data fitting with a rather large number of adjustable parameters would not have been very convincing. Our results cannot be regarded as quantitative, but they do indicate a strong attraction between specifically adsorbed Tl^+ and NO_3^- ions. The NO_3^- — NO_3^- repulsion is significant and will be discussed in connection with Dr. Payne's on KNO_3 adsorption.

I would now like to ask Dr. Parsons a question he may not find surprising, namely, is one justified in using the concepts of average charge and potential in dealing with a surface that is partially covered with rather large ions? Dr. Parsons pointed out in 1959[1]

[1] K. M. Joshi and R. Parsons, *Electrochim. Acta*, 4, 129 (1961).

the need for a three-dimensional solution of the Poisson equation. Moreover, one would also have to consider other interactions than purely electrostatic ones. The case corresponding to $x_2 - x_1 < 0$ certainly should give some trouble. What is then the significance of $\phi_M - \phi_2$? I realize that an answer to my question could well be, you give us a better way of treating such cases, but Dr. Parson's thoughts on this question should be of interest.

Finally, I would like to ask Dr. Parsons his present position on the selection of the electrical variable, charge on the electrode *vs.* potential, in the treatment of adsorption. The dust has not settled, and this question has led to rather spirited discussion. It is unfortunate that Professor Frumkin is not present, as he certainly would also have had something to say on this point. Anyhow, the arguments of one school of thought should be of general interest.

Roger Parsons: The analysis of the $TlNO_3$ system is most interesting, and the interaction coefficients seem reasonable. Use of both r parameters equal to unity seems likely to be fairly near to the correct value.

In the case of flat orientation of large ions I do not think that the errors in the use of average potentials and charges are more serious than in the case of small ions at the same adsorbed charge density. I agree that the vertical orientation gives more trouble, and this is included in a very qualitative way in the idea of screening the sulfonate charge in the diffuse layer. Undoubtedly a more sophisticated model is desirable, but not much progress has been made in this direction as far as explaining experimental results is concerned.

I believe that there is some degree of agreement that charge is the preferable variable for ionic adsorption, but this is not so for neutral molecule adsorption. I still retain the opinion that it is preferable in the latter case, but it is very difficult to make a conclusive test of this or the opposite view. Tests can be devised for congruent isotherms (those for which the interaction parameters are independent of electrical conditions), but there is no *a priori* reason to assume that the isotherm for a given substance is congruent.

E. Gileadi: Equation [1] in this paper takes into account the obvious activity coefficient of the species in solution, but seems to neglect activity coefficients on the surface. Apart from lateral interaction effects which cause a change in the free energy of adsorption, there is an important entropy term which must be introduced when an adsorbed species occupies more than one site on the surface ($r > 1$). This accounts for the nonrandom distribution of occupied (and free) sites on the surface. Calculations of this type have been given by Miller[2] for the relatively simple case of $r = 2$, but as far as I know none have so far been published for higher values of r. Some preliminary calculations by Hurwitz and Gileadi for $r = 4$ show that this effect can be quite substantial and can alter the shape of the isotherm. The additional difficulty which arises here is that the form of the entropy term depends not only on the value of r but also on the shape of the adsorbed molecule.

It would seem therefore that the isotherms given here are applicable mainly for liquid electrodes and would not apply to solid electrodes with well-defined and localized adsorption sites.

Roger Parsons: Yes, I agree that Eq. [1] is likely to be useful only for liquid electrodes where there are no definite sites on the metal surface. In this case the entropy contribution is included according to the Flory-Huggins model.

[2] A. R. Miller, *Proc. Cambridge Phil. Soc.*, 35, 293 (1939).

Richard Payne: I think several important points arise from this paper.

1. It is stated that the lines in Fig. 3 are approximately parallel at low coverages, whereas in actual fact, they diverge. The slope at $q = -10\ \mu C/cm^2$, for example, is 0.019 $cm^2/\mu F$; whereas at $q = 8\ \mu C/cm^2$, it is 0.0043 $cm^2/\mu F$. This suggests strongly that the standard free energy of adsorption of the flat form falls off from the linear charge dependence assumed in the analysis. I think this is confirmed by the discrepancy between the measured and calculated charge dependence of the amount adsorbed which the authors attribute to neglect of cross-interaction coefficients. The discrepancy could also be attributed to decrease of $d \ln \beta_1/dq$ with q which would mean that the flat form would not replace the vertical form as rapidly as predicted by the theory.

2. I would also like to make two other points in connection with the peaks in Fig. 3. It is suggested that the lines should become horizontal if the center of charge of the adsorbed species is in the diffuse layer. I disagree with this, since it neglects the contribution to ϕ^{m-2} of replaced solvent dipoles. I think it would be difficult to explain the charge dependence of the amount adsorbed for many neutral adsorbates without taking this factor into account. Second, the authors state that the divergence of the lines in Fig. 3 at high coverages can be explained in terms of $(\partial q/\partial \phi^{m-2})_{q'}$, the capacity measured at constant amount adsorbed which I think is only partially true. It is not possible to explain the zero and negative slopes of ϕ^{m-2} *vs.* q' at constant q without taking into account the contribution of the replaced solvent dipoles.

3. The value of the parameters used in the calculation which are listed under Fig. 5 seem unrealistic in certain respects. If the area occupied by a solvent molecule is taken as 10Å^2 then according to the experimental saturation areas of the two forms, *i.e.*, 53 and 32 Å^2 in the corresponding values of r_1 and r_2 should be roughly 5 and 3, respectively, rather than the 2 and 1 assumed in the calculation. How sensitive is the calculation to the values chosen for r_1 and r_2?

I think the value $\beta_1^{max} = 1$ should read $\ln \beta_1^{max} = 1$. This leads to $\Delta G_1^{max} = 576$ cal/mole which is more than an order of magnitude lower than the usual values found for ionic adsorption ($\sim$ 20 kcal/mole). Using the value $S = 12$ we find $\Delta G_2^{max} = -1.43$ kcal which again is much too low. It seems that with this value of S the difference between ΔG_1^{max} and ΔG_2^{max} is also unrealistically large (*i.e.*, a factor of 2.303 log $12 \simeq 2.5$). Can the authors comment on this point?

Roger Parsons: 1. This explanation is certainly a possible one. I had assumed that the flat orientation of the toluene sulfonate would behave in the same way as the benzene in disulfonate reported previously. In fact, the number of points in this low coverage region in Fig. 3 is rather small (4 concentrations or so), and the slopes of these plots cannot be given with complete confidence.

2. I do not entirely agree. As I suggest in the remarks on your paper, it is possible to obtain the quadratic dependence of free energy of adsorption on charge if only the thickness of the inner layer is increased by the adsorption. Then the change of sign of the slope of ϕ^{m-2} *vs.* q' follows with the charge corresponding to zero slope (maximum adsorption) depending on dipolar or ionic properties. An alternative explanation is in terms of the average dielectric constant of the inner region in which the dipoles may also play a part. In the real system it may well be that all these phenomena contribute.

3. I have discussed the value of the parameter r for some single adsorption systems briefly elsewhere[3] and suggested that the value found was smaller than would be expected from the known size of the water

[3] Roger Parsons, *J. Electroanalyt. Chem.*, 8, 93 (1964).

molecule and that this might be due to the existence of clusters of water molecules on the mercury surface. Variation in the relative values of r_1 and r_2 changes some features of the curves such as those in Fig. 5. In particular, the limit at large positive changes (left-hand side of Fig. 5) is $\theta = r_2/r_1$ so that this ratio determines the relative heights of the peak and the saturation coverage at positive charges.

The caption under Fig. 5 should read ln β_1^{max}. This value is arbitrary, and the actual value would depend on the concentration range for which the curves in the figure apply. The difference between ΔG_1^{max} and ΔG_2^{max}, however, does have real significance. In the absence of similar analyses for simpler systems, it is only possible to express an opinion about the magnitude used here, but I believe this difference is not too large; if it were much smaller it would become close to RT, and there would be no clear predominance of the vertical form over any range of the variables.

J. R. Macdonald: Your implicit assumption that there are no stable intermediate states for the adsorbed molecules between completely flat and standing-up straight conditions seems reasonable to me. On the other hand, in the situation where there are appreciable concentrations of molecules in both these two stable states, one would expect thermal equilibrium between them; thus a proportion of them at any instant should be undergoing transitions from one state to the other. Should not your treatment include the effects of the molecules in these intermediate positions?

Roger Parsons: It is indeed true that under conditions where the energies of the two forms of adsorbed species are comparable intermediate orientations must also have similar energies. However, the solution of the complete problem of the energy of the system as a function of orientation of each toluene sulfonate ion would be difficult. It seems likely that the main features of the present simplified solution would still be present since in most regions one form or the other would predominate.

B. E. Conway: It may be of interest to note that a two-position treatment for adsorption also applies to the neutral molecule, pyridine. This is indicated by the fact that (*a*) the apparent standard free energy of adsorption of pyridine on Hg decreases in a discontinuous manner with increasing coverage θ expressed to the power $\theta^{3/2}$ to allow for dipole repulsion effects;[4] and (*b*) by the fact that the surface pressure ϕ-surface excess Γ relation shows two linear regions with different slopes which can best be interpreted in terms of a disorientation-orientation transition in the double layer.[5] Similar effects are observed in the sorption of pyridine in montmorillonite.[6]

In regard to the Flory-Huggins type of treatment you mentioned in which the different areas of the adsorbate molecules (solvent and solute) are taken into account, it may be mentioned that Shinoda and Hildebrand[7] have found for the analogous lattice problem in three-dimensional solutions of spherical molecules of different sizes that the required volume-fraction statistics represent the solution behavior less satisfactorily than do mole fraction statistics. This may be due to the shapes of the molecules involved. However, for tetraalkylammonium salts the size factor can be significant in the activity coefficients.[8] The lattice theory may be quantitatively applicable only to those solutes that approach the ideal condition of occupying some simple multiple number of the solvent sites laterally (as in polymer solutions, or diphenyl in benzene). Similar problems would, it seems, arise in the case of the Flory-Huggins type of treatment for a two-dimensional phase.

[4] B. E. Conway and R. G. Barradas, *Electrochim. Acta*, **5**, 319, 349 (1961).

[5] B. E. Conway, R. G. Barradas, P. G. Hamilton, and J. M. Parry, *J. Electroanal. Chem.*, **10**, 480 (1965); cf. L. Gierst, "Transactions of Symposium on Electrode Processes," Philadelphia 1959, p. 109, E. Yeager, Editor, John Wiley & Sons, Inc., New York (1961).

[6] R. Greene-Kelley, *Trans. Faraday Soc.*, **51**, 412, 425 (1955).

[7] K. Shinoda and J. Hildebrand, *J. Phys. Chem.*, **61**, 789 (1957).

[8] B. E. Conway and R. E. Verrall, *J. Phys. Chem.*, **70**, 1473 (1966).

The Structure of the Mercury-Solution Electrical Double Layer in the Presence of Adsorbed Oxyanions

Richard Payne

Air Force Cambridge Research Laboratories, L. G. Hanscom Field, Bedford, Massachusetts

ABSTRACT

The unusual adsorption characteristics of oxyanions are described with special reference to the adsorption of nitrate ions from KNO_3 solutions. The adsorption energy is shown to be linearly dependent on the charge in contrast to the behavior previously found for mixed solutions of NH_4NO_3 (and also NH_4ClO_4) with NH_4F at constant ionic strength where the dependence is approximately quadratic. The reasons for the differences are discussed in terms of the structure of the inner region of the double layer. The capacity of the inner region of the double layer is analyzed and related to the form of the adsorption isotherm and the Esin and Markov coefficient. Arguments are advanced in favor of using the mean ionic activity rather than the salt activity in the isotherm.

The unusual electrocapillary properties of inorganic oxyanions like nitrate and perchlorate were first recognized by Grahame and Soderberg (1) in a systematic study of the specific adsorption of anions. They concluded from their measurements that the nitrate ion is relatively weakly adsorbed, probably by Van der Waals-type adsorption forces rather than the stronger forces characteristic of the adsorption of the iodide ion for example. This viewpoint seemed to be confirmed by recent measurements of the adsorption of nitrate (2) and perchlorate (3) ions from mixed solutions of NH_4NO_3 and NH_4ClO_4, respectively, with NH_4F at constant ionic strength, which suggested that specifically adsorbed anions are replaced by solvent molecules at sufficiently positive values of the electrode charge in much the same way that weakly held organic adsorbates are desorbed at the extremes of polarization. However, studies of KNO_3 and $HClO_4$ solutions appear to indicate fundamental differences in the characteristics of the ad-

sorption process for a given anion depending on the nature of the solution. Thus the adsorption of nitrate ions from pure KNO_3 solutions more closely resembles that of the strongly adsorbed iodide ion than the adsorption of nitrate ions from the mixed ammonium salt solutions. This result is somewhat surprising and apparently casts some doubt on the validity of Grahame's analysis (4). The problem is here reconsidered with special reference to the behavior of the KNO_3 system.

Experimental

The differential capacity of the double layer at a dropping mercury electrode was measured for seven concentrations of KNO_3 ranging from 0.01-1M using the a-c bridge method described previously (5). The internal precision of the measurements was better than 0.05%. The potential was measured with a precision of 1 mv with respect to a calomel reference electrode in 0.1M KCl. In order to minimize uncertainties due to variations in the liquid junction potential (LJP), a 0.1M KNO_3 solution was always maintained in contact with the reference electrode. The liquid junction was made in a solution-sealed stopcock and was left undisturbed throughout the measurements. As before, a second liquid junction of the type KNO_3 (0.1M) $|KNO_3(x\text{M})$ was deliberately introduced. The junction was again maintained in a solution-sealed stopcock. The LJP in this case could be calculated from the Henderson equation using published values (6) of t^+, the cation transference number. Since t^+ is close to 0.5 for KNO_3 solutions, the LJP is small and can be accurately computed. The reproducibility of this arrangement was repeatedly checked by measuring the potential of zero charge (pzc) using the streaming mercury electrode method (7), and also by checking the pzc against published values (8) and the value found independently (9) for 1M KNO_3 using a 1M KCl calomel reference electrode in direct contact with the KNO_3. The agreement found was usually better than 1 mv.

Solutions were prepared volumetrically from permanganate distilled water and AR grade KNO_3 previously recrystallized from the same water. No trace of electroreducible or surface active impurities was detected during the measurements. Mercury was purified in the usual way by extraction with dilute HNO_3 followed by multiple distillation *in vacuo*. Capillaries were prepared and silicone treated as described previously (10). Solutions were freed from oxygen by bubbling with filtered and presaturated oxygen-free nitrogen. The pzc was measured for each solution by the method of the streaming mercury electrode (7). All measurements were made in a water thermostat controlled to ±0.05°C.

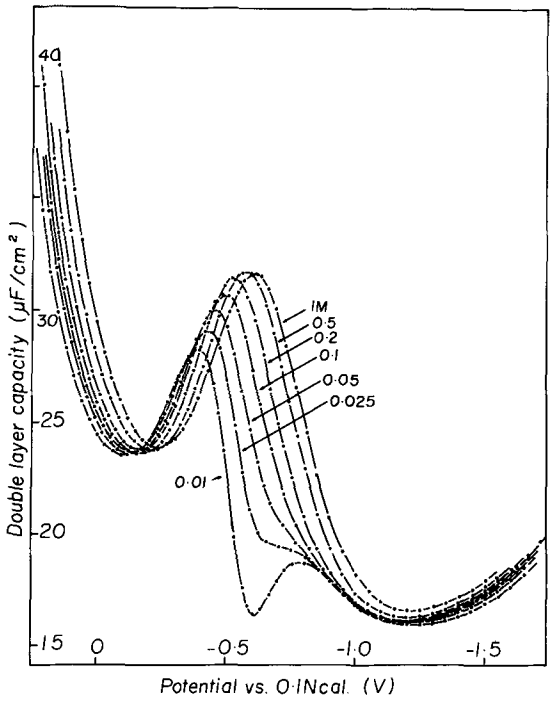

Fig. 1. Differential capacity of the electrical double layer at a mercury electrode in contact with aqueous KNO_3 solutions at 25°C.

Results

The differential capacity of the double layer is shown as a function of the potential for seven concentrations of KNO_3 in Fig. 1. The characteristic capacity hump which occurs close to the pzc decreases in height as the bulk concentration of KNO_3 decreases due to the effect of the diffuse layer capacity at the lower concentrations. The occurrence of specific adsorption at the pzc, even in the most dilute solution, is suggested by the fact that the capacity minimum due to the effect of the diffuse layer capacity occurs at a potential of ~60 mv more negative than the pzc owing to the effect of the superimposed steeply rising inner layer capacity. It will be shown, however, that most of the concentration dependence of the capacity in Fig. 1 is due to the effect of the diffuse layer, in contrast with the behavior of the halide anion systems where the concentration dependence of the inner layer capacity is much more important.

The capacity was integrated twice with respect to the potential using a digital computer (Elliot 803) as described previously (10). Integration constants were taken from the measured zero charge potentials and published interfacial tension data of Gouy (11). The measured potentials were converted to an E^- scale with the aid of published values of the mean activity coefficient and cation transference number (6). The computed data were in the form of values of the capacity (C), potential measured with respect to a hypothetical anion reversible electrode (E^-), interfacial tension (γ) and the function $\xi^- = \gamma + qE^-$ all interpolated to integral values of the surface charge density on the metal (q). The capacity potential and interfacial tension for each solution at the pzc are recorded in Table I.

The surface excess of cations (Γ^+) was calculated in the usual way (12) by plotting ξ^- against $2RT/F$ ln $a_\pm$ for constant values of q and differentiating graphically according to the thermodynamic equation

$$-d\xi^- = 2RT/F \cdot \Gamma^+ \, d \ln a_\pm - E^- \, dq \qquad [1]$$

where $a_\pm$ is the mean activity and constant temperature and pressure are understood.

The charge dependence of Γ^+ is shown for several concentrations of the salt in Fig. 2. The flatness of the variation on the anodic side first noted by Grahame and Soderberg (1) distinguishes this system from systems like KCl and KI where Γ^+ goes through a well-defined minimum (13). This difference is due to the smaller charge dependence of the specific adsorption of the nitrate ion as will be shown. The flat maximum

Table I. Coordinates of the electrocapillary maximum and values of the cathodic minimum capacity for aqueous KNO_3 solutions at 25°C

C, mole/liter	C_{min}, μF/cm²	$-E_{zero}$[a], v	γ_{zero}[b], dyne/cm	C_{zero}, μF/cm²
0.01	15.89	0.548	425.2	18.30
0.025	15.94	0.554	424.9	23.11
0.05	15.96	0.560	424.5	26.34
0.1	16.00	0.571	424.1	28.67
0.2	16.05	0.585	423.4	30.40
0.5	16.22	0.600	422.1	31.53
1	16.56	0.617	420.9	31.59

[a] E_{zero} is emf of the cell
Hg | Hg_2Cl_2 | 0.1M KCl ¦ 0.1M KNO_3 ¦ xM KNO_3 | Hg
[b] Interpolated from data of Gouy (11).

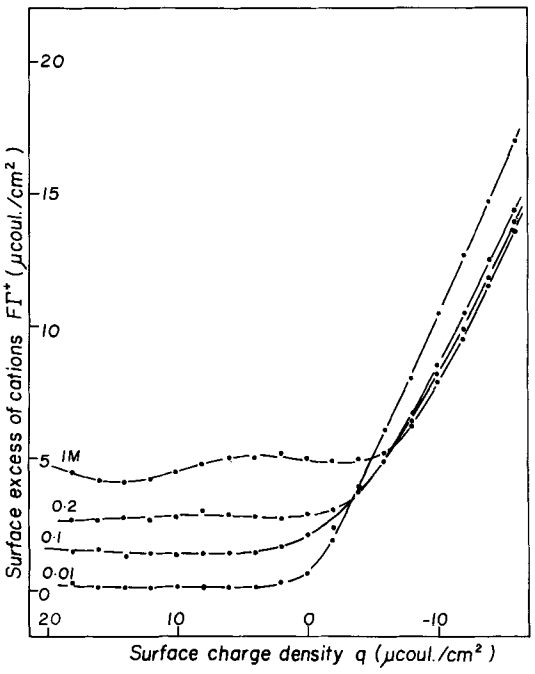

Fig. 2. Charge due to the surface excess of cations as a function of the concentration of KNO_3 and the charge on the metal.

in Γ^+ for the 1M solution close to $q = 4\mu C/cm^2$ suggests that the anion adsorption approaches saturation coverage (14), although this effect may be an artifact resulting from errors inherent in the graphical differentiation. Since Γ^+ is close to zero for $q \gtrsim 4\mu C/cm^2$ in the 0.01M solution, the charge on the solution side of the interface (q^s) is almost wholly due to specifically adsorbed anions in this region if specific adsorption of cations is discounted. Although measurements in solutions more dilute than 0.01M were not made, the results in Fig. 2 suggest that a plot of Γ^+ *vs.* log $a_\pm$ would be asymptotic to $\Gamma^+ = 0$ at infinite dilution, in which case a similar plot of the surface excess of anions (Γ^-) would be asymptotic to the value $-q/F$. Since there is no diffuse layer charge all of q^s is made up of the charge due to specifically adsorbed anions (q^1) so that q^1 apparently approaches the value $-q$ at infinite dilution. This is somewhat surprising since q^1 should presumably approach zero when the bulk concentration of anions is zero. Because of the uncertainty in the diffuse layer calculation under conditions where Γ^+ is close to zero (15), it could be assumed that this effect is due to errors in the measurements or the analysis. This point is discussed in more detail below.

The values of Γ^+ were used to calculate the surface excess of anions (Γ^-) by difference from q^s/F

$$\Gamma^- = q^s/F - \Gamma^+ \qquad [2]$$

The charge due to diffuse layer anions (q^d) was then calculated from Gouy-Chapman diffuse layer theory assuming no specific adsorption of cations. The charge due to specifically adsorbed anions was found by subtracting the diffuse layer concentration from the total surface excess of anions

$$q^1 = F\Gamma^- - q^d \qquad [3]$$

The values of q^1 obtained in this way were then used directly in the subsequent analysis which was developed by Parsons (12) and Grahame (4).

In Fig. 3 q^1 is shown as a function of q for several concentrations of KNO_3. It is evident that the curves are approximately linear and parallel for $q \geq 4\mu C/cm^2$, the slope of the linear segment being

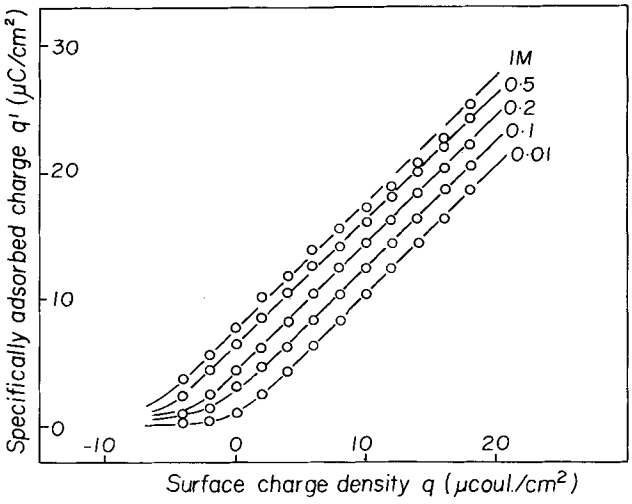

Fig. 3. Charge due to specifically adsorbed nitrate ions as a function of the charge on the metal and concentration of KNO_3.

close to 1.0 in good agreement with the result found by Grahame and Soderberg for 0.1M KNO_3. The systematic deviations from the line of unit slope for the most concentrated solution can be reasonably attributed to errors of graphical differentiation which are most serious at the extremes of the concentration range. The maximum deviation is $\sim 0.8\ \mu C/cm^2$, which is probably within the experimental error. The potential difference (ϕ^{m-2}) generated across the inner region of the double layer by specifically adsorbed anions was calculated by subtracting RT/F ln $a_\pm$ and the potential difference across the diffuse layer (ϕ_2) from E^-. The resultant values of ϕ^{m-2} were then plotted against q^1 for integral values of q. The results of this plot are shown in Fig. 4. As was found previously for KCl (16) and sodium benzenedisulfonate solutions (14) the data can be represented by a series of parallel straight lines. The appreciable scatter of the points is again attributable to errors introduced by the graphical differentiation. This is particularly troublesome at the lower concentrations where Γ^+ is close to zero. Under these conditions the calculation of ϕ_2 and q^d from diffuse layer theory is extremely sensitive to errors in Γ^+.

The capacity was analyzed with the aid of diffuse layer theory and values of dq^1/dq obtained by graphical differentiation of the plots in Fig. 3. The capacity of the inner region (C^i) was first obtained through the relationship

$$1/C = 1/C^i + 1/C^d(1 + dq^1/dq) \qquad [4]$$

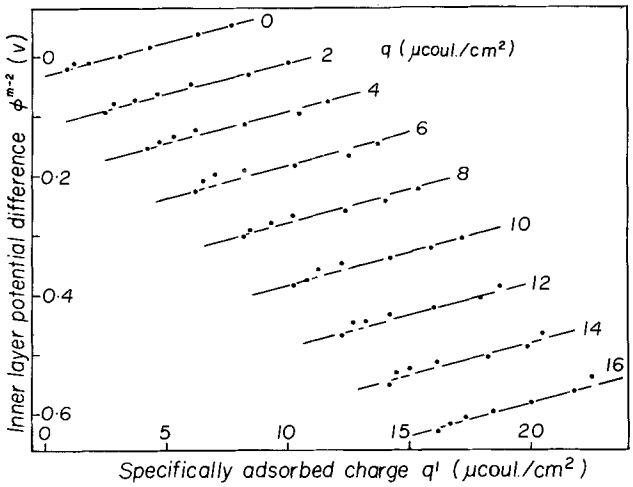

Fig. 4. Potential difference generated across the inner region of the double layer by specifically adsorbed anions.

where C^d is the capacity of the diffuse double layer. C^i was then further resolved into components measured at constant charge and at constant amount adsorbed through the identity

$$1/C^i = 1/{}_qC^i + 1/{}_{q1}C^i \cdot dq^1/dq \quad [5]$$

where ${}_qC^i$ the capacity of the inner layer measured at constant amount adsorbed and ${}_{q1}C^i$ the capacity measured at constant charge on the metal are defined by

$${}_qC^i = (\partial q/\partial \phi^{m-2})_{q1} \quad [6]$$

and

$${}_{q1}C^i = (\partial q^1/\partial \phi^{m-2})_q \quad [7]$$

As in all previously studied systems ${}_{q1}C^i$ is independent of the amount adsorbed (in view of the linearity of the plots in Fig. 4) and can therefore be replaced by the corresponding integral capacity ${}_{q1}K^i$. The value of ${}_{q1}K^i$ in the present system is 96 $\mu F/cm^2$.

The total inner layer capacity C^i and the capacity at constant amount adsorbed ${}_qC^i$ are shown as a function of q for several concentrations of KNO_3 in Fig. 5 and 6. The curves in both cases are almost independent of the salt concentration. This is somewhat surprising since C^i is expected to depend strongly on specific adsorption of the anion and hence on the bulk concentration of KNO_3. It appears that most of the concentration dependence of the measured capacity in Fig. 1 can be attributed to variation of the diffuse layer capacity. The constancy of ${}_qC^i$ is to be expected

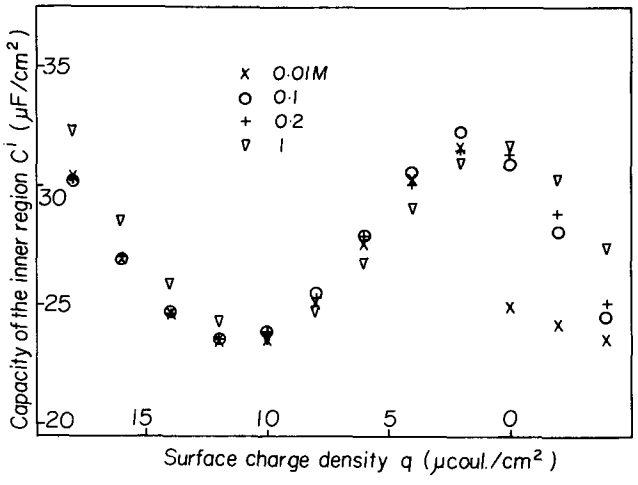

Fig. 5. Differential capacity of the inner region of the double layer as a function of the charge on the metal and concentration of KNO_3.

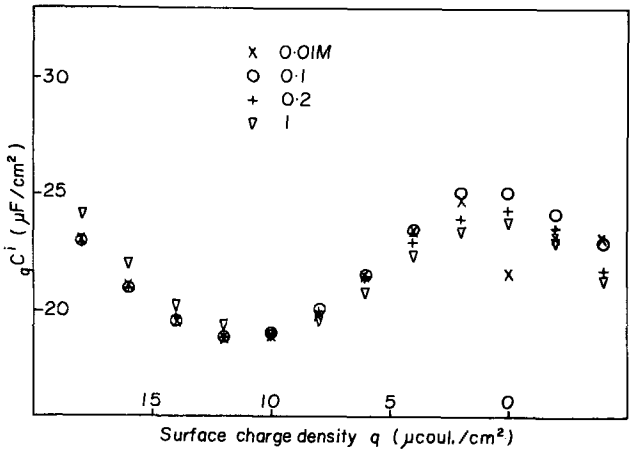

Fig. 6. Component of the inner layer capacity measured at constant amount adsorbed as a function of the charge on the metal and concentration of KNO_3.

since the plots of ϕ^{m-2} *vs.* q^1 in Fig. 4 are parallel. ${}_qC^i$ could also have been calculated for each experimental point in Fig. 4 by interpolating ϕ^{m-2} at the appropriate value of q^1 and then differentiating the corresponding values of q with respect to ϕ^{m-2}. Since the lines are parallel, the results of this calculation are independent of q^1.

Discussion

Adsorption Isotherm

The data were fitted to a single constant charge isotherm using the method described by Parry and Parsons (14). In order to test the correctness of maintaining constant charge rather than constant potential in this system the criterion devised by Frumkin et al. (17) was applied. According to Frumkin the charge (q) and potential (ϕ) in the case of a constant charge isotherm are related by the equation

$$q = (\phi - \theta\phi_N)/[(1-\theta)/C_o + \theta/C'] \quad [8]$$

where ϕ_N is the pzc corresponding to a coverage $\theta = 1$. ϕ and ϕ_N are measured with respect to the pzc for $\theta = 0$. C_o and C' are the capacities corresponding to $\theta = 0$ and $\theta = 1$, respectively. When $q = 0$; *i.e.* at the pzc, Eq. [8] reduces to

$$\phi_{q=0} = \theta\phi_N \quad [9]$$

so that the pzc should be a linear function of the coverage if a constant charge isotherm is obeyed. Figure 4 shows that this is so for the present system as was found previously for nitrate and perchlorate ion adsorption from mixed solutions of NH_4F with NH_4NO_3 and NH_4ClO_4, respectively. However, it should be pointed out as mentioned by Frumkin *et al.* that if $C_o = C'$ the corresponding equations for constant potential adsorption

$$q = C_o\phi(1-\theta) + C'(\phi - \phi_N)\theta \quad [10]$$

$$\phi_{q=0} = \phi_N\theta/[C_o/C'(1-\theta) + \theta] \quad [11]$$

also reduce to Eq. [9]. Although this condition seldom occurs in adsorption of organic compounds, it appears in view of the small dependence of C^i on concentration (Fig. 5) in this system that C_o and C' may be similar so that the value of the test is correspondingly reduced. It is possible within the limitations of the somewhat crude approximations of Frumkin's treatment to extend the argument to consider adsorption at constant values of q other than zero. In this case the constant charge equation, Eq. [8], can be rearranged to give

$$\phi = q/C_o + \theta[\phi_N + q(1/C' - 1/C_o)] \quad [12]$$

whereas the constant potential equation, Eq. [10], gives

$$\phi = [q + C'\theta\phi_N]/[C_o(1-\theta) + C'] \quad [13]$$

According to Eq. [12] ϕ should be a linear function of θ with a slope that increases (or becomes less negative) with increasing q by an amount $(1/C' - 1/C_o)$, whereas Eq. [13] predicts a more complex dependence. The relationship of Eq. [12] to the plots of ϕ^{m-2} *vs.* q^1 in Fig. 4 is obvious. Since these plots are parallel it follows that $C' \approx C_o$ in this system as was shown earlier (Fig. 5). Again this does not necessarily confirm the correctness of the constant charge isotherm since both [12] and [13] reduce to the common equation

$$\phi = q/C_o + \theta\phi_N \quad [14]$$

when $C' = C_o$. However, in the $NH_4NO_3 + NH_4F$ system C' and C_o are not equal and the plots of ϕ^{m-2} *vs.* q^1 (or θ) are linear with a slope which becomes increasingly positive with q in agreement with Eq. [12]. It appears, therefore, that a constant charge isotherm is appropriate to this system, and in the ab-

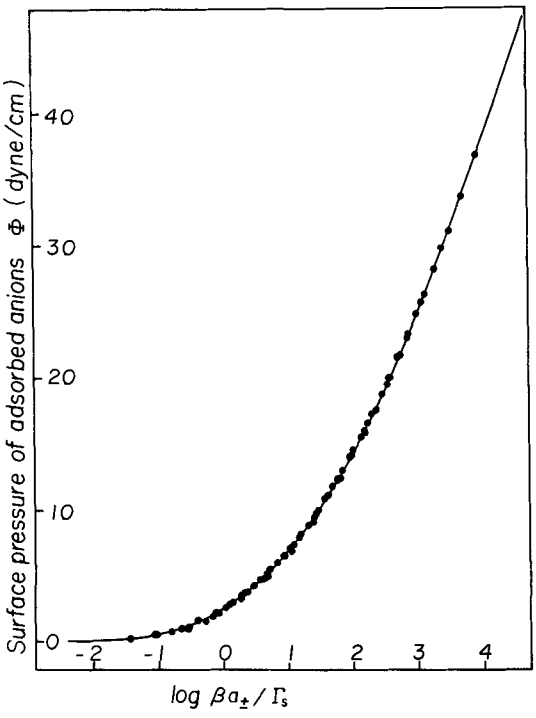

Fig. 7. Composite curve of the surface pressure of nitrate ions specifically adsorbed from KNO_3 solutions. The range of q covered is 0-18 $\mu C/cm^2$.

sence of any indications to the contrary it seems reasonable to assume that the same is true for the present system.

The surface pressure (Φ) of specifically adsorbed anions was calculated as described elsewhere (14, 18). The individual curves of Φ *vs.* log $a_\pm$ for various constant values of q were fitted together to give the composite curve shown in Fig. 7. The solid line was calculated from a Frumkin isotherm (19),

$$\ln[\theta/(1-\theta)] + A\theta = \ln(\beta a_\pm/\Gamma_s) \qquad [15]$$

with the following constants

$$\begin{aligned} &A/2.303 = 3 \\ &\left\{\begin{array}{l} \Gamma_s = 1.59 \times 10^{14}\ \text{molecule/cm}^2 \\ q_s^1 = 25.4\ \mu C/cm^2 \end{array}\right. \\ &\log\beta = 14.83 + 0.205\,q \end{aligned} \qquad [16]$$

where A is the dimensionless lateral interaction coefficient, Γ_s the saturation coverage, q_s^1 is equal to $F\Gamma_s$, and β is related to the standard free energy of adsorption at zero coverage (ΔG°) by

$$\beta = \exp(-\Delta G^\circ/RT) \qquad [17]$$

The variation of ΔG° with q (Fig. 8) showed a slight sigmoid tendency which was regarded as small enough to be neglected. The largest deviation of Φ from the common curve in Fig. 7 was no more than 0.3 dyne/cm.

The constants of the isotherm are remarkably similar to those previously found for the adsorption of nitrate ions from NH_4NO_3 + NH_4F solutions (2) which also obeys a Frumkin isotherm with $A/2.303 = 1$, $q_s^1 = 24.7\ \mu C/cm^2$ and $\log\beta = 14.95 + f(q)$[1]. Thus the anomalously large apparent area of the adsorbed nitrate ion (~60 Å^2) is again emphasized. The lateral interaction coefficient is larger by a factor of 3 for the KNO_3 system. This has the effect of spreading the adsorption over a wider concentration range in the lower and intermediate range of coverage. This suggests that the lateral interactions may be screened out to some extent by the constant high electrolyte concentration in the mixed electrolyte system. The same factor would lead to variation of the interaction coefficient with concentration in the KNO_3 system which would mean that the adsorption could not be represented by a single isotherm.

[1] $f(q)$ in this system is nonlinear.

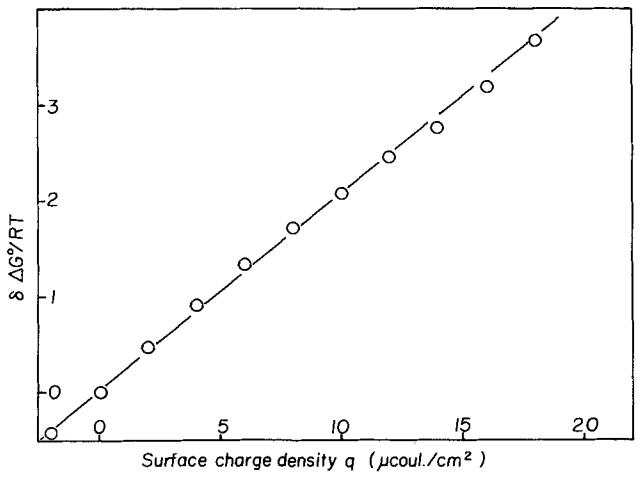

Fig. 8. Charge dependence of the standard free energy of adsorption of nitrate ions from KNO_3 solutions.

It is interesting to note that the plot of ϕ^{m-2} *vs.* q^1 at $q = 0$ in Fig. 4 does not extrapolate to $\phi^{m-2} = 0$ at $q^1 = 0$ but to a value which is ~25 mv positive. When the isotherm values of q^1 are used to calculate the diffuse layer potential difference, the same plot is curved but now properly extrapolates to the origin, suggesting therefore that the isotherm values of q^1 may be more accurate than the values obtained by graphical differentiation. The source of this discrepancy appears to be the diffuse layer potential difference which, according to the graphical analysis, does not approach zero at low concentrations. This is another way of stating that the specifically adsorbed charge appears to be asymptotic to a value of $-q/F$ rather than zero at infinite dilution as was discussed earlier. The divergence of the ϕ^{m-2} *vs.* q^1 plots calculated directly and from the isotherm at $q = 0$ can

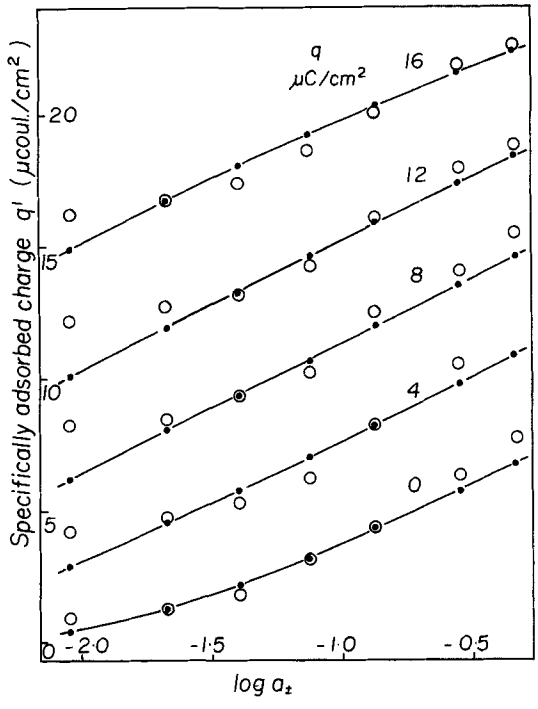

Fig. 9. Comparison of the charge due to specifically adsorbed ions calculated directly according to Eq. [1] (open circles) with values calculated from the isotherm (closed circles).

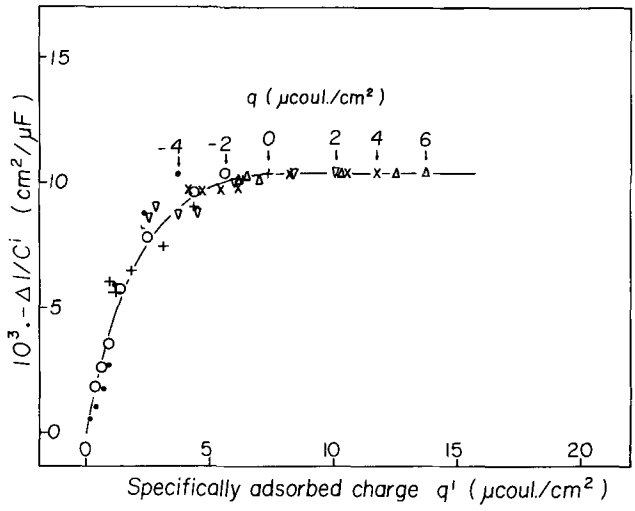

Fig. 10. Change of the inner layer capacity produced by adsorption of nitrate ions from KNO_3 solutions as a function of the amount adsorbed.

evidently be accounted for by a systematic error in ξ^- of no more than 0.2 dyne/cm. This is due to the extreme sensitivity of the calculation of ϕ_2 from diffuse layer theory to the value of q^1 under these conditions. In Fig. 9 are compared the values of q^1 calculated by the two methods. It is apparent that the directly calculated values are asymptotic to a value close to $q^1 = -q$ at the low concentration end whereas the isotherm values are asymptotic to $q^1 = 0$ (as they clearly must be if they are to fit a single common isotherm). This behavior is also evident in other systems.[2] Thus, although the deviations in Fig. 9 could be accounted for by very small errors in the measurements, they are nevertheless believed to be real and represent a small dependence of the isotherm constants on the charge or concentration or both. For this reason the directly calculated values of q^1 were used in the analysis.

As is well known, the change of the capacity produced by adsorption is characteristic of the adsorption isotherm and under favorable circumstances can be used to identify the isotherm and evaluate its constants (20, 21). The change of the inner-layer capacity ($-\Delta 1/C^i = 1/C^i - 1/{}_qC^i$) is shown as a function of q^1 in Fig. 10. As mentioned earlier, $\Delta 1/C^i$ reaches a limiting value as was found previously for the adsorption of iodide ions from formamide solutions (18). Now according to Eq. [5]

$$-\Delta 1/C^i = 1/{}_{q1}K^i \cdot dq^1/dq \qquad [18]$$

or

$$-\Delta 1/C^i = 1/{}_{q1}K^i \cdot d \ln \beta/dq \cdot dq^1/d \ln \beta \qquad [19]$$

The last factor on the R.H.S. of Eq. [19] is characteristic of the adsorption isotherm. Since ${}_{q1}K^i$ and $d \ln \beta/dq$ are constant in this system, it follows that the shape of the $-\Delta 1/C^i$ *vs.* q^1 curve is the same as that of $dq^1/d \ln \beta$ *vs.* q^1. It is easily shown that the Frumkin isotherm leads to the relationship

$$dq^1/d \ln \beta = q^1{}_s\{[(1-\theta)]^{-1} + A\}^{-1} \qquad [20]$$

leading to a maximum value of $dq^1/d \ln \beta$ at $\theta = 0.5$ whereas a virial type of isotherm gives

$$dq^1/d \ln \beta = (1/q^1 + 2B/F)^{-1} \qquad [21]$$

where B is the second virial coefficient leading to the limiting value of $F/2B$ when $2B >> F/q^1$. It appears, therefore, that the present system might be better described by a virial form of isotherm. The value of B given by Eq. [19] and [21] is 440Å²/mol.

[2] See for example ref. (16).

As was pointed out previously, this ambiguity between the Frumkin and virial forms of the adsorption isotherm can arise when the lateral interaction coefficient A is large because under these conditions (and at sufficiently small values of θ) the Frumkin isotherm reduces to the virial equation. However, it follows from Eq. [18] that where the plots of ϕ^{m-2} *vs.* q^1 (Fig. 4) are linear and plots of q^1 *vs.* q (Fig. 3) are also parallel at the high concentration end, $\Delta 1/C^i$ must reach a limiting value which in general will be different for each value of q. This behavior was noted by Parsons (20) for the aq. KI system in which the charge dependence of the limiting value of $\Delta 1/C^i$ is evidently due primarily to the variation of ${}_{q1}K^i$ reported by Grahame (4) for this system. Where ${}_{q1}K^i$ is also independent of q (parallel plots of ϕ^{m-2} *vs.* q^1 in Fig. 4) and the q^1 *vs.* q plots are both linear and parallel at the high concentration end, $\Delta 1/C^i$ will reach a common limiting value for all values of q as found in the present system.

A modification of isotherms based on the Langmuir isotherm to take into account the different sizes of the adsorbing particles and the solvent molecules they replace was recently proposed by Parsons (22). The modified Frumkin isotherm is

$$\beta a = \theta e^{A\theta}/r(1-\theta)^r \qquad [22]$$

where r is the number of solvent molecules replaced by one adsorbate molecule. This isotherm leads to a maximum in $d\theta/d \ln \beta$ when $\theta = (1 + \sqrt{r})^{-1}$ so that when r is large the curve of $d\theta/d \ln \beta$ (or $-\Delta 1/C^i$) against θ is highly asymmetric. This seems likely to be the case in this system in view of the low saturation coverage and may account for the apparent limiting value of $-\Delta 1/C^i$. In other words the descending branch of the curve to the right of the maximum may have been eliminated by the assumptions mentioned previously. In this case the fit to a simple Frumkin isotherm would have to be regarded as empirical. From the value of 59Å² previously deduced for the saturation area and a value of 6Å² taken as the area occupied by a water molecule we obtain a value for r of ~10 leading to a maximum in $-\Delta 1/C^i$ when $\theta \approx 0.25$ or $q^1 \approx 7$ μC/cm². According to Fig. 10 $-\Delta 1/C^i$ indeed reaches its maximum value close to this point. It therefore seems reasonable to conclude that Parsons' modification of the Frumkin isotherm will describe the adsorption and that the limiting value of $-\Delta 1/C^i$ found is due to small errors introduced by the simplifying approximations necessarily made in the analysis.

Capacity of the Inner Region

The component of the capacity of the inner region measured at constant amount adsorbed (${}_qC^i$) is independent of the amount adsorbed within the experimental error. Similar behavior has been observed for all previously studied systems of anion adsorption from solutions of a single salt (4, 14, 16, 18). A small charge dependence of ${}_{q1}K^i$ (the reciprocal slope of the plots of ϕ^{m-2} *vs.* q^1 in Fig. 4) observed for the adsorption of iodide ions from both aqueous and formamide solutions of KI is of doubtful significance.

The behavior of the KNO_3 system contrasts sharply with that of mixed solutions of NH_4NO_3 and NH_4F at constant ionic strength (2) in which the adsorption of the nitrate ion results in a marked decrease of ${}_qC^i$ with increasing amount adsorbed. The same behavior was also found for perchlorate ion adsorption under similar conditions (3). The change in the total inner layer capacity produced by the adsorption of nitrate ions from the mixed solutions is shown as a function of concentration and electrode charge in Fig. 11. As was noted previously, these curves closely resemble those frequently found in the adsorption of neutral organic substances [see for example ref. (23)] and, as shown by Parsons (21), are characteristic of a quadratic charge (or potential) dependence of the

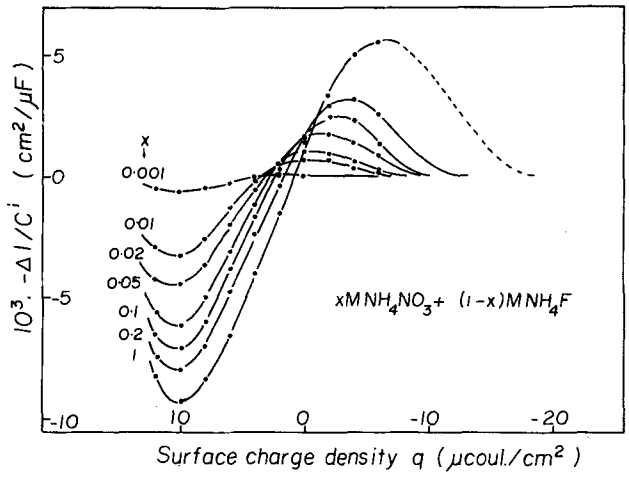

Fig. 11. Change of the inner layer capacity resulting from adsorption of nitrate ions from mixed solutions of NH_4NO_3 and NH_4F as a function of the charge on the metal and composition of the solution.

standard free energy of adsorption. They can be compared with the corresponding curves for the KNO_3 system in Fig. 12 which apparently exhibit the limiting value of $-\Delta 1/C^i$ characteristic of a virial form of the adsorption isotherm with a linear charge dependence of the adsorption energy as discussed earlier.

Since the specific adsorption of ions presumably results in the replacement of adsorbed solvent molecules it seems reasonable to assume that the capacity will depend on the amount adsorbed and, because the ions will in general be less polarizable than the replaced solvent molecules, the capacity would be expected to decrease. At the same time the average effective thickness of the layer will depend on the amount adsorbed and also on the size of the ion. For an ion like the nitrate ion which presumably adsorbs in a flat position on the electrode, the thickness of the layer should be little affected. It seems unlikely, therefore, that the expected decrease in the dielectric constant (ϵ^i) of the inner layer resulting from the adsorption would be compensated by a corresponding decrease in the thickness (x_2) as suggested by Grahame (4). Certainly the general occurrence of this effect in both aqueous and nonaqueous solutions (which of course was not known to Grahame) makes the possibility of accidental compensation of this kind seem unlikely. It is suggested, therefore, that the behavior of the mixed electrolyte system rather than

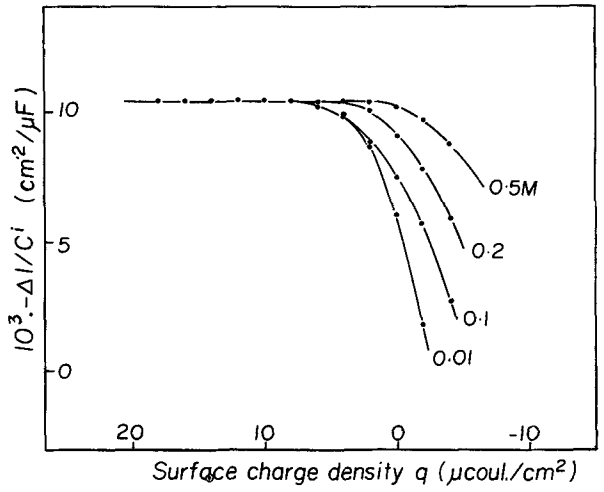

Fig. 12. Change of the inner layer capacity resulting from adsorption of nitrate ions from KNO_3 solutions as a function of concentration and the charge on the metal.

that of the KNO_3 system is more consistent with a realistic physical model of the inner region.

The fundamental change in the character of the adsorption of ions like nitrate and perchlorate when the composition of the solution is changed is difficult to understand. The quadratic charge dependence of the adsorption energy found for the mixed electrolyte system was previously attributed, by analogy with the adsorption of organic substances, to competitive adsorption of the ion with solvent dipoles. However, the fact that the pure KNO_3 solutions behave differently suggests that the fluoride ion, which is supposedly nonspecifically adsorbed, rather than the solvent is the competing species. It seems likely that the fluoride ion is specifically adsorbed to some extent at extreme positive polarizations although this possibility unfortunately can only be inferred, as in the case of inorganic cations (24), from indirect evidence because of the gross uncertainties in the diffuse layer correction mentioned earlier. It does not seem likely on the other hand that fluoride ions could be sufficiently strongly adsorbed under any conditions to replace adsorbed nitrate ions. The curves in Fig. 11 tend to confirm the original interpretation since the quadratic charge dependence of the adsorption energy is already well developed close to the pzc where specific adsorption of fluoride ions can almost certainly be discounted. It is therefore necessary to look elsewhere for an explanation of the difference between the two types of systems.

Grahame (4) wrote the part of the potential difference across the inner region resulting from the specifically adsorbed charge as

$$_{q1}\phi^{m-2} = \frac{-4\pi n^i e^o (x_2 - x_1)}{\epsilon^i} \qquad [23]$$

where x_1 is the distance of the center of the ion from the metal surface, n^i is the number of singly charged specifically adsorbed ions and e^o is the electronic charge. It is clear, however, as Frumkin indicated in his theoretical treatment for the adsorption of neutral substances (25), that Eq. [23] should include a second term to account for the contribution of solvent dipoles replaced in the adsorption process. $_{q1}\phi^{m-2}$ should therefore be written

$$_{q1}\phi^{m-2} = \frac{-4\pi n^i}{\epsilon^i}[e^o(x_2 - x_1) - n_w\bar{\mu}] \qquad [24]$$

where n_w is the number of solvent dipoles of average moment in the direction of the field $\bar{\mu}$ which are replaced by one specifically adsorbed ion. At sufficiently positive values of q (the electrode charge) the solvent dipoles will be oriented by the field with the negative end of the dipole facing the metal so that their removal will result in a positive shift of the electrode potential. The effect should also increase with increasing q as the degree of orientation, and hence $\bar{\mu}$ increases.

It was noted previously that the plots of ϕ^{m-2} *vs.* q^1 for the mixed electrolyte system are not parallel: the slope decreases with q and eventually reverses sign close to the limit of anodic polarization. This is a further manifestation of the quadratic charge dependence of the adsorption energy in view of the approximate relationship (26)

$$(\partial\phi^{m-2}/\partial q^1)_q = 2RT/F \cdot d\ln\beta/dq \qquad [25]$$

If it is assumed that the main contribution to variation of ϕ^{m-2} at constant q is through $_{q1}\phi^{m-2}$ as defined by Eq. [24] it follows that the condition for $(\partial\phi^{m-2}/\partial q^1) = 0$ is

$$e^o(x_2 - x_1) = n_w\bar{\mu} \qquad [26]$$

It would not be possible to explain these experimental results in terms of Grahame's expression for $_{q1}\phi^{m-2}$

(Eq. [23]) which would require an infinite value of the dielectric constant or zero or negative values of x_2—x_1, which seem to have no physical significance. It is clear therefore that Eq. [23] is only valid for the limiting case where the ion becomes a point charge and the dielectric a structureless continuum, neither of which are likely to be good approximations to the real situation. It therefore seems more reasonable to interpret the charge independent values of $(\partial\phi^{m-2}/\partial q^1)_q$ found for KNO_3 and other single salt systems in terms of Eq. [24] in preference to Eq. [23]. The constancy of $(\partial\phi^{m-2}/\partial q^1)_q$ would then reflect the constancy of $1/\epsilon^i(\epsilon^o(x_2 - x_1) - n_w\bar{\mu})$ in Eq. [24]; $x_2 - x_1$ would therefore have to increase with q in order to offset the expected increase in $\bar{\mu}$ according to which the results for the mixed electrolyte system were interpreted. It is not, however, clear why this should occur for the single salt and not for the mixed electrolyte system.

The slope of ϕ^{m-2} *vs.* q^1 for the mixed electrolyte system becomes approximately constant at 0.0051 $cm^2/\mu F$ for small negative values of q suggesting that the contribution of oriented dipoles to ϕ^{m-2} is small in this region as would be expected. The corresponding slope for pure KNO_3, however, is 0.0104 $cm^2/\mu F$ which is larger by a factor of 2. Therefore, $x_2 - x_1$ is apparently larger for the KNO_3 system over the whole range of polarization which suggests that imperfect imaging in the diffuse layer of the adsorbed ions occurs, leading to apparently increased values of x_2 as suggested by Dutkiewicz and Parsons (27). Certainly the most important difference between the KNO_3 and the NH_4NO_3 + NH_4F systems lies in the composition of the diffuse layer. Some evidence for the effect of this on the adsorption process is found in the smaller value of the lateral interaction coefficient in the isotherm for the mixed electrolyte system which suggests that the mutual repulsion of the adsorbed ions is being partially screened out by the high electrolyte concentration in the diffuse layer. The indication of a small concentration dependence of the isotherm constants for the KNO_3 system also tends to confirm this. Further studies of mixed electrolyte systems will be required to resolve this problem.

Distance Ratio

According to the Grahame-Parsons analysis of the inner layer capacity the distance ratio $(x_2 - x_1)/x_2$ is given directly by the capacitance ratio

$$ {}_qK^i/{}_{q^1}K^i = (x_2 - x_1)/x_2 \qquad [27] $$

It can easily be shown that when the effect on ϕ^{m-2} of the replaced solvent dipoles is taken into account according to Eq. [24] the capacitance ratio now gives

$$ {}_qK^i/{}_{q^1}K^i = (x_2 - x_1)/x_2 - n_w\bar{l}/x_2 \qquad [28] $$

where $\bar{l}$ is the mean component of the length of the solvent dipole in the direction of the field. The capacitance ratio therefore no longer gives the distance ratio directly.

As was discussed at length in the previous section ${}_qK^i$ and ${}_{q^1}K^i$ are independent of the amount adsorbed for the KNO_3 system and since K^i also does not vary much with q the capacitance ratio is almost independent of q and q^1, and has a value close to 0.25 in close agreement with the value reported by Parry and Parsons for the benzenedisulfonate ion. The capacitance ratio for NH_4NO_3 + NH_4F solutions on the other hand is much lower; it also decreases with q from a value of 0.12 at $q = 0$ to zero at $q = 10$ $\mu C/cm^2$ and is negative for larger values of q as would be expected from the earlier discussion.

The distance ratio can be calculated by an alternative method devised by Grahame, but subsequently modified by Parry and Parsons, in which the adsorption energy is arbitrarily expressed as the sum of a "chemical" term ($F\Phi'$) analogous to the Stern specific adsorption potential and an electrical term ($F\phi_1$) where ϕ_1 is the potential at an anion site. The isotherm is written

$$ \theta/1 - \theta = a_{\pm} \exp(\Phi' + \phi_1) F/RT \qquad [29] $$

By expressing the difference in potential between the inner and outer Helmholtz planes $\phi_1 - \phi_2$ as a fraction $\gamma/(\beta + \gamma)$ of ϕ^{m-2} Eq. [29] can be used to determine a distance ratio $\gamma/(\beta + \gamma)$ as a function of q and q^1. Replacement of ϕ_1 in Eq. [29] by $\gamma/(\beta + \gamma)$. ϕ^{m-2} + ϕ_2 leads to the equation which is plotted in Fig. 13. Values of $\gamma/(\beta + \gamma)$ calculated from the slopes are compared with the corresponding values of $(x_2 - x_1)/x_2$ calculated from Eq. [27] in Fig. 14. $\gamma/(\beta + \gamma)$ is also almost independent of q and as found in all other systems of this type is larger than $(x_2 - x_1)/x_2$. This was previously attributed (14) to breakdown of the constant field approximation in Grahame's method of calculation due to discreteness of charge effects as a result of which a fraction of ϕ^{m-2} greater than the distance ratio is dropped between the IHP and OHP. An alternative explanation is possible however in terms of the contribution of the displaced solvent dipoles to the capacitance ratio (Eq. [28]) previously neglected in the calculation of $(x_2 - x_1)/x_2$. It may be significant that for both KI (4) and KCl (16) $\gamma/(\beta + \gamma)$ approaches the value of $(x_2 - x_1)/x_2$ calculated from Eq. [27] close to the pzc but increases rapidly with increasing q. This is consistent with Eq. [28] since the contribution of the second term should be small close to the pzc, but should increase with q to give values of the capacitance ratio smaller than the true distance ratio. The KNO_3 results which do not show this con-

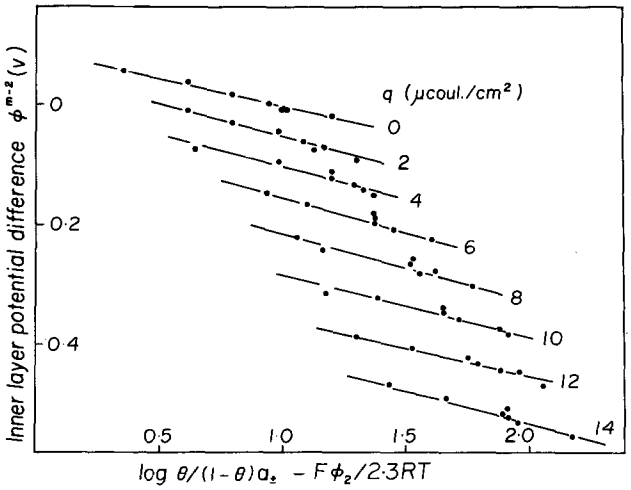

Fig. 13. Plot of Eq. [29] for various values of the electrode charge.

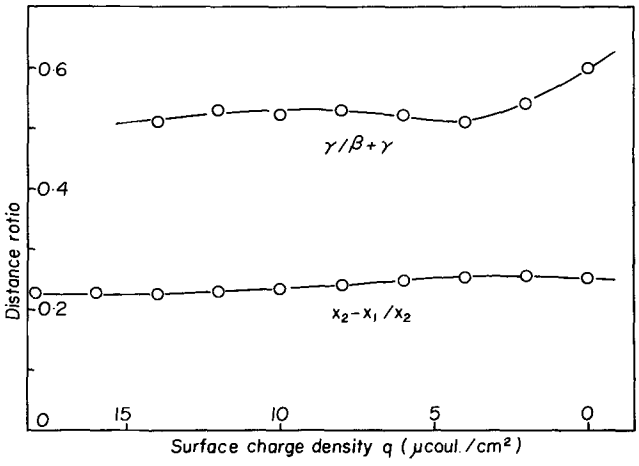

Fig. 14. Charge dependence of the distance ratio calculated by two methods.

Table II. Properties of the double layer in the presence of specifically adsorbed nitrate ions

q, $\mu C/cm^2$	$(x_2 - x_1)/x_2$	$\gamma/(\beta + \gamma)$	$F\Phi'/2.303RT$	$-F(\partial E^+/\partial\mu)_q$
−4	0.238			
−2	0.239			
0	0.250	0.60	1.20	0.95
2	0.254	0.54	1.12	0.97
4	0.254	0.51	0.98	0.98
6	0.248	0.52	1.00	0.98
8	0.241	0.53	0.98	0.99
10	0.234	0.52	0.90	0.99
12	0.229	0.53	0.91	0.99
14	0.225	0.51	0.74	1.02
16	0.227			1.02
18	0.228			1.04

vergence of $\gamma/(\beta + \gamma)$ and $(x_2 - x_1)/x_2$ are probably unreliable close to the pzc because of the scatter in the plots in Fig. 13 resulting from errors in ϕ_2 values calculated from diffuse layer theory.

Values of the specific adsorption potential Φ' obtained from the intercepts in Fig. 13 are recorded in Table II. $F\Phi'/2.303RT$ in this system is evidently close to 1.0 compared with ~2.8 found for the system KI in formamide (18).

In a recent paper Dutkiewicz and Parsons (27) compared the adsorption of iodide ions from pure KI solutions with that from mixtures of KI and KF at constant ionic strength from which they conclude that the salt activity rather than the anion activity (*i.e.*, the mean ionic activity) should appear in the anion adsorption isotherm. This, however, seems inconsistent since it amounts to equating the chemical potential of adsorbed anions to the chemical potential of the salt in solution. Further, it does not seem possible to consider the adsorption of neutral salt, since not only are the anions specifically adsorbed into the inner layer whereas the cations are in the diffuse layer, but also because the ions are adsorbed to different extents except at the pzc. As was pointed out previously (18), this argument also affects the constants of the isotherm deduced by fitting the experimental surface pressure of adsorbed anions to the integrated isotherm. The surface pressure measured at constant charge as defined by Parsons (12) is

$$\Phi = \xi^+ - \xi^+_0 = \int \Gamma^- d\mu \qquad [30]$$

where ξ^+ is equal to $\gamma + qE^+$, μ is the chemical potential of the salt, and ξ^+_0 is the limiting value of ξ^+ at infinite dilution. According to Eq. [30] differentiation of Φ with respect to ln $a_\pm^2$ gives the surface excess of anions, but it is clear that what is actually being measured is adsorption of neutral salt since, if q is kept constant, adsorption of anions must be accompanied by adsorption of an equal number of cations. Φ, therefore, cannot be regarded as the surface pressure of anions because it contains a contribution from adsorption of cations. This is another way of stating that the anion adsorption isotherm should contain $a_\pm$ rather than $a_\pm^2$ because differentiation of Φ as defined by Eq. [30] when plotted as a function of ln $a_\pm$ will obviously give values of Γ^- which are too large by a factor of two. Thermodynamically the adsorption of a given number of ions resulting from a given change in the chemical potential of the ion in solution will produce the same decrease in the interfacial tension irrespective of the state of the adsorbed ions; it seems, therefore, reasonable to assume that Φ as defined by Eq. [30] contains equal contributions from cations and anions. This appears to be equivalent to the assumption of equal activities of anion and cation in the solution, *i.e.*, $a_+ = a_- = a_\pm$. The plot of $\Phi/2$ *vs.* ln $a_\pm$ has the correct slope and is now consistent with the anion adsorption isotherm based on the mean ionic activity rather than the salt activity. The surface pressures of adsorbed anions shown in Fig. 7 were calculated in this way with small corrections for the contribution of diffuse layer anions. It should be mentioned that the value of the lateral interaction coefficient in the isotherm and also the standard free energy of adsorption calculated from the curve fitting procedure depend on the choice of the activity of the adsorbate in solution. The amounts adsorbed and the saturation coverage, however, will be correct in any case if the fit has been made correctly.

In view of the experimental evidence described by Dutkiewicz and Parsons in support of the idea of using the salt activity in the adsorption it is of interest to make a similar comparison for the KNO_3 system and the mixed NH_4NO_3 + NH_4F system. This is done in Fig. 15 and 16 where the amounts of specifically adsorbed nitrate ions are plotted against log $a_\pm$ and log $a_\pm^2$, respectively. It appears that the agreement is better when log $a_\pm$ rather than log $a_\pm^2$ is used in disagreement with the result found for the KI and KI + KF systems. The agreement of the log $a_\pm$ plots for the nitrate systems is less satisfactory than that of the log $a_\pm^2$ plots found for the iodide systems, as might be expected in view of the weaker adsorption of nitrate and the fact that different cations were involved in the two systems compared. Furthermore, the agreement is much better at the lower values of q and only deteriorates at the more positive values which were not reached in the iodide system. It would, therefore, be of considerable interest to extend the iodide measurements to positive values of q and also

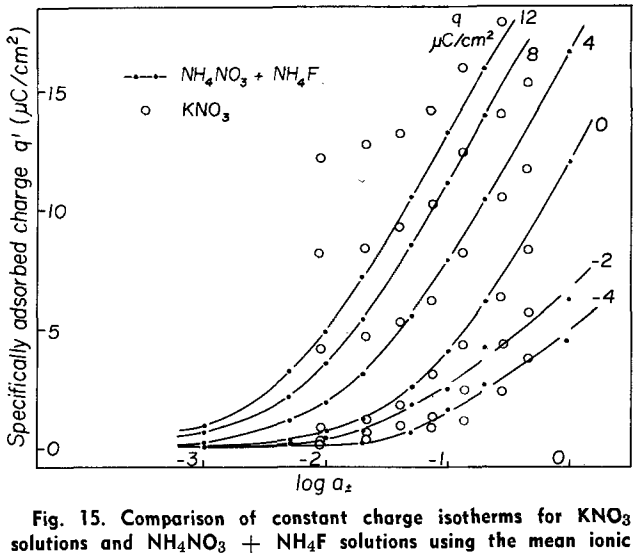

Fig. 15. Comparison of constant charge isotherms for KNO_3 solutions and NH_4NO_3 + NH_4F solutions using the mean ionic activity as the concentration variable.

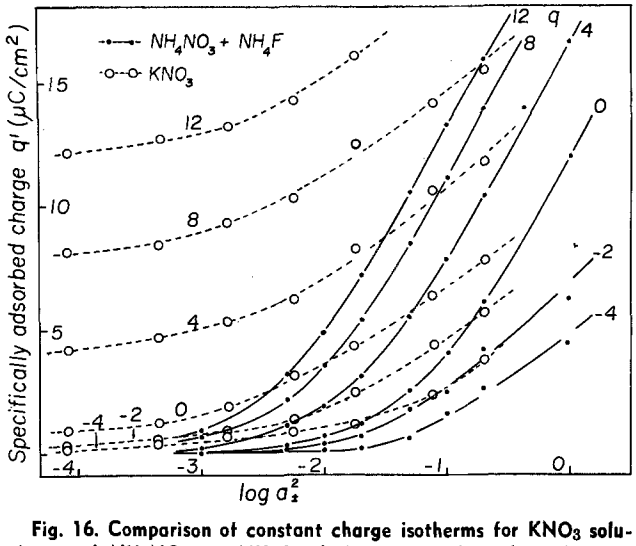

Fig. 16. Comparison of constant charge isotherms for KNO_3 solutions and NH_4NO_3 + NH_4F solutions using the salt activity as the concentration variable.

to study other systems in order to determine the effect of the supporting electrolyte on the adsorption process.

Esin and Markov Coefficient

Equation [1] can be written in the alternative form

$$-d\xi^+ = \Gamma^- d\mu - E^+ dq \qquad [31]$$

where E^+ is now the potential measured with respect to a cation reversible electrode and ξ^+ is correspondingly defined as $\gamma + qE^+$. Cross differentiation in Eq. [31] gives a form of the Esin and Markov coefficient (28)

$$(\partial E^+/\partial\mu)_q = -(\partial\Gamma^-/\partial q)_\mu \qquad [32]$$

The surface excess of anions can be divided into the contributions of specifically adsorbed and diffuse layer anions so that Eq. [32] can be written

$$(\partial E^+/\partial\mu)_q = -1/F\,[(\partial q^1/\partial q)_\mu + (\partial q_-{}^d/\partial q)_\mu] \qquad [33]$$

In the present system the diffuse layer concentration of anions does not vary much with q for positive values so that the second term on the right-hand side of Eq. [33] can be neglected. The Esin and Markov coefficient is therefore equal to $-1/F(\partial q^1/\partial q)_\mu$. E^+ is shown as a function of the salt chemical potential for integral values of q in Fig. 17. The plots are evidently linear for $q \geq 2$ μC/cm^2 with slopes which are similar and close to unity (see Table II). This is in agreement with the $\partial q^1/\partial q$ values obtained from plots of q^1 *vs.* q (Fig. 3). However, this does not constitute independent confirmation of the correctness of the values since the uncertainties introduced into the calculation of q^1 by the diffuse layer correction are inherent in the assumption that $(\partial q_-{}^d/\partial q)_\mu = 0$ in Eq. [33]. It is interesting to note that the Esin and Markov coefficient is close to unity at the extreme of anodic polarization which suggests that diffuse layer behavior is obeyed. The reason for this is that Γ^+ is actually almost independent of q although the (constant) value of Γ^+ is positive for all but the most dilute solutions, whereas diffuse layer behavior predicts limiting repulsion. The Esin and Markov coefficient therefore cannot be regarded as a reliable criterion of the occurrence of specific adsorption under these conditions. However, the occurrence of specific adsorption is confirmed by the fact that the slope of the plots in Fig. 17 does not decrease to the theoretical value of 0.5 at $q = 0$ predicted by diffuse layer theory. The curvature at the low concentration end for $q = 0$ indicates the approach to diffuse layer behavior at low concentration but specific adsorption of anions is not completely absent at all concentrations until the charge reaches -12 μC/cm^2.

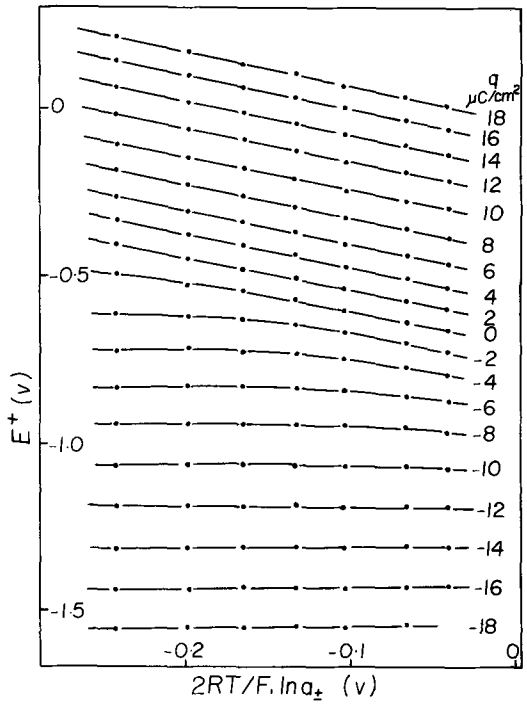

Fig. 17. Esin and Markov plots for aqueous KNO_3 solutions at 25°C.

The Esin and Markov is directly related to the anion adsorption isotherm since

$$(\partial E^+/\partial\mu)_q = (\partial q^1/\partial \ln\beta)_\mu \cdot d\ln\beta/dq \qquad [34]$$

As pointed out by Parsons (20) $(\partial q^1/\partial \ln\beta)_\mu$ is characteristic of the adsorption isotherm. Since $\ln\beta$ is evidently a linear function of q in this system (Fig. 8) it would appear that a Langmuir type of isotherm is incorrect since this would predict a maximum value in $(\partial q^1/\partial \ln\beta)_\mu$, and hence in the Esin and Markov coefficient, at $\theta = 0.5$ which is not found (see Table II). Although this conclusion is again dependent on the approximations involved in neglecting the diffuse layer contribution in Eq. [33] and possible deviations of $d\ln\beta/dq$ from constancy, a virial type behavior or more likely the modified Langmuir behavior of Eq. [22] is suggested.

The plots in Fig. 17 for extreme cathodic values of q show a small but apparently significant positive slope in contrast with the predictions of diffuse layer theory according to which the slope should be zero as anions undergo limiting repulsion. This suggests that anions are being readsorbed as the electrode charge becomes more negative. Similar behavior has been observed in other aqueous solutions (9) and cannot apparently be completely explained by specific adsorption of cations. Further study and analysis of these results will be required before the possibility of systematic experimental errors can be eliminated.

REFERENCES

1. D. C. Grahame and B. Soderberg, *J. Chem. Phys.*, **22**, 449 (1954).
2. R. Payne, *J. Phys. Chem.*, **69**, 4113 (1965).
3. R. Payne, *ibid.*, In press.
4. D. C. Grahame, *J. Am. Chem. Soc.*, **80**, 4201 (1958).
5. G. J. Hills and R. Payne, *Trans. Faraday Soc.*, **61**, 316 (1965).
6. R. Parsons, "Handbook of Electrochemical Constants," Butterworths Scientific Publications, London (1959).
7. D. C. Grahame, E. M. Coffin, J. I. Cummings, and M. A. Poth, *J. Am. Chem. Soc.*, **74**, 1207 (1952).
8. B. E. Conway, "Electrochemical Data," Elsevier Publishing Co., New York (1952).
9. R. Payne, Unpublished data.
10. R. Payne, *J. Electroanal. Chem.*, **7**, 343 (1964).
11. G. Gouy, *Ann. Chim. Phys.*, **29**, 145 (1903).
12. R. Parsons, *Trans. Faraday Soc.*, **51**, 1518 (1955).
13. D. C. Grahame, *Chem. Rev.*, **41**, 441 (1947).
14. J. M. Parry and R. Parsons, *Trans. Faraday Soc.*, **59**, 241 (1963).
15. K. M. Joshi and R. Parsons, *Electrochim. Acta*, **4**, 129 (1961).
16. D. C. Grahame and R. Parsons, *J. Am. Chem. Soc.*, **83**, 1291 (1961).
17. A. N. Frumkin, B. B. Damaskin, V. M. Gerovich, and R. I. Kaganovich, *Doklady Akad. Nauk SSSR*, **158**, 706 (1964).
18. R. Payne, *J. Chem. Phys.*, **42**, 3371 (1965).
19. A. N. Frumkin, *Z. Physik. Chem. (Leipzig)*, **116**, 466 (1925).
20. R. Parsons, *J. Electroanal. Chem.*, **7**, 136 (1964).
21. R. Parsons, *ibid.*, **5**, 397 (1963).
22. R. Parsons, *ibid.*, **8**, 93 (1964).
23. M. Breiter and P. Delahay, *J. Am. Chem. Soc.*, **81**, 2938 (1959).
24. A. N. Frumkin, "Advances in Electrochemistry and Electrochemical Engineering," vol. 1, p. 88, Interscience Publishers, New York (1961).
25. A. N. Frumkin, *Z. Physik.*, **35**, 792 (1926).
26. R. Parsons, *Trans. Faraday Soc.*, **55**, 999 (1959).
27. E. Dutkiewicz and R. Parsons, *J. Electroanal. Chem.*, **11**, 100 (1966).
28. R. Parsons, "Proceedings of the Second International Congress on Surface Activity," Vol. III, p. 38, Butterworths Scientific Publications, London (1957).

Discussion

Roger Parsons: I would like to suggest that the main reason for the difference of behavior of NO_3^- ion in mixtures with F^- compared with pure nitrate solutions is the fact that the inner layer thickness x_2 for F^- is smaller than that for NO_3^-. This is suggested by the fact that the inner layer capacity in pure fluoride solutions at positive charges is higher than that in nitrate solutions in spite of the greater specific adsorption in the latter which would tend to raise the capacity.

The tendency for quadratic dependence of adsorption free energy on electrode charge follows then from the fact that the introduction of nitrate ions to a fluoride solution tends to increase the inner layer thickness. The resulting quadratic behavior was discussed previously,[1] and this would automatically lead to ϕ^{m-2} $-q_-^{1}$ plot whose slope changed sign. It is also possible that the reduction in the interactive parameter in the NO_3^- isotherm is due to the lowered value of x_2 in the system containing fluoride.

The KF + KI system seems to be simpler because as Grahame[2] showed x_2 seems to be very similar for F^- and I^-. Hence, this system is a more satisfactory one for examining the functional dependence of adsorption on bulk activity. Nevertheless, it is certainly true that the comparison of single and mixed systems should be extended to more positive charges than we have so far studied.[3]

The significance of the dipole term in Eq. [24] is not very clear. If such a term is introduced, it is probably necessary to use a different value for ϵ^i, the apparent dielectric constant of the inner layer.

Finally, I would like to ask why there is no evidence of an approach to saturation in the adsorption isotherm of Fig. 3 which extend to charges equal if not higher than the value calculated as the maximum in the Frumkin isotherm. Similarly, do the results at more positive charges show a descending branch of the curve in Fig. 10 which again would be expected from this analysis?

Richard Payne: I agree with Dr. Parsons that the results for the mixed fluoride and nitrate solutions could be explained in terms of a variation in thickness of the inner layer as the amount of adsorbed nitrate increases rather than the replacement of oriented dipoles or decrease in the dielectric constant. However, it does not seem likely that the mean thickness of the layer would be appreciably increased by specific adsorption of nitrate ions in the flat orientation especially at the low coverages involved. Also, since the diffuse layer charge changes sign in the middle of the concentration range, it does not seem possible to attribute any thickness variation to variation in composition of the diffuse layer, *i.e.*, at concentrations above $\sim 0.1N$ the diffuse layer is populated by cations at all charges. It is therefore not possible to conclude with certainty that a thickness change will accompany the adsorption process. On the other hand, if it is assumed, as seems extremely likely, that the solvent dipoles in the inner layer are oriented at positive charges then the replacement of dipoles by adsorbed ions must result in a potential shift of the kind observed.

I also agree that the KF + KI system would be more appropriate as a test of the bulk activity factor, insofar as the iodide ion is simpler than the nitrate ion. On the other hand, the fluoride ion will be more strongly solvated than iodide so that there is really no reason to believe that the similarity between F^- and I^- will be any greater than that between F^- and NO_3^- in their effect on the thickness of the inner layer.

It seems appropriate to introduce the dipole term in Eq. [24] under conditions where it can be assumed that the dipole is permanently oriented. Under these conditions, there can be no orientational contribution to the dielectric constant although the oriented dipole will of course generate a potential difference. It seems more realistic to make this approximation in which the dipoles are fixed in a dielectric medium the polarizability of which is the sum of the contributions of the atomic and molecular polarizabilities of all the species present with no contribution of permanent dipoles, which should be almost independent of the potential. In Dr. Macdonald's paper, it is assumed that the high-frequency value of $\epsilon^i = 6$ is appropriate with the possibility of a variable contribution from orientation of permanent dipoles which may or may not be present. The assumption in Eq. [24] is that its effect is small.

The reasons for the apparent discrepancy between the plots in Fig. 3 and the saturation coverage given by the isotherm are given in answer to Professor Delahay's question. The absence of the descending branch in Fig. 10 predicted by the Frumkin isotherm is due to the fact that $-\Delta 1/C^i$ was calculated directly rather than from the isotherm values of q^1 as explained in my paper. It was pointed out that insofar as the plots in Fig. 3, 4, and 8 can be regarded as linear the value of $-\Delta(1/C^i)$ in Fig. 10 must be constant as it is at sufficiently positive values of q where the curvature of q' *vs.* q disappears. If we assume instead that the first two terms on the RHS of Eq. [19] are constant as given by the analysis, but that the last term $dq^1/d \ln \beta$ is given by the Frumkin isotherm, then the plots of $-\Delta C^i$ would have a maximum value occurring at half coverage. In actual fact although the surface pressure data fits a Frumkin isotherm closely, it appears that the fit is approximate and that the apparent limiting value is more like the actual behavior, which has also been observed for the adsorption of iodide ions from aqueous solutions[4] and formamide solutions.[5]

Paul Delahay: First, I would like to note that the relative weak dependence of the amount of specifically adsorbed NO_3^- on the concentration for KNO_3 is also observed for $TlNO_3$. The spread between 0.01 and 1M solution is of the order 6 $\mu C/cm^2$ in both cases.

In Eq. [16] Dr. Payne uses a saturation coverage of 25.4 $\mu C/cm^{-2}$. How does he justify this value since no saturation coverage of that order is apparent from Fig. 3. The plot in Fig. 3 is still quite linear up to 25 $\mu C/cm^{-2}$. The value used by Dr. Payne corresponds to the ratio of $3H_2O/NO_3^-$, but does not seem justified by experiment.

Second, I note that Dr. Payne's value of $A = 3$ is of the same order as the value of A we found for NO_3^--NO_3^- interaction in $TlNO_3$, namely, 2-5.5 (depending on the charge on the electrode). The question is, How does he account for the difference between $A = 1$ for $NH_4NO_3 + NH_4F$ and $A = 3$ for KNO_3?

Finally, why does Dr. Payne seem to rule out cation specific adsorption to explain the anomalous feature of the Esin and Markov?

Richard Payne: The apparent absence of the approach to saturation in Fig. 3 is partly due to the fact that

[1] Roger Parsons, *J. Electroanal. Chem.*, 5, 397 (1963).

[2] D. C. Grahame, *J. Am. Chem. Soc.*, 80, 4201 (1958).

[3] E. Dutkiewicz and R. Parsons, *J. Electroanal. Chem.*, 11, 100 (1966).

[4] R. Parsons, *J. Electroanal. Chem.*, 7, 136 (1964).

[5] R. Payne, *J. Chem. Phys.*, 42, 3371 (1965).

parallel straight lines have been drawn through all the points including the 1M points which actually begin to fall off above $q \approx 10$ $\mu C/cm^2$. The approach to saturation is more apparent in the curves shown in Fig. 9. Also, as I have stressed in my paper, the values of q^1 have been calculated directly rather than by the isotherm fitting method, whereas the saturation coverage of 25.4 $\mu C/cm^2$ was found from the isotherm. Although the fit of the experimental surface pressures to the theoretical curve (Fig. 7) derived from the isotherm is well within the experimental error I have still preferred to use directly calculated values of q^1 because of the uncertainty of the diffuse layer correction in this system. I have also stressed that I believe the fitting of data of this kind to an isotherm by the surface pressure method is an insensitive procedure and that the result tends to obscure much of the fine detail. It seems likely that both the interaction parameter and the saturation coverage depend on the charge on the metal so that the value given by the isotherm should be regarded as an averaged quantity.

In reply to the question concerning specific adsorption of cations and the Esin and Markov coefficient, the effect referred to was observed only in dilute solutions. In other words, the system is close to limiting repulsion of anions for the higher concentrations as predicted by diffuse layer theory, whereas at the lower concentrations, there appears to be positive adsorption of anions which increases with the negative charge on the metal. The effect has been observed with KNO_3, Na_2SO_4, and NaOH solutions and also appears in the electrocapillary data of Oldfield[6] for NaOH, LiOH, and KOH solutions. Since the effect is only apparent in dilute solutions, it does not appear possible to explain it in terms of specific adsorption of cations. The effect appears to be real, but the possibility that it is due to some defect in the experimental method has not yet been eliminated.

The question of the difference between the lateral interaction parameters for KNO_3 and $NH_4NO_3 + NH_4F$ is difficult to answer. First, it should be pointed out that these parameters probably vary with the charge and composition of the solution as mentioned earlier. The difference could be attributed to partial screening of the electrostatic charge by fluoride ions in the mixed electrolyte system. Alternatively, the difference could be due to difference in the diffuse layer composition and the effects that this might exert on the lateral component of the polarizability of the solvent dielectric or on the nature of the imaging of ions and dipoles in the OHP.

B. E. Conway: I wish to comment on some aspects of the specific behavior exhibited in the adsorption of cations and anions in the double-layer. In two dimensions, the concentrations of ions in the double-layer under most conditions are equivalent to concentrations in three-dimensional solutions of several molar. At such high concentrations, three-dimensional electrolyte solutions exhibit rather specific variations in their activity coefficients connected with the hydration of the ions and the close interaction of such hydrated ions. The specificity of such effects is believed to be connected with the structure forming or structure breaking influence of such ions in the water solvent.[7] In two dimensions in the double-layer, it appears that more attention must be paid to the possible role of such solvent-structure effects if specificities in ion adsorption are to be accounted for. The presence of oriented or dielectrically saturated water in the interphase will, however, make the detailed consideration of such effects a somewhat different problem from that involved in bulk aqueous solutions. The orientation of solvent by the electrode field[8] may occur competitively or cooperatively with that caused by the ions in the double-layer, depending on their charge and that of the electrode.

Richard Payne: In reply to Professor Conway's comments, it does not seem likely to me that the solvent structural effects he mentions will be important in the interphase since the structure of the solvent layer will presumably be determined primarily by the large field due to the electrode charge rather than by lateral solvent-solvent interactions. There is no evidence to suggest that any of the unusual structural properties of bulk water are retained in the adsorbed state, and indeed calculations of the electrostatically generated pressure in the double layer together with the known effects of pressure on the structure of bulk water lead one to the same conclusion.[9] The structure of the solvated ion in the bulk solution will, of course, affect the adsorption inasmuch as the solvation energy contributes to the adsorption energy. Bockris, Müller and Devanathan[10] in fact regard the solvation energy as a major factor in the adsorption process. However, this factor obviously does not affect the charge (or potential) dependence of the adsorption which is due to a variety of other factors. It seems to me that specific metal-ion and metal-solvent forces, ion size, ion and solvent polarizability and other purely electrostatic effects are likely to be more important than the structural effects mentioned by Professor Conway.

J. Ross Macdonald: While I agree that one should take account of the effect of the dipole moment of displaced solvent molecules, as you have done, I question the appropriateness of your method of doing so. For one thing, the ion which replaces one or more solvent dipoles will have an induced dipole moment and, in addition, its charge and the image of this charge in the conducting electrode will form a nonideal dipole. I do not see where you have taken account of these partially compensating effects.

Second, in a treatment of adsorption of ions from gas onto a conducting electrode, Barlow and I found that inclusion of images and induced polarization did, in fact, lead to an infinite effective dielectric constant under some conditions. Perhaps a discrete charge and dipole treatment of the present situation might lead to the same possibility here. Do you have any comments on this point?

Richard Payne: I agree with Dr. Macdonald that the introduction of the dipole term in Eq. [24] is a crude approximation and that other terms involving induced polarization of both solvent molecules and ions and the images of these induced dipoles in the metal and in the solution should be taken into account in any calculation of ϕ^{m-2}. However, no attempt was made to calculate the dipole term in Eq. [24] using the ordinary dipole moment of water. This term was included as a first order correction to the potential generated by the adsorbed ions. μ can be regarded as the effective dipole moment taking into account the contribution of the dipole imaging and other effects on ϕ^{m-2} of removing the dipole. It seems likely in any case that these effects will be second order, as was in fact assumed by Macdonald and Barlow[11] in a previous paper.

[6] Oldfield, Thesis, London, 1951.

[7] Frank and Evans, *J. Chem. Phys.*, 13, 507 (1945); Frank and Wen, *Discussions Faraday Soc.*, 24, 133 (1957); Frank, *Proc. Roy. Soc., London*, A247, 481 (1958).

[8] J. O'M. Bockris, M. A. V. Devanathan, and K. Müller, *Proc. Roy. Soc., London*, A274, 55 (1963); B. E. Conway, "Theory and Principles of Electrode Processes," Ronald Press, New York (1965).

[9] See J. R. Macdonald and C. A. Barlow, Jr., *J. Chem. Phys.*, 36, 3062 (1962).

[10] J. O'M. Bockris, K. Müller, and M. A. V. Devanathan, *Proc. Roy. Soc.*, 274, 55 (1963).

[11] J. R. Macdonald and C. A. Barlow, Jr., *J. Chem. Phys.*, 39, 412 (1963).

Some Aspects of the Thermodynamics of the Platinum Hydrogen Electrode

A. N. Frumkin, N. A. Balashova, and V. E. Kazarinov

Institute of Electrochemistry, Academy of Sciences of the USSR, Moscow and Moscow State University

ABSTRACT

The presence of adsorbed hydrogen results in essential differences in the thermodynamics of the surface phenomena on the platinum electrode compared to the mercury one. Thus in this case the point of zero charge (in the conventional sense) does not coincide with the maximum of the electrocapillary curve. The value of the potential difference between the electrode and the solution depends not only on the surface charge but also on the amount of adsorbed hydrogen. Additional complications arise in the presence of specifically adsorbed cations and anions in the solution. The experimental data used in this paper have been obtained by the charging curves method, by direct determinations of anion and cation adsorption, and by the measurements of the potential shift with changing composition of the solution under isoelectric conditions.

A platinum electrode obtained by platinization or activation of smooth platinum by alternating anodic and cathodic polarization in the potential range of ψ_r from $\psi_r = 0$ to $\psi_r = 0.5$-0.6, as referred to hydrogen electrode in the same solution, can be considered a reversible system in acid solutions. Therefore, in interpreting its surface properties, it is possible to make use of Gibbs thermodynamics. Thereby, it should be taken into consideration that, in addition to free charges and ions forming the electric double layer, there is adsorbed hydrogen on the electrode surface. It can be assumed that within the potential range indicated no adsorbed oxygen is present on the electrode surface. In the presence of strongly adsorbed anions or cations (I^-, Cd^{2+}), the condition of reversibility of adsorption processes may be violated. In that case a thermodynamic treatment would give only approximate results.

In the case of alkaline solutions, the above assumptions seem to be valid only within a narrower potential range and only for solutions containing singly charged cations of alkali metals. In the presence of doubly charged cations, such as Ba^{2+}, complications may arise (1)

Let us consider first the case of an acidified or alkalized solution of a binary electrolyte (2), assuming the concentration of the H^+ or OH^- ions to be small compared to that of the salt ions.[1] At constant temperature and pressure, the state of the system is determined by the chemical potentials of hydrogen μ_H, of the hydrogen ion μ_{H+} and of the salt ions μ_s, which we shall express in electric units. We shall set the interface in such a way that the Gibbs adsorption of water $\Gamma_{H_2O} = 0$. Then for $d\sigma$, where σ is the surface density of the free energy, we shall have

$$d\sigma = -\Gamma_H d\mu_H - \Gamma_{H+} d\mu_{H+} - (\Gamma_{C+} + \Gamma_{A-}) d\mu_s \quad [1]$$

where Γ_H, Γ_{H+}, Γ_{C+}, and Γ_{A-} are Gibbs surface densities of hydrogen, hydrogen ion, cation and anion of the salt, respectively, also expressed in electric units.

Evidently

$$\psi_r = (\mu_H)_o - \mu_H \quad [2]$$

where $(\mu_H)_o$ is the value of μ_H in equilibrium with molecular hydrogen at given temperature and pressure. Now

$$\Gamma_{H+} = \Gamma_{A-} - \Gamma_{C+} \quad [3]$$

The quantity Γ_{H+} can be considered to be the density of the electrode surface charge ϵ, assuming that with an excess of C^+ cations, the presence of H^+ ions in the ionic part of the double layer can be neglected (see footnote 1) and that being adsorbed, all hydrogen ions give off their charges to the metal and change to H atoms. In other words, we assume that the potential determining H^+ ions are not adsorbed specifically or that jointly the specifically adsorbed H^+ ion and the negative surface charge can be identified with an H atom. Equating Γ_{H+} with ϵ is somewhat conditional. In fact, specifically adsorbed ions, such as I^- or Cd^{2+}, are shown by experiment to form covalent bonds with the electrode surface (4). Therefore, it could be assumed that in Cd^{2+} adsorption, some of the Cd^{2+} ions change to atoms, giving off positive charges to the surface. Hence two separate quantities Γ_{Cd+} and Γ_{Cd} could be introduced, just as it was done in considering the electrocapillarity of thallium amalgams (5). However, since in the case under consideration we cannot vary independently μ_{Cd} and μ_{Cd2+}, such separation would be aimless. Therefore, within the frame of the thermodynamic treatment it would be reasonable to consider formally all ions disappearing from the solution, except the H^+ ions, to be adsorbed as ions, although such an assumption would have to be essentially corrected in developing a molecular theory of the electric double layer on the Pt electrode (see below).

Let us designate by A_H the amount of hydrogen adsorbed per unit surface. The quantity A_H is not identical with Γ_H, as part of the hydrogen disappearing from the bulk of the solution, when a unit surface is formed, is ionized and expended in its charging. Obviously the following relationship exists between A_H and Γ_H

$$\Gamma_H = A_H - \Gamma_{H+} = A_H - \epsilon \quad [4]$$

From Eq. [1], [2], [3], and [4] it is possible to deduce some relationships between measurable quantities (2, 6). No allowance will be made for hydrogen solubility in the metal and the possible effect of dissolved hydrogen on the electrode process. We shall also assume the quantity μ_{H+} to remain constant with changing ψ_r, that is that the changes in the value of

[1] In practice, the last condition was often not fulfilled, since in an experimental determination of ionic adsorption the use of solutions with a low concentration of H^+ or OH^- ions makes it difficult to keep the pH of the solution constant. However, at least in the case of Cs^+ ions, this could not lead to a significant error in the determination of the charge of adsorbed cations, since when the ratio $[H^+]:[Cs^+]$ is decreased 10 times, adsorption of Cs^+ from $0.01N$ Cs_2SO_4 solution at $\psi_r = 0$ increases only by 30% (3), as it follows also from Fig. 1. Even at the same concentration, the Cs^+ ions seem to displace considerably the H^+ ions from the ionic side of the double layer.

$[H^+]$ caused by those in A_H are small compared to $[H^+]$.[2]

Let us consider the case of a solution of a constant salt composition (μ_s = const). Since

$$\left(\frac{\partial\Gamma_H}{\partial\mu_{H+}}\right)_{\mu_H} = \left(\frac{\partial\Gamma_{H+}}{\partial\mu_H}\right)_{\mu_{H+}} \quad [5]$$

or

$$\left(\frac{\partial\Gamma_H}{\partial\mu_{H+}}\right)_{\psi_r} = -\left(\frac{\partial\Gamma_{H+}}{\partial\psi_r}\right)_{\mu_{H+}} \quad [5a]$$

$$\left(\frac{\partial\Gamma_{H+}}{\partial\psi_r}\right)_{\mu_{H+}} = \left(\frac{\partial\psi_r}{\partial\mu_{H+}}\right)_{\Gamma_H}\left(\frac{\partial\Gamma_H}{\partial\psi_r}\right)_{\mu_{H+}} \quad [6]$$

The quantity Γ_{H+} can be determined experimentally directly from the change in the hydrogen ion concentration in the solution in contact with the electrode polarized to the potential ψ_r, or, according to Eq. [3], from the difference between the anion and cation adsorptions. Some examples of the dependence of Γ_{H+} upon ψ_r are given in Fig. 1 and 2 (7).

The curves in these figures, as well as in others, are extended into the oxygen region, which, however, will not be discussed in the present paper. Now, evidently

$$\left(\frac{\partial\Gamma_H}{\partial\psi_r}\right)_{\mu_{H+}} = -\left(\frac{\partial Q}{\partial\psi_r}\right)_{\mu_{H+}} \quad [7]$$

where Q is the quantity of electricity to be supplied to the electrode per unit surface to shift its potential from some initial value to the value ψ_r, assuming that the quantity of hydrogen dissolved in the bulk of the solution, which is in equilibrium with the electrode, can be neglected compared to the amount of adsorbed hydrogen. Finally, the quantity $\left(\frac{\partial\psi_r}{\partial\mu_{H+}}\right)_{\Gamma_H}$ is determined from the change in the electrode potential, as referred to hydrogen electrode in the same solution, with changing $[H^+]$ under isoelectric conditions, *i.e.*, at open circuit (constant Γ_H).[3] Thus Eq. [6] can be verified quantitatively. A roughly approximate verification of this kind has already been carried out (2). There the quantity $\left(\frac{\partial\psi_r}{\partial\mu_{H+}}\right)_{\Gamma_H}$ was determined from the change in ψ_r when passing from acidified to alkalized solutions, *i.e.*, μ_{H+} was changed within too wide limits. The values of the derivatives in Eq. [6] were equated with the half-sum of the values obtained experimentally for the lowest and the highest *p*H. At present similar measurements are made using improved technique.[4]

Of interest is another deduction from Eq. [1] and [4]. With the solution composition constant

$$\frac{\partial\sigma}{\partial\psi_r} = \Gamma_H = A_H - \epsilon \quad [10]$$

Thus, the maximum of the "electrocapillary curve" of the platinum hydrogen electrode lies not at $\epsilon = 0$, but at $A_H - \epsilon = 0$ and does not coincide with the point of zero charge in the usual sense of this term, *i.e.*, the potential at which the quantity $\epsilon = \Gamma_{A-} - \Gamma_{C+}$ vanishes. According to (2), the point of zero charge of platinum in solution of N NaCl + 0.01N HCl lies at $\psi_r = 0.16$, whereas the quantity $A_H - \epsilon$ vanishes at $\psi_r \approx 0.3$. Such a discrepancy may seem to be unexpected if we proceed from the derivation of Lippman's equation, suitable for the concept of an ideal polarizable mercury electrode, *e.g.*, in the form given by Grahame (10) or Parsons (47). However, Lippman himself understood perfectly well that what the right-hand side of his equation expresses is the capacitance of a unit surface at constant potential (11). Evidently, in the case of a hydrogen-adsorbing metal, the last quantity cannot coincide with the surface charge in the sense of the electrostatic theory of the double layer. In 0.01N Cs_2SO_4 + 0.01N H_2SO_4 the point of zero charge lies at $\psi_r = 0.30$ (3, 7) (0.19 *vs.* NHE) and is close to the potential of the maximum of σ. This coincidence is, however, an accidental one.

The platinum electrode potential ψ, measured against a constant reference electrode, such as the normal hydrogen electrode, depends not only on Γ_{H+}, but on A_H as well. In fact

[2] When the above conditions are fulfilled, the state of the system at a given initial solution composition is completely determined by the quantity of electricity Q supplied to the electrode from some initial moment of time. In this sense, the behavior of the electrode does not differ from that of an ideal or completely polarized electrode, although in this case, the condition of the absence of the exchange of charges between the electrode and the solution, which is usually considered to be the criterion of ideal polarizability, is not fulfilled.

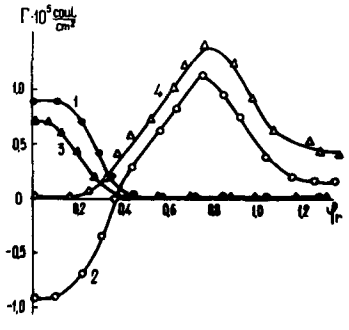

Fig. 1. Dependence of Γ_{Cs+} (1) and Γ_{H+} (2) in 0.018N Cs_2SO_4 + 0.002N H_2SO_4 and Γ_{Cs+} (3) and $\Gamma_{SO_4 2-}$ (4) in 0.01N Cs_2SO_4 + 0.01N H_2SO_4 on ψ_r.

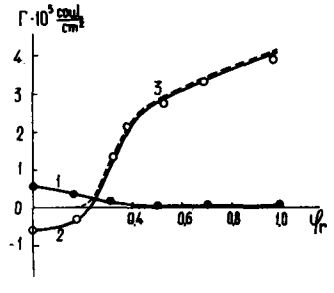

Fig. 2. Dependence of Γ_{Na^+} (1), Γ_{H+} (2) and Γ_{Br-} (3) in 10^{-3}N NaBr + 10^{-3}N H_2SO_4 on ψ_r.

[3] Changes in the electrode state in which the quantity Γ_H, determining the total amount of electricity stored on the electrode, remains constant were suggested to be called isoelectric (8). Isoelectric measurements can be carried out readily in the case of electrodes with developed surface (platinized platinum, activated carbon), for which the condition Γ_H = const. can be fulfilled easily in practice when replacing the solution. These measurements have something in common with the coulostatic method developed by Delahay and collaborators (46), since in both cases changes in the electrode potential at open circuit are observed. The problems to be solved in the two cases were, however, different.

[4] From Eq. [6] by simple transformations (9) it is possible to obtain the relationship

$$\left(\frac{\partial\psi_r}{\partial\mu_{H^+}}\right)_{\Gamma_H} = 1:\left[\left(\frac{\partial A_H}{\partial\Gamma_{H^+}}\right)_{\mu_{H^+}} - 1\right] \quad [8]$$

or

$$\left(\frac{\partial\psi}{\partial\mu_{H^+}}\right) = \left(\frac{\partial A_H}{\partial\Gamma_{H^+}}\right)_{\mu_{H^+}}:\left[\left(\frac{\partial A_H}{\partial\Gamma_{H^+}}\right)_{\mu_{H^+}} - 1\right] \quad [9]$$

where ψ is the potential measured against normal hydrogen electrode.

Equations [8] and [9] determine the dependence of the hydrogen electrode potential on the *p*H of the solution with Γ_H remaining constant, *i.e.*, under isoelectric conditions. The quantity $\left(\frac{\partial A_H}{\partial\Gamma_{H^+}}\right)_{\mu_{H^+}}$ is negative in most cases; if $\left|\left(\frac{\partial A_H}{\partial\Gamma_{H^+}}\right)_{\mu_{H^+}}\right| >> 1$, Eq. [9] turns into the usual relationship for the reversible hydrogen electrode.

$$d\psi = d\mu_{H+} - d\mu_H \quad [11]$$

Now, let us put (2)

$$d\psi = \left(\frac{\partial\psi}{\partial A_H}\right)_{\Gamma_{H+}} dA_H + \left(\frac{\partial\psi}{\partial\Gamma_{H+}}\right)_{A_H} d\Gamma_{H+}$$

$$= X dA_H + Y d\Gamma_{H+} \quad [12]$$

From [11] and [12] it follows

$$X\left(\frac{\partial A_H}{\partial\mu_H}\right)_{\mu_{H+}} + Y\left(\frac{\partial\Gamma_{H+}}{\partial\mu_H}\right)_{\mu_{H+}} = -1 \quad [13]$$

$$X\left(\frac{\partial A_H}{\partial\mu_{H+}}\right)_{\mu_H} + Y\left(\frac{\partial\Gamma_{H+}}{\partial\mu_{H+}}\right)_{\mu_H} = 1 \quad [14]$$

From [13], [14], [4], and [5] we obtain

$$X = -\left(\frac{\partial A_H}{\partial\mu_{H+}}\right)_{\mu_H} : Z \quad [15]$$

$$Y = \left[\left(\frac{\partial A_H}{\partial\mu_{H+}}\right)_{\mu_H} + \left(\frac{\partial A_H}{\partial\mu_H}\right)_{\mu_{H+}}\right] : Z \quad [16]$$

where

$$Z = \left(\frac{\partial\Gamma_{H+}}{\partial\mu_{H+}}\right)_{\mu_H}\left(\frac{\partial A_H}{\partial\mu_H}\right)_{\mu_{H+}} - \left(\frac{\partial\Gamma_{H+}}{\partial\mu_H}\right)_{\mu_{H+}}\left(\frac{\partial A_H}{\partial\mu_{H+}}\right)_{\mu_H}$$

$$= \left(\frac{\partial\Gamma_H}{\partial\mu_H}\right)_{\mu_{H+}}\left(\frac{\partial\Gamma_{H+}}{\partial\mu_{H+}}\right)_{\mu_H} - \left(\frac{\partial\Gamma_H}{\partial\mu_{H+}}\right)^2_{\mu_H} \quad [17]$$

If $\left(\frac{\partial A_H}{\partial\mu_{H+}}\right)_{\mu_H} = 0$, *i.e.*, atomic hydrogen adsorption does not depend on the composition of the solution, according to Eq. [15], $X = 0$. In this case, the presence of adsorbed hydrogen has no effect on the potential difference. In actual fact, however, the value of A_H depends on pH, increasing when passing from acid to alkali at small and medium coverages and decreasing at large coverages (2, 6). As all the quantities appearing in the right-hand sides of Eq. [15], [16], and [17] are measurable, it is possible to calculate from these equations the contribution of atoms and ions to the potential difference at the electrode-solution interface. Unfortunately, there are no sufficiently accurate values of the quantities $\left(\frac{\partial A_H}{\partial\mu_{H+}}\right)_{\mu_H}$ and $\left(\frac{\partial\Gamma_{H+}}{\partial\mu_{H+}}\right)_{\mu_H}$ available at present. The results of a roughly tentative calculation from the data obtained in (2) are presented in Fig. 3. Since in this case the measurements of Γ_{H+} were made in N NaCl + 0.01N HCl and in N NaCl + 0.05N KOH, the results of the calculation can give an approximate idea of the quantities X and Y for the intermediate value of pH, *i.e.*, for a neutral solution. More accurate measurements of this kind are to be made at a later date. In spite of the tentative nature of the data in Fig. 3, it is possible to draw some conclusions from them regarding the mechanism of the appearance of the potential difference on the platinum hydrogen electrode. At small coverages, the quantity X is positive, *i.e.*, in the atomic hydrogen coverage the negative dipole end is turned toward the solution. With increasing coverage, the sign of polarity changes, the effect continuing to increase in absolute value as $\psi_r = 0$ is approached. As already pointed out in the literature,

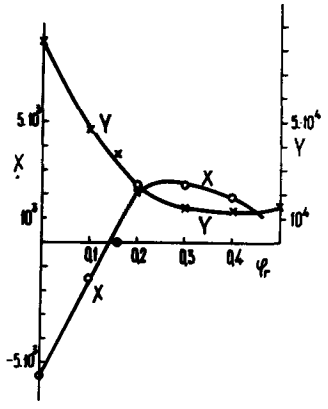

Fig. 3. Dependence of the quantities $X = \left(\frac{\partial\psi}{\partial A_H}\right)_{\Gamma_{H+}}$ and $Y = \left(\frac{\partial\psi}{\partial\Gamma_{H+}}\right)_{A_H}$ on ψ_r in N NaCl solution. Ordinates in farads^{-1} x cm^2.

the change in polarity with increasing coverage is in agreement with the results of the work function measurements (12). It follows from a comparison of the X and Y curves that the contribution of the adsorbed hydrogen atom to the establishment of the potential difference is approximately by an order of magnitude less than that of the adsorbed ion. The quantity Y^{-1} is the electrode capacitance at constant A_H. At ψ_r = 0.3-0.5, it is equal to *ca.* 70 μf/cm^2 and decreases to 12 μf/cm^2 with ψ_r approaching zero. The decrease in capacitance can be partially due to the substitution of cations for anions in the ionic side of the double layer, but the effect of the increasing surface coverage with adsorbed hydrogen on the capacitance should be taken into consideration as well. In actual fact, as is clear from Fig. 3, the increase in Y with decreasing ψ_r becomes appreciable beginning with ψ_r = 0.3, whereas the point of zero charge, as is evident from Fig. 6 in Frumkin and Slygin's work, in neutral N NaCl should lie at ψ_r = 0.18. It should be noted that within the range of ψ_r = 0.3-0.5 the capacitance values are high. Numerous a-c measurements on smooth electrodes at sufficiently high frequencies give capacitance values of 15-20 μf/cm^2 in the double layer region. It is possible that this value should be even smaller if allowance is made for the roughness factor. The reliability of the values obtained from the adsorption measurements depends on the correct estimation of the platinized electrode surface. The calculation of adsorption per cm^2, and hence of the quantities X and Y, given in this paper is based on the assumption that at ψ_r = 0, there is one H atom for each Pt atom, and 1.31 x 10^{15} atoms/1 cm^2 of the Pt surface.[5] The determination of the surface area by this method leads to values which are in agreement with the Pt surface measurements by the BET method (14, 15). Thus, the discrepancy between the results of the capacitance determination from adsorption measurements and from impedance is a real one. The most probable explanation would be to suppose the establishment of equilibrium between the adsorbed anion and the platinum surface to be a slow process, which is in agreement with the covalency of the Pt-anion bond under equilibrium conditions. It should be noted that the capacitance of the Pt electrode in the double layer region in a 0.1N H_2SO_4 solution, determined from adsorption measurements (without control however of the condition A_H=const being

[5] There are some discrepancies in the estimation of the latter value. Thus, Fisher, Chon, and Aston (13) give the value 1.195 x 10^{15}. These discrepancies are too small, however, to account for those between the results of the two methods of the capacitance determination.

observed) amounts to as little as 36 ± 5 μf/cm² (3), *i.e.*, is much less than in solutions of halides.

If the establishment of the potential difference at the platinum electrode-solution interface cannot be understood without taking into account the contribution of the atomic coverage, it is not possible either to assume, as Bowden and Rideal (16) did some time ago, the total potential difference established to be determined by the dipole moment of the adsorbed atoms. As pointed out by Frumkin (17), it is impossible to fulfill the conditions of equilibrium between electrode, solution, and adsorbed gas at a given electrode potential without taking into consideration the electric double layer. Let us explain this for the simplest case of the equilibrium hydrogen electrode. Under the assumption made, the quantity A_H depends only on μ_H and hence on ψ_r

$$A_H = f(\psi_r) \qquad [18]$$

On the other hand, if we designate the effective dipole moment of the Pt-H bond as d, we shall have

$$\psi = \psi_r - (\mu_{H+})_o + \mu_{H+} = \frac{4\pi A_H d}{e} + \text{const} \qquad [19]$$

where e is the elementary charge and $(\mu_{H+})_o$ the value of μ_{H+} at molar concentration of the H^+ ions. It is evident that the quantity A_H, determined from [19], in the general case cannot be the solution of Eq. [18]. This conclusion remains valid if, under the assumption about the equilibrium state of the system, we assume O_{ads} to be present on the surface along with H_{ads}. At the first glance, the results of the adsorption measurements of the cations from dilute NaOH and CsOH solutions seem to be at variance with this conclusion (18) (Fig. 4). In this case the cation adsorption practically does not depend on ψ_r. In other words, the change in the potential difference seems to be due to that in the atomic coverage, a decrease in the amount of adsorbed H and an increase in that of adsorbed O. In actual fact, however, the constancy of Γ_{C+} is probably of a random nature, since the adsorption effect in alkaline solutions is made up of two items: cation adsorption, associated with H_{ads} ionization, and adsorption by hydrated surface oxide groups, which are of a weakly acid nature and take up cations in alkaline solutions. With increasing ψ_r, the first effect decreases, whereas within a certain potential range, the second effect increases, resulting in the approximate constancy of Γ_{C+}. Such an explanation is supported by the following observations. In the presence of Br^- or I^- ions (as well as of Cl^- ions at higher concentrations, which displace oxygen from Pt surface) in alkaline solutions at not too small ψ_r, Γ_{C+} decreases with increasing ψ_r (Fig. 5) (7, 18, 19). In $Ca(OH)_2$ and $Ba(OH)_2$ solutions containing doubly charged cations Ca^{2+} and Ba^{2+}, which seem to be strongly chemisorbed by hydrated surface oxides, with increasing ψ_r in the hydrogen region Γ_{C+} increases (Fig. 6) (1). Of particular interest is the approximate constancy of Γ_{C+} in the hydrogen region, which is also observed, although within a narrower range of ψ_r values, in

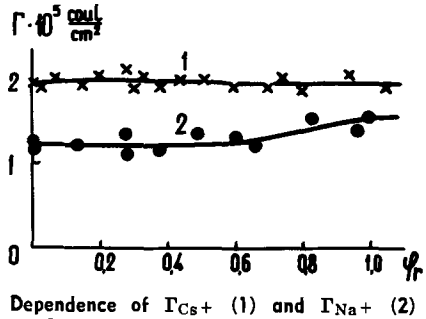

Fig. 4. Dependence of Γ_{Cs+} (1) and Γ_{Na+} (2) in 10^{-2}N CsOH and 10^{-2}N NaOH on ψ_r.

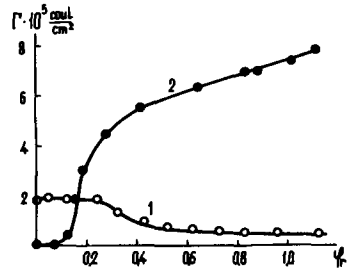

Fig. 5. Dependence of Γ_{Cs+} (1) and Γ_{I-} (2) in 10^{-2}N CsOH + 10^{-2}N CsI on ψ_r.

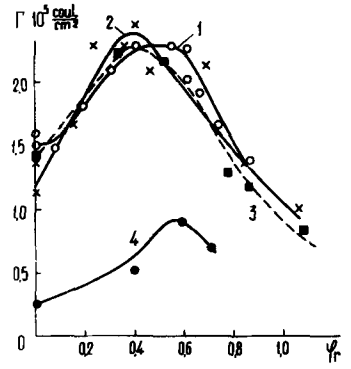

Fig. 6. Dependence of adsorption values on ψ_r: 1, Ca^{2+} in 10^{-3}N $Ca(OH)_2$; 2, Ba^{2+} in 10^{-3}N $Ba(OH)_2$; 3, Ba^{2+} in 10^{-3}N $Ba(OH)_2$ + 1N NaOH; 4, Ca^{2+} in 10^{-3}N $Ca(OH)_2$ + 1N NaOH.

acidified solutions of sulfates (Fig. 1). In this case, the change in ψ_r at a practically constant Γ_{C+} is partly determined by that in the effective dipole moment of the Pt-H bond. As pointed out earlier, at small coverages the dipole of this bond is turned toward the solution with its negative, at large coverages—with its positive end. Another factor leading to an increase in the absolute value of the negative potential difference at constant Γ_{C+} in the range of small ψ_r, which we have also mentioned earlier, is the decrease in the capacitance of the electric double layer with increasing A_H.

The thermodynamic theory outlined here can be extended to other hydrogen adsorbing metals. As shown by Tyurin and Tsybulevskaya (20), who studied the dependence of the charging curves of disperse rhodium on the *p*H of the solution, an empiric relationship is valid in the case of the rhodium electrode

$$A_H = f_1 (pa^{-0.52}) \qquad [20]$$

where p is the equilibrium pressure of molecular hydrogen, a is the activity of hydroxonium ion, and f_1 is some functional dependence. Equation [20] can also be written as

$$A_H = f_2 (\mu_H - 0.26\,\mu_{H+}) \qquad [21]$$

whence from [11], [15], and [16] it follows

$$\left(\frac{\partial A_H}{\partial \Gamma_{H+}}\right)_{\psi} = -\left(\frac{\partial \psi}{\partial \Gamma_{H+}}\right)_{A_H} : \left(\frac{\partial \psi}{\partial A_H}\right)_{\Gamma_{H+}}$$

$$= \left[\left(\frac{\partial A_H}{\partial \mu_H}\right)_{\mu_{H+}} + \left(\frac{\partial A_H}{\partial \mu_{H+}}\right)_{\mu_H}\right] : \left(\frac{\partial A_H}{\partial \mu_{H+}}\right)_{\mu_H}$$

$$= -\frac{1 - 0.26}{0.26} = -2.8$$

The relatively low value of $\left|\left(\frac{\partial A_H}{\partial \Gamma_{H+}}\right)_{\psi}\right|$ (com-

pared to platinum) can be partly due to the Rh surface which apparently always carries a positive charge in the hydrogen region (21). It also points to a considerable and constant polarity of the Rh-H bond, with the negative dipole end turned toward the solution.

Let us consider some other possible changes in the composition of the solution.

Adsorption of cations and anions of the electrolyte, on one hand, and hydrogen adsorption, on the other, exert a mutual influence (6). It follows from [1], [3], and [4] that

$$\left(\frac{\partial A_H}{\partial \mu_s}\right)_{\psi_r,\mu_{H^+}} = \left(\frac{\partial(\Gamma_{A^-} - \Gamma_{C^+})}{\partial \mu_s}\right)_{\psi_r,\mu_{H^+}} - \left(\frac{\partial(\Gamma_{A^-} + \Gamma_{C^+})}{\partial \psi_r}\right)_{\mu_s,\mu_{H^+}} \quad [22]$$

Equation [22] can be verified experimentally, although this has not been done yet. In fact, adsorption of cations and anions on platinum can be directly estimated from experiment, primarily by the method of radioactive tracers (7). Then, by the charging curves method, it is possible to find the quantity $\left(\frac{\partial \Gamma_H}{\partial \mu_s}\right)_{\psi_r,\mu_{H^+}}$, and hence $\left(\frac{\partial A_H}{\partial \mu_s}\right)_{\psi_r,\mu_{H^+}}$. From [22], by elementary transformations, we obtain

$$\left(\frac{\partial \psi}{\partial \mu_s}\right)_{\epsilon,\mu_{H^+}} = -\left[\frac{\partial(\Gamma_{A^-} + \Gamma_{C^+})}{\partial \epsilon}\right]_{\mu_s,\mu_{H^+}} - \left(\frac{\partial \psi}{\partial \epsilon}\right)_{\mu_s,\mu_{H^+}} \left(\frac{\partial A_H}{\partial \mu_s}\right)_{\psi_r,\mu_{H^+}} \quad [23]$$

With $\frac{\partial A_H}{\partial \mu_s} = 0$, Eq. [23] changes to a relation which is well known from the thermodynamics of electrocapillary phenomena (22, 27).

At the present time, experimental data are available on the adsorption on platinum of the cations Na^+, Cs^+, Ca^{2+}, Ba^{2+}, Cd^{2+}, Tl^+ and the anions SO_4^{2-}, $H_2PO_4^-$, Cl^-, Br^-, I^- from acid and partly from alkaline solutions (1, 3, 4, 7, 18, 19, 23) which, however, will not be presented here. Let us consider briefly only a few of the specific features of this adsorption.

The behavior of adsorbed Na^+ and Cs^+, as well as of Ca^{2+} and Ba^{2+} in acid solutions is on the whole similar to their behavior at the mercury-solution interface.[6] But the difference in their adsorptivities, which increases in the sequence: $Na^+ < Cs^+ < Ca^{2+} < Ba^{2+}$ is much greater. The maximum charge of adsorbed cations remains within 5 — 10 x 10^{-6} coul/cm^2 for acid and 10 — 25 x 10^{-6} coul/cm^2 for alkaline solutions at the bulk concentrations of the order of 10^{-2} mol. The cations Cd^{2+} and Tl^+ show a pronounced specific adsorptivity (to a lesser degree also Zn^{2+} and Pb^{2+}). In the case of Cd^{2+} the maximum charge reaches the value 60 x 10^{-6} coul/cm^2, and the coverage reaches large fractions of a monolayer. The adsorptivity of anions increases in the sequence $SO_4^{2-} < Cl^- < Br^- < I^-$; the maximum charge of adsorbed anions increases in this sequence from 15 to 140 x 10^{-6} coul/cm^2. Some specific adsorptivity is observed also in the case of the least adsorbable ion SO_4^{2-}, since the adsorption of SO_4^{2-} and Cs^{2+} maintains a small, but still measurable, value at the point of zero charge in acidified Cs_2SO_4 solution as well. One of the characteristic differences between specific adsorption of ions on Pt and that on mercury is that in the former

[6] Added in proof: New data show that the difference in the behavior of Ba^{2+} at both interfaces is much greater than it was supposed earlier.

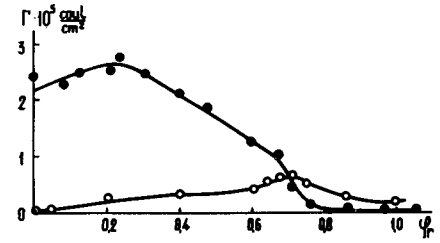

Fig. 7. Dependence of $\Gamma_{Cd^{2+}r}$ and $\Gamma_{SO_4^{2-}}$ in 10^{-2}N $CdSO_4$ + 10^{-2}N H_2SO_4 on ψ_r.

case the phenomenon of superequivalent adsorption is much less pronounced. Considerable adsorption of halogen ions on platinum is accompanied over a wide potential range by slight adsorption of cations only (Fig. 2). The same holds true in the case of adsorption of the anion SO_4^{2-} in the presence of the Cd^{2+} ion (Fig. 7). In the latter case, however, it is this small quantity of adsorbed anions and the positive charges on Pt corresponding to them which determine the ultimate positive sign of the potential difference between metal and solution to be observed at potentials more positive than the point of zero charge of platinum in absence of specific adsorption. Hence it follows that the effective charge of specifically adsorbed cations Cd^{2+} must be very small. It would be possible to estimate this charge quantitatively by measuring, *e.g.*, $\left(\frac{\partial \psi}{\partial \Gamma_{Cd}}\right)_{\Gamma_{A^-}}$ and $\left(\frac{\partial \psi}{\partial \Gamma_{A^-}}\right)_{\Gamma_{Cd}}$ in $CdSO_4$ + H_2SO_4 solutions with varying concentration of both components. At the present time, however, such data are not available. The results of an attempt to estimate the effective charge of adsorbed Tl^+ ions in (23) cannot be agreed with.

Adsorptivity of ions can also be determined from the potential shift on introduction of an ion under isoelectric conditions into a solution containing only weakly, or not at all, specifically adsorbable ions.[7] Such "adsorption" potentials of anions (24) (Cl^-, Br^-, I^-) and cations (25) (Tl^+, Cd^{2+}, Zn^{2+}, Pb^{2+}) were determined by Obrucheva on platinized and smooth platinum [see also (26)]. A supporting electrolyte was used, *e.g.*, *N* H_2SO_4. Let us designate the chemical potential and the surface density of the surface active ion by μ_i and Γ_i, respectively. We assume its concentration to be so small, compared to that of other ions in the solution, that it can be varied, maintaining the chemical potentials of the other ions in the solution practically constant. Under these conditions, the variables to be taken into consideration are μ_H and μ_i. From the relation

$$d\sigma = -\Gamma_H d\mu_H - \Gamma_i d\mu_i \quad [24]$$

it follows

$$\left(\frac{\partial \Gamma_H}{\partial \mu_i}\right)_{\mu_H} = \left(\frac{\partial \Gamma_i}{\partial \mu_H}\right)_{\mu_i} \quad [25]$$

whence

$$\left(\frac{\partial \psi_r}{\partial \mu_i}\right)_{\Gamma_H} = -\left(\frac{\partial \psi_r}{\partial \Gamma_H}\right)_{\mu_i} \left(\frac{\partial \Gamma_H}{\partial \mu_i}\right)_{\mu_H} = \left(\frac{\partial \psi_r}{\partial \Gamma_H}\right)_{\mu_i} \left(\frac{\partial \Gamma_i}{\partial \psi_r}\right)_{\mu_i} = \left(\frac{\partial \Gamma_i}{\partial \Gamma_H}\right)_{\mu_i} \quad [26]$$

Taking into consideration Eq. [4], Eq. [25] can be written as

$$\left(\frac{\partial \psi_r}{\partial \mu_i}\right)_{\Gamma_H} = 1 : \left[\left(\frac{\partial A_H}{\partial \Gamma_i}\right)_{\mu_i} - \left(\frac{\partial \epsilon}{\partial \Gamma_i}\right)_{\mu_i}\right] \quad [27]$$

[7] Evidently, the isoelectricity condition cannot be fulfilled at potentials which are so close to the reversible hydrogen potential that the hydrogen content in the bulk of the solution becomes comparable to the amount of hydrogen adsorbed on the electrode surface.

We shall assume the adsorptivity of the ion i to be so large that, in spite of small concentration, it will displace from the ionic part of the double layer other ions with charges of the same sign. Then in the case of the surface-active anion

$$\epsilon = \Gamma_{i-} - \Gamma_{C+} \qquad [28]$$

and the surface-active cation

$$\epsilon = \Gamma_{A-} - \Gamma_{i+} \qquad [28a]$$

where C^+ and A^- are cation and anion which do not show significant specific adsorptivity. From [27], [28], and [28a], it follows for the case of anion adsorption[8]

$$\left(\frac{\partial\psi_r}{\partial\mu_i}\right)_{\Gamma_H} = 1 : \left[\left(\frac{\partial A_H}{\partial\Gamma_{i-}}\right)_{\mu_i} - 1 + \left(\frac{\partial\Gamma_{C+}}{\partial\Gamma_{i-}}\right)_{\mu_i}\right] \qquad [29]$$

and for the case of cation adsorption

$$\left(\frac{\partial\psi_r}{\partial\mu_i}\right)_{\Gamma_H} = 1 : \left[\left(\frac{\partial A_H}{\partial\Gamma_{i+}}\right)_{\mu_i} + 1 - \left(\frac{\partial\Gamma_{A-}}{\partial\Gamma_{i+}}\right)_{\mu_i}\right] \qquad [29a]$$

The expressions in square brackets determine the sign and value of the potential shift under isoelectric conditions with increasing concentration of the i ion, assuming the adsorption equilibrium to be maintained all the time. These expressions differ from those obtained in the case of the mercury electrode not only in that they contain the term $\left(\frac{\partial A_H}{\partial\Gamma_i}\right)_{\mu_i}$, but also in that the quantity $\left(\frac{\partial\Gamma_{C+}}{\partial\Gamma_{i-}}\right)_{\mu_i}$ and, accordingly, $\left(\frac{\partial\Gamma_{A-}}{\partial\Gamma_{i+}}\right)_{\mu_i}$ are small (unless the potential lies in the immediate vicinity of the point of zero charge). The latter fact is due to the insignificance of the value of superequivalent adsorption on the Pt electrode, already mentioned earlier.[9] In the expression in square brackets in Eq. [29] all items are always negative. Therefore, the quantity $\left(\frac{\partial\psi_r}{\partial\mu_i}\right)_{\Gamma_H}$ should be negative, as would be expected in the case of anion adsorption, and less than unity in absolute value, approaching unity on complete displacement of adsorbed hydrogen by the anion. The last conclusion is at variance with some results of Obrucheva (24), since, when the concentration of Br^- and I^- was increased ten times, with H_2SO_4 used as a supporting electrolyte, under certain conditions adsorption shifts of the potential in the direction of more negative values equal to 0.12v or even larger were observed, which would correspond to $\left(\frac{\partial\psi_r}{\partial\mu_i}\right)_{\Gamma_H} \sim -2$. It is possible, however, that in more dilute solutions adsorption equilibrium was not established. In the case of cation adsorption (Eq. [29a]), the second and the third items in square brackets are always positive. Usually, the first item is also positive, and the positive value of the sum determines in the case of cation adsorption the shift of ψ_r in the direction of higher values. In some cases, however, *e.g.*, in adsorption of Cd^{2+} from acid solution of $CdSO_4$, at small values of ψ_r, Γ_{i+} increases with increasing ψ_r (7). Probably, this is the result of the competition between Cd^{2+} and H for sites on the platinum surface (Fig. 7). At large enough negative values of $\left(\frac{\partial A_H}{\partial\Gamma_{i+}}\right)_{\mu_i}$, the quantity $\left(\frac{\partial\psi_r}{\partial\mu_{i+}}\right)_{\Gamma_H}$ may become negative, and the adsorption of the cation may cause a potential shift toward more negative values. Such effects were actually observed in the case of the adsorption of the Tl^+ ion in the vicinity of the reversible hydrogen potential and were explained by the displacement of adsorbed hydrogen (25). It should be emphasized, however, that these data are of a strictly qualitative nature, and the verification of the quantitative theory of adsorption shifts of potential in the case of specific ion adsorption on platinum necessitates further study.

Measurements of adsorption shifts of potential also give an independent method of determination of the changes in the shape of the charging curve with changing composition of the solution since all the values of ψ_r obtained in passing from the values $\mu_i = (\mu_i)_1$ to $\mu_i = (\mu_i)_2$ at Γ_H = const. evidently can give a charging curve corresponding to the solution with $\mu_i = (\mu_i)_2$, provided the charging curve of the solution with $\mu_i = (\mu_i)_1$ is known (28).

Recently much attention has been given to adsorption of organic substances on electrodes of the platinum type, and valuable results have been obtained by Bockris and co-workers (29). Assuming that this kind of adsorption can be considered to be a reversible process, which does not seem to be true in all cases, the following relation can be used for a system with constant concentration of all components except adsorbed hydrogen and organic substance

$$d\sigma = -\Gamma_H d\mu_H - \Gamma_{org} d\mu_{org} \qquad [30]$$

where Γ_{org} and μ_{org} are adsorbed amount and chemical potential of the organic substance (30).

Taking into consideration Eq. [4], it follows from [30] that

$$\left(\frac{\partial A_H}{\partial\mu_{org}}\right)_\psi - \left(\frac{\partial\epsilon}{\partial\mu_{org}}\right)_\psi = -\left(\frac{\partial\Gamma_{org}}{\partial\psi}\right)_{\mu_{org}} \qquad [31]$$

whence

$$\left(\frac{\partial\mu_{org}}{\partial\psi}\right)_{\Gamma_{org}} = -\left(\frac{\partial\mu_{org}}{\partial\Gamma_{org}}\right)_\psi \left(\frac{\partial\Gamma_{org}}{\partial\psi}\right)_{\mu_{org}} = \left(\frac{\partial A_H}{\partial\Gamma_{org}}\right)_\psi - \left(\frac{\partial\epsilon}{\partial\Gamma_{org}}\right)_\psi \qquad [32]$$

Equation [32] can also be written in the form

$$\left(\frac{\partial\Delta G_{org}}{\partial\psi}\right)_{\Gamma_{org}} = -\left(\frac{\partial\epsilon}{\partial\Gamma_{org}}\right)_\psi + \left(\frac{\partial A_H}{\partial\Gamma_{org}}\right)_\psi \qquad [33]$$

where ΔG_{org} is the standard free energy of adsorption of organic substance. In the case of the mercury electrode, the change in adsorptivity of organic substance with the potential is determined by the first term in the right hand side of Eq. [33]. To compare the values of the first and of the second terms, let us put it as it is usually done (31)

$$\epsilon = \epsilon_1\left(1 - \frac{\Gamma_{org}}{\Gamma_\infty}\right) + \epsilon_2\frac{\Gamma_{org}}{\Gamma_\infty} \qquad [34]$$

where Γ_∞ is the limiting adsorption of organic substance and ϵ_1 and ϵ_2 the charge per unit surface on uncovered and covered parts of the surface, respectively. Similarly, we can put

[8] If $A_H = 0$, Eq. [29], as it is easy to show, becomes identical with the relation deduced recently by Dutkievicz and Parsons (48) (loc. cit., Eq. [14]) to determine the shift of the potential of a mercury electrode in a KF solution, caused by the adsorption of I- ions at constant charge.

[9] For the mercury electrode in the case of specific adsorption of anions, the quantity $\left(\frac{\partial\Gamma_{C^+}}{\partial\Gamma_{i^-}}\right)_{\mu_i}$ is close to 0.3 (27).

$$A_H = (A_H)_1 \left(1 - \frac{\Gamma_{org}}{\Gamma_\infty}\right) + (A_H)_2 \frac{\Gamma_{org}}{\Gamma_\infty} \quad [35]$$

It follows from [34] and [35] that

$$\frac{\partial \epsilon}{\partial \Gamma_{org}} = \frac{1}{\Gamma_\infty}(\epsilon_2 - \epsilon_1) \quad [36]$$

$$\frac{\partial A_H}{\partial \Gamma_{org}} = \frac{1}{\Gamma_\infty}[(A_H)_2 - (A_H)_1] \quad [37]$$

For many organic substances and over a wide potential range, in the case of the mercury electrode $|\epsilon_2|$ is known to be several times less than $|\epsilon_1|$, which fact determines the desorbing action of the electric field. Judging by the few experimental data available (32), a similar relation should exist between $(A_H)_2$ and $(A_H)_1$. Thus, the relative importance of the first and the second terms in the right-hand side of Eq. [33], as the factors determining the value of $\left(\frac{\partial \Delta G_{org}}{\partial \psi}\right)_{\Gamma_{org}}$, depends in order of magnitude on the ratio of A_H and $|\epsilon|$. Taking into consideration that the maximum value of A_H in the hydrogen region is $\sim 2 \times 10^{-4}$ coul/cm^2, and the maximum value of ϵ for the Pt electrode, *e.g.*, in acid sulfate solutions, is of the order of 10^{-5} coul/cm^2, it is evident that the second term in the right-hand side of Eq. [36] is of great importance. Even at the positive boundary of the hydrogen region and within the so-called "double layer" region, in which in the case of solutions without surface-active anions the amount of hydrogen adsorbed on platinum surface, small as it is, is not equal to zero, ϵ and A_H can be of the same order of magnitude and the presence of the term $\left(\frac{\partial A_H}{\partial \Gamma_{org}}\right)_\psi$ should be taken into consideration in determining the dependence of ΔG_{org} on ψ. Hence it follows that the relations deduced for the mercury electrode are not applicable for the determination of the position of the adsorption maximum of neutral molecules relative to the point of zero charge in the case of the platinum electrode. Whereas the point of zero charge of platinum at low pH values lies in the hydrogen region, due to the desorbing action of hydrogen, the potential of maximum adsorption should be shifted into the double layer region. The magnitude of this shift is limited by the appearance on the platinum surface not only of positive charges, but also of adsorbed oxygen. The mutual influence of adsorption of organic substance and oxygen cannot be considered using thermodynamic methods owing to the irreversibility of oxygen adsorption, but there is no doubt that the presence of the latter also reduces the adsorption of organic molecules. The shift of the potential of maximum adsorption in the direction of more positive values relative to the point of zero charge must decrease in the presence of surface-active anions, since at not too small ψ_r the latter decrease A_H and increase ϵ.

It should be noted that in considering the thermodynamics of adsorption of organic substances on the Pt electrode, we assumed the molecule to be adsorbed without dissociation. In actual fact, the adsorption of many compounds, e.g., aliphatic alcohols, involves dehydrogenation (33), which makes the treatment of the process somewhat more complicated. This case should be considered separately.

A suggestion was made to determine the point of zero charge of platinum from the potential at which adsorption of organic substance does not depend on the electrolyte concentration (34). This conclusion could be considered to be justified only if the quantity A_H were proved to remain unchanged with changing electrolyte concentration.

Finally, it should be noted that Eq. [33] is applicable not only to adsorption of a neutral molecule, but also to that of the surface active cations and anions, present as an addition to the supporting electrolyte, provided their concentration is so small that it can be varied, keeping the concentration of the supporting electrolyte practically constant. In this case, the quantity Γ_{org} in Eq. [33] should be substituted by the surface density of the ion being adsorbed Γ_i.

ADDENDUM

Of essential importance for the development of the theory of the double layer on platinum is the determination of the potential of zero charge $\psi_{\epsilon=0}$. The following methods were used for this purpose: direct determination of the quantity Γ_{H^+} from the changes of the hydrogen ion concentration caused by the adsorption process (I); determination of the potential at which anion and cation adsorptions, expressed in electric units, become equal (II); determination of the deviation of a thin platinum wire in an electric field (III); determination of the dependence of the force which must be applied in order to establish a contact between two crossed platinum wires on the potential (IV); determination of the potential corresponding to the maximum contact angle (V). The last method is a roughly approximate one. Some results obtained by the above methods are listed in Table I.

As it is evident from Table I, the data obtained by different methods are in fair agreement. In the case of minimum specific adsorption $\psi_{\epsilon=0} = 0.16$-0.19. This quantity shifts in the direction of more negative values in adsorption of the anions Cl^- and Br^- and in the direction of more positive values in adsorption of the ion Cd^{2+}.

In addition to investigations by the above mentioned methods, attempts have been made to determine the value of $\psi_{\epsilon=0}$ from the position of the minimum on the differential capacitance-potential curve, this minimum being assumed to correspond to the maximum diffusivity of the electric double layer. The use of this method, which gives reliable results for metals that do not adsorb hydrogen, such as mercury (38), gallium (39), silver (40), lead, tin, etc. (41, 42), involves, however, considerable difficulties in the case of the platinum electrode, on whose surface adsorbed hydrogen and oxygen are present, since in this case the pseudocapacity of ionization of these gases is superimposed on the double layer capacity. Additional difficulties arise due to the slowness of the process of adsorption equilibrium establishment during the formation of the double layer on platinum, which was discussed earlier. Although, in principle, measurements carried out in dilute solutions at sufficiently high frequencies should give correct values of $\psi_{\epsilon=0}$, the difficulties arising in such measurements do not seem to have been overcome as yet. The values of $\psi_{\epsilon=0}$, obtained by various investigators from the capacitance measurements of the Pt electrode (43, 44), show great divergences. Moreover, the potential corresponding to the minimum observed on the differential capacitance curve greatly depends on pH, which has been recently confirmed by Gileadi, Rubin, and Bockris (45). As already shown by Frumkin and Slygin, due to the polarity of the Pt-H bond, a dependence of $\psi_{\epsilon=0}$ on pH should exist. But the linear rela-

Table I. Zero charge potential of platinum in different solutions

Solution	$\psi_{\epsilon=0}$, v, NHE	Method of measurements, reference	
$2 \cdot 10^{-5}N$ H_2SO_4	0.16	III	(35)
N Na_2SO_4 + $10^{-2}N$ H_2SO_4	0.11	I	(19)
$10^{-3}N$ Na_2SO_4 + $10^{-3}N$ H_2SO_4	0.18	II	(7)
$10^{-2}N$ Cs_2SO_4 + $10^{-2}N$ H_2SO_4	0.19	II	(3)
$1.8 \cdot 10^{-2}N$ Cs_2SO_4 + $2 \cdot 10^{-2}N$ H_2SO_4	0.19	II	(3)
$2 \cdot 10^{-5}N$ HCl	0.19	III	(35)
N NaCl + $10^{-2}N$ HCl	0.06	I	(19)
$10^{-3}N$ NaCl + $10^{-3}N$ HCl	0.10	II	(7)
$10^{-3}N$ NaBr + $10^{-3}N$ H_2SO_4	0.04	II	(7)
N NaBr + $10^{-2}N$ HBr	−0.02	I	(19)
$10^{-2}N$ $CdSO_4$ + $10^{-2}N$ H_2SO_4	0.65	II	(7)
N NaBr + $5 \cdot 10^{-2}N$ NaOH	−0.26	I	(19)
$10^{-2}N$ CsI + $10^{-2}N$ CsOH	−0.58	II	(7)
$10^{-2}N$ KCl	0.20	IV	(37)
$10^{-3}N$ KCl	0.20	IV	(37)
N Na_2SO_4 + $10^{-2}N$ H_2SO_4	0.27	V	(36)

tionship between the supposed value of $\psi_{\epsilon=0}$ and pH, established in (45), cannot be explained on the basis of the theory and makes it probable that the minimum observed reflects to some extent the minimum coverage of the surface with adsorbed hydrogen and oxygen rather than the maximum diffusivity of the double layer (44). This is in agreement with the relation between the slopes of the $\Gamma_{H^+,\psi}$ and the $\Gamma_{H,\psi}$ curves in solution containing the SO_4^{2-} ion (3, 7), which shows that in this case, in the so-called double layer region the amount of adsorbed hydrogen and oxygen on the surface is commensurable with the double layer charge. Thus, in 0.1*N* H_2SO_4, within the potential range 0.3-0.8, the value of $\partial\Gamma_{H^+}/\partial\psi$ is equal to 36 ± 5 μf/cm^2, whereas the value of $-\partial\Gamma_H/\partial\psi$, determined from the slope of the charging curve, is ~70 μf/cm^2 at ψ = 0.3-0.5 and 150 μf/cm^2 at ψ = 0.5-0.8 (3). An even greater discrepancy is observed at higher pH (2). Only in the presence of specifically adsorbed anions, such as Cl^- and Br^-, the capacitance values, determined from the adsorption measurements and the charging curves coincide over some potential range, *i.e.*, the surface is practically free of adsorbed H and O.

It should be also kept in mind that a certain lowering of the differential capacitance values with increasing dilution is not necessarily connected with increased diffusivity of the double layer and can be caused by an exclusion of a part of the surface, which is especially pronounced if the surface is not perfectly smooth or markedly inhomogeneous.

On the whole we think that the capacitance minimum of the platinum electrode, corresponding to the maximum diffusivity of the double layer, has not yet been established. It appears therefore doubtful whether the value of $\psi_{\epsilon=0}$ equal to 0.48 at pH = 3 obtained by capacity measurements (45) really corresponds to the point of zero charge of platinum. The question of the relationship between the potential of zero charge and that of maximum adsorption of neutral molecules in the case of the Pt electrode was discussed earlier.

REFERENCES

1. N. Balashova and M. Kulesneva, *Elektrokhimiya*, **1**, 155 (1965).
2. A. Frumkin and A. Slygin, *Acta physicochim. URSS*, **5**, 819 (1936).
3. V. Kazarinov and N. Balashova, *Doklady Akad. Nauk SSSR*, **157**, 1174 (1964).
4. N. Balashova and V. Kazarinov, *Elektrokhimiya*, **1**, 512 (1965).
5. A. Frumkin and A. Gorodetzkaya, *Z. physik. Chem. (A)*, **136**, 451 (1928); A. Frumkin and A. Titievskaya, *Zhur. Fiz. Khim.*, **31**, 485 (1957); **32**, 157 (1958); A. Frumkin, "Surface Phenomena in Chemistry and Biology," p. 189, J. Danieli, K. Pankhurst and A. Riddiford, Editors, Pergamon, London (1958).
6. A. Frumkin, "Advances in Electrochemistry," vol. 3, p. 328, P. Delahay, Editor, Interscience, New York (1963).
7. N. Balashova and V. Kazarinov, *Uspekhi Khim.*, **31**, 1721 (1965); *Collec. Czech. Chem. Comm.*, **30**, 4184 (1965); A. Frumkin, G. Mansurov, V. Kazarinov, and N. Balashova, *ibid.*, **31**, 806 (1966); G. Mansurov, V. Kazarinov, and N. Balashova, *Elektrokhimiya*, In press.
8. E. Ponomarenko, A. Frumkin, and R. Burshtein, *Isvest. Akad. Nauk SSSR, Ser. Khim.*, 1549 (1963).
9. A. Frumkin, *Elektrokhimiya*, **2**, 387 (1966).
10. D. Grahame, *Chem. Revs.*, **41**, 441 (1947).
11. G. Lippman, *Ann. chim. phys.*, (5), **5**, 494 (1875).
12. J. Mignolet, *J. chim. phys.*, **52**, 19 (1957).
13. R. Fisher, H. Chon, and J. Aston, *J. phys. Chem.*, **68**, 3420 (1964).
14. G. Chomchenko, A. Pletyushkina, and G. Vovchenko, "Catalytic reactions in the liquid phase" Akad. Nauk Kaz. SSR, Alma Ata, 1963.
15. M. Tarasevich, K. Radyushkina, and R. Burshtein, *Elektrokhimiya*, In press.
16. P. Bowden and E. Rideal, *Proc. Roy. Soc.*, (A), **120**, 59 (1928); P. Bowden, *ibid.*, **125**, 446 (1929).
17. A. Frumkin, *Sov. Phys.*, **4**, 260 (1933).
18. V. Kazarinov, N. Balashova, and M. Kulesneva, *Elektrokhimiya*, **1**, 975 (1965).
19. A. Slygin, A. Frumkin, and V. Medvedovsky, *Acta physicochim. URSS*, **4**, 911 (1936).
20. Yu. Tyurin and A. Tsybulevskaya, *Doklady Akad. Nauk SSSR*, **159**, 1140 (1964).
21. G. Chomchenko, A. Lunev, and K. Bogdanovskaya, *Elektrokhimiya*, **1**, 1352 (1965).
22. A. Frumkin, *Z. physik. Chem.*, **103**, 55 (1923).
23. B. J. Bowles, *Electrochim. Acta*, **10**, 717, 731 (1965).
24. A. Obrucheva, *Zhur. Fiz. Khim.*, **32**, 2155 (1958); *Doklady Akad. Nauk SSSR*, **141**, 1413 (1961); **142**, 859 (1962).
25. A. Obrucheva, *ibid.*, **120**, 1072 (1958).
26. A. Frumkin, "Transactions of the Symposium on Electrode Processes," p. 1, E. Yeager, Editor, Wiley & Sons, Inc., New York (1961); *Electrochim. Acta*, **5**, 266 (1961).
27. A. Frumkin, *Zhur. Fiz. Khim.*, **30**, 2066 (1956); R. Parsons, Proc. Sec. Congr. Surf. Act., Electrical Phenomena, p. 38, Butterworths, London (1957).
28. A. Frumkin, G. Mansurov, N. Balashova, and V. Kazarinov, *Elektrokhimiya*, In press.
29. H. Dahms and M. Green, *This Journal*, **110**, 1075 (1963); J. O'M. Bockris, and D. Swinkels, *ibid.*, **111**, 736 (1964); J. O'M. Bockris, D. Swinkels, and M. Green, *ibid.*, **111**, 743 (1964).
30. A. Frumkin, *Doklady Akad. Nauk SSSR*, **154**, 1432 (1964).
31. A. Frumkin and B. Damaskin, "Modern Aspects of Electrochemistry," J. O'M. Bockris and B. Conway, Editors, Vol. 3, p. 149 (1964).
32. M. Breiter and S. Gilman, *This Journal*, **109**, 622 (1962); O. Khasova, Yu. Vasiliev, and V. Bagotsky, *Elektrokhimiya*, **1**, 84 (1965).
33. O. Petry, B. Podlovchenko, A. Frumkin, and Hira Lal, *J. Electroanal. Chem.*, **10**, 253 (1965); B. Podlovchenko, O. Petry, A. Frumkin, and Hira Lal, *ibid.*, **11**, 12 (1966).
34. H. Dahms and M. Green, *This Journal*, **110**, 466 (1963).
35. N. Balashova and A. Frumkin, *Doklady Akad. Nauk SSSR*, **20**, 449 (1938).
36. A. Gorodetzkaya and B. Kabanov, *Phys. Ztschr. Soviet Union*, **5**, 419 (1934).
37. T. Voropaeva, B. Deryaguin, and B. Kabanov, *Dokl. Akad. Nauk SSSR*, **128**, 881 (1959); *Zhur. Koll. Khim.*, **24**, 396 (1962).
38. M. Vorsina and A. Frumkin, *Doklady Akad. Nauk SSSR*, **24**, 918 (1939).
39. A. Frumkin, N. Grigoryev and I. Bagotskaya, *Elektrokhimiya*, **2**, 329 (1966).
40. D. Leikis, *Dokl. Akad. Nauk SSSR*, **135**, 1429 (1960); I. Dagaeva, D. Leikis, and E. Sevastyanov, *Elektrokhimiya*, **2**, 820 (1966).
41. T. Borisova, B. Ershler, and A. Frumkin, *Zhur. Fiz. Khim.*, **22**, 925 (1948); T. Borisova and B. Ershler, *ibid.*, **24**, 337 (1950).
42. A. Frumkin, *Svensk. Kim. Tid.*, **77**, 300 (1965).
43. V. Kheifets and B. Krasikov, *Zhur. Fiz. Khim.*, **31**, 1992 (1952).
44. T. Birintseva and B. Kabanov, *Doklady Akad. Nauk SSSR*, **132**, 868 (1960); *Zhur. Fiz. Khim.*, **37**, 2600 (1963).
45. E. Gileadi, B. Rubin, and J. O'M. Bockris, *J. Phys. Chem.*, **69**, 3335 (1965).
46. P. Delahay and D. Mohilner, *J. Am. Chem. Soc.*, **84**, 4247 (1962); P. Delahay, *J. Phys. Chem.*, **67**, 135 (1963); **68**, 981 (1964).
47. R. Parsons, "Modern Aspects of Electrochemistry," Vol. 1, p. 103, J. O'M. Bockris, Editor, Butterworths, London (1954).
48. E. Dutkiewicz and R. Parsons, *J. Electroanal. Chem.*, **11**, 100 (1966).

Discussion

M. W. Breiter: The paper stresses the important aspects in which the adsorption of inorganic and organic species on platinum differs from that on mercury because of simultaneous adsorption of hydrogen atoms or oxygen atoms. The general predictions of the thermodynamic treatment given first by Frumkin and Slygin[1] are in good agreement with the numerous results of direct measurements of ion adsorption on platinum by the above authors. The influence[1] of the composition of the electrolyte on hydrogen adsorption is also reflected by the heats of hydrogen adsorption[2,3] at the same coverage in different electrolytes. The heat decreases with increasing adsorbability and concentration of the anion. The decrease of the heat is paralleled[4,5] by less negative values of the corresponding entropy change at small hydrogen coverage ($\theta < 0.1$). If organic species are chemisorbed, the resulting decrease of hydrogen adsorption may be used as a measure of the coverage with organic species. A quantitative method was suggested recently.[6]

An attempt was made some time ago to apply the thermodynamic treatment[1] to the determination of halide ion adsorption from the measurements[7] of hydrogen adsorption on smooth platinum in 1M $HClO_4$ with additions of HCl or HBr at halide ion concentrations of 10^{-3} and 10^{-2}M. However the changes of Q (see Eq. [7] in the paper) with the chemical potential of HCl and HBr, respectively, were not large enough to warrant a computation under the condition of having the same surface state at different anion concentrations. The technique developed by Gilman[8] appears useful for the study of halide ion adsorption on platinum.

S. Schuldiner: This paper gives an excellent thermodynamic treatment of the Pt hydrogen electrode. Many useful relations are derived which are of value. The initial assumption of the authors that the potential range from 0 to 0.5-0.6v *vs.* the hydrogen electrode in the same solution can be considered as a reversible system in acid solution is open to question. Work at the U. S. Naval Research Laboratory has shown that the reversible H^+/H_2 reaction determines potential on a Pt electrode in acid solution only up to 0.18v *vs.* NHE. Furthermore this work and others has shown that a large part of the hydrogen associated with a Pt electrode is irreversibly sorbed. Thus, the potential range Frumkin, Balashova, and Kazarinov assume to be valid for the reversible hydrogen electrode appears to be much less than claimed.

A. N. Frumkin (communicated): It is not important for the theory developed by us whether the equilibrium of the reaction H^+/H_2, to which Dr. Schuldiner's remark refers, is realized in practice. The theory presumes only the existence of an equilibrium for the ionization reaction of adsorbed hydrogen. The existence of this equilibrium is proved by the complete reversibility of the charging curves in the potential range indicated and by the independence of the length and shape of the charging curves from the time of measurement, which varied from 10 to 100 min, when employing our method (platinized platinum electrodes with 5-10 mg Pt-black/cm^2 of visible surface).[9] Apparently, owing to the wide use of fast pulse methods in recent years it has become unusual to treat the surface of the platinum hydrogen electrode as an equilibrium system.

F. G. Will: In Eq. [7] of the thermodynamic treatment, it is assumed that the amount of charge supplied to the electrode to shift its potential from one to another value in the hydrogen adsorption region is not substantially affected by molecular hydrogen in the electrolyte. With the lightly platinized electrodes used in this study, this assumption can lead to significant errors, depending on the particular conditions of charging. Recent, still unpublished calculations show that an even more significant error may be introduced by neglecting the diffusion of atomic hydrogen from the surface of the electrode into its interior. The magnitude of this error will again depend on transition times, surface roughness, and the size of the platinum black grains.

With regard to the relative contributions of adsorbed atomic hydrogen and of hydrogen ions to the potential difference at the platinum solution interface, it seems surprising that the contribution of the ions should be an order of magnitude larger. While it is granted that this would be true for the particular electrolytes (1N NaCl + 0.01N HCl and 1N NaCl + 0.05N KOH) considered in this study, it appears highly unlikely that it is also true for many acid electrolytes. In the case of the latter, a near 1:1 ratio between surface platinum atoms and adsorbed hydrogen atoms is found. From studies in the gas phase[10,11] it is known that the work function of platinum is changed by as much as 1 electron volt when hydrogen is adsorbed. Certainly, then, the effect of adsorbed ions cannot be one order of magnitude larger.

E. Gileadi: I would like to agree with Dr. Will that the surface area measured from a hydrogen charging curve at very low current densities may be substantially in error due to hydrogen diffusion from the bulk of the metal. On the other hand, the authors find agreement between their area measurement and B. E. T. measurement so that their hydrogen charging method probably cannot be very much in error.

A. N. Frumkin (communicated): Contrary to Dr. Will's comments, the data presented by Marvet and Petry[12] also show that hydrogen solubility in the electrolyte and the metal could not affect the results obtained. The question as to how the presence of dissolved hydrogen could be taken into consideration in the equations derived by us, should this be necessary, will be dealt with elsewhere.

Dr. Will's remark regarding the relationship between the quantities designated by us X and Y seems to be founded on a misunderstanding. The contribution of the adsorbed H atoms to the potential difference set up at the interface is by an order of magnitude less than that of the adsorbed Na^+ and Cl^- ions per one adsorbed particle. The maximum amount of adsorbed Na^+ and Cl^- ions is, however, in about the same proportion less than the maximum amount of adsorbed hydrogen atoms. As the result, the contribution of the ions and of the atoms to the potential difference being set up become comparable, which deter-

[1] A. Frumkin and A. Slygin, *Acta Physicochim. URSS.*, 5, 819 (1936).

[2] W. Böld and M. Breiter, *Z. Elektrochem.*, 64, 897 (1960).

[3] M. Breiter and B. Kennel, *ibid.*, 64, 1180 (1960).

[4] M. Breiter, *Elektrochim. Acta*, 7, 25 (1962).

[5] M. W. Breiter, *Ann. N. Y. Acad. Sci.*, 101, 709 (1963).

[6] M. W. Breiter and S. Gilman, *This Journal*, 109, 622 (1962).

[7] M. W. Breiter, *Electrochim. Acta*, 8, 925 (1963).

[8] S. Gilman, *J. Phys. Chem.*, 68, 2098, 2112 (1964).

[9] R. Marvet and O. Petry, *Elektrokhimiya*, 1, 1225 (1965).

[10] Ref. (12) of the paper.

[11] Sachtler, Rootsaert, and Van Reijen.

[12] R. Marvet and O. Petry, *Elektrokhimiya*, 1, 1225 (1965).

mines the shape of the charging curves observed. In the case of ions with pronounced specific adsorptivity, such as Tl^+ ions, when maximum ion adsorption becomes comparable with hydrogen adsorption owing to the covalent bond between the metal and the adsorbed ion, Y should approach X.

E. Gileadi: I would like to refer to two of the topics mentioned in this paper, namely, the position of the potential of zero charge on Pt and the interpretation of the potential dependence of organic adsorption on Pt.

The potential of zero charge on platinum has been investigated in our laboratory in some detail by two methods.[13] One method depends on the study of the effect of natural salt concentration on the potential dependence of organic adsorption[14] and the other is the well-known measurement of differential double layer capacity as a function of potential in highly purified dilute solutions of $HClO_4$. Results obtained by the two methods were found to be in good agreement, and I would like to concentrate on those obtained by the capacitance method.

Fig. EG 1 shows a typical C-V plot in highly purified, dilute $HClO_4$ solution. The pretreatment of the electrode was found to be of very great importance, and in particular the absorption of hydrogen into the bulk of the metal must be controlled. The curve marked "without H" in Fig. EG 1 was obtained on an electrode which has been treated for 3 hr at 450°C in an atmosphere of purified argon. Calculations based on independent measurement of the diffusion coefficient of hydrogen in Pt carried out in our laboratory[15] confirmed that under these conditions all the hydrogen was eliminated from the metal. Prolonged heating (overnight) had no further effect. The curve marked "with H" was obtained after keeping the electrode at a potential of 0.2v r.h.e. for 5 min, allowing for hydrogen diffusion into the metal. Figure EG 2 gives similar results in alkaline solutions.

[13] E. Gileadi, S. D. Argade, and J. O'M. Bockris, *J. Phys. Chem.*, 70, 2044 (1965).

[14] H. Dahms and M. Green, *This Journal*, 110, 466 (1963).

[15] E. Gileadi, M. A. Fullenwider, and J. O'M. Bockris, *This Journal*, in press.

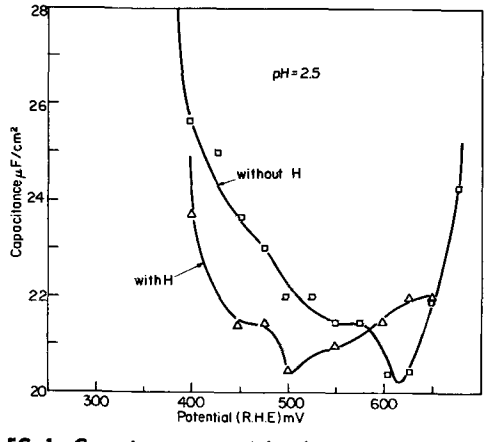

Fig. EG 1. Capacitance-potential relationship in dilute $HClO_4$ solution.

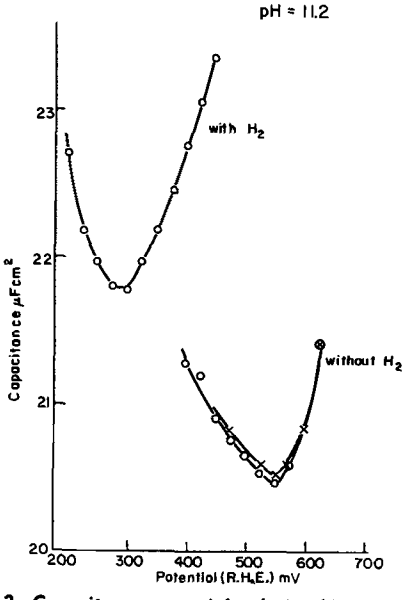

Fig. EG 2. Capacitance-potential relationship in dilute $NaClO_4$ + NaOH solution at high pH.

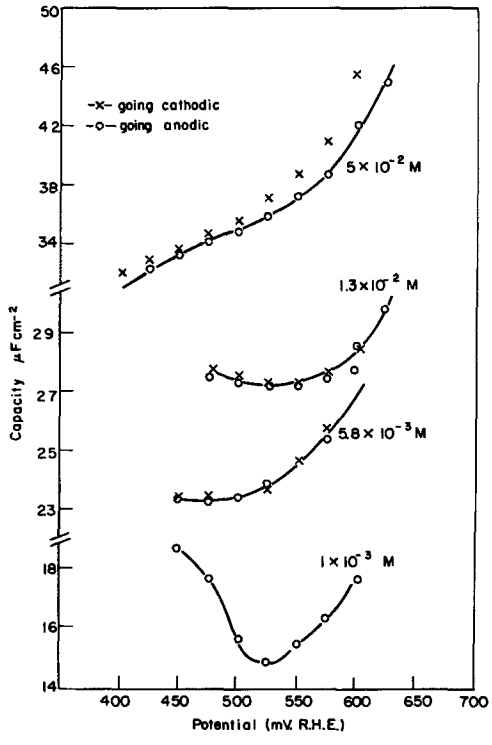

Fig. EG 3. Variation of the shape of the C-V plots with increasing $HClO_4$ concentration.

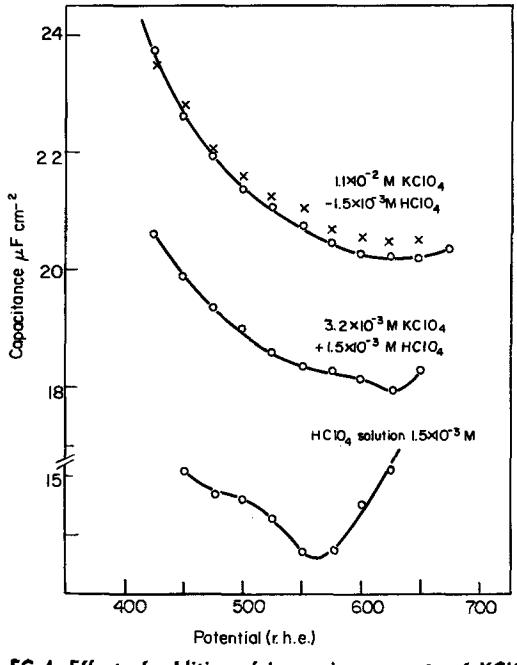

Fig. EG 4. Effect of addition of increasing amounts of $KClO_4$ on the shape of the C-V curves.

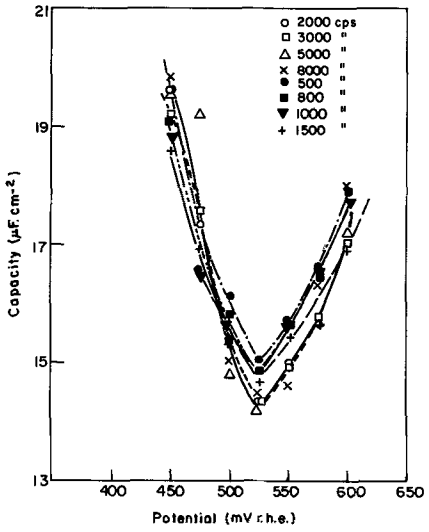

Fig. EG 5. Differential capacity measurements on platinum in 0.001N $HClO_4$ solution as a function of frequency.

Two types of experiments were performed to prove that the capacitance minimum observed here does in fact correspond to the maximum diffusivity of the double layer, *i.e.*, to the potential of zero charge. Figure EG 3 shows the variation of the shape of the C-V plot with increasing concentration of $HClO_4$. In Fig. EG 4, the effect of increasing the total ionic strength by addition of $KClO_4$ is shown. In both cases the capacitance minimum characteristic of the potential of zero charge in dilute solutions disappears as soon as the total concentration of electrolyte exceeds $5 \times 10^{-3}N$.

In Fig. EG 5, the effect of frequency on the C-V plot in the vicinity of the potential of zero charge is given for a frequency range of 0.5×10^3 to 8×10^3 cps. A very small frequency variation is observed, which can be attributed to the lack of complete symmetry between the working and counter electrode, and to a certain extent to a possible slight roughness of the surface.

On the basis of the effect of concentration and frequency on the C-V plot we then conclude that the capacitance minimum observed in our measurements in very dilute solution corresponds to the potential of zero charge. The value of the potential of zero charge, measured *vs.* a constant reference electrode, varies linearly with pH to an extent of 60 mv/pH unit and has a value of $V_{pzc} = 0.56 \pm 0.025$v independent of pH when measured *vs.* a reversible hydrogen electrode in the same solution.

The disagreement between the results presented by Frumkin *et al.* in this paper and our own recent result may be at least in part due to the different pretreatment of the electrode. Our values refer to a "hydrogen free" Pt electrode, while the results of Frumkin *et al.* and probably all other results reported so far refer to a "hydrogen loaded" electrode. Figures EG 1 and EG 2 indicate that the effect of hydrogen in the metal is at least in the right direction to resolve this discrepancy.

I would like to turn now to the question of the interpretation of the potential dependence of adsorption of neutral organic molecules on Pt. In several publications from our laboratory in recent years[16-19] this dependence has been interpreted in terms of a "competition with water" model while according to the present papers of Frumkin *et al.*, this is more likely due to essentially a competition with hydrogen and oxygen adsorbed on the surface.

We are in agreement with the relevant Eq. [33] in this text, which gives the variation of the free energy of adsorption of organic with potential at constant Γ_{org} as a function of the derivatives of the charge and the hydrogen coverage A_H with respect to Γ_{org} at constant potential

$$\left(\frac{\partial \Delta G_{org}}{\partial \psi}\right)_{\Gamma_{org}} = -\left(\frac{\partial \epsilon}{\partial \Gamma_{org}}\right)_{\psi} + \left(\frac{\partial A_H}{\partial \Gamma_{org}}\right)_{\psi}$$

The relative importance of the two terms on the r.h.s. of this equation for the Pt system is, however, disputed. Moreover, to explain the decrease of coverage with potential above 0.5v a similar equation would have to be assumed for adsorbed oxygen. It is doubtful if such an equation would be valid, due to the irreversible nature of oxygen adsorption, as pointed out by Frumkin in a previous publication.[20]

Several experimental facts do not seem to be in agreement with the theory proposed here by Frumkin.

1. Peak adsorption on Pt occurs at about 0.45v (NHE) in $1N$ H_2SO_4. The coverage decreases roughly symmetrically on either side of V_{max}, yet at 0.2v, $\theta_H = 0.5$ while at 0.7v (*i.e.*, at an equal distance on the anodic side of V_{max}) the coverage by oxygen is probably not more than 0.05.

2. In a study of hydrocarbon adsorption on Pt on open circuit it was found[21] that ethylene displaced hydrogen from the electrode surface. On the other hand, it was found to have essentially no effect on oxygen coverage in the same system.[22] Thus

$$|(\partial A_H/\partial \Gamma_{org})_\psi| >> |(\partial A_o/\partial \Gamma_{org})_\psi|$$

and an unsymmetrical $\theta - \psi$ relationship would be predicted.

3. In the adsorption of naphthalene and n-decylamine on Ni an increase of coverage with increasing cathodic potential occurred in a region where coverage by hydrogen also increased.

In conclusion, we agree that hydrogen adsorption may have an effect on the potential dependence of organic adsorption in certain systems. However, it appears highly unlikely that our results for *e.g.*, ethylene[17] and benzene[18] adsorption can be interpreted even partially on this basis.

The pH dependence of the potential of zero charge and the effect of pH on organic adsorption are consistent with our interpretation of the $\theta - V$ relationship. Figure EG 6 shows $\theta - V$ plots for the adsorption of benzene on Pt from mixtures of H_2SO_4 and Na_2SO_4 maintaining a constant concentration of $SO_4^=$ ions.[18] A plot of the potential of zero charge and the potential of maximum adsorption *vs.* pH is given in

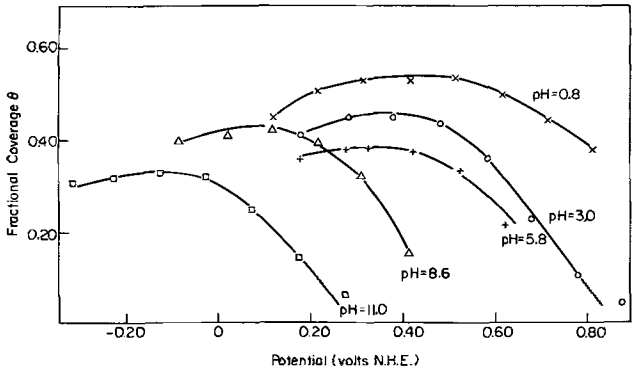

Fig. EG 6. The adsorption of benzene on Pt as a function of potential and pH.

[16] J. O'M. Bockris, M. Green, and D. A. J. Swinkels, *This Journal*, 111, 736, 743 (1964).

[17] E. Gileadi, B. T. Rubin, and J. O'M. Bockris, *J. Phys. Chem.*, 69, 3335 (1965).

[18] W. Heiland, E. Gileadi, and J. O'M. Bockris, *ibid.*, 70, (1966).

[19] E. Gileadi, *J. Electroanal. Chem.*, 11, 137 (1966).

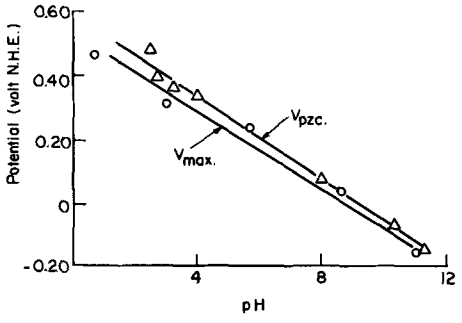

Fig. EG 7. pH dependence of the potential of zero charge and the potential of maximum adsorption on Pt.

Fig. EG 7. The two lines are parallel within experimental error with V_{max} slightly cathodic to V_{pzc} at all pH values as expected according to the water competition model.[16]

A. N. Frumkin (Communicated): A number of attempts have been made at the Institute of Electrochemistry to use for the platinum-hydrogen electrode the method of the point of zero charge determination from the capacitance minimum in dilute solutions, first proposed by one of the authors.[23] Although Birintseva and Kabanov[24] observed at $\psi = 0.18$v the appearance of a minimum on the C, ψ curves in 0.01 and 0.001*N* H_2SO_4, which disappeared with increasing concentration (C, the capacitance per unit electrode surface; other designations, the same as in our paper), *i.e.*, in agreement with the point of zero charge determination, in our paper we pointed out with good reason, as it seems to us, that the difficulties involved in these measurements have not yet been overcome. Recently Burshtein, Pshenichnikov, and Shevchenko, of the same Institute, apparently obtained more reliable results. The experiments were carried out with a smooth Pt electrode, which after reduction in hydrogen at 450°C and outgassing *in vacuo* at 900°, had been activated in the solution by the application of sawtooth cathodic and anodic pulses in the interval of ψ_r values from 0.0 to 1.6v. As can be seen from Fig. AF 1, at higher concentrations a minimum is observed at $\psi \sim 0.55$v, which is, undoubtedly, a pseudocapacity minimum due to ionization of adsorbed hydrogen and oxygen. As the solution is diluted, however, a deeper minimum appears at $\psi = 0.23$v, *i.e.*, close enough to the pzc determined by direct adsorption measurements. The position of this minimum on the ψ-axis does not change when the concentration of the acid is changed from 0.01 to 0.002*N* and appears therefore to be pH independent. Further measurements will show how far this result can be considered conclusive.

Comparing the results of his measurements by the differential capacitance method with the data on the pzc given in our paper, Dr. Gileadi suggests that the difference in the surface state of the electrode is one of the reasons for the discrepancy observed. In Dr. Gileadi's opinion, his own data refer to a "hydrogen free" electrode, whereas our data are for a "hydrogen loaded" one. In this connection, we would like to make two observations. The term "hydrogen loaded" does not correctly describe the surface state of the electrodes used by us, as under cathodic polarization the electrode can be loaded with hydrogen to various degrees. In actual fact, our aim was to establish the conditions for the equilibrium relative to the ionization reaction of adsorbed hydrogen as given by Eq. [2]. Such conditions, as will be shown below, really can be established. As regards the surface treatment carried out by Dr. Gileadi, there is no doubt that no equilibrium is established on the surface of a smooth electrode deactivated by prolonged heating at 450°C without subsequent activation by alternating anodic and cathodic polarizations. Measurements of the electronic work function of platinum, however, performed at the Institute of Electrochemistry by Fokina, Shurmovskaya, and Burshtein have shown that in order to remove strongly adsorbed or dissolved gases from the surface of solid smooth platinum it is necessary to carry out degassing *in vacuo* at 900°C. In addition, as it follows from a series of studies by Bagotsky and collaborators,[25] previously degassed platinum absorbs appreciable amounts of oxygen from the solution already at the potential $\psi_r \sim 0.4$v. Therefore, we suppose that the minimum observed by Dr. Gileadi in the experiments with 0.001*N* $HClO_4$ is likely to be connected with the position of the pzc of a somewhat oxidized platinum surface. In fact, according to the data of Balashova and Frumkin,[26] in dilute H_2SO_4 the pzc of oxidized platinum lies at $\psi \sim 0.5$v, *i.e.*, it is strongly shifted in the positive direction.

At any rate, the shift in the minimum on the capacitance curve along the ψ-axis with changing pH of the solution, observed by Dr. Gileadi, as well as by Kheifets and Krasikov,[27] shows adsorbed oxygen (or hydrogen) to be present on the metal surface, since otherwise it would be impossible to account for this pH dependence by means of any theory. Unfortunately, Dr. Gileadi does not mention whether he observed the dependence of the depth of this minimum

[20] A. M. Franklin, *Doklady Akad. Nauk. SSSR*, 154, 1432 (1964).

[21] L. W. Niedrach, *This Journal*, 111, 1309 (1964).

[22] J. O'M. Bockris, H. Wroblowa, E. Gileadi, and B. J. Piersma, *Trans. Faraday Soc.*, 61, 2531 (1965).

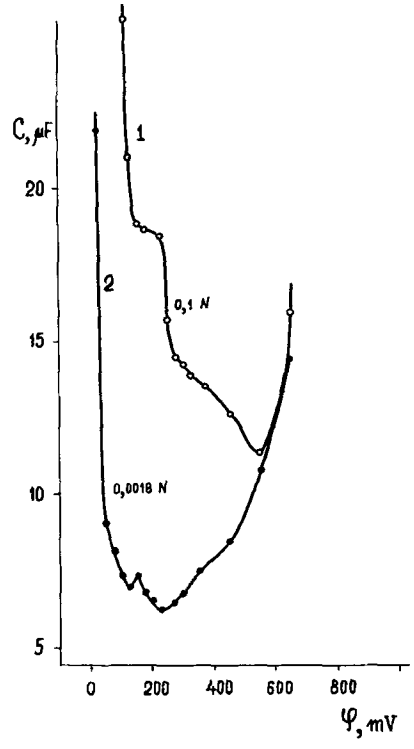

Fig. AF 1. Dependence of the capacitonce of an activated Pt electrode on the potential vs. NHE in dilute solutions (Burshtein, Pshenichnikov and Shevchenko). 1. 0.1N H_2SO_4; 2. 0.0018 NH_2SO_4; frequency: 1. 10,000; 2. 5100 cps.

[23] T. Borisova, B. Ershler, and A. Frumkin, *Zhur. Fiz. Khim.*, 22, 925 (1948).

[24] T. Birintseva and B. Kabanov, *Zhur. Fiz. Khim.*, 37, 2600 (1963).

[25] V. Lukianycheva and V. Bagotsky, *Doklady Akad. Nauk SSSR*, 155, 160 (1964); V. Lukianycheva, V. Tikhomirova, and V. Bagotsky, *Elektrokhimya*, 1, 262 (1965).

[26] N. Balashova and A. Frumkin, *Doklady Akad. Nauk SSSR*, 20, 449 (1938).

[27] V. Kheifets and B. Krasikov, *Zhur. Fiz. Khim.*, 31, 1992 (1952).

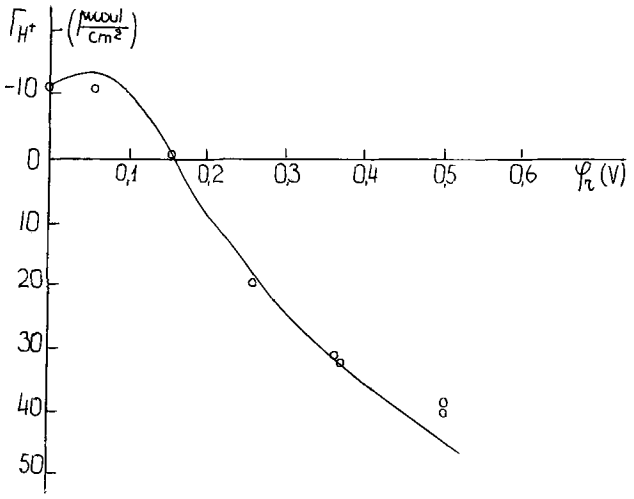

Fig. AF 2. Dependence of Γ_{H+} on ψ_r for a platinized platinum electrode in *N* KCl + 0.01*N* HCl. The full drawn curve has been calculated from Eq. [6]; the circles represent experimental values (Frumkin, Petry, and Marvet).

on the concentration of the solution only in acid solutions or at other pH as well. This point is an important one.

From our point of view, it was most important to show that under the conditions of our experiments, the surface of the platinum electrode could really be treated as an equilibrium system, so that Gibbs thermodynamics could be applied to it. At present, Frumkin, Petry, and Marvet have been able to prove experimentally the correctness of this assumption, at any rate for the case of a platinized platinum electrode. In Fig. AF 2 the values of Γ_{H+} in the function of ψ_r determined experimentally in *N* KCl + 0.01*N* HCl solution are compared with those calculated by means of Eq. [6] of our paper from the values of $\left(\frac{\partial \Gamma_H}{\partial \psi_r}\right)_{\mu_{H+}}$ and $\left(\frac{\partial \psi_r}{\partial \mu_{H+}}\right)_{\Gamma_H}$.

The calculated values were obtained by the integration of the $\left(\frac{\partial \Gamma_{H+}}{\partial \psi_r}\right)_{\mu_{H+}}$ curve determined from Eq. [6] using the value of Γ_{H+} at $\psi_r = 0$ found experimentally. Good agreement between calculated and experimental values corroborates the correctness of our assumption as well as of the determination of the pzc by the method designated in our paper as method I.

In the second part of his discussion, Dr. Gileadi presents some arguments against the thermodynamic treatment of the dependence of the adsorption of organic substances on the potential, which was suggested by one of the authors.[28] According to Dr. Gileadi, the relations like our Eq. [33] are quantitatively inapplicable to the oxygen region of the charging curve owing to the irreversibility of oxygen adsorption. This is quite correct and was emphasized in our paper. It is not clear, however, how a model based on "competition with water" can be quantitatively used in this potential range when the measurements of the anion adsorption show that in the case of anions, which are not adsorbed specifically, the tension of the electric field of the double layer, due to positive surface charges and negative charges of adsorbed anions, decreases rather than increases with rising ψ_r.[29] The increase in the latter quantity depends completely on that in the number of adsorbed oxygen atoms and on the dipole nature of the Pt — O bond.

Our treatment refers to the idealized case of organic substance adsorption when an equilibrium relative to adsorption of all components is established on the surface. Naturally in the case of chemisorption of such substances as ethylene, when adsorbed hydrogen [30,31] appears on the platinum surface and methane and ethane can be detected in the gas phase,[31] it is not possible to explain all the phenomena observed in terms of a thermodynamic theory. The general parallelism, however, between the position of the potential of maximum adsorption and the supposed pzc determined as it has been done by Dr. Gileadi, follows from our interpretation of the physical significance of this potential and the relationship between the adsorption of organic substances and that of electrochemically active gases.

Hideaki Kita: 1. According to the statement on the fourth paragraph, the H^+ ions in the ionic part of the double layer are adsorbed giving off their charges to the metal and changing to H atoms. Thus, the quantity Γ_{H+} is identified with the charge density on the electrode.

If we extend this identification further, Γ_{H+} can also be the quantity of adsorbed hydrogen atoms thus formed. Since Γ_H is the symbol for the surface density of hydrogen atom, these quantities, Γ_{H+} and Γ_H, appear not to be separated definitely from each other.

On the other hand, if we understand the quantity Γ_{H+} as the surface density of hydrogen ion as defined in paragraph 3, the charge density of electrode surface would be negligibly small according to the statement in paragraph 4 that the presence of H^+ ions in the ionic part of the double layer can be neglected at the conditions of an excess of C^+ cations.

2. Equation [2] can be taken as applicable only for the case where the step, $H^+ + e^- = H(ads)$, is in equilibrium, since the hydrogen electrode reaction occurs irreversibly at the polarization of ψ_r. Hence, the quantity A_H, which is understood to be the amount of hydrogen disappeared from the bulk of solution according to the statement in paragraph 5 cannot be the equilibrium quantity and must not be introduced in the thermodynamical equations.

In short, interrelations among Γ_{H+}, Γ_H, and A_H do not seem to be clear enough.

A. N. Frumkin (Communicated): 1. The quantities Γ_H and Γ_{H+} may become equal (but opposite in sign) if no measurable amount of adsorbed hydrogen in the atomic form is present on the electrode surface. Such case was considered by one of the authors earlier.[32]

2. The exchange current of the reaction $H^+ + e^- \rightleftarrows H_{ads}$ at $[H^+] = 10^{-2}N$ is of the order of 10^{-1} amp/cm^2. The maximum current density, used by us in the measurements of the charging curves, calculated per cm^2 of true electrode surface, did not exceed 10^{-6} amp/cm^2. Thus, the equilibrium conditions for the above reaction were realized.

S. Gilman: It was suggested that the discrepancy between the results of capacitance determination from adsorption measurements and from the impedance might be explained on the basis of slow establishment of equilibrium between the adsorbed anion and the platinum surface. While the observation need not be general for all anions, evidence has been found[33]

[28] A. Frumkin, *Doklady Akad. Nauk SSSR*, 154, 1432 (1964).

[29] A. Slygin, A. Frumkin, and V. Medvedovsky, *Acta physicochim. URSS*, 4, 911 (1936); N. Balashova and V. Kazarinov, *Usp. Khim.*, 34, 1721 (1965).

[30] R. Burshtein, V. Tiurin, and A. Pshenichnikov, Proc. 14th Internat. Symp., Brighton, September 1964, p. 315, D. Collins, Editor, Pergamon Press (1965); *Doklady Akad. Nauk SSSR*, 160, 629 (1965); V. Tiurin, A. Pshenichnikov, and R. Burshtein, *Electrokhimiya*, In press.

[31] L. Niedrach, *This Journal*, 111, 1309 (1964).

[32] B. Bruns and A. Frumkin, *Z. physik. Chem.* (A), 147, 125 (1930).

[33] S. Gilman, *J. Phys. Chem.*, 68, 2098, 2112 (1964).

that (at potentials below *ca.* 0.8v in acid solution) the adsorption-desorption of chloride and phosphate ions is rapid and reversible. An alternative explanation for low capacitance is naturally surface contamination,[34] although it is not altogether certain that the high values measured at clean smooth Pt electrodes [34,35] are entirely free of pseudocapacitance.

A. N. Frumkin (Communicated): Our paper was concerned with the discrepancy between the calculated value of $Y^{-1} = \left(\frac{\partial \Gamma_{H^+}}{\partial \psi}\right)_{A_H}$ and the capacitance determined by the a-c measurements at a high enough frequency, the former quantity proving to be much larger than the latter. Since the presence of pseudocapacity of the ionization reaction of adsorbed hydrogen could have affected only the second quantity, taking it into consideration would have resulted only in the increase in this discrepancy.

In the case of I^- adsorption from NaI solutions on a platinized Pt electrode, it takes hours for the equilibrium to be established.[36] Such a delay was not observed in the case of ions without specific adsorptivity, which shows that it cannot be caused by the diffusion difficulties or by the presence of impurities in the solution. The effect of the latter moreover could not be of great importance in the case of platinized electrodes with a highly developed surface. The adsorption process of such anions as I^- on platinum is in many respects similar to that of oxygen chemisorption from the solution. Slow establishment of the equilibrium in this case is a well known fact and has been the object of a number of investigations (*e.g.*[37]). In the case of the chlorine anion, these phenomena are much less pronounced, but hardly absent altogether. The technique used by Dr. Gilman is probably not quite suitable for the investigation of very slow processes.

G. C. Barker: I do not question any of the experimental facts reported by Professor Frumkin and his co-workers. I merely wish to point out that the specific adsorption of certain metals on platinum is an effect far more striking than might be suspected from adsorption potential measurements. Our unpublished work, based largely on studies of the rate of increase of the part of the interfacial impedance connected with the reduction of hydrogen ions and the oxidation of adsorbed hydrogen atoms, suggests that hydrogen adsorption sites are readily occupied by adsorbed metal atoms sometimes even when the solution concentration of the ion metal is as low as 10^{-8}M. The adsorption for potentials in the range in which hydrogen is adsorbed is very marked for Cd and Tl and strong adsorption of the ions of Pb, Bi, and Sn in the same potential region is also observed with strongly acid solutions (HCl, $HClO_4$). Generally the adsorbed metal is displaced when the platinum electrode is anodically polarized and this displacement (due to oxygen adsorption) rather than the oxidation of organic matter is usually the main reason why platinum electrodes are "activated" by anodic polarization. Often the solutions used in studies of the kinetics of the formation and oxidation of molecular hydrogen contain copper and lead ions at concentrations up to 10^{-7} — 10^{-6}M and such concentrations are sufficient to rapidly displace a substantial amount of the adsorbed hydrogen from a smooth platinum electrode and so greatly lower the activity of the electrode. The fall in activity is generally accelerated in stirred solution as the adsorption usually seems to be a diffusion-controlled process. It might also be mentioned that, if a smooth platinum electrode is suspended in a sealed glass cell lined with platinum, the surface of which has been platinized, after saturating the solution with hydrogen and subjecting the electrode to brief anodic polarization occasionally during the first few days, the activity of the electrode (studied by a-c means) remains almost constant for months without further activation. This shows clearly that if adequate precautions are taken to remove from the solution organic matter and ions tending to be strongly adsorbed, a spontaneous fall in activity such as has been suggested from time to time in the literature does not occur. Clearly such falls are due to faulty experimental techniques. Professor Frumkin states that adsorbed Cd is covalently bound to the electrode, and it seems likely that the same may be true in other cases where almost complete coverage (judging from the effect on the impedance) is obtained at potentials considerably more positive than that for bulk deposition of the metal. As has been suggested earlier by Professor Frumkin, the strong adsorption is presumably connected with the formation of a two-dimensional intermetallic compound. Mössbauer studies of the bonding of specifically adsorbed tin on platinum made recently by Bowles and Cranshaw at Harwell suggest that the adsorbed tin is very strongly bound to the electrode.

Reply by *M. W. Breiter*: Study of the deposition of copper ions on smooth platinum from acidic solutions (1M $HClO_4$) was carried out by me at potentials more anodic than the potential of copper deposition about two years ago. The results were not published because of the presence of small amounts of organic impurities leading to an anodic wave in the oxygen region during an anodic sweep. It was observed that copper ions may be deposited at potentials up to 0.25v more anodic than the deposition potential. The layer formed is less than a monolayer and considered by me as an adsorbed layer of Cu atoms. Thicker layers are formed at the potential of copper deposition. The layers can be removed by anodic stripping.

H. D. Hurwitz: Without using the original method of Gibbs, it seems to me that we may formulate the problem of the nonideal polarized interphase in an equivalent manner starting from the equation of Gibbs-Duhem and the electroneutrality condition

$$\Gamma'_{H^+} + \epsilon = \Gamma_{A^-} - \Gamma_{C^+} \qquad [1]$$

At constant T one has

$$(d\sigma)_T = -\Gamma_{A^-} d\mu_{A^-} - \Gamma_{C^+} d\mu_{C^+} - \Gamma'_{H^+} d\mu_{H^+} - A_H d\mu_H - \epsilon d\psi \qquad [2]$$

In [1] and [2] one has stated that the Gibbs surface defined by $\Gamma_{H_2O} = 0$ is permeable to H^+ and H. The quantities Γ_{A^-}, Γ_{C^+}, A_H and the charge ϵ have been defined in the paper. As for Γ'_{H^+}, the surface excess of H^+, it has been assumed to vanish in the model of Frumkin *et al.* in order to fit with the interpretation of the value of ϵ.

For the condition of electrochemical equilibrium respectively at the working electrode and at the reference electrode, one has

$$\mu_{H^+} - F\psi = \mu_H \qquad [3]$$

$$\mu_{H^+} - F\psi^{ref} = (\mu_H)_0 \qquad [4]$$

and

$$\psi_r = \psi + \frac{(\mu_H)_0 - \mu_{H^+}}{F} \qquad [5]$$

with ψ_r the cell potential.

From Eq. [2] and [3] one deduces easily that

$$(d\sigma)_T = -\Gamma_{A^-} d\mu_{A^-} - \Gamma_{C^+} d\mu_{C^+} - [\Gamma'_{H^+} + \epsilon] d\mu_{H^+} - [A_H - \epsilon]\, d\mu_H \qquad [6]$$

[34] S. Gilman, *Electrochim. Acta*, 9, 1025 (1964).

[35] M. Breiter, *J. Electroanal. Chem.*, 7, 38 (1964).

[36] N. Balashova and V. Kazarinov, *Elektrokhim.*, 1, 512 (1965).

[37] V. Nesterova and A. Frumkin, *Zhur. Fiz. Khim.*, 26, 1178 (1952).

Another way to write [2] is obtained in making use of [1], [3], and [4], thus

$$(d\sigma)_T = -\Gamma_{A-}d\mu_{AH} - \Gamma_{C+}d\mu_{COH} - F[\epsilon - A_H]d\psi_r \quad [7]$$

in which

$$d\mu_{AH} = d\mu_{A-} + d\mu_{H+};\ d\mu_{COH} = d\mu_{C+} - d\mu_{H+}$$

According to the definition $\epsilon = \Gamma_{H+}$ and assumption $\Gamma'_{H+} = 0$, Eq. [6] transforms into Eq. [1] of Frumkin *et al.*, and relations [3] and [4] of this work are readily inferred and may be extended to the case where H^+ is not only in state of contact adsorption ($\Gamma'_{H+} \neq 0$).

From [6] it is observed that at μ_{A-} and μ_{C+} constant, $[\Gamma'_{H+} + \epsilon]$ and $[A_H - \epsilon]$ are thermodynamically independent variables. Therefore, by exact differential property, $d\psi$ could be written in terms of these coordinates, or by introducing an analytical change of coordinates* in terms of either $[A_H + \Gamma'_{H+}]$ and $[\Gamma'_{H+} + \epsilon]$ or A_H and Γ_{H+}, according to the approximation of Frumkin. Equation [12] of Frumkin with X^{-1} the pseudocapacitance of adsorption and Y^{-1} a capacitance of the double layer suggests that such change of coordinates has been used.

Equation [10] of Frumkin *et al.* may be easily shown to follow from Eq. [7] given above.

* With $X = [A_H - \epsilon]$; $Y = [\Gamma'_H + \epsilon]$ and $U = X + Y$; $V = Y$ the Jacobian $J(X,Y/U,V)$ of the transformation $X,Y \rightarrow U,V$ is unity.

Ion Pairing Mechanisms in Electrode Processes

L. Gierst, L. Vandenberghen,[1] E. Nicolas, and A. Fraboni

Free University of Brussels, Brussels, Belgium

ABSTRACT

The influence of "bulk" ion pairing on electrode processes is easily detected when its main effect is to decrease the activity of the depolarizer. On the other hand, when association with the adsorbed ions of the supporting electrolyte forms a more electroactive entity, it is known that it can be more difficult to distinguish between direct discharge, or via ion pairs. However, a broad intercomparison (under strictly identical experimental conditions) of the influence of the nature and concentration of the supporting cation (Li^+, Na^+, K^+, Cs^+, Mg^{2+}, Ca^{2+}, Ba^{2+}) on depolarizers of various electronic charge, allows to detect the abnormal behaviors, which are not determined by the pure "static" ψ effect. An indirect method has also been used, which essentially consists in modifying the double layer profile by adding, at constant concentration, increasing amounts of tensioactive ions having the same charge as the electrode, *e.g.*, iodide at not too negative charge densities.

The occurrence of chemical ion pairing as a concomitant rate-determining factor in electrode processes is generally easily detected from the effect of suitable composition changes at constant double layer structure: a typical case is the action of the sulfate ion on cation reduction, recently studied in our laboratory (15). However, it has been pointed out (1, 2) that, in the case of anion reduction proceeding at sufficiently negative potentials in not too concentrated solutions, the variations of the apparent rate constant produced by changing the concentration of the supporting electrolyte can be referred either to the usual ψ effect acting on the "bulk" species or to a prior charge-decreasing process involving ion-pairing with the supporting cations, which helps to circumvent the repulsive interaction with the electrode. In some cases, sudden changes in α_0 values (for want of more definite proof) seem even to suggest that each mechanism could be rate-determining within separate potential ranges (3).

Exact diagnosis of the type of mechanism unfortunately is made more difficult by the conjunction of three circumstances:

1. Since no double layer model of sufficient accuracy is available (if it should be, it would probably be hardly adaptable to electrode kinetics), the fact that a given electrochemical reaction follows closely the predictions derived from the Frumkin relation coupled with for instance the Gouy-Chapman theory, does not constitute in itself an overwhelming argument (2).

2. There is some tendency to focus the investigations on electrochemical reactions which present quite abnormal characteristics, without paying enough interest to reactions more apt to bring clearer information. Some of these latter reactions have occasionally received only superficial attention, or have been investigated with inadequate methodology, enough however to hinder their reexamination.

3. Most of the available data cannot be directly compared, since experimental conditions (such as drop time, compositions, temperature) and measured quantities (average or instantaneous currents, 45° tangent of half-wave potentials, etc. . . .) are highly variable.

The method adopted here consists in reassessing the basic characteristics of a sufficient number of these reactions, under strictly standardized conditions.[2]

The systematic intercomparison of the results obtained allows the identification of the various types of behavior and relates them specifically to their corresponding rate-determining mechanisms. Additional evidence may be gained from a more general comparison considering other data relative to behaviors which are known to be affected by ion pairing.

The present study is limited to concentrated solutions (0.1 and 1*N*) of supporting electrolytes with the most common mono- and divalent cations. As far as the charge of the depolarizer is concerned, it is worthwhile to distinguish: (*a*) the "formal" charge z^0 calculated from valencies and stoichiometry; (*b*) the "bulk" charge z_B which prevails in solution and may vary with the concentration of the supporting electrolyte [for highly charged anions, z_B is generally close to −2 in 1*N* solutions (8)]; (c) the "apparent" charge z_K which best fits the Frumkin equation if it is assumed that there is no prior labile association with the supporting cation, and when ψ is controlled by the supporting electrolyte concentration; (*d*) the "actual" charge z_δ of the electroactive entity itself.

[1] Excerpts from dissertations to be submitted to the Faculty of Sciences as partial fulfillment of the requirements for Ph.D. degree.

[2] Since no claim for originality is made, the extended list of references pertaining to each of the various depolarizers used has been deliberately omitted. Such references are easily available in systematic polarographic surveys (6, 7).

The connection between z_K and z_δ constitutes one of the problems dealt with in this paper.[3]

A first approach consists in modifying the ψ potential without affecting the cationic composition. Besides the use of amalgam electrodes already used successfully (2), this result may be achieved by suitable substitution of the anion of the supporting electrolyte, using anions of increasing adsorbability, and as far as the potentials at which measurements are made are not too negative with respect to the point of nul charge. A more indirect way, usable through the whole potential range, is based on the substitution of the supporting cation itself; it can indeed be presumed that the specific interactions with the electrode (affecting ψ values), and with the depolarizer [controlling the prior chemical step(s)], are not following the same sequence.

Instrumentation and Reagents

All the data presented have been derived from the analysis of instantaneous maximum current-time polarographic curves, obtained with a controlled drop-time of 4 sec. The experiments were carried out at 25° ± 0.2°C, in a conventional three-electrode cell, with a separate high-impedance circuit for the measurement of potentials. The I-E curves were recorded at slow scanning rates, with at least a hundred drops for the rising section of each wave.

Triply distilled water and doubly distilled mercury were used. The various supporting electrolytes were made from A.R. products (after recrystallization, when needed, and calcination each time it was possible). In the particular case of the pyrophosphate ion fresh solutions were prepared daily, to avoid appreciable hydrolysis. It has been verified, for each supporting electrolyte, and after careful deoxygenation, that the residual current recorded at high sensitivity, was devoid of any waves or steps indicative of the presence of significative amounts of electroactive or adsorbable foreign species.

The depolarizers were generally determined according to standard procedures and used without further purification, at concentrations of the order of $10^{-3}N$. Sodium chlorite was purified following the procedure of Weiner (9).

Processing Data and Presentation of Results

Each depolarizer has been systematically studied in supporting electrolytes of Li^+, Na^+, K^+, Cs^+, Mg^{++}, Ca^{++}, Ba^{++} each in 0.1 and 1N (as long as solubility or pH incompatibilities were not insuperable).

After graphical deduction of the charging current component (evaluated separately with the supporting electrolyte alone), I/I_d plots were constructed, and the diffusional character of the limiting current, was checked by conventional means. Log $\chi = f(E)$ plots were then established, using the values tabulated by Koutecky (10).

In most of the cases, for which first order surface reactions were encountered, the apparent rate constants v can be calculated from the well-known relation (10)

$$\log v = \log \chi + \log \sqrt{\frac{7}{12}\frac{D_o}{t_d}} + \eta(E) \qquad (a)$$

where D_o is the diffusion coefficient in $cm^2\ sec^{-1}$ t_d the drop-time (4 sec)

$$\eta(E) = -\log\left[1 - \sqrt{\overrightarrow{D}/\overleftarrow{D}}\exp \cdot (F(E-E_o)/RT)\right] \qquad (b)$$

being a positive correction term to be added only when the process is not entirely irreversible ($Eu^{+++} + \epsilon \rightleftharpoons Eu^{++}$ and $Cr^{+++} + \epsilon \rightleftharpoons Cr^{++}$ for instance). However, as only relative changes of log v are of interest, and since D_o values are slightly generally affected by composition changes,[4] insignificantly anyway with respect to the χ variations themselves, intercomparison of the rate constants has been based mostly on log χ values.

In the few cases (NO_3^-, NO_2^-) where reduction was proceeding at very negative potentials, thus preventing the evaluation of the diffusion current (which merged into the reduction wave of the supporting cation), relatively large concentrations of the depolarizer were used, and the foot of the wave was recorded at high sensitivity. After proper correction, if any was needed, for the supporting cation current, the apparent rate constants were obtained from the classical steady-state relation

$$v = \frac{I}{nF[C]_\infty A_d} \qquad (c)$$

which is sufficiently accurate in the case where I values do not exceed a few per cent of the diffusion current (A_d being the electrode area at the drop time).

Intercomparison of Data

Comparison of half-wave potentials, the easiest and most precise quantities to obtain, has been discarded, because the mere fact that potentials are shifted with composition makes it more difficult to evaluate the influence of the double layer structure (which of course varies both with composition and potential). It has been preferred to select, for each system, a "median" potential[5] for which all v or χ values have been calculated. When E shifts or α slopes are large, some extrapolation may be required, the extent of which was never found objectionable, in view of the reasonable straightness and parallelism of the Tafel plots.

The next step was to calculate, for each system and each supporting electrolyte, values of the purely formal quantity $\Delta\psi'$ defined by

$$\Delta\psi' = \frac{RT}{F}\frac{\Delta \ln (\chi \text{ or } v)}{z_K - \alpha_0 n_\alpha} \qquad (d)$$

using as reference level the (χ, v) values observed in the 1N sodium solution.

$\Delta\psi'$ represents the change in ψ potential which would account for the recorded variations, with the *a priori* assumption that the system obeys the Frumkin relation strictly. As shown later, although sometimes completely incorrect, such an arbitrary calculation is however useful, because it allows easy intercomparison, and the immediate diagnosis of any "atypical" behavior.

Within defined pH and potential ranges, some oxygenated anions are electroreducible only after undergoing a fast protonation reaction, which, among other things, leads to a decrease of the negative charge of the "bulk" particles (more rarely, this prior chemical step is sufficiently slow to give rise to a decrease in the limiting current, which becomes then kinetically controlled). Such cases will be presented and discussed later.

$\alpha_0 n_\alpha$ was calculated from the experimental $d \ln v/dE$ slopes, with a correction $\Delta\alpha_\psi$ for $d\psi/dE$, estimated on the basis of thermodynamic and not of "actual" ψ' values. Typical correction terms were, respectively, about +0.1 and +0.2, for z_B being −1 and −2.

[3] For the sake of clarification, the case of the uranylcarbonate ion in N sodium carbonate could be considered briefly as an example. Its formal charge z_o is −4 [$UO_2(CO_3)_3^{4-}$], while the "bulk charge" z_B is of the order of −2 [$UO_2(CO_3)_3Na_2^{2-}$]. If [Na^+] is modified, the corresponding variation of the apparent rate constant leads to $z_K = -2$, by applying the Frumkin relation. However, if a fast prior association with Na^+ is required before discharge may occur, the actual z_δ value may be only −1.

[4] H_3O^+ ions excepted, typical extreme deviations never exceeded 10%.

[5] The "median" potential is chosen in order to have $O < i < id$ for all compositions.

All $\Delta\psi'$ values[6] are finally fitted into the ψ_R—E diagram, using the ψ_R curve calculated for $Na^+ = 1N$ as reference line (for ψ_R see "Thermodynamic Data"). The actual ordinate ψ'' is thus equal to ψ_R (Na^+ $1N$) $+\Delta\psi'$. This way of presentation (purely arbitrary again) does not mean that any special consideration is given to the validity of the ψ_R curve: it is merely dictated by the fact that (*i*) experimental results in $1N$ sodium solutions were the most abundant, and that (*ii*) $\Delta\psi_R$ variations when Na^+ is replaced by 0.1 and $1N$ divalent cations are small, allowing thus a better detection of non-ψ effects.

Thermodynamic Data

It is well known that negatively charged mercury surfaces are characterized by charge density-potential curves which are very little affected by the nature of the cation and its charge (11). In accordance with this fact, the few measurements of charge distribution based on the Gibbs equation tend to fail to show any significant amount of "specific" adsorption.[7] This results in part from the low intrinsic sensitivity of the method.

"Reference" ψ_R values have been calculated by assuming that the charge density of the diffuse part of the double layer equals that of the electrode, save in the sign. ψ_R has been calculated using the classical Gouy-Chapman relation (13), neglecting thus all second-order effects (which are by no means easily amenable to quantitative evaluation).

Such $\psi_R - E$ plots have been constructed (Fig. 1) for $Z = 1$, $Z = 2$, and $N = 1$ and 0.1, on the basis of Grahame results (11). Z and N are, respectively, the electronic charge and the normality of the supporting cation.

It should be stressed that no particular confidence is placed in these curves (they are, for instance, grossly incorrect for Cs^+), which will be merely used as a canvas delineating trends more than describing actual behavior. In fact, one of the aims of the present paper is to check by kinetic measurements to what extent ψ_R values may be used to explain or predict the influence of composition.

The same graph includes (interrupted line) the ψ potentials relative to $1N$ iodide solutions, as calculated by Grahame (14), and the corresponding $\Delta\psi$ curve, which represents the ψ_R-lowering due to the iodide adsorption.

[6] For IO_3^-, the $\Delta\psi'$ values have been increased by 15 mv. This procedure will be justified in the Discussion.

[7] We mean by "specific" : "depending on the species," without relating this expression to any particular hypothesis on the nature of the forces involved.

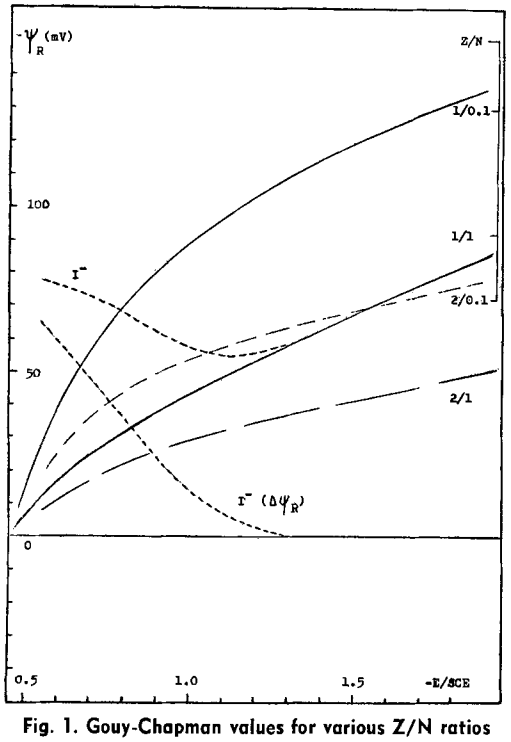

Fig. 1. Gouy-Chapman values for various Z/N ratios

Experimental

Depolarizers with formal electronic charge varying between +3 and —8 have been investigated. The behavior of neutral species will not be discussed here, since ψ effects are generally small, as compared with salting out interference.

Cationic depolarizers.—The selection of suitable cations was determined by the following requirements (besides the obvious condition of nonreversibility).

The cation must be present in its true cationic form. Possibility of complexation with the supporting anion has thus to be recognized. Perchlorate medium unfortunately cannot be used systematically, since potassium and cesium salts have low solubilities. In the particular case of multicharged cations in sulfate medium, ion pairing may be important and leads then to a significant decrease of the activity coefficient. [A systematic study, conducted at constant cationic strength with variable amounts of sulfate, has shown, for all the cations studied (Eu^{+++}, Cr^{+++}, Co^{++}, Ni^{++}, H^+) that changes in rate constants with composition are quantitatively accounted for, assuming fast dissociation of ion pairs prior to discharge itself, with reasonable *p*K's values for association (15)].

Another possible complication results from the presence of hydrolyzed species, which are generally more electroactive than the cation itself (possibly in part through specific adsorption). This situation may be avoided by sufficient *p*H lowering, which, in turn, restricts the range of usable potentials, prohibiting *inter alia* the study of ions like Ga^{+++}, Al^{+++}, and most of the rare earth trivalent cations. Fe^{++}, too, is preferentially reduced under the form $Fe(OH)^+$, as shown by Ivanov and Jofa (16), and reconfirmed by our own results.

Generally speaking, the over-all discharge process has to be devoid from kinetic complications like any slow prior chemical step or change in the surface reactivity by electrodeposition. In the particular case of Ni^{++}, for which the limiting current is controlled by a nonelectrochemical step involving rearrangement of the water-shell (17, 18), it is still possible to draw reliable conclusions, if small relative values of current are compared, in which case the prior step is kept under conditions of labile equilibrium.

These considerations have so far limited the exploration to the ions Eu^{+++} and Cr^{+++} (slightly acid perchlorate solutions), Ni^{++} and H^+ (chloride and perchlorate solutions), and Co^{++} (sulfate and perchlorate solutions). Some limited information is also at hand for Zn^{++} (nitrate medium) (19), Fe^{++} and Mn^{++} (perchlorate solutions).

Tables Ia and b, and Fig. 2 embody all the kinetic data now gathered. They will be analyzed and compared with the other corresponding results in the Discussion section.

Anionic depolarizers (Tables IIa, IIb, and III; Fig. 3-5).—The study of mononegative anions is of considerable interest, because association with the supporting cation can be expected to be the smallest, at least when $Z = +1$. Consequently this could afford the opportunity of disentangling, from the complex pattern of behaviors, the basic features of the "pure" ψ effect when it acts on anions.

Under such circumstances, comparison with kinetic ψ'' values obtained with cations can be worth-

Table Ia

Depol.	E	$\alpha_o n_a$	$z_K - \alpha_o n_a$	log χ 1N Na$^+$	Δ log χ (*vs.* Na$^+$ 1N) Li$^+$ 0.1	Li$^+$ 1	Na$^+$ 0.1	Na$^+$ 1	K$^+$ 0.1	K$^+$ 1	Cs$^+$ 0.1	Cs$^+$ 1
Eu^{3+}	−0.66	0.38	2.62	−0.17*			0.90	0				
Cr^{3+}	−0.8	0.41	2.59	−0.81	1.28	0.07	1.26	0	1.23		1.16	
Mn^{++}	−1.48	0.8	1.2	−0.8			0.75	0				
Fe^{++}	−1.32	0.7	1.3	−0.8			0.6	0				
Ni^{++}	−1	0.5	1.5	−0.85	1.07	0.1	0.94	0	0.94	−0.1	0.75	−0.25
Co^{++}	−1.28	0.31	1.69	−0.02	1.16	0.21	1.06	0	0.87	−0.18	0.15	−0.61
H^+	−1.56	0.45	0.55	0.02	0.34	0.16	0.25	0	0.19	−0.07	0.02	−0.18
Zn^{++} **	−1	0.25	1.75	−2.5			1.2	0				

* Eu^{3+} : $\log \chi - \log \left[1 - \sqrt{\frac{\vec{D}}{\overleftarrow{D}}} \exp. \frac{F}{RT} (E - E_o) \right]$.

** Zn^{++} : J. Koryta, *Electrochim. Acta*, 6, 67 (1962).

Table IIa

Depol.	E	$\alpha_o n_a$	$z_K - \alpha_o n_a$	log χ 1N Na$^+$	Δ log χ v (*vs.* Na$^+$ 1N) Li$^+$ 0.1	Li$^+$ 1.	Na$^+$ 0.1	Na$^+$ 1	K$^+$ 0.1	K$^+$ 1	Cs$^+$ 0.1	Cs$^+$ 1
IO_3^-	−1.1	0.96	−1.96	−0.61	−1.22	0.11	1.35	0	−1.49	−0.22	−0.95	0.11
BrO_3^-	−1.64	0.88	−1.88	−0.15	−1.76	−0.42	−1.50	0	−1.23	0.17	−0.20	0.87
NO_3^-	−1.55	0.7	−1.7	−6.52*	−1.70	−0.16	−1.33	0	−1	0.1	−0.08	0.77
NO_2^-	−1.76	0.7	−1.7	−4.74*	−1.58	−0.2	−1.24	0	−1	0.14	−0.1	0.90
ClO_2^-	−1.8	0.37	−1.37	0.07	−1.42	0	−1.28	0	−1.21	0	−0.1	0.83
ReO_4^-	−1.35	0.65	−1.65	−1.07	−1.59		−1.16	0	−0.81		−0.032	

* NO_3^-, NO_2^- : log v by Eq. (c).

while, in order to appreciate the magnitude of the deviations, and their possible origin.

The following anions were studied, under controlled conditions, for which their reduction is pH-independent: BrO_3^- and IO_3^- (at pH) > 11.5, to avoid occurrence of the prior protonation mechanism), ReO_4^- (at pH ≥ 13, to suppress the catalytic water discharge), ClO_2^- (at 9 < pH < 13, to eliminate both the protonation mechanism and the prewave which occurs in strongly alkaline medium), NO_2^- and NO_3^- (these reactions are pH-insensitive within a large range). The reduction of palladite (PdO_2^-) and periodate ($H_3IO_6^=$) have been investigated at pH 13. The fact that these reactions are pH-dependent, with d ln v/d pH ≃ −1 at constant double layer structure, with no indication of any "kinetic" limiting current, leads to the conclusion that the electroreduction itself is preceded by a fast protonation step

$$(PdO_2^= + H^+ \rightleftharpoons PdO_2H^- \qquad (e)$$

$$H_3IO_6^= + H^+ \rightleftharpoons H_4IO_6^-) \qquad (f)$$

and involves mononegative particles. This deduction is confirmed by the order of magnitude of the ψ effects. However, since composition changes may alter the protonation equilibrium, these reactions will be discussed separately.

Similarly, some mononegative anions (like O_2H^- or SbO_2^-), although predominating in solution at the

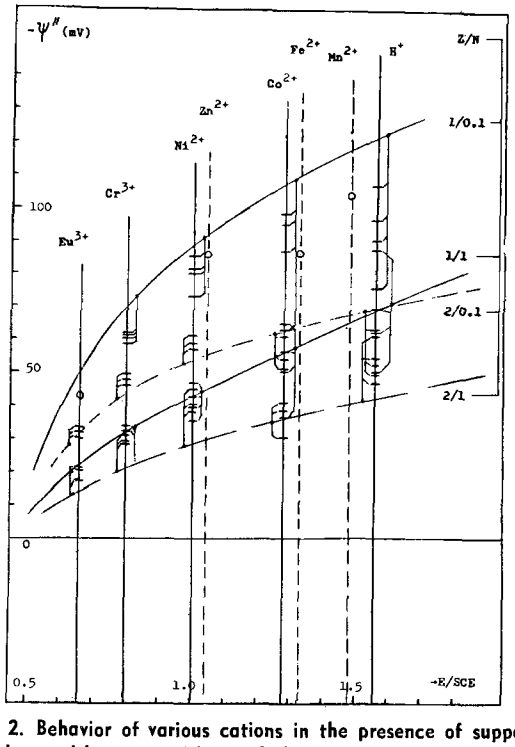

Fig. 2. Behavior of various cations in the presence of supporting electrolytes with monopositive and dipositive cations, expressed in terms of ψ'' (see details under Symbols and Units).

Table Ib

Depol.	Δ log χ (*vs.* Na$^+$ 1N) Mg^{++} 0.1	Mg^{++} 1	Ca^{++} 0.1	Ca^{++} 1	Ba^{++} 0.1	Ba^{++} 1
Eu^{3+}	0.44	−0.06	0.39	−0.09	0.34	−0.25
Cr^{3+}	0.76	−0.03	0.73	−0.14	0.62	−0.14
Ni^{++}	0.47	0.05	0.4	−0.07	0.34	−0.12
Co^{++}	0.10	−0.52	−0.09	−0.48	−0.17	−0.76
H^+	−0.07	−0.08	−0.17	−0.15	−0.19	−0.22

Table IIb

Depol.	Δ log χ (*vs.* Na$^+$ 1N) Ca^{++} 0.1	Ca^{++} 1	Ba^{++} 0.1	Ba^{++} 1
IO_3^-	2.26	3.12	1.78	2.50
BrO_3^-	1.29	2.11	1.33	2.16
NO_3^-	0.76	1.25	1.07	1.56
NO_2^-	0.95	1.90	1.03	1.82
ClO_2^-	0.80	1.43	0.72	1.32
ReO_4^-	0.61	1.16	0.98	1.32

Table III

Depol.	E	$\alpha_0 n_a$	$z_K - \alpha_0 n_a$	log χ 1N Na+	Δ log χ (*vs.* Na+ 1N) Li+ 0.1	Li+ 1	Na+ 0.1	Na+ 1	K+ 0.1	K+ 1	Cs+ 0.1	Cs+ 1
$CrO_4^=$	−0.7	0.6	−2.6	−0.7	−0.87	0.24	−1.07	0	−1.2	−0.25	−0.83	−0.04
	−0.9			1.05	−1.61	0.16	−1.54	0	−1.57	−0.18	−0.92	0.37
UC*	−1.08	0.6	−2.6	1.1	−2.51	−0.5	−2.1	0	−1.74	0.05	−0.79	1.19
$S_4O_6^=$	−0.82	0.19	−2.19	0.66	−1.41	−0.05	−1.03	0	−0.66	0.37	−0.17	≧0.9
	−1.3			1.13	−2.25	−0.26	−1.35	0	−0.53	0.53	−0.17	≧1.1
UPP**	−0.82	0.4	−3.4	−0.67		0.24	−2.7	0		0.10		0.56

* UC = uranyl carbonate.
** UPP = uranyl pyrophosphate pH 9.1.

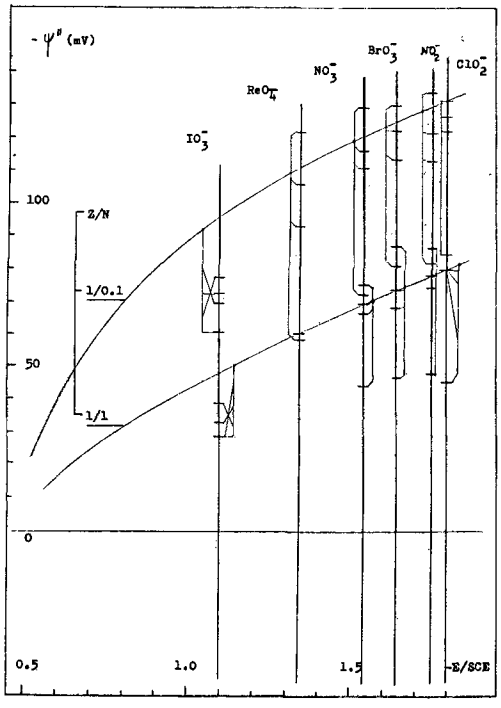

Fig. 3. Behavior of mononegative anions for supporting electrolytes with monopositive cations, expressed in terms of ψ'. (See details under Symbols and Units.)

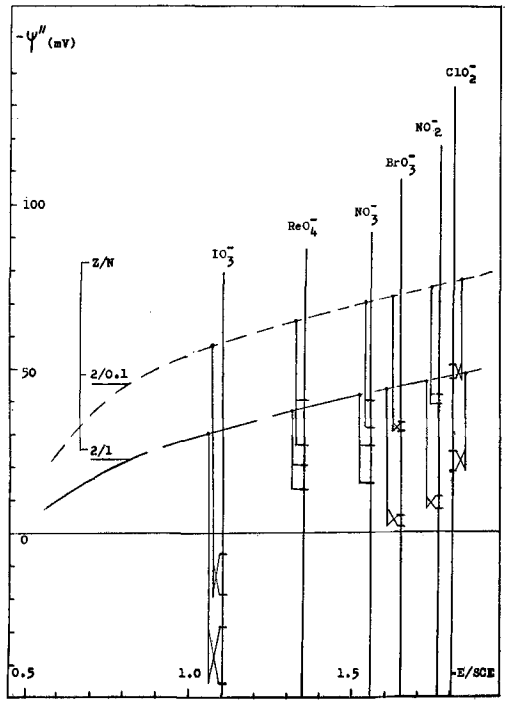

Fig. 4. Behavior of mononegative anions for supporting electrolytes with dipositive cations, expressed in terms of ψ'. (See details under Symbols and Units.)

pH values which were used, were found to be only reducible under their neutral monoprotonated form. Since pH and supporting electrolyte concentration can be varied independently, the identification of the apparent charge of the dischargeable species presents no difficulties. However, if hydroxides are used as supporting electrolyte, both effects combine and the overall kinetics may appear quite complex.

A few multicharged anions have been studied: $CrO_4^=$ (at pH > 13, to suppress the protonation mechanism), $S_4O_6^=$ (in neutral unbuffered solutions), $UO_2(CO_3)_3^{4-}$ (0.1N in carbonate, to stabilize the complex), $(UO_2)_2(P_2O_7)_3^{8-}$ (0.1N in pyrophosphate, for the same reason). These two last systems were carefully investigated, in order to delineate compositions for which direct discharge of the complex is the rate-determining step, without any prior decomplexation reaction.

Supporting cations.—pH requirements have very often precluded the use of Mg^{++} (and sometimes Ca^{++}). It was essential to check whether the buffering action of Mg^{++}, Ca^{++}, and even Ba^{++} (second pK) was not influencing the electrode processes. Precipitation between multicharged species ($|z_B Z| \geqq 4$) imposed another rather strict limitation.

Results Obtained with Anion Substitution

As pointed out earlier, difficulties which may arise when trying to distinguish between ψ-effect and a prior association stem from the fact that varying the supporting cation affects both mechanisms the same way, when the depolarizer is an anion. It is therefore obvious that this obstacle might be evaded, if the double layer structure could be modified in a controlled way, without appreciably shifting the chemical equilibriums under consideration. For that purpose, the simplest method consists in replacing the usual supporting anion (ClO_4^-, F^-, OH^-) by another which is as tensioactive as possible. Iodide is thus the best choice.

For 1N solutions, this substitution brings a negative variation $\Delta\psi_R$, which persists at rather negative potentials (see Fig. 1). Such a method, however, must be used with caution, since the relative smallness of $\Delta\psi_R$ values which occur at negative potentials, tend to render objectionable any second order factor capable of blurring the resulting "pure" ψ effect. In particular, the anion substitution is accompanied by a variation of the mean activity coefficient $\gamma^{\pm}$, which can act both on the activity of the depolarizer, and on the double layer. As far as the former effect is concerned, it is

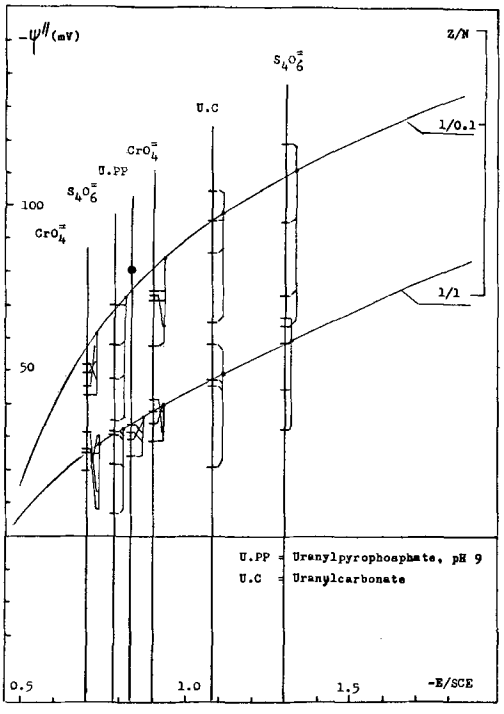

Fig. 5. Behavior of multicharged anions with supporting electrolytes with monopositive cations, expressed in terms of ψ''. (See details under Symbols and Units.)

safe to assume as a first approximation that the depolarizer activity coefficient simply follows $\gamma^{\pm}$ (20). Such a trend has been confirmed experimentally, by measuring the χ values for the reduction of uranylcarbonate (at —0.92v) and comparing them (Table IV) to the corresponding $\gamma^{\pm}$ of the various supporting electrolytes selected in view of the inactivity of their anions.

The fact that rate constants vary more than $\gamma^{\pm}$ suggests that the simultaneous double layer modification acts cooperatively (as it can be inferred from the Gouy-Chapman theory, amended with the crude first approximation that activities must replace concentrations). As a matter of fact, when working at constant activity with the same supporting electrolytes, the χ values (Table V) are practically identical (with the exception of the perchlorate medium, for which a positive deviation is observed).

As a result of these experiments, it appears necessary to make the substitution of the inactive anion for iodide, by using a salt having the closest mean activity coefficient to it. In N solutions, sodium acetate is the best choice ($\gamma_{(NaI)} = 0.736$ *vs.* $\gamma_{(NaAc)} = 0.757$).

Table IV

Supporting* electrolyte	$\gamma^{\pm}$	χ (−0.92v)
NaAc	0.757	1.115
$NaClO_4$	0.629	1.00
$NaClO_3$	0.589	0.71
$NaNO_3$	0.548	0.508

* Each 0.9N + 0.05M in Na_2CO_3.

Table V

Salt*	χ (−0.92v)
NaAc	0.485
$NaClO_4$	0.875
$NaClO_3$	0.55
$NaNO_3$	0.51

* Concentrations adjusted for $\gamma^{\pm} = 0.548$.

Table VI

Depolarizer	$\Delta \log \chi(-0.82v)$	$(z_A - \alpha_o n_\alpha)$ calc.	$z_A(\pm 0.3)$
$CrO_4^=$	−0.85	−1.57	−2.2
$S_4O_6^=$	−0.87	−1.61	−1.8
$UO_2(CO_3)_3^{4-}$	−0.45	−0.83	−1.4
$(UO_2)_2(P_2O_7)_3^{8-}$	−0.33	−0.61	−1.0

These solutions have thus been used, with small additions of tensio-inactive complexing agents, when required.

The depolarizers were chosen in order to allow measurements of $\Delta\chi(Ac^- \rightarrow I^-)$ at the same potential (—0.82v/SCE, for which $\Delta\psi_R$ (I^-) amounts to —32 mv). Table VI embodies the $\Delta \log \chi$ value, together with values found for $(z_A - \alpha_o n_\alpha)$, and the derived corresponding electronic charges z_A themselves (the subscript A refers to charges found in the anion substitution method).

Comparative Analysis of Results

Intercomparison of Fig. 1, 2, 3, 4, and 5 permits one to draw some direct conclusions regarding the effect of the various supporting electrolytes investigated. In this respect, it should be recalled (*i*) that all ψ'' values have been normalized by equalization of ψ'' (Na^+ 1N) to the corresponding ψ_R and (*ii*) that ψ'' is nothing but a purely formal quantity which expresses in terms of potential the resultant of all the actual rate-determining factors, even if some are nonelectrical in nature.

Cationic depolarizers.—Comparison between ψ'' and ψ_R (Fig. 2) is of special interest, since non-ψ effects can be expected to be minor, as the depolarizers are not capable of ion pairing with the supporting cations. Despite the fact that too few systems are available to draw definite conclusions, it appears that both concentration and potential changes exhibit the trends predicted by the Gouy-Chapman theory (crossing of the 2/0.1 and 1/1 curves in particular), although the absolute values of the variations are generally lower than expected (for 1/0.1 data in particular). Closer examination of the figure proves that in some cases factors specific to the depolarizers themselves are determining.

On the other hand, as far as the nature of the supporting cation is concerned, excellent regularity in sequences is always observed, the rate constants decreasing in the orders $Li^+ > Na^+ > K^+ > Cs^+$ and $Mg^{++} > Ca^{++} > Ba^{++}$. It is noteworthy that (*i*) Cs^+ is markedly retarding all reactions (Co^{2+}, H^+), and that (*ii*) divalent cations do not show very large differences (less than the corresponding for Li^+, Na^+, and K^+).

Most of these findings are not new (4): it was however useful to restate them in a "standardized" way in view of rendering intercomparison with the other cases more coherent.

Anionic depolarizers.—Mononegative anions in presence of supporting electrolytes with monopositive cations (1/0.1 and 1/1).— Reduction potentials for the various anions investigated happen to be more negative than —1.1v. Although rate constants obtained for periodate and palladite reductions are within the potential gap, they will be presented later, for the reason given above.

Examination of Fig. 3 shows that most of the ψ'' values are in satisfactory agreement with the corresponding ψ_R curves, except for Cs^+. There is a good concordance between the sequential intervals, Na^+ and K^+ being usually the closest together.

However, iodate presents a completely abnormal behavior [already discovered before this work, ref. (5, 21)]. Instead of being $Li^+ < Na^+ < K^+ < Cs^+$, the sequences are $K^+ < Na^+ < Li^+$, Cs^+ (1N) and $K^+ < Na^+ < Li^+ < Cs^+$ (0.1N), and they remain perturbed even in 0.01N solutions. Li^+ and Na^+ media

are obviously characterized by abnormally high rate constants. It is this fact which leads us to shift downward all iodate ψ'' values, in order to give a reasonable position for Cs^+ (see discussion part for further arguments).

A closer inspection of Fig. 3 discloses that, although not inverted, Li^+ (0.1N) values for BrO_3^- and ClO_2^- are somewhat too low. This tendency is exalted in 1N medium for ClO_2^-, but vanishes with BrO_3^-. It should be noted that Cs^+ 0.1N seems to be the most accelerating with ReO_4^-, the only anion for which 0.1 Cs^+ ψ'' overtakes 1N Na^+ ψ_R. These slight deviations, as insignificant as they may look, will however find definite correspondences with relevant data presented in the next section.

Mononegative anions in presence of supporting electrolytes with divalent cations.—For most of the depolarizers, Mg^{++} was not utilizable, in view of *p*H prerequisites. Figure 4 reveals that large positive deviations from the ψ_R curves, varying from system to system, are systematically observed.

When the deviation is important (IO_3^-, BrO_3^-, ClO_2^-, NO_2^-), the normal sequence $Ba^{++} > Ca^{++}$ is reversed. On the other hand, the concentration effect (0.1 → 1N) is in reasonable agreement with the calculated (0.1N/1N)ψ_R differences, though generally somewhat smaller.

Multicharged anions with $Z = 1$ supporting electrolytes.—As a result of solubility and *p*H incompatibilities, not enough information is now available when $Z > +1$, and, even for $Z = 1$, relatively few comparable data have been obtained up to date.

Inspection of Fig. 5 shows that $S_4O_6^=$ and uranylcarbonate ions present a "normal" behavior, in marked contrast with $CrO_4^=$ and uranylphosphate ions (*p*H 9.1) for which the Li^+ inversion is again observed. Comparison of chromate ψ'' values at the two potentials indicated, reveals that the extent of deviation seems to decrease with more negative potential.

Cationic effects on "complex" electrochemical reactions.—A number of electrochemical reaction schemes include concentration- or rate-controlling steps (*e.g.*, decomplexation, protonation, etc.), easily distinguished from ψ effects. When they involve anions, such reactions generally respond to cationic effects. Diagnosis of the relevant mechanisms is of interest, since it may sometimes help to devise appropriate mathematical corrections, allowing the deduction of the undesirable chemical effect from the main electrochemical step, with the resulting possibility of obtaining usable ψ'' values. A few pertinent examples will be briefly discussed.

Occurrence of a prior fast nonelectrochemical reaction.—Two typical cases are afforded by the electroreduction of periodate (22) and palladite ions in alkaline medium. For both processes, the study of the influence of variable *p*H at constant double layer structure, and vice versa, shows conclusively that a labile protonation step occurs before the discharge which involves a mononegative particle (Eq. *e*, *f*).

The net pseudomonomolecular rate constants can then be affected by any shift undergone in the prior equilibrium. For periodate in 0.1N alkaline hydroxides, all the polarization curves are practically coincident around the potential of nul charge. However, in 1N solutions, differences in rate constants become obvious, the equilibrium (*f*) being shifted forward from Li^+ to Cs^+ (for LiOH, this is mostly due to incomplete dissociation). As a result, 1N ψ'' values calculated without taking this circumstance into account, are in error. After proper correction, however, the ψ'' values are cogent with the others so far obtained.

Palladite reduction (25) will be considered with some more detail, since, in contrast with periodate, Ba^{++} and Ca^{++} salts are sufficiently soluble (Ca^{++} however is useless for our purposes, in view of its *p*H buffering action).

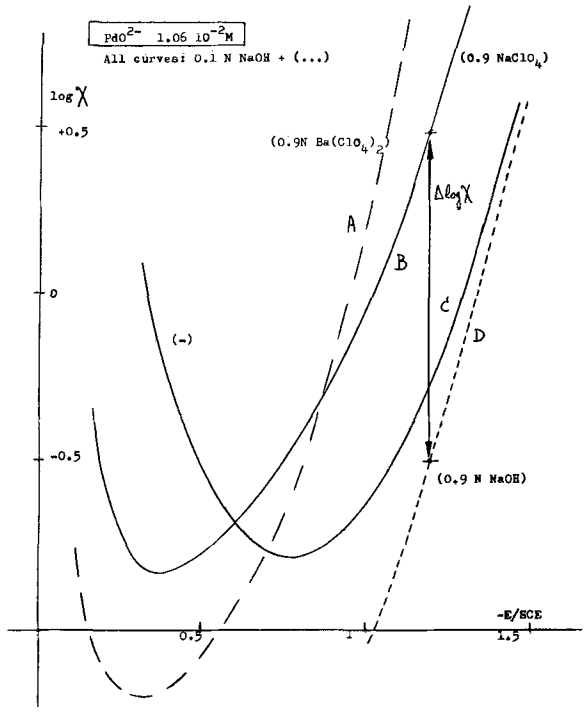

Fig. 6. Effect of composition on the polarization curves for palladite reduction.

Examination of Fig. 6 (which embodies only a few selected polarization curves) leads to the following conclusions.

1. At the same sodium concentration (1N : curves B and D), the over-all apparent rate constants decrease by an order of magnitude when *p*H is raised by one unit, independently of the potential. This fact demonstrates the existence of a prior protonation step (which is fast, as evidence by the attainment of the true diffusion current in all cases).

2. At the same *p*H (13), and variable [Na^+] (0.1 and 1N : curves C and B), the usual ψ effect predominates, with the resulting crossing of the two curves near the point of nul charge, at which ψ reverses itself. The order of magnitude of the effect corresponds to $z_k \simeq -1$ (with $\alpha_o \simeq 0.25$).

3. Comparison between curves C and D (NaOH 0.1 and 1N) is instructive because it shows the complex behavior which is observed when *p*H influence is studied without controlling ionic strength : pure *p*H effect around the point of null charge, and, at sufficiently negative potentials, nearly complete compensation between retarding *p*H- and accelerating ψ effects [periodate reduction behaves the same way under similar condition (22). As it is with periodate, the series $Li^+ \rightarrow Cs^+$ is also somewhat perturbed by shifts in the prior equilibrium in 1N alkaline hydroxides].

4. When equinormal Ba^{++} is substituted for Na^+ (curves A and B), conflicting effects are observed : the net rate constant increases at negative potentials, but drops to attain a nearly constant lowering ($\Delta \log \chi \simeq -0.3$) at potentials more positive than the point of nul charge.

This behavior may be explained assuming that the prevailing bulk species $PdO_2^=$ is appreciably associated with Ba^{++} (*p*K's for 2-2 ion-pairing are currently over 2), thus bringing a shift toward deprotonation for the prior chemical step. Simultaneously, the same Ba^{++} ions are increasing the discharge rate constant of PdO_2H^-, the more as the potential is made negative. It results from this that $\Delta\psi''$ calculated for Ba^{++} are cogent only if a suitable correction is made for the first chemical effect. The proposed mechanism

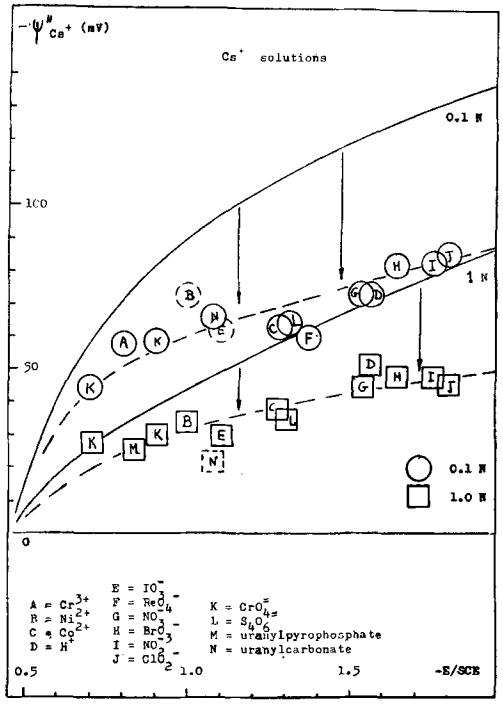

Fig. 7. Effect of Cs^+ as supporting cation on electrode reactions involving depolarizers of various charges expressed in terms of ψ''.

also indicates that $BaPdO_2$ ion pairs are not electroactive (probably for want of any hydroxyl groups, a rather common behavior in oxyanion reduction).

Occurrence of rate-limiting steps.—The existence of large cationic effects has already been demonstrated in the case of the "kinetic" prewave presented by ClO_2^- in very alkaline media (23, 24).[8]

A different example, now under study in this laboratory, is afforded by the reduction of ReO_4^- at $pH \geq 13$.

It is well known (26) that perrhenate waves are generally exalted and distorted by simultaneous catalytic hydrogen evolution. However, at *p*H 13 and before the start of the hydrogen wave, a relative well-defined limiting current is observed, which corresponds to a net 7-8 electron process. This current was observed to fall with increasing *p*H, the easier as the supporting cation is changed according to the series $K^+ < Na^+ < Li^+ << Ba^{++}$. In all cases, the amplitude decreases to a limiting value coresponding to a net 3-electron reduction. Meanwhile, the wave is shifted along the potential axis, in accordance with the expected behavior of a "normal" mononegative anion. These characteristics are explainable, by assuming that :

1. The rate-determining step is always the slow transfer of the first electron.

2. The following steps include a purely chemical process (possibly a disproportionation mechanism involving Re^{IV}), which, although usually too fast to allow detection, slows down by the increase in *p*H, and is notably affected by selective cationic effects (probably of the ion-pairing type).

These few examples illustrate the multiplicity of situations where cations may exert specific influence. Fortunately, such behaviors present peculiarities which permit their easy distinction from the simplest cases first considered above.

The Discussion Section will be devoted essentially to these latter cases, for which mechanism diagnosis remains to be debated.

Discussion

Results obtained with cationic depolarizers show that their behavior generally follows predictions from the Frumkin theory, using the simple Gouy-Chapman model, although some systematic deviations are indicated. For all of the systems, dilution of $Z = 1$ supporting electrolytes does not quite bring the expected increase in apparent rate constants. These deviations, however, remain marginal and would perhaps reflect some specific adsorption (or size effect) of the depolarizers themselves. The decelerating effect of Cs^+ is noticeable; it presents the same order of magnitude for all depolarizers, irrespective of their charge (Fig. 7). For 1*N* Cs^+ solutions, ψ'' varies very little with potential, with the consequence that experimental α values observed in that medium need hardly any correction for the double layer effect.[9]

In the case of multicharged anions, the supporting anion substitution method shows that z_A (which can be expected to equal z_δ) is close to —2 for the chromate and tetrathionate ions, and that, accordingly, no prior association is needed. [Using thallium amalgams, Frumkin (2) found the same result for persulfate.]

For uranylcarbonate, however, $z_K \simeq -2$ and $z_A \simeq -1.4$, a discrepancy which suggests some limited prior interaction with Na^+. In the case of the rather bulky uranylpyrophosphate anion z_A is around —1, while $z_K \simeq -3$. These conflicting values are indicative of an extensive amount of prior labile ion pairing. Besides, the surprisingly low value of z_A is perhaps explainable in terms of a size effect and the subsequent lowering of the effective ψ value acting on the anion.

Regarding the mononegative depolarizers (the only ones for which it was possible to compare mono- and divalent supporting cations), examination of the ψ'' values reveals that the extent of deviation observed in Li^+ medium is closely related to (*a*) the amount of "abnormal" acceleration due to divalent cations, and (*b*) the reversal in the usual Ba^{++}-Ca^{++} series (as found with cationic depolarizers).

Figure 8 in which the relative $\Delta\psi''$ charges resulting from the substitution $Na^+ \rightarrow Li^+$ have been plotted *vs.* the same quantities for $Ba^{++} \rightarrow Ca^{++}$, illustrates this correlation, and shows furthermore that the extent of deviation from the normal behavior increases according to the sequence

$$ReO_4^- < NO_3^- < NO_2^- < BrO_3^- < ClO_2^- < IO_3^- \quad (g)$$

The contrasting behavior of ReO_4^- and IO_3^- appears clearly in Fig. 9 which embodies a larger number of monopositive supporting cations. It should be noted that these intercomparisons are vitiated to some extent by the fact that the various depolarizers have been studied at their "median" reduction potentials which vary from —1.1 to —1.8v. (The potential depend-

[8] We recently found (37) that this prewave results from the catalytic reduction of ClO_2^- by minute amounts of ferrite ions, electrogenerated by reduction of ferrate. The so-called "desorption dip" observed about —1.6 v/SCE coincides with further reduction to metallic iron. The large cationic effects previously observed are essentially linked to the fact that each particular sample of any hydroxide is differently contaminated by iron traces. Recent experiments conducted with rigorous control of the ferrate content have shown that the catalytic wave depends in fact very little on the cationic composition (as can be expected for such a mechanism).

[9] Using the average cesium ψ'' values, it is possible to compute the charge densities for the diffuse part of the double layer. After algebraic addition to the corresponding electrode charge densities, the amount of specific adsorption may finally be evaluated. Such work is now extended to a larger concentration range and complete results will be published later.

For Cs+ 1*N*, "kinetic" q_i can be compared to independent thermodynamical data recently obtained (q_i') (12). The agreement between the two sets of results is satisfactory, in view of the inherent imprecision of the Gibbs method at low q_i', and the approximations involved in the Gouy-Chapman theory for the diffuse part, which affect our q_i values.

Table VII

$-E$	q_{III_g}	q_i	q_i'
0.92	—10	3.1	1.8
1.05	—12	4.1	4.8
1.17	—14	5.1	6.8

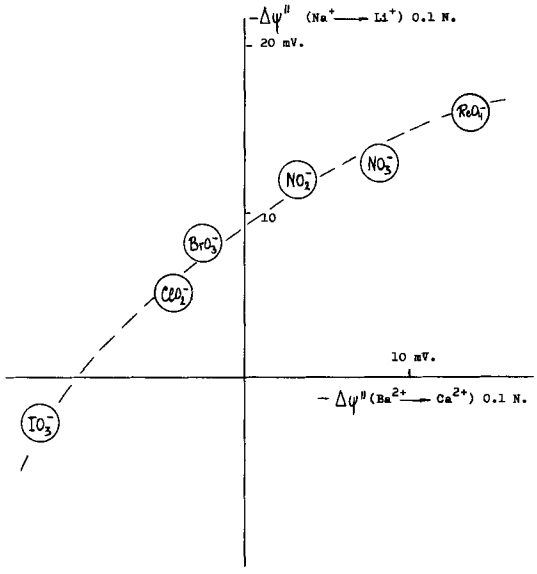

Fig. 8. Comparative effect of the substitutions $Na^+ \rightarrow Li^+$ and $Ba^{2+} \rightarrow Ca^{2+}$ (0.1N) expressed in terms of ψ''.

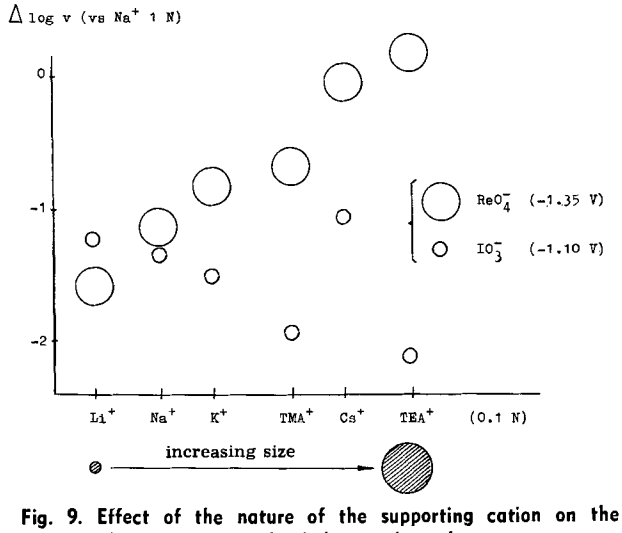

Fig. 9. Effect of the nature of the supporting cation on the variations of rate constants for iodate and perrhenate.

ence of the observed effects is demonstrated the best with the palladite system, Fig. 6, curves A, B, which permits the measurements of rate constants over a large potential interval, due to the particularly low α value. It can be shown from that figure that the charge-reducing effect of Ba^{++} is only effective when ψ is repulsive enough.) The fact, however, seems of relatively secondary importance, and affects the deductions drawn later only slightly (more particularly, IO_3^- and ReO_4^- median potentials are relatively close).

It is of particular interest to note that there is a remarkably close correlation between series (*g*) and many other sequences which characterize other types of anion behavior, as exemplified by: (*a*) B coefficients of viscosity in aqueous solutions (27); (*b*) adsorption potentials at the water-air interface (38, 39); (c) selectivity coefficients of anionic exchange resins of the Dowex 1 or 2 type (40); (*d*) effect on salting out chromatography (41); (*e*) coadsorption with tetrapropylammonium ions at the air-water interphase (42); (*f*) coadsorption with tetraalkylammonium ions on negatively charged mercury (32); (*g*) distribution coefficients between water and an organic phase (chloroform) in the presence of a large cation as extractant (*e.g.*, tetraphenylarsonium) (34, 35).

Table VIII permits direct intercomparison between these different sequences which, for this purpose,

Table VIII. Anionic series (increasing "cavity-pairing" downward)

	1	2	3	4	5	6	7	8
F⁻	OH⁻				OH⁻	IO_3^-	IO_3^-	IO_3^-
			Ac⁻					ClO_2^-
			IO_3^-					
			OH⁻		Ac⁻			
					CN⁻			BrO_3^-
Cl⁻			BrO_3^-		ClO_2^-	NO_2	BrO_3^-	
			NO_2^-		BrO_3^-			NO_2^-
						BrO_3^-		
					NO_3^-			
Br⁻	NO_3^-	NO_3^-	NO_3^-	NO_3^-			NO_3^-	NO_3^-
	MnO_4^-				ClO_3^-			
I⁻						NO_3^-	MnO_4^-	
						MnO_4^-		
	ClO_3^-		SCN⁻		SCN⁻	ClO_3^-		
		ClO_4^-				ClO_4^-		
	SCN⁻		ClO_4^-		ClO_4^-	ReO_4^-		ReO_4^-

Column 1, anion adsorption at the air-water interphase (38, 39); 2, coadsorption with tetrapropylammonium at the air-water interphase (42); 3, selectivity coefficients of anionic exchange resins of the Dowex 1 or 2 type (40); 4, salting out chromatography (41); 5, coadsorption with tetraalkylammonium ions on negatively charged mercury (32); 6, distribution coefficients between water and an organic phase (chloroform) in the presence of a large cation as extractant (*e.g.* tetraphenylarsonium) (34, 35); 7, B coefficients of viscosity in aqueous solutions (27); 8, sequence found in this work (increasing "electrostatic ion-pairing" upward) (cf. Fig. 8)

Table IX. Ionic behavior in water

← increasing	Field strength Water structure ordering Salting-out	decreasing →
La^{+++},Mg^{++},Ca^{++},Ba^{++}		
	Li^+,Na^+,K^+,Cs^+,Me_4N^+,Et_4N^+, etc.	
	F^-,OH^-,IO_3^-,Cl^-,Br^-,I^-,ClO_4^-,MnO_4^-,ReO_4^-, etc.	
$Fe(CN)_6^{\equiv}$,$CO_3^{=}$,$SO_4^{=}$		
"mostly electrostatic" ion-pairing		"cavity sharing" (28)

have been "normalized" with respect to the halide ions (horizontal double lines), except for the series found in this work, for which IO_3^- and ReO_4^- have been chosen as reference levels, since halides cannot be investigated.

The obvious conclusion that stems from inspection of Table VIII is that the deviations observed in the electrochemical behavior are merely a new aspect of a more general phenomenon. There is at present a growing amount of evidence supporting the concept (originated by Gurney) that interaction between oppositely charged ions increases if they both exert the same type of structural influence on the water molecules that surround them (27). These order-making or order-destroying effects are related to thermodynamic quantities like the partial ionic entropies, or the B coefficient of viscosity. Recent works by de Jong (30), Bregman (33), Ling (43), Eisenman (29), and Diamond (28), among others, may be considered to a certain extent as attempts to quantify the Gurney concept, in terms of quantities like ion field strength, polarizability, and suitable spatial configurations.

Table IX lists several ions, tentatively positioned according to their charge and the extent of their water-ordering character. According to the Gurney concept, association can be expected to prevail mostly between oppositely charged ions of the same type. Association (or pairing, the two words being taken as equivalent) between water-ordering ions is typified by $MgSO_4$ or LiOH. On the other hand, entities like Et_4NI or Ph_4AsClO_4 are examples of the inverse type of interaction (essentially pairing by "cavity-sharing," or, in other words, "cavity pairing").

In the case of a cavity-type water-depolymerizing anion like ClO_4^- or ReO_4^-, the other interacting cavity may be a cation of the same type (free or part of

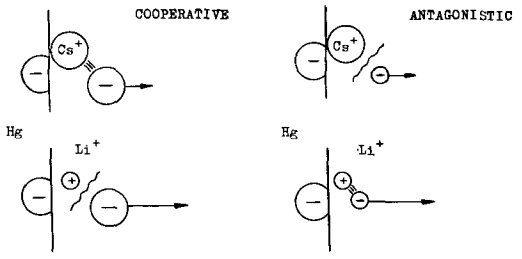

Fig. 10. Coupled ψ and pairing effects. Anion discharge on negatively charged mercury: ≡ interaction; ~ lack of interaction; → amount of ψ repulsion.

an exchange resin, Table VIII, col. 3, 6) or any weakly charged interphase (col. 1). Columns 2, 4, 5 correspond to a more complex situation for which three different "cavities" interact together. The unexpected order-making of the iodate ion results essentially from the fact that its oxygen atoms have very small π-bonds with the central iodine atom and are thus able to interact strongly with water.

Regarding the reactions considered in the present work, the characteristics of the deviations or reversals observed indicate that the responsible factor is linked with ion pairing of the first type (water-ordering partners). Negatively charged mercury acts itself as a "cavity" macro-ion (more or less similar to ClO_4^- at very negative potentials) and, as such, specifically adsorbs cavity-type cations like Cs^+. In this case, ψ is accordingly lowered and so is the repulsion between mercury and the anionic depolarizer. However, if the latter is also of the cavity-type, interaction with adsorbed Cs^+ ions contributes to increase its local concentration, and significant increase of the apparent rate constant is observed (Fig. 9 and 10).

On the other hand, when lithium is the supporting cation, ψ is more repulsive (due to the lack of interaction with mercury). However, if the reducible anion is of the water-ordering type (IO_3^-, *e.g.*), the local ion pairing tends to circumvent the repulsion, and sequence reversal may be observed. Figure 10 illustrates schematically the four limiting cases which can be encountered.

Although little doubt exists about the fact that occurrence of ion pairing and deviating behaviors are linked, it still remains to be established whether the association affects only the local concentration of the depolarizer, or whether its reactivity itself is enhanced.

Experiments now under way using proton-donor cations (NH_4^+, $CH_3NH_3^+$, etc.) and electrodes other than mercury (Pt, Au) show further sequences of the same type which strongly suggest that reactivity may indeed be enhanced provided that the reduction requires a protonation step. It is believed that the transition complex involved a water-molecule which can be subjected to considerable electrostriction when ion pairing occurs, the effect of which being to decrease the activation energy of the rate-determining step. This concept will be presented and discussed later.

Conclusions

Within the range of compositions and concentrations to which the present study is restricted, deviations from the "average" ψ effect appear to be intimately related to the extent of association. Although "mostly electrostatic" ion pairing is the most frequent factor responsible for the increases in rate constant, a cavity ion pairing mechanism is indicated in the case of perrhenate in tetraalkylammonium solutions. The direction and the amplitude of the observed effects can be accounted for on the basis of the Gurney concept which stresses the importance of the water-ion interaction.

The present investigation points out that specific conclusions about rate-determining factors require the preliminary intercomparison of as many systems as possible, in order to allow the definition of a "standard" type of behavior, regardless of any *a priori* assumption for the double layer model. It appears, however, that the simple Gouy-Chapman, despite its intrinsic defects, predicts values which are in rather reasonable agreement with the order of magnitude of the kinetic effects observed, as far as the cases for which specific adsorption or deviating mechanisms occurs are carefully excluded.

Acknowledgments

Two of the authors (L. V. and E. N.) gratefully acknowledge the tenure of Research Studentship, respectively from I.R.S.I.A. (Institute of Industrial and Agricultural Scientific Research) and F.N.R.S. (National Foundation for Scientific Research).

SYMBOLS AND UNITS

A	electrode area, cm^2
C	concentration in $mole/cm^3$ $(C)_\infty$ = bulk conc.
D_o	diffusion coefficient in $cm^2.\ sec^{-1}$ ($\vec{D}$, $\overleftarrow{D}$ for particles respectively involved in forward and reverse steps)
E	electrode potential *vs.* saturated calomel electrode
I	current (amp.) I_d diffusion current
i	current density (amp/cm^2)
n_α	number of electrons transferred in the rate-determining step
N	normality of the supporting cation
Z	charge of the supporting cation
z	charge of the depolarizer
α	apparent transfer coefficient
α_o	corrected for the ψ effect
δ	plane of closest approach for the supporting cation
δ'	plane of closest approach for the depolarizer
ψ	potential in the diffuse part of the double layer, with respect of the bulk of the solution

ψ',ψ'',ψ_R see definition under Intercomparison Data Caption of Fig. 2, 3, 4, 5. The curves are ψ_R values, for various Z/N, calculated from the Gouy-Chapman theory. Each vertical line corresponds to the potential at which the rate constants have been measured (depolarizer indicated above). ψ'' values are plotted under the form of small intersecting horizontal bars. The corresponding ψ_R curve is identified by the intersecting dot on the lateral bracket. The downward succession of the prongs along the bracket follows the "normal" sequences

Li^+, Na^+, K^+, Cs^+ — (Mg^{++}) if any, Ca^{++}, Ba^{++}

It results from this convention that any crossing corresponds to a reversed sequence.

REFERENCES

1. W. H. Reinmuth, "Transactions of the Symposium on Electrode Processes," Philadelphia, 1959, p. 143, John Wiley & Sons, Inc., New York (1961).
2. A. N. Frumkin, O. A. Petry, and N. V. Nikolaeva-Fedorovich, *Electrochim. Acta*, **8**, 177 (1963).
3. L. Gierst, "Transactions of the Symposium on Electrode Processes," Philadelphia 1959, p. 109, John Wiley & Sons, Inc., New York (1962).
4. A. N. Frumkin, *Trans. Faraday Soc.*, **55**, 156 (1959).
5. P. Delahay and C. Mattax, *J. Am. Chem. Soc.*, **76**, 5314 (1954).
6. L. Meites, "Polarographic Techniques," 2nd ed., pp. 615-711, Interscience, New York.
7. T. A. Kryukova, S. I. Siniakova, and T. V. Arefieva, "Polarographic Analysis," Moscow (1959).
8. C. W. Davies, "Ion Association," Butterworth, London (1962).
9. R. Weiner, *Z. Elektrochem.*, **52**, 234 (1948).
10. J. Koutecky, *Coll. Czec. Chem. Communs.*, **18**, 591 (1953).
11. D. C. Grahame, *Chem. Rev.*, **41**, 441 (1947); *J. Am. Chem. Soc.*, **76**, 4821 (1954); *This Journal*, **98**, 343 (1951).
12. H. Wroblova, Z. Kovac, and J. O'M. Bockris, *Trans. Faraday Soc.*, **61**, 1523 (1965).

13. G. Gouy, *J. Phys.* (*Paris*), **9**, 457 (1910); D. Chapman, *Phil. Mag.*, **25**, 475 (1913).
14. D. C. Grahame, *J. Am. Chem. Soc.*, **80**, 4021 (1958).
15. P. Herman, Mémoire de licence U.L.B. (1964).
16. V. F. Ivanov and E. A. Jofa, *Doklady Akad. Nauk. S.S.S.R.*, **137**, 1149 (1961).
17. J. Dandoy and L. Gierst, *J. Electroanal. Chem.*, **2**, 116 (1961).
18. N. S. Hush and J. W. Scarrott, *ibid.*, **7**, 26 (1964).
19. J. Koryta, *Electrochim. Acta*, **6**, 67 (1962).
20. E. A. Guggenheim, *Phil. Mag.*, **19**, 588 (1935).
21. J. J. Tondeur, Thèse de doctorat U.L.B. (1962).
22. L. Jensovsky, *Coll. Czec. Chem. Communs*, **22**, 181 (1957).
23. N. Konopik and E. Berger, *Monatsh.*, **84**, 666 (1953).
24. Sh.S. Shchegol, Trudy 4-go Sov. Elektrochimii Moscva, p. 215.
25. O. Tomicek, J. Cihalik, J. Dolezal, V. Simon, and J. Zyka, *Chem. Listy*, **46**, 714 (1952).
26. Ch. Rulfs and P. J. Elving, *J. Am. Chem. Soc.*, **73**, 3284 (1951).
27. R. W. Gurney, "Ionic Processes in Solution," chap. 10, 11, 16, McGraw-Hill Book Co., New York (1953).
28. R. M. Diamond, *J. Phys. Chem.*, **67**, 2513 (1963).
29. G. Eisenmann, in "Membrane Transport and Metabolism," p. 163, publ. by Kleinzeller and Kotyk, Acad. Press N. Y. (1961).
30. P. H. Teunissen and H. G. Bungenberg de Jong, *Koll. Beihefte*, **48**, 33 (1949).
31. J. Lyklema and J. Overbeek, *J. Coll. Science*, **16**, 595 (1961).
32. L. Gierst, J. J. Tondeur, and E. Nicolas, *J. Electroanal. Chem.*, **10**, 397 (1965).
33. J. I. Bregman, *Ann. N. Y. Acad. Sci.*, **57**, 130 (1953).
34. R. Bock and G. M. Beilstein, *Z. Anal. Chem.*, **44**, 192 (1963).
35. R. Bock and J. Jainz, *Fresenius Z. Anal. Chem.*, **198**, 315 (1963).
36. a. P. Lukovtsev, Trudy 4-go Sov. Elektrochimii Moscva, pp. 302, 773; b. I. Turyan and A. Tsinman, *Doklady Akad. Nauk. S.S.S.R.*, **136**, 5 (1961).
37. L. Gierst *et al.*, *J. Electroanalyt.*, To be published.
38. A. N. Frumkin, *Z. physik Chem.*, **109**, 34 (1929).
39. J. E. B. Randles, *Trans. Faraday Soc.*, **52**, 1573 (1956).
40. R. Kunin, "Ion Exchange Resins," p. 62, John Wiley & Sons, Inc., New York (1963).
41. A. G. Breyer, Ph.D. Thesis, Rutgers U. (1958).
42. A. N. Frumkin, S. Reichstein, and R. Kulvarskaya, *Kolloid Z.*, **40**, 9 (1929).
43. G. Ling, *J. gen. Physiol.*, **43**, Suppl., 149.

Discussion

F. C. Anson: Professor Gierst should be complimented on providing so much valuable new information on double layer structure in a very large number of supporting electrolytes. I would like to ask three questions about this work.

1. Do you regard the departure of any particular reactant from the "normal" behavior established for each supporting electrolyte as a sufficient or merely a necessary indication of the occurrence of ion pairing?

2. Whenever ion pairing is invoked to explain rate enhancement must it not also be assumed that the ion paired species, which has a lower charge and can therefore more readily cross the diffuse layer, has at least as large a standard electrode reaction rate constant as the unpaired starting material?

3. Is any commitment made or intended as to where the ion pairing takes place, *i.e.*, in the bulk of the solution, only within the diffuse layer, or both?

L. Gierst: 1. Any departure from the "normal behavior" is of course in itself not automatically indicative that ion pairing is the responsible factor. What we have shown, however, is that the sequence of results found in our experiments are very similar to many others, for which there is clear evidence that ion pairing is the controlling factor. Furthermore, all these sequences follow the order which can be predicted from such thermodynamic quantities as ionic entropies or B coefficient of viscosity, if we accept Gurney's views about the water structure effect.

2. The influence of pairing on the intrinsic reducibility of a given anion is difficult to assess. Present experiments indicate that enhancement in reactivity is in fact observed at least for oxyanions of the "water-organizing" type, when their reduction involves protonization. This matter will be presented in detail in a later paper.

3. Since the supporting cation concentration is increased in the diffuse part of the double layer, the amount of ion pairing is accordingly larger there, especially if cationic specific adsorption occurs. It remains difficult at present to delineate the role of the local electrical field since it acts on both electrolytic dissociation and water structure (cf. the recent contributions to that topic by Hurwitz and Sanfeld[1] and by Nürnberg[2]).

[1] H. Hurwitz, A. Sanfeld, and A. Streicher, *Electrochim. Acta*, **9**, 975 (1964); A. Sanfeld and A. Streicher-Sanfeld, *Trans. Faraday Soc.*, **62**, 1907 (1966).

[2] H. Nurnberg, *Discussions Faraday Soc.*, 1965, 39.

H. B. Urbach: Professor Gierst, have you made calculations of the ion recombination from Brönsted's theory and have you correlated your results with these calculations?

L. Gierst: No, since our experiments were carried out in nonideal solutions and some vital parameters are not available. It should perhaps be mentioned that the sequence of results found are following the order for "effective" radii of hydrated ions, proposed by Nightingale[3] on the basis of his phenomenological theory of ionic solution.

G. J. Hills: Ion association is a well-established general phenomenon in electrolyte solutions, although it is seldom possible, except in dilute nonaqueous solutions of low permittivity, to specify the nature and degree of the association. In concentrated aqueous solutions, the variety of local ion and solvent interactions is large, and in the absence of any obvious discriminating procedures, it is often necessary and desirable to express the total interaction in purely thermodynamic terms which contain all of the general and specific interactions of any pair of ionic species. These thermodynamic features will inevitably influence the ionic distribution at the interface, and this paper is concerned to delineate the way in which this influence occurs.

Just how far this can be done in terms of ion pairing is doubtful. These are complex concentrated systems in which the electrostatic interactions cannot yet be quantified. The term "ion pair" implies a long-lived species, the electrochemical characteristics of which are not taken into account here. It is not easy to see how far the effects described can be further quantified except perhaps by using more dilute solutions, *e.g.*, without supporting electrolyte, or by using cation reversible (membrane) electrodes to take into account the effective lowering of γ_+.

I should be glad of some further clarification of the "median potential" and some further reassurance that (*a*) no specific adsorption took place (IO_3^-) and (*b*) that the charging current was successfully eliminated. Indeed the broad sweep of results presented here could usefully be complemented by a detailed description of the procedures and results of a single system in which all the approximations could be assessed.

[3] E. Nightingale, *J. Phys. Chem.*, **63**, 1382 (1959).

L. Gierst: 1. Concentrated ionic aqueous solutions are not easily amenable to thermodynamic analysis and, besides, there are still many conflicting views about the water structure, and the way it is affected by ions (see Kavanau's[4] monograph, for example). We do not believe, however, that this fact should be a sufficient reason to abandon the field. One of the main conclusions we draw from the present work is that a general picture of what happens starts to emerge. In that respect, intercomparison of as many types of behavior as possible must be pursued in order to pinpoint the responsible factors. Quantitative thermodynamic explanations will probably follow, but must be based on sufficient prior experimental evidence (see also 1. in our reply to Dr. Anson).

2. IO_3^- is not adsorbed at the potentials under consideration (—0.65v *vs.* e.c.m.).

3. Capacity currents were carefully deduced, of course.

4. Procedures used were based on the classical Koutecky theory.[5] We did not find it useful to produce the polarization curves themselves, which would have increased the size of the paper considerably.

H. Hoffmann: Dr. Gierst presents a wealth of excellent experimental data which may be used for further improvement of the Gouy-Chapman theory of the double layer.

The authors use the procedure of anion substitution of the supporting electrolyte to distinguish between ψ-effects and effects which are due to ion association. The substitution certainly should also influence the association equilibrium of the anion depolarizer with the supporting cations since I^- ions will form complexes with the cations and two coupled association equilibria will result.

The existence of water structure enforced ion pairs is concluded from the data which is of particular interest since such associates are normally not considered and have not yet been discovered by other techniques. Therefore these data should stimulate investigations with different methods which are directly sensitive to ion pair formation.

L. Gierst: The mentioned difficulty was circumvented as far as possible by using two anions (iodide and acetate), the sodium salts of which have very close mean activity coefficients.

B. E. Conway: In regard to the interesting ion-pairing effects discussed by Professor Gierst, it may be useful to record that we have recently[6] determined the components of charge Γ_{K^+} and Γ_{Cl^-} for KCl adsorption in aqueous solutions containing various concentrations of pyridine, the surface excess (Γ_{Py}) of which could be independently determined from the derivative $-(\partial\gamma/\partial\mu_{Py})_{E,\mu_{KCl}}$ by means of appropriate electrocapillary measurements. In the presence of adsorbed pyridine, both Γ_{K^+} and Γ_{Cl^-} increase almost equally both on the cathodic and anodic branches as the Γ_{Py} increases. The effect is largest in the strongest KCl and pyridine solutions. The parallel increase of the Γ_{K^+} and Γ_{Cl^-} seems to be most easily explained by supposing that ion pairing in the double layer is enhanced by the presence of adsorbed pyridine. The concentration of pyridine in the bulk was insufficient to lower the bulk dielectric constant significantly so that the species in solution were still presumedly free hydrated K^+ and Cl^- ions.

L. Gierst: The observed enhancement is very interesting. It could perhaps reflect the fact that the transition between the pyridine layer and the "bulk" water is not really sharp, and that the boundary region (including the hydrated nitrogen groups) possesses a rather low "microscopic" dielectric constant, favoring local ion pairing. There is some similitude between this behavior and the fact that large organic cations, when they are specifically adsorbed, also tend to pair with anions of suitable type.[7]

[4] J. L. Kavanau, "Water and Solute Water Interactions," Holden-Day, Inc., San Francisco, London, Amsterdam (1964).

[5] J. Koutecky, *Coll. Czech. Chem. Commun.*, 18, 591 (1953).

[6] B. E. Conway, R. G. Barradas, P. Hamilton, and J. M. Parry, *J. Electroanal. Chem.* (1965).

[7] L. Gierst, J. Tondeur, and E. Nicolas, *J. Electroanalyt. Chem.*, 10, 397 (1965).

Panel Discussion on Adsorption at Solid Electrodes

I. The Application of Multipulse Potentiodynamic Sequences to the Study of Surface Intermediates in the Electrochemical Oxidation of Organic Substances

S. Gilman

General Electric Research and Development Center, Schenectady, New York

In the electrochemical oxidation of complex organic molecules on platinum electrodes, it may be anticipated that parallel and sequential reaction steps will occur. Such complex systems do not lend themselves well (1) to study by the steady-state treatments of classical kinetics. However, through the use of pulse techniques, it is often possible to isolate individual reaction steps and to characterize surface intermediates. Early application of such techniques was made in the study of the adsorption and oxidation of methanol (2, 3).

In this paper, I shall discuss the manner in which some particular aspects of the adsorption and reaction of organic compounds (encountered in the study of C_2 hydrocarbons) were examined by means of the "multipulse potentiodynamic" method first developed in connection with the study of CO adsorption (4).

Experimental

The electronic instrumentation, test vessel, etc., have been described previously (4). The test electrode used in most of the measurements, was a length of C.P. grade smooth platinum wire. A platinized wire was used only in the last section as indicated. All potentials are referred to that of a reversible hydrogen electrode in the adsorbate-free electrolyte.

Discussion

Study of the Mechanism and Kinetics of Activated Adsorption (of Ethane)

Use of a linear anodic sweep in the measurement of adsorption kinetics.—The organic adlayer may be "stripped" by means of a linear anodic sweep (l.a.s.) and the coverage determined from the corresponding charge. In the sequence of Fig. 1, steps A-C serve to clear the surface of previously adsorbed material. Step *D* (which is optional) serves to prereduce the surface, but the low potential prevents the adsorption of ethane in the allotted time. In step E, atomic hydrogen is rapidly removed from the surface and the

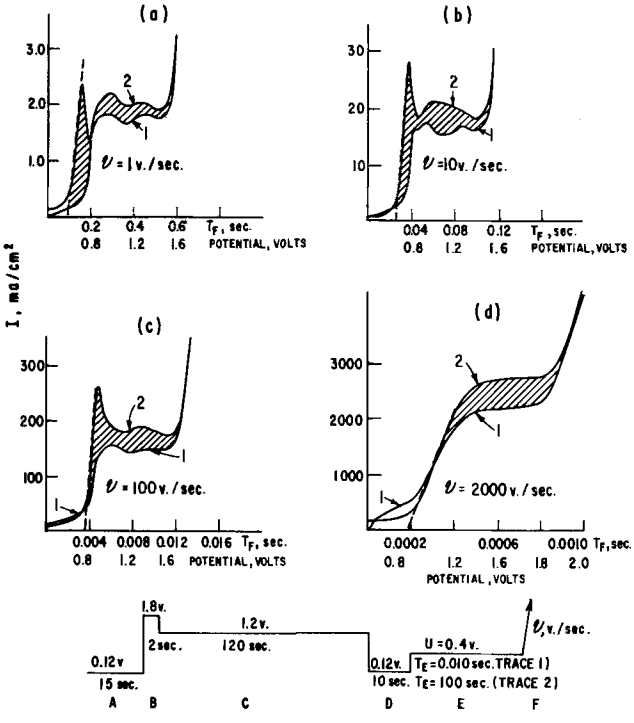

Fig. SG1. Linear anodic sweep traces corresponding to the "clean" surface (traces "1") and to the surface partially covered with ethane (traces "2"). The 1*N* $HClO_4$ solution was saturated with ethane at 60°C. The electrode was smooth, having a "roughness factor" (R.F.) of 1.5 based on hydrogen adsorption. After Gilman, ref. (5).

adsorption of ethane occurs at 0.4v for 100 sec. The potential sequence was chosen in such a way at the beginning of step E, the solution adjacent to the surface was well equilibrated with the bulk solution and transport of the hydrocarbon was by ordinary diffusion (5). Traces "1" of Fig. SG1a-SG1d were obtained in the absence of hydrocarbon and correspond to the "clean" surface. The current corresponds mainly to surface oxidation until copious evolution of molecular oxygen sets in at *ca.* 1.6v.[1] Traces "2" correspond mainly to combined oxidation of the surface and of adsorbed ethane.[2] Let us call the difference in areas under curves 1 and 2, Q_E' (hatched areas). Let us also assume the existence of a charge, Q_E which bears the following relationship to the absolute coverage with ethane

$$Q_E = nF\,\Gamma_E \qquad [1]$$

where Γ_E is the coverage of the surface with various adspecies (in moles/cm²), and n is the average number of electrons required for oxidation and desorption of an ethane adspecies. Then Q_E may be used as a measure of absolute coverage if n is known and remains constant; Q_E is a measure of relative coverage if n is constant, but the value of n is not known.

The experimental charge $Q_E' = Q_E$ if the following conditions hold:

1. All organic material is desorbed by the time traces 1 and 2 (Fig. SG1) merge.
2. Capacitive corrections are negligible.
3. Traces "1" and "2" comprise identical surface oxidation charges.
4. Negligible readsorption and/or oxidation of ethane occurs during the sweep.
5. The desorption of organic material is entirely oxidative (not due to electrostatic repulsion).

An indirect test of the validity of such assumptions is made by exploring the dependence of Q_E' on the sweep speed. It was found (5) for ethane that Q_E' remains constant for sweep rates ν as small as 1 v/sec to somewhat under 100 v/sec (with dependence on surface coverage, as well as on ν). Decreasing charge at higher values of ν was found to correspond to retention of a portion of the adlayer past the region of oxygen evolution. A more direct test of the equality of Q_E' and Q_E may be made for rapidly adsorbed substances. For CO (4), ethylene and acetylene (6) a plot of the anodic stripping charge *vs.* the square root of adsorption time is linear until high coverages are achieved. This suggests diffusion-controlled adsorption. The slopes of such plots were found in excellent agreement with a diffusion law if it was assumed that the values of n (of Eq. [1]) correspond to complete oxidation of the adlayer to CO_2 and H_2O (as in the steady-state situation). Hence the method has been validated for these quite diverse compounds. Similar validation has been reported for even more complex molecules (7, 8).

An explanation may now be offered for the apparent equality of the surface oxidation charge (by the end of the sweep) both in the presence and absence of an adsorbed organic substance.[3] The kinetics of oxidation of the surface is such that the charge (after the first small fraction of a second) depends strongly on the potential, but only slightly (approximately on the logarithm) of the time (9). The organic material may be regarded as blocking sites temporarily and hence slightly decreasing the time of surface oxidation. This causes a negligible error.

Correction for surface oxidation might also be made by cathodically reducing the surface and measuring the corresponding charge. This is, however, best avoided where possible since reduction is sluggish (9) and may lead to error through incomplete reduction or through simultaneous oxidation of dissolved organic material (both lead to positive error in determination of surface coverage with the organic material).

It is to be noted that in this application, the l.a.s. trace is used only to derive the charge, Q_E, corresponding to the adsorption process preceding the sweep (other wave forms may be used but are generally not as satisfactory). Hence variations (with sweep speed) of such characteristics of the trace as peak voltage, current, etc., have no bearing on the problem. This seems a point previously misunderstood by other investigators [see, for example ref. (11, 12)].

Results of the kinetic measurements.—The kinetics of ethane adsorption may be examined through recording Q_E or the hydrogen codeposition charge (see below) as a function of time at various constant potentials. Over a range of several tenths of a volt, the "true" rate of adsorption was found (5) to follow the law

$$\frac{d\theta_E}{dt} = KC(1-\theta_E)^2 \qquad [2]$$

or the integral law

$$1/\theta_F = KCt + 1 \qquad [3]$$

where $\theta_F = 1 - \theta_E$, and C is the concentration of dissolved ethane. Equation [2] implies an adsorption step which is second order in unoccupied[4] (by ethane) surface sites and relatively field-independent. A reasonable mechanism is

[1] There may be considerable IR drop (due to residual resistance between the Luggin capillary and the working electrode) included in the nominal potential at high sweep speed. This, however, does not effect the measured charge which is the only quantitative consideration in such measurements.

[2] By "adsorbed ethane" we mean "the adlayer resulting from the adsorption of ethane" which may have a composition quite different from that of the parent molecule.

[3] The charge corresponding to oxidation of the surface is not necessarily identical in presence and absence of the organic adsorbate at constant potentials less than *ca.* 1.6v.

[4] The possibility that such sites are occupied by inorganic species (*e.g.*, H_2O) is not ruled out.

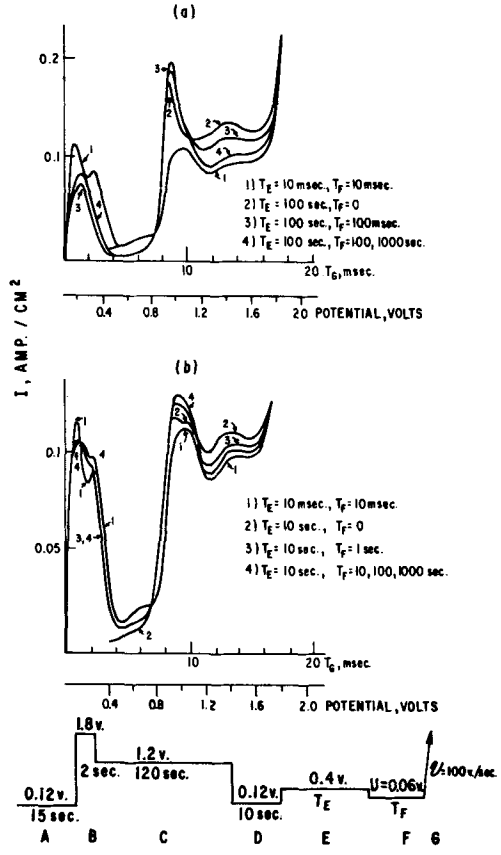

Fig. SG2. Linear anodic sweep traces obtained during desorption of adsorbed "ethane." The 1*N* $HClO_4$ solution was saturated with ethane at 60°C; the smooth Pt electrode had a R.F. = 1.5. T_E and T_F are adsorption and desorption time intervals, respectively. After Gilman, ref. (13).

$$C_2H_6 \text{ (dissolved)} \rightarrow \underset{|}{\overset{C_2H_5}{S}} + \underset{|}{\overset{H}{S}}$$

$$H \rightleftarrows H^+ + e^- + S$$
$$|$$
$$S$$

where S = Surface site.

Study of the Kinetics and Mechanism of Desorption (of Adsorbed Ethane)

Figure SG2 presents traces corresponding to desorption of a portion of the ethane adlayer. As in Fig. SG1, adsorption was allowed to occur at 0.4v (step E). In step F the desorption proceeded under the influence of (low) potential U and the desorption process could be followed as a function of time (T_F) by application of l.a.s. (G). In Fig. SG2a, trace 1 corresponds to the clean surface. Trace 2 corresponds to 100 sec of adsorption, with no desorption. Traces 3 and 4 correspond to 100 sec of adsorption, followed by 100 msec and 100-1000 sec of desorption, respectively. We see that the material desorbing (type II) corresponds mainly to the portion of the adlayer which oxidizes at relatively high potentials during the l.a.s., while the nondesorbable residue (N.D.R.) (type I) corresponds mainly to the more electrochemically reactive material. The N.D.R. is retained at potentials as low as —0.2v (13). Hence this experiment serves to characterize two types of surface intermediates.

By measuring (from traces such as those of Fig. SG2) the charge, ΔQ_E corresponding to desorption, it was possible (13) to establish the kinetic law

$$\frac{-d\theta_E}{dt} = H' \exp\left[(\alpha n' FU/RT) + m\theta_E\right] \qquad [4]^5$$

[5] In ref. (13) the "+" was accidentally omitted between the two terms in the exponential term of Eq. [4].

where $\alpha = 0.5$ and $n' = 2$ electrons. Equation [4] suggests the following mechanism for the desorption

C_2H_2 (adsorbed) + $2e^-$ + $2H^+ \rightarrow C_2H_4$ (adsorbed)

$C_2H_2 \rightarrow$ Further hydrogenation (to ethane) and desorption.

The first step is rate-determining. A similar chemical hydrogenation (involving hydrogen atoms) step is also permissible.

Identification of Surface Intermediates

Type I intermediates.—The adsorption of C_1 "oxygenated" molecules (HCOOH, CO_2, etc.) results in nondesorbable adlayers resembling the "type I" ethane oxidation intermediate (14, 15). The "type I" intermediate is therefore believed to comprise one or more C_1 oxygenated surface structures.

Type II intermediates studied with linear anodic sweeps.—Figure SG3 presents traces obtained in the adsorption of ethylene and acetylene. The traces for both adsorbates are similar to those for the type II oxidation intermediate of ethane. Also, (temperatures under 60°C) the adlayers of all three substances may be hydrogenated and desorbed as ethane (16). When ethylene is adsorbed at potentials of 0.4v or less, a current flows corresponding to the abstraction of (approximately) 2 hydrogen atoms/molecule. These results suggest that at moderate potentials and temperatures, the type II intermediate, and adsorbed ethylene and acetylene have a common average stoichiometry corresponding to C_2H_2.

Type II intermediate studied by linear cathodic sweeps.—Figure SG4 presents linear cathodic sweep traces corresponding to the codeposition of hydrogen on a surface partially covered with adsorbed ethylene. Trace I corresponds to H-deposition on the "clean" surface. The area above the trace (preceding large-scale evolution of molecular hydrogen) corresponds to approximately a monolayer of hydrogen atoms. Traces 2-6 correspond to the hydrogen required to complete a mixed monolayer of hydrogen atoms and organic material. A rather high sweep speed is required to prevent desorption of the organic material (5, 6, 13). The areas defined by trace 1 and any sub-

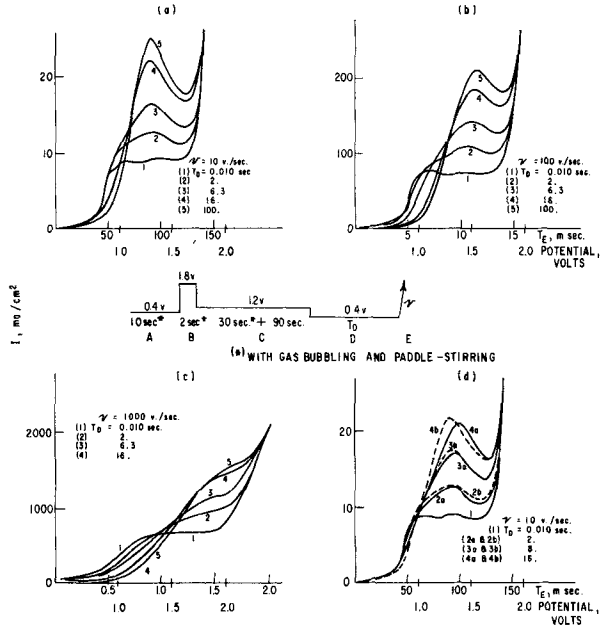

Fig. SG3. Linear anodic sweep traces for adsorbed ethylene and acetylene. The traces were recorded during l.a.s. E of the specified sequence. T_D is the adsorption time. The solid traces (a-c) and the dashed traces (d) were obtained in 1N $HClO_4$ saturated with a gas mixture of 1.08% ethylene + 98.92% argon (30°C). The solid traces (d) were obtained in 1N $HClO_4$ saturated with a gas mixture of 0.105% acetylene + 99.985% argon (30°C). Electrode roughness factor = 1.4. After Gilman, ref. (6).

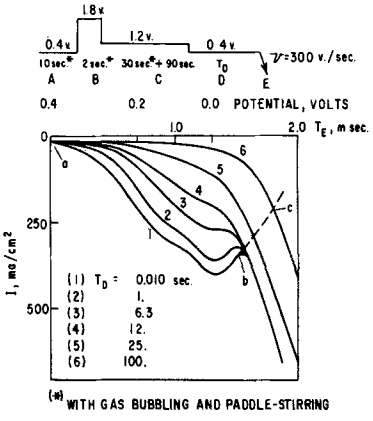

Fig. SG4. Linear cathodic sweep traces corresponding to codeposition of hydrogen on a surface partially covered with ethylene. The traces were measured during sweep E of the specified sequence. T_D is the adsorption time. The solution was 1N $HClO_4$ saturated with a gas mixture of 1.08% ethylene + 98.92% argon (30°C). After Gilman, ref. (6).

sequent trace, represents a charge, $\Delta(sQ_H)$ corresponding to (hydrogen) sites blocked by organic material. This is related to the absolute coverage with the ethylene by

$$\Delta(sQ_H) = mF\,\Gamma_{ENE}\ (ENE = \text{ethylene}) \qquad [5]$$

Analogous to Eq. [1]

$$Q_{ENE} = nF\,\Gamma_{ENE} \qquad [6]$$

Combining Eq. [5] and [6]

$$\Delta(sQ_H)/Q_{ENE} = m/n \qquad [7]$$

The quantity m/n (sites/electron) may serve as an indication of the number of valences per adspecies for simple molecules [*e.g.*, for CO, acc. to ref. (4)]. For the more complex hydrocarbons, it may serve, at least, as a characterization of the structure. For ethylene and acetylene at low potentials, m/n was found constant with a value (*ca.* 0.3) corresponding to 3 valences/adsorbed entity, based on simple assumptions. At higher potentials, m/n (ethylene) was found to increase to values that would correspond to ultimate dehydrogenation to adsorbed carbon (17).

Interconversion of Surface Intermediates

The skeletal oxidation scheme for ethane may be represented by

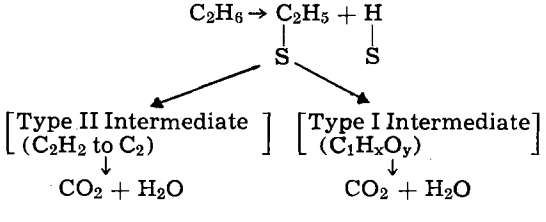

Possible conversions of the type II to type I intermediate were investigated by means of the pulse sequence appearing in Fig. SG5. Higher temperatures were examined to favor conversion. A platinized surface was employed to minimize the rate of transport (per geometric cm^2) during the time allotted for conversion. The functions of the various steps in the sequence of Fig. SG5 are:

A-C. Pretreatment
D. Adsorption at 0.3v
E. Oxidation of adlayer at 0.8v [to reduce the ratio, (type I)/(type II)].

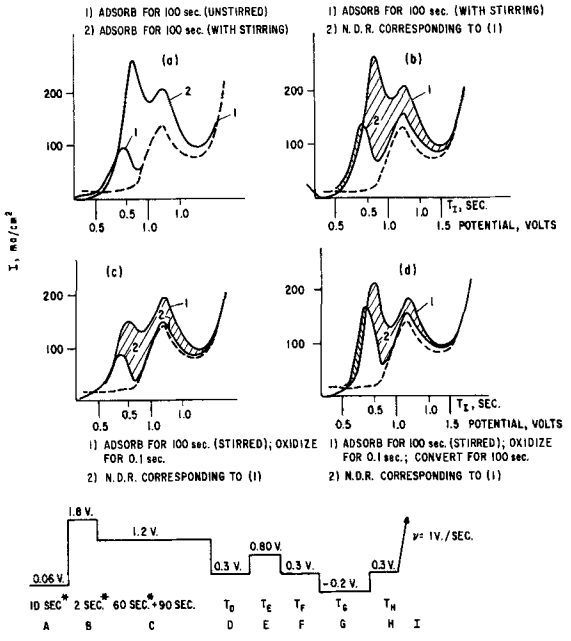

Fig. SG5. Use of linear anodic sweep traces for determination of the nondesorbable residue during readsorption of acetylene. Electrode B (R.F. = 138) was used. The electrolyte was 85% phosphoric acid saturated with ethylene at 120°C. The dashed trace corresponds to the clean surface and was obtained in the absence of adsorbate with T_D = 1 sec, $T_E = T_F = T_G = T_H = 0$. (a) Trace 1, corresponds to ethylene adsorbed for T_D = 100 sec (quiescent solution). $T_E = T_F = T_G = T_H = 0$. Trace 2, corresponds to ethylene adsorbed for 100 sec (stirred solution). $T_E = T_F = T_G = T_H = 0$. (b) Trace 1, corresponds to ethylene adsorbed for T_D = 100 sec (stirred solution) + 90 sec (quiescent solution) $T_E = T_F = T_G = T_H = 0$. Trace 2, corresponds to the nondesorbable residue for the conditions of trace 1. T_D = 100 sec (stirred solution + 90 sec (quiescent solution) $T_E = T_F$ = 0, T_G = 1 sec (to desorb), T_H = 0.1 sec (to reduce concentration of adsorbed and dissolved hydrogen). (c) Trace 1, corresponds to ethylene adsorbed for T_D = 100 sec (stirred solution) and 90 sec (quiescent solution), and partially oxidized for T_E = 0.1 sec with $T_F = T_G = T_H = 0$. Trace 2, corresponds to the nondesorbable residue for the conditions of trace 1. T_D = 100 sec (stirred solution) + 90 sec (quiescent solution), T_E = 0.1 sec, T_F = 0, T_G = 1 sec (to desorb), T_H = 0.1 sec (to reduce concentration of adsorbed and dissolved hydrogen). (d) Trace 1, Corresponds to ethylene adsorbed for T_D = 100 sec (stirred solution) + 90 sec (quiescent solution), partially oxidized for T_E = 0.1 sec and readsorbed for T_F = 100 sec. $T_G = T_H = 0$. Trace 2, Corresponds to the nondesorbable residue for the conditions of trace 1. T_D = 100 sec (stirred solution) plus 90 sec (quiescent solution) T_E = 0.1 sec, T_F = 100 sec, T_G = 1 sec, T_H = 0.1 sec.

F. Possible conversion (type II → type I) step at 0.3v
G. Desorption step: remove type II at —0.2v so that separate amounts of types I and II may be determined.
H. Preoxidation step (0.1 sec): to decrease the concentration of hydrogen, hence preventing the corresponding oxidation current during the sweep.
I. Linear anodic sweep: for alternative determinations of type I and of total I + II.

The durations of the various steps was adjusted to provide the conditions listed with Fig. SG5a-SG5d. The dashed traces of the figure correspond to the "clean" surface. The traces marked N.D.R. correspond only to the nondesorbable residue (type I). The other traces correspond to the entire adlayer (1 + II).

In Fig. SG5a, traces 1 and 2 correspond to the entire adlayer obtained after 100 sec (quiescent solution) and 100 sec (stirred solution). The traces of Fig. SG5a acts as control experiment for the conversion step of Fig. SG5d. In Fig. SG5b, trace 1 corresponds to the total

adlayer after 100 sec (with stirring) and 90 sec (quiescent solution) which is the "original condition" for the remaining experiments of Fig. SG5b-SG5d. Trace 2 corresponds to the N.D.R. portion of trace 1. The difference between areas under 1 and 2 (large hatched area minus small hatched area) is the charge corresponding to the type II portion of the adlayer. In Fig. SG5c, adsorption for 100 sec (stirred solution) + 90 sec (quiescent solution) was allowed and then the ratio of type II/type I was increased by briefly oxidizing at 0.8v. The total remaining adlayer is characterized by trace 1 of Fig. SG5c and the type I fraction of that adlayer is characterized by trace 2 of the figure. In Fig. SG5d, time is allotted for conversion of type II to type I in the adlayer containing a high ratio of type II/type I. Trace 2 of Fig. SG5d reveals that there is accumulation of appreciable additional type I compared with trace 2 of Fig. SG5c. This increase is approximately twice that which would have accumulated from the solution during the time allotted for conversion (twice the charge corresponding to trace 1 of Fig. SG5a). However, this possible conversion is approximately 1/5 the amount which could be accumulated from the solution in the absence of a "reservoir" of type II (1/5 the amount represented by trace 2 of Fig. SG5b). Hence one may conclude that the conversion of type II to type I is not an important path of the over-all reaction of ethane to yield $CO_2 + H_2O$.

Acknowledgment

This work is a part of the program under contract (Contract No. DA-44-009-ENG-4909) with the U.S. Army Engineer Research and Development Laboratories, Ft. Belvoir, Virginia, to develop a technology that will facilitate the design and fabrication of practical military fuel cell power plants for operation on ambient air and hydrocarbon fuels.

REFERENCES

1. K. J. Laidler, "Chemical Kinetics," p. 327, McGraw-Hill Book Co., New York (1965).
2. M. W. Breiter and S. Gilman, *This Journal*, **109**, 623 (1962).
3. S. Gilman and M. W. Breiter, *ibid.*, **109**, 1099 (1962).
4. S. Gilman, *J. Phys. Chem.*, **67**, 78 (1963).
5. S. Gilman, *Trans. Faraday Soc.*, **61**, 2546 (1965).
6. S. Gilman, *ibid.*, **62**, 466 (1966).
7. S. B. Brummer, J. I. Ford, and M. J. Turner, *J. Phys. Chem.*, **69**, 3424 (1965).
8. E. J. Cairns and A. M. Breitenstein, Abstract No. 172, Spring Meeting of the Society, May 1966.
9. S. Gilman, *Electrochim. Acta*, **9**, 1025 (1964).
10. B. E. Conway, E. Gileadi, and H. Angerstein-Kozlowska, *This Journal*, **112**, 341 (1965).
11. E. Gileadi and B. E. Conway, "Modern Aspects of Electrochemistry," Vol. 3, Chap. V, Butterworths, London (1965).
12. S. Srinivasan and E. Gileadi, *Electrochim. Acta*, **11**, 321 (1966).
13. S. Gilman, *Trans. Faraday Soc.*, **61**, 2561 (1965).
14. L. W. Niedrach, S. Gilman, and I. Weinstock, *This Journal*, **112**, 1161 (1965).
15. L. W. Niedrach, in "Hydrocarbon Fuel Cell Technology," B. Baker, Editor, Academic Press, New York (1965).
16. L. W. Niedrach, *This Journal*, **111**, 1309 (1964).
17. S. Gilman, *Trans. Faraday Soc.*, **62**, 481 (1966).

Discussion

E. Gileadi: Dr. Gilman claims that C_2H_6, C_2H_4, and C_2H_2 all give rise to the same surface species on adsorption on a bright Pt electrode through partial dehydrogenation of ethane and ethylene. Two types of experiments carried out in our laboratory indicate that this is not the case.

1. The kinetics of the anodic oxidation of ethylene and acetylene have been studied by Bockris and coworkers in recent years.[1-3] A fundamentally different behavior was observed for the two compounds, indicative of different reaction paths and different rate determining steps. If ethylene were to dehydrogenate on the surface spontaneously, as claimed by Dr. Gilman, and give rise to an acetylenic residue, both compounds should behave kinetically in an identical manner.

2. An experiment has been performed[4] in which a Pt electrode was allowed to reach its rest potential in 1*N* H_2SO_4 and was then potentiostated at this potential (with obviously no current flowing through the circuit). Ethane or ethylene was then rapidly introduced into the cell and the current transient was recorded. In the case of ethane (and similarly for propane), an anodic current transient was observed, corresponding to a surface dehydrogenation followed by ionization of the hydrogen atom produced. No current was produced upon addition of ethylene to the solution, indicating that no dehydrogenation occurred. This is further confirmed by results of Niedrach published in 1964[5] where hydrogen was found on the surface of Pt electrodes in solutions containing saturated hydrocarbons at open circuit, but not in the case of ethylene.

The difference in the adsorption behavior of unsaturated and saturated hydrocarbons can be easily understood in a tentative manner. An unsaturated hydrocarbon can be chemisorbed on the surface by opening an ethylenic or acetylenic bond and using the orbitals thus made available for the formation of covalent bonds to the surface. In the case of saturated hydrocarbons the required orbital can only be made available by rupture of some of the existing C-H or C-C bonds, the former being usually the case.

The various peaks of current obtained during anodic stripping of organic compounds are often interpreted in terms of various species formed on the surface during the adsorption process which takes place at a lower potential. This is a prime example of a case in which the measuring technique may influence the system and cause major errors in the interpretation of results.

The anodic oxidation of a hydrocarbon molecule on the surface involves several steps, giving rise to intermediates associated with one or more adsorption pseudocapacitance peaks. The occurrence of several peaks is indicative of the existence of several different species on the surface during the anodic sweep. This in itself, however, does not constitute sufficient proof that the same species existed on the surface at the potential at which adsorption was taking place, before the sweep was started.

S. Gilman: The suggestion of similar adlayers in the adsorption of ethylene and acetylene is based on three types of evidence:

1. The traces obtained when the adlayer is "stripped" by means of a linear anodic sweep (Fig. SG3) are almost identical for the two adsorbates when comparison is made at equal surface coverage.

2. The number of hydrogen sites obscured per mole-

[1] H. Wroblowa, B. J. Piersma, and J. O'M. Bockris. *J. Electroanal. Chem.*, 6, 401 (1963).

[2] J. O'M. Bockris, H. Wroblowa, E. Gileadi, and B. J. Piersma, *Trans. Faraday Soc.*, 61, 2531 (1965).

[3] J. W. Johnson, H. Wroblowa, and J. O'M. Bockris, *This Journal*, 111, 863 (1964).

[4] E. Gileadi, G. Stoner, and J. O'M. Bockris, Interim Technical Progress Report Contract No. Da-44-009-AMC-469(T), U. S. Army Engineer Research and Development Lab., Fort Belvoir, Va.; September 1965 to April 1966.

[5] L. W. Niedrach, *This Journal*, 111, 1309 (1964).

cule adsorbed is almost the same for the two adsorbates.[6]

3. When ethylene is adsorbed at 0.4v (30°C) under conditions of diffusion control, an anodic current contribution is observed.[6] This current corresponds approximately to that calculated for abstraction of two hydrogen atoms per molecule adsorbed. Because adsorption is diffusion-controlled, it is not possible that this current corresponds to partial or complete oxidation of additional nonadsorbed molecules, but this is possible in the study of ethane, in ref. (4). Since the presumed hydrogen abstraction charge for ethylene is only 1/6 the total charge for complete conversion of the adlayer to CO_2 and H_2O, it may easily be overlooked through compensation [*e.g.*, by O_2 reduction, as may have been the case in ref. (4)] or through slow hydrogenation of additional ethylene ("self-hydrogenation"). The latter possibility is suggested by the observation that the open-circuit potential goes through a minimum in the lengthy equilibrations studied by Niedrach.[5]

While the evidence suggests that acetylenic structures are present in the adlayers of ethane, ethylene, and acetylene, the evidence also suggests that the adlayers at "steady state" are by no means identical. The ethane adlayer contains additional species (type I) which cannot be removed by hydrogenation.[7] The steady-state coverages for ethylene and acetylene are significantly different[8] presumably because of the different steric requirements of the two different parent molecules. Hence it would be anticipated that the steady-state rates of oxidation of the three different adsorbates would differ, as found in footnotes 1 and 3.

The question of whether ethylene is associatively or dissociatively adsorbed in the absence of electrolyte has been a controversial subject for over thirty years.[9] The results are probably sensitive to the experimental conditions.[10] In view of the complexity of the problem area, Dr. Gileadi's attempt to predict the structure of the adlayer from the electronic structure of the parent molecule is therefore probably an oversimplification.

I agree with Dr. Gileadi's argument that the appearance of "waves" during a linear anodic sweep is not conclusive evidence for the existence of structurally different adspecies before the application of the sweep. It is for this reason that I do not rely on such evidence in my own work. In Fig. SG2 and SG5, for instance, the distinction between type I and type II species is made on the basis of whether the material may be desorbed (presumably through hydrogenation) at low potentials (a chemical differentiation). It happens that the chemically differentiated species also seem to be represented by two waves (with considerable overlap) in this particular case.

E. Gileadi: We find that the adsorption of ethylene and benzene on platinized Pt in 1*N* H_2SO_4 is reversible with respect to a change of potential in the range of 0.1-0.7v re. RHE. This observation in fact serves as our main criterion for reversibility of the adsorption process in these systems and makes the study of adsorption isotherms here meaningful.

S. Gilman: In the experiments of Dr. Gileadi and coworkers, only the surface concentration of radioactive carbon is determined. The method is not very sensitive (precise) and provides no information on the structure of the adlayer. Voltammetric measurements reveal[8] that the ethylene adlayer changes in structure at potentials above *ca.* 0.5v (probably corresponding to increasing dehydrogenation) and that this results in a dependence of steady-state surface coverage on the path taken to reach the potential of interest. It seems possible that Dr. Gileadi's isotherms do not have the usual thermodynamic significance (a balance between reversible adsorption and desorption) but represent a balance between rates of adsorption and hydrogenation (at low potentials) or between rates of adsorption and oxidation to CO_2 and H_2O (at high potentials).

[6] S. Gilman, *Trans. Faraday Soc.*, **62**, 466 (1966).
[7] S. Gilman, *Trans. Faraday Soc.*, **61**, 2561 (1965).
[8] S. Gilman, *Trans. Faraday Soc.*, **62**, 481 (1966).
[9] "Chemisorption" by D. O. Hayward and B. M. W. Trapnell, 2nd ed., p. 251, Butterworths, Washington (1964).
[10] D. W. McKee, *J. Am. Chem. Soc.*, **84**, 1109 (1962).

II. Structure and Composition of Organic Adsorption Layers on Pt Electrodes—Relation to Reaction Kinetics

S. B. Brummer

Tyco Laboratories, Inc., Waltham, Massachusetts

The study of organic adsorption on Pt electrodes has been stimulated recently by interest in the mechanism of the reactions at the anode in fuel cells. Work from our own laboratory has been concerned with the HCOOH reaction (1-4), which one might hope to be a simple model system, and with a more complex reaction, the oxidative adsorption of C_3H_8 (5, 6). The aim of these continuing studies is to investigate the nature of the adsorbate and to relate the findings to the overall reaction kinetics of the parent compound.

The measurement of θ on solid electrodes is a difficult experimental problem. The capacity method, which has been so useful for the Hg-solution interface, is inappropriate and one has to adopt other procedures. An obviously appealing method, because of its directness, is the radioactive tracer technique (7, 8) where the amount of adsorbed fuel is "counted" without any apparent uncertainty. The disadvantage of this technique is the long time scale required for the counting and the necessity to use very rough electrodes to achieve sufficient sensitivity.

Another fairly direct method which has been widely used to estimate θ is anodic stripping. This was originally done after removing the electrode from the solution of the adsorbate (9). This procedure has the advantage of not having complications due to charge from readsorption during the stripping transient. Also, because the stripping may be done very slowly, no correction for contemporaneous electrode oxidation is necessary. The disadvantages are the cumbersomeness of the technique and the likelihood of removing loosely adsorbed material. *In situ* anodic stripping is then to be preferred, particularly where the adsorption process is complex and the adsorbate may comprise more than one material. This procedure has been used extensively by Breiter (10), Gilman (11), and Giner (12) as well as in our own work. The usual disadvantage of the procedure is the large correction which must be made for electrode oxidation. The main advantage is the high versatility of the method for complex adsorbate analysis. Within certain limits, the method may be thought of as "direct."

Another method, which is particularly useful for Pt electrodes but not so direct, is H-atom deposition. Here, adsorption is permitted to occur, and a cathodic charging curve (galvanostatic or linear potential sweep) is applied to estimate the fraction of the electrode which is available for H-atom deposition. This fraction, $\theta_H{}^c$, is assumed to be equal to that part of the electrode not occupied by the organic adsorbate ($\theta_H{}^c = 1 - \theta_{org}$). This assumes that $\theta_H{}^c$ is less than unity only for steric reasons (*i.e.*, site blockage) and

that no desorption occurs during the $\theta_H{}^c$ measurement. The latter is easy to verify experimentally; the former is less certain for it is well known that the heat of adsorption of H atoms depends on their coverage (13). Thus different interactions between H atoms and the organic adsorbate than between H atoms might lead to inclusion of a nonsteric effect on the measured value of $\theta_H{}^c$. Opposing such an effect is the observation that for finite θ_{org}, the hydrogen overpotential is higher than for a clean surface so that the possible effects of any H-organic interactions would be opposed by the more cathodic potential of the electrode. Recently (14), we have investigated this problem by comparing θ_{org} obtained above with those obtained using anodic hydrogen charging. Here, after allowing adsorption (at E_{ads}), the potential is lowered to a potential positive of the reversible hydrogen potential (E_1) so as to deposit H atoms onto part of the surface. These are then stripped to yield $\theta_H{}^{anodic}$, which is the ratio of the charge found for H_{ads} compared to that found at the same potential (E_1) on a clean electrode. Since the H atom concentration on a clean electrode decreases with increasing potential, we can adjust the amount of hydrogen on the electrode for a given θ_{org} by adjusting the potential E_1. We find a good 1:1 correlation between $\theta_H{}^{anodic}$ and $\theta_H{}^c$ over the whole range from 0-1 in θ. Since nonsteric effects, if they were significant, would show up strongly in the $\theta_H{}^{anodic}$ data, this is good evidence that the main effect in the cathodic measurement is steric.

In any complex system, it is strongly advised to use more than one of the above methods. Thus for the hydrocarbon case (5, 6). we found that the average oxidation state of the adsorbate varies with time and potential of adsorption. Any conclusions about the kinetics and the steady-state extent of adsorption, drawn solely from anodic charging data would, then, be in error. Conclusions drawn from other methods would not be affected but, by combining anodic stripping with one of the other methods much more detailed information about the adsorbate and its participation in the electrode reaction can be obtained.

Identity of adsorbed species.—The major point to be made here is that very often the adsorbed species do not have the same chemical composition as the original adsorbate. This view has attained wide acceptance for a number of fuels. Thus for HCOOH (1, 2, 15), methanol (15, 16), and for saturated hydrocarbons (5, 6, 17, 18) there can be little doubt that the adsorbate is either a reaction-intermediate or the product of a side-reaction. In addition, in some instances, the situation is more complex in that the adsorbate is not a single species, but consists of a number of materials of varying oxidation state, perhaps none of which is the original fuel.

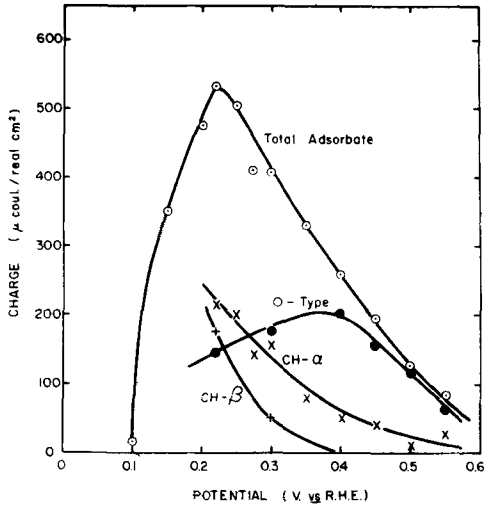

Fig. SB1. Adsorption of C_3H_8 on smooth Pt from 13M H_3PO_4 solution at 130°C.

An example is given in Fig. SB1 (14) for the adsorption of C_3H_8 on Pt from H_3PO_4 solutions at 130°C. The method of examining the structure of the adsorbate and of discriminating the different species was indicated in part earlier (6) and will be described more fully later (14). We see that while the total adsorbate concentration appears to show a fairly simple dependence on potential (Q *vs.* E is almost linear above 0.2v suggesting a Temkin isotherm) the adsorbate actually consists of at least three species. We divide these species into two broad classes, the O-type and the CH-type. The basis of this distinction is whether we judge that most of the C-H bonds in the original fuel have been replaced by C-O bonds (14). The oxidation state of these adsorbed species is very different. Thus the O-type has an $[e]$ value[1] of 1.3 ± 0.05 whereas, for example, the CH-β type releases ~4 electrons per site when oxidized. Because of these variations in oxidation state, Fig. SB1 is not a true representation of the relative amounts of the various species. Thus for example, at 0.3v, $\theta_o \simeq 0.65$, $\theta_{CH\text{-}\beta} \simeq 0.1$ and $\theta_{CH\text{-}\alpha} \simeq 0.25$; total coverage ~1. At 0.2v, total coverage is also about unity, but there is a larger amount of charge to oxidize the adsorbate because of the larger contribution of CH-species.

The important conclusion that we can draw from the above data is that measuring "isotherms" for the adsorption of the parent fuel is not likely to be very helpful in analyzing the kinetics of the reactions of the fuel.

Relation of adsorbed species to over-all reaction.—Earlier, we suggested that $HCOOH_{ads}$ is not HCOOH itself. An important reason for this suggestion was the observation that the oxidation current decreases as θ increases (1). Similarly, Giner (15, 18) has reported a decline in oxidation rate with time for a number of organic oxidations which he related to the accumulation of an adsorbed species. The frequently observed variations of oxidation rate with time seem to be the result of the accumulation of relatively refractory adsorbed species. Giner (15, 18) has suggested that this species is similar to "reduced CO_2" (12). The exact relationship of this species to the general mechanism of the oxidation of organic species must vary from compound-to-compound but its frequent presence is very suggestive. Two basically different mechanisms involving reduced CO_2 can be postulated, *e.g.*

$$\text{Fuel} \xrightarrow[\text{steps}]{\text{sequence of}} \text{reduced } CO_2 \xrightarrow{\text{slow}} CO_2 \quad [1]$$

$$\left.\begin{array}{l} \text{Fuel} \longrightarrow CO_2 \\ \downarrow \text{ "reduced } CO_2\text{"} \xrightarrow{\text{slow}} CO_2 \end{array}\right\} \quad [2]$$

In [2], the main reaction proceeds on that part of the surface not occupied by reduced CO_2; in [1], the oxidation of reduced CO_2 is the rate-limiting step. For HCOOH, at low E, [2] is probably applicable. For C_3H_8, [1] appears to be the mechanism [here we tentatively equate O-type material with reduced CO_2; more information on this point will be published later (14)].

The important conclusions we can draw from the above data are:

1. Simple current-potential curves should be interpreted with extreme caution and only in the context of adsorption data.
2. Application of isotherm theory is only of marginal relevance in these complex systems.
3. We must use experimental methods which can can give us information on the chemical composition of the adsorbates and on their relation to the original fuel and to the over-all reaction.

[1] $[e]$ is the number of electrons released per covered site when the adsorbate is completely oxidized to CO_2.

In these ways, we can expect to continue the significant improvement in our understanding of these complex reactions.

The author is pleased to acknowledge support by the U. S. Army Engineer Research and Development Laboratories, Fort Belvoir, Va.

REFERENCES

1. S. B. Brummer and A. C. Makrides, *J. Phys. Chem.*, **68**, 1448 (1964).
2. S. B. Brummer, *ibid.*, **69**, 562 (1965).
3. S. B. Brummer and J. I. Ford, *ibid.*, **69**, 1355 (1965).
4. S. B. Brummer, *ibid.*, **69**, 1363 (1965).
5. S. B. Brummer, J. I. Ford, and M. J. Turner, *ibid.*, **69**, 3424 (1965).
6. S. B. Brummer and M. J. Turner, "Hydrogen Fuel Cell Technology," p. 409, Academic Press, New York (1965).
7. M. Green and H. Dahms, *This Journal*, **110**, 466 (1963).
8. J. O'M. Bockris and D. A. J. Swinkels, *ibid.*, **111**, 736 (1964).
9. T. O. Pavela, *Ann. Acad. Sci. Fennicae, Ser. A.*, **2**, 59 (1954).
10. M. W. Breiter, *Electrochim. Acta*, **8**, 447 (1963).
11. S. Gilman, *J. Phys. Chem.*, **67**, 78 (1963).
12. J. Giner, *Electrochim. Acta*, **8**, 857 (1963).
13. See for example review by A. N. Frumkin, "Advances in Electrochemistry and Electrochemical Engineering," Vol. 3. John Wiley & Sons, Inc., New York (1963).
14. S. B. Brummer and M. J. Turner, In press.
15. J. Giner, *Electrochim. Acta*, **9**, 63 (1964).
16. O. A. Petry, B. I. Podlovchenko, A. N. Frumkin, and Hira Lal, *J. Electroanal. Chem.*, **10**, 253 (1965).
17. S. Gilman, *Trans. Faraday Soc.*, **61**, 2546 (1964).
18. J. Giner, Abstract at C. I. T. C. E. Meeting, London, 1964.

Discussion

M. W. Breiter: The conclusion that intermediates and not formic acid molecules are adsorbed on platinum in acidic solutions at room temperature appears very doubtful on the basis of my recent studies[1] in which small amounts of formic acid were quickly added to 1*M* $HClO_4$ at 0.2v under conditions such that only a small amount of intermediates can be formed anodically. At concentrations C $\geq$ 0.01*M* HCOOH the adsorbed amounts of formic acid agreed well with the corresponding amounts of previous measurements made under repetitive cycling between 0.05v and about 1.5v at 0.03 v/sec. Decomposition of formic acid molecules into intermediates and hydrogen atoms can be ruled out at 30°C on smooth platinum on the basis of the small rates observed by Giner[2] and Gottlieb[3] at room temperature. The question of the adsorbed intermediate is open in the more complex case of methanol. Our techniques do not allow us to distinguish between adsorbed species of a different nature and the same species adsorbed with different heats of adsorption on the heterogeneous platinum surfaces. The conclusions on the nature of the adsorbed species are mainly based on the interpretation of kinetic data, not on direct evidence.

S. B. Brummer: The experiment of Breiter[4] showed that at 0.2v, $HCOOH_{ads}$ could not simply be an intermediate of the oxidation reaction since too little charge apparently flowed after he introduced HCOOH into the solution. One possible alternative to his conclusion that $HCOOH_{ads}$ is HCOOH itself is the presence of reduction reactions to give an adsorbed species which is more reduced than HCOOH itself. Then, $i_{obs} = (i_a - i_c)$, where i_a is the current for oxidation (to CO_2) of HCOOH and i_c is the current for reduction of HCOOH to an adsorbed product. Then

$$Q_{obs} = \int (i_a - i_c)\, dt \qquad [1]$$

Such a process cannot be excluded on the basis of Breiter's data. Another possibility to obtain an adsorbed product which is not HCOOH itself is from the chemical decomposition of HCOOH on the electrode. Breiter rules this out on the basis of the HCOOH decomposition rate as reported by Gottlieb.[5] This rate, he says, is too slow, which indeed it is. However, this decomposition rate refers to a "poisoned" catalyst, *i.e.*, the Pt already has a full layer (about 0.75 of a monolayer[6]) of $HCOOH_{ads}$. The current for HCOOH oxidation decreases with increase in θ[6,4] and it seems extremely probable that the chemical decomposition rate is also much faster on a clean electrode, as used by Breiter.[7] Thus, the evidence is not conclusive.

The reasons for our view that $HCOOH_{ads}$ is not HCOOH are to some extent kinetic in origin. Thus i_a decreases with increase in θ.[6] Additional evidence on this point arises from the work of Giner[8,9] and also from our measurement of the charge to oxidize $HCOOH_{ads}$. We found[10] 285 μC/real cm^2, in good agreement with Breiter's own value.[11] This is too much to correspond to a close-packed monolayer of HCOOH (230 μC/real cm^2) and yet this material only occupies ~75% of the available surface. Incidentally, this species cannot be $COOH_{ads}$, which is sometimes suggested, since a compact monolayer of this material only provides 115 μC/real cm^2.

E. Gileadi: I would like to make two remarks to Dr. Brummer's presentation. First, I cannot agree with Dr. Brummer's point of view just made in his talk that the study of adsorption isotherms is useless. It is perhaps the most important single measurement one can make in adsorption studies and can lead to very valuable information regarding the state of the adsorbed species on the surface, its surface bond energy, and the type and magnitude of lateral interactions on the surface. In addition this kind of measurements can lead to better understanding of the anodic oxidation process involved, as has been demonstrated in the case of ethylene[12,13] and benzene.[14,15] It is clear, on the other hand, that adsorption isotherms can only be considered when the adsorption process is reversible. This was shown to be the case for ethylene[13] and benzene[15] which were studied in our laboratory. For

[1] M. Breiter, *Electrochim. Acta*, **10**, 503 (1965).

[2] J. Giner, *Electrochim. Acta*, **8**, 857 (1963); *ibid.*, **9**, 63 (1964).

[3] M. Gottlieb, *This Journal*, **111**, 465 (1964).

[4] M. W. Breiter, *Electrochim. Acta*, **10**, 503 (1965).

[5] M. H. Gottleib, *This Journal*, **111**, 465 (1964).

[6] S. B. Brummer and A. C. Makrides, *J. Phys. Chem.*, **68**, 1448 (1964).

[7] Incidentally, even without this consideration, it's doubtful if the rate of the reaction HCOOH $\rightarrow$ CO_2 + H_2 is germane to the identity of $HCOOH_{ads}$.

[8] J. Giner, *Electrochim. Acta*, **8**, 857 (1963).

[9] J. Giner, *Electrochim. Acta*, **9**, 63 (1964).

[10] S. B. Brummer, *J. Phys. Chem.*, **69**, 562 (1965).

[11] M. W. Breiter, *Electrochim. Acta*, **8**, 447 (1963).

[12] H. Wroblowa, B. J. Piersma, and J. O'M. Bockris, *J. Electroanal. Chem.*, **6**, 401 (1963).

[13] E. Gileadi, B. T. Rubin, and J. O'M. Bockris, *J. Phys. Chem.*, **69**, 3335 (1965).

[14] J. O'M. Bockris, H. Wroblowa, E. Gileadi, and B. J. Piersma, *Trans. Faraday Soc.*, **61**, 2531 (1965).

[15] W. Heiland, E. Gileadi, and J. O'M. Bockris, *J. Phys. Chem.*, **70**, 1207 (1966).

the system studies by Dr. Brummer, rapid surface reactions clearly occur and adsorption equilibrium is not maintained. An attempt to obtain adsorption isotherms for such a system would obviously be futile.

My second point refers to the need to study adsorption always by several methods. Here I am in complete agreement with Dr. Brummer. A comparative study of adsorption of several compounds by the radiotracer method and by two electrochemical methods is under way in our laboratory, and we hope to be able to report these results in the near future.

S. B. Brummer: I understand Dr. Gileadi's concern to elaborate the adsorption isotherm. My main point is that where the adsorbate is not chemically identical with the adsorbing fuel or where there is more than one adsorbate, this is not a particularly useful thing to do. In this instance, the main concern must be to find out the composition of the adsorbates, their distribution-with-potential and their relation to the overall reaction. This appears to be the approach which is most relevant to the study of the anodic reactions of organic fuels.

H. B. Urbach: I am in agreement with Dr. Brummer's observation in his talk that the adsorption isotherms of many molecules described in the literature have not taken into account the fact that a Faradaic current is generally present. This would indicate that the observed values of surface coverage represent a steady state rather than an equilibrium. I would like to propose the following quantitative relation (based on the assumption of a Langmuir isotherm) between the observed coverage, θ, the theoretical equilibrium value, θ_{eq}, and the current, i

$$\frac{\theta}{\theta_{eq}} = \left(1 - \frac{i}{i_L} - \frac{i}{i_A}\right)\left(1 - \theta_{eq}\frac{i}{i_L}\right)^{-1}$$

where i_L is the diffusion limited current and i_A is the adsorption limited current defined by

$$i_A = nFk_a a_o$$

where n is the number of electrons, F is the faraday, k_a is the adsorption rate and a_o is the bulk activity of the adsorbed species.

S. B. Brummer: The presence of faradaic current certainly does necessitate a correction to the concentration of the adsorbate at the electrode-solution interface. However, one must be cautious in the application of simple models to calculate the concentration of the electroactive species at the interface, since this frequently is not the original adsorbing material, but is the product of a (number of) irreversible surface reactions. In such a case, it would not be appropriate to derive a θ_{eq} from the observed θ and the faradaic current.

S. Schuldiner: An assumption is made that organic and H atom adsorption is additive to one monolayer. This does not take into account that both the adsorption and absorption of H atoms can be influenced by the presence of organic species.

S. B. Brummer: In analyzing the structure of the adsorbed species, we have made use of cathodic H-atom deposition and we have assumed that $\theta_{org} = 1 - \theta_H$. ($\theta_H$ is the fraction of H-atom deposition charge compared with an organic-free surface, and θ_{org} is defined as the fraction of the surface occupied by organic.) This procedure assumes:

(*a*) That the organic is not desorbed or reduced during the cathodic H-atom charging. Conditions can be chosen to ensure that these assumptions are true.

(*b*) That at finite θ_{org}, the only reason that θ_H is < 1 is because of site coverage by the organic. Thus we assume that the interaction energy (or whatever determines the fall of H-atom adsorption energy with increase in coverage) is similar in magnitude between H-organic as between H-H. This is of course not likely to be true in general. One factor which tends to help this to be more probable, *i.e.*, to ensure that all the surface not occupied by organic is charged with H-atoms during the charging process, is that in presence of organic the H_2-overvoltage is higher. This helps to deposit H-atoms on the organic-free surface, despite unfavorable energy considerations. In recent experiments, we have compared the values of θ_{org} obtained above with those obtained from anodic H-atom stripping. In the latter case, the effect of interactions would be more deleterious because the potential (say in the range $+0.03$ to $+0.1$v *vs.* R.H.E.) can be changed so as to alter the initial (organic-free) H-atom coverage considerably. We appear to get good ($< 10\%$) agreement for values of θ_{org} determined cathodically and those determined anodically from potentials where the H-atom coverage on a clean electrode is as low as 0.6 of a monolayer. This we regard as good evidence that in this case (C_3H_8 in H_3PO_4) the assumption of only steric hindrance is reasonable.

(*c*) The assumption that the surface of the Pt is just as much or as little receptive to H-adsorption is not necessary. We only assume that in the short time involved in the cathodic measurement the difference between the behaviors with or without the organic adsorbate is negligible. In experiments we have recently carried out with the adsorption of n-hexane, we find no difference whether or not we allowed the possibility of H-adsorption. Hence, in this case at least, this possibility does not have to be considered.

A. Reed and E. Yeager: We are attempting to use infrared attenuated total reflection methods to examine the adsorption of organic species from aqueous solutions on germanium. The intensity of the C-H stretching frequency ca. 2900 cm^{-1} is used as a measure of the amount of adsorption. Particular systems under study include the Tritons, octanol, and stearic acid. D_2O has been used as the solvent rather than H_2O since the O-H stretching frequency of ordinary water masks the C-H absorption band.

Several difficulties are involved in such studies. First is the difficulty of differentiating between optical absorption due to the adsorbed species and that due to species in the bulk solution. Another problem is the preparation of a clean, well-defined surface without destroying the optical quality of the germanium surface. Presently the method is limited by signal-to-noise ratio, but some improvement of this appears possible.

In the case of stearic acid, we have cast monolayer films on the germanium by a modified Langmuir-Blodgett technique. With the germanium plate in contact with solution containing negligible stearic acid, the monolayer spectrum is quite evident. Work is continuing in this area, and we hope to report data under controlled conditions in the near future.

Technical Notes

Effect of Polarization Field on Electroluminescence

S. Kawashima

Broadcasting Science Research Laboratories, Japan Broadcasting Corporation, Setagaya, Tokyo, Japan

Many investigations about brightness waves of electroluminescence (EL) have been published (1). Generally speaking, in the brightness waves produced by sinusoidal wave excitation, two emission peaks, primary and secondary, appear for each half-cycle of the applied voltage. Since their emission mechanisms are considered to be different (2), analyses of them are rather complicated.

On the other hand, in the case of excitation by using pulse voltage, emission peaks appear only at the rise and fall of the pulse voltage, and the secondary peak usually does not appear. Hence, analyses of the phenomena become rather easy. Nudelman and Matossi (3) observed the brightness waves of ZnS:Cu,Pb, separately, on blue and green emissions by using pulse voltage and analyzed the decay curve of the brightness waves. They concluded that the excitation process is due to inelastic collision of accelerated electrons with luminescence centers and that the green emission is due to the electronic transition via the conduction band, while the blue emission is due to the one within the luminescence centers. ,Briggs (4) observed the brightness waves of Zn(S, Se) phosphors, also separately on blue and red emissions, by the use of pulse voltage having pulse width of 2 to 40 μsec, and found that the voltage dependence of emission intensity can be expressed as $B = B_0 \exp(-C/V^{1/2})$ in the same way as in the case of sinusoidal voltage excitation. Tanaka (5) measured the brightness waves of ZnS:Cu, Pb phosphor by using a pulse voltage having very short rise and fall times. He found that the decay curve of the emission at the fall of pulse voltage follows bimolecular law and that the time constant of the decay curve increases with increase of temperature.

In the present work, build-up of brightness waves under excitation by pulse voltage superposed with d-c voltage were studied and compared with steady-state brightness waves.

Experimental Method

A ZnS:Cu,I phosphor which exhibits only blue emission and a ZnS:Cu,Al phosphor which exhibits only green emission were used in order to facilitate the analyses of the phenomena. A "vacuum type" EL cell using no embedding material was used lest errors be introduced. Namely, phosphor powders were coated on a metal plate electrode with alcohol, and then were dried. "Nesa" electrode was placed on the phosphor layer, and the cell was mounted in a vacuum chamber. Two sheets of Mylar film were inserted between the two electrodes and the phosphor layer to prevent the carrier injection from the electrodes.

The pulse generator used is capable of producing both a-c and d-c pulses. D-c pulse was obtained by cutting the a-c component with the diode. For superposition of d-c voltage on the pulse voltage, a battery was connected to the output of the pulse generator in series with the EL cell. This pulse generator can supply voltages of 1500 peak-to-peak volts (vpp) at maximum and of frequencies ranging from 50 to 10,000 pulse per second (pps). Both the rise and decay time of the pulse voltage were below 0.5 μsec even an EL cell of about 30 pF was loaded.

The light emitted from the EL cell was detected by means of a type 1P21 photomultiplier tube whose output was displayed on a Tektronix 545 oscilloscope coupled with dual-beam preamplifiers.

Results

1. Brightness waves are independent of whether the EL cell is operated by a-c pulse or d-c pulse. Further, in the case of excitation by pulse, sinusoidal and half-wave sinusoidal voltage, superposition of a d-c voltage on the exciting voltage does not affect the brightness wave.

In Fig. 1, the brightness wave produced by half-wave sinusoidal voltage is compared with that when positive or negative d-c voltage is superposed on it. The peak height of the half-wave voltage in this figure is about 500v and the superposed d-c voltage is 360v. It is interesting that there is almost no difference between these brightness waves, although the superposed d-c voltage is nearly the same order in magni-

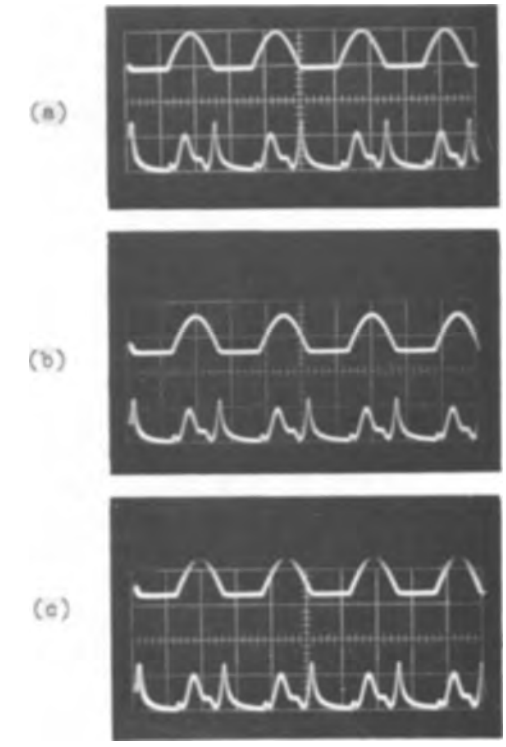

Fig. 1. Brightness waves under half-wave sinusoidal voltage. Frequency is 50 cps, phosphor used is ZnS:Cu,I. a (Top), no bias; b (center), negative bias; c (bottom), positive bias.

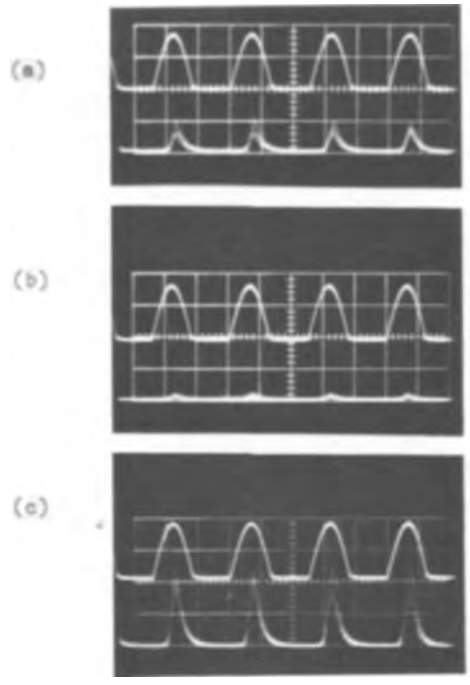

Fig. 2. Effects of superposed d-c voltage on the brightness waves of evaporated EL cell. Frequency of half-wave sinusoidal voltage is 150 cps and zero-to-peak voltage is about 180v. EL cell is made of evaporated ZnS:Mn thin film. a (Top), no bias; b (center) negative bias; c (bottom), positive bias.

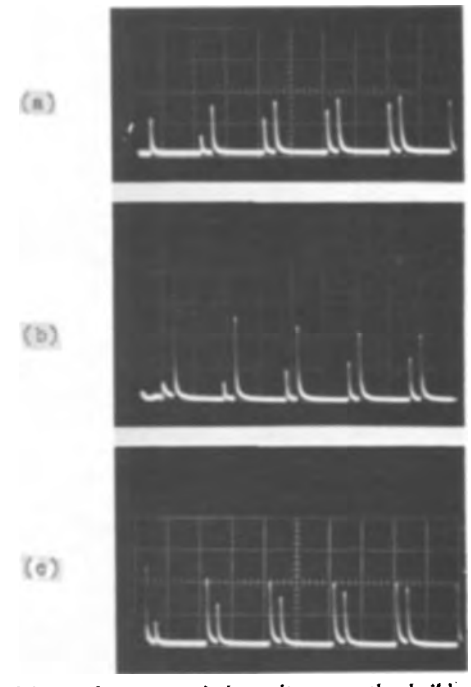

Fig. 3. Effects of superposed d-c voltage on the build-up characteristics. a (Top), no bias; b (center), negative bias on negative pulse; c (bottom), positive bias on negative pulse.

tude as the half-wave sinusoidal voltage and the shapes of these brightness waves are considerably complicated. It is inferred from this that an internal field, *i.e.*, a polarization field, which cancels the superposed d-c field, is set up in the phosphor crystal.

Brightness waves of an evaporated EL cell when excited by half-wave sinusoidal voltage are shown in Fig. 2. Here, as is clear from the figure, effects of the superposed d-c voltage are conspicuous. This EL cell was prepared by evaporating a ZnS:Mn phosphor in vacuum on a Nesa glass and by using aluminum as the metal electrode. Since the electrodes are in contact with the phosphor layer, it is expected that carrier injection from the electrodes takes place. Consequently, it is believed that brightness waves are greatly varied, because a polarization field large enough to cancel the superposed d-c field hardly grows up in this case.

2. Since the polarization field has not been set up in the EL cell or in the phosphor particles before the field application, it is expected that unusual phenomena may be found in the build-up of the brightness wave, as the build-up process of such a polarization field proceeds. Then, the build-up characteristics of the brightness wave were measured by using a pulse voltage superposed with a positive or negative d-c voltage. Frequency of the pulse voltage was 1000 pps, pulse width was 200 μsec, and the polarity of the pulse voltage was negative in all cases. Pulse voltage of 600 vpp was applied to the EL cell of about 100μ in thickness. D-c voltage superposed was +1000 or −1000v. Since the build-up of brightness wave is very sensitive to the historical state of the EL cell, the irradiation of infrared light was given to the cell in all cases before the field application so as to prevent the fluctuation of results.

The experimental results are given in Fig. 3. Let the emission peaks corresponding to the rise and fall of the pulse voltage be denoted by P_r and P_f, respectively. In general, when the EL cell was excited by the pulse voltage having a pulse width much shorter than the pulse-off period, the height of P_r was slightly smaller than that of P_f. In the case of d-c pulse excitation, both P_r and P_f increase gradually and approach the steady-state height. However, when a negative voltage of the same polarity as that of the pulse voltage is superposed, P_f is very large from the outset and then decreases gradually to the steady-state height, while P_r increases gradually. The opposite is the case with the superposition of a positive d-c voltage.

These facts show that the excitation due to the polarization field must be taking place, and that the transient process in which the polarization reaches the steady state corresponds to the bulid-up of the brightness wave.

3. The polarization field observed in the above experiments is not attributable to Mylar films used for electrical insulation. In order to ascertain this, similar experiments were performed by using pulse voltage of frequency 100 pps. It was found that the brightness wave reaches steady state within nearly a same number of cycles of the applied voltage as in the case of 1000 pps. If a polarization field is set up in Mylar film, it is expected that the brightness wave reaches steady state after a fixed period determined by the capacitance of the Mylar film. Consequently, it is concluded that the polarization field is set up within each phosphor particle.

Discussion

Experimental results described in the previous section provide a clear evidence for the new model of EL proposed by Fischer (6), that the excitation due to polarization field takes place during the EL process. That the delayed emission mechanism proposed by Zalm (7) takes place in this "vacuum"-type EL cell could be easily ascertained by the experiment using a sinusoidal voltage superposed with a short pulse voltage on it. Consequently, P_f of the brightness wave under a d-c pulse excitation corresponds to the emission from the region that has been previously excited at the rise of the pulse voltage, while P_r corresponds to the emission from the region that has been excited at the fall of the pulse voltage. Hence, it is concluded that the excitation due to the polarization field takes place at the fall of the d-c pulse voltage in almost the same degree as that due to the applied field. The re-

sult of experiment 3 also supports this inference and shows that the polarization field is set up within each phosphor particle. Therefore, the excitation and emission process in the case of d-c pulse excitation, can be interpreted in the following way. At field application, carrier generation from conducting lines within the crystal (6) or impact ionization at a local high field region (8) occurs. Generated free electrons are swept toward the positive electrode side and recombine with luminescence centers which have been produced at previous excitation process, giving rise to the emission peak corresponding to P_r while generated holes are rapidly trapped in unexcited luminescence centers and ionize them. As this process proceeds, a polarization field due to the ionized luminescence centers and excess electrons which have been swept to the positive electrode side and trapped there, grow up so as to be large enough to cancel the applied field.

At field removal, excitation process due to this polarization field occurs in almost the same degree of magnitude as that due to the applied field, giving rise to the light pulse corresponding to P_f.

On the other hand, in the case of a-c pulse and superposition of a d-c voltage, the polarization field is considered to be set up so that the applied field at an instant just before the field reversal is almost canceled in the steady state. Therefore, since the excitation at the field application and reversal are both nearly equal in magnitude to that due to the applied peak-to-peak voltage, light peaks P_r and P_f in these cases are considered to be the same in shapes and heights as those in the case of d-c pulse excitation, respectively.

Experimental results that steady state brightness waves produced by using sinusoidal and half-wave sinusoidal voltage are not affected by the superposition of a d-c voltage on the exciting voltage, are also explained in a similar way.

Experimental result shown in Fig. 3 can be interpreted by considering build-up of the polarization field. When a negative d-c voltage is superposed on a negative pulse voltage, the intense negative field is applied at the initial rise of the negative pulse voltage, giving a strong excitation. Consequently, the light peak at initial fall of the pulse voltage is large. Since a polarization field is built-up gradually, P_f at the fall of the successive pulses become small in height and approach steady-state height. On the other hand, when a positive high field is superposed on the negative pulse voltage, excitation at the fall of the pulse voltage is more intense than that at the rise, during the first several pulses. Hence, it is understandable that light peaks at the rise of the first several pulses are large in height and decrease to the steady-state height.

Manuscript received Jan. 4, 1966; revised manuscript received May 3, 1966.

Any discussion of this paper will appear in a Discussion Section to be published in the June 1967 JOURNAL.

REFERENCES

1. J. F. Waymouth, *Phys. Rev.*, **95**, 941 (1954); F. E. Morehead, *This Journal*, **105**, 461 (1958); D. R. Frankl, *Phys. Rev.*, **111**, 1540 (1958).
2. C. H. Haake, *J. Appl. Phys.*, **28**, 117 (1957).
3. S. Nudelman and F. Matossi, *This Journal*, **101**, 546 (1954).
4. G. R. Briggs, *Bull. Amer. Phys. Soc.*, **2**, 155 (1958).
5. S. Tanaka, *J. Phys. Soc. Japan*, **14**, 1123 (1959).
6. A. G. Fischer, *This Journal*, **110**, 733 (1963).
7. P. Zalm, *Philips Research Repts.*, **11**, 353 (1956).
8. W. Lehmann, *This Journal*, **104**, 45 (1957); K. Maeda, *J. Phys. Soc. Japan*, **15**, 205 (1960).

The Chemical Polishing of Single Crystal α-Alumina Using Silicon

J. D. Filby

Royal Radar Establishment, Malvern, Worcestershire, England

Epitaxial layers of silicon grown on single crystal alumina promise to be very useful for electronic devices. Details have been published of the preparation of these layers by either the hydrogen reduction of silicon tetrachloride (1, 2), or trichlorosilane (3, 4), or the pyrolysis of silane (2-4). The alumina substrates are normally prepared by mechanically polishing down to $< 1\mu$ diamond grade followed by a chemical polish to remove the mechanically damaged layer. A variety of chemical polishes have been used, the most common being based on either orthophosphoric acid, lead fluoride, or sodium borate. The resultant surface finish however is not usually of a very high standard, an orange-peel effect often being obtained as well as occasional small etch pits or facets. In addition the removal of the last traces of some of the polishing mediums from the substrate surface is difficult.

The work of Reynolds and Elliott (5) at the Post Office Research Station on the vacuum deposition of silicon on single crystal alumina suggests that it might be possible to polish chemically the alumina with silicon. This technique would have the advantage that polishing could be carried out in the silicon deposition apparatus thus eliminating contamination by residue from other chemical polishes or by handling between the polishing and deposition processes.

An investigation into the feasibility of such a polishing process has been carried out using silane diluted with hydrogen in a system operating at approximately atmospheric pressure. The apparatus essentially consisted of a water-cooled vertical quartz reaction chamber connected via suitable valves and flowmeters, to sources of high purity hydrogen and a 3% silane in hydrogen mixture. The system could be evacuated to 10^{-4} mm Hg. The alumina substrates were cut on the $(1\bar{1}02)$ or $(2\bar{1}\bar{1}3)$ planes from single crystal boules grown by the Verneuil process. They were mechanically polished down to 20μ diamond grade before placing on a susceptor in the reaction chamber. The original susceptor was made of silicon and induction heated. It contained a vitreous carbon insert to assist in the initial coupling.

Figure 1 is a micrograph of the $(1\bar{1}02)$ surface of alumina after heating at 1240°C for 30 min in a flow of 20 liters/min hydrogen and 25 cc/min of 3% SiH_4/H_2 mixture. The surface is very uneven consisting mainly of a large number of very shallow pits each associated with a globule. The globules were obviously molten at the operating temperature and therefore cannot consist entirely of silicon. Microprobe x-ray analysis has shown that in addition to silicon the globules contain an appreciable amount of aluminum. This explains how they could be molten at 1240°C as silicon-aluminum alloys can have a melting point as low as 577°C.

It has been previously suggested (1) that alumina can be etched by silicon at elevated temperatures according to the reaction

Fig. 1. Silicon-aluminum alloy globules and associated etch pits on a $(1\bar{1}02)$ alumina surface.

Fig. 2. Tracks left on the $(1\bar{1}02)$ alumina surface by migrating alloy droplets.

$$2Si + Al_2O_3 \xrightarrow{H_2} 2SiO\ (g) + Al_2O\ (g)$$

The above result indicates that, if the attack is severe enough, in addition to these two volatile compounds some free aluminum is also obtained. The exact mechanism for the formation of the free aluminum is doubtful. The reduction of alumina by silicon to form aluminum is thermodynamically unfavorable at 1240°C. However such thermodynamical calculations assume equilibrium conditions whereas the present reaction takes place in a flow system under conditions far removed from equilibrium.

The existence of silicon/aluminum globules on the alumina surface is obviously detrimental to obtaining a smooth finish. This is due to the enhanced etching rate of the alloy compared to pure silicon which results in pits if the globules are stationary and tracks, Fig. 2, if they are mobile on the substrate surface. This is not the first time that rapid attack of alumina by a silicon alloy has been observed. It has previously been reported (6) that silicon/gold alloys etch alumina at temperatures as low as 750°C.

To avoid the formation of alloy droplets the silane concentration in the gas flow was reduced. Figure 3 is a micrograph of the surface of a substrate after 20 min in a gas flow containing 10 cc/min of 3% SiH_4/H_2 mixture, other conditions were similar to those for the previous sample. The attack was now fairly uniform, and no alloy droplets were observed. However, the etching rate was very slow, only 2μ of material being removed in 20 min, and traces of scratches left by the 20μ diamond grade are still clearly visible.

To obtain more reasonable polishing rates higher temperatures were indicated and so the silicon susceptor was replaced by one of high purity graphite.

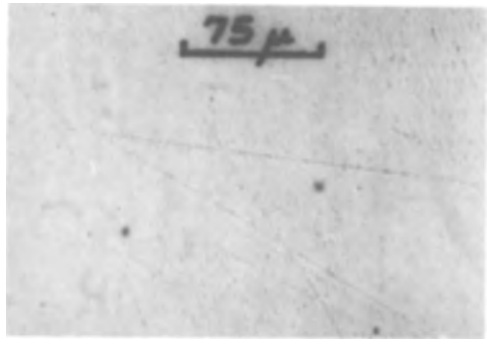

Fig. 3. Partially polished $(1\bar{1}02)$ alumina surface. Remains of mechanical scratches still visible.

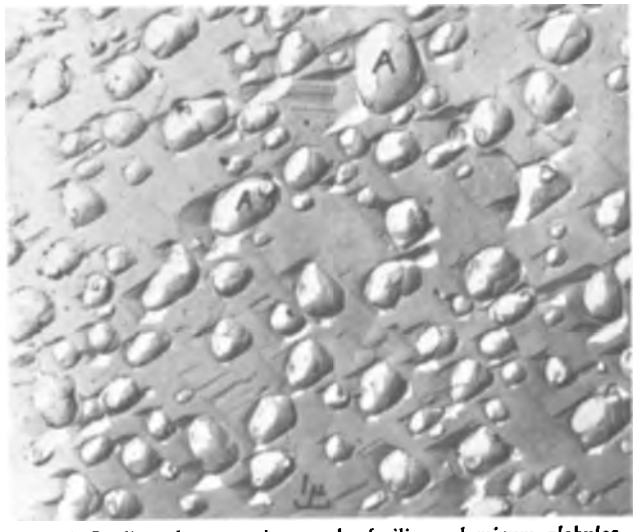

Fig. 4. Replica electron micrograph of silicon-aluminum globules, A, and etch pits on $(2\bar{1}\bar{1}3)$ alumina surface.

Fig. 5. Replica electron micrograph of etch pits on $(2\bar{1}\bar{1}3)$ alumina surface after alloy globules have been removed.

Figures 4-6 are replica electron micrographs of the $(2\bar{1}\bar{1}3)$ surfaces of two alumina samples which were etched by silicon at 1370°C for 8 min in a gas flow of 40 liters/min H_2 and 100 cc/min 3% SiH_4/H_2. The sample in Fig. 5 and 6 was subsequently heated *in situ* at 1250°C in a hydrogen flow of 20 liters/min for 20 min.

The surfaces of both these samples were sufficiently polished to remove the scratches left by the mechani-

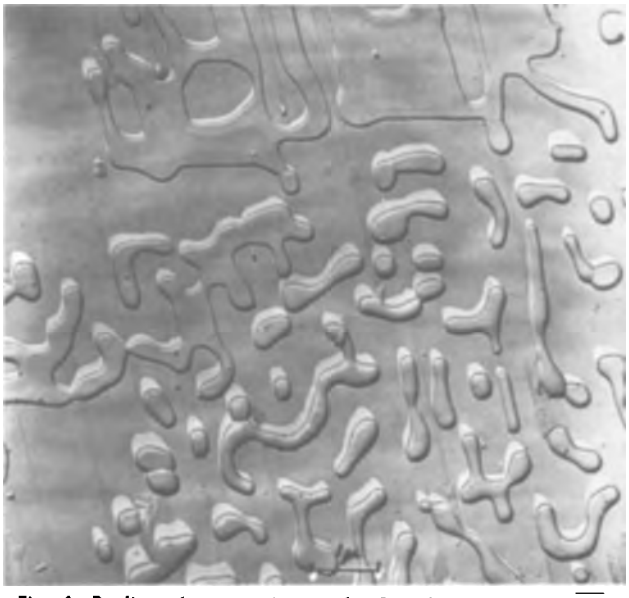

Fig. 6. Replica electron micrograph of etch figures on $(2\bar{1}\bar{1}3)$ alumina surface.

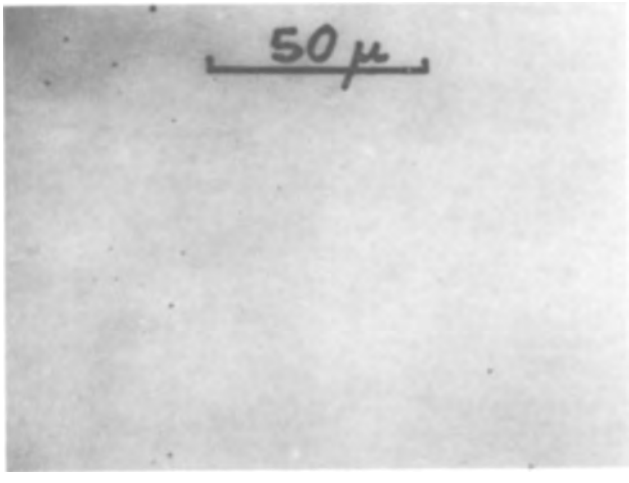

Fig. 7. Surface of $(1\bar{1}02)$ alumina polished with silicon at 1380°C

cal polishing. However small silicon/aluminum globules, approximately 1μ diameter, were obtained, and these had etched small pits. Fig. 4, which they almost fill. These alloy droplets were easily removed by the treatment described above of heating the substrate in hydrogen only. Auxiliary experiments have shown that during the removal of the droplets by this process any etching of the alumina surface is confined to the regions beneath the globules.

It is now possible to see the shape of the etch pits in more detail, Fig. 5. The sides are smooth and inclined at an angle of approximately 4° to the $(2\bar{1}\bar{1}3)$ substrate surface. They must therefore correspond to high index crystallographic planes. The fact that the pit sides are faceted in this manner and that the globules all penetrate the substrate in the same crystallographic direction indicates that the etching rate of the alloy is orientation dependent.

Figure 6 is a replica electron micrograph of another area of the surface shown in Fig. 5. In this region globules have not been formed and the etch figures consist of flat bottomed regions which have undergone uniform attack. A large proportion of the edges of these etched regions are approximately aligned along the same crystallographic directions as those traced by the intersection of the $(2\bar{1}\bar{1}3)$ alumina surface and the etch pit facets in Fig. 5. As the etched areas in Fig. 6 are all of similar depth, ~ 800Å, a continuation of the etching process should result in the removal of a uniform layer, *i.e.*, a polished surface should be obtained. The presence of alloy globules on another part of this sample indicates, however, that the silane concentration in the gas stream is still slightly too high.

A uniformly polished surface was obtained on $(1\bar{1}02)$ alumina at 1380°C using a gas flow of 20 liters/min of H_2 and 50 cc/min of 3% SiH_4/H_2. Figure 7 shows the completely featureless surface obtained over a wide area after polishing for 17 min. Examination by replica electron microscopy also failed to reveal any surface imperfections. Under the above conditions the alumina was removed at a rate of ½ μ/min.

This investigation has demonstrated that it is possible to polish chemically single crystal alumina using only the gases normally present in the silicon deposition plant. The presence of a graphite susceptor, necessary in this work to obtain the high substrate temperature (~ 1400°C) required for polishing, would not be satisfactory for the subsequent process of depositing the single crystal silicon layer on the alumina. This difficulty may be overcome by using a silicon carbide coated graphite susceptor which is compatible with both the high temperature and purity requirements. A silicon or silicon coated graphite susceptor could still be used if a very slow polishing rate was acceptable. This could be the case if the bulk of the polishing were done by the chemical techniques at present in use and the above technique was used only as a final cleaning and polishing procedure in the deposition plant.

Acknowledgments

The author gratefully acknowledges the expert assistance of D. G. Coates and P. J. Born for the electron micrographs and x-ray microanalysis results. British Crown Copyright. Reproduced with permission of the Controller, Her Britannic Majesty's Stationery Office.

Manuscript received June 6, 1966.

Any discussion of this paper will appear in a Discussion Section to be published in the June 1967 JOURNAL.

REFERENCES

1. H. M. Manasevit and W. I. Simpson, *J. Appl. Phys.*, **35**, 1349 (1964).
2. H. M. Manasevit, A. Miller, F. Morritz, and R. Nolder, *Trans. A.I.M.E.*, **233**, 540 (1965).
3. B. A. Joyce, R. J. Bennett, R. W. Bicknell, and P. J. Etter, *ibid.*, **233**, 556 (1965)
4. J. L. Porter and R. G. Wolfson, *J. Appl. Phys.*, **36**, 2746 (1965).
5. F. H. Reynolds and A. B. M. Elliot, *Phil. Mag.*, **13**, 1073 (1966).
6. J. D. Filby and S. Nielsen, Third International Vacuum Congress, Stuttgart, June 1965.

Preparation of GaAs Specimens for Transmission Electron Microscopy

E. Biedermann and K. Brack

IBM Deutschland, IBM Laboratories, Boeblingen, Germany

The thinning of semiconductor specimens for transmission electron microscopy by the well-known jet etch technique (1, 2) requires special etching solutions for each material in order to obtain satisfactorily clean and smooth crystal surfaces. In the following note, we report on difficulties and results that were obtained in the preparation of GaAs specimens with different etching solutions.

Experimental

The apparatus we used is essentially identical to that of ref. (1). The GaAs specimens were [111]-oriented crystal wafers with a diameter of 3 mm and a thickness of 0.3 mm. Two different etching solutions have been used:

1. NaOCl-H_2O solution (ratio 1:5) at 80°C. (This solution is commonly used in GaAs device fabrication for chemical surface polishing.)
2. HCl-H_2O_2-H_2O solution (ratio 40:4:1) at 20°C.

Both solutions had been found to fulfill the basic requirements of giving reasonable etching rates of a few microns per minute on both the As and the Ga-sides of the specimens, at the same time yielding optically smooth and clean surfaces on both crystal faces.

Results and Discussion

In Fig. 1 and 2 transmission electron micrographs are shown of GaAs specimens prepared with etching solution 1 and 2, respectively. The microscope used is a Siemens Elmiscope I. The typical difference between the two preparation methods is evident. With solution 1 (Fig. 1) a coarse grainy structure appears all over the crystal which at first sight might be attributed to a high concentration of small precipitation particles. With solution 2, however, the crystals appear clear and almost faultless. Only a few of the familiar crystal defects, dislocations and stacking faults are found (shown in Fig. 2).

We conclude, therefore, that the grainy structure of Fig. 1 is not an intrinsic property of the GaAs crystal. It must, instead, be caused by the reaction of solution 1 with the GaAs surface. Our efforts to obtain more information on a possible surface layer by transmission electron diffraction, however, failed. No reflexes besides those of the GaAs crystal could be found. Thus, we are presently not in a position to give a detailed interpretation of the observed transmission contrast in Fig. 1. For the preparation of transmission specimens of GaAs, however, only solution 2 can be recommended.

Acknowledgments

The authors wish to thank Miss Heide Winkler for her capable assistance in preparation and electron microscopy.

Manuscript received April 25, 1966; revised manuscript received July 9, 1966.

Any discussion of this paper will appear in a Discussion Section to be published in the June 1967 JOURNAL.

REFERENCES

1. G. R. Booker and R. Stickler, *Brit. J. Appl. Phys.*, **13**, 446 (1962).
2. E. S. Meieran, *J. Appl. Phys.*, **36**, 2544 (1965).

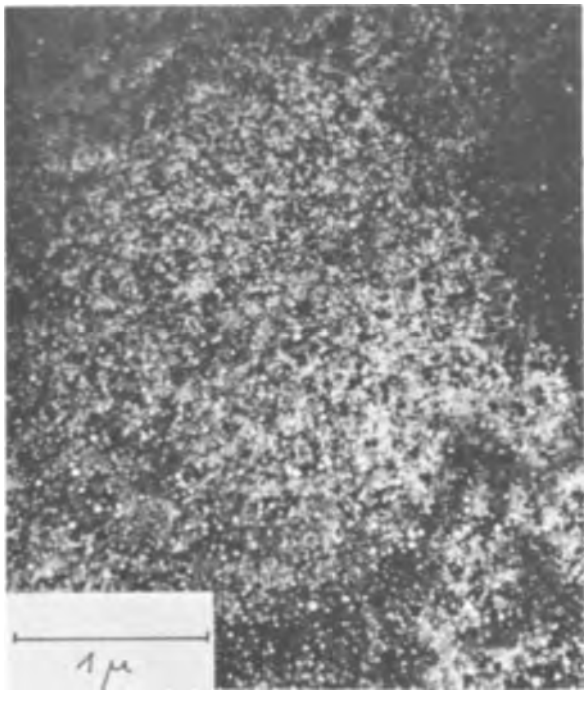

Fig. 1. Electron transmission micrograph of a GaAs sample thinned down with NaOCl + H_2O. The grainy structure is produced by the NaOCl etch.

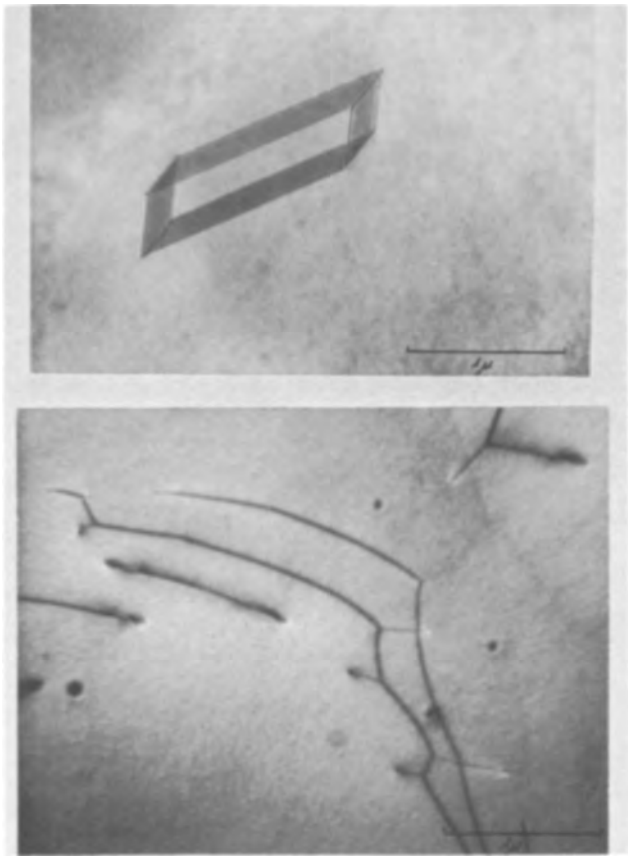

Fig. 2. Electron transmission micrographs of HCl-H_2O_2-H_2O etched GaAs samples. Usual crystal defects are shown (compare Fig. 1).

The Vapor Pressures of Titanium Tetrabromide and Chromium Carbonyl

A. A. Boni

Department of the Aerospace and Mechanical Engineering Sciences, University of California, San Diego, La Jolla, California

For $TiBr_4$ solid-gas equilibrium, three independent results have been previously published (1-3). The results of Hall *et al.* (1) are lower than the results of Seki (2) by approximately one order of magnitude, but agree well with the data of Keavney and Smith (3). Furthermore, the heats of sublimation were found to be 16.2, 12.15, and 16.17 kcal/mole, respectively. The data of Seki (4) were obtained by the use of a glass spring manometer and those of Keavney and Smith (3) with a manometer utilizing mineral oil as the working fluid. The results of Hall *et al.* (1), however, were derived from measurements made on liquid titanium tetrabromide together with the heat of fusion and ΔC_p for the sublimation process.

The solid-gas equilibrium vapor pressure of chromium carbonyl has been obtained by Wilkerson (5) and by Hieber *et al.* (6). These results are in complete agreement, but differ considerably from those of Windsor and Blanchard (7).

Experimental

We have measured the equilibrium vapor pressure above $TiBr_4$ and $Cr(CO)_6$ by using a precision fused quartz-spiral, bourdon-tube gauge which is sold commercially by the Texas Instruments Company (Model No. 140A). The vapor pressure of the sample was determined by measuring the rotation of the bourdon tube from its equilibrium position due to the pressure of the vapor. The equilibrium position is defined by a zero pressure difference between the inside of the tube and the exterior environment, which was evacuated in order to provide a constant absolute reference pressure. The angular deflection of the tube is determined by the unbalance of a pair of photocells which were previously aligned in the equilibrium position. The quoted accuracy of the gauge is 0.003 mm Hg minimum resolution and 0.006 mm Hg repeatibility. In order to determine the pressure-rotation curve of the bourdon-tube, a McLeod gauge was used. The system was completely evacuated to a pressure level of less than 10^{-4} mm Hg for a period of several days. A small quantity of dry argon gas was admitted to the system and the pressure was read with the McLeod gauge. The system was then reevacuated and filled again in order to obtain calibration curve over the pressure range from 10^{-3} to 10 mm Hg.

The bourdon tube was connected to a sample reservoir and the vacuum pumping system through an all-glass apparatus. Pump oil from the diffusion pump was prevented from backstreaming into the system by using a liquid nitrogen cold trap. When a vapor pressure measurement was made, the cold trap was excluded from the system in order to prevent condensation of the sample vapor. The complete system was checked for leaks with a helium leak detector and the leak rate was found to be less than 1×10^{-9} scc/sec of helium, which was quite acceptable for the purposes of our measurements.

The test crystals were transferred from sealed glass ampoules in which they were received into glass sample reservoirs in a dry box which was filled with dry argon in order to prevent contamination of the sample. The purity of these samples was guaranteed by the respective manufacturers to be a minimum of 99.5%. The sample reservoir was surrounded with dry ice while still in the inert atmosphere and was then rapidly attached to the test apparatus. The test apparatus itself had been evacuated overnight to a pressure level of less than 10^{-4} mm Hg. The sample reservoir was evacuated for a period of several hours while maintaining the dry-ice bath. The dry-ice bath was then removed, and for a period of one day the crystals were distilled under vacuum into another sample reservoir which was connected to the remainder of the system. The rejected parts of the sample were then sealed off.

In order to obtain data at temperatures both above and below room temperature, the reservoir containing the test sample was surrounded by a water bath. The bath was heated with a standard electric heating unit, the heat input of which was controlled by a mercury thermoregulator. Low temperatures were attained by using an ice bath. Uniform composition of the water bath was maintained by using an electrical stirring unit, and the temperature was measured with an iron-constantan thermocouple. This system was capable of achieving over-all temperature control to within $\pm$ 0.3°C.

All portions of the system which were not in contact with the constant temperature bath were wrapped with electrical heating tape and heated to a temperature larger than the heat bath temperature at which the measurement was made in order to prevent condensation of the sample vapor in the system. The quartz bourdon tube itself was heated with a thermostat-controlled heating unit which is built into the instrument.

Table I. Vapor pressure of titanium tetrabromide

Temperature, °K	Pressure, mm Hg	$(\log P)_{obs} - (\log P)_{calc}$*
275.3	0.0130	+0.008
276.2	0.0143	+0.005
277.5	0.0156	−0.016
278.3	0.0182	+0.013
280.4	0.0221	0.000
283.9	0.0312	−0.009
290.8	0.0677	+0.024
291.8	0.0703	−0.003
294.8	0.0990	+0.017
296.6	0.1120	0.000
298.2	0.1330	+0.008
307.6	0.2820	−0.003
311.2	0.4030	−0.020

* Calculated from Eq. [2].

Table II. Vapor pressure of chromium carbonyl

Temperature, °K	Pressure, mm Hg	$(\log P)_{obs} - (\log P)_{calc}$*
274.0	0.0130	+0.007
277.2	0.0182	−0.004
287.2	0.0547	+0.004
293.0	0.1040	+0.020
294.7	0.1198	+0.013
301.7	0.2180	−0.021
310.7	0.5030	−0.006

* Calculated from Eq. [3].

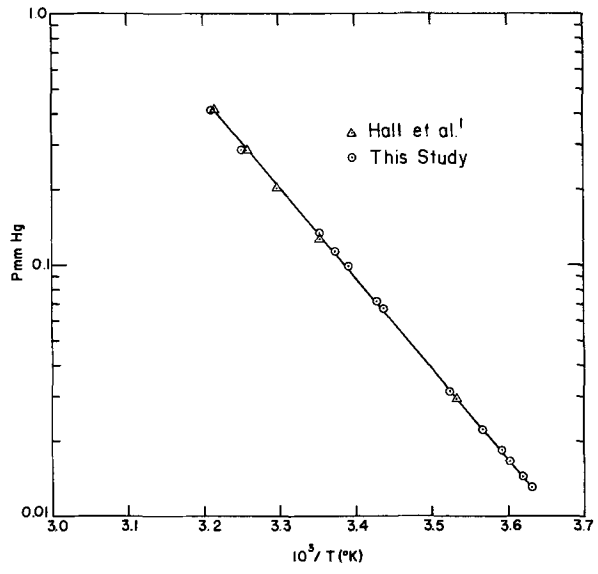

Fig. 1. Vapor pressure of titanium tetrabromide

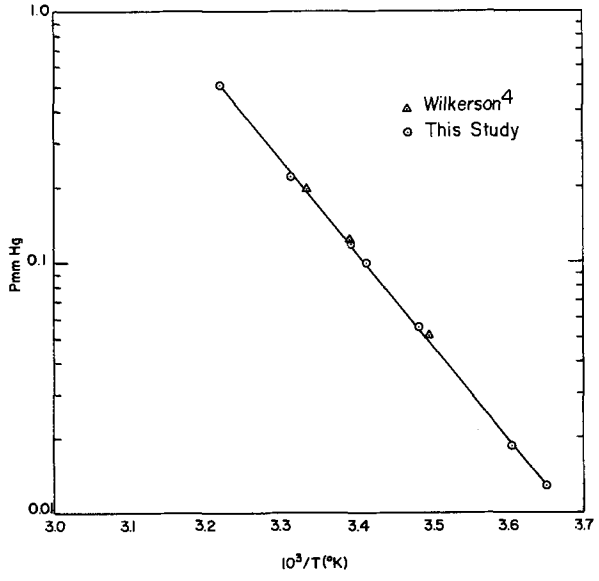

Fig. 2. Vapor pressure of chromium carbonyl

Results

The experimental data are presented in Tables I and II and plotted in Fig. 1 and 2. The heat of sublimation may be obtained from these data by integrating the Clausius-Clapeyron equation relating the equilibrium properties of the solid to those of the equilibrium vapor. After integration, a relationship of the following form is obtained

$$4.575 \log_{10} p = -(\Delta H/T) + B \qquad [1]$$

Results for $TiBr_4$.—A least squares fit of our data (see Table I) results in the following expression for the vapor pressure of $TiBr_4$

$$\log_{10} p \text{ (mm Hg)} = -(3621/T) + 11.26 \qquad [2]$$

Thus we find for the heat of sublimation, ΔH, the value 16,570 ± 200 cal/mole. We may compare this with that obtained in ref. (1) by using their vapor pressure equation to calculate a heat of sublimation corresponding to a temperature in the middle of the range reported in this study, *e.g.*, 293°K. This results in a value of 16,240 cal/mole. Thus, we are in good agreement with the results of Hall *et al.* (1).

Results for $Cr(CO)_6$.—For $Cr(CO)_6$, we obtained the relation

$$\log_{10} p \text{ (mm Hg)} = -(3737.7/T) + 11.750 \qquad [3]$$

Therefore, our value for the heat of sublimation is 17,092 ± 200 cal/mole, which is in good agreement with Wilkerson's estimate of 17,200 cal/mole and 17,180 cal/mole as reported by Hieber *et al.*

Acknowledgment

The author wishes to acknowledge helpful discussions with S. S. Penner and K. G. P. Sulzmann during the course of this study. This research was supported by the Advanced Research Projects Agency (Project DEFENDER) under Contract No. DA-31-124-ARO-D-257, monitored by the U.S. Army Research Office-Durham; IRPA Report No. 66-70.

Manuscript received April 11, 1966; revised manuscript received July 5, 1966.

Any discussion of this paper will appear in a Discussion Section to be published in the June 1967 JOURNAL.

REFERENCES

1. E. H. Hall, J. M. Blocher, Jr., and I. E. Campbell, *This Journal*, **105**, 271 (1958).
2. S. Seki, *J. Chem. Soc. Japan*, **62**, 581 (1941).
3. J. J. Keavney and N. O. Smith, *J. Phys. Chem.*, **64**, 737 (1960).
4. I. Nitta and S. Seki, *J. Chem. Soc. Japan*, **62**, 581 (1941).
5. T. Wilkerson, The University of Michigan, ORA Report No. 02822-3T, AFOSR 1151 (1961); Ph.D. Thesis (1961).
6. W. Hieber and E. Romberg, *Z. anorg. u. allgem. Chem.*, **221**, 332 (1935).
7. M. M. Windsor and A. A. Blanchard, *J. Am. Chem. Soc.*, **56**, 823 (1934).

Brief Communication

Selected Area Deposition of Single Crystal Silicon on Amorphous Quartz

J. D. Filby and S. Nielsen

Royal Radar Establishment, Malvern, England

The authors recently reported progress toward the deposition of single crystal layers of silicon on amorphous quartz (1), showing that crystallites as large as 300μ in diameter could be achieved using an ultrathin layer of alloy (2), a variation of the V.L.S. process (3). In this work silicon was sublimed or evaporated on to a quartz substrate held at a temperature between 700° and 800°C. Immediately prior to the deposition of the silicon, the quartz surface was washed and degreased and coated with a layer of gold 1-2000Å thick. It was proposed that the gold produced an ultrathin gold-silicon alloy layer over the substrate surface and that this alloy layer influenced the nucleation and growth of the silicon, thus enabling the large crystallites to be formed. Further progress is now reported which enables single crystal regions of silicon to be deposited on preselected areas of the amorphous quartz.

It was first noticed that a selected area deposition on the quartz surface was often obtained accidentally (*e.g.*, Fig. 1). It was thought that this was caused by preferential deposition in a groove or depression on the quartz surface. Certainly preferential deposition was observed in artificially induced grooves, but the effect was not reproducible.

Experiments using ultrathin silicon-gold alloy layers have shown that the alloy attacks most substrates, including sapphire (4), magnesium oxide, quartz, tantalum pentoxide, and silicon nitride. The attack can remove a considerable thickness of the substrate and, since silicon takes part in the attack, very little deposition of silicon is obtained. This suggests that, if it is possible to prevent the attack in selected areas, preferential deposition could be obtained in those areas. One possible technique for protecting the quartz is to evaporate on it a metal which does not alloy with either silicon or gold below 1000°C. Two suitable metals are tantalum and tungsten and areas of these, 25μ square, were evaporated on to amorphous quartz substrates using electron microscope grids as masks. The evaporation took place in a conventional mercury pumped system at a pressure of $\sim 10^{-5}$ mm Hg using a Varian e-gun evaporation source. A 1000Å thick layer of gold was then evaporated over the entire substrate surface from a resistance-heated tantalum boat. Finally the substrate was transferred to a sublimation apparatus (5) where silicon was sublimed on to it at the rate of 1 μ/hr, the substrate temperature being in the range 850°-950°C.

Tantalum was used as the protective metal for the sample shown in Fig. 2. The only deposit between the protected areas consists of solidified silicon-gold alloy, whereas each of the tantalum areas is covered by a layer of silicon approximately 5μ thick. The silicon layers sit on top of quartz mesas, approximately 2μ

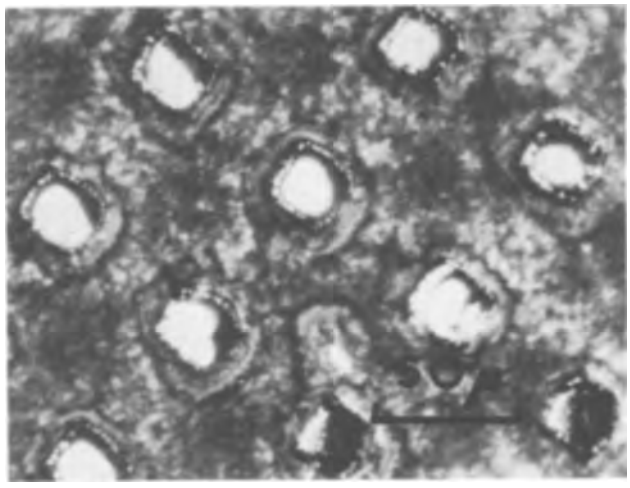

Fig. 2. Single crystal silicon areas deposited on amorphous quartz in regions preselected by covering with a tantalum film.

Fig. 1. Single crystal silicon grown in a groove on amorphous quartz

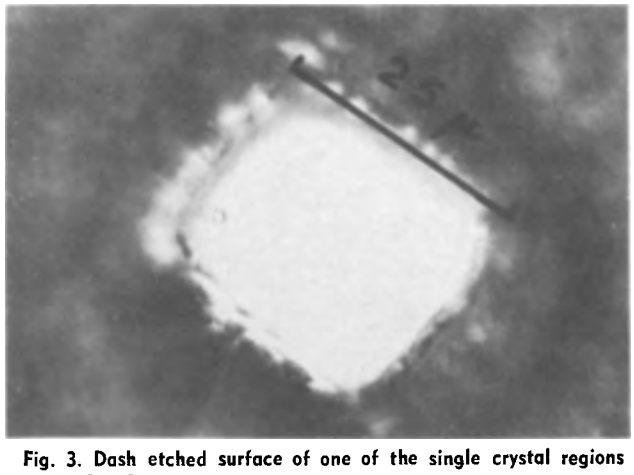

Fig. 3. Dash etched surface of one of the single crystal regions shown in Fig. 2.

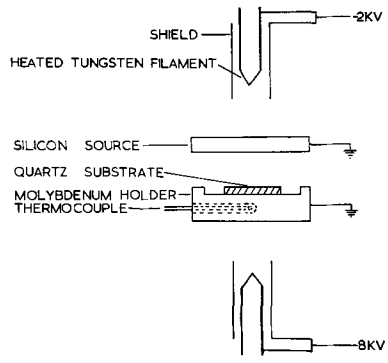

Fig. 4. Schematic diagram of evaporation apparatus

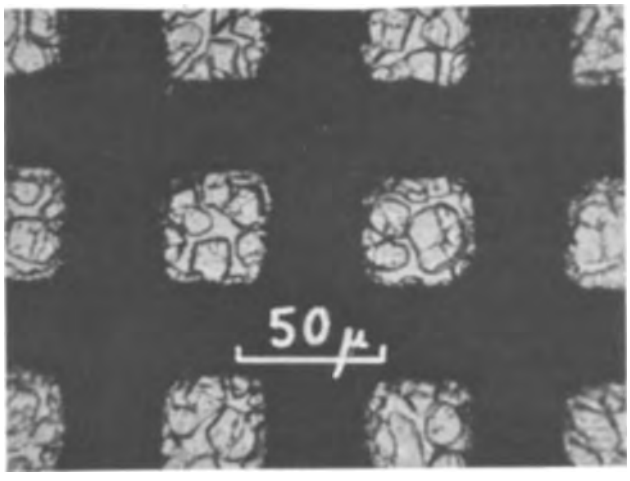

Fig. 5. Early stage of growth on tantalum protected regions of polycrystalline silicon layer obtained by evaporation.

high, created by the etching of the unprotected quartz during the deposition process.

Examination of the silicon areas to ascertain whether they were single crystal was difficult. They were too small to examine individually by electron or x-ray reflection diffraction techniques, and electron transmission studies were complicated by the necessity to hold and thin these small areas. The evidence accumulated, however, indicates that the silicon areas are single crystal. The patterns obtained from an x-ray Laue back reflection examination of the region containing the silicon islands includes spots, as well as the diffuse rings due to the amorphous quartz. These spots could only have originated from the silicon areas, indicating that they are crystalline. Treating the sample with a Dash etch to reveal stacking faults produced no effect (Fig. 3). This etch normally reveals grain boundaries and in the case of amorphous or finely polycrystalline silicon very bad staining is obtained. Its lack of effect on the present sample is strong evidence that the silicon islands are in fact single crystal. Although selected area deposition using tantalum areas on quartz in the presence of an ultrathin layer of gold has been demonstrated in many experiments, the effect could not be obtained consistently, suggesting that the many variables in the system are not easy to control.

For some device purposes the ultrathin alloy zone crystallized technique has the disadvantage that the alloying metal, in this case gold, is incorporated in the silicon layer up to the limit of solid solubility at the deposition temperature. Also the existence of the alloy between the silicon islands means that they are not always electrically isolated from each other. Possible ways of eliminating the need for the gold layer have therefore been studied.

It has been the authors' experience that, besides reducing the temperature required for epitaxial deposition, the ultrathin layer of gold generally lowers the minimum temperature at which silicon will chemically attack the substrate. This suggests that silicon would still attack quartz, in the absence of gold, if the temperature were high enough. An attempt was therefore made to deposit selective areas of single crystal using a higher temperature instead of an ultrathin alloy. To achieve the higher substrate temperatures it proved necessary to use an evaporation rather than a sublimation procedure. The evaporation apparatus is shown diagrammatically in Fig. 4 and is similar to that used by Gasson (6).

Preliminary experiments showed that for an evaporation rate of approximately 1μ/min no silicon was deposited on plain quartz substrates above 1325°C, as measured by the thermocouple in the substrate holder. The measured temperature may, of course, be different from the actual temperature of the substrate surface. Having established the temperature above which deposition on the quartz surface did not take place, the plain quartz samples were replaced by those containing areas protected by tantalum or tungsten spots. These were heated to 1350°C and silicon evaporated on them at the above rate. Examination showed that there was no deposit on the unprotected areas, but that the protected areas were covered by irregular grains of silicon. Although the grains are quite large, single crystals covering the whole of a protected area have not been observed to date. The grain size at an early stage of the silicon deposition on areas of tantalum on quartz is shown in Fig 5.

If the substrate temperature was raised to above that for the formation of a liquid alloy between silicon and tantalum or tungsten (1385° or 1400°C, respectively), then no silicon was deposited at all, and the substrate was etched one and a half times more rapidly by the alloy than by the silicon. This resulted in a series of pits in the "protected" areas.

Acknowledgments

The authors gratefully acknowledge the expert assistance of W. H. Wilgoss. British Crown Copyright. Reproduced with permission of the Controller, Her Britannic Majesty's Stationery Office.

REFERENCES

1. J. D. Filby and S. Nielsen, *This Journal*, **112**, 957 (1965).
2. J. D. Filby and S. Nielsen, *Microelectronics and Reliability*, **5**, 11 (1966).
3. R. S. Wagner and W. C. Ellis, *Appl. Phys. Letters*, **4**, 89 (1964).
4. J. D. Filby and S. Nielsen, Third International Vacuum Congress, Stuttgart, June 1965.
5. J. D. Filby and S. Nielsen, *Brit. J. Appl. Phys.*, **17**, 81 (1966).
6. R. C. Newman, *Microelectronics and Reliability*, **3**, 121 (1964).

Manuscript received July 11, 1966.

Any discussion of this paper will appear in a Discussion Section to be published in the June 1967 JOURNAL.

Periodic Variation of Exchange Current Density of Hydrogen Electrode Reaction with Atomic Number and Reaction Mechanism

Hideaki Kita

Research Institute for Catalysis, Hokkaido University, Sapporo, Japan

ABSTRACT

A survey of recent results shows that the activity log i_o is a periodic function of the atomic number for each long period. It is concluded that the bulk properties of electrode dominate its activity. Also, log i_o decreases linearly with heat of adsorption or increases linearly with work function for the transition metals, but remains unchanged for the metals following them (the ascending metals). These relations are qualitatively interpreted by the catalytic and the electrochemical mechanism for the transition and the ascending metals, respectively.

The hydrogen electrode reaction

$$2H^+ + 2e^- = H_2 \qquad [1]$$

is one of the simplest and the most fundamentally important reactions among various kinds of heterogeneous catalyses, and its solid understanding would be a milestone in the approach toward complicated features of catalysis. The electrochemical study of catalysis generally has the advantage in comparison with chemical studies that one can easily follow a reaction over a wide range of experimental conditions, especially of free energy difference between reactants and products, which makes it possible to observe kinetics even on a catalyst of little activity. The hydrogen electrode reaction has been studied most extensively on various metals, and work on it has accumulated increasingly especially during the last decade. Most of this work is much more reliable than earlier work, in the sense that particular precautions have been taken against contamination of solution and electrode surface.

The present comprehensive survey of the results shows that the activity of metals for the reaction, expressed by the exchange current density i_o (amp/cm^2), varies widely, namely from the largest value reported on Pd, of log i_o = −1.2, to the lowest one on Pd, of −12.9, and it varies even on the same metal, for example, from −3.15 to −7.04 on Au. Such variations in the activity should be caused by several factors, such as bulk property of the electrode material, surface state of the electrode, and composition of the solution.

The present paper is concerned with the decision about the determining factor for the activity and with the elucidation of the mechanism for the hydrogen electrode reaction. This is done by relating the activity of various metals to their properties such as atomic number, heat of atomization of the metal, heat of adsorption of hydrogen on the metal, work function, etc.

Review of Results Reported and the Determining Factor

Table I shows the results of observations and experimental conditions, reported during the past ten years mainly till 1964 (1-61), which were available to the author. The exchange current density, i_o, was determined by extrapolating the current density, i, to $\eta = 0$ according to the Tafel equation

$$\eta = a + b \log i$$

where a and b are constants and η is the overvoltage, defined as[1]

$$F\eta = \mu(e^-) - \mu(e^-)_{eq} \qquad [2]$$

in terms of the chemical potentials, $\mu(e^-)$ and $\mu(e^-)_{eq}$, of metal electrons under working and equilibrium conditions.

Activity and atomic number (62).—In Fig. 1, the logarithm of the exchange current density is plotted against the atomic number of electrode metals; the symbols, ●, ●, and ○, represent the values obtained, respectively, in acidic, alkaline, and neutral solutions. In the case where two linear parts appear in the η-log i plot, i was extrapolated from the part at lower η.[1]

Table I and Fig. 1 are discussed below.

1. *Periodicity of the activity.*—The results on the same metal fluctuate considerably, especially in cases of Rh, Pd, W, Au, and Pd, but still the log i_o values of the respective metals studied are basically a periodic function of the atomic number, as shown by the dotted lines in Fig. 1; in other words, in each long period of the Periodic Table, the activity increases first with atomic number, reaches a maximum at the metals of group VIII, decreases quite sharply with a minimum at the metal of IIB or IIIB, and then increases again with further increase of the atomic number. The activity varies in a particularly similar way in the second and the third long periods, revealing precise periodicity. It may be noted that the third metal of any triad of group VIII shows a tendency to have the highest activity. The present distinct max-

[1] Overvoltage as used in this paper, is the negative value of the potential of the test electrode referred to that of the reversible electrode under the same conditions.

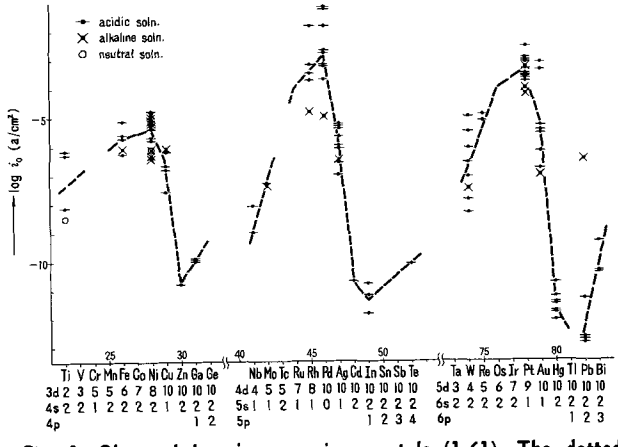

Fig. 1. Observed log i_o on various metals (1-61). The dotted lines indicate the periodic variation of log i_o with the atomic number. —●—, acidic solution; X, alkaline solution; ○, neutral solution.

Table I. List of reported values of log i_o (amp/cm^2) and b on various metals

Metal	Electrode: Form	Electrode: Treatment	Solution: Conc	Solution: Preelectrolysis	Temp, °C	Rest potential[a]	Range of observation in log i (amp/cm^2)	b, mv	log i_o, amp/cm^2	Reference
Ag			1N HCl	1 amp/cm^2, 3.1 × 10^4 Coulomb	Room temp		−6 ~ −1	60 ± 5 130 ± 5	−5.4 ± 0.4 (−3.7 ± 0.4)	(1)
	Wire	Chem. polished, heated in H_2 at 600°C for 2 ~ 3 hr	5N HCl	1 amp/cm^2, 10^5 Coulomb			−3 ~ +2	120	−5.3	(2)
	Wire	Chem. polished	1N H_2SO_4	Conducted, no details			−4 ~ −2	110	−5.7*	(3)
	Wire	Sealed into glass bulb	1N NaOH	10 ma/cm^2, 20 hr	30		−7.5 ~ −3	120	−6.50	(4)
	Wire	Heated in H_2 at 700°C for 1 hr, sealed into glass bulb	0.4N HCl	10 ma/cm^2, 60 hr	23 ± 2		−7 ~ −3	57 ± 2 101 ± 9	−6.6 −5.35	(5)
	Wire	Sealed into glass bulb	0.1N NaOH	10 ma/cm^2, 2 days 0.1 amp/cm^2, 36 hr	25		−7 ~ −2	122	−6.5	(6)
	Single or polycrystal	Electropolished, held in hot H_2 for a few days, gently anodized	2N H_2SO_4	Conducted, no details	Room temp	+0.35 ~ +0.45v, occasionally 0 ~ +18 mv	−7.5 ~ −2.7	59 116	~−6*	(7)
	Wire	Sealed into glass bulb	0.1N HCl 0.1N DCl	0.1 amp/cm^2, 24 ~ 36 hr	26 ± 1		−5.5 ~ −2	72 ± 7 12 (5) ± 5 72 ± 7 122 ± 5	−6.10 ± 0.2 −4.80 ± 0.15 −7.05 ± 0.2 −5.40 ± 0.15	(8)
	Foil	Heated in H_2 at 450°C for 24 hr, sealed with paraffin	2N H_2SO_4	0.1 amp, 60 hr	Room temp		−2.3 ~ −1.3	120	−5.4	(9)
	Wire	Sealed in Teflon, anodic, cathodic polarizations	1.11 or 0.26N NaOH	~30 ma, ~60 hr	21 ± 2	4.5 ± 0.9 mv	−5 ~ +1	43 ± 2 309 ± 5	−5.35 ± 0.4	(10)
Au	Wire	Anodic polarization	8N H_2SO_4				−3 ~ −1	130	−3.15	(11)
	Bead	Anodic, cathodic polarizations (40 ma, 200 sec)	2N H_2SO_4	50 ma, a week	29 ± 1		−3 ~ −0.5	27	−3.4*	(12)
	Wire	Sealed into glass bulb	0.1N HCl 0.1N NaOH	27 ma/cm^2, 42 hr 180 ma/cm^2, 43 hr		Value of r.h.e.	−5.63 ~ −2.41[b] −5.92 ~ −3.68[b]	71 97 119	(−6.83) −5.64 −7.04	(13)
	Foil	Cleaned chemically	0.1N HCl	Conducted, no details		Value of r.h.e.	−6 ~ −3	123	−5.5*	(14)
	Wire	Sealed into glass bulb	0.1N DCl 0.1N HCl	0.1 amp/cm^2, 24 ~ 36 hr	26 ± 1		−5 ~ −1.5	120 ± 5 110 ± 5	−6.23 ± 0.22 −5.60 ± 0.18	(8)
	Wire	Sealed with paraffin or araldite scraped with sharp glass bar	2N H_2SO_4		20		−3 ~ −1	116 ± 4	−5.36	(15)
Bi	Plate	Previously polarized	0.9N HCl 0.9N H_2SO_4 0.9N $HClO_4$	Conducted, 20 ~ 25 hr			−7 ~ −1	118 ± 5 101 ± 5 100 ± 5	−9.32 −10.45 −10.4	(16)
Cd	Wire	Heated in H_2 at 200°C	0.5N H_2SO_4	1 ma/cm^2, 15 ~ 20 hr	Room temp		−5 ~ −2	135 ± 12	−10.77 ± 0.75	(17)

Table I. (Continued)

Metal	Electrode: Form	Electrode: Treatment	Solution: Conc	Solution: Preelectrolysis	Temp, °C	Rest potential[a]	Range of observation in log i (amp/cm²)	b, mv	log i_0, amp/cm²	Reference
Cu	Wire	Sealed into glass bulb	0.1N HCl 0.01N NaOH	75 ma/cm², 37 hr 0.36 ma/cm², 14 hr			$-4.51 \sim -3.47$[b] $-5.19 \sim -3.75$[b]	114 ± 8 107 ± 6	-6.84 -6.09	(13)
	Wire	Heated to red hot in H_2, sealed into glass bulb	0.1N HCl	0.25 amp/cm², 24 hr	38 ± 1		$-5 \sim -1$		-6.21*	(18)
		Sealed into glass bulb	0.1N HCl 0.1N DCl	0.1 amp/cm², 24 ~ 36 hr	26 ± 1		$-5.5 \sim -2$ $-5.5 \sim -2$	120 ± 5 120 ± 5	$-6.7 \pm 0..15$ -7.6 ± 0.15	(8)
Fe	Wire	Sealed into glass bulb	0.01N HCl 0.1N NaOH	18 ma/cm², 36 hr 25 ma/cm², 35 hr			$-4.06 \sim -3.19$[b] $-4.09 \sim -2.16$[b]	118 ± 15 120 ± 2	-6.29 -6.06	(13)
	Wire	Sealed into glass bulb	0.5N HCl 0.5N DCl	15 ma/cm², 20 hr				133 ± 4 134 ± 4	-5.18 ± 0.1 -5.77 ± 0.14	(19)
	Cylindrical	Mounted on Teflon holder, etched in 0.5M H_2SO_4	0.5M H_2SO_4	Conducted, no details	25 ± 0.03		$-3.9 \sim -1.6$	118	-5.65*	(20)
Ga	Solid Liquid		0.1N HCl	Conducted, no details	20.5 35		$-6 \sim -3$	113 93	-10.0 -10.1	(21)
	Solid Liquid		1N H_2SO_4		28 32		$-5 \sim -3$	95 95	-9.9* -10.0*	(22)
Hg	Pool	Redistillation	1.005N HCl		25 ± 0.02		$-4.6 \sim -1$	118 ± 2	-11.53 ± 0.05	(23)
	Pool	Triply distilled, then distilled in vacuum	0.1N HCl	Conducted, no details	21 ± 0.1		$-6 \sim -1$	116	-12.11*	(24)
	Pool	Purified in vacuum apparatus	0.1N HCl	Conducted, no details	0		$-11 \sim -8$	$\alpha = 0.54$ $\alpha = 1.54$		(25)
	Pool		0.1M HCl solution of H_2O, CH_3OH, C_2H_5OH, n-C_3H_7OH		20 ± 0.5			117 107 104 102	-11.8 -11.5 -10.8 -10.8	(26)
	Drop	Triply distilled	0.1N $HClO_4$	1 ma/cm², overnight	25		$-4 \sim -1.7$	118	-11.82	(27)
	Pool	Redistilled, anodic polarization in HNO_3-$Hg_2(NO_3)_2$, distillation in vacuum	1N HCl solution of CH_3OH 1N DCl solution of CH_3OD	Conducted, no details Conducted, no details	27		$-4 \sim -2$ $-4 \sim -3$	119* 119*	-10.8* -11.3*	(28)
In			0.1M $HClO_4$	1 ma/cm², overnight	25		$-3.5 \sim -1.15$	118	-11.85	(29a)
	Cylindrical	Electropolished in 2:1 mixture of CH_3OH and HNO_3 at 0.3 ma/cm², cathodic polarization at 1v overnight	0.1M $HClO_4$ 0.01M $HClO_4$	10 ma, 16 hr	30.0 ± 0.2		$-6.3 \sim -2.8$	$\alpha = 0.530$ ±0.04 $\alpha = 0.48$ ±0.02	-11.19 ± 0.07 -10.8 ± 0.3	(29c)
Mo	Wire	Flushed in vacuum, sealed into glass bulb	0.1N HCl 0.1N NaOH	75 ma/cm², 37 hr 0.24 amp/cm², 71 hr			$-5.52 \sim -3.48$[b] $-3.34 \sim -1.80$[b] $-4.74 \sim -3.72$[b] $-3.58 \sim -2.10$[b]	80 ± 4 104 ± 4 80 ± 3 116 ± 8	-7.30 -6.40 -7.35 -6.35	(13)
Nb			1N HCl				$-3 \sim -1$	110	-9*	(29b)

Table I. (Continued)

Metal	Electrode: Form	Electrode: Treatment	Solution: Conc	Solution: Preelectrolysis	Temp, °C	Rest potential[a]	Range of observation in log i (amp/cm²)	b, mv	log i_o, amp/cm²	Reference
Nb cont'd	Plate	Polished with emery paper, cathodic polarization (5 ma/cm², 1 hr)	1N H_2SO_4 1N NaOH	10 ma/cm², 6 hr			−5 ~ −2.3	low 130 low 140	— −6.75 — −7.50	(29d)
		Polished with emery paper, cathodic polarization (5 ma/cm², 96 hr)	1N H_2SO_4 1N NaOH	10 ma/cm², 6 hr			−5 ~ −2.3	low 120 low 140	— −6.33 — −6.15	
	Sheet (passive state)	Purified by a zone-refining method, mounted in Teflon holder, cleaned in HCl	0.145N HCl	4 ~ 5 ma, 50 hr	25 ± 0.1		−6 ~ −2	57 343	−8.06	(29e)
Ni	Wire	Sealed into glass bulb	1.0N HCl 0.1N NaOH	0.1 amp/cm², 18 hr	20 ± 0.5		−6 ~ −2.3 −7.7 ~ −3.3	109 ± 9 101 ± 4	−5.4 ± 0.1 −6.4 ± 0.2	(30)
	Disk	Electrodeposition (15 ma/cm², 10 min)	0.5M $NiSO_4$		45 ± 0.05		−3 ~ −1.3	120	−6.1	(31)
	Single crystal (100) (110) (111)	Anodic treatment in 70% H_2SO_4	0.1N $HClO_4$ 0.15N $HClO_4$ 0.15N $HClO_4$		25		−6 ~ −3	100 155 150	−4.85 −5.2 −5.2	(32)
	Cross section of rod	Polyethylene sleeved	2N NaOH	25 ma, 3 ~ 4 hr	26 ~ 28		−6 ~ −1	100*	−4.9*	(33)
	Wire	Sealed into glass bulb	0.1N HCl 0.1N DCl	0.1 amp/cm², 24 ~ 36 hr	26 ± 1		−5 ~ −1.35	118 ± 3 124 ± 3	−5.87 ± 0.15 −6.35 ± 0.15	(8)
		Heated to red hot in H_2, sealed into glass bulb	0.1N HCl	0.25 amp/cm², 24 hr	38 ± 0.1		−5 ~ −1	95*	−5.24	(18)
	Cylinder	Anodic (10 ~ 100 ma/cm²) & cathodic (2 ma/cm², 5 min) polarization	0.1N NaOH	10 ~ 15 ma/cm², 18 ~ 124 hr	30	0 ± 2 mv	−6 ~ −2.5	89	−5.03	(34)
	Small sphere	Sealed into glass bulb	0.95N NaOH	3.5 ma, 48 ~ 72 hr	22 ± 1		−3 ~ +2	104 ± 9	−5.32	(35)
	Cross section of rod	Mounted in Pyrex holder by Kel-F wax, polishings, treated by chromic acid/sulfuric acid	1M $HClO_4$ pH = 0.04 1M $NaClO_4$ + 0.01M NaOH pH = 10.8	30 ma, 6 hr	25 ± 0.1		−6 ~ −1.2 −5 ~ −1.5	125 105	−5.7 −5.0	(36)
	Single crystal (100) (110) (111)	Chem. polished	4N KOH				−5.5 ~ −2	89 ~ 93	−5.0	(37)
	Wire	Heated in H_2 at 700°C	0.5N H_2SO_4 0.5N NaOH	1 ma/cm²,15 ~ 20 hr	Room temp			124 ± 10 96 ± 10	−5.22 ± 0.53 −6.10 ± 0.10	(17)
	Evaporated film		NaOH pH = 13.68	20 ~ 30 ma/cm², 30 ~ 50 hr	Room temp		−4.8 ~ −0.8	90*	−5.1*	(38)
Pb		Cathodic polarization (0.1 ~ 1 ma/cm²)	0.1, 0.01N H_2SO_4		20		−6.6 ~ −2.8	118	−12.9*	(39)
			1N H_2SO_4 1N HCl				−4.2 ~ −0.5	120 117	−12.7 −12.9	(40)
	Wire	Chem. polished	0.5N H_2SO_4 0.5N NaOH	1 ma/cm², 40 hr 1 ma/cm², 16 hr	Room temp		−5 ~ −1.3	125 ± 14 129 ± 4	−11.33 ± 1.40 −6.47 ± 0.26	(17)

Table I. (Continued)

Metal	Electrode: Form	Electrode: Treatment	Solution: Conc	Solution: Preelectrolysis	Temp, °C	Rest potential[a]	Range of observation in log i (amp/cm²)	b, mv	log i_o, amp/cm²	Reference
Pd	Wire	Anodic polarization	$2N$ H_2SO_4		Room temp		$-4.4 \sim 0$	29 0	-2.7	(41)
	Bead β-phase	Anodic (5 ma, 15 min) cathodic (50 ma, 30 min) polarizations	$1.05N$ H_2SO_4 pH = 0.40	Conducted, no details	39 ± 1		$-2.0 \sim -0.5$	40 0		(42)
		Anodic (10 ma, 30 min) cathodic (50 ma, 30 min) polarizations	$0.514N$ H_2SO_4 $+0.5N$ Na_2SO_4 pH = 0.84	Conducted, no details	39 ± 1		$-2.0 \sim -0.6$	42 126	-1.25*	
	Membrane α-phase	Anodic polarization (10 ma, 45 min)	$2N$ H_2SO_4 pH = 0 $0.3N$ H_2SO_4 + $0.7N$ Na_2SO_4 pH = 0.9	Conducted, no details	31 ± 2	$+49.5$ mv	$-4.5 \sim -0.5$ $-4.5 \sim -1.4$	(42) 124 (30) 125	-1.2* -1.85*	(43)
	Wire	Sealed into glass bulb	$0.1N$ HCl $0.1N$ NaOH	0.24 amp/cm², 13 hr 0.12 amp/cm², 38 hr		Value of r.h.e.	$-2.89 \sim -1.41$[b] $-4.13 \sim -3.08$[b]	99 125	-3.25 -5.01	(13)
	Wire α-phase	Sealed into glass bulb	$0.1N$ HCl $0.1N$ DCl	0.1 amp/cm², $24 \sim 36$ hr	26 ± 1		$-5 \sim -1.5$ $-5 \sim -2.2$	(25 ± 3) 110 ± 10 (25 ± 3) 120 ± 10	-2.8* -3.7*	(8)
	Membrane		$2N$ H_2SO_4		20		$-4 \sim -2$	120	-3.2*	(44)
	Wire	Palladized	$1.0N$ HCl		25 ± 0.2		$-3.4 \sim 0$	29.5	-2.5*	(45)
Pt	Bead		0.05M NaOH + 0.22M Na_2SO_4	$5 \sim 10$ ma, a week	25 ± 1	± 0.5 mv	$-4.8 \sim -2.2$	126	-3.25*	(46)
	Wire		$1N$ H_2SO_4		20	$< +2$ mv	$-7 \sim -2$	129	-3.65*	(47)
	Wire	Heated in H_2 at 600°C for 10 min, anodic polarization (0.1 amp/cm², 10 sec)	$1N$ HCl	0.1 amp/cm², 10 hr	23 ± 2		$-3 \sim -1$	29 ± 1	-3.0	(5)
	Wire	Anodic (0.01 coulomb/cm²), cathodic polarizations	$0.1N$ NaOH	10 ma/cm², $25 \sim 30$ hr	25		$-5 \sim -3$	114 ± 11	-4.17	(48)
	Bead	Anodic polarization	$1N$ H_2SO_4	$5 \sim 10$ ma, overnight	25 ± 1	± 0.5 mv	$-4 \sim -0.6$	25	-3.1*	(49)
	Small sphere	Soaked in chromic + sulfuric acid mixture for 24 hr, anodic & cathodic polarization (0.1 amp/cm², 5 sec)	$1N$ H_2SO_4 0.5M HCl	Conducted, 15 hr 10 ma/cm², 18 hr	25.0 25 ± 0.5	Value of r.h.e.	$-4 \sim +0.4$ $-3.4 \sim -1$	26* 27.8 ± 1.4	-3.6* -2.59 ± 0.09	(50) (51)
	Wire	Platinized	$0.1N$ HCl $0.1N$ DCl	0.1 amp/cm², $24 \sim 36$ hr	26 ± 1			30 ± 2 31 ± 2	-3.16 ± 0.1 -3.33 ± 0.1	(8)
	Wire	Heated in H_2, sealed into glass bulb, anodic polarization (10 ma/cm², 10 sec)	$0.5N$ HCl $0.5N$ DCl	15 ma/cm², 20 hr				29 ± 3 26 ± 6	-3.33 ± 0.14 -3.62 ± 0.45	(20)
	Foil	Anodic polarization ($1 \sim 2$ ma/cm²), cathodic polarization ($i < 1$ ma/cm²) till potential reached the value of r.h.e.	$0.1N$ Na_2CO_3 pH = 11	Conducted, 15 hr	25 ± 0.5		$-5.5 \sim -1$	58 ± 2 260 ± 60	-3.83 -2.58	(52)
	Wire	Anodic polarization	$0.5N$ H_2SO_4 $0.5N$ NaOH	1 ma/cm², $15 \sim 20$ hr	Room temp			30 ± 1 117 ± 8	-3.53 ± 0.05 -4.06 ± 0.09	(17)
Re	Wire	Mounted in Teflon holder, cleaned in HCl	$0.037N$ HCl $0.145N$ HCl	$4 \sim 5$ ma, 50 hr	25 ± 0.1		$-6 \sim -2$	43 29.2	-4.95 -5.14	(29e)

Table I. (Continued)

Metal	Electrode: Form	Electrode: Treatment	Solution: Conc	Solution: Preelectrolysis	Temp, °C	Rest potential[a]	Range of observation in log i (amp/cm²)	b, mv	log i_o, amp/cm²	Reference
	Wire	Sealed into glass bulb	0.01N HCl 0.01N NaOH	Conducted, no details 6 ma/cm², 20 hr		Value of r.h.e.	$-3.38 \sim -3.08$[b] $-4.18 \sim -3.51$[b]	55 ± 3 119 ± 3	-3.80 -4.85	(13)
Rh	Bead	Anodic, cathodic polarizations	1M H_2SO_4	Conducted, no details	27 ± 1		$-5 \sim -0.5$	27.5	-3.0*	(53)
	Bead	Anodic, cathodic polarization (0.3 amp/cm², 90 min)	2N H_2SO_4		25 ± 1		$-3.5 \sim 0$	120	-1.85*	(54)
	Wire	Anodic polarization (10 ma/cm²)	0.5N H_2SO_4	1 ma/cm², 15 ~ 20 hr	Room temp			28 ± 2	-3.22 ± 0.06	(17)
Si	Single crystal (111) n- & p-types	Treated with solutions; HF:HNO_3 = 1:2 & 42% HF	2N H_2SO_4 2.5N HF		20 20		$-6 \sim -1$ $-6 \sim -1$	180 170	-6.0 -7.7*	(55) (56)
Te	Rod		1N HCl	30 ~40 ma/cm², 20 hr	30		$-6 \sim -2$	53 115	-10.1* -6.4*	(57)
Ti	Wire		0.5M NaCl		30		$-5.7 \sim -2.7$	154	-8.45*	(58)
		10 min in hot 1N NaOH, 1 ~ 2 min in hot 2N H_2SO_4, polished with glass powder	1N H_2SO_4 1N HCl				$-5 \sim -2.5$	135 130	-6.07 $-6..30$	(59)
	Plate	10 min in hot 1N NaOH, 1 ~ 2 min in hot 2N H_2SO_4, cathodic polarization in 2N H_2SO_4 (5 ma/cm², 1 hr)	2N H_2SO_4				$-5 \sim -1.5$	119	-8.15*	(60)
W	Wire	Heated in H_2 at 600°C for 2 ~ 3 hr	5N HCl	1 amp/cm², 10^6 Coulomb	25		$-3 \sim +2$	110	-5.0	(2)
	Wire	Heated in vacuum at 3000°C for 1 min, in H_2 at 1000°C for 2 ~ 3 min	0.1N HCl	10 ma/cm², 60 hr	23 ± 2			60 ± 3 105 ± 13	-6.11 -5.55	(5)
		Cleaning with molten $NaNO_3$	0.5N HCl 0.5N DCl	15 ma/cm², 20 hr				70 ± 5 112 ± 9 69 ± 6 101 ± 4	-7.87 ± 0.31 -6.30 ± 0.23 -8.34 ± 0.27 -7.10 ± 0.42	(20)
	Wire	Cleaning with molten $NaNO_3$, heating in H_2 at 200°C	0.5N H_2SO_4 0.5N NaOH	1 ma/cm², 15 ~ 20 hr	Room temp			84 ± 6 116 ± 3 80 ± 1 100 ± 4	-6.63 ± 0.22 -5.90 ± 0.09 -7.53 ± 0.10 -6.60 ± 0.26	(17)
Zn			1N H_2SO_4		20		$-4.6 \sim -1.8$	120	-10.8*	(61)

* Values estimated from figures; ( ) uncertain values; [a] values of rest potential are referred to the reversible hydrogen electrode (r.h.e.) in the same solution and hydrogen atmosphere; [b] the region where a straight Tafel line is observed.

imum of the activity at metals of group VIII is also found in other heterogeneous catalyses, *e.g.*, the isotopic exchange in molecular hydrogen (63), the hydrogen-oxygen reaction (64), the synthesis and decomposition of ammonia (65), and the recombination of atomic hydrogen (66). The metals of group VIII have thus the largest activity for a host of important heterogeneous catalyses.

A similar periodicity for the hydrogen electrode reaction has been suggested by Bockris (29b) and recently by Khomutov (67) with regard to the overvoltage of metals at a certain definite current density. In the former work, however, the periodicity in the first long period is incomplete because of lack of observations, and in the latter only those in hydrochloric or sulfuric acid are included. Moreover, only one or two values for each metal are used in these works; this appears insufficient for remarks on the points 2 and 3.

2. *Effect of composition of the solution on activity.*— The log i_o value for the same electrode material fluctuates apparently without correlation with pH by 1 ~ 2 in most cases, whereas the fluctuation is much larger in the cases of Rh, Pd, and Pb, amounting to *ca.* 6 at most on Pb. The latter group of metals might have to be re-examined, since the observations in alkaline solution are scanty and extremely scattered. No correlation of activity is found either with respect to variation of the anion of the acid as seen, for example, in the case of Ni in Table I, where the log i_o values are, respectively, —5.4 (1*N* HCl) (30), —5.87 (8) and —5.24 (18) (both 0.1*N* HCl), —5.22 (0.5*N* H_2SO_4) (17), —5.2 (0.15*N* $HClO_4$) (32), and —5.7 (1M $HClO_4$) (36).

The activity appears similarly to have no correlation with the kind of solvent in the electrolyte solution, as exemplified by the log i_o values of the mercury electrode, *i.e.*, —11.8, —11.5, —10.8, and —10.8, respectively, for 0.1M HCl solution in water, methyl alcohol, ethyl alcohol, and n-propyl alcohol (26). The log i_o values in heavy water are, however, smaller in all cases than those in ordinary water, and its isotopic difference varies from 0.95 for Ag to 0.17 for Pt, being 0.55 on an average (8,20).

3. *Effect of treatment of the electrode.*—The electrode of nickel, which is one of the metals studied in detail, was subjected to a wide variety of treatments, as seen from the third column of Table I, *i.e.*, reduction of a wire in hydrogen atmosphere, electrodeposition of Ni from $NiSO_4$ solution, anodic or chemical polishing of a single crystal, quenching of the melt in helium atmosphere, evaporation of Ni on a glass wall, etc. However it is apparent from Fig. 1 that the log i_o values of nickel electrodes subjected to the above treatments are not very different from each other. Hence, the activity appears to depend not so much on the treatment as on the atomic number. The same is the case with most of the other metals.

Piontelli, Bicelli, and LeVecchia (32) and Weininger and Breiter (37) observed Tafel lines individually on (100), (110), and (111) lattice planes of the fcc crystal of Ni; Piontelli *et al.* observed with anodically treated electrodes that the log i_o values of the respective lattice planes differed by 0.35 at most, while Weininger *et al.* found, with chemically polished electrodes, practically no difference in the log i_o values between the lattice planes.

4. *Liquid and solid surfaces.*—It is of interest that the activity of liquid mercury conforms to the periodicity of the activity of solid electrodes as illustrated in Fig. 1. In the case of gallium, the activity is much the same whether the electrode is in the liquid or solid state, as observed in the respective cases at temperatures slightly above or below the melting point of 29.78°C (Table I).

These facts indicate that it is not essential in determining the activity of hydrogen electrode reaction whether the electrode is solid or liquid, which provides evidence for the crystal plane model of the catalyst and against the distribution model originating from the active center theory of Taylor (68a) and developed recently by Russian authors (68b).

Determining factor of the activity (62).—The above mentioned points 1 to 4 lead us to conclude that bulk property of the electrode material is the determining factor for the activity of hydrogen electrodes. In other words, the activity of a metal depends not so much on the kind of solvent, the electrolyte and its composition (point 2) as on the atomic number of the electrode metal. Further, the activity depends neither on the surface treatment (point 3), nor on the state of aggregation, *i.e.*, liquid or solid, of the electrode (point 4) within the fluctuation of results. Hence the periodic variation of the activity (point 1) is primarily effected by the bulk property of electrode material and only secondarily by other factors such as the solution and the surface state.

Activity and Properties of the Metal

The question arises from the above conclusion as to what property of electrode material effects essentially the activity. Many physical properties such as heat of atomization of the metal, melting point, metallic radius and work function are known to show periodic gradation within the long periods. These quantities are now considered in comparison with the periodic variation of the activity.

It may be noted qualitatively from the electron configuration of outer shells of the element attached to Fig. 1 that the activity in each long period increases first with successive addition of an electron to the d-orbital, reaches a maximum at nearly filled d-orbital, decreases quite sharply after its completion, with one or two electrons in the s-orbital, and then increases again with further addition of electrons to the p-orbital. In the following discussions, we denote the transition metals including IB metals by "d-metals" and the metals following them in the Periodic Table by "sp-metals."

The heights of the dotted line in Fig. 1 at the atomic number of each electrode metal are taken as the representative values for the respective metals and are denoted by [log i_o] in what follows.

Heat of atomization of the metal, $-\Delta H_{atom}$.—The heat of atomization of the metal is one of the measures of the cohesive strength of metal atom in the bulk. Surface metal atom may have unsaturated valencies directed outward from the surface on account of the absence of neighboring atoms above it. Thus unsaturated valencies may form bond with adsorbate, *e.g.*, intermediates of the hydrogen electrode reaction in the present case, with a strength depending on the nature of the metal, especially the cohesive strength of

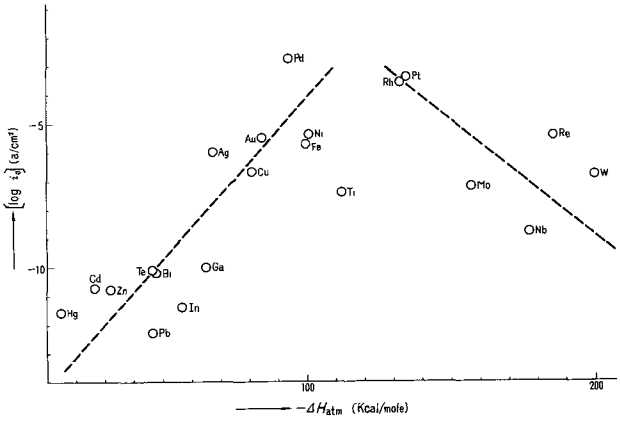

Fig. 2. Log i_o *vs.* heat of atomization of electrode metals, $-\Delta H_{atom}$

metal atom in the bulk. The [log i_o] values of respective metals are plotted against their heat of atomization after Sanderson (69) in Fig. 2. As seen in the figure, there exists a definite correlation between them and even an optimum value of the heat of atomization. The same relation is expected with respect to the melting point of the metal which changes with the atomic number in a way similar to that of the heat of atomization.

Metallic radius.—The metallic radius in any long period may also be taken as a measure of the cohesive strength, since it might appear that the smaller the radius the greater must be the strength of binding. This quantity, however, does not give any significant relation to the activity, as exemplified by W, Re, and Pt in the third long period whose metallic radii are almost the same, *i.e.*, 1.37, 1.37 and 1.38Å, whereas the [log i_o] values are quite different, *i.e.*, —6.8, —5.4, and —3.4, respectively. Hence the heat of atomization of the metal seems to be more closely related to the activity of the hydrogen electrode reaction.

Heat of adsorption of hydrogen, $-\Delta H_{ads}$.—The heat of adsorption of an adsorbate may not be the sole function of the heat of atomization of metal, since chemical bonds are usually more or less polarized. Eley (70) has proposed that the heats of chemisorption of gases on metals may be computed by means of Pauling's equation of bond energies (71), namely, in case of hydrogen chemisorption as

$$-\Delta H_{ads} = E(M-M) + 46.12(X_M - X_H)^2 \quad [3]$$

where $E(M - M)$ is the bond energy between metal atoms measured from the lowest potential energy and X_M or X_H is the electronegativity of metal atom or hydrogen atom, respectively. It has been pointed out by Stevenson (72) that if the electronegativities of metal atoms are calculated from their work function, ϕ, by the formula

$$X_M = 0.355\phi \quad [4]$$

and the values for $E(M - M)$ are taken as 1/6 of the heat of sublimation in the case of metals with "closest packed" lattices, a good agreement is obtained between the calculated and the observed heats of adsorption. In Fig. 3, the [log i_o] values are plotted against the heat of adsorption, $-\Delta H_{ads}$, as calculated by Eq. [3] and [4] and with the approximation of 1/6 of the heat of atomization (69) for $E(M - M)$. It is interesting to see from Fig. 3 that the behavior of d-metals is distinctly different from that of sp-metals, namely, the activity of d-metals has a tendency to decrease with increase of $-\Delta H_{ads}$, whereas the activity of sp-metals remains almost unchanged. Conway and Bockris (73) have studied hydrogen overvoltage

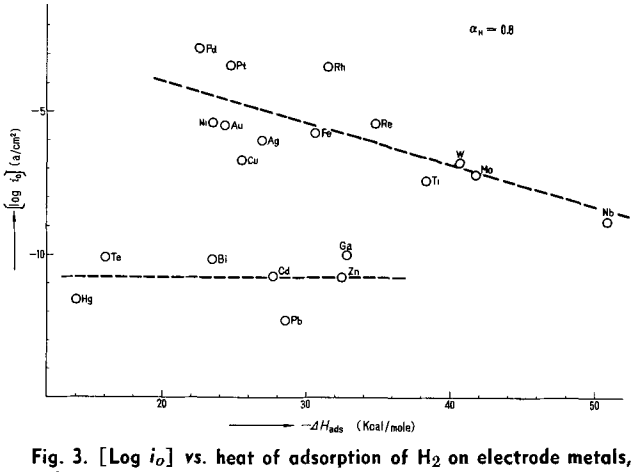

Fig. 3. [Log i_o] *vs.* heat of adsorption of H_2 on electrode metals, $-\Delta H_{ads}$.

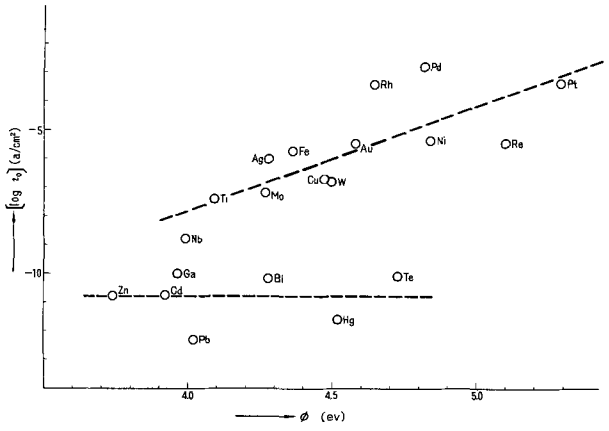

Fig. 4. [Log i_o] *vs.* work function of electrode metals, ϕ

on metals at a constant current density of 1 ma/cm² in comparison with $-\Delta H_{ads}$. The log i_o value and thus the activity should increase with decrease of the overvoltage quoted above, provided that the increment of the logarithm of the unidirectional current density per unit increase of overvoltage be universally constant. Their result is similar under this convention to the present one for the transition metals but not for the sp-metals, *i.e.*, some of them (Pb, Hg, and Tl) gained while others (Cd and Ga) lost in activity with increase of $-\Delta H_{ads}$. This discrepancy is attributed to the difference of the log i_o values they quoted from the present ones.

Work function, ϕ.—The correlation of work function, which is known to be a periodic function of the atomic number, with the activity is investigated by plotting the [log i_o] values against Michaelson's values of the work function (74) in Fig. 4. The activity of d-metals increases with work function, but that of the sp-metals remains again almost unchanged as seen in Fig. 4. The latter finding is not in agreement with that of Conway and Bockris (73).

Other properties.—The electronegativity of metal atoms, X_M, changes periodically with the atomic number with maxima and minima, respectively at IB and IIB metals in each period. The plot of [log i_o] against X_M does not, however, reveal any distinct correlation but only a rough tendency of decrease of [log i_o] with increase of X_M. Other properties such as mass magnetic susceptibility, electric resistance, and type of lattice are also periodic functions of the atomic number, but are not in a distinct correlation with the activity.

Reaction Mechanism of the Hydrogen Electrode Reaction

The facts shown in Fig. 3 and 4 definitely indicate that different mechanisms are operating on the respective groups of metals, *i.e.*, on the d-metals and the sp-metals, where the [log i_o] value of the former decreases or increases linearly with the heat of adsorption of H_2 or the work function, while that of the latter remains unchanged. This indication is supported by experimental results on the separation factors, S_D or S_T, of deuterium or tritium defined as

$$S_D(\text{or } S_T) = [C_H/C_D(\text{or } C_T)]_{gas}/[C_H/C_D \text{ (or } C_T)]_{soln}$$

where C_H, C_D, and C_T are the atomic concentrations of the isotopes, H, D, or T, with respect to the total amount of hydrogen atoms. A number of observations have been reported on various metals and conditions. Recent results obtained at a definite current density (17, 75-78), are summarized in Fig. 5, where ↘ and ↗ are the values of S_D in acidic and alkaline solution, ↙ and ↖ are those of S_T, respectively, all obtained at a current density of 0.01 amp/cm², and similar sym-

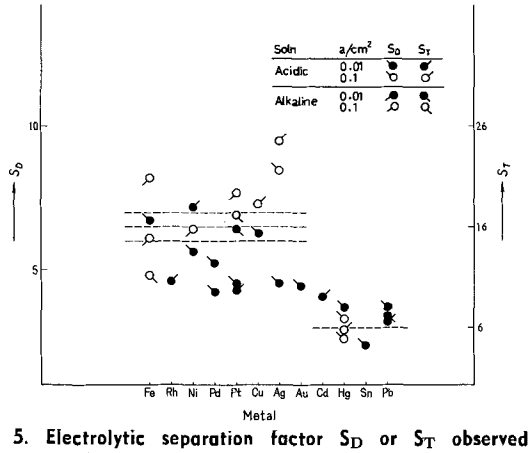

Fig. 5. Electrolytic separation factor S_D or S_T observed on various metals (17, 75-78). The dotted lines represent the theoretical values of $S_D = 6 \sim 7$ or 3 and $S_T = 16$ or 6 (80 ~ 82).

bols with open circles are values obtained at 0.1 amp/cm². As seen from Fig. 5, these results are widely scattered, but it can be concluded, in extension of the previous conclusion by Horiuti and Okamoto (79), that the separation factors fall into two groups: the larger values are those of the d-metals and the smaller ones those of the sp-metals. The dotted lines in Fig. 5 represent the theoretical values of Horiuti and his co-workers, *i.e.*, 6 ~ 7 of S_D (80) or 16 of S_T (81) for the former group and 3 of S_D (82) or 6 of S_T (81) for the latter group, respectively. The S_D and S_T scales in Fig. 5 are graded differently so that S_D = 6.5 and S_T = 16 on the one hand and S_D = 3 and S_T = 6 on the other hand fall, respectively, on the same levels. Some observed values of S_T, *viz.*, 4.1 on Ni in 0.5*N* NaOH and 6.0 and 4.4 on W in 0.5*N* H_2SO_4 and 0.5*N* NaOH solutions (17), are exceptionally small, but they are reported to increase with repetition of measurements and hence were not included in Fig. 5. The appearance of the two groups of separation factors supports the view that different mechanisms are operative on the respective groups of metals.

Horiuti and his co-workers (80, 82) have attributed the catalytic mechanism to the hydrogen electrodes of Ni, Au, Cu, Pt (at high η), and Pb (in alkaline solution) and the electrochemical mechanism to those of Hg, Sn, Pt (at low η), and Pb (in acidic solution); the catalytic mechanism proceeds through the two steps

$$H^+ + e^- \rightarrow H(a),\ 2H(a) \not\rightarrow H_2 \quad [5a], [5b]$$

and the electrochemical mechanism through

$$2H^+ + e^- \rightarrow H_2{}^+(a),\ H_2{}^+(a) + e^- \not\rightarrow H_2 \quad [6a], [6b]$$

respectively, with the rate-determining step signified by $\not\rightarrow$, where (a) denotes an adsorbed state. Recent results on the hydrogen electrode reaction on nickel, *i.e.*, the existence of a cathodic saturation current (35) and the coincidence of the experimental heat of activation with the theoretical one (83), confirm the catalytic mechanism.

We now proceed to interpret the results obtained in Fig. 3 and 4 applying the catalytic or the electrochemical mechanism respectively to the d- or sp-metals.

The unidirectional rate of an elementary step, v_+, has been given in general form by Horiuti (84) as

$$v_+ = (RT/h\nu)p^{\ddagger}/p^{\mathrm{I}} \quad [7]$$

where ν is the stoichiometric number of the rate-determining step and $r^{\ddagger}$ and r^{I} are factors defined as follows. Consider a macroscopic assembly, $\mathfrak{A}$, which consists of electrode, electrolyte solution, and 1 atm hydrogen gas at a definite temperature but comprises none of the critical system of the rate-determining step. The term $p^{\ddagger}$ is defined as the factor by which the partition function, $\Omega\mathfrak{A}$, of $\mathfrak{A}$ is multiplied by addition of a critical system to $\mathfrak{A}$ to form $\mathfrak{A}^{\ddagger}$, *i.e.*

$$p^{\ddagger} = \Omega\mathfrak{A}^{\ddagger}/\Omega\mathfrak{A} \quad [8a]$$

where $\Omega\mathfrak{A}^{\ddagger}$ is the partition function of $\mathfrak{A}^{\ddagger}$. It follows from the properties of the partition function that $p^{\ddagger}$ is the Boltzmann factor of the Helmholtz free energy increase of $\mathfrak{A}$ caused by the addition of the critical system to it, *i.e.*, that of its chemical potential

$$\mu(\ddagger) = -RT \ln p^{\ddagger} \quad [8b]$$

The factor p^{I} is similarly defined as

$$p^{\mathrm{I}} = \Omega\mathfrak{A}^{\mathrm{I}}/\Omega\mathfrak{A} \quad [9a]$$

where $\Omega\mathfrak{A}^{\mathrm{I}}$ is the partition function of $\mathfrak{A}^{\mathrm{I}}$ which is formed by addition of the initial system, I, of the rate-determining step to $\mathfrak{A}$. The factor p^{I} is similarly the Boltzmann factor of the chemical potential, $\mu(\mathrm{I})$, of I, *i.e.*

$$\mu(\mathrm{I}) = -RT \ln p^{\mathrm{I}} \quad [9b]$$

The factor $p^{\ddagger}$, as defined by Eq. [8a], has been expressed as (84)

$$p^{\ddagger} = \mathrm{N}^{\ddagger}\Omega\mathfrak{A}^{\ddagger}_{\sigma^{\ddagger}(\ddagger)}/\Omega\mathfrak{A}$$

where $\mathrm{N}^{\ddagger}$ is the total number of seats, $\sigma^{\ddagger}$, of the critical system and $\Omega\mathfrak{A}^{\ddagger}_{\sigma^{\ddagger}(\ddagger)}$ is the partition function of $\mathfrak{A}^{\ddagger}_{\sigma^{\ddagger}(\ddagger)}$, *i.e.*, the particular state of $\mathfrak{A}^{\ddagger}$ with a single critical system accommodated in a particular $\sigma^{\ddagger}$; $\Omega\mathfrak{A}^{\ddagger}$ is in consequence the total sum of $\Omega\mathfrak{A}^{\ddagger}_{\sigma^{\ddagger}(\ddagger)}$ over-all $\sigma^{\ddagger}$'s, *i.e.*, $\mathrm{N}^{\ddagger}\Omega\mathfrak{A}^{\ddagger}_{\sigma^{\ddagger}(\ddagger)}$. Dividing both the numerator and the denominator of the above equation by the partition function, $\Omega\mathfrak{A}_{\sigma^{\ddagger}(0)}$, of $\mathfrak{A}^{\ddagger}_{\sigma^{\ddagger}(0)}$, *i.e.*, the particular state or $\mathfrak{A}$ where it has particular $\sigma^{\ddagger}$ unoccupied with certainty, we have (84)

$$p^{\ddagger} = N^{\ddagger}q^{\ddagger}\theta_{\sigma^{\ddagger}(0)} \quad [10]$$

where

$$q^{\ddagger} \equiv \Omega\mathfrak{A}^{\ddagger}_{\sigma^{\ddagger}(\ddagger)}/\Omega\mathfrak{A}_{\sigma^{\ddagger}(0)}$$

is the Boltzmann factor of the reversible work, $\epsilon(\ddagger)$, required to bring $\ddagger$ from its reference state to the preliminarily evacuated $\sigma^{\ddagger}$, *i.e.*

$$\epsilon(\ddagger) = -RT \ln q^{\ddagger} \quad [11]$$

and

$$\theta_{\sigma^{\ddagger}(0)} \equiv \Omega\mathfrak{A}_{\sigma^{\ddagger}(0)}/\Omega\mathfrak{A}$$

is the probability of $\sigma^{\ddagger}$ being unoccupied.

The probability $\theta_{\sigma^{\ddagger}(0)}$ is further developed in general form with respect to the adsorbate A, inclusive of I or part of it, as (84)

$$\theta_{\sigma^{\ddagger}(0)} = (p^{iA(a)}/q^{iA(a)})\theta_{\sigma^{\ddagger}(iA)} \quad [12]$$

where $q^{iA(a)}$ is the Boltzmann factor of the reversible work, $\epsilon(iA)$, required to bring i samples of $A(a)$ from their reference state to the preliminarily evacuated $\sigma^{\ddagger}$, *i.e.*

$$\epsilon(iA) = -RT \ln q^{iA(a)} \quad [13]$$

$p^{iA(a)}$ is the Boltzmann factor of $i\mu(A.a)$ or i times the chemical potential, $\mu(A.a)$, of $A(a)$, *i.e.*

$$i\mu(A.a) = -RT \ln p^{iA(a)} \quad [14]$$

and $\theta_{\sigma^{\ddagger}(iA)}$ is the probability of $\sigma^{\ddagger}$ being occupied by $iA(a)$.

The unidirectional rate of the hydrogen electrode reaction is now expressed in terms of current density, i_+, from Eq. [7] and [10] as

$$i_+ = 2e(kT/Ah)N^{\pm}q^{\pm}\theta_{\sigma^{\pm}(0)}/p^{\mathrm{I}} \qquad [15]$$

or from Eq. [7], [10] and [12] as

$$i_+ = 2e(kT/Ah)N^{\pm}q^{\pm}p^{iA(a)}\theta_{\sigma^{\pm}(iA)}/p^{\mathrm{I}}q^{iA(a)} \qquad [16]$$

remembering that $\nu = 1$ for both the catalytic and the electrochemical mechanism, where A is the surface area and e the elementary charge; the factor 2 cares for the transfer of two elementary charges at every occurrence of the step [5b] or [6b] in the steady state. Equations [15] and [16] are now applied to the respective mechanisms below.

Catalytic mechanism.—As regards the catalytic mechanism stated by [5a] and [5b], we have

$$\mathrm{I} = 2\,\mathrm{H}(a), A = \mathrm{H}(a) \text{ and } i = 2. \qquad [17a], [17b], [17c]$$

The chemical potential, $\mu(\mathrm{H}.a)$, of $\mathrm{H}(a)$ is expressed, on account of the partial equilibrium of step [5a], as

$$\mu(\mathrm{H}.a) = \mu(\mathrm{H}^+) + \mu(e^-)$$

or as

$$\mu(\mathrm{H}.a) = (1/2)\mu(\mathrm{H}_2) + F\eta \qquad [18]$$

from Eq. [2] and the relation

$$\mu(\mathrm{H}_2) = 2\mu(\mathrm{H}^+) + 2\mu(e^-)_{\mathrm{eq}} \qquad [19]$$

for the equilibrium of reaction [1].

The unidirectional current density is derived from Eq. [15], [17a], [9b], and [18] at $\eta = 0$ where $i_+ = i_o$ as

$$i_o = K_1 q^{\pm}\theta_{\sigma^{\pm}(0)} \qquad [20a]$$

or from Eq. [16] and [17a] to [17c] at $\eta = 0$ as

$$i_o = K_2(q^{\pm}/q^{2\mathrm{H}(a)})\theta_{\sigma^{\pm}(2\mathrm{H})} \qquad [20b]$$

where

$$K_1 = 2e(kT/Ah)N^{\pm}\exp\{\mu(\mathrm{H}_2)/RT\}$$

and

$$K_2 = 2e(kT/Ah)N^{\pm}$$

are, respectively, common to an electrode material in order of magnitude.

According to Horiuti-Polanyi's principle (85) that $\epsilon(\pm)$ varies by a positive proper fraction, α, of the variation of reversible work, $\epsilon(\mathrm{I})$, of the initial system, *i.e.*

$$\epsilon(\pm) = \alpha\epsilon(\mathrm{I}) + \text{const} \qquad [21]$$

the factor $q^{\pm}$ of Eq. [20a] and [20b] is approximately expressed by Eq. [21], [11], and [17a] as

$$-RT\ln q^{\pm} = \alpha_c\epsilon(2\mathrm{H}) + \text{const} \qquad [22a]$$

where α_c is a particular value of α for the catalytic mechanism. The reversible work $\epsilon(2\mathrm{H})$ defined as $-RT\ln q^{2\mathrm{H}(a)}$ is, on the other hand, expressed in terms of the heat of adsorption, $-\Delta H_{\mathrm{ads}}$, approximately as

$$\epsilon(2\mathrm{H}) = -RT\ln q^{2\mathrm{H}(a)} = \Delta H_{\mathrm{ads}} + R + \text{const} \qquad [22b]$$

where R is the repulsive potential of $2\mathrm{H}(a)$ in $\sigma^{\pm}$ with respect to the surrounding $\mathrm{H}(a)$'s.

The dependence of i_o on $-\Delta H_{\mathrm{ads}}$ is now discussed in the two limiting cases where the electrode surface is practically bare or practically fully occupied by $\mathrm{H}(a)$, *i.e.*, $\theta_{\sigma^{\pm}(0)} \simeq 1$ or $\theta_{\sigma^{\pm}(2\mathrm{H})} \simeq 1$, respectively.

1. $\theta_{\sigma^{\pm}(0)} \simeq 1$; here we have $R = 0$. From Eq. [20a], [22b], we obtain

$$\log i_o = -\alpha_c\Delta H_{\mathrm{ads}}/2.3RT + \text{const}$$

The above equation indicates an increase of $\log i_o$ with increase of the heat of adsorption, $-\Delta H_{\mathrm{ads}}$.

2. $\theta_{\sigma^{\pm}(2\mathrm{H})} \simeq 1$; here we obtain, assuming $R =$ const, the following equation from Eq. [20b], [22a], and [22b]

$$\log i_o = (1-\alpha_c)\,\Delta H_{\mathrm{ads}}/2.3RT + \text{const}$$

which shows an increase of $\log i_o$ with decrease of $-\Delta H_{\mathrm{ads}}$.

Case 2, where $\theta_{\sigma^{\pm}(2\mathrm{H})} \simeq 1$, is qualitatively in agreement with results for the d-metals in Fig. 3, but case 1 is not. From the slope of the dotted line for the d-metals, the value of α_c is estimated at about 0.8. This value satisfies the necessary condition that α_c is the positive proper fraction. The coverage of $\mathrm{H}(a)$ on electrode surface has been studied by various methods and concluded to be almost unity at $\eta = 0$ on Pt (86, 87) which has a relatively low value of $-\Delta H_{\mathrm{ads}}$ as seen from Fig. 3. The other d-metals with higher heat of adsorption hence may safely be taken to satisfy condition 2. As regards the IB metals of the Periodic Table, however, no reliable data of $-\Delta H_{\mathrm{ads}}$ or coverage seem to have been reported because of their slow rate of adsorption.

Conway and Bockris (73) have discussed the relation between $-\Delta H_{\mathrm{ads}}$, calculated by Eq. [3] using the respective values of the electronegativity of the metals, and the work function and found that $-\Delta H_{\mathrm{ads}}$ increases with decrease of the work function. The same relation is also derived from Eq. [3] and [4] identifying $E(\mathrm{M}-\mathrm{M})$ with 1/6 times the heat of atomization, and hence the relation of $\log i_o$ to the work function of the d-metals shown in Fig. 4.

Electrochemical mechanism.—As regards the electrochemical mechanism stated by [6a] and [6b], we have

$$I = \mathrm{H}_2^+(a) + e^-, A = \mathrm{H}_2^+(a), \text{ and } i = 1. \qquad [23a], [23b], [23c]$$

Thus the chemical potential, $\mu(\mathrm{I})$, of I is expressed on account of the partial equilibrium of step [6a] as

$$\mu(\mathrm{I}) = 2\mu(\mathrm{H}^+) + 2\mu(e^-)$$

or by Eq. [2] and [19] as

$$\mu(\mathrm{I}) = \mu(\mathrm{H}_2) + 2F\eta \qquad [24]$$

The unidirectional current density is derived from Eq. [15], [23a], [24], and [9b] at $\eta = 0$ where $i_+ = i_o$ as

$$i_o = K_1 q^{\pm}\theta_{\sigma^{\pm}(0)} \qquad [25a]$$

or from Eq. [16], [9b], [23a] to [23c], [14], and [2] at $\eta = 0$ as

$$i_o = K_2[q^{\pm}/q^{\mathrm{H}_2^+(a)}\exp\{-\mu(e^-)_{\mathrm{eq}}/RT\}]\theta_{\sigma^{\pm}(\mathrm{H}_2^+)} \qquad [25b]$$

The factor $q^{\pm}$ in Eq. [25a] and [25b] is expressed similarly to Eq. [22a], from Eq. [21], [11], and [23a], as

$$-RT\ln q^{\pm} = \alpha_E\{\epsilon(\mathrm{H}_2^+) + \mu(e^-)^2{}_{\mathrm{eq}}\} + \text{const} \qquad [26]$$

where α_E is a particular value of α for the electrochemical mechanism and $\mu(e^-)$ is independent of the electrode material as seen from Eq. [19], *i.e.*

$$\mu(e^-) = \text{const} \qquad [27]$$

The reversible work $\epsilon(\mathrm{H}_2^+)$, defined as $-RT\ln q^{\mathrm{H}_2^+(a)}$, has been discussed by Horiuti (88, 89) and is expressed by Eq. [3.3.H_2^+] and [5.1] of ref. (88), with additional term R for the repulsive potential of $\mathrm{H}_2^+(a)$ due to surrounding kindred species as

$$\epsilon(\mathrm{H}_2^+) = \epsilon(\mathrm{H}_2^+)_0 + FE_P + R$$

[2] Here the symbol, $\epsilon(e^-)$, is replaced by $\mu(e^-)$, since the electron is transferred into the conduction band of electrode material where we have no seat such as $\sigma^{\pm}$ on the electrode surface.

where E_P is the electrostatic potential of plane P on which $H_2^+(a)$ resides, and $\epsilon(H_2^+)_0$ is $\epsilon(H_2^+)$ minus its electrochemical part. We have from Eq. [5] in ref. (89)

$$\epsilon(H_2^+)_0 = \alpha_H \epsilon(H) + \epsilon(H^+)_0 - 2.7 \text{ ev}$$

where α_H is a positive proper fraction, $\epsilon(H)$ the reversible work required to bring $H(a)$ from its reference state to the preliminarily evacuated site, $\epsilon(H^+)_0$ that of $H^+(a)$ minus the electrostatic part which is taken as a constant in the absence of a specific adsorption potential, and 2.7 ev is the dissociation energy of H_2^+ in vacuum. It has been shown by Horiuti (88), on the other hand, that $\Delta E_P = -\alpha_w \Delta\phi$ from which we have

$$E_P = -\alpha_w \phi + \text{const}$$

where α_w is a positive proper fraction. Expressing $\epsilon(H)$ as

$$\epsilon(H) = (1/2)\,\Delta H_{ads} + \text{const}$$

the reversible work $\epsilon(H_2^+)$ is given finally from the above four equations as

$$\epsilon(H_2^+) = \alpha_H \Delta H_{ads}/2 - \alpha_w F\phi + R + \text{const} \quad [28]$$

The dependence of i_o on $-\Delta H_{ads}$ or ϕ is now discussed for the two limiting cases where the electrode surface is practically bare or practically fully occupied by $H_2^+(a)$, *i.e.*, $\theta_{\sigma+(0)} \simeq 1$ or $\theta_{\sigma+(H_2^+)} \simeq 1$, respectively.

1. $\theta_{\sigma+(0)} \simeq 1$; here we have $R = 0$. From Eq. [25a] and [26] to [28], we obtain

$$\log i_o = -\alpha_E\{\alpha_H \Delta H_{ads}/2 - \alpha_w F\phi\}/2.3RT + \text{const} \quad [29a]$$

2. $\theta_{\sigma+(H_2^+)} \simeq 1$; here we obtain from Eq. [25b], [26] to [28], [23b], [23c], and [13], assuming R = const,

$$\log i_o = (1-\alpha_E)\{\alpha_H \Delta H_{ads}/2 - \alpha_w F\phi\}/2.3RT + \text{const} \quad [29b]$$

Remembering that $-\Delta H_{ads}$ increases with decrease of ϕ as pointed out by Conway and Bockris (73), one can see from Eq. [29a] and [29b] that the increase of ϕ compensates more or less that of ΔH_{ads}, so that the log i_o's may run almost invariably with $-\Delta H_{ads}$ or with ϕ in either case of $\theta_{\sigma+(0)} \simeq 1$ or $\theta_{\sigma+(H_2^+)} \simeq 1$, in agreement with the results shown in Fig. 3 and 4 for the sp-metals. If we plot the work function against the heat of adsorption calculated by the Eley-Stevenson's method, we obtain the relationship with respect to the sp-metals as shown in Fig. 6. One can see that the work function decreases linearly with increase of the heat of adsorption with slope of −1.0. From this value, assuming $\alpha_H = \alpha_c$, we obtain 0.4 for α_w which again satisfies the necessary condition that α_w is a positive proper fraction.

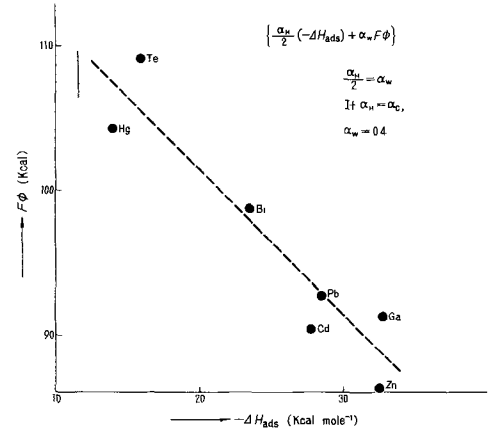

Fig. 6. $F\phi$ *vs.* $-\Delta H_{ads}$ with respect to sp-metals

Conclusion

1. Survey of the results on the hydrogen electrode reaction reported during the ten years previous to 1964 shows that the logarithm of the exchange current density, log i_o, is a periodic function of the atomic number for each long period.

2. The above periodic variation is primarily effected by the bulk property of electrode material but secondarily by the other factors such as the solution and the surface state of the electrode.

3. Two distinct relations are found between [log i_o] (the height of the dotted line in Fig. 1 at the atomic number of respective metals) and the heat of adsorption $-\Delta H_{ads}$, or the work function ϕ, where the [log i_o] value of d-metals depends linearly on $-\Delta H_{ads}$ or $-\phi$, while that of sp-metals runs practically invariably.

4. The above relations are qualitatively interpreted on the basis of the catalytic mechanism for the d-metals and of the electrochemical mechanism for the sp-metals respectively.

Acknowledgments

The present author wishes to express his sincere thanks to Professor J. Horiuti for his encouragement and stimulating discussions given throughout this work. He wishes also to express his thanks to Dr. I. Toyoshima for his deep interest and discussions on the present work.

SYMBOLS

i_o, activity	exchange current density, amp/cm^2
[log i_o]	height of the dotted line in Fig. 1 at the atomic number of respective metals
$-\Delta H_{atom}$	heat of atomization of metal, kcal/g-atom
$-\Delta H_{ads}$	heat of adsorption of hydrogen, kcal/mole
X_M	electronegativity of metal atom, ev
ϕ	work function of metal, ev
S_i	separation factor of isotope i
I	initial system of rate-determining step
$+$	critical system of rate-determining step
$\sigma+$	seat on the electrode surface which is available for $+$
$N+$	number of seats on electrode surface
A	surface area, cm^2
e	elementary charge
$\mu(\delta)$	chemical potential of species δ, kcal/mole
p^δ	Boltzmann factor of $\mu(\delta)$
$\epsilon(\delta)$	reversible work required to bring δ from its reference state to the preliminarily evacuated seat or site which accommodates δ, kcal/mole
q^δ	Boltzmann factor of $\epsilon(\delta)$
η	overvoltage, defined as $\{\mu(e^-) - \mu(e^-)_{eq}\}/F$, V
$\mathfrak{A}$	macroscopic assembly consisting of electrode, electrolyte solution, and 1 atm hydrogen gas at a definite temperature but comprising none of the critical system
$\mathfrak{A}^\delta$	macroscopic assembly formed by addition of δ to $\mathfrak{A}$
$\mathfrak{A}_{\sigma+(0)}$	particular state of $\mathfrak{A}$ with a particular seat $\sigma+$ being unoccupied with certainty
$\mathfrak{A}_{\sigma+(\delta)}$	particular state of $\mathfrak{A}$ with a particular seat $\sigma+$ being occupied by δ with certainty
$\Omega\mathfrak{A}$'s	partition function of $\mathfrak{A}$'s defined above
$\theta_{\sigma+(0)}$	probability of $\sigma+$ being unoccupied
$\theta_{\sigma+(\delta)}$	probability of $\sigma+$ being occupied by δ
α's	positive proper fractions
R	repulsive potential

REFERENCES

1. J. O'M. Bockris and B. E. Conway, *Trans. Faraday Soc.*, **48**, 724 (1952).

2. J. O'M. Bockris and A. M. Azzam, *ibid.*, **48**, 145 (1952).
3. H. Gerischer and W. Mehl, *Z. Elektrochem.*, **59**, 1049 (1955).
4. I. A. Ammar and S. A. Awad, *J. Phys. Chem.*, **60**, 1290 (1956).
5. J. O'M. Bockris, I. A. Ammar, and A. K. M. S. Huq, *J. Phys. Chem.*, **61**, 879 (1957).
6. M. A. V. Devanathan, J. O'M. Bockris, and W. Mehl, *J. Electroanal. Chem.*, **1**, 143 (1959).
7. A. A. Antoniou and F. E. W. Wetmore, *Can. J. Chem.*, **37**, 222 (1959).
8. B. E. Conway, *Proc. Roy. Soc.*, **A256**, 128 (1960).
9. K. Gossner, Chr. Löffler, and G. M. Schwab, *Z. phys. Chem.*, **28**, 229 (1961).
10. T. Yamazaki and H. Kita, *J. Research Inst. Catalysis, Hokkaido Univ.*, **13**, 77 (1965).
11. M. Breiter, H. Kammermeier, and C. A. Knorr, *Z. Elektrochem.*, **60**, 454 (1956).
12. S. Schuldiner and J. P. Hoare, *J. Phys. Chem.*, **61**, 705 (1957).
13. N. Pentland, J. O'M. Bockris, and E. Sheldon, *This Journal*, **104**, 182 (1957).
14. D. J. G. Ives, *Can. J. Chem.*, **37**, 213 (1959).
15. K. Gossner and C. Löffler, *Z. Phys. Chem. N. F.*, **37**, 123 (1963).
16. U. W. Palm and V. E. Past, *Zhur. Fiz. Khim.*, **38**, 773 (1964).
17. J. O'M. Bockris and S. Srinivasan, *Electrochim. Acta*, **9**, 31 (1964).
18. B. E. Conway, E. M. Beatty, and P. A. DeMaine, *ibid.*, **7**, 39 (1962).
19. J. O'M. Bockris and D. F. A. Koch, *J. Phys. Chem.*, **65**, 1941 (1961).
20. E. J. Kelly, *This Journal*, **112**, 124 (1965).
21. St. G. Christov and L. Rajceva, *Z. Elektrochem.*, **66**, 486 (1962).
22. K. Sabo and I. Bagotskaja, *Doklady Akad. Nauk SSSR*, **149**, 139 (1963).
23. A. J. De Bethune, *J. Am. Chem. Soc.*, **71**, 1556 (1949).
24. B. Post and C. F. Hiskey, *ibid.*, **72**, 4203 (1950).
25. A. Mituya, *J. Research Inst. Catalysis, Hokkaido Univ.*, **4**, 228 (1956).
26. S. Minc and J. Sobkowski, *Bull. Akad. Polon. Sci.*, **8**, 29 (1959).
27. J. N. Butler and A. C. Makrides, *Trans. Faraday Soc.*, **60**, 938 (1964).
28. B. E. Conway and M. Salomon, *J. Chem. Phys.*, **41**, 3169 (1964).
29a. J. N. Butler and A. C. Makrides, *Trans. Faraday Soc.*, **60**, 1664 (1964).
29b. J. O'M. Bockris, *ibid.*, **43**, 417 (1947).
29c. J. N. Butler and M. Dienst, *This Journal*, **112**, 226 (1965).
29d. A. L. Rotinyan and N. M. Kozhevnikova, *Zhur. Fiz. Khim.*, **37**, 1818 (1963).
29e. M. J. Joncich, L. S. Stewart, and F. A. Posey, *This Journal*, **112**, 717 (1965).
30. J. O'M. Bockris and E. C. Potter, *J. Chem. Phys.*, **20**, 614 (1952).
31. J. Yeager, J. P. Cels, E. Yeager, and F. Hovorka, *This Journal*, **106**, 328 (1959).
32. R. Piontelli, L. P. Bicelli, and A. La Vecchia, *Accad. Nazionale Dei Lincei VIII*, **27**, 312 (1959).
33. M. A. V. Devanathan and M. Selvaratnam, *Trans. Faraday Soc.*, **56**, 1820 (1960).
34. A. C. Makrides, *This Journal*, **109**, 977 (1962).
35. H. Kita and T. Yamazaki, *J. Research Inst. Catalysis, Hokkaido Univ.*, **11**, 10 (1963).
36. A. K. M. S. Huq and A. J. Rosenberg, *This Journal*, **111**, 270 (1964).
37. J. L. Weininger and M. W. Breiter, *ibid.*, **111**, 707 (1964).
38. A. Matsuda and T. Ohmori, *J. Research Inst. Catalysis, Hokkaido Univ.*, **10**, 203 (1962).
39. S. Jofa, *Zhur. Fiz. Khim.*, **19**, 117 (1945).
40. W. Palm and V. Past, *Doklady Akad. Nauk SSSR*, **146**, 1374 (1962).
41. R. Clamroth and C. A. Knorr, *Z. Elektrochem.*, **57**, 399 (1953).
42. J. P. Hoare and S. Schuldiner, *This Journal*, **102**, 485 (1955).
43. J. P. Hoare and S. Schuldiner, *ibid.*, **104**, 564 (1957).
44. H. Shiratori, *Denkikagaku* (Electrochemistry), **29**, 765 (1961).
45. J. C. Barton and F. A. Lewis, *Z. Phys. Chem.*, **33**, 99 (1962).
46. S. Schuldiner, *This Journal*, **107**, 426 (1954).
47. K. J. Vetter and D. Otto, *Z. Elektrochem.*, **60**, 1072 (1956).
48. I. A. Ammar and S. Darwish, *J. Phys. Chem.*, **63**, 983 (1959).
49. S. Schuldiner, *This Journal*, **106**, 891 (1959); *ibid.*, **108**, 384 (1961).
50. E. Yeager, "Transactions of the Symposium on Electrode Processes," John Wiley & Sons, Inc., New York (1961).
51. R. Parsons, *Trans. Faraday Soc.*, **56**, 1340 (1960).
52. T. Hisano, *Denkikagaku* (Electrochemistry), **31**, 98 (1963).
53. S. Schuldiner, *This Journal*, **107**, 452 (1960).
54. J. Hoare, *ibid.*, **107**, 820 (1960).
55. E. A. Efimov and I. G. Erusalimchik, *Doklady Akad. Nauk SSSR*, **124**, 609 (1959).
56. E. A. Efimov, I. G. Erusalimchik, and G. P. Sokolova, *Zhur. Fiz. Khim.*, **36**, 1005 (1962).
57. I. A. Ammar and S. A. Awad, *This Journal*, **103**, 182 (1956).
58. N. Hackerman and C. D. Hall, Jr., *ibid.*, **101**, 321 (1954).
59. Ya. M. Kolotyrkin and P. S. Petrov, *Zhur. Fiz. Khim.*, **31**, 659 (1957).
60. A. T. Petrenko, *ibid.*, **36**, 1527 (1962).
61. A. L. Rotinyan, N. P. Fedotieff, and Li Un Sok, *ibid.*, **31**, 1259 (1957).
62. H. Kita, *J. Research Inst. Catalysis, Hokkaido Univ.*, **13**, 151 (1965).
63. M. A. Avdeenko, G. K. Boreskov, and M. G. Slin'ko, Sbornik. Problemy kinetiki i kataliza. IX. Izotopy v katalize. Izd. Akad. Nauk SSSR, Moscow, p. 61 (1957).
64. G. K. Boreskov, M. G. Slin'ko, A. G. Filippova, and R. N. Gur'yanova, *Doklady Akad. Nauk SSSR*, **94**, 713 (1954).
65. O. F. Shcheglov, G. K. Boreskov, and M. G. Slin'ko, *ibid.*, **105**, 123 (1955).
66. S. Katz, G. B. Kistiakowsky, and R. F. Steiner, *J. Am. Chem. Soc.*, **71**, 2257 (1949). B. J. Wood and H. Wise, *J. Chem. Phys.*, **29**, 1416 (1958).
67. N. E. Khomutov, *Zhur. Fiz. Khim.*, **39**, 532 (1965).
68a. H. S. Taylor, *Proc. Roy. Soc.*, **A108**, 105 (1925).
68b. S. Z. Roginsky, Catalysis and Adsorption on Non-uniform Surfaces, Acad. Sci. SSSR, Moscow (1948).
69. R. T. Sanderson, "Chemical Periodicity," Reinhold Publishing Co., New York (1964).
70. D. D. Eley, *Discussions Faraday Soc.*, **8**, 34 (1950).
71. L. Pauling, "The Nature of the Chemical Bond," Cornell University Press, Ithaca, N. Y. (1940).
72. D. P. Stevenson, *J. Chem. Phys.*, **23**, 203 (1955).
73. B. E. Conway and J. O'M. Bockris, *J. Chem. Phys.*, **26**, 532 (1957).
74. H. B. Michaelson, *J. Appl. Phys.*, **21**, 536 (1950).
75. Y. Takahashi, S. Oka, and M. Oikawa, *Bull. Chem. Soc. Japan*, **31**, 220 (1958).
76. J. O'M. Bockris, S. Srinivasan, and M. A. V. Devanathan, *J. Electroanal. Chem.*, **6**, 205 (1963).
77. H. v. Buttlar, W. Vielstich, and H. Barth, *Z. Elektrochem.*, **67**, 650 (1963).
78. M. v. Stackelberg and W. Jahns, *ibid.*, **62**, 349 (1958).
79. J. Horiuti and G. Okamoto, *Sci. Papers Inst. Phys. Chem. Research, Tokyo*, **28**, 231 (1936).
80. G. Okamoto, J. Horiuti, and K. Hirota, *ibid.*, **29**, 223 (1936).
81. J. Horiuti and T. Nakamura, *J. Research Inst. Catalysis, Hokkaido Univ.*, **2**, 73 (1951-3); *J. Chem. Phys.*, **18**, 395 (1950).
82. J. Horiuti, T. Keii, and K. Hirota, *J. Research Inst. Catalysis, Hokkaido Univ.*, **2**, 1 (1951-3).
83. H. Kita and O. Nomura, *ibid.*, **12**, 107 (1964).
84. J. Horiuti, *ibid.*, **1**, 8 (1948-51).
85. J. Horiuti and M. Polanyi, *Acta Physicochim. USSR*, **2**, 505 (1935).
86. M. Breiter, C. A. Knorr, and W. Wölkl, *Z. Elektrochem.*, **59**, 681 (1955).
87. F. G. Will and C. A. Knorr, *ibid.*, **64**, 270 (1960).
88. J. Horiuti, *J. Research Inst. Catalysis, Hokkaido Univ.*, **3**, 52 (1954).
89. J. Horiuti, Proc. IInd International Congress of Surface Activity, Vol. II Solid-Gas Interface, p. 280, Butterworth Science Pub., London (1957).

Discussion

M. W. Breiter: A large amount of experimental data has been compiled for the interesting attempt to correlate the exchange current densities of hydrogen evolution on different metals with bulk properties of these metals. However, as discussed under A, the results in Fig. 1 and 2 of the paper may be interpreted in a different way. Some of the basic assumptions concerning the interpretation of the results in Fig. 3 and 4 are reexamined under B.

(*A*) As demonstrated[1,2] a "volcano"-type curve is to be expected when the exchange current densities of the Volmer reaction, of the Tafel reaction, and of the Heyrovsky reaction are plotted for different metals *vs.* the heat of hydrogen adsorption on these metals. If this result is accepted in contrast to the derivation of a linear relationship between the logarithm of the exchange current densities and the heat of adsorption in the paper, the three volcano curves in Fig. 1 may be easily correlated to $-\Delta H_{ads}$. The metals with relatively large values of $-\Delta H_{ads}$ are located on the left side of each of the long periods while the metals with small heat of adsorption are on the right side. Metals with intermediate values (d-metals) are located in the middle. A volcano type curve may be drawn through the points in Fig. 2. This results from the fact that ΔH_{ads} increases with ΔH_{atom}.

(*B*) Heats of adsorption calculated from Eq. [3] and [4] correspond to negligible hydrogen coverage in the gas phase ($\theta << 1$). Therefore these approximate values of $-\Delta H_{ads}$ should be used in the comparison between $-\Delta H_{ads}$ and exchange current densities only in the case that a small coverage has been established on the respective metal under H_2– evolution (as on mercury for instance). Experimental determinations [3,4] of $-\Delta H_{ads}$ as function of coverage show that the values of $-\Delta H_{ads}$ in Fig. 3 are too large for Pt, Rh, and Pd. The same statement applies to the d-metals Au, Cu, Ag, and the sp-metals Zn, Cd, Pd, Hg, Te since perceptible adsorption from the molecular gas was not found[5] at 300°K and $p_{H2} \approx 0.1$ mm Hg.

Any conclusions on the reaction mechanism from the results in Fig. 4 are very doubtful as it is demonstrated by two recent discussions[6,7] of electrode reactions and electrode material.

Hideaki Kita: It must be mentioned that the heat of adsorption is not the simple function of $-\Delta H_{atom}$ but also the function of the work function as shown by Eley and Stevenson.

Decrease of the heat of adsorption with coverage is taken into account in the present paper by R in Eq. [22b] of the text. This value is taken to be independent of electrode metal at $\theta_{\sigma^{\mp}(2H)} \simeq 1$ as a first approximation since R is the repulsive potential among hydrogen atoms on the surface, and the metal atoms would effect this potential only secondarily.

I agree with your opinion that IB metals, Cu, Ag, and Au, are poor adsorbents for hydrogen under very small pressure. However, in the region where we observe a Tafel relation, the situation is totally different as seen from the fact that, for example, the overvoltage of 0.4v corresponds to the very high pressure of 10^{16} mm Hg. The log i_o extrapolated from such conditions is generally a function of overvoltage and thus coverage (cf first paragraph in the reply to Dr. Schuldiner) which might be much higher than that obtained by the usual adsorption study of a gas-solid system. For the sp-metals, H_2^+-desorption mechanism is applied. It is open to question whether the surface is considerably covered with $H_2^+(a)$ or practically bare.

Roger Parsons: It is very useful to have confirmation of the Balandin volcano-like behavior of the exchange currents given by the two equations following [22b]. This prediction was first given independently by Professor Gerischer[8] and myself.[9] In fact, we gave the more general result that this type of behavior would occur for any mechanism involving adsorbed atomic hydrogen as an intermediate, and I extended the description to a heterogeneous surface described by Temkin's isotherm.

In regard to Dr. Kita's predictions for the mechanism involving slow discharge of the molecular hydrogen ion, I believe that equations [29a] and [29b] also lead to a Balandin volcano curve with heat of adsorption, because the coefficient α_w is likely to be very small. This coefficient in fact expresses the relation between the potential at the site of the reacting ion to the potential on the electrode and is given [according to ref. (88)] by

$$\alpha_w = \frac{1}{1 - X_p \cdot \frac{\partial}{\partial E_p}\left(\frac{\partial E}{\partial X}\right)_a + \frac{G F^2}{N_A R T}\textcircled{H}(1-\textcircled{H}) \cdot \frac{4\pi X_p}{D_p}} \qquad [1]$$

where X_p is the distance of the plane containing the centers of the reacting ions from the electrode, E_p is the average potential of this plane (bulk of the solution taken as zero), and D_p is the dielectric constant in this region. G is the number of sites in the plane at X_p, $\textcircled{H}$ is the fraction of these occupied by H^+ or H_2^+ ions and $1 - \textcircled{H}$ the fraction occupied by H atoms or empty. $(\partial E/\partial X)_a$ is the field strength at $X_p + dX$. Equation [1] may thus be written as

$$\alpha_w = \frac{1}{1 + \frac{C_D + C_{ads}}{C_H}}$$

where C_H is the capacity of the inner region $O < X < X_p$, C_D is the capacity of the diffuse layer, which is assumed in the model to begin at $X_p + dX$ and C_{ads}

[1] R. Parsons, *Trans. Faraday Soc.*, 54, 1053 (1958).

[2] H. Gerischer, *Bull. Soc. Chim. Belg.*, 67, 506 (1958).

[3] W. Böld and M. Breiter, *Z. Elektrochem.*, 64, 897 (1960).

[4] A. Frumkin, "Advances in Electrochemistry," P. Delahay, Editor, p. 366, Interscience Publishers, New York (1963).

[5] G. Ehrlich, Proc. of the 3rd Intl. Congress on Catalysis, W. M. H. Sachtler, G. C. A. Schuit, and P. Zwietering, Editors, pp. 113-145, North Holland Publishing Co., Amsterdam (1965).

[6] R. Parsons, *Surface Science*, 2, 418 (1964).

[7] A. N. Frumkin, *Elektrokhim.*, 1, 394 (1965).

[8] H. Gerischer, *Bull. Soc. Chim. Belg.*, 67, 506 (1958).

[9] R. Parsons, *Trans. Faraday Soc.*, 54, 1053 (1958).

is an adsorption capacity. It is well known that the diffuse layer capacity far exceeds the inner layer capacity except in very dilute solutions. Hence under the conditions of most hydrogen overvoltage experiments $C_D/C_H >> 1$. With G given the reasonable value of 10^{15} sites cm^{-2}, the value of C_{ads} is $6200\textcircled{H}(1-\textcircled{H})\mu F\ cm^{-2}$, so that C_{ads}/C_H will be large compared with unity except where H is very small or very close to unity. Hence it appears that α_w will be considerably less than the value of 0.5 required to substantiate the predictions of this theory given in the paper. It seems more probable that the exchange current of a hydrogen molecule ion mechanism depends on the heat of adsorption of hydrogen in the same way as that of the ion + atom mechanism discussed earlier by Gerischer and myself.

In fact there are objections to the hydrogen molecule ion mechanism which have been thoroughly discussed by many authors. One, to the model itself, is worth mentioning here. It seems improbable that the same adsorption sites will be occupied by H, H^+, and H_2^+ especially on metals such as mercury which adsorb hydrogen very weakly.

Finally, I should like to comment on the use of Eley's equation for weakly chemisorbed gases. This type of equation has had reasonable confirmation for gases which are strongly chemisorbed. However, it has an obvious defect for weak chemisorption since it predicts that for any metal M and any gas X_2 the M — X bond strength cannot fall below half the bond strength of X_2. Thus in the limit it makes an impossible prediction. Therefore, it seems reasonable to recommend extreme caution in applying this equation to weak chemisorption.

Hideaki Kita: It is unlikely at $\textcircled{H} \simeq 0$ or $\textcircled{H} \simeq 1$ that the coefficient α_w is very small. In the presence of a supporting electrolyte or in case of a concentrated solution, the factor $(\partial E/\partial X)_a$ in the above Eq. [1] of Dr. Parson's comment is expected to be small because of the lesser extent of the diffuse double layer. Thus the second term of the denominator of Eq. [1] might not be so large as pointed out in the comments. According to ref. (88) of my paper, the value of $\alpha_{w,o}$ defined as [Eq. (20.1α) of ref. (88)]

$$\alpha_{w,o} = 1/\left\{1 - X_p \frac{\partial}{\partial E_p}\left(\frac{\partial E}{\partial X}\right)_a\right\}$$

is estimated at 0.53 at 300°K for 1N uni-uni-valent neutral electrolyte solution, which is in agreement with the above expectation. The value of 0.4 for α_w obtained from the slope of Fig. 6 in my paper indicates that $\textcircled{H}$ is either very small or very close to unity.

The treatment in ref. (88) is developed in a general way by taking into account possible states of a physically identical site being either empty or occupied by one of H^+, H_2^+, and H exclusively. The probability of each state depends on many factors such as electrode material, overvoltage, solution, etc. It is concluded (88) that the reversible work, $w(\delta_i)$, required to fill up a specified, unoccupied site with δ_i [Eq. (3.4.ϵ) of ref. (88)] decreases in the following order on mercury

$$w(H) >> w(H^+) > w(H_2^+) > 0$$

Hence the probability of a site occupied by H on Hg might be extremely small.

I admit more or less an uncertainty included in the estimation of $-\Delta H_{ads}$ by the Eley-Stevenson method with respect to the sp-metals, although Eq. (3) of the text does not have the term corresponding to the bond strength of X_2. Nevertheless, the conclusion still holds valid, which is obtained from Fig. 3 of the text that the activity of the sp-metals does not depend on the heat of adsorption.

S. Schuldiner: Dr. Kita's compilation of log i_o's and comparisons with metallic properties are very interesting and useful. Such comparisons often appear to give real correlations, but on closer examination one realizes that limitations of data accuracy and assumed wide regions of linear behavior are really not justified. For example, the use of the extrapolated Tafel equation to zero overvoltage to obtain i_o is incorrect. The Hammett[10] relation to determine i_o correctly or Dolin, Ershler, and Frumkin's[11] $1/R_\eta$ as a characteristic of the rate of the over-all reaction would give much more reliable measures of catalytic activity. Of course, the range of orders of magnitude reflected in Fig. 1 are so broad that accuracy may not be too important. But accuracy is important in the other figures, because only with accurate data can one draw meaningful relations.

A fault of the Kita technique can be illustrated from his conclusion that the catalytic mechanism hold for d metals. Using the finding of several authors that a Pt electrode has an H_{ad} coverage of about unity and since Pt has a relatively low value of $-\Delta H_{ad}$, he concludes that other d metals with higher heats of adsorption must have essentially fully covered surfaces. Dr. Kita ignores the fact that Au has a very low H_{ad} coverage and that its $-\Delta H_{ad}$ is about the same as Pt.

In fact, one can justifiably draw one, or better, two parallel plateaus for the d metals from Pd to Re in Fig. 3. Just because the metals below Re appear to lie on a slope does not justify the extrapolation of this slope through the more active metals. A similar argument may be made for the data in Fig. 4. Here Ag, Fe, Au, Ni, and Re are essentially on a plateau and Rh, Pd, and Pt are on a higher plateau. Another factor not considered in this treatment is the change of $-\Delta H_{ad}$ with degree of coverage with H_{ad}. Also the fact that some metals (Pd, Pt, Fe, Ni, etc.) are known to absorb significant amounts of H atoms in their surface layers can in effect change both $-\Delta H_{ad}$ and the electrode material.

Hideaki Kita: 1. The value of log i_o obtained by the extrapolation of the Tafel line might not necessarily be in agreement with those obtained for example from i *vs.* η plot in the region near the reversible potential or the isotopic exchange reaction at $\eta = 0$. In case of the extrapolation, log i_o is expressed as

$$\log i_o = \log i - \eta \frac{\partial \log i}{\partial \eta}$$

which reduces to — a/b when Tafel line holds, but in general is a function of overvoltage or current density. Thus, the log i_o of the present paper is taken as a measure of the activity under the working condition of electrodes where the Tafel line is observed. Its accuracy depends on those of a and b.

2. About the coverage on Au, it must be mentioned that the kinetics on Au reported by many workers (Table I and Fig. 1 of the text) fluctuate very much and hence it might be required to re-examine.

3. The primary fact in Fig. 3 and 4 of the text is the separation of activities into two groups of d- and sp- metals. Further analysis of the tendency in the d-metals would require much precise values for log i_o and $-\Delta H_{ads}$.

4. The change of $-\Delta H_{ads}$ with coverage is taken into account in the present paper by R in Eq. [22b] of the text which is obviously zero in case 1 where

[10] Hammett, *J. Am. Chem. Soc.*, **46**, 7 (1924).

[11] Dolin, Ershler, and Frumkin, *Acta Physicochim. URSS*, **8**, 779 (1940).

$\theta_{\sigma^{\ddagger}(0)} \simeq 1$ and is taken to be independent of electrode metal as a first approximation in case 2 where $\theta_{\sigma^{\ddagger}(2H)} \simeq 1$ because the change of ΔH_{ads} is governed mainly by the repulsive interactions among hydrogen atoms on the surface.

5. There is a parallelism between the tendency to absorb hydrogen in the bulk of metal[12] and the heat of adsorption. However, the effect of surface layer absorption may be considered as a secondary one as seen from the results of nickel electrodes which were prepared by various kinds of treatments (Table I and Fig. 1 of my paper) and resulted in almost the same activity.

D. B. Matthews: The dependence of log i_o for the hydrogen evolution reaction on the electronic work function Φ reported by Professor Kita[13] differs from the correlation obtained by Matthews[14] which is in qualitative agreement with the work of Conway and Bockris.[15] The correlation obtained by Matthews[14] is shown in Fig. DM1.

The significance of such correlations is questionable in view of uncertainties in the value of Φ and i_o. Nevertheless, the correlation obtained by Matthews[14] is compatible with the present state of knowledge of the mechanism of the hydrogen evolution reaction. Thus the three groups of metals distinguishable in Fig. DM 1 correlate with three mechanisms of the hydrogen evolution reach on and with the three groups of protium-tritium separation factors measured on these metals.[16] Thus the slow discharge mechanism is believed to be operative on the low i_o group of metals (Hg, Pb, Cd, Sn, etc.), the slow electrochemical discharge mechanism on the medium i_o group of metals (Ag, Au, Ni, Fe, Cu, W, etc.) and the slow catalytic recombination mechanism on the high i_o group of metals (Pt, Pd, Ir, etc.)

The correlation shown in Fig. DM1 takes on even more significance when viewed in the light of the work of Conway and Bockris,[15] because the present correlation was obtained using the values of Φ assembled by Conway and Bockris.[15] Only the i_o values have been changed in order to take into account recent developments in technique which have led to new and/or better data. Thus the weak correlation obtained by Conway and Bockris[15] for the low i_o group of metals is greatly strengthened by the addition of data accumulated between 1957 and 1966.

The interpretation of these results remains the same as that proposed by Conway and Bockris.[15] The dependence of i_o on Φ arises primarily through the dependence of the heat of adsorption of atomic hydrogen on the electrode on Φ.

[12] cf. D. P. Smith, "Hydrogen in Metals," (1947).

[13] H. Kita, Abstract, No. 153. Electrochem. Soc. Symposium on Electrode Processes, Cleveland (1966).

[14] D. B. Matthews, Ph.D. Thesis, University of Pennsylvania (1965).

[15] B. E. Conway and J. O'M. Bockris, *J. Chem. Phys.*, 26, 532 (1957).

[16] J. O'M. Bockris and S. Srinivason, *Electrochim. Acta*, 9, 31 (1964).

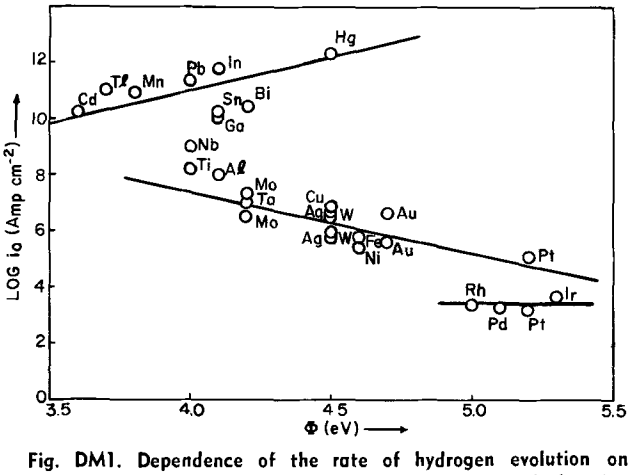

Fig. DM1. Dependence of the rate of hydrogen evolution on metal electrodes in acid solution on the electronic work function Φ of the metal.

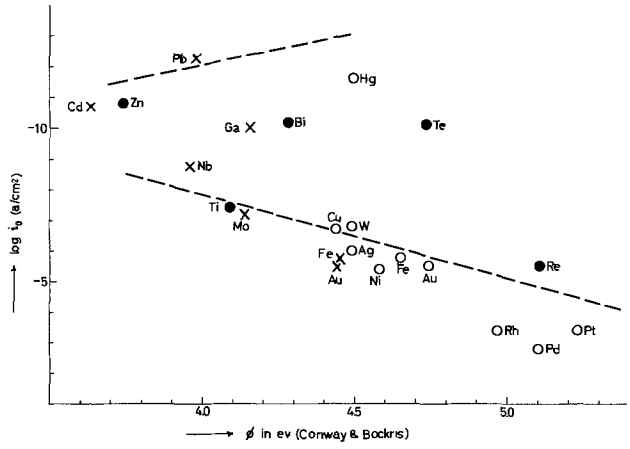

Fig. HK1. Log i_o vs. work function of electrode metals. Solid circles represent results not included in Fig. 1 of Conway and Bockris.[15]

Hideaki Kita: In Fig. HK-1 the present values of log i_o are plotted against the value of Φ quoted by Conway and Bockris.[17] Dotted lines in Fig. HK-1 are taken from Fig. 1 in the publication of Conway and Bockris.[17] From the comparison of these figures large difference can be noticed for the sp-metals. Namely, in the present paper the activity is taken as independent of Φ for the sp-metals, whereas in the paper of Conway and Bockris[17] and Fig. 1 therein, it is taken as dependent on Φ. Since the present values are obtained from Fig. 1 of my paper as averaged ones, they might be more reliable than those of Fig. 1 of Conway and Bockris.

Further division of the d-metals in Fig. 1 of my paper is questionable in view of uncertainties in the values of log i_o and Φ.

Frank Ludwig and *Ernest Yeager*: Dr. Kita has listed data for hydrogen discharge on platinum and platinized-platinum in Table I of his paper as well as in various figures. Some of these data probably need to be re-examined. Various electrochemists including A. N. Frumkin have suspected for some time that diffusion control may be involved in some and perhaps all of the hydrogen overpotential measurements on both bright and platinized-platinum in acid media reported in the literature. Consequently we have undertaken a study of hydrogen overpotential on bright platinum using the rotating disk-ring technique.[18] Preliminary results are now available.

The dependence of the overpotential measured on a bright platinum disk on rotation rate is shown in Fig. L-Y1. These measurements were made by the interrupter technique. Both activated and nonactivated electrodes exhibit a similar dependence. The usual precautions were taken to minimize impurity effects. The activation procedure consisted of maintaining the disk at a potential of +0.8v against a reversible hydrogen electrode in the same solution for 1 min, a

[17] B. E. Conway and J. O'M. Bockris, *J. Chem. Phys.*, 26, 532 (1957).

[18] A. Frumkin and L. Nekrasov, *Doklady Akad. Nauk. SSSR*, 126, 115 (1959); Y. Ivanov and B. Levich, *ibid.*, 126, 1029 (1959).

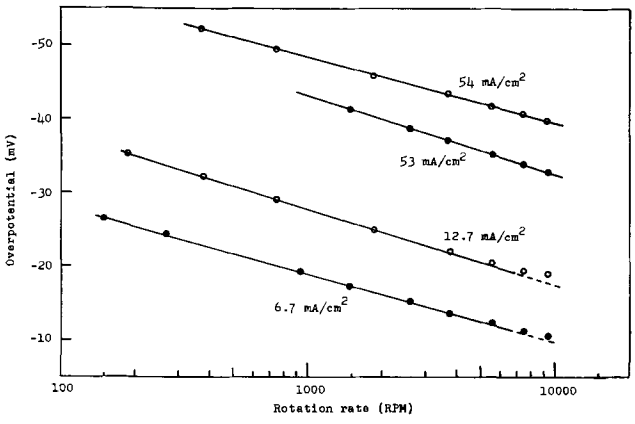

Fig. L-Y1. Dependence of hydrogen overpotential at bright platinum on rotation rate in 1*N* HCl at 25°C at constant current (—●—, activated platinum; —○— nonactivated platinum; slopes, 9.9 ± 0.9 mv/decade).

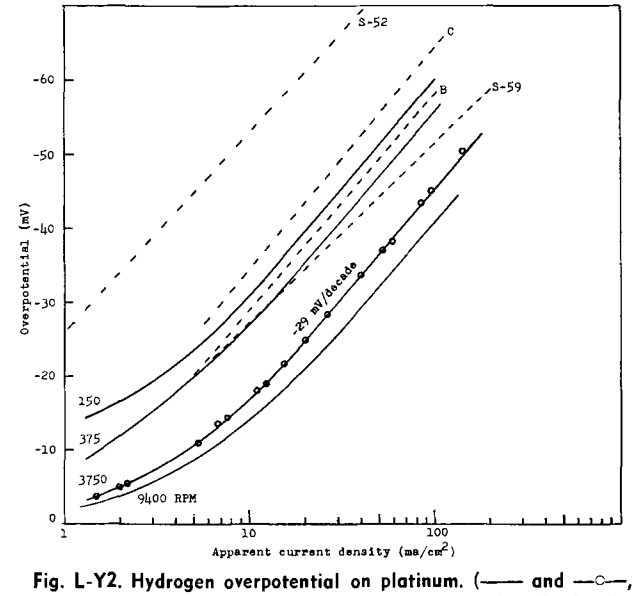

Fig. L-Y2. Hydrogen overpotential on platinum. (—— and —○—, present work at different electrode rotation rates, 1*N* HCl, bright, activated platinum at 25°C; S-52, Schuldiner[19] in 1952, 1*N* H_2SO_4, unstirred, bright activated platinum at 25°C; S-59, Schuldiner[19] in 1959, 1*M* H_2SO_4, bright activated platinum, stirred with 500 ml/min of gas flow through the solution at 25°C; C, Conway[20], 0.1*N* HCl, unstirred, platinized-platinum at 26°C; B, Bockris[21], 1*N* HCl, unstirred, bright activated platinum at 23°C).

condition insufficient to liberate any oxygen or chlorine and far less strenuous than that used by other authors for activation [see, for example, ref. (21)].

Figure L-Y2 shows the usual overpotential *vs.* log *i* plots for various rotation rates and also earlier data obtained by other workers. The curve for 3750 rpm was measured with increasing current at a constant rotation rate. Virtually identical results were obtained with decreasing current. The curves designated 150, 375, and 9400 rpm were calculated by applying corrections to the 3750 rpm curve with the correction determined from the dependence of the potential on rotation rate at constant current. Curves evaluated directly experimentally at other fixed rotation rates showed essentially identical slopes and similar dependence of the intercepts on rotation rates but reproducibility of the intercepts was somewhat poor.

In interpreting these results let us dismiss the idea that increased efficiency of mass transport of the hydronium ion to the electrode surface is responsible for the depression of the hydrogen overpotential with increased rotation rate. The concentration of HCl (1*M*) is just too high for this explanation to be valid. We believe that supersaturation of the solution with dissolved molecular hydrogen is involved. In particular the concentration of hydrogen in solution greatly exceeds the bulk value because of nucleation and transport problems, and increases with current density. This explanation was suggested by Yeager, Oey, and Hovorka[22] in 1953 and by M. Breiter *et al.*[23] in 1956. It should be understood that bubble formation relieves supersaturation only at the surface of the bubble and that substantial supersaturation is to be expected over the average of the electrode surface because of mass transport limitations associated with the diffusion of dissolved molecular hydrogen to the growing bubbles.

The —30 mv/decade slope can result from pure kinetic control with the desorption-recombination step rate determining, from pure diffusion control, or from mixed diffusion-kinetic control. To explain the present results on the basis of mixed diffusion-kinetic control, however, the rate of the back reaction must not be negligible and must in fact increase in direct proportion to the current density. Such is a reasonable possibility if the extent of supersaturation of the solution adjacent to the electrode is large compared to the bulk concentration of H_2 and the rate of transport of H_2 from the electrode surface is approximately proportional to the concentration of the dissolved H_2 at the electrode surface, *i.e.*

$$i = \kappa\,[(C_{H_2})_e - (C_{H_2})_\infty] = \kappa(C_{H_2})_e$$

with $(C_{H_2})_e >> (C_{H_2})_\infty$, where $(C_{H_2})_e$ and $(C_{H_2})_\infty$ are the concentrations of dissolved H_2 adjacent to the electrode and in the bulk of the solution, respectively, and κ is a proportionality constant. Our results indicate that, depending on the activation of the platinum, control may range from pure mass transport to combined mass transport-kinetic.

If the constant κ is directly proportional to $\omega^{-1/2}$, a slope of +15 mv/decade would be expected for plots of the type shown in Fig. L-Y1 for either pure diffusion control or combined diffusion-kinetic control provided the net rate is small compared to either the forward or reverse internal rates. The somewhat lower slopes evident in Fig. L-Y1 probably reflect complications associated with bubble formation in the vicinity of the electrode surface. Supersaturation is probably not uniform across the disk.

Only a few preliminary measurements have been made with the ring technique. The open-circuit potential of the ring exhibits approximately 30% of the overpotential measured on the disk by the interrupter method and is subject to a interesting oscillation phenomena which remains to be studied further. One would not expect the ring potential, however, to give a reliable indication of the average supersaturation at the disk surface since bubbles develop as the liquid spirals across the disk and the ring.

We believe that these observations are at least sufficient to require a re-examination of the whole question of the significance of now accepted overpotential measurements on platinum in acid media.

The authors acknowledge partial support of this research by the U.S. Office of Naval Research.

Roger Parsons: I would like to support the suggestion that the over-all process of hydrogen evolution

[19] S. Schuldiner, *This Journal*, 99, 488 (1952); *ibid.*, 106, 891 (1959).

[20] B. Conway, *Proc. Roy. Soc.*, A256, 128 (1960).

[21] J. O'M. Bockris, I. Ammar, and A. Huq, *J. Phys. Chem.*, 61, 879 (1957).

[22] E. Yeager, T Oey, and F. Hovorka, *J. Phys. Chem.*, 57, 268 (1953).

[23] M. Breiter, H. Hammermaier, and C. Knorr, *Z. Elektrochem.*, 60, 34 (1956).

on active platinum electrodes is controlled by diffusion of molecular hydrogen. Results I obtained about 13 years ago[24] showed that the rate of the over-all reaction was unusually reproducible over a period of up to 16 days while the a-c impedance changed rather rapidly with time. Hence, it is probable that the over-all process does not depend on anything happening at the electrode surface. Similarly, the activation energy for the over-all process was about 5 kcal which is the order expected for a diffusion process. These results were interpreted somewhat differently in the paper cited. The more recent work by Frumkin's co-workers also supports the diffusion mechanism.

G. C. Barker (communicated): From discussion remarks there now seems to be recognition of the fact that the polarization observed with clean smooth platinum and with some other metals is largely concentration polarization resulting from nucleation difficulties in the formation of gaseous hydrogen. I wish merely to point out that bubble formation at a clean surface free from re-entrant cavities is made difficult by the fact that the metal surface is wetted by the solution.[25] With a more hydrophobic platinum surface produced by deposition of one or more monolayers of stearic acid, bubble formation occurs much more readily and, despite the contamination of the surface the overpotential during hydrogen deposition in unstirred solution, is often smaller than for a completely clean surface. Ready formation of bubbles during gas deposition at electrodes is often indicative of surface contamination.

B. E. Conway (communicated): An analysis of the type given by Kita was first developed by Ruetschi and Delahay[26] and by Conway and Bockris[27] who took into account the electronegativity difference between H and various metals in their calculation of MH bond energies in relation to the electronic work function ϕ_e. In the further development of relations between ϕ_e, the heat of adsorption of H and the exchange current i_o, or overpotential at a given c.d., it seems that more attention must be paid to the extent of H-coverage prevailing in the steady state at various metals and the effect this has on the ϕ_e and the current at a given potential. A treatment of this type given by Parsons[28] leads to a pyramidal relation between i_o and the standard free energy ΔG_H^o of adsorption of hydrogen for both ion discharge (I) and atom-ion desorption (II) mechanisms. However, as we have pointed out elsewhere,[29] it seems that I will tend to prevail with low coverage θ_H by H at numerically small or positive ΔG_H^o values with a consequent increase of i_o with decreasing ΔG_H^o, while II tends to prevail with the catalytic and adsorptive metals having more negative ΔG_H^o and the $i_o - \Delta G_H^o$ relation will then be on the descending part of the pyramidal relation, *i.e.*, i_o will decrease for a desorption step with increasing strength of adsorption of H as predicted previously.[27]

Hideaki Kita (communicated): The change of the heat of adsorption of hydrogen with θ_H is taken into account by R in Eq. [22b] of the paper, the value of which might be primarily determined by the nature of hydrogen atom, since R is the measure of mutual interaction among hydrogen atoms on the surface. Hence, in the first approximation R might be taken almost independent of metals and then be assumed to be constant at relatively high coverage. The relationship between log i_o and $-\Delta H_{ads}$ obtained under the above conditions with respect to the catalytic mechanism (case 2 of the paper) is qualitatively in agreement with the results (Fig. 3 of the paper) for the d-metals which are the catalytic and adsorptive metals.

The pyramidal relation between log i_o and $\{-\Delta H_{ads} + F\phi_e\}$ could be also expected as seen from Eq. [29a] and [29b] of the paper for the electrochemical mechanism where the rate is governed by the neutralization of the adsorbed hydrogen molecule ion $H_2^+(a)$, *i.e.*

$$H_2^+(a) + e^- \rightarrow H_2$$

However, the compensating effect between the changes of $-\Delta H_{ads}$ and ϕ_e by metals as discussed in the present paper depresses the above expected relation to a great extent, so that the log i_o may not apparently depend on $-\Delta H_{ads}$ or ϕ_e as shown from the results for the sp-metals (Fig. 3 and 4 of the paper). Hence it is concluded that the electrochemical mechanism is operative on the sp-metals.

[24] R. Parsons, *Trans. Faraday Soc.*, **56**, 1340 (1960).

[25] G. C. Barker, Dissertation, Cambridge University (1946).

[26] P. Ruetschi and P. Delahay *J. Chem. Phys.* **23**, 195 (1955).

[27] B. E. Conway and J. O'M. Bockris, *ibid.*, **26**, 532 (1957).

[28] R. Parsons, *Trans. Faraday Soc.*, **54**, 1053 (1958).

[29] B. E. Conway, in "Progress in Reaction Kinetics," Vol. IV, G. Porter, Editor, Pergamon Press, Oxford (in press, 1966); B. E. Conway, "Theory and Principles of Electrode Processes," Ronald Press, New York (1965).

The Pressure Coefficient of the Hydrogen Electrode Reaction

G. J. Hills and D. R. Kinnibrugh

Chemistry Department, The University, Southampton, England

ABSTRACT

The various criteria for the mechanism of the hydrogen electrode reaction are considered with particular reference to the pressure coefficient of the reaction rate. The techniques of studying electrode processes at pressures up to 1500 atm are described, and the volume of activation derived for the hydrogen evolution reaction has been found to be −3.4 ml mole^{-1}. This negative value is not in accord with either of the two mechanisms usually proposed for this reaction. It suggests that the rate-determining step is the stage

$$e(\text{metal}) \rightarrow e(\text{aq})$$

i.e., the emission and hydration of metallic electrons.

This paper is concerned with the measurement and interpretation of the pressure coefficient of the hydrogen evolution reaction on mercury. The reaction has been studied at moderate current densities and under applied hydrostatic pressures up to 1500 atm. The partial pressure of molecular hydrogen remained throughout at ~1 atm, and the principal effect of the applied pressure was to influence the free energy of activation *via* the volume of activation.

Pressure coefficients of reactions in condensed phases are peculiarly sensitive to the role played by the solvent, the free volume of which is a function of

changes in electric charge density, of degree of solvation, and of other intermolecular factors. By determination of the volume of activation for the hydrogen evolution reaction, it was hoped to delineate still further the exact mechanism of the rate-determining step and to offer additional evidence for one or other of the theories usually proposed.

Activation Parameters as Diagnostic Criteria

The mechanism of most reactions is discernible by analysis of the reaction order which, in effect, is to sense the response of the reaction to changes in the chemical potential of significant components. Additional intensive variables include the temperature and pressure of the system and, for charge-transfer reactions, the electrode potential. For electrode processes, the two coefficients $\left(\frac{\partial \ln i}{\partial \eta}\right)_{T,P,\mu}$ and $\left(\frac{\partial \ln i}{\partial \mu}\right)_{T,P,\eta}$ are the most commonly used criteria and, in the absence of complicating features, often delineate unambiguously the path of an electrode reaction. Complications can arise principally because the distribution of interfacial chemical potentials and that of the interfacial electrical potential are mutually interdependent. This is clearly to be seen in the hydrogen evolution reaction on mercury

$$2H^+ + 2e \xrightarrow[Hg]{} H_2 \qquad (A)$$

The electrochemical reaction orders of this electrode process have been summarized by Conway and Salomon (1) from which it is clear that in dilute solutions of hydrochloric acid

$$\left(\frac{\partial \ln i}{\partial \eta}\right)_{T,P,\mu} = \frac{F}{2RT} \qquad [1]$$

and that with an interfacial composition stabilized by supporting electrolyte,

$$\left(\frac{\partial \eta}{\partial \mu_{HCl}}\right)_{T,P,i} = \frac{RT}{F} \qquad [2]$$

Without supporting electrolyte, the corresponding reaction order is zero because the activity of hydrogen ions in the outer Helmholtz plane and the potential, ψ_1, of that plane are related by the theory of the diffuse double layer, such that

$$\left(\frac{\partial \eta}{\partial \mu_{HCl}}\right)_{T,P,i} = 0 \qquad [3]$$

These criteria by themselves do not distinguish between two possible rate-determining steps of the overall mechanism, A, namely

$$H^+ + e \xrightarrow[slow]{} H;\ 2H \xrightarrow[fast]{} H_2 \qquad (B)$$

$$H^+ + e \xrightarrow[fast]{} H;\ H + H^+ + e \xrightarrow[slow]{} H_2 \qquad (C)$$

The reaction scheme C has been strenuously advocated by Horiuti (2, 3) and others (4, 5) and requires that the interface be saturated with either atomic hydrogen or the hydrogen molecule ion, H_2^+, regarded as an intermediate in the second, slow stage of C. The experimental evidence for this is often denied, and additional evidence (6, 7) from studies of isotope separation factors has been adduced to support the former scheme, B. We have therefore been concerned to examine the other criteria to see if they support one or other of these proposed mechanisms.

Both the temperature and the pressure derivatives of the rate of the hydrogen evolution reaction can conveniently be examined in terms of the appropriate form of the transition state theory, as applied to this system, *i.e.*

$$i = nFa_{H^+}\frac{kT}{h}\exp-\frac{\Delta G_o^{\neq}}{RT}\exp-\frac{\alpha\eta zF}{\beta RT} \qquad [4]$$

The temperature derivative

$$\left[\frac{\partial \ln (i/T)}{\partial (1/T)}\right]_{a_{H^+},P,\eta}$$

then leads, approximately at least, to the enthalpy of activation (8). Before the details of the approximations are called into question, it may be noted that the observed value is unremarkably high, ~22 kcal mole^{-1} (9). It can be attributed to a number of energetic processes, which may include the desolvation of hydronium ions, the reaction of atomic hydrogen with its surroundings, and the emission of electrons from the metal. It involves intra- as well as intermolecular transformations, it is always a complex quantity and it is seldom a discriminating factor (10).

The corresponding pressure-derivative leads to the volume of activation, *i.e.*

$$RT\left(\frac{\partial \ln i}{\partial P}\right)_{T,\eta,a_{H^+}} = -\Delta V^{\neq} \qquad [5]$$

It is invariably the case that $\Delta V^{\neq}$ is controlled by intermolecular changes only, *i.e.*, it is particularly sensitive to changes in intermolecular separation and in solvent free volume. For reactions which involve a charged, activated state, *i.e.*, where an extra degree of polarity is generated, there is an associated negative volume of activation, and the reaction is therefore accelerated by pressure (11). It might be supposed that for neutralization reactions where ions are discharged, the opposite would be obtained, and we sought to confirm this.

The various assumptions underlying the significance of the derived volume of activation are discussed later. The fact that $\Delta V^{\neq}$ was in fact found to be large and negative required a re-examination of both mechanisms referred to above.

Experimental

The measurement of hydrogen overpotential at a mercury electrode is a simple and well-established procedure. The system must be scrupulously clean, and the worst effects of surface-active or electro-active impurities can be avoided if a freshly formed mercury electrode is used.

It was decided here that a dropping mercury electrode was undesirable, not so much because of the difficulty of controlling such a system inside a pressure vessel [this has been done twice before (12, 13)], but rather because of the associated charging current. Instead, an extruded mercury drop electrode was used which could be generated and rejected at will by an electromechanical device, which in turn could be remotely operated within a pressure vessel. Three problems therefore presented themselves: (*i*) the design of a high-pressure system; (*ii*) the construction of a miniaturized electrode cell assembly able to transmit hydrostatic pressures, and (*iii*) its coupling to a mechanically driven piston capable of generating accurately mercury drops of known surface area.

Apparatus.—The design and assembly of the high-pressure vessel, pump, gauges, and ancillary equipment presented few problems. The technique of so doing is described elsewhere (14, 15) and the present equipment is summarized in Fig. 1.

The cell presented many more problems and that shown in Fig. 2 was evolved only after many other designs had failed. It consists essentially of a number of concentric glass cylinders able to move telescopically in order to transmit the pressure from the pump oil to the solution within the cell. Additional seals of mercury prevented ingress of the oil into the cell either through the sliding joints or through the

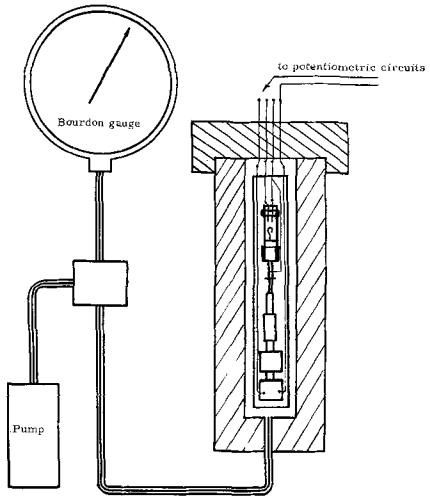

Fig. 1. High-pressure system

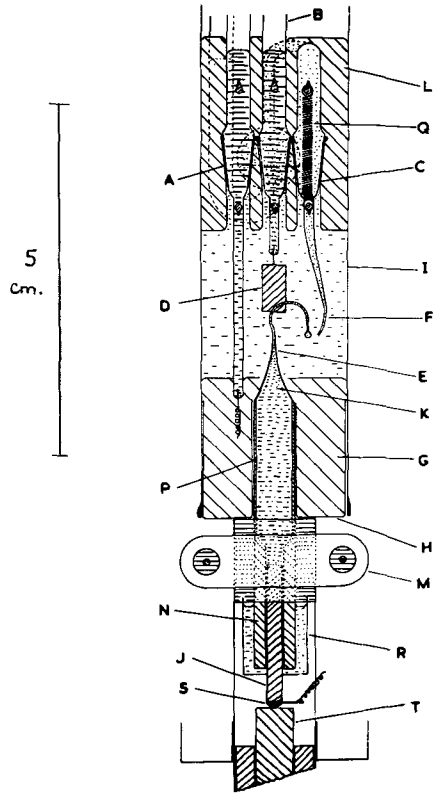

Fig. 2. Miniature cell for high-pressure overvoltage studies: A, B, C, B5 glass cone-socket joints; D, palladized palladium electrode; E, extruded mercury electrode; F, micro Luggin capillary; G, mercury pool; H, hollow glass syringe plunger; I, matching barrel to H; J, stainless steel piston; K, mercury reservoir; L, mercury seal; M, micrometer clamp; N, glass sheath to piston; P, upper end of N sliding into another barrel; Q, steel retaining springs; R, Teflon cup filled with water; S, insulating pad; T, micrometer screw.

fixed conical joints. All mercury exposed to the solution was maintained at a cathodic overpotential with relation to a large working anode of palladized palladium, presaturated with molecular hydrogen.

The extruded mercury drop electrode was generated at the end of a thin hooked capillary by movement of a stainless steel piston, through a Teflon bush, into precision-bore glass tubing which formed the base of the electrode capillary. This piston was driven by a micrometer plunger, the barrel of which was linked

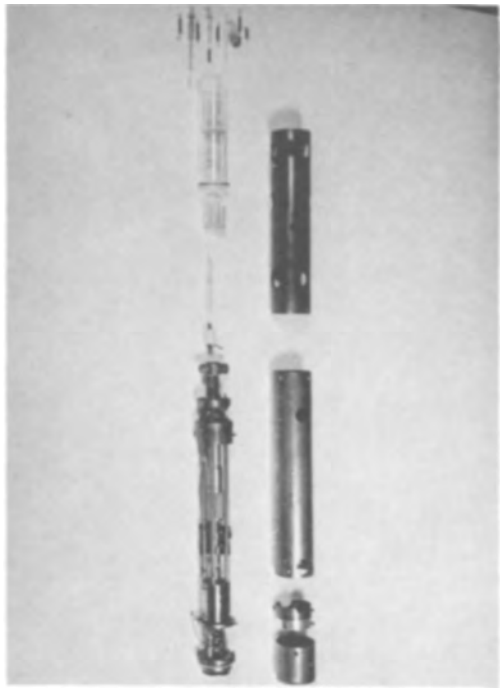

Fig. 3. Pulse-driven micrometer piston and cell

to a digital pulse-operated rotary solenoid (Ledex type 2E, N.S.F. Ltd.) by a micro gear-head (size 11, Vactric Control Ltd.) with a reduction ratio of 24.79:1. The apparatus is illustrated in Fig. 3 and its exact mode of operation will be described elsewhere (16). It need only be noted here that existing drops could be dislodged by an electric pulse applied to the electrode and that subsequently the volume of each extruded drop was directly proportional to the number of succeeding pulses applied to the drive. In terms of the characteristics of the rotary solenoid, the gear-head, the micrometer, and the area of the piston, the absolute volume of each drop could, in principle, be calculated. There is, however, always the possibility that when the drop breaks away, the mercury recedes into the capillary or a small drop is left. The first possibility was minimized by siliconing the capillary and by ensuring that the break-away was followed immediately by 5 pulses which then began a new drop. Even so, there was felt to be residual uncertainty as to the absolute area of each drop and to overcome the initial end-effects and the eventual distortion by sagging, it was decided to determine the current density from the linear part of the variation of observed current with surface area. For a constant density of mercury this is readily seen to be proportional to $n^{2/3}$, where n is the number of pulses.

The current flowing to the mercury electrode was determined potentiometrically, and the potential of the electrode itself was measured with respect to a microcalomel electrode joined to the cell by a very small "whisker" of drawn tubing filled with 1M KCl solution and serving as a Luggin capillary.

Procedure.—All the glass fitments were cleaned by boiling in perchloric acid solution. They were rinsed and soaked in conductivity water, dried in air, and assembled. The cell was mounted on the piston head, the capillary electrode filled with mercury (under vacuum) and the cell filled with hydrogen saturated oxygen-free solution. A short period of pre-electrolysis was allowed, using a sacrificial platinum electrode, and finally the system was sealed with mercury. It is seen in operation in Fig. 4.

The assembled apparatus was sheathed in a protective brass cylinder, to which electrical connections

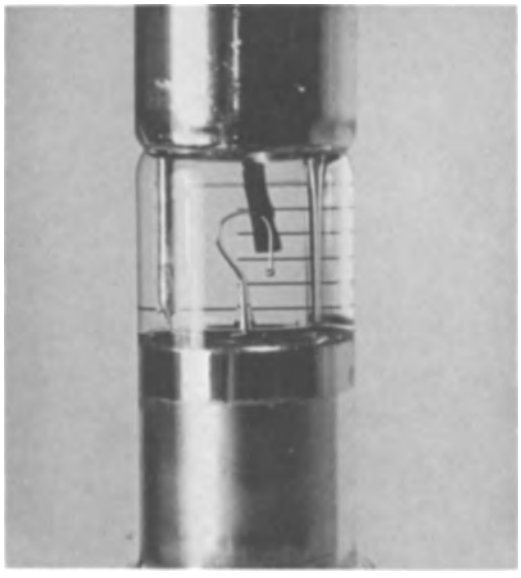

Fig. 4. Extruded mercury drop with upper and lower mercury seals

were soldered. This was inserted into the pressure vessel which was topped up with kerosene, sealed, and connected to the pump.

The proper functioning of the electrode was checked by various tests at 1 atm including the measurement of interfacial capacity. The pressure cycle was carried out in steps of 250 atm. At the highest pressures unstable conditions were often detected, and a new system had then to be used with another set of ascending pressures.

Results

The results relate to measurements made on the cell

$$Hg \mid 0.1M\ HCl \,||\, 1M\ KCl \mid Hg_2Cl_2 \mid Hg$$

Cathodic currents were measured as a function of overpotential, electrode area, and applied hydrostatic pressure.

At a particular value of overpotential and applied pressure, the current was measured at successive values of pulses, n, used to inject mercury into the electrode capillary. The observed current was a linear function of $n^{2/3}$, the slope of which was related, as above, to the current density. The results for one particular value of the overpotential are shown in Table I; the results for all values of η are summarized in Table II.

Table I. Observed currents, I, in μa at a fixed applied potential (—1.350v) as a function of electrode area and of applied hydrostatic pressure

	Pressure, atm				
n	250	500	750	1250	1500
15	1.68	1.92	2.18	2.20	2.63
25	2.45	2.69	3.04	3.07	3.60
35	3.16	3.34	3.85	3.81	4.40
45	3.79	3.99	4.48	4.53	5.16
55	4.34	4.58	5.10	5.32	5.87
65	4.89	5.33	5.60	6.17	6.54
75					7.17
$dI/dn^{2/3}$, amp $\times 10^{-7}$	3.20	3.34	3.53	3.60	3.90
i, $\times 10^{-4}$ amp cm^{-2}	1.26	1.32	1.39	1.42	1.54

Table II. A summary of observed current densities ($-\log_{10} i$) as a function of applied potential and applied hydrostatic pressure

Applied potential	Applied pressure, atm				
	250	500	750	1250	1500
−1.350	3.900	3.879	3.857	3.848	3.812
−1.400	3.418	3.383	3.391	3.370	3.334
−1.425	3.180	3.152	3.152	3.141	3.098
−1.450	2.934	2.913	2.906	2.883	2.857

The applied overpotentials are referred to the equilibrium potential of the above cell which is also pressure dependent. An allowance must be made for this pressure dependence and, in the absence of every relevant partial molar volume, it was determined experimentally using the cell

$$H_2,Pt \mid 0.1M\ HCl \,||\, M\ KCl \mid Hg_2Cl_2 \mid Hg$$

which utilizes a platinized platinum electrode and which has a more easily observed equilibrium emf. The HCl solution was saturated at 1 atm pressure, and it was assumed that its solution concentration remained, throughout the range of pressures, the same as that of the working cell.

The equilibrium emf of this cell was found to be a linear function of pressure and equal to 8.0×10^{-6}v atm^{-1}. This corresponds to a decrease in $\left(\frac{\partial \log i}{\partial P}\right)_{T,\mu,\eta}$ of 7.6×10^{-5} atm^{-1} in terms of the observed Tafel slope of 106 mv. This correction has therefore to be added to the observed pressure coefficient of current density. Results are summarized in Fig. 5 and 6 which show, respectively, Tafel slopes at 250 and 1500 atm, and the variation of (uncorrected) current density with pressure for four overvoltages. The average slope for all the measurements leads to a final pressure coefficient of cathodic current density of $13.8_5 \times 10^{-5}$ log^{-1} atm^{-1}.

Discussion

The significance of the pressure coefficient.—Although there is some scatter of the data presented in

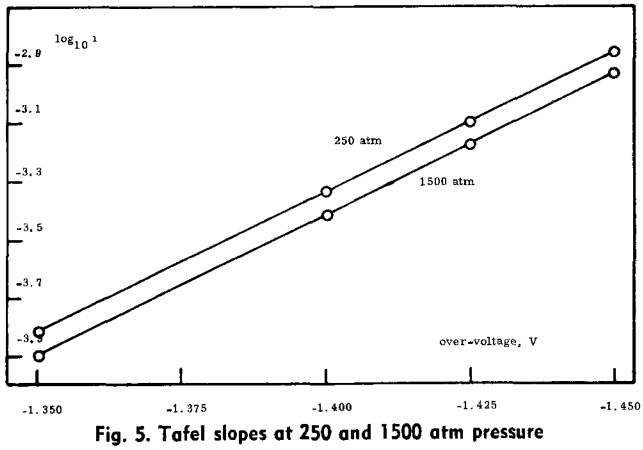

Fig. 5. Tafel slopes at 250 and 1500 atm pressure

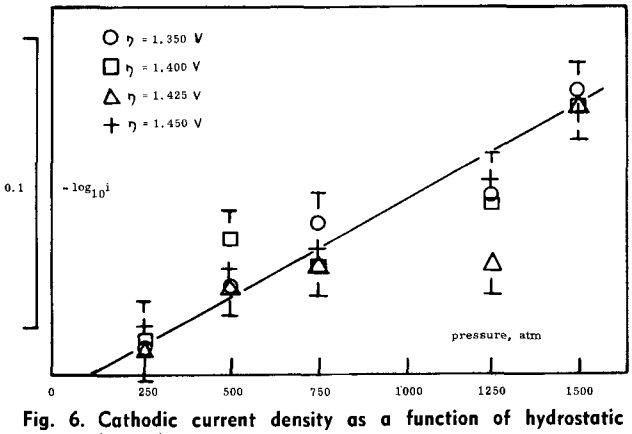

Fig. 6. Cathodic current density as a function of hydrostatic pressure; (|— —|) denotes limits of error.

Fig. 6, the results from a number of independent measurements confirm the sign and magnitude of the pressure coefficient. For a single, simple process this can then be translated into the corresponding volume of activation

$$\Delta V^{\ddagger} = -RT\left(\frac{\partial \ln i}{\partial P}\right)_{T,\mu,\eta} = -3.40 \pm 0.15 \text{ ml mole}^{-1} \quad [6]$$

The first requirement of the analysis is therefore to confirm that the coefficient relates predominantly to the single charge-transfer process under consideration.

There will normally be several contributions to the pressure coefficient of a rate process in solution, most of them not directly connected with the rate-determining step. Thus, the compression of the solution will increase the density and the volume concentration of all the components. The compressibility of water is not high, and over the range of pressures considered here, (~1500 atm), the total compression would not exceed a few per cent. A more serious change in composition arises in systems which are incompletely dissociated. An increase in pressure may then cause a large increase in ionic concentration because of the electrostrictive contraction of solvent resulting from ionization. This is no scope for such an effect in the present system.

Even if the stoichiometric concentration is not significantly altered by pressure, it is still possible that the absolute bulk activity of the reactants will change. The pressure-derivative of activity coefficient is related to the relative partial molar volumes, *i.e.*

$$2RT\left(\frac{\partial \ln \gamma_{\pm}}{\partial P}\right)_{T,\mu} = \overline{V} - \overline{V}_0 \quad [7]$$

For dilute solutions of hydrochloric acid, it may safely be estimated from the Debye-Hückel theory in terms of the pressure coefficient of solvent dielectric constant. Such a calculation suggests that this is also a very small effect.

It has also to be remembered that because the measurements are ultimately related to the standard hydrogen electrode, both working and reference electrodes have a common standard state. The thermodynamic effect of pressure on the bulk phase components is therefore zero.

The last and most important potential complication to the simple significance of $\Delta V^{\ddagger}$ is the possible effect of pressure on ionic distribution in the double layer. There is no evidence that pressure seriously disturbs the structure of the double layer, especially at cathodic potentials. The equilibrium between hydrogen ions in the bulk of the solution and those in the outer Helmholtz plane is an electrostatic one and is unlikely to be significantly influenced by pressure.

It may therefore be concluded that at high pressures, as at 1 atm, the rate of the hydrogen evolution reaction in dilute solution without supporting electrolyte is independent of the chemical potential of dissolved HCl and that the observed pressure-coefficient represents the volume of activation of the rate-determining process.

The significance of the volume of activation.—As indicated earlier, atoms and molecules are relatively incompressible whereas the free volume of a molecular assembly is sensitive to compressive stresses either from an externally applied pressure or from internal electrostrictive forces arising, for example, from the creation or introduction of charged centers. Thus, reactions in solution which proceed through a charged or polar activated state have negative volumes of activation and are therefore accelerated by applied pressure (11).

It is therefore surprising that the hydrogen evolution reaction, in which charge in the solution disappears, should also have a negative volume of activation. To appreciate this apparent anomaly, it is necessary to consider each aspect of the supposed rate-determining steps. The simple charge-transfer step

$$H^+(aq) \xrightarrow[Hg]{+e} H(ads) \quad (D)$$

can be resolved into at least three separate stages: (*i*) the dehydration of the hydronium ion and/or its transfer to the reaction site, (*ii*) the neutralization step in which a hydrogen atom is formed and then (possibly) adsorbed, (*iii*) the transfer of an electron from the mercury.

It is not easy to estimate the partial molar volume of hydration of a hydrogen ion. It may be noted with certainty that $\overline{V}^{\circ}$ for HCl does not differ from that of, say, NaCl. Mukerjee (17) and Conway and Desnoyers (18) have gone further than this and have reasonably argued (from size considerations and suitable extrapolations) that $\overline{V}^{\circ}_{H^+(aq)} = -5$ ml g-ion^{-1}. Whatever the significance of this result, it is evident that dehydration of the hydronium ion involves a large increase in volume.

Hills and Payne (19) made a detailed study of the effect of the transfer of ions into the double layer at mercury electrodes. They showed that when a specifically adsorbed ion displaces water molecules from the inner layer, there is a considerable increment of volume of the system. It follows that any similar process involving the transfer of hydrogen ions or atoms to the metal surface will likewise involve a positive volume change.

It may, however, be remarked that migration of hydrogen ions at 25°C requires a negative volume of activation, ~ −3 ml mole^{-1} (20), and that transfer of hydrogen ions from the outer Helmholtz plane to the reaction site might therefore involve the same process of contraction. This argument is untenable because the negative volume of activation of protonic migration is common to most ions and is associated with disengagement of water molecules from the structured solvent in the path of the ion (20).

Finally, some speculation may be made concerning the size of the hydrogen atom. There is evidence that this is a relatively large molecule and, for example, its disappearance in the gaseous recombination reaction

$$H^+ + H \rightarrow H_2^+ \quad (E)$$

is accompanied by a large decrease in volume (21). The volume of formation of hydrogen atoms would no doubt be influenced by its degree of adsorption on the metal surface. This cannot be a large factor on mercury and even if the process of adsorption largely nullified the partial molar volume of formation of atomic hydrogen, it is still difficult to see how the neutralization of the hydrogen ion can give rise to other than an increment of volume and *inter alia* to a positive volume of activation.

It remains to consider the transfer of electrons from the metal. Only if this is the predominant stage of the neutralization reaction and one with a large negative volume change, could adequate compensation for the other contributions be achieved. It is possible that the appearance of negative charges in the inner part of the double layer could give rise to further degrees of electrostriction, although the experimental evidence of Hills and Payne (19) is against this. They showed that the net volume of the interface (*i.e.*, of the inner layer) was independent of the degree of polarization beyond −10 μC cm^{-2} and therefore inferred that the closest packing of the water molecules had already been achieved. However, there is a distinction between a uniform potential gradient and that arising from discreet electronic charges, and it is therefore necessary to consider in greater detail the interaction between electrons and water. Before this is done, some

consideration will be given to the second possible rate-determining charge-transfer step, namely the ion-atom step

$$H^+_{(aq)} + H \xrightarrow[Hg]{e} H_2 \qquad (F)$$

This reaction continues to be advocated in spite of strong arguments against it. Experimental evidence for the existence of the intermediate ion, H_2^+, is strong, although frequently denied. It has been estimated (5) that in the gaseous state, the free energy change of reaction B is ~ -60 kcal mole^{-1}. This would accommodate the energy of desolvation of the proton and allow a high concentration of H_2^+ in solution. The small size of this ionic species has already been commented on and, if the activated state has a similar structure, then the observed negative volume of activation could readily be accounted for. Indeed, the pressure coefficient reported here might be considered to be the strongest evidence so far for the ion-molecule mechanism.

This mechanism also satisfies all the other criteria provided the activity of atomic hydrogen or of the hydrogen molecule ion is constant, *i.e.*, independent of potential. In the present formulation this implies a "coverage" of unity. Observed interfacial capacities of mercury in HCl solution allow no significant coverage, *i.e.*, displacement of water molecules. although they would not be inconsistent with a high concentration of H_2^+. Even so, the activity of H_2^+ is still dependent on the steady-state concentration of hydrogen atoms. If this activity is potential-dependent, and there is no reason why it should not be, the electrochemical reaction order could not lead to the Tafel slope observed.

One must therefore return to the slow ion-discharge step, A, and reconsider the evidence for electron emission as the principal feature of the rate-determining step. The inner layer adjacent to the electrode is known to be populated only with water molecules; cations are excluded and anions are further repelled. The main act of charge transfer can therefore be considered to be the transfer of electrons from the metal surface to the outer Helmholtz plane.

The possibility that classical electron emission is the rate-determining step of the hydrogen evolution reaction has been considered earlier (22), but rejected on the grounds that it leads to impossibly small rate constants. A rough calculation in terms of the thermionic work function of mercury, 4.5 ev (23) and the probable depth of the potential well of a hydrated electron, $\sim$ 2 ev (24) leads to an energy of electron abstraction of $\sim$60 kcal mole^{-1} which is nearly three times the observed activation energy. There is, however, the possibility of tunneling and, in spite of recent arguments to the contrary (6, 7), Christov (25, 26) maintains that this is an important feature of the hydrogen electrode reaction. Bockris (22) argues otherwise and suggests that the "work of forming the transition state is almost entirely made up of that of stretching the bond between the cation and the hydration sheath." If this were so, it would certainly be detected as a positive volume of activation as it is in most translational processes (27, 28).

Support for the independent existence of the aquated electron has recently come from several sources (24, 29, 30). The electrochemical consequences have been examined by Yurkov (31) and further evidence for its importance in electrode processes is furnished by the work of Barker (30) who studied photoemission currents at the mercury electrode in aqueous systems. In contrast with electrode systems *in vacuo*, the energy barrier associated with electron abstraction in the present system is strongly potential-dependent, since almost all of the potential gradient occurs in the double layer and the effective work function is altered. In the absence of electron scavengers, the photoemission current was negligible, since the hydrated electrons were continuously returning to the electrode. In acid solutions, an appreciable photocurrent was observed and was attributed almost entirely to electron-capture by the hydronium ion which is known to be a fast reaction [$k = 2.36 \times 10^{10}$ mole^{-1} sec^{-1} (30)]. The partial molar volume of the electron in water is not known, but in keeping with every other small ion, it must be negative. The transfer of electrons through the inner layer to the reaction zone beyond would therefore also require a negative volume of activation and this would not conflict with the results from the equilibrium studies of Hills and Payne (19). The pressure coefficient reported here is therefore advanced as further evidence for the participation of the aquated electron in electrode processes.

The assumption that the rate-determining step of the hydrogen electrode reaction is simply

$$e(\text{metal}) \rightarrow e(\text{aq})$$

would go far to explain the great sensitivity of this reaction to the nature and state of the metal surface, to the presence of adsorbed material and, even for a pure metal surface, to its thermionic work function. It follows that the succeeding steps of the reaction are all fast. Electron capture by the hydronium ion leads to hydrogen atoms which react immediately and exothermically with further hydronium ions to form the hydrogen molecule ion. This in turn also acts as an electron scavenger and reacts immediately to form molecular hydrogen. This mechanism is in accord with much of the independent experimental evidence; it does not invalidate any of the other criteria mentioned above and the results of the analysis of reaction order remain the same. At least, in the case of the hydrogen evolution reaction on mercury, the heat of adsorption of hydrogen on mercury no longer appears a necessary feature of the argument. This will conflict with many other theories and it may be that they will need to be re-examined in the light of this fresh experimental evidence.

Acknowledgments

The authors wish to thank the United Kingdom Central Electricity Generating Board for a scholarship for one of them (D.R.K.). They also wish to thank the Courtaulds Educational Trust for the gift of high-pressure apparatus.

LIST OF SYMBOLS

a	activity
ev	electron volt
F	the faraday
$\Delta G_0^{\pm}$	standard molar free energy of activation
h	Planck's constant
i	current density
I	total current
k	rate constant
k	Boltzmann's constant
m	molality
n	number of pulses
n	number of electrons transferred in the electrode reaction
P	pressure
R	gas constant
T	absolute temperature
v	volt
$\bar{V}$	partial molar volume
$\bar{V}_o$	partial molar volume at infinite dilution
$\Delta V^{\pm}$	volume of activation
α	energy transfer coefficient
β	stoichiometric number
$\gamma_{\pm}$	mean molal activity coefficient
μ	chemical potential
η	overvoltage

REFERENCES

1. B. E. Conway and M. Salomon, *Electrochim. Acta*, **9**, 1599 (1964).
2. J. Horiuti, T. Keii, and K. Hirota, *J. Research Inst. Catalysis, Hokkaido Univ.*, **2**, 1 (1951).

3. J. Horiuti, "Transactions of the Symposium on Electrode Processes," pp. 17-34, E. Yeager, Editor, John Wiley & Sons, Inc., New York (1961).
4. O. M. Poltarak, *Zhur. Fiz. Khim.*, **27**, 599 (1953).
5. D. J. G. Ives, *Can. J. Chem*, **37**, 213 (1959).
6. M. Salomon and B. E. Conway, *Discussions Faraday Soc.*, **39**, 223 (1965).
7. J. O'M. Bockris, S. Srinivasan, and D. B. Matthews, *Discussion Faraday Soc.*, **39**, 239 (1965).
8. J. O'M. Bockris, "Modern Aspects of Electrochemistry," Vol. I, p. 197, J. O'M. Bockris, Editor, Butterworths, London (1954).
9. B. Post and C. F. Hiskey, *J. Am. Chem. Soc.*, **72**, 4203 (1950).
10. S. B. Brummer and G. J. Hills, *Trans. Faraday Soc.*, **57**, 1816 (1961).
11. E. Whalley, "Advances in Physical Organic Chemistry," V. Gold, Editor, Academic Press, New York, 2 (1964).
12. S. G. Mairanovskii, M. G. Gonikberg, and A. A. Opekunov, *Doklady Akad. Nauk S.S.S.R.*, **123**, 312 (1958).
13. G. J. Hills and R. Payne, *Trans. Faraday Soc.*, **61**, 316 (1965).
14. G. J. Hills, *Talanta*, **12**, 1317 (1965).
15. G. J. Hills and P. J. Ovenden, "Advances in Electrochemistry and Electrochemical Engineering," Vol. IV, P. Delahay and C. W. Tobias, Editors, Interscience Publishers, Inc., New York (1966).
16. D. R. Kinnibrugh, Thesis (Southampton) 1965; G. J. Hills and D. R. Kinnebrugh, To be published.
17. P. Mukerjee, *J. Physic. Chem.*, **65**, 740 (1961).
18. B. E. Conway and J. E. Desnoyers, *Can. J. Chem.*, In press: *see J. Phys. Chem.*, **68**, 2305 (1964).
19. G. J. Hills and R. Payne, *Trans. Faraday Soc.*, **61**, 326 (1965).
20. G. J. Hills, P. J. Ovenden, and D. R. Whitehouse, *Discussion Faraday Soc.*, **39**, 207 (1965).
21. C. A. Coulson, *J. Chem. Soc.*, **1965**, 778.
22. J. O'M. Bockris, "Electrochemistry," Proceedings of the 1st Australian Conference, Pergamon Press, London, pp. 691-710 (1964).
23. O. Klein and E. Lange, *Z. Elektrochem.*, **44**, 542 (1938).
24. E. J. Hart and J. W. Boag, *J. Am. Chem. Soc.*, **84**, 4090 (1962).
25. S. G. Christov, *Z. Phys. Chem.*, **214**, 40 (1960).
26. S. G. Christov, *Electrochim. Acta*, **4**, 194, 306 (1961).
27. S. B. Brummer and G. J. Hills, *Trans. Faraday Soc.*, **57**, 1823 (1961).
28. S. B. Brummer, *J. Chem. Phys.*, **42**, 1636 (1965).
29. S. Gordon, E. J. Hart, M. S. Matheson, J. Rabani, and J. K. Thomas, *Discussion Faraday Soc.*, **36**, 193 (1963).
30. G. C. Barker, Report to C.I.T.C.E. Meeting Moscow (1963).
31. V. A. Yurkov, *Soviet Electrochemistry*, Vol. II, Consultants Bureau, N. Y. p. 85 (1961).

Discussion

Dennis B. Matthews: First let me correct some wrong impressions one might obtain from the paper by Hills and Kinnibrugh. The impression has been given that the work of Bockris, Srinivasan, and Matthews[1] excludes electron tunneling. Such is not the case, however, as the theory of charge transfer at electrodes proposed by Bockris and Matthews[2, 3] is strongly dependent on electron tunneling. Also, the work of Christov[4, 5] is concerned with proton tunneling and not with electron tunneling.

Although by far the major contribution of this paper is the new experimental results, I would like to touch on several points regarding the interpretation of the results, in particular on the newly proposed mechanism

$$Me^- \rightarrow e^-(aq) \qquad [1]$$

First, such a mechanism would lead to no hydrogen isotope effect for the hydrogen evolution reaction, in contrast with experiment. Second, the energetics of reaction [1] are such as to lead to a negligible rate of reaction. Consider the potential energy profile for electron transfer from the metal to the solvent (Fig. DM 1).

The electronic work function Φ for mercury is about 4.5 ev while the solvation energy of the electron L_e is about 2 ev or less. This means that in order for the electron to undergo tunnel transfer from the metal to the solvent, it must undergo excitation from the Fermi level by about 2.5 ev or greater ($\simeq$60 kcal mole^{-1}) in contrast to observed value of 21 kcal mole^{-1} for the activation energy of the hydrogen evolution reaction on mercury.

[1] J. O'M. Bockris, S. Srinivasan and D. B. Matthews, *Discussion Faraday Soc.*, 39, 239 (1965).

[2] J. O'M. Bockris and D. B. Matthews, *J. Electroanalyt. Chem.*, 9, 325 (1965).

[3] J. O'M. Bockris and D. B. Matthews, *Proc. Roy. Soc. Series A, London*, in press.

[4] St. G. Christov, *Z. Phys. Chem.*, 214, 40 (1960).

[5] St. G. Christov, *Electrochim. Acta*, 4, 194, 306 (1961).

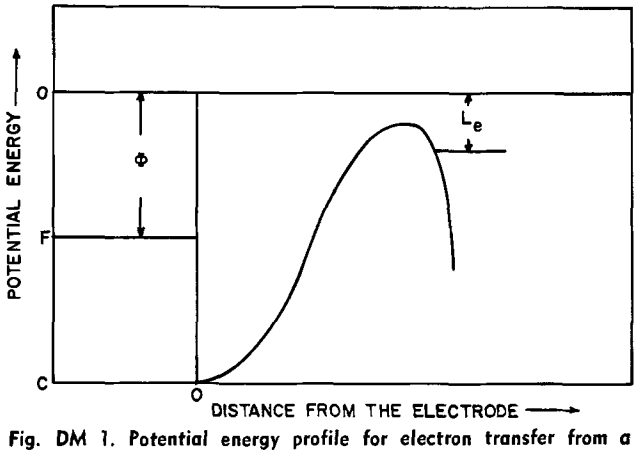

Fig. DM 1. Potential energy profile for electron transfer from a metal to the solvent.

L. I. Kristalik (communicated): Very interesting results on the dependence of the cathodic hydrogen evolution rate on hydrostatic pressure have been obtained in the Hills and Kinnibrugh paper, but it seems to me that the interpretation of these data is not rigorous. The authors maintain that the derivative of the logarithm of the current with respect to pressure at a constant overvoltage is directly determined by the change in the volume on activation

$$RT\left(\frac{\partial \ln i}{\partial p}\right)_\eta = -\Delta V^{\neq} \qquad [1]$$

In reality, however, $\Delta V^{\neq}$ determined by Eq. [1] is not the true value of the change in the volume on transition from the H_3O^+ ion in the double layer and the electron in the metal to the activated complex, but some effective value $\Delta V_r^{\neq}$. The true volume change during activation is determined not by the pressure dependence of the current at a constant overvoltage but by that at a constant potential

$$RT\left(\frac{\partial \ln i}{\partial p}\right)_\phi = -\Delta V_{id}^{\neq} \qquad [2]$$

At a constant overvoltage, however, the change in the pressure results in that of the total potential difference equal to the change in the equilibrium potential.

The situation is in many respects similar to the relations to be encountered in the investigation of the temperature dependence of the electrode processes rates where the determinable real activation energy (at η = const) does not represent the true energy change of the transition from the initial to the activated state (ideal activation energy), but differs from it by a quantity proportional to the latent heat of the over-all electrode process, which cannot be determined experimentally.[6]

Likewise, $\Delta V_r^{\neq}$ differs from $\Delta V_{id}^{\neq}$ by a similar quantity associated with the pressure dependence of the equilibrium potential.

It can be readily seen that

$$\left(\frac{\partial \ln i}{\partial p}\right)_{\phi} = \left(\frac{\partial \ln i}{\partial p}\right)_{\eta} - \left(\frac{\partial \ln i}{\partial \phi}\right)_{p} \frac{d\phi_e}{dp}$$

$$= \left(\frac{\partial \ln i}{\partial p}\right)_{\eta} + \frac{\alpha F}{RT}\frac{d\phi_e}{dp} \quad [3]$$

where ϕ_e is the equilibrium value of ϕ.

$$F\phi_e = \mu_e + \mu_{H3O^+} - \mu_{H2O} - \frac{1}{2}\mu_{H_2} \quad [4]$$

It follows from Eq. [2]-[4] that

$$RT\left(\frac{\partial \ln i}{\partial p}\right)_{\eta} = -\Delta V_{id}^{\neq} + \frac{\alpha}{2}\overline{V}_{H_2} + \alpha\overline{V}_{H2O} - \alpha\overline{V}_{H3O^+} \quad [5]$$

The same result can be obtained by the differentiation of the kinetic equation of the H_3O^+ ions discharge. The derivative $d\mu_e/dp$ is omitted in Eq. [5]. It is difficult to estimate it accurately, but its value can be shown to be not large.

The partial molar volume of dissolved hydrogen is $\overline{V}_{H_2}$ = 26 cm³/mole [7] $\overline{V}_{H2O} - \overline{V}_{H3O^+} = -\overline{V}_{H^+}$ can be estimated to be +5 cm³ [ref. (17), (18) in Hills and Kinnibrugh's paper].

From these values, α = 1/2 and the experimentally obtained value $\Delta V_r^{\neq} = -RT(\partial \ln i/\partial p)_{\eta} = -3.4$ cm³, we have

$$\Delta V_{id}^{\neq} \simeq -3.4 + 6.5 + 2.5 = +5.6 \text{ cm}^3/\text{mole}$$

Although the accuracy of the determination of this value is not very high, there is no doubt that $\Delta V_{id}^{\neq}$ is positive. Therefore, it is not necessary to assume the electron emission from the metal to be the slow step of the process. By the way, it does not seem possible that the dependence of the overvoltage on *p*H of the solution could be explained on the basis of this assumption.

G. J. Hills: The issue raised by Dr. Krishtalik is an important one. The fact that we have already taken it into account was no doubt obscured by our definition of η as "overvoltage." In fact, throughout this paper, η is the overpotential, and the scale of overpotential was derived from the observed pressure coefficient of the reference electrode cell

$$\text{Pt, } H_2 \mid \text{HCl} \,\|\, \text{1M KCl} \mid Hg_2Cl_2 \mid \text{Hg}$$
(partial pressure, 1 atm)

It follows that the overpotential is equated to the derived overvoltage for the cell

$$\text{Hg} \mid H_2, \text{HCl} \mid \text{Pt}$$

assuming only that ohmic and concentrational overpotentials are negligible.

The advantage of this procedure is that the standard states of both working and reference electrodes are the same and that there are ∴ no differential pressure effects on the thermodynamic properties of the system. In more specific terms, changes in chemical potential of the initial and final states embracing the transition state are compensated by corresponding changes in the reference electrode.

There is no question of differentiating at constant potential. The appropriate differential is

$$\left(\frac{\partial \ln i}{\partial P}\right)_{T,\eta}$$

Roger Parsons: I think that this is an elegant piece of experimental work, and the results are presented in the most satisfactory form, namely as the result of pressure changes on the rate at constant overpotential. However, I believe that the interpretation requires some modification.

If the rate is expressed in terms of the overpotential, then the corresponding free energy of activation may be expressed in a form such as

$$\Delta G^{\neq} = \mu^{\neq} - (1-\alpha)\mu_{H^+} - \frac{\alpha}{2}\mu_{H_2}$$

where $\mu^{\neq}$ is the standard chemical potential of the activated complex, μ_{H^+} that of the hydrogen ion solution, μ_{H_2} that of the final product, molecular hydrogen, in this case dissolved in solution, and α is the cathodic transfer coefficient. This equation is quite general independent of the mechanism of the hydrogen electrode reaction.

The pressure coefficient of the electrode reaction rate at constant overpotential is then

$$-RT\left(\frac{\partial \ln i}{\partial P}\right)_{\eta} = \left(\frac{\partial \Delta G^{\neq}}{\partial P}\right)_{\eta} = \Delta V^{\neq}$$

$$= \overline{V}^{\neq} - (1-\alpha)\overline{V}_{H^+} - \frac{\alpha}{2}\overline{V}_{H_2}$$

It is likely that the largest contribution to $\Delta V^{\neq}$ is $\overline{V}_{H_2}$, the partial molal volume of dissolved hydrogen, and this would explain the negative value experimentally found whatever is the mechanism.

The usual assumption that the discharge mechanism is rate-determining on mercury would suggest that $\overline{V}^{\neq} - (1-\alpha)\overline{V}_{H^+}$ is approximately zero if one uses the approximate model proposed by Temkin[8] in which the electrical properties of the activated state correspond to a charge of $(1-\alpha)$ (cf. the Marcus and Hush theories of electron transfer reactions).

G. J. Hills: Dr. Parsons raises a question similar to that of Dr. Kristalik but not so easily answered. The initial and final states are undoubtedly pressure-dependent and the terms $\overline{V}_{H^+}$ and (especially) $\overline{V}_{H_2}$ are finite and large.

However, both terms contribute to the corresponding two pressure coefficients $(\partial E/\partial P)_i$ and ∴ $(\partial \ln i/\partial P)_{\eta}$ of the reference electrode.

This apparent compensation may not, however, completely eliminate the contributions to $\Delta\overline{V}^{\neq}$ from the initial and final states. On qualitative grounds it is clear that to whatever degree the transition state

[6] M. I. Temkin, *Zhur. fiz. Khim.*, 22, 1081 (1948).

[7] I. R. Krichevsky and A. A. Ilyinskaya, *Zhur. fiz. Khim.*, 19, 621 (1945). No corrections have been made here for a certain dependence of $\overline{V}_{H_2}$ on pressure and solution composition (change in the activity of dissolved H_2) since such corrections cannot change the orders of magnitudes of the values obtained. A more detailed analysis, which cannot be given here, shows that the corrections associated with the activity coefficients of H_3O^+ and H_2O are almost exactly compensated for by the change in the activity coefficient of the activated complex (L. I. Krishtalik, *Elektrokhimiya*, In press; *Zhur. fiz. Khim.*, In press).

[8] M. I. Temkin, Trudy Soveshchaniya po Elektrokhimii Moscow, 181 (1953).

volume is influenced by the partial molar volumes of H^+ and H_2, the fact that these are, respectively, negative and positive is support for the view that the

$$2H^+ \xrightarrow[Hg]{2e} H_2$$

conventional mechanism should have a positive volume of activation, which experimentally it has not.

Dr. Kristalik also raises the important issue of the pH dependence and *inter alia* of the 1st-order reaction mechanism required to explain it. I would agree that the simple step

$$e_{Hg} \rightarrow e_{aq}$$

would not by itself satisfy this criterion. It is likely, however, that the rate-determining process requires a particular cavity or solvent cage for the aquation of the electron to be permanent and that this is a function of hydrogen ion concentration in the outer Helmholtz plane. A similar agreement would presumably be required to sustain the observed H_2/D_2 separation factor.

R. A. Marcus: I should like to comment on the interpretation of the extremely interesting data of the authors on pressure effects for electrode reactions, and to suggest that the experimental data may well be consistent with conventional mechanisms.

For simplicity, we consider first the case of a simple redox reaction. The derivative of a theoretical expression[9] for the rate constant with respect to pressure may be equated to the corresponding derivative of the expression $k_{rate} = (kT/h)\exp(-\Delta F^{\ddagger}/kT)$. As shown later, one finds thereby that ln k_{rate} depends on pressure only through a term $E(P) - E_o'(P)$, if work terms w^r and w^p are neglected and if [1] is assumed.

$$V^{\ddagger} \cong \frac{1}{2}(V^r + V^p), \text{ when } \alpha = 0.5 \text{ and } w^r \cong w^p \cong 0 \quad [1]$$

[$E(P) - E_o'(P)$ is the cell potential minus the "standard" cell potential for the prevailing medium, pressure P, and temperature. V^r, V^p, and $V^{\ddagger}$ are the volumes of the system before reaction, after reaction, and in the activated state, respectively. α is the transfer coefficient. w^r and w^p are the work terms to transport the reactant and the product to the electrode, respectively.]

The assumption embodied in Eq. [1] can be tested by plotting ln i *vs.* $E(P) - E_o'(P)$ and seeing if all points lie on the same curve, regardless of P. (i = current of forward step.) Deviations permit the determination of a "volume excess" at $\alpha = 0.5$, $V^{\ddagger} - \frac{1}{2}(V^r + V^p)$. It should be noted that approximation [1] is merely a rough conjecture, designed hopefully to account for major volume changes such as those discussed by the authors.

When there is more than one step in the reaction the preceding remarks apply to each step if all properties mentioned are taken to be those for that step. [For any step one then plots its ln k_{rate} *vs.* its $E(P) - E_o'(P)$.]

When the reaction is not a simple redox one but is some proton or other transfer there is some reason to believe that an equation of the same functional type (*i.e.*, the same as Eq. [3] below) applies to k_{rate} for any step, at least when $\alpha \cong 0.5$. Now, however, the E_o' is one corrected for any change of standard translational entropy during the reaction because of adsorption or because of gain or loss of particles.[10] One would again conclude that ln k_{rate} (at a given surface coverage) for any step would depend only on $E(P) - E_o'(P)$ for that step if assumption [1] were valid.

A preliminary examination of the authors' Fig. 5 and 6 suggests, interestingly enough, that a plot of ln i *vs.* $E(P) - E_o'(P)$ follows the above behavior, using $E_o'(P)$ for the over-all reaction. To be sure, the more detailed significance of this result depends on the mechanism, and, in particular, on the difference between the pressure dependence of $E_o'(P)$ for the slow step and that for the over-all reaction and, in some cases, on the pressure dependence of surface coverage.[11] We omit any detailed discussion here, although one could readily formulate such a treatment, utilizing mechanistic considerations in the literature[11] and, if one wished, using [1] as above.

When the work terms w^r and w^p are not negligible, they exhibit a pressure dependence because of the usual volume changes caused by bringing the charges together. By differentiation of a theoretical expression for k_{rate} containing these terms[12] and utilization of the preceding results (*e.g.*, in the following notation, utilizing the value found for $d\lambda/dP$ from data when $w^r \simeq w^p \simeq 0$) one obtains an expression for the pressure dependence of the current. Some model could then be introduced for dw^r/dP and dw^p/dP.

To conclude these remarks we justify below the statement regarding a plot of ln i *vs.* $E(P) - E_o'(P)$ for a redox reaction. At any temperature and pressure, the rate constant of the forward step, k_+, for reaction [2] was given by [3], when $w^r \simeq w^p \simeq 0$.[9]

$$A_{ox} + e - M \underset{k_-}{\overset{k_+}{\rightleftharpoons}} A_{red} + M \quad [2]$$

$$-kT \ln k_+/Z = \frac{1}{4}\lambda(1 + \Delta/\lambda)^2 \quad [3]$$

where $Z \cong 10^4$ cm sec^{-1}. $\Delta = ne(E - E_o')$ at pressure P. λ is an intrinsic reorganization term which depends on differences of properties of A_{ox} and A_{red} (*e.g.*, differences of bond lengths in the coordination shell, etc.). k_- is obtained from k_+ by replacing Δ by $-\Delta$.

When $\Delta << \lambda$, the transfer coefficient is 0.5 and, in this region, differentiation of [3] yields [4] since $d\Delta/dP = V^p - V^r$.

$$-kT(\partial \ln k_+/\partial P)_E = \frac{1}{4}d\lambda/dP + \frac{1}{2}(V^p - V^r) \quad [4]$$

However, from the relation $k_+ = (kT/h)\exp(-\Delta F^{\ddagger}/kT)$ one also finds that the left side equals $V^{\ddagger} - V^r$. Thus

$$\frac{1}{4}d\lambda/dP = V^{\ddagger} - \frac{1}{2}(V^r + V^p) \quad [5]$$

Hence, when assumption [1] is made, $d\lambda/dP$ vanishes and, one sees from [3], the statement has been proved for reaction [2]. The actual value of $V^{\ddagger} - \frac{1}{2}(V^r + V^p)$ can be evaluated from ln i *vs.* $E(P) - E_o'(P)$ plots. Points for different pressures will fall on different though parallel lines if this "volume excess" is nonzero. On theoretical grounds $d\lambda/dP$ is expected to be small for redox reactions, an examination of the expression[9] for λ shows.

In concluding these remarks I should like to add that the authors are to be congratulated for their interesting and, for electrochemistry, pioneering study of pressure effects. It would be useful to make simi-

[9] R. A. Marcus, *J. Chem. Phys.*, 43, 679 (1965), or earlier papers of the author cited therein.

[10] Such a correction was made [*J. Chem. Phys.*, 43, 3477 (1965)] for E_o' in reactions of solvated electrons, because their reactions with simple redox systems involve a loss of one particle and so a decrease in the standard translational entropy of the system.

[11] In considering possibilities of mechanism we have been guided by the excellent discussion in R. Parsons, *Trans. Faraday Soc.*, 54, 1053 (1958). When the slow step on mercury is the discharge reaction, $H_3O^+ + e(Hg) \rightarrow H_2O + H - Hg$ (see Parsons) and when the surface coverage is small, only the pressure dependence of the difference between the $E_o'(P)$ of the slow step and that of the over-all reaction, $H_3O^+ + e(Hg) \rightarrow H_2O + \frac{1}{2}H_2 + Hg$ is relevant. This term depends on $V^{M-H} - V^M$, where M denotes electrode and surrounding solution.

[12] Ref. (1), Eq. (82).

lar studies for redox systems at electrodes, since they may be simpler to understand.

B. E. Conway: I do not think that it is necessary for the volume of the final state molecule H_2, or even of adsorbed H, to be considered in the basic kinetic interpretation of volumes of activation $\Delta V^{\neq}$. Only the volume change between the initial state and the activated state is involved in any kinetic process. The volume change must, however, be deduced with proper consideration of any pressure variation of the reference electrode potential ϕ (which will be determined by the volume change in the single electrode process $2H_3O^+ + 2e \rightleftharpoons 2H_2O + H_2$, at equilibrium), as I have pointed out elsewhere.[13] This matter, Professor Hills claims, has apparently been taken into account by calculating his pressure effects at constant overpotential. We also pointed out in the above reference the similarity, noted by Kristalik here, to the problem of temperature effects at constant overpotential η which leads to the determination of an apparent activation energy discussed by Temkin.[14] It is the pressure dependence of the hydrogen electrode potential which we considered previously[13] which introduces the partial molar volumes of H^+ and H_2 considered by other contributors to this discussion.

The negative $\Delta V^{\neq}$ may, in fact, be connected with penetration of the proton from the outer layer where it is in the "$H_9O_4^+$" configuration, to a more compressed configuration in the inner layer[15] at the interface of the electrode. In H_2O itself, the H_3O^+ entity in $H_9O_4^+$ occupies effectively a relatively large volume since it tends to promote structure around it as the $H_9O_4^+$ hydrogen bonded complex. It seems possible that under conditions near the surface where the water is already electrostricted by the double-layer field,[16] the volume of the hydrated proton may well become decreased. Such an effect may not, however, be expected to apply to other cations owing to the special relation of the hydrated proton to the water structure.[17]

[13] See discussion on pp. 577-578 in "Chemical Physics of Ionic Solutions," B. E. Conway and R. G. Barradas, Editors, John Wiley & Sons, Inc., (Electrochemical Society Series), New York (1966).

[14] M. I. Temkin, *Zhur. Fiz. Khim.*, 22, 1081 (1948).

[15] B. E. Conway, *Discussions Faraday Soc.*, 39, 266, 277 (1965).

[16] J. R. McDonald, *J. Chem. Phys.*, 22, 1859 (1954).

[17] For example see review by B. E. Conway, "Modern Aspects of Electrochemistry," Vol. III, Chap. 2, J. O'M. Bockris and B. E. Conway, Editors, Butterworths, London (1964).

Some Problems in Electrodeposition

J. A. Harrison, S. K. Rangarajan, and H. R. Thirsk

Department of Physical Chemistry, The University of Newcastle-upon-Tyne, England

ABSTRACT

The investigations described refer predominantly to the study of the kinetics of electrocrystallization by potentiostatic methods. Experimental and theoretical investigations have been made over many years of both metallic, cathodic, and nonmetallic, anodic deposition processes, and it is shown how these are beginning to fit into a framework. Theoretical work from the school is described in which a fairly complete description (including diffusion in the solution and on the surface), of an electrode process has been formulated. This is given for potentiostatic conditions and for the application of small a.c. and is discussed in general terms. Some possibilities arise for a stricter examination of the diffusion phenomena.

Fundamental studies of electrodeposition, or more specifically electrocrystallization, in the sense of including both anodic and cathodic processes is a major interest of but few schools of electrochemistry. Quite recently a number of reviews of work have been published, and two in particular give a very wide survey of the present position (1, 2), so wide, in fact, that the nonspecialist might, with apparent justification, query the usefulness of the present paper. At the outset, we therefore wish to make the point that, to-date, little of the speculation concerning the fundamental mechanisms relevant to deposition has been proved; our object in describing in outline, in the present paper, the more recent work of the Newcastle School includes, as one of its major aims, the hope that the expression of our own ideas will stimulate a continued and unbiased examination and development of both theory and experiment.

Nonmetallic Deposition

Much of the experience in the study of electrocrystallization, forming the background for the present paper, has arisen through studies of nonmetallic deposition explored, in the main, by potentiostatic techniques in the nonsteady state. The method was first employed successfully in the examination of a well-known phase change, that of $PbSO_4 \rightarrow PbO_2$ (3), and the same method was subsequently used for direct deposition, in the investigation of the deposition of α and β lead dioxide on to platinum (4). The power of the experimental procedure lay in the fact that the growth of the new phase proceeded on isolated sites with, initially, no overlapping and, moreover, the types of deposit formed were in many cases ideal for electron optical studies defining topology, structure, and epitaxy.

Methods of handling the kinetic data, obtained as current time transients, using the ideas of a potential dependent nucleation process followed by growth according to a simple geometric scheme and indeed, analogous to methods of treating solid reactions, has been adequately described in a number of papers; we quote here the most important (4, 5, ref. 2, p. 168-201).

In the above publications the ideas concerning the evaluation of the values of the potential dependent rate constants for one-, two- and three-dimensional centers growing freely by electrodeposition were formulated together with a discussion of cases with a random distribution of growth centers, in which the effect of overlapping could be dealt with in order to permit the kinetic evaluation of the current/time transients.

Two references above refer to specific systems (3, 4), the others are quite general in application. Other papers relevant to single systems are: (*a*) formation of calomel on mercury (7), (*b*) formation of cadmium hydroxide on cadmium amalgams (8), (c) electrodeposition of γ MnO_2 on platinum (9); formation of thallous chloride on thallium amalgams (10).

Reactions on mercury and mercurous amalgam substrates have been particularly informative kinetically, and the deposits lend themselves to electron optical studies. A general account of such studies was given very recently (11). We shall complete this section of the paper and deal with very recent work with such systems in which some further progress and confirmation in interpretation has been made.

Further reference to the mechanism of formation of calomel on mercury is necessary. This process was discussed structurally in some detail in earlier work (12, 13). From the kinetic evidence (7) it was deduced that the highly oriented deposit was formed on the surface by the laying down in that position of layers of a monomolecular order in height. This finding was at variance with the conclusions arrived at much later by other workers using a galvanostatic-ellipsometric technique (14) who based their conclusions on a dissolution-precipitation sequence. This involved the dissolution of mercury as Hg_2Cl^+, which partially disproportionated to Hg^o and mercuric species and when Hg_2Cl^+ attained a certain critical surface concentration, calomel was supposed to precipitate in the solution. A reinvestigation of the process was thought necessary in view of the importance we attach to our general proposals for electrocrystallization in these systems; this has now been completed, and we consider that the earlier proposals (7) are confirmed. The system was examined, in the first place, potentiostatically and also by impedance measurements. The potential-time profiles given in Fig. 1 were used, selected on the basis of the galvanostatic and potentiostatic transients shown schematically in Fig. 2.

Figure 2A and B are galvanostatic transients (the dotted line is the reversible potential for the system) and C and D potentiostatic transients. According to Ives *et al.* (16a, b, c) transients of type A were supposed to be due to the anodic dissolution of mercury, involving mainly mercuric entities, and B to the formation of a layer (monolayer) of "chloromercury" with subsequent growth or rearrangement of this layer.

Calomel was considered to form by the disproportionation of the "chloromercury." In the work by

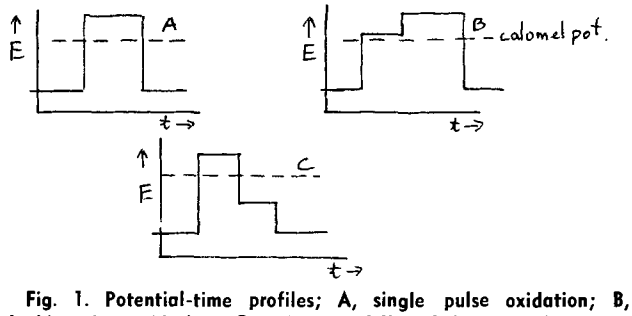

Fig. 1. Potential-time profiles; A, single pulse oxidation; B, double-pulse oxidation; C, oxidation followed by reduction.

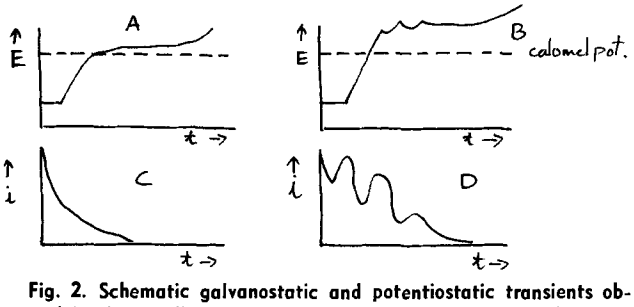

Fig. 2. Schematic galvanostatic and potentiostatic transients observed in the anodic polarization of Hg in Cl^- solutions. A and C under dissolution conditions; B and D for electrocrystallization conditions.

Armstrong *et al.* (15), for potentials held at less than the calomel reversible potentials, and particularly in solutions of concentration 2M, linear plots of i. vs. $t.^{-1/2}$ were obtained with t as little as 100 μsec indicative of mass transfer control for dissolution transients. At intermediate potentials +ve to the reversible potentials single peaks were obtained with an integrated charge of about 500 μC; at higher potentials this peak split into several peaks as in the earlier work of Bewick *et al.* (13). The nature of the complex associated with the diffusion process was examined by impedance measurements.

The current for the diffusion controlled process followed the equation

$$i = nFC_oD_o^{1/2}/\pi^{1/2}t^{1/2} \qquad [1]$$

where C_o is the concentration of the complex at the electrode surface. From the potential dependence of the current at constant time a two-electron transfer process was indicated.

In confirmation of these results from the Faradaic impedance, at lower frequencies the value of the Warburg impedance may be written as

$$|Z| = RT/n^2F^2C_o(D_o\omega)^{1/2} \qquad [2]$$

Again, from the variation of Z with potential, $n = 2$. From an assumption of $D_o = 10^{-5}$ cm^2 sec^{-1} estimates of $(C_o)_{\eta=0}$ were made giving satisfactory evidence for $HgCl_4^{2-}$ as the dissolving species. This evidence seems to be in essential agreement with (16) but makes the proposal of the Hg_2Cl^+ intermediate of Bockris (15) and Hills and Ives (17) unlikely. The evidence reaffirms the previous conclusions (7) concerning the mechanism of the electrocrystallization of the calomel by two-dimensional growth in monolayers with the additional ideas that, as in the case of mercuric oxide formation (18 and below) and thallous chloride (10) the multilayer peaks may well be due to the generation and growth of screw dislocation by a Frank-Read mechanism.

A somewhat similar impedance study was made in the examination of the growth of mercuric oxide on mercury (18) where again there is evidence for the dissolution of a mercury complex at a potential just negative to the Hg/HgO reversible potential; a similar analysis of the impedance results identifies this as an uncharged $Hg(OH)_2$ complex, which continues to be produced even when a HgO monolayer is formed. The covalently bonded, orthorhombic HgO is formed in these experiments with the (010) plane parallel to the mercury surface, that is the zig-zag HgO chains lie in the surface (Fig. 3).

The crystallite size was extremely small ($< 2\mu$ in diameter). An extension of the double pulse method employed previously to nucleate crystals at a high potential and then grow them on at lower potentials was used. Providing, and this is our usual assumption, that the slow stage in the growth process is the incorporation of the material at the periphery, then

$$i'/i = k'/k \quad \text{where } i \text{ and } k \text{ correspond to } \eta_1 \qquad [3]$$

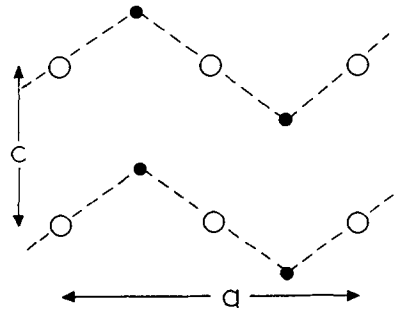

Fig. 3. The (010) plane of mercuric oxide: • O; ○ Hg

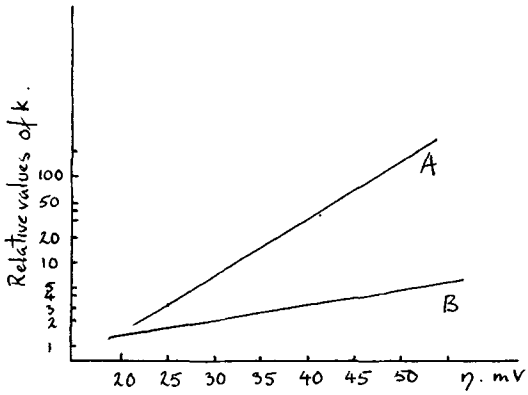

Fig. 4. Relative values of growth constant for HgO in M NaOH: A, multilayer rising section; B, multilayer falling section.

and i' and k' to η_2; $\eta_1 > \eta_2$. The potential was changed just before the current maximum since it was considered that the proportion of the current due to other causes was a minimum at that point and i' was taken as the minimum current after the potential step. Relative values of k are plotted in Fig. 4 as a function of potential.

The problem of the multilayer peak, as observed in the growth of TlCl (10) mercurous oxalate (19) and calomel (7, 15) is discussed further in this paper. A somewhat more elaborate model is chosen than in any previous treatment of the geometric model [see ref. (4), (5), (2)], in that two crystal growth rate constants, k_1 parallel to the electrode and k_2 orthogonal to the surface, are employed. t^3 dependence rather than the t^2 dependence follows for cylindrical growth.

The equation is of the form

$$i = nFk_2[1 - \exp(-\pi M^2 k_1{}^2 A t^3/3\rho^2)] \exp(-\pi M^2 k_1{}^2 A t^3/3\rho^2) \quad [4]$$

(M = molecular weight, ρ density, A, the nucleation rate constant) so that, for example, the plot in Fig. 5

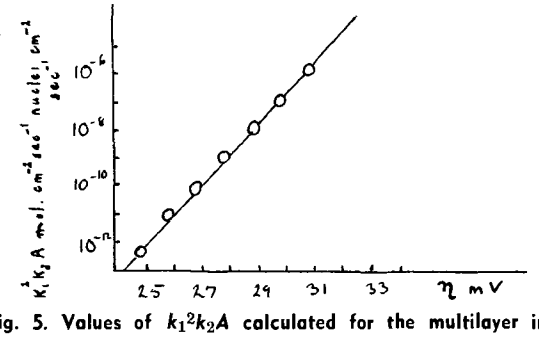

Fig. 5. Values of $k_1{}^2k_2A$ calculated for the multilayer in 5M NaOH from data as for Fig. 6.

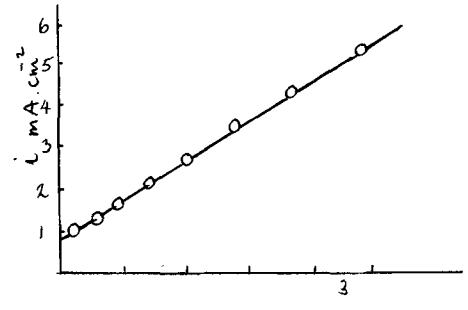

Fig. 6. Plot of i. vs. t.^{3} (unit of base 13.3 x 10^{-3} sec^3). η = 26 mv, 5M NaOH.

is of $k_1{}^2k_2A$ derived from Fig. 6. k_2 can be found from the relation from the transient, that is the current at the maximum $i_m = nFk_2/4$. We are still confronted with the difficulty of separating k_1 and A which in many of our studies appears as a composite constant k_1A, and this problem has been discussed elsewhere, for example (11).

To date we have not made any significant experimental determination in this problem excepting in the possibilities referred to briefly in the section on relaxation methods. An appendia to the paper on mercuric oxide does however discuss overlap with growing centers in three-dimensional systems with two growth constants; this will not be discussed further here.

Relaxation Methods

Relaxation methods, to be discussed here, are still potentiostatic in character but operate through a programmed pulse train. From the description of experiments involving the nonsteady state of electrode processes and designed to determine rate constants of fast reactions, it emerges clearly that the electrocrystallization process is in competition with diffusion processes; indeed, the measurable effect due to the electrode reaction, in which the interest lies, may be small.

It is intended, in this section, to give a brief outline of recent work on nucleation and crystal growth using as an illustration the deposition of PbO_2 on platinum showing how potentiostatic relaxation techniques may be employed; a more complete account is in the course of publication (20).

From solutions of the differential equations for an assumed reaction sequence, expressions for the variation of observable parameters in terms of the rate constants of the reaction steps may be obtained; the chosen parameters are, yield of product, and time.

It is helpful to consider steady and nonsteady states of the following reaction scheme

$$A \underset{k_1'}{\overset{k_1}{\rightleftharpoons}} B \xrightarrow{k_2} C \quad [5]$$

where any one of the rate constants k_1, k_1', and k_2 may be potential dependent. The steps are linked through the coverage θ of the adsorbed state B.

The time-dependent coverage is given by

$$\Omega\, \partial\theta/\partial t = k_1C_A(1 - \theta) - k_1'(\theta) - k_2\theta \quad [6]$$

where Ω, in moles cm^{-2}, is the saturation coverage for a monolayer, k_1' and k_2 are in moles cm^{-2} sec^{-1}, k_1 in cm sec^{-1}, C_A in moles cm^{-3}, and it is assumed the rate constants are independent of coverage, *i.e.*, no site interaction.

In the steady state the over-all rate R may be written as

$$R = k_2\theta = k_1k_2C_A/(k_1C_A + k_1' + k_2) = \partial C_c/\partial t$$

At low coverage, when $k_1' > k_1\, C_A$, $R \simeq k_1k_2C_A/k_1'$ [7]

and at high coverage, when $k_1C_A > k_1'$, $R \simeq k_2$ [8]

For the nonsteady state it is assumed that in the simplest case $\theta = 0$ at the beginning of each potential pulse. The time dependence of the coverage θ is then obtained by integration of Eq. [6].

$$\theta = k_1C_A/(k_1C_A + k_1' + k_2)[1 - \exp\{-(k_1C_A + k_1' + k_2)t/\Omega\}] \quad [9]$$

and the rate of formation of product is

$$R = k_2\theta \quad [10]$$

Equation [10] has a steady-state value identical with Eq. [7] and gives for the characteristic a (relaxation) time τ

$$\tau = \Omega/(k_1C_A + k_1' + k_2) \quad [11]$$

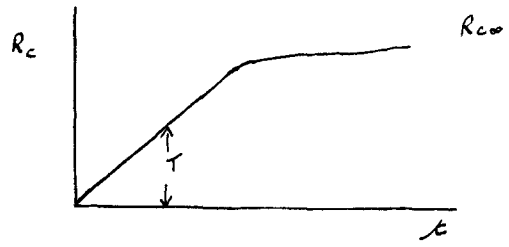

Fig. 7. Sketch of the steep approach of the yield to the steady-state value.

It will be seen that the rate constant of the over-all reaction depends on the smallest k_1, that is the slowest step of the sequence, but the relaxation time is determined by the largest k_1. Thus, by means of a relaxation technique it is possible to determine the rate constants of the fast steps in reaction sequences, particularly if the over-all rate is low.

To examine the time dependence of the yield of product, $C_c = 0$ when $t = 0$, and integration of [10] gives

$$C_c = k_1k_2C_At(k_1C_A + k_1' + k_2) - k_1k_2C_A\Omega/(k_1C_A + k_1 + k_2)^2 [1-\exp-\{k_1C_A + k_1' + k_2)\ t/\Omega\}] \quad [12]$$

where C_c is the integral yield after time t, the length of the applied pulse.

If R_c is the yield per second, *i.e.*, $R_c = C_c/t$

$$R_c = R_{c\infty} - R_{c\infty}(\tau/t)(1-\exp-t/\tau) \quad [13]$$

where $R_{c\infty}$ is the steady-state value given by [7]. A sketch of the function showing the steep approach of the yield to the steady-state value is shown in Fig. 7.

In practice it is usually impossible to measure the yield for a single pulse, and so a suitable program of repetitive pulses is employed. R_c is calculated from the total yield and the over-all time of polarization T, where $T = \Sigma t$. In choosing the pulse program it is important to select a duty ratio such that the condition $\theta = 0$ at the beginning of each pulse is satisfied.

The relaxation time may be estimated from plots of yield *vs.* pulse time as in Fig. 7. The potential and concentration dependence of the relaxation times so obtained provide tests on the interpretation of reaction mechanisms in addition to those obtained by more conventional measurements, the distinction being that relaxation measurements refer to the fast steps in the mechanism.

The application of the technique may be illustrated by considering the electrodeposition of PbO_2. We will consider a mechanism suggested in an earlier paper.

$$OH^- \rightleftharpoons OH_{ads} + e \quad (a)$$

$$OH_{ads} + Pb^{2+} + OH^- \rightarrow PbO_2 + 2H^+ + e \quad (b)$$

This is formally analogous to the discharge-electrochemical mechanism of the hydrogen evolution reaction. In examples of crystal growth there is, however, a complicating factor in that the free formation of the lattice must be preceded by the nucleation of growth centers. This nucleation process proceeds by the same mechanism as the lattice formation, but the activation energy will be modified by the electrochemical surface free energy of the embryonic nucleus. The formation of nuclei will therefore have a different (longer) relaxation time than the crystal growth process. The study of these relaxation times should enable a more detailed model to be built up of the initial stages of aggregation.

The nucleation of lead dioxide was studied with the pulse train shown in Fig. 8a; that of the subsequent

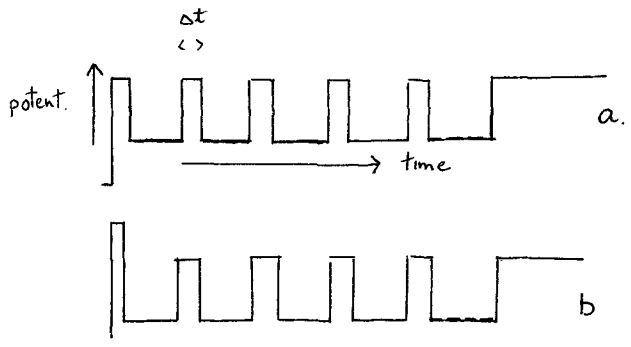

Fig. 8. Pulse trains to examine nucleation and crystal growth

growth by that of 8b. For the experiments the electrolysis of an aqueous solution of molar sodium acetate and molar acetic acid was undertaken for a series of polarization pulse times at the potential of + 2.3 or + 2.5v and the base potential of + 120 mv. Since nucleation requires a higher activation energy than crystal growth, an initial single high potential pulse was applied to form a number of nuclei on the electrode surface (4). This pulse was followed by a train of pulses having a lower amplitude which tested the relaxation of crystal growth. As the pulse length was below that required to form nuclei, further nucleation could be neglected during this polarization. The base potential chosen was low enough to permit the relaxation of the growth of the centers but high enough to maintain the stability of the deposit. The value was varied to examine possible effects. The final section of the profile was a continuous application of the polarization potential.

The current-time curves observed for the formation of lead dioxide, in the absence of the section of the pulse train used to investigate the relaxation effects, Fig. 8a, b, are illustrated in Fig. 9a, b, [see ref. (20)]. The initial section of the plots can be shown to be proportional to t^3, and this is due to the combined effects of the progressive nucleation of growth centers coupled with the three-dimensional growth of these centers (2). If nuclei are first formed by an initial short polarization at a high potential, the initial section of Fig. 9b is proportional to t^2, *i.e.*, three-dimensional growth of a fixed number of centers. The relaxation of nucleation and of crystal growth can be simply investigated by using the form of these curves. If the pulse train shown in Fig. 8b precedes the polarization at the upper potential and the total length of the polarization "on" time (Σt) is chosen to be equal to that required to reach point B in Fig. 9a then, if there has been no relaxation of the formation of nuclei, the initial current on finally maintaining the continuous polarization will correspond to that at point B, and there will be no current-time transient. On the other hand if relaxation has been complete, then

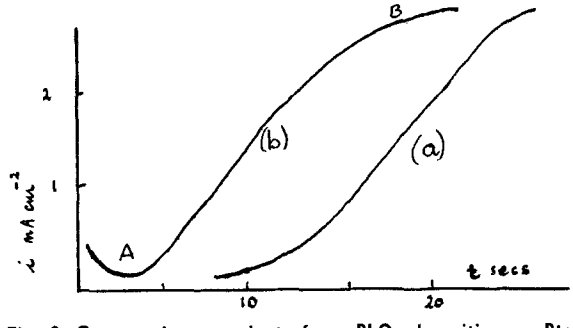

Fig. 9. Current time transients for α-PbO_2 deposition on Pt: (a) at constant η = 275 mv; (b) nuclei preformed at η = 425 mv for 0.1 sec and then grown at 275 mv. Sol. 0.1M $PbAc_2$, M NaAc, M HAc.

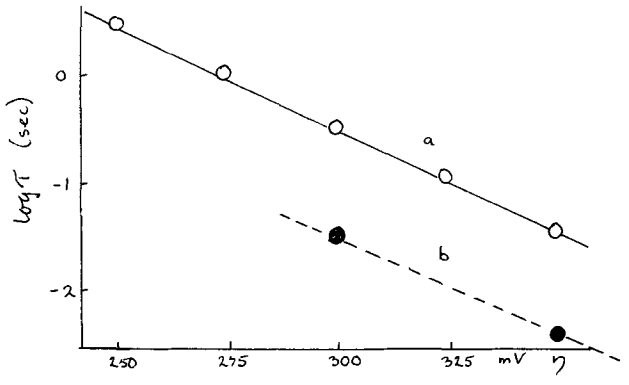

Fig. 10. Effect of base potential and η on relaxation times: a, base potential +50 mv; b, base potential +100 mv.

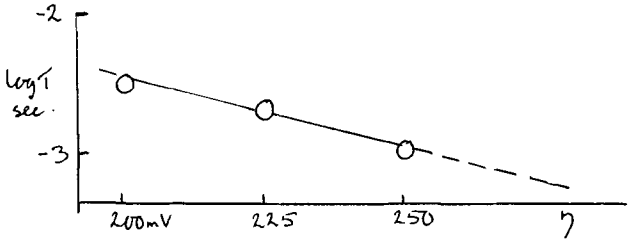

Fig. 11. Variation of relaxation time of crystal growth of α-PbO_2 with overpotential. Nuclei formed at 425 mv for 0.1 sec.

the system will be found initially at point A and the complete current-time curve of Fig. 9a will be traced. In practice the relaxation is sharp.

The variation of the relaxation times with polarization potential is illustrated in Fig. 10 for a solution 0.1M with respect to lead acetate and molar with respect to acetic acid and sodium acetate. The lines given refer to two different base potentials, positive to the reversible βPbO_2 potential.

The relaxation of lattice growth was measured in a similar manner to that of nucleation. In the event of no relaxation, the initial current on maintaining the final steady potential of Fig. 8b was that corresponding to point B on Fig. 9b, while in the event of complete relaxation, the current corresponded to A and the complete curve was again traced. The variation of the relaxation time with potential is illustrated for the same solution in Fig. 11.

A variation of the relaxation time with overpotential is observed for the crystal growth of lead dioxide, showing that the fastest process is again a charge transfer step. In this case the relaxation time however decreases with overpotential so that the forward direction of the charge transfer, that is, the discharge reaction, has the highest rate constant. According to the mechanism which has been suggested, *i.e.*, Eq. (*a*) and (*b*), this could be assigned to either of the stages. Further information can, however, be obtained from the fact that the relaxation is only observable over a restricted potential range. According to the arguments which have been given above, this can be explained if the highest rate constant is assigned to a preequilibrium, the slowest step succeeding this equilibrium. For such a mechanism the relaxation can only be observed for a restricted portion of the potential range in which a significant yield due to the over-all reaction may be obtained. The fastest step must therefore be attributed to the forward reaction of Eq. (*a*), and crystal growth takes place in a layer of adsorbed hydroxyl radicals present at high coverage. The same conclusion was drawn previously from an examination of the concentration dependence of the over-all rate constants.

Some Problems Concerning the Electrocrystallization of Metals

Metal electrodeposition is a complex phenomenon, and electrodeposits formed on solid metals have a complicated geometry. It is therefore not surprising that little is known in detail about the primary processes involved. In the past, inference about the kinetics of electrodeposition has usually been made from stationary current voltage measurements. In some cases galvanostatic potential-time curves and, rarely, potentiostatic current-time curves have been measured. Some measurements have been made using a-c techniques. On solid metals, the results are not easily interpreted. This has led us to start to investigate the kinetics of metal deposition on mercury and graphite substrates where the initial stages of crystal growth can be observed. We have also attempted to show the limitations of the older measurements theoretically. What follows is for the most part an abbreviated review of this work and our personal approach to the problem.

Theories of the mechanism of the electrodeposition of metals have tended to follow vapor phase studies and assume that lattice growth occurs from mobile adsorbed species (adatoms) on the surface. They are formed electrochemically at the metal solution interface by discharge of the "aqueous metal ion." An alternative route into the lattice is by direct deposition of the metal ions at the growth sites (step lines). Diagramatically the two mechanisms for a general electrochemical reaction are as follows:

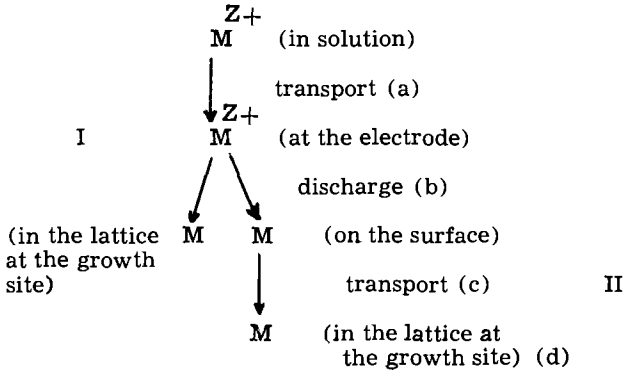

Mechanism I will be discussed first in view of the experimental work available for soft metals, and then work on the transition metals. Mechanism II is then considered when (*i*) the lattice growth step (d) alone is rate determining; (*ii*) deposition (b) and surface diffusion (c) are important. It is also shown in this section how this theory (which assumes a parallel step line model) can be extended to include the lattice growth step (d).

Recent experimental data, some of which are now under investigation, are mentioned, to show how the theory is related to measurement.

A recent review (1) has assumed that the adatom mechanism II occurs exclusively. Evidence for this mechanism however derives from the low melting point metals, mercury, lead, zinc, cadmium, tin, and silver. These metals have rather weak surface bonds, and adatoms might be expected to form easily and be mobile on the surface. Unfortunately, these metals have a large exchange current and diffusion in the solution can become the main mode of transport to the growth site. Gerischer (21) (Mehl and Bockris have carried out essentially similar experiments) has shown that, if silver is dissolved potentiostatically in a stirred silver perchlorate solution to a stationary current, then the concentration overpotential is in excess of that calculated from the Nernst diffusion theory for linear diffusion. This extra overpotential has been

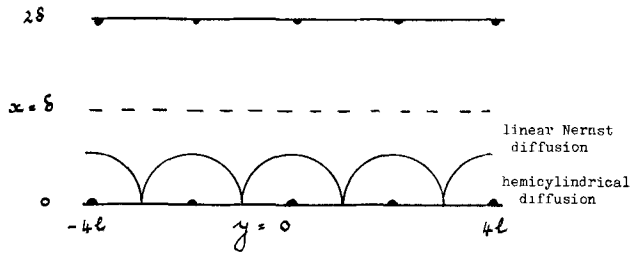

Fig. 12. Model used to calculate the effect of the discrete nature of an electrode surface along x = 0. The line sinks are separated by impervious material.

attributed to adatoms on the surface. However, this is not necessarily true as material can also arrive at the site by hemicylindrical diffusion.

In Fig. 12 the surface of a metal on to which ions are being electrodeposited by mechanism I is visualized as a row of line sinks, the step lines, where material is incorporated on to the lattice. Each line sink receives material from a linear Nernst diffusion of thickness δ and a hemispherical diffusion zone radius l. $2l$ is distance between the step lines. The method of Kasper (22) can then be used to calculate, in the stationary state, the relative concentration changes in the solution due to linear and hemicylindrical diffusion (23). The result is

$$\frac{\Delta C}{\Delta C_{\text{Nernst}}} = \frac{l}{\delta\pi} \ln \frac{16\,\delta^2}{\pi^2 a^2} + \frac{2l}{\delta\pi} \sum_{1}^{\infty} \ln \left\{ \frac{1 + \cosh \dfrac{\pi n l}{\delta}}{\cosh \dfrac{\pi n l}{\delta} - 1} \right\} \quad [14]$$

where ΔC is the total concentration change in the solution and a is here an arbitrary radius, of atomic dimensions, surrounding the line sink. If $a = 2 \times 10^{-8}$ cm and $\delta = 10^{-3}$ cm then $\Delta C/\Delta C_{\text{Nernst}}$ can be evaluated as a function of l/δ. This curve has a limiting value of approximately 1.3 when l/δ is small. In experiments on a solid metal such as silver, it would seem likely that the step lines are generated by dislocations in the surface and l/δ would be small. In agreement with this, Gerischer (21) gives $\Delta\eta/\Delta\eta_{\text{Nernst}}$ (identical to $\Delta C/\Delta C_{\text{Nernst}}$ when the total overpotential is small) as 1.5. The interpretation of the excess polarization as due solely to adatoms on the surface, is therefore not unambiguous.

An interesting aspect of Eq. [14] is that when at the other extreme l/δ is large $\Delta C/\Delta C_{\text{Nernst}}$ is also large. Thus it should be possible to measure high rates of reaction by, for example, the deposition at constant potential of silver or mercury onto graphite or on a noble metal. This would perhaps alleviate the need for very high-speed electronic equipment for these reactions.

The electrodeposition of the low melting point metal copper from acidified cupric sulfate solution onto a plated copper electrode, has recently been reinvestigated (24) by means of a rotating disk. This shows that the lattice growth step on a cathode of this type is very fast and the mechanism is dominated by the cuprous/cupric redox couple. Similar conclusions have been drawn by previous workers (25).

The high melting point metals, on the other hand, have low exchange currents, and diffusion effects in the solution are less likely. A complicating feature, however, when such transition metals are deposited from aqueous solution is the possibility of complex formation or the codeposition of hydrogen. Gierst (26) has suggested from polarographic and galvanostatic measurements that for nickel, in solutions of simple salts the hydrated nickel is discharged, the rate of dehydration of the ion at the surface being the rate-determining step. The depression of the polarographic limiting current on adding an inert electrolyte was interpreted in these experiments as a double layer effect, the shift of the Gouy layer potential.

Another example is the potentiostatic deposition of Co on to mercury from unbuffered potassium nitrate solutions where in addition to the metal a hydroxide can also be formed (27). We propose that this occurs by a mechanism

$$Co^{2+} + H_2O \rightleftharpoons H^+ + CoOH^+ \xrightarrow{2e} Co + OH^-$$

$$Co^{2+} \downarrow \text{ on the electrode surface}$$

$$Co(OH)_2 \text{ or } CoO \quad [15]$$

This mechanism depends on the fact that, due to the differing diffusion constants of H^+ and OH^-, a gradient of OH^- ions can exist in the region adjacent to the interface. An alternative mechanism would be the liberation of OH^- ions from H_2O in the interfacial region.

$$H_2O \xrightarrow{e} \tfrac{1}{2}H_2 + OH^- \quad [16]$$

This would mean the absorption of a hydrogen atom or molecule into the oxide film, as the production of gaseous hydrogen, even at high rates of formation of oxide, is usually not observed. There is evidence that in general cathodic oxide formation is greatly influenced by the amount of indifferent electrolyte present. In mechanism [15] this could occur by changing the concentration of the reducible species Co^+OH. Mechanism [16] would allow these effects as an alteration of the activity of OH^- in the interfacial region. Similar phenomena of the formation of cathodic oxide or hydroxide occur during the reduction of the chromate anion. When the aquo-complex is replaced by the thiocyanate complex this complication is removed and the potentiostatic initial current, as a function of potential, shows the usual Tafel slope. The current-time curves from this complex onto mercury, and other metals onto graphite, show that the growth of a metallic layer can be interpreted in terms of nucleation and lattice growth in a similar way to the deposition of nonmetal films.

When the slow step in an electrocrystallization process is incorporation at the edge of a growing nucleus and all transport processes to the nucleus are fast, then, in the early stages of growth, before overlapping becomes important, simple geometrical arguments can be used to predict the form of the potentiostatic current time curves. If one considers a single hemispherical nucleus growing on a surface, then if $V(t)$ is the volume of the nucleus at any time, r is the radius, and $i(t)$ the current

$$i_{(t)} \propto \frac{\partial V_{(t)}}{\partial t} \propto \frac{\partial}{\partial r}\left(\frac{2}{3}\pi r_{(t)}^3\right) \cdot \frac{\partial r}{\partial t} \propto 2\pi r_{(t)}^2 \quad [17]$$

$$r_{(t)} \propto t$$

and

$$i_{(t)} \propto t^2$$

Another possibility is that if the slow step is round the basal periphery (for instance by the movement of adatoms along the basal plane), then the rising transient can be calculated as follows

$$i_{(t)} \propto 2\pi r_{(t)}^2 \frac{\partial r}{\partial t} \propto 2\pi r_{(t)}$$

$$r_{(t)} \propto t^{1/2}$$

$$i_{(t)} \propto t^{1/2} \quad [18]$$

The constant of proportionality involves the lattice growth and nucleation rate constants and is easily

Table I

t^3	t^2	t	$t^{1/2}$	e^t	$t^{3/2}$	
Progressive 3 D periphery none	Instantaneous 3 D periphery none	Instantaneous 2 D periphery none	Instantaneous 3 D basal periphery none	Progressive 2 D Top area none	Progressive 3 D basal periphery none	a) b) c) d)
	Progressive 2 D periphery none	Progressive 1 D periphery none	Instantaneous 3 D periphery planar diffusion		Progressive 3 D periphery planar diffusion	a) b) c) d)

a) Type of nucleation; b) geometry; c) site of slow step; d) transport in solution.

calculated as shown in many previous publications from this school [see for example (2)]. Similar relations can be written for other combinations of geometry, reaction site, and mode of transport to the growing center and type of nucleation. These equations are not, however, unique, as can be seen by reference to Table I, in which some possible dependences are given. For example, it is generally not possible to distinguish directly between adatoms and diffusion in the solution although a possible way is given later. A knowledge of the geometry by means of electron diffraction is a prerequisite. Not all of these dependences, some of which are new, have been observed, but it seems likely that in practice even more complicated cases will occur, particularly that of preceding chemical reaction. An important example is when another electrochemical reaction goes simultaneously with the growing metal layer. Arguments similar to that used in deriving Eq. [17] and [18] then show that, depending on whether the second reaction goes preferentially on the growing metal lattice (either at the edge or on top of the nuclei) or on the uncovered substrate, then different potentiostatic current time curves are obtained. In fact, a whole family of dependences can be formulated easily and are too numerous to be given easily in a table. These dependences are, however, not unique, as in the example Table I, and extra evidence is necessary to deduce a reaction mechanism. An example investigated in this laboratory, among other noble metal depositions (27), is the reduction of the $PtCl_4^{2-}$ anion at a pyrographite electrode. Here there is the possibility of discharge from the various complexes in solution and also the possibility of the catalytic deposition of hydrogen either at the edges or on top of the growing nuclei, depending on the potential. We think it might be possible to explain in these terms the polarographic curves for the reduction of the $PtCl_4^{2-}$ anion, about which there is some controversy in the literature. Because of the 3-4 sec drop time used in polarography, quite a large number of platinum nuclei must be present on the mercury in these experiments, and in our experience this can have a profound effect on the current flowing.

At longer times when overlap becomes important, provided that the slow step is at the edge, the current-time curve can be calculated theoretically in a few simple cases. This has been demonstrated for the formation of some nonmetallic lattices on Hg, *e.g.*, calomel and references given in the section on nonmetallic deposition.

When the slow step is not at the edge and lattice growth is no longer governed by purely geometrical considerations, it is more difficult to set up a model to calculate the current time-transient. This has proved to be the case for the nickel thiocynate complex, mentioned above; here the kinetics are controlled by the rate of discharge, surface diffusion and lattice growth (28).

As this is a system which has been investigated in some detail it would be useful here to give the principal results. The potentiostatic current time curves, which correspond, by the amount of charge, to the formation of a monolayer one unit cell thick, have a maximum similar to that for the formation of some nonmetallic films, *e.g.*, calomel. A symmetrical curve would be expected if the slow step is at the edge that is if (*d*), in scheme II, alone is rate determining. The curves are, however, unsymmetrical. This immediately suggests that some process precedes lattice incorporation. Possibly this could be a preceding chemical reaction in the solution or the diffusion of adatoms to the growth site. The initial currents, plotted as a function of potential, show a Tafel slope corresponding to the discharge step. At higher negative potentials the initial current becomes kinetically controlled by the rate at which the preceding chemical reaction

$$Ni^{2+} + SCN^- \rightleftharpoons Ni\,SCN^+ \xrightarrow{2e} Ni + SCN^-$$

can produce the reducible species. In the region at lower potentials where the initial current is the discharge rate and this is followed by the effects of crystal growth, in that the curves go through a maximum, the inescapable conclusion would seem to be that these two processes are linked by adatom diffusion on the surface. The experimental fact that by switching instantaneously to more positive potentials some of the charge is removable, presumably that in transit to the growth site, gives more confidence in this suggestion. In such a complex situation, especially when overlap is important, the easiest way of reproducing the current-time curves is by means of simulation, and this has been attempted. At short times the problem can be approached analytically, if the number of nuclei is constant, by means of the parallel step line model shown in Fig. 13.

This model was originally proposed for the growth of solids from the gas phase by the adatom mechanism. The more difficult problem of how diffusion in the solution can be included in the theory will be discussed later. If c is the concentration of adatoms on the surface at a point between the step lines, then for a cathodic deposition at constant potential

$$\frac{\partial c}{\partial t} = D\frac{\partial^2 c}{\partial x^2} + k_1' - k_2'c \qquad [19]$$

where

$$k_1' = \frac{i_o}{ZF}\exp\left[\frac{\alpha Z\eta_1 F}{RT}\right],$$

$$k_2' = \frac{i_o}{ZFc_o}\exp\left[\frac{(\alpha-1)Z\eta_1 F}{RT}\right]$$

D is the adatom diffusion constant, c_o is the adatom

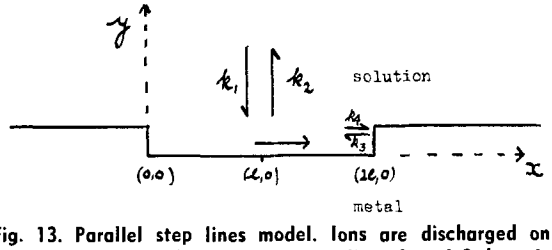

Fig. 13. Parallel step lines model. Ions are discharged on the surface from solution between the step lines 0 and 2 *l*, and then diffuse along the surface to the step lines.

concentration at the equilibrium potential, and the other symbols have their usual electrochemical significance. The boundary conditions are as follows

$$c = c_o \qquad 0 > x > l \qquad t = 0 \qquad [20]$$

$$c = c_o \qquad x = 0 \qquad t > 0 \qquad [21]$$

$$\frac{\partial c}{\partial x} = 0 \qquad x = l \qquad t > 0 \qquad [22]$$

These equations can be solved by the Laplace transform method to give a current-time transient. The result will not be quoted here as it is not directly amenable to experimental verification. It is more interesting to calculate the effect of an experiment of the type proposed by Gerischer (21). This involves polarizing the electrode to a stationary state at a potential η_1 and then instantaneously switching the potential to a second smaller overpotential η_2 (at constant l) such that this initial current is zero. This applies only to very rapid reactions where at short times the double layer charging can be neglected. These are just the reactions where changes in the solutions are expected. An experimental test of whether transport is by adatoms or diffusion in the solution to the step lines is suggested by the theory (23). As a result of a Gerischer experiment the theory gives

$$0 = i_{t\to 0} = ZFk_2 \left[\frac{k_1}{k_2} - \frac{k_1'}{k_2'} + \frac{k_1' - k_2' c_o}{k_2' l} \left(\frac{D}{k_2}\right)^{1/2} \frac{\sinh\left(\frac{k_2'}{D}\right)^{1/2} l}{\cosh\left(\frac{k_2'}{D}\right)^{1/2} l} \right] \qquad [23]$$

where the quantities without a prime belong to η_2. By substitution of the rate constants in terms of i_o and overpotential then

$$i_o \exp\frac{\alpha Z\eta_1 F}{RT} \left[\exp\left[\frac{ZF}{RT} (\eta_2 - \eta_1) \right] - 1 \right] = -i_{stat} \qquad [24]$$

where i_{stat} is the stationary current at η_1. This consequence of the theory could presumably be tested, after correcting the η values for concentration changes in the solution, by comparing it with

$$i_o \exp\frac{\alpha Z\eta_1 F}{RT} \left\{ \exp\left(-\frac{Z\eta_2 F}{RT} \right) - \exp\left(-\frac{Z\eta_1 F}{RT} \right) \right\} = -i_{stat} \qquad [25]$$

This equation is derived by considering a Gerischer experiment in which concentration changes, only, occur in the solution. It must be noted that these equations may equally well be deduced from any other model provided that, in one case, concentration changes take place before, and, in the other case after, electron transfer.

Equilibrium at step lines during metal growth is probably only achieved for metals with high exchange currents (29). In other cases it is necessary to replace boundary conditions [22] by [26]

$$D\frac{\partial c}{\partial x} = k_4 c - k_3 \qquad [26]$$

where k_4 is the rate constant governing growth at the step lines and k_3 that of the back reaction. A solution of Eq. [19] with [20], [26], and [22] corresponding to a Gerischer experiment can be obtained using the Laplace transform method. This leads when the metal deposition is relatively irreversible, *i.e.*, $k_3 = 0$ and the potentials such that $k_2' = 0$, $k_1 = 0$ to

$$i = -\frac{2ZFDk_2k_4^2k_1'}{l} \sum_0^\infty \frac{\exp -(D\alpha_n^2 + k_2)t}{(D^2\alpha_n^2 l + Dk_4 + k_4^2 l) D^2\alpha_n^2} \qquad [27]$$

that is, a transient due only to the removal of adatoms and the lattice continues to grow during the transient. In Eq. [27] α_n is the root of the transcendental equation

$$l\alpha_n \tan l\alpha_n = \frac{k_4 l}{D} \qquad [28]$$

It would therefore be possible, by setting up calibration curves in terms of the parameters $k_4 l/D$ and D/l^2, to compare the experimental and theoretical results. Experimental data are not sufficiently adequate at present to test these equations.

It seems that only by a detailed fitting of an equation of this type can unequivocal evidence for the adatom mechanism be obtained. These equations, however, presuppose that diffusion of adatoms along the surface is the only mode of transport to the growth sites. A more complete theory has been formulated (30). Differential equations corresponding to Eq. [19] can be written for potentiostatic conditions as follows

$$D\left[\frac{\partial^2 c}{\partial x^2} + \frac{\partial^2 c}{\partial y^2}\right] = \frac{\partial c}{\partial t} \qquad 0 \leqslant x < l \qquad y > 0 \qquad [29]$$

$$D_a\frac{\partial^2 c}{\partial x^2} + k_1 c - k_2 C_a = \frac{\partial C_a}{\partial t} \qquad 0 \leqslant x < l \qquad y = 0 \qquad [30]$$

As before x is the distance co-ordinate in the surface as shown in Fig. 13. y extends into the solution. In contrast to the previous, C_a,D_a, now refer to adatoms, and C,D, to the ions in solution. c^o,$c_a{}^o$ are now the concentrations at the equilibrium potential. The boundary conditions corresponding to [20], [21], and [22] now become sets for the x and y directions, respectively.

Initial conditions

$$C_{(x,y,t)} = c^o \qquad t = 0 \qquad [31]$$

$$C_{a(x,t)} = c_a{}^o \qquad t = 0 \qquad [32]$$

Boundary conditions

$$\begin{aligned} C_{(x,y,t)} &= c^o && y \to \infty \\ \frac{\partial c}{\partial x} &\to 0 && x = 0 \\ c_a &\to c_a{}^o && x = 0 \\ D\frac{\partial c}{\partial y} &= k_1 c - k_2 c_a && y = 0 \qquad 0 < x \leqslant l \\ D\frac{\partial c}{\partial x} &= D_a\frac{\partial c}{\partial x} = 0 && x = l,\ \delta \to 0 \qquad y \geqslant 0 \end{aligned} \qquad [33]$$

To make the problem symmetrical in both phases it is of advantage to rewrite Eq. [29]-[33] in terms of a surface layer of thickness δ. It can be shown that solving the amended equations and allowing $\delta \to 0$ gives a correct solution of [29], [30]. The transform of the solution is complicated and is at present being programmed for the computer. It is hoped later to publish potentiostatic i/t curves as a function of k_1, k_2, D, D_a, l, which can be directly compared with experimental data in the literature. However, it is pos-

sible to discuss limiting cases. The actual transform of the solution is

$$\bar{i} = ZF(k_1c^o - k_2c_a^o)\,(p\sqrt{pD}/x_{oo}(p))\cdot\left\{1 + \left(\frac{k_2\sqrt{pD}}{x_{oo}(p)}\right)(S_1(p))^{-1}\right\} \quad [34]$$

where

$$x_{oo}(p) = (k_1 + \sqrt{pD})p + k_2\sqrt{pD}$$

$$S_1(p) = \sum_0^\infty \epsilon_m \left(k_1 + \sqrt{\left(p + \frac{1}{\tau_m}\right)D}\right) p/x_{m.o(p)}$$

$$x_{m.o(p)} = \left(k_1 + \sqrt{\left(p + \frac{1}{\tau_m}\right)D}\right)\left(p + \frac{1}{\tau_m{}^a}\right) + k_2\sqrt{\left(p + \frac{1}{\tau_m}\right)D}$$

where

$$\epsilon_m = 1\ ,\ m = 0$$
$$= 2\ ,\ m = 1, 2 \ldots..$$

$$k_1 = i_o/ZFC_o \exp\left(\frac{\alpha ZF\eta}{RT}\right),$$

$$k_2 = i_o/ZFC_a^o \exp\left[\frac{(\alpha - 1)ZF\eta}{RT}\right]$$

also

$$\frac{1}{\tau_m} = \frac{m^2\pi^2 D}{l^2}\ ,\ \frac{1}{\tau_m{}^a} = \frac{m^2\pi^2 D_a}{l^2}$$

$\bar{i}$ is the Laplace transform of the current defined by

$$\bar{i}(p) = L\,i_{(t)} = p\int_0^\infty \exp - pt \cdot i_{(t)}\,dt \quad [35]$$

For two limiting cases the inverse transforms of [34] can immediately be written down

(*i*) Allowing $D_a \to \infty$ leads to a dependence

$$i_{(t)} = i_o\left[\exp\frac{\alpha ZF\eta}{RT} - \exp\frac{(\alpha - 1)ZF\eta}{RT}\right] \cdot \exp k_1{}^2\frac{t}{D}\operatorname{erfc}\left(k_1\sqrt{\frac{t}{D}}\right) \quad [36]$$

Equation [36] is the well-known equation for semi-infinite diffusion to a planar electrode, and at long times reduces to $i \propto t^{-1/2}$

(*ii*) When diffusion in the solution is neglected by allowing $D \to \infty$ the equations published earlier (6) are reproduced. A particularly significant property of these equations is that when $t \to \infty$ a stationary state is reached, namely

$$i_{t\to\infty} = \frac{ZF}{l}(k_1c^o - k_2c_a^o)\tanh\left(\sqrt{\frac{k_2}{D_a}}\cdot l\right)\left(\sqrt{\frac{D_a}{k_2}}\right) \quad [37]$$

By putting $l \propto 1/\eta$ in this equation then at low overpotential the stationary i/η curve can be calculated for surface diffusion alone.

In an actual current time transient represented by [34] it can be shown that, if surface diffusion is important, it might be expected that the stationary state for surface diffusion would appear before the decay for diffusion in the solution and a plateau would appear.

The a-c method for measuring the impedance of an electrochemical system, and interpreting this in terms of i_o and α, is well known. An early attempt to obtain the elements of an equivalent circuit analogous to the potentiostatic case with diffusion in the solution given above was made by Lorenz (31). His measurements probably represent the largest body of evidence in favor of the adatom mechanism, and it is important to look at his method of calculation in view of the ambiguous nature of the potentiostatic and galvanostatic measurements mentioned earlier. The Lorenz calculation is, however, approximate. An accurate solution for this model can be obtained easily for a small a-c perturbation, from [34]. Using the previous nomenclature and also

$$\Delta i = |\Delta i| \cos(\omega t + \phi) \quad [38]$$

then from [34]

$$\Delta i = \text{real part of } \frac{i_oZF|\Delta\eta|}{RT}\cdot\left\{j\omega\sqrt{\frac{j\omega D}{x_{oo(j\omega)}}}\left[1 + k_2\sqrt{\frac{j\omega D}{x_{oo(j\omega)}S(j\omega)}}\right]\right\} \quad [39]$$

where $j = \sqrt{-1}$, $k_1 = i_o/ZFc_o$, $k_2 = i_o/ZFc_a^o$.

The limiting cases of this will now be briefly discussed under some simplifying conditions. The reader is referred to the original papers for the details

(*i*) When

$$\frac{D_a}{2} >> k_2 \text{ and } \omega << \frac{D_a}{2}$$

Equation [39] reduces to the well known equation derived by Randles. These conditions are then sufficient to ensure that bulk diffusion and the electrochemical step alone are rate determining. Experimental work based on this limiting case is well understood. The equivalent circuit elements are then the Warburg impedance in series with the transfer resistance and in parallel with the double layer impedance.

(*ii*) When surface diffusion is rate determining a sufficient condition is

$$\frac{k_1 l}{D} \to 0 \quad [40]$$

Equation [39] now reduces to the one published earlier (6).

(*iii*) In actual experiments the region where mixed control operates, that is when

$$\frac{k_1}{D} \to 0 \qquad \sqrt{\frac{k_2}{D_a}}\cdot l >> l \quad [41]$$

will dominate the behavior. This aspect of the theory is new and will be discussed further. It is shown by inserting this condition into [39] that the equivalent circuit in this limit is now a transfer resistance in series with both Warburg impedance and an impedance consisting of a capacity in parallel with surface diffusion impedance. If

$$\frac{\omega}{k_2} << \left(\sqrt{\frac{k_2}{D_a}}\cdot l\right)^{-1}$$

then the surface diffusion impedance (Zad) becomes very significant and of the form

$$RT\sqrt{\frac{k_2}{D_a}}\cdot\frac{l}{ZFi_o}$$

That is Zad degenerates into a pure resistance. The faradaic reaction now exhibits classical behavior, in that the impedance R_D, C_D exhibit a linear dependence, as found *e.g.*, for deposition at amalgam electrodes, where the metal lattice is continuously removed. However the intercept of the $R_D/\omega^{-1/2}$ plot is no longer RT/ZFi_o but $(RT/ZFi_o)\ (1 + \sqrt{k_2/D_a}\cdot l)$. The Lorenz treatment coincides with the above only under the special conditions

$$\frac{\omega}{k_2} << \left(\sqrt{\frac{k_2}{D_a}}\cdot l\right)^{-1}$$

If $\omega >> k_2$ then the discrepancy between Lorenz and this work would be expected to be significant. A detailed calculation of the impedance as a function of frequency is being made and will be published later [30].

The next step is to relax boundary condition $c = c_a^o$ at $x = 0$ in [33] by replacing it by

$$D_a\left(\frac{\partial c}{\partial x}\right)_{x=0} = k_4(c_a - c_a^o) \qquad [42]$$

This is exactly equivalent to replacing [22] by [26], and treats the case when equilibrium is not maintained at the step line and there is a finite rate of incorporation at the step line. The most interesting result is that from the general equation a number of steady states are possible showing that a square law dependence between i and η cannot prove by itself that surface diffusion is rate determining.

To sum up the implications of the new theoretical considerations presented in outline in the previous pages, it would seem that solutions of the diffusion problem for much more realistic general models are possible. Important limiting cases and a heuristic approach can give valuable pointers to experimental interpretations, while emphasizing that less general models can give an utterly misleading interpretation of the experiment, especially when different combinations of events can lead to similar results.

Conclusion

We have endeavored, in this paper, to review the very recent theoretical and experimental developments arising particularly from our own investigations and the activities of the research group with which we are associated. Electrodeposition has been treated in the broadest possible sense including the deposition of both metallic and nonmetallic phases.

Thus, progress in this field allows one to characterize the various steps in a very general type of electrochemical reaction. Nonmetallic and metallic deposits behave very similarly, the differences being a reflection of the electronic properties of the individual lattice structures. In many cases nonmetallic films grow with the slow step at the edge; this is not surprising in view of the complex nature of these lattices. Metallic lattices which are simpler chemically tend to form at much higher rates and therefore preceding transport processes can become rate determining.

As shown by the time dependence these processes can be detected and experiments designed to overcome the effects of diffusion in the solution by, for example, growing a large constant number of nuclei at the outset potentiostatically, and then growing these at a much lower potential as shown in the text. More sophisticated relaxation technique such as a-c impedance, or trains of pulses can be used to elucidate the mechanism of deposition or dissolution of various complexes in solution and species adsorbed on the surface. In general it would seem to us that metal deposition is likely to be dominated by study of complexes and equilibria in solution as precursors to lattice growth.

We have found the technique of growing lattices of a known structure on inert substrates to be a powerful one which, in fact, corresponds to the method of measuring initial rates, common in chemical kinetics. Lattices grow with well-defined crystal habits and as thin films lending themselves to electron optical examination. It should be possible to determine experimental rate constants especially for the formation of metal lattices and we feel that it is with these that future theories of electrocrystallization will be concerned.

The theoretical treatment of the diffusion problems involved are clearly possible with more realistic models, and this will undoubtedly permit the design of more soundly based experiments to test the relative importance of surface diffusion in the over-all scheme; this is a matter which we think to be of particular importance and where, to date, we consider considerable uncertainty to lie.

Acknowledgment

Finally we must express our gratitude to our many colleagues for frequent and continual discussion, without which progress would be negligible.

REFERENCES

1. J. O'M. Bockris and A. Damjanovic, "Modern Aspects of Electrochemistry," Vol. III, Butterworths, London (1964).
2. M. Fleischmann and H. R. Thirsk, "Advances in Electrochemistry and Electrochemical Engineering," Vol. III, Interscience Publishers Inc., New York (1963).
3. M. Fleischmann and H. R. Thirsk, *Trans. Faraday Soc.*, **51**, 71 (1955).
4. M. Fleischmann and M. Liler, *ibid.*, **54**, 1370 (1958).
5. M. Fleischmann and H. R. Thirsk, *Electrochim. Acta*, **1**, 146 (1958).
6. *Idem, ibid.*, **2**, 22 (1960).
7. A. Bewick, M. Fleischmann, and H. R. Thirsk, *Trans. Faraday Soc.*, **58**, 2200 (1962).
8. M. Fleischmann, K. S. Rajagopalan, and H. R. Thirsk, *ibid.*, **59**, 741 (1963).
9. M. Fleischmann, H. R. Thirsk, and I. Tordesillas, *ibid.*, **58**, 1865 (1962).
10. M. Fleischmann, J. Patterson, and H. R. Thirsk, *ibid.*, **61**, 1256 (1965).
11. M. Fleischmann and H. R. Thirsk, *Electrochim. Acta*, **9**, 757 (1964).
12. H. R. Thirsk, *Proc. Phys. Soc.*, **B66**, 129 (1953).
13. E. H. Boult and H. R. Thirsk, *Trans. Faraday Soc.*, **50**, 376 (1954).
14. J. O'M. Bockris, M. A. V. Devanathan, and A. K. N. Keddy, *Proc. Roy. Soc.*, **A279**, 327 (1964).
15. R. Armstrong, M. Fleischmann, and H. R. Thirsk, *Trans. Faraday Soc.*, **61**, 2238 (1965).
16a. R. H. Cousens, D. J. G. Ives, and R. W. Pittman, *J. Chem. Soc.*, 3973, **1953**; b, H. P. Dibbs, D. J. G. Ives, and R. W. Pittman, *ibid.*, 3370, **1957**; c, D. C. Cornish, H. P. Dibbs, F. S. Feates, D. J. G. Ives, and R. W. Pittman, *ibid.*, 4101, **1962**.
17. G. J. Hills and D. J. G. Ives, *J. Chem. Soc.*, **305**, 311, 318 (1951).
18. R. Armstrong, M. Fleischmann, and H. R. Thirsk, To be published.
19. R. Armstrong, Unpublished work.
20. M. Fleischmann, J. Mansfield, H. R. Thirsk, H. Wilson, and Lord Wynne-Jones, To be published.
21. H. Gerischer and R. P. Tischer, *Z. Elektrochem.*, **61**, 1159 (1957).
22. C. Kasper, *Trans. Electrochem. Soc.*, **77**, 353 (1940).
23. M. Fleischmann and J. A. Harrison, To be published.
24. O. R. Brown and H. R. Thirsk, *Electrochim. Acta*, **10**, 383 (1965).
25. J. O'M. Bockris and M. Enyo, *Trans. Faraday Soc.*, **58**, 1187 (1962).
26. L. Gierst, "Transactions of the Symposium on Electrode Processes," E. Yeager, Editor, John Wiley & Sons, Inc., New York (1961).
27. D. J. Astley and J. A. Harrison, Unpublished work.
28. M. Fleischmann, J. A. Harrison, and H. R. Thirsk, *Trans. Faraday Soc.*, **61**, 2742 (1965).
29. M. Fleischmann and J. A. Harrison, To be published.
30. M. Fleischmann, S. K. Rangarajan, and H. R. Thirsk, To be published.
31. W. Lorenz, *Z. Phys. Chem.* (Frankfurt), **19**, 377 (1959).

Discussion

H. Gerischer: I would like to make a short comment on this very important and stimulating paper which concerns the model used for describing the electrolytic deposition and dissolution of a metal. In this model as represented in Fig. 13 the assumption is made that only the rate of the reaction step in which an atom (or ion) moves perpendicularly to the surface plane depends on the electrical charge in the double layer, *i.e.*, on the electrode potential. This model has given a great deal of very valuable information and can give more. It is therefore of very great value to have now a rigorous mathematical solution for this model as given in this paper. One may not forget, however, that this model has a serious weakness in the way in which the transfer of atoms from kink sites to the surface planes is treated. This process is obviously not independent of electrode potential in contradiction to the model used here. I think that this is one of the reasons for the fact that no limitation of the anodic dissolution rate of a metal can be observed. It is obviously very difficult to modify the kinetics in this model as to take into account this kind of complication in the calculations. In a very preliminary way, we have already had to apply such a treatment to the surface migration and the exchange of adatoms with kink sites, but these ideas have to be developed much further in such a rigorous way as shown in this paper.

H. Thirsk: I think we are very conscious of the fact that the complete model examined mathematically is still very much simplified. The boundary condition in a sense summarizes our assumptions concerning the nature of the surface diffusion involved; that is, the step is a continuous line-sink/source and this is dependent on the assumption that the mean free path of the diffusing atoms is much greater than the mean distance between two consecutive sinks and that equilibrium is maintained for the exchange and is not influenced by mass transfer through the solution. We have not tried to treat the effects of the potential field at this present stage, although I am certain the probable importance of such a complication has been raised in earlier papers in electrocrystallization, written in collaboration with Dr. M. Fleischmann.

H. B. Urbach: I would like to confirm Professor Gerischer's remarks concerning the electrostatic character of the mechanism of surface migration of adatoms. The question of the mechanism of transport resolves itself into two alternatives. Is the mechanism a random walk (pure diffusion) process or is it an electrostatic process? Naumevets and Gavrilyuk[1] in the U.S.S.R. have actually observed, by means of the field ion microscope, that the motion of particles at a gas-solid interface is influenced by the direction of the local fields impinging on the interface. They were in fact able to influence the direction of motion of the adatoms at will. Their calculations showed that the observed forces were consistent only with an electrostatic interpretation based on the interaction of dipoles (the adsorbed adatom complex with its image) and the field. Prior to my discovery of the Russian paper, I had performed an analysis[2,3] of the mathematical problem associated with the electrolyte-metal interface where it is expected that the field intensity at the interface would be much greater than at the gas metal interface. It is based on taking the tangential (to the interface) component of the gradient of the scalar product of the dipole moment and the field intensity and is similar to the Russian analysis.

H. Thirsk: We are assuming a normal surface diffusion process. I must say that I had not thought of the Russian work to be of immediate relevance to electrodeposition, although of great elegance and interest. However, in view of your mathematical treatment indicating that the effect would be greater in electrolytic deposition, the whole assumption merits further consideration. We look forward to more information on your calculations.

R. G. Buck: Inasmuch as you have obtained an exact solution for the current transform in the potentiostatic case, you could make direct use of the result realizing that it gives, on substitution of $j\omega$ for the transform variable, the frequency dependence of the impedance. Use of the transform in this manner would save the effort required to invert the transform. Providing it is electrochemically sound and experimentally feasible to apply a small amplitude sinusoidal ripple potential in addition to the d-c bias, the impedance spectrum could be measured and could be compared by curve fitting with the derived impedance function. This type of experiment related to work of Sluyters[4] seems to be a reasonable way of getting at the rate constants for the cases where coupling occurs between mass transport and a slow surface reaction.

H. Thirsk: We have dealt with the a-c case by substituting $j\omega$, but the i *vs.* t relationships are of direct interest to us in the nonsteady state following the application of a potential jump.

E. Gileadi: A new relaxation technique is suggested in this paper for the measurement of the rate of the fast charge transfer reaction in a reaction sequence such as given in Eq. [5]. I would like to ask whether this method is considered by the authors in any way superior to the long established bridge method first suggested by Frumkin, Dolin, and Erschler[5] in 1940. Is the accuracy of the measurement improved? If a fast charge transfer step is at quasi-equilibrium, followed by a slower rate-determining step, a substantial pseudocapacity may arise, in which case the system is less than ideally suitable for application of potential steps, unless very small electrodes are used.

H. Thirsk: What we are proposing is a method of studying electrochemical process by relaxation methods employing a potentiostat with a fast rise time. The possibility of the method is the point of interest and not the question as to whether another method is more accurate. In any case, I am unaware of the satisfactory application of an a-c bridge method of the type you describe to crystal growth problems of a type precisely relevant to the present paper. We are fully aware of the problems of pseudocapacity.

J. O'M. Bockris (communicated): We welcome Professor Thirsk's summary of the work which his team has been carrying out in Newcastle. In a general way, we think that the goals which they seem to seek in

[1] A. M. Gavrilyuk and A. G. Naumevets, *Sov. Phys.—Solid State*, 5, 2043 (1964).

[2] H. B. Urbach *et al.*, Report AFCRL-64-539, Contract No. AF 19(628)-3234 prepared for the Air Force Cambridge Research Laboratories, Cambridge, Massachusetts.

[3] H. B. Urbach, *Electrochim. Acta*, In press.

[4] Sluyters.

[5] A. Frumkin, P. Dolin, and B. Ershler, *Acta Physicochim. URSS*, 13, 779 (1940).

their work,—rate-determining step and path,—are those which we seek, too, at the University of Pennsylvania. We would like, nevertheless, to make some comments on the studies carried out at Newcastle.

(*i*). Much of the work summarized in Professor Thirsk's paper is work done not on electrodeposition in any conventional sense, but, rather, on electrocrystallization, for example, the formation of thallous chloride on thallium amalgams. Although these studies are complementary to those of metal deposition, which Thirsk *et al.* also study, there are of course considerable differences in growth of A on B (the most frequent objective of the Newcastle work) and electrodeposition of A on A, for instance of Cu on copper substrate.

(*ii*). The technique which Thirsk *et al.* use predominantly is that of the potentiostatic transients. It is a powerful one. Nevertheless, conclusions regarding the rate-determining step based on behavior at times such that monolayer build-up is in its early stages need not always be valid in respect to the steady state at longer times.

(*iii*). There seems to be a danger in relying too much on one technique. The number of steps between the observations of the transients and the model is a long one, and, if unconfirmed by an alternative method, the model may not always be secure.

Thus, electron microscopy, with Thirsk *et al.* use, does have special disadvantages in electrochemical studies because it is impractical to use it *in situ*. We would like here to mention the use of the Nomarski system of optics for *in situ* studies of metal deposition. This uses polarized light; it allows microscopy and interferometry in the same small apparatus and can be used to make studies, *e.g.*, of the movement of growth steps over the crystal surface. Ellipsometric techniques perhaps may be developed usefully here, as well.

The differences between Professor Thirsk's work and ours are in details of some models.

The mechanism of the formation of calomel.—This is that mechanism in which the Newcastle and Philadelphia groups have come into definite disagreement. The disagreements have significance outside a direct interest in the mechanism of calomel formation, because the mechanism of anodic crystallization reactions, the main area in which the Newcastle group has worked, is to be treated either along a dissolution precipitation path or along that of anion deposition and subsequent crystal growth steps. Although, of course, both types of mechanisms may function under different conditions, were the latter type of mechanism (which the Newcastle group have proposed be true for calomel, too) to be disproved in this case, it would tend to suggest some revision in other mechanisms. A second reason why the disagreement is important has to do with the fact that the counter case to that of the Newcastle work is based on an ellipsometric technique which has the advantage of giving direct information on the state of the surface and the disadvantage[6] of being brand new in electrochemistry.

The principal pieces of experimental evidence which made Bockris, Devanathan, and Reddy[7] favor the dissolution-precipitation mechanism for calomel formation are:

(*i*) The fact that, in galvanostatic transient measurements of mercury dissolution, the current passes for a significant time (corresponding to the dissolution of many layers of Hg) before the ellipsometer registers any new phase on the surface. This time increases with decreasing current density. Constant electrode potential close to that of calomel electrode is, however, established in much earlier time.

(*ii*) The fact that the time (analogous to a transition time) which elapses between the switching on of a galvanostatic current and the beginning of ellipsometer signals of a new phase is stirring-dependent. At low current densities effective stirring prevents the formation of calomel completely.

(*iii*) The (very significant) fact that the ellipsometric studies indicate a continuation of film growth of calomel after the current has been cut off during the initial period of growth.

These three facts seem to be consistent only with a dissolution-precipitation model, which is also what is found with Ni.[8]

It does seem that, in his paper at this meeting, Professor Thirsk has not perhaps been quite sufficiently revealing in the presentation of the position, *e.g.*, he did not call attention to the above facts. Further, the formula for the complex which dissolves has been overstressed at the expense of the controversy concerning the basic model. Bockris, Devanathan, and Reddy found their work to be consistent with Hg_2Cl^+ (as has Hills and Ives[9]), and Thirsk prefers $HgCl_4^{2-}$. This seems of lesser importance than the type of mechanism for the anodic formation of halide films.

What chance can there be that both mechanisms occur? Most of the Newcastle work was done under potentiostatic conditions where the initial currents would be several orders of magnitude greater than with the Philadelphia work. The dissolution-precipitation stage would be immeasurably quick on the Newcastle time scale for potentiostatic work, or, possibly the mechanism actually changes. Alternatively, could the presence of impurities in one solution have given nucleation centers for crystallization on the metal which changed this stage from what was observed in the other?

The main thing which must be done is to establish independent verifications of the ellipsometric results, for, if verified, the position is then quite unambiguous.[10]

Is surface diffusion a step in over-all metal deposition mechanism?—Professor Thirsk's position is that he doubts it. For low melting point metals, he favors diffusion in solution, and considers that a hemicylindrical diffusion model with a growth step serving as a line sink can explain experimental facts. Our position is that, at least on Cu, Ag, and Ga, surface diffusion is involved in the mechanism of deposition, and, at low overpotentials (and with certain preparation of the electrode surface), may be rate-determining.

The surface diffusion position is, we submit, past the hypothesis stage. For example: (i) In systems where a surface diffusion model has been proposed, support comes from the reasonable values (*e.g.*, 0.1 of total coverage) of the adion concentrations at the reversible potential. Certainly, the equations we have used concern a crude model for the surface and surface diffusion, but were it wrong, as Professor Thirsk implies it might be, c_o values (verified by independent work and techniques) would hardly be in the region expected.

(*ii*) It was shown by Mehl and Bockris[11] (1957) that an analysis of galvanostatic transients for silver dissolution gives also i_o, the exchange current density for the transfer reaction, on the assumption of rate-determining surface diffusion control near the reversible potential. At overpotentials above 100 mv's, there is behavior clearly indicating charge transfer

[6] Although Reddy, Genshaw, and Bockris [A. K. N. Reddy, M. Genshaw, and J. O'M. Bockris, *J. Electroanalyt. Chem.*, **8**, 406 (1964)] have shown that in respect to platinum oxides, the ellipsometric studies agree almost exactly with coulometric ones.

[7] J. O'M. Bockris, M. A. V. Devanathan, and A. K. N. Reddy, *Proc. Roy. Soc.*, **A279**, 327 (1964).

[8] J. O'M. Bockris, A. K. N. Reddy, and M. G. B. Rao, To be published.

[9] G. H. Hills and D. J. G. Ives, *J. Chem. Soc.*, 305, 311 (1951).

[10] The solution of the ellipsometric equations is quite easy for calomel because the films are not conducting.

[11] W. Mehl and J. O'M. Bockris, *J. Chem. Phys.*, **27**, 818 (1957).

control and i_o can be readily obtained in a direct way, without the application of surface diffusion theory. The values agree well.

(*iii*) Despic and Bockris found that the parameters of the surface diffusion steps, and hence whether it was rate-determining, was dependent on solution purity. This would, of course, effect only surface diffusion.

Particularly (*ii*) and (*iii*) seem to offer strong evidence for surface diffusion as one of the consecutive steps[12] before lattice building commences. Although the evidence from our own work extends only over Cu, Ag, and Ga, we suggest that surface diffusion is always a step in metal deposition processes (not necessarily rate determining, of course).

Another point concerns the prediction which Professor Thirsk makes concerning the metals for which surface diffusion is most likely to occur. He considers it to be the high melting point, or "hard" metals, where the bond strength to the adatoms will be high. If the question is the competition between diffusion from site A to site B via the surface or via the solution, then we are dealing with alternative parallel paths and the easier will be favored. If the bond strength of substrate to surface atom is high, then the heat of activation for surface diffusion will tend to be high and hence a tendency (not necessarily resultful) will arise to take the solution path and *vice versa* for the soft metals. Of course, the reverse indications pertain to the rate-determining step.

In respect to the initial contributions to the surface diffusion kinetics, the 1957 note of Mehl and Bockris[11] gave the first quantitative values of surface adion concentrations and the first equations in which galvanostatic transients were related to surface diffusion velocity, rate of charge transfer and adion concentration. Gerischer and Tischer's[13] work, reported in the same year, was qualitative.[14] The 1957 equations also allowed determination of the fast rate constant as well as the slow one (cf. Eq. [11] of Thirsk).

H. R. Thirsk (communicated): We are grateful to Professor Bockris for his comments on our paper, since this seems to justify a rather more detailed treatment of certain aspects of our work which still do not seem to be well understood. To consider the general points raised by Professor Bockris:

(*i*) *Electrodeposition.*—If this term means anything at all, it must refer to the growth of a deposit on a substrate due to the passage of a current across the interface. It is irrelevant whether the process is anodic or cathodic. The question of A on A or A on B is equally of importance in either process.

(*ii*) *The potentiostatic technique.*—Admittedly we have used this method very extensively. It has the major advantages of allowing an analysis of the nonsteady state to be undertaken. Galvanostatic methods must always involve drastic approximations when the treatment of nonsteady state conditions is required, since electrochemical rate constants are potential dependent.

(*iii*) Other techniques.—*In situ* techniques are obviously very desirable. Although the techniques of electron diffraction and electron microscopy cannot be used for *in situ* investigations in electrodeposition, they are nevertheless extremely necessary for (*a*) the examination of the surface of the substrate, and (*b*) the identification of the nature of the electrodeposited material. As I understand it, I would not be happy in using ellipsometry as a means of identifying a surface layer without confirmation by other techniques.

[12] J. O'M. Bockris and G. Razumney, in "The Electrocrystallization of Metals," in press, Plenum.

[13] H. Gerischer and R. P. Tischer, *Z. Elektrochem.*, **61**, 1159 (1957).

[14] But, Lorenz [W. Lorenz, *Z. Elektrochem.*, **58**, 912 (1954)] discussed surface diffusion quantitatively in 1954.

We consider now the criticisms made of our treatment of the kinetics of formation of calomel, since this is a particularly well defined problem. The observations which seem to us the most important in this case are the following. The deposits of calomel which are formed electrochemically invariably have the (110) plane parallel to the electrode surface[15] independently of crystal size. Potentiostatic experiments at high chloride ion concentrations give i—t transients which follow the equation

$$i = nFC_oD_o^{1/2}/\pi^{1/2}t^{1/2}$$

and are consistent with the view that the mercury is dissolving as $HgCl_4^{2-}$.[16] Potentiostatic experiments at lower chloride ion concentrations give a series of peaks, the charge under each peak being constant at $\sim$ 100 μC cm^{-2} [16,17] in both HCl and KCl solutions. Exactly equivalent galvanostatic observations have been reported by Ives *et al.*,[18] though Bockris *et al.*[19] using only one solution (1*M* KCl) have not been able to reproduce these results. "Adsorption" prewaves are found for the anodic polarography of chloride ions at [Cl$^-$] 10^{-3}M.[20-23] These adsorption waves arise from the formation of one monomolecular layer of Hg_2Cl_2 on the electrode surface.

So far as these observations are concerned, which we believe can only be explained on the basis of the mechanism which we have described in detail previously, the only point in dispute between ourselves and Professor Bockris concerns the form of the galvanostatic transients which should be observed. Since both the Newcastle and Birkbeck College groups have published C-E curves demonstrating the cleanliness of their systems, dare I suggest that a possible cause of the discrepancy could arise from contamination of the electrode surface.

The points considered by Professor Bockris and thought by him to favor a dissolution precipitation mechanism are now taken in turn:

(*i*) We agree. The arrest close to the calomel potential is due to the dissolution of $HgCl_4^{2-}$ and also to the high differential capacity at this point.

(*ii*) Again we agree. Under galvanostatic conditions with a reversible dissolution reaction the electrode potential (and of necessity the rate of change of electrode potential) is a function of stirring conditions.

(*iii*) This point concerns the behavior of an electrode on open circuit. Here the significant principle is that the net current crossing the interface shall be zero. Thus further growth of a calomel film

$$2Hg + 2Cl^- \rightarrow Hg_2Cl_2 + 2e$$

is possible since this can be compensated for by the reaction

$$2e + HgCl_4^{2-} \rightarrow Hg + 4Cl^-$$

Thus the points raised by Bockris *et al.* do not unambiguously favor either mechanism.

There are some further internal inconsistencies in the dissolution-precipitation model to which attention should be drawn. These are

[15] E. H. Boult and H. R. Thirsk, *Trans. Faraday Soc.*, **50**, 376 (1954).

[16] R. D. Armstrong, M. Fleischmann, and H. R. Thirsk, *Trans. Faraday Soc.*, **61**, 2239 (1965).

[17] A. Bewick, M. Fleischmann, and H. R. Thirsk, *Trans. Faraday Soc.*, **58**, 2200 (1962).

[18] D. C. Cornish, S. N. Das, D. J. G. Ives, and R. W. Pittman, *J. Chem. Soc.*, **1966A**, 111, and earlier work by the same authors.

[19] J. O'M. Bockris, M. A. V. Devanathan, and A. K. N. Reddy, *Proc. Roy. Soc.*, **279A**, 327 (1964).

[20] R. Haul and E. Scholz, *Z. Elektrochem.*, **52**, 226 (1948).

[21] A. A. Vlcek, *Coll. Czech. Chem. Comm.*, **19**, 221 (1954).

[22] T. Biegler, *J. Electroanal. Chem.*, **6**, 357 (1963).

[23] R. D. Armstrong, M. Fleischmann, and J. Koryta, *Coll. Czech. Chem. Comm.*, **30**, 4342 (1965).

(*i*) The formation of calomel is written

$$Hg_2Cl^+ + Cl^- \rightarrow Hg_2Cl_2 \qquad [1]$$

Now Hg_2Cl_2 is a solid, and as is well known, the formation of a solid from a solution requires (*a*) appreciable supersaturation, (*b*) nucleation and subsequent growth of small crystals of the solid. Thus the kinetics of reaction [1] cannot be described by rate constants of a type which would be appropriate if Hg_2Cl_2 were a solution soluble species, but rather by a nucleation rate and an expression for the rate at which nuclei, once formed, grow. This Professor Bockris does not attempt to do. It would also be interesting to know the fate of small crystals once formed in the vicinity of the electrode. Does passivation occur because these crystals fall onto the mercury surface due to gravitational forces?

(*ii*) The disproportionation reaction

$$\text{"Mercuric Entities"} + Hg^o \rightleftharpoons Hg_2Cl^+ \qquad [2]$$

is considered first order in "Mercuric Entities." Neglecting for the moment the fact that the evidence for Hg_2Cl^+ is slight, the first order approximation for [2] requires

$$[\text{Mercuric Entities}] << [Hg^o]$$

which cannot possibly be true, since $[Hg^o] \approx 10^{-7}$M.[24]

I think a cautionary word about the structural aspects of the three systems Professor Bockris and his collaborators have studied to date is relevant; I am referring to the calomel, nickel, and platinum passivation. The nature of the passivating layer in the first case is well known and might incidentally make a better subject for the polarized light in active studies than most systems; the second case is structurally far more difficult and I would have considerable reservations concerning the proposals without good secondary evidence from something other than ellipsometry.

[24] H. C. Moser and A. F. Voigt, *J. Am. Chem. Soc.*, 79, 1837 (1957).

Here, also, at the *p*H of the experiments from an estimation using recent data, it should be noted that

$$\frac{[NiOH^+]}{Ni^{2+}} \approx 2 \times 10^{-7}$$

and the final product in the oxide layer (Jones, Wynne-Jones) was much nearer to $NiO_{1.84}$.

The platinum oxide system is even less well understood. We would certainly not expect the same kinetic analysis to suffice for these three very dissimilar system.

Metal deposition.—Professor Bockris bases his experimental evidence for the adatom mechanism on essentially galvanostatic measurements. Clearly here, theoretically, he is at a disadvantage, in that the exact mathematical analysis of such transients is impossible. Potentiostats have been used for many years simply to obviate this difficulty. As is shown in our paper we believe previous estimates of the adatom contribution to be totally due to hemicylindrical diffusion to dislocation or growth sites on the solid metal surface.

In the past, not sufficient was known about the nature of nucleation and subsequent growth in metal deposition to define this complex problem sufficiently. It is, however, a change of phase and has parallels in the chemistry of solid reactions and metallurgy. We suggest that from the point of view of surface diffusion studies the A on A system, because of the structure of metal A, is far too complex. On the other hand when a metal ion is deposited potentiostatically on an inert substrate it is easy to control the number and formation of nuclei and observe growth alone. We hope further that measurement of lattice incorporation constants, as have been very successfully measured in this Department for nonconducting salts and for solid-solid transformations for suitable systems will shed some light on the kinetics of metal deposition.

An Ellipsometric Determination of the Mechanism of Passivity of Nickel[1]

J. O'M. Bockris, A. K. N. Reddy, and B. Rao

The Electrochemistry Laboratory, The University of Pennsylvania, Philadelphia, Pennsylvania

ABSTRACT

The capacity of nickel in acid solution have been followed by means of ellipsometry under conditions of potentiostatic control of the material at various points in the passivation current-potential diagrams and also with automated equipment which allows the recording of the ellipsometer reading under transient conditions. It is found possible to evaluate the refractive index, thickness, and light adsorption of the film at all parts of the process. The film begins to form at the first inflection on the current-potential diagram, but after the current reaches its maximum point, it does not change further in thickness. When the current begins to descend, there is a parallel rapid increase in the electronic conductivity of the film. Passivation arises from a critical increase in semiconduction of the film on the surface. The increase in electronic conductivity reduces the field available for the encouragement of anodic dissolution and transport through the film. Hence, dissolution ceases, *i.e.*, passivity, occurs.

The phenomenon of passivity has been studied for over a century. In fact, the first theory of passivity was intuited in 1844 when Faraday stated: "My strong impression is that the surface . . . is oxidized, or that the superficial particles of the metal are in such relation to the oxygen of the electrolyte as to be equivalent to an oxidation, and that having their affinity for oxygen satisfied and not being dissolved by the acid . . . there is no renewal of the metallic surface. . . ." With these words, Faraday glimpsed the critical role of the surface in determining the stability of a metal in a corrosive environment. In addition, he not only distinguished two possible modes of interaction between the reactive metal surface and oxygen (*viz.*,

[1] Paper summarized by Halina Wroblowa (Mrs. J. O'M. Bockris) at the Cleveland Meeting.

oxidation and an oxygen-metal relationship which is equivalent to surface oxidation), but also implied the difficulty of deciding between these alternatives.

Despite Faraday's century-old statement of the fundamental problem in passivity, no definitive solution has been forthcoming. The critical issue has, however, been cast into modern terminology, and the two principal views are that the basic cause of passivity is a three-dimensional oxide film with particular properties or a two-dimensional chemisorbed oxygen film. Of course, these two views are only the basic themes, and modern proponents have developed several subtle variations of them (1-14).

The resolution of the controversy has been delayed by continued reliance on the measurement of the electrical characteristics of the metal-solution interface, *viz.*, the potential, current, or capacity. Such measurements do not always lead to an unambiguous determination of the mechanism of electrochemical phenomena at interfaces. What has been lacking is an *in situ*, preferably nonelectrochemical method of revealing the state of an electrode surface under the normal conditions of electrochemical experimentation. A technique which satisfies these requirements is ellipsometry, but while its principles have been available for several decades (15-17), it is only recently that the difficulties of applying it to electrochemical systems have been overcome (18).

Ellipsometry is based on the sensitivity with which polarized light reflects changes in the state of a metal surface. In particular, the technique is based on the measurement of the changes which surface films induce in the polarization state of reflected light. These changes (represented by a relative phase retardation Δ and a relative amplitude diminution ψ) of an elliptically polarized light beam reflected from a film-covered surface are related to the complex refractive index n_F^* and thickness L_F of the film, by the film-optics equation (17)

$$\tan \psi e^{i\Delta} = f(n_F, \kappa_F, L_F, n_M, \kappa_M, n_1, \theta_i, \lambda)$$

$$\tan \psi e^{i\Delta} = \frac{r_{p,12} + r_{p,23}\, e^X}{1 + r_{p,12}\, r_{p,23}\, e^X} \Big/ \frac{r_{s,12} + r_{s,23}\, e^X}{1 + r_{s,12}\, r_{s,23}\, e^X} \qquad [1]$$

where $r_{p,12}$, $r_{p,23}$, $r_{s,12}$ and $r_{s,23}$ are the Fresnel reflection coefficients (19). The subscripts p and s refer to the reflection coefficients for the light vibrations, parallel and perpendicular to the plane of incidence. The subscripts 1, 2, 3 refer to the medium, film and substrate, respectively (Fig. 1). Further,

$$r_{p,12}, r_{p,23}, r_{s,12}, r_{s,23} = f(n_F, \kappa_F, L_F, n_M, \kappa_M, n_1, \theta_i, \lambda)$$

$$r_{p,12} = \frac{n_F^* \cos\theta_i - n_1 \cos\theta_t}{n_F^* \cos\theta_i + n_1 \cos\theta_t} \qquad [2]$$

$$r_{s,12} = \frac{n_1 \cos\theta_i - n_F^* \cos\theta_t}{n_1 \cos\theta_i + n_F^* \cos\theta_t} \qquad [3]$$

$$r_{p,23} = \frac{n_3^* \cos\theta_t - n_F^* \cos\theta_t'}{n_3^* \cos\theta_t + n_F^* \cos\theta_t'} \qquad [4]$$

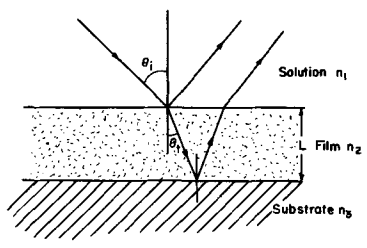

Fig. 1. Basic principle of ellipsometry

$$r_{s,23} = \frac{n_F^* \cos\theta_t - n_3^* \cos\theta_t'}{n_F^* \cos\theta_t + n_3^* \cos\theta_t'} \qquad [5]$$

$$X = -4\pi i\, n_F^* \cos\theta_t\, L_F/\lambda \qquad [6]$$

$$n_F^* = n_F + i\kappa_F \qquad [7]$$

$$n_3^* = n_M + i\kappa_M \qquad [8]$$

where $i = \sqrt{-1}$ and θ_i is the angle of incidence at the metal surface; θ_t is the angle of refraction in the film; θ_t' is the angle of refraction in the metal; n_1 is the refractive index of the medium (sulfuric acid solution in the present case); λ is the wavelength of the light used; n_M and κ_M are the refractive index and absorption coefficient of the metal; n_F, κ_F, and L_F are the refractive index, absorption coefficient, and thickness of the film, respectively.

Ellipsometry is particularly noted for the fact that monolayer films are theoretically expected to give easily measurable changes in the parameters of the polarized light. It constitutes, therefore, an excellent method of making *in situ* examination of the formation, growth, and characteristics of anodic films. In the present communication, a detailed report is given of a steady-state ellipsometric study (20) of the passivation of nickel in acid solution.

Experimental

Electrolyte.—All the experiments were carried out at room temperature (~20°C) in solutions of 0.01*N* H_2SO_4 + 0.5*M* K_2SO_4 (pH = 3.15) kept under a prepurified nitrogen atmosphere.

Electrodes.—Nickel tape of 99.5% purity (thickness 0.0375 cm) was found to have sufficient mirror finish to be used as the reflecting electrode. The counter electrode consisted of a rectangular platinized platinum sheet, and the reference electrode, a saturated calomel electrode. The cell arrangement is shown in Fig. 2.

Electrode preparation.—After degreasing in hot alcohol, the nickel tape was washed in conductivity water. In order to remove air-formed oxides, it was etched for 2 min in a 50-50 mixture of nitric and sulfuric acids, washed in conductivity water, and then maintained at a potential of — 0.25v (*vs.* NHE) by means of a Wenking 61-R potentiostat. The optical constants of the nickel were found to be consistent with those given in the literature for pure nickel surfaces (21).

Cell.—The cell (4.5 x 2.19 x 4.65 cm) was made of transparent Corning synthetic fused quartz (refractive index n = 1.458). The top of the cell was made of Teflon, with openings for the electrode and the gas.

Electrochemical measurements.—Steady-state experiments.—The current density-potential curve was obtained using a Wenking 61-R potentiostat, the current being measured by a Sargent SR recorder via a Keithley 610 electrometer. Steady state was assumed to exist when, in a period of 15 min, the current changed by less than 1% of the total current.

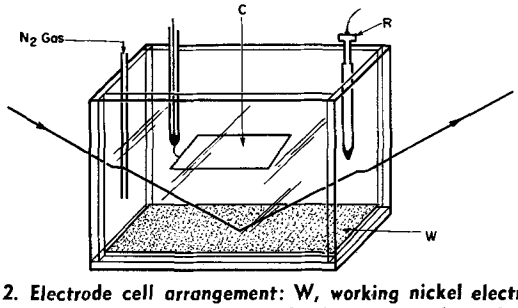

Fig. 2. Electrode cell arrangement: W, working nickel electrode; R, saturated calomel electrode; and C, the counter electrode.

Galvanostatic reduction.—The electrode was maintained at steady state in the passive region by means of a potentiostat; thereupon a switch with a rise time of ~ 10 μsec was used to impose a constant cathodic current on the nickel electrode. The resulting potential-time transients were recorded using a Tektronix RM-35A oscilloscope and a C-12 Polaroid camera.

Potentiostatic reduction.—The procedure consisted of switching from a potential in the passive region to a more negative one, and recording the current-time plots on a Sargent SR recorder. Care was taken to choose a lower, final potential which was, significantly above the potential for hydrogen evolution, so that the only cathodic process could be the reduction of the surface entity.

Ellipsometric measurements.—A standard procedure (22) was adopted for finding the extinction positions of the polarizer and analyzer. From the settings thus determined, a calculation was made of the values of the relative phase retardation, Δ, and the relative amplitude diminution, ψ, of the vibrations parallel and perpendicular to the plane of incidence. In this calculation, cell corrections (23) were introduced to take into account the fact that the incident and reflected light beams were not entering and leaving the cell at normal incidence.

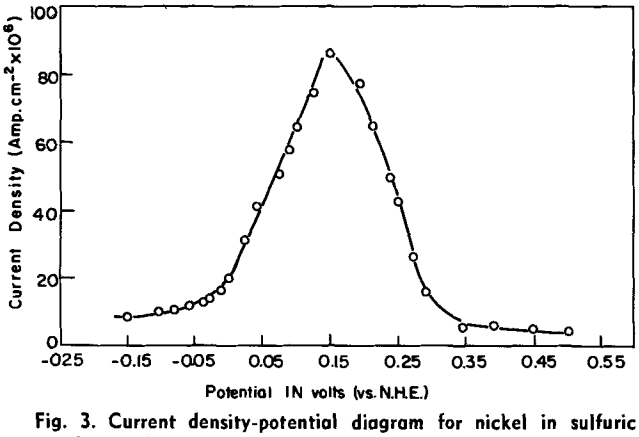

Fig. 3. Current density-potential diagram for nickel in sulfuric acid solutions (pH = 3.15).

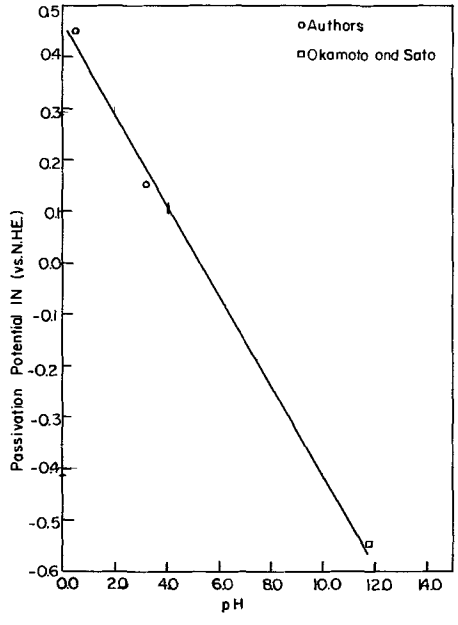

Fig. 4. pH vs. E_{pp} during the passivation of nickel in sulfuric acid solutions (pH = 3.15).

Results

Steady-state current density-potential plots.—The current density-potential curve for the pretreated nickel foil electrode in acid solutions of 0.5M SO_4^{--} concentration (pH = 3.15) is shown in Fig. 3. The passivation potential E_{pp} was + 0.15v (*vs.* NHE). The transition from the active to the passive state is clear. The pH dependency of the passivation process is given in the form of E_{pp} — pH plot in Fig. 4 with a slope of 95 mv/pH unit.

Galvanostatic reduction.—The potential-time curves obtained from the galvanostatic reduction are shown in Fig. 5. The potential falls rapidly to the value at which hydrogen evolution occurs after passing through a potential arrest. At a galvanostatic current density of 0.1 ma cm^{-2}, about 100 μC cm^{-2} are used at the arrest.

Potentiostatic reduction.—Typical current-time curves for the potentiostatic reduction of passive nickel are shown in Fig. 6. After an initial fall in current, there is a region of constant cathodic current, signifying a reduction process. This region corresponds to about 21 mC/apparent cm^2 when the reduction

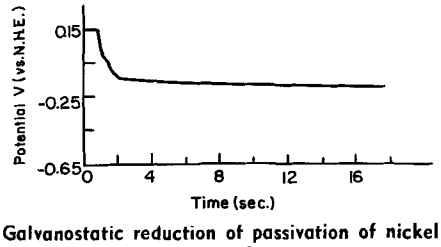

Fig. 5. Galvanostatic reduction of passivation of nickel at a constant current density of 0.1 ma cm^{-2}.

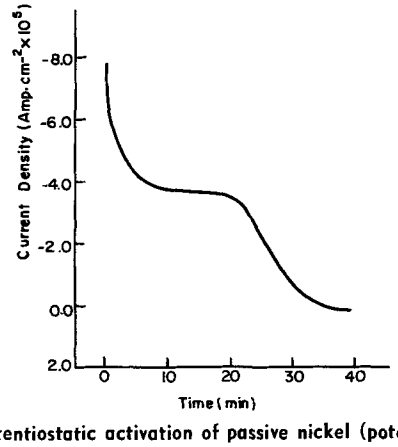

Fig. 6. Potentiostatic activation of passive nickel (potential before activation: +0.17v (vs. NHE).

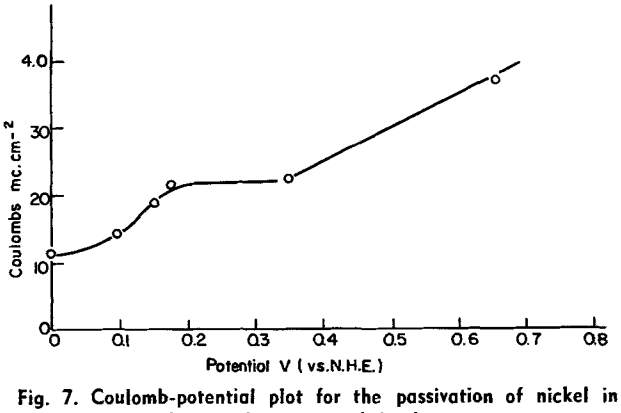

Fig. 7. Coulomb-potential plot for the passivation of nickel in acid solutions (under steady-state conditions).

was commenced on an electrode maintained at a steady-state potential of +0.3v. The quantity of electricity used for this reduction process depends on the initial steady-state potential from which the reduction was commenced (Fig. 7).

To check whether the potentiostatic reduction is effective in reducing the material on the nickel surface, an ellipsometric examination was carried out after the potentiostatic transient. It was found that the optical constants of the surface after potentiostatic reduction were the same as those of bare nickel.

Steady-state ellipsometry.—The steady-state values of Δ and ψ as a function of the potential of the nickel electrode are shown in Fig. 8 and 9. Figure 10 shows a $\Delta - \psi$ plot during the passivation of nickel, and Fig. 11 projects a three-dimensional plot of the variation

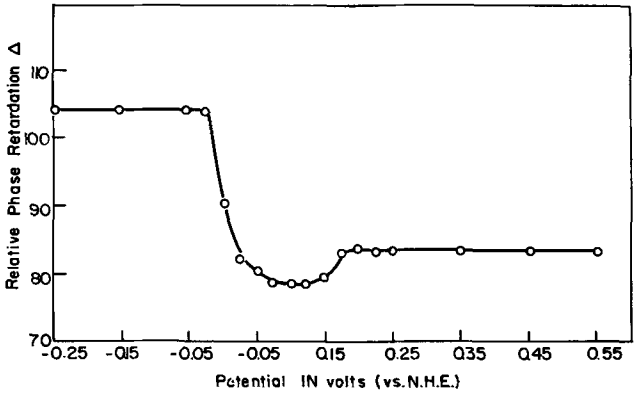

Fig. 8. Variation of relative phase retardation Δ as a function of potential, during the steady-state anodic passivation of nickel in sulfuric acid solution (pH = 3.15).

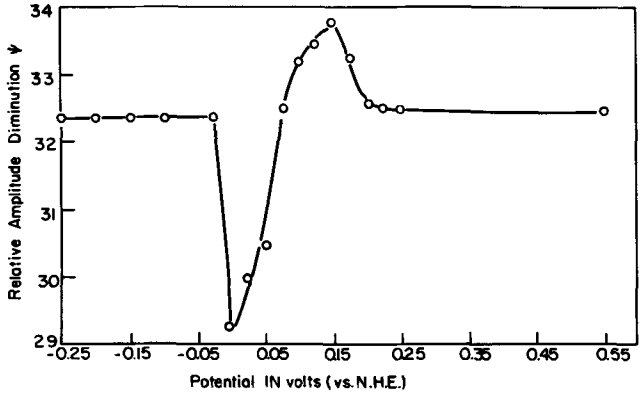

Fig. 9. Change of relative amplitude diminution ψ as a function of potential during the anodic passivation of nickel.

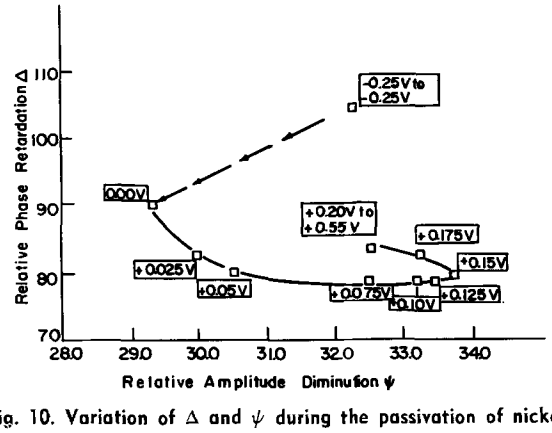

Fig. 10. Variation of Δ and ψ during the passivation of nickel

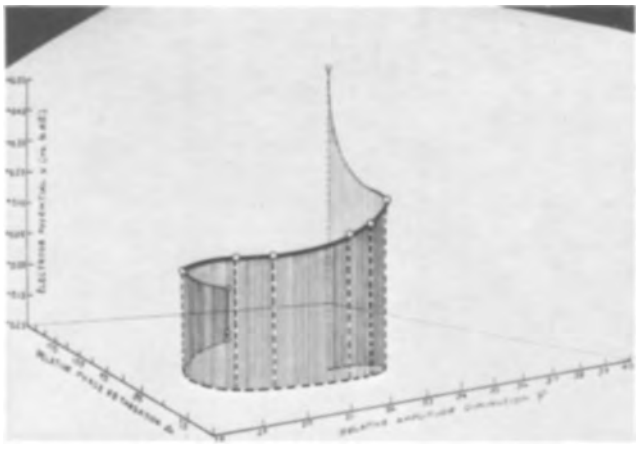

Fig. 11. Three-dimensional plot of the variation of Δ, ψ during the passivation of nickel.

of Δ, ψ as a function of the applied potential. Between — 0.250 and — 0.025v (*vs.* NHE), it is seen that there is no change in either Δ or ψ. There is, however, a drastic change ($\sim$ 14° in Δ and $\sim$ 3° in ψ) in Δ and ψ in the potential range between —0.025 and 0.000v. A feature of the observed Δ—ψ plot is that there is a characteristic inflection precisely at the passivation potential. In fact, an inflection of this type may be regarded as the ellipsometric criterion of passivation.

Discussion

Anodic dissolution of nickel.—At — 0.250v, it can be taken that the nickel is in a film-free condition, since the nickel has been etched and potentiostated at a potential in the immunity domain of the potential-pH diagram (24) for nickel. This expectation has also been confirmed by a comparison between the optical constants of nickel calculated from the Δ and ψ at — 0.250v and those found in the literature for pure nickel.

Since there is no change in either Δ or ψ in the potential range between — 0.250 and — 0.025v (*vs.* NHE), it means that one is working with a film-free nickel electrode. In this potential range, however, the current-potential curve indicates an increasing anodic current. Hence, the nickel must be dissolving anodically without film formation.

Previous electrochemical studies (25, 26) and the chronoellipsometric investigations (27) indicate that the nickel dissolves anodically via a soluble intermediate

$$Ni + OH^- \rightleftharpoons Ni\,OH_{ads} + e$$

$$NiOH_{ads} \rightarrow NiOH^+ + e$$

This mechanism is quite similar to the well-established mechanism for the anodic dissolution of iron in acid solutions (28).

Evaluation of the ellipsometric data.—The problem with the rigorous film-optics Eq. [1] is that, while only two quantities, Δ and ψ, are experimentally determined, there are three characteristics n_F, κ_F, and L_F, of the film, which have to be evaluated. Under these circumstances, the following procedure was adopted:

(*A*) At the outset, certain ranges for the maximum expected variation of film thickness (L), refractive index (n_F), and absorption coefficient (κ_F) were chosen on the following basis: For the thickness, a minimum of zero and a maximum of 100Å were considered; the minimum corresponds to a film-free surface and the maximum value is based on the fact that passive films thicker than 100Å have not been reported (29). The limits of film refractive index were taken to be 1.0 (physically adsorbed oxygen) and 4.0 (to allow for the maximum value found in the literature for solid oxides) (30). The absorption

index of the film was taken to be between 0.0 (a nonabsorbing film) and 1.9 (the absorption index of the metal).

(*B*) Choosing some particular value, L_F, (say 10Å), the film optics equation was used to calculate Δ and ψ for various values of n_F and κ_F chosen within the range stated above. A typical calculation of Δ and ψ from assumed values of n_F, L_F, and κ_F is given below. The following constants are known: n_1 the refractive index of the medium 1.334; n_M, the refractive index of the metal 1.793; κ_M, the absorption index of the metal — 1.834; θ_i the corrected angle of incidence 68.05°; and finally the wavelength of the light used 5461Å. A value of $L_F = 54$Å, $n_F = 3.1$, and $\kappa_F = -1.2$ were chosen for the typical calculation. Then the following quantities were calculated in the order given below

$$\cos\theta_t = \left[1 - \frac{n_1^2 \sin^2\theta_i}{(n_F + i\kappa_F)^2}\right]^{1/2}$$

$$= 0.948 - i\,0.049$$

$$\cos\theta_t' = \left[1 - \frac{n_1^2 \sin^2\theta_i}{(n_M + i\kappa_M)^2}\right]^{1/2}$$

$$= 1.030 - i\,0.044$$

$$X = -4\pi i(n_F + i\kappa_F)\cos\theta_t L_F/\lambda$$
$$= 0.160 - i\,0.357$$
$$e^X = 0.797 - i\,0.298$$

Making use of these results in Eq. [2]-[5], the Fresnel reflection coefficients come out to be

$$r_{p,12} = -0.011 - i\,0.159$$
$$r_{p,23} = 0.021 - i\,0.371$$
$$r_{s,12} = -0.741 + i\,0.098$$
$$r_{s,23} = -0.113 + i\,0.357$$

The above values are then used to calculate the numerator and denominator of Eq. [1]:

$$\text{NUM} = \frac{r_{p,12} + r_{=0.23}\,e^X}{1 + r_{p,12}\,r_{p,23}\,e^X} = -0.119 - i\,0.482$$

$$\text{DEN} = \frac{r_{s,12} + r_{s,23}\,e^X}{1 + r_{s,12}\,r_{s,23}\,e^X} = -0.816 + i\,0.235$$

Thus,

$$(\tan\psi\cos\Delta + i\tan\psi\sin\Delta) = -0.022 + i\,0.585$$
$$\tan\psi\cos\Delta = -0.022$$
$$\tan\psi\sin\Delta = 0.585$$

$$\therefore \tan\Delta = -26.547$$
$$\Delta = 92.157$$
$$\tan\psi = 0.585/0.999$$
$$\psi = 30.345$$

In practice, one chooses the lower limit of n_F, *viz.*, 1.0, and carries out calculations by varying κ_F in steps of 0.05 from 0 to 1.9. Then, the calculations are repeated for values of n_F increasing in steps of 0.05 from 1.0 to 4.0. Then, the whole set of calculations are repeated for other values of film thickness increasing in steps of 1.0Å within the range 0 — 100Å. In all, some 10^5 calculations of Δ and ψ were made.

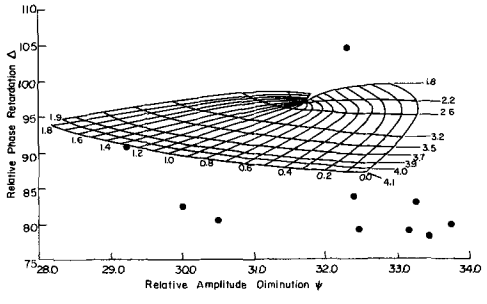

Fig. 12. Δ — ψ computed reactions for a film of constant thickness 40Å. The black circles ○ represent the experimental Δ — ψ plots observed during the passivation of nickel.

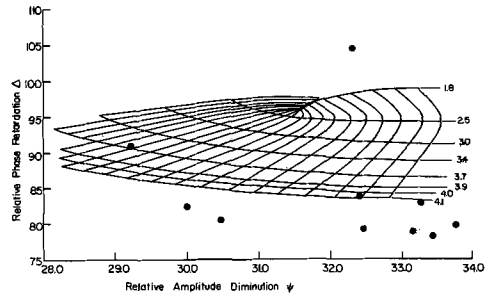

Fig. 13. Δ — ψ computed relation for film of constant thickness 50Å.

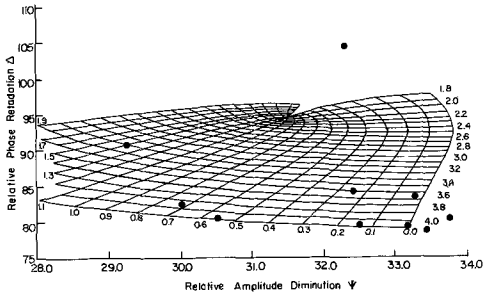

Fig. 14. Δ — ψ relations (computed) for a film of thickness 60Å

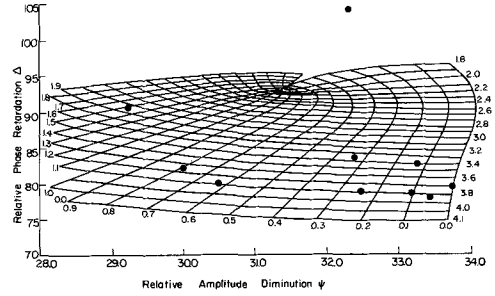

Fig. 15. Computed Δ — ψ relations for a film of constant thickness 70Å.

(*C*) For every value of film thickness, the values of the calculated Δ and ψ are plotted by joining points which correspond to the same κ_F but varying n_F, and those which correspond to the same n_F but varying κ_F. The former give rise to "vertical" lines and the latter to "horizontal" lines. In this way, one obtains, for every value of film thickness, a grid of lines in the Δ — ψ diagram.

(*D*) Finally, the experimental Δ — ψ plots are superimposed upon the calculated Δ — ψ grid for the various thicknesses (Fig. 12-17).

By this comparison between the experimental and calculated Δ— ψ diagrams, it can be demonstrated that for film thicknesses of less than 45Å, the experimental Δ, ψ values do not fall inside the grid in the calculated diagram (Fig. 12).[2] Thus, the film that is formed at 0.0v (*vs.* NHE) cannot be less than 45Å. For higher thicknesses, however, there is a fit. Thus, the values of film thickness, refractive index and absorption coefficient are in the range shown in Fig. 18-20.

[2] At potentials greater than 0.0 (*vs.* NHE), the value of the minimum thickness consistent with the ellipsometric values is 70Å.

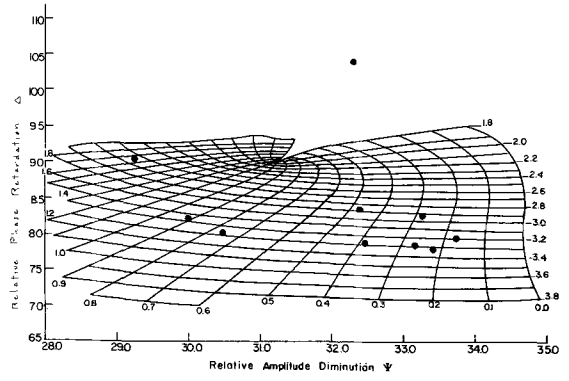

Fig. 16. Computed $\Delta - \psi$ relations for a film of thickness 90Å

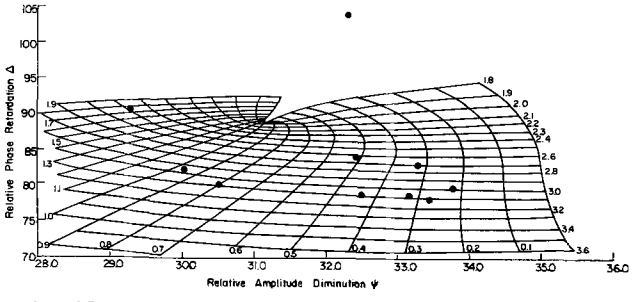

Fig. 17. $\Delta - \psi$ computed relations for a film of constant thickness 100Å.

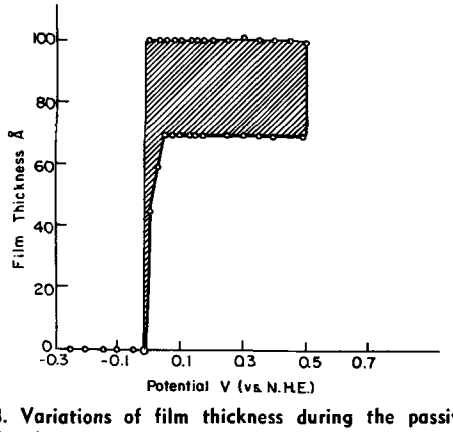

Fig. 18. Variations of film thickness during the passivation of nickel. The thick line refers to the minimum thickness that can be attained.

To narrow down these film characteristics more definitively, the potentiostatic activation results were used. From the quantity of electricity used to reduce the surface film present at various steady-state potentials, the film thickness was calculated. The film formed at 0.0v (*vs.* NHE) was taken, on the basis of chronoellipsometric data (27), to be nickel hydroxide. Using the molecular weight and density of nickel hydroxide, with a roughness factor of 2, the $Ni(OH)_2$ film thickness was calculated to be 60Å (20). In the case of the films present at other potentials, there is uncertainty in the particular compounds present. But, whatever the nickel compound (subhydroxide, various nickel oxides NiO_x), the film thickness at potentials more anodic than 0.0v (*vs.* NHE) turned out to be within 10% of the initial value, *viz.*, 60Å.

Since the potentiostatic activation experiments have yielded a value of film thickness of 60 ± 6Å, the $\Delta - \psi$ diagrams calculated for a 60 ± 6Å film can be used to read off those values of n_F and κ_F which correspond to the experimentally-observed values of Δ and ψ.

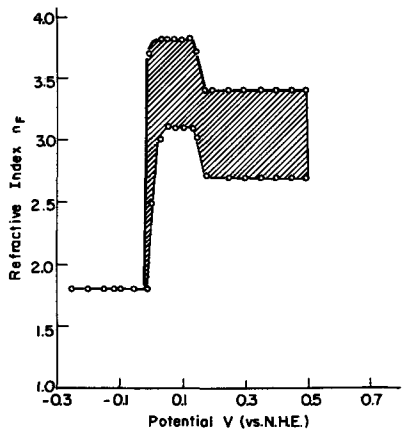

Fig. 19. Variation of refractive index. n_F as a function of potential, during the passivation of nickel. The thick line refers to the minimum refractive index of the film that can be obtained by using a value of film thickness computed from coulometry.

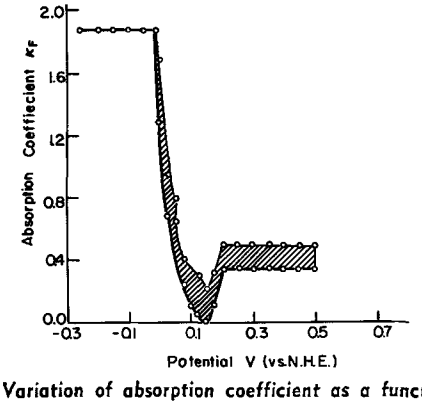

Fig. 20. Variation of absorption coefficient as a function of potentials during the passivation of nickel. The thin line refers to the maximum κ_F that can be obtained.

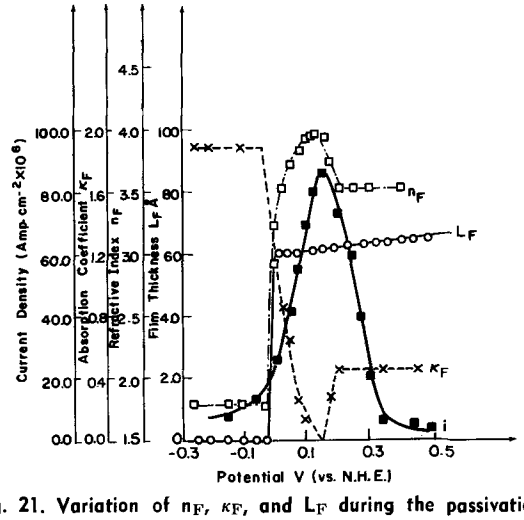

Fig. 21. Variation of n_F, κ_F, and L_F during the passivation of nickel in acid solutions.

Thus, one obtains the film thickness (L_F), refractive index (n_F) and absorption coefficient (κ_F) which have been reported earlier (20). Figure 21 shows a three-way plot of the variation of n_F, κ_F, and L_F as a function of potential.

Film formation.—The sudden large change in Δ and ψ in a narrow 25 mv potential range between — 0.025 and 0.000v (*vs.* NHE), is the ellipsometric evidence of film formation. This film has been shown by unambiguous interpretation of the ellipsometric data to be not less than 45Å, and with the help of coulometric data to be about 60Å.

It will be noticed, however, that the onset of film formation is not accompanied by any decrease in the dissolution current (the gradient of the current-potential line, however, is decreased). The inescapable conclusion is that the film formed at 0.0v (*vs.* NHE) does not *per se* cause passivity. It can only be a precursor or prepassive film.

Analysis of the chronoellipsometric data (27) on the mechanism of precursor film formation supports a dissolution-precipitation mechanism (18). Nickel dissolves anodically to form a soluble intermediate, $NiOH^+$, which accumulates near the electrode until there is precipitation of $Ni(OH)_2$.

The potential at which film formation takes place can be estimated by the following calculations: Assuming that, for a prepassive film to form by precipitation in solution, the current for anodic dissolution i_a is greater than the limiting current i_L required for the ionic species ($NiOH^+$) to form the precipitate, one has, say

$$(i_a)_{\text{film formation}} = 10\, i_L$$

$$(i_o)_a\, e^{\eta F/RT \cdot 3/2} = 10 \cdot \frac{DzF}{\delta} c_{NiOH^+} \qquad [9]$$

Taking the concentration of the $NiOH^+$ species from chronoellipsometric data (27) as 10^{-3} m/l and $(i_o)_a$ (28) as 7×10^{-7}, Eq. [9] can be expressed as

$$(\eta F/RT)\,(3/2) = 2.303 \log (1.4 \times 10^6)$$

$$\eta = +\,0.248\text{v}$$

Taking into account the reversible potential for nickel dissolution at this pH (3.15), as — 0.2v (*vs.* NHE), the potential of inflection where the film formation should occur is + 0.048v (*vs.* NHE), in excellent agreement with the experimentally observed value of + 0.000v (*vs.* NHE).

Passivation process.—It is seen (Fig. 21) that the quantities n and κ undergo two marked qualitative change, the first of which is associated with film formation. The second of these two changes is that which is more important from the view point of the mechanism of passivity, for it occurs at the potential at which the current begins to fall, *i.e.*, at the passivation potential. The decreasing trend of κ, which began at the film formation potential, is reversed and κ begins to increase.

The absorption coefficient is known from classical optics to be related to the electrical conductivity, σ_ν, of the film at optical frequencies (31)

$$\sigma_\nu = n\kappa\nu \qquad [10]$$

where σ_ν is the e.s.u. conductivity at the frequency.

Thus the changes in κ_F are a direct measure of the potential-variation of electrical conductivity at the optical frequencies (under steady-state conditions) during the passivation of nickel in acid solutions (pH = 3.15). There is a decrease in the electrical conductivity until the passivation potential, and immediately afterwards an increase in the conduction is observed. Further, the final values of conductivity are of the order observed with semiconductors at optical frequencies (32). This indicates that the passivation process is associated with the formation of a semiconducting film. Although the difference in conduction of a metal and a semiconductor at zero frequency would be many orders of magnitude, at optical frequencies (10^{14} cps), this difference would be expected to be much smaller, since the relaxation time of the electrons in the metal is 10^{12} sec^{-1}, and thus only a small response would be expected from the electrons in the metal to radiation of 10^{14} cps (33).

Composition changes in the passivation process.—The changes of refractive index from an initial precursor film of $Ni(OH)_2$ to the final semiconducting passive film probably arise from the anodic oxidation of $Ni(OH)_2$. Some indications concerning the nature of the passive film can be obtained by comparing the refractive indices calculated theoretically for various types of oxides with those experimentally observed from ellipsometry.

It is possible to calculate the refractive indices (real) from the well-known Lorentz-Lorenz equation

$$\frac{n^2-1}{n^2+2}\frac{M}{d} = \frac{4\pi}{3} N\alpha_o \qquad [11]$$

where M and d are the molecular weight and density of the material, respectively; α_o is the total molar polarizability of the molecule comprising the material, and n is the real refractive index of the material medium. The important aspect of the calculations is to obtain the value of the molar polarizability α_o of the molecule. For a diatomic molecule, α_o is given by

$$\alpha_o = \frac{b_1 + 2b_2}{3} \qquad [12]$$

where b_1 and b_2 are polarizabilities in the direction of line centers joining the two atoms and perpendicular to the line of centers, respectively, are given by

$$b_1 = \frac{\alpha_1 + \alpha_2 + 4\alpha_1\alpha_2/r^3}{1 - 4\alpha_1\alpha_2/r^6} \qquad [13]$$

$$b_2 = \frac{\alpha_1 + \alpha_2 - 2\alpha_1\alpha_2/r^3}{1 - \alpha_1\alpha_2/r^6} \qquad [14]$$

where α_1 and α_2 are the electronic polarizabilities of the atoms 1 and 2 comprising the molecule and r is the bond distance between them.

There exists an apparent uncertainty in the available electronic polarizability data, as also in the averaging of the individual polarizabilities (in three mutually perpendicular directions) to obtain the molar polarizability α_o. It was assumed that the structure of the nickel oxide would also represent the nonstoichiometric nickel oxides (NiO_x, $x \geq 1$).

Nickel oxide has a cubic structure with the unit cell side, a = 4.17Å. The densities of the various nonstoichiometric oxides were calculated on a proportional basis of the oxygen present in those compounds. The following electronic polarizability data were taken

$$\alpha_{Ni^{++}} = 0.27 \times 10^{-24}\ \text{cc/mole}$$

$$\alpha_{O^{--}} = 2.4 \times 10^{-24}\ \text{cc/mole}$$

It was further assumed that a proportional increase of $\alpha_{O^{--}}$ takes place with change of radius of the O^{--} with increasing nonstoichiometry ($O_{1.0} \rightarrow O_{1.7}$).

The above electronic polarizability data were fed into Eq. [12] to [14] to calculate the molar polarizability, α_o. Using Eq. [11] and the above information, the refractive index of the medium was calculated. It was found that the refractive indices of the compounds $NiO_{1.5}$ — $NiO_{1.7}$ varied from 3.3. — 3.7. The experimentally observed value of the refractive index in the passive region was 3.5. Thus, a comparison between the experimental and calculated values establishes that the passive layer is of composition $NiO_{1.5\text{-}1.7}$.

But the conversion of $Ni(OH)_2$ to a nonstoichiometric oxide has been studied by Briggs and Wynne-Jones (34). Using x-ray diffraction studies in conjunction with electrochemical measurements, they suggested the actual final product to be $NiO_{1.7}$ in agreement with ellipsometric determinations. It has been established, therefore, that in the anodic conversion

of the precursor film $Ni(OH)_2$ to the final passive film, a nonstoichiometric change takes place, and that this change is associated with a marked increase of electronic conductivity and a marked decrease of corrosion rate.

The existence of a semiconducting passive film does not preclude the possibility of oxygen chemisorbing on its surface. In fact, such a chemisorbed oxygen layer must be involved in the evolution of oxygen at ~ 1.5v. When, however, one attempts a galvanostatic reduction, the charge used ($\sim$100 μC cm^{-2}) indicates that only the chemisorbed oxygen on top of the passive oxide is reduced before the potential falls to that corresponding to hydrogen evolution. That the passive oxide is not reduced under galvanostatic conditions is proved by the fact that after such an experiment the ellipsometer still reveals a film-covered surface even in the presence of hydrogen evolution.

Mechanism of anodic passivation.—The present results have brought out several clear diagnostic criteria which permits for the first time a direct testing of the various suggestions regarding the mechanism of passivity. It has been demonstrated unambiguously that a thick (not less than 45Å) three-dimensional film is formed at a potential distinctly cathodic to the passivation potential and that this is a necessary, but not sufficient, condition for passivity. It is the conversion of this precursor film into a semiconductor that constitutes the essential step in the mechanism of passivation, because the development of electronic conductivity prevents high-field ion transport through the film and thus prevents metal dissolution. Metal dissolution is thus drastically reduced and the metal has become passive.

Most of the theories of passivity (1-14) are at variance with either or both of the fundamental experimental conclusions that have emerged from this study. It appears that with regard to the mechanism of precursor film formation, the view of Müller which is based on a dissolution-precipitation mechanism is in closest correspondence with facts indicated by ellipsometry. The existence of electronic (13) conductivity has been stressed by Weil (13), by Vetter (12), and by Pryor (14). But, an integrated view requires a picture, not only of what characteristics the passive film must have, but also an indication of how and when they are introduced. The present study leads to a unified picture of the passivation process: a prepassive film is formed by a dissolution-precipitation mechanism, and this film starts becoming an electronic conductor at the passivation potential. The essential cause of passivity is neither a monolayer nor a multilayer of oxide. It is the conversion in the multilayer from ionic to electronic conduction at the passivation potential probably by the introduction of nonstoichiometry.

Acknowledgment

The authors acknowledge financial support from the Aeronautical Systems Command, U.S. Air Force, under Contract No. AF 33(616)-8150, and from the National Aeronautical and Space Administration, under Contract No. NsG-325. They also thank Dr. S. Roberts for helpful suggestions regarding the computational methods. One of us (A.K.N.R.) thanks the Council of Scientific and Industrial Research, India, for the grant of leave of absence.

REFERENCES

1. H. H. Uhlig, *Z. Elektrochem.*, **62**, 626 (1958).
2. Ya. M. Kolotyrkin, *ibid.*, **62**, 624 (1958).
3. B. N. Kabanov, *Tr. Savestich. po. Elektrokhim. Akad. Nauk. SSSR. Otd. Khim. Nauk*, p. 138 (1953).
4. K. Schwabe and G. Dietz, *Z. Elektrochem.*, **62**, 751 (1958).
5. M. Fleischmann and H. R. Thirsk, *This Journal*, **110**, 663 (1963).
6. G. W. Akimov and W. P. Batrakava, *Izd. Akad. Nauk. SSSR* (1956).
7. U. R. Evans, *Z. Elektrochem.*, **62**, 619 (1958).
8. W. J. Müller, *ibid.*, **30**, 401 (1922).
9. W. A. Mueller, *This Journal*, **107**, 157 (1960).
10. K. F. Bonhoeffer and U. F. Franck, *Z. Elektrochem.*, **55**, 180 (1951).
11. G. Okamoto and N. Sato, *Trans. Jap. Inst. Metals*, **2**, 113 (1961).
12. K. J. Vetter, *Z. physik. Chem.*, **4**, 165 (1955).
13. K. G. Weil, *Z. Elektrochem.*, **62**, 638 (1958).
14. M. J. Pryor, *This Journal*, **106**, 557 (1959).
15. P. Drude, *Ann. Physik. Chemie*, **39**, 481 (1890).
16. L. Tronstad, *Z. physik. Chem.*, **142**, 241 (1929).
17. A. B. Winterbottom, *Det Kgl Norske Videnskab Selakabe Skrifterer*, 1 (1955).
18. A. K. N. Reddy and J. O'M. Bockris, "Symposium on Ellipsometry," Washington, D. C., p. 229 (1963).
19. M. Born and E. Wolf, "Principles of Optics," p. 30, Pergamon Press, New York (1959).
20. A. K. N. Reddy, M. G. B. Rao, and J. O'M. Bockris, *J. Chem. Phys.*, **42**, 2246 (1965).
21 S. Roberts, *Phys. Rev.*, **114**, 104 (1959).
22. G. N. Ramachandran and S. Ramoseshan, "Handbuch der Physik.," Band XXV/1, p. 1, Springer-Verlag, Berlin (1961).
23. A. K. N. Reddy, To be published.
24. M. Pourbaix, N. de Zaubov, and E. Deltombe, "Proceedings of the International Committee of Electrochemical Thermodynamics and Kinetics," p. 193, Butterworths, London (1957).
25. G. Okamoto and N. Sato, *This Journal*, **110**, 605 (1963).
26. A. K. N. Reddy, B. Rao, and J. O'M. Bockris, To be published.
27. A. K. N. Reddy and B. Rao, To be published.
28. J. O'M. Bockris, D. Drazic, and A. R. Despic, *Electrochim. Acta*, **4**, 325 (1961).
29. K. J. Vetter, "Electrochemische Kinetik," p. 431, Springer-Verlag, Berlin (1960).
30. H. H. Landolt and R. Brönstein, "Zahlenwerte und Functionen Aus Physik und Chemie," 8, Jeil. Optische Konstanten, Springer-Verlag, Berlin (1954).
31. M. Born and E. Wolf, "Principles of Optics," p. 601, Pergamon Press, New York (1959).
32. R. J. Archer, *This Journal*, **104**, 619 (1957).
33. R. P. Feynmann, "Lectures on Physics," Vol. II, Sect. 18, Addison-Wesley, Reading (1964).
34. G. W. D. Briggs and W. F. K. Wynne-Jones, *Electrochim. Acta*, **7**, 241 (1962).

Discussion

W. Mehl: The work by Bockris, Reddy, and Rao shows that ellipsometric measurements can lead to significant contributions to the understanding of passivation phenomena. It also shows, however, that the interpretation of ellipsometer readings in terms of parameters which are meaningful to electrochemistry is by no means simple and straightforward; rather it requires additional assumptions and numerical data obtained by other means. It is interesting to note for example that the value of the thickness of the passivating oxide film was actually not determined in this work by ellipsometry but rather by an electrical method. The optical method does permit one, however, to follow the all-important changes of the electrode surface at the Flade potential (which can be either a "passivation" or an "activation" potential depending on the direction of the potential sweep).

Weil[1] and Vetter[2] have shown that the thickness of the oxide film for passive iron is potential dependent

[1] K. G. Weil, *Z. Elektrochem.*, 59, 711 (1955).

[2] K. J. Vetter, *Z. Elektrochem.*, 58, 230 (1954).

and with an acidic electrolyte a linear relationship was found between film thickness and the difference between the applied potential and the Flade potential. This would lead in the steady state to a value $d = 0$ for the film thickness at the Flade potential, and one could now argue that the smallest value for the thickness of a passivating oxide film is that of a monolayer. On nickel Arnold and Vetter[3] measured a thickness of the passivating oxide film of about 40Å. They did, however, speculate that at the Flade potential a nonporous monolayer was formed, which grew only at more anodic potentials to the above-mentioned thickness of 40Å.

What struck me most about this work was the similarity between the model proposed here for the passivation of nickel and the model proposed by Bonhoeffer, Vetter, Weil, and Pryor[4] and Gohr and Lange[5] for the passivity of iron. Nickel and iron are chemically rather similar elements; this agreement is thus very reasonable.

Going into the details of the work presented here, two points seem to be somewhat questionable. The first and minor point is the high index of refraction found for the surface oxide. The value 3.5 is very high for a nickel compound; the highest value reported previously was 2.4 for NiO.[6] It can perhaps be argued that the value for FeO (cubic) is 2.3 while the value for Fe_2O_3 (rhombohedric) is 3.0.[6] Nevertheless, it seems unsatisfactory to calculate by a somewhat involved method an index of refraction of 3.5 for $NiO_{1.5\text{-}1.7}$ without showing that the same method leads to the correct value for NiO.

The second and more important objection is concerned with the passivation mechanism proposed by the authors. The mechanism proposed in the section on "Composition changes in the passivation process" of the paper has to be reconciled[7] with the observed values of the Flade potential. For iron this was for a long time a controversial point. From the work of Franck[8] it was known that the pH dependence of the Flade potential for iron E_{Fe}^F follows the relationship

$$E_{Fe}^F = 0.58 - 0.058\ pH$$

Only fairly recently Vetter[9] and Gohr and Lange[5] have shown that it can be reconciled with the following electrode mechanism

$$2Fe_3O_4 + H_2O \rightarrow 3\ \gamma\text{-}Fe_2O_3 + 2H^+ + 2e^-$$

i.e., passivation is preceded by the formation of Fe_3O_4. The Flade potential is now defined as that potential at which the oxygen partial pressure reaches the value for the equilibrium between γ-Fe_2O_3 and Fe_3O_4.

While in acidic solutions, Fe_3O_4 is dissolved so rapidly that no continuous film can form below (at potentials more negative than) the Flade potential, this oxide is rather stable in alkaline solutions and the existence of a prepassive film below the Flade potential has been shown.[10,11] The ideas of Pryor are somewhat different from those of Vetter, but they also involve a similar sandwich structure.

For nickel, Arnold and Vetter[3] have shown that the pH dependence of the Flade potential is described by

$$E_{Ni}^F = 0.355 - 0.058\ pH$$

The value for E_{Ni}^F at pH = 3.15 obtained by the present authors agrees excellently with the above expression while the other point of Fig. 4 and the value taken from Okamoto [ref. (11) of the authors] do not.

It appears from the present paper that the authors propose for the electrode mechanism responsible for passivation the mechanism of the nickel hydroxide electrode, but the potential of this electrode is unfortunately roughly 1v more positive[12] than the experimental values given above for the Flade potential.

In spite of these objections to certain details, I find the demonstration of the importance of the Flade potential by ellipsometric measurements most impressive.

J. O'M. Bockris and H. Wroblowa (partially communicated): Ellipsometry determines the situation in a passivation process, and this can essentially be read from the last figure in the paper. The result contains elements of several theories associated with the names of Muller, Ibl, Vetter, and Pryor. It does not correspond to anyone of these theories. Further, there are gaps in our knowledge of the causes for the happenings which ellipsometry indicates: the most important of these is the reason for the rise in conductivity; the explanation offered in terms of a change of valency state of the metal and a consequent increase in conductivity is largely speculative. An alternative speculation could be in terms of the effects of ionic adsorption at the prepassive oxide-solution layer and effects of the ionic field on the conductance of the oxide (cf. the effects found by Paul Schmidt for cation adsorption on the conductance of surface films of oxide).

Note that ellipsometry is a technique in which the use of computors is virtually essential. This is probably the reason for the long delay in realization of a technique ideally suited to electrode studies, the theory of which has been available for several decades.

The refractive index which ellipsometry gives for the passive film is indeed high. However, values as high and higher do characterize some transition metal oxides and sulfides. If one solves the Lorenz-Lorentz equation for refractive index (n), it can be seen that the theoretical value of n would be expected to increase rapidly as the polarizability approaches $(3M)/(4\pi N_A \rho)$ where M = molecular weight, ρ = density, and N_A = Avogadro's number. It is likely that the effective polarizability of oxygen is greater in a nonstoichiometric oxide than in a stoichiometric oxide.

Regarding the validity of the calculation method for refractive indices which we used in our paper, the method was indeed tested by us for NiO. The theory (which we later used to interpret the value of $n = 3.5$ in the passive region) gave $n = 2.47$ whereas experimental values for the refractive index of NiO were 2.2-2.5.

Regarding the thermodynamics of the active and passive transition for which we have suggested an oxidation to $NiO_{1.5}$-$NiO_{1.7}$ (on the basis that this would fit, by calculation the refractive index determined ellipsometrically): calculation of the standard potential for a transition of $Ni(OH)_2$ to this nonstoichiometric oxide would be impossible to make in the absence of appropriate thermodynamic data (which would be clearly difficult to obtain). The value reported by Conway and Gileadi refers to bulk phases of a different constitution from that suggested in our papers. It lies 1v above the observed passivation potential. The potential of the NiO-Ni_3O_4 couple lies below that determined by us. The range for various oxidation potentials of NiO thus extends over more than a volt and includes that determined.

Regarding the pH dependence on the passivation potential; that experimentally reported here agrees

[3] K. Arnold and K. J. Vetter, *Z. Elektrochem.*, **64**, 407 (1960).

[4] M. J. Pryor, *This Journal*, **106**, 557 (1959).

[5] H. Gohr and E. Lange, *Naturwiss.*, **43**, 12 (1956).

[6] "Landolt-Bornstein," K. H. and A. M. Hellwege, Editors, vol. 8, p. 198, Springer, Berlin (1962).

[7] K. G. Weil and K. F. Bonhoeffer, *Z. physik. Chem. N. F.*, **4**, 175 (1955).

[8] U. F. Franck, *Z. Naturforsch.*, **4a**, 378 (1949).

[9] K. J. Vetter, *Z. Elektrochem.* **62**, 642 (1958).

[10] K. Heusler, K. G. Weil, and K. F. Bonhoeffer, *Z. physik. Chem. N. F.*, **15**, 149 (1958).

[11] B. N. Kabanov and D. Leikis, *Acta physiocochim. USSR*, **21**, 769 (1946).

[12] B. E. Conway and E. Gileadi, *Can. J. Chem.*, **40**, 1933 (1962).

with the observations of Okanoko and Sato [ref. (25) of our paper], although it differs from that of Arnold and Vetter [ref. (3) of Mehl's comments]. The latter authors record only three points through which one could draw lines with slopes between 58 and 90 mv.

Regarding the constancy of film thickness; cf. our reply to Dr. Vermilyea's comment later in the discussion of our paper.

H. R. Thirsk: I think that in many ways the choice of the word "precipitation" by the authors is unfortunate. The optical measurements imply a coherent layer on the surface with quite well-defined structural and electrical properties. It is as reasonable to consider such a layer as deposited as it would be so described in metal deposition. I think this is a matter more of semantics than electrodics, and I would urge some agreement on what word to use.

J. O'M Bockris (communicated): Professor Thirsk's comment could only be made in the absence of contact with the unpublished chrono-ellipsometric evidence in the nickel passivation. The dependence of τ on i from this work is consistent only with metal dissolution terminated at τ with the formation of a substance, the solubility product of which follows from the measurements as equal to that of $Ni(OH)_2$.

Other strong evidence is available to support a dissolution-precipitation mechanism for nickel at $pH = 3.1$: (*a*) τ is affected by stirring; (*b*) The growth of the deposit is linear with respect to time (cf. unpublished work by Reddy and Bhimasina-Rao on transient ellipsometry), where the ellipsometer is balanced in times of the order of 0.02 sec.

Thus, the prepassive layer cannot be formed in the sense of a Faradaic process of OH^- or water discharge but must be "precipitated," the Ni first forming $Ni(OH)^+$ and then $Ni(OH)_2$ when the critical concentration is exceeded.

D. A. Vermilyea: In both the passive and the prepassive conditions the steady current is determined by the rate at which the film dissolves. Suppose the film changes from insulating to semiconducting during the transition, as found by the authors, but dissolves at the same rate. Because of the reduced electronic field the ion transport would decrease, giving a temporarily reduced current. Continued dissolution will then reduce the film thickness until ion transport is again in balance with dissolution rate, and the current will then be equal to that in the prepassive condition. The authors' observations show, however, that the film thickness remains unchanged after the transition while the steady current decreases. It is therefore not a change in the rate of ion transport which is responsible for passivity, but rather a decrease in the dissolution rate of the film. It is then the dissolution rate which should be considered in connection with the observed changes in film properties.

H. Wroblowa and J. O'M Bockris: According to the mechanism suggested in the paper, under conditions of anodic polarization, the prepassive film does not dissolve chemically, nor is the steady-state current equal to the rate of this film's dissolution. This situation arises from the fact that the vicinity of the electrode is always saturated with the corresponding nickel ions, as shown below.

Upon anodic polarization, the bare metal surface dissolves to form $NiOH^+$ ions which diffuse away from the electrode. This corresponds to the exponential rise of current with potential (cf. Fig. 21). The limiting diffusion current density is

$$i_{L,NiOH^+} \frac{2FD\, c_{NiOH^+}}{\delta\, 1000}$$

where $D_{NiOH^+} \cong 10^{-5}$ cm/sec, $\delta \cong 5 \times 10^{-2}$ cm for an unstirred solution, and c_{NiOH^+} corresponds to the saturation concentration in moles/liter, *i.e.*, $c_{NiOH^+} = K/OH^-$ where K is the solubility product [$K = (NiOH^+)\ (OH^-)$]. When with increasing potential the current becomes higher than $i_{L,NiOH^+}$, the prepassive film of $Ni(OH)_2$ precipitates on to the electrode and cannot dissolve since the saturation concentration of $NiOH^+$ ions is continuously maintained at the saturation value by the nickel dissolution current and the high field transport through the film. This corresponds to the region between the potential at which the film first appears and the passivation potential (cf. Fig. 21).[13]

(The fact that in this region the thickness changes little, although the current increases some five times, can be easily explained by the increased rate of diffusion away of $NiOH^+$ ions, arising from the increased value of c^* with potential. This would be expected because of a *p*H decrease expected for currents above[14] $\sim 4 \times 10^{-5}$ amp cm^{-2}, resulting in corresponding increase of c^*_{NiOH}.)

Under those conditions the rate of chemical dissolution of the prepassive film is practically equal to 0. Thus, passivation cannot be connected with the changes in the dissolution rate of the film, but with the observed appearance at the passivation potential, of the electronic conductivity which decreases the field across the film and consequently decreases the rate of the nickel ion transport through it.

B. N. Kabanov: The passivation theory of metals suggested by Bockris, Reddy, and Rao, according to which passivation is caused by an increase in the electronic conductivity of a nonpassivating thick (not less than 45Å) phase layer, is simple and elegant and unites the theories of Müller, Bonhöffer, and Vetter. This theory has been verified for a particular case of the passivation of commercial nickel in 0.5M K_2SO_4 solution at $pH = 3.15$.

However, in principle, the theory is not applicable to a large group of systems in which passivation occurs before a thick nonpassivating layer of a non-electron conducting substance is formed on the metal surface.

Such systems include primarily those in which the metal is passivated by an amount of oxygen smaller than that required to form a continuous monoatomic layer, *e.g.*, platinum in HCl solutions,[15] iron is not very strong (say 0.1N) NaOH solutions.[16] One oxygen monolayer suffices for zinc passivation in dilute KOH solutions,[17] for indium passivation in citric acid and other solutions,[18] etc.

In some systems (*e.g.*, iron in acid sulfate solutions, zinc in alkaline solutions) a phase oxide layer can be formed as well (not necessarily as the result of precipitation from the solution, but often owing to the reaction occurring in the solid phase without the metal ions passing into the solution). There are a number of cases, however, when the phase layer is formed only after passivity has set in, *i.e.*, after a strong slowing down of the process of anodic oxidation of the metal, which is due to adsorption of oxygen or other atoms.[17]

[13] It may be seen from Fig. 21 that the film appears exactly at the potential where an inflection appears on the i-E curve and the current starts to increase linearly, rather than exponentially, with E.

[14] This is the value of the limiting current of hydrogen ions produced in the reaction

$$Ni + H_2O \rightarrow NiOH^+ + H^+ + 2e^-$$

[15] B. Ershler, *Z. Fiz. Khim.*, **14**, 357 (1940); **18**, 131 (1944).

[16] B. Kabanov and D. Leikis, *Doklady Akad. Nauk SSSR*, **58**, 1685 (1947).

[17] T. Popova, V. Bagotzky, and B. Kabanov, *Z. Fiz. Khim.*, **36**, 1433 (1962); B. Kabanov, *Izv. Acad. Nauk SSSR, Otd. Khim. Nauk*, **1962**, 980.

[18] T. Popova and N. Symonova, *Izv. Acad. Nauk SSSR, Ser. khim.*, **1963**, 1187.

At the present time one cannot draw a general conclusion about the applicability of the theory of Bockris *et al.* to the passivation of different metals. In our opinion, the wide diversity of cases of metal passivation cannot be explained by any single theory. A large group of passivation phenomena can be accounted for by a concept, which I should call adsorption theory of passivity. In the paper under consideration[19] (Tables 1 and 2) I have been wrongly ascribed the point of view that the passivating layer "acts as barrier layer and prevents the particles of the solution from reaching the electrode surface." According to my concept, for metal passivation to occur a strong chemical bond between the passivating agent (O, OH, SO_4, I, etc.) and the metal surface is required.

In some cases the formation of nonpassivating oxide or salt layers does exert an indirect influence on passivation. The thickness of the nonpassivating layer may vary in different cases from 1-2 molecules to 50-100Å. As a rule, after the passivating layer has been formed (or the nonpassivating layer has been transformed into the passivating one), it proves to be permeable to ions. Therefore, the statement of the authors of the paper under discussion that after passivation the ion penetration and hence continued corrosion (dissolution) of the metal stops should be considered as an over simplification.

It should be noted that the bond between the passivating agent and metal atoms (in the case of a weak bond between the metal atoms) might facilitate the tearing away of this group of atoms from the electrode, *i.e.*, bring about the activation of the metal by the same substance, which in other cases or under different conditions causes passivation (O, OH, SO_4, etc.).

J. O'M Bockris (communicated): Of course, there is no doubt of the literal correctness of Professor Kabanov's assertion that our use of an ellipsometric technique to show that the passivation of nickel in solution of *p*H 3.15 occurs by dissolution-precipitation of a prepassive hydroxide layer, followed by an increase in its electronic conductivity at higher potentials (and hence its passivation) does not constitute a mechanism determination applicable to all systems. There is no doubt, for example (as also determined ellipsometrically[20]) that metals which become passive in the sense that, at a given potential and reaction, they suddenly cease to be good electrocatalysts (*e.g.*, Pt in the oxidation of ethylene) do so by forming a thin film and that there is a considerable change in surface properties whilst the amount of O is less than that which would correspond to a monolayer.

In respect to the mechanism of the cessation of dissolution or corrosion of a substrate at a given potential, it may be that there are systems where the mechanism which we have established for one system involving Ni is not general. However, it does not seem too much to submit that the application of ellipsometric technique under potentiostated conditions makes a radical break in the history of the examination of passivity and corrosion and that it gives so much more direct information compared with that obtained before (which was always interpretive, *e.g.*, current-potential behavior) that it would be perhaps incautious to be confident concerning the mechanism in other systems, until typical ones have been examined ellipsometrically. In unpublished work, we have established a qualitatively similar phenomenology with Fe to that with Ni, and it appears that in the presence of Cl^- ions, the rise in electronic conductivity does not occur, an interesting indication of the mechanism of the effect of the depassivating action of Cl. We make two specific points:

1. The description we made of the mechanism associated with Professor Kabanov's papers represented our understanding of it. The occurrence of "a strong chemical bond between the passivating agent and the metal surface" is not by itself a statement of a mechanism.

2. Regarding Professor Kabanov's penultimate paragraph, there is perhaps some misunderstanding. It may well be that the permeation coefficient (and the corresponding mobility) of the metal ion in the film is unchanged on passivation. We have no information on this point from the ellipsometry. The point is that the electronic conductivity increases so that the field gradient in the film is reduced and hence ionic transport through the film is reduced. It is this reduction of the rate of transport of the metal cation through the film (which may well have unchanged permeability to the ions concerned) which is the immediate cause of the reduced dissolution rate, or passivation.

S. Schuldiner: It was observed that the film thickness found on a passive Ni electrode was ≈60Å. This demonstrates that a film thickness above 60Å is unnecessary for passivation, but does it prove that the effective film has to be this thick?

J. O'M. Bockris (communicated): Dr. Schuldiner's question is indeed well taken. It is, of course, analogous to that of Professor Kabanov.

There can of course be no "virtually certain" answer until a dozen or so systems exhibiting metal-dissolution passivation have been measured. I can give two points in favor of the answer that it is essential that the film which "causes" passivity must be more than a mono-layer in thickness.

(*A*). Under conditions of transient ellipsometry, measuring down to 0.02 sec, and a correspondingly timed potential transient, the film is still 10-20Å thick for nickel in a solution of $pH = 3.1$.

(*B*). What the steady-state measurements indicate is that there is a quite sudden (in respect of the potential at which it switches on) deposit of a film which at this switch-on potential attains a thickness which hardly varies as the potential is increased. At the point at which the thickness-potential plot suddenly rises to its final value, the current inflects, its rate of increase with potential rapidly falling. Chronoellipsometry shows the deposit to have a solubility product equal to that of $Ni(OH)_2$. At potentials positive to the switch-on point of the layer, the current rises still, with decreasing rate of rise; and then, at the passivation potential, the electronic conductance rises from zero to a large value. These are facts. It is difficult, for the Ni case under the given conditions, to avoid from these facts, a model in which the critically important factor is the change in conductance with potential. But, in this case, the film must have a corresponding lattice, *i.e.*, must be "several monolayers" thick. Of course, no claim is made particularly for the 60Å which was ellipsometrically determined for Ni under steady-state measurements as being a critically low value of film thickness for passivation in general. What is claimed to have been established is that before passivation occurs a film is layed down, in the case reported, 60Å thick. The critical point is that this thick film lies down before passivation. This is the fact which is inconsistent with the views of those workers who agree with the evidence, long available from coulometry, that a film in the 50-100Å region is associated with passivity but maintain that it is not the cause of it, the latter being often attributed to effects on the double layer potential difference of an adsorbed O layer. The present results show that the passivation is associated with a rise in the electronic

[19] *Editorial Note*: In the preprint of the paper the authors included two tables (1, Views of Various Authors on the Theory of Passivity and 2, Summary of Our Conclusions Compared with Other Authors) which they have chosen to withdraw from final publication.

[20] A. K. N. Reddy, M. Genshaw, and J. O'M. Bockris, *J. Electroanal. Chem.*, 78, 406 (1964).

conductance of the film, *i.e.*, not with the action of a monolayer.

Clearly, it can always be argued, *cf.* Professor Kabanov's comment, that the qualitative result is not a general one; and this possibility can only be met by extending the ellipsometric work to several systems. But it must be taken into account that the model which the ellipsometry so unambiguously suggests contains elements from various theories formerly suggested for metal dissolution passivation, and eliminates one of two classes of such theories. It seems quite probable, on the present evidence, that a qualitatively similar model will be favored by the forthcoming evidence for the other transition metals.

F. W. Will: It is agreed that the ellipsometric method is a valuable *in situ* method for the study of surface films on electrodes. Its major shortcoming, however, is that it does not lead to an unambiguous identification of the species constituting the surface films. Furthermore, little is known about the effect of the ionic double layer and of adsorbed species on the elliptically polarized light.

It ought to be mentioned that other *in situ* methods have emerged recently that are of considerable importance. (The advantage of two of these, like x-ray diffraction and infrared absorption techniques, lies in the fact that an unambiguous identification of surface species is possible.

J. O'M. Bockris (communicated): X-ray analysis of electrodeposits *in situ* has been made occasionally, *e.g.*, by placing a rotating disk electrode so that it is half out of solution and submitting the top half to the beam. The difficulty is not only that the deposits hitherto must be relatively thick, but of course the x-rays decompose the aqueous layer and this may lead to unexpected electrode reactions. Infrared studies have been attempted (through thin film electrodes, from the back, to avoid absorption by water). Hitherto, no successful identification of a surface compound has been thus recorded. Electron microscopy could hypothetically be used were a machine of sufficient power constructed so that the electron energies could overcome absorption in the solution. Its cost would be astronomical. Electron spin resonance gives quite good theoretical predictions for sensitivity in detecting radicals with unpaired spins. Attempts at its use in electrode reactions have not yet succeeded.

A general difficulty concerning the first three of these is that of solution absorption. In ellipsometry, the effect of the solution is not simply corrected for, but is an essential part of the analysis of the effects of the three media, solution, film, and metal, on the state of the polarization of light. Further, ellipsometry not only gives evidence concerning the identity of a new phase, but also a determination of its thickness down to monolayer values and its properties in respect to light absorption (*i.e.*, in many cases, its electronic conductance). Again, it lends itself to automation and can hypothetically be made to give information on the above parameters on a micro second time scale (in Reddy and Bhimasina-Rao's unpublished, work, the time was as little as 0.02 sec). A laser as a source in ellipsometry could give a considerable increase in range of applicability, for example, adsorption on electrodes could be measured. By varying the frequency of the incident radiation, a kind of ellipsometric spectroscopy could be produced.

I do not think these facts and prospects are consistent with the implication of Dr. Will's comment that ellipsometry is one of several techniques for looking at electrode surfaces *in situ*. In respect to detecting and measuring the appearance and behavior of a new phase on an electrode in solution, the ellipsometric method (under potentiostatic control) seems to have considerable advantages over any other method as yet publicly discussed.

Re Dr. Will's thought that ellipsometry gives ambiguity in respect to the identification aspects of a new phase: it rests on the assumption that the refractive index determined is already that of the bulk; and if it is known and sufficiently different from that of alternative possibilities, the phase can be identified. There may indeed be difficulty here if one of these conditions is not fulfilled, but no more difficulty than exists in x-ray analysis which also depends normally on comparison with spectra of known entities.

Oxide Involvement in Some Anodic Oxidation Reactions

B. E. Conway, N. Marincic, D. Gilroy, and E. Rudd

Department of Chemistry, University of Ottawa, Ottawa, Ontario, Canada

ABSTRACT

A comparative study of the involvement of surface oxides of platinum in the anodic oxidation of (*a*) formate, (*b*) hydrocarbons, and (*c*) hydrazine has been made. In case (*a*) the oxidation has also been studied in two rigorously dehydrated nonaqueous solvents, acetonitrile and propylene carbonate, to which were successively added initially traces and later larger quantities of water. Activation and inhibition effects arise and are related to the water content of the solutions. The oxide coverages were determined at various potentiostatically held potentials E by cathodic galvanostatic and differentiated galvanostatic transients for ascending and descending directions of change of E. Complications which may arise in the quantitative interpretation of results obtained from the repetitive potentiodynamic method are illustrated.

In cathodic organic reductions, the two general pathways of direct electron transfer or of indirect electrochemical hydrogenation by adsorbed H atoms produced by discharge from the solution have for many years been recognized (1-3). A similar situation arises in anodic oxidation: the anodic reaction pathway may be one in which direct electron withdrawal with subsequent reaction of the resulting free radical ion or free radical with the solvent occurs; alternatively, it may be one in which surface oxides (or adsorbed oxygen-containing species,[1] *e.g.*, OH or O) are produced in a charge-transfer step from entities in the solution or from the sol-

[1] The distinction between "surface oxides" and adsorbed O or OH is to some extent an academic one. A film of the order of a monolayer cannot be described in terms of formal stoichiometry, particularly if there is heterogeneity of adsorption sites originally at the bare metal. Surface films must presumably become of the order of 20-50 atomic layers thick before they can be spoken of in terms of bulk behavior and corresponding stoichiometry and thermodynamic behavior (13). However, recent ellipsometric studies (48) indicate a qualitative change of the properties of the surface "oxide" on Pt at *ca.* 0.9-1.0v to those more characteristic of a bulk species. Presumably this oxide may be identified with the so-called "dermasorbed" oxygen proposed by Schuldiner.

vent, and then react in the steady-state with substrate reductant either diffusing to the surface or coadsorbed at the electrode surface. These two types of process were first discussed for anodic oxidation of organic molecules by Fichter and by Perkin (4, 5) for some hydroxylation, halogenation and pseudohalogenation reactions with benzene and other organic substrates. More recently, this type of reaction has been considered in anodic hydrocarbon oxidation mechanisms (6, 7) and in the electrochemical oxidation of formate ion (8). The presence of adsorbed O species (henceforth we shall refer to the adsorbed oxygen-containing species as simply "O" except where otherwise explicitly stated) can also be responsible for initial passivation effects as suggested by Kolotyrkin (9) and treated by Breiter *et al.* (10). When the surface coverage by "O" species is potential dependent (as it usually is) this can give rise to kinetic inhibition effects which manifest themselves in the current-potential curve as a reversal which is most marked in processes such as dissolution of iron, but also arises in anodic oxidations of hydrogen and organic substrates. This type of effect, it seems, was first treated by Nord (11), developed by Bagotskii and Vasilev (12; *cf.* 13) and treated in detail for a variety of reaction mechanisms by Gilroy and Conway (8) in terms of the adsorption isotherm for the inhibiting species. The latter authors also showed that self-inhibition effects with reversal of current-potential relations can occur in the absence of coadsorbed oxides when the products of a reaction step (*e.g.*, in formate oxidation) occupy more sites than the reactant. Passivity effects in hydrocarbon oxidation through involvement of adsorbed O have also been proposed by Bockris *et al.* (7) and their mechanism of the effect involves changes in the type of surface oxide species present (*v.* 8; *cf.* 12); the importance of conductance changes in the oxide film in passivation of metals (*e.g.*, Ni) has been stressed by Bockris and Reddy (14) on the basis of interpretations of ellipsometric measurements and this must be considered an important advance (*cf.* 13) in the experimental understanding of the onset of effective passivity in metal dissolution. Such effects are, however, probably not necessarily involved in passivation of those anodic oxidation reactions which do not involve metal dissolution.

In most of the organic oxidation reactions in which passivation effects have been indicated, little attempt has been made until recently to characterize (in relation to the kinetics) the nature and extent of adsorption of the passivating species, *e.g.*, by electrochemical transient techniques. In the present paper, we have examined comparatively [*cf.* ref. (12) for other systems] the potentiostatic current-potential behavior for anodic oxidations of several simple substances: formate ion in aqueous KOH; hydrazine in acid and alkaline solutions; ammonia in alkaline (KOH) solution; and C_2H_4 and C_3H_8 in perchloric and phosphoric acids. The kinetic behavior has been related to determinations both of the extent of surface oxide coverage as a function of potential and the corresponding H atom accommodations at more cathodic potentials evaluated by use of the differential galvanostatic charging method from potentiostatically controlled anodic potentials. An important aspect of the present work is the use of completely nonaqueous solutions in one or two cases, with subsequent controlled additions of small concentrations of water, in order to establish semiquantitatively the role of water in (*a*) producing the surface oxide and (*b*) the corresponding kinetic effects of this oxide in current-potential curves, since the extent of surface oxide coverage can then be determined not only by anode potential but by the concentration of added water. Related matters concerning the hysteresis of the current-potential curves and irreversibility in formation and reduction of surface oxides at Pt are examined. Here we shall concentrate on recording the principal experimental observations.

Experimental

Procedures.—Steady-state potentiostatic procedures have been employed in most of this work using a Wenking short rise-time potentiostat. Current-potential relationships were determined, point by point, manually at controlled intervals of time sufficiently long (30 sec-1 min) for surface charging processes to have become completed. Further long-time effects which may be associated with deactivation or poisoning (15) were thus avoided. In some experiments, the potentiodynamic procedure was also used, the potentiostat then being controlled by a Servomex type LF 141 function generator (using single ramp and repetitive linear voltage-time characteristics).

In most of the measurements, galvanostatic reduction transients were taken from the potentiostatically held potentials and differentiated by means of an operational amplifier using the procedure of Kozlowska and Conway (16). Both direct and differentiated transients were displayed simultaneously on a dual-beam oscilloscope. This method gives much better resolution of structure in the charging curve than is apparent in the latter itself and provides information analogous to that available from the potentiodynamic method, except that steady-current kinetics apply and this facilitates quantitative interpretations of rate effects (17, 18). The differentiated transient gives directly the reciprocal of the electrode capacitance (including adsorption pseudocapacitance) as a function of potential, and the distances (times) between the minima in C give precise estimates of the corresponding charges passed between various potentials in the charging curves, without the necessity of integrations.

Systems studied. Formate.—Potassium formate for experiments in aqueous medium was recrystallized from water and dried under vacuum for 48 hr. For experiments in nonaqueous media, triethylammonium formate[2] was prepared *in situ* by adding a controlled amount (stoichiometric quantity) of formic acid to a known weight of triethylamine in the solvent. The exact amounts were determined outside the cell in a separate experiment by means of a conductance titration. Separate kinetic experiments showed that a slight excess of the amine did not interfere with the kinetics of oxidation of the formate ion.

The reactants were purified as follows: formic acid was dried over anhydrous $CuSO_4$ and the triethylamine over $LiAlH_4$. The components were mixed slowly in a bath cooled in liquid N_2 to about −10°C until part of the solution became solid. The containing vessel was maintained in a polyethylene bag to minimize contamination by atmospheric moisture.

The solvents used were water, acetonitrile and propylene carbonate.

Distilled water was redistilled from alkaline permanganate and distilled once again in a stream of purified N_2 directly into the cell.

Acetonitrile was distilled *in vacuo* once from anhydrous $CuSO_4$ and once from P_2O_5 (19-22) and finally into the cell. All operations were conducted in a stream of N_2 dried by passage through a solid reactant drying train and passed through three liquid air traps. The dried cell and all ancillary apparatus were contained in a polyethylene bag into which a steady stream of dry N_2 (from boiling liquid N_2) was passed during the preparation of the solutions and during the runs.

In some experiments, final drying of the solution was achieved *in situ* in the cell by lowering into the liquid a large ampoule containing a molecular sieve material, previously baked out in a vacuum oven. After agitation for 12 hr, the ampoule was withdrawn

[2] Most inorganic formates were insufficiently soluble to be used. Tetramethylammonium formate was prepared, but could not be obtained in a sufficiently dry state.

and the runs commenced. This procedure gave the driest solutions (see below).

Propylene carbonate was dried over anhydrous $CuSO_4$ and distilled *in vacuo*. The electrolyte was made up as in the case of the acetonitrile solutions. Drying with P_2O_5 or the molecular sieve was impracticable owing to chemical reactions which were observed to take place.

Hydrazine and hydrazine sulfate.—Hydrazine was prepared from the analytical grade chloride or sulfate salts by distilling from strong aqueous KOH. The resulting aqueous solution of "hydrazine hydrate" was redistilled and the middle fraction was made up in aqueous H_2SO_4 or KOH to give various concentrations in the 1*N* supporting electrolyte of acid or alkali. Nitrogen was used for bubbling the solutions, and a rotating wire electrode was used in some experiments to achieve uniform stirring. In other experiments, a rotating disk electrode (23) was used to examine the role of diffusion control.

Hydrocarbons.—A number of experiments were carried out on the oxidation of ethylene and propane at various temperatures at platinized Pt electrodes in hydrogen peroxide purified H_3PO_4 (85%) and in analytical grade $HClO_4$ which has a better impurity level (with respect to anodically oxidizable impurities) than has H_3PO_4. The cell was capable of being operated up to 150°C and was provided with an internal heater and thermostat, and presaturator tubes for the purified gas supplies. Potentiostatic preelectrolysis for 24-hr periods at a sacrificial electrode was found to be beneficial in diminishing background current in the absence of hydrocarbon. The potential was set to that giving a maximum current, viz. at *ca.* 0.8v E_H, since the background current suffers passivation effects at higher potentials. Oxide co-coverage and H accommodation were determined during the steady-state hydrocarbon oxidation runs by the galvanostatic procedure mentioned above. In some runs, the rate of charging of the platinum electrode itself (in the absence of hydrocarbon) could be studied by rapid controlled current measurements for known times, provided that the electrode was large enough. From the known capacitance of a platinized electrode per cm^2, it is easy to show that the current-potential relation for anodic charging of the electrode can be measured up to 10^{-2} amp cm^{-2} (apparent) without increasing the coverage by oxide by more than 10% if the measurements are made over *ca.* 20-sec intervals or less.

Reference electrodes.—The hydrogen reference electrode was used in most of the solutions including the nonaqueous ones where it also seems to function satisfactorily (*cf.* 24). In the KOH solutions, the Hg/HgO electrode was used with a sealed probe communicating to the compartment of the cell otherwise used for the hydrogen reference electrode. The probe was terminated by a 7/10 joint wetted with the solution. Liquid junction potential corrections were made where necessary.

Electrode preparation.—Platinum wires, previously cleaned in acetone, were sealed in glass bulbs in a stream of hydrogen as described previously (25). The electrodes were mounted in the cell in sliding tubes according to techniques developed previously. In all experiments, the electrodes were subjected to the following electrochemical pretreatment before steady-state kinetic observations were commenced: polarization at 0.5 cps (triangular pulse) between the potentials −0.2 to +1.6v E_H for 10 min. This achieved best reproducibility of the current-potential curves.

Palladium electrodes were prepared similarly. Platinized Pt electrodes were prepared by the usual method (26) for obtaining a black velvety deposit; this procedure was preferred to the method employing no additive which leads to coarser and less reproducible deposits.

Results and Discussion

Formate oxidation.—A number of studies of formic acid oxidation on platinum have been reported (27-31) using various approaches, particularly the potentiodynamic one (31). A detailed constant current study was reported by Conway and Dzieciuch (32) who examined (*a*) the electrochemical behavior in terms of steady-state consecutive reaction kinetics and (*b*) the involvement of electrochemically detectable intermediates. In aqueous medium, the steady-state (potentiostatic) log i-v curve is characterized by reversals of the direction of the current-potential relations for the ascending and descending directions (with much hysteresis) which can be treated theoretically in terms of inhibition effects discussed previously (8, 11, 12). Theoretically (8), the maximum current in a single electron, ion-discharge controlled anodic oxidation inhibited by a single "univalent" oxide species should arise at *ca.* half coverage of the electrode by such a species. The differential (cathodic) galvanostatic measurements from controlled-potential steady states indicate, however, that surface oxide coverage at the potential of the current maximum is quite small ($<$ *ca.* 0.2) on smooth Pt in the oxidation of formate in alkaline solutions. In neutral solutions (8), however, the current maximum occurs at *ca.* 1v E_H and adsorbed species are then hardly detectable at this potential [*cf.* ref. (30) for the HCOOH case]. This situation could arise because (*a*) the formate oxidation occurs only on a small fraction of the surface which is then covered relatively to a greater degree by oxide or (*b*) because inhibition arises from coadsorption of another, electroinactive species arising from the decomposition of formate ion itself. The latter possibility seems likely and is consistent with conclusions (*cf.* 30) of other workers who have examined formic acid oxidation. Such a species may be the "reduced CO_2" entity of Giner (33) or an adsorbed dehydrogenated formate ion "CO_2^-," but the inhibiting species discussed by other workers is only found at rather lower potentials. Alternatively, the mechanism suggested previously (32) involving the steps.

$$HCOO^- + M \rightarrow M/HCOO^\cdot + e$$
$$M/HCOO^\cdot \rightarrow M/H + M/CO_2$$
$$M/H \rightarrow H^+ + e$$
$$M/CO_2 \rightarrow CO_2$$

can explain the observed behavior if the discharge step is not rate-determining. Self-inhibition (8) can arise since, in the second step, two adsorption sites are formally required for each one occupied by the

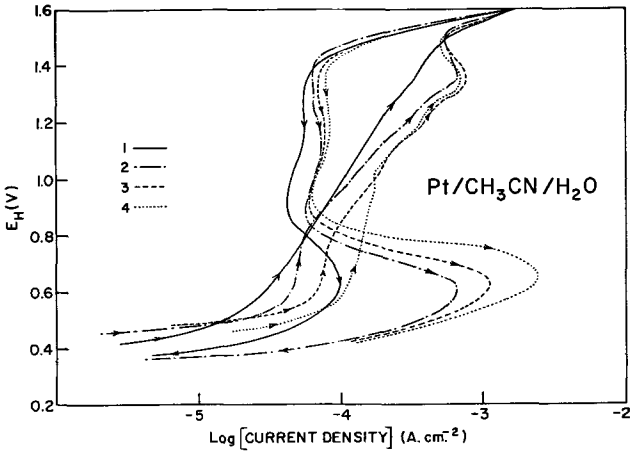

Fig. 1. Potentiostatic steady-state log i-E curves for formate oxidation in anhydrous and water-containing acetonitrile (Pt; 5°C). Points taken at 50 mv intervals. 1, 0 ml; 2, 2 ml; 3, 5 ml; 4, 10 ml solution.

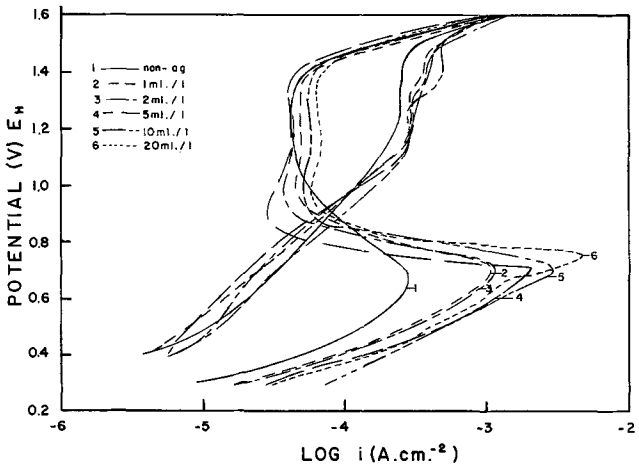

Fig. 2. Potentiostatic steady-state log i-E curves for formate oxidation in anhydrous and water-containing propylene carbonate (Pt; 5°C). Points taken at 50 mv intervals.

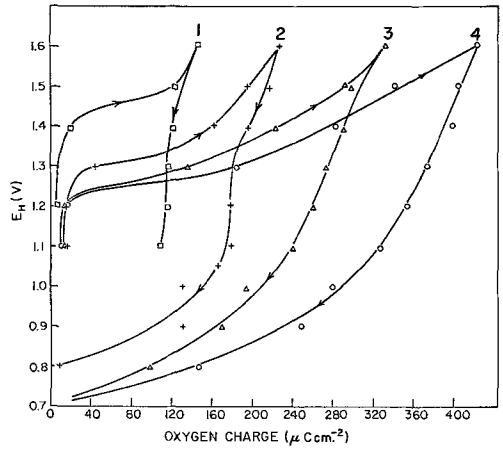

Fig. 3. Oxide coverage on Pt for formate oxidation in acetonitrile as a function of potential and water content (5°C). Numbers on curves correspond to those in Fig. 1.

reactant. A current-potential curve with reversal then arises and the auto-inhibiting species are adsorbed H and CO_2. The coverage by the adsorbed species ($HCOO^{\cdot}$) must be potential-dependent in order to explain (8) the reversal of the log i-E curve, and this requirement is met for the reaction scheme above. Oxide coverage seems to become appreciable only at higher anodic potentials of 1.0-1.2v, in the direction of ascending electrode potentials.

The experiments in nonaqueous media [other than formic acid itself; *cf.* (32), (34)] have been performed in order to examine the effects of controlled amounts of water in the solution. Under these conditions, surface coverage of the electrode by oxide can be controlled by the water content as well as by potential. The results in acetonitrile and propylene carbonate are shown in Fig. 1 and 2, and the general features are similar; the corresponding oxide coverages as a function of potential and water content are shown in Fig. 3. The oxide coverages in terms of charge Q_o can be related to the water concentration c through a relation similar to a Langmuir adsorption isotherm (Fig. 4) by plotting c/Q_o *vs.* c; satisfactory linear relations are obtained. Presumably, the adsorption is an electrochemical one involving a process which can be represented formally as an electrochemical equilibrium (below the O_2 reversible potential)

$$Pt + H_2O_{(ads)}\,Pt \rightleftharpoons \text{“}Pt(OH)\text{”} + H^+ + e$$

The important conclusion from the results in Fig. 1 and 2 is that the current for formate ion oxidation

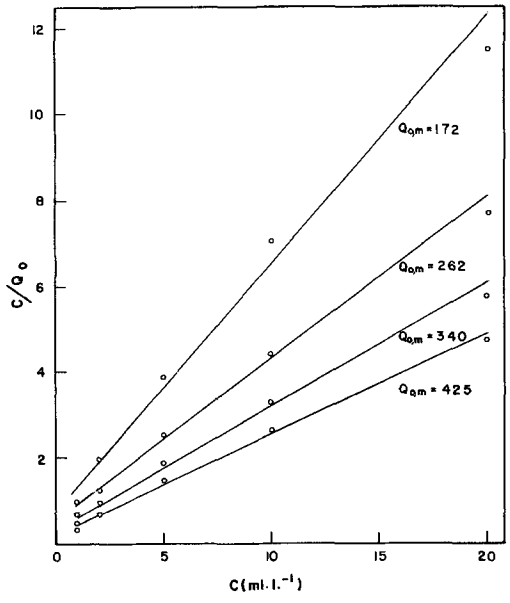

Fig. 4. Test of electrochemical Langmuir isotherm for oxide charge as a function of water concentration for various maximum charges $Q_{o,m}$ at the higher potentials.

does not become appreciable in the descending current-potential curve until almost all the electrochemically detectable oxide has been removed (Fig. 3). However, the magnitude of the current maximum is related to the amount (in terms of charge for cathodic oxide reduction) of oxide that was present at higher anodic potentials and not to the total apparent free surface available. The effect is not connected with, *e.g.*, specific poisoning by acetonitrile, since the results in a chemically very different solvent (propylene carbonate) are remarkably similar (Fig. 2). The reaction therefore seems to proceed only on that fraction of the surface that has just become reduced from previously being in an oxide-covered state. Since the minimum current seems to arise at a potential for which oxide again just cannot be detected, this current presumably does not arise from reactions such as

$$Pt/OH + HCOO^- \rightarrow Pt + CO_2 + H_2O + e$$

or

$$Pt/O + HCOO^- \rightarrow Pt/OH + CO_2 + e$$

Similarly, if the chemical step

$$Pt/HCOO^{\cdot} + Pt/OH \rightarrow Pt + CO_2 + H_2O$$

were involved, the rate would tend to be maximal at *ca.* half coverage by both species (cf. 6,8). It seems that these mechanisms involving “O” are likely to participate appreciably in the kinetics only at higher anodic potentials, as suggested previously (8).

The general similarity in the log i-E curves and in the hysteresis in formation and reduction of the oxide at various contents of water (Fig. 3) in the solution, suggests that oxide may be present in patches on the surface (at each of which normal oxidation and reduction occurs with associated kinetics of formate oxidation) rather than as a uniform, but correspondingly more dilute, layer with fractional coverage dependent on water content.

The behavior in various concentrations of KOH in aqueous medium is also of interest. At smooth Pt, the oxide charge at 0.8, 1.0, and 1.2v (E_H) decreases with increasing formate ion concentration in 0.1M KOH aq. (Fig. 5).

At 1.4v, it only decreases to a small value rather critically at 6-7 molar formate, and at 1.6v there is only a small steady decrease. In 0.5M KOH aq., (Fig. 6) however, the oxide charges at various potentials do

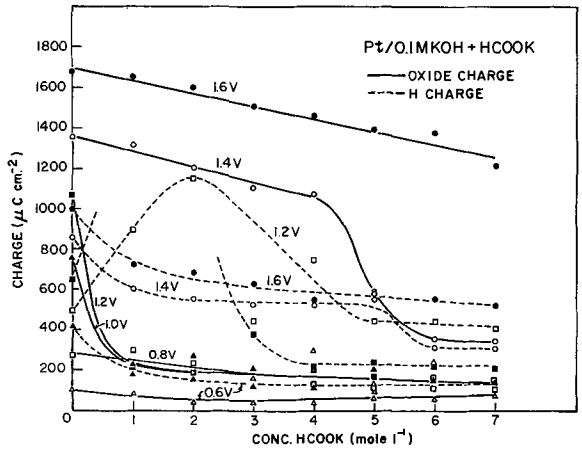

Fig. 5. Oxide charge and H accommodation at smooth Pt for formate oxidation in 0.1M KOH aq. as a function of HCOOK concentration and potential (E_H).

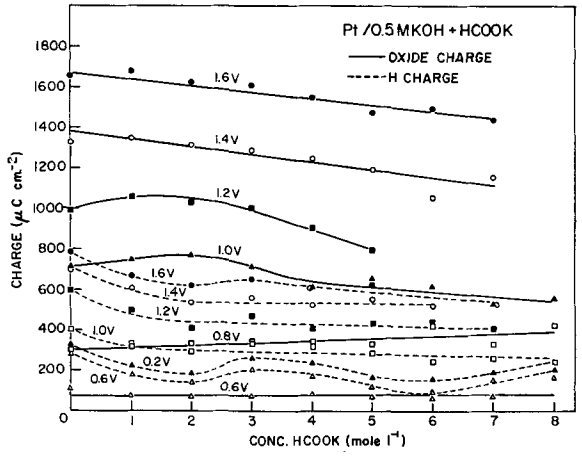

Fig. 6. Oxide charge and H accommodation at smooth Pt for formate oxidation is 0.3M KOH aq. as a function of HCOOK concentration and potential (E_H).

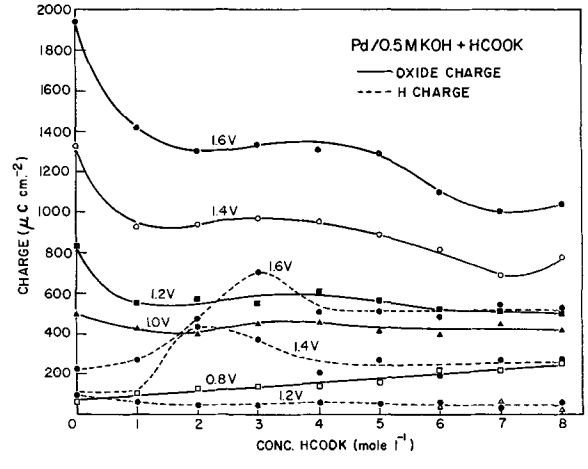

Fig. 7. Oxide charge and H accommodation at smooth Pd for formate oxidation in 0.5M KOH aq. as a function of HCOOK concentration and potential (E_H).

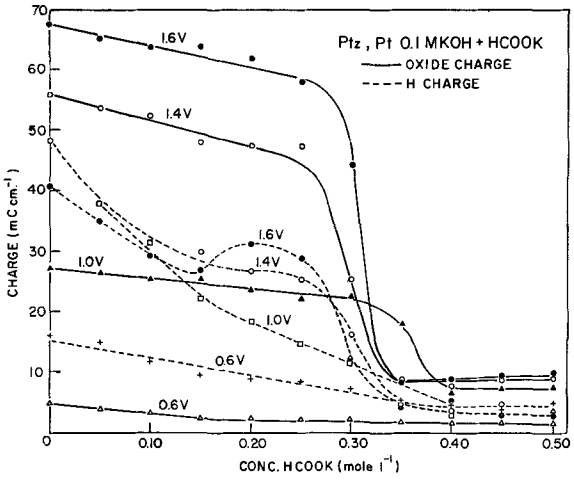

Fig. 8. Oxide charge and H accommodation at platinized platinum for formate oxidation in 0.1M KOH aq. as a function of HCOOK concentration and potential (E_H).

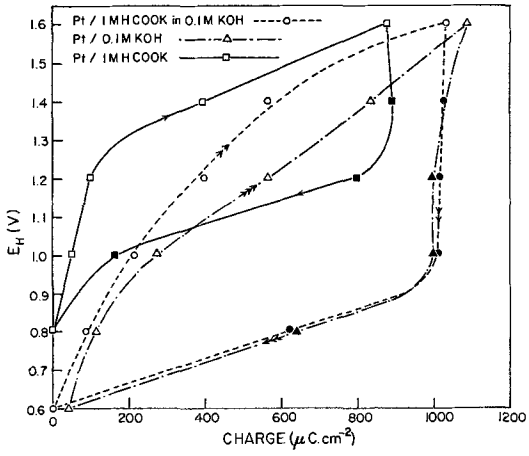

Fig. 9. Comparison of oxide charges at smooth Pt under various conditions in aqueous formate oxidation.

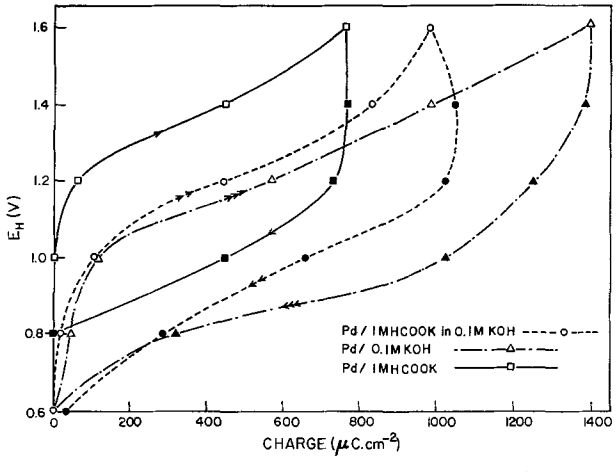

Fig. 10. Comparison of oxide charges at smooth Pd under various conditions in aqueous formate oxidation.

not show any sharp decrease in the presence of formate but only a progressive small diminution at 1.2-1.6v (E_H). Analogous effects arise at Pd electrodes (Fig. 7). On platinized platinum, however, a very marked critical decrease of oxide coverage arises between 0.3 and 0.4M formate in 0.1M KOH aq. (Fig. 8).

Similarly, the hydrogen accommodation (at more cathodic potentials) measured in differential transients from various anodic potentials, decreases in a similar way.

Oxide charges determined under various conditions are compared in Fig. 9 (Pt) and 10 (Pd) for various potentials.

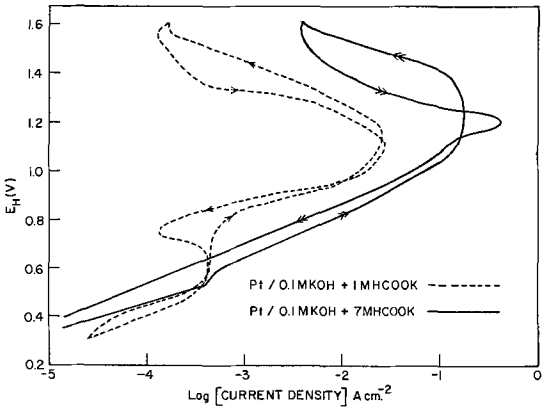

Fig. 11. Comparison of potentiostatic steady-state log i-E curves for formate oxidation at smooth Pt in 1 and 7M HCOOK in aq. 0.5M KOH.

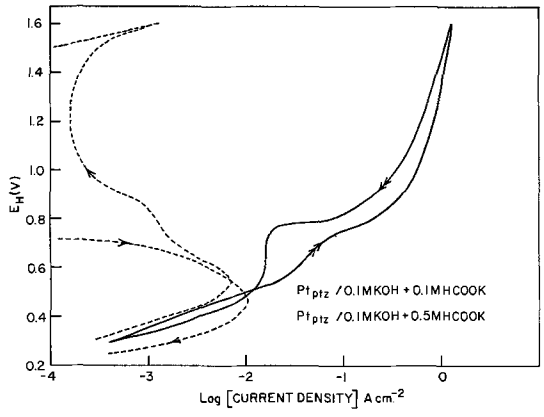

Fig. 12. Comparison of potentiostatic steady-state log i-E curves for formate oxidation at platinized Pt in 0.1 and 0.5M HCOOK in 0.1M aq. KOH.

Corresponding to the relation between oxide coverage and KOH/HCOOK ratio discussed above, a marked dependence of the shapes of the log i-E curves for formate oxidation on formate ion concentration is apparent in Fig. 11 and 12 for smooth and platinized Pt electrodes.

Some inhibition effects still arise around 0.55-0.75v (E_H), but the behavior above 0.8v is quite different when the formate to KOH ratio is high: the hysteresis is much diminished and much higher currents pass at higher anodic potentials when the oxide coverage is found to be diminished (Fig. 5-8). Again, the kinetic behavior changes critically between 0.1 and 0.5M formate in 0.1M KOH at platinized Pt (Fig. 12). At higher KOH concentration (0.5M), the critical change in the kinetics occurs between 1 and 3.5M formate. There is evidently a critical competitive situation between adsorption of oxide species and "formate" species depending on the KOH concentration. Presumably at sufficiently high formate concentrations, the rate of reaction between discharged formate species and the oxide produced by discharge of OH^- (or from water) is large enough to maintain a low steady state oxide coverage. Also there will be mutual inhibition effects; the presence of a greater coverage by formate species will tend to inhibit oxide formation by discharge from OH^- ion, *cf.* the inhibition of oxygen evolution in the aqueous Kolbe reaction (32).

Hydrazine oxidation.—Mechanisms.—It is found experimentally (cathodic transients) that no significant oxide coverage is involved in hydrazine oxidation up to 1.0v and surface oxide only appears in oxidation in acid media at low concentrations <0.01M when diffusion control just becomes significant. It remains on

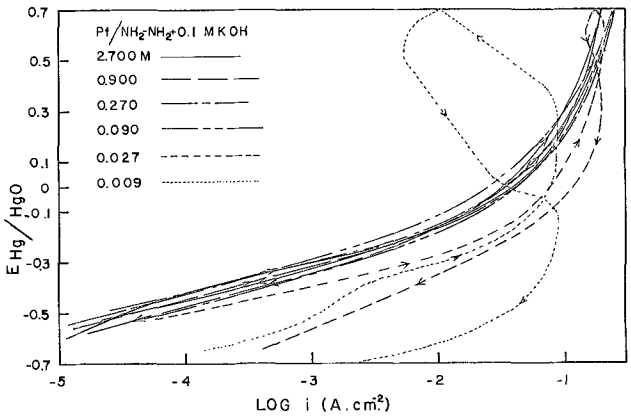

Fig. 13. Potentiostatic log i-E relations for N_2H_4 oxidation at smooth Pt in 0.1M KOH aq. at various concentrations and 25°C (oxide coverage and associated hysteresis only arises at low concentrations when diffusion control begins to become significant).

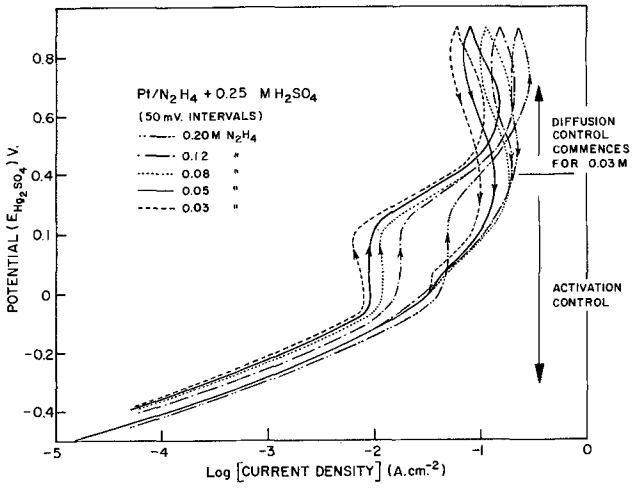

Fig. 14. As in Fig. 13, but with 0.25M H_2SO_4 at 25°C

the electrode to lower potentials in a descending i-E curve and then well-known hysteresis and current oscillations characteristic of passivity are observed (Fig. 13 and 14). Under most conditions, only dehydrogenation and dissociation steps need therefore be considered. Following physical adsorption, possible consecutive reaction steps involving dissociation of the N-N bond in hydrazine are:

Scheme A

$$N_2H_4 \rightarrow NH_2 + NH_2 \qquad \text{I}$$

$$NH_2 \rightarrow NH + H \qquad \text{II}$$

$$(H + OH^- \rightarrow H_2O + e) \qquad \text{IIa}$$

or

$$NH_2 + OH^- \rightarrow NH + H_2O + e \qquad \text{IIb}$$

followed by

$$NH \rightarrow N + H \text{ (with IIa)} \qquad \text{III}$$

or

$$NH + OH^- \rightarrow N + H_2O + e \qquad \text{IIIb}$$

$$2N \rightarrow N_2 \qquad \text{IV}$$

Alternatively, a scheme B involving progressive dehydrogenation with the indicated chemisorbed species (without N-N dissociation), may be involved

$$N_2H_4 \rightarrow N_2H_3 + H \text{ (or } N_2H_4 + OH^- \rightarrow N_2H_3 + H_2O + e \text{ Va)} \qquad \text{V}$$

$$(H + OH^- \rightarrow H_2O + e) \qquad \text{(IIa)}$$

$$N_2H_3 \rightarrow N_2H_2 + H \text{ (with IIa)} \qquad \text{VI}$$

$$N_2H_2 \rightarrow N_2H + H \text{ (with IIa)} \qquad \text{VII}$$

$$N_2H \rightarrow N_{2(ads)} + H \text{ (with IIa)} \qquad \text{VIII}$$

$$N_{2(ads)} \rightarrow N_2 \qquad \text{IX}$$

or steps of type Va in reactions VI, VII, and VIII. In scheme B, N_2H_3 may be singly bonded to the surface, and succeeding radicals may be bonded through two sites. It has been concluded previously (44) that a mechanism involving free-radical intermediates is preferable to one (45) involving dissociated hydrogen. However, these two types of reaction must be related since successive dehydrogenation would leave adsorbed species on the electrode as in the schemes A and B.

The kinetics in the presence of added acid or alkali are characterized by: (*a*) current-potential relations (Fig. 13 and 14) with continuously increasing slopes towards a limiting current, but with initial slopes at low current density of about 0.1-0.12v (*ca.* 2.3 $2RT/F$); (*b*) reaction orders in acid (Fig. 15) which are between 0.3 and 1 and tend to decrease with increasing concentration[3] but show no systematic dependence on potential; and (*c*) reaction orders in alkali which are near zero (Fig. 13) at moderate and high concentrations but tend to become negative at low concentrations (ascending curves prior to diffusion control and oxide formation).

The absence of surface oxide at potentials where it is normally formed suggests that (*a*) adsorbed species from N_2H_4 inhibit its formation and/or (*b*) it is removed as fast as it is formed by reaction with N_2H_4 or derived radicals so that its steady-state concentration on the surface is always small. When diffusion-controlled conditions are approached and the electrode is starved of hydrazine, oxide formation can be detected (Fig. 13); it is removed on stirring the solution when the latter is near the critical concentration for diffusion control. The present results seem to indicate that the presence of oxide, when at appreciable coverage, is inhibitive rather than catalytic as was concluded previously (46). In NH_3 oxidation, oxide is found even at quite high concentrations of NH_3.

[3] Further studies at more closely spaced concentration intervals are in progress. The upper and lower limits are, however, restricted by the limited solubility of the salt and the onset of diffusion control, respectively.

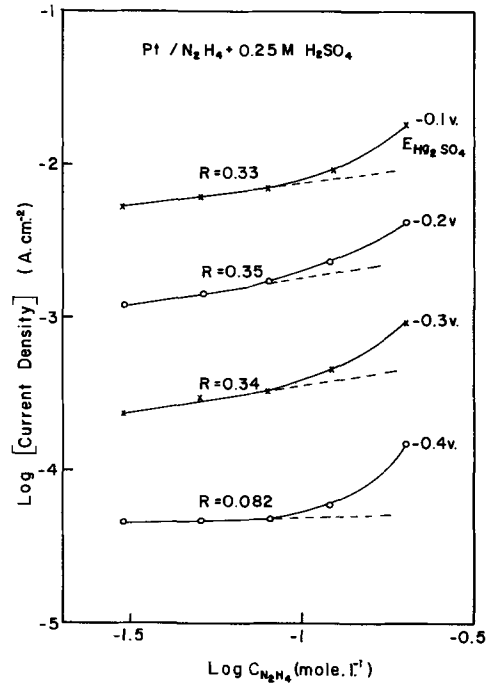

Fig. 15a. Rates of N_2H_4 oxidation at smooth Pt as a function of concentration at various potentials (0.25M H_2SO_4 at 25°C).

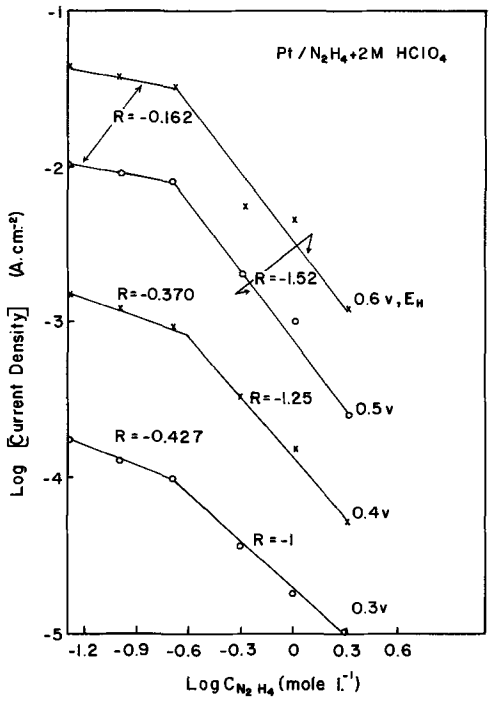

Fig. 15b. As in 15a but in 2M $HClO_4$ at 25°C. (Differences from Fig. 15a arise because of greater degree of ionization.)

Tafel slopes and reaction orders.—The initial region of the log i-E relations ($b \doteq 2.3\ 2RT/F$) corresponds either to an electrochemical step of ionization of an intermediate, the surface coverage of which is independent of V or to a primary discharge process in the first step of the reaction (*e.g.*, $N_2H_4 + OH^- \rightarrow N_2H_3 + H_2O + e$ or $N_2H_4 + OH^- \rightarrow NH_2 + NH + H_2O + e$). Other steps in the sequences A or B above would tend to give Tafel slopes less than $2.3\ 2RT/F$ (*cf.* 36, 37). The approach to a limiting current (*cf.* 44) suggests (35, 36) that either (*a*) a recombination controlled process such as IV becomes rate-determining with coverage θ_N by the intermediate tending limitingly to unity or (*b*) a first order chemical dissociation step becomes rate-limiting. The limiting current is not diffusion controlled except at the lowest concentration. The possibility (*a*) is to some extent supported in alkaline solution since the reaction order $\mathcal{R}$ is initially small or zero (Fig. 13). Except at complete coverage, *e.g.*, by N or N=N species in reactions IV or IX, respectively, $\mathcal{R}$ will be a function of potential.

This conclusion may be reached by deducing the reaction order as a function of potential in one or two cases and relating it to the Tafel slope; in fact, this procedure turns out to be useful for the examination of mechanisms giving this type of current-potential behavior. Several examples will be considered.

If the reaction involves successive electrochemical dehydrogenation steps (*cf.* 44) similar to Va, and if the rate-determining step were, say, the desorption IX, the velocity of IX is

$$v_9 = k_9\,\theta_{N_2} \qquad [1]$$

and θ_{N_2} (N_2 is chemisorbed "N=N") can be expressed in terms of c through K_5 and three potential-dependent quasi-equilibrium constants for prior steps if V is involved (case I), and through four potential-dependent equilibrium constants if Va is involved (case II). Then

$$v_9 = \frac{k_9 K_5 K_6 K_7 K_8 \exp 3VF/RT \cdot c}{1 + cK_5 + cK_6 \exp VF/RT + cK_7 \exp 2VF/RT + cK_8 \exp 3VF/RT} \quad [2]$$

and correspondingly for the electrochemical pathway in Va

$$v_9 = \frac{k_9 K_5 K_6 K_7 K_8 \exp 4VF/RT \cdot c}{1 + cK_5 \exp VF/RT + cK_6 \exp 2VF/RT + cK_7 \exp 3VF/RT + cK_8 \exp 4VF/RT} \quad [3]$$

where potential-dependent equilibrium constants have been introduced for steps VI, VII, and VIII if they proceed like Va by proton transfer; the latter type of step seems more likely and is consistent with a similar step in the oxygen evolution reaction (36).

The reaction orders may be readily obtained for both these cases as a function of potential by appropriate differentiations and give, in general, relations of the type

$$\mathcal{R} = 1/[1 + c f(K, V)] \quad [4]$$

where $f(K,V)$ is the sum of terms such as K_5, $K_6 \exp VF/RT$, $K_7 \exp 2VF/RT$ in Eq. [2] or corresponding terms in Eq. [3]. It is clear that quite generally $\mathcal{R}$ will tend to decrease with increasing c and increasing potential, but the relation to the latter will not be simple since it involves sums of exponentials in V. If in some cases, one of the exponential terms in V together with its K value in the product were predominant in the denominator of Eq. [2] or of Eq. [3], then $\mathcal{R}$ would be simply related to V by

$$\ln\left(\frac{1}{\mathcal{R}} - 1\right) = \ln c + \ln K_n + n\, VF/RT \quad [5]$$

where K_n is now a particular equilibrium constant for the step involving the n'th electron transfer. Hence

$$d \ln\left(\frac{1}{\mathcal{R}} - 1\right)/dV = nF/RT \quad [6]$$

Similar conclusions would follow if another first order chemical step were rate-determining. For a second order recombination step, $\ln\left(\frac{2}{\mathcal{R}} - 1\right)$ would be a function of c and V.

If the mechanism involves the second-order recombination desorption IV (scheme A)

$$v_4 = k_4 \theta_N^2 \quad [7]$$

and if θ_N is related to coverage by antecedant species

$$\theta_N = \Pi K . \theta_{NH_2} \quad [8]$$

where ΠK is a combination of quasi-equilibrium constants; also, if two-site adsorption is involved, *e.g.* in step 1,

$$\frac{\theta_{NH_2}}{(1 - \theta_{NH_2} - \Sigma\theta_x)^2} = K_1 c \quad [9]$$

where $\Sigma\theta_x$ is the coverage by other species on the surface and may be potential dependent. An explicit expression in terms of c is unwieldly but in terms of θ, the reaction order is

$$\mathcal{R} = 2(1 - \theta_{NH_2} - \Sigma\theta_x)/(1 + \theta_{NH_2} - \Sigma\theta_x) \quad [10]$$

θ_{NH_2} will be potential dependent if I is an electrochemical step such as

$$N_2H_4 + OH^- \rightarrow NH_2 + NH + H_2O + e$$

or if $\Sigma\theta_x$ is potential dependent. A simple form for the Tafel slope may be obtained for IV only when $\Sigma\theta_x$ is negligible; then

$$b = \frac{1 - \theta_{NH_2}}{1 + \theta_{NH_2}} \cdot \left(\frac{RT}{2F}\right) \quad [11]$$

where only θ_{NH_2} is potential dependent; b is therefore related to the reaction order at any potential by

$$b = \frac{1}{\mathcal{R}}\left(\frac{RT}{F}\right) \quad [12]$$

and includes any case where the b refers simply to a tangent of slope $dV/d \ln i$ in a curve approaching a limiting current.

In 0.1M KOH, the reaction velocity initially has little dependence on concentration, but at low concentration the rate tends to increase (Fig. 13) with decreasing concentration until it becomes diffusion controlled, whereupon an inhibition and reactivation effect of the type found in other anodic oxidations is observed. The current for descending potentials is then greater at low potentials than that for ascending potentials, *i.e.*, an activation analogous to that in formate oxidation occurs. The behavior at low concentrations implies a negative reaction order, similar to that observed in ethylene oxidation (6). In that case, a reaction between adsorbed ethylene and the surface oxide was envisaged.

The velocity of any process involving an adsorbed intermediate N_2H_x (x = 0, 1, 2, or 3) can be expressed in terms of coverages of intermediates in prior steps and the corresponding equilibrium constants (providing prior steps are not entirely irreversible; *cf.* 36, 43). This implies that the reaction order in N_2H_x, with which the intermediates and first chemisorbed species will be in adsorption equilibrium, will always tend to be positive (or zero for full coverage). A competitive adsorption situation (*cf.* 6) is required to account for a negative reaction order.

If a step such as

$$N_2H_3 \rightarrow N_2H_2 + H$$

for example, (following the initial adsorption) were involved as a rate-determining process, its velocity would be

$$v_6 = k_6 \theta_{N_2H_3} (1 - \theta_{N_2H_3}) \quad [13]$$

since two sites for adsorption of N_2H_3 and H would be required (*cf.* 8, 49). If N_2H_3 were in equilibrium with N_2H_4 in the bulk at concentration c through the electrochemisorption

$$N_2H_4 \rightarrow N_2H_3 + H^+ + e$$

then

$$v_6 = k_6 \frac{K_{5a}c}{1 + K_{5a}c}\left(1 - \frac{K_{5a}c}{1 + K_{5a}c}\right) \quad [14]$$

where K_{5a} is an electrochemical equilibrium "constant" (potential dependent)

Hence

$$v_6 = \frac{k_6 K_{5a} c}{(1 + K_{5a}c)^2} \quad [15]$$

which gives a potential dependent rate and a reaction order

$$\mathcal{R}_6 = (1 - K_{5a}c)/(1 + K_{5a}c) \quad [16]$$

after differentiating v_6 w.r.t. c and multiplying by c/v_6. Equation [16] gives first order kinetics at low concentration, zero when $K_{5a}C = 1$ and negative order kinetics when $K_{5a}C > 1$ (limitingly $\mathcal{R}_6 = -1$ as $K_{5a}C >> 1$). This is in the wrong direction to explain the trend of $\mathcal{R}$ in the present results for alkaline solutions.

It may be suggested tentatively that an adsorbed O or OH radical mechanism of the type involved in ethylene oxidation (6) therefore seems the only one that could account for the negative reaction order at low concentrations. In these terms, the reaction $OH^- + Pt \rightarrow$ "PtOH" $+ e$ would proceed on a surface appreciably covered by N_2H_x species at a rate given (*cf.* 38) by

$$v_{OH} = k_{OH}C_{OH^-}\,(1 - \theta_T)\, e^{\beta VF/RT}\, e^{-(1-\beta)r\theta_T/RT} \quad [17]$$

where θ_T is the total coverage by adsorbed species and $r\theta_T$ is a Temkin term reflecting the change of energy of adsorption of OH with increasing coverage θ_T (*cf.* 13, 38, 39). The reaction with hydrazine then would be envisaged as a chemical one (*cf.* 46).

$$N_2H_x + x\text{"PtOH"} \rightarrow xH_2O + N_2$$

with the OH^- discharge initially rate-determining.[4] v_{OH} in Eq. [17] would tend to be smaller (cf. 6) as θ_T (due to increased $\theta_{N_2H_x}$) were increased. Hence a negative reaction order is predictable as in the ethylene oxidation (6). Equation [17] also gives the correct Tafel slope of 2.3 $2RT/F$. The limiting current obtained at high potentials must result from a chemical step, *e.g.*, IV or IX, could not be rate-determining at lower potentials since they could only give rise to slopes $< 2.3\ 2RT/F$. At lower potentials, $\theta_{OH} << 1$ in the steady-state, since no intermediates are detectable in cathodic transients from anodic potentials.

At the higher concentrations of N_2H_4 where $\mathcal{R} \doteq 0$, but the Tafel slope is still 2.3 $2RT/F$, a direct electrochemical reaction with an adsorbed species at full coverage seems the only possibility, *e.g.*

$$N_2H_3 + OH^- \rightarrow N_2H_2 + H_2O + e$$

with $\theta_{N_2H_3} \rightarrow 1$.

In acid solutions, the reaction order behavior is more normal and $\mathcal{R}$ is fractional and tends to decrease with increasing concentration of N_2H_4 (Fig. 15) as required for any direct adsorption process I or V or for following steps indirectly dependent on the primary adsorption step. There is less tendency for a limiting current to be reached and the Tafel slope is *ca.* 2.3 $2RT/F$ over a wide range of current densities.

Shape of current-potential relation.—The shape of the current-potential relation for alkaline solutions indicates an approach to a limiting current which could arise because of activation or diffusion control. The latter possibility is excluded (except at much lower concentrations) since the currents passing in the limiting region are independent (within 2%) of rotation rate at the rotating disk electrode. The Tafel slopes at lower potentials eliminate the possibility of IX or IV being rate-determining and hence giving at higher coverage a limiting current, although this may still arise if the mechanism changes with increasing potential.

The limiting behavior must therefore originate from the potential-independent rate of some chemical step along the sequences described above. At higher potentials, it is evident that some preceding step is unable to meet the current that would normally be associated exponentially with increasing potential, and this step must presumably be a chemical step of dissociation such as II, III, etc., or VI, VII, etc., or possibly the primary adsorption step itself (I or V).

The kinetics of oxidation of successive H atoms in N_2H_4, NH_3 and similarly in the case of hydrocarbons poses some special problems in electrochemical kinetics since current contributions arise from successive steps in the reaction and not just in one step in the reaction. A simpler but analogous case arises in the hydrogen evolution reaction proceeding by the mechanism

$$H^+ + e + M \rightarrow MH$$

$$MH + H^+ + e \rightarrow H_2$$

where current passes in both steps of the coupled mechanism; a similar situation occurs in the mechanism of the oxygen evolution reaction (36).

Thus, in the chemical scheme B (V-IX), the coverages by N-containing intermediates in the steady state will be indirectly dependent on potential since the H atoms produced in the dissociation steps will be removed with increasing velocity at higher anodic potentials when their steady-state coverage may well approach zero, so that in scheme B with chemical (rather than electrochemical) dissociation steps, it is difficult to speak of equilibria in steps prior to the rate-determining one since entities in the prior steps are "drained off" rapidly by electrochemical H ionization in side-reactions. The "equivalent circuits" for the indirect (*e.g.*, steps such as V coupled with IIa) and direct (*e.g.*, Va and following analogous steps) dehydrogenations are of some special interest and can be represented (neglecting capacitance contributions for simplicity) as

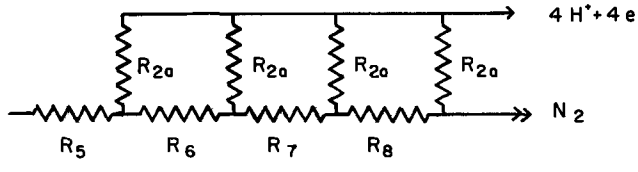

for the chemical dehydrogenation pathways in B and

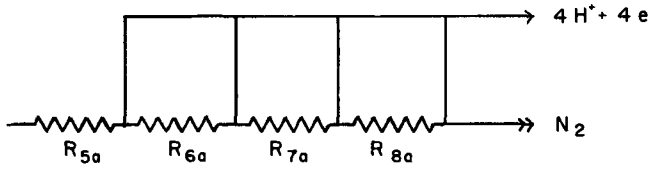

for electrochemical dehydrogenation steps. R_9 and R_5 to R_8 in the chemical pathway are resistance analogues corresponding to reciprocal chemical rates while R_{5a} — R_{8a} are potential-dependent analogue resistances.

Hysteresis.—No hysteresis characteristic of co-adsorbed oxide (contrast the cases of formate and hydrocarbon oxidation) is observed, and no oxide can be detected as mentioned above. However, in alkaline media, the descending current line is always above the one for ascending anodic potentials suggesting that with increasing potential, increasing coverage by intermediates is involved and these remain on the electrode at a nonequilibrium concentration as the potential is lowered.

[4] This would apply only, of course, at moderately anodic potentials.

Conversely, in acid media, the hysteresis is in the opposite sense and the descending curves are somewhat lower than the ascending ones. Hysteresis characteristic of oxide formation is again only observed at low concentrations when diffusion control is approached (Fig. 14). Rotation of the electrode then causes the oxide to disappear presumably by reaction with the N_2H_4 which can then reach the electrode. Similar effects occur in hydrocarbon oxidation at the region of the peak current.

Hydrocarbon oxidation.—Passivation effects in hydrocarbon oxidation at Pt are well known but, the involvement of co-adsorbed oxide has not been examined in detail quantitatively. Wroblowa, Piersma and Bockris (6) mentioned the coverage by oxide at Pt in ethylene oxidation, but it is unclear if this coverage was measured during the ethylene oxidation. In Fig. 16-18 are shown the current-potential relations for ethylene and propane oxidation in phosphoric acid together with the corresponding oxide charges (Q_o) and H accommodations (Q_H) at more cathodic potentials (fast galvanostatic discharge). The H charge is independent of potential and hence probably does not include any contribution from H participating in rehydrogenation of adsorbed C skeletal species (40); this is supported by the fact that the Q_H in the presence of hydrocarbon is less than that determined at the same electrode in its absence (*cf.* 40) (Fig. 16, 18).

In the hydrocarbon oxidations studied, significant oxide charge appears just at the beginning of the inhibition inflection and continues to increase with increasing anode potential. The coverage is much less

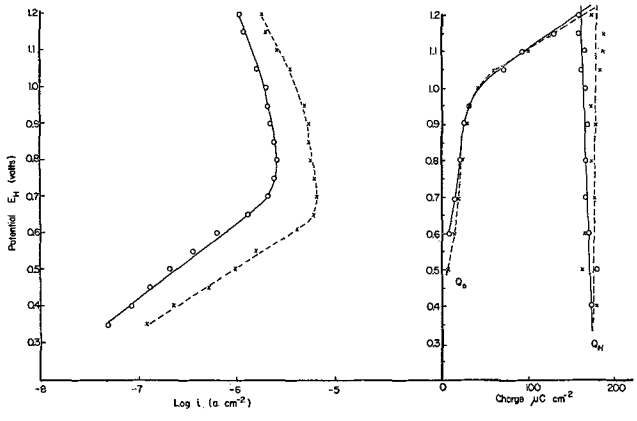

Fig. 16. Potentiostatic log i-E curves for ethylene oxidation with oxide charge Q_o and hydrogen accommodation Q_H as a function of potential, determined in the presence of ethylene. ○, 60°C, x, 90°C, both Q_H and Q_o values. Corrected to real cm^2 on basis of Q_H = 0.21 mC cm^{-2} at 25°C. Solution 1M $HClO_4$ (similar results in H_2SO_4).

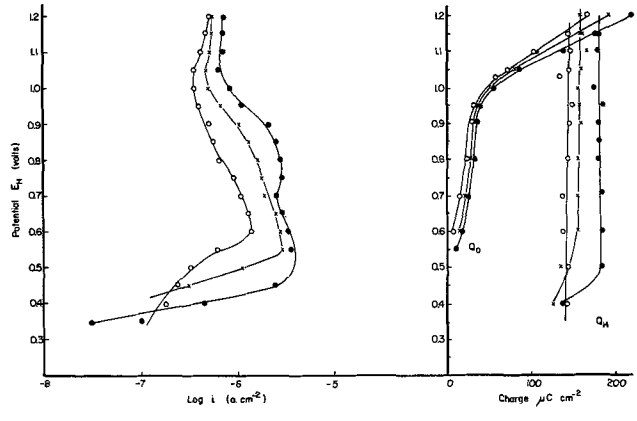

Fig. 17. As in Fig. 16 but for propane in 85% H_3PO_4. ○, 90°C, x, 120°C, •, 150°C, all Q_o and Q_H corrected to real cm^2 at 25°C.

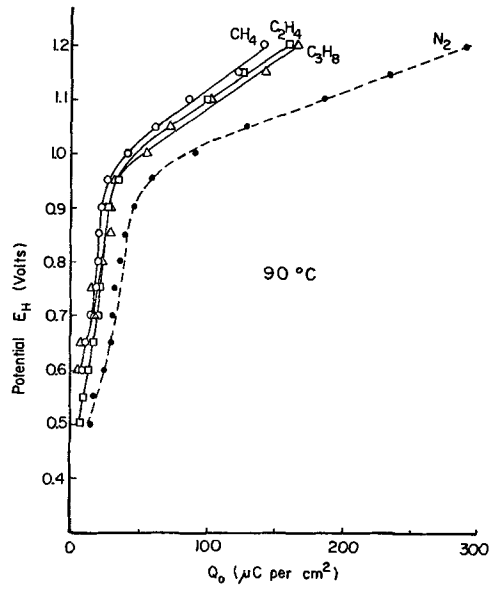

Fig. 18. Comparisons of oxide coverage in hydrocarbon oxidations at 90°C in 85% H_3PO_4. Q_o includes d.l. charges at all potentials (same in Fig. 16 and 17).

than 0.5 at the current maximum (*cf.* 8) and suggests that the catalytic reaction may proceed only on a fraction of the available surface but that this fraction is then relatively more covered by oxygen species. This view is in accord with general theories of active centers in catalysis. The extent of the inhibition in anodic current is however less than that in formate oxidation and a relatively potential-independent current passes above *ca.* 0.8v E_H. Since the oxide coverage is then appreciable, this current may be maintained by reaction of the adsorbed hydrocarbon with the surface oxide (*cf.* the N_2H_4 case). Below *ca.* 0.55v (E_H), surface oxide is undetectable by the differential charging method and the hydrocarbon oxidation proceeds in an uninhibited manner. The kinetic involvement of an oxide at these lower potentials in a mechanism such as that envisaged by Bockris *et al.*, (6 ,7) cannot, however, be excluded since anodic discharge of "OH" species at the surface may still proceed at a relatively high rate but the steady-state or equilibrium coverage could be small. The detectable limit by transient studies is somewhat arbitrary and Q_o ten or one hundred times smaller at lower potentials may still be kinetically significant. Direct measurements of the current densities for oxide charging at large platinized electrodes indicates that the rates can be quite high (10^{-1} amp cm^{-2}) at relatively low anodic potentials (*ca.* 0.3v E_H) and the potential is seemingly determined mainly by the extent of oxide coverage that has accumulated during the rate measurements (if these are sufficiently fast, three decades of anodic charging current density can be examined with less than 10% oxide coverage on the electrode). This "accumulated oxide charge" effect can be extrapolated out approximately by making measurements at various time intervals or charging rates; the polarization in charging is then quite small; however, it is indicated significantly by shifts of the pseudocapacitance maximum with increasing charging (or discharging) rate at higher rates or at greater sweep speeds.

Sweep-rate effects in processes involving surface oxides.—For a number of processes, *e.g.*, formate and formic acid oxidation, significant oxidation rates arise in regions of potential where the oxide coverage is appreciable and potential-dependent. The currents passing as a function of potential in a potentiodynamic sweep experiment can therefore be determined by (*a*)

the Faradaic current i_F for the over-all oxidation reaction; (b) what may be called the "pseudo"-Faradaic current i_c associated with the charging of the adsorption pseudo-capacitance C (this current is zero in the steady state at a given potential except when the over-all reaction proceeds by a chemical depolarization of an electrochemically formed film of adsorbed species); and (c) the non-Faradaic double-layer charging current, $i_{d,l}$; normally $i_{d,l} << i_c, i_F$.

Current peaks can arise in potentiodynamic runs for two reasons: (a) because of an intrinsic inhibition effect such as we have discussed previously (8); and (b) because the adsorption capacitance C is usually potential-dependent (38, 39) and the charging current ($i_c = CdV/dt$) is hence a maximum when C is a maximum. However, if there is any "irreversibility" (this is of course a relative matter; see below) in the charging process producing or removing surface oxide as the potential is changed, then C itself may depend at a given potential on the rate of sweep dV/dt ($= S$). Effects of this kind are quite marked at Pt (41); similarly the coverage attained at a given potential in a sweep may depend on S since the coverage will usually be "out of phase" with the potential (42).

The charging current for a process such as

$$M + H_2O \underset{k_{-1}}{\overset{k_1}{\rightleftharpoons}} MOH + e + H^+$$

is given (42) as a function of potential by

$$i_c = k_1 (1 - \theta)\, e^{V/b} - k_{-1}\, \theta\, e^{-V/b} \qquad [18]$$

if the symmetry factor is 0.5 and the Tafel slopes for the above processes are b. In the nonsteady state

$$i_c = C\, dV/dt = k \frac{d\theta}{dV} \cdot \frac{dV}{dt} \qquad [19]$$

where k is a proportionality constant relating charge to coverage θ.

Hence θ, at a given potential, is a function of S and V, determined by the differential equation

$$\theta = \frac{e^{V/b} - k \dfrac{d\theta}{dV} \cdot \dfrac{S}{k_1}}{e^{V/b} + \dfrac{1}{K_1} e^{-V/b}} \qquad [20]$$

where $K_1 = k_1/k_{-1}$ and a reduced sweep-rate S/k_1 is introduced. The relative effect of S on coverage at a given potential therefore depends, as expected, on how large is the rate-constant k_1 for the charging process. This result, it will be seen, is analogous to that which we previously calculated for rate effects in galvanostatic charging (42). Equation [20] must be solved numerically.[4a] The derived θ as a function of V for various values can then be used in a kinetic inhibition equation (8) to obtain the shape of an inflected current-potential relation for i_F for some oxidation process as a function of S when i_c and i_F are comparable in the same range of potentials. Qualitatively, the effect of S is shown in Fig. 19. It is to be noted, as we have mentioned previously (42), that the principal difficulties with the sweep method arise when it is used repetitively so that neither a steady current nor a steady state is ever involved and V is $f(t)$. The use of the potentiodynamic successive individual pulse method (single potential ramps) applied by Gilman (e.g., 40) appears preferable (42) since in the sweep, the charge passed is related to steady-state conditions obtaining prior to the initiation of the sweep; in this respect, the method is analogous to that employed here using the differential galvanostatic procedure. However, some complications can still arise if the potential range swept includes any region where new Faradaic processes arise.

[4a] Quantitative calculations on this effect are in progress, using a computer solution for Eq. [20].

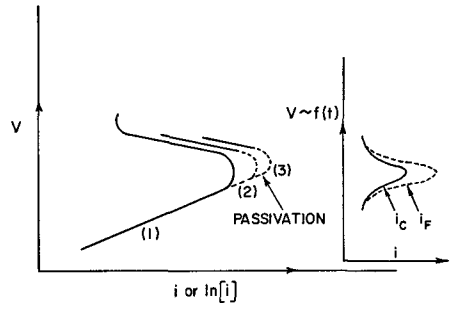

Fig. 19. Current-potential relations (schematic) for an inhibited process at increasing sweep speeds (no diffusion control). 1, Steady-state; 2, 3, increasing S. Inset: Faradaic and pseudocapacitative current contributions.

Acknowledgments

Grateful acknowledgment is made to the Defence Research Board for the award of Grant No. 5412-01 supporting part of this work and to the U.S. Army Engineer Research and Development Laboratory, Fort Belvoir, for the award of Contract No. CP-70A1-63-4 in support of other parts of it. One of us (E.J.R.) acknowledges the award of a Fellowship from General Motors of Canada, Ltd.

REFERENCES

1. M. von Stackelberg and T. Weber, *Z. Elektrochem.*, **56**, 806 (1952).
2. M. Bruner and S. J. Dluska, *Bull. Acad. Science, Crakow*, 691 (1907).
3. J. O'M. Bockris, "Modern Aspects of Electrochemistry," Chap. 4, Vol. I, Butterworths, London (1954).
4. F. Fichter and M. Stocker, *Ber.*, **47**, 2003 (1914).
5. F. M. Perkin, *Chem. News*, **91**, 55 (1905); *ibid.*, **92**, 66 (1905); see also C. J. Brockman, "Electro-Organic Chemistry, "John Wiley & Sons, Inc., New York (1926).
6. H. Wroblowa, B. J. Piersma, and J. O'M. Bockris, *J. Electroanal. Chem.*, **6**, 401 (1963).
7. J. O'M. Bockris, H. Wroblowa, E. Gileadi, and B. J. Piersma, *Trans. Faraday Soc.*, **61**, 2531 (1965).
8. D. Gilroy and B. E. Conway, *J. Phys. Chem.*, **69**, 1259 (1965); H. Kozlowska and B. E. Conway, In preparation.
9. Y. M. Kolotyrkin, *Z. Elektrochem.*, **62**, 664 (1958).
10. M. Breiter, K. Franke, and C. A. Knorr, *ibid.*, **63**, 226 (1959).
11. H. Nord, *Acta Chem. Scand.*, **18**, 681 (1964).
12. V. S. Bagotskii and Y. B. Vasilev, *Electrochim. Acta*, **9**, 869 (1964).
13. E. Gileadi and B. E. Conway, "Modern Aspects of Electrochemistry," Vol. III, Chap. V, Butterworths, London (1964).
14. J. O'M. Bockris and A. Reddy, *J. Chem. Phys.*, **42**, 2046 (1965).
15. W. R. Busing and W. Kauzmann, *ibid.*, **20**, 1129 (1952).
16. H. A. Kozlowska and B. E. Conway, *J. Electroanal. Chem.*, **7**, 109 (1964).
17. B. E. Conway, E. Gileadi, and H. A. Kozlowska, *This Journal*, **112**, 341 (1965).
18. B. E. Conway, *J. Electroanal. Chem.*, **8**, 486 (1964).
19. D. S. Berns and R. M. Fuoss, *J. Am. Chem. Soc.*, **82**, 5585 (1960).
20. G. J. Janz and S. S. Danyluk, *ibid.*, **81**, 3846 (1959).
21. I. M. Kolthoff and F. G. Thomas, *J. Phys. Chem.*, **69**, 3049 (1965).
22. J. F. O'Donnell, J. Ayres, and L. K. Mann, *Anal. Chem.*, **37**, 1161 (1965).
23. J. Wojtowicz and B. E. Conway, *J. Electroanal. Chem.*, To be published.
24. J. O'M. Bockris, *Discussions Faraday Soc.*, **1**, 95 (1947).
25. J. O'M. Bockris and B. E. Conway, *J. Sci. Inst.* **25**, 8 (1948).

26. J. H. Ellis, *J. Am. Chem. Soc.*, **38**, 737 (1916).
27. R. Munson, *This Journal*, **111**, 372 (1964).
28. A. Kutschker and W. Vielstich, *Electrochim. Acta*, **8**, 985 (1963).
29. R. P. Buck and C. R. Griffith, *This Journal*, **109**, 1005 (1962).
30. S. B. Brummer, *J. Phys. Chem.*, **69**, 562 (1965); *cf.* S. B. Brummer and A. C. Makrides, *ibid.*, **68**, 1448 (1964).
31. M. W. Breiter, *Electrochim. Acta*, **8**, 457 (1963); *cf.* S. Gilman, *J. Phys. Chem.*, **67**, 78 (1963).
32. B. E. Conway and M. Dzieciuch, *Can. J. Chem.*, **41**, 38, 55 (1963).
33. J. Giner, *Electrochim. Acta*, **8**, 857 (1963); *ibid.*, **9**, 63 (1964).
34. H. A. Kozlowska and B. E. Conway, To be published.
35. J. O'M. Bockris and A. M. Azzam, *Trans. Faraday Soc.*, **48**, 145 (1952).
36. J. O'M. Bockris, *J. Chem. Phys.*, **24**, 817 (1956).
37. B. E. Conway and P. L. Bourgault, *Can. J. Chem.*, **40**, 1690 (1962).
38. B. E. Conway and E. Gileadi, *ibid.*, **42**, 90 (1964).
39. E. Gileadi and B. E. Conway, *J. Chem. Phys.*, **39**, 3420 (1963); see also *Electrochim. Acta*, **8**, 143 (1963).
40. S. Gilman, *Trans. Faraday Soc.*, **61**, 2546 (1965); *ibid.*, **61**, 2561 (1965).
41. B. E. Conway and D. Gilroy, To be published.
42. B. E. Conway, E. Gileadi, and H. A. Kozlowska, *This Journal*, **112**, 341 (1965).
43. B. E. Conway, "Theory and Principles of Electrode Processes," Ronald Press Inc., New York (1965).
44. S. Szpak, P. Stonehart, and T. Katan, *Electrochim. Acta*, **10**, 563 (1965).
45. T. O. Pavela, *Suomen Kemistilehti*, **30B**, 240 (1957).
46. S. Karp and L. Meites, *J. Am. Chem. Soc.*, **84**, 906 (1961).
47. D. M. King and A. J. Bard, *ibid.*, **87**, 419 (1965).
48. A. Reddy, M. A. V. Devanathan, and J. O'M. Bockris, *J. Electroanal. Chem.*, **6**, 61 (1963); see also *J. Chem. Phys.*, **42**, 2246 (1965).
49. A. Johnson, H. Wroblowa, and J. O'M. Bockris, *Electrochim. Acta*, **9**, 639 (1964).

Discussion

E. Gileadi: There seems to be some degree of disagreement between our results and yours with regard to the effect of hydrocarbons on oxide formation on Pt. We have measured the potential at which formation of a measurable amount of oxide is observed in 1*N* H_2SO_4 solutions saturated with N_2, ethylene, or butadiene.[5] Ethylene seemed to have no effect on the potential of oxide formation, while in the presence of butadiene an approximately 0.1v shift toward more positive potentials was observed. Similarly the quasi-passivation region observed in hydrocarbon oxidation on Pt starts at a higher anodic potential in the case of butadiene than in the case of ethylene and other olefins studied.

B. E. Conway: It must be remembered that our curves for cathodic charge in the oxygen region include the double-layer contribution and that our results refer to platinized Pt.

It is difficult to establish precisely the potential at which "oxide" is just detectable in galvanostatic cathodic transients (*e.g.*, see our Fig. 18), unless these are differentiated.[6] However, at a given potential well in the "oxide" region, the Q_o is undoubtedly appreciably smaller in the presence than in the absence of hydrocarbon.

S. Gilman: Low values of "oxide charge."—The charge corresponding to oxidation of the Pt surface (Q_o) may be smaller in the presence than in the absence of an organic substance (at low potentials where the surface is partially covered with the organic material). However, some of the effects of concentration of organic material on Q_o appear suspicious (*e.g.*, Fig. 5). Negative errors in Q_o may be caused by accidental oxidation of the organic compound during the cathodic pulse used to reduce the surface and to evaluate Q_o. For instance, at a concentration of 4*M*, diffusion (non-steady-state linear diffusion) alone would allow an 800 μC error (due to formate oxidation) to occur during less than 1 μsec. One way to avoid such difficulty is to reduce the surface at a constant potential[7] chosen sufficiently low so that oxidation of the organic substance may not occur.

High values of hydrogen codeposition charge.—Values of hydrogen coverage in the presence of hydrocarbons at low potentials (*e.g.*, Fig. 16) seem too high according to my experience. Hydrogenation-desorption of the adlayer is a common problem with the hydrocarbons[8] and may be responsible for an error in the data. Such desorption may apparently occur at very high sweep speeds (using linear sweeps) or current densities (using galvanostatic pulses) as well as at low sweep speeds. Hence the conditions of such an experiment must be chosen with great care.[9]

Activation of the surface through oxide reduction.—The enhancement of anodic current which has been observed following reduction of the passivated Pt surface may be due to such effects as: (*a*) a smaller surface concentration of relatively inactive species; (*b*) a more favorable coverage of the surface with active intermediates. For example[10] the oxidation of CO is first order in adsorbed CO and first order in "vacant sites" and hence is "self-poisoned" at high coverages with CO.

B. E. Conway: We do not consider the diffusion effect mentioned by Dr. Gilman as likely to account for the dependence of Q_o on formate concentration for the following reasons: (*a*) at a given formate concentration, the Q_o is dependent on the [formate]; [KOH] ratio; (*b*) the Q_o behavior with varying formate concentration also depends critically on the nature of the electrode, *e.g.*, if it is Pd, or smooth or platinized Pt. Thus the concentration at which the decrease of Q_o arises depends on the KOH concentration and the nature of the electrode surface.

While we had considered in our paper the point regarding rehydrogenation desorption of hydrocarbon residues at low potentials (and mentioned Gilman's work in this respect), the results we obtained with fast galvanostatic pulses seem to indicate in our work that this is not an appreciable effect under our conditions; the reasons are (*a*) the Q_H is less in the presence of hydrocarbon than in its absence; (*b*) the Q_H is more or less independent of the potential from which the cathodic galvanostatic transient was initiated.

The matter of surface activation in the direction of descending potentials in the formate oxidation we agree could in principle be explained in such terms as Dr. Gilman suggests. However, the important point is

[5] J. O'M. Bockris, H. Wroblowa, E. Gileadi, and B. J. Piersma, *Trans. Faraday Soc.*, **61**, 2531 (1965).

[6] H. Kozlowska and B. E. Conway, *J. Electroanal. Chem.*, **7**, 109 (1964).

[7] S. Gilman, *J. Phys. Chem.*, **67**, 1898 (1963).

[8] S. Gilman, *Trans. Faraday Soc.*, **61**, 2546 (1965); **62**, 466 (1966).

[9] S. Gilman, *Trans. Faraday Soc.*, **62**, 466 (1966).

[10] S. Gilman, *J. Phys. Chem.*, **68**, 70 (1964).

that the extent of the activation depends on the previous degree of "oxide" coverage and that a maximum in the descending i-v curve is always seen. This must imply a potential dependent adsorption of some inhibiting intermediate as we have discussed elsewhere.[11]

M. W. Breiter: It has been claimed in the short abstract of this paper and in several other papers of Professor Conway and co-workers that the differential galvanostatic technique should be preferred to the potentiostatic sweep technique because the charging conditions are better defined. The claim is based on a kinetic treatment of galvanostatic charging in which the adsorption is assumed Langmuirian. However, this assumption is rarely fulfilled for the heterogeneous surfaces of solid metals. If a more complex isotherm or the superposition of several Langmuir isotherms with different adsorption coefficients is required for the adequate description of the adsorption on a heterogeneous surface like platinum, only numerical solutions are possible for galvanostatic and potentiostatic charging. The charging conditions are equally complex. A computer analysis of potentiostatic and galvanostatic charging has been made by me recently in which the capacitive charging was considered in both methods and the effect of the ohmic potential drop between Luggin capillary and test electrode for the sweep technique. The treatment is more comprehensive than the recent treatment of the charging processes by Professor Gileadi.

A similar statement applies to the study of the oxygen layer by the two techniques. A qualitative discussion of the inhibiting effect of the oxygen layer on the anodic oxidation of methanol at platinum was given for different sweep rates by Dr. Gilman and myself. Any attempt to interpret the inhibiting effect by Langmuirian kinetic expressions appears futile to me. Since only a blocking of the very active centers (less than 10% of the surface area) seems to be involved in the inhibition of the H_2 oxidation and the oxidation of many organic species on platinum, a kinetic treatment is difficult and should not be based on expressions for the total surface area which is electrochemically available for the formation of the oxygen layer.

B. E. Conway: The calculations Dr. Breiter has performed seem to confirm what we have previously implied[12-14] namely that the sweep and galvanostatic procedure will not always give the same results. In the sweep method for a charging process, the current depends on potential in a complex way, being determined by the sweep rate and the adsorption pseudocapacitance at any given potential. The pseudocapacitative charging current, therefore, corresponds to various degrees of polarization in the charging process, and neither steady-state current nor chemical steady-state kinetics apply; the potential also is not constant. It is in this sense that the sweep method is more complex in regard to interpretation of the kinetics of charging processes than is the direct or differential[15] galvanostatic method.

When a current-potential curve which shows a passivation inversion is involved, further complications can arise, as we point out in the paper, since the rate of formation of the passivating species can depend on sweep speed. The current maximum is then a complex function of sweep rate because both pseudo-Faradaic currents (*e.g.*, for surface oxide formation) and Faradaic currents for the over-all reactions are involved, and the latter depends in a critical way on the coverage produced by the former at a given potential in the sweep. Again, the galvanostatic analysis of the kinetics is simpler. Treatment of inhibition effects under Temkin conditions was the basis of our earlier paper.[11]

E. Gileadi: We have recently calculated the variation of the apparent adsorption pseudocapacity with potential, current density,[16] and sweep rate[17] for the simple case of a single adsorbed intermediate, for galvanostatic and potential sweep transients, respectively. The physical quantity which is indicative of the degree of departure of the system from quasi-equilibrium is the current density. Its magnitude, relative to the values of the forward and reverse specific rate constants, essentially determines the behavior of the system. Thus, as long as the current density is maintained constant, a simple qualitative physical interpretation can be made[16] even for complex systems, and an algebraic solution of the problem is possible for the simple case.

In potential sweep transients the quasi-equilibrium is disturbed to a degree which is indirectly related to the sweep rate. Since the current density can vary an order of magnitude or more during the transient, the reaction may be almost at equilibrium part of the time and far away from equilibrium at other times during the same transient. Thus it is hard to see how a single sweep rate equivalent to a given current density during a galvanostatic transient can be defined. No algebraic solution is possible here, even for the simplest case unless the further assumption that the reverse reaction is negligible during the transient is made. Further the IR correction, either numerically or by a compensation method, is much more simple when galvanostatic transients are used.

On the other hand I do agree that for the purpose of obtaining the charge associated with the adsorbed species on the surface only, either method can be used with equal success. Also in more complicated systems involving several types of surface sites, several intermediates or if a Temkin type adsorption isotherm applies, one has to resort to numerical computation in any case.

S. B. Brummer: The authors attempt to indicate that passivation in the current-potential behavior for a number of organic reactions at Pt electrodes is the result of inhibition by surface oxides formed as the potential is raised. In a number of instances, however, they do not observe any oxide, or at least an insufficient amount of oxide, to be present. They postulate alternatively a mechanism for the inhibition in terms of coverage of the electrode by an inhibiting adsorbed species, perhaps an intermediate in the reaction.

The difficulty with such an explanation is that for almost every case that has been studied (*e.g.*, $HCOOH$[18,19], C_3H_8[20,21]; an exception is CO[22,23]) there is no appreciable coverage of the electrode in the appropriate potential region. Thus, to take HCOOH as an example, neither H-atom deposition nor anodic stripping shows the presence of any adsorbed material. Thus the authors' explanation, which requires high

[11] D. Gilroy and B. E. Conway, *J. Phys. Chem.*, 69, 1259 (1965).

[12] B. E. Conway, E. Gileadi, and H. A. Kozlowska, *This Journal*, 112, 341 (1965).

[13] B. E. Conway, *J. Electroanal. Chem.*, 8, 486 (1964).

[14] B. E.. Conway, "Theory and Principles of Electrode Processes," Ronald Press Inc., New York (1965).

[15] H. A. Kozlowska and B. E. Conway, *J. Electroanal. Chem.*, 7, 109 (1964).

[16] B. E. Conway, E. Gileadi, and H. Angerstein-Kozlowska, *This Journal*, 112, 341 (1965).

[17] S. Srinivasan and E. Gileadi, *Electrochim. Acta*, 11, 321 (1966).

[18] S. B. Brummer and A. C. Makrides, *J. Phys. Chem.*, 68, 1448 (1964).

[19] S. B. Brummer, *J. Phys. Chem.*, 69, 562 (1965).

[20] S. B. Brummer, J. I. Ford, and M. J. Turner, *J. Phys. Chem.*, 69, 3424 (1965).

[21] S. B. Brummer and M. J. Turner, "Hydrocarbon Fuel Cell Technology," Academic Press, New York (1965).

[22] S. Gilman, *J. Phys. Chem.*, 67, 78 (1963).

[23] S. B. Brummer and J. I. Ford, *J. Phys. Chem.*, 69, 1355 (1965).

coverage of the electrode, is not possible unless it be assumed that the inhibiting adsorbed species cannot be oxidized at all, even at potentials approaching O_2 evolution, and yet is reversibly desorbed at relatively cathodic potentials. At the very least, such material should show up as an inhibitor of the transient oxidation of the electrode[24] and/or should show a double layer "desorption" peak.

A possible alternative to the authors' explanation, which appears to agree with the data for HCOOH oxidation,[18, 19] is to postulate that a nonelectrochemical (*e.g.*, adsorption) step is rate-limiting and that all subsequent steps are fast. For example:

$$\text{HCOOH solution} \rightleftharpoons \text{HCOOH}_{\text{electrode}} \quad [1]$$

$$\text{HCOOH}_{\text{electrode}} \xrightarrow{\text{slow}} \text{H}_{\text{ads}} + \text{COOH}_{\text{ads}} \quad [2]$$

$$\text{H}_{\text{ads}} \xrightarrow{\text{fast}} \text{H}^+ + \text{C} \quad [3]$$

$$\text{COOH}_{\text{ads}} \xrightarrow{\text{fast}} \text{CO}_2 + \text{H}^+ + \text{C} \quad [4]$$

(Whether or not the initial species is HCOOH or $HCOO^-$ is not relevant to the present discussion.) In this scheme, [2] is slow and, therefore, θ_{COOH} must be small. The slow step must be nonelectrochemical because of the almost potential-independent current frequently observed.[18, 25] The authors' suggestion that H_{ads} could be the inhibiting species for their mechanism would hardly seem likely. Nor can the "reduced CO_2" species of Giner[26, 27] be used to explain the phenomenon since this species is only found on the electrode at lower potentials.

An additional complication could also arise because of rejection of the reactant from the double layer by anion or solvent adsorption as the potential is raised. This was tentatively suggested previously,[18] on the basis of the current-coverage relationships at various potentials. Such an effect, depressing $HCOOH_{electrode}$, could account for a decrease (or an increase for that matter, if the conditions were appropriate) of the rate of reaction [2] with increase in potential. The extent of this decrease is difficult to estimate without more definite information that is presumably available about the Pt-solution double layer.

B. E. Conway: The difficulty mentioned by Dr. Brummer is recognized in our paper, and in fact we have specifically suggested both with respect to formate and hydrocarbon oxidations that the reactions may be proceeding only on an active fraction of the total sites available for kinetic processes (*cf.* active centers in catalysis) and that the inhibition occurs on these active sites. In fact, in general chemical terms, the active sites would tend to be the first to be oxidized since they would tend to be stronger Lewis bases, or less noble, than the bulk of the metal. It seems that some inhibiting species, the surface concentration of which is potential dependent, is clearly required to account for the rather symmetrically reversed i-v curves that are normally involved in formate and other oxidations.

It is of interest that in alkaline solutions (although not in neutral or acid solutions) "oxide" can be detected in the cathodic transients to an appreciable extent in the "inhibition" region (Fig. 5 and 6).

A nonelectrochemical step is difficult to accept as rate limiting since a well-defined Tafel region arises initially in the direction of ascending anodic potentials[28] and current reversal occurs at higher potentials. A nonelectrochemical step could give a limiting current but, it seems, not a subsequent change of sign of Tafel slope for formate oxidation.

The "limiting" current observed by Brummer [his ref. (18)] may arise only apparently since the anode potential was only taken up to 0.75v. In our work with $HCOO^-$ ion, a true current reversal occurs at rather higher potentials (after an apparent limiting current) and would not be seen at such low potentials as Dr. Brummer went up to. Similarly the coverage by the intermediate studied by Dr. Brummer in his ref. (19) has already diminished to near zero by *ca* 0.65v E_H; the reducible species seen in our experiments only appears at higher potentials and therefore may more legitimately be identified as an "oxide" species.

This matter also brings up another point of general importance, namely that the course of an electrochemical reaction cannot simply be judged on the basis of adsorption studies alone. These must be used in conjunction with the steady-state kinetic characteristics of the reaction, *e.g.*, Tafel slopes, current reversal effects and reaction orders.

Finally, all our work has referred to formate ($HCOO^-$) ion in neutral or alkaline solutions, so that the species HCOOH is not actually the primary reactant under our conditions; thus the formate ion is probably not necessarily adsorbed in the same way as the formic acid molecule to which Dr. Brummer's discussion refers. The conclusions made previously for formic acid oxidation probably are not entirely applicable to the formate ion case, particularly under our conditions of alkalinity.

J. O'M. Bockris (communicated): I think that the usual difficulty of determining oxide as apart from adsorbed OH is not difficult any more and taking this into account would help to clarify some points in the paper of Conway and co-workers.

Thus, there is difficulty only if there is a monolayer. Then, it is adsorbed O (or OH) if the oxygen has a single bond and adsorbed oxide. However, if it is more than one bonded and coordinated by the metal on more than one side, it is a two-dimensional oxide.

This is the structural definition: the empirical definition arises from the ellipsometry which switches in in the neighborhood[29] of 0.9v.

Thus, in the section of their paper on Hydrocarbon oxidation, Conway *et al.* do not distinguish between adsorbed OH and oxide. They refer, for example, to the absence of oxide giving the rate "lack of inhibition." It is adsorbed O (or OH) which exits at these more negative potentials, and this must get into organic oxidations in some way from stoichiometric grounds: one does not have to have an oxide. Again, ellipsometry would be the main distinguishing point.

I think that, in reference to the Bagotsky and Vasiliev paper, we must note that the maxima there observed below that near 0.9v is certainly due to a pseudocapacitance charging process as implicitly pointed out by Bagotsky and Vasiliev[30] who found that in the steady-state no such curves could be seen.

B. E. Conway (communicated): The question of the identity of "surface oxide" at Pt was discussed in our paper, and the distinction between adsorbed oxygen species and oxide was recognized in our footnote in relation to the ellipsometric evidence. In our own and other electrical transient measurements, no distinction can, of course, be made between one type of species and another. However the well-known hysteresis in the formation and reduction of "oxide" at Pt undoubtedly arises in part from the irreversible transformation that occurs between "adsorbed" species and a two-dimensional "phase oxide." It is worth noting that quite independent evidence for the effect of ad-

[24] Compare the recent results of Gilman, [*J. Phys. Chem.*, 69, (1965)] on Cl^- adsorption.

[25] See also the early work of Muller and Tanaka.

[26] J. Giner, *Electrochim. Acta*, 8, 857 (1963).

[27] J. Giner, *Electrochim. Acta*, 9, 63 (1964).

[28] D. Gilroy and B. E. Conway, *J. Phys. Chem.*, 69, 1259 (1965).

[29] A. Reddy, Genshaw, and J. O'M. Bockris.

[30] V. Bagotsky and Y. Vasiliev, *Electrochim. Acta*, 9, 869 (1964).

sorbed O atoms in causing modification of the arrangement of metal atoms in the adsorbent surface has been obtained by low energy electron diffraction studies;[31] these changes in surface structure in the presence of adsorbate O-species may be similar to those encountered at the platinum anode surface above 1v.

We agree regarding the Bagotsky and Vasiliev results. In our work all the maxima observed are, however, true kinetic inhibition maxima since they were observed in the steady state[32] and arise presumably because of the presence of an inhibiting species, the surface concentration of which is dependent on potential.[32,33]

M. C. B. Hotz (communicated): Some years ago we made some conductivity measurements on aqueous solutions of hydrazinium perchlorate and hydrazinium chloroplatinate using platinized-platinum electrodes. We noted a change of conductivity with time; the chloroplatinate ion was found to have been reduced to metallic platinum. and evidence was obtained for production of chloride ion in the perchlorate solution. The reactions were much faster when platinized-platinum electrodes were used than with bright platinum, and we believed that the reduction was due to molecular hydrazine produced by the reaction

$$N_2H_5^+ + H_2O \rightleftharpoons H_3O^+ + N_2H_4$$

Even if Professor Conway used a substantial excess of perchloric acid, the possibility of this reaction cannot be ruled out.

B. E. Conway: We agree that free N_2H_4 can arise by hydrolysis; this effect may in fact be enhanced near the electrode surface where at anodic potentials the *p*H in the double-layer will tend to be higher than in bulk owing to repulsion of hydronium ions. Nevertheless, the concentration of free N_2H_4 must be very much smaller than that of $N_2H_5^+$ in 1M strong acid solutions. However, if the free energy of activation for oxidation of N_2H_4 were sufficiently less than that for $N_2H_5^+$, the disadvantageous difference of concentration of these two species could be outweighed by different rate constants for the respective oxidation reactions. Since the kinetic features of the reaction in acid and alkaline solutions are so different these possibilities must, however, be largely ruled out.

T. O. Rouse (communicated): The authors have presented an interesting correlation between water content in nonaqueous solutions and inhibition of formate oxidation by platinum "oxide." Some ambiguity still exists when the results for anhydrous propylene carbonate (PC) are considered (curve 1, Fig. 2). It is unfortunate that the log *i vs. V* curve for anhydrous acetonitrile or the oxide coverages for PC are not presented. If we assume, as the authors do, that the behavior in the two systems is comparable, it would appear that little or no oxide is present throughout the potential range in anhydrous PC. A comparison between curves 1 and 2 of Fig. 2 indicates considerable inhibition occurs between 0.8 and 1.1v when appreciable water is present, even though the authors are unable with their present technique to detect oxide formation over much of this range. The lack of inhibition in the anhydrous case in this potential range reinforces the authors' contention that the reaction in this range does not proceed via an oxide intermediate. However, it also follows that between 0.8 and 1.0v range, the reaction does not proceed only on sites just freshly uncovered of oxide. The reaction proceeds most readily when presumably little or no oxide was present at the higher potentials (the anhydrous situation).

Have the authors considered in greater detail the situation in anhydrous acetonitrile and PC?

B. E. Conway: The question concerning the results for anhydrous solutions in the case of CH_3CN arises from an error in the caption of Fig. 1 in the preprint. The solid line in this figure actually represents the behavior for the anhydrous case as it does in Fig. 2. The other solutions contained 2, 5, and 20 ml l^{-1} of water. The same applies to the curves in Fig. 3. It is likely (see Fig. 4) that even our best anhydrous solution still contained electrochemically significant traces of water; in all respects, however, the results in acetonitrile and propylene carbonate are entirely comparable, including the oxide coverages as a function of water content. Further work carried out in the absence of formate but with $NaClO_4$ as the electrolyte in CH_3CN confirms the dependence of oxide coverage on water content.

We agree regarding the remaining comments concerning the role of oxide as inhibitor or coreactant.[32]

[31] L. H. Germer, R. M. Stern, and A. U. MacRae, Metal Surfaces, Joint Seminar, Metal Parks, Ohio, 287 (1962) publ. 1963, *C.A.*, **61**, 15782 (1964); *cf.* L. H. Germer, *Scientific American*, p. 32 (March 1965).

[32] D. Gilroy and B. E. Conway, *J. Phys. Chem.*, **69**, 1259 (1965).

[33] B. E. Conway, "Theory and Principles of Electrode Processes," p. 203, Ronald Press, New York (1965); E. Gileadi and B. E. Conway, "Modern Aspects of Electrochemistry," Vol. 3, Chap. V, J. O'M. Bockris and B. E. Conway, Editors, Butterworths, London (1964).

Electrochemistry of Surface Oxides

A. C. Makrides

Tyco Laboratories, Inc., Waltham, Massachusetts

ABSTRACT

The electrochemical properties of surface oxides, particularly as they affect redox reactions at electrodes, are discussed. Experimental results on the effects of surface oxides on hydrogen evolution on nickel, on redox reactions on iron, on the hydrogen peroxide reactions on gold, and on oxygen evolution on lead are presented and discussed. The kinetics of formation and reduction of surface oxides are also examined with particular reference to gold electrodes where extensive measurements have been obtained.

Surface oxides play a role in a number of electrochemical reactions either directly by modifying the energetics of adsorption of reactants or intermediates or indirectly by changing the potential distribution at the surface. Some aspects of the electrochemistry of surface oxides have been of particular interest at our laboratory and have been explored in some detail. In particular, we have been concerned with the effects of oxides on oxygen reduction and evolution, on the hydrogen peroxide reactions, on the hydrogen reaction, and on the kinetics of simple redox reactions involving ions in solutions. In addition, we have studied the kinetics of formation and reduction of surface oxides using the gold electrode as a model system. In this paper we present a summary of these series of investigations and outline some of the general features of electrochemical reactions on superficially oxidized electrodes.

Experimental

The range of conditions covered by the investigations referred to is too wide to permit a detailed description here of the experimental procedures. In general, three-compartment, Pyrex cells were used and only glass, Teflon, and the electrode came in contact with the solution.

Solutions were made up of triply distilled water (one distillation being from dilute, alkaline $KMnO_4$) and C.P. or A.R. or recrystallized reagents. Purification included in some cases preelectrolysis or treatment with hydrogen peroxide. Certain potential sequences for cleaning the electrode were used, and these are described below or appropriate references are given. Gases were of highest purity available and were further purified by passage through appropriate traps or diffusion barriers, depending on the gas. Finally, the cells were thermostated to ± 0.1°C of the desired temperature.

Results and Discussion

Kinetics of formation and reduction of very thin oxide films.—The gold system was chosen for a detailed study of the kinetics of formation and reduction because of certain features which simplify its experimental study: the electrode can be electropolished with relative ease and it can be cycled between negative potentials (*vs.* RHE) and about + 2.0v without any permanent change in its surface or bulk properties; the reduction of anodically formed gold oxide films is particularly straightforward, the potential-time curve during most of the reduction occurring at a more or less constant potential; and, finally, the reproducibility of the measurements is very good generally about ± 3% in charge and ± 2 mv in potential.

The general technique we have used is to measure by cathodic, galvanostatic pulses the charge required for the reduction of a film formed anodically at a fixed potential. The cathodic pulse was generally of the order of 10 ma/cm^2; in fact, in the range of 1-100 ma/cm^2, the charge does not depend (< 1% variation) on the cathodic current density. This is true whether the film is allowed to reach a steady-state thickness or whether its formation is interrupted at a shorter time and the film reduced cathodically.

The steady-state charge (Q_∞) determined as described above, and corrected for double-layer charging, is shown as a function of potential in Fig. 1. Data previously published (1) are also given in this figure. The charge is a linear function of potential in the range of interest here with a slope of 1.25 x 10^{-3} coul/v.

The equivalent thickness of the anodic film has not been determined independently, but we know from results presented previously (1) that a monolayer of oxide corresponds to about 400 μC/cm^2 and has a thickness of about 10Å. Figure 1 shows, therefore, that a continuous transition occurs, as the potential is increased, from one to two equivalent layers (and beyond this to about three equivalent layers). We are dealing, therefore, with very thin films which range in thickness between 10 and 30Å. At potentials higher than 2.0v, the protective character of the film breaks down and films of essentially unlimited thickness can be grown (2).

The data in Fig. 1 suggest that the rate of growth of the film becomes negligibly small at a field which is independent of the thickness (E/Q_∞ = const.). It was attractive, therefore, to examine the model proposed by Mott (3, 4) for the growth of very thin films, which has already been applied to films of the same order of thickness as those encountered here. Of the two possible rate-determining steps, transport of ions through the oxide and reaction at an interface, the latter is rate controlling in the very thin film region. Without going into details of this model, which has been discussed at great length in the literature (5), the rate expression is

$$dX/dt = u \exp (X_1/X) \qquad [1]$$

with $X_1 = qaV/kT$, $u = u_0 \exp(-W/kT)$, and $u_0 = N'\Omega\nu$. Here, q is the charge on the ion, a the half-width and W the height of the energy barrier at the interface, N' the number of ions per unit surface area at kinks, etc., ν their frequency of vibration, and Ω the volume of oxide per metal ion. Since X_1 is of the order of 10^{-6} to 10^{-5} cm for the case considered here [and previously, (4)], Eq. [1] may be integrated approximately to yield

$$X_1/X = \ln [(X_1 u/X_\infty) t] \qquad [2]$$

Thus, at constant potential the thickness depends on time through an inverse logarithmic relation.

We have examined in detail the relation between Q and t over a sixfold range of time (~2.10^{-4} to 3.10^2 sec) and over the range of potentials included in Fig. 1 (E = 1.4 to 1.9v). These results, which encompass the kinetics of formation of the first monolayer (Q < 400 μC/cm^2), will be discussed in detail elsewhere (6). In the present context, we may simply state that the kinetics predicted by the Mott model are not obeyed during the formation of these very thin films, but on the contrary one observes a direct logarithmic relation between Q and t as shown in Fig. 2 for E = 1.8v.

This result was not entirely unexpected, since inverse logarithmic X-t relations have been rarely found in practice, direct logarithmic relations being more frequent. A direct logarithmic relation for oxidation has been attributed by Hauffe and Ilschner (7) to electron tunnelling being rate-determining for the growth of very thin films; however, such an explanation is obviously not applicable to the anodic formation of very thin films.

Grimley and Trapnell (8) have discussed the rate of growth of very thin films under conditions of saturation by chemisorbed, field-creating ions and have derived a linear law for both n- and p-type oxides assuming that the field is constant and independent of the oxide thickness. For a more complicated case, namely, for conditions of equilibrium between neutral

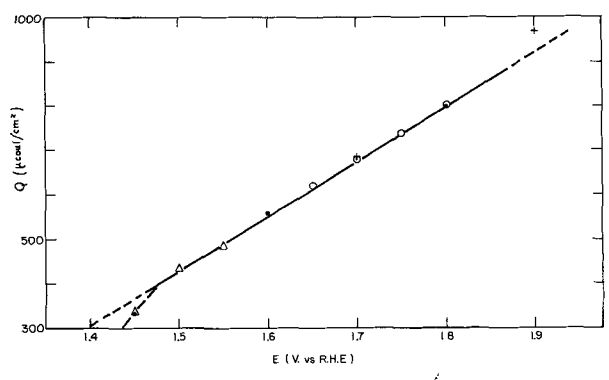

Fig. 1. Steady-state charge for reduction of anodic film on gold as a function of potential of formation ($NHClO_4$, 30°C).

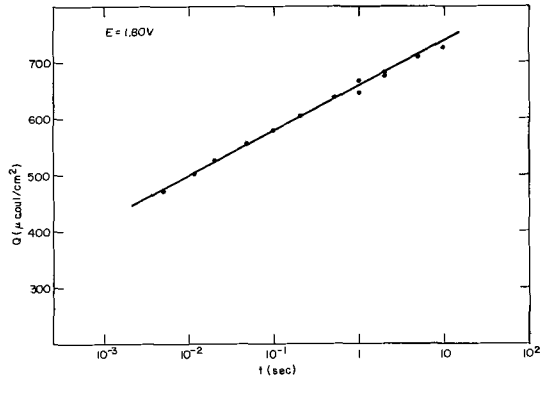

Fig. 2. Charge for reduction of anodic film formed on gold at 1.80v *vs.* RHE as a function of time of formation ($NHClO_4$, 30°C).

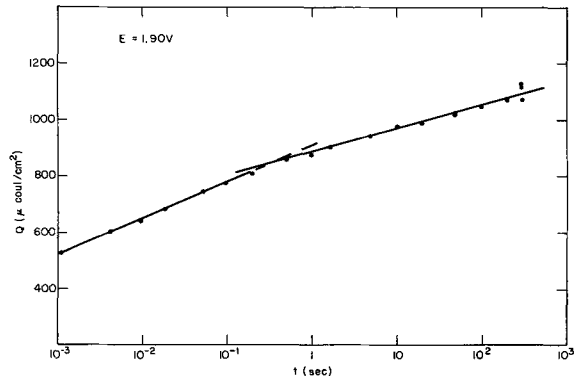

Fig. 3. Charged for reduction of anodic film formed on gold at 1.90v *vs.* RHE as a function of time of formation ($NHClO_4$, 30°C).

pairs and adsorbed ions, and for coverages by ions well below unity, they find an inverse logarithmic law if surface reactions (creation or destruction of vacant sites) are rate-determining.

It may be useful here to refer again to Fig. 1 and to emphasize that one of the implicit assumptions of these models may not hold true for our results in the very thin film region. In these models, the film is treated essentially as a continuum. In the calculation of the field, the thickness is assumed to be continuously variable by amounts presumably small in comparison to the thickness of a single layer. In fact, since we are dealing with a very few layers, in this case two or three, such a concept of film thickness is questionable. The fact that the charge measured is highly reproducible both for a given electrode and from electrode to electrode, suggests that layers are formed sequentially and that it is extremely unlikely that we are dealing with a film of variable thickness which happens to yield an average, equivalent thickness between, say, one and two layers. We must, therefore, examine the kinetics of growth of each layer separately and probably consider that during the formation of a layer, the thickness of the film is essentially constant. Results at 1.90v bear out this point (Fig. 3): we observe here a change in the kinetic constant as we go from the second layer (400-800 $\mu C/cm^2$ to a third (>800 $\mu C/cm^2$).

The two surface reactions which can be rate-determining are the reactions at the film-solution and at the metal-film interfaces. We may describe these in electrochemical terms, if we wish, and represent them by the usual chemical symbols. If we assume that the formation of oxygen ions (be they O^-, $O^=$, OH^-, etc.) is slow, we can attribute the logarithmic kinetics to an Elovitch-type relation as proposed for monolayer formation on platinum (9), that is to a relation of the type

$$\frac{dQ}{dt} = i = nFk \exp(-mQ) \exp(\alpha nFE/RT)$$

However, the physical basis of such a relation is obscure, particularly as a layer builds up to saturation; furthermore, m must be assumed to vary (arbitrarily) as each layer is formed; finally, it is not clear how this kinetic model can account for the gradual build-up of successive layers. A model easier to interpret can be constructed using the same general postulates as in the Mott theory, but modifying these for the particular conditions encountered here. The rate-limiting reaction is still assumed to be the passage of metal ions from metal to film, but the condition of constant potential drop across the film is abandoned. With this postulate, a direct logarithmic rate law can be derived, the rate constant being a function of the applied potential and of the film thickness. This model accounts for the general features of the kinetics of formation of anodic films on gold and also for their kinetics of reduction (1, 10). However, certain features of the reduction kinetics, *e.g.*, a dependence of the rate at a fixed reduction potential on the potential of formation of the film, are still not clear.

Effects of Surface Oxide Films on Electrochemical Processes

A number of reactions occur under conditions where the electrode may have either an adsorbed layer of oxygen or a very thin oxide film. We consider here a number of systems studied at our laboratory specifically for possible effects of oxide films on the reaction kinetics.

Hydrogen evolution on nickel.—We showed some time ago (11) that nickel electrodes in alkaline solution at 30°C behave in two distinct ways with respect to the hydrogen evolution reaction: electrodes in what we called the "initial state" show Tafel slopes of about 0.130v, exchange currents of about 2×10^{-5} amp/cm², and stoichiometric numbers $\nu = 2$; electrodes in a state arrived at by passivation show Tafel slopes of about 0.080v, exchange currents of about 0.8×10^{-5} amp/cm², and stoichiometric numbers of $\nu = 1$. Further studies with this system suggest strongly that the passive film formed on anodic polarization is reduced very sluggishly and that, in fact, in 0.1*N* NaOH solutions the anodically formed film, or some residual part of it, is present even at potentials of —0.200v *vs.* RHE.

Nickel electrodes can be prepared in an apparently completely reduced state by pretreatment with cathodic pulses of the order of 200 ma/cm². Results on the hydrogen reaction on such electrodes are shown in Fig. 4 and 5. The behavior of the same electrode after a passivating treatment is also shown in Fig. 4 and 5. The effect of the residual oxide or chemisorbed oxygen layer on the kinetics of the hydrogen reaction is to change the mechanism from

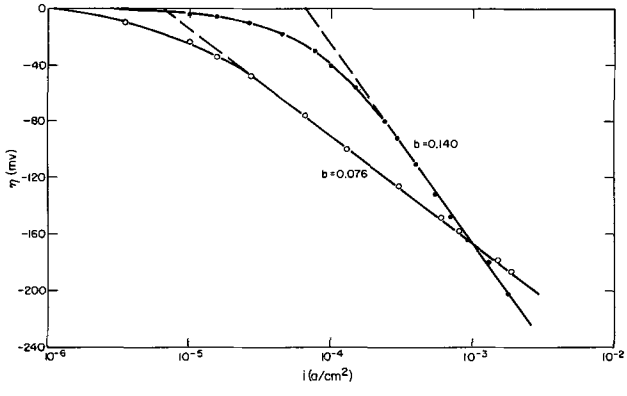

Fig. 4. Hydrogen overpotential on Ni in reduced state (●) and after anodic passivation (○) (0.1N NaOH, 30°C).

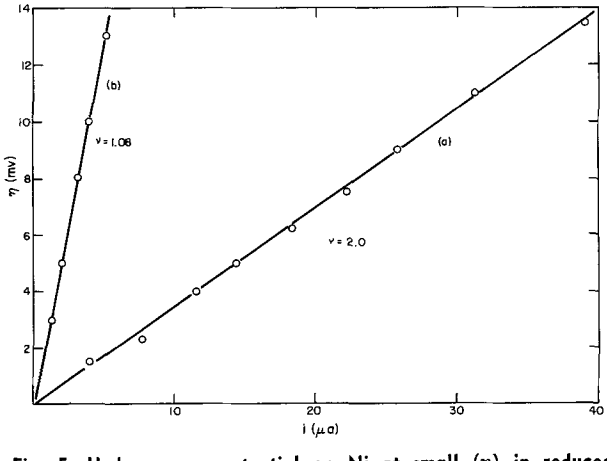

Fig. 5. Hydrogen overpotential on Ni at small (η) in reduced state (a) and after anodic passivation (b) (0.1N NaOH, 30°C).

$$H^+ + e \rightarrow H_{ads} \quad \text{(slow)}$$

$$H_{ads} + H_{ads} \rightleftharpoons H_2$$

to the sequence

$$H^+ + e \rightleftharpoons H_{ads}$$

$$H + H^+ + e \rightarrow H_2 \quad \text{(slow)}$$

with the consequent changes in the Tafel parameters and stoichiometric numbers given above. This change is probably also accompanied by a substantial decrease of θ_o, the extent of coverage by adsorbed hydrogen at the equilibrium potential; the value of θ_o for electrodes cycled to anodic potentials is vanishingly small.

Redox reactions on passive electrodes.—The kinetics of redox reactions involving ions in solution, specifically the Fe^{+3}/Fe^{+2} couple, were studied on passive electrodes of Ni, Fe, Ti, and Fe-Cr electrodes (12).

Aside from specific effects, *e.g.*, changes in the energy of adsorption of reactants or of intermediates, surface oxides may influence the kinetics of an electrochemical reaction by providing a barrier to electron transfer between the metal and an ion or molecule at the oxide/electrolyte interface. With thick films, the oxide is the electrode, and the chemical character of the bulk oxide and its electrical properties, *e.g.*, its semiconducting properties, determine its electrode characteristics. At the other extreme, very thin oxide films may be considered as simply providing a barrier through which electrons must tunnel in order to participate in the reaction. The electrical characteristics of films of intermediate thickness, in the range of about 30 to 200Å, are probably influenced strongly by the underlying metal.

A simple way of examining the general electrochemical effects of surface oxides is to compare the kinetics of an elementary electron transfer reaction on oxide-covered and oxide-free electrodes. Specific effects, *e.g.*, adsorption, should be at a minimum for the redox couple chosen. The Fe^{+++}/Fe^{++} couple was selected for study because its kinetic behavior on oxide-free electrodes is straightforward. Furthermore, since its reversible potential falls in about the middle of the potential region over which a number of common metals and alloys are passive, both the oxidation of ferrous ion and the reduction of ferric ion can be followed without gross interference from corrosion reactions.

Overpotential measurements for the Fe^{+++}/Fe^{++} couple on passive Ni, Fe, Ti, and Fe-Cr alloys carried out in solutions of fixed ionic strength but of varying *p*H. Tafel lines were generally obtained with exchange currents between 10^{-7} and 10^{-5} amp/cm^2. Typical polarization curves are shown in Fig. 6 (12).

The cathodic transfer coefficients are about 0.45 for this redox reaction on essentially all passive electrodes studied. The anodic transfer coefficients are less, particularly on Ti and Fe electrodes. The sum of the apparent transfer coefficients, calculated from the anodic and cathodic polarization curves, is significantly less than unity.

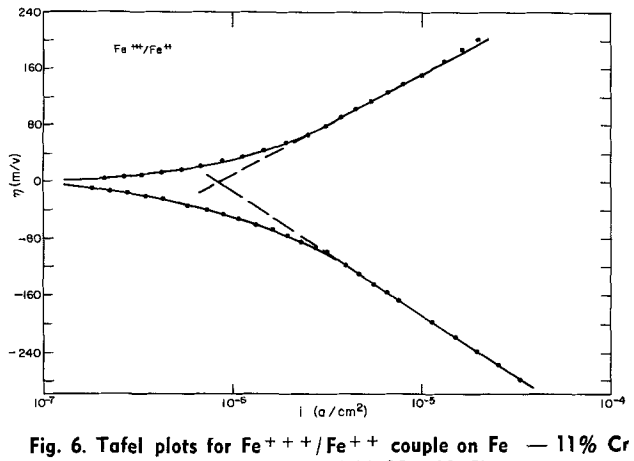

Fig. 6. Tafel plots for Fe^{+++}/Fe^{++} couple on Fe — 11% Cr alloys (C = 0.050M, pH = 2.2, M $MgSO_4$, 30°C).

The polarization behavior of the Fe^{+++}/Fe^{++} couple on passive Ni and Ti can be summarized by an expression of the form (potentials in units of RT/F)

$$i = i_o \{\exp(-\alpha_r \eta) - \exp[\beta_r(1-\gamma)\eta]\}$$

with the sum of the apparent transfer coefficients, α_c and α_a, being given by

$$\alpha_c + \alpha_a = \alpha_r + \beta_r(1-\gamma) = 1 - \gamma\beta_r$$

and an apparent stoichiometric number is

$$\nu = \pm\, i_o \Big/ \left(\frac{\partial i}{\partial \eta}\right)_{\eta=0} = 1 - \gamma\beta_r$$

The fraction of the overpotential drop within the film is given by γ. These equations are followed by passive Ni at *p*H = 2.3 and by Ti at *p*H = 1.5 and for $T \leq 20$°C. The coefficient γ is 0.15 for Ni and 0.60 for Ti. Fe, Ni at low *p*H, and Ti at higher temperatures show a more complicated behavior on anodic polarization. A limiting anodic current, which is unrelated to diffusion of Fe^{+2} in solution is observed on these passive metals under these conditions, and it appears that here $\gamma \simeq 1$.

These results show that an appreciable fraction of the total potential drop on anodic polarization occurs within the passive film. This potential drop is probably associated with changes in the average oxidation state of cations between the inner and outer layers of the surface oxide.

Other reactions.—We have examined a number of other cases where it has been postulated that oxide or chemisorbed oxygen (or OH) films are involved in the kinetics. For example, the H_2O_2 reactions on gold have been assumed to involve adsorbed OH groups (13) or adsorbed oxygen (14). In this particular case, we find that the H_2O_2 reactions proceed on a surface which is free of oxide and, in fact, essentially free of any other adsorbed intermediate (15). For example, the double layer capacity of a gold electrode in a N_2-saturated, *N* $HClO_4$ solution containing 0.1M H_2O_2 is the same as in *N* $HClO_4$; also, chronopotentiograms in H_2O_2 show no evidence for the adsorption of an intermediate prior to H_2O_2 oxidation or reduction. This result is in harmony with our studies of oxidation of gold since these show that no significant amount of adsorbed oxygen should be present in the relevant potential region.

Another reaction studied in some detail was oxygen evolution on lead dioxide. Here, we are dealing with a bulk oxide electrode, but one where the possibility of specific effects was strongly suggested by other work. It has been reported (16, 17) that α- and β-PbO_2 electrodes show different mechanisms for oxygen evolution (substantially different Tafel slopes and exchange currents). Previous work with this system was carried out using PbO_2 electrodes deposited under arbitrary conditions. Actually, it appears that PbO_2 electrodes as commonly prepared are highly porous and, consequently, the reported kinetic results (including values of the Tafel constant for oxygen evolution) are in error. We have prepared low surface area α- and β-PbO_2 electrodes and for these we find no difference in the kinetic parameters for oxygen evolution (18) and no evidence for adsorbed intermediates during oxygen evolution. Therefore, specific effects attributable to the structure of the oxide are minor with this system.

REFERENCES

1. S. B. Brummer and A. C. Makrides, *This Journal*, **111**, 1122 (1964).
2. S. B. Barnartt, *ibid.*, **106**, 722, 991 (1959).
3. N. F. Mott, *Trans. Faraday Soc.*, **43**, 429 (1947).
4. N. Cabrera and N. F. Mott, *Repts. Progr. Phys.*, **12**, 163 (1949).

5. See, for example, L. Young, "Anodic Oxide Films," Academic Press, New York (1961).
6. A. C. Makrides, S. B. Brummer, and M. Pate, To be published.
7. K. Hauffe and B. Ilschner, *Z. Elektrochem.*, **58**, 382 (1959).
8. T. B. Grimley and B. M. W. Trapnell, *Proc. Roy. Soc.*, **A234**, 405 (1956).
9. W. Böld and M. W. Breiter, *Electrochim. Acta*, **5**, 145 (1961); S. Gilman, **9**, 1025 (1964).
10. S. B. Brummer, M. J. Turner, and A. C. Makrides, To be published.
11. A. C. Makrides, *This Journal*, **109**, 977 (1962).
12. A. C. Makrides, *ibid.*, **111**, 392, 400 (1964).
13. J. O'M. Bockris and L. Oldfield, *Trans. Faraday Soc.*, **51**, 249 (1955).
14. G. Bianchi, F. Mazza, and T. Mussini, *Electrochim. Acta*, **7**, 457 (1962).
15. A. C. Makrides and M. Pate, To be published.
16. P. Rüetschi, R. T. Angstadt, and B. D. Cahan, *This Journal*, **106**, 547 (1959).
17. P. Rüetschi, J. Sklarchuk, and R. T. Angstadt, Proc. 3rd Intl. Symp. Batteries, p. 89, D. H. Collins, Editor, Macmillan, New York (1963).
18. A. C. Makrides, A. B. Gancy, and J. Bradspies, To be published.

Discussion

Roger Parsons: It seems to me that the introduction of the factor $(1 - \gamma)$ into the anodic transfer coefficient and not into the cathodic transfer coefficient means that the proposed model will not produce a Nernst equation of the correct form. At least at the reversible potential the anodic and cathodic transfer coefficient must add up to unity. Thus it seems that, if this model applies, there must be a change in transfer coefficient near the reversible potential. Is this observed? Do the electrodes obey the Nernst equation for systems like Fe^{3+}/Fe^{2+}?

A. C. Makrides: Professor Parsons' comments on the requirement that the transfer coefficients must add to unity at the reversible potential is, of course, correct. These electrodes obey the Nernst relations (see reference cited above), which suggests that they are sufficiently good electronic conductors so that electrons are close to equilibrium when no current flows. Under conditions of current flow, this is no longer true and a potential drop appears within the film; the apparent transfer coefficients must be changing, therefore, as one departs from equilibrium.

B. E. Conway: It may be of interest to note that Meyer[1] considered the effects of barrier layer type oxide films on the kinetics of electrode processes occurring at the film-solution interface. This treatment gives rise to an over-all apparent transfer coefficient α given by

$$\alpha = \alpha_f \alpha_r / (\alpha_f + \alpha_r)$$

where α_f is the symmetry factor for the film charge transfer process and α_r is the transfer coefficient for the interface reaction. Generally the apparent α is less than the α_r, and this may account for some high anodic Tafel slopes observed. Meyer also gave a treatment for the equilibrium condition for a redox system at an oxide covered electrode.

The kinetics of oxygen evolution at gold or gold palladium alloys were studied by MacDonald and Conway[2] who took into account the role of the oxide film on the oxygen evolution kinetics at gold.

We have found that a direct logarithmic growth law for the oxide may also be demonstrated at Pt in terms of the charge Q_o required for reduction of the surface oxide. In this case, however, the film grows only to a thickness much less than that attainable in gold.

Finally it may be of interest to record that the Kolbe reaction in aqueous solution is another example of a process that occurs in the steady state on an oxide covered surface, *e.g.*, at Pt and in some cases at gold.[3]

A. C. Makrides: The comments of Professor Conway on the Meyer model are appreciated, but as we have shown in connection with one of these studies,[4] the assumption of a barrier to electron transfer in the film and of a potential drop across this barrier which depends on the current does not lead to reasonable values for the apparent transfer coefficients. According to this model, the apparent cathodic and anodic transfer coefficients for the over-all reaction are

$$\alpha_c = \frac{\alpha_f \alpha_r}{\alpha_f + \alpha_r} \qquad \alpha_a = \frac{\beta_f \beta_r}{\beta_f + \beta_r}$$

where $\alpha_f + \beta_f = 1$ and $\alpha_r + \beta_r = 1$, with the subscripts f and r referring to the film and to the redox reaction in solution, respectively. If $\alpha_f \simeq \beta_f \simeq 0.5$, then for $\alpha_r \simeq \beta_r \simeq 0.5$, we expect $\alpha_c = 0.25$ and $\alpha_a = 0.25$. Typical values for the apparent coefficients in our case are $\alpha_c = 0.45$ and $\alpha_a = 0.36$. If we choose α_f so as to make the cathodic apparent coefficient agree with the experimental value, then the apparent anodic coefficient is not reasonable. For example, if $\alpha_f = 0.90$ and $\alpha_r \simeq \beta_r \simeq 0.5$, then $\alpha_c = 0.35$, reasonably close to 0.45, but α_a is now only 0.08, far from the experimental value.

H. Gerischer: It is very interesting and important to characterize oxide layers on metals by their behavior in electron transfer reactions. It is only regrettable that these processes are not yet fully understood; for example I cannot yet see a satisfactory interpretation for the unusual charge transfer coefficients you have obtained for the anodic and cathodic reactions. The assumption that a constant part of the voltage variation is lost in the interior of the oxide for the driving force of the redox reaction remains to be understood. Without external electronic current you can obtain the equilibrium redox potential. This means electronic equilibrium is realized in the over-all electrode. It seems now very unlikely that just in the region of equilibrium potentials the charge transfer coefficient should vary so rapidly, and this is even more unlikely since this coefficient remains remarkably constant in the other regions of your Tafel plots. The loss of free energy of the electrons in the redox reaction going on should therefore be related to the transport of electrons through the oxide layer to give such as analogous semilogarithmic correlation. In this case the same values for the ineffective part of the voltage should be found for different redox reactions. Has this already been investigated?

A. C. Makrides: The point raised by Professor Gerischer is a very real difficulty with our attempt to interpret the observed kinetics. As he points out, it is not likely that the transfer coefficient will vary rapidly at potentials close to equilibrium and then remain constant at substantial overpotentials. We have tried to explain this behavior by assuming a structure of the film which might account for rectification in one direction, namely, in the direction of increasingly positive potentials. It was proposed that in a mixed valency oxide there is a change in the average oxidation state as one proceeds from the metal to the solution interface even in these very thin films. A structure of this kind will show rectification in the observed direc-

[1] R. E. Meyer, *This Journal*, **107**, 847 (1960).

[2] MacDonald and B. E. Conway, *Proc. Roy. Soc. London*, **A269**, 419 (1962).

[3] Dickenson and Wynne-Jones, *Trans. Faraday Soc.*, **58**, 382 (1962); Vigh, Ph.D. Thesis, Ottawa (1966).

[4] A. C. Makrides, *This Journal*, **111**, 392 (1964).

tion. However, this is a speculative suggestion and although it is in harmony with other results from studies of the reduction characteristics of passive films, there is no solid evidence that it is valid.

James P. Hoare: I wish to take this opportunity to commend Dr. Makrides and his group at Tyco Laboratories for the excellent work they have done with these interesting electrochemical systems. This work brings to mind several controversial areas which offer excellent opportunity for those in attendance to express their viewpoints.

In these cases discussed, the electrode under investigation may be considered as an inert electrode at least in the experimental regions where the electrode kinetics were studied. The role of the inert electrode in electrode kinetics is to act as a source or sink for electrons and the catalytic surface on which the electrode reaction may take place. One facet of such studies relates to the effect which the presence of a thin film on the electrode surface has on the catalytic activity of the surface for a given electrode process.

Consider, for example, the oxygen-platinum system. Under ordinary conditions a monolayer film of adsorbed oxygen is formed on the platinum surface.[5] The nature of this film is still not unambiguously determined since the dispute between a layer of oxide and a layer of adsorbed oxygen atoms is not settled.[6] Even the latest ellipsometric evidence[7] may be adequately explained by oxygen dissolved in the metal surface layers. There is evidence from potential sweep data,[8] steady-state polarization data,[9] and rotating ring studies[10] that the reduction of oxygen is inhibited by the presence of adsorbed oxygen on Pt electrodes. It also appears to be true for Pd,[11] Rh, and Ir electrodes. However, the presence of a layer of adsorbed oxygen seems to increase the rate of reduction of H_2O_2.[12] Possibly the reduction of O_2 is electron-transfer controlled, and the film inhibits the transfer of electrons whereas the reduction of H_2O_2 can proceed chemically, accelerated by the presence of adsorbed oxygen. In the absence of oxide, the decomposition of H_2O_2 most likely proceeds by a local cell process[13] which is a slower one than the chemical process.

When oxygen is dissolved in the Pt metal through anodization and when the adsorbed oxygen on the surface is removed by reduction with H_2 or a redox system, the electrode surface is a better catalyst for many electrode reactions, as demonstrated by the preanodized indicator electrode in electroanalytical systems.[14] By treating the Pt with HNO_3, it is possible to cause even more oxygen to be dissolved in the Pt as an alloy of O and Pt atoms as found from x-ray and vacuum fusion analyses.[15] Such electrodes have a relatively low overvoltage for the reduction of O_2 and for the reduction of H_2O_2.[16] However, the overvoltage for the evolution of O_2 is the same for HNO_3-treated[16] and untreated Pt anodes.[17] For the evolution of O_2 on Pt anodes, the electrode reaction takes place on an oxide surface which is the same for treated and untreated electrodes, but for the reduction of O_2 it takes place on a bare surface so that the presence of dissolved oxygen makes a difference between the rates on a treated and untreated Pt electrode.

It appears that the evolution of oxygen on Pt and Rh anodes takes place on an electronically conducting film of adsorbed oxygen since the film does not grow with prolonged anodization[5] and since the double layer capacity does not fall as oxygen is adsorbed.[18] In this case the film is the catalytic surface on which the electrode reaction takes place. With respect to Pd anodes, the adsorbed oxygen film actually participates in the evolution of oxygen by the decomposition of PdO_2 to PdO and O_2.[11] The current goes into the conversion of PdO to PdO_2. On Au anodes, the evolution of O_2 probably proceeds with difficulty on the oxide covered surface since the films of Au_2O_3 are likely to be ionic conductors as shown by continued growth of the film with anodic polarization[19] and by a lowering of the double layer capacity as oxygen is adsorbed on Au.[20] However, these films of Au_2O_3 are poorly adherent and easily flake off.[19] In this case the current goes into the simultaneous formation of Au_2O_3 and the evolution of O_2, probably on bare gold sites.[21]

It is seen, then, that one must distinguish between oxygen adsorbed on the surface and that dissolved in metal surface layers in studying the effects of adsorbed oxygen films on the electrode kinetics. Another point to be considered is the possibility that the film is the catalytic surface on which the reaction may proceed or that it may actually participate in the electrode reaction itself.

A. C. Makrides: Dr. Hoare's comments on the solution of oxygen in platinum point out one of the difficulties in interpreting results from anodic oxidation experiments with noble metals. In the particular case discussed by us, the over-all kinetics are such that it is unlikely that any appreciable amount of oxygen is dissolved into the metal. In general, one expects this process to be relatively slow around room temperature. Because of this difficulty, it seems to me that the explanation of certain observations on the electrochemical behavior of platinum in terms of dissolved oxygen should be treated with caution.

T. O. Rouse and J. L. Weininger: At this meeting of the Theoretical Division of the Society we are reporting the study of a redox reaction at a Li-doped semiconducting single crystal NiO electrode.[22] Comparison with the results obtained in the present paper is appropriate, although it should be pointed out that our electrode is structurally well-defined whereas some uncertainty exists regarding the structure of the passive layer.

In our case, it was first necessary to characterize the semiconducting electrode quite thoroughly. The initial results indicated a potential distribution across both the solution side and the semiconductor side of the interface in the absence of a faradaic process.[23] This potential distribution has now been demonstrated

[5] K. J. Vetter, "Elektrochemische Kinetik," Springer-Verlag, Berlin (1961), p. 502; F. P. Bowden, *Proc. Roy. Soc.*, A125, 446 (1929); W. Böld and M. W. Breiter, *Electrochim. Acta*, 5, 145 (1961).

[6] M. W. Breiter and J. L. Weininger, *This Journal*, 109, 1135 (1962).

[7] A. K. N. Reddy, M. Genshaw, and J. O'M. Bockris, *J. Electroanal. Chem.*, 8, 406 (1964).

[8] M. W. Breiter, *Electrochim. Acta*, 9, 441 (1964); W. Vielstich, *Z. Instrumkde*, 71, 29 (1963).

[9] J. P. Hoare, *This Journal*, Submitted for publication.

[10] L. Myuller and L. N. Nekrasov, *J. Electroanal. Chem.*, 9, 282 (1965); *Electrochim. Acta*, 9, 1015 (1964).

[11] J. P. Hoare, *This Journal*, 112, 1129 (1965).

[12] G. Bianchi, F. Mazza, and T. Mussini, *Electrochim. Acta*, 7, 457 (1962); 10, 445 (1965).

[13] J. P. Hoare, *This Journal*, 112, 608 (1965).

[14] *e.g.*, F. C. Anson, *J. Am. Chem. Soc.*, 81, 1554 (1959); D. G. Davis, *Talanta*, 3, 335 (1960); I. M. Kolthoff and E. R. Nightingale, *Anal. Chim. Acta*, 17, 329 (1957).

[15] J. P. Hoare, S. G. Meibuhr, and R. Thacker, *This Journal*, Submitted for publication.

[16] J. P. Hoare, *This Journal*, 110, 245 (1963); 112, 849 (1965).

[17] J. P. Hoare, *This Journal*, 112, 602 (1965).

[18] S. Schuldiner and R. M. Roe, *This Journal*, 110, 332 (1963); J. P. Hoare, *Nature*, 204, 71 (1964).

[19] S. Barnartt, *This Journal*, 106, 722 (1959); J. P. Hoare, 110, 245 (1963).

[20] M. C. Banta and N. Hackerman, *This Journal*, 111, 114 (1964); J. P. Hoare, *Electrochim. Acta*, 9, 1289 (1964).

[21] J. P. Hoare, *Electrochim. Acta*, 11, 311 (1966).

[22] T. O. Rouse and J. L. Weininger, Paper presented at the Cleveland Meeting of the Society, Theoretical Div., Extended Abstract No. 179, May 1966.

[23] T. O. Rouse and J. L. Weininger, *This Journal*, 113, 184 (1966).

quantitatively[22] in the presence of the redox couple ferrocyanide-ferricyanide.

The extension of the double layer across the electrode interface is in agreement with the work reported by the author. In our chronopotentiometric study we obtained different results with regard to the electrode reaction. We found that the oxidation of $Fe(CN)_6^{-4}$ proceeds in a kinetically irreversible manner. The reduction of $Fe(CN)_6^{-3}$ is hindered. Consequently, there is a pronounced rectification effect at the semiconductor electrode, which will also be reported by Greef and co-workers at this meeting.[24]

Our findings are that the exchange current, i_o, for the oxidation of ferrocyanide depends on the degree of doping of the NiO electrode, on the concentration of the oxidized and reduced species, C_O and C_R, in the solution, and on *p*H. Linear relations of i_o with $\sqrt{C_O \cdot C_R}$ and with *p*H, respectively, show that a portion of the double layer extends into the solution. The quantitative estimation of the two diffuse portions of the double layer is obtained from galvanostatic measurements. An apparent transfer coefficient, α, of 0.5 is obtained from plots of E *vs.* $\log\left[1-\left(\frac{t}{\tau}\right)^{1/2}\right]$, based on the kinetic expression of E as a function of time at constant current density for an irreversible electrode process

$$\eta = \frac{RT}{\alpha nF}\log\left[1-\left(\frac{t}{\tau}\right)^{1/2}\right] + \frac{RT}{\alpha nF}\log\frac{i}{i_o}$$

where E is the electrode potential at time t, and τ is the transition time when diffusion control is established. The theoretical implication of $\alpha = 0.5$, *i.e.*, a coefficient of 120 mv/decade in the right-hand terms of the above equation, is that the potential distribution is that shown in Fig. TOR1, where η stands for overvoltage, ϕ for potential, the subscripts refer to the bulk of the solid phase, the surface, and the solution, and the superscript ^{o} denotes equilibrium or condition of rest potential. It is seen that on applying an overvoltage $\eta = \phi_B - \phi_B^o$, a corresponding overvoltage, η_S, of the same magnitude appears at the electrode surface. Thus, the electrode polarization due to the anodic reaction appears across the Helmholtz portion of the double layer.

Our experimental results are in agreement with a model which predicts that an appreciable potential drop in the solution will occur only for a large concentration for charge carriers in the semiconducting oxide. The remarkable similarity in exchange currents and apparent transfer coefficients between our work and the author's previous results[25] indicates that the anodic films also contain a large number of charge carriers (of the order of 10^{20} cm^{-3}). Because NiO is a mixed valency semiconductor one can discuss valence states in terms of charge carriers, *e.g.*, Ni(III) in the lattice of NiO is equivalent to a hole (defect-electron). At the surface the concentration of the charge carrier depends on the applied potential. Therefore, it seems possible that the properties of some passive films can be deduced from a comparison of experimental results with semiconductor theory. Further experimental work on both anodically formed and single crystal NiO is needed to complete such a description.

[24] R. Greef, D. Yohe, and E. Yeager, Paper presented at the Cleveland Meeting of the Society, Theoretical Div., Extended Abstract No. 180, May 1966.

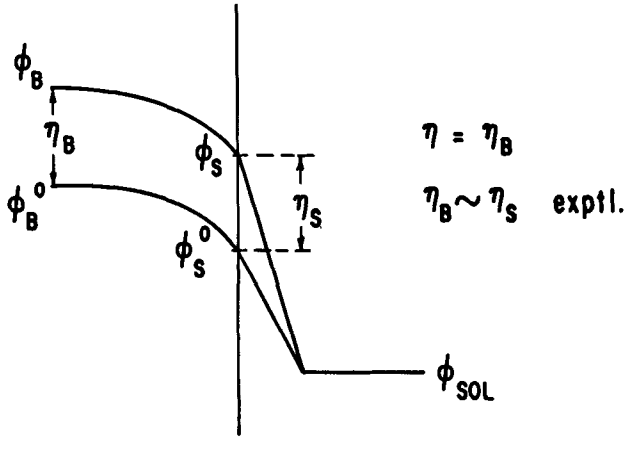

Fig. TOR1. Effect of redox couple

A. C. Makrides: The results quoted by Drs. Rouse and Weininger are very interesting, and it is quite likely that we will not understand passive films until we have examined in some detail the electrochemical behavior of analogous bulk oxides. It is indeed remarkable that there is such a similarity in exchange currents and apparent transfer coefficients for these redox reactions on single crystal NiO electrodes and on passive nickel electrodes. This is probably more than a coincidence, and further work with these systems will certainly be extremely interesting.

Paul C. Milner: In the formation of very thin oxide films on gold, what pertinence do continuum models have, especially during the formation of less than a monolayer? If layers form successively and should be treated individually, what halts the growth of a layer at a particular potential? Thermodynamics (as in the Temkin isotherm)? Kinetics (because of varying dissolution rates or because of formation rates dependent on the degree of completion of the layer being formed)? Both? Is the reduction process the reverse of the formation process? In reduction at constant current, is the effective current density constant or does it depend on the amount of oxide remaining in the layer being reduced?

In the oxygen evolution reaction at α-PbO_2, is it certain that there has been no recrystallization of the surface to give β-PbO_2, the thermodynamically stable form in acid solutions? This might take place fairly readily by way of the plumbous ions which are present in the solution in fairly sizeable quantities at potentials close to the equilibrium lead dioxide/lead sulfate potential. Are previous results semiquantitatively explicable on the basis of porous electrode theory?

A. C. Makrides: The questions formulated by Dr. Milner are of course very much to the point and parallel those raised in the paper. In the formation of very thin oxides, one questions the applicability of a continuum model, and this objection was raised above. The factors which limit the growth of the particular layer are undoubtedly kinetic and they must arise from a lowering of the field as the layer grows.

The oxygen evolution studies on α-PbO_2 were carried out on electrodes which were potentiostatically held above the reduction potential at all times. Recrystallization did not occur as was evident from studies in dilute $HClO_4$(0.01*N*) where differences between the α and β modifications were noted. Previous results can be explained with the usual assumption of a change in the apparent Tafel slope when dealing with porous electrodes. The difference of a factor of two in this constant is consistent with what one expects from theory.

A. Riga and E. Yeager: As part of a study of the electrochemical properties of single crystal lithiated nickel

[25] A. C. Makrides, *This Journal*, **111**, 392 (1964).

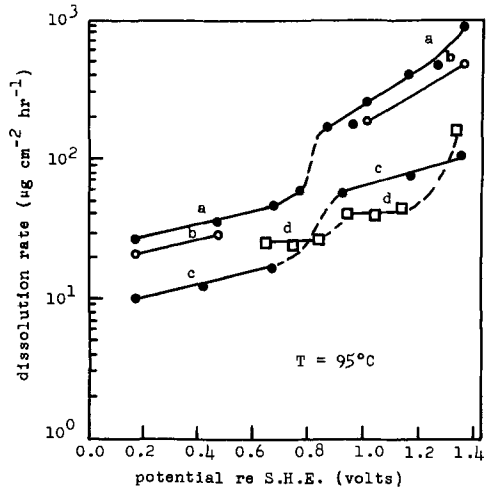

Fig. AR1. Dissolution rates of lithiated NiO as a function of potential. Curve a, 1M HCl, x = 1.1%; b, 1M HCl, x = 0.92%; c, 1M HCl, x = 0.85%; d, 0.5M H_2SO_4, x = 0.80%.

oxide, we have measured the rates of dissolution as a function of the potential of the oxide relative to the solution. Dissolution rates have been determined at controlled potentials in HCl and H_2SO_4 solutions by subsequently analyzing the solutions for nickel spectrophotometrically. Elevated temperatures (95°C) have been used to increase the otherwise very slow rates of dissolution to a point where measurements would be carried out over a few hours. The use of a Teflon cell with Kel-F window permitted *in situ* photomicrographs. Experimental details will be presented in a paper now in preparation.

In Fig. AR1 is shown the dependence of the logarithm of the dissolution rates on potential for lithiated single crystal nickel oxide prepared by the method of Cech and Alessandrini[26] and infused with lithium at 1600°C with a technique similar to that used by Rouse and Weininger.[27] The dissolution of $Li_xNi_{(1-x)}O$ with $x = 0.9\%$ was followed as a function of time for 5 to 6 hr at potentials of +0.5, 1.0, and 1.4v re standard hydrogen electrode (SHE) and the rates found to be constant over this period of time. From Fig. AR1, it can be seen that the dissolution rate increased very substantially over the relatively narrow voltage range of +0.8 to 0.9v re SHE. The flat band potential and the anodic peak in the voltammetry curve ascribed to the $Ni^{+2} - Ni^{+3}$ conversion also fall in this range. A pronounced change in the mode of attack at potentials below +0.8v and above 0.9v re SHE is evident in the photomicrographs. Typical micrographs are shown in Fig. AR2 for 1*N* HCl. At potentials cathodic to 0.8v re SHE, the surface is uniformly attacked with no etch pits evident at magnifications of 800 fold. At potentials anodic to 0.9v re SHE, etch pits of the type shown in Fig. AR2b develop with the number of etch pits per unit area generally constant after the first 10 to 20 min.

Some tendency for an exponential dependence of the dissolution rate on potential above and below the region of rapid change is apparent in Fig. AR1, but the range of dissolution rates is too limited for a good test of such a relationship within the precision of the measurements. The dependence of the dissolution rate on carrier concentration remains to be fully established.

The dependence of the dissolution rate on potential shown in Fig. AR1 can be explained on the basis that dissolution involves the transmission of the cations and anions of the lattice over potential energy barriers, the heights of which are dependent on the potential drop across the oxide-solution interface. If the cation barrier is higher than that for anions, then an increase in dissolution rate with increasing anodic potential would be expected. This explanation is similar to that of Engell.[28] While such an explanation has obvious appeal to the electrochemical kineticist (particularly those of the Tafel school), the predominant factors may not be so much the effects of the applied potential directly on the heights of the potential energy barriers but rather the effects of the applied potential on the adsorption of ions on the oxide surface and the valency state or carrier concentration in the equivalent of a plane of closest approach within the oxide phase.

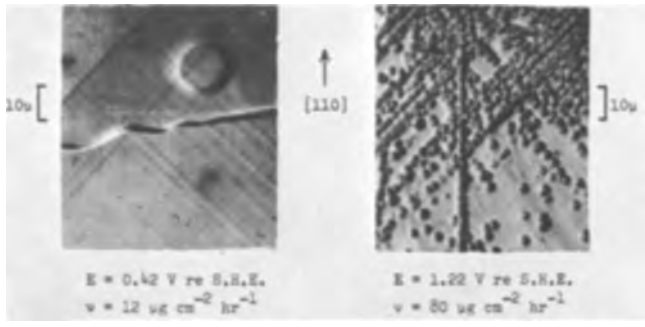

Fig. AR2. Photomicrography (in situ) $Li_xNi_{(1-x)}O$ (x = 1%) 3 hr in 1M HCl at 95°C.

We are pleased to acknowledge the help of Dr. R. Greef and Mr. D. Yohe in this work and the financial support of this research by the Office of Naval Research.

J. L. Weininger and M. W. Breiter: Reference is made to our work on the anodization[29] and hydrogen evolution[30] on single crystal and polycrystalline nickel electrodes. Although our measurements were made in 4*N* KOH as compared to 0.1*N* NaOH in the author's work there was generally a great difference between the experimental results on a freshly prepared surface and one which had been through one or more passivation cycles. Similar Tafel slopes (0.130 and 0.090 mv/decade) and even exchange currents of the same order of magnitude (10^{-5} μa/cm^2) were observed. We apparently differ, however, in interpretation. What is meant by an "electrode in a state arrived at by passivation"? In our case, the equivalent of about ten monolayers of $Ni(OH)_2$ and higher oxide was produced on the metallic surface. Subsequently, the oxides were reduced at —300 mv (*vs.* RHE) for 8 min. After this treatment we obtained the experimental behavior comparable to that of the author's passivated electrode.

It is readily agreed that the kinetics of hydrogen reduction is complex and that under different experimental conditions, and different pretreatment of the nickel electrode, the extent to which the steady state is determined by the Volmer, Heyrovsky, or Tafel reaction may vary. But there was no indication that anodic-cathodic cycling produces a more tenacious oxide film. Our conclusions of a rate-determining Volmer reaction are based on the measurements of cath-

$$Ni + H_2O + e = Ni - H + OH^-$$

odic current-potential curves and the capacities at negative overvoltage. The possibility that nickel hydroxide may be present at $\eta = 0$ in 0.1*N* NaOH makes the application of the stoichiometric number ν as a criterion doubtful.

[26] R. Cech and E. Alessandrini, *Trans. Am. Soc. Met.*, 51, 150 (1959).

[27] T. Rouse and J. Weininger, *This Journal*, 113, 184 (1966).

[28] *e.g.*, H. J. Engell, *Z. Physik. Chem. N. F.*, 7, 158 (1956); *Z. Elektrochem.*, 60, 905 (1956).

[29] J. L. Weininger and M. W. Breiter, *This Journal*, 110, 484 (1963).

[30] J. L. Weininger and M. W. Breiter, *This Journal*, 112, 707 (1964).

Charge Transfer Processes at Organic Insulator Electrodes

W. Mehl, J. M. Hale, and F. Lohmann

Cyanamid European Research Institute, Cologny/Geneva, Switzerland

ABSTRACT

Charge transfer reactions at insulator electrodes are discussed in terms of the model developed for such processes at semiconductor electrodes. A simplifying condition here is that only such reactions are possible which lead to the injection of holes into the valence band or of electrons into the conduction band. Measurements at anthracene electrodes showed complete agreement with the predictions derived from the model including the possibility of having reversible charge transfer reactions.

Insulators are, by classical definition, materials which provide electrical insulation, *i.e.*, which permit the passage of no current or only a small amount even at high applied voltages. A project using insulators as electrode materials for electrochemical studies would thus not seem to be a very promising one.

Since the development of the energy-band theory of the electronic structure of solids by the application of quantum mechanics to the solid state, it has been understood, however, that insulators should be able to carry currents if somehow electrons can be raised into the conduction band which is normally empty (1). In certain cases, this can be done by excitation with light or heat; another possibility is the injection of charges from suitably chosen contacts (1,2). We shall discuss here the conditions under which electrons can pass from electrolyte solutions into insulators.

The interface between insulators and electrolytes has to be discussed as a part of the general problem of the interface between semiconductors and electrolytes because insulators can be defined as semiconductors with a large interval between the Fermi-level and the allowed energy bands, e.g., at least 1 ev.

The band representation of an insulator-electrolyte interface is shown in Fig. 1 for two important cases (3). In Fig. 1a the concentration of electrons at the contact is higher than in the bulk of the material: we define this as an "ohmic contact for electrons." In Fig. 1b, the concentration of holes at the contact is higher than in the bulk of the material; we define this as an "ohmic contact for holes." With these definitions, we can now formulate the subject of this paper as an investigation of the question under which circumstances electrolytic contacts to insulators are ohmic.

Redox Reactions at Insulator Electrodes

At insulator electrodes only those redox reactions can take place which result in the net injection of electrons in the conduction band or in the net injection of holes in the valence band. A formula for the exchange current of a redox reaction at an insulator electrode can be derived with the aid of any of the theories which describe the Franck-Condon restricted transitions of electrons involving solvated species.

$$i_o^n = F\nu C_R \exp\left\{ -\frac{\lambda}{4kT}\left[\left(\zeta - \frac{-\Delta\epsilon_s^n - kT\ln C_O/C_R}{\zeta\lambda}\right)^2 + \frac{4\Delta\epsilon_s^n}{\lambda}\right]\right\} \quad [1a]$$

$$i_o^p = F\nu C_O \exp\left\{ -\frac{\lambda}{4kT}\left(\zeta + \frac{\Delta\epsilon_s^p + kT\ln C_O/C_R}{\zeta\lambda}\right)^2\right\} \quad [1b]$$

Here i_o^n and i_o^p are the electron exchange current with the conduction band and the hole exchange current with the valence band, respectively: ν is the velocity of movement along the reaction coordinate, C_O is the concentration of the oxidized species, and C_R that of the reduced species at the outer Helmholtz plane at the equilibrium potential. λ is an energy parameter which in magnitude equals the energy required to reorient the solvation atmosphere about the oxidized species until it becomes identical with that about the reduced species in equilibrium. ζ is the number of electrons involved in the electron transfer reaction, $\Delta\epsilon_s$ is the magnitude of the forbidden gap between the Fermi level and the allowed energy state for the carrier in the surface (the bottom of the conduction band for an electron and the top of the valence band for a hole) at the equilibrium potential. Equations [1a] and [1b] can be derived from the theories of Dewald (8), who used Marcus' theory of the electron transfer reaction, Gerischer (5) and Dogonadze and Chizmadzhev (6) under equivalent approximations. These are (*i*) the energy distribution of electrons, holes, oxidized and reduced species are described by Boltzmann statistics; (*ii*) the cross section through the potential energy surface for the reaction, made by the reaction coordinate, consists of two intersecting parabolae.

As the penetration of a medium by an electric field depends on the concentration within the medium of free charges, the potential difference applied across an insulator electrode-electrolyte interface will be shared between the interior of the insulator and the Helmholtz inner layer in such a manner that most of the potential drop occurs across the insulator (9). This argument is valid only if surface states can be excluded. Any assumptions about the potential distribution at the insulator-electrolyte interface have thus always to be verified by experiments.

Let us assume that all of the interfacial potential variation exists within the solid. The $\Delta\epsilon_s$ can be expressed through the Nernst equation

$$\Delta\epsilon_s^n = \Delta^n + e_o(E_R - E_{FB}) = \Delta^n + e_o(E_s - E_{FB}) + kT\ln C_O/C_R \quad [2a]$$

$$\Delta\epsilon_s^p = \Delta^p - e_o(E_s - E_{FB}) - kT\ln C_O/C_R \quad [2b]$$

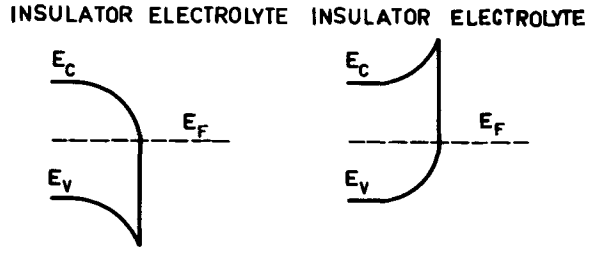

Fig. 1. Schematic energy-band diagram for injecting electrolytic contacts in thermal equilibrium.

Δ^n and Δ^p are the intervals of energy between the Fermi level and the conduction band and valence band, respectively, in the bulk of the insulator; E_R is the equilibrium potential, E_s the standard potential of the redox system, and E_{FB} the flat band electrode potential of the insulator; e_o is the electronic charge. Insertion of these relations into Eq. [1a] and [1b] yields the simplified forms

$$i_o^n = F\nu C_R \exp\left\{\frac{-[\zeta^2\lambda + \Delta^n + e_o(E_s - E_{FB})]^2}{4\,\zeta^2\lambda\, kT}\right\} \quad [3a]$$

$$i_o^p = F\nu C_O \exp\left\{\frac{-[\zeta^2\lambda + \Delta^p - e_o(E_s - E_{FB})]^2}{4\,\zeta^2\lambda\, kT}\right\} \quad [3b]$$

Two consequences of these formulas are of special interest for this investigation: (*i*) the exchange current is proportional to either C_O or C_R whereas at a metal electrode $i_o \alpha \sqrt{C_O C_R}$; (*ii*) the magnitude of the exchange current is determined by the standard potential of the redox couple. If the couple is strongly oxidizing with $E_s - E_{FB} >> 0$ then $i_o^p >> i_o^n$; furthermore, when $e_o(E_s - E_{FB}) \sim \Delta^p$ the exchange current has the order of magnitude that it takes at a metal.

A similar relationship was derived previously and confirmed experimentally for germanium electrodes (5).

For insulators, concentration polarization of the charge carriers in the solid is of major importance for the discussion of the current voltage characteristic. The relevant boundary value problem has recently been discussed in detail (10). Expressed in terms of the steady-state current with the assumption of first order kinetics, the boundary condition at the insulator-electrolyte interface has the form

$$i_n = A_n\,(n^* C_O^* - N_c C_R^*) \quad [4a]$$

$$i_p = A_p\,(N_v C_O^* - p^* C_R^*) \quad [4b]$$

in which the A's are constants, the asterisks connote the transition state of the electron transfer reaction, and N_c, N_v are the densities of states in the conduction band and the valence band. The forward and backward currents are equal to the exchange current at the equilibrium potential, whence

$$i_o^n = A_n n_o^*\, C_O^* = A_n N_c C_R^* \quad [5a]$$

$$i_o^p = A_p N_v C_O^* = A_p p_O^*\, C_R^* \quad [5b]$$

The carrier concentrations at the equilibrium potential are distinguished with a zero subscript. Only the concentration of the carriers in the solid phase varies with the current because of our assumption that all the potential drops in the insulator. Hence

$$i_n = i_o^n\left(\frac{n^*}{n_o^*} - 1\right) \quad [6a]$$

$$i_p = i_o^p\left(1 - \frac{p^*}{p_o^*}\right) \quad [6b]$$

$$n = n_o^*\left(1 + \frac{i_n}{i_o^n}\right) \quad [7a]$$

$$p = p_o^*\left(1 - \frac{i_p}{i_o^p}\right) \quad [7b]$$

We thus come to the important conclusion that the partial electron and hole currents are limited on the anodic and cathodic sides respectively to the values of the exchange currents. The total current shows this limitation in the one carrier problem.

Transport Problem for Insulators

A one-carrier current passing through an insulator is necessarily associated with a space charge because each injected carrier contributes one excess charge to the insulator, negative in the case of electrons, positive in the case of holes. The physical situation is closely analogous to the familiar case of the formation of a space charge in a vacuum tube.

For the formulation of the transport problem for electrons in the conduction band of an insulator we consider a crystal of thickness d through which a current is passing. We assume an electrolyte to make an ohmic contact for electrons at $x = d$ while, for $x = 0$ we assume we have a metallic contact which is non-ohmic for holes. Let $E(x)$ be the electric field at a distance x from the metal contact, $n(x)$ the number of electrons per unit volume, and μ their mobility. $\psi(x)$ is the electrostatic potential in the insulator, ϵ the dielectric constant, and ϵ_o is the permittivity of free space.

The exact theory is based on three equations: a current flow equation, Poisson's equation, and an equation relating the electrostatic field vector to the gradient of the scalar potential

$$i = e_o\, n(x)\, \mu\, E(x) \quad [8]$$

$$\frac{dE(x)}{dx} = \frac{-4\pi}{\epsilon\epsilon_o} e_o\, n(x) \quad [9]$$

$$E(x) = -\frac{d\psi}{dx} \quad [10]$$

As boundary condition we have Eq. [7a] which in the one carrier case reduces to

$$n^* = n_o^*\left(1 - \frac{i}{i_o}\right) \quad [11]$$

and a relation between the potentials corresponding to the bottom of the conduction band at the metal ($x = 0$) and electrolyte ($x = d$) interfaces

$$\psi_d - \psi_o = -V_D - \eta \quad [12]$$

V_D is the degree of bending of the bands under equilibrium conditions, and η is the applied overpotential (zero at equilibrium) defined negative for cathodic polarization. Substituting for E in Poisson's equation in terms of n, and integrating from $x = d$ to $x = 0$, we find

$$\frac{1}{n^2} = \frac{1}{(n^*)^2} - \frac{8\pi e_o^2 \mu}{\epsilon\epsilon_o i}(d - x) \quad [13]$$

Combination of Eq. [8], [10], and [13] and subsequent integration from $x = d$ to x yields the current voltage relation at $x = d$

$$\frac{12\pi e_o^3 \mu^2 (n^*)^3}{\epsilon\epsilon_o i^2}(V_D + \eta) = \left[1 - \frac{8\pi e_o^2 \mu\, d\,(n^*)^2}{\epsilon\epsilon_o i}\right]^{3/2} - 1 \quad [14]$$

If n^* is large enough so that

$$i << \frac{2\mu k\, T n^*\, d}{(L_D^*)^2} \quad [15]$$

where L_D^* is the Debye length in the insulator surface, Eq. [14] reduces to Child's law for solids

$$-i = \frac{9}{32\pi}\epsilon\epsilon_o \mu \frac{(V_D + \eta)^2}{d^3} \quad [16]$$

Since $n^* \to 0$ for $-i \to i_o$, this relationship can only be observed for currents $i < i_o$.

In this derivation of Child's law with the proper boundary conditions we have neglected any diffusion current, any carrier density present in thermal equilibrium, and any traps. Lampert (11) has shown, that the first approximation is not very serious. The second approximation means only that any linear current-

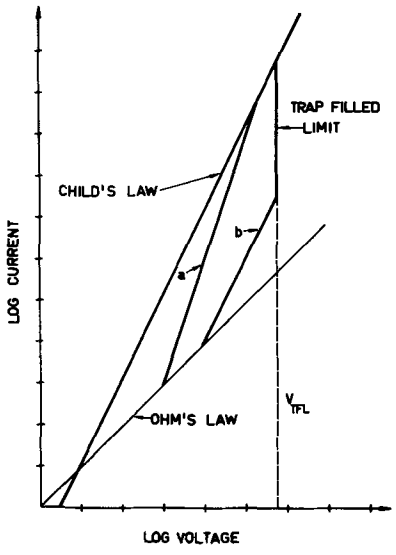

Fig. 2. Schematic current-voltage characteristic for one carrier space charge limited current: (a) quasi continuum of trapping states with exponential energy distribution; (b) single set of trapping states lying in energy above the Fermi level.

voltage relationship at very low voltages is not covered by this treatment. The third approximation is very serious, however, because a perfect solid has never been found. In a real crystal, charges residing in traps set up a space charge which impedes injection into the crystal in the steady state. In many cases, however, the traps are filled at a threshold voltage called the trap-filled limit (2, 11), V_{TFL}, at which the current rises steeply. Thereafter the current is limited by the mobile space charge in transit within the solid and the current-voltage curve obeys Child's law. Rose (2) and Lampert (11) have dealt in detail with the voltage dependence of the space charge limited (S.C.L.) currents for various trap distributions and trap levels. Some of their results are summarized in Fig. 2.

Band model.—Anthracene is the best investigated organic insulator and is therefore well suited as a model substance. A schematic structural representation of the anthracene molecule is given in Fig. 3 (15) together with the averaged values for the bond lengths. The anthracene crystal is monoclinic with two

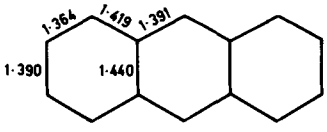

Fig. 3. Schematic structural representation of an anthracene molecule with averaged values for bond lengths (in Angstrom units).

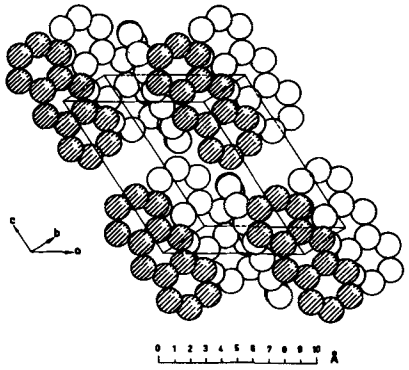

Fig. 4. Unit cell structure for anthracene

molecules per unit cell. The unit cell structure is shown in Fig. 4 (15). If $\vec{a}$, $\vec{b}$, $\vec{c}$ are the unit cell vectors, then $\alpha = \frac{1}{2}(\vec{a} + \vec{b})$, $\beta = \frac{1}{2}(-\vec{a} + \vec{b})$ and $\vec{c}$ connect the geometrical centers of nearest neighbor molecules.

The drift mobility of injected carriers has been shown to decrease with increase in temperature (12, 13) so that the band approximation can be used to describe the behavior of injected electrons and holes. This was confirmed by theoretical calculations which showed that the structure of the bands appropriate to an excess electron or hole can be calculated with the tight binding approximation (14). Le Blanc has called the band which contains the excess electrons the "electron band" and the one which contains the excess holes the "hole band" rather than using the conventional expressions "conduction band" and "valence band" (14). This was done in order to emphasize the fact that one is dealing with the electronic states of two distinct systems rather than two states of the same system.

Experimental Details

Single crystals of anthracene were grown by three conventional methods: a modified Bridgeman technique, vacuum sublimation, and growth from solution. Semiconductor grade purity is required for our measurements. We started off with material of the best available commercial purity (Fluka "For Scintillation") which showed the characteristic blue fluorescence of anthracene. Most of the tetracene, a very efficient fluorescence quencher and a common impurity for anthracene, was thus already removed. This material was further purified by zone-refining it up to 80 times, depending on the quality of the starting material.

The solution grown crystals have the highest degree of structural perfection and show the greatest mechanical strength. They are relatively thin (20-200μ) so that the high field strengths which are often desired can be obtained more conveniently. Inadvertently, however, impurities were introduced into these crystals from solution so that the trap density was always considerably higher for these crystals than for other types. The electrochemical phase boundary reaction was, however, unaffected by these impurities.

The melt-grown crystals were unmatched in purity but they showed frequently poor mechanical strength. In rapidly cooled crystals up to 500 dislocations per cm^2 were counted, usually accompanied by cracks (31). By careful annealing, it was possible to reduce this number to 10 and less. The crystals cleave readily parallel to the $\vec{a},\vec{b}$-plane (Fig. 4) which is also the prominent plane of the melt- or sublimation-grown crystals (16). Structural perfection and chemical purity of sublimation-grown crystals take up an intermediate position between the melt-grown and the solution-grown types.

Samples varying in thickness from 0.05 to 5 mm were prepared from melt-grown crystals by cutting with a chemical saw followed by cleavage. The crystals were cemented with an epoxy resin between two electrolytic half-cells made of glass. The cells were mounted on aluminum carriages, which moved on tracks made of the same material and which could be fixed to incorporate the crystals (Fig. 5). The electrolyte was stored in vessels V_1 and V_2 so that repeated washing of the crystals with the solutions was possible. The electric field was applied by means of two platinum electrodes K_1 and K_2 with a Keithley power supply type 240 or 242. The current was measured with a Keithley electrometer type 610B. Light intensities were determined with a calibrated photomultiplier Philips 150 UVP. During the measurement the cell was kept in a Faraday cage; only shielded cable was used.

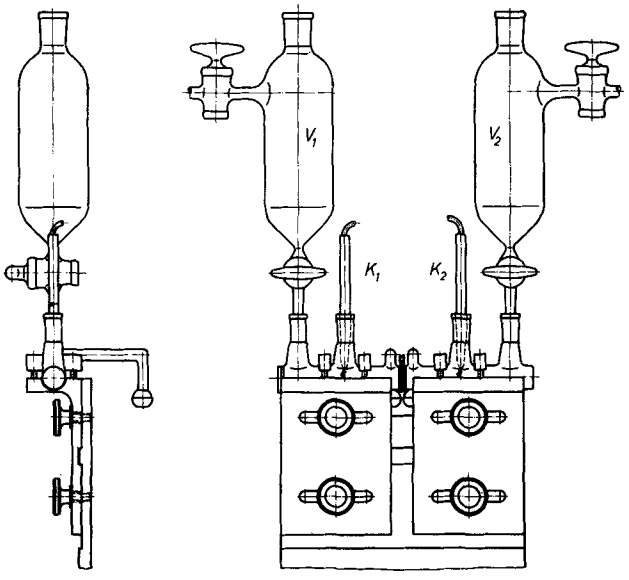

Fig. 5. Measuring cell. K_1, K_2, platinum electrodes; V_1, V_2, electrolyte storage vessels.

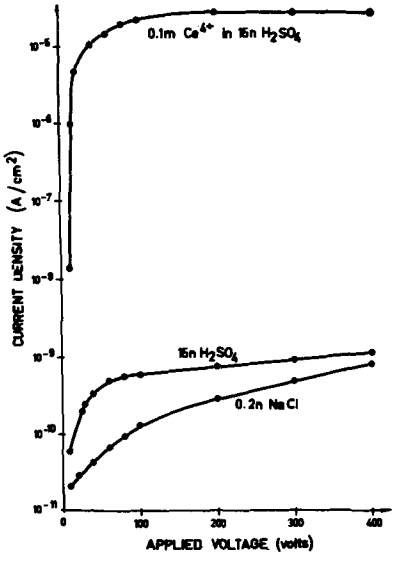

Fig. 6. Cathodic limiting current with various electrolytes. The negative compartment contained a 0.2N NaCl solution.

Redox Reactions

Anthracene has a width of the forbidden gap of about 4 ev (17) and is thus a perfect insulator. The hole band is completely filled, and the electron band is completely empty. Charge transfer across the anthracene-electrolyte interface is possible only with such redox systems which lead to either

Mn^{4+}/Mn^{3+}	10^{-2} mol/l
Ce^{4+}/Ce^{3+}	10^{-2} mol/l

injection of holes into the hole-band or electrons into the electron band.

Mn^{4+}/Mn^{3+}	10^{-2} mol/l
Ce^{4+}/Ce^{3+}	10^{-2} mol/l

Figure 6 shows a current voltage curve which was obtained when both electrode compartments (Fig. 5) were filled with 0.2M NaCl-solution. The current is independent of the polarity of the applied voltage. Surface currents and currents through the cement probably contribute appreciably to our measured value which we shall be using as reference scale only. Also plotted in Fig. 6 are current values which were obtained when the half-cell with the positive electrode was filled with a solution of 0.1M $Ce(SO_4)_2$ in 15N H_2SO_4 while the other half-cell was filled with the NaCl-solution. On voltage reversal the zero current was measured. As 15N H_2SO_4 alone also injects holes to a certain degree, this effect has also been plotted.

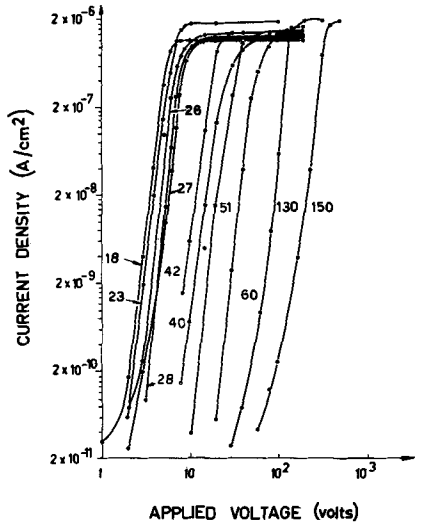

Fig. 7. Cathodic current-voltage curves at various thicknesses (in microns) of the anthracene crystals Electrolyte: 10^{-2}M $Ce(SO_4)_2$ in 0.5M H_2SO_4.

Table I. Hole exchange currents for various redox systems

System		Electrolyte	Standard redox potential (NHE)	i_o^p, amp/cm²
I_3^-/I^-	0.1M	1M KI	+0.54	5×10^{-8}
$IrCl_6^{2-}/IrCl_6^{3-}$	0.1M	0.5M HCl	+0.96	5×10^{-6}
$Cr_2O_7^{2-}/Cr^{3+}$	0.1M	2M H_2SO_4	+1.10	5×10^{-7}
Mn^{3+}/Mn^{2+}	0.1M	7.5M H_2SO_4	+1.5	1×10^{-4}
MnO_4^-/Mn^{2+}	0.1M	0.5M H_2SO_4	+1.5	5×10^{-5}
Ce^{4+}/Ce^{3+}	0.1M	2M H_2SO_4	+1.44	2×10^{-5}
		2.5M H_2SO_4	+1.40	1×10^{-4}
Fe^{3+}/Fe^{2+}		0.5M H_2SO_4	+0.77	10^{-11}
$Fe(CN_6)^{3-}/Fe(CN_6)^{4-}$		1M H_2SO_4	+0.69	10^{-11}

Figure 7 provides a proof that the limiting currents are indeed caused by a phase boundary reaction. It is shown that the limiting current does not depend on the thickness of the sample while the rest of the curve does, as predicted by S.C.L. current theory.

In Table I exchange currents for various redox systems are listed showing at least qualitatively the predicted dependence of these currents on the redox potential. (The table also shows that the system I_3^-/I^- is obviously not covered by our model.)

Both for the systems Mn^{4+}/Mn^{3+} in 15N H_2SO_4 and Ce^{4+}/Ce^{3+} in 15N H_2SO_4 the exchange current at an anthracene electrode is roughly equal to that for the same system at a metal electrode assuming equal concentration of the reduced and the oxidized component.

Vetter (18, 19) found the following values at a platinum electrode

15N H_2SO_4	$i_o = 1.3 \times 10^{-5}$ amp/cm²
1N H_2SO_4	$i_o = 2.3 \times 10^{-4}$ amp/cm²

The values for the exchange currents at the anthracene electrode are

15N H_2SO_4	$i_o = 2 \times 10^{-5}$ amp/cm²
15N H_2SO_4	$i_o = 8 \times 10^{-5}$ amp/cm²

here only the concentration of the oxidized component is of interest.

Considering the high inaccuracy which is inherently connected with the measurement of exchange currents, the excellent agreement of the values for the exchange currents measured on anthracene with those measured on platinum has to be considered somewhat fortuitous Nevertheless, these results have to be considered as an experimental proof of our prediction that redox reactions can be "reversible" at insulator electrodes.

The similarity in the magnitude for the exchange current of the redox systems Ce^{4+}/Ce^{3+} (E_S = 1.4v) and Mn^{4+}/Mn^{3+} (E_S = 1.5v) measured at platinum and at anthracene electrodes proves according to Eq. [3b] that $e_o(E_s - E_{FB}) \cong \Delta^p$. The injection of electrons into the electron band is possible with the system Li^+/e^- ($E_s = -3.0$v). This reaction will be discussed in more detail in the following paragraph. The rate of this reaction is so high that we were not able to determine it. It seems thus very likely that also for this system $e_o(E_s - E_{FB}) \cong \Delta^n$. We have thus as a rough estimate of the distance between hole and electron-band $\Delta\epsilon$ = 4.5v. This value agrees very well with a recently quoted value (17) $\Delta\epsilon$ = 4.4v which was determined from photoconductivity data.

Corrosion.—The hole injecting contacts are highly oxidizing, and thus an oxidative attack of the anthracene crystal is inevitably connected with the hole injection process. Very little is known about this process.

The reaction of anthracene with a solution of $Ce(SO_4)_2$ in sulfuric acid, however, was used commercially at the turn of this century for the manufacture of anthraquinone (20). Measurements of the infrared absorption spectrum of partially oxidized crystals did indeed show that anthraquinone was formed on the electrode surface; nothing is known about intermediates and about the reaction mechanism.

It was found that the rate of dissolution of the oxide film increased with increasing concentration of sulfuric acid in the supporting electrolyte. Because of this effect we tried to make most measurements in 15*N* sulfuric acid.

Reactions of Anthracene Ions on Anthracene Electrodes

Helfrich and Schneider (21) have shown that electrons can be transferred to an anthracene crystal from negative anthracene ions dissolved in tetrahydrofuran (THF). They prepared the ions by reduction of anthracene, dissolved in THF, with sodium. Injection of electrons can also be achieved from the blue solution of lithium in ethylenediamine (22) but in this case, the anthracene crystal itself is attacked by the reducing agent and the situation is more complicated. Figure 8 shows a current potential-plot determined with this system. No limiting current was found indicating that all electrochemical processes are fast and that the shape of the curve is completely determined by concentration polarization of electrons in the bulk of anthracene. A trap-filled limit can be recognized as can be transition into the $i = kV^2$ relationship of Child's law.

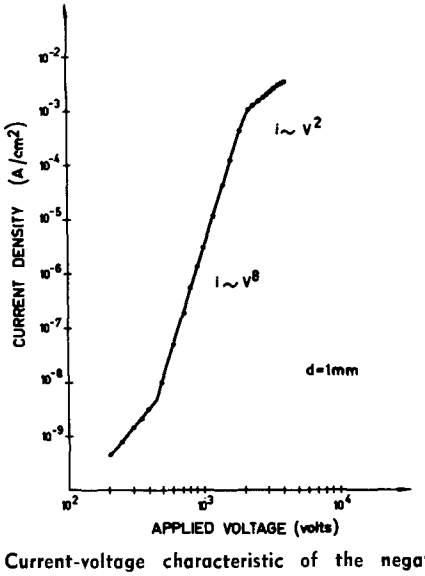

Fig. 8. Current-voltage characteristic of the negative space charge limited current.

The injection of holes by oleum (23) or a solution of anthracene and $AlCl_3$ in nitromethane (21) is similar to the lithium/ethylenediamine case; the strong electron acceptors attack the anthracene crystal directly, and these systems are thus not very suitable for an investigation of the electron exchange reaction. Hole injection by anthracene cations in solution can be studied if these are generated electrolytically. Stable anthracene cations can be produced electrolytically from a solution of anthracene in trifluoroacetic acid in the presence of boron trifluoride (24).

The reaction rate constant k for homogeneous electron transfer processes of the kind $X + X^- \rightarrow X^- + X$, where X is an aromatic hydrocarbon molecule and X^- is the paramagnetic radical ion can be determined from the broadening of hyperfine lines in the EPR spectrum of X^- as a function of the concentration of X (25). For aromatic hydrocarbons the value for k is about 10^7 to 10^9 liter mole^{-1} sec^{-1} (25, 26). For the anthracene system [anthracene] + [anthracene]$^-$ → [anthracene]$^-$ + [anthracene] the value k = 4.8 $\pm 1.10^8$ liter mole^{-1} sec^{-1} was recently found for a solution in dimethylformamide (26).

According to Marcus (27) a relationship of the form $(10^{-11}\ k_h)^{1/2} = 10^{-4}\ k_{el}$ should exist between the chemical (k_h) and electrochemical (k_{el}) rate constants for redox systems, provided the extent of overlap between molecular orbital and electrode orbital is about the same as between two molecular orbitals. In our case the approximation should certainly be a good one as the hydrocarbon forms the electrode. Unfortunately, it is not quite clear, however, if these reactions are covered by Marcus' theory (29). Nevertheless, thus far the rate constants for electron transfer at metal electrodes involving ions of aromatic hydrocarbons have turned out to be too large for determination by electrochemical means (30), and the rate constants at anthracene electrodes should also be very large.

We have tried to get some information on these rate constants by measurements with a rotating disk electrode made from anthracene. A rotating disk electrode was made by mounting solution grown crystals with paraffin on the hollow shaft of a trubore stirrer. The arrangement permitted measurements from 20 to 1000 rpm. Electrical contact to the anthracene was made with a droplet of mercury (23). In case of a diffusion limited current i the following relationship between i and ω, the speed of rotation should be obtained (31)

$$\frac{i}{\omega^{1/2}} = \frac{\xi F C_O D^{2/3}}{1.6\bar{\nu}^{-1/6}} \qquad [17]$$

where C_O is the concentration of active species in the

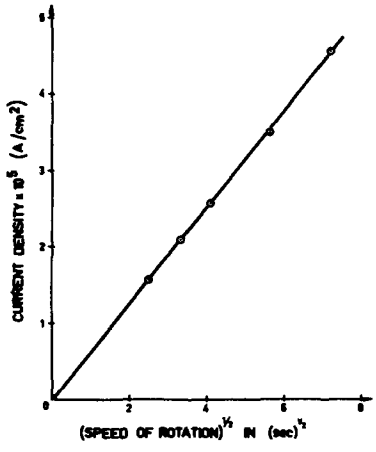

Fig. 9. Dependence of the current density at a rotating anthracene disk electrode on the speed of rotation for anthracene cations.

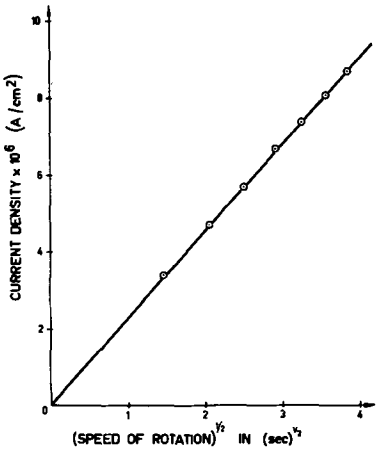

Fig. 10. Dependence of the current density at a rotating anthracene disk electrode on the speed of rotation for anthracene anions.

bulk of the solution, D is the diffusion coefficient, and $\bar{\nu}$ the kinematic viscosity of the solution used.

Equation [17] was verified both with solutions of positive anthracene ions in a mixture of trifluoroacetic acid and boron trifluoride-water (Fig. 9) and with solutions of negative anthracene ions in dimethylformamide (Fig. 10). In each case, the ions were generated electrolytically. From these measurements, the following diffusion coefficients were determined:

$$D\,(\text{anthracene}^+) = 2 \times 10^{-6}\,\text{cm}^2\,\text{sec}^{-1}$$

$$D\,(\text{anthracene}^-) = 8 \times 10^{-6}\,\text{cm}^2\,\text{sec}^{-1}$$

The rate constants for the exchange reactions were in both cases too high to be determined. As a lower limit of the exchange current for the exchange reaction between the anthracene electrode and positive ions $i = 2 \times 10^{-1}$ amp/cm² was determined, and for that between the electrode and negative ions 4×10^{-1} amp/cm². These values were obtained by extrapolating from our experimental data (24) to 1M solutions of ions.

Double Injection

In the cell depicted in Fig. 5 one vessel was filled with a solution of anthracene and $AlCl_3$ in nitromethane as hole injecting agent and the other vessel

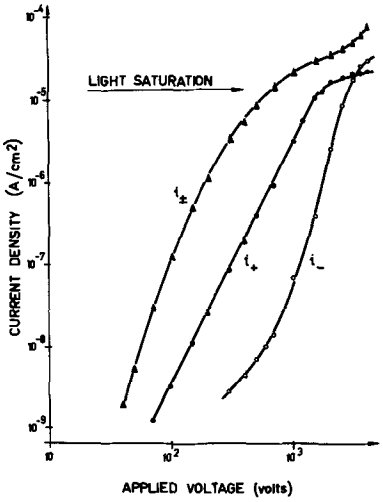

Fig. 11. Current-voltage characteristic of the space charge compensated current $i_\pm$ and the positive i_+ and negative i_- space charge limited current. Positive injecting contact: solution of anthracene and $AlCl_3$ in nitromethane. Negative injecting contact: solution of lithium metal in ethylenediamine.

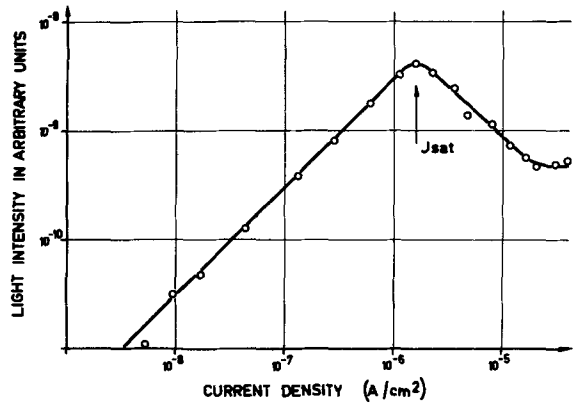

Fig. 12. Intensity of emitted light as function of double injection current.

with a solution of lithium in ethylenediamine as electron injecting agent. With a properly oriented electric field (positive electrode in the oxidizing agent, negative electrode in the reducing agent) simultaneous injection of electrons and holes is then possible. As predicted by theory (11), it is observed that in this case the current is several orders of magnitude larger than the space charge limited current at the same applied voltage (Fig. 11). Also recombination of holes and electrons leads to the excitation of the fluorescence spectrum of anthracene. With a photomultiplier the intensity of the light emission was measured as a function of the current density and linearity was found over four orders of magnitude (21, 32, 33). The result is interpreted as being due to the formation by recombination of holes and electrons of the first excited singlet state of anthracene, which is responsible for the emission of the fluorescence spectrum. When the current reached the limiting value for the hole injection reaction, the light intensity saturated and decreased with further increase of voltage and current (Fig. 12).

This observation fits very well into our model of the injecting processes: as long as the contacts are ohmic, all the current near them is carried by either electrons or holes through diffusion. As soon as the hole-limiting region is reached, the current at the hole contact is obviously carried partially at least by electrons. The oxidation products at the electrode surface can now provide centers for radiationless recombination resulting in a decrease in the intensity of light emission. Figure 13 shows a cross-section through a luminescing anthracene crystal. The light intensity is highest near the positive contact which is proved by changing the contacts.

Acknowledgments

Many thanks are due to Mr. G. Duccini for his patient efforts to increase the quality of our anthracene crystals and to Miss E. Pobitschka for valuable contributions to the experiments.

LIST OF SYMBOLS

A_n, A_p	Constants in the boundary condition for the concentration polarization of charge carriers in the solid
C_O	Concentration of oxidized ions in solution
C_R	Concentration of reduced ions in solution
D	Diffusion coefficient of ions in solution
d	Thickness of the insulator
E	Electric field
E_{FB}	Flat band electrode potential
E_R	Equilibrium potential
E_s	Standard potential
e_o	Electronic charge
F	Faraday constant
i	Current
i_o	Exchange current

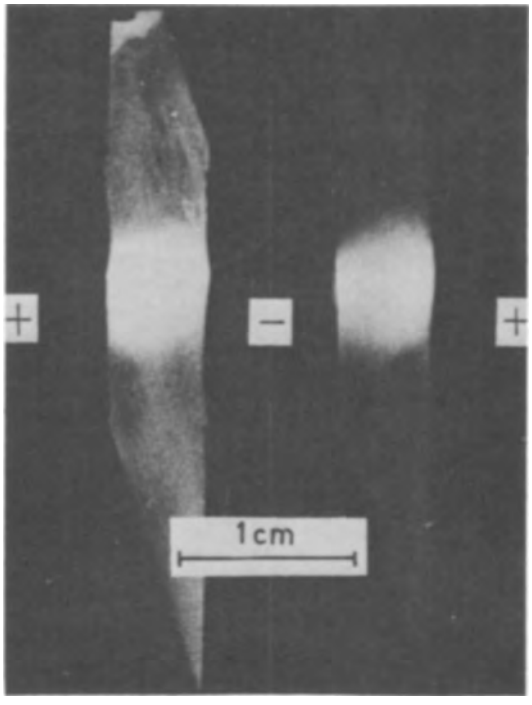

Fig. 13. Photograph of cross section through luminescing anthracene crystal. The second photograph was taken after exchange of the contacts. Positive injecting contact, oleum; negative injecting contact, solution of lithium metal in ethylenediamine; contact area, 0.2 cm^2; current, 2 x 10^{-6} amp/cm^2.

i_o^n	Electron exchange current with the conduction band
i_o^p	Hole exchange current with the valence band
k	Boltzmann constant
L_D	Debye length
n	Electron density
p	Hole density
T	Absolute temperature
V_D	Degree of banding of bands under equilibrium conditions
x	Distance variable
Δ^n	Interval of energy between Fermi-level and the conduction band in the bulk of the insulator
Δ^p	Interval of energy between Fermi-level and the valence band in the bulk of the insulator
ϵ	Dielectric constant
ϵ_0	Permittivity of free space
$\Delta\epsilon_s^n$	Forbidden gap between Fermi-level and conduction band in the surface of the insulator
$\Delta\epsilon_s^p$	Forbidden gap between Fermi-level and valence band in the surface of the insulator
$\Delta\epsilon$	Forbidden gap between valence and conduction band
ζ	Number of electrons involved in the electron transfer reaction
η	Overpotential
λ	Energy parameter
μ	Mobility of carrier
ν	Velocity of movement along the reaction coordinate
$\bar{\nu}$	Kinematic viscosity
ω	Speed of rotation
*	Connotes the transition state of the electron transfer reaction

REFERENCES

1. N. F. Mott and R. W. Gurney, "Electronic Processes in Ionic Crystals," Clarendon Press, Oxford (1940).
2. A. Rose, "Concepts in Photoconductivity and Allied Problems," Interscience Publishers, Inc., New York (1963).
3. H. K. Henisch, "Rectifying Semiconductor Contacts," Oxford University Press, London (1957).
4. R. A. Marcus, *Can. J. Chem.*, **37**, 155 (1959); *Ann. Rev. Phys. Chem.*, **15**, 155 (1964); *J. Chem. Phys.*, **24**, 966, 979 (1956); **26**, 867, 872 (1957); *Discussion Faraday Soc.*, **29**, 21 (1961).
5. H. Gerischer in "Advances in Electrochemistry and Electrochemical Engineering," Vol. 1, P. Delahay, Editor, Interscience Publishers, Inc., New York (1961).
6. R. R. Dogonadze and Yu. A. Chizmadzhev, *Proc. Acad. Sci. USSR*, **144**, 463 (1962); **145**, 563 (1962).
7. N. S. Hush, *J. Chem. Phys.*, **28**, 962 (1958); *Discussion Faraday Soc.*, **29**, 113, 133, 244 (1960); *Trans. Faraday Soc.*, **57**, 557 (1961).
8. J. F. Dewald in "Semiconductors," N. B. Hannay, Editor, Reinhold Publishing Co., New York (1959).
9. V. A. Myamlin and Yu. V. Pleskov, *Russ. Chem. Rev.*, **32**, 207 (1963).
10. J. M. Hale and W. Mehl, *Surface Science*, **4**, 221 (1966).
11. M. A. Lampert, *Rept. Progr. Phys.*, **27**, 329 (1964).
12. R. G. Kepler, *Phys. Rev.*, **119**, 1226 (1960).
13. O. H. LeBlanc, Jr., *J. Chem. Phys.*, **33**, 626 (1960).
14. O. H. LeBlanc, Jr., *ibid.*, **35**, 1275 (1961)
15. A. McL. Mathieson, J. M. Robertson, and V. C. Sinclair, *Acta Cryst.*, **3**, 245 (1950).
16. F. R. Lipsett, *Can. J. Phys.*, **35**, 284 (1957).
17. G. Castro and J. F. Hornig, *J. Chem. Phys.*, **42**, 1459 (1965).
18. K. J. Vetter, *Z. physik. Chem.*, **196**, 360 (1951).
19. K. J. Vetter and G. Manecke, *ibid.*, **195**, 270 (1950).
20. German Pat. 158 609, Feb. 18, 1902, Farbwerke vorm. Meister Lucius & Brüning in Höchst a.M.
21. W. Helfrich and W. G. Schneider, *Phys. Rev. Letters*, **14**, 229 (1965).
22. W. Büchner and W. Mehl, *Z. physik. Chem. (Frankfurt)*, **44**, 376 (1965).
23. W. Mehl, *Ber. Bunsenges. Physik. Chem.*, **69**, 583 (1965).
24. F. Lohmann and W. Mehl, To be published.
25. R. L. Ward and S. I. Weissmann, *J. Am. Chem. Soc.*, **80**, 1518 (1958).
26. T. Layloff, T. Miller, R. N. Adams, H. Fäh, A. Horsfield, and W. Proctor, *Nature*, **205**, 382 (1965).
27. R. A. Marcus, *J. Phys. Chem.*, **67**, 853 (1963).
28. A. C. Aten, J. Dieleman, and G. J. Hoijtink, *Discussion Faraday Soc.*, **29**, 182 (1960).
29. R. A. Marcus, *J. Chem. Phys.*, **43**, 2654 (1965).
30. A. C. Aten and G. J. Hoijtink, "Advances in Polarography. Proceedings of the second International Congress, Cambridge 1959," I. S. Longmuir, Editor, Vol. 2, p. 777, Pergamon Press, Oxford (1960).
31. V. G. Levich, *Acta Physicochim. URSS*, **17**, 257 (1942); **19**, 117 (1944).
32. W. Mehl and W. Büchner, *Z. physik Chem. (Frankfurt)*, **45** (1965).
33. W. Mehl, "Proceedings of the International Symposium on Luminescence Munich, Sept. 5-9, 1965," N. Riehl and H. Kallmann, Editors, Thiemig, Munich (1966).

Discussion

H. Gerischer: One interesting question I feel arises from your observations that strong acidic solutions such as H_2SO_4 at higher concentrations can inject holes. What is the redox reaction in this case? I suppose it could be the reduction of oxygen if this oxidant is present in high enough concentrations. This reduction may then be catalyzed by the acid. That the H_2SO_4 is reduced itself seems to be very unlikely for these concentrations if it was pure. As another possibility, one could ask whether protons could be associated with the aromatic molecules on the surface by some kind of π-bonding. If this would be the mechanism of hole injection by protons directly, the anthracene molecules will be hydrogenated by this injection. Is there any indication available what mechanism may occur?

W. Mehl: An investigation of the role played by sulfuric acid in the hole injection reaction is in progress in our laboratory and the suggestions by Professor Gerischer are most helpful. No conclusive evidence for a particular mechanism has thus far been obtained.

R. E. Visco: We have been studying a system similar to that described by Dr. Mehl.[1,2] In nonaqueous aprotic solvents it is possible to generate electrochemically the radical cation, $R^{+\cdot}$, and the radical anion, $R^{-\cdot}$, of aromatic hydrocarbons. We have generated these radicals for rubrene and 9-10 diphenylanthracene in acetonitrile and recently in benzonitrile. Using the treatment of Feldberg[3] it has been possible to estimate a lower limit for the chemical rate constant for the homogeneous cation-anion annihilation reaction to give an electronically excited state of the hydrocarbon. We estimate a rate constant of 5×10^6 liters mole $^{-1}$ sec^{-1} as the lower limit. Despite the observation of singlet fluorescence, the excited state formed as a consequence of the ion-ion annihilation reaction may be either the first excited singlet or the lowest lying triplet. Our data at present do not allow an unambiguous determination since two triplets can undergo a subsequent annihilation to give an excited singlet.

J. L. Weininger: The outstanding features of this very interesting work, as well as the questions arising from it, are related to exchange currents of various redox couples at the anthracene electrode, the charge transport within the anthracene crystals, and the space charge distribution at the interface.

The measurements of the exchange currents demonstrate very clearly the importance of matching up energy states at the electrode surface with those of the redox couple at the solution-side of the interface, *i.e.*, that these must be in close proximity on an energy scale to give large exchange currents at equilibrium. In measuring the exchange current, how is the chemical interaction with anthracene prevented? A strongly oxidizing couple, or the large potential differences used, should result in oxidation of the anthracene to anthraquinone. Alternately, there may be present some adsorbed material or products of photooxidation, which should strongly affect the electrode kinetics on the semiconducting or insulating electrode. Similarly, reduction to the negative anthracene ion should change the condition of the surface. As an example, in work on semiconducting single crystal NiO electrodes[4] we have found that the mere evolution of hydrogen suffices to alter irreversibly the nature of the semiconducting electrode, possibly by changing the doping of the surface layer.

The experimental data on the Ce (IV)/Ce(III) and Mn(IV)/Mn(III) exchange show that the exchange currents, $i_{o,p}$ and $i_{o,M}$, respectively, for the hole conduction at an insulator electrode and at a Pt electrode, are of the same magnitude. One of the authors has shown[5], with the same assumptions as those used in deriving Eq. [3] that

$$i_{o,p}/i_{o,M} = \exp - [(E_F - E_V)/2kT]$$

If $i_{o,M} \sim 2.7\, i_{o,p}$, then $-(E_F - E_V) \sim 2kT$ which is about the limit of applicability of Boltzmann statistics. Have the authors considered the consequences of the band-gap picture becoming degenerate, *i.e.*, $-(E_F - E_V) < 2kT$, both on the redox reaction at the interface and on the charge transport within the electrode?

What conclusions can one reach regarding the charge transport within the insulator (with dark conduction of 10^{-19} ohm^{-1}cm^{-1}), into which a substantial number of charge carriers, corresponding to a conductivity of 10^{-8} ohm^{-1} cm^{-1} are injected? Neither hole-hopping nor transport in bands can be singled out as the appropriate mechanism of conduction. One difficulty is the identification and influence of traps known to be present. What are these traps? Do they only limit conduction by capturing charge carriers, or do they also facilitate charge transport by providing suitable donor and acceptor levels? Further electrochemical work on anthracene electrodes with deliberate doping or special structural defects would be of particular interest. In this connection the work of Hoesterey and Letson[6] is a first quantitative study of the effect of controlled impurities on the conductivity of anthracene. As for structural defects, what would be the results of electrochemical measurements on the anthracene crystals with their original large number of dislocations as contrasted to the annealed crystal electrodes which were used here?

The linear relation between the cathodic exchange current and the concentration of ceric ion is in accord with the potential drop being almost entirely on the insulator side of the interface. For the same system Pope and co-workers[7] have reported a dependence on the 0.6 power, *i.e.*, $i_o \propto c_{Ce(IV)}^{0.6}$. This latter discrepancy may be due to surface states. It is mentioned here to indicate the pitfalls and experimental difficulties besetting studies of semiconductor electrodes. The authors are to be commended for tackling the insulator electrode in a semiquantitative manner and for their experiments resulting in luminescent recombination of electrons and holes as well as the exchange current measurements.

W. Mehl: Dr. Weininger raises a number of very basic questions which deserve a much more thorough discussion than can be given here. Some of the points

[1] R. E. Visco and E. A. Chandross, *J. Am. Chem. Soc.*, **86**, 5350 (1964).

[2] E. A. Chandross, J. W. Longworth, and R. E. Visco, *J. Am. Chem. Soc.*, **87**, 3259 (1965).

[3] S. W. Feldberg, *J. Am. Chem. Soc.*, **88**, 390 (1966).

[4] T. O. Rouse and J. L. Weininger, Paper presented at the Cleveland Meeting of the Society, Theoretical Div., Extended Abstract No. 179, May 1966.

[5] W. Mehl, *Ber. Bunseng. Phys. Chem.*, **69**, 583 (1965).

[6] D. C. Hoesterey and G. M. Letson, *J. Phys. Chem. Solids*, **24**, 1609 (1963).

[7] M. Pope, H. Kallmann, A. Chen, and P. Gordon, *J. Chem. Phys.*, **36**, 2486 (1962).

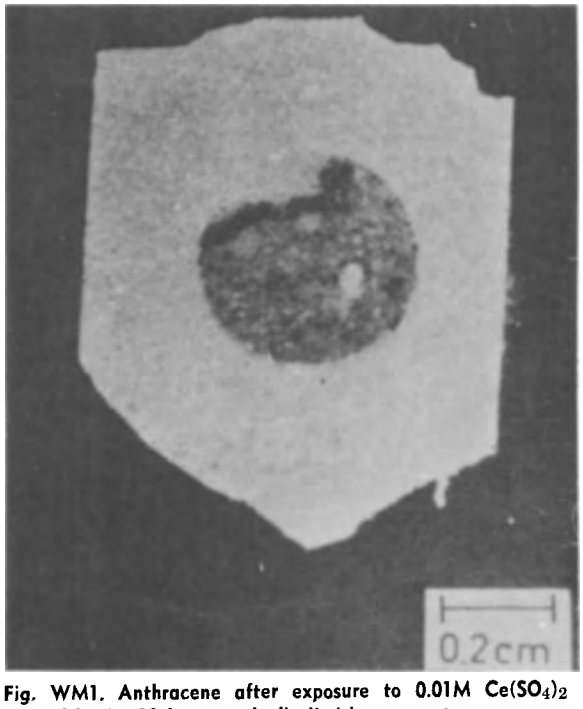

Fig. WM1. Anthracene after exposure to 0.01M $Ce(SO_4)_2$ + 0.5M H_2SO_4 for 12 hr at cathodic limiting current.

mentioned are dealt with in some detail in a forthcoming publication.[8] Briefly it can be said at this point that in order to achieve hole injection in anthracene crystals fairly strong oxidation agents have to be used, and the formation of an anthraquinone film at the electrode surface is indeed a major problem. In accordance with our model the formation of such a film can, however, be prevented if one works in the limiting current region. Apparently in this case anthracene radical ions which are formed on the anthracene surface transfer their charge under the influence of the electrical field to the bulk of the crystal and the surface remains unattacked. This is demonstrated in Fig. WM1 which shows a photograph of an anthracene electrode which has been exposed for 12 hr to a 0.01M solution of $Ce(SO_4)_2$ in 0.5M sulfuric acid while a cathodic limiting current was flowing. The dark part is the unoxidized anthracene surface opposite a mercury drop which served as contact at the rear of the crystal. The light area is a thick oxide film. If a current smaller than the limiting current is drawn through the crystal, an oxide film forms resulting in a reduction of the limiting current. Special precaution has therefore to be taken in order to be able to make, *e.g.*, meaningful measurements of the concentration dependence of the exchange current.

It has also been found that surface oxides completely inhibit the injection of electrons from reducing agents, and only after these oxides have been removed can appreciable electron currents be measured.

The question of trap distribution etc. has been dealt with extensively by Helfrich and Mark.[9]

[8] W. Mehl and J. M. Hale, "Insulator Electrode Reactions" in "Advances in Electrochemistry and Electrochemical Engineering," P. Delahay and C. W. Tobias, Editors, Vol. 7, Interscience Publishers, Inc., New York, To be published.

[9] W. Helfrich and P. Mark, *Z. Physik*, 171, 527 (1963).

Electrochemical Behavior of Semiconductors under Illumination

H. Gerischer

Institute of Physical Chemistry, Technical University, Munich, Germany

ABSTRACT

In contrast to metals, the average free energy of electrons can be changed in semiconductors to a great extent by illumination. Especially the concentration of minority electronic carriers can differ by orders of magnitude from the equilibrium value. This has two major effects on electrode processes: (*a*) change of charge distribution and potential drops in the space charge layer; and (*b*) variation of the rate of electrode reaction in which minority carriers are involved. Some examples are given for those effects at various semiconductors.

A great number of photogalvanic or photovoltaic effects are known, often summarized under the name "Bequerel effects." Many of these phenomena are the consequence of photochemical reactions in the electrolyte; others are connected with irreproducible changes in the electrode composition. We shall limit our considerations here to such cases where the "photoelectrochemical" effect is caused by absorption of light in a semiconducting electrode, and the composition of the electrode is not changed.

The absorption of light by an electrode means that electrons are excited and that the statistical equilibrium of energy distribution among solid-state electrons is disturbed. At the energy level and local position where the electron has absorbed the light quantum a hole is left and the excited electron is transferred to energy states above the normally occupied levels. Due to the strong interaction between the electrons in the metal themselves and between the electrons and the atomic constituents of the lattice, the excess energy is distributed rapidly over the solid and is converted into lattice vibrations, *i.e.*, heat. As one of the consequences of this rapid energy exchange, electron emission from a solid surface by excitation with light has a very small efficiency. In accordance with this, the currents attributed to electron emission from electrode surfaces, as investigated by a few authors (1, 2) in the past years at the dropping mercury electrode, are relatively small. This subject is discussed in the following paper by Barker, Gardner, and Sammon.

Inside a metallic conductor the mean free energy of the electrons cannot be changed noticeably, even under strong illumination, because too many electrons with energies near the Fermi level are present and equalize the average value. The situation is quite different for a semiconductor. Although there is similar interaction between the electrons and lattice atoms as in a metal and although the exited electrons and holes rapidly lose some of their excess energy, there is a barrier for the final restitution of statistical equilibrium given by the slow transition from band to band, *i.e.*, the slow recombination of electrons and holes. By slow, we understand this rate relative to that one of energy exchange between electronic and vibrational quantum states in the same energy band of electrons.

As a consequence of this retarded redistribution of excess energy in a semiconductor, electrons and holes are accumulated under illumination in equal amounts on energy levels near the band edges until a steady state has been reached where the recombination compensates the generation of electron hole pairs by light.

This process of electronic excitation is illustrated in Fig. 1 for a metal and for a semiconductor.

How much the effective free energy of electrons and holes is altered in the steady-state depends on the recombination rate and on the number of electrons and holes present under equilibrium conditions. If we assume that the energy distribution of each of the electronic carriers corresponds to equilibrium distribution in their separate energy bands also under illumination, then the change in free energy relative to equilibrium can be expressed by the following equations

$$\Delta\mu_{e^-} = RT \ln\left(1 + \frac{\Delta n^*}{n_0}\right) \qquad [1]$$

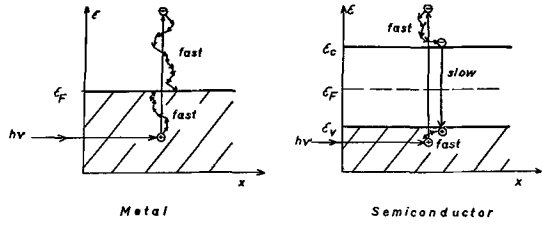

Fig. 1. Light absorption and energy redistribution in a metal and a semiconductor.

$$\Delta\mu_p = RT \ln\left(1 + \frac{\Delta p^*}{p_o}\right) \quad [2]$$

In the absence of specific traps for the electrons or holes, the excess concentrations Δn^* and Δp^* must be equal to fulfill the condition of electroneutrality in the interior of the semiconductor. n_o and p_o are the equilibrium concentrations related to the band gap energy ΔE_g by

$$n_o \cdot p_o = n_i^2 = N_c \cdot N_v \cdot \exp\left(-\frac{\Delta E_g}{RT}\right) \quad [3]$$

Equations [1] and [2] show that the change in free energy under illumination is much greater for minority carriers than for majority carriers. When the equilibrium concentration of minority carriers is very small, an enormous change in free energy can be caused for those species by illumination. We must therefore expect that all important chemical and electrochemical effects will be due to this large deviation from equilibrium for the minority carriers, while the respective change in activity of majority carriers will have minor or negligible importance.

We can calculate the concentration change of electronic carriers in the semiconductor under illumination by standard procedures (3). To do this for the simplest case, we will assume that the illuminated specimen is n- or p-type and that the increase of minority carrier concentration remains small compared with the equilibrium concentration of majority carriers. We then have the situation as designed in Fig. 2 for a n-type material.

From the diffusion theory, the steady-state equation for the region where light absorption is negligible is given by

$$D_n \cdot \frac{\partial^2 \Delta p^*}{\partial x^2}$$

$$= r(p_o \cdot \Delta n^* + n_o \Delta p^* + \Delta n^* \cdot \Delta p^*) \approx r \cdot n_o \cdot \Delta p^* \quad [4]$$

where $n_o >> p_o$, $\Delta p^* << n_o$, and r is the rate constant for recombination.

Since $\Delta p^* \to 0$ for $x \to \infty$, the solution is

$$\Delta p^* = \Delta p_o \cdot \exp\left(-\frac{x}{L_p}\right) \quad [5]$$

where Δp_o^* is the concentration change in the surface region where the light is absorbed, and L_p is the mean free path for diffusion of holes.

$$L_p = \sqrt{\frac{D_p}{r \cdot n_o}} = \sqrt{D_p \cdot T_p} \quad [6]$$

and $(1/r \cdot n_o) = T_p$ = mean life time of holes.

The surface concentration change Δp_o^* is obtained by introducing the production of carriers in the surface area as a boundary condition for the flux of carriers into the interior. This assumption is justified as long as the depth of the region of light absorption is small compared with L_p.

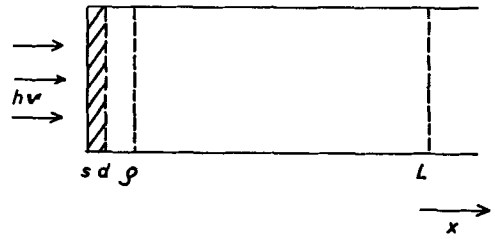

Fig. 2. Model assumed for discussion of photoresponse by illumination of the surface: s, surface; s-d, main light absorption region; s-ρ, space charge layer; s-L, mean free path of minorities.

$$-D_p \cdot \left(\frac{\partial \Delta p}{\partial x}\right)_{x=0} = I_L - I_{SR} \quad [7]$$

where I_L is the absorbed light intensity in quantum units and I_{SR} the surface recombination rate.

The result is

$$\Delta p_o^* = \frac{I_L - I_{SR}}{D_p/L_p} = \sqrt{\frac{T_p}{D_p}} \cdot (I_L - I_{SR}) \quad [8]$$

Introducing $D_p/L_p \cdot p_o = I_{p,o}$, the saturation current for transfer of holes from the interior to the surface, we get

$$\frac{\Delta p_o}{p_o} = \frac{I_L - I_{SR}}{I_{p,o}} \quad [9]$$

The concentration of electrons is altered by the same amount, but, according to our assumption, Δn^* remains small compared to n_o. Therefore an equal flux of electrons, as given in Eq. [7] for holes, flows from the light absorption area in the interior. Also, when the majority carriers have a different mobility, their migration rate is controlled by the diffusion coefficient of the minority carriers as long as $D_n \cdot n >> D_p \cdot p$. The Dember potential difference (the equivalent of diffusion potentials in electrolytes) which gives the force for equalizing the two migration rates remains insignificant under this condition (3).

Up to now we have not included in our considerations the space charge in a semiconductor surface region which is of great importance for electrochemical experiments. The carrier distribution in this space charge zone determines the potential difference between the surface and the interior. This is the most important part of the electrical double layer in the semiconductor electrode (4-10). Any change in this potential difference causes an equivalent change in the electrode potential. Simultaneously, the space charge layer structure controls the drift of electrons and holes through the surface region. This seriously complicates the discussion of photoeffects in a semiconductor because we have to deal now with a double layer which is not in the equilibrium state but only under steady-state conditions.

We shall see that the main effects of illumination on electrochemical processes at semiconductors are due to the two following principle deviations from equilibrium condition in the steady-state situation: (*i*) deviation from equilibrium for minority carrier concentration in the region under the surface outside the space charge layer, as given in Eq. [4]-[9]; and (*ii*) deviation from equilibrium for charge distribution in the space charge layer to distribute the flow of electrons and holes to the interior and the surface as necessary.

Before we come to the details, I would like to recall in this connection the late J. F. Dewald, who was one of the most brilliant scientists who has dealt with semiconductor electrochemistry. In one of his fundamental papers (8) he gave a stimulating outlook on the great importance of photoeffects at semiconductors for the understanding of electrochemical reactions.

Space Charge Capacitance under Illumination

The space charge distribution controls the capacitive charging currents during rapid variation of the electrode potential at a semiconductor. That has been discussed theoretically by various authors and proven experimentally for germanium electrodes (4-7, 11-13). The easiest case to discuss is an intrinsic semiconductor with carrier concentration: $n_o = p_o = n_i$. In this case the space charge capacity is

$$C_{sc} = \left(\frac{2\epsilon\epsilon_o e_o^2}{kT}\right)^{1/2} \cdot \sqrt{n_i} \cdot \cos h \frac{\Delta\psi_s}{2\phi} \quad [10]$$

$$\Delta\psi_s = \psi_s - \psi_i$$

$$\phi = \frac{kT}{e_o} = \frac{RT}{F}$$

ψ_s = electrostatic potential in the surface, ψ_i = electrostatic potential in the interior of the semiconductor, and the other symbols are standard.

Under illumination, the concentration at the interior end of the space charge layer may be changed to: $n_o^* = n_i + \Delta n^* = p_o^*$, where Δn^* depends on the illumination intensity. For an intrinsic semiconductor the recombination kinetic is of second order, and therefore we have no linear relationship between light intensity and Δn^*. Nevertheless the simple relation of Eq. [10] remains valid; one has only to replace n_i by $n_i + \Delta n^*$. The relation between space charge capacities with and without illumination at the same $\Delta\psi_s$ is therefore

$$\left(\frac{C_{sc^*}}{C_{sc}}\right)_{\Delta\psi_S} = \sqrt{1 + \frac{\Delta n^*}{n_i}} \qquad [11]$$

Easiest to compare is the value at $\Delta\psi_s = 0$, because this is the minimum in the capacity curve. Since we cannot measure absolute $\Delta\psi_s$ values, it is very helpful to have such a diagnostical reference point in the capacity *vs.* electrode potential plots. Plotting the log C_{sc} values against electrode potential, measured against an arbitrary reference electrode, a linear shift in vertical direction for the log C_{sc} values should be found when the minima are brought to the same point in the potential scale.

As an example such a plot is given in Fig. 3 for an intrinsic Ge electrode. The capacities have been measured in this case by a rapid pulse method (11). These measurements were made while going continuously through the interesting range of polarization in about 1 sec, to avoid changes of the Helmholtz layer potential drop.

With n- or p-type materials, the capacity is little changed under illumination as long as the majority carriers are enriched in the surface region by the polarization potential. On the other hand, there is a great increase in capacity in the depletion range of polarization, especially in the case of inversion. A quantitative analysis will not be given here. In principle, the changes of the capacity values under illumination can be used to gain information about the carrier distribution and the surface potential.

Photovoltage under Constant Current

The theory of surface photovoltage for a semiconductor interface in contact with nonconducting gases was developed by Brattain and Bardeen (14) for the case when the charge is kept constant in the space charge layer. Brattain and Garrett (15), and later Dewald (6), applied this theory to semiconductor electrodes. This instantaneous photovoltage always has the tendency to flatten the energy bands, *i.e.*, to diminish the potential difference at the interface caused by excess charge, due to the increase in capacity. It changes sign therefore with the sign of excess charge present at the applied polarization, and this effect can be used to indicate the flat band condition or zero point of space charge. This technique has been used, *e.g.*, by Pleskov and Tyagai (16).

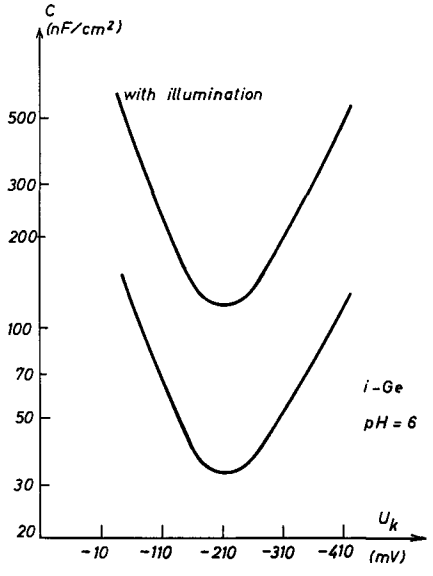

Fig. 3. Capacity data without and with illumination for i-Ge-electrodes in phosphate buffer solution at pH 6.

As Dewald pointed out, this theory is only applicable to describe the so-called instantaneous photoeffect where one assumes that the time for reaching the steady state of carrier distribution under illumination is small compared with the time of discharge of the double layer by an electrochemical reaction. This is a rather serious limitation for the quantitative analysis of photovoltage at semiconductor electrodes since in nearly all systems electrochemical reactions occur simultaneously.

Therefore we shall discuss here photovoltages under the condition of a constant current. Since the electrochemical reactions at a semiconductor electrode are normally controlled by the surface concentration of one type of carrier, this condition means that the concentration of the discharge determining electronic carrier is kept constant at the surface. Only in such cases, where more than one electrochemical reaction with charge transfer in different bands occurs simultaneously, as is the case in some corrosion processes, this boundary condition is not longer justified. The discussion of such conditions is much more complicated (17), and theoretical conclusions are difficult to verify.

Under the above assumption, the steady-state photovoltage can be derived from Eq. [2] and [8] for a surface reaction which is controlled by holes, *i.e.*, an oxidation process via the valence band. On the other hand, from Eq. [1] and the relation for Δn^*, corresponding to Eq. [8], the photovoltage for a reduction reaction via the conductance band as the rate-determining step can be calculated.

If we assume that the charge distribution in the space charge layer corresponds to equilibrium in spite of the fact that there is a flow of carriers through this layer, we can apply the equilibrium correlation for holes, to calculate the surface potential from

$$\rho_{\mu_p} = s_{\mu_p} + F\,(\psi_s - \psi_\rho) \qquad [12]$$

The index ρ means the value at the termination of the space charge layer in the interior and index s the surface values. From Eq. [2] we obtain the photovoltage $\Delta\psi_R^*$

$$\Delta\psi_{R^*} \equiv \psi_s^* - \psi_s - (\psi_\rho^* - \psi_\rho)$$

$$= \frac{1}{F}\left[\rho_{\mu_p}^* - \rho_{\mu_p} - (s_{\mu_p}^* - s_{\mu_p})\right] \qquad [13]$$

With $^*\psi_s = \psi_\rho = \psi_i$ (no Dember potential) and $s_{\mu_p}^* = s_{\mu_p}$ (p_s = const as boundary condition), we get from Eq. [2] and [9] for an electrode process controlled by holes at constant current

$$\Delta\psi_R^* = \frac{\Delta\mu_p^*}{F} = \frac{RT}{F}\ln\left(1 + \frac{\Delta p^*}{p_o}\right)$$

$$= \frac{RT}{F}\ln\left(1 + \frac{I_L - I_{RS}}{I_{p,o}}\right) \qquad [14]$$

Contrary to the instantaneous photopotential this reaction controlled photovoltage $\Delta\psi_R^*$ does not change its sign with the sign of the surface charge. Equation [14] shows further that the magnitude of $\Delta\psi_R^*$ depends mainly on p_o, so that in this case a large effect can be found only for n-type materials.

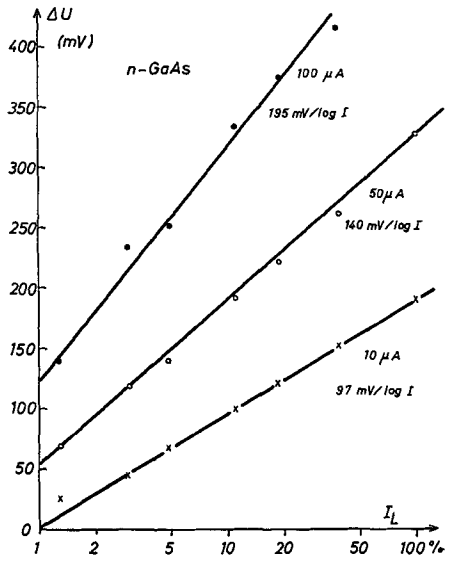

Fig. 4. Photovoltage in relation to light intensity for n-GaAs-electrodes (0.001 ohm cm) under constant anodic current in 1N H_2SO_4.

The photovoltage as measured in a galvanic cell against a reference electrode has the opposite sign of $\Delta\psi_R^*$, since a galvanic cell of this type includes the potential difference $(\psi_i - \psi_s)$ as one of the additive potential jumps at the interfaces of the cell. We see, therefore, that the electrode potential of a semiconductor with an anodic process at constant current is shifted to the negative (cathodic) direction by illumination.

Analogously, an electrode under cathodic polarization and with rate control by electrons will show the corresponding photovoltage

$$\Delta\psi_R^* = -\frac{\Delta\mu_n^*}{F} = -\frac{RT}{F}\ln\left(1+\frac{\Delta n^*}{n_o}\right) = -\frac{RT}{F}\ln\left(1+\frac{I_L - I_{RS}}{I_{n,o}}\right) \quad [15]$$

This photovoltage has the negative sign in $\Delta\psi_s$; therefore the electrode potential is shifted to more positive (anodic) values.

We have tried to verify these simple relations with GaAs electrodes where we know that the anodic dissolution is controlled by holes (18, 19) and the cathodic hydrogen evolution by electrons (20). A plot of the photovoltage ΔU_L in the galvanic cell formed by the reference electrode and the GaAs electrode is represented in Fig. 4 for a n-type electrode at three different currents. The photovoltage at p-type electrodes was negligible under anodic polarization as expected.

According to Eq. [8] we can expect that $\Delta p^* \sim \log I_L$ when $I_{RS} << I_L$. It is found indeed that a linear relation exists between ΔU_L and log I_L for the region $I_L >> I_{p,o}$ as shown in Fig. 4. But in disagreement with the theory above, the slope of this linear relationship is greater than the theoretical value 2.3 RT/F = 60 mv, indicating that this theory is not yet complete.

It is not difficult to see qualitatively where our assumptions will not be justified under the experimental conditions. In the derivation of Eq. [14], we have assumed that the equilibrium distribution is retained in the space charge layer. But if $I_L >> I_{p,o}$ and $I_{SR} << I_L$, the majority of electron hole pairs which are produced in the space charge layer have to drift to the interior. We have used light from a mercury lamp which is absorbed within a depth smaller or comparable with the extension of the space charge layer (compare Fig. 2). Therefore, an additional potential difference is necessary to adjust the flow rate of both carriers to the steady-state condition of equal drift rate through the space charge layer. This additional value of $\Delta\psi^*_{SC}$ is like a diffusion potential (Dember potential) for carrier drift through the space charge layer. We cannot yet present a rigorous calculation of this effect, but the results in Fig. 4 indicate a relationship similar to Eq. [4].

The experimentally obtained relation for large enough illumination intensities is approximately as follows

$$\Delta U_L = -(1+a)\frac{RT}{F}\cdot\ln I_L + \text{const} \quad [16]$$

The sign and magnitude of $\Delta\psi^*_{SC}$ depends on the excess charge at the surface. For enrichment of rate-controlling carriers in the space charge layer, the sign is the same as $\Delta\psi^*_R$. That is certainly the case for an inversion layer as we had in the experiments of Fig. 4. For depletion of rate-controlling carriers in the space charge, the sign is opposite to $\Delta\psi^*_R$.

A proof for this explanation of the photoresponse in Fig. 4 could be given by the following experiment. If one uses a thin slice electrode with a thickness comparable to the mean free path of minority carriers, and illuminates this slice from the back side, which is in contact with air, then the minority carrier concentration at the inner side of the space charge of the electrode should vary linearly with I_L. But in contrast to the direct illumination of the electrode surface itself, a smaller number of electron hole pairs is drifting under this condition to the electrode surface from the interior. When the surface recombination is negligible, pratically no drift should transverse the space charge layer to the electrode surface, and $\Delta\psi^*_{SC}$ should be very small.

The photovoltage under constant current for such a slice electrode under illumination of the front and back electrode sides has been studied. We found indeed that at small current the photovoltage under illumination of the back side had about the theoretical slope of 60 mv. Such experiments seem to allow us to distinguish between these two sources of photovoltage.

But as seen already in Fig. 4 the constant current load of the electrode itself also causes a deviation of the equilibrium distribution in the space charge layer since the slope of the ΔU_L — log I_L plots increases for greater currents. The reason is that the anodic current applied to the electrode needs an additional voltage difference in the space charge layer to drive the excess holes, necessary for the reaction, to the surface. This effect would be negligible only for the case where $j << I_{p,o}$. Unfortunately, this condition cannot be fulfilled in such experiments since other difficulties then arise.

At n-type GaAs of 0.1 ohm cm the saturation current $I_{p,o}$ is of the order of 10^{-6}-10^{-5} amp cm^{-2}. If we used anodic currents of the order of 10^{-6} amp cm^{-2}, then the surface concentration of electrons was changed under strong illumination to such an extent that in parallel to the anodic process hydrogen discharge occurred which consumes electrons. Under these conditions the external current is no longer equivalent to the anodic reaction rate, and the assumption, p_s = const, no longer holds. Therefore, we had to do our experiments at higher anodic polarization, and the results under too weak illumination cannot be compared with theory.

The technique of backside illumination for thin slices may be a useful device to supplement the analytical tools for studying semiconductor electrode reactions by investigating the effects of carrier injection from other sources, as was first done in the transistor-

like arrangements of Brattain and Garrett (15) or Pleskov (21).

It may be mentioned briefly that the shift of corrosion potential under illumination with cathodic control of the oxidant in an etching solution with injection of holes can be explained in the same way as a photovoltage under constant current, as was shown earlier for germanium (22). Much more difficult to discuss is the corrosion situation with hydrogen evolution as the cathodic process because both bands are then involved in the surface reactions, and again no simple boundary condition for the space charge layer surface can be given. In general, it may be concluded that the photovoltage at electrodes where electrochemical reactions disturb the balancing conditions for the motions of electrons and holes have to be analyzed with great caution.

Photocurrent under Constant Electrode Potential

Another experimental condition very easy to verify is the control of electrode potential under illumination. When only one electrode reaction controlled by one kind of charge carriers determines the faradaic current, the illumination must in any case increase the electrode reaction rate. Assuming again equilibrium distribution throughout the space charge layer, the surface concentration of both carriers at constant $\Delta\psi_s$ should be proportional to their concentration at the inner side of the space charge layer at distance ρ from the surface.

$$n_s = n_\rho^* \exp\left(+\frac{\Delta\psi_s}{\phi}\right)$$

$$p_s = p_\rho^* \cdot \exp\left(-\frac{\Delta\psi_s}{\phi}\right) \qquad [17]$$

With the assumption that the current is proportional to either n_s or p_s, the increase in current should be directly proportional to this increase in carrier concentration at point ρ

$$\Delta j_p^* = \Delta p_\rho^* \cdot \exp\left(-\frac{\Delta\psi_s}{\phi}\right)$$

$$\Delta j_n^* = \Delta n_\rho^* \cdot \exp\left(\frac{\Delta\psi_s}{\phi}\right) \qquad [18]$$

These equations show how greatly the photocurrent depends on the value of $\Delta\psi_s$.

So far, this kind of photoresponse seems to be easily understood. Unfortunately, it is largely impossible to fulfill the assumptions in this derivation over a greater region of light intensities. The reason is once again the necessity for the flow of carriers through the space charge layer disturbing the equilibrium distribution there. Worse than in the preceding section, in the case of a photocurrent at constant potential, a unipolar drift through the space charge layer becomes necessary which increases rapidly with illumination intensity. Therefore, the relation between Δj^* and Δp_ρ^* or Δn_ρ^* will no longer be linear.

Another simple correlation can only be expected under saturation current conditions where the transport of the reacting carriers to the surface is rate determining, that is in the potential range of saturation current for the electrode reaction. This can be verified experimentally for an electrode specimen where these carriers are in the minority. We have then an inversion layer at the surface, if the electrode is biased into reversal direction. If the applied voltage is high enough, then all carriers which reach the space charge region are then separated by the strong electrical field in this inversion layer. One kind of carrier only moves to the surface; the other is either held back or is rapidly transferred to the interior. The quantum efficiency for the photocurrent for illumination of the front side will reach at high polarization the value of one since the chance for recombination will then become very small.

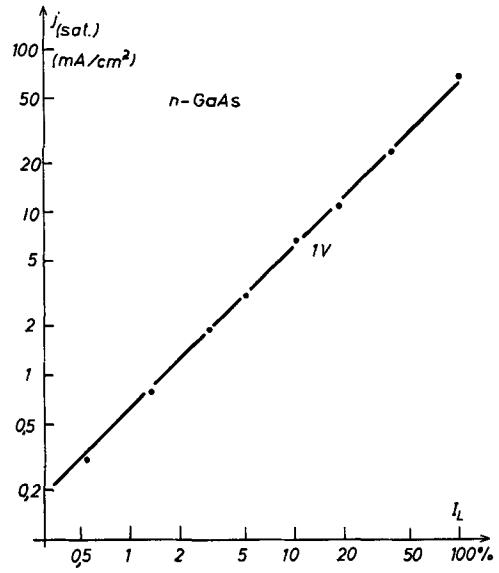

Fig. 5. Saturation current light intensity plot for n-GaAs under anodic polarization of +1v.

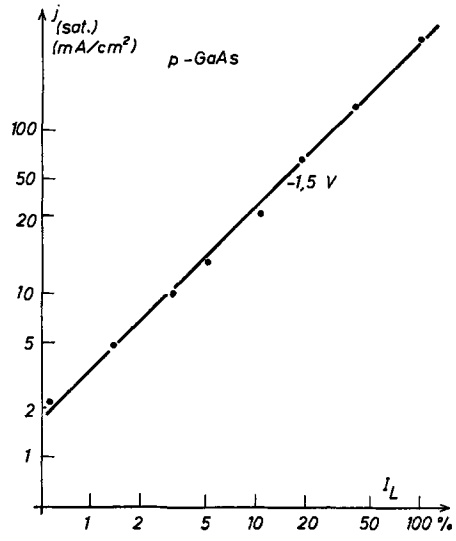

Fig. 6. Saturation current light intensity plot for p-GaAs under cathodic polarization of —1.5v.

Figure 5 represents the result of such an experiment for a n-type GaAs electrode under anodic polarization showing the linearity of photocurrent with light intensity.

Figure 6 gives the analogous results for p-type GaAs under cathodic polarization.

Photodecomposition of a Semiconductor Electrode with Large Energy Gap

Photoeffects at semiconductors are more pronounced as the band gap energy increases. This can be concluded from Eq. [1] and [2] since either n_o, p_o, or both concentrations are extremely small in such a semiconductor. The electrochemical reactions will then be controlled simply by one type of charge carrier, and simultaneous reactions in both bands at the same electrode become very improbable. Typical examples for such systems are CdS (b and gap: 2.4 ev) and ZnO (band gap: 3.2 ev).

Williams (23) has discussed the photovoltaic effect for this and other binary compounds in a very stimu-

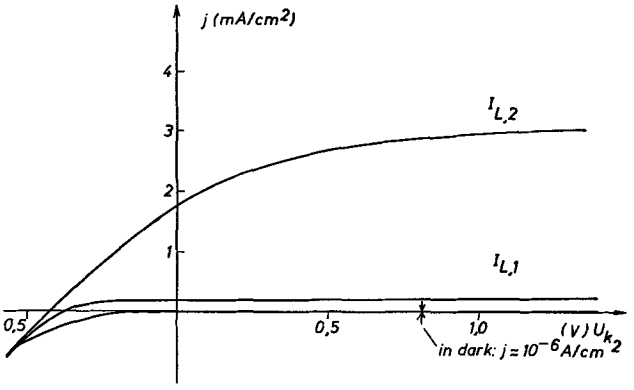

Fig. 7. Current voltage curves for CdS in 1N KCl (pH 5.6) under illumination.

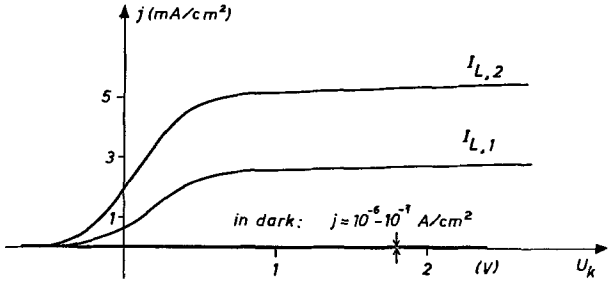

Fig. 8. Current voltage curves for ZnO in H_2SO_4 (pH 3) under illumination.

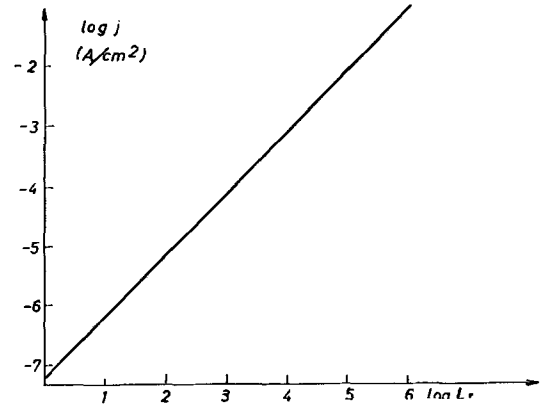

Fig. 9. Photocurrent in dependence on light intensity for ZnO electrode in saturation region.

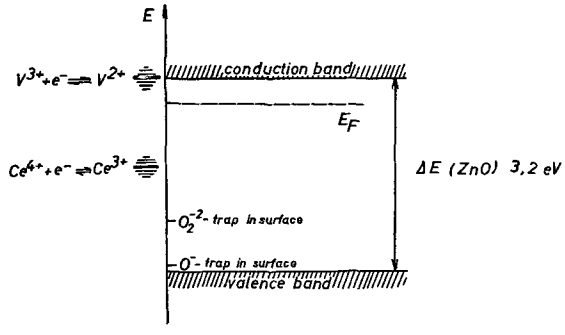

Fig. 10. Schematic correlation between semiconductor and electrolyte electronic energy levels for ZnO electrode.

lating paper. He observed that CdS is decomposed under illumination with anodic polarization into Cd^{+2} ions and sulfur. Two electrons are liberated in this process, which must be written as

$$CdS + 2h\nu \rightarrow Cd^{2+} \cdot aq + S + 2e^-_{CdS} \qquad [19]$$

By this reaction the semiconductor becomes negatively charged with respect to the solution as long as the electrons are not led away from the CdS electrode. This can be done by anodic polarization. Therefore, an anodic current flows through the electrode under illumination as shown in the current voltage curves for a CdS electrode in Fig. 7. The anodic saturation current at sufficiently high anodic polarization is proportional to the light intensity, as Williams already has found.

Without illumination, the anodic current is extremely small and depends on the rate of chemical dissolution of the crystals and on the metal excess in the ZnO. The behavior of ZnO electrodes is very similar as shown in Fig. 8. The cathodic branch of the current voltage curve represents hydrogen evolution (including some reduction to metallic zinc on the surface), and it is not influenced by illumination, as in the case of CdS electrodes. In the anodic region ZnO is decomposed under illumination, to give $Zn^{2+} \cdot aq$ and oxygen according to the following reaction

$$2ZnO + 4h\nu \rightarrow 2Zn^{2+} \cdot aq + O_2 + 4e^-_{ZnO} \qquad [20]$$

The photocurrent under sufficiently high anodic polarization increases linearly with light intensity as shown in Fig. 9. The quantum efficiency reaches the value of one within the limits of the accuracy of our analysis.[1]

This behavior can be explained in full analogy to the results with nonpolar or less polar semiconductors like Ge or GaAs. Figure 10 gives a schematic representation of the energy correlation between the bands in ZnO at flat band situation and the electronic energy terms in an electrolyte characterized by the electronic energy levels of two typical redox systems. Since all obtainable specimens of ZnO are n-type and the reduction of hydrogen ions can occur easily via electron transfer from the conduction band, the conduction band must be in the region of the electronic levels of the hydrogen redox system to allow this kind of charge transfer (7, 24, 25). This picture is confirmed by data of Dewald (8) on the electrode potential for flat band situation derived from capacity measurements.

Due to the large band gap in ZnO, no interacting redox energy levels in the electrolyte can be expected in the energy region of the valence band, because this energy would correspond to redox couples with standard potentials in the order of +3v.

Under illumination at flat band condition, the holes produced by the light diffuse through the crystal until they can recombine with an electron. Few holes reach the surface, but since there is no electron donor of this energy level available in the solution, these holes will be reflected to the interior, if they are not to recombine there.

It seems to be only a small chance that a hole may be trapped on the surface. A trapped hole on the surface is something like an O^- ion on the surface when we accentuate the partial ionic character of the chemical bond in the ZnO crystal. Such an incompletely charged ion is more weakly bonded to the crystal lattice and may therefore be able to change its local position in the lattice. By such a process, a stable trap level should be formed above the normal valence band energy levels. If such an O^- ion is able to accept a second hole, the bond to the lattice will be completely broken and an adsorbed O atom will be formed. Such surface traps have already been discussed frequently, *e.g.*, by Collins and Thomas (26) and by Heiland (27).

As our results indicate, the second hole may be more easily trapped at the neighboring oxygen ion forming in the second step primarily $(O\text{-}O)^{-2}$ ionic

[1] After this paper was written, an investigation of the behavior of ZnO electrodes under illumination was published by Lohmann (28) in which fully analogous current voltage curves are reported as given here.

groups with two remaining bonds attached to the lattice. In this way more energy can be gained by the formation of the O-O bond and the O_2 molecule structure is obtained on the surface. This process is emphasized by the observation that almost no hydrogen-peroxide could be found in the solution as a product of the photodecomposition. (Analytical results indicated a small formation of H_2O_2, but to less than 6% and confirmed, on the other hand, the production of O_2 by the illumination with about 95% efficiency.) After addition of two more holes the final molecular oxygen bond is formed by retaining two electrons from the original lattice bonds. Thereafter the O_2 molecule can easily be desorbed from the surface. Such hypothetical energy levels for O^- and $(O\text{-}O)^{-2}$ are included in the schematic plot of Fig. 10.

The probability for this process described above will become very high under anodic polarization. Since no inversion layer can be formed for such a semiconductor, due to the fact that the thermal generation of holes is by far too slow, the surface area is depleted of electrons, and the space charge is built up only by the immobile positively charged donors. The Mott-Schottky approximation is valid in describing the charge distribution. For our purpose, it is only important to know that under anodic polarization a strong electrical field is built up in the space charge layer which completely separates electrons and holes generated in this area. The electrons are driven to the interior, and the holes accumulate at the surface. The same happens with holes produced further inside in so far as they reach the space charge layer by diffusion. This situation is represented in Fig. 11.

Obviously, the formation of oxygen at the surface according to the reaction described above now becomes very probable since the complete separation of electrons and holes in the space charge layer fully prevents recombination at the surface. If the space charge layer is extended so far into the interior as to include the whole region of light absorption, the quantum efficiency for this charge separation and the following decomposition reaction should approach the value of one, as was confirmed in the experiments.

The current transfer to the electrolyte is completed by Zn^{2+} ions easily leaving their surface position in the lattice at those points where the neighboring oxygen ions have already left their normal lattice places. Rate determining for this photochemical decomposition are the reactions of the holes in the surface. The overall reaction may be summarized in the following steps

$$ZnO + 4h\nu \rightleftharpoons ZnO + 4e^- + 4p^+$$
$$O_s^{-2} + p^+ \rightarrow O_s^- \quad \text{slow}$$
$$O_s^- + O_s^{-2} + p^+ \rightarrow (O\text{-}O)^{-2} \quad \text{slow}$$
$$(O\text{-}O)^{-2} + 2p^+ \rightarrow O_2 \quad \text{fast}$$
$$2Zn_s^{2+} + aq \rightleftarrows 2Zn^{2+} \cdot aq \quad \text{fast}$$
$$2Zn + 4h\nu \rightarrow 2Zn^{2+} \cdot aq + O_2 + 4e^- \qquad [21]$$

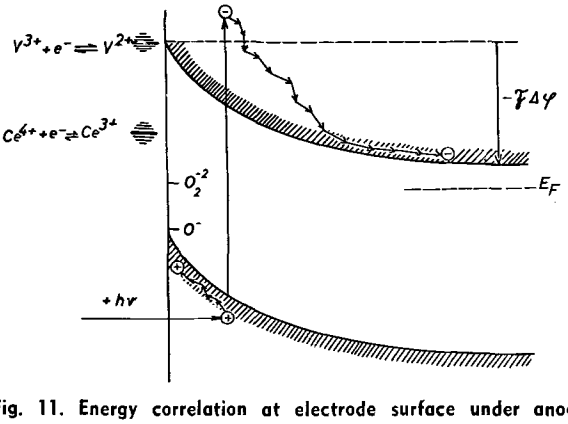

Fig. 11. Energy correlation at electrode surface under anodic polarization.

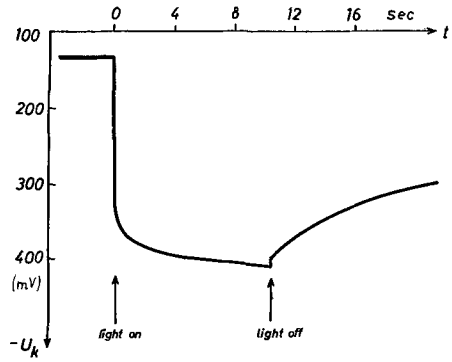

Fig. 12. Photoresponse of ZnO electrode at zero current in H_2SO_4 (pH 3).

The photochemical decomposition of CdS can be described analogously due to the accumulation of holes on the surface.

The photoresponse of a ZnO electrode in an open circuit is seen in Fig. 12. Characteristically, a very small fast photovoltage is built up after the beginning of illumination, followed by a slower increase of the photovoltage over a relatively long period. The photovoltage disappears very slowly after stopping the illumination apart from a first fast drop. This can be explained by the small efficiency of the hole trapping process in Eq. [21] without an applied anodic polarization, due to the unprevented recombination. In an open-circuit electrons accumulate in the electrode in parallel with the rate of the irreversible oxygen formation in the surface. This causes the observed slow photo response in the negative direction. The fast response must represent the Dember potential. A steady state is reached when electrons leave the surface by means of a cathodic reaction at the same rate as holes are consumed in the anodic reaction Eq. [21]. This cathodic reaction for electrons will be the hydrogen evolution

$$2H^+ \cdot aq + 2e^- \rightarrow H_2 \qquad [22]$$

or any other electron accepting reduction process. We have observed, in agreement with this assumption, that the restitution of the reference potential in the dark is largely accelerated by a depolarizing redox system (as *e.g.* H_2O_2). Further, the photopotential in an open circuit is smaller in the presence of such a depolarizer.

All these experiments indicate clearly that the reactions of minority carriers are the controlling processes in such systems. For any process in which a crystal lattice is to be destroyed, holes will play this part in a semiconductor, since their presence weakens directly the strength of a chemical bond in a crystal. The equivalent role for electrons can only be expected at such semiconductors where electrons are the minority carriers and their reactions with electron acceptors in the electrolyte will control the reactivity. The last examples show that the combination of photochemical and electrochemical investigations can be very useful for the understanding of semiconductor reactions.

Acknowledgments

The author would like to thank his co-workers Miss I. Mattes, W. Mindt, and H. Tributsch for making the experiments analyzed in this paper. He would also like to thank Dr. M. H. Miles for correcting the English text. He is further much indebted to Professor G. Heiland for delivering the single crystals of ZnO used in these experiments.

REFERENCES

1. M. Heyrovsky and R. G. W. Norrish, *Nature*, **200**, 880 (1963); M. Heyrovsky, **206** 1356 (1965).
2. G. C. Barker, Paper given at the 14th meeting of CITCE, Moscow 1963.

3. *e.g.* W. Shockley, "Electrons and Holes in Semiconductors," 8. edit., D. van Nostrand Co., London (1963); R. Wiesner in "Halbleiterprobleme," III, p. 59, W. Schottky, Editor, F. Vieweg, Braunschweig (1956); J. Tauc, "Photo- and Thermoelectric Effects in Semiconductors," Pergamon Press, Oxford (1962); S. M. Ryvkin, "Photoelektrische Erscheinungen in Halbleitern," Akademie-Verlag, Berlin (1965).
4. K. Bohnenkamp and H. J. Engell, *Z. Elektrochem.*, **61**, 1184 (1957).
5. M. Green in "Modern Aspects of Electrochemistry," J. O'M. Bockris, Editor, vol. 2, p. 343, Butterworth, London (1959).
6. J. F. Dewald in "Semiconductors," ACS Monograph No. 140, N. B. Hannay, Editor, p. 727 Reinhold Publishing Corp., New York (1959).
7. H. Gerischer in "Advances in Electrochemistry and Electrochemical Engineering," Vol. 1, p. 139, P. Delahay, Editor, Interscience Publishers, New York, London (1961).
8. J. F. Dewald in "The Surface Chemistry of Metals and Semiconductors," H. C. Gatos, Editor, p. 205, J. Wiley & Sons, Inc., New York (1960).
9. H. U. Harten in "Festkörperprobleme," III, p. 81, F. Sauter, Editor, F. Vieweg, Braunschweig (1964).
10. V. A. Miamlin and Yu. V. Pleskov, *Usp. Khim.*, **32**, 470 (1963).
11. W. H. Brattain and P. J. Boddy, *This Journal*, **109**, 574 (1962).
12. M. Hofmann-Pérez and H. Gerischer, *Z. Elektrochem.*, **65**, 771 (1961); H. Gerischer, M. Hofmann-Pérez and W. Mindt, *Z. Elektrochem.*, **69**, 130 (1965).
13. J. Boddy, *J. Electroanalyt. Chem.*, **10**, 199 (1965).
14. W. H. Brattain and J. Bardeen, *Bell Syst. Tech. J.*, **32**, 1, (1953).
15. W. H. Brattain and C. G. B. Garrett, *ibid.*, **34**, 129 (1955).
16. Yu. V. Pleskov and V. Tyagai, *Doklady Acad. Nauk. SSSR*, **141**, 1135 (1961).
17. R. M. Lazarenko-Manervich, *Zhur. Fiz. Khim.*, **36**, 2066 (1962).
18. Yu. V. Pleskov, *Doklady Akad. Nauk. SSSR*, **143**, 1399 (1962).
19. H. Gerischer, *Z. Elektrochem.*, **69**, 578 (1965).
20. H. Gerischer, *Z. physik. Chem. N.F.*, In press.
21. Yu. V. Pleskov, *Doklady Akad. Nauk SSSR*, **130**, 302 (1960).
22. H. Gerischer and F. Beck, *Z. physik. Chem. N.F.*, **23**, 113 (1960).
23. R. Williams, *J. Chem. Phys.*, **32**, 1505 (1960).
24. H. Gerischer, *Z. physik. Chem. N.F.*, **27**, 48 (1961); F. Beck and H. Gerischer, *Z. Elektrochem.*, **63**, 943 (1959).
25. H. Gerischer in "The Surface Chemistry of Metals and Semiconductors," H. C. Gatos, Editor, p. 177, J. Wiley & Sons, Inc., New York (1960); *Record of Chem. Progress*, **23**, 135 (1962).
26. Collins and Thomas, *Phys. Rev.*, **112**, 388 (1958).
27. G. Heiland, *J. Phys. Solids*, **22**, 227 (1961).
28. F. Lohmann, *Z. Elektrochem.*, **70**, 87 (1966).

Discussion

W. Mehl: The depth of penetration of light seems to play an important role in the investigation of the photoeffects of electrode processes. As the extinction coefficient varies strongly with frequency near the absorption edge, I wonder if the author has done measurements in this frequency range.

H. Gerischer: The wavelength of the light is indeed a very important parameter. We have usually used light with energy much higher than the band gap. The light is absorbed then in a range very near to the surface and with relatively low anodic polarization the space charge layer is extended far enough into the interior as to achieve the situation indicated in Fig. 2. This is shown in the current-voltage curves by the fact that the anodic currents does not further increase with increasing voltage. For light with energy close to the band gap the current increases over a much greater voltage range as can be seen in a Fig. HG1.

In this figure, photocurrents at CdS electrodes are shown for two different wavelengths. The current under illumination of light with 4080Å wavelength reaches the saturation value at a polarization of 1v while the current under illumination with 5400Å light

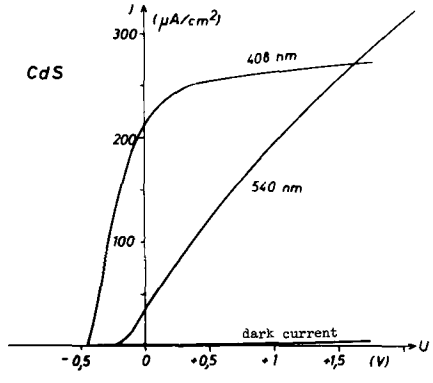

Fig. HG1

continues to increase up to much higher voltages. Since the space charge layer according to the Schottky-Mott theory for such systems expands proportionally to $\sqrt{u}$, it is possible to obtain from such measurements information on the absorption coefficient of the light of a particular wavelength.

W. W. Harvey: The quantitative discrepancies between measured photoeffects for GaAs electrodes reported by Professor Gerischer and the predictions of the relations developed in his paper are likely the result of inadequacies in the physical model. In single-crystal germanium electrodes (to which the model does pertain) the mean lifetime of the minority carriers is sufficiently long that the minority carrier diffusion length is generally large in comparison to the extent of the space charge region. Consequently, thermal generation of carriers in the latter region makes a small contribution to the limiting flux of minority carriers arriving at the surface by diffusion from the interior. In essence, then, for germanium it is necessary to take into account thermal generation of carriers only in the body and at the surface.

Turning now to a compound semiconductor such as GaAs, we note first that the best available crystals have lifetimes which are orders of magnitude smaller than those of germanium and silicon. Thus the diffusion lengths of minority carriers in compound semiconductors are generally very short, and it will no longer be valid to neglect thermal generation in the space charge region in comparison to that taking place within several diffusion lengths of the surface. Moreover, the statistical theory of generation and recombination of charge carriers in semiconductors indicates an enhancement of the net rate of generation in the field of the space charge. In semiconductors of short body lifetime and large gap, therefore, the major contribution to the limiting current of minority carriers arriving at the electrode surface may (in the absence of illumination) be made by thermal generation in the region of space charge (see, for example, Pleskov's initial paper[1] on GaAs electrochemistry and

[1] Yu. V. Pleskov, *Doklady Akad. Nauk SSSR*, **143**, 1399 (1962).

Myamlin's treatment[2] of anodic limiting currents for silicon electrodes).

The foregoing considerations lead me to question not only the applicability of Professor Gerischer's model to the semiconductor electrodes considered in his paper, but also whether, in fact, for the thin-slice experiments with GaAs the thickness was comparable with the diffusion length (certainly not with the "mean free-path," as stated) of the minority carriers. As I showed some years ago,[3,4] for thin-slice electrodes it is necessary to take into account thermal generation in the vicinity of the back surface. For n-type germanium, the measured limiting anodic current at the front surface increased linearly with the intensity of light incident upon the back surface, and a family of intersecting lines was obtained whose slopes were determined by the magnitude of recombination velocity at the back surface. Similar considerations probably also apply to the GaAs experiments reported by Professor Gerischer, with the additional complications resulting from space-charge generation.

H. Gerischer: I agree with you that the analysis of the thin slice experiments with GaAs is rather questionable. The deviations in results from the assumptions of our simplified model can be caused to a substantial extent by the effects you have mentioned. We found rather poor reproducibility of these results with slices made from different crystals which obviously indicates a great influence of the recombination properties in the surface region. Much more work will have to be done before we understand the details.

Concerning the limiting current under saturation conditions, I think that the situation is much clearer since recombination at the surface where minority carriers are consumed becomes very unlikely then. Also in the exhaustion layers, recombination should be very small. I would expect therefore that in this case the influence of field strength on recombination should not be detectable. Our results with regard to the saturation current under illumination are in good agreement with this assumption.

[2] V. A. Myamlin, *Doklady Akad. Nauk SSSR*, 139, 1153 (1961).

[3] W. W. Harvey, *J. Phys. Chem. Solids*, 14, 82 (1960).

[4] W. W. Harvey, *J. Phys. Chem.*, 65, 1641 (1961).

G. C. Barker (communicated): Professor Gerischer is clearly correct in suggesting that when there is a minority carrier drift in the space charge region it is not possible to derive an expression for the potential drop across the region that is both simple and exact. This is a difficulty which will persist, and I wonder what attempts have been made to tackle this problem theoretically. It clearly is one which also arises in connection with transistors, and I would imagine that workers in the transistor field must have given some thought to it. Of course it is easy today to construct electrical analogues of the diffuse double layer near an electrode and of the related space charge region within a semiconductor or within an ion exchange membrane. Further one can see that, in principle, it is possible to devise an analogue circuit which also takes account of drift of current carriers. The latter step is, however, more difficult and less elegant than the simulation of a space charge or a diffuse double layer at equilibrium, and I am not sure whether the effort would be worth while.

My second comment has to do with the results obtained with zinc oxide and cadmium sulfide crystals. I would like to ask what happens when the illuminated and anodically polarized crystal is in contact with a solution containing a common or related ion. Is there still corrosion of CdS in a sulfide solution and enhanced dissolution of zinc oxide in slightly alkaline solution. According to the mechanism proposed in the ZnO case there is no removal of holes at the interface by electrons supplied by ions or water molecules at the interface and I suspect that Professor Gerischer may say that the mechanism is unchanged in alkaline solution. However, it has to be noted that the $OH\text{-}OH^-$ standard potential is thought to be in the vicinity of 3v *vs.* NHE and direct transfer of electrons from adsorbed OH^- ions to holes in the valence band seems not impossible.

Finally I would suggest the addition of aliphatic alcohols or other organic OH scavengers to the anodically polarized ZnO system. Such additions might throw some light on the mechanism by which holes are consumed at the surface though I doubt whether it would be possible to distinguish between reactions induced by OH radicals and those induced by O^- ions formed in the way suggested in Professor Gerischer's paper.

Photocurrents Produced by Ultraviolet Irradiation of Mercury Electrodes

II. Factors Influencing Photocurrents Caused by Electron Emission

G. C. Barker, A. W. Gardner, and D. C. Sammon

Atomic Energy Research Establishment, Harwell, Didcot, Berkshire, England

ABSTRACT

The influence on the photocurrent of factors such as wavelength, scavenger concentration, ionic strength, diffusion coefficient of the hydrated electron, and the nature of products of the scavenging reaction, is considered. The discussion is illustrated by experimental data obtained by a variety of methods, and some preliminary results for substantially monochromatic light are described which lead to approximate relative rate constants for the scavenging of hydrated electrons by some simple inorganic ions and molecules.

The presence of certain reducible solutes (1-3) in an inert electrolyte solution in contact with a uv irradiated mercury electrode gives rise to a photocurrent (i_p) proportional at low concentration (C_s) to $C_s^{1/2}$. This current might be caused by: (*a*) homogeneous or heterogeneous photolysis (4) followed by reduction at the electrode of one or more products of the photolytic reaction; (*b*) excited water molecules (5) that

are formed at the electrode surface and react with the solute as they diffuse away from the surface; (*c*) excited mercury ions at the surface that react with solute present in the compact part of the double layer; (*d*) hydrogen atoms formed by the dissociation of adsorbed water molecules (6) that reduce the solute as they diffuse away from the electrode surface, their oxidation at the electrode surface being a fairly slow process; (*e*) hydrated electrons formed directly at the interface by electron transfer to water molecules situated in the compact part of the double layer. These electrons, although thermodynamically unstable as regards oxidation by the electrode, return to the electrode fairly slowly (apparent rate constant of the order of 100 cm s^{-1}) and some of them diffuse away from the electrode. While so doing they are captured by the solute molecules or ions; (*f*) a variant on (*e*) involving the indirect formation of hydrated electrons (1) at varying distances from the electrode surface. The electrons ejected from the electrode leave with a variable amount of kinetic energy and travel some distance through the solution before being hydrated.

Although at high solute concentration currents due to (*a*) may occur with certain solutes (NO_3^-, BrO_3^-) this mechanism cannot account for the concentration dependence of the photocurrents considered in this paper. Mechanism (*c*), could lead to a current that is not linearly related to C_s, but is not consistent with (*i*) the observed rather slight dependence of i_p on supporting electrolyte concentration (1) and (*ii*) the insensitivity of i_p to the charge on the solute ion or molecule when the ionic strength is small. All of the remaining mechanisms involve the diffusion away from the electrode of an entity produced by the radiation, and each is superficially consistent with the observed concentration dependence. In the present paper attention is largely focussed on mechanisms (*e*) and (*f*). Studies of the influence of ionic strength on i_p show that the current is partly if not entirely due to one of these mechanisms, and comparative and competitive photocurrent experiments lead to rate constants for electron scavenging in fair agreement with those obtained in other ways. Although H atoms may well be formed they probably contribute little to the photocurrent as scavenging rate constants are often two or more orders of magnitude smaller than the corresponding rate constants for the scavenging of hydrated electrons (13). The same may be true for excited water molecules.

Experimental

In all experimental work the test electrode has been a dropping mercury electrode (DME) as the initial experiments showed clearly that surface contamination could greatly influence the potential dependence of i_p when H_3O^+ is the scavenger. Advanced polarographic equipment has been used exclusively to study i_p as such equipment makes it possible to measure a minute photocurrent in the presence of a very much larger faradaic current due either to the reduction of the scavenger or to the reduction of small amounts of species such as oxygen arising from slow photolysis of the electron scavenger.

Measurements of i_p have invariably been made at controlled potential. Five related experimental approaches have been employed. In the first experiments (MP 1) square wave modulated light from a 100w medium pressure mercury lamp was used, the lamp (quartz envelope) being mounted alongside a quartz polarographic cell (solution light path *ca.* 5 mm). The potential dependence of the amplitude of the square wave (225 cps) component of the photocurrent was studied with a square wave polarograph (SWP). Later a more elaborate apparatus (MP 2) was used to make more precise comparative measurements of i_p for different scavengers. A four electrode cell was used (DME, reference electrode, cathodically polarized mercury pool counter electrode, and Ag polarizing electrode) with a solution light path of about 1 cm. The mean value of the lamp voltage was automatically regulated by controlling the temperature of the air in a quartz jacket surrounding a 100w medium pressure lamp, and the lamp current waveform was regulated electronically. Appreciably higher light intensity than in the MP 1 experiments was obtained by forming an image of the mercury discharge in the plane of the test electrode using quartz lenses. The square wave component of i_p was again measured with a SWP.

To study the residual current in the absence of a scavenger a 250w high-pressure mercury arc (compact source) was used. Square wave modulated intense light was obtained in these experiments (HP) by placing a slotted rotating disk in the light path. As in the MP 2 work an image of the arc was formed at the surface of the test electrode. The solution light path was *ca.* 2 cm.

Recently in comparative and competitive scavenging experiments substantially monochromatic 2537Å light from a low-pressure mercury discharge lamp (5w Vycor envelope) has been used. In these experiments (LP) rectangular modulation of the light was needed, and this was produced by increasing the power dissipated in the lamp by a factor of *ca.* 4 for a time interval of about 1/25 sec starting about 2.5 sec after the start of growth of the mercury drop, this delay time being controlled by a pulse polarograph (PP). This polarograph was used to study the potential dependence of the average change in the current supplied to the DME at constant potential over a time interval of 1/50 sec starting 1/50 sec after the increase in light intensity. Owing to the diffuse nature of the light source no attempt was made to focus light on the test electrode, and the lamp was merely mounted alongside a cell with a cylindrical quartz section which surrounded the mercury drop (solution light path *ca.* 1 cm). The current flowing through the lamp was stabilized, and the laboratory temperature was held constant to $\pm$ 0.5°C.

Studies have been made of the time dependence of i_p using the HP apparatus, by varying the phase of the modulation relative to the phase of the current sampling circuit of the SWP. Also an inexpensive 25 J electronic flash source (xenon in Pyrex envelope, flash duration 400 μsec) has been used for the same purpose. The variation of i_p with time at substantially constant potential was studied with an oscilloscope connected to the output terminals of the main current amplifying circuit of the PP. This instrument controlled the potential of the DME, and it also could be used to record the potential dependence of the integrated charge lost by the DME during the light flash.

The transparency of the various solutions to the radiations employed was studied with a Unicam spectrophotometer Type SP 500, and quantitative deductions from experimental data have not been made without applying corrections if the absorption of any wavelength contributing appreciably to the photocurrent exceeded 5%. Such absorption was only of importance in work with NO_3^- and NO_2^- and prior exposure to uv light was minimized as far as possible in experiments with these scavengers.

With both the SWP and the PP measurements were made at predetermined times in the drop life and the constancy of the mercury flow rate was monitored by measuring the double layer capacity of the DME at the measurement time using the normal circuits of the polarographs. Information such as the potential dependence of i_p was usually automatically recorded, and over the years some 10^5 bits of recorded information have accumulated. Throughout the paper experimental values of i_p are expressed in arbitrary units. "Saturation" photocurrents (amp cm^2) were not larger than $2\ 10^{-6}$ (MP 1), 10^{-5} (MP 2), $4\ 10^{-5}$ (HP), $2\ 10^{-6}$ (LP), and 10^{-3} (unfiltered flash).

Solutions were prepared from triply distilled water.

Reagent grade chemicals were used, and in some instances, where freedom from impurities which might act as scavengers was important, recrystallization or calcination was resorted to, usually without producing a marked improvement. A complicated pretreatment of the solutions which is mentioned later was made use of in studies of the residual current. Normally the solutions were deoxygenated (often before forming the mercury pool counter electrode to avoid H_2O_2 formation) by bubbling purified nitrogen through the solution in the cell, hydrogen or argon being used occasionally. Anaesthetic grade N_2O was used without purification as it contained virtually no oxygen and negligible amounts of other impurities which were either polarographically reducible (NO,NO_2) or which could act as electron scavengers. Solutions containing known concentrations of N_2O were prepared by mixing known volumes of N_2O saturated electrolyte solution and argon saturated electrolyte solution and then rapidly injecting the mixture into an argon filled cell. Alternatively if an exact knowledge of the N_2O concentration was not vital, solutions containing N_2O at a low concentration were obtained by introducing a known volume of electrolyte solution into the cell, saturating this with N_2O, and then bubbling argon through the cell at controlled rate for a known length of time. The N_2O concentration decreased exponentially with time, and concentrations down to 10^{-4}M could be obtained with an accuracy better than 10% if the temperature of the solution and of the inflowing gas was held constant.

Early measurements were made at the ambient temperature (20° ± 2°C). Recent measurements (LP) have been made in a small thermostatted room (17° ± 0.5°C).

Diffusion Coefficient of the Hydrated Electron

The diffusion coefficient of the hydrated electron has been determined by studying the transient change in the electrical conductivity[1] of very dilute NH_4OH solutions (~3 10^{-6}M) when irradiated with a pulse of 4 Mev electrons from a linear accelerator. These solutions were prepared from conductivity water taking steps to destroy organic matter and to eliminate CO_2 and other inorganic impurities and then were carefully deoxygenated and saturated with hydrogen to destroy OH radicals formed by the decay of H_2O^+. A large voltage had to be applied to the electrodes of the conductivity cell to obtain a signal well above interference signals from the accelerator, and this voltage was applied in the form of a rectangular pulse starting shortly before the accelerator pulse (~3 μsec duration) and lasting 10^{-4}—5 10^{-4} sec. Figure 1 is typical of the results obtained. During the accelerator pulse an increase in conductivity is observed which is partly due to the formation of hydrated electrons in the solution and partly to H_3O^+ ions (~3 10^{-7}M)

[1] Similar experiments have recently been reported by Schmidt and Buck. The Argonne workers find a value for D_e of 4.7 10^{-5} cm^2 sec^{-1} in agreement with the later value here reported.

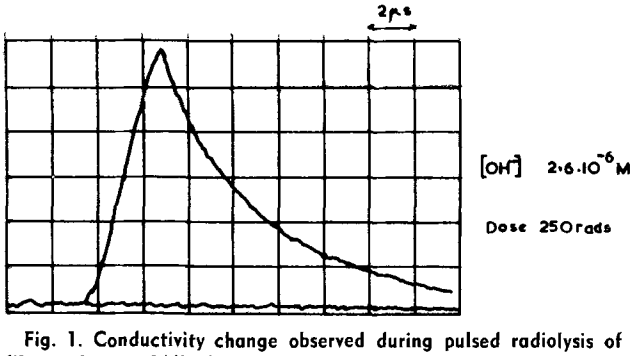

Fig. 1. Conductivity change observed during pulsed radiolysis of dilute solution of NH_4OH.

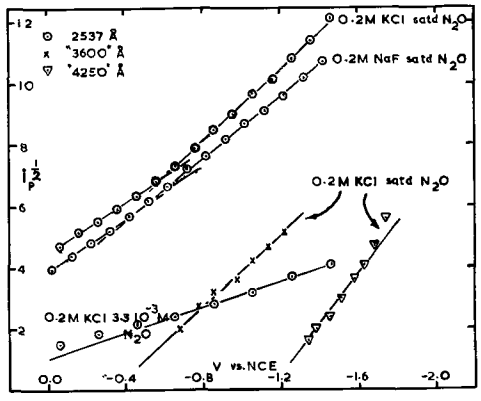

Fig. 2. Influence of wavelength on i_p

formed by the decomposition of H_2O^+. The H_3O^+ ions are mainly consumed by OH^- ions in the solution, and the hydrated electrons are removed somewhat more slowly by reaction with H_3O^+, and with OH radicals, as well as by a second order reaction of the electrons with themselves. One thus might expect the conductivity decay to be rather complex, but in reality it is almost exactly a simple exponential decay. As the consumption of H_3O^+ by OH^- tends to produce a solution which contains hydrated electrons and an equivalent deficit of OH^- ions, this simple first order decay of the change in conductivity indicates that the electron mobility is almost equal to that of the OH^- ion. In the present paper a value for *De*, the diffusion coefficient of e^-_{aq} of 5 10^{-5} cm^2 sec^{-1} is used.

Photoemission of Electrons

It is to be expected that the photoemission of electrons using monochromatic light will be influenced by the potential of the electrode in much the same way as the yield for photoemission into a vacuum is affected by the quantum energy.

Ignoring for the moment possible complications introduced by the discreteness of the charges in the double layer the effective work function should decrease steadily as the potential becomes more negative and, as has been suggested by Delahay (3), a linear relation between $i_p^{1/2}$ and potential should be observed. Such a relation holds for emission *in vacuo* and some degree of linearity is predicted by Fowlers theory (14). Figure 2 shows the dependence of $i_p^{1/2}$ on potential for several solutions containing N_2O. This electron scavenger is ideal for such studies as experiment suggests that electron capture over a wide range of potential is an irreversible process and that the way in which i_p varies with potential is unaffected by reactions following the scavenging reaction. The photocurrent is time invariant for elapsed times in the range 0.1-20 msec and, as it is unlikely that N_2O^- has a half-life in neutral or slightly alkaline solution larger than 0.1 sec, the complete photocurrent mechanism is probably

$$e^-_{aq} + N_2O \rightarrow N_2O^- \qquad (a)$$

$$N_2O^- \rightarrow N_2 + O^- \text{ (fast homogeneous reaction)} \qquad (b)$$

$$O^- + H_2O \rightarrow OH + OH^- \text{ (neutral or slightly alkaline solution)} \qquad (c)$$

Almost all the OH radicals so formed will be directly or indirectly reduced (*e.g.*, $OH + Cl^- \rightarrow Cl + OH^-$, $Cl + e \rightarrow Cl^-$) at all accessible potentials. Over a wide range of potential the capture of a hydrated electron by N_2O leads to the loss of a further electron by the electrode, and two electrons are thus permanently lost by the electrode.

Considering first the results for substantially monochromatic 2537Å light it is seen that the plots for

0.2M KCl and 0.2M NaF saturated with N_2O (3.1 10^{-2}M) at atmospheric pressure appear to have two linear portions which intersect at potentials close to the ECM potentials (E_{ecm}) for these solutions. Superficially the presence of specifically adsorbed Cl^- at the interface does not greatly influence the plot (the slightly smaller values of i_p for the fluoride solution are probably due to a trace of mercurous ion). Extrapolation to the potential axis of the linear portions for $E > E_{ecm}$ gives a value of 0.85 ± 0.15v *vs.* NCE for the apparent threshold potential when 2537Å radiation is used. With solutions saturated with N_2O a substantial fraction of the hydrated electrons are captured, and the photocurrents are comparable with the saturation photocurrent i_{ps}. With lower values of C_s the experimental accuracy decreases somewhat but for a scavenger concentration of 3.3 10^{-3}M there is still some indication of a change in slope near E_{ecm}.

The general behavior with 2537Å light seems to be indicative of photoemission, but the change in slope suggests that emission may be slightly influenced by ions adsorbed at the electrode. It was shown earlier (1) that the photocurrent produced by H_3O^+ is not noticeably dependent on the nature of the cations adsorbed at the surface when the electrode carries a large negative charge. Early work also showed that the magnitude of the current was little affected by the electrolyte concentration for concentrations between 1 and 0.2M. Thus it would seem that the factor influencing the rate of emission of electrons with light of constant wavelength (or polychromatic light of constant chromatic composition) is the potential of the electrode with respect to the bulk of the solution, rather than some factor closely connected with the double layer structure and composition. One suspects immediately that the current is produced mainly by electrons having energies sufficiently large to travel distances large compared with the half-thickness of the diffuse double layer. However, it would be remarkable if the electrical double layer did not in some way affect the potential variation of the photocurrent.

The change in the slope of the $i_p^{1/2}$ plots near the ECM may possibly be due to discreteness of the charge in the double layer. With an idealized compact double layer of constant thickness one imagines that the effective work function of the mercury surface would decrease steadily as the potential became more negative, the rate of decrease of work function being only slightly smaller than the rate of change of potential if e^-_{aq} is formed indirectly. Let us assume that the probability of emission of electrons is determined by some function such as $\exp \gamma/f$ where f is the local field strength at the mercury surface. [Functions such as this arise in field emission (7).] Introducing discreteness of charge into the picture gives a change from a uniform field to one with large fluctuations from the average value. Negative fluctuations due to a surface excess of cations will have a greater effect on emission than the positive ones due to an excess of anions. Expressed somewhat differently, the presence of discrete negative charges only tends to suppress emission over a small fraction of the surface, and the average rate is much the same as if the negative charge is evenly distributed over the plane of closest approach for the anions. A surface excess of cations, however, greatly enhances emission over a small fraction of the total surface and produces a larger increase in the average rate as compared with the value when the charge is smoothed out over the plane of closest approach. Tentatively the change in slope thus will be attributed to preferential emission in the vicinity of adsorbed cations. This effect should presumably be most readily detected at high scavenger concentration but it should still influence i_p at low scavenger concentration if the average range of the electrons prior to thermalization is large compared with the thickness of the compact part of the double layer.

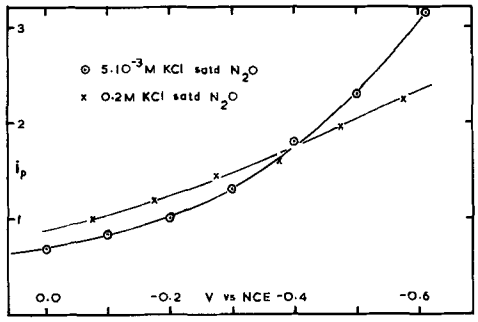

Fig. 3. Influence of ionic strength on N_2O photocurrent

Influence of Adsorbed Anions on the Ψ Potential

Although at high ionic strength i_p is not very sensitive to the ionic strength, double layer effects can be detected at low ionic strength.

Figure 3 shows the variation with potential of the "saturation" photocurrent for 0.2M and 5 10^{-3}M KCl saturated with N_2O (no correction has been made for the slight decrease with increasing electrolyte concentration of the solubility of N_2O). At $E < E_{ecm}$ the current is larger for the more dilute solution. This effect is predicted qualitatively by theory given later. Due to electromigration of electrons in the diffuse double layer, the current approaches more closely i_{ps}. More surprising is the decrease in current when the electrolyte concentration is reduced if the electrode is positively charged. A similar but smaller decrease was observed with 2 10^{-2}M KCl when the electrode carried an appreciable positive charge. According to the model introduced by Grahame (8) which is often used in the interpretation of electrocapillary data, specific adsorption of anions produces a reversal in the sign of the Ψ potential. The photocurrent measurements suggest that if such a reversal does occur it is quite localized and that the Ψ potential over an appreciable fraction of the surface changes sign when the sign of the charge on the electrode changes. The decrease in photocurrent can be attributed to electromigration of hydrated electrons in regions where the Ψ potential is positive in sign. If this interpretation of the experimental results is correct, the study of photoemission at electrodes may cast new light on the structure of the double layer.

Energetics of Photoemission

It was suggested in Part I (1) that photoemission should commence close to the ECM with light of wavelength 2500Å as the quantum energy then roughly equals the work function of mercury. This naïve suggestion ignored many factors, one of which was the change in energy level on transferring an electron from *vacuo* to a medium of finite electronic polarizability. There is some doubt as to the effective dielectric constant of water when a fast moving charge is involved, but it is conceivable that the change in energy level could be sufficient to account for the threshold potential for 2537Å light. Taking the effective radius of the free electron in water to be of the order of 2Å, an effective dielectric constant of 2 would produce a change of energy level of about 40 kcal, *i.e.*, 1.7 ev. The conversion of a thermal electron to a hydrated electron involves a further change in energy level. It is currently believed (9) that the heat of hydration is about 50 kcal. This is with respect to the electron *in vacuo* and the heat of hydration for a thermal electron in water is presumably appreciably smaller, possibly no larger than 10-15 kcal. Clearly the possibility that there may be a small number of free electrons in water containing hydrated electrons cannot be ruled out.

It is generally assumed that when hydrated electrons are formed homogeneously by light absorption by cer-

tain anions they are formed directly within the solvent cage round the ion. However, as Dainton (10) has pointed out, the rapid approach to a limiting quantum yield in scavenging experiments is not consistent with theory based on such a small separation of the partners. This difficulty vanishes if it is assumed that free electrons are ejected from the ions and that these electrons travel a short distance before becoming hydrated. In this case also one can postulate emission made possible not by the hydration energy of the hydrated electron but by the polarizability of the medium.

It will be clear by now that the mechanism which we favor for the photocurrent is indirect formation of hydrated electrons some distance away from the electrode. Three distinct steps are envisaged. First the ejection of an electron from the electrode,[2] second the thermalization of the electron, and finally its hydration. The last step may take place fairly slowly, and thermal electrons may travel a short distance before hydration takes place. Undoubtedly an appreciable fraction of the ejected electrons will return to the electrode before being hydrated, but those which escape from the double layer region are eventually converted into hydrated electrons. All the experimental facts known to us are consistent with this mechanism, but as the evidence in some instances cannot be regarded as conclusive the general behavior if the photocurrent were caused by hydrated electrons formed directly at the interface is briefly considered in later sections.

Influence of Wavelength

An obvious parameter to vary is wavelength. The importance of doing this has long been recognized, but the work of early workers (11) did not lead to results of permanent value. Unfortunately the photocurrent is often small, and after the insertion of a monochromator in the light path the current may be too small to measure.

In Fig. 2 there are two plots of $i_p^{1/2}$ obtained with 0.2M KCl saturated with N_2O and the flash source. Combinations of Wratten filters were used to vary the position of the pass band and to reduce the bandwidth of the light path. The characteristics of the shorter wavelength radiation were maximum intensity I_m close to 3600Å, 0.5 I_m at 3450 and 3750Å, 7.5% I_m at 3200Å and 2% I_m at 3000Å. Those of the longer wavelength radiation were I_m close to 4250Å, 9.5% I_m at 4000Å, 31% I_m at 4400Å, 1% I_m at 3800Å, 1% I_m at 4800Å. These radiations were not as monochromatic as one would wish, but they provide some semiquantitative information about the behavior when long wavelengths are used. In both cases the plot of $i_p^{1/2}$ against potential is fairly linear. There are no reliable points for potentials more negative than about —1.6v *vs.* NCE because at such potentials the reduction of N_2O commences and a spurious photocurrent due possibly to heating of the interface by the absorbed radiation is observed. The "4250Å" radiation was closer to being monochromatic than the "3600Å" radiation and consequently the apparent threshold potential obtained by extrapolation of data for the former radiation is more reliable. Extrapolation gives —1.14 ± 0.05v *vs.* NCE for the "4250Å" radiation and —0.36 ± 0.1v *vs.* NCE for the "3600Å" radiation, the latter value being in all probability somewhat too positive due to the presence of wavelengths somewhat shorter than 3600Å.

Approximate though these results are they serve to show that the apparent threshold potential changes considerably as the wavelength increases, changing by 1.99 ± 0.25v when the wavelength changes from 2537Å (4.86 ev) to 4250Å (2.92 ev). Actually the change in threshold potential should be somewhat larger than the change in work function as ejected energetic electrons presumably lose a little energy while passing through the compact part of the double layer. It should be mentioned that our results do not agree with the recent work of Heyrovsky (2b). For N_2O and several other scavengers the rate of change of threshold potential with quantum energy (E/ev) was found by him to be close to 0.5. Such a value and a mechanism based on electron emission are mutually inconsistent.

[2] The quantum efficiency is dependent on wavelength and potential and is about 0.07% at —1.5v *vs.* SCE for 2537Å light.

Influence of Scavenger Concentration

Results reported earlier (1) for solutions containing H_3O^+ ions were interpreted on the basis of scavenging by H_3O^+ of hydrated electrons diffusing away from the electrode surface. A simplified model was employed in which all the hydrated electrons are deposited in a deposition plane distance δ away from the surface. Capture within the region $0 < x < \delta$ is ignored but for $x > \delta$ hydrated electrons are consumed by

$$e^-_{aq} + S \rightarrow S^- \qquad (d)$$

and

$$i_p/i_{ps} = Q\delta/(1 + Q\delta) \qquad [1]$$

where $Q = (k_sC_s/D_e)^{1/2}$, D_e is the diffusion coefficient of the hydrated electron, k_s is the rate constant of the scavenging reaction ($M^{-1}s^{-1}$), C_s is the scavenger concentration, i_p is the photocurrent, and i_{ps} is the saturation photocurrent for $C_s \rightarrow \infty$. In the derivation of [1] it is assumed that hydrated electrons move only by diffusion and that their motion is uninfluenced by the field in the diffuse double layer. Strictly i_p and i_{ps} refer to 1 cm² of electrode surface.

The aperiodic equivalent electrical circuit for this model is the one shown in Fig. 4a. The diffusion of e^-_{aq} in the region $x > 0$ is represented by the motion of charge along a resistive transmission line (12) (no inductance) with constant series resistance R_{tl} and shunt capacity C_{tl} per unit length, and the homogeneous capture of hydrated electrons is allowed for by uniformly distributing shunt resistance R_s along the line for $x > \delta$. The deposition of e^-_{aq} is represented by an infinite impedance current generator of magnitude i_{ps} at $x = \delta$, and the photocurrent i_p is the difference between i_{ps} and the current at $x = 0$. The short circuit at this point implies diffusion-controlled capture of electrons by the electrode.

$$R_{tl} = \theta/D_e, C_{tl} = 1/\theta, \text{ and } R_s = \theta/k_sC_s \quad [2], [3], \text{ and } [4]$$

where θ is arbitrarily chosen (it is connected with the equivalence of voltage and hydrated electron concentration) and has the dimensions ohm cm sec^{-1} if the circuit refers to 1 cm² of electrode surface.

In the rapidly attained steady state (see later section) for constant i_{ps} the shunt capacity is of no importance and looking to the right the impedance at $x = \delta$ equals $(R_{tl}R_s)^{1/2}$. The circuit thus reduces to

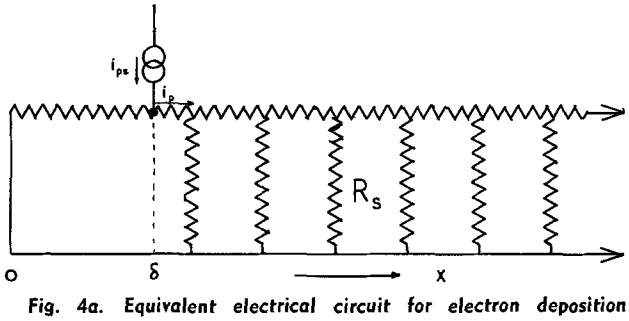

Fig. 4a. Equivalent electrical circuit for electron deposition model: exact circuit.

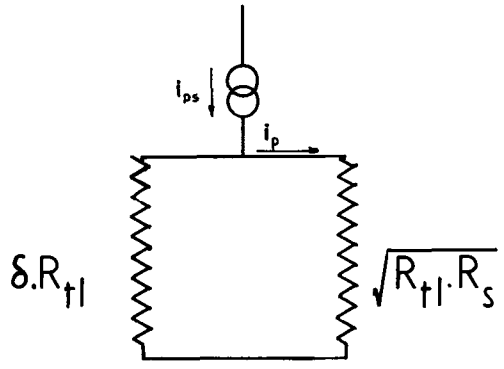

Fig. 4b. Equivalent electrical circuit for electron deposition model: reduced form for constant light intensity.

the one in Fig. 4b. The injected current i_{ps} is now partitioned between two resistors of value $R_{tl}\delta$ and $(R_{tl}R_s)^{1/2}$ and Eq. [1] readily follows.

If it cannot be assumed that every encounter of a hydrated electron with the electrode results in transfer to the electrode the short circuit at $x = 0$ is replaced by a resistance $R_e = \theta/k_e$, where k_e (cm sec^{-1}) is the electron transfer rate constant (the apparent rate constant if dissociation of e^-_{aq} precedes transfer and is the rate-controlling step). In this case

$$i_p/i_{ps} = Q\delta'/(1 + Q\delta') \qquad [5]^3$$

where $\delta' = \delta + D_e/k_e$. Thus the apparent range prior to hydration is increased by D_e/k_e and the δ values given later could possibly be attributed to a value for k_e of the order of 10^2 cm sec^{-1}.

Distributed Deposition of Charge

To estimate the effect of distributed charge deposition and to take account of scavenging in the region in which hydrated electrons are formed, it is necessary first to derive an expression for the photocurrent produced by deposition at the plane x^1 when the scavenger concentration is uniform for $x > 0$. The equivalent circuit for zero electron concentration at $x = 0$ takes the form shown in Fig. 5. The semi-infinite line used previously is replaced by an infinite line with the same electrical characteristics, and zero concentration at $x = 0$ is obtained by placing at $-x^1$ a negative image of the current source at x^1. The photocurrent di_p is the difference between the current di_{ps} deposited at x and the current flowing at $x = 0$, and

$$di_p = di_{ps}\,(1 - \exp\text{-}Qx) \qquad [6]$$

Thus, if the rate of deposition of charge is $F(x)$

$$i_p/i_{ps} = \int_0^\infty (1 - \exp\text{-}Qx)F(x)\,dx / \int_0^\infty F(x)\,dx \qquad [7]$$

As yet the form of $F(x)$ is unknown and only two special cases will be considered.

(*i*) $F(x) = A(2\delta - x)$ for $0 < x < 2\delta$ and 0 for $x > 2\delta$, A being a constant. This might be approximately

[3] Equation [5] holds for scavenging of other entities produced by radiation (H atoms excited H_2O molecular) after appropriate changes in parameters.

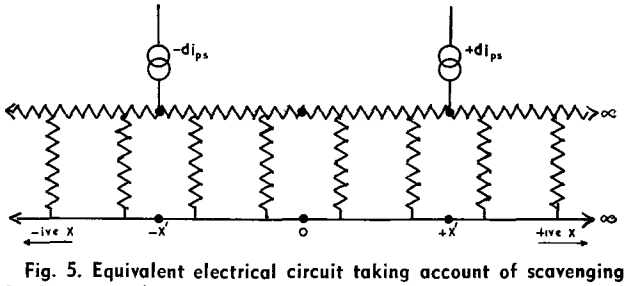

Fig. 5. Equivalent electrical circuit taking account of scavenging for $0 < x < \delta$.

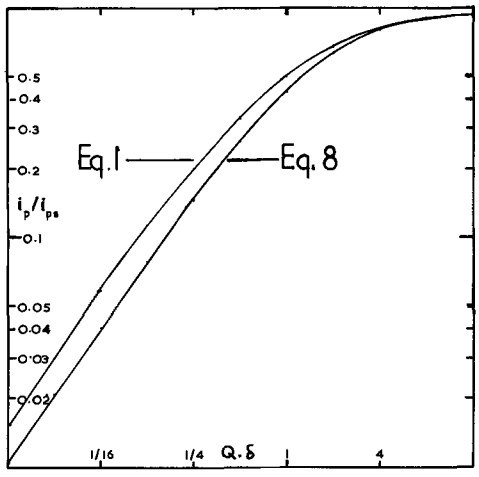

Fig. 6. Dependence of i_p/i_{ps} on $Q\delta$

applicable when unfiltered polychromatic light from a high-pressure mercury arc or from a flash source is used. Equation [7] leads to

$$i_p/i_{ps} = 1 - \tfrac{1}{2}Q^{-2}\delta^{-2}\exp\text{-}2Q + \tfrac{1}{2}\delta^{-2}Q^{-2} - \delta^{-1}Q^{-1} \qquad [8]$$

Figure 6 shows that the variation of i_p/i_{ps} with $Q\delta$ predicted by this equation is similar to that given by Eq. [1].

(*ii*) $F(x) = A\exp\text{-}x/\delta$. This case arises if the hydration of thermal electrons is a slow process. Using Eq. [7] it follows that i_p/i_{ps} is given by Eq. [1]. Without exact knowledge of $F(x)$ there must be uncertainty about the variation of i_p at high C_s and, of course, i_{ps} cannot be readily determined. However, the order of magnitude of the apparent range prior to

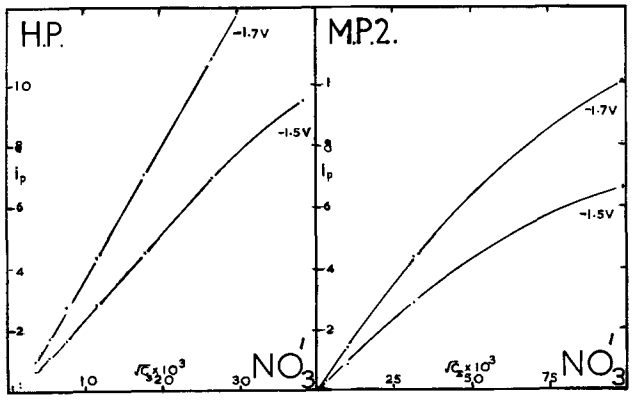

Fig. 7a and b. Dependence of i_p on $C_s^{1/2}$:KNO_3 in 1M KCl

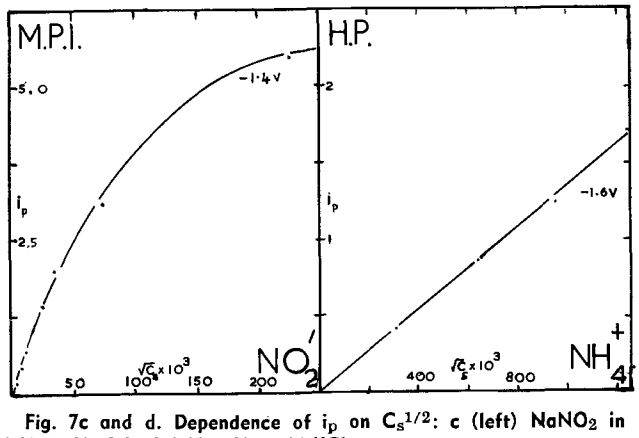

Fig. 7c and d. Dependence of i_p on $C_s^{1/2}$: c (left) $NaNO_2$ in 0.2M KCl; d (right) NH_4Cl in 1M KCl.

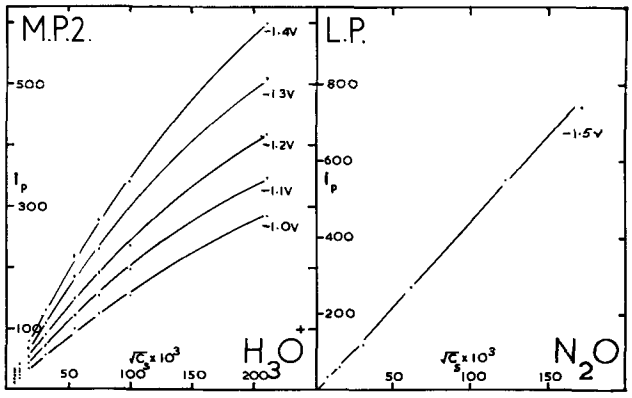

Fig. 8. Dependence of i_p on $C_s^{1/2}$: a (left) $HClO_4$ in 1M KCl; b (right) N_2O in 0.2M KCl.

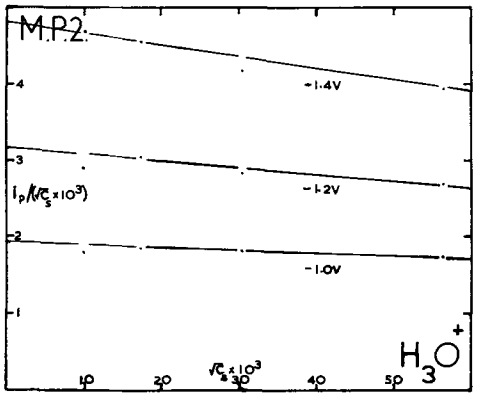

Fig. 9. Variation of i_p $C_s^{-1/2}$ with $C_s^{1/2}$

hydration probably can be estimated using Eq. [1] or [8].

There is no uncertainty about the variation of i_p when C_s is small. Provided that the light intensity is not so large as to cause depletion of the solution, and that due allowance is made for competing scavenging by impurities and by the solvent, it is to be expected that i_p at low C_s will be proportional to $C^{1/2}$. This expectation has been confirmed by us (1) and by Delahay (3) and it is well borne out by the graphs in Fig. 7 and 8.[4] In the NH_4^+ case the linearity is maintained to the highest concentration as k_s in this case is unusually small. In other cases (H_3O^+, NO_3^-, NO_2^-) some departure from linearity is observed at high scavenger concentration which cannot in the H_3O^+ case be attributed to light absorption, although this is a contributory factor with NO_3^- and NO_2^-. Only the experimental data for H_3O^+ are suitable for the evaluation of δ. For localized deposition and the two types of distributed deposition considered earlier i_p/i_{ps} can be written in the approximate form

$$i_p/i_{ps} \cong AQ\delta(1 - BQ\delta) \qquad [9]$$

Thus a plot of $i_p/C_s^{1/2}$ against $C_s^{1/2}$ should be linear up to moderately large values of $Q\delta$ with a slope ABi_{ps} $\delta^2 k_s/D_e$. If Eq. [1] is used $AB = 1$, while Eq. [8] leads to a value for AB of 1/3. Three such plots based on the H_3O^+ data are given in Fig. 9. The slopes lead to values for δ of 34, 41, and 48Å, respectively, at the potentials —1.0, —1.2, and —1.4v *vs.* SCE if $AB = 1$, and to values larger by the factor $3^{1/2}$ if $AB = 1/3$. A value for k_s of 1.4 10^{10} M^{-1} sec^{-1} is here assumed, and i_{ps} is obtained by extrapolation.

It is to be expected that δ will increase as the potential becomes more negative if during the thermalizing process the electrons travel an appreciable distance. Slow hydration after very rapid thermalizing should not lead to a dependence of δ on potential if the

[4] All potentials refer to SCE.

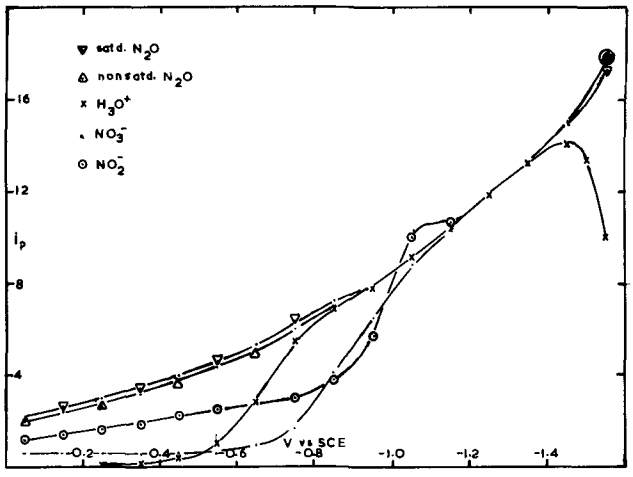

Fig. 10. i_p curves for various scavengers in 0.2M KCl normalized at —1.3v, 2537Å radiation.

transfer of electrons back to the electrode is a diffusion controlled process. It is doubtful whether the experimental data are sufficiently precise for the above potential dependence of δ to be regarded as significant. However, evidence for such a dependence is also provided by measurements of i_p/i_{ps} using a high and a low value of C_s. For H_3O^+ this current ratio increases by 18 ± 5% when the potential is changed from —1.0 to —1.4v *vs.* SCE. A similar but slightly smaller increase has been found for N_2O in 0.2M KCl. These results suggest that the rather long range of the electrons prior to hydration cannot be entirely attributed to slow hydration of thermal electrons.

Dependence of i_p on Potential and Nature of Scavenger

Photocurrents are observed with many inorganic and organic scavengers, but it is profitable, when considering evidence for electron emission, to give most attention to simple systems in which there is no strong adsorption of the scavenger at the interface and which are relatively free from complications introduced by homogeneous or heterogeneous photolysis of the scavenger. Thus in the present paper only experimental results for scavenging by N_2O, H_3O^+, NO_3^-, NO_2^- and by the ions of Cd, Zn, and Ni are considered in any detail. Even some of these systems turn out to be quite involved.

Although polychromatic light is often entirely satisfactory for comparative measurements of i_p at low C_s using different scavengers, it is generally desirable in studies of the potential dependence to use either monochromatic light of wavelength below 3000Å or at least polychromatic light (line or continuum) containing no wavelengths longer than 3000Å. These desiderata were not fully appreciated in our early work and effects to be observed with light of short wavelength were sometimes partly masked.

In Fig. 10 are plotted photocurrent curves for various scavengers in 0.2M KCl. The curves are normalized at —1.3v *vs.* SCE; 2537Å radiation was used, the scavenger concentration was 10^{-3}M and 0.2M KCl was used to avoid light absorption by mercurous ions (the solubility of Hg_2Cl_2 increases as the Cl^- concentration increases). An important feature of the curves is their tendency to coalesce at values of the potential more negative than —1.2v *vs.* SCE. The fall in i_p in the H_3O^+ case at potentials more negative than —1.5v is, of course, due to the fall in scavenger concentration at the electrode surface connected with the onset of the h.e.r. This coalescence points to a common factor which we believe to be electron emission followed by scavenging of hydrated electrons.

At more positive potentials the behavior is more complex. Only with N_2O does i_p increase smoothly as

the potential becomes more negative. With H_3O^+ hardly any photocurrent is observed until the potential reaches —0.45v *vs.* SCE. Shortly after this potential the current rises rapidly and the curve then merges into the N_2O curve. With NO_3^- as the scavenger a small current is observed at the most positive potential which can be used. This current at first changes only slowly as the potential becomes more negative, but in the vicinity of —0.8v *vs.* SCE the i_p curve rises fairly rapidly to join the N_2O curve. NO_2^- behaves in yet another way. An appreciable current roughly equal to half the normalized current for N_2O is observed at potentials positive with respect to —1.0v but i_p increases rapidly at about —1.0v and the current curve slightly overshoots the N_2O curve before joining it at still more negative values of the potential. These peculiar but not unexpected effects can be attributed to reactions involving the unstable products of the scavenging reactions. Only in the case of N_2O do such reactions not influence the shape of the i_p/E curve although electron scavenging in this case is followed by homogeneous and heterogeneous reactions.

If the entity S^- formed by electron capture is stable in solution (possibly only because second order reactions of S^- in pairs are unimportant due to the low concentration) it may be oxidized by the electrode and the captured electron, if this happens, is returned to the electrode. In such circumstances i_p clearly will be small. Thus the rather rapid increase in the H_3O^+ photocurrent might be attributed to the cessation of the oxidation of either H atoms formed by electron capture or H_2^+ ions formed heterogeneously at the electrode surface [homogeneous formation is too slow (13) a process to account for suppression of i_p at small values of elapsed time]. Examination of the rising part of the curve shows that it resembles in shape a polarographic wave for an irreversible reduction, rising from 10-90% of its "limiting" value in a potential interval of about 200 mv. This is consistent with a totally irreversible oxidation process involving 1 electron and having an α value of about 0.5. However, the position of the "wave" seems to be not markedly temperature dependent, a fact which is possibly not consistent with a high degree of irreversibility. As some results considered later suggest that i_p for H_3O^+ at more negative potentials is partly due to the participation of H atoms (formed in the scavenging reaction) in the atom-ion reaction[5]

$$H + H_3O^+ + e \rightarrow H_2 + H_2O \quad \text{(irreversible c.t.r.)} \quad [e]$$

it is possible that the rapid rise in i_p is due to competition between this reaction and the oxidation reaction

$$H_2O + H \rightarrow H_3O^+ + e \quad \text{(irreversible c.t.r.)} \quad [f]$$

If the rates of both reactions are similarly influenced by temperature, the "half-wave" potential will be insensitive to changes in temperature.

Speculative explanations for the behavior of NO_3^- and NO_2^- can also be advanced. In the NO_3^- case the half-life of NO_3^{2-} may be sufficiently long to permit oxidation of it at the electrode surface when the potential is more positive than —1.0v *vs.* SCE. At more negative potentials this oxidation ceases and NO_3^{2-} is removed by

$$NO_3^{2-} + H_2O \rightarrow NO_2^- + OH + OH^- \quad \text{(homogeneous)} \quad [g]$$

The OH radicals are then directly or indirectly reduced by the electrode and hence the capture of one electron leads, when the potential is very negative, to the permanent loss of 2 electrons by the electrode. The small current observed at the most positive potential which can be employed with 0.2M KCl might be due to incomplete oxidation (see next section) of NO_3^{2-} or even to scavenging of H atoms formed by the radiation. In this connection it should be noted that the H atom scavenging reaction is presumably

$$H + NO_3^- \rightarrow NO_2 + OH^- \quad \text{(homogeneous)} \quad (h)$$

and if the reduction of NO_2 is a rapid charge transfer reaction

$$NO_2 + e \rightarrow NO_2^- \quad \text{(c.t.r.)} \quad [i]$$

the small contribution of the H atoms to the photocurrent might conceivably change only slowly with potential.

In the NO_2^- case the variation of i_p with potential is similar to the d-c polarogram for NO in a buffered solution of *p*H 7. The latter exhibits a large step following a small slowly rising wave, and the half-wave potential for the large step is roughly coincident with the rapid increase in the photocurrent. Also, if the solution is made strongly alkaline, the large step in the polarogram vanishes and so does the greater part of the step in the photocurrent curve. Thus it is likely that these two steps are due to the same electrode reaction. Presumably NO_2^{2-} is formed by electron capture in the photocurrent case and this unstable entity is possibly rapidly converted to NO

$$NO_2^{2-} + H_2O \rightarrow NO + 2OH^- \quad \text{(homogeneous)} \quad [j]$$

The NO then tends to be reduced at the electrode surface, but the polarographic experiments suggest that this reaction is slow, and little therefore of the NO formed would actually be reduced during the small time between the increase in light intensity and the current measuring time. Thus at potentials positive with respect to the sudden rise in i_p the photocurrent probably is roughly equal to the rate of capture of hydrated electrons. What happens at more negative potentials is less certain but the sudden increase in i_p, we believe, is initiated by a sudden change in the mechanism by which NO is reduced at the electrode surface. At more negative potentials than —1.0v *vs.* SCE it seems likely that reaction (j) may be followed by

$$NO + e \rightarrow NO^- \quad \text{(c.t.r.)} \quad [k]$$

and that NO^- (possibly after conversion to HNO) may be further reduced. In strongly alkaline solution (1M NaOH) the situation is clearer as polarographic experiments suggest that the reduction of NO then stops at NO^- and thus the capture of a hydrated electron by NO_2^- in strongly alkaline solution presumably leads to the permanent loss by the electrode of 2 electrons if the potential is very negative.

From the above discussion it is evident that the capture of a hydrated electron does not generally result in the permanent loss of 1 electron by the electrode. It is thus necessary to introduce a type of stoichiometric number which we shall term the electron transfer number v_s. This number, which may not in all cases be an integer, is defined as the number of electrons permanently lost by the electrode as a result of the capture of a hydrated electron in the solution. Thus the saturation current i_{ps} is the product of v_s and i_d, the rate of deposition of charge in the solution. The value of v_s may change in the presence of other scavengers and in what follows the superscript o is used to indicate the absence of other scavengers. A knowledge of v_s^o for different scavengers is often vital for the evaluation of rate constants from photocurrent data.

Electron Scavenging Followed by Oxidation of Reaction Product

The approximate equivalent electrical circuit (1 cm^2 of interface) for the case in which the product S^- of the scavenging reaction is stable as regards reaction with the solvent, and with any solute present, but is oxidized by a heterogeneous charge transfer process

[5] Or in the related reaction where the H_3O^+ is replaced by a water molecule, *i.e.*

$$H + H_2O + e \rightarrow H_2 + OH^-$$

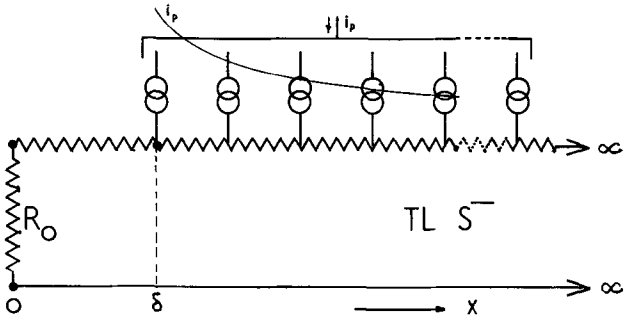

Fig. 11. Equivalent circuit taking account of oxidation of S^-

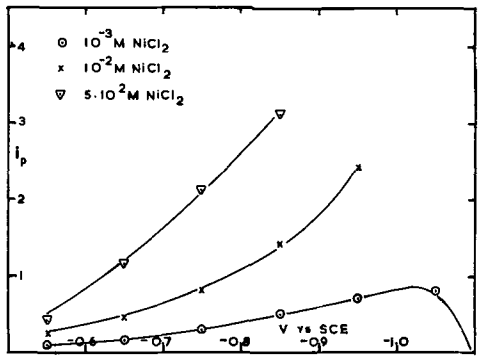

Fig. 12. Photocurrent observed with 0.2M KCl containing $NiCl_2$; polychromatic light.

involving only 1 electron, is the one shown in Fig. 11. The formation of S^- in the solution is represented by a vast number of current generators distributed along the length of a semi-infinite resistive transmission line connected with the linear diffusion of S^-. A resistance R_o linking the input terminals ($x = 0$) of the line takes account of the finite rate of oxidation of S^- at the electrode surface. The various electrical components are defined by

$$R_{tl} = \theta/D_{S-},\ C_{tl} = \theta^{-1},\ R_o = \theta/k_o \quad [10],\ [11],\ [12]$$

where k_o is the rate constant of the charge transfer process and D_{S-} is the diffusion coefficient of S^-. Using the localized electron deposition model the current generators supply current per unit length equal to $i_p\, Q \exp -Q(x-\delta)$ for $x > \delta$ where i_p is the photocurrent which would be observed if S^- were not oxidized. The actual photocurrent i_p^o is the difference between the total injected current and the current flowing through R_o. For large values of elapsed time a generator di_p at x gives rise to a photocurrent di_p^o given approximately by

$$di_p^o = di_p(x + D_{S-}/k_o)\,(\pi D_{S-}t)^{-1/2} \quad [13]$$

where t is the elapsed time since the application of the current di_p (*i.e.*, since the start of irradiation). It readily follows that the total observed photocurrent i_p^o is given approximately by

$$i_p^o = i_p(Q^{-1} + \delta + D_{S-}/k_o)\,(\pi D_{S-}t)^{-1/2} \quad [14]$$

if (*a*) the light intensity (alternatively the increase in light intensity) is constant for $t > 0$, (*b*) i_p is appreciably smaller than i_{ps}.

If $k_o \to \infty$ the photocurrent, which is connected solely with the diffusion of S^- away from the electrode, is small and relatively independent of C_s. Inserting typical values for the parameters ($D_{S-} = 10^{-5}$ cm^2 sec^{-1}, $k_s = 2\ 10^{10}$ M^{-1} sec^{-1} $C_s = 10^{-3}$M) it is found that $i_p^o/i_p \cong 5\ 10^{-4}\ t^{-1/2}$. In our experimental work with light from mercury discharges t has not usually been smaller than $2\ 10^{-3}$ sec, and hence any photocurrent produced by ions such as Cd(II) or Zn(II) should have been quite small. Experiment (MP1) showed that with these ions at concentrations up to 10^{-3}M i_p^o/i_p was not larger than 0.03 (taking for i_p one half of the H_3O^+ i_p for the same concentration of H_3O^+). This somewhat negative result is not inconsistent with electron capture followed by oxidation of S^-, but it clearly is desirable to repeat these experiments with more sensitive apparatus.

With 0.2M KCl containing Ni^{2+} or Mn^{2+} measurable photocurrents were observed up to the potentials at which reduction of the scavenger occurred. The results (MP.1) for Ni^{2+} are given in Fig. 12. At constant potential the photocurrent is roughly proportional to $C_s^{1/2}$ and as pulsed radiolysis (15) has shown that k_s for scavenging of e_{aq}^- by Ni^{2+} corresponds to diffusion control, it is conceivable that the photocurrent is due to slow oxidation of Ni^+ at the electrode surface. If the experimental data are fed into Eq. [14] it is found that k_o only increases slowly as the potential becomes more positive and has a value of the order of 0.25 cm sec^{-1} at -0.8v *vs.* SCE electrode. It is, however, doubtful whether this interpretation of the results is correct. It can be envisaged that electron capture sometimes may not lead instantaneously to the formation of S^- but rather to the formation of a type of ion pair e_{aq}^- S, the formation of S^- from the ion pair being an appreciably slower process than electron capture. So far no evidence for such a mechanism has been revealed by photocurrent studies using many different scavengers. This mechanism tends to destroy the linear relation between i_p and $C_s^{1/2}$ as the average life of the "ion pair" is dependent on its average distance from the electrode at the time it is formed, which increases as C_s diminishes (it is here assumed that encounters of "ion pairs" with the electrode will lead to rapid electron transfer to the electrode). It seems possible, however, that the Ni^{2+} photocurrent may be due to rapid reaction of a small fraction of the excited Ni^+ ions formed by electron capture with water molecules

$$Ni^{+*} + H_2O \to Ni^{2+} + H + OH' \quad \text{(homogeneous)} \quad [l]$$

the remainder being de-excited in other ways and oxidized by the electrode. This hypothetical photocurrent mechanism leads to the observed dependence of i_p on C_s.[6]

The photocurrent observed with Mn^{2+} is slightly smaller and can be similarly interpreted in at least two ways. Clearly all these systems require further study, but this is not a task to be lightly undertaken, especially in the case of ions of metals such as Pb, Tl, Cd, In, Cu, and Zn, because of the small value of i_p^o and the occurrence of apparent photocurrents due simply to heating of the interface by the absorbed radiation. With unfiltered light from a flash source or a high pressure mercury arc, i_{ph}, the heating current connected with the temperature coefficient of the double layer charge density, when largest is of the same order of magnitude as the residual photocurrent at the most negative potential in the absence of added scavenger.

Residual Photocurrent

The hydrated electron has a finite life in water and in dilute electrolyte solutions of pH < 9, decaying by the reaction

$$e_{aq}^- + H_2O \to H + OH^- \quad \text{(homogeneous)} \quad [m]$$

Early pulsed radiolysis experiments indicated a half-life of the order of 50 μsec, but more recent work (16) using lower electron concentrations and water stored in silica or polythene has given a value close to 500 μsec. Treating the decay reaction as a scavenging reaction the product k_sC_s has a value of about $2\ 10^3$ sec^{-1}, and a residual photocurrent is to be expected

[6] Yet another explanation would be that on arrival at the interface some of the Ni^+ ions are reduced although a substantial fraction are oxidized.

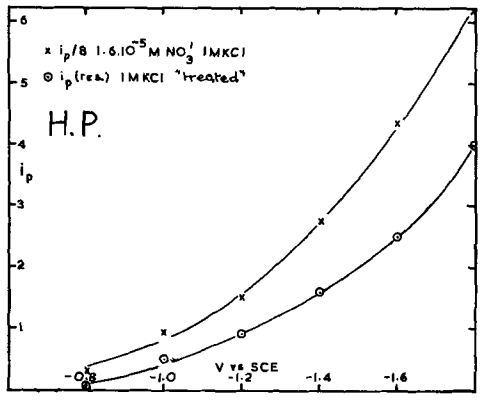

Fig. 13. Photocurrent produced by NO_3^- and the corresponding residual photocurrent.

which should be about 300 times smaller than $i_{ps}(v_s = 1)$.

The residual current has been studied using various light sources. The HP data are possibly the most reliable as greatest care was then taken in the preparation of solutions and also the measured currents then greatly exceeded the noise level of the SWP. Figure 13 shows the potential dependence of residual current with the measurement time interval adjusted to make the measurements insensitive to i_{ph} (the heating photocurrent). A scaled down i_p curve for NO_3^- ($1.6\ 10^{-5}$M) obtained under identical conditions is included in the figure, and it will be seen that the two currents vary in much the same way with potential. C_e^0, the electron concentration at the hypothetical deposition plane calculated using NO_3^- data, a value of $k_{NO_3^-}$ assumed later, and the equation

$$i_p = FC_e^0(k_sC_sD_e)^{1/2} \quad (1) \qquad [15]$$

did not exceed 10^{-11} mole cm^{-3} in these experiments and consequently removal of e_{aq}^- by the diffusion controlled second order reaction [17]

$$e_{aq}^- + e_{aq}^- \rightarrow H_2 + 2\ OH^- \quad \text{(homogeneous)} \quad [n]$$

was not of importance.

Calculations of the electron half-life based on the relative magnitudes of the residual and NO_3^- photocurrents (assuming $v_s = 1$ for the residual current) yielded values in the range 100-200 μsec for 1M solutions of KCl, Na_2CO_3, and Na_2SO_4 (solutions which were first made 10^{-2}M in SO_3^{2-}, irradiated with light from a high-pressure mercury lamp, oxygenated to destroy SO_3^{2-}, deoxygenated and irradiated to destroy H_2O_2). This treatment destroys impurities such as NO_3^-, NO_2^- but generally it did not reduce the residual i_p by more than a factor of 3. The *p*H after treatment was ~9 for the Cl^- and SO_4^{2-} solutions.

The slight discrepancy between the half-life deduced from the residual current and that now accepted by radiation chemists cannot be attributed to impurities in our solutions that are reduced at potentials more positive than −1.6v *vs.* SCE.

It is possible that the half-life may decrease in relatively concentrated electrolyte solutions. It has been suggested that there is some slight tendency for ion pair formation between inert cations at high concentration and hydrated electrons (18). Accelerated decay thus might be connected with the scavenging by protons produced by field dissociation of water molecules lying between the electron and the cation.

Time Dependence of the Photocurrent

As few experimental studies have been made of the time dependence of i_p it would be inappropriate to discuss this dependence at length, but it is important to show that the results so far obtained do not clash with the electron emission mechanism. Adopting once more the localized deposition model it follows from the solution of a closely related problem in heat conduction (19) (involving radiation from a semi-infinite rod with appropriate initial and boundary conditions) that for irradiation of constant intensity starting at $t = 0$

$$i_p/i_{ps} \cong Q\delta\ (1 - Q\delta)^{-1}\ [(\pi C_sk_st)^{-1/2} \exp - k_sC_st + \text{erf}\ (k_sC_st)^{1/2}] \qquad [16]$$

if i_p is appreciably smaller than i_{ps} and $t >> \delta^2/D_e$. It is assumed that $v_s = 1$. For small values of t, i_p tends to be large but a pseudosteady state is rapidly established, the current for $t = 2(k_sC_s)^{-1}$ being only 5% larger than the steady-state value. For diffusion-controlled scavenging ($k_s = 2\ 10^{10}$M^{-1} sec^{-1}) and a typical scavenger concentration (10^{-4}M) the steady state is virtually attained in 1 μsec.

Studies have been made (HP) of the variation of i_p with elapsed time using square wave modulated light and 1M KCl containing H_3O^+ at concentrations between 10^{-4}M and 1M. No variation was observed for values of t between the minimum value imposed by the SWP (~500 μsec) and the maximum value (~2.5 msec). More recently the i_p waveform at substantially constant potential for filtered (3200-3800Å) light produced by the flash source has been studied oscilloscopically. With 0.2M KCl solutions containing H_3O^+ at concentrations from 10^{-4}M upwards the waveform shape was independent of C_s and at all times it appeared to be almost identical with that observed when a uv vacuum photocell was irradiated. Even the residual current waveform at potentials where this current is largest, although slightly affected by a current connected with heating of the electrode-solution interface, was similar in shape to the light waveform.

In the case of the H_3O^+ photocurrent it is believed that at $E < -1.0$v *vs.* SCE $v_s = 2$. The results of the experiments with the flash source indicate that for steady illumination the current associated with the transfer of the second electron would attain a constant value in a time not greater than 100 μsec for H_3O^+ concentrations above 10^{-4}M. H atoms formed homogeneously have only a short distance to travel to arrive at the electrode and, although some must inevitably diffuse away from the electrode, the fraction so doing for values of the elapsed time greater than 100 μsec is small if the reduction of H_3O^+ ions by reaction (*e*) is a rapid process. There should however, be some slight variation in i_p for very small values of elapsed time. As yet our experimental techniques have not permitted a search for this second order effect.

Influence of Ionic Strength

Thus far the influence of the nature and concentration of the inert supporting electrolyte has not been considered and it has been implicitly assumed that the diffuse double layer field is insufficiently large to influence the motion of hydrated electrons. Studies of the influence of this field when it is large are of considerable diagnostic importance. Clearly the motion of electrons will be affected in much the same way as the motion of charged reactants and the diffusion problem is closely related to the dynamic Ψ effect which has been studied theoretically by many workers (20). A relatively simple approach is outlined below.

In the absence of a scavenger the diffusion equation when Ψ, the potential relative to the bulk of the solution, is time invariant is

$$\partial C_e/\partial t = D_e\ \partial/\partial x\ [\partial C_e/\partial x - FC_e/RT \cdot d\Psi/dx] \qquad [17]$$

A term must be added to the right-hand side when a scavenger is present, and since the system is at equilibrium as regards the spatial variation of C_s, this is $-k_sC_sC_e \exp(-z_s\Psi F/RT)$, where C_e is the hy-

drated electron concentration (mole cm^{-3}) and z_s is the number of positive charges carried by the scavenger. The complete equation is

$$\partial C_e/\partial t = D_e\,\partial/\partial x\,[\partial C_e/\partial x - (FC_e/RT)\,d\Psi/dx] - k_s C_s C_e \exp(-z_s\Psi F/RT) \quad [18]$$

After making the substitution $V = C_e \exp(-\Psi F/RT)$ this equation can be written in the form

$$\partial V/\partial t = \exp(-\Psi F/RT)\,\partial/\partial x\,[D_e \exp(+\Psi F/RT)\,\partial V/\partial x] - k_s C_s V \exp(-z_s\Psi F/RT) \quad [19]$$

This is the equation for the motion of charge along a resistive transmission line with nonuniform series resistance, nonuniform shunt capacity, and nonuniform shunt resistance; R_{tl}, C_{tl}, and R_s are defined by

$$R_{tl} = \theta/D_e \exp -\Psi F/RT \quad [20]$$

$$C_{tl} = \theta^{-1} \exp \Psi F/RT \quad [21]$$

$$R_s = \theta(k_s C_s)^{-1} \exp(z_s - 1)\,\Psi F/RT \quad [22]$$

Thus it follows that for localized deposition the equivalent electrical circuit is the one shown in Fig. 14, if it is assumed that the heterogeneous rate constant for the transfer of electrons from the solution to the electrode is infinite. The only important differences between this circuit and the one in Fig. 4a are that the resistance per unit length at any point is increased by the factor $\exp -\Psi F/RT$ where Ψ is the potential at the corresponding plane in the solution, and that the electron concentration is now proportional to the product of V, the line voltage, and $\exp \Psi F/RT$ instead of being proportional to V.

For very low $k_s C_s$ it is evident from the circuit that the diffuse double layer field increases the stationary concentration of e^-_{aq} at $x = \delta$ and, hence i_p, by the factor

$$\phi = \delta^{-1} \int_0^\delta \exp -\Psi F/RT \cdot dx \quad [23]$$

Further, for a 1:1 supporting electrolyte and a value of δ appreciably larger than the half-thickness of the diffuse double layer, on writing ϕ in the form

$$\phi = 1 + \delta^{-1} \int_0^\delta (\exp -\Psi F/RT - 1)\,dx \quad [24]$$

we see that the factor reduces to

$$\phi = 1 + \Gamma_+/C_{se}\delta \quad [25]$$

where Γ_+ is the surface excess (mole cm^{-2}) of the univalent cations of supporting electrolyte and C_{se} is the electrolyte concentration (mole cm^{-3}). Thus with a 10^{-2}M solution ϕ is of the order of 40 when the potential is very negative with respect to E_{ecm} if δ = 40Å. In practice the increase in i_p is considerably smaller, but this is not unexpected for reasons mentioned below.

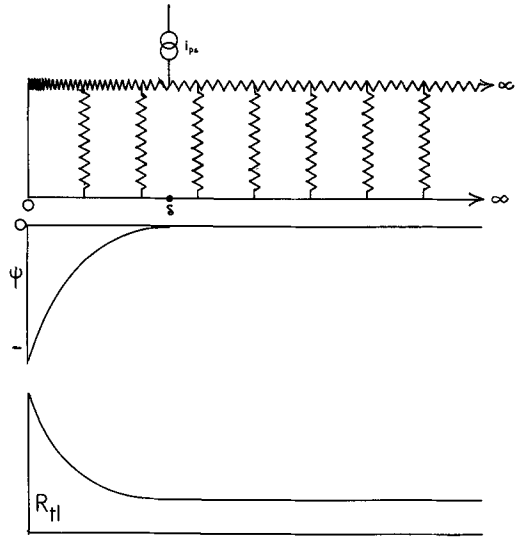

Fig. 14. Influence of the double layer field on the equivalent circuit when deposition is localized.

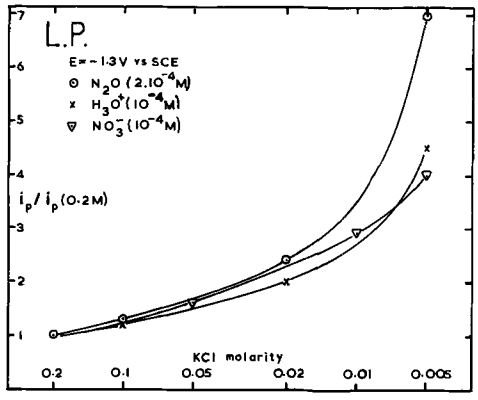

Fig. 15. Influence of ionic strength on i_p

In Fig. 15 are given the results of some preliminary studies of the influence of ionic strength on i_p for three scavengers (H_3O^+, N_2O, and NO_3^-). The data refer to KCl solutions and 2537Å light and undesirably high scavenger concentrations had to be employed ($1\text{-}2.10^{-4}$M). The figure shows that the ratio of i_p to i_p for the same scavenger concentration in 0.2M KCl increases as the ionic strength falls, the variation being roughly the same for each of the three scavengers. These results suggest that the photocurrent is caused partly, if not entirely, by a diffusing negatively charged entity.

A detailed comparison with theory will not be made for several reasons. First because the equivalent circuit in Fig. 14 becomes inexact if there is slight ion pair formation between the cations of the supporting electrolyte and the hydrated electrons. The effect of the diffuse double layer field is then reduced. An alternative circuit taking account of ion pair formation can be written down immediately, but such a circuit is of no immediate value as no quantitative information about ion pair formation is available and absolutely nothing is known about the effect of slight dielectric saturation in the double layer region on pair formation. The second and most important reason is concerned with discreteness of charge in the diffuse double layer. Due to random motion of ions in the double layer *it seems* inevitable that the average velocity of translation of a charged particle through the layer will be considerably larger than that predicted by classical theories of the layer. What is needed to make a comparison between theory and experiment is the time average of $\exp -\Psi F/RT$ while all that is currently available is $\exp -\bar{\Psi}F/RT$ where $\bar{\Psi}$ is the time average of Ψ. The final and less compelling reason is that due allowance must be made for distributed deposition of charge. In principle the single current generator in Fig. 14 should be replaced by an infinite number of generators distributed along the line.

A marked increase in residual photocurrent with decreasing ionic strength for 1:1 electrolytes was first observed by Heyrovsky (3a). A change in concentration from 0.1 to 10^{-3}M produced a tenfold increase. We have recently observed a fourfold increase with KCl solutions on reducing the concentration from 0.2 to 2 10^{-3}M. Such changes are to be expected as the stationary electron concentration in the solution outside the double layer rises as the ionic strength falls and a larger fraction of the deposited hydrated electrons decay in the solution (or react with trace impurities). Heyrovsky found that the effect became progressively smaller as the cationic charge increased. This is qualitatively predicted by theory since for

constant double layer charge the integral $\int_0^s \exp - \Psi F/RT$ decreases as the cationic charge increases.

Slow Heterogeneous Oxidation of the Hydrated Electron

It was indicated earlier that the possibility of slow direct transfer of electrons from the solution to the electrode cannot be ruled out *a priori*. Taking slow transfer into account the equivalent circuit in Fig. 14 has to be modified. The short circuit at $x = 0$ is replaced by a resistance R_e' defined by $R_e' = \theta/k_e \exp - \Psi^o F/RT$ where k_e is the heterogeneous rate constant for the transfer of electrons from hydrated electrons at the interface to the electrode. Clearly the introduction of this resistance will tend to make the photocurrent for constant C_s much more sensitive to ionic strength. The experimental facts seem to rule out the possibility of slow direct transfer (coupled possibly with direct formation of e^-_{aq}) as the main path for electron transfer from the solution to the electrode.

There remains the possibility that direct transfer of an electron from e^-_{aq} to the electrode may be a moderately slow process ($K_e < 10$ cm sec^{-1}) and that transfer to the electrode is preceded by the dissociation reaction

$$e^-_{aq} \underset{k_r}{\overset{k_d}{\rightleftharpoons}} e^- + H_2O \qquad [o]$$

Making use of standard diffusion theory for a chemical reaction followed by a fast charge transfer reaction, and assuming an infinite rate constant for the latter reaction, the apparent heterogeneous rate constant for electron transfer is $k_d\ (D_e'/k_r)^{1/2}$ and the reaction layer thickness is $(D_e'/k_r)^{1/2}$, where D_e' is the diffusion coefficient of a free thermal electron. To account for the rather slow variation in the photocurrent with ionic strength the reaction layer thickness would have to be somewhat larger than the half-thickness of the diffuse double layer for 5 10^{-3}M KCl solution. Assuming a value for the reaction layer thickness of the order of 50Å, and a value for D_e' of 10^{-1} cm^2 sec^{-1}, a value for k_r of the order of 4 10^{11} sec^{-1} (pseudo-first order rate constant) is obtained. Such a value would mean that thermal electrons travel some distance before becoming hydrated.

The equivalent circuit for this system ($v_s = 1$) takes the form shown in Fig. 16 if the influence of the double layer field is neglected. The deposition of thermal electrons in the solution is represented by distributed current generators, but these now supply current to $TL(e^-)$ which is connected with the linear diffusion of free electrons in the solution. The short-circuit at $x = 0$ implies instantaneous capture of any free electron arriving at the electrode surface. $TL(e^-)$ is linked by distributed resistance to the line $TL(e^-_{aq})$ which represents the linear diffusion of hydrated electrons in the solution. These linking resistances are connected with the homogeneous conversion of e^- into e^-_{aq} and the reverse process and the linking resistance per unit length of line is given by $R_l = \theta/k_d$ if the series resistance, shunt capacity, and shunt resistance of $TL(e^-_{aq})$ are defined by Eq. [2], [3], and [4]. The resistance and capacity per unit length of $TL(e^-)$ are defined by

$$R_{tl}(e^-) = \theta k_r/D_e'k_d \text{ and } C_{tl}(e^-) = k_d/k_r\theta$$

It is assumed that unbound electrons are not captured by scavengers but this is not an essential assumption. If it is not made, the scavenging of unbound electrons is represented by shunt resistance distributed uniformly along $TL(e^-)$.

The most general form of the circuit contains a resistance R_e' (defined above) linking the terminals of $TL(e^-_{aq})$ at $x = 0$ to take account of slow transfer of electrons from hydrated electrons at the interface to the electrode. If there is an appreciable field in the region of the diffuse double layer, the circuit is basically the same but $R_{tl}(e^-)$, R_l, and $R_{tl}(e^-_{aq})$ are increased by the time average of exp $- \Psi F/RT$ and the shunt capacities of the two lines are reduced by the same factor. Apart from possible complications introduced by pair formation and by capture of unthermalized electron the resulting circuit should be reasonably exact. Unfortunately it is impossible at the present time to assess accurately the relative importance of the various components in the circuit, and it is not clear how the various uncertainties are to be resolved conclusively.

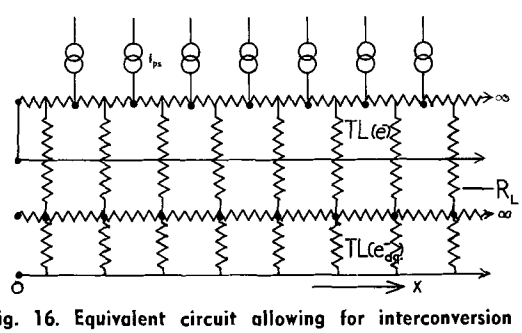

Fig. 16. Equivalent circuit allowing for interconversion of e^- and e^-_{aq}.

Comparative, Competitive, and Successive Scavenging

Perhaps the most crucial test of the proposed mechanism is to ascertain whether relative rate constants deduced from photocurrent measurements bear any resemblance to those obtained by pulsed radiolysis. This may demand a knowledge of the electron transfer numbers for the scavenging reactions.

Comparative Scavenging

From earlier discussion it follows that when the scavenger concentration is very large i_p approximates to v_s^o times the rate of deposition of electrons in the solution (i_d). Thus for two scavengers A and B, the ratio v_A^o/v_B^o, in principle, can be determined by making measurements of the photocurrent with high concentrations of A and of B. This method cannot always be used owing to light absorption by the scavengers at high concentration. However, in such determinations it may not be necessary to use light of very short wavelength and the possibility of evaluating v_s^o ratios for uv absorbing species such as NO_3^- and NO_2^- using "violet" light is currently being investigated. Once v_A^o/v_B^o has been evaluated k_A/k_B can be determined by making measurements with very low concentrations of A and of B as

$$i_p(A)/i_p(B) = v_A^o(k_AC_A)^{1/2}/v_B^o(k_BC_B)^{1/2} \qquad [26]$$

It is, of course, here assumed that the electron transfer numbers are independent of C_s, and that a high scavenger concentration does not influence the rate of deposition of hydrated electrons in the solution. The latter is not a permissible assumption if the scavenger is strongly adsorbed at the interface, and it is possible for v_s^o to vary with C_s in a range of potential in which a heterogeneous charge transfer reaction following electron scavenging is not completely diffusion-controlled. Consequently i_p measurements must be made at a potential where the variation of i_p with potential is independent of the reaction scheme.

Competitive Scavenging

Competitive experiments with solutions containing two scavengers A and B also lead to relative electron transfer numbers and to relative rate constants. The term $-k_sC_sC_e$ in the diffusion equation (1) has to be replaced by $-(k_AC_A + k_BC_B)C_e$ and it follows that for constant light intensity and $i_p << i_d$ the rate of capture of electrons is proportional to

$$(k_A C_A + k_B C_B)^{1/2}$$

As each electron captured by A and B leads to the permanent loss by the electrode of v_A and v_B electrons, respectively, the current at constant potential is

$$i_p = i_d G (v_A k_A C_A + v_B k_B C_B)/(k_A C_A + k_B C_B)^{1/2} \quad [27]$$

where G is a constant. By varying C_A/C_B, v_A/v_B and k_A/k_B can be determined. Low scavenger concentrations must be used in such determinations.

If the two scavenger concentrations are very large and almost all the emitted electrons are captured, the observed photocurrent is given by

$$i_p \cong i_d (v_A k_A C_A + v_B k_B C_B)/(k_A C_A + k_B C_B) \quad [28]$$

If $v_A = v_B$ the current tends to be independent of C_A/C_B, but if $v_A > v_B$ the introduction of a large concentration of A into a solution already containing B at a high concentration produces a marked increase in current. The earlier remarks about light absorption apply in this case also, and it is desirable (*a*) that the electron transfer numbers should be independent of scavenger concentration and (*b*) that there should be no interactions between the over-all photocurrent mechanisms. Ambiguity may result if an entity produced directly or indirectly by electron capture reacts with the other scavenger to produce an intermediate capable of oxidation or reduction. If $v_A = 0$ (*e.g.*, due to oxidation of A^-) Eq. [27] and [28] reduce to

$$i_p = i_d G v_B k_B C_B/(k_A C_A + k_B C_B)^{1/2} \quad (i_p << i_d) \quad [29]$$

and

$$i_p \cong i_d v_B k_B C_B/(k_A C_A + k_B C_B) \quad [30]$$

Extensive use has been made of these two equations which do not demand a knowledge of v_B for the evaluation of k_A/k_B.

If $k_B C_B << k_A C_A$ Eq. [27] can be written in the approximate form

$$i_p \cong i_d\, G v_A (k_A C_A)^{1/2} [1 + (2v_B - v_A) k_B C_B/2 v_A k_A C_A] \quad [31]$$

Thus by studying the change in i_p produced by the addition of a small amount of B it is possible to decide between the three following possibilities

$$2v_B > v_A$$

$$2v_B = v_A$$

$$2v_B < v_A$$

It has to be borne in mind that any conclusion so arrived at may not hold for v_A^0 and v_B^0, the transfer numbers in the absence of other scavengers.

Successive Scavenging

One further way of evaluating homogeneous rate constants deserves mention. Consider the reaction scheme

$A + e^-_{aq} \rightarrow A^-$	(homogeneous)	[p]
$A^- + B \rightarrow C$	(homogeneous)	[q]
$C \rightarrow D + e$	(fast c.t.r.)	[r]

where B does not react with e^-_{aq}. The photocurrent associated with electron capture by A (and possibly with following reactions which for simplicity are omitted from the scheme) is reduced when species B is present because ultimately some of the captured electrons are returned to the electrode by charge transfer reaction (r). This reaction scheme is encountered with alcoholic solutions. The aliphatic alcohols are known to be efficient scavengers for H atoms and OH radicals and scavenging reaction usually involves hydrogen abstraction from the α carbon atom.

Two distinct types of behavior can be distinguished if reaction (r) is diffusion-controlled. The behavior is simplest when v_A^0 is unity. Then, if reaction (q) is a moderately rapid homogeneous reaction and a small amount of B is present, at normal values of the elapsed time almost all A^- is converted into the intermediate C and this is virtually all oxidized at the electrode. Thus the observed photocurrent is very small in comparison with the value prior to the introduction of scavenger B.

More interesting is the behavior when v_A is larger than unity due to a charge transfer reaction involving A^- at the electrode surface. In this case the reaction, which may be written formally

$$A^- + e \rightarrow A^{2-} \quad [s]$$

competes with homogeneous reaction (q) for A^- and the current is very small only if the concentration of B is so large that there is little possibility of A^- (formed within the very thin electron scavenging reaction zone) arriving at the electrode surface. Without writing down any equations it is evident that an appreciable current will be observed if $k_A C_A$ is comparable with $k_B' C_B$ where the superscript ' denotes scavenging of a species other than e^-_{aq}. An approximate expression for the current is most readily obtained by the equivalent circuit approach and Fig. 5 is directly applicable if reaction (r) is diffusion-controlled. The current generator di_{ps} is identified with the deposition of A^- in the solution by reaction (p) and the transmission line takes account of linear diffusion of this entity, while the distributed shunt resistance allows for the homogeneous consumption of A^- by scavenger B. In this instance we are interested in the rate of arrival of A^- at the electrode surface and making use of equations analogous to [2], [3], and [4] this current is found to be

$$di_p = di_{ps} \exp - (k_B' C_B/D_B)^{1/2} x \quad [32]$$

where D_B is the diffusion coefficient of B. Now for small $k_A C_A$ the rate of deposition of A^- in the solution is approximately

$$\alpha\, i_d (k_A C_A) \exp - (k_A C_A/D_e)^{1/2} x$$

and using Eq. [32] it follows that the rate of arrival of A^- at the electrode is proportional to $i_d k_A C_A\, (Q + Q')^{-1}$ where $Q = (k_A C_A/D_e)^{1/2}$ and $Q' = (k_B' C_B/D_{A^-})^{1/2}$. For each A^- ion or molecule arriving at the electrode v_A^0 electrons are permanently lost by the electrode if the presence of scavenger B does not influence the transfer number.

Thus for constant light intensity[7] and constant C_A

$$i_p \propto [1 + (Q'/Q)]^{-1} \quad [33]$$

and a plot of the reciprocal of i_p against $C_B^{1/2}$ is linear and permits the evaluation of k_B' if D_B, D_e, and k_A are known.

We have discussed this special type of successive scavenging at some length because it appears to be the only conclusive way of evaluating v_s^0 for i_p when e^-_{aq} is scavenged by H_3O^+.

Scavenging Rate Constants

The evaluation of rate constants (strictly relative rate constants) using equations given in the preceding section is a task which is as yet hardly begun. Values for a variety of electron scavenging reactions are tabulated in Table I. To make comparison with pulsed radiolysis data easier we have assumed that for our solutions (1 and 0.2M) the rate constants deduced from pulsed radiolysis and chemical experiments at low ionic strength should be multiplied by antilog-$0.2z$ where z is the number of electronic charges carried by the scavenger ion or molecule. This correction is nu-

[7] Equation [33] is also valid for varying light intensity if i_p approaches its pseudosteady-state value rapidly.

Table I. Comparison of rate constants deduced from i_p measurements with pulsed radiolysis values [K_A(pr)]

System	Scavenger A	Scavenger B	Method	C_A (M)	C_B (M)	Potential, v *vs.* SCE
(a)	H_3O^+	N_2O	Compet. LP	0, 10^{-3}-10^{-2} 0, 10^{-2}-10^{-1}	$3.1\ 10^{-2}$ $7.9\ 10^{-3}$	−0.2 to −0.4
(b)	H_3O^+	N_2O	Compar. LP	0, 10^{-3}	$1.56\ 10^{-3}$	−1.3
(c)	Zn(II)	H_3O^+	Compet. LP	0, 10^{-2}-10^{-1}	10^{-3}	−0.8
(d)	Cd(II)	N_2O	Compet. LP	0, 10^{-3} 0, 10^{-3}-10^{-2}	$2.2\ 10^{-3}$ $3.1\ 10^{-2}$	−0.1 to −0.4
(e)	Zn(II)	N_2O	Compet. LP	0, 10^{-2}-10^{-1} 0, 10^{-2}-10^{-1}	$3.1\ 10^{-2}$ $1.8\ 10^{-3}$	−0.1 to −0.6 −0.8
(f)	Ni^{2+}	N_2O	Compet. LP	0, 10^{-4}-10^{-2} 0, 10^{-2}	$1.8\ 10^{-3}$ $3.1\ 10^{-2}$	−0.1 to −0.4 −0.1 to −0.4
(g)	NO_3^-	N_2O	Compet. LP	0, $3.3\ 10^{-3}$	$5\ 10^{-3}$	−0.1 to −0.4
(h)	NO_2^-	N_2O	Compet. LP	0, $3.3\ 10^{-3}$	$5\ 10^{-3}$	−0.1 to −0.7
(i)	Cd(II)	NO_2^-	Compet. LP	0, 10^{-3}	$3.3\ 10^{-3}$	−0.05 to −0.2
(j)	NO_3^-	H_3O^+	Compar. MP2	10^{-4}	10^{-4}	−1.1 to −1.3
(k)	NO_2^-	NO_3^-	Compar. MP2	10^{-4}	10^{-4}	−1.2 to −1.5

Table I. (Continued)

System	Assumed	Equations used	k_A(p.r.)* 10^{10} M^{-1} sec^{-1}	$k_A(i_p)\phi$ 10^{10} M^{-1} sec^{-1}	Comments
(a)	$v_A = 0$ $k_{N_2O} = 0.56$ (15)	[29] [30], [29]	1.4 (25) 1.4	1.5 ~1	
(b)	$v_A^\circ = v_B^\circ$	[26]	1.4	1.8	
(c)	$v_A = 0$	[29]	0.06 (26)	0.046	Zn^{2+} partially complexed
(d)	$v_A = 0$ $v_A = 0$	[29] [30], [29]	2.1 (15) 2.1	3.6 ~2	Cd^{2+} largely complexed
(e)	$v_A = 0$ $v_A = 0$	[30], [29] [29]	0.06 0.06	~0.1 0.05	
(f)	$v_A = 0$ $v_A = 0$	[29] [30], [29]	0.9 (15) 0.9	1.5 ~1	Little complexing of Ni^{2+}
(g)	$v_A \approx 0.35$	[27]	1.76 (15)	≈2.0	
(h)	$v_A \approx 1$	[27]	0.63 (15)	≈0.5	pH 5.5
(i)	$v_A = 0$ $k_{NO_2^-} = 0.63$ (15)	[29]	2.1	~3	
(j)	$v_A^\circ = v_B^\circ$	[26]	1.76	2.0	Medium 1M KCl
(k)	$v_B^\circ = v_B^\circ$ $k_{NO_3^-} = 1.76$ (27)	[26]	0.63	0.49	Medium 1M NaOH

$\phi\ k_A(i_p)$ refers to 0.2M KCl unless otherwise indicated. No allowance for uncertainty in the assumed values of $k_{H_3O^+}$ and k_{N_2O} is made nor have any small corrections for the effect of ionic scavengers on the dynamic ψ effect been applied.

* Pulsed radiolysis rate constants have been multiplied by anti-log $-0.2Z_s$.

merically slightly smaller than is predicted by the Brönsted theory (21), but an examination of experimental data (22) for a variety of reactions suggests that the assumed correction is more realistic (at least for 0.2M solutions) than the theoretical value.

Several of the rate constants have been obtained by competitive experiments with N_2O as one scavenger and a metallic ion as the second scavenger. In these experiments v_s for the second scavenger was virtually zero and hence a knowledge of v_s for the first scavenger was not needed. In much of the work i_p was rather small and undesirably high scavenger concentrations had to be used to minimize errors due to low signal to noise ratio and due to slight drifts in the zero of the pulse polarograph. The equations used in the interpretation of the data were in some instances thus not strictly applicable. Similar difficulties sometimes were encountered in competitive experiments between H_3O^+ and metallic ions. The results are only to be regarded as preliminary results but there is little possibility that they are greatly in error and they are included in the paper because they show clearly that the studied N_2O photocurrents are largely, if not entirely due to electron capture.

One important fact should be borne in mind when considering the results of competitive experiments. The entity formed by electron capture by one of the scavengers may react with the second scavenger. Unstable metal ions formed by electron capture are likely to react slowly with H_3O^+. The rate constants in Table I suggest that the reaction of Zn^+ with H_3O^+ must be fairly slow ($k' < 10^8 M^{-1}\ sec^{-1}$) and also that the second order rate constants for the capture by N_2O of the species formed when e^-_{aq} is captured by the ions of Zn, Cd, and Ni are $< 10^{10}\ M^{-1}\ sec^{-1}$. However, exploratory experiments with solutions containing H_3O^+ and Ni^{2+} suggest that Ni^+ may react rather rapidly with H_3O^+, as the introduction of Ni^{2+} did not produce the expected reduction in i_p. This fact may be not unrelated to the anomalously large photocurrent observed with Ni^{2+} which was discussed earlier. In this connection it should be mentioned that if a solution contains a very large amount of scavenger A, all the deposited electrons will be rapidly converted into A^- and, if A^- is scavenged by B at low concentration, the photocurrent can be regarded as one due to the outward diffusion, and slow capture by B of A^-. Further if the second scavenging reaction is diffusion-controlled, the photocurrent will be of the same order of magnitude as if scavenger A were not present.

Some rate constants obtained by comparative scavenging are also included in Table I. In the interpretation of these results relative values of v_s° were needed, and the reasons for choosing the values indicated in the table are summarized below. The main foundation stones in our calculations of absolute rate constants (0.2 and 1M electrolyte) have been values of 1.4 10^{10} and 5.6 10^9 $M^{-1}\ sec^{-1}$ for the scavenging of e^-_{aq} by H_3O^+ and N_2O, respectively.

N_2O.—It was mentioned earlier that the most probable value for $v_{N_2O^\circ}$ in neutral solution is 2. This electron transfer number is not likely to change in acidified solutions as OH radicals will presumably be formed even more readily by the homogeneous reaction

$$O^- + H_3O^+ \rightarrow OH + H_2O \qquad [t]$$

The addition of EtOH to 0.2M KCl (natural *p*H) saturated with N_2O (1 atm) reduces the photocurrent, and for a solution which is 1M with respect to EtOH the photocurrent at potentials more positive than −1.6v *vs.* SCE is only about 10% of the value without ethanol. Some indication of a rapid rise at more negative potentials (<1.7v *vs.* SCE) is seen, and with an acidified solution (10^{-4}M H_3O^+) a rapid increase in photocurrent at about −1.4v *vs.* SCE is detected. These results can be interpreted in terms of the following reaction scheme

$$e^-_{aq} + N_2O \rightarrow N_2O^- \qquad [a]$$

$$N_2O^- \rightarrow N_2 + O^- \qquad [b]$$

$$O^- + H_2O \rightarrow OH + OH^- \qquad [c]$$

$$OH + CH_3CH_2OH \rightarrow H_2O + CH_3CHOH \qquad [t]$$

$$CH_3CHOH + H_2O \rightarrow CH_3CHO + H_3O^+ + e \quad \text{(rapid c.t.r. at } E > -1.4\text{v)} \qquad [u]$$

Some of these steps may well be bypassed (*e.g.*, O^- may react directly with EtOH). The reverse of reaction (u) is in all probability the first step in the reduction of acetaldehyde, and we believe it is relevant that the polarographic reduction of this compound [23] in solutions of *p*H ~ 7 commences at a somewhat more negative potential than the rise in the photocurrent (neutral solution). Thus the suppression of i_p by EtOH is to be attributed to the oxidation of the α ethanol radical and the accompanying return of the scavenged electron to the electrode. It should be noted that the experimental data indicate that the oxidation of this radical at potentials more positive than −1.4v must be a moderately rapid process.

H_3O^+.—The evidence for a value for v_s^0 in this case of 2 is; (*i*) The addition of ethanol to 0.2M KCl 10^{-3}M H_3O^+ at first produces a fairly rapid fall in i_p at potentials positive with respect to —1.4v *vs.* SCE. Further additions have a progressively smaller effect, and with a solution 0.5M with respect to EtOH the photocurrent is still roughly half the value in the absence of EtOH. It is well established that EtOH is an efficient H atom scavenger and that the main product of the scavenging reaction is the α ethanol radical. In the absence of a competing reaction virtually all the H atoms produced by electron capture should thus be converted to these radicals and as bimolecular combination of radicals (H or CH_3CHOH) is ruled out by the low concentrations prevailing in the photocurrent experiments (LP) almost all the captured electrons should be returned to the electrode by reaction (u). This is not in accordance with the experimental facts, and hence it may be concluded that there is a competing reaction which might be the well-known atom-ion reaction (e). The reaction must be quite fast at potentials in the range —0.8 to —1.3v *vs.* SCE and able to compete effectively with the scavenging of H by EtOH. A plot of the reciprocal of i_p against the square root of the EtOH concentration is fairly linear up to 1.5M EtOH and using Eq. [33] a value of the rate constant for scavenging of H by EtOH of 2.8 10^7M^{-1} sec^{-1} is obtained [assuming $k_{H3O+} = 1.4\ 10^{10}$M^{-1} sec^{-1} (see Table I), $D_e = 5\ 10^{-5}$ cm^2 sec^{-1}, $D_H = 5\ 10^{-5}$ cm^2 sec^{-1}]. The corresponding values obtained by other methods are 1.5 10^7 and 1.65 M^{-1} sec^{-1} (24). The measure of agreement is rather striking and supports the interpretation placed on the experimental results.

(*ii*) The "saturation" photocurrent for N_2O is almost identical with that for H_3O^+ at a concentration smaller by the ratio of the rate constants.

(*iii*) The addition of small amounts of H_3O^+ to 0.2M KCl containing ~5 10^{-3}M N_2O produces a small but progressive increase in i_p. If $v_{H3O+} = 1$ while $v_{N2O} = 2$, a progressive decrease should be observed. This however, does not prove that $v_{H3O+}{}^0 = 2$ as H atoms react slowly with N_2O ($k'_{N2O} = 1.25\ 10^4$M^{-1} sec^{-1}) producing OH radicals which would be reduced by the electrode.

NO_3^-.—It was suggested earlier that v_s^0 in this case is 2 when the photocurrent is well developed. The supporting evidence for this is that the addition of small amounts of NO_3^- to 0.2M KCl, ~4 10^{-3} MN_2O leads, at the more negative potentials, to an increase in i_p. If a value for v_{N2O} of 2 is assumed it follows that v_{NO3-} is certainly not unity. At more positive potentials the effective value of $v_{NO3-}{}^0$ solution produces a decrease in i_p. This indicates an effective value of v_s smaller than unity. This evidence however, does not show conclusively that the transfer number has these values when NO_3^- is the only scavenger present.

NO_2^-.—The experimental evidence in this case is even weaker but, such as it is, it suggests that at potentials positive with respect to —0.9v *vs.* SCE the effective electron transfer number in the presence of N_2O is close to unity since the introduction of small amounts of NO_2^- into 0.2M KCl containing N_2O at concentrations in the range 10^{-3} to 5 10^{-3}M seems to have little effect on the photocurrent. Other facts leading tentatively to the same conclusion were mentioned earlier. In 1M NaOH for reasons given earlier v_{NO2-} is assumed to be 2 at potentials more negative than —1.3v *vs.* SCE.

The rate constants deduced from comparative experiments (MP 2) which are given in Table I agree reasonably well with values obtained by pulsed radiolysis. This suggests that the relative electron transfer numbers have been assigned the correct values, but it is possible that the absolute values may not be correct. In particular we have found it difficult to accept a value for $v_{H3O+}{}^0$ of 2 despite the fact that the atom-ion reaction has long been considered by some workers to be important in the normal hydrogen evolution reaction at electrodes.[8] However, all attempts to establish a value of unity have so far failed.

Second Order Reactions

In all experiments other than those with the flash source the stationary electron concentration at any point in the solution has not exceeded 10^{-8}M, and the concentrations of species, produced as a consequence of electron capture, which are consumed heterogeneously have also been very small. If a long-lived entity is produced which is not rapidly consumed by a homogeneous or heterogeneous reaction, its concentration in the solution near the electrode surface slowly rises as time progresses, and second order reactions between such entities and with other species slowly become more likely. It is conceivable that the behavior under intense radiation of some of the systems considered in this paper may change with flash illumination. This change in most cases should be detectable as the linearity between photocurrent and light intensity should be affected. High intensity radiation should in the future cast light on disproportionation reactions between unstable species and fast reactions such as reaction (o). With low light intensities the behavior is in all cases simplest, and the photocurrent is expected to be proportional to light intensity. The latter expectation has been confirmed by experiment (HP) with solutions containing both large and small (10^{-4}M) concentrations of H_3O^+.

Conclusions

All the reliable experimental facts currently available indicate that photocurrents characterized by a dependence on the square root of the scavenger concentration are mainly due to the photoemission of electrons from the electrode surface. The dependence of the apparent threshold potential on wavelength, the values of relative rate constants deduced from competitive and comparative scavenging experiments, and the influence of ionic strength on the photocurrent are the main evidence for this conclusion. The apparent range deduced from the departure from linearity of the relation between current and the square root of the scavenger concentration indicates that the electrons travel an appreciable distance through the solution before becoming hydrated, a conclusion which is supported by the slight dependence of apparent range on potential and by variations with potential in the ratio of nonsaturation current to a "saturation" current with potential. No reliable evidence is yet available to show whether after thermalization the electrons travel a further distance prior to hydration, but it is possible that this happens, and also that the return of hydrated electrons to the electrode may be preceded by dissociation of the hydrated electron. The hard core of evidence for electron emission has in the present paper been embellished with much speculation mainly concerned with the nature of the reactions following the scavenging reaction. It will be remarkable if none of it proves to be wrong, but such speculative excursions from reality are unavoidable at the present time. It is clear that the study of photocurrents offers to the electrochemist and to the radiation chemist a simple way of studying fast homogeneous processes and a way to extend our understanding of the processes which follow electron capture. It should also clarify the mechanisms of certain slow charge transfer reactions and cast new light on the structure of the electrical double layer.

Acknowledgment

We gratefully acknowledge the benefit received from discussions with Dr. J. H. Baxendale.

REFERENCES

1. G. C. Barker and A. W. Gardner, (Part I), paper presented at CITCE Meeting, Moscow, Sept. 1963, To be published.

[8] As indicated earlier the second step may be + H + H_2O + e → H_2 + OH^- rather than (*e*).

2. (a) M. Heyrovsky, "Polarography 1964," G. J. Hills, Editor, Macmillan London, in press; (b) *idem., Nature*, **206**, 1356 (1965).
3. P. Delahay and V. S. Srinivasan, *J. Phys. Chem.*, In press.
4. H. Berg and H. Schweiss, *Electrochim. Acta*, **9**, 425 (1964); H. Berg, *Z. Chem.*, **2**, 237 (1962); M. Eisenberg and H. P. Silverman, *Electrochim. Acta*, **5**, 1 (1961); J. J. Surash and D. M. Hercules, *J. Phys. Chem.*, **66**, 1602 (1962).
5. F. S. Dainton and S. R. Logan, *Trans. Faraday Soc.*, **61**, 715 (1965).
6. M. Heyrovsky and R. G. W. Norrish, *Nature*, **200**, 880 (1963).
7. R. Gomer, "Field Emission and Field Ionization," Harvard University Press, Cambridge, Mass.
8. D. C. Grahame, *Chem. Rev.*, **41**, 441 (1947).
9. J. Jortner, *Rad. Res., Supplement* 4, 24 (1964).
10. F. S. Dainton and P. Fowles, *Proc. Roy. Soc.*, **287**, 312 (1965).
11. F. P. Bowden, *Trans. Faraday Soc.*, **27**, 505 (1931).
12. G. C. Barker, "Transactions of the Symposium on Electrode Processes," E. Yeager, Editor, J. Wiley & Sons, Inc., New York (1963).
13. M. Anbar and P. Neta, "Tables of Bimolecular Rate Constants," Israel Atomic Energy Commission, I. A. 992, p. 18.
14. R. H. Fowler, *Phys. Rev.*, **38**, 45 (1931).
15. J. H. Baxendale, E. M. Fielden, and J. P. Keene, *Nature*, **201**, 468 (1964); *Proc. Roy. Soc.*, **286**, 320 (1965).
16. J. H. Baxendale, Private communication.
17. S. Gordon, E. J. Hart, M. S. Matheson, J. Rabani, and J. K. Thomas, *J. Am. Chem. Soc.*, **85**, 1375 (1963).
18. See ref. (9) p. 33.
19. H. S. Carslaw and J. C. Jaeger, "Conduction of Heat in Solids," p. 111, Clarendon Press, Oxford (1948).
20. B. Levich, *Doklady Akad. Nauk SSSR*, **67**, 309 (1949); L. Gierst, see ref. (12) p. 109; H. Matsuda and P. Delahay, *J. Phys. Chem.*, **64**, 332 (1960); S. K. Rangarajan, *Can. J. Chem.*, **41**, 983 (1963).
21. See A. A. Frost and R. G. Pearson, "Kinetics and Mechanism," p. 150, J. Wiley & Sons, Inc., New York (1961).
22. Moelwyn Hughes, "Physical Chemistry," p. 1227, Pergamon Press, London (1957); G. Capski and H. A. Schwartz, *J. Phys. Chem.*, **66**, 471 (1962).
23. P. J. Elving and V. Rutner, *Ind. Eng. Chem., Anal. Ed.*, **18**, 176 (1946).
24. See ref. (13) p. 10.
25. S. Gordon, E. J. Hart, M. S. Matheson, J. Rabani, and J. K. Thomas, *Discussion Faraday Soc.*, **36**, 193 (1963).
26. See ref. (13) p. 10.
27. E. J. Hart, S. Gordon, and J. K. Thomas, *J. Phys. Chem.*, **68**, 1271, 1524 (1964).

Discussion

P. Delahay (discussor) and *G. Tessari*: Dr. Barker has presented some good evidence to support his general mechanism, and I do not plan to question this mechanism here. I shall also leave for the Discussion of Photocurrents some points of theory on electron emission. My comments will rather cover three points in the analysis of experimental data.

First, I would suggest caution in drawing conclusions from plots of the square of the photocurrent against potential, and particularly from variation in the slope of this plot. Such a dependence is not of analytical character, and indeed calculated plots (square root of current against field) are not linear when the range of field is sufficiently large. This comment applies particularly to Dr. Barker's detailed implications he derived from his Fig. 2.

Second, I like to stress the importance of irradiation with monochromatic light or the best that can be achieved toward that aim. Furthermore, it is important that currents be compared for equal fluxes of photons at different wavelengths. Analysis of the electrode potential and wavelengths dependence demands that kind of experimental information. Comparison of results, otherwise, becomes more tentative.

Third, the study of the time dependence of photocurrents is essential whenever consecutive solvated electron-scavenger reactions are involved. The course of these reactions may be affected by potential and by wavelengths, and these effects may escape in measurements involving only a narrow range of time. Dr. Tessari recently found a pronounced time dependence for N_2O in 0.1M NaF long after irradiation had stopped. Dr. Barker has warned us about this effect, but I like to stress the necessity of experimental study before the deduction of detailed mechanisms.

In conclusion, I believe we can all admire Dr. Barker's extensive pioneering work, but we should realize, as he does, that mechanisms can only be tentative, at least in certain cases. More definitive results hopefully may result by consideration of the experimental points I raised. I hope so anyhow.

G. C. Barker: I find myself in broad agreement with the comments made by Professor Delahay. Exact linearity in the plot of $i_p^{1/2}$ against field over a wide range of field certainly is not predicted by theory, but results obtained for emission *in vacuo* often fit a plot of $i_p^{1/2}$ against quantum energy over a range of 1 or more electron volts. Also of the methods available for the determination of the apparent threshold potential the $i_p^{1/2}$ *vs.* potential plot is the only nonsubjective method.

It is clearly essential when studying the emission of electrons rather than their subsequent fate to work with monochromatic light of variable wavelength and also to have some knowledge of the incident light intensity. Our experiments show that the yield at constant potential falls progressively as the wavelength increases. In this connection it should be mentioned that the current units in the case of the data plotted in Fig. 2 of our paper vary with wavelength.

I am somewhat puzzled by the slow variation in potential with time observed for N_2O in 0.1M NaF solution. This I would not expect as OH radicals should rapidly be directly or indirectly reduced at the electrode surface. Of course fluorine may be produced as an intermediate, but it is not easy to see why this should not be rapidly reduced. This system is one which we have not yet studied oscilloscopically. Only long-term average current measurements have been made with 0.2M saturated with N_2O and using 2537Å radiation.

P. J. Boddy: The result reported by Professor Delahay that the electrode potential changes abruptly to a more positive value during a brief light pulse and then subsequently drifts even more positive by a few millivolts over times of the order of tens of milliseconds is not necessarily inconsistent with Dr. Barker's mechanisms (e) and (f). The only necessary assumption is that the photo-emitted electrons are stopped (*i.e.*, reduced to ordinary diffusional motion) by collisions with molecules or ions before travelling more than approximately one Debye length (appropriate to the particular solution) away from the electrode surface. The extra positive charge left on the metal surface as a result of electron emission gives rise to a small increase in the field at the surface, and this of course is the origin of the immediate electrode potential change. The additional negative charges appearing in the solu-

tion phase (and it is immaterial now whether these are electrons, hydrated electrons, or anions) will not in general be distributed in a way consistent with the already existing potential profile in the diffuse part of the double layer and will hence have a tendency to drift either toward or away from the electrode as the electrostatics demands. If in fact the over-all tendency is to drift away from the electrode, then, since the field due to the additional positive charge on the electrode is acting over a greater distance, a positive increase in the electrode potential could be expected.

P. Delahay: Dr. Boddy made an interesting point, but I am not sure whether he is right for the following reasons: (*A*) Diffusion surely must occur well beyond the diffuse double layer in a time of 50 msec in a 0.1 or a 1M electrolyte. (*B*) The same effect should be observed regardless of the scavenger, but is hardly found when 1M $HClO_4$ is used instead of N_2O.

Regardless of whether Dr. Boddy is right or wrong, the drift of potential we observed at open circuit would result in a current-time dependence at constant potential (Dr. Barker's conditions). My original comment still stands about the necessity of considering time dependence.

H. Gerischer: The very good efficiency of H_3O^+ ions as irreversible electron scavengers seems very surprising to me. I would have expected that, due to the very negative redox potential of dissolved hydrogen atoms, each H-atom approaching the electrode surface would be reoxidized. Reaction (f) which you have discussed should be very fast if no other stabilization of the hydrogen atom occurs. Such a stabilizing process would be the formation of $H_2^+ \cdot aq$ in a homogeneous reaction between $H \cdot aq + H_3O^+$. According to your Fig. 10, the scavenger efficiency of the H^+ ions decreases rapidly in a critical range of polarization. Does this not indicate that some stabilization of the H atoms takes place due to interaction with an unknown species which prevents reoxidation of those radicals below this critical potential range?

G. C. Barker: The variation of the H_3O^+ photocurrent with potential might be interpreted in the way suggested by Professor Gerischer, but there are some additional experimental facts to be considered. Experiment suggests that when this photocurrent is well developed and, tending to vary with potential in the same way as the N_2O photocurrent, the electron transfer number is the same for both photocurrents. Now LP experiments with solutions which were saturated with N_2O and which contained a relatively small ($\sim 10^{-4}$M) amount of H_3O^+ have shown that when the potential is such that the reduction of H_3O^+ is largely diffusion controlled there is a substantial apparent fall in the N_2O photocurrent. This is due to the production of OH^- ions by the photocurrent mechanism which react homogeneously with hydrogen ions which otherwise would have been reduced at the electrode surface. In such LP experiments it is of course the change in current produced by the rectangular light pulse which is measured, and little change will be observed when the H_3O^+ reduction is largely diffusion controlled if, for each electron lost by the electrode as a consequence of photo-emission, one OH^- ion is produced. The behavior points to OH^- and N_2 as the final products of the N_2O photocurrent reaction and thus to a value for $v_{N_2O}^{\circ}$ of 2. It follows that $v_{H_3O^+}^{\circ}$ is probably 2 at potentials more negative than —0.9v *vs.* SCE. Such a value suggests that the H atoms participate in a charge transfer reaction leading to the loss of a further electron by the electrode. The reaction is presumably either the so-called atom-ion reaction or the related reaction in which the H_3O^+ ion is replaced by a water molecule. At potentials more negative than —0.9v the reaction in question must take place much more rapidly than the oxidation of hydrogen atoms, the latter reaction being the main path for the removal of hydrogen atoms only at much more positive values of the potential.

Panel Discussion on Electrode Photocurrents

Introductory Remarks

Paul Delahay

The topic of electrode photocurrents was selected for discussion for two reasons: (*a*) recent work, and particularly that of Dr. Barker and co-workers, is of interest in relation to current, intensive work on the solvated electron; (*b*) electron emission from a metal into a solvent such as water is a poorly understood phenomenon which possibly may be of significance in the interpretation of double layer phenomena and electrode processes. The first aspect was treated in detail in Dr. Barker's paper, and I like to examine briefly the second problem.

We recently pointed out (1) that Fowler's treatment (2) of the effect of an electrical field on photoemission in vacuum could provide a basis for the interpretation of electrode photocurrents. This matter was further examined by Mr. Susbielles (3) and led to the following conclusions: (*A*) The calculated photocurrent-field curves for monochromatic irradiation have the same general shape as the experimental saturation photocurrent-electrode potential curves (in the absence of secondary complications due to consecutive solvated electron-scavenger reactions). (*B*) Plots of the square root of the photocurrent against field for monochromatic irradiation are essentially linear (although the relationship is not a simple analytical one). (*C*) The photocurrent at a given field increases with frequency of irradiation much in the same way as for photoemission in vacuum. These conclusions were obtained either by assuming that the transmission coefficient for electron emission is equal to unity or by calculating the transmission coefficient as a function of energy.

These results hopefully should allow determination of the field at the electrode and might lead to a new kind of information on double layer phenomena. However, preliminary experimental results do not seem to confirm these calculations. The square root dependence seems to be observed experimentally, but the effect of wave length, according to Tessari's recent work (4), differs from the calculated behavior. It is possible that electrode contamination accounts for these abnormal results, but this may well not be the case. We plan further work in this respect. One might also argue that the theoretical model is not a realistic one.

REFERENCES

1. P. Delahay and V. S. Srinivasan, *J. Phys. Chem.*, **70**, 420 (1966).
2. R. H. Fowler, *Phys. Rev.*, **38**, 45 (1931).
3. P. Delahay and G. G. Susbielles, Unpublished work.
4. P. Delahay and G. Tessari, Unpublished work.

Discussion

H. Gerischer

I would like to contribute only two very brief comments to this discussion. The most problematic question in connection with photocurrents by electron emission seems to me to be the emission process itself. One will have to take into account the probability of reflection at the boundary between condensed phases. It is unlikely that the interaction with the liquid phase can be taken into account by considering electrical polarization forces solely. Specific interactions with higher electronic states of the solvent molecules may provide some preferential energy ranges for electrons entering into the solution. This may be shown in the unexpected dependence of the photoemission on wavelengths which Professor Delahay has reported.

On the other hand, electrons emitted into the solution will be scattered by the ions of the electrolyte. I would expect therefore that the mean distance which will be reached by the electrons should decrease with increasing electrolyte concentration. This would increase the probability of recapturing electrons by the electrode.

We have tried to study the emission processes and recapturing process separately by using very short light flashes (of the order of 1-2 μsec). Until now, however, we could not reach high enough resolution for the analyzing electronic system to find the true response of the cell (dropping mercury electrode). Obviously the recapturing process has a too short time constant, which is in agreement with the assumption, made by Dr. Barker, that the electrons reach distances below 100Å. The mean free life time, with the assumption of 100% recapturing efficiency at the electrode, should be then of the order of 10^{-7} sec, which is indeed too fast for our measuring circuit.

R. A. Marcus

The subject of hydrated electrons has been one of considerable interest to chemists in the past few years. This printed version of my remarks will be abbreviated to avoid duplicating a description given elsewhere of the reaction theory and properties of this species. There are several points which should be mentioned, however, as well as one experiment which has so far eluded some chemical kineticists but which may be accessible to electrochemists.

Experimental data on the hydrated electron are of several types: visible absorption spectra, "thermodynamic" (as determined from the ratio of the forward and reverse rate constants of $e + H_2O \rightleftharpoons H + OH^-$), reaction rates of solvated electrons, and mobility measurements. The second item indicates that the solvation free energy is quite large, about —35 kcal mole^{-1} perhaps. Reactions of a solvated electron with simple redox systems are extremely rapid, principally because its standard potential is so negative (about —2.7v), and partly because its intrinsic reorganization parameter [¼λ in our equations (1)] is so low: Per reactant, ¼λ is about 5, 10, and 15 kcal mole^{-1} for the solvated electron, Fe^{+2} — Fe^{-3}, and $Co(NH_3)_6^{+2}$ —$Co(NH_3)_6^{+3}$ species, respectively (1). (¼λ for the reaction is essentially the sum of those for the two reactants.)

Most of the homogeneous reactions of the solvated electron are so fast that they are diffusion-controlled. [It may be recalled that $(1/k_{obs}) = (1/k_{act}) + (1/k_{diff})$, where k_{obs}, k_{act}, and k_{diff} are the observed, activation-controlled, and diffusion-controlled rate constants, respectively (1). When $k_{act} >> k_{diff}$, then $k_{obs} \cong k_{diff.}$) The theory indicates that the rates for reaction with redox systems having typical λ's are diffusion-controlled or almost so, when the standard potential is less negative than —1.5 to —2.0v or less positive than +1.0 to +0.5v (1). To learn more about the chemical behavior of the solvated electron, *i.e.*, to study k_{act}, it would be useful to investigate reactions with redox reactants having E_o's outside this interval. Although the interval outside is an elusive one for stable redox systems, it may be accessible for study with the short-lived species which are generated electrochemically.

When the second reactant is strongly oxidizing, its reaction with the solvated electron is so exothermic that an excited state of the product could form. Chemiluminescence could then ensue, either by emission from this excited state or from one formed from it. A theory of chemiluminescent electron transfer reactions has been described elsewhere (2) and applied to the solvated electron reaction (1). It appears that no chemiluminescence has been observed in solution as yet, however, as a result of a hydrated electron reaction. The electrochemist may have a better chance of observing it:

Let us suppose that the potential of an electrochemical cell is switched back and forth between large positive and large negative values in the presence of a suitable reducible species. Let us suppose further that the electrode is illuminated, either with steady or with synchronized pulsed illumination. During part of the negative half of the cycle photoelectrons are ejected, and during part of the positive half the reducible species yields some powerful unstable oxidizing agent, if it was suitably chosen. Reaction between this oxidizer and the solvated electron can then occur if the concentration of the former is high enough. The system could then be examined for chemiluminescence.

The theory of reactions of solvated electrons can readily be adapted to the calculation of the scavenging rate of metal electrodes for these electrons. One finds that at typical potentials reaction is extremely efficient. Similarly, it could be adapted to calculate the rate of spontaneous emission of electrons as a function of potential. It is clear from the redox potential of the solvated electron[1] that the potential would have to be very negative.

[1] For the effective E_o' for use in the theory should take (1) —2.9v (Stockholm convention) rather than the actual one of —2.7v, to correct for the effects of changes of standard translational entropy. The value of $\lambda/4$ is that cited earlier in the present remarks.

REFERENCES

1. R. A. Marcus, *Adv. Chem. Series*, **50**, 138 (1965); *J. Chem. Phys.*, **43**, 3477 (1965). The first volume is entirely devoted to solvated electrons and contains articles by many contributors.
2. R. A. Marcus, *J. Chem. Phys.*, **43**, 2654 (1965).
3. R. A. Marcus, *ibid.*, **43**, 679 (1965) or references cited therein

Hydrocarbon Fuel Cells with Fluoride Electrolytes

Elton J. Cairns[1]

General Electric Research and Development Center, Schenectady, New York

ABSTRACT

Fuel cell investigations using saturated hydrocarbon fuels with aqueous cesium salt electrolytes and Teflon bonded platinum electrodes have shown that the acidic system CsF-HF-H_2O comprises a suitable set of electrolytes for high performance hydrocarbon fuel cells. The effects of electrolyte composition and temperature on cell performance were studied with emphasis on propane as the fuel. Cell performance was also determined as a function of the molecular structure of the fuel using the homologous series of normal paraffins from C_1 to C_{16}. Maximum performance at 150°C was obtained at the composition F/Cs = 2.0, H_2O = 10 mole %. The HF-H_2O azeotrope showed good performance at 110°C on several hydrocarbons. No current or voltage cycling was observed under any conditions, in contrast to other acidic electrolytes.

During the last several years, there has been an increased interest in obtaining fuel cells which can carry out the direct anodic oxidation of saturated hydrocarbons to carbon dioxide and water at useful current densities and low overvoltages. Most of the early hydrocarbon fuel cell work was concerned with acidic electrolytes (1-3) because hydroxide electrolytes react with the products of the anodic oxidation process, yielding formate and carbonate in place of hydroxide (1). An invariant alkaline electrolyte suitable for use with such fuels as methanol, carbon monoxide, and ethylene was reported by Cairns and MacDonald (4), who found that fuel cell operation at temperatures as high as 200°C could be achieved at atmospheric pressure with aqueous Cs_2CO_3 or Rb_2CO_3 electrolytes. Further work with methanol using the Cs_2CO_3 electrolyte indicated that the temperature range between 100° and 200°C provided significant performance increases over the lower temperature region below 100°C (5).

The investigations using Cs_2CO_3 and Rb_2CO_3 electrolytes were extended to include saturated hydrocarbons, but unexpectedly low current densities were obtained, a result which was attributed to the very low solubilities of the saturated hydrocarbons in strong carbonate solutions (6). Meanwhile, higher current densities had been achieved using strong acid electrolytes in the same temperature range (7, 8).

With the above results in mind, an attempt was made to increase the solubility of the hydrocarbons in the cesium-salt electrolyte by substituting fluoride anion for a portion of the carbonate anion. This choice was made because HF is known to increase the solubility of hydrocarbons in aqueous solution (9), and because the fluoride anion is not expected to be specifically adsorbed on the electrodes (10, 11). The effect of fluoride content of the Cs_2CO_3-CsF-HF-H_2O electrolyte system on the rate of the anodic oxidation of propane was studied at 150°C. The effect of the chain-length of the normal paraffin fuel molecule on the rate of anodic oxidation was studied at 150° and 105°C.

[1] Present address: Chemical Engineering Division, Argonne National Laboratory, Argonne, Illinois.

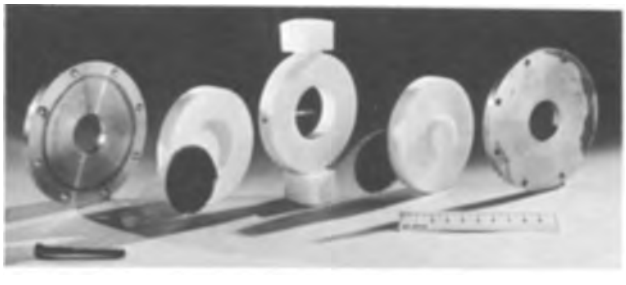

Fig. 1. Photograph of cell parts

Experimental

The fuel cell was constructed of PTFE and platinum in order to minimize any possible contamination of the electrodes and electrolyte. Figure 1 shows the cell parts arranged in the order of assembly. The fuel and oxygen compartments were 3.81 cm in diameter (11.38 cm^2 area) and 0.3 cm deep; the electrolyte compartment was the same size (the 1.2 cm thick electrolyte spacer in the center of Fig. 1 was replaced by a thinner one). The electrodes were made from platinum black (~20 m^2/g) and PTFE by procedures similar to those already reported (12), and contained 50 mg Pt/cm^2. The 45-mesh platinum gauze electrode support also served as current collector. The active geometric area of each electrode was 11.38 cm^2. The cell was held together by Monel end plates and bolts; the PTFE surfaces were self-gasketing.

The assembled fuel cell was mounted, together with an identical cell, which contained reversible hydrogen reference electrodes, in the apparatus shown schematically in Fig. 2. The dashed line represents a forced-convection air thermostat. The electrolyte was circulated by gravity from a PTFE reservoir through the reference cell and the fuel cell to a lower reservoir, from which it was returned to the upper reservoir by

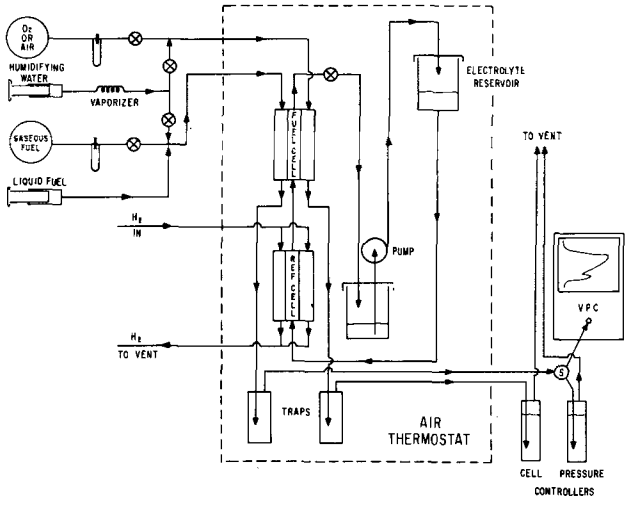

Fig. 2. Schematic diagram of apparatus

an all-PTFE bellows pump. The circulation rate was 4 to 10 cc/min. All surfaces which contacted the electrolyte were PTFE, except for the electrodes themselves which were Pt and PTFE.

The gaseous hydrocarbon fuels were metered by means of a needle valve and a capillary-tube flow meter, and the liquid fuels were fed by a constant-speed syringe drive. Fuel vaporization, where necessary, was carried out with an electrically heated vaporization unit in the feed line (13). Product analysis could be carried out on a chromatograph as desired, using sampling valves in the exit lines.

The normal saturated hydrocarbon fuels and their purities were: methane, Matheson ultra high purity, 99.95% min.; ethane, Matheson, cp, 99.0% min.; propane, Matheson instrument grade, 99.5% min.; butane, Matheson instrument grade, 99.5% min.; pentane, Phillips research grade, 99.84%; hexane, Phillips research grade, 99.99%; octane, Phillips research grade, 99.85%; decane, Phillips research grade, 99.49%; hexadecane, Phillips pure grade, 99.0% passed through silica gel for further purification. The oxygen was electrolytic grade, 99.6% minimum purity. The electrolytes were prepared from Cs_2CO_3 having less than 100 ppm impurities, purified using procedures already reported (14, 15), from Baker and Adamson reagent grade 48% HF, with less than 20 ppm impurities, and from quartz-redistilled H_2O. Electrolyte compositions were determined by acid-base titrations for HF, and by a gravimetric method for Cs as Cs_2SO_4; water was determined by difference.

The electrical measurements were carried out using a modified Kordesch-Marko interrupter (16, 17), yielding potentials on a resistance-free basis. The reference electrode was a reversible hydrogen electrode in the same electrolyte at the same temperature as the cell. All potentials reported are on a resistance-free basis unless otherwise specified. The current density-voltage data were usually measured starting at open circuit, increasing the current in a stepwise manner, and taking readings after electrical steady-state was indicated on a strip-chart recorder. Usually, a period 2-5 min was required to reach steady state at each current. Little or no hysteresis was observed when readings were taken by stepwise decreases in current, except at current densities below about 2 ma/cm².

Results and Discussion

Cesium-salt electrolytes at 150°C.—In order to investigate the effect of replacing the carbonate anion of the Cs_2CO_3 electrolyte by fluoride anion, the temperature of 150°C was selected because the cell C_3H_8(Pt)/85 w/o (weight per cent) Cs_2CO_3/(Pt)O_2 had shown the highest performance at that temperature (6). After taking the current density-voltage data for that cell, the electrolyte (about 200 cc) was drained from the system, a small (1-2 cc) sample was taken for analysis, and an addition of 25 cc of 48% HF was made, converting a portion of the Cs_2CO_3 to CsF. The electrolyte was then reconcentrated to a composition having a boiling point of 160°C, and returned to the system. After gathering current density-voltage data, the sampling and HF addition procedures were repeated.

The results for the performance of the propane anode are summarized in Fig. 3, where the numbers on the curves indicate the number of 25 cc HF additions that had been made to the initial Cs_2CO_3 electrolyte prior to taking the data. The first few additions resulted in essentially no change in anode performance. The shape of these curves is characteristic of a mass-transport limited electrode reaction and the low value of the limiting current density is probably associated with the very low solubility of propane in the electrolyte. Beginning with the seventh HF addition, the shape of the current density-voltage curve changed to a semilogarithmic form, characteristic of an electrochemical rate limiting process, and the current density at a given overvoltage increased by nearly

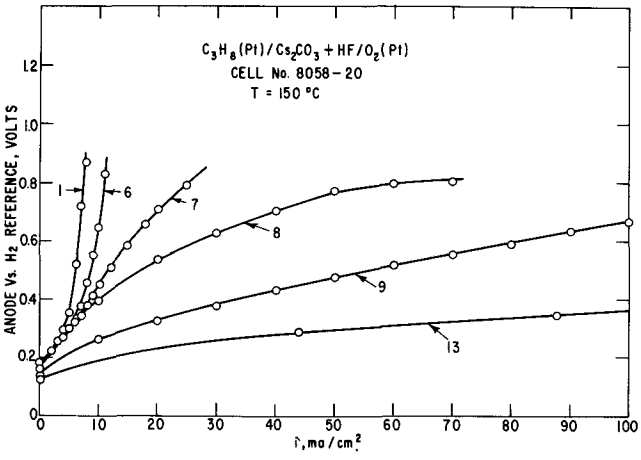

Fig. 3. Propane anode performance for various numbers of HF additions to the initial Cs_2CO_3 electrolyte.

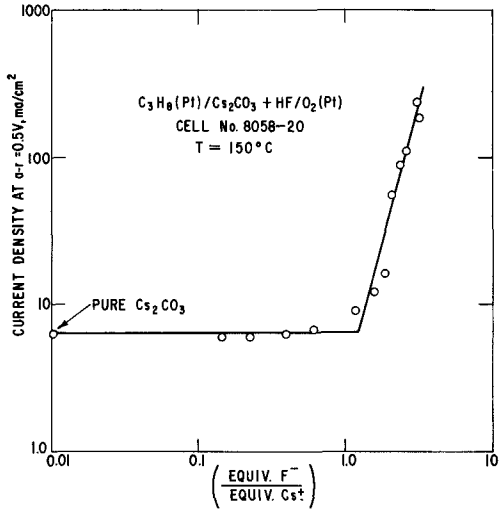

Fig. 4. Effect of fluoride:cesium ratio (by equivalents) on the anode current density at 0.5v *vs.* rhe, for propane on platinum black at 150°C.

two orders of magnitude. The large increase of current density necessitated a concomitant increase in the solubility-diffusion coefficient product for propane in the electrolyte.

The results shown in Fig. 3 were related quantitatively to the electrolyte composition by plotting the current density at an anode *vs.* reference potential of 0.5v as a function of the fluoride:cesium ratio in the electrolyte (as determined by analysis), as shown in Fig. 4. The datum point at $F^-/Cs^+ = 0.01$ is actually the 25 mole % Cs_2CO_3 —75 mole % H_2O point, and it is clear that substitution of the fluoride anion for the carbonate anion has no effect on the rate of propane oxidation, until the F^-/Cs^+ ratio exceeds a value of 1.2. It is probably significant that the electrolyte is still alkaline at a F^-/Cs^+ ratio of 1.0, and at about 1.2, the electrolyte becomes acidic, accompanying an increase in anodic oxidation rate. Further additions of HF cause an exponential increase of current density with F^-/Cs^+ ratio. The slope of the ascending portion of the line in Fig. 4 corresponds to the equation

$$i_{(E_{ar}=0.5)} = k\left(\frac{F^-}{Cs^+}\right)^{3.7} \qquad [1]$$

which indicates a very strong dependence of the propane oxidation rate on the HF content of the electrolyte. The F^-/Cs^+ ratio was not increased beyond 3.3 because further HF additions would bring the boiling point below 160°C (18).

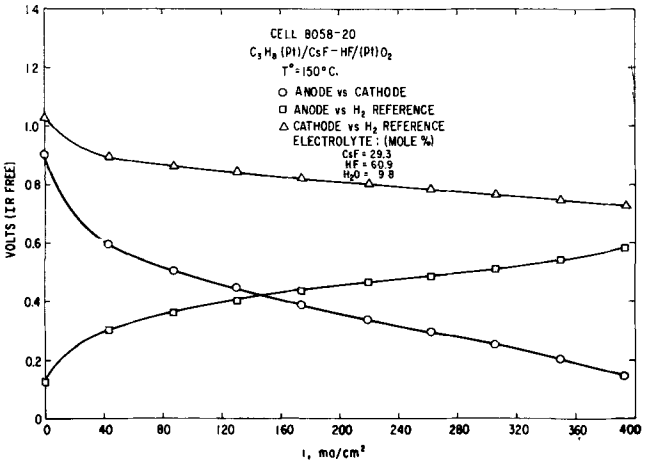

Fig. 5. Performance of propane at 150°C using optimum electrolyte composition

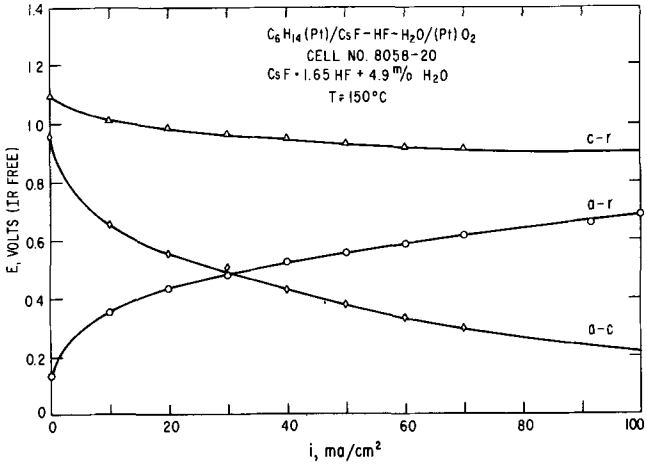

Fig. 7. Hexane performance at 150°C

The results shown in Fig. 3 and 4 suggest that the solubility-diffusion coefficient product for propane in the electrolyte was increased sufficiently by the HF additions so that at F^-/Cs^+ ratios above about 2, the diffusion of dissolved fuel no longer limited the anode performance. Furthermore, additional increases in the HF content of the electrolyte resulted in improvements in the rate of the electrochemical oxidation process at a given overvoltage, probably aided by the lack of fluoride anion adsorption.

The current density-voltage curves for the propane cell having an electrolyte of the optimum composition for operation at 150°C are shown in Fig. 5. The HF:CsF ratio was 2.08, and the water content was 9.8 mole %, corresponding to curve 13 of Fig. 3. A current density of 400 ma/cm² was obtained at a resistance-free cell voltage of nearly 0.2v; the anode *vs.* reference potential was 0.58v at 400 ma/cm². The maximum power density was 80 mw/cm², at about 0.3v, resistance-free.

Several other normal saturated hydrocarbon fuels were tested in the same cell at 150°C, using an electrolyte of the composition HF:CsF = 1.65, H_2O = 4.9 mole %. The methane performance is shown in Fig. 6. Note that current densities above 100 ma/cm² were obtained, indicating that methane is not as unreactive as might have been expected based on the usual organic chemistry experience at these temperatures. The current density supported by the methane anode at anode *vs.* reference potentials below about 0.3v is greater than that from the other saturated hydrocarbons, probably because of the higher H:C ratio of methane, and the absence of C-C bonds associated with the formation of a difficultly oxidized species on the anode surface (19). The maximum power density for methane was about 25 mw/cm², near 0.3v anode *vs.* cathode.

The current density-voltage curves for n-hexane at 150°C using the electrolyte HF:CsF = 1.65 H_2O = 4.9 mole % are presented in Fig. 7, from which it can be seen that the current densities obtained are similar to those for methane, and lower than those for propane. The maximum power point for n-hexane was 21 mw/cm², resistance-free.

The results for all of the normal saturated hydrocarbons investigated can be summarized by plotting the current density at selected anode potentials against the number of carbon atoms in the fuel molecule, as shown in Fig. 8. All of the normal saturated hydrocarbons, methane to n-octane, could be oxidized at practical current densities at 150°C, and all showed reactivities within a factor of five of one another. The data of Fig. 8 can be used to reconstruct the current density-voltage curves for the anodes.

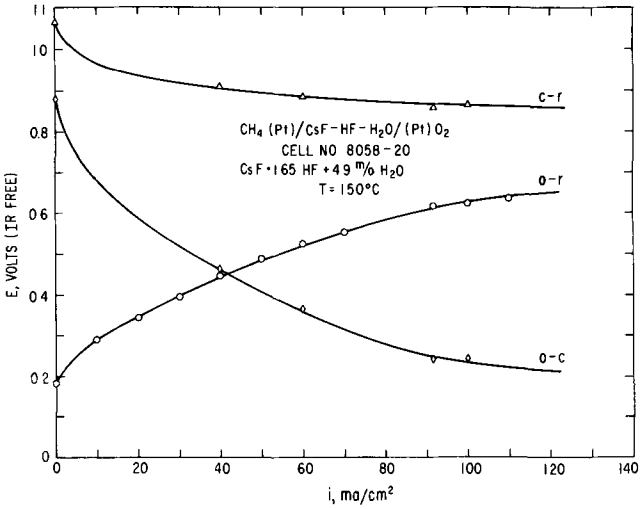

Fig. 6. Methane performance at 150°C

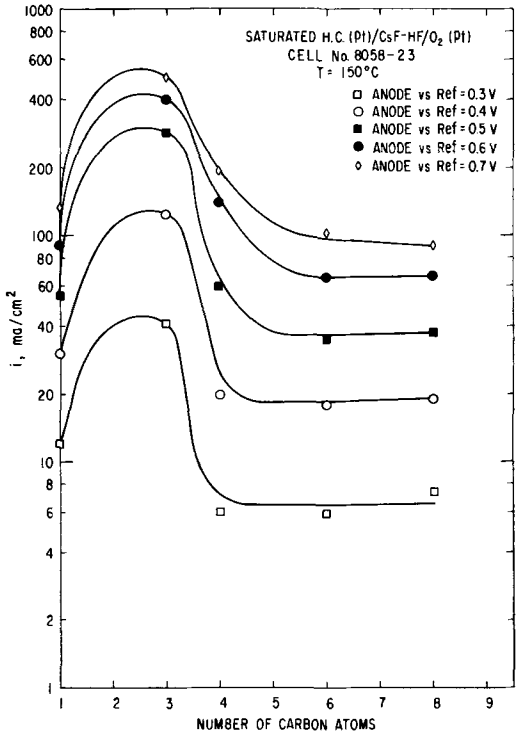

Fig. 8. Effect of fuel carbon number on rate of anodic oxidation at 150°C.

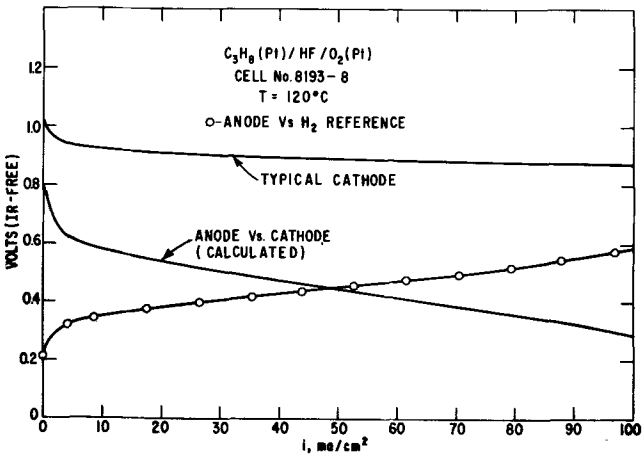

Fig. 9. Propane performance at 115°C, using 36 mole % HF electrolyte

Hydrofluoric acid azeotrope electrolyte at 105°C.— Because of the fact that the rate of anodic oxidation of propane increased rapidly with increasing HF content in the CsF-HF-H_2O system, it was decided that the HF concentration should be maximized by eliminating the CsF. The operating temperature was maximized by using the 36 mole % HF azeotrope (bp~ 115°C) (18) as the electrolyte. The elimination of the CsF made it necessary to operate the cell at temperatures in the range 105°-115°C, since the boiling-point elevation caused by the cesium fluoride could no longer be used to achieve the higher operating temperatures.

The current density-voltage curve for propane on platinum black (50 mg Pt/cm²) is given in Fig. 9, together with a typical cathode curve and the corresponding anode *vs.* cathode curve. The current density at a given anode potential is lower for the HF azeotrope at 115°C than for the optimum CsF-HF-H_2O electrolyte at 150°C (Fig. 5), but the propane performance at 105°C is still high enough to have practical interest, the maximum power density being 30 mw/cm², resistance-free.

The performances of methane, ethane, propane, butane, pentane, hexane, octane, decane, and hexadecane were determined at 110°C, in addition to that of propane, the usual fuel. These fuels fell into three classes: gas at both room temperature and the cell operating temperature (CH_4, C_2H_6, C_3H_8, C_4H_{10}), liquid at room temperature and gas at the cell temperature (C_5H_{12}, C_6H_{14}), and liquid at both temperatures (C_8H_{18}, $C_{10}H_{22}$, $C_{16}H_{34}$). There were no differences in cell performance which could be attributed to the physical state of the fuel in the cell, except for the fact that in general, the fuels which were liquids in the cell had lower partial pressures than the gaseous ones, resulting in relatively lower performance for octane, decane, and hexadecane. The performance results for the various normal saturated hydrocarbon fuels at 110°C are summarized in Fig. 10. The curve shapes are similar to those of Fig. 8, and generally agree with those found for hydrocarbons on Pt black in other strong acid electrolytes (20, 21).

The current densities obtained for the various hydrocarbons at 110°C in hydrofluoric acid are significantly higher per unit weight of Pt than those obtained with other acidic electrolytes at the same temperature, suggesting that there is a significant difference specific to HF. It is possible that this difference is related to the relative absence of anion adsorption with the HF electrolyte (22).

It should be mentioned that under no conditions has either current or voltage cycling been observed with

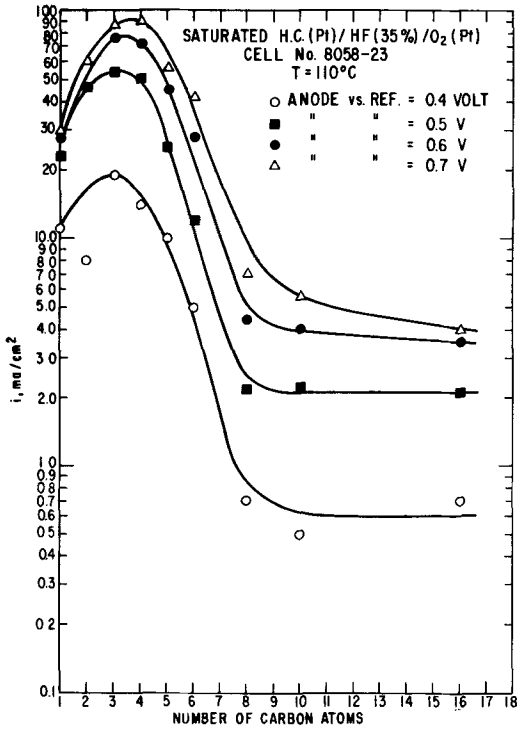

Fig. 10. Effect of fuel carbon number on rate of anodic oxidation at 110°C.

any of these fluoride electrolytes when operating on any hydrocarbon fuel, in contrast to other acid electrolytes (20, 23, 24).

Product identification and material balances.—Product identification was carried out on the chromatograph connected to the anode exit stream as indicated in Fig. 2. In order to prevent HF vapor from entering the chromatograph, a bubbler containing a saturated aqueous KF solution was placed in the fuel exit stream, efficiently absorbing the HF vapor. The product identification analyses showed that only CO_2 and H_2O were produced from the propane fuel.

Material balances, in which fuel disappearance rates as well as CO_2 production rates were measured and compared to the current drawn from the cell, indicated that the CO_2 yield was 95 ± 10% of theoretical, and the fuel consumption rate was about 100 ± 10%. These values correspond to measurements made in the temperature range 100° to 166°C, and at current densities from 5 to 100 ma/cm², using both HF-H_2O and CsF-HF-H_2O electrolytes. The major source of error was the measurement of the very low gas flow rates involved (sometimes less than 1 cm³/min).

Conclusions

1. The ternary system CsF-HF-H_2O comprises a set of electrolytes useful for high-performance saturated hydrocarbon fuel cells operating near 150°C, the performance increasing with increasing HF content.

2. The maximum performance is obtained using C_2-C_4 normal saturated hydrocarbons. Somewhat lower performance is obtained with C_1 and n-C_5-C_{16} paraffins.

3. Good performance is obtained with normal paraffins (particularly C_2-C_4) with the HF-H_2O azeotrope at 105°C.

4. Complete conversion of propane to CO_2 and H_2O has been observed for the temperature range 105° to 166°C, over a wide range of current densities for both the HF-H_2O and the CsF-HF-H_2O electrolytes.

5. No current or voltage cycling has been observed under any conditions.

Acknowledgments

It is a pleasure to thank Mr. G. J. Holm for his aid in performing the experiments, and Mr. L. D. Sangermano and Dr. E. L. Simons for their analyses of the electrolyte solutions.

This work is a part of the program under contracts DA-44-009-AMC-479(T) and DA-44-009-ENG-4909, ARPA Order No. 247 with the U.S. Army Engineer Research & Development Laboratories, Ft. Belvoir, Virginia, to develop a technology which will facilitate the design and fabrication of practical military fuel cell power plants for operation on ambient air and hydrocarbon fuels.

Manuscript was received June 8, 1966. This paper was presented at the San Francisco Meeting May 9-13, 1965.

Any discussion of this paper will appear in a Discussion Section to be published in the June 1967 JOURNAL.

REFERENCES

1. M. J. Schlatter, in "Fuel Cells," Vol. 2, G. J. Young, Editor, Reinhold Publishing Co., New York (1963).
2. G. J. Young and R. B. Rozelle, *ibid.*
3. W. T. Grubb, in Proc. 16th Ann. Power Sources Conf., Atlantic City (May 1962).
4. E. J. Cairns and D. I. MacDonald, *Electrochem. Tech.*, **2**, 65 (1964).
5. E. J. Cairns and D. C. Bartosik, *This Journal*, **111**, 1205 (1964).
6. E. J. Cairns and G. J. Holm, Presented at Electrochem. Soc. Meeting, Washington, D. C. (Oct. 1964), Abstr. No. 30; see also extended abstracts of the Battery Div., **9**, 75 (1964).
7. W. T. Grubb and L. W. Niedrach, in Proc. 17th Ann. Power Sources Conf., Atlantic City (May 1963).
8. R. Jasinski, J. Huff, S. Tomter, and L. Swette, *Ber. Der. Bunsenges*, **68**, 400 (1964).
9. E. B. Butler, C. B. Miles, and C. S. Kuhn, Jr., *Ind. Eng. Chem.*, **38**, 147 (1946).
10. D. C. Grahame, *Chem. Rev.*, **41**, 441 (1947).
11. A. N. Frumkin, in "Advances in Electrochemistry and Electrochemical Engineering," Vol. 3, P. Delahay, Editor, John Wiley & Sons, New York (1963).
12. L. W. Niedrach and H. R. Alford, *This Journal*, **112**, 117 (1965).
13. H. A. Liebhafsky and E. J. Cairns, "Fuel Cells and Fuel Batteries," chap. 8, John Wiley & Sons, New York (to be published).
14. E. L. Simons, E. J. Cairns, and L. D. Sangermano, *Electrochem Tech.*, **2**, 355 (1965).
15. E. L. Simons, E. J. Cairns, and L. D. Sangermano, *Talanta*, **13**, 199 (1966).
16. K. Kordesch and A. Marko, *This Journal*, **107**, 480 (1960).
17. E. J. Cairns and A. D. Tevebaugh, Saturated Hydrocarbon Fuel Cell Program, Technical Summary Report No. 3, Part I, Task IV, Jan. 1-June 30, 1963, Contract No. DA-44-009-ENG-4909, ARPA Order No. 247 Project No. 8A72-13-001-506, USAERDL.
18. E. J. Cairns, *Electrochem. Tech.*, **4**, (1966).
19. L. W. Neidrach, in "Hydrocarbon Fuel Cell Technology," B. S. Baker, Editor, Academic Press, New York (1965).
20. H. Binder, A. Köhling, H. Krupp, K. Richter, and G. Sandstede, *This Journal*, **112**, 355 (1965).
21. W. T. Grubb and C. J. Michalske, in Proc. 18th Ann. Power Sources Conf., Atlantic City (May 1964).
22. E. J. Cairns and E. J. McInerney, To be published.
23. R. P. Hamlen and E. J. Szymalak, *Electrochem. Tech.*, **4**, 172 (1966).
24. E. R. White and H. J. R. Maget, in Proc. 19th Ann. Power Sources Conf., Atlantic City (May, 1965).

The Effect of Anodic Films on the Gaseous Oxidation of Tantalum

R. E. Pawel and J. J. Campbell

Metals and Ceramics Division, Oak Ridge National Laboratory, Oak Ridge, Tennessee

ABSTRACT

The influence of anodic films up to 3000Å thick on the subsequent high-temperature oxidation characteristics of tantalum was studied. At a given temperature, the anodic films decreased the gross oxygen consumption rate to an extent dependent on their thickness and also delayed the onset of the "breakaway" increase in the oxidation rate common to this metal. The result that very thin anodic films pass comparatively large quantities of oxygen to the metal while postponing the appearance of the crystalline oxide phases permitted some oxygen solution effects during the early stages of oxidation to be observed.

While a considerable amount of interest exists in studies of the properties and behavior of anodic oxide films formed on the "valve-metals," only a few investigators have attempted to assess quantitatively the effect of an existing anodic film on the subsequent thermal oxidation characteristics. Polling and Charlesby (1) used optical and gravimetric techniques to observe the changes in thickness of anodic oxide layers on zirconium during gaseous oxidation at elevated temperatures. They found that in the thin-film range, oxidation proceeded along the same path as if the anodic layer were formed thermally. From this and other observations, they concluded that there was no essential difference between the thermal and anodic oxide films for this metal over the range of conditions used in their experiments.

Lakhiani and Shreir (2) observed the anodization of niobium at several temperatures in a variety of electrolytes. When the metal was anodized at low current density, (1 ma/cm^2), the growth of the initial oxide layer, its breakdown, and the development of a nonprotective oxide was observed to be qualitatively similar to the events during the early stages of thermal oxidation. The breakdown of the protective film in this case, by virtue of the physical similarity, was likened by Lakhiani and Shreir to a form of Vermilyea's "field crystallization," (3) where regions of crystalline oxide were assumed to nucleate within the film and consume the amorphous oxide. While Vermilyea (3, 4) had visualized field crystallization, at least for films on tantalum, in a different way, *i.e.*, a mechanical displacement process beginning at the oxide-metal interface, it may still be that the important event responsible for film breakdown in both cases is indeed closely related.

Some comparisons of the general behavior of the thermal and anodic oxidation processes of tantalum and niobium have also been made by Harvey, Draper,

and Wilman (5-7). They likewise picture that for both metals an initially amorphous, anodic-like film forms during the decreasing-rate period of thermal oxidation. Breakaway was proposed to be associated with the formation of "crystal nuclei," followed by cracking of the overlying amorphous pentoxide film.

Also of interest in comparing thermal and anodic oxide films is the growing amount of information on the high-temperature annealing characteristics of anodic films (4-9). If an anodized tantalum specimen is held in vacuum at elevated temperatures, the anodic film will lose oxygen to the metal with no apparent change in thickness, resulting in drastic changes to its electrical properties. At temperatures above 500°C, the anodic films have been reported to crystallize and/or dissolve into the metal. In any case, there appears to be considerable mobility in these films at temperatures above 200°-300°C.

Although the similarities noted above between the anodization process and of some of the important low-temperature thermal-oxidation characteristics might indicate that similar mechanisms, if not identical systems, are involved, it has been established elsewhere that several important differences also exist, particularly for the oxidation of tantalum. For example, effects of oxygen solution and the appearance of the metallic suboxides of tantalum during thermal oxidation (10-11) present a complication that is not faced during anodic oxidation. For specimens oxidizing, prior to breakaway, in the temperature range 300°-550°C, at least two crystalline oxides other than the pentoxide have been identified. The particular physical form associated with suboxide growth (platelets) is difficult to rationalize in terms of conventional oxidation behavior.

The present paper reports the results of a series of experiments in which anodized tantalum specimens were subjected to further oxidation in dry oxygen at elevated temperatures. The characteristics of the anodic films are compared to the thermally formed oxide products especially with regard to the delaying effect an existing anodic film exerts on the "breakaway" process.

Experimental Procedure

For the kinetic studies, tantalum specimens were prepared from 1 × 2 cm and 1 × 4 cm coupons cut from 0.020-in. sheet. The coupons were annealed in vacuum for 2 hr at 1600°C, mechanically polished through 0.3μ alumina, and finally electropolished in a 90% H_2SO_4-10% HF solution. (Nominal analysis of tantalum is about 99.7-99.8% with Nb, Fe, W, and Si being major metallic impurities; interstitial content after vacuum anneal is approximately 200-300 ppm.) A short length of 0.010-in. tantalum wire was discharge welded to one end of the specimen to serve as electrical contact during anodization and support during subsequent handling. Several anodization procedures were utilized, including (*i*) anodizing in 0.5% Na_2SO_4 after boiling the specimens in distilled water to remove, or at least nullify the effect of, any residual fluoride from the electropolish; and (*ii*) anodizing the electropolished specimen in 0.2% KF. These procedures result in highly adherent and poorly adherent anodic films, respectively. However, when heated for short times at 400°C or above, both types of film were adherent, and each resulted in specimens which behaved similarly for the experiments reported in this paper. Our present results are thus based on anodic films formed in the above dilute electrolytes. As is the case for many other properties of anodic films, it is highly probable that films formed in different media, particularly concentrated solutions, would exhibit behavior different in degree, if not in kind, from that reported here.

The specimens were anodized at constant voltage by allowing the current to discharge through a variable resistor in series with the cell. The current density was generally maintained at less than 20 ma/cm² by manually reducing the series resistance as anodization proceeded. In order to utilize a voltage-thickness calibration, the specimens were anodized for an arbitrary "standard" time of 3 min, sufficiently long so that the film thickness was insensitive to minor variations in the anodization time. Our previously reported value (12) of 16.7Å per applied volt was used to obtain the oxide film thickness.

The specimens were heated quickly in oxygen to the desired reaction temperature and the oxidation rates were measured by a manometric technique previously described (13). Pressure changes during an experiment were small enough (generally less than 15 mm Hg) to consider the oxidation conducted at constant pressure. All oxidation experiments were carried out in dry oxygen at atmospheric pressure.

The development of stresses in the oxidizing specimens was followed in a series of "flexure" experiments. Tantalum coupons, 1 × 4 cm, prepared as noted above, were anodized and one side protected with a thin film of vapor-deposited aluminum. The flexure of such specimens during oxidation was measured and converted to maximum bending stress values in a manner already reported (14).

Results and Discussion

The initial stages of the gaseous oxidation of tantalum metal in the intermediate temperature range 400°-600°C have been described on both kinetic and phenomenological bases (10, 11). These studies have shown that this part of the oxidation process is comparatively complicated, distinguished by the formation and growth of platelets of oxide rather than reasonably uniform oxide films. Platelet formation is related to oxygen solution effects and the particular mode of formation of the suboxides of tantalum. If the tantalum specimen surface is electro- or chemically polished so that a disturbed surface layer is not present, these developments during oxidation can be followed easily in a hot-stage microscope or by standard metallography.

As oxidation proceeds, the formation of the pentoxide is associated with an abrupt increase in the oxidation rate. While there is still disagreement in the literature concerning the particular phenomenon or "important event" responsible for the increased rate, all investigators agree that the bulk of the pentoxide, once formed, offers little resistance to oxygen permeation and thus serves poorly as a protective oxide film. It seemed reasonable to us to suggest that the films formed on tantalum during the postbreakaway part of gaseous oxidation were poorly protective because of the manner in which they were formed and not necessarily because of some inherent property.

The nonuniform oxide morphology which exists during the decreasing-rate period of oxidation prior to breakaway certainly does not resemble the product of anodic oxidation, although as will be discussed later, a superficial anodic-like layer may enhance platelet formation. However, because of the differences in properties, studies of the thermal oxidation of anodized tantalum permit certain aspects of the early stages of this process to be emphasized.

Vacuum treatments.—In this phase of the research, we have been concerned with the oxidation characteristics of anodized specimens at temperatures below which the rate of crystallization or oxide dissolution becomes appreciable. Preliminary experiments in which anodized specimens with films 250Å and thicker were held in vacuum showed that at temperatures as high as 500°C the dissolution rate of the oxide was extremely low. Such vacuum treatments could, however, result in a lessening in the degree of protection afforded an anodized specimen during subsequent oxidation. Vermilyea (7) and Smith (9) have pointed out that while the thickness of the anodic film on tanta-

lum remains constant during low-temperature annealing (at least the interference color does not change perceptibly), some oxygen from the oxide is taken into the metal with a resulting large change in the electronic properties of the oxide. In addition, Vermilyea showed a slight sharpening of the diffraction halos from the essentially amorphous oxide films during such treatments. We have also observed by electron diffraction similar structural changes during annealing of films stripped from the metal (15). Actual crystallization of the stripped films within reasonable times did not occur at temperatures below 550°-600°C (6, 8, 15); higher temperatures appear to be required for complete crystallization of films-in-place on the metal.

While films held in vacuum at 500°C were stable for long periods of time, or dissolved extremely slowly, an appreciable rate of anodic film dissolution was observed on specimens held at 600°C, the films exhibiting a behavior very much like that reported by Pemsler for diffusion-controlled film dissolution on zirconium (16) and hafnium (17). Of particular interest was the observation that the dissolution process in the case of b.c.c. tantalum also was not completely isotropic; *e.g.*, several interference colors sharply defined by the grain boundaries existed after annealing an anodized polycrystalline specimen. Furthermore, observations on annealed anodized single-crystal cylinders with <110> axes indicated that the dissolution rate at this temperature was almost uniform (at least along the [110] zone) except within about ±10° of a (100). At the (100), the dissolution rate, at least for the first few hours, was observed to be slightly more than twice as great as the other areas. In all regions, the dissolution rate decreased with time. However, while the amount dissolved on the (100) showed a parabolic time dependence, at least up to 24 hr, our rather limited data for dissolution in the slower region could not be satisfactorily described in this way over this time range.

Oxidation.—If the anodized tantalum specimens were held in dry oxygen at atmospheric pressure instead of vacuum, dissolution of the films was not generally observed. Instead, at temperatures of at least 500°C, the films exhibited a very high degree of stability and resistance to thickening as well as dissolution. Insofar as could be judged from the lack of change in the interference color of an anodic film before and after such treatments, the film thickness and the appearance of the metal surface was not altered despite the fact that oxygen solution was occurring through the film into the metal.

Anodized tantalum specimens having film thicknesses of approximately 250-2500Å were oxidized for extended periods of time at 500° and 600°C in order to assess systematically the degree of protection which results and to observe the eventual "failure" of the film. For example, after 24 hr at 500°C for films 500Å and thicker, visual comparison with an as-anodized, standard specimen revealed no significant changes in the interference colors or general specimen appearance; unanodized specimens subjected to the same treatment underwent substantial oxidation, with white scales of the pentoxide as the prominent feature. While it quickly became apparent that the degree of protection at a given temperature was directly dependent on the thickness of the anodic layer, it was also observed that imperfections in the films play an important role. Anodic films exhibiting low leakage currents formed on well electropolished surfaces were more efficient in "protecting" the metal from oxidation. Local breakdown of the film at a point of weakness may, instead of being self-healing, lead to an accelerated deterioration of the remainder of the film. This is particularly noticeable in the case of films less than 250Å in thickness where the oxidation behavior is difficult to reproduce. Once local breakdown has occurred, the metal oxidizes rapidly and the voluminous pentoxide which is formed propagates the disturbance. The topography more closely resembles the breakdown of the slowly oxidizing (100) face of niobium (13) than that of any stage of oxidation of plain electropolished tantalum.

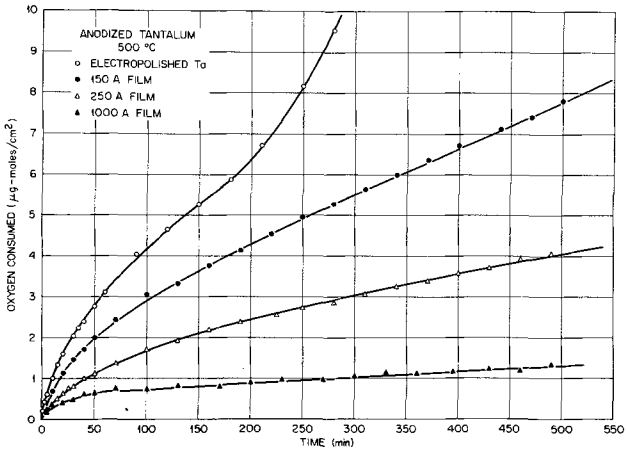

Fig. 1. Effect of anodic film thickness on the oxidation rate of polycrystalline tantalum at 500°C. ○ plain electropolished tantalum; ● 150Å anodic film; △ 250Å anodic film; ▲ 1000Å anodic film.

While it was difficult to tell by visual inspection if the anodized specimens were undergoing change during the exposure to oxygen prior to breakdown, metallographic examination, flexure experiments, and x-ray analysis indicated that oxygen was being dissolved into the metal in substantial quantities. Smyth *et al.* (9) as part of their studies of the dielectric properties of anodic films, have also reported that oxygen penetrates the film to the metal during heat treatment in air. Furthermore, because of the nature of the property changes, they were able to conclude that the oxygen passes through the film itself and not by way of cracks or pores.

Kinetics.—The effect of thin anodic oxide films on the early stages of oxidation of tantalum is illustrated quantitatively in Fig. 1 which shows the kinetics of oxygen uptake at 500°C for plain electropolished tantalum and anodized tantalum having film thicknesses of 150, 250, and 1000Å. During the decreasing-rate period of reaction for plain tantalum, most of the total oxygen consumed is going into solution in the metal. After about 10 min, platelets of a suboxide of tantalum extending into the metal begin to form; after about 3 hr, the increasing oxidation rate signals the occurrence of "breakaway," and the specimen is soon covered with a thickening, porous film of the pentoxide. On the other hand, the presence of an anodic film obviously impedes the reaction to an extent dependent on the film thickness. Since the film thickness does not change appreciably during this period,[1] the oxygen consumed is thus going into solution in the metal. Nevertheless, compared to plain tantalum, the appearance of oxide platelets in the metal beneath the anodic film is postponed, both on a time basis and on the basis of the total oxygen consumed. It may be that the oxygen concentration in the metal surface layers beneath the anodic film remains less than that during oxidation of the plain metal. Another possibility is that the presence of the anodic film affects the pertinent surface energies so as to make it energetically expensive for a new oxide phase to form. In either case, a greater total amount of oxygen would be necessary to initiate platelet formation. Because of this, or the associated increased strain energy, the observation

[1] It might be argued that the refractive index of the film and perhaps the metal change in such a direction and with such magnitude so as to mask the observation of a thickness change. While in principle this is possible, the probability is small that such an effect would not be noticed over the wide range of film thicknesses, annealing times, and temperatures studied.

that platelets formed on anodized tantalum are generally larger than those on plain tantalum is consistent with either explanation. Also postponed on both bases is the breakaway increase in the oxidation rate. While comparatively thick anodic films, 1000Å and up, afford effective protection for long times, films as thin as 40Å produce dramatic differences in breakaway oxidation behavior compared to the plain tantalum. It is to be noted, however, that films in this thickness range pass oxygen at a rate comparable to that used during the oxidation of the plain tantalum. Thus, an anodic oxide film on tantalum has the unusual property of serving both as a semi-inert barrier film and as a repressor of the formation of the crystalline oxides during subsequent thermal oxidation.

The effect of temperature on the oxidation kinetics of anodized specimens was also studied. The oxidation rate curves at temperatures from 425° to 575°C for plain tantalum and for anodized tantalum with film thicknesses of 250 and 1000Å are presented in Fig. 2, 3, and 4. The protection afforded by these films is seen to persist over the whole temperature range. Films thicker than 1000Å were generally even more resistant; for example, even at 600°C a 3000Å film prevented breakaway for at least 4 hr. However, the thicker films become increasingly susceptible to electrical breakdown during their formation, especially in poorer quality films where certain flaws are "activated" at comparatively low voltages. In such films,

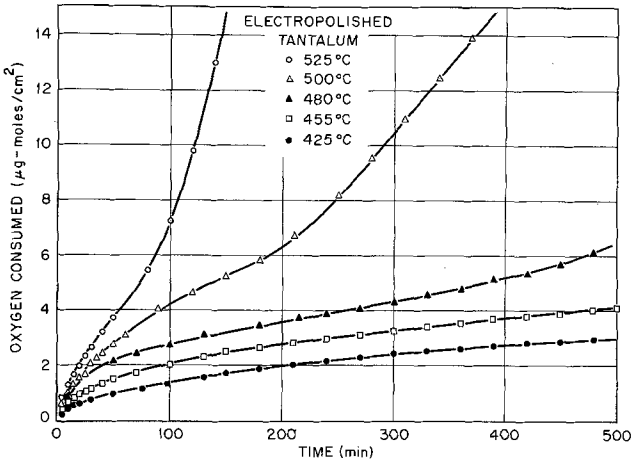

Fig. 2. Effect of temperature on the oxidation rate of electropolished polycrystalline tantalum. ● 425°C; □ 455°C; ▲ 480°C; △ 500°C; ○ 525°C.

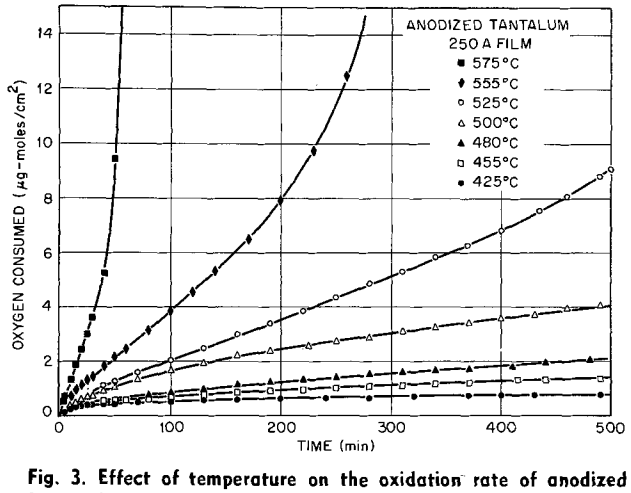

Fig. 3. Effect of temperature on the oxidation rate of anodized polycrystalline tantalum having a film thickness of 250Å. ● 425°C; □ 455°C; ▲ 480°C; △ 500°C; ○ 525°C; ♦ 555°C; ■ 575°C.

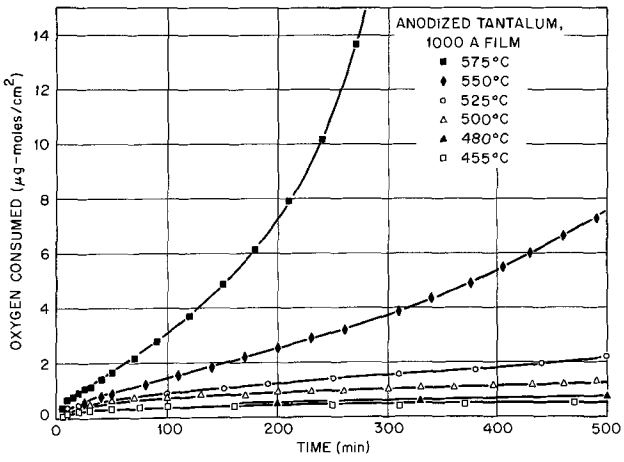

Fig. 4. Effect of temperature on the oxidation rate of anodized polycrystalline tantalum having a film thickness of 1000Å. □ 455°C; ▲ 480°C; △ 500°C; ○ 525°C; ♦ 550°C; ■ 575°C.

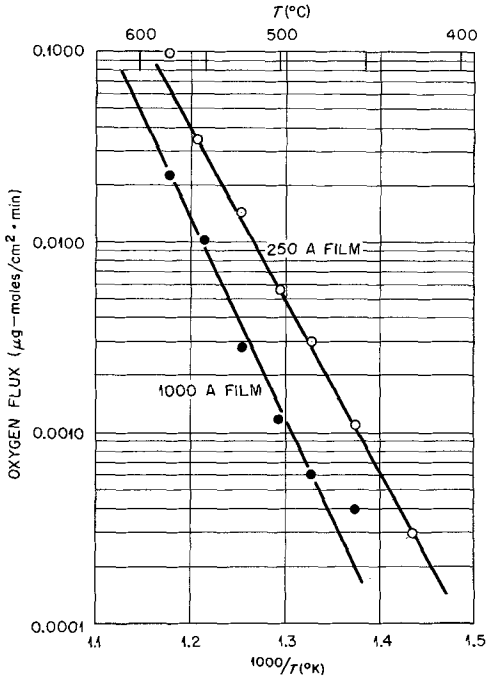

Fig. 5. Oxygen permeation rates through anodic oxide film on polycrystalline tantalum. ○ 250Å film; ● 1000Å film.

breakaway oxidation is initiated quickly in these local regions, resulting in a general loss of oxidation resistance. Vermilyea (4) has described in detail the importance and nature of some of the imperfections in anodic films. Presumably, flaws in the thinner films also represent points of weakness with respect to oxidation as well as electrical and chemical attack, and eventual breakdown of the films would begin at these points.

It is difficult to place much confidence in the pertinence of a particular analytical expression describing the prebreakaway oxidation kinetics of anodized tantalum. After an initial decreasing-rate period, the time dependence is more-or-less linear until the onset of breakaway. The oxygen consumption rates in this region were obtained from the data in Fig. 3 and 4 and are plotted as a function of reciprocal temperature in Fig. 5. Within the limits of accuracy of the experimental values, the data for the 250 and 1000Å films describe two near-parallel lines differing by a factor of about four in ordinate values. That the rate ratio for oxygen consumption at each temperature is ap-

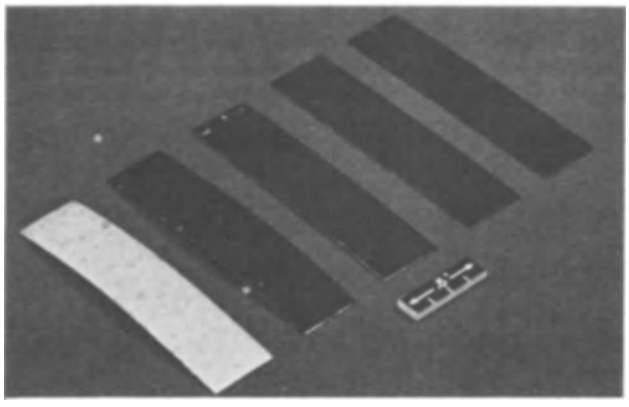

Fig. 6. Flexure and surface appearance of plain and anodized tantalum after oxidation for 2 hr at 530°C. From left to right, the specimens are plain electropolished tantalum and tantalum having film thicknesses of 40, 80, 160, and 250Å, respectively. The underside of each specimen was protected by a vapor-deposited aluminum layer.

proximately equal to the inverse of the thickness ratio is evidence in favor of the oxygen mass transport mechanism in the anodic film as being rate controlling. The decreasing rate period at the beginning of the reaction is, in this light, simply a transient in the approach to a steady-state diffusion condition. If the above reasoning is correct over the whole temperature range, the activation energy for oxygen transport in amorphous anodic films on tantalum is, from Fig. 5, about 45,000 cal/mole.

Flexure.—The fact that the thin anodic films suppressed the formation of additional oxide while allowing oxygen to penetrate to the metal during exposure to oxygen permitted a critical test to be made of the authors' earlier conclusion (14) that oxygen solution effects, rather than the formation of oxide, were primarily responsible for the observed surface stresses in the preliminary stages of tantalum oxidation. Thus, measurements were made of the flexure of thin anodized specimens exposed to oxygen on one side. The occasion of a definite flexure of such specimens during a period of time when no additional oxide was observed to form seemed conclusive evidence that oxygen in solution is a major source of stress.

A typical set of tantalum specimens used in the flexure experiments is shown in Fig. 6. This photograph illustrates the flexure and surface appearance of plain tantalum and tantalum with anodic oxide films thicknesses of 40, 80, 160, and 250Å after oxidation for 2 hr at 530°C. The plain tantalum surface is heavily oxidized and the specimen is bent. The anodized specimens show varying degrees of flexure but, with the exception of the 40Å specimen, show no metallographic or x-ray evidence of additional oxides. Despite their dark appearance in the figure, the surfaces of these specimens are still bright, in sharp contrast to that of the plain tantalum. In the microscope, the 40Å specimen shows only little physical evidence of the comparatively large amount of oxygen taken into solution. Distortion markings and a few large platelets, common to the earliest stages of oxidation of plain tantalum are visible. The topography of the plain tantalum specimen and 40Å anodized tantalum specimen is compared in Fig. 7 and 8. Specimens with thicker anodic films exhibit essentially the same microstructure as in the as-anodized condition.

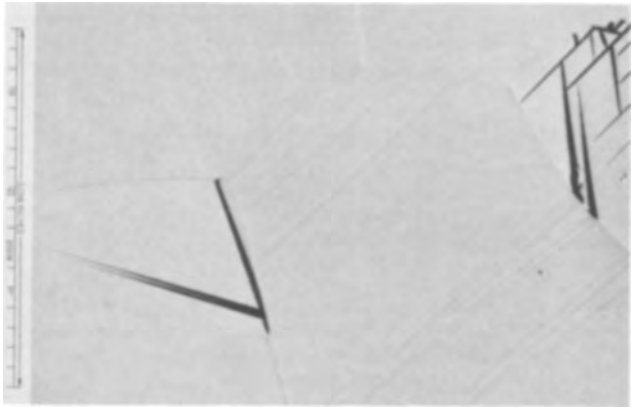

Fig. 8. Surface appearance of anodized polycrystalline tantalum having a film thickness of 40Å after 2 hr in oxygen at 530°C.

Quantitative measurements of the degree of flexure were made during oxidation of the anodized specimens. As shown in Fig. 9, the maximum bending stress, computed from the physical properties and radius of curvature of the specimen as a function of time, varied similarly to the total amount of oxygen going into solution, reaching a value of about 16,000 psi after 6 hr of oxidation. Because of the obviously different set of boundary conditions applicable in this case, the actual surface stress and stress distribution due to oxygen solution cannot be computed in the manner previously reported for plain tantalum (14). However, since the total strain energies in both cases (for specimens with very thin anodic films, at least) are about the same, it is reasonable to suspect stresses in the surface region to approach that observed in plain tantalum, approximately 50,000 psi compression.

X-ray results.—X-ray data consistent with the above arguments were also obtained. Before and after exposure to oxygen, diffraction measurements were made through the anodic film of the lattice spacing of metal planes parallel to the surface. Lattice param-

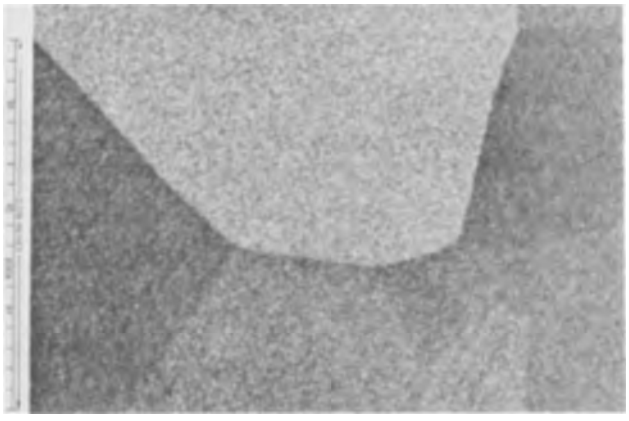

Fig. 7. Surface appearance of plain electropolished polycrystalline tantalum after 2 hr in oxygen at 530°C.

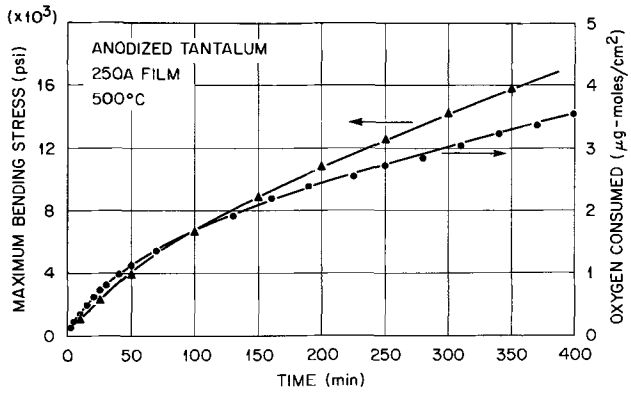

Fig. 9. Comparison of the bending stress and oxidation rate curves for anodized polycrystalline tantalum (250Å) at 500°C.

eters were also determined by the Debye-Scherrer techniques for thin surface layers filed from the metal. The results by these two techniques correlated very well if it was assumed that an oxygen concentration gradient existed in the metal. For the case of both plain tantalum and anodized tantalum, exposure to oxygen at 500°C quickly increased the tantalum lattice parameter, calculated from the interatomic spacings of planes parallel to the surface, to 3.330Å, a dilation of about 0.025Å compared to unoxidized control specimens. This dilation, since it is limited only to a thin surface layer and because of the constraints imposed by the remainder of the specimen outside the gradient, is larger by about a factor of two than that which would result from the same uniform concentration of oxygen (18). On the basis of a uniform distribution, the appropriate lattice parameter would have been 3.317Å, corresponding to an oxygen concentration of about 3.7 a/o (atomic per cent) (19). It was observed that this latter parameter value agreed much better with that obtained from similar specimens by the Debye-Scherrer method, 3.312-3.314Å, especially considering the deeper section employed. Since a rather steep oxygen concentration gradient may develop during oxidation, the maximum oxygen concentration immediately beneath the surface may rise to values higher than that reported here.

Conclusions

The results of this investigation have shown that anodic films formed on electropolished tantalum specimens can exert a surprisingly great influence on the gaseous oxidation characteristics. Films as thin as 40Å, for example, were observed to double the length of the "protective" period for tantalum at 500°C. During the time that the anodic films remain protective, they are substantially amorphous in structure, and pass oxygen to the underlying metal without "growing" or changing in thickness. The activation energy for oxygen permeation of these films was calculated to be about 45,000 cal/mole. The anodic films appear to slow down the oxidation process in two ways: (*i*) the oxygen flux is reduced, being related inversely to the film thickness; and (*ii*) the nucleation of the crystalline suboxides of tantalum is postponed to higher total oxygen levels. This may be a result of a changed oxygen concentration gradient near the surface, or of a change in other properties at the metal surface due to the film. The anodic films lose their protective properties as breakdown occurs first at localized points and then spreads across the specimen mainly by lateral growth of the fast-oxidizing regions. Presumably these localized points are associated with imperfections in the film or metal causing crystalline oxides to form more quickly at the metal-anodic oxide interface. While the films dissolve into the metal at measurable rates when held in vacuum at temperatures above 500°C, their retarding effects during oxidation may be observed at temperatures of at least 600°C. The occurrence of oxygen solution in the metal during oxidation of anodized tantalum was observed by several methods. Flexure and x-ray measurements correlated well with the concept that high stress levels exist along the oxygen concentration gradient in the metal.

Acknowledgments

The authors would like to thank J. V. Cathcart for his assistance during the course of this investigation and in the preparation of the manuscript. We also acknowledge the efforts of C. J. Sparks and R. M. Steele for the x-ray measurements. Research on this paper was sponsored by the United States Atomic Energy Commission under contract with the Union Carbide Corporation.

Manuscript was received June 23, 1966. This paper was presented at the Philadelphia Meeting, Oct. 9-14, 1966.

Any discussion of this paper will appear in a Discussion Section to be published in the June 1967 JOURNAL.

REFERENCES

1. J. J. Polling and A. Charlesby, *Acta Met.*, **2**, 667 (1954).
2. D. M. Lakhiani and L. L. Shreir, *Nature*, **188**, 49 (1960).
3. D. A. Vermilyea, *This Journal*, **102**, 207 (1955).
4. D. A. Vermilyea, *Acta Met.*, **1**, 282 (1953); *This Journal*, **104**, 485 (1957); *Acta Met.*, **5**, 113 (1957). and *This Journal*, **110**, 250 (1963).
5. J. Harvey and P. H. G. Draper, *J. Inst. Metals*, **92**, 136 (1963-1964).
6. J. Harvey and H. Wilman, *Acta Cryst.*, **14**, 1278 (1961).
7. P. H. G. Draper and J. Harvey, *Acta Met.*, **11**, 873 (1963); and P. H. G. Draper, *Acta Met.*, **11**, 1061 (1963).
8. L. D. Calvert and P. H. G. Draper, *Can. J. Chem.*, **40**, 1943 (1962).
9. D. M. Smyth, G. A. Shirn, and T. B. Tripp, *This Journal*, **110**, 1264, 1271 (1963); and *ibid.*, **111**, 1331 (1964).
10. P. Kofstad, *J. Inst. Metals*, **91**, 209 (1962-1963); *ibid.*, **90**, 253 (1961-1962); and P. Kofstad and J. Krudtaa, *J. Less-Common Metals*, **5**, 477 (1963).
11. R. E. Pawel, J. V. Cathcart, and J. J. Campbell, *Acta Met.*, **10**, 149 (1962); and *This Journal*, **107**, 956 (1960).
12. R. E. Pawel, *Rev. Sci. Instruments*, **35**, 1066 (1964).
13. R. E. Pawel, J. V. Cathcart, and J. J. Campbell, *AIME Symposium, Columbium Metallurgy*, p. 442, Interscience, New York (1961).
14. R. E. Pawel, J. V. Cathcart, and J. J. Campbell, *This Journal*, **110**, 551 (1963).
15. R. E. Pawel and J. J. Campbell, *This Journal*, **111**, 1230 (1964).
16. J. P. Pemsler, *ibid.*, **105**, 315 (1958).
17. J. P. Pemsler, *ibid.*, **106**, 1067 (1959).
18. J. D. Eshelby, *Solid State Phys.*, **3**, 112, Academic Press, New York (1956).
19. E. Gebhardt and H. D. Seghezzi, *Z. Metallk.*, **50**, 521 (1959).

Acknowledgments

The financial support of the Naval Air Engineering Center, Philadelphia, Pennsylvania, is gratefully acknowledged. The authors wish to thank Dr. J. O'M. Bockris for helpful discussions. The cooperation of Mr. F. S. Williams and Mr. E. Taylor of N.A.E.C. is also acknowledged.

Manuscript was received March 7, 1966; revised manuscript was received June 30, 1966. The opinions and assertions expressed are the private ones of the authors and are not to be construed as official or reflecting the views of the Department of the Navy or Naval Service at large.

Any discussion of this paper will appear in a Discussion Section to be published in the June 1967 JOURNAL.

REFERENCES

1. L. Cailletet, *Compt. Rend.*, **58**, 327 (1864).
2. J. O'M. Bockris, J. McBreen, W. Beck, and L. Nanis, To be published.
3. M. A. V. Devanathan and Z. O. J. Stachurski, *Proc. Roy. Soc.*, **A270**, 90 (1962).
4. M. A. V. Devanathan and Z. O. J. Stachurski, *This Journal*, **111**, 619 (1964).
5. M. A. V. Devanathan, Z. O. J. Stachurski, and W. Beck, *ibid.*, **110**, 886 (1963).
6. R. C. Frank, *J. Appl. Phys.*, **29**, 1263 (1958).

Technical Notes

Corrosion of Zircaloy-2 by Hydrogen Peroxide at Elevated Temperature

R. J. Davis, T. H. Mauney, and J. R. Hart

Reactor Chemistry Division, Oak Ridge National Laboratory, Oak Ridge, Tennessee

It has been shown that fission fragment (1, 2) or fast neutron (3) bombardment accelerates the corrosion of Zircaloy-2 by oxygenated aqueous media. The corrosion occurs at constant rates, and for fast neutron bombardment the corrosion rate, R, in terms of weight gain ($\mu g/cm^2/day$) and neutron flux of energies greater than 1 Mev, ϕ ($n/cm^2/sec$) is

$$R = 7 \times 10^{-12}\phi$$

The acceleration of corrosion in hydrogenated media (3) under fast neutron bombardment is much less or perhaps nil. Ionizing (β-γ) irradiations (4, 5) do not accelerate Zircaloy-2 corrosion in oxygenated aqueous media.

Since β-γ radiations do not accelerate corrosion, it has been concluded in the past (1, 2) that the heavy particle effect was due to damage in the metal or oxide, but not due to species generated in the aqueous solution. This conclusion followed from the fact that β-γ radiations produce the same species in solution as do heavy particles, and it was assumed that the concentrations were not enough different to explain the results.

Cox (6) recently pointed out that some in-pile loop results (7) indicate accelerated corrosion of Zircaloy-2 exposed to solution, one second downstream of the irradiated part of the loop. This suggested the possibility that hydrogen peroxide, probably the only specie with a half-life approaching one second, was responsible for the corrosion. [The authors had (7) considered this possibility, but did not believe the data justified any conclusions.] Subsequently Jenks (8) showed that corrosion effects of the two types of radiations could be qualitatively explained by assuming that corrosion is accelerated by low concentrations of H_2O_2 and that the acceleration increases with concentration. It was estimated that in water at 280°C, a steady-state H_2O_2 concentration in the neighborhood of 10^{-5}M would exist under reactor irradiation at moderate intensities. Furthermore, the concentration would increase with dissolved oxygen in stoichiometric excess and would decrease with dissolved hydrogen in excess. The concentration of H_2O_2 under β-γ irradiation would be much lower. These findings suggested the following experiment.

Experimental

Specimens of Zircaloy-2 were exposed to 10^{-5}M H_2O_2 at 280°C for 297 hr. A control group of specimens was exposed in the same set-up to oxygenated water.

The peroxide exposure was accomplished by the feed and bleed system shown in Fig. 1. Hydrogen peroxide solution (0.05M) was pumped into an autoclave by a pulse-feeder pump at the rate of about 800 cc/hr. The autoclave was completely liquid-filled, and the solution in the autoclave was stirred with a magnetically operated dash pot stirrer. The solution

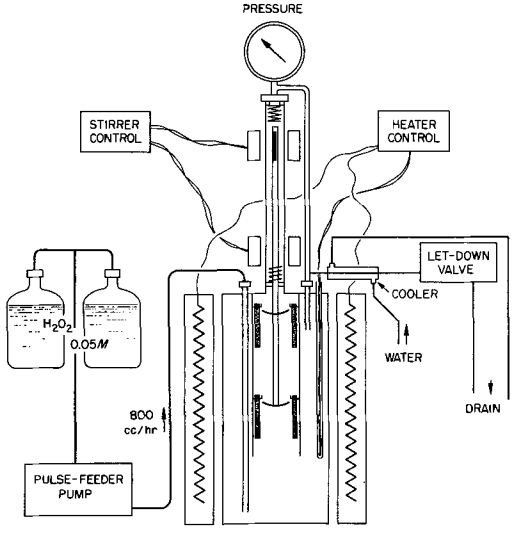

Fig. 1. Feed and bleed autoclave system

Table I. Summary of weight gains

Weight Gain Results			
Specimens exposed to:	10^{-5}M H_2O_2		Oxygenated water
Specimens pretreated by:	Prefilming 20 hr	Chemical polishing	Chemical polishing
No. of specimens	4	2	8
Weight gain, avg value ($\mu g/cm^2$)	91*	88	104
Weight gain, range ($\mu g/cm^2$)	80-100*	87-90	89-119

* Total weight gains including that during 20-hr prefilming.

coming out of the autoclave was quickly cooled to room temperature, and then bled out of the system at 1500 psi through a let-down valve. Periodic samples of the output solution were analyzed and found to contain about 10^{-5}M (range 0.6 to 1.2 x 10^{-5}M) hydrogen peroxide. All parts of the system which were heated were constructed of titanium.

The controls were run in the same autoclave at the same temperature for the same length of time. The autoclave was initially filled with the same 0.05M peroxide solution which quickly decomposed on heating to provide an environment of oxygenated water. No peroxide was pumped through the system.

Both sets of specimens were chemically polished in $HF-HNO_3$ and some of them were prefilmed by exposure to 280°C water for 20 hr before exposure to the peroxide. Corrosion was measured by weight gain.

The weight gains are summarized in Table I.

Discussion

The data demonstrate that corrosion of Zircaloy-2 by oxygenated water is not enhanced by continuous feeding of hydrogen peroxide at a concentration of 10^{-5}M.

Estimates (8) of peroxide concentrations in oxygenated water indicate that the 10^{-5}M is about the peroxide concentration which exists during irradiation by a fast neutron flux of 10^{13} n/cm²/sec (> 1 Mev). This flux, in turn, is known to result in a corrosion rate of about 70 $\mu g/cm^2$/day.

From the observed rates of 7-8 $\mu g/cm^2$/day, it followed that hydrogen peroxide in solution is not responsible for the corrosion acceleration which results from irradiation by fast neutrons.

Manuscript received June 27, 1966. Research was sponsored by the United States Atomic Energy Commission under contract with the Union Carbide Corporation.

Any discussion of this paper will appear in a Discussion Section to be published in the June 1967 JOURNAL.

REFERENCES

1. G. H. Jenks, "Fluid Fuel Reactors," pp. 232-245, J. A. Lane, H. G. MacPherson and Frank Mason, Editors, Addison-Wesley Co., Inc., Reading, Mass. (1958).
2. G. H. Jenks, "Corrosion of Zirconium Alloys," pp. 41-57, ASTM Special Tech. Pub. No. 368, ASTM, Philadelphia, Pa., 1063.
3. G. H. Jenks and R. J. Davis, *This Journal*, In press.
4. G. O. Heston and M. D. Silverman, ORNL-CF-56-2-2, February 1956.
5. D. J. Harrop, N. J. M. Wilkins, and J. N. Wanklyn, "The Effect of Gamma Dose on Zirconium and Zircaloy-2 Relevance to Corrosion," AERE-R-4779, 1964.
6. B. Cox, Private communication.
7. W. A. Burns, "Effects of Fast Neutron Irradiation, Fabrication History, and Water Oxygen on the Environmental Behavior of Zirconium Alloys," BNWL-88, August 1965, p. 23.
8. G. H. Jenks, "Effects of Reactor Operation on HFIR Coolant," ORNL-3848, October 1965.

Electroluminescence and Photoresponse of Ta_2O_5 and TiO_2 Diodes

T. W. Hickmott

General Electric Research and Development Center, Schenectady, New York

Electroluminescence has been observed from rectifying Ta-Ta_2O_5-Au and Ti-TiO_2-Au diodes under d-c forward bias and the photoresponse of such diodes has been measured in the visible portion of the spectrum. In each case, the photoresponse threshold is approximately equal to the energy of electroluminescent radiation from the diode.

Tantalum strips, 1 mm wide and ~6000Å thick, were deposited on heated glass microscope slides by electron beam evaporation through a mask (1). Titanium strips of high resistivity, indicative of low purity of the metal, were deposited on microscope slides by sputtering in argon. Oxide films were formed by anodizing at constant current, followed by curing at constant voltage until the current through the oxide decreased to low levels. For tantalum, 0.5% H_2SO_4 was used as electrolyte while a formic acid electrolyte was used to anodize titanium (2). The thickness of the oxide film is proportional to the final forming voltage; for Ta_2O_5, the thickness is ~17 Å/v, for TiO_2, ~22Å/v. Diodes of 1 mm² area were formed by evaporating semitransparent Au or Cu electrodes, 200Å thick, through a mask. Procedures used to measure conductivity, electroluminescence and photoresponse have been described (3, 4).

Both Ta-Ta_2O_5-Au and Ti-TiO_2-Au diodes are rectifying, with high conductivity occurring when the Au counterelectrode is positive. Figure 1 shows the

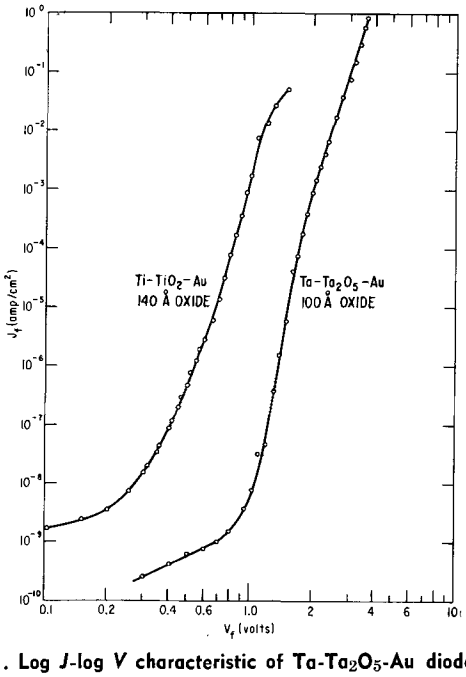

Fig. 1. Log *J*-log *V* characteristic of Ta-Ta_2O_5-Au diode and Ti-TiO_2-Au diode. $T = 295°K$.

current-voltage characteristic under forward bias for a Ta-Ta_2O_5-Au and a Ti-TiO_2-Au diode formed to 5v. The current density, J, was derived from the measured currents by using the geometric area of the diode. The J-V characteristic of the Ta-Ta_2O_5-Au diode is very similar to that reported by Standley and Maissel (5). Below 0.9v, currents reached a steady-state value very slowly after applying a step voltage; it was necessary to wait several minutes to record each value of current. In the steeply rising portion of the J-V curve there was no appreciable drift of current values until high current densities were reached. The J-V characteristic of the Ti-TiO_2-Au diode closely resembles the J-V characteristic of a Nb-Nb_2O_5-Au diode of comparable thickness although the currents are higher. Anodic films are difficult to form on titanium and the quality of anodized TiO_2 films is much poorer than anodized films on Ta or Nb.

High field electroluminescence of valve metals such as Al or Ta under reverse bias or during anodization has been known for many years (6). Very faint visible radiation may be observed under such conditions. Only in Nb-Nb_2O_5-Au diodes has electroluminescence been reported to occur in rectifying oxide films at low diode voltages under d-c forward bias (3).

Electroluminescent radiation from Nb-Nb_2O_5-Au diodes was detected by means of a cooled 7102 photomultiplier with S-1 sensitivity, and glass filters were used to show that it had energy between 1.2 and 1.3 ev (electron volts), independent of diode voltage or oxide thickness. Figure 2 shows the ratio of photomultiplier current, I_p, to diode current, I_f, and I_f, at different diode voltages, V_f, for a Ta-Ta_2O_5-Au and Ti-TiO_2-Au diode with the same oxide thicknesses as in Fig. 1. The diode temperature was ~0°C. The operating conditions of the photomultiplier were the same as used in measurements of electroluminescence from Nb-Nb_2O_5-Au diodes. The energy of electroluminescent radiation can only be determined approximately because of the spectral characteristics of the filters. For Ta-Ta_2O_5-Au diodes, no radiation with energy greater than 1.8 ev was detected. The peak electroluminescent intensity lies between 1.5 and 1.7 ev, appreciably higher than for Nb_2O_5 diodes. For Ti-TiO_2-Au diodes, emitted radiation had energy between 1.2 and 1.4 ev. Electroluminescence from Ta_2O_5 diodes also

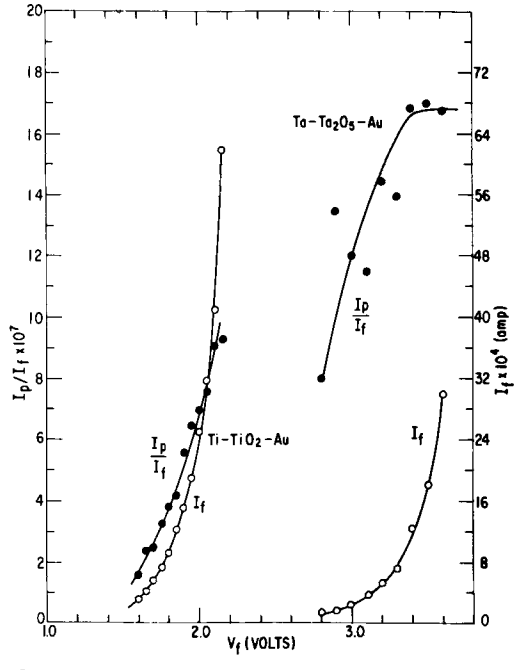

Fig. 2. Relative electroluminescent efficiency and diode current for Ta-Ta_2O_5-Au diode (100Å oxide) and Ti-TiO_2-Au diode (140Å oxide).

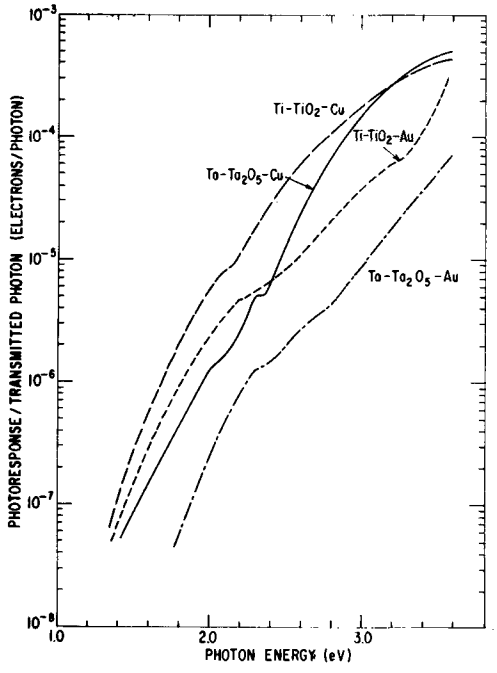

Fig. 3. Photoresponse/transmitted photon of Ta_2O_5 and TiO_2 diodes.

differed from electroluminescence from Nb_2O_5 and TiO_2 diodes in that $I_p \alpha I_f$ above 3.2v while $I_p \alpha I_f^2$ for the latter two oxides.

The observation of photoconductivity in the system valve metal/anodic oxide/electrolyte generally requires uv-radiation (7). For Ta_2O_5, the threshold for photoconductivity is 4.3 ev (8), for Nb_2O_5, 3.3 ev radiation (9). In contrast the threshold for photoconductivity in Nb-Nb_2O_5-metal diodes, where the metal counter electrode is Au, Ag, or Cu, is 1.2 ev, the same energy as electroluminescence from Nb_2O_5 diodes (3). The short-circuit photoresponse/transmitted photon for Ta-Ta_2O_5-Au, Ta-Ta_2O_5-Cu, Ti-TiO_2-Au, and Ti-TiO_2-Cu diodes is shown in Fig. 3. In each case, the oxide is so thin (5v) that optical interference phenomena in the oxide do not affect the photoresponse (4). Corrections have been made for the variation of transmission of the metal counter electrode with wavelength in calculating the photoresponse/transmitted photon.

As is the case with Nb_2O_5 diodes, the threshold for photoresponse in TiO_2 diodes, 1.3 ev, is the same with Au and Cu counter electrodes and is approximately equal to the energy of electroluminescence from Ti-TiO_2-Au diodes. In contrast, while the threshold for photoconductivity in Ta-Ta_2O_5-metal diodes is shifted into the visible it differs by 0.4 ev when Au and Cu counter electrodes are used. The quantum efficiency of Nb_2O_5, Ta_2O_5, or TiO_2 diodes is markedly smaller with Au counter electrodes than with Cu counter electrodes. For TiO_2 and Ta_2O_5 diodes with Cu counter electrodes, there is an inflection in the photoresponse at 2.1 ev while diodes with Au counter electrodes show a similar inflection at 2.3 ev. This is the energy of the maximum value of the transmission of thin evaporated films of these metals; similar inflections occur in the photoresponse of thin Nb_2O_5 with Cu and Au counter electrodes (4). Maximum photovoltages for the diodes of Fig. 3 due to intense visible radiation have been measured by focusing the light from a 40w zircon arc lamp onto the diodes. Maximum photovoltages at 295°K were; Ta-Ta_2O_5-Au, 0.94v, Ta-Ta_2O_5-Cu, 0.79v, Ti-TiO_2-Au, 0.39v, and Ti-TiO_2-Cu, 0.18v. The values for Au diodes are about 0.1v less than has been reported for maximum photovoltages developed when an electrolyte contact was made to the oxide and excitation was done with uv radiation (10).

Electroluminescence and photoresponse of Ta_2O_5 and

TiO_2 diodes is very similar to that in Nb_2O_5 diodes. It has been proposed that hole injection in Nb-Nb_2O_5-Au diodes occurs in an impurity band 1.2 ev below the conduction band of the oxide (3). Similar impurity bands may occur in oxides such as Ta_2O_5 and TiO_2.

In general, the conduction, optical and dielectric breakdown properties of oxide films whose thickness is large enough (>100Å) that tunneling is not an important conduction mechanism appear to fall in two groups, depending on the band gap of the individual oxides. Insulators such as Al_2O_3, SiO_2, or SiO characterized by band gaps of about 8v, have electrical properties significantly different from oxides such as TiO_2 or Nb_2O_5 whose band gaps are around 3v. Ta_2O_5 with a band gap of 4.5v, appears to occupy an intermediate position.

Acknowledgment

The assistance of J. R. Rairden in providing tantalum films, of D. T. Marple in loaning a photomultiplier and filters, and of J. A. Bergeron for the loan of a monochromator is gratefully acknowledged.

Manuscript received June 16, 1966.

Any discussion of this paper will appear in a Discussion Section to be published in the June 1967 JOURNAL.

REFERENCES

1. J. R. Rairden and C. A. Neugebauer, *Proc. IEEE*, **52**, 1234 (1964).
2. D. M. Cheseldine, *This Journal*, **111**, 1005 (1964).
3. T. W. Hickmott, *J. Appl. Phys.*, **37**, October 1966.
4. T. W. Hickmott, *ibid.*, **37**, November 1966.
5. C. L. Standley and L. I. Maissel, *ibid.*, **35**, 1530 (1964).
6. H. F. Ivey, "Electroluminescence and Related Effects," Supp. 1 of "Advances in Electronics and Electron Physics," p. 161, Academic Press, Inc., New York (1963).
7. L. Young, "Anodic Oxide Films," p. 129, Academic Press, Inc., New York (1961).
8. L. Apker and E. A. Taft, *Phys. Rev.*, **88**, 58 (1952).
9. R. E. Salomon, G. B. Adams, and W. M. Graven, *This Journal*, **110**, 1163 (1963).
10. J. Rupprecht, *Naturwiss.*, **47**, 127 (1960).

The Cathodoluminescence of Terbium Activated Indium Orthoborate

Frank J. Avella

General Telephone & Electronics Laboratories, Inc., Bayside, New York

Cathodoluminescence from Tb^{3+} in a borate matrix was demonstrated over forty years ago by Nichols and Howes (1); however, no Tb activated borates have been reported to cathodoluminesce with significant efficiency as compared with other green-emitting phosphors. Indeed, the same statement applies to non-borate phosphors activated by Tb. In 1964 Wanmaker and Bril (2) described the photoluminescence of Tb^{3+} in alkaline earth borates, but did not report on the cathodoluminescence. Concomitant investigation of the same systems in these laboratories showed $3CaO \cdot B_2O_3$:Tb to have the best response to cathode ray excitation of any Tb activated phosphor then known. This paper describes the cathodoluminescence of Tb^{3+} in a new host, $InBO_3$. Data are presented which show that $InBO_3$ is the most efficient host yet reported for the cathodoluminescence of Tb^{3+}. Furthermore, it is shown that $InBO_3$:Tb is comparable in efficiency and luminous output to Zn_2SiO_4:Mn, a widely used commercial phosphor. Comparisons are also made with related Tb activated phosphors.

$InBO_3$:Tb is prepared by reaction between the constituent oxides using conventional multiple firing techniques in air. $InBO_3$ is white to light yellow in body color and crystallizes in the rhombohedral crystal system with the calcite structure (3). Since the Tb^{3+} ion is larger than In^{3+}, $TbBO_3$ has the hexagonal vaterite structure (4). Therefore, partial substitution of In by Tb is equi-valent but not isostructural. Optimum activator concentration is 0.02 to 0.03 g-atom/mole of phosphor, and no lattice distortion is evident from routine x-ray powder diffraction analyses.

For cathodoluminescence measurements the phosphors were settled at optimum densities on 1-in. square sheets of conductive glass, which were then positioned in a demountable cathode ray tube and excited at 15 kv. Emission spectra were recorded directly in terms of relative energy by the method of Wiggins (5), and C.I.E. color coordinates (6) and values of lumen equivalent (7) were calculated therefrom. The luminous output was measured with an RCA 1P21 photomultiplier equipped with a Kodak Wratten 106 filter. Persistence was determined using a pulsed defocused electron beam for excitation and an oscilloscope for recording the decay characteristics.

The cathodoluminescence spectrum from Tb^{3+} in $InBO_3$ (Fig. 1) is dominated by the group of emission lines between 530 and 567 nm arising from $^5D_4 \rightarrow {}^7F_5$ electronic transitions. Fifteen distinct lines are resolved in this group with the two at 542 and 550 nm being most intense. A very small fraction of the emitted energy is produced by $^5D_4 \rightarrow {}^7F_{6,4,3}$ transitions and appears at 476-513, 577-603, and 614-640 nm, respectively. This nearly total domination of the spectrum by transitions to the $^7F_5$ levels distinguishes the Tb^{3+} emission in $InBO_3$ from that reported for other borate hosts. Wanmaker and Bril (2) show relatively intense $^5D_4 \rightarrow {}^7F_{6,4,3}$ transitions from ultraviolet excited

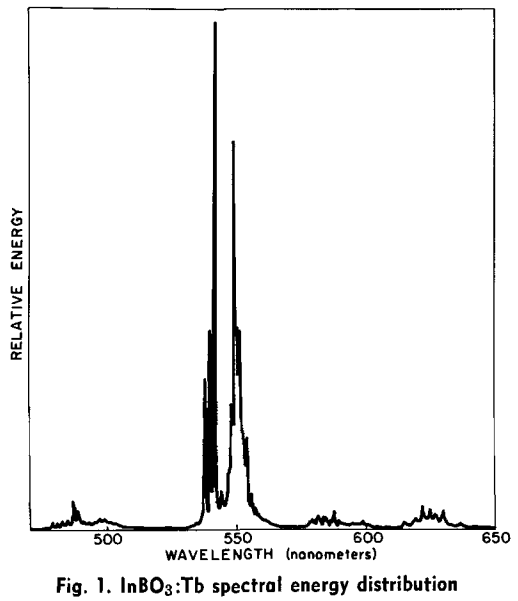

Fig. 1. $InBO_3$:Tb spectral energy distribution

Table I. Cathodoluminescence data for green-emitting phosphors

Phosphor	Relative luminosity	Decay to $I_0/10$ (msec)	C.I.E. color coordinates x	y	Lumen equivalent (lumen/rad watt)	Relative conversion efficiency
$Zn_{0.72}Cd_{0.28}S$:Ag	100	0.05	0.27	0.62	500	1.00
Zn_2SiO_4:Mn	60	15	0.22	0.71	540	0.56
Y_2O_3:Tb	15	—	—	—	—	—
$InBO_3$:Tb	65	15	0.31	0.66	610	0.54
$3CaO \cdot B_2O_3$:Tb	25	4	0.32	0.63	550	0.23
YBO_3:Tb	20	5	0.31	0.64	570	0.17
$M^{III}BO_3$:Tb (M^{III} = Sc,Lu,Gd,La)	15	—	—	—	—	—

$3CaO \cdot B_2O_3$: 0.06Tb. In the Sr and Ba analogues they show these transitions to be considerably reduced in intensity relative to the $^5D_4 \rightarrow {}^7F_5$, but not to the degree observed here for $InBO_3$:Tb. A similar comparison can be made with the $Tb_{0.2}Na_{0.2}Zn_{0.7}B_2O_4$ reported by Brixner (8).

Table I presents cathodoluminescence data on the Tb activated orthoborates with Y_2O_3:Tb (9), Zn_2SiO_4:Mn, and $Zn_{0.72}Cd_{0.28}S$:Ag cathode ray phosphors included for comparison. In terms of relative luminosity, $InBO_3$:Tb is slightly superior to Zn_2SiO_4:Mn and considerably superior to $3CaO \cdot B_2O_3$:Tb and the other Tb activated phosphors. The ratio of relative luminosity to lumen equivalent yields a value for the efficiency with which the exciting energy is converted into luminous energy. In Table I the sulfide phosphor is arbitrarily assigned a conversion efficiency of 1.00. Despite its high value of lumen equivalent resulting from the intense $^5D_4 \rightarrow {}^7F_5$ transitions, $InBO_3$:Tb is comparable to Zn_2SiO_4:Mn in efficiency and is considerably more efficient than the other Tb activated borates.

Acknowledgment

The author is indebted to V. Qvistorff for assistance in the experimental work; to C. S. Wiggins for spectral measurements; to A. K. Levine, F. C. Palilla, and O. J. Sovers for helpful discussions and suggestions.

Manuscript received May 17, 1966.

Any discussion of this paper will appear in a Discussion Section to be published in the June 1967 JOURNAL.

REFERENCES

1. E. L. Nichols and H. L. Howes, *J. Opt. Soc. Am.*, **13**, 573 (1926.)
2. W. L. Wanmaker and A. Bril, *Philips Research Repts.*, **19**, 479 (1964).
3. E. M. Levin, R. S. Roth, and J. B. Martin, *Am. Mineral.*, **46**, 1030 (1961).
4. R. E. Newnham, M. J. Redman, and R. P. Santoro, *J. Am. Ceram. Soc.*, **46**, 253 (1963).
5. C. S. Wiggins, To be published.
6. "The Science of Color," Chap. 8, Optical Society of America, Washington, D. C. (1963).
7. O. J. Sovers and L. J. Bodi, *J. Opt. Soc. Am.*, **55**, 1643 (1965).
8. L. H. Brixner, *This Journal*, **112**, 984 (1965).
9. G. Gashurov, Private communication.

The Ga-As-Si Ternary Phase System

M. B. Panish

Bell Telephone Laboratories, Incorporated, Murray Hill, New Jersey

Studies of the condensed phase diagram of the Ga-As-Si ternary system have been undertaken because of the current interest in gallium arsenide p-n junctions made by diffusion or solution growth. This work is a continuation of previous studies done in this laboratory on the ternary phase diagrams of group four elements with gallium and arsenic (1). These elements are of particular interest because of their "amphoteric" nature when in solid solution with GaAs and other III-V compounds.

Unlike the Ga-As-Sn and Ga-As-Ge ternary systems (1), the GaAs primary phase field is not the most extensive one in the phase diagram. Most of the data in this study, however, have been obtained in that phase field since it is the study of GaAs which is the primary objective of this work.

Binary Phase Systems

Ga-As.—Gallium and arsenic form a single congruently melting compound, GaAs, with a melting point of 1238°C (2). Thurmond (3) has utilized the solubility measurements of Köster and Thoma (2) and Hall (4), along with an adaptation of the regular solution treatment of Vieland (5) to construct the binary GaAs liquidus curve. The melting point of GaAs was recently measured by this author (6) and a value of 1237° ± 2°C was obtained.

GaSi.—Gallium and silicon form a simple eutectic system with a eutectic temperature of 30°C at 5×10^{-8} a/o (atom per cent) silicon (7). The binary liquidus was studied by Keck and Broder (8) and Klemm *et al.* (9), and their experimental data were used by Thurmond and Kowalchik (7) to construct a binary liquidus curve which is consistent with other thermodynamic data. The latter binary phase diagram has been used in this work.

As-Si.—The binary phase diagram for the As-Si system which has been constructed by Hansen (10) from the data of Klemm and Pirscher (11) was used for this work. This system contains two compounds, SiAs which melts congruently at 1083°C and $SiAs_2$ which decomposes below the melting point. There is one eutectic point between Si and SiAs at 1073°C and 40.5 a/o As and another at 786°C and about 90 a/o arsenic between As and $SiAs_2$. The peritectic temperature for $SiAs_2$ is 944°C.

Experimental

Semiconductor grade arsenic and silicon with purities better than 99.99% were used in this work. Reclaimed gallium with purity better than 99.99% was used and for many of the runs reclaimed GaAs with purity better than 99.99% was used instead of the elements. The use of GaAs was necessary when the relative amounts of Ga and As were high in order to prevent explosions resulting from the exothermic reaction of the elements. On the high arsenic side of the phase diagram GaAs and As were used as the source of arsenic and gallium. It was possible to heat these mixtures to the molten state without explosions if the heating was done slowly in the range 700°-825°C ($\approx$ 10°C/hr).

Fused silica capsules with a volume of about 2 cc which were about 2/3 filled with melt were used for the differential thermal analysis experiments. The experimental details are similar to those which have already been described for the study of the Ga-As-Zn system (12) except that the cells used in this work

Table I. Thermal effects in the Ga-As-Si system

Atom per cent							
Ga	As	Si	T_1	T_2	T_3	T_4	T_5
82.0	15.0	3.0	1017	766	*	—	—
70.0	15.0	15.0	1020	1008	*	—	—
50.0	12.5	37.5	1149	1034	*	—	—
50.0	30.0	20.0	1136	1092	*	—	—
50.0	40.0	10.0	1186	1090	*	—	—
42.5	42.5	15.0	1175	1115	*	—	—
35.0	35.0	30.0	1126	≈1125	*	—	—
27.5	27.5	45.0	≈1214	1124	*	—	—
17.0	17.0	66.0	1268 ± 5°C	1122	*	—	—
38.25	44.25	17.5	1177	1115	1032	—	—
30.0	40.0	30.0	1131	≈1116	1031	—	—
35.0	50.0	15.0	1172	1040-1050	1030	—	—
20.0	50.0	30.0	1100	≈1058	1030	—	—
19.8	52.2	28.1	1105	1027	—	905	≈760
19.0	56.5	24.5	1098	1015	—	908	770

* A ternary eutectic or peritectic occurs in the gallium corner of the phase diagram at a temperature below 100°C but is not observable by the method used in this work.

were similar in shape but much smaller in volume than those used previously.

For most of the previous DTA studies with GaAs it has been convenient to hold the molten mixtures in the fused silica DTA cells at 200°-300°C above the temperature at which the first solid is expected to precipitate, and in general temperatures above 1250°C were not required since the highest melting compound was GaAs at 1238°C. For the system containing silicon, however, the 200°-300°C criteria would require temperatures much above 1250°C. In this work it was found that melts containing up to 30 a/o silicon required homogenization temperatures of about 1300°C and for mixtures containing more than 30 a/o Si homogenization temperatures of 1350°C and above were necessary. The practical working limit for fused silica in this work was found to be 1350°C and this limited the range of silicon compositions which could be studied.

X-ray analysis of the differential thermal analysis samples was done by the standard powder technique.

Results

The temperatures at which thermal effects were observed when melts of various compositions were cooled are given in Table I. T_1 represents the temperature at which the surface of primary crystallization is reached, T_2 is the temperature at which a second solid phase precipitates, and T_3 is the temperature at which a ternary eutectic or peritectic transition occurs.

Some of the data given in Table I are plotted in Fig. 1 through 4. The melting point of pure Si was taken as 1410°C (7). Figures 1 through 4 show the thermal effects observed for DTA samples with starting compositions along cuts A through D in the ternary system (Fig. 5). For these samples, lines attributable to the presence of GaAs and Si were always observed in the x-ray powder photographs. Solid solubility of Si in GaAs or As or Ga in Si was not observed.[1]

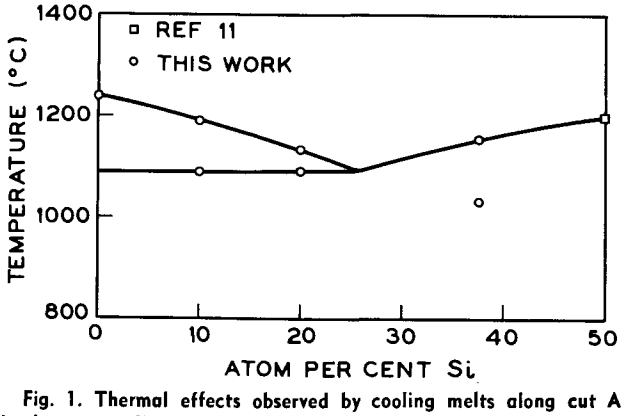

Fig. 1. Thermal effects observed by cooling melts along cut A in the ternary diagram.

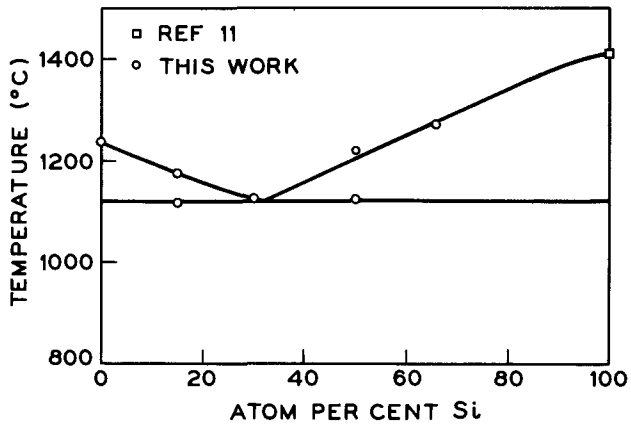

Fig. 2. Thermal effects observed by cooling melts along cut B (the GaAs-Si pseudobinary) in the ternary diagram.

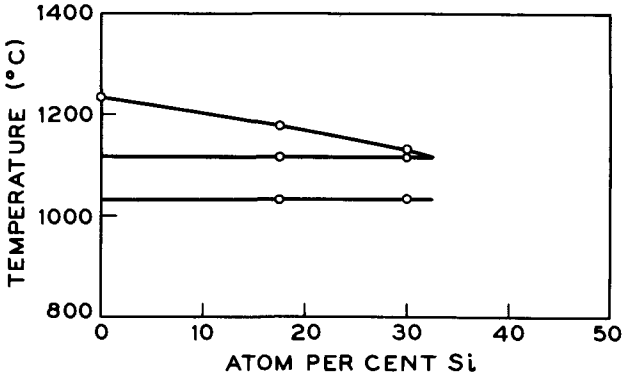

Fig. 3. Thermal effects observed by cooling melts along cut C in the ternary diagram.

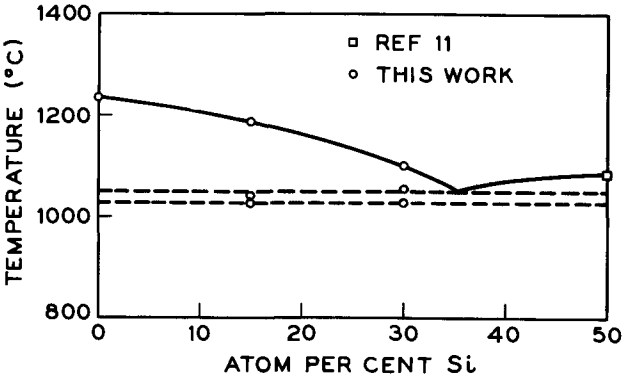

Fig. 4. Thermal effects observed by cooling melts along cut D in the ternary diagram.

DTA cooling curves were obtained for several other compositions not on cuts A-D in the ternary system. The data obtained from these experiments were used with the data from cuts A-D to construct the ternary phase diagram as described below.

Construction of the Ternary Diagram

The Ga-As binary diagram of Thurmond (3), the Ga-Si binary diagram of Thurmond and Kowalchik (7), and the As-Si binary diagram of Klemm and

[1] It should be noted that the precision of the x-ray powder photographs was insufficient to reveal small degrees of solid solubility. These studies simply reveal the solid solubility to be sufficiently small, that for the purpose of constructing the ternary diagram, it can be assumed that the liquidus compositions of cooling melts is along tie lines drawn through the primary phase and the melt compositions.

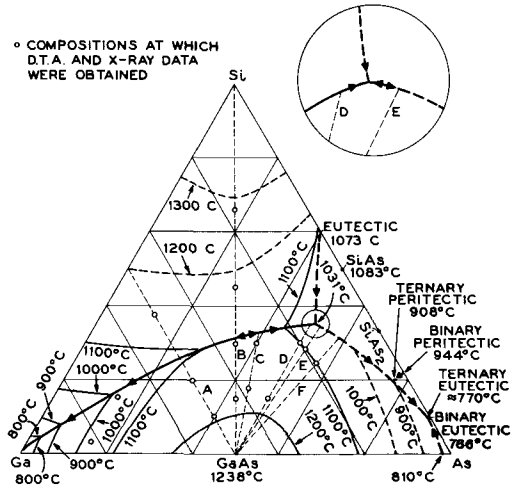

Fig. 5. Ga-As-Si ternary phase diagram. Concentrations are in atom per cent.

Pirscher (11) were used as the boundaries of the ternary diagram (Fig. 5) without modification.

By analogy with the Ga-As-Ge system the T_2 thermal effect for cuts A, B, C, and D (Fig. 5) was taken to be due to the intersection of the cooling melt with a second primary phase field. The major fields separated by the curve drawn through T_2 intersection points on these cuts are the Si primary phase field on the Si side of the diagram and the GaAs primary phase field on the GaAs side of the diagram. The curve representing the boundary between Si and GaAs primary phase field was further delineated from DTA data obtained from several other experimental points outside of cuts A, B, C, and D in the ternary system.

The T_3 thermal effect noted for cuts C and D at 1031°C is consistent with a ternary eutectic from which Si, GaAs, and SiAs precipitate. The location of the eutectic was established as being between cuts D and E on Fig. 5 from the shapes of the DTA cooling curves. The cooling curves for samples on cut D showed T_3 as the last thermal effect. The cooling curves for the two data points on the 1100° isotherm on cuts E and F had thermal effects at about 908° and 770°C. These result from a ternary peritectic and a ternary eutectic which correspond to the 944° and 786°C thermal effects on the Si-As binary, respectively.

The x-ray photographs of DTA samples from cuts C, D, E, and F did not show definitive evidence for the presence of SiAs and $SiAs_2$. There were many additional weak lines not attributable to GaAs or Si. These were, however, difficult to measure. There are no standard powder patterns available for comparison for SiAs and $SiAs_2$.

Electron beam microprobe studies of several of the cooled DTA samples provided data which is essentially in agreement with the phase diagram in Fig. 5. A sample from cut B contained only GaAs and Si, while one on cut D contained large crystals of GaAs plus a much more finely divided group of crystals some of which were GaAs and others a phase containing As and Si. A sample from cut E was similar to that on cut D, and one on cut F contained GaAs plus two closely associated phases containing silicon and arsenic. No region characteristic of the 770°C ternary eutectic was observed. It is probable that the 908°C ternary peritectic reaction is incomplete.

It was noted that for cuts A and B the shape of the liquidus in the GaAs primary phase field was almost identical to that previously reported for the Ga-As-Ge system. Isotherms up to 1100°C in the Ga rich region of that phase field were therefore drawn with the Ga-As-Ge diagram as a guide. The 1200°C isotherm was drawn on the basis of cuts A-D. The 1100°C isotherm in the arsenic rich region was drawn through the experimental points.

Because of the high pressures involved, these studies were not extended to the high arsenic portion of the phase diagram and the curves in that portion of the diagram are therefore drawn to be consistent with the available data. Similarly, because of the high temperatures required, not much experimental data was obtained in the Si primary phase field. Isotherms in this region were simply drawn smoothly through the experimental data available.

Conclusions

A major portion of the ternary condensed phase diagram of the Ga-As-Si system has been constructed on the basis of differential thermal analysis studies. The diagram consists primarily of the primary phase fields of Si and GaAs with smaller fields due to SiAs and $SiAs_2$. No ternary compounds were observed.

Acknowledgments

The author is indebted to C. D. Thurmond for his helpful suggestions during the course of this work. The aid of Mr. S. Sumski with some of the experimental work, and of Miss D. R. Margel for the x-ray analysis is gratefully acknowledged. Electron beam microprobe analyses were done by H. Schreiber.

Manuscript received May 25, 1966.

Any discussion of this paper will appear in a Discussion Section to be published in the June 1967 JOURNAL.

REFERENCES

1. M. B. Panish, *J. Less Common Metals*, **10**, 416 (1966).
2. W. Köster and B. Thoma, *Z. Metallkunde*, **40**, 291 (1955).
3. C. D. Thurmond, *J. Phys. Chem. Solids*, **26**, 785 (1965).
4. R. N. Hall, *This Journal*, **110**, 385 (1963).
5. L. Vieland, *Acta. Met.*, **11**, 137 (1963).
6. M. B. Panish, *This Journal*, **113**, 861 (1966).
7. C. D. Thurmond and M. Kowalchik, *Bell System Tech. J.*, **39**, 169 (1960).
8. P. H. Keck and J. Broder, *Phys. Rev.*, **90**, 521 (1953).
9. W. Klemm, L. Klemm, E. Nohman, H. Volk, E. Orlander, and H. A. Klein, *J. anorg. u. allgem. chem.*, **256**, 239 (1948).
10. M. Hansen, "Constitution of Binary Alloys," McGraw-Hill Book Co., New York (1958).
11. W. Klemm and P. Pirscher, *Z. anorg. chem.*, **247**, 211 (1941).
12. M. B. Panish, *J. Phys. Chem. Solids*, **27**, 291 (1966).

The Influence of Crystallographic Defects on Device Performance

J. M. Fairfield and G. H. Schwuttke

IBM Components Division, East Fishkill Laboratory, Hopewell Junction, New York

Imperfections in the crystallographic structure of silicon diodes influence their reverse characteristics (1-5), and an understanding of this phenomenon is necessary for the effective design of high-quality semiconductor devices. Usually investigators have shown a statistical or circumstantial relation between crystal imperfections and device performance; however, Queisser and Goetzberger (4) have shown that excessive leakage currents may occur at stair rod dislocations, and Barson (6) has observed such leakages at arbitrary points on stacking faults in epitaxial material.

This paper describes a study of the effects of crystallographic imperfections introduced during typical fabrication procedures and shows that leakage currents do occur at edge dislocations. It also discusses methods by which such imperfections can be controlled and their effects minimized. This investigation has been accomplished by studying simple diffused silicon diodes that were made using standard diffusion techniques. Their reverse characteristics were measured and compared with the crystallographic perfection of the silicon wafers, examined by means of transmission x-ray diffraction microscopy.

Procedure

Silicon wafers were cut from Czochralski crystals, lapped, and chemically polished. Planar diffused P^+—N and N^+—P diodes were made using standard SiO_2 masking techniques and boron or phosphorus diffusions. For the boron diffusion, we used a two-step process consisting of a capsule deposition cycle at 1108°C (using a Si-B powder source) (7) and an oxidation drive-in cycle at 1150°C. The phosphorus diffusion was a single-cycle dynamic process (1000°C) with PH_3 as the source (8). In both cases, the wafers were supported vertically in a quartz boat. The junction depths were typically 1-2μ, and surface concentrations were about 10^{19} atm/cc for the boron and 10^{20} atm/cc for the phosphorus diodes. Alternate rows were made with diffused guard rings to suppress surface breakdown (9). The geometry of these diodes is shown in Fig. 1.

The crystallographic perfection of these silicon wafers was examined at specific points in the process by means of x-ray transmission diffraction microscopy (10). Large-area topographs of entire wafers were recorded using the Scanning Oscillator Technique (SOT) and the imperfections were identified [see ref. (10)]. Initially, the wafers were dislocation free. (There were some bulk precipitation effects through the crystal; however, these had no significant effect upon the reverse characteristics of the diodes.) The x-ray technique is particularly well adapted to this type of study because it is nondestructive: the wafers may be examined and reexamined at any or all points in the process.

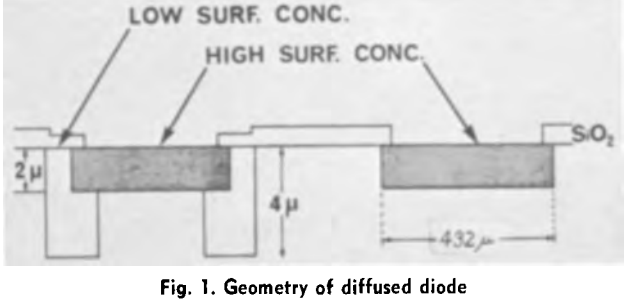

Fig. 1. Geometry of diffused diode

The reverse I-V characteristics were studied by probing the diffused diodes on the wafers. The diodes were classified as either reasonably hard or soft using the following two requirements for a hard diode. (*I*) Low current: the voltage at 20 μa reverse current must be within 10% of the voltage at 200 μa. (*II*) High current: the voltage at 200 μa must be within 10% of true avalanche breakdown voltage.

In this way the wafers were mapped for device performance and compared with the x-ray topographs. In addition, the soft diodes were examined for microplasmas to determine the nature and location of the leakage currents within the device area. The locations of the microplasmas were noted and compared to the crystallographic structure.

Results and Discussion

From the consideration of device performance, the most significant crystallographic defects in this study are bands of dislocations created during the heat cycling of the diffusion processing (in both phosphorus and boron diffused wafers). These are illustrated in Fig. 2 and 3, which are examples of x-ray topographs of diffused wafers, by the anomalous contrast near the edges. These dislocations are nucleated at the edges of

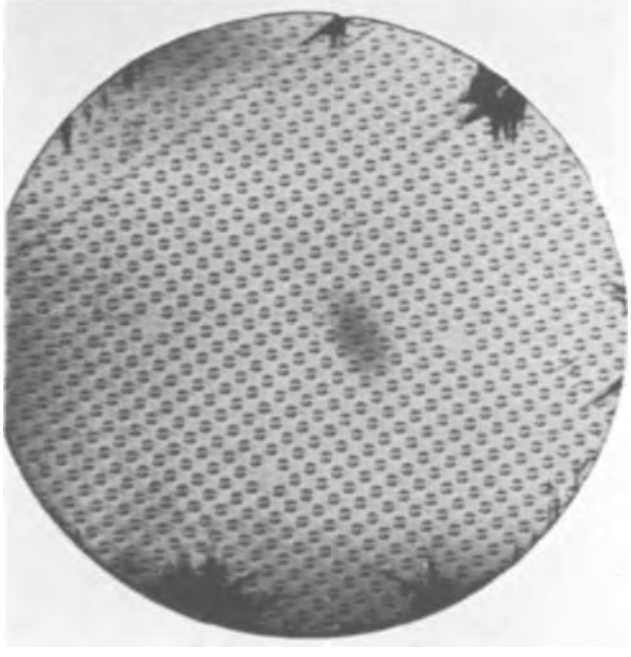

Fig. 2. Large-area SOT topograph of boron-diffused wafer. Heavy contrast near periphery of wafer results from edge dislocations nucleating at chips. Lesser contrast to right of wafer can be related to strain during heat cycles. (Note also that diffraction contrast, due to elastic strain from the oxide mask, delineates the diffused diodes.)

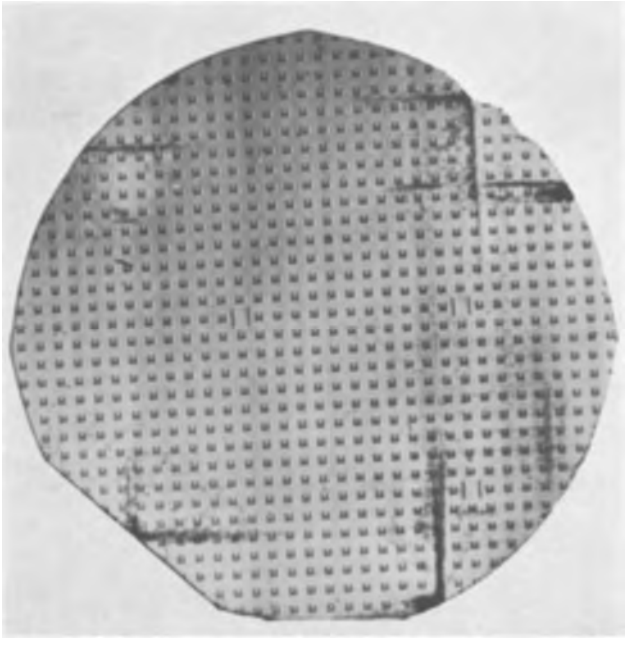

Fig. 3. Large-area SOT topograph of phosphorus-diffused wafer showing the same heavy contrast as Fig. 2.

the wafers and extend a few tenths of an inch into the interior. Favored points of nucleation are small chips, scratches, and other forms of physical damage introduced before the heat cycling. (These occasionally include points of apparent microalloying.) An example of dislocations nucleated at scratches is illustrated in Fig. 4. Finally, lesser degrees of imperfection could be associated with mechanical strain during the heat cycles, due to faulty support in the diffusion boat (see Fig. 2).

These dislocations significantly degrade the hardness of the diode reverse characteristics. Diodes in the undamaged areas yielded 90% as reasonably hard; whereas, those diodes in the areas of dislocations yielded about 20% as hard. A typical wafer yield map

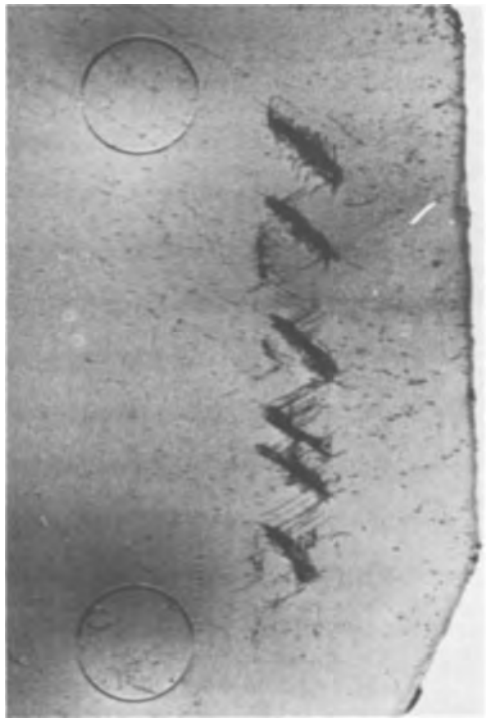

Fig. 4. Small area topograph of diffused silicon wafer illustrating dislocations nucleating at scratches on the wafer surface.

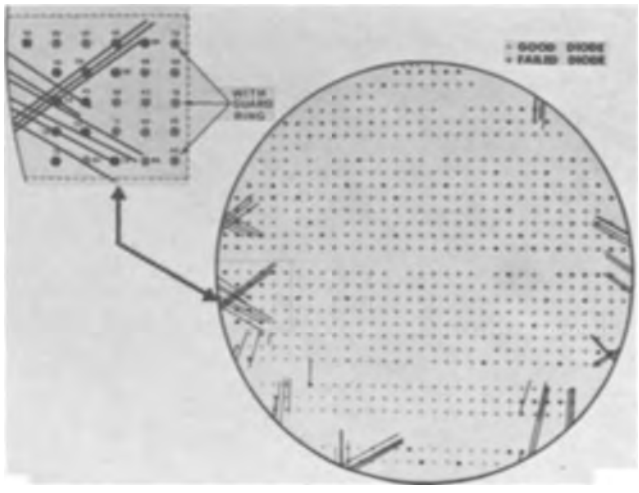

Fig. 5. Typical wafer yield map of a diffused wafer (boron). Heavy lines indicate bands of dislocations as indicated from the topograph. Area set off by broken line is enlarged to give reverse voltages at 20 μa. Apparent variations in such voltages of good diodes are due either to the presence (or lack) of the guard ring or to significant variations in wafer resistivity near the edge.

is shown in Fig. 5. The true avalanche breakdowns varied between 60 and 110v and reflected the background doping of the material. With only a few exceptions, all diodes with dislocations in their active areas were soft.

The reverse characteristics of failed diodes are "soft" rather than linear with specific points of discontinuity (as, for example, a double break characteristic). Goetzberger and Shockley have shown that such softness can be due to metallic precipitation in the active region of the diode (11). The microplasma structure of many soft diodes indicates that the high leakage currents occur at specific points along the dislocations; this is illustrated in Fig. 6. Thus, it is reasonable that metallic precipitates nucleate as specific points along the dislocations and cause the excessive leakage currents at sub-avalanche voltages, in the manner discussed by Goetzberger and Shockley. It has been suggested previously that microplasmas associated with stair-rod dislocations can be caused by

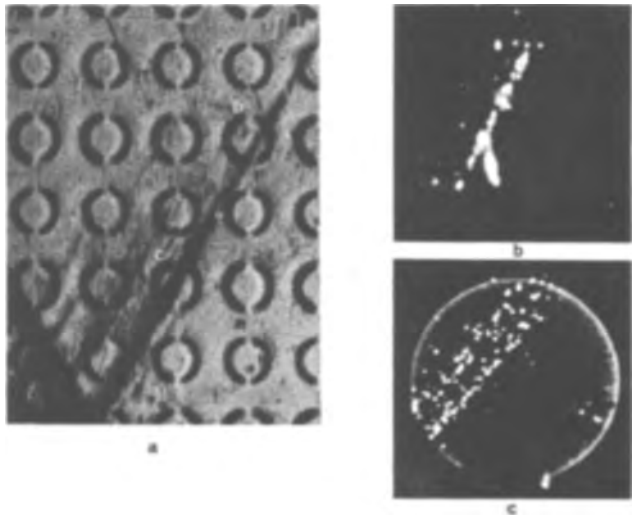

Fig. 6. X-ray topograph and microplasma structure of soft diodes: (a) topograph; (b) microplasma structure of diode marked "b"; (c) microplasma structure of diode marked "c". These microplasmas were always red.

metallic precipitates at these dislocations (4).

Finally, the diffused guard ring did not significantly effect the yield factors (although it did raise the apparent avalanche breakdown by about 25%). Thus, the mechanism of softness seems to be similar. It should be noted, however, that microplasmas for soft diodes without guard rings tended to be at or very near the outer periphery of the planar diodes.

One obvious method of reducing device softness from this mechanism is to eliminate the sources of nucleation for these dislocations. The chips, scratches, etc., from which these dislocations nucleate, usually occur during handling. Thus, one should carefully avoid any procedure that might result in physical damage. Some of the sources that we have found for this damage are listed below:

1. Handling wafers with stainless steel tweezers, or other hard objects.
2. Poor cleaning precedures. Cotton swabs can introduce scratches. If ultrasonic cleaning is used, chipping may occur if wafers are in contact with each other or other hard substances (*e.g.*, wire cleaning boats).
3. Contaminated or poorly designed diffusion boats. Wafers should be supported so as to eliminate strain during diffusion. Also contaminants, including devitrified quartz, may introduce strains during diffusion.
4. Failure to remove saw damage at the edges during polishing procedures.

In general, one should handle wafers as little as possible and use extreme care when it is necessary. Diffused wafers can be made that are virtually free of such damage as illustrated in Fig. 7. The yield of the wafer illustrated in Fig. 7 is well over 90%.

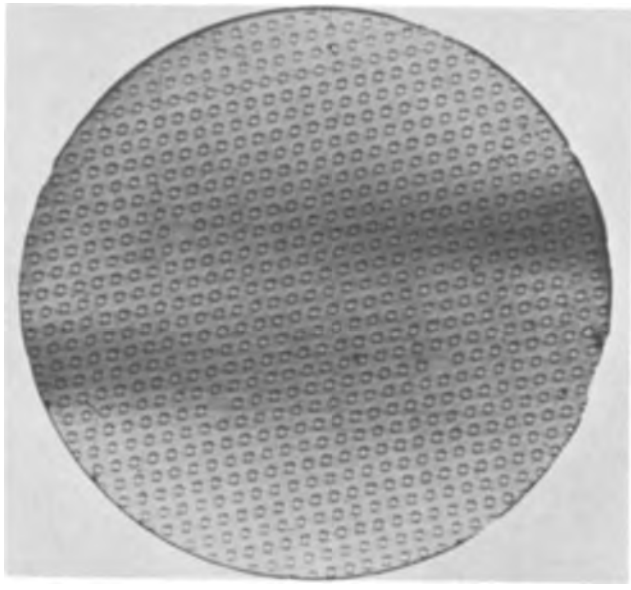

Fig. 7. Large area SOT topograph of diffused wafer without dislocations.

Acknowledgments

The authors gratefully acknowledge the x-ray work of C. Hoogendoorn and T. A. Hansen and the help of R. Racicot for diffusions. The research reported in this paper was sponsored in part by the Air Force Cambridge Research Laboratories, Office of Aerospace Research, Contract No. AS 19(628)-5059.

Manuscript received July 15, 1966. This paper was presented at the Cleveland Meeting, May 1-6, 1966.

Any discussion of this paper will appear in a Discussion Section to be published in the June 1967 JOURNAL.

REFERENCES

1. A. Chynoweth and G. L. Pearson, *J. Appl. Phys.*, **29**, 1103 (1958).
2. F. Barson, W. J. Armstrong, and W. E. Mutter, *This Journal*, **111**, 1263 (1964).
3. G. H. Schwuttke, Electron Device Meeting, Washington, D. C., October 1963.
4. H. J. Queisser and A. Goetzberger, *Phil. Mag.*, **8**, 1063 (1963).
5. E. D. Jungbluth and P. Wang, *J. Appl. Phys.*, **36**, 1967 (1965).
6. F. Barson, IBM East Fishkill, Hopewell Junction, N. Y., private communication.
7. M. C. Duffy and W. J. Armstrong, *Electrochem. Tech.*, **4**, 475 (1966).
8. R. P. Donovan and A. M. Smith, New York meeting of Electrochemical Society, October 1963, Abstract 150.
9. A. Goetzberger, B. McDonald, R. Haitz, and R. M. Scarlett, *J. Appl. Phys.*, **34**, 1591 (1963).
10. G. H. Schwuttke, *J. Appl. Phys.*, **36**, 2712 (1965).
11. A. Goetzberger and W. Shockley, *ibid.*, **31**, 1821 (1960).

Brief Communications

Galvanic Effects in Vacuum Deposited Thin Films

M. Hacskaylo

Physical Electronic Laboratory, Melpar, Inc., Falls Church, Virginia

and R. T. Foley

Chemistry Department, The American University, Washington, D. C.

During the investigation of the electrical properties of vacuum-deposited dielectric films, formed in layered configurations, some interesting galvanic effects have been observed. The purpose of this communication is to report the observations and present an explanation.

The "thin films" referred to are those in the micron- and millimicron thickness range and should not be considered in the thicknesses of those fabricated for solid electrolyte galvanic cells (1, 2). Techniques for vacuum depositing the capacitor configuration have been described in detail by Feldman and Hacskaylo (3, 4). Aluminum and gold electrodes were deposited from tungsten boats. The CeO_2 films (5) were deposited at both fast (approximately 2000 Å/min) and slow (approximately 200 Å/min) rates using com-

mercial material[1] from tungsten boats, and at slow rates only from boron nitride liners (6). Film thicknesses were measured with a Zeiss interference microscope. Cerium (IV) oxide films formed at the slow deposition rate had a slight straw color, whereas the films formed at the fast rate were colorless. The dielectric layers were analyzed by x-ray diffraction and all exhibited characteristic CeO_2 patterns. Cerium metal was detected in the films formed at a slow rate. However, after heating to 500°C in air, the films lost their coloration and Ce metal was no longer detected. Films formed at the faster rate gave no indication of Ce metal. The starting material for the deposition was determined to be CeO_2 species, whereas the residue in the tungsten boats after the deposition consisted of Ce metal without traces of CeO_2. Suboxides, if present, were not detected.

A typical configuration and deposition sequence is as follows: glass substrate (25 x 25 x 1 mm), aluminum (1600Å), CeO_2 (1.0μ), aluminum (300Å). The top and bottom electrodes were suitably isolated by the dielectric layer, and the common cell plate area was 0.50 cm^2.

The voltages of the samples were measured by a Hewlett-Packard VTVM model 410B across a 4000 ohm load, and the current was measured with two Weston microammeters, model 301 (0-50 μa and 0-200 μa ranges full scale with internal resistances of 1140 and 660 ohm, respectively). The values of the voltages and current densities reported here have been recalculated taking into consideration all external resistances.

Galvanic effects (*i.e.*, an emf developed between the top and bottom metallic electrodes) in these films are readily produced by introducing traces of moisture. For example, the moisture generated by cupping a hand over the cell was sufficient to generate an open circuit voltage of 0.1-0.2v and a short circuit current of about 30 μa/cm^2. When a drop of water was placed on the top electrode of an Al-CeO_2-Al sample an open circuit voltage of 0.8v was measured with a short circuit current of 350 μa/cm^2. The top film (electrode exposed to water) of the array that exhibited the galvanic effect was always positive, *i.e.*, acted as the cathode, whereas the bottom was negative. In a typical experiment, the lower and the upper films were electrically connected across a 4000 ohm load and the current and voltage were measured simultaneously. The sample was then moistened with a drop of water, and placed on a hot plate. The output was recorded at 20 sec intervals. The results are shown

[1] American Potash and Chemical Corporation.

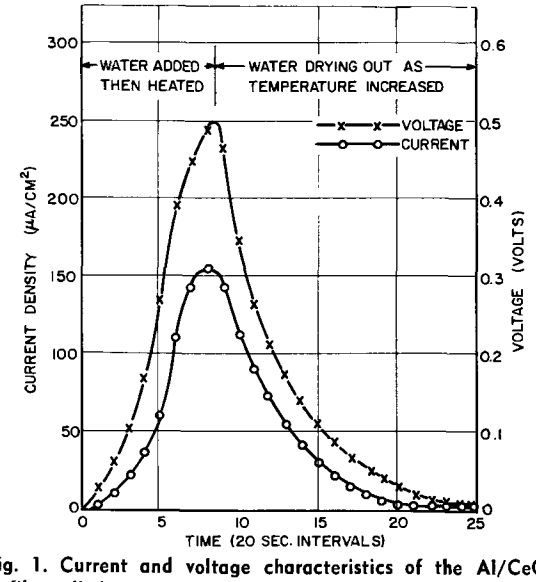

Fig. 1. Current and voltage characteristics of the Al/CeO_2/Al thin film cell that was moistened and then heated to dryness. Lower electrode, Al, 1800Å; CeO_2, 1.5μ; top electrode, Al, 500Å.

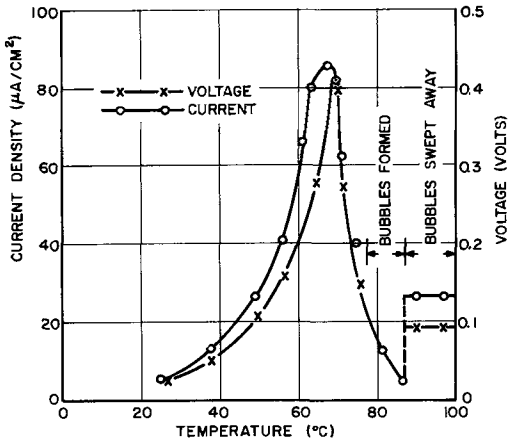

Fig. 2. Temperature dependence of current and voltage characteristics of Al/CeO_2/Al thin film cell immersed and heated in water.

in Fig. 1. The voltage and current increased with temperature up to a point at which the water appeared to have evaporated. When the sample appeared to be completely dry the output decreased to zero. The peak output during the test was 160 μa/cm^2 at 0.5v. The sample was then immersed in distilled water and the water heated. The current, voltage, and water temperature were recorded, as indicated in Fig. 2. The current and voltage exhibited peaks at about 68°C of 85 μa/cm^2 and 0.42v, respectively. The output of the galvanic cell decreased irregularly from 68° to 85°C reaching a fairly constant voltage of 0.1v and 28 μa at 100°C. The output remained constant for about 15 min. The experiment described above and illustrated in Fig. 2 exhibited galvanic effects for 2.5 hr. A similar cell was totally immersed in water at room temperature and it exhibited a voltage of 0.32v and a current density of 18 to 25 μa/cm^2 for 65 hr.

During the immersion of the cell in water, definite physical changes were observed. The top electrode lost its metallic appearance. The portion of the CeO_2 film that was not covered with the top electrode was unaffected by the water or current flow. The bottom aluminum electrode changed from a metallic to a milky translucent appearance. This transformation occurred only underneath the area covered by the top electrode.

A number of cells were made in which the thickness and materials of the electrodes were varied. Gold and aluminum electrodes were interchanged. The galvanic action corresponding to these variations is given in Table I. It was observed that it was necessary for water to diffuse through the top plate before an appreciable galvanic effect would occur. This was manifested by a time delay in the beginning of the effect. The presence of a "thick" top layer (2.5μ) prevented

Table I. Galvanic characteristics of vacuum-deposited thin film cells with various materials and thicknesses

Top electrode		Dielectric CeO_2	Bottom electrode			
Material	Thickness, Å	Thickness, μ	Material	Thickness, Å	Open circuit voltage, v	Short circuit current, μa/cm^2
Al	300	1.0	Al	1600	0.48	30
Al	550	1.5	Al	3000	0.80	120
Al	1000	1.5	Al	1400	0.48	85
Al	6000	0.8	Al	4500	0.80	350
Al*	1070	1.5	Al	300	0.35	75
Al	1070	1.9	Al	300	0.23	30
Al	25000	1.4	Al	2000	0	0
Au	300	3.0	Al	2800	0.62	160
Au	500	1.1	Al	5000	0.60	140
Au	300	0.9	Au	2100	0	0
Au	500	1.0	Au	2500	0	0

* Al-CeO_2 layers heated to 500°C in air for 45 min prior to top plate deposition.

the diffusion of water as well as the exhibition of the galvanic effect. When a film of gold was deposited for the top plate, galvanic action was observed when water diffused through the film. However, when a gold film was used for the bottom electrode (*i.e.*, the one coated with CeO_2 and with air access restricted to it) there was no galvanic action even though water had diffused through the top electrode of aluminum or gold. The galvanic action is apparently not affected by the Ce content of the CeO_2 film.

The effect is not restricted to samples with CeO_2 as the dielectric component. A thin film cell was constructed with $PbCl_2$ as the dielectric film separating the two Al electrodes. When water was placed on the top electrode an open circuit voltage of 0.6v and a short circuit current of about 1000 $\mu a/cm^2$ was observed. The cell functioned for only a few minutes.

A few other general observations can be made concerning the phenomena. When the cells were subjected to heat but no moisture, no galvanic effect was produced. There was no evidence of a photovoltaic effect upon illumination with white or u.v. light.

It appears reasonable to explain all of these observations in terms of an air-depolarized galvanic cell. The lower film, next to the glass substrate, functions as the anode. The usual polarization of the aluminum electrode is limited by a restricted oxygen supply. The (corrosion) current is increased by the presence of chloride ions ($PbCl_2$ experiment). The reaction product is a hydrated aluminum oxide.

The electrolyte is the added water or moisture containing dissolved oxygen. The high cross-sectional area to length ratio allows sufficient electrical conductivity. The CeO_2 acts simply as a separator holding the electrolyte. The use of inorganic separators in conventional batteries is being investigated currently (7). It is unlikely that CeO_2 contributes ionic conductivity as temperatures in the 700°-800°C range would be required before appreciable values of specific conductivity would be achieved (8).

The cathode is the upper electrode at which the reaction

$$2H_2O + O_2 + 4e \rightarrow 4OH^-$$

takes place. Thus, the reaction takes place whether the top electrode is Au or Al. The active metal is required at the anode. The temperature dependence of the cell immersed in water is approximated by the temperature relationship of iron corrosion in water when the rate controlling step is diffusion of dissolved oxygen to the cathode as discussed by Uhlig (9).

These observations are of interest in several areas of electrochemistry. First, they illustrate troublesome effects encountered in the preparation of solid state devices such as thin-film capacitors. Second, they confirm accepted mechanisms of the electrochemical theory of corrosion which would have galvanic cells operating at the microscopic scale. Third, the implication is that similar effects can operate over an extended period of time and limit the shelf life of solid-state batteries. Finally, the observations suggest the development of air-depolarized thin-film batteries recognizing, of course, the inherent limitation of capacity.

Acknowledgment

It is a pleasure to acknowledge the efforts of W. C. Conlon for sample preparation, Dr. Hannibal de-Schmertzing for chemical and x-ray analysis and Dr. Charles Feldman for valuable discussions.

Manuscript received July 18, 1966.

Any discussion of this paper will appear in a Discussion Section to be published in the June 1967 JOURNAL.

REFERENCES

1. J. N. Mrgudich, P. J. Bramhall, and J. J. Finnegan, IEEE Transactions on Aerospace and Electronic Systems, Vol. AES-1, No. 3, 290 (1965).
2. J. L. Weininger, *This Journal*, **105**, 439 (1958).
3. C. Feldman and M. Hacskaylo, *Rev. Sci. Instruments*, **33**, 1459 (1962).
4. M. Hacskaylo and C. Feldman, *J. Appl. Phys.*, **33**, 3042 (1962).
5. G. Hass, J. B. Ramsey, and R. Thun, *J. Opt. Soc. Am.*, **48**, 324 (1958).
6. F. J. Hemmer and J. R. Piedmont, *Rev. Sci. Instruments*, **33**, 1355 (1962).
7. W. N. Carson, "Electrodeposited Inorganic Battery Separators," NAS 5-9168.
8. D. Singman, *This Journal*, **113**, 502 (1966).
9. H. H. Uhlig, "Corrosion and Corrosion Control," p. 84, John Wiley & Sons, Inc., New York (1963).

Corrosion and Growth of Silver Crystals under Hydrothermal Conditions

R. R. Monchamp, R. C. Puttbach, and J. W. Nielsen

Airtron Division, Litton Precision Products, Inc., Morris Plains, New Jersey

In a recent paper Levinson and Carter (1) discussed a limited observation of silver corrosion and the morphology of the resultant silver crystals.

The formation of silver crystals under hydrothermal conditions has been observed in this laboratory during the growth of ruby using K_2CO_3 (2), $Y_3Fe_5O_{12}$ using K_2CO_3, and ZnO using KOH (3).

Silver corrosion has also been noted by Laudise and Kolb in some of their ZnO work (4) and by Hill and Harker (5) in the hydrothermal growth of BeO using KOH as the solvent.

In the hydrothermal growth of ruby in K_2CO_3 at high pressures (>1000 atm), we have observed only slight silver attack; however, when the working pressure was below 1000 atm and the concentration was less than 3*M*, severe corrosion occurred. We have reported previously that under these latter conditions it appears that the silver can contains two immiscible fluids (6). Silver attack and growth of silver crystals occurred at the interface region of the fluids. This attack and growth is similar to that reported by Levinson and Carter (1) and Harker and Hill (5).

With ZnO in KOH and $Y_3Fe_5O_{12}$ in K_2CO_3 under conditions commonly used for crystal growth (7), only a single fluid phase exists; however, silver corrosion and growth of silver crystals is still observed. Thus it should be stressed that a two-phase fluid condition is not necessary for the corrosion and growth of silver.

The corrosion in the single phase cases occurs below the baffle in the nutrient zone, and the growth of silver crystals occurs predominantly on the top of the can and just at the baffle area. To a lesser degree some silver crystals have been observed on the seed support ladder and also within grown ZnO or $Y_3Fe_5O_{12}$ crystals. It is significant that the major part of the silver growth takes place at the baffle plate and top

of the can which are the two locations of the largest temperature changes within the fluid.

We propose that the following mechanism is operative in all the examples cited. The initial attack of silver is caused by oxygen dissolved in the basic solutions and in the air entrapped in the silver can during its closure. In the nutrient zone, the hottest part of the can, a soluble silver complex is formed which is convectively transported to the cooler regions of the can. Because of thermal disturbance of the equilibrium a disproportionation reaction occurs which yields metallic silver and a silver complex of higher oxidation number.

Similar thermally dependent disproportionation reactions are popularly used for the vapor phase growth of III-V compounds. The lack of thermodynamic data for the possible silver species at the elevated pressures and temperatures makes it impossible to assign definite oxidation states to the silver in the transporting complex ions. In the single phase, growth occurs in the two regions where the temperature drops are greatest, at the baffle plate (its purpose is to divide the fluid into two temperature regions), and the top of the can where the heat loss to the ambient is greatest. In the two-phase system the same mechanism is applicable except that the disproportionation in this case may not be due to a thermal disturbance of the equilibrium. Rather the equilibrium is displaced by the relative solubilities of the species in both phases. As a result of the solubility change at the interface, the equilibrium is displaced so that this is the region in the silver can where the greatest attack and crystal growth are noted.

Support for the above proposition has been obtained in two independent experiments. First in the case of ZnO, a 2½ times increase in reactor volume size and thus in the amount of solvent greatly increased the amount of silver corrosion although the measured conditions remained the same. Second, in the growth of $Y_3Fe_5O_{12}$, H_2O_2 was added to the system to try to produce oxidizing conditions. Whereas no silver attack was observed in previous experiments, the addition of H_2O_2 caused the most severe case of corrosion and silver crystal growth ever observed even though the exact conditions were duplicated.

For crystal growth it is highly desirous to eliminate this silver corrosion for many reasons. Having proposed the above mechanism it is obvious that an effective remedy would be the inclusion of a reducing agent within the can. In the ZnO crystal growth 2-3g of metallic zinc added to 2830 ml of 6M KOH have been found to eliminate completely any trace of silver corrosion. Furthermore, zinc does not add any contamination since it is oxidized to Zn^{+2} which is already present as a dissolved species. The obvious metals to add for ruby and $Y_3Fe_5O_{12}$ are aluminum and yttrium, respectively. Additions of metallic aluminum to the K_2CO_3 solution used for ruby have also eliminated any traces of silver attack which were noted under the single phase condition. It is observed that the solubility of oxygen in K_2CO_3 is much less than in KOH.

Manuscript received Aug. 11, 1966.

Any discussion of this paper will appear in a Discussion Section to be published in the June 1967 JOURNAL.

REFERENCES

1. S. Levinson and F. L. Carter, *This Journal*, **113**, 756 (1966).
2. R. R. Monchamp, R. C. Puttbach, "Hydrothermal Growth of Large Ruby Single Crystals," Interim Engineering Progress Report No. V, Air Force Contract AF 33(657)-10508, Airtron Division, Litton Precision Products, Inc., Morris Plains, N. J., ASD Project Nr. 8-132, June 30, 1964.
3. R. R. Monchamp, R. C. Puttbach, "The Growth of Zinc Oxide Crystals," Interim Engineering Progress Report No. VII, Air Force Contract AF 33(657)-8795, Airtron Division, Litton Precision Products, Inc., Morris Plains, New Jersey, ASD Project Nr. 7-988, February 29, 1964.
4. R. A. Laudise and E. D. Kolb, Private communication.
5. V. G. Hill and R. I. Harker, "Development of Hydrothermal Method for Growing Large, High Purity Single Crystals of Beryllium Oxide," Progress Report No. 7, Air Force Contract AF 33(615)-1712, Tempress Research Inc., State College, Pa., BPSN64-6899-17371-737101. May 31, 1966.
6. R. R. Monchamp, R. C. Puttbach, and J. W. Nielsen, "Hydrothermal Growth of Large Ruby Crystals," Final Report, AF Contract AF 33(657)-10508, Airtron Division, Litton Precision Products, Inc. Morris Plains, N. J., ASD Project Nr. 8-132, October 1965.
7. R. A. Laudise, E. D. Kolb, and A. J. Caporaso, *J. Am. Ceram. Soc.*, **47**, 9 (1964).

Current Distribution on a Rotating Disk below the Limiting Current

John Newman

Inorganic Materials Research Division, Lawrence Radiation Laboratory, and Department of Chemical Engineering, University of California, Berkeley, California

ABSTRACT

The uniform current density on a rotating disk electrode at the limiting current is not achieved at lower currents because the edge of the disk is more accessible than the center as a result of the ohmic potential drop in the solution. The current distribution is calculated for well-stirred solutions and also for lower rotation speeds where surface overpotential, concentration overpotential, and ohmic drop are all significant. The current density at the center can vary between 50 and 100% of the average current density, and the ohmic potential drop to the center of the disk is 27.3% greater for the uniform current than for the primary current distribution.

The rotating disk electrode is popular for studying both diffusion in electrolytic solutions and the kinetics of moderately fast electrode reactions because the hydrodynamics (1,2) and the mass-transfer characteristics (3) are well understood and because the current density on the disk electrode is supposed to be uniform. However, the current distribution is uniform only at the limiting current where the concentration of the reactant is zero at the electrode surface. In the other extreme, the primary current distribution (7), applicable in the absence of concentration overpotential and surface overpotential, shows an infinite current density at the edge and a value equal to half the average current density at the center of the disk.

It is of interest to assess the degree of nonuniformity of the current distribution due to the nonuniform ohmic potential drop. Newman (4) has indicated how to treat current distribution in cells where the potential distribution in the bulk of the solution and the concentration distribution in the diffusion layer must be calculated simultaneously. These ideas are applied in the present paper to the specific case of a rotating disk electrode. It is assumed that the disk electrode, of finite size, is embedded in an infinite, insulating plane and that the walls of the cell and the counter electrode are removed to infinity. Dilute-solution theory, with constant diffusion coefficients, mobilities, and activity coefficients, is assumed to be applicable. For simplicity, only two cases are treated, metal deposition from a single-salt solution and electrode reactions with an excess of supporting electrolyte, in which the transference number of the reactant is zero.

Those readers who wish to skip the mathematical development can go directly to the section on results, keeping in mind that the current distribution depends on several important parameters defined in Eq. [21], [27], [30], and [37].

Concentration Profile in the Diffusion Layer

The concentrations differ from their bulk values only in a thin region near the electrode surface, and in this region the fluid velocity can be approximated by (1-4)

$$v_r = a\,r\,y\,\Omega\sqrt{\Omega/\nu} \text{ and } v_y = -a\,y^2\,\Omega\sqrt{\Omega/\nu} \quad [1]$$

where $a = 0.51023$. This approximation, which is valid for large values of the Schmidt number $Sc = \nu/D$, can be expected (5, 6) to cause an error of about 3% in calculated rates of mass transfer when $Sc = 1000$. The concentration is to be determined from the equation

$$v_r\frac{\partial c}{\partial r} + v_y\frac{\partial c}{\partial y} = D\frac{\partial^2 c}{\partial y^2} \quad [2]$$

or

$$a\,y\,\Omega\sqrt{\Omega/\nu}\left[r\frac{\partial c}{\partial r} - y\frac{\partial c}{\partial y}\right] = D\frac{\partial^2 c}{\partial y^2} \quad [3]$$

where only the dominant diffusion term $D\partial^2 c/\partial y^2$ needs to be included on the right because of the thinness of the diffusion layer. This equation applies to diffusion of a single salt if D denotes the diffusion coefficient of the salt. The equation also applies to a minor ionic component in a solution with supporting electrolyte where ionic migration can be neglected. Then D denotes the ionic diffusion coefficient.

Since the diffusion layer is thin, it is appropriate to replace the normal distance y by the variable

$$\zeta = y\,(a\nu/3D)^{1/3}\sqrt{\Omega/\nu} \quad [4]$$

In terms of this variable the concentration in the diffusion layer can be expressed as a series solution

$$c = c_\infty\left[1 + \sum_{m=0}^{\infty} A_m (r/r_o)^{2m}\theta_m(\zeta)\right] \quad [5]$$

This is a power series in r, but only even powers are included since the concentration must be an even function of r.

The functions $\theta_m(\zeta)$ satisfy the differential equation

$$\theta_m'' + 3\zeta^2\theta_m' - 6m\zeta\theta_m = 0 \quad [6]$$

which can be obtained by substituting the series [5] into Eq. [3].

The boundary conditions are

$$\theta_m = 1 \text{ at } \zeta = 0 \text{ and } \theta_m = 0 \text{ at } \zeta = \infty$$

In this way the concentration given by Eq. [5] equals the bulk value c_∞ far from the disk, and the concentration at the surface of the electrode is

$$c_o = c_\infty\left[1 + \sum_{m=0}^{\infty} A_m (r/r_o)^{2m}\right] \quad [7]$$

The coefficients A_m are yet to be determined.

The normal current density i at the electrode surface is related to the derivative of the concentration

$$\frac{i}{nF} = \frac{D}{1-t}\frac{\partial c}{\partial y}\bigg|_{y=0} = \frac{Dc_\infty}{1-t}\left(\frac{a\nu}{3D}\right)^{1/3}\sqrt{\frac{\Omega}{\nu}}\sum_{m=0}^{\infty} A_m\left(\frac{r}{r_o}\right)^{2m}\theta_m'(0) \quad [8]$$

where t is the transference number and c the concentration of the reactant and n is the number of electrons

Table I. Derivatives at the surface of the functions in the concentration series

m	$\theta_m'(0)$	m	$\theta_m'(0)$
0	−1.11984652	6	−2.47384276
1	−1.53298792	7	−2.59428724
2	−1.80549058	8	−2.70452088
3	−2.01572374	9	−2.80646029
4	−2.18998277	10	−2.90150549
5	−2.34045076		

produced when one reactant ion or molecule reacts. With excess indifferent electrolyte, $t = 0$. The calculation of the current density by this series requires values of $\theta_m'(0)$, which are given in Table I.

Potential Distribution outside the Diffusion Layer

In the region where the concentrations are uniform, the potential satisfies Laplace's equation

$$\nabla^2\Phi = 0 \qquad [9]$$

For this problem we use rotational elliptic coordinates ξ and η related to the cylindrical coordinates r and y by [see ref. (7)]

$$y = r_o\xi\eta \text{ and } r = r_o\sqrt{(1+\xi^2)(1-\eta^2)} \qquad [10]$$

In this coordinate system Laplace's equation is

$$\frac{\partial}{\partial\xi}\left[(1+\xi^2)\frac{\partial\Phi}{\partial\xi}\right] + \frac{\partial}{\partial\eta}\left[(1-\eta^2)\frac{\partial\Phi}{\partial\eta}\right] = 0 \qquad [11]$$

Since the ohmic drop for a small disk is concentrated in the solution near the disk, we adopt the following boundary conditions:

$$\left.\begin{array}{l}\partial\Phi/\partial\eta = 0 \text{ at } \eta = 0 \text{ (on the insulating annulus).}\\ \Phi = 0 \text{ at } \xi = \infty \text{ (far from the disk).}\\ \Phi \text{ well behaved at } \eta = 1 \text{ (on the axis of the disk).}\end{array}\right\} \qquad [12]$$

These imply that the disk electrode is embedded in a sufficiently large insulating plane and that the counter electrode is far enough away so that the current distribution is not influenced by its position.

The solution of Eq. [11] satisfying conditions [12] can be expressed as a series

$$\Phi = \frac{RT}{ZF}\sum_{n=0}^{\infty} B_nP_{2n}(\eta)M_{2n}(\xi) \qquad [13]$$

where $P_{2n}(\eta)$ denotes the Legendre polynomial of order $2n$ and $M_{2n}(\xi)$ is a Legendre function of imaginary argument satisfying the differential equation

$$\frac{d}{d\xi}\left[(1+\xi^2)\frac{dM_{2n}}{d\xi}\right] = 2n(2n+1)M_{2n} \qquad [14]$$

and the boundary conditions

$$M_{2n} = 1 \text{ at } \xi = 0 \text{ and } M_{2n} = 0 \text{ at } \xi = \infty \qquad [15]$$

The coefficient RT/ZF is introduced with regard for the expression to be used later for the concentration overpotential. For the two cases treated in this paper we have

$$\left.\begin{array}{l}Z = -z_+z_-/(z_+-z_-) \text{ for the single salt}\\ Z = -n \text{ with supporting electrolyte}\end{array}\right\} \qquad [16]$$

At $\xi = 0$, Eq. [13] yields

$$\Phi_o = \frac{RT}{ZF}\sum_{n=0}^{\infty} B_nP_{2n}(\eta) \qquad [17]$$

This should be regarded as the potential just "outside" the diffusion layer or as the potential extrapolated to the electrode surface if the actual current distribution prevails, but there is no concentration variation near the electrode surface. Effects due to the concentration variation are to be included in the concentration overpotential.

The current density is related to the derivative of the potential just outside the diffusion layer

$$i = -\kappa_\infty\left.\frac{\partial\Phi}{\partial y}\right|_{y=0} = \frac{-\kappa_\infty}{r_o\eta}\left.\frac{\partial\Phi}{\partial\xi}\right|_{\xi=0} = \frac{-\kappa_\infty}{r_o\eta}\frac{RT}{ZF}\sum_{n=0}^{\infty} B_nP_{2n}(\eta)M_{2n}'(0) \qquad [18]$$

where κ_∞ is the conductivity of the bulk solution. From the properties of Legendre functions one finds that

$$M_{2n}'(0) = -\frac{2}{\pi}\frac{(2^n n!)^4}{[(2n)!]^2} \qquad [19]$$

Since the diffusion layer is thin, the current density evaluated from the potential derivative outside the diffusion layer (Eq. [18]) must equal the current density evaluated from the concentration derivative at the electrode surface (Eq. [8]). See also ref. (4). This provides a relationship between the coefficients B_n of the potential series and the coefficients A_m of the concentration series.

$$B_n = \frac{\pi}{4}N\sum_{m=0}^{\infty} Q_{n,m}A_m \qquad [20]$$

where

$$N = -\sqrt{\frac{r_o^2\Omega}{\nu}}\left(\frac{a\nu}{3D}\right)^{1/3}\frac{nZF^2Dc_\infty}{RT(1-t)\kappa_\infty} \qquad [21]$$

and

$$Q_{n,m} = (4n+1)\frac{4\theta_m'(0)}{\pi M_{2n}'(0)}\int_0^1 \eta(1-\eta^2)^m P_{2n}(\eta)\,d\eta \qquad [22]$$

This relationship is obtained by equating the two expressions for the current density, multiplying by $\eta P_{2n'}(\eta)$, integrating with respect to η from zero to one, and making use of the orthogonality relation

$$\int_0^1 P_{2n}(\eta)P_{2n'}(\eta)\,d\eta = \begin{cases}1/(4n+1) & \text{if } n = n'\\ 0 & \text{if } n \neq n'\end{cases} \qquad [23]$$

and the relation

$$(r/r_o)^2 = 1 - \eta^2 \text{ at } \xi = 0 \qquad [24]$$

Some values of $Q_{n,m}$ are given in Table II.

Overpotentials

The potential V of the metal disk electrode is the sum of the potential drop in the solution Φ_o, the concentration overpotential η_c, and the surface overpotential η_s

$$V = \Phi_o + \eta_c + \eta_s \qquad [25]$$

The three terms on the right will vary with radial position on the disk in such a way that V is constant. The potential drop in the solution Φ_o is evaluated from Eq. [17].

For the concentration overpotential we adopt the expression [see ref. (4)]

Table II. Matrix $Q_{n,m}$ relating the coefficients of the potential series to the coefficients of the concentration series

n	$m = 0$	$m = 1$	$m = 2$	$m = 3$	$m = 4$	$m = 5$
0	1.11985	0.76649	0.60183	0.50393	0.43800	0.39008
1	0.34995	−0.0	−0.09404	−0.12598	−0.13687	−0.13931
2	−0.05905	−0.14147	−0.09521	−0.05315	−0.02310	−0.00220
3	0.02221	0.03649	0.06208	0.06398	0.05647	0.04643
4	−0.01112	−0.01675	−0.02237	−0.03138	−0.03666	−0.03818
5	0.00649	0.00943	0.01191	0.01450	0.01812	0.02141
6	−0.00417	−0.00595	−0.00733	−0.00862	−0.00996	−0.01161
7	0.00287	0.00405	0.00492	0.00569	0.00643	0.00719
8	−0.00207	−0.00290	−0.00350	−0.00401	−0.00448	−0.00494
9	0.00155	0.00217	0.00260	0.00296	0.00329	0.00359
10	−0.00120	−0.00167	−0.00200	−0.00226	−0.00250	−0.00272

$$\eta_c = -\frac{RT}{ZF}\left[\ln\left(\frac{c_\infty}{c_o}\right) - t\left(1 - \frac{c_o}{c_\infty}\right)\right] \quad [26]$$

This applies approximately to metal deposition from a solution of a single salt. It also applies approximately to the reaction of a minor component from a solution with excess indifferent electrolyte, in which case $t = 0$.

The current density and the surface overpotential are assumed to be related by the expression

$$i = i_o\left(\frac{c_o}{c_\infty}\right)^\gamma\left[\exp\left\{\frac{\alpha ZF}{RT}\eta_s\right\} - \exp\left\{-\frac{\beta ZF}{RT}\eta_s\right\}\right] \quad [27]$$

where i_o is the exchange current density at the bulk concentration and is assumed to be proportional to the concentration to the γ power. Thus the exchange current density at the surface concentration c_o is expressed as $i_o \cdot (c_o/c_\infty)^\gamma$ in Eq. [27]. It is convenient to refer the current density to the limiting current density

$$i_{lim} = -\frac{nF\,Dc_\infty}{1-t}\left(\frac{a\nu}{3D}\right)^{1/3}\sqrt{\frac{\Omega}{\nu}}\,\theta_o'(0) \quad [28]$$

so that Eq. [27] becomes

$$\frac{i}{i_{lim}} = \frac{J}{N\theta_o'(0)}\left(\frac{c_o}{c_\infty}\right)^\gamma\left[\exp\left\{\frac{\alpha ZF}{RT}\eta_s\right\} - \exp\left\{-\frac{\beta ZF}{RT}\eta_s\right\}\right] \quad [29]$$

where

$$J = i_o r_o ZF/RT\,\kappa_\infty \quad [30]$$

These expressions for the overpotentials have been used so that conclusions of some generality can be drawn without introducing too many parameters. The evaluation of the concentration overpotential requires only the concentration values in the bulk and at the surface, but not a detailed knowledge of the concentration profile. In the case of the solution with supporting electrolyte, there are other species besides the limiting reactant whose concentrations are not being calculated but should perhaps enter into the determination of the overpotential. An example would be the product species in a redox reaction. The present results could be applied approximately to such a case since the product species is not so decisive in the determination of the current distribution, or the calculations could be refined to include the concentration of the product species.

The overpotential relationships cited in this section constitute an additional connection between the coefficients A_m of the concentration series and the coefficients B_n of the potential series. The concentration at the surface and the current density must adjust themselves so that the overpotentials add up to the applied voltage V according to Eq. [25]. However, it is not possible to obtain an explicit expression similar to Eq. [20].

Numerical Calculation Method

In numerical calculations it is necessary to truncate the concentration and potential series. The potential series works very well, but the coefficients A_m of the concentration series are found to have alternating signs, large absolute values, and considerably different values depending on how many terms in the series are retained. This can be avoided, to some extent, by re-expressing the concentration on the surface in terms of orthogonal polynomials

$$c_o = c_\infty\left[1 + \sum_{l=0}^{\infty} a_l P_{2l}(r/r_o)\right] \quad [31]$$

Then the coefficients a_l are small, decrease in magnitude with increasing l, and are roughly independent of the number of terms retained in the series. Furthermore, they can be evaluated by an integration over the surface concentration

$$a_l = (4l+1)\int_o^1\left(\frac{c_o}{c_\infty} - 1\right)P_{2l}(r/r_o)\,d(r/r_o) \quad [32]$$

It does become a little more difficult to evaluate the current density according to Eq. [8], and the problems arising from the fact that the coefficients A_m are large and of alternating sign are not entirely eliminated. This can be seen from the expression for the Legendre polynomial of order 20

$$\begin{aligned} P_{20}(x) = [&34{,}461{,}632{,}205\,x^{20} - 167{,}890{,}003{,}050\,x^{18} \\ &+ 347{,}123{,}925{,}225\,x^{16} - 396{,}713{,}057{,}400\,x^{14} \\ &+ 273{,}491{,}577{,}450\,x^{12} - 116{,}454{,}478{,}140\,x^{10} \\ &+ 30{,}117{,}537{,}450\,x^8 - 4{,}461{,}857{,}400\,x^6 \\ &+ 334{,}639{,}305\,x^4 - 9{,}699{,}690\,x^2 \\ &+ 46{,}189]/262{,}144 \end{aligned} \quad [33]$$

The coefficients become as large as 1.5×10^6; yet the absolute value of $P_{20}(x)$ is never greater than one for the range of interest! Consequently the calculation of the contribution to the current density arising from the Legendre polynomial of order 20 in Eq. [31] requires accurate values for $\theta_m'(0)$ as given in Table I. Because of these difficulties it was decided to truncate the series [5 and 31] at $m = 10$ and $l = 10$.

The coefficients B_n and A_m or a_l were calculated by an iterative procedure:

1. The current density and the surface concentration were specified at the center of the disk. As an initial guess this was taken to apply to the whole disk so that $a_o = A_o = c_o/c_\infty - 1$ and all the other coefficients are zero.
2. The coefficients B_n were calculated according to Eq. [20].
3. The potential outside the diffusion layer was calculated at selected values of r according to Eq. [17].
4. The potential V of the electrode was calculated by applying Eq. [25] to the center of the disk where η_c and η_s could be calculated from the specified current density and surface concentration.
5. The overpotential $\eta = \eta_c + \eta_s$ was calculated at selected values of r from Eq. [25].
6. At these same values of r, the overpotential η and the assumed current density were used to calculate the surface concentration c_o by a trial-and-error solution of Eq. [26] and [27].
7. The coefficients a_l were calculated according to Eq. [32]. In order to achieve convergence it was usually necessary to average these in some way with the previous set of a_l.
8. The current density was calculated from Eq. [8].
9. The calculations enumerated in items 2 through 8 above were repeated until no significant changes occurred in the values.

This procedure was modified slightly for the well-stirred case ($N = \infty$) where all the concentrations have their bulk values.

Results

Primary and limiting current distributions.—As a point of departure it is worthwhile to examine two limiting cases. The primary current distribution corresponds to a uniform potential Φ_o in the solution just outside the diffusion layer and was calculated by Newman (7). The current density on the disk is

$$i = 0.5\,i_{avg}/\sqrt{1 - (r/r_o)^2} \quad [34]$$

and the total current to the disk is

$$I = 4\kappa_\infty r_o \Phi_o \quad [35]$$

This result is shown in Fig. 1. In the case of the primary current distribution, the surface overpotential

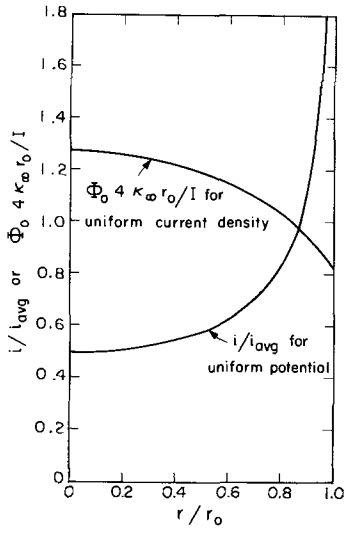

Fig. 1. Primary current distribution and potential distribution for a uniform current density.

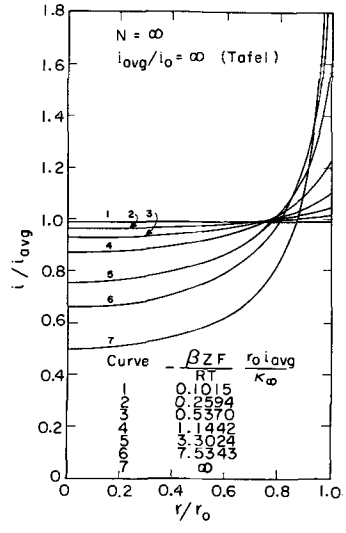

Fig. 3. Secondary current distribution for Tafel polarization

and concentration overpotential are negligible, and the current distribution is completely determined by the ohmic drop in the solution, with the result that the current density is infinite at the edge of the disk and is half of the average value at the center of the disk.

Levich (3) has shown that the current density is uniform on the disk surface and is given by Eq. [28] when the current is limited by the rate of mass transfer of a reactant to the disk. The corresponding potential Φ_0 just outside the diffusion layer can be calculated from Eq. [17] and [20] with $A_0 = -1$ and all the other A's set equal to zero. The result is shown in Fig. 1, normalized in such a way that it can be compared conveniently with the value $\Phi_0 4\kappa_x r_0/I = 1$ for the primary current distribution. For the same total current, the current density at the center of the disk is twice as high as the primary current, and this requires a potential 27.3% higher in order to force the higher current density to the center of the disk. At the same time the current density at the edge of the disk is finite, and the potential is lower than for the primary distribution.

Secondary current distribution.—If the rotation speed is high, so that $|i| << |i_{lim}|$, then the concentration overpotential is negligible, and the so-called secondary current distribution prevails. The current distribution is then determined by the balance between the surface overpotential and the ohmic drop in the solution. The result is shown in Fig. 2 and 3 for two limiting cases corresponding to linear polarization and to Tafel polarization.

For sufficiently small current densities $|i| << i_0$, Eq. [27] becomes linear, and the slope of the polarization curve at zero current is

$$\left.\frac{di}{d\eta_s}\right|_{i=0} = (\alpha+\beta)\frac{ZF}{RT}i_0 \qquad [36]$$

The parameter J is thus similar to that identified by Hoar and Agar (8) for the characterization of the influence of electrolytic resistance, polarization, and cell size on current distribution. In the linear range the current distribution depends only on the parameter $(\alpha + \beta)J$, as shown in Fig. 2 with $\alpha + \beta = 1$. In particular, the current distribution i/i_{avg} does not depend upon the level of the current. The curve for $J = \infty$ is the primary current distribution.

At higher currents where the condition $|i| << i_0$ no longer holds, the current level becomes important. This can be characterized by the dimensionless ratio

$$\delta = |i_{avg}|\frac{ZFr_0}{RT\kappa_\infty} \qquad [37]$$

In the other extreme, when $|i| >> i_0$, one of the exponential terms in Eq. [27] is negligible, and Tafel polarization is said to apply

$$\eta_s = -\frac{1}{\beta}\frac{RT}{ZF}(\ln|i| - \ln i_0) \qquad [38]$$

(For current flow in the opposite direction, the term involving α would be retained.) In the Tafel region the actual value of the exchange current density is no longer important in determining the current distribution since it just contributes an additive constant to the surface overpotential, as shown in Eq. [38]. The current distribution i/i_{avg} is completely determined by the parameter $\beta\delta$ and is shown in Fig. 3. Curve 7 for $\beta\delta = \infty$ is the primary current distribution.

It does not seem worthwhile to plot the current distribution for intermediate current levels between the linear and Tafel regions. Instead Fig. 4 and 5 give just the values for i/i_{avg} and Φ_0 at the center of the disk. The current ratio can vary between 0.5 and 1.0 in the extreme cases of the primary current distribution and the uniform current distribution. The ohmic drop to the center of the disk is expressed in Fig. 5 in the

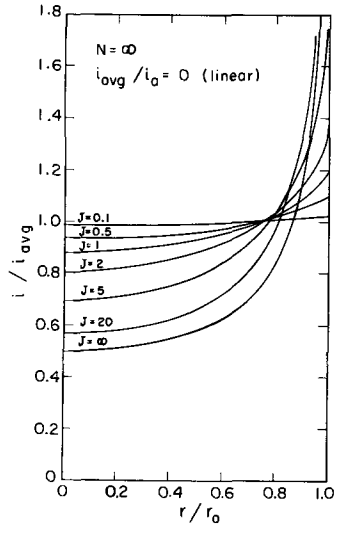

Fig. 2. Secondary current distribution for linear polarization

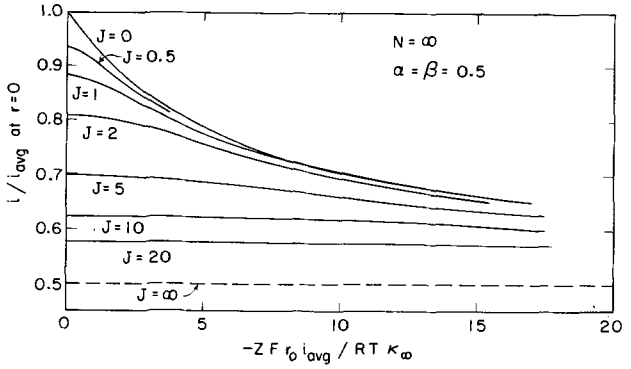

Fig. 4. Current density of the center of the disk when concentration polarization is absent.

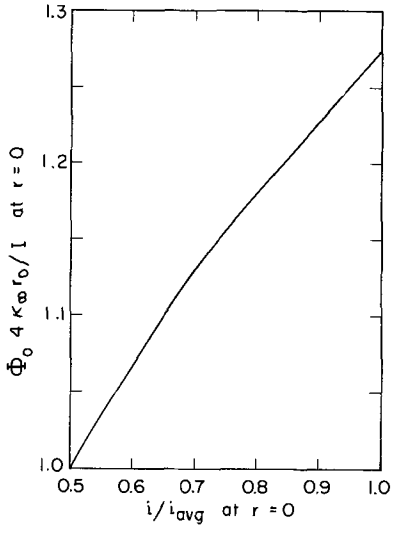

Fig. 5. Correction factor for resistance to center of disk

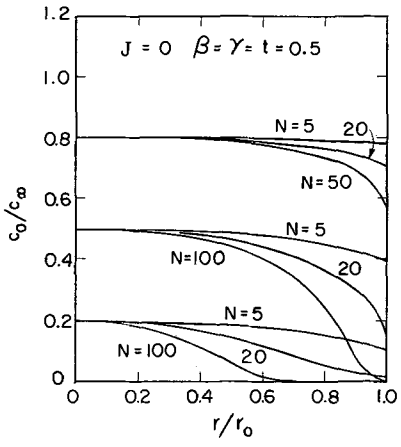

Fig. 6. Surface concentration for Tafel kinetics

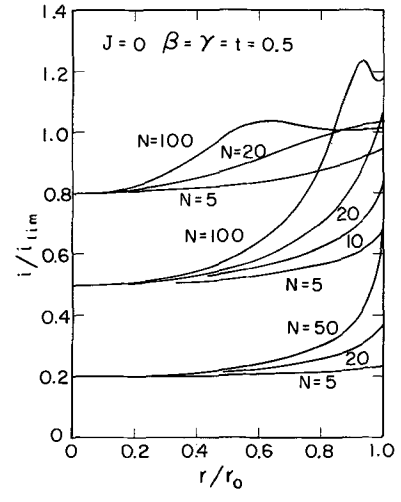

Fig. 7. Current distribution for Tafel kinetics with an appreciable fraction of the limiting current.

form $\Phi_0 4\kappa_\infty r_0/I$, a dimensionless effective resistance which can vary between the values 1.0 for the primary current distribution and 1.273 for the uniform current distribution. For large currents the Tafel results apply. As the current is decreased, the distribution becomes more uniform but approaches at low currents the linear results for the given value of J rather than a completely uniform current density. At intermediate current levels, all four parameters J, δ, α, and β can affect the current distribution. Figures 4 and 5 show the effect of J and δ when $\alpha = \beta = 0.5$.

Effect of concentration polarization.—The current density can also be limited by the rate of mass transfer of the reactants to the electrode. An important parameter in this regard is N, defined in Eq. [21]. This parameter is proportional to the square root of the Reynolds number $\mathrm{Re} = r_0^2\Omega/\nu$, the one-third power of the Schmidt number $Sc = \nu/D$, and the ratio c_∞/κ_∞. It represents the importance of the ohmic potential drop relative to the concentration overpotential at a given fraction of limiting current. An increase in disk size r_0 increases the distance over which current flows and thus increases the magnitude of the variation of the potential Φ_0. An increase in rotation speed Ω is accompanied by an increase in current at a given fraction of limiting current and thus increases the potential variation due to the ohmic drop. On the other hand, supporting electrolyte can be added so that κ_∞ increases but not c_∞. This reduces the importance of the ohmic drop.

Since the limiting current density is given by Eq. [28], the condition for the concentration overpotential to be negligible and for the secondary current distribution to apply, $|i_{avg}| << |i_{lim}|$, can be expressed as $\delta << N$.

Figures 6 and 7 show the concentration and current distributions on the disk for Tafel kinetics and for various levels of current and rotation speed. The corresponding curves on the two graphs can be found by the relationship between the current and the surface concentration at the center of the disk: $i/i_{lim} = 1 - c_0/c_\infty$ at $r = 0$. The higher currents correspond to lower surface concentrations.

The distributions of concentration and of current shown on Fig. 6 and 7 become more nonuniform for larger values of N, but they still become limited by the rate of mass transfer. The local current density is able to exceed the average limiting current only because the current is less than that value near the center of the disk. This situation can be compared to a disk with an insulator in the center and an annular or ring electrode. For such a system the local limiting current density would be infinite at the inner edge of the ring electrode and would decrease toward the outer edge. Some of the curves on Fig. 7 show this situation: the current rises as the local overpotential increases with increasing r but begins again to decrease after the concentration has effectively gone to zero and the increasing overpotential can have no more effect.

Figure 8 shows the correction factor for the current density at the center of the disk. The curve for $N = \infty$ corresponds to no concentration polarization and was shown on Fig. 4. The curves for $N = 5$, 10, and 20 depart from the curve for $N = \infty$ and terminate with a uniform current at their respective limiting currents.

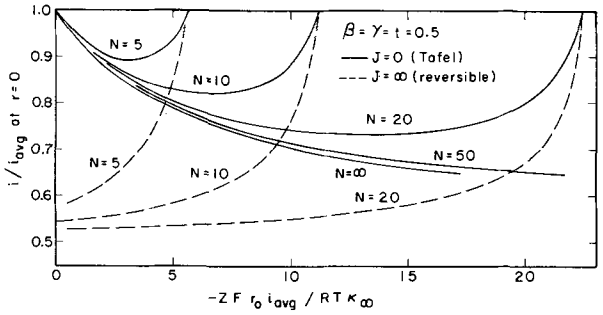

Fig. 8. Current density at the center of the disk

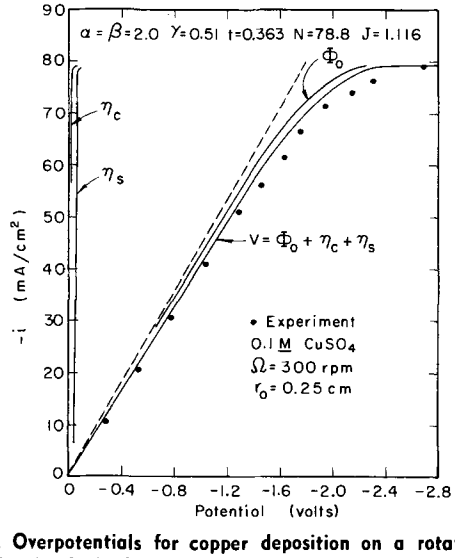

Fig. 9. Overpotentials for copper deposition on a rotating disk. Dashed line is ohmic drop for the primary current distribution.

For a sufficiently large value of the exchange current density, the surface overpotential is negligible compared to the ohmic drop in the solution and the concentration overpotential. The electrode is then said to be reversible. The current-density ratios for reversible electrodes are shown as dashed curves on Fig. 8. The distribution is more nonuniform than for Tafel kinetics, becomes more nonuniform for larger values of N, and still becomes uniform at the limiting current.

Copper deposition. Figure 9 shows a polarization curve for copper deposition from a solution containing no supporting electrolyte. Measured potentials reported by Hsueh and Newman (9) have been corrected (7) for the fact that the reference electrode was not at infinity. The following parameters were used in the calculation of the surface overpotential, the concentration overpotential, and the ohmic drop at the center of the disk:

n = −2, Z = 1, κ_∞ = 0.00872 (ohm-cm)$^{-1}$ [ref. (10)],
i_0 = 1 ma/cm², $\alpha = \beta = 2$, γ = 0.51 (ref. 11),
r_o = 0.25 cm, Ω = 300 rpm = 31.416 rad/sec
i_{lim} = 79.20 ma/cm²,
D = 0.642 x 10^{-5} cm²/sec [integral value, ref. (12)],
t = 0.363 (ref. 13), ν = 0.94452 x 10^{-2} cm²/sec,
J = 1.116, N = 78.8.

Most of the polarization is due to ohmic drop in the solution since the conductivity is so low. The curve shows how the ohmic resistance changes as limiting current is approached due to the current density becoming more uniform. The agreement with the experimental values is considerably better than that obtained with the ohmic drop for the primary current distribution (dashed line). Possible explanations for the discrepancy which remains are uncertainties in the surface overpotential and the fact that the insulating plane of the disk was not infinite, but would allow current to flow in the region above the plane of the disk. The discrepancy is roughly equal to the correction for the fact that the reference electrode is not at infinity.

Conclusions

The present results can be applied most simply to practical problems in studies of electrode kinetics if the actual current density at the center of the disk and the potential drop to the center of the disk can be obtained, perhaps by means of Fig. 4, 5, and 8, from the measured average current density and the parameters N, J, α, β, γ, and t related to the properties of the solution and the electrode reaction and the size and rotation speed of the disk electrode. Since some of these properties probably are not known in advance, trial-and-error calculations are involved.

The rotating disk is usually used for moderately fast reactions, that is, reactions for which the exchange current density is not too low. The effect of mass transfer can be corrected for (by assuming a uniform current density) or eliminated by an extrapolation to infinite rotation speed. However, the effect of a nonuniform current density is not eliminated. To assess the degree of nonuniformity, one should calculate or estimate J, δ, and N. Unless J and δ are both small, there will be a significant nonuniformity, and unless $\delta << N$ a correction must be made for the different concentration at the electrode surface.

Suppose that the 0.1M $CuSO_4$ solution studied earlier is made 1.53M in H_2SO_4 for the purpose of suppressing the ohmic potential drop in the solution. For the same current density, say 70 ma/cm², the values of the parameters N, δ, J, and t would be

N = 1.6 instead of 78.8,
δ = 2.5 instead of 78,
J = 0.037 instead of 1.116,
t = 0 instead of 0.363.

These changes are primarily results of the increased conductivity (0.548 instead of 0.00872 ohm^{-1}-cm^{-1}).

It should be noted that with the addition of sulfuric acid the current density is now above the limiting current since the contribution of migration to the mass transfer has now been suppressed by the high electrical conductivity. We might next try to eliminate the mass transfer effect altogether by increasing the rotation speed. If the criterion is taken to be $N = 20\ \delta$, the rotation speed must now be increased to 290,000 rpm, at which speed the flow becomes turbulent at about r = 0.18 cm. Few people would consider operating even at speeds as high as 30,000 rpm. Nevertheless, let us assume that mass transfer effects can be ignored.

With δ = 2.5 and β = 1 and $J \approx 0$, the results presented earlier indicate that the current density at the center of the disk is 79% of the average current density and the ohmic drop is 29.5 mv.

Finally one might note that the a-c resistance to a disk should be somewhat different from the actual value since the a-c resistance would correspond more closely to the primary current distribution. For the same reason it would be inconsistent to use current step methods to study electrode kinetics with the rotating disk. In current step methods the initial jump of the potential is taken as a measure of the ohmic drop. This would be proper for a sphere where the initial current distribution is the same as the quasi-steady current distribution (before mass-transfer limitations become important).

Acknowledgment

This work was supported by the United States Atomic Energy Commission.

NOMENCLATURE

a	0.51023
a_l	coefficients in series for surface concentration
A_m	coefficients in series for concentration
B_n	coefficients in series for potential
c	concentration of reactant, mole/cm^3
c_o	concentration at electrode surface, mole/cm^3
c_∞	bulk concentration, mole/cm^3
D	diffusion coefficient, cm^2/sec
F	Faraday's constant, coulomb/equiv
i	normal current density at electrode surface, amp/cm^2
i_o	exchange current density, amp/cm^2
i_{avg}	average current density, amp/cm^2
i_{lim}	limiting current density, amp/cm^2
I	total current to the disk, amp
J	dimensionless exchange current density (see Eq. [30])
M_{2n}	a Legendre function (see Eq. [14] and [15])
n	number of electrons produced when one reactant ion or molecule reacts
N	parameter related to significance of mass transfer (see Eq. [21])
P_n	Legendre polynomial of order n
$Q_{m,n}$	see Eq. [22] and Table II
r	radial coordinate, cm
r_o	radius of disk, cm
R	universal gas constant, joule/mole-deg
Re	$= r_o^2\Omega/\nu$, Reynolds number
Sc	$= \nu/D$, Schmidt number
t	transference number of reactant
T	absolute temperature, °K
v_r, v_y	velocity components, cm/sec
V	potential of metal disk electrode, volt
y	normal distance from disk, cm
z_i	charge number of species i
Z	see Eq. [16]
α,β,γ	parameters in kinetic expression (see Eq. [27])
δ	dimensionless average current density (see Eq. [37])
ζ	dimensionless normal distance (see Eq. [4])
η	elliptic coordinate (see Eq. [10])
η_c	concentration overpotential, volt
η_s	surface overpotential, volt
θ_m	functions in concentration series
κ_∞	conductivity of bulk solution, ohm^{-1}-cm^{-1}
ν	kinematic viscosity, cm^2/sec
ξ	elliptic coördinate (see Eq. [10])
Φ	electrostatic potential, volt
Φ_o	external potential extrapolated to electrode surface, volt
Ω	rotation speed, radians/sec

Manuscript received May 4, 1966.

Any discussion of this paper will appear in a Discussion Section to be published in the June 1967 JOURNAL.

REFERENCES

1. Th. v. Kármán, *Z. angew. Math. u. Mechanik*, **1**, 233 (1921).
2. W. G. Cochran, *Proc. Cambridge Phil. Soc.*, **30**, 365 (1934).
3. B. Levich, *Acta Physicochim. U.R.S.S.*, **17**, 257 (1942).
4. John Newman, The Effect of Migration in Laminar Boundary Layers, UCRL-16665, February, 1966.
5. D. P. Gregory and A. C. Riddiford, *J. Chem. Soc.*, **1956**, 3756.
6. John Newman, *J. Phys. Chem.*, **70**, 1327 (1966).
7. John Newman, *This Journal*, **113**, 501 (1966).
8. T. P. Hoar and J. N. Agar, *Discussions Faraday Soc.*, **1**, 162 (1947).
9. Limin Hsueh and John Newman, *Electrochim. Acta*, To be published.
10. B. Fedoroff, *Ann. Chim.*, **16**, 154 (1941).
11. Tor Hurlen, *Acta Chem. Scan.*, **15**, 630 (1961).
12. John Newman and Limin Hsueh, *Electrochim. Acta*, To be published.
13. J. J. Fritz and C. R. Fuget, *J. Phys. Chem.*, **62**, 303 (1958).

Studies on the Oxygen Gradients in Oxidizing Metals

V. The Oxidation of Oxygen-saturated Zirconium

J. P. Pemsler

Ledgemont Laboratory, Kennecott Copper Corporation, Lexington, Massachusetts

ABSTRACT

Oxygen-saturated zirconium was oxidized at temperatures between 840° and 1300°C. In the range 1100°-1300°C a parabolic film growth rate was observed which is more rapid than that observed during oxidation of oxygen-free metal. However, rational rate constants k_r, which characterize transport properties through the film, are identical. In the range 840°-975°C a rapid initial growth is followed by a parabolic rate more rapid than that observed on oxygen-free metal. Values of k_r are somewhat larger for oxidation of oxygen-saturated metal, the difference becoming greater at the higher temperature. Oxygen solution during oxidation of oxygen-free zirconium at 840°-975°C is believed to result in a more protective film due to the formation of voids within the film.

During the high-temperature oxidation of zirconium, significant quantities of oxygen dissolve in the metal substrate simultaneously with the growth of oxide, so that a metal zone rich in oxygen forms beneath the oxide layer. At sufficiently high-temperature oxygen solution may account for the major portion of the weight gain of the sample. The role that this oxygen solution plays in the mechanism of oxidation has not been clearly understood. In previous papers (1-3) evidence has been presented that oxygen solution obeys diffusion kinetics and remains parabolic for sufficiently thick samples. However, the kinetics of the oxide film growth is complex (4). Between 550° and 650°C film growth is approximately parabolic with an activation energy of about 30 kcal/mole. Between 750° and 910°C no normal rate law is obeyed; a rapid initial growth is followed by a much slower growth. At 975°C coincident with void formation the rate increases. Between 1100° and 1300°C voids no longer form, and the rate becomes parabolic and rapid with an activation energy of 35 kcal/mole.

Several inconclusive studies concerned with the effect of dissolved oxygen on the oxidation rate of zirconium have been previously published. Osthagen and Kofstad (5) reported an increase in the rate of oxidation when dissolved oxygen is present in zirconium. The rate increased gradually between 0 and 4 a/o (atomic per cent), then rapidly between 4 and 10 a/o, where it leveled off. Interpretations concerning the

mechanism of oxidation were made based on these observations. Cox and Harder (6) criticized this work on the basis of the fact that no examination of the microdistribution of oxygen in the samples was made. They find that the increases in oxidation rate of Zircaloy-oxygen alloys up to about 0.5 fraction saturated can be ascribed largely to inhomogeneous distribution of oxygen and that the closer a homogeneous oxygen distribution is approached, the closer the oxidation rate approaches that of low oxygen-containing material.

The difficulties inherent in the above studies are: (*i*) the inability to obtain homogeneous zirconium-oxygen alloys and (*ii*) the brittle nature of the high oxygen content alloys which prevents formation of an adherent oxide layer.

It is the purpose of this paper to determine the effect of oxygen solution on the kinetics of film formation by oxidizing sound metallurgical samples which are saturated with oxygen.

Experimental

The zirconium used in this investigation was obtained in the form of rods, and the analysis has been given previously (3). Tapered zirconium disks 1.5 cm in diameter and ranging in thickness from about 0.9 to 1.25 mm were oxidized for 1 hr at 1100°C. This resulted in an oxide film about 110μ thick, which when dissolved into the disk would just saturate the metal substrate with oxygen where the disk was about 1 mm in thickness. After oxidation, oxygen was removed from the system and the sample annealed in vacuum at 1100°C for 36 hr. This was sufficient time to diffuse the oxide film into the sample and to create a nearly homogeneous oxygen distribution throughout the metal substrate. In this manner, disks were produced which had a thin residual oxide coating on their thin end and metal which was about 85% saturated on the thick end. Between these extremes was metal of gradually increasing oxygen content all the way up to the saturation value where the metal met the remaining oxide film as shown in Fig. 1. The temperature of the furnace was then adjusted to the temperature of the final oxidation, and oxygen was admitted. Samples were oxidized for the appropriate length of time and the experiment concluded. Samples were then sectioned, and the oxide film thickness formed on metal that was saturated and near-saturated with oxygen was measured.

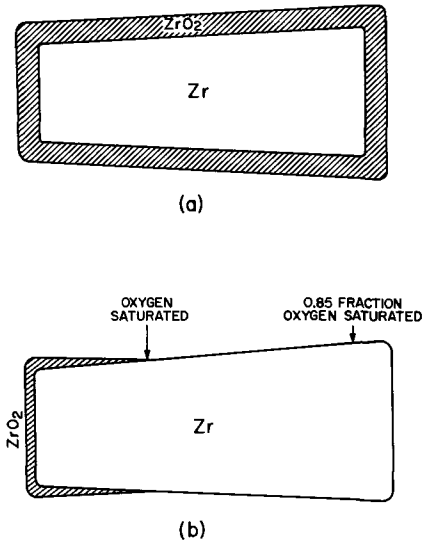

Fig. 1. Preparation of oxygen-saturated zirconium: (a) zirconium disk oxidized for 1 hr at 1100°C; (b) oxidized disk vacuum annealed 36 hr at 1100°C.

Difficulty was found in growing sound oxides on oxygen-saturated samples at temperatures below 840°C. In order to minimize possible thermal cycling effects due to cooling of samples diffused at 1100°C to the final oxidation temperature of 750°C or lower, additional experiments were performed using 0.1 mm thick foil and a preoxidation and oxygen dissolution temperature of 840°C.

Results

Oxidation of oxygen-saturated metal at temperatures of 750°C and below resulted in a spotty white oxide, even for times as short as 1 hr. This occurred whether the sample was a disk saturated at 1100°C or a foil saturated at 840°C. The white oxide resulted in a cracked film, and it was not possible to obtain meaningful kinetic data at 750°C and lower.

Film growth data at temperatures of 840°-1300°C are shown in Fig. 2-5, along with the corresponding data for the oxidation of samples with negligible initial oxygen content (henceforth called "oxygen-free" zirconium). Open circles represent film thickness on oxygen-free zirconium, filled circles represent data obtained from oxygen-saturated zirconium, and the lines without circles represent the total weight gain obtained during oxidation of oxygen-free zirconium (3) (*i.e.*, film thickness plus oxygen in solution expressed as equivalent film thickness).

Oxidation of oxygen-saturated zirconium in the range 1100°-1300°C conforms to a parabolic film growth rate which is more rapid than that observed during oxidation of oxygen-free material. The increased film growth on the oxygen-saturated zirconium brings the film thickness up to that approximately equivalent to the total weight gain found on oxygen-free zirconium oxidized for the same period of time. This does not say that the total weight gain is the same in both cases since oxygen-saturated zirconium is already equivalent to $ZrO_{0.4}$ and needs

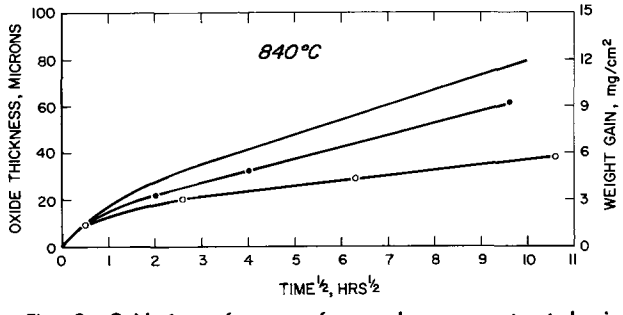

Fig. 2. Oxidation of oxygen-free and oxygen-saturated zirconium at 840°C. ○ Film thickness on oxygen-free zirconium; ● film thickness on oxygen-saturated zirconium; ——— total weight gain on oxygen-free zirconium.

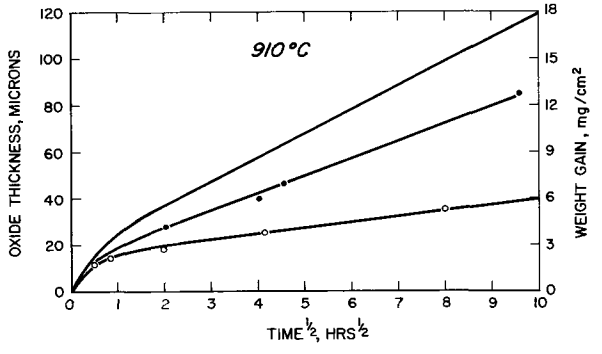

Fig. 3. Oxidation of oxygen-free and oxygen-saturated zirconium at 910°C: ○ Film thickness on oxygen-free zirconium; ● film thickness on oxygen-saturated zirconium; ——— total weight gain on oxygen-free zirconium.

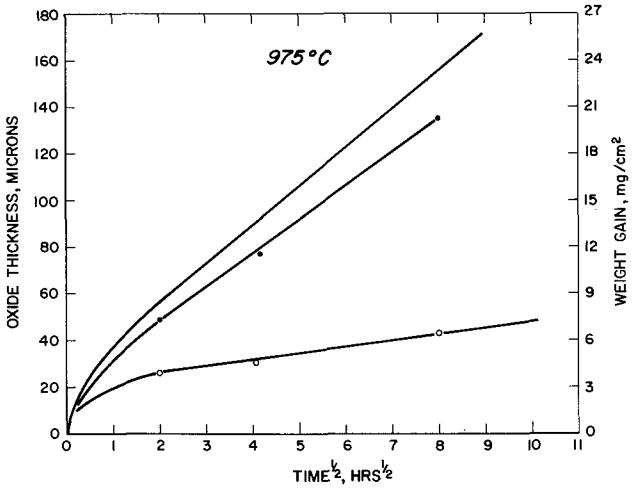

Fig. 4. Oxidation of oxygen-free and oxygen-saturated zirconium at 975°C. ○ Film thickness on oxygen-free zirconium; ● film thickness on oxygen-saturated zirconium; ——— total weight gain on oxygen-free zirconium.

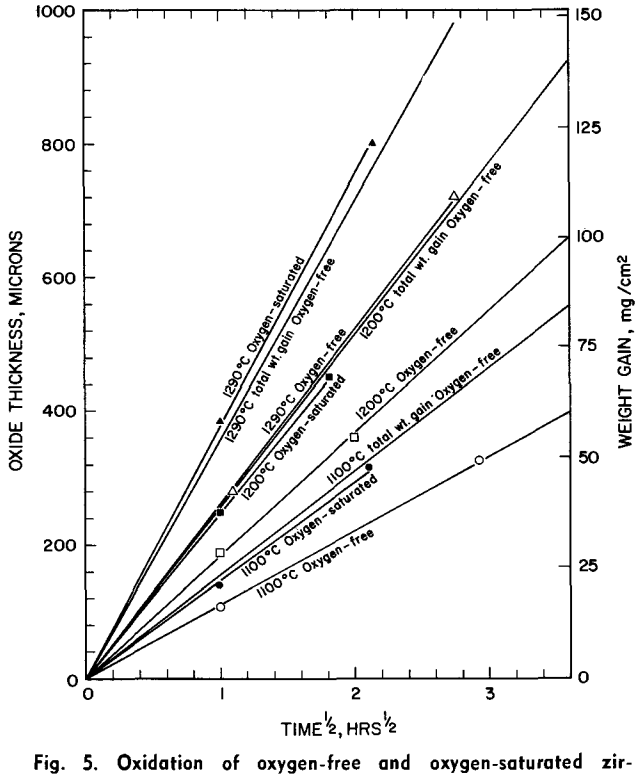

Fig. 5. Oxidation of oxygen-free and oxygen-saturated zirconium at 1100°-1300°C.

only 1.6 atoms of oxygen per zirconium atom to bring it to ZrO_2.

At 840°, 910°, and 975°C the film formation rate is more rapid on oxygen-saturated zirconium than on oxygen-free metal. The kinetic curves for both materials are similar: a rapid initial rate is followed by a parabolic region. Unlike the oxidation behavior at 1100°-1300°C, the increase in oxide film thickness is not sufficient to result in a weight gain equivalent to that observed as the total weight gain for oxygen-free metal.

During oxidation of oxygen-free zirconium at 975°C, after about 4 hr voids are found at the oxide/metal interface; at later times these voids continue to form at the oxide/metal interface and are also found buried within the oxide (4). No such voids were found during oxidation of oxygen-saturated zirconium. Furthermore, with oxygen-free zirconium, taper sections at 910°C show a band of small voids which form between about one and four hours within the oxide (4). Taper sections on saturated material did not reveal such a structure.

Similar to oxygen-free zirconium, oxidation of oxygen-saturated zirconium at 1025° and 1050°C resulted in the formation of large voids and a highly irregular oxide/metal interface. It was therefore difficult to evaluate any differences in the oxidation behavior at these temperatures.

Discussion

Zirconium is generally considered to oxidize by an anion vacancy diffusion mechanism. The transport processes through the oxide film are supposed to be

$$Zr = Zr^{+4} + 2\square_{O}^{=} + 4e^{-} \quad \text{at the metal/oxide interface} \quad [1]$$

and

$$O_2 + 4e^{-} + 2\square_{O}^{=} = 2\,O^{=} \quad \text{at the oxygen/oxide interface} \quad [2]$$

where $\square_{O}^{=}$ is an oxygen ion vacancy.

During oxidation of oxygen-free zirconium the simultaneous process of oxygen solution into the metal substrate occurs at the metal/oxide interface, and also generates oxygen ion vacancies according to the reaction

$$O^{=} = O_{(M)} + \square_{O}^{=} + 2e^{-} \quad [3]$$

where $O_{(M)}$ indicates an interstitial oxygen atom in the metal lattice.

As a result of the occurrence of the reaction in Eq. [3], whether oxygen-free or oxygen-saturated zirconium is being oxidized, the reaction at the metal/oxide interface should not be written as in Eq. [1] but must rather be written as

$$(ZrO_{0.4})_{sat} = Zr^{+4} + 1.6\square_{O}^{=} + 3.2e^{-} \quad [4]$$

where $(ZrO_{0.4})_{sat}$ represents oxygen-saturated zirconium which has the composition $ZrO_{0.4}$.

The oxygen ion vacancy concentration in the oxide at the oxide/metal interface is determined by the thermodynamic equilibrium between the oxide and oxygen-saturated metal. This value will be the same whether oxygen-free or oxygen-saturated zirconium is being oxidized. It might then be expected that the transport rate of oxygen ions across the film would be the same in both cases. In order to examine this, we will make use of the rational rate constant, k_r, defined by the equation

$$\frac{\dot{n}}{A} = \frac{1}{2}\frac{k_r}{\Delta x} \quad [5]$$

where $\dot{n}/A$ is the rate of oxygen transport in g-atom/cm²-sec, Δx is the instantaneous film thickness of the oxide layer, and k_r is in units of equivalents/cm²-sec for unit thickness. The factor 1/2 is due to the fact that oxygen is divalent. For oxygen-free zirconium $\dot{n}/A$ must be read from the total weight gain curve, while the corresponding value of Δx is obtained from the film growth curve; values of k_r may then be calculated from Eq. [5]. For oxygen-saturated zirconium $\dot{n}/A$ and the corresponding value of Δx are read from the same curve. Values of k_r are then calculated from the equation

$$\frac{\dot{n}}{A} = \frac{1}{1.6}\frac{k_r}{\Delta x} \quad [6]$$

which expresses the fact that the metal phase was present initially as oxygen-saturated zirconium corresponding to $ZrO_{0.4}$.

Values of $\dot{n}/A$ and Δx from 840°-1300°C were obtained from Fig. 2 through 5. Data for calculating k_r for oxygen-free zirconium in the temperature range 550°-750°C were obtained from a previous investi-

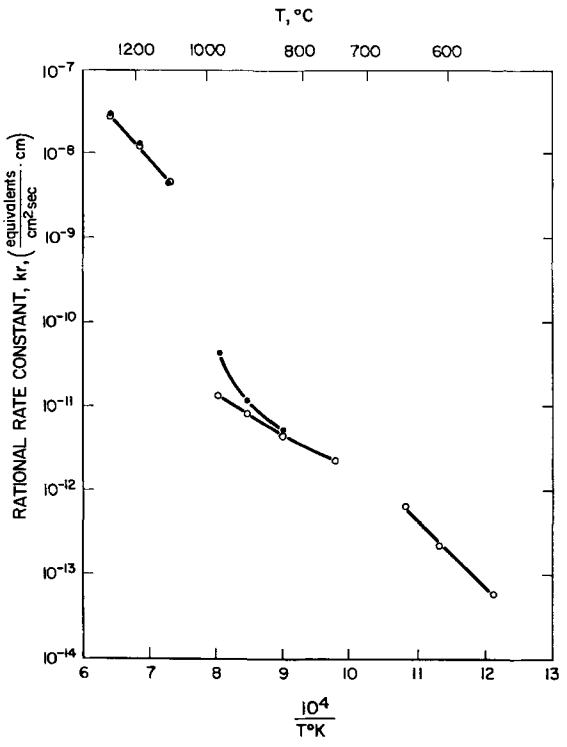

Fig. 6. Arrhenius plot of the rational rate constant, k_r, for oxidation of oxygen-free and oxygen-saturated zirconium. ○ oxygen-free zirconium; ● oxygen-saturated zirconium.

gation (4). Data for oxygen-saturated zirconium in this temperature range could not be obtained for reasons discussed previously. In the temperature range of 1100°-1300°C the calculations are straightforward. At temperatures below 1100°C where the simple parabolic rate law does not hold, $\dot{n}/A$ is read directly from the parabolic portion of the curve, while Δx is obtained by extrapolating the parabolic portion of the film growth curve to zero time and subtracting the intercept value of the ordinate from the observed film thickness. If the period during which the rapid initial growth occurred is short, then the value of k_r obtained by this procedure should be a good approximation to the true value.

An Arrhenius plot of k_r is shown in Fig. 6. In the temperature range 1100°-1300°C where the film is believed to be the high defect tetragonal oxide, values of k_r for oxygen-free and oxygen-saturated metal are identical, indicating that the transport properties of the film are the same whether it grows on oxygen-free or oxygen-saturated zirconium. In the temperature range 840°-975°C values of k_r are somewhat larger for the oxidation of oxygen-saturated metal, the difference becoming greater at the higher temperature. Thus, at 840°-975°C the process of oxygen solution during oxidation results in a more protective film than would occur were there no oxygen solution. It has been previously stated that the formation of voids is suppressed during the oxidation of oxygen-saturated zirconium. These voids have been ascribed to a condensation of oxygen ion vacancies triggered by the tetragonal/monoclinic transformation in zirconia (4). Since oxygen solution is a source of anion vacancies, it is reasonable that void formation might be accelerated by the additional contribution of vacancies formed during the process of oxygen solution. That void formation is not altogether eliminated by eliminating the oxygen solution process is apparent from observations on oxygen-saturated zirconium oxidized at 1025° and 1050°C.

Since the decrease in the rate appears to parallel the increase in void formation, it is reasonable to associate the two phenomena although it is not obvious by what mechanism the presence of voids in the oxide film would decrease the transport rate through the oxide. It has been shown that under certain circumstances nonlattice diffusion through the oxide predominates during the oxidation of zirconium (4), and the initiation and termination of these unidirectional paths may be affected by the occurrence of voids within the oxide.

Although there is a difference in film growth behavior of oxygen-free and oxygen-saturated zirconium in the range 840°-975°C, the shape of the film growth curves are nevertheless similar. These data are consistent with the hypothesis previously advanced (4) wherein the rate is determined by transport through an initial tetragonal oxide which transforms to the monoclinic structure.

It is interesting to speculate on the reasons why an adherent oxide film could not be obtained when oxidizing oxygen-saturated zirconium at temperatures below 840°C. It may be related to the increased embrittlement of the oxygen-saturated metal at the lower temperatures. The strains produced at the metal/oxide interface during oxide growth could then cause cracking in the brittle oxygenated metal, and hence an accelerated attack. It is also possible that the tetragonal phase, hypothesized to occur at the metal/oxide interface, may not be stabilized to as low a temperature during oxidation of oxygen-saturated zirconium. The monoclinic oxide may exhibit less plasticity than the high defect tetragonal oxide and undergo cracking while still quite thin.

Current work is directed toward investigating nonlattice mechanisms in the oxide film and details of the role of the tetragonal/monoclinic inversion on the kinetics.

Acknowledgment

The author is pleased to acknowledge the valuable assistance and suggestions of J. K. Litchfield and stimulating discussions with J. B. Lightstone.

Manuscript received March 22, 1966. This paper was presented at the Philadelphia Meeting, Oct. 9-14, 1966.

Any discussion of this paper will appear in a Discussion Section to be published in the June 1967 JOURNAL.

REFERENCES

1. J. P. Pemsler, *J. Nuclear Materials*, **7**, 16 (1962).
2. J. P. Pemsler, *This Journal*, **111**, 381 (1964).
3. J. P. Pemsler, *ibid.*, **112**, 477 (1965).
4. J. P. Pemsler, *Electrochem. Technol.*, **4**, 128 (1966).
5. K. Osthagen and P. Kofstad, *This Journal*, **109**, 204 (1962).
6. B. Cox and B. R. Harder, *ibid.*, **110**, 1110 (1963).

The Mechanical Properties of Thin Anodic Films on Aluminum

D. H. Bradhurst[1] and J. S. Llewelyn Leach

Department of Metallurgy, Imperial College of Science and Technology, London, England

ABSTRACT

The measured stresses associated with the growth of oxide on the surface of aluminum are much lower than those calculated from the Pilling-Bedworth ratio. The magnitude of the stresses in alumina formed anodically on pure aluminum is shown to be dependent on the rate of formation. Some experiments are described which show that, even at low temperatures, the presence of a large ionic flux will permit the deformation of alumina providing a mechanism by which the growth stresses can be relieved.

The degree of protection against corrosion or oxidation afforded by the oxide film on a metal surface depends in part on its integrity, its thickness, and on the diffusion constants in the oxide.

The ultimate thickness to which an oxide film may grow before it cracks, *i.e.*, the protective thickness, depends on its ability to withstand or relieve the stresses which may arise during growth. If the accumulated stress exceeds the strength of the film, cracking or detachment will occur resulting in an increase in the corrosion rate.

In order to improve corrosion resistance by increasing the protective thickness of the oxide film, data are required both on the stresses which are produced during film growth and on the mechanical properties of oxide films. Considerable effort has been directed toward understanding the diffusion processes, for example in the Wagner-Hauffe (1) theory of oxidation. However, attempts to investigate experimentally the factors influencing the protective thickness to which an oxide grows have been few (2, 3).

Anodic films on aluminum are especially suited to initial studies in this field due to the ease with which films having reproducible properties may be formed and separated from the metal. In addition, the relatively low mechanical strength of pure aluminum makes it possible to study the mechanical properties of the oxide while it is still attached to the metal. The mechanical properties of these films are substantially different from the bulk material (4); it was therefore essential to make measurements directly on oxide rather than to attempt the extrapolation from the known properties of oxides in bulk.

This paper describes experiments made to measure the stresses in anodic films under different conditions of growth and some observations which support the concept that plastic deformation of a growing oxide film may occur at room temperature, if the ionic diffusion is sufficient. The stresses in the oxide were calculated from measurements of the bending of aluminum foils anodized on one side only while the evidence for low-temperature plasticity was obtained from measurements of the deformation of thin wires covered with a layer of oxide.

Experimental

The aluminum, on which the anodic films were formed, was 99.99% pure and in the form of wire 0.01 cm diameter or foil 0.005 cm thick.

Foil specimens were prepared by cutting to form parallel-sided strips either 6.00 or 8.00 cm in length which were then lightly rolled to remove the burred edge and finally annealed. The surfaces of the specimens were de-oxidized in chromic-phosphoric acid solution, etched in sodium hydroxide solution, washed in distilled water, and allowed to dry.

An electrical contact was made to one end of the strip which was then mounted in a glass tube using a cold setting resin. One side of the specimen was coated with Lacomit, a flexible lacquer, and allowed to dry.

Deflections of up to 0.4 cm were measured to a precision of $\pm$ 0.001 cm. However, reproducibility was not good. At a current density of 1 ma/cm^2 deflection *vs.* oxide thickness curves were reproduced to within about $\pm$ 20%. This figure was probably greater at lower current densities, although a precise estimate of the variation was not made in these experiments.

The annealed aluminum wires of lengths between 9 and 15 cm were mounted, using the cold setting resin, in tubular glass end-pieces. Some wires were mounted with only the air-formed oxide film on them and these are described as "clean" wires. Other wires, before mounting, had been anodized to produce thick (3000Å) oxide films. These films were formed in ammonium borate solution (*p*H 9.7) at a constant current density of 5 ma/cm^2 up to the required voltage (v), usually 200v. This was then held constant for 5 min by which time the current had decayed to a small value and the oxide thickness (θ) was given by the relation $\theta = 15v$ Å. The constancy of this relation was checked, using foil specimens, by measurements of surface capacity.

During measurements on foils the anodic oxide films were formed at constant current density. The values of current density and the solutions used varied from test to test but, with the exception of interruptions necessary for measurements of the zero field deflection, constant current conditions were used throughout any one test. In addition to the ammonium borate solution similar to that used for anodizing the wires, two 3% ammonium citrate solutions of *p*H 6 and 9.7 (adjusted with ammonium hydroxide) were used during stress measurements on the foils.

In order to determine the stress in the oxide film from the observed bending of the foil during anodizing, the force required to deflect the strip was measured by means of a sensitive torsion balance. The stress, S, within an oxide film grown on the exposed surface of the strip can be calculated from the expression

$$S = \frac{2F \cdot l}{A\,(t-d)} \qquad [1]$$

where F is the force required to bend the strip a given distance (obtained from the torsion balance measurements), l is the length of the strip of thickness t, and A the cross-sectional area of the oxide film of thickness d. Alternatively, the expression

$$S = \frac{E \cdot t^2 \cdot x}{3\,l^2 \cdot d} \qquad [2]$$

[1] Present address: Australian Atomic Energy Commission, Research Establishment, Sutherland, New South Wales, Australia.

may be used, where E is the Young's modulus of aluminum, and x the deflection of the end of the strip.

The techniques used for the measurements of the mechanical properties of anodic oxide films under static conditions, *i.e.*, when negligible ionic diffusion is present in the film, have been described previously (4). For measurements of the deformability of oxide films during growth, the following technique was used.

Stress-strain curves were obtained for both clean and anodized wires, using an "Instron" hard beam recording tensometer. Similar anodized specimens were then mounted as for the tensile tests, but re-immersed in the anodizing solution, and loaded by hanging a weight on the lower glass end-piece so that the load corresponded to a known point on the stress-strain curve. A small anodic current was then passed which was recorded together with the voltage. The additional extension of the wire, if any, was observed using a travelling microscope focussed on the end of the wire. The current density was increased in steps, the voltage, current, and extension being continuously observed. Experiments were made to determine both the critical load, and the critical current at which additional extension of the wires occurred.

Results

Stresses in the oxides.—Two main factors were found to influence the deflection of the aluminum strips during anodic oxide growth. The primary factor was the stress inherent in the film, but superimposed on this was a voltage dependent deflection which always acted on the strip in such a way as to indicate an apparent compressive stress in the oxide film. In order to eliminate this "electrostatic" effect, deflection measurements were made at zero field, by switching off the current and allowing the strip to come to rest under the influence of the stresses in the film.

Both methods already outlined for the calculation of stress were used, and the results are compared in Fig. 1, which shows the deflection with and without the applied field for an aluminum strip anodized at 3.3 ma/cm^2 current density. The deflection is plotted as a function of the film thickness (which is proportional to the anodizing voltage). The stress in the film calculated from Eq. [1] and [2] is shown on the same axes. The similar values of stress obtained by both methods show that the Lacomit protective layer does not alter the elastic properties of the aluminum strip to any significant extent at these small deflections.

The stress in the oxide calculated from the deflection of the foils was in general not a function of the thickness of the oxide and in many cases was nearly constant. In some experiments, however, the stress appeared to decrease as the oxide thickened, as in Fig. 1, and in others the stress increased as the oxide thickness increased. In view of this lack of consistency the data have been presented in the form shown in Fig. 2 where the vertical lines on the stress axis represent the total range of stress observed in each experiment for oxide films of thicknesses within the range 150-3000Å. These results are shown in Fig. 2 as a function of the current density used for anodizing.

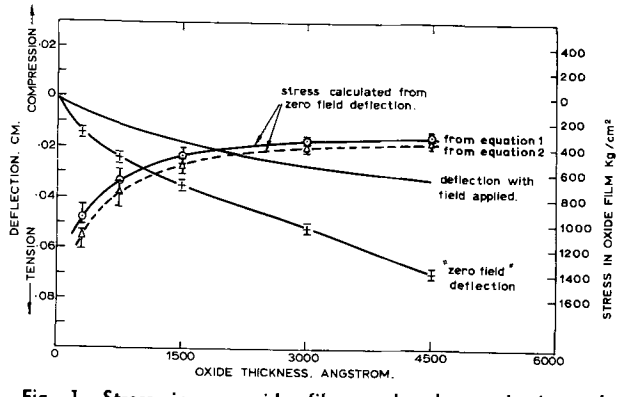

Fig. 1. Stress in an oxide film produced on aluminum by anodizing in ammonium borate solution (pH 9.7) at 3.3 ma/cm^2. Stress was calculated using Eq. [1] (calibration) and Eq. [2] (theoretical).

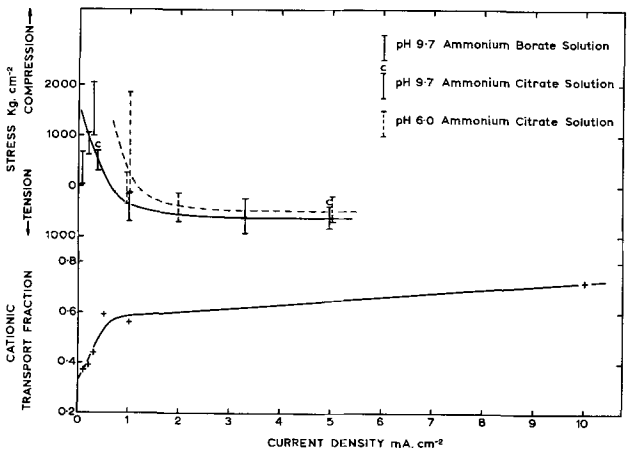

Fig. 2. Curve 1, stress in anodic oxide films on aluminum as a function of current density of formation (in ammonium borate and ammonium citrate solutions); curve 2, fraction of cationic transport in oxide films on aluminum as a function of current density of formation [determined by Davies et al. (6)] in ammonium citrate solution.

It may be seen that the current density is important in determining the nature of the stress developed in the film. At low current density there is a greater tendency for compressive stress to develop. The results shown for 3% solutions of ammonium citrate and ammonium borate of *p*H 9.7 are similar. The results obtained for 3% ammonium citrate solution (of unadjusted *p*H 6) also exhibit a similar trend, but the current density at which stress reversal occurs appears to be somewhat higher than for the more alkaline solutions.

Davies *et al.* (5, 6) have shown that during anodic oxidation of aluminum in ammonium citrate solution the relative amounts of the two ionic species diffusing in the oxide are dependent on the rate of oxidation. The anodic films referred to in Davies' work were formed in 3% ammonium citrate solution which was the electrolyte used for the stress measurements shown as dotted lines in Fig. 2. His results (6), expressed as the cationic transport fraction, are included in Fig. 2 for comparison with the stress data.

The measurements of stresses in anodic oxide films reported by Vermilyea (7) are in qualitative agreement with the results obtained in the present work. The effect of the forming voltage on the measured stress is qualitatively the same for both investigations. The effect of rate of formation of the oxide on the stresses observed is also noted by Vermilyea, but a detailed investigation and interpretation was not attempted.

Deformation of the oxides.—The results of the deformation experiments during anodic growth are shown in Fig. 3 and 4. The results of a typical experiment appear in Fig. 3 in which the extension of a previously anodized wire, loaded with 35.5g, is shown as a function of time during the course of further anodizing. The current density was increased in steps, rapid deformation commencing only when the current density exceeded the leakage current density. During such an experiment the voltage across the film usually did not exceed 240v and was always less than the dielectric breakdown voltage which, under these conditions, is about 350-400v.

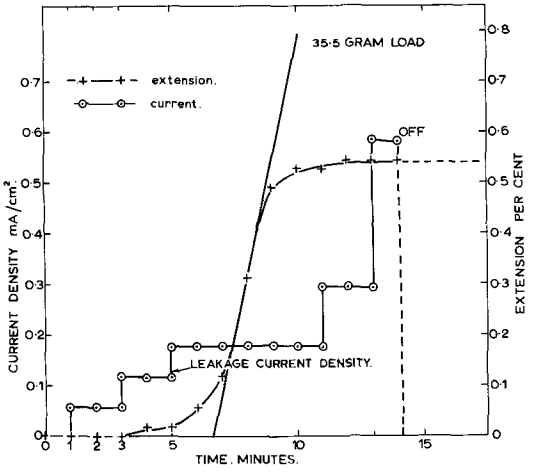

Fig. 3. Extension of a loaded anodized wire as a function of time as the anodic current is increased.

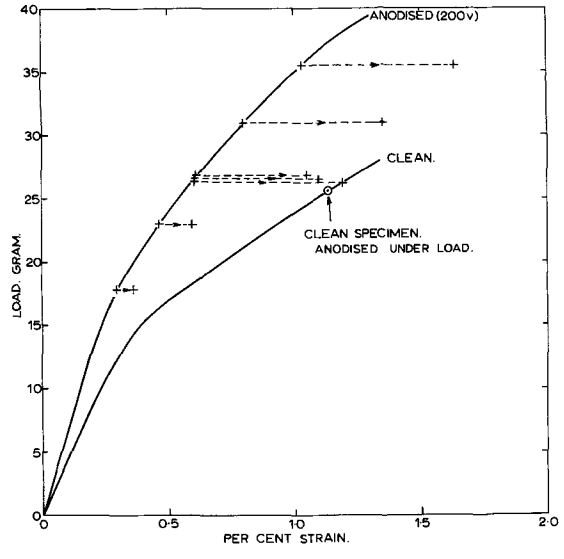

Fig. 4. "Additional" extension produced by passing anodic current through anodized wires under tensile load.

The extension recorded in this experiment together with data from other experiments are shown in Fig. 4 as a function of load; each dotted line represents one experiment. The load, voltage, and current data for each experiment are given in Table I.

Changes in the length of the wire due to grown-in stresses in the oxide may be shown to be small compared with the extensions observed. Experimentally this was demonstrated by anodizing two freely suspended wires of similar length to the test specimens. Measurements at current densities of 0.1 and 5 ma/cm² showed that no significant change in length of the wires occurred.

A blank experiment was carried out on a clean wire loaded at 26.6g. No extension occurred during a period of 1 hr during which anodizing was carried out at different current densities in the range from 0.125 to 7.5 ma/cm².

Discussion

Stress measurements.—Stresses in growing oxide films are sometimes assumed to arise from the volume change which occurs when a specific quantity of metal is converted into metal oxide. Experimental evidence shows that this is an oversimplification and that in many instances other factors may partly or wholly determine the nature and magnitude of the stress which develops in a growing oxide film. These factors include the nature of the diffusing ionic species involved in the film formation, epitaxy, surface roughness, and residual stresses in the metal. The evidence obtained from the present experiments supports the suggestion that the nature of the diffusing species is of primary importance in determining the stress in oxide films.

Table I. Load, voltage, and current data for results appearing in Fig. 4.

Effective load, g	Current density for deformation, ma/cm²	Leakage current density, ma/cm²	Maximum voltage reached, v
35.5	0.125-0.16	0.125	220
31	0.12-0.18	0.14	212
26.6	0.08-0.33	0.10	215
26.6	0.10-0.19	0.13	222
23	0.24-0.33	0.11	225
16.8	1.36-2.72	0.1	275
16.8	7.0	probably 0.1	275
26.6	7.5		350
26.6*	0.125-7.5	0.125	350

* "Clean wire" experiment.

The specimens used in these experiments were chemically polished and annealed, and the anodic film produced is known to be extremely fine grained. Stresses within the film arising from surface roughness and residual stresses were therefore minimized and epitaxial stresses confined to a few atom layers. As the volume ratio for aluminum oxide is greater than 1, compressive stress is expected if it can be shown that film growth proceeds by the inward diffusion of oxygen. A rough calculation of the magnitude of this compressive stress may be made under these conditions. The linear elastic strain at the metal oxide interface is given by $\sqrt[3]{V_R}$ where V_R is the volume ratio for γ-alumina ($= 1.28$). This corresponds to a linear strain of 0.0857 and a stress of 36,000 kg/cm² [Young's modulus for the film is 4.2 x 10^5 kg/cm² (4)].

The observation of compressive stress at low current density appears qualitatively consistent with this model, although the observed compressive stress (up to 2000 kg/cm²) is much less than the calculated value. The work of Davies *et al.* (5, 6) seems to offer a possible explanation. There it was shown that, at low current density (0.1 ma/cm²), the anodic film formed on aluminum predominantly by oxygen movement although cations did pass into solution. At higher current densities the proportion of cationic movement increased as shown in Fig. 2, and it also contributed to the film formation. At the low current density the requirement for film formation by the inward diffusion of oxygen is fulfilled, thus giving rise to the compressive stress as observed. The occurrence of tensile stress in the aluminum oxide films formed at the higher current densities suggests that the volume ratio is no longer the predominant stress-determining factor under conditions where the film forms by the movement of both ions. Oxide formed by movement of metal ions would be expected to form without restraint at the oxide-environment interface and to be relatively free of stress.

Furthermore, it seems reasonable that the low values of compressive stress might be explained in terms of the cationic movement through the oxide film even at low current density. There are now many instances (7-9) in the literature where the concept of two moving species has been invoked to explain oxidation phenomena.

A second possible explanation, namely, the occurrence of plastic deformation of the oxide film in the crystallographic sense, seems at first sight very unlikely at room temperature due to the absence of sufficient thermal activation to allow movement of dislocations or of lattice ions. However, during oxidation there is a significant ionic flux, which in the case

of anodic oxidation is field-activated and related to the ionic current flowing. The results of the experiments on thin wires suggest that deformation of the oxide by a creep mechanism must be considered possible under conditions where a sufficiently high ionic current is passing through the oxide film as can occur during anodic growth.

Oxide deformation experiments.—The influence of the presence of a thin oxide film on the mechanical properties of aluminum has been considered by a number of workers including Barrett (10) and Holt (11). Two effects are recognized. The first, for very thin films, operates by pinning surface dislocation sources, thereby increasing the elastic strain which the underlying metal can tolerate before yielding. In the second type, of which the present results are an example, the whole stress-strain curve is raised as may be seen in Fig. 4. In this case the film is thick enough to act not only in pinning surface dislocation sources but also as a barrier preventing the escape of dislocations having internal sources. The series of extensions indicated as dotted lines in Fig. 5 show how the influence of the film is removed during the passage of an ionic current slightly in excess of the experimentally determined "critical" value. Deformation of the film undoubtedly occurred during extension of the wires since cracking of the film would have been accompanied by a transient voltage drop due to the finite quantity of charge required to heal the crack by anodizing. No such transients were observed, and it seems likely from previous work on the mechanical breakdown of these films (4) that the sensitivity of this method would have been sufficient to detect any cracks formed.

Creep deformation of alumina in bulk is not normally significant at temperatures less than 1000°C (10). However, during anodic oxidation the current density may be sufficient for the ionic diffusion flux in the direction of the applied field to equal that attained by thermal diffusion at a much higher temperature.

Nabarro (12) has derived an equation for the creep rate ds/dt resulting from thermal motion of single ions in a lattice. The expression

$$\frac{ds}{dt} = \frac{D P a^3}{A^2 kT} \qquad [3]$$

involves the diffusion coefficient D, the applied stress P, the volume of a vacancy a^3, and the grain size A. In the form given the equation applies only when $Pa^3/kT < 1$.

Such a relation implies that the ionic movement is thermally activated whereas in the present case of anodic oxidation the ionic movement is primarily field activated. In order to employ this equation to interpret the present results, it is necessary to eliminate D from the equation and to incorporate a term involving the ionic current.

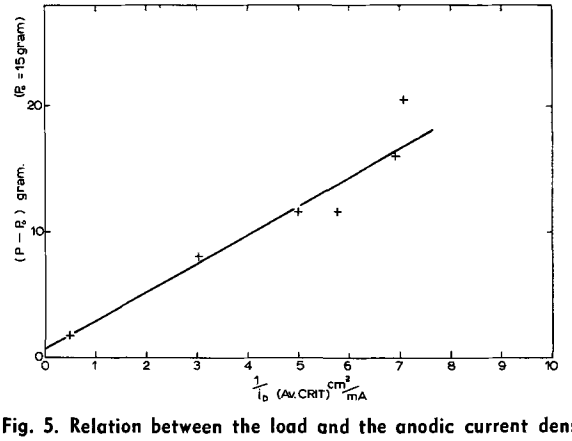

Fig. 5. Relation between the load and the anodic current density for initiation of extension.

The equation for ionic conduction in the presence of a high field has been shown to have the form

$$J = 2qan\nu \exp\frac{-W}{kT} \exp\frac{+qaE}{kT}$$

where W is the height of the activation barrier for ionic movement, q, a, and E are the ionic charge, the jump distance, and the applied field, n is the number of moving ions per cubic centimeter, and ν is the vibration frequency of a lattice ion.

The thermally activated diffusion coefficient D is given by the equation

$$D = \frac{1}{6} a^2 \nu \exp\left(\frac{-W}{kT}\right)$$

In the present circumstances additional diffusion arises from field activation, and it is suggested that an enhanced diffusion coefficient should be used defined as

$$D = \frac{1}{6} a^2 \nu \exp\left(\frac{-W}{kT}\right) \exp\left(\frac{qaE}{kT}\right)$$

The resulting equation for the deformation rate has the form

$$\frac{ds}{dt} = \frac{a^4 PJ}{12A^2 kTnq}$$

which shows that the deformation rate should be proportional to the product PJ and terms which are approximately constant for a given material and temperature.

In the present experiments it has not been found possible to show a relation between the rate of deformation, the current, and the load. In the deformation equation as formulated, J represents the ionic flux whereas the currents shown in Fig. 3 are total currents and the leakage current densities in Table I are those for zero oxide growth. The relatively large and to some extent irreproducible leakage current leads to uncertainty in the true value of J, particularly at low current densities. Experimentally, it is found that the current density required to initiate the additional extensions is inversely proportional to the applied load as seen in Fig. 5.

It might be expected that, in a material such as alumina which contains two ionic species, both species must diffuse to permit deformation. In the present experiments it has only been possible to show that at high stresses the minimum current for deformation approaches the leakage current below which no oxide is formed and presumably no ions move. Davies (5, 6) has shown that, even at very low rates of anodic oxide formation, there is some movement of cations even though the formation of the oxide occurs exclusively by anionic movement. Thus this system does not seem suitable for testing whether or not deformation can occur with only one ion diffusing.

In the present experiments the stresses which were relieved by diffusion were tensile in character. However, there seems to be no appropriate reason why the compressive stresses which should result from anionic movement in the oxidation of these metals could not be relieved by similar processes.

In previous studies (4) it was shown that the deformability of anodic oxide films at room temperature and in the absence of a diffusion flux was considerably greater than that of the oxide in bulk. This deformation which was shown to be entirely elastic was as large as 2%. This is greater than the largest total extension measured in the present work, independently supporting the suggestion that the additional extension observed is not due to fracture of the oxide.

The small grain size of this anodic oxide (13), which may account for properties previously reported (4), also provides ample internal surface to which the dif-

fusing ions may be added to allow extension or from which they may be removed to allow compression of the oxide film.

The results of the present experiments show that, in the presence of an ionic diffusion flux, the mechanical properties of the oxide film are still further changed from those of the bulk material. Thus measurements made of the plasticity of oxides in bulk and in the absence of the large fluxes of ions associated with oxidation processes are of little help and can be misleading when applied to the solution of oxidation problems. It is interesting to consider the possibility of deliberately enhancing the ability of these oxides to relieve the grown in stresses and thus improve their protective nature by increasing the protective thickness.

Acknowledgments

The authors wish to thank Professor J. G. Ball for his support throughout this work and for the provision of laboratory space in his department. The financial support for the work and the provision of a stipend for one of them (D.H.B.) by the Central Electricity Generating Board is also gratefully acknowledged.

Manuscript received Dec. 21, 1965.

Any discussion of this paper will appear in a Discussion Section to be published in the June 1967 JOURNAL.

REFERENCES

1. K. Hauffe, *Progr. in Metal Phys.*, **4**, 71 (1953).
2. A. Y. Nehru, Ph.D. Thesis, London (1963).
3. N. B. Pilling and R. E. Bedworth, *J. Inst. Metals*, **29**, 529 (1923).
4. D. H. Bradhurst and J. S. Ll. Leach, *Trans. Brit. Ceram. Soc.*, **62**, 793 (1963).
5. J. A. Davies, J. P. S. Pringle, R. L. Graham, and F. Brown, *This Journal*, **109**, 999 (1962).
6. J. A. Davies, J. Domeij, J. P. S. Pringle, and F. Brown, *ibid.*, **112**, 675 (1965).
7. D. A. Vermilyea, *ibid.*, **110**, 345 (1963).
8. E. C. Potter and G. M. W. Mann, 1st International Congress on Metallic Corrosion, p. 417, Butterworths, London (1961).
9. U. R. Evans, *This Journal*, **110**, 1290 (1963).
10. C. S. Barrett, P. M. Aziz and I. Markson, *J. Metals*, **5**, 1655 (1953).
11. D. B. Holt, *Acta Met.*, **10** [11], 1021 (1962).
12. F. R. N. Nabarro, Report on the Conference on the Strength of Solids, Bristol 1947, pp. 75-90, Physical Society (1948).
13. H. G. Wilsdorf, *Nature*, **168**, 600 (1951).

Diffusion Coefficients, Oxygen Activities, and Defect Concentrations Across a p-Type Oxide Layer on a Metal

F. S. Pettit

Advanced Materials Research and Development Laboratory, Pratt & Whitney Aircraft, Division of United Aircraft Corporation, North Haven, Connecticut

ABSTRACT

Oxygen activities, diffusion coefficients of metal ions, and defect concentrations across an oxide layer on nickel, cobalt, iron, and manganese have been determined from the parabolic rate constants for growth of the oxide on the metal in different pressures of oxygen. Theoretical expressions are presented which account for the observed results.

During the oxidation of a metal where a dense, thick, adherent oxide is formed and the oxide thickness increases in accordance with the parabolic rate law, the oxide composition varies from that of the oxide in equilibrium with the metal to that of the oxide in equilibrium with the gas. Consequently, within the oxide layer, parameters such as diffusion coefficients, activities of metal and oxygen, and the concentration of atomic defects change continuously from the metal/oxide interface to the oxide/gas interface. The purpose of this paper is to show that, for cases where the oxidation rate is pressure dependent (*i.e.*, cation deficient oxides), one may use equations derived by Wagner (1) to obtain diffusion coefficients, oxygen activities, and the concentration of atomic defects across the oxide layer by determining parabolic rate constants for growth of the oxide in fixed pressures of oxygen.

Theoretical Considerations

Metal deficit oxides on metals are usually formed by diffusion of metal ions and electron holes across the oxide with the slower moving cations determining the oxidation rate. The diffusion coefficient of oxygen is usually small compared to that of metal and the flux of oxygen ions can be neglected. For thick oxide layers where the effect of space charge boundary layers is negligible, Wagner (1) has shown that the flux of metal ions and the flux of electron holes across the oxide can be written as

$$\tilde{j}_M = -(\tilde{C}_M D^*_M/RT)\left(\frac{d\mu_M}{dx} + z_M F \frac{d\rho}{dx}\right) \quad [1]$$

$$\tilde{j}_\oplus = -(\tilde{C}_\oplus D^*_\oplus/RT)\left(\frac{d\mu_\oplus}{dx} + F\frac{d\rho}{dx}\right) \quad [2]$$

where the symbols are as follows:

$\tilde{j}_M$, $\tilde{j}_\oplus$ the flux of metal ions and the flux of electron holes, respectively, in equivalents per unit area; per unit time.

$\tilde{C}_M$, $\tilde{C}_\oplus$ the concentration of metal ions and electron holes, respectively, in equivalents per unit volume.

D^*_M, $D^*_\oplus$ the self-diffusion coefficient of metal ions and electron holes, respectively (cm^2/sec).

μ_M, $\mu_\oplus$ the chemical potential of metal ions and electron holes, respectively (cal/mole).

z_M the valence of the metal ion (eq./mole).

F Faraday constant (cal/eq. volt).

ρ the electrical potential (volts).

R the gas constant (cal/mole-deg).

T absolute temperature.

x reaction coordinate across the oxide layer (cm).

In view of electroneutrality requirements, $\tilde{j}_\oplus = -\tilde{j}_M$. Thus on rearranging Eq. [1] and [2] and then sub-

tracting Eq. [2] from Eq. [1], the expression for the flux of metal ions may be written as

$$\tilde{j}_M = -(1/RT)\left(\frac{\tilde{C}_M D^*_M \tilde{C}_\oplus D^*_\oplus}{z_M \tilde{C}_M D^*_M + \tilde{C}_\oplus D^*_\oplus}\right)\left(\frac{d\mu_M}{dx} - z_M \frac{d\mu_\oplus}{dx}\right) \quad [3]$$

For an electronic conductor, $D^*_M << D^*_\oplus$. Furthermore, within the oxide, the following relations are valid

$$\mu^o_M = \mu_M - z_M \mu_\oplus \quad [4]$$

$$d\mu^o_M = -(z_M/z_o)\, d\mu_o \quad [5]$$

where μ^o_M and μ_o are the chemical potentials of metal and oxygen, respectively, and z_o is the valence of oxygen. Substitution of Eq. [4] and [5] into Eq. [3] yields

$$\tilde{j}_M = (z_M \tilde{C}_M D^*_M / z_o RT)\, d\mu_o/dx \quad [6]$$

or

$$\int_o^x \tilde{j}_M\, dx = (\tilde{C}_M)\int_{a'_o}^{a_o} (z_M D^*_M/z_o)\, d\ln a_o \quad [7]$$

where a'_o is the activity of oxygen at the metal/oxide interface (*i.e.*, $x = 0$) and a_o is the oxygen activity in the oxide layer at a distance x from the metal/oxide interface. In view of Eq. [7], one may write

$$\int_o^x \tilde{j}_M\, dx \Big/ \int_o^{x_T} \tilde{j}_M\, dx = \tilde{C}_M \int_{a'_o}^{a_o} (z_M/z_o) D^*_M\, d\ln a_o \Big/ \tilde{C}_M \int_{a'_o}^{a''_o} (z_M/z_o) D^*_M\, d\ln a_o \quad [8]$$

where x_T is the total oxide thickness and a''_o is the oxygen activity at the oxide/gas interface. The integrals on the left-hand side of Eq. [8] can be integrated provided $\tilde{j}_M$ is independent of x. This will be the case for oxides with small homogeneity ranges. Furthermore, according to Wagner's theory of metal oxidation (1) the numerator and denominator on the right-hand side of Eq. [8] are equal to the "rational rate constant," k_r, for growth of the oxide in atmospheres with oxygen activities of a_o and a''_o, respectively. The rational rate constant and the parabolic rate constant, k_p are interrelated by,

$$k_r = z^2_o \tilde{V}\, k_p / 2M^2_o \quad [9]$$

where $\tilde{V}$ is the equivalent volume of the oxide, and and M_o is the molecular weight of oxygen. k_p is defined as

$$(\Delta m/A)^2 = k_p\, t \quad [10]$$

where $(\Delta m/A)$ is the weight gain per unit area and t is the time. Substitution of Eq. [9] into Eq. [8] and integration of the left-hand side of Eq. [8] yields

$$x/x_T = k_p^{(a_o)}/k_p^{(a''_o)} \quad [11]$$

where $k_p^{(a_o)}$ and $k_p^{(a''_o)}$ are parabolic rate constants for oxidation of the metal in gas atmospheres with oxygen activities of a_o and a''_o, respectively, and the quantity (x/x_T) is a normalized reaction coordinate. For a given temperature, one may determine k_p experimentally at different oxygen pressures over the interval a'_o to a''_o, and Eq. [11] can then be used to determine (x/x_T) for specific values of a_o. From this information the oxygen activity across an oxide layer formed in a gas with an oxygen activity of a''_o can be obtained. Furthermore, if the concentration of atomic defects as a function of a_o is known, the defect concentration across the oxide layer can also be determined.

Finally, the variation of the self-diffusion coefficient across the oxide layer can be determined if D^*_M is known as a function of a_o. From the definition of the "rational rate constant" and Eq. [9], k_p can be written as

$$k_p = 2(M_o/z_o \tilde{V})^2 \int_{a'_o}^{a_o} (z_M/z_o) D^*_M\, d\ln a_o \quad [12]$$

For a given temperature a'_o is constant and Eq. [12] can be differentiated with respect to a_o for constant a'_o (2, 3). This differentiation yields

$$(dk_p/d\ln a_o)_{a'_o} = 2(z_M/z_o)(M_o/z_o \tilde{V})^2 D^{*(a_o)}_M \quad [13]$$

where (z_M/z_o) has been assumed to be constant and $D^{*(a_o)}_M$ is the self-diffusion coefficient of metal ions in an oxide with an oxygen activity of a_o. Equation [13] can be used to calculate $D^{*(a_o)}_M$ as a function of a_o providing $(dk_p/d\ln a_o)_{a'_o}$ is known. $(dk_p/d\ln a_o)_{a'_o}$ can be determined by plotting k_p *vs.* $\ln a_o$ and calculating the slope of the resulting curve for given values of a_o.

In the following sections of this paper, parabolic rate constants for the growth of oxides on nickel, cobalt, iron, and manganese will be used to determine self-diffusion coefficients of metal ions, defect concentrations, and oxygen activities across oxide layers on these metals.

Growth of NiO *on Nickel*

Fueki and Wagner (4) have studied the oxidation of nickel and determined parabolic rate constants as a function of oxygen pressure. Their results for a temperature of 1190°C are given in Fig. 1 where the parabolic rate constants are plotted *vs.* the logarithm of

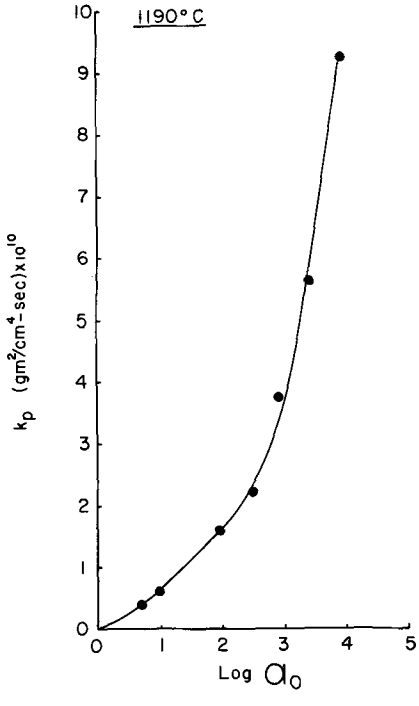

Fig. 1. Parabolic rate constants for the growth of NiO on nickel as a function of oxygen activity in the gas phase. The range of oxygen activities covered correspond to oxygen pressures from the Ni/NiO equilibrium to 1 atm [Fueki and Wagner (4)].

the oxygen activity in the gas phase.[1] (In the present paper unit oxygen activity will be taken for the oxide in equilibrium with the metal as a reference basis, *i.e.*, $a_o = 1$ for metal/oxide equilibrium.) The data presented in Fig. 1 were used with Eq. [11] to determine the normalized reaction coordinate, x/x_T, for specific values of a_o. The results of these calculations, which are presented in Fig. 2, give the activity of oxygen across an oxide layer formed on nickel by oxidation in 1 atm of oxygen at 1190°C. Fueki and Wagner have used Eq. [13] to determine self-diffusion coefficients of nickel in NiO as a function of oxygen pressure. Since the oxygen activity across a layer of NiO on nickel is given in Fig. 2, the results of Fueki and Wagner were used with the data of Fig. 2 to obtain values for the self-diffusion of nickel across a layer of NiO formed on nickel in 1 atm of oxygen at 1190°C. These results are presented in Fig. 2 and show that D^*_{Ni} is a linear function of the normalized reaction coordinate.

Growth of CoO on Cobalt

Pettit and Wagner (5) have studied the oxidation of cobalt at 1150°C and determined parabolic rate constants as a function of oxygen pressure. These data, which are presented in Fig. 3, were used to determine a_o as a function of x/x_T with the help of Eq. [11]. The activity of oxygen across a layer of cobaltous oxide formed on cobalt by oxidation in 1 atm of oxygen at 1150°C is given in Fig. 4. The self-diffusion coefficient of cobalt in cobaltous oxide was obtained as a function of oxygen activity by graphically determining the slope of the curve in Fig. 3, (*i.e.*, $(dk_p/d \ln a_o)_{a'_o}$) for given values a_o, and then $D^{*(a_o)}_{Co}$ was calculated

[1] Fueki and Wagner performed experiments at low oxygen pressures by using CO_2 which contained small amounts of CO. The buffer capacity of such mixtures is poor, and the establishment of the equilibrium oxygen pressure can be questioned because of evolution of CO during the oxidation reaction and because of the presence of a diffusion boundary layer adjacent to the oxide surface. Pettit and Wagner (5) found such effects to be negligible for the oxidation of cobalt in CO_2-CO mixtures containing as little as 2 v/o (volume per cent) CO. The smooth curve formed by the data of Fueki and Wagner (see Fig. 1) suggests that these effects are also negligible for the oxidation of nickel in CO_2 containing 0.25 v/o (volume per cent) CO. Moreover the shape of the curve in Fig. 1 is predominantly fixed by the results obtained in oxygen containing atmospheres. Therefore, the results obtained in CO_2-CO mixtures are not critical in the present paper.

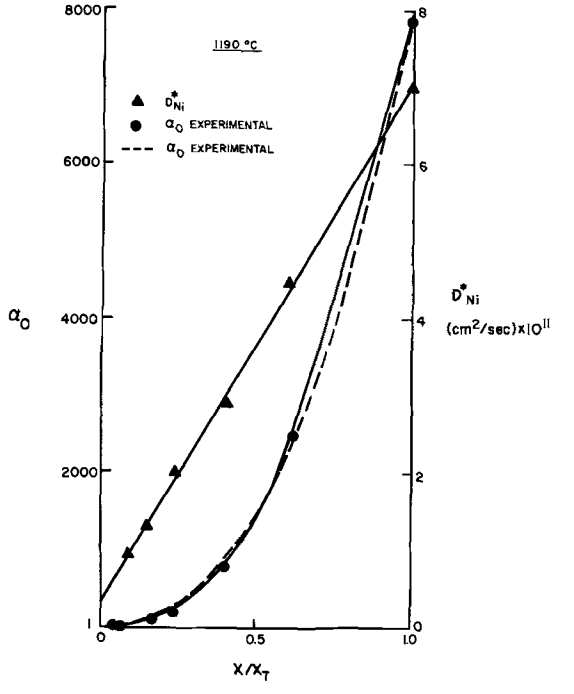

Fig. 2. Oxygen activity and the self-diffusion coefficient of nickel across a layer of NiO formed on nickel by oxidation in oxygen at 1 atm.

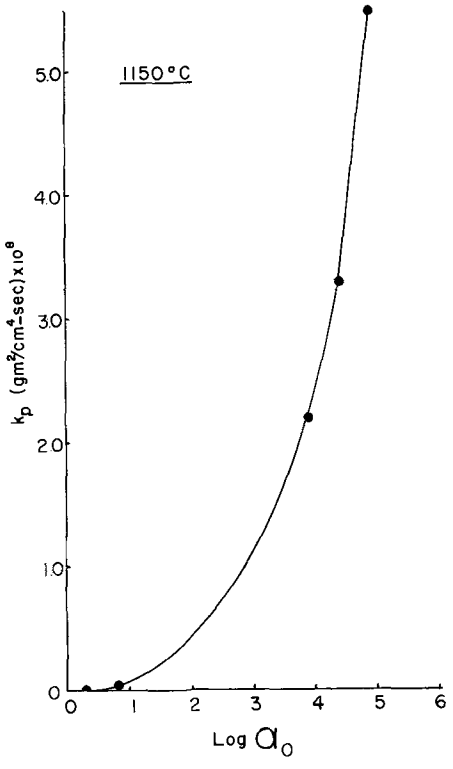

Fig. 3. Parabolic rate constants for the growth of CoO on cobalt as a function of oxygen activity in the gas phase. The range of oxygen activities covered correspond to oxygen pressures from the Co/CoO equilibrium to 1 atm [Pettit and Wagner (5)].

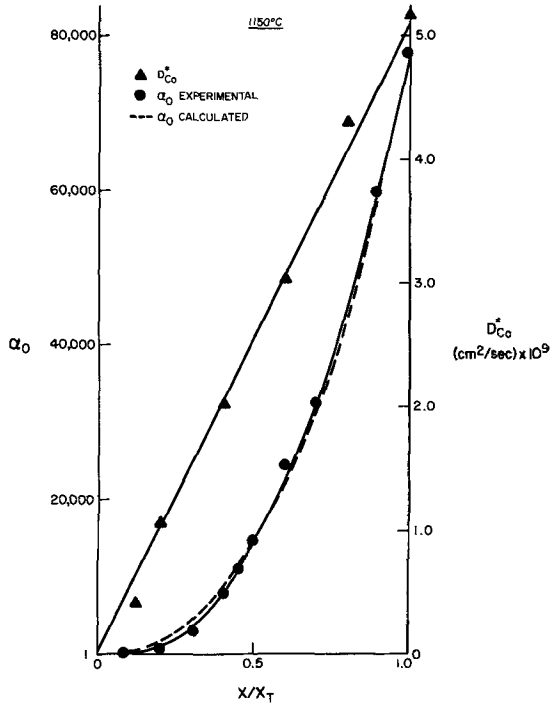

Fig. 4. Oxygen activity and the self-diffusion coefficient of cobalt across a layer of CoO formed on cobalt by oxidation in oxygen at 1 atm.

with the help of Eq. [13]. The results of the calculations are presented in Fig. 4 where D^*_{Co} has been plotted *vs.* the normalized reaction coordinate. It can be seen that D^*_{Co} is a linear function of the normalized reaction coordinate. Self-diffusion coefficients for cobalt in cobaltous oxide have been determined by

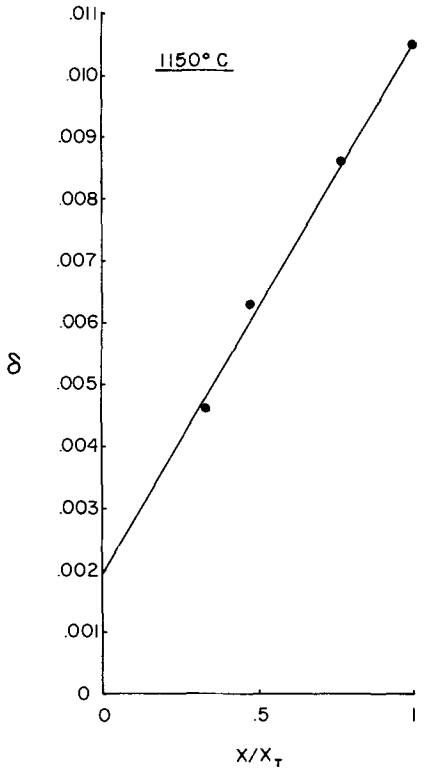

Fig. 5. Cobalt deficit across a layer of $Co_{1-\delta}O$ formed on cobalt by oxidation in oxygen at 1 atm pressure.

Carter and Richardson (6) from measurements using radioactive tracers. A value for D^*_{Co} of 9 x 10^{-9} cm^2/sec was obtained for 1148°C and 1 atm of oxygen. In the present work D^*_{Co} was found to be 5.2 x 10^{-9} cm^2/sec for a temperature of 1150°C and 1 atm of oxygen.

Eror (7) has determined the cobalt deficit, δ, in $Co_{1-\delta}O$ using gravimetric techniques. Eror's results for 1150°C are given in Table I. Eror's data give δ as a function of a_o. Since a_o across the oxide layer is given in Fig. 4, the cobalt deficit across the oxide layer was obtained. The cobalt deficit across an oxide layer formed on cobalt by oxidation in 1 atm of oxygen at 1150°C is presented in Fig. 5. Figure 5 shows that the cobalt deficit is a linear function of the normalized reaction coordinate.

Growth of FeO *(Wüstite) on Iron*

Equation [11] has been obtained for the growth of oxides which have small homogeneity ranges, since it has been assumed that the flux of metal ions is independent of the reaction coordinate. This is not the case for wüstite, since at 1100°C, $Fe_{0.95}O$ is in equilibrium with iron while $Fe_{0.87}O$ is in equilibrium with Fe_3O_4. Therefore, the flux of iron ions near the iron/wüstite interface can be greater than the flux of iron ions near the wüstite/gas interface by as much as 10%. For wüstite, Eq. [11] gives values of x/x_T which are about 10% too large. The error in x/x_T is largest (*i.e.*, 10%) for small values of x/x_T and decreases as x/x_T increases, approaching zero as x/x_T approaches unity. Thus even though wüstite exhibits a large homogeneity range, Eq. [11] can be used as approximation.

Table I. Cobalt deficit, δ, in $Co_{1-\delta}O$ for the oxide in equilibrium with oxygen at 1150°C

δ	P_{O_2}	a_o
0.0046	4.7 × 10^{-2}	3.7 × 10^{3}
0.0063	1.5 × 10^{-1}	1.2 × 10^{4}
0.0086	5.1 × 10^{-1}	4.0 × 10^{4}
0.0105	1.0	7.8 × 10^{4}

Pettit (8) has studied the oxidation of iron in CO-CO_2 mixtures under conditions such that wüstite was the only stable oxide. Parabolic rate constants for the growth of $Fe_{1-\delta}O$ on iron for a temperature of 1100°C are presented in Fig. 6 as a function of oxygen activity in the gas phase. These data were used with Eq. [11] to determine a_o across a layer of wüstite formed on iron by oxidation in a CO-CO_2 mixture with a CO_2/CO ratio equal to 4 (see Fig. 7). The data presented in Fig. 6 were also used with Eq. [13] to determine D^*_{Fe} across the wüstite layer; D^*_{Fe} was found to be 1 x 10^{-7}

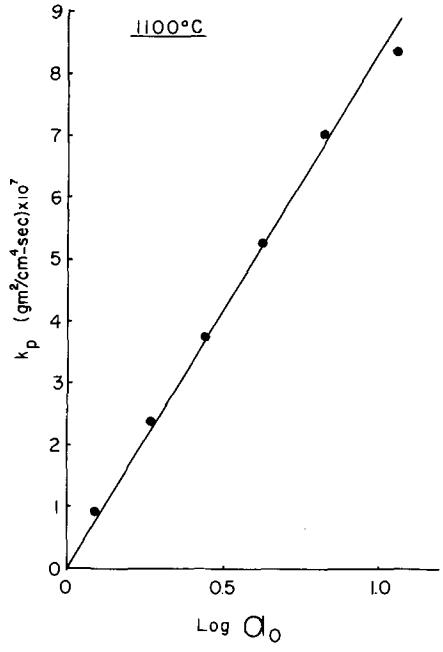

Fig. 6. Parabolic rate constants for the growth of wüstite on iron as a function of oxygen activity in the gas phase. The range of oxygen activities covered correspond to CO_2/CO ratios from 0.36 (*i.e.*, iron-wüstite equilibrium) to 4 [Pettit (8)].

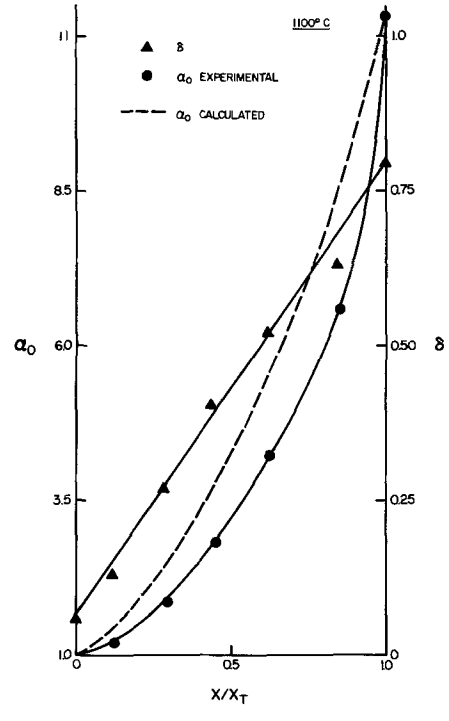

Fig. 7. Oxygen activity and the iron deficit across a layer of $Fe_{1-\delta}O$ formed on iron by oxidation in a CO-CO_2 mixture with CO_2/CO = 4.

cm²/sec for all values of x/x_T, *i.e.*, $Fe_{0.95}O$ to $Fe_{0.88}O$. Levin and Wagner (9) have extrapolated data obtained by Birchenall *et al.* (10) to 1100°C and found D^*_{Fe} to be 0.9 x 10^{-7} and 2.2 x 10^{-7} for wüstite of the composition $Fe_{0.95}O$ and $Fe_{0.91}$, respectively.

Darken and Gurry (11) have determined the iron deficit, δ, in wüstite as a function of a_o at 1100°C. These results along with oxygen activities presented in Fig. 7 were used to obtain δ as a function of the normalized reaction coordinate. As can be seen in Fig. 7, δ is a linear function of the normalized reaction coordinate. Engell (12) used an electrochemical method to measure δ across a FeO layer formed on iron at 900°C and found that δ was a linear function of the reaction coordinate.

Growth of MnO *on Manganese*

Fueki and Wagner (13) have studied the oxidation of manganese in CO-CO_2 mixtures over the temperature interval 800°-1200°C. The oxide layer was found to be MnO, and marker experiments revealed that manganese ions played the major role of material transport in manganese oxide. Parabolic rate constants for the growth of MnO on manganese are presented in Fig. 8 for a temperature of 1100°C. The activity of oxygen and D^*_{Mn} across a layer of MnO formed on manganese by oxidation in a CO-CO_2 mixture with $CO_2/CO = 100$ (*i.e.*, $a_o = 10^{6.64}$) were obtained from these data with the help of Eq. [11] and [13]. The results are presented in Fig. 9. D^*_{Mn} was found to be a linear function of the normalized reaction coordinate.

Discussion of Results

In developing the equations which were used to obtain the preceding results, it was not necessary to make any assumptions with regard to the dependence of D^*_M on a_o. If the self-diffusion coefficient is assumed to be proportional to the concentration of atomic defects which in turn is related to the activity of oxygen by (14)

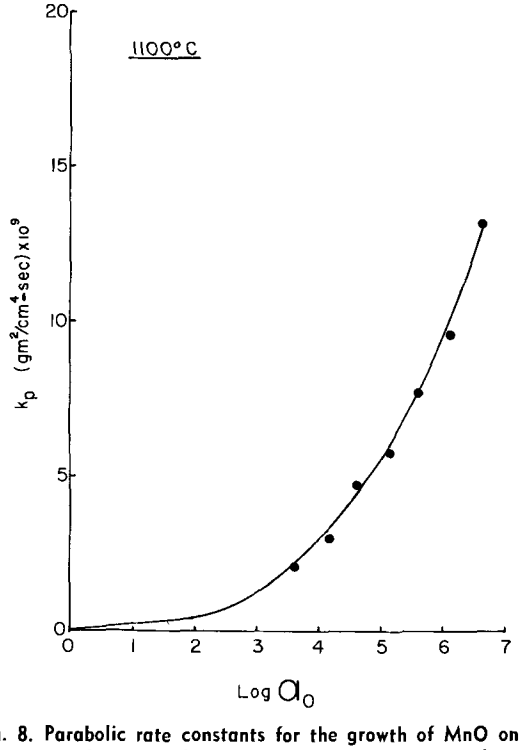

Fig. 8. Parabolic rate constants for the growth of MnO on manganese as a function of oxygen activity in the gas phase. The range of oxygen activities correspond to oxygen pressures from the Mn/MnO equilibrium to the oxygen pressure for a CO-CO_2 mixture with $CO_2/CO = 100$ [Fueki and Wagner (13)].

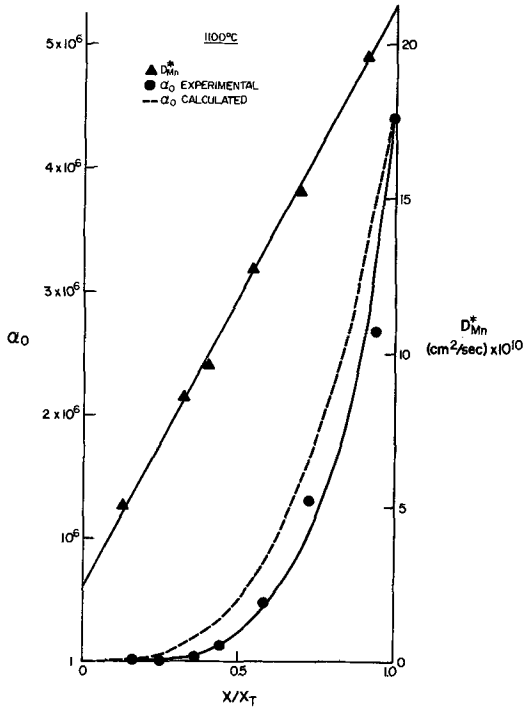

Fig. 9. Oxygen activity and the self-diffusion coefficient of manganese across a layer of MnO formed on manganese by oxidation in a CO-CO_2 mixture with $CO_2/CO = 100$.

$$C_d = C_d^{(o)} a_o^n \qquad [14]$$

then the self-diffusion coefficient can be written as

$$D^*_M = D^{*}_{M}{}^{(o)} a_o^n \qquad [15]$$

where C_d is the concentration of defects in the oxide (*i.e.*, one type of defect mechanism is assumed to predominate; for the oxides under consideration in this paper cation vacancies and electron holes), $C_d^{(o)}$ and $D^{*}_{M}{}^{(o)}$ are the defect concentration and self-diffusion coefficient in an oxide with an oxygen activity of unity and n is a parameter which indicates the degree of association between atomic and electronic defects. In the present discussion n will be assumed to be constant for a given temperature. Substitution of Eq. [15] into Eq. [8], and integration, yields

$$a_o^n = 1 + (a''_o{}^n - 1)x/x_T \qquad [16]$$

If n is known, Eq. [16] may be used to calculate a_o as a function of the normalized reaction coordinate for a given a''_o. The following values of n were used to calculate a_o, 1/2.55 for NiO (4), 1/2.5 for CoO (5), 1/3 for FeO (15), and 1/3 for MnO (13). Calculated and experimental values of a_o across oxide layers on nickel, cobalt, iron, and manganese are compared in Fig. 2, 4, 7, and 9, respectively. Calculated values of a_o for MnO and FeO are slightly larger than experimental values. However, as mentioned previously, Eq. [11] is an approximation for oxides with large homogeneity ranges.

Substitution of Eq. [16] into Eq. [14] and [15] gives the following expressions for the defect concentration and for D^*_M

$$C_d = C_d^{(o)} (1 + (a''_o{}^n - 1)x/x_T) \qquad [17]$$

$$D^*_M = D^{*}_{M}{}^{(o)} (1 + (a''_o{}^n - 1)\, x/x_T) \qquad [18]$$

In Eq. [17] and [18] $C_d^{(o)}$, $D^{*}_{M}{}^{(o)}$, and a''_o are constants and thus C_d and D^*_M should be linear functions of x/x_T. The defect concentration across oxide layers on iron and cobalt are in agreement with Eq. [17]. Furthermore, the self-diffusion coefficients for metal ions across oxide layers on nickel, cobalt, and manga-

nese agree with Eq. [18]. The self-diffusion coefficient of iron across a layer of wüstite on iron was found to be virtually constant in the present study. These results do not agree with Eq. [18] nor with the results obtained by extrapolating the data of Birchenall *et al.* (9) to 1100°C although the value of D^*_{Fe} obtained in the present studies was of the same order of magnitude as the extrapolated values. These results are difficult to explain since atomic disorder in wüstite is complicated (16, 17).

The results obtained for nickel and cobalt show that Eq. [14] and [15] are valid for these systems, and therefore the disorder type in NiO and CoO does not appear to change throughout the oxygen activity range covered by the available data. The results obtained for manganese indicate that these equations are also valid for MnO; however MnO has been found to be an n-type semiconductor at low oxygen activities (7). Even then a metal deficit may be present; however it is also possible that MnO coexisting with the metal contains an excess of the metal. Thus Eq. [14] and [15] cannot be used for MnO because at present there is not sufficient experimental data to present a rational treatment of the oxidation process. Substitution of Eq. [15] into Eq. [12] and integration yields the following expression for the parabolic rate constants of nickel and cobalt

$$k_p = 2\ (M_o/z_o \tilde{V})^2 (D^*_{M^{(o)}}/n)\ (a''^n_o - 1) \qquad [19]$$

If the oxidation rate is expressed in terms of the total oxide thickness (*i.e.*, $x^2_T = 2kt$), then Eq. [19] becomes

$$k = D^*_{M^{(o)}}\ (a''^n_o - 1)/n \qquad [20]$$

For oxygen pressures in the vicinity of 1 atm, $a''^n_o >> 1$ for p-type oxides and Eq. [20] can be written as

$$k/D^*_{M}{}^{(a''_o)} = 1/n \qquad [21]$$

Equations [19], [20], and [21] are equivalent to an equation introduced by Mott and Gurney (18) under the assumption that the defect gradient across the oxide layer was linear. Carter and Richardson (14) have suggested that the Mott and Gurney equation is not valid for the oxidation of cobalt because experimentally determined k/D^*_{Co} ratios did not agree with the theoretical k/D^*_{Co} ratio of 3 which they obtained from the Mott and Gurney equation. Equation [21] shows that for $k/D^*_{Co} = 3$, n must equal 1/3. A value of n equal to 1/3 corresponds to the following reaction

$$Co^{++} + 1/2\ O_2 = CoO + V_{Co} + 2\oplus \qquad [22]$$

where V_{Co} indicates a cobalt vacancy. In other words, k/D^*_{Co} equals 3 only when there is no association of cobalt vacancies and electron holes. If some association occurs, n will be greater than 1/3. In the present study at 1150°C, a value of $n = 1/2.5$ for cobaltous oxide gave oxygen activities which were in good agreement with experimental values. For $n = 1/2.5$, Eq. [21] gives $k/D^*_{Co} = 2.5$ which agrees with the experimental value of 2.59 determined by Carter and Richardson at 1148°C.

Acknowledgments

The writer is indebted to Vincent Nevins for his technical assistance and to H. Schmalzried, J. B. Wagner, Jr., and R. Dils for helpful discussions.

Manuscript received Jan. 5, 1966; revised manuscript received July 19, 1966.

Any discussion of this paper will appear in a Discussion Section to be published in the June 1967 JOURNAL.

REFERENCES

1. C. Wagner, "Diffusion and High Temperature Oxidation of Metals," "Atom Movements," ASM 1951, Cleveland, p. 153 (1951).
2. C. Wagner, *Proc. Internat. Committee Electrochem. Thermodyn. and Kinetics* (CITCE), **7**, 361 (1957).
3. F. S. Pettit, *J. Phys. Chem.*, **9**, 68 (1964).
4. K. Fueki and J. B. Wagner, Jr., *This Journal*, **112**, 384 (1965).
5. F. S. Pettit and J. B. Wagner, Jr., *Acta Met.*, **12**, 41 (1964).
6. R. E. Carter and F. D. Richardson, *Trans. AIME*, **200**, 1244 (1954).
7. N. G. Eror, PhD Thesis, Northwestern University, Evanston, Ill., (1965).
8. F. S. Pettit, Dr. Eng. Thesis, Yale University, New Haven, Conn. (1962).
9. R. Levin and J. B. Wagner, Jr., *Trans. AIME*, **233**, 159 (1965).
10. L. Himmel, R. F. Mehl, and C. E. Birchenall, *ibid.*, **197**, 827 (1953).
11. L. S. Darken and R. Gurry, *J. Am. Chem. Soc.*, **67**, 1398 (1945).
12. H. J. Engell, *Z. Elektrochem.*, **63**, 835 (1959).
13. K. Fueki and J. B. Wagner, Jr., *This Journal*, **112**, 970 (1965).
14. R. E. Carter and F. D. Richardson, *J. Metals*, **7**, 336 (1955).
15. D. M. Smyth, *J. Phys. Chem. Solids*, **19**, 167 (1961).
16. C. E. Birchenall, "The Mechanisms of Diffusion in Solids," "Reactivity of Solids," p. 24, Elsevier Publishing Co., Princeton, N. J. (1961).
17. D. Tannhauser, *J. Chem. Solids*, **23**, 25 (1962).
18. N. F. Mott and R. W. Gurney, "Electronic Processes in Ionic Crystals," p. 257, Clarendon Press, Oxford (1948).

The Parabolic Oxidation Kinetics of Niobium

J. S. Sheasby[1] and G. R. Wallwork

School of Metallurgy, University of New South Wales, Kensington, N. S. W., Australia

and W. W. Smeltzer

Department of Metallurgy and Metallurgical Engineering, McMaster University, Hamilton, Ontario, Canada

ABSTRACT

The rate of growth and properties of the first layer of compact γ-Nb_2O_5 to form are important for elucidation of the oxidation reaction for niobium. It was found possible to maintain this oxide in contact with the metal for sufficient time in the temperature range 720°-825°C to make measurements of its growth rate at various oxygen pressures. This layer, which accounts for the major proportion of the oxygen uptake during the time of its formation, was found to grow at a parabolic rate by a process in which the dominant diffusing species is oxygen. The growth rate of this oxide was highly sensitive to the environmental pressure of oxygen; but it was not pervious to molecular oxygen.

The oxidation of niobium has been studied by many workers and the literature was reviewed recently by Seybolt (1). This metal exhibits unusual oxidation features for at each temperature and pressure the oxidation rate is found to follow a complex series of time laws. However, the reaction rate becomes time independent over the temperature range 400°-1200°C at pressures not too far removed from atmospheric. Particularly at lower temperatures the time independent reaction is usually preceded by a short period of approximately parabolic oxidation behavior.

The defect structure of γ-Nb_2O_5, the modification that forms on specimens oxidized below about 830°C (2, 3) is not well known. However, there is agreement on the basis of marker studies (4) that the most mobile ionic species in this oxide is oxygen. Also, the suboxides, NbO_x and NbO_z, and lower oxides, NbO and NbO_2, have been observed at the metal/oxide interface during oxidation (2, 5-7). During oxidation oxygen dissolves in the metal core of specimens. On the basis of microhardness measurements Klopp *et al.* (6) have calculated the diffusion coefficient of oxygen in niobium.

The parabolic oxidation stage before onset of linear kinetics has been shown by Pawel *et al.* (8) to involve the growth of a protective layer of γ-Nb_2O_5 which cracks at some critical thickness. Kofstad and Kjollesdal (9) further define the linear kinetics as representing a rate-determining transport of oxygen ions through an oxide barrier next to the metal having an approximately constant thickness. This type of mechanism for the transition from parabolic to linear reaction kinetics has been given also in the description of the oxidation behavior of tantalum (10).

A most tractable and important part of the oxidation mechanism appears to be the growth of the first γ-Nb_2O_5 layer. This paper describes an investigation into the growth of this layer where experimental conditions have been selected in order that formation of this compact scale would account for over 95% of the total oxygen consumed by a specimen.

Experimental Procedure

Specimens were cut in the form of squares approximately 1.2 cm^2 from sheets 1 mm thick produced by Fansteel. The hardness of the niobium was V.P.N. 150 (50g load) and the grain size approximately 25μ diameter. Oxidation runs were performed in a conventional all-glass vacuum system with a silica reaction tube using commercial oxygen dried over phosphorous pentoxide.

Experimentation showed that surface preparation of the metal was important. The preparation that was least prone to blistering and hence failure of the oxide formed was abrasion up to 600 grade silicon carbide paper. Above 830°C, the γ-αNb_2O_5 transition appeared to disrupt the oxide layer at an early stage of the reaction.

Niobium oxidizes more heavily on the edges of specimens than on the main faces. Hence, except for short oxidation times at low oxygen pressures kinetic data for a specimen as a whole is not meaningful. The technique used was to oxidize specimens for varying periods of time under different conditions. The rate constants of oxidation were then estimated from scale thickness measurements taken by microscopic examination of polished cross-sections of specimens.

Estimates of specimen self heating upon reaction were made by suspending specimens on 5 mil Pt/Pt-Rh thermocouple wires with the thermocouple bead embedded in the specimen suspension hole. Typically, on lowering a specimen into the hot zone of a furnace at 788°C at an oxygen pressure of 40 Torr the specimen temperature rose 50°C above the furnace temperature. The specimen then cooled to a steady value in about 6 min. To minimize such non-isothermal conditions specimens were oxidized attached to a thermocouple connected to a high-speed recorder. By adjusting the specimen position in the furnace hot zone temperature control within ± 5°C was attained on entry and ± 1°C throughout the reaction.

Results

A series of specimens was oxidized for increasing periods of time at 788°C and 750 Torr oxygen to demonstrate that the first layer of oxide to form on a niobium specimen was protective. Scale thickness measurements are presented in Table I. The evaluations of the parabolic oxidation rate constants for growth of the compact scale from results for these exposures were reproducible within 10%. The rate of γ-Nb_2O_5 scale formation was equivalent to 8.4×10^{-6} $(gO)^2$ cm^{-4} min^{-1} which may be compared to the measured rate of oxygen solution into the metal of

Table I. Thickness of oxide formed on niobium after reaction at 788°C 750 Torr oxygen

Time, min	Oxide thickness, μ	Parabolic rate constant, μ^2/min	Time, min	Oxide thickness, μ	Parabolic rate constant, μ^2/min
5	40.8	334	45	136	402
			60	152	384
20	87.6	383	60	158	365
25	94	354	120	220	403
40	120	360	120	208	361

[1] Present address: Faculty of Engineering Science, University of Western Ontario, London, Ontario, Canada.

Table II. Parabolic rate constants of Nb_2O_5 scale formation

Temperature, °C	Pressure, Torr	Time, min	Oxide thickness, μ	Parabolic rate constant, μ^2/min
825	750	45	162	583
825	750	45	162.8	585
825	100	60	148	365
825	100	60	168	470
825	10	120	140	163
825	10	30	67.5	152
825	1	120	24	4.8
825	1	30	8.3	2.3
788	750	60	149	370
788	100	120	188	294
788	10	200	168	141
788	4	60	66.0	72.6
788	2	120	74.3	46.1
788	1	180	61.8	21.8
768	750	60	114.4	218
768	100	60	98.5	161.5
768	10	120	105.1	92.0
768	1	180	53.8	16.1
720	200	2	13.9	96
720	100	26	37.8	55
720	10	45	35.5	28
720	1	90	36.7	15

$1.4 \times 10^{-9}(gO)^2$ cm^{-4} min^{-1}. Oxidation of the metal was therefore associated predominantly with formation of the oxide scale. As one is restricted to the study of the rate of formation of the first layer of scale, the scale measurement technique is not practical under all oxidation conditions. However, a reasonable range was covered and the values obtained for temperatures in the range 720°-825°C are given in Table II and plotted in Fig. 1.

Oxidized specimens exhibited compact oxide on the main faces surrounded by a frame of cracked oxide. The amount of this edge oxide increased with increasing temperature. In cross-section the black oxide is an almost featureless compact layer, Fig. 2, though at low pressures the oxide/metal interface tended to be irregular and at high temperatures a line of porosity formed beneath the oxide/gas interface, Fig. 3. In polarized light the γ-Nb_2O_5 layer appeared to be composed of columnar grains with the major axis normal to the metal surface, Fig. 4. Scales formed at 760 Torr showed a gradation of color from black at the metal/oxide interface to white at the oxide/gas interface. Scales formed at lower pressures exhibited a greater proportion of dark oxide until at 1 Torr oxygen the scale was completely black. Color gradients evident in polarized light suggested a stoichiometry gradient but this aspect was not pursued when it was found that the ratio of black to white oxide depended on the rate at which a specimen was quenched to room temperature. After etching (11), layers of NbO and NbO_2 could be seen at the metal interface of all the oxidized specimens. These oxides are shown in the taper section of Fig. 5 and their identification was confirmed by x-ray diffraction.

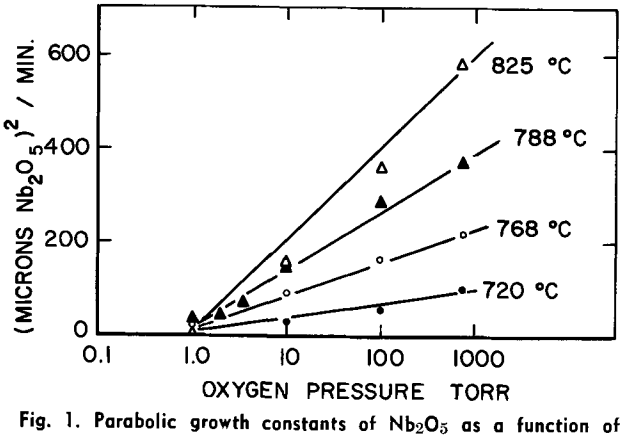

Fig. 1. Parabolic growth constants of Nb_2O_5 as a function of oxygen pressure.

Fig. 2. Cross section of a specimen oxidized for 45 min at 800°C, oxygen pressure 750 Torr. Magnification 75X.

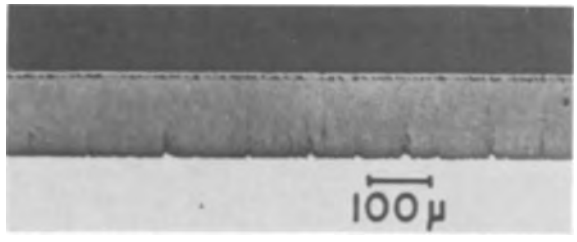

Fig. 3. Cross section of a specimen oxidized for 120 min at 825°C, oxygen pressure 10 Torr. Magnification 100X.

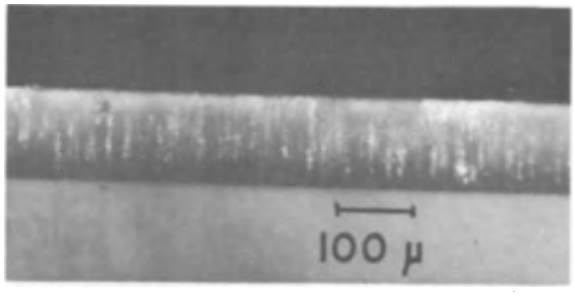

Fig. 4. Cross section in polarized light of a specimen oxidized for 105 min at 800°C, oxygen pressure 10 Torr. Magnification 100X.

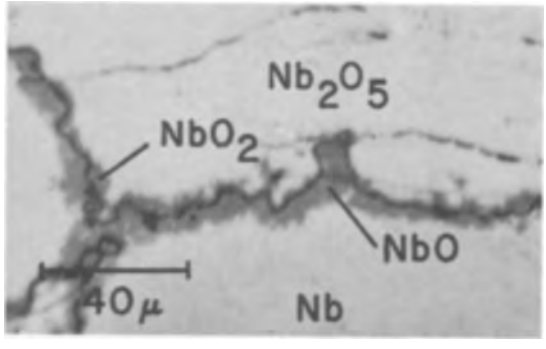

Fig. 5. Taper section of a specimen oxidized for 240 min at 720°C, oxygen pressure 10 Torr. Taper 10:1; etch Ence and Margolin (11) "H", showing γ-Nb_2O_5, NbO_2, NbO, and Nb metal. Magnification 500X.

In so far as could be ascertained by light microscopy, the adherent scales were essentially compact. The mechanism of their growth appeared to be consistent with previous findings for predominant diffusion of oxygen. This was evidenced by the sustained appearance of polishing defects from the initial speci-

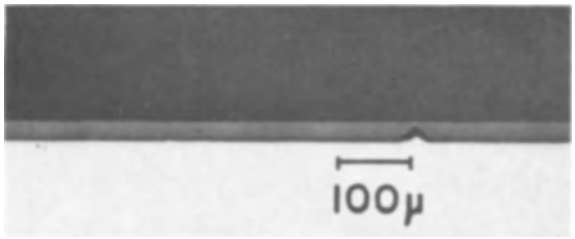

Fig. 6. Cross section of a specimen oxidized for 5 min at 719°C, oxygen pressure 750 Torr. Magnification 100X.

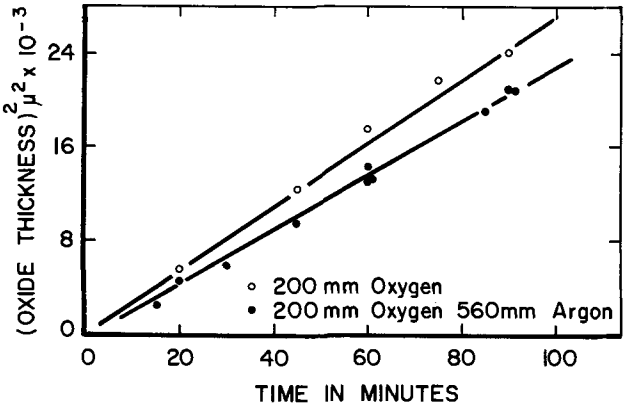

Fig. 7. Oxidation of niobium at 777°C, 200 Torr oxygen. Effect of 560 Torr argon.

men preparation on the free oxide surface of specimens oxidized below 800°C. However, a line of pores was observed in the oxide just beneath the oxide/gas interface, Fig. 3, for specimens oxidized above 800°C.

The scales appeared to be impervious to molecular oxygen. As illustrated in Fig. 6, voids were occasionally seen in an otherwise compact scale. Since the metal interface has not receded as far under the void as elsewhere, the void was acting as a barrier to oxygen transport and not as a short circuit for molecular oxygen. To obtain confirmatory evidence, specimens were oxidized in oxygen atmospheres containing an argon mole fraction of 0.74. If molecular oxygen transport through pores in a scale was playing an effective role in the reaction mechanism, the presence of argon would be expected to markedly reduce the magnitude of the reaction kinetics (10). The plots of the results for this experiment shown in Fig. 7 illustrate, however, that argon had little effect on the magnitude of the parabolic reaction rate.

Discussion

Although the oxidation behavior of niobium under all possible conditions of temperature, oxygen pressure, and specimen geometry is most complex, the formation of a compact γ-Nb_2O_5 scale under well-defined conditions at relatively high temperatures may be represented by a parabolic equation. Relatively minor amounts of oxygen were associated with formation of thin layers of NbO and NbO_2 adjacent to the metal surface and oxygen solution in the metal. Since oxygen solution in the metal core obeyed parabolic kinetics, the occurrence of parabolic γ-Nb_2O_5 scale growth demonstrated that one stage of the oxidation reaction before onset of linear kinetics is an example of a multiphase diffusion process.

The evidence from this investigation, with exception of porosity observed in the scales formed at temperatures above 800°C, suggested that oxygen was the migrating species in the scales. The line of porosity in scales near the oxide/gas interface (Fig. 3) perhaps could be interpreted as showing a minor amount of metal migration. This evidence, nevertheless, is ambiguous for the pores encased in the scale could be caused by formation of voids at the metal/oxide interface during the early stages of the reaction by condensation of vacancies and/or local separation of the scale from the metal by plastic deformation. Accordingly, the present findings substantiate previous marker measurements (4) to the effect that oxygen is the major diffusion species.

Since the parabolic rate constants were unusually sensitive for an ionic transport process to the environmental oxygen pressure (Fig. 1), it was necessary to demonstrate that the apparently compact scale was impervious to molecular oxygen. The evidence against such a possibility was twofold. First, voids in an otherwise compact layer (Fig. 6) acted as a barrier to oxygen transport, and not as a short circuit as it would be if the compact scale were porous to molecular oxygen. Second, the presence of an inert gas in the oxidizing atmosphere had little effect on the parabolic rate of scale formation (Fig. 7). Stringer (10) has shown recently that when there is a possibility of molecular oxygen transport through pores greatly reduced oxidation rates can be obtained in such reaction conditions.

Insufficient data are available to attempt an analysis of the parabolic kinetics or the sensitivity of these kinetics to oxygen pressure. If γ-Nb_2O_5 exhibits the same lattice defect structure as α-Nb_2O_5, concentrations of two types of oxygen vacancies in an oxide scale would depend on the levels of oxygen activity. Singly and doubly ionized oxygen vacancies have been shown to predominate in α-Nb_2O_5, at high and low oxygen pressures (12), respectively, but information is not available on their mobilities. The parabolic rate constants at pressures less than 1 Torr oxygen follow a different pressure dependency (Fig. 1). It is feasible accordingly that the complex pressure dependency of the parabolic kinetics is associated with the concentrations and mobility properties of two types of oxygen vacancies in the oxide scale at different oxygen pressures. Experimental work is being carried out in an attempt to elucidate these features.

Acknowledgments

This contribution is based on a thesis submitted by J. S. Sheasby to the School of Graduate Studies, University of New South Wales in partial fulfillment of the requirements for the Ph.D. degree. He wishes to acknowledge financial assistance from the Australian Government. The studies completed at McMaster University were carried out under the auspices of the U.S. Air Force Office of Scientific Research, Office of Aerospace Research. The authors were indebted to A. E. Jenkins, University of New South Wales, and J. Stringer, Battelle Memorial Institute, for helpful discussions.

Manuscript received April 25, 1966.

Any discussion of this paper will appear in a Discussion Section to be published in the June 1967 JOURNAL.

REFERENCES

1. A. U. Seybolt, *Advances in Physics*, **12**, 1 (1963).
2. H. J. Goldschmidt, *J. Inst. Metals*, **87**, 235 (1958-1959).
3. N. Terao, *Japanese J. Appl. Physics*, **2**, 156 (1963).
4. J. V. Cathcart, J. J. Campbell, and G. P. Smith, *This Journal*, **105**, 443 (1958).
5. N. Norman, *J. Less Common Metals*, **4**, 52 (1962).
6. H. Inouye, "Columbium Metallurgy," p. 649, Metals Society, A.I.M.E., Conf. 1960.
7. T. L. Kolski, *Trans. ASM*, **55**, 119 (1962).
8. R. E. Pawel, J. V. Cathcart, and J. J. Campbell, "Columbium Metallurgy," p. 667, A.I.M.E. Conf. 1960.
9. P. Kofstad and H. Kjöllesdal, *Trans. A.I.M.E.*, **221**, 285 (1961).
10. J. Stringer, *This Journal*, **112**, 1083 (1965).
11. E. Ence and H. Margolin, *J. Metals*, **6**, 246 (1954).
12. P. Kofstad, *J. Phys. Chem. Solids*, **23**, 1571 (1962).

Correlation Between Ellipsometric and Electrical Measurements on Passive Iron

J. L. Ord

Department of Physics, University of Waterloo, Waterloo, Ontario, Canada

and D. J. DeSmet[1]

Department of Physics, University of Illinois, Urbana, Illinois

ABSTRACT

Optical measurements of surface layers on passive iron electrodes are compared with electrical measurements of capacitance and other overpotential parameters. Results of these studies show that the surface layer on the electrode may be regarded as consisting of more than one part. Specifically, in neutral electrolyte there is a thin conducting layer of constant thickness present on the surface in addition to an electrically limiting layer of variable thickness, while in acid electrolyte there is a layer located outside the electrically limiting layer which grows at a constant rate to large thickness. This thick layer can be removed by holding the electrode at a potential slightly below the passive region. Changes in thickness of the electrically limiting layer, determined optically, are consistent with a field dependent conduction mechanism.

Many experimental investigations of passivity have employed electrical and electrochemical methods to determine the state of a passive electrode. The properties of the passive electrode, such as layer thickness, are then deduced from these measurements (1). These indirect determinations inevitably depend on a number of assumptions concerning the state of the electrode, such as the roughness of the surface, the potential profile between the electrode and the electrolyte, the position of the current limiting barrier, etc. Also, only the simplest measurements can be performed without disturbing the system in some manner.

Optical measurements (2, 3) avoid most of these difficulties, since one can use an ellipsometer to measure the thickness of a film without altering the system being studied. Even though the interpretation of optical measurements may involve certain assumptions about the system, these assumptions will be independent of those made for the electrical measurements. If both methods yield results which agree, this lends credence to the assumptions.

Experimental studies of passive iron electrodes (4-7) indicate that the thickness of the passive layer, obtained from the interpretation of electrochemical measurements, increases linearly with the passivating potential when the current density is held constant. The present work has been undertaken in order to determine whether this relationship could be verified by ellipsometric measurements. This work was further motivated by the observation that a passive iron electrode held at constant potential in acid electrolyte slowly changes its capacitance with time, although the current density remains constant.

Experimental

Electrodes were prepared from single crystals of iron obtained from Research Crystals Inc. of Richmond, Virginia. The crystal was first turned to a diameter of 0.2 in. and cut to a length of 0.3 in., and then a small hole was drilled along the axis for the mounting assembly. The surface on which the optical measurements were made was prepared by grinding a flat surface of about 0.08 x 0.3 in. on the side of the cylinder, followed by hand lapping of this surface on a tungsten carbide plate. The electrode was then clamped between Teflon washers in the electrode assembly (8), given a brief chemical polish, x-rayed to check the orientation, and finally reduced in neutral electrolyte to remove any film left by the chemical polish. The orientation of the surface on which the data presented in this work were obtained was 8° off a (110) plane.

The cell in which the experiments were performed consists of an equilateral hollow prism. A platinum cathode is mounted permanently in the cell, and standard taper joints are used to mount the electrode assembly, the reference electrode, and a gas dispersion tube. The surface of the sample under study was mounted vertically in this cell.

The electrical equipment and circuitry are similar to those used in an earlier work (7). A mercurous sulphate electrode with a 0.1*N* K_2SO_4 salt bridge is used as a reference electrode, and all potentials are given with respect to this reference. The two electrolytes used in this work were (*i*) an equivolume mixture of 0.15*N* sodium borate and 0.15*N* boric acid, of *p*H 8.4 and (*ii*) 1.0*N* sulphuric acid. These electrolytes have been used in several studies of the passivity of iron (5, 7, 10). Electrolytes were bubbled with argon for at least 12 hr prior to the beginning of an experiment in order to free the system of dissolved gases. This bubbling was continued throughout the course of an experiment.

The ellipsometer used was a Gaertner Model L119, in which light passes through the compensator before reflection. Monochromatic light of wavelength 5461Å was used throughout the experiments. All measurements were made by holding the compensator fixed at an angle of 45° with respect to the plane of incidence and varying the polarizer and analyzer orientations alternately until a null was found. Iris diaphrams of about 1 mm in diameter were placed adjacent to the cell immediately before and after reflection, so that the optical measurements were made on a portion of the surface of about 1 mm in diameter. The angle of incidence for all results contained herein was 60°. A computer program written by McCrackin and Colson (9) was used in the calculations of the theoretical curves needed in order to estimate the thickness and refractive index of the thin films from the polarizer and analyzer readings.

Results

The first measurements were performed on an iron electrode in the neutral borate buffer electrolyte. The electrode was first reduced cathodically and then

[1] Present address: Department of Physics, University of Alabama, University, Alabama.

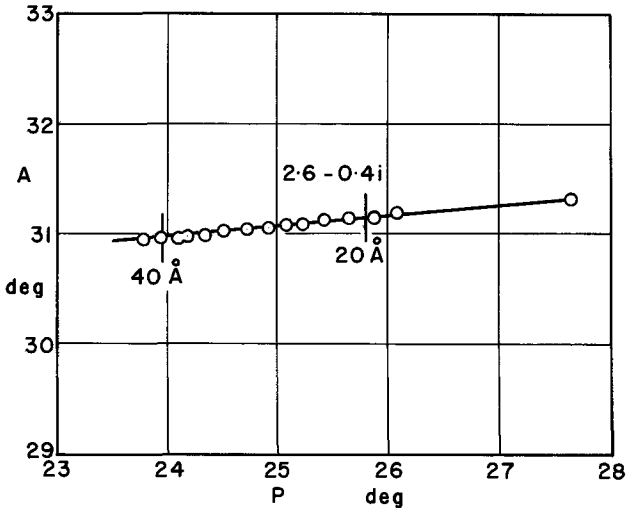

Fig. 1. A vs. P for galvanostatic oxidation of iron at 5 $\mu a/cm^2$ in borate buffer. The curve is a theoretical curve for a layer of index 2.6-0.4i on a substrate of index 3.50-3.66i. Points on the curve corresponding to thicknesses of 20 and 40Å are indicated.

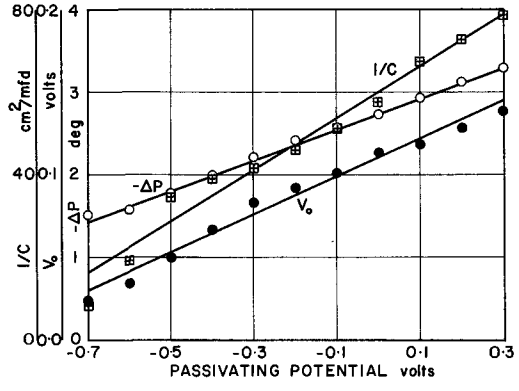

Fig. 2. V_0, $1/C$, and $-\Delta P$ as a function of passivating potential for galvanostatic oxidation of iron at 5 $\mu a/cm^2$ in borate buffer.

transferred to the optical cell. The initial optical measurement on the surface agreed closely with the measurement made when the electrode was reduced cathodically in the optical cell at the end of the experiment. This optical measurement is assumed to be characteristic of a bare iron surface. A constant oxidation current was then applied to the system and was interrupted at regular intervals for short periods of time (60-80 sec), during which the null settings of the polarizer and analyzer were determined.[2] The open circuit transients were recorded and analyzed to determine the values of the parameters V_0 and i_0 appearing in the expression relating the current density, i, to the overpotential, V

$$i = i_0 \exp (V/V_0) \qquad [1]$$

The analysis of the transient also yields a value for the capacitance of the electrode.

The results of this experiment for an oxidation current density of 5 $\mu a/cm^2$ are plotted in Fig. 1 and 2. Figure 1 shows the analyzer setting at null, A, and the corresponding polarizer setting, P, for each open circuit transient. These parameters are chosen to represent the optical data since they are the numbers read directly from the instrument for the zone used for most measurements (11). A theoretical curve for a layer of index 2.6-0.4i on a substrate of index 3.50-3.66i, which fits the experimental points well, is shown in the figure. (Points on the curve corresponding to 20 and 40Å are marked.) Other curves corresponding to slightly different values of the layer index can be found which fit the experimental data almost as well, and this introduces an uncertainty of about 20% in the determination of the absolute thickness of the layer. The relative layer thickness, however, varies almost linearly with the polarizer setting for all such curves, thus ΔP is a good measure of relative thickness.

In Fig. 2, ΔP, V_0, and $1/C$ are shown as functions of the passivating potential (the potential on the oxidation transient at which the circuit is opened). One can see by examining this figure that V_0 and $1/C$, which are presumed directly proportional to the thickness of the electrically limiting layer, and ΔP, the change in the polarizer setting from that of a film-free electrode, all vary linearly with passivating potential. However if these parameters are extrapolated to their respective zeros, V_0 and $1/C$ are found to intersect the potential axis at the same point while ΔP still indicates the presence of a layer. Thus the electrically limiting layer is not the only layer present on the surface.

A similar experiment in acid electrolyte is complicated by the dissolution of the layer into the electrolyte and by the high current density required to passivate the electrode. The electrode geometry in the optical cell is not suitable for passivation at high current density, hence the electrode is passivated in another cell and transferred to the optical cell while passive. This technique is also used with neutral electrolyte when active state reaction products are to be excluded from the cell, as it is not convenient to exchange the electrolyte in the optical cell during an experiment.

The simplest optical measurements which can be performed in acid electrolyte are those made on an electrode in the so-called "steady state." To reach this state the potential is held constant until the current shows no further time dependence. Usually an hour is sufficient to reach this state after the potential has been raised by a 0.1v increment, and a somewhat longer time is required when the potential is lowered by the same amount.

In the first experiment attempted in acid electrolyte, the electrode was passivated and allowed to reach a steady state at a low potential in the passive region. The P and A values were then determined, and a 20-sec open circuit transient was recorded to determine the values of the electrical parameters. The potential was then raised by 0.1v increments and the measurements were repeated after the electrode reached a steady state. The values for the electrical parameters obtained from this experiment differ little from those reported in an earlier work (7), but the optical results show little regularity and are not reproducible, *i.e.*, the P and A values at null do not return to their initial values when the electrode is returned to a steady state at the initial potential.

A very simple experiment shows the reason for this behavior. If the electrode is held in a steady state at a fixed potential, and both optical measurements and open circuit transients are repeated at regular intervals for several days, then results such as those shown in Fig. 3 and 4 are obtained. Figure 3 shows the optical data alone. The curve in Fig. 3 is a theoretical curve for a layer of index 1.65-0.4i on a substrate of index 3.50-3.66i. (Actually a layer of thickness 35Å and index 2.6-0.4i, the passive layer found in neutral electrolyte, is assumed to lie between the 1.65-0.4i index layer and the substrate, but this assumption shifts the curve only slightly.) This value of index is chosen since it gives a theoretical curve which fits the experimental data well, except at high thickness, and it is needed in order to estimate the magnitude of the thick-

[2] Subsequent measurements with a following ellipsometer show that the null settings do not change appreciably over a brief open circuit transient.

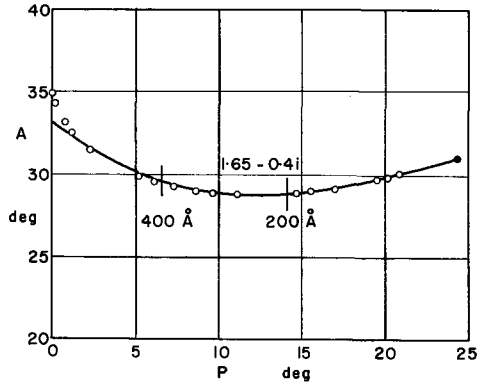

Fig. 3. *A vs. P* for an iron electrode in a "steady state" at 0.7v in 1*N* H_2SO_4. The curve is a theoretical curve for a layer of index 1.65-0.4*i* with the 200 and 400Å points indicated.

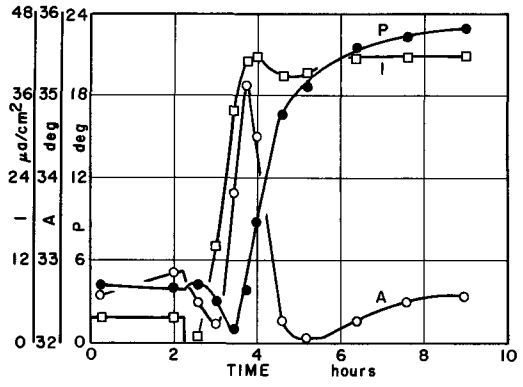

Fig. 5. *I*, *P*, and *A* as a function of time for an iron electrode lowered to a potential of —0.05v from 0.7v in 1*N* H_2SO_4.

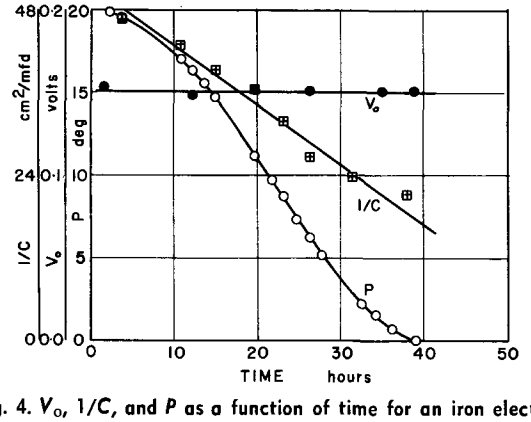

Fig. 4. V_o, 1/*C*, and *P* as a function of time for an iron electrode in a "steady state" at 0.7v in 1*N* H_2SO_4.

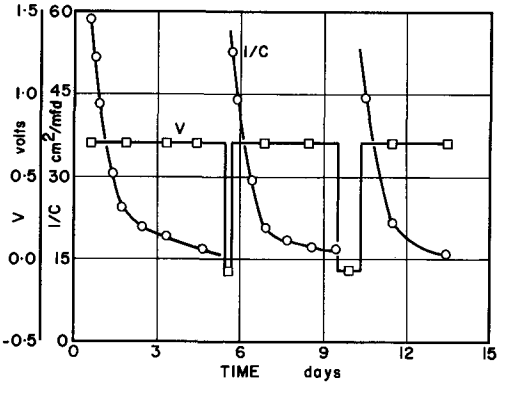

Fig. 6. 1/*C* as a function of time for an iron electrode in 1*N* H_2SO_4 cycled between the potentials shown in the figure.

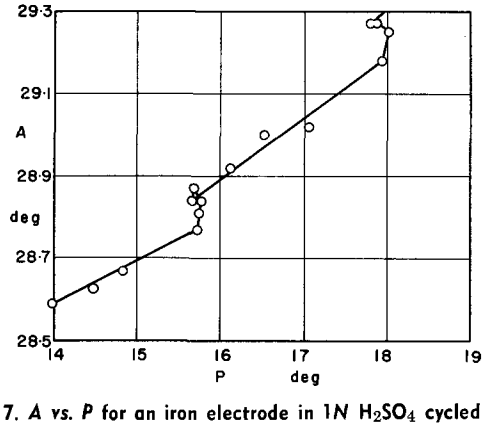

Fig. 7. *A vs. P* for an iron electrode in 1*N* H_2SO_4 cycled between 0.2 and 0.7v at the times indicated in Fig. 8.

ness involved. The correlation between the thickness of the film and the electrical parameters of the system is shown in Fig. 4, in which *P*, V_o, and 1/*C* are plotted as functions of time (again *P* is chosen to represent thickness). This figure shows that V_o has no appreciable time dependence, but 1/*C* has a time dependence similar to that of *P*.

These figures show that a relatively thick film builds up on the electrode with time. The buildup of this film has little or no effect on the steady state current density and V_o, although it does affect 1/*C*. This effect on capacitance is not caused by the concentration of reaction products in the electrolyte, since a complete change of electrolyte has no effect on the dependence of capacitance on time.

This thick layer can be removed from the electrode in a few hours by lowering the potential to a point at which the current density in the steady state is an order of magnitude higher than it is in the passive region. The results obtained by doing this are shown in Fig. 5. Note that the optical changes lag behind the change in current density, and that several hours are required after the current becomes constant before the layer is completely removed. During the layer removal, the *P* and *A* values do not retrace the locus shown in Fig. 3. Hence the layer removal process does not proceed by uniform thinning. Figure 6 shows the effect on 1/*C* of a number of cycles of buildup and removal of the layer.

Since the layer which builds up approximately linearly with time does not affect the current density or V_o, it is not the electrically limiting layer. In order to detect the electrically limiting layer optically the potential is switched back and forth between 0.2 and 0.7v at regular time intervals. The results of this experiment are plotted in Fig. 7 and 8. (Note that the scales used for *P* and *A* are greatly expanded over the scales used in Fig. 3. The experimental accuracy required to detect changes in the thickness of the electrically limiting layer and the extent of scatter in the results both show up clearly in this figure.)

Figure 7 shows the optical data alone. A *P-A* locus is obtained whose structure cannot be produced by changes in thickness of a single layer with a constant refractive index. Figure 8 gives the times and potentials at which measurements were made. Reference to Fig. 3 gives the amount that the outer layer was allowed to grow before the switching was started.

Discussion

The optical results in neutral electrolyte show that a dielectric layer with thickness up to 40Å is present

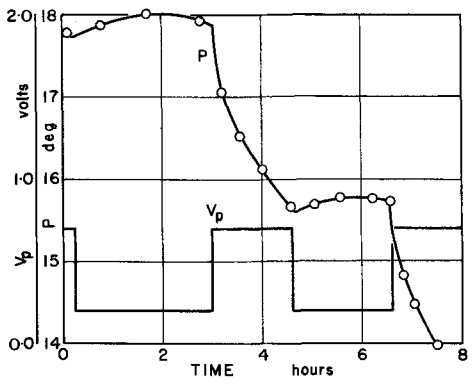

Fig. 8. P vs. time for an iron electrode in 1N H_2SO_4 cycled between the potentials shown in the figure.

on the surface of the electrode. Nagayama and Cohen (10) deduced this result earlier using cathodic reduction measurements. Recently Kruger and Calvert (12) obtained similar optical results in this system. The electrical measurements in neutral electrolyte are in agreement with those presented in an earlier paper (7) in which it is concluded that V_0 is proportional to the thickness of the electrically limiting layer, and the reciprocal capacitance is a linear function of layer thickness, provided a parallel plate model is valid and the roughness factor remains constant.

The V_0 and $1/C$ data plotted in Fig. 2 show that the electrically limiting layer changes in thickness by a factor of five across the passive region. The optical data show that over this region the total thickness of the dielectric layer on the surface changes by a factor of slightly more than two. Therefore the electrically limiting layer does not make up the total thickness of the dielectric layer. If the change in thickness of the dielectric layer in the passive region is attributed to a change in the thickness of the electrically limiting layer only, a two-layer model results with a 15Å conducting layer in series with an electrically limiting layer of variable thickness up to about 25Å. Two-layer models have been proposed by other workers (10) for this system. Extremely accurate measurements would be required to determine whether the two layers have different indices of refraction.

The results in acid electrolyte show that the steady state is not truly steady, although V_0 and the current density are independent of time. A layer builds up on the surface at an approximately constant rate for several days. The only electrical parameter which changes as this layer builds is the capacitance. To interpret this behavior we choose a model in which the electrode surface is covered by a thin electrically limiting layer which is in turn covered by a layer which builds up with time to a considerable thickness.

The effect of several cycles of buildup and removal of the outer layer on capacitance is shown in Fig. 6. The fact that the capacitance values follow this cycling shows that the changes in the capacitance are not due to changes in the roughness factor. This conclusion is also supported by the fact that the current (which is also area dependent) does not follow the capacitance variations. The cycling experiment also changes the thickness of the electrically limiting layer, hence it is not possible to conclude whether the changes in the capacitance of the passive layer are due to the buildup of the outer layer, or to some change in the structure of the electrically limiting layer with time.

The optical detection of changes in the thickness of the electrically limiting layer is complicated by the continuous buildup of the thick outer layer. Direct analysis of the optical data for thickness and refractive index is difficult. We will attempt to show only that the optical data are consistent with the electrochemical mechanism proposed for thickness changes of the passive layer (4, 6).

It is usually assumed that the steady-state current density gives a measure of the oxidation current required to balance the dissolution of the passive layer. It is assumed further, but not without reservation (13), that the dissolution rate is the same when the thickness of the layer is varying as it is when the thickness is held constant in the steady state. The current density through the layer depends exponentially on the field within the layer. The rate of change of thickness of the layer is proportional to the difference between the instantaneous field-limited current density and the steady-state current density. The thickness changes which result when the potential is switched back and forth between 0.2 and 0.7v at intervals of a few hours can be predicted from this mechanism. When the potential is raised, the exponential field dependence causes the current density to increase greatly, and produces a relatively rapid buildup of the layer until the field falls to a value at which the oxidation current balances the layer dissolution. When the potential is lowered, the exponential field dependence lowers the current density by a smaller amount, hence the layer thickness decreases relatively slowly.

The data presented in Fig. 7 and 8 are consistent with all of these predictions. Changes in the thickness of a layer of constant refractive index would generate a smooth P-A locus. The expanded scale used in Fig. 7 shows the P-A locus to have a structure which is shown in Fig. 8 to correlate with the potential switching. Hence layers of differing refractive indices must be present on the surface and undergo simultaneous changes in thickness after the potential is switched. In the proposed model the passive layer has an index of 2.6-0.4i whereas the outer layer has an index of 1.65-0.4i, and the thickness of both layers will be changing after a switch in the potential.

The variation of P with time during growth of the outer layer at fixed potential is shown in Fig. 4 (P decreases as the thickness increases). Figure 8 shows what happens to a segment of Fig. 4 when the potential is switched back and forth. When the potential is switched down, P first increases, then begins to decrease. (If the lower potential is maintained long enough P will eventually decrease at the rate shown in Fig. 4.) This result is consistent with a decrease in the thickness of the passive layer (at a time-dependent rate) opposing the steady increase in the thickness of the outer layer. When the potential is switched up, P decreases very rapidly at first, but eventually decreases at the rate shown in Fig. 4. This result is consistent with an increase in the thickness of both the passive layer (at a time-varying rate) and the outer layer. The magnitude of the change in P attributed to the change in thickness of the passive layer is similar to that measured in neutral electrolyte for the same change in potential.

Acknowledgment

The authors are indebted to Mr. W. J. Woitowetch for his assistance in preparing electrodes, and to Mr. P. H. Cress for his assistance with the computer program. This work received partial support from the National Research Council of Canada under Grant No. A-1151, and from the Research Board of the University of Illinois.

Manuscript received May 2, 1966; revised manuscript received July 21, 1966.

Any discussion of this paper will appear in a Discussion Section to be published in the June 1967 JOURNAL.

REFERENCES

1. J. L. Ord, *This Journal*, **112**, 46 (1965).
2. L. Tronstad, *Trans. Faraday Soc.*, **29**, 502 (1933).
3. J. Kruger, *This Journal*, **110**, 654 (1963).

4. K. G. Weil, *Z. Elektrochem.*, **59**, 711 (1955).
5. N. Sato and M. Cohen, *This Journal*, **111**, 512 (1964).
6. J. L. Ord and J. H. Bartlett, *ibid.*, **112**, 160 (1965).
7. J. L. Ord, *ibid.*, **113**, 213 (1966).
8. H. G. Feller and J. Osterwald, *ibid.*, **111**, 119 (1964).
9. F. L. McCrackin and J. P. Colson, NBS Technical Note 242 (1964).
10. M. Nagayama and M. Cohen, *This Journal*, **109**, 781 (1962).
11. F. L. McCrackin, E. Passaglia, R. R. Stromberg, and H. L. Steinberg, *J. Research Nat. Bur. Standards A*, **67**, 363 (1963).
12. J. Kruger and J. P. Calvert, *This Journal*, **112**, 180C, Abstract No. 71 (1965).
13. K. J. Vetter, *ibid.*, **110**, 597 (1963).

Environmental Factors Affecting the Critical Potential for Pitting in 18-8 Stainless Steel

H. P. Leckie and H. H. Uhlig

Department of Metallurgy, Massachusetts Institute of Technology, Cambridge, Massachusetts

ABSTRACT

The concept of a critical potential below which pitting of 18-8 and other passive alloys does not occur in aqueous Cl^- media is affirmed. Increasing Cl^- concentration shifts the critical potential to more active values. The potential is shifted to more noble values by presence of other anions, *e.g.*, ClO_4^-, SO_4^{--}, NO_3^-, OH^-, sufficient concentrations of which act as pitting inhibitors. Lowering of temperature similarly enobles the critical potential. The shift at 0°C exceeds the oxidation-reduction potential for $Fe^{++} \rightarrow Fe^{+++} + e$ accounting for resistance of 18-8 to pitting in $FeCl_3$ solutions at ice temperature but not at room temperature. The critical potential is not affected appreciably in the acid *p*H range; it moves markedly in the noble direction in the alkaline range corresponding to observed resistance to pitting in alkaline Cl^- media. These results are interpreted in terms of competitive adsorption of Cl^- and other anions for sites on the alloy surface. Only at a sufficiently high surface concentration of Cl^- is oxygen, making up the passive film, displaced locally, and passivity thereby destroyed resulting in a pit. The special behavior of NO_3^- inhibition and factors affecting reproducibility of measurements are discussed.

The tendency for 18-8 and other stainless steels to corrode locally by pitting when immersed in chloride solutions including sea water was recognized soon after stainless steels became available. Early investigations showed that pitting corrosion is an electrochemical process in which the pit acts as a fixed anode and the remainder of the passive surface is cathode (1). Early measurements also showed a so-called "break through" or "critical" potential at which pitting initiates. Recent measurements of such critical potentials for stainless steels are reported by Rosenfeld and Maximtschuk (2), Rocha (3), Brauns and Schwenk (4), Defranoux (5), Pourbaix *et al.* (6), Herbsleb (7), Tomashov *et al.* (8), and by Fokin *et al.* (9). An excellent review of the subject has been published by Kolotyrkin (10).

It was not clear, however, from early short-time laboratory investigations whether pitting in any degree would occur below the so-called critical potential, or whether pitting was only delayed in time. Discussions on this matter continue to the present day. Perhaps the first satisfactory demonstration that pitting can be permanently suppressed came from an experiment in which 18-8 stainless steel was immersed at room temperature in 10% $FeCl_3$ inhibited with 3% $NaNO_3$. No pitting or appreciable weight loss of duplicate specimens occurred over a period of 25 years (1, 11). A similar specimen immersed in 10% $FeCl_3$ without NO_3^- addition was riddled with pits within a few hours. Uhlig and Gilman (11) explained the observed inhibition in terms of a supposed shift of the critical potential for pitting, brought about by nitrate addition, to a value more noble than the oxidation-reduction potential of ferric chloride. This explanation is confirmed by results reported in this paper.

Actually, the satisfactory inhibition of pitting by polarizing a passive metal to a potential below (more active than) its critical value has been practiced for many years, even though the corresponding explanation was not understood. For example, cathodic protection of stainless steels against pittting in sea water by attaching an equal or greater area of iron has been used with success over a period of years (12). Similarly aluminum in practice has been cathodically protected against pitting by coupling it to a galvanically more active metal like zinc (13). The iron in galvanic contact with stainless steel polarizes it below the critical potential of the latter (approximately 0.2v, hydrogen scale in 3% NaCl). Iron cannot, in any case, polarize 18-8 to its open circuit anode potential, as is required for the cathodic protection of nonpassive metals, since the anode potentials of the two metals are nearly the same. Iron by the same token is not suited to protecting aluminum because its approximate corrosion potential in 3% NaCl (—0.4v) is more noble than the critical potential of aluminum (—0.48v) (14); the corresponding more favorable corrosion potential of zinc, on the other hand, is —0.8v. Obviously zinc does not and cannot polarize aluminum to its very active anode potential in the order of —1.7v; it is only required that aluminum be polarized to a value more active than its critical potential. Protection of any passive metal against pitting continues as long as all portions of the metal surface are adequately polarized to a value below (more active than) its critical potential in the given environment.

The importance of the critical potential both to an understanding of the pitting mechanism and to practical applications, as mentioned above, suggests the value of a systematic study of critical potentials for 18-8 stainless steels focussed first on environmental factors, and second on metallurgical factors. Environmental factors make up the subject of the present paper.

Experimental

Stainless steel electrodes (17.7% Cr, 8.7% Ni) were prepared as cylinders measuring 4 mm diameter and 1.4-2 cm long. The original cast type 304 rod was homogenized in vacuum at 1050°C for 20 hr and water quenched; it was then swaged to diameter, annealed at 1050°C for 1 hr, and again water quenched. The elec-

trode was drilled and tapped allowing attachment to a threaded small diameter Ni wire. The nickel wire was enclosed within a glass tube and a water-tight seal was maintained by means of a Teflon gasket between glass and electrode held in constant contact by a rubber grommet and nut attached to the nickel wire at the other end. Specimens were polished to 3/0 emery paper followed by pickling in a solution containing 15% HNO_3, 2% HF by volume at 60°C for 5 min. The latter treatment produced a smooth shiny surface.

The all-glass cell used for polarization studies incorporated the following features: (*i*) provision for a centrally located anode surrounded by four equispaced platinum cathodes, (*ii*) inlet for gas agitation and deaeration, and (*iii*) a further inlet to permit a Luggin capillary from a saturated calomel reference electrode to reach near the anode surface.

All electrolytes were deaerated for one or more hours using prepurified nitrogen which was further purified before entering the cell by passing it over copper turnings at 400°C. The cell was placed in a large constant temperature cabinet maintained by heating or refrigeration to 25° ± 0.2°C. This cabinet also permitted tests to be carried out between temperature limits of —1° and 50°C. At the latter temperature, the limits of control were ±1°C.

Reproducible measurements demanded a crevice-free mounting and a homogeneous alloy surface. Either crevices or concentration gradients at some portion of the electrode surface, *e.g.*, caused by carbide precipitation, tend to lower the critical potential in chloride solutions, causing scatter of results. Deaeration of electrolyte as practiced in the present measurements helped avoid crevice corrosion if there was any tendency in this direction.

For polarization measurements, a Wenking potentiostat was employed in conjunction with a chart recorder capable of measuring current to 0.1 μamp. A potentiostatic step-by-step polarization technique was followed, in most cases allowing a period of 5 min to elapse at each 50 mv potential increment before recording the current. In neutral halide solutions, where the critical and passive current densities are not large, the electrode was first held at a potential in the passive region for a period of 15 min before further polarizing in the noble direction. In this way a more nearly steady-state condition was achieved. Where no passive breakdown (pitting) occurred, polarization was continued in most instances to 1.2v (H_2 scale), a value approaching or being within the transpassive region. To obtain more exact values of the critical potential, the step-by-step technique was often supplemented by current-time curves at a constant potential maintained close to the approximate critical value. The final breakdown potential called V_c was taken as the most active (least noble) value for which no continued increase of current with time (corresponding to pitting) was observed over a period of about 24 hr. Reproducibility of critical potentials obtained in this manner was within ±5 mv. Because such measurements were unduly time-consuming, much of the data was obtained with no more than 5 min intervals between shifts of potential. Critical potentials of this kind are labeled V'_c, values of which in 1*N* NaCl, for example, are found to be about 0.09v more noble than values of V_c (Fig. 1). This difference represents the probable order of magnitude between all the short-time and steady-state critical potentials presently reported. Incidence of pitting by current-time curves was confirmed by examination of the electrode under a low power microscope.

Results and Discussion

The potentiostatic anodic polarization curves (5 min each point) of 18-8 stainless steel in deaerated 0.1*N* NaCl and 1*M* H_2SO_4 are shown in Fig. 2. In H_2SO_4 no pitting occurs; the increase of current above about 1.0v in the transpassive region corresponds to uniform corrosion with CrO_4^{--} formation, whereas in the passive region Cr^{+++} forms instead (plus Fe and Ni corrosion products). In 0.1*N* NaCl, on the other hand, the current increases at the critical potential V'_c equal to 0.36v, denoting the onset of visible pitting. The upward sweep of potential at higher current densities is related to polarization effects at anodic regions constituting the pits. Corrosion products within the pits, the inner surface of which is in the active state, are mostly Fe^{++} combined with Ni^{++} and probably Cr^{+++}. The critical potential observed in Fig. 2 is unaffected by

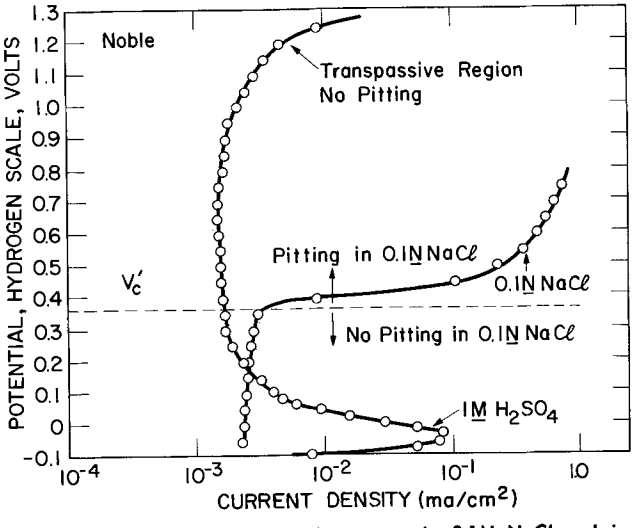

Fig. 2. Potentiostatic polarization curves in 0.1*N* NaCl and in 1*M* H_2SO_4 showing critical potential in chloride solution, 25°C.

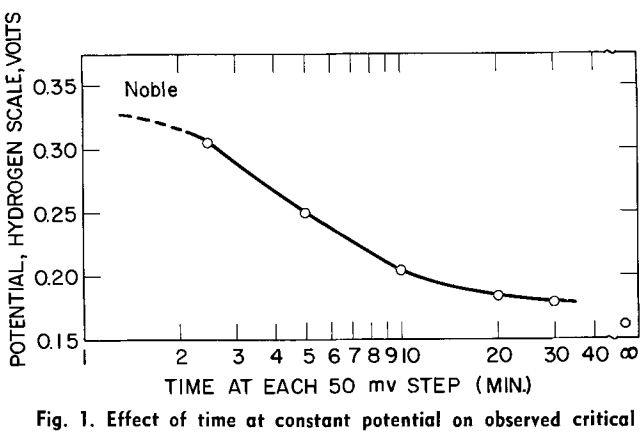

Fig. 1. Effect of time at constant potential on observed critical potential for pitting in 1*N* NaCl, 25°C.

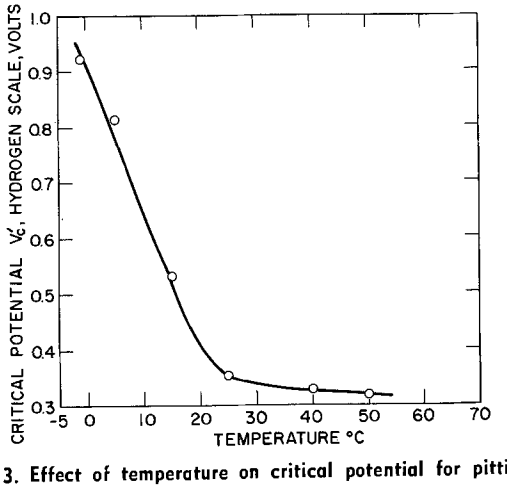

Fig. 3. Effect of temperature on critical potential for pitting in 0.1*N* NaCl.

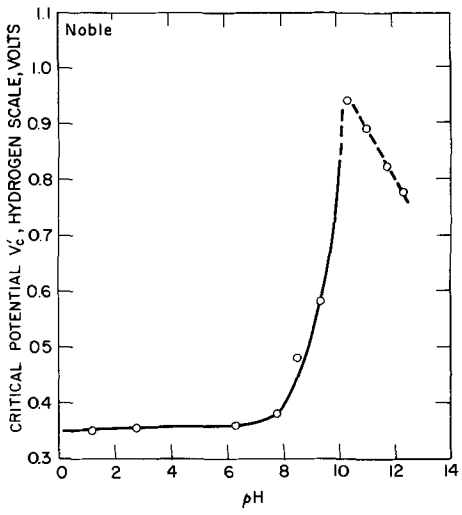

Fig. 4. Effect of pH on critical potential for pitting in 0.1N NaCl, 25°C.

aeration of the electrolyte provided crevice corrosion is avoided.

The effect of temperature of 0.1*N* NaCl on V'_c for 18-8 within the range —1.0° to 50°C is shown in Fig. 3. The critical potential does not change sensitively above room temperature, but there is a remarkable shift of potential in the noble direction below room temperature. At 0°C, V'_c is more noble than the oxidation-reduction potential for $Fe^{++} \rightarrow Fe^{+++} + e$. From this behavior it could be predicted that 18-8 would be appreciably more resistant to pitting at low compared to room temperatures. This prediction was confirmed in preliminary experiments in which 18-8 sheet specimens immersed in 0.5*M* $FeCl_3$, 0.5*M* NaCl solution at 0°C clearly showed no pitting, weight loss, or visible reduction of $FeCl_3$ after 24-hr immersion, whereas control specimens at 25°C were badly pitted and the brown-yellow $FeCl_3$ solution had reduced to green $FeCl_2$. In another experiment lasting two weeks, with some variation of temperature in the neighborhood of 0°C, specimens of 18-8 similarly did not show pitting nor did the $FeCl_3$ solution undergo reduction.

The critical potential is not greatly affected in acid 0.1*N* NaCl ranging in pH from 1 to 7 (adjusted by HCl additions) as shown in Fig. 4. In alkaline solutions, pH 7-10 (adjusted by NaOH additions), however, the critical potential becomes much more noble corresponding to increased resistance to pitting. Brauns and Schwenk (4) reported a similar shift of potential in the noble direction on addition of 0.5*N* NaOH to 1*N* NaCl. It has been known for some time that NaOH (15) or Na_2CO_3 (16) additions to NaCl effectively inhibit pitting of stainless steels. Furthermore, Uhlig and Morrill (17) showed that pitting of 18-8 in 4% NaCl at 90°C decreases markedly as the pH is increased above 7. Rocha (3) presented data at 50°C showing only small effect of pH on critical potentials in the acid range of pH, similar to data of Fig. 4.

Above pH 10, Fig. 4 shows that the apparent value of V'_c decreases with pH. However, the increases of current observed at corresponding values of potential do not correspond to pitting but to attainment instead of the transpassive state with formation of CrO_4^{--}. This shift is in accord with the analogous anodic reaction for pure Cr

$$Cr + 4H_2O \rightarrow CrO_4^{--} + 8H^+ + 6e$$

the potential for which also moves in the active direction as (H^+) decreases or pH increases. The calculated slope of potential *vs.* pH, according to the above reaction, is —0.08 v/pH unit which is in reasonable agreement with the corresponding observed slope of Fig. 4 equal to —0.09 v/pH unit.

The comparatively small shift of V'_c in the acid region was confirmed by determining values in 0.25, 0.5, and 1*N* HCl. Potentiostatic curves showed that, within the limitations of the few experimental points that were obtained, the critical value V'_c shifts in the active direction a maximum of only about 0.05v which is probably accounted for mostly by increasing Cl^- activity rather than by change of H^+ activity. It is of interest that characteristics of passivity can be maintained in an acid so strong as 1*N* HCl, although the passive and critical current densities are higher than for neutral chloride solutions by orders of magnitude.

The effect of increasing Cl^- concentration in neutral NaCl solution is to shift V_c in the active direction by about 0.09v for a 10-fold change in concentration. This compares with a 0.13v shift for Al found by Kaesche (14). Data are given in Fig. 5 for steady-state conditions, each point representing the final value derived from numerous potentiostatic polarization measurements at potentials near V_c extending over hours. Note that these values are somewhat more active than corresponding values of V'_c cited previously. Values of V_c in volts are linear with logarithm of Cl^- activity, following the equation

$$V_c = -0.088 \log(Cl^-) + 0.168$$

Rosenfeld *et al.* (2) and Kolotyrkin *et al.* (18) reported that various anions when added to chloride solutions shift the critical potential to more noble values, accounting for an increased resistance to pitting. Pourbaix *et al.* (6) noted a similar shift of potential on adding HCO_3^- to NaCl solutions, and Brauns and Schwenk (4) reported analogous behavior for OH^- or SO_4^{--} additions. This effect can be noted in the potentiostatic curves of Fig. 6 for 18-8, showing that V'_c in 0.1*N* NaCl moves to more noble values with increasing Na_2SO_4 concentration. At and above 0.15*M* Na_2SO_4 no pitting occurs at all, the observed current increase being characteristic of transpassivity in absence of Cl^-. In other words, sufficient SO_4^{--} added to a Cl^- solution inhibits pitting of 18-8. Other anions also act as inhibitors, the amount necessary for complete inhibition varying with the anion. In all cases, the greater the Cl^- concentration, the greater is the required amount of inhibiting anion. Based on potentiostatic measurements extending over hours, it was found that the logarithm of the minimum amount of anion for inhibition expressed in terms of anion activity, is linear with the logarithm of the corresponding Cl^- activity. This relation for inhibition by SO_4^{--}

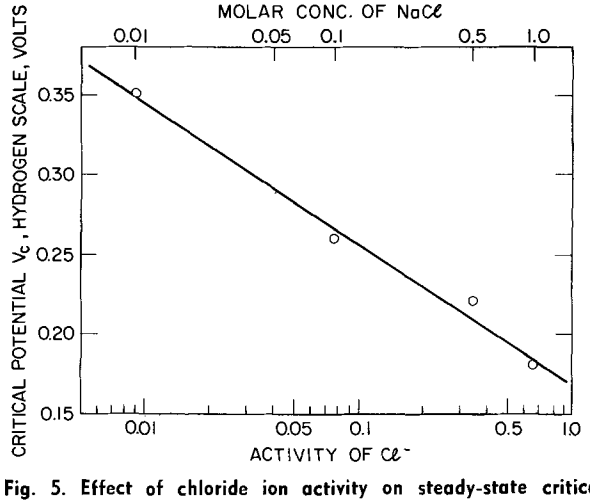

Fig. 5. Effect of chloride ion activity on steady-state critical potential for pitting, 25°C.

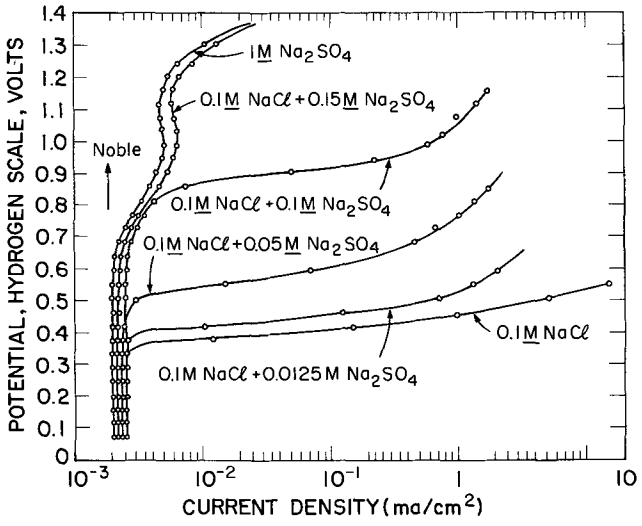

Fig. 6. Potentiostatic polarization curves in 0.1M NaCl showing increasingly noble values of the critical potential with additions of Na_2SO_4, 25°C.

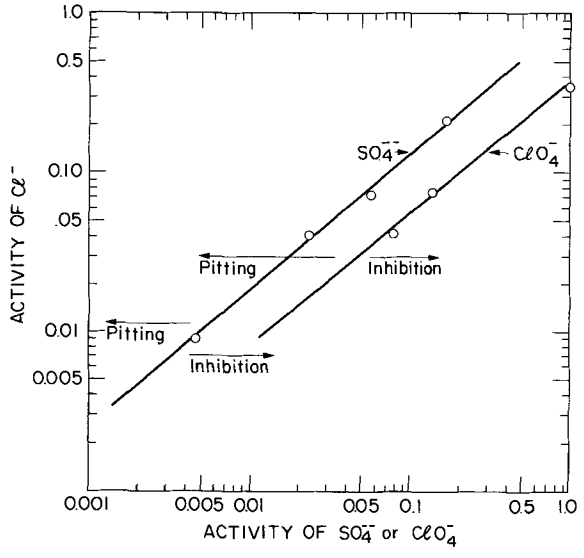

Fig. 7. Activity of SO_4^{--} or ClO_4^- required to inhibit pitting as a function of Cl^- activity, 25°C.

and by ClO_4^- is shown in Fig. 7. Similar data for OH^- and NO_3^- inhibition are shown in Fig. 8. The corresponding equations expressing minimum anion activity necessary to inhibit pitting of 18-8 in a solution of given Cl^- activity are as follows

$$\log (Cl^-) = 1.62 \log (OH^-) + 1.84$$
$$= 1.88 \log (NO_3^-) + 1.18$$
$$= 0.85 \log (SO_4^{--}) - 0.05$$
$$= 0.83 \log (ClO_4^-) - 0.44$$

These equations express the fact that efficiency of inhibition for $(Cl^-) > 0.1$ decreases in the order: $OH^- > NO_3^- > SO_4^{--} > ClO_4^-$. In solutions of unit activity Cl^-, for example, corresponding to 1.5*N* NaCl, values for the activity of OH^-, NO_3^-, SO_4^{--}, and ClO_4^- required for inhibition are respectively 0.07, 0.24, 1.15, and 3.4.

Uhlig and Gilman (11) found a comparable equation to hold: $\log (Cl^-) = 1.92 \log (NO_3^-) + 1.34$ expressing the activity of NO_3^- necessary to inhibit pitting of 18-8 in $FeCl_3$ solutions of given Cl^- activity. This equation agrees reasonably well with the present equation obtained potentiostatically in NaCl-$NaNO_3$

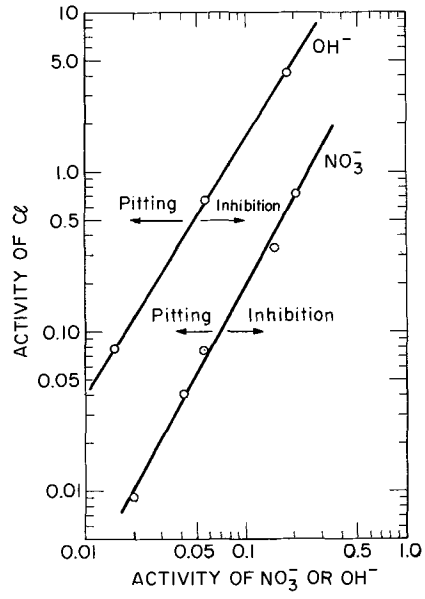

Fig. 8. Activity of OH^- or NO_3^- required to inhibit pitting as a function of Cl^- activity, 25°C.

mixtures, especially considering the fact that activity coefficients of $FeCl_3$ solutions required estimation from values for $LaCl_3$ solutions.

Figure 8 shows that in 0.1*N* NaCl, corresponding to an activity of Cl^- = 0.078, the required activity of OH^- for inhibition = 0.015, corresponding to *p*H 12.2. This value is consistent with the critical *p*H shown in Fig. 4 for inhibition of pitting in 0.1*N* NaCl up to potentials corresponding to onset of transpassivity remembering that steady-state values V_c are approximately 0.09v more active. In other words, corrected potentiokinetic values of Fig. 4 shift the curve down and to the right, which then places the critical potential at a *p*H of 11 or 12, above which the alloy does not pit if polarized to approximately 1v.

The potentiostatic curves for 18-8 in Cl^- solutions to which the other anions cited above are added, resemble those shown in Fig. 6 for SO_4^{--} additions, with the exception of NO_3^-. For nitrate additions, the critical potential for pitting is shifted in the noble direction, but further polarization of the alloy in a given ratio NO_3^-/Cl^- electrolyte may inhibit pitting again. This behavior was first pointed out by Brauns and Schwenk (4) and is shown in Fig. 9. It is reason-

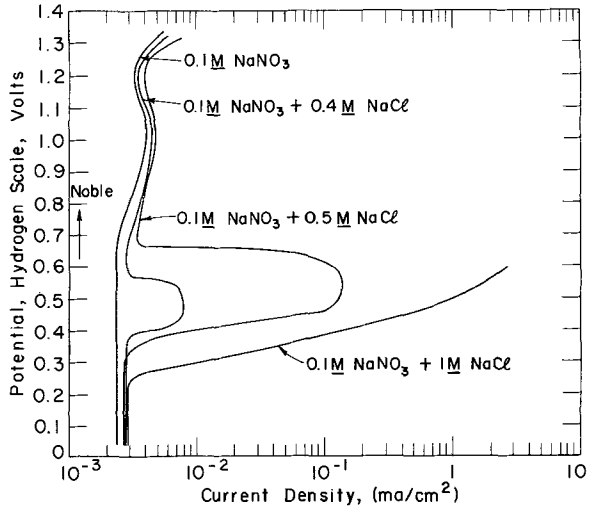

Fig. 9. Potentiostatic polarization curves in 0.1*N* $NaNO_3$ containing increasing amounts of NaCl, 25°C.

ably explained by the reduction of nitrates by Fe^{++} produced as an anodic corrosion product of 18-8 both generally and within pits in the less noble portion of the passive region. On exceeding the oxidation-reduction potential for $Fe^{++} \rightarrow Fe^{+++} + e^-$ (standard potential = 0.77v), surface concentration of Fe^{+++} then predominates over Fe^{++} concentration, and reduction of NO_3^- is diminished. Hence, at some potential more noble than V'_c, NO_3^- becomes available in greater concentration to inhibit pitting, and previously formed pits may be repassivated provided their geometry and adequate stirring of electrolyte allow sufficient NO_3^- to enter the pit cavities.

Analogous behavior does not occur with the other anions that were investigated because they are not readily reduced by Fe^{++}. The inhibiting concentrations of NO_3^- shown in Fig. 8 are those which produced no breakdown in any portion of the passive region, allowing 5 min at each potential, the electrolyte behaving essentially as do solutions of $NaNO_3$ free of Cl^-. Brauns and Schwenk (4) reported, as we do, that OH^- and SO_4^{--} additions enoble values of V_c, but they found that NO_3^- additions, contrary to our results, do not affect the critical potential. It is likely that their observation is explained by the appreciable reduction of NO_3^- by Fe^{++} accruing during prolonged anodic polarization below the $Fe^{++} \rightarrow Fe^{+++} + e$ potential. At faster rates of potential change, as in our measurements, NO_3^- does not have time to reduce, and V_c therefore moves toward more noble values with increasing NO_3^- concentrations, similar to the shift which occurs with SO_4^{--} or OH^- additions. In agreement, Herbsleb (7) showed through potentiokinetic measurements of 18-8 that a critical potential V_c in 1M NaCl + 0.5M $NaNO_3$ solution, which we find according to Fig. 8 to be in the inhibiting range, is observed only at slow (0.2 v/hr) but not at fast (2 v/hr) rates of potential change. It is expected that rate of stirring also enters such observations, fast rates tending to dilute surface concentration of Fe^{++} and thereby decreasing the rate of NO_3^- reduction.

Theory of the critical potential.—Hoar, Mears, and Rothwell (19) described initiation of pitting as one preceded by adsorption of aggressive ions, *e.g.*, Cl^-, on a supposed oxide film, followed by penetration of the film (without exchange) under the influence of an electrostatic field. When the field across the film-solution interface reaches a critical value, pitting occurs. Other ions may also penetrate the passive oxide, depending on size and charge, contaminating the oxide and making it a better ionic conductor, thereby favoring oxide growth. The oxide is presumably either undermined by vacancy condensation at the metal interface or it releases cations rapidly at the electrolyte interface so that in either case pitting proceeds. The induction period for pitting to occur is related to the time required for supposed penetration of ions through the oxide film. Streicher (20) previously expressed a less detailed but similar viewpoint.

It would seem from this model of pitting behavior that anions other than Cl^-, *e.g.*, SO_4^{--}, ClO_4^-, NO_3^-, OH^-, should in some measure accelerate pitting by contaminating the supposed oxide, whereas in fact they are inhibitors as present and previously published data show. Inhibition occurs despite applied potentials across the passive film that otherwise readily cause pitting in absence of inhibitor. Also, oxide films, being soluble in acids, ought to be thinner or more porous hence more easily penetrated at low *p*H than at high *p*H values, yet the critical potential is not appreciably altered in 0.1N NaCl on going from *p*H 7 to 1 (Fig. 4). Furthermore, anion size appears to be less important than specific interaction of anions with the metal surface. For example, Cl^- is more effective than SO_4^{--} in causing pitting of passive iron in presence of CrO_4^{--}, but SO_4^{--} is more effective than Cl^- in presence of NO_2^- (21).

An alternative model, which in the authors' opinion offers advantages in describing the facts, is based on reversible competitive adsorption of aggressive ions like Cl^- with oxygen for sites on the stainless steel surface. Adsorbed oxygen rather than metal oxide is considered to make up the passive film (22). This is the model discussed in detail by Kolotyrkin (10, 23). Also Rosenfeld and Maximtschuk (2), and Brauns and Schwenk (4) in their discussion of pitting mechanism refer to a similar model. Oxygen normally has higher affinity than Cl^- for adsorption sites on a stainless steel surface, but as the potential of the alloy is shifted in the positive (noble) direction, more Cl^- ions move into the double layer. At a sufficient concentration corresponding to the critical potential, Cl^- ions succeed at favored sites in destroying passivity by displacing adsorbed O ions. The anodic overvoltage for dissolution of alloy ions is then appreciably reduced wherever the metal is in contact with Cl^- compared to metal in contact with adsorbed O, and hence metal ions rapidly enter solution resulting in a pit. Preferred transport of Cl^- (transference number of Cl^- in 0.1N NaCl = 0.61) into anodic areas because of the continuous corrosion current, and still higher transference number of Cl^- in heavy-metal chlorides, insures that the anode areas remain active. The induction time for pitting is explained in part by the slow process of competitive adsorption. When anions other than Cl^- are present, these also tend to adsorb on the passive alloy surface displacing Cl^-. Hence, in their presence the competitive process requires a shift of potential to still more noble values so as to enable Cl^- ion to reach a concentration in the double layer adequate to displace oxygen of the passive film thereby destroying passivity locally. Should pitting not occur up to a potential of about 1.0v, which is the order of magnitude open-circuit cathode (oxygen) potential of 18-8 in aerated electrolytes, pitting is effectively inhibited because it then becomes impossible for Cl^- to displace oxygen on the metal surface at any available galvanic potential. The more readily an anion adsorbs on the passive surface, and the higher its affinity for the metal surface, the more effectively does it exclude Cl^- and inhibit pitting. Hence OH^- is usually a better inhibitor than is ClO_4^-, the latter adsorbing least of all common anions.

Rosenfeld and Maximtschuk (2) using radioactive Cl^{36} proved that more Cl^- adsorbs on Cr, the passive properties of which 18-8 approximates, as the potential of Cr is shifted in the noble direction. They also showed that SO_4^{--} or OH^- added to chloride solutions decreases adsorption of Cl^- and that at sufficiently high concentrations of either anion, practically no adsorption of Cl^- occurs at all, even in the noble potential region. These results support the mechanism of pitting described above based on competitive adsorption.

Following from the supposition that the amount of anion adsorbing depends on its activity in solution in accord with the Freundlich adsorption isotherm, and that pitting is inhibited when a critical ratio of anion to Cl^- activity is reached, it was shown (11) that the relation log (Cl^-) = constant + n_1/n_2 log (anion) should hold where n_1 corresponds to the exponent in the Freundlich adsorption isotherm: amount adsorbed = $k_1(Cl^-)^{1/n_1}$ and n_2 is the corresponding exponent for inhibitor ion. This equation describes the present data and it also describes the amount of CrO_4^{--} or NO_2^- needed to inhibit pitting of iron in presence of Cl^- or SO_4^{--} where again competitive adsorption is the probable underlying mechanism (21).

With reference to the constants for the above equation listed earlier for various inhibiting ions, it is noted that values of n_2 as judged from the coefficients for log (OH^-) and log (NO_3^-) are smaller than for log (SO_4^{--}) and log (ClO_4^-) assuming that n_1 for adsorption of (Cl^-) is the same in all cases. These values are perhaps in line with the expected higher

affinity of OH^- and NO_3^- for the metal surface compared to SO_4^{--} or ClO_4^-. At low concentrations of Cl^- ($<0.01N$), however, the critical activities of inhibiting ion may be no longer in the same order, indicating that some additional factor enters the adsorption mechanism. The part played by Cl^- concentration may explain why Rosenfeld and Maximtschuk (2) found efficiency of inhibition to decrease in the order $NO_3^- > ClO_4^- > SO_4^{--}$ whereas we find $NO_3^- > SO_4^{--} > ClO_4^-$.

The critical potential is insensitive to pH in the acid region presumably because H^+ does not competitively adsorb on the passive 18-8 surface in this range. In the alkaline region, however, OH^- in sufficient concentration is available for adsorption; its high affinity for the metal surface makes it an effective inhibitor at relatively low concentrations. At temperatures below room temperature, the chemical affinity of 18-8 for oxygen is probably not changed appreciably judging from the small change in Flade potential of Fe with temperature. However, affinity of 18-8 for H_2O at low temperatures may increase appreciably making it more difficult for Cl^- to displace both adsorbed H_2O and oxygen, and accounting for the marked noble shift of potential. It would be difficult to explain such a high temperature coefficient on the basis of any supposed change of anion diffusion rate through an oxide lattice.

It should be noted that the effect of increasing Cl^- concentration to shift V_c in the negative (active) direction can account for an apparent induction time for pitting in stagnant solutions because the small continuous passive current serves to transport NaCl to the alloy surface. This is one of the reasons why crevices, if they exist, are the first to pit because they harbor higher concentrations of Cl^-. This factor, and also perhaps nonuniform composition alloy surfaces, or exposed edges compared to faces of cold-rolled alloy (7) (caused probably by differing crystal orientation), may account for the scattered values of critical potentials reported in the literature. It may also account for an apparent induction time beyond the time normally required for competitive adsorption to occur.

Our present results support the view that for specific environmental conditions and nonstagnant electrolytes, the critical potential is observed at well-defined reproducible values. On the other hand, whether pits once formed will again repassivate at some potential lower than the critical value as reported by Pourbaix *et al.* (6) depends, in our opinion, on accidental favorable geometry of the pit cavities and a stirring rate high enough to mix electrolyte inside the pits with electrolyte outside.

Acknowledgment

This research was supported by the Office of Saline Water, United States Department of the Interior, on Contract No. 14-01-0001-404, to whom the authors express their appreciation.

Manuscript received April 15, 1966. This paper was presented at the Philadelphia Meeting, Oct. 9-14, 1966.

Any discussion of this paper will appear in a Discussion Section to be published in the June 1967 JOURNAL.

REFERENCES

1. "Corrosion Handbook," p. 165, H. H. Uhlig, Editor, John Wiley & Sons, Inc., New York (1948).
2. I. Rosenfeld and W. Maximtschuk, *Z. Physik. Chem.*, **215**, 25 (1960).
3. H. Rocha, *Werkstoffe u. Korrosion*, **11**, 352 (1960).
4. E. Brauns and W. Schwenk, *Archiv. Eisenhüttenw.*, **32**, 387 (1961).
5. J. Defranoux, *Corrosion Sci.*, **3**, 75 (1963).
6. M. Pourbaix, L. Klimzack-Mathieu, Ch. Mertens, J. Meunier, Cl. Vanleugenhaghe, L. De Munch, J. Laureys, L. Neelemans, and M. Warzu, *ibid.*, **3**, 217 (1963).
7. G. Herbsleb, *Werkstoffe u. Korrosion*, **16**, 929 (1965).
8. N. Tomashov, G. Chernova, and O. Marcova, *Corrosion*, **20**, 166t (1964).
9. M. Fokin, M. Kurtepov, V. Zhuravlev, and B. Oreshkin, First Int. Symposium on Desalination, Washington, D. C. (1965).
10. Ya. Kolotyrkin, *Corrosion*, **19**, 261t (1963).
11. H. Uhlig and J. Gilman, *ibid.*, **20**, 289t (1964).
12. F. L. LaQue in "Corrosion Handbook," p. 416, H. H. Uhlig, Editor, John Wiley & Sons, New York (1948).
13. R. Mears, *ibid.*, p. 49
14. Estimated from data of H. Kaesche, *Z. Physik. Chem. N.F.*, **34**, 87 (1962).
15. J. Matthews and H. Uhlig, *Corrosion*, **7**, 419 (1951).
16. F. Schafmeister and W. Tofaute, *Tech. Mitt. Krupp*, **3**, 223 (1935).
17. H. Uhlig and M. Morrill, *Ind. Eng. Chem.*, **33**, 875 (1941).
18. Ya. Kolotyrkin, G. Golovina, and G. Florianovitch, *Proc. Acad. Sci., USSR*, **148**, 1106 (1963).
19. T. Hoar, D. Mears, and G. Rothwell, *Corrosion Sci.*, **5**, 279 (1965).
20. M. A. Streicher, *This Journal*, **103**, 375 (1956).
21. S. Matsuda and H. Uhlig, *ibid.*, **111**, 156 (1964).
22. H. H. Uhlig, *Z. Elektrochem.*, **62**, 626 (1958).
23. Ya. Kolotyrkin, *This Journal*, **108**, 209 (1961).

A Dilatometric Study of the Cathodic Hydrogenation of Nickel

Kenneth A. Moon and Edward T. Clegg

United States Army Materials Research Agency, Watertown, Massachusetts

ABSTRACT

Hydrogen content and specimen elongation were measured as functions of reaction time during cathodic hydrogenation of nickel strip specimens of various thicknesses. In contrast to earlier work, the hydride appears to have a composition close to NiH. The reaction follows the parabolic rate law. The relation between elongation and hydrogen content depends on specimen thickness in a manner which can be simply interpreted in terms of the elastic and plastic properties of the hydride and metal, together with a residual stress in the newly formed hydride about 10^5 psi.

There has been a renewed interest in recent years in the role of volume changes in reactions where a new phase forms on the surface of a metal (1). Most of the work (2-7) has employed strip-deflection measurements as an indication of the stresses produced by the reaction. Only two papers (8, 9) are known to us in which dimensional changes of a specimen were reported. In this paper we report the results of a dilatometric study of the cathodic hydrogenation of thin strip specimens of nickel, in which both elongation and hydrogen content were followed as functions of time and specimen thickness. The results have been interpreted in terms of a residual compressive stress in the newly formed hydride, with subsequent relaxation conditioned by specimen dimensions and the elastic and plastic properties of the solids.

Nickel forms a hydride of reported (10-12) composition about $NiH_{0.7}$. The hydride has a fcc arrangement of nickel atoms, as in pure nickel, but the lattice constant is 6% greater (13, 14). The decomposition pressure of the hydride is about 20 kbar (15), but surface concentrations of hydrogen atoms equivalent to pressures exceeding this can be maintained in cathodic discharge by using a high current density and a suitable catalyst (16), although it has not so far been possible to obtain a hydride layer thicker than about 30μ. The amount of hydrogen which passes beyond the interphase surface to dissolve in the nickel core is negligibly small (11). Janko (17) has shown that hydrogenation and subsequent dehydrogenation of a nickel single crystal leave the outer layers of the crystal only slightly disoriented. The reaction is not perfectly reversible, as shown by x-ray diffraction (17), electrical resistance changes (18, 19), and microscopic examination (14).

Materials and Procedures

The nickel specimens were purchased from the H. Cross Company in the form of rolled "A" nickel strips 0.476 cm wide and of nominal thickness 0.5, 1, 2, 4, 8, and 12 mils. The calculated thicknesses, assuming a density of 8.9 g/cc, were 0.00124, 0.00250, 0.00468, 0.00980, 0.0197, and 0.0296 cm. Specimens 5.2 cm long were cut from the strips. To provide for mounting in the dilatometer, two 0.11-cm-diameter holes spaced 4.8 cm apart were punched near the ends of the specimens. In calculations, we used 4.6 cm as the effective specimen length, because the ends of the specimens were shielded from the electric current by the silica specimen holders of the dilatometer. Before use, the specimens were rinsed with ether and annealed for 4 hr at 900°C in a stream of hydrogen purified by permeation through palladium-silver alloy. Heating and cooling rates were 4°/min. After annealing, the stream of pure hydrogen was continued until the specimen was removed just before the start of a hydrogenation.

The dilatometer was constructed of fused silica, as shown in Fig. 1. The differential transformer was a Schaevitz Engineering Company Model 100SS-L. The power supply and amplifier was a Daytronic Corporation Model 300-C-60, and its recorder output was connected to a L&N Model H AZAR recorder. The specimens were mounted in the dilatometer by means of a silica pin through the upper hole in the specimen and corresponding holes in the transmission rod, and a platinum pin (for electrical connection) through the lower hole in the specimen and corresponding holes in the dilatometer body. After causing the assembly to settle into a stable position by gentle tapping, no further change occurred (in absence of hydrogenation) even with the ½ mil specimens. In several experiments, nickel reinforcing plates were fastened to the ends of a ½-mil specimen; the results were similar to those obtained in absence of reinforcing plates. Six sensitivity ranges were available, varying from ±0.1 in. to ±0.001 in. full scale. All scales used in this work were calibrated periodically with a special jig using a commercial micrometer. The force exerted by the dilatometer spring on the specimen was 37g.

Cathode current was supplied from a Harrison Laboratories Model 6202A power supply. The reported current density is subject to systematic errors due to uncertainty in the corrections applied to account for end effects and for the wire used to make electrical connection. The anode consisted of two identical perforated platinum sheets arranged symmetrically opposite the specimen faces about 6 cm from the faces. The electrolyte was 1250 ml of 1*N* sulfuric acid, in which 0.45g of thiourea was dissolved just before use. Before use, the electrolyte was brought to room temperature, preelectrolyzed with platinum electrodes, and then raised into position around the specimen. Voltage was applied to the specimen before the electrolyte touched it. Electrolyte temperature and room temperature remained constant within a few tenths of a degree throughout all runs, usually between 21° and 22°.

At the time chosen for terminating the hydrogenation, the electrolyte was removed, a central portion of the specimen was cut out with scissors, and this portion was rinsed with pure water and dropped to the bottom of a glass tube immersed in liquid nitrogen. Only a few seconds elapsed from the termination of hydrogenation to the chilling of the specimen. The tube was then connected to the hydrogen-analysis apparatus and the air and liquid oxygen were pumped away for a ten-minute period during which the specimen was kept at liquid-nitrogen temperature. The ap-

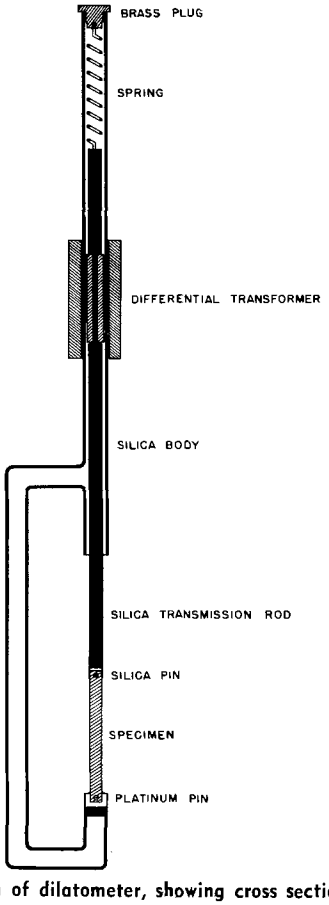

Fig. 1. Sketch of dilatometer, showing cross section through axis. Clamps, adjusting screws, etc., are not shown.

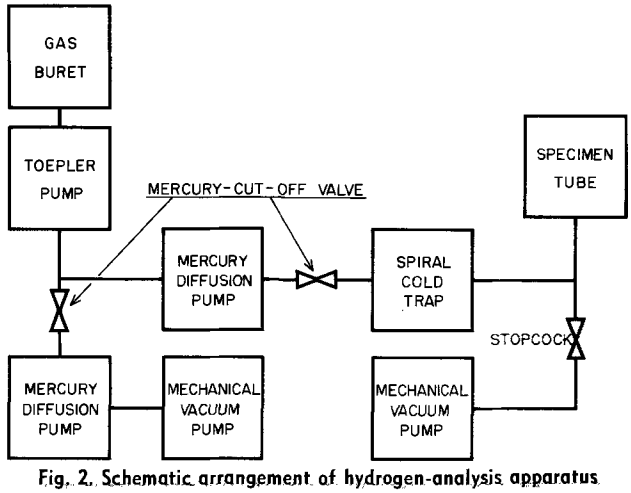

Fig. 2. Schematic arrangement of hydrogen-analysis apparatus

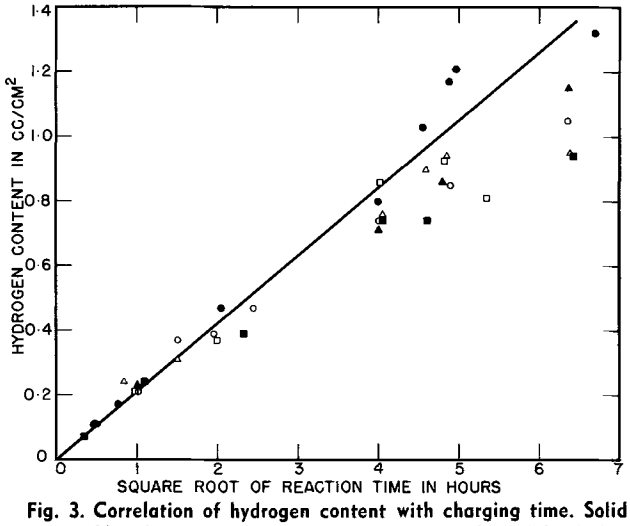

Fig. 3. Correlation of hydrogen content with charging time. Solid squares, ½-mil specimens; solid triangles, 1-mil; solid circles, 2-mil; open circles, 4-mil; open triangles, 8-mil; open squares, 12-mil.

paratus was a glass vacuum system of conventional design, as shown in Fig. 2. At the end of the 10-min period, the condensation trap was chilled with liquid nitrogen, the valves were adjusted to the positions for collecting hydrogen, and the specimen tube was allowed to warm up. When the water had evaporated from the specimen tube, the specimen was heated to 250° and the evolved hydrogen was transferred to the gas buret and measured.

Results and Discussion

Figure 3 shows hydrogen content *vs.* reaction time for our experiments in which cathode current density was 75 ma/cm². Hydrogen content is expressed in cubic centimeters of hydrogen gas (STP) per square centimeter of specimen surface area, ignoring the area of the edges. The reaction initially follows the parabolic rate law, whereas earlier workers (20) obtained a linear relation between hydrogen content and square root of reaction time only after an initial induction period. We presume that the induction period was due to an oxide layer on the specimens. The parabolic kinetics indicate that the reaction is controlled by volume diffusion in an unbroken surface layer of uniform thickness. For long reaction times the reaction becomes stationary and eventually retrograde, with poor reproducibility. This is not unexpected. The hydride is unstable at atmospheric pressure, so any paths which may exist for the outward passage of hydrogen molecules from the hydride layer will set up a counter-current reaction and bring the over-all reaction to a steady state. If such a path arises during the course of hydrogenation (*e.g.*, a crack), its conductance for hydrogen molecules will increase as time passes, because of localized shrinkage due to loss of interstitial hydrogen. We doubt that there is any need (15) for more elaborate arguments to explain the limited penetration of the hydride layer. An analogous situation exists in the oxidation of metals (1, p. 30), except in that case a failure of the surface layer produces an increase in the reaction rate, since the oxide is stable.

Earlier workers (10-12) have concluded that the hydride composition is about $NiH_{0.7}$, but our ½-mil specimens attain a hydrogen content about 1 cc/cm², corresponding to a minimum hydrogen content in the hydride equal to $NiH_{0.96}$. The reason for the discrepancy is unknown, but it might be due to oxygen impurity in the electrodeposited nickel specimens used in the earlier work. Since the hydrogen atoms in the hydride occupy octahedral interstitial sites (21), the

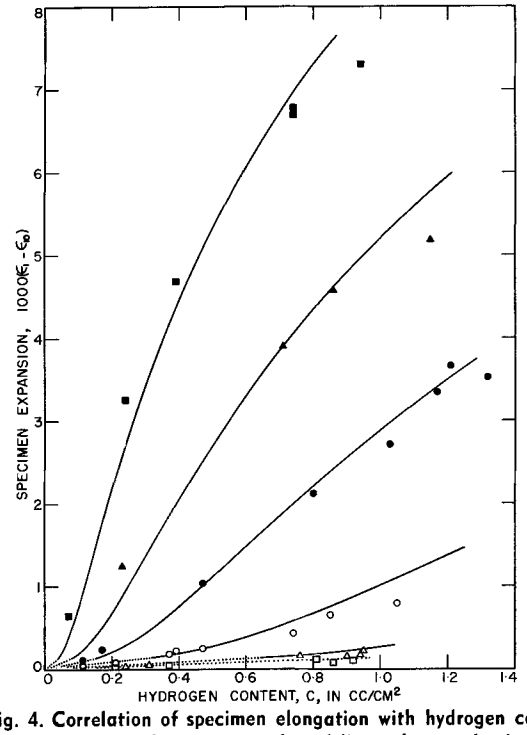

Fig. 4. Correlation of specimen elongation with hydrogen content. Solid lines, theory, plastic range; dotted lines, theory, elastic range; point symbols same as in Fig. 3.

probable upper limit of the hydride composition is NiH. Since our minimum value for the average hydride composition is very close to this upper limit, we conclude that the homogeneity range of the hydride is quite narrow.

Figure 4 shows the relation between specimen elongation and hydrogen content for the cathode current density of 75 ma/cm². A few experiments were run at other current densities, and the results suggest that the elongation *vs.* hydrogen content relationship is independent of current density. This is to be expected in view of the evidence, cited above, that the homogeneity range of the hydride is narrow.

We present here a simplified theoretical treatment which gives some insight into the results shown in Fig. 4. We assume that the hydride composition is NiH, and the density of nickel is 8.9 g/cc, so that the thickness of the unreacted nickel core is given by

$$T = T_o - BC \qquad B = 1.18 \times 10^{-3} \qquad [1]$$

where T_o is the initial specimen thickness in centimeters and C is the hydrogen content as defined above. If we let $R^{1/3}$ be the ratio of lattice parameter of hydride to that of nickel, to a good approximation

$$2D = R(T_o - T) \qquad R^{1/3} = 1.06 \qquad [2]$$

where D is the thickness of the hydride layer in centimeters. We next make some simplifying assumptions concerning the nature of the stress system in the specimen, since a rigorous analysis appears to be prohibitively difficult. We imagine the specimen sliced into a large number of laminae parallel to the faces of the specimen. We assume that in each lamina there is a uniform plane state of stress with one principal direction along the dilatometer axis and the other perpendicular to the dilatometer axis and parallel to the faces of the specimen. Edge effects are ignored. Coherency stresses at the metal/hydride interface are ignored; they must be of very short range, and exist in pairs of opposing effects relative to elongation of the specimen. We assume that the distension of the laminae is the same for all laminae. Thus, the nickel

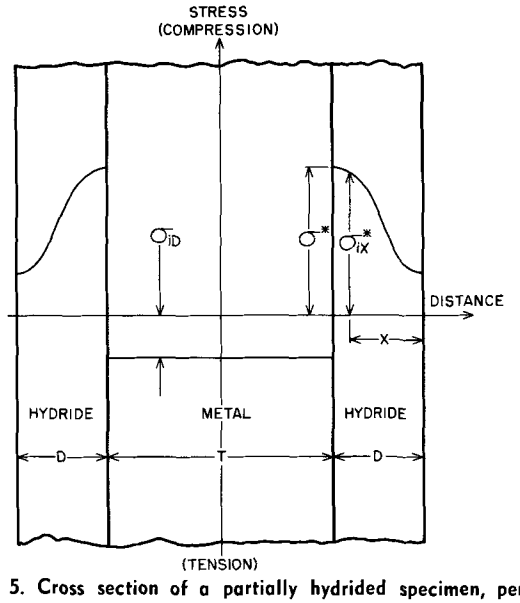

Fig. 5. Cross section of a partially hydrided specimen, perpendicular to specimen faces, showing the assumed distribution of stress.

core can be treated as a single lamina, but not the hydride laminae, since in them the strain (relative to the state of zero stress) will depend on their position relative to the reaction interface. The residual compressive stress in the newly formed hydride is assumed to have a fixed value σ^*, regardless of any strains existing in the nickel from which it was formed. Figure 5 shows the situation schematically.

We use the symbols σ_{iy}, ϵ_{iy}, E, ν, and σ^*_{ix}, ϵ^*_{ix}, E^*, ν^* for the stress, strain, Young's modulus, and Poisson's ratio of the nickel and hydride, respectively. Subscript i (1 or 2) refers to the principal directions in the laminae, 1 being the direction of the dilatometer axis. Subscript x indicates the depth of the hydride lamina relative to the outer surface of the hydride. The symbol y is the instantaneous value of the thickness of the hydride layer; that is, y increases from 0 to D during the course of the hydrogenation. Balance of forces gives $T\sigma_{1D} = T_0E\epsilon_{10} + 2\int_0^D \sigma^*_{1x}dx$, and $T\sigma_{2D} = 2\int_0^D \sigma^*_{2x}dx$, where $\epsilon_{10} = 3.685(10^{-8})/T_0$ is the initial strain due to the dilatometer spring. We assume that Hooke's law applies in the hydride laminae; that is, $E^*\epsilon^*_{ix} = \sigma^*_{ix} - \nu^*\sigma^*_{jx}$. (Note that this implies absence not only of plastic flow or cracking in the hydride, but also of any interdependence of strain and composition in the hydride.) Noting that $\epsilon^*_{ix} = \epsilon^* - (\epsilon_{iD} - \epsilon_{ix})$, where $\epsilon^* = (1-\nu^*)\sigma^*/E^*$ is the initial residual strain in the hydride, and combining all the above equations, we obtain

$$T(\sigma_{1D} - \sigma_{2D}) = T_0E\epsilon_{10} + 2E^*\{\int_0^D (\epsilon_{1y} - \epsilon_{2y})dy - D(\epsilon_{1D} - \epsilon_{2D})\}/(1+\nu^*) \quad [3]$$

$$T(\sigma_{1D} + \sigma_{2D}) = T_0E\epsilon_{10} + 2E^*\{\int_0^D (\epsilon_{1y} + \epsilon_{2y})dy - D(\epsilon_{1D} + \epsilon_{2D}) + 2D\epsilon^*\}/(1-\nu^*) \quad [4]$$

We first consider the case where strains in the nickel core are purely elastic, so that by Hooke's law, $E\epsilon_{iD} = \sigma_{iD} - \nu\sigma_{jD}$. In this case the solution of Eq. [3] and [4] is

$$\epsilon_{1D} - \epsilon_{1O} = (1/2)\epsilon_{1O}(1+\nu)(a_1F + + a_nF^n..) + (1/2)(1-\nu)(\epsilon_{1O} + 2R\sigma^*/E)(b_1F + + b_nF^n..) \quad [5]$$

where $F = BC/T_o$, $a_1 = b_1 = 1$, $a_n/a_{n-1} = 1 - RE^*(1+\nu^*)(n-1)/E(1+\nu)n$, and $b_n/b_{n-1} = 1 - RE^*(1-\nu^*)(n-1)/E(1-\nu)n$. Note that for small F, $(\epsilon_{1D} - \epsilon_{1O})$ is proportional to F, the slope being $\epsilon_{1O} + R\sigma^*(1-\nu)/E$.

The other case we consider is that in which specimen distension is great enough to produce plastic flow in the nickel core, but not in the hydride. Instead of Hooke's law, we use the Prandtl-Reuss equations of plastic flow in the form presented by Hill (22). Reduced to the form appropriate for our stress system, these are

$$d\epsilon_{iD} = (d\sigma_{iD} - \nu d\sigma_{jD})/E + (2\sigma_{iD} - \sigma_{jD})d\bar{\sigma}_D/2\sigma_DH'_D \quad [6]$$

where the generalized stress $\bar{\sigma}_D = (1/2)\{3(\sigma_{1D} - \sigma_{2D})^2 + (\sigma_{1D} + \sigma_{2D})^2\}^{1/2}$ is the same function, H, of a generalized plastic strain integral that stress is of plastic strain in a uniaxial tensile test. Rostoker's work (23) suggests that for nickel this functional relationship is of the form $(\bar{\sigma} - \bar{\sigma}_o)^2 = K\bar{\epsilon}^P$ where $\bar{\sigma}_o$ is the stress at the elastic limit, so the derivative H' in Eq. [6] is equal to $K/2(\bar{\sigma}_D - \bar{\sigma}_o)$. To simplify the computations, we have made the assumption $RE^* = E$ and $\nu^* = \nu$, in which case exact solutions are possible for the elastic range, as follows (with subscript D henceforth omitted)

$$\sigma_1 - \sigma_2 = E\epsilon_{10}e^F \quad [7]$$

$$(\bar{\sigma}/E)^2 = \epsilon^{*2}(e^F-1)^2/(1-\nu)^2 + \epsilon_{10}\epsilon^*(e^{2F}-e^F)/(1-\nu) + (\epsilon_{10}e^F)^2 \quad [8]$$

$$\epsilon_1 = \epsilon_{10}e^F + \epsilon^*(e^F-1) \quad [9]$$

For the plastic range

$$d\ln(\sigma_1 - \sigma_2) = dF - 3EF(\bar{\sigma} - \bar{\sigma}_o)d\bar{\sigma}/K\bar{\sigma}(1+\nu) \quad [10]$$

$$\frac{d\bar{\sigma}}{dF}\left\{4\sigma + \frac{EF(\bar{\sigma} - \bar{\sigma}_o)}{K\bar{\sigma}}\left[\frac{9(\sigma_1 - \sigma_2)^2}{1+\nu} + \frac{(\sigma_1 + \sigma_2)^2}{1-\nu}\right]\right\} = 4\sigma^2 + \frac{2\sigma^*}{R}[\sigma_1 + \sigma_2] \quad [11]$$

$$\frac{d\epsilon_1}{dF} = \epsilon^* + \frac{(\sigma_1 - \sigma_2)(1+\nu)}{2E} + \frac{(\sigma_1 + \sigma_2)(1-\nu)}{2E} + \frac{(2\sigma_1 - \sigma_2)(1-F)(\bar{\sigma} - \bar{\sigma}_o)}{K\sigma}\frac{d\bar{\sigma}}{dF} \quad [12]$$

The curves in Fig. 4 were constructed from Eq. [7]-[12], using numerical integration in the plastic range. We used the values $\nu = 0.31$ and $E = 3\text{x}10^7$ psi (24). By trial and error we selected as best values: $\epsilon^* = 0.0035$, $\sigma_o = 6000$ psi, and $K = 10^{11}$ psi^2. The values of σ_o and K cannot be compared directly with known experimental values because these two properties are strongly dependent on grain size, purity, specimen history, and testing conditions. However, we note in Fig. 5 of ref. (23) that for six specimens K ranged from $1.2\text{x}10^{10}$ to $8.0\text{x}10^{10}$ psi^2, and σ_o ranged from 2920 to 8810 psi. The value of ϵ^* would be 0.06 if no reorganization of the nickel lattice occurred at the reaction interface. Presumably the interface is semicoherent, and dislocation climb accounts for the discrepancy between 0.06 and 0.0035 (25). The value 0.0035 corresponds to $\sigma^* = 1.3\text{x}10^5$ psi, which is comparable to residual stresses found in some other systems (2, 3, 6, 7, 26), but is an order of magnitude greater than values reported previously (4, 5) for nickel hydride. Although the agreement between theory and experiment in Fig. 4 is only approximate, we cannot reasonably adjust σ^* appreciably lower than $8\text{x}10^4$ psi. In both of the earlier studies (4, 5) the estimate of the thickness of the hydride layer is open to criticism, and we believe that our value for the residual stress is to be preferred.

Acknowledgment

The authors are grateful to Mrs. Anna Hansen for performing the numerical integrations.

Manuscript received Feb. 21, 1966; revised manuscript received Aug. 1, 1966.

Any discussion of this paper will appear in a Discussion Section to be published in the June 1967 JOURNAL.

REFERENCES

1. U. R. Evans, "The Corrosion and Oxidation of Metals," Edward Arnold Ltd., London (1960).
2. P. D. Dankov and P. V. Churaev, *Doklady Akad. Nauk SSSR*, **73**, 1221 (1950).
3. W. Jaenicke and S. Leistikow, *Z. physik. Chem. (Frankfort)*, **15**, 175 (1958).
4. Z. Szklarska-Smialowska and M. Smialowski, *Bull. Acad. Polon. Sci., Ser. sci. chim. geol. geogr.*, **6**, 427 (1958).
5. A. T. Sanzharovskii and O. S. Popova, *Zhur. Prikl. Khim.*, **34**, 2120 (1961).
6. R. E. Pawel, J. V. Cathcart, and J. J. Campbell, *This Journal*, **110**, 551 (1963).
7. W. Jaenicke, S. Leistikow, and A. Stadler, *ibid.*, **111**, 1031 (1964).
8. J. Herenguel, D. Whitwham, and J. Boghen, *Compt. rend.*, **243**, 2060 (1956).
9. D. Whitwham, J. Boghen, and J. Herenguel, *Rev. Aluminium*, **34**, 611 (1957).
10. B. Baranowski, *Bull. Acad. Polon. Sci., Ser. sci. chim. geol. geogr.*, **7**, 897 (1959).
11. B. Baranowski and M. Smialowski, *ibid.*, p. 663.
12. B. Baranowski and M. Smialowski, *J. Phys. Chem. Solids*, **12**, 206 (1959).
13. A. Janko, *Bull. Acad. Polon. Sci., Ser. sci. chim.*, **8**, 131 (1960).
14. T. Boniszewski and G. C. Smith, *J. Phys. Chem. Solids*, **21**, 115 (1961).
15. B. Baranowski, *Bull. Acad. Polon. Sci., Ser. sci. chim.*, **10**, 451 (1962).
16. H. Jarmolowicz and M. Smialowski, *J. Catalysis*, **1**, 165 (1962).
17. A. Janko, *Bull. Acad. Polon. Sci., Ser. sci. chim.*, **10**, 613 (1962).
18. Z. Sklarska-Smialowska, *ibid.*, **8**, 305 (1960).
19. D. J. van Ooijen, *J. Phys. Chem. Solids*, **23**, 1173 (1962).
20. B. Baranowski, *Bull. Acad. Polon. Sci., Ser. sci. chim. geol. geogr.*, **7**, 907 (1959).
21. E. O. Wollan, J. W. Cable, and W. C. Koehler, *J. Phys. Chem. Solids*, **24**, 1141 (1963).
22. R. Hill, "The Mathematical Theory of Plasticity," p. 39, Oxford University Press, London (1950).
23. W. Rostoker, Armour Research Foundation, Illinois Institute of Technology, Report ARL-63-245, June, 1963.
24. C. J. Smithells, "Metals Reference Book," 2nd ed., vol. 2, p. 571, Butterworth, London (1955).
25. J. W. Christian in "Decomposition of Austenite by Diffusional Processes," p. 375, Interscience, New York (1962).
26. R. Pinner, *Electroplating and Metal Finishing*, **9**, 391 (1956); **10**, 7 (1957).

The Heat-Treatment of Anodic Oxide Films on Tantalum

V. The Thermal Redistribution of Incorporated Phosphorus

D. M. Smyth

Research and Development Laboratories, Sprague Electric Company, North Adams, Massachusetts

ABSTRACT

Dielectric measurements and radiotracer techniques have been used to follow the migration of incorporated phosphorus in anodic oxide films on tantalum during heat-treatment at temperatures above 400°. The phosphorus moves away from the tantalum, accumulating into a region of very high phosphorus content on the tantalum side of the phosphorus-containing layer. Little or no migration occurs on the other side of the layer. Redistribution is much more extensive when heat-treatment is carried out in air than when the ambient is a vacuum.

The effect of anodization electrolyte on the dielectric properties of heat-treated, anodized tantalum was reported in the preceding paper in this series (1). In particular, it was found that phosphoric acid has a profound effect, and this was correlated with a non-uniform incorporation of significant amounts of phosphorus in the anodic oxide, as reported by Randall, Bernard, and Wilkinson (2), and with the observation that the incorporated phosphorus inhibits the rate of diffusion of oxygen through the oxide during heat-treatment. The result is that the heat-treated oxide has an inner, shallow gradient of conductivity in the phosphorus-free region adjacent to the tantalum, and an outer, steep gradient of conductivity in the phosphorus-containing region which had formed adjacent to the electrolyte. The distinction between the two gradients increased with increasing H_3PO_4 concentration in the anodization electrolyte.

This work was based on the results of heat-treatments carried out at 400°, and it appeared that the distribution of phosphorus in the oxide was not affected by the heating. Efforts to extend these experiments to higher temperatures of heat-treatment led to substantial deviations from the earlier results. This is the subject of the present paper.

Experimental

The experimental details have been described previously (1, 3-5). Unless specifically stated otherwise, all work reported here concerns samples anodized in 14.6M H_3PO_4 (the commercial 85% acid) to 75v with the heat-treatment being carried out in air. Dielectric measurements were made in a 40% aqueous solution of H_2SO_4.

Results and Discussion

The pertinent results are shown in Fig. 1 in the form of plots of log frequency *vs.* the reciprocal series capacitance. As shown previously (5), this is equivalent to a plot of log conductivity *vs.* position in the film with the Ta_2O_5-electrolyte interface at $1/C = 0$. The measurements were made over a frequency range of 50-3200 Hz at two temperatures, 34° and 0°. The results were then all normalized to 34° by use of the activation energy of conduction of 0.6 ev previously reported (5). This, in effect, extends the frequency range at 34° to 55,000 Hz. The mathematical basis for this is contained in the expressions

$$\sigma_0 = Ae^{-E/kT} \quad [1]$$

$$\sigma_0 = \omega\epsilon\epsilon_0 \quad [2]$$

where [1] represents the temperature dependence of semiconduction, and [2] expresses the relationship between σ_0, the level of conductivity which defines the boundary between effective dielectric and effective electrode and the frequency ($\omega = 2\pi f$). These relations are discussed in detail in ref. (5). This technique is used to extend the data range to frequencies which would otherwise be prohibitive because of the low sample impedance.

According to our usual interpretation of these data, each plot in Fig. 1 represents a portion of a conductivity profile across the heat-treated oxide. The data do not extend to sufficiently high frequencies to show

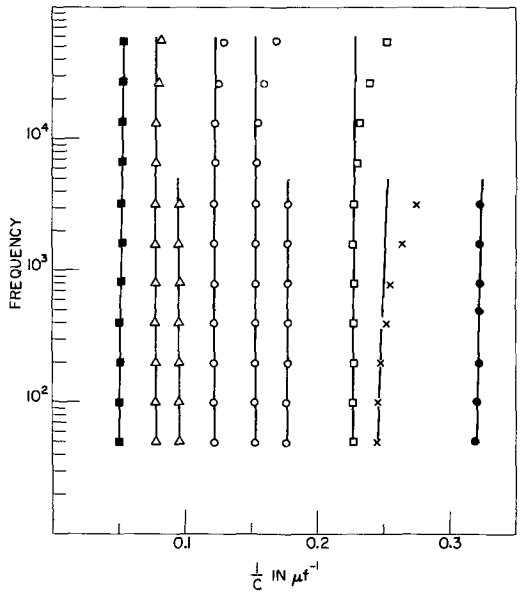

Fig. 1. Effect of time and temperature of heat-treatment on the dielectric properties of tantalum anodized in 14.6M H_3PO_4. From right to left: • unheated; X 300°, ½ hr; □ 400°, 1 hr; ○ 500°, ¼ hr, ½ hr, 1 hr; △ 550°, ¼ hr, 4 hr; ■ 600°, ¼, ½, 1 hr (same curve).

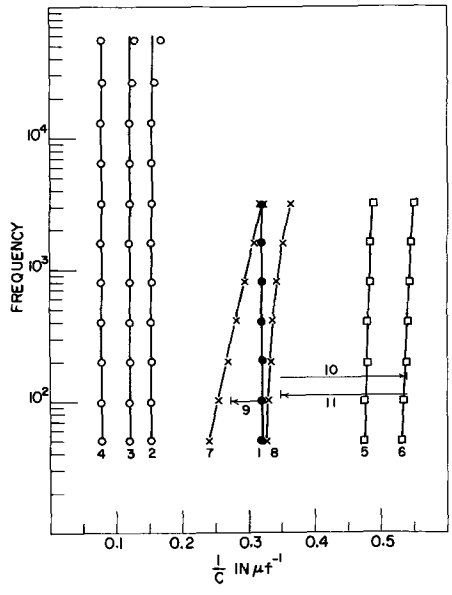

Fig. 3. Effect of reformation and bias on the dielectric properties of tantalum anodized in 14.6M H_3PO_4 and heat-treated. Numbered sequence: 1, • unheated; 2, ○ 500°, ½ hr; 3, ○ 500°, 1 hr; 4, ○ 500°, 4 hr; 5, □ reformed, 75v, ½ hr; 6, □ reformed, 75v, 3½ hr; 7, X 20v bias (after relaxation from 6); 8, X 50v bias; 9, 3 hr, no bias; 10, 1 hr, 75v; 11, 18 hr, no bias.

the profile all the way to the Ta-Ta_2O_5 interface which presumably lies in the vicinity of the curve shown for an unheated sample, *i.e.*, at about $1/C = 0.3\ \mu f^{-1}$. In each case, the effective dielectric thickness at low frequencies is represented by the region between the conductivity profile and $1/C = 0$.

The results show two main factors. As the heat-treatment conditions become increasingly severe in terms of either temperature or time, the interface between effective dielectric and effective electrode moves toward the Ta_2O_5-air interface, and it becomes sharper in the sense that it remains nearly vertical to higher frequencies. This effect reaches saturation for heat-treatment at 600°. The effect of the phosphorus content becomes particularly evident at 600°, since samples formed in 0.01M H_2SO_4, for instance, undergo almost complete physical deterioration at this temperature. The anodic oxide film is extensively disrupted by powdery, white oxide, whereas those samples anodized in 14.6M H_3PO_4 survive with clear, unimpaired oxide films.

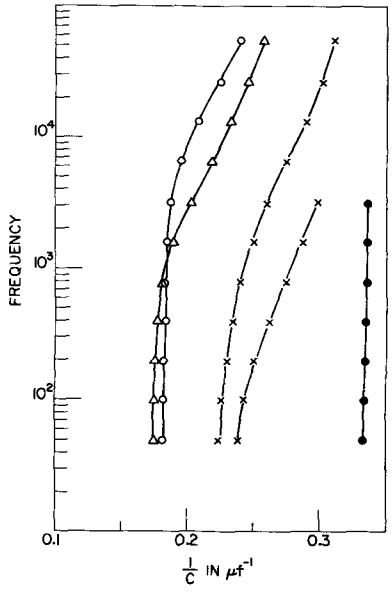

Fig. 2. Effect of heat-treatment on the dielectric properties of tantalum anodized to 37.5v in 14.6M H_3PO_4, then to 75v in 0.01M H_2SO_4. From right to left: • Unheated; X 300°, ½ hr; X 300°, 4 hr; ○ 500°, ½ hr; △ 550°, 1 hr.

Figure 2 shows similar results obtained from samples anodized first to 37.5v in 14.6M H_3PO_4 and then to 75v in 0.01M H_2SO_4. It has been shown that the oxide film formed from this type of anodic oxidation contains a phosphorus-containing layer sandwiched between outer and inner phosphorus-free layers (2). It is seen that heat-treatment has less effect on this type of sample.

When samples which have been anodized in 14.6M H_3PO_4 and extensively heat-treated in air are subjected to reanodization at the original anodization voltage, the results are rather complicated. Some of this behavior is shown in Fig. 3. Reanodization decreases the capacitance to values substantially below the original, preheated value. Moreover, a distinct change in interference color indicates that additional oxide growth has occurred. The dielectric properties of the reanodized samples drift with time, however. Without bias the capacitance returns to the vicinity of the preheated value and becomes much more frequency-dependent. From the results shown in Fig. 3 it appears that the application of a substantial bias, as is done during reanodization, results in a severe polarization effect which decays very slowly. This behavior is not understood at the present time.

If we are to accept the dielectric behavior at face value, the results indicate that the dielectric-electrode interface, and hence the interface between phosphorus-containing and phosphorus-free oxide, is moving toward the Ta_2O_5-air interface during heat-treatment at 400° and above. This movement is greatly reduced when the phosphorus-containing layer is sandwiched between two phosphorus-free layers (anodization in H_3PO_4, followed by anodization in H_2SO_4). Fortunately, the radiotracer technique described by Randall, Bernard, and Wilkinson offers a direct test of this interpretation (2).

In the initial radiotracer experiment, two samples were anodized to 75v in 14.6M H_3PO_4 containing P^{32}. The anodization was carried out at 1 ma/cm^2 to 75v

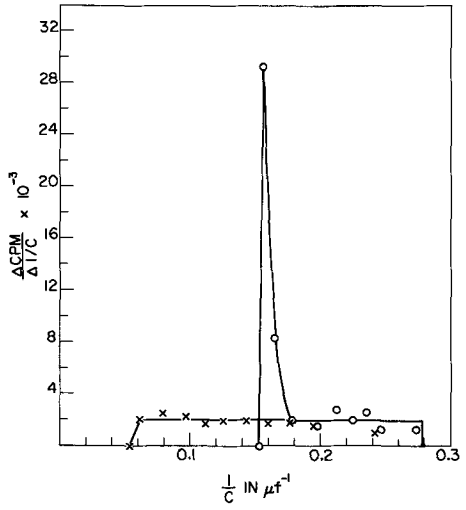

Fig. 4. Effect of heat-treatment on the distribution of phosphorus in anodized tantalum. X Unheated; ○ heated, 500, 1 hr, in air.

and then at 0.1 ma/cm^2 to the same voltage. The samples were not held at constant voltage. Two other samples were similarly anodized to 37.5v in the radiotracer H_3PO_4 and then to 75v in 0.01M H_2SO_4. One sample of each kind was heated at 500° in air for 1 hr. The phosphorus profile across the oxide was then determined for each sample by the removal of successive thin layers of oxide in HF. The results are shown in Fig. 4 and 5 in which $\Delta CPM/\Delta 1/C$ has been plotted against 1/C. ΔCPM represents the difference in counts-per-minute of the sample before and after a particular etching and therefore is the amount of activity removed by the etching. $\Delta 1/C$ is the related difference in the reciprocal series capacitance and thus represents the thickness of oxide removed. It follows that $\Delta CPM/\Delta 1/C$ is proportional to the concentration of phosphorus in the dissolved oxide, and this has been plotted against position in the film as determined by 1/C. These plots thus represent the distribution of phosphorus in the oxide. In the case of the heated samples, a portion of the oxide adjacent to the tantalum is conducting, and the capacitance values are consequently greater than those of the unheated samples. In order to get a meaningful geometric picture of the phosphorus distribution, a constant value of 1/C has been added to each value for the heated samples in order to normalize the results at the Ta_2O_5-electrolyte interface. In actuality, the residual radioactivity and the reciprocal series capacitance went to zero at the same point in the oxide for the heat-treated samples. This correlation has been discussed previously (1).

The initial observation was that the total radioactivity of the samples was unchanged, within experimental accuracy, by the heat-treatment. Hence no phosphorus was lost from the films. The results show that the interface between phosphorus-containing and phosphorus-free oxide has indeed moved toward the Ta_2O_5-air interface as a result of heat-treatment. The movement has taken place in a very peculiar manner. The phosphorus has accumulated into a concentrated region at the interface, apparently by the complete depletion of the phosphorus content of the oxide on the side toward the tantalum. The phosphorus content of the oxide on the other side of the accumulation region has not been disturbed. Moreover, in the case of the buried phosphorus-containing layer, the accumulation has occurred only on the tantalum side of the layer.

The radiotracer analysis confirms the conclusions drawn from the capacitance measurements. The apparent movement of the boundary between conducting and nonconducting oxide is in good agreement with the movement of the boundary between phosphorus-containing and phosphorus-free oxide. Moreover, the high concentration of phosphorus at the interface accounts for the observation that the log f *vs.* 1/C plots shown in Fig. 1 remain vertical to higher frequencies as the extent of heat-treatment is increased. However, the nature of the accumulation of phosphorus is most peculiar and deserves further consideration. First of all, the migration is clearly against the direction of the concentration gradient; and, second, in the case of the buried layer, Fig. 5, the migration took place only on the side facing the tantalum. It is interesting to note that for the latter situation, the two sides of the phosphorus-containing layer differ greatly in oxygen deficiency and conductivity during and after heat-treatment, according to the model discussed previously (1). This is depicted schematically in Fig. 6. Possibly the phosphorus diffuses more readily where the oxygen vacancy concentration is high, or the potential distribution in the oxide may be very important.

A further attempt was made to clarify the situation as follows. Two identical samples were made, as before, to have buried radiophosphorus-containing layers. One of these was heated at 500° for 1 hr in air, while the other was heated at 500° for 1 hr in a vacuum of 5 x 10^{-7} Torr. The latter sample was then reanodized at 50v for 1 hr in 0.01M H_2SO_4 in order to form an outer, insulating layer so that capacitance measurements could be used to determine the thick-

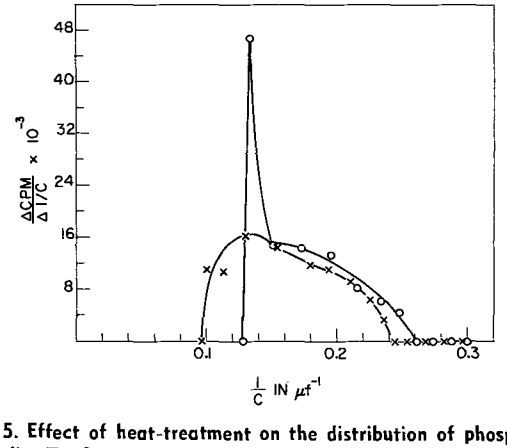

Fig. 5. Effect of heat-treatment on the distribution of phosphorus in anodic Ta_2O_5 with a buried phosphorus-containing layer. X Unheated; ○ heated 500°, 1 hr, in air.

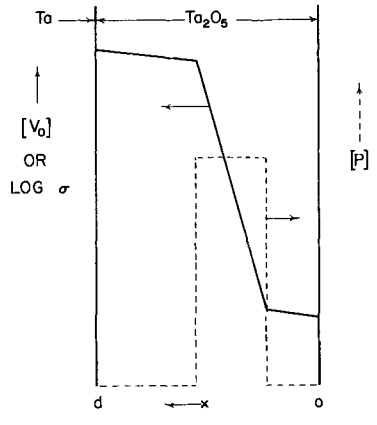

Fig. 6. Schematic representation of oxygen deficiency (V_o), conductivity σ, and phosphorus concentration (P) across anodic oxide formed in H_3PO_4.

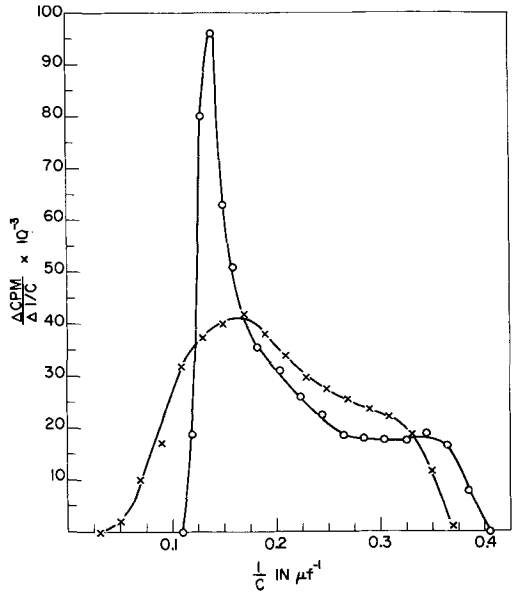

Fig. 7. Effect of ambient atmosphere on the redistribution of phosphorus in anodic Ta_2O_5 during heat-treatment. ○ 500°, 1 hr, in air; X 500°, 1 hr, in vacuum.

ness of oxide removed during each etching of the phosphorus profile determination. Prior to this reanodization the capacitance was extremely high, indicating that the oxide film was oxygen deficient and conducting throughout. The reanodization should not affect the distribution of phosphorus in the oxide (2). The usual radiotracer analyses indicated the phosphorus distributions shown in Fig. 7. (Again the results have been normalized so that the apparent Ta_2O_5-electrolyte interfaces coincide, in this case at $1/C = 0.52\ \mu f^{-1}$.) The sample heated in air behaved as before, but the vacuum-heated sample shows much less rearrangement of phosphorus.

The behavior of the vacuum-heated sample could be explained in two ways. Some initial migration of phosphorus could have occurred prior to the completion of the oxygen depletion throughout the film, at which point migration ceased; or, a form similar to that of the air-heated sample may have initially formed, and, after the entire region became oxygen-deficient and conducting, the sharp hump of phosphorus content may have started to decay by ordinary diffusion. The latter explanation is preferred, since all of the air-heated samples have shown an abrupt interface at the junction between phosphorus-containing and phosphorus-free oxide. In addition, all of the dielectric measurements have indicated a sharp boundary, even for very small amounts of boundary movement. No transient situation has ever been seen in an air-heated sample which would suggest a phosphorus distribution similar to that of the vacuum-heated sample in Fig. 7.

If the preferred sequence just described is correct, it suggests that the original accumulation of phosphorus is a field-driven process, since ordinary diffusion behavior occurs once the film becomes uniformly conducting (ordinary diffusion behavior in the sense of the flattening of peaks and rounding of edges of a concentration profile). A field-driven mechanism seems more likely to build up the sharp peak of concentration of phosphorus than a diffusion process. Even if there were a tendency for the phosphorus-containing region to separate into a phosphorus-rich phase and a phosphorus-free phase, it seems unlikely that the phosphorus-rich phase would separate out into such a neat pile. It would be more likely to collect into isolated clumps. Thus, although the precise mechanism is not clear, it appears more likely that the phosphorus is driven by an electric field associated with the boundary between the two conductivity gradients.

The extent to which the phosphorus accumulates is quite remarkable. According to Randall *et al.*, the concentration of phosphorus in the phosphorus-containing region of a tantalum oxide film formed in 14.6M H_3PO_4 corresponds to about a phosphorus atom for each five tantalum atoms (2). The radiotracer work reported here shows accumulations of phosphorus up to at least ten times that present prior to heat-treatment. It is thus a major constituent of that portion of the oxide. Oxides of niobium and tantalum with high contents of phosphorus are not unknown. Shtin and Sharova have described amorphous precipitates obtained by the addition of phosphoric acid to solutions of niobium and tantalum (6, 7). Compositions of $2M_2O_5 \cdot P_2O_5 \cdot 6H_2O$ and $M_2O_5 \cdot P_2O_5$ (after calcining at 1000°) were reported, where M = Ta or Nb. A variety of crystalline compounds having the general composition $A_2O_5 \cdot 9M_2O_5$ have been characterized by Waring and Roth, where A = P, As, or V, and M = Ta or Nb (8). Although the relationship between these various materials and the amorphous, phosphorus-containing, anodic films is not clear, the chemical compatibility of phosphorus with niobium and tantalum oxides is demonstrated.

Acknowledgment

The author gratefully acknowledges the assistance of Dr. J. J. Randall, Jr., and Mr. Stanley Szpak, who carried out the radiotracer analysis, and the experimental assistance of Miss Marjorie Cutler.

Manuscript received June 13, 1966.

Any discussion of this paper will appear in a Discussion Section to be published in the June 1967 JOURNAL.

REFERENCES

1. D. M. Smyth, T. B. Tripp, and G. A. Shirn, *This Journal*, **113**, 100 (1966).
2. J. J. Randall, Jr., W. J. Bernard, and R. R. Wilkinson, *Electrochim. Acta*, **10**, 183 (1965).
3. D. M. Smyth, G. A. Shirn, and T. B. Tripp, *This Journal*, **110**, 1264 (1963).
4. D. M. Smyth and T. B. Tripp, *ibid.*, **110**, 1271 (1963).
5. D. M. Smyth, G. A. Shirn, and T. B. Tripp, *ibid.*, **111**, 1331 (1964).
6. A. P. Shtin and A. K. Sharova, *Razdelenie Blizkikh po Svoistam Redkikh Metal*, **1962**, 107; (*C. A.*, *58*, 9858)
7. *Idem.*, *Tr. Inst. Khim., Akad. Nauk S.S.S.R., Ural'sk. Filial* **1963** (7), 91; (*C. A.*, *61*, 8948)
8. J. L. Waring and R. S. Roth, *Acta Cryst.*, **17**, 455 (1964).

Effects of Growth Conditions on Microstructures in CdS:Cu Single Crystals

Arthur Dreeben

RCA Laboratories, Radio Corporation of America, Princeton, New Jersey

ABSTRACT

The sublimation temperature used to grow large boules of CdS:Cu affects the concentration of incorporated copper, while temperature differences along the boule affect the distribution of the impurity in the crystal. Lower sublimation temperatures tend to form crystals with dislocation tangles in which decorated loops, helices, dipoles, and cardioid configurations have been identified. Rapid growth leads to polygonization and formation of grain boundaries where precipitates, which are affected by the degree of crystallographic misorientation around the boundary, differ in size and geometry from those in the grains.

It was previously shown that the acceptor elements copper, silver, and gold form precipitates in CdS crystals (1). In the case of copper, the presence of extraneous phases shaped as needles, rods, or disks were related to different concentrations of the copper impurity. Gold, under the initial growth conditions, formed a single type of discrete hexagonal platelets lying in the CdS (0001) plane. Later, two kinds of platelets, differing in size, orientation, composition, and associated dislocations, were identified as resulting from a variation in growth conditions (2).

In this paper, the influence of growth conditions on microstructures directly observable in CdS:Cu single crystals by optical microscopy is described in terms of crystal perfection and a variety of decorated dislocations, some of which have not previously been identified in II-VI compounds.

Crystal Growth

The crystals were grown from the vapor phase in a pointed quartz tube which slowly advanced into a decreasing temperature gradient, as shown in Fig. 1, to produce boules 1-2 in. long and ½ in. in diameter (1, 3). The sintered CdS charge, containing the added impurity, sublimes at the temperature, T_{max}, and, as the growth run starts, the tip of the tube is at temperature T_2. In practice, the position of the tube is adjusted so that T_2 is 14°-20° lower than T_{max}. At the end of the run, the crystal boule is between the gradient temperatures, T_3 and T_4, at the moment when slow cooling to room temperature begins.

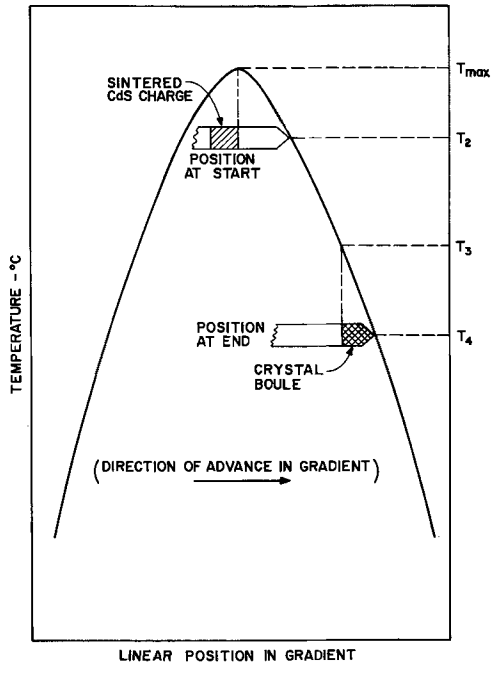

Fig. 1. Temperature profile and growth tube positions for preparing CdS crystal boules.

Although many parameters undoubtedly influence the growth characteristics of the crystal, the present work indicates that the amount and distribution of copper in the boule, the morphology of the precipitate phase, and the types of dislocations depend to some extent on T_{max} and $\Delta t = (T_3 - T_4)$. Grain boundary formation in the boule depends on T_{max} and also on the rate at which the growth tube passes through the gradient, slower rates favoring fewer grains. The results pertain to as-grown crystals slowly cooled at the same rate to room temperature, and will be illustrated with reference to crystallographically oriented, mechanically polished slices from representative boules.

Effects of Growth Conditions

Copper concentration.—The concentration of copper found in the boules is always less than that originally in the corresponding CdS charges, some copper (along with other impurities) concentrating in the unsublimed CdS.[1] This result, obtained consistently in many growth runs, was often obvious from the distinct difference in color and transparency between charges and the resulting boules. The observation was confirmed by chemical analyses. For example, 0.04-0.05 w/o Cu were found in two representative boules prepared with T_{max} at 1227°C, from charges containing 1 and 1.5 w/o copper. There was, in addition, an indication from only a few experiments that the final amount of copper in the boules may also depend on the particular T_{max} used, more copper apparently being incorporated at higher temperatures. A quantitative relationship between copper concentration and temperature has not been established, but this trend was suggested by chemical analyses of a few boules for which T_{max} differed by about 20°. For smaller differences, the effect was not well defined.

The total amount of copper in as-grown samples is partly in solid solution and partly precipitated. Examination of many boules revealed variations in the color and precipitation patterns of individual crystal slices from a given boule, thus showing that the copper is not always homogeneously distributed. In general, there is a larger amount of copper at the higher temperature end, T_3. This concentration gradient appears to result from the progressive change in charge composition caused by the fractionation effect, re-

[1] Similar fractionation effects have also been observed by others using this growth method (17).

ferred to above, and from the temperature difference across the boule as it grows. This difference, which reaches 40°-60° toward the conclusion of a growth run, is sustained by the boule for many hours, and it has previously been shown that temperature differences of 20° cause a similar marked segregation of copper in CdS crystals (4). Slight variations in precipitate segregation were occasionally found in adjacent regions of a boule over which the local temperature difference was small compared with Δt. Chemical analyses have shown that such samples may, nevertheless, have virtually the same amounts of total copper. These effects are influenced by slight fluctuations in growth rate and are related to a temperature dependence of solubility (5).

Precipitation and dislocations.—Precipitation in the interior of a CdS:Cu crystal grown with T_{max} = 1228°C, and containing about 0.05 w/o copper, occurred in the form of rods with a tendency to align in hexagonal arrays in the basal plane (1). However, other boules, grown in the same way, but with T_{max} =1217°C, had the same final amount of copper, but entirely different precipitation patterns and dislocation arrays which will be described. Temperatures were maintained at ± 1°-2° as shown by periodic, recorded monitoring for extended periods. This variation would occur as a gradual drift rather than as abrupt changes. The 11° difference between the nominal T_{max} values, which were the only deliberately altered parameter, is, therefore, regarded as a significant factor in determining the microstructure characteristics. Some contribution, however, from another, presently undefined parameter, is not entirely excluded. Previous evidence (1) indicated that the precipitate phase was copper sulfide; however, changes in composition may also accompany the changes in morphology.

Precipitation in the present crystals is characterized by randomly distributed particles and dislocation tangles. As viewed in the basal plane, the crystals often have relatively clear subgrains, partially denuded by preferential precipitation along the low angle boundaries that enclose them, as seen in Fig. 2. These boundaries extend in depth, approximately parallel to the c-axis, with many decorations emanating from them and extending into the clear areas in which the observed patterns change with the focal length selected.

Helical dislocations are among the several configurations observed in these crystals. The example in Fig. 3 shows evidence of climb, while others were clearly seen to be held up by precipitates in their paths. Heavier local precipitates, similar in appearance to those acting as obstacles, are also found in linear arrays not directly associated with other dislocations. In Fig. 4, for example, the symmetry of the decorations taken in pairs suggests that they occur at sites where successive turns of a helical dislocation intersect the (0001) plane.

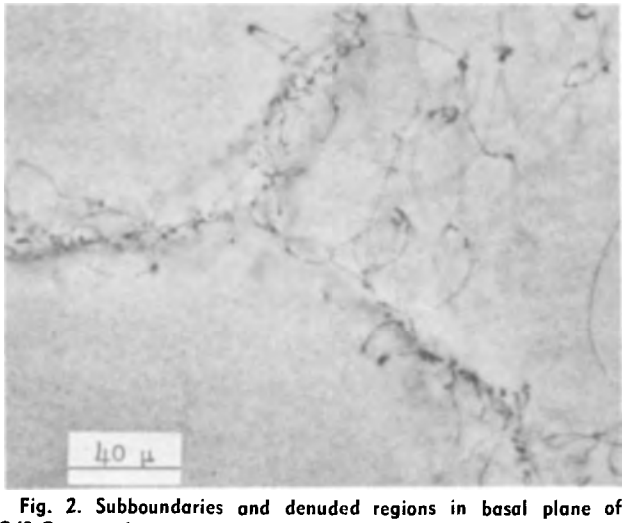

Fig. 2. Subboundaries and denuded regions in basal plane of CdS:Cu crystal.

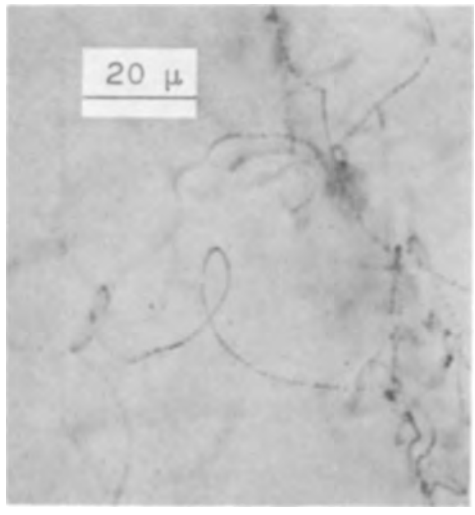

Fig. 3. Helical dislocation

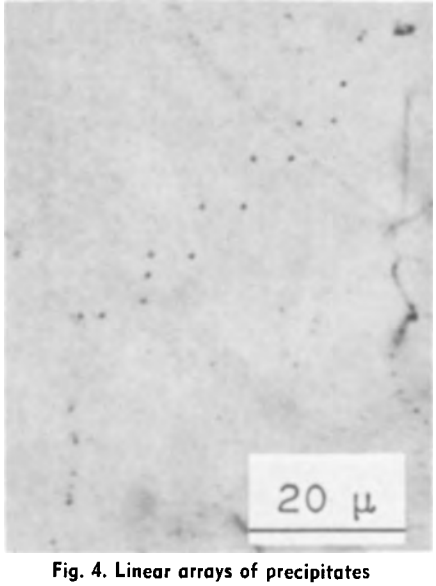

Fig. 4. Linear arrays of precipitates

Some illustrations of elliptically shaped loops lying in the basal plane with their major axis in crystallographic a-directions, are seen in Fig. 5A. The two loops in Fig. 5B lie in the [11$\bar{2}$0] direction, but one is about 10μ below the other. The formation of such a succession of coaxial loops may occur from the repulsion between successive turns of a growing helix as observed and discussed by Dash for the formation of prismatic loops in silicon doped with gold (6). When the present work was concluded, Möhling and Peibst (7), employing the Lang technique, reported their observation of helical dislocations and prismatic rings in pure CdS platelets. These configurations were also thought to have been formed by the Dash mechanism, and even in the pure crystals, the presence of trace impurities was believed necessary for the generation and climb of the dislocations.

Another typical dislocation form is comprised of two curved segments extending toward each other from subboundaries to meet at a cusp where a more prominent circular precipitate is found. Often, several parallel systems of this type are grouped together as

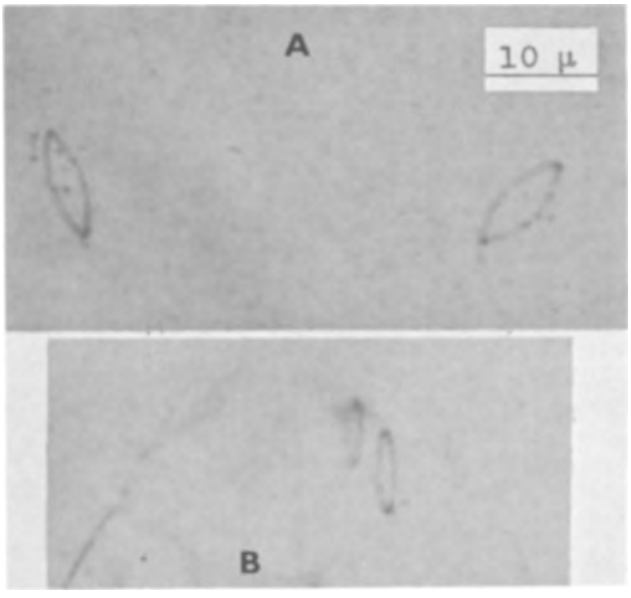

Fig. 5. Dislocation loops in basal plane

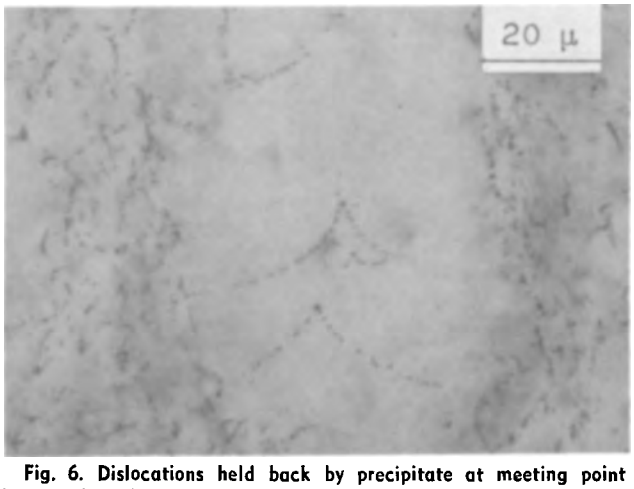

Fig. 6. Dislocations held back by precipitate at meeting point between boundaries.

shown in Fig. 6. Although these curved decorations generally lie in the basal plane, a portion of an arm will occasionally incline into the crystal. Other similar hairpin-like configurations, not necessarily between boundaries, have additional parallel extensions as in Fig. 7A, or segments closer together as in Fig. 7B. All of these formations are suggestive of dislocation dipoles that can result from an obstacle in the path as discussed by Gilman and Johnston (8), and Stokes and Olsen (9). Barber and Tighe (10) have pointed out that a smaller obstacle results in a larger curvature of a dipole.

An example of well-formed cardioid decorations observed within these hexagonal crystals, is shown in Fig. 8. Configurations of this type suggest the operation of a Frank-Read source (11), or a recent modification by Damiano and Brown (12), to account for the generation and multiplication of dislocations nucleated at inclusions, to form closed loops in a (0001) plane of hexagonal zinc crystals.

So far, only the new dislocations resulting from growth conditions employing a relatively low T_{max} have been described. It will now be shown that more rapid growth leads to the formation of gross defects. The growth rate can be affected by increasing either T_{max} or the rate of advance into the gradient. It was found that even at 1234°C, or at a rate of 0.02 in./hr (twice the usual rate) the boules contained more grain boundaries and polygonized regions. The boundaries of

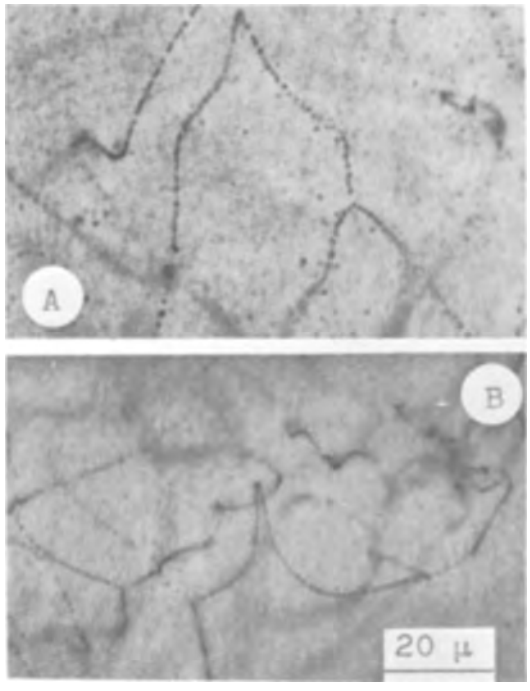

Fig. 7. Dislocation dipoles in (0001) plane

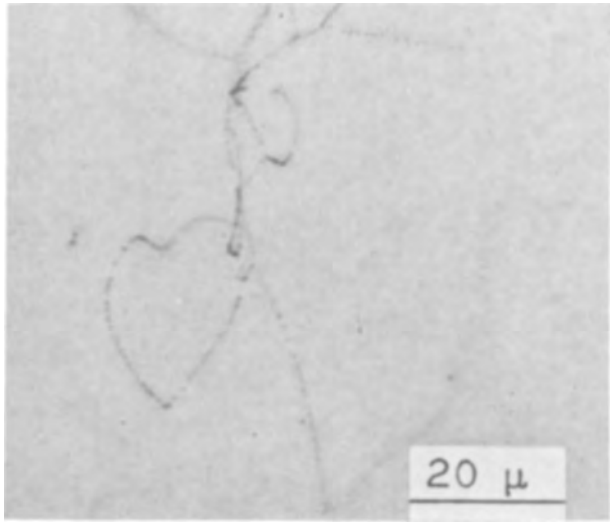

Fig. 8. Cardioid dislocation in basal plane

the hexagonal polygonization network shown in Fig. 9, for example, are decorated with disk-shaped precipitates[2] previously found to occur in single crystals with copper concentrations of about 0.8-1.0 w/o (1). This heavy segregation at the boundaries has substantially denuded the enclosed regions, many of which nevertheless contain rod-like precipitates characteristic of 0.2 w/o copper (1).

In another crystal, the grain boundary shown in Fig. 10 extended along the entire boule, parallel to the growth axis, and it can be seen that here, also, the preferential precipitation along the boundary has denuded the surrounding areas. The grain below the boundary has a (0001) face parallel to the plane of observation, while the angular misorientation of the upper grain is 17° with respect to the c-axis. The boundary extends through the crystal inclined at an angle of 10° to the plane of observation. The lines visible in Fig. 10B, extending into this region, are not

[2] Some details, such as the shape of the precipitates in this case, can be seen with greater clarity under the microscope than they can in the photomicrograph.

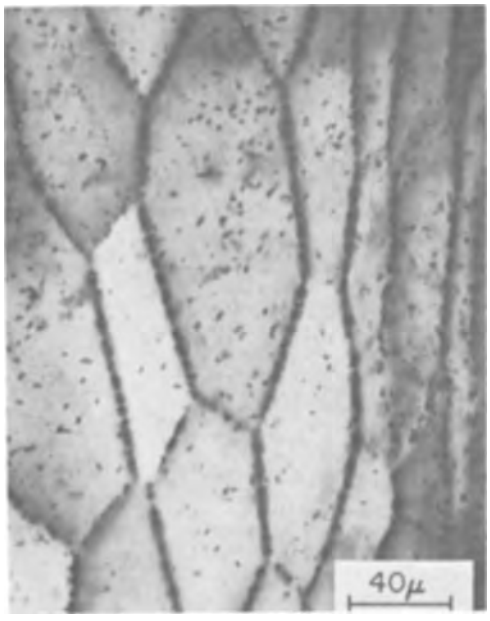

Fig. 9. Polygonization in CdS:Cu crystal

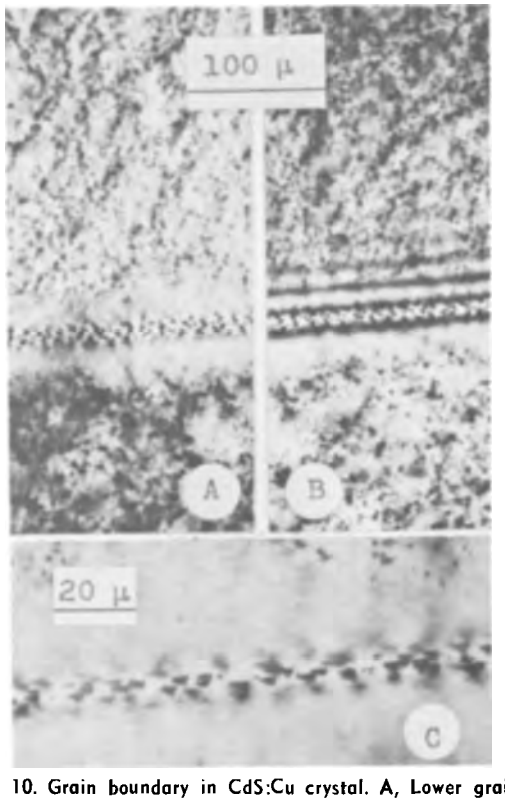

Fig. 10. Grain boundary in CdS:Cu crystal. A, Lower grain with (0001) face, upper grain misoriented by 17°; B, same field between crossed polaroids showing strain birefringence bands; C, high magnification showing discrete triangular precipitates in boundary region.

dislocation lines, but rather strain birefringence bands seen between crossed polaroids. It is noteworthy that in this higher energy boundary region, the nature of the precipitate is quite distinct from that in either grain. The outstanding differences, as seen under high magnification in Fig. 10C, are the larger size and triangular shape of the discrete platelets which are oriented with their bases along a $[2\bar{1}\bar{1}0]$ direction, and an apex pointed in a $[01\bar{1}0]$ direction toward the lower (0001) grain.

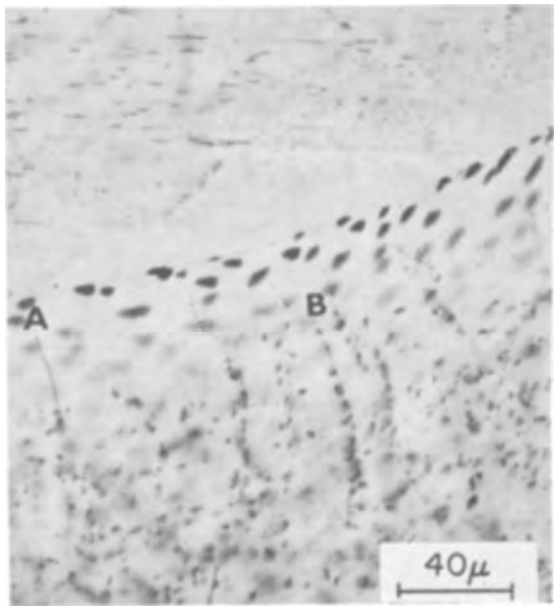

Fig. 11. Grain boundary in CdS:Cu crystal with greater misorientation than in Fig. 10; upper grain, $(10\bar{1}0)$ face; lower grain—c-axis inclined away from boundary at 29° angle. Note larger size of boundary precipitates compared with Fig. 10C, and dislocation lines at A and B.

Another example of this kind of boundary, in a similar crystal, is shown in Fig. 11, but here there is an even greater crystallographic misorientation of the two grains. The upper grain is a $(10\bar{1}0)$ face in which the precipitate needles are normal to the c-axis, [0001], and parallel to the a-direction, $[11\bar{2}0]$. Although the boundary itself does not lie entirely in this $[11\bar{2}0]$ direction, a flat side of the larger precipitates in the boundary region, is oriented this way. In the lower grain, the c-axis is inclined at an angle of 29° to the face, rotated away from the boundary about an a-axis approximately parallel to the $[11\bar{2}0]$ direction in the upper grain. The discrete precipitates in this boundary are almost twice the size of those in Fig. 10C, suggesting that different energies are associated with the two boundaries. Changes in these boundary precipitates have also been observed as a function of the impurity concentration in the grains. Similar effects, related to the orientation of grains have been reported for precipitation along boundaries in metals (13, 14). These effects may also depend on differences in nucleation rates within boundaries and on differences in precipitate growth rates which result from the more rapid solute diffusion along the boundaries (15). It is possible that there is also a local variation of composition (16).

Although these boundaries seem to be the source for some dislocations (at A and B, Fig. 11, for example), there is no extensive system of tangles as with the sub-boundaries previously described (see Fig. 2). The reason may be related to differences in local energies associated with the two kinds of boundaries.

Summary and Conclusions

Effects of growth conditions on large, vapor phase grown crystals of CdS:Cu have been examined. The concentration of copper incorporated in a boule has some dependence on the sublimation temperature, while its distribution in the crystal is sensitive to temperature differences that exist during growth and cooling. Crystals prepared using a sublimation temperature of about 1217°C often have dislocation tangles and sub-boundaries that act as sources for dipoles and

helices from which single loops are also formed. Cardioid decorations suggest the operation of a modified Frank-Read mechanism. If crystal growth is too rapid, polygonization and grain boundary formation increase. The boundaries act as sinks for precipitates which differ in geometry and size from particles in the grains. The size is affected by the degree of misorientation between grains.

Acknowledgments

The author wishes to thank W. M. Anderson for much of the crystal preparation, Mrs. M. Ippolito for the chemical analyses, and G. Neighbor and E. Krieger for the x-ray diffraction data. He is also grateful to M. S. Abrahams for critically reading the manuscript.

The research reported in this paper was sponsored by the Department of Defense, Advanced Research Projects Agency, Materials Sciences Office, under Contract No. SD-182.

Manuscript received April 15, 1966; revised manuscript received Aug. 5, 1966.

Any discussion of this paper will appear in a Discussion Section to be published in the June 1967 JOURNAL.

REFERENCES

1. A. Dreeben, *This Journal*, **111**, 174 (1964).
2. A. Dreeben, *ibid.*, **112**, 493 (1965).
3. W. W. Piper and S. J. Polich, *J. Appl. Phys.*, **32**, 1278 (1961).
4. A. Dreeben and R. H. Bube, *This Journal*, **110**, 456 (1963).
5. A. Dreeben, To be published.
6. W. C. Dash, *Phys. Rev. Ltrs.*, **1**, 400 (1958).
7. W. Mohling and H. Peibst, *Phys. Stat. Sol.*, **12**, 145 (1965).
8. J. J. Gilman and W. G. Johnston, *Solid State Phys.*, **13**, 147 (1962).
9. R. J. Stokes and K. H. Olsen, *Phil. Mag.*, **8**, 957 (1963).
10. D. J. Barber and N. J. Tighe, *ibid.*, **11**, 495 (1965).
11. W. T. Read, "Dislocations in Crystals," McGraw-Hill Book Co., Inc., New York (1953).
12. V. V. Damiano and N. Brown, *Trans. Met. Soc., AIME*, **230**, 926 (1964).
13. P. J. E. Forsyth, G. J. Metcalfe, R. King, and B. Chalmers, *Nature*, **158**, 875 (1946).
14. W. Gruhl and D. Amman, *Acta Met.*, **3**, 347 (1955).
15. S. Amelinckx and W. Dekeyser, *Solid State Phys.*, **8**, 325 (1959).
16. J. H. Westbrook, *Met. Rev.*, **9**, 415 (1964).
17. M. Aven and W. Garwacki, *Appl. Phys. Ltrs.*, **5**, 160 (1964).

Preparation and Properties of Pyrolytic Silicon Nitride

V. Y. Doo, D. R. Nichols, and G. A. Silvey

IBM Components Division, East Fishkill Facility, Hopewell Junction, New York

ABSTRACT

Silicon nitride has very attractive electrical, physical, and chemical properties which are of great interest for microelectronic devices. Until recently, most methods that have been reported in literature produce silicon nitride in the form of powder, needles, ribbons, or flakes. Recently, Sterling and Swann reported that continuous films of silicon nitride have been obtained. A new pyrolytic method for preparing pinhole-free continuous silicon nitride film is described. Films have been successfully prepared in the temperature range of 750°-1100°C. Some physical and chemical properties of those films are summarized.

Silicon nitride has many attractive properties, such as high electrical resistivity (~10^{14} ohm-cm), high dielectric strength (~10^7 v/cm), and extremely high resistance against chemicals, which are of great interest for microelectronic devices.

Several methods (1-6) of preparing silicon nitride have been reported in the literature. Most of those methods yield silicon nitride in the form of powder, needle, ribbon, or flake. Commercial silicon nitride particles are produced by heating elemental silicon in either nitrogen (1-3) or in dehydrated ammonia (4). Silicon nitride powder also has been prepared by heating silane and dehydrated ammonia (5). Sterling and Swann (6) reported that silicon nitride film has been obtained by the reaction of silane and ammonia at a pressure of about 0.1 Torr under r.f. discharge. Kuntz (9) reported preparation of nitride films by the reaction of silicon tetrafluoride with ammonia in the temperature range of 1200°-1900°C.

Film Preparation and Structural Properties

In the pyrolytic process described here, silane and ammonia react in the presence of excess hydrogen. It is known that silane decomposes at about 500°C. The presence of excess hydrogen suppresses the premature decomposition of silane. The deposition of silicon nitride is performed in a quartz reaction chamber. The apparatus is similar to that used in silicon epitaxial growth. The gases are mixed prior to entry into the reaction chamber. The flow rate of hydrogen is 4 liters/min with the silane-to-ammonia ratio of 1 to 20-40. The substrate temperature ranged from 750°-1100°C. The substrates used were single crystal silicon unless otherwise specified. The growth rate (G) is plotted as

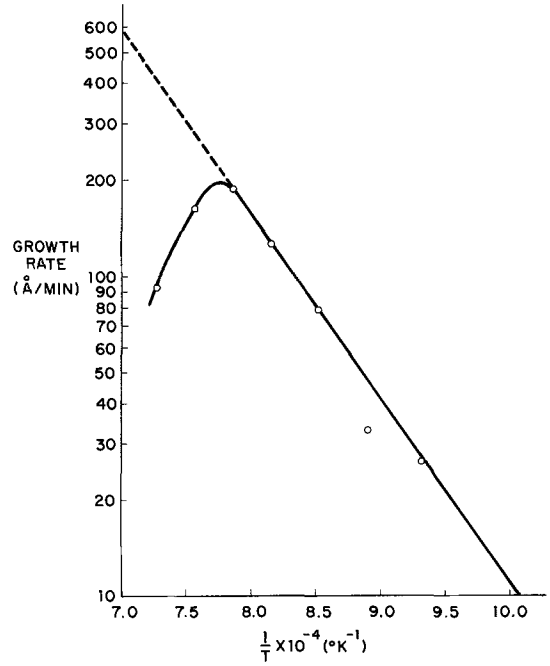

Fig. 1. Growth rate vs. inverse of substrate temperature

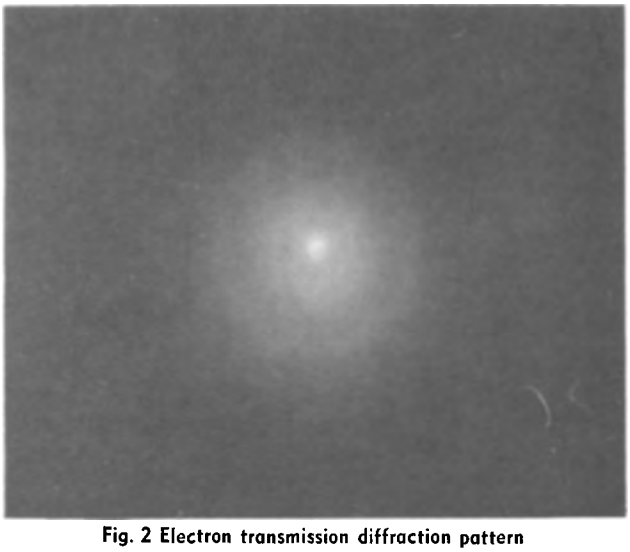

Fig. 2 Electron transmission diffraction pattern

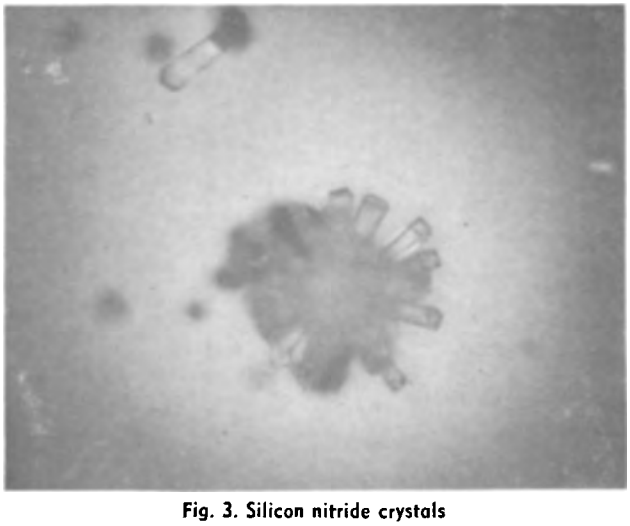

Fig. 3. Silicon nitride crystals

a function of reciprocal temperature ($1/T$) as shown in Fig. 1. Note the maximum growth rate occurred at 1000°C. In the temperature range between 750°-1000°C, the points are essentially on a straight line from which an activation energy of about 26.5 kcal/mol was obtained. The decrease in growth rate at temperatures above 1000°C is probably caused by the depletion of silane in the region near the substrate due to the premature decomposition of silane.

The structure of the silicon nitride films was investigated. The transmission diffraction pattern shows two very diffused rings as shown in Fig. 2. This indicates that the films are amorphous. The transmission electron micrographic examination confirmed this conclusion. Scattered large crystals of silicon nitride, however, were observed on films grown at 1100°C. Figure 3 shows some of those crystals.

Cracks have been observed on thick silicon nitride films ($>1\mu$) deposited on silicon substrates. The density of cracks increases with increasing film thickness and film growth rate. Usually cracks started to appear on films grown at 500 Å/min. Figure 4 shows an extremely high density of cracks on a 4μ thick film was grown at 950°C with a growth rate of 850 Å/min which is a factor of seven higher than the normal rate. Cracks were also found on films less than 1μ thick after annealing at high temperatures. Figure 5 shows the cracks of a 0.7μ film after annealing for 15 min at 1200°C in a nitrogen atmosphere.

Occurring with the cracks was substrate warping along an axis almost perpendicular to the cracks. The

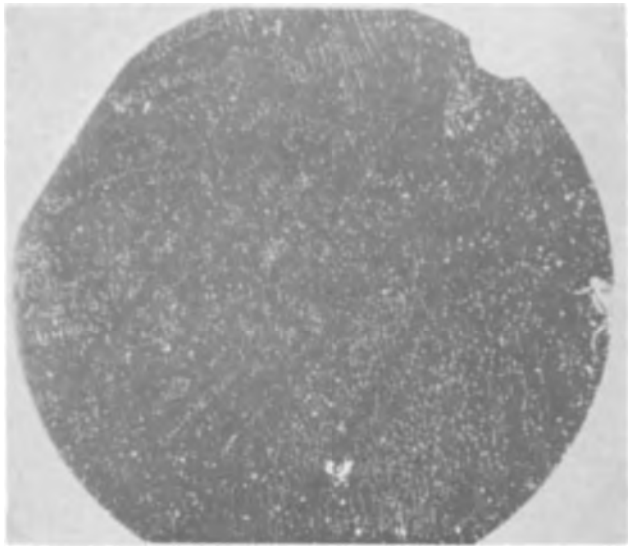

Fig. 4. Cracks on a 4μ silicon nitride film grown at 950°C at unusually high rate (850 Å/min).

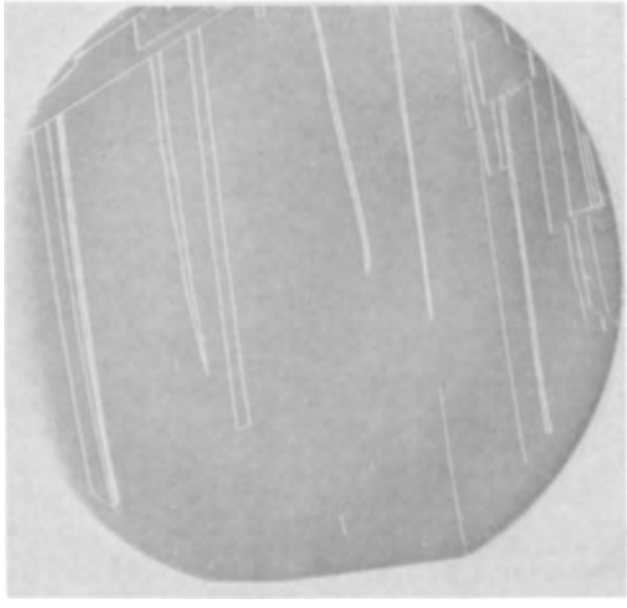

Fig. 5. Cracks on a 0.7μ silicon nitride film after annealing at 1200°C for 15 min.

cracks and warping apparently are caused by strong interfacial stresses between the silicon nitride and silicon substrate. The origin of the interfacial stresses was not determined. The structural mismatch, the difference in thermal expansion coefficient, and the densification of the film during annealing could have generated sufficient interfacial stresses to cause cracking and warping.

Physical and Chemical Properties

Some physical and chemical properties of the silicon nitride films have been investigated. The infrared absorption peak of commercial silicon nitride crystals is reported at 10.7μ (7). Sterling and Swann (6) reported that the IR absorption peak of the silicon nitride films prepared by r.f. discharge is very broad, from $10\text{-}14\mu$ with a maximum at 12μ. The films prepared by the pyrolytic process show a peak from $10\text{-}12\mu$. Figure 6 shows a typical IR absorption spectrum. No shifting of the peak position was detected after the film was annealed in nitrogen 3 hr at 1100°C.

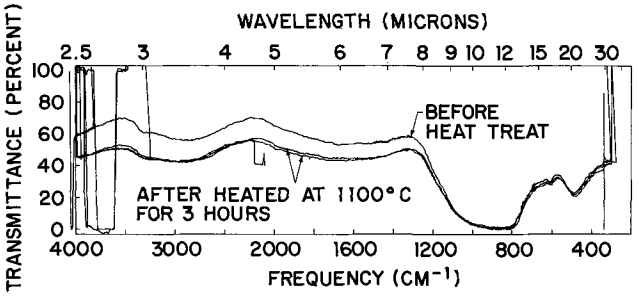

Fig. 6. Infrared spectrum of silicon nitride film, as grown and after annealing at 1100°C for 3 hr in N_2 atmosphere.

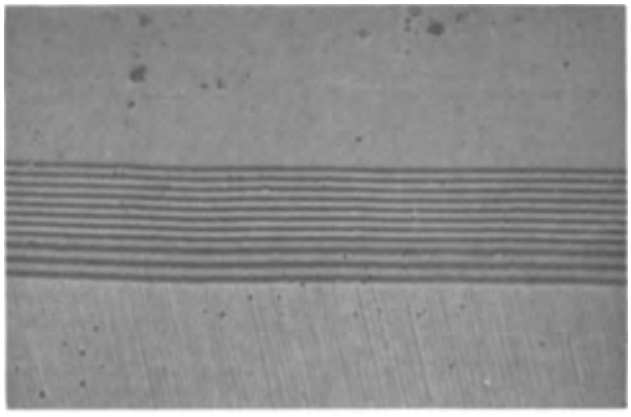

Fig. 7. Interference fringes of silicon nitride deposited on a SiO_2 coated-silicon substrate.

The index of refraction was determined by measuring the film thickness and the number of interference fringes from a monochromatic incident light whose wavelength is known. Figure 7 shows the interference fringes on a bevel of the silicon nitride film which was deposited on an oxidized silicon substrate. Note the difference in inter-fringe spacing between the silicon nitride and silicon dioxide that was caused by their difference in index of refraction. Since the index of refraction of steam oxide is known, the measured difference in inter-fringe spacing provides another method of determining the index of refraction of the silicon nitride film. The measured index of refraction of silicon nitride is about 2.0-2.06.

The dielectric constant was determined by capacitance measurements. Aluminum dots of about 0.1 in. diameter were evaporated onto the film. The capacitance between the aluminum dot and the silicon substrate was then measured. The measured capacitance per unit area is plotted against the reciprocal of film thickness as shown in Fig. 8. The straight line indicated in the figure corresponds to a dielectric constant of 6.34 $\pm$ 0.08.

The density of the commercial silicon nitride crystals is 3.44 g/cm³ (8). The pyrolytic silicon nitride films showed a density of 3.02-3.21 g/cm³.

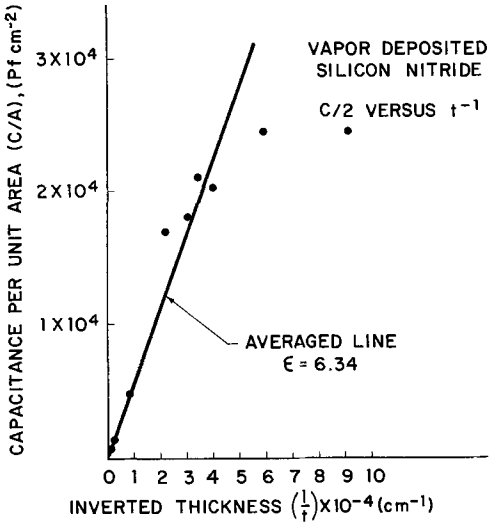

Fig. 8. Capacitance per unit area vs. reciprocal film thickness

The dielectric strength of the silicon nitride was determined by the breakdown voltage of approximately 10^7 v/cm.

As previously stated silicon nitride has extremely high resistance to chemicals. Only hydrofluoric acid attacks it at room temperature. The etch rate of the as-grown films in 48% HF at room temperature was found to be 75-100 Å/min. Because of its high chemical inertness, the permeability to impurity diffusion of silicon nitride may be very low. In diffusion experiments, it was found that many impurities which silicon dioxide fails to mask are held back by silicon nitride. The results of those experiments will be reported subsequently.

Acknowledgment

The authors wish to thank Dr. R. E. Jones and Messrs. J. S. Makris and J. Regh for their assistance in this investigation.

Manuscript received March 31, 1966; revised manuscript received July 1, 1966.

Any discussion of this paper will appear in a Discussion Section to be published in the June 1967 JOURNAL.

REFERENCES

1. E. T. Turkdogan, P. M. Bills, and V. A. Tippet, *J. Appl. Chem.*, **8**, 295 (1958).
2. L. Weiss and T. Engelhardt, *Z., anorg. Chem.*, **65**, 38 (1910).
3. P. Popper and S. N. Ruddlesden, *Trans. Brit. Ceram. Soc.*, **60**, 603 (1961).
4. W. Kaiser and C. D. Thurmond, *J. Appl. Phys.*, **30**, 427 (1959).
5. H. Jenkner and H. W. Schmidt, German Pat. 1,136,-315, September 1962.
6. H. F. Sterling and R. C. G. Swann, *Solid-State Elec.*, **8**, 653 (1965).
7. W. Pliskin, Private communication.
8. I. Weiss and T. Engelhardt, *Z., anorg. Chem.*, **65**, 38 (1910).
9. U. E. Kuntz, U. S. Pat. 3,226,194, December 28, 1965.

Semiconductor Joining by the Solid-Liquid-Interdiffusion (SLID) Process

I. The Systems Ag-In, Au-In, and Cu-In

Leonard Bernstein

Research & Development Laboratory, Fairchild Semiconductor, Palo Alto, California

ABSTRACT

The acronym SLID is used to describe a process whereby high-temperature phases are formed by diffusion in the presence of liquid. A technique is discussed which utilizes these phenomena in producing high-temperature-stable bonds which have been fabricated at low temperatures. The binary systems Ag-In, Au-In, Cu-In among others exhibit these characteristics. Photomicrographs and electron probe microanalysis data are presented to identify and describe the phases formed in these bonds. Some applications for the use of this joining technique are suggested in addition to the feasibility of extending this method to the use of ternary and higher order alloy SLID systems.

Semiconductor device fabrication, electronic component part assembling, and all other sequential processes which require a number of brazing or soldering steps, have, for a long time, been hampered by the fact that successive operations must be performed at lower and lower temperatures to avoid remelting and the possibility of disturbing a joint made in a previous operation. In many cases, this severely limits the use of the particular component. For example, a device which requires five soldering operations during assembly might use at its last stage an alloy whose melting point is so low that it would be virtually destroyed in use under any conditions that were the least bit severe. In addition, many of the inherent properties of the materials and device characteristics may never be realized due to limited operating temperatures imposed by the low-temperature processes and/or materials. Another shortcoming of conventional bonding techniques is that components can be rated at no higher temperatures than that temperature at which the assembly operation was performed.

It was therefore concluded that if some multicomponent system for bonding materials could be designed, which did not have the built-in temperature limitations, it would find immediate practical application.

Many of the properties of metals and alloys are structure sensitive. The phases which occur in alloys and constitute their structure are represented as areas of homogeneity in equilibrium phase diagrams. By developing or removing these phases, one of the properties of systems that can be changed irreversibly is the melting range of the constituents of the system. If this can be accomplished while a metallurgical bond is produced between two components, then this bond, if its components undergo a phase transformation, can melt at a different temperature than that at which its transformation occurred (the temperature at which the bond was made).

It is the purpose of this paper to describe a technique whereby bonds can be made at a low temperature and subsequently withstand higher temperature use. If necessary, these bonds can withstand further fabrication processes without melting or otherwise being adversely affected. The physical mechanisms describing these phenomena can be understood by a study of phase equilibria and diffusion theory. This process occurs by solid-liquid interdiffusion, hereafter referred to as SLID. This differs from conventional diffusion or wide-gap brazing techniques which may or may not occur in the presence of liquid phase but which do, however, rely on diffusion into the bulk body to be bonded to for their properties. SLID, since it most generally requires a separate preform, requires diffusion to occur within its self-contained structure only.

Although many systems are capable of producing bonds meeting the aforementioned requirements, this paper will concentrate on a discussion of experiments in the three simple binary systems: Ag-In, Au-In, and Cu-In. As seen from the discussion in the section below on Theory, this joining technique relies on the use of a laminated system, in which at least one layer is composed of a low-melting phase (in this case indium) and at least one layer is high melting (*i.e.*, Au, Ag, Cu, etc.).

From the theory and experimental data presented, other binary, ternary, and complex multicomponent systems having similar characteristics will be suggested.

Although the terms brazing and soldering have been strictly defined by both the American Welding Society and American Society for Metals by a fabrication temperature criterion, they have in common usage come to mean much more. For example, soft solders, in addition to being used at temperatures below 800°F, are accepted as being composed of the elements Pb, Sn, In, Bi, etc. Hard "solders," on the other hand, are by strict definition really brazes. They are primarily composed of the precious metals. The hard solders have properties such as strength, thermal conductivity, thermal fatigue, etc., differing greatly from the soft solders. With the growth of the semiconductor industry, a new class of alloys became generally commercially available. These materials such as the Au-Sn, Au-Ge, and Au-Si eutectics are used at soft soldering temperatures but have hard solder or braze properties. The materials used in this study are a combination of "hard" and "soft" solders. Since, the process is a diffusion limited one, however, the fabrication temperature may fall in either the strictly defined soldering or brazing range. It does have the capability, however, of being fabricated at low temperatures and having subsequent braze joint properties, such as remelt temperature, thermal conductivity and fatigue, strength, etc.

Review of the literature.—Much has been written in the past with regard to solid-state bonding of materials (1-11) utilizing diffusion phenomena and the physical mechanisms and principles describing and governing these phenomena (6, 12-31). With the growth of nuclear technology, new impetus was given to the interdiffusional aspects of diffusion bonding problems (32-38), particularly relating to the formation of intermetallic phases in fabricating clad fuel elements and isothermal mass transfer in liquid metals. A literature search indicated that very little had been written describing techniques utilizing the mechanism of liquid

phase diffusion with its subsequent transformations to enhance bonding. Harman (39-42) extended the well known mercury amalgam techniques to gallium, limiting his study to powder mixtures, but attributed the high-temperature characteristics of the bond to a liquid phase sintering mechanism (41). A more recent study (43) describes some more practical liquid diffusion soldering techniques with particular emphasis on avoiding formation of pores and intermetallic compounds in the seam joints of structural members.

The semiconductor industry has created new problems pertaining to material interfaces subjected to elevated temperatures in fabricating electronic devices and in subsequent use (44-62).

Theory.—Many families of systems have characteristics which lend themselves to SLID bonding. These systems must have one component with a low melting point, and another with a high melting point and an equilibrium phase diagram such that elevated temperature processing will result in a phase transformation of the liquid component to a higher melting point material. Systems with peritectic reactions are typically of this type. Examination of the phase diagrams (63) shown in Fig. 1, 2, and 3 will aid in the comprehension of this phenomenon.

If one placed two blocks of silver and indium together and permitted them to lie in intimate contact for an extended period of time (days or weeks) at a temperature corresponding to T_0 in Fig. 1, (at this temperature no liquid phase is present at any time) there will develop layers in this system corresponding to each one-phase region crossed by this horizontal line T_0. These phases will form by isothermal diffusion. If diffusion is permitted to continue until close to equilibrium conditions are reached, according to Gibb's phase rule no more than two layers could exist in this system. These phases would correspond to any two adjacent phases of the system, depending on the gross composition of the sample. If the gross composition falls within a one-phase region, the system will be composed of but a single phase. Diffusion theory (6) dictates that there can be no two-phase layers in isothermal diffusion structures. All of the phases predicted by the equilibrium diagrams, however, do not always appear (33-35) as distinct layers (6, 64).

In the silver-indium system the following phases can be present at the same time at temperature T_0: α, ζ', γ', ϕ, and In.

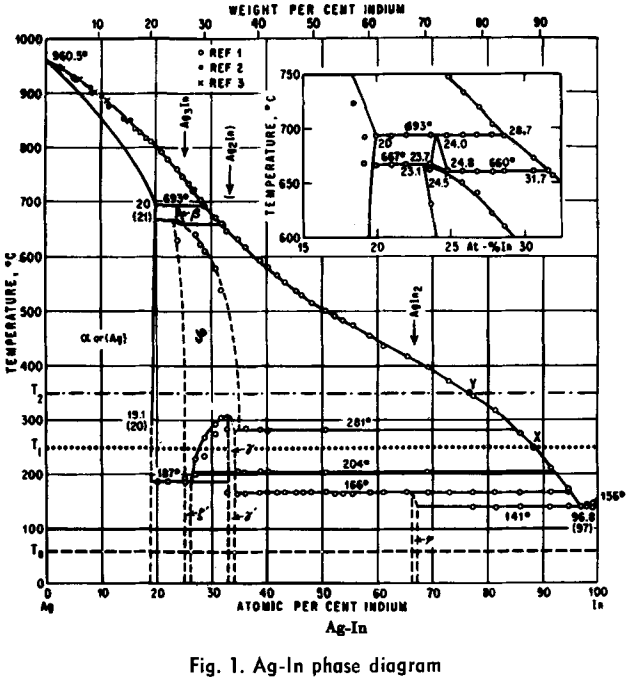

Ag-In

Fig. 1. Ag-In phase diagram

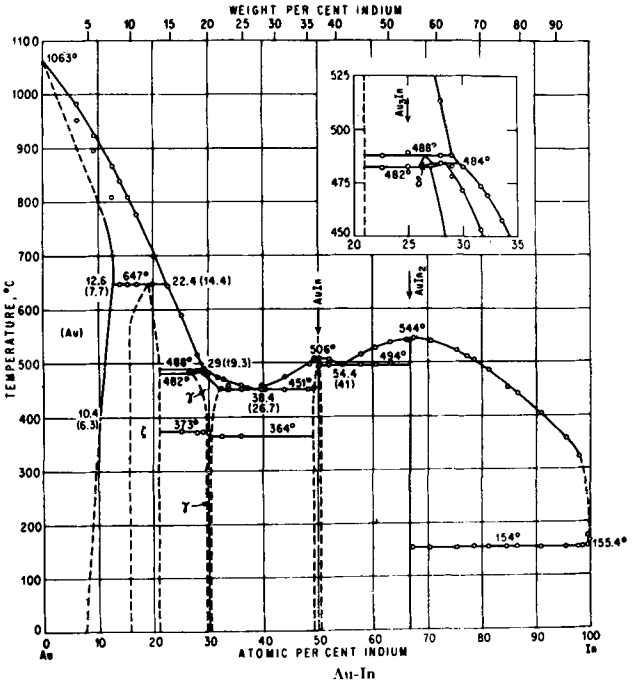

Au-In

Fig. 2. Au-In phase diagram

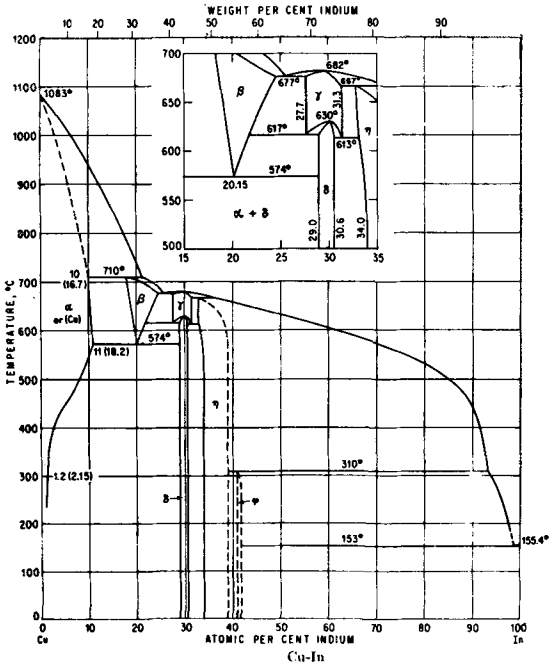

Cu-In

Fig. 3. Cu-In phase diagram

At temperatures above the melting point of indium, T_1 and T_2 shown in Fig. 1, this system can be used for producing high-temperature bonds. At temperature T_1, liquid indium will form and dissolve a given quantity of silver, as shown by composition X on the phase diagram. The saturated liquid will be separated from the silver substrate by finite layers of γ and ζ. Indium from liquid X will, in time, diffuse through γ and ζ while silver is diffusing in the opposite direction until complete transformation of the liquid to the solid phases takes place. As soon as the last of the liquid phase disappears, the system is capable of withstanding temperatures of greater than 600°C (the probable decomposition point of ζ) before liquid phase reappears. Only if the system were inadvertently heated to where liquid phase forms would danger (64) of creating a low-temperature bond exist.

At temperature T_2, indium from the liquid of composition Y need only diffuse through the ζ phase to complete the reaction with $\alpha : \alpha + \text{In} \rightarrow \zeta$.

The feasibility of producing high-temperature diffusion bonds in the presence of liquid phase was demonstrated by the work of a number of investigators. Castleman and Seigle (33) encouraged the growth of the high melting point phases δ and ϵ by annealing an Al-Ni diffusion couple above its eutectic temperature of 640°C. Lashko and Lashko (43) eliminated the liquid phase completely from the seam area of diffusion bonds in a variety of systems by annealing at elevated temperatures.

Powell and Braun (65), in their study of diffusion in the Au-In system below the melting point of indium, discovered inadvertently the effect of a molten zone, due to faulty temperature control, on the structure of the intermediate phases (see their Fig. 3b). The structural change associated with the phase transformation in turn affects the values for the diffusion coefficients. Investigating the mechanism of peritectic reactions, Sartell and Mack (64) pointed out the importance of structure and its effect on the nature of the diffusion process.

In the diffusion of Cd, In, and Sn in Ag, Tomizuka and Slifkin (6) found that, for temperatures below 600°C, the effects of grain boundaries become significant. Achter, Birks, and Brooks (67) in measuring grain boundary diffusion of Zn and Cu using electron-probe techniques determined that the ratio of grain boundary diffusion coefficient of lattice diffusion coefficient, D_B/D_L, to be approximately 10^6. Similar results were obtained for self diffusion in Ag by LeClaire (14) and in Ni by Upthegrove and Sinnott (68) with the ratios increasing with decreasing temperature. McLean (69) points out that, nevertheless, the diffusant will not usually penetrate much further along the grain boundaries than through the lattice, because the diffusing substance, when it has travelled further along a boundary, will diffuse sideways into the single crystals neighboring the boundaries. With diffusion times on the order of 100 hr, D_B/D_L must be approximately 10^5 for grain boundary diffusion to penetrate twice as far as lattice diffusion.

The Au-In (55) and Cu-In (55) systems, shown in Fig. 2 and 3 can be expected to produce bonds capable of withstanding minimum temperatures of 451°C and 667°C, respectively, after complete liquid diffusion. The physical mechanism accounting for SLID bonding in these systems is similar to that described for the Ag-In system.

The SLID process goes through five distinct stages during the bonding cycle:

Wetting.—During this stage the conventional surface free energy relationships (45, 70-84) play primary roles in achieving optimum wetting.

Alloying.—During this stage there must be some liquid solubility, even if only extremely limited, of the high melting component or components and the surfaces to be bonded, in the low melting phase or phases. This stage terminates when the liquid is completely saturated according to the appropriate phase diagram.

Liquid diffusion.—In this stage the liquid and solid components begin to interdiffuse to form more of the high melting point components.

Gradual solidification.—The quantity of liquid phase diminishes and the bond gradually solidifies until all liquid disappears.

Solid-diffusion.—During the preceding two stages, diffusion in the solid state is also taking place, but after complete solidification, solid diffusion is the only mechanism driving the reaction to equilibrium as dictated by the appropriate phase diagram.

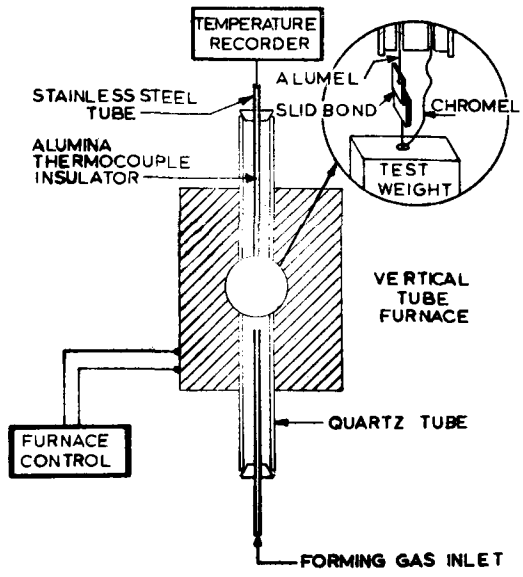

Fig. 4. Apparatus for determining unbonding temperatures of SLID bonds.

Experimental Procedure and Results

Clad materials were chosen for the preforms for SLID bonding. Three variables, temperature, time, and gross composition, control the process. Temperature was varied between 200°-450°C; time from 10-120 min; gross composition was controlled by adjusting thickness of layers such that equilibrium composition was always in the solid solution region. All bonds were made in a tube furnace in a gas ambient (hydrogen, forming gas, nitrogen or argon) low in oxygen or water vapor using parts 0.175 x 0.250 in. stamped from clad sheets, 5-40 mils thick.

The formation of internal In_2O_3 bands in silver-indium alloys has been studied by Rapp and coworkers (85) and the thermodynamic stability of In_2O_3 is well known (86). Oxygen and water vapor content therefore must be kept low to minimize their effects on wetting and diffusion. All parts were well cleaned using conventional cleaning and degreasing techniques. The importance of cleanliness and its effects on diffusion were pointed out by Rhines (6) and on bonding by Williams (5).

Bonded couples were evaluated in a furnace shown schematically in Fig. 4. To determine the temperature capabilities of the systems, the 0.175 x 0.250 in. parts were bonded in a lap joint configuration so that the bond area was approximately 0.175 x 0.175 in. The sample was suspended in the hot zone of a vertical tube furnace connected to a chromel-alumel thermocouple via a clamping fixture. A weight was hung from one leg of the thermocouple wire, which placed the couple in tension, in such a way that when the sample broke, the thermocouple circuit would open. The load on the bond was applied as a shear stress, and it was assumed that when continuous liquid phase formed in the interfacial bond region, rupture would occur. As a calibration of the test equipment used, rupture tests were periodically run on standard simple eutectic bonds (Au-Sn mp 280°C; Au-Ge mp 356°C; Al-Si mp 577°C; Ag-Cu mp 779°C) which always broke within 3°C of their respective melting points.

After bonding, samples were prepared metallographically by angle (approximately 15°) lapping. Some samples were subjected to electron probe x-ray microanalysis (87) for phase identification in the bond regions.

Figures 5, 6, and 7 show the high temperature results of some SLID bonds made in the Ag-In, Au-In, and Cu-In systems respectively. The anomalous low-tem-

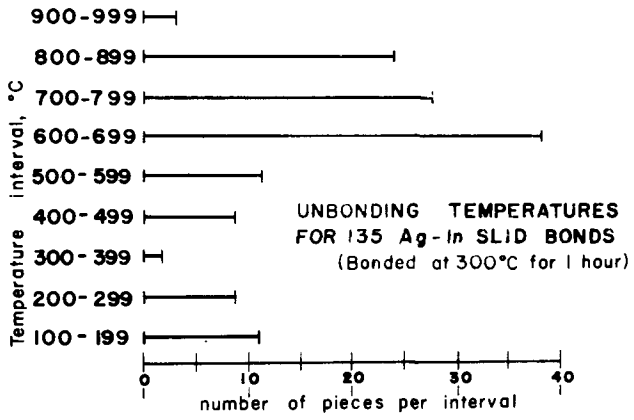

Fig. 5. Unbonding temperatures for Ag-In SLID bonds

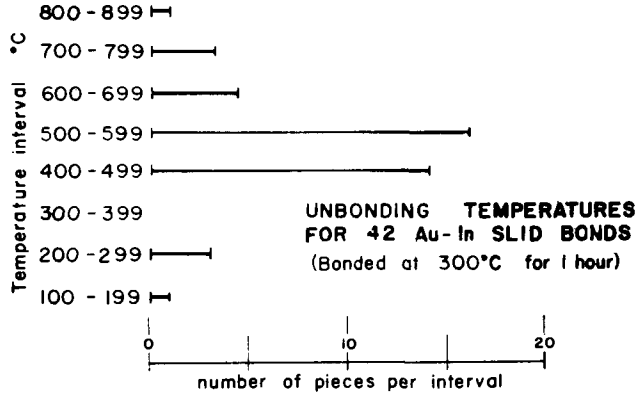

Fig. 6. Unbonding temperatures for Au-In SLID bonds

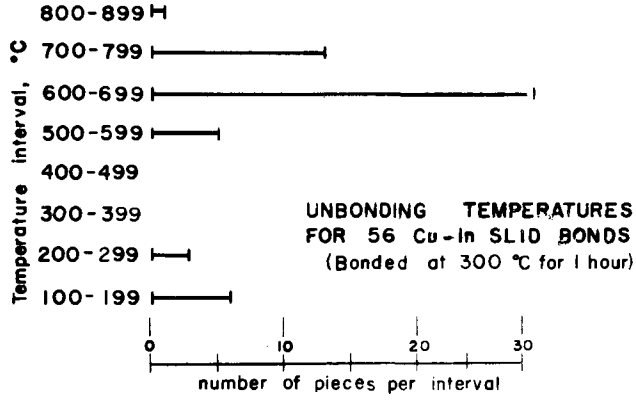

Fig. 7. Unbonding temperatures for Cu-In SLID bonds

perature ruptures found in all three binary systems were correlated with incomplete transformation to high-temperature phases in the interface. This is thought to be due to only partial completion of one or more of the five bonding stages for reasons such as poor wetting, unsatisfactory mating of parts, the kinetics of a particular reaction, etc. In the silver and copper systems, this anomaly accounted for 16% of the units tested; in the gold system, 9%. In one ternary system investigated (88), no low-temperature results were observed, possibly due to the lesser sensitivity of this system to the aforementioned effects.

Table I shows the results of electron probe x-ray microanalysis on some of the bonds made. In Table II the identification and extent of formation of phases in the Ag-In system is shown as observed from metallographic taper sections of SLID bonds. Tables III and IV show similar results, respectively, for the Cu-In and Au-In systems. Figures 8-13 are photomicrographs of some of the bonds identified in the previous tables.

Some hybrid bonds were made for the purpose of determining feasibility of the technique in complex systems. These were made in the following systems: those involving a third or fourth element; those to silicon surfaces; and those to surfaces in order to produce hermetic enclosures. The results were described in detail elsewhere (88). In general, however, it can be reported here that in those cases in which the phase diagrams indicated a favorable condition, SLID bonding occurred.

Table I. Electron probe x-ray microanalysis of interfacial bond regions

Sample No.	Bond	Diffusion cycle	Phase chemistries (analytically measured in wt %)	Probable interface identification
1922	Ag/In/Ag	250°C for 15 min	In-10; Ag-90	Minor: Ag with In in solid sol'n. continuous layer
			In-35; Ag-65	Major: Ag_2In; continuous layer
			In-68; Ag-32	Minor: $AgIn_2$: discontinuous layers
2011	Au/In/Au	200°C for 10 min	In-12; Au-88	Minor: $\zeta(Au_4In)$; continuous layer of rose-pink color
			In-21; Au-78	Major: $\gamma(Au_9In_4)$; continuous layer of grey-white
			In-54; Au-46	Major: $AuIn_2$; blue-white with dark stains after etching; continuous layer
2000	Cu/In/Cu	300°C for 10 min	In-50; Cu-50	Minor: η continuous layer
			In-56; Cu-44	Major: ϕ continuous layer

Table II. Metallographic taper-section of SLID bonds in the Ag-In* system

Specimen No.	Diffusion cycle	Probable interface identification
32	200°C/30 min	Major: Ag_2In (pink) + $AgIn_2$ (white) Minor: black & white, discontinuous—unreacted In plus Ag compounds
33	250°C/30 min	Major: pink, continuous layer—Ag_2In Minor: white, continuous layer—$AgIn_2$ Very minor: black & white, discontinuous—unreacted In plus Ag compounds
34	300°C/30 min	Minor: α solid solution Very major: pink; Ag_2In (practically complete bond area) Very Minor: white; $AgIn_2$ No unreacted In present
35	350°C/30 min	Major: α solid solution Major: Ag_2In No $AgIn_2$ present
36	400°C/30 min	Major: α solid solution Major: Ag_2In

* Black and white photomicrography is unable to distinguish subtle color differences between phases which the eye can. These tables therefore may differ from the corresponding figures.

Discussion

It appears on examination of cross sections that there is most liquid available for bonding in the Ag-In system and the least in the Au-In system for a given temperature level. These observations agree with what one would expect from the phase diagrams. From Tables III, IV, and V, the interdiffusion of indium is greatest with gold and least with copper. Wetting of

Table III. Metallographic taper-sections of SLID bonds in the Cu-In system

Specimen No.	Diffusion cycle	Probable interface identification
47	200°C/30 min	Major: white, continuous bands plus columnar growth of $\eta + \phi$ phases Major: black and white, continuous phase of unreacted In plus Cu compounds
45	250°C/30 min	Major: white, continuous bands plus columnar growth of $\eta + \phi$ phases Minor: black and white, discontinuous phase of unreacted In plus Cu compounds
46	300°C/30 min	Major: white, continuous bands plus columnar growth of $\eta + \phi$ phases Minor: black and white, discontinuous phase of unreacted In plus Cu compounds
44	350°C/30 min	Major: white, continuous bands plus columnar growth of $\eta + \phi$ phases Minor: black and white, discontinuous phase of unreacted In plus Cu compounds
48	400°C/30 min	Only traces of black and white phases remain. Region consists primarily of $\eta + \phi$.

Table IV. Metallographic taper sections of SLID bonds in the Au-In system

Specimen No.	Diffusion cycle	Probable interface identification*
2011	200°C/10 min	No α detectable Minor: rose-pink ζ Very very minor: cream colored γ Minor: white, AuIn plus $AuIn_2$ (equal volume to ζ) Very Major: (approx. 80% by volume of bond): black and white phase, probably unreacted In plus Au compounds No voids found in this bond structure
49	200°C/30 min	Very minor: yellow α Major: ζ Major: γ + AuIn + $AuIn_2$ Minor: black and white
53	250°C/30 min	Minor: α Major: ζ Major: γ Major: AuIn (white) Major: $AuIn_2$ (blue-white) No black and white phase appears. Between the ζ and γ phases some Kirkendall looking voids appear.
52	300°C/30 min	Minor: α Major: ζ Very major: γ Very minor: AuIn plus $AuIn_2$ Kirkendall voids still present
51	350°C/30 min	Minor: α (thicker than @ 300°C) Major: ζ Major: γ (equal volume to ζ) No white phases present
50	400°C/30 min	Minor: α (thicker than @ 350°C) Major: ζ Major: γ (thinner than ζ)

* All phases present, at all temperatures, appear as continuous bond structures except the black and white phase which is discontinuous.

Fig. 8. Ag-In SLID bond made at 200°C for 30 min. Etchant: 2g $K_2Cr_2O_7$, 8 ml H_2SO_4; 4 ml NaCl (sat. sol.), 400 ml H_2O; swab for 10 to 30 sec; at temperatures as low as 200°C transformation of indium to higher melting phases is complete.

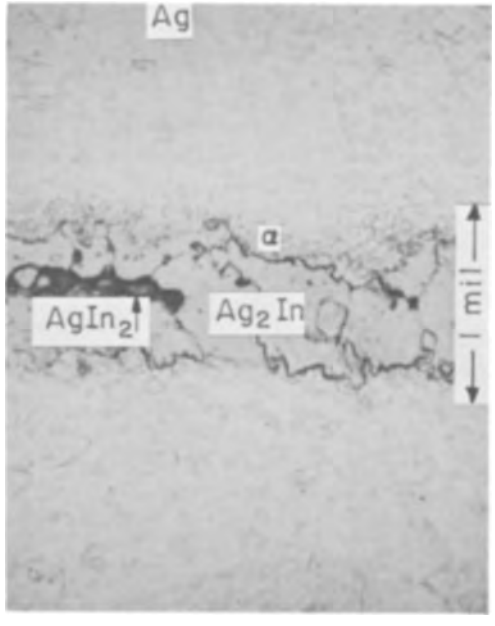

Fig. 9. Ag-In SLID bond made at 300°C for 30 min. Etchant: same as Fig. 8. The darkened area of the silver adjacent to Ag_2In is solid solution.

the indium to Ag, Cu, or Au appears to be most critical in the silver system, probably due to its high oxygen solubility, and least critical in the gold system.

From the high-temperature rupture results shown in Fig. 5, 6, and 7, bonds made at 300°C in these systems withstood subsequent loads at 400°-900°C in most cases. These results have been correlated with phases identified in the bond regions and shown in Tables II, III, and IV.

Ag-In *system.*—At temperatures up to 400°C for 30 min no Ag_3In could be detected either metallographically or by electron probe techniques. It would be interesting to photograph the α-Ag_2In interface with an electron microscope in an attempt to detect this phase which should exist according to diffusion theory. All of the phases formed during the diffusion cycles grew in layers only. We would, therefore, not expect any short-circuiting effects in diffusion usually associated with columnar phase growth. When bonding at 300°C and above, for all practical purposes, only high-temperature phases exist.

Cu-In *system.*—Although all of these bonds withstood elevated temperatures without rupturing, electron probe results and metallographic analysis seem to indicate that some lower melting phases persist even at the 400°C diffusion cycle. The phase transformation in this system does seem sluggish. Perhaps the black and white phase which shows up in Fig. 12, but unfortunately not in Fig. 13 is very discontinuous, thereby enabling one to apply a load to the bond region up to temperatures at which the copper-rich

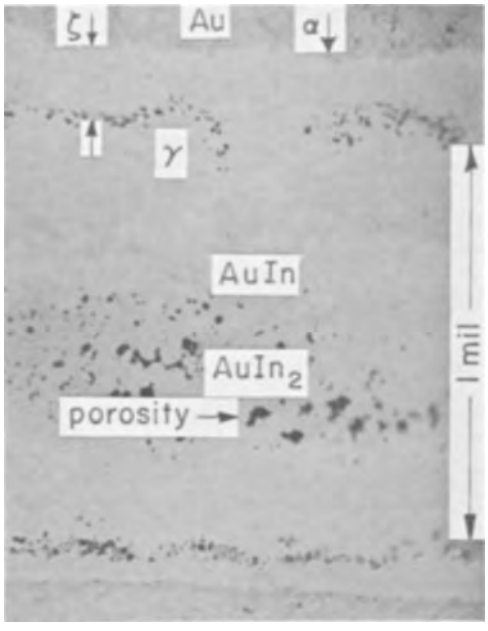

Fig. 10. Au-In SLID bond made at 250°C for 30 min. Visual identification is clearer than B&W photomicrographs due to the vivid color contrast of phases. Porosity shown in center is due to factors such as mating and pressure not investigated in this study.

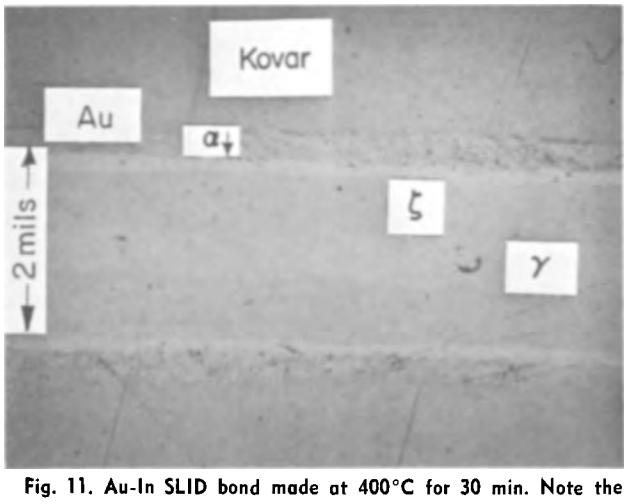

Fig. 11. Au-In SLID bond made at 400°C for 30 min. Note the complete absence of voids and phases richer in indium than γ.

phases melt. Results shown in Fig. 7 indicate this possibility.

Au-In *system.*—This system produced the most colorful phases. Transformations occurred very rapidly and at very low temperatures. Table IV shows that an increase of time at 200°C from 10 to 30 min resulted in a decrease in the quantity of the lowest melting phase in the bond area from 80% of the volume to a minor portion. At 250°C and above, the structure is composed entirely of high melting phases. At 250° and 300°C small voids appear in the interface between the ζ and γ phases. If the voids are the result of the Kirkendall effect it is not understood why they should not also appear at temperatures above 300°C. At temperatures of 350° and 400°C, voids entirely in the γ phase, appear, which are probably due to density difference between the phases.

Conclusions

The processes thus far described and experimented with are feasible, not only theoretically, but in a practical manufacturing process for producing high-temperature bonds using lower temperature processing

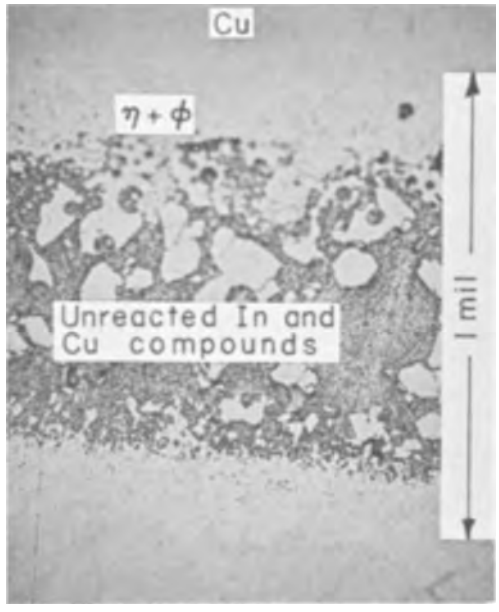

Fig. 12. Cu-In SLID bond made at 200°C for 30 min. Unreacted indium darkens in metallographic preparation due to pick-up of alumina abrasive.

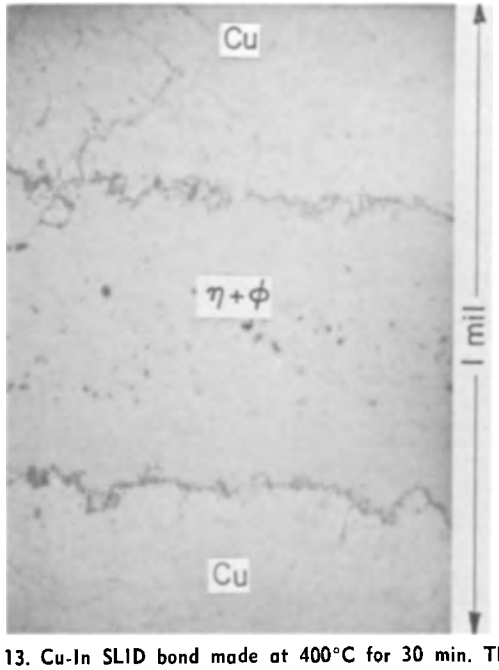

Fig. 13. Cu-In SLID bond made at 400°C for 30 min. The two phases in the bond interface could not be differentiated using common etchants.

conditions for a multitude of both semiconductor and nonsemiconductor brazing or bonding applications.

It is expected that by going to more complex systems, one could combine the effects of different elements to achieve optimum results. For example, the greater quantity of liquid in the Ag system compared to Au at comparable temperature levels together with the fast diffusion of the Au system would suggest a Ag-Au-In SLID bond; the improved oxidation resistance of tin alloys compared with indium might result in a Au-Ag-In-Sn system. The systems of Ni, Pd, Pt, Fe, Co, and Mn seem promising when combined with In and/or Sn. The specific contributions of other elements and fabrication techniques affecting the phase diagrams and diffusion phenomena provide unlimited conditions for future experiments.

Acknowledgments

The author would like to thank S. Prussin for the many stimulating discussions early in the investigation which led to the development of the technique and H. Bartholomew for the many suggestions and ingenious gadgets in addition to being a patient "sounding board."

Manuscript received Jan. 25, 1966; revised manuscript received June 1, 1966. This paper was presented at the San Francisco Meeting, May 9-13, 1965 while employed at Alloys Unlimited, Inc.

Any discussion of this paper will appear in a Discussion Section to be published in the June 1967 JOURNAL.

REFERENCES

1. S. Storcheim, J. L. Zambrow, and H. H. Hausner, *Trans. AIME*, **200**, 269 (1954).
2. L. S. Castleman and L. L. Seigle, *Progr. Repts., Sylvania Electric Products,* Bayside, N. Y. (Aug. 1956 and Feb. 1958).
3. M. J. Albom, *Welding J.*, **43**, 491, 499 (June 1964).
4. J. M. Williams, Thesis, M.I.T. (June 1956).
5. J. M. Williams and M. B. Bever, *Trans. Am. Soc. Metals*, **L11**, 585 (1960).
6. F. N. Rhines, "Surface Treatment of Metals," *Trans. Am. Soc. Metals*, Cleveland, 122 (1941).
7. M. J. Albom, *Welding J.*, **41**, 491-s (1962).
8. W. Feduska and W. L. Horigan, *ibid.*, **41**, 28-s (1962).
9. *I.* M. Barta, *ibid.*, **43**, 241-s (1964).
10. E. M. Passmore, *ibid.*, **42**, 186-s (1963).
11. J. A. Hoffman *et al., ibid.*, **41**, 160-s (1962).
12. R. A. Wolfe and H. W. Paxton, *Trans. AIME*, **230**, 1426 (1964).
13. A. D. LeClaire, *Progr. in Metal Phys.*, **1**, 373 (1949).
14. A. D. LeClaire, *ibid.*, **4**, 307 (1953).
15. A. D. LeClaire, *Brit. J. Appl. Phys.*, **13**, 433 (1962).
16. A. D. LeClaire, *Phil. Mag.*, **7**, 141 (1962).
17. A. C. Smigelskas and E. O. Kirkendall, *Trans. AIME*, **171**, 130 (1947).
18. D. Lazarus, "Solid State Physics," Vol. 10, pp. 71-126, Academic Press, New York (1960).
19. D. Lazarus, "Impurities and Imperfections," p. 107, Am. Soc. Metals, Cleveland (1955).
20. C. Kittel, "Introduction to Solid State Physics," 2nd ed., John Wiley & Sons, New York (1957).
21. L. S. Darken, *Metals Tech.*, p. 1-13, (August 1942).
22. L. S. Darken, *Trans. AIME*, **175**, 184 (1948).
23. R. F. Mehl and F. N. Rhines, *ibid.*, **137**, 301 (1940).
24. D. D. Van Horn, *Trans. Am. Soc. Metals*, **L1**, 185 (1959).
25. J. B. Clark and F. N. Rhines, *ibid.*, **L1**, 199 (1959).
26. J. S. Kirkaldy, *Can. J. Phys.*, **35**, 435 (1957); **36**, 899, 907, 917 (1958); **37**, 30 (1959); **40**, 208 (1962); **41**, 2166, 2174 (1963); **42**, 1643 (1964).
27. W. Jost, "Diffusion in Solids, Liquid and Gases," Academic Press, New York (1952).
28. C. Zener, "Imperfections in Nearly Perfect Crystals, John Wiley & Sons, New York (1952).
29. J. Bardeen and C. Herring, Atom Movements, Am. Soc. Metals, Cleveland (1951).
30. C. E. Birchenall, Reactivity of Solids-4th Int. Symposium on the Reactivity of Solids, Elsevier Publishing Co., Amsterdam (1960).
31. L. E. Toth and A. W. Searcy, *Trans. AIME*, **230**, 690 (1964).
32. L. S. Castleman, *Nuclear Sci., Eng.*, **4**, 209 (1958).
33. L. S. Castleman and L. L. Seigle, *Trans. AIME*, **209**, 1173 (1957).
34. L. S. Castleman and L. L. Seigle, *ibid.*, **210**, 589 (1958).
35. G. V. Kidson, *J. Nuclear Materials*, **1**, 21 (1961).
36. A. K. Covington, J. D. Baird, and A. A. Woolf, *J. Nuclear Energy*, **16**, 355 (1962).
37. A. D. LeClaire and I. J. Bear, *ibid.*, **2**, 229 (1956).
38. J. D. Baird, *ibid.*, **11**, 81 (1960).
39. G. G. Harman, *Rev. Sci. Instr.*, **31**, 717 (1960).
40. G. G. Harman, *ibid.*, **32**, 465 (1961).
41. G. G. Harman, NBS Tech. Note #140.
42. G. G. Harman, U. S. Patent No. 3,141,238.
43. N. F. Lashko and S. V. Lashko, *Tsvet. Metally*, **8**, 86 (1964).
44. L. Bernstein, *Semi. Prod.*, **4** [2], 29 (1961); **4** [8], 35 (1961).
45. L. Bernstein, *ibid.*, **6** [2], 16 (1963); **6** [12], 23 (1963).
46. D. B. Wittry, J. M. Axelrod, and J. O. McCalden, "Properties of Elemental and Compound Semiconductors," Metallurgical Soc. Conferences, **5**, 89, Interscience Publishers, New York (1960).
47. I. A. Lesk, *Trans. AIME*, **233**, 578 (1965).
48. T. A. Longo and B. Selikson, *Semi. Prod.*, **6** [11], 12 (1963).
49. R. Schmidt, Solid-State Device Research Conference, Univ. of New Hampshire (1962).
50. G. A. Dodson, *ibid.*
51. J. P. Jan and W. B. Pearson, *Phil. Mag.*, **8**, 279 (1963).
52. C. Weaver and L. C. Brown, *ibid.*, **7**, 1 (1962).
53. M. B. McNeil, *This Journal*, **110**, 1169 (1963).
54. F. Lee, Paper presented at the Toronto Meeting of the Society, May 1964, Abstract No. 58.
55. J. A. Cunningham, AIME Conference, Technical Conference on Materials Science and Technology in Integrated Electronics, San Francisco, California, Sept. (1965).
56. M. Khorouzan and L. Thomas, *ibid.*
57. J. R. Howell and J. W. Kanz, ibid.
58. D. G. Cummings, Wescon Session 16B Papers, San Francisco, Calif., July (1965).
59. L. E. Colteryahn and D. D. Shaffer, *ibid.*
60. L. E. Colteryahn and J. F. Kersey, *ibid.*
61. J. R. Howell and J. W. Kanz, *ibid.*
62. D. G. Cummings, *ibid.*
63. By permission from "Constitution of Binary Alloys," by Max Hansen, McGraw-Hill Book Co., New York (1958).
64. J. A. Sartell and D. J. Mack, *J. Inst. Metals*, **93**, 19 (1964-65).
65. G. W. Powell and J. D. Braun, *Trans. AIME*, **230**, 694 (1964).
66. C. T. Tomizuka and L. Slifkin, *Phys. Rev.*, **96**, 610 (1954).
67. M. R. Achter, L. S. Birks, and E. J. Brooks, *J. Appl. Phys.*, **30**, 1825 (1959).
68. W. R. Upthegrove and M. J. Sinnott, *Trans. ASM*, **L**, 1031 (1958).
69. D. McLean, "Grain Boundaries in Metals," Clarendon Press, Oxford (1957).
70. C. M. Adams, *J. Metals*, **12**, 73 (1960).
71. P. Kozakevitch, "The Physical Chemistry of Metallic Solutions and Intermetallic Compounds," Symposium, **1**, 84 Chemical Publishing Co., New York (1960).
72. G. Tammann and A. Ruhenbeck, *Z. anorg. u allgem. Chem.*, **223**, 192 (1935).
73. F. J. Bondi, *Chem. Revs.*, **52**, 417 (1953).
74. C. M. Adams, *J. Metals*, **12**, 1 (1960).
75. A. J. Wall and D. R. Milner, *J. Inst. Metals*, **90**, 10 (1962).
76. J. W. Taylor, "Progress in Nuclear Energy," p. 398, Pergamon Press, Inc., New York (1953).
77. W. D. Kingery, *J. Am. Ceram. Soc.*, **36**, 11 (1953).
78. G. Economos and W. D. Kingery, *ibid.*, **36**, 12 (1953).
79. M. Humenick, Jr., and W. D. Kingery, *ibid.*, **37**, 1 (1954).
80. W. D. Kingery, *ibid.*, **37**, 2 (1954).
81. W. D. Kingery and F. A. Halden, *Amer. Ceram. Bull.*, **34**, 117 (1955).
82. M. Humenick, Jr., and N. M. Parikh, *J. Am. Ceram. Soc.*, **39**, 60 (1956).
83. W. M. Armstrong, A. C. D. Chaklader, and J. F. Clarke, *ibid.*, **45**, 115 (1962).
84. J. C. Williams and J. W. Nielsen, *ibid.*, **43**, 5 (1959).
85. R. A. Rapp, D. F. Frank, and J. V. Armitage, *Acta Met.*, **12**, 505 (1965).
86. L. E. Epstein, *Ceram. Age*, April, 37 (1954).
87. Analysis performed at Advanced Metals Research Corporation in Burlington, Massachusetts.
88. L. Bernstein and H. Bartholomew, *Trans. AIME*, **236**, 405 (1966).

Superconducting Niobium Stannide (Nb_3Sn) Films on Metallic Substrates

T. L. Chu and J. R. Gavaler

Westinghouse Research Laboratories, Pittsburgh, Pennsylvania

ABSTRACT

Niobium stannide, Nb_3Sn, has been transported from a sintered source material onto various substrates by hydrogen halides in the presence of a temperature gradient. The superconducting transition temperature of the deposited films was found to depend, among other factors, strongly on the separation between the source and the substrate. At large separations, the deposited films were nonstoichiometric due to the differences in reactivities of niobium and tin toward hydrogen halide and the ease of reduction of niobium and tin halides with hydrogen. At small separations, the films deposited on metallic substrates were found to have a superconducting transition temperature of 18°K and a critical current density of up to 6×10^4 amp cm^{-2} in magnetic fields of 50 kG.

Niobium stannide Nb_3Sn, a Type II superconductor, has been prepared by metallurgical and chemical techniques. The sintering of a stoichiometric mixture of the elements was the method first used to prepare this compound. Three intermetallic phases are known to exist in the Nb-Sn system. Nb_3Sn does not form below 805°±5°C and exists as an equilibrium phase up to the melting point of the compound, approximately 2000°C (1). Because of the brittleness of niobium stannide, the sintering process is usually carried out after a mixture of niobium and tin has been fabricated into its final form. Various techniques have been devised to produce niobium stannide wires capable of carrying currents higher than 10^5 amp cm^{-2} at 4.2°K in fields of 100 kG (2).

The sintering technique is not sufficiently flexible for producing niobium stannide in forms desirable for other purposes. Chemical approaches have produced interesting results. For example, the simultaneous reduction of mixtures of niobium and tin chlorides with hydrogen in a flow system has been used for the deposition of niobium stannide on substrate surfaces in the temperature range of 900°-1200°C (3-5). The chemical reaction is represented by the equation

$$3NbCl_4(g) + SnCl_2(g) + 7H_2(g) = Nb_3Sn(s) + 14HCl(g)$$

The reductions of niobium and tin chlorides show different dependence on temperature and on H_2/halide molar ratios because of their differences in activation energies and free energy changes. Thus, the composition of the deposited material depends on the substrate temperature and the composition of the reactant. Although deposited material with a composition deviation as much as 5% from stoichiometry was found to retain a single phase β-tungsten structure, this compositional variation resulted in significant changes in transition temperature (6). Thus, the stoichiometry of the deposited material, and therefore the control of substrate temperature and reactant composition are of extreme importance. Under proper conditions, niobium stannide has been prepared in various forms such as films on metallic substrates which have been used to construct solenoids capable of generating fields in excess of 100 kG (7).

Chemical approaches are more flexible for the preparation of niobium stannide. However, the thermal reduction technique requires the precise control of reactant composition and substrate temperature, and the yield of the reduction process is only moderate. We have investigated the usefulness of the chemical transport technique, because of its inherent simplicity, for the deposition of niobium stannide films on various substrates. Using this technique, niobium stannide has been efficiently transported from a sintered source material onto substrate surfaces by hydrogen halides in the presence of a temperature gradient. Aside from other factors, the superconducting transition temperature of the deposit was found to depend on the separation between the substrate and the source material. At small separations, the deposited films have transition temperatures of 18°K and a critical current density of up to 6×10^4 amp cm^{-2} in magnetic fields of 50 kG. The chemical transport of niobium stannide under various conditions and the properties of resulting deposits are described in this paper.[1]

Experimental

The transport of solid substances by chemical reactions has been used widely for the preparation of electronic materials during recent years (8). Niobium stannide reacts reversibly with hydrogen halides, such as hydrogen chloride and hydrogen bromide to yield a mixture of metallic halides. For example

$$Nb_3Sn(s) + 14HBr(g) = 3NbBr_4(g) + SnBr_2(g) + 7H_2(g)$$

Where $NbBr_4$ and $SnBr_2$ are assumed to be the predominant species. Since the hydrogen reduction of most metallic halides becomes thermodynamically more favorable at higher temperatures, hydrogen halides are capable of transporting niobium stannide from a low temperature region to substrates at higher temperatures. In the source region, hydrogen bromide reacts with the source material to produce $NbBr_4$, $SnBr_2$, and H_2, which are transported to the substrate region at higher temperatures. The reverse reaction takes place in the substrate region because of the change in temperature, depositing Nb_3Sn.

The transport of niobium stannide onto various substrates by hydrogen halide was carried out using both closed tube and flow system techniques. Sintered niobium stannide plates, prepared by pressing a blend of niobium and tin powder and sintering at 900°-1400°C for various durations, were used as the source material. Substrates used for the deposition of niobium stannide included quartz, stainless steel, silver, Hastelloy, and many other common metals. Matheson anhydrous hydrogen bromide and hydrogen chloride, of 99.8 and 99.0% purity, respectively, were used as transport agents, and the noncondensable impurities were

[1] Subsequent to the submission of our paper, a paper "The Growth of Single Crystals of Nb_3Sn by Chemical Transport," by J. J. Hanak and H. S. Berman was presented at the Internation Conference on Crystal Growth, Boston, June 20-24, 1966. In this work, Nb_3Sn single crystals were grown by the conventional chemical transport technique in contrast to the close-spacing transport for the deposition of thin films emphasized in our paper.

removed by evacuating the solid which was refrigerated with liquid nitrogen. Fused silica tubes of 2.5 cm I.D. or 2.5 x 2.5 cm cross-section were used horizontally as reaction tubes in most experiments.

To carry out the closed-tube transport, the reaction tube containing the source material and the substrate was evacuated to 10^{-5} Torr or less, a known amount of the transport agent was distilled in, and the reaction tube was sealed. When a large substrate-source separation, say 10 cm or more, was desired, the reaction tube was placed in a horizontal tube furnace containing two independently controlled temperature zones. The region of the tube containing the substrate was placed in the high temperature zone, 800°-1000°C, and the source material was usually maintained at 600°-800°C. When a small substrate-source spacing was desired, the substrate was placed on the bottom of a square cross-sectioned tube, and the source plate was placed at about 1 mm above the substrate. To establish a temperature gradient across the reaction tube, only the bottom side of the tube was heated by a flat horizontal heater. The substrate thus assumes a higher temperature than the source material. However, the temperature difference between the source and the substrate, determined by the geometry of the reaction tube, is small and cannot be varied at will.

In many close-spacing experiments, the substrates were heated resistively so that the temperature difference between the substrate and the source material could be readily adjusted. A fused silica tube of 2.5 cm diameter, enclosed in a horizontal furnace, was used as the reaction tube. One end of the tube was provided with inlet tubes for the transport agent and the diluent, and the other end was provided with two demountable electric leads and the exhaust tube. The metallic substrates, in the form of hair-pins, were connected to the electric leads. Two sintered niobium stannide plates were placed approximately 1 mm above and below the substrate. After the reaction tube was purged with the diluent, such as helium, the reaction tube was heated to approximately 700°C to prevent the condensation of metal halides on the wall of the reaction tube. The wire substrate was then further heated resistively to about 850°C, and a temperature difference between the source and substrate of 50°C or more was readily achieved. The transport agent was then introduced at a low flow rate, say 5 ml/min, and the flow of the transport agent and the diluent was maintained through the transport process. Alternatively, the reaction tube was evacuated and backfilled with the transport agent to a pressure of 10-15 cm. The transport process then was carried out in a closed system under similar temperature conditions as in the flow system.

The superconducting transition temperature of niobium stannide specimens was determined by conventional techniques. The measurement of the resistive voltage drop across a specimen was used when electrical contacts could be applied to the specimen. For small or irregular specimens, the specimen was placed inside a small coil which was a part of a tank circuit, and its resonant frequency was measured. When the specimen becomes superconducting, the inductance of the coil decreases, resulting in a decrease in the frequency. The critical current density of niobium stannide deposited on wire substrates was measured on specimens approximately 2 cm long. The ends of the test specimen were copper plated and then indium soldered onto heavy copper leads. When the voltage drop across the specimen exceeded 5 μv, the sample was considered to have passed from the superconducting to the normal state.

Results and Discussion

The transport of niobium stannide by hydrogen halides has been established in both closed tube and gas flow systems under a variety of conditions. Since the separation between the source material and the substrate was found to be the most important variable determining the transition temperature of the deposit, the following discussion is divided into two parts according to the source-substrate separation used in the transport experiments.

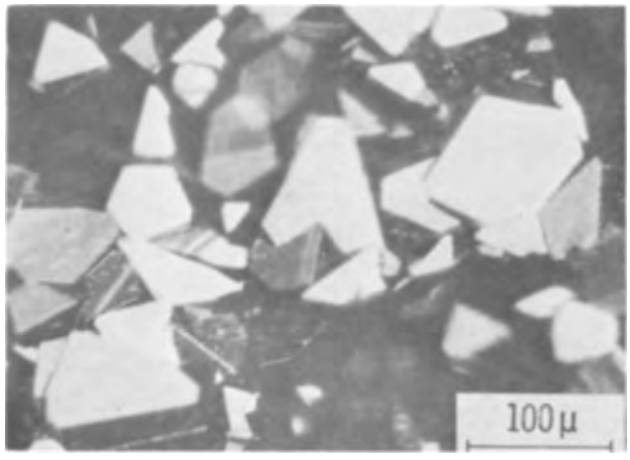

Fig. 1. Niobium stannide transported onto a quartz substrate by hydrogen bromide in a closed tube with a source-substrate separation of 10 cm. This film, approximately 250μ thick, had transition temperature of 13°-18°K, indicating that the film was nonstoichiometric.

Transport of niobium stannide with large source-substrate separation.—In most transport experiments, a bright metallic film was deposited in the high temperature zone of the reaction tube. The transport rate was determined predominately by the composition and pressure of the transport agent, the source and substrate temperatures, and the distance between the source and the substrate. For example, a film 250μ thick was deposited at a rate of 3 μ/hr using hydrogen bromide at 2.5 atm as the transport agent. The source and substrate were 10 cm apart and their temperatures were 600° and 900°C, respectively. This film was found to be polycrystalline and consisted of many crystallites 20-30μ wide (Fig. 1). It was also found to be a single phase material by Picklesimer's anodization technique (9). The source material used in this transport experiment was sintered at 1200°C for 20 hr and had a transition temperature of over 18°K. However, the transition temperature of the transported film was found to be in the range of 13°-18°K. This broad transition of the transported film indicates its nonstoichiometry. This is due to the difference in reactivity of niobium and tin toward hydrogen bromide and the difference in the ease of reduction of niobium and tin bromides. Thus the composition of the film changed gradually as the transport proceeded. Niobium stannide films prepared by using other substrate temperatures or using source material sintered at different temperatures (900°, 1050°, and 1400°C) had similar or lower transition temperatures.

Among the metallic substrates used in the transport process, silver and Hastelloy were found to be relatively inert in hydrogen bromide up to about 900°C. At substrate temperatures below 800°C, the deposited films had low transition temperature, less than 10°K, indicating that they were not stoichiometric. At substrate temperatures of 950°C or higher, the substrates were severely attacked. Therefore most experiments were carried out at substrate temperatures of 850°-900°C, and the temperatures of the source material were maintained 250°-300°C lower. Under these conditions, the properties of the transported films were also found to be affected by the sintering temperature of the source material. When the source material was sintered at low temperatures, both silver and Hastelloy substrates were attacked to some extent. The deposited

Table I. Deposition of Nb_3Sn films on silver and Hastelloy substrates by chemical transport using a source-substrate separation of 10 cm

Sintering temp of source Nb_3Sn, °C[a]	Substrate temp, °C	Film quality	Transition temp, °K[b]
900, 1050, 1200, and 1400	≤800	Fair to good	10
900, 1050, 1200, and 1400	≥950	Very poor, substrate severely attacked	5-18 depending on source material
900	850-900	Poor	10-18
1050	850-900	Poor	10-18
1200	850-900	Fair	13-18
1400	850-900	Good	9-13

[a] All sintering times were a minimum of 4 hr after an initial sintering of 70 hr at 900°C.
[b] The transition temperatures given were measured on films deposited on metallic substrates whenever possible. In cases where the deposits on metallic substrates were not of sufficiently good quality for measurement, the transition temperatures given are for films deposited on quartz under the same experimental conditions.

films, with transition temperatures in the range of 10°-18°K, were not tightly adherent and were of poor appearance. The degree of attack was found to decrease with increasing sintering temperature of the source material. The substrates were not significantly attacked when the source material was sintered at 1400°C, and continuous and adherent films were obtained. However, these films exhibited lower transition temperatures, 9°-13°K, due to the presence of excess niobium in the films. Thus, the attack on substrate when using source material sintered at low temperatures was probably due to the alloying of tin with the substrate at the deposition temperature. The source material sintered at very high temperatures, say 1400°C, was likely to be tin-deficient due to evaporation, thus minimizing the attack of the substrates. Results of a number of experiments showing the effects of substrate temperature and the temperature of the source material are summarized in Table I. Similar results were obtained when a hydrogen-hydrogen bromide mixture was used as the transport agent. Therefore the transport technique using a large source-substrate separation was not able to produce films of stoichiometric niobium stannide.

Close-spacing transport of Nb_3Sn.—When niobium stannide is transported by using a large source-substrate separation, the composition of the resulting material varies along the length of the reaction tube due to the difference in reactivity of niobium and tin halides. By using a very small source-substrate separation, all components of the source material can be transported simultaneously and quantitatively to the substrate. The change in composition between source and substrate is therefore extremely small. This advantage has been utilized for the transport of chemical compounds which differ widely in properties, such as the III-V semiconducting compounds (10).

When the source-substrate spacing was 1 mm and the external heating of substrate was used, as described earlier, the source temperature was estimated to be approximately 20°C lower than the substrate. Despite the much smaller temperature gradients, the deposition rate of Nb_3Sn by the close-spacing technique was similar to that achieved by the large-spacing transport technique. For example, niobium stannide films were deposited on quartz substrates at 850°C at a rate of approximately 3 μ/hr by using hydrogen bromide at 2.5 atm as the transport agent. When a niobium stannide plate sintered at 900°C for 70 hr was used as the source material, the film was found to have a sharp transition temperature in the range of 17°-18°K. Similar results were obtained by using source material sintered at 1050° and 1200°C. These results confirm that sintered Nb_3Sn can be chemically transported with no significant change in stoichiometry. According to the composition-transition temperature relation of vapor deposited Nb_3Sn (5, 6), the deviation of the transported film from stoichiometry is presumably less than 2%. However, the deposition of niobium stannide on silver and Hastelloy substrates was also complicated in many cases by the attack on the substrates. Results of a series of experiments are summarized in Table II. At substrate temperatures of 800°C or below and 950°C or above, the close-spacing transport technique yielded results very similar to those obtained by the large-spacing transport technique. However, at substrate temperatures of 850°-900°C, the use of source material sintered at 900°, 1050°, or 1200°C yielded deposits with high transition temperatures, in contrast with the large-spacing transport technique (cf. Table I). But the attack of the substrate during the transport process prevented the formation of adherent films. The deposited films obtained from source material sintered at 1400°C exhibited low transition temperature, due presumably to a tin deficiency in the source material.

Table II. Deposition of Nb_3Sn films on metallic substrates by close-spacing technique using external heating of substrates

Sintering temp of source Nb_3Sn, °C	Substrate temp, °C	Film quality	Transition temp, °K
900, 1050, 1200, and 1400	≤800	Fair to good	≤10
900, 1050, 1200, and 1400	≥950	Very poor, substrate severely attacked	5-18, depending on source material
900	850-900	Poor	17->18
1050	850-900	Poor	17->18
1200	850-900	Fair	17->18
1400	850-900	Good	11-14

When the substrate was heated resistively in the close-spacing transport experiments, a considerably larger temperature difference between the substrate and the source material, and consequently a corresponding higher deposition rate, 5 μ/min or higher, were achieved. This rate was obtained in both closed and flow systems and was about 100 times that obtained by the external heating technique. This high deposition rate of niobium stannide sufficiently eliminated the attack of the substrate to permit the deposition of high quality, adherent, and continuous films. When a helium-hydrogen bromide mixture was used as the transport agent in a flow system or when hydrogen bromide at a pressure of 10-15 cm was used as the transport agent in a closed system, films with high transition temperature, ≥18°K, were deposited reproducibly on Hastelloy substrates. A typical film deposited on Hastelloy at 850°C is shown in Fig. 2.

Fig. 2. Niobium stannide film deposited on a Hastelloy substrate by the close-spacing transport technique. The source and substrate temperatures were 800° and 850°C, respectively, and the transition temperature of this film was 18°K.

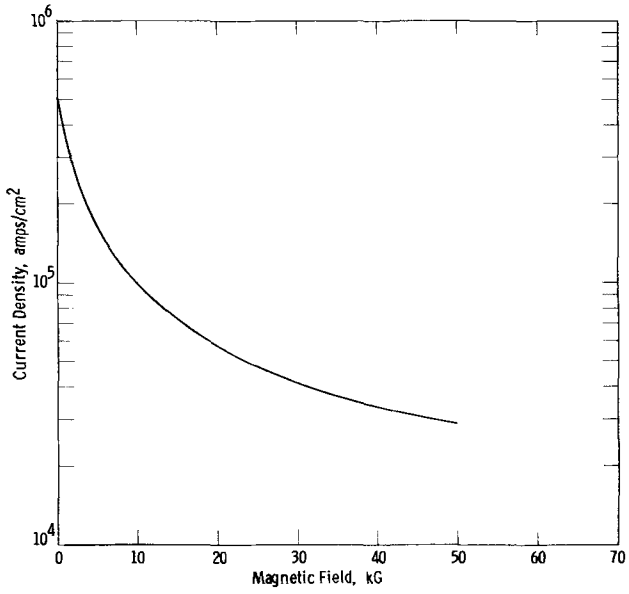

Fig. 3. A typical current density *vs.* field curve of niobium stannide films deposited on Hastelloy by the close-spacing transport technique.

This film, deposited at a rate of approximately 2 μ/min, was 30μ thick and had a transition temperature of 18°K. The current density of a number of niobium stannide films transported by the close-spacing technique was measured in magnetic fields up to 50 kG. A typical current density *vs.* external field curve is shown in Fig. 3. The current density was approximately 6 x 10^5 amp/cm^2 in zero field and was 3 x 10^4 amp/cm^2 in a field of 50 kG. The highest current densities achieved thus far, measured in a field of 50 kG, were greater than 6 x 10^4 amp/cm^2. Thus, it has been demonstrated that by using a large temperature difference between the source and the substrate, niobium stannide films with good superconducting properties can be deposited on a metallic substrate. This technique is considerably simpler than the thermal reduction technique in a flow system and has potential applications for the construction of superconducting solenoids.

Summary and Conclusions

Niobium stannide, Nb_3Sn, has been transported from a low temperature zone to higher temperature regions by using hydrogen bromide or hydrogen chloride as a transport agent, as expected from thermochemical considerations. It has been established that the large-spacing transport technique, in which the source material and the substrate are 10 cm or more apart, is not readily adaptable for the deposition of stoichiometric Nb_3Sn films. This is due mainly to the differences in reactivities of niobium and tin toward hydrogen halide and the ease of reduction of niobium and tin halides with hydrogen. On the other hand, the close-spacing technique has been proven to be capable of reproducibly depositing niobium stannide films with good superconducting properties.

To accomplish the deposition of adherent niobium stannide films on metallic substrates, it is essential to carry out the transport process at high rates to minimize the attack of the substrates. The resistance heating of substrates provided a large temperature difference between the substrate and the source material and therefore, a high transport rate. Niobium stannide films deposited on Hastelloy substrates were found to have high transition temperatures, $\geq$18°K, and reasonable current densities. The feasibility and reproducibility of this process for the preparation of stoichiometric niobium stannide have been established.

Acknowledgment

We wish to thank Drs. J. K. Hulm and S. A. Autler for their encouragement during the course of this work, Mr. W. T. Reynolds for supplying the sintered niobium stannide plates, and Dr. C. K. Jones and Mr. A. Patterson for their contribution in the transition temperature and current density measurements.

Manuscript reecived May 14, 1966; revised manuscript received Aug. 1, 1966.

Any discussion of this paper will appear in a Discussion Section to be published in the June 1967 JOURNAL.

REFERENCES

1. H. J. Levinstein and E. Buehler, *Trans. Met. Soc. AIME*, **230**, 1314 (1964).
2. See, for instance, J. E. Kunzler, E. Buehler, F. S. L. Hsu, and J. H. Wernick, *Phys. Rev. Letters*, **6**, 89 (1961); D. L. Martin, M. G. Benz, C. A. Bruch, and C. H. Rosner, *Cryogenics*, **2**, 161 (1963).
3. J. J. Hanak, in "Metallurgy of Advanced Electronic Materials," p. 161, G. E. Brock, Editor, Metallurgical Society Conferences, Vol. 19, Interscience, New York (1963).
4. J. J. Hanak, K. Strater, and G. W. Cullen, *RCA Rev.*, **25**, 551 (1964).
5. G. W. Cullen, *Trans. Met. Soc. AIME*, **230**, 1494 (1964).
6. J. J. Hanak, G. D. Cody, J. L. Cooper, and M. Rayl, "Proceedings of 8th International Conference on Low Temperature Physics," p. 353, Butterworth Scientific Publications, Ltd., London (1963).
7. H. C. Schindler and F. R. Nyman, *RCA Rev.*, **25**, 570 (1964).
8. See, for instance, H. Schaefer, "Chemical Transport Reactions," Academic Press, New York (1964).
9. M. L. Picklesimer, "Anodization as a Metallographic Technique for Zirconium Base Alloys," U. S. Atomic Energy Commission, Oak Ridge Nat. Lab, Rpt. 2296, 1957.
10. See, for instance, F. H. Nicholl, *This Journal*, **110**, 1165 (1963).

The Application of Gas Chromatography to the Analysis of Gas/Vapor Atmospheres in Semiconductor Processes

R. Nuttall

Ferranti Limited, Wythenshawe, England

ABSTRACT

Some of the problems which have been investigated using gas chromatography are discussed. The atmospheres examined are those concerned with the epitaxial deposition of silicon, the components estimated including the chlorides of boron, silicon, and phosphorus. The results indicate the source of some of the variations observed in the epitaxial process and also suggest a common feature of the reactions involving silicon chlorides.

Gas chromatography is a method by which gases and vapors may be separated. It depends for its operation on the differences in the distribution coefficients of the gases and vapors (components) between a fixed phase and a gaseous mobile phase. In practice the sample of mixed components is injected into a carrier gas stream, usually hydrogen or helium, which passes through a column containing a suitable absorbent. The components separate in the column according to their distribution coefficient with regard to the carrier gas and the absorbent and pass out of the end of the column in a specific order as the individual components. These are detected as they emerge by using a thermal conductivity cell or one of the many other types of detectors. The components are detected and registered on a recorder, but as they are not identified nor is the quantity present indicated directly it is necessary to calibrate the equipment initially with known components. This requires measuring their retention time, *i.e.*, the time taken for the sample to reach the detector after injection and also to measure the sensitivity to a given quantity of a component. It is not proposed to discuss the theory or the many other aspects of gas chromatography further in view of the large range of literature available on the subject (1-4).

Apparatus

Figure 1 shows the apparatus used in the investigations and is typical of the standard commercial units available. The basic differences from the commercial units were (*a*) the whole system was constructed from Teflon and stainless steel because of the reactivity of the components to be examined; (*b*) the sampling valve used was based on a design described by Hamlin (5); and (*c*) an auxiliary flow of hydrogen for sampling purposes was incorporated. There are several references (6-8) to work carried out in investigating inorganic halides by gas chromatographic techniques in the literature, and the column packing which gave the most satisfactory separation of the compounds investigated was similar to that described by Abe (6). The column details were: support material, Kieselguhur, 72-85 grade; stationary phase, 15% silicone oil, 85% support material; column temperature, 50°C for chlorides, 90°C for bromides or mixtures of chlorides and bromides. The column length was 300 cm and was constructed from 3/16 in. ID stainless steel tubing. Other column packings which were investigated and proved unsatisfactory due to poor resolution and "tailing" were: support material, powdered Teflon 72-85 grade; stationary phases, Kel-F40 oil, Apiezon grease, Squalene and liquid paraffin.

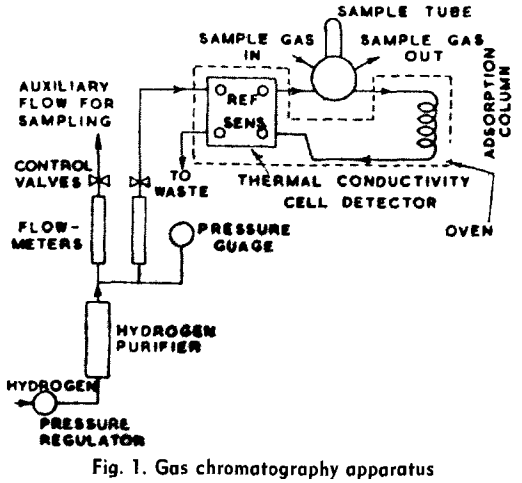

Fig. 1. Gas chromatography apparatus

A typical differential chromatogram obtained with this equipment is shown in Fig. 2. The area under the peak is a measure of the concentration of the component, and its position is indicative of the particular component. Where good resolution is obtained the peak height will be a measure of the concentration.

The peaks shown are for $SiCl_4$,$SiHCl_3$, SiH_2Cl_2, and HCl. This chromatogram was obtained during the investigations subsequently carried out and was typical of reaction 9, Table I.

Results of Investigations

Two-component systems.—(*a*) The effect of water vapor on the composition of certain two-component systems found in the epitaxial silicon field were investigated. The mixtures were $SiCl_4/PCl_3$ and $SiCl_4/BCl_3$. The equipment could not be adapted readily to estimate accurately differences in concentrations of two components less than 1% so that all the studies had to be carried out with initial concentrations greater than 1%.

Figure 3 shows the change of $PCl_3/SiCl_4$ concentration with evaporation using dry hydrogen and wet hydrogen. An initial concentration of molar ratio 0.1 $PCl_3/SiCl_4$ was used. The wet hydrogen was produced by first passing the hydrogen through water at 20°C before passing it into the $PCl_3/SiCl_4$. It is interesting to note that an increase in the relative concentration of $PCl_3/SiCl_4$ is observed using wet hydrogen, suggesting that the $SiCl_4$ is preferentially hydrolyzed. This is fortunate in that in $SiCl_4$ doped with trace amounts of PCl_3 the amount of PCl_3 is relatively unaffected by contact with moist air.

Figure 4 shows the results obtained by evaporation of a mixture of 10% BCl_3 in $SiCl_4$ using wet and dry hydrogen. In this case the tendency is for the BCl_3

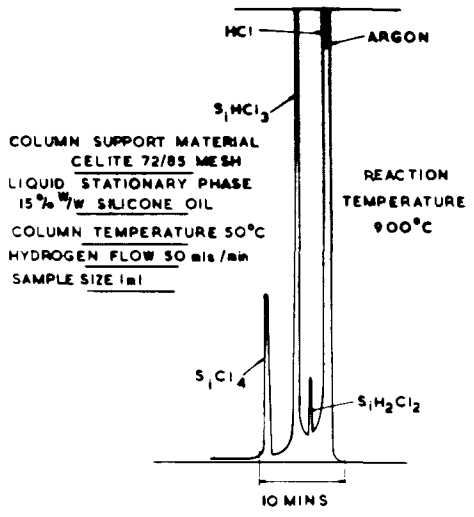

Fig. 2. Gas chromatogram showing presence of $SiCl_4$, $SiHCl_3$, Si_2HCl_2, and HCl produced when $SiHCl_3$ in argon is passed over a hot substrate.

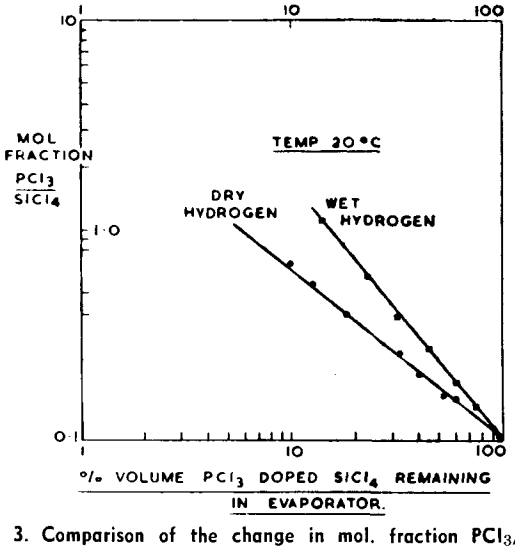

Fig. 3. Comparison of the change in mol. fraction $PCl_3/SiCl_4$ with evaporation using wet and dry hydrogen as carrier gas.

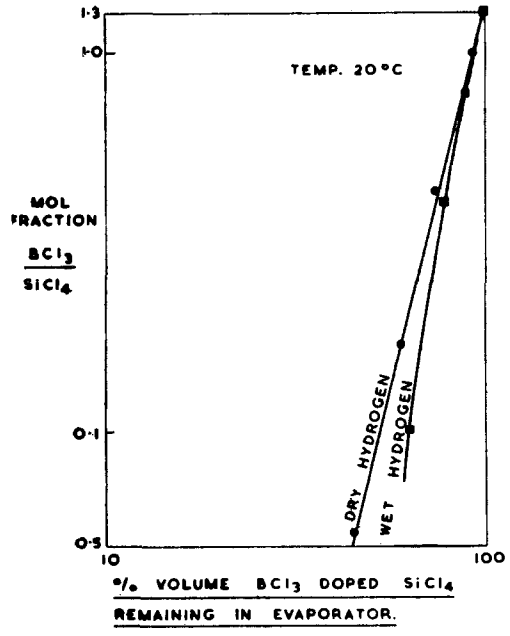

Fig. 4. Comparison of change in mol. fraction $BCl_3/SiCl_4$ using wet and dry hydrogen as carrier gas.

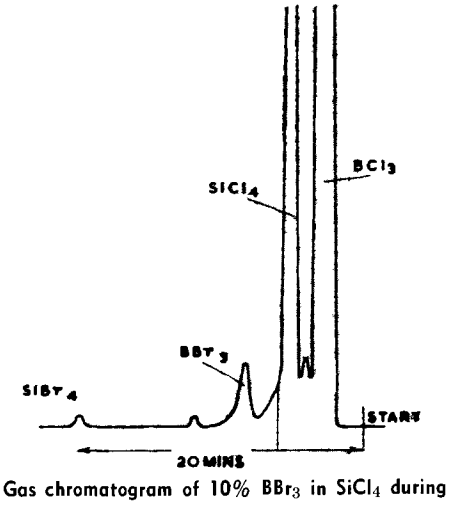

Fig. 5. Gas chromatogram of 10% BBr_3 in $SiCl_4$ during evaporation.

to be hydrolyzed preferentially, which may account for the fact that $SiCl_4$ doped with trace quantities of BCl_3 appears to lose its boron content on repeated handling and storing. This is reflected in the resistivity and type of epitaxial layers produced from such $SiCl_4$. The tendency is for the epitaxial layers of silicon produced to revert to n-type conductivity when the $SiCl_4$ is repeatedly removed from the equipment for storage, unless great care is taken to avoid ingress of air.

(b) The behavior of $BBr_3/SiCl_4$ mixtures on evaporation was also investigated. Figure 5 shows a chromatogram obtained during the evaporation of 10% BBr_3 in $SiCl_4$. It can be seen that the bulk of the boron in the vapor phase is present as the chloride and that other mixed halides are present. The presence of the chloride has already been reported using infrared transmission for detection (9). In further experiments several other small peaks have been observed which could correspond to the other silicon and boron chlorobromides judging from the boiling points of these compounds recorded in the literature. The identification of similar compounds on a basis of boiling point/retention time (2) is possible in some cases, and in view of the similarity of the compounds involved in this particular case it would be expected that the retention time would be a function of the bp of the compound. Figure 6 shows the change in peak heights of BCl_3 and $SiCl_4$ during the evaporation of 10% BBr_3 in $SiCl_4$. The behavior of the BCl_3 is interesting in that the number of moles present in the vapor phase remains relatively constant after an initial decrease. On standing the behavior is repeated. The $SiCl_4$ decreases steadily at a faster rate than expected because a proportion is converted to the relatively involatile $SiBr_4$ and other chlorobromides. Only the BCl_3 and $SiCl_4$ peak heights have been plotted as these are the only components which have high concentrations in the vapor phase.

Examination of the oxidation, reduction, and etching reactions associated with $SiCl_4$.—*Equipment.*—The equipment used to study the reaction products produced by the various reactions associated with $SiCl_4$ is shown in Fig. 7. This is simply a modified version of the standard vertical epitaxial deposition cell described in the literature (10, 11) with provision to take a continuous flow of gas from just above the wafer surface and pass this through the sampling valve on the gas chromatographic equipment.

Procedure.—Initially the gas chromatograph was calibrated with individual known compounds and, in some

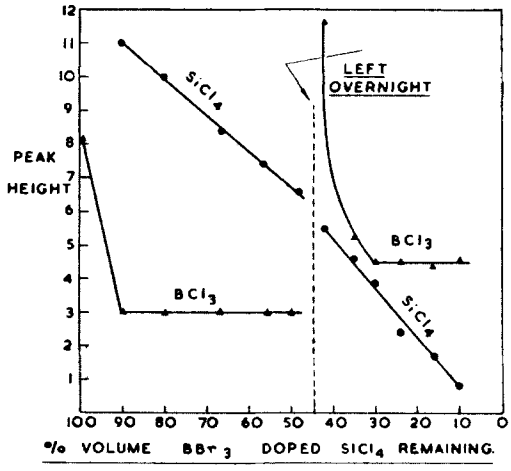

Fig. 6. Change in peak height of the components BCl_3 and $SiCl_4$ on the evaporation of 10% BBr_3 in $SiCl_4$.

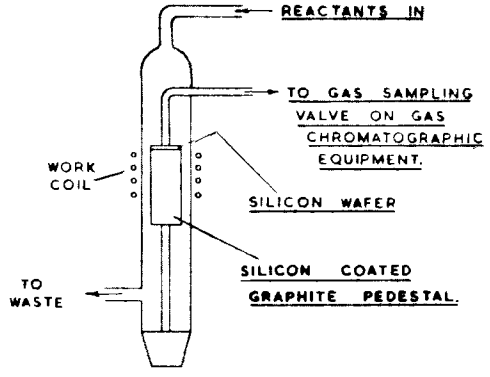

Fig. 7. Reaction cell

cases, mixtures of these compounds. The compounds were selected as being those expected to be found during the studies, and any unexpected peaks were identified during the experiments by again using known compounds. Unfortunately, it was soon apparent that quantitative measurements would be unreliable as the equipment did not have facilities for changing the sensitivity with the accuracy necessary for reliable quantitative measurement. This change in sensitivity was necessary because of the large variations in peak height which was found during these experiments. It was, however, possible to assess whether the particular component was there as a major or minor constituent. The experiments were carried out by taking gas samples from the reaction cell while various reactions were in progress. The reaction conditions, namely temperature and concentration, were varied and samples again taken.

Results.—Table I shows the reactions studied and the results from the chromatograms obtained.

In addition to these results it was observed that all the reactions involving $SiCl_4$ or $SiHCl_3$ as one of the reactants did not commence until 850°C. Only above 850°C were any peaks other than the reactants observed, and their presence coincided with the initiation of reaction at the surface of the silicon substrate. This suggests that the reactions are surface dependent, *i.e.*, heterogeneous. The reactions involving water vapor did tend to show a small HCl peak below 850°C due to some homogeneous hydrolysis taking place. This increased in height rapidly above 850°C, with the deposition of silicon dioxide on the silicon substrate.

Consider the reactants studied in the order indicated.

Table I. Results obtained from reaction studies

	Reactants	Components observed on gas chromatogram
[1]	$SiCl_4 + H_2$ Molar Ratio $\frac{SiCl_4}{H_2} < 0.28$	$SiCl_4$(M), $SiHCl_3$(L), SiH_2Cl_2(T) + HCl(M)
[2]	$SiCl_4 + H_2 + Si$ Molar Ratio $\frac{SiCl_4}{H_2} > 0.28$	$SiCl_4$(M), $SiHCl_3$(M), SiH_2Cl_2(L) + HCl(M)
[3]	$SiCl_4 + A + Si$	$SiCl_4$(M) + Cl_2(T)
[4]	$SiCl_4 + H_2 + H_2O$	$SiCl_4$(M) + HCl(M)
[5]	$SiCl_4 + H_2 + CO_2$	$SiCl_4$(M) + HCl(M)
[6]	$SiCl_4 + A + H_2O$	$SiCl_4$(M) + HCl(M)
[7]	$Si + HCl + H_2$	$SiCl_4$(L), $SiHCl_3$(M), SiH_2Cl_2(L) + HCl(M)
[8]	$SiHCl_3 + H_2$	$SiCl_4$(L), $SiHCl_3$(M), SiH_2Cl_2(L) + HCl(M)
[9]	$SiHCl_3 + A$	$SiCl_4$(L), $SiHCl_3$(M), SiH_2Cl_2(L) + HCl(M)
[10]	$SiHCl_3 + H_2 + H_2O$	$SiHCl_3$(M) + HCl(M)

M, Major constituents; L, minor constituents; T, trace constituents.

1. The reaction of H_2 with $SiCl_4$ above 850°C produces the deposition of silicon at molar ratios $SiCl_4/H_2 < 0.28$ and also the intermediate products $SiHCl_3$ SiH_2Cl_2 + HCl. SiH_3Cl was also detected, but as its peak tended to be masked by the HCl peak its presence was not always conclusive. Above molar ratios $SiCl_4/H_2 > 0.28$ the silicon substrate is etched (10) and reaction 2 applies.

2. The reaction products are identical to those in reaction 1, but all the peak heights show a marked increase. The appearance of the silicon wafer after etching is similar to that obtained using HCl/H_2, being of a mirror finish free from oxide.

3. The reaction of $SiCl_4$ with Si using an argon carrier gas results in etching of the silicon. Chlorine was detected during this reaction and, of course, $SiCl_4$. The appearance of the wafer was similar to that produced by chlorine etching, *i.e.*, any oxide remained unattacked. Large quantities of an involatile deposit which consists of polymerized $SiCl_2$ molecules (12) were observed on the cell walls at the exhaust end of the cell. Because $SiCl_2$ polymerizes so readily and is then relatively involatile it cannot be observed on the gas chromatogram. It should be noted that this reaction is useful in replacing chlorine as an etchant in the examination of oxidized wafers for pinholes in situations where the use of chlorine is hazardous from safety aspects and also where its purity is suspect. When the substrate was silicon heavily doped with phosphorus, PCl_3 was observed on the chromatogram.

4 and 5. In the reaction of $SiCl_4$ with H_2O using a hydrogen carrier gas, only HCl and $SiCl_4$ (and CO_2 in reaction 4) were observed on the chromatogram. No other intermediates were observed. The oxide deposition rate was very temperature dependent (13) and was indicated on the chromatogram by a rapid increase in the HCl peak height with increasing temperature. As the H_2O concentration was decreased the simultaneous deposition of Si and SiO_2 was observed, and this coincided with the appearance of $SiHCl_3$, SiH_2Cl_2 on the chromatogram.

6. In the above reaction using argon as the carrier gas HCl and $SiCl_4$ were observed, but there was a suggestion that more homogeneous hydrolysis was taking place prior to deposition than with hydrogen. There was a small HCl peak observed when pedestal and slice were at room temperature, but this increased rapidly above 850°C. If the H_2O concentration was decreased below a specific level, then both deposition

of SiO_2 and etching of the silicon substrate were observed.

7. The reaction of HCl with the silicon substrate using a hydrogen carrier gas results in reaction products as found for the reduction of $SiCl_4$. The etch rate was not greatly temperature dependent. The most predominant peak, excluding HCl, was $SiHCl_3$.

8. The reduction of $SiHCl_3$ with H_2 results in the deposition of silicon and the production of $SiCl_4$, SiH_2Cl_2, ($SiHCl_3$) and HCl. This reaction does not remove silicon at high molar ratios and temperature, but the deposition rate does decrease above 1200°C (11).

9. On passing $SiHCl_3$ in argon over the heated Si substrate apparent disproportionation of the $SiHCl_3$ occurs, *i.e.*, $2SiHCl_3$ $SiH_2Cl_2 + SiCl_4$.

HCl was also present, and some polymer was deposited on the walls on the reaction cell which suggests that the reaction $SiHCl_3 \rightarrow SiCl_2 + HCl$ is also taking place. There was no apparent deposition of silicon or etching of the silicon substrate, which also suggests that the reaction is independent of the substrate material. This was confirmed by using graphite as the substrate when the same chromatogram was produced.

10. The reaction of $SiHCl_3$ with H_2O using a hydrogen carrier gas deposits SiO_2 on the silicon substrate. Only $SiHCl_3$ and HCl were observed on the chromatogram, and the oxide deposition rate was very temperature dependent.

Discussion

As previously stated a common feature of all the reactions studied using $SiCl_4$ and $SiHCl_3$ as one of the reactants was the fact that no reaction involving the surface occurred before 850°C. Not until this temperature was reached did any change in the chromatogram occur, and this coincided with some surface reaction. This would therefore suggest that each reaction proceeds through the same initiation step. In all the reactions which initially contained reactants consisting of H_2, Cl_2, and Si, the same components were also observed on the chromatogram. It would appear therefore that, depending on the concentrations of Cl: Si: H involved in the vapor phase and the reaction temperature, a reaction balance is attained consisting of $SiCl_4$, $SiHCl_3$, SiH_2Cl_2, $SiHCl_3$, HCl, Si, and $SiCl_2$. Lever (16) and Sedgwick (17) have considered these reactions on a theoretical basis, but a quantitative comparison of their results with those obtained in these experiments is not feasible due to the limitations of the particular equipment used. This would, however, be possible with more sophisticated equipment having facilities to enable the sensitivity to be changed accurately during the actual tracing of the chromatogram.

Conclusion

The experiments described suggest that gas chromatography can be a valuable tool in investigating many problems found in the semiconductor field. It is limited in investigating solids and liquids at low vapor pressure or reaction products which are short lived, *e.g.*, in the silicon deposition studies described it was impossible to detect $SiCl_2$ monomer as this readily polymerized to an involatile solid. However, it may be feasible to estimate the amount of $SiCl_2$ by difference, but this would, of course, involve a total analysis of all the gases passing out of the system.

Acknowledgment

The author wishes to thank Mr. D. King and Mr. C. Rowbottom for their able assistance in constructing and operating the chromatographic equipment.

Manuscript received Feb. 16, 1965; revised manuscript received Aug. 8, 1966. This paper in its original form was presented at the Electronic Materials Convention, Birmingham University, September 1964.

Any discussion of this paper will appear in a Discussion Section to be published in the June 1967 JOURNAL.

REFERENCES

1. J. H. Know, "Gas Chromatography," Methuen Monograph.
2. H. Purnell, "Gas Chromatography," J. Wiley & Sons, Inc., New York (1962).
3. "Gas Chromatography," A series of International Symposiums held under the Auspices of the Analysis Instrumentation Division of the Instrument Society of America. Published by Academic Press, New York.
4. Glossary of Terms relating to Gas Chromatography British Standard 3282: 1963 British Standards Institution.
5. A. G. Hamlin, G. Inveson, and T. R. Phillips, *Anal. Chem.*, **35**, 2037 (1963).
6. Yasuhiko Abe, *Bunseki Kagaku*, **9**, 795 (1960).
7. J. Joklik, *Collection Czechoslov. Chem. Communs.*, **26**, 2079 (1961).
8. N. A. Palamarchuk, S. V. Syavtsillo, N. M. Turkel'-taub, and V. T. Shemyatenkova, *Tr. Komis po Analit Khim., Akad Nauk SSSR, Inst. Geokhim i Analit Khim.*, **13**, 277 (1963).
9. K. J. Miller and M. J. Grieco, *This Journal*, **110**, 1252 (1963).
10. H. C. Theuerer, *ibid.*, **108**, 649 (1961).
11. R. Nuttall, *ibid.*, **111**, 317 (1964).
12. E. G. Bylander, *ibid.*, **109**, 1171 (1962).
13. W. Steinmaier and J. Bloem, *ibid.*, **111**, 296 (1964).
14. J. M. Charig and B. A. Joyce, *ibid.*, **109**, 957 (1962).
15. Schafer, *Z. anorg. u. Allgem. Chem.*, **286**, 27 (1956).
16. R. F. Lever, *IBM J. Research and Devel.*, **8**, 460 (1964).
17. T. O. Sedgwick, *This Journal*, **111**, 1381 (1964).

Nondestructive Determination of Thickness and Perfection of Silica Films

Lawrence A. Murray and Norman Goldsmith

Electronic Components and Devices, Radio Corporation of America, Somerville, New Jersey

ABSTRACT

Analysis of the infrared reflection system of silica on silicon shows that the silica film thickness can be deduced from both the short-wavelength interference pattern and the reflection height of the 9μ silicon-oxygen resonance. Marked disagreements between these two independent measurements can be ascribed to a lack of comparative perfection of the oxide film. The effect of heat-treatment on both the reflectivity at 9μ and the etch rate of deposited silica films is discussed.

Experimental

Prior to oxide growth, silicon wafers were prepared by either chemical or mechanical polishing. Both n- and p-type substrates were used, with resistivities varying from 0.001 to 50 ohm-cm. These samples were steam-oxidized at 1000°C.

The reflection spectra were recorded with a Perkin-Elmer "Infracord" double-beam spectrophotometer equipped with two reflectance attachments. The instrument was adjusted to read 100% with gold reflectors in both beams. The angle of incidence was 26.5°. When a polished silicon wafer was placed in the sample position, the trace in the 2.5-15μ region varied from 39 to 37%. The spectra of the oxidized wafers were measured, and the points of interest were recorded. The oxide thickness for each sample was then determined by the Tolansky method to an estimated accuracy of ±150Å. Figure 1 shows a typical reflection spectrum of a silica film on silicon with the pertinent points indicated.

Thickness Determined from Interference

For oxide thicknesses between 4500 and 9000Å, a minimum reflectivity exists in the short wavelength region because of interference. The thickness, d, of the film can be determined by the following usual equation (1):

$$d = \frac{P\lambda_{min}}{2(n^2 - \sin^2\theta)^{1/2}} \qquad [1]$$

where n is the index of refraction of the silica and θ is the angle of incidence. The order number, P, is 1/2 for such films.

For films thicker than 9000Å, a maximum appears with order number of unity. Figure 2 shows the variation of d with λ_{min}, with n taken as that of fused silica and $\sin^2\theta$ as 0.2. This method has been used for film thicknesses exceeding 50,000Å by first determining P and then multiplying the value read from Fig. 2 by 2P.

Thickness as a Function of R_{max}

In the neighborhood of 9μ, the silica lattice begins to absorb energy as a result of resonant stretching of the silicon-oxygen bonds. In this region, the indices of refraction (n) and absorption (k) change rapidly. The variable k increases at wavelengths short of resonance and then falls rapidly beyond the resonance wavelength, while n increases to a maximum just beyond resonance. In principle, reflectivity as a function of film thickness can be calculated (2) from a knowledge

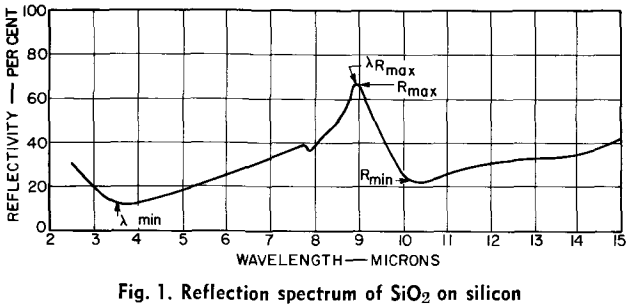

Fig. 1. Reflection spectrum of SiO_2 on silicon

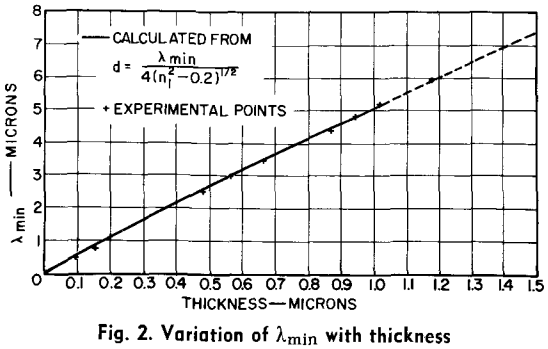

Fig. 2. Variation of λ_{min} with thickness

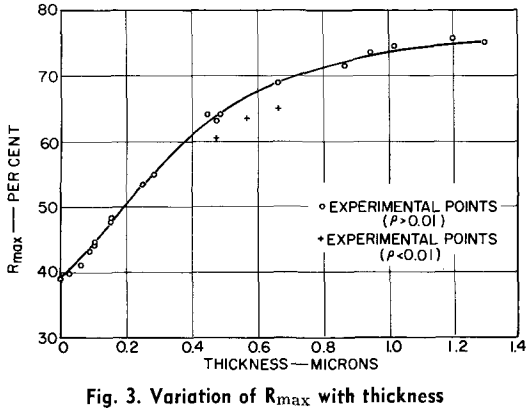

Fig. 3. Variation of R_{max} with thickness

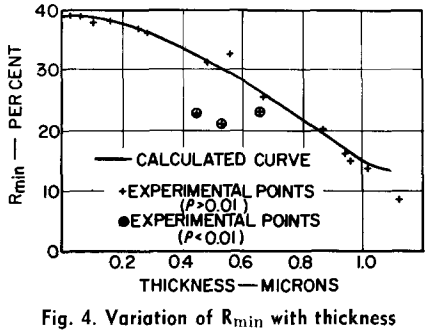

Fig. 4. Variation of R_{min} with thickness

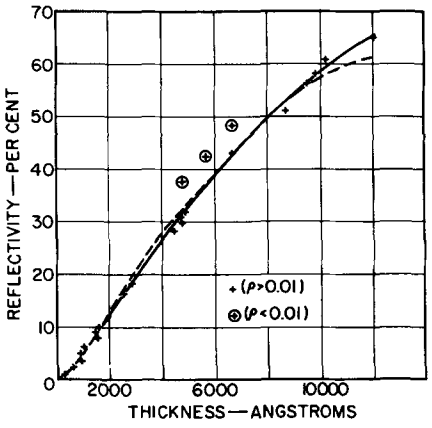

Fig. 5. Variation of $R_{max} - R_{min}$ with thickness

of n and k of the film, n of the substrate, and the angle of incidence.[1] This tedious calculation was not performed because conflicting values for n and k are given in the literature (3, 4). The value of λR_{max}, the wavelength of maximum reflectivity near 9μ, is itself a function of thickness, requiring the use of varying values of n and k in the calculation.

The experimentally determined values of reflectivity as a function of thickness are shown graphically in Fig. 3. The reflectivity of fused silica, equivalent to an infinite film thickness, was found to be 75%. These results are applicable only to the particular angle used in this work and to wafers having nonpolished rear surfaces. The measured reflectivity is dependent on both the angle of incidence and, as indicated, the reflectivity of the back surface. With these quantities held constant, measurement of the reflectivity near 9μ is a practical method for the determination of the thickness of silicon dioxide films on silicon for layers thinner than 7000Å.

Thickness as a Function of R_{min}

At wavelengths beyond the 9μ resonance, the refractive index again decreases to a low value, and normal reflection characteristics reappear. Experimentally it was found that a pronounced reflection minimum exists in the 10.5μ region, and that the value of R_{min} is dependent on thickness. In this region, n for fused silica is approximately 2.2 (3, 4). For the thicknesses considered the quarter-wave plate conditions are approximated [*i.e.*, $n_2 = (n_1 n_3)^{1/2}$ and $d = \lambda/4n_2$]. The oxide layer then begins to act as an antireflection coating, and the reflectivity decreases as the film thickness increases. The experimental points are shown in Fig. 4, along with a computed reflection curve.

[1] The equations in ref. (2) do not include a term for the reflectivity from the back of the substrate. This reflection may be accounted for by adding an additional term, $R_b \exp(-2\,n\nu)$, to the calculated reflectivities. For the wafers used in this study, R_b is estimated to be 0.08. Because unpolarized light is used, the computations must be made for both parallel and perpendicular polarization, and the two reflectivities must be averaged.

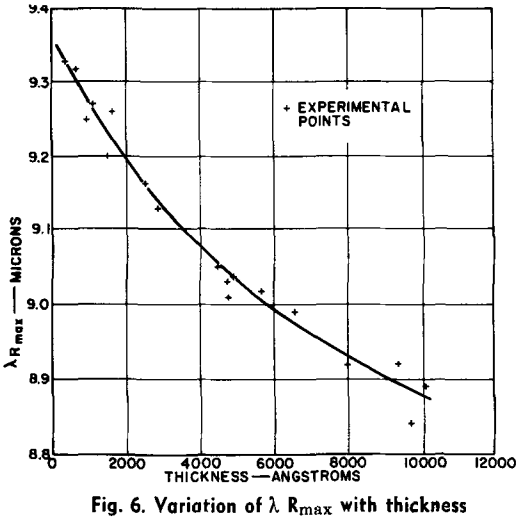

Fig. 6. Variation of λR_{max} with thickness

Thickness as a Function of R_{max}-R_{min}

As thickness increases, R_{max} saturates; however, R_{min}, which was constant at low values, begins to rise and then decreases as R_{max} saturates. Thus, a plot of $(R_{max})-(R_{min})$ is quasi-linear. The practical result of this behavior is that the difference in the two reflectivities yields accurate values of thickness over the range from 300 to 10,000Å. Figure 5 shows the variation of $(R_{max})-(R_{min})$. Low-resistivity points are further from the curve, and there is some disagreement between calculation and experiment at oxide thicknesses near 10,000Å. This thickness range spans that commonly used in device processing and is a useful method for in-process control of oxide thickness.

Resistivity of the Substrate

For most substrates, the amount of light absorbed by the wafer is negligible because the absorption coefficient is small. Provided the resistivity is greater than 0.01 ohm-cm, there is little influence from the substrate on radiation traversing the substrate. The anomalous reflectivity of the 10^{19} p-type sample is caused by plasma resonance which occurs in heavily doped low-mobility semiconductors (5). Measurements of film thickness using the 9μ reflection height, cannot be made reliably on in-process wafers which have surface concentrations exceeding 10^{19}. In fact, for doping levels of 10^{21}, a pronounced minimum in the reflectivity occurs in the region of 3μ, which also invalidates the use of the interference equation to determine the film thickness.

Variation of λ_{max} with Thickness

The wavelength at which R_{max} occurs depends on the thickness of the oxide, as shown in Fig. 6. Although the accuracy in determining thickness is poor because of the slow variation of λ_{max} with thickness, a knowledge of the approximate value of this point is useful as a check on other measurement values. The extreme values, $d \to 0$ and $d \to \infty$, occur at wavelengths at which n and k, respectively, are reported to reach their maximum value (3).

Oxide-Perfection Studies

The use of infrared transmission to study the properties of deposited silicon dioxide films has been reported previously (6). Similar information can be obtained from a study of the reflection spectrum, obviating the need for specially prepared high-resistivity substrates. The reflection spectrum of a silica film obtained by the controlled oxidation of silane at low temperatures is shown in Fig. 7.

Comparison of the thickness predicted from the short wavelength minimum and that indicated by the 9μ reflection height shows that the latter method predicts a much smaller thickness than actually exists. Furthermore, the wavelength of the maximum is shifted to-

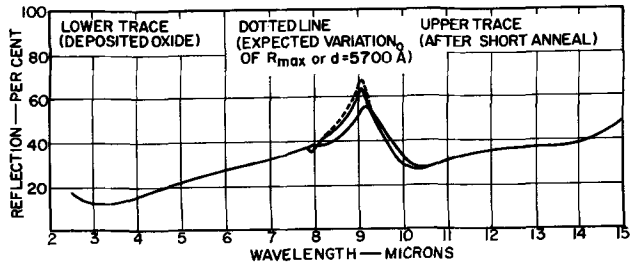

Fig. 7. Deposited SiO_2 reflection spectrum before and after heat-treatment.

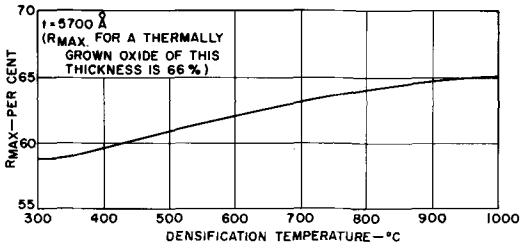

Fig. 8. R_{max} of deposited oxide as a function of densification temperature.

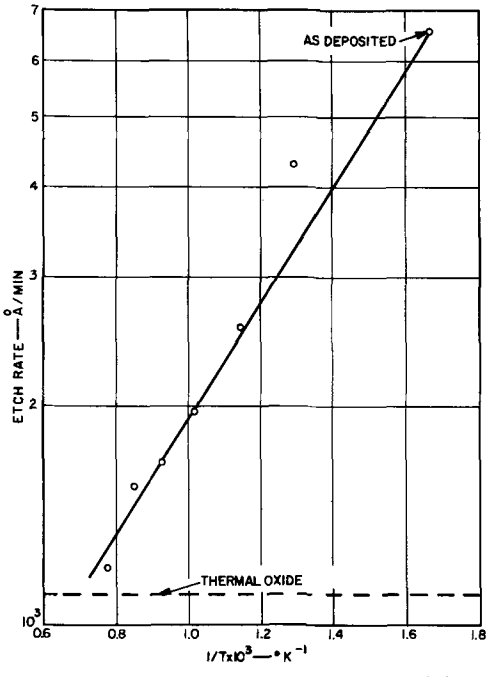

Fig. 9. Etch rate of deposited oxide as a function of densification temperature.

ward longer wavelengths. These facts imply that the bonding in the deposited film differs from that of the grown films, resulting in differing values for the optical constants responsible for the reflection height. As reported (6), the deposited films etched faster than thermally grown oxides.

For study of the densification of the films, samples were heat-treated at various temperatures in argon or oxygen. The results did not depend strongly on the ambient. After heat-treatment, the reflectivity increased and the etch rate decreased. Figure 8 shows the variation of reflectivity at 9μ with heat-treatment temperature for one sample. Although the length of heat-treatment influenced the reflection height for short periods, in all cases the reflectivity became sensibly constant after certain treatment times. These times varied from 1 hr at 500°C to less than 1 min at 1000°C. All values reported are for the saturated case. For the sample shown, a calculation of thickness determined from the short wavelength pattern predicts that the reflectivity should reach 70%. However, the temperature-reflectivity curve saturates at 68%, indicating that a structure comparable to that of a steam-grown oxide was not reached. When the sample was heat-treated at 1000°C in steam, however, the predicted reflectivity was reached.

The variation of the etch rate in buffer etch[2] with the temperature of densification was also determined. The results of such a measurement are shown in Fig. 9. The etch rate does not quite reach the rate of thermally grown oxide, yet because it is required in many

[2] 682 cc H_2O, 164 cc HF, 1 lb NH_4F at 25°C.

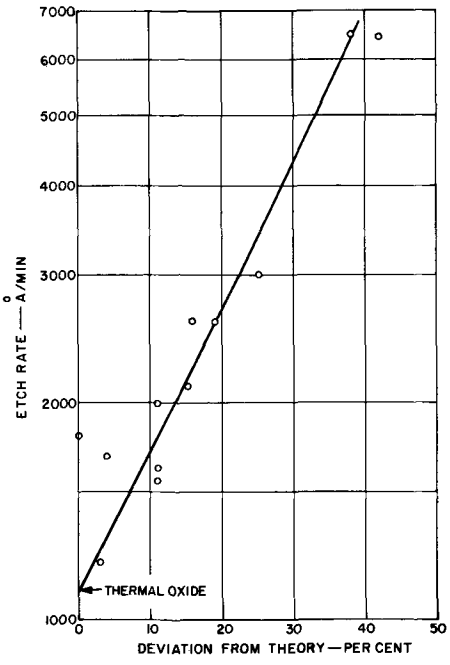

Fig. 10. "Perfection Index" vs. etch rate of deposited oxide

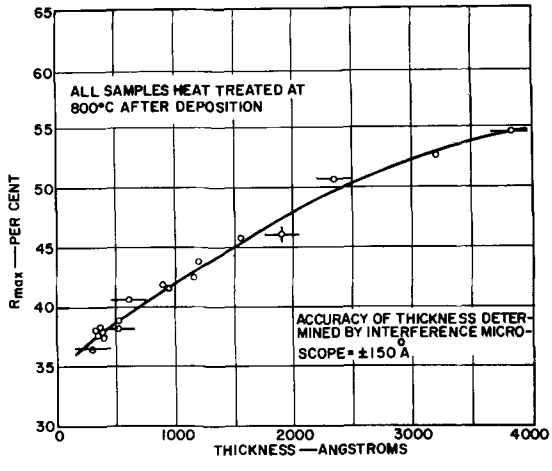

Fig. 11. R_{max} of deposited oxide (700°C) on GaAs as a function of thickness.

instances during device fabrication, a nondestructive method for etch-rate determination is useful.

Empirically, the convenient relationship $A = \log 100/(140 - R_{max})$ is used to express the 9μ peak height. The percentage deviation of the deposited film from the expected value can then be defined as $\%D = 100\ (A - A'/A)$, where A' refers to the measured value, and A to the value expected for the known thickness. The deviation curve as a function of etch rate in Fig. 10 shows a fair correlation, particularly in view of the fact that measurement of reflectivity results in large errors in the computed value of A', especially at peak heights very close to the expected values.

Sometimes, densification at elevated temperatures is not feasible, as in the case of silica layers deposited on gallium arsenide by the pyrolysis of ethyl silicate. In this instance, however, the thermal history of the sample is controlled, and the thickness can be obtained from a measurement of R_{max}. Figure 11 shows the variation of R_{max} with thickness.

Acknowledgment

The authors thank E. Jordan for preparing the samples and for many helpful discussions, W. Stever and

J. DiPiazza for their assistance, and J. White for the use of his gallium arsenide curves.

Portions of this work were supported by the Air Force Avionics Laboratory, Wright-Patterson Air Force Base, under contract AF33(657)11615.

Manuscript received Dec. 10, 1965; revised manuscript received July 5, 1966. This paper was presented at the San Francisco Meeting, May 9-13, 1965.

Any discussion of this paper will appear in a Discussion Section to be published in the June 1967 JOURNAL.

REFERENCES

1. E. A. Corl and H. Wimpfheimer, *Solid-State Elec.*, **7**, 755 (1964).
2. M. Born and E. Wolf, "Principles of Optics," pp. 624-627, Pergamon Press, London (1959).
3. I. Simon and H. O. McMahon, *J. Chem. Phys.*, **21**, 23 (1953).
4. N. Neuroth, *Glastech. Ber.*, **11**, 420 (1955).
5. L. Murray, J. Rivera, and P. A. Hoss, Submitted to J. Appl. Phys.; see also *Bull. Am. Phys. Soc.*, May, 1965.
6. W. Pliskin and H. S. Lehman, Paper presented at the Toronto Meeting of the Society, May 1964.

Controlled Vapor-Liquid-Solid Growth of Silicon Crystals

R. S. Wagner and C. J. Doherty

Bell Telephone Laboratories, Incorporated, Murray Hill, New Jersey

ABSTRACT

The experimental procedure for controlled vapor-liquid-solid, or VLS, crystal growth is discussed for silicon. The hydrogen reduction of $SiCl_4$ was used as transport reaction, and gold as the liquid-forming impurity. The stability of the liquid droplet, which is the main criterion for controlled VLS growth, is discussed in detail. It is shown that an adverse temperature gradient or an oversupply of silicon from the vapor may render the liquid droplet unstable, thereby terminating controlled VLS growth. Silicon crystals can be grown epitaxially on perfect or imperfect silicon substrates. The control of both location of crystal growth and of diameter and length of the crystals is demonstrated.

The vapor-liquid-solid (VLS) method of crystal growth, discussed in detail by Wagner and Ellis (1, 2) is distinctly different from the commonly used vapor-solid (VS) technique. In the VLS method the crystal grows from a supersaturated liquid solution. The supersaturation of the vapor can be kept small enough to suppress the VS deposition, yet large enough to vapor deposit at the liquid alloy. Atoms arriving from the vapor diffuse, in a concentration gradient, through the liquid and deposit at the solid-liquid interface. The liquid solution is formed by alloying a proper material with the substrate crystal. Many advantages are obtained if silicon crystals are grown by the VLS method using the hydrogen reduction of $SiCl_4$ (3). For this process many metals such as gold, platinum, or nickel can be used as liquid-forming agents (2). It has been shown (2) that silicon atoms are preferentially deposited on the liquid alloy. The vapor-liquid deposition rate can be orders of magnitude larger than the vapor-solid deposition rate. The difference in deposition rates increases with decreasing deposition temperature. Therefore, silicon crystals can be grown at deposition temperatures as low as 800°C. In addition, the liquid alloy protects the growing crystal, at the solid-liquid interface, from oxidation, etc., and from foreign particles which could result in the formation of crystalline defects. Highly perfect crystals can be grown by the VLS method at a low deposition temperature, because crystal growth occurs via the liquid-solid transformation. The VLS method is uniquely suited to grow silicon crystals on selected sites on a silicon substrate. Furthermore, both the diameter and the length of the VLS crystal are controllable.

It is the objective of this paper to describe in detail the experimental procedure for controlled VLS growth of silicon crystals. Three factors should be emphasized. First, great care must be taken to keep undesired impurities from the deposition region. Second, a temperature gradient may be either advantageous or adverse during VLS growth, depending on geometry. Third, the supply of silicon from the vapor must be kept within certain limits determined by the transport process of silicon through the liquid alloy.

Sample preparation and deposition apparatus.— Single crystal silicon wafers, preferably with {111} main faces are used as substrates because the usual VLS growth direction for this material is <111>. An exact orientation of the substrate surface is not necessary for subsequent VLS growth. Even a {211} surface may be used. The VLS crystals grown on such a substrate are then inclined by 19.47° with respect to the <211> substrate normal. The number of the dislocations in the substrate crystal has no observable effect on VLS growth. Dislocation-free crystals were successfully grown on dislocation-free and on plastically deformed crystals containing up to 10^7 dislocations/cm^2. We have never observed the growth of silicon whiskers (4) from dislocations which terminate at the substrate surface. We found for silicon, the growth of whisker crystals invariably occurs by the VLS mechanism only, on the site of the liquid alloy.

The silicon substrate crystals (1-100 ohm-cm, n- or p-type) were prepared using the following procedure: (*i*) The main faces are ground with 600 grit Carborundum. (*ii*) The wafers are washed in acetone and toluene to remove any traces of mounting wax. (*iii*) They are next washed in Alconox solution. (*iv*) The wafers are etched for 5 min in 1:4(HF, HNO_3) solution followed by an etch in 1:2:6 (HF, acetic, HNO_3) for 5 min. Subsequently the wafers are rinsed in deionized filtered water and dried at 110°C.

The gold (99.999% purity) used for alloying may be prepared by filing, slicing a fine wire or sheet, or by evaporation through a mask. Of these the sliced wire or sheet is the least contaminated material. The gold pieces were cleaned in acetone and toluene and boiled in Alconox solution. This was followed by an etch in aqua regia for a few minutes. The particles were rinsed in deionized, filtered water and dried. In most cases the gold pieces were placed either manually or with the aid of a mask on the silicon substrate.

The apparatus used for controlled VLS growth of silicon is discussed in ref. (2). In the present work, two different heating systems were used. In one, the reaction tube of silica was placed inside a resistance furnace. With such a system a rather long isothermal deposition zone can be obtained, and an adverse temperature gradient avoided. The other system consisted of a graphite tube, serving as an r-f susceptor, placed inside the reaction tube. The graphite tube was first

baked at 1200°C and subsequently coated with silicon. It was found that frequently numerous fine silicon whiskers grew inside the graphite tube. The whisker crystals were removed from the tube by scraping and more silicon deposited. This procedure was repeated until no more whisker crystals were observed. For both heating systems, the silicon substrate crystal was placed either on a silicon or silica support situated in the isothermal deposition zone. Great care was taken to keep the whole deposition apparatus as clean as possible. The hydrogen used for the experiment was purified by a palladium diffuser. The temperature in the deposition zone was controlled to within ±2°C. The $SiCl_4$ to hydrogen mole ratio used in the experiment ranged from 0.01 to 0.1, with a total hydrogen flow rate of 300-1000 cc/min. It should be noted that etching of the silicon substrate may occur, even for an extremely small hydrogen to $SiCl_4$ mole ratio, if an isothermal reaction zone is used. In such a system the ratio of HCl to unreacted $SiCl_4$ increases along the deposition zone. Therefore, the proper location of the silicon substrate for subsequent VLS growth must be found empirically; it depends strongly on the geometry of the reaction zone, the total gas flow and hydrogen to $SiCl_4$ mole ratio. The silicon substrate was placed in a down stream region where no silicon deposit occurred on a clean silica substrate. This deposition region is also useful for VLS growth of silicon crystals on silicon substrates partly masked with SiO_2.

Alloying and initial VLS growth.—The most difficult and least understood aspects of VLS growth are the alloying process of the impurity agent with the substrate and the initial stages of VLS growth, the rise of the liquid droplet from the substrate. It has been found that alloying gold with the silicon substrate is difficult to control. The temperature at which the liquid alloy forms may vary from 600°C to well over the melting point of gold (1063°C). For freshly cleaned gold and silicon, the alloying temperature is about 600°-800°C. An oxide layer on the silicon substrate may prevent alloying at the gold-silicon eutectic temperature (370°C).

The shape of the liquid droplet, determined by the liquid-solid contact angle, depends on the rate of temperature increase during alloying. We have not found a satisfactory procedure to control the spreading of the liquid over the substrate surface. It is suggested that the spreading may be controlled to some extent by masking the substrate around the intended alloy region with an SiO_2 layer. This would result in preferred dissolution of silicon from the substrate interior and also would control the shape of the droplet. The observed contact angle at 1050°C is about 10°-20° which would indicate good wetting of the substrate by the liquid. This contact angle is however most likely not the equilibrium contact angle but rather a consequence of the dissolution kinetics.

The small contact angle remains constant or decreases slightly when $SiCl_4$ is introduced to the carrier gas. However, sometimes a sudden increase in contact angle is observed. The sequence of events during alloying and the initial VLS growth is shown in Fig. 1 (5). In Fig. 1a is shown a piece of gold on the silicon substrate before alloying. In Fig. 1b the temperature has been increased to about 1050°C. Figure 1c, photographed after about 10 min of VLS deposition, shows a marked increase in contact angle. As a consequence, the diameter of the growing crystal decreases during the initial stage of VLS growth. Finally, in Fig. 1d, photographed after about 30 min of VLS growth, the contact angle has become stabilized. From this point on, there is no more change and the diameter of the growing crystal remains constant if the deposition temperature is held constant. The gradual increase in contact angle results in the formation of a tapered section at the base of a VLS crystal as shown in Fig. 1. At the substrate surface the crystal is either six or three sided, depending on deposition temperature

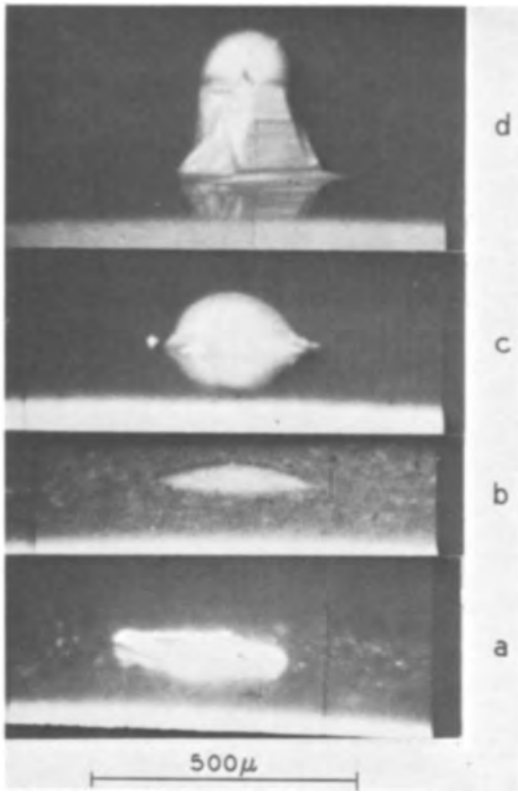

Fig. 1. Time lapse sequence of alloying and initial VLS growth. (a) Gold particle on silicon substrate at room temperature, (b) liquid droplet of gold-silicon alloy at 1050°C, (c) and (d) after 10 and 30 min respectively of growth at 1050°C. Magnification 100X.

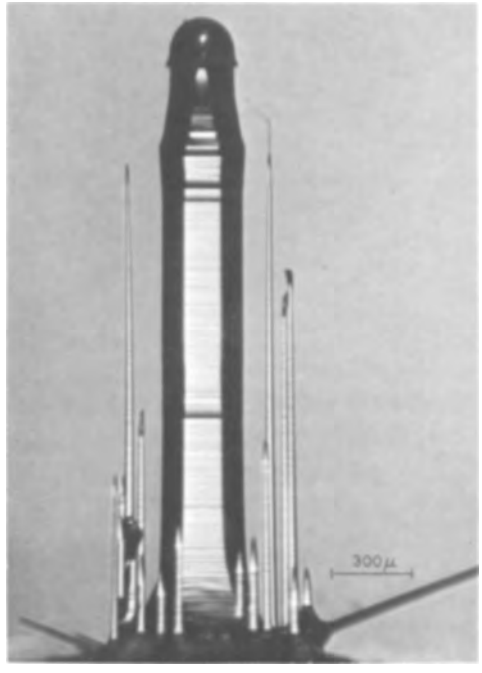

Fig. 2. Break up of liquid alloy during initial VLS growth giving rise to formation of main crystal surrounded by fine whiskers. Magnification 100X.

and time. At temperatures higher than about 1050°C, the VS deposition is considerable at the base, resulting in a three-sided form.

In the first stage of VLS growth, the liquid alloy is very sensitive to a temperature gradient or oversupply from the vapor phase. Apparently the droplet is not in a stable configuration. Too much vapor supply

may result in a partial break up of the liquid into smaller droplets, each new droplet then giving rise to VLS growth as shown in Fig. 2. Once the crystal grows beyond the tapered section, it is rather stable with respect to changes in temperature and deposition rate. The effect of a temperature gradient or deposition oversupply on the stability of a liquid droplet is discussed in detail in the following sections of this paper.

Vapor Supply

At steady state VLS growth, the same number of silicon atoms which enter the liquid from the vapor are deposited at the solid-liquid (S-L) interface. This flux of silicon atoms diffuses through a concentration difference ΔC across the liquid alloy of thickness L. The value of ΔC is an important factor for the stability of the liquid alloy. We assume for the following discussion that convective mixing in the liquid is negligible and a disk-like shape of the liquid alloy. In Fig. 3 is shown a section of the silicon liquidus Si_L and the deposition isotherm T_E. With no vapor deposit the composition of the liquid will be C_E, the equilibrium concentration. For steady state VLS growth, the composition of the liquid is C_L at the liquid-gas interface and C_g at the liquid-solid interface. C_g, which may be very small, is the supersaturation required for nucleation and growth of new crystal layers.

The concentration gradient in the liquid disk is given by

$$\frac{\Delta C}{L} = \frac{V}{D} \qquad [1]$$

where V is the speed of advancement of the S-L interface and D is the diffusion coefficient of silicon in the liquid alloy. From the phase diagram Fig. 3 it follows that for a given V, D, and L the concentration difference in the liquid $\Delta C = C_L - C_E$ (atom fraction) corresponds to a liquidus supercooling ΔT. Homogeneous nucleation theory (6) predicts a ΔT_{max} of about 300°C for pure Si or a liquid Si alloy. For $\Delta T > 300$°C the supercooling is high enough to nucleate silicon crystal by homogeneous nucleation in the liquid alloy. This sets an upper limit for ΔC during VLS growth, ΔC can be about 0.25 for $T_E = 950$°C. It has been found experimentally that this consideration is extremely important in order to avoid instability of the liquid alloy by nucleation. For example for $L = 10^{-2}$ cm, $D = 5\text{x}10^{-5}$ cm²/sec, and $T_E = 950$°C the critical growth velocity $V_{max} \sim 3.5$ mm/hr.

The VLS growth rate V (cm/sec) for a given total gas flow f (cm³/sec), a $SiCl_4/H_2$ mole ratio m_R and for a reaction tube of cross section A (cm²) can be estimated as

$$v = \frac{f m_R M}{A V_o} \qquad [2]$$

where M = molecular weight of $SiCl_4$, V_o = standard volume of perfect gas, and ρ = density of solid silicon. The assumptions implicit in Eq. [2] are a dynamic system of high flow rate, a condensation coefficient of unity for the liquid alloy and the absence of the disproportionation reaction. It is also assumed that silicon atoms on the side faces of the growing crystal do not migrate to the liquid. For $f = 6$ cm³/sec, $m_R = 0.014$, and $A = 5$ cm² the calculated VLS growth rate $V = 0.3$ mm/hr. For these conditions in the temperature range 950°-1100°C, the observed growth rate is only slightly larger than the calculated value.

Both Eq. [1] and [2] are only crude approximations of the true state of affairs. Convective mixing of the liquid alloy, which may be considerable when using r-f heating, will increase the critical velocity V_{max}. A more static reaction system (slow flow rate) will increase V because of higher impingement rate of $SiCl_4$ molecules. The reader is referred to a more rigorous calculation of the vapor phase deposition rate of silicon given by Shepherd (7). Finally, ΔT_{max} may be much smaller than 300°C if heterogeneous nucleation sites are present in the liquid alloy or on the surface of the liquid.

It is evident from the previous discussion that a sudden decrease in deposition temperature T_E during VLS, results in a sudden increase in ΔC and therefore ΔT. During the transient the ΔT can become large enough for homogeneous or heterogeneous nucleation. In Fig. 4 is shown a silicon crystal which was originally grown at 1000°C. During growth the temperature was suddenly reduced to 600°C for about 30 sec and subsequently raised to 950°C. The breakup of the liquid alloy is dramatic, giving rise to the formation of numerous small crystals which are in random orientation with respect to the main crystal.

Effect of Temperature Gradient on VLS Growth

Pfann (8) has shown that a liquid alloy zone in contact with solid solvent material can migrate through the solvent material under the influence of a temperature gradient. This phenomenon, called temperature-gradient zone melting (TGZM), arises be-

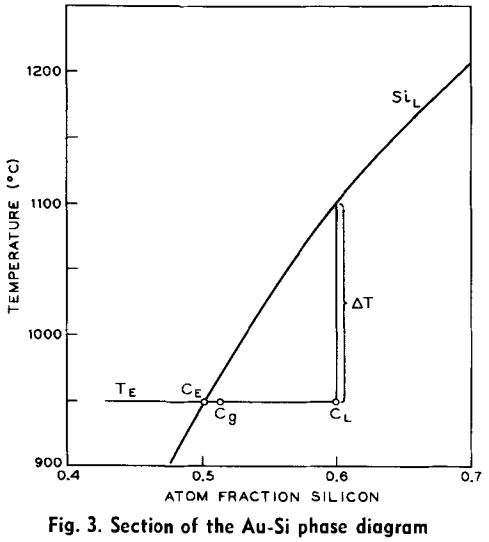

Fig. 3. Section of the Au-Si phase diagram

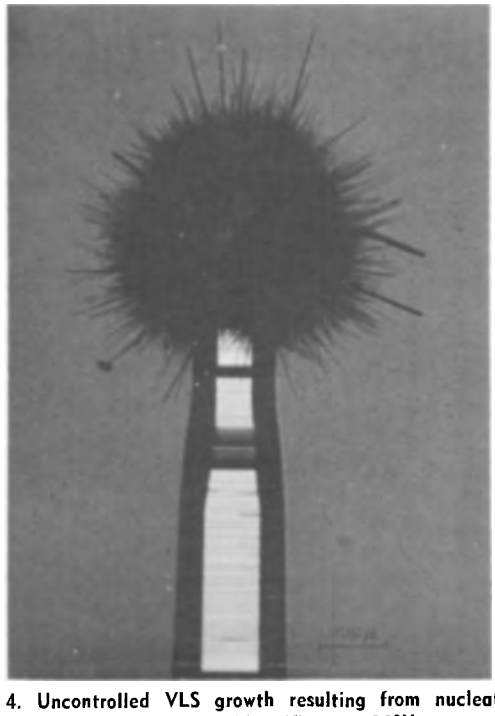

Fig. 4. Uncontrolled VLS growth resulting from nucleation of silicon crystals in liquid alloy. Magnification 250X.

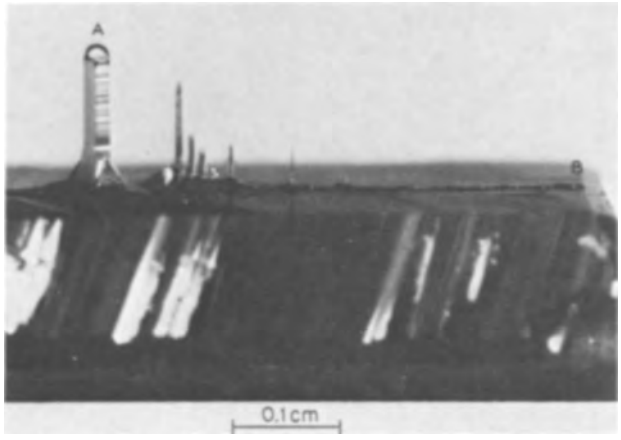

Fig. 5 Adverse effect of a lateral temperature gradient on VLS growth. A single alloy droplet, initially at position A, broke up into smaller droplets which migrated toward a higher temperature region. All droplets but the smallest one at position B gave rise to VLS crystals. Magnification 30X.

cause of continuous melting and freezing of solvent at the hotter or colder section of the liquid zone. The liquid alloy droplet on a silicon substrate comprises such a system if a temperature gradient is imposed. If the gradient is such that the substrate interior is hotter than the substrate surface, the liquid alloy will migrate into the substrate, until no more liquid is exposed to the vapor. It is evident that VLS growth is impossible under such condition. If the temperature gradient is along the substrate surface, the alloy droplet may move along the substrate toward a higher temperature region. The silicon entering the liquid from the vapor will be preferentially deposited at the colder side of the droplet. This gives rise to the build up of silicon on the substrate surface in the form of a ramp. On a (111) substrate, the ramp surface can be an extremely smooth (111) face. An additional consequence of a lateral temperature gradient can be that the liquid droplet may break up into smaller droplets. During TGZM on the substrate surface the liquid-solid contact angle becomes nonuniform, being smallest at the hot end of the liquid zone. This can lead to partial break up of the liquid droplet. This is shown in Fig. 5, where a large lateral temperature gradient was imposed during growth. The initial position of the alloy droplet was close to A where the largest crystal grew. The droplet broke up during migration giving rise to smaller crystals. The smallest droplet migrated to B. The liquid droplet can rise from the substrate surface even with a lateral temperature gradient, if the VLS growth rate is larger than the rate of TGZM.

From the previous section it follows that a temperature gradient in which the vapor-liquid interface is hotter than the S-L interface would be of great advantage during VLS growth. The liquid supercooling, ΔT as shown in Fig. 3, could be reduced by an amount equal to the temperature difference across the liquid alloy. By this means the stability of the liquid could be greatly improved.

Control of Diameter

The diameter of a VLS crystal is controlled by three factors, namely the initial amount of gold used for alloying, the deposition temperature, and the vapor-solid (V-S) deposition rate which also depends on the deposition temperature. For a given deposition temperature, the amount of gold determines the diameter of the growing crystal. The volume of the liquid droplet is given by the phase diagram. For a given amount of gold, the diameter of the crystal can be varied over a wide range by simply changing the

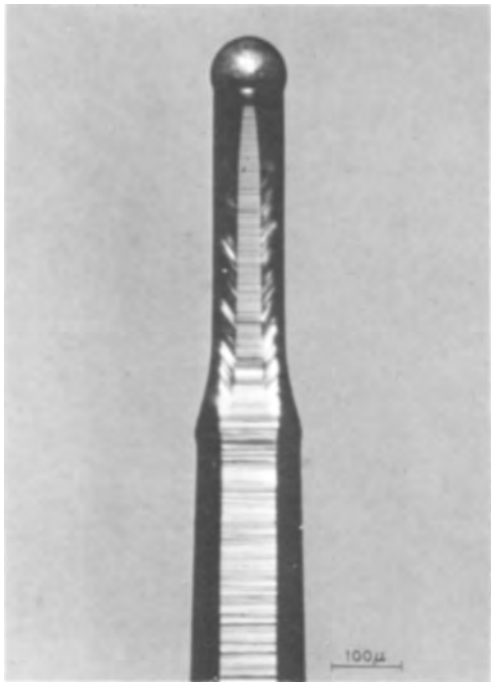

Fig. 6. Change of diameter during VLS growth, the lower section was grown at 1050°C, the top section at 950°C. Magnification 250X.

deposition temperature. Figure 6 is a photograph of an end-section of a VLS crystal. The lower part has been grown at about 1050°C, the upper part at about 950°C. Note the gradual decrease in cross-section which occurred during the temperature change. It is advisable to reduce or even stop completely the $SiCl_4$ supply and to reduce the temperature gradually. Too rapid a temperature change may cause a "pinching off" of small droplets from the main body of the liquid, giving rise to the formation of branches. An increase in diameter can be obtained by raising the deposition temperature. In this case it is helpful to increase the $SiCl_4$:H_2 mole ratio during the gradual temperature increase. This prevents remelting of silicon at the S-L interface which may cause the (111) interface to become unstable. In the extreme case the droplet may run down the side faces of the crystal, leading to subsequent uncontrolled growth.

Crystals grown at temperatures higher than about 950°C have hexagonal cross-section, with {211} side faces. At lower temperatures the cross-section becomes twelve-sided by the formation of six {110} faces. This change in morphology probably occurs because of the increase in liquid surface tension with decreasing temperature. The meniscus of the liquid droplet tends to be more circular. The edge angle of the crystal increases from 120° to 150° by changing from a six-sided to a twelve-sided morphology.

If the temperature is increased, for example from 850° to 1050°C, the {110} side faces will rapidly disappear by V-S deposition until the crystal is six-sided. While at this temperature the V-S deposit on the {211} side faces is extremely small, the {110} faces must be very favorable nucleation sites for V-S deposition. There is yet another change in morphology at a deposition temperature close to 1100°C; the crystal becomes three-sided. Three of the six {211} faces grow at the expense of the other {211} faces. At this temperature, the rate of evaporation of gold from the liquid is considerable. When all the gold has been consumed, the tip of the crystal will be bounded by three {111} faces.

Finally, the diameter of the crystal depends on the amount of V-S deposit. This sharply increases with deposition temperature. It has been estimated (2)

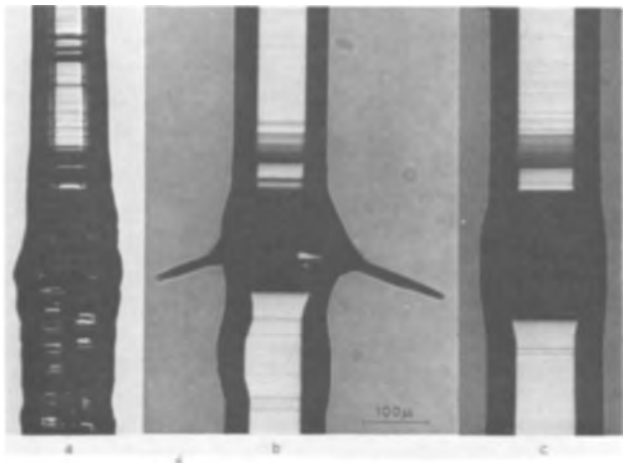

Fig. 7. Continuation of VLS growth after the crystal was cooled to room temperature and kept for 16 hr in (a) air, (b) and (c) in dry hydrogen. In (b) two side branches formed during regrowth. Magnification 250X.

that the VLS and V-S growth rates become comparable between 1200°-1300°C.

Regrowth.—It may be desirable, for practical purposes, to stop VLS growth, cool the crystal to room temperature, keep it there for a considerable time and subsequently continue growth. This procedure has been carried out many times and the following observations were made. It was found that the crystal must be kept in a nonoxidizing atmosphere such as hydrogen. Exposing the crystal to air may result in polycrystalline deposit on the existing side faces if the subsequent deposition temperature is below 1100°C; however, the newly VLS grown side faces are not affected. Second, it is also desirable to keep the initial regrowth deposition temperature slightly higher than the previous one. This results in proper melt-back during alloying and avoids formation of branches.

Figure 7 shows three silicon crystals which were regrown at 1000°C after being kept at room temperature for about 16 hr. The crystal in Fig. 7a was exposed to air. The regrown top section has the usual high degree of perfection; the lower section, however, is overgrown with polycrystalline deposit. The crystals in Fig. 7b and 7c were kept in a dry hydrogen atmosphere after cooling. Branches which formed upon regrowth are shown in Fig. 7b, and perfect regrowth is shown in Fig. 7c.

VLS growth of crystal patterns.—A goal of controlled VLS growth is the preparation of arrays of silicon crystals on silicon substrates. The growth of such arrays is not very difficult if all the experimental results discussed in the previous chapters are considered in detail. In Fig. 8 are shown six growth patterns of different form and dimension. Crystals of up to 1.5 cm in length have been grown with a maximum diameter of about 0.3 mm. The smaller the diameter of the crystal, the fewer are the difficulties encountered. For the growth of a crystal pattern, it is very important to use an isothermal reaction zone. A lateral temperature gradient may distort the intended growth pattern by TGZM during the initial stages of growth. The length of the crystals on an individual substrate may vary considerably, depending on the position of the crystals in the reaction tube. In Fig. 8b, the substrate was situated perpendicular to the gas flow. The outermost crystals were close to the susceptor wall. In Fig. 8f, the crystal array grew parallel to the gas flow direction. The crystals growing "downstream" are shorter, reflecting the depletion of $SiCl_4$ along the reaction tube. This effect can be eliminated by proper geometrical design of the

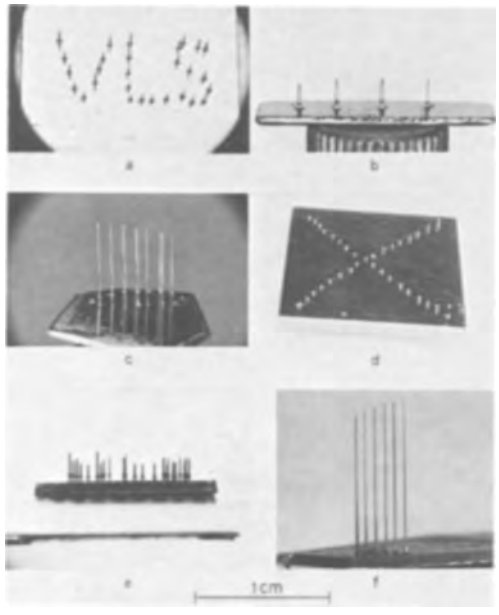

Fig. 8. Controlled VLS growth of silicon crystals in various arrays on silicon substrates. Magnification 5X.

reaction zone. X-ray measurements, using the Lang technique, have shown that the crystals in an array are "epitaxial" with respect to each other and therefore with the substrate. The observed angular misorientation between the crystals is smaller than 140 sec of arc, which is the resolution of the measurement technique employed.

Arrays of crystals have been grown with as many as 30 crystals on a 1 x 2 cm substrate. When conditions of cleanliness and proper temperature and gas phase conditions were observed, one crystal grew on each and every site where a gold particle had been placed manually. Another method, more suitable for production of arrays of many crystals, was to place a mask or template of pyrolytic graphite on the substrate crystal. An impurity particle was placed in each hole in the template and alloying was accomplished with the template in place. Subsequently, the template was removed and the VLS growth begun. Patterns of alloy dots also were made by evaporation of impurity agents through a mask onto the wafer. However, not every alloy dot produced only one crystal. A center crystal normally grew surrounded by fine whiskers of micron dimension. More work will be required to eliminate the breaking up of evaporated alloy dots.

Summary

Silicon crystals can be grown readily by the VLS technique under controlled conditions. Both the location of growth, the diameter of the crystal, and its ultimate length can be controlled. However, two important points must be considered, the presence of undesired impurities in the deposition region and the stability of the liquid alloy droplet. The first point requires extreme cleanliness of substrate, alloying agent, reaction tube, and carrier gas. The second point demands the absence of undesirable temperature gradients during alloying and VLS growth and proper adjustment of the total $SiCl_4$ concentration in the carrier gas. A temperature gradient may cause the alloy droplet to migrate into the substrate interior, or along the substrate surface, or may cause the formation of kinking or branching during growth (9). Proper gas composition is necessary to keep the concentration gradient in the liquid, and therefore the corresponding liquidus supercooling, small enough to avoid nucleation of silicon crystals in the liquid. It has been shown that the diameter of a VLS crys-

tal depends both on the amount of the alloying agent used and also on the deposition temperature. Crystals with sections of different diameter can be prepared simply by changing the deposition temperature during growth. The growth of arrays of crystals in various patterns has been demonstrated.

Crystalline defects have been studied in silicon crystals grown by the VLS technique. The majority of these crystals are highly perfect. However, some crystals contain defects such as dislocation, impurity striation, elastic strain, and second phase entrapment. The origin of such defects and their prevention will be discussed in a forthcoming paper (9).

Acknowledgments

We are grateful to W. G. Pfann and H. C. Theuerer for many helpful discussions.

Manuscript received April 11, 1966; revised manuscript received July 8, 1966.

Any discussion of this paper will appear in a Discussion Section to be published in the June 1967 JOURNAL.

REFERENCES

1. R. S. Wagner and W. C. Ellis, *Appl. Phys. Letters*, **4**, 89 (1964).
2. R. S. Wagner and W. C. Ellis, *Trans. Met. Soc. AIME*, **233**, 1053 (1965).
3. H. C. Theuerer, *This Journal*, **108**, 649 (1961).
4. S. Mendelson, *J. Appl. Phys.*, **36**, 2525 (1965).
5. R. S. Wagner, C. J. Doherty, and S. M. Arnold, *J. Metals*, **17**, 1031 (1965).
6. D. Turnbull, *J. Appl. Phys.*, **21**, 1022 (1950).
7. W. H. Shepherd, *This Journal*, **112**, 988 (1965).
8. W. G. Pfann, "Zone Melting," p. 254, John Wiley & Sons, Inc., New York (1966).
9. R. S. Wagner, Unpublished work.

Electrode Overvoltages in Molten Fluorides

The Anodic Behavior of Nickel Electrodes in Fluoride Melts

S. Pizzini, R. Morlotti, and E. Römer

High Temperature Chemistry, Euratom C.C.R. ISPRA, Varese, Italy

ABSTRACT

Anodic overvoltage measurements on nickel electrodes in NiF_2-KF, LiF-NaF-KF, NaF-KF, and LiF-KF melts of eutectic composition have been carried out by the galvanostatic, potentiostatic, and potential-sweep methods at temperatures ranging from 450° and 800°C. In oxide-free melts no activation overvoltage for the anodic and cathodic reactions has been observed. It was, however, observed that nickel behaves as a "covering-layer electrode" in the presence of traces of oxides, added to the melts as NiO, or resulting from the hydrolysis of the residual water in the melt after a high vacuum drying process. The semiconducting behavior of nonstoichiometric NiO surface layers has been considered and the results of the present work have been compared with the literature data on the Ni/NiO electrode in molten salts.

It does not seem to be widely recognized at present that the corrosion behavior of metallic electrodes in halide melts depends mainly on the oxidizing environment, if the corrosion of metal electrodes, due to reactions with the dissolved water, hydroxides, or halide-acids, is taken as an exception rather than a common phenomenon (1).

It was, however, shown, in the excellent reviews of Grimes (2) and of Baes (3) that nickel-base alloys exhibit very good corrosion resistance to fluoride melts, provided that a careful preparation of the melt and of the covering atmosphere is carried out. Littlewood and Argent (4) observed that unknown or uncontrolled factors affect the Nernst potential of nickel in alkali-chloride melts. Moreover it was shown in some previous investigations, dealing with overvoltage measurements on aluminum electrodes in molten KHF_2 (5), on lead electrodes in molten PbF_2-NaF eutectic mixtures (6), and on iron electrodes in molten alkali fluorides (7) that the contamination of the melts by oxides or water leads to the open circuit or anodic passivation of the electrode.

This paper deals with the anodic behavior of nickel in oxide-containing fluoride melts together with the kinetics of the anodic dissolution and cathodic deposition reactions in oxide-free fluoride melts.

Experimental Procedures

Suprapur or Pro Analysis LiF, NaF, and KF were supplied by Merck A. G. and used without further purification. NiF_2 was prepared by hydrofluorination of $NiCl_2 \cdot 6H_2O$, supplied as Reagent Pure by Merck A. G., or by high vacuum decomposition of $NiF_2 \cdot 2H_2O$ supplied by BDH. The products obtained contained more than 99% of NiF_2. Spectrographically standardized nickel rods were obtained from Johnson & Matthey or from Leytess Metal Inc.

Cells were assembled in vacuum tight quartz containers (see Fig. 1) for atmosphere control and the experiments were performed under high vacuum as well as under dry (10 ppm H_2O max) and deoxygenated argon, which was purified by passage through Linde's Molecular Sieves and Zr-Ti (50-50) chips at 600°C.

The tensiometric cell consists of a nickel working electrode and a nickel reference electrode. A Luggin capillary of about 0.5 to 0.1 mm diameter connects the reference electrode compartment to the electrode compartment.

The emf of the tensiometric cell has been shown reproducible within 1 mv in concentrated NiF_2 solutions or in NiO saturated melts. In Ni^{2+}-free melts the emf of the tensiometric cell is of course poorly reproducible. As insulating material, boron nitride (BN), supplied by Union Carbide, was used.

This cell design allows cylindrical symmetry of the current density distribution and avoids convective motions due to thermal gradients near the electrode surface. Any screening effects due to the reference electrode are avoided too. Temperature, measured in the hole (F) with a 1 mm diameter chromel-alumel thermocouple, was kept constant to ± 0.5°C.

The fluoride mixtures were dried under high vacuum prior to melting with step-wise increasing temperature from 100° up to 400°-450°C.

The high vacuum drying process was followed and standardized with samples of LiF in BN crucibles using an Omegatron-Type mass spectrometer (8) for residual gas analysis and by a polarization technique on Pt microelectrodes in LiF-NaF-KF melts for the analysis of dissolved hydrolysis products (9). It was shown that water can be removed at temperatures lower than 550°C without hydrolysis. Results are

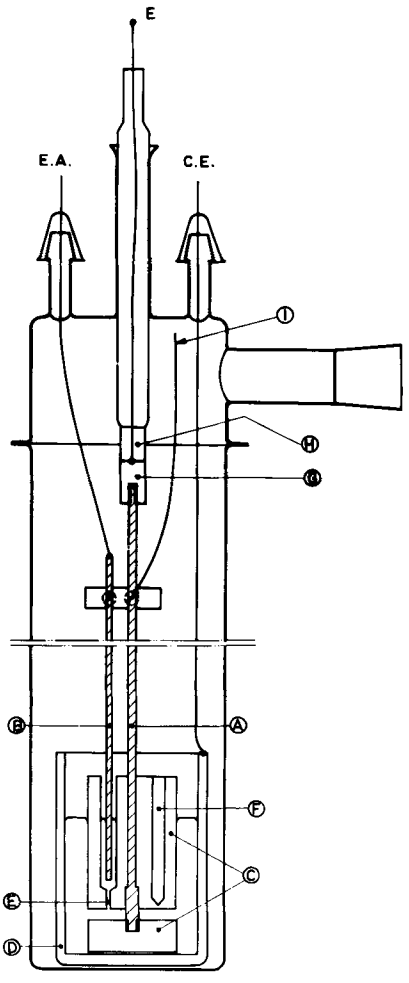

Fig. 1. Assembly of the cell. A, Nickel electrode; B, nickel reference electrode; C, BN insulators; D, graphite crucible; E, Luggin capillary; F, thermocouple hole; G-H, Inox to Kovar-glass joints; I, auxiliary silver lead to the electrode; E, silver lead to the electrode; EA, silver lead to the reference electrode; CE, silver lead to the counter electrode.

given in Table I, where the partial pressures are indicated as the ratios p/P (p = partial pressure, P = total pressure) .

From this table [see also ref. (8) for more detailed information] it is seen that the partial pressure of the species with mass 20 (HF) increases with temperature above 600°C. The same statement applies to species with mass 49, which corresponds to BF_3, resulting from reaction of B_2O_3 (contained in BN) with HF.

Furthermore anodic limiting current measurements on Pt electrodes in LiF-NaF-KF melts (9) demonstrated that the content of hydrolysis-products (as OH^-) in the melt is of the same order or smaller than the one calculated from chronopotentiometric measurements in the same melts pretreated with HF and H_2 (10) or with $NH_4HF_2+H_2$ (11), and ranges between 10^{-5} and 10^{-4} moles cm^{-3}. With reference to the results of ref. (11) it is worthwhile to consider that the absence of reducible materials was qualitatively indicated ($i\tau^{1/2} < 5x10^{-3}$ amp cm^{-2} $sec^{1/2}$) whereas no information was given on the presence of oxidable materials.

Overvoltage measurements have been carried out by the galvanostatic, potentiostatic, and potential sweep methods.

In the galvanostatic measurements, the AMEL Model 561 or 557 potentiostats (rise time less than 10^{-3} sec) were used as constant d-c supply or the John Fluke Model 351.

In the potentiostatic measurements, a d-c amplifier was used as a high impedance buffer amplifier, because the input impedance of the 557 AMEL Potentiostat was considered too low (10^5 ohms). A fully transistorized delay time unit supplied by the Electronic Service of C.C.R. Euratom Ispra, was used as a source of triggering pulses for the oscillograph (Tektronics 535 A) and as electronic relays for the modulation of the potentiostat. A high speed noise-free, Claire Model Hg 1002 relay was used Oscillograms were recorded by use of a Polaroid camera. Chronopotentiograms were also recorded by a Sargent Recorder, whose input impedance was increased by Keithley Electrometer Model 610 R used as a pre-amplifier.

Results and Discussion

Cathodic and anodic processes at nickel electrodes in oxide free melts.—In molten NiF_2-KF (10-90% in moles) eutectic the reaction[1]

$$(\alpha)\ {}_{I}Ni^{2+} \rightleftharpoons {}_{II}Ni^{2+}$$

is shown to occur at 800°C without activation overvoltage and concentration (diffusion + reaction) polarization up to relatively high current densities (2 amp/cm^2). The measured polarization merely corresponds to the ohmic drop across the electrolyte, as the ϵ *vs.* c.d. plot (not reported here) shows satisfactory evidence for Ohm's law behavior. The blue color of the melt, after contacting it with nickel metal, and the appearance of unidentified peaks in the x-ray powder spectra of the solidified mixture, probably indicates a certain solubility of Ni metal in NiF_2 containing melts (12). Apparently this process does not influence the anodic dissolution and cathodic deposition of nickel.

This result, together with previous ones (5-7) indicates that in fluoride melts also the condition of a zero or extremely low activation overvoltage for the cathodic reduction and anodic dissolution of metals can be considered as a general rule (13, 14).

In oxide-free and Ni^{2+}-free or very dilute NiF_2 solutions in LiF-NaF-KF (46.5-11.5-42 mole %) melts the rate-controlling step for the anodic dissolu-

[1] For the nomenclature used in this paper see section on Symbols and ref. (28).

Table I. Partial pressures of the residual gases over LiF for an ultra-high vacuum drying process [ref.(8)]

	Normalized partial pressures[a]							
Mass	300°C	400°C	450°C	500°C	550°C	600°C	650°C	700°C
2	n.d.	n.d.	n.d.	n.d.	n.d.	n.d.	n.d.	n.d.
16	$4 \cdot 10^{-2}$	$5.1 \cdot 10^{-2}$	$7.8 \cdot 10^{-2}$	$1.2 \cdot 10^{-1}$	$7.3 \cdot 10^{-2}$	$6.5 \cdot 10^{-2}$	$2.1 \cdot 10^{-2}$	$2.2 \cdot 10^{-2}$
17	$1.6 \cdot 10^{-2}$	$1.7 \cdot 10^{-1}$	$2.2 \cdot 10^{-1}$	$1.4 \cdot 10^{-1}$	$6.1 \cdot 10^{-2}$	$3.2 \cdot 10^{-2}$	$2.1 \cdot 10^{-2}$	$2.2 \cdot 10^{-2}$
18	$6.4 \cdot 10^{-1}$	$5.9 \cdot 10^{-1}$	$5 \cdot 10^{-1}$	$4.7 \cdot 10^{-1}$	$4.6 \cdot 10^{-1}$	$2.3 \cdot 10^{-1}$	$1.1 \cdot 10^{-1}$	$1.4 \cdot 10^{-1}$
19	$4.8 \cdot 10^{-2}$	$4.5 \cdot 10^{-2}$	$4.1 \cdot 10^{-2}$	$4 \cdot 10^{-2}$	$4.3 \cdot 10^{-2}$	$2.6 \cdot 10^{-2}$	$2.8 \cdot 10^{-2}$	$2.2 \cdot 10^{-2}$
20	$2.4 \cdot 10^{-3}$	$1 \cdot 10^{-3}$	$2.5 \cdot 10^{-3}$	$5.3 \cdot 10^{-3}$	$1.2 \cdot 10^{-1}$	$1.9 \cdot 10^{-1}$	$2.3 \cdot 10^{-1}$	$2.2 \cdot 10^{-1}$
28	$5.6 \cdot 10^{-2}$	$5.1 \cdot 10^{-2}$	$6.6 \cdot 10^{-2}$	$5.3 \cdot 10^{-2}$	$7.3 \cdot 10^{-2}$	$9.1 \cdot 10^{-2}$	$1.7 \cdot 10^{-1}$	$2.7 \cdot 10^{-1}$
49	—	—	—	—	$2.4 \cdot 10^{-3}$	$2.2 \cdot 10^{-1}$	$2.7 \cdot 10^{-1}$	$1.5 \cdot 10^{-1}$
P	$2 \cdot 10^{-6}$	$3 \cdot 10^{-6}$	$2.5 \cdot 10^{-6}$	$5.5 \cdot 10^{-6}$	$6.5 \cdot 10^{-6}$	$7.7 \cdot 10^{-6}$	$7 \cdot 10^{-6}$	$1 \cdot 10^{-5}$

[a] Partial pressures expressed as p/P ratios, where p is the partial pressure as measured with the Omegatron gauge and P is the total pressure as measured with an ionization manometer; temperature ± 20°C.

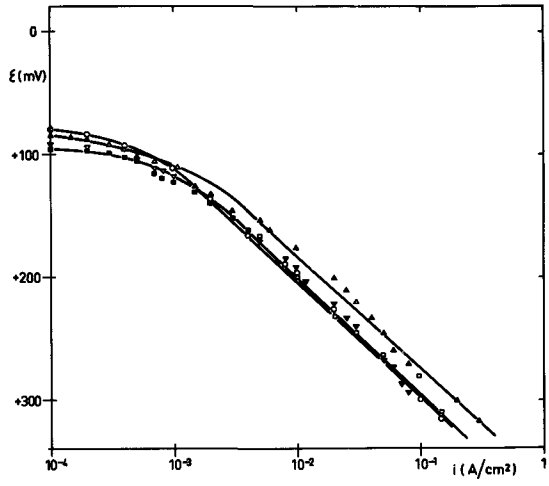

Fig. 2. ϵ *vs.* log d-c plot for the anodic dissolution of nickel in oxide-free KF-NaF-LiF melts. T is 550°C (from galvanostatic measurements).

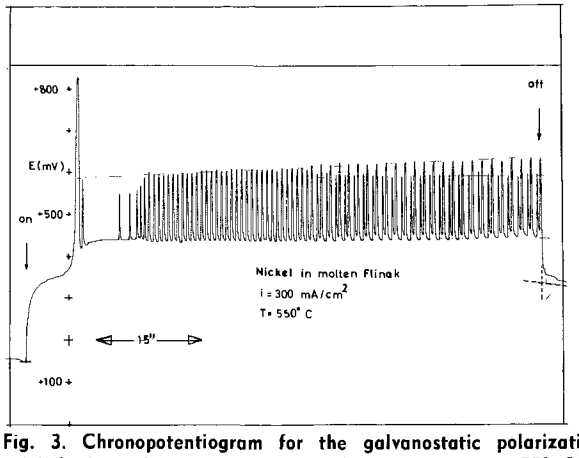

Fig. 3. Chronopotentiogram for the galvanostatic polarization of nickel electrodes in oxide-free KF-NaF-LiF melts at 550°C.

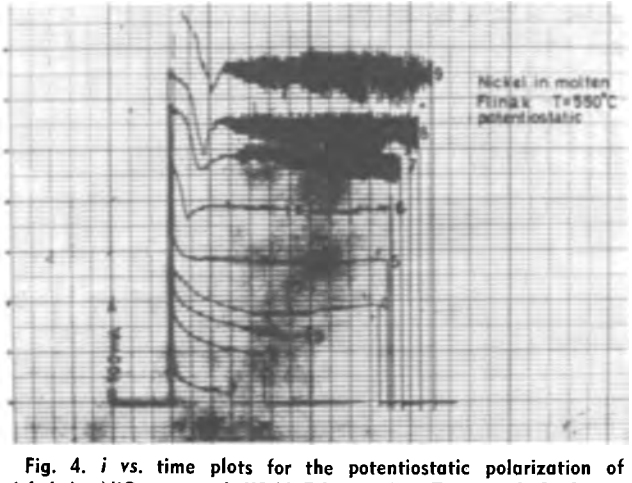

Fig. 4. *i vs.* time plots for the potentiostatic polarization of nickel in NiO-saturated KF-NaF-LiF melts. T = 550°C. 1. + 100 mv; 2. + 200 mv; 3. + 250 mv; 4. + 300 mv; 5. + 350 mv; 6. + 400 mv; 7. + 450 mv; 8. + 500 mv; 9. + 550 mv. Ni/NiO oxide reference electrode.

tion process of nickel has been shown to be the mass-transfer across the diffusion layer.

The Tafel law is followed in the c.d. range 10^{-3} to 10^{-1} amp/cm² as shown in Fig. 2, where the steady-state polarization values are plotted; the slope of the Tafel plot closely corresponds to $RT/2F$, in good agreement with the theoretical slope for a diffusion-controlled anodic dissolution process (15).

No evidence has been obtained in these dilute solutions of an activated rate-determining step.

Anodic processes at nickel electrodes in oxide-containing melts.—Evidence has been given on the influence of oxides (dissolved or as surface layers) on the anodic dissolution process.

It was, in fact, observed that both saturation of the melt with NiO and relatively high partial pressures of water lead to the open circuit passivation of the electrode. Traces of O^{2-} or OH^- resulting from hydrolysis of residual water in the melt (9) are also sufficient for the passivation of the electrode under current flow. The anodic polarization of both active and passive electrodes in alkali fluoride melts leads at a certain critical c.d. or voltage (according to the kind of experimental technique), to an instability shown by oscillations of the electrode voltage or of the cell current as is shown in the following figures.

Figure 3 shows the beginning of the oscillation of the electrode voltage of nickel electrodes in LiF-NaF-KF melts.

The high overvoltage peak, which is observed in Fig. 3, corresponds to the sudden passivation of the electrode. No peaks have been detected in the polarization of passive electrodes in LiF-NaF-KF and LiF-KF (50-50% in moles) melts. The oscillatory behavior of the electrode has also been found less reproducible in frequency than on initially active electrodes.

Figure 4 shows the corresponding instability of the cell current observed by the potentiostatic method at potentials higher than + 400 mv *vs.* a Ni reference electrode in a NiO saturated LiF-NaF-KF melt at 550°C. It is assumed that under these circumstances the Ni reference electrode works as a Ni/NiO electrode.

Figure 5 shows the potentiostatic anodic and cathodic polarization of a passive nickel electrode, determined by the potentiodynamic (potential-sweep) method at a traverse rate of 0.1 v/min, in NaF-KF (40-60% in moles) melts at 800°C. The anodic and cathodic activation of the electrode is observed; it is also worthwhile to observe that passivation occurs without the characteristic passivation loop (29, 30).

The dashed line shows the corresponding ϵ *vs.* c.d. plot obtained by the galvanostatic method in a sep-

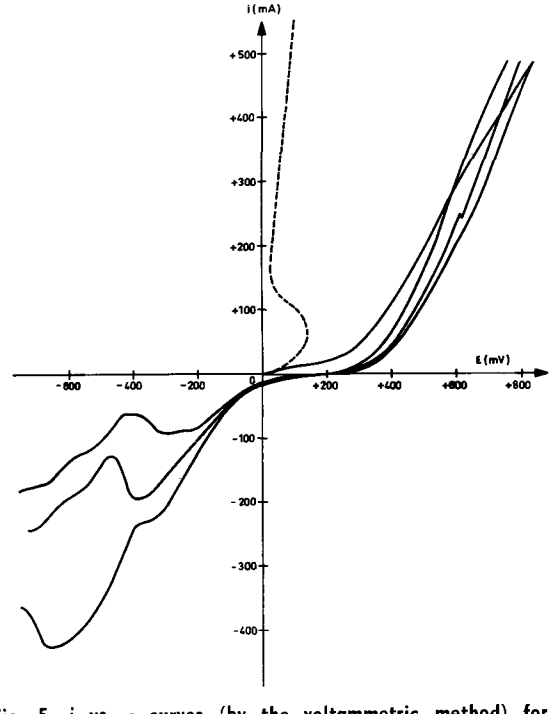

Fig. 5. *i vs.* ϵ curves (by the voltammetric method) for the cathodic and anodic polarization of Ni in NaF-KF melts at 800°C. Sweep 0.1 v/min. The dashed line (from galvanostatic measurements) reports the corresponding iR drops.

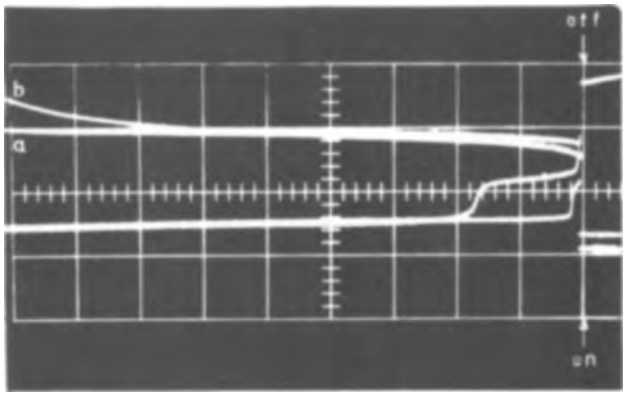

Fig. 6. Oscillograms for the anodic polarization of nickel electrodes in LiF-KF melts at 560°C. $P = 10^{-3}$ Torr. X axis, 50 m sec/cm; y axis, 200 mv/cm; c.d., 900 ma/cm^2.

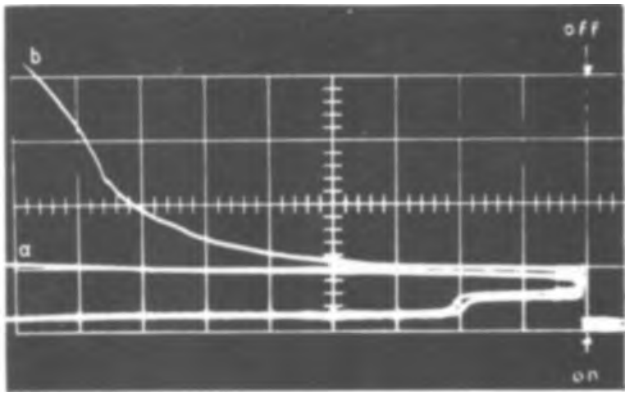

Fig. 7. Oscillograms for the anodic polarization of nickel electrodes in LiF KF melts at 560°C. $P = 10^{-3}$ Torr. X axis, 50 m sec/cm; y axis, 500 mv/cm; c.d., 1.1 amp/cm^2.

arate experiment. The increase of layer thickness in the passive zone is indicated by the deviation from linearity of the experimental curve.

The cathodic activation (due to the reduction of the oxide layer) takes place at a potential very close to the reference potential, whereas the anodic activation occurs at a potential between + 300 and 400 mv *vs.* the reference electrode.

Figures 6 and 7, which refer to the anodic polarization of nickel at 560°C in LiF-KF melts, show the galvanostatic charging curves and the corresponding potential decay curves oscillographically recorded at current densities higher than the critical current density.[2] The corresponding curves in NiO saturated LiF-KF melts and NiO saturated LiF-NaF-KF melts are quite similar.

The transition times, as well as the persistency of the voltage plateau which is observed at about + 200 mv *vs.* the reference electrode, clearly depend both on the total charge passed and on the previous history of the electrode. For this reason any attempt to plot the transition times in an i *vs.* $\tau^{1/2}$ plot is unsuccessful.

In order to account for this active-passive behavior of nickel let us suppose that the passivation of nickel electrodes at open circuit or under current in Li^+-free and in Li^+-containing melts results from an insulating NiO surface film. Indeed we shall discuss the anodic behavior of nickel in terms of the mass transport and charge transfer reactions across the phase boundaries Ni/NiO and NiO/solution as well as across the bulk of NiO.

All the possible reactions occurring at a Ni/NiO electrode, considering both the case of a stoichiometric and a nonstoichiometric oxide layer, are reported in

[2] In each figure two traces are reported: curve (a) refers to the first polarization, curve (b) to a subsequent polarization at the same c.d.

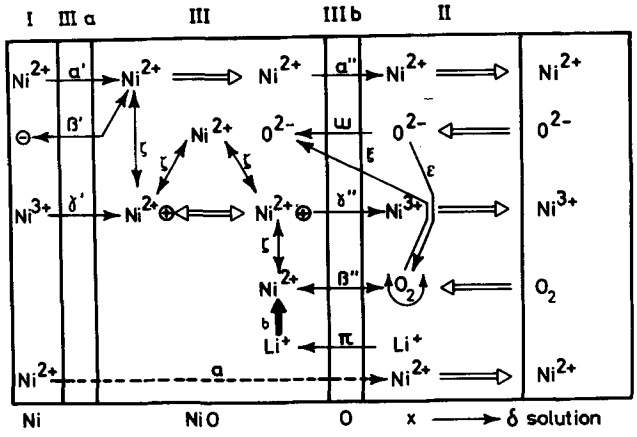

Fig. 8. Phase-scheme according to ref. (28) for a Ni/NiO_{1+x}/ electrode. I indicates the metal phase, III the oxide phase, II the solution phase, IIIa and IIIb being the interphases between the metal and the oxide phase and between the oxide and the solution phase, respectively. → Indicates a charge-transfer process at the interphases IIIa IIIb or in the bulk of the oxide-phase. Open arrow indicates a mass-transfer process across the bulk of a phase. Solid dark arrow indicates the substitutional exchange of a lattice position. $Ni^{2+}\oplus$ indicates a positive hole in the lattice and δ is the thickness of the diffusion layer.

the phase-diagram of Fig. 8 (5) on the basis of the generally accepted conduction mechanism in NiO (16-21). In this diagram the reactions which involve the exchange of electrons have been described (reaction ζ) in terms of jumps of holes between $Ni^{2+}\oplus$ and Ni^{2+}, where Ni^{2+} is a nickel ion in a regular position of the cationic sublattice and $Ni^{2+}\oplus$ corresponds to a hole freed from a cation-vacancy and trapped at a Ni^{2+} site (*i.e.*, corresponds to a Ni^{3+}-ion).

In the same diagram the build-up of nonstoichiometric NiO due to excess oxygen dissolution is indicated by the reaction

$$\beta'' + \zeta + \xi : \tfrac{1}{2}{}_{II}O_2 + 2_{III}Ni^{2+} \hookrightarrow {}_{III}O^{2-} + 2_{III}Ni^{2+}\oplus \quad [1]$$

and the substitutional Li^+ dissolution in the cationic sublattice is indicated by

$$\pi + \sigma + \zeta : {}_{II}Li^+ + {}_{III}Ni^{2+} \rightarrow {}_{III}Li^+(Ni^{2+}) + {}_{III}Ni^{2+}\oplus \quad [2]$$

In the latter case the mass balance is satisfied by the simultaneous occurrence of the reaction

$$(\omega) \qquad {}_{II}O^{2-} \rightarrow {}_{III}O^{2-}$$

However, if the rates of the reactions [1] and [2], both of which lead to a nonstoichiometric oxide layer, are lower than the rate of the Ni diffusion by cation vacancies or grain boundaries into the oxide layer, the NiO surface layer remains at its stoichiometric composition, according to the reaction

$$_{I}Ni + 2_{III}Ni^{3+} \rightarrow 3_{III}Ni^{2+} \quad [3]$$

which corresponds to the coupling of the reactions

$$(\alpha') \qquad {}_{I}Ni^{2+} \rightarrow {}_{III}Ni^{2+}$$

and

$$(\beta') \qquad 2_{I}e + 2_{III}Ni^{3+} \rightarrow 2_{III}Ni^{2+}$$

where ${}_{I}Ni^{2+} + 2_{I}e$ corresponds, according to the formalism used in this paper, to ${}_{I}Ni$.

Evidence has been found from the results of the present work and from the comparison of these results with the literature data, that the surface layer is of stoichiometric composition over a broad range of experimental conditions.

As the present measurements have been done under high vacuum or under oxygen-free argon, it appears that reaction [1] does not affect the stoichiometry of the surface layer.

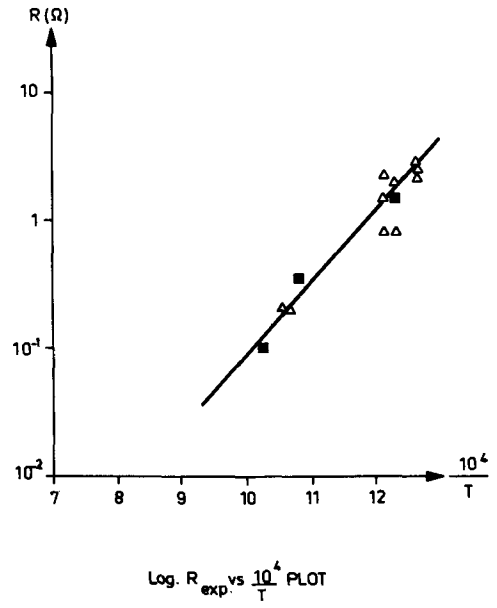

Fig. 9. Log R vs. $1/T$ plot for the electrical resistivity of the NiO layer on nickel electrodes. △ LiF-NaF-KF melts; ■ LiF-KF melts; R is given in ohm/cm^2.

Furthermore, measurements of the self-diffusion coefficients of oxygen and nickel in NiO single crystals in the temperature range 700°-1400°C (22-24) indicate that the diffusion of oxygen in NiO is of several orders of magnitude lower than that of Ni.[3]

From the iR drops, measured on passive nickel electrodes at different temperatures, corrected for the corresponding iR drops due to the electrolyte resistance [about 20-50 mv at 1 amp/cm^2, as measured at iron electrodes, which are perfectly reversible in dilute solutions of FeF_2 in alkali fluoride melts (7)], the value of the d-c resistance of the passivating layer has been obtained.

The slope of the Arrhenius plot[4] obtained with these experimental resistance values, as it is seen in Fig. 9, where R is given in ohm-cm^{-2}, is in quite good agreement with the figures given in ref. (17, 20, 21) for the nearly stoichiometric NiO.

The work of Hill *et al.* (25) indicates that in the molten Li_2SO_4-K_2SO_4 eutectic melt the Ni/NiO electrode behaves reversibly up to about 650°C, where a break in the emf *vs.* T plot is observed. They accounted for this result by suggesting a deviation from the stoichiometry of NiO at temperatures higher than 650°C due to the Li^+-dissolution in solid solution, and supposing a high solubility of the solid solution at temperatures lower than 650°C.

This result is qualitatively in agreement with our results, as it was also shown that in Li^+-containing melts the surface layer is nearly stoichiometric, at least at temperatures lower than 650°C. We do not agree, however, with the suggestion of a high solubility of the Li_2O-NiO solid solution at low temperatures, as it seems much more probable that a slow rate-determining step affects the over-all rate of reaction [2].

We found in fact (26) that reaction [1], which was investigated on sintered pellets of NiO at oxygen partial pressures between 3 to 760 Torr, is a very slow one in the same temperature range.

Finally it is worthwhile to note that the curves of the cathodic reduction of the oxide layer in Fig. 5 (cathodic activation) demonstrate that the reduction occurs at the reversible potential with an uncertainty of few millivolts (which is of the same order as the emf of the tensiometric cell) under the assumption that the reference electrode reaction is that of an oxide electrode.

It appears indeed that the anodic dissolution of nickel at passive electrodes is described by reaction [4] (see Fig. 8)

$$\alpha' + Ni^{2+}\text{-transfer} + \alpha'' \qquad [4]$$

at current densities or potentials lower than the critical transition current or the transpassive potential, respectively, at temperatures lower than 650°C in Li^+ containing melts and at higher temperatures in Li^+-free melts.

As for the activation of passive nickel electrodes and the oscillatory behavior of nickel under strong anodic polarization, only a qualitative picture of the phenomenon results from the experimental data. We discuss only the case of the activation of a passive nickel electrode, which is assumed as before to be initially covered with a layer of nearly stoichiometric nickel oxide. Differing from the iron-oxide system, the stability range of the wüstite-type NiO_{1+x} phase is not well defined and the higher nickel oxides are known to be unstable as bulk phases at high temperature.

Furthermore, x-ray diffraction patterns obtained at room temperature from these higher oxides do not reveal a structure different from that of NiO (27).

However, the steps in the potential decay curves (see Fig. 6 and 7) and the reproducibility of the activation potential (see Fig. 5) seem to indicate the formation of a higher nickel oxide surface phase with good electronic and (or) ionic conductivity under sufficiently strong anodic polarization.

The proposed model for such an electrode is given in Fig. 10, where the oxide phase (NiO_{1+y}) is supposed to have a composition near to Ni_3O_4 ($y \leq 0.33$).

If only electronic conduction is supposed, via electron holes or electrons only the reactions

$$(\epsilon) \qquad {}_{II}O^{2-} \rightarrow \tfrac{1}{2}\,{}_{II}O_2 + 2_{IV}e$$

$$(\epsilon') \qquad {}_{II}O^{2-} + 2_{IV}\oplus \rightarrow \tfrac{1}{2}{}_{II}O_2$$

$$(\lambda) \qquad {}_{II}Ni^{2+} \rightarrow {}_{II}Ni^{3+} + {}_{IV}e$$

$$(\lambda') \qquad {}_{II}Ni^{2+} + {}_{IV}\oplus \rightarrow {}_{II}Ni^{3+}$$

should occur in the transpassive[5] range, as the fluo-

[3] $D^{O}_{NiO} = 1.0 \times 10^{-5} \exp(-54\ \text{kcal}/RT)\ \text{cm}^2\ \text{sec}^{-1}$ (22)
$D^{Ni}_{NiO} = 1.7 \times 10^{-4} \exp(-56.0\ \text{kcal}/RT)\ \text{cm}^2\ \text{sec}^{-1}$ (23)
$D^{Ni}_{NiO} = 1.83 \times 10^{-3} \exp(-45.6\ \text{kcal}/RT)\ \text{cm}^2\ \text{sec}^{-1}$ (24)

[4] Which is taken as a measure of the activation energy of the electrical resistivity according to the relationship
$\rho = \rho^0 A \exp(\Delta E/RT)$

[5] The transpassive range (28-30) is considered here as the anodic c.d. range lying at c.d. higher than the activation current.

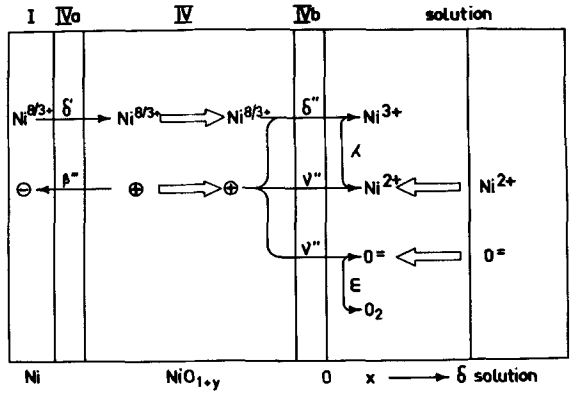

Fig. 10. Phase-scheme, according to ref. (28) for a Ni/NiO_{1+y} electrode. I indicates the metal phase, II the solution phase, IV a magnetite-type NiO_{1+} phase, IVa and IVb the interphases between the metal and the oxide phase, and between the oxide and solution phase, respectively. → Indicates a charge-transfer process. Open arrow indicates a mass-transfer process. δ is the thickness of the diffusion layer.

rine discharge reaction occurs at much more anodic potentials, as compared with the potential at which activation occurs (see Fig. 5).

However, the melt is a very dilute solution of both Ni^{2+} and $O^{=}$ and reactions ϵ, ϵ', λ, and λ' should occur under diffusion limiting current conditions.

Actually, from previous measurements which have been carried out in fluoride melts (9) in order to investigate the oxygen evolution reaction on bright platinum electrodes, there is the evidence that the limiting current for the anodic reaction

$$O^{=} \rightarrow \tfrac{1}{2} O_2 + 2e$$

in melts prepared with the same experimental procedure ranges between 2-10 ma/cm^2. It is apparent that other reactions, different from the ϵ and λ ones, are to be considered, as their contribution to currents as high as 500 ma, observed in the transpassive range, is negligible.

We consider indeed a mass transfer reaction, indicated as $Ni^{8/3+}$ transfer[6] in Fig. 10, which occurs, simultaneously with the ϵ and λ ones, across a very thin layer of NiO_{1+y}. It is worthwhile to note that the cracking of this layer could be responsible for the oscillatory behavior of nickel electrodes observed both under galvanostatic and potentiostatic polarization and of the high currents observed in the transpassive range.

In this latter case, under potentiostatic polarization (by the potential-sweep method) both the reactions

$$\delta' + Ni^{8/3+}\text{-transfer} + \delta''$$

and

$$(\alpha) \qquad {}_{I}Ni^{2+} \rightarrow {}_{II}Ni^{2+}$$

occur, at a rate which only depends on the characteristics of the *i vs.* ϵ curves for the separate reactions.

As the activation potential and that of the potential steps seem to be independent of the oxygen partial pressure over the melt, we postulate that the over-all anodic activation reaction is

$$3\,NiO + O^{2-} \rightarrow Ni_3O_4 + 2e \qquad [5]$$

The coupling of reaction [5] with reaction [6]

$$NiO + 2e \rightarrow Ni + O^{2-} \qquad [6]$$

(which is the electrode reaction at the reference electrode) corresponds to the reaction

$$Ni + Ni_3O_4 \rightleftharpoons 4\,NiO \qquad [7]$$

From the figures for the activation potential (+380 mv at 800°C) and of the steps in the potential decay curves (+ 200 mv at 550°C) we obtain for the free energy of reaction [7]

$\Delta G_7 = -2FE = -9000 \pm 460$ cal at 550°C and $\Delta G_7 = -16.000 \pm 460$ cal at 800°C.

Acknowledgments

The authors wish to acknowledge Dr. G. Sternheim for many stimulating discussions, Dr. M. A. Bredig (Oak Ridge National Laboratory) for his suggestions about nickel solubility in molten fluorides, Dr. Vos and Mr. Toussaint for their x-ray analyses and Dr. Becker and Mr. Termanini for the construction of the electronic relay.

Manuscript received April 22, 1966; revised manuscript received July 7, 1966. This paper was presented at the San Francisco Meeting, May 9-13. 1965.

Any discussion of this paper will appear in a Discussion Section to be published in the June 1967 JOURNAL.

[6] ${}_{IV}Ni^{8/3+} = \frac{1}{3}\,{}_{IV}Ni^{2+} + \frac{2}{3}\,{}_{IV}Ni^{3+}$ [ref. (28)]

SYMBOLS

ϵ	Potential difference measured at the terminals of the tensiometric cell
$I^{Me^{z+}}$	Corresponds to $Me - z_I e$, where the subscripts at the left indicates the phase (28)
I	Metal phase
II	Solution phase
III or IV	Oxide phases
$\ominus$	Indicates an electron
$Me^{2+} \oplus$	Indicates a hole trapped at a cationic site
$\oplus$	Indicates a free electron hole

REFERENCES

1. A. E. Jenkins, "Proceedings of the First Australian Conference," p. 149, Pergamon Press, New York (1965).
2. W. R. Grimes, ORNL 3708.
3. C. F. Baes, Jr., Paper presented at the IAEA Meeting, Wien (1965).
4. R. Littlewood and E. J. Argent, *Electrochim. Acta*, **4**, 155 (1961).
5. S. Pizzini, G. Sternheim, and A. Magistris, *Corrosion Sci.*, **4**, 345 (1964).
6. S. Pizzini and L. Agace, *ibid.*, **5**, 193 (1965).
7. S. Pizzini and E. Römer. To be presented at the 1st EUCHEM Conf., Trondheim.
8. G. Trevisan and S. Pizzini, In press, Proc. 3rd Int. Vacuum Congress, Stuttgart, July 1965.
9. S. Pizzini and R. Morlotti, *Electrochim. Acta*, **10**, 1033 (1965).
10. D. L. Manning, *J. Electroan. Chem.*, **6**, 227 (1963).
11. S. Senderoff and G. W. Mellors, *This Journal*, **113**, 66 (1966).
12. M. A. Bredig, "Molten Salt Chemistry," M. Blander, Editor, Interscience Publishers, New York (1964).
13. R. Piontelli, *Ann. N. Y. Acad. Sci.*, **79**, 1025 (1960).
14. R. Piontelli, Proc. 1st Austr. Conf. El., p. 932, Pergamon Press, New York (1965).
15. K. Vetter, "Electrochemische Kinetik," Springer, Berlin (1964).
16. M. Verwey *et al.*, *Philips Research Repts.*, **5**, 173 (1950).
17. R. R. Heikes and W. D. Johnston, *J. Chem. Phys.*, **26**, 582 (1957).
18. S. Van Houten, *J. Phys. Chem. Solids*, **17**, 7 (1960).
19. F. J. Morin, "Semiconductors," N. B. Hannay, Editor, Reinhold Publishing Co., New York (1960).
20. S. P. Mitoff, *J. Chem. Phys.*, **35**, 3, 882 (1961).
21. R. W. Wright and J. P. Andrews, *Proc. Phys. Soc. (London)*, **A62**, 446 (1949).
22. M. O'Keeffee and N. J. Moore, *J. Chem. Phys.*, **65**, 1438 (1961).
23. R. Lindner and Å. Åkerstrom, *Discussion Faraday Soc.*, **23**, 133 (1957).
24. J. Shi Choi and W. Moore, *J. Chem. Phys.*, **66**, 1308 (1962).
25. D. C. Hill, B. Porter, and A. S. Gillespie, *This Journal*, **105**, 4081 (1958).
26. S. Pizzini and R. Morlotti, Unpublished results.
27. J. J. Lander, *Acta Cryst.*, **4**, 148 (1951).
28. F. Lange and H. Göhr, "Thermodynamische Electrochemie," Hütig Verlag, Heidelberg (1962).
29. M. Pourbaix and F. Vanderrelden, *Corrosion Sci.*, **5**, 81 (1965).
30. N. D. Green and R. B. Leonard, *Electrochim. Acta*, **9**, 45 (1964).

The Oxidation of Silicon Carbide at 1150° to 1400°C and at 9 x 10^{-3} to 5 x 10^{-1} Torr Oxygen Pressure

Earl A. Gulbransen, Kenneth F. Andrew, and Fred A. Brassart

Research Laboratories, Westinghouse Electric Corporation, Pittsburgh, Pennsylvania

ABSTRACT

A kinetic study was made of the oxidation of high-purity silicon carbide using a dynamic-type reaction system. Two types of oxidation behavior were found. Passive oxidation occurred for conditions where silica films were formed on the surface. Active oxidation occurred for conditions where volatile silicon monoxide was formed. The transition conditions between the two types of oxidation were studied as a function of oxygen pressure and temperature. The transition temperatures and pressures were related to thermochemical conditions for the reaction of silicon carbide with silica to form silicon monoxide and carbon monoxide.

The oxidation of silicon carbide has been studied extensively at normal pressure where silica films are formed (1-7). Several of the workers (2, 6, 7) showed that amorphous silica films were formed during oxidation below 1300°C and cristobalite at 1300°C and higher.

Webb, Norton, and Wagner (8) suggest that, in the oxidation of carbides, protective oxide films form provided the carbide does not react with its oxide. If reaction occurs, rupture of the oxide may occur.

At low oxygen pressures Ervin (1) showed high rates of reaction could occur with the formation of silicon monoxide. Following Wagner's analyses (9) of the analogous silicon oxidation reaction we will call this fast region of oxidation the active region, and the slow region where silica films are formed, the passive region. The purpose of this paper is to extend Ervin's (1) work and to study the transition conditions for the two regions of oxidation.

Thermochemical Analyses

Table I shows the reactions which can occur in the silicon carbide oxygen system and associated reactions. Reactions [1]-[4] show large positive values for log K_p. Rupturing of the oxide film could occur when silica films are formed. Oxidation can also occur without the formation of an oxide film by reactions [2] and [4]. Reaction [5] shows silicon carbide dissociates under vacuum conditions if silicon vapor is removed. The solid phase reactions of silicon carbide with silica, reactions [6] and [7], can occur if the gaseous reaction products are removed. Reactions [6] and [7] can be compared to the reaction between silicon and silica. The silicon monoxide equilibrium pressures (for reactions [6] and [8]) can be calculated from the data of Table I. If sufficient silicon monoxide exists in the gas phase, reactions [6] and [8] can be reversed with the formation of silica films on silicon.

Apparatus and Samples

The apparatus and method have been described (11, 12). A Cahn (13) type of vacuum microbalance was used in the flow reaction system.

Table I. Thermochemical analyses, silicon carbide-oxygen system

Reactions	Equilibrium constants (log K_p) (10) 1127°-1527°C		
	1127°	1327°	1527°
[1] $SiC(s) + 3/2O_2(g) \rightleftarrows SiO_2(s) + CO(g)$	30.60	26.26	22.89
[2] $SiC(s) + O_2(g) \rightleftarrows SiO(g) + CO(g)$	14.17	13.51	12.99
[3] $SiC(s) + 2O_2(g) \rightleftarrows SiO_2(s) + CO_2(g)$	36.61	30.96	26.58
[4] $SiC(s) + 3/2O_2(g) \rightleftarrows SiO(g) + CO_2(g)$	20.18	18.22	16.69
[5] $SiC(s) \rightleftarrows Si(s) + C(s)$	−2.828	−2.428	−2.018
[6] $SiC(s) + 2SiO_2(s) \rightleftarrows 3SiO(g) + CO(g)$	−18.70	−11.98	−5.58
[7] $SiC(s) + 3SiO_2(s) \rightleftarrows 4SiO(g) + CO_2(g)$	−29.12	−20.02	−13.00
[8] $1/2Si(s) + 1/2SiO_2(s) \rightleftarrows SiO(g)$	−4.106	−2.520	−1.347

Single crystals of light green silicon carbide were obtained through the courtesy of Hamilton (14). Most of the crystals had small twin crystals attached at some point on the surface. The crystals were of high-purity grade having a total impurity level of 10^{15}-10^{17} atoms/cc.

The crystals had the α-SiC 6H structure (15, 16). The basal plane (0001) was in the surface. No attempt was made to distinguish the silicon and carbon faces of the crystals.

The crystals weighed 0.01-0.025g, had surface areas of 0.12 to 0.28 cm^2, and were 0.06 to 0.07 cm thick. Individual crystals were suspended from the end of the balance by using 0.06 cm diameter quartz fibers. Reagent grade oxygen was used in all experiments.

Method.—The method in brief was to heat the sample to temperature in vacuum. After equilibrium was achieved, oxygen was added to the desired pressure over a time period of 1 to 1½ min to prevent serious disturbances to the sample and balance. During this period of changing pressure, the sample may have undergone reaction under varying oxidation conditions.

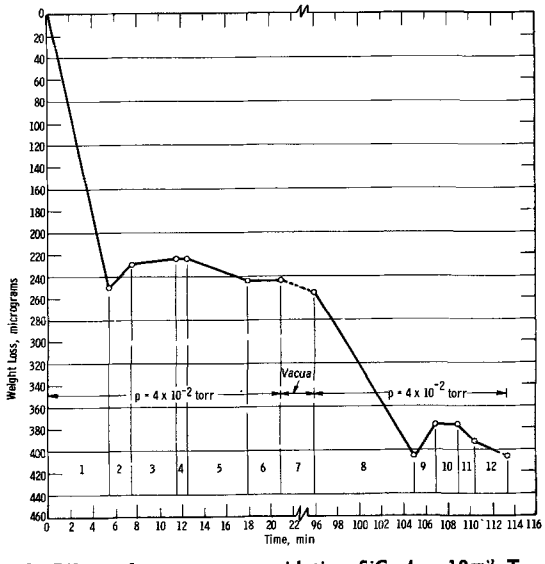

Fig. 1. Effect of temperature oxidation SiC, 4 x 10^{-2} Torr O_2 pressure. Flow 1.0 x 10^{18}-2.26 x 10^{18} atoms O/sec.

Zones of reaction

1 1300°
2 1270°-1250°
3 1250°
4 Temperature Raised
5 1275°-1300°
6 1300°
7 1300°-~75 min
8 1300°
9 1277°-1250°
10 Temperature raised
11 1275°-1300°
12 1300°

Results and Discussion

Active and passive oxidation processes.—Figure 1 shows a series of experiments at 4 x 10^{-2} Torr oxygen pressure which were made to evaluate the transition conditions between active and passive oxidation.

Zone 1 of Fig. 1 shows an active type of oxidation occurs at 1300°C. Passive oxidation occurs with the formation of an oxide film as shown in zone 2 at 1250°C. The rate of oxidation decreases in zone 3 as the silica film grows in thickness.

Active oxidation occurs again on raising the temperature to 1300°C in zones 4 and 5. The presence of a silica film prevents the occurrence of a rapid type of active oxidation. Removal of the oxide film by reactions [6] and [7] was a slow process at 4 x 10^{-2} Torr pressure.

To remove the silica film at a more rapid rate, it was necessary to heat the sample in vacuum. A test was made on the effect of heating in a vacuum at 1300°C for 75 min (zone 7). A rapid weight loss type of oxidation occurred on reoxidizing in zone 8.

These experiments show two basic oxidation processes occur in the oxidation of silicon carbide. The first was a weight loss or active type of reaction. Volatile silicon monoxide was formed together with carbon monoxide. Protective oxides may exist on the surface, but these were not formed during oxidation under the given conditions. The second was a weight gain or passive type of oxidation. Here, a silica film was formed. Since carbon monoxide was also formed, fast reactions could occur due to rupturing of the oxide film.

We term oxidation reactions occurring slowly in the active region in the presence of previously formed silica films as intermediate types of oxidation reactions.

Effect of pressure on transition temperature for active and passive oxidation.—Figure 2 shows weight change *vs.* time curves at pressures of 9 x 10^{-3}, 4 x 10^{-2}, 1 x 10^{-1}, and 5 x 10^{-1} Torr at 1300°C. Figure 2 shows passive oxidation occurs at 1300°C for pressures of 1 x 10^{-1} and 5 x 10^{-1} and active oxidation for pressures of 9 x 10^{-3} and 4 x 10^{-2} Torr. Similar plots were made for the same pressures at 1350° and 1400°C. Active oxidation was found to occur at 1350°C for 9 x 10^{-3} and 4 x 10^{-2} Torr pressures and passive oxidation at 1 x 10^{-1} and 5 x 10^{-1} Torr pressures. At 1400°C, active oxidation was found to occur for 9 x 10^{-3}, 4 x 10^{-2}, and 1 x 10^{-1} Torr pressures.

The weight gain curves at 1300°, 1350°, and 1400°C initially show fast rates of oxidation. After several minutes of oxidation, a protective film of silica was formed and the rates of oxidation decreased. We conclude that the transition pressure at 1300°C was between 4 x 10^{-2} and 1 x 10^{-1} Torr, at 1350°C it was about 1 x 10^{-1} Torr, and at 1400°C the transition pressure was above 1 x 10^{-1} Torr.

Light microscopic observations on the reacted samples were made. One side showed lightly etched regions while the other side was smooth. The edge near where the original crystal was grown also showed evidence of selective reaction.

We interpret the weight loss curves as reaction of both Si and C atoms from the SiC surface. The initial

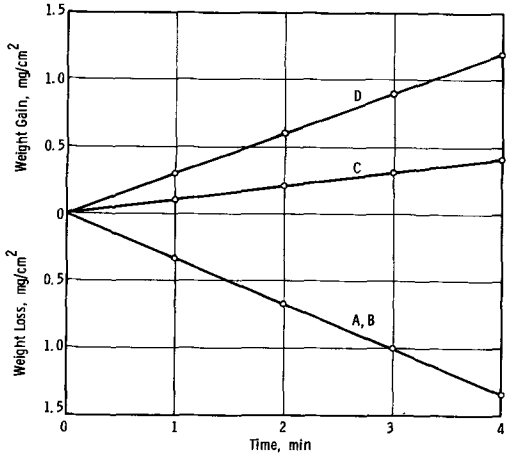

Fig. 2. Oxidation of SiC, effect of pressure, 1300°C: A, 9 x 10^{-3}; B, 4 x 10^{-2}; C, 1 x 10^{-1}; D, 5 x 10^{-1} Torr.

weight losses were a linear function of time. Since an oxide film was not formed and the reaction products were removed by the gas flow, no evidence was found for a change in the mechanism of reaction as the reaction proceeded.

We interpret the weight gain curves as the difference between oxygen reacted to form silica and the weight of carbon lost by reaction with oxygen. For each 32g of oxygen reacted with silicon, 12g of carbon were reacted with oxygen. From stoichiometry, the weight of silica formed was 3 times the weight gain.

Kinetics of active type oxidation of SiC.—Table II shows a summary of the kinetic data for the active or weight loss region of oxidation. The following reactions were proposed to account for the oxygen consumed in the reaction.

$$SiC(s) + O_2 \rightleftarrows SiO(g) + CO(g) \quad [2]$$

$$SiO(g,s,l) + \tfrac{1}{2} O_2 \rightleftarrows SiO_2(s) \quad [9]$$

Reaction [2] occurs at the sample-gas interface while reaction [9] occurs after the SiO(g) leaves the surface and condenses on the furnace tube. Total oxygen consumed was the sum of that used in reactions [2] and [9], *i.e.*, 3 atoms of O per SiC molecule.

The data at 9 x 10^{-3} Torr for 1300°, 1350°, and 1400°C show little effect of temperature on the rate of oxidation. Pressure or gas flow had a major effect on the kinetics of oxidation. This was seen in values of dn'/dt at 1400°C for the three pressures 9 x 10^{-3}, 4 x 10^{-2}, and 1 x 10^{-1} Torr. The data indicates a $P^{0.8}$ dependence. We would suggest that gas diffusion of oxygen to the reaction interface was rate controlling.

Kinetics of the passive-type oxidation of SiC.—Figure 2 also shows weight gain curves. These curves show part of the initial fast stage of the reaction since part of the oxidation was not observed while the oxygen pressure and gas flow were adjusted. After several minutes of reaction, a protective film was formed and the rates of oxidation decreased to small values.

Table II. Summary kinetic data oxidation SiC, active region

Temp, °C	Reaction conditions: Pressure, Torr	Flow, atoms O/sec	Kinetic data: Wt. loss, g/sec	dn'/dt, molecules/cm²-sec	Efficiencies: Flow, %	Kinetic theory, %	Comments, type reaction
1250	9 x 10^{-3}	2.2 x 10^{17}	1.87 x 10^{-7}	1.47 x 10^{16}	3.8	1.0	Intermediate
1300	9 x 10^{-3}	2.26 x 10^{17}	1.56 x 10^{-6}	8.6 x 10^{16}	32	6.1	Active
1350	9 x 10^{-3}	2.08 x 10^{17}	1.65 x 10^{-6}	8.9 x 10^{16}	36	6.4	Active
1400	9 x 10^{-3}	1.23 x 10^{17}	1.31 x 10^{-6}	1.67 x 10^{17}	49	12.3	Active
1300	4 x 10^{-2}	1.74 x 10^{18}	7.5 x 10^{-7}	8.5 x 10^{16}	2.0	1.4	Intermediate
1350	4 x 10^{-2}	1.86 x 10^{18}	8.6 x 10^{-7}	6.8 x 10^{16}	2.1	1.1	Intermediate
1400	4 x 10^{-2}	1.62 x 10^{18}	5.22 x 10^{-6}	6.6 x 10^{17}	15	11	Active
1400	1 x 10^{-1}	1.33 x 10^{19}	9.3 x 10^{-6}	1.2 x 10^{18}	3.2	8	Active

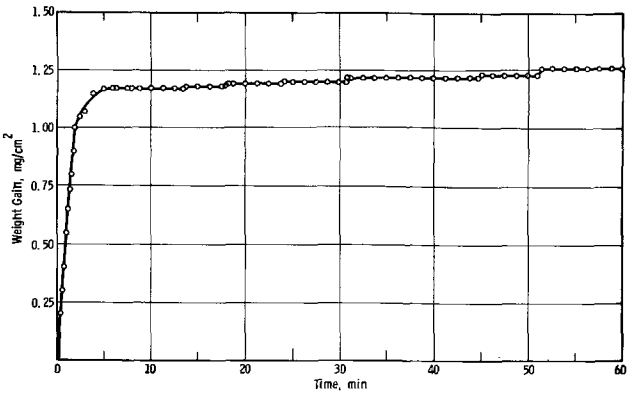

Fig. 3. Oxidation SiC, 1250°C and 4 x 10^{-2}

Figure 3 shows a weight gain *vs.* time curve, after the initial period, for the oxidation of SiC at 1250°C and 4 x 10^{-2} Torr pressure. Figure 3 shows a rapid oxidation for the first 5 min after which a slow reaction was found. A fast rate of oxidation of 7.5 x 10^{-6} g/cm²-sec was observed in the early stages of reaction. This rate decreased to 2.7 x 10^{-8} g/cm²-sec during the slow part of the oxidation. The oxidation in the latter stages of reaction appeared to occur in small increments. This suggested a cracking and healing of the silica film on the SiC for conditions near transition.

Table III shows a summary of the data for the weight gain region of oxidation. It was of interest to calculate the thickness of silica films, required for slow reaction, from an analysis of curves as shown in Fig. 3. These thickness values are given in Table II in units of grams per square centimeter and in angstroms.

Mass spectrometer study of the reaction products.—A liquid helium cooled trap was attached to the reaction system, and the gases were collected from the 1350°C and 9 x 10^3 Torr experiment. The gas analysis showed carbon monoxide as the major reaction product. We also conclude that carbon monoxide was not oxidized in the furnace tube after leaving the SiC surface.

Flow and kinetic theory efficiencies.—To compare this oxidation reaction with other fast oxidation reactions, it is of interest to calculate the flow and kinetic theory efficiencies. The flow efficiency is calculated as the ratio of the oxygen gas which reacts to the oxygen gas passed over the sample. The equation is

$$E = \frac{3\,dn/dt}{F} \qquad [10]$$

Table IV. Comparison theoretical and experimental values of maximum oxygen pressures for oxide free surfaces on silicon carbide

Temp, °C	Theoretical, p_{O_2}(max) Torr	Experimental, p_{O_2}(max) Torr	Ratio, p_{O_2} theory/p_{O_2} expt.
1200	3.5×10^{-2}	10^{-2}	3.5
1300	2×10^{-1}	$4 \times 10^{-2} - 1 \times 10^{-1}$	~3
1400	1.5	5×10^{-1}	3

Here F is the flow rate in atoms of O passing over the specimen per second and dn/dt is the actual reaction rate in molecules of SiC reacting per second. Table II gives values of the flow efficiencies for the various reaction conditions. Flow efficiencies up to 49% were calculated for active oxidation.

The kinetic theory efficiencies were calculated from the expression for the number of collisions of oxygen molecules with the surface per cm²-sec, n, and the rate of oxidation dn'/dt. The expression is

$$\epsilon = \frac{dn'/dt}{n} \qquad [11]$$

Table II gives the values for the various reaction conditions. Kinetic theory efficiencies up to 12.3% were calculated.

Calculation of transition conditions between active and passive oxidation.—Wagner (9) considered the transition between active and passive oxidation of silicon for various partial pressures of oxygen in a flowing oxygen-helium gas mixture. The following equation was developed for calculating the maximum partial pressure of oxygen, p_{O_2} (max), for maintaining an oxide free surface of silicon

$$p_{O_2}\,(\max) \cong \tfrac{1}{2}\,(D_{SiO}/D_{O_2})^{1/2}\,p_{SiO}\,(eq) \qquad [12]$$

Here p_{SiO} (eq) is the equilibrium pressure of silicon monoxide from Eq. [8] of Table I. D_{SiO} and D_{O_2} were the diffusion coefficients of SiO and O_2 in the boundary layer gas mixture. Wagner estimated D_{SiO}/D_{O_2} to have a ratio of 0.64 from the molecular weights and diameters of SiO and O_2 molecules.

The same analysis can be made to calculate the transition conditions for the oxidation of silicon carbide. Since mass spectrometer analyses showed the formation of carbon monoxide, Eq. [6] of Table I was used to calculate the equilibrium values for p_{SiO}. A ratio of 0.64 was assumed for D_{SiO}/D_{O_2} and a value of ½ for the exponent of the ratio. Values of p_{SiO} were taken from Eq. [6] of Table I.

Table IV shows the theoretical and experimental values for the values of p_{O_2} (max) and the ratio of the theoretical and experimental values for 1200°, 1300°, and 1400°C. The theoretical values were larger

Table III. Summary kinetic data oxidation SiC, passive region

Reaction conditions			Kinetic data			Oxide thickness	
Temp, °C	Pressure, Torr	Flow, atoms O/sec	Wt. gain, g/sec	dn'/dt, molecules/cm²-sec	dA/dt, Å/sec	Min. SiO_2 thickness, g/cm²	Min. thickness, Å
1150	9×10^{-3}	2.04×10^{17}	4.0×10^{-8}	5.0×10^{15}	10.3	3.6×10^{-4}	1.8×10^{4}
1150	4×10^{-2}	1.67×10^{18}	5.2×10^{-7}	6.5×10^{16}	134	1.4×10^{-3}	7.1×10^{4}
1150	1×10^{-1}	1.05×10^{19}	3.6×10^{-6}	4.5×10^{17}	930	3.3×10^{-3}	1.7×10^{5}
1150	5×10^{-1}	1.26×10^{18}	2.4×10^{-7}	3.0×10^{16}	62	—	—
1200	9×10^{-3}	2.65×10^{17}	5.3×10^{-8}	2.9×10^{15}	6	3.4×10^{-4}	1.7×10^{4}
1200	9×10^{-3}	1.29×10^{17}	1.7×10^{-8}	2.2×10^{15}	4.5	1.4×10^{-4}	0.7×10^{4}
1200	4×10^{-2}	1.48×10^{18}	6.0×10^{-8}	7.5×10^{15}	16	2.3×10^{-4}	1.1×10^{4}
1200	1×10^{-1}	1.13×10^{19}	2.1×10^{-7}	2.7×10^{16}	56	1.3×10^{-3}	6.5×10^{4}
1250	4×10^{-2}	2.1×10^{18}	9.7×10^{-7}	1.2×10^{17}	248	2.1×10^{-3}	1.03×10^{5}
1250	1×10^{-1}	1.13×10^{19}	7.7×10^{-7}	1.0×10^{17}	207	1.7×10^{-3}	8.7×10^{4}
1250	5×10^{-1}	1.6×10^{19}	1.1×10^{-6}	1.4×10^{17}	290	3.3×10^{-3}	1.7×10^{5}
1300	1×10^{-1}	1.13×10^{19}	2.0×10^{-7}	2.5×10^{16}	52	1.1×10^{-3}	5.5×10^{4}
1300	5×10^{-1}	1.52×10^{18}	6.0×10^{-7}	7.5×10^{16}	155	1.7×10^{-3}	8.5×10^{4}
1350	1×10^{-1}	1.28×10^{19}	3.9×10^{-6}	3.1×10^{17}	64	5.6×10^{-3}	2.8×10^{5}
1350	5×10^{-1}	1.68×10^{18}	4.8×10^{-6}	6.0×10^{17}	1240	2.9×10^{-3}	1.5×10^{5}

than the experimental values. The differences were probably within the limits of error.

Manuscript received Feb. 24, 1966; revised July 25, 1966. This paper was presented at the Cleveland Meeting, May 1-6, 1966. The work described here was supported in part by the United States Army Research Office, Durham, North Carolina.

Any discussion of this paper will appear in a Discussion Section to be published in the June 1967 JOURNAL.

REFERENCES

1. G. Ervin, *J. Am. Ceram. Soc.*, **41**, 347 (1958).
2. P. J. Jorgensen, M. E. Wadsworth, and I. B. Cutler, *ibid.*, **42**, 613 (1959).
3. P. J. Jorgensen, M. E. Wadsworth, and I. B. Cutler, *ibid.*, **43**, 209 (1960).
4. R. F. Adamsky, *J. Phys. Chem.*, **63**, 305 (1959).
5. K. Motzfeldt, *Acta Chem. Scand.*, **18**, 1596 (1964).
6. G. I. Finch and H. Wilman, *Trans. Faraday Soc.*, **33**, 337 (1937).
7. H. G. Heine and P. Scherer, *Helv. Phys. Acta*, **13**, 489 (1940).
8. W. W. Webb, J. T. Norton, and C. Wagner, *This Journal*, **103**, 112 (1956).
9. C. Wagner, *J. Appl. Phys.*, **29**, 1295 (1958).
10. JANAF Thermochemical Tables, The Dow Chemical Co., Midland, Mich. (1960). Si (s,l,g), SiO_2 (s), SiC (s): Dec. 31, 1962; SiO (g): Sept. 30, 1963; C (g): March 31, 1961.
11. E. Gulbransen, K. Andrew, and F. Brassart, "Vacuum Microbalance Techniques," Vol. 4, p. 127, Paul Waters, Editor, Plenum Press, New York (1965).
12. E. Gulbransen, K. Andrew, and F. Brassart, *Carbon*, **1**, 413 (1964).
13. L. Cahn, *Instruments and Control Systems*, **35**, 107 (1962).
14. D. Hamilton, *This Journal*, **105**, 735 (1958).
15. A. R. Verma, Butterworths Scientific Publications, London 1953, p. 102.
16. R. S. Mitchell, *Z. Krist.*, **109**, 1 (1957).

The Mechanism of Demineralization at Carbon Electrodes

S. Evans and W. S. Hamilton

Research Division, Rocketdyne, A Division of North American Aviation, Inc., Canoga Park, California

ABSTRACT

The results of coulometric and mass-balance analyses were used to establish the mechanism of demineralization and regeneration at chemically treated carbon paste electrodes. The chemical treatment results in the formation of weak acid groups on many carbon surfaces. The acid groups are ionized in the cathodic cycle by the electrochemical generation of hydroxyl ion. Anionic groups thus produced result in depletion of cations from solution. During regeneration, the hydrogen which was adsorbed on the carbon during the demineralization cycle is oxidized, giving rise to acid conditions. The anionic groups are thus converted back to the acid form, and cations are released to the solution.

Several mechanisms have been proposed to account for the adsorption of alkali or acid on carbon. Schilow (1) postulated that such adsorption arose by interaction with acidic and basic oxides on carbon surface. Garten and Weiss (2) explained the adsorption of cations from basic solution (*e.g.*, NaOH) on cathodically polarized charcoal and platinized charcoal by the reduction of quinone to hydroquinone. Recently it has been reported that considerable adsorption of alkali occurred under experimental conditions which excluded the presence of quinone or hydroquinone groups (3). Frumkin and co-workers (4) proposed an electrochemical theory wherein activated charcoal functions as a gas electrode in the presence of oxygen or hydrogen. In the presence of hydrogen, hydrogen ion appears in solution, leaving the charcoal negatively charged; the negatively charged surface attracts an equivalent quantity of cations. The electrochemical sorption of active gases (oxygen, hydrogen) on activated carbon has been used in analytical radiochemistry for the selective adsorption of ions from solution (5, 6).

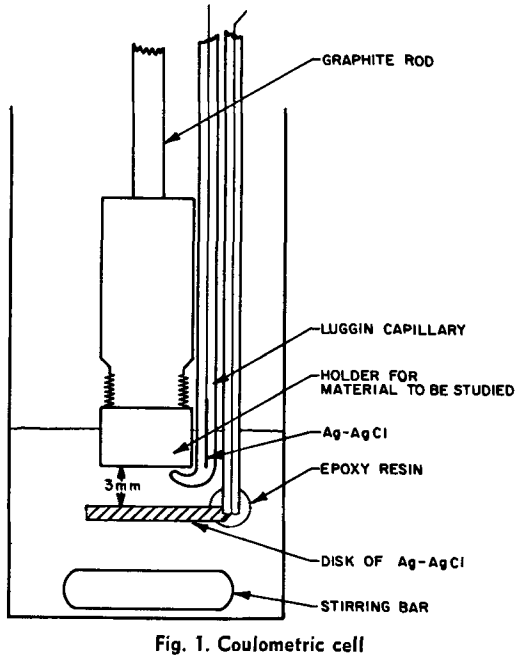

Fig. 1. Coulometric cell

In contrast to the above studies, the objective of this effort is to elucidate the mechanism of exchange of cations from neutral NaCl solutions. Coulometric and mass-balance experiments were used to establish the relationship between coulombs passed and extent of exchange.

Experimental

The cell (Fig. 1) was a small glass vial in which the three electrodes were fixed in the positions shown. The auxiliary electrode was made by anodizing a disk of porous silver in HCl solution. The test electrode (Fig. 2) consisted of a Teflon cup threaded to fit a Teflon plunger through which a ¼-in.-diameter graphite rod was cemented. A graphite disk was placed between the graphite rod and the carbon paste to improve electrical contact to the paste. A 25-mg sample of the material to be studied was supported on a disk of Whatman No. 42 filter paper. The potential at the test electrode was detected through a Luggin capillary which contained a silver wire coated with silver chloride. This Ag-AgCl electrode was in contact with the electrolyte (*e.g.*, 300 ppm NaCl). The electronic instrumentation has been described previously (7).

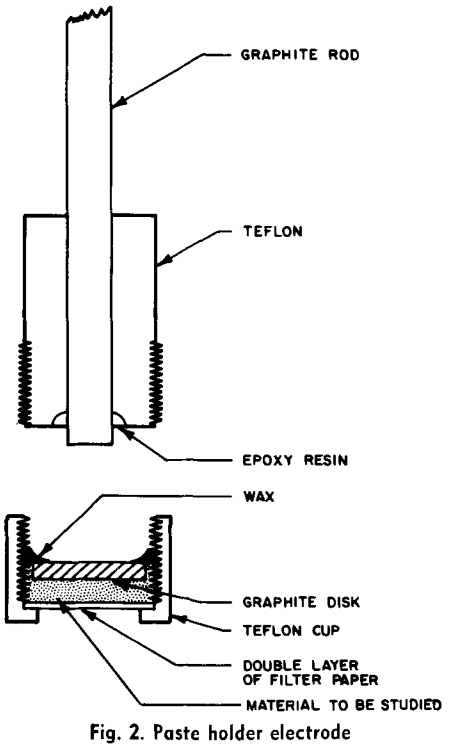

Fig. 2. Paste holder electrode

The materials studied included Air-Spun graphite, Norit-A, Carbolac-1, the sulfonic acid exchange resin Dowex 50W-X4 (J. T. Baker), and the carboxylic acid ion-exchange resin Amberlite IRC-50 (Mallinckrodt). The carbon materials (Air-Spun graphite, Norit-A, and Carbolac-1) were oxidized in a mixture of nitric and sulfuric acids in accordance with a procedure developed at the University of Oklahoma (8).

The cation exchange capacity of the above materials was determined chemically by suspending a sample in 0.2M NaOH for about 24 hr. The material was then filtered, washed with deionized water, and vacuum dried. A 25-mg portion of the dried sample was suspended in 10 cc of 0.12M HCl solution for about 24 hr. The solution was filtered and the filtrate was analyzed for sodium. The concentration of sodium ion in solution can be expressed in terms of milliequivalents of sodium adsorbed per gram of material.

All of the test solutions were analyzed for sodium ion with a Beckmann DU Spectrophotometer with flame attachment and were titrated potentiometrically for chloride ion.

Table I. Coulometric studies of acid-treated Norit-A

Test No.	Polarity (test electrode)	Coulombs	Efficiency, % Na+	Efficiency, % Cl-	pH	Milliequivalent[a] Ads/g	Milliequivalent[b] Des/g
B-1	–	1.44	76	95	5	0.45	
B-2	+	1.44	64	98	5		0.38
B-3	–	2.00	87	93	5	0.72	
B-4	+	1.44	100	96	5		0.60
B-5	–	1.44	96	91	5	0.57	
B-6	–	1.44	93	94	5	0.55	
B-7	–	1.44	94	94	5.5	0.56	
B-8	–	1.44	86	93	6	0.51	
B-9	–	1.44	72	98	8	0.43	
B-10	–	1.44	28	89	10	0.17	
B-11	–	1.44	9	92	11	0.05	
B-12	+	1.70	106	110	6		0.75
B-13	+	2.62	97	96	5		1.05
B-14	+	1.44	102	94	5		0.61
B-15	+	1.44	60	97	4		0.36
B-16	+	1.44	22	93	3		0.12
B-17	–	1.44	74	101	5	0.44	
B-18	–	1.44	88	97	5	0.52	
B-19	+	1.44	109	90	5		0.65

[a] Milliequivalents Na^+ adsorbed per gram of Norit-A.
[b] Milliequivalents Na^+ released to solution per gram of Norit-A.
Stock solution: 300 ppm NaCl (as prepared); 119 ppm Na^+ (as determined by analysis); 183 ppm Cl^- (as determined by analysis).

Table II. Coulometric studies of weak-acid ion-exchange resin

Test No.	Polarity (test electrode)	Coulombs	Efficiency, % Cl-	Efficiency, % Na+	pH	Milliequivalent Ads/g	Milliequivalent Des/g
JA-1	–	0.72	85	82	5	0.22	
JA-2	–	1.64	88	95	5	0.57	
JA-3[a]	–				5		
JA-4	–	2.54	94	95	5	0.88	
JA-5	–	2.16	96	92	5	0.72	
JA-6	–	2.25	89	85	5	0.71	
JA-7	–	2.50	91	82	5	0.75	
JA-8	–	3.06	93	74	5	0.83	
JA-9	–	2.30	90	50	8	0.41	
JA-10	–	1.66	93	35	9	0.21	
JA-11[b]	–	2.22	94	60	7.5	0.49	
JA-12	+	5.02	99	105	5		1.94
JA-13	+	4.83	103	102	5		1.8
JA-14	+	3.66	94	82	4		0.94
JA-15	+	2.27	92	35	3.5		0.29
JA-16	+	2.74	100	8	3		0.077
JA-17[c]	–	3.56	92	88	5	1.15	

[a] Electrode kept on open circuit for 2 hr.
[b] Current = 0.1 mamp.
[c] Solution = 1000 ppm NaCl.

Results

Ion Uptake and Release

The tabulated results of several experiments are shown in Tables I and II. An entire series of experiments was performed sequentially (*e.g.*, B-1 through B-19) with one 25-mg sample of the material. Each experiment in a series involved pipetting 10 cc of 300 ppm NaCl solution into the cell and passing a constant current (0.2 ma) between the paste electrode and the auxiliary Ag-AgCl electrode. The efficiencies were calculated from the ratio of the coulombic equivalent of the measured change in sodium or chloride ion concentration to the actual number of coulombs passed. The approximate *p*H at the paste electrode was determined by contacting a piece of *p*H indicator paper to the bottom surface of the test electrode. The recorded values are therefore not the *p*H of the bulk solution.

The results of six replicate experiments with different samples of acid-treated Norit-A were similar; some of the results of one series of experiments are shown in Table I. The minimum number of tests for a series was 40. During this time there was no evidence of electrode deterioration. Alternate cathodic and anodic cycles resulted in removal and release of sodium ion, respectively.

At high efficiencies for sodium ion (Table I) there was no change in surface *p*H and a mass-balance analysis for sodium ion was experimentally obtained. Decrease in the efficiency for sodium ion uptake or release was accompanied by an increase and decrease in surface *p*H, respectively; under these conditions a mass balance for NaCl was not obtained. One test series was carried out in a nitrogen atmosphere; the results were much the same as those shown in Table I. There was no release of sodium ion to the solution when the electrodes were allowed to remain on open circuit for several hours.

It can be seen (Table II) that similar results were obtained when a weak-acid ion-exchange resin (Amberlite IRC-50) was used as the active material.

Representative data from all of the experiments were condensed and are plotted in Fig. 3. Each point represents one sequential experiment of a test series. The cumulative number of equivalents of sodium adsorbed on the electrode during a continuous series of cathodic cycles (*e.g.*, JA-1 through JA-11) is plotted against the efficiency for each cycle.

It can be seen (Fig. 3) that with Air-Spun graphite (HJ), acid-treated Air-Spun graphic (HI), and a 2:1 mixture of Norit A and Air Spun graphite (HD), exchange capacities were low, and the exchange process

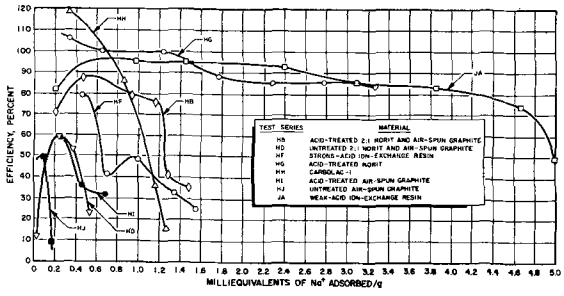

Fig. 3. Exchange characteristics of cation-exchange materials

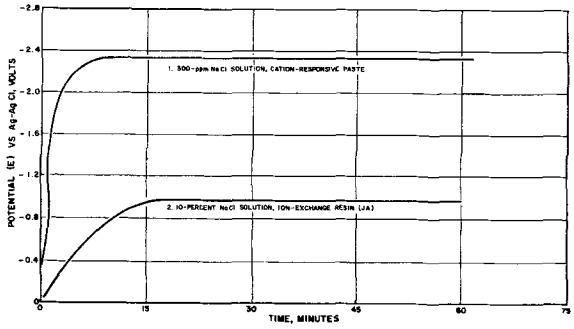

Fig. 5. Potential of paste electrode during demineralization (0.2 ma/mp).

was inefficient. The exchange was accompanied by rapid changes in pH.

The strong acid ion-exchange resin mixed with untreated Norit-graphite (HF) has a capacity of the order of 1.55 millieq./g. The process, however, is inefficient and is accompanied by pH changes.

The Carbolac-1 (HH), has been electrochemically titrated to the extent of 1.3 millieq. of acid per gram. Titration of Carbolac-1 with NaOH (9) yielded 1.8 millieq./g.

The total exchange capacity of the acid-treated Norit and graphite mixture (HB) was of the order of 3 millieq./g; the process was efficient for the exchange of 1.2 millieq./g. Changes in pH were observed only after exchange had occurred to this extent (*i.e.*, 1.2 millieq./g). This material was studied extensively. The exchange characteristics were similar when nitrogen was present. Good reproducibility was found in replicate experiments.

The exchange capacity of acid-treated Norit-A (HG) varied from about 2.6 to 3.5 in the six replicate experiments. In test series HG (Fig. 3), exchange corresponding to 3.3 millieq./g occurred relatively efficiently with only small change in pH. The material was successfully regenerated with H_2SO_4.

The weak-acid ion-exchange resin, Amberlite IRC-50 (JA, Table II), exchanged efficiently to the extent of 4.7 millieq./g with no changes in pH. Regeneration of this material occurred with equal efficiency (Fig. 4). Test JA-17, in 1000 ppm NaCl solution (Table II), was 88% efficient, demonstrating good recycling capability. There was no significant release of sodium ion to the solution when the electrode was allowed to remain on open circuit for 2 hr (JA-3).

Electrode Potential

The potential of the test electrode with respect to the Ag-AgCl electrode contained in the Luggin capillary was monitored for each of the constant-current experiments.

Demineralization (ion uptake).—A typical potential curve obtained during a demineralization cycle (0.2 ma, 300 ppm NaCl, test electrode is cathode) consisted of two regions (curve 1, Fig. 5); an initial region of rapid potential change generally covering the range from 5 to 10 min, followed by a region of constant potential. All of the curves were of similar shape; the magnitude of the potential in the constant-potential region varied from about 2 to 2.8v for carbon-paste materials. The value was about two times greater in experiments with the weak-acid resin (test series JA) where no carbon paste was present and where the entire electrochemical reaction took place on the graphite backing. Potential measurements with this electrode during demineralization in a 10% NaCl solution were of the same general shape (curve 2, Fig. 5).

A current interruptor technique (7) was used in a few of the experiments to establish the extent of the IR contribution to the potential measured between the reference electrode contained in the Luggin capillary and the test electrode. It was found that during the demineralization cycle the magnitude of the IR drop rose continuously for the first several minutes at constant current and achieved a steady value during the constant-potential region of the curve.

The assumption was made that the difference between the end potential during a demineralization cycle and the potential recorded immediately on breaking the circuit is a measure of the IR drop. Values determined in this manner were in qualitative agreement with these determined using a current interruptor technique. The value of the final IR drop for various materials has been plotted with respect to the efficiency of removal of sodium ion for the cycle in which the recording was made (Fig. 6). It can be seen that when demineralization was occurring efficiently the magnitude of the final IR drop was high. At such times no surface pH changes were detected.

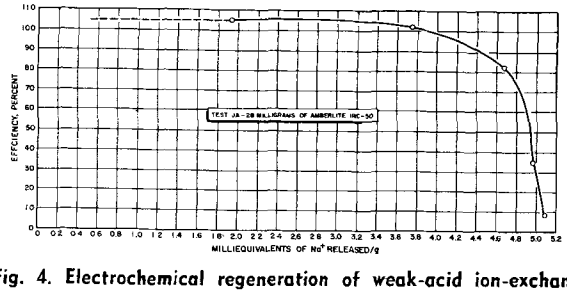

Fig. 4. Electrochemical regeneration of weak-acid ion-exchange resin.

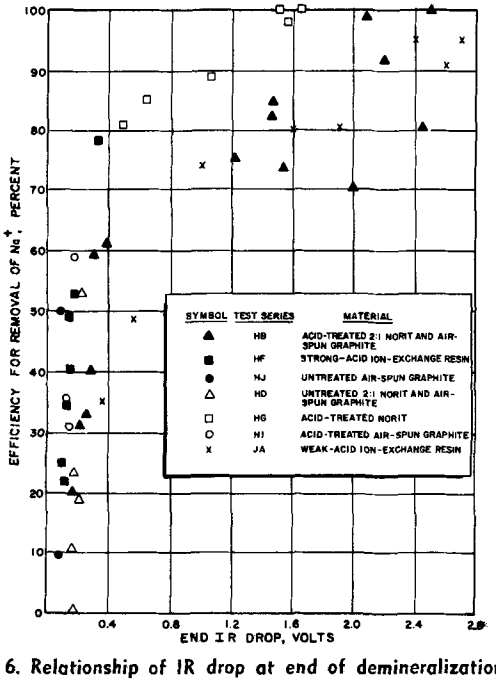

Fig. 6. Relationship of IR drop at end of demineralization cycle to measured efficiency of the cycle.

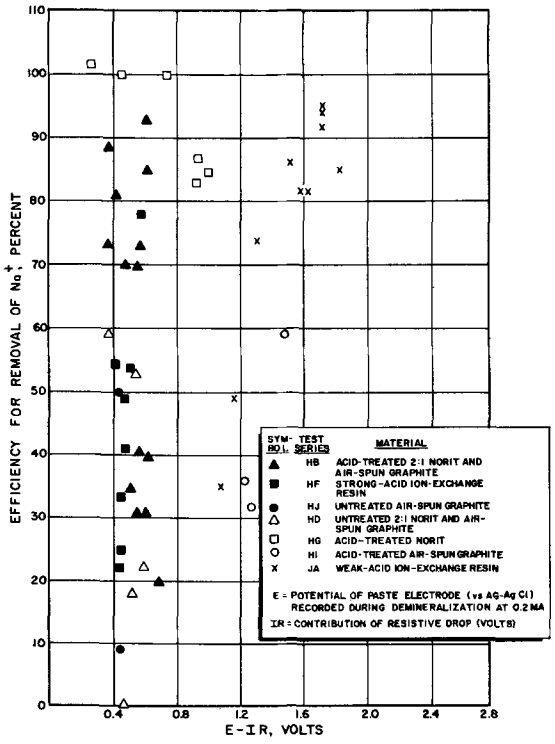

Fig. 7. Relationship of E-IR at end of each cycle to efficiency for the cycle.

At low demineralization efficiencies, the IR drop was low and appeared to be independent of the material used, and the surface *p*H was higher (generally between 10 and 11).

Subtraction of the IR drop from the final potential should give a measure of the remaining forms of polarization. It appears (Fig. 7) that for the bulk of the materials studied, the value E-IR is relatively independent of the demineralization efficiency. Exceptions are the weak-acid resin where the electrochemical reaction was occurring at the graphite backing and the acid-treated Air-Spun graphite.

Regeneration.—The potentials at which regeneration occurred varied with the previous history of the electrode. When regeneration followed immediately after demineralization (cathodic pretreatment), polarization was low. The regeneration process could be achieved below a few tenths of a volt with respect to the Ag-AgCl reference. Prolonged regeneration generally resulted in potential values between 0.6 and 1v. Regenerations undertaken a day after demineralization exhibited higher values (between 0.6 and 1v *vs.* Ag-AgCl). It seems probable that hydrogen adsorbed during demineralization was oxidized during regeneration.

A series of experiments was designed to highlight the above behavior. A 25-mg sample of acid-treated Norit was placed in an NaOH solution to determine the effect of chemical conversion of surface groups. The material was then placed in the holder electrode and studied. The results are shown in Table III. The

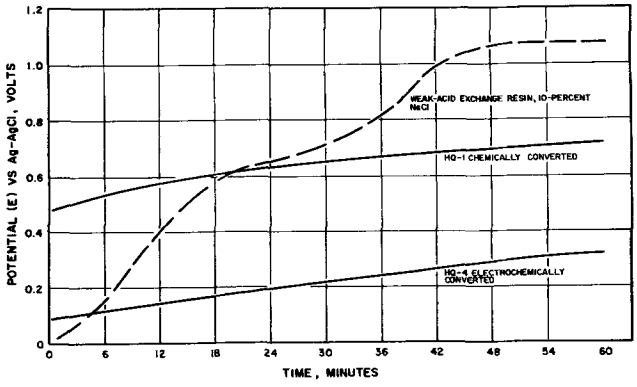

Fig. 8. Potential of paste electrode during regeneration (0.2 mamp).

chemically converted material was regenerated at 0.2 ma in two steps (HQ-1 and HQ-2). Electrochemical demineralization followed (HQ-3). The material was again regenerated (HQ-4, 5, and 6). Potentials recorded during regeneration (Fig. 8) of a surface which was chemically converted (HQ-1) were higher than those recorded on regeneration of an electrochemically converted surface (HQ-4). The dashed curve represents regeneration of a weak-acid exchange resin (which had been previously used for electrochemical demineralization) in a 10% NaCl solution. In this latter case, the electrochemical processes were taking place at the graphite backing. The two steps indicate that hydrogen was adsorbed on the graphite backing during demineralization and that it is reoxidized during the first plateau.

Open-Circuit Exchange

The extent of exchange occurring at acid-treated Norit-A and Amberlite IRC-50 in various concentrations of neutral NaCl solution is shown in Table IV. The materials were continuously stirred in NaCl for 5 days, and then were filtered, washed thoroughly with deionized water, and vacuum dried. The adsorbed sodium ion was regenerated to the solution (see Experimental section).

The exchange capacity in NaOH was also evaluated (Table IV). The values determined for acid-treated Norit-A varied from batch to batch; the variation was between 2.5 and 3.5 millieq./g.

Discussion

The reactions which occurred at the Ag-AgCl auxiliary electrode involved the removal and release of chloride ion.

$$\text{Anode reaction:} \quad Ag + Cl^- - e^- = AgCl \quad [1]$$

$$\text{Cathode reaction:} \quad AgCl + e^- = Ag + Cl^- \quad [2]$$

When demineralization and regeneration proceeded efficiently, a mass-balance analysis for sodium chloride was obtained. Changes in chloride ion concentration were in quantitative agreement with Eq. [1] and [2], and it is concluded that sodium ion was adsorbed and released when the test electrode was cathode and anode, respectively.

Table III. Regenerative experiments

Test No.	Polarity, (test electrode)	Coulombs	Efficiency, % Cl⁻	Efficiency, % Na⁺	*p*H	Milliequivalents per gram Des
HQ-1	+	0.74	100	74	3	0.23
HQ-2	+	0.74	70	45	2.5	0.14
HQ-3	−	2.24				
HQ-4	+	0.82	90	100	5.5	0.33
HQ-5	+	0.72	95	81	5	0.24
HQ-6	+	0.72	87	81	3	0.24

Table IV. Open-circuit exchange

Solution	Na⁺ Adsorbed, milliequivalents per gram: Acid-treated Norit	IRC-50
0.03% NaCl	0.14	0.07
0.1% NaCl	0.21	0.09
0.3% NaCl	0.41	0.09
1.0% NaCl	0.35	0.13
10.0% NaCl	0.47	0.17
0.2M NaOH	3	6

Mechanism of Demineralization

The primary electrochemical reaction which occurs when the test electrode is made the cathode, is

$$H_2O + e^- = H_{ads} + OH^- \quad [3]$$

The basic condition localized about the cathode provides an environment favorable to the ionization of weak-acid groups

$$RCOOH + OH^- + RCOO^- + H_2O \quad [4]$$

and gives rise to the demineralization reaction

$$RCOO^- + Na^+ = RCOONa \quad [5]$$

where

R carbon (Norit)
COOH = any suitable acid group

The faradaic reaction involves the adsorption of hydrogen on the carbon surface and the generation of OH^- (Eq. [3]); at constant current, the true efficiency (Eq. [3]) is approximately 100%. The efficiency for demineralization is of this order only when Eq. [4] and [5] occur equally efficiently.

The results showed that at high efficiency (Eq. [5]), no change in *p*H occurred. The OH^- generated was efficiently used in demineralization (Eq. [4]). Marked *p*H changes were observed at low efficiencies. In such cases, the OH^- which was generated did not result in ionization of the acid (Eq. [4]), and the *p*H rose.

While weak-acid, ion-exchange resins can be titrated with NaOH, the reaction with neutral NaCl solution is small (10) as seen in Table IV. A weak-acid, carboxylic resin is slightly ionized

$$RCOOH = RCOO^- + H^+$$

Anionic groups (*e.g.*, $RCOO^-$) are necessary for exchange, and the weak acid groups are predominantly nonionic at low *p*H. The efficient removal of sodium ions from NaCl solution at carboxylic acid ion-exchange resins (test series JA) provides direct confirmation of the mechanism presented. The demineralization reaction is analogous to the titration of an ion exchange resin, but in this example, the base for the titration is electrochemically generated.

The groups on the carbon surface need not be carboxylic. Evidence has been presented for other weak acid groups which have exchanged with sodium ion (11). Recently the acidity of various carbon surfaces has been determined by neutralization with bases of various basicities (11). The results of the coulometric titration of Carbolac-1 (test series HH) were in agreement with those obtained by direct titration with NaOH (9). The exchange capacity of Norit-A was found to be of similar magnitude when determined chemically or electrochemically.

The increase in the IR drop during demineralization can be explained in terms of the cell design. The volume of the paste electrode compartment was about 0.016 cc compared to a bulk solution volume of 10 cc. At high demineralization efficiencies, electrolysis of the solution in the paste electrode compartment resulted in the depletion of sodium chloride (by Eq. [5] and ionic transport) with no concomitant change in *p*H. This resulted in an increase in the IR drop. A steady value of IR drop was observed after a steady-state diffusion rate from the outer solution had been attained. It was found that the magnitude of this IR drop depended on the stirring rate, confirming that it was controlled by the rate of diffusion of bulk solution into the paste electrode compartment.

When demineralization was not efficient, the OH^- produced was not consumed, and there was no marked change in the contribution of the IR drop. Examination of the results (Fig. 6) indicated that at high efficiencies the magnitude of the contribution of IR drop was substantial. A marked decrease in drop at low efficiencies was accompanied by a rise in *p*H. Subtraction of the IR drop from the measured potential (Fig. 7) indicated that the contribution of other forms of potential was relatively independent of efficiency. The values associated with the carboxylic acid ion-exchange resin were higher, since the current density was greater at the graphite backing.

It is concluded that the potential recorded during efficient demineralization consisted mostly of IR drop; the magnitude of which is peculiar to the design of the paste holder electrode. The extent of this contribution can be markedly decreased by proper design of electrodes.

The electrochemical reaction did not involve the evolution of hydrogen on the graphite surface. Recently it has been reported (12) that hydrogen gas is not formed free, but is adsorbed by the active carbon. Experiments with coherent electrodes, wherein acid-treated Norit-A was affixed to a carbon backing have been performed in this laboratory. There was no visual evidence of gas evolution. The potential recorded during demineralization was too low to account for hydrogen evolution. This work is being prepared for publication.

Mechanism of Regeneration

The main electrochemical reaction which occurs when the test electrode is made the anode, is

$$H_{ads} - e = H^+ \quad [7]$$

This results in a localized low *p*H which aids the recombination to form acid groups.

$$RCOONa + H^+ = RCOOH + Na^+ \quad [8]$$

At high regeneration efficiency there was no change in *p*H. The hydrogen was adsorbed during previous cathodic (demineralization) cycles. Oxidation waves for hydrogen have been observed after the cathodic cycle (13), as evidenced from the appearance of a limiting current during anodic potentiostatic scanning experiments. An equivalent limiting current was noted for potentiostatic curves obtained after a demineralization cycle (14). No such limiting current appeared on the fully oxidized surface. It can be seen (test series HQ) that an electrochemically converted surface is regenerated at lower potentials than one which was converted chemically (Fig. 8). The chemical conversion was accomplished without the adsorption of hydrogen.

$$RCOOH + NaOH = RCOONa + H_2O \quad [9]$$

The localized acidic condition which resulted in recombination to the acid form (RCOOH) was created by the oxidation of water.

$$H_2O - e = \tfrac{1}{2} O_2 + 2H^+ \quad [10]$$

Figure 8 shows that regeneration of the carboxylic acid resin (test series JA) involves the oxidation of hydrogen which was adsorbed to a limited degree on the graphite backing, and subsequently, the oxidation of water. The quantity of hydrogen adsorbed was greater with carbon paste electrodes; the hydrogen was adsorbed on the carbon paste material. Since the oxidation of hydrogen is energetically easier than the oxidation of water, the incorporation of acid-treated Norit with ion-exchange resins would result in more favorable conditions for regeneration.

Exchange Capacity

Figure 3 shows that the acid treatment of Norit and of the Norit-graphite mixture increased the cation capacity. It is proposed that the acid-treatment resulted in the formation of weak-acid exchange groups. Acid-treated Norit exhibited exchange characteristics superior to any of the carbon-type materials studied

(Fig. 3) and is competitive with commercial ion-exchange resins.

Strong-acid exchange groups are almost completely ionized under any conditions so that their exchange characteristics are relatively independent of pH (10). Such materials exchange with sodium ion in NaCl solution and are not amenable to electrochemical control. The bulk of the exchange at such groups (test series HF) is not electrochemically induced. The pH changes which occurred during demineralization did not appear to be dependent of the efficiency.

Manuscript received May 12, 1966; revised manuscript received July 14, 1966. This work was supported by the Office of Saline Water, Department of the Interior, under Contract 14-01-0001-334.

Any discussion of this paper will appear in a Discussion Section to be published in the June 1967 JOURNAL.

REFERENCES

1. E. J. Miller, *J. Phys. Chem.*, **36**, 2967 (1932).
2. V. A. Garten and D. E. Weiss, *Austr. J. Chem.*, **8**, 68 (1955).
3. R. Burshtein and E. A. Ponomarenko, *Russ. J. Phys. Chem.*, **39**, 140 (1965).
4. R. Burshtein and A. Frumkin, *Z. Phys. Chem.*, **A141**, 219 (1929).
5. A. N. Mosevich and E. L. Mordbey, *Zhur. Fizi. Khim.*, **34**, 1900 (1960).
6. D. N. Strazhesko, I. A. Tarkovskaya, and G. F. Yankovskaya, ONR Technical Report ONRL-C-18-65, London, England, 17 November 1965.
7. S. Evans, *This Journal*, **113**, 165 (1966).
8. J. W. Blair and G. W. Murphy, *American Chemical Society Advances in Chemistry Series*, **27**, 206 (1960).
9. V. A. Garten, D. E. Weiss, and J. B. Willis, *Austr. J. Chem.*, **10**, 295 (1957).
10. F. Helfferich, "Ion Exchange," Chap. IV, McGraw-Hill Book Co., Inc., New York (1962).
11. H. P. Boehm, E. Diehl, W. Heck, and R. Sappok, *Angew. Chem.*, **3**, 669 (1964).
12. W. Tomassi, H. Jankowska, S. Pietrzyk, and J. Bryeka, *Electrochim. Acta*, **10**, 605 (1965).
13. J. Farrar, S. Evans, and G. Seele, "Mechanism of Electrode Demineralization," Final Report to U.S. Department of the Interior, Office of Saline Water, 30 June 1964.
14. S. Evans and W. S. Hamilton, "Mechanism of Electrode Demineralization," Final Report to U.S. Department of the Interior, Office of Saline Water, 30 July 1965.

Short-Pulse Techniques

II. Perturbation Times in Alkali-Halide Systems

B. J. Piersma,[1] Sigmund Schuldiner, and T. B. Warner

U. S. Naval Research Laboratory, Washington, D. C.

ABSTRACT

A new technique involving the perturbation of a system from equilibrium using very short galvanostatic pulses and miniature cells has been applied to study the electrical double layer at Pt electrodes. The perturbation time, the time required for the double layer to begin charging, was determined for hydrogen- and alkali metal-halide systems and for reversible hydrogen systems in several acids and NaOH. The perturbation time was essentially independent of charging current density and of the anion in solution but was strongly dependent on the cation species and electrolyte concentration. Models to explain the absence of electrode polarization during the initial flow of charge into the double layer are discussed. A model which involves a very fast faradaic process and which is consistent with the experimental observations is proposed. It is suggested that the perturbation time, which is less than 100 nanosec for 1M solutions, represents the time required for movement of ions into or out of the compact double layer.

In a previous paper (1), a galvanostatic short-pulse technique was developed to study the kinetics of the I_3^-/I^- reaction on a Pt electrode. Oscilloscopic traces at very short times (less than 0.1 μsec) showed delays or perturbation times in the charging of the electrical double layer from the equilibrium potential. It was suggested that a short-pulse technique could be applied to determine the perturbation times of ions in the compact double layer. This study was undertaken to explore this possibility further.

[1] National Academy of Sciences-National Research Council Postdoctoral Research Associate at NRL.

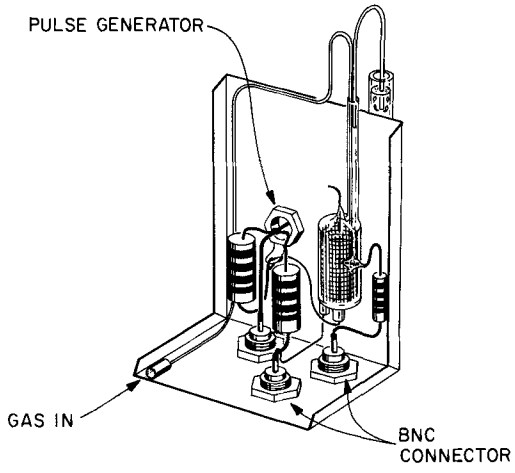

Fig. 1. Miniature cell

Experimental

The miniature glass cells (Fig. 1) used were designed to be terminated coaxial cables. This minimized the effects of overshoot and ringing inherent in short-pulse measurements. Two central Pt wires, approximately 1 cm long and 0.025 cm diameter, were less than 0.05 cm apart and served as the working and reference electrodes. The counter electrode was a Pt gauze cylinder of size approximately the inside dimensions of the cell (about 1 cm diameter x 1 cm length). Two 22 gauge Teflon tubes, one of which was supplied with a female luer fitting, were sealed in the cell with polyethylene, as shown in Fig. 1. Solution was added or removed with a gas-tight syringe (Hamilton Model 1001). Gas was bubbled through the cell from a glass pipe system connected to the cell with a male luer fitting.

The basic circuit is similar to that used previously (1, 2), and is shown in Fig. 2. The cell was mounted

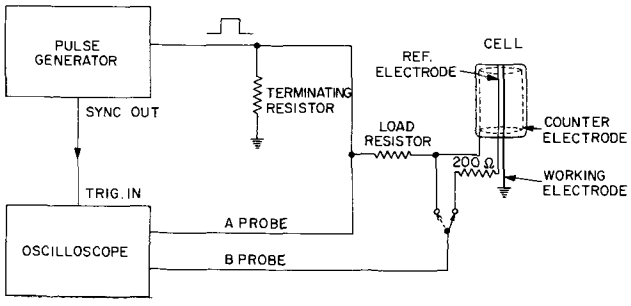

Fig. 2. Block diagram of basic electrical circuit

in an aluminum chassis which was attached directly to the pulse generator (E-H Research Laboratories, Inc., Model 121) with a BNC connector. The leads from the cell to BNC connectors on the chassis were made as short as possible, being only a few millimeters long. Since changes in electrolyte concentration varied the solution resistance, the terminating resistor and load resistor were changed such that the output impedance of the pulse generator was matched and the cell IR drop was not excessive. The 200 ohm resistor connected to the reference electrode reduced ringing and overshoot by balancing the impedance in the cable to the oscilloscope. Measurements were made with a Tektronix Type 585 oscilloscope. Long current pulses to examine system cleanliness were obtained with an Electro-Pulse Model 3450D pulse generator (4).

Values of the charging currents were determined as usual (1). The shape of the pulse itself was constantly checked using a dummy circuit with only resistive components. A typical trace of an acceptable pulse is shown in Fig. 3. During the course of the experiments the pulse generator required periodic adjustments to retain the flatness of the pulse and the short rise times (4 nsec). The experimental technique was also carefully examined using dummy cells with known resistive and capacitative components to completely insure that the perturbation times observed with the electrolytic cells were not instrumental artifacts.

The purification systems for hydrogen and helium were as described previously (3). Chlorine was Matheson, research grade, and was used without further purification. Other reagents were as follows: KI, I_2, KBr, Br_2, LiCl, NaCl, KCl, NaOH, HCl, H_2SO_4, and HNO_3 all "Baker Analyzed" reagent; RbCl and CsCl were prepared from hydroxide solutions by reaction with HCl and recrystallized. All solutions were prepared with triply distilled H_2O (3). All systems were at equilibrium at open circuit.

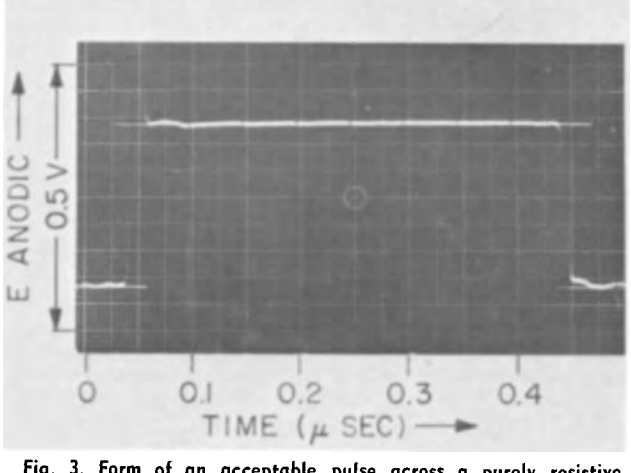

Fig. 3. Form of an acceptable pulse across a purely resistive dummy circuit.

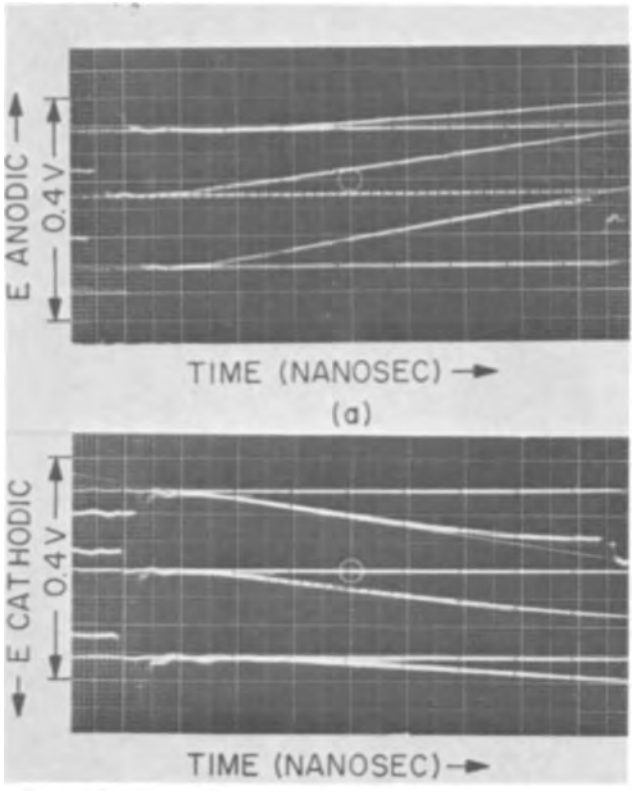

Fig. 4. Oscilloscope traces of pulses in 1M KI/0.0025M I_2 systems, i = 2.2 amp/cm². (a) Anodic pulses, time scales: lowest trace 50 nsec/cm, middle trace 40 nsec/cm, upper trace 20 nsec/cm; (b) Cathodic pulses, time scales: lowest trace 20 nsec/cm, middle trace 40 nsec/cm, upper trace 50 nsec/cm. Note: Each major division = 1 cm on oscilloscope screen.

After the cell had been suitably cleaned,[2] solution was added and He (in chloride systems Cl_2 was substituted) was bubbled through the cell, for about 1 hr, to reduce the oxygen concentration in the system. Gas flow was stopped during the few seconds required for measurements because of the large effects of gas bubbles on the cell resistance. Pulses were applied repetitively at rates of 100-500 cps. For the pulses used (less than 0.5 μsec) this spacing was sufficient (1) so that the electrodes were at equilibrium at the onset of each perturbation.

Results

Initial studies were carried out with KI solutions containing 0.0025M I_2 for comparison with previous results (1). Typical charging curves for anodic and cathodic pulses are given in Fig. 4. As the concentration of the KI solution was decreased, the cell resistance increased and the terminating and load resistors were changed to keep the IR drop within the limits of the oscilloscope screen at the more sensitive amplitude ranges (0.1-0.5 v/cm). The effect of changing the charging current on the perturbation time was examined carefully for the KI/I_2 system.

After the KI/I_2 system had been thoroughly examined, KBr/Br_2 and KCl/Cl_2 systems were studied in a similar manner. For the latter system, Cl_2 was bubbled through the cell rather than an inert gas. The study was then extended to MCl/Cl_2 systems with different cations and to reversible hydrogen systems with several electrolytes. All of the systems examined were reversible systems to provide stable base potentials. In an attempt to obtain a clean cell with an H_2SO_4/H_2 system after KI/I_2 solutions had been used,

[2] The cleaning procedure included: (i) warm (approx. 60°C) concentrated NaOH solution, (ii) warm conc. HNO_3, (iii) warm 50% HNO_3/50% H_2SO_4, (iv) 10-12 rinses with triply distilled H_2O over a period of 24 hr. Each step was followed with 10-12 rinses with triply distilled H_2O.

it was found, by using the reported cleanliness tests (4), that it was extremely difficult to remove all traces of iodide from the Pt electrodes. It was thus necessary to use different cells for the different halides and for the acid/H_2 systems studied. In light of these results, the recent suggestion by Devanathan and Tilak (5) of treating Pt electrodes with KI solution prior to capacity measurements to obtain a base capacity of 20 $\mu F/cm^2$ would seem open to question. This treatment might explain the difference in their results from those obtained in this laboratory (3), *i.e.*, a capacity of 40 $\mu F/cm^2$ was obtained with bright Pt, in the so-called double layer region of potentials, in a highly purified system, containing H_2SO_4.

The effect of changing the charging current on the perturbation time in the 1.0M KI/0.0025M I_2 system is presented in Table I, together with the double layer capacitance. These data are representative of the reproducibility obtainable with this technique. The perturbation times were determined from the oscilloscopic traces in two different ways. As seen from Fig. 4, the perturbation time is readily obtained by simply measuring the time between the onset of the pulse and the point at which double layer charging begins. Alternatively, the IR drop was measured at pulse cutoff and this value was marked off from the initial foot of the pulse. The time at which the polarization, due to charging of the double layer, became larger than this IR drop was taken as the perturbation time. Identical perturbation times were obtained with these two procedures, within the scatter of measurements, being in general ±3 nanosec. Scatter of data in more dilute solutions in some cases became as large as ±10 nanosec. Here the smaller charging currents used (because of higher solution resistance) resulted in slower charging of the double layer. Since perturbation times were also longer in the more dilute solutions, the scatter was always less than ±10%. With more dilute solutions, the IR correction method was more precise since a sharp break due to double layer charging was not obtained. Close examination of oscilloscope traces at every current density used (0.1 to 5 amp/cm^2) indicate small transition regions before double layer charging becomes linear.

The variation of perturbation time, t_p, with concentration is shown in Fig. 5, for KI/I_2, KBr/Br_2, and KCl/Cl_2 systems. It is evident that: (*a*) a good linear relation between the perturbation time, t_p, and log concentration is obtained, (*b*) anodic pulses result in different perturbation times from cathodic pulses, however, t_p becomes the same at a salt concentration of about 5M, and (*c*) changing the anion has surprisingly little influence on t_p. Further experiments to examine the influence of the nature of the anion on t_p are summarized in Table II. It is evident that the anion has very little to do with the perturbation times observed.

The variation of t_p with concentration of MCl/Cl_2 systems with different cations is given in Fig. 6 and 7 for anodic pulses and cathodic pulses, respectively. In addition to the linear t_p *vs.* log concentration relations and the differences between $t_{p,a}$, anodic and $t_{p,c}$ cathodic, a rather startling dependence on the cation is observed. The largest difference is between H^+ and the first alkali metal ion Li^+, while the higher alkali metal ions, K^+, Rb^+, and Cs^+, give similar behavior.

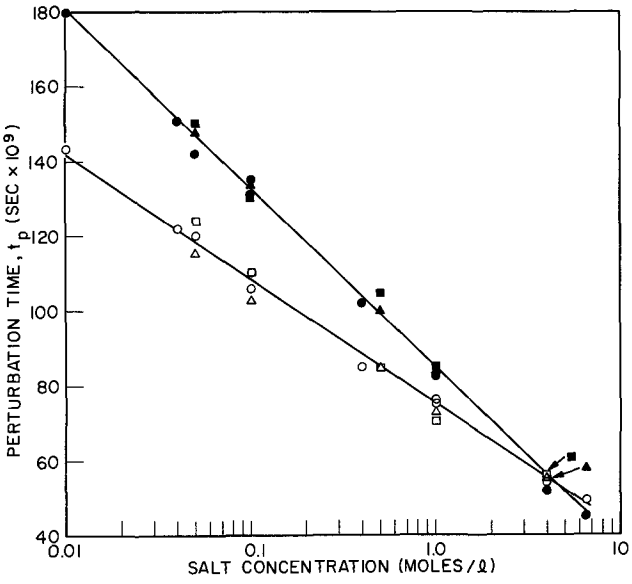

Fig. 5. t_p *vs.* log conc. for KI/I_2: (⊙) cathodic, (●) anodic, KBr/Br_2 (△) cathodic, (▲) anodic and KCl/Cl_2 (□) cathodic, (■) anodic systems.

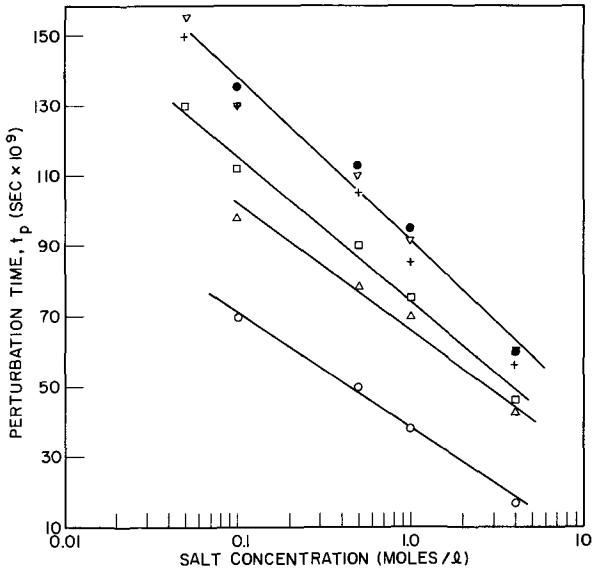

Fig. 6. t_p *vs.* log conc. from anodic charging in MCl/Cl_2 systems: (⊙) H^+, (△) Li^+, (□) Na^+, (+) K^+, (▽) Rb^+, (●) Cs^+.

Discussion

The experimental observations which must be considered in discussion of the perturbation times are summarized as follows:

(*i*) $t_p \neq f(i)$ within the limits of i used (0.1-5 amp/cm^2)

(*ii*) $t_p \neq f(E_{rev})$

Table I. Perturbation times and double layer capacitances at different current densities for 1.0M KI/0.0025M I_2 solution

Current density, amp/cm^2	Cathodic pulse t_p, sec × 10^9	Cathodic pulse C_{dl}, $\mu F/cm^2$	Anodic pulse t_p, sec × 10^9	Anodic pulse C_{dl}, $\mu F/cm^2$
1.65	75	6.3	85	7.5
2.49	74	7.1	83	8.3
3.09	76	6.1	80	7.3
3.34	74	6.4	82	6.9
4.76	75	7.3	84	8.6
Averages	75 ± 1	6.6 ± 1	83 ± 3	7.7 ± 1

Table II. Perturbation times in reversible hydrogen systems

1M solutions	t_p, Cathodic, sec × 10^9	t_p, Anodic, sec × 10^9
H_2SO_4	19	38
HNO_3	18	36
HCl	20	40
NaOH	70	78

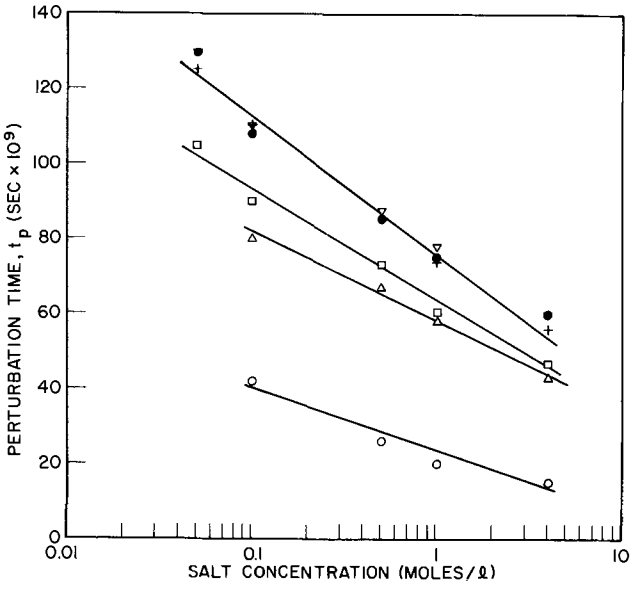

Fig. 7. t_p vs. log conc. from cathodic charging in MCl/Cl_2 systems: (○) H^+, (△) Li^+, (box with dot) Na^+, (+) K^+, (triangle up side down with dot) Rb^+, (●) Cs^+.

(*iii*) $t_p = f(\text{cation})$, $t_{p,H+} < t_{p,Li+} < t_{p,Na+} < t_{p,K+} \approx t_{p,Rb+} \approx t_{p,Cs+}$
$t_p \neq f(\text{anion})$, $t_{p,SO_4^=} \approx t_{p,NO_3^-} \approx t_{p,Cl^-} \approx t_{p,Br^-} \approx t_{p,I^-}$

$$(iv)\quad \frac{dt_p}{d\log \text{conc.}} = -\text{const.},$$

$$\left(\frac{dt_{p,a}}{d\log \text{conc.}}\right) > \left(\frac{dt_{p,c}}{d\log \text{conc.}}\right)$$

(*v*) $t_{p,a} > t_{p,c}$ for conc. $< 4M$
$t_{p,a} \approx t_{p,c}$ for conc. $> 4M$

A prime consideration for a model to explain the perturbation time is the fact that energy is being passed into the double layer while the measured potential difference across the double layer remains constant. The observations tend to indicate that two processes are involved, *i.e.*, one which is time dependent but independent of the charging current and which determines t_p, and another process which can use the charge passed during t_p without altering the potential difference, *i.e.*, without charging the double layer.

The latter process can be understood on a physical basis from the equation for a capacitor if we assume that the double layer does act essentially as an ideal unit area capacitor

$$C = \frac{Q}{E} = \frac{\epsilon}{4\pi d}$$

where the dielectric constant in the double layer $\epsilon \approx 6$ and the distance d, normally the distance between the plates of a capacitor, is equated to the thickness of the compact layer and is approximately 3.5Å. To obtain constant E while Q changes requires either a change in the dielectric constant, ϵ, or a change in the double layer thickness, d, *i.e.*, a change in position of the outer Helmholtz plane. If we assume for $E = 0.6$v, that $Q = 10$ μcoul/cm^2 and $d = 3.5$Å, then $\epsilon = 6.6$. Hence, for a typical change in Q from an anodic pulse of 1 amp/cm^2 during a perturbation time of 100 nanosec, $\Delta\epsilon = 0.06$, *i.e.*, the dielectric constant would have to increase by about 1% to give the required result. Alternatively, if we assume constant ϵ, the thickness d would have to decrease by about 1% during the anodic perturbation time. Whether ϵ and d would have to increase or decrease would of course depend on the potential with respect to the potential of zero charge, p.z.c., *i.e.*, whether Q increases or decreases. In any case, the changes required are on the order of 1%, which seems entirely reasonable.

A more detailed model is obtained by examining the chemical nature of a change in ϵ or a change in d. The dielectric constant is increased by removal of ions from the double layer, either by mass transfer or by neutralization through charge transfer, or by a relaxation of restriction on the movement of dipoles. Since a net transfer of ions into or out of the double layer would result in actual charging of the capacitor, *i.e.*, a change in E with Q, this cannot occur during the perturbation time. Further, the time required for ions to move into or out of the double layer is very possibly on the same order as the observed perturbation times. Grahame (6) has suggested, from calculations for a simple RC circuit and based on data from a mercury electrode, that the time required for establishment of ionic equilibrium within the double layer is on the order of 100 nanosec.

The double layer thickness is changed by a shift of the outer Helmholtz plane. This could occur by a slight relaxation of the plane, *e.g.*, by a movement of the cations within their solvation sheaths. The kinds of shifts involved, *i.e.*, approximately 0.05Å, could readily be achieved simply by a movement of the cations within the sheaths of water molecules surrounding them, and as such do not require movement of ions into or out of the double layer.

The perturbation time can be viewed either as the time required for the transfer of ions, *i.e.*, a type of inertia which must be overcome before ions can begin to move, or as the time required to saturate some initial process in the compact layer, *e.g.*, dielectric saturation, before the effects of the charging pulse are communicated to the diffuse layer and the bulk of the solution. By this we mean that either the ions require a finite time, *i.e.*, t_p, before they can begin to move, quite analogous to the relaxation times observed in solution, or that they can respond at faster times but that some initial process must be first satisfied. Any consistent model must include the cation dependence and anion and charging current independence of the perturbation times. The process which accepts energy without changing the potential difference across the double layer could involve dipole rotation or orientation, a movement of electrical center of ions in the outer Helmholtz plane, or an electron transfer process with the transfer of an equivalent number of oppositely charged ions out of or into the compact layer (or possibly only the shift of the outer Helmholtz plane), the charge on the electrode remaining effectively constant. These processes are very likely not separable, but for purposes of argument we shall discuss them separately.

From the frequency dependence of the double layer resistance and capacitance at solid electrodes measured by a-c impedance methods, Bockris and coworkers (7, 8) proposed a relaxation time for water dipoles. To explain relaxation times of about 10^{-8} sec on Hg and about 10^{-6} sec on Cu in primarily sulfate solutions, they assumed that water molecules which are adsorbed on the electrode are restricted in motion so that their relaxation time is made large enough for it to fall within the frequency range of measurement. The relaxation of water dipoles at the copper-solution interface was considered as qualitatively resembling that in ice, with a relaxation time of 10^{-3} sec, rather than that in water, 10^{-10} sec. A slow relaxation process in the oriented water layer at charged interfaces has also been proposed from the effects of superimposing an a-c field over a d-c polarizing potential at a dropping mercury electrode (9). Another indication of the times involved in the motion of water dipoles can be taken from water-water exchange rates (10). The substitution rates of the first-hydration-shell water molecules by ligands for alkali-metal cations have been reported for Li^+ as

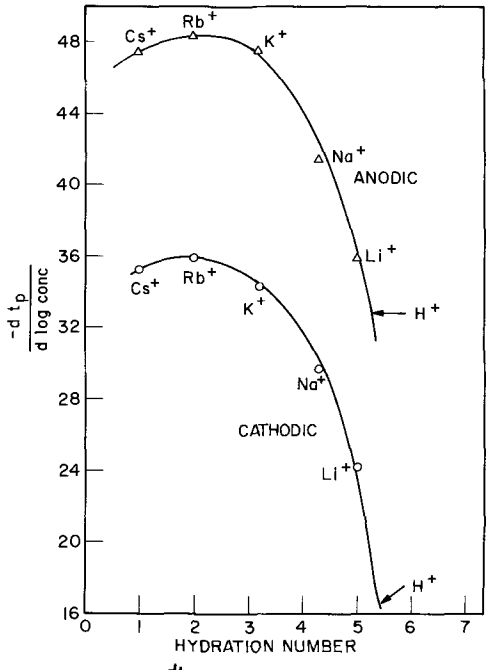

Fig. 8. — $\frac{dt_p}{d \log c}$ vs. hydration number (11).

0.47-9.0 x 10^8/sec and for Cs^+ as 2.1-50 x 10^8/sec. The water molecules held in the first hydration shell, particularly for Li^+, should be somewhat analogous to water oriented in the double layer. It would appear that the times involved for the rotation and orientation of water dipoles in the double layer agree reasonably well with the observed perturbation times. The influence of cations on the perturbation time may be attributed to hydration and to the effect of ordering of the water dipoles in the compact layer by the cations. A correlation of the perturbation times with hydration number (11) is shown in Fig. 8. In this case the change in t_p with concentration has been plotted since this is a constant for each cation. It is interesting to note that if this correlation is correct, the hydration number for H^+ is between 5 and 6. Initially it would appear that the cation effect on t_p is in the wrong direction. For example, following the suggestion of Samoilov (12) that the larger cations (K^+, Rb^+, and Cs^+) have a negative hydration number, *i.e.*, are structure breaking, the rotation of water dipoles would be expected to be easier and thus faster for these cations. However, if we view the process as one which must become saturated, *i.e.*, completed, before double layer charging begins, then the least oriented systems should require more time to become fully oriented. For example, the double layer with Li^+ would be expected to have a more ice-like water structure than a double layer with Cs^+. Thus it should require less time for the dipoles to become completely oriented in the field in the presence of Li^+ since a higher degree of order is already established. Of course the water dipoles adsorbed directly on the Pt surface should be highly oriented at potentials away from the p.z.c. (13, 14), so that the molecules which rotate are possibly in the diffuse layer. This model also explains the concentration dependence. As the solution becomes more dilute, there are fewer ions, resulting in a more loose structure in the double layer and thus longer times are required to completely orient the water dipoles. The similarity in perturbation times for K^+, Rb^+, and Cs^+ are well in agreement with the suggested negative hydration or structure breaking properties of larger cations. Anions, which are not strongly hydrated, would thus not be expected to influence the perturbation times in this model.

The one experimental observation which is completely contrary to this model and which cannot be explained is that of the current independence of t_p. If the process occurring during the transition time is the orientation of dipoles and double layer charging begins when this orientation is essentially complete, *i.e.*, the dielectric is saturated, then t_p would have to depend on the amount of charge flowing into the double layer. Any model which proposes the completion of a process in the compact layer before the double layer begins to charge up must be dependent on charge and hence t_p would have to change with charging current density. For a given system, t_p was found to be independent of the charging current over more than one order of magnitude. The apparent independence of t_p on the reversible potential could also argue against this model. For example, for 1M systems of KI/I_2, KBr/Br_2, and KCl/Cl_2, the reversible potentials differ by about 1v, as seen from the following equilibria (15)

$$3\,I^- = I_3^- + 2e^-, \quad E_o = +0.536v$$

$$2\,Br^- = Br_{2(aq)} + 2e^-, \quad +1.087v$$

$$2\,Cl^- = Cl_2 + 2e^-, \quad +1.3595v$$

It is expected that a shift of potential difference across the double layer would strongly affect the structure of the adsorbed layer and orientation of water dipoles. The possibility does exist that the p.z.c. would shift in such a direction to balance this change in equilibrium potential. Recent determinations of the p.z.c. of Pt in halide solutions using radiotracer methods indicate that the p.z.c. does shift in the positive direction in going from I^- to Cl^- solutions, possibly by as much as 0.7v (16). The change in equilibrium potential could therefore be accompanied by a corresponding shift in p.z.c. such that the double layer structure would not be altered appreciably. In the absence of more detailed information, this point will not be further considered except to indicate that it need not be a serious consideration.

In a recent study, Grantham (17) has concluded that there is a complete absence of relaxation times of water molecules in the double layer in the range 10^{-8}-10^{-2} sec, and attributes the observed frequency dependence of resistance and capacitance to improper electrode design. On the basis of this and other studies (18), Devanathan (5) concludes that water molecules are not oriented in up and down positions (14) but are adsorbed flat and are insensitive to field. This conclusion seems premature with the lack of evidence on a-c frequency variation of the double layer resistance and capacitance at frequencies above about 10^5 c.p.s. on solid electrodes, which is just the range where the relaxation process should become important, and particularly in light of the success which the water dipole model has had in interpreting organic adsorption. On the basis of the previous argument our results suggest that it is not the saturation of dielectric constant as brought about by dipole orientation which determines the perturbation time. However, our results do definitely establish that a perturbation time exists, which may be similar to the frequency variation observed in a-c impedance measurements, and the rotation of dipoles should not be ruled out, even though t_p is not determined by such a process.

A model which permits a t_p independent of charge is based on the specific adsorption of ions, particularly anions. We first postulate, in line with earlier reasoning, that two fundamentally different processes occur, the first of which is the means by which charge is used up without actual charging of the double layer and may include more than one type of process, *i.e.*, dipole orientation, charge transfer, ion movement within solvation sheaths, etc., and a second process which involves the movement of ions into or out of

the compact layer and determines t_p. The first process has been considered on a physical basis and we shall now examine it in greater detail. Following the double layer model of Grahame (6), the charge on the metal will equal the sum of charges in the inner and outer Helmholtz layers and the charge in the diffuse layer

$$-q_M = q_i + q_o + q_d$$

where the q's will be negative for anions and positive for cations. In the presence of specific adsorption, which is expected for the systems examined here, there will be additional charge in the inner layer and hence also in the outer layer to maintain a constant q_M at a given potential difference (with respect to the p.z.c.), *i.e.*, superequivalent or contact adsorption. Thus ions could undergo discharge in the inner layer and a corresponding transfer of oppositely charged ions out of the outer layer, or possibly only a shift of the outer Helmholtz plane, would maintain constant q_M. Charge transfer, which could be a fast process from ions already present in excess in the inner layer, with a corresponding shift of the outer Helmholtz plane could therefore occur while the charge on the metal remains constant and thus energy could be used up without actual charging of the double layer capacitor.

Two cases should be distinguished, one for electrodes positive to the p.z.c., which is the case for most of the equilibrium systems considered here, and one for electrodes negative to the p.z.c., which is probably the case for reversible hydrogen systems on Pt. In the first case, an anodic pulse would require electron transfer from anions specifically adsorbed on the Pt with a simultaneous shift of cations within their hydration sheaths away from the electrode. The actual movement of cations during this time may be suggested, however, in view of the proposal that the perturbation time is determined by the time required for appreciable movement of ions into the double layer, this would seem less likely than the smaller movement of many cations corresponding to a single anion discharge. A cathodic pulse would then require reduction of atoms to anions in the inner layer with a corresponding movement of the outer Helmholtz plane toward the electrode surface. Since the amounts of specifically adsorbed ions become appreciable, particularly for the halide systems (19), this process would not be limited by the charging current in the times under consideration. For the second case, *i.e.*, electrode surface negative to the p.z.c., an anodic pulse would require discharge of atoms to form cations (probably $H \rightarrow H^+ + e^-$) with a subsequent shift of anions away from the electrode. A cathodic pulse would then involve electron transfer to H^+ to form H atoms and movement of anions toward the surface.

Following a recent suggestion by Delahay (20), the amounts of specifically adsorbed ions participating in this process can be examined using the relation

$$q_{measured} = q + \frac{V_{sr}}{V_{sr} + V_{tr}} ZF\Gamma$$

where q is that due to the usual double layer charging process and the other term is due to a Faradaic process, where V_{sr} is the rate of the charge separation process and V_{tr} is the rate of the mass transfer process. During t_p, $q = O$, so that from the charging current and t_p, the surface excess should be obtained directly. For typical values of $i = 1$ amp/cm^2 and $t_p = 100$ nanosec, we obtain $ZF\Gamma_- = 0.1$ μcoul/cm^2, assuming that V_{tr}, the term relating to mass transfer, is zero since mass transfer has not yet begun. This gives a surface excess of $\Gamma_- = 10^{-12}$ g.equiv./cm^2 for anions involved in the Faradaic process and if we assume that cations are pushed out of the double layer, a Γ_+ of 10^{-12} g.equiv./cm^2 would be required. This value compares well with the Γ_+ reported from radiotracer measurements on Pt electrodes for alkali halide systems (16). At high enough current densities, essentially all of the superequivalently adsorbed anions, *i.e.*, those adsorbed in excess of the amount expected on the basis of the charge on the metal surface and hence balanced by cations in the outer Helmholtz plane and the diffuse layers, should be used up in the Faradaic process. Thus at high enough current densities, this should be a method for determining directly the amount of superequivalent or contact adsorption.

This process should not be particularly sensitive to the ions in solution, so long as they are adsorbed in sufficient excess to satisfy the charge requirements during the perturbation time and the rate of electron transfer is sufficiently fast. The cation effect must be explained in terms of the second process, *i.e.*, in terms of the actual movement of ions into or out of the double layer. These two processes should not be viewed as occurring exclusively but that some diffusion will begin during t_p and only when appreciable mass transfer can occur does the potential begin to change. The fact that both processes occur together is seen from the slight curvature in the charging curves between the flat initial region and the linear double layer charging region. The manner in which cations can influence the diffusion process is difficult to see, however, their influence is an experimental fact. The effect of cations is most probably related to hydration and the structure of the solution as already discussed.

Summary

The experimental observations obtained using the discussed short pulse technique are new and perhaps somewhat difficult to accept in light of the commonly accepted concepts of the double layer structure. However, when comparisons are made with well established relaxation times observed in bulk solution, the results appear reasonable. It should be remembered that the results refer to events in the double layer which occur before the charging process and which have not been previously examined. Further, it should be remembered that every effort was made to eliminate instrumental artifacts and we feel that the results presented reflect actual properties of the double layer. The model proposed has limitations but it does essentially account for the experimental observations. Further measurements particularly using doubly and triply charged cations are required before a more detailed model can be proposed. These results tend to confirm the recent suggestion of Delahay that two processes can occur in the charging process, however, they suggest that the Faradaic contribution is less than 1% of the total charge. Finally these results point to the discrete particle nature of the electrical double layer and the method holds real promise for obtaining more detailed information about the structure of the double layer at electrodes.

Acknowledgment

The authors are grateful to Mr. C. H. Presbrey, Jr. for assistance with the electronic circuits and adjustments of the pulse generator.

Manuscript received June 23, 1966.

Any discussion of this paper will appear in a Discussion Section to be published in the June 1967 JOURNAL.

REFERENCES

1. S. Schuldiner and C. H. Presbrey, Jr., *This Journal*, **111**, 457 (1964).
2. C. H. Presbrey, Jr. and S. Schuldiner, *ibid.*, **108**, 985 (1961).
3. S. Schuldiner and R. M. Roe, *ibid.*, **110**, 332 (1963).
4. S. Schuldiner and T. B. Warner, *J. Phys. Chem.*, **68**, 1223 (1964).
5. M. A. V. Devanathan and B. V. K. S. R. A. Tilak, *Chem. Rev.*, **65**, 635 (1965).
6. D. C. Grahame, *ibid.*, **41**, 441 (1947).

7. J. O'M. Bockris, W. Mehl, B. E. Conway, and L. Young, *J. Chem. Phys.*, **25**, 776 (1956).
8. J. O'M. Bockris and B. E. Conway, *ibid.*, **28**, 707 (1958).
9. R. Narayan, V. K. Venkatesan, and K. S. G. Doss, *J. Sci. Industr. Res.*, **20B**, 450 (1961).
10. J. L. Kavanau, "Water and Solute-Water Interactions," Holden-Day, Inc., San Francisco (1964).
11. T. N. Andersen and J. O'M. Bockris, *Electrochim. Acta*, **9**, 347 (1964).
12. O. Ya. Samoilov, *Discussions Faraday Soc.*, **24**, 141 (1957).
13. N. F. Mott and R. J. Watts-Tobin, *Electrochim. Acta*, **4**, 79 (1961).
14. J. O'M. Bockris, M. A. V. Devanathan, and K. Muller, *Proc. Roy Soc.*, **274**, 55 (1963).
15. A. J. deBethune and N. A. Swendeman Loud, "Standard Aqueous Electrode Potentials and Temperature Coefficients at 25°C," C. A. Hampel, Skokie, Ill. (1964).
16. N. A. Balashova and V. E. Kazarinov, *Elektrokhimiya*, **1**, 512 (1965).
17. D. H. Grantham, Ph. D. Dissertation, Iowa State Univ., Ames, Iowa (1962).
18. B. B. Damaskin, *Zhur. Fiz. Khim.*, **32**, 2199 (1958); *Russ. Chem. Rev.*, **30**, 78 (1961); D. C. Grahame, *J. Am. Chem. Soc.*, **68**, 301 (1946); W. Lorenz, *Z. Physik. Chem.*, **26**, 424 (1960); V. I. Melik-Gaikazyan, *Zhur. Fiz. Khim.*, **26**, 560 (1952); V. I. Melik-Gaikazyan and P. I. Dolin, *Doklady Akad. Nauk SSSR*, **64**, 409 (1949).
19. H. Wroblowa, Z. Kovach, and J. O'M. Bockris, *Trans. Faraday Soc.*, **61**, 1523 (1965).
20. P. Delahay, Preprints of Symposium on Electrode Processes, p. 1, Electrochem. Soc. Meeting, Cleveland, May 1966.

Electrochemical Processes in Thin Films

II. Preliminary Quantitative Treatment of Film Stabilization by the Marangoni Effect

E. N. Lightfoot and V. Ludviksson

Department of Chemical Engineering, University of Wisconsin, Madison, Wisconsin

ABSTRACT

This paper is concerned with the mechanism of formation of stable supermeniscus electrolyte films, observed on gas diffusion electrodes. The Marangoni effect associated with surface tension gradients in liquids is considered and found to give film characteristics which are in agreement with many observations made to date. By numerical example it is shown that a temperature gradient of −0.4 C/cm in water or a concentration gradient of 0.035 mole/liter·cm in aqueous KOH solution each can produce a typical liquid film, 1μ thick and unlimited in height. This mechanism is shown to provide more vigorous water recirculation in films than vapor phase transport, and a preliminary unsteady-state analysis is shown to give the right magnitude for the climbing rates observed for the spreading of many hydrocarbons on vertical surfaces. The mechanism is unable to explain effects observed in the absence of concentration or temperature gradients, but apparently could have a pronounced effect under operating conditions of gas diffusion electrodes.

Recently there has been published a number of reports showing experimental evidence for the existence of stable films of electrolyte above the intrinsic meniscus on gas-diffusion electrodes. This evidence has been obtained both by indirect measurements, *i.e.*, measurements of current densities as a function of height above the meniscus (1-5, 8, 13) and by direct observation (6, 7). As yet no satisfactory explanation for the existence of these films is available. Electrocapillary, double-layer and surface-energy-of-formation effects, which are often suggested, appear too weak to produce the observed film thickness (*ca.* 1/20 to 2μ). Gravitational flow, made possible by concentration polarization and vapor phase water transport (9), appears likely in the large scale systems used by Will (1) and others. However, calculations have shown (10) that for such small pore radii as are found in fuel-cell electrodes, vapor transport becomes incapable of supplying even the reactant water needed for such processes as

$$O_2 + 2H_2O + 4e = 4\,OH^-$$

let alone allowing the formation of a flowing film. However, the probable existence of such films in microporous systems has been shown (8) and since all above-cited analyses agree that the thickness of these supermeniscus films has a large effect on electrode performance, a search for better understanding of the film behavior is well justified.

No single known effect appears capable of explaining all observed characteristics of supermeniscus films, and it is possible that such films are produced by some truly novel phenomenon. However, it seems more likely that they are produced by a more or less subtle combination of well known forces, and the probable effects of such forces should be very carefully reviewed before more esoteric ones are sought. The well known Marangoni effect is one possible source of stabilization and is treated in this paper.

As suggested in the first paper of this series (9), surface tension gradients resulting from either temperature or concentration inequalities provide a possible mechanism for water transport and film stabilization. It is the purpose of this paper to give a convenient basis for discussion of this mechanism, and to assess its importance under conditions likely to occur in practical electrochemical devices.

Qualitative Description of Mechanism

From a qualitative standpoint the importance of surface tension gradients in promoting the spreading of liquid films has long been known. Examples of such effects include "tears of strong wine" and the tendency for liquids, such as lubricating oils, to "crawl" out of open containers. The explanation of such phenomena, commonly included in the term "Marangoni effect," was suggested as early as 1855 by Thomson (11). More recently a very convincing demonstration of the nature of what may be called the "oil-can" effect was given by Bascom, Cottington, and Singleterry (12). The basic mechanism both here and in the case of tears of strong wine is the evaporation of one component of a mixture from the upper regions of a meniscus or a surface diffused primary film. If the liquid layer remaining has a higher surface tension than the bulk liquid, then the surface layer, and some

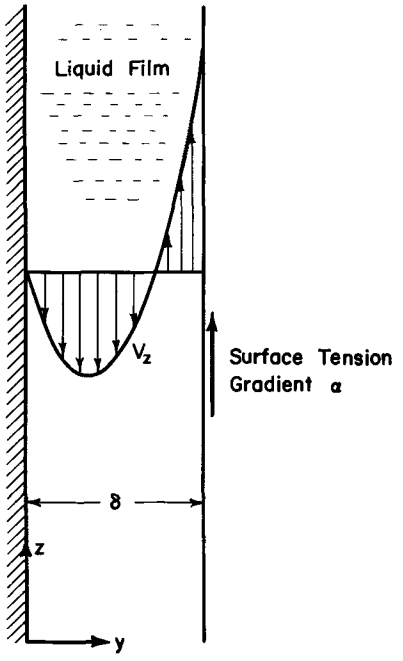

Fig. 1. Liquid film on a vertical, solid surface stabilized by surface tension gradient.

bulk liquid with it will be pulled upward. By analogy, if electrochemical reaction on an electrode can give rise to appreciable surface tension gradients in the upper regions of the meniscus or on a previously wetted electrode, by virtue of concentration or temperature inequalities, then a stable electrolyte film can be maintained or even formed spontaneously as observed by Müller (6). It is our purpose to explore this possibility.

Since, to our knowledge, no quantitative treatment of surface spreading has been attempted we begin by describing a simple model system quantitatively.

Quantitative Description of a Surface Tension Supported Film

For our present purposes it is sufficient to consider steady one-dimensional flow in a thin film on a flat vertical plate as shown in Fig. 1. Extension to a system in which film thickness is appreciable relative to the local radius of curvature is easily accomplished, but gives no further information at the level of the present treatment.

The film behavior is governed by the following relations. (*i*) a momentum balance (the equation of motion); (*ii*) a flux equation (Newton's law of viscosity); (*iii*) a set of boundary conditions.

These relationships may be written in the following form:

$$-\frac{d\tau_{yz}}{dy} + \rho g_z = 0 \qquad [1]$$

$$-\mu\frac{dv_z}{dy} = \tau_{yz} \qquad [2]$$

As boundary conditions we shall use:

$$\text{B.C. 1} \qquad \text{at } y = 0 \qquad v_z = 0 \qquad [3]$$

$$\text{B.C. 2} \qquad \text{at } y = \delta \qquad \tau_{yz} = \tau_0 \qquad [4]$$

Implicit in Eq. [1] to [4] is the assumption of local equilibrium, *i.e.*, the local film behavior is independent of upstream or downstream conditions other than those imposed by the requirement of conservation of mass. This assumption, amply justified by analysis and experiment for the much thicker and faster moving films encountered in steam condensation and elsewhere, should not introduce any appreciable error. Thus, these simple equations are in fact quite general.[1] The second boundary condition permits a nonzero shear stress at the gas-liquid interface. In the special but likely case of negligible velocity gradients in the gas phase, and infinite radius of curvature, this surface stress can be equated to the local surface tension gradient

$$\tau_0 = -\frac{d\sigma}{dz} = -\alpha \qquad [5]$$

We can now easily integrate [1] and [2] to get

$$v_z = \left(\frac{\alpha\delta}{\mu}\right)\eta - \left(\frac{\rho g\delta^2}{\mu}\right)\left(\eta - \frac{1}{2}\eta^2\right) \qquad [6]$$

where $\eta = y/\delta$. Thus, the local velocity profile is parabolic, and as shown in Fig. 1 it may have regions of both negative and positive velocity. The flow average velocity

$$\langle v_z \rangle = \frac{1}{2}\left(\frac{\alpha\delta}{\mu}\right) - \frac{1}{3}\left(\frac{\rho g\delta^2}{\mu}\right) \qquad [7]$$

can clearly either be positive, negative, or zero.

For the common case where μ and ρ do not vary significantly with position, it is convenient to write Eq. [7] in dimensionless form

$$Re = \frac{1}{2}R^2 Mr - \frac{1}{3}R^3 \qquad [8]$$

where $Re = Q/\nu P$, a film Reynolds number and $Q/P = \delta \langle v_z \rangle$ is the volumetric flow rate per unit width of film, $R = \delta(g/\nu^2)^{1/3}$, a dimensionless film thickness; and $Mr = (\alpha^3/\rho^3 g^2 \nu^2)^{1/3}$, a dimensionless group characteristic of films which we call Marangoni number. This Reynolds number *vs.* film thickness relation is plotted in Fig. 2. For positive Marangoni numbers, which give a stable film, there is clearly a flow maximum of

$$Re_{max} = 1/6\, Mr^3 \qquad [8a]$$

when the dimensionless film thickness is equal to the Marangoni number ($R = Mr$). There are also two film thicknesses yielding no flow

$$R = 0 \text{ and } R = 3/2\, Mr$$

Note that so far we have not specified the value of δ, nor can we evaluate its magnitude from the above

[1] For multicomponent systems the fluid velocity must be the mass-average velocity. For these, and for nonisothermal systems, the possible variation of μ across the film requires, in principle, that the equations of energy conservation and continuity of species also be used. However, calculations to be published later have shown that, for the very large length-to-thickness ratios typical of these films, temperature and concentration variation across the film will always be negligible in practice.

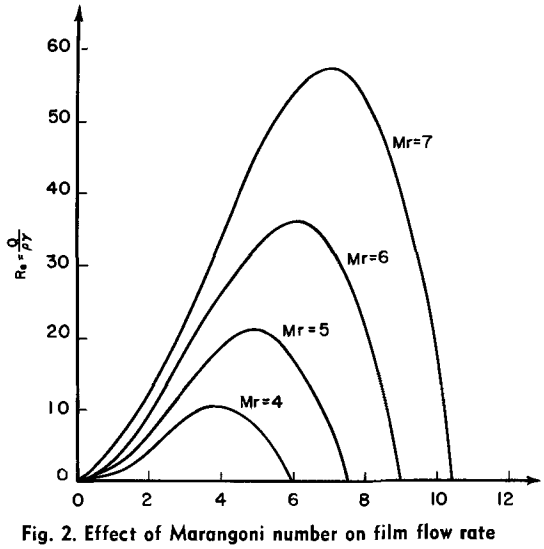

Fig. 2. Effect of Marangoni number on film flow rate

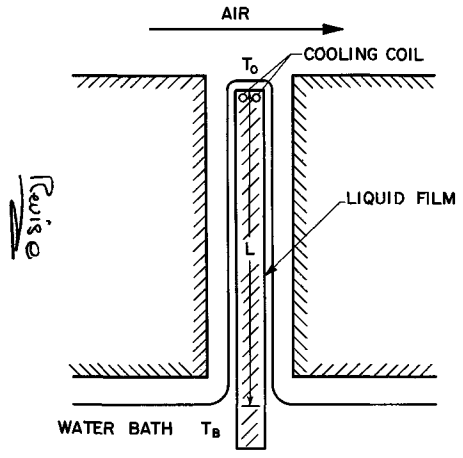

Fig. 3. Vertical plate covered by a liquid film with evaporation possible at the top.

information alone. Therefore, we have to provide one additional restriction. For the purpose of illustration we now consider the slightly more complex system of Fig. 3. We picture here a vertical plate of height L in contact with water at temperature T_B at the lower edge and a cooling device at the top maintaining it locally at a temperature of T_0 where $T_0 < T_B$. On both sides there are closely placed surfaces isolating the system from radiation and convective currents. We now consider some limiting cases.

No net flow in film.—If we assume that the air above the assembly in Fig. 3 is saturated with vapor at T_0, then no evaporation from the film will take place and no net flow of liquid will occur. This means $< v_z >$ must equal zero and now δ is fixed by Eq. [7]

$$\delta_{loc} = \frac{3}{2}\frac{\alpha}{\rho g}$$

since the solution $\delta = 0$ is not physically interesting in our analysis.

As an illustration let us consider a plate 10 cm high and with a temperature difference between bottom and top $T_B - T_0 = 4°C$. Further we let the properties of water be given by $\rho = 1$ g/cc, $\mu = 1$ cp, and $\partial\sigma/\partial T = -0.163$ dyne/cm °C. For this system we expect a nearly linear temperature gradient over the height of the plate with an average value of $dT/dz = -0.4°C/cm$. With the above physical data this gradient will give a film of thickness

$$\delta = \frac{3}{2} \cdot 0.163 \cdot 0.4 \frac{1}{980.1} = 10^{-4}\,\text{cm}$$
$$= 1\ \text{micron}$$

This is of the order of magnitude observed in many electrochemical systems and the temperature gradient of 0.4°C/cm is not unreasonable for many physically interesting situations. The maximum velocity observed is obviously in the surface, and its value provides a measure of the recirculation rate in the film

$$v_{max} = \frac{\alpha\delta}{\mu} - \frac{\rho g \delta^2}{2\mu}$$
$$= \frac{0.163 \cdot 0.4 \cdot 10^{-4}}{0.01} - \frac{1 \cdot 980 \cdot 10^{-8}}{2 \cdot 0.01}$$
$$= 1.64 \cdot 10^{-4}\,\text{cm/sec} = 0.59\,\text{cm/sec}$$

The system thus described is dynamic but steady with the film stabilized by opposition of body and surface forces.

Film with net upward flow.—If the ambient air is unsaturated and evaporation occurs at the top of our wetted plate, then there will be a net upward flow equal to the evaporation rate

$$Q_{Film} = \delta < v_z > P = Q_{evap}$$

where P is the wetted perimeter of the plate. If we neglect vapor phase transport along the film height, which will often be reasonable for small pores (10), Q will not vary with position. For the system under consideration, in which a pure fluid is flowing and T_0 is fixed, evaporation will determine the film thickness until the maximum flow rate is reached. However, for conditions permitting evaporation at a volumetric rate greater than $1/6\ Mr^3\ P_\nu$ (see Eq. [8a]) the supply capacity of the film is reached. Evaporation rate is then controlled by the surface tension-gravity balance and Eq. [8a] applies. At this maximum rate the thickness of the steady state film is given by

$$\delta_{lim} = \left(\frac{\alpha}{\rho g}\right)$$

where δ_{lim} is really that value of δ which corresponds to the smallest maximum flowrate $(Q/\rho)_{max}$ over the film height. For the conditions of the above numerical example $(\alpha/\rho g)$ is essentially constant over the film height and the film thickness providing the maximum volumetric flow is $2/3\mu$. This corresponds to an evaporation rate of $4.83 \cdot 10^{-9}$ cm³/sec cm. The maximum velocity, that of the surface, is 0.785 cm/hr.

If instead of the evaporation process at the top of the film we postulate a long plate with the same temperature gradient, the film will tend to climb up the plate. Such unsteady flows are quite complex and cannot be discussed in detail here. However, a semi-quantitative description can be obtained rather easily (see appendix at the end of paper) if surface curvature of the advancing film is neglected. On this basis it appears that an advancing front moves up the wall at a dimensionless velocity $3/16\ Mr^2$ and with a thickness $3/4\ Mr$. Behind the advancing front the film gradually broadens to a dimensionless thickness Mr corresponding to that for maximum steady flow rate. The speed of the advancing front is about $8 \cdot 10^{-5}$ cm/sec for our illustrative problem, which is very close to the climbing rates of $4 \cdot 10^{-5}$ to $8 \cdot 10^{-5}$ cm/sec observed for many hydrocarbons which give comparable film thickness (12).

It is clearly important to investigate further the dynamics of film formation as well as the much more complex problems associated with electrochemical processes on the wetted surface. In such systems surface tension gradients will result from concentration inequalities (concentration polarization) as well as thermal. These will be treated in future papers of this series.

Discussion

The above simple analysis together with the qualitative but detailed discussion of Bascom, Cottington, and Singleterry (12), provide a picture of stable "Marangoni films" suitable for our present purposes. It only remains to assess their probable importance in electrochemical processes.

First it is important to note that only very small gradients of surface tension are needed to produce films of the thickness believed to exist on electrodes. Thus, it was shown that a few tenths of a degree per centimeter are needed to produce 1μ thick films. Correspondingly small concentration gradients are required for isothermal films, especially for such electrolytes as KOH, the surface tension of which increases rapidly with concentration as shown in Fig. 4. In fact, one can show that for KOH a change in concentration of 0.035 mole/liter/cm of plate height has the same effect as the temperature gradient of −0.4°C/cm in the previous illustrative example.

Second, it should be pointed out that the vertical circulation produced in stable but dynamic films by

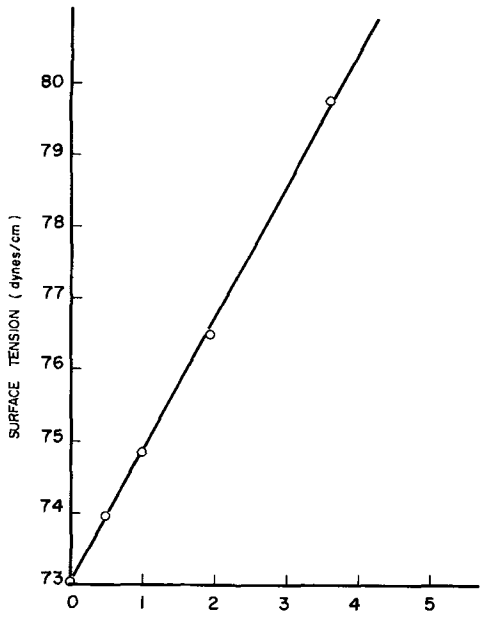

Fig. 4. Surface tension of aqueous solutions of KOH vs. molar concentration.

surface tension gradients tends to reduce concentration polarization in much the same way as the vapor-phase water recirculation predicted for large systems in the first paper of this series. It may therefore provide a further explanation for the small amount of concentration polarization observed in these films to date.

Third, it should be remembered that gravitational influences tend to become small in most electrode structures while surface forces tend to become predominant. Thus, more pronounced surface tension effects can occur, with the primary restraint provided by viscous forces and mass-balance requirements. It seems, therefore, entirely possible that complex dynamic patterns could be obtained in porous electrodes such as those used in ion-exchange membrane cells.

Very little reliable quantitative data are yet available for actual electrochemical operations. However, it may be of interest to compare the results of above equations with typical data of Bennion. He calculates the concentration profile in the film necessary to supply the reaction water by vapor-phase transport. These profiles show gradients from ~0.07 mole/liter cm to 1.0 mole/liter cm. A typical current of 50 μa/cm needs in his estimate a gradient of about 0.55 mole/liter cm at the bottom of the film to supply the reaction water in the area of the fastest reaction rate. At the same time our proposed mechanism requires a gradient of only 0.042 mole/liter cm to supply the reaction water for this value of the current. Thus, the surface tension mechanism is much more powerful than the vapor phase transport mechanism even in large systems.

Despite the rather encouraging agreement with experimental data which these illustrations show, there are still some observations left unexplained by this mechanism. Müller (6) has recently reported the existence of stable films in the apparent absence of surface tension gradients and the growth of a concentrated electrolyte film over a dilute one, apparently against a downward directed surface tension gradient. The explanation of these phenomena can apparently not be found in the Marangoni effect.

However we think the explanation need not necessarily be sought in a previously unknown physical effect but rather in the correct interpretation of already known factors or combination of them. A much more thorough analysis of the Marangoni effect is possible and an unsteady-state analysis is intended.

The dynamic aspects required by the Marangoni effect and the vapor recirculation mechanism for film stabilization can be tested by closer study of the hydrodynamics of supermeniscus films using tracer methods. This paper lays the ground for the interpretation of such experiments.

Although surface tension gradients may not be the only factor determining the film behavior they certainly are likely to arise and have an important effect under operating conditions of a gas diffusion electrode.

Manuscript received Dec. 13, 1965; revised manuscript received June 13, 1966.

Any discussion of this paper will appear in a Discussion Section to be published in the June 1967 JOURNAL.

APPENDIX

Preliminary Analysis of Unsteady-State Behavior

The spreading (*i.e.*, unsteady) behavior of liquid films is quite complex and cannot be described accurately without allowance for surface curvature at the advancing film front. It must, therefore, be left to a later paper. We can, however, demonstrate some important transient film characteristics by the following very simple analysis.

We begin once again with a very simple system: a film initially of zero height and the following assumptions: (*i*) constant surface tension gradient α in the direction of film flow, (*ii*) negligible film curvature; and (*iii*) negligible mass transfer with respect to the vapor phase. Since inertial effects in the film can be safely neglected the film may be described by

$$Re = \frac{1}{2}R^2 Mr - \frac{1}{3}R^3 \qquad (A)$$

$$\frac{\partial R}{\partial \tau} = -\frac{\partial Re}{\partial Z} \qquad (B)$$

At

$$\tau = 0, \quad Z = 0, \quad 0 < R < Mr \qquad (C)$$

Here $\tau = \nu t/L^2$, a dimensionless time, $Z = z/L$, a dimensionless distance from the top of the intrinsic meniscus, $L = (\nu^2/g)^{1/3} = \delta/R$. Equation (B) states the requirement of mass conservation for a nonvolatile film. Equations (A) and (B) are readily combined to obtain a formal relation for film thickness as a function of position and time. For the assumed boundary conditions this relation takes the simple form

$$Z = (R\,Mr - R^2)\tau \qquad (D)$$

Equation (D) is used in Fig. 5 to show calculated film shapes for several times (solid lines). It is seen immediately that the calculated R is a double-valued function of position: a physically meaningless result obtained by neglect of surface curvature. Analogous

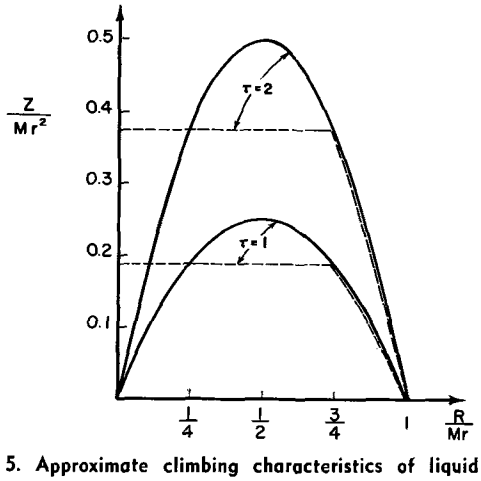

Fig. 5. Approximate climbing characteristics of liquid films

multiple-valued profiles are obtained for concentration waves in fixed sorbent beds when solute dispersion is neglected and for shallow-water waves if viscous dissipation is not taken into consideration.

Just as in these analogous situations a useful asymptotic result can be obtained by replacing the double-valued front by a combination of sharp (or discontinuous) and diffuse portions satisfying the same mass balance. Such an asymptotic front is represented in Fig. 5 for $\tau = 1$ by a heavy dotted line. The position Z_d of the sharp portion of the front, and the film thickness R_d where it meets the diffuse portion, are determined for our boundary conditions by means of the mass-balance relation:

$$\left(\frac{dZ}{d\tau}\right)_d R_d = \int_0^{R_d} \frac{dZ}{d\tau}\, dR \qquad \text{(E)}$$

$$(R_d\, Mr - R_d^2)\, R_d = \int_0^{R_d} (R\, Mr - R^2)\, dR$$

$$= \frac{1}{2} R_d^2\, Mr - \frac{1}{3} R_d^3 \qquad \text{(F)}$$

so that

$$R_d = \left(\frac{3}{4}\right) Mr \qquad \text{(G)}$$

$$Z_d = \frac{3}{16} Mr^2\, \tau \qquad \text{(H)}$$

Thus we find that the film climbs at a steady rate expressed by Eq. (H), and that the advancing front is three-quarters as wide as the steady-state film corresponding to maximum flow rate (see Eq. [8a]). The dimensionless speed $dZ_d/d\tau = 3/16\, Mr^2$, at which this front advances is just slightly in excess of the dimensionless average velocity $Re_{max}/R_{max} = 1/6\, Mr^2$ of the steady film at maximum flow. However, it is also important to note the final thickness of the climbing film $R_{max} = Mr$ is only approached asymptotically for $\tau/Z \to \infty$ as seen from Eq. (D).

These conclusions are probably sound even though they are based on an incomplete model of the film front. The correspondingly idealized description of concentration waves has, for example, been shown to be: (*i*) a proper limiting solution for large τ/Z (14),(*ii*) a useful engineering approximation (15). Equations (G) and (H) can then most probably be considered useful approximations for the large length-to-thickness ratios of postulated electrochemical films.

REFERENCES

1. F. G. Will, *This Journal*, **110**, 145 (1963).
2. F. G. Will, *ibid.*, **110**, 152 (1963).
3. E. A. Grens, R. M. Turner, and T. Katan, *Advanced Energy Conversion*, **4**, 109 (1964).
4. D. N. Bennion and C. W. Tobias, *This Journal*, **113**, 589 (1966).
5. D. N. Bennion, Ph.D. Thesis, University of California, Berkeley, Calif., June 1, 1964.
6. R. H. Müller, *This Journal*, **113**, 943 (1966).
7. R. H. Müller, *ibid.*
8. T. Katan, S. Szpak, and R. A. Botosan, "Development of Improved Electrodes for Fuel Cells," Prepared under Bureau of Naval Weapons Contract NOw 64-0597-f. May, 1965.
9. E. N. Lightfoot, *This Journal*, **113**, 614 (1966).
10. V. Ludviksson and E. N. Lightfoot, Unpublished calculations.
11. J. Thomson, *Phil. Mag.*, **10** (4th ser.), 330 (1855).
12. W. D. Bascom, R. H. Cottington, and C. R. Singleterry, *Adv. Chem. Ser.*, **43**, 355 (1964).
13. H. J. R. Maget and R. Rothlein, *This Journal*, **112**, 1034 (1965).
14. S. Goldstein, *Proc. Royal Soc. (London)*, **A219**, 151, 171 (1953).
15. E. N. Lightfoot, R. J. Sanchez-Palma, and D. O. Edwards, "New Chemical Engineering Separations Techniques," H. M. Schoen, Editor, p. 83, Interscience Publishers, New York (1962).

Technical Notes

Automatic Registration of Electrolyte Specific Gravity in Lead-Acid Batteries

Jeanne Burbank

U. S. Naval Research Laboratory, Washington, D. C.

and Emmanuel Goldstein[1]

Quanta Laboratories Incorporated, Falls Church, Virginia

The refraction of light is a fundamental property of matter and a manifestation of the interaction of electromagnetic radiation with the electrons belonging to atoms, ions, and molecules. The laws of refraction are well known, and numerous basic studies are available; only a few representative articles and reviews are cited for examples here (1-8). Refractive index is the ratio of the speeds of light in two media, and tables giving these indices for various pure liquids, gases, many solids, and solutions list the speed in the given material relative to air or vacuum as a standard (9, 10).

For determination of the refractive index of liquids, a small sample is sometimes removed from the bulk material and the index measured by visual observation with a refractometer. Continuously recording instruments are available, but their application has usually been limited to pipelines and processing tanks handling large volumes of a single material. Several are described as research instruments (2, 5, 11-20).

Measuring the refractive index is relatively so simple and the amount of sample required so small that these determinations may be used as an alternative to density or specific gravity measurements (2, 11, 12). It is frequently desired to monitor the specific gravity of a solution during the course of a production operation, and a continuously recording refractometer may be used conveniently for this purpose under suitable conditions.

It is common practice to follow changes in specific gravity of the sulfuric acid electrolyte in the lead-acid cell. The "over-riding importance" of this as-

[1] Present address: Alpha Micro-Optics Company, Beltsville, Maryland.

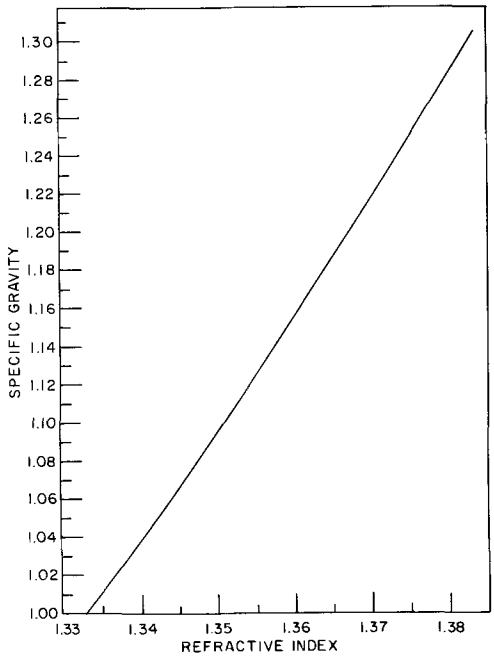

Fig. 1. Relation of specific gravity and refractive index of aqueous H_2SO_4 solutions at 20°C (10).

pect of the behavior of the lead-acid battery has recently been emphasized by Robinson and Heinson (21). Specific gravity gives an indication of the condition as well as the state of charge of the cell, and the end-of-charge is determined by constancy in the readings. For these determinations, small samples of electrolyte are usually removed periodically by hand, and the specific gravity determined by hydrometer. In large batteries, the specific gravity is measured only on selected pilot cells because of the excessive time and labor required to sample each individual cell.

The reaction of the lead cell is usually written

$$PbO_2 + Pb + 2H_2SO_4 = 2PbSO_4 + 2H_2O$$
$$\text{charge} \longleftrightarrow \text{discharge}$$

and Vinal (22) presents a full description of the electrolyte and the variation of specific gravity with the state of charge of the cell. Figure 1 shows the relation of specific gravity to refractive index of aqueous H_2SO_4 solutions throughout the concentration range employed in batteries (3, 10, 23-25), and clearly indicates that refractive index may be used to follow changes in specific gravity of the electrolyte in the lead-acid battery.

It was to fill the need of a simple inexpensive continuously recording device to monitor the electrolyte in individual cells of large batteries that the present work was undertaken; however the instrument described is not limited to this use and was originally developed for other applications (26).

The Instrument and Its Use in a Battery

A compact inexpensive dipping refractometer was fashioned from a U-shaped rod, the two ends of which were sealed in a mounting head. The head may be of a suitable material and geometry to fit as a plug in any desired container, and the length of the probe is chosen so that the rod is partially or totally immersed in the liquid being monitored. Within the mounting head a miniature light source and photodetector were located at either end of the tubulation. The amount of light falling on the detector depends on the loss through the walls of the rod, which in turn is a function of the indices of refraction of the material of the rod and the medium surrounding it. The rod is chosen so that its index of refraction is greater than that of the medium it is used to monitor. Any change in refractive index of the surrounding medium results in a change in the critical angle of total internal reflection for the light traveling through the rod and, therefore, in the amount of radiation falling on the photodetector. The sharp radius of curvature at the tip of the probe produces an area particularly sensitive to changes in refractive index of the medium. The signal output from the photodetector may be readily converted by conventional instrumentation for registration on standard recorders.

To illustrate the application of this instrument to lead-acid battery monitoring, the probe was fabricated from glass rod, the light source and photodetector circuit were powered from an external battery, the photodetector replacing one arm in a bridge circuit. The bridge imbalance was sensed by a Keithley electrometer amplifier-microammeter. The output of this device fed a standard L&N 20-mv multipoint recorder. Initial bridge balance for a null was accomplished by variable resistive arms in the bridge circuit. A number of cells could be monitored at one time by using a probe and bridge circuit for each cell, and a nonshorting switch to scan the cells, connected to a recorder through a coupling circuit, if necessary. The instrument may be modified for internal calibration and temperature compensation.

A commercial 30 amp-hr cell was used in this work. The cell was charged and the specific gravity adjusted to 1.257. A small hole was drilled in the cell top and the probe partially submerged in the electrolyte at the edge of the element. The cell was cycled at the 4- and 8-hr rates. During the cycling, samples of electrolyte were temporarily removed at intervals and the specific gravity measured by conventional methods. The probe was calibrated by preliminary submersion in a series of standard sulfuric acid solutions. The tests described here were carried out at room temperature. A small sheet of polyethylene was placed in the cell between the probe and the cell element to serve as a deflector for gas bubbles for some of the tests.

Results and Discussion

A photograph of a section of recorder chart showing the registration of the change in refractive index and cell voltage for a capacity discharge of the cell is shown in Fig. 2. A comparison of this recording with the usual plot of specific gravity readings taken during such a discharge (22) shows that the two are indistinguishable. At the end of a charge when the negative plates began to gas vigorously, the refractometer readings became erratic owing to the hydrogen bubbles in the electrolyte. This was eliminated by placing the plastic sheet between the element and the probe to shield it from direct impingement of the bubbles.

Several interesting phenomena were observed during this work, which suggest that this instrument or

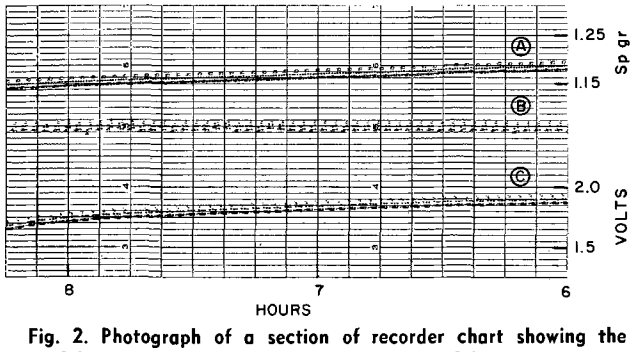

Fig. 2. Photograph of a section of recorder chart showing the final 2.25 hr of a capacity discharge at the 8-hr rate at room temperature. A, Specific gravity (refractive index); B, discharge current, 5 amp; C, cell voltage.

modifications of it may be useful for more fundamental electrochemical investigations. The lead-acid cell used for this test contained no provision for stirring the electrolyte, and during charge as the positive plates began to gas significantly, before the negatives finished, the refractive index passed through a maximum. As the charge continued, the specific gravity decreased again as mixing took place and ultimately rose to the final and constant value. These effects are attributed to oxygen bubbles carrying high density electrolyte to the top of the cell from the reaction of charge at the positive plate. This was followed by a second rise as the negative plates finished charge and began to gas freely, and ultimately by a leveling off as the electrolyte became thoroughly mixed. The rates of these changes might be used, under suitable experimental conditions, to measure the difference in rates of charge of the positive and negative plates, and in diffusion rate studies.

Immediately on application of the charge or discharge current, the indicator showed a transitory response that may merit further investigation. It is possible that the deflection was caused by differences in the rates of response of the anions and cations to the application of the electric field. The response time of the device is essentially limited only by the time constant of the photodetector and its associated circuitry. Capillary probes may be used, and the sensitive tip placed in close proximity to an electrode surface, within the diffusion layer. This suggests its possible use for estimating concentration gradients near the surface of an electrode, supplementing Schlieren, interferometric, and analytical techniques (27-29).

Manuscript received June 22, 1966; revised manuscript received Sept. 1, 1966. This paper was presented at the Philadelphia Meeting, Oct. 9-14, 1966.

Any discussion of this paper will appear in a Discussion Section to be published in the June 1967 JOURNAL.

REFERENCES

1. J. R. Partington, "An Advanced Treatise on Physical Chemistry," Vol. IV-Physico-Chemical Optics," Section X parts A and D., Longmans, Green and Co., New York (1953).
2. L. W. Tilton and J. K. Taylor, "Physical Methods in Chemical Analysis," 2nd rev. ed., G. W. Berl, Editor, Vol. I, p. 412, Academic Press, New York (1960).
3. K. Fajans, H. Kohner, and W. Geffcken, *Z. Elektrochem.*, **34**, 1 (1928).
4. A. Heydweiller, *Phys. Z.*, **26**, 526 (1925).
5. A. Fink, *Osterr. Chem. Ztng.*, **55**, 93 (1954).
6. C. A. Clemens, *Ind. and Eng. Chem.*, **13**, 813 (1921).
7. O. Bryngdahl, *Acta Chim. Scand.*, **11**, 1017 (1957).
8. G. Spacu and E. Popper, *Z. Physik. Chem.*, **B25**, 460 (1934).
9. Landolt-Börnstein, Physikalisch-Chemische Tabellen II Erg. Vol. 2, 1931.
10. "Handbook of Chemistry and Physics," 46th ed., p. D 127, The Chemical Rubber Co., Cleveland (1965-1966).
11. T. R. P. Gibb, Jr., "Optical Methods of Chemical Analysis," 1st ed., Chap. VII, p. 319 ff, McGraw-Hill Book Co., Inc., New York (1942).
12. J. Reilly and W. N. Rae, "Physico-Chemical Methods," 4th ed. revised, Vol. II, p. 224 ff., Methuen and Co. Ltd. London (1943).
13. S. Claesson, *Arkiv Kemi. Mineral. Geol.*, **23A**, 1 (1946).
14. P. Donzelot and G. Gamus, *Compt. rend.*, **224**, 336 (1947).
15. D. Zaukelies and A. A. Frost, *Anal. Chem.*, **21**, 743 (1949).
16. H. E. Jones, L. E. Ashman, and E. E. Stahly, *ibid.*, **21**, 1470 (1949).
17. G. R. Thomas, C. T. O'Konski, and C. D. Hurd, *ibid.*, **22**, 1221 (1950).
18. N. R. Trenner, C. W. Warren, and S. L. Jones, *ibid.*, **25**, 1685 (1953).
19. D. J. Fraade and O. D. Larison, *ISA Journal*, **6**, 34 (1959).
20. L. E. Maley, *ISA Trans.*, **1**, 245 (1962).
21. R. G. Robinson and J. T. Heinson, "Batteries 2," D. H. Collins, Editor, p. 407, Pergamon Press, New York (1965).
22. G. W. Vinal, "Storage Batteries," 4th ed., John Wiley & Sons Inc., New York (1955).
23. V. H. Veley and J. J. Manley, *Proc. Roy. Soc.*, **76A**, 469 (1905).
24. A. Hantzsch and F. Durigen, *Z. physik Chem.*, **136**, 1 (1928).
25. H. Kohner and M. L. Gressmann, *ibid.*, **A144**, 137 (1929).
26. E. Goldstein, "A Refractive Liquid Level Sensor," in preparation.
27. A. Brenner, *Proc. Am. Electroplaters' Soc.*, **1941**, 28.
28. N. Ibl, Y. Barrada, and G. Trumpler, *Helv. Chim. Acta*, **37**, 583 (1954).
29. L. Stephenson and J. H. Bartlett, *This Journal*, **101**, 571 (1954).

Blue Luminescence in Calcium Chlorovanadates

M. A. Aia and Paul Lublin

The Bayside Laboratory, Research Center of
General Telephone & Electronics Laboratories Inc., Bayside, New York

Reports on luminescence in the vanadates of calcium have been widely scattered and inconsistent, probably owing to the scarcity of definitive x-ray diffraction data on the alkaline earth vanadates. The phase diagram for CaO-V_2O_5 shows 3 phases, $CaO \cdot V_2O_5$, $2CaO \cdot V_2O_5$, and $3CaO \cdot V_2O_5$ (1). In 1926 Robl (2) reported reddish-brown photoluminescence for $Ca_2V_2O_7$. A few years later Schloemer (3) reported very weak red luminescence for CaV_2O_6. In an extensive study of alkaline earth vanadates Rothschild (4) observed no measurable luminescence in either $Ca_2V_2O_7$ or $Ca_3(VO_4)_2$. Brixner and co-workers (5, 6) were the first to prepare large crystals (monoclinic) of $Ca_3(VO_4)_2$ suitable for structural studies, but these were not luminescent at room temperature. European patents (7, 8) have disclosed luminescence in the halovanadates of Sr, Ba, Mg, and Zn, but not those of Ca. Kotera and Sekine (9) have reported strong blue luminescence under 2537Å excitation in what they reported was $Ca_2V_2O_7$, although they added large excesses of CaO, as well as 3% by weight NH_4ClO_4, before firing. We prepared $Ca_2V_2O_7$, but observed no measurable luminescence at room temperature; in agreement with Rothschild (4). However, we did observe bright blue luminescence in calcium chlorovanadates under excitation by short-wave ultraviolet light. We found that all of our luminescent compositions contained $Ca_5Cl(VO_4)_3$ with the hexagonal structure of the well-known phosphate mineral, apatite.

Experimental

Luminescent calcium chlorovanadates were prepared by heating mixtures of high-purity $CaCO_3$, NH_4VO_3, and $CaCl_2$ (100-200% excess Cl) in covered silica crucibles for up to 20 hr in air at 450°C, followed by mortaring and refiring at 1000°C for 1 hr. Calcium chlorovanadates of lower brightness were

prepared by heating nonluminescent, chloride-free calcium orthovanadates with Ca/V mole ratios $\geqq 1.67$ in a dried stream of 10% HCl — 90% O_2 for 1 hr at 800°C. X-ray diffraction analysis confirmed the formation of the apatite structure. At higher temperatures, or in the absence of O_2, large quantities of vanadium chlorides were volatilized, leaving black, nonluminescent residues. Similar problems occurred when NH_4Cl was used as the source of chloride in the air-firing process. We also prepared $Ca_5F(VO_4)_3$ with the apatite structure and found no visible luminescence at room temperature or at liquid nitrogen temperature.

X-ray diffraction data were obtained from a calibrated Philips-Norelco Diffractometer, using Ni-filtered CuKα radiation and scanning at 1°/min. Photoluminescence data were obtained in the region 200-700 nm on an Aminco-Bowman spectrophotofluorometer using a xenon lamp as the source and an RCA 1P28 or 6217 photomultiplier as the detector. Cathodoluminescence was tested in a demountable cathode-ray tube operated at a 15-kv accelerating potential and a 0.5 $\mu a/cm^2$ anode current density on the phosphor screen. The phosphor was settled at 5 mg/cm^2 on 1 x 1 in. plates of Corning EC (electrically conducting) glass.

Structural Studies.—Klement and Harth (10) prepared calcium halovanadates with the apatite structure from melts of NaCl, NaBr, and NaI, but did not give data on either the luminescence or the cell parameters for these compounds. The d-spacings and relative intensities of $Ca_5Cl(VO_4)_3$ differ considerably from those of the corresponding chlorophosphate due to the larger a unit-cell dimension of the chlorovanadate and to the greater scattering power of V *vs.* P. Lattice parameters of both the fluorovanadate and chlorovanadate of Ca are compared to those of the corresponding phosphates in Table I. The parameters were determined by the method of least squares.

It is not yet known whether the same structural differences that exist between the chloro and fluorophosphates (13) also exist between the chloro and fluorovanadates.

We prepared chlorovanadates and fluorovanadates of Sr and Ba and found that these also had the apatite structure, with larger lattice parameters than those of the corresponding calcium vanadates. The results will be presented in a more comprehensive report on x-ray diffraction studies of group II vanadates.

Luminescence studies.—The blue emission band of calcium chlorovanadate is similar to that of $CaWO_4$ (14) although slightly narrower. The emission under short uv extends from approximately 340 to 590 nm and peaks at 445 nm, as compared to $CaWO_4$ which peaks at 450 nm. It is known that the true emission peak for $CaWO_4$ is close to 425 nm; hence the true emission peak for calcium chlorovanadate probably lies near 420 nm. The excitation band is also broad (220-380 nm), and overlaps that of the emission band. Peak excitation was obtained near 305 nm as compared to 274 nm for $CaWO_4$, which is consequently much brighter under 2537Å light. The absolute values of the excitation peaks are in doubt because the apparent excitation curves were not readily corrected for the varying output of the xenon source as the range 200-400 nm was scanned. Unlike $CaWO_4$, the chlorovanadates exhibited only very weak blue emission when excited by cathode rays.

The intensity of photoluminescence, as well as the structure of the material, was considerably influenced by the Ca/V mole ratio of the chlorovanadate phosphors and best results were obtained when excess $CaCO_3$ was added, as shown in Table II. The brightest phosphor (Ca/V = 2.5) actually consisted of 3 phases which were present in the following amounts by weight: $Ca_5Cl(VO_4)_3$ about 50%, $Ca_3(VO_4)_2$ about 40%, CaO about 10%. On a molar basis the CaO content was close to 25%. The $Ca_3(VO_4)_2$ was identified by comparing the d-spacings to those we obtained from a single crystal.[1] Similar samples prepared without chloride did not exhibit either luminescence or apatite structure until they were refired in an atmosphere of 10% HCl —90% O_2 at 800°C. In no case was $CaCl_2$ or its hydrates detectable by x-ray diffraction analysis. Because neither the excitation nor the fluorescence peaks for photoluminescence shifted detectably with the appearance of free CaO in the x-ray diffraction patterns, the luminescence appears to originate in the vanadate groups and not in the CaO. This was confirmed by experiments, in which CaO was leached out with dilute HCl without loss in brightness.

The brightness of samples containing free CaO was found to deteriorate on prolonged standing in ambient air. Concurrently, the formation of $Ca(OH)_2$ was detected by x-ray diffraction. The free CaO seemed to be leached out with 2% HCl solution, as evidenced by the disappearance of the intense diffraction lines at d = 2.40 and 1.70Å. However, an even more intense line at d = 2.77Å was not affected. Furthermore, the HCl treatment sometimes caused the surface of the white powders to turn yellow and in no case improved the initial brightness significantly. The persistent, intense line at d = 2.77Å is puzzling since it was not observed in either pure $Ca_5Cl(VO_4)_3$ or $Ca_3(VO_4)_2$ and was believed due entirely to CaO, in which case it should have been diminished by the HCl treatment.

Despite the proximity of the ionic radius of Mn^{2+}, Tb^{3+}, or Ho^{3+} to that of Ca^{2+}, it was not possible to obtain efficient emission at room temperature by adding $MnCl_2$, Tb_2O_3, or Ho_2O_3 to the calcium chlorovanadates even when Na^+ was added (as NaCl) for charge compensation. The results were somewhat better with Eu_2O_3 doping. The range 0.04-0.16 mole Eu per mole $Ca_5Cl(VO_4)_3$ was investigated; both the blue host emission and the characteristic red Eu^{3+} emission were obtained, the former in lowest yield and the latter in highest yield at 0.04 Eu (1% by wt). As with many other self-activated phosphors, the

[1] Single crystals kindly supplied by L. H. Brixner of the DuPont Laboratories.

Table I. Comparison of unit-cell sizes of halovanadates and halophosphates of calcium

Apatite* compound	a, Å	c, Å	c/a	Ref.
$Ca_5Cl(VO_4)_3$	10.16	6.79	0.668	This work
$Ca_5Cl(PO_4)_3$	9.63	6.78	0.704	(11, 12)
$Ca_5F(VO_4)_3$	9.67	7.01	0.725	This work
$Ca_5F(PO_4)_3$	9.37	6.88	0.735	(13)

* 2 molecules per unit-cell; the hexagonal space group of apatite is $P\ 6_3/m = C^2_{6h}$.

Table II. Effect of Ca/V mole ratio on intensity of photoluminescence and structure of calcium chlorovanadates (Cl/V mole ratio = 1.0)

Mole ratio Ca/V	Relative intensity* at 445 nm (τ_X = 305 nm)	Phases found (x-ray diffraction)
1.67 (theor.)	18	$Ca_5Cl(VO_4)_3$
2.0	87	$Ca_5Cl(VO_4)_3$ + $Ca_3(VO_4)_2$** + CaO
2.5	105	Ditto but more CaO
3.0	60	Ditto but still more CaO

* Intensities are given *vs.* $CaWO_4$ (Sylvania No. 2402) excited at λ = 274 nm where the power output of the xenon source was less than at 305 nm.

** The 4 more intense x-ray diffraction lines for monoclinic $Ca_3(VO_4)_2$ in the range 4-90 degrees 2θ occur at d = 3.307 (25), 2.943 (100), 2.832 (20), and 2.698Å (50). Relative intensities are given in parentheses.

intensity of photoluminescence in all the calcium chlorovanadates prepared, doped or undoped, was much higher at liquid nitrogen temperature than at 25°C. For example, at 77°K, the respective emissions of Tb^{3+} (yellow-green) and Ho^{3+} (blue-green) were clearly visible in samples doped with the appropriate rare earth oxide, although at room temperature no luminescence at all was seen under uv excitation.

We prepared $Sr_5Cl(VO_4)_3$, $Sr_5F(VO_4)_3$, $Ba_5Cl(VO_4)_3$, and $Ba_5F(VO_4)_3$ powders with the apatite structure and found they were efficiently excited by long-wavelength uv, as might be expected (8). The excitation peak for all four of these compounds was in the wavelength region 338-348 nm; the emission from the strontium vanadates was bright yellow-white at room temperature while that from the barium vanadates was bright green-white. These phosphors were also much brighter when reduced to the temperature of liquid nitrogen.

Discussion and Conclusions

It is significant that chloride is essential in the preparation of luminescent calcium vanadates since, without it, the apatite structure is not formed. There is little doubt that the blue luminescence arises in the tetrahedrally coordinated VO_4 groups of $Ca_5Cl(VO_4)_3$ and that the process is critically affected by the local site symmetry. For example, there is no visible fluorescence in $Ca_5F(VO_4)_3$ which may have a slightly different structure. It now seems possible that the blue-emitting materials prepared by Kotera and Sekine (9) actually contained $Ca_5Cl(VO_4)_3$ since all the essential ingredients were present in their procedure. A large influence of the cations (*i.e.*, Ca^{2+}, Sr^{2+}, or Ba^{2+}), as well as the halide ions on the luminescence in halovanadates with the apatite structure has also been suggested by the present work.

Acknowledgment

The authors wish to thank J. T. Ragusin and A. Calvano for their help in performing the experiments and analyses.

Manuscript received May 17, 1966; revised manuscript received Aug. 1, 1966.

Any discussion of this paper will appear in a Discussion Section to be published in the June 1967 JOURNAL.

REFERENCES

1. A. N. Morozov, *Metallurg.*, **12**, 21 (1938); $CaO-V_2O_5$ phase diagram reproduced by R. Kohlmuller and J. Perraud, *Bull. Soc. Chim. France*, **1964**, 642.
2. R. Robl, *Z. angew Chem.*, **39**, 608 (1926).
3. A. Schloemer, *J. prakt. Chem.*, **133**, 51 (1932).
4. S. Rothschild, *Br. J. Appl. Phys.*, Suppl. **4** S32 (1955).
5. L. H. Brixner, P. A. Fluornoy, and K. Babcock, *This Journal*, **111**, 873 (1964).
6. L. H. Brixner and P. A. Fluornoy, *ibid.*, **112**, 303 (1965).
7. K. T. Wilke and H. Kotschy, Czech. Pat. 102, 182 (1962).
8. H. F. Ward and P. Chambers, Brit. Pat. 946,073 (1964).
9. Y. Kotera and T. Sekine, *Bull. Chem. Soc. Japan*, **27**, 13 (1954).
10. R. Klement and R. Harth, *Chem. Ber.*, **94**, 1452 (1961).
11. X-Ray Powder Data File, Am. Soc. Testing Mater., Philadelphia, Card No. 12-263 (1964).
12. A. N. Akhavan-Niaki, *Ann. Chim.* (*Paris*), **6**, 51 (1961).
13. R. W. Mooney and M. A. Aia, *Chem. Revs.*, **61**, 433 (1961).
14. F. A. Kroeger, "Some Aspects of the Luminescence of Solids," Elsevier Publishing Co., New York (1948); available as Out of Print Book from University Microfilms, Inc., Ann Arbor, Michigan.

The System $PbNb_2O_6$ and Its Bearing on the Growth of Single Crystals of the Ferroelectric Polymorph

V. G. Hill and R. I. Harker

Tem-Pres Research, Incorporated, State College, Pennsylvania

Lead metaniobate exists as tetragonal, rhombohedral, and orthorhombic polymorphs. Francombe (1) and Roth (2, 3) showed that the orthorhombic modification, which was first discovered by Goodman (4) is metastable at atmospheric pressure. Francombe also reported that the most stable low temperature phase was the rhombohedral polymorph, which transforms at 1200°-1250°C to the tetragonal form. The orthorhombic polymorph is a ferroelectric material with a Curie point of 560°C (5). It is unique among the structures which contain a highly polarizable ion with a noble gas electronic configuration, in that it is not pseudo-cubic. Good single crystals of this polymorph are desirable for electronic studies and devices because polycrystalline materials are neither reliable nor as strongly ferroelectric.

Polycrystalline samples are obtained by firing at temperatures above 1250°C. Columnar crystals 2-3-mm in length have been obtained by heating the material above 1350°C and then crystallizing the melt by slow cooling (1). In both cases, the tetragonal polymorph was formed stably at high temperatures, preserved metastably on cooling, and prevented from passing through a rather sluggish inversion to the stable rhombohedral form. The resultant material then passed through the enantiotropic inversion to the ferroelectric, metastable orthorhombic form.

No data was found in the literature on the effect of pressure on the stability relations of the orthorhombic form. The calculated specific gravities of the orthorhombic, tetragonal, and rhombic polymorphs are 6.7, 6.5, and 7.3, respectively. On the basis of these figures, and disregarding the effect of temperature, increasing pressure might be expected to increase the stability field of the rhombohedral polymorph at the expense of the tetragonal polymorph. However, considering the metastable equilibrium similarly, pressure might be expected to increase the field of the orthorhombic form relative to the tetragonal form. It was argued that if the latter consideration prevailed, then high pressure techniques might be used to grow large crystals of the ferroelectric form. An alternative growth method might also be indicated by the phase relations.

Starting Materials and Equipment

The phase relationships in the system were determined using (*a*) externally heated cold seal test tube vessels of Stellite or René in conjunction with a Tem-Pres Model HR-1B-4 hydrothermal unit (6, 7, 8), (*b*) internally heated hydrostatic pressure apparatus, Tem-Pres Model PV-3C-2 (7), and (*c*) eternally heated uniaxial pressure device, Tem-Pres Model SJ-100 (9). The sample, and a small amount of water or other solvents where necessary, were sealed in gold or platinum tubes for reaction in the first two

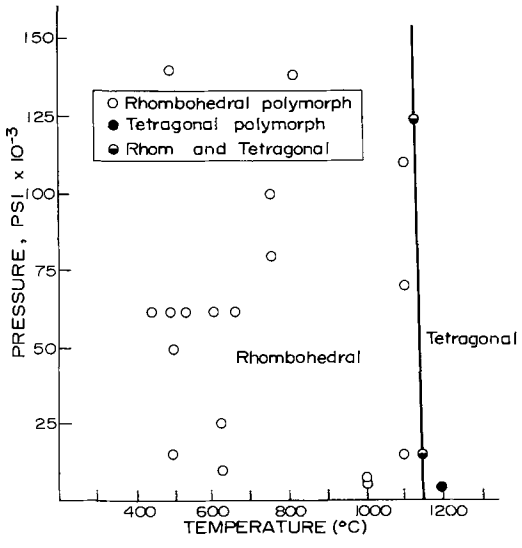

Fig. 1. Phase diagram of the system $PbNb_2O_6$

units. In the uniaxial press, the sample was a small wafer surrounded by a nickel ring sandwiched between platinum foil disks, and pressed between the faces of carbide anvils. The duration of the runs varied, depending on the conditions employed. Runs were from half an hour, when very high pressure and high temperature runs were made, to about two weeks for runs at the lowest temperatures and pressures. Runs made at atmospheric pressure in platinum wound quench furnaces were on samples sealed in 2.5 or 5 mm diameter platinum tubes to prevent changes in the compositions of mixtures due to volatilization of lead.

Phases were identified by x-ray diffraction methods, supplemented with the petrographic microscope.

The starting materials used were: (*i*) Stoichiometric mixture of PbO and Nb_2O_5: This mixture was prepared by grinding the weighed amounts of the two previously dried oxides under acetone for about 2 hr. (*ii*) Polycrystalline rhombohedral $PbNb_2O_6$: This was prepared by heating the stoichiometric mixture to 1000°C for about 1 hr in a sealed platinum tube. (*iii*) Polycrystalline orthorhombic $PbNb_2O_6$: This was prepared by firing the rhombohedral form at 1250°C in a sealed platinum tube for 1 hr.

Experimentation and Results

Figure 1 shows the stability relations among the phases in the system $PbNb_2O_6$ as determined in this work. The orthorhombic form has no stability field in the p-t range studied. When the mixed oxides were used as starting material a mixture of rhombohedral $PbNb_2O_6$, a pyrochlore type compound (probably $3PbO \cdot 2Nb_2O_5$), and orthorhombic $PbNb_2O_6$ were formed below 500°C and pressures over 50,000 psi. The orthorhombic $PbNb_2O_6$ obtained was probably a solid solution containing excess Nb_2O_5. The $3PbO \cdot 2Nb_2O_5$ phase and orthorhombic $PbNb_2O_6$ formed metastably in runs of a few days, but rhombohedral $PbNb_2O_6$ resulted when the duration of the run exceeded seven days.

On the basis of the data obtained, the only possibility of obtaining single crystals of the orthorhombic form is by metastable transformation. This approach introduces the problem of avoiding the sluggish transformation to the stable rhombohedral polymorph. There is also the problem of going through the tetragonal-orthorhombic transformation without damaging the crystal extensively. A study was therefore made of the effects of dopants on both the tetragonal-rhombohedral and tetragonal-orthorhombic transformations. It was found that the addition of up to 4% ZrO_2 or TiO_2 did not affect the equilibrium phase relations shown in Fig. 1, but had a marked effect of decreasing the rate of inversion when the reaction was done "dry." Under "wet" or hydrothermal conditions the rate of this inversion to the rhombohedral form was increased by the dopants and the doped orthorhombic polymorph easily inverted to the rhombohedral polymorph in its stability field.

Since it was not possible to stabilize the orthorhombic polymorph by using dopants, the tetragonal-orthorhombic inversion was studied to determine if crystal damage could be minimized. The D.T.A. curve for orthorhombic $PbNb_2O_6$ was obtained between 300° and 650°C at a heating rate of 10°C/min. An exothermic reaction was detected at 560° ± 10°C at 1 atm pressure. The peak obtained on the heating cycle was relatively sharp while that on the cooling cycle was somewhat broadened. It was also found that the observed orthorhombic to tetragonal inversion temperature increased slightly with increased particle size. This may be simply the result of the restraining effect of the larger crystal. The rate of inversion to the rhombohedral form was very sluggish and this form was not detected in material which had been through three heating and cooling cycles encompassing the inversion. Attempts were made to study the effects of pressure on the orthorhombic to tetragonal inversion using a Tem-Pres high pressure D.T.A. attachment (10). However, the small enthalpy involved (about 8% that of cryolite) prevented detection of the inversion with any degree of certainty.

The Bridgman method of crystal growth was selected for more detailed study as a possible method for growing the orthorhombic polymorph. Because of the high melting temperatures involved, and the variable valences possible for niobium, precautions had to be taken to prevent the loss of oxygen from the composition; otherwise a darkening of the crystals resulted. A stoichiometric mixture of PbO and Nb_2O_5 was first heated to 900°C and homogenized by grinding. The product was transferred to a special Bridgman crucible which was sealed by arc welding, and then fired at 1200°C for 2 hr. Finally the entire contained charge was melted by heating to 1350°C. In these experiments the sealed crucible was lowered through the furnace at 4-6 cm/hr, which corresponded to an initial cooling rate of less than 0.4°C/hr and a mean rate of 4°C/hr until the temperature of the charge was 1150°C. At this temperature the charge was cooled rapidly to 650°C in order to avoid inversion to the rhombohedral form. The slow cooling was again resumed in an attempt to minimize the disrupting effect of the inversion. Various programs including much slower and much faster cooling rates of the tetragonal polymorph were tried in an effort to reduce significantly the damage done to the crystals. It was found that when the melt was slowly cooled from

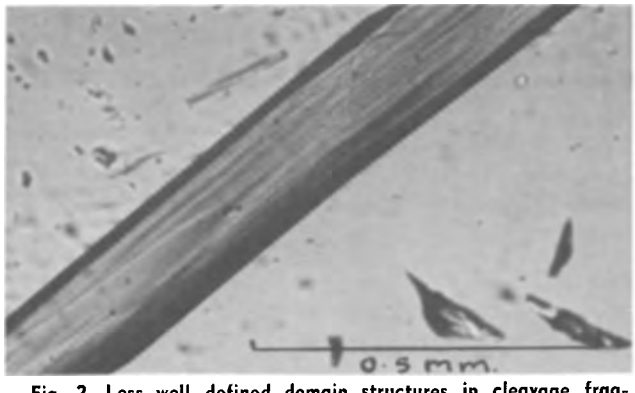

Fig. 2. Less well defined domain structures in cleavage fragments from $PbNb_2O_6$ which was cooled slowly to 1250°C, and then cooled rapidly to room temperatures.

Fig. 3. Intricate domain structures in orthorhombic $PbNb_2O_6$ which was cooled slowly. Thin cleavage fragment as seen in transmitted light.

1350° to 1200°C, and then immediately removed from the furnace the resulting product showed only minor amounts of cracking. Some fragments of this did not show the usual coarse domain structures, and their quality was good, see Fig. 2. The fine domains in these were of the order of 0.002 mm as compared to 0.01 mm in other specimens, see Fig. 3.

Petrographic examination of thin sections from other specimens showed that several nuclei developed in the cone of the crucible but a dominant one finally extended into the main body of the crucible. One section did not extinguish under crossed incols, but the cleavage and domain structures appeared to have the same orientation throughout the main mass of the sample, indicating that a large single crystal existed before the inversion took place and shattered the material.

Examination of the surfaces of uncleaved and freshly cleaved flat flakes showed an intricate pattern of related features, in addition to the obvious cracks (Fig. 4). These features do not resemble any of the domain patterns which had been seen in transmitted light, and perhaps are not related to them. We conclude that they are growth features exposed by cleavage along a single crystallographic plane.

The products from these runs were cracked to varying degrees. Some of the pieces (weighing 1-3g) appeared to be fragments from a single crystal. This was supported by x-ray diffractometer tracings obtained from polished faces of these fragments. In all cases the only reflections obtained were the different orders from the same plane.

Laue photographs from the upper surface of the melted products of the other runs indicate that the surfaces contained areas which were misoriented with respect to the main mass. This was probably confined to the upper surface which definitely appeared to be a polycrystalline mosaic, and usually cracked.

The crystals grown varied in color from colorless to pale straw.[1] Examination of the larger fragments with a binocular microscope showed that they are all cracked, badly strained, and twinned. Many of them have a well developed network of fractures. By petrographic examination of thin fragments and sections, a marked mosaic structure bounded by (110) twin pairs was apparent. Domain structures as small as 0.005 mm were observed, but size and density varied. A few pieces, however, do not contain domain structures but instead a fibrous or interwoven pattern. These fragments would immediately develop a domain structure when stressed by simple mechanical techniques such as squeezing or probing. It logically follows that the preparation of the thin sections may have induced much twinning and domain structure. It was also noted that some of the features developed

[1] Nonstoichiometric $PbNb_2O_6$, which was formed when the material was fired in air varied in color from pale green to much deeper green, and was opaque in thicker sections.

Fig. 4a.

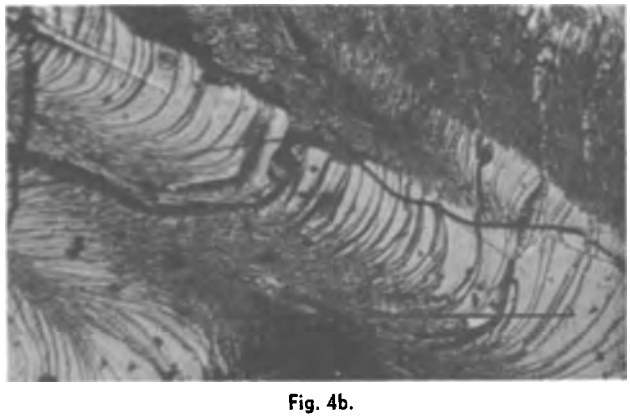

Fig. 4b.

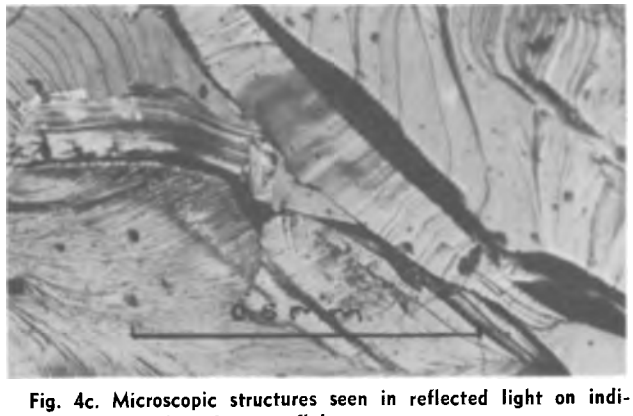

Fig. 4c. Microscopic structures seen in reflected light on individual orthorhombic cleavage flakes.

by mechanical stress strain relaxed in a few minutes while the samples were under the microscope.

Discussion of Results

It appears that orthorhombic lead metaniobate, even when doped with small amounts of ZrO_2, has no stability field at temperatures below 1150°C and pressures up to 25 kilobars and it is, therefore, unlikely that large single crystals of this material can be grown hydrothermally. A choice of methods involving the growth of the tetragonal phase in its stability field and converting this to the orthorhombic phase remains. The tetragonal to orthorhombic inversion produces a discontinuous change in cell dimension, and large anisotropic strains develop. Francombe and Lewis (5) relate this to the appearance of spontaneous ferroelectric strain, and an increase in the covalent character of the Pb-O bonds. The latter could result in 001-type cleavage as was found in orthorhombic $PbNb_2O_6$. This mechanism could explain the frequent fracturing of crystals grown by the Bridg-

man technique. The crystals tend to fracture but the degree of fracturing has no simple relationship to conditions of growth of the crystals. The rapid quenching of the run after the tetragonal phase has crystallized, but before it inverts to the rhombohedral phase, seems to result in an improved product. It was also observed that the crystals became twinned and even fractured because of ordinary handling. In some experiments, clean $PbNb_2O_6$ splinters were observed to develop cracks and otherwise relieve strain under the microscope. Annealing the crystals at the Curie point does relieve some of the stresses but results in increased fracturing.

The ability to re-orient the crystallographic axes of the crystals by mechanical stresses does, however, appear to offer some hope for a method of producing single domain crystals, or at least crystals with fewer large domains from a crystal which has passes through the Curie point.

Acknowledgments

The authors wish to express their thanks to Dr. W. C. Luth, formerly of the Materials Research Laboratory, The Pennsylvania State University for performing some of the runs in the internally heated pressure vessel system. This work was sponsored by the U.S. Air Force Materials Laboratory, Wright-Patterson Air Force Base, under contract AF 33(615)-1712 R. L. Hickmott, project engineer.

Manuscript received May 31, 1966; revised manuscript received July 14, 1966.

Any discussion of this paper will appear in a Discussion Section to be published in the June 1967 JOURNAL.

REFERENCES

1. M. H. Francombe, *Acta Cryst.*, **9**, 683 (1956).
2. R. S. Roth, *ibid.*, **10**, 437 (1957).
3. R. S. Roth, *J. Research Nat. Bur. Stand.*, **62**, 27 (1959).
4. G. Goodman, *J. Am. Ceram. Soc.*, **36**, 309 (1953).
5. M. H. Francombe and B. Lewis, *Acta Cryst.*, **11**, 696 (1958).
6. O. F. Tuttle, *Geol. Soc. Am. Bull.*, **60**, 1727 (1949).
7. R. Roy and O. F. Tuttle, "Physics and Chemistry of the Earth," Vol. 1, pp. 138-180, Pergamon Press, London and New York (1956).
8. W. C. Luth and O. F. Tuttle, *Am. Min.* **48**, 1401 (1963).
9. R. Roy, *Min. Ind.*, **29**, No. 5 (1960).
10. R. I. Harker, *Am. Min.*, **49**, 1742 (1964).

Epitaxial InAs on Semi-Insulating GaAs Substrates

G. R. Cronin, R. W. Conrad, and S. R. Borrello

Texas Instruments Incorporated, Dallas, Texas

The preparation of high-purity indium arsenide has been reported by several laboratories working with crystals grown from the melt (1-3). Both horizontal ingot growth and vertical pulling techniques have been employed in obtaining high-purity n-type material with excess carrier concentrations of about 1-2 x 10^{16}/cm^3 at 300°K. Excess carrier concentrations less than 10^{16}/cm^3, however, have not been easily achieved. By extensive purification of both indium and arsenic, Effer (2) prepared an apparently uncompensated sample of InAs whose electron concentration at 77°K was 8.0 x 10^{15}/cm^3 with a mobility of 75,700 cm^2/v-sec. Vapor growth of InAs has been achieved by a halide transport technique analogous to that which transports GaAs (4-6). Some difficulty of electrical evaluation exists, however, unless measurements can be made on discrete crystals of vapor grown material or the material is deposited on an insulating substrate. In this series of experiments the substrate chosen for deposition was chromium-doped GaAs since the semi-insulating property of this material allows unambiguous electrical evaluation of the deposit. Furthermore, semi-insulating GaAs is readily available, easy to polish, and has the same crystal structure as InAs.

Experimental

The reactor and flow systems are shown in Fig. 1. All hydrogen is purified by palladium diffusion. The HCl required for indium transport is prepared as needed by bubbling hydrogen through pure $AsCl_3$ in a gas-saturator system. The arsenic trichloride used in these experiments is distilled from commercial reagent grade anhydrous $AsCl_3$. Distillation is accomplished with a twelve foot column packed with Pyrex helices and operated with a reflux ratio of about 30 to 1. The distilled $AsCl_3$ contains no detectable impurities. This mixture of $AsCl_3$ and hydrogen passes through a quartz tube filled with quartz chips and heated to about 880°C. The reduced arsenic condenses on the cool walls of the quartz tube outside the reduction furnace and the resulting HCl-hydrogen mixture is introduced into the reactor. An advantage of this technique is that the HCl is prepared as needed and storage of the compressed gas in steel containers is unnecessary.

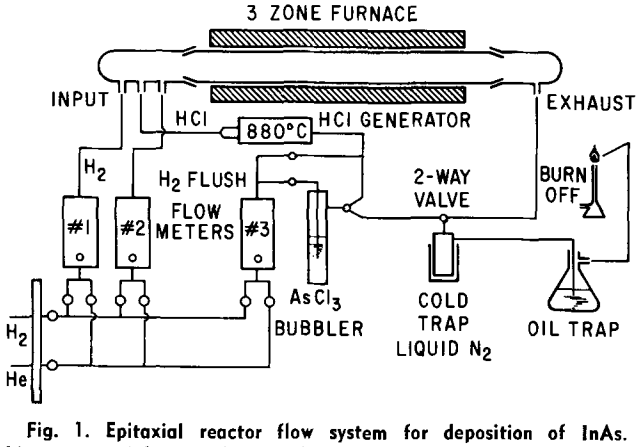

Fig. 1. Epitaxial reactor flow system for deposition of InAs. Lines are stainless steel up to flow meters, Teflon lines beyond.

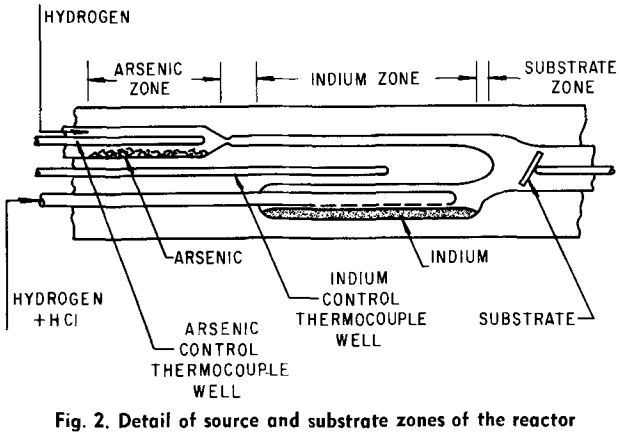

Fig. 2. Detail of source and substrate zones of the reactor

Table I. Temperature and flow conditions for epitaxial InAs deposition

	Temperature, °C	Flow rate, cc/min
Arsenic	430	30 (H_2)
Indium	870	60 (HCl/H_2)
Substrate	740	—
Excess hydrogen flush	—	30
$AsCl_3$ reduction furnace	880	—

A detailed sketch of the reactor proper is shown in Fig. 2. A three-zone furnace is used to provide independent control over the arsenic, indium, and substrate zones of the reactor. Typical operating conditions of flow rates and temperatures are shown in Table I. Temperatures are controlled to within ± 1°C with proportional control equipment. Arsenic vapor is transported to the substrate zone by passing hydrogen over heated arsenic. Indium transport is achieved with the volatile monochloride prepared by passing a mixture of pure HCl and hydrogen over elemental indium maintained at a temperature of 870°C. Both the arsenic and the indium are commercially available research grade materials, 99.9999% pure.

GaAs substrates, 30 mils thick, were cut on the (100) orientation and polished on a paper pad wet with sodium hypochlorite solution after the manner of Reisman and Rohr (7).

Initially, three substrate orientations were examined: the (100), (111)A, and (111)B. Since the best crystalline structure and highest growth rate were obtained with the (100), all further work was done on (100) substrates. Polishing time is approximately 2 hr during which time about 3 mils are removed from the surface of the substrates. Since the substrates are polished in batches and some storage is necessary, they are given one further chemical etch individually just before being placed in the reactor. This final etch consists of 15 cc of $5H_2SO_4$-H_2O-H_2O_2 mixture for 5 min followed by 5 additional minutes in the same solution to which 5 cc of H_2O have been added. The latter etching is carried out in a rotating beaker.

Hall coefficient and resistivity measurements were made by either of two procedures: (*i*) an a-c technique using ultrasonically cut six-armed specimens to which contacts were indium-soldered, and (*ii*) a d-c method using rectangular shaped samples, contacts being made with indium plated phosphor bronze strips. Both methods yielded the same results and were used interchangeably.

The epitaxial layer thicknesses were determined by microscopic examination of cleaved edges or by bevel lap techniques. Single crystallinity and epitaxial orientation were established by optical microscopy and x-ray diffraction.

In addition, spectral transmission measurements were made on the epitaxial layers and the absorption coefficient in the absorption edge region was found to be the same as that for melt-grown material.

Results

Under the operating conditions shown in Table I, we have observed growth rates of 30-40 μ/hr on (100) oriented substrates. Figure 3 shows the surface and cleaved edge of a layer produced under these conditions. The layer is easily seen under a microscope because of a faint but distinct color difference. For the purpose of obtaining clearer pictures the cleaved edge shown in Fig. 3 was stained for about 1 sec in the same sodium hypochlorite solution used to polish the substrates. This solution darkens the substrate but leaves the InAs layer apparently unchanged. The defect density revealed by etching the surface with a 3:1 mixture of HNO_3-HF is relatively low. The smooth cleavage characteristics on (110) planes, similar to bulk material, are generally associated with smooth, shiny layers having low surface defect density.

For our particular reactor system, any significant departure from the arsenic temperature and HCl-H_2 mixture flow rate shown in Table I adversely affects the physical properties of the deposits. Figure 4 shows the etched surface and cleaved edge of a layer prepared under arsenic-deficient conditions. The poor surface and cleavage characteristics and irregular interface are typical of layers grown indium-rich and are suggestive of alloying between excess indium and the GaAs substrate. Growth under indium-deficient conditions generally results in sharp, planar interfaces but dull surfaces with high defect densities and poor cleavage characteristics.

In general, most of the surface irregularities we have observed have the appearance of line defects lying in <110> directions. They bear a marked resemblance to line defects which have been observed in both GaAs(8) and silicon (9). Although these defects appear to originate at the epitaxial interface, we believe that in general they are not only a result of substrate imperfections but also appear to be associated with incorrect vapor composition. Analogous effects of vapor composition on the morphology of epitaxial GaAs layers has been described by Ewing and Greene (10).

The electron mobilities and excess carrier concentrations at room temperature and 77°K for a number of samples are shown in Table II. Samples 1 through 6 were prepared at or near the operating conditions of Table I. Samples grown over a wide range of temperature and flow rate conditions have invariably been n-type. Material with excess electron concentrations less than $2 \times 10^{16}/cm^3$ seems to be rather easily obtained. The best sample we have prepared has an electron mobility at 77°K of 7.04×10^4 $cm^2/v\text{-}sec$ at 6.1×10^{15} electrons/cm^3.

We have also obtained samples which, unlike melt-grown material, show unusually low excess electron

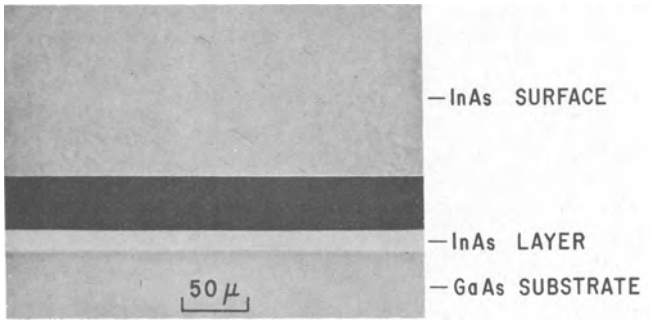

Fig. 3. Etched surface (upper) and cleaved edge (lower) of InAs layer prepared under optimized conditions (Table I).

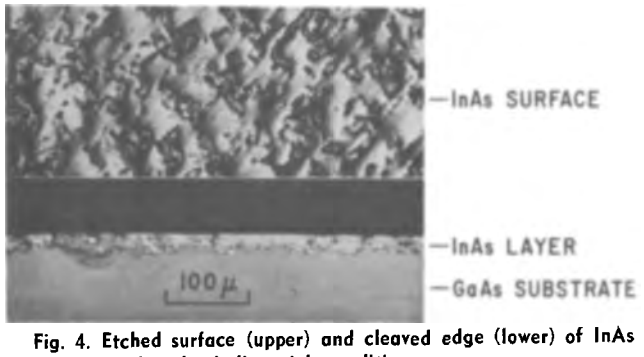

Fig. 4. Etched surface (upper) and cleaved edge (lower) of InAs layer prepared under indium-rich conditions.

Table II. Hall and resistivity data for InAs layers on GaAs* substrates

Sample No.	Layer thickness, μ	Room temperature			77°K		
		Resistivity, ohm-cm	Mobility, $cm^2/v\text{-}sec$	Excess carrier conc, cm^{-3}	Resistivity, ohm-cm	Mobility, $cm^2/v\text{-}sec$	Excess carrier conc, cm^{-3}
1	24	2.7×10^{-2}	2.1×10^{4}	1.1×10^{16}	1.4×10^{-2}	5.9×10^{4}	7.6×10^{15}
2	16	2.0×10^{-2}	2.0×10^{4}	1.7×10^{16}	1.1×10^{-2}	4.8×10^{4}	1.2×10^{16}
3	14	2.2×10^{-2}	1.9×10^{4}	1.5×10^{16}	1.2×10^{-2}	5.3×10^{4}	9.8×10^{15}
4	20	3.2×10^{-2}	2.3×10^{4}	8.7×10^{15}	1.5×10^{-2}	7.0×10^{4}	6.1×10^{15}
5	28	8.7×10^{-2}	1.7×10^{4}	4.2×10^{15}	4.2×10^{-2}	5.9×10^{4}	2.5×10^{15}
6	24	2.0×10^{-2}	2.1×10^{4}	1.5×10^{16}	1.3×10^{-2}	5.8×10^{4}	8.2×10^{15}
7	15	1.6×10^{-1}	5.8×10^{3}	6.8×10^{15}	5.6×10^{-1}	3.2×10^{3}	3.5×10^{15}
8	14	8.7×10^{-1}	3.6×10^{3}	2.0×10^{15}	3.3×10^{1}	3.9×10^{2}	4.8×10^{14}

* Chromium-doped, semi-insulating (10^{8} ohm-cm at 300°K), (100) ± 0.5° oriented.

concentrations (see samples 7 and 8 of Table II). These samples also show low mobilities at both room temperature and 77°K, suggesting a high degree of compensation. This kind of material is obtained only when arsenic temperatures much higher than optimum are used. However, we have not been able to prepare p-type InAs by this method.

Two possible explanations for the dependence of the electrical properties of epitaxial InAs on the vapor composition can be proposed. First, large deviations from the optimum vapor composition may promote the formation of physical defects. At high arsenic concentrations, arsenic interstitials and indium vacancies are the simplest point defects which could show acceptor properties (11). Second, changes in vapor composition might significantly alter the vapor-solid segregation coefficients of residual impurities present in the arsenic.

Acknowledgment

The authors wish to acknowledge the support of the Air Force Avionics Laboratory under Contract AF 33(615)-2913 with the Reconnaissance Division, and contract AF 33(615)-1272 with the Electronic Technology Division.

Manuscript received May 11, 1966; revised manuscript received August 19, 1966.

Any discussion of this paper will appear in a Discussion Section to be published in the June 1967 JOURNAL.

REFERENCES

1. R. H. Harada and A. J. Strauss, *J. Appl. Phys.*, **30**, 121 (1959).
2. D. Effer, *This Journal*, **108**, 357 (1961).
3. G. R. Cronin, M. E. Jones, and O. Wilson, *ibid.*, **110**, 582 (1963).
4. D. Effer, *ibid.*, **112**, 1020 (1965).
5. G. R. Antell and D. Effer, *ibid.*, **106**, 509 (1959).
6. D. Effer and G. R. Antell, *ibid.*, **107**, 252 (1960).
7. A. Reisman and R. Rohr, *ibid.*, **111**, 1425 (1964).
8. T. Gabor, *ibid.*, **111**, 821 (1964).
9. C. A. Lenie, *SCP and Solid State Technol.*, **7**, 41 (1964).
10. R. E. Ewing and P. E. Greene, *ibid.*, **111**, 1266 (1964).
11. F. A. Kröger, "The Chemistry of Imperfect Crystals," John Wiley & Sons, New York (1964).

The Repeatability of the Anode Effect in Cryolite-Alumina Melts

B. J. Welch and R. J. Snow

School of Chemical Technology, The University of New South Wales, Kensington, New South Wales, Australia

Hitherto, studies of the anode effect have been primarily confined to correlations with the critical current density (1-3), but the various correlations between concentration and the point of anode effect have not been in substantial agreement.

The complexity of factors affecting these correlations has recently been illustrated by both Piontelli (3) and Schmitt (4). Piontelli found that correlations between critical current density and alumina concentration held only for a fixed orientation and design of the working anode. Results of Schmitt's investigations showed that, at a fixed critical current density, the alumina concentration decreased as the temperature increased.

Because the anode is often consumed at an uneven rate during electrolysis the true surface area could change. Also the true surface area for different carbons varies considerably, so the differences between correlations of apparent critical current density are not surprising.

Provided the total cell resistance is low the cell voltage would be less dependent on these variables, and therefore, a more reproducible parameter than critical current density. This is because the overpotential at the anode is high (5) while the cathode overvoltage is small (3), and therefore the only current dependent contribution to the cell voltage would be that arising from the cell resistance.

In this work the reproducibility of the point of anode effect was studied for an anode of fixed surface area by simultaneously determining the cell voltage and apparent geometric current density at the point of anode effect. The reproducibility was studied as a function of alumina concentration by making successive measurements with all other conditions constant and also by doing repeat experiments for constant conditions.

Experimental

A schematic view of the cell arrangement is presented in Fig. 1. The exposed surface area of a Union Carbide A.U.C. grade graphite rod (A) was defined by a boron nitride insulator (B), and this graphite surface was used as the working anode. The counter electrode (C) had a much larger surface area than the anode and was positioned so that the inter electrode distance was kept to a practical minimum to reduce the cell resistance. Concentric insulated inconel (D, E) tubes served as electrode contact leads.

A protective argon atmosphere was maintained within the sealed furnace tube at all times. All measurements were made at 985° ± 2°C using a constant solvent composition of Na_3AlF_6 + 5 w/o AlF_3 + 5 w/o CaF_2.

The anode effects were induced by slowly increasing the applied potential to the cell using a variable stabilized d-c power supply. The current and cell voltage were simultaneously recorded on an E.A.I.

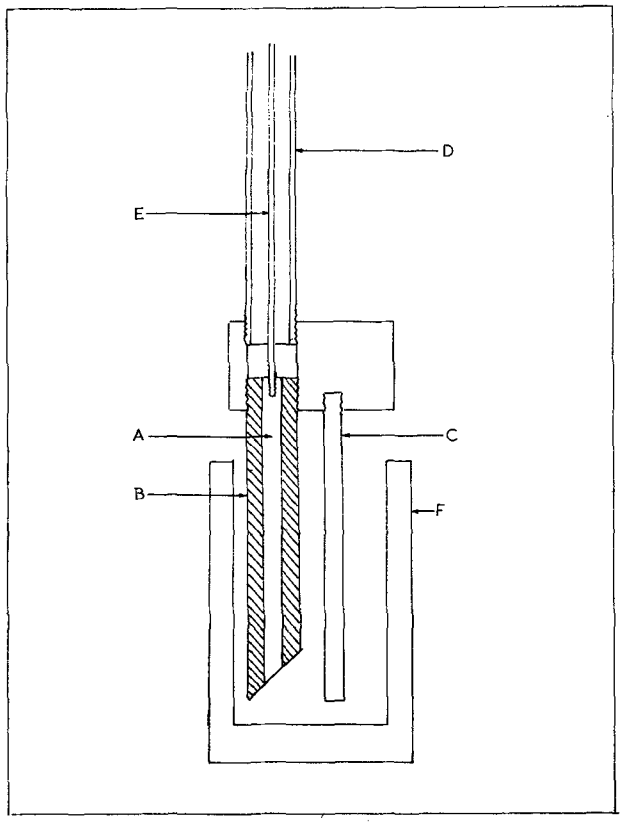

Fig. 1. Schematic view of cell assembly: A, graphite anode rod; B, boron nitride insulator; C, counter electrode; D, E, concentric inconel electrode leads; F, graphite crucible.

model 1130 X-Y Recorder. For each new electrode assembly a short period of electrolysis was carried out to present a uniform electrode surface before measurements were made.

Results

The point of the anode effect was determined for melts containing between 2 and 8 w/o alumina. At least 10 determinations of the point defining the anode effect were carried out during an experiment, and repeat experiments were also carried out for a given melt composition.

The results obtained for the critical current density as a function of alumina concentration are plotted in Fig. 2, and they are compared with curves constructed from the data of Piontelli (3).

The mean critical cell voltage *vs.* alumina concentration curve is presented in Fig. 3. Table I summarizes the variations observed during an experiment for repeated measurements of the parameters describing the point of anode effect.

It is seen from Table I that, for all alumina concentrations, both the accuracy and reproducibility of the critical cell voltage is better than those observed for the critical current density. The variations observed in the cell voltages were generally random in nature. During a series of measurements the values of the critical current density decreased with each successive measurement. Although the rate of decrease as a function of measurement was not always the same, the decrease was invariably more gradual for lower alumina concentrations. This was probably due to the change in angle of the anode surface, which was sometimes (particularly for higher alumina concentrations) apparent from the appearance of the electrode surface after an experiment. This explanation would be consistent with Piontelli's observation.

Because of this the initial measurements were considered to be the more comparable data, and therefore the initial critical current density, as well as the mean values are presented in Fig. 2.

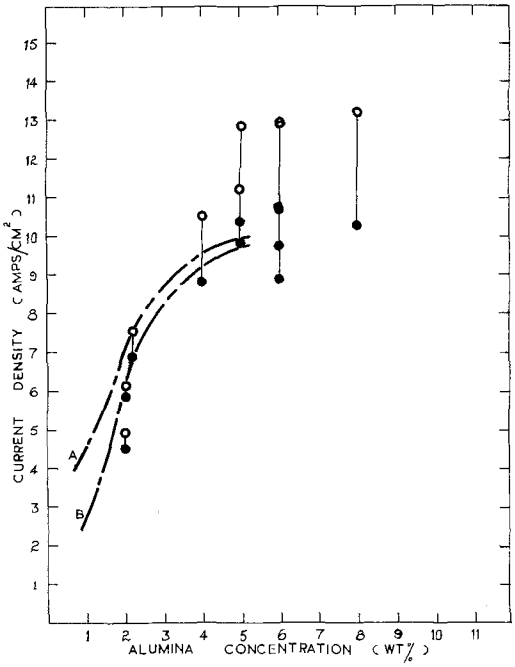

Fig. 2. Variation in critical current density with alumina concentration. Curve A, from Piontelli's data for hemispherical anode; curve B, from Piontelli's data for plane anode, ○ initial critical current densities, • mean values of critical current density.

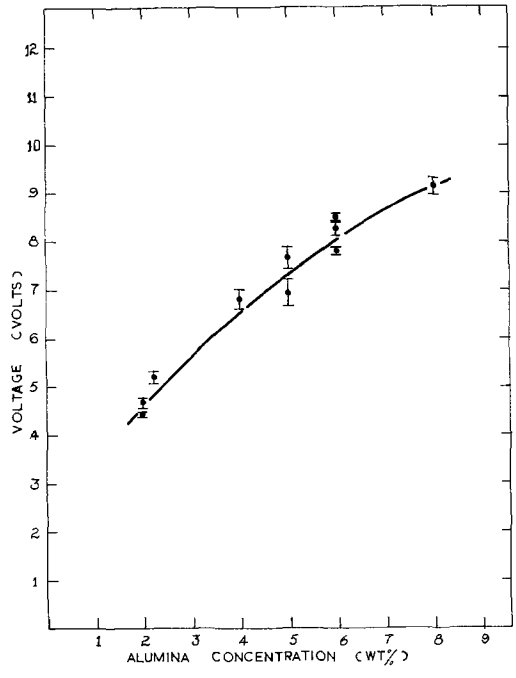

Fig. 3. Variation in cell voltage at point of anode effect with alumina concentration.

The scatter from the best curve would be less for the initial measurements than the mean measurements, but both curves would differ from Piontelli's results. This would be expected because of the different carbon type and anode design.

Conclusions

For applications such as *in situ* analysis of alumina concentrations in a Hall Heroult cell, it is evident that the critical cell voltage is a more reproducible parameter for designs where the cell has a low resistance. The variations in critical current density are more

Table I. Accuracy and reproducibility of measurements for the point of anode effect at 985° ± 2°C

Alumina concentration, w/o	Number of measurements	Variation of critical cell voltage, % of mean	Variation of critical anode current density, % of mean
2.00	10	2.3	11.2
2.00	20	1.1	2.9
2.23	50	2.3	4.6
4.00	19	2.9	10.2
4.98	33	3.0	14.6
4.99	31	4.0	6.0
6.00	25	1.6	6.3
6.00	29	1.0	12.4
6.00	31	0.9	20.2
7.98	26	2.0	12.1

pronounced because of their dependence on both the anode carbon and its orientation which in turn is dependent on previous electrolysis of the electrode.

Manuscript received Aug. 15, 1966.

Any discussion of this paper will appear in a Discussion Section to be published in the June 1967 JOURNAL.

REFERENCES

1. I. K. Delimarskii and B. E. Markov, "Electrochemistry of Fused Salts," (English Translation) Sigma Press, Washington, p. 290 (1960).
2. A. I. Belyaev, *Usp. Khim.*, **25**, 1288 (1956).
3. R. Piontelli, in "Proceedings of the First Australian Conference on Electrochemistry," Gutman and Friend, Editors, p. 932, Pergamon Press, London (1964).
4. H. Schmitt, in "Extractive Metallurgy of Aluminum," Vol. 2, "Aluminum," G. Gerard, Editor, p. 169, Interscience Publishers, New York (1963).
5. B. J. Welch and N. E. Richards, in "Extractive Metallurgy of Aluminum," Vol. 2, "Aluminum," G. Gerard, Editor, p. 15, Interscience Publishers, New York (1963).

Discussion Section

This Discussion Section includes discussion of papers appearing in the *Journal of The Electrochemical Society*, Vol. 112, No. 8, 9, 10, and 12 (August, September, October, and December 1965), and Vol. 113, No. 1, 3, 5, and 6 (January, March, May, and June 1966).

Notes on the Chemical Polishing of Gallium Arsenide Surfaces

R. D. Packard (pp. 871-872, Vol. 112, No. 8)

K. E. Mironov[1]: The chemical polishing of compound semiconductor gallium arsenide by means of etching with solutions based on mineral acids is usually explained by the considerable viscosity increasing in such etchants, but the chemical nature of etchant must be more responsible for polishing action.

From some papers[2-5] it is possible to produce the dependence of action mode for such etchant as H_2SO_4: H_2O_2: H_2O. Minimal etch rates for GaAs corresponds to 2-4% of H_2O_2 content in solutions. Selective or polishing action of such etchants is dependent on acid concentration. There are typical triangular etch pits on the {111} faces in the presence of less than 35% H_2SO_4; only conic pits instead of typical triangular ones on the Ga{111} face and polishing action for any other face, if the acid content is between 35-67%, and polishing action only, if etchant content is more than 67% H_2SO_4.

The viscosity of concentrated H_2SO_4 solutions changes in a rather complicated manner because of acid monohydrate formation.[6] Smoother and more regular changes increase the quantity of undissociated molecules in these solutions.[7] Therefore, it seems more correct to connect the polishing action of etchants on the base of concentrated acid with a predominance of undissociated H_2SO_4 species that are forming in such solutions in the presence of the hydrogen peroxide, the peroxomonosulfuric acid H_2SO_5.[8] The latter may also help for polishing action of etchants.

A viscosity maximum for water solutions of HNO_3 corresponds to 70% of acid. The etchants based on the concentrated HNO_3 with the addition of strong HCl reveal the polishing. The dilution of such etchant with the glycerin does not make the increase of HNO_3 dissociation since this one usually decreases in alcohol solutions. Therefore the action of such etchant or an etchant diluted by glycol, ethanol, or benzene as stated by Dr. Packard has to retain polishing action. The high viscosity of etchants containing undissociated inorganic acids promote the polishing action of these mixtures.

R. C. Packard[9]: I have no basic quarrel with Dr. Mironov's thesis that the degree of acid dissociation is a highly important variable. I agree that the etching solution viscosity is important. Dr. Mironov makes the point that the degree of dissociation of inorganic acid, as well as solvent viscosity (alcohol *vs.* glycol, *etc.*), helps determine the final etchant viscosity. This is true. As stated in the cited paper, etches are usually aqueous solutions containing reagents which react with the semiconductor to form soluble reaction products. Dr. Mironov agrees that the chemical nature of the etchant is responsible for the polishing action. However, as I pointed out, the etch rate is dependent on the rate of reactant in-diffusion and product out-diffusion, which is dependent only on solution viscosity, for a given system. Thus, with a normally fast mineral-acid etch, the etching solution viscosity must be a limiting factor.

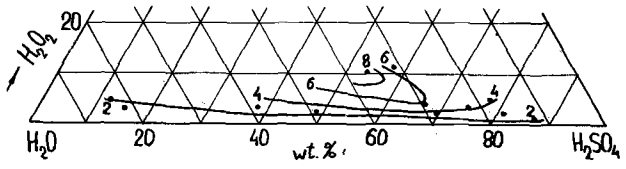

Fig. 1. Lines of equal solution rate for GaAs etching with mixtures H_2SO_4:H_2O_2:H_2O. Figures attached to the lines correspond to values of solution velocity, μ/min.

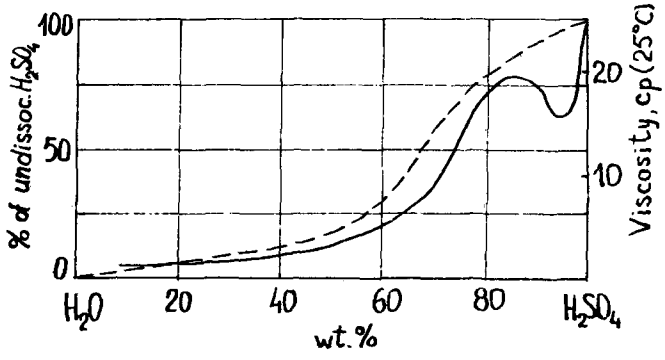

Fig. 2. The viscosity (solid line)[6] and undissociated molecules H_2SO_4 (broken line)[7] *vs.* weight per cent of acid in mixtures H_2O — H_2SO_4.

The Double Layer Capacitance of Silver in Perchlorate Solution

L. Ramaley and C. G. Enke (pp. 947-950, Vol. 112, No. 9)

D. I. Leikis, E. S. Sevastianov, and I. G. Dagaeva[10]: It is suggested in the paper cited that in 1N sodium perchlorate solutions the electric double layer (edl) on silver is similar to edl on mercury, if the potential of zero charge (pzc) of silver is assumed to be equal to —0.7v (NHE), as was shown by one of the authors of the present paper.[11] The authors of the paper under discussion consider, however, that be-

[1] Institute of Inorganic Chemistry, Sib. Dep. of Academy of Sciences of the USSR, Novosibirsk, 90, Moscow, USSR.

[2] F. A. Cunnell, J. T. Edmond, and W. R. Harding, *Solid State Electronics*, 1, 97 (1960).

[3] J. W. Faust, "Compound Semiconductors," Vol. 1, "Preparation of III-V Compounds," p. 445. Reinhold Publishing Corp., New York (1962).

[4] R. L. Petrussevich, E. S. Sollertinskaja, and O. I. Pavlov, *Solid State Physics* (Sov. ed.), 4, 1378 (1962).

[5] L. N. Vozmilova, N. G. Maljuta, and G. A. Kataev, *J. Phys. Chem.* (Sov. ed.), 38, 2725 (1964).

[6] Spravochnik Khimika, "Handbook for Chemist," 2nd ed., pp. 717, Khimia, Moscow-Leningrad (1964).

[7] H. S. Harned and B. B. Owen, "The Physical Chemistry of Electrolytic Solutions," 2nd ed., Reinhold Publishing Corp., New York (1950).

[8] J. M. Monger and O. Redlich, *J. Phys. Chem.*, 60, 797 (1956).

[9] Present address: Melpar Space Science Laboratory, 15 Mercer Road, Natick, Massachusetts 01760.

[10] Institute of Electrochemistry, Academy of Sciences of the USSR, Moscow, USSR.

[11] D. I. Leikis, *Doklady Akad. Nauk SSSR*, 135, 1429 (1960).

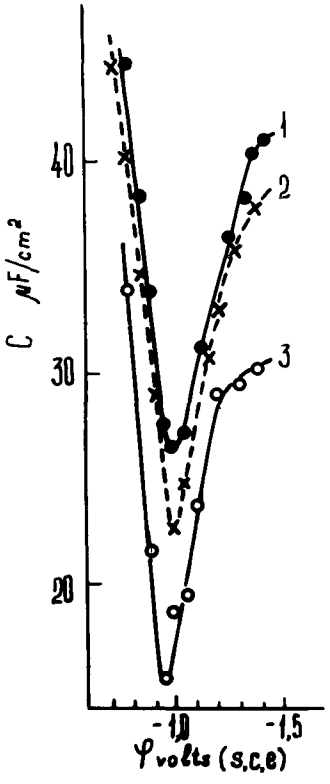

Fig. 1. Dependence of differential capacitance on potential for a silver electrode in Na_2SO_4 solutions of various concentrations: curve 1, 10^{-2}N solution; curve 2, 5×10^{-3}N solution; curve 3, 10^{-3}N solution.

fore drawing final conclusions regarding the problem in question, it would be necessary to have further proofs of the correctness of the value of pzc established. Due to improved experimental technique,[12] we have been able lately to carry out the differential capacitance measurements on silver more carefully, both with respect to accuracy and in solutions of lower concentrations. As can be seen from Fig. 1 the differential capacitance curves on the silver electrode in dilute solutions show a well-pronounced minimum, which becomes deeper with increasing dilution of the solution. The latter fact clearly points to this minimum reflecting the change in the diffusedness of edl with the potential. Hence, $\varphi = -0.7$v (NHE) is really pzc of silver in the solution containing no surface-active ions. This value of pzc agrees with that obtained.[11] A comparison of the differential capacitance curves for silver in 0.01 and 0.001N Na_2SO_4 solutions[13] with those for mercury (taken from [14]) has shown them to coincide almost completely near pzc. This permits us to draw the conclusion that the structures of edl in dilute solutions of electrolytes for the metals being compared are similar. It is shown in[13] that pzc of silver does not depend on pH (in the pH range from 3.4 to 12). This supports the conclusion that the differential capacitance minimum obtained corresponds to pzc of silver.

Another problem—the nature of frequency dispersion—is also considered in the original paper. In particular, in the case of silver this phenomenon is suggested to be due to the surface inhomogeneity of solid metal. Such a suggestion seems to be quite likely. As shown in [11], the difference in the shape of the desorption peak on the capacitance curves in solutions containing a surface-active organic substance in the case of silver and mercury also seems to be due to the inhomogeneity of the silver surface. It should be pointed out, however, that the dispersion data presented in the original paper have been obtained on an electrode which was not sealed into a quartz capillary, *i.e.*, there was still a possibility for a thin electrolyte film to be formed between silver and the capillary. The formation of such a film, as shown in [15,16] may also cause frequency dispersion. The latter may also be caused by some roughness of the surface,[17] which was present, as it follows from the data in the original paper, even in the case of polished silver electrodes.

In our opinion, owing to the above considerations, it is impossible to interpret quantitatively the experimental results for frequency dispersion as being due only to surface inhomogeneity of the metal.

L. Ramaley[18] and **C. G. Enke**[19]: The fine work reported above is noted with great interest by these authors who are pleased to have some of their suggestions concerning the similarity of the double layer structures on Ag and HG supported. However, there is one point concerning the construction and use of the test electrode in our experiments which needs to be clarified. A spherical silver electrode was formed at the end of a fine silver wire. This electrode was immersed in the electrolyte so that the solution surface intersected the silver wire above the sphere but well below the wire-glass seal. Therefore, the observed frequency dispersion could not have been caused by a thin electrolyte film between the silver and the capillary. A similar affect could be caused by creeping of the solution up the wire, but the area involved would be much less significant than in the case of the capillary action which was presumed to exist.

Vapor Phase Deposition and Etching of Silicon

W. H. Shepherd (pp. 988-994, Vol. 112, No. 10)

W. J. Riedl[20]: The contributions in the field of thermodynamic approach to the growth of epitaxial silicon are based on the assumption of the occurrence of chemical reactions either in the gas phase[21] or only on the surface of silicon seed as stated by Dr. Shepherd. Chemical equilibria considered in these two cases are different. Taking into account three reactions

$$SiCl_{4\,gas} + 2H_{2\,gas} = 4HCl_{gas} + Si_{solid} \qquad (i)$$

$$SiCl_{4\,gas} + Si_{solid} = 2SiCl_{2\,gas} \qquad (ii)$$

$$Si_{solid} = Si_{gas} \qquad (iii)$$

Equilibrium concentrations of all components can be computed by solving the following system of equations

$$\frac{(4n_1)^4}{(1-n_1-n_2)\,(w-2n_1)^2(1+w+n_1+n_2+n_3)} = K_1(T) \quad [1]$$

$$\frac{(2n_2)^2}{(1-n_1-n_2)\,(1+w+n_1+n_2+n_3)} = K_2(T) \quad [2]$$

[13] E. A. Budniskaya, D. I. Leikis, E. S. Sevastianov, and A. I. Shurpach, "Elektrokhimiya," In press.

[13] I. G. Davaeva, D. I. Leikis, and E. S. Sevastianov, "Elektrokhimiya," In press.

[14] B. B. Damaskin and N. V. Nikolaeva-Fedotovich, *Zhur. Fiz. Khim.*, 26, 1484 (1962).

[15] D. I. Leikis, E. S. Sevastianov, and L. L. Knots, *Zhur. Fiz. Khim.*, 37, 1633 (1964).

[16] R. de Levie, *J. Electroanalyt. Chem.*, 9, 117 (1965).

[17] R. de Levie, *Electrochim. Acta*, 10, 113 (1965).

[18] Present address: College of Natural Science, Department of Chemistry, Chemistry Building, Michigan State University, East Lansing, Michigan 48823.

[19] Alfred P. Sloan Research Fellow.

[20] Tele- and Radio Research Institute, Warsaw, Poland.

[21] W. Steinmaier, Philips Research Reports, 18, 75 (1963).

$$\frac{n_3}{1+w+n_1+n_2+n_3} = P_{Si}(T) \qquad [3]$$

The constant $K_2(T)$ experimentally determined by Schäfer and Nickl[22]

$$\log K_2(T) = 10.081 - 16427\,T^{-1} \qquad [4]$$

seems to be reliable.

According to Brewer[23], Kubaschevski and Evans[24], and Glassner[25], enthalpy of liquid $SiCl_4$ is $H_{298} = -150.1$ kcal mol^{-1}. Heat of evaporation of this compound in the boiling temperature 330°K is $L_{330} = 6.859$ kcal mol^{-1}.[23] Taking into account the change in the heat capacity within the range 298°-330°K[25] it has been found that $L_{298} = 7.228$ kcal mol^{-1}. Hence, enthalpy of gaseous $SiCl_4$ is $H_{298} = (-150.1 + 7.228)$ kcal mol^{-1}. Using the thermodynamic data given by Wenner[26], Rossini[27], Kubaschevski and Evans[24], listed by Glassner[25], the following equation has been derived

$$\log K_1(T) = -12380\,T^{-1} - 2.51 \log T + 1.2\,10^{-4}\,T + 16.50 \qquad [5]$$

The most reliable values of the saturated vapor pressure over solid silicon seem to be those given by Ceplayeva, Priselkov, and Karelin[28], who applied for measurements the integral variant of the effusion method. Their results have been discussed and compared with those of other authors by Nesmeyanov[29] who represented them by an equation which, expressed in atmospheres, has the form

$$\log P_{Si}(T) = -101.65421 - 11185.64\,T^{-1} + -0.00685812T + 35.81091 \log T \qquad [6]$$

Solving the system of Eq. [1]-[3] gives concentrations of all components at equilibrium states. In higher concentrations of $SiCl_4$ Eq. [3] can be neglected. If, however, equilibria on the boundary gas-silicon surface are considered under assumption of chemical changes occurring on the surface only, the neglect of silicon vapor pressure, which is then higher than partial pressure of $SiCl_2$ especially over 1500°K, probably should not be done. If silicon condensation occurs in the temperature $T < T_s$ at some distance from the seed surface the temperature of which is T_s, this condensation seems to be a consequence of the reverse process given by Eq. [3] rather than by Eq. [2] for the following reason. The decomposition of $SiCl_2$ streaming away from the seed surface, with the formation of solid silicon requires

$$\frac{p^2_{SiCl_2}(T)}{p^2_{SiCl_2}(T_s)} \cdot \frac{p_{SiCl_4}(T_s)}{p_{SiCl_4}(T)} > \frac{K_2(T)}{K_2(T_s)} \qquad [7]$$

If, for example, $T = 1350$°K, $T_s = 1600$°K, the temperature gradient being 450°/cm, the temperature $T = 1350$°K is attained outside of the diffusion layer, where the concentration of $SiCl_4$ equals the initial value. Since, according to the computed values from Eq. [1-3] for the above mentioned conditions, equilibrium pressure of $SiCl_4$ on the surface is very small and that of $SiCl_2$ much smaller in the bulk of the gas than on the surface, then

$$\frac{p^2_{SiCl_2}(1350)}{p^2_{SiCl_2}(1600)} \cdot \frac{p_{SiCl_4}(1600)}{p_{SiCl_4}(1350)} < \frac{K_2(1350)}{K_2(1600)} = \frac{0.82\,10^{-2}}{0.65}$$

As a result, the decomposition of $SiCl_2$ in the gas phase at some distance from the hot silicon surface should not occur.

Details will be given in a more extensive paper.

SYMBOLS

H	molar enthalpy
$K_1(T), K_2(T)$	equilibrium constants of the reactions 1 and 2
L	molar heat of evaporation
n_1, n_2, n_3	extents of reactions 1, 2, and 3
p_i	partial vapor pressure of a component "i"
$P_{Si}(T)$	saturated vapor pressure of silicon
T	absolute temperature
T_s	absolute temperature on the surface of silicon seed
w	number of moles H_2 per mole $SiCl_4$ before any reaction occurs

Reaction of Nickel Carbonyl with Carbon Disulfide

S. H. Pitts, Jr. (pp. 1054-1055, Vol. 112, No. 10)

R. B. Barclay and A. R. Popley[30]: The effect of CS_2 on the decomposition of $Ni(CO)_4$ was investigated at AWRE several years ago and, on the basis of information obtained at that time, we must disagree with Pitts' main conclusion that the breakdown of the $Ni(CO)_4$ under these circumstances is inherently different from straight thermal decomposition.

With reference to the infrared analysis of the residual gases we have always found residual $Ni(CO)_4$ which decomposes often in the form of a fine powder and not on the sides of the container. This was only discovered because attempts to use mass spectographic methods of analysis had produced visible films on the side of the sample tube and when none were found in the initial infrared analysis further investigation led to the discovery of this fine powder. It is suggested that this could, in part, explain the discrepancies in pressure rise found by Pitts. Further evidence that not all $Ni(CO)_4$ was decomposed in the reaction chamber comes from the analysis of the nickel film. If it is assumed that all the nickel in the carbonyl is deposited, then a mass balance calculation on the system shows that almost 50% more S occurs in the plate than is fed into the system. Errors in measuring the system volume or the initial pressure of CS_2 could not be large enough to account for this difference, and the conclusion must be that undecomposed $Ni(CO)_4$ is present. In addition the assumption that all the sulfur from the CS_2 has been incorporated in the plate gives a calculated pressure increase factor of 2.8 which is in agreement with the recorded pressure increases.

Further discrepancies in pressure rise may have been caused by the rapid initial decomposition of the carbonyl during the time which it takes the system to equilibrate, *i.e.*, the "minimum time to admit $Ni(CO)_4$ to the reaction flask to an equilibrium pressure."

On the basis of the data on oxidation obtained by Pitts, calculation shows that the weight gain is consistent with the balance of his analysis being oxygen since it corresponds to that expected if all the Ni were converted to oxide. The high amount of oxygen in the plate is more consistent with oxygen in the system than an extensive breakdown of CO.

We have formulated the following hypothesis based on data from practical plating experiments.

[22] H. Schaefer and J. Nickl, *Z. anorg. Chem.*, 274, 250 (1953).

[23] L. Brewer, "Chemistry and Metallurgy of Miscellaneous Materials: Thermodynamics," McGraw-Hill Publishing Co., New York (1950).

[24] O. Kubaschewski and E. Evans, "Metallurgical Thermochemistry," Academic Press, New York (1951).

[25] A. Glassner, "The Thermochemical Properties of the Oxides, Fluorides, and Chlorides to 2500°K," Report ANL-5107, U. S. Government Printing Office, Washington, D. C.

[26] R. R. Wenner, "Thermochemical Calculations," McGraw-Hill, Publishing Co., New York (1941).

[27] F. D. Rossini, "Selected Values of Chemical Thermodynamic Properties," National Bureau of Standards, Washington, D. C. (1952).

[28] A. W. Ceplayeva, J. A. Priselkov, and W. W. Karelin, *Westnik M. G. U.*, 5, 36 (1960) (in Russian).

[29] A. N. Nesmeyanov, "Vapor Pressure of the Chemical Elements," Publ. House of the Academy of Sciences of USSR., Moscow (1961) (in Russian).

[30] United Kingdom Atomic Energy Authority, Atomics Weapons Research Establishment, Aldermaston, Berkshire, England.

Mechanism of decomposition.—The reaction scheme suggested in the literature[31] is as follows

$$Ni(CO)_4 \rightleftharpoons Ni(CO)_3 + CO \quad [I]$$

$$Ni(CO)_3 \rightarrow Ni + 3CO \quad [II]$$

(*a*) Reaction [I] is rate controlling and leads to the following rate equation

$$-dp/dt = kp/(1 + k'p_{CO}) \quad [1]$$

(*b*) If $Ni(CO)_4$ is weakly adsorbed and CO strongly adsorbed, Eq. [1] reduces to

$$-dp/dt = k''p/p_{CO} \quad [2]$$

(*c*) If $Ni(CO)_4$ were strongly adsorbed the reaction would be simple first order.

This reaction scheme was further developed by Tonosaki[32,33] who showed that Eq. [1] was obeyed in the early stages and Eq. [2] in the later stages of the reaction.

This led to the following results

$$\text{Stage 1.} \quad (1 + 3bp_o)k_m - bv = k_1 \quad [3]$$

$$\text{Stage 2.} \quad 3p_o k_m - v = k_2 \quad [4]$$

where

$$k_m = 2.303\, t^{-1} \log P_o/p$$
$$v = (P_t - P_o)/t$$

b, k_1, and k_2 are positive constants, P_o is the initial pressure of $Ni(CO)_4$, P_t the total pressure at time t. A plot of k_m against v should give two straight lines of slope $(1 + 3\ P_o b)/b$ and $3\ P_o$, respectively.

The above equations were applied to the results obtained by plating brass disks with or without accelerator. In the cases where no accelerator was used two distinct stages were found. However, the later stage did not agree with Tonosaki's Eq. [4] because the gradient of the line was greater than that for the first stage instead of smaller. This might be interpreted as a return to Eq. [3] but when an accelerator was added it was found that the second stage gave a line of negative slope which is completely incompatible with either Eq. [3] or [4].

It therefore seems possible that there may be a third stage to the decomposition of $Ni(CO)_4$ possibly involving an entirely different reaction to that set out in Eq. [I] and [II], and further investigation is being carried out on this point.

It may be that the first stage of decomposition suggested by Tonosaki has been missed in the case of plating the brass disks because few readings were taken early in the run. Thus, the first line obtained by plotting k_m against v could be that represented by Eq. [4]. Two runs without accelerator in fact gave good agreement with the idea that the first line obeyed Eq. [4]. The fact that Eq. [4] is valid over a considerable portion of the run (~30 min) shows that only the rate of breakdown has been effected not the fundamental mechanism.

Effect of temperature and accelerators.—If the rate of desorption controls the reaction, then the addition of an accelerator which was adsorbed in preference to CO would be expected to produce the same effect as raising the temperature, namely, a lowering of the partial pressure of CO at the surface of the plate with a consequent increase in the rate of decomposition. The effect of an accelerator is in fact like that of temperature.

Other evidence can be adduced to support the idea that the accelerator action is a surface phenomenon. It is found that progressive increases in accelerator concentration do not lead to proportional increases in the rate of decomposition: in fact conditions of saturation seem to occur where very little further change in rate is induced by increasing the accelerator concentration. This agrees with the saturation effect found by Pitts. The accelerator is gradually consumed, being incorporated into the plate, and analysis of the surface layer and bulk of the plate has shown that a surface concentration of S exists which is about 50% higher than that in the bulk metal. If the accelerator was acting through the formation of NiS nuclei, this surface concentration would not be expected.

Toward the end of plating the proportion of accelerator to carbonyl will be greater and, since it is well known that large concentrations of S bearing compounds can cause the breakdown of $Ni(CO)_4$, there will be a tendency toward decomposition to NiS and CO: this might be expected to give rise to higher surface S concentrations for plates deposited over a longer time but evidence on this point is still lacking.

S. H. Pitts, Jr.: We appreciate the stimulating comments. While experiments can be urged as supporting a similarity in thermal and CS_2-promoted $Ni(CO)_4$ decomposition theories, proof is lacking. We observed that in nickel plating by induced heat, decomposition of the carbonyl will often occur in the gas phase as well as on the surface. This is independent of CO desorption and does not occur at room temperature.

It is not clear from the discussion by what method the presence of residual $Ni(CO)_4$ was established and if the amount was significant. When 13-15% CS_2 was used, we found no more than 5% $Ni(CO)_4$ in the reacted mixtures by infrared analysis. Tests also were made to decompose any residual carbonyl by heating it in a pressure monitored container. The pressure increase was insignificant. We performed another qualitative test that indicated an absence of $Ni(CO)_4$ in an expended reaction mixture. The addition of more CS_2 gave no further reaction; the addition of more $Ni(CO)_4$ caused another pressure increase. A CS_2 concentration of 13-15% in the initial charge mixture is the optimum to give complete conversion of both CS_2 and $Ni(CO)_4$. At higher concentrations, infrared analysis showed residual CS_2. Lower concentrations gave reacted mixtures that contained unreacted $Ni(CO)_4$.

To produce the mass balance calculations of Barclay and Popley to give 50% more sulfur than was charged and a pressure increase factor of 2.8 requires using 50 mm as the pressure of the $Ni(CO)_4$ in the initial reaction mixture (which was incorrect). The actual $Ni(CO)_4$ pressure in the typical run was only 17.9 mm (21.4-3.5) as described in the fourth paragraph. Also, the reported sulfur and nickel content of the deposited material may have been misleading. The elemental analysis was made on a composite material collected from numerous runs in which the CS_2 pressure was as low as 0.6 mm. It is not necessarily representative of this typical run. If, for example, a CS_2 charge of 2 mm was used instead of 3.5 mm in the mass balance calculations for complete consumption of CS_2 and $Ni(CO)_4$, both the nickel and the sulfur content approximate those found analytically.

It is thought that errors in the initial gas charges are at a minimum. The normal time for charging the system with $Ni(CO)_4$ was 15 sec. The maximum pressure change possible in this period due to the reaction could be only 10% of the total charged as determined from a plot of pressure *vs.* time.

Surface nucleation and growth was a visual observation. The formation of NiS nuclei was not implied.

The extent to which sulfur bearing compounds cause the breakdown of $Ni(CO)_4$ is questionable. In this investigation only H_2S and CS_2 were found to cause it. Sulfur compounds that we found to be ineffective

[31] E. H. Bawn, "The Kinetics of the Decomposition of Nickel Carbonyl," *Trans. Faraday Soc.* (1935).

[32] Tonosaki and Suginuma, *Bull. Inst. Phys. and Chem. Res.*, 22, 1014 (1943).

[33] Tonosaki, "The Thermal Decomposition of $Ni(CO)_4$, Vapor, IV," Tohoku University Science Report, I. Vol. 37.

were sulfur dioxide, methanethiol, carbonyl sulfide, and diethyl sulfide.

A more comprehensive investigation seems necessary to elucidate these reaction mechanisms. We hope Barclay and Popley will publish their work.

An Electrochemical Model for the Oxidation of Zirconium

D. H. Bradhurst, J. E. Draley, and C. J. Van Drunen (pp. 1171-1177, Vol. 112, No. 12)

H. H. Uhlig[34]: It was pointed out in a paper by the undersigned[34a] that thin film oxidation data obeying the cubic equation can often be expressed equally well by the two-stage logarithmic equation. This is the case for data presented in Fig. 9 of the present paper by Bradhurst *et al.*, which are plotted in terms of the cubic equation. The corresponding two-stage logarithmic behavior of the same data are shown in Fig. 1 below. The two heavy lines follow points through the single straight line representing the

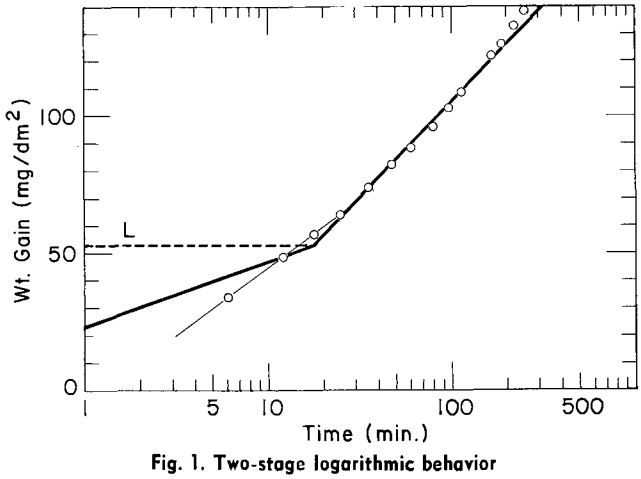

Fig. 1. Two-stage logarithmic behavior

cubic equation as given in Fig. 9; individual points are experimental values supplied by courtesy of J. Draley who also pointed out that the initially obtained points are not as precise as those obtained for longer times. Some correction of weight gain values should be made because of oxygen dissolving in the metal, but such corrections do not affect the present discussion.

The significance of two-stage logarithmic oxidation kinetics has been described in terms of an initial constant density space charge in the growing thin oxide film, with control of oxidation being vested in rate of transfer of electrons from metal to oxide.[35] Beyond a critical thickness L of the oxide, the trapped excess charge dissociates in part, leading to a diffuse space charge and to a higher oxidation rate constant in the usual logarithmic equation $y = k_o \ln (t/\tau + 1)$ where y is the thickness of oxide (or weight of oxygen in the oxide per unit area), k_o is the reaction rate constant, t is time and τ is a constant.

The value of L can be estimated[36] from the work function of the metal, and from the electron affinity v of oxygen adsorbed on the oxide equal to 3.6 ev.

$$L = k_o \left| \frac{e(\phi - v)}{kT} - 1 \right|$$

Taking the thermionic work function of Zr equal to 4.12 ev[37] and the value of k_o from the slope of the first-stage oxidation step in the figure equal to 23/2.3 = 10 mg/dm² the calculated value of L = 52 mg/dm². This compares with the observed value of 53 mg/dm². The observed value of L for lines through the individual points is 68 mg/dm². If the averaged work function of 3.84 ev is substituted [36], the calculated value becomes 19 mg/dm² which is still the right order of magnitude.

The fact that thin film oxidation data for zirconium follow the cubic equation or the two-stage logarithmic equation, combined with the reasonable correspondence of calculated and observed values of L lend support to the view that the oxidation rate is controlled not by diffusion of ions or migration of electric charge through an oxide film, but instead by rate of electron transfer from metal to oxide at the metal-oxide interface.

D. H. Bradhurst[38], **J. E. Draley, and C. Van Drunen:** We have looked at semi-log plots of our oxidation data a number of times. We have never seen good evidence for any straight line portions. Referring to Professor Uhlig's figure, we believe the points best form one continuous curve. Incidentally, the first point (at least 6 min) is plotted a little lower that we have used it. Perhaps we made an error when sending it to him. This small revision, plus additional points from the original recorder trace between 6 and 42 min, confirm to us continuation of the longer time curvature to shorter times. (For this run, reliable data could not be taken at time less than 6 min.)

We appreciate Professor Uhlig's interest in our data. We do not believe that the oxidation of zirconium under our conditions fits his oxidation model. Accordingly, we feel we can offer no evidence to confirm or deny the general validity of his model.

The Valency of Aluminum Ions and the Anodic Disintegration of the Metal

M. E. Straumanis and K. Poush (pp. 1185-1188, Vol. 112, No. 12)

L. Rédey[39]: The authors prove that the black deposit formed on the aluminum anode contains fine aluminum particles, as a result of partial disintegration of electrode. They point out that this phenomenon explains why the apparent valency of aluminum ions leaving the anode is lower than 3. This statement is highly probable in my opinion too.

However there are some circumstances in which metal particles are not observable, but, instead of this, hydrogen evolution occurs during the anodic dissolution of aluminum. Although the apparent valency of aluminum ions entering solution is lower than 3 in this case too, it is unnecessary to assume the formation of Al^+ ions, in spite of the fact that the phenomenon may not be explained by disintegration of anode. Several authors established that, for example in solution of halogen ions, hydrogen gas evolved on aluminum anode and only a small quantity of metal particles were detectable and the apparent valency of aluminum ions was 1.7-2.8 depending on circumstances. A plausible explanation of this phenomena is the mixed electrode behavior of the aluminum anode. At the same time two electrochemical processes take place on its surface

$$Al \rightarrow Al^{3+} + 3e^-$$

and

$$2H^+ + 2e^- \rightarrow H_2$$

The evolution of hydrogen gas is the result of local currents flowing on the anode. Therefore, the quan-

[34] Corrosion Laboratory, Massachusetts Institute of Technology, Cambridge, Massachusetts.

[34a] H. H. Uhlig, J. Pickett, and J. MacNairn, *Acta Met.*, 7, 111 (1959).

[35] H. H. Uhlig, *Acta Met.*, 4, 541 (1956).

[36] V. Nwoko and H. H. Uhlig, *This Journal*, 112, 1181 (1965).

[37] H. Michaelson, *J. Appl. Phys.*, 21, 536 (1950).

[38] Present address: Australian Atomic Energy Commission, Southerland, N. S. W., Australia.

[39] Polytechnical University of Budapest, Inorganic Chemistry Institute, Budapest XI., Gellert-ter 4, Budapest.

tity of evolved hydrogen is equivalent to the surplus of dissolved aluminum (considering the Faraday law and apart from occasional disintegration of metal). The action of local currents is not identical with so-called self-dissolution; the latter proceeds without external polarizing current. Besides the presence of activating anions also external anodic polarizing current is necessary[40] to get that strong local current observed under some conditions (up to a few hundred ma/cm^2). Namely, the local currents become stronger if the extent of anodic polarization increases.

Under the conditions in question formation of Al^+ ions is improbable because the estimated value of standard redox potential of Al^+/Al^{3+} electrode (in aqueous solution) is -2.76v.[41] That is, the Al^+ ions would be extremely unstable and they could not exist in the solution for a perceptible period.

M. E. Straumanis[42]: I am very much pleased by Professor L. Rédey's statement that Al goes into solution as an Al^{3+} ion, pointing out the extreme instability of Al^+. Nevertheless, there still might be the possibility that the Al^+ just formed returns within a very short period of time to the anode and gives up simultaneously or successively two more electrons. Since it is impossible at present to decide experimentally how the removal of the electrons occurs at the anode, we have the right to assume that Al^{3+} ions are formed at once. A further possibility that the Al^+ ions, if formed, disappear by the self-reduction, and oxidation reaction

$$3Al^+ \rightarrow 2Al + Al^{3+} \qquad [1]$$

is ruled out because of the presence of comparatively large particles (embedded in the oxide layer[43]) which could not be formed in reaction [1][44], and because the coulometric measurements with Al-amalgam as an anode showed the formation of only Al^{3+} ions within the limits of error.[45] The same occurs at an In-amalgam electrode, where only In^{3+} ions are formed, the results falling within an error limit much narrower than in the case of Al.[46] The coulometric measurements are the strongest evidence in favor of Al^{3+} and In^{3+} ion formation in the first step during anodic dissolution[47], although In^+ is much more stable than Al^+. Therefore, intermediate steps[48], may be registered only under specific experimental conditions.

Thus, the deviation from Faraday's law during anodic dissolution of metals is explained by the partial surface disintegration of the metal and by the increase of the self-dissolution rate in case of active metals when under anodic current.[49] Professor Rédey is also correct in stating that anodic dissolution may occur without disintegration. In fact, such a dissolution with no disintegration, or more correctly, with hardly detectable disintegration was also observed in this laboratory.[49] Furthermore, similar observations were made by King *et al.*,[50,51] working with Mg. It depends entirely on experimental conditions whether or not spalling of the oxide or hydroxide films is accompanied by spalling (disintegration) of the anodic metal. If the amounts of the latter are small, they may react quickly with the electrolyte under H_2 evolution, thus escaping microscopic detection.[52]

If the protective oxide layer is partially spalled of an active metal anode (by the impact of cations going into solution), the self-dissolution rate of the bare metal spots increases due to activity of the metal or due to the action of local cathodes now exposed to the electrolyte.[49] So, there is no reason why the action of local elements should be excluded from contributing to the self-dissolution rate.

[40] L. Rédey, Untersuchung des Potentials Polarisierter Anoden, Periodica Polytechnica, Budapest, 4, 219 (1960).

[41] N. Lohonyai and L. Rédey, Beiträge zum elecktrochemischen Verhalten der Aluminium (I) ionen. Periodica Polytechnica, Budapest, 6, 121 (1962).

[42] University of Missouri at Rolla, Graduate Center for Materials Research, Rolla, Missouri.

[43] M. E. Straumanis and K. Poush, *This Journal*, 112, 1185, Fig. 3 (1965).

[44] M. E. Straumanis and D. L. Mathis, *J. Less-Common Met.*, 4, 213 (1962).

[45] M. E. Straumanis and K. Poush, *This Journal*, 112, 1185, Table I. (1965).

[46] M. E. Straumanis and R. L. Martin, *Z. anorg. u. allgem. Chem.*, 334, 321, Table 2. (1965).

[47] M. E. Straumanis, *This Journal*, 113, 636 (1966).

[48] R. E. Visco, *This Journal*, 112, 932 (1965); 113, 636 (1966).

[49] M. E. Straumanis, *This Journal*, 105, 284 (1958); 108, 1087 (1961).

Anomalously Large Photovoltages in a New Photovoltaic Cell

P. N. Ramachandran and R. E. Salomon (pp. 42-45, Vol. 113, No. 1)

M. Hartl[53]: Ramachandran and Salomon previously have reported on this high voltage photovoltaic effect at low temperatures in anodized zirconium electrodes coated with an evaporated layer of copper or gold.[54] On similar investigations using anodized and sandwich-contacted tantalum electrodes[55] we could find only a small increase (factor 2) of the photovoltage at low temperatures. Measuring the photoeffect also in anodized sandwich-contacted zirconium electrodes[56] we got similar results as in anodized tantalum, *i.e.*, no high voltage photovoltaic effect. According to our investigations we suppose that the difference in the applied measuring methods could explain the different results.

Contrary to Ramachandran and Salomon, who used a high impedance electrometer together with an auxilliary bucking circuit, we compensated the photovoltage in a low impedance circuit (sensitive current instrument for null detection) and this in particular for the following reason:

Using a high impedance electrometer (with or without compensation or bucking circuit) the time constant of the measuring circuit is given by the capacitance and series resistance of the photovoltaic element in the oxide layer. Our measurements show[55,56] that the short-circuit photocurrent and therewith the series resistance of tantalum and zirconium oxide largely increases with decreasing temperature. Together with the relatively high capacitance of the thin oxide layers (nF/cm^2) we got time constants of hours measuring the photovoltage in ZrO_2 layers with an electrometer at -150°C. In this case we also found high but not reproducible values of the photovoltage. But we believe that unintentional charging of the capacitance of the oxide layer may be the reason for this effect, because the high time constant of the measuring circuit does not allow the corresponding discharge. It is possible that the photoemission, as discussed below, together with a bucking circuit produces this charging of the capacitance.

We therefore determined the photovoltage[55,56] by a low impedance compensation circuit. For null detection (photovoltage equal to the compensation voltage) we used a low impedance current measuring instrument, whose sensitivity was sufficient to measure the expected short circuit photocurrent.

[50] J. L. Robinson and P. F. King, *This Journal*, 108, 36 (1961).

[51] P. F. King, *This Journal*, 113, 536 (1966).

[52] M. E. Straumanis and B. K. Bhatia, *This Journal*, 110, 357 (1963).

[53] Institut für Technische Elektronik, Technische Hochschule, München, Germany.

[54] P. N. Ramachandran and R. E. Salomon, *J. Phys. Chem. Solids*, 24, 583 (1963).

[55] M. Hartl, *Z. Naturforsch.*, 20b, 392 (1965).

[56] M. Hartl and K. Achtziger, *Phys. Stat. Sol.*, 14, 355 (1966).

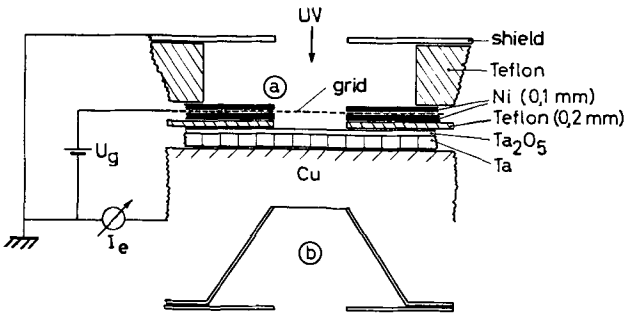

Fig. 1. Schematic set-up of the electrodes used to measure the photoemitted electrons out of an anodized tantalum sheet with a counter electrode in the form of: (a) a fine meshed copper grid mounted between two nickel disks at a small distance (0.3 mm) from the surface of the oxide layer, or (b) a cone made of an anodized tantalum sheet, which could be used instead of the grid. The illuminated area was 3 mm in diameter in both cases.

Therewith the time constant is given by the capacitance of the oxide layer and the input resistance of the current sensitive instrument and was below 0.1 sec in our experiments. It may be mentioned that this compensation circuit (for detail see [56]) seen from the side of the oxide layer, has, in balance ($I = 0$), an "infinitely" high input resistance which is still comparatively infinite, if the sensitivity of the null detecting instrument is high enough to measure the expected short-circuit photocurrent under the given conditions. With this sensitive compensation circuit, we could measure the photocurrent-voltage-characteristic in the proximity of the photovoltage, which was never higher than 2v in gold contacted ZrO_2 layers, produced by an anodization voltage (U_A) up to 60v. Besides the discussed problem of measuring the photovoltage in sandwich-contacted oxide layers with an electrometer, the so far unpublished results of our investigations, concerning the photoeffect in uncontacted oxide layers, may help to explain

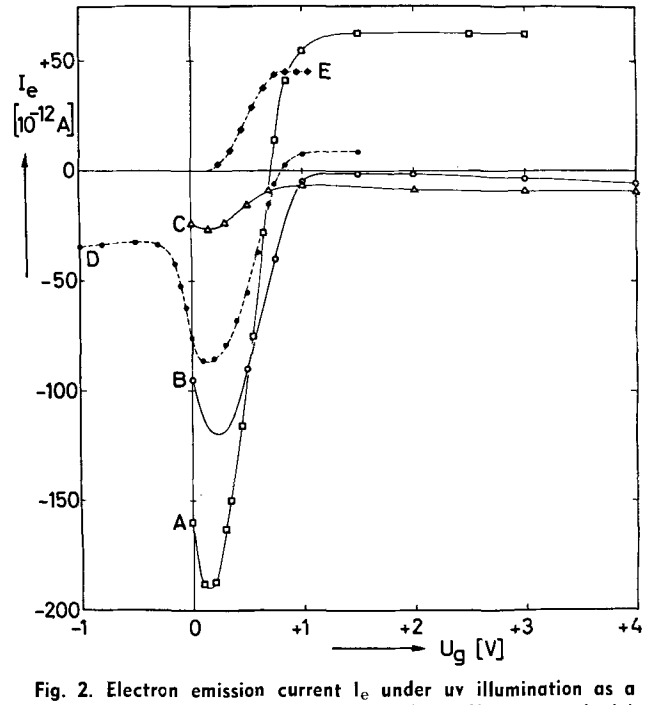

Fig. 2. Electron emission current I_e under uv illumination as a function of the applied grid (or cone) voltage U_g measured: (a) with the grid in Fig. 1a and a tantalum sheet anodized with a formation voltage of 4v: A at + 20°C; B at —10°C; C at —35°C; and D at +25°C at a reduced intensity of light: (b) with the cone in Fig. 1b and a tantalum sheet anodized with a formation voltage of 3v: E at +25°C.

the unusual photoeffect observed by Ramachandran and Salomon. Also in our experiments the conducting path to the surface of the oxide layers was obtained by photoelectron emission. We again used the described low impedance circuit.

Figure 1 shows the mounted electrodes: the chemically polished anodized tantalum sheet (0.1 mm thick) is attached to a copper rod, which was used as electrical lead to the tantalum and also as heat conductor from and to the probe. A fine-meshed copper grid (wire distance 40μ) in a short distance (0.3 mm) above the surface of the oxide layer serves as counter electrode (a in Fig. 1). In this set up, only simultaneous illumination of both electrodes is possible; however the conduction path is defined clearly. To avoid photoemission from the counter electrode while measuring the photoemission from the oxide layer alone, the grid in Fig. 1 was replaced by a cone made of anodized tantalum sheet (b in Fig. 1). The electrode chamber could be evacuated (10^{-5} Torr) by an oil diffusion pump. The light spot (0.25 x 0.25 mm) of an Osram mercury super pressure lamp (HBO 100 W/2) was focused on the probe to get high-intensity photon flux.

Figure 2 shows the current (I_e)-voltage (U_g) characteristics of an anodized tantalum sheet under illumination. Curves A and D in Fig. 2 are measured at room temperature and at different light intensities L_A and L_D ($L_A > L_D$). With sufficient positive grid voltage, current saturation is obtained. The magnitude of this saturation current corresponds to the number of photoemitted electrons out of the oxide layer on the tantalum, and thus is proportional to the intensity of light. Lowering the positive grid voltage, the electron current from the oxide layer to the grid drops to zero at a certain grid voltage U_{go}. This grid voltage U_{go} compensates a photovoltage U_o between the tantalum electrode and the copper grid. It may be mentioned that the photovoltage obtained by this "contactless" measuring method is influenced by the difference in the work functions of the oxide layer and the counter electrode and also by the different number and energy distribution of the photoemitted electrons out of the two electrodes. At lower positive grid voltages than U_{go} the electron flow from the grid to the surface of the oxide layer should also reach a saturation value at sufficient high negative grid voltage. Curve D in Fig. 2 shows that this negative saturation current, which would correspond to the photoelectron emission out of the grid, cannot be obtained. With increasing the negative grid voltage, the negative current decreases from a maximum (between $U_g = U_{go}$ and $U_g = 0$) to a lower value. This specific voltage current characteristic can be explained by the fact that the surface of the oxide layer will be charged to grid potential by the electrons from the grid. Increasing the negative grid potential (and thus increasing the surface potential of the oxide layer to the same values by the assumed charging), an increasing component of the photoemitted electrons from the grid flows to the grounded shield and reduces the measured current from the grid to the oxidized tantalum electrode. Measuring the temperature dependence of the photovoltage U_o with I_e set to zero, we obtained curve A in Fig. 3 for the same oxide coated tantalum electrode as investigated in Fig. 2, and curve C for a chemically polished tantalum electrode without an oxide layer. By comparison curve D in Fig. 3 gives the temperature dependence of the photovoltage in an anodized tantalum electrode coated with an evaporated transparent layer of gold. The similarity of the temperature dependence between the diagrams A and D in Fig. 3 above room temperature (and the difference between A and C) confirms our assumption that the measured photovoltage, identical with U_{go}, is mainly due to the photovoltage in the oxide layer. The large increase of U_o with decreasing temperature below room temperature

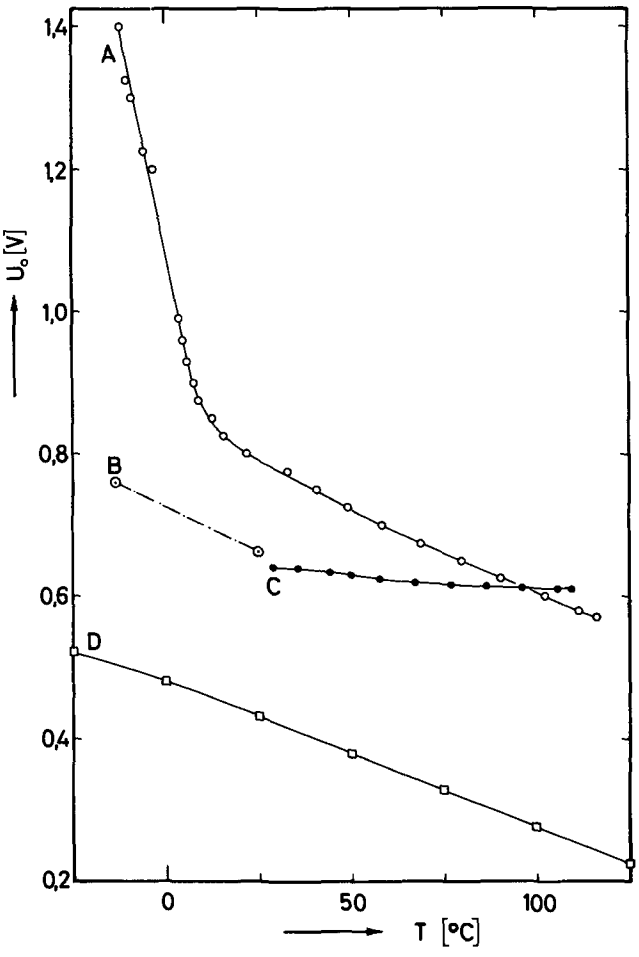

Fig. 3. Photovoltage U_0 as a function of the temperature T measured: A with a low impedance compensation circuit ($I_e = 0$) and B directly with a high impedance electrometer (10^{14} ohm) using the same probe as in Fig. 2a curves A-D. By comparison: C: not anodized tantalum measured as A; D: sandwich contacted anodized tantalum (different intensity of light and oxide thickness corresponding to a formation voltage of 24v.)

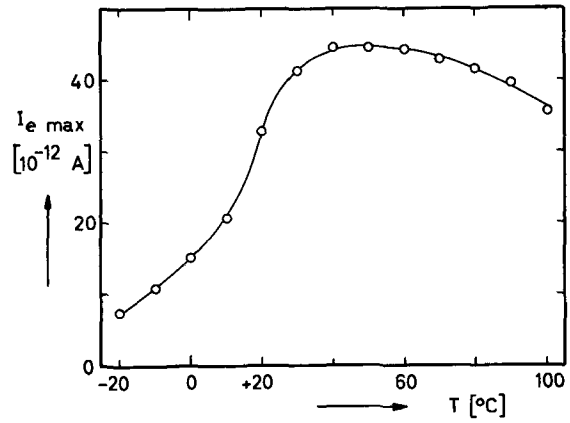

Fig. 4. Maximum electron emission current $I_{e\,max}$ (saturation value of curve E in Fig. 2) out of anodized tantalum (formation voltage 6v) as a function of temperature T.

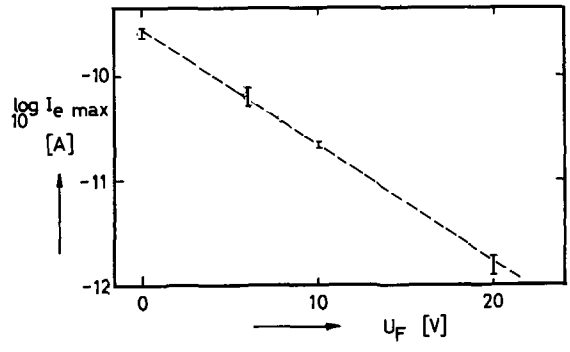

Fig. 5. Maximum electron emission current $I_{e\,max}$ out of anodized tantalum as a function of the oxide thickness corresponding to the given anodization voltage U_A.

is surprising and our curve A seems to lead to the high photovoltages observed by Ramachandran and Salomon. But measuring on the other hand the photovoltage between the grounded grid and the anodized tantalum electrode with a high impedance electrometer directly, without bucking or compensating voltage, we got the two points of curve B in Fig. 3 showing no unusual voltage increase.

To clear this discrepancy we measured the complete current (I_e) voltage (U_g) characteristic also at lower temperatures. Our results are curves B and C in Fig. 2. These curves demonstrate that photoemission out of the anodized tantalum at low temperatures cannot be observed under the given conditions (Fig. 1*a*), and hence a compensation of the photovoltage is not possible with electron current flow only in one direction.

Using the anodized tantalum cone in Fig. 1b instead of the grid (a) it could be shown that the photoemission out of an anodized tantalum electrode is measurable in the investigated lower temperature range. Curve E in Fig. 2 shows the emission current I_e as a function of cone voltage. The saturation current $I_{e\,max}$ at positive cone voltage as a function of temperature is given in Fig. 4. The fact that the saturation point of the emission current as function of the applied voltage (U_g) is nearly independent of temperature, also excludes a larger change of the photovoltage as found in Fig. 3 curve A.

Figure 5 shows the decrease of this saturation current, which also is the maximum photoemission current $I_{e\,max}$, with increasing thickness of the oxide layer. According to the results given in Fig. 4 and 5 it might be supposed that the photoemission out of the relatively thick oxide layers investigated by Ramachandran and Salomon cannot be measured with the used instruments at low temperatures; but without measurable electron emission out of the oxide layer the photovoltage should not be determinable.

However, if the electron emission out of the oxide layer can be neglected against that out of the counter electrode, curve B and C in Fig. 2 should approach zero ($I_e = 0$) with increasing positive grid voltage. The fact that we, however, measured an emission current opposite to the applied field and nearly independent of the positive grid voltage, indicates an additional phenomenon, which could not be explained at present. But according to the shape of curve B and C in Fig. 2 (quite different from A and D) and according to the facts of small electron emission out of the oxide layer and of the directly measured low photovoltage (curve B in Fig. 3), we believe that this negative emission current at positive grid voltage (measured up to + 10v) is not caused by higher photovoltage but more likely by surface charging of the oxide layer, similar to that found with the negative grid voltage even at room temperature (curve D in Fig. 2). The reason for this charging could be any auxiliary voltage (as in our experiments the applied grid voltage, or any other compensating resp. bucking voltage) or perhaps electrons with higher energies emitted by a heated counter electrode.

Although our investigations are not carried out under the same experimental conditions as applied by Ramachandran and Salomon and also were for a different purpose, we hope, however, to have shown some of the problems which should be discussed by Ramachandran and Salomon to clear their measured unusual photoeffect.

Acknowledgment.—The author is indebted to Professor Dr. M. Knoll, the Director of the Institut für Technische Elektronik der Technischen Hochschule München, for encouraging this work and wishes to thank Dipl. Ing. H. Hippmann for some measurements, Dipl. Ings. U. Büktas and Graul for helpful criticisms during the preparation of the manuscript, and the Bundesministerium für wissenschaftliche Forschung for financial support.

Detection of Thermal Reaction in Mixed Oxide Powders by Electrical Resistance Measurements

A. N. Copp, M. Nakahira, and G. W. Brindley (pp. 237-239, Vol. 113, No. 3)

J. Deren and J. Haber[57]: Copp, *et al.*, consider the possibility of employing the measurements of electrical conductivity to the investigation of the solid-state reactions in semiconducting oxide systems. There are several remarks which we would like to mention in connection with this problem.

1. Measurements of the electrical conductivity may be a useful experimental technique mainly in studying first stages of the reaction in the polycrystalline mixtures. A solid-state reaction must begin at the intergranular boundaries, and the first steps of the reaction must comprise the structural changes of surface layers, surface migration, formation of surface compounds, etc. As in many cases the conductivity of polycrystalline material is determined by the conductivity of surface layers and intergranular contacts; these changes will entail the changes of electrical conductivity and its activation energy before any new phase is formed in the amount sufficient to be detected by the x-ray diffraction. The results illustrated in Fig. 1 show that even at comparatively low temperatures irreversible changes of electrical conductivity of the $MgO+Cr_2O_3$ mixture are observed[58] although no formation of new phases could be detected by x-ray technique. These changes are related to surface processes, as shown by the investigation of chemical, microscopic, and adsorptive properties.[59-61]

2. It seems that in many cases additional information may be obtained by measuring the electrical conductivity not only as a function of temperature but also as function of the pressure (pressure of oxygen in case of oxide mixtures). The dependence of conductivity on pressure at constant temperature follows the equation: $\sigma = k \cdot p^{\pm 1/n}$, n being dependent on the nature of the oxide and conditions of the experiment. In the case of the reaction between two oxides characterized by different n, the changes of n may supply some information about the first steps of the reaction.[62]

3. In many solid-state reactions metastable intermediate products are formed in small quantities. Their formation may have a pronounced influence on the electrical conductivity, as these compounds appear mainly at the surface of crystallites.[58-61]

4. Once a new phase of the product is formed, it may determine the over-all electrical conductivity. It seems that the growth of crystallites of this phase influences the electrical conductivity to a smaller degree only. It also seems doubtful whether direct relationship between the changes of electrical conductivity and the conversion can be expected.

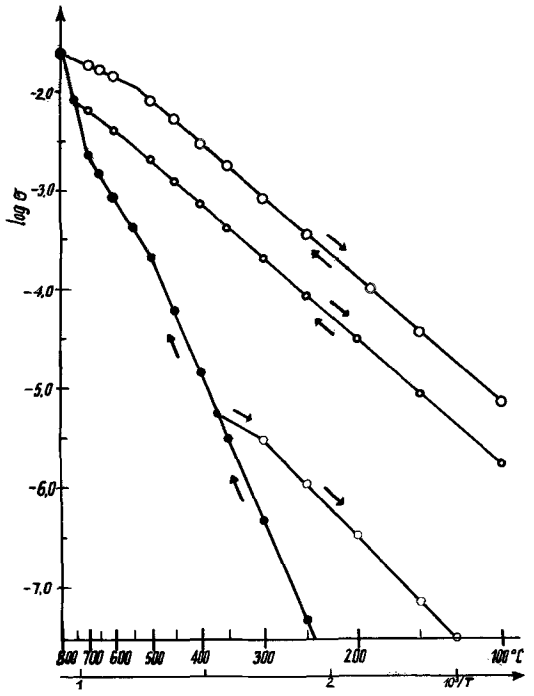

Fig. 1.

5. Measurements of electrical conductivity may also give valuable information concerning the phase diagrams of the oxide systems. In such applications a very critical approach, however, must be adopted since the so-called singular points[63] do not necessarily correspond to a new phase.[59,64]

6. There are two important aspects of the application of conductivity measurements as a method of investigation of the solid-state reactions. As seen from the above discussion the electrical conductivity of an oxide mixture depends on many different factors, and unambiguous conclusions can be drawn only if several various experimental techniques are used simultaneously. In this respect the measurements of electrical conductivity must be considered as a supplementary technique. The second problem refers to the question as to whether electrical conductivity is the most useful property from the point of view of the investigations in this field. It may be suggested that measurements of the work function may give more straightforward information concerning the surface state of the reacting polycrystalline mixture.

A. N. Copp, M. Nakahira, and G. W. Brindley[65]: We are pleased to receive the comments and to have our attention drawn to some recent publications that were overlooked in our own article. We agree entirely with their comment 1 that several different techniques are necessary to avoid unambiguous conclusions; however, we still emphasize that the readily observable breaks in log resistivity (or conductivity) *vs.* $1/T$ curves appear to correspond to the onset of reactions between the components. In their comments 1, 3, and 4, Deren and Haber appear to agree with our general thesis, which we refrained from expressing in as much detail as they supply.

[57] Department of Inorganic Chemistry, School of Mining and Metallurgy, Krakow, Poland.

[58] A. Bielanski, J. Deren, and Z. Barutowicz, *Z. anorg. u. allgem. Chem.*, **305**, 169 (1960).

[59] A. Bielanski, J. Deren, and E. Duczyminska, *Z. anorg. u. allgem. Chem.*, **316**, 75 (1962).

[60] J. Deren and J. Haber, *Z. anorg. u. allgem. Chem.*, **342**, 277 (1966).

[61] J. Deren and J. Haber, *Z. anorg. u. allgem. Chem.*, **342**, 288 (1966).

[62] A. Bielanski, J. Deren, J. Haber, and E. Polaczkowa, *Z. anorg. u. allgem. Chem.*, **294**, 269 (1958).

[63] V. N. Yeremienko and A. M. Baynysh, *Problems of Powder Metallurgy*, **1**, 57 (1954) (in Russian).

[64] A. Bielanski and J. Deren, *Roczniki Chem.*, **29**, 1145 (1955).

[65] Materials Research Laboratory, Pennsylvania State University, University Park, Pennsylvania.

The Growth of Pink Magnesium Aluminate ($MgAl_2O_4$) Single Crystals

C. O. Dugger (pp. 306-307, Vol. 113, No. 3)

L. H. Brixner[66]: The author states in the last paragraph of this paper that the hydrolysis of a fluoride to an oxide might be considered a new technique for growing single crystals. It is probably correct that he was the first to adopt this method specifically for the preparation of single crystalline $MgAl_2O_4$, but as a fundamental technique it is not novel. We used the hydrolysis of both fluoride and chlorides in what we call "flux-reaction technique" for the preparation of transparent single crystalline ferrites of the type $BaFe_{12}O_{19}$ and $SrFe_{12}O_{19}$ in 1959.

Otherwise Dr. Dugger's paper is a fine piece of experimental work and, if he succeeds in growing larger crystals, he may indeed have a novel host for Cr^{+3}.

C. O. Dugger: I wish to thank Dr. Brixner for calling my attention to his use of chloride and fluoride hydrolysis in the growth of oxide single crystals.[67]

The solid-state chemical equation (solid-phase hydrolysis) to form $BaFe_{12}O_{19}$ from the reactants BaF_2 and Fe_2O_3, as suggested by Dr. Brixner, included one mole of water. The source of water in this reaction was not discussed by Dr. Brixner in his above referenced paper. Also in this paper the source of water was not established in the molten phase hydrolysis of the chlorides. Assuming the mechanism for chloride and fluoride hydrolysis is similar, Dr. Brixner's technique in bringing about the hydrolysis reaction and the temperature at which he added Fe_2O_3 to the molten solution was different from the technique used by the undersigned. The major differences in the two techniques were:

(*A*) Dr. Brixner bubbled oxygen into molten $BaCl_2$ (mp 962°C) while in the preparation of $MgAl_2O_4$ single crystals, extreme care was taken to exclude any oxygen in the carbon furnace chamber in which the starting mixture, BaF_2, MgF_2, and Al_2O_3 was heated.

(*B*) At 1250°C, Dr. Brixner introduced Fe_2O_3 into the molten solution while this author added oxides possessing waters of crystallization to hydrated fluorides at room temperature and then heated the well ground, isostatically pressed mixture to the molten phase.

At present, the exact mechanism for the conversion of MgF_2 to MgO and the chemical formation of $MgAl_2O_4$ from Al_2O_3 is not known. It has been suggested that the chemical reaction MgF_2 and Al_2O_3 to form $MgAl_2O_4$ is a metathetical reaction. Experimental evidence does not support this suggestion. Our laboratory findings indicate that the conversion of MgF_2 to MgO is a hydrolysis reaction.

It appears that the solid and molten phase fluoride hydrolysis-solution technique, for growing high quality stoichiometric oxide single crystals, has the potential of becoming another good method for growing single crystals of some refractory oxides once more is known about the technique.

Adsorption and Oxidation of Butane on Platinum Black in H_2SO_4

J. A. Shropshire and H. H. Horowitz (pp. 490-492, Vol. 113, No. 5)

S. B. Brummer[68]: The authors come to the conclusion that the strong dependence of the initial rate of adsorption of butane on potential in the range 100-300 mv *vs.* the reversible hydrogen electrode (RHE) arises from blockage of butane adsorption sites by adsorbed hydrogen atoms. They conclude, also, that butane adsorbs only in type II (most anodic) H-sites. These conclusions are of great interest and, if confirmed, would be of considerable significance not only in relation to hydrocarbon adsorption on Pt but also in connection with the energetics of H atom adsorption itself. However, some of the authors' experimental techniques appear inappropriate to the study of this system. In addition, the conclusions they draw appear inconsistent with what is generally known about hydrocarbon adsorption on Pt and also with their own data.

Concerning the experimental techniques used by the authors, we would note, as they mentioned, that the early part of the adsorption occurs on a partly oxide covered electrode but, also, as is not mentioned, over a range of potentials.[69] This leads to an intercept of the Q_B *vs.* τ plots of Fig. 5 (Q_B is charge to oxidize adsorbed butane, τ is the time of adsorption). One could hardly agree that the claimed constancy for the intercepts of the Q_B *vs.* τ plots is very convincing (cf. Fig. 5). In any case, when the maximum adsorption is small (*e.g.*, at 0.0v *vs.* SCE) the true initial rate would be concealed by this intercept. One might note also that if the composition of the adsorbed layer varies with potential, which important point the authors completely ignore, the presence of partially oxidized residues adsorbed at high potentials during the return from the "burn off scan" will have profound effects on the kinetics of further adsorption. It would have been considerably better if the authors had really adsorbed at constant potential and if they had measured Q_B in such a way as to avoid readsorption during the "burn off scan."

The major query about the authors' procedures, however, is their assumption that Q_B is a measure of adsorbed butane. The explicit assumption that they make here is that the oxidation state of the adsorbed material is constant, independent of time and potential of adsorption. Further, they assume that the adsorbed material is butane itself. Neither of these assumptions is likely on general grounds and in fact there is a considerable body of evidence to the contrary. Thus, it has been shown for C_3H_8,[70, 71] for C_2H_6,[72] and for various hydrocarbons including C_4H_{10} itself,[73, 74] that the adsorbed material is not the original hydrocarbon and that its oxidation state is a function of time of adsorption and potential. For C_3H_8, this was shown to be true even at 80°C,[70, 71] for C_2H_6 it was shown even as low as 60°C[72] and, in both cases, it would be true at lower temperatures. Recent results[75] show similar behavior for n-C_6H_{14} and there can be little doubt that this is a general effect for the adsorption of saturated hydrocarbons from acid solutions onto Pt electrodes. Thus "adsorption rates" of butane derived from Q_B *vs.* τ plots are unlikely to be correct. Similarly, the reported variation of this "adsorption rate" with potential is of dubious significance.

The authors take no account of this effect. In fact, in their section "additional evidence in support of Type II site adsorption," they explicitly require that the adsorbate be butane itself. This "supporting evidence" based on this asumption cannot then be valid.

It could perhaps be argued that since the authors corrected the "rates" derived from their Q_B *vs.* τ plots for butane oxidation, the reported slopes do represent

[66] Pigments Department, Experimental Station, E. I. du Pont de Nemours & Company, Wilmington, Delaware.

[67] L. H. Brixner, *J. Am. Chem. Soc.*, 81, 3841 (1959).

[68] Tyco Laboratories, Incorporated, Waltham, Massachusetts 02154.

[69] "Over a range of potentials," because the potentiostat would take at least 2.5 sec to provide the charge to lower the potential from 1.1v (the end of the "burn off" scan) to the working potential. Much of this charge would be passed over a range of potentials where adsorption of butane would occur.

[70] S. B. Brummer, J. I. Ford, and M. J. Turner, *J. Phys. Chem.*, 69, 3424 (1965).

[71] S. B. Brummer and M. J. Turner, "Hydrocarbon Fuel Cell Technology," p. 409, Academic Press, New York, 1965.

[72] S. Gilman, *Trans. Faraday Soc.*, 61, 2546 (1965).

[73] J. Giner, Paper presented at 15th CITCE Meeting, London (Sept. 1964).

[74] L. W. Niedrach and M. Tochner, Report by General Electric Co. to USAERDL, Fort Belvoir, Va., on Contract No. DA-44-009-AMC-479(T), Dec. 1965.

[75] S. B. Brummer and M. J. Turner, In press.

the true rate of adsorption of butane. However, they used the "steady state" oxidation rate of butane for this purpose and the transient rate of oxidation under the conditions of adsorption onto a clean surface is always much higher. Thus for HCOOH oxidation,[76-79] methanol oxidation,[77] saturated hydrocarbon oxidation[73, 80, 81] and unsaturated hydrocarbon oxidation,[73, 82] the oxidation current always falls rapidly with time during the initial time period. The authors appear to have overlooked this fact in correcting their Q_B *vs.* τ plots. Had they made this correction appropriately they could have obtained the correct adsorption kinetics from their Q_B *vs.* τ plots. However, their overriding assumption which stated simply is that butane either oxidizes to CO_2 or is adsorbed as unchanged butane would not be any more true.[83] One must conclude, then, that the reported "adsorption rates" may be seriously in error.

The important conclusion which the authors say their data point to is that the adsorption rate is first order in free surface (Fig. 7) and occurs only on type II H-sites. Notwithstanding that the "supporting evidence" for this supposition is based on the assumption of 4 sites per adsorbed molecule so that the rate should depend on $(1 - \theta_H)^4$, the evidence is not convincing.[84] Firstly, we note that the data of Fig. 7 refer on the one hand to "adsorption rates" determined at various potentials and on the other to "free surfaces" $[= (1 - \theta_H) = \theta_F]$ determined in absence of C_4H_{10}. The variation in adsorption rate with potential could be due to a number of factors but if the authors' theory were correct then at fixed potential (*e.g.*, in the data of Fig. 5) we expect the observed adsorption rate to decline as butane covers the free surface. Yet, as Fig. 5 of their paper shows, Q_B increases linearly with τ. Indeed this linearity is the basis of the authors' "adsorption rates." The extent of coverage of the electrode by adsorbed C_4H_{10} during the authors' adsorption experiments may be estimated from their results. Thus for the electrode of Fig. 5, Q_B apparently increases at 39 ma at +0.05v *vs.* SCE. Comparing with Fig. 6, and allowing for the steady state oxidation current at +0.05v as given in Table II, shows that this electrode contained 26.5 mg of Pt. From Table I, Q_H^s is 1.265 coul. Adsorption of butane after 40 sec at 0.05v is 2.3 coul and then Q_B/Q_H^s is 1.82. The maximum value, Q_B^s/Q_H^s, is 3.3 and, making the authors' assumptions of 4 sites per molecule, eventual maximum coverage of the relevant sites[85] and adsorption by butane *per se*, this corresponds to coverage by butane of 55% of the electrode surface. Despite this, the Q_B *vs.* τ plots of Fig. 5 show no curvature and, even on a "rate" *vs.* θ_F relation, the rate should have diminished by 55% in 40 sec. If the dependence on θ_F^4 implied by the authors' other assumption were true, the rate should have diminished to ~4% of its original value by this time.

Had the previously mentioned transient oxidation current correction been applied, the initial adsorption rate at low butane coverage would be higher than that at high coverages. There is almost certainly then some dependence on free surface but it is not that claimed by the authors. The only way in which this dependence can be established is to study adsorption *vs.* free surface and time at fixed potential. Figure 7 of the author's article shows merely that a parameter, which is related to the rate of adsorption, changes with the potential of adsorption in a similar way to the way in which H atoms are adsorbed on Pt in the absence of butane. It does not show what the authors claim.[86]

J. A. Shropshire and H. H. Horowitz: The authors would like to thank Dr. Brummer for taking sufficient interest in our paper to offer comments and trust that the following discussion will help to eliminate any misunderstandings that may still exist.

Considerable difficulty would be avoided if it were not immediately assumed that all adsorption-electrooxidation data obtained on active platinum black need be equivalent to that obtained on smooth platinum, often annealed, microelectrodes. It would be very desirable, if it were possible, to study the rate of adsorption of hydrocarbons on smooth platinum electrodes using what have become more or less standard techniques. Unfortunately, diffusion limits the rate of hydrocarbon accumulation on platinum microelectrodes suspended in electrolyte, and true adsorption rates, therefore, cannot be determined. Furthermore, smooth platinum microelectrodes do not behave in the same manner as platinum black electrodes with regard to hydrocarbon adsorption and oxidation, as discussed below. While the use of the porous electrode-flowing electrolyte system required the application of less elegant electrochemical techniques, it nevertheless has demonstrated its merit in showing the existence of an adsorption rate limitation, which correlated with the limiting current observed with actual fuel cell electrodes.

The most stringent requirement of the porous electrode system was that only slow voltage sweeps were possible due to the long charging time of the electrode. An appreciable amount of fuel adsorption, therefore, occurred during the scan and return, giving an apparent intercept of about 10% of maximum coverage. However, most of the coulombs in this intercept reached the electrode during the scan, after the adsorption period and not prior to it. Therefore, the adsorption did occur on an essentially clean surface. In fact, since the intercept was constant, independent of adsorption voltage, it would have been valid for us to subtract it from the raw data of Fig. 5 to obtain curves passing through the origin. A sawtooth rather than triangular voltage form was used to minimize the time available for adsorption after burn-off and prior to the start of the next nominal adsorption period. Since most of the return time is spent in reducing platinum oxides in a potential region where arriving butane is oxidized, the maximum time for fuel adsorption at uncontrolled potential is less than one second, and would have permitted less than 1% coverage to occur.

With the regard to the possible change in composition of the adsorbed butane with potential, we must stress again that desorption of the adsorbed material yielded essentially pure butane identified by gas chromatography. The identification of the adsorbed material is not assumed. Furthermore, this butane is not formed by hydrogenation of fragments since the desorption process consumed no more coulombs than those required to hydrogenate the newly vacated sites. Surely evidence for partial oxidation obtained from kinetic data and adsorption isotherms taken on smooth platinum at lower temperatures must yield to this

[76] S. B. Brummer and A. C. Makrides, *J. Phys. Chem.*, **68**, 1448 (1964).

[77] J. Giner, *Electrochim. Acta*, **9**, 63 (1964).

[78] M. W. Breiter, *Electrochim. Acta*, **10**, 503 (1965).

[79] R. P. Buck and L. R. Griffith, *This Journal*, **109**, 1005 (1962).

[80] S. B. Brummer, Report by Tyco Laboratories to USAERDL, Fort Belvoir, Va., on Contract No. DA-44-009-AMC-410(T), Oct. 1964.

[81] J. O'M. Bockris, E. Gileadi, and G. Stoner, Report to USAERDL, Fort Belvoir, Va., on Contract No. DA-44-009-AMC-469(T), Apr. 1966.

[82] J. O'M. Bockris, H. Wroblowa, E. Gileadi, and B. J. Piersma, *Trans. Faraday Soc.*, **61**, 2531 (1965).

[83] And the finally adsorbed material would of course still not be butane itself.

[84] E. J. Cairns [Ref. (6) of June 1965] has reported that for C_3H_8 in HF at 90°C, the adsorption kinetics follow a third order law in free surface.

[85] If we were to accept the conclusion of adsorption only on type II sites, both $Q_B{}^s/Q_H{}^{II}$ and $Q_B{}^{40\ sec}/Q_H{}^{II}$ would be about double these values, but the estimate of coverage would not be altered.

[86] Incidentally, we may note that the authors claim that only ~ 50% of the surface is occupied by C_4H_{10} is certainly not true for C_3H_8[69, 70] and n-C_6H_{14}[75] where coverage by hydrocarbon approaches unity.

Table I.

Electrode form	50 Mg Pt black	1 cm² Smooth Pt
Saturation butane coverage, millicoulombs	8000	0.6
Coverage in 20 sec, millicoulombs (25% of saturation)	2000	0.15
Typical scan time, sec/v	20	0.01
Avg scan current, ma (assuming peak requires 1/3 v)	300	50
Correction for oxidation, millicoulombs (25% of coverage)	500	0.04
Observed oxidation current, ma (assuming 20 sec adsorption)	25	0.002

actual product isolation and analysis. Moreover, data of Niedrach[87] for both ethane and propane adsorption-desorption on high area platinum black completely substantiate this observation. Both these adsorbed paraffins were desorbed substantially unchanged with at most a few per cent of cracked products. It should be noted that only with high surface area porous electrodes is the isolation of desorbed material possible. One hundred mg of platinum black can adsorb and desorb 0.15 cc of butane at STP.

The discussion of the correction for steady-state oxidation during adsorption is very important and needs amplification and clarification for this and other papers. Steady-state oxidation rates in this study were not taken from separate experiments but were measured during the actual adsorption simply by reading the current delivered by the potentiostat. The ability to do this is again a function of the massiveness of the porous electrode system. This is certainly an advantage of the porous electrode over microelectrodes. With low area electrodes and fast scans, the currents are low and the ratio of the current during adsorption to that during the scan is low. These two factors make it virtually impossible to detect anodic oxidation during adsorption on microelectrodes even though it may be quite significant. An example giving order of magnitude numbers will illustrate this important point. Assume that a high area electrode and a microelectrode each reach 25% of saturation coverage with butane after 20 sec adsorption, and during that period each oxidize 25% of what they adsorb. A simple calculation shows that under typical scanning conditions easily detectable scan currents of the order of 10^2 ma are obtained, but the oxidation current is 25 ma in the case of the large electrode and a practically undetectable 0.002 ma in the case of the small one, as shown in Table I.

It was undoubtedly for this reason that a number of authors claimed to measure hydrocarbon adsorption at potentials of 0.5-0.7v *vs.* reversible hydrogen. On porous electrodes, the oxidation currents would be so high at these potentials that it would be obviously impossible to measure saturation coverages. Thus the use of high surface area electrodes has permitted us to verify by actual isolation of the desorbate that butane does not change its composition on the surface under our conditions and has provided an *in situ* method for correcting the adsorption for steady-state oxidation. Both features combine to make a consistent picture.

Much has been made of the fact that one molecule of butane appears to adsorb on four platinum sites. It is appealing to assume one carbon atom per platinum atom at saturation; but no attempt was made to tie this to the kinetics of the adsorption process. In fact, little can be learned about the reaction order since the rate measurements extended to less than 25% coverage of the surface. Maximum coverages were of the order of 6200 millicoulombs. The linear adsorption rate range extended for 500-1500 millicoulombs as shown in Fig. 5 of the paper. Therefore, only an 8-25% change in slope would be expected rather than the 55% calculated by Dr. Brummer on the basis of first order kinetics. We do agree with him that an adsorption rate proportional to the fourth power of the fractional free surface is unlikely on the basis of these data. Perhaps the initial adsorption is virtually irreversible even though it requires four sites. This point should be investigated further.

[87] L. W. Niedrach, *This Journal*, 111, 1309 (1964).

Explosion of a Chemical Polishing Solution

S. F. Bubar and D. A. Vermilyea (pp. 519, Vol. 113, No. 5)

R. H. Buck[88]: During a period of stay at the Department of Metallurgy, University of Florida, I also had the same experience as the authors but using glycerine (10 parts) as the viscous agent in a nitric acid (5 parts) hydrofluoric acid (5 parts) chemical polishing solution for zirconium. Water was to be added later to control the polishing. A stoppered plastic container in which the fresh solution was stored, ruptured violently about 4 hr after mixing due to reaction occurring within the bottle. On the other hand, a titanium etching solution containing 40 HNO_3/15HF/45H_2O remained stable for months.

Although the exact nature of the chemical reaction causing the explosion is open to speculation it is perhaps pertinent to point out that the presence of concentrated sulfuric acid is usually necessary to bring about the nitration of glycerine to nitroglycerine[89,90] in a reasonable time by promoting anhydrous conditions. A more likely reaction in this case is the oxidation of glycerine in a highly oxidizing medium. Karrer[90], for example, states that strong nitric acid alone will cause oxidation of glycerine, a trihydric alcohol, to glyceric acid. The oxidation may, of course, proceed further and become degradative. The explosion could thus have been caused by a rise in temperature due to the nondissipated heat of reaction, accentuated by the viscosity of the mixture, combined with pressure build-up from the gaseous decomposition products of the reaction. One can visualize a similar reaction occurring in the case of lactic acid (α-hydroxy propionic acid). Lactic acid and glycerine are chosen because they are relatively stable, viscous, and miscible with water in all proportions, properties conferred by the presence of hydroxyl groups. Although these same groups are capable of easy oxidation to corresponding acids, it is difficult to think of less vulnerable organic alternatives having the required physical properties. The role of the viscous agent in chemical polishing is generally thought to be partly physical, but the specificity of some of the reagents used is still not wholly explained. Thus glycerine, glycols, lactic acid, acetic acid, and phosphoric acid[91] have been used.

Inquiries have revealed that the occurrence of such explosions is fairly common. In one case a glycerine/HF/HNO_3 mixture was prepared on the liter-scale and stored in a screw-topped glass bottle—with disastrous consequences. It is not only in the industries concerned with microelectronics or refractory metals that heed should be given: a standard etch for aluminum (Vilella's etch) contains 10 parts HNO_3/20 parts HF/30 parts glycerine. Further in this context, it is relevant to point out the additional hazard recently investigated in connection with perchloric acid/acetic anhydride electropolishing solutions[92] where the reaction between acetic anhydride and water

[88] United Kingdom Atomic Energy Authority, Atomic Weapons Research Establishment, Aldermaston, Berkshire, England.

[89] C. V. King, *This Journal*, 112, 251C (1965).

[90] P. Karrer, "Organic Chemistry," American Elsevier Co. Inc., New York (1950).

[91] D. C. Cornish, *Proc. Joint* IERE-IEE Conference on "Application of Thin Films in Electronic Engineering," Paper 14, Imperial College, London (July 1966).

[92] R. K. Bartlett and H. S. Turner, *Chem. and Ind.* 1933 (November 20, 1965).

caused a young metallurgy student to lose the sight of both eyes.

Solutions containing an organic moderator with HNO_3 and HF should certainly not be stored after use. In view of their increasing industrial use in connection with refractory metals and semiconductors, periodic warnings about their hazards such as issued in *This Journal*[89] might serve to reach the worker at the bench.

On the Potential/*p*H Diagrams of the Cu-NH_3-H_2O and Zn-NH_3-H_2O Systems

H. E. Johnson and J. Leja (pp. 630, Vol. 113, No. 6), Discussion Section)

F. Letowski and J. Niemiec[93]: The argument of Messrs. Johnson and Leja, that there are no two substances with alternately reversed acid-basic characteristics, which has been presented in the response to our contribution, is of rather a vague character and seems to be hardly acceptable from our point of view. The point of the matter is that the mathematical equations, called also by us, in abbreviation, equilibria [17] and [15], are, in fact, the two peculiar cases (expressions) describing the same equilibrium between Cu_2O and $Cu(NH_3)_2^+$ at definitely different *p*H conditions.

The general Cu_2O-$Cu(NH_3)_2^+$ equilibrium equation has been derived on the basis of the following data: $\mu^o_{Cu(NH_3)_2^+} = -15{,}510$ cal, $\mu^o_{Cu_2O} = -34{,}980$ cal, $\mu^o_{H_2O} = -56{,}690$ cal, and $K_{NH_3} = 10^{9.22}$, and its mathematical form is as follows

$$pH = -8.43 - \log [Cu(NH_3)_2^+] + 2 \log ([NH_4^+] + [NH_3]) - 2 \log (10^{-9.22} + 10^{-pH}) \quad [1]$$

This has been deduced by using the relationships

$$[NH_4^+] = \frac{[H^+] \cdot C_A}{K_{NH_3} + [H^+]} \text{ and } [NH_3] = \frac{K_{NH_3} \cdot C_A}{K_{NH_3} + [H^+]} \quad [2]$$

where C_A is the total, "analytical" ammonia contents in solution, amounting to the sum

$$C_A = ([NH_4^+] + [NH_3])$$

The general Cu_2O-$Cu(NH_3)_2^+$ equilibrium equation under discussion undergoes simplification to become transformed into Eq. [17], if $pH >> 9.22$. Then $[NH_3] >> [NH_4^+]$ and some simplifications can be made

$$\log ([NH_4^+] + [NH_3]) \approx \log [NH_3],$$
$$\log (10^{-9.22} + 10^{-pH}) \approx \log 10^{-9.22} = -9.22$$
$$\text{and } pH = 10.01 - \log [Cu(NH_3)_2^+] + 2 \log [NH_3] \quad [17]$$

Equation [17], which is a simplified expression of the general equation given above in the case when $[NH_3] >> [NH_4^+]$, loses its practical sense and does not represent the Cu_2O-$Cu(NH_3)_2^+$ equilibrium state when NH_3 and NH_4^+ concentrations become comparable or when $[NH_3] << [NH_4^+]$. In the latter case, the general equation assumes the form of Eq. [15] (according to Mattson) and is valid if $pH << 9.22$. Then

$$\log ([NH_4^+] + [NH_3]) \approx \log [NH_4^+]$$
$$\log (10^{-9.22} + 10^{-pH}) \approx \log 10^{-pH} = -pH, \text{ and}$$
$$pH = 8.43 + \log [Cu(NH_3)_2^+] - 2 \log [NH_4^+] \quad [15]$$

If, on the other hand, the concentrations (activities) of NH_3 and NH_4^+ are comparable, *i.e.*, at *p*H values close to 9.22, the equilibrium may not be described either by Eq. [17] or by [15]. In such a case, the general Cu_2O-$Cu(NH_3)_2^+$ equilibrium equation should be used which would take into account the sum of NH_3 and NH_4^+ concentrations.

H. E. Johnson and **J. Leja**: We wish to thank Messrs. Letowski and Niemiec for their discussion.

[93] Institute of Inorganic Chemistry and Rare Elements Metallurgy, Technical University, Wybrzeze Wyspianskiego 27, Wroclaw, Poland.